META 2026 Dublin – Ireland

The 16th International Conference on Metamaterials, Photonic Crystals and Plasmonics

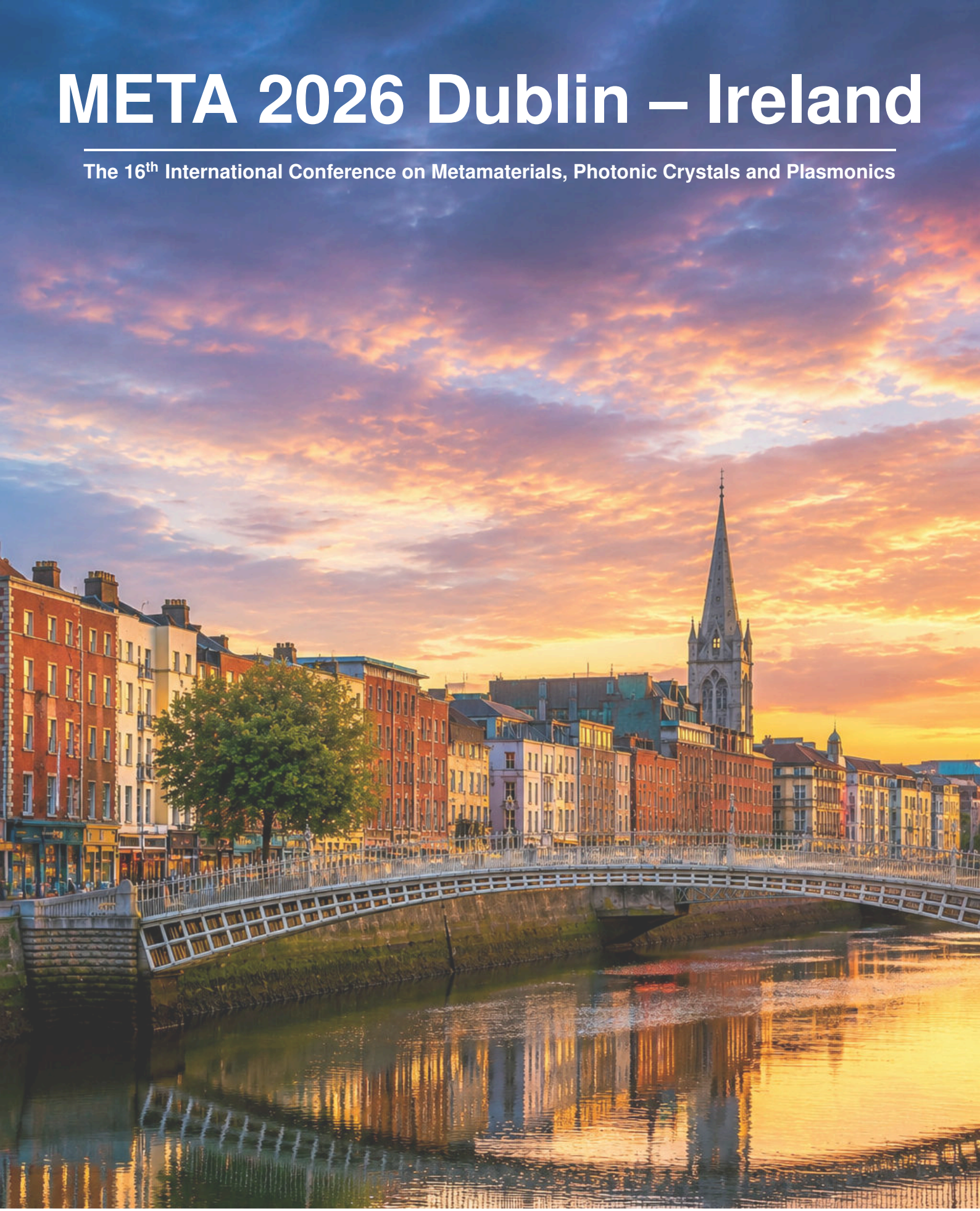

14–17 July 2026
Dublin, Ireland

Proceedings

metaconferences.org

ISSN 2429-1390

SILVER SPONSOR

AIP Publishing

Proudly sponsoring META 2026

Our mission is to advance, promote, and serve the **physical sciences** for the benefit of humanity by **breaking barriers to open, fair research** communication and empowering researchers to accelerate global progress.

Explore our resources and programs designed to connect your work to a legacy of foundational discoveries and new ideas, and to a community of peers and institutions around the world.

Learn more at publishing.aip.org

Textured Broadband Antireflective Windows & Lenses

Thorlabs' Textured Antireflective (AR) Windows and Lenses have subwavelength nanostructures etched directly into the bulk optic substrate.

Compared to traditional thin-film AR coatings, these textured surfaces offer:

- Lower Reflectance Over a Broad Wavelength Range
- Lower Angular Sensitivity
- Higher Laser-Induced Damage Threshold

With options available for UV, VIS, and NIR applications, our textured AR optics are ideal for applications that require high-power lasers and long-term beam stability.

Enhanced Optical Performance

- <0.25% Average Reflectance per AR Surface
- ≥98% Transmission Over Specified Wavelength Range
- Excellent Broadband Operation
- High Resistance to Laser-Induced Damage

Built for High-Power & Precision Applications

Ultrafast Lasers | Imaging Systems | Spectroscopy | Quantum Optics | Vacuum Systems | Industrial Photonics

Our textured AR windows and lenses are offered in diameters ranging from 1/2" – 1.5" with unmounted and mounted options available.

Textured AR Lenses

Textured AR Windows

Münchner Weg 1 | 85232 Bergkirchen, Germany | +49 (0) 8142 4269800 | www.thorlabs.com

META 2026 Dublin – Ireland

The 16th International Conference on Metamaterials, Photonic Crystals and Plasmonics

Dublin, Ireland · 14–17 July 2026

Dates	14–17 July 2026
Venue	Trinity College Dublin, The University of Dublin, College Green, Dublin 2, D02 PN40, Ireland
Website	metaconferences.org
Contact	contact@metaconferences.org
Indexing	SCOPUS indexed
ISSN	2429-1390
Partners	Trinity College Dublin, Ireland · Paris-Saclay University, France

PERMANENT PROCEEDINGS REPOSITORY

The official permanent repository of the META Conference Proceedings is available at:

https://metaconferences.org/proceedings/

This repository provides long-term public access to the proceedings volumes of all editions of the International Conference on Metamaterials, Photonic Crystals and Plasmonics (META).

EDITED BY

Ortwin Hess	Trinity College Dublin, Ireland
Said Zouhdi	Paris-Saclay University, France

© 2008–2026 META Conference · ISSN 2429-1390 · All rights reserved

Preface

META 2026

This volume constitutes the official proceedings of **META 2026**, the 16th International Conference on Metamaterials, Photonic Crystals and Plasmonics, held on 14–17 July 2026 at Trinity College Dublin, The University of Dublin, Ireland.

Since its first edition in 2008, the META conference series has grown into one of the largest international forums devoted to metamaterials, photonic crystals, plasmonics and nanophotonics. The present volume reflects that breadth: it spans topological and non-Hermitian photonics, quantum metaphotonics, chiral and magnetoelectric phenomena, acoustic and phononic metamaterials, metasurfaces and flat optics, inverse design and machine learning, nanofabrication, biosensing and the industrial exploitation of metasurface devices.

META 2026 gathered authors from **44 countries** across five continents. Following evaluation by the Scientific Advisory Committee and the Technical Program Committee, with the support of the symposium and special-session organisers, **933 contributions** were accepted for presentation and are collected here: 5 plenary lectures, 27 keynote lectures, 1 tutorial, 731 invited and contributed oral presentations and 169 poster presentations, organised in 6 symposia, 24 special sessions, 15 general-session topics and a pre-conference workshop.

Every contribution in this volume was reviewed for originality, technical soundness and relevance to the conference scope, and is published in the form provided by its authors. The peer-review and publication policy is detailed on the following page.

We warmly thank the members of all committees and the session organisers for the quality of the scientific selection, Trinity College Dublin for hosting the conference in an exceptional setting, our sponsors and partner institutions, and above all the authors and participants who make META what it is. We hope this volume will serve as a lasting record of the conference and a useful reference for the community.

Dublin, July 2026 — *The Editors*

Ortwin Hess — Trinity College Dublin, Ireland
Said Zouhdi — Paris-Saclay University, France

Peer Review & Publication Policy

META 2026

Peer Review

All contributions submitted to META 2026 were evaluated by members of the Scientific Advisory Committee and of the Technical Program Committee, with the support of the symposium and special-session organisers. Submissions were assessed on the basis of extended abstracts or full papers; acceptance was notified together with the presentation category (plenary, keynote, invited, oral or poster).

Selection Criteria

Reviewers were asked to assess each submission against the following criteria:

- originality and novelty of the work;
- technical soundness and scientific rigour;
- relevance to the scope of the conference;
- clarity of the presentation.

Publication Ethics

Authors certify that their contribution is original, that it does not infringe any third-party rights, and that all sources are duly acknowledged. Each paper is published as supplied by its authors, who bear full responsibility for its content. At least one author of each contribution registered for and presented the work at the conference.

Indexing & Archiving

The META proceedings are published under **ISSN 2429-1390** and are **indexed in SCOPUS**. The present volume is archived and available at metaconferences.org/proceedings.

SUGGESTED CITATION OF THIS VOLUME

Proceedings of the 16th International Conference on Metamaterials, Photonic Crystals and Plasmonics (META 2026), O. Hess and S. Zouhdi, Eds., Dublin, Ireland, 14–17 July 2026. ISSN 2429-1390.

Copyright

© 2026 the respective authors. All rights reserved. Reproduction of any part of this volume requires the permission of the authors concerned.

Contents

§ Preface 5

§ Peer Review & Publication Policy 6

§ Welcome from the General Chairs 8

§ META 2026 at a Glance 9

§ The META Conference Series 10

§ Sponsors & Partners 12

§ META Awards 15

§ Organization & Committees 17

§ Plenary Talks 23

§ Keynote Talks 29

§ Pre-Conference Workshop 44

§ Conference Papers & Indexes 98

Talk type colour code used throughout this volume:

PLENARY 35 min KEYNOTE 30 min INVITED 20 min

ORAL 15 min POSTER Session

DUBLIN, IRELAND • 14–17 JULY 2026

Welcome to META 2026

Dear Colleagues and Friends,

It is our distinct honour and pleasure to welcome you to **META 2026**, the 16th International Conference on Metamaterials, Photonic Crystals and Plasmonics, hosted this year by **Trinity College Dublin** in the historic city of Dublin, Ireland, from 14 to 17 July 2026.

Since its inception, the META series has grown into one of the world's foremost forums on metamaterials, nanophotonics and the physics of light–matter interaction, uniting a global community of physicists, engineers and material scientists. This year's conference brings together **over 900 researchers from 45 countries**, spanning academia and industry, featuring **five plenary lectures**, **twenty-seven keynote presentations**, **six thematic symposia**, **twenty-four special sessions** and hundreds of contributed talks and posters spanning the most exciting frontiers of the field.

Beyond the science, we warmly invite you to experience the culture, history and renowned hospitality of Dublin — a UNESCO City of Literature and home to one of Europe's oldest universities. We are confident that META 2026 will be a memorable occasion for scientific exchange, new collaborations and lasting friendships.

We gratefully thank our sponsors, partners, committee members and authors, whose dedication makes this conference possible. We wish you a stimulating and enjoyable conference.

"Where light meets matter, new science begins."

Ortwin Hess
META 2026 General Chair
Trinity College Dublin, Ireland

Said Zouhdi
Founder & General Chair
Paris-Saclay University, France

META 2026 at a Glance

A snapshot of the 16th edition of the world's leading forum on metamaterials, nanophotonics and the physics of light.

900+
PARTICIPANTS

43
COUNTRIES

930+
PRESENTATIONS

5
PLENARY LECTURES

27
KEYNOTE LECTURES

6
SYMPOSIA

24
SPECIAL SESSIONS

Trinity College Dublin, Ireland • 14–17 July 2026

Proceedings · SCOPUS Indexed • Open Access

SINCE 2002
The META series in numbers

16	10,000+	50+	6,000+	200+
CONFERENCES	PARTICIPANTS	COUNTRIES	PAPERS PRESENTED	KEYNOTE & PLENARY

✓ 24 Special Sessions ✓ 3 Journal Awards ✓ Open-Access Proceedings

The META Conference Series

The META Conference traces its origins to the landmark **Bianisotropics 2002** meeting held in Marrakesh, Morocco, one of the earliest international conferences dedicated to advanced electromagnetic materials. As the field of metamaterials rapidly emerged during the early 2000s, the conference naturally evolved into **META**, reflecting the birth of a new scientific discipline.

The inaugural meeting, in 2002, welcomed **Prof. Victor G. Veselago**, whose pioneering theory of negative-index media laid the foundations of modern electromagnetic metamaterials. The same year, the conference founders edited *Advances in Electromagnetics of Complex Media and Metamaterials* (Springer, NATO Science Series), widely recognised as the first international scientific book to feature the term “Metamaterials” in its title.

Today, META is one of the world’s leading conference series in metamaterials, plasmonics, photonic crystals and nanophotonics. Over sixteen editions, it has welcomed more than **10,000 researchers from over 50 countries**, providing an interdisciplinary forum where physics, materials science, optics, engineering and emerging quantum technologies converge. META is recognised for bringing together pioneers of the field with early-career researchers in an environment that fosters scientific excellence, innovation and international collaboration. Its peer-reviewed proceedings are published in **open access** at metaconferences.org/proceedings.

THE META JOURNEY

From the origins of metamaterials to a global conference series

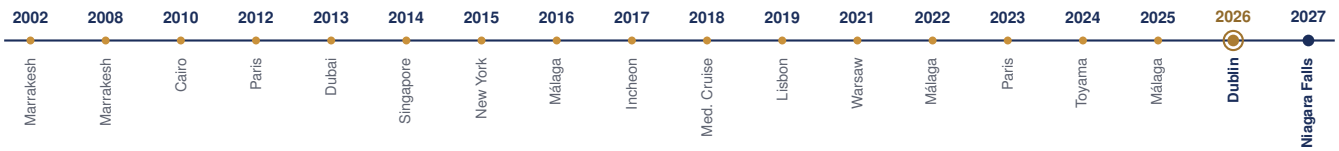

2002 Bianisotropics (origin) · 2008 first META · 2026 host · 2027 next edition

Next edition — META 2027 • Niagara Falls, Canada · 13–16 July 2027

Did you know?

- Prof. Victor Veselago attended the inaugural conference in 2002.
- The term “Metamaterials” appeared in one of the earliest dedicated international books, edited by the conference founders.
- META has been organised across Europe, Asia, Africa and North America.

META 2026 • PROGRAM BOOKLET

Sponsors & Partners

The organisations whose generous support makes META 2026 possible — in photonics, optics and scientific publishing.

Sponsors & Partners

META 2026

We gratefully acknowledge the following organisations whose generous support contributes to the success of META 2026.

SILVER SPONSORS

Technology & Research Partners

AIP Publishing

Publisher of APL Quantum — publishing.aip.org

AIP Publishing advances the physical sciences by connecting researchers through high-quality journals and innovative publishing services. As publisher of *APL Quantum*, it supports excellence in photonics, quantum science and emerging technologies.

ZEISS

Optical and Photonics Solutions — zeiss.com

Seeing beyond

ZEISS is a global technology leader in optics and optoelectronics, providing advanced microscopy, imaging and semiconductor manufacturing solutions that enable cutting-edge scientific research.

Phasics

Wavefront Sensing Technologies — phasics.com

Phasics develops innovative wavefront sensing and quantitative phase imaging systems for industrial inspection, biomedical imaging and advanced optical metrology.

MetacMed

Metamaterials for Medical Technologies — metacmed.eu

A European Doctoral Network funded by Horizon Europe, dedicated to metamaterials and medical technologies, fostering interdisciplinary research and international training.

MAGNIFIC

Multifunctional Nanophotonics — euproject-magnific.com

A Horizon Europe Doctoral Network developing next-generation multifunctional nanophotonic materials and devices for future photonic technologies.

SmartIR

Active Light Control across IR, THz & Visible smartir.co.uk

SmartIR develops smart optical devices that actively control, shape and detect light across the infrared, terahertz and visible ranges, combining advanced materials, photonics and intelligent sensing for space, defence and industrial applications.

Frontiers

Open-Access Publisher & Open Science Platform frontiersin.org

Frontiers is one of the world's leading open-access publishers and open science platforms, making millions of peer-reviewed research articles openly available and advancing discovery across research, health and technology.

PARTNERS & SUPPORTERS

Academic & publishing partners

Trinity College Dublin

HOST INSTITUTION

One of Europe's oldest and most prestigious universities.

Université Paris-Saclay

FOUNDING ACADEMIC PARTNER

Ranked among the world's leading research universities.

Fáilte Ireland

SUPPORTER

Ireland's National Tourism Development Authority.

Thorlabs

PHOTONICS INSTRUMENTATION

Global supplier of photonics equipment supporting research worldwide.

Advanced Devices & Instrumentation

Best Poster Award · Science Partner Journal

APL Quantum (AIP Publishing)

META Award · AIP Publishing

Laser & Photonics Reviews

Best Talk Award · Wiley

Nanophotonics

Best Talk Award · Wiley

Interested in becoming a META sponsor? Contact contact@metaconferences.org.

META Awards

META recognises outstanding scientific contributions through a series of awards, presented in partnership with leading international journals.

APL Quantum META Award

PRESENTED BY APL QUANTUM · AIP PUBLISHING

Honours a landmark contribution to the physics and applications of metamaterials, nanophotonics and quantum science.

Best Poster Award

PRESENTED BY ADVANCED DEVICES & INSTRUMENTATION

Celebrates the most compelling poster, rewarding clarity, originality and scientific impact among the contributed posters.

Best Talk Award

PRESENTED BY LASER & PHOTONICS REVIEWS · WILEY & NANOPHOTONICS · WILEY

Two outstanding oral presentations are distinguished for the quality of their science and the excellence of their delivery, underlining the breadth of excellence across the technical program.

Award recipients are announced during the conference. We warmly thank our award partners for their generous support.

META 2026 • PROGRAM BOOKLET

Organization & Committees

General Chairs · Scientific Advisory Committee · Technical Program Committee · Symposia Organizers

Organization & Committees

META 2026

META 2026 General Chairs

Ortwin Hess
META 2026 General Chair
Trinity College Dublin
Ireland

Said Zouhdi
META General Chair
Paris-Saclay University
France

Scientific Advisory Committee

13 members

Andrea Alù	US	Nader Engheta	US	Vladimir Shalaev	US
Harry Atwater	US	Ortwin Hess	IE	David R. Smith	US
Alexandra Boltasseva	US	Yuri Kivshar	AU	Nikolay Zheludev	UK
Federico Capasso	US	Susumu Noda	JP		
Che Ting Chan	HK	Dorota A. Pawlak	PL		

Technical Program Committee

48 members

Guillermo Acuna	CH	Denis Garoli	IT	Marco Miniaci	FR
Pierre-Michel Adam	FR	Li Ge	US	Khaled Mnaymneh	CA
Antonio Ambrosio	IT	Tommaso Giovannini	IT	Taiichi Otsuji	JP
Ashod Aradian	FR	Alexander Govorov	US	Willie Padilla	US
Benfeng Bai	CN	Tatjana Gric	LT	Dorota Pawlak	PL
Maha Ben Rhouma	FR	Jean-Philippe Groby	FR	Lucia Petti	IT
Henri Benisty	FR	Yael Gutierrez	ES	Virginie Ponsinet	FR
Jamal Berakdar	DE	Han Htoon	US	Giorgio Quaranta	CH
Svetlana Boriskina	US	Kotaro Kajikawa	JP	Junsuk Rho	KR
Debashis Chanda	US	Eugene Kamenetskii	IL	Junichi Takahara	JP
Pai-Yen Chen	US	Howard Lee	US	Takuo Tanaka	JP
Johan Christensen	ES	Jensen Li	HK	Hong Wei	CN
Sébastien Cueff	FR	Qiang Li	CN	Weiren Zhu	CN
Alfredo De Rossi	FR	Yang Li	CN	Arcady Zhukov	ES
Alexander F. Dmitriev	SE	Anatole Lupu	FR		
Monika Fleischer	DE	Konstantinos Makris	GR		
Andrea Fratalocchi	SA	Martin McCall	UK		

Symposia Organizers

META 2026

SYM I — Hybrid Nanomaterials and Metastructures for Photonics, Sensing and Energy

Jérôme Plain
Univ. of Technology of Troyes
France

Alexander Govorov
Ohio University
USA

Davy Gérard
Univ. of Technology of Troyes
France

Pedro H. Martinez
Nanyang Technological University
Singapore

SYM II — New Trends in Nanophotonics and Advanced Materials

Junsuk Rho
POSTECH
Korea

Hakjoo Lee
CAMM
Korea

Namkyoo Park
Seoul National University
Korea

Seong Ok Han
Korea Inst. of Energy Research
Korea

SYM III — Advanced Passive and Active Metasurfaces and Zero-Index Materials

Howard Lee
Univ. of California, Irvine
USA

Pin Chieh Wu
National Cheng Kung University
Taiwan

Wen-Hui (Sophia) Cheng
National Cheng Kung University
Taiwan

Symposia Organizers

META 2026

SYM IV — Chirality, Magnetism, and Magnetoelectricity in Metamaterial Structures

Eugene Kamenetskii

Ben Gurion Univ. of the Negev

Israel

SYM V — Architectured Elastic and Acoustic Metamaterials & Phononic Crystals

Marco Miniaci

Politecnico di Torino

Italy

Jensen Li

HKUST

Hong Kong

Jean-Philippe Groby

LAUM–CNRS / Univ. du Mans

France

Vincent Pagneux

LAUM–CNRS

France

Vicent Romero-García

UPV

Spain

Stefano Laureti

University of Calabria

Italy

Symposia Organizers

META 2026

SYM VI — Advanced Techniques for Computational Electromagnetics

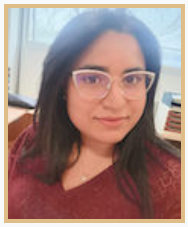

Maha Ben Rhouma
Gustave Eiffel Univ. — ESYCOM
France

Special Sessions Organizers (24 sessions)

SP1 Tatjana Gric LT

SP2 Anatole Lupu FR, Henri Benisty FR

SP3 Weiren Zhu CN, Zhenfei Li CN, Jin Zhang FI

SP4 Jamal Berakdar DE, Andrei Afanasev US

SP5 Sébastien Cueff FR, Yael Gutierrez ES

SP6 Fei Ding DK, Sergey I. Bozhevolnyi DK

SP7 Guillermo Acuna CH, Peter Zijlstra NL, Hiroshi Sugimoto JP

SP8 Debashis Chanda US

SP9 Dorota Pawlak PL, Virginie Ponsinet FR

SP10 Konstantinos Makris GR, Li Ge US

SP11 Alessandro Veltri EC, Ashod Aradian FR

SP12 Hong Wei CN

SP13 Matthew Singer US

SP14 Eugene Kamenetskii IL

SP15 Lucia Petti IT, Massimo Rippa IT

SP16 David R. Smith US, Okan Yurduseven UK

SP17 Giuseppina Simone IT

SP18 Philippe Tassin SE

SP19 Khaled Mnaymneh CA

SP20 Gonzalo Álvarez-Pérez IT, Huatian Hu IT

SP21 Carlos Alberto Maciel Escudero DE, Jorge Olmos Trigo ES, Mario Zapata Herrera ES

SP22 Chiara Deriu IT, Tommaso Giovannini IT, Chiara Cappelli IT, Laura Fabris IT

SP23 Jérémie Margueritat FR, Aurélien Crut FR

SP24 Yu Zhang US

META 2026 • PROGRAM BOOKLET

Plenary Talks

Five flagship plenary lectures by world-leading figures in photonics, plasmonics and metamaterials.

SUPPORTED BY OUR SILVER SPONSORS

META 2026 Plenary Program

Five flagship plenary lectures by world-leading figures in photonics, plasmonics and metamaterials.

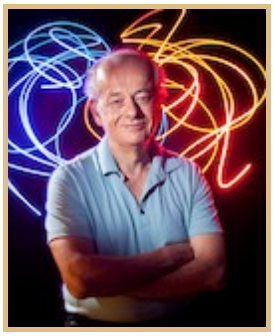

Federico Capasso

Harvard University, USA

Metasurfaces: From Classical to Quantum Optics

Alexandra Boltasseva

Purdue University, USA

Materials-Driven Photonics: Tunable and Extreme Light Control

Jeremy J. Baumberg

University of Cambridge, UK

Precision Nanogap Metamaterials for Tracking Bioanalytes

Rachel Grange

ETH Zurich, Switzerland

Quadratic Nanomaterials for On-Chip Classical & Quantum Devices

Ruwen Peng

Nanjing University, China

Metasurfaces for Classical and Quantum Light Control

Supported by our silver sponsors

AIP Publishing · ZEISS Seeing beyond · Phasics EXOSENS GROUP · MetaMed · MAGNIFIC · SMARTIR · frontiers

Plenary Talks

META 2026

PLENARY 5 plenary lectures · 35 minutes each including Q&A

PLENARY LECTURE 1

PLENARY · 35 min

Jeremy J. Baumberg

University of Cambridge, UK

Directs the NanoPhotonics Centre at the University of Cambridge and the Cambridge Nano Doctoral Training Centre. A leading innovator in nanoscale optical materials. **Fellow of the Royal Society**, Optica and the Institute of Physics. Recipient of the IoP Faraday Gold Medal (2017), the Royal Society Rumford Medal (2014) and the IoP Mott Lectureship (2005).

TALK TITLE

Precision Nanogap Metamaterials for Tracking Bioanalytes using SERS and SEIRA

ABSTRACT

I will discuss a range of recent key advances that give robust, repeatable, and recleanable nanogap plasmonic sensors, as well as midIR metamaterials enabling real-time flow electrochemistry.

PLENARY LECTURE 2

PLENARY · 35 min

Alexandra Boltasseva

Purdue University, USA

Ron and Dotty Garvin Tonjes Distinguished Professor of Electrical and Computer Engineering at Purdue University. PhD from the Technical University of Denmark (2004). **Fellow of NAI, MRS, IEEE, Optica and SPIE.** Former Editor-in-Chief of *Optical Materials Express*. Recipient of the **2023 R.W. Wood Prize** (Optica), 2022 Guggenheim Fellowship, MRS Outstanding Young Investigator (2013) and IEEE Photonics Society Young Investigator Award (2013).

TALK TITLE

Materials-Driven Photonics: Toward Tunable and Extreme Light Control

ABSTRACT

We study tailorable and dynamically tunable properties of transparent conducting oxides (TCOs) and transition metal nitrides (TMNs) for applications in all-optical modulators and flat optics. We also investigate metal-to-insulator transition in ultra-thin TMN films operating in the so-called transdimensional regime.

PLENARY LECTURE 3

PLENARY · 35 min

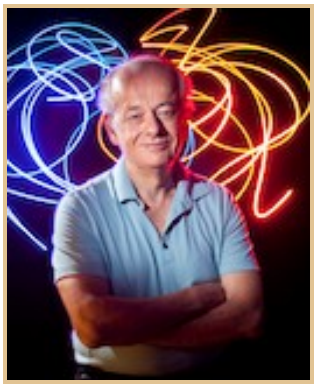

Federico Capasso

Harvard University, USA

Robert Wallace Professor of Applied Physics at Harvard University. Co-inventor of the quantum cascade laser and a pioneer of metasurfaces and flat optics. **Member of the U.S. National Academies of Sciences and Engineering.** Recipient of the IEEE Edison Medal, the Balzan Prize and the King Faisal Prize for Science.

TALK TITLE

Metasurfaces: From Classical to Quantum Optics

ABSTRACT

We demonstrate a generalized Hong-Ou-Mandel effect using metasurfaces and graph theory, enabling controlled multi-photon bunching, antibunching, and entanglement across parallel matrix-encoded spatial modes. Our theoretical framework predicts the device's behavior and facilitates the design of dual graphs representing both metasurface-based multiport interferometer designs and the complex non-classical correlations they generate

PLENARY LECTURE 4

PLENARY · 35 min

Rachel Grange

ETH Zurich, Switzerland

Full Professor of Photonics at ETH Zurich (since 2025); previously Associate and Assistant Professor there. Research on integrated optics and nonlinear nanophotonics with metal-oxides — notably thin-film lithium niobate and barium titanate — for classical and quantum devices.

TALK TITLE

Quadratic Nanomaterials for On-Chip Classical and Quantum Devices

ABSTRACT

Here I will present our recent progress in top-down fabrication of lithium niobate devices and bottom-up approaches, including the assembly of randomly oriented nanocrystals and sol-gel processes, to generate nonlinear classical and quantum signals. Finally, I will describe how these platforms are suited for nonlinearities in machine learning.

PLENARY LECTURE 5

PLENARY · 35 min

Ruwen Peng

Nanjing University, China

Distinguished Professor in the School of Physics, Nanjing University, and principal investigator at the National Laboratory of Solid State Microstructures. Research in nanophotonics, metamaterials, plasmonics, photonic quasicrystals and phononic transport. Recipient of the National Science Foundation for Distinguished Young Scholars (China, 2006), the Chinese Young Women Scientists' Award (2011) and the Xie Xide Award (2013).

TALK TITLE

Metasurfaces as a Platform for Classical and Quantum Light Control

ABSTRACT

In this talk, we present metasurfaces as a platform for classical and quantum light control. The approaches achieve potential applications in optical display, data storage, information encryption, and quantum information networks.

META 2026 • PROGRAM BOOKLET

Keynote Talks

Twenty-seven keynote lectures spanning the most active frontiers of nanophotonics and metamaterials.

SUPPORTED BY OUR SILVER SPONSORS

Keynote Talks

META 2026

KEYNOTE 27 keynote lectures · 30 minutes each including Q&A

KEYNOTE 1

KEYNOTE · 30 min

Ali Adibi

Georgia Institute of Technology, USA

Joseph M. Pettit Professor of Electrical and Computer Engineering, Georgia Tech. Pioneer in nanophotonics and computational imaging.

TALK TITLE

Hybrid Techniques for Inverse Design and Knowledge Discovery in Large-Scale Multifunctional Nanophotonic Devices

ABSTRACT

This talk is focused on a new class of inverse design tools for large-scale nanophotonic structures by combining rigorous gradient-based techniques with machine learning tools. By combining these two classes of design tools, dimensionality of the design space and the computation requirement can be reduced by 2-3 orders of magnitude.

KEYNOTE 2

KEYNOTE · 30 min

Girish S. Agarwal

Texas A&M University, USA

Distinguished Professor of Physics, Texas A&M. Renowned for fundamental contributions to quantum optics.

TALK TITLE

QED of Chiral Waveguides Coupled to Quantum Emitters

ABSTRACT

Waveguide QED is a quantum platform in which photons mediate long range interactions in a one dimensional channel. This talk highlights waveguide QED with quantum emitters, emphasizing quantum interference (Fano minima and transparency), chiral interactions, quantum nonreciprocity, and steady state entanglement, together with squeezed bath stabilization and dissipative phase transitions.

KEYNOTE 3

KEYNOTE · 30 min

Esther Alarcón Lladó

NWO-I AMOLF Institute, The Netherlands

Tenured Group Leader at the NWO-I AMOLF Institute and, since 2023, Professor by special appointment on Nanoelectrochemistry at the University of Amsterdam; chair of the Dutch Physics Council. She earned her PhD from the University of Barcelona in 2009, held Marie Curie and Ambizione Energy postdoctoral fellowships at A*STAR (Singapore), LBNL Berkeley and EPFL Lausanne, and in 2016 founded the 3D Photovoltaics group at AMOLF, working at the interface of optics, nanotechnology and electrochemical scanning probe microscopy.

TALK TITLE

Managing light and matter at the nanoscale for sustainable energy conversion

ABSTRACT

We realized a 1D coupled nanolaser chain enabling topologically protected bright zero modes. Our design exploits coupling sign inversion through photonic crystal barrier engineering. We present the design parameters, numerical simulation results, and preliminary experimental results from the first fabricated structures.

KEYNOTE 4

KEYNOTE · 30 min

Harry Atwater

California Institute of Technology, USA

Otis Booth Leadership Chair, Division of Engineering and Applied Science, Caltech. Pioneer in solar energy science and plasmonics. **Member of the National Academy of Engineering.**

TALK TITLE

Wavefront Shaping and Harnessing Coherence with Guided Mode Metastructures

ABSTRACT

Guided mode metastructures are key building blocks for design of electro-optic active metasurfaces for wavefront shaping, and in metasurfaces that enable spatial coherence in the far field radiation emitted from thermal radiation sources and luminescent emitters.

KEYNOTE 5

KEYNOTE · 30 min

Gerrit E.W. Bauer

TU Delft (NL) & Tohoku University (JP)

Professor at Delft University of Technology and Tohoku University. His scientific work is in theoretical condensed matter physics.

TALK TITLE

Advances in Ferronics

ABSTRACT

Compared to magnetic materials, the dynamics of the ferroelectric order has received little attention from the scientific community. Here I review recent progress in understanding ferrons, the elementary excitations of the ferroelectric order.

KEYNOTE 6

KEYNOTE · 30 min

Philippe Ben-Abdallah

Institut d'Optique - CNRS, France

Research Director at CNRS and head of the Thermoplasmonics group at the Charles Fabry Laboratory. Research on near-field radiative heat transfer and thermal management at the nanoscale.

TALK TITLE

Thermal Photonics in Nonreciprocal and Time-Modulated Many-Body Systems

ABSTRACT

This talk explores thermal photonics in nonreciprocal many-body systems, revealing novel heat-flow control via spin-caloritronic effects. I also present a phase-tunable Floquet approach to manipulate radiative heat transfer, enabling directional flow, reversible pumping and reconfigurable flux in time-modulated networks, paving the way for programmable thermal photonic devices.

KEYNOTE 7

KEYNOTE · 30 min

Robert W. Boyd

University of Ottawa, Canada & University of Rochester, USA

Canada Excellence Research Chair in Quantum Nonlinear Optics, University of Ottawa; M. Parker Givens Professor of Optics, University of Rochester. Author of two books and over 200 research papers. Fellow of OSA and APS.

TALK TITLE

Highly Nonlinear Photonic Materials Based on Metamaterials, Plasmonics, and Nanostructuring

ABSTRACT

This contribution reviews advances in the development of highly nonlinear materials by the combination of methods devised from the fields of metamaterials, plasmonics, and structured surfaces. We also review how these materials have led to the development of new photonics applications, including applications in quantum information technologies.

KEYNOTE 8

KEYNOTE · 30 min

Louise Bradley

Trinity College Dublin, Ireland

Professor at the School of Physics, Trinity College Dublin. Research in nanophotonics, plasmonic metasurfaces, sensing and quantum technologies.

TALK TITLE

Engineering Strong Light–Matter Coupling in Dielectric Metasurfaces

ABSTRACT

Interest in exciton-polaritons for quantum devices, quantum sensing and low-threshold lasing applications continues to grow. Consequently, the realization of robust, room temperature strong-coupling systems is the subject of extensive effort. Herein, strong light-matter coupling is engineered in dielectric metasurfaces coupled with two-dimensional dichalcogenide material WS2

KEYNOTE 9

KEYNOTE · 30 min

Igal Brener

Sandia National Laboratories, USA

Senior Scientist at Sandia National Laboratories and Nanophotonics thrust co-leader at the Center for Integrated Nanotechnologies. Research in dielectric and semiconductor metamaterials, nonlinear nanophotonics and ultrafast optoelectronics.

TALK TITLE

Semiconductor Metasurfaces for Enhanced Nonlinearities and Control of Single Photon Emission

ABSTRACT

We integrate epitaxial GaAs quantum dots into III- V semiconductor metasurfaces for efficient, position-tolerant light extraction and tunable functionality. Huygens designs boost collected photoluminescence tenfold and enable bunched and super-bunched emission. Symmetry-engineered quadromer lattices provide multiresonant qBIC control and greatly enhance four-wave mixing and nonlinear optical phenomena.

KEYNOTE 10

KEYNOTE · 30 min

Zhigang Chen

Nankai University, China

Chair Professor at Nankai University. Research in nonlinear optics, topological photonics, and optical trapping and manipulation. **Fellow of Optica and the American Physical Society.**

TALK TITLE

Kagome-Inspired Topological Photonics: From Lattice Design to Robust Control of Light

ABSTRACT

I will present our recent advances in Kagome-inspired photonic lattices and their structural extensions, including super-honeycomb, breathing Kagome, disclination-based, and fractal-like geometries. These systems enable the realization of diverse topological states, such as higher-order boundary modes, vortex states carrying orbital angular momentum, and flatband-induced localization.

KEYNOTE 11

KEYNOTE · 30 min

Alberto Corigliano

Politecnico di Milano, Italy

Full Professor of Structural Mechanics, Politecnico di Milano. Research in MEMS, mechanical metamaterials and multiphysics modeling.

TALK TITLE

Metastructures for Spatial Signal Processing and Energy Confinement

ABSTRACT

This work critically discusses micro- and meso-scale graded metastructures as spatial signal processing platforms, with emphasis on achieving tonotopicity, advanced control of wave propagation, and elastic energy confinement. Illustrative examples include graded micro- and meso-scale arrays and bio-inspired, cyclically symmetric phononic pseudo-crystals.

KEYNOTE 12

KEYNOTE · 30 min

F. Javier García de Abajo

ICFO — The Institute of Photonic Sciences, Spain

ICREA Research Professor at ICFO, Barcelona. Leading theoretician in nanophotonics and electron–light interactions. Fellow of the American Physical Society and Optica.

TALK TITLE

Probing Nanoscale Optical Nonlocal and Nonlinear Effects Through Free Electrons

ABSTRACT

We explore how free electrons probe nanomaterials' nonlocal and nonlinear optical responses with unmatched spatial resolution, examining harmonic generation, Kerr nonlinearities, and interference of inelastically scattered electrons, while lateral deflections from finite momentum transfers reveal nonlocal effects.

KEYNOTE 13

KEYNOTE · 30 min

Rob Devlin

Metalenz, USA

Co-founder and CEO of Metalenz, the first company to bring metasurface technology to mass markets, with more than 150 million metasurface optics integrated into consumer devices for 3D sensing. Recipient of Optica's Kevin P. Thompson Optical Design Innovator Award (2025).

TALK TITLE

Scaling the Metasurface Market: From Flat Optics to Sensor-Integrated Intelligence

ABSTRACT

From lab breakthrough to mass-market deployment, this presentation explores the commercialization of metasurfaces at Metalenz-highlighting key drivers, technical challenges, and emerging applications. Metasurfaces are no longer just flat optical elements; they are evolving into system-level platforms for intelligent perception, enabling more perceptive, accurate, and efficient vision systems.

KEYNOTE 14

KEYNOTE · 30 min

Bahram Djafari-Rouhani

University of Lille, France

Emeritus Professor of Physics at the University of Lille. Pioneer in the field of phononic crystals and metamaterials. Recipient of the Bloch Prize (Phononics 2013).

TALK TITLE

Topological Phononic and Photonic Modes in Optomechanic Crystals

ABSTRACT

In this work we present a theoretical investigation of structures that simultaneously support localized topological phononic and photonic modes, enabling enhanced optomechanical interactions. Two platforms are considered: (i) a one-dimensional nanobeam engineered within the framework of the Su-Schrieffer-Heeger (SSH) model and (ii) a two-dimensional honeycomb membrane.

KEYNOTE 15

KEYNOTE · 30 min

Bert Hecht

University of Würzburg, Germany

Professor of Experimental Physics at the University of Würzburg. Research on near-field optical microscopy, plasmonics and the enhancement of light–matter interaction on the nanometer scale.

TALK TITLE

Nanorobots Steered by Light

ABSTRACT

Plasmonic nanoantennas can be used to redirect scattered light, causing momentum transfer via photon recoil. By exploiting different degrees of freedom of light, such as helicity and photon energy, several antennas can be driven selectively with minimal crosstalk to neighboring structures even at subwavelength distance.

KEYNOTE 16

KEYNOTE · 30 min

Yu-Jung Lu

Academia Sinica, Taiwan

Associate Research Fellow at the Research Center for Applied Sciences, Academia Sinica. Research in active plasmonics, nanophotonics and metasurfaces.

TALK TITLE

Plasmonic HfN-Gated Monolayer MoS_2 for Giant Trion Modulation and Scalable Optoelectronic Devices

ABSTRACT

We demonstrate a chip-scale, gate-tunable light-emitting platform that integrates scalable monolayer MoS2 with a HfN plasmonic gate electrode. The favorable band alignment enables giant trion modulation, yielding a PL modulation depth of 24%.

KEYNOTE 17

KEYNOTE · 30 min

Angela Madeo

TU Dortmund University, Germany

Professor at TU Dortmund. Specialist in enriched continuum models and mechanical metamaterials.

TALK TITLE

Modeling Boundary Effects in Acoustic Metamaterials by a Relaxed Micromorphic Continuum

ABSTRACT

To accurately describe elastic wave propagation in these materials characterized by their heterogeneities or microstructures, it is essential to adopt non-local or enriched modeling approaches. In this context, we propose the relaxed micromorphic model (RMM), which effectively captures these phenomena by treating the material as continuum with enriched kinematics.

KEYNOTE 18

KEYNOTE · 30 min

Bumki Min

KAIST, Republic of Korea

Professor in the Department of Physics, KAIST. Research in metamaterials and metadevices, micro- and nano-optics, 2D optical materials, and time-varying photonics.

TALK TITLE

Photonic Time Crystals: Transport, Emission, Squeezing

ABSTRACT

Photonic time crystals provide a unified setting for studying wave transport, light-matter interaction, and quantum fluctuations in driven media. Here we show that seemingly different phenomena in these systems, including transport, emission, and squeezing, can be understood within a common Floquet framework that connects classical and quantum descriptions.

KEYNOTE 19

KEYNOTE · 30 min

Hiromi Okamoto

Institute for Molecular Science, Japan

Professor of chemistry at the Institute for Molecular Science, Japan. Research in nano- and micro-scale optical imaging of materials, and plasmonic and chiral materials.

TALK TITLE

Chiro-optical micro-/nano-imaging and near-field interaction

ABSTRACT

We developed chiral photoinduced force microscopy (PiFM) to visualize nanoscale chiro-optical responses using circularly polarized light. Chiral and achiral plasmonic nanostructures were imaged, revealing local chiral fields and probe-induced chirality. This approach enables nanometer-scale chiro-optical imaging beyond conventional near-field techniques.

KEYNOTE 20

KEYNOTE · 30 min

Romain Quidant

ETH Zurich, Switzerland

Professor at ETH Zurich (Mechanical and Process Engineering). Research in nano-optics and optomechanics, with applications from fundamental physics to biomedicine. Recipient of three ERC grants.

TALK TITLE

Meta-Optics Based Optomechanics

ABSTRACT

We discuss the use of metaoptics in optomechanics. By exploiting resonant silicon meta-atoms, we achieve enhanced optomechanical performance and deterministic control over optical forces. We show that engineering multipolar Mie resonances allows for switching between attractive and repulsive forces, directly mirroring the behavior of two-level systems.

KEYNOTE 21

KEYNOTE · 30 min

Vladimir M. Shalaev

Purdue University, USA

Scientific Director for Nanophotonics at Birck Nanotechnology Center and Distinguished Professor of Electrical and Computer Engineering at Purdue University. **Fellow of IEEE, APS, SPIE, MRS and Optica.** Recipient of the APS Frank Isakson Prize, Optica Max Born Award, IEEE Photonics William Streifer Award, Rolf Landauer Medal and the UNESCO Medal.

TALK TITLE

Metamaterials at Crossroads: From Quantum to Space-Time Photonics

ABSTRACT

We discuss quantum photonics based on the recently discovered single-photon emitters in silicon nitride and the avalanche-enhanced optical modulation in silicon at single-photon intensities. Then, we show that transparent conducting oxides (TCOs) operating in the near-zero index (NZI) regime can enable extreme time-varying media.

KEYNOTE 22

KEYNOTE · 30 min

Giuseppe Strangi

Case Western Reserve University, USA

Professor of Physics at Case Western Reserve University, where he leads the Nanoplasm Lab. Research in metamaterials, epsilon-near-zero media and optical biosensing. **Fellow of Optica and the European Physical Society.**

TALK TITLE

Chirality in Light–Matter Interaction

ABSTRACT

Chiral metasurfaces enable strong control of light matter interaction at the nanoscale. Planar plasmonic architectures generate superchiral electromagnetic fields that enhance chiroptical responses beyond natural systems. These engineered platforms support enantioselective sensing, molecular spectroscopy, and quantum photonics by amplifying weak optical signatures of molecular chirality.

KEYNOTE 23

KEYNOTE · 30 min

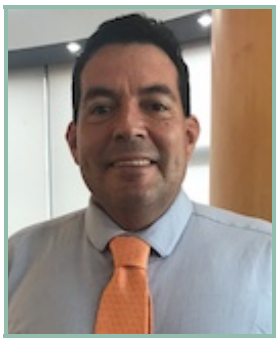

Michael E. Tobar

University of Western Australia, Australia

Professor of Physics at the University of Western Australia, where he leads the Quantum Technologies and Dark Matter Research Lab. Former ARC Laureate Fellow. Research in precision and quantum measurement, frequency metrology and dark-matter detection.

TALK TITLE

Electric Dipole Moments via Electromagnetic Duality

ABSTRACT

We present a duality-based framework that maps EDM physics onto Zeeman structure. Stark-induced dipoles are represented through a magnetic current description of microscopic polarization, while intrinsic dipoles remain tied to spin. A Bohr scale dipole unit and pseudo angular momentum organize dipole operators and selection rules.

KEYNOTE 24

KEYNOTE · 30 min

Jelena Vučković

Stanford University, USA

Jensen Huang Professor of Global Leadership and Professor of Electrical Engineering, Stanford University. **Member of the National Academy of Sciences** and External Scientific Member of the Max Planck Institute for Quantum Optics. Fellow of APS, Optica and IEEE.

TALK TITLE

Inverse designed, densely integrated classical and quantum photonics

ABSTRACT

Recent breakthroughs in photonics design, along with new nanofabrication approaches and heterogeneous integration play crucial roles in building photonics for applications including optical interconnects and quantum technologies. This design breakthrough is named photonic inverse design, and refers to efficiently searching through the space of all possible photonic device geometries.

KEYNOTE 25

KEYNOTE · 30 min

Eli Yablonovitch

UC Berkeley, USA

James & Katherine Lau Chair Professor of Engineering, UC Berkeley. Father of the photonic bandgap concept, who coined the term "photonic crystal". **Member of the National Academy of Sciences, National Academy of Engineering and the American Academy of Arts and Sciences.** Recipient of the Buckley Prize, the Isaac Newton Medal and the IEEE Photonics Award.

TALK TITLE

Can Physics and Optical Science Expedite Artificial Intelligence?

ABSTRACT

Artificial Intelligence (AI) requires intensive optimization calculations and is now demanding nuclear power for data centers. All the variables in an AI model must converge, to expedite the calculations. Data center energy is dominated by data communication which costs 1pJ/bit, about 6 orders of magnitude higher than the Landauer Limit.

KEYNOTE 26

KEYNOTE · 30 min

Anatoly V. Zayats

King's College London, UK

Chair in Experimental Physics and Head of the Photonics & Nanotechnology Group, King's College London; Co-Director of the London Centre for Nanotechnology. Research in nanophotonics, plasmonics, metamaterials and optical spin–orbit coupling. **Fellow of Optica**, the Institute of Physics and SPIE; elected Member of Academia Europaea.

TALK TITLE

Generating Optical Merons through Spin–Orbit Coupling in Anisotropic Metamaterials

ABSTRACT

We will discuss the enhanced spin-orbit coupling in strongly anisotropic metamaterials which provides efficient conversion of polarisation state of the transmitted light and results in meron-type topological structures of the electromagnetic field. Flexible control of polarisation and its topological properties is important for optical manipulation, communications, metrology and quantum technologies.

KEYNOTE 27

KEYNOTE · 30 min

Nikolay Zheludev

University of Southampton, UK, and Texas A&M University, USA

Professor Zheludev is a **Fellow of the Royal Society** and a Member of the US National Academy of Engineering. His honours include the European Physical Society Quantum Electronics and Optics Prize, the Faraday Gold Medal, the Thomas Young Medal, Singapore's President's Science and Technology Award, and the Institute of Physics Singapore President Gold Medal.

TALK TITLE

Optical metrology a myriad times finer than Robert Hook's and a million times faster than Eadweard Muybridge's

ABSTRACT

By training metrological estimators, employing topologically structured light, and engineering the flow of Fisher information, optical metrology can surpass conventional resolution limits by orders of magnitude-achieving atomic-scale precision at megahertz acquisition rates.

META 2026 • PROGRAM BOOKLET

Pre-Conference Workshop

COST TETRA Workshop on Biophotonics & Biometamaterials · 13–14 July 2026.

Pre-Conference Workshop

META 2026

COST · TETRA 5th Workshop on Biophotonics and Biometamaterials

Workshop Info

Dates: 13–14 July 2026 **Location:** Beckett Room, Trinity Conference Centre – Arts Building

Day 1 — Monday 13 July 2026

09:00 – 09:10 Registrations

09:10 – 09:20 **Presentation of the Workshop**
Tatjana Gric — Vilnius Tech, Lithuania

09:20 – 09:40 **COST travel reimbursement rules: presentation of the Grant Holder Manager**
Fikret Alpay Teksen — Vilnius Tech, Lithuania

09:40 – 10:30 Affinity Diagramming

10:30 – 11:00 ***Refreshment Break***

CANCER DIAGNOSTICS AND TREATMENT

11:00 – 11:30 **Wavelets–Fourier decomposition for wide-beam scattering and image-based analysis: bridging photonic metasurfaces and biomedical tissue diagnostics**
Kofi Edee — University of Clermont Auvergne, France

11:30 – 12:00 **A miniaturized implantable antenna for brain signal monitoring**
Moti Haridim — HIT—Holon Institute of Technology, Israel

IMAGING TECHNIQUES

12:00 – 12:30 **Multi-photon imaging and compositional analysis by spectral deconvolution in noninvasive vascular scaffolds**
Steve Smith — South Dakota Mines, USA

12:30 – 13:00 **Partial Mueller polarimetry for real-time diagnostic imaging of biological tissues**
Tatiana Novikova — École Polytechnique, France

13:00 – 13:30 **Aggregated plasmonic gold nanoparticles for surface-enhanced Raman spectroscopy**
Miklos Veres — HUN-REN Wigner Research Centre for Physics, Hungary

13:30 – 13:40 Group Photo

13:40 – 15:00 ***Lunch Break***

NOVEL METAMATERIALS

15:00 – 15:30 **Atomistic theory of hot carriers in metallic nanoparticles**
Johannes Lischner — Imperial College London, UK

15:30 – 16:00 **Metamaterials: from theory to applications**
Tatjana Gric — Vilnius Tech, Lithuania

16:00 – 16:30 **Effects of the order-to-disorder transition on plasmonic metasurfaces**
Jerome Plain — University of Technology of Troyes, France

Day 2 — Tuesday 14 July 2026

BIOPHOTONICS MEETING MEDICINE

09:00 – 09:30 **Early-stage testicular cancer detection via a multi-antenna Vivaldi sensor configuration** *(online)*
Fikret Alpay Teksen — Vilnius Tech, Lithuania

09:30 – 10:00 **Biophotonics for psychological stress measurements**
Victoria Barygina — Università di Firenze, Italy

10:00 – 10:30 **From biometamaterials to regulatory readiness: COST Action TETRA and in silico NAMs for biomedical efficacy and safety**
Ivana Vinković Vrček — Inst. of Medical Research & Occupational Health, Croatia

10:30 – 11:00 ***Refreshment Break***

FUTURE TRENDS

11:00 – 11:30 **Compact and efficient Quantum Dot based room-temperature THz sources**
Edik Rafailov — Aston University, UK

11:30 – 12:00 **Targeted gold nanorod conjugates for photothermal treatment of cancer**
Anatoliy Pinchuk — University of Colorado, USA

12:00 – 13:00 Storyboarding

13:00 – 15:00 ***Lunch Break***

15:00 – 16:00 Post-Up Activity

COST Action CA23125 — TETRA (The metamaterial formalism approach to recognize cancer)
More info: www.cost.eu

META 2026 · DUBLIN, IRELAND · 14–17 JULY 2026

Conference Papers

Full texts of the plenary, keynote, invited, oral and poster contributions presented at META 2026

933
Papers
in this volume

32
Lectures
5 plenary · 27 keynote

36
Sessions
6 symposia · 24 special · 6 general

169
Posters
5 thematic groups

Trinity College Dublin · The University of Dublin · Ireland
metaconferences.org · ISSN 2429-1390

Proceedings Contents

Plenary Presentations 98

Metasurfaces as a platform for classical and quantum light control 99
Ruwen Peng, Mu Wang

From Classical to Quantum Metasurfaces for Multiphoton Interferometry 100
Federico Capasso

Materials-Driven Photonics: Toward Tunable and Extreme Light Control 101
Alexandra Boltasseva

Precision nanogap metamaterials for tracking bioanalytes using SERS and SEIRA 102
Jeremy J. Baumberg

Quadratic Nanomaterials for On-Chip Classical and Quantum Devices 103
Rachel Grange

Keynote Presentations 104

Generating Optical Merons through Spin-orbit Coupling in Anisotropic Metamaterials 105
Vittorio Aita, Anastasiia Zaleska, Anatoly Zayats

How can light be used for measurements a myriad times finer than those of Robert Hooke and a million times faster than those of Eadweard Muybridge? 107
Nikolay I. Zheludev

Probing nanoscale optical nonlocal and nonlineareffects through free electrons 108
F. Javier García de Abajo

Metastructures for spatial signal processing and energy confinement 109
Raffaele Ardito, Marcello Cazzola, Chiara Gazzola, Jacopo Maria De Ponti, Marco Miniaci, Prisca Viviani, Alberto Corigliano

Chirality in Light Matter interaction 111
Giuseppe Strangi

Managing light and matter at the nanoscale for sustainable energy conversion 112
Esther Alarcón Lladó

Kagome-Inspired Topological Photonics:From Lattice Design to Robust Control of Light 113
Zhigang Chen

Meta-optics based optomechanics 114
Adeel Afridi, Bruno de Melo, Bin Lu, Nadine Meyer, Romain Quidant

Scaling the Metasurface Market: From Flat Optics to Sensor-Integrated Intelligence 116
Rob Devlin

Wavefront Shaping and Harnessing Coherence with Guided Mode Metastructures 117
Julie Belleville, Martin Thomaschewski, Komron Shayegan, Yae-Chan Lim, Gloria Halka, Arun Nagpal, Nimisha Ramprasad, Lior Michaeli, Harry Atwater

Can Physics and Optical Science Expedite Artificial Intelligence? 119
Eli Yablonovitch

Metamaterials at Crossroads: from Quantum to Space-Time Photonics 120
Vladimir M. Shalaev

Highly Nonlinear Photonic Materials Based on Metamaterials, Plasmonics, and Nanostructuring 121
Robert Boyd

Inverse designed, densely integrated classical and quantum photonics 123
Jelena Vuckovic

Thermal Photonics in Nonreciprocal and Time-Modulated Many-Body Systems 124
Philippe Ben Abdallah

Advances in Ferronics 126
Gerrit Bauer

Engineering Strong Light-Matter Coupling in Dielectric Metasurfaces 127
A. Louise Bradley, Y. Zhang, X. Zhang, K. Mamaeva, N. Jia, J. Schulz, J. Dobie

Chiro-Optical Micro-/Nano-Imaging and Near-Field Interaction 129
Hiromi Okamoto

QED of Chiral Waveguides Coupled to Quantum Emitters 130
Girish Agarwal

Plasmonic HfN-Gated Monolayer MoS□ for Giant Trion Modulation and Scalable Optoelectronic Devices 132
Yu-Jung Lu

Nanorobots Steered by Light 133
Bert Hecht

Semiconductor metasurfaces for enhanced nonlinearities and control of single photon emission 134
Igal Brener

Photonic Time Crystals: Transport, Emission, Squeezing 135
Bumki Min

Electric Dipole Moments via Electromagnetic Duality 136
Michael Tobar

Topological Phononic and Photonic Modes in Optomechanic Crystals 138
Nouh Krai, Hicham Mangach, Abdellatif Gueddida, Gaëtan Lévêque, Yan Pennec, Marco Miniaci, Bahram Djafari Rouhani

Modeling boundary effects in acoustic metamaterials by a relaxed micromorphic continuum 140
Angela Madeo

Hybrid Techniques for Inverse Design and Knowledge Discovery in Large-scale Multifunctional Nanophotonic Devices 141
Reza Marzban, Jamshid Hassanpour, Jiu Chang, Hamed Abiri, Ali Adibi

Tutorial 142

Chiro-Optical Microscopy - Near-Field and Far-Field 143
Hiromi Okamoto

Hybrid Nanomaterials and Metastructures for Photonics, Sensing and Energy 144

Green Hydrogen Produced from Water Splitting at Photocatalytic Titanium Dioxide Thin Films on Gold Nanoislands 145
Nicolas Albenge, Florian Laible, Jonas Rathgeb, Timo Braun, Sandra Glocker, Bjarne Gutbrod, Leah Schynowski, Udo Weimar, Nicolae Barsan, Monika Fleischer

Very-large scale reconfigurable surfaces for dynamic control of THz and millimeter waves 147
Said Ergoktas

Engineering Local Field Enhancement with Single-Crystal Noble Metal Plasmonics 148

Jacob Syme, Tashfin Shaife, Rebbeca Storck, Hannah Martinelli, Albert Adserias, Finlay MacNab, Sasan V. Grayli, Gary Leach

Control of photo-induced absorption and chemical functionalization within plasmonic nanostructures **150**
Marlo Vega, Thomas Prieur, Julien Moreau, Paul-Ludovic Karsenti, Céline Molinaro, Olivier Soppera, Paul Charette, Michael Canva, Jean-François Bryche

Terahertz Slow- and Fast-Light Switching Through Liquid-Crystal-Integrated Plasmon-Induced Transparency Fano-resonant Metamaterials **151**
Rafał Kowerdziej, Ilario Bisignano, Dmitriy Yavorskiy, Marek Olifierczuk, Antonio Ferraro, Giuseppe Emanuele Lio, Norbert Pałka, Jerzy Wróbel, Roberto Caputo

Hybrid integrated nonlinear photonics with resonant 2D materials **154**
Alessandro Bile, Domenico de Ceglia, Daniele Ceneda, Maria Cristina Larciprete, Marco Centini

Metasurfaces with phase singularity for sensorapplications: a theoretical and experimental study **156**
Theo Girerd, Sébastien Cueff, Fabien Mandorlo, Taha Benyattou, Xavier Letartre, Cécile Jamois, Lydie Ferrier, Lotfi Berguiga

Flexible and Stackable Stickers to Prepare Quasi-3D Metasurfaces **158**
Shunsuke Murai, Koichi Okamoto

Tailoring Optical Dispersion using Nonlinear Geometric-phase Metasurfaces **159**
Mikko Huttunen, Madona Mekhael, Roman Calpe, Robert Fickler, Tommi Hakala

Polarization-resolved nonlinear chiroptical scattering **160**
Ventsislav Valev

Sensing chiral molecules using achiral plasmonic metasurfaces: limitations and perspectives **161**
Obren Markovic, Shuhui Yang, Mathieu Nicolas, Catherine Schwob, Mathieu Mivelle, Guillaume Demesy, Nicolas Bonod, Souhir Boujday, Bruno Gallas

Chiral surface plasmons and their spin-hall effect on top of helix arrays **163**
Paul de Bollivier, Vage Karakhanyan, Roland Salut, Miguel A. Suarez, Nicolas Martin, Thierry Grosjean

Dielectric Mie Nanostructures and Metasurfaces for Quantum Emitter Control **164**
Antoine Azéma, Swaroop Palai, Jonas Muller, Etienne Palleau, Frank Fournel, Vincent Larrey, Guilhem Larrieu, Gonzague Agez, Jean-Marie Poumirol, Vincent Paillard, Peter R. Wiecha, Laurence Ressier, Aurélien Cuche

Precision Synthesis and Functionalization: Uniform, Size- and Shape-Tunable Gold and Silver Nanostructures for Advanced Platforms **166**
Kyoungweon Park, Aklilu Worku, Angela Campo, Richard Vaia

Photochemical Synthesis of Gold Nano- and Microplates on Substrates **167**
Svetlana Neretina, Brendan Nieukirk, Runze Tang

High-Q Band-folded Lattice Resonances for Low-threshold Lasing **168**
Shaojun Wang

Chirality-Induced Response in Chiral Inorganic Materials **169**
Yoshihiko Togawa

Self-assembled Plasmonic Metamaterials with Hyperbolic Dispersion for Applications in Sensing **170**
Anastasiia Zaleska, Mayela Romero-Gomez, Anatoly Zayats, Wayne Dickson

Broadband Infrared Unidirectional Absorption by non-Hermitian Multilayer Structure **171**
Wakana Kubo

Revising Model Reactions in Plasmonic Chemistry **173**
Olga Guselnikova

Self-assembly of Artificial Proteins as Scaffold for Advanced Nanophotonics **174**
Liudmila Trotsiuk, Nathan Epalle, Rémi Chassagnon, Régis Parvaud, Valérie Marchi, Marielle Valerio-Lepiniec, Agathe Urvoas-Cisse, Philippe Minard, Erik Dujardin

Ultrafast switching from strong to weak coupling in hybrid plasmonic-photonic microcavities 176
Benedict Morris, Sergei Kostcheev, Luis Dos Santos, Khanh-Van Do, Anna Rumyantseva, Shuwen Zeng, Renaud Bachelot, Bruno Palpant

Chemical Reactions Driven by Plasmonic Hot Carriers 178
Seunghoon Lee

Locally asymmetric plasmonic photocatalysis driven by light's polarization 179
Lucas Vazquez Besteiro

Circular Dichroism Enhancement via CPL□Induced Chiral Growth of Core-Shell Plasmonic Particles 180
Koichiro Saito, Yoshie Ishikawa

Single-Particle Spectroscopy on Chiral Plasmonic Nanostructures 181
Wei-Shun Chang, Angel Thomas, Vidhi Singla, Oscar Avalos Ovando, Manita Khatri, Misbah ul Ain, Trang Nguyen, Tamie Vo, Alexander O. Govorov

Plasmonic Nanosensor for Force Sensing in Live Cells 182
Won Park

Optical Activity Modulation in Chiral Metasurfaces using Structured Light 184
Paula Laborda Lalaguna, Shun Hashiyada, Nikolaj Gadegaard, Jörg B. Götte, Stephen M. Barnett, Kayn A. Forbes, Yoshito Y. Tanaka, Malcolm Kadodwala

Enhanced Photoluminescence through Excitation - Surface Lattice Resonance Coupling in Aluminum Metasurfaces 185
Ali Sraj, Eloise Garcelon, Jerome Martin, Davy Gérard, Liudmila Trotsiuk, Alexandre Chevillot-Biraud, Stéphanie Lau-Truong, Nordin Felidj, Anne-Laure Baudrion

Van der Waals metasurfaces from strong coupling to topology 187
Andreas Tittl

Colloidal Photonic Crystal Slabs for Hybrid Plasmon Photon Mode Engineering in Sensing and Energy Applications 188
Swagato Sarkar, Tobias A. F. Koenig, Larysa Baraban, Andreas Fery

Permittivity-Engineered Dielectric Media of Hybrid Nanomaterials and Tunable Microcavity Metastructures for Enhanced Exciton-Light Interactions 190
Pedro Ludwig Hernandez-Martinez, Hilmi Volkan Demir

Hybrid Oxide-Phase-Change Heterostructures for Thermally Tunable Mid-Infrared Photonics 192
Daniele Ceneda, Martina Mercurio, Roberto Macaluso, Nunzio Timpanaro, Marco Centini, Maria Cristina Larciprete

When Grain Boundaries Create Plasmons: Localized Resonances in Hyperdoped polysilicon films 194
Mohamad Bahsoun, Jesse Groenen, Sebastien Joulié, Cecile Marcelot, Robin Cours, Sebastien Kerdiles, Mathieu Opprecht, Caroline Bonafos, Jean-Marie Poumirol, Jean-Marie Poumirol

In-plane Directed Power Flow in Anisotropic Hyperbolic Materials 195
Eric Seabron, Eric Jackson, Michael Meeker, Andrew Lang, Rhonda Stroud, Daniel C. Ratchford, Brandon K. Durant, Xitlali G. Suarez, Chase Ellis, Joseph Tischler

Metasurfaces for photon management in a thermophotovoltaic system 198
Vadim Zakomirnyi, Anna Rumyantseva, Sergei Kostcheev, Demetrio Macias, Renaud Bachelot, Davy Gerard

Chiral sensing with dielectric nanophotonics 200
Alberto G. Curto

Smart ways to achieve tunable chiral assemblies 201
Ziwei Zhou, Ningwei Sun, Nina Tverdokhleb, Artur Movsesyan, Anja Maria Steiner, Patrick T. Probst, Vaibhav Gupta, Bo Yin, Nicolas Pazos-Perez, Ramon A. Alvarez-Puebla, Mirjam Hofmaier, Martin Müller, Holger Merlitz, Olga Guskova, Yaroslava G. Yingling, Franziska Lissel, Tobias A. F. Konig, Zhiming Wang, Alexander O. Govorov, Nicholas A. Kotov, Andreas Fery

Near-Field Optical Chirality on Achiral Gold Nanoparticles under Linear Polarization 203

Minyu Chen, Sylvie Marguet, Davy Gérard, Lucas Vázquez Besteiro, Safi Jradi, Alexander O. Govorov, Tao Xu, Renaud Bachelot

The Interaction of Vortex Light with Chiral Assemblies **204**
Thierry Verbiest, Weizhen Liu, Yovan de Coene

In situ plasmon-induced polymerization of chiral polymer thin films for enantioselective sensing in fM range **205**
Amine Khitous, Céline Molinaro, Olivier Soppera

Surface Lattice Resonance Engineering via Plasmonic Nanoparticle Self-assembly, Transfer, and Laser Treatment **206**
Tomas Tamulevičius, Gvidas Klyvis, Klaudijus Midveris, Muhammad Haris, Tomas Klinavičius, Asta Tamulevičienė, Mindaugas Juodėnas, Domantas Peckus, Joel Henzie, Sigitas Tamulevičius

Emission of Quantum Dots within Plasmonic Patch Arrays sustained by Surface Lattice Resonance **208**
Agnes Maitre, Hugo Saint-Olive, Fengzhi Gu, Louis Agard, Willy Daney de Marcillac, Thomas Pons

Thermoplasmonics-driven polymerization from the macroscale to the nanoscale **209**
Céline Molinaro, Amine Khitous, Mathieu Bastide, Sylvie Marguet, Olivier Soppera

Photothermal effects in metal layers **212**
Benoit Rogez, Quanbo Jiang, Zakaria Marmri, Franck Thibaudau, Jerome Wenger, Guillaume Baffou

Operando Quantification and Mapping of Interfacial Charge-Transfer Efficiency in Hybrid Materials **214**
Olivier Henrotte

Symmetry breaking bu biomolecules in chiral nanophotonics **217**
Malcolm Kadodwala

Chiral Shape Transformation of Colloidal Silver Nanostructures using Circularly Polarized Light **218**
Gil Markovich, Daniel Feferman, Bar Reuven, Monika Ghalawat, Lucas Besteiro, Alexander O. Govorov

Molecular Bridges in MXenes: Tunable Charge Transport and Chemiresistive Sensing **219**
Yudhajit Bhattacharjee

Controlling Polaritonic Contributions to Material Properties **220**
Matthew Sheldon

Hybrid AI design of reconfigurable and compactplasmonic Arithmetic and Logic Units **222**
Amine Khitous, Nicolas Gros, Léo Martin, Florian Dell'ova, Aurélie Bertaux, Ouassila Labbani Narsis, Gérard Colas des Francs, Christophe Nicolle, Alexandre Bouhelier, Erik Dujardin

Experimental benchmark of AI-Optimized, Reconfigurable, All-Optical Plasmonic Arithmetic and Logic Units **224**
Amine Khitous, Nicolas Gros, Léo Martin, Florian Dell'Ova, José Valderrama-Botia, Aurélie Bertaux, Ouassila Narsis Labbani, Gérard Colas des Francs, Christophe Nicolle, Alexandre Bouhelier, Erik Dujardin

All-Dielectric Photo-Thermo-Optical Metasurfaces for All-Optical Spatio-Temporal Wavefront Control **227**
Gopal Narmada Naidu, Giulia Tagliabue

Near-Field Coupling in Plasmonic Nanoarrays: Tailoring Radiative and Non-Radiative Losses Through Gap Engineering **228**
Benedict Morris, Bruno Palpant

Single plasmon transport in 1D nanowire **229**
Gérard Colas des Francs

Multiplexed label-free (bio)molecular analytics using plasmonic nanoparticles **230**
Tomas Lednicky, Guilherme Lopes, Baihui Li, Matthias Urban, Andrea Csaki, Wolfgang Fritzsche

Modeling and Design of Nonlinear Metastructures for All-Optical Modulation and THz Generation **231**

Giulia Crotti, Unai Arregui Leon, Pietro Baldin, Andres Valladares Y Tacchi, Andrea Schirato, Giuseppe Della Valle

Plasmon-induced spin selectivity for controlling reaction intermediates in relevant chemical transformations 233
Karolina Kukrálová

EC-SERS - a combination of electrochemistry and Raman spectroscopy for selective detection of organic contaminants in complex water matrices 235
Jana Rosenkranzova

Advancements in laser photo-acoustic spectroscopy towards imaging of absorption and chirality in nanostructures and metamaterials 238
Emilija Petronijevic

Automated computation on AI-designed all-optical Boolean microprocessors by an interfacial robot driving a non-linear optical bench. 239
Léo Martin, Alice Nyaga, Fayçal Houssaini, Amine Khitous, Nicolas Gros, Aurélie Bertaux, Ouassila Narsis Labbani, Gérard Colas des Francs, Christophe Nicolle, Alexandre Bouhelier, Abdenbi Mohand-Ousaid, Erik Dujardin

New trends in nanophotonics and advanced materials 242

Engineering Electromagnetic Descriptors at the Nanoscale with Plasmonic Nanoantennas 243
Mario Zapata, Javier Aizpurua

Can Surface Plasmon Carry Heat? 244
Jungmin Nam, Kuk Hyun Yun, Bong Jae Lee

Polarization-Programmable Optics using Chiral Dielectric Metastructures 245
Soo Jin Kim

Subspace-protected topological phases 247
Masatoshi Sato

Fluctuation-induced Hall-like lateral forces in a chiral-gain environment 248
Daigo Oue, Mário Silveirinha

Metasurface concepts for polarisation control 249
Ilya Shadrivov

Numerical analysis of directional guided modes on highly anisotropic metasurface 250
Maxim Nikitin, Andrei Lavrinenko, Battulga Munkhbat, Osamu Takayama

Meta-optics based multidimensional imager 251
Fengjun Li, Zilan Deng, Xiangping Li

DRUM: From Diabolic to Exceptional Point and Phase-Tunable Hysteresis toward Controllable Artificial Neurons 252
Stefano Biasi, Bülent Aslan, Davide Olivieri, Stefano Gretter, Lorenzo Pavesi

Chirality in Non-Hermitian Photonic Crystals 254
Masaya Notomi, Yuto Moritake, Taiki Yoda

Temporal Dispersion Effects in Optical Spectra of Exciton-Plasmon Systems at Strong Coupling 256
Sancenia Johnson, Gabrielle Williams, Tigran Shahbazyan

High-Entropy Alloy-Based Metasurfaces for plasmon absorber in mid infrared wavelength 258
Yoshiaki Nishijima, Makoto Ohashi, Yuya Hoshimiya

Finite-Barrier Bound States and Flat Bands Enabled by p-Orbitals 259
Tao Liu, Han-Rong Xia, Duanduan Wan, Meng Xiao

Chirped Pulse Propagation and Control in Reverberant non-Hermitian Settings Enabled Through Complex Time Delay 260
Isabella Giovannelli, Thomas M. Antonsen, Steven Anlage

Plasmonic Nanostars: Engineering Optical Tunability for Enhanced Efficiency 262
Nicolas Pazos Perez

Copper-based plasmonic nanohole arrays for electromagnetic field enhancement 264
Madiha Amrani, Tô Nguyet, Gaëtan Lévêque, Mohamed El Ghafiani, E. H. El Boudouti, Yan Pennec, Rabah Boukherroub, Bahram Djafari-Rouhani

Metasurface□Driven Control of Quantum Emitters: From Visible Nanolasers to Telecom Photonics 266
Giovanni Mattei

Two Distinct Quasi-Bound States in the Continuum in an Amorphous Silicon Metasurface 268
Hicham Mangach, Pascal Szriftgiser, Gaëtan Lévêque, Yan Pennec, Bahram Djafari-Rouhani

Self enhanced generative metasurface inverse design 270
Mathys Le Grand, Pascal Urard, Loumi Trémas, Damien Maitre, Louis-Henri Fernandez-Mouron, Régis Orobtchouk

Spatial Fourier filtering with metagratings 272
Mahmoud A. A. Abouelatta, Karim Achouri

Foundry-Ready Multi Laser Terahertz Bandwidth Photonic Isolator via Electro-optic Synthetic Motion 273
Kyunghun Han, Yiliang Bao, Junyeob Song, David Long, Sean Bresler, Daron Westly, Jason Gorman, Thomas LeBrun, Kartik Srinivasan, Vladimir Aksyuk

Miniaturized Full-Color Waveguide Combiner for AR Headsets: Wide Field-of-View and High Resolution via Compound Metagratings 274
Oksana Shramkova

Enhancing the Sensitivity of Low-cost Zero-Reflection Metasurfaces for Clinical Translation 276
Nurten Koc, Ali Belarouci, Serap Aksu

Plasmon Assisted Up Conversion for High Performance Photochromic Smart Windows 277
Ovidio Peña-Rodríguez, Chang Woo Kim, Edgardo Gabriel Santoro, Umapada Pal, Young Soo Kang

Photonic integrated circuits on fiber tips for lab-on-fiber sensing 279
Arthur Bouamra, Pieter Vijn, René P. J. van Veldhoven, Jui-Hung Chen, Shuo-Yen Tseng, Andrea Fiore

Attosecond Extreme-Ultraviolet Skyrmion Pulses from High Harmonic Generation 280
David Marco, Luis Plaja, Carlos Hernandez-Garcia

Nanoscale Photonic Topological Insulators 282
Xiaoyong Hu

Hard and Soft: Exploiting Nanoplasmonics in Sensing Applications 283
Luca De Stefano, Valeria Nocerino, Bruno Miranda, Principia Dardano

Optical Phenomena in Time-Varying Transparent Conductors 284
Marcello Ferrera, Wallace Jaffray, Sven Stengel

Tailoring valley polarization and optical nonlinear effect in transition-metal dichalcogenides 285
Mu Wang, Ruwen Peng

Advanced Manufacturing Tools for Data□Processing Fiber Photonics Fabrication 286
Marcos D. Vozer Felisberto, Andrey Machnev, Thomas W. Burkle, Maxwell H. Jancich, Babak Seradjeh, Phillip Richerme, Alexander Gumennik

Chiral Diffraction from Quasiperiodic Monotile Lattice Based on Aperiodic Hat Tiling 289
Yuto Moritake

Silicon Nitride Photonics for High-Performance Systems 291
Frederic Gardes, Ilias Skandalos, Yaonan Hou, Dun Qiao, Huiwen Deng, X. Yu, Jaeseong Park, Chong Chen, Mingchu Tang, Michelle Paparella, Lifeng Bao, Elliot Sandell, Thalia Dominguez Bucio, Jérémy Moeyaert, Thierry Baron, Peter Smowton, Huiyun Liu, Alwyn Seeds, Stelios Simos, T. Moschos, Miltos Moralis-Pegios, Isaac Johnson, Theodore Rangarajan, James Gates, Nikos Pleros

Spatiotemporal Metasurface for Unconventional Control of Electromagnetic Waves 293

Anatoly Efimov, Chun-Chieh Chang, Simo Pajovic, Wilton J. M. Kort-Kamp, Hou-Tong Chen, Diego A. R. Dalvit, Abul Azad

Symmetry-Broken q-BIC Dielectric Metasurfaces for Enhanced Linear and Nonlinear Light-Matter Interactions **295**
Wen-Hui (Sophia) Cheng, Hung-Yi Wu, Tzu-Hsiang Liu, Hsin-Yu Shen

Femtosecond Laser Direct-Written Optical Fiber Microstructure Devices for Laser Applications **296**
Xuewen Shu

Novel Materials for UV Plasmonic Nanostructures **298**
Michael Foltýn, Tomáš Šikola, Michal Horák

Plasmonic Enhancement of Second Harmonic Generation from a van der Waals Crystal **300**
Hong Liu

3D topological photonics: 3D Chern photonic insulators and electromagnetic axions **302**
Chiara Devescovi, Antonio Morales-Perez, Maia G. Vergniory, Aitzol Garcia Etxarri

Dirac-Polariton Bose-Einstein Condensation at Room Temperature via Bound States in the Continuum in a WS□ Monolayer **303**
Bruno Miranda, Silvia Romano, Scott Duhey, Aidar Kemelbay, Arian Gashi, Vito Mocella, Ivo Rendina, Adam M. Schwartzberg, Gianluigi Zito

Manipulate Multispectral 3D Polarization Structures with Optical Metasurfaces **304**
Xianzhong Chen, Hammad Ahmed, Chunmei Zhang

Breakdown of the Kirchhoff's law of thermal radiation by a spatiotemporally modulated nonreciprocal metasurface **305**
Diego A. R. Dalvit, Anatoly Efimov, Chun-Chieh Chang, Simo Pajovic, Wilton J. M. Kort-Kamp, Dongsung Kim, Hou-Tong Chen, Abul Azad

Theory of Dispersive Space-Time Interfaces **306**
Alessandra Contestabile, Maria Antonietta Vincenti, Giuseppe Castaldi, Michael Scalora, Marcello Ferrera, Vincenzo Galdi, Carlo Rizza

Exciton Polarons in 2D semiconductors **308**
Carlos Alberto Maciel Escudero, Giuseppe Meneghini, Jamie Fitzgerald, Ermin Malic

Janus Vortex Meta-Laser **310**
Lili Gui, Yiyuan Xu, Hao Chen, Kun Xu

SPDC in Thin-Film LN: From Tunable Polarization Entanglement to Doubly-Resonant Metasurfaces **311**
Maximilian Weissflog, Saniya Shinde, Shaun Lung, Jinyong Ma, Sina Saravi, Thomas Pertsch, Andrey Sukhorukov, Frank Setzpfandt

Closed-form conditions for parametric amplification in open photonic time crystals **312**
Adrià Canós Valero, Sergei Gladyshev, David Globosits, Stefan Rotter, Egor A. Muljarov, Thomas Weiss

Cavity-Enhanced Superfluorescence and Lasing Transitions in Two-Dimensional Single-Crystal Perovskite Superlattices **315**
Jae Yong Suh

Towards Realization of Ideal Anapole Excitations **317**
Radoslaw Kolkowski, Matti Kaivola, Sagar Sehrawat, Andriy Shevchenko

Material and Device Optimizations for Wavelength-Selective Infrared Devices **319**
Tadaaki Nagao, Keisuke Watanabe, Thien Duc Ngo

Programmable Broadband Nonlinear Infrared Imaging with Dielectric Metasurfaces **320**
Ze Zheng

Shining Light on 2D Antiferromagnets **322**
Viktoriia Radovskaia, Mengxing Na, Theo H. Rasing, Alexey V. Kimel, Dmytro Afanasiev

Chiral Photonic Environments for Coherent Control of Valley Excitons **324**
Hassan Lamsaadi, Aurélien Cuche, Hugo Lourenço Martins, Vincent Paillard, Sébastien Weber, Jean-Marie Poumirol, Gonzague Agez

Optical Properties Tuning of Quantum Emitters in WSe2 Monolayers 325
Javier Martín-Sánchez

Photonic Inverse Design using differentiable electromagnetic solver for CMOS image sensors and Photonic Integrated Circuits 327
Hyunsung Park, Jaekwan Kim, Subeom Song, Junho Lee, Yongseob Yun, Sungmo Ahn, Choonlae Cho, Sooyeon Lee, Sookyoung Roh, Seokho Yun

Hybrid Photonic Crystal Platforms: Enabling High-Efficiency Photonic Devices and Novel Functionalities 328
Tae-Yun Lee, Hansol Lee, Lakjong Jeong, Heonsu Jeon

Limited Size Object Microscopy - Smaller Objects, Higher Resolution 329
Giorgio Adamo, Taeyong Chang, Eng Alk Chan, Nikolay I. Zheludev

Subwavelength metamaterials for modal and thermo-optic control in silicon interferometers 330
Aitor Villafranca Velasco, Irene Olivares, Irena Stolic, Raquel Fernández de Cabo, Alejandro Sánchez-Sánchez, Daniele Melati, Carlos Alonso-Ramos, David González-Andrade

Competing Lattice and Defect Dynamics Govern Terahertz-Driven Ferroelectricity in Quantum Paraelectric SrTiO3 332
Jingbo Qi

Advanced Contactless Manipulation of Micro- and Nanostructures: from Optical Forces to Acoustic Tweezers 334
Maria G. Donato, Silvie Bernatova, Antonino Foti, Pietro Giuseppe Gucciardi, Maria Antonia Iatì, Alessandro Magazzù, Andrea Mandanici, Onofrio Maria Maragò

Thermalization Speed of Highly Multimode Nonlinear Systems 335
Emmanouil Theodoros Kokkinakis, Konstantinos G. Makris, Demetrios N. Christodoulides

Advancements in Silicon Nitride Platform 337
Khaled Mnaymneh

Electrostatic Repulsion as a Governing Mechanism in Near- and Far-Field Optical Binding of Gold Nanoparticles 339
Marques Manuel

Foundry Enabled Chip-scale Photonics Technology and Applications 340
Yeshaiahu (Shaya) Fainman

Wide-angle Nonreciprocal Thermal Emitters with Strong Contrast Between Absorptivity and Emissivity 341
Georgios Veronis, Md Tanvir Emrose, Ming Zhou, Gabriel Nedelea, Roya Ebrahimi Meymand, Shanhui Fan

Compact High-Q Photonic Crystal Cavities with Improved Robustness to Disorder 342
Nicoletta Granchi, Camilla Gonzini, Matteo Lodde, Gabriele Calusi, René P. J. van Veldhoven, Andrea Fiore, Guillermo Arregui, Francesca Intonti

Graded-index metamaterials for on-chip control over mode exchange 344
Raquel Fernández de Cabo, Alejandro Sánchez Sánchez, Daniele Melati, Carlos Alonso Ramos, Aitor Villafranca Velasco, David González Andrade

Mechanistically Guided Plasmonic Dendrites for Selective CO□ Reduction 346
Anjalie Edirisooriya, Zelio Fusco, Ning Lyu, Christin David, Fiona Beck

Lasers that run cool on their own 348
Chun-Wei Chen, Michel J. F. Digonnet, John Ballato, Peter D. Dragic, Martin Bernier, Enkeleda Balliu

Perovskite Superfluorescence and High Temperature Macroscopic Quantum Effects 349
Kenan Gundogdu

Reversible metal electrodeposition for high-contrast active optical and metamaterials 350
Po-Chun Hsu

From Simulation to Design: AI-Solvers andAI-Optimizers for Electromagnetics 351
Raphael Pestourie

Topology Optimized High-Q Photonic Crystal Resonators for the THz Band 353
Stephen Hanham

Intelligent Nanofabrication for Nanophotonics: Quantifying and Understanding Process Variability 355
Wenhan Zhang, Ben Mills, Kevin MacDonald

Manipulating matter with vector twisted light 356
Mohamed Babiker

Programmable Nanophotonics with the Plasmonic Phase-Change Material In3SbTe2 357
Lukas Conrads, Matthias Wuttig, Thomas Taubner

Tailorable Light Driven Reaction with Phase-changing Material Metasurface 358
Ning Lyu, Anjalie Edirisooriya, Dawei Liu, Zelio Fusco, Shenyou Zhao, Fiona Beck, Christin David

Hot Carriers in Balance: Molecularly Functionalised Nanogaps Resolve Wavelength-Dependent Plasmonic Charge Generation 359
Ishaan Lohia, Santiago Rodríguez-Jiménez, Charlie Readman, Christine Joy Querebillo, Rowena Davies, Gregory Q. Wallace, Duncan Graham, Erwin Reisner, Bart de Nijs

Solution-Processed Quantum Light Sources Spanning the Visible to the Infrared 360
Jennifer Hollingsworth, Eric G Bowes, Han Htoon

Self-powered refractory NIR plasmonic photodetectors with compact, broadband, and quantitative spectroscopy 361
Eslam Abubakr, Saito Saito, Hironori Suzuki, Tetsuo Kan

Bound-State-in-the-Continuum Lasing Modes inInGaAs Nanowire Photonic Crystals 363
Bogdan-Petrin Ratiu, Ji Tong Wang, Kyle S. Netherwood, Nicolae-Coriolan Panoiu, Li Qiang, Sang Soon Oh

Circularly polarized Raman scattering for optical spin detection in silicon metasurfaces 364
Guillermo Serrera, Rasmus H. Godiksen, Lex M. Dedding, Tom T.C. Sistermans, Ershad Mohammadi, T. V. Raziman, Søren Raza, Pablo Albella, Alberto G. Curto

Boosting nonlinear optical response in resonant metal-dielectric metasurfaces at visible and UV spectrum 365
Crina Cojocaru, Shroddha Mukhopadhyay, Michael Scalora, Jose Trull

Advancements in Chiral Nanophotonics via Block Copolymer Supramolecular Assembly and Plasmonic Antenna-Reactor Catalysis 368
Dong Ha Kim

Tailoring Light-Sound Interactions in Photonic Integrated Circuits 369
Moritz Merklein

Photonic cluster state Generation from a Telecom-Emitting Quantum Dot 370
Giora Peniakov, Reza Hekmati, Johannes Michl, Mohamed Helal, Moritz Meinecke, Jochen Kaupp, Yorick Reum, Andreas Pfenning, Sven Höfling, Tobias Huber-Loyola

Liquid crystalline polymer photonics for all-optical signal modulation 372
Sara Nocentini, Daniele Martella, Francesco Riboli, Camilla Parmeggiani, Diederik Wiersma

Plasmon-Driven pn Junctions in Graphene Revealed by Raman Spectroscopy and Flexural Phonon Coupling 373
Maciej Wiesner, W. Strupinski, Jayanta Sarkar, Aleksandra Trzaskowska, Nojoon Myoung, Andriy Serebryannikov

Semiconductor Nanocrystal Optoelectronics for Classical and Quantum Light Generation 375
Emek Goksu Durmusoglu, Hilmi Volkan Demir

III-Nitrides based Integrated Nonlinear Photonics 377
Changzheng Sun, Bing Xiong, Jian Wang, Lai Wang, Zhibiao Hao, Yanjun Han, Hongtao Li, Lin Gan, Yi Luo

Optics of 3D Second-Harmonic Photonic Crystals from Colloidal Self-Assembly Templating 379
Thomas Kainz, Ülle-Linda Talts, Rachel Grange, Ullrich Steiner, Viola Vogler-Neuling

Resolving Surface Plasmon Dispersion with Fabry-Pérot-Assisted Extraordinary Optical 381

Transmission
Youssef El Badri, Hicham Mangach, Mustapha Bahich, Yan Pennec, Bahram Djafari-Rouhani, Younes Achaoui

Tunable resonances in doubly anisotropic, high-index MoS2 nanoplatelets **383**
Bingying You, Tom T.C. Sistermans, Alberto G. Curto

Near field imaging and spectroscopy of complex stacking of semiconductors **385**
Laure Tailpied, Clément Gureghian, Frederic Fossard, Jean-Sebastien Mérot, Fernando Gonzalez-Posada-Flores, Jean-Baptiste Rodriguez, Gregory Vincent, Thierry Taliercio, Baptiste Fix

All-Solid Multicore Fibre Probe for Background-Free Raman Spectroscopy **387**
Stephanos Yerolatsitis, Thomas Wright, András Kufcsák, Alexandra Adams, Tom Quinn, Sohan Seth, Kevin Dhaliwal, James Stone

Multilevel Spatial Programming of Photonic Devices with Phase-Change Materials **390**
Chirine Saadi, Capucine Laprais, Fouad Bentata, Xavier Letartre, Guillaume Saint-Girons, Patrice Genevet, Nicolas Baboux, Lotfi Berguiga, Sébastien Cueff, Ecole Centrale de Lyon

Topological Eutectic Heterostructure Plasmonic Metasurfaces for THz Lasing and Amplification **391**
Konstantinos Kouderis, Anousha Khamsavi, Kingshuk Bandopadhyay, Hamid Reza Darabian, Dorota Anna Pawlak, Chao Tang, Victor Ryzhii, Taiichi Otsuji

Long-lived subradiance via cavity-mediated collective interaction **393**
Kyu-Young Kim, Jin Hee Lee, Woong Bae Jeon, Dong Hyun Park, Suk-In Park, Jin Dong Song, Changhyoup Lee, Je-Hyung Kim

Laser Processing of Metallic Surfaces for Radiative Cooling and Autonomous Dew Water Harvesting **394**
Pablo Pou-Alvarez, Anne Mongruel, Mónica Fernandez-Arias, Antonio Riveiro, Daniel Beysens, Juan Pou

Metasurfaces for Laser Cooling and Trapping of Atoms and Integrated Cold-Atom Platforms **395**
Thu Hac Huong Le, Ryohei Takei, Sota Kagami, Akafumi Takamizawa, Yuichi Kurashima, Taisei Motomura

Polymer-Based Passive Radiative Cooling Films for Thermal Management **397**
Emma Spotorno, Paola Stagnaro, Lucia Conzatti, Roberto Utzeri, Simona Losio, Francesco Bisio, Michele Magnozzi, Maurizio Canepa

Wave Localisation in Aperiodic and Correlated Disorder Photonic Structures **399**
Marian Florescu, Alex Meek, Kriss Stokkereit

Phase nanoengineering of complex oxides for spin-wave devices **400**
Edoardo Albisetti

Micron Scale Spontaneous Parametric Down Conversion in Periodically Poled Layered Semiconductors **401**
Leone Di Mauro Villari, Andrea Alessandrini, Benjamin Braun, Simone Paganelli, Chiara Trovatello, Lee Rozema, Andrea Marini

Visible-Near Infrared Hyperbolic Polariton along Hyperbolic Metamaterials' interface **403**
Jingbo Sun, Ji Zhou

Quantum photonic sources based on 2D materials **404**
Xifeng Ren

Plasmonic tunnel junction electroluminescence: Effects of magnetic fields and resonant cavities **405**
Douglas Natelson, Shusen Liao, Ken Ssennyimba, Jaime Abad-Arredondo, Qian Ye, Alessandro Alabastri, Antonio Fernández-Domínguez, Francisco García-Vidal, Kexin Xie

Ultra-weak force measurement with optical levitation in vacuum **406**
Yu Zheng, Long Wang, Yuan Tian, Fang-Wen Sun

Coherent Terahertz Light Generation, Modulation, and Detection with Layered Superconducting Quantum Metamaterials **407**
Mingqi Zhang, Samane Kalhor, Haonan He, Yongyu Zou, Maryam Allamki, Toshiaki Hattori, Takanari Kashiwagi, Kaveh Delfanazari

Topology Optimization on Weakly-confining InP Platform Enables Ultra-compact Low-loss Triplexer 408
Hao Jiang, Yijun Chen, Shuang Zheng, Minming Zhang

3D printed coupled micro-potentials for photonic quantum gases 409
Julian Schulz, Kirankumar Karkihalli Umesh, Sven Enns, Frank Vewinger, Georg von Freymann

Optical Properties of Twisted Bilayer Graphene 411
Tobias Stauber, Miguel Sánchez Sánchez, Igor Vasilevskiy, José González

Artificial magnetism and passivity in plasmonic clusters with spatial dispersion 413
Ranjeet Dwivedi, Kevin Vynck, Alexandre Baron, Ashod Aradian

DNA origami-based photonic crystals for visible light 414
Gregor Posnjak, Tim Liedl

Polarization control of photons with photonic crystal devices 415
Xiulai Xu

Magnonic Waveguide Networks for Spin-wave Computing 416
Rudolf Bratschitsch

Machine Learning for Inverse Design 417
Philippe Tassin

Wave-Based Photonic Computing: From Complexity-Driven Reservoirs to Engineered Phase Encoding 418
Gerard McCaul, Girish Tripathy, Luana Olivieri, Giulia Marcucci, Juan Sebastian Totero Gongora

Optical reconfiguration of Exceptional Points on chip 419
Angel Ortega-Gomez, Jonathan Dearlove, Nikolaos Farmakidis, Mingde Du, Iñigo Liberal, Harish Bhaskaran

Non-Reciprocal Silicon Photonic Resonators with 2D CuCrP□S□ 420
Mahmoud Rasras, Ghada Dushaq

Light-Driven Order: Shift and Injection Raman Forces Driving Coherent Phonons 421
Habib Rostami, J. Luke Pimlott

Infrared Silicon Metalenses through Deep-UV for Thermal Imaging 422
Kai Sun, Jordan Scott, Xingzhao Yan, Jun-Yu Ou, Otto L. Muskens

Van der Waals hybrid photonic devices 423
Yuichiro Kato

Spatio-Temporal Metalattices in ENZ Transparent Conductors 425
Sven Stengel, Wallace Jaffray, Farhan Ali, Mustafa Ozlu, Colton B. Fruhling, Maria Antonietta Vincenti, Domenico de Ceglia, Michael Scalora, Alexandra Boltasseva, Vladimir M. Shalaev, Andrea di Falco, Marcello Ferrera

Spectral Design of Disordered Photonic Metamaterials 426
Aaron Shih, Mathias Casiulis, Stefano Martiniani, Frank Scheffold

Bulk-radiation Correspondence in Radiative Photonic Lattices 427
Xinyi Yuan, Grazia Salerno

Imaging-based, time-resolved detection of rare microparticles in continuous flow 430
Raphael Hauer, Christian Hill, Ulrich Hohenester

Fundamental Passive Components for Topological Photonic Integrated Circuits 432
S. Okada, Qianshuo Wang, Liyan Hu, Raku Yamaji, Xingxiang Wang, Xiao Hu, Tomohiro Amemiya

Plasmon-Induced Fluorescence Enhancement in Aminoporphyrin Thin Film Coupled with Gold Nanocubes Array 433
Giuseppe Di Maio, Roberto Termine, Caterina Damiano, Emma Gallo, Massimo La Deda

A New Effective Medium Approximation for Nanostructure on a Layered Films 434
Kotaro Kajikawa

Harnessing Effective Medium Birefringence for Broadband Chirality Generation in Resonant 435

Metasurfaces
Chloe Doiron, Andrew Kim, Lisa Hackett, Sadhvikas Addamane, Taisuke Ohta, Alexander Cerjan

On-chip Integrated Intelligent Photonic Computing **437**
Kun Liao

Localization and diffusive transport in photonic correlated disorder materials **438**
Nicoletta Granchi, Gabriele Calusi, Kris Stokkereit, Matteo Lodde, Camilla Gonzini, Andrea Fiore, Marian Florescu, Francesca Intonti

Label-free and Label-based approaches for tapered fiber photometry in the deep brain **439**
Massimo De Vittorio, Ferruccio Pisanello

Self-Hybridized Exciton-Polaritons in Two-Dimensional-Perovskite Microcrystals **440**
Martina Borreani, Alexander Schleusener, Sudhir K. Saini, Lin-Han Li, Miao-Ling Lin, Ping-Heng Tan, Vincenzo Caligiuri, Roman Krahne

Flat Optics for Multispectral Grafted Vortex Beams and OAM Combs **441**
Hammad Ahmed, Xianzhong Chen

Autonomous Agentic Systems for MetamaterialDesign and Research **443**
Willie Padilla

Coherent Thermal Wavefront Manipulation Using Hierarchical Metasurfaces **444**
Yungui Ma

Progress in the development of efficient Quantum Dot based room temperature THz sources **445**
Edik Rafailov

Single-shot polarization-resolved microscopy of nanomaterials **446**
Julien Flamant, Nathan Ullberg, Baptiste Marthy, Khosro Kamali, Patrick Ferrand, Mikael Käll, Guillaume Baffou

Multifunctional Optical Metasurfaces and Their On-Chip Integration **447**
Bo Xiong, Minjun Xie

Direct Nanoimprint Lithography as an Additive Full-Wafer Manufacturing Platform for All-Inorganic Metaoptics and AR Waveguides **449**
James Watkins

Synthesis of Colloidal Nanoalloys by Ultrafast Laser Irradiation **450**
Andrés Guerrero Martínez, Guillermo González Rubio

Polarization-Controlled Lattices of Sub-Wavelength Photonic Spin Skyrmions **451**
Andrei Afanasev

Fast and High efficiency photo-thermal conversion in optical nanocavity **452**
Giuseppe Nicoletta, Giuseppe Emanuele Lio, Roberto Caputo, Antonio Ferraro

Ultra-Fast Optical Response of Al:ZnO Metasurfaces in the near infrared range **453**
Stefania Benedetti, Tersilla Virgili, Luca Bursi, Michele Guizzardi, Andrea Villa, Alessandro di Bona, Sergio D'Addato, Andrea Mescola, Gian Carlo Gazzadi, Arrigo Calzolari

Polarisation control in time-varying low-index films **455**
Wallace Jaffray, Sven Stengel, Alexandra Boltasseva, Vladimir M. Shalaev, Maria Antonietta Vincenti, Domenico de Ceglia, Michael Scalora, Carlo Rizza, Marcello Ferrera

Tunable Achiral Metamaterial Substrates for Enantiomer Detection **457**
Maryam Mirahmadi, Ali Douaki, Vincenzo Caligiuri, Denis Garoli, Roman Krahne

Tunable Polaritonic Topologies Generated by qBIC Metasurfaces **458**
Connor Heimig, Enrico Baù, Jonas Biechteler, Florian Mangold, Julian Schwab, Manobina Karmakar, Leonardo de S Menezes, Haoran Ren, Stefan A. Maier, Harald Giessen, Andreas Tittl

Advanced passive and active metasurfaces and zero-index materials 461

Plasmonic Semiconductor Laser Particles Across Surface-Supported, Metal-Coated, and Metalattice Configurations 462
Sangyeon Cho

Nanofocusing of Orbital Angular Momentum Beams for Chirality Imaging 463
Zhenrong Zhang

Cross-Shaped Metasurface for Advanced Spectral-Scanning LiDAR 464
Hongyan Fu, Yaqi Han

Broadband Metamaterial Absorbers for Highly Sensitive Molecular Detection 465
Takuo Tanaka

Timetronics vs Electronics 467
Venugopal Raskatla, Jinxiang Li, Giorgio Adamo, Kevin MacDonald, Nikolay I. Zheludev

Generalized Lorentz Framework for Active Semiconductor Plasmonics at the Deep Nanoscale 468
Xuewen Chen

Topological metasurface for wavefront manipulation 469
Qinghua Song

Metasurface-Enabled Solid-State Photon Sources 471
Fei Ding

Continuous-Wave Chiral Exciton-Polariton Lasers Across the Visible and Infrared 472
Siying Peng

Enhancing Light-Matter Coupling via Topology Optimized Cavities on 2D Excitonic Material 473
Brandon Triplett, Davide Cassara, Morris M. Yang, Karthik Pagadala, Federico Capasso, Vladimir M. Shalaev, Alexandra Boltasseva

Rigorous and approximate electromagnetic simulators for free-form light-emitting device optimization 474
Min Seok Jang

Engineering spontaneous emission with metasurfaces 475
Benjamin Vest

Out-of-equilibrium nonlinear optical dynamics in ultraviolet epsilon-near-zero materials 476
Matteo Silvestri, Luca Assogna, Davide Tedeschi, Carino Ferrante, Andrea Marini

Octave-Spanning Terahertz Quarter-Wave Plates Based on Over-Coupled Fabry-Perot Resonances in Reflective Metal-Dielectric-Metal Metasurfaces 478
Tae Gwan Park, Chun-Chieh Chang, Hou-Tong Chen

Building Uncooled Infrared Camera based on One Atom Thick Graphene 480
Debashis Chanda

Dynamic Surface-Lattice Resonance Metasurface for Time-Varying Photonics 481
Jonathan Weber, Adam Ball, Dhruv Fomra, Sumit Goswami, Benjamin Diroll, Thirumalai Venkatesan, Nathaniel Kinsey

New Materials for Large Scale, Roll-to-Roll Metasurfaces 483
Vivian Ferry

Dual-layer metasurfaces supporting bound states in the continuum for torque sensing 484
Alexander Schossmann, Michael Tofferl, Maximilian Saiko, Alexander Bergmann, Peter Banzer

All-glass metasurface laser optics based on self-generation of nano-particles 486
Eyal Feigenbaum

Harnessing Epsilon-Near-Zero Effects: Fiber Lasers, Thermo-Optic Dynamics, and Beyond 488
Qian Li

Flat Optics with Computational Imaging for Biomedical Applications 489
Sunil Vyas, Cheng Hung Chu, J. Andrew Yeh, Yuan Luo

Nonlocal Meta-Optics: Addressing Fundamental Scaling Constraints in Imaging Systems 490
Bohan Zhang, Yuanmu Yang

Nanophotonic Devices and Metasurfaces using High Mobility Transparent Conductive Oxides 491
Sudipta Biswas, Saika Muntaha Bari, Sandra Achieng, Alan Wang

Deciphering Chirality via Super-Resolution Near Field Chiral Absorption 493
Yang Zhao

Probing Molecular Dynamics in Optical Nanocavities: Decoding Ensemble Signatures 494
Hector Pascual Herrero, Joni Spencer, Alvine Yu, Elizabeth M. Y. Lee, Regina Ragan

Unconventional Semiconductors forSwitchable Photonics 496
Marina Leite

Can Nanostructures and Metasurfaces Affect the Casimir Force? 497
Jeremy Munday

Confinement-Induced Nonlocality and Optical Nonlinearity in Transdimensional Plasmonics 498
Igor Bondarev

Nonlocal flat optics for frequency-angle selective light control 499
Jung-Hwan Song, Qitong Li, Zhepeng Zhang, Fenghao Xu, Jorik van de Groep, Skyler Selvin, Andrew Mannix, Mark L. Brongersma

Graphene-based Acive Metasurface for Mid-IR Transmission Modulation 500
Jinseok Kong, Heonhak Ha, Junhyung Kim, Jiwon Kang, Min Seok Jang

Novel Metaphotonic Structures for Enhanced Light-matter Interaction 503
Seyed Enjavi, Reza Marzban, Ashkan Zandi, Amin Khavasi, Saeed Javadizadeh, Hamed Abiri, Abhirupa Saha, Ali Adibi

Squeezing Light Fields for Ultrafast Detectors and Single Photon Sources 504
Maiken Mikkelsen

Time Reflection of Guided Light in Optically Switched Metasurfaces: Generating Magnetic Field on the Nanoscale 505
Shivakh Rawat, Samyobrata Mukherjee, Gennady Shvets

Chalcogenide Metamaterials for High-Speed Tunable Photonics 506
Jesse Frantz, Arash Nemati, Jason Myers, Robel Bekele, Vinh Nguyen, Yajun Gao, Adam Overvig, Andrea Alù

Towards dynamic metasurfaces and nanophotonics in barium titanate on insulator 507
David Barton, Sarah Berman, Sina Abedini Dereshgi, Ethan Ray

Chirality, magnetism, and magnetoelectricity: Separate phenomena and joint effects in metamaterial structures 509

Theory of Spin-Chiral Phonon Coupling in Chiral Crystals 510
Dapeng Yao, Gen Tatara

Orbital optical chirality: Spectrally and spatially resolved measurements of multipolar chiroptical responses for optical vortex beams 512
Yoshito Y. Tanaka

Strong coupling of chiral light with chiral matter: a macroscopic study 514
Sergey Dyakov, Natalia Salakhova, Ilia Smagin, Denis Baranov, Ilia Fradkin, Nikolay Gippius

Nonlinear magnetization dynamics as a route to nonreciprocal phases, spin superfluidity, and analogue gravity 515
Benedetta Flebus, Vincent Flynn

Breaking of time-reversal symmetry and Onsager reciprocity in chiral molecule interfaced with 516

an environment
Jonas Fransson

Nonlinear terahertz magnetoelectric coupling of electromagnons in multiferroics **517**
Youtarou Takahashi

Zero-frequency chiral magnonic edge states protected by non-equilibrium topology **518**
Rembert Duine, Pieter Gunnink, Joren Harms, Alexander Mook

Gaussian quantum state preparation of ferromagnetic magnons **519**
Marco Brühlmann, Monika Mycroft, Yunyoung Hwang, Jorge Puebla, Rostyslav Serha, Andrii Chumak, Carlos Gonzalez Ballestero

Symmetry Principles and Topology-Driven Design of Knot-Particle Metasurfaces **520**
Nadav Goshen, Yarden Mazor

Dynamical orbital magneto-electric response in complex materials **521**
Yuriy Mokrousov

Pure moving optical media at microwave frequencies using magnetochiral metasurfaces **522**
Toshiyuki Kodama

Intrinsic Hyperbolic Anisotropy for Low-Loss Polarization Control and Chiral Light-Matter Interaction **524**
N. Melchioni, A. Mancini, G. Venturi, L. Nan, A. Efimova, S. Chiodini, A. Ambrosio

Rotation and Self-Ordering of Nanoparticles by Optical Forces Carrying Angular Momentum **526**
Hajime Ishihara

Photoinduced magnetic phase transitions in the Kondo-lattice model **528**
Masahito Mochizuki, Ryo Hamano

GHz acoustic vortex for the manipulation of orbital angular momentum of light **529**
Alessandro Pitanti, Paulo Santos

Analyzing Nanoscopic Light-Matter Interactions Using Reconfigurable Photonic Integrated Circuits **530**
Marko Šimić, Johannes Bütow, Jörg S. Eismann, Sarah Lindner, Peter Banzer

Magnetic Multipole Dependent Dichroism Arising from Vortex Light **532**
Akbar Salam

Emergent Spin-Orbital Berry Curvature Fluxes in pseudo-Nodal Semimetals **534**
Peter C. Schmitz, Dongwook Go, Yuriy Mokrousov

Excitonic Charge Density Waves in Moire Ladders **535**
Paula Mellado, Javiera Cabezas, Francisco Muñoz

RKKY-like interactions between two magnetic skyrmions **537**
Xiangrong Wang

Microwave radiation from high chirality vortex dynamics. **540**
Feodor Yu. Ogrin

Feedback effects of electromagnetic interactions in bianisotropic media **542**
Kei Sawada

Towards compact microfluidic chips for efficient chiral recognition **543**
David Ayuso

Chiral Metamaterials with Twisted Metallic Wire Structures **544**
Ming-Li Chang, Che Ting Chan

When Chirality Protection Fails: Bulk-Mediated Reflection of Surface Spin Waves **546**
Oleksandr Serha

Symmetry Behavior of Chiral Disorder Metamaterials **547**
Simone Zanotto

Pushing micro-focused BLS to the Nanoscale: Modeling and Nanophotonic Enhancement for Magnon Detection 549
Ondřej Wojewoda, Michal Urbánek

Momentum Space Enabled Functionalities in Chiral Metasurfaces 550
Alexander Antonov, Connor Heimig, Tao Jiang, Dmytro Gryb, Leonardo de S Menezes, Maxim Gorkunov, Andreas Tittl

Topology Optimized Aluminum Chiral Nanogap Antennas for DUV Circular Dichroism Enhancement 552
Atsushi Taguchi

On the relation between local optical chirality andcircular dichroism in enantiomeric sensing 554
Diana Shakirova, Adrià Canós Valero, Thomas Weiss

Spin-Wave Amplification via Phase-Transition-Driven Temporal Interfaces 555
Pawel Gruszecki, Krzysztof Sobucki

Strong Coupling of Chiral Magnons in Altermagnets 557
Peng Yan

Relationship between Antiferromagnetic Spin Pumping and Magnetic Resonance 558
Masahiro Sato, Hogara Watanabe

Chiral structures nanofabrication with optical skyrmions 561
Takashige Omatsu

Magnetoelectric effects in truly and falsely chiral media 562
Omar Jesus Franca Santiago, Stefan Yoshi Buhmann

Resonances and reversal in local and global chirality responses 563
Itamar Kimchi

Topological polarization textures and emergent chirality in ferroelectric materials 565
Svitlana Kondovych

From Skyrmions to Twistons to Hopfions: Topological Textures Beyond Homotopy Groups of Spheres 566
Maria Azhar, Sandra Shaju, Trishita Das, Ross Knapman, Alessandro Pignedoli, Yijie Shen, Karin Everschor-Sitte

Local and non-local phenomena in curvilinear and 3D magnets 568
Oleksandr Pylypovskyi

Emergent Magnetoelectricity in Stacked VdW Magnets 570
Yong P. Chen

Chiral Polaritonics and Molecular Lasing: Concept, Challenges, and future Directions 572
Kai Mueller, Denis Baranov, Christian Schaefer

Persistent Energy Fluxes and Angular momentum in Non-reciprocal Electromagnetic Systems 573
Ivan Latella

Nonreciprocal nonlinear magneto-optical metasurfaces 574
Jialong Wang, Dongchen Ma, Yi Shuai, Jun Qin, Qing Zhang, Lei Bi

On the efficiency of enantiomer separation using optical evanescent fields near waveguides 576
Sebastian Golat, Francisco J. Rodriguez-Fortuno

Bottom-Up Engineered Hybrid Plasmonic Broken L-Shaped Metamaterial Platforms Reveal Broadband Enhanced Optical Chirality 578
Ufuk Kilic, Raymond Smith, Shawn Wimer, Yousra Traouli, Sema G. Kilic, Eva Schubert, Christos Argyropoulos, Mathias Schubert

Theory of Electric Polarization in Inhomogeneous Crystals Based on the Quantum Transport Equation 581
Shuichi Murakami, Yuta Suzuki, Nobuhiro Arai, Manato Fujimoto, Yang Gao, Di Xiao

Magnetic Helicity of Chiral Molecules 582

Ivanina Ilieva, Christof Holzer, Carsten Rockstuhl, Ivan Fernandez-Corbaton

Hot-Electron Generation and Photoinduced Chirality in Plasmonic Nanocrystals 584
Alexander O. Govorov

Tailoring Smith-Purcell radiation using moiré photonic crystals and chiral materials 585
Thomas Delplace, Loris Cavenaile, Bjorn Maes

Quantum materials in chiral cavities 586
Ceren Dag

Geometric Phase Modulation in Circularly Birefringent Plasmonic Structures 588
Pasha Goz, Akash Das, Andre Yaroshevsky, Yuri Gorodetski

Giant Magneto-Impedance Effect in Magnetic Microwires: Challenges, Advances and Perspectives 591
Arcady Zhukov, Alvaro Gonzalez, Paula Corte-Leon, Jesus Olivera, Valentina Zhukova

An Electromagnetically Driven Vaterite-based Panacea Platform 593
Pavel Ginzburg, Hani Barhom, Andrey Machnev, Andrey Ushkov, Denis Kolchanov, Pavel Bezrukov

Photonics for Thermal Management in Photovoltaics 595
George Perrakis, Anna Tasolamprou, Maria Kafesaki

Self-Polarizing Chiral Cavities for Control of Quantum Emitters 597
Behrooz Semnani, Anya Houk, M. Soltani, Athena Xu, M. Bajcsy

Microscopic Hopfield Theory of Hyperbolic Phonon Polaritons in Layered Materials 598
Yu Zhang

Photoelectron chiral dichroism from tailored light: symmetry and helicity 600
Ofer Neufeld

Evaluating Surface-Enhanced Chiroptical Spectroscopy on Nanostructured Aluminum Substrates in the Deep-UV 602
Bjoern Reinhard

Nonreciprocal Neural Networks for Decoupled Bidirectional Computing via Magneto-Optical SSPP Transmission Lines 604
Xiaomeng Li, Enzong Wu, Hongsheng Chen, Zuojia Wang

Spin relaxation near surfaces via gyromagnetic coupling to Rayleigh vorticity baths 605
Mamoru Matsuo, Hiroshi Funaki, Ryotaro Sano, Ai Yamakage, Tatsuhiko Ikeda

Phononics and acoustic metamaterials 606

Resonator Cascades in a 3D Lattice as a Broadband Acoustic Metamaterial 607
Frieder Lucklum

Practical Design of Helmholtz Resonators Considering Geometry and Acoustic Losses 610
Vicente Cutanda Henriquez, Frieder Lucklum

Transmission enhancement through a barrier induced by global and local mirror symmetries in periodic waveguides 611
Elie Salemeh, Simon Félix, Vincent Pagneux

Ultrafast Electronic and Acoustic Dynamics in Nanocrystalline Silicon 612
Tânia Ribeiro, Tiago E. C. Magalhaes, Houssem Rezgui, Gloria Conte, Oili Ylivaara, Jouni Ahopelto, Clivia M. Sotomayor-Torres

Optical probing of the vibrational and thermal dynamics of single metal nanoparticles 614
Nathan Berrit, Noëlle Lascoux, Clément Panais, Sylvie Marguet, Natalia Del Fatti, Aurélien Crut

Radiation Control in Fluid-Loaded Metamaterial Waveguides with Space and Time Modulation 615
Emanuele Riva, Alper Erturk

Coherent control of acoustic phonons in phononic waveguides 616
Chushuang Xiang, Edson Rafael Cardozo de Oliveira, Sathyan Sandeep, Konstantinos Papatryfonos, Martina Morassi, Luc Le Gratiet, Abdelmounaim Harouri, Isabelle Sagnes, Aristide Lemaitre, Omar Ortiz, Martin Esmann, Norberto Daniel Lanzillotti-Kimura

Wave Transport in Valley Phononic Crystals 617
Myung-Joon Lee, Il-Kwon Oh

Numerical Study of Viscoelastic Soil Effects in Seismic Metamaterials 619
Stefano Laureti

Coupled Inertial Amplification and Local Resonance Band Gaps 621
Cetin Yilmaz

Verification of a two-fold topological phase transition ruled by third-nearest-neighbor hoppings 623
Rafael Mendez-Sanchez, Yonatan Betancur-Ocampo, Bryan Manjarrez-Montañez, Angel Martínez-Argüello, Alejandro Franco-Medrano, Enrique Flores-Olmedo, Gabriela Báez

Non-reciprocal communication with signal amplification 625
Xinxin Guo, Zhenwei Xu, Ulrich Kuhl, Nicolas Noiray

From Acoustic Spin, Elastic Spin to Phonon Spin 626
Jie Ren

Wide-area Topological Higher-order Modes in Heterostructured Kagome Phononic Crystal 628
Yusuke Hata, Yuri Fukaya, Kenji Tsuruta

Complex Topological Phases Driven by Beyond-Nearest-Neighbor Interactions 629
Amir Rajabpoor Alisepahi, Siddhartha Sarkar, Kai Sun, Jihong Ma

Space-multiplexing Metalens for Multiple Ultrasonic Bessel Vortex Beams 631
Jie Zhu, Qian Cheng

Experimental Investigation of Resonant Microdisks for the Creation of a Multiple-Scattering Acoustic Medium 632
Ch. Ghaisas, S. C. Baltogiannis, Y. Zhang, D. Garcia, B. Tallon, L. Belliard, Olga Boyko

Sub-THz electromechanics and optomechanics 634
Hong Tang

Omnidirectional and anomalous acoustic absorptionwith an array of wiremeshes 635
Juan Pablo Escudero, Jean-Philippe Groby, Vincent Pagneux

Finite-Size Effects in Mechanical Metamaterials: The Role of Interfaces 636
Svenja Hermann

Mode conversion for elastic waves via temporal interfaces 637
Cong Chen, Zhanyu Li, Xiaoming Zhou, Gengkai Hu

Flat Band Skin Effect in Mechanical Metamaterials 640
Xulong Wang, Guancong Ma

Transient Growth Boundaries in Nonnormal Lattices 642
Ioannis Kiorpelidis, Konstantinos G. Makris

Elastic Willis Metamaterials: Parameter Characterization and Wave Matching Application 644
Joo Hwan Oh

Nanocrystalline Silicon for Optomechanics 646
Gloria Conte, Omid R. Ranjbar-Naeini, Manjunath Balagopalan, Cristiana F. Alves, Oliver Schraidt, Oili Ylivaara, Jouni Ahopelto, Clivia M. Sotomayor-Torres

On the Interpretation of Aeroacoustic Metadevice Performance in Terms of Spacetime Curvature 648
Giada Colombo, Umberto Iemma

Tackling the Long-Wavelength Challenge in Underwater Noise Reduction with Metabarriers 650
Marco Miniaci

Acoustic Purcell effects in phase-transitioning nanodroplets 651
Chengzhi Shi

Generalization of exceptional point: high-dimensional coalescing non-Hermitian spaces 652
Guancong Ma

On the Quest of a Boundary Integral Formulationfor Aeroacoustics of Metacontinua in CurvedSpacetime 653
Umberto Iemma, Giada Colombo

Band-structure calculations of phononic crystals in the hard-scatterer limit 655
Arkadii Krokhin, Dmitrii Shymkiv

Optical imaging of sub-GHz acoustic waves in topological phononic crystals 656
Osamu Matsuda

Trapping GHz Rayleigh Waves with Phononic Crystals 658
Daniel Torrent, Liangshu He, Fernando Soldevila, Yabin Jin, Pawel Packo, Agustín Mihi

Color Holographic Imaging Based on an Acoustic Metasurface 659
Hong-Gen Chen, Hao-Wen Dong, Yue-Sheng Wang

Odd active solids 660
Anton Souslov

Phononic Topological Waveguides for Gigahertz Applications 661
Monika Devi Koijam, Yan Pennec, Clivia M. Sotomayor Torres, Bahram Djafari-Rouhani

Quantum Valley Hall-Based Continuously Tunable Phononic Wave Coupler 663
Keita Funayama, Kenichi Yatsugi, Hiroya Tanaka, Hideo Iizuka

Helmholtz Resonator-Induced All-Angle Self-Collimation in Square-Lattice Sonic Crystals 665
David Ramirez Solana, Muhammad Gulzari

Ultrafast nanomechanics of single MoS2 nanotubes 669
Francesco Banfi

Self-Organized Multimode Phonon Lasing in a Silicon Optomechanical Nanobeam 670
David Alonso Tomás, Daniel Navarro-Urrios

Localization and antilocalization of sound in a phononic crystal with symmetric disorder 671
Jose Sanchez-Dehesa, Francisco Cervera, Martin Ibarias, Dmitrii Shymkiv, Arkadii Krokhin

Nanoscale Local Electromechanical Sources for GHz Phononics 672
Tapani Makkonen, Oili Ylivaara, Omid R. Ranjbar-Naeni, Clivia M. Sotomayor Torres, Jouni Ahopelto

Eigenmode steering with time-varying acoustic metamaterials 673
Wai Chun Wong, Gregory Chaplain, Jensen Li

Advanced Techniques for Computational Electromagnetics 675

Advanced electromagnetic simulations for free electrons and nanoscale optical fields 676
F. Javier García de Abajo

Computational Nanophotonics for AR Optics: From Performance Targets to Artifact□Robust Designs 677
Christina Spaegele

Topologically structured doughnuts: optical skyrmions, superoscillations, and axion probes 678
Nikitas Papasimakis

A universal scattering anomaly near bound states in the continuum 679
Ya Yan Lu

Separating partially coherent light 680
Charles Roques-Carmes

Simulation and Optimization of Large-Scale Metasurfaces **681**
Jens Niegemann, Shin-Sung Kim, Thibault Leportier, Han-Hsiang (Michael) Cheng

Photo-Excited Silicon-Based Quarter-Wave Plate for Terahertz Applications **683**
Shohei Tsuzuki, Jun Shibayama

Near-field focusing and amplification of tip-substrate radiative heat transfer **684**
Milo Vescovo, Philippe Ben-Abdallah, Riccardo Messina

Time Modulation of Near-Field Radiative Heat Transfer **686**
Mauro Antezza

Numerical advances in the computation of radiative heat transfer between nanostructures **687**
Brahim Guizal, Omar Tada, Mauro Antezza, Youssef Jeyar

BIC-Enhanced Partial LDOS in Terahertz Metasurfaces **688**
Jie Ji, D. Peeters, W. Holman, T. X. Hoang, D. van Mechelen, J. Gomez Rivas, Jose Sanchez-Gil

Time-Frequency Structured Light for Analog Processing of Broadband Waveforms **690**
Majid Goodarzi, Geunweon Lim, Connor Rowe, Benjamin Crockett, Xinyi Zhu, Hao Sun, Jose Azana

High-Speed Chemical Identification Enabled by Terahertz Parametric Wavelength Conversion **692**
Kosuke Murate, Sota Mine, Kodo Kawase

Theory and experiments on GaN waveguide polariton lasers **694**
Olha Bahrova, Valentin Develay, I. Septembre, D. Bobylev, Christelle Brimont, L. Doyennette, B. Alloing, H. Souissi, E. Cambril, S. Bouchoule, T. Ackemann, Jesus Zuniga Perez, Thierry Guillet, Guillaume Malpuech, Dmitry Solnyshkov

Understanding and Designing High Harmonic Generation from Nanostructured Surfaces **696**
Gavin Crowder, Jesse Thompson, Lora Ramunno

Inverse design frameworks towards realistic freeform flat optics **697**
Joao Cunha, Filipe Camarneiro, Diogo Aguiam

Nonreciprocal Surface Plasmons in a Metasurface Formed by Magnetically Biased Plasmonic Cylinders **699**
Ioannis Katsantonis, Costas Valagiannopoulos, Anna Tasolamprou

Nonlocal metasurfaces for Quantitative Phase Microscopy **701**
Ann Roberts

Realization of Photonic Parallel Spaces and Overlapping Optical Devices **703**
Yun Lai

Adaptive Tapering Strategy for Waveguide Dielectric Laser Accelerators under Pulsed Operation **704**
Davide Guarnera, Hatou Yvelin Donkeng, Roberta Palmeri, Giorgio Sebastiano Mauro, Nunzio Salerno, Alberto Bacci, Santi Concetto Pavone, Giuseppe Torrisi, Andrea Locatelli, Gino Sorbello

How many channels can a photonic device support? **705**
Paul Virally, Pengning Chao, Alessio Amaolo, Alejandro Rodriguez, Sean Molesky

The photonic gearbox: ultra-high local density of states via cylindrical-symmetry breaking **707**
Alessio Amaolo

Multiscale simulations of electronic excitations of molecules coupled to plasmonic nanostructures **709**
Stefano Corni

Manipulating waves with metamaterials in multiple dimensions (x,y,z)/(x,y,z,t) **710**
Victor Pacheco-Peña

Miexciton enhanced fluorescence in monolayer WS2 /Si Huygens metasurface **712**
Junichi Takahara

Radiative heat transfer measurements at small scales in systems involving several bodies **713**
Victor Guillemot, Ana Isabel F. Tresguerres-Mata, Riccardo Messina, Valentina Krachmalnicoff, Remi Carminati, Philippe Ben-Abdallah, Wilfrid Poirier, Yannick De Wilde

Scattering Symmetries in Metagratings 714
Karim Achouri

Application of Spatial Symmetries in Plasmonic Lattice Design 715
Kristian Arjas, Grazia Salerno, Päivi Törmä

Enabling Meta-surface Design with Neural Network Technologies. 716
Denis Rideau, Mathys Le Grand, Damien Maitre, Loumi Tremas, Habib Mohamad, adam Fuchs, Pascal Urard, Valerie Serradeil, James Downing

Machine-Learning Assisted Design of Tunable Metasurfaces 720
Alexander Wolff, Lukas Mueller, Janis Krieger, Lars Franke, Ralf Stemler, Steffen Klingel, Marco Rahm

Cooperative absorption in random particulate media: achieving spectral selectivity 721
Cédric Blanchard, Cristina Gila, Timothée Guerra, Olivier Rozenbaum

Deep Learning-Enhanced Dual-Comb Ghost Imaging with Minimally Invasive Probes 722
Myoung-Gyun Suh

Photonic driven dual-mode thermoregulation: from static to dynamic design evolution 723
Muluneh G. Abebe, Eva Loccufier, Jozefien Geltmeyer, Karen De Clerck, Bjorn Maes

Photoluminescence of Pyrolytic Carbon Dots on Plasmonic Metasurfaces 724
Pierre Berini

Advancing Machine Learning-Assisted Quantum Photonic Device Design and Optimization 726
Alexander V. Kildishev, Vladimir M. Shalaev, Alexandra Boltasseva, Yuheng Chen, Vaishnavi Iyer, Pranshu Maan

From Design to Fabrication: Limits & Manufacturing Tolerances in Optical Metasurfaces and Meta-Modulators 727
Sonia Freddi, Alfonso Nardi, Michael Scalora, Agostino Di Francescantonio, Sofia Martins, Johann Osmond, Attilio Zilli, Marco Finazzi, Michele Celebrano, Maria Antonietta Vincenti, Monica Bollani

Dynamically Reconfigurable Waveguide-Fed Metasurface Apertures: From Theory to Application 729
David R. Smith

Optical Nonlinearities in Materials with Nonlocal Response 730
Gonzalo Alvarez-Perez, Huatian Hu, Cristian Ciracì

Useful and detrimental thermal radiationin near-field energy-conversion devices such as thermophotovoltaics 731
P-Olivier Chapuis

Thin-film lithium niobate channel waveguides: numerical analysis and perturbational modelling 733
Manfred Hammer, Behnood Taheri, Henna Farheen, Jens Förstner

Unconventional Geometric Phases in Optics 735
Shubo Wang

Adaptive photonics with phase-change materials: multiphysics modelling and design 736
Dmitry Chigrin

High-Fidelity Fullwave Solvers and Reduced-Order Models for the Design of Complex Nanostructured Photonic Devices 737
Mahmoud Elsawy, Alexis Gobe, Stéphane Lanteri

Advanced in Topology Optimization for Metaphotonics and Integrated Optics 740
Antonio Calà Lesina

SCRIBEed GRIN-Lenses by Topology Optimization 741
Rasmus Christiansen, Dajie Xie, Paul Braun

Engineering Optical Nonlinearities Using Nanostructured Materials 743
Luca Razzari

Radiative decay of surface plasmon propagating in thin metal film 744
Arkadii Krokhin, Andrey Bozhko

Metamaterials: novel trends and applications 746

Design of Reconfigurable and Non-Reciprocal Soft-matter Photonic Devices 747
Peter Ropač, Zala Korenjak, Matjaž Humar, Miha Ravnik

High-Precision Nanofabrication and Characterization of Metamaterials Using ZEISS FIB-SEM Technology 749
Olena Vertsanova, Martina Schenkel

The interaction of nanoplasmonic hot carriers with adsorbates 750
Johannes Lischner

Nanostructured GLAD optical coatings for reflectance and birefringence control 751
Lina Grineviciute, Darija Astrauskyte, Lukas Ramalis

Lattice Resonances in Bipartite Arrays of Nanodisks 753
Juan Jose Alvarez Serrano, Vincenzo Aglieri, Juan Ramon Deop-Ruano, Muhammad Sohaib, Andrea Toma, Alejandro Manjavacas

Prelude to the search for natural vibrations of tensegrity-inspired cellular metamaterials 754
Anna Al Sabouni-Zawadzka, Adam Zawadzki, Wojciech Gilewski, Maciej Kołodziejczak

Scalable Metafibres for Advanced Imaging via On-Fibre Wavefront Engineering and Wavefront Shaping 756
Fei He, Rafael Fuentes Dominguez, Terry Wright, George Gordon

Nitride-based nanoparticles for metasurfaces 759
Ermelinda Salvaggio, Jérémie Béal, Gregory Abadias, Sophie Camelio, David Babonneau, Davy Gerard, Christophe Couteau, Jérôme Plain

Abnormal hot carrier thermalization at van Hove singularities in twisted bilayer graphene 760
Nianze Shang, Chen Huang, Kaihui Liu, Zhipei Sun

Wavelet-Fourier Modal Method for very Large-Beam Scattering in Photonics and Biophotonics 761
Kofi Edee

Multiphoton Luminescence and Second Harmonic Imaging in 2D Materials 762
Arik Ahmed, J. Pierce Fix, Sheikh Parvez, Jane Peabody, Nicholas J. Borys, Steve Smith

Laser-induced formation of plasmonic nanostructures 763
Rodrigas Liudvinavicius, Kernius Vilkevicius, Evaldas Stankevicius

Integration of metamaterial phase-shifting ICs in 3D-printed packages for wireless communication 764
Adam Pander, Kentaro Soeda, Daisuke Kitayama, Hibiki Kagami, Yoshinori Yamaguchi, Kuniaki Konishi, Junji Yumoto, Hiroyuki Takahashi

Super□Resolution Interferometric Lithography Beyond the Diffraction Limit Enabled by a Tuneable Metasurface 766
Mohammad Mahdi Jafarizadeh Jazi, Leila Yousefi

Constructive homogenization of dispersed random media 769
Vladimir Mityushev

Design of an Airy-Beam-Generating Element Made with High-Refractive-Index and Low-Reflectance Metasurface in the 28 GHz Band 770
Yuta Tanaka, Mahiro Ochiai, Takehito Suzuki

Electron-Driven Photon Sources for Ramsey Interferometry with Electron Beams 771
Nahid Talebi

Application of Metamaterials in Soft and Biodegradable Electronics 773
Seung-Kyun Kang

High-efficiency nonlinear optical response of silicon based metasurfaces in the visible and UV spectrum 775
Shroddha Mukhopadhyay, Crina Cojocaru, Maria Antonietta Vincenti, Michael Scalora, Jose Trull

Multilayer Gap Plasmons in Periodic Perfect-Conductor-Dielectric Structures 777
Michael Haftel, Justin Case, Anatoliy Pinchuk

Parity-Time and quasi-normal modes in Photonics, Plasmonics, Acoustics 778

Emergence of higher-order exceptional points in composite non-Hermitian quantum systems 779
Jan Wiersig, Weijian Chen

Light Trapping by Non-Hermitian Thin Films 780
L. Grineviciute, I. Lukosiunas, J. Nikitina, I. Meskelaite, D. Gailevicius, Kestutis Staliunas

Photonic neuromorphic computing using non-Hermitian zero modes in coupled nanolaser arrays 781
Kaiwen Ji, Giulio Tirabassi, Cristina Masoller, Ge Li, Alejandro M. Yacomotti

Pumped and active dissipative media with non-Hermitian periodic potentials 783
Salim Benadouda Ivars, Muriel Botey, Kestutis Staliunas, Ramon Herrero

Phase conjugation and focusing in multimode non-Hermitian systems 785
Konstantinos G. Makris, Demetri Psaltis

Sensing with complex Bragg gratings over parity-time states 787
Tianyi Hao, Pavel Cheben, Jens H. Schmid, Pierre Berini

Topology in space, time, and space-time 789
Alexander Szameit

Mode-cleaning in multimode fibers via chiral non-Hermitian modulations 790
Muriel Botey

A quantum particle in a potential well with an absorbing barrier - non-Hermitian tunneling 792
Eva-Maria Graefe

New Advances in Metamaterials and Their Functional Applications 793

Geometric Tailoring of Anisotropic Metamaterials for Elastic Wave Steering 794
Jianlong Chen, Dong Yan, Chao Wan, Guangyan Liu, Kai Zhang

Direct tensor processing with coherent light 796
Yufeng Zhang, Kaizhi Wang, Zhipei Sun, Xuhan Guo

Chiral fields and ultrafast chiral spectroscopy 798

Manipulating chiral effects with plasmonic nanostructures 799
Yuanyang Xie, Alexey Krasavin, Anatoly Zayats

Non-dichroic Chiral Photoelectron Spectroscopy 801
Letizia Fede, Debobrata Rajak, Chris Sparling, David Ayuso, Sylvain Betoule, Valérie Blanchet, Piero Decleva, Dominique Decamps, Stéphane Petit, Bernard Pons, Yann Mairesse, Andres Ordonez

Nonlinear Light-Matter Interactions for Ultrafast Chiral Detection in Confined Environments 802
Stefanos Koufidis, Jacob Edginton, David Ayuso

Twisted light generates robust many-body states for practical quantum computing 804
F. J. Rodríguez, Luis Quiroga, Neil Johnson

Dynamically Tuneable Helicity in Twisted Electromagnetic Resonators 816
Emma Paterson, Jeremy Bourhill, Michael Tobar, Maxim Goryachev

Attosecond Chiral Interferometry with Free Electron Lasers 818
Davide Faccialà, J. Terentjevas, A. Senftleben, J. Mikosch, M. Ruberti, A. Schneider, M. Padovani, A. G. Lohr, A. Roos, P. Martin Maier, P. C. Flores, R. Heilemann, E. A. Christou, J. Ghosh, L. Oberti, L. Germeroth, M. Mirahmadi, C. Vozzi, K. Prince, M. Di Fraia, S. Patchkovskii, O. Plekan, T. Baumert, K. Ueda, P. Kolorenc, V. Averbukh, C. Callegari, D. Ayuso, O. Smirnova

Tailored laser fields for driving nonlinear interactions with chiral molecules 819
Aude Rodriguez, Jacob Edginton, Alexander Löhr, Justas Terentjevas, Patricia Vindel-Zandbergen, Andrés Ordóñez, Josh Vogwell, Olga Smirnova, David Ayuso, Laura Rego

Controlling Intensity and Polarization at Deep Subwavelength Scale with Plasmonic Metastructures 821
Viktor Podolskiy, Brandon Gomes, Jiaren Tan, Hooman Barati Sedeh, Yuruo Zheng, Jacob LaMountain, Sean Morrison, Anatoly Zayats, Natalia Litchinitser

Functional materials for tunable and reconfigurable photonics 823

Polymer plasmons and gating for active metaoptics 824
Magnus Jonsson

Metamaterial devices and metalenses for optical beam steering 825
Daniele Melati, Sarra Salhi, Jian Cao, Gervasio D'Anzieri, Zindine Mokeddem, Hachim Lahbib, Warren Kut King Kan, Sandeep Yadav Golla, Constantine Papakonstantinou, Amir Hossein Masominia, Laurent Vivien, Carlos Ramos, Eric Cassan, Pavel Cheben, Jens H. Schmid, Xiaochen Xin, Winnie N. Ye

Integrated Optical Phased Arrays for AR Displays, Biophotonics, Trapped Ions, & Beyond 827
Jelena Notaros

Active and Reconfigurable Free-Space Photonics using Phase-Change Metamaterials 830
C. David Wright, Joe Shields, Guoce Yang, Carlota Ruiz de Galarreta, Mengyun Wang, Stuart Kendall, Joe Pady, Nikolaos Farmakidis, David B. Phillips, Jacopo Bertolotti, Andrea Alù, Harish Bhaskaran

Broadband Optical Properties and Thermal Stability of Thermal Evaporated GST and GSST Thin Films for Reconfigurable Metalens Applications 832
João Borlido, Ricardo Machado, Bernardo Dores, José Rodrigues, Filipa Mota, Eliana Vieira, Julien Legendre, Ioannis Draganidis, Georgia Papadakis, Diogo Aguiam, José Correia

Analysis of the fast dynamics of optical properties in phase change materials 834
Sebastian Walfort, Nils Holle, Julia Vehndel, Niklas Vollmar, Nils Weber, Joel Billermann, Martin Salinga

A Fabrication-Friendly All-optical Integrated Photonic Phase-change Memory with Plasmonic Enhancement 835
Joseph Pady, Junchao Song, Emanuele Gemo, Joe Shields, Stuart Kendall, Nikolaos Farmakidis, Harish Bhaskaran, Ivonne Bente, Wolfram Pernice, C. David Wright

Self-Consistent Optical-Thermal Modeling of VO2 Nanoparticles for Tunable Photonic Applications 838
Peter Kepič, Jiří Kabát, Tereza Bačová, Filip Ligmajer

Semimetallic nanostructures as multifunctional materials for nanophotonics 839
Fernando Chacon-Sanchez, Johann Toudert, Rosalia Serna

Phase transitions for tunable nanophononics 840
Sandeep Sathyan, Ornella Colmegna, Helmut Karl, Sébastien Cueff, Norberto Daniel Lanzillotti-Kimura

Nanoresonators and metasurfaces for nonreciprocal photonics 841
Sergey Kruk

Canalization-based super-resolution imaging using an individual van der Waals thin layer 842
Jiahua Duan, Aitana Tarazaga Martín-Luengo, Christian Lanza, Stefan Partel, Kirill Voronin, Ana Isabel F. Tresguerres-Mata, Gonzalo Alvarez-Perez, Alexey Y. Nikitin, Javier Martín-Sánchez, Pablo Alonso González

Room-temperature zero differential thermal emitters enabled by the controllable metal-insulator transition in rare-earth perovskite nickelates 844
Luigi Matera, Laurent Divay, Luis Moreno Vicente-Arche, Manuel Bibes, Paolo Bortolotti, Julian Peiro, Lucia Iglesias

Coherent Spin-Photon Interfaces based on Molecular Rare-Earth Systems 846
Diana Serrano

The Old Brewster Effect Meets New Phase-Change Materials for Optical Switching 848

Gonzalo Santos, Diego Pérez, Josef Resl, Maria Losurdo, Yael Gutiérrez, Fernando Moreno

Scalable Tunable Phase-Change Metasurfaces by soft Nanoimprint Lithography: from dielectric/PCM hybrid architectures to volatile VO2 photonics 849
Magali Putero

Near-Unity Optical Switching by Sb2S3/Si Hybrid Metasurfaces 851
Amin Zamani, Gabriel Sanderson, Meibao Qin, Lu Zhang, Qiwei Miao, Sara Moujdi, Ze Zheng, Mohammadhossein Momtazpour, Christopher J. Mellor, Wending Zhang, Ting Mei, Zakaria Mansouri, Lei Xu, Mohsen Rahmani

Reproducible 2D Structural Color Platforms for Reliable pH Sensing Applications 854
Jing Qian, Yekaterina Tskhe, Luke Madden, Enrique Azuaje-Hualde, David Hoey, A. Louise Bradley, Larisa Florea, Colm Delaney

Quantum metaphotonics 856

Integrated Single-Photon Emitters with Plasmonic Nanostructure 857
Keyu Jin, Lian Shen

Non-Reciprocal Photon-Pair Generation from Nonlinear Metasurfaces 858
Jinyong Ma, Xiwen Qiu, Tongmiao Fan, Tuomas Haggren, Hark Hoe Tan, Chennupati Jagadish, Andrey Sukhorukov

Metamaterials with Varactors: Manipulating Spoof Surface Plasmon Polaritons 859
Jinhui Shi, Zhaoqi Jiang, Zheng Zhu, Wenjia Li, Chunying Guan

Diffractive Optical Elements Empowered Spectropolarimetry via Single-Shot Imaging 860
Bing Lei, Jianyu Weng, Xiaoyu Cao, Zong Xiang, Xinyu Ma, Jie Li, Zhe Xie, Wei Wang, Jianhua Shi

Enhanced light-matter interactions: fundamentals and sensing applications 862

Nanomaterials and Nanostructures for Semi-Transparent and Color Photovoltaics 863
Ilya Sychugov

AI-driven Design and Synthesis of Plasmonic Nanoparticles 864
Jose Luis Montaño-Priede, Ana Sánchez-Iglesias, Anish Rao, Marek Grzelczak

Engineering Optical Sensitivity in Plasmonic Metasurfaces: from LSPR to high-Q Surface Lattice Resonances 866
Kartikey Pandey, Mathias Dolci, Yun Luo, Stéphanie Lau-Truong, Sarra Gam-Derouich, Alexandre Chevillot-Biraud, Nordin Felidj, Claire Mangeney

Engineering High-Q Dielectric Metasurfaces for Enhanced Light-Matter Interaction and Multimodal Biosensing 868
Jose Francisco Algorri, Dimitris Zografopoulos, Luis Rodriguez-Cobo, Adolfo Cobo, Mohammed Janneh, Patrizio Vaiano, Marco Pisco, Andrea Cusano

Nanoimprinted Chiral Photonic Architectures for Circularly Polarized Photoluminescence 871
Agustín Mihi, Jose Mendoza-Carreño, Xiaoyu Qi, Luis A. Pérez, Miquel Garriga, Isabel Alonso

Photoelectrochemical Chiral Nanofabrication by Circularly Polarized Light 872
Takuya Ishida, Tetsu Tatsuma

Mie Voids for Refractive Index Measurement of Unknown Water under High-Pressure 874
Hiromasa Niinomi, Hiroki Nada, Tetsuya Hama, Kazuhiro Gotoh, Yumiko Kodama, Tomoya Oshikiri, Masaru Nakagawa, Yuki Kimura

Exploring the Origins of Circular Dichroic Optical Forces at the Nanoscale 876
Junsuke Yamanishi

Ultimate Magneto-Optical Bounds at the Nanoscale 878
Jorge Olmos

A single photon source for the THz regime 879
Diego Martin Cano, Caspar Groiseau, Antonio I. Fernandez-Dominguez, Miguel Angel Martinez-Garcia, Carlos Sanchez Munoz

Optically Enhancing or Detecting Single Molecules on DNA Origamis 881
Sébastien Bidault

Modelling the Purcell Enhancement on Nonlocal Metasurfaces 882
Joshua T. Y. Tse, Taisuke Enomoto, Shunsuke Murai, Katsuhisa Tanaka

Structural colours using transition metal dichalcogenide nanostructures 883
Ida Juliane Bundgaard, Yonas Lebsir, Catarina Ferreira, Christos Tserkezis

Few-molecule nonlinear vibrational spectroscopy with dual-resonant plasmonic nanocavities 884
Christophe Galland, Zhiyuan Xie, Nobuaki Oyamada, Francesco Ciccarello, Wen Chen

Tip-Enhanced Sum Frequency Generation: Nonlinear Molecular Responses and Electrophotonic Effects Observed beyond the Diffraction Limit 886
Atsunori Sakurai, Shota Takahashi, Tatsuto Mochizuki, Toshiki Sugimoto

Optical Fields with Spatially Modulated ChiralityToward Chiral Trapping and Separation 889
Atsushi Kamegaya, Shun Hashiyada, Yoshito Y. Tanaka

Ultrasensitive label-free miRNA sensing realized by a Q-tunable plasmonic metasurface 891
Daiki Kawasaki, Takuo Tanaka

Single-molecule mass distribution sensing of proteins with high-Q silicon nitride microresonators 894
Koji Masuda, Abdullah Alabbadi, Linda Kasiarova, Pascal Del'Haye, Tobias Herr, Jiri Damborsky, Martin Marek, Stanislav Mazurenko, Josef Sivic, Frank Vollmer

Bio-Inspired Nanophotonics 896

Strategies for Infrared Management and Thermal Insulation Inspired from Biological Organisms 897
Amandine Marchand, Kevin Delmote, Olivier Deparis, Sébastien Mouchet

Switchable nonlocal organic metasurfaces 899
Dongqing Lin, Yulong Duan, Magnus Jonsson

Bio-inspired photonic devices as a platform for quantum photonics 900
Oliver Trojak, Sean Gorsky, Fabrizio Sgrignuoli, Felipe Pinheiro, JinDong Song, Luca DalNegro, Luca Sapienza

Spatial Memory of Hot Carriers in Disordered Plasmonic Structural Colors 901
Manobina Karmakar, Ayon Jyoti Karmakar, Aritra Biswas, Mahdi Soudi, Tianyi Guo, Pablo Cencillo Abad, Prasanta Kumar Datta, Debashis Chanda

Metasurface tongues as universal liquid sensors 902
Justin Sperling, Finlay Walton, Daniel Osborne, Badri Aekbote, Anthony Perri, Rebecca Setford, Hanyu Gao, Liam Wilson, Chad Sipperley, Rudolf Schick, Baptiste Poursat, Caroline Gauchotte-Lindsay, William Peveler, Alasdair Clark

Structural Dyes by Design: Physics-Guided Photonic Colour Modules on Commodity Substrates 903
Hannah Sanford-Crane

Dynamically Tunable Structural Colors 905
Aritra Biswas, Debashis Chanda

Reversible and Dynamic Photonic Bandgap Modulation via Chemical Reactions in Liquid Crystalline Polysaccharides 906
Cecile Chazot, Simona Fine, Nina Hildenhagen, Bart Jan Ravoo

Tunable “Meta”-Optical Fibers for Ultrawide-FieldBio-Imaging 908
Howard Lee, Andrew Palmer, Yucheng Jin, Jin Yan, Harvey Lin, Albert Teoh, Emma Wallace-Wilmot, Sophia Turean

When ‘meta' meets ‘materials': innovative materials, fabrication, functionalities 909

Exploiting strong confinement of light in hybrid self-assembled metamaterials 910
Anton Bykov, Nicolas Spiesshofer, Charalambos Louca, Tabitha Jones, Lille Borresen, Nima Taghipour, Jeremy J. Baumberg

Light and molecules at the nanoscale 911
Pablo Alonso-González

Publishing in Nature Portfolio 912
Rachel Won

Interband plasmonic elemental materials for sustainable nanophotonics: widening the spectral range 913
Johann Toudert, Fernando Chacon-Sanchez, Rosalia Serna

Chiroptical Emergence in Disordered Plasmonic Assemblies 915
Aso Rahimzadegan, Zihao Lu, Thomas G. Parton, Sinuhe Perea-Puente, Antonio Carone, Jessica Ma, Emeline Raguin, Bruno Frka-Petesic, Aurimas Narkevicius, Junyoung Kwon, Heather F. Greer, Nicholas A. Kotov, Kevin Vynck, Silvia Vignolini

Disorder silica microsphere coating for efficient sub-ambient radiative cooling 917
Jorge Burgos, Ares Lládos, Sara Nuñez-Sánchez, Ceferino López, Juliana Jaramillo, Pedro David García

Silicon metasurfaces for thermal control of classical and quantum light 919
Agostino Di Francescantonio, Omer Can Karaman, Giulia Tagliabue

Designer metasurfaces from the bottom-up 920
Beniamino Sciacca

Directed Self-Assembly of Block Copolymers for Ultra-High-Resolution Gold Metasurfaces and Photonic Crystals 921
Achmad Putranto, Hong Li, Martin Kogelschatz, Guillaume Fleury, Sébastien Cavalaglio, Badreddine Smiri, David Fuard, Camille Petit-Etienne, Raphael Ramos, Redouane Borsali, Marc Zelsmann

Engineered 3D Topological Eutectics: Tailoring Dirac-Rashba Interfaces via Directional Solidification for Advanced Spin-Orbitronics 922
Kingshuk Bandopadhyay, Krzysztof Markus, Andrzej Materna, Federico Mazzola, Dorota Anna Pawlak

Tamm plasmon laser diodes 924
Joel Bellessa, Maël Laupretre, Clémentine Symonds, Jean Michel Benoit, Aristide Lemaitre

Photoluminescence Modulation in Self-Coupled Molecular Cavities 925
Evan S. Hyunkoo Kang

US Defense Perspective on Past and Future of Metamaterials 926
Mark S. Spector

Geometry Matrix: From Physical Model to Computational Framework 927
Alonso Moreta, Mateo Perez, Karen Caicedo, Ashod Aradian, Alessandro Veltri

Silicon Nanoparticle Monolayer Coating for Glossy, Non-Iridescent and Tunable Reflective Colors 928
Hiroshi Sugimoto, Jialu Song, Keisuke Moriasa, Mojtaba Karimi Habil, Minoru Fujii

Nanometer-Precision Optical Metrology of Large Area Nanoimprinted Metasurfaces 929
Jaime Gomez Rivas, Masoumeh Goudarzi, Sunghwan Jo, Maira Perez Sosa, Yu-Chen Wei, Matthijs Berghuis, Mohammad Ramezani, Agustín Mihi

Metasurface Stickers for Tailoring Photoluminescence and Inducing Chirality 930
Shunsuke Murai, Koichi Okamoto

Phase Transition Driven Nanoparticle Assembly in Multicomponent Systems based on Liquid Crystals 932
Piotr Lesiak, Natalia Kasian, Anna Kozanecka-Szmigiel, Jan Bolek, Karol Kakarenko, Natalia Kowalska, Wiktor Lewandowski, Tomasz Woliński

Optical Metrology of Chiral and Strain Engineered Metasurfaces 933
Fabian Haake, Marcello Pozzi, Theresa Stecher, Henning Galinski

Engineering Silicon Optical Properties via Metal-Assisted Chemical Etching 934
Gilles Bourret

Nondestructive testing of metamaterials by Photoacoustic and Photothermal Techniques 935
Roberto Li Voti, G. Leahu, E. Petronijevic, C. Skubisz, A. Maurizi, G. Lalle, G. Cesarini, M. C. Larciprete, M. Centini, A. Belardini, C. Sibilia

Non-Hermitian Photonics - Topological, Disordered and Quantum systems 936

Non-Ergodic Extended Phase for Electromagnetic Waves in 3D Non-Hermitian Disordered Media 937
Marcus Prado, Romain Bachelard, Robin Kaiser, Felipe Pinheiro

Anomalous surface response in a non-Hermitian Weyl semimetal 939
Yidong Chong, Shuxin Lin, Rimi Banerjee, Zheyu Cheng, Kohei Kawabata, Baile Zhang

Solitons Mediated by Skin-Mode Localization and Band Nonreciprocity 940
Kun Ding

Machine Learning for Drawing Phase Diagrams of Nonlinear Optical Resonators with 1D Su-Schrieffer-Heeger Lattice 942
Chukwunaedum Patrick Izediuno, Ghada Alharbi, Zeeshan Ahmad, Stephan Wong, Sang Soon Oh

Measurement-Induced Crossover of Quantum Jump Statistics in Postselection-Free Many-Body Dynamics 944
Kazuki Yamamoto, Ryusuke Hamazaki

Topological insulator-based quantum optical sensor arrays 945
Harry Zheng, Arnab Banerjee, Peter Bermel

Scattering Properties of non-Hermitian Resonant Systems Explored Through the Generalized Wigner-Smith Operator 947
Nadav Shaibe, Jared Erb, Thomas M. Antonsen, Steven Anlage

Topological perfect transition in one-dimensional multi-orbital photonic lattices 949
Polette Parra-Palavecino, Diego Roman-Cortes, Rodrigo Vicencio

Programmable Anisotropic Exceptional Points in Passive Multiport Scattering Networks 951
Kaiyuan Wang, Niall Byrnes, Matthew Foreman

Nano-Lasers, Spasers, and Nanostructures with Quantum Elements 953

Temporal coherence properties of an aluminum nanocone lattice laser 954
Tiziana Cesca, Elizabeth Mendoza-Sandoval, Giuseppe Pirruccio, Giovanni Mattei

Quantum Nonlinear Response of Emitter Lattices 956
Blas Durá-Azorín, Antonio I. Fernandez-Dominguez, Alejandro Manjavacas

Chiral light from exceptional points in a coupled nanolaser ring array 957
Kaiwen Ji, Melissa Hedir, Ramy El Ganainy, Li Ge, Alejandro M. Giacomotti

Assembled Nanocrystal Lattice Nanolasers 959
Mindaugas Juodėnas, Nadzeya Khinevich, Gvidas Klyvis, Domantas Peckus, Joel Henzie, Tomas Tamulevičius, Sigitas Tamulevičius

Vortex nanolaser based on a photonic disclination cavity 961
Hong-Gyu Park

Optical Response of Active Plasmonic Nanoshells with Retardation and Gain Saturation Effects 963
Luis Cerdán

Controlling light-matter interactions with engineered nanolaser patterns 965
Dávid Vass, Miklós Waldhauser, Virág Szünstein, András Szenes, Balázs Bánhelyi, Mária Csete

Design for a qBIC laser based on a TiO2metasurface 967
Justin Schulz, Jack Dobie, Yongliang Zhang, A. Louise Bradley

Robust Perovskite Quantum Dots for Microcavity Photonics 970
Yu-Hsun Chou

Plasmonics and Nanophotonics: Fundamentals and Applications 972

Twist photonics in 2D materials 973
Yunyun Dai

Universal detection of layer-breathing modes in two-dimensional materials enabled by plasmonic nanocavity 974
Miao-Ling Lin, Heng Wu, Ping-Heng Tan

Chiral Plasmonic Nanoparticles 976
Jianfang Wang

Controllable Self-Assembly of Gold Nanoparticles with Concave Geometries 977
Limin Qi

Transition Metal-CO Bond: sigma-bonding or pi-bonding? 978
Zhen-Chao Dong

Rational Design and Applications of Intrinsically Chiral Plasmonic Nanoparticles 979
Xiaolu Zhuo, Yilin Chen, Shengyan Wang, Zhongyi Chen, Ruiqian Zhang, Jianfang Wang

Plasmonic Control of Dark Excitons and Valley Coherence in TMDC Monolayers under Ambient Conditions 980
Lei Shao

Interaction between Plasmonic Nanostructures and 2D Semiconductor Materials 981
Hong Wei

Controlling Activity and Selectivity through Charge-Flow Engineering in Plasmonic Catalysis 982
Yicui Kang, Bart de Nijs, Emiliano Cortés

Quantum Quasinormal Mode Theory for Spatio-Temporally Resolved Magnetodielectric Cavity Quantum Electrodynamic 985
Lars Meschede, Daniel D. A. Clarke, Ortwin Hess

Commercialization of Metasurface and Nanophotonic Devices 988

Building the Innovation Pipeline: Leveraging Princeton Core Facilities and Statewide Resources for Photonics Commercialization 989
Alexander Norman

Azopolymer photomorphing as holographic lithography for reconfigurable structured surfaces 990
Marcella Salvatore, Stefano Luigi Oscurato

A Scalable Structural-Color Nanocavity Platform for Stain-Free Digital Pathology 991
Qizhe Chen, Qiaoqiang Gan

Twenty Years of Research in Subwavelength Grating Metamaterial Integrated Photonics:From Fundamentals to Real-World Impact 993
J. Gonzalo Wanguemert Perez, Alejandro Ortega-Moñux, Robert Halir, Pavel Cheben, Jens H. Schmid, José Dario Sarmiento-Merenguel, Alejandro Maese-Novo, Pablo Ginel-Moreno, Iñigo Molina-Fernández

Photonic Band Gap Robustness of Stealthy Hyperuniform Metamaterials 994
Manuel Gallego, Uzair Malik, Yezhezi Zhang, Michael A. Klatt, Claire F. Gmachl

Application focused meta-surface design: workflow, methods & examples 996
Lieven Penninck, Chris Beckerleg, Bavo Robben

Metal oxide metasurfaces elaborated by nanoimprint and derived methods 997
David Grosso, B. Kerzabi, M. Abbarchi, M. Putero, A. Gourdin, M. Bouabdellaoui, E. Daher, L. Weber

Applications of azopolymers in planar diffractive optics and dynamic microstructure lithography 999
David McGee, Christopher Baker, Coleman Huetz, Brielle Zemer

Plasmonically powered organic light emitting devices for advanced display applications 1000
Haridas Mundoor, Michael Fusella, Gearht VanVoorhis, Mathew Philippou, Renata Saramak, Vinod Menon, Nicholas Thompson, Mike Weaver, Julie Brown

Metasurface Electrodes for Enhanced Light-Matter Interactions in Organic Light-Emitting Materials and Devices 1001
Deirdre O'Carroll, Sneha Sreekumar, Keshan Perera, Haydee Pacheco

Agentic photonic simulation with Tidy3D 1003
Zongfu Yu, Yannick Augenstein

Inverse Designed Flat Optics for Extended Depth of Focus Laser Beam Shaping 1004
Rajesh Menon, Apratim Majumder, Tina M. Hayward, Nicole Brimhall, Vishwa Pal, Kamal P. Singh

Metaoptics metrology using a wave front sensor 1006
Matthieu Ansquer, Nolan Chan, Benoit Wattellier

Towards chiral and magnetoelectric quantum electrodynamics 1008

Mechanisms of noise immunity in quantum nonlinear and nonreciprocal dynamics 1009
Nicholas Rivera

Triangular cross-section Möbius resonators: electromagnetic helicity and experimental observation of mode-dependent Berry phases 1010
Jeremy Bourhill, Emma Paterson, Maxim Goryachev, Michael Tobar

Spin-selective Structural Phase Transitions in Chiral Crystals Driven by Chiral Phonon Condensation 1012
Shun Asano, Youichi Yanase

Deterministic generation of a large-scale multi-photon GHZ state 1014
Zu-En Su, Dan Cogan, Oded Kenneth, David Gershoni

Exponentially-enhanced sensing with a frequency-encoded bosonic Kitaev chain 1015
Paul-Édouard Blanchard, Alexander McDonald, Philippe St-Jean

Enhanced Microwave-to-Optical Quantum Transduction with Optomechanical Nanobeam Heterostructures 1016
Akihiko Sekine, Ryo Murakami, Yoshiyasu Doi

Cavity control of Kondo physics in two-dimensional materials 1017
Jun Mochida, Yuto Ashida

Induced angular momentum from axion electrodynamics of metals and insulators 1019
Flavio Nogueira, Anastasiia Chyzhykova, Vira Shyta

Large topological magneto-optical effect from atomic-scale skyrmion-like texture 1020
Yoshihiro Okamura

Valley assisted Orbital angular momentum of light detection 1021
Jiang Hao, Yan Zhang, Weibo Gao

Extraction of Circularly Polarized Single Photons from Linearly Polarized Emitters 1024
Sarah Lindner, Peter Banzer

Bulk-Edge Correspondence in Photonic Spacetime Insulators 1025

João Câmara Serra, Rudin Kraja, Foster Sabatino, Alexander Khanikaev, Mário Silveirinha

Time-Varying Metamaterials for Synthetic Motion 1028
Satoshi Tomita

Inverse Design in Nanophotonics: From Diffusion Models to Time-Domain Adjoint Optimizations 1029
Mingyu Park, Seunghyun Lee, Jinseong Bae, Donghyun Kim, Chanik Kang, Kyungmin Kim, Donghyun Park, Dongjin Seo, Soobin Um, Haejun Chung

Theoretical prediction and experimental testing of photon emission directionality in spontaneous and stimulated emission 1031
Valerica Raicu, Michael Stoneman

Landau polaritons and cavity-driven attractive interactions in single and bilayer graphene 1033
Giacomo Scalari, Elsa Jöchl, Felix Helmrich, Lucy Hale, Lorenzo Graziotto, Atac Imamoglu, Tobia Nova, Jérôme Faist

MEQED and Bianisotropy 1035
Eugene Kamenetskii

Quantum Noise Spectroscopy of Chiral Quantum States 1036
Benjamin Lawrie

Plasmonic Nanomaterials for Bio-diagnostics, Environmental Monitoring and Food Safety 1038

Vanadium Dioxide Nanoparticles: A Platform for Tuning Localized Surface Plasmons 1039
Michal Horák, Jiří Kabát, Rostislav Řepa, Jordan A. Hachtel, Peter Kepič, Vlastimil Křápek, Andrea Konečná, Tomáš Šikola

Correlation Spectroscopy based Nanobiosensor: Application for Cu-Zn Superoxyde Dismutase detection 1041
Mohand Chalal, Abdelhak Dhibi, Nordin FELIDJ, Nadia Djaker

Decoding Intracellular Microenvironment by SERS 1043
Aleksandra Szaniawska, Agnieszka Girstun, Katarzyna Bogusz, Justyna Grzeda, Aleksandra Miszczak, Hubert Sobiech, Katarzyna Wlecial, Andrzej Kudelski

Multimetallic plasmonic nanoparticles for colorimetric sensing 1045
Vincenzo Amendola

Low-Power Plasmonic Strategies for Nanoscale Analyte Transport and Trapping 1046
Aliaksandra Rakovich, Marciano Palmo do Carmo, David Mack, Diane J. Roth, Miao Zhao, Ancin M. Devis, Francisco Rodriguez-Fortuño, Stefan A. Maier, Paloma A. Huidobro

Fluorescence-based chiral sensingwith silicon metasurfaces 1049
Tom T.C. Sistermans, Artemijs Krimovs, Robert Pal, Alberto G. Curto

Smart materials for thermal management by utilizing environmental sensing 1051
Duncan Sutherland, Xavier Gonzalez

Resonant Heat Transfer for Efficient Off Grid Photothermal Desalination 1052
William Schmid, Qian Ye, Aleida Machorro-Ortiz, Peter Nordlander, Naomi J. Halas, Alessandro Alabastri

Micro and Nanolasers for Biomolecular Detection 1054
Soraya Caixeiro

Hybrid Photonic-Electronic Tapered Optical Fibers for Multimodal Neural Interfacing 1055
Ferruccio Pisanello, Linda Piscopo, Barbara Spagnolo, Antonio Balena, Sneha Pottekad, Claudia Lattebovio, Giulio Mastrototaro, Muhammad Fayyaz Kashif, Cinzia Montinaro, Stella Aslanoglou, Mohammadrahim Kazemzadeh, Antonio Qualtieri, Massimo De Vittorio

Disordered Plasmonic Metasurfaces: From Scalable Fabrication to Imaging Applications 1057
Doeun Kim, Juhwan Kim, Gyurin Kim, Youn Ju Na, Hyeon-Ho Jeong

Silver Bullet - Vaterite-Based Metamaterials for Controllable ROS Generation in Biomedicine **1059**
Pavel Bezrukov, Hani Barhum, Pavel Ginzburg

Free-Electron-Driven Chip-Scale Mercury-Free Broadband UV Light Sources with Ultrahigh Germicidal Efficiency **1061**
Vijay Kumar Sharma, Hilmi Volkan Demir

Engineering FRET mechanism via plasmonic systems for ultra-sensitive biosensing **1062**
Vincenzo Caligiuri, Olga Favale, Ferdinanda Annesi, Angela Candreva, Massimo La Deda, Marco Filice, Marzia Marciello, Antonio De Luca

Towards Point-of-Care and Food Safety Applications of SERS for Shiga Toxin Detection **1065**
Alessia Milano, Amalia D'Avino, Valentina Marchesano, Domenico Sagnelli, Massimo Rippa, Bryan Guilcapi, Lu Zhou, Maurizio Brigotti, Gianluigi Ardissino, Stefano Morabito, Lucia Petti

On-chip biosensing by Surface Plasmon Resonance of antibiotic and insecticide residues in real samples **1068**
Salvatore Moschetto, Kelment Zahoaliaj, Mario Prosa, Andrea Lorenzoni, Jeroen Peters, Stefano Toffanin, Erik Beji, Margherita Bolognesi

Hybrid Plasmonic-Photonic Platforms for Enhanced Biosensing and Optical Information Processing **1070**
Alessio Buzzin, Nicolas Hanine, Lorenzo Giannini, Michela Baiocchi, Angelica Focardi, Ahmadreza Alaeddini, Badrul Alam, Rita Asquini

DNA identification using surface-enhanced Raman spectroscopy and surface plasmon resonance **1073**
Andrzej Kudelski

Thermal management of plasmonic nanoparticles using 2D materials for single-molecule biosensing **1074**
Peter Zijlstra

Electronic precursors to bond formation and controller reaction pathways in single-molecule junctions **1075**
Kristina Rusimova

Plasmonic nanofibers for neurochemical monitoring **1076**
Jean-Francois Masson, Maryam Hojjat Jodaylami, Ailsa Geddis

Self-Assembly Nanostructures for Highly Sensitive SERS Platforms **1077**
Maria Alessandra Cutolo, Francesco Galeotti, Sara Spaziani, Giuseppe Quero, Mohammed Janneh, Alberto Micco, Andrea Irace, Giovanni Breglio, Marco Pisco, Andrea Cusano

Pesticide Recognition in Water Using Silver Plasmonic SERS Nanostructures Assisted by PCA **1078**
Massimo Rippa, Alessia Milano, Valentina Marchesano, Domenico Sagnelli, Bryan Guilcapi, Amalia D'Avino, Anna De Girolamo Del Mauro, Lucia Petti

Low-Cost Flexible SERS Platforms for On-Site Detection of Bacterial and Viral Pathogens in Wastewater **1080**
Amalia D'Avino, Alessia Milano, Valentina Marchesano, Bryan Guilcapi, Domenico Sagnelli, Massimo Rippa, Lucia Petti

Photonics on multimode optical fibers **1082**
Linda Piscopo, Di Zheng, Muhammad Fayyaz Kashif, Annabella La Grasta, Tadele Orbula Otomalo, Liam Collard, Alessandra Corrado, Antonio Balena, Cinzia Montinaro, Massimo De Vittorio, Ferruccio Pisanello

Topological Bound States in the Continuum in Photonic Crystal Slabs for Label-Free Biosensing **1084**
Karen Caicedo, Silvia Romano, Gianluigi Zito, Ivo Rendina, Vito Mocella

Flowthrough Raman readout in plasmonic nanopores for sequencing applications **1086**
Francesco De Angelis

Metamaterials and Metasurfaces as Platforms for Next-Generation Electromagnetics: Fundamentals, Applications and Future Trends 1087

Communicating and Computing with Microwave Networks 1088
Matteo Nerini, Bruno Clerckx

Universal Wave-Control Framework for Reconfigurable Microwave Systems 1089
Philipp del Hougne

Compressive Metasurfaces for Communications and Imaging Applications 1091
Okan Yurduseven, David R. Smith

Self-Organized Photonic Metasurface Synthesis Inspired by Morphogenesis 1092
Thomas Fromentèze, Marco Gandolfi, Andrea Locatelli, Costantino De Angelis, Emebet Woldu Hadgu, Rapha¨el Pestourie

Physical Neural Networksfor Wireless Communications 1093
Marco Di Renzo

Analysis and Simulation of Intrinsic Response Time of Time-Varying Metasurfaces 1094
Sheng Lei, Alex Man Hon Wong

Transformer-based Neural Network Enabled Subpixel-Resolution in Wide-Field Meta-Microscope 1096
Shanshan Hu, Tao Li

A Machine-Learning-Enabled Metasurface Adapting to the Environment 1098
Thijs van Rossum, Thomas Koschny, Philippe Tassin

Topological Insulator Metamaterials 1100

Reconfigurable Topological Insulators and Acoustic Devices Based on an Electroacoustic Material Platform 1101
Michael Leamy

A spectral localizer approach for Floquet insulators 1103
Stephan Wong, Alexander Cerjan, Justin Cole

CVD-Synthesized PtTe□ Nanoribbon Arrays for Tunable Mid-IR Polarized Photocurrent via SPP Control 1104
Christian Martella, Alessandro Molle

Magnetic Response Enhancement in Topological Insulator Metamaterial Hybrid Layers 1105
Qiang Sun, Eitan Dvorquez, Felipe A. Pinto, Mohan C. Mathpal, Jeronimo R. Maze, Brant C. Gibson, Andrew D. Greentree

Terahertz non-linear optics in van der Waals topological insulator metamaterials 1106
Miriam Serena Vitiello

Graphene and Topological Insulator Metamaterials for Terahertz Applications 1107
Klaas-Jan Tielrooij

Exceptional points can enable lower-Q modes to lase first 1108
Julius Kullig, Qi Zhong, Jan Wiersig, Ramy ElGanainy

Directional Solidification as a Platform for Bulk Plasmonic and Metamaterial Composites 1109
Dorota Anna Pawlak, Kingshuk Bandopadhay, Krzysztof Markus, Andrzej Materna, Ali Abbas, Hamid Reza-Darabian, Piotr Piotrowski, Monika Tomczyk, Katarzyna Sadecka, Nada Aghad

Topological Metamaterials Driven Study of the Dielectric Response of the Cancerous Biological Tissue 1110
Tatjana Gric

Inverse design, topology optimization, and machine learning 1111

Algorithm-driven Design for Functionally Multiplexed Metasurfaces 1112
Wei Ma, Yuhang Wang

Adjoint-Based Characterization of Anisotropic and Bianisotropic Metamaterials Guided by Group Theory 1114
Edgar Bustamante, Denis Ridzal, Ihab Fathy El-Kady

Large-Scale Photonic Inverse Design for Co-Optimized Photonic Systems 1116
Geun Ho Ahn

Resolution and Robustness Bounds for Reconstructive Spectrometers 1117
Yidong Chong, Changyan Zhu, Hsuan Lo, Jianbo Yu, Qi Jie Wang

Symmetry-Informed Deep Learning for Scattering Parameter Prediction 1119
Viktor Aadland Lilja, Philippe Tassin

Inverse design of OPA beam steering correction meta optics 1121
Joao Cunha, Filipe Camarneiro, João Borlido, Patrícia C. Sousa, Diogo Aguiam

Quantum Matter and Dynamics in Hybrid Metamaterial Platforms 1123

Engineering van der Waals Materials for Quantum Optical Emission 1124
Shengxi Huang

Topological plasmonics: A study of a non-Hermitian Su-Schrieffer-Heeger chain 1126
Flore K. Kunst

Nonlocal and nonlinear nanophotonics 1127

Integrated Nonlinear Photonics for Compact Terahertz and Quantum Devices 1128
Shima Rajabali

GaAs nanowires as a tunable source of polarization-entangled photons 1129
Elise Bailly-Rioufreyt, Zoya Polshchykova, Grégoire Saerens, Wenhe Jia, Helena Weigand, Thomas Dursap, Andreas Maeder, Philippe Regreny, Robert Chapman, Alexandre Danescu, Nicolas Chauvin, José Penuelas, Rachel Grange

Metasurface-controlled external cavity tunable lasers 1131
Zahra Basiri, Alessandro Tomasino, Gabriel Juelg, Andrea Lanfranchi, Ileana-Cristina Benea-Chelmus

Enhancing the Kerr-effect in nonlinear media for mid-IR single-photon detection at room temperature 1133
Richarda Niemann, Ke-Sean J. Peter, Maxwell J. Tolchin, Jon-Paul Maria, Sahin Ozdemir, Nathaniel Kinsey, Durdu Guney, Joshua D. Caldwell

Phonon-Enhanced Sum-Frequency Generation Spectro-Microscopy of Hexagonal Boron Nitride 1135
Niclas Sven Mueller, Alexander P. Fellows, Nasim Mirzajani, Purbita Kole, Mira Kreßler, Kyoungpyo Lee, Ben John, Andrew E. Naclerio, Tao Yang, Christian Carbogno, Katayoun Gharagozloo-Hubmann, Damián Baláž, Ryan A. Kowalski, Hendrik H. Heenen, Christoph Scheurer, Karsten Reuter, Joshua D. Caldwell, Martin Wolf, Patryk Kusch, Xiaoqin Li, Piran R. Kidambi, Martin Thämer, Alexander Paarmann

Probing Low-Frequency Excitations with Visible Light and Electron Beams 1137
Leila Rocio Prelat, Eduardo J.C. Dias, F. Javier García de Abajo

Limitations and Opportunities in Second Order Nonlinear Optical Materials: The Role of the Penn Gap 1139
Jacob Khurgin

Using material and structural resonances to shape photon pair emission by four-wave mixing 1140
Hua Li, Omer Can Karaman, Valeria Vento, Giulia Tagliabue, Christophe Galland

Nonlinear Self-Action Driven by Quasi-Bound States in the Continuum **1142**
Alfonso Nardi, Sonia Freddi, Michael Scalora, Agostino Di Francescantonio, Johann Osmond, Attilio Zilli, Marco Finazzi, Michele Celebrano, Monica Bollani, Maria Antonietta Vincenti

A Boundary Element Method Solver for Dispersive Feibelman Parameters in Plasmonics **1144**
Ulrich Hohenester, Lorenz Huber

Mapping Nonlocal Bulk Continuum to Few Surface Modes **1145**
Runzhi Zou, Qiang Zhou, Pu Zhang, Xue-Wen Chen

On An Integral-Equation Method in Quantum Hydrodynamics: Efficiency and Convergence Issues **1147**
Christos Mystilidis, Xuezhi Zheng, Christos Tserkezis

Probing the extreme optical field around plasmonic nanocavities **1148**
Hongli Zhou, Shunping Zhang

Lattice Resonances in Periodic Arrays of Time-Modulated Scatterers **1149**
Juan Ramon Deop-Ruano, María Blanco de Paz, Diego M. Solís, Alejandro Manjavacas

Nonlocal metasurfaces controlling the geometric phase and direction of light **1150**
Adam Overvig

Single-cycle optical nonlinearity of transparent conducting oxides explained **1151**
Ieng-Wai Un, Subhajit Sarkar, Yonatan Sivan

Hydrodynamic model for nonlocal electrodynamics effects in ultra-confined plasmons **1152**
André Jorge Chaves, Tiago Barbosa, Line Jelver, Simão Cardoso, Diego Costa, Leonardo Campos, Ingrid Barcelos, N. Asger Mortensen, Nuno Peres

Nonlocal and Nonlinear Effects in Plasmonics from a Time-Dependent Density Functional Theory Perspective **1154**
Antton Babaze, Javier Aizpurua, Andrei G. Borisov

Controlling the optical response of 2D semiconductors with THz pulses **1156**
Tommaso Venanzi, Marzia Cuccu, Edith Wietek, Xiaoxiao Sun, Raul Perea-Causin, Samuel Brem, Daniel Erkensten, Takeshi Taniguchi, Kenji Watanabe, Ermin Malic, Manfred Helm, Stephan Winnerl, Alexey Chernikov

Mid-infrared nonlinearity in heavily-doped semiconductor nanoantennas and waveguides **1158**
Michele Ortolani, Raffaella Polito, Maria Gambelli, Enrico Bau, Andreas Tittl, Luca Lucia, Adel Bousseksou, Raffaele Colombelli, Gregoir Beaudoin, Isabelle Sagnes, Huatian Hu, Gonzalo Alvarez-Perez, Cristian Ciraci, Enrico Talamas Simola, Monica De Seta, Sara Cibella, Francesco Mattioli, Andrea Notargiacomo, Marialilia Pea, Tommaso Venanzi, Valeria Giliberti

Remote Nonlinear Imaging of Hyperbolic Phonon Polaritons using Sum-Frequency Microscopy **1160**
Richarda Niemann, Gonzalo Álvarez-Pérez, Ana Isabel F. Tresguerres-Mata, Enrique Teran-Garcia, Dorotheé Mader, Niclas Sven Mueller, Sören Wasserroth, Martin Wolf, Aitana Tarazaga Martín-Luengo, Javier Martín-Sánchez, Pablo Alonso-Gonzáles, Alexander Paarmann

Prospects to bypass metal nonlocal phenomena using phonon-polaritons **1162**
Jacob Terndrup Heiden, Eduardo J.C. Dias, Minhyuk Kim, Martin Nørgaard, Vladimir A. Zenin, Sergey G. Menabde, Hu Young Jeong, N. Asger Mortensen, Min Seok Jang

Nonreciprocal plasmons in nanostructured graphene **1164**
Joel D. Cox

Quantum Plasmonics in Metals and Emerging Applications of Graphene Plasmons **1166**
P. André Gonçalves

Quantum Hydrodynamic Theory with a frequency-dependent kinetic-energy kernel in real-space **1167**
Lucian A. Constantin, Fabio Della Sala

Shaping Light and Matter in Non-Perturbative Light-Matter Coupling Regimes **1168**
Erika Cortese, Johannes Bürger, Simone Di Muzio, Dario Ballarini, Simone De Liberato

Geometric Phase Wavefront Shaping in Nonlinear Meta-Optics: From Tensor-Driven Phase to **1169**

Nonlocal Metasurfaces
Luca Carletti

Quantum and emitter-size effects in emitter-plasmon interactions **1170**
Tadele Orbula Otomalo, Gabriel Gil, Gonzalo A-Perez, Huatian Hu, Ferruccio Pisanello, Stefano Corni, Fabio Della Sala, Cristian Ciraci

Tunability of nonlinear plasmonics in nanostructured 2D materials **1171**
Line Jelver, Joel D. Cox

Excitation of Dark Modes and Multipole Plasmons via Surface-Response Function **1173**
Fan Yang

Electro-Optic Phonon Polaritons **1174**
Michael Spencer, Olga Minakova, Maximilian Frenzel, Joanna M. Urban, Martin Wolf, Sebastian F. Maehrlein

Nonlocal Optical Response of Phonon-Polaritonic Nanoparticles **1176**
Yina Wu, Fadil Iyikanat, Vahagn Mkhitaryan, Eduardo J. C. Dias, Andrea Konečná, Jordan A. Hachtel, F. Javier García de Abajo

New trends in light-matter interaction at the nanoscale 1178

The Impact of Dark Excitons on Polariton Spatiotemporal Dynamics in 2D Semiconductors **1179**
Jamie Fitzgerald, Roberto Rosati, Ermin Malic

Electrical excitation of surface plasmons and light **1181**
Elizabeth Boer-Duchemin

Organic Hyperbolic Metamaterials and Nanostructures for Light-Matter Interactions **1182**
Sara Núñez Sánchez

Brewster Quasi-BICs in Out-of-Plane Symmetry Broken Nanodisk Metasurfaces **1183**
Beatriz Castillo, Lucia Hidalgo-Orteaga, Antonio García-Martín, Diego Romero Abujetas, José Antonio Sánchez-Gil

Electron-beam spectroscopy simulations using the T-matrix method **1185**
Elli Stamatopoulou, Carsten Rockstuhl

Within and Beyond the Photon Beam: 3D Electrokinetic Mapping to Manipulation of Optical Matter **1187**
Roger Bresoli Obach, B. Louis, J. Hofkens, H. Masuhara, M. I. Marques, J. Olmos, R. Delgado-Buscalioni

Quantitative Analytical Model for Scattering-type Scanning Near-field Optical Spectroscopy **1189**
Kirill Voronin, Rainer Hillenbrand, Alexey Y. Nikitin

Tailoring the Optical Properties of Random Metasurfaces for Multifunctional Applications **1190**
Alejandro Reyes-Coronado, Jonathan A. Urrutia-Anguiano, Isabel Y. Rojas-Martinez

Active light steering with electron beams **1192**
Eduardo J.C. Dias, Álvaro Rodríguez-Echarri, Theis Rasmussen, F. Javier García de Abajo, Joel D. Cox

Multi-Electron Effects in Free-Electron Beams: Light Generation and Electron-Electron Correlations **1194**
Valerio Di Giulio, Rudolf Haindl, Armin Feist, Claus Ropers

Free electrons shape light, light shapes free electrons **1197**
Alvaro Rodriguez Echarri

Scaling Up Light-Matter Interactions - Challenges in Fabrication **1198**
Rijil Thomas

Directional Energy Delivery at the Nanoscale: The Iris-Gated Approach for Photothermal Applications **1200**
Javier González-Colsa, Jose M. Saiz, Alfredo Franco, Dolores Ortiz, Francisco González, Fernando Bresme, Pablo Albella

Chiral Cavities Made from Lattices of Highly Electromagnetically-Chiral Scatterers 1201
Lukas Rebholz, Carsten Rockstuhl, Ivan Fernandez-Corbaton

Novel quantum effects in (Surface-Enhanced) Raman Scattering from molecular systems 1203
Adrian Juan-Delgado, Ruben Esteban, Lukas A. Jakob, Jean-Baptiste Trebbia, Shu Hu, Rakesh Arul, Roberto A. Boto, Quentin Deplano, Philippe Tamarat, Rémi Avriller, Niclas Sven Mueller, Diego Martın-Cano, Paloma A. Huidobro, Jeremy J. Baumberg, Brahim Lounis, Javier Aizpurua

Light management in high-refractive index semiconductor nanowires 1206
Nicklas Anttu

Photonic time crystals assisted by high-Q resonances 1207
Puneet Garg, Viktar Asadchy, Carsten Rockstuhl

Color Routing and Beam Steering of Single-Molecule Emission with a Spherical Silicon Nanoantenna 1209
Maria Sanz-Paz, Nicole Siegel, Guillermo Serrera, Javier Gonzalez-Colsa, Fangjia Zhu, Karol Kolataj, Minoru Fujii, Hiroshi Sugimoto, Pablo Albella, Guillermo Acuna

Theoretical characterization of tip-enhanced nanocavities for active control of vibrational signals 1211
Isabel Pascual Robledo, Philippe Roelli, Iris Niehues, Javier Aizpurua, Rainer Hillenbrand

Imaging the spatial distribution of tunneling-induced luminescence beyond the diffraction limit of light 1213
Elysé Laurent, Ricardo Javier Peña Roman, Sarah Miller, Aditi Raman Moghe, Etienne Lorchat, Séverine Le Moal, Elizabeth Boer-Duchemin, Luiz Fernando Zagonel, Stéphane Berciaud, Eric Le Moal

Nanoscale heat flow in laser-heated silicon nanospheres probed by pump-probe cathodoluminescence 1215
Saskia Fiedler, Evelijn Akerboom, Théo Soler, Loriane Monin, Hiroshi Sugimoto, Minoru Fujii, Wiebke Albrecht, Albert Polman

Infrared Magnetoplasmonics in Transparent Conductive Oxide Nanocrystals 1217
Alessio Gabbani

Surface-Enhanced Raman Scattering: Integrating Theoretical and Experimental Perspectives 1218

SERS Chemosensing of Metal Ions: Transduction Strategies and Interface Design 1219
Luca Guerrini

Time-Dependent Surface Enhanced Raman Scattering Simulations 1220
Giulia Dall'Osto, Stefano Corni

Operando SERS: From Molecular Spectroscopy to Plasmon-Driven Photochemistry 1221
Shashank Kumar Gahlaut, Ilko Bald, Radwan M. Sarhan, Biswajit Bhattacharyya

Plasmonic Nanopore Geometry Effects in Flow-Through Single-Molecule SERS 1222
Kirill Khabarov, Xinxin Liu, Ilaria Micol Baldi, Frank Niklaus, Francesco De Angelis

Materials for Surface-Enhanced Raman Spectroscopy Detection of Per- and Poly-fluoroalkyl Substances in Aqueous Film-Forming Foams 1224
Chuntao Wang, Kushal Biswas, Sangmin Jeong, Anila Bello, Dhimiter Bello, Michael Ross

From AI Design to SERS Spectral Shaping and Nanoplastics Detection with Metal Film over Nanospheres 1226
Cosmin Farcau, Ioana Cârdan, Ana Maria Mihaela Gherman, Fran Nekvapil

Simulating Surface-Enhanced Spectroscopies: The ωFQFμ Model 1228
Pablo Grobas Illobre, Tommaso Giovannini, Chiara Cappelli

Theoretical Investigation of Vibrational Imaging Induced by Electronically Forbidden Transitionsin Tip-Enhanced Raman Scattering 1230
Mamoru Tamura, Hiroyuki Ikagawa, Hajime Ishihara

Zwitterionic polymeric coacervates as plasmonic boxes for one-pot SERS biomarkers detection in biofluids 1233
Caterina Dallari, Francesca Torrini, Luisa Ponticelli, Silvia Bagnoli, Benedetta Nacmias, Valentina Bessi, Francesco Saverio Pavone, Paolo Arosio, Caterina Credi

SERS behavior of the antiepileptic drug cenobamate 1235
Lydia Federica Gervasini, Annachiara D'Urso, Emilio Ciusani, Alessia Cutri, Sebastiano Trusso, Paolo Maria Ossi, Andrea Lucotti, Matteo Tommasini

Nanoscale Phononics : Energy Transport, Light-Matter Coupling, and Emerging Applications 1237

Inelastic light scattering by metallic nanocrystals: symmetry, shape and chirality 1238
Lucien Saviot

Driving giant monochromatic THz strain waves in metal heterostructures by electronic pressure 1239
Matias Bargheer

Modeling the Acousto-Plasmonic Coupling: Raman Energy Density Framework 1241
Nicolas Large

Energy transfer from hot holes to phonons in photoexcited Germanium: ultrafast heating of Raman-active modes 1243
Jelena Sjakste, Raja Sen, Nathalie Vast

Unveiling Acoustic Phonon Dynamics via Time-Resolved Brillouin Spectroscopy of optophononic Resonators 1245
Carlos Montenegro, Elham Mehdi, Sandeep Sathyan, Edson Rafael Cardozo de Oliveira, Isabelle Sagnes, Martina Morassi, Aristide Lemaître, Norberto Daniel Lanzillotti-Kimura

Plasmon-Enhanced Brillouin Light Scattering Investigations of Acoustoplasmonic Metasurfaces 1246
Thomas Vasileiadis

Nanostructuration for Ultra-High Frequency Acoustic Wave Emission and Detection using Femtosecond Laser Pulses 1247
Arnaud Devos

Thermal Metamaterial Design for Phonon Heat Management at Low Temperature 1249
Boris Brisuda, Jon Canosa Diaz, Thierry Crozes, Jean-François Robillard, Olivier Bourgeois

Acoustic Phonons, Vibronic Coupling, and Room-Temperature Super-Radiance in Engineered, Icosahedral Virus Capsids 1251
Bogdan Dragnea

Approaching Ultimate Quality Factors in Nanomechanical Resonators Made of Silicon Carbide 1252
Eva Weig

Energy transport and switching in finite disordered networks 1254
Yann Chalopin

Non-Diffusive Nanoscale Phonon Heat Transport in 2D Materials 1256
Sebin Varghese, Jordi Tur Prats, Albert Beardo, Francesc Xavier Alvarez, Klaas-Jan Tielrooij

Anisotropic phonon dynamics at the nanoscale in a nanophononic SiN membrane 1258
Valentina Giordano, Silvia Mazzoleni, Stéphane Pailhès, Filippo Bencivenga

Surface Acoustic Waves and Spin Waves interaction in iron thin film 1259
Pauline Rovillain, Anupam Sharma, Florian Millo, Louis Christienne, Jean-Yves Duquesne, Mahmoud Eddrief, Franck Fortuna, Laura Thévenard, Catherine Gourdon, Massimiliano Marangolo

Experimental realization of Algorithm-designed Nanophononic Metasurfaces 1261
Michele Diego, Matteo Pirro, Jade Hardouin, Gabrielle Mazevet-Schargrod, Junior Rognon, Byunggi Kim, Roman Anufriev, Masahiro Nomura

Acoustic vibrations of single gold nanodisks supported on solid substrates 1263
Nathan Berrit, Clément Panais, Noëlle Lascoux, Sylvie Marguet, Natalia Del Fatti, Aurélien Crut

The optomechanics way to probe a single living cell 1265
Hilario Boggiano, Louis Waquier, Cherif Belacel, Ivan Favero

Mapping electrostatic and Casimir forces above metallic nanostructures using suspended nanowires 1266
Lucas Judéaux, Philip Heringlake, Hugo Weltz, Cattleya Dousset, Benjamin Pigeau, Olivier Arcizet

Vibrational dynamics of self-assembled nanoparticles 1269
Mohammad Imran Shaik, Nicholas Blanchard, Benoit Mahler, Jérémie Margueritat

Cavity Quantum Materials and Polaritonic Devices: From Microscopic Theory to Functionality 1272

Probing Cavity Polaritons via Scattering of Frequency-Entangled Biphoton States 1273
Andrei Piryatinski, Nishaant Jacobus, Sameer Dambal, Eric R. Bittner, Yu Zhang, Ajay R. S. Kandada

Cavity coupling of van der Waals heterostructures 1275
Gunda Kipp, Hope M Bretscher, Gaetan Membrez, Ethan Koskas, Lorenzo Graziotto, Felix Helmrich, Luca Somboli, Benedikt Schulte, Dorothee Herrmann, Kateryna Kusyak, Matthew W. Day, Sivasruthi Kesavan, Toru Matsuyama, Xinyu Li, Sara Maria Langner, Jesse Hagelstein, Felix Sturm, Alexander M. Potts, Christian J. Eckhardt, Yunfei Huang, Kenji Watanabe, Takashi Taniguchi, Angel Rubio, Dante M. Kennes, Michael Sentef, Emmanuel Baudin, Guido Meier, Christian Reichl, Giacomo Scalari, Werner Wegscheider, Marios H. Michael, James McIver, Jérôme Faist

Restoring Bloch's Theorem for Cavity Exciton Polaron-Polaritons 1278
Michael A. D. Taylor, Yu Zhang

META Quantum Nanophotonics Workshop 1280

Engineering Quantum Light with Perovskite Quantum Dots 1281
Yury Rakovich, Alexey Y. Nikitin, Virginia Martínez-Martínez, Andrey Rogach, Igor Aharonovich

Telecom-wavelength quantum nanophotonics with self-assembled quantum dots 1283
Nir Rotenberg

Subradiant entangled states in plasmonics and the quantization of radiative systems 1284
Angela Demetriadou

Quantum optical metasurfaces for photon pair generation 1287
Igal Brener

Ultrasensitive nanothermometry with single organic dye molecules 1288
Mohammad Musavinezhad, Jan Renger, Stephan Gotzinger, Alexey Shkarin, Vahid Sandoghdar

Thermalization of photons in disordered scattering media 1289
Valentina Krachmalnicoff, L. Soncin, Y. De Wilde, R. Pierrat, R. Carminati

Enhanced Plasmon-Emitter Coupling and Emission at the Single-Molecule Level 1290
R. Margoth Cordova Castro

Plasmonics and Nano-Optics 1292

Epsilon-near-zero mode in highly doped GaN thin films 1293
Julia Ingles-Cerrillo, Maria Villanueva-Blanco, Benjamin Damilano, Stéphane Vézian, Miguel Montes Bajo, Adrian Hierro

Symmetry enhanced modal design for magnetic emission from plasmonic core-satellite resonators 1296

Joshua Davis, Sébastien Bidault, Mathieu Mivelle, Mona Tréguer-Delapierre, Alexandre Baron

Nanostructured Cd(Zn)O for mid-infrared, near-field enhancement 1299
Miguel Montes Bajo, Pablo Ibañez-Romero, Javier Yeste, Eduardo Martínez Castellano, Maria Villanueva-Blanco, Andrea C. Illana, Fernando Gonzalez-Posada, Thierry Taliercio, Vicente Muñoz-Sanjosé, Adrian Hierro

Tunable coupling between conducting polymer nanoantennas and epsilon-near-zero thin films 1302
Suraya Kazi, Yulong Duan, Magnus Jonsson

Nanophotonics and Plasmonics Applications: Optical Antennas, Quantum Photonic Devices, and Beyond 1304

Switching Quantum Dot Microresonators by Ultrafast Laser Pulses 1305
Pietro Castronovo, Marco Reale, Susan A Rigter, Cherie R. Kagan, Christopher B. Murray, Salvatore Lorenzo, Erik C. Garnett, Peter Schall, Emanuele Marino, Alice Sciortino, Fabrizio Messina

Coupling-Controlled Exceptional Points in Intersubband Polaritonic Metasurfaces 1308
Beomjoon Kim, Hyeongju Chung, Gerhard Boehm, Mikhail A. Belkin, Jongwon Lee

Solving the Helmholtz equation with analog systems at telecommunications wavelengths 1311
Ross Macdonald, Andrew Naylor, Victor Pacheco-Peña

Chiral and Hyperbolic Metamaterials 1314

Inverse Faraday Effect and Gyrotropy in Time-Varying ENZ Films 1315
Domenico de Ceglia, Carlo Rizza, Michael Scalora, Maria Antonietta Vincenti, Wallace Jaffray, Sven Stengel, Marcello Ferrera

Carrier Drift Modulation and Hyperbolic Time Crystals 1318
Evgeniy Narimanov, Boris Shapiro

Metasurfaces: Flat Optics, FSS, HIS, and Beyond 1320

Reconfigurable Optical Imaging via a Wavelength-Driven Multifunctional Metasurface 1321
Hongliang Li, Yang Xiao, Yuning Ye, Jisen Wen, Xuechao Yu

SuperLattice Plasmon Mode in a Grating of 2D Electron Strips 1324
Alexey Shuvaev, A. R. Khisameeva, V. M. Muravev, K. R. Dzhikirba, A. A. Zabolotnykh, P. A. Gusikhin, M. S. Ryzhkov, D. A. Khudaiberdiev, A. S. Astrakhantseva, I. V. Kukushkin, A. Pimenov

Strong Coupling between quasi-bound states in the continuum and monolayer WS□ on a Si□N□ metasurface 1326
Yongliang Zhang, Oisin McCormack, Na Jia, Hodjat Hajian, Jack Dobie, Justin Schulz, Xia Zhang, Owen Moynihan, Brain Corbett, A. Louise Bradley

Wafer-scale fabrication of quartz-monolithic metalenses for the ultraviolet 1330
Jaewon Jang, Hui Jae Cho, Yeonsang Park

Colorimetric thermography by a long-infrared dual-band metalens 1332
Zhendong Luo, Peng Zhang, Yang Zhao, Mu Ku Chen

Passive and Reconfigurable Terahertz Logic Metasurfaces via Frequency and Orientation Multiplexing 1334
Mohammadhossein Momtazpour, Lei Xu, Dou Feng, Anjali Chaudhary, Dominic Craske, Costas Tsakonas, Cuifeng Ying, Demosthenes Koutsogeorgis, Miguel Navarro-Cía, Mohsen Rahmani

Deep-UV Photonic-Crystal Surface-Emitting Lasers with Sub-Degree Beam Divergence 1336
Philippe Tassin, Dogukan Apaydin, Hjalmar Andersson, Lukas Uhlig, Sarina Graupeter, Joachim Ciers, Giulia Cardinali, Erik Strandberg, Tim Wernicke, Michael Kneissl, Ulrich Theodor Schwarz, Asa Haglund

Tunable Emission Enhancement in Ge Filmsthrough All-Dielectric Metasurfaces 1338

Jon Schlipf, Diana Ryzhak, Giovanni Capellini, Paul Oleynik, Yuji Yamamoto, Inga Anita Fischer

Metamaterial-Based Devices 1340

Monolithic integrated meta-mirror color filter for 5K PPI OLED pixel 1341
Chi-Sun Hwang, Yong Hae Kim, Hyunsu Cho, Sunghoon Hong

Extreme field enhancement and anapoles in high-index tunable metamaterials 1343
Zoltan Sztranyovszky, Nicolas Spiesshofer, Caleb Todd, Rakesh Arul, Jeremy J. Baumberg, Angela Demetriadou

High-Efficiency Off-Grid-Positioned Metasurface Color Router for Sub-Micron CMOS Image Sensors 1346
PoHan Fu, Chin-Chuan Hsieh

Photonic Crystals and Electromagnetic Bandgap Structures 1348

Perovskite Anti-Resonant Reflection Optical Waveguide Fibre 1349
Christian Johnson-Richards, Luke Cording, Noel Healy

Effects of randomness on self-assembled photonic crystals 1352
Duanduan Wan

Emergence of Rashba Spin-Orbit Coupling in Staggered-Gyromagnetic Photonic Crystals 1353
Yao-Ting Wang, Wenlong Gao, Hua-Shin Lin

Symposia, Special-Session and Workshop Posters 1356

On-chip Neural Network for High-speed, Energy-efficient and Integrated Computation 1357
Xueyun Li, Shining Zhu, Tao Li

From Translucent to Transparent Wood 1359
Ilya Sychugov

Multiscale QM/Classical Modeling of SERS Spectra in Amino Acids and Nucleobases 1360
Sveva Sodomaco, Chiara Cappelli

Topological edge state waveguide fed antennas 1362
Shih-Hui Gilbert Chang

Gradient-Momentum Engineering in Metasurface for Continuous and Asymmetric Beam Steering 1363
Hsiu-Ping Su, Po-Sheng Huang, Pin Chieh Wu

Multiscale analysis of anisotropic composites 1365
Natalia Rylko

Spectral and Polarization Control of Smith-Purcell Radiation via Chiral Dielectric Gratings 1366
Loris Cavenaile, Thomas Delplace, Muluneh G. Abebe, Bjorn Maes

Experimental Study of Mechanically Graded Tensegrity-Inspired Cellular Metamaterials 1369
Anna Al Sabouni-Zawadzka, Adam Zawadzki, Wojciech Gilewski, Maciej Kołodziejczak

Dynamical superradiance in vibrationally dressed molecules 1371
Lukas Freter, Piper Fowler-Wright, Javier Cuerda, Brendon Lovett, Jonathan Keeling, Päivi Törmä

Surface-Enhanced Raman Spectroscopic Observation of SuFEx Processes at Metal Surfaces 1374
Aleksandra Miszczak, Justyna Grzeda, Hubert Sobiech, Jan Dudziński, Michał Barbasiewicz, Andrzej Kudelski, Aleksandra Szaniawska

Flat band Engineering in Polymer Acoustic Lieb Lattices 1376
Anusha Rehman, Riccardo Carlo Moroni, David Hutchins, Peter J. Thomas, Rudolf Roemer, Katarzyna Majewska, Stefano Laureti

Self-configuring linear diffractive optical networks for adaptive imaging through multimode fibres 1379
Jérôme Don Jayamanne, José C. A. Rocha, Unė G. Būtaitė, Joel Carpenter, David B. Phillips

Free-Electron Coupling to Surface Polaritons Mediated by Small Scatterers 1381
Leila Rocio Prelat, Eduardo J.C. Dias, F. Javier García de Abajo

Long-range coupling through photonic molecules 1383
Romina Abarca-Ramirez, Diego Roman-Cortes, Rodrigo Vicencio

Hyperbolic Super□Resonance and Long□Range Quantum Entanglement 1385
Evgeniy Narimanov, Eugene Demler

Observing Exceptional Lines in Scattering Matrices 1387
Wenzhe Liu, Jingyi Zhao, Xinhao Wang, Lei Shi, Che Ting Chan, Jian Zi

Nanopopcorn-Based SERS Nanosensors for Intracellular pH Mapping 1389
Katarzyna Bogusz, Katarzyna Wleciał, Agnieszka Girstun, Andrzej Kudelski, Aleksandra Szaniawska

Magnetic Properties and Applications of Glass-coated Ferromagnetic Microwires 1391
Valentina Zhukova, Paula Corte-Leon, Mihail Ipatov, Juan Maria Blanco, Arcady Zhukov

Beyond optical chirality density: tensor-based description of electromagnetic chirality 1393
Ilia Smagin

Programmable synthetic frequency dimension platform for on-chip topological photonics 1395
Xiaolong Su, Weiwei Liu, Bing Wang, Peixiang Lu

Angle-Induced Double Resonance of Quasi-Guided Modes for Enhanced Second-Harmonic Generation 1397
Sooseong Ji, Jaesung Kim, Jongwon Lee

3D Stokes Polarimetry of Dipolar Near-Fields 1400
Guillermo Serrera, Yael Gutiérrez, José J. Gil, Fernando Moreno

Flexible and Programmable Semiconductor Plasmonic Platforms for Near-Infrared Meta-Optics 1401
Debmalya Mukhopadhyay, Bivas Saha

A Dynamically Beam Steerable Metasurface Antenna with Sidelobe Suppression 1404
Enez Furkan Cihan, Nursel Akçam

Quantisation of polariton modes for dispersive resonators 1409
Jakub Skorka, Ben Yuen, Angela Demetriadou

Chiral sensing along dielectric waveguides: effective index splitting and mode coupling 1412
Alice de Corte, Tom T.C. Sistermans, Ankit K. Singh, Bjorn Maes, Alberto G. Curto

Parametric studies to approximate configurations optimal for asymmetrical responses 1414
Miklós Waldhauser, Ákos Sebők-Papp, Dávid Vass, András Szenes, Balázs Bánhelyi, Mária Csete

Coupled nanolaser arrays: towards the realization of bright topological lasers 1417
Amina Saadani, Kenneth Syddall, Kaiwen Ji, Juan Ariel Levenson, Kamel Bencheikh, Alejandro M. Yacomotti

Low-Contrast Bound States in the Continuum Metasurfaces Enabling Single Nanoparticle Sensing 1419
Keisuke Watanabe, Samuel Crowther, Masanobu Iwanaga, Frank Vollmer, Tadaaki Nagao

Externally Driven Quantum Dynamics in Plasmonic Nanocavities 1421
Ishita Jena, Angus Crookes, Ben Yuen, Angela Demetriadou

Time-varying Metamaterials on a Drone Rotor Blade 1424
Pavel Ginzburg, Dmytro Vovchuk, Anna Mikhailovskaya, Konstantin Grotov, Mikhail Tsukerman, Omer Tsidki, Sergey Geyman, Mykola Khobzei, Vladyslav Tkach, Toms Salgals, Natalja Muračova, Vjaceslavs Bobrovs

Metallic Nanohelices as Chiral Metasurfaces & Applications in Chiral Sensing 1426
Thu Hac Huong Le

Surface Light Localization in Topological Multilayers 1428
Eva Otero, Ivan Toftul, Yuri Kivshar, Crina Cojocaru, Jose Trull

Revolutionizing semiconducting SERS application for resistant pollutants via nanoarchitectonics 1430
Yunqing Kang, Yusuke Yamauchi, Julio Gutiérrez Moreno, Olga Guselnikova

High-performance Wide-angle Metalens for Optical Receiver 1432
Wei-Hsiang Lai, Pin Chieh Wu

Structural Coloring via Hyperuniform Arrays of Tapered Si Nanostructures on Glass 1434
Hanna Kylhammar, Mikko Kjellberg, Srinivasan Anand

Physically intuitive coupling engineering for realizing the proposed spectral response at the resonator with drop waveguide 1436
Yae Jun Kim, Yu Sung Choi, Jae Won Ahn, Jae Woong Yoon

Tunable Thermal Emissivity for Thermal Infrared Camouflage Enabled by a Zigzag Metallic Glass Structure 1438
Yu-Ching Shih, Wei-Han Wang, Chia-Hsuan Lee, Hsuen-Li Chen

Resonant dielectric metasurfaces in Silicon Nitride for enhanced third harmonic generation in the UV 1440
Shroddha Mukhopadhyay, Maria Antonietta Vincenti, Radu Malureanu, Crina Cojocaru, Michael Scalora, Jose Trull

Quantum Nanophotonic Control in Non-Perturbative Light-Matter Coupling Regimes 1442
Erika Cortese, Johannes Bürger, Simone Di Muzio, Dario Ballarini, Simone De Liberato

Effects of TE-TM splitting on bistability and nonlinear spin dynamics in resonantly driven spinor exciton-polaritons 1444
Ting Wei Chen, Szu-Cheng Cheng

Near-field observation of energy transfer in nonlocalmetasurfaces 1446
Jie Ji, Wouter Holman, Djero Peeters, Jaime Gomez Rivas

Structural diversity of pentatwinned plasmonic nanoparticles 1449
Ana Sánchez-Iglesias, Marek Grzelczak

Waveguide-Driven Nanoparticle-on-Mirror Nanocavities for Integrated On-Chip Raman Spectroscopy 1451
Daniel Arenas Ortega, Elena Pinilla Cienfuegos, Alejandro Martínez

Inverse-Designed Ultra-Compact 1 x 3 Beam Splitter on a Cladding-Free Photonic Crystal Platform 1455
Jinseong Bae, Donghyun Park, Minjin Kim, Sejeong Kim, Haejun Chung

Tunable nonlinearities of nonlocal free-electron gas in plasmonic heavily doped semiconductors 1458
Huatian Hu, Gonzalo Alvarez-Perez, Antonio Valletta, Marialilia Pea, Michele Ortolani, Cristian Ciraci

Thermally Addressable Au/PDLC Multilayer metamaterial: A Platform for Tunable Epsilon-Near-Zero Response 1460
Vimala Sridurai, Geetha G. Nair

Leveraging Stochastic Textures in Chiral Nematics for multi-modal Physical Unclonable Functions (PUFs) 1463
Mauro Daniel Luigi Bruno, Giuseppe Nicoletta, Roberto Caputo, Maria Penelope De Santo, Riccardo Cristoforo Barberi, Antonio Ferraro

Exploring the coupling of TPMSs: What utility canthey provide? 1465
Alonso Cuartero Mondoño, Andrea Bergamini

Topological Eutectic Heterostructures: Quantification of Their 2D-morphology 1467
Krzysztof Markus, Kingshuk Bandopadhyay, Andrzej Materna, Andriy. M. Gusak, Dorota Anna Pawlak

All-Dielectric Slotted-Disk Metasurface Sensor Based on quasi-Bound States in the Continuum 1469
Jack Dobie, Oisin McCormack, Yongliang Zhang, Justin Schulz, A. Louise Bradley

Mid□Infrared Metasurfaces for Exosome□Based Liquid Biopsy in Hepatocellular Carcinoma 1471

Riccardo Di Santo, Benedetta Niccolini, Flavio Di Giacinto, Marco De Spirito, Raffaella Polito, Andrea Notargiacomo, Michele Ortolani, Alessandra Di Gaspare, Fabrizio Pizzolante, Gabriele Ciasca, Marialilia Pea

Colloidal lithography for correlated disorder light-trapping structures **1473**
Laura de Almeida, Jean-Baptiste Doucet, Guilhem Almuneau, Stephane Collin, Inès Revol

Meta-devices based on liquid photonic devices **1476**
Yin Zhou, Zihan Geng, Mu Ku Chen

Breaking Reciprocity with Self-Oscillators **1478**
Alexander Stoychev, Ulrich Kuhl, Nicolas Noiray

Generalized Space-Time reconfigurable Metasurfaces in synthetic dimension **1481**
Yinglan Li, Chengzhi Qin, Bing Wang, Peixiang Lu

Inverse Designed Metasurfaces for SpatiallyIsolated Optical Skyrmions **1483**
Donghyun Park, Jinseong Bae, Jiwoo Kim, Sejeong Kim, Haejun Chung

Optimization of Broadband Sound Absorber Consisting of Helmholtz Resonator Array **1486**
Jia-Hong Sun, Yu-Shao Chang, Jin-Chen Hsu

Causality and free-space propagation for the second quantization of radiative nanophotonic systems **1488**
Luke Hands, Ben Yuen, Angela Demetriadou

Light emission from metals - photluminescence and electroluminescence **1491**
Imon Kalyan, Ieng-Wai Un, Kaiqiang Lin, John M. Lupton, Sebastian Bange, Yonatan Sivan

Phase-Change Extraordinary Optical Transmission Metasurfaces for Reconfigurable Spatial Filtering in the Mid-Infrared **1493**
Stuart Kendall, Joe Shields, Joe Pady, Carlota Ruiz de Galarreta, Jacopo Bertolotti, C. David Wright

Structural and Electronic Transitions in Pure and Au-Decorated VO2 Nanoporous Thin Films under Thermal and Photothermal Excitations **1495**
Claudia Pernilla Hallqvist, Charlotte Lea Oceane Nani, Edoardo Casadei, Cristina Mancarella, Francesco Bisio, Michele Magnozzi, Maurizio Canepa, Andrea Li Bassi

Equivalent Circuit Analysis of a Time-Varying Edge-Coupled Split-Ring Resonator **1497**
Theocharis Manassis, Guido Valerio, Theodosios Karamanos

Optimising Microwave Cavities for nonzero Helicity with Machine Learning **1500**
Emma Paterson, Jeremy Bourhill, Maxim Goryachev

Polarisation Conversion in Bulk Hyperbolic Crystals **1502**
Katherine Stevens, Rebecca Craig, Mark Cunningham, Sonja Franke-Arnold, Rair Macedo

Towards a BIC-based optomechanical polarization modulator **1505**
Chiara Brugnoni, Giuseppe Emanuele Lio, Grazia Salerno, Simone Zanotto, Alessandro Tredicucci, Alessandro Pitanti

Elasticity-Driven Wrinkled PDMS Structures for Tailoring Optical Properties Across the Hyperspectral Range **1508**
Urszula Malecka, Patrycja Wytrych, Tomasz Stefaniuk

Ultrasonic Needle Beam Generation in Water Using a Complex-Amplitude-Encoded Polymer Trapped-Air Acoustic Mirror **1511**
Hafiz Muhammad Imran, Marco Ricci, Rocco Zito, Stefano Laureti

Finite Element Simulation of Strain Measurement in Auxetic Materials via FBG Sensors **1513**
Katarzyna Majewska, Riccardo Carlo Moroni, Stefano Laureti

Fabry-Pérot and Friedrich-Wintgen Bound States inthe Continuum in a Plasmonic Double T-Cavity **1515**
Amina Rezzouk, Soufyane Khattou, Madiha Amrani, Adnane Noual, E. H. El Boudouti, Bahram Djafari-Rouhani

Auxetic Materials for Biomimicry: Designing for Tendon-Like Behavior **1517**
Riccardo Carlo Moroni, Katarzyna Majewska

Photonic Fiber Bragg Grating Sensor Network for Detection and Micro-Doppler Characterization of Small UAVs 1519
Rodions Marstupa, Aleksandrs Olins, Mykola Khobzei, Vladyslav Tkach, Serhii Haliuk, Sandis Migla, Toms Salgals, Vjaceslavs Bobrovs, Dmytro Vovchuk

Plasmonics, Nano-Optics and Nanophotonics 1521

Control of Chiroptical Response with Chiral Plasmonic Nanoparticles 1522
Ruiqian Zhang, Xiaolu Zhuo, Jianfang Wang

Harmonizing Plasmonic and Photonic Effects to Boost Photocatalytic H2 Production 1524
Tharishinny Raja Mogan, Jiajia Zhang, Li Shiuan Ng, Siew Kheng Boong, Carice Chong, JinnKye Lee, Haitao Li, Hiang Kwee Lee

Carbon Nanodot Superparticles as a new family of Optical Metamaterials 1527
Caterina Tortorici, Riccardo Rubino, Laureline Roffi, Vincenzo De Michele, Rodrigo Szostak, Fabrizio Messina, Alice Sciortino

Optical Control of Lasing Modes in Quantum Dot Superparticles 1530
Marco Reale, Pietro Castronovo, Marco Cannas, Emanuele Marino, Alice Sciortino, Fabrizio Messina

Enhanced hot-carrier generation and dissociation in porous gold nanorods 1533
Katarzyna Kluczyk-Korch, Tomasz Antosiewicz

Exciton-Plasmon Strong Coupling in Gold Nano-Bipyramid Arrays 1535
Kseniia Mamaeva, Hodjat Hajan, Jamie Somers, Teodora Faraone, Colm Delaney, Larisa Florea, A. Louise Bradley

Deterministic Photon Addition in a Waveguide Mode 1538
Kristina Malinowski, Holland Frieling, Benjamin Koltenbah, Pankaj Jha, Harry Atwater

Pole expansion of the optical scattering matrix via rescaled scattering channels 1541
Elias Fösleitner, Adrià Canós Valero, Zoltan Sztranyovszky, Egor A. Muljarov, Kirill Koshelev, Thomas Weiss

Can real motion be synthetically emulated? 1543
Kyan Louisia, Francisco J. Rodríguez-Fortuño

Probing Strongly Coupled Multi-Resonant Plasmonic Cavities and Excitons in ITR-PEEM 1545
Sacha Schwarz, Raphael Gherman, Alex Currie, Jean-François Bryche, Guillaume Beaudin, Dominique Drouin, Serge Ecoffey, François Fillion-Gourdeau, Pierre Levesque, Paul Charette, Steve MacLean

Detection and Quantification of Mid-Infrared through Raman thermometry in Plasmonic Bilayer Metasurface 1547
Anju Sajan, Christopher Sumner, Rohit Chikkaraddy

Direct Laser Writing of Ag-Au Thin Films for Plasmonic Sensing Platform 1549
Kernius Vilkevičius, Tomas Rakickas, Evaldas Stankevičius

Benchmark Study Using Machine Learning Surrogate Models for Predicting Optical Spectra of Tungsten Bronze Nanospheres Based on Mie Theory 1552
Yuanchao Lu, Ruixing Li

Enhanced Strong Coupling in Two-Dimensional Dichalcogenide Materials and a Bowtie Nanoantenna Plasmonic Array 1556
Na Jia, Bhera Ram Tak, Luke Doolan, Yongliang Zhang, Riley Gatensby, Jonathan N. Coleman, Richard G. Hobbs, A. Louise Bradley

Spatial Dispersion in Optical Properties of Planar Lattices of Plasmonic Nanoparticles Revealed by Müller Matrix Ellipsometry 1560
Eugene Bortchagovsky, Dai Fang, Monika Fleischer, Dietrich R. T. Zahn

Eigenmodes of Finite Rectangular Lattices 1563
Jussi Kelavuori, Roman Calpe, Benjamin Asamoah, Tommi Hakala, Mikko Huttunen

Single-Particle Study of Spin Crossover Compounds for Reconfigurable Photonic Integration 1565

Lucas Mascaro Burguera, Ramón Torres Cavanillas, Alejandro Regueiro, J. Ignacio Echevarría, Eugenio Coronado, Jorge Parra, Pablo Sanchis, Javier Hernández Rueda, Elena Pinilla Cienfuegos

Design of exotic plasmonic lattice dispersions **1567**
Joel Lehikoinen, Päivi Törmä

Interparticle Spacing-Driven Ultrafast Dynamics in Gold Nanoparticle Superlattices **1570**
Pietro Castronovo, Cristian Gonzalez, Giuseppe Ammirati, Shengsong Yang, Daniele Catone, Alessandra Paladini, Patrick O'Keeffe, Cherie K. Kagan, Christopher B. Murray, Antonio Emanuele, Emanuele Marino, Fabrizio Messina, Alice Sciortino, Alice Sciortino

Temporal Interfaces in a Kretschmann-Raether Geometry **1573**
Harry Donegan, Miraculous Joseph Bhaseen, Francisco J. Rodríguez-Fortuño, Anatoly Zayats

Mode and Pitch Multiplexed Guided-Mode Resonance Active Metasurfaces, for Multi-Wavelength Control **1575**
Julie Belleville, Martin Thomaschewski, Harry Atwater

Wavelength-Guided Plasmonic Control of CO□ Reduction: From Model Nanostructures to Gold Dendritic Electrodes **1578**
Anjalie Edirisooriya, Manuka Suriyage, Zelio Fusco, Ning Lyu, Shenyou Zhao, Christin David, Fiona Beck

Cd(Zn)O gap antennas on polar substrates **1580**
Maria Villanueva-Blanco, Pablo Ibañez-Romero, Julia Ingles-Cerrillo, Javier Yeste, Vicente Muñoz-Sanjosé, Maria del Carmen Martínez-Tomás, Miguel Montes Bajo, Adrian Hierro

Switchable n-type conducting polymer nanoantennas **1583**
Suraya Kazi, Pravallika Bandaru, Yulong Duan, Shangzhi Chen, Magnus Jonsson

Vortex Excited Plasmon Resonances in Metal Nanodisks Governed by Symmetry and Size **1584**
Daisuke Tanaka, Kayn A. Forbes, David Andrews

Single-photon generation from strongly coupled Au-metasurface-WSe2 monolayers via photon blockade **1586**
Andergachew Berhe, Haroldo Hattori, Andrey Miroshnichenko

TMOKE Enhancement via Hybrid Fabry-Perot-Plasmonic Modes in Magnetoplasmonic Multilayers **1589**
Elkin Sepúlveda, Edgar J. Patino, Mario Zapata

The Topography Makes the Potential: A Covariant Wave Equation for Surface Plasmon Polaritons on Arbitrary Weakly Curved Interfaces **1591**
Florian Bönsel, Flore K. Kunst

Mixing Lateral Casimir Forces: Rotating Particle Above a Moving Surface **1593**
Stéphane Azar, Francisco J. Rodríguez-Fortuño

Fast Computation of Hot-Spot-Enhanced Hot-Carrier Generation in Plasmonic Nanoclusters **1595**
Pablo M. Uribe-Pizarro, Alan McGaughey, Francisco Ramirez-Cuevas

Room-Temperature Lasing in quasi-2D Perovskite Coupled with High-Q Plasmonic Metasurfaces **1597**
Yen-Yu Wang, Ning-Hao Lee, Lin-Chyn Yuan, Chia-Yu Lai, Jia-Wern Chen, Chen-Yu Wang, Tzu-Yu Peng, Chu-Chen Chueh, Yu-Jung Lu

Tip-Enhanced High-Harmonic Generation in an STM Nanojunction Driven by Mid-Infrared Pulses **1600**
Atsunori Sakurai, Shota Takahashi, Tatsuto Mochizuki, Tsuneto Kanai, Toshiki Sugimoto

Enhanced Raman scattering on tip-on-mirror platforms **1603**
Víctor Camús, Daniel Arenas-Ortega, Alejandro Martínez, Elena Pinilla-Cienfuegos, Ana Cros, Núria Garro

Ultranarrow Linewidth Surface Lattice Resonances in Aluminum Bowtie Metasurfaces **1605**
Bhera Ram Tak, Robert O'Meara, Nebras Alattar, Hodjat Hajian, Richard G. Hobbs

Plasmonic Response in Mg-Al Bimetallic Nanoparticles **1607**
Marwan Alam, Katarzyna Kluczyk-Korch, Tomasz Antosiewicz

Lithium Niobate Photonic Moiré Superlattice forTelecoms Wavelengths 1610
Romae Grierson-Copeland, Christian Richards-Johnson, Noel Healy

Metamaterials, Metasurfaces and Their Applications 1612

Temporal Disorder in Two-Dimensional Phononic Time Crystals: A Numerical Study 1613
Takamichi Terao

Research on Hydrogel-Based Flexible Underwater Acoustic Metamaterials 1616
Haoyu Zhao, Lei Zuo, Jinxin Zhao, Kai Zhang

Diversity-Optimized Dataset Generation Pipeline for High-Reflectivity Metamirror Inverse Design 1618
Swarali Talele, Liam Shelling Neto, Stefanie Kroker

Chiral Meta-atoms for Geometric-phase Manipulation in Metasurfaces Operating in the Visible Range 1620
Mircea Giloan

Mid-infrared Hyperbolic Metamaterial for the Silicon-Germanium Technology Platform 1622
Jon Schlipf, Enrico Talamas Simola, Fritz Berkmann, Leonetta Baldassare, Giovanni Capellini, Monica de Seta, Luciana di Gaspare, Inga Anita Fischer, Damiano Marian, Michele Ortolani, Michele Virgilio

Polarization needle beam metalens for large-volume super-resolution photoacoustic neuroimaging in expanded tissue 1624
Yongjae Jo, Inki Kim

Autoregressive Transformer for Inverse Design of Optical Multilayer Thin-Film Structures 1626
Kewen Ding, Peng Dai, Mike Pivnenko, Daping Chu

Hyperbolic metamaterials for efficient single photon emission 1629
Manobina Karmakar, Pavel Klok, Katarina Rovenská, Peter Kepič, Thomas Possmayer, Beáta Idesová, Filip Ligmajer, Leonardo de S Menezes

Dual-Band Beam-Switching Cavity-Excited Antenna Based on Scattering Constellations 1632
Yumeng Wang, Zeqiang Lin, Alex Man Hon Wong

Retrieving colors hidden in a grey Fabry-Pérot cavity through coherent absorption 1635
Giuseppe Emanuele Lio, Giulio Carotta, Lorenzo Lavista, Andrea Camposeo, Giacomo Venturi, Agnese Guernieri, Alessandro Pitanti, Simon A. R. Horsley, Giuseppe C. La Rocca, Alessandro Tredicucci, Simone Zanotto

Broadband tunable second-harmonic generation using local-to-nonlocal intersubband polaritonic metasurfaces 1638
Jaesung Kim, Gerhard Boehm, Mikhail A. Belkin, Jongwon Lee

Fundamental Limits to the Design of AchromaticMetasurfaces 1641
Nicolas Kossowski, Roman Buisine, Adelin Patoux, Rémi Colom, Patrice Genevet, Samira Khadir

Transmissive Metasurface for Efficient Underwater Sound Focusing with a Wide Incident Angle 1643
Jin-Chen Hsu, Jia-Feng Lai, Jia-Hong Sun

Transfer Learning for Data-Efficient Modeling of Composite Metasurface Unit Cells 1645
Alexander Wolff, Lukas Mueller, Steffen Klingel, Marco Rahm

Spatial Electric-Field-Induced Chiral Discrimination in Planar Plasmonic Nanostructures 1647
Chung-Kai Tseng, Tang-Chun Liu, Almudena Marti-Morant, Chao-Yi Tai

Towards Tunable Nanophotonics Filters using Quantum Confined Stark Effect 1650
Tanneguy Blandin, Mathieu Arribat, Antoine Monmayrant, Aurélie Lescestre, Jean-Yves Duboz, Olivier Gauthier-Lafaye

Inducing anisotropy in time via spacetime interfaces 1653
Andrew Naylor, Victor Pacheco-Peña

Fundamental Study on Lamb Wave Control Using Resonator-Based Acoustic Metasurfaces 1656
Kent Hora, Toshihiko Sugiura

Genetic Algorithm-based 3D-Metamaterials for Radar Range Extension **1658**
Dmytro Vovchuk, Dmitry Dobrykh, Konstantin Grotov, Anna Mikhailovskaya, Mykola Khobzei, Vladyslav Tkach, Anton Kharchevskii, Toms Salgals, Vjaceslavs Bobrovs, Pavel Ginzburg

High-Index Plasmonic Metamaterials for Mid-Infrared Upconversion **1660**
Caleb Todd, Nicolas Spiesshofer, Zoltan Sztranyovszky, Rakesh Arul, Angela Demetriadou, Jeremy J. Baumberg

Efficient bio-sensor based on terahertz metasurface **1663**
Pradeep Tiwari, Deepak Kala, Maciej Sakowicz

Polarization dynamics of waves propagating in complex media: application to moving media **1665**
Aymeric Braud, Renaud Gueroult

Parity Resolved Origin Optimization for Efficient Multipolar Modeling of Metasurfaces **1670**
Hossein Allahverdizadeh, Karim Achouri

Scattering properties of a cylindrical scatterer with time-modulated permittivity **1672**
Jiaruo Yan, Ioannis Katsantonis, Mohamed Mostafa, Viktar Asadchy, Maria Kafesaki

Ultrashort Bright Envelope Solitons in Ferromagnetic Metamaterials Placed in High-Intensity Magnetic Biased Fields **1675**
Feodor Yu. Ogrin, Alexandra V. Zhabova, Mariya D. Amel'chenko, Sergei V. Grishin, Sergei A. Nikitov

Robust Design of a Reconfigurable Linear-to-Circular Polarization Metasurface via LHS **1677**
Gregorio J. Molina-Cuberos, Ángel J. García-Collado, Ismael Barba, José Margineda

Optically Transparent Metasurface Reflector for Radar Visibility Enhancement of Vehicles **1680**
Sergei Geiman, Dmytro Vovchuk, Denis Kolchanov, Mykola Khobzei, Vlad Tkach, Vjaceslavs Bobrovs, Hagit Gilon, Eyal Cohen, Eran Yungar, Pavel Ginzburg

300-μm Gaussian Beams from Meta-Grating Couplers for Ultra-Stable Lasers **1683**
Max Schittenhelm, Mika Gaedtke, Steffen Sauer, Sebastian Häfner, Stefanie Kroker

Elimination of Beam Walk-off in Second Harmonic Generation **1686**
Edvinas Aleksandravičius, Darius Gailevičius, Kęstutis Staliūnas

Zero-angle polarizers based on periodically structured dielectric thin films **1688**
Julianija Nikitina, Rytis Buzelis, Kestutis Staliunas, Lina Grineviciute

Optical properties of Ge metasurfaces realized on a Si photonics platform for wavelength-selective absorption **1690**
Paul Oleynik, Wei-Han Chen, Jon Schlipf, Oliver Skibitzki, Christian Wenger, Inga Anita Fischer

Optical responses from zero optical-path-length object **1692**
Da Yong Lee, Moongul Byun, Robert Magnusson, Jae Woong Yoon

Anomalous Reflecting Nonlocal Metasurfaces **1695**
Marten Musiol, Liam Shelling Neto, Steffen Sauer, Sebastian Häfner, Stefanie Kroker

Multi-frequency Amplification of Underwater Acoustic Signals **1698**
C. W. Park, H. J. Lee, J. H. Park, W. Choi

Temporal Coupled Mode Theory for a Single Floquet-Sheet Resonator **1700**
Yao-Ting Wang, Hsu-Hui Chou

Beam Steering in the Sub-Terahertz Band Using a Microbridge-Array Based Reconfigurable Intelligent Surface **1703**
Steffen Klingel, Lars Franke, Marco Rahm

Assessing Monolithic and Thin-Film Silicon Metasurfaces for Ultrafast Pulse Applications **1706**
Klaudijus Midveris, Gvidas Klyvis, Erika Jonaitytė, Tomas Klinavičius, Andrius Žutautas, Mindaugas Juodėnas

Physics-Guided Inverse Design of Broadband Low-Frequency Underwater Acoustic Metamaterials **1708**
Krupali Donda, Vatsal Patel, Yash Shah, Vimi Patel

Conditional Diffusion Modeling for Low-Frequency Underwater Acoustic Absorber Design **1711**
Vatsal Patel, Vimi Patel, Yash Shah, Krupali Donda

Actively Tunable EIT in Strongly Coupled Toroidal Terahertz Metamaterials 1713
Lavi Kumar Vaswani, Bhagwat Singh Chouhan, Rohith K. M., Sirsendu Ghosal, Anuraj Panwar, P. K. Giri, Gagan Kumar

Interference Induced Complex Nonlinearities in Metal-ITO Metasurfaces 1715
Christopher Stevens, Matthew Klein, Ashley Luo, Dennis Walker, Joshua Hendrickson, Ivan Avrutsky, Shivashankar Vangala, Maxim Sukharev

Photonic Crystals, Lasers and Photonic Devices 1717

Enhancement of Spontaneous Decay Rate in Hybrid Photonic Nanocavities 1718
Themistoklis Deloudis, Angus Crookes, Angela Demetriadou

Solution-processed microcavities incorporating luminescent hybrid Copper(I) iodides 1721
Federica Bortoletto, Emma Contini, Ullrich Steiner, Andrea Dodero

Multimode Waveguiding Photonic-Crystal Gratings 1724
Lucciano Antonio Letelier Carreño, Lina Grineviciute, Simas Melnikas, Kestutis Staliunas

Spatially coherent quantum dot emission using guided mode resonances 1726
Nimisha Ramprasad, Harry Atwater

Stabilization of Whispering Gallery Microresonators by Hidden Solvent Dynamics 1728
Marco Reale, Antonino Madonia, Simonpietro Agnello, Marco Cannas, Emanuele Marino, Alice Sciortino, Fabrizio Messina

Topological Transitions in Bilayer Photonic CrystalSlabs 1731
Bo Wang, Junjie Li

Thermal optical and mechanical tuning in all-silicon and hybrid nanopillars 1734
Víctor González Morote, David Alonso-Tomas, Nestor Eduardo Capuj, Albert Romano-Rodriguez, Daniel Navarro-Urrios

Independent control of dispersion band and linewidth of guided-mode resonances by using dual-ridge unit-cell structures 1738
Joong Hyeon Pyo, Yu Sung Choi, Robert Magnusson, Jae Woong Yoon

Controlling topologically-protected edge states via synthetic space manipulation in photonic crystals 1741
Bartosz Janaszek, Tomasz Śmiarowski, Anna Tyszka-Zawadzka, Paweł Szczepański

Floquet-Engineered Switching of Dissipation between Driven and Undriven States 1743
Hidemasa Yamane

Nonlinear Topological States in Photonic Crystals: Modal Structure and Dynamics 1746
Tomasz Śmiarowski

Micro/Nano Fabrication and Characterization 1748

Establishing a Library of Metasurface Building Blocks through Coherence-Controlled Holographic Microscopy 1749
Ondrej Cervinka, Vlastmil Weiss, Martin Hrtoň, Petr Bouchal, Petr Liška, Filip Ligmajer, Tomáš Šikola, Petr Viewegh

Retrieving structural and optical parameters of 2D photonic crystals through angle-resolved spectroscopy: Addressing the electron microscope limitations 1751
Anand Eswara Rao Aryasomayajula, Viswanath P

Structural Colour Transmission of Novel Superimposed Gratings Fabricated via Two-Photon Polymerisation 1754
Jamie Somers, Jing Qian, Colm Delaney, Pascal Landais, A. Louise Bradley

Wrinkle-Mediated Plasmonic Metasurfaces for Large-Area Photoresponsive Devices 1757

Swagato Sarkar, Tobias A. F. Koenig, Andreas Fery

Hybrid Silica-Perovskite Microcavities for High Quality-Factor Whispering-Gallery Resonance **1759**
Luke Cording, Christian Johnson-Richards, Hei Chit Leo Tsui, Pablo Docampo, Noel Healy

Uniformity-Enhanced Gas-Phase Catalyst Etching of Silica Glass for Metalens Fabrication **1762**
Yusuke Kataoka, Kohei Sano, Yoshitaka Ono, Yasuo Hayashi

Automated SEM-Based Metrology for Wafer-Scale Characterization of Nanostructured Metamaterials **1764**
Naga Anirudh Peyyety, E. Butzen, I. Harder, T. Waldsauer, S. Bauerdick, K. Gieb

Meta-lenses phase characterization by phase retrieval **1767**
Jialuo Cheng, Bowen Liu, Yin Zhou, Lei Shi, Zihan Geng, Mu Ku Chen

Effective Optical Response of Multilayer Thin Films Using a Single-Layer Model for Photonic Applications **1770**
Mohammad Al-Kuhaili, Reem Abubaker

Author Index **1776**

Session Index **1812**

Country Index **1813**

PLENARY LECTURES

Plenary Presentations

5 contributions · pp. 99–103

Metasurfaces as a platform for classical and quantum light control

Ruwen Peng*, and Mu Wang

National Laboratory of Solid State Microstructures, School of Physics, and Collaborative Innovation Center of Advanced Microstructures, Nanjing University, Nanjing 210093, China
*Corresponding author: rwpeng@nju.edu.cn

***Abstract*— In this talk, we present metasurfaces as a platform for classical and quantum light control. The approaches achieve potential applications in optical display, data storage, information encryption, and quantum information networks.**

***Keywords*— metasurfaces, polarization manipulation and multiplexing, transparent matte materials.**

Part I. Matesurfaces for polarization manipulation and multiplexing: from classical to quantum

It is well known that manipulating the polarization of light on the microscale or nanoscale is essential for integrated photonics and quantum optics. In this talk, we present our recent classical and quantum studies on polarization manipulation and multiplexing via optical metasurfaces. One is to break the limitation of polarization multiplexing in optical metasurfaces with engineered noise [1,2], and the other is to realize the generation, transformation and multichannel distribution of entangled photons with dielectric metasurface [3-5]. Very recently we have further carried out multiprotocol quantum key distributions based on a single metasurface [6]. The approaches achieve potential applications in optical display, data storage, information encryption, and quantum information networks.

Part II. Matte surfaces with broadband transparency

The long-standing paradox between matte appearance and transparency has deprived traditional matte materials of optical transparency. In this talk, we present the solution to this centuries-old optical conundrum by harnessing the potential of disordered optical metasurfaces [7,8]. Through the construction of a random array of meta-atoms tailored in asymmetric backgrounds, we have created transparent matte surfaces that maintain clear transparency regardless of the strength of disordered light scattering or their matte appearances. Our work introduces an unprecedented frontier of transparent matte materials in optics, offering unprecedented opportunities and applications.

References

[1] Bo Xiong, Yu Liu, Yihao Xu, Lin Deng, Chao-Wei Chen, Jia-Nan Wang, Ruwen Peng*, Yun Lai, Yongmin Liu*, Mu Wang*, "Breaking the limitation of polarization multiplexing in optical metasurfaces with engineered noise", Science 379, 294-299 (2023).

[2] Feng-Jun Li, Shuai Wang, Rui Zhong, Meng-Xia Hu, Yue Jiang, Meijiu Zheng, Mu Wang, Xiangping Li, Ruwen Peng*, and Zi-Lan Deng*, "Metasurface polarization optics: From classical to quantum", Applied Physics Reviews 11, 041332 (2024).

[3] Ya-Jun Gao, Zheng Wang, Yue Jiang, Ru-Wen Peng*, Zi-Yu Wang, Dong-Xiang Qi, Ren-Hao Fan, Wen-Jie Tang, and Mu Wang*, "Multichannel distribution and transformation of entangled photons with dielectric metasurfaces", Physical Review Letters 129, 023601 (2022).

[4] Ya-Jun Gao, Xiang Xiong, Zhenghan Wang, Fei Chen, Ru-Wen Peng*, and Mu Wang*, "Simultaneous generation of arbitrary assembly of polarization states with geometrical-scaling -induced phase modulation", Physical Review X 10, 031035 (2020).

[5] Yajun Gao, Rui Zhong, Xianglin Mao, Hulin Zhang, Yue Jiang, Chenyu Bao, Chuanfeng Li, Ruwen Peng*, and Mu Wang*, "Interference-induced entanglement engineering on a metasurface", Physical Review Letters 136, 023601 (2026).

[6] Yue Jiang, Rui Zhong, Hu-Lin Zhang, Zheng Wang, Yi-Fei Liu, Ren-Hao Fan, Dong-Xiang Qi, Wen-Jie Tang, Ziyu Wang, Ruwen Peng*, and Mu Wang*, "A multichannel metasurface for multi-protocol quantum key distributions", Nano Letters 25, 7442-7449 (2025).

[7] Hongchen Chu, Xiang Xiong, Ya-Jun Gao, Jie Luo, Hao Jing, Cheng-Yao Li, Ruwen Peng*, Mu Wang*, Yun Lai*, "Diffuse reflection and reciprocity-protected transmission via a random-flip metasurface", Science Advances 7, eabj0935 (2021).

[8] Hongchen Chu, Xiang Xiong, Nicholas X. Fang, Feng Wu, Runqi Jia, Ruwen Peng*, Mu Wang*, Yun Lai*, "Matte surfaces with broadband transparency enabled by highly asymmetric diffusion of white light", Science Advances 10, eadm8061 (2024).

From Classical to Quantum Metasurfaces for Multiphoton Interferometry

Federico Capasso
Harvard John A. Paulson School of Engineering and Applied Sciences,
Harvard University, Cambridge, MA 02138, USA

Multiphoton interference and entanglement are fundamental to quantum information science, but necessary extensions to higher-dimensional systems remain challenging due to imperfections and complexity of scaling conventional optical setups.

Here we demonstrate a generalized Hong-Ou-Mandel effect using metasurfaces and graph theory, enabling controlled multi-photon bunching, antibunching, and entanglement across parallel matrix-encoded spatial modes.[1] Our theoretical framework rigorously predicts the device's behavior and facilitates the design of dual graphs representing both metasurface-based multiport interferometer designs and the complex non-classical correlations they generate. Experimentally, we show that a single-layer metasurface induces strong multiphoton interference simultaneously across multiple Jones matrix–encoded diffraction orders—violating the classical limit and effectively implementing higher-order Hadamard interferometers.
These results highlight the potential of metasurface-based quantum graphs for scalable, low-decoherence quantum information infrastructure.

1. Kerolos M. A. Yousef, Marco D'Alessandro, Matthew Yeh, Neil Sinclair, Marko Loncar Federico Capasso *Science* **389**, 416 (2025)

Materials-Driven Photonics: Toward Tunable and Extreme Light Control

Alexandra Boltasseva[1*]

[1] Elmore Family School of Electrical and Computer Engineering, Birck Nanotechnology Center and Purdue Quantum Science and Engineering Institute, Purdue University, West Lafayette, IN 47907, USA

*Corresponding author: aeb@purdue.edu

***Abstract*— We study tailorable and dynamically tunable properties of transparent conducting oxides (TCOs) and transition metal nitrides (TMNs) for applications in all-optical modulators and flat optics. We also investigate metal-to-insulator transition in ultra-thin TMN films operating in the so-called transdimensional regime. We also discuss the tailorability of 2D transition-metal carbides and nitrides (MXenes) for tailorable photonic devices.**

***Keywords*— tunable photonics, switchable materials, transparent conducting oxides, MXenes.**

Tailorable and dynamically tunable materials are crucial for advancing nonlinear and quantum optics, as well as optical technologies at large including IT, classical and quantum communication, imaging, sensing and energy conversion. Recently, transparent conducting oxides (TCOs) and transition metal nitrides (TMNs) have attracted attention for photonic applications as they exhibit enhanced light-matter interactions, particularly in their metallic/plasmonic regime and near the so-called epsilon near zero (ENZ) region. Here, we explore the static and dynamic tailorability and tunability of optical properties in TCOs and TMNs. Both homogeneous TCOs and TMNs, as well as structured devices made from them, were investigated for tunability of their optical interactions such as harmonic generation and optical modulation. We also report on investigations of ultra-thin TMN films where interesting metal-to-insulator transitions happen in the so-called transdimensional regime. We also discuss the customizability of 2D transition-metal carbides and nitrides (MXenes) to enable new pathways for tailorable photonic devices.

Precision nanogap metamaterials for tracking bioanalytes using SERS and SEIRA

Jeremy J Baumberg[1]

[1] Nanophotonics Centre, Cavendish Laboratory, Department of Physics, University of Cambridge, CB3 0US, UK

***Abstract*— Sensing of trace analytes, or of molecules at the metal interface that controls catalysis or battery electrochemistry, is challenging. Optical vibrational spectroscopies have huge potential, because they can be enhanced at nanostructured metal surfaces, but have been hard to control. I will discuss a range of recent key advances that give robust, repeatable, and recleanable nanogap plasmonic sensors, as well as midIR metamaterials enabling real-time flow electrochemistry.**

***Keywords*— metamaterials, plasmonics, sensing, SERS, SEIRA, electrochemistry, flow**

Quadratic Nanomaterials for On-Chip Classical and Quantum Devices

Rachel Grange

ETH Zurich, Department of Physics, Institute for Quantum Electronics, Optical Nanomaterial Group, Switzerland
*Corresponding author: grange@phys.ethz.ch

***Abstract*— Nonlinear materials used in telecommunications, lasers and quantum technologies are typically bulk single crystals. To access more sophisticated features in on-chip devices such as parametric or electro-optic effects, thin-film lithium niobate has recently emerged as a promising platform, albeit with significant fabrication constraints. Here I will present our recent progress in top-down fabrication of lithium niobate devices and bottom-up approaches, including the assembly of randomly oriented nanocrystals and sol-gel processes, to generate nonlinear classical and quantum signals. Finally, I will describe how these platforms are suited for nonlinearities in machine learning.**

***Keywords*— nonlinear optics, photonic integrated circuit, spontaneous parametric down conversion, lithium niobate, barium titanate**

KEYNOTE LECTURES

Keynote Presentations

27 contributions · pp. 105–141

Generating Optical Merons through Spin-orbit Coupling in Anisotropic Metamaterials

Vittorio Aita[1] , Anastasiia Zaleska[1], and Anatoly V. Zayats[1,*]

[1]Department of Physics and London Centre for Nanotechnology, King's College London, United Kingdom

*Corresponding author: anatoly.zayats@kcl.ac.uk

***Abstract*— We will discuss the enhanced spin-orbit coupling in strongly anisotropic metamaterials which provides efficient conversion of polarisation state of the transmitted light and results in meron-type topological structures of the electromagnetic field. Flexible control of polarisation and its topological properties is important for optical manipulation, communications, metrology and quantum technologies.**

***Keywords*— spin-orbit coupling, anisotropic metamaterials, optical field topologies.**

I. Introduction

Polarisation-controlled light–matter interactions underpin advanced applications in optical communication, sensing, photochemistry, and quantum optics. Precise spatial and temporal structuring of optical fields, combined with engineered material responses, enables control over spin–orbit coupling and the formation of topologically complex photonic states [1–5]. In particular, uniaxial materials support spin–orbit interactions that facilitate vortex beam generation. Uniaxial metamaterials provide enhanced anisotropy and chiral responses beyond natural media. Plasmonic nanorod-based metamaterials exhibit tunable dispersion regimes associated with epsilon-near-zero behavior and hyperbolic dispersion. In the hyperbolic regime. Although accessing extraordinary modes of the metamaterial requires oblique incidence to interact with longitudinal field components, tight focusing of structured scalar or vector beams enables excitation at normal incidence. Here, we experimentally demonstrate polarisation control of vector vortex beams using an anisotropic plasmonic metamaterial operating in hyperbolic regimes [6–9]. We observe azimuthal polarisation conversion and the formation of second-order meron-like polarisation topologies.

II. Results and Discussion

We studied experimentally and theoretically how strongly anisotropic plasmonic nanorod metamaterials interact with tightly focused vector beams to reshape their polarisation through spin–orbit coupling. In the epsilon-near-zero (ENZ) regime of the nanorod-based metamaterial, the longitudinal field component of the beam is heavily damped inside the metamaterial, resulting in the azimutalisation of the polarisation state of the beam upon transmission. Such azimuthalisation is observed for most beams except pure radial beams, for which longitudinal component is essential. Away from ENZ wavelengths, no polarisation conversion is observed. In the hyperbolic dispersion regime (wavelengths longer than ENZ), strong anisotropy enables significant spin–orbit conversion even for simple circularly polarized beams. Tight focusing produces vortex polarisation structures upon transmission, where components with opposite spin and different orbital angular momentum combine to create spatially varying polarisation. Analysis of Stokes parameters reveals synthetic polarisation textures consistent with second-order meron topologies.

III. Conclusion

We investigated how vector beams with strong longitudinal fields interact with a strongly anisotropic metamaterial and how this interaction drives spin–orbit coupling effects. The optical response depends on the dispersion regime: in the epsilon-near-zero regime, the metamaterial converts the input polarization into an azimuthal state, whereas in the hyperbolic regime it produces vortex-like polarisation patterns with second-order meron topology. This topological behavior is governed by the metamaterial anisotropy and the spin conversion of the incident beam. Combining strongly anisotropic and nonlinear metamaterials, dynamic generation of merons and control over their topologies can be achieved.

Acknowledgments

This work was supported by the UK EPSRC Project EP/Y015673/1 and ERC iCOMM project 789340.

References

[1] Y. Shen, Q. Zhang, P. Shi, L. Du, X. Yuan, and A. V. Zayats, "Optical skyrmions and other quasiparticles of light," Nat. Photon., vol. 18, pp. 15–25 (2024).

[2] J. Wu, A. Yu. Bykov, A. Zaleska, and A. V. Zayats, "Spectral synthesis of temporal response of nonlinearity through tuneable electron and phonon dynamics in a metamaterial," npj Nanophotonics, vol. 3, 2, 2026.

[3] Y. Shen, B. Yu, H. Wu, C. Li, Z. Zhu, and A. V. Zayats, "Topological transformation and free-space transport of photonic hopfions," Adv. Photon., vol. 5, 015001 (2023).

[4] H. J. Putley, B. Davies, F. J. Rodríguez-Fortuño, A. Yu. Bykov, and A.V. Zayats, “Mixing skyrmions and merons in topological quasicrystals of evanescent optical field,” Optica, vol. 12, pp. 614-619 (2025).
[5] Y. Xie, A. V. Krasavin, D. J. Roth, and A. V. Zayats, “Unidirectional chiral scattering from single enantiomeric plasmonic nanoparticles,” Nature Commun., vol. 16, 1125, 2025.
[6] V. Aita, D. J. Roth, A. Zaleska, A. V. Krasavin, L. H. Nicholls, M. Shevchenko, F. J. Rodríguez-Fortuño, and A. V. Zayats, “Longitudinal field controls vector vortex beams in anisotropic epsilon-near-zero metamaterials,” Nature Commun., vol. 16, 3807, 2025.
[7] K. A. Forbes, V. Aita, and A. V. Zayats, “Generating optical angular momentum through wavefront curvature,” APL Photonics, vol. 10, 020801, 2025.
[8] V. Aita and A. V. Zayats, “Enhancement of optical spin-orbit coupling in anisotropic ENZ metamaterials,” IEEE Photon. Journ., vol. 15, 0600108, 2023.
[9] V. Aita, A. Zaleska, H. J. Putley, and A. V. Zayats, “Polarisation conversion and optical meron topologies in anisotropic epsilon-near-zero metamaterials," ACS Photonics, vol. 12, pp. 2909–2915, 2025.

How can light be used for measurements a myriad times finer than those of Robert Hooke and a million times faster than those of Eadweard Muybridge?

N. I. Zheludev [1,2]

[1] University of Southampton, ORC, SO16 7NF, Southampton, UK
[2] Texas A&M University, Hagler Institute, Texas, TX 77843-3572, USA

Abstract— **By training metrological estimators, employing topologically structured light, and engineering the flow of Fisher information, optical metrology can surpass conventional resolution limits by orders of magnitude—achieving atomic-scale precision at megahertz acquisition rates.**

***Keywords*— metrology, structured light, Fisher Information.**

We review recent advances in nanoscale optical metrology based on the analysis of coherently scattered light. By combining structured optical fields with optimisation of Fisher information flow, positions and dimensions of nanoscale objects can be measured with precision that reaches the atomic scale, exceeding limits traditionally imposed by diffraction and even thermal (Brownian) motion.

We further discuss the conceptual transition from high-precision parameter estimation to true high-resolution imaging, and introduce emerging principles for super-resolution imaging of finite-size objects beyond conventional optical limits. These developments establish a unified framework linking structured illumination, information theory, picophotonic localisation metrology and optical superesolution.

REFERENCES

[1] M. Weimar *et al.*, *Controlling the Flow of Information in Optical Metrology* (2025). https://doi.org/10.48550/arXiv.2508.13640
[2] T. Chang, G. Adamo, N. I. Zheludev, *Super-resolution imaging of limited-size objects*, **Nature Photonics** (in press, 2026). https://arxiv.org/abs/2602.00719
[3] T. Liu *et al.*, *Picophotonic localization metrology beyond thermal fluctuations*, **Nature Materials 22**, 844–847 (2023). https://doi.org/10.1038/s41563-023-01543-y

Probing nanoscale optical nonlocal and nonlinear effects through free electrons

F. Javier García de Abajo[1,2,*]

[1]ICFO-Institut de Ciencies Fotoniques, The Barcelona Institute of Science and Technology, 08860 Castelldefels (Barcelona), Spain
[2]ICREA-Institució Catalana de Recerca i Estudis Avançats, Passeig Lluís Companys 23, 08010 Barcelona, Spain
*javier.garciadeabajo@nanophotonics.es

***Abstract*— We explore how free electrons probe nanomaterials' nonlocal and nonlinear optical responses with unmatched spatial resolution, examining harmonic generation, Kerr nonlinearities, and interference of inelastically scattered electrons, while lateral deflections from finite momentum transfers reveal nonlocal effects.**

***Keywords*— nonlinear optics, nanoscale optics, free electrons, nonlocal effects.**

We discuss different strategies for leveraging free electrons to quantify the nonlocal and nonlinear optical response of nanomaterials with unprecedented spatial resolution. In particular, we examine the ability of free electrons to probe harmonic generation as well as Kerr nonlinearities through the changes that these optical effects produce in the spectra of shaped electrons, and through the interference of inelastically scattered electron components. In addition, finite momentum transfers in the electromagnetic interaction between free electrons and nanomaterials result in lateral electron deflections that can be used to assess nonlocal effects.

ACKNOWLEDGMENTS

This work was supported by the European Research Council (101141220-QUEFES), the Spanish MICIU (PID2024-157421NB-I00 and Severo Ochoa CEX2024-001490-S), the European Commission (101017720-eBEAM), and the Catalan CERCA Program.

Metastructures for spatial signal processing and energy confinement

Raffaele Ardito[1], Marcello Cazzola[1], Chiara Gazzola[1],
Jacopo M. De Ponti[1],Marco Miniaci[2], Prisca Viviani[1], A. Corigliano[1*]
[1]Department of Civil and Environmental Engineering, Politecnico di Milano, Italy
[2]Department of Structural, Geotechnical and Building Engineering, Politecnico di Torino, Italy
*Corresponding author: alberto.corigliano@polimi.it

***Abstract* — This work critically discusses micro- and meso-scale graded metastructures as spatial signal processing platforms, with emphasis on achieving tonotopicity, advanced control of wave propagation, and elastic energy confinement. Illustrative examples include graded micro- and meso-scale arrays and bio-inspired, cyclically symmetric phononic pseudo-crystals.**

***Keywords* — metamaterials, metastructures, rainbow effect, tonotopic effect.**

I. Introduction

Structures with self-adapting abilities must be endowed with efficient sensors sending information to systems embedded in the structures themselves, able to interpret and classify the sensed signals which are finally used to activate feedback and actuation mechanisms.

The path from sensing to adaptation is hindered in many cases from the low intensity of the sensed signals and from the lack of autonomous energy sources. The possibility to efficiently govern energy fluxes, guiding them along pre-defined paths, confining and amplifying energy in pre-defined locations represents a major step toward self-adaptive structures.

This contribution will leverage on recent results in the field of elastic metastructures which could effectively be used for controlled and efficient information transport, mechanical energy confinement and signal amplification in adaptive structures.

Among different elastic wave control mechanisms, a recent line of work employs graded arrays of resonators embedded in a host structure to manipulate wave propagation by taking advantage of the interaction between the structure and the resonators [1]-[3]. The term graded refers to the smooth variation of a particular parameter of the resonators along space, allowing to control the propagation of waves in a broadband regime. This modulation strategy promotes a wavenumber transformation that, in turn, activates a spatial decrease of the wave velocity when the wave enters inside the array [1], [2]. Array guided waves slow down as they transverse the array with different frequency components localizing at specific spatial positions, resulting in a so-called *rainbow* effect, which replicates tonotopic phenomena found e.g. in the human ear apparatus.

Examples discussed will include graded resonator arrays at micro and meso-scales, additive manufactured devices containing liquids, and bio-inspired cyclically symmetric phononic pseudocrystals exhibiting broadband elastic-wave attenuation.

II. Methods and Results

Our approach is based on the design of elastic structures in which wave propagation is spatially controlled by locally tailoring the dispersion relation. While this approach has been previously demonstrated in elastic waveguides embedding local resonators [1], in this work we exploit two additional mechanisms: (i) the coupling between elastic periodic structures and liquids, and (ii) the use of a cyclically symmetric phononic pseudocrystals.

Under the hypothesis of adiabatic variation of the effective properties of the medium, the structure is assumed to be locally periodic. Dispersion properties are therefore described by local dispersion curves obtained by imposing Bloch–Floquet periodicity conditions. Numerical analyses are performed using COMSOL Multiphysics, employing the Solid Mechanics and Pressure Acoustics modules to account for the fully coupled elastic–acoustic problem.

The presence of a fluid within the periodic elastic metastructure provides an additional degree of freedom for controlling the dispersion characteristics. Previous works [4] have shown that introducing a fluid inside cubic unit cells equipped with flexible membranes on the top and bottom surfaces allows the opening of band gaps at lower frequencies, with the membranes acting as elastic springs and the fluid contributing an added mass to the system.

In the present work, we extend this approach by introducing openings between adjacent unit cells, enabling the concurrent propagation of acoustic waves through the fluid domain. This configuration promotes strong coupling between acoustic and

elastic waves, allowing for selective transmission or attenuation of waves in the coupled fluid–solid medium.

ACKNOWLEDGMENTS

This work is supported by the ERC advanced grant IMMENSE (Grant Agreement 101140720), funded by the European Union. MM acknowledges funding from the European Research Council (ERC) under the European Union's Horizon Europe research and innovation programme through the POSEIDON project (Grant Agreement No. 101039576) and from the DREAM project, financed by the European Union – NextGenerationEU under the National Recovery and Resilience Plan (NRRP), Mission 4, Component 2, Investment 1.2.

REFERENCES

[1] J.M. De Ponti, A. Colombi, E. Riva, R. Ardito, F. Braghin, A. Corigliano, R.V. Craster, "Experimental investigation of amplification, via a mechanical delay-line, in a rainbow-based metamaterial for energy harvesting," Appl. Phys. Lett. 117, 2020.

[2] J.M. De Ponti, L. Iorio, G.J. Chaplain, A. Corigliano, R.V. Craster, R. Ardito, "Tailored Topological Edge Waves via Chiral Hierarchical Metamaterials," Phys. Rev. Applied 19, 034079, 2023.

[3] L. Carpentier, A. Gueddida, G. Lévêque, R. Alcorta-Galvan, C. Croënne , M. Miniaci, B. Djafari-Rouhani, Y. Pennec, "Elliptic pillars based metasurface for elastic waves focusing in a plate," APL Materials, 12 (4), no. 041102, 2024.

[4] L. Wu, Y. Li, "Harnessing Bulging or Sloshing Modes to Design Locally Resonant Liquid-Solid Metamaterials," Journal of Sound and Vibration 510 (October): 116280, 2021.

Chirality in Light Matter Interaction

Giuseppe Strangi[1,2,*]

[1]Department of Physics, Case Western Reserve University, Cleveland, OH, USA
[2]Nanoscience Laboratory for Human Technologies, University of Calabria and CNR-NANOTEC, Rende, Italy
*Corresponding author: gxs284@case.edu

***Abstract*—Chiral metasurfaces enable strong control of light matter interaction at the nanoscale. Planar plasmonic architectures generate superchiral electromagnetic fields that enhance chiroptical responses beyond natural systems. These engineered platforms support enantioselective sensing, molecular spectroscopy, and quantum photonics by amplifying weak optical signatures of molecular chirality.**

***Keywords*— chirality, metasurfaces, superchiral fields, nanophotonics, chiroptical sensing.**

I. Introduction

Chirality is a fundamental property of systems lacking mirror symmetry and plays a critical role in molecular chemistry, biology, and optical physics. In optical systems, chirality governs the interaction between matter and circularly polarized electromagnetic fields, producing phenomena such as optical rotation and circular dichroism. Detecting weak chiral optical signals remains challenging because natural chiroptical responses are typically small. Recent advances in nanophotonics have introduced metasurfaces composed of subwavelength nanostructures capable of tailoring electromagnetic chirality and amplifying light matter interactions.

II. Methods

The investigated platform consists of planar plasmonic metasurfaces designed to break spatial inversion symmetry. Arrays of nanoscale metallic resonators support localized plasmonic modes that generate highly confined electromagnetic fields. By controlling geometry and material composition, the metasurfaces produce resonant field distributions with enhanced optical chirality density. These superchiral electromagnetic environments increase the interaction strength between electromagnetic fields and nearby chiral molecules.

III. Results and Discussion

Both numerical and experimental studies show that planar plasmonic metasurfaces can generate intrinsic superchiral electromagnetic fields comparable to those typically associated with three dimensional chiral structures. Localized plasmonic resonances create electromagnetic hotspots where optical chirality density is strongly enhanced. Molecules placed within these regions experience amplified chiroptical interactions, leading to stronger circular dichroism signals and improved sensitivity in molecular detection. These results highlight the potential of metasurface platforms for biosensing, enantioselective spectroscopy, and nanoscale photonic control.

IV. Conclusion

Engineered chiral metasurfaces provide a powerful strategy for controlling light matter interaction through enhanced electromagnetic chirality. The generation of superchiral fields enables improved detection of molecular chirality and opens new opportunities in biosensing, nonlinear optics, and quantum photonics.

Acknowledgments

The author acknowledges the support of the Project PRIN 2022 ”Enantioselex” and the NSF -EAGER ”Developing Optical Forces to Advance Separations in Biosensing.”

References

[1] A. Lininger, G. Palermo, A. Guglielmelli, G. Nicoletta, M. Goel, M. Hinczewski, and G. Strangi, “Chirality in light matter interaction,” *Advanced Materials*, vol. 35, Art. no. 2107325, 2023.
[2] G. Palermo and G. Strangi, “Intrinsic superchirality in planar plasmonic metasurfaces,” *Nano Letters*, vol. 24, 2024.
[3] G. Palermo, G. E. Lio, M. Esposito, L. Ricciardi, M. Manoccio, V. Tasco, A. Passaseo, A. De Luca, and G. Strangi, “Biomolecular sensing at the interface between chiral metasurfaces and hyperbolic metamaterials,” *ACS Applied Materials & Interfaces*, vol. 12, pp. 30181–30188, 2020.

Managing light and matter at the nanoscale for sustainable energy conversion

Esther Alarcón Lladó

NWO-I AMOLF , The Netherlands

For the successful large-scale deployment of solar energy conversion technologies, whether for generating electrical power or facilitating chemical processes, we require the design of nano-architectures that effectively control light-scattering.[1] One powerful approach to achieving this control is through the design of metasurfaces, which are engineered materials with tailored optical properties. Light can be directed and distributed by precisely structuring the spatial frequencies within these metasurfaces, thereby allowing light to be guided in specific directions, absorbed at specific locations, or transmitted according to the desired outcome.[2-4]

The fine control over light-matter interactions requires fine control over nano-fabrication. At the same time, for any of these new photonic concepts to be implemented in real devices for sustainable energy generation, their fabrication must be scalable. In this talk, we will first discuss the robustness of broadband metasurface light scattering on fabrication imperfections.[3] We will then delve into the development of scalable methods for metasurface fabrication with nanoscale feature control, from deterministic top-down approaches to self-assembled methods.[5]

[1] K. Jaeger et al., “Optics for Terawatt-Scale Photovoltaics – Review and Perspectives”, Optica Open 2025
[2] E. C. Garnett, B. Ehrler, A. Polman, E. Alarcon-Llado, “Photonics for photovoltaics: advances and opportunities”, ACS Photonics 8, 61 (2020)
[3] N. Tavakoli et al., “Over 65% Sunlight Absorption in a 1 μm Si Slab with Hyperuniform Texture,” ACS Photonics, 9, 1206 (2022)
[4] A. Tiede et al., “Blob detection for photonics metasurface designing: angular and spectral control of scattering light”, Advanced Photonics (2026)
[5] A. Lambertz et al., “Practical design rules for correlated disordered nanopatterns via polymer blend lithography”, in review

Kagome-Inspired Topological Photonics: From Lattice Design to Robust Control of Light

Zhigang Chen
The MOE Key Laboratory of Weak-Light Nonlinear Photonics,
TEDA Applied Physics Institute and School of Physics,
Nankai University, Tianjin, China
zgchen@nankai.edu.cn

***Abstract*— Kagome-type lattices offer a versatile platform for exploring topological photonics, owing to their unique symmetry, flatband features, and rich band topology. In this talk, I will present our recent advances in Kagome-inspired photonic lattices and their structural extensions, including super-honeycomb, breathing Kagome, disclination-based, and fractal-like geometries. These systems enable the realization of diverse topological states, such as higher-order boundary modes, vortex states carrying orbital angular momentum, and flatband-induced localization. By integrating real-space structural design with momentum-space topology, we uncover new mechanisms for robust manipulation of light. These results highlight a unifying framework for engineering complex topological photonic states, with potential applications in integrated photonics and optical information processing.**

***Keywords*— Topological photonics, Kagome lattice, flatband localization, orbital angular momentum**

Levitation optomechanics with meta-atoms

Adeel Afridi[1], Bruno de Melo[1], Bin Lu[1], Nadine Meyer[1], Romain Quidant[1,*]

[1]Department of Mechanical and Process Engineering, ETH Zurich, Switzerland

*Corresponding author: rquidant@ethz.ch

***Abstract*— We discuss the use of meta-optics in levitated optomechanics. By replacing silica nanoparticles with resonant silicon meta-atoms, we achieve enhanced optomechanical performance and deterministic control over optical forces. We show that engineering multipolar Mie resonances allows for switching between attractive and repulsive forces, directly mirroring the behavior of two-level systems.**

***Keywords*— Metasurfaces, dielectric nanophotonics, optomechanics, optical forces.**

I. Introduction

Traditional levitated optomechanics primarily utilizes silica nanoparticles, which are typically restricted to being "high-field seekers" (attracted to intensity maxima). Unlocking the full potential of ultra-weak force sensing and quantum state preparation, could benefit smarter particles that offer higher polarizability, and tunable interaction signs. This talk presents a new paradigm in optomechanics by utilizing meta-atoms - high-permittivity dielectric nanoparticles (such as silicon) that support strong Mie resonances. We start by introducing theoretically the specificities of trapping silicon meta-atoms. We then present experimental demonstrations of both deterministic control over the sign of optical forces on suspended metasurfaces and 'trapping in the dark' of individual Si meta-atoms.

II. Methods

The research combines rigorous analytical modeling with advanced experimental nanophotonics:

- **Theoretical framework:** We employ Mie theory and electrodynamics to model the optomechanical coupling of silicon nanoparticles. This includes calculating the complex polarizability and its dependence on laser detuning relative to magnetic and electric Mie resonances.
- **Experimental realization:** We utilize a hybrid optical platform where a metasurface, composed of engineered silicon meta-atoms, is pattern into a suspended nanomembrane and place into a standing wave.
- **Force characterization:** Optical forces are probed within a phase-controlled standing wave. Using homodyne detection and lock-in techniques, we extract the phase and amplitude of the membrane's displacement to determine the direction (attractive vs. repulsive) and magnitude of the exerted light pressure.

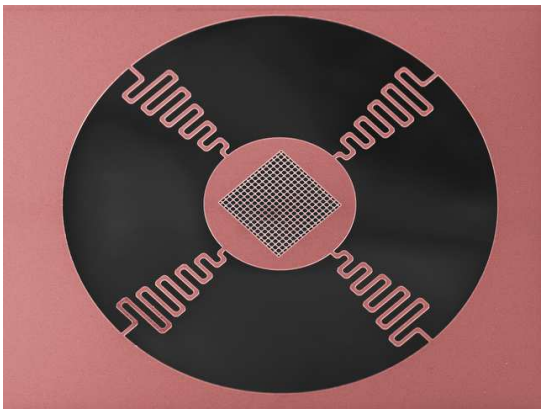

Fig. 1 SEM micrograph of a suspended array of silicon meta-atoms.

III. Results and Discussion

Our results demonstrate that meta-atoms offer several advantages over standard silica particles in levitation optomechanics:

- **Enhanced performance:** Silicon meta-atoms provide significantly higher trap frequencies and depths due to their high refractive index, facilitating easier access to the center-of-mass **ground-state cooling** regime in vacuum.
- **Sign reversal:** By adjusting the detuning of the trapping laser relative to the particle's resonances, we show that the sign of the polarizability can be flipped. This enables "low-field seeking" behavior, where particles can be trapped at intensity minima.

- **Multipolar control:** Experimentally, we confirm that by tailoring the geometry of meta-atoms to engineer the coherent superposition of multipolar modes (dipolar, quadrupolar, and octupolar), we can deterministically switch between **attractive and repulsive forces**. This mirrors the behavior of two-level systems but at a macroscopic, engineered scale.

IV. Conclusion

The integration of Mie-resonant meta-atoms into optomechanical systems represents a significant leap forward. By moving beyond the dipole approximation of simple dielectric particles, we achieve a level of control over optical forces previously reserved for atomic systems. These findings pave the way for high-precision force sensing, the study of non-equilibrium thermodynamics at the nanoscale, and the development of scalable, on-chip optomechanical devices for quantum technologies.

V. Acknowledgments

This work was supported by the European Research Council through the grant ERC-SyG Q-Xtreme #951234.

References

[1] S, Lepeshov, N. Meyer, P. Maurer, O. Romero-Isart, and R. Quidant, “Levitated optomechanics with meta-atoms,” Phys. Rev. Lett. 130, 233601, 2023.

[2] A. Afridi, B. Melo, N. Meyer, and R, Quidant, “Controlling the sign of optical forces using metaoptics”, Nature Comm. 17, 1163, 2026.

[3] I. Toftul, M. Petrov, R,. Quidant, and Y. Kivshar, “Optical supertorque induce by Mie-resonant modes”, ACS Photonics 12, 3447, 2025.

[4] B. Lu et al, in preparation.

Scaling the Metasurface Market: From Flat Optics to Sensor-Integrated Intelligence

Rob Devlin, Co-founder and CEO, Metalenz, USA
rob.devlin@metalenz.com

Metasurfaces began as a promising academic research direction. At Metalenz, they have transitioned from lab demonstrations into over 150 million deployed consumer devices, manufactured at commercial scale in existing semiconductor foundries. This presentation examines the path from research breakthrough to commercialization and the emergence of a rapidly growing metasurface market, highlighting key milestones, technical challenges, and lessons learned along the way.

Moving beyond miniaturization, Metalenz is now co-designing metasurface hardware and perceptual AI to enable sensing capabilities that conventional optics cannot deliver. This new platform technology unlocks new information from light—bringing advanced sensing capabilities to mass-market machine vision and consumer devices for the first time.

Metasurfaces are no longer just flat optical elements; they are becoming system level solutions for intelligent perception, enabling the perceptive, accurate, and efficient vision systems that will power the next decade of intelligent machines.

Wavefront Shaping and Harnessing Coherence with Guided Mode Metastructures

Julie Belleville, Martin Thomaschewski, Komron Shayegan, Yae-Chan Lim, Gloria Halka, Arun Nagpal, Nimisha Ramprasad, Lior Michaeli and Harry A. Atwater

Thomas J. Watson Laboratories of Applied Physics
California Institute of Technology, USA
*Corresponding author: haa@caltech.edu

***Abstract*— Guided mode metastructures are key building blocks for design of electro-optic active metasurfaces for wavefront shaping, and in metasurfaces that enable spatial coherence in the far field radiation emitted from thermal radiation sources and luminescent emitters.**

***Keywords*— guided metastructures, wavefront shaping, thermal focusing, receiprocity breaking.**

I. Introduction

Active metasurfaces that enable dynamic modulation of reflection and transmission amplitude, phase, and polarization, using resonantly excited materials electro-optic active media, are powerful design elements for meta-imaging and computation. We report the design and realization of nanostructured high quality factor dielectric active metasurfaces that enable both phase and amplitude modulation. They employ perovskite electro-optic active media (lithium niobate and barium titanate) with incorporated driving electrodes that introduce local refractive index modifications in the active medium that couple to high Q factor resonant modes, in an externally applied electric field. We show that coupling of multiple spectral resonances has interesting and beneficial implications for beam steering and wavefront shaping..

Thermal radiation and luminescence emission are normally pictured as arising from the collective action of mutually incoherent sources of dipole radiation. However, by coupling thermal and luminescent emission to waveguide structures and surface-propagating modes, we can achieve considerable control over the angular and spectral properties of radiation. I will discuss several examples, including i) electro-optical phase gradient modulation for beam steering and wavefront shaping ii) thermal beaming from surface plasmon-coupled resonators, an iii) reciprocity-breaking in magneto-electric semiconductors and Weyl semimetals, and iv) optical concentration in external luminescent solar concentrators.

II. Wavefront shaping with Electro-optic metasurfaces

Electro-optically tunable active metasurfaces that enable dynamic modulation of reflection and transmission amplitude, phase, and polarization using resonantly excited materials and phenomena are powerful design elements for meta-imaging and computation. As flat, low-profile optical elements, active metasurfaces have potential serve as cascadable, programmable components in optical meta-imaging systems, such as lens-less cameras and single-photon imaging systems. In this talk, I will discuss active metasurface designs with high quality factor, local, resonant elements, tunable via electrooptic control. Ferroelectric oxides such as lithium niobate and barium titanate play a pivotal role in enabling precise electrical control of the intensity, frequency, and phase of an optical signal. Here, we report on design of visible and near infrared frequency tunable lithium niobate and barium titanate metasurfaces. Our device incorporates high-quality factor guided mode resonances for efficient beam manipulation with electrically driven, independent phase control of their constituent subwavelength elements.

III. Tailoring Thermal Emission

In metastructures that support surface waves, there is a strict relationship between the momentum or in-plane wave-vector and the energy or wavelength at which the radiation outcouples. We design and demonstrate a structure with self-focused (i.e. lensing) thermal emission with a collective resonance, the Rayleigh anomaly, which imparts long-range, in-plane spatial coherence combined with local resonances to realize a spatial phase profile across the finite aperture. We then find the optimal scatterer profile using particle-swarm optimization that produces focal points for thermal emission at varying distances and operational wavelengths.

IV. Reciprocity Breaking in Weyl Semimetals

The magneto-optic response of magnetic Weyl semimetals is characterized by non-diagonal permittivity governed by the nontrivial Berry curvature that exists between recombinant Weyl nodes. We have observed reciprocity breaking in the magnetic Weyl semimetals $Co_3Sn_2S_2$, and CoMnGa confirmed via observation of a net reflectance modulation that is nearly an order of magnitude higher than that of the typical transverse magneto-optical Kerr effect in ferromagnets, without the concurrent application of any external magnetic field, and discuss implications of these findings.

V. External Luminescent Concentrators

Finally, we report designs for metasurface-based external luminescent solar concentrators that couple luminescence excited by broadband radiation (sunlight) into surface modes and subsequently via metasurface elements into the far field, and we describe the conditions leading to net optical concentration of sunlight onto a solar cell. We model a prototype system based on II-VI semiconductor quantum dots whose emission is matched to the absorption edge of an InGaP solar cell.

Acknowledgments

This work was supported by the AFOSR, Meta, and the Space Solar Power Project.

Can Physics and Optical Science Expedite Artificial Intelligence?

Eli Yablonovitch

Electrical Engineering and Computer Sciences Dept.,
UCLA/University of California, Berkeley, USA
eliy@eecs.berkeley.edu

Abstract: Artificial Intelligence (AI) requires intensive optimization calculations and is now demanding nuclear power for the data centers. All the variables in an AI model must converge together, to expedite the calculations. Data center energy is dominated by data communication which costs ~1pJ/bit, about 6 orders of magnitude higher than the Landauer Limit.

Metamaterials at Crossroads: from Quantum to Space-Time Photonics

Vladimir M. Shalaev

School of Electrical and Computer Engineering, Birck Nanotechnology Center and Purdue Quantum Science and Engineering Institute, Purdue University, West Lafayette, IN 47906, USA

Corresponding author: shalaev@purdue.edu

***Abstract*— We discuss quantum photonics based on the recently discovered single-photon emitters in silicon nitride and the avalanche-enhanced optical modulation in silicon at single-photon intensities. Then, we show that transparent conducting oxides (TCOs) operating in the near-zero index (NZI) regime can enable extreme time-varying media with novel and unique phenomena, including photonic time crystals and 4D space-time metamaterials.**

***Keywords*— metamaterials, quantum metamaterials, space-time metamaterials, photonic time crystals.**

Highly Nonlinear Photonic Materials Based on Metamaterials, Plasmonics, and Nanostructuring

Robert W. Boyd

The Institute of Optics, University of Rochester, Rochester, NY USA

Department of Physics, University of Ottawa, Ottawa ON Canada

robert.boyd @ur.rochester.edu

***Abstract*— This contribution reviews advances in the development of highly nonlinear materials by the combination of methods devised from the fields of metamaterials, plasmonics, and structured surfaces. We also review how these materials have led to the development of new photonics applications, including applications in quantum information technologies.**

***Keywords*— metamaterials, nonlinear optics, plasmonics, structured surfaces.**

I. Introduction

Materials with superior nonlinear optical properties are expected to play a key role in the development of future photonic devices and protocols for applications including quantum technologies, machine learning, and image acquisition and processing. revolutionized electromagnetic wave control. Recent research approaches on means to achieve these enhanced optical properties include the following: Optical materials display greatly enhanced nonlinear optical response at wavelengths for which the real part of the permittivity vanishes (this is the so-called epsilon-near-zero, or ENZ condition). Recent work stresses the development of both homogeneous ENZ materials and of metamaterials designed to display ENZ behavior at desired wavelengths. One example of this latter approach is the use of metal-dielectric multilayer stacks, with the optical materials and layer thicknesses selected to produce ENZ behavior at any wavelength in the visible range REF. Still another approach entails the fabrications of nanoscale optical cavities comprised of one linear end mirror and one nonlinear end mirror. These cavities display highly nonlinear and complex dynamic behavior because of the interplay between cavity resonances and the resonance behavior of the nonlinear cavity end mirror. The usefulness of these novel materials will be illustrated by examples of their use in several current applications.

II. Methods

One critical application of these novel photonic materials is in the field of nonlinear optics (NLO). NLO plays a key role in creating quantum states of light used in the field of light-based quantum information. A well-known example is the process of spontaneous parametric down-conversion (SPDC), which is routinely used to produce entangled photon pairs. In SPDC, an intense laser beam excites a second-order, that is, a $\chi^{(2)}$, NLO crystal. Some fraction of the photons in the incident beam split into two photons of lower energy. These daughter photons constitute an entangled photon pair; the properties of one photon are inherently linked to the properties of the other photon. This entangled state is an example of a quantum state of light, that is, a state that cannot be described using classical physics.

The relationship between NLO and the creation of quantum states of light exists at a very fundamental level. Most common light sources, such as sunlight, lasers, discharge lamps, and LED light bulbs, produce classical light. Several mathematical procedures have been developed for distinguishing classical from quantum light. For example, if the Wigner distribution function of a light field is anywhere negative, that light field is necessarily nonclassical. Classical light cannot be transformed into quantum light by means of a linear transformation. Only a nonlinear transformation can turn classical light into quantum light. There has been considerable recent interest in other situations involving quantum light and NLO. For example, the process of high-order harmonic generation (HHG) is modified when excited by quantum light [1,2]. Also, it has recently been reported that quantum states of light can be generated by the interaction of a strong pump beam with properly prepared metasurface [3].

Quantum states of light lend themselves to applications not possible with classical light. The field of quantum sensing is concerned with developing means to perform measurements more precisely through use of quantum light. A specific sort of quantum sensing is quantum imaging, a research area that seeks to produce "better" images using quantum methods. The image can be better in one of several different ways, that is, it might possess better spatial resolution, might display better

signal-to-noise ratio, or might be able to be formed using a very small number of photons.

III. Conclusion

We have reviewed recent approaches to the development of highly nonlinear materials based on a metamaterials platform. In addition, we have illustrated the utility of this approach by means of some applications that are enabled by use of these materials.

Acknowledgments

This work was supported by the US Office of Naval Research through MURI award N00014-20-1-2558 and through award N00014-19-1-2247 and by the US National Science Foundation under Award 2138174. This work was also supported by the Natural Sciences and Engineering Research Council of Canada under the Alliance Consortia Quantum Grant ALLRP 578468 - 22 and Discovery Grant RGPIN/2017-06880 and by the Canada Research Chairs program under award 950-231657.the AMBER Centre for fabrication support.

References

[1] 1. Gorlach, Alexey, et al. Nature Physics 19.11 (2023): 1689-1696.
[2] Lange, C.S., T. Hansen, and L. B. Madsen. Physical Review A 109.3 (2024): 033110
[3] Black, A. N., L. D. Nguyen, B. Braverman, K. T. Crampton, J. E. Evans, and R. W. Boyd, Optica 10, 952-958, 2023.
[4] T.Santiago-Cruz, S. D.Gennaro, O.Mitrofanov,et al.,"Resonant metasurfaces for generating complex quantum states," Science 377(6609), 991–995 (2022).

Inverse designed, densely integrated classical and quantum photonics

Jelena Vuckovic

Stanford University, USA
*Corresponding author: jela@stanford.edu

Abstract— **Recent breakthroughs in photonics design, along with new nanofabrication approaches and heterogeneous integration play crucial roles in building photonics for applications including optical interconnects and quantum technologies. This design breakthrough is named photonic inverse design, and refers to efficiently searching through the space of all possible photonic device geometries, within fabrication constraints, and by employing fast electromagnetic solvers and optimization tools. Additionally, new photonic platforms have been developed which enable functionalities beyond silicon on insulator, including silicon carbide, diamond, and Titanium:sapphire on insulator, as well as ultra-strong electro-optic materials, such as strontium and barium titanate. With these new approaches to design and fabrication, novel optoelectronic devices and systems have been designed and demonstrated, including error-free and fast chip-to-chip and on-chip optical interconnects compatible with commercial foundries, chip scale Ti:sapphire lasers and amplifiers, CMOS compatible isolators and laser frequency stabilizers, and silicon carbide and diamond chip-scale quantum technologies**

.

Thermal Photonics in Nonreciprocal and Time-Modulated Many-Body Systems

Philippe Ben-Abdallah[1*]

[1]Laboratoire Charles Fabry, UMR 8501, Institut d'Optique, CNRS, Université Paris-Saclay, 2 Avenue Augustin Fresnel, 91127 Palaiseau Cedex, France
*Corresponding author: pba@institutoptique.fr

Abstract— This talk explores thermal photonics in nonreciprocal many-body systems, revealing novel heat-flow control via spin-caloritronic effects. I also present a phase-tunable Floquet approach to manipulate radiative heat transfer, enabling directional flow, reversible pumping and reconfigurable flux in time-modulated networks, paving the way for programmable thermal photonic devices.

***Keywords*— Near-field radiative heat transfer, nonreciprocal media, spacetime modulation.**

I. Introduction

In the first part of this talk, I will examine thermal photonic phenomena in nonreciprocal many-body systems [1] composed of magneto-optical materials. When driven out of equilibrium by temperature gradients and spatially varying magnetic fields, these systems display unconventional radiative behaviors, including photonic analogs of condensed-matter effects such as the thermal Hall effect [2,3] and the inverse spin Hall effect [4]. These results (Fig.1) reveal new possibilities for controlling heat currents through spin-caloritronic mechanisms.

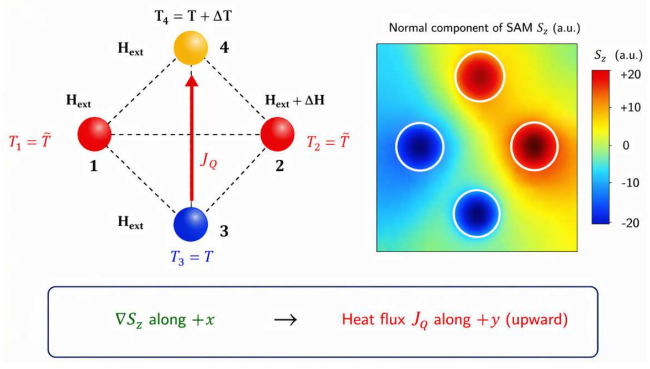

Fig. 1 Principle of inverse spin thermal Hall effect in a non-reciprocal network of C4 symmetry made with magneto-optical nanoparticles under spatially variable external magnetic field H_{ext} along the x-direction where no temperature gradient exists (T1 = T2). This spatial variation of external field induces a gradient in the same direction of light's spin angular momentum (SAM) Sz which, in turn gives rise to a transversal heat flux Jq.

In the second part, I will introduce a tunable approach to control thermal emission (Fig.2) and radiative heat transport based on Floquet interference between elastic and inelastic scattering channels arising from time-modulated permittivities [5]. By adjusting the modulation phases, one can achieve directional heat flow (Fig.3), reversible heat pumping, and reconfigurable splitting of radiative flux in many-body systems [6,7].

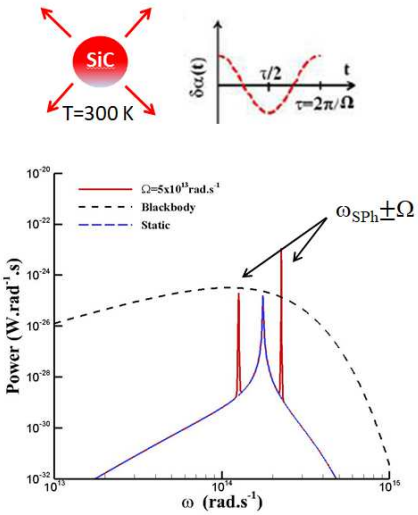

Fig. 2 Power spectrum of thermal emission at T = 300 K of a static and modulated dipole associated to a SiC nanoparticle 100 nm radius under a sinusoidal variation at the frequency Ω. The dashed line corresponds to the blackbody emission.

II. Conclusion

Together, these results reveal a unified mechanism to control radiative heat currents through spin-angular-momentum engineering and time modulation. They establish that nonreciprocity—whether induced by magnetic fields or

temporal modulation—enables transverse and programmable heat transport at the nanoscale. This opens the way toward actively controlled thermal photonic devices, where heat flow can be steered, reversed, or dynamically reconfigured using external fields and modulation protocols.

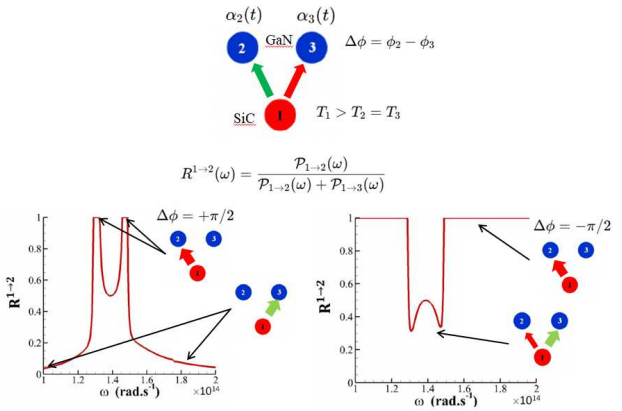

Fig. 3 Phase-controlled splitting of radiative heat flux in a three-nanoparticle SiC-GaN-GaN network. Splitting ratio R1→2, defined from the net absorbed power, with a polarizability variation $\delta\alpha = 0.1$. The SiC nanoparticle (red) acts as a hot source at T1 = 400 K, while the two GaN nanoparticles (blue) serve as colder outputs held at T2 = T3 = 300 K. Panels (left) and (right) correspond to relative modulation phases $\varphi = +\pi/2$ and $\varphi = -\pi/2$, respectively at the frequency $\Omega = \omega_{LO} - \omega_{TO}$ of GaN.

References

[1] S.-A. Biehs, R. Messina, P. S. Venkataram, A. W. Rodriguez, J. C. Cuevas, and P. Ben-Abdallah, "Near-field radiative heat transfer in many-body systems," Rev. Mod. Phys. 93, 025009, 2021.

[2] P. Ben-Abdallah, Phys. Rev. Lett. 116, 084301, 2016.

[3] A. Ott, P. Ben-Abdallah, and S.-A. Biehs,"Circular heat and momentum flux radiated by magneto-optical nanoparticles", Phys. Rev. B 97, 205414,
2018.

[4] P. Ben-Abdallah, "Inverse spin thermal Hall effect in nonreciprocal photonic systems", Phys. Rev. Lett. 134, 113804, 2025.

[5] R. Yu and S. Fan, "Time-modulated near-field radiative heat transfer", PNAS 121, e2401514121, 2024.

[6] P. Ben-Abdallah, "Interference-controlled radiative heat transport in time-modulated networks", Phys. Rev. B 113, L161407 (2026).

[7] R. Messina and P. Ben-Abdallah, "Many-Body Floquet Theory for Radiative Heat Transfer in Time-Modulated Systems", Phys. Rev. B, 113, 035404 (2026).

Advances in Ferronics

Gerrit E.W. Bauer

Advanced Institute for Materials Research (AIMR) & IMR & CSIS
Tohoku University, Aoba-ku, Katahira 2-1-1, Sendai/Miyagi 980-8577 Japan
bauer.gerrit.ernst.wilhelm.d8@tohoku.ac.jp

***Abstract*— Compared to magnetic materials, the dynamics of the ferroelectric order has received little attention from the scientific community. Here I review recent progress in understanding ferrons, the elementary excitations of the ferroelectric order.**

***Keywords*— ferroelectrics, domain walls, ferrons**

The duality between electric and magnetic dipoles in electromagnetism only partly applies to condensed matter. This becomes evident when inspecting the elementary excitations of the magnetic and ferroelectric orders, viz. spin and polarization waves that are quantized into magnons and ferrons, respectively. Magnons are transverse Goldstone modes at GHz frequencies that carry magnetic dipoles, while ferrons (in displacive ferroelectrics) are longitudinal Higgs modes at THz frequencies that carry electric dipoles. The ferrons and magnons have received asymmetric attention from the condensed matter community in the past [1]: While magnonics is an established and flourishing subfield in magnetism at the brink of contributing to quantum information, ferronics is still non-existent but dedicated workshops attract much interest [2].

Recent results on field-dependent heat conductance [3] as well as ballistic propagation [4,5] and diffuse transport [6] of ferrons illustrate the potential of dipole-carrying elementary excitations for applications in thermal, information, and communication technologies.

New developments include the prediction of "multiferrons" [7,8], chimera quasiparticles that emerge when ferroelectricity meets chiral phonons, as well as a polarization transfer force on ferroelectric domain walls [9] that may lead to ferron current-induced polarization switching, a new functionality in ferroelectrics that until now has been reserved for magnetic devices.

Acknowledgments

This work was supported by JSPS Kakenhi Grants No. 22H04965 and No. 24H02231.

References

[1] G.E.W. Bauer, P. Tang, R. Iguchi, J. Xiao, K. Shen, Z. Zhong, T. Yu, S.M. Rezende, J.P. Heremans, and K. Uchida, Perspective: Polarization transport in ferroelectrics, Phys. Rev. Applied 20, 050501 (2023).

[2] Ferrons and Magnons: Friends or Foes? https://www.spice.uni-mainz.de/ferronics-vs-magnonics-home/

[3] B.L. Wooten, R. Iguchi, P. Tang, J. Kang, K. Uchida, G.E.W. Bauer, and J.P. Heremans, Electric field–dependent phonon spectrum and heat conduction in ferroelectrics, Sci. Adv. **9**, eadd7194 (2023).

[4] J. Choe, T. Handa, C. Huang, A. Liston, J. Cox, J. Stensberg, Y. Hong, D. G. Chica, D. Xu, F. Tay, et al., Observation of Coherent Ferrons, arXiv:2505.22559.

[5] K. Shen, P. Tang, X. Chen, Y. Gao, Y. Fan, Z. Guo, Y. Wei, H. Jiang, X. Zhang, M. Wang, et al., Observation of ferron transport in ferroelectrics, arXiv:2505.24419.

[6] B. Zhang, R. Duan, S. S. Mishra, S. Jana, J. Kim, T. T. Caiwei, Y. J. Tan, W. Wang, P. T. C. Ietro, Z. Liu, and R. Singh, Electric-field Control of Giant Ferronics, arXiv:2509.06057.

[7] M. Pols, C. P. Romao, D.M. Juraschek, Multiferrons: lattice excitations with finite polarization and magnetization, arXiv:2510.15703

[8] P. Tang and G.E.W. Bauer, Multiferroic-like Quasiparticles in Ferroelectrics, arXiv:2510.18588 .

[9] H. Yang, P. Yan, and G.E.W. Bauer, Polarization transfer force on ferroelectric domain walls, submitted.

Engineering Strong Light-Matter Coupling in Dielectric Metasurfaces

Y. Zhang[1], X. Zhang[1], K. Mamaeva[1,2], N. Jia[1], J. Schulz[1], J. Dobie[1,2] and A. L. Bradley [1,2*]

[1] School of Physics and CRANN, Trinity College Dublin, College Green, Dublin 2, Ireland
[2] IPIC, Tyndall National Institute, Dyke Parade, Cork, Ireland
*Corresponding author: bradlel@tcd.ie

***Abstract*— Interest in exciton-polaritons for quantum devices, quantum sensing and low-threshold lasing applications continues to grow. Consequently, the realization of robust, room temperature strong-coupling systems is the subject of extensive effort. Herein, strong light-matter coupling is engineered in dielectric metasurfaces coupled with two-dimensional dichalcogenide material WS_2.**

***Keywords*— metasurfaces, strong coupling, WS_2 monolayer, Rabi splitting. quasi-bound states in the continuum**

I. Introduction

Room-temperature strong light-matter interactiion has been demonstrated in a range of material configurations using two-dimensional dichalcogenides, quantum dots and J-aggregrates coupled with dielectric and metallic metasurfaces as well as single plasmonic nanoresonators[1-5]. These systems provide complementary opportunities to access regimes of many, few or single excitons, to maximise the Rabi splitting, to control the decay rate of the coupled system or to optimize the pumping of the polariton branches. Among these materials, monolayer WS_2 is particularly well suited for room-temperature strong coupling due to its large exciton binding energy and robust A-exciton resonance in the visible spectral range.

Herein, strong coupling between the A-exciton of monolayer WS_2, located at 614 nm, and a quasi-bound state in the continuum (q-BIC) supported by dielectric metasurfaces is investigated. The metasurface is comprised of meta-atoms of disks incorporating an asymmetric slot, which enables the excitation of high-Q factor q-BIC modes with accompanying large field enhancement at the surface. Both the resonance energy and Q-factor of the metasurface can be systematically tuned by adjusting the disk height, radius, slot width, and lattice periodicity. This high degree of geometric control allows the q-BIC resonance to be engineered to tailor the radiative damping of the nanoresonator while maintaining spectral overlap with the A-exciton. Additional flexibility in controlling the strongly coupled system is achieved by modifying the local dielectric environment, for example through the introduction of a dielectric overlayer on top of the WS_2 monolayer.

II. Methods

A schematic of the slotted disk metasurface is presented in Figure 1. The lower slot edge is fixed at y_{min} = – 20 nm with respect to the disk centre. The slot width is changed by tuning y_{max}. Finite difference time domain simulations are carried out using a commercial software, Lumerical. The metasurface is simulated using a normally incident plane-wave polarized along the x-axis parallel to the slot. Periodic boundary conditions are used in the x and y directions with perfectly matched layers in z[4]. The transmittance measurements are made using normally incident white light, with the transmitted signal is fibre-coupled to a spectrometer.

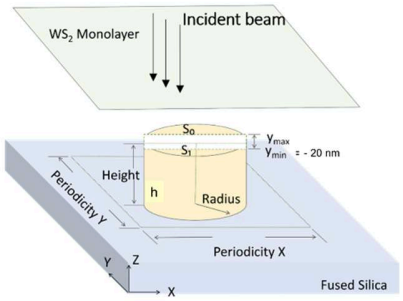

Fig. 1 Unit cell geometry of a WS_2 monolayer on top of a slotted-disk dielectric metasurface.

III. Results and Discussion

In the first instance, a TiO_2 metasurface is explored. TiO_2 has a refractive index of ~2.6 and negligible absorbance at the energy of the monolayer WS_2 A-exciton. For a metasurface suspended in air a maximum Rabi splitting of 64 meV at room temperature is observed[4]. Critical coupling is achieved when

radiative losses of the q-BIC mode match the non-radiative losses of the WS_2. It is demonstarted that this condition can be achieved, corresponding to polaritonic critical coupling in the strong coupling regime, with a maximum absorbance of 0.5 in each of the polariton branches.

In the second case, tuning of the dielectric environment for a strongly coupled system comprised of monolayer WS_2 coupled with a Si_3N_4 slotted-disk metasurface on a fused silica substrate is investigated. Si_3N_4 has a refractive index of ~2 with negligible absorbance at the A-exciton wavelength. In air a maximum Rabi splitting of 29 meV is observed. The addition of a 100 nm-thick PMMA layer on top of the WS_2 monolayer increases the Rabi splitting to 36 meV. The PMMA layer enhances the field confinement and suppresses radiative losses. Excellent agreement is observed between the experimental and simulations results.

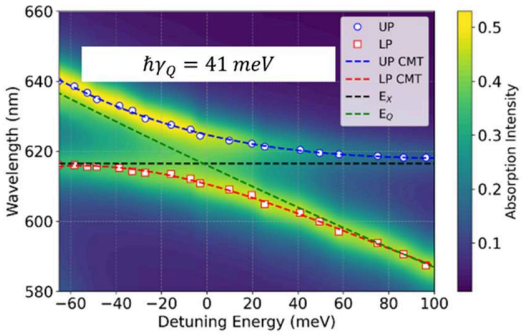

Fig. 2 Si slotted-disk metasurface: Absorbance colourmap as a function of detuning energy $\Delta = E_Q - E_X$ for a q-BIC damping rate of 41 meV. The corresponding Rabi splitting a zero detuning is 45 meV. The exciton full-width-half-maximum linewidth is 27 meV.

Si is CMOS compatible with well-established nanoscale fabrication. While it has a high refractive index of ~ 4 at the wavelength of the monolayer WS_2 A-exciton, it has non-negligible absorption ($k = 0.02$) and, consequently, has not been =explored for strong coupling applications in this wavelength range. A slotted disk metasurface on a fused silica substrate is investigated. In this case both the exciton and Si metasurface exhibit non-radiative losses. Firstly, it is demonstrated that a large Rabi splitting of 48 meV can be observed. Achieving critical coupling requires matching the total radiative and non-radiative losses in the hybridized system. Therefore, the cavity radiative losses must be tuned to match the total of the non-radiative losses. It is demonstrated that this can be achieved in the Si slotted disk metasurface with a small reduction in the overall Rabi splitting, as shown in Fig. 2. Critical coupling can be engineered and enhanced pumping of the upper and lower polariton branches realized. This works illustrates the potential of Si metasurfaces for polaritonic critical coupling.

IV. Conclusion

We have demonstrated strong coupling between the A-exciton of monolayer WS_2 and the q-BIC modes of slotted-disk metasurfaces fabricated from three different dielectric materials. The strength of the light–matter interaction, quantified by the Rabi splitting, can be systematically tuned by engineering the radiative losses of the metasurface through control of the slot width or by modifying the surrounding dielectric environment. In particular, matching the refractive indices of the substrate and superstrate reduces radiative losses and leads to an enhanced Rabi splitting.

However, the condition for maximum Rabi splitting does not correspond to the condition of optimal pumping of the polaritonic states. In many photonic systems, limited independent tunability of the resonance energy, radiative and non-radiative losses prevent simultaneous access to both the strong-coupling and critical-coupling regimes. It has been shown that polaritonic critical coupling can be engineered in both low-loss and intrinsically lossy dielectric metasurfaces at room temperature, providing maximum absorbance in the polaritonic branches. These results establish q-BIC metasurfaces aa versatile and scalable design framework for polaritonic devices, opening new opportunities for CMOS-compatible integrated platforms, low-threshold nonlinear optics, and actively engineered light–matter interactions in nanophotonic systems.

Acknowledgments

This work was supported by Research Ireland under awards SFI-21/FFP-P/10187, 12/RC/2276_P2, PIADS: 18/EPSRC-CDT/3585 and ACM: 18/EPSRC-CDT/3581_26. The authors thank the Advanced Microscopy Laboratory, CRANN for fabrication support.

References

[1] D. Friedrich, J. Qin, B. Schurr, T. Tufarelli, H. Groß, and B. Hecht, "Anticrossing of A Plasmonic Nanoresonator Mode and A Single Quantum Dot at Room Temperature," *Advanced Science,* vol. 12, no. 36, p. e06676, 2025.

[2] J. Lawless, C. Hrelescu, C. Elliott, L. Peters, N. McEvoy, and A. L. Bradley, "Influence of Gold Nano-Bipyramid Dimensions on Strong Coupling with Excitons of Monolayer MoS2," *ACS Applied Materials & Interfaces* vol. 12, ed, 2020, pp. 46406-46415.

[3] D. Melnikau *et al.*, "Rabi Splitting in Photoluminescence Spectra of Hybrid Systems of Gold Nanorods and J-Aggregates," *The Journal of Physical Chemistry Letters,* vol. 7, no. 2, pp. 354-362, 2016/01/21 2016, doi: 10.1021/acs.jpclett.5b02512.

[4] X. Zhang and A. L. Bradley, "Polaritonic critical coupling in a hybrid quasibound states in the continuum cavity–WS_2 monolayer system," *Physical Review B,* vol. 105, no. 16, 2022-04-21 2022.

[5] J. Zhong *et al.*, "Room-Temperature Strong Coupling of Few-Exciton in a Monolayer WS2 with Plasmon and Dispersion Deviation," *Nano Lett.,* vol. 24, p. 1579, 2024.

Chiro-Optical Micro-/Nano-Imaging and Near-Field Interaction

Hiromi Okamoto[1,*]

[1]Institute for Molecular Science, National Institute of Natural Sciences, Okazaki, Japan
*Corresponding author: aho@ims.ac.jp

***Abstract*— We developed chiral photoinduced force microscopy (PiFM) to visualize nanoscale chiro-optical responses using circularly polarized light. Chiral and achiral plasmonic nanostructures were imaged, revealing local chiral fields and probe-induced chirality. This approach enables nanometer-scale chiro-optical imaging beyond conventional near-field techniques.**

***Keywords*— chiro-optical effects, optical near field, microscopy, photoinduced force microscopy.**

I. Introduction

Observing the internal structure of chiro-optical responses in nano- and micro-scale materials is essential for understanding their chiral properties. We have developed near-field and far-field microscopic imaging methods based on chiro-optical effects. To visualize the geometric structure of chiro-optical responses, particularly at the nanoscale, near-field optical techniques are required. We therefore developed an aperture-type near-field optical microscopy method and achieved chiro-optical imaging of both chiral and achiral plasmonic materials. However, the spatial resolution was limited by the aperture diameter of the near-field probe, typically a few tens of nanometers.

Recently, photoinduced force microscopy (PiFM) has emerged as a new near-field imaging technique. Based on atomic force microscopy, PiFM visualizes optical near-fields by detecting forces between the sample near-field and the polarized probe, and can in principle achieve sub-nanometer spatial resolution. Using this detection principle, we developed chiral PiFM by introducing circularly polarized light and demonstrated nanoscale visualization of chiro-optical responses in chiral plasmonic materials [1].

In this report, we present chiral PiFM imaging of achiral materials to clarify the imaging mechanism. We also describe an analysis of optical forces, including gradient and scattering forces, acting on chiral materials [2], which forms the basis of PiFM.

II. Methods

A critical issue in PiFM measurements of chiro-optical effects is the elimination of photothermal effects. To distinguish optical forces from photothermal contributions, heterodyne frequency modulation (HFM) is required [3]. We employed HFM combined with frequency-modulation atomic force microscopy (FM-AFM) to selectively detect optical forces.

III. Results and Discussion

Chiral PiFM measurements near chiral gold nanostructures revealed differences in the optical forces acting on the probe under left- and right-circularly polarized light, demonstrating the feasibility of nanoscale chiro-optical imaging. Although achiral gold nanosphere dimers do not exhibit macroscopic chiro-optical effects, chiral PiFM revealed localized chiro-optical effect with positive and negative signals depending on position. Furthermore, weak chiral PiFM signals were observed even for single spherical nanoparticles, which should exhibit no intrinsic local chirality signals. This effect is attributed to probe-induced chirality arising from the probe shape and configuration.

IV. Conclusion

We demonstrated near-field chiral optical forces using chiral PiFM, enabling visualization of nanoscale chiral fields around both chiral and achiral nanoparticles. These results indicate the potential of chiral PiFM for broad applications in materials science, nanophotonics, and biochemical analysis.

Acknowledgments

The author thanks Drs. J. Yamanishi, H.-Y. Ahn, Profs. M. Sadgrove, and K. T. Nam for their contributions. This work was supported by Grant-in-Aid for Scientific Research (KAKENHI No. JP22H05135).

References

[1] J. Yamanishi, H.-Y. Ahn, H. Okamoto, "Nanoscopic observation of chiro-optical force," Nano Lett. vol. 23, pp. 9347–9352, 2023.
[2] J. Yamanishi et al., "Heterodyne frequency modulation in photoinduced force microscopy," Sci. Adv. vol. 8, eabq2604, 2022.
[3] J. Yamanishi et al., "Optical gradient force on chiral particles," Phys. Rev. Appl. 9, 024031, 2018.

QED of Chiral Waveguides Coupled to Quantum Emitters

Girish S. Agarwal[1,*]

[1] Texas A&M University, College Station, Texas 77843, USA
*Corresponding author: Girish.Agarwal@ag.tamu.edu

***Abstract*—Waveguide QED is a fundamentally quantum platform in which photons mediate long-range interactions in a one-dimensional channel. This talk highlights waveguide QED with quantum emitters, emphasizing quantum interference (Fano minima and transparency), direction-dependent interactions, quantum nonreciprocity under strong driving, and steady-state entanglement, together with squeezed-bath stabilization and dissipative phase transitions.**

***Keywords*— waveguide QED, chiral waveguides, quantum emitters, transparency, nonreciprocity, entanglement, squeezed bath, time crystals**

I. Introduction

Waveguide quantum electrodynamics provides a cavity free route to strong light matter interaction, where propagating photons in a one dimensional channel interact strongly with quantum emitters. We survey how chirality, interference, and engineered environments in waveguide platforms enable tunable transparency, direction dependent interactions, nonreciprocal transport, and steady state entanglement.

II. Many-atom Fano resonances

In the single-photon scattering theory considered here, a chain of N waveguide-coupled emitters can exhibit multiple Fano minima in reflection (equivalently, transparency peaks in transmission), with up to $N-1$ such minima as the detuning is scanned, and their positions/visibility depend strongly on the inter-emitter phase $\phi = kL$ [1]. In the analytic result, both r and t share the same collective (many-atom, spacing-dependent) denominator that encodes multiple scattering, while r has a numerator proportional to the collective interference function μ_N. Therefore, whenever $\mu_N = 0$, the reflection vanishes (a Fano minimum) and the chain becomes transparent. Since kL enters the same collective scattering factors that set this interference, changing kL strongly shifts and can even suppress these minima.

The double-emitter case allows for multiple photon transport channels, enabling destructive interference. The reflection amplitude is

$$r^{(2)} = -\frac{2ie^{ikL}\Big[\sin(kL) + \big(\Delta_k/\Gamma\big)\cos(kL)\Big]}{\big(\Delta_k/\Gamma + i\big)^2 + e^{2ikL}}. \tag{1}$$

This immediately shows a Fano minimum when the numerator is zero, i.e., $\Delta_k^{\min} = -\Gamma\tan(kL)$, so the transparency point is tunable purely by the spacing phase kL.

III. Transparency for many atoms

For a periodic chain of disparate emitters at $kL = n\pi$, the transmission coefficient is [2]:

$$t = \frac{1}{1 + i\Gamma\sum_{j=1}^{N}\big(\omega_k - \omega_j + i\Gamma_0\big)^{-1}}. \tag{2}$$

The key factor that modifies the spectrum is this additive effect of the inverse detunings. If Γ_0 is small enough to drop, Eq. (2) directly leads to the perfect-transparency condition:

$$\sum_{j=1}^{N}\frac{1}{\Delta_{k(j)}} = 0, \qquad \Delta_{k(j)} \equiv \omega_k - \omega_j. \tag{3}$$

Each emitter contributes a reflection pathway $\propto 1/\Delta_{k(j)}$; arranging detunings so these contributions cancel makes the reflected waves destructively interfere and yields $r = 0$, $t = 1$. A simple practical choice is pairwise equal-and-opposite detunings for even N. This multi-emitter transparency is distinct from the well-known EIT.

This transparency persists even under strong-field conditions [3]. In chiral waveguide QED (asymmetric coupling to forward- and backward-propagating modes), a two-qubit system can exhibit complete forward transmission and zero reflectivity, irrespective of input power, when the qubits are detuned antisymmetrically (one above and one below the central waveguide frequency) and the phase separation satisfies $\phi = n\pi$.

IV. Chiral waveguide induced interactions

A chiral waveguide (direction-dependent coupling) mediates not only collective decay but also a coherent exchange interaction between different emitters. The coherent waveguide-mediated interaction between a pair of qubits (j,l) can be written as

$$H_{jl} = -\frac{i}{2}\left[\left(\Gamma_{j\leftarrow l} - \Gamma^*_{l\leftarrow j}\right)S_j^+ S_l^- + \left(\Gamma_{l\leftarrow j} - \Gamma^*_{j\leftarrow l}\right)S_l^+ S_j^-\right]. \tag{4}$$

Here $S_j^{\pm}$ are the raising/lowering operators of qubit j, and $\Gamma_{i\leftarrow j}$ is the (generally complex and ϕ-dependent) waveguide-mediated coupling for excitation transfer from qubit j to qubit i; its direction is fixed by the spatial ordering along the 1D waveguide. Eq. (4) can be separated into a symmetric exchange channel plus an antisymmetric (chiral) channel. The

antisymmetric contribution has the form of a Dzyaloshinskii–Moriya interaction (DMI). In a nonchiral waveguide, one has $\Gamma_{\rightarrow} = \Gamma_{\leftarrow}$, and only the symmetric exchange term remains.

V. Quantum nonreciprocity and Quantum criticality

Ref. [3] studies transmission and reflection from a chiral waveguide coupled to qubits for arbitrary input powers and reports quantum nonreciprocity and a critical coupling regime. Here, nonreciprocity means that forward and backward propagation can give different transmissions. A key point is that, while a corresponding classical two-oscillator setup can remain reciprocal, in the quantum two-qubit system asymmetric detunings break reciprocity, revealing distinctive quantum nonlinear effects. In particular, for suitable asymmetric detunings and chiral couplings, forward propagation can enter a critical coupling regime for qubits where the coherent field amplitude transmission vanishes entirely at specific driving powers, while the backward transmission remains finite. This regime enables an exceptionally high degree of nonreciprocity in both coherent and incoherent parts of the transmitted field. The same quantum criticality already appears in the one-qubit case: as the input power is varied, the coherent transmission develops a pronounced dip at a critical power, approaching zero on resonance.

VI. Chiral effects due to DMI

The Dzyaloshinskii–Moriya interaction (DMI) can generate nonreciprocal quantum entanglement: with all parameters fixed and only the driven port exchanged, the steady-state two-qubit entanglement differs [4]. For representative phases and detuning patterns, forward driving exhibits a broad high-concurrence region, while backward driving is much weaker.

An especially simple limit occurs at the pure-state transparency points: the system can end up in a pure state because certain decohering channels do not participate, which also yields power-independent perfect transparency. At these pure-state transparency points, the concurrence becomes analytic. For symmetric detuning (the two qubits detuned equally), DMI is essential: it provides an additional coherent coupling channel that enables cancellation of the drive-populated "bright" component, so the dynamics stays in the "dark" manifold and the steady state becomes pure. Without DMI, the steady state remains mixed.

VII. Squeezed-bath stabilized entanglement

In an extended atomic array coupled to a squeezed vacuum, the bath fluctuations can drive the array into a pure dark state decoupled from the environment [5]. A particularly simple and striking result is that for an even number of atoms, the stabilized dark state can be a dimerized state consisting of maximally entangled atomic pairs. These pairs mimic the squeezed field by showing reduced fluctuations in one polarization quadrature and amplified fluctuations in another. Equivalently, the squeezed bath transfers its pair correlations to atoms, producing pairwise entanglement and protecting it by pushing the system into a dark manifold.

VIII. Squeezed bath and time-crystalline phase

In open (dissipative) quantum systems, continuous time crystals can appear as nonequilibrium phases with persistent oscillations even though the Hamiltonian and dissipation are time independent. In [6], the collective-spin model is coupled to a broadband squeezed vacuum reservoir. The key message is: squeezing reshapes the dissipative phase transition and the time-crystal phase. In particular, increasing squeezing can sharpen the dissipative phase transition.

IX. Conclusion

Chiral waveguides provide a unified platform to study and control quantum interference, directional photon transport, and waveguide-induced interactions at the single- and few-emitter level. We discuss how these systems also support quantum nonreciprocity and steady-state entanglement, and how engineered environments such as squeezed baths can stabilize correlations and enable time-crystalline behavior.

Acknowledgments

The funding of the Robert A Welch Foundation (Grant No. A-1943) is gratefully acknowledged.

References

[1] D. Mukhopadhyay, G. S. Agarwal, "Multiple Fano interferences due to waveguide-mediated phase coupling between atoms," *Phys. Rev. A*, 100, 013812 (2019).

[2] D. Mukhopadhyay, G. S. Agarwal, "Transparency in a chain of disparate quantum emitters strongly coupled to a waveguide," *Phys. Rev. A*, 101, 063814 (2020).

[3] Q. Miao, G. S. Agarwal, "Transparency, nonclassicality, and nonreciprocity in chiral waveguide quantum electrodynamics," *Phys. Rev. Research*, 7, 013138 (2025).

[4] Z. Zhang, Q. Miao, G. S. Agarwal, "Quantum nonreciprocity from qubits coupled by Dzyaloshinskii–Moriya interaction," arXiv:2602.11284.

[5] R. Gutiérrez-Jáuregui, A. Asenjo-Garcia, and G. S. Agarwal, "Dissipative stabilization of dark quantum dimers via squeezed vacuum," *Phys. Rev. Research*, 5, 013127 (2023).

[6] Z. Zhang, Q. Miao, G. S. Agarwal, "Time crystals and nonequilibrium dissipative phase transitions mediated by squeezed bath," *Phys. Rev. A*, 112, 033708 (2025).

Plasmonic HfN-Gated Monolayer MoS_2 for Giant Trion Modulation and Scalable Optoelectronic Devices

Yu-Jung Lu[1,2*]
[1]Research Center for Applied Sciences, Academia Sinica, Taipei 11529, Taiwan
[2]Department of Physics, National Taiwan University, Taipei 10617, Taiwan
*E-mail: yujunglu@gate.sinica.edu.tw

We demonstrate a chip-scale, gate-tunable light-emitting platform that integrates scalable monolayer MoS_2 with a HfN plasmonic gate electrode. The favorable band alignment enables giant trion modulation, yielding a PL modulation depth of ~ 24%.

Abstract

Absorption in atomically thin materials remains a key bottleneck for realizing ultrathin, high-performance optoelectronics. Although many strategies have been explored to enhance light-matter interaction in two-dimensional (2D) semiconductors [1], translating these approaches into scalable monolayer devices with consistently improved performance has remained challenging. We address this issue by demonstrating wafer-scale integration of monolayer single-crystal MoS_2 photodetectors with a nitride-based plasmonic metasurface to achieve a high detectivity of 2.58×10^{12} Jones with a record-low dark current of 8 pA and long-term stability over 40 days [2]. We observed an enhancement factor greater than 100 compared to control devices, which can be attributed to the local optical field-enhanced photogating effect by the resonant HfN plasmonic metasurface. Building on this unique photogating concept, we further report a chip-scale, gate-tunable light-emitting platform that integrates monolayer MoS_2 with a work-function-controllable HfN gate electrode. Owing to the favorable band alignment, the device enables efficient charge accumulation and giant trion modulation, yielding a photoluminescence (PL) modulation depth of ~ 24% across tunable regions exceeding 5,000 μm^2 [3]. To further amplify the emission, we introduce resonant nanoparticle-on-mirror (NPoM) plasmonic cavities, achieving a 46-fold emission enhancement due to the Purcell effect while preserving the gate-tunable trion control. Finite-difference time-domain (FDTD) simulations reveal strong optical field confinement in the NPoM cavity, which facilitates efficient plasmon-trion coupling. Taken together, these results demonstrate a room-temperature, CMOS-compatible approach for realizing actively reconfigurable 2D light sources, paving the way for on-chip integrated photonics, visible light communication, dynamic display technologies, tunable emission platforms, and advanced active control of light–matter interactions in atomically thin semiconductors. Overall, these works provide unique approaches [1-4] for energy-efficient on-chip plasmonic circuitry for next-generation optical communication, computation, and quantum information processing. The detailed mechanisms and potential applications of this technology will be explored further in the presentation.

Reference

[1] Hao-Yu Lan, Yu-Hung Hsieh, Zong-Yi Chiao, Deep Jariwala, Min-Hsiung Shih, Ta-Jen Yen, Ortwin Hess, **Yu-Jung Lu***, Gate-Tunable Plasmon-Enhanced Photodetection in a Monolayer MoS_2 Phototransistor with Ultrahigh Photoresponsivity. ***Nano Lett.*** 21, 3083–3091 (2021)

[2] Wei-Ren Syong, Jui-Han Fu, Yu-Hsin Kuo, Yu-Cheng Chu, Mariam Hakami, Tzu-Yu Peng, Jason Lynch, Deep Jariwala, Vincent Tung, and **Yu-Jung Lu***, Enhancing Photogating Gain in Scalable MoS_2 Plasmonic Photodetectors *via* Resonant Plasmonic Metasurfaces. ***ACS Nano*** 18, 5446–5456 (2024).

[3] Tzu-Yu Peng†, Cheng-Han Lin†, Kai Qi, Jui-Han Fu, Chen-Yu Wang, Jyun-Wei Huang, Jia-Wern Chen, Zheng-Zhe Chen, Hung-Wei Shiu, Yao-Wen Chang, Liang-Yan Hsu, Min-Hsiung Shih, Vincent Tung*, and **Yu-Jung Lu***. Giant Trion Modulation in Scalable Monolayer MoS_2 *via* Plasmonic HfN Gates. ***Nature Photonics*** Accepted (2026)

[4] Jason Lynch†, Tzu-Yu Peng†, Jing-Wei Yang, Ben R. Conran, Bongjun Choi, Cindy Yueli Chen, Zahra Fakhraai, Clifford McAleese, **Yu-Jung Lu***, Deep Jariwala*, High-temperature-resilient hyperbolicity in a mixed-dimensional superlattice. Matter (Cell Press) 8, 102290 (2025)

Nanorobots Steered by Light

Bert Hecht[1,*]

[1] Nano-Optics and Biophotonics group, Experimental Phyiscs 5, Institute of Physics, University of Würzburg, Germany
*Corresponding author: bert.hecht@uni-wuerzburg.de

***Abstract*— Plasmonic nanoantennas can be used to redirect scattered light, causing momentum transfer via photon recoil. By exploiting different degrees of freedom of light, such as helicity and photon energy, several antennas can be driven selectively with minimal crosstalk to neighboring structures even at subwavelength distance. Placing up to 4 such nanothrusters on a single micron-sized platform results in an object whose position and orientation can be controlled precisely in 6 degrees of freedom in 2D. By equipping such structures with plasmonic-tweezer elements, interactions with the environment become possible. We discuss nanorobots - less than 1μm in size - interacting with bacteria in aqueous solution driving at speeds of tens of up to 50μm/s.**

***Keywords*— light-driven nanorobots, photon recoil, plasmonic tweezer, optical forces**

Semiconductor metasurfaces for enhanced nonlinearities and control of single photon emission

Igal Brener

Center for Integrated Nanotechnologies, Sandia National Laboratories, USA
ibrener@sandia.gov

***Abstract*—We integrate epitaxial GaAs quantum dots into III–V semiconductor metasurfaces for efficient, position-tolerant light extraction and tunable functionality. Huygens designs boost collected photoluminescence tenfold and enable bunched and super-bunched emission. Symmetry-engineered quadromer lattices provide multiresonant qBIC control and greatly enhance four-wave mixing and nonlinear optical phenomena.**

***Keywords*— metasurfaces, quantum dots, nonlinear optics, quantum, four wave mixing, emission**

The integration of epitaxial semiconductor quantum dots (QDs) into nanophotonic architectures is a cornerstone of scalable quantum information systems, increasingly leveraging the unique capabilities of III–V semiconductor metasurfaces. Unlike plasmonic or conventional dielectric platforms, metasurfaces fabricated from high-index semiconductors enable monolithic integration of emitters—such as local-droplet-etched (LDE) GaAs QDs[1]—directly within the resonator body. Subwavelength control of light via Mie-resonant architectures and nonlocal modes maximizes modal overlap while eliminating the lossy interfaces inherent to hybrid material platforms. Beyond linear control, the field is rapidly advancing toward nonlinear optical metasurfaces, with a major focus on improving parametric processes and harmonic generation, including access to higher-order nonlinearities.

Using Huygens metasurfaces, [2] we create a position-tolerant environment that delivers a tenfold increase in collected photoluminescence, [3] while the broad resonance bandwidth simultaneously captures emission from multiple excitonic complexes. This enables a single-emitter, dual-mode source that produces both antibunched single photons ($g^{(2)}(0) < 0.5$) from neutral excitons and superbunched photons ($g^{(2)}(0) > 2$) from charged complexes under identical pumping conditions. By incorporating these design rules into a voltage-tunable heterostructure that exploits the quantum-confined Stark effect, we can tune distant QDs into spectral resonance with shared nonlocal modes, yielding an order-of-magnitude enhancement in free-space outcoupling. [4]

Future designs that control and enhance interactions between quantum dots will require tailored control over optical fields, modal structure, and the spectral placement of multiple high-Q resonances; further improvements to nonlinear and parametric processes (e.g., SPDC or FWM) in metasurfaces [5] will demand similar advances. To address these needs, we recently developed a multiresonant nonlocal metasurface design paradigm. [6, 7] We employ a symmetry-based, rational framework built around "quadromer" lattices (four elements per unit cell) that uses double band folding and selection rules to realize multiple quasi-bound states in the continuum (qBIC) resonances whose free-space polarizations, Q-factors, mode profiles, and spectral separations can be selected predictably and with strong fabrication robustness. Applying this paradigm to nonlinear processes has enabled several-orders-of-magnitude enhancement of four-wave mixing relative to unpatterned films. Together, active electrical tuning and robust quadromer design establish a scalable framework for investigating cooperative emission and advanced nonlinear optics in future photonic integrated circuits.

Acknowledgments

This work was supported by the U.S. Department of Energy, Office of Basic Energy Sciences, Division of Materials Sciences and Engineering and performed performed, in part, at the Center for Integrated Nanotechnologies, an Office of Science User Facility operated for the U.S. Department of Energy (DOE) Office of Science.

References

1. M. Gurioli, Z. Wang, *et al.*, "Droplet epitaxy of semiconductor nanostructures for quantum photonic devices", Nat Mater **18**, 799 (2019).
2. M. Decker, I. Staude, *et al.*, "High-Efficiency Dielectric Huygens' Surfaces", Advanced Optical Materials **3**, 813 (2015).
3. S. Prescott, P. P. Iyer, *et al.*, "Mie metasurfaces for enhancing photon outcoupling from single embedded quantum emitters", Nanophotonics **14**, 1917 (2024).
4. S. Prescott, P. P. Iyer, *et al.*, "Voltage-Tunable Nonlocal Metasurface for Enhanced Outcoupling of Emission from Quantum Dots", Nano Lett. (2026).
5. T. Santiago-Cruz, S. D. Gennaro, *et al.*, "Resonant metasurfaces for generating complex quantum states", Science **377**, 991 (2022).
6. S. C. Malek, C. F. Doiron, *et al.*, "Robust multiresonant nonlocal metasurfaces by rational design", Nanophotonics **14**, 449 (2025).
7. S. C. Malek, T. Norden, *et al.*, "Giant Enhancement of Four-Wave Mixing by Doubly Zone-Folded Nonlocal Metasurfaces", ACS Nano **19**, 35609 (2025).

Photonic Time Crystals: Transport, Emission, Squeezing

Bumki Min[1]

[1] Department of Physics, Korea Advanced Institute of Science and Technology, Republic of Korea
*Corresponding author: bmin@kaist.ac.kr

***Abstract*— Photonic time crystals, whose optical properties vary periodically in time, provide a unified setting for studying wave transport, light-matter interaction, and quantum fluctuations in driven media. Here we show that seemingly different phenomena in these systems, including transport, emission, and squeezing, can be understood within a common Floquet framework that connects classical and quantum descriptions. This perspective highlights photonic time crystals as a general platform for nonequilibrium photonics, where time-periodic modulation reshapes how light propagates, interacts, and fluctuates.**

***Keywords*— photonic time crystals, transport, emission, squeezing**

Electric Dipole Moments via Electromagnetic Duality

Michael E. Tobar[1,*]

[1]Quantum Technologies and Dark Matter Research Laboratory, Department of Physics, The University of Western Australia,
*Corresponding author: michael.tobar@uwa.edu.au

***Abstract*—We present a duality based framework that maps electric dipole moment physics onto Zeeman structure. Stark induced dipoles are represented through a magnetic current description of microscopic polarization, while intrinsic dipoles remain tied to spin. A Bohr scale dipole unit and pseudo angular momentum organize dipole operators and selection rules.**

***Keywords*— electric dipole moments, Stark effect, Zeeman effect, electromagnetic duality, equivalence currents.**

I. Introduction

Electric dipole moments (EDMs) provide exceptionally sensitive probes of discrete symmetries and are central to searches for new CP-violating physics. Intrinsic EDMs remain unobserved at current sensitivity (e.g., for the electron) [1], while induced orbital EDMs arise routinely through parity mixing in static electric fields, for example in the linear Stark effect. This work develops a symmetry-driven operator framework that maps the Stark sector onto a Zeeman-like structure under electromagnetic duality, making explicit a classical–quantum correspondence between equivalence-current methods and quantum polarization textures. The full treatment and derivations are given in [2].

II. Dual Ohanian viewpoint and magnetic probability current

Ohanian's construction expresses the spin magnetic moment in terms of an effective bound probability current derived from a microscopic magnetization field [3]. By electromagnetic duality, we introduce an electric-sector analogue based on the wavefunction's microscopic polarization $\vec{P}(\vec{r})$. A nonzero curl defines an *effective magnetic probability current density*

$$\vec{J}_m(\vec{r}) \;=\; -\epsilon_0^{-1}\,\nabla \times \vec{P}(\vec{r}), \tag{1}$$

which provides a field-equivalence (topological) representation of internal polarization textures. Importantly, the induced orbital EDM originates physically from parity mixing and charge displacement; $\vec{J}_m$ is an equivalent representation of the same internal structure rather than an additional causal mechanism. In this language, the dipole expectation can be written compactly as

$$\langle \hat{\vec{d}} \rangle \;=\; -\frac{\epsilon_0}{2}\int \vec{r}\times \vec{J}_m(\vec{r})\, d^3r, \tag{2}$$

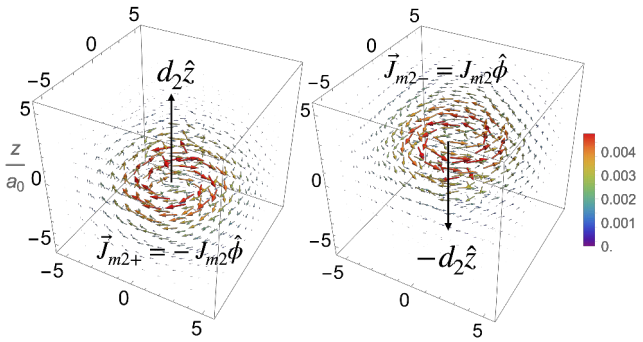

Fig. 1. Illustration of the dual-current picture: polarization textures with nonzero curl admit an equivalent magnetic probability-current representation, plotted for the $n = 2$ Stark states of the hydrogen atom

emphasizing the direct analogy with bound-current representations of magnetic dipoles. This mirrors classical equivalence-current methods in electromagnetics, where impressed electric excitations can be traded for equivalent magnetic currents that reproduce the same exterior fields.

III. Hydrogenic hidden symmetry and pseudo angular momentum

Within the hydrogenic Coulomb problem, the orbital angular momentum $\vec{L}$ and Runge–Lenz operator $\vec{A}$ generate a hidden dynamical symmetry that organizes the degenerate n manifolds. For a finite-mass nucleus, the internal (relative-coordinate) Hamiltonian is written using the reduced mass μ, and for bound states ($H < 0$) a scaled Runge–Lenz operator $\vec{A}_{\rm sc} = \vec{A}/\sqrt{-2\mu H}$ has the dimensions of angular momentum. The combinations $\vec{J}_\pm = (\vec{L} \pm \vec{A}_{\rm sc})/2$ generate the familiar $SO(4) \simeq SU(2) \times SU(2)$ structure of the Coulomb problem and satisfy standard $SU(2)$ commutation relations within a fixed n manifold. In the presence of a static electric field, the Stark interaction couples to the Runge–Lenz sector, and the relevant two- (or few-) level parity subspace can be organized by an effective angular-momentum–like degree of freedom: a *pseudo angular momentum* $\vec{J}_p$ in parity space. This pseudo angular momentum obeys the usual $SU(2)$ algebra and provides the appropriate quantum numbers for Stark eigenstates in the parabolic basis.

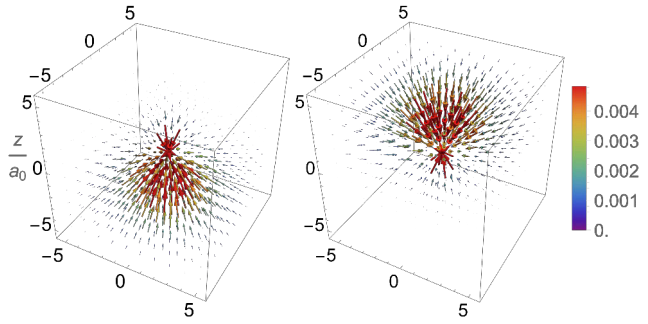

Fig. 2. Runge–Lenz structure used to construct the pseudo angular momentum in parity space for Stark mixing, plotted for the $n = 2$ Stark states of the hydrogen atom

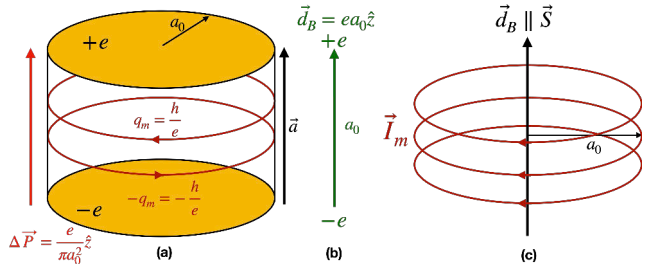

Fig. 3. Semi-classical representations of the Bohr EDM scale, $\vec{d}_B$. (a) Idealized quasi-1D "unit cell" of quantized permanent polarization, $\Delta\vec{P} = \frac{e}{\pi a_0^2}\hat{z}$, for which $\nabla \times \vec{P} \neq 0$ implies an *effective* magnetic current on the radial surface (a dual representation of the polarization texture, not a literal magnetic-charge flow). For mnemonic purposes this surface current can be pictured as two fictitious opposite magnetic charges $\mp q_m = \mp\frac{h}{e}$ circulating in opposite senses, associated with pseudo-spin (pseudo-angular momentum) in parity space rather than mechanical orbital motion. (b) Classical Bohr EDM: two point charges $\pm e$ separated by the Bohr radius a_0. (c) Schematic of an intrinsic Bohr-scale EDM connected to the position-space spin vector $\vec{S}$, represented equivalently by an effective azimuthal magnetic current $\vec{I}_m$ at radius $\sim a_0$.

IV. Bohr-scale dipole unit and orbital dipole operator

We define the natural electric dipole unit (Bohr-scale EDM) as $d_B \equiv e a_\mu$, where a_μ is the Bohr radius defined using the reduced mass. This scale is equivalent to a classical dipole formed by two charges $\pm e$ separated by a_μ, and it also matches the dipole obtained from a polarization quantum in a quasi one-dimensional "cell" picture (Fig. 3). The orbital dipole operator can be written in a Landé-like form,

$$\hat{\vec{d}}_{\rm orb} \;=\; g_E\, d_B\, \frac{\hat{\vec{J}}_p}{\hbar}, \tag{3}$$

where g_E is an electric analogue of the Landé factor determined by the hydrogenic symmetry within a fixed n manifold. As a concrete example, for $n = 2$ Stark mixing of the $2s$ and $2p_{m=0}$ orbitals produces states with permanent induced EDMs $\langle d \rangle = \pm 3 d_B$, corresponding to $g_E = 3$ for that parity doublet.

V. Broader relevance

Beyond atomic physics, the same dual-current language naturally connects to "impressed source" formulations used in engineered resonant and radiating structures. In particular, modified axion electrodynamics can be expressed in terms of effective impressed polarization and magnetization backgrounds, which in turn generate equivalent current sources [6]. Within the present framework, the $\vec{E}\cdot\vec{B}$ interaction admits dual magnetic-current signatures that mirror those appearing in the Stark-sector representation, suggesting a common symmetry-informed viewpoint for electric-dipole responses driven by weak background fields. The dual formulation also gives a new basis to describe magneto-electric couplings between Zeeman and Stark states.

VI. Conclusion

We presented a symmetry-based electromagnetic-duality formulation for EDMs that casts Stark-induced orbital dipoles into a Zeeman-like operator structure. A Bohr-scale dipole unit and a pseudo angular momentum in parity space organize orbital dipole operators, while the magnetic probability-current description provides a compact dual representation of internal polarization textures. The approach is intended to be pedagogical and symmetry driven, and may be useful wherever current-equivalence ideas are routinely employed in quantum and classical electrodynamics.

References

[1] Tanya S. Roussy, Luke Caldwell, Trevor Wright, William B. Cairncross, Yuval Shagam, Kia Boon Ng, Noah Schlossberger, Sun Yool Park, Anzhou Wang, Jun Ye, and Eric A. Cornell. An improved bound on the electron's electric dipole moment. *Science*, 381(6653):46–50, 2023.

[2] Michael E. Tobar, Dual magnetic and electric dipole symmetry: pseudo angular momentum in parity space and the electric Landé g-factor. *arXiv preprint* arXiv:2511.07692, 2025.

[3] Hans C. Ohanian. What is spin? *American Journal of Physics*, 54(6):500–505, 06 1986.

[4] C. Abel, S. Afach, N. J. Ayres, C. A. Baker, G. Ban, G. Bison, K. Bodek, V. Bondar, M. Burghoff, E. Chanel, Z. Chowdhuri, P.-J. Chiu, B. Clement, C. B. Crawford, M. Daum, S. Emmenegger, L. Ferraris-Bouchez, M. Fertl, P. Flaux, B. Franke, A. Fratangelo, P. Geltenbort, K. Green, W. C. Griffith, M. van der Grinten, Z. D. Grujić, P. G. Harris, L. Hayen, W. Heil, R. Henneck, V. Hélaine, N. Hild, Z. Hodge, M. Horras, P. Iaydjiev, S. N. Ivanov, M. Kasprzak, Y. Kermaidic, K. Kirch, A. Knecht, P. Knowles, H.-C. Koch, P. A. Koss, S. Komposch, A. Kozela, A. Kraft, J. Krempel, M. Kuźniak, B. Lauss, T. Lefort, Y. Lemière, A. Leredde, P. Mohanmurthy, A. Mtchedlishvili, M. Musgrave, O. Naviliat-Cuncic, D. Pais, F. M. Piegsa, E. Pierre, G. Pignol, C. Plonka-Spehr, P. N. Prashanth, G. Quéméner, M. Rawlik, D. Rebreyend, I. Rienäcker, D. Ries, S. Roccia, G. Rogel, D. Rozpedzik, A. Schnabel, P. Schmidt-Wellenburg, N. Severijns, D. Shiers, R. Tavakoli Dinani, J. A. Thorne, R. Virot, J. Voigt, A. Weis, E. Wursten, G. Wyszynski, J. Zejma, J. Zenner, and G. Zsigmond. Measurement of the permanent electric dipole moment of the neutron. *Phys. Rev. Lett.*, 124:081803, Feb 2020.

[5] David Vanderbilt. *Berry Phase in Electronic Structure Theory, Electric Polarization, Orbital Magnetization and Topological Insulators*. Cambridge University Press, 2018.

[6] Michael E. Tobar, Ben T. McAllister, and Maxim Goryachev. Modified axion electrodynamics as impressed electromagnetic sources through oscillating background polarization and magnetization. *Physics of the Dark Universe*, 26:100339, 2019.

Topological Phononic and Photonic Modes in Optomechanic Crystals

Nouh Krai[1], Hicham Mangach[1], Abdellatif Gueddida[1], Gaëtan Lévêque[1], Yan Pennec[1], Marco Miniaci[1,2], Bahram Djafari-Rouhani[1*]

[1] Univ Lille, CNRS, Centrale Lille, Junia, UPHF, UMR 8520-IEMN, F59000 Lille, France
[2] Dipartimento di Ingegneria Strutturale, Edile e Geotecnica, Politecnico di Torino, Italy
*Corresponding author: bahram.djafari-rouhani@univ-lille.fr

***Abstract* — In this work we present a theoretical investigation of structures that simultaneously support localized topological phononic and photonic modes, enabling enhanced optomechanical interactions. Two platforms are considered: (i) a one-dimensional nanobeam engineered within the framework of the Su–Schrieffer–Heeger (SSH) model and (ii) a two-dimensional honeycomb membrane.**

***Keywords* — Topological phononics and photonics, Optomechanics, localized modes, nanobeam cavities, SSH model.**

I. Introduction

In recent years, significant interest has emerged in the design of optomechanical (OM) cavities exhibiting high quality factors, and strong OM couplings due to their potential for information processing and communication technologies [1]. ~~This~~ Our work primarily focused on the design of cavities embedded in nanobeam phoxonic crystals, where the localization of acoustic and optical modes occur, respectively, in the few GHz and in the telecom wavelength (1550nm) range, and the OM coupling rates can achieve about 0.5 MHz [2-4]. In parallel, topological concepts have enabled the realization of robust, localized edge states in both photonics [5-6] and phononics [7-10], offering enhanced resilience against fabrication imperfections or structural disorders. In this work, we aim to bridge these two approaches by proposing structures that simultaneously host topological phononic and photonic localized modes. By engineering the spatial overlap of their electromagnetic and mechanical fields, we demonstrate a platform for achieving strong and robust optomechanical interaction.

II. Topological Structures and Localized Phononic and Photonic Modes

We discuss two types of topological structures, namely (i) a one-dimensional (1D) nanobeam where a Dirac gap is created by using the dimerization scheme of the well-known Su-Schrieffer-Heeger (SSH) model [10] and (ii) a 2D honeycomb membrane where a Valley-Hall Dirac gap originates from the breaking of the C_{3v} to C_3 symmetry.

The initial 1D OM device is constituted by a cavity inside a periodic nanobeam. The latter is made of a Si-based array of holes and stubs where proper engineering of the geometrical parameters produces acoustic and optical bandgaps, respectively in the GHz and telecom range. Several conventional cavities have been designed in this type of nanobeam [2-4, 12]. In this work, we propose to extend such designs to topological cavities inspired by the SSH model. In this model, the original unit cells are paired by making long and short distances between neighboring unit cells (Fig. 1). The dimerized structure exhibits a Dirac bandgap where two different topologies can be distinguished depending on whether the super-cell is built from long-distance or short-distance initial unit cells. Then, an association of two crystals with different topologies creates an interface that can support a localized (cavity) mode inside the Dirac gap. This scheme can be applied to both phononic and photonic band structures to create the topological OM cavity. Two types of interface profiles are considered, namely a step profile at the junction of the two crystals, or an adiabatically graded interface where the parameters are gradually changed from the center towards both sides. The optical and acoustic frequencies for both profiles are very close to each other, however the progressive variation of the parameters allows to achieve high optical quality factor and stronger OM coupling. An example is illustrated for a 7 GHz acoustic mode, an optical mode at 1546nm with a quality factor of 6.2 10^4, and an OM coupling rate of $g/2\pi$= 785 kHz. Finally, we have checked the robustness of the topological OM cavity against imperfections and disorder, in comparison to a conventional cavity. From several realizations of disorder, it can be concluded that the topological cavity exhibits a much better stability and reduced fluctuations of resonance frequencies, quality factors and OM coupling rates.

A second structure consists of a periodic silicon-based honeycomb two-dimensional membrane to realize the analog of the quantum valley Hall effect (QVHE) for both photonic and phononic band diagrams [9]. The lattice is constituted by an array of triangular holes embedded within hexagons and circular holes located at the vertices (Fig. 2). Both phononic and photonic modes that are symmetrical with respect to the mid-

plane of the membrane exhibit Dirac cones at the K/K' point of the Brillouin zone. Introducing an asymmetry in the size of the holes breaks the spatial normal mirror symmetry of the structure and gives rise to the opening of Dirac gaps, occurring respectively at 0.332 THz and 8.85 MHz, whose widths increase with the amount of asymmetry (Fig. 2). We investigate the Berry curvature distributions and Chern numbers of the bands as a function of the asymmetry. Then, robust photonic and phononic interface states are predicted to exist at the boundary of two topologically different crystals. We study the propagation of the localized interface modes at the junction of the two crystals. By considering different interface configurations, such as bearded and zigzag, we demonstrate the robustness of the topological modes at sharp bends through the analysis of the Fourier components of the forward and backward waves. We also emphasize that the output interface connecting the waveguide to the surrounding environment can have a significant impact on backscattering and cannot be overlooked in practical applications.

ACKNOWLEDGMENTS

This work was supported by the European Union's Horizon Europe research and innovation program under grant agreement MAGNIFIC (GA No 101091968) and the CHIST-ERA Call 2021 under GA No CHIST-ERA-20-NOEMS-003. MM also acknowledges support from the European Research Council (ERC) under the European Union's Horizon Europe research and innovation programme (POSEIDON, Grant Agreement No. 101039576) and the DREAM project (which received funding from the European Union Next-GenerationEU – National Recovery and Resilience Plan – NRRP, Mission 4, Component 2, Investment 1.2).

REFERENCES

[1] A. H. Safavi-Naeini, D. Van Thourhout, R. Baets, and R. Van Laer, "Controlling phonons and photons at the wavelength scale: integrated photonics meets integrated phononics", Optica 6, 213 (2019).

[2] M. Oudich, S. El-Jallal, Y. Pennec, B. Djafari-Rouhani, J. Gomis-Bresco, D. Navarro-Urrios, C. M. Sotomayor Torres, A. Martınez, and A. Makhoute, "Optomechanic interaction in a corrugated phoxonic nanobeam cavity", Phys. Rev. B 89, 245122 (2014).

[3] J. Gomis-Bresco et al, "A one-dimensional optomechanical crystal with a complete phononic band gap", Nat. Commun. 5, 4552 (2014).

[4] A. Gueddida, B. Djafari Rouhani, Y. Pennec, A. Di Donato, L. Pierantoni, A. Korovin, D. Mencarelli, "Coupling of integrated waveguide and optomechanic cavity for microwave phonon excitation in si nanobeams", Photonics 7, 67 (2020).

[5] T. Ozawa, H.M. Price, A. Amo, N. Goldman, M. Hafezi, L. Lu, M.C. Rechtsman, D. Schuster, J. Simon, O. Zilberberg, I. Carusotto, "Topological Photonics". Reviews of Modern Physics91, 015006 (2019).

[6] G. Lévêque, P. Szriftgiser, A. Amo, Y. Pennec, "Relation between Interface Symmetry and Propagation Robustness along Domain Walls Based on Valley Topological Photonic Crystals". APL Photonics 9, 126107 (2024).

[7] T.W. Liu, F. Semperlotti, "Experimental Evidence of Robust Acoustic Valley Hall Edge States in a Nonresonant Topological Elastic Waveguide". Phys. Rev. Applied 11, 014040 (2019).

[8] X. Xi, I. Chernobrovkin, J. Košata, M.B. Kristensen, E. Langman, A.S. Sørensen, O. Zilberberg , A. Schliesser, "A soft-clamped topological waveguide for Phonon", Nature 642, 947 (2025).

[9] M. Miniaci, R.K. Pal, B. Morvan, M. Ruzzene, "Experimental Observation of Topologically Protected Helical Edge Modes in Patterned Elastic Plates", Phys. Rev. X 8, 031074 (2018).

[10] M. Miniaci, F. Allen, R.K. Pal, Spectral flow of a localized mode in an elastic media", Phys. Rev. Applied, 20, 064018 (2023).

[11] W.P. Su, J.R. Schrieffer, A.J. Heeger, "Solitons in Polyacetylene", Phys. Rev. Lett 42, 1698 (1979).

[12] A. Gueddida, L. Carpentier, G. Lévêque, Y. Pennec, B. Djafari-Rouhani, "Elastic Wave Focusing and Optomechanical Coupling in a Nano-Opto-Electro-Mechanical Device" Proceedings of Antennas and Electromagnetic Structures (AES) 2024.

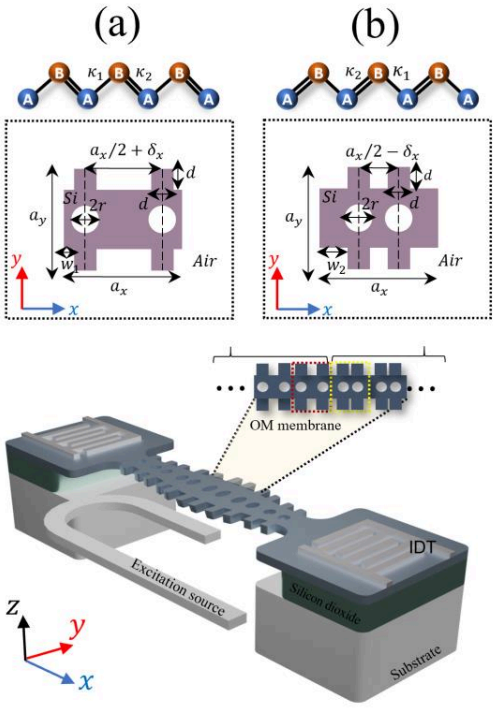

Figure 1: Schematic view of the topological optomechanical cavity. Panels (a) and (b) illustrate unit cells with long and short distances between holes and stubs, with a spacing parameter δ_x.

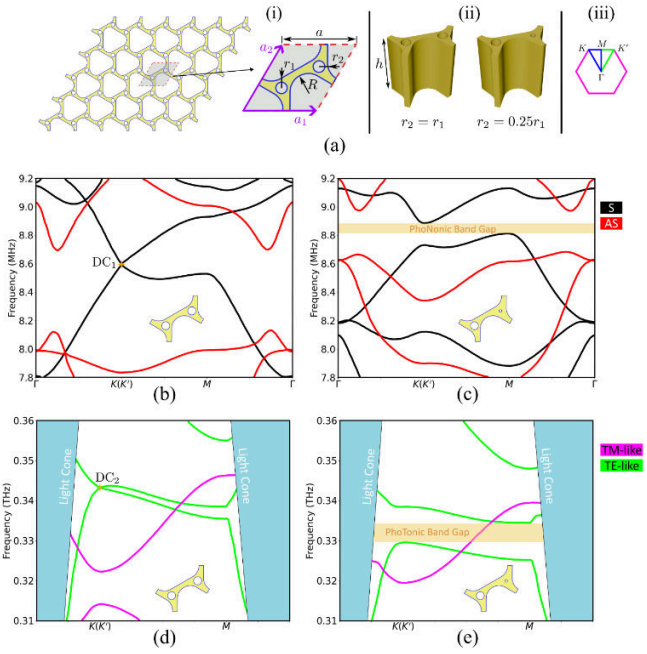

Figure 2: (a) In-plane and out-of-plane views of the unit cell before and after symmetry breaking, and its first irreducible Brillouin zone. (b, c) Phononic dispersion curves, respectively, before and after symmetry breaking. The black and red colors, respectively, illustrate the symmetrical (S) and anti-symmetrical (AS) modes with respect to the mid-plane of the plate. (d, e) Same as (b, c) for the photonic dispersion curves.

Modeling boundary effects in acoustic metamaterials by a relaxed micromorphic continuum

Angela Madeo[1,*]

[1] TU Dortmund University, Germany
*Corresponding author: angela.madeo@tu-dortmund.de

***Abstract*— Exploring the dynamical response of mechanical metamaterials within the framework of elastic wave propagation has gathered increasing attention in recent decades. To accurately describe elastic wave propagation in these materials – characterized by their heterogeneities or microstructures – it is essential to adopt non-local or enriched modeling approaches. In this context, we propose the relaxed micromorphic model (RMM), which effectively captures these phenomena by treating the material as continuum with enriched kinematics. A crucial micro-mechanical effect addressed by this model is the presence of band gaps, for which waves with specific frequencies cannot propagate through the material. Our previous studies have demonstrated that the RMM adequately describes the bulk behavior of mechanical metamaterials. Challenges arise, however, when considering finite-size metamaterial blocks, where boundary effects can significantly influence behavior due to reduced dimensions. Consequently, it becomes necessary to enhance the relaxed micromorphic model framework to account for these boundary effects. We will illustrate how incorporating boundary forces facilitates accurate modeling of finite-size metamaterial specimens within the framework of micromorphic elasticity.**

***Keywords*— relaxed micromorphic model, acoustic metamaterials, boundary effects, elastic wave propagation, band gaps**

Hybrid Techniques for Inverse Design and Knowledge Discovery in Large-scale Multifunctional Nanophotonic Devices

Reza Marzban, Jamshid Hassanpour, Jiu Chang, Hamed Abiri, and Ali Adibi

School of Electrical and Computer Engineering, Georgia Institute of Technology

Abstract: This talk is focused on a new class of inverse design tools for large-scale nanophotonic structures by combining the unique features of rigorous gradient-based techniques (e.g., topological optimization) with machine learning tools. It is shown that by combining these two classes of design tools, the dimensionality of the design space as well as the computation requirement for training the algorithms can be reduced by 2-3 orders of magnitude. This will result in a powerful tool for not only designing large-scale and multifunctional nanophotonic devices but also obtaining helpful insight into the device operation and the importance of different design parameters in achieving the desired performance measures.

Bio: Ali Adibi is the director of Bio and Environmental Sensing Technologies (BEST) and a professor and Joseph M. Pettit chair in the School of Electrical and Computer Engineering, Georgia Institute of Technology. He is also a member of the Winship Cancer Research Center at the Emory University. His research group has pioneered several structures in the field of integrated nanophotonics for both information processing and sensing. He has also pioneered new sensing solutions for medical diagnosis as well as AI algorithms for diagnosis and prognosis in medicine. He is the author of more than 260 journal papers and 600 conference papers. He has served as the editor, conference chair, and technical committee members in over 30 different conferences and journals. He has also led several multidisciplinary research teams in the areas of integrated optics and metaphotonics for sensing, interconnection, and imaging. He is the recipient of several awards including Presidential Early Career Award for Scientists and Engineers, Packard Fellowship, NSF CAREER Award, and the SPIE Technology Achievement Award. He is also a fellow of OSA, SPIE, and AAAS.

TUTORIAL

Tutorial

1 contribution · pp. 143–143

Chiro-Optical Microscopy — Near-Field and Far-Field

Hiromi Okamoto[1,*]

[1]Institute for Molecular Science, National Institute of Natural Sciences, Okazaki, Japan
*Corresponding author: aho@ims.ac.jp

***Abstract*— Chiro-optical microscopy enables spatially resolved analysis of material chirality. This tutorial reviews near-field and far-field chiro-optical microscopic techniques, including aperture-type methods, photoinduced force microscopy, and high-precision CD imaging, and summarizes their applications to nano- and micro-scale chiral materials.**

***Keywords*— chiro-optical effects, microscopy, near-field microscopy, photoinduced force microscopy.**

I. Introduction

Chiro-optical effects provide valuable information on the chirality of materials and are widely applied in chemistry, materials physics, biosciences, and related fields. Chiro-optical spectroscopy, typified by circular dichroism and optical rotation, is therefore recognized as a powerful tool for analyzing material chirality. Despite its high potential, the application of chiro-optical spectroscopy is sometimes limited because of generally weak signals and interference from linear-polarization effects; consequently, only a few studies have reported chiro-optical imaging of inhomogeneous anisotropic samples. Nevertheless, the development of chiro-optical microscopic imaging methods is expected to have a significant impact on a wide range of research fields related to chiral materials. In this tutorial, fundamental techniques of chiro-optical microscopy are reviewed, and applications to nano- and micro-scale materials, such as plasmonic materials and microcrystals, are summarized.

II. Methods of Chiro-Optical Microscopy

A few different types of microscopic techniques have been employed to achieve chiro-optical microscopy, depending on the detection method and the spatial resolution required.

Aperture-type near-field optical microscopy: With aperture-type near-field microscopy, circular dichroism (CD) imaging using circularly polarized light [1], as well as polarimetric imaging using linearly polarized light [2], can be achieved. In the former case, the sample is illuminated with far-field radiation modulated between left- and right-circular polarization, and the response field near the sample is collected by a near-field aperture probe and detected in intensity. Lock-in detection yields the difference between the responses under left- and right-circularly polarized illumination, providing the CD signal. Near-field CD images are obtained by scanning the sample relative to the probe. In the latter case, the sample is illuminated with a linearly polarized field through the near-field aperture, and the forward-scattered light is detected in the far field. The ellipticity and polarization rotation angle are measured using polarization optics, and scanning the sample yields near-field ellipticity and optical rotation images. Using these methods, spatial resolutions of several tens of nanometers have been achieved.

Photoinduced force microscopy: As an alternative near-field approach, photoinduced force microscopy based on atomic force microscopy (AFM) was developed recently. In this method, both the sample and the probe are illuminated with light, and the force exerted on the probe due to light-induced polarization is detected by the AFM mechanism. Chiro-optical images can be obtained by introducing left- and right-circularly polarized illumination [3]. Spatial resolutions of several tens of nanometers have been demonstrated, and resolutions of a few nanometers, or better, are anticipated in principle.

Far-field high-precision CD microscopy: Even with conventional far-field optics, precise and accurate CD imaging free from linear dichroism is not straightforward for non-uniform anisotropic samples, and only a few reliable reports exist. A major source of linear dichroism artifacts is the use of a photoelastic modulator (PEM), which is commonly employed in conventional CD spectrophotometers. To achieve reliable CD imaging, we developed a new method of circular polarization modulation instead of using a PEM. With this approach, we achieved reliable high-precision CD microscopic measurements of non-uniform anisotropic chiral materials [4].

References

[1] T. Narushima and H. Okamoto, “Strong nanoscale optical activity localized in two-dimensional chiral metal nanostructures,” J. Phys. Chem. C, vol. 117, pp. 23964-23969, 2013.
[2] S. Hashiyada, T. Narushima, and H. Okamoto, “Imaging Chirality of Optical Fields near Achiral Metal Nanostructures Excited with Linearly Polarized Light,” ACS Photon., vol. 5, pp. 1486-1492, 2018.
[3] J. Yamanishi, H.-Y. Ahn, and H. Okamoto, “Nanoscopic Observation of Chiro-Optical Force,” Nano Lett., vol. 23, pp. 9347-9352, 2023.
[4] T. Narushima and H. Okamoto, “Circular Dichroism Microscopy Free from Commingling Linear Dichroism via Discretely Modulated Circular Polarization,” Sci. Rep., vol. 6, 35731, 2016.

SYMPOSIUM 1

Hybrid Nanomaterials and Metastructures for Photonics, Sensing and Energy

61 contributions · pp. 145–241

Green Hydrogen Produced from Water Splitting at Photocatalytic Titanium Dioxide Thin Films on Gold Nanoislands

Nicolas Albenge[1,*], Florian Laible[1], Jonas Rathgeb[1], Timo Braun[1], Sandra Glocker[1], Bjarne Gutbrod[1], Leah Schynowski[2], Udo Weimar[2], Nicolae Barsan[2], Monika Fleischer[1]

[1]Institute for Applied Physics and Center LISA[+], University of Tübingen, Germany
[2]Institute of Physical and Theoretical Chemistry and Center LISA[+], University of Tübingen, Germany
*Corresponding author: nicolas.albenge@uni-tuebingen.de

***Abstract*—Gold nanoislands are hybridized with a titanium dioxide thin film combining visible light absorbing structures with UV absorbing photocatalysts for light-induced water splitting. A custom reactor is built to measure the amount of hydrogen generated. Design considerations and first hints to the generation of green hydrogen are presented.**

***Keywords*— green hydrogen, plasmonic photocatalysis, nanoislands, thin films.**

I. Introduction

Annually only about 1% of the 100 million tonnes of hydrogen (H_2) production worldwide is environmentally sustainable. Green H_2 can be generated directly from solar energy via water splitting in plasmonic photocatalysis, holding the potential to be more efficient than industrially used, indirect H_2 generation methods including e.g. electrolysis.
High-energy charge carriers in plasmonically excited metal nanostructures can drive chemical reactions via charge transfer and an increase in temperature [1]. Titanium dioxide (TiO_2) generates charge carriers upon photo-absorption of UV light, but they can recombine before taking part in redox reactions. Combining TiO_2 with gold (Au) nanostructures, UV and visible light is absorbed, more charge carriers form through energy transfer, and an electric field originating from the space charge region reduces charge recombination and promotes their separation [2].

II. Methods

After sputtering of Au on glass substrates, a dewetting process at 360 °C for 33 min leads to the formation of Au nanoislands. Next, a TiO_2 thin film is evaporated (see Fig. 1a). Several samples fabricated in this manner are mounted vertically in a polydimethylsiloxane (PDMS) base. The resulting highly absorbing array is submerged in a closed reactor and irradiated by a halogen lamp through a window. Generated H_2 is carried by an airflow to gas sensors able to detect H_2 (see schematic in Fig. 1b).

III. Results and Discussion

Scanning electron microscope measurements show Au nanoislands with sizes from 10 nm to 20 nm. Transmission

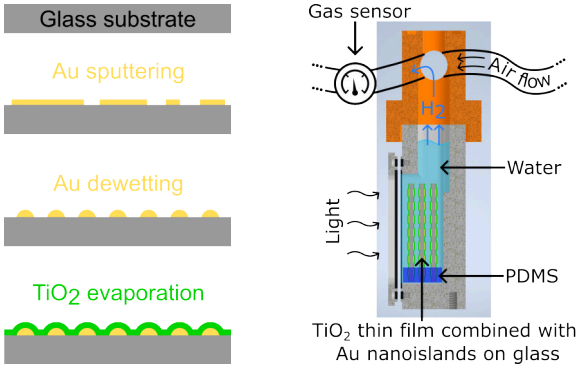

(a) (b)

Fig. 1: Schematic drawing of the fabrication process (a) and the reactor setup (b)

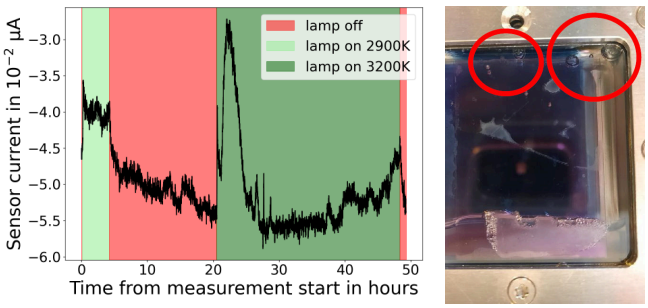

(a) (b)

Fig. 2: Sensor current during an H_2 measurement with the halogen lamp turned on and off (a) and accumulated H_2 bubbles inside the reactor most likely preventing continuous H_2 measurements (b).

UV-Vis spectroscopy yields absorbance peaks at roughly 610 nm. In Fig. 2a the sensor response shows enhanced signals while the lamp is illuminating the reactor. During the second illumination phase with enhanced light intensity (highlighted with a darker green area) the signal drops again after roughly 2 h. One possible explanation is an accumulation of H_2 bubbles

inside the reactor chamber, which can not be transported to the gas sensors by the air flow (see Fig. 2b).
As further design considerations, annealing the TiO_2 could enable transitions from amorphous to crystalline anatase films and improve water splitting rates [3]. An evaporation and dewetting process of platinum can lead to the formation of platinum nanoislands acting as cocatalysts improving H_2 evolution [4].

IV. Conclusion

We have demonstrated the fabrication of a hybrid system combining Au nanoislands exhibiting plasmonic responses with visible light and photocatalytic TiO_2 thin films. First traces of H_2 generation are observed. Future work will extend the design to improve H_2 detection and generation.

Acknowledgments

The authors thank C. Simo and the members of the Fleischer group for helpful discussions. Experimental support by R. Löffler, M. Turad and the members of the metal and glass workshop is gratefully acknowledged.

References

[1] S. Linic, U. Aslam, C. Boerigter and M. Morabito, "Photochemical transformations on plasmonic metal nanoparticles," *Nature Materials*, vol. 14, pp. 567–576, 2015.
[2] X. Zhang, Y. L. Chen, R. Liu and D. P. Tsai, "Plasmonic photocatalysis," *Reports on Progress in Physics*, vol. 76, pp. 1–41, 2013.
[3] J. Abed, M. AlMheiri, F. Alexander, N. S. Rajput, J. Viegas and M. Jouiad, "Enhanced solar absorption of gold plasmon assisted TiO_2-based water splitting composite," *Solar Energy Materials and Solar Cells*, vol. 180, pp. 228–235, 2018.
[4] F. Wang, R. J. Wong, J. H. Ho, Y. Jian and R. Amal, "Sensitization of Pt/TiO_2 Using Plasmonic Au Nanoparticles for Hydrogen Evolution under Visible-Light Irradiation," *ACS Applied Materials & Interfaces*, vol. 9, pp. 30575–30582, 2017.

Very-large scale reconfigurable surfaces for dynamic control of THz and millimeter waves

Said Ergoktas[1,2]

[1]Department of Physics, University of Bath, UK
[2]Center for Photonics, University of Bath, UK
*Corresponding author: mse38@bath.ac.uk

In this talk, I will go through brief history of our research on graphene-based terahertz (THz) devices leading to our latest work on very large-scale reconfigurable surfaces for dynamic control of THz and millimeter-wave.[1]

Keywords: graphene, terahertz, spatial light modulator, mm-wave

Reconfigurable intelligent surfaces (RIS) that can program terahertz (THz) and millimeter-wave fields in real time are a key missing hardware layer for next-generation wireless links, sensing, and non-invasive imaging. Progress has been limited by the scarcity of efficient, electrically tunable THz materials and by the challenge of scaling from single devices to large, densely addressable arrays. Here we present a very-large-scale programmable THz surface that merges graphene electro-optical modulators with mature thin-film transistor (TFT) active-matrix backplanes. The resulting platform implements >300,000 individually addressable, subwavelength pixels over a large area, enabling spatially structured control of transmission and reflection across the THz/mm-wave spectrum. We demonstrate electronically generated transmission patterns and masks with high uniformity and reproducibility and show millisecond-scale switching suitable for dynamic operation. In reflection mode, the multilayer architecture is engineered to operate near a reflection singularity, providing strong amplitude and phase reconfiguration and enabling large phase excursions associated with a topological transition in the complex reflection response. To highlight functionality beyond static patterning, we demonstrate (i) single-pixel mm-wave imaging of concealed metallic objects using structured masks and computational reconstruction, and (ii) dynamic beam steering and beam shaping via reconfigurable diffraction patterns, including vortex-beam generation. These results establish a scalable route to real-time, software-defined THz wavefront control for imaging and emerging THz communication systems.

REFERENCES

1. Malevich, Y., Ergoktas, M.S., Bakan, G. *et al.* Very-large-scale reconfigurable intelligent surfaces for dynamic control of terahertz and millimeter waves. *Nat Commun* **16**, 2907 (2025).

Engineering Local Field Enhancement with Single-Crystal Noble Metal Plasmonics

Jacob Seigo Syme[1], Tashfin Shaife[1], Rebecca Storck[1], Hannah Martinelli[1], Albert Adserias[1], Finlay MacNab[1], Sasan V.-Grayli[2], Gary W. Leach[1,*]

[1]Department of Chemistry, Simon Fraser University, Burnaby, Canada
[2] Department of Physics, Simon Fraser University, Burnaby, Canada
*Corresponding author: gleach@sfu.ca

***Abstract*— We describe a platform for single-crystal plasmonic nanomaterials and metasurfaces enabling engineered local field enhancements and new opportunities in nanophotonics, sensing, and energy harvesting. Engineered hot spots, metasurfaces and optically active nanostructures provide tailored fields, large SERS sensing response, controlled scattering for flat optics, and improved photo- and electro-catalytic activity.**

***Keywords*— single-crystal noble metals, engineered hot spots, metasurfaces, optical activity**

I. Introduction

Material quality plays a critical role in the performance of nanometer-scale plasmonic structures and represents a significant hurdle to large-scale device integration. Progress has been hindered by the challenges of realizing scalable, high quality, metal deposition strategies, and by poor pattern transfer and device fabrication yields characteristic of most metal deposition approaches, which yield polycrystalline metal structure. Here we highlight a novel, scalable and versatile platform to deposit ultrasmooth, single-crystal (SC) gold films ideal for subtractive patterning of nanostructures through ion beam milling, and high definition, sub-wavelength SC nanostructures through lithographic patterning methods to yield SC metasurfaces[1,2]. Here we describe complementary strategies to achieve enhanced local fields from SC plasmonic structures where we utilize the geometry and crystallinity of SC gold metasurfaces to manipulate the wavelength-dependent optical responses and plasmonic local near-field distributions of metallic nanostructures.

II. Results and Discussion

We employ a solution deposition method in the presence of anionic additives to give shape-controlled, single-crystal plasmonic gold nanostructures on Ag(100) and Au(100) substrates. Together with lithographic patterning. this chemistry yields metal deposition with precise geometry and location control to provide SC, plasmonic gold metasurfaces with tailored optical response that leverages their individual and collective responses. SC Au(100) metasurfaces comprised of square pyramidal nanostructures with dominant Au(111) facets have been fabricated to tailor the local plasmonic fields to provide resonant enhancement of the surface enhanced Raman scattering (SERS) spectra (Fig. 1). Finite Difference Time Domain (FDTD) simulations guide the design of the metasurfaces through nanostructure size and periodicity to provide local field enhancement resonant with the 785 nm laser employed for SERS measurements. This resonant enhancement provides significantly larger SERS response from Raman marker molecules such as benzoic acid (BA), compared to the SERS response from BA-covered SC gold surfaces comprised of SC square pyramids of random disposition.[3]

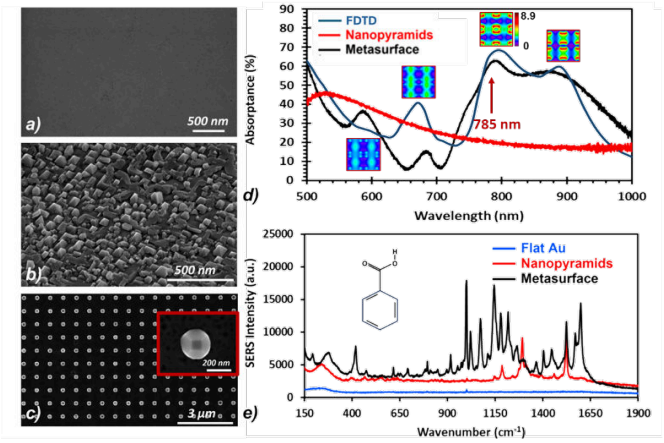

Fig. 1 SEM images of (a) flat Au, (b) randomly distributed square nanopyramids resulting from Au deposition in the presence of sulfate additives, and (c) a 250 nm diameter truncated square pyramid, 700 nm period, gold metasurface. (d) Experimental absorptance spectrum of the benzoic acid-coated randomly distributed nanopyramids (red), and the experimental (black) and FDTD simulated (blue) absorptance of the benzoic acid-coated metasurface shown in panel (c). Insets show the FDTD unit cell electric field distributions of the optical resonances appearing at 580, 680, 785, and 900 nm. (e) 785 nm SERS response from the benzoic acid-coated surfaces displayed in panels (a)–(c).

While it is common wisdom that metal-supported metasurfaces display poor SLR quality factors due to rapid dissipation of plasmonic excitation into the bath of electron density provided by the supporting metal surface, we are currently developing new strategies to produce SC metal-

supported, plasmonic metasurfaces with large surface lattice resonance (SLR) response.

One popular approach to achieve large local field enhancement is via the un-patterned deposition of solution-grown plasmonic nanocrystals onto a substrate. This approach relies on the fortuitous formation of hot spots that are not easily predictable but can give rise to enormous local field enhancements that drive large SERS response, that in some cases afford single-molecule sensitivity. Here, we describe our attempts to access more reproducible and quantitative SERS responses through the engineering of "hot spots" in single-crystal metal films through focused ion beam and helium ion beam milling. We design optical cavities, resonant antennas, and structures with nanometer-scale gaps through Finite Difference Time Domain (FDTD) simulation software, pattern high-quality SC metal films to create the desired engineered hot spots and employ SERS response as a measure of local field enhancement.

SC films of plasmonic metals and their alloys have also been employed for water splitting and CO_2 reduction reaction (CO2RR) electrocatalysis. We have identified optimal PtAu(100) and PtAg(100) alloy compositions for the hydrogen evolution reaction (HER) and shown that Au:Cu(100) SC alloy composition controls the CO2RR product distribution, yielding large (~60%) faradaic efficiency for C_2H_4 reduction products. Deposition of high surface area materials shows that these electrocatalytic processes can be enhanced through light exposure via plasmon-assisted electrocatalysis.

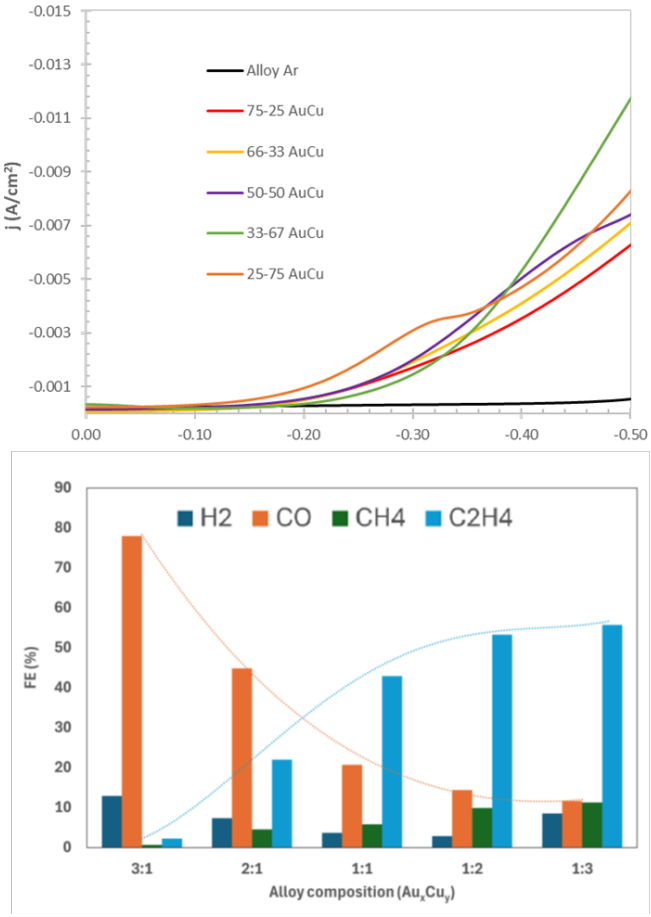

Fig. 2 Top: Linear sweep voltammograms of SC AuCu(100) alloy films of varying composition. The results show composition-dependent electro-chemical current production and overpotential. Bottom: SC AuCu(100) alloy product distributions. The results show composition-dependent.Faradaic efficiencies. Higher carbon content CO2RR products are correlated with alloys of higher copper content.

III. Conclusion

We have demonstrated a versatile and enabling platform for single-crystal plasmonics and nanophotonics applications. SC metals provide superior materials properties with reproducible and predictable, high-fidelity pattern transfer and tailored, enhanced local fields for SC metasurfaces, engineered hot spots and optically active nanostructures, with application in nanophotonics, sensing and energy harvesting.

Acknowledgments

We acknowledge financial support from the Natural Sciences and Engineering Research Council of Canada, the Canada Foundation for Innovation, the British Columbia Knowledge Development Fund, CMC Microsystems and Simon Fraser University.

References

[1] V. Grayli, S., Zhang, X., MacNab, F. C., Kamal, S., Star, D. and Leach, G. W.*, "Scalable, Green Fabrication of Single-Crystal Noble Metal Films and Nanostructures for Low-Loss Nanotechnology Applications," ACS Nano. **14,** 7581–7592, 2020.

[2] V. Grayli, S., Kamal. S. and Leach, G. W.*, "High performance, single crystal gold bowtie nanoantennas fabricated via epitaxial electroless deposition," Scientific Reports, **13,** 12745, 2023.

[3] V. Grayli, S., Zhang, X., Star, D. and Leach, G. W.*, "Tailoring Plasmonic Fields with Shape-Controlled Single-Crystal Gold Metasurfaces," ACS Appl. Mat. and Interfaces, **16**, 35410−35420, 2024.

Control of photo-induced absorption and chemical functionalization within plasmonic nanostructures

M.Vega[1,2,3], T. Prieur[1,2,3], J. Moreau[3], PL Karsenti[1,2], C. Molinaro[4,5], O. Soppera[4,5], P. Charette[1,2], M. Canva[1,2], J-F Bryche[1,2*]

[1]Laboratoire Nanotechnologies Nanosystèmes (LN2) - IRL3463, CNRS, Univ. de Sherbrooke, INSA Lyon, École Centrale de Lyon, Univ. Grenoble Alpes, Canada
[2]Institut Interdisciplinaire d'Innovation Technologique (3IT), Univ. de Sherbrooke, Canada
[3]Laboratoire Charles Fabry, LCF, CNRS, IOGS, Univ. Paris-Saclay, France
[4]Université de Haute Alsace, CNRS, IS2M UMR 7361, F-68100 Mulhouse, France
[5]Université de Strasbourg, F-67081 Strasbourg, France
*Corresponding author: jean-francois.bryche@cnrs.fr

***Abstract*— We demonstrate how thermal energy distribution within excited plasmonic metasurfaces can be used for local modification of chemical functionalization for biosensing applications.**

***Keywords*— Thermoplasmonics, pump-probe spectroscopy, Surfaced enhanced Raman spectroscopy, plasmonic biosensors.**

I. Introduction

Through several projects, we have studied plasmonic couplings, between propagative (SPP) and localized surface plasmons (LSP) in nanostructures [1,2,3]. The coupled mode has demonstrated interest in biosensing applications, notably in SPR and SERS (Raman spectroscopy) [3,4]. In addition, metal nanoparticles behave as heat sources by absorbing and converting light into thermal energy, resulting [5,6] in an interesting new pathway to manipulate at the nanoscale chemical functionalization.

II. Methods

We measured the transient reflectivity of a metasurface consisting of a 2D array of nano-cross shaped particles using pump-probe spectroscopy. These were compared with numerical simulations based on the Three-Temperature Model [6,7], which accounted for non-thermal electron ballistic displacement to determine the relative contribution of non-thermalized (N), thermalized electrons (T_e) and lattice temperatures (T_l). Additionally, the potential sensing performance was evaluated using a custom SPRI setup and TERS instrument [4,5].

III. Results and Discussion

We showed experimentally and numerically that non-thermal energy density and temperature inside the two arms of the nano-crosses can be controlled with the polarization of the pump pulse [7]. We then exploited the repartition of the three different energy baths (N, T_e, T_l) to degrade the chemical functionalization on the nanoparticles with a spatial resolution as low as 20 nm. We extended our study to several shapes of nanoparticles to optimize the control of the electronic temperature distribution on and around the gold nanostructures.

IV. Conclusion

We have demonstrated control at the nanoscale of the electronic and lattice temperatures and used it to locally modify the chemical functionalization of plasmonic biosensors. Future work will extend toward biosensing applications as well as understanding relative contribution of non-thermal and thermal effects on chemical modification. A complementary analysis based on thermopolymers is underway [8] to offer new understanding of ultrafast thermoplasmonic phenomena.

Acknowledgments

This work was supported by the French government ('France 2030' and ANR-11-IDEX-003) and by the Natural Sciences and Engineering Research Council of Canada with Discovery Grant; as well as the Fonds de Recherche du Québec, CMC Microsystems, MNT Voucher, Mitacs for their grants.

References

[1] J.-F. Bryche *et al.,* "Experimental and numerical investigation of biosensors plasmonic substrates [...]," Micro and Nano Engineering, vol. 2, pp. 122–130, 2019.
[2] M. Vega *et al.,* "Plasmonic Film with Diluted Nanostructures for Light Energy Harvesting and Sensing," ACS Appl. Opt. Mater., vol. 3, pp. 2329–2338, 2025.
[3] R. Gherman *et al.,* "A comprehensive study of plasmonic mode hybridization in gold nanoparticle-over-mirror (NPoM) arrays," Nanophotonics, vol. 14, pp. 5347–5361, 2025.
[4] J.-F. Bryche *et al.,* "Spatially-Localized Functionalization on Nanostructured Surfaces for Enhanced Plasmonic Sensing Efficacy," Nanomaterials, vol. 12, p. 3586, 2022.
[5] C. Beltrami *et al.,* "Surface plasmon resonance imaging signal amplification for the detection of micro-RNAs in the context of organ donation," Biophotonics in Point-of-Care III. SPIE, p. 15, 2024.
[6] P. Bresson *et al.,* "Improved two-temperature modeling of ultrafast thermal and optical phenomena [...]," Phys. Rev. B, vol. 102, 2020.
[7] J.-F. Bryche†, M. Vega† *et al.,* "Ultrafast Heat Transfer at the Nanoscale: Controlling Heat Anisotropy," ACS Photonics, 2023.
[8] A. Khitous *et al.,* "Unveiling Localized Plasmonic Activation comparing Photochemically and Thermally Initiated Polymerization." American Chemical Society (ACS), chemrxiv-2025.

Terahertz Slow- and Fast-Light Switching Through Liquid-Crystal-Integrated Plasmon-Induced Transparency Fano-resonant Metamaterials

R. Kowerdziej [1,*], I. Bisignano [2,3], D. Yavorskiy [4,5], M. Olifierczuk [1], A. Ferraro [6], G. E. Lio [7], N. Pałka [8], J. Wróbel [1,5], R. Caputo [9]

[1] Institute of Applied Physics, Military University of Technology, 2 Kaliskiego St., 00-908, Warsaw, Poland
[2] Research Center for Materials Nanoarchitectonics (MANA), National Institute for Materials Science (NIMS), Tsukuba, Ibaraki 305-0044, Japan
[3] Faculty of Pure and Applied Sciences, University of Tsukuba, Tsukuba, Ibaraki 305-8577, Japan
[4] CENTERA Laboratories, Institute of High Pressure Physics PAS, 29/37 Sokołowska St., 01-142 Warsaw, Poland
[5] Institute of Physics PAS, 32/46 Lotników Avenue, 02-668 Warsaw, Poland
[6] Consiglio Nazionale delle Ricerche – Instituto di Nanotecnologia (CNR-Nanotec), via P. Bucci cubo 33c, Rende, CS, 87036, Italy
[7] Department of Physics E. Fermi, University of Pisa, Largo Bruno Pontecorvo 3, 56127, Pisa, Italy
[8] Institute of Optoelectronics, Military University of Technology, 2 Kaliskiego St., 00-908, Warsaw, Poland
[9] Physics Department, University of Calabria, via P. Bucci cubo 31c, Rende, CS, 87036, Italy
*Corresponding author: rafal.kowerdziej@wat.edu.pl

***Abstract* — Active and hybrid Fano-resonant plasmon induced transparency (PIT) metasurfaces are identified as an emerging technology in terahertz optics. Here, we introduce Fano-resonant liquid crystal integrated PIT metasurface for terahertz slow- and fast-light switching. Our findings support active Fano-resonant metasurfaces as compelling candidates for state-of-the-art nonlinear and slow- and fast-light devices.**

***Keywords* — active metamaterials, terahertz physics, liquid crystal photonics, plasmon-induced transparency, fast light, slow light.**

I. Introduction

The resonance phenomenon was revealed by Galileo Galilei in 1602 as he examined musical strings. It was later found that a variety of resonances, including mechanical, acoustic, and electromagnetic, are prevalent features of numerous classical and quantum systems. Typically, the spectral lineshape of these resonances is articulated through the Lorentzian formalism, with its dynamic variables originating from a basic linear differential equation [1]. In 1961, Ugo Fano encountered a remarkable resonance phenomenon while investigating the autoionizing states of atoms, which has been subsequently termed the Fano resonance [2].

In contrast to the Lorentzian resonance, the Fano resonance occurs when a discrete quantum state engages with a continuum of states, resulting in a unique shape in the absorption spectrum, σ(E), which adheres to the specific pattern outlined by the well-known Fano formula [3,4]:

$$\sigma(E) = D^2 \frac{(q+\Omega)^2}{1+\Omega^2} \quad (1)$$

where E represents the energy, $q = cot\delta$ is the Fano parameter, δ denotes the phase shift of the continuum. Additionally, the parameter Ω is defined as: $\Omega = \frac{2(E-E_0)}{\Gamma}$, where Γ and E_0 denote the resonance width and energy, respectively. Finally, the value D^2 can be expressed as $D^2 = 4sin^2\delta$ [4].

Current technological developments are advancing towards the incorporation of these attributes for application in plasmonics, and the progress in metaphotonics has led to numerous instances of resonant optical phenomena associated with the physics of Fano resonances [5,6]. Fano-resonant metamaterials have attracted considerable attention as an efficient and highly precise toolkit for designing innovative photonic chips with exotic functionalities, unveiling a wide range of applications in sensors, laser technology, switching mechanisms, as well as nonlinear and slow-light devices [7-9]. Interestingly, under specific circumstances, a Fano resonance can be seen as the plasmonic counterpart of plasmon-induced

transparency (PIT) [1,5-7]. These circumstances involve: (i) a sufficiently small frequency detuning between the two resonances being coupled; (ii) significant differences in resonance linewidths; and (iii) appropriate resonance amplitudes[5-7]. Hence, the emergence of Fano resonances is attributed to the interference among two or more oscillators, giving them a natural susceptibility to variations in geometry or the surrounding environment.

In consideration of the broad spectrum of opportunities and the ongoing evolution of Fano-resonant metamaterials that rely on the PIT effect, there is a current lack of multifunctional platforms that facilitate the management of both slow- and fast-light effects throughout a wide spectral range. Hence, it is critical to pursue further advancements in this sector.

In light of the previously mentioned limitations, we hereby introduce the notion of an active and hybrid Fano-resonant terahertz PIT metamaterial that facilitates the management of both slow- and fast-light effects over an extensive spectral range.

II. Hybrid and Active Plasmon-Induced Transparency Fano-Resonant Metamaterial

The spatial distribution and geometric dimensions of PIT microstructured metamaterial is shown in Fig. 1(a). The whole structure is composed of unit cells having a square shape with sides measuring 100 µm. A top-view image of the fabricated metasurface is presented in Fig. 1(b). To achieve fast and reproducible spectral tuning of PIT peaks, the metamaterial was hybridized with a 20-µm-thick layer of 1825 nematic liquid crystal (NLC) mixture, as shown in Fig. 1(c).

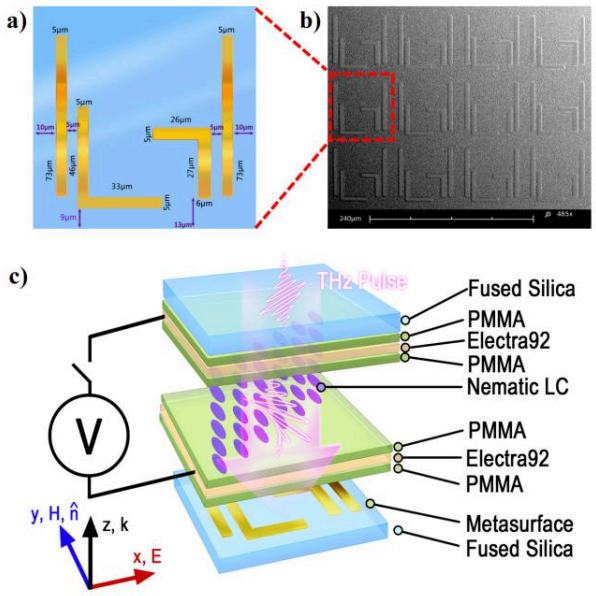

Fig. 1. Hybrid and active Fano-resonant PIT metamaterial. (a) Unit cell geometry. (b) SEM image of fabricated microstructured Fano-resonant metasurface. (c) Scheme of the liquid crystal integrated metamaterial cell.

III. Results and Discussion

Our efforts began with the design and optimization of the metasurface architecture, employing numerical simulations. To provide an explanation for the origin of the two PIT peaks, we first executed simulations of the individual meta-atoms that constitute the foundation of the final Fano-lineshape metasurface, as seen in Fig. 2.

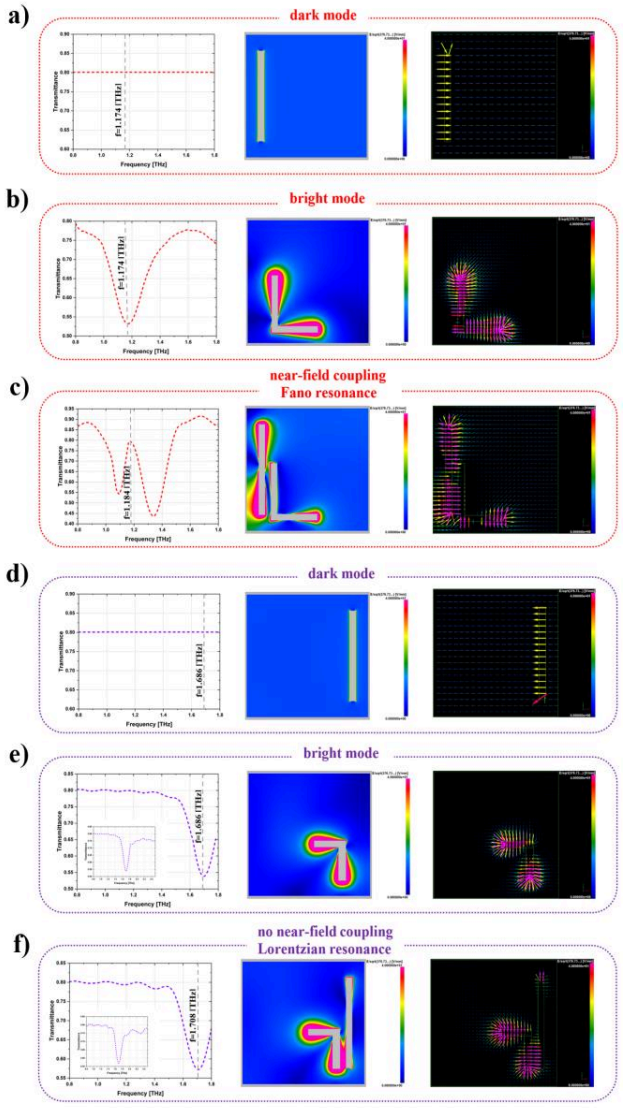

Fig. 2. Simulated transmittance amplitude and corresponding electric as well as vector field distribution at resonance frequency of (a) the sole left bar, (b) the sole left L-shaped element, (c) both left elements, (d) the sole right bar, (e) the sole right L-shaped element, and (f) both right elements.

It has been proven that the first Fano-resonant peak of plasmon-induced transparency (PIT1) results from the near-field coupling between the dark and bright meta-atoms, which are represented by the sole left bar, and the sole left L-shaped element, respectively. On the contrary, the meta-atoms located on the right do not exhibit near-field coupling, which results in a collective response that takes the form of a Lorentzian resonance. As a result, the PIT2 peak is produced from the interference of the Fano-resonant response (PIT1) and the

aforementioned Lorentzian resonance.

Significantly, our approach combines simulation, optimization techniques, and experimental insights. A comparison of the simulated and experimental results for the Fano-resonant PIT metamaterial is shown in Fig. 3. Figure 3(c) provides the group delay, calculated by:

$$t_g = \frac{d\varphi(\omega)}{d\omega} \qquad (2)$$

A heightened phase dispersion is observed around the transparency windows, resulting in a greater group index (n_g), which can be expressed as:

$$n_g = \frac{c}{h}\frac{d\varphi(\omega)}{d\omega} \qquad (3)$$

where, c is the velocity of light in free space, h is the substrate thickness and φ is the transmission phase of the MM structure. In Fig. 3(d), we have represented the group index value as a function of frequency to allow for a quantitative interpretation of the group index values within the transparency windows. It is evident from the figure that the normal dispersion of the group index is paired with anomalous dispersion surrounding the transparency windows. Crucially, group index (n_g) changes from a positive to a negative value depending on THz frequency, thus affirming the occurrence of slow- and fast-light effects.

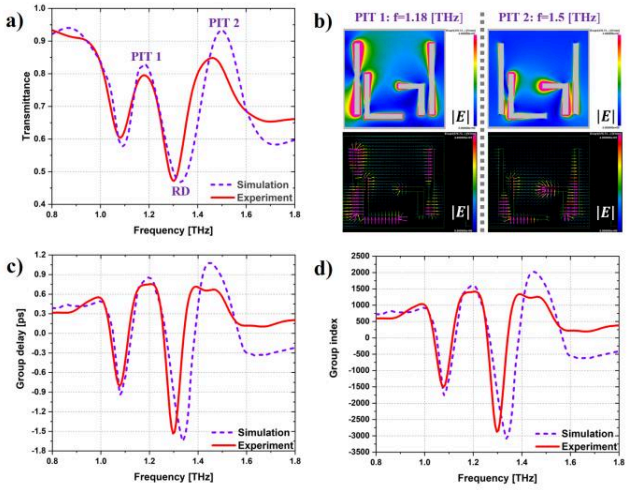

Fig. 3. A comparison of simulated and experimental outcomes. (a) Transmittance amplitude of the Fano-resonant PIT metamaterial. (b) The distribution of electric and vector fields at the resonance frequencies for both PIT1 and PIT2. (c) Group delay and (d) group index.

In the final section of the study, we utilized the sensitivity of the LC to an external stimulus, specifically an electric field, which enabled us to reorient the molecules within the LC mixture. This approach allowed us to assess the tunable parameters of the Fano-resonant metamaterial at THz frequencies. The chosen outcomes are displayed in Fig. 4. The experimental data evidently reveal that the Fano-lineshape PIT metamaterial can be effectively adjusted, achieving an intensity change of as much as 2.5% and a spectral range of up to 22 GHz, merely by varying the magnitude of the AC bias voltage, as depicted in Fig. 4(b). These values approach the theoretical limits of 5.5% for intensity tunability and 30GHz for spectral tunability [see Fig. 4(a)].

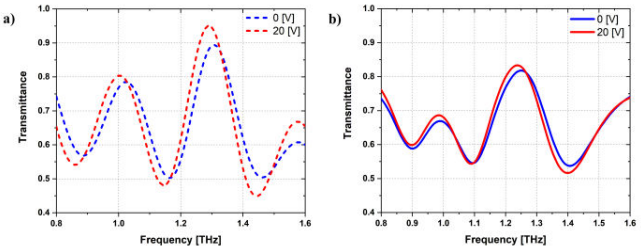

Fig. 4. Fano-resonant PIT metamaterial (a) simulated and (b) experimental transmittance amplitude tunability for off- (0[V]) and on-state (20[V]).

Following the outlined methodology, we also established the tunability of both terahertz group delay (t_g), and group index (n_g).

IV. Conclusion

We have introduced a concept of Fano-resonant PIT THz metamaterial for active control of both terahertz group delay (t_g), and group index (n_g). Notably, the group index varies from a positive to a negative value depending on THz frequency, thus corroborating the manifestation of slow- and fast-light effects. The results of our study endorse active Fano-resonant metasurfaces as noteworthy candidates for leading-edge nonlinear devices, including those designed for slow and fast light functionalities.

Acknowledgments

This research was supported by the National Science Centre under grant SONATA BIS-12 No. 2022/46/E/ST7/00454, entitled “Tunable and ultrafast terahertz hybrid metamaterials based on plasmon-induced transparency effect.”

References

[1] B. Luk’yanchuk, N. I. Zheludev, S. A. Maier, N. J. Halas, P. Nordlander, H. Giessen, C. T. Chong, "The Fano resonance in plasmonic nanostructures and metamaterials." *Nature materials* 9.9 (2010): 707-715.

[2] U. Fano, "Effects of configuration interaction on intensities and phase shifts." *Physical review* 124.6 (1961): 1866.

[3] G. E. Lio, A. Ferraro, R. Kowerdziej, A. O. Govorov, Z. Wang, R. Caputo, “Engineering Fano-Resonant Hybrid Metastructures with Ultra-High Sensing Performances”. Adv. Optical Mater. 2023, 11, 2203123.

[4] M. F. Limonov, M. V. Rybin, A. N. Poddubny & Y. S. Kivshar, "Fano resonances in photonics." *Nature photonics* 11.9 (2017): 543-554.

[5] J.-P. Connerade, A. Lane, "Interacting resonances in atomic spectroscopy." *Reports on Progress in Physics* 51.11 (1988): 1439-1478.

[6] C. Yan, K.-Y. Yang, O. J. F. Martin, "Fano-resonance-assisted metasurface for color routing." *Light: Science & Applications* 6.7 (2017): e17017-e17017.

[7] W. X. Lim, M. Manjappa, Y. K. Srivastava, L. Cong, A. Kumar, K. F. MacDonald, R. Singh, "Ultrafast all-optical switching of germanium-based flexible metaphotonic devices." *Advanced materials* 30.9 (2018): 1705331.

[8] S.-E. Mun, H. Yun, C. Choi, S.-J. Kim, and B. Lee, “Enhancement and Switching of Fano Resonance in Metamaterial.” *Adv. Opt. Mater.* 2018, 6(17), 1800545.

[9] C. Wu, A. B. Khanikaev, G. Shvets, "Broadband slow light metamaterial based on a double-continuum Fano resonance." *Physical review letters* 106.10 (2011): 107403.

Hybrid integrated nonlinear photonics with resonant 2D materials

A. Bile[1], D. de Ceglia[2], D. Ceneda[1], M. C. Larciprete[1], M. Centini[1]*

[1] Sapienza Università di Roma, Dept. SBAI, Italy
[2] University of Brescia, Dept. of Information Engineering, Italy
*Corresponding author: marco.centini@uniroma1.it

***Abstract*— We present a hybrid integrated platform based on patterned 3R MoS_2 enabling compact visible second harmonic generation. Band edge localization and counter propagating excitation provide efficient vertical emission from nanoscale nonlinear regions, supporting scalable integrated nonlinear and quantum photonic architectures.**

***Keywords*— nonlinear photonics, 2D materials, integrated waveguides, second harmonic generation, quantum photonics.**

I. Introduction

Two dimensional transition metal dichalcogenides exhibit exceptionally strong second order nonlinear susceptibilities enhanced by excitonic resonances and reduced dimensionality [1], [2]. Integrating these materials into dielectric waveguides enables ultracompact frequency conversion platforms operating in the visible spectral range. However, strong absorption near excitonic transitions imposes strict constraints on device geometry and field localization.

Hybrid integrated architectures combining silicon nitride waveguides with resonant MoS2 nanoelements offer a route toward efficient nonlinear interaction within nanometric volumes. The present work investigates a band edge engineered structure capable of maximizing pump localization while enabling vertical extraction of the generated second harmonic.

II. Methods

The device consists of a Si3N4 ridge waveguide patterned with 11 periodically spaced 3R phase MoS_2 resonators positioned above a SiO_2 substrate (Fig. 1). Counter propagating pumps at 890 nm excite a band edge resonance that localizes the fundamental field inside the MoS_2 elements while minimizing propagation losses. The generated second harmonic at 445 nm radiates vertically through leaky modes supported by the hybrid structure.

Full wave electromagnetic simulations are performed using a nonlinear polarization model under the undepleted pump approximation. The MoS_2 nonlinear susceptibility is taken from experimentally reported resonant values [3]. Device parameters are optimized to balance absorption, field enhancement, and phase interference between distributed nonlinear sources [4].

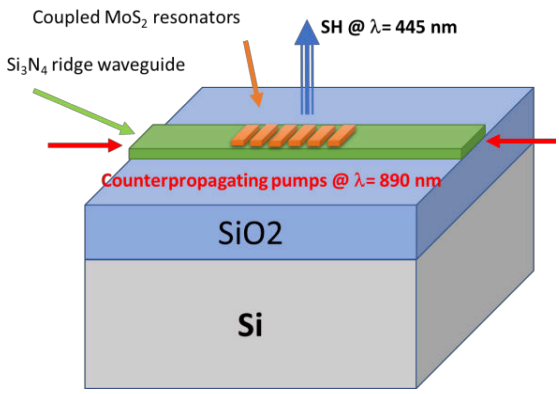

Fig. 1 Sketch of the Hybrid Si_3N_4 waveguide with coupled MoS_2 resonators excited by counter propagating pumps. Vertical radiation corresponds to the generated second harmonic.

III. Results and Discussion

The optimized structure achieves efficient frequency conversion within an interaction area of approximately 1 µm². Simulations predict second harmonic conversion efficiencies approaching 0.004 percent at moderate (300 MW/cm^2) peak pump intensities. The band edge resonance produces strong spatial confinement of the fundamental field, enhancing the effective nonlinear interaction length despite the atomic scale thickness of MoS_2.

The optimized structure consists of 11 MoS_2 stripes, each 30 nm thick and 100 nm wide, separated by 102 nm air gaps. The field distributions associated with the corresponding band edge mode are shown in Fig. 2. The fundamental pump field exhibits strong longitudinal localization inside the MoS2 array, forming a standing wave pattern that maximizes the nonlinear polarization. The generated second harmonic displays efficient vertical radiation and spatial confinement consistent with coherent emission from the coupled resonators.

Directional emission control emerges from coherent interference between distributed nonlinear sources. Figure 3

shows the upward and downward normalized radiated second harmonic power as a function of MoS_2 spacing. Results were normalized to a single MoS_2 patch having the same total MoS_2 width as the device to quantify the effect of band-edge enhancement. The response remains broadband over tens of nanometers, supporting ultrafast excitation and robust tolerance to fabrication variations.

These features indicate compatibility with spontaneous parametric down conversion and correlated photon generation in visible integrated platforms.

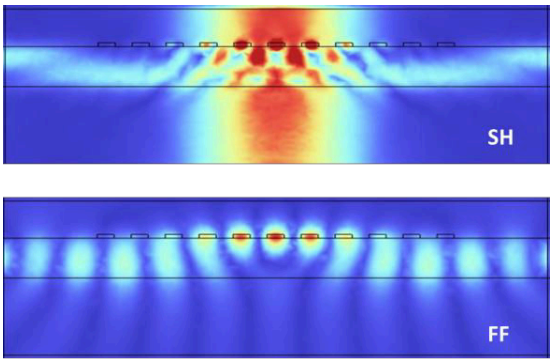

Fig. 2 Simulated electric field intensity distributions for the optimized structure composed of 11 MoS_2 stripes separated by air gaps. The fundamental frequency (bottom) is strongly localized within the array, while the generated second harmonic (top) radiates vertically from the interaction region.

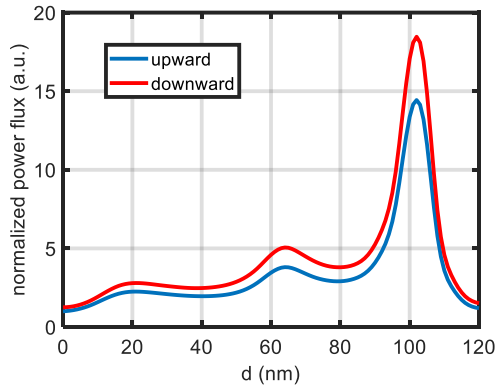

Fig. 3 Upward (blue) and downward (red) radiated second harmonic power as a function of MoS2 element spacing.

IV. Conclusion

We demonstrate a hybrid resonant photonic architecture capable of ultracompact visible second harmonic generation using patterned 2D materials. The platform supports directional emission control, nanoscale nonlinear interaction, and compatibility with CMOS fabrication. These results establish a pathway toward scalable visible frequency nonlinear and quantum photonic circuits based on resonant 2D materials.

Acknowledgments

This work was supported by the European Union under the Italian National Recovery and Resilience Plan (NRRP) of Next Generation EU partnership PE0000023-NQSTI.

References

[1] Xie, Z.; Zhao, T.; Yu, X.; Wang, J. Nonlinear Optical Properties of 2D Materials and Their Applications. Small 2024, 20, 2311621.

[2] Malard, L. M.; Alencar, T. V.; Barboza, A. P. M.; Mak, K. F.; De Paula, A. M. Observation of Intense Second Harmonic Generation from MoS_2 Atomic Crystals. Phys. Rev. B 2013, 87, 201401.

[3] Zograf, G.; Küçüköz, B.; Polyakov, A. Y.; Yankovich, A. B.; Ranjan, A.; Bancerek, M.; Agrawal, A. V.; Olsson, E.; Wieczorek, W.; Antosiewicz, T. J.; Shegai, T. O. Ultrathin 3R-MoS_2 metasurfaces with atomically precise edges for efficient nonlinear nanophotonics. Commun. Phys. 2025, 8, 271.

[4] Bil,e A.; de Ceglia, D.; Ceneda, D.; Larciprete, M. C.; and Centini, M. Compact Second-Harmonic Generation in the C-Exciton Band of 3R-MoS_2 for Integrated Quantum Photonics, ACS Photonics 2026 13 (1), 1-13

Metasurfaces with phase singularity for sensor applications: a theoretical and experimental study

Théo Girerd[1], Sebastien Cueff[2], Fabien Mandorlo[1], Taha Benyattou[1], Xavier Letartre[2], Cécile Jamois[1], Lydie Ferrier[1], Lotfi Berguiga[1,*]

[1]INSA Lyon, Ecole Centrale de Lyon, CNRS, Université Claude Bernard Lyon 1, CPE Lyon, INL, UMR5270, 69621 Villeurbanne, France

[2]Ecole Centrale de Lyon, INSA Lyon, CNRS, Université Claude Bernard Lyon 1, CPE Lyon, INL, UMR5270, 69130 Ecully, France

*Corresponding author: lotfi.berguiga@cnrs.fr

***Abstract*—Photonic structures with phase singularities are studied theoretically and experimentally for sensing applications. Our theoretical framework provides a better understanding of the phase behaviour near critical coupling. We demonstrated that the sensitivity and detection limit of the Goos-Hänchen sensor can be improved theoretically by a factor of 100 000.**

***Keywords*— Photonic sensors, phase singularity, Goos-Hänchen shitf, Tamm plamon photonic crystal, Bloch Surface Wave.**

I. Introduction

Photonic sensors are a rapidly growing area of scientific research, driven by demand in fields such as health, safety, the environment and food. In the health sector, early diagnosis remains critical for many diseases, including cancer, infectious diseases, cardiovascular diseases and autoimmune diseases. Therefore, developing sensitive photonic sensors capable of detecting molecules with low molecular weight and/or present in low concentrations remains a technical and scientific challenge. In nanophotonics, resonant metasurfaces have been studied and developed for their ability to amplify light locally and thus improve the detection of biomolecules on their surface. Photonic structures with phase singularity are sensors that lead to a very low limit of detection. Two interrogation methods exploiting phase singularity are currently in use: i) phase interrogation using polarimetric or interferometric methods [1], or ii) the Goos–Hanchen effect, which involves measuring the lateral displacement of the reflected beam [2]. This paper explores photonic sensors with phase singularity theoretically and experimentally, providing new insights into sensors with phase interrogation as well as those using the Goos–Hanchen effect when critical coupling and its phase singularity are approached.

II. Methods

In this paper, a phenomenological approach with Temporal Coupled Mode Theory is used to model the reflectivty of photonic structures. Deduced analytical equations describing the sensitivity for sensor interrogated in phase or by the Goos-Hänchen effect have been established[3–5]. The physical parameter that describe the phase sensitivty and the Goos-Hänchen are established and allow to predict the limit of detection versus the physical parameters.

III. Results and Discussion

The phase sensitivity S_ϕ and the Goos-Hänchen sensitivty S_{GH} are described by the following two equations:

$$S_\phi = \frac{2}{\lambda_{res}} \frac{Q}{r_{min}} S_\lambda \quad and \quad S_{GH} = -\frac{3\sqrt{3} a \lambda_{res}}{8\pi^2 c} \left(\frac{Q}{r_{min}}\right)^2 S_\lambda \tag{1}$$

The sensitivities are governed by the quality factor Q, the sensitivity in wavelength S_λ, the wavelength resonance λ_{res} and for Goos-Hänchen effect by the dispersion in angle $a = \frac{d\omega_{res}}{d\theta}$, with ω_{res} the pulsation at resonance. The phase sensitivity and Goos-Hänchen sensitivity explode when the minimum of reflectivity at resonance r_{min} tends toward zero in other words when the critical coupling is approached. For phase sensitivity this variation is linear with the ratio Q/r_{min} and for Goos-Hânchen this variation is squared.

Experimental measurements are performed using an interferometric setup with holography [6] on Tamm plasmon nanostructures. Critical coupling was achieved during nanofabrication by tuning the grating geometry to the nanometre scale. The phase sensitivity relation has been verified.
Using the same experimental setup and photonic structures, the Goos–Hanchen shift can be estimated by Fourier imaging. This shows that a giant Goos–Hanchen shift is possible (up to 2 mm). This also allows us to verify the validity of our theoretical framework concerning the Goos–Hanchen shift versus Artmann's usual equation [7].

IV. Conclusion

With the developed theoretical framework, we pointed out that for metasurface with phase singularities, sensitivity and limit of detection can be pushed at very high value and at very low level respectively. We explored phase singularity and we showed experimentally the link between the phase of the reflected light and the Goos-Hänchen shift thanks to Fourier imaging. Theoretically with Goos-Hänchen sensors the sensitivity and limit of detection can be pushed by 5 orders of magnitudes. It is possible by a better understanding of the Goos-Hänchen shift behavior around the critical coupling.

REFERENCES

1. Kabashin, A. V., Kravets, V. G. & Grigorenko, A. N. Label-free optical biosensing: going beyond the limits. *Chemical Society Reviews* **52,** 6554–6585 (2023).
2. Zhu, S., Jaffiol, R., Crunteanu, A., Vézy, C., Chan, S.-T., Yuan, W., Ho, H.-P. & Zeng, S. Label-free biosensing with singular-phase-enhanced lateral position shift based on atomically thin plasmonic nanomaterials. *Light: Science and Applications* **13** (Jan. 2024).
3. Berguiga, L., Ferrier, L., Jamois, C., Benyattou, T., Letartre, X. & Cueff, S. Ultimate phase sensitivity in surface plasmon resonance sensors by tuning critical coupling with phase change materials. *Optics Express* **29,** 42162–42175 (2021).
4. Berguiga, L., Girerd, T., Letartre, X., Benyattou, T., Jamois, C., Mandorlo, F. & Ferrier, L. Exploring phase sensitivity and limit of detection near the critical coupling of metasurfaces and its phase singularity. *arXiv* (2025).
5. Berguiga, L., Cueff, S., Ferrier, L., Mandorlo, F., Benyattou, T., Letartre, X. & Jamois, C. A formalism for giant Goos-Hänchen shift in metasurface sensors with phase singularity. *arXiv* (2025).
6. Girerd, T., Mandorlo, F., Jamois, C., Benyattou, T., Ferrier, L. & Berguiga, L. Optical sensing based on phase interrogation with a Young's interference hologram using a digital micromirror device. *Optics Express* **32,** 3647 (Jan. 2024).
7. Pollès, R., Mihailovic, M., Centeno, E. & Moreau, A. Leveraging beam deformation to improve the detection of resonances. *Physical Review A* **94** (Dec. 2016).

Flexible and Stackable Stickers to Prepare Quasi-3D Metasurfaces

Shunsuke Murai[1,*], Koichi Okamoto[1]

[1]Department of Physics and Electronics, Graduate School of Engineering, Osaka Metropolitan University, Japan
*Corresponding author: murai@omu.ac.jp

***Abstract*— We present a strategy for preparing quasi-three-dimensional metasurfaces using flexible and stackable metasurface stickers. By integrating periodically arranged metasurface structures with incoherent light sources, the angular radiation distribution can be effectively controlled, enabling highly directional emission. The flexibility and stackability of the polymer-embedded metasurface stickers allow facile assembly of multilayer architectures, providing additional degrees of freedom for tailoring optical responses. Potential applications include directional light sources and other functional photonic devices based on reconfigurable quasi-3D metasurfaces.**

***Keywords*—Metasurface stickers; Directional emission; Polymer-embedded nanostructures**

I. Introduction

Metasurfaces enable compact control of light through subwavelength nanostructures, yet most implementations remain limited to rigid, two-dimensional platforms. Extending metasurface functionality toward three-dimensional configurations while maintaining simplicity and reconfigurability is highly desirable, particularly for controlling emission from incoherent light sources. In this work, we propose flexible and stackable metasurface stickers as a practical route to realize quasi-3D metasurfaces and directional light emission.

II. Methods

The metasurface structures were designed as periodic nanoantenna arrays to engineer the angular radiation characteristics through collective lattice effects. The nanostructures were fabricated on a sacrificial substrate and subsequently embedded into a flexible polymer layer, forming a freestanding metasurface sticker. These stickers can be attached to light-emitting substrates or stacked in multiple layers to create quasi-3D configurations. Optical characterization was performed by measuring far-field emission patterns under incoherent illumination, allowing direct evaluation of the angular radiation distribution and directionality.

III. Results and Discussion

A single metasurface sticker significantly modified the emission pattern of an incoherent light source, producing enhanced intensity in specific angular directions. Stacking multiple stickers provided additional control over the radiation distribution, indicating effective out-of-plane structuring through layer stacking. This approach enables angular emission engineering without complex fabrication or precise alignment, while preserving mechanical flexibility and reconfigurability.

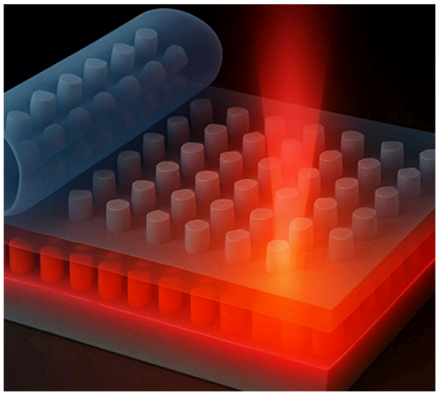

Fig. 1: Sketch of the metasurface-based directional lightsource; an emitter sandwiched between two metasurfaces [4].

IV. Conclusion

Flexible and stackable metasurface stickers provide a simple and scalable platform for preparing quasi-3D metasurfaces. The demonstrated control of directional emission from incoherent light sources highlights their potential for compact directional lighting and other reconfigurable photonic applications.

Acknowledgments

This work was partly supported by the Nanotechnology Hub, Kyoto University. We gratefully acknowledge financial support from Kakenhi (25K01501, 25K21709), provided by JSPS, Japan, and the Futaba foundation.

References

[1] S Murai, et al., *J. Mater. Chem.* C 11, 472-479 (2023)
[2] R Kamakura et al., *J. Appl. Phys.* 124, 213105 (2018)
[3] S Murai, et al., *J. Appl. Phys.* 129 183101 (2021)
[4] TY Lo, et al., *Adv. Opt. Mater.*, e02518 (2025)
[5] S Murai et al., *ACS Appl. Opt. Mater.* 3, 2006-2012 (2025)
[6] H Gao et al., *Nanophotonics* 14, 4627 (2025)
[7] J He et al., *ACS Photonics* 12, 4608-4615 (2025).

Tailoring Optical Dispersion using Nonlinear Geometric-phase Metasurfaces

Mikko J. Huttunen[1,*], Madona Mekhael[1], Roman Calpe[2], Robert Fickler[1], Tommi Hakala[2]

[1]Photonics Laboratory, Physics Unit, Tampere University, Tampere, Finland
[2]Center for Photonics Sciences, University of Eastern Finland, Joensuu, Finland
*Corresponding author: mikko.huttunen@tuni.fi

***Abstract*— We demonstrate nonlinear metasurfaces utilizing nonlinear geometric phase, providing accurate phase control of nonlinear signals via adjusting the orientation of metasurfaces. Demonstrated metasurfaces could be used as thin coatings for nonlinear applications benefitting of dispersion fine-tuning, such as for frequency conversion of ultrashort pulses using very thin nonlinear materials.**

***Keywords*— nonlinear metasurfaces, geometric phase, dispersion engineering, ultrafast optics.**

I. Introduction

Dispersion engineering is instrumental in many ultrafast applications, such as frequency conversion/characterization of ultrashort pulses using very thin nonlinear materials [1]. Nonlinear metasurfaces are emerging as a promising candidate to provide new possibilities for fine-tuning the dispersion engineering capabilities of existing technologies dominantly based on chirped mirror coatings [2]. Here, we discuss and present our latest work to develop metasurface-based coatings enabling fine-tuning of dispersion.

II. Methods and Results

The approach is based on earlier work on phasematching metasurfaces using multipass cell configuration [3]. Here, we extend the concept and study a stack of two metasurfaces, consisting of randomly positioned three-bladed gold nanogears (Fig. 1a). Due to the symmetry (C_{3v}) of nanogears, their linear response is isotropic, but second-harmonic generation (SHG) response exhibits an orientation-dependent geometric phase [4]. By rotating the second metasurface, the phasematching curves of SHG responses shift (Fig. 1b), demonstrating the phase control. Extracted phase is shown in Fig. 1c, demonstrating up to 2π phase control.

III. Conclusion

We have demonstrated nonlinear metasurfaces utilizing nonlinear geometric phase, providing accurate and up to 2π phase control of nonlinear signals via adjusting the metasurface orientations.

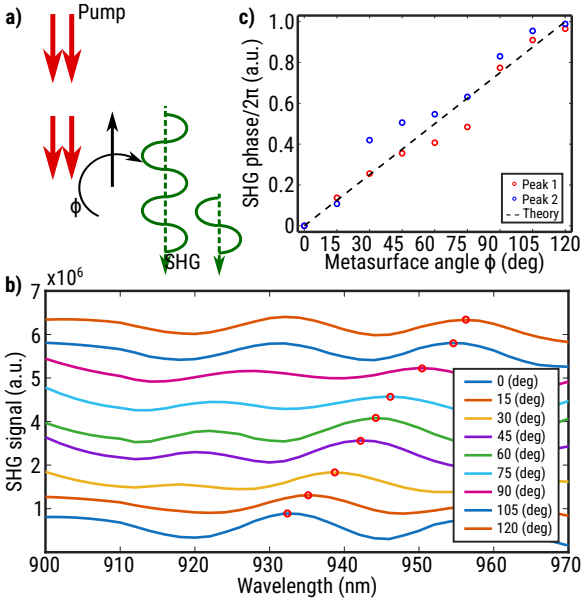

Fig. 1 a) Schematic of the experiment showing a stack of two metasurfaces of varying relative orientation. b) Measured SHG intensities as functions of pump wavelength and 2nd metasurface angle φ. c) Extracted relative phases of the SHG peaks with pump beam near 930–960 nm (highlighted with red circles in b) and 920–940 nm.

Acknowledgments

We acknowledge the support of the Research Council of Finland via projects (308596 and 332399), and via the Flagship of Photonics Research and Innovation (PREIN) (320165 and 320166).

References

[1] M. Zavelani-Rossi, *et al.* "Pulse compression over a 170-THz bandwidth in the visible by use of only chirped mirrors," *Opt. Lett.* vol. 26, pp. 1155–1157, 2001.
[2] N. Vermeulen, *et al.* "Post-2000 nonlinear optical materials and measurements: Data tables and best practices" *J. Phys. Photonics* vol. 5, p. 035001, 2022.
[3] M. Mekhael, *et al.* "Phase-matched second-harmonic generation from metasurfaces inside multipass cells" ACS Photonics vol. 11, pp. 682–687, 2024.
[4] G. Li, *et al.* "Continuous control of the nonlinearity phase for harmonic generations" *Nature Mater.* vol. 14, pp, 607–612, 2015.

Polarization-resolved nonlinear chiroptical scattering

Ventsislav K. Valev[1,*]

[1]Department of Physics, University of Bath, United Kingdom
*Corresponding author: v.k.valev@bath.ac.uk

***Abstract*— Recent reports of nonlinear chiroptical scattering include hyper-Rayleigh, hyper-Mie, hyper-Tyndall and hyper-Raman optical activity. All were observed as differences in scattered light intensity that depend on the handedness of incident light and of the scatterers. Here, we demonstrate that the polarization state of the scattered light constitutes an independent set of chiroptical observables.**

***Keywords*— metamaterials, nanophotonics, chirality, nonlinear scattering, nanomaterials.**

I. Introduction

Although nonlinear optical activity in scattered light was theoretically proposed in 1979,[1] its experimental realization has emerged only in the past few years. Light scattering is conventionally classified into three regimes determined by the ratio of particle size to wavelength: Rayleigh scattering for subwavelength particles, Mie scattering for particles comparable to or larger than the wavelength, and the intermediate Tyndall regime. These classifications extend naturally to nonlinear optics. Because in nonlinear optics the light-matter interactions are governed by *hyper*polarizabilities, when scattering occurs at harmonic frequencies of the incident field, the processes are termed hyper-Rayleigh, hyper-Mie, and hyper-Tyndall scattering.

If the scatterers are chiral – that is, they lack mirror symmetry – the scattered light can exhibit *optical activity*. Here, optical activity refers to any change of light properties that is directly related to chirality. In 2019, we reported the first experimental observation of hyper-Rayleigh optical activity at the second harmonic.[2] This effect was observed as a difference in the intensity of second-harmonic light that depends on the chirality of the scatterers. Because even- and odd-order nonlinear processes obey different selection rules and probe distinct material responses, extending these studies to third-harmonic hyper-Rayleigh optical activity constituted a significant advance.[3] We subsequently demonstrated hyper-Mie optical activity, again as a change in detected intensity (at third-harmonic frequency).[4] We also reported hyper-Tyndall optical activity.[5]

The scattering phenomena described above are elastic, conserving energy within the light–matter system. In contrast, Raman scattering is inelastic, involving energy exchange with material excitations. When such inelastic scattering occurs in conjunction with nonlinear frequency conversion, the process is termed hyper-Raman scattering. We further showed that chiral nanoparticles can induce effective chirality in otherwise achiral molecules, giving rise to both Raman and hyper-Raman optical activity.[6] In both cases, the chiroptical effects were recorded as changes in the detected intensity.

II. Results and Discussion

Here we present several recent advances. First, while hyper-Rayleigh, hyper-Mie and hyper-Tyndall optical activity were so far only demonstrated at up to three wavelengths, we now show second- and third-harmonic spectra that extend over hundreds of nm, thereby establishing these effects as spectroscopic tools.

Next, we show that nonlinear chiroptical scattering is encoded directly in the polarization state of the generated harmonic field. Rather than relying on intensity differences between left- and right-handed excitation, we resolve how chirality governs the polarization of the scattered harmonic light itself. Remarkably, strong enantiomorph-dependent polarization signatures persist even under linearly polarized excitation, where chiroptical effects are often presumed negligible. In symmetry terms, our work extends harmonic optical activity beyond intensity-based metrics, analogous to the conceptual shift from conventional Raman optical activity to dual circular-polarization detection.

References

[1] L. D. Andrews, T. Thirunamachandran, “Hyper−Raman scattering by chiral molecules”, J. Chem. Phys. Vol. 70, 1027, 1979.
[2] J. T. Collins, K. R. Rusimova, D. C. Hooper, H.-H. Jeong, L. Ohnoutek, F. Pradaux-Caggiano, T. Verbiest, D. R. Carbery, P. Fischer, V. K. Valev, “First Observation of Optical Activity in Hyper-Rayleigh Scattering”, Phys. Rev. X Vol. 9, 011024, 2019.
[3] L. Ohnoutek, H.-H. Jeong, R. R. Jones, J. Sachs, B. J. Olohan, D. M. Răsădean, G. Dan Pantoş, D. L. Andrews, P. Fischer, V. K. Valev, “Optical activity in third-harmonic Rayleigh scattering: a new route for measuring chirality”, Laser Photonics Rev. Vol 12, 2100235, 2021.
[4] L. Ohnoutek, J.-Y. Kim, J. Lu, B. J. Olohan, D. M. Răsădean, G. Dan Pantoş, N. A. Kotov, V. K. Valev, “Third harmonic Mie scattering from semiconductor nanohelices”, Nat. Photonics Vol. 16, 126-133, 2022.
[5] B. J. Olohan, E. Petronijevic, U. Kilic, S. Wimer, M. Hilfiker, M. Schubert, C. Argyropoulos, E. Schubert, S. R. Clowes, G. Dan Pantoş, D. L. Andrews, V. K. Valev, “Chiroptical Second-Harmonic Tyndall Scattering from Silicon Nanohelices”, ACS Nano Vol. 18, 16766–16775, 2024.
[6] R. R. Jones, J. F. Kerr, H. Kwon, S. R. Clowes, R. Ji, E. Petronijevic, L. Zhang, G. Dan Pantoş, B. Smith, T. Batten, P. Fischer, D. Wolverson, D. L. Andrews, V. K. Valev, “Chirality conferral enables the observation of hyper-Raman optical activity”, Nat. Photonics Vol. 18, 982–989, 2024.

Sensing chiral molecules using achiral plasmonic metasurfaces: limitations and perspectives

Obren Markovic[1], Shuhui Yang[1], Mathieu Nicolas[1,2], Catherine Schwob[1], Mathieu Mivelle[1], Guillaume Demesy[2], Nicolas Bonod[2], Souhir Boujday[3], B. Gallas*,[1]

[1]Sorbonne Université, CNRS, Institut des NanoSciences de Paris, INSP, F-75252 Paris, France

[2] Aix-Marseille Univ, CNRS, Centrale Marseille, Institut Fresnel, 13013 Marseille, France

[3]Sorbonne Université, CNRS, Laboratoire de Réactivité de Surface, LRS, F-75252 Paris, France

*Corresponding author: bruno.gallas@sorbonne-universite.fr

***Abstract*—Multipolar modes can be used to generate superchiral fields in the vicinity of plasmonic resonators. However, small systematic shape errors can produce linear polarization effects that can propagate in the CD to produce a spurious signal. Polarimetry allows estimating the sensitivity limits to the detection of chiral molecules.**

***Keywords*— metasurfaces, optical activity, plasmonics.**

I. Introduction

Chirality is central to the reactivity of biological molecules, with its characterization traditionally relying on the differential absorption of right- and left-circularly polarized light—an effect known as circular dichroism (CD). This approach enables the monitoring of both the configuration of simple molecules and the conformation of complex systems such as peptides or proteins. However, the weak interaction of light with these molecules severely limits detection sensitivity, particularly in studies of chiral object-surface interactions.

To enhance this interaction, photonic resonators, especially those based on localized surface plasmon resonances, have been proposed. These resonators engineer local electromagnetic fields at resonance, generating so-called superchiral fields. To date, such fields have primarily been produced using chiral resonators, but their use can introduce strong artifacts that may be mistaken for the presence of chiral molecules near the resonators [1]. In contrast, we propose the use of metasurfaces containing achiral resonators for chiral molecule detection. In this approach, superchiral fields are controlled by the polarization of the excitation light [2,3,4], offering a promising alternative for artifact-free chiral sensing. However, even such metasurfaces may exhibit irreducible artifacts.

II. Methods

Achiral plasmonic resonators can generate local chiral fields even under linear polarization excitation, as illustrated in Fig. 1 [2,3]. These fields are proposed to significantly enhance the interaction between light and chiral matter, enabling detection through variations in far-field CD [5,6].

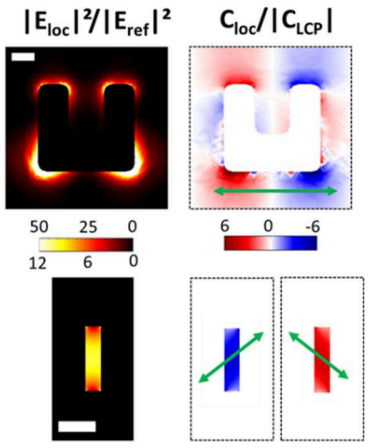

Fig. 1 Calculated near field intensity and chirality density of arrays of U-shaped resonators and nanoslits. The scale bar is 50 nm, the orientation of the linear polarization of the exciting light is indicated by a green arrow.

The resonators are typically fabricated using lithography techniques, which provide precise control over their shape. However, systematic fabrication errors may still occur, introducing residual linear birefringence and dichroism. These artifacts can propagate into the measured CD signal, producing an apparent CD effect known as LBLD. The impact of LBLD can be quantitatively assessed through full polarimetric characterization of the resonators [1].

III. Results and Discussion

Arrays of U-shaped gold resonators and nanoslits in gold films were fabricated using conventional e-beam lithography,

as shown in Fig. 2(a) and (b). Despite the apparently ideal resonator shapes observed in SEM images, the measured Circular Dichroism (CD) could never be fully suppressed (Fig. 2(c) and (d)).

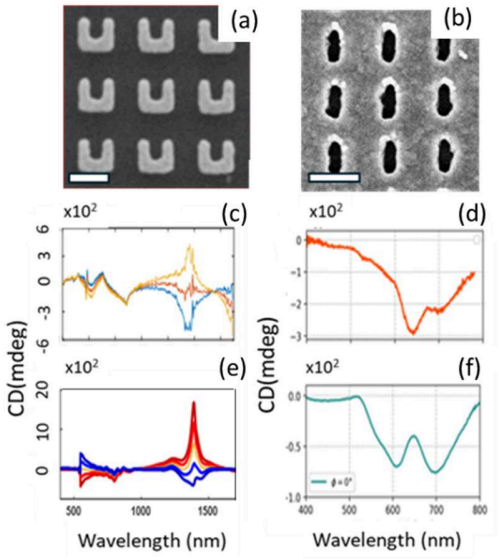

Fig. 2 SEM images of (a) U-shaped resonators and (b) nanoslits. The scale bar is 200 nm. Measured CD (note the x10^2 factor) for (c) U-shaped resonators and (d) nanoslits. In (c), different azimuthal angles (in steps of 0.1°) have been tested. Calculated CD for (e) asymmetry in arm length of 1 nm, (f) skew of 1 nm in nanoslit shape.

To investigate this discrepancy, numerical simulations of shape asymmetries were conducted using RCWA [1,7]. For U-shaped resonators, asymmetries in arm length, width, and base tilt were systematically tested. The best agreement with experimental measurements was achieved for an arm length asymmetry of just 1 nm (Fig. 2(e)). Similarly, for nanoslits, a skewness deviation of only 1° from the ideal shape was sufficient to reproduce the observed residual CD magnitude (Fig. 2(f)).

These effects are attributed to the LBLD phenomenon, which propagates into the CD signal [1]. While the calculated shape deviations are too subtle to be detected in SEM images, they are sufficient to induce spurious CD signals on the order of hundreds of millidegrees—larger than the typical CD values of most chiral biomolecules (usually a few millidegrees). Although the noise in the measurements (Fig. 2(c-d)) remains low, detecting CD variations caused by a chiral analyte would require a single, metasurface and a highly controlled experimental setup. Even minor deviations in measurement conditions could lead to significant fluctuations in spurious CD (Fig. 2(c)).

IV. Conclusion

We have demonstrated that even simple achiral metasurfaces can generate strong superchiral near fields, showing great promise for the detection of chiral biomolecules. However, conventional lithography techniques used to fabricate these metasurfaces can introduce systematic shape errors. These imperfections result in spurious CD through the LBLD effect, with magnitudes significantly exceeding those expected from interactions with chiral analytes. Numerical simulations reveal that shape deviations as small as a few nanometers, too subtle to be visualized using standard imaging techniques, are sufficient to induce these artifacts. In contrast, polarimetric measurements prove highly sensitive to such deviations, offering a means to identify and characterize the origin of spurious CD signals. This stresses the importance of precise fabrication control and comprehensive polarimetry measurement techniques in developing reliable chiral sensing platforms.

Acknowledgments

This work was supported by ANR-23-CE42-0019 and by the France 2030 program through grant ANR-24-EXLU-0001.

References

[1] O. Markovic, W. Chaabani, C. Schwob, M. Mivelle, and B. Gallas, “From Ideal to Real: Chiroptical Consequences of Asymmetries in Plasmonic Nano-Slit Metasurfaces”, ACS Photonics, vol. 12, pp. 6360-6367, 2025.

[2] M. Nicolas, S. Yang, C. Méthivier, S. Boujday, and B. Gallas, "Probing Peptide Adsorption Kinetics and Regioselectivity via Multipolar Plasmonic Modes of Gold Resonators", Appl. Phys. B: Opt. Mat. vol. 131, pp. 162, 2025.

[3] Cui, L., Yang, X., Reynier, B., Schwob, C., Bidault, S., Gallas, B., Mivelle, M. "Achiral magnetic photonic antenna as a tunable nanosource of superchiral light", ACS Photonics, vol. 10, pp. 3850-3857, 2023.

[4] Mathieu Nicolas, Per Magnus Walmsness, Jayeeta Amboli, Lu Zhang, Guillaume Demesy, Nicolas Bonod, Souhir Boujday, Morten Kildemo, Bruno Gallas, "True circular dichroism in optically active achiral metasurfaces and its relation to chiral nearfields", ACS Appl. Opt. Mater., vol. 1, pp. 1360-1366, 2023.

[5] Tang, Y. O.; Cohen, E. “Optical Chirality and Its Interaction with Matter”, Phys. Rev. Lett., vol. 104, pp. 163901, 2010.

[6] Maoz, B. M.; Chaikin, Y.; Tesler, A. B.; Bar Elli, O.; Fan, Z.; Govorov, A. O.; Markovich, G. “Amplification of Chiroptical Activity of Chiral Biomolecules by Surface Plasmons”, Nano Lett., vol. 13, pp. 1203−1209, 2013.

[7] Besbes, M. SimPhotonics_FMM Matlab Toolbox for modeling nanophotonic devices, 2023.

Chiral surface plasmons and their spin-hall effect on top of helix arrays

Paul de Bollivier, Vage Karakhanyan, Roland Salut, Miguel A. Suarez, Nicolas Martin,

Thierry Grosjean*

[1]FEMTO-ST Institute, CNRS, University Marie et Louis Pasteur, Besançon, France
*Corresponding author: thierry.grosjean@univ-fcomte.fr

***Abstract*— We demonstrate the existence of a new type of surface plasmons supported by arrays of gold nanohelices. A spin Hall effect is observed in the free-space outcoupling of these surface plasmons, revealing a spin-dependent deflection in the emitted radiation. These results highlight the chiral nature of the plasmonic modes sustained by nanohelix arrays and provide new opportunities for controlling spin-dependent light–matter interactions in plasmonic systems.**

***Keywords*— Nanohelices, helix-array, surface plasmons, chirality, helicity, surface wave, spin-hall effect, metamaterials.**

Helical plasmonic structures exhibit remarkable chiroptical properties and have attracted significant interest in nanophotonics and metamaterials. Arrays of metallic helices have been shown to operate as broadband circular polarizers [1] and to exhibit negative refraction under large wave illumination [2]. When locally excited, these systems can also support the propagation of optical analogs of magnetic spin waves along the helix axis [3]. In these configurations, the observed response arises from volumetric plasmonic modes within the helix arrays.

Here, we demonstrate the existence of surface plasmons propagating on top of a helix array, whose electromagnetic fields decay along the helix axis both within the array and in the free space above it.

Through finite-difference time-domain simulations, we first predicted the optical properties of the chiral surface plasmons, including their dispersion relation. To demonstrate the existence of these surface waves experimentally, we fabricated homochiral arrays of six-turn gold-coated carbon helices. The helix cores were produced by focused ion beam-induced deposition of carbon, followed by the deposition of a thin gold layer to support plasmonic excitations.

Using a custom optical setup enabling far-field observation along the propagation direction of the surface plasmons in the metamaterial (horizontal axis), the array was illuminated normal to the surface (vertical axis) with a tightly focused laser beam at wavelengths in the telecommunication band. Under these conditions, we observed the free-space outcoupling of the surface plasmons, revealing a pronounced spin Hall effect and highlighting the intrinsic chiroptical nature of the plasmonic wave.

ACKNOWLEDGMENTS

This work was supported by the French Agence Nationale de la Recherche under project CIFOM (ANR-23-CE42-0021), the CNRS under project CIPOM, the French Renatech network, MIMENTO and SMARTLIGHT technological platforms, and the Région Bourgogne Franche-Comté

References

[1] J. K. Gansel, M. Thiel, M. S. Rill, M. Decker, K. Bade, V.Saile, G. von Freymann, S. Linden, and M. Wegener, “Gold helix photonic metamaterial as broadband circular polarizer,” science, vol. 325, no. 5947, pp. 1513–1515, 2009.

[2] C. Wu, H. Li, Z. Wei, X. Yu, and C. T. Chan,“Theory and experimental realization of negative refraction in a metallic helix array”, Physical Review Letters, vol. 105, no. 24, p. 247401, 2010.

[3] V. Karakhanyan, R. Salut, M. A. Suarez, N. Martin, and T. Grosjean, “Optical spin waves,” Nano Letters, vol. 24, no. 27, pp. 8296-8302, 2024.

Dielectric Mie Nanostructures and Metasurfaces for Quantum Emitter Control

Antoine Azéma[1,3], Swaroop Palai[1,2], Jonas Muller[3], Etienne Palleau[2] Frank Fournel[4], Vincent Larrey[4], Guilhem Larrieu[3], Gonzague Agez[1], Jean-Marie Poumirol[1], Vincent Paillard[1], Peter R. Wiecha[3], Laurence Ressier[2], and Aurélien Cuche[1,*]

[1]CEMES-CNRS, Université de Toulouse, CNRS, UPS, Toulouse, France
[2]LPCNO, Université de Toulouse, CNRS, INSA, UPS, 135 Avenue de Rangueil, 31077 Toulouse, France
[3]LAAS-CNRS, Université de Toulouse, CNRS, INP, Toulouse, France
[4]Université Grenoble Alpes, CNRS, CEA-Leti Minatec, Grenoble, France
*corresponding author: aurelien.cuche@cemes.fr

***Abstract*— Enhancing single-photon sources efficiency via optically resonant nanostructures is crucial for quantum communications. High-refractive-index dielectric nanostructures offer appealing optical properties through Mie resonances, with reduced absorption, and compatibility with CMOS technology. This study explores experimentally and numerically how silicon nanoantennas and metasurfaces influence the spontaneous emission and directionality of model quantum emitters.**

***Keywords*— dielectrics, nanoantennas, metasurfaces, single photon, quantum emitters.**

Improving the brightness and efficiency of single photon sources by the mean of optically resonant nanostructures is a major stake for the development of efficient nanodevices for quantum communications.
For a couple of decades, these resonant nanostructures have mainly been made of noble metal that sustain strong localized plasmon resonances (LSPR) that can be used to manipulate, concentrate or redirect visible light. Such properties have led to numerous actual or potential applications in integrated optics, sensors, nonlinear optics, field-enhanced spectroscopies, or photovoltaics. Recently, an alternative emerged with high refractive index dielectric nanostructures, which offer the same range of applications as plasmonics by manipulating Mie optical resonances instead of LSPR [1].

These resonances can be efficiently tuned by modifying the size, shape, and material of those nanostructures (e.g. silicon, n ~ 4) [2]. Furthermore, high index dielectric nanostructures offer several key advantages when compared to their metallic counterparts: absorption losses are far weaker for wavelengths longer than the direct band gap, access to semiconductor (CMOS) technology for nanostructure fabrication, and presence of intrinsic strong magnetic and electric resonances, providing an unique opportunity to spatially separate and redistribute the energy of the magnetic and electric parts of the electromagnetic field in the near field, otherwise inextricably connected in the far field [3].

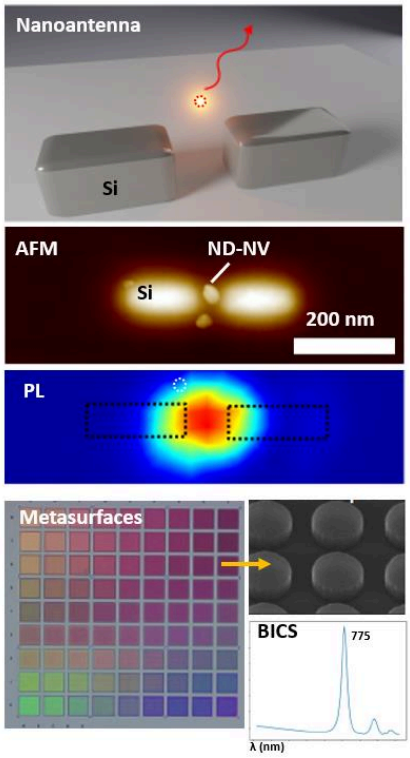

Fig. 1 Top: illustration of a Si nanoantenna coupled to a quantum emitter (ND-NV), and corresponding characterizations [5]. Bottom : metasurfaces made of Si nanodiscs.

In this work, we examine how both simple and complex high-index dielectric nanoantennas influence the spontaneous emission and directional properties of model quantum emitters. In particular, color centers in nanodiamonds are an ideal model system exhibiting single photon emission properties at room temperature [4], making them particularly suitable for proof-of-concept experiments in quantum nano-optics. By modifying the LDOS through nanostructuring, we use time-resolved photoluminescence measurements and Fourier imaging to show that the photodynamics and the directivity of these emitters can

be significantly enhanced when coupled to a nanoantenna, even at the single-photon level. Our experimental results are in good agreement with multipolar analysis and numerical simulations based on the Green Dyadic Method – GDM [6]. Additionally, we numerically investigate the potential of two-dimensional silicon nanostructure arrays, known as metasurfaces, for controlling these photodynamic processes.

ACKNOWLEDGMENTS

This work was supported by Programme Investissements d'Avenir through the grants ANR-10-LABX-0037-NEXT (MILO) and NanoX n° ANR-17-EURE- 0009 (Q-META), by the HiLight ANR project ANR-19-CE24-0026, by LAAS-CNRS micro and nanotechnologies platform member of the French Renatech network, by the Région Midi-Pyrénées via the Institute for Quantum technologies in Occitanie (IQO) (PhD grant), and by the computing facility center CALMIP of the University of Toulouse under grants P12167 and P1107.

REFERENCES

[1] H. Kallel et al, "Tunable enhancement of light absorption and scattering in Si1xGex nanowires", Phys. Rev. B, vol. 12: 085318, 2012.

[2] P.R. Wiecha et al., "Strongly directional scattering from dielectric nanowires", ACS Photonics, vol. 4: pp 2036–2046, 2017.

[3] M. Montagnac et al., "Control of light emission of quantum emitters coupled to silicon nanoantenna using cylindrical vector beams", Light : Science and Applications, vol. 12 (1), 239, 2023.

[4] M. Humbert et al., "Versatile, rapid and robust nanopositioning of single-photon emitters by AFM-nanoxerography", Nanotechnology, vol. 33, 215301, 2022.

[5] M. Humbert et al., "Large-scale controlled coupling of single-photon emitters to high index dielectric nanoantennas using AFM nanoxerography", Nanoscale, vol. 15, 599-608, 2023.

[6] R. Hernandez et al., "Directional silicon nano-antennas for quantum emitter control designed by evolutionary optimization" JOSA B, vol. 41 (2), A108-A115, 2024.

Precision Synthesis and Functionalization: Uniform, Size- and Shape-Tunable Gold and Silver Nanostructures for Advanced Platforms

Kyoungweon Park, [1,2*] Aklilu Worku,[1,2] Angela Campo[1], Rich Vaia [1]

[1] Materials & Manufacturing Directorate, Air Force Research Laboratory, Wright-Patterson Air Force Base, Ohio, USA [2] AV inc., Dayton Ohio, USA

*Corresponding author: kyoungweon.park@avinc.com

***Abstract*— Silver nanostructures offer superior optical response over gold at a lower cost. However, scalable aqueous synthesis with precise size and shape control remains challenging. This talk presents advances in aqueous synthesis and robust functionalization, demonstrating how these scalable silver nanoplatforms can match or exceed gold's performance in real-world applications.**

***Keywords*— plasmonic nanoparticles, silver nanostructure, scalable synthesis.**

Silver nanostructures are exceptional candidates for next generation plasmonic, catalytic, and sensing applications, offering superior optical response, higher conductivity, and better cost-effectiveness than gold. While the polyol process enables scalable synthesis, it often limits size and shape precision and complicates functionalization. Achieving similar scalability in aqueous systems remains a significant challenge due to the difficulty of regulating the seed facets that govern growth. Furthermore, robust functionalization is essential for integrating these sensitive materials into advanced platforms. This talk presents recent advances in the scalable aqueous synthesis of silver nanoparticles, focusing on strategies to control seed facets, morphology, and surface chemistry across large batches. We also highlight scalable functionalization approaches that ensure reliable integration into high-performance systems. Finally, by comparing silver and gold counterparts, we demonstrate how silver nanostructures can match or exceed the efficiency of gold in real-world applications.

Photochemical Synthesis of Gold Nano- and Microplates on Substrates

Svetlana Neretina[1,*], Brendan Niuekirk[1], Runze Tang[1]

[1]College of Engineering, University of Notre Dame, Indiana, USA
*Corresponding author: sneretina@nd.edu

***Abstract*— We introduce a photochemical synthesis that yields periodic arrays of highly faceted gold nanoplates with deterministic shape control. Light-driven solution chemistry enables uniform, device-ready architectures compatible with large-area patterning. This approach provides a scalable platform for integrating plasmonic nano- and microplates into metasurfaces, optical components, and next generation photonic devices.**

***Keywords*— gold nanoplates, microplates, periodic arrays, synthesis.**

High-Q Band-folded Lattice Resonances for Low-Threshold Lasing

Shaojun Wang[1*],

[1]School of Optoelectronic Science and Engineering, Soochow University, Suzhou 215006, China
*Corresponding author: swang.opto@suda.edu.cn

***Abstract*—We present dielectric metasurface nanolasers leveraging non-local lattice resonances and band-folding to achieve high-Q electric quadrupole modes with superior field–gain overlap. Via Pancharatnam–Berry phase encoding, we enable low-threshold, directional, circularly polarized lasing, offering a compact, full-polarization-controllable source for quantum photonics and sensing.**

***Keywords*— metalaser, nonlocal metasurfaces, PB phase, low-threshold, directional lasing.**

I. Introduction

Addressing the bottlenecks of limited integrability in traditional semiconductor lasers and high optical losses in plasmonic nanolasers[1], we present a novel architecture for dielectric metasurface micro/nanolasers based on non-local lattice resonances. By employing a Brillouin zone band-folding strategy, we precisely lock the high-Q modes of tightly bound in-plane electric quadrupole lattices into the spectral region above the light cone yet below the Rayleigh anomaly[2]. This approach maintains an ultra-high quality factor while achieving significant spatial overlap between the near-field and the gain medium, fundamentally overcoming the challenges of field-gain separation inherent in out-of-plane magnetic dipole Bound States in the Continuum (BIC) modes and the difficulties of integrating gain materials within nanopores[3].

Furthermore, we demonstrate in-situ encoding of Pancharatnam-Berry (PB) geometric phases[4] via translational and rotational perturbations of diatomic unit cells. This establishes a critical pathway from efficient near-field light-matter interactions to far-field highly directional circularly polarized emission. Ultimately, this work provides a new paradigm for light sources characterized by high Q, low power consumption, superior beam quality, full-polarization controllability, and ease of integration, paving the way for next-generation intelligent sensing and quantum photonic systems.

Acknowledgments

This work was financially supported by the National Natural Science Foundation of China (62411540033, 62275184, 22502132), the Natural Science Foundation of Jiangsu Province (SBK20250201842), the Engineering Research Center of Digital Imaging and Display of Education Ministry of China, the Engineering Research Center of Digital Graphic and Next-generation Printing of Jiangsu Province, and the Priority Academic Program Development (PAPD) of Jiangsu Higher Education Institutions.

References

[1] F. Freire-Fernández, S.-M. Park, M. J. H. Tan, and T. W. Odom, "Plasmonic lattice lasers," *Nature Reviews Materials*, vol. 10, no. 8, pp. 604–616, 2025.

[2] Z. Zhang, C. Xu, C. Liu, M. Lang, Y. Zhang, M. Li, W. Lu, Z. Chen, C. Wang, S. Wang, *et al.*, "Dual control of enhanced quasi-bound states in the continuum emission from resonant c-Si metasurfaces," *Nano Letters*, vol. 23, no. 16, pp. 7584–7592, 2023.

[3] Y. Zeng, X. Sha, C. Zhang, Y. Zhang, H. Deng, H. Lu, G. Qu, S. Xiao, S. Yu, Y. Kivshar, *et al.*, "Metalasers with arbitrarily shaped wavefront," *Nature*, vol. 643, no. 8074, pp. 1240–1245, 2025.

[4] T. Chervy, S. Azzini, E. Lorchat, S. Wang, Y. Gorodetski, J. A. Hutchison, S. Berciaud, T. W. Ebbesen, and C. Genet, "Room temperature chiral coupling of valley excitons with spin-momentum locked surface plasmons," *ACS Photonics*, vol. 5, no. 4, pp. 1281–1287, 2018.

Chirality-Induced Response in Chiral Inorganic Materials

Yoshihiko Togawa[1,*]

[1]Department of Physics and Electronics, Osaka Metropolitan University, Sakai, JAPAN
*Corresponding author: ytogawa@omu.ac.jp

***Abstract*—Chirality-dependent generation, propagation, and transfer of angular momenta of the chiral phonons are demonstrated with chiral quartz crystals under the steady heat flow.**

***Keywords*— Quartz, Chiral Phonon, Angular Momentum**

I. Introduction

It has been clarified that the spin polarization phenomena initially found in chiral organic molecules occur even in chiral inorganic crystals. The spin signals appear in a variety of chiral materials from molecules to crystals irrespective of electrical conductivity ranged from metals to insulators. As a manifestation of chirality, which corresponds to time-even pseudo scalar, works as a microscopic chiral term in driven chiral media and hybridizes translational and rotational degrees of freedom, a polarization of angular momenta appears under charge or thermal flow. In this study, we investigate chirality-dependent generation, propagation, and transfer of angular momenta of the chiral phonons with chiral quartz crystals under the steady heat flow [2].

II. Methods

Quartz is an insulative and diamagnetic material which has a trigonal crystal structure with the space group of $P3_121$ (No. 152) or $P3_221$ (No. 154). The former has a right-handed helical arrangement of SiO_4 tetrahedrons along the c axis, while the latter has the left-handed one. A quartz sample is set on a heat bath with a resistive heater on the other end for the thermal power apply, as used in the conventional setup for the steady-state thermal conductivity measurement. For the signal detection via an inverse spin Hall effect, two electrodes of tungsten (W) or platinum (Pt) were deposited by a sputtering method in the center part of the quartz, which is located between the heater and thermal bath.

III. Results and Discussion

The temperature dependence of the detected signal coincides with those of the thermal conductivity and Seebeck coefficient. The signals change the polarity with regard to the handedness of quartz. In addition, they show the opposite polarity when replacing the detection electrode from W to Pt. Furthermore, a dependence of the signal intensity on the electrode thickness is consistent with that expected for the inverse spin Hall effect. These results indicate that chirality-dependent angular momenta are generated and carried by the thermally driven chiral phonons in the quartz crystal and could be extracted from the quartz as a spin signal.

IV. Conclusion

We have demonstrated that heat flow can generate the spin signal in chiral quartz. A comprehensive understanding of these nontrivial features will clarify the mystery of chirality-induced dynamical responses such as chirality-induced spin selectivity (CISS).

Acknowledgments

This work was supported by JSPS KAKENHI Grant Nos. 22H01944, 23H01870 and 23H00091; by JSPS International Joint Research Program (JRPLEAD with UKRI) (Grant No. JPJSJRP20241710); by the Grant of the OML Project by the National Institutes of Natural Sciences (NINS Program No. OML012301); and by JST ERATO from JST (Grant No. JPMJER2503).

References

[1] Y. Togawa, A. S. Ovchinnikov, and J. Kishine, "Generalized Dzyaloshinskii-Moriya Interaction and Chirality-Induced Phenomena in Chiral Crystals," Journal of the Physical Society of Japan **92**, 081006 (2023), Special Topics DMI.

[2] A. Inui, R. Aoki, Y. Nishiue, K. Shiota, Y. Kousaka, H. Shishido, D. Hirobe, M. Suda, J. Ohe, J. Kishine, H. M. Yamamoto, and Y. Togawa *et al*., "Chirality-Induced Spin-Polarized State of a Chiral Crystal $CrNb_3S_6$," Physical Review Letters 124, 166602 (2020).

[3] K. Shiota, A. Inui, Y. Hosaka, R. Amano, Y. Onuki, M. Hedo, T. Nakama, D. Hirobe, J. Ohe, J. Kishine, H. M. Yamamoto, H. Shishido, and Y. Togawa, "Chirality-induced spin polarization over macroscopic distances in chiral disilicide crystals," Physical Review Letters 127, 126602 (2021).

[4] K. Ohe, H. Shishido, M. Kato, S. Utsumi, H. Matsuura, and Y. Togawa, "Chirality-Induced Selectivity of Phonon Angular Momenta in Chiral Quartz Crystals," Physical Review Letters 132, 056302 (2024).

Self-assembled Plasmonic Metamaterials with Hyperbolic Dispersion for Applications in Sensing

Anastasiia Zelaska, Mayela Romero-Gomez, Anatoly Zayats and Wayne Dickson*

Department of Physics, King's College London, London, UK
*Corresponding author: wayne.dickson@kcl.ac.uk

***Abstract*— Plasmonic metamaterials with hyperbolic dispersion are characterized by a transition from elliptic to hyperbolic dispersion at a tunable epsilon-near-zero frequency. Their self-assembled fabrication provides unique opportunities for tailoring their constituents, but importantly, hybridizing them with functional layers for ultrasensitive sensing.**

***Keywords*— metamaterials, plasmonics, sensing.**

I. Introduction

Plasmonic metamaterials based on self-assembled arrays of gold nanorods have demonstrated excellent sensitivity to a range of stimuli, including biological molecules[1], ultrasound[2] and hydrogen[3]. The flexibility of the electrochemical fabrication approach not only enables the constituent plasmonic material to be varied [4], but also allows the morphology of the meta-atoms comprising the metamaterial to be tailored, for example, to maximize the electromagnetic field enhancement[5]. In this work we will summarise the development of these plasmonic metamaterials for applications in ultra-sensitive sensing, with a particular emphasis on how the underlying plasmonic metamaterial can be hybridized with suitable transduction layers for sensing targets in the gas phase.

II. Methods

The plasmonic metamaterials are fabricated using electrochemical growth of metallic nanorods within nanoporous aluminium oxide templates, producing highly quasi-ordered self-assembled arrays with tunable geometry and composition. This scalable approach enables the realization of nanorod metamaterials based on different plasmonic materials, including gold, copper, and aluminium, providing either stability (gold), additional functionality (copper) (Fig. 1a–c), or bringing the epsilon-near-zero (ENZ) response into the deep ultraviolet (Fig. 1d–f). Post-fabrication electrochemical modification provides an additional mechanism to both tailor the optical response of the metamaterial and provide sensitivity to different stimuli for applications in sensing. In the case of hydrogen sensing, electrochemical functionalization with palladium provides a reversible sensing mechanism, while copper can readily be anodized (Fig. 1b-c) to create Cu_2O or CuO shells for VOC detection.

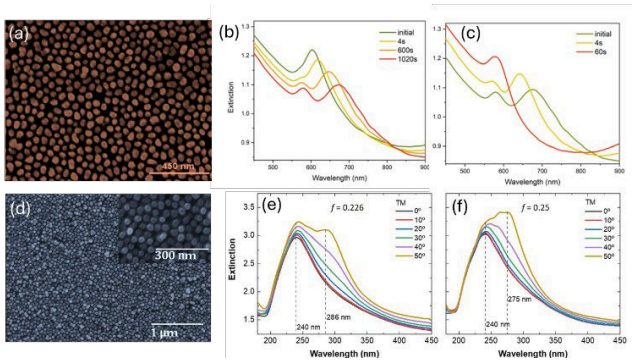

Fig. 1. Plasmonic Metamaterials comprised of copper (a-c) or aluminium (d-f). The electrochemistry of copper enables both wide tunability of the ENZ condition (b, c) with a controllable shell-thickness of copper (II) oxide while aluminium metamaterials bring the ENZ into the deep ultraviolet (e, f).

III. Results and Discussion

These self-assembled nanorod metamaterials can be engineered to provide highly sensitive detection of a range of stimuli. This work will focus on their functionalization with palladium for high-specificity hydrogen detection, metal oxides for VOC detection, and intrinsic deep UV sensitivity to biological molecules.

IV. Conclusion

This work demonstrates the flexibility of self-assembled metamaterials for adaptation to a wide range of stimuli for ultrasensitive sensing.

References

[1] A. V. Kabashin et al., "Plasmonic nanorod metamaterials for biosensing," Nature materials, vol. 8, no. 11, pp. 867-871, 2009.
[2] V. V. Yakovlev et al., "Ultrasensitive non-resonant detection of ultrasound with plasmonic metamaterials," Advanced Materials, vol. 25, pp. 2351-2356, 2013.
[3] M. E. Nasir, W. Dickson, G. A. Wurtz, W. P. Wardley, and A. V. Zayats, "Hydrogen detected by the naked eye: optical hydrogen gas sensors based on core/shell plasmonic nanorod metamaterials," Advanced Materials, vol. 26, pp. 3532-3537, 2014.
[4] A. Zaleska, A. V. Krasavin, A. V. Zayats, and W. Dickson, "Copper-based core–shell metamaterials with ultra-broadband and reversible ENZ tunability," Materials Advances, vol. 5, pp. 5845-5854, 2024.
[5] R. M. Córdova-Castro, A. V. Krasavin, M. E. Nasir, A. V. Zayats, and W. Dickson, "Nanocone-based plasmonic metamaterials," Nanotechnology, vol. 30, p. 055301, 2019.

Broadband Infrared Unidirectional Absorption by non-Hermitian Multilayer Structure

Wakana KUBO*

[1] Department of Electrical Engineering and Computer Science,
Tokyo University of Agriculture and Technology,
*Corresponding author: w-kubo@cc.tuat.ac.jp

***Abstract*—We demonstrate a non-Hermitian four-layer structure exhibiting broadband unidirectional absorption in the infrared region. By precisely designing layer thicknesses, directional absorption is achieved over a wide spectral range. This approach offers a promising route toward thermal management applications, such as infrared heat-shielding and thermal smart window technologies.**

***Keywords*— Non-Hermitian photonics, Unidirectionality, Infrared region, Multilayer, Thermal smart glass**

I. Introduction

Non-Hermitian photonics has emerged as a powerful platform for realizing strong light–matter interactions, enabling unique phenomena such as optical unidirectionality and the non-Hermitian skin effect.[1] These distinctive optical phenomena open promising opportunities for applications in the visible and infrared (IR) spectral regions, including optical isolators, asymmetric absorbers, and thermal radiation control.

Representative demonstrations of non-Hermitian unidirectionality have been reported in photonic structures in the visible light region.[2] Furthermore, non-Hermitian unidirectionality has also been explored beyond the visible regime. However, the reported unidirectional responses are typically restricted to narrow spectral bands or specific operating wavelengths. For applications in thermal control, unidirectional absorption must be achieved over a broadband spectral range that follows the blackbody radiation spectrum. To date, broadband unidirectional infrared absorption based on non-Hermitian multilayer structures has not yet been reported, particularly in a form compatible with blackbody radiation spectra.

In this study, we design and experimentally demonstrate a non-Hermitian unidirectional multilayer structure spectrally matched to blackbody radiation using the transfer-matrix formulation. We further investigate the thermal radiation shielding effect of the proposed non-Hermitian structure to discuss its potential application as a functional thermal smart window.

II. Methods

A multilayer structure composed of alternating calcium fluoride (CaF_2) and bismuth (Bi), serving as low-loss and high-loss materials, respectively, was employed to realize non-Hermitian optical responses in the infrared (IR) region.

To achieve unidirectionality of the multilayer structure, the thicknesses of the four layers were designed using the electromagnetic transfer-matrix formulation.

$$\mathrm{M} = \prod_{j=1}^{N} \begin{pmatrix} cos\beta_j & isin\frac{\beta_j}{q_j} \\ iq_j sin\beta_j & cos\beta_j \end{pmatrix},\ j = 1, 2, 3, \cdots N$$

Here, β_j is the phase thickness of the *j*-th layer defined as

$\beta_i = k_0 n_j d_j cos\theta_j$. Eq. (3)

The optical admittance q_j depends on the polarization of the incident light.

$q_j(\mathrm{TE}) = n_j cos\theta_j$, $q_j(\mathrm{TM}) = \frac{n_j}{cos\theta_j}$, Eq. (4)

where n_j, d_j, and k_0 are the refractive index, the thickness of the *j*-th layer, and the wavenumber in vacuum.

III. Results and Discussion

Figure 1(a) presents a schematic of the four-layer structure designed to match the blackbody radiation spectrum at 373 K. Figure 1(b) presents the calculated absorption spectra of the four-layer structure under forward (red line) and backward (black line) illumination.

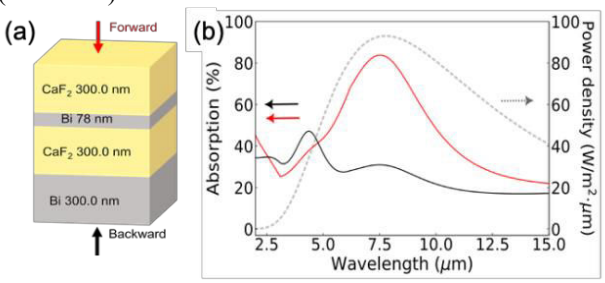

Fig. 1 (a) Schematic of the four-layer structure designed to match the blackbody radiation spectrum at 373 K. (b) Calculated absorption spectra of the four-layer structure under forward (red line) and backward (black line) illumination. The gray dashed line presents the blackbody radiation spectrum at 373 K.

The absorption spectrum under forward illumination showed an absorption of 83.9% at a wavelength of 7.5 μm and showed good agreement with the blackbody radiation spectrum at 373 K (gray dashed line). In contrast, the absorption spectrum under backward illumination exhibited an absorption of 30.9% at 7.5 μm, indicating that the absorption difference between forward and backward illumination was 53.0%. These results demonstrate that broadband infrared unidirectionality was numerically realized through transfer-matrix formulation and appropriate selection of high-loss and low-loss materials.

To realize broadband infrared unidirectional absorption, we fabricated a four-layer structure on Cu substrate using thermal evaporation. Figure 3(a) shows a photograph of the fabricated four-layer structure. The left and right samples correspond to film stacks of forward and backward structures, respectively.

Figure 3(b) presents the cross-sectional SEM image of the four-layer structure. The measured film thicknesses of the forward structure were 194 ± 80 nm (bottom Bi layer), 377 ± 93 nm (CaF_2 layer), 77 ± 2 nm (Bi layer), and 319 ± 45 nm (top CaF_2 layer), respectively.

Figure 3(c) presents the measured absorption spectra of the sample under forward (red line) and backward (black line) illumination. Two peaks of nearly perfect absorption were observed, with absorption values of 99.1% and 98.4% at 4.7 and 7.2 μm. In contrast, the absorption under backward illumination at these wavelengths was 27.1% and 20.4%, indicating a modulation depth of 52% at 4.7 μm.

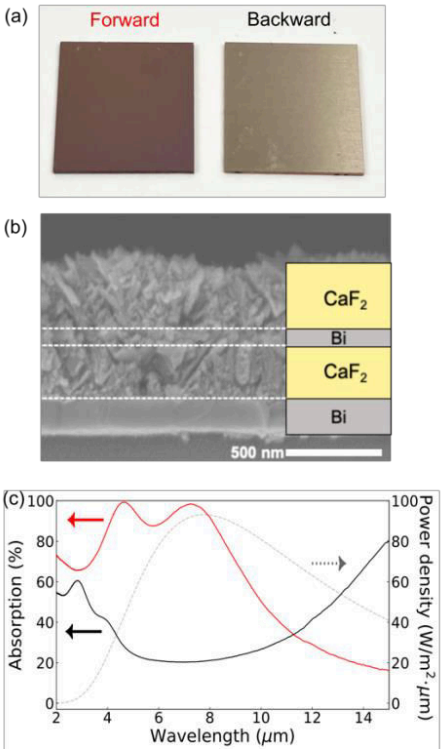

Fig. 2 (a) Photograph of the fabricated four-layer structure. The left and right samples correspond to film stacks of forward and backward structures, respectively. (b) Cross-sectional SEM image of the four-layer structure. (c) Measured absorption spectra of the sample under forward (red line) and backward (black line) illumination. The dashed line presents the blackbody radiation spectrum at 373 K.

This result demonstrates broadband infrared unidirectional absorption for the first time.

Finally, we examined the functionality of the four-layer structure as a smart glass for shielding thermal radiation. The forward and backward structures were heated using a hot plate, and the resulting temperatures were monitored by an IR camera (Fig. 3(a)). Owing to nearly perfect absorption of thermal radiation from the heat source, the forward structure exhibited a higher temperature of 64.9 °C. In contrast, the backward structure reflected a portion of the incident thermal radiation, resulting in a lower substrate temperature of 62.8 °C compared with the forward structure. These results suggest that the non-Hermitian structure exhibiting broadband infrared unidirectional absorption can function as an effective thermal shielding glass.

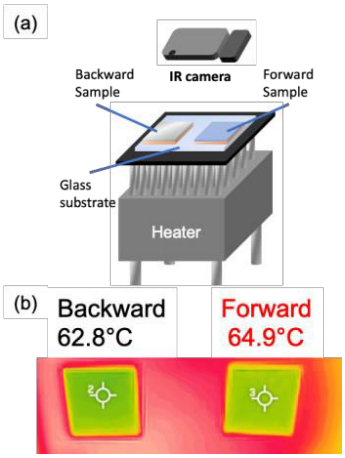

Fig. 3 (a) Experimental setup for observing the thermal shielding effect of the four-layer structure. (b) Infrared (IR) camera images of the non-Hermitian structures with forward (right) and backward (left) film-stack configurations.

Conclusion

In summary, we proposed and experimentally demonstrated a non-Hermitian four-layer structure that exhibits broadband unidirectional absorption in the infrared region.[3] By designing the individual layer thicknesses based on the transfer-matrix formulation, the absorption peak under forward illumination can be spectrally matched to the blackbody radiation spectrum at different temperatures, while the absorption under backward illumination is strongly suppressed. These results suggest potential applications in thermal smart windows.

Acknowledgments

This work was supported by JSPS KAKENHI Grant Number JP24H02232.

References

[1] J. Doppler *et al.*, "Dynamically encircling an exceptional point for asymmetric mode switching," *Nature,* vol. 537, no. 7618, pp. 76-79, 2016.

[2] L. Feng *et al.*, "Demonstration of a large-scale optical exceptional point structure," *Opt. Express,* vol. 22, no. 2, pp. 1760-1767, 2014.

[3] A. Yamamoto, B. Ganbat, W. Kubo, " Broadband Infrared Unidirectional Absorption by non-Hermitian Structure", in preparation.

Revising Model Reactions in Plasmonic Chemistry

Olga Guselnikova[1]

1 Institute of Applied Physics, Vienna University of Technology, Vienna 1040, Austria

*Corresponding author: olga.guselnikova@tuwien.ac.at

***Abstract*— Progress in plasmonic chemistry demands reliable model reactions to elucidate energy transfer, mechanisms, and materials discovery. We show PNTP azo coupling on Au nanoparticles is unsuitable, as plasmonic heating induces Au–S cleavage and thiol oxidation. We propose alkoxyamine homolysis, offering simpler kinetics, identifiable products, and robust mechanistic interpretation for catalysis.**

***Keywords*— plasmon catalysis, azo-coupling, alkoxyamine, photocatalysis**

I. Introduction

Plasmonic catalysis relies on model reactions to understand energy transfer mechanisms and guide materials discovery. The azo coupling of 4-nitrothiophenol (PNTP) has been widely used as a model reaction; however, uncertainties remain regarding its mechanistic simplicity and reliability under plasmon excitation. This work reassesses its validity and proposes a more suitable alternative..

II. Methods

Gold nanoparticles coated with PNTP were subjected to laser-induced plasmon excitation. Reaction progress and surface chemical changes were monitored using Raman spectroscopy and X-ray photoelectron spectroscopy (XPS), focusing on N 1s and S 2p spectral regions to track bond changes and oxidation processes.

Local temperature effects during plasmon excitation were evaluated experimentally and theoretically to determine whether heating could induce ligand desorption and surface chemical transformation.

To identify a more suitable model reaction, alkoxyamine homolysis was investigated as an alternative system, monitored via electron paramagnetic resonance (EPR) spectroscopy due to its well-defined radical products and established kinetic behavior.

III. Results and Discussion

Experimental observations reveal:

• Successful PNTP azo coupling confirmed by Raman and XPS analysis

• Significant Au–S bond cleavage during irradiation, evidenced by S 2p spectral changes

• Concurrent thiol oxidation detected in N 1s spectra

• Plasmonic heating raises local temperatures above thiol desorption thresholds

• Reaction kinetics involve multiple competing pathways rather than a simple mechanism

These findings demonstrate that PNTP coupling involves ligand desorption and oxidation processes, complicating mechanistic interpretation and violating requirements for a simple model reaction.

In contrast, alkoxyamine homolysis proceeds via a single bond-cleavage event, producing identifiable radicals with well-understood kinetics, enabling reliable mechanistic analysis.

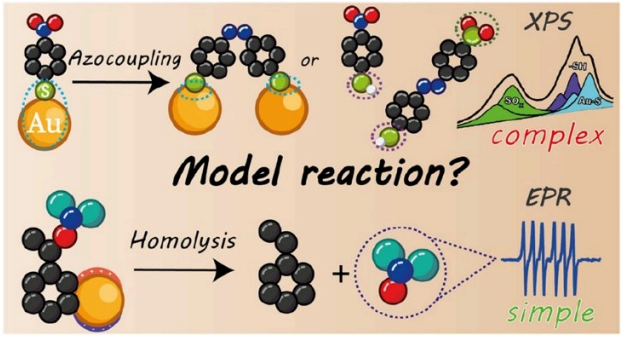

Figure 1. Comparison of PNTP azo coupling and AA homolysis as model reactions for plasmon catalysis fundamental studies.

IV. Conclusion

The PNTP azo coupling reaction is unsuitable as a universal model reaction for plasmonic catalysis because plasmonic heating induces surface bond cleavage and complex reaction pathways. Alkoxyamine homolysis offers a simpler, kinetically well-defined alternative suitable for mechanistic studies. Adoption of reliable model reactions will accelerate progress in plasmon-driven catalysis.

References

[1] Gorbunova et al., *ACS Catalysis*, 2025, DOI: 10.1021/acscatal.5c01129

Self-assembly of Artificial Proteins as Scaffold for Advanced Nanophotonics

Liudmila Trotsiuk[1*], Nathan Epalle[2], Rémi Chassagnon[1], Régis Parvaud[1], Valerie Marchi[3], Marielle Valerio-Lepiniec[2], Agathe Urvoas-Cisse[2], Philippe Minard[2], Erik Dujardin[1*]

[1]ICB, CNRS UMR-6303, Université Bourgogne Europe, France
[2]Institute for Integrative Biology of the Cell (I2BC), CEA, CNRS, Université Paris-Saclay, France
[3]Rennes Institute of Chemical Sciences, CNRS, University of Rennes 1, France
*Corresponding authors: Liudmila.Trotsiuk@gmail.com, Erik.Dujardin@cnrs.fr

***Abstract*— We demonstrate a proof of concept for artificial protein assemblies as programmable scaffolds for the selective positioning of quantum emitters that opens new avenues for engineered light–matter interactions in nanophotonics.**

***Keywords*— self-assembly, protein origami, quantum emitters, collective emission.**

I. Introduction

In nature, the spontaneous process of protein self-assembly, driven by specific intermolecular interactions, leads to the formation of highly symmetrical and periodic structures such as viral capsids and cytoskeletal filaments, demonstrating nanometer-scale precision and remarkable structural reproducibility [1]. Such precision and periodicity are particularly attractive for nanophotonics, where accurate control over emitter positioning is essential for enhancing light-matter interactions and enabling engineered optical properties beyond those achievable with disordered materials [2]. However, the use of natural proteins in nanophotonic applications remains challenging due to their limited stability, structural fragility, and restricted tunability. To overcome these limitations, we demonstrate the concept of artificial protein origami as a platform for the selective and controlled arrangement of quantum emitters that can result in plethora of optical phenomena.

II. Methods

The strategy of protein origami is based on the assembly of small and stable artificial α-helical repeat proteins (α-Rep) that serve as modular building blocks.[3] To induce controlled assembly, we mix two types of proteins: “bricks” and “staples” (Figure 1a) [4,5]. Each brick consists of a central region (green region) containing a defined number of α-helical repeats and two distinct α-Rep termini (red and blue). Staples proteins (Fig. 1a, orange) are small proteins that are designed to recognize and bind selectively to complementary interfaces on the blue and red termini of two adjacent bricks thus driving the formation of a superhelical structure (Fig. 1a, right). By bridging neighboring bricks, staples effectively lock and stabilize them at a predetermined orientation and distance. The resulting superhelices can further interact with each other and assembling into more complex 3D structures such as chiral fibers, sheets, and multilayer structures with Moiré patterns [4,5].

Notably, the original protein sequences are designed with amino acids that do not contain any thiol groups. Subsequent introduction of cysteine residues enables site-specific functionalization, creating anchoring points for covalent attachment of various quantum emitters, such as fluorescent gold clusters, quantum dots, and molecular dyes.

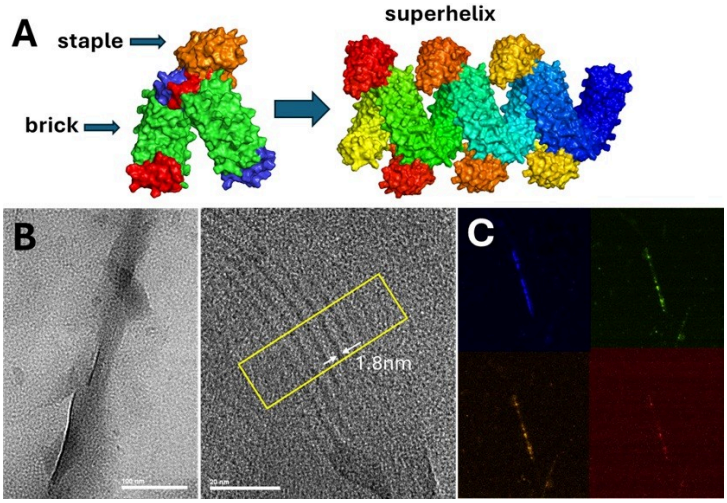

Fig. 1: (A) the model of brick and staple assembly forming a superhelix. (B) TEM of assembled protein origami with attached gold clusters. (C) FLIM images of origami with luminescent gold clusters. Blue and partially green regions represent proteins’ autofluorescence, while green, orange and red regions correspond to the PL of clusters.

III. Results and Discussion

We employed functionalized bricks in which four cysteine residues were introduced into the middle of the inner surface of the central region (Figure 1a, green). In this configuration, the attached emitters are positioned and confined within the

internal cavity of the superhelix. Upon complete binding of emitters to the bricks, a densely packed one-dimensional chain of emitters is expected to form along the helix axis. Owing to the small diameter of the superhelical inner cavity (~4 nm), glutathione-stabilized gold nanoclusters were selected as emitters. Gold clusters were first attached to the bricks via ligand exchange, followed by induction of self-assembly through the addition of staples. Transmission electron microscopy (TEM) images (Figure 1b) confirm the formation of assembled protein origami structures where individual helices are organized into extended sheet-like architectures.

Fluorescence Lifetime Imaging Microscopy (FLIM) was performed to verify cluster attachment. The gold clusters exhibit broad luminescence (FWHM ≈ 90 nm) in the 500–700 nm range, with a maximum at 600 nm. Emission was recorded in four spectral channels (Figure 1c). The blue and partially green channels correspond to protein autofluorescence, enabling localization of the protein structures, while the green-orange-red channels arise from gold cluster emission. As shown in Figure 1c, the cluster luminescence is strongly colocalized with the protein structures, confirming their successful attachment.

IV. Conclusion

We have demonstrated proof of concept for using artificial protein assemblies as scaffolds for the selective positioning of quantum emitters. By selecting appropriate brick designs, the inter-emitter distance and periodicity can be precisely controlled at the nanometer scale. This programmable spatial organization enables the formation of ordered emitter arrays within well-defined 3D architectures. The presented concept opens new pathways for applications in nanophotonics, including engineered light-matter interactions, collective phenomena, and the development of functional photonic nanomaterials.

Acknowledgments

This work was supported by the French National Research Agency with the frame of ProteOrigami project (ANR-21-CE09-0045). L. T. and E. D. thank CNRS Centre-Est regional office for financial support.

References

[1] N. Jaison, K. Yadav, H. Yang, and V. Yadav, “Biocrystallization: Harnessing natural scaffolds for stable protein crystal formulations,” New Biotechnology, vol. 90, pp. 257-267, 2025.

[2] A. Vaskin, R. Kolkowski, A. F. Koenderink, and I. Staude, “Light-emitting metasurfaces,” Nanophotonics, vol. 8 (7), pp. 1151-1198, 2019.

[3] A. Urvoas, A. Guellouz, M. Valerio-Lepiniec, M. Graille, D. Durand, D. C. Desravines, et al., "Design, production and molecular structure of a new family of artificial alpha-helicoidal repeat proteins (alphaRep) based on thermostable HEAT-like repeats", J Mol Biol, 404, 307-27, 2010

[4] L. Moreaud et al., “Design, synthesis, and characterization of protein origami based on self-assembly of a brick and staple artificial protein pair,” PNAS, vol. 120 (11), p. e2218428120, 2023.

[5] J. Miller, A. Urvoas, B. Gigant, M. Ouldali, A. Arteni, A. Mesneau, et al., "Engineering of brick and staple components for ordered assembly of synthetic repeat proteins", J Struct Biol, 215, 108012, 2023.

Ultrafast Switching from Strong to Weak Coupling in a Hybrid Plasmonic-Photonic Microcavity

Benedict S. Morris[1,*], Sergeï Kostcheev[2], Luis Santos[1], Khanh-Van Do[1], Anna Rumyantseva[2], Shuwen Zeng[2], Renaud Bachelot[2], and Bruno Palpant[1]

[1] LuMIn, Université Paris-Saclay, CNRS, ENS Paris-Saclay, CentraleSupélec, Gif-sur-Yvette, France
[2] L2n, Université de Technologie de Troyes, Troyes, France
*Corresponding author: benedict.morris@centralesupelec.fr

***Abstract*— Ultrafast optical absorption can modify gold nanoparticle optical properties. We exploit this subpicosecond reversible change to explore strong coupling physics in a plasmonic-photonic microcavity. We show that our hybrid system can be tuned from strong to weak coupling by all optical pumping, opening new pathways for sensing applications.**

***Keywords*— Rabi splitting, plasmonic nanoarray, pump-probe spectroscopy, femtosecond laser, sensing.**

Metallic nanoparticles, through the localised surface plasmon resonance (LSPR) phenomenon, exhibit distinct optical absorption that depends on particle geometry, volume, material, environment, and spatial distribution. This resonance can be altered by a small perturbation in the environment of the particles; hence, they are used for efficient sensing applications. Despite the considerable detection sensitivity that can be achieved [1], there is still a need for a short-timescale detection of light molecules in dilute conditions.

To address this sensing challenge, we pursue a new hybrid technology [2], [3] by coupling gold nanorods (AuNRs) to a photonic cavity composed of two Bragg mirrors. This novel approach combines the sensitivity of plasmonic and photonic devices allowing us to propose a new generation of optical sensors.

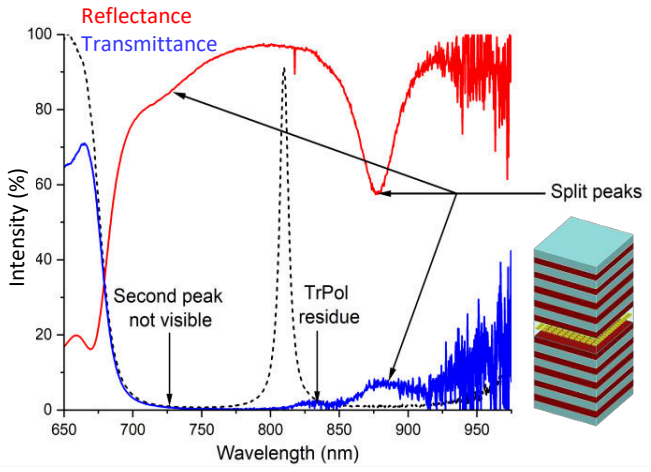

Fig. 1: Bare cavity transmittance (black dotted line) compared to hybrid cavity transmittance (blue line) and reflectance (red line) where the Rabi splitting is clearly visible.

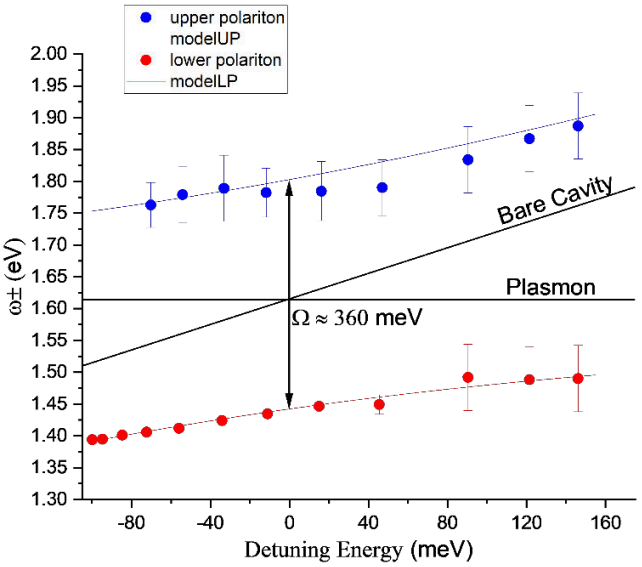

Fig. 2: Anti-crossing curve of our hybrid cavity showing large Rabi Splitting at zero detuning.

Within this hybrid framework, the strong and ultrastrong coupling regimes emerge as rich domains of electromagnetic interaction, where a large diversity of physical phenomena is enabled. To experimentally explore these regimes, we fabricate a plasmonic metasurface placed at the anti-node of a first-order Bragg microcavity, through electron-beam lithography and evaporation. We achieve robust, strong coupling (coupling strength $g \approx 0.10$), at ambient room temperature conditions. Then, after validating the stationary FDTD simulations with experimental results, the simulations are used to investigate the effects of the metasurface filling factor and position in the cavity on the coupling to the photonic resonance.

The coupling regime between our two resonators is highly dependent on each individual oscillator. Therefore, any change in the plasmonic resonator will have repercussions on the system's overall response. On the other hand, due to the LSPR dependence on the nanoparticle optical properties, any change in the dielectric function of the particles affects the plasmon resonance. Incidentally, when subject to subpicosecond laser pulses, high absorption in gold nanoparticles can lead to an ultrafast modification of the gold's dielectric function [4], therefore leading to a transient change in the plasmon resonance.

We therefore study, through pump-probe measurements, the effect of the AuNRs' transient modulation after absorption of short laser pulses on the coupling regime. We demonstrate that the reversible ultrafast modification of the AuNRs' complex permittivity results in a subpicosecond switch in coupling regimes. The spectral and time-domain signatures of these coupling regimes are both sensitive to the AuNR environment, opening a new pathway for high sensitivity sensing due to additional information compared to conventional stationary spectral data alone.

REFERENCES

[1] Y. Xu *et al.*, 'Optical Refractive Index Sensors with Plasmonic and Photonic Structures: Promising and Inconvenient Truth', *Adv. Opt. Mater.*, vol. 7, no. 9, p. 1801433, May 2019, doi: 10.1002/adom.201801433.

[2] R. Ameling, D. Dregely, and H. Giessen, 'Strong coupling of localized and surface plasmons to microcavity modes', *Opt. Lett.*, vol. 36, no. 12, p. 2218, Jun. 2011, doi: 10.1364/OL.36.002218.

[3] D. G. Baranov *et al.*, 'Ultrastrong coupling between nanoparticle plasmons and cavity photons at ambient conditions', *Nat. Commun.*, vol. 11, no. 1, p. 2715, Jun. 2020, doi: 10.1038/s41467-020-16524-x.

[4] X. Hou, N. Djellali, and B. Palpant, 'Absorption of Ultrashort Laser Pulses by Plasmonic Nanoparticles: Not Necessarily What You Might Think', *ACS Photonics*, vol. 5, no. 9, pp. 3856–3863, Sep. 2018, doi: 10.1021/acsphotonics.8b01012.

Chemical Reactions Driven by Plasmonic Hot Carriers

Seunghoon Lee[1,2*]

[1]Department of Chemistry, Dong-A University, South Korea
[2]Department of Chemical Engineering, Dong-A University, South Korea
*Corresponding author: seunghoon@dau.ac.kr

***Abstract*— Plasmonic hotspots generate hot carriers that drive chemical transformations, while enhanced fields enable in situ SERS readout. We demonstrate visible-light degradation of polyethylene microplastics by Au nanoparticle clusters and CPL-driven chiral growth from achiral Au nanocubes, arising from asymmetric hot-electron distributions and validated by CDS and SEM.**

***Keywords*— Hot carrier, Plastic degradation, SERS, Chirality.**

I. Introduction

Plasmonic metal nanoparticles (NPs) can efficiently merge the reactivity and energy harvesting abilities with enhanced plasmonic performance for sustainability. In this presentation, I will introduce the ability of plasmonic nanostructures to induce efficient energy transfer for plasmonic catalysis based on hot electron-mediated chemical reactions. Colloidally assembled nanostructures, e.g., Au particle-in-a frame and bimetallic assembled Au@M (M=Pd, Pt) nanostructures with catalytically active metals, exhibited superior performance over their constituent nanostructure counterparts in plasmonic sensing, surface-enhanced Raman scattering (SERS), and plasmonic catalysis. These model systems allow us to study the synergy effect of hot spots in plasmonic catalysis. The assembled NPs with hot spots can induce efficient light-to-chemical energy conversion as increasing non-radiative plasmon decay to the catalyst surface. We monitored the plasmon-mediated chemical reactions using SERS and dark-field scattering spectroscopy to study hot carrier-induced chemical conversion. Also, we thoroughly investigated the chirality transfer from circularly polarized light (CPL) to achiral Au nanocubes with hot carrier-mediated chemical reactions without involving any chiral molecule stimulators. Theoretical simulations, including hot-electron surface maps combined with experimental growth time and wavelength dependence of the chiral growth, reveal that the plasmon-induced chirality transfer is mediated by the asymmetric distribution of hot electrons on achiral Au nanocubes under CPL excitation. We expect these studies to provide a new direction for developing efficient plasmonic catalysts.

II. Results and Discussion

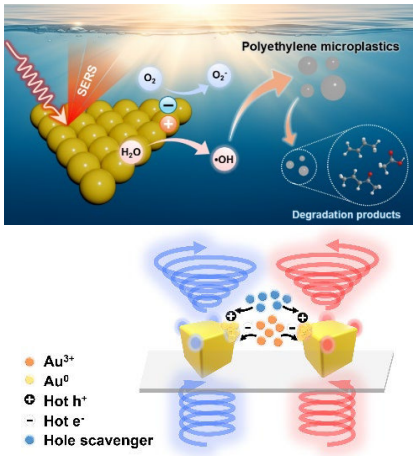

III. Conclusion

Plasmonic hot carriers provide a versatile route to drive chemical reactions, while plasmon-enhanced spectroscopy directly tracks the underlying pathways. By employing plasmonic nanostructures, we demonstrate visible-light microplastic degradation and CPL-induced chirality transfer, establishing design principles that connect hot-carrier generation, and nanoscale chemical and structural evolution.

Acknowledgments

This work was supported by he National Research Foundation of Korea (NRF) grant funded by the Korean government (MSIT) (RS-2022-NR071775, RS-2023-00220748).

References

[1] S. Lee, H. Hwang, W. Lee, D. Scherbarchov, Y. Wy, J. Grand, B. Auguié, D. H. Wi, E. Cortés, and S. W. Han, *ACS Energy Lett.* vol. 5, pp 3881-3890, 2020.
[2] S. Lee, C. Fan, A. Movsesyan, J. Bürger, F. J. Wendisch, L. de S. Menezes, S. A. Maier, H. Ren, T. Liedl, L. V. Besteiro, A. O. Govorov, and E. Cortés, Angew. Chem. Int. Ed., 63, pp. e202319920, 2024.
[3] J. Yang, M. Kang, R. K. Chitumalla, E. Cortés, J. Jang and S. Lee, J. Am. Chem. Soc. vol. 148, pp. 3462-3471, 2026.

Locally asymmetric plasmonic photocatalysis driven by light's polarization

L. V. Besteiro[1*]

[1]CINBIO, University of Vigo, Campus Universitario de Vigo, Lagoas Marcosende, 36310 Vigo, Spain

[*]corresponding author: lucas.v.besteiro@uvigo.es

***Abstract*: Light-to-matter chirality transfer can modify achiral plasmonic structures illuminated with circularly polarized light, inducing chiral growth on achiral plasmonic seeds by photocatalytically imprinting the reduced symmetry of the local fields onto the nanoparticle. We will discuss how different energy-transfer mechanisms can drive such asymmetric geometric transformations, discussing recent experimental demonstrations.**

Plasmonic nanostructures offer strong resonant responses in the UV-to-IR spectral range, which has led to their use in many optical and energy-related applications. Plasmonic photocatalysis stands as a prominent example of the latter, with plasmonic nanostructures serving as nanoscale antennas funneling radiant energy into their local environment. This talk will cover a particular subset of plasmonic photocatalytic setups with two defining characteristics: (i) the light-driven process modifies the geometry of the plasmonic nanoparticle or the optical properties of its immediate environment, and (ii) does so preserving local asymmetries induced by impinging circularly polarized light (CPL). This creates chiral features in initially achiral shapes, hence transferring chirality from light to the nanostructures, and contrasting with common strategies yielding chiral plasmonic systems, where chirality is seeded from molecules or introduced through top-down fabrication methods. The presentation will cover theoretical considerations underpinning light-to-matter chirality transfer in plasmonics,[1] a discussion about the physical energy-transfer mechanisms driving this phenomenon,[2,3] as well an overview of experimental work going from pioneering examples[4,5] to recent progress.[6,7]

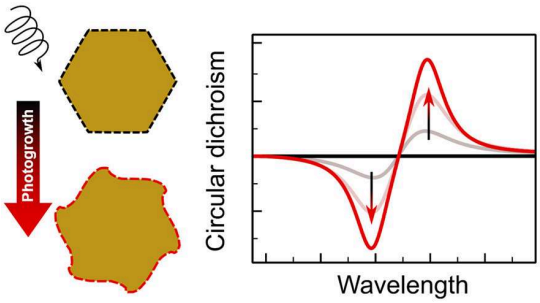

Figure 1. Diagram representing chiral growth of an achiral plasmonic nanostructure under CPL.[1]

References

1. L. V. Besteiro *et al.*, "Local Growth Mediated by Plasmonic Hot Carriers: Chirality from Achiral Nanocrystals Using Circularly Polarized Light," *Nano Lett.*, vol. 21, no. 24, pp. 10315–10324, 2021.
2. A. Movsesyan *et al.*, "Creating Chiral Plasmonic Nanostructures Using Chiral Light in a Solution and on a Substrate: The Near-Field and Hot-Electron Routes," *Adv. Opt. Mat.*, vol. 11, no. 18, p. 2300013, 2023.
3. O. Ávalos-Ovando *et al.*, "Universal imprinting of chirality with chiral light by employing plasmonic metastructures," *Appl. Phys. Rev.*, vol. 10, no. 3, p. 031412, 2023.
4. K. Saito and T. Tatsuma, "Chiral Plasmonic Nanostructures Fabricated by Circularly Polarized Light," *Nano Lett.*, vol. 18, no. 5, pp. 3209–3212, 2018.
5. A. Horrer *et al.*, "Local Optical Chirality Induced by Near-Field Mode Interference in Achiral Plasmonic Metamolecules," *Nano Lett.*, vol. 20, no. 1, pp. 509–516, 2020.
6. S. Lee *et al.*, "Unraveling the Chirality Transfer from Circularly Polarized Light to Single Plasmonic Nanoparticles," *Angew. Chem. Int. Ed*, p. e202319920, 2024.
7. M. Ghalawat *et al.*, "Chiral Symmetry Breaking in Colloidal Metal Nanoparticle Solutions by Circularly Polarized Light," *ACS Nano*, vol. 18, no. 41, pp. 28279–28291, 2024.

Circular Dichroism Enhancement via CPL-Induced Chiral Growth of Core–Shell Plasmonic Particles

Koichiro Saito[1,*], Yoshie Ishikawa[1]

[1]National Institute of Advanced Industrial Science and Technology (AIST), Japan
*Corresponding author: koichiro.saito@aist.go.jp

***Abstract*— Synthesizing chiral plasmonic nanoparticles under circularly polarized light avoids the need for chiral molecules. However, their g-factors have remained low. Here, we achieve an approximately eightfold enhancement of the g-factor by inducing chiral Ag growth on MnO_2-coated gold nanorods.**

***Keywords*— chirality, plasmonic nanoparticles, circularly polarized light, colloidal synthesis**

I. Introduction

Chiral plasmonic nanoparticles with intrinsically asymmetric morphologies hold great promise for applications such as chiral sensing and asymmetric catalysis. Synthesizing chiral plasmonic nanoparticles using circularly polarized light (CPL) as the chiral source offers the advantage of not requiring any chiral molecules. We previously demonstrated that circularly polarized light can drive a photochemical reaction that deposits silver onto gold nanorods (AuNRs) dispersed in solution, yielding rod-shaped chiral plasmonic nanoparticles (AuNR@Ag) that exhibit circular dichroism (CD) [1]. Although such colloidal synthesis is suitable for large-scale production, the resulting g-factors have remained relatively low.

In this study, we synthesized AuNR@MnO_2 by inducing chiral deposition of manganese oxide around colloidal AuNRs under circularly polarized light. We then deposited Ag onto these AuNR@MnO_2 structures under CPL irradiation to obtain AuNR@MnO_2@Ag. The colloidal solution of the core-shell nanostructures exhibited a g-factor approximately eight times larger than that of conventional AuNR@Ag.

II. Methods

AuNR@MnO_2 were synthesized by irradiating left- or right-handed circularly polarized light (CPL) from a red LED ($\lambda \approx 630$ nm) onto a dispersion of Au nanorods (AuNRs) containing citrate and permanganate. Subsequently, AuNR@MnO_2@Ag was obtained by adding citrate and silver nitrate to the AuNR@MnO_2 dispersion and irradiating CPL under the same conditions. Based on the absorbance and CD spectra of the dispersions, the g-factor values were calculated.

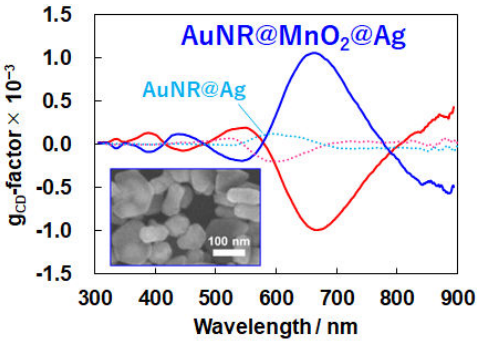

Fig. 1 CD spectra of AuNR@MnO_2@Ag synthesized under left-handed (red) or right-handed (blue) CPL. Inset: SEM image of the AuNR@MnO_2@Ag sample prepared under right-handed CPL.

III. Results and Discussion

The AuNR@MnO_2@Ag structures were predominantly rectangular in shape, although a small number of plate-like particles were observed due to excessive silver overgrowth. The maximum g-factors of AuNR@MnO_2@Ag and AuNR@Ag synthesized under right-handed CPL were 1.06×10^{-3} and 0.13×10^{-3}, respectively (Fig.1). The MnO_2 between the AuNR cores and the deposited Ag likely acts as a nanoscale spacer, potentially resulting in plasmonic coupling. This plasmon coupling could lead to a significant increase in the g-factor compared to AuNR@Ag.

IV. Conclusion

We achieved a large CD enhancement through CPL-induced chiral growth in core–shell plasmonic nanoparticles. Further chiral growth of these structures is expected to yield even greater enhancements. In the future, catalytic or sensing functions could be incorporated into these chiral structures by appropriately selecting material combinations.

Acknowledgments

This work was supported by JSPS KAKENHI (Grant No. JP 25H01642).

References

[1] K. Saito, Y. Nemoto and Y. Ishikawa, “Circularly Polarized Light-Induced Chiral Growth of Achiral Plasmonic Nanoparticles Dispersed in a Solution,” Nano Lett. 2024, 24, 12840.

Single-Particle Spectroscopy on Chiral Plasmonic Nanostructures

Wei-Shun Chang[1*], Angel Rose Thomas[1], Vidhi Singla[1], Oscar Avalos Ovando[2], Manita Khatri, Misbah ul Ain, Trang Nguyen[1], Tamie Vo[1], Alexander O Govorov[3]
[1]Department of Chemistry and Biochemistry, University of Massachusetts Dartmouth, North Dartmouth, Massachusetts, 02747, United States
[2]Department of Nanoscience, Joint School of Nanoscience and Nanoengineering, University of North Carolina at Greensboro, Greensboro, North Carolina 27401, United States
[3]Department of Physics and Astronomy, Ohio University, Athens, OH, 45701, United States
[*]Corresponding author: wchang2@umassd.edu

***Abstract*— We present a novel approach for a chiral dark-field spectromicroscopy that enables high-throughput, artifact-free measurements of plasmonic nanostructures at the single-particle level. This method reliably quantifies the intrinsic chirality of nanoparticles and elucidates plasmon-coupled circular dichroism in hybrid plasmonic systems.**

***Keywords*— circular dichroism, circular differential scattering, plasmon-coupled circular dichroism, chiral plasmonics.**

I. Introduction

Engineering the chirality of plasmonic nanostructures is essential for applications in biosensing, chiral catalysis, and enantioselective separation. Because optochirality is strongly regulated by nanostructure morphology, establishing reliable structure–chirality relationships remains challenging. Single-particle measurements could overcome this obstacle by resolving sample heterogeneity. Dark-field scattering (DFS) microscopy has emerged as a promising technique for measuring circular differential scattering (CDS) from individual nanoparticles; however, its accuracy is often compromised by artifact signals.

II. Methods

We have developed a custom-built DFS microscope with hyperspectral imaging capability that enables high-throughput, artifact-free measurement of CDS spectra from single plasmonic nanostructures. This method employs unpolarized excitation to maintain circular polarization at the sample plane and detection optics comprising a broadband quarter-waveplate and a Wollaston prism. (Figure 1) A sequential measurement by manipulating quarter waveplate orientation allows us to identify the intrinsic CDS signal while eliminating the artifact signal originating from linear dichroism. [1]

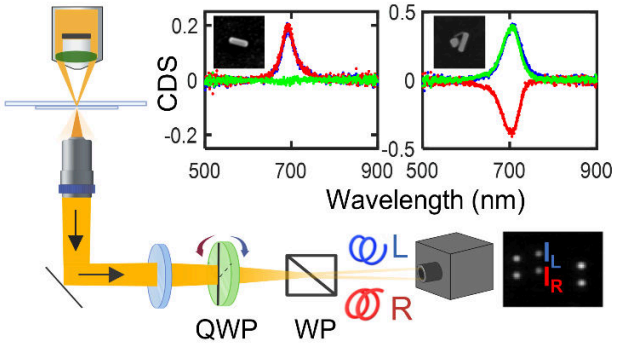

Fig. 1 Schematics of custom-built chiral DFS microscope.

III. Results and Discussion

Experimental results show:

- Measurements of intrinsic CDS of single chiral nanostructures.
- Identification of artifact CDS signal in uncoupled achiral Au nanorods.
- Observation of plasmon-coupled circular dichroism of single hybrid nanostructures composed of Au nanorods and DNA.

IV. Conclusion

We have demonstrated a precise measurement of the CDS of single achiral and chiral nanostructures. Additionally, the plasmon-coupled circular dichroism of DNA-functionalized Au nanorods is also unambiguously probed.

Acknowledgments

This work is supported by the National Science Foundation (CHE-2247710, CAT) and by UMass Dartmouth's Marine and Undersea Technology (MUST) Program funded by the Office of Naval Research (N00014-23-1-2141). The electron scanning electron microscope is supported by the National Science Foundation under Grant No. 1726239.

References

[1] A. R. Thomas, V. Singla, O. Avalos-Ovando, T. Nguyen, T. Vo, A. O. Govorov, and W.-S. Chang "Artifact-free Dark-field Scattering Microspectroscopy for Single-particle Chiral Measurements at the Nanoscale," ACS Nano, vol 4, pp. 3530-3540 (2026)

Plasmonic Nanosensor for Force Sensing in Live Cells

Won Park

[1]Department of Electrical, Computer & Energy Engineering, University of Colorado, Boulder, CO, USA

*Corresponding author: won.park@colorado.edu

***Abstract*— This paper presents a novel force sensor based on plasmonic modulation of upconverted luminescence. The short-range nature of plasmonic interaction enables high sensitivity. The nanosensor was used to monitor the cell-substrate interaction in live cell culture. It reveals mechanical forces in sub-cellular resolution.**

***Keywords*— surface plasmon, upconverted luminescence, biosensing, force sensing.**

I. Introduction

Upconverting nanoparticles (UCNPs) are excited by infrared light and emit visible and ultraviolet photons. The use of infrared excitation is attractive for chemical and biological sensing as it is absorbed minimally by water and many organic compounds and does not induce any background autofluorescence, leading to superior signal-to-noise ratio [1]. Compared to other frequency upconversion mechanisms such as two-photon fluorescence and high harmonic generation, UCNPs show far greater efficiencies [2], Furthermore, UCNPs do not photobleach or blink, making them ideal agents for imaging and sensing [3]. Considering these advantages, it is unsurprising that research on UCNP-based sensors has been steadily increasing over the years [4].

In this paper, we present a sensing platform based on the Purcell effect, which influences the emission process. Since the optical interaction responsible for the Purcell effect is a short-range interaction with strong distance dependence, any changes in the distance between the UCNPs and the nanoresonator modifies the luminescence properties. To build a sensor based on this mechanism, one should employ a molecule or a material that changes its length or volume in response to the environmental conditions or analytes one wants to detect. In this work, we report a straightforward yet powerful example of this sensing scheme which allows optical detection of mechanical forces. Sensors capable of quantitatively measuring physical forces are critical for a wide range of fields such as biology, medicine, and robotics. In biology and medicine, the interplay between physical forces and cell functions has long been a fundamental subject of research. Physical forces play an important role in many biological processes such as stem cell differentiation, initiation of transcriptional programs, morphogenesis, cell migration, malignancy, and wound healing. In robotics, high quality tactile sensing would enable more delicate and complex operations such as grasp control, dexterous manipulation or object recognition.

II. Sensing Principle

Our nanosensor is composed of a gold nanodisk, a polydimethylsiloxane (PDMS) layer and UCNPs (Fig. 1a). The UNCPs are $NaYF_4:Yb^{3+},Tm^{3+}$ nanoparticles which, under 980 nm excitation, emit multiple luminescence bands, as shown in Fig. 1(b). In this work, we use the two strongest emission bands centered at 645 and 800 nm. The finite-difference time-domain (FDTD) simulations showed that a gold nanodisk with a diameter of 150 nm and a thickness of 30 nm is the best choice. As shown in Fig. 1(b), the nanosensor structure exhibits a main plasmonic peak centered at around 770 nm and a smaller peak near 610 nm. The resulting Purcell enhancement of 645 and 800 nm emission results in exponentially decaying intensity ratio as a function of distance. This distance dependent PL intensity ratio provides the basis for the force sensing.

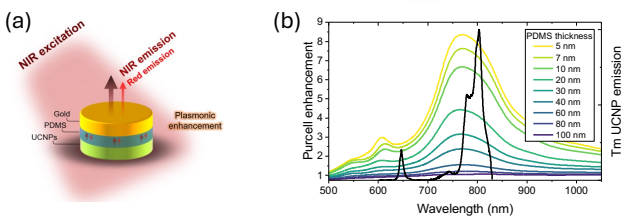

Fig. 1 (a) Schematic of the nanosensor composed of a gold nanodisk, a flexible polymer (PDMS), and UCNPs. (b) Calculated Purcell enhancement factor for various PDMS thicknesses. The size of the gold nanodisk is chosen to exhibit a large enhancement at 800 nm and minimal enhancement at 645 nm. That is, the gold disks are 150 nm in diameter and 30 nm in thickness.

III. Results and Discussion

To make the nanosensors, we developed a novel fabrication process that combines laser interference lithography (LIL), self-

assembly of UCNPs, pattern transfer and dry/wet etching. A detailed description of the fabrication process is given in a recent publication [5]. Fig. 2 shows the samples at various stages of the fabrication process.

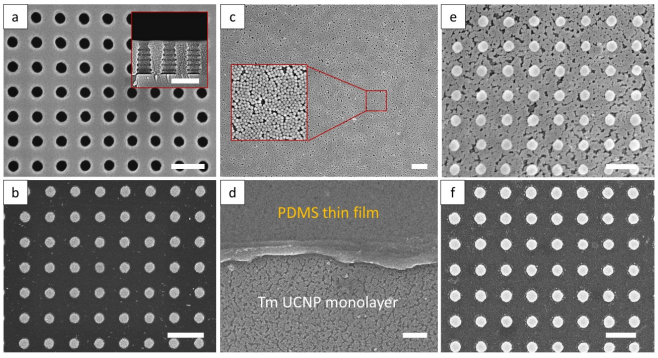

Fig. 2 Scanning electron micrographs (SEMs) of (a) nanohole array on a negative photoresist produced by laser interference lithography (Inset: cross-sectional view of the nanoholes revealing the modulated sidewall profile due to the interference pattern), (b) gold nanodisk array obtained by gold evaporation on the nanohole array shown in (a) and a subsequent lift-off, (c) monolayer of UCNPs obtained by the interfacial self-assembly method (Inset: a higher magnification view of the self-assembled monolayer), (d) PDMS thin film deposited on the UCNP monolayer shown in (c). Here, we deliberately etched the PDMS layer partially to reveal the underlying UCNP monolayer for better visualization. (e) Gold nanodisks transferred onto the PDMS surface after dry etch and (f) the final sensor array after etching away the extra UCNPs outside the gold nanodisks. All scale bars indicate 500 nm.

The fabricated nanosensors were characterized by a custom-built force characterization setup in which the nanosensors were strained by a pressurized gas. Fig. 3 shows the sensor response as a function of applied force. The PL intensity ratio increases gradually in the force range of 70 ~ 740 nN. It was not clear whether the nanosensor reached saturation at ~740 nN, because that was the maximum force we could generate using the gas pressure chamber. The force sensitivity (defined as the ratio of signal change per applied force change) obtained from the slope of Fig. 3 was 2 μN^{-1}. This corresponds to a pressure responsivity of 35 GPa^{-1}, which is two orders of magnitude larger than that of the alkaline earth UCNP force sensor [6].

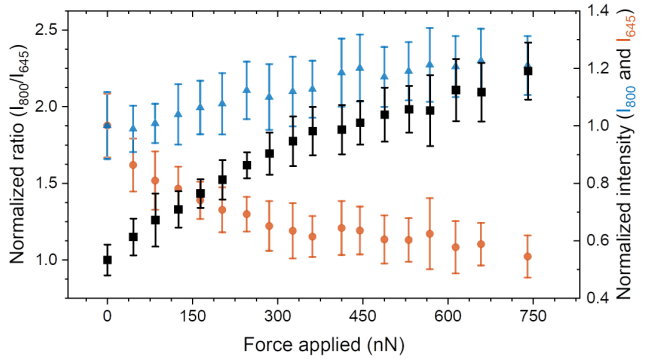

Fig. 3 PL intensity ratio as a function of applied force.

Finally, we performed force sensing experiments in live cell cultures. For these experiments, cells were grown on top of the nanosensor array and the fluorescence signal was imaged by a two-photon microscope. The results revealed that the cell-substrate adhesion force is around 20-30 nN and it varies spatially as the cells divide and migrate. This is the first direct measurement of cell-substrate mechanical interaction.

IV. Conclusion

We present a novel force sensor based on the plasmon modulated upconversion luminescence. By exploiting the short-range nature of plasmon interaction, the nanosensor is responsive to nanoscale deformations, which in turn allows for precise sensing of small forces. Since the near-infrared light interacts minimally with biological tissues, the use of near-infrared excitation makes the nanosensors well suited for biosensing applications. Furthermore, the new nanosensor employs a ratiometric sensing scheme in which one luminescence band serves as the signal while the other one acts as reference. The ratiometric sensing is much robust against environmental variations than the fluorescence intensity-based sensing scheme. The nanosensors are also very small, ~150 nm in diameter, and fabricated in a massive array. This enables sensing with high spatial resolution. This feature is particularly attractive for tactile sensing in robots where most tactile sensors lack high spatial resolution.

Acknowledgments

The work is supported in part by the National Science Foundation (CBET 2029559, TIP 2432516), National Institute of Health (R21 GM140347), Department of Education (GAANN P200A180012, P200A210111) and Colorado Office of Economic Development and International Trade (DO 2023-2330).

Competing Interest

The author has a stake in Irradiant Sensing Corporation.

References

[1] B. Zhou, B. Shi, D. Jin, and X. Liu, "Controlling upconversion nanocrystals for emerging applications," *Nature Nanotechnology,* vol. 10, no. 11, pp. 924-936, Nov 01 2015, doi: 10.1038/nnano.2015.251.

[2] F. Auzel, "Upconversion and anti-Stokes processes with f and d ions in solids," (in English), *Chem Rev,* vol. 104, no. 1, pp. 139-73, Jan 2004, doi: 10.1021/cr020357g.

[3] S. Wu *et al.*, "Non-blinking and photostable upconverted luminescence from single lanthanide-doped nanocrystals," *Proc Natl Acad Sci U S A,* vol. 106, no. 27, pp. 10917-21, Jul 7 2009, doi: 10.1073/pnas.0904792106.

[4] M. S. Arai and A. S. S. de Camargo, "Exploring the use of upconversion nanoparticles in chemical and biological sensors: from surface modifications to point-of-care devices," *Nanoscale Adv,* vol. 3, no. 18, pp. 5135-5165, Sep 14 2021, doi: 10.1039/d1na00327e.

[5] T. Ba Tis, C. Sabo, B. Xu, C. Corbella Bagot, E. Rappeport, and W. Park, "A scalable fabrication method for gold nanodisk-upconverting nanoparticle hybrid nanostructures," *Nanoscale,* vol. 16, no. 15, pp. 7690-7699, Apr 18 2024, doi: 10.1039/d3nr06644d.

[6] C. A. McLellan *et al.*, "Engineering Bright and Mechanosensitive Alkaline-Earth Rare-Earth Upconverting Nanoparticles," *J Phys Chem Lett,* vol. 13, no. 6, pp. 1547-1553, Feb 17 2022, doi: 10.1021/acs.jpclett.1c03841.

Optical Activity Modulation in Chiral Metasurfaces using Structured Light

Paula L. Lalaguna[1,*], Shun Hashiyada[2], Nikolaj Gadegaard[3], Jörg B. Götte[4], Stephen M. Barnett[4], Kayn A. Forbes[5], Yoshito Y. Tanaka[2] and Malcolm Kadodwala[1]

[1]School of Chemistry, University of Glasgow, United Kingdom
[2]Research Institute for Electronic Science, Hokkaido University, Japan
[3]School of Engineering, University of Glasgow, United Kingdom
[4]School of Physics and Astronomy, University of Glasgow, United Kingdom
[5]School of Chemistry, University of East Anglia, United Kingdom
*Corresponding author: Paula.LabordaLalaguna@glasgow.ac.uk

Abstract

We demonstrate a real-time, all-optical method for tuning optical activity in chiral metasurfaces without altering the metasurface geometry. By employing tightly focused circularly polarized Laguerre–Gaussian beams carrying different combinations of spin and orbital angular momentum, we achieve dynamic control of the dichroism through selective excitation of optically dark multipolar modes.

Keywords— metasurfaces, orbital angular momentum, chirality, vortex beams.

Enhanced Photoluminescence through Excitation - Surface Lattice Resonance Coupling in Aluminum Metasurfaces

A.Sraj[1], E.Garcelon[1], J.Martin[1], D.Gérard[1], L.Trotsiuk[1], A.Chevillot-Biraud[2], S.Lau-Truong[2], N.Felidj[2] and A-L.Baudrion*[1]

[1]1 L2n, CNRS UMR7076, Université de Technologie de Troyes, France.
[2]ITODYS, UMR7086, Université Paris Cité, France
*Corresponding author: anne_laure.baudrion@utt.fr

***Abstract*—We demonstrate high photoluminescence (PL) enhancement from colloidal quantum dots (QDs) using aluminum (Al) metasurfaces by matching excitation wavelengths to Surface Lattice Resonances (SLR). By tuning lattice periods, we prove excitation-SLR coupling is the dominant mechanism. These findings provide a robust framework for designing high-efficiency, QD-based nanophotonic devices.**

***Keywords*— metamaterials, Aluminum, Surface Lattice Resonance, Photoluminescence enhancement.**

I. Introduction

Plasmonic metasurfaces supporting **Surface Lattice Resonances (SLRs)** have emerged as a premier platform for tailoring light-matter interactions at the nanoscale. These collective modes arise from the diffractive coupling of localized surface plasmons, resulting in high quality-factor resonances associated with significantly extended near-field confinement compared to isolated nanoparticles[1]. Such properties are highly appealing for enhancing the optical response of weak emitters.

Strategies to amplify the **photoluminescence (PL)** of colloidal **quantum dots (QDs)** have prioritized emission matching[2][3], where the metasurface resonance is spectrally aligned with the peak emission wavelength of the QDs. However, this approach often isolate the critical role of the absorption rate. Recent theoretical studies[4] suggest that the local field enhancement at the excitation wavelength may be the dominant contributor to the overall PL signal. In this work, we utilize **aluminum (Al) nanodisk arrays** to experimentally investigate this mechanism. Al is an ideal material for this study due to its low cost, and plasmonic response across the UV-visible spectrum. By precisely engineering the lattice periodicity, we demonstrate that matching the SLRs to the specific excitation laser wavelengths results in **high PL enhancement** of blue and green emitting perovskites QDs used in our study. Our findings shift the focus from emission to excitation matching, providing a more effective rule for high-brightness nanophotonic devices.

II. Methods

The Al nanoparticle arrays were fabricated using standard **Electron Beam Lithography (EBL)**, resulting in a samples with lattice periods ranging from **200 nm to 500 nm**. Following the synthesis of the **colloidal QDs** via room temperature method[5], they were deposited onto the arrays by **spin-coating** to ensure a uniform emitter layer. The collective optical response of the arrays was characterized using **extinction spectroscopy**. Finally, **Fluorescence Lifetime Imaging Microscopy (FLIM)** was employed to measure the **PL increase** and **lifetime reduction** of the QDs on the SLR-excitation matched arrays relative to the background.

III. Results and Discussion

The **FLIM** measurements demonstrate that **fluorescence lifetimes are maximally reduced** specifically when the **excitation wavelength is matched to the SLR mode**. Under this resonance condition, we achieve interesting brightness gains, with **PL enhancement factors of up to 3.7 for green emitting perovskites QDs (515 nm) and up to 10 for blue emitting perovskites QDs (466 nm)**

relative to the background. These findings confirm that excitation-SLR matching is the dominant driver for maximizing emission in Al-based metasurfaces.

IV. Conclusion

In conclusion, we have experimentally demonstrated that **excitation-SLR coupling** is the primary mechanism for achieving **PL enhancement** in Al metasurfaces. By selectively matching the lattice periodicity to the excitation wavelength, we achieved high PL intensity and significant **lifetime reduction** for blue perovskite quantum dots. These results redefine the rules for high-performance nanophotonic platforms, shifting the focus toward excitation-matched resonances to maximize the efficiency of colloidal quantum emitters.

Acknowledgments

The authors thank the Graduate School NANO-PHOT (Ecole Universitaire de Recherche, PIA3, contract ANR-18-EURE-0013), the Région Grand Est for their financial support through a Ph.D. scholarship.

References

[1] V. G. Kravets et al. “Plasmonic Surface Lattice Resonances: A Review of Properties and Applications”. In: ChemicalReviews 118.12 (2018). PMID: 29863344, pp. 5912–5951. doi: 10 . 1021 / acs . chemrev . 8b00243. eprint: https ://doi.org/10.1021/acs.chemrev.8b00243. url: https://doi.org/10.1021/acs.chemrev.8b00243.

[2] Darren C. J. Neo et al. “Subwavelength Plasmonic Color Tuning of Quantum Dot Emission”. In: ACS Photonics 6.1 (2019), pp. 93–98. doi: 10 . 1021 / acsphotonics . 8b01586. eprint: https : / / doi . org / 10 . 1021 / acsphotonics .8b01586. url: https://doi.org/10.1021/acsphotonics.8b01586.

[3] N. I. Cade et al. “The Plasmonic Engineering of Metal Nanoparticles for Enhanced Fluorescence and Raman Scattering”. In: Journal of Optics A: Pure and Applied Optics 11.11 (2009), p. 114021. doi: 10.1088/1464-4258/11/11/114021.

[4] Frederic Laux, Nicolas Bonod, and Davy Gérard. “Single Emitter Fluorescence Enhancement with Surface Lattice Resonances”. In: The Journal of Physical Chemistry C 121.24 (2017), pp. 13280–13289. doi: 10.1021/acs.jpcc.7b04207. eprint: https://doi.org/10.1021/acs.jpcc.7b04207. url: https://doi.org/10.1021/acs.jpcc.7b04207.

[5] Xiaoming Li et al. “CsPbX3 Quantum Dots for Lighting and Displays: Room-Temperature Synthesis, Photolumi-
nescence Superiorities, Underlying Origins and White Light-Emitting Diodes”. In: Advanced Functional Materials
26.15 (2016), pp. 2435–2445. doi: https : / / doi . org / 10 . 1002 / adfm . 201600109. eprint: https : / / advanced . onlinelibrary.wiley.com/doi/pdf/10.1002/adfm.201600109. url: https://advanced.onlinelibrary.wiley.
com/doi/abs/10.1002/adfm.201600109

Van der Waals metasurfaces from strong coupling to topology

Andreas Tittl[1,*]

[1]Nano-Insitute Munich, Faculty of Physics,
Ludwig-Maximilians-Universität München, Germany
*Corresponding author: andreas.tittl@physik.uni-muenchen.de

***Abstract*— Van der Waals metasurfaces are redefining the landscape of nanoscale light-matter interaction by merging structural design flexibility with deterministic atomic-layer assembly. Leveraging quasi-bound states in the continuum (qBICs), we demonstrate a progression from high-Q visible resonators to intrinsic strong coupling and ultralow-power nonlinearities in heterostructure metasurfaces. Finally, we show how material anisotropy enables topological charge splitting for robust polaritonic flatband formation.**

***Keywords*— van der Waals materials, metasurfaces, bound states in the continuum, intrinsic strong coupling, topology.**

I. Introduction

The emergence of van der Waals (vdW) materials has unlocked a new paradigm for materials engineering, characterized by the ability to isolate individual crystal planes and restack them into customized vertical heterostructures. Unlike conventional semiconductors, these crystalline solids allow for the assembly of artificial structures without the constraints of lattice matching or dangling bonds, providing unparalleled control over their optoelectronic properties. By patterning these layered stacks into resonant metasurfaces, we can combine the rich physics of 2D semiconductors, such as stable room-temperature excitons and high refractive indices, with the precise radiative loss management of bound states in the continuum (BICs). This monolithic integration transforms the vdW crystal into an active optical cavity, enabling the exploration of complex light-matter interactions and exotic topological phases within an atomically engineered platform.

II. Methods

Our methodology combines mechanical exfoliation of bulk vdW crystals (hBN, WS_2, ReS_2) onto fused silica substrates with top-down nanofabrication. Standard processes include electron-beam lithography (EBL) to define resonator geometries and reactive ion etching (RIE) for pattern transfer. For heterostructure metasurfaces, dry transfer techniques are utilized to stack atomic layers prior to nanopatterning. Optical characterization is performed via white-light transmittance microscopy and angle-resolved Fourier-space spectroscopy

III. Results and Discussion

We first demonstrate that nanostructured vdW materials can support high-quality (Q) resonances over the full visible spectrum. Using low-index ($n \approx 2$) hBN, we realize qBIC metasurfaces with experimental Q factors above 300 spanning wavelengths from 400 to 1000 nm [1]. We then extend this concept to excitonic vdW materials, demonstrating intrinsic strong light-matter coupling in self-hybridized bulk WS_2 metasurfaces with a Rabi splitting of 116 meV [2]. Moving to vertically integrated heterostructures, we show that patterning an hBN/WS_2/hBN stack into a BIC-driven metasurface allows for the atomic-layer assembly of optical cavities. These heterostructure metasurfaces exhibit exceptional nonlinearities, with the strong-coupling regime saturating at excitation fluences three orders of magnitude lower than conventional cavity systems [3]. Finally, we demonstrate that material-intrinsic anisotropy in ReS_2 can be harnessed to fundamentally transform the photonic topological landscape. By splitting integer topological charges into momentum-separated half-integer singularities, we drive the formation of robust, polarization-controllable photonic and polaritonic flatbands [4].

IV. Conclusion

Our results highlight the potential for the monolithic integration of metasurfaces and 2D materials to achieve unprecedented control over light-matter interactions. These findings pave the way for low-threshold polariton lasers and topologically protected quantum photonic circuits operating under ambient conditions.

Acknowledgments

This work has received major support from the German Research Foundation (DFG), the European Research Council (ERC), and the European Innovation Council (EIC).

References

[1] L. Kühner et al., Advanced Materials 35, 2209688 (2022).
[2] T. Weber et al., Nature Materials 22, 970-976 (2023).
[3] L. Sortino et al., Nature Photonics 19, 825-832 (2025).
[4] C. Heimig et al., arXiv:2509.01258 (2025).

Colloidal Photonic Crystal Slabs for Hybrid Plasmon Photon Mode Engineering in Sensing and Energy Applications

Swagato Sarkar[1,2,*], Tobias A.F. König[1], Larysa Baraban[2], Andreas Fery[1]

[1] Leibniz-Institut für Polymerforschung Dresden e. V., Dresden, Germany
[2] Institute of Radiopharmaceutical Cancer Research, Helmholtz-Zentrum Dresden-Rossendorf, Dresden, Germany
*Corresponding author: sarkar@ipfdd.de, s.sarkar@hzdr.de

***Abstract*— Hybrid plasmonic photonic metasurfaces enable strong field confinement with reduced optical losses, but scalable implementations remain challenging. This work presents colloidal photonic crystal slabs as a versatile platform for engineering hybrid modes. Applications ranging from charge transfer and photocatalysis to surface-enhanced Raman scattering and biosensing are demonstrated.**

***Keywords*— colloidal metasurfaces, hybrid plasmon-photon modes, photonic crystal slabs, surface enhanced Raman scattering, biosensing.**

I. Introduction

Plasmonic nanostructures provide extreme electromagnetic field confinement but are inherently limited by optical losses, whereas dielectric photonic structures offer low-loss propagation with reduced nanoscale localization. Hybrid plasmonic-photonic geometries combine these complementary advantages, enabling strong and spectrally selective field enhancement with improved energy efficiency.

Most hybrid metasurfaces rely on top-down fabrication, which limits scalability. In contrast, template-assisted self-assembly (TASA) offers a bottom-up alternative that enables large area fabrication with nanoscale precision. Colloidal photonic crystal slabs (cPhCs) based on directed nanoparticle assembly on thin waveguides have therefore emerged as a general platform for hybrid plasmon photon mode engineering, with relevance to sensing and energy conversion [1].

II. Methods

CPhCs were fabricated by TASA of gold nanoparticles into periodic 1D lattices on dielectric waveguides. Interference lithography and wrinkle-assisted patterning were employed to define templates over centimeter-scale areas [1-3]. Recently, confinement-based printing was used to enable rapid and reproducible pattern transfer onto a variety of substrates [3].

Optical characterization was performed using angle-resolved ultraviolet-visible-near-infrared spectroscopy and confocal Raman spectroscopy under normal and oblique incidence [1,5]. Charge transfer and photocatalytic activity were assessed using two-terminal electrical measurements and dye degradation assays [2,3]. Finite-difference time-domain simulations were used to model electromagnetic field distributions and hybrid-mode dispersion [1,4,5]. The concept of hybrid plasmon-photon mode formation in colloidal photonic crystal slabs, along with the corresponding scalable fabrication workflow, is summarized schematically in Fig. 1.

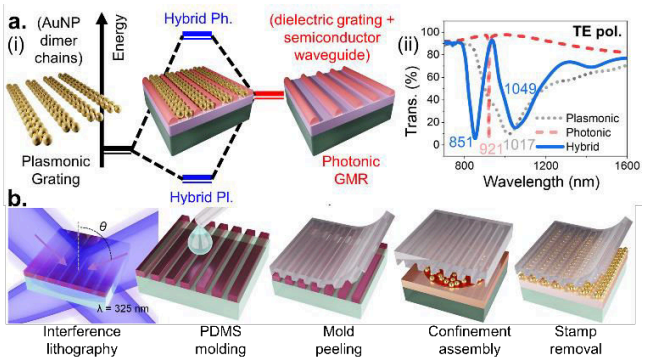

Fig. 1 Hybrid plasmon-photon mode concept and fabrication. (a) Schematic of mode hybridization between plasmonic nanoparticle gratings and photonic guided-mode resonances, with representative TE-polarized transmission spectra [1]. (b) Scalable fabrication via laser interference lithography, PDMS molding, and nanoparticle stamping.

III. Results and Discussion

Periodic colloidal nanoparticle lattices on waveguides serve as efficient optical couplers, giving rise to hybridized waveguide plasmon-polariton modes with well-defined dispersion relations [1]. Unlike conventional metallic gratings, nanoparticle chains enable excitation of hybrid modes for electric field components both parallel and perpendicular to the lattice direction, significantly expanding polarization

accessibility.

Figure 2 provides an overview of the applications of linear AuNP chain assemblies fabricated via TASA, covering both hybrid plasmon-photon and purely plasmonic functionalities. These hybrid modes facilitate efficient energy funneling into the waveguide, enabling broadband photo-enhanced charge injection in Au TiO_2 heterostructures [2]. Large-area devices exhibit measurable photocurrents and enhanced photoresponsivity under guiding conditions, while ultrafast spectroscopy reveals polarization-dependent charge-transfer dynamics influenced by nanoparticle ligand shells. Imprint-based colloidal printing further enables narrow-linewidth hybrid modes and plasmon-induced hot-electron-driven photocatalysis on the centimeter scale [3].

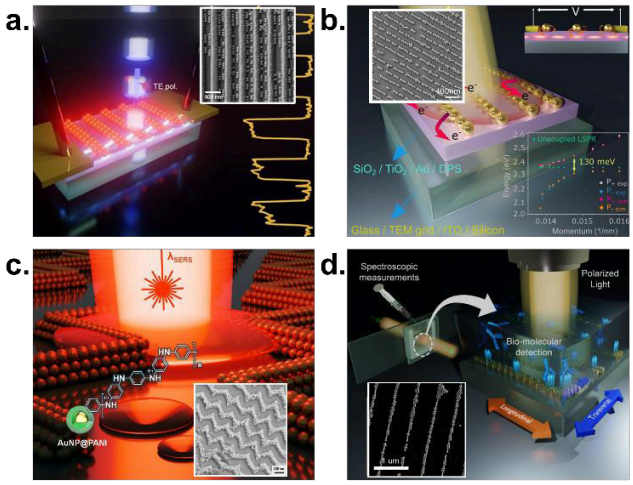

Fig. 2. 1D/2D AuNP chain assemblies fabricated via TASA. (a, b) Hybrid plasmon-photon architectures based on nanoparticle chains coupled to waveguide modes, towards plasmonic charge transfer/ photodetection as well as photocatalytic activity [1-3]. (c, d) Plasmonic chain assemblies supporting surface-enhanced Raman scattering and biosensing through strong localized field enhancement and polarization-dependent response [4, 6].

Purely plasmonic supracolloidal assemblies fabricated via wrinkle-based templates exhibit strong interparticle coupling and isotropic optical responses, enabling tunable plasmonic resonances for SERS applications [4]. However, integrating colloidal nanoparticle lattices into photonic crystal slabs yields low-loss hybrid plasmon-photon metasurfaces optimized for surface-enhanced Raman scattering. Angle-resolved SERS excitation reveals hybrid guided mode resonances and mode degeneracy, while systematic variation of lattice periodicity and nanoparticle concentration demonstrates robust performance against structural disorder. Maximal Raman enhancement is achieved when hybrid resonances spectrally coincide with the excitation wavelength [5].

Finally, linear nanoparticle assemblies fabricated via both interference lithography and wrinkle-assisted patterning exhibit pronounced polarization-dependent refractive index sensitivity. Proof-of-concept biosensing experiments demonstrate the detection of tumor necrosis factor alpha, highlighting the potential of hybrid plasmonic modes for scalable biointerfaces [6].

IV. Conclusion

Colloidal photonic crystal slabs provide a scalable, versatile platform for engineering hybrid plasmon-photon modes with controlled dispersion, reduced losses, and enhanced robustness. By bridging fundamental hybrid-mode physics with applications in energy conversion, spectroscopy, and biosensing, this approach establishes general design principles for large-area hybrid nanophotonic metastructures.

Acknowledgments

Tobias A.F. König acknowledges Volkswagen Foundation for financial support through the Freigeist Fellowship. Larysa Baraban and Andreas Fery acknowledge the financial support of DFG, German Research Foundation, for the funding of project 451785257 (GRK 2767-‘Supracolloidal Structures’) and project BA 4986/10.

References

[1] S. Sarkar, V. Gupta, M. Kumar, J. Schubert, P. T. Probst, J. Joseph, and T. A. König, “Hybridized guided-mode resonances via colloidal plasmonic self-assembled grating,” ACS Applied Materials & Interfaces, vol. 11, no. 14, pp. 13752-13760, 2019.

[2] [2] S. Sarkar, V. Gupta, T. Tsuda, J. Gour, A. Singh, O. Aftenieva, A. M. Steiner, M. Hoffmann, S. Kumar, A. Fery, and J. Joseph, “Plasmonic charge transfers in large-scale metallic and colloidal photonic crystal slabs,” Advanced Functional Materials, vol. 31, no. 19, p. 2011099, 2021.

[3] V. Gupta, S. Sarkar, O. Aftenieva, T. Tsuda, L. Kumar, D. Schletz, J. Schultz, A. Kiriy, A. Fery, N. Vogel, and T. A. König, “Nanoimprint lithography facilitated plasmonic-photonic coupling for enhanced photoconductivity and photocatalysis,” Advanced Functional Materials, vol. 31, no. 36, p. 2105054, 2021.

[4] Z. Yu, S. Sarkar, S. Seçkin, N. Sun, A. K. Ghosh, S. Wießner, Z. Zhou, and A. Fery, “Two-dimensional wrinkle-assisted zigzag plasmonic chains for isotropic SERS enhancement,” Scientific Reports, vol. 15, no. 1, p. 3662, 2025.

[5] S. Seçkin, S. Sarkar, F. Schneider, G. Yi, K. Gaur, A. J. Meixner, S. Reitzenstein, D. Zhang, and T. A. F. König, “Robust hybrid plasmon-photon modes in colloidal metasurfaces revealed by angle-resolved SERS,” manuscript submitted.

[6] [6] T. H. Tonmoy, S. Seçkin, M. Hoffmann, I. Çela, G. Yi, A. Alsadig, S. Sarkar, C. Rossner, T. A. König, A. Fery, and L. Baraban, “Enhanced refractive index sensitivity of linearly assembled gold nanoantennae for biosensing applications,” Small, p. e10159, 2025.

Permittivity-Engineered Dielectric Media of Hybrid Nanomaterials and Tunable Microcavity Metastructures for Enhanced Exciton–Light Interactions

Pedro Ludwig Hernandez-Martinez[1] and Hilmi Volkan Demir[1,2]

[1]*LUMINOUS!* Centre of Excellence for Semiconductor Lighting and Display,
School of Electrical and Electronic Engineering and School of Physical and Mathematical Sciences,
Nanyang Technological University, 639798, Singapore
[2]Department of Electrical and Electronics Engineering, Department of Physics,
UNAM−National Nanotechnology Research Center, and Institute of Materials Science and Nanotechnology,
Bilkent University, Ankara 06800, Turkey
*corresponding author, E-mail: pedro@ntu.edu.sg, HVDEMIR@ntu.edu.sg

***Abstract*—We present hybrid nanomaterial platforms that combine permittivity engineered dielectric media with tunable photonic metastructures to control excitonic interactions. Near-zero epsilon environments enable dramatic enhancement of nonradiative energy transfer between quantum emitters, while multiresonant microcavity arrays support room-temperature exciton polaritons in colloidal nanoemitters with strong coupling and tunable light-matter interactions.**

***Keywords*— hybrid nanomaterials, epsilon-near-zero (ENZ) media, energy transfer, exciton polaritons, microcavity metastructures.**

I. Introduction

The ability to control excitation energy flow and light–matter interactions at the nanoscale is central to the development of advanced photonic and optoelectronic technologies. Here, we present two complementary strategies for engineering excitonic interactions in hybrid dielectric media [1,2] containing nanomaterial systems of (i) tunable photonic metastructures supporting room-temperature exciton–polariton formation and (ii) permittivity-engineered dielectric environments enabling ultrahigh nonradiative energy transfer.

II. Methods

Förster-type nonradiative energy transfer between excitonic nanostructures was systematically analyzed using an analytical electrodynamic framework describing dipole–dipole interactions in complex dielectric media [2]. Donor–acceptor systems consisting of quasi-zero-dimensional quantum dots and quasi-two-dimensional quantum wells were modeled to derive the dependence of the transfer rate on the background medium permittivity. The dielectric screening factors governing the interaction were obtained from the electric field generated by excitonic dipoles in the surrounding medium. Parametric sweeps of the complex permittivity were performed to identify resonant conditions in epsilon-near-zero regimes and quantify the resulting enhancement of energy transfer. The resulting FRET rates were calculated using the expression:

$$\gamma_{trans} = \frac{2}{\hbar}\mathrm{Im}\left[\int dV\left(\frac{\varepsilon_A(\omega)}{4\pi}\right)\mathbf{E}_{in}(\mathbf{r})\cdot\mathbf{E}_{in}^{*}(\mathbf{r})\right] \quad (1)$$

where the integration is across the acceptor volume, $\varepsilon_A(\omega)$ is the dielectric function of the acceptor, and $E_{in}(\boldsymbol{r})$ is the effective electric field created by an exciton at the donor side.

Exciton–photon coupling in the microcavity system was analyzed using a coupled oscillator model describing the interaction between cavity photon modes and excitonic transitions in colloidal quantum wells[1]. The photonic dispersion of the multilayer cavity was calculated using a transfer-matrix formalism, while the excitonic response was modeled as a Lorentz oscillator. Diagonalization of the coupled system yields the upper and lower polariton branches and their Hopfield coefficients, allowing extraction of the Rabi splitting, detuning dependence, and strong-coupling conditions.

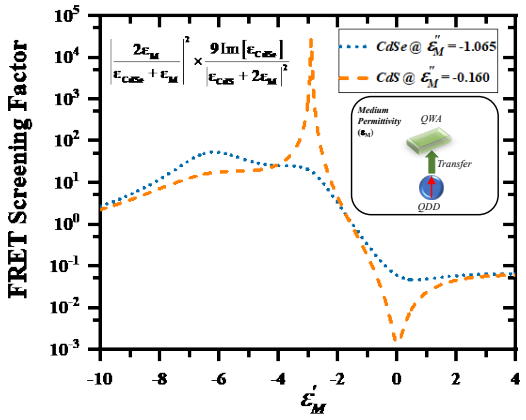

Fig. 1 Schematic representation of FRET from donor quantum dot to acceptor quantum well. FRET screening factor for CdSe (blue line, $\varepsilon_M'' = -1.065$) and CdS (red line, $\varepsilon_M'' = -0.160$) as a function of the real part of the medium permittivity.

III. Results and Discussion

Here, we investigated Förster-type nonradiative energy transfer (FRET) between semiconductor nanostructures embedded in complex dielectric media with engineered permittivity. Analytical derivations of the FRET rate for donor–acceptor pairs composed of quasi-0D quantum dots (QDs) and quasi-2D quantum wells (QWs) reveal that the transfer efficiency can be dramatically enhanced when the background medium approaches epsilon-near-zero (ENZ) conditions. In this regime, the dielectric screening factor exhibits a resonance when the denominator approaches zero, leading to a singular enhancement of dipole–dipole coupling. Using realistic material parameters achievable through digital metamaterial implementations (e.g., effective permittivity ε_M=-2+i), the FRET rate can be enhanced by more than two orders of magnitude, reaching enhancement factors up to 229-fold for QD donor-QD acceptor (QDD–QDA) pairs and 321-fold for QD donor-QW acceptor (QDD–QWA) configurations relative to vacuum.

Complementary to this near-field control mechanism, we also demonstrated tunable strong coupling between excitons and cavity photons in a multiresonant microcavity metastructure platform fabricated using binary lithography and reflow (BLR). This architecture enables nanometer-scale control of cavity length variations (<5 nm) across arrays of microcavities on a single chip. The platform was integrated with gradient core–crown CdSe/$CdSe_xS_{1-x}$ colloidal quantum wells, which exhibit enhanced photostability and large exciton binding energies (~200 meV). Angle-resolved spectroscopy reveals clear exciton–polariton formation at room temperature with a Rabi splitting of ≈ 50 meV and a Rabi quality factor Q_R ≈ 3.3, confirming a robust strong-coupling regime.

IV. Conclusion

With these results, we show that combining permittivity-engineered dielectric media with tunable photonic metastructures provides a powerful approach for controlling excitonic interactions and hybrid light–matter states. Such hybrid platforms open new opportunities for efficient excitonic energy transport, tunable polaritonic devices, and integrated photonic architectures for sensing, light generation, and energy-harvesting applications.

Acknowledgments

The authors acknowledge support from Singapore Agency for Science, Technology and Research (A*STAR) MTC program under grant number M21J9b0085, Ministry of Education, Singapore, under its Academic Research Fund Tier 1 (MOE-RG62/20). HVD also gratefully acknowledges the support from TUBA.

References

[1] N. V. Cam, M. A. Rahman, S. Akhil, E. G. Durmusoglu, T. T. H. Do, P. L. Hernandez-Martinez, C. Dabard, D. Arora, S. Uddin, G. Zamiri, H. Wang, S. T. Ha, N. A. Mortensen, H. V. Demir, J. K. W. Yang "Tunable Multiresonant Microcavity Exciton-Polaritons in Colloidal Quantum Wells", Nano Letters 25, 6109 (2025).

[2] P. L. Hernández-Martínez, A. C. Yucel, and H. V. Demir, "Ultraefficient Förster-Type Nonradiative Energy Transfer Enabled by the Complex Dielectric Medium with Tuned Permittivity" J. Phys. Chem. C 125, 12405, 2021.

Hybrid Oxide–Phase-Change Heterostructures for Thermally Tunable Mid-Infrared Photonics

Daniele Ceneda[1], Martina Mercurio[1], Roberto Macaluso[2], Nunzio Timpanaro[2], Marco Centini[1], Maria Cristina Larciprete[1]
[1]Department of Basic and Applied Sciences for Engineering, Sapienza Università di Roma, Rome, Italy
[2] Department of Engineering, University of Palermo, Palermo, Italy
*Corresponding author: mariacristina.larciprete@uniroma1.it

***Abstract*— We present our research activity on hybrid oxide heterostructures, in particular combining strongly anisotropic molybdenum trioxide, MoO_3, with thermochromic vanadium dioxide, VO_2. The integration of these two materials required careful control of the deposition sequence and interface quality in order to preserve both the polar dielectric properties of MoO_3 and the phase-change behavior of VO_2. By combining α-MoO_3 with VO_2 in multilayer architectures, we demonstrate reversible thermal modulation of the infrared optical response, leading to dynamic tuning of phonon-polariton resonances supported by the α-MoO_3 layer.**

***Keywords*— polar materials, thermochromic materials, phase-change, heterostructures.**

I. Introduction

Controlling electromagnetic radiation in the mid-infrared (mid-IR) spectral region is crucial for a wide range of emerging technologies including thermal emission engineering, chemical sensing, infrared imaging, and free-space optical communications. In this context, polar dielectric materials capable of supporting phonon polaritons have attracted increasing attention due to their ability to confine and manipulate infrared radiation at sub-wavelength scales.

Among them, the van der Waals crystal α-MoO_3 is particularly interesting because of its strong in-plane optical anisotropy and the presence of multiple Reststrahlen bands that enable polarization-dependent propagation of phonon polaritons [1]. These properties make α-MoO_3 an attractive material for mid-IR photonic components and metasurfaces. However, the realization of large-area thin films that preserve the intrinsic anisotropic optical response remains challenging.

At the same time, achieving dynamic tunability of infrared optical properties represents a key step toward adaptive photonic systems. Phase-change materials such as vanadium dioxide (VO_2) provide a promising solution, as they exhibit a reversible metal–insulator transition (MIT) accompanied by significant changes in their optical constants [2].

In this work we investigate large-area oxide thin films and their integration into hybrid heterostructures combining α-MoO_3 and VO_2. By coupling a polaritonic material with a thermochromic phase-change layer, we develop a platform capable of dynamically modulating the infrared optical response through temperature control.

II. Methods

Large-area, hybrid heterostructures were fabricated by integrating α-MoO_3 layers with VO_2 thin films using pulsed laser deposition (PLD). The growth parameters were carefully optimized by tuning substrate temperature, oxygen partial pressure, laser fluence, and deposition rate in order to obtain films with high crystalline quality and uniform thickness over centimeter-scale substrates. In these multilayer systems the thermally induced phase transition of VO_2 will enable reversible modulation of the optical response of the structure.

III. Results and Discussion

The optical response of the deposited films was investigated by Fourier-transform infrared spectroscopy (FTIR). Measurements performed at near-normal incidence revealed the characteristic Reststrahlen bands associated with the α-MoO_3 crystal structure [3]. In particular, three phonon-related spectral regions were identified: the x-Reststrahlen band (approximately 820–972 cm^{-1}), the y-Reststrahlen band (545–851 cm^{-1}), and the z-Reststrahlen band located between 962 and 1010 cm^{-1}, indicating that the polaritonic properties of the material are preserved in the multilayer configuration.

Furthermore, temperature-, polarization-, and angle-dependent FTIR measurements were performed to investigate the interaction between the phonon-resonances of α-MoO_3 and the phase-dependent optical properties of VO_2.

When α-MoO_3 and VO_2 are combined into multilayer heterostructures, the phase transition of VO_2 leads to measurable changes in the infrared spectral response of the

system. In particular, temperature-resolved FTIR spectra reveal a modulation of the phonon-polariton resonances associated with the α-MoO_3 layer when the VO_2 film switches from the insulating to the metallic phase.

This thermally induced modulation demonstrates that the interaction between anisotropic phonon polaritons and phase-change materials can be exploited to get a strong dynamic range of mid-IR optical properties of the resulting heterostructure. The ability to control phonon-resonances over large areas represents an important step toward practical reconfigurable infrared photonic devices.

IV. Conclusion

In summary, we investigated oxide thin films and hybrid heterostructures combining α-MoO_3 and VO_2 for tunable mid-infrared photonics. Optimized pulsed laser deposition enabled the realization of large-area α-MoO_3 films with clearly observable Reststrahlen bands. The integration of VO_2 phase-change layers provides an effective mechanism for active control of the infrared optical properties through the thermally driven metal–insulator transition. Furthermore, the use of tungsten-doped VO_2 allows tuning of the transition temperature toward room temperature, enabling more practical operating conditions [4-5].

Our results demonstrate that coupling anisotropic polar materials with phase-change oxides offers a versatile approach for the development of dynamically reconfigurable photonic components in the mid-infrared, including tunable emitters, adaptive metasurfaces, and polarization-dependent optical devices.

Acknowledgments

The work was financed by the European Union—NextGenerationEU (Bando PRIN 2022, Directorial Decree n. 104—February 02, 2022, Project code: 2022ZRN4LX). The opinions expressed are those of the authors only and should not be considered representative of the European Union or the European Commission's official position. Neither the European Union nor the European Commission can be held responsible for them.

References

[1] W.Ma, P.Alonso-González, S.Li, A.Y.Nikitin, J.Yuan, J.Martín-Sánchez, J.Taboada-Gutiérrez, I.Amenabar, P.Li, S.Vélez, C.Tollan, Z.Dai, Y.Zhang, S.Sriram, K.Kalantar-Zadeh, S.-T.Lee, R.Hillenbrand and Q.Bao, "In-Plane Anisotropic and Ultra-Low-Loss Polaritons in a Natural van der Waals Crystal", Nature vol. 562, pp. 557–562, 2018.

[2] M.A.Kats, D.Sharma, J.Lin, P.Genevet, R.Blanchard, Z.Yang, M.M.Qazilbash, D.Basov, S.Ramanathan and F. Capasso, "Ultra-thin perfect absorber employing a tunable phase change material," Appl. Phys. Lett. Vol. 101, pp. 221101, 2012.

[3] M.C:Larciprete, D.Ceneda, C.Yang, S.A.Dereshgi, F.V.Lupo, M.P.Casaletto, R.Macaluso, M.Antezza, Z.Zhang, M. Centini and K.Aydin, "Large-Area Polycrystalline α-MoO_3 Thin Films for IR Photonics. J. Phys. D: Appl. Phys. vol. 57 (13), pp. 135107, 2024.

[4] M.C.Larciprete, D. Ceneda, D. Scirè, M. Mosca, D. Persano Adorno, S. Abedini Dereshgi, R. Macaluso, R. Li Voti, C. Sibilia, T. Cesca, G.Mattei, K.Aydin and M.Centini, "Tunable IR perfect absorbers enabled by tungsten doped VO_2 thin films", APL Mater. vol. 11, pp. 091107, 2023.

[5] A.Bile, D.Ceneda, V.E.S. Maryam, D.Scirè, G.Buscarino, M.Mosca, D.Persano Adorno, R.Macaluso, R.Li Voti, C.Sibilia, T.G. Folland, K.Aydin, M.Centini and M.C.Larciprete, "Room-temperature tuning of mid-infrared optical phonons and plasmons in W-doped VO_2 thin films", Optical Materials vol. 154, pp. 115732, 2024.

When Grain Boundaries Create Plasmons: Localized Resonances in Hyperdoped polysilicon films

1

Mohamad Bahsoun[1], Jesse Groenen[1], Sébastien Joulié[1], Cécile Marcelot[1], Robin Cours[1], Sébastien Kerdiles[2], Mathieu Opprecht[2], Caroline Bonafos[1] and Jean-Marie Poumirol[1]

[1]CEMES, CNRS, University Toulouse, France
[2]LETI, CEA-University of Grenoble-Alpes France
*Corresponding author: jean-marie.poumirol@cemes.fr

***Abstract*— We report an innovative approach for fabricating large-area, silicon-based plasmonic metasurfaces without engineered nanostructures. We show that hyperdoped polysilicon layers annealed under out-of-equilibrium conditions, exhibit enhanced light–matter tunable interactions. These remarkable optical properties originate from naturally formed metal–dielectric interfaces at grain boundaries, which support localized surface plasmon resonances.**

***Keywords*— nanoplasmonics, doped semiconductor, coupled dipoles**

I. Introduction

Advances in nanofabrication enabling subwavelength metasurfaces have been central to the success of plasmonics. However, despite rapid progress, the widespread commercialization of plasmonic metasurfaces remains hindered by challenges in scalable manufacturing and deployment in real-world devices.

II. Results and Discussion

Hyper doped polysilicon films were obtained by laser thermal annealing of a 23 nm phosphorus doped silicon-on-insulator substrate. In such extremely out-of-equilibrium conditions, concentrations of electrically active dopants beyond the equilibrium solid solubility limit can be achieved in localized regions[2]. Automated Crystal Orientation Mapping in TE performed on the samples annealed above full-melt conditions, reveals that the polycrystalline layer consists of randomly oriented nanograins separated by grains boundaries with grain size distribution ranging from 5 nm to 50 nm (see insert fig.1). Fourier-transform infrared spectroscopy shows that on these polycrystalline samples the shape of the transmission is strongly altered and the transmission minimum is no longer localized at zero frequency as it is the case for doped Si monocrystal[1]. This is a clear sign that the optical signature is no longer dominated by free carriers. Using electrodynamics simulations we confirmed that surface plasmon resonances can emerge intrinsically from unpatterned polysilicon layers composed of nanometric grains, without the need for any external nanostructuring.

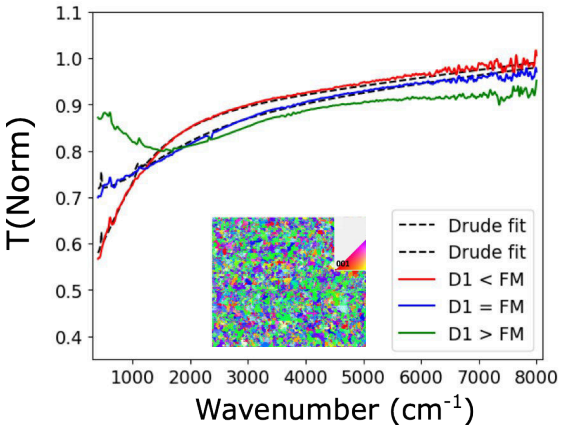

Fig. 1 Normalized transmittance. Continuous lines, measured on unpatterned hyper- doped Si layers bellow full melt, at full melt and over full melt. Insert ACOM images (orientation maps)

III. Conclusion

This behaviour, which cannot be achieved in polycrystalline noble metals, arises from the strong dielectric contrast between metallic-like silicon grains and dielectric grain boundaries. The resulting high packing density promotes strong dipole–dipole coupling, which dominates the plasmonic response of the material. Ultimately, near-field coupling elevates the size-distribution of doped nanograins to a central parameter controlling the plasmonic response, even if grain dimensions lie nearly three orders of magnitude below the excitation wavelength.

Acknowledgments

This work was partly supported by ANR DIAAPASON (ANR-24-CE09-4555) and by the Tremplin project PLASMONIX from CNRS-Physique

References

[1] J-M . Poumirol et. al. « Hyper doped silicon nanoantennas and metasurfaces for tunable infrared plasmonics » ACS photonics vol. 8, 5 pp. 1393–1399, 2021.
[2] N. Chery et. al. and Y. T. Lee, “Study of recrystallization and acticvation processes in thin and highly doped silicon-on-insulator layers by nanosecond laser thermal annealing,”journal of applied physics vol. 131, 6 2022.

In-plane Directed Power Flow in Anisotropic Hyperbolic Materials

Eric Seabron[1,2], Eric Jackson[1], Michael Meeker[1], Andrew Lang[1], Rhonda Stroud[1,3], Daniel C. Ratchford[1], Brandon K. Durant[1], Xitlali G. Suarez[1], Chase Ellis[1], Joseph Tischler[1,4*]
[1]Naval Research Laboratory, Washington DC, USA
[2]Howard University, Washington DC, USA
[3]Arizona State University, Phoenix AZ, USA
[4] University of Oklahoma, Norman, OK USA
*Corresponding author: tischler@ou.edu

***Abstract*—We harness the anisotropic nature of Calcite to modify and control the light-matter interactions in the mid-IR. We introduce hyperbolic Calcite as a polar dielectric with in-plane anisotropic permittivity as a platform that supports cavity-like volume phonon polaritons (vPhPs) with significant modal volume compression due to the Calcite's hyperbolic dispersion.**

***Keywords*— metamaterials, hyperbolicity, nanostructuring, anisotropy, calcite.**

I. Introduction

The study of phonon polaritons (PhPs) in polar dielectrics is essential for advancing mid-infrared (mid-IR) radiometry, λ ~ 3-30 μm, for sensing, vibrational spectroscopy, black-body radiation sources, and other photonic applications [1-9]. Polar dielectric materials support PhP modes within the "reststrahlen band", the spectral region between the material's transverse and longitudinal optical Transverse and Longitudinal optical phonons [10]. Compared to plasmon polaritons, PhPs have much longer scattering lifetimes, resulting in lower optical losses making them attractive materials platforms for infrared photonics [11]. Hyperbolic polar dielectrics have a unique optical dispersion which arises when the permittivity tensor have both a negative (metallic-like) and positive (dielectric-like) component leading to hyperbolic shaped isofrequency dispersion curves. Due to the unbounded nature of the hyperbola shaped isofrequency dispersion, the physics supports coupling in very high-k limit which leads to subwavelength optical volume confinement. Hence, hyperbolic polar dielectrics can support PhP resonances with very high figure of merit which has been experimentally shown in a myriad of material platforms including hBN, β-Ga2O3, and InGaAs [12-17]. Hyperbolic materials can be found naturally or engineered as metamaterial. Current work focuses on understanding and controlling aspects of hyperbolic resonators such as physical attributes and crystal orientation to allow for the manipulation and emergence of interesting polariton behavior [14,18,19]. Developing in-plane anisotropy, where both the "metallic" and "dielectric" axis lie in-plane, is a unique geometry that is difficult to realize experimentally because it is very challenging to fabricate using conventional methods for creating metamaterials [20]. Although research has been done using 1D BNNTs and 2D hBN to study in-plane anisotropy, process and applications are limited by the difficulty of engineering microstructures into hBN based nanomaterials [21].

Recent studies show the first experimental observation of hyperbolicity in calcite, which is unique because its optical properties are highly dependent on the crystalline plane normal to the optical axis. Hence, we can easily achieve in-plane anisotropy by cleaving the crystal surface on the <100> plane [22-24]. Hyperbolic materials with in-plane anisotropy are a rare property, in part because they cannot be produced artificially using conventional methods for creating layered optical metamaterials. This makes Calcite particularly flexible material platform for studying novel hyperbolic optical physics and may have niche applications for novel mid-infrared photonic devices such as thermal radiation sources, sensors, spectrometers, waveguides, and polarizers.

II. Methods

In this work we use FTIR spectroscopy and COMSOL Finite Element Analysis (FEA) simulations to explore the exotic behavior of resonators in hyperbolic Calcite with extreme in-plane anisotropy. We experimentally show that engineering the permittivity tensor of Calcite resonators can tune the resonant frequency of strongly confined volume PhP modes in the mid-IR. Here we present a successful theoretical model which describes the hyperbolic dispersion relation, poynting vector, and selection rules for light coupling to polar dielectric resonators with extreme in-plane anisotropy.

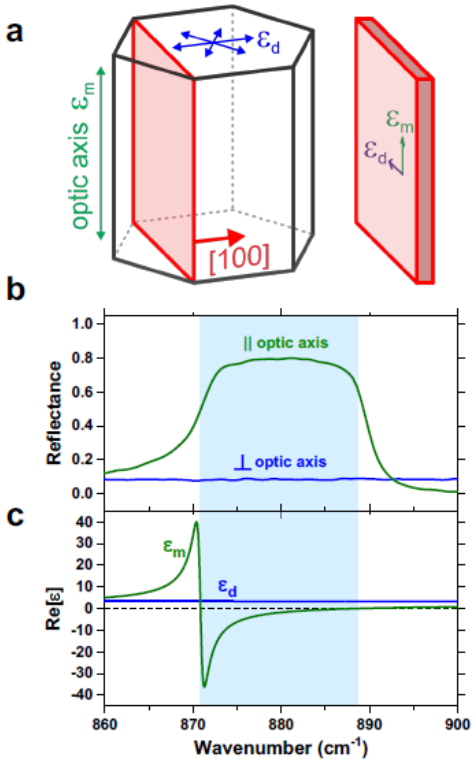

Fig. 1: Optical properties of bulk calcite. (a) Illustration depicts how the (100) sample is cut from hexagonal crystal unit cell. (b) Reflectance measurements of (100) calcite polarized parallel (green curve) and perpendicular (blue curve) to the optic axis (green curve), demonstrating optical anisotropy in the sample plane. (c) real part of the in-plane permittivity measured for (100) calcite along the optic axis (green curve) and perpendicular to the optic axis (blue curve), revealing the metallic-like and dielectric nature of the permittivities for each respective axis in the sample plane.1 Unit cell geometry of the proposed metamaterial.

Strongly coupled resonator structures in calcite supports PhP modes in its lower Rhestralen band (850-900cm-1) and its upper Rhestralen band (1350-1600cm-1) depending on the orientation of the incident polarization relative to the crystalline axis (supplemental figure 1) [19,22]. For this study we will focus on the lower Rhestralen band due to its unique behavior supporting volume PhP modes. Reports using the <001> surface of Calcite show that the "metallic-like" extraordinary axis is pointed into the substrate, hence the in-plane permittivity is isotropic and shouldn't have any polarization dependance; this represents the most studied hyperbolic crystal geometry. Our experiments using <100> plane of Calcite showed that the R-band reflectivity acquired using FTIR has a strong polarization dependance. Our results show the lower R-band the incident light is most strongly coupled when the polarization is parallel to the extraordinary axis, as shown in figure 1a. From the experimental data in figure 1ab, the lower R-band's bulk calcite, which is highlighted in blue, reveals Calcite's Type I Hyperbolic character which will support volume PhP modes. In figure 1b, we further explored the polarization dependance of bulk Calcite by recording the polarization dependent reflectivity in the middle of the R-band, ~879cm-1, on both <001> "isotropic" plane (red) and <100> "anisotropic" plane (black). Our results revealed a natural Malus' law trend for the anisotropic plane which validates our theory that the in-plane anisotropy is a direct cause of its polarization dependance.

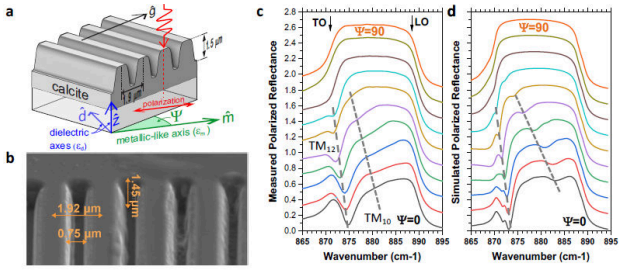

Fig. 2: Figure 2: Tuning of hyperbolic modes within 1D resonators. (a) Illustration of resonator geometry where resonators have a fixed pitch of 1.9 mm and height of 1.5 mm and are rotated with respect to the calcite optic axis (green arrow) by the angle Y. The orientation of the incident polarization for the measurements shown in subsequent panels is indicated by the red arrow. (b) Scanning electron microscope image of resonator grooves etched into (100) calcite. (c) Measured and (d) simulated polarized reflectance

III. Conclusion

Our study achieved novelty through validated hypotheses and established the influence of in-plane anisotropy on the behavior of Volume PhP modes supported by hyperbolic polar dielectrics such as Calcite. We confirmed that modal conservation and k-vector selection rules are independent of permittivity orientation, with the isofrequency surface oriented by the permittivity tensor and the k-vector selected by resonator geometry. Additionally, our validated characteristic equation allows predictability of modes given knowledge of resonator geometry and permittivity in one orientation, enabling derivations for other rotations. We comprehensively demonstrated the polariton physics within hyperbolic polar dielectrics with extreme in-plane anisotropy, showcasing its influence on frequency dependence based on resonator size, shape, and orientation. Furthermore, our findings revealed how in-plane anisotropy can manifest large changes in power flow direction from a small shift in resonator orientation relative to the in-plane extraordinary optic axis. We foresee Anisotropic Calcite as a valuable materials platform for investigating unconventional anisotropic hyperbolic materials and metamaterials. Leveraging its bulk properties for nanostructuring distinguishes it from 2D polar dielectric materials, while its low-loss characteristics for strong, high-Q resonances differentiate it from more lossy plasmonic hyperbolic materials. These attributes suggest potential applications for spectrometers and beam splitters using hyperbolic materials in various fields.

Our future work will utilize our novel physical model and cavity-resonance physics to establish a framework for enhanced power flow control, frequency tuning, and increased resonance lifetime (Q-value) for Volume PhP modes in 2D resonators and unconventional geometries. Additionally, our research aims to delve deeper into the relatively unexplored physics of surface

PhPs in the Upper R-band, particularly with extreme in-plane anisotropy. Overall, our study paves the way for further exploration and practical applications in the realm of anisotropic materials, offering insights and possibilities for advancements in various technological domains.

ACKNOWLEDGMENTS

E.M.S., M.A.M., B.K.D., and X.G.J. acknowledges support from the National Research Council Research Postdoctoral Fellowship. E.M.J., A.C.L., R.M.S. D.C.R., J.G.T. and C.T.E. acknowledge funding from the Office of Naval Research and the U.S. Naval Research Laboratory's Nanoscience Institute NSI 6.1 Base Program.

REFERENCES

[1] M. Autore, P. Li, I. Dolado, F. J. Alfaro-Mozaz, R. Esteban, A. Atxabal, F. Casanova, L. E. Hueso, P. Alonso-González, J. Aizpurua, A. Y. Nikitin, S. Vélez, and R. Hillenbrand, "Boron nitride nanoresonators for phonon-enhanced molecular vibrational spectroscopy at the strong coupling limit," Light: Sci. Appl. 7(4), 17172 (2018).

[2] T. G. Folland, L. Nordin, D. Wasserman, and J. D. Caldwell, "Probing polaritons in the mid- to far-infrared," J. Appl. Phys. 125(19), 191102 (2019).

[3] A. D. Dunkelberger, C. T. Ellis, D. C. Ratchford, A. J. Giles, M. Kim, C. S. Kim, B. T. Spann, I. Vurgaftman, J. G. Tischler, J. P. Long, O. J. Glembocki, J. C. Owrutsky, and J. D. Caldwell, "Active tuning of surface phonon polariton resonances via carrier photoinjection," Nat. Photonics 12(1), 50–56 (2018).

[4] A. D. Dunkelberger, D. C. Ratchford, A. B. Grafton, V. M. Breslin, E. S. Ryland, D. S. Katzer, K. P. Fears, R. J. Weiblen, I. Vurgaftman, A. J. Giles, C. T. Ellis, J. G. Tischler, J. D. Caldwell, and J. C. Owrutsky, "Ultrafast active tuning of the Berreman mode," ACS Photonics 7(1), 279–287 (2020).

[5] R. Berte, C. R. Gubbin, V. D. Wheeler, A. J. Giles, V. Giannini, S. A. Maier, S. De Liberato, and J. D. Caldwell, "Sub-nanometer thin oxide film sensing with localized surface phonon polaritons," ACS Photonics 5(7), 2807–2815 (2018).

[6] E. Shkondin, T. Repän, M. E. Aryaee Panah, A. V. Lavrinenko, and O. Takayama, "High aspect ratio plasmonic nanotrench structures with large active surface area for label-free mid-infrared molecular absorption sensing," ACS Appl. Nano Mater. 1(3), 1212–1218 (2018).

[7] T. G. Folland, G. Lu, A. Bruncz, J. R. Nolen, M. Tadjer, and J. D. Caldwell, "Vibrational coupling to epsilon-near-zero waveguide modes," ACS Photonics 7(3), 614–621 (2020).

[8] H. Lu, X. Liu, L. Wang, Y. Gong, and D. Mao, "Ultrafast all-optical switching in nanoplasmonic waveguide with Kerr nonlinear resonator," Opt. Express 19(4), 2910–2915 (2011).

[9] M. Ren, B. Jia, J.-Y. Ou, E. Plum, J. Zhang, K. F. MacDonald, A. E. Nikolaenko, J. Xu, M. Gu, and N. I. Zheludev, "Nanostructured plasmonic medium for terahertz bandwidth all-optical switching," Adv. Mater. 23(46), 5540–5544 (2011).

[10] K. Feng, W. Streyer, Y. Zhong, A. J. Hoffman, and D. Wasserman, "Photonic materials, structures and devices for Reststrahlen optics," Opt. Express 23(24), A1418–A1433 (2015).

[11] J. B. Khurgin, "Relative merits of phononics vs. plasmonics: the energy balance approach," Nanophotonics 7(1), 305–316 (2018).

[12] A. J. Hoffman, L. Alekseyev, S. S. Howard, K. J. Franz, D. Wasserman, V. A. Podolskiy, E. E. Narimanov, D. L. Sivco, and C. Gmachl, "Negative refraction in semiconductor metamaterials," Nat. Mater. 6(12), 946–950 (2007).

[13] S. Dai, Z. Fei, Q. Ma, A. S. Rodin, M. Wagner, A. S. McLeod, M. K. Liu, W. Gannett, W. Regan, K. Watanabe, T. Taniguchi, M. Thiemens, G. Dominguez, A. H. C. Neto, A. Zettl, F. Keilmann, P. Jarillo-Herrero, M. M. Fogler, and D. N. Basov, "Tunable phonon polaritons in atomically thin van der waals crystals of boron nitride," Science 343(6175), 1125–1129 (2014).

[14] J. D. Caldwell, A. V. Kretinin, Y. Chen, V. Giannini, M. M. Fogler, Y. Francescato, C. T. Ellis, J. G. Tischler, C. R. Woods, A. J. Giles, M. Hong, K. Watanabe, T. Taniguchi, S. A. Maier, and K. S. Novoselov, "Sub-diffractional volume-confined polaritons in the natural hyperbolic material hexagonal boron nitride," Nat. Commun. 5(1), 5221 (2014).

[15] S. Dai, Q. Ma, T. Andersen, A. S. McLeod, Z. Fei, M. K. Liu, M. Wagner, K. Watanabe, T. Taniguchi, M. Thiemens, F. Keilmann, P. Jarillo-Herrero, M. M. Fogler, and D. N. Basov, "Subdiffractional focusing and guiding of polaritonic rays in a natural hyperbolic material," Nat. Commun. 6(1), 6963 (2015).

[16] Matson, Joseph, et al. "Controlling the propagation asymmetry of hyperbolic shear polaritons in beta-gallium oxide." Nature communications 14.1 (2023): 5240.

[17] Narimanov, Evgenii E., and Alexander V. Kildishev. "Naturally hyperbolic." Nature Photonics 9.4 (2015): 214-216.

[18] C. T. Ellis, J. G. Tischler, O. J. Glembocki, F. J. Bezares, A. J. Giles, R. Kasica, L. Shirey, J. C. Owrutsky, D. N. Chigrin, and J. D. Caldwell, "Aspect-ratio driven evolution of high-order resonant modes and near-field distributions in localized surface phonon polariton nanostructures," Sci. Rep. 6(1), 32959 (2016).

[19] Breslin, Vanessa M., et al. "Hyperbolic phonon polariton resonances in calcite nanopillars." Optics Express 29.8 (2021): 11760-11772.

[20] Poddubny, Alexander, et al. "Hyperbolic metamaterials." Nature photonics 7.12 (2013): 948-957.

[21] T. Low, A. Chaves, J. D. Caldwell, A. Kumar, N. X. Fang, P. Avouris, T. F. Heinz, F. Guinea, L. Martin-Moreno, and F. Koppens, "Polaritons in layered two-dimensional materials," Nat. Mater. 16(2), 182–194 (2017).

[22] Mukhopadhyay, S., Ellis, C. T., Ratchford, D. C., Jackson, E. M., Tischler, J. G., Reinecke, T. L., & Johannes, M. D. (2021). Natural hyperbolicity in bulk calcite. Journal of Applied Physics, 130(14).

Metasurfaces for photon management in a thermophotovoltaic system

Vadim Zakomirnyi[1], Anna Rumyantseva[1], Sergei Kostcheev, Demetrio Macias, Renaud Bachelot, Davy Gérard[1,*]

[1]Light, nanomaterials, nanotechnologies (L2n), Université de Technologie de Troyes & CNRS, Troyes, France
*Corresponding author: davy.gerard@utt.fr

***Abstract*— Metasurfaces provide powerful opportunities for tailoring the spectral and angular properties of thermal radiation, which is crucial for improving the efficiency of thermophotovoltaic (TPV) energy conversion. In this work we investigate a metasurface designed for photon management in TPV systems. The structure operates as a spectral filter that suppresses undesired thermal radiation while transmitting photons within the useful spectral range of a low-bandgap photovoltaic cell. Numerical electromagnetic simulations reveal resonant field localization near 1.8 µm associated with modes supported by the periodic nanostructure. The resulting transmission spectrum demonstrates selective filtering in the near-infrared region relevant for TPV operation. These results highlight the potential of metasurface-based optical filters for improving photon utilization in high-temperature thermophotovoltaic systems.**

***Keywords*— dielectric metasurfaces, thermophotovoltaics, energy.**

I. Introduction

A significant fraction of the energy consumed in high-temperature industrial processes is dissipated as waste heat. Recovering even a modest portion of this energy represents a major technological and environmental challenge [1,2], with the potential to reduce both primary energy demand and CO_2 emissions. For example, in cement production, processes operating at temperatures between 800 and 1400 °C generate large radiative heat fluxes that remain largely underutilized.

Thermophotovoltaic (TPV) conversion represents a particularly promising approach in this temperature range [1-4]. By converting thermal infrared radiation into electrical power through low-bandgap photovoltaic cells, TPV systems enable direct radiative heat-to-electricity conversion. In principle, their efficiency can exceed that of thermoelectric generators under similar conditions. In practice, however, TPV performance is strongly limited by the spectral mismatch between the broadband thermal emission of hot surfaces and the narrow spectral response of the photovoltaic cell. Sub-bandgap photons are not converted and therefore contribute to thermal losses, while supra-bandgap photons generate excess heat through carrier thermalization. Both mechanisms reduce the overall conversion efficiency.

Metasurfaces offer a powerful approach to address this limitation by enabling spectral and angular control of thermal radiation. In this work, we investigate a metasurface designed for photon management in thermophotovoltaic systems. The classical approach to improve TPV efficiency relies on the use of a selective emitter, that is, a metasurface designed to emit in a selected wavelength range when heated [5-8]. Here, the proposed structure operates as a spectral filter that suppresses unwanted thermal radiation while transmitting photons within the useful spectral range of the photovoltaic cell. By tailoring the geometry of the metasurface unit cell, the spectral response of the structure can be engineered to improve the overlap between thermal emission and the spectral sensitivity of the TPV cell.

The spectral selectivity arises from resonant electromagnetic modes supported by the periodic nanostructure. These resonances produce strong localization of the electric field within the metasurface unit cell, leading to enhanced interaction between the incident radiation and the nanostructured material [9-11]. As a result, the transmission spectrum exhibits pronounced spectral features in the near-infrared region around 1.8 µm, which is close to the bandgap wavelength of typical InGaAs photovoltaic cells used in thermophotovoltaic systems.

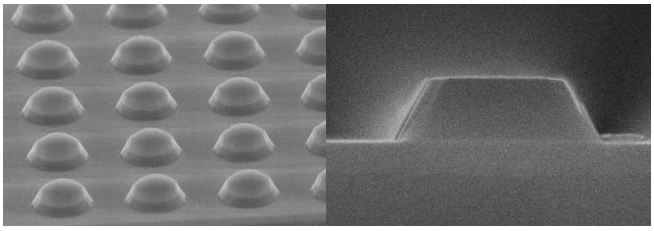

Fig. 1 SEM image of the large scale fabricated metasurface (left) and closer view on unit cell geometry (right). Size of the pillar in the unit cell is 1 µm at the top and 1.2 µm at the bottom. The structure was fabricated on Si substrate, then covered with 300 nm of SiC layer. Bottom part of nanopillar is SiO_2 and upper part is from SiC both with 300 nm thicknesses. Lattice period is 2 µm.

II. Results and Discussion

Fabrication was performed on double-side polished 4-inch intrinsic silicon wafers using contact photolithography followed by physical vapor deposition (PVD) and lift-off processes. This approach allows patterning of centimetre-scale metasurface areas while remaining compatible with scalable and cost-effective manufacturing techniques.

The metasurface in form of a square array of dielectric nanopillars was formed from several dielectric materials chosen for their optical performance and compatibility with high-temperature operation. The lower part of the resonator consists of a SiO_2 section that forms the base of the nanopillar, while the upper part is composed of a SiC layer. The thickness of both layers is approximately 300 nm. In addition, a continuous SiC layer with a thickness of 300 nm is deposited on the substrate, providing both optical functionality and improved thermal robustness. Silicon carbide is particularly attractive for thermophotovoltaic applications due to its high thermal stability and favourable optical properties in the near-infrared spectral range [11,12].

The resonators show a truncated-cone geometry, with a top diameter of approximately 1 µm and a bottom diameter of about 1.2 µm, which results from the lithography and lift-off process. The lattice period of the array is 2 µm. Scanning electron microscopy (SEM) characterization shown on Figure 1 confirms that the fabricated geometry closely matches the design parameters used in the numerical simulations.

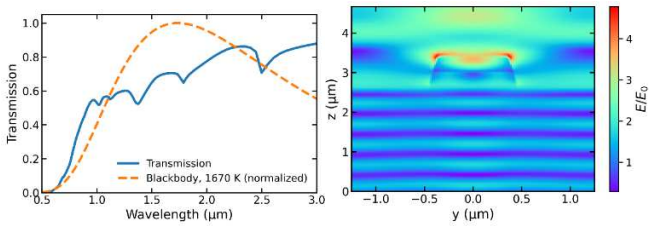

Fig. 2 Electromagnetic response of the metasurface. (left) Calculated transmission spectrum of the metasurface in the near-infrared spectral range relevant for thermophotovoltaic conversion. (right) Simulated near-field distribution at the resonance wavelength of approximately 1.8 µm, showing strong field localization near the metasurface structure.

The periodic arrangement of these dielectric resonators enables the excitation of resonant electromagnetic modes in the near-infrared spectral region as shown on Figure 2. These resonances play a key role in shaping the spectral transmission of the metasurface and form the basis for the photon-management functionality targeted in thermophotovoltaic systems. Simulated spectral response of the optical metasurface revealing selective transmission in the near-infrared range which is important for thermophotovoltaic conversion. The simulated near-field distribution shown in Fig. 2 (right panel) demonstrates strong localization of the electromagnetic field at the resonance wavelength. The electric field is concentrated in the vicinity of the nanopillar structure, indicating the excitation of resonant modes supported by the metasurface. This field confinement enhances the interaction between the incident radiation and the nanostructured material, enabling effective spectral filtering of the incoming thermal radiation.

III. Conclusion

The presented metasurface demonstrates the potential of nanophotonic structures for photon management in thermophotovoltaic systems. By engineering the spectral response of the metasurface, it is possible to selectively transmit photons within the useful spectral range of the photovoltaic cell while suppressing unwanted radiation. Such metasurface-based filters represent a promising platform for improving photon utilization and enhancing the overall efficiency of thermophotovoltaic energy conversion systems.

Acknowledgments

This work is supported by the European Union under the HORIZON Research and Innovation Action (grant ID 101160642).

References

[1] Bitnar, B., Durisch, W., and Holzner, R., "Thermophotovoltaics on the move to applications," *Applied Energy* **105**, 430–438 (2013).
[2] Datas, A., and Martí, A., "Thermophotovoltaic energy in space applications: Review and future potential," *Solar Energy Materials and Solar Cells* **161**, 285–296 (2017).
[3] Lenert, A., Bierman, D. M., Nam, Y., Chan, W. R., Celanovic, I., Soljačić, M., and Wang, E. N., "A nanophotonic solar thermophotovoltaic device," *Nature Nanotechnology* **9**, 126–130 (2014).
[4] LaPotin, A., Schulte, K. L., Steiner, M. A., et al., "Thermophotovoltaic efficiency of 40%," *Nature* **604**, 287–291 (2022).
[5] Greffet, J.-J., Carminati, R., Joulain, K., Mulet, J.-P., Mainguy, S., and Chen, Y., "Coherent emission of light by thermal sources," *Nature* **416**, 61–64 (2002).
[6] Li, W., and Fan, S., "Nanophotonic control of thermal radiation for energy applications [Invited]," *Optics Express* **26**, 15995–16021 (2018).
[7] Overvig, A. C., Mann, S. A., and Alù, A., "Thermal Metasurfaces: Complete Emission Control by Combining Local and Nonlocal Light-Matter Interactions," *Physical Review X* **11**, 021050 (2021
[8] Ijaz, S., Kang, D., Rana, A. S., Kim, J., Chani, M. T. S., Zubair, M., et al., "Metasurface Absorber–Emitter Pair-Integrated High-Efficiency Thermophotovoltaic System," *ACS Photonics* **12**, 3829–3839 (2025).
[9] Liu, W., Li, Z., Cheng, H., Chen, S., and Tian, J., "Dielectric Resonance-Based Optical Metasurfaces: From Fundamentals to Applications," *iScience* **23**, 101868 (2020).
[10] Bonod, N., and Kivshar, Y., "All-dielectric Mie-resonant metaphotonics," *Comptes Rendus Physique* **21**, 425–442 (2020).
[11] Babicheva, V. E., and Evlyukhin, A. B., "Mie-resonant metaphotonics," *Advances in Optics and Photonics* **16**, 539–658 (2024).
[12] Inampudi, S., Cheng, J., Salary, M. M., and Mosallaei, H., "Unidirectional thermal radiation from a SiC metasurface," *Journal of the Optical Society of America B* **35**, 39–46 (2018).

Chiral sensing with dielectric nanophotonics

Alberto G. Curto[1,2]

[1] Photonics Research Group, Ghent University-imec, 9052 Ghent, Belgium
[2] Center for Nano- and Biophotonics, Ghent University, 9052 Ghent, Belgium

*Corresponding author: alberto.curto@ugent.be

***Abstract*— Chiral molecules can have different biological functionalities depending on their handedness. Identifying chirality, however, is limited by low sensitivity, restricting detection to high concentrations and large volumes. We present several experimental and theoretical examples of dielectric metasurfaces and waveguides to enhance the sensitivity of chiral molecular detection.**

***Keywords*— circularly polarized luminescence, circularly polarized Raman scattering, circular dichroism, metasurfaces, integrated photonics, waveguides.**

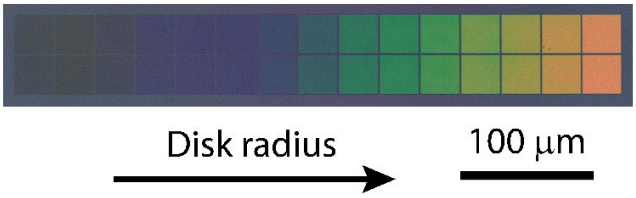

Fig. 1 – Metasurfaces made of crystalline silicon on glass.

Chirality is omnipresent in biochemistry, where molecules with opposite handedness can have markedly different biological functionalities. Detecting molecular chirality, however, is plagued by low sensitivity, limiting its use to high concentrations and large volumes. In this presentation, we introduce three examples of dielectric nanophotonic structures for chiral sensing, in particular, silicon metasurfaces and dielectric waveguides.

By sustaining optical resonances of electric and magnetic dipole origin, high-index metasurfaces can strongly enhance the sensitivity of chiral molecular detection in small volumes [1-3]. First, we will discuss our experimental results on enhancing circularly polarized luminescence from chiral molecules using crystalline silicon metasurfaces. Our results combine fluorescence enhancement [4] with controlled circular polarization. To this end, we developed a microscope with polarization modulation and photon-counting capabilities to measure smaller chiral analyte volumes than are possible with commercial systems.

Second, we will present enhanced circularly polarized Raman scattering in silicon metasurfaces. Our experimental results agree with a tensorial theory of polarized Raman scattering, demonstrating the relevance of the multipolar Mie resonances in metasurfaces for controlling excitation and emitted polarizations.

Last, we introduce a theoretical framework for predicting both optical rotation and circular dichroism induced by a chiral analyte, incorporated either as a coating or within the core of a cylindrical dielectric waveguide, for sensing applications. Our approach incorporates the Pasteur parameter into a mode solver to predict an effective index splitting explained by mode coupling theory. We explore the waveguide parameter space to identify optimal radii and refractive indexes to maximize optical rotation and circular dichroism.

Overall, both metasurfaces and waveguides open exciting paths to reach previously unmeasurable sensitivities for chiral optical spectroscopies at lower molecular concentrations and smaller analyte volumes.

ACKNOWLEDGMENTS

This work was financially supported by the European Research Council (ERC) under the European Union's Horizon 2020 Research and Innovation Program (Grant Agreement 948804, CHANSON).

REFERENCES

[1] E. Mohammadi, A. Tittl, K. L. Tsakmakidis, T. V. Raziman, and A. G. Curto, "Dual Nanoresonators for Ultrasensitive Chiral Detection," ACS Photonics, vol. 8, no. 6, 2021
[2] T. V. Raziman, R. H. Godiksen, M. A. Müller, and A. G. Curto, "Conditions for Enhancing Chiral Nanophotonics near Achiral Nanoparticles," ACS Photonics, vol. 6, no. 10, 2019
[3] E. Mohammadi, T. V. Raziman, and A. G. Curto, "Nanophotonic Chirality Transfer to Dielectric Mie Resonators," Nano Lett, vol. 23, no. 9, 2023
[4] S. Murai, G. W. Castellanos, T. V. Raziman, A. G. Curto, and J. G. Rivas, "Enhanced Light Emission by Magnetic and Electric Resonances in Dielectric Metasurfaces," Adv Opt Mater, vol. 8, no. 16, 20203.

Smart ways to achieve tunable chiral assemblies

Ziwei Zhou[1]*, Ningwei Sun[1], Nina Tverdokhleb[1,2,3], Artur Movsesyan[4], Anja Maria Steiner[1], Patrick T. Probst[1], Vaibhav Gupta[1], Bo Yin[5], Nicolás Pazos-Peréz[6], Ramón A. Álvarez-Puebla[6,7,] Mirjam Hofmaier[1], Martin Müller[1], Holger Merlitz[1], Olga Guskova[1,2], Yaroslava G. Yingling[8], Franziska Lissel[1,9], Tobias A. F. König[1,2], Zhiming Wang[4], Alexander O. Govorov[10], Nicholas A. Kotov[11,12,13]*, and Andreas Fery[1,14,15]*

[1]Leibniz-Institut für Polymerforschung Dresden e.V., Dresden, Germany.

[2]Technische Universität Dresden, Dresden Center for Computational Materials Science (DCMS), Dresden, Germany.

[3]Dresden Center for Computational Materials Science (DCMS), TU Dresden, Dresden, Germany.

[4]Institute of Fundamental and Frontier Sciences, University of Electronic Science and Technology of China, China.

[5]Ansys Inc., 2600 Ansys Dr. Canonsburg, PA 15317, USA.

[6]Department of Physical and Inorganic Chemistry Universitat Rovira i Virgili, Tarragona, Spain.

[7]ICREA, Passeig Lluís Companys 23, Barcelona, Spain.

[8]Department of Materials Science and Engineering, North Carolina State University, Raleigh, North Carolina 27695, USA.

[9]Faculty of Chemistry and Food Chemistry, Technische Universität Dresden, Dresden, Germany.

[10]Department of Physics and Astronomy, Ohio University, Athens, Ohio 45701, USA.

[11]Department of Chemical Engineering, University of Michigan, Ann Arbor, MI, USA.

[12]Biointerfaces Institute, University of Michigan, Ann Arbor, MI, USA.

[13]Department of Materials Science and Engineering, University of Michigan, Ann Arbor, MI, USA.

[14]Center for Advancing Electronics Dresden (cfaed), Technische Universität Dresden, Dresden, Germany.

[15]Department of Physical Chemistry of Polymeric Materials, Technische Universität Dresden, Dresden, Germany.

*Corresponding author: zhou@ipfdd.de, kotov@umich.edu, fery@ipfdd.de

***Abstract*— Chiral nanomaterials enable advanced optics, sensing and catalysis, yet laboratory fabrication of non-mirror-symmetric structures often demands delicate, equipment-intensive steps. We present simple, efficient routes to tunable plasmonic chirality by assembling achiral nanoparticles with abundant chiral biomolecules. These bio-guided assemblies transfer and amplify**

chirality, yielding switchable chiral responses without complex lithography.

***Keywords*— metamaterials, plasmonic chirality, nanoparticle assembly**

I. Introduction

Traditional plasmon-coupled circular dichroism (PCCD) suffers from inherently weak signals due to the size mismatch between chiral molecules and achiral nanoparticles[1,2]. Consequently, researchers have long attempted to enhance PCCD via the creation of strong plasmonic hotspots; however, such approaches have yielded limited improvements, and PCCD intensity still remains far below that of structural circular dichroism (CD)[3].

II. Methods

In our work, we shift the focus from engineering plasmonic hotspots to investigating the conformation of chiral molecules. By applying a simple yet effective strategy—namely, the in-situ stretching of biomolecules anchored to plasmonic nanoparticles (Fig 1)—we achieve a substantial enhancement of PCCD, with a circular dichroism of 1.18 degree and a dissymmetry factor of 0.2.

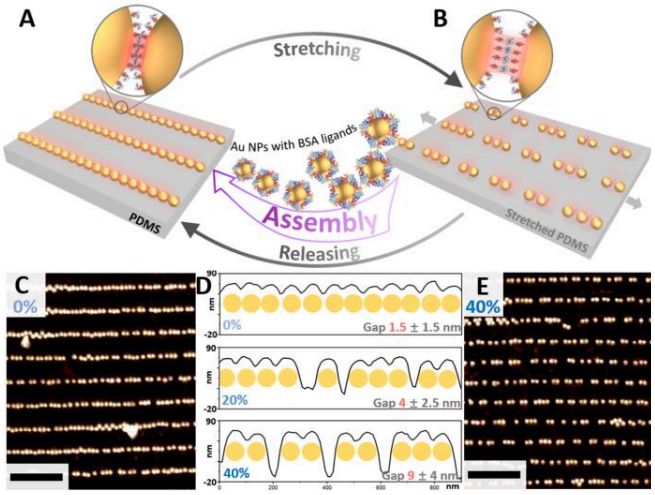

Fig. 1 Novel 1D chiral assembly of Au nanoparticles coated with BSA protein, which can be stretched due to the elastic PDMS substrate (A,B). During stretching the distance between nanoparticles increased gradually (C-E).

III. Results and Discussion

The enhanced PCCD originates not from intensified plasmonic hotspots, but from the conformational modulation of biomolecules bridging adjacent nanoparticles. In-situ stretching redistributes asymmetric electrostatic fields, amplifying chiral near-field interactions and producing a CD signal of 1.18° with a dissymmetry factor of 0.2 (Fig 2A). This lever-like mechanism enables reversible switching over 100 cycles (Fig 2B), demonstrating dynamic and tunable chiroptical activity beyond conventional hotspot-based strategies.

Molecular dynamics simulations (Fig 2C-E) indicate that the enhanced PCCD arises from stretching-induced recovery of protein secondary structures, which leads to a substantial amplification and directional alignment of molecular dipoles along the extension axis, thereby strengthening asymmetric near-field coupling.

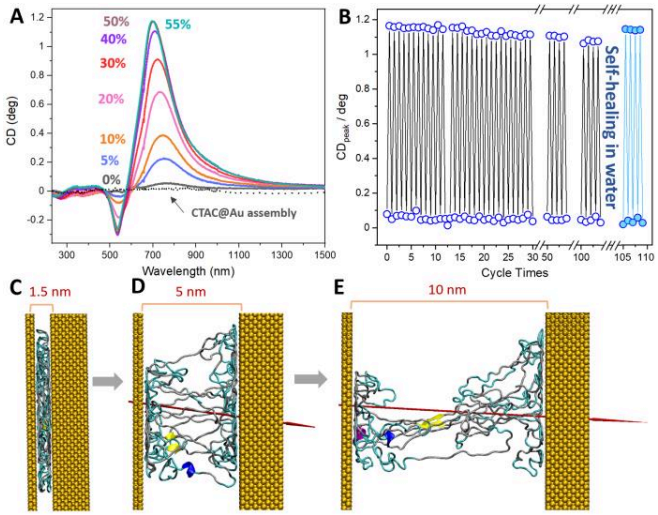

Fig. 2 Conformation-induced enhancement and switching of PCCD in BSA@Au assemblies. (A) CD spectra of BSA@Au assemblies under different stretching ratios. (B) Reversible PCCD switching over 100 cycles. (C–E) Molecular dynamics simulations illustrating protein stretching between nanoparticles accompanied by secondary structure recovery and dipole amplification along the extension direction.

IV. Conclusion

Our findings establish molecular conformation control as a new paradigm for plasmonic chirality amplification, enabling robust, reversible and stimuli-responsive chiroptical activity beyond conventional structural asymmetry.

Acknowledgments

This work was supported by Alexander von Humboldt foundation, DFG RTG 2767, Projektnummer 451785257, DFG via the “Responsible Electronics in the Climate Change Era - REC²” Cluster of Excellence (EXC 3035, Project-ID 533607596) and Leibniz Research Association “Advanced Materials Safety”.

References

[1] Govorov, A. O. Plasmon-Induced Circular Dichroism of a Chiral Molecule in the Vicinity of Metal Nanocrystals. Application to Various Geometries. The Journal of Physical Chemistry C 115, 7914-7923 (2011).

[2] Zhang, Q. et al. Unraveling the origin of chirality from plasmonic nanoparticle-protein complexes. Science 365, 1475-1478 (2019).

[3] Cao, Z. et al. Chirality Transfer from Sub-Nanometer Biochemical Molecules to Sub-Micrometer Plasmonic Metastructures: Physiochemical Mechanisms, Biosensing, and Bioimaging Opportunities. Adv Mater 32, e1907151 (2020).

Near-Field Optical Chirality on Achiral Gold Nanoparticles under Linear Polarization

Minyu Chen[1,2] Sylvie Marguet[3], Davy Gerard[1], Lucas Vázquez Besteiro[4], Safi Jradi[1] Alexander Govorov[5], Tao Xu[2], Renaud Bachelot[1,2]*

[1]Light, Nanomaterials & Nanotechnologies (L2n) Laboratory, CNRS UMR 7076. University of Technology of Troyes, France

[2]School of Mechatronic Engineering and Automation & School of Microelectronics, Shanghai University, China

[3]Université Paris Saclay, CEA, CNRS, NIMBE, Gif sur Yvette, France

[4]CINBIO, Universidade de Vigo, 36310 Vigo, Spain

[5]Department of Physics and Astronomy, Ohio University, Athens, OH, 45701 USA

*Corresponding author: renaud.bachelot@utt.fr

***Abstract*— It is shown that linearly polarized light can generate and control chiral near fields in geometrically achiral gold nanotriangles. Using plasmon-assisted 2-photon polymerization, near fields are recorded as permanent polymer structures. Polarization and wavelength tuning reveal transitions between achiral and chiral configurations linked to different plasmonic modes and symmetry breaking.**

***Keywords*—nanoplasmonics, chirality,2-photon polymerization.**

I. Introduction

In nanoplasmonics, chirality plays a crucial role in the interactions between light and matter. While the majority of research has focused on the interaction of chiral nanostructures with chiral light, recent studies reveals that achiral plasmonic nanostructures can exhibit chiral near fields under linearly polarized excitation.[1]

II. Methods

To study this effect, we employed plasmon-assisted 2-photon polymerization as a tip-free near-field recorder that converts near fields into permanent 3D polymer nanostructures,[2] enabling direct readout of the near-field and its evolution with incident polarization angle and wavelength (see Fig. 1)

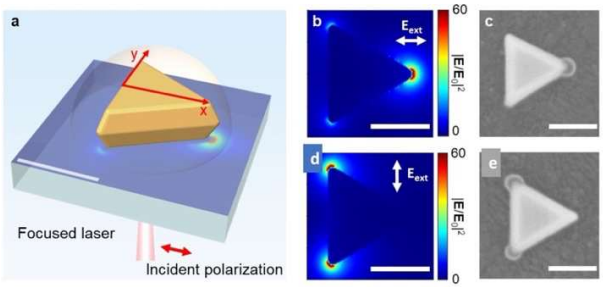

Fig. 1 a) Schematic diagram of plasmon-triggered 2-photon polymerization method. b),d) FDTD-simulated intensity maps at λ=780 nm under different incident polarizations directions (white arrows). c);e) corresponding SEM images of individual gold nanoprisms after irradiation.

III. Results and Discussion

On C3v-symmetry gold nanotriangles (NT), 2D symmetry breaking was quantified through the in-plane chirality factor V_{min}, defined from the loss of mirror symmetry of the polymer with respect to the three mirror planes of the NT and evaluated from both SEM images and FDTD simulations. Near-field dissymmetry maps derived from simulations and AFM topographies further resolved the redistribution of chiral hot spots. By jointly tuning polarization and wavelength, we revealed a controllable transition between achiral and chiral polymer configurations correlated with the modal composition of the plasmonic response (dipolar versus edge-dominated higher-order modes).

IV. Conclusion

These results establish a practical route to engineer and permanently record polarization-tunable planar dissymmetry in achiral nanoantennas, with implications for chiral sensing, enantioselective photochemistry, and nanophotonic devices.

Acknowledgments

This work was supported by the French National Research Agency, the Région Grand Est and the European Union.

References

[1] S. Hashiyada et al. “Imaging Chirality of Optical Fields near Achiral Metal Nanostructures Excited with Linearly Polarized Light”. ACS Photonics, Vol. 5, pp. 1486-1492, 2018.

[2] X. Zhou et al. “lasmon-based photopolymerization: near-field probing, advanced photonic nanostructures and nanophotochemistry”. J. Optics Vol. 16, pp 114002 (17 pages), 2014.

The Interaction of Vortex Light with Chiral Assemblies

Thierry Verbiest[1,*], Weizhen Liu[1], Yovan de Coene[1]

[1]Department of Chemistry, KULeuven, Belgium
*Corresponding author: thierry.verbiest@kuleuven.be

***Abstract*— In this work we investigated the interaction of vortex light carrying orbital angular momentum with chiral nanomaterials.**

***Keywords*— nanomaterials, vortex light.**

I. Introduction

Although the optical properties of a material can be understood using the more than 150 years old Maxwell's equations, the fundamental structure-property relationship between light and matter remains very relevant. Particularly interesting are the optical properties of chiral materials, a class of materials that is of fundamental importance in all scientific fields. Chiral molecules are molecules that are not superimposable on their mirror image. They exist in two different forms that are mirror images, called enantiomers. The standard procedure for differentiating between enantiomers is to evaluate and compare their interaction with circularly-polarized light. Whereas the real part of the refractive index of a freely moving chiral molecule imparts a phase retardation between the left- and right-hand circularly polarized field components, the complex part informs on the handedness-dependent light losses in the material. The most convenient experimental methods to evaluate these effects are circular dichroism (CD) and optical rotation (OR).

Maxwell's equations tell us that electromagnetic radiation carries both energy and momentum along its trajectory. Apart from linear momentum along its trajectory, light can carry a nonzero angular momentum. When light is circularly polarized, the photons carry a spin angular momentum (SAM) of $\sigma\hbar$ where σ can either be +1 (for left-circularly polarized light) or -1 (for right-circularly-polarized light). Less well known is that photons can also carry orbital angular momentum (OAM) of $l\hbar$ where l can be any integer number. For example vortex light or Laguerre-Gaussian light carries orbital angular momentum. The total angular momentum is then the sum of a spin part depending on polarization and an orbital part with a certain spatial distribution of the momentum vector [1]. In this context, helical dichroism (HD) has been introduced as the OAM analogue of CD [2]. It quantifies the differential optical response of chiral structures when illuminated with vortex beams of opposite angular momentum.

II. Results and Discussion

Helical dichroism is defined as

$$\mathrm{HD} = 2\frac{\mathrm{R}_{+l} - \mathrm{R}_{-l}}{\mathrm{R}_{+l} + \mathrm{R}_{-l}}$$

where R+ℓ and R−ℓ represent the transmission, reflection, or scattering intensities of right- or left-handed structures under a vortex beam with topological charge |ℓ|.
We present here a series of experimental results of helical dichroism on chiral nanostructures.

Several chiral nanostructures were investigated using vortex light and reflection measurements. The samples were either composed of gold or polymer.

Helical dichroism on the order of 10% were observed, much higher than what is usually found in CD, and highly dependent on the topological charge used. In this presentation we will discuss the influence of beam size, size of the nanostructures and other experimental variables that affect helical dichroism.

Acknowledgments

This work was supported by the KULeuven via a C1 research project.

References

[1] L. Allen, M. W.Beijersbergen, R. J. C. Spreeuw, and J. P.Woerdman, "Orbital angular momentum of light and the transformation of Laguerre-Gaussian laser modes," *Phys. Rev. A* 45, p. 8185-8189,1992

[2] W. Brullot, M.K. Vanbel, T. Swusten and t. Verbiest, "Resolving enantiomers using the optical angular momentum of twisted light", Science Advances, Vol 2, e1501349, 2016.

In situ plasmon-induced polymerization of chiral polymer thin films for enantioselective sensing in fM range

A. Khitous[1,2], C. Molinaro[1,2], O. Soppera[1,2,*]

[1] Université de Haute Alsace, CNRS, IS2M UMR 7361, F-68100 Mulhouse, France
[2] Université de Strasbourg, France
*Corresponding author: olivier.soppera@uha.fr

***Abstract*— Harnessing plasmonic near-fields, we grow molecularly imprinted nanolayers exactly where light probes matter. The resulting chiral plasmonic interfaces enable absolute enantioselective sensing with sub-femtomolar sensitivity.**

***Keywords*— sensor, chirality, SPR, MIP, photopolymerization.**

I. Introduction

The ability to discriminate molecular enantiomers with high sensitivity and absolute selectivity remains a major challenge in bioanalysis, pharmaceutical chemistry, and asymmetric synthesis. Here, we introduce a plasmon-driven near-field photopolymerization (NFPP) strategy enabling the *in situ* growth of molecularly imprinted polymer (MIP) nanolayers directly onto gold-coated plastic optical fibers (POF@Au).

II. Results and Discussion

By harnessing the strongly confined electromagnetic near-field generated under surface plasmon resonance (SPR), polymerization is spatially restricted to the nanometric sensing volume. This self-aligned process ensures nanometer-scale control over film growth, perfectly matched to the plasmonic probing depth. Using S-propranolol as a model chiral target, the resulting POF@Au@MIP sensors exhibit an ultralow limit of detection of 0.34 fM and complete enantioselectivity, with no detectable response to the opposite R-enantiomer.

Importantly, the detection dynamics and sensitivity can be finely tuned through irradiation time, directly linking optical excitation conditions to structural and analytical performance. The ultra-thin nature of the imprinted layer, combined with the intrinsic sensitivity of SPR to refractive index changes within its evanescent field, explains the sub-femtomolar detection limit. The formulation strategy and photochemical polymerization route further ensure negligible non-specific adsorption, enabling quantitative detection of a target enantiomer even in the presence of a 100-fold excess of its mirror image.

Beyond this proof of concept, the NFPP approach provides a scalable and versatile platform for engineering chiral plasmonic interfaces with molecular precision. Because molecular imprinting relies on target-directed templating, the methodology is inherently adaptable to a wide range of analytes by tuning monomer composition and stoichiometry.

III. Conclusion

This work establishes near-field-controlled polymer growth as a powerful route toward next-generation enantioselective plasmonic sensors and functional nanophotonic interfaces.

Acknowledgments

The authors acknowledge ANR for funding (POPCORN grant number ANR-21-CE09-0035 and PEPR LUMA, Project Sunrise ANR-23-EXLU-0003). This work of the Interdisciplinary Institute HiFunMat, as part of the ITI 2021–2028 program of the University of Strasbourg, CNRS and Inserm, was supported by IdEx Unistra (ANR-10-IDEX-0002) and SFRI (STRAT'US project, ANR-20-SFRI-0012) under the framework of the French Investments for the Future Program.

References

1. Khitous, A.; Lartigue, L.; Moreau, J.; Soppera, O. Insights into Photopolymerization at the Nanoscale Using Surface Plasmon Resonance Imaging. Small **2024**. DOI: 10.1002/smll.202401885.
2. Khitous, A.; Molinaro, C.; Abdallah, S.; Chen, M. Y.; Marguet, S.; Laurent, G.; Vidal, L.; Malval, J. P.; Fiorini-Debuisschert, C.; Adam, P. M.; et al. Spatial Distribution of the Photopolymerization Induced by Localized Surface Plasmons: Impact of the Morphology of the Au Nanoparticles. J Phys Chem C **2024**, 128 (31), 13097-13107. DOI: 10.1021/acs.jpcc.4c03148
3. Khitous, A.; Molinaro, C.; Gree, S.; Haupt, K.; Soppera, O. Plasmon-Induced Photopolymerization of Molecularly Imprinted Polymers for Nanosensor Applications. Advanced Materials Interfaces **2023**, 10 (7), 2201651, https://doi.org/10.1002/admi.202201651. DOI: https://doi.org/10.1002/admi.202201651.
4. Arcadio, F.; Noël, L.; Del Prete, D.; Maniglio, D.; Seggio, M.; Soppera, O.; Cennamo, N.; Bossi, A. M.; Zeni, L. Soft molecularly imprinted nanoparticles with simultaneous lossy mode and surface plasmon multi-resonances for femtomolar sensing of serum transferrin protein. Scientific Reports **2023**, 13 (1). DOI: 10.1038/s41598-023-38262-y.
5. Khitous, A.; Molinaro, C.; Thomas, C.; Haupt, K.; Soppera, O. Synthesis and Integration of Hybrid Metal Nanoparticles Covered with a Molecularly Imprinted Polymer Nanolayer by Photopolymerization. In Sensors, **2023**; Vol. 23.

Surface Lattice Resonance Engineering via Plasmonic Nanoparticle Self-assembly, Transfer, and Laser Treatment

T. Tamulevičius[1,2,3,*], G. Klyvis[1], K. Midveris[1], M. Haris[2], T. Klinavičius[1], A. Tamulevičienė[1,3], M. Juodėnas[1], D. Peckus[1,2], J. Henzie[4], S. Tamulevičius[1,2]

[1]Institute of Materials Science, Kaunas University of Technology, Kaunas 51423, Lithuania
[2]Physics Department, Kaunas University of Technology, Kaunas 51368, Lithuania
[3]UAB Nanoversa, Kaunas 51423, Lithuania
[4]International Center for Materials Nanoarchitectonics, National Institute for Materials Science, Tsukuba 305-0044, Japan
[*]Corresponding author: tomas.tamulevicius@ktu.lt

***Abstract*— Broad LSPRs in noble-metal nanostructures are engineered by arranging nanoparticles into well-defined arrays, where scattered light couples into plasmonic lattices. Self-assembly, transfer, and laser treatment of chemically synthesized nanoparticles onto thin films enable wave-guided SLRs with multiple high-Q-factor modes, thereby enabling applications in photonics, sensing, and anticounterfeiting.**

***Keywords*— Surface lattice resonance, self-assembly, nanoparticle transfer, laser treatment.**

I. Introduction

Resonant absorption and scattering in plasmonic nanostructures find numerous applications from optical sensing to photocatalysis, but their further development and exploitation might be limited as localized surface plasmon resonance (LSPR) is broad in its nature. Arranging plasmonic material nanoparticles into well-defined periodic arrays enables coupling of the scattered light into the pitch-determined Rayleigh anomalies, resulting in high-Q-factor modes known as surface lattice resonances or plasmonic lattices [1]. Clean room technologies deliver high-resolution patterning, but related vacuum thin film deposition has some drawbacks in material microstructure and roughness. Whereas wet colloid synthesis delivers nearly ideal nanostructures that are also reasonably monodispersed under careful synthesis condition control [2]. The experimentally measured LSPR-related extinction spectra of colloids are directly related to the deviations in size and material properties, which were traced back to the size distribution employing a deep neural network (DNN) based spectral analysis [3],[4]. Lithography methods define pattern dimensions at the design stage directly, whereas template-based assembly allows tailoring of the plasmon resonances via deposition of different average size nanostructures, deposition of multimers [5], or via additional laser treatment of nanoparticles [6].

II. Methods

The PDMS deposition templates were soft lithography replicated from the clean-room-made silicon masters. The silver and gold nanoparticles were synthesized using seeded-growth colloidal chemistry. Gold and silver nanosphere size distributions were analyzed using a DNN trained with theoretically simulated data. Nanoparticles were assembled in PDMS templates via capillarity-assisted particle deposition (CAPA) and transferred onto different substrates via an established process employing water-soluble PVA film [7]. The laser treatment was carried out via motorized sample translation with respect to the Yb:KGW femtosecond laser beam. Optical response of the nanoparticle lattices was analyzed under a darkfield microscope and in the angular resolved UV-Vis-nIR transmission spectroscopy. Electrochemical performance was tested as the photoelectrochemical response in the three-electrode configuration. Experimental findings were compared with numerical simulations.

III. Results and Discussion

Size distributions of the Ag [3] and Au [4] colloids of different average-sized spherical nanoparticles were analyzed with the developed DNN software and revealed the significance of the dielectric function dispersion and its size dependence. The silver nanocubes were deposited in the template and transferred onto the different thickness TiO_2 layer of fused quartz substrate, exhibiting multiple W-SLR resonances red shifting with the increasing thin film thickness. The angular resolved polarized light transmission measurements identified the hybridized TM and TE W-SLR modes in the waveguide structure. Gold nanoparticle arrays were transferred onto electrically conductive ITO substrates and demonstrated photoelectric response in the visible spectra that was attributed

to the presence of the hybridized optical resonances. Carefully adjusting the laser power used to treat gold nanoparticle arrays resulted in different colors being seen under the dark field illumination, which was attributed to different effects, including remelting of multimers into bigger nanoparticles, fracturing of the particles into the smaller ones, and others. Local laser treatment changed the SLR position as well as enabled micrometric resolution patterns from nanoparticles applicable for anticounterfeiting applications.

IV. Conclusion

Chemically synthesized nanoparticle colloids with template-based particle self-assembly enables origination of plasmonic metasurfaces with tailored optical properties and deliver a manifold of practical applications where optical resonances are in play.

Acknowledgments

The work was supported by the European Economic Recovery and Resilience Plan "New Generation Lithuania" and the budget of the Republic of Lithuania, Project No. 02-002-P-0001.

References

[1] M. Juodėnas, *et al.*, "Surface Lattice Resonances in Self-Assembled Arrays of Monodisperse Ag Cuboctahedra," ACS Nano, Vol. 13, No. 8, 9038–9047, 2019.

[2] N. Khinevich, *et al.*, "Size and Crystallinity Effect on the Ultrafast Optical Response of Chemically Synthesized Silver Nanoparticles" J. Materiomics, Vol. 10, 3, 594-6002023, 2024.

[3] T. Klinavičius *et al.*, "Deep Learning Methods for Colloidal Silver Nanoparticle Concentration and Size Distribution Determination from UV–Vis Extinction Spectra" J. Phys. Chem. C, Vol. 128, 23, 9662–9675, 2024.

[4] T. Klinavičius *et al.*, "How to Select the Proper Gold Permittivity for Generating Training Data for Deep Neural Networks for Analysis of the Nanoparticle Colloid Size Distributions from Their UV–Vis–NIR Extinction Spectra? J. Phys. Chem. C, 129, 39, 17616–17631, 2025

[5] N. Khinevich, *et al.*, "Wavelength-tailored Enhancement of Raman Scattering on a Resonant Plasmonic Lattice," Sens. Actuator B-Chem., Vol. 394, 134418, 2023.

[6] T. Tamulevičius, *et al.*, "Optical device with ordered scatterer arrays for secure identity and a method of producing the same" US12134280B2, 2021.

[7] M. Monshi, *et al.* "Graphene-Enhanced Resonant Arrays of Silver Nanoparticles for Sustained Detection of Raman Signature" J. Phys. Chem. C, Vol. 129, 33, 14983–14992, 2025.

Emission of Quantum Dots within Plasmonic Patch Arrays sustained by Surface Lattice Resonance

Agnès Maître[1,*], Hugo Saint Olive[1], Fengzhi Gu[1], Louis Agard[1], Willy Daney de Marcillac[1], Thomas Pons[2]

[1]Institut des NanoSciences de Paris, Sorbonne Université, CNRS, France
[2]Laboratoire de physique et d'étude des matériaux, ESPCI, Sorbonne université, CNRS, France
*Corresponding author: agnes.maitre@insp.jussieu.fr

***Abstract*— We study both esperimentally and theoretically arrays of plasmonic patch antennas, exhibiting ultra thin surface lattice resonance modes. Those modes will be coupled to quantum dot in order to engineer their fluorescence.**

***Keywords*— plasmonics, surface lattice resonance, quantum dots, fluorescence**

I. Introduction

On a plasmonic nano cylinder grating, Surface Lattice Resonance exhibit ultrathin absorbance peaks. We propose to combine those resonance with the emission of quantum dots embedded in antennas, in order to control and enhance their emission,

II. Methods

On a plasmonic nanocylinder grating, Surface Lattice Resonance are modes which propagate along the surface, hybridizing the large width local surface plasmon resonance, with the Rayleigh anomaly (corresponding to the diffracting mode propagating along the surface) [1,2]. SLR mode have very thin width which can be used to engineer the fluorescence of quantum dots.

A patch antenna made of a thin dielectric layer between a gold layer and a thin nanocylinder **Erreur ! Signet non défini.**gold patch has demonstrated and its capabilities to control both dynamics and directivity of quantum dots embedded inside the dielectric layer [3,4] thanks to a large Purcell factor.

We aim to realise arrays of patch antennas in order to combine surface lattice resonances and the high resonance of patch antenna in order to reach strong coupling of the quantum dots within such structure.

III. Results and Discussion

We perform (figure 1) simulation for arrays of patch antennas exhibiting for incident white light illumination ultra thin peaks, whose width is one order of magnitude thinner than the antenna patch resonance, and with similar amplitude. Experimental realization of arrays of antennas without the quantum dots show under white light normal incidence exhibit thins peaks in the absorbance characteristic of surface lattice resonance

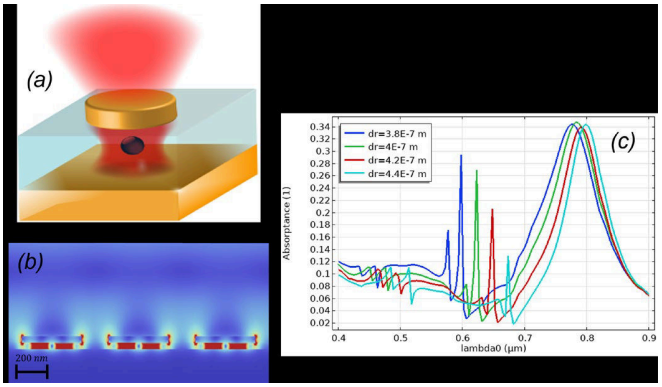

Fig. 1. a) Schematics of a single patch antenna. b) field amplitude for an array of patch antennas with a period dr. c) absorbance of the patch antenna array under white light illumination under normal incidence

IV. Conclusion

We demonstrated experimentally and theoretically surface lattice resonance for arrays of patch antennas. Ongoind work is devoted to the study of the coupling of quantum dots within these arrays.

Acknowledgments

This work is supported by ANR-21-CE42-0029 Nanowhisper, ANR-23-CE09-0029-01 Colime, CNRS énergie 2026 Dephy

References

[1] V.G. KRAVETS et Al "Plasmonic surface Lattice Resonances: A 5912 (2018).
[2] M. DEWYNTER et AL. "Broadening the Plasmonic Spectral Range of Metallic Metasurfaces Using Dual-Material Arrays". Nano Letters , 26, 6, 2223, 2026
[3] Amit Raj DHAWAN et AL. "Extreme multiexciton emission from deterministically assembled single emitter subwavelength plasmonic patch antenna, Light Sci Appl 9, 33, 2020.
[4] Amit Raj DHAWAN et AL. "Fabrication of Efficient Single-Emitter Plasmonic Patch Antennas by Deterministic In Situ Optical Lithography using Spatially Modulated Light". Adv. Mater , 34, 2108120, 2022.,

Thermoplasmonics-driven polymerization from the macroscale to the nanoscale

Céline Molinaro[1,2,*], Amine Khitous[1,2], Mathieu Bastide[1,2], Sylvie Marguet,[3] Olivier Soppera[1,2]

[1]Université de Haute Alsace, CNRS, IS2M UMR 7361, Mulhouse, France
[2]Université de Strasbourg, Strasbourg, France
[3]Université Paris-Saclay, CEA, CNRS, NIMBE, Gif-sur-Yvette, France
*Corresponding author: celine.molinaro@uha.fr

***Abstract* — We developed a thermopolymerizable formulation that polymerizes above 130°C. Using continuous wave and femtosecond laser regimes, we generated millimetric polymer dots (collective heating) and nanometric shells (confined heating) on dense gold nanoparticles. Surprisingly, on colloidal nanotriangles, directional polymer lobes were formed, challenging the assumption of uniform temperature distribution within nanoparticles.**

***Keywords*— thermoplasmonics, gold nanoparticles, polymerization**

I. Introduction

Localized surface plasmon induced polymerization of free-radical acrylate monomers is an efficient, smart, and versatile method for preparing metal/polymer hybrid nanoparticles (NPs) with accurate control of the thickness and spatial distribution of the polymer on the NP surface. Through decay processes, the plasmon emitted light, hot charge carriers and heat. While the photochemical pathway is well known for generating hybrid NPs,[1] thermoplasmonic effects have not been used in this context.

Yet, accurately controlling and observing the temperature distribution generated by illuminated gold nanoparticles (NPs), i.e. thermoplasmonics, is critical for diverse applications. In biology, it enables photothermal therapy [2] while in chemistry, it drives catalysis [3], NP reshaping [4], and solar energy production [5].

Here, we investigated thermoplasmonic route to graft polymer onto gold NPs. The polymer (i.e. thermopolymerizable formulation), acting as a thermal probe, will be used to characterize thermoplasmonics heat generation effects at the macroscopic scale and at the single NP scale.

II. Methods

We developed a thermopolymerizable formulation combining a thermal initiator (DIAMS) and a triacrylate monomer (PETA). This formulation remains transparent in the visible range and only polymerizes above 130°C [6].

The experimental principle is the following: a droplet of the thermopolymerizable formulation is deposited on the gold NPs sample. Then the sample is illuminated with controlled power, exposure time and polarization. The sample is then rinsed with ethanol. If the polymerization threshold temperature has been reached (or exceeded), polymer is on the sample. If not, no polymer is observed.

First, we validated the thermopolymerization principle for thermoplasmonics using a high-density gold NP sample (prepared by gold evaporation followed by thermal dewetting). Illumination at 532 nm, close to the plasmonic resonance, was performed using two laser regimes: continuous wave (cw) and femtosecond (fs) pulses (pulse duration 60fs with 5 kHz frequency). While polymer dots are visible to the naked eye at the macroscale, nanoscale experiments were conducted on TEM grids and further characterized on high resolution TEM (ARM200F JEOL).

We then applied the same process to colloidal gold nanotriangles (NTs), using fs-pulses illumination at 800 nm (Ti:Sapphire 140 fs with a repetion rate of 80 MHz).

III. Results and Discussion

First, we investigated thermopolymerization using two distinct laser regimes: a continuous wave and fs pulses laser illumination (see figure 1), on dense gold NPs samples. In cw laser illumination, 100-µm thick polymer dot are observed. While its size might be surprising compared to the nanometric size of the NPs, this observation aligns with collective heating effect [7], already well-known theoretically. When multiple NPs are illuminated with a cw laser, the temperature rises homogenously across the illuminated area.

In contrast, fs pulses laser illumination generates polymer with a totally different behavior. The polymer is visible to the naked eye due to the change of color induced by the shift of the plasmon resonance in the polymerized area (Fig. 1, below).

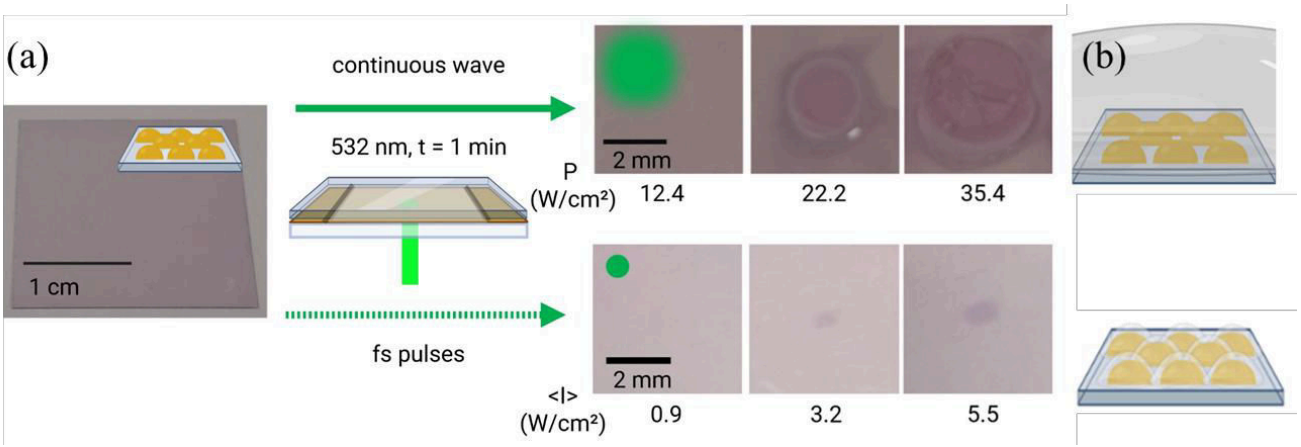

Fig. 1 (a) Experimental results obtained in cw (on top)[2] and fs pulses (below) illumination for various irradiance and (b) associated illustration of the polymerization obtained. [8]

To determine the polymer distribution at the nanoscale, experiments on TEM grids were conducted (Fig. 2), revealing nanometric polymer shells around individual NPs. Here, the heat is confined at the vicinity of each NPs.

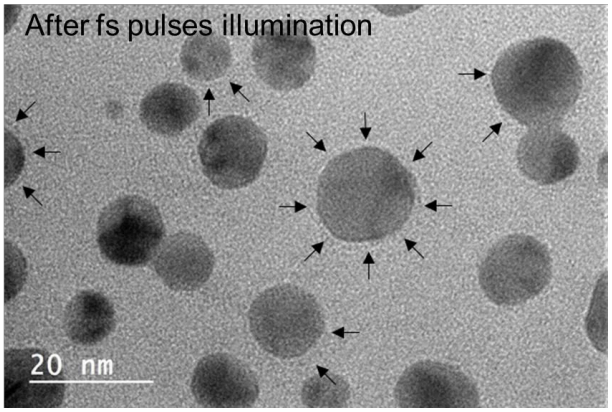

Fig. 2 TEM images of the gold NPs after fs pulses illumination at 5.5 W/cm² with the thermopolymerizable formulation. [8]

By tailoring the laser regime on the same gold sample, we demonstrate the ability to control the heat generation between collective and confined heating through the generation of polymer structures ranging from millimetric to nanometric scales through thermoplasmonics. Notably, the same thermopolymerizable formulation was used in both cases, confirming its ability to polymerize at a defined temperature threshold at the macroscale and at the nanoscale. [8]

Building on this result, which provides us with a temperature probe functional at the nanoscale, we applied this method to colloidal NTs, illuminated near their plasmon resonance at 800 nm. Surprisingly, directional polymer lobes, along the tip or the edge of the NT excited by the incident polarization, were observed (Fig. 3). [9] This experimental result was unexpected from a theoretical point of view, which instead predicted a homogeneous temperature distribution. [7] The interpretation of this observation remains under discussion, given the three mechanisms following the plasmonic excitation (field enhancement, hot electrons and heat generation). We emphasize here that the thermopolymerizable formulation exhibits no absorption in the visible range,ruling out any photochemical pathway. Regarding hot electrons, their contribution to the polymerization process is unlikely, as the thermal iniator molecules (DIAMS) are diluted in a dielectric matrix (i.e. the monomer), preventing efficient transfer to trigger a reaction via this mechanism. Thus, only heat generation might explain these polymer lobes.

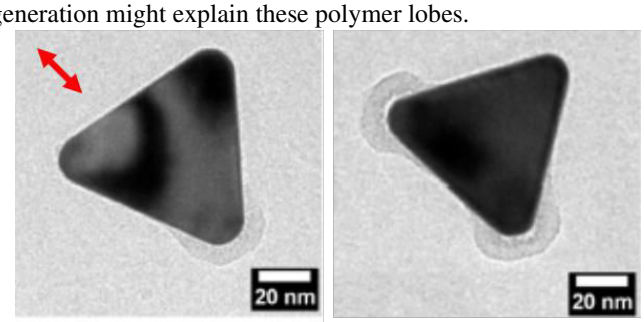

Fig. 3 TEM images of nanotriangles after their illumination at 0.53 mW at 800 nm in the presence of the thermopolymerizable formulation. The red arrow depicts the polarization direction. [9]

IV. Conclusion

In conclusion, by addressing the laser regime in a specific way, it is possible to generate nanometric to almost millimetric polymer through thermoplasmonics, opening new pathway for grafting thermoresponsive materials accross scales. Furthermore, validating a temperature probe based on polymerization, functional at both macroscopic and nanometric scales will enable deeper exploration of the thermoplasmonic of nanoparticles.

Acknowledgments

This work was partly carried out at the IPCMS-Ultrafast user facility funded by PEPR LUMA (reference ANR-22-EXLU-0002).

References

[1] A. Khitous et al., “Spatial distribution of the photopolymerization induced by localized surface plasmons : impact of the morphology of the Au nanoparticles,” The Journal of Physical Chemistry C, vol. 128, pp. 13097-13107, 2024.

[2] X. Huang et al., “Plasmonic photothermal therapy (PTTT) using gold nanoparticles,” Lasers in Medical Science, vol. 23, pp. 217-228, 2008.
[3] A. Baldi, et al., “Pulsed photothermal heterogeneous catalysis”, ACS Catalysis, vol. 13, pp. 3419-3432, 2023.
[4] C. Molinaro et al., “From plasmon-induced luminescence enhancement in gold nanorods to plasmon-induced luminescence turn-off: a way to control reshaping”, Physical Chemistry Chemical Physics, vol. 20, pp. 12295-12302, 2018.
[5] B. Yang et al., “Thermoplasmonics in solar energy conversion: materials, nanostructured designs, and applications,” Advanced Materials, vol. 34, pp. 2107351, 2022.
[6] C. Molinaro et al., “Chemical method based on thermally activated free radical polymerization to determine the temperature in thermoplasmonics,” ACS Applied Polymer Materials, vol.6, pp. 5331-5338, 2024.
[7] G. Baffou et al., “Photoinduced heating of nanoparticle arrays,” ACS Nano, vol. 7, pp. 6478-6488, 2013.
[8] C. Molinaro et al., “Controlled polymerization at macroscale and nanoscale through thermoplasmonics”, Plasmonics, 2025
[9] A. Khitous et al., “Unveiling localized plasmonic activation comparing photochemically and thermally initiated polymerization”, ChemRxiv, 2025.

Photothermal effects in metal layers

Benoit Rogez[1,2*], Quanbo Jiang[1,2], Zakaria Marmri[3], Franck Thibaudau[3], Jérôme Wenger[2], Guillaume Baffou[2]

[1] L2n, CNRS-University of Technology of Troyes, UMR 7076, France
[2] Institut Fresnel, CNRS-Aix Marseille University, UMR 7249, France
[3] CINaM, CNRS-Aix Marseille University, UMR 7325, France

*Corresponding author: benoit.rogez@utt.fr

***Abstract*— Photothermal heating of metal layers, especially gold, is often neglected given gold is a poor light absorber, and good heat conductor. This picture is, however, not always true, and we have recently shown, both experimentally and theoretically, that photothermal heating of gold films can have unexpected behaviour and effects when working at the micro to nano-scale.**

***Keywords*— Photothermal heating, Nano-scale temperature measurement, Quantitative Phase Imaging.**

I. Introduction

Up to now, most photothermal studies have been focused on Nanoparticle-based systems, mainly because of a many applications in nanomedicine, nanofabrication, nanocatalysis,… Recently, however, more and more applications rely on light interaction with a metal film (SPR, SERS, Plasmonic trapping,…) where photothermal effects are often overlooked, mostly for two reasons. First, because it is generally assumed that, if any light could be absorbed by the gold film and converted into heat, its exceptional thermal conductivity would quickly disperse the heat, leading to a negligeable temperature increase. Second, because measuring temperature at the nanoscale remains quite challenging, and only few techniques allow a precise and accurate measurement.

Combining optical microscopy and numerical reconstruction, Quantitative Phase Microscopy has recently emerged as an easy-to-implement, label-free, and calibration-free technique to measure temperature at the nanoscale with sub-Kelvin accuracy. Using this technique, we studied photothermal effect on various thin metal film geometry and plasmonics nanostructures and we will discuss the origin of the light-to-heat conversion in this case, as well as potential ways to better control it. Finally, we'll discuss the potential effects of photothermal effect on metal layer considering the case of plasmonic trapping.

II. Methods

Quantitative Phase Microscopy (QPI) regroups an ensemble of optical imaging techniques which give access to both the intensity and the phase/shape of the wavefront of light. Thanks to its sensitivity in phase, QPI has been shown to be able to detect temperature variation at the nanoscale thanks to the so-called mirage effect. Indeed, upon heating, the refractive index of the medium - either a liquid, or a polymer - decreases, and induces a variation in the phase of the transmitted light (Fig.1). Using numerical reconstruction, this variation of phase can then be converted into a 3D temperature map, with nanometric resolution, and sub-Kelvin accuracy [1].

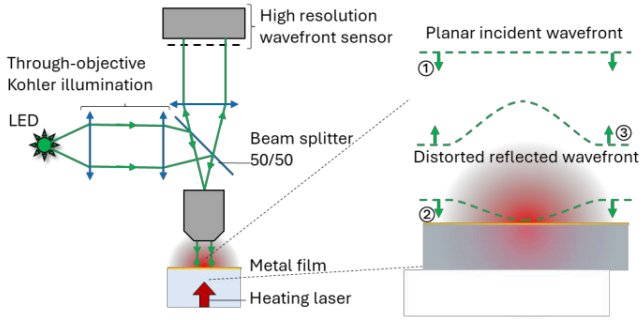

Fig. 1: Principle of wavefront sensor-based QPI measurement of temperature. The laser-induced temperature profile is illuminated with a planar wavefront. Because of refractive index variation, this wavefront is distorted and imaged onto a high resolution wavefront sensor.

Being label-free, QPI-based temperature measurement does not require calibration and can work over an extended temperature range (several hundred of °C), making it an easy and accurate way to measure temperature increase in solution.

Using this technique, we experimentally measured photothermal heating on metal layers, either plasmonic or non-plasmonic (Fig.2a)) and developed a set of numerical tool to allow easy retrieval of the 3D temperature map from the 2D phase images (Fig.2b-d) (available free of charge as supplementary material of [2]).

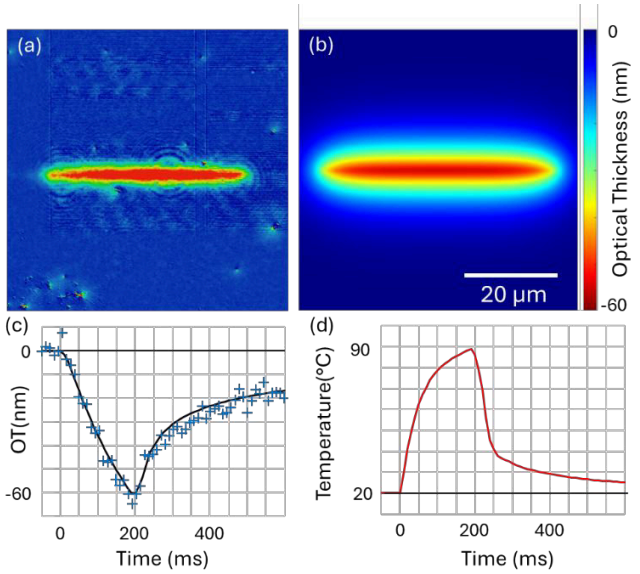

Fig. 2: Heating of a metal layer with a 200-ms line-shaped laser pulse. (a) Experimental optical thickness (OT) at the end of the laser pulse (200 ms). (b) Best-fitting simulated OT. (c) Comparison of the experimental (dots) and simulated OT. (d) Corresponding temperature determined from the simulation.

III. Results and Discussion

We then study more specifically the case of plasmonic trapping. Here, a 5 mW infra-red laser is focused on a plasmonic nano-aperture, and the resulting plasmonic field enhancement allows optical trapping of nanoparticles down to a few nanometer in diameter.

In this configuration, the general belief is that, even though light absorption near the nanohole is enhanced due to plasmonic resonance, the relatively thick gold film (100 nm or more) should quickly dissipate the heat, and limit the temperature increase to a few degrees. Our experimental measurement however showed a temperature increase of several tens of degrees (Fig.3). Using the previously developed numerical models, we were able to attribute this high temperature increase to (1) absorption not on the gold film nor on the plasmonic nanostructure but on the adhesion layer, (2) “not so efficient” heat dissipation by the gold film.

The main consequence of this local heating was the formation of a long-range (several tens of micrometers) thermal trap, governing the diffusion of nanoparticles around the nano-aperture localized plasmonic trap. This thermophoretic effects could be stronger than the optical trap itself, and allowed us to explain the otherwise unexplainable effects of nanoparticule coating on trapping efficiency [3,4].

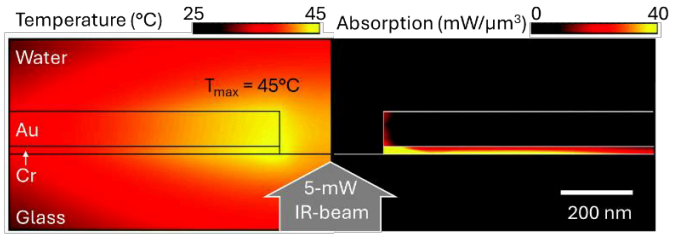

Fig. 3: Temperature increase (left) and local power density absorbed (right) when a 5 mW laser beam (1064 nm) is focused onto a 200 nm diameter nanohole on a 100 nm thick gold film with 13 nm Cr adhesion layer. Most of the absorption happens within the adhesion layer, leading to high temperature increase.

These results helped us understand how to control the photothermal heating to reduce its unwanted effects, or even take advantage of it.

IV. Conclusion

We have presented an easy-to-implement and accurate method to measure temperature at the nanoscale based on QPI, as well as numerical tool to retrieve and/or predict photothermal heating on metal layers. We used these tools to study local heating induced in plasmonic trapping experiments and showed that heat generation on, and near metal layer can have major effects on the system behavior, and should therefore not be overlooked. We hope these tools will help better understanding some still unexplained phenomena observed when in application based on light-metal layer interaction.

Acknowledgments

This work was supported by the French “Agence Nationale de la Recherche” (Grants No. ANR-18-CE42-0013 and ANR-17-CE09-0026-01) and the European Research Council (ERC) under the European Union's Horizon 2020 research and innovation programme (grant agreement no. 723241)

References

[1] G. Baffou et al. Thermal Imaging of Nanostructures by Quantitative Optical Phase Analysis. ACS Nano 2012, 6, 3, 2452–2458
[2] B. Rogez et al. Thermoplasmonics of metal layers and nanoholes. APL Photonics, 6, 101101, 2021.
[3] Q. Jiang, et al. Adhesion Layer Influence on Controlling the Local Temperature in Plasmonic Gold Nanoholes. Nanoscale 12, 2524-2531, 2020
[4] Q. Jiang,. Quantifying the Role of the Surfactant and the Thermophoretic Force in Plasmonic Nano-Optical Trapping. Nanoletters 20,12, 8811-8817, 2020

Operando Quantification and Mapping of Interfacial Charge-Transfer Efficiency in Hybrid Materials

Olivier Henrotte[1]*

[1]Nanoinstitute Munich, Ludwig-Maximilians-Universität München, 80539 München, Germany

*Corresponding author: O.henrotte@lmu.de

***Abstract*— Hybrid semiconductor–metal photocatalysts often show strong activity, yet the fraction of photogenerated carriers that reaches the solid–liquid interface and drives redox chemistry remains poorly quantified. Herein, I will present operando, spatially resolved quantification of interfacial charge-use efficiency across hybrid systems.**

***Keywords*—metal-semiconductor, scanning electrochemical microscopy, quantum efficiency, interfacial charge-transfer.**

I. Introduction

Photocatalytic performance at solid–liquid interfaces is governed by coupled processes spanning multiple length and time scales: light absorption and carrier generation, ultrafast relaxation and trapping, charge transport through heterogeneous media, and finally interfacial charge transfer to solution-phase species. Standard bulk metrics (e.g., rates, apparent quantum yields, product selectivity) generally convolve these steps, complicating mechanistic interpretation and limiting rational design. This becomes particularly severe in hybrid semiconductor–metal architectures, where interfacial states, junction energetics, and nanoscale morphology can introduce spatially varying reactivity and multiple parallel pathways.

A central, often implicit quantity is the interfacial charge-use efficiency—the fraction of photogenerated carriers that (i) survive recombination, (ii) reach the solid–liquid interface, and (iii) execute productive redox chemistry. While optical spectroscopies can reveal excited-state dynamics, they do not necessarily report on the chemically useful carrier flux at the interface under operando conditions. Conversely, purely electrochemical measurements typically lack the spatial resolution needed to separate heterogeneous regions. Bridging this gap requires correlative, operando measurements that link local structure and illumination conditions to spatially resolved redox activity, enabling a quantitative view of which parts of a hybrid architecture actually "use" photogenerated charge in solution.

Here, I present an operando strategy aimed at extracting and mapping interfacial charge-use efficiency across a hierarchy of hybrid material systems with increasing architectural complexity: (i) a 2D MoS_2 monolayer as a geometrically well-defined model interface; (ii) planar arrays of Au or Pt nanoislands on a semiconductor film (TiO_2) to probe how metal identity and morphology modulate interfacial reactivity; and (iii) a one-dimensional junction geometry based on a TiO_2 nanotube decorated only at the tip with Au nanoislands, which enables direct tests of axial charge transport and spatial separation of solution-phase redox processes.

II. Methods

Our methodology combines structural and optical mapping with operando scanning electrochemical microscopy (SECM) and reaction–diffusion modelling to quantify interfacial charge-use efficiency in hybrid photocatalysts. Morphology is characterized by SEM, optical response by scanning spectrophotometer microscopy, and local photochemical activity by light-coupled SECM (Figure 1.a,b). A calibrated diffusion model converts the SECM probe signal into the corresponding surface reaction rate, enabling extraction of external and internal quantum efficiencies.[1], [2]

III. Results and Discussion

Using operando light-coupled SECM on a monolayer MoS_2 model interface, we quantified where photogenerated charges become chemically productive at the solid–liquid interface. Oxidation signatures remain confined to the illuminated region, whereas reduction products are detected far from the excitation spot (Figure 1.c), consistent with long-range lateral electron transport (up to ≥80 μm).[1]

Beyond spatial mapping, we revealed that the A-exciton internal quantum efficiency (IQE) exceeds the C-transition IQE, even though EQE may still be larger for C when absorption is stronger. Collectively, these results show that MoS_2 activity cannot be rationalized solely by "defect = active site"; rather, carrier transport and extraction geometry determine where oxidation vs reduction occurs, and excitation energy selects which carrier population is most chemically productive.[1]

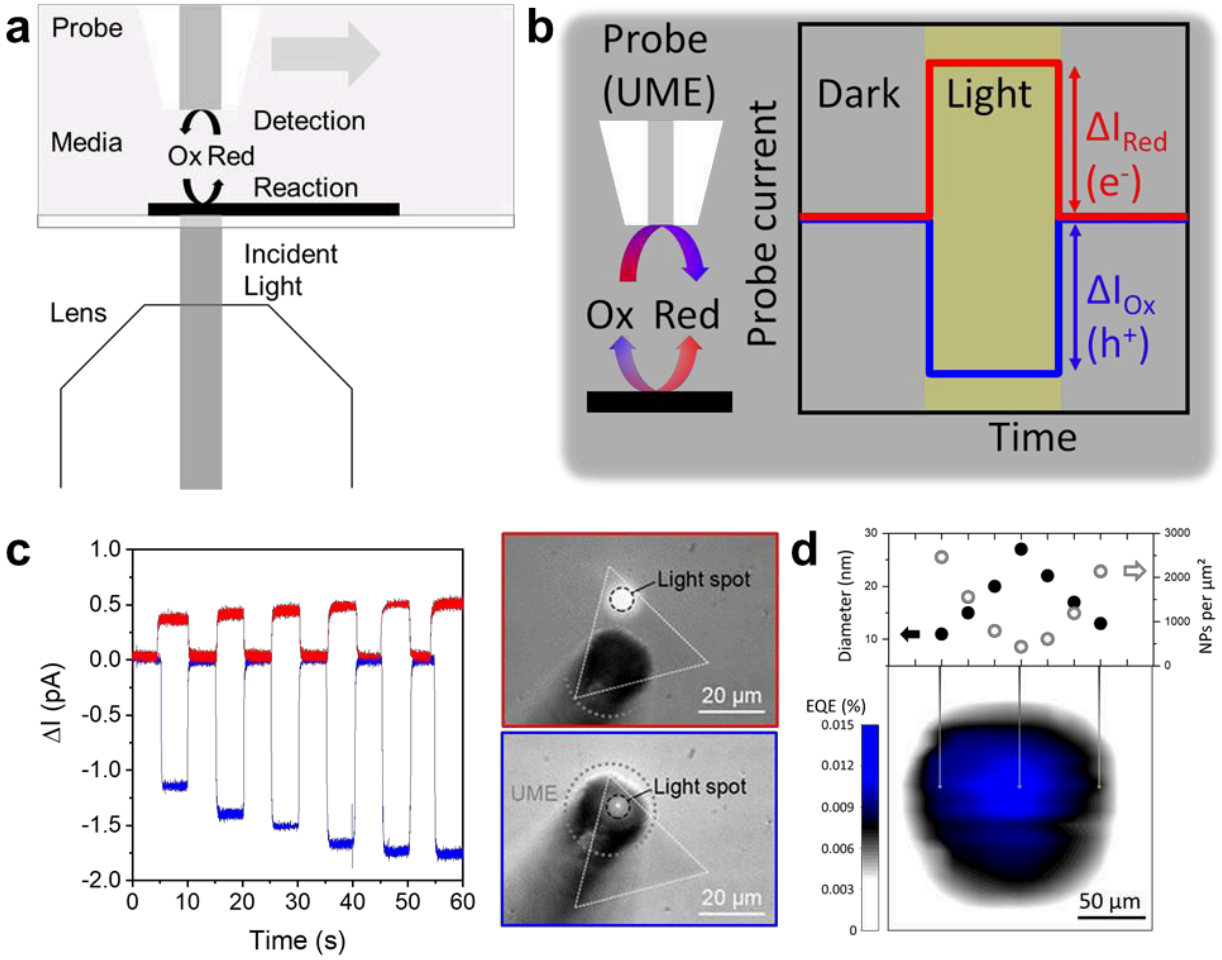

Figure 1. (a) Schematic of the light-coupled scanning electrochemical microscopy (SECM) configuration. (b) Conceptual diagram illustrating signal acquisition for either a reduction (red) or oxidation (blue) process occurring at the investigated material and detected at the probe. (c) Unaligned (Top) and aligned (Bottom) excitation–detection measurements on a MoS_2 monolayer, highlighting the spatial separation of reduction (electron-driven; red) and oxidation (hole-driven; blue) sites as a function of light-excitation position and power. (d) Top: Au nanoparticle population along the array centerline (diameter, left axis, filled symbols; number density, right axis, open symbols). Bottom: external quantum efficiency (EQE) map of the Au nanoparticle array measured by SECM. Experimental conditions: (c) λ_{LED} = 660 nm, r_T = 0.1 µm, RG = 25, Z = 5 µm; (d) λ_{LED} = 595 nm, r_T = 5 µm, RG = 5, Z = 20 µm. Electrolyte: 1 mM ferrocene dimethanol in 0.1 M KCl.

We extended this methodology to semiconductor-metal hybrid systems via Au nanoisland arrays on planar TiO_2. The Au/TiO_2 arrays exhibit peak EQE at the plasmon resonance (around the ~595 nm region for the studied arrays), and the measured EQE varies systematically with nanoisland statistics (size distribution and number density) (Figure 1.d). Wavelength-dependent analysis supported by theory indicates that the dominant carrier channel changes with excitation: interband ("d-hole") contributions dominate at shorter wavelengths, while plasmonic hot holes dominate at longer wavelengths.[2] This provides a direct explanation for why optical absorption alone is not predictive— greater absorption does not necessarily translate into higher chemical yield unless the relevant carrier population is efficiently extracted and coupled to interfacial charge transfer.

Applying nanoscale SECM to a tip-decorated TiO_2 nanotube bearing Au nanoparticles, we observed a bipolar, nanodiode-like behavior: oxidation is confined to Au-decorated regions (consistent with hot-hole-driven chemistry), while reduction products emerge in spatially distinct locations, consistent with hot-electron injection into TiO_2 followed by transport and interfacial transfer elsewhere. In other words, a single illuminated hybrid structure can sustain spatially separated oxidation and reduction zones through engineered charge separation and transport. [2]

IV. Conclusion

Across these three platforms—2D MoS_2, planar semiconductor–metal nanoisland arrays, and 1D nanotube-based junctions—I aim to show that interfacial charge-use efficiency is not a bulk property but an architecture-dependent, spatially heterogeneous quantity that must be measured operando. In MoS_2, oxidation and reduction are spatially separated and IQE depends strongly on excitation channel (A

exciton vs C transition), demonstrating that productive photochemistry is governed by transport and extraction geometry rather than absorption alone. In Au/TiO_2 nanoisland arrays, we established a quantitative workflow linking morphology and optical response to chemically specific reactivity maps, and we demonstrated that wavelength selects distinct hot-carrier pathways—explaining why absorption is an incomplete predictor of chemical yield. Finally, the plasmonic nanodiode concept shows that geometry can encode spatially programmed redox chemistry, and the tip-only Au design demonstrate this principle in a cleaner and more quantitative ways.

Taken together, these studies support a practical design message for hybrid photocatalysts: improving performance requires engineering not only light harvesting, but also the routes by which specific carrier populations reach the solid–liquid interface and react with solution species—and validating these pathways through operando, spatially resolved quantification.

ACKNOWLEDGMENTS

This work was supported by the EU Horizon Europe Marie Skłodowska-Curie grant agreement No. 101205585.

REFERENCES

[1] O. Henrotte *et al.*, "Spatially resolved photocatalytic active sites and quantum efficiency in a 2D semiconductor," *Nat. Commun.*, vol. 16, no. 1, p. 6904, Jul. 2025, doi: 10.1038/s41467-025-62284-x.

[2] O. Henrotte *et al.*, "Local Photochemical Nanoscopy of Hot-Carrier-Driven Catalytic Reactions Using Plasmonic Nanosystems," *ACS Nano*, vol. 17, no. 12, pp. 11427–11438, 2023, doi: https://doi.org/10.1021/acsnano.3c01009.

Symmetry breaking bu biomolecules in chiral nanophotonics

Malcolm Kadodwala
University of Glasgow, UK

***Abstract*— Chiral biomolecules adsorbed on enantiomorphic silicon metasurfaces break mirror symmetry by perturbing electromagnetic boundary conditions. This interfacial coupling forms meta-diastereomers, hybrid states whose linear and circular dichroism depend on combined molecular and structural handedness. The resulting stereostructural sensitivity enables discrimination of protein conformation and antibody–antigen binding without near-field enhancement mechanisms.**

Chiral Shape Transformation of Colloidal Silver Nanostructures using Circularly Polarized Light

Gil Markovich[1,*], Daniel Feferman[1], Bar Reuven[1], Monika Ghalawat[1,2], Lucas V. Besteiro[3], Alexander O. Govorov[4]

[1]School of chemistry, Tel Aviv University, Tel Aviv, Israel
[2] Advanced Institute for Materials Research, Tohoku University, Sendai, Japan
[3] CINBIO, University of Vigo, Vigo, Spain
[4] Department of Physics and Astronomy and Nanoscale and Quantum Phenomena Institute, Ohio University, Athens, Ohio, US

*Corresponding author: gilmar@post.tau.ac.il

***Abstract*— Localized plasmon induced galvanic replacement reaction in colloidal silver nanostructures was used to transform their shape using circularly polarized light illumination. We break their shape symmetry and obtain chiral nanostructures exhibiting substantial circular dichroism. Electric field induced nanostructure alignment facilitates such symmetry breaking, using circularly or linearly polarized light.**

***Keywords*— silver nanostructures, circularly polarized light, galvanic replacement reaction, symmetry breaking, plasmon resonance.**

Molecular Bridges in MXenes: Tunable Charge Transport and Chemiresistive Sensing

[1]Yudhajit Bhattacharjee

[1]Leibniz-Institut für Polymerforschung Dresden e. V. ; bhattacharjee@ipfdd.de

Abstract: MXenes, a family of 2D transition metal compounds, have emerged as promising materials due to their tunable surface chemistry and exceptional electrical properties, making them ideal candidates for flexible electronics and sensor applications. In this work, we present a versatile strategy to adjust interlayer spacing and interfacial interactions within $Ti_3C_2T_x$ - MXenes through molecular cross-linking, achieved by sequential ligand exchange with homologous diamines. Initially, oleylamine ligands were employed to exfoliate and stabilize MXene flakes in organic solvent, facilitating their uniform dispersion. The delaminated flakes were then reassembled into thin films through controlled cross-linking using diamines with varied aliphatic chain lengths, enabling precise modulation of interlayer spacing. Grazing incidence X-ray scattering (GIXRD/GIWAXS) revealed a systematic increase of interlayer distance with increasing chain length, while density functional theory (DFT) calculations corroborated these results, indicating precise tunability based on a molecular length scale. We performed charge transport measurements of the resulting films, demonstrating a strong correlation: as the interlayer spacing increases, the electrical conductivity shows a distinct trend. Notably, longer ligands led to more separated layers, which introduced broader tunneling barriers, while shorter linkers improved inter-flake coupling, increasing conductivity.[1] Beyond conductivity, the cross-linked MXene films exhibited promising chemiresistive sensing behavior. When exposed to volatile organic compounds and water vapor, they responded with significant resistance changes. A pronounced selectivity towards H_2O was observed. This selectivity is attributed to the modified interfaces of MXenes, where molecular cross-linkers act as both spacers and functional moieties, facilitating the adsorption of polar analytes and enabling rapid, reversible chemiresistive responses. By strategically tuning interlayer spacing, interface structure, and surface chemistry through molecular cross-linkers, this work demonstrates how molecular design directly influences both electronic transport and chemiresistive sensing properties in MXene systems.[1]

Key words: MXene, Charge transport, Density Functional Theory (DFT), Hybrid nanomaterials, Molecular Cross-linking, Vapor sensing

Reference:

1. **Y. Bhattacharjee***, L. Mielke, M. Al-Hussein, S. Singh, K. Schaefer, B Rodriguez-Barea, Q Li, A K. Ghosh, A. Erbe, C. Herrmann, Y. Vaynzof, A. Fery, H. Schlicke*. Molecular Cross-linking of MXenes: Tunable Interfaces and Chemiresistive Sensing. ***Adv. Funct. Mater***. 2025, e18884.

Controlling Polaritonic Contributions to Material Properties

Matthew Sheldon[1,*]

[1]Department of Chemistry, University of California, Irvine, USA
*Corresponding author: m.sheldon@uci.edu

***Abstract*— We show that engineered plasmonic cavities can control how light matter coupling contributes to material behavior. Across recent studies, cavity symmetry and optical state density reshape polariton character, radiative energy transport, and thermoelectric response. These results establish photonic design as a route to tuning spectroscopy, chemistry, and charge transport.**

***Keywords*— plasmonic nanocavities, polaritons, vibrational strong coupling, local density of optical states, thermoelectric response.**

I. Introduction

Optical cavities are increasingly viewed not only as spectroscopic environments but as platforms for controlling material behavior. In plasmonic nanocavities, the local density of optical states, radiative damping, and mode symmetry can all be engineered on subwavelength length scales. These features make plasmonic systems especially attractive for studying how light matter interactions contribute to chemical and physical properties under both weak and strong coupling conditions.

This presentation synthesizes three recent studies from our laboratory that together support a unified picture. First, the symmetry of a plasmonic cavity can change the radiative character of the hybrid states formed under vibrational strong coupling. Second, resonant cavities can modify a thermally driven chemical transformation by enhancing localized radiative energy transfer. Third, photonically structured plasmonic environments can alter the apparent thermoelectric response of a metal nanostructure. Taken together, these results argue that polaritonic and near polaritonic contributions to material properties can be intentionally controlled through photonic design.

II. Results and Discussion

Our first study addressed a basic question in polariton science: which states become optically bright or dark after strong coupling, and how does that depend on cavity symmetry. Using subradiant quadrupolar plasmonic resonators, we found that the usual expectation from bright cavity systems can be inverted. In these structures, the hybrid polariton states acquire subradiant character, while the collective molecular states that are usually spectrally hidden become comparatively accessible. This result shows that cavity symmetry directly shapes the optical character of the coupled states and opens a route for probing molecular contributions that are often difficult to observe in conventional cavity geometries.

Our second study connected this state engineering perspective to chemical reactivity. We examined the thermal dehydration of copper sulfate pentahydrate on resonant plasmonic nanocavity substrates and found that vibrational coupling lowered the onset temperature of dehydration by as much as fourteen degrees Celsius. Spatially resolved Raman mapping showed that the strongest modification occurred in regions of highest optical state density near the nanocavity hotspots. These observations support a mechanism in which resonant electromagnetic modes enhance radiative energy exchange between the cavity and the molecular film, reducing local thermal resistance and changing how thermal energy is delivered to the reacting material. In this study, weak and strong coupling modify the intrinsic thermal transfer properties of the chemical system itself, changing how energy is exchanged, transported, and ultimately used to drive reaction.

Our third study extended this broader idea beyond chemistry and into electronic transport. In structurally uniform gold nanowires placed adjacent to plasmonic nanodisk antennas, we observed spatially correlated photovoltage signals that tracked the local photonic environment. Because the devices were designed to minimize known structural sources of Seebeck coefficient variation, the results point to a photonic contribution to the apparent thermoelectric response. The data are consistent with a photothermoelectric mechanism in which the engineered photonic landscape modifies the effective Seebeck coefficient through photon electron interactions. This finding suggests that photonic structure can be used not only to control optical absorption and local heating, but also to tune electronic transport behavior in metals.

Across these three studies, several common themes emerge. The first is that mode symmetry matters because it determines whether coupled states are radiative, subradiant, or spectroscopically silent. The second is that local density of optical states matters because it defines where light matter interaction is strongest and where modified behavior is most likely to appear. The third is that photonic modes can influence material properties through transport phenomena, not only through static spectral signatures. These themes provide a coherent framework for understanding how optical cavities

contribute to spectroscopy, chemistry, and charge transport in plasmonic systems.

III. Conclusion

Across these three studies, several common themes emerge. The first is that mode symmetry matters because it determines whether coupled states are radiative, subradiant, or spectroscopically silent. The second is that local density of optical states matters because it defines where light matter interaction is strongest and where modified behavior is most likely to appear. The third is that photonic modes can influence material properties through transport phenomena, not only through static spectral signatures. These themes provide a coherent framework for understanding how optical cavities

References

[1] J. E. Yim, Z. T. Brawley, and M. T. Sheldon, "Subradiant plasmonic cavities make bright polariton states dark," Nanophotonics 13, 2035 to 2045, 2024.

[2] Z. T. Brawley, S. Pannir-Sivajothi, J. E. Yim, Y. R. Poh, J. Yuen-Zhou, and M. Sheldon, "Vibrational weak and strong coupling modify a chemical reaction via cavity-mediated radiative energy transfer," Nature Chemistry 17, 439 to 447, 2025.

[3] B. Zhao, A. Lee, J. E. Yim, Z. Brawley, E. Brass, and M. Sheldon, "Photonic Contributions to the Apparent Seebeck Coefficient of Plasmonic Metals," Nano Letters 25, 12386 to 12392, 2025.

Hybrid AI design of reconfigurable and compact plasmonic Arithmetic and Logic Units

Amine Khitous,[1] Nicolas Gros,[2] Léo Martin,[1] Florian Dell'Ova,[1] Aurélie Bertaux,[2] Ouassila Narsis Labbani,[2] Gérard Colas des Francs,[2] Christophe Nicolle,[3] Alexandre Bouhelier,[1] Erik Dujardin[1 *]

[1] Laboratoire Interdisciplinaire Carnot de Bourgogne (ICB), Université Bourgogne Europe CNRS UMR 6303, 21000 Dijon, France.
[2] Connaissances et Intelligence Artificielle Distribuée (CIAD), Université Bourgogne Europe ER 7533, 21000 Dijon, France.

*Corresponding author: Erik.Dujardin@cnrs.fr

***Abstract*— We recently introduced the concept of all-optical arithmetic and logic units (ALU) in single plasmonic cavities. The first prototype showed the sub-optimal addition of two 1-bit numbers and all 2-input logic gates. In the absence of an established design theory for such holistic devices, we have developed a new hybrid AI approach that optimizes the design beyond the performances of the initial intuitive demonstrator and paves the way to more complex optical Boolean computing.**

***Keywords*— optical computing, plasmonics, hybrid AI, non-linear optics.**

I. Introduction

Photonics has revolutionized information transfer, but processing and computing remain provided by microelectronic solutions that face fundamental limitations, including the interconnect bottleneck: circuits of smaller switching devices need longer and narrower interconnects, where most energy is dissipated.

We recently proposed a new concept of micrometric, all-optical and interconnect-free, reconfigurable Arithmetic and Logic Units (ALU) of increasing computing capacity. The shape of a 2D single crystalline gold microcavity defines a set of plasmon modes to be used as reconfigurable computation channels.[1,2] The plasmonic landscape, optically excited by N Boolean inputs encoded into two polarization states of focused fs-pulsed laser spots, generates a remote optical Boolean calculus at the ALU output ports. The arithmetic or logic function is directly realized by the relationship between the inputs and outputs. Unlike all information paradigms that rely on concatenated switching devices to realize logic gates, Shannon's theory of information does not apply to our holistic devices and we need to uncover the specific rules governing our ALU design and operation for given Boolean functions. The first prototype to demonstrate experimentally this concept, though sub-optimally, was a cavity with a double hexagon (DH) shape.[1,2] To improve the device performance, we have created a hybrid AI (HAI) tool able to propose candidate cavity shapes as well as optimal excitation/detection condition and successfully shown that they outperform the DH prototype in realizing the 1-bit Full-Adder function.

II. Methods

A robust Boolean function is achieved in plasmonic modal ALU devices when the transmittance, probed here as the non-linear photoluminescence (NPL) transmittance, between the input and output ports obeys the truth table with a high Boolean contrast (i.e. a large difference between '0' and '1' output values). This condition can be expressed for any Boolean function and used to identify where and when an output signal fulfils it.[2] We have created a purpose-conceived hybrid AI framework that that comprises two genetic algorithms to tests millions of cavity shapes and excitation/detection schemes, check the viability of the proposal based on a specific set of ontologies [3] and assesses the optical response of the cavity with a 30 000x acceleration factor compared to standard simulation tools to finally provide most promising solutions.[4]

III. Results and Discussion

Within a few computation days, this DALHAI tool has identified optimal coherent drive conditions for the DH cavity and a set of 5 cavities with increasing overall Boolean contrast for the joint (AND, XOR) Boolean function that implements the 1-bit Full-Adder function. As Fig. 1 shows, the performance is increased by a factor of 200% compared to the optimized DH case.

Experimental realization and testing of such plasmonic ALUs and the effective assessment of the computation quality was carried out and will be introduced but detailed in a separate contribution. In particular, the cavity shapes are realized, from the geometrical description by the HAI, by focused ion beam (FIB) milling of single crystalline gold microflakes. The optical Boolean computation is obtained by implementing the coherent 2-beam excitation of the cavity [5] and controlling the

excitation parameters (beam positions, linear polarization set encoding the Boolean inputs and relative phase-shift between the two incident fs-pulsed beams).

We will also discuss the extension and generalization of our approach towards more complex Boolean functions taking the 2xN-bit Full-Adder as a user case requiring 2N inputs and N+1 outputs.

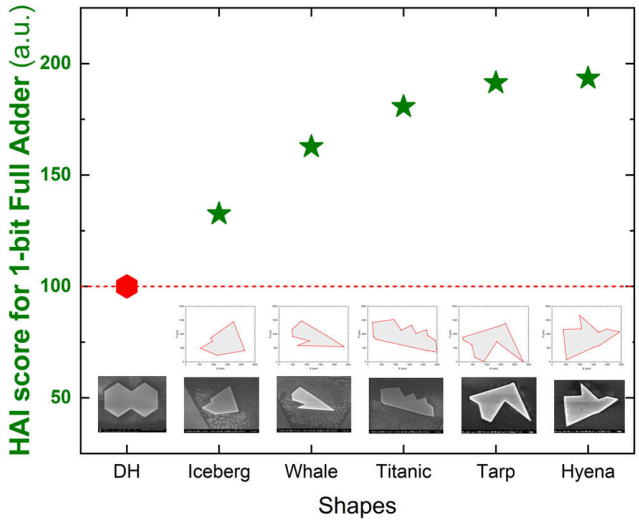

Fig. 1: Optimal 1-bit Full-Adder Boolean contrast (normalized to the one of the DH cavity) for the series of HAI-design plasmonic cavities. Each simulated score corresponds to a specific set of excitation conditions (input locations, linear polarization set, phase shift between exciting pulses). In inset: geometric shape provided by the HAI (top row) and SEM images of the nanofabricated cavities from single crystalline flakes (bottom row). [6].

IV. Conclusion

Our hybrid AI tools successful uncover better performing cavities achieving the targeted 1-bit and 2-bit Full-Adder functions. These results are extremely promising as no established criteria for shaping a cavity and operation scheme for a chosen Boolean function is available. In the process, we have identified several limitations that suggest improvement steps to further generalize our approach in order to reach more complex Boolean functions.

Acknowledgments

This work has been partially funded by the French Agence Nationale de la Recherche (ANR-20-CE24−0001 DALHAI, ANR-25-TSIA-0001 CAIPOP, ANR-25-CE24-7238 POMMARD, ISITE-BFC ANR-15-IDEX-0003), the REMONTADA project of the EIPHI Graduate School (ANR-17-EURE-0002). The authors also acknowledge the support of CNRS MITI (Project BOTAI 2023-24). Device nanofabrication and characterization was performed at the technological platforms SMARTLIGHT, ARCEN Carnot at ICB and MIMENTO at FEMTO-ST under program Investment for the Future (ANR-21-ESRE- 0040), the Région de Bourgogne Franche-Comté, the CNRS, and the French Renatech+ network.

References

[1] Kumar, U *et al.*, “Interconnect-Free Multibit Arithmetic and Logic Unit in a Single Reconfigurable 3 μm2 Plasmonic Cavity”, ACS Nano 2021, 15, 13351−13359

[2] Dell’Ova, F., Brûlé, Y., Gros, N., Bizouard, J., Shakirova, D., Bertaux, A., ... & Dujardin, E. (**2024**). Compact implementation of a 1-bit adder by coherent 2-beam excitation of a single plasmonic cavity. ACS photonics, 11(2), 752-761.

[3] Labbani Narsis, O., Dujardin, E., Nicolle, C., Gros, N. "From Human Cognitive Expertise to Ontological Formalization: Bridging the Knowledge Gap for Nanophotonic Calculator Design and Simulation." Joint Ontology Workshops (JOWO) - 14th International Conference on Formal Ontology in Information Systems (FOIS 2024), Jul 2024, Enschede, Netherlands. (hal-05411152)

[4] Manvendra Janmaijaya, et al., "ESPLANADE: Efficient Simulation of Plasmonic Logic and Arithmetic NAnoDEvice", Submitted for publication, hal-05411342

[5] F. Dell'Ova, et al., " Coherent two-beam steering of delocalized nonlinear photoluminescence in a plasmon cavity", Opt Express 2022 30, 10, 17517-17528

[6] A. Khitous, N. Gros, L. Martin, F. Dell'Ova, A. Bertaux, O. Labbani Narsis, G. Colas des Francs, C. Nicolle, A. Bouhelier, E. Dujardin, 2026, in preparation.

Experimental benchmark of AI-Optimized, Reconfigurable, All-Optical Plasmonic Arithmetic and Logic Units

Amine Khitous,[1 *] Nicolas Gros,[2] Léo Martin,[1] Florian Dell'Ova,[1] José Valderrama-Botia,[1]Aurélie Bertaux,[2] Ouassila Narsis Labbani,[2] Gérard Colas des Francs,[2] Christophe Nicolle,[3] Alexandre Bouhelier,[1] Erik Dujardin[1 *]

[1] Laboratoire Interdisciplinaire Carnot de Bourgogne (ICB), Université Bourgogne Europe CNRS UMR 6303, 21000 Dijon, France.

[2] Connaissances et Intelligence Artificielle Distribuée (CIAD), Université Bourgogne Europe ER 7533, 21000 Dijon, France.

*Corresponding authors: Amine.Khitous@ube.fr, Erik.Dujardin@cnrs.fr

***Abstract*: The recent demonstration of the concept of all-optical arithmetic and logic units (ALU) in single plasmonic cavities able to perform all 2-input, 2-output operations required to add two 1-bit numbers has prompted the need for a conceptual breakthrough to design processors able to deliver higher Boolean complexity. In the absence of established blueprinting theory for such holistic devices, we have developed a new hybrid AI approach that optimizes the design beyond the performances of the initial intuitive demonstrator. We present here the experimental testing of the AI-designed ALU structures and operation conditions and benchmark our design approach for future optical processors of higher complexity.**

***Keywords*: metamaterials, optical full adders, interconnect-free arithmetic logic unit (ALU), coherent plasmonic interference, 2D plasmonic cavity, nonlinear photoluminescence (NPL).**

I. Introduction

The development of integrated optical computing architectures is a central challenge in modern nanophotonics, driven by the need to overcome the fundamental limitations of electronic processors [**1**]. While transistor performance has continued to improve, signal routing through metallic interconnects has emerged as the dominant bottleneck, imposing severe constraints in terms of power consumption, footprint and clockrate at advanced technology nodes [**2**]. Optical approaches offer an attractive alternative, benefiting from high bandwidth and low dissipation, yet conventional photonic platforms remain limited by diffraction and bulky interconnect architectures [**3**].

Plasmonic nanostructures provide a promising downsizing route for optical computing by confining electromagnetic fields below the diffraction limit. In this context, nonlinear photoluminescence (NPL), arising from hot-electron dynamics in metals, offers a powerful virtual local probe of plasmonic mode localization and interference.[**3**] Understanding and controlling the spatial distribution of NPL is therefore crucial for encoding and reading out Boolean logic states in plasmonic devices [**4-6**].

Recent demonstrations of plasmonic logic gates within single cavities have highlighted the potential of interconnect-free optical computation. The Boolean output contrast delivered by these demonstrators are nevertheless modest as not optimization procedure has been applied, thereby highlighting the need for an optimal design approach towards viable Boolean scalability [**5,6**]. We have recently elaborated a new a hybrid artificial intelligence (HAI) framework that predicts optimal cavity geometries and excitation parameters for the 2x1-bit Full-Adder and associated 1-input logic gates.[**7**,**8**] In this work, we experimentally benchmark the performances of the HAI proposals by nanofabricating the HAI-inverse-designed cavities, explore the determinant coherent conditions to generate a contrasted output and establish the performance roadmap of this new series of optical computing devices. By jointly optimizing the cavity geometry and the excitation conditions, we realize reconfigurable all-optical plasmonic arithmetic and logic units, culminating in the experimental demonstration of a cascade-free 1-bit optical full adder within a single plasmonic cavity with a 200% output contrast improvement.

II. Methods

2D plasmonic cavities were fabricated by focused ion beam milling chemically synthesized single-crystal gold microflakes deposited on a transparent glass substrate with a 10-nm nominal conductive indium tin oxide layer. [**5,6**] The milling of the polygonal shapes of the cavities was directly implemented from the Hybrid AI output files by simply adjusting the ion dose to

Proceedings of META 2026 · Dublin, Ireland · 14–17 July 2026 · ISSN 2429-1390 · pp. 224–226

the microflake thickness.

HAI approach was employed to optimize both the excitation conditions and the geometries of the plasmonic cavities. In our setup, two laser beams coherently illuminate each cavity at distinct positions, and the logical information is encoded in the polarization of each beam (810 nm, 140 fs, 80 MHz), representing "0" or "1," as illustrated in **Fig.1**, which shows both the experimental instrument and the cavity irradiation scheme. With two beams and two polarization states, four input configurations are possible (00, 01, 10, 11).

In this work, we focus on a 2×1-bit full adder, which requires a XOR gate to perform the sum and an AND gate to generate the carry. To perform an addition correctly, both the XOR and AND gates must operate simultaneously for the same input configuration. The Boolean contrast (ε), defined as the measure of distinguishability between the logical states "0" and "1" based on their output intensities, was enhanced through HAI-guided optimization (**Fig.1.b-c**). The AI proposed several optimized cavity shapes, and the Boolean contrast of the 2×1-bit full adder was systematically compared between AI-predicted simulations and experimental measurements, demonstrating excellent agreement and validating the effectiveness of the AI-driven design framework.

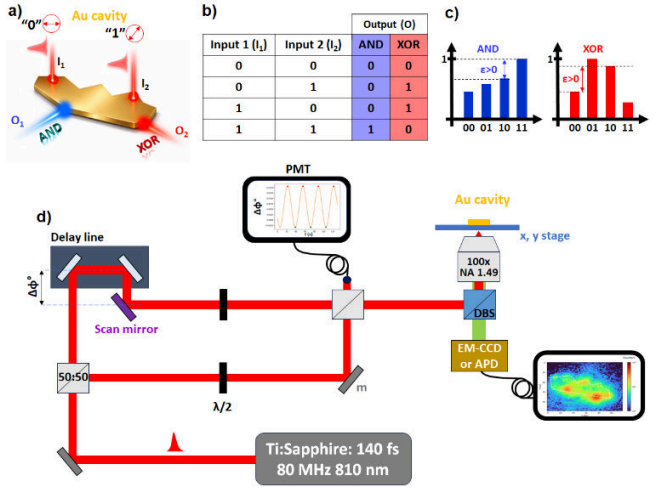

Fig.1: (**a**) Conceptual schematic of the plasmonic cavity. (**b**) Combined truth tables of the output positions simultaneously implementing AND and XOR logic (full-adder operation) within a single plasmonic cavity. (**c**) Bar-plot representation of the AND and XOR logic gates, highlighting a positive Boolean contrast (ε). (**d**) Schematic of the experimental setup used for optical characterization of the full-adder.

III. Results and Discussion

First, the geometry and excitation conditions (polarization, beam positions, and relative phase shift between the two irradiation beams) of the plasmonic cavities were optimized for logic-gate operations using an AI-driven framework that combines accelerated simulations with evolutionary algorithms. Five geometries (Whale, Mountain, Titanic, Hyena, and Tent) outperformed the reference double-hexagon (DH) design [**3**], achieving up to a twofold improvement (**Fig. 2**). SEM images of the AI-designed structures are shown in **Fig. 2**.

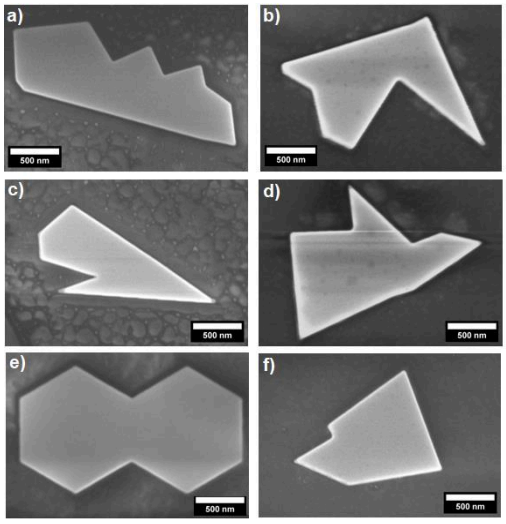

Fig. 2: SEM images of the studied structures: titanic (**a**), tent (**b**), hyena (**c**), whale (**d**), mountain (**e**), and double hexagon (**f**).

The experimental implementation of the AI-predicted excitation conditions demonstrated that these structures achieve Boolean scores (**Fig. 3**) up to four times higher than those obtained from designs based on experimental intuition [**6**]. As an illustrative example, the Titanic geometry exhibits both logic gates of the adder at a phase shift of 40°, with a contrast of 77% for the AND gate and 22% for the XOR gate, resulting in a Boolean score of 22%, compared to only 3% reported in our previous studies [**6**]. The logic-gate locations are clearly spatially separated, which facilitates their identification. Furthermore, **Fig. 3** demonstrates the realization of a fully optical, interconnection-free 2×1-bit adder.

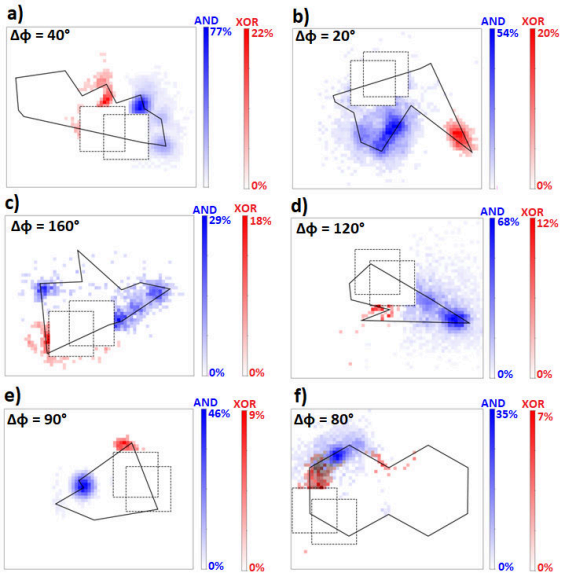

Fig. 3: Optimal 1-bit adder maps obtained experimentally under the excitation conditions predicted by the AI, for the studied structures: titanic (**a**), tent (**b**), hyena (**c**), whale (**d**), mountain (**e**), and double

hexagon (**f**).

Moreover, we demonstrate that the position of the logic gate can be controlled by tuning the phase shift between the two beams. **Fig.4** presents an example of the variation of the Boolean score of the Titanic geometry as a function of the phase shift, highlighting the reconfigurability of the plasmonic-cavity-based adder. Interestingly, the experimental trends of the Boolean scores for the XOR and AND gates are in good agreement with theoretical predictions.

These cavities exhibit phase-dependent reconfigurability, where $\Delta\varphi$ controls beam interference, enabling switching between AND and XOR functions without altering the geometry. For example, in the Titanic structure, $\Delta\varphi \approx 0°$ favors AND, while $\Delta\varphi \approx \pm 120°$ favors XOR.

IV. Conclusion

In conclusion, AI-driven optimization enables the design of plasmonic cavities with high performance and reconfigurability. NPL generation is governed by confined cavity transport modes and strongly depends on beam polarization and position, with sharp corners serving as efficient output points. The optimized geometries outperform the reference double-hexagon design, achieving up to twofold improvement in Boolean contrast. Phase-dependent control allows dynamic switching between AND and XOR gates without changing the cavity, while long-range plasmon propagation and local hot-electron transport explain the observed NPL patterns. These results confirm the accuracy of AI predictions and highlight a physical performance plateau set by intrinsic plasmonic constraints, demonstrating that AI-assisted inverse design is a powerful strategy for creating robust, high-performance, and reconfigurable plasmonic logic devices.

Acknowledgments

This work has been partially funded by the French Agence Nationale de la Recherche (ANR-20-CE24−0001 DALHAI, ANR-25-TSIA-001 CAIPOP, ANR-25-CE24-7238 POMMARD), ISITE-BFC ANR-15-IDEX-0003), the REMONTADA project of the EIPHI Graduate School (ANR-17-EURE-0002). The authors also acknowledge the support of CNRS MITI (Project BOTAI 2023-24). Device nanofabrication and characterization was performed at the technological platforms SMARTLIGHT, ARCEN Carnot at ICB and MIMENTO at FEMTO-ST under program Investment for the Future (ANR-21-ESRE- 0040), the Région de Bourgogne Franche-Comté, the CNRS, and the French Renatech+ network.

References

[1] Rizzo, A., Novick, A., Gopal, V., Kim, B. Y., Ji, X., Daudlin, S., ... & Bergman, K. (**2023**). Massively scalable Kerr comb-driven silicon photonic link. Nature Photonics, 17(9), 781-790.

[2] Thraskias, C. A., Lallas, E. N., Neumann, N., Schares, L., Offrein, B. J., Henker, R., ... & Tomkos, I. (**2018**). Survey of photonic and plasmonic interconnect technologies for intra-datacenter and high-performance computing communications. IEEE Communications Surveys & Tutorials, 20(4), 2758-2783.

[3] Teulle, A., Marty, R., Viarbitskaya, S., Arbouet, A., Dujardin, E., Girard, C., Colas des Francs, G. (**2012**) Scanning optical microscopy modeling in nanoplasmonics, JOSA B, 29(9), 2431-2437.

[4] Kumar, U., Viarbitskaya, S., Cuche, A., Girard, C., Bolisetty, S., Mezzenga, R., Colas des Francs, G., Bouhelier, A., Dujardin, E. (**2018**) Designing Plasmonic Eigenstates for Optical Signal Transmission in Planar Channel Devices, ACS Photonics, 5, 2328−2335

[5] Kumar, U., Cuche, A., Girard, C., Viarbitskaya, S., Dell'Ova, F., Al Rafrafin, R., ... & Dujardin, E. (**2021**). Interconnect-free multibit arithmetic and logic unit in a single reconfigurable 3 μm2 plasmonic cavity. *ACS nano*, *15*(8), 13351-13359.

[6] Dell'Ova, F., Brûlé, Y., Gros, N., Bizouard, J., Shakirova, D., Bertaux, A., ... & Dujardin, E. (**2024**). Compact implementation of a 1-bit adder by coherent 2-beam excitation of a single plasmonic cavity. ACS photonics, 11(2), 752-761.

[7] Labbani Narsis, O., Dujardin, E., Nicolle, C., Gros, N. "From Human Cognitive Expertise to Ontological Formalization: Bridging the Knowledge Gap for Nanophotonic Calculator Design and Simulation." Joint Ontology Workshops (JOWO) - 14th International Conference on Formal Ontology in Information Systems (FOIS 2024), Jul **2024**, Enschede, Netherlands. (hal-05411152)

[8] Janmaijaya, M., El Vaigh, C. B., Gros, N., Bertaux, A., Labbani, O. N., Kumar, S., ... & Dujardin, E. (**2025**). ESPLANADE: Efficient Simulation of Plasmonic Logic and Arithmetic NAnoDEvice.

All-Dielectric Photo-Thermo-Optical Metasurfaces for All-Optical Spatio-Temporal Wavefront Control

Gopal Narmada Naidu*, Giulia Tagliabue

Laboratory of Nanosciene for Energy Technologies, EPFL, Switzerland
*Corresponding author: gopal.naidu@epfl.ch

***Abstract*— All-dielectric photo-thermo-optical metasurfaces could enable high speed all-optical spatiotemporal wavefront control. We demonstrate reconfigurable metasurface optical responses driven by thermo-optic nonlinearities and present an inverse thermal design framework for programmable temperature profiles. Together, these capabilities advance dynamic meta-optics, photothermal catalysis, and next-generation spatial light modulation for photonic and energy applications.**

***Keywords*— photo-thermal, thermo-optic, all-dielectric metasurfaces, inverse design, temperature shaping, reconfigurable, wavefront control.**

I. Introduction

Precise spatiotemporal control of optical wavefronts is central to emerging technologies including imaging, optical communications, holography, and laser processing. Conventional spatial light modulators based on liquid crystals are limited by millisecond response times, restricting their applicability in high-speed optical systems. Metasurfaces composed of subwavelength nanoresonators provide a compact platform for manipulating amplitude, phase, and polarization with high spatial resolution. However, achieving rapid and fully optical reconfigurability remains a major challenge. Thermo-optic nonlinearities and photothermal effects in high index dielectrics provide a promising route toward all-optical high-speed modulation.[1], [2], [3]

II. Methods

Combining electromagnetic simulations, topology optimization, and machine learning based design strategies, we efficiently explore high-dimensional design spaces, achieving optimized wavefront control while overcoming the computational limits of traditional iterative approaches. We further develop an inverse thermal design framework for dielectric metasurfaces composed of amorphous silicon nanoresonators, wherein a precomputed library of absorption spectra as a function of geometry and temperature is constructed using full wave electromagnetic simulations and target temperature distributions are mapped onto metasurface layouts. Coupled optical and thermal simulations are performed to evaluate steady state and transient temperature fields under optical illumination.

III. Results and Discussion

Silicon exhibits a strong thermos-optic coefficient, enabling substantial refractive index modulation with modest temperature variations. Coupled optical and thermal simulations of silicon dielectric metasurfaces reveal that optical and thermal dynamics can be partially decoupled, enabling optical modulation faster than thermal relaxation.[4] Motivated by these findings, we developed an inverse thermal design framework that maps target temperature profiles onto metasurface layouts, enabling precise nanoscale thermal control. We demonstrate that thermo-optical nanoresonators enable dynamic reconfigurability through wavelength or intensity multiplexing without complex unit cells. Furthermore, we show that engineered thermal distributions enhance photo-thermocatalytic performance by exploiting nonlinear temperature-dependent reaction kinetics to improve catalytic efficiency, while more broadly providing a general framework for optimizing other photothermal processes including solar evaporation and separation technologies.[5] Finally, this work aims to extend these concepts to realize fully reconfigurable all-optical metasurfaces with independent amplitude, phase, and polarization control.

IV. Conclusion

We present an inverse designed all-dielectric photo-thermo-optical metasurface platform for high-speed all-optical spatiotemporal wavefront control. The combination of thermo-optic nonlinearities and programmable temperature shaping establishes a scalable strategy for dynamic meta optics, photothermal catalysis, and next generation spatial light modulation.

Acknowledgments

This work was supported by the Swiss National Science Foundation (Starting Grant No. 211695).

References

[1] G. P. Zograf, M. I. Petrov, S. V. Makarov, and Y. S. Kivshar, *Adv. Opt. Photon.*, vol. 13, no. 3, pp. 643–702, Sep. 2021
[2] A. Archetti, R.-J. Lin, N. Restori, F. Kiani, T. V. Tsoulos, and G. Tagliabue, *Nanophotonics*, vol. 11, no. 17, pp. 3969–3980, 2022
[3] A. Naef, E. Mohammadi, T. V. Tsoulos, and G. Tagliabue, *Advanced Optical Materials*, vol. 11, no. 20, p. 2300698, Oct. 2023
[4] O. C. Karaman, G. N. Naidu, A. R. Bowman, E. N. Dayi, and G. Tagliabue, *Laser & Photonics Reviews*, vol. 19, no. 24, p. e01014, Dec. 2025
[5] G. N. Naidu, O. C. Karaman, and G. Tagliabue, 2025. [Online]. https://arxiv.org/abs/2510.15697

Near-Field Coupling in Plasmonic Nanoarrays: Tailoring Radiative and Non-Radiative Losses Through Gap Engineering

Benedict S. Morris[1, *] and Bruno Palpant[1]

[1] LuMIn, Université Paris-Saclay, CNRS, ENS Paris-Saclay, CentraleSupélec, Gif-sur-Yvette, France
*Corresponding author: benedict.morris@centralesupelec.fr

***Abstract*— Absorption losses in plasmonic nanoparticles limit their performance in many optical and photonic applications by dissipating energy as heat and damping resonance strength. Using finite-difference time-domain simulations (FDTD), we demonstrate that near-field coupling in dense, periodic nanoparticle arrays can significantly mitigate these losses.**

***Keywords*— Critical coupling, finite-difference time-domain (FDTD) simulations, electric field enhancement.**

When interparticle distances are small, for the free carriers inside a given particle, the field enhancement of neighbouring particles reduces the effect of the field enhancement at the tip of the particle under study. As a result, the internal electric field—and thus the associated Ohmic losses and optical absorptance—are substantially reduced (Fig. 1), despite intense field enhancement in the narrow interparticle gaps. By comparing our results to analytical theory of electric dipole arrays [1], we show that engineering the gaps in periodic arrays allows fine tuning of the non-radiative to radiative losses ratio [2]. In addition to this tailoring of losses, we show that near-field coupling can induce both red- and blue-shifting of the plasmon resonance wavelength. This interplay between the near-field enhancement and the electric field inside the nanoparticles suggests a route to exploit densely packed plasmonic arrays for optical devices, achieving high resonance strength and field enhancement while minimizing thermal losses and associated damping.

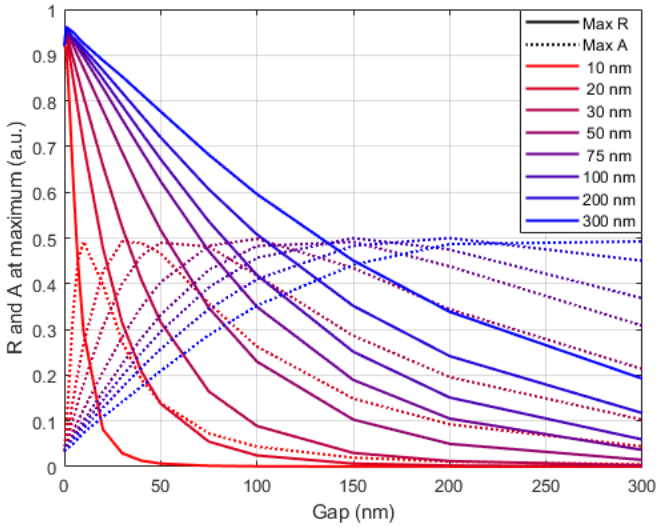

Fig. 1: Maxima of reflectance (solid lines) and absorptance (dotted lines) for different nanorod lengths (in nm) as a function of gap. The nanorods are 10 nm wide by 10 nm high.

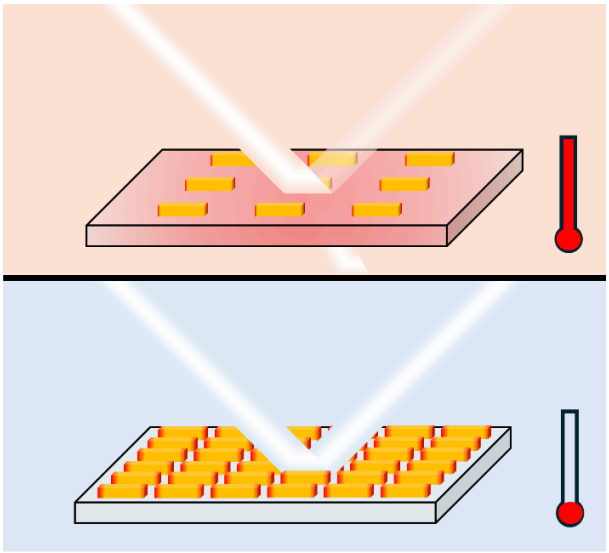

Fig. 2 : Small interparticle gaps lead to mirror-like behaviour with high values of enhanced near-field and reduced thermal losses.

References

[1] R. Alaee, M. Albooyeh, and C. Rockstuhl, "Theory of metasurface based perfect absorbers," 50, 503002.
[2] B. S. Morris, and B. Palpant, "Near-Field Coupling in Plasmonic Nanoarrays: Tailoring Radiative and Non-Radiative Losses Through Gap Engineering," Submitted.

Single plasmon transport in 1D nanowire

Gérard Colas des Francs

Laboratoire ICB UMR 6303 CNRS/Université Bourgogne Europe, Dijon, France

gcolas@ube.fr

***Abstract*—Waveguide quantum electrodynamics (wQED) explores the interaction between emitters and guided modes in *e.g.* optical nanofibers and plasmonic nanowires. We develop a dedicated formalism that naturally introduces coupling constant into a non Hermitian effective Hamiltonian. This facilitates the physical interpretation of plasmon transport including the role of propagation losses.**

***Keywords*— quantum plasmonics, wQED, non Hermitian.**

I. Introduction

Waveguide quantum electrodynamics (wQED) exploits evanescent coupling to mediate photon-photon interactions—otherwise weak—in direct analogy to cavity quantum electrodynamics (cQED). Quantum emitters coupled to a plasmon waveguide have been demonstrated to implement single-photon optical transistors [1], two-qubit entanglement [2], [3], long-range energy transfer [4], and nanowire lasers [5].

Theoretical treatments of wQED generally follow two complementary approaches. Effective Hamiltonian models describe emitter–waveguide interactions using *ad hoc* coupling constants, allowing compact expressions for single photon transmittivity [6], [7]. In contrast, continuous formulations based on the electromagnetic Green's tensor provide a description of the electromagnetic environment [2], [8]. In this work, we derive effective non-Hermitian Hamiltonians directly from the quantized electromagnetic Green's tensor of a plasmonic nanowire. This formulation naturally incorporates propagating SPPs and losses within a unified description.

II. Modulation of the single plasmon transport

The electromagnetic field is quantized within the Langevin type model [9] and we follow the procedure described by Castellini *et al* [10], but adapted to propagative modes to obtain the interaction Hamiltonian associated to a single emitter coupled to a plasmonic nanowire.

We consider a silver nanowire of radius 50 nm coupled to a single emitter located at 15 nm from its surface. We assume an emission at the telecom wavelength $\lambda = 1.5\,\mu\text{m}$, for which the nanowire supports a single mode SPP_0. The various contributions to the reflectivity and transmitivity are presented in Fig. 1. Single photon reflectivity and transmittivity achieve $R_0 = 50\%$ and $T_0 = 10\%$ at zero detuning $\omega = \omega_0$.

We extend our formalism to several emitters and demonstrate a significative improvement of the single plasmon modulation ($R_0 = 86\%$ and $T_0 = 2\%$ for 5 emitters).

Fig. 1. Modal reflectivity R_0 and transmittivity T_0 associated to the fundamental SPP_0 mode and to high order $\sum_{n\geq 1} R_n = \sum_{n\geq 1} T_n = \sum_{n\geq 1}$.

III. Conclusion

We have developed a Green-function-based effective Hamiltonian to single-plasmon transport in nanowires. The modal analysis clarifies the respective roles of guided and non-guided contributions in determining transport properties.

References

[1] D. Chang, A. Sörensen, E. Demler, and M. Lukin, "A single-photon transistor using nanoscale surface plasmons," *Nature Physics*, vol. 3, pp. 807–812, 2007.

[2] D. Dzsotjan, A. S. Sorensen, and M. Fleischhauer, "Quantum emitters coupled to surface plasmons of a nanowire: A Green's function approach," *Physical Review B*, vol. 82, p. 075427, 2010.

[3] A. Gonzalez-Tudela, D. Martin-Cano, E. Moreno, L. Martin-Moreno, C. Tejedor, and F. J. Garcia-Vidal, "Entanglement of two qubits mediated by one-dimensional plasmonic waveguides," *Physical Review Letters*, vol. 106, p. 020501, 2011.

[4] J. de Torres, P. Ferrand, G. Colas des Francs, and J. Wenger, "Coupling emitters and silver nanowires to achieve long-range plasmon-mediated fluorescence energy transfer," *ACS Nano*, vol. 10, pp. 3968–3976, 2016.

[5] E. Bermudez-Urena and *et al*, "Plasmonic waveguide-integrated nanowire laser," *NanoLetters*, vol. 17, pp. 747–754, 2017.

[6] J. Shen and S. Fan, "Coherent photon transport from spontaneousemission in one-dimensional waveguides," *Optics Letters*, vol. 30, p. 2001, 2005.

[7] Y. Chen, M. Wubs, J. Mørk, and A. Koenderink, "Coherent single-photon absorption by single emitters coupled to one-dimensional nanophotonic waveguides," *New Journal of Physics*, vol. 13, p. 103010, 2011.

[8] A. Asenjo-Garcia, J. Hood, D. Chang, and H. Kimble, "Atom-light interactions in quasi-one-dimensional nanostructures: A Green's-function perspective," *Physical Review A*, vol. 95, p. 033818, 2017.

[9] L. Knoll, S. Scheel, and D. Welsch, *Coherence and Statistics of Photons and Atoms*. John Wiley & Sons, Inc., 2001, ch. QED in dispersing and absorbing media.

[10] A. Castellini, H. R. Jauslin, B. Rousseaux, D. Dzsotjan, G. Colas des Francs, A. Messina, and S. Guérin, "Quantum plasmonics with multi-emitters: Application to adiabatic control," *The European Physical Journal D*, vol. 72, p. 223, 2018.

Multiplexed label-free (bio)molecular analytics using plasmonic nanoparticles

Tomas Ledničky, Guilherme Lopes, Baihui Li, Matthias Urban, Andrea Csáki, Wolfgang Fritzsche*

Department of Nanobiophotonics,
Leibniz Institute of Photonic Technology (Leibniz-IPHT) Jena, Germany
*Corresponding author: wolfgang.fritzsche@ipht-jena.de

***Abstract*— Nanoscale noble metal structures show the effect of localized surface plasmon resonance (LSPR), based on interaction of light with conduction electrons in the metal. As the observed resonance wavelength is influenced by the refractive index, modification with specifically binding biomolecules realizes label-free biosensors, also possible in array format for multiplexing.**

***Keywords*— gold nanoparticles, biosensing, DNA hybridization, sensor arrays.**

I. Introduction

Besides composition (material) size and shape of noble metal nanostructures, also the refractive index of the surrounding influences the resonance wavelength due to the effect of localized surface plasmon resonance (LSPR). By monitoring the resonance wavelength using VIS spectroscopy, refractive index sensing is so possible. By modifying the surface with certain receptors (molecules like antibodies, aptamers or DNA, which bind a target molecule highly specifically), a molecular detection with high specificity is provided. When using arrays of gold nanostructure spots each modified with a different receptor molecule, multiplexing is possible.

II. Methods

Chemically synthesized gold nanoparticles 80 nm diameter were spotted in an array pattern (spot diameter ca. 120 µm, center-to-center distance of 275 µm, Fig. 1) and modified by a second spotting run with various receptor molecules, such as single-stranded DNA [1, 2]. An imaging spectrometer setup using spectrally filtered light provided by 6 LEDs of different wavelengths spanning the VIS range is used to monitor the LSPR peak with a time-resolution in the lower second range upon incubation with target molecules (complementary DNA) [3]. Sensorgrams, plots of the resonance wavelength over time, are used to visualize the changing peak wavelength upon incubation with various buffers and/or target molecule solutions.

III. Results and Discussion

Experimental results show:

- Multiplexed label-free monitoring of DNA hybridization kinetics
- No significant cross-talk between different targets
- Strong agreement between simulated and measured spectra

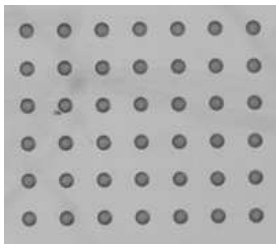

- Fig. 1 Optical transmission micrograph of a gold nanoparticle sensor array (spot diameter about 120 µm)

IV. Conclusion

We have demonstrated a multiplexed, label-free monitoring of molecular interactions for DNA using gold nanoparticle sensor arrays with VIS spectroscopic imaging readout.

Acknowledgments

We thank Florian Seier for initial DNA multiplexing experiments. This work was supported by the BMFTR, funding program Photonics Research Germany (13N15717) and is integrated into the Leibniz Center for Photonics in Infection Research (LPI). The LPI, initiated by Leibniz-IPHT, Leibniz-HKI, UKJ and FSU Jena, is part of the BMFTR national roadmap for research infrastructures.

References

[1] A. Pittner, S. Wendt, D. Zopf, A. Dathe, N. Grosse, A. Csaki, W. Fritzsche, O. Stranik: Fabrication of micro-patterned substrates for plasmonic sensing by piezo-dispensing of colloidal nanoparticles. Analytical and Bioanalytical Chemistry 411, 1537-1547 (2019).

[2] Zopf, D.; Pittner, A.; Dathe, A.; Grosse, N.; Csáki, A.; Arstila, K.; Toppari, J. J.; Schott, W.; Dontsov, D.; Uhlrich, G.; Fritzsche, W.; Stranik, O., Plasmonic Nanosensor Array for Multiplexed DNA-based Pathogen Detection. ACS Sensors 2019, *4* (2), 335-343.

[3] S. Kastner, M. Urban, A.-K. Dietel, A. Csaki, W. Fritzsche: Cost-Effective and Robust Multispectral Light-Emitting Diode Device for the Readout of Plasmonic Microarray Sensors. Advanced Photonics Research 2200252 (2023) https://doi.org/10.1002/adpr.202200252

Modeling and Design of Nonlinear Metastructures for All-Optical Modulation and THz Generation

G. Crotti[1,+], U. Arregui Leon[1,+], P. Baldin[1], A. Valladares Y Tacchi[1], A. Schirato[1,2], and G. Della Valle[1,*]

[1]Dipartimento di Fisica, Politecnico di Milano, Italy
[2]Department of Physics and Astronomy, Rice University, Houston (TX), USA
*Corresponding author: giuseppe.dellavalle@polimi.it

***Abstract*— Nonlinear metastructures combining nanoscale electromagnetic resonances and material nonlinearities, offer unprecedented opportunities in photonics. Here, we review our recent results in the field, where finite-element-method numerical analysis is exploited to model and design a variety of nonlinear metastructures, for the ultrafast all-optical control and THz generation.**

***Keywords*— metasurfaces, nanoantennas, hot carriers, difference-frequency generation, terahertz, ultrafast photonics.**

I. Introduction

Photonic nanostructures, including metasurfaces, made of nonlinear materials have attracted increasing interest for the unprecedented possibility of boosting and tailoring the optical nonlinearities of the constituent media. Most research in the field has focused on two main directions, depending on the kind of nonlinearity to be exploited (see for instance, [1-3] and references therein): (i) nonlinearities mediated by photoinduced hot carriers for the all-optical modulation of light; (ii) instantaneous nonlinearities for light generation at the nanoscale.

II. Results and Discussion

Semiconductor metasurfaces have been demonstrated to be all-optically reconfigurable via photogenerated hot carriers for several years [4,5]. However, most works in the field have assumed a photoinduced permittivity modulation which is either homogeneous across the structure, or spatially inhomogeneous in a way that is not actively involved in the reconfiguration process. Here, we report on semiconductor metasurfaces designed to enhance the effect of photoinduced transient spatial inhomogeneities. The key idea is to exploit the symmetries presiding over the optical response of the metastructure and to induce, via photogenerated hot carriers and the subsequent third-order nonlinearity, a transient modulation of these symmetries. We originally introduced the concept by the all-optical modulation of the left-right inversion symmetry in a nonlocal AlGaAs metasurface, leading to efficient and ultrafast (sub-picosecond) modulation of light [6]. More recently, we consider a heterostructure metasurface where the meta-atom includes two nanowires made of AlGaAs, geometrically identical but with different stoichiometric compositions. We theoretically predict the possibility to modulate the discrete translational symmetry of the system, by effectively halving the metasurface periodicity (via photoinduced hot carrier), and thus transiently suppressing the first diffracted order over a relatively broad spectral range.

Second-order processes in nanostructures made of non-centrosymmetric crystals have attracted an increasing interest in the last few years, especially for second harmonic generation (SHG) and difference frequency generation (DFG) at the nanoscale [1,2,7]. DFG in all-dielectric nanoantennas boosted by phonon-polariton resonances has been also proposed for the nonlinear generation of THz radiation from infrared pump pulses [8,9]. Following a multipolar theory approach, we report on a strong influence of the illumination scheme on the DFG process. For example, in <111>-oriented AlGaAs nanopillars an efficient control of the THz radiation pattern is enabled by acting on the polarization state of the single pump in an intrapulse-DFG scheme. When resorting to an interpulse-DFG scenario, it is possible to control the far-field pattern of a Z-cut $LiNbO_3$ nanocylinder by changing from two co-polarized to two cross-polarized infrared pumps, at almost no cost in terms of conversion efficiency.

III. Conclusion

A design strategy based on the concept of transient symmetry modulation has been proposed to exploit hot-carrier mediated third-order nonlinearities in semiconductor metasurfaces. The efficiency of this approach opens new perspectives for the design of high speed all-optically reconfigurable nanophotonic devices.

All-dielectric metastructures can also enable THz generation from infrared pumps with advanced functionalities, such as wide-angle beam steering or nonlinear routing, by simply acting on pump polarization in the DFG process. Extending this analysis to nanoantenna arrays opens the way to all-optically reconfigurable metasurfaces for THz photonics.

ACKNOWLEDGMENTS

[+] These authors contributed equally: G.C., U.A.L.

This work is funded by the European Union− Next Generation EU PNRR − M4C2 I1.1 - PRIN 2022 - Progetto HOTMETA, ID 2022LENW33, CUP:D53D2300229 0006. We also acknowledge the EU's Horizon 2020 METAFAST project under grant agreement no. 899673, and EU's Horizon Europe research and innovation programme under the MSCA PATHWAYS HORIZON-MSCA-2023-PF-GF no. 101153856.

REFERENCES

[1] L. Carletti, M. Gandolfi, D. Rocco, A. Tognazzi, D. de Ceglia, M. A. Vincenti and C. De Angelis, "Reconfigurable nonlinear response of dielectric and semiconductor metasurfaces," Nanophotonics, vol. 10, pp. 4209-4221, 2021.

[2] P. Vabishchevich and Y. I. Kivshar, "Nonlinear photonics with metasurfaces," Photonics Research, vol. 11, pp. B50-B64, 2023.

[3] M. Maiuri, A. Schirato, G. Cerullo and G. Della Valle, "Ultrafast All-Optical Metasurfaces: Challenges and New Frontiers," ACS Photonics, vol. 11, pp. 2888-2905, 2024.

[4] M. R. Shcherbakov, P. P. Vabishchevich, A. S. Shorokhov, K. E. Chong, D.-Y. Choi, I. Staude, et al. "Ultrafast All-Optical Switching with Magnetic Resonances in Nonlinear Dielectric Nanostructures," Nano Letters, vol. 15, pp. 6985-6990, 2015.

[5] G. Della Valle, B. Hopkins, L. Ganzer, T. Stoll, M. Rahmani, S. Longhi, Y. S. Kivshar, C. De Angelis, D. N. Neshev, G. Cerullo, "Nonlinear Anisotropic Dielectric Metasurfaces for Ultrafast Nanophotonics," ACS Photonics, vol. 4, pp. 2129-2136, 2017.

[6] G. Crotti, A. Schirato, O. Pashina, O. Sergaeva, M. Petrov, C. De Angelis, and G. Della Valle, "Ultrafast switching of a metasurface quasi-bound state in the continuum via transient optical symmetry breaking," Light: Science & Applications, vol. 14, 240, 2025.

[7] L. Carletti, A. Locatelli, O. Stepanenko, G. Leo, and C. De Angelis, "Enhanced second-harmonic generation from magnetic resonance in AlGaAs nanoantennas," Optics Express, vol. 20, pp. 26544-26550, 2015.

[8] U. Arregui Leon, D. Rocco, L. Carletti, M. Peccianti, S. Maci, G. Della Valle, and C. De Angelis, "THz-photonics transceivers by all-dielectric phonon-polariton nonlinear nanoantennas," Scientific Reports, vol. 12, 4590, 2022.

[9] U. Arregui Leon, L. Carletti, D. Rocco, C. De Angelis and G. Della Valle, "THz Generation via Optical Rectification in Nanomaterials: Universal Modeling Approach and Effective $\chi^{(2)}$ Description," Laser & Photonics Review, vol. 18, 2300669, 2024.

Plasmon-induced spin selectivity for controlling reaction intermediates in relevant chemical transformations

Karolina Kukrálová[1*], Elena Miliutina[1], Vladislav Buravet[1], Anastasiia Tulupova[1], Yingying Cai[2], Christian Rossner[1,2], Václav Švorčík[1], Oleksiy Lyutakov[1]

[1]Department of Solid State Engineering, UCT Prague, Czech Republic

[2]Leibniz Institute of Polymer Research Dresden, Technische Universität Dresden, Germany
*Corresponding author: kukraloa@vscht.cz

***Abstract*— Chiral-induced spin selectivity (CISS) is a well-known phenomenon where molecular chirality filters electron spins. This lecture proposes Plasmon-Induced Spin Selectivity (PISS) as an electromagnetic analogue. We demonstrate how chiral plasmonic fields align spins during transitions, utilizing this mechanism to drive and control spin-dependent chemical transformations in nanostructured environments.**

***Keywords*— plasmon, chiral, spin-selectivity, water splitting, ammonia production, CO_2 reduction.**

INTRODUCTION

Chiral-induced spin selectivity (CISS) is a well-known phenomenon where the structural asymmetry of chiral molecules acts as a filter for electron spins. As electrons move through these helical or asymmetric frameworks, the interaction between their motion and the molecular electrostatic field favors the transmission of one spin orientation over the other. This effect is widely utilized to improve the efficiency of electrochemical processes, such as water splitting, by suppressing unwanted side reactions. It can be utilized also in the electrochemistry, to enhance efficiency and selectivity of chemical transformations.

Commonly spin polarization is traditionally achieved using magnetic materials and in case of CISS it relies on the spin-orbit coupling of electrons within asymmetric molecular structures. Our recent studies report the observation of spin selectivity induced by chiral plasmonic field. Plasmon-Induced Spin Selectivity (PISS) emerges as a powerful alternative, utilizing chiral plasmonic fields to align electron spins. This mechanism has been proved effective in water splitting, where spin-polarized electrons favor the production of triplet oxygen over undesired hydrogen peroxide. Similar thermodynamic benefits are currently being explored for nitrogen and carbon dioxide reduction. By aligning electron spins, PISS can lower activation barriers and suppress hydrogen evolution. Controlling spin states facilitates the stabilization of key intermediates in these complex multi-electron processes, potentially enabling more efficient pathways toward ammonia synthesis and high-order hydrocarbon production.

I. METHODS

A seed-mediated colloidal method facilitated by a chiral amino acid or peptide was used for the preparation of chiral MeNPs. The 432-helicoid III particles exhibit specific chiral morphology resulting in a high value of g-factor but there are more MeNPs that can be used.

The electrodes combining a redox active layer with AuNPs were prepared by electrodeposition and drop-casting.

Evidence for PISS was established through electrochemical experiments by measuring presence of hydrogen peroxide, ammonia production and creation of C2+ products.

II. RESULTS AND DISCUSSION

Experimental results show:

- Chiral MeNPs were created with a g-factor equal to 0,2 and they were coupled with redox active layers.
- Created systems were used in electrochemical and photoelectrochemical regime for water splitting, nitrogen and carbon dioxide reduction.
- While hydrogen peroxide typically competes as a main product of water splitting, our system demonstrated a significant preference for triplet oxygen formation.
- Plasmon triggering positively affect reaction kinetics (observed for both chiral and achiral MeNPs).
- Critically, performance metrics under illumination substantially outperformed those in dark, indicating that plasmonic excitation actively mediates spin-alignment.
- Utilization of chiral plasmon apparently affects reaction selectivity and effectivity in the case of nitrogen and CO_2 reduction.

III. Conclusion

We have demonstrated an apparent impact of illumination i.e. plasmon induced spin selectivity on the amount of reaction products in the case of relevant electrochemical transformations. Light-driven enhancement confirms the efficacy of PISS in modulating reaction pathways, providing a robust experimental foundation for utilizing chiral plasmonic nanostructures to bypass conventional thermodynamic barriers in multi-electron transfer processes.

Acknowledgments

This work was supported by This work was supported by the GACR under project 26-21905S and by the Project OP JAK_Amulet, No CZ.02.01.01/00/22_008/0004558, of the Ministry of Education, Youth and Sports, which is cofunded by the European Union.

References

[1] B. P. Bloom, Y. Paltiel, R. Naaman and D. H. Waldeck, "Chiral Induced Spin Selectivity," Chemical Reviews, vol. 124, pp. 1950–1991, 2024.

[2] S. W. Im, R. M. Kim, J. H. Han, I. H. Ha, H. Lee, H. Ahn, E. Jo and K. T. Nam, "Synthesis of chiral gold helicoid nanoparticles using glutathione," Nature Protocols, vol. 20, pp. 1082–1096, 2025.

[3] A. Tulupova et al., "Light Entrapment by Plasmonic Chiral Lock for Enhancement of 2D Flakes Catalytic Activity," ACS Applied Materials & Interfaces, vol. 17, pp. 32553–32565, 2025.

[4] D. Zabelin et al., "Chiral 2D flakes with single atoms inclusion for spin-controlled oxygen evolution," Journal of Power Sources, vol. 641, 236839, 2025.

EC-SERS - a combination of electrochemistry and Raman spectroscopy for selective detection of organic contaminants in complex water matrices

Jana Rosenkranzova[1,*], Elena Miliutina[1], Sarka Zapletalova[1], Vasilii Burtsev[1], Andreii Trelin[1], Vaclav Svorcik[1], Oleksiy Lyutakov[1]

[1]Department of Solid State Engineering, University of Chemistry and Technology, 166 28 Prague, Czech Republic

*Corresponding author: rosenkrj@vscht.cz

***Abstract*— Pharmaceutical contaminants in wastewater are a growing environmental concern. Electrochemical surface-enhanced Raman spectroscopy (EC-SERS) with mesoporous gold sensitively detects trace organics by electrochemically controlling analyte selective accumulation on plasmon active surface, enhancing spectral intensity, and reducing matrix interference on SERS-active nanostructures. Several model pharmaceutical pollutants to assess analytical performance.**

***Keywords* — electrochemical surface-enhanced Raman spectroscopy, mesoporous gold, wastewater, pharmaceutical pollutants, trace detection, SERS, EC-SERS, environmental monitoring.**

I. Introduction

The rapid and reliable detection of trace amounts of hazardous organic compounds in complex media remains a major challenge in modern analytical chemistry, particularly in environmental analysis. This problem is especially important for wastewater, where pharmaceuticals and other organic micropollutants are often present at very low concentrations in the presence of numerous interfering substances [1]. This matrix complexity significantly limits the applicability of conventional analytical methods and creates a demand for highly sensitive, selective, and reproducible analytical approaches [2].

In this context, EC-SERS represents a highly promising strategy for trace-level detection [3]. By combining the molecular specificity of Raman spectroscopy with the signal amplification provided by plasmonic nanostructured surfaces and the controllability of electrochemical techniques, EC-SERS enables enhanced analyte adsorption, improved signal reproducibility, and selective detection in complex media [3]. The application of an electrochemical potential can promote the preconcentration of target molecules on the substrate surface, influence their orientation and interaction with the metal, and help suppress background interference [4]. These features make EC-SERS particularly attractive for the analysis of wastewater samples containing trace organic contaminants.

This work aimed to develop and validate an EC-SERS method based on mesoporous gold substrates for the detection of trace analytes (pharmaceutical contaminants) in wastewater. Special attention was paid to diclofenac, carbamazepine, and ibuprofen, which were selected as model analytes to evaluate the analytical performance of the proposed approach. These compounds are widely recognised as important pharmaceutical pollutants due to their extensive use, persistence in wastewater, and potential environmental impact [5]. The study focused on assessing the sensitivity, reproducibility and applicability of the mesoporous gold-based EC-SERS platform developed for the determination of these pharmaceutical contaminants in complex wastewater matrices.

II. Methods

Mesoporous gold was used as the SERS-active substrate and working electrode for EC-SERS, fabricated following Lim et al. [6]. PS-b-PEO (10 mg) was dissolved in 3 mL THF, heated to 40°C, and stirred for 30 min, then 1.5 mL absolute ethanol, 1 mL 40 mM HAuCl4, and 2.5 mL deionized water were added dropwise and stirred for 1 h. This micellar solution was used for gold electrodeposition by chronoamperometry (Edc = −0.5 V, t = 1200 s) in a three-electrode cell (FTO glass working electrode, Ag/AgCl reference, platinum grid counter). After deposition, substrates were rinsed seven times with THF and deionized water to remove residual micelles.

The mesoporous gold layer was characterized by UV–Vis absorption spectroscopy (Lambda 850, UV WinLab™), SEM and EDX (LYRA3 GMU, Tescan, 10 kV, 600 pA), and XRD (Empyrean, Malvern Panalytical, Cu Kα, 8.04 keV, λ = 1.54151 Å, 45 kV, 30 mA). Surface morphology and layer thickness were additionally evaluated by AFM scratch profiling (Icon, Bruker, peak force tapping mode).

The simulated wastewater was prepared using the composition from Aiyuk and Verstraete [7]. The prepared solution was diluted ten times prior to use.

EC-SERS measurements were conducted using a closed electrochemical flow cell positioned within a DXR3 Raman Microscope (Thermo Fisher Scientific), as illustrated in Fig. 1B. Spectral acquisition was performed with a standard 10× objective, a 25 μm slit aperture, an exposure time of 10 s, and signal averaging over 10 accumulations. The laser power was

adjusted in the range of 0.5–10 mW, employing excitation wavelengths of 785 nm and 532 nm. Subsequently, the optimal deposition potential for EC-SERS was systematically evaluated within a potential window extending from open-circuit conditions (no externally applied potential) up to 0.8 V.

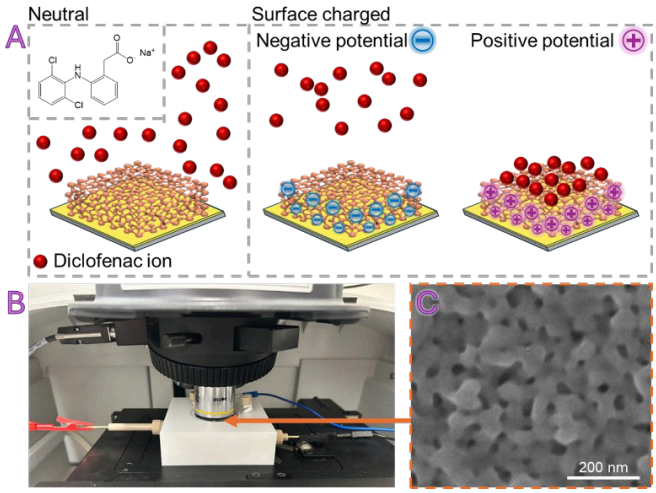

Fig. 1: (A) Schematic of the sensing mechanism via plasmon-enhanced EC-SERS on mesoporous gold; (B) electrochemical cell inside Raman spectrometer; (C) SEM of mesoporous gold (working electrode).

III. Results and Discussion

The EC-SERS method regulates the spatial distribution of analyte molecules near a SERS-active surface by applying an external electrode potential. Diclofenac, used as a model compound, is mainly anionic in solution, so its interfacial behaviour at the electrode is dominated by electrostatic interactions. Without an applied potential, diclofenac is randomly distributed in the bulk, and its interaction with the SERS-active surface depends mainly on diffusion and weak nonspecific adsorption. As a result, the analyte concentration near the surface, and thus the SERS signal intensity, remain relatively low.

When a positive potential is applied, the electrode surface becomes positively charged, electrostatically attracting negatively charged diclofenac anions to the near-electrode region. This leads to their accumulation in the electrical double layer, decreases their average distance from the metal surface, increases their probability of entering SERS-active "hot spots," and produces a strong enhancement of the Raman signal.

When a negative potential is applied, the electrode becomes negatively charged and repels diclofenac anions. This lowers the analyte concentration near the surface, suppresses adsorption, and decreases the fraction of molecules in SERS-active regions, reducing the SERS signal intensity. This concept was used for substrate regeneration, allowing the same substrate to be reused multiple times without a substantial decrease in signal. These processes are illustrated schematically in Fig. 1A.

Mesoporous gold served as the working electrode in the EC-SERS platform due to its high surface area, well-defined porosity, and excellent conductivity. These features provide many active sites for analyte adsorption, promote SERS hot spot formation, and enable effective electrochemical modulation at the electrode–electrolyte interface [8]. Its tuneable pore morphology is an additional advantage: in this study, pores of 40–60 nm may restrict penetration of larger matrix components into the inner enhancement-active regions while still allowing smaller analyte molecules to reach the surface.

Diclofenac, ibuprofen, and carbamazepine were studied as model pharmaceutical contaminants in pure water and wastewater. Diclofenac and ibuprofen were reliably detected down to 10^{-6} mol L^{-1}, whereas carbamazepine gave a much weaker EC-SERS response under the same conditions. This difference arises from their acid–base properties: at pH ~5, diclofenac and ibuprofen are mainly anionic and are strongly attracted to the positively polarised electrode, leading to interfacial preconcentration and stronger signals. In contrast, carbamazepine remains mostly neutral at this pH, experiences little electrostatic attraction, accumulates less at the interface, and therefore shows a lower EC-SERS signal.

This behaviour was clearly observed in pure water, where diclofenac and ibuprofen showed strong signals at low concentrations, while carbamazepine remained much less detectable. In wastewater, conditions are more complex because of a highly heterogeneous matrix containing many potentially interfering constituents, including natural organic matter, proteins, humic and fulvic substances, surfactants, inorganic salts, and various dissolved organic and inorganic species. At pH ~5, some of these components—especially humic and fulvic substances—carry a net negative charge and compete with the target analytes for adsorption at the positively polarised electrode surface. In addition, larger macromolecular and colloidal or aggregated species can block active surface sites or hinder mass transport to the most enhancement-effective regions of the electrode.

Mesoporous gold offers a key advantage: its tuneable 40–60 nm pore size can be adjusted during synthesis to restrict larger matrix components from reaching internal SERS hot spots, while allowing smaller analyte molecules to diffuse in and interact with the active regions. Thus, mesoporous gold serves as a conductive working electrode, a SERS-active substrate, and a structurally selective interfacial layer that improves analyte detection in complex media. The same electrode can be used for up to six consecutive measurements without noticeable performance loss, demonstrating its stability and suitability for wastewater analysis.

IV. Conclusion

In conclusion, a mesoporous-gold-based EC-SERS platform was shown to detect low concentrations of pharmaceutical organic analytes in wastewater. Diclofenac, carbamazepine, and ibuprofen were used as model compounds to evaluate performance in the presence of environmentally relevant contaminants. The combination of electrochemical control with mesoporous gold substrates enabled sensitive, reproducible, and reliable detection in complex aqueous matrices. The substrate also retained its performance over at least six measurement cycles, demonstrating high reusability.

Acknowledgments

The authors acknowledge the assistance provided by the Advanced Multiscale Materials for Key EnablingTechnologies project, supported by the Ministry of Education, Youth, and Sports of the Czech Republic. Project No. CZ.02.01.01/00/22_008/0004558, Co-funded by the European Union.

References

[1] P.M. Choi, B.J. Tscharke, E. Donner, J.W. O'Brien, S.C. Grant, S.L. Kaserzon, R. Mackie, E. O'Malley, N.D. Crosbie, K.V. Thomas, J.F. Mueller, Wastewater-based epidemiology biomarkers: Past, present and future, TrAC Trends Anal. Chem. 105 (2018) 453–469. https://doi.org/10.1016/j.trac.2018.06.004.

[2] N. Sims, B. Kasprzyk-Hordern, Future perspectives of wastewater-based epidemiology: Monitoring infectious disease spread and resistance to the community level, Environ. Int. 139 (2020) 105689. https://doi.org/10.1016/j.envint.2020.105689.

[3] C.L. Brosseau, A. Colina, J.V. Perales-Rondon, A.J. Wilson, P.B. Joshi, B. Ren, X. Wang, Electrochemical surface-enhanced Raman spectroscopy, Nat. Rev. Methods Primer 3 (2023) 79. https://doi.org/10.1038/s43586-023-00263-6.

[4] X. Tang, R. Wen, C. Ji, J. Wei, Y. Han, L. Wu, Electrochemical potential enhanced EC-SERS sensor for sensitive and label-free detection of acetamiprid, Microchem. J. 206 (2024) 111524. https://doi.org/10.1016/j.microc.2024.111524.

[5] E.S. da Silva, R.W. Becker, M.C.V.M. Starling, E.C. Machado, A.P.V. Reis, A.P. Aguilar, T.A. de O. Mendes, C. Sirtori, C.C. Amorim, An integrated analysis of the use and potential risks of pharmaceutical drugs in hospital wastewater: Consumption and occurrence by suspect screening analysis, and antibiotic resistance, Sci. Total Environ. 973 (2025) 179132. https://doi.org/10.1016/j.scitotenv.2025.179132.

[6] H. Lim, K. Kani, J. Henzie, T. Nagaura, A.S. Nugraha, M. Iqbal, Y.S. Ok, M.S.A. Hossain, Y. Bando, K.C.W. Wu, H.-J. Kim, A.E. Rowan, J. Na, Y. Yamauchi, A universal approach for the synthesis of mesoporous gold, palladium and platinum films for applications in electrocatalysis, Nat. Protoc. 15 (2020) 2980–3008. https://doi.org/10.1038/s41596-020-0359-8.

[7] S. Aiyuk, W. Verstraete, Sedimentological evolution in an UASB treating SYNTHES, a new representative synthetic sewage, at low loading rates, Bioresour. Technol. 93 (2004) 269–278. https://doi.org/10.1016/j.biortech.2003.11.006.

[8] M.A. Correa-Duarte, I.B. Becerril-Castro, R.A. Alvarez-Puebla, The Role of Porosity in SERS, Adv. Opt. Mater. 13 (2025) e01376. https://doi.org/10.1002/adom.202501376.

Advancements in laser photo-acoustic spectroscopy towards imaging of absorption and chirality in nanostructures and metamaterials

Emilija Petronijevic[1,*], Claudia Skubisz[1], Grigore Leahu[1], Concita Sibilia[1], Roberto Li Voti[1], Alessandro Belardini[1]

[1]Department SBAI, Sapienza University of Rome, Italy
*Corresponding author: emilija.petronijevic@uniroma1.it

***Abstract*— We use photo-acoustic effect do reveal scattering-free absorption signals at the nanoscale. We present microscope-enriched laser photo-acoustic spectroscopy with full tunability of a conventional chiro-optical set-up.**

***Keywords*— metamaterials, plasmonics, nano-photonics, photo-acoustic spectroscopy.**

I. Introduction

Photo-thermal techniques are still unconventional, but extremely useful in characterization of absorbed light at the nanoscale [1-3]. Direct characterization of absorption is highly important in nano-photonics and plasmonics, where nanostructured media can be tailored to resonantly enhance absorption. Moreover, characterizing different absorption of left and right circular polarizations, i.e. circular dichroism (CD), is important for the field of chiral nanophotonics.

We apply photo-acoustic spectroscopy (PAS) to convert absorption-induced periodic heating into an acoustic signal, thus enabling contactless, scattering-free, non-destructive, low-postprocessing absorption characterization.

II. Results and Discussion

We enrich PAS set-up with multiple tunable components present in conventional chiro-optical set-ups. The laser is widely tunable in the near-IR and visible range, in power, polarization, spot-size, position on the sample, incidence angle. Moreover, in PAS, tunable modulation frequency could potentially allow for depth scanning. We successfully apply it to measure absorption and chirality in different nanostructures and metamaterials [4-6].

III. Conclusion

We believe that PAS is yet to become attractive for mapping chirality at the nanoscale with multiple degrees of freedom.

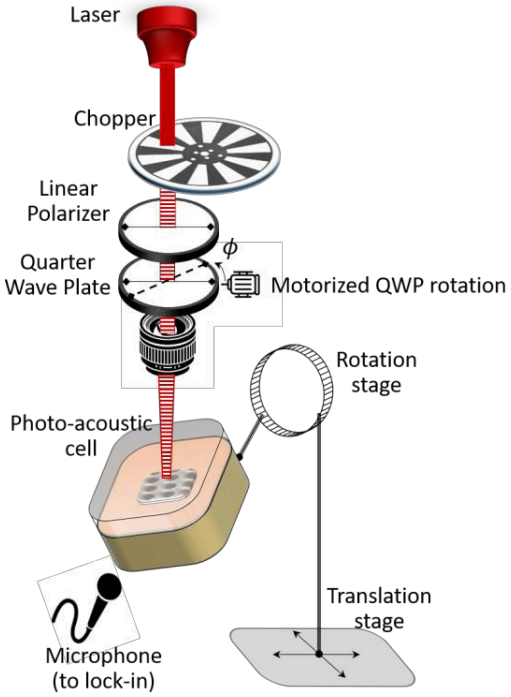

Figure 1 Laser photo-acoustic spectroscopy set-up.

References

[1] P. Spaeth et al., Photothermal circular dichroism of single nanoparticles rejecting linear dichroism by dual modulation, ACS Nano 15(10), 16277–16285 (2021).
[2] E. Petronijevic et al., Nanostructured materials for circular dichroism and chirality at the nanoscale: towards unconventional characterization [Invited], Opt. Mater. Express 12(7), 2426-2937 (2022).
[3] G. Leahu et al., Diffracted Beams from Metasurfaces: High Chiral Detectivity by Photothermal Deflection Technique, Adv. Opt. Mater. 9, 2100670 (2021).
[4] E. Petronijevic et al., Listening to nanostructures' absorption with many degrees of freedom: widely tunable photo-acoustic characterization, Eur. Phys. J. Plus 140-613 (2025).
[5] C. Skubisz et al., Photo-acoustic technique with widely tuneable laser: metasurface circular dichroism response, J. Eur. Opt. Society-Rapid Publ. 20, 1 (2024).
[6] E. Petronijevic et al., Photo-acoustic spectroscopy detects nanostructures against resonant and absorbing substrates, J. Eur. Opt. Society-Rapid Publ. 21, 49 (2025).

Automated computation on AI-designed all-optical Boolean microprocessors by an interfacial robot driving a non-linear optical bench.

Léo Martin,[1 *] Alice Nyaga,[2] Fayçal Houssaini,[1] Amine Khitous,[1] Nicolas Gros,[3] Aurélie Bertaux,[3] Ouassila Narsis Labbani,[3] Gérard Colas des Francs,[1] Christophe Nicolle,[3] Alexandre Bouhelier,[1] Abdenbi Mohand-Ousaid,[2] Erik Dujardin[1 *]

[1] Laboratoire Interdisciplinaire Carnot de Bourgogne (ICB), Université Bourgogne Europe CNRS UMR 6303, 21000 Dijon, France.

[2] FEMTO-ST Institute, AS2M, Université M. et L. Pasteur, 25000 Besançon, 25000, France.

[3] Connaissances et Intelligence Artificielle Distribuée (CIAD), Université Bourgogne Europe ER 7533, 21000 Dijon, France.

*Corresponding authors: Leo_Martin@etu.ube.fr, erik.dujardin@cnrs.fr

***Abstract* — We demonstrate all-optical Boolean computing with an interfacial robot, BOTAI, that autonomously drives a multi-beam non-linear optical setup. The system interprets operating instructions from a hybrid artificial intelligence to position, encode and time fs-pulsed laser beams carrying the input Boolean operands onto a single 2D plasmonic microcavity and acquires the non-linear photoluminescence response that is processed in the Boolean computation result. BOTAI demonstrates the fully automated Boolean logic operations with sub-100 nm positioning accuracy.**

***Keywords* — plasmonics, non-linear optics, optical computing, robotics.**

I. Introduction

All-optical arithmetic and logic units (ALUs) represent a promising pathway toward ultrafast and energy-efficient computing. We have recently demonstrated that two-dimensional plasmonic cavities carved from ultrathin crystalline gold microplates can operate as reconfigurable all-optical ALUs, already achieving basic logic gate operations as well as a 1-bit full-adder [1-3]. To optimize their performance, we are developing a hybrid artificial intelligence (HAI) framework that predicts optimal cavity geometries and excitation parameters [4].

Experimental validation of HAI-optimized structures demands ultra-precise positioning, fast polarization flipping and temporal synchronization of the input fs-pulsed beams, which become increasingly challenging for human operators as system complexity grows. Hence, we introduce BOTAI, an interfacial robot that autonomously drives our two-beam optical bench with sub-pixel accuracy. This system establishes the foundation for scaling to N-bit ALU processors with $N \geq 2$, where manual operation becomes impractical and automation is essential for exploring complex Boolean operations.

II. Methods

Principle of single cavity All-Optical ALU

The Boolean ALU is a planar polygonal plasmonic structure (~3 × 2 µm²) nanofabricated into crystalline gold microflakes deposited on a transparent substrate. Two synchronized femtosecond laser beams (810 nm, 140 fs pulses, 80 MHz) are focused onto designated input ports on the structure perimeter. Logical input bits are encoded as linear polarization states, while the plasmonic response is controlled by adjusting the inter-pulse temporal delay, modulating the interference between excited surface plasmon modes. Since the absolute phase offset varies between experiments, the measurement protocol scans the full 2π phase range while recording the output observable encoded in non-linear photoluminescence (NPL) maps. This provides complete optical responses for all relative phase shifts. The HAI framework determines the ALU geometry and optimizes excitation conditions - input port coordinates, polarization states encoding "0" and "1" and the relative phase shift - while simulating the optical response and ensuring implementation of targeted arithmetic and logic functions.

Optical Setup

Figure 1 illustrates the dual-beam coherent excitation setup.

The laser output is split into two independent paths with equal intensity. Beam 1 is focused directly onto the first input port, while Beam 2 passes through a motorized delay line before being steered to the second input port. Both beams are focused through a 100× objective (N.A. 1.49) to approximately 300 nm diameter spots with 15-20 mJ/cm² fluence. The resulting NPL is filtered via a dichroic beam splitter and recorded as 2D spatial maps on an EMCCD camera.

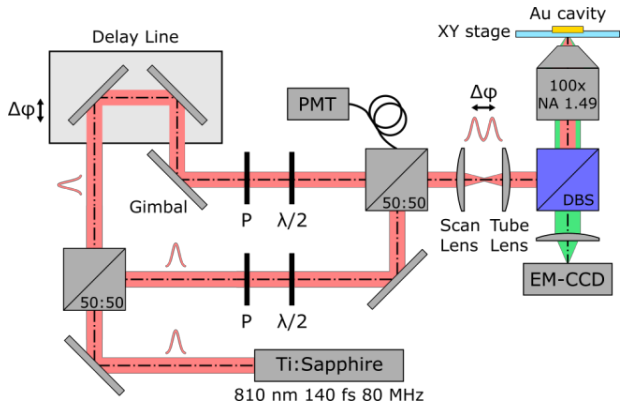

Fig. 1. Dual-beam optical setup for coherent excitation of the 2D plasmonic ALU cavities

Robotic Control and Automation

The BOTAI robot autonomously controls the experimental setup through a Python-programmed interface managing seven motorized components: Andor Luca EMCCD camera (structure recognition and NPL acquisition), Mad City Labs NanoDrive XY stage (sub-100 nm sample positioning), Newport Picomotor 8742 gimbal (two-axis beam steering), Newport DL125 delay line (pulse phase-shift modulation), Thorlabs K-Cube polarizers ×2 (Boolean input encoding), and Zurich Instruments UHF lock-in amplifier (phase monitoring and camera fire signal acquisition). BOTAI interprets optimal measurement parameters - targets structure geometry, input port locations and polarization angles encoding "0" and "1" - and autonomously executes the complete measurement sequence.

Computer Vision for Structure and Beam Detection

Automatic structure localization employs Otsu thresholding on brightfield images, followed by morphological filtering and contour extraction. Candidate structures are filtered by area and ranked via Hu moment shape matching against HAI reference geometry. The best candidate undergoes polygon alignment optimization maximizing intersection area between reference and detected contours. Critical corrections account for OpenCV's pixel-corner convention and systematic detection biases.

Laser fluorescence spot detection uses intensity thresholding, Gaussian blur, and mean position calculation of maximum-valued pixels, achieving sub-pixel accuracy. A fluorescence-to-810 nm offset correction is applied to determine the incident focus spot position.

Closed-Loop Positioning

The gimbal alignment positions Beam 2 to port I2 with respect to port I1 location through iterative error minimization (Δ = target - spot), converting pixel errors to motor steps via calibrated proportional coefficients. Iteration continues until $|\Delta| < 0.5$ pixel, with final verification via 5-frame averaging.

Once both input beams are positioned, XY stage alignment brings port I1 of the cavity to beam 1 position using the same proportional correction method, converging within 6 iterations maximum. The port I2 of the cavity is concomitantly brought to beam 2.

Automated Measurement Protocol

Upon operator selection of the target HAI-designed structure,[5] BOTAI executes the following autonomous sequence:

1. Beam 1 localization by centroid detection of laser's residual fluorescence focal spot
2. Structure detection: Computer vision identifies and localizes the selected geometry on the camera field of view
3. Beam 2 positioning: closed-loop gimbal directs the second excitation beam to port I2 relative to Beam 1
4. Structure alignment: closed-loop XY stage positions the structure such that ports I1 and I2 coincide with Beams 1 and 2 respectively
5. Optical contact search: Two-phase delay line scan (coarse then fine) determines pulses temporal overlap
6. Sequential acquisition, for each input Boolean configuration of the 2-input ALU (00, 01, 10, 11):
   a. Polarizer angles setup
   b. Structure position verification
   c. Delay Line scan starting from optical contact
   d. NPL map recording

When the output locations (for example the AND and XOR function corresponding to the CARRY and SUM of the 1-bit Full Adder) are known, direct readout of the computation result is possible. For newly designed cavities, the Boolean gate locations are automatically provided as described in [2].

III. Results and Discussion

Automated Positioning and Measurements

Closed-loop control of the XY stage and gimbal beam steering converges within a maximum of six iterations, achieving sub-pixel accuracy better than 0.5 pixel (< 25 nm) and maintaining positional stability throughout the complete four-configuration measurement sequence.

Applied to a HAI-designed plasmonic cavity (~3 × 2 µm gold monocrystal), this autonomous procedure successfully executes the full measurement protocol and enables correct simultaneous realization of XOR and AND logic gates (i.e. SUM and CARRY of a 1-bit full adder), confirming accurate beam positioning on input ports I1 and I2. This automated procedure demonstrates repeatability exceeding that achievable by manual

alignment performed by a human operator.

Limitations and Perspectives

The system currently lacks adaptive beam positioning based on NPL response. A human operator can modulate beam positions according to real-time NPL feedback, whereas BOTAI executes fixed HAI instructions. Implementation of an additional feedback loop analyzing NPL response quality could enable adaptive beam optimization.

The architecture facilitates future expansion to 4-beam configurations required for more complex 2×2-bit ALUs with 3-bit outputs ("11"+"11" = "110"), the optical setup is currently under construction.

IV. Conclusion

We have demonstrated autonomous robotic control of a complex non-linear optical setup for all-optical Boolean computing. The BOTAI system successfully interprets HAI-generated instructions, performs sub-pixel beam and structure positioning, and acquires complete NPL characterization datasets. This robot-AI integration enables systematic exploration of plasmonic computing architectures and paves the way for increased Boolean complexity through multi-beam configurations. Future developments will incorporate adaptive positioning strategies and extend to $2N \geq 4$ input beams for advanced arithmetic operations.

Acknowledgments

This work has been partially funded by the French Agence Nationale de la Recherche (ANR-20-CE24−0001 DALHAI, ANR-25-TSIA-001 CAIPOP, ANR-25-CE24-7238 POMMARD), ISITE-BFC ANR-15-IDEX-0003), the REMONTADA project of the EIPHI Graduate School (ANR-17-EURE-0002). The authors also acknowledge the support of CNRS MITI (Project BOTAI 2023-24). Device nanofabrication and characterization was performed at the technological platforms SMARTLIGHT, ARCEN Carnot at ICB and MIMENTO at FEMTO-ST under program Investment for the Future (ANR-21-ESRE- 0040), the Région de Bourgogne Franche-Comté, the CNRS, and the French Renatech+ network.

References

[1] Upkar Kumar *et al.*, “Interconnect-Free Multibit Arithmetic and Logic Unit in a Single Reconfigurable 3 μm2 Plasmonic Cavity”, ACS Nano 2021, 15, 13351−13359

[2] F. Dell'Ova, et al., " Coherent two-beam steering of delocalized nonlinear photoluminescence in a plasmon cavity", Opt Express 2022 30, 10, 17517-17528

[3] Florian Dell’Ova *et al.*, “Compact Implementation of a 1-Bit Adder by Coherent 2,-Beam Excitation of a Single Plasmonic Cavity”, ACS Photonics 2024, 11, 2, 752–761

[4] Ouassila Labbani Narsis, et al., "From Human Cognitive Expertise to Ontological Formalization: Bridging the Knowledge Gap for Nanophotonic Calculator Design and Simulation." Joint Ontology Workshops (JOWO) - 14th International Conference on Formal Ontology in Information Systems (FOIS 2024), Jul 2024, Enschede, Netherlands. (hal-05411152)

[5] Manvendra Janmaijaya, et al., "ESPLANADE: Efficient Simulation of Plasmonic Logic and Arithmetic NAnoDEvice", Submitted for publication, hal-05411342

SYMPOSIUM 2

New trends in nanophotonics and advanced materials

149 contributions · pp. 243–460

Engineering Electromagnetic Descriptors at the Nanoscale with Plasmonic Nanoantennas

Mario Zapata-Herrera [1, *] and Javier Aizpurua[1,2,3]

[1]Donostia International Physics Center (DIPC),
Paseo Manuel de Lardizabal 4 20018, Donostia-San Sebastián, Spain
[2]IKERBASQUE, Basque Foundation for Science, 48009 Bilbao, Spain
[3]Department of Electricity and Electronics,
University of the Basque Country, 48940 Leioa, Spain
*Corresponding author: mzapatah@gmail.com

***Abstract*— We present a unified framework for engineering electromagnetic descriptors in plasmonic nanoantennas to control nanoscale light–matter interactions. Full-wave simulations show how geometry, symmetry, and lattice coupling tune LDOS, chirality, and decay channels. Nanogap cavities and surface-lattice-resonant arrays enable tailored emission, polarization selectivity, and vibrational sensing, validated experimentally.**

***Keywords*— Plasmonic nanoantennas, Surface lattice resonances, SEIRA, FEM, chirality.**

Plasmonic nanoantennas enable the engineering of light-matter interactions at the nanoscale by reshaping electromagnetic boundary conditions and achieving subwavelength confinement. Their capability to localize and redistribute electromagnetic energy provides controlled access to a broad variety of optical observables. These electromagnetic descriptors constitute a quantitative framework for describing nanophotonic systems, supporting prediction, comparison between architectures, and experimental design. Here, we present a computational strategy based on full-wave three-dimensional finite-element simulations in COMSOL Multiphysics to engineer key quantities such as the local density of optical states (LDOS), optical chirality density, radiative and non-radiative decay rates, field enhancement factors, and lattice-mediated coupling for realistic applications.

Particularly, we show that nanogap cavities yield strong Purcell enhancement, while symmetry-broken and intrinsically chiral nanoantennas produce polarization-selective and circular dichroic responses. In periodic arrays, surface lattice resonances (SLRs) induce spectral narrowing and collective enhancement, improving linewidth control and sensing figure of merit (FOM) [1].

These collective modes can also mediate molecular chirality transfer, enabling tunable circular dichroism in achiral nanoparticle lattices through controlled coupling with chiral molecules [2]. At the near-field level, gap-confined fields and polarization-dependent modal distributions govern hot-spot localization and plasmon-driven chemistry. Such descriptor-level control underpins enhanced refractometric sensing in nanoparticle arrays [1], SEIRA-based detection of molecular vibrational fingerprints in resonant infrared nanoantennas [3], and polarization- resolved super-resolution SERS imaging in gap-engineered systems [4].

Together, these results establish a descriptor-driven approach to nanophotonics in which geometry, symmetry, and collective effects are systematically engineered to tailor emission, chirality, and vibrational responses. The proposed models not only guide device design but also are validated by experimental realizations, reinforcing their predictive capability for advanced nanophotonic materials.

Acknowledgments

This work has been partially funded by the Basque Government under the research project ELKARTEK KK-2022/00041 and the Guipuzkoa Quantum program's 2022 call under the research project QUANTUM SEIRA (2022-QUAN-000034-01).

References

[1] U. F. S. Roggero, et al. Optics Express 33, 14: 30328-30341, 2025.
[2] E. Goerlitzer, et al. ACS Photonics 10, 6: 1821–1831, 2023.
[3] S. Merino, et al. Spectro. Act Part A, 345, 15, 126772, 2026.
[4] D. Shoup,et. al., Anal. Chem. 96, 28, 11422–11429, 2024.

Can Surface Plasmon Carry Heat?

Jungmin Nam[1], Kuk Hyun Yun[1], Bong Jae Lee[1,*]

[1]Department of Mechanical Engineering, KAIST, South Korea
*Corresponding author: bongjae.lee@kaist.ac.kr

***Abstract*—This presentation outlines our recent endeavors in developing an efficient heat spreader made of a nanoscale metallic film, beginning with experimental investigations to demonstrate in-plane heat transfer along a thin metal film via surface plasmon.**

***Keywords*— surface plasmon, in-plane heat transfer, thin metal film.**

I. Introduction

The thermal conductivity of nanoscale thin films is significantly constrained by the classical size effect, occurring when film thickness becomes comparable to or smaller than the mean free path of primary heat carriers such as phonons and electrons. This reduction in thermal transport efficiency hinders effective heat dissipation from localized hot spots, thereby compromising the performance and reliability of highly integrated microelectronic devices. As traditional thermal management techniques reach their physical limits, there is a critical need for advanced strategies rooted in a fundamental understanding of extreme-scale heat transfer phenomena

II. Results and Discussion

In 2023, a novel heat transfer mechanism was identified involving surface plasmon polaritons (SPPs) generated at the interfaces of thin metallic films. These electromagnetic surface waves, which couple photons with free electrons, can achieve propagation lengths extending over several centimeters in the mid-infrared regime. Initial investigations demonstrated that SPPs can enhance the in-plane thermal conductivity of a 100 nm Ti film by approximately 25% [1].

Subsequent research focused on noble metals, specifically Au and Ag thin films supported by SiO_2 substrates. This work emphasized the necessity of incorporating thickness-dependent permittivity to account for electron-boundary scattering. Results indicated that such size effects reduce predicted plasmon thermal conductivity by approximately 30% compared to bulk-property models [2]. For these systems, an optimal thickness of 20 nm was identified to maximize SPP-mediated transport when utilizing a 10 nm Ti adhesive layer.

To determine the global conditions for maximum enhancement, a comparative analysis across various metals (Al, Ag, Au, Cu, and Pt) was conducted [3]. This study established that metals characterized by high plasma frequencies and low damping coefficients provide superior channels for plasmonic heat transfer.

Finally, numerical validation confirmed that while different mathematical approaches (complex-β vs. complex-ω) yield different local propagation lengths, the predicted overall thermal conductivity remains consistent, ensuring the robustness of these theoretical models [4].

III. Conclusion

This research establishes a comprehensive theoretical and experimental framework for utilizing surface plasmon polaritons as a primary heat dissipation channel in supported thin films. By optimizing material selection and film geometry, SPP-mediated heat transfer will offer a scalable and effective solution for mitigating thermal management challenges in next-generation microelectronics.

Acknowledgments

This work was supported by the National Research Foundation of Korea (NRF) grant funded by the Korea government (MSIT) (No. RS2024-00442068).

References

[1] D. Kim, S. Choi, J. Cho, M. Lim, and B.J. Lee, "Boosting Thermal Conductivity by Surface Plasmon Polaritons Propagating along a Thin Ti Film," Physical Review Letters, 130, 176302, 2023.

[2] D. Kim, J. Nam, and B.J. Lee, "Plasmon Thermal Conductivity of Thin Au and Ag Films," Physical Review B. 108, 205418, 2023.

[3] K.H. Yun, D. Kim, and B.J. Lee, "Maximum Plasmon Thermal Conductivity of a Thin Metal Film," Physical Review B, 109, 165415, 2024.

[4] K.H. Yun and B.J. Lee, "Impact of Surface Plasmon Dispersion Relations on Plasmon Thermal Conductivity in Thin Films: A Complex- β and Complex-ω Perspective," International Communications in Heat and Mass Transfer, 172, 110542, 2026.

Polarization-Programmable Optics using Chiral Dielectric Metastructures

Soo Jin Kim*

School of Electrical Engineering, Korea University, Seoul, Republic of Korea
*Corresponding author: kimsjku@korea.ac.kr

***Abstract*— We demonstrate symmetry broken dielectric metasurfaces that leverage the nonlocal guided mode resonances to enable efficient spin selective polarization control and chirality resolved detection. Moreover, we propose metastructures which produce globally biased optical chirality in the near and far field regime, supported by coupled mode design rules.**

***Keywords*— dielectric metasurfaces, nonlocal resonances, chiral optics, polarimetry, Stokes parameters.**

I. Introduction

Chiral meta optics afford the spin dependent manipulation and sensing of light in a compact planar film, with applications in polarization resolved imaging, molecular detection, and integrated photonics. However, there remain several challenging issues in realizing strong chirality in a single layered dielectric metastructure. For example, strong intrinsic chirality often relies on three-dimensional geometry or loss engineering, and realizing a perfectly planar intrinsic chiral metastructure still remains elusive. Here we exploit symmetry breaking along with collective guided mode resonances to realize efficient planar intrinsic chirality and various chiroptical functions including the spin selective polarization control and chirality resolved detection. Additionally, we leverage the nonlocal resonances in periodic dielectric arrays to offer an ability to enhance chiral light matter interaction and produce globally biased optical chirality in the near and far field regime.

II. Results and Discussion

We demonstrate chirality-resolved polarization meta-optics using a symmetry-broken dielectric metasurface in which the meta-atoms are arranged in a periodic array that supports a nonlocal guided-mode resonance. In the operating spectral range, the optimal coupling of local and nonlocal resonances provides steep dispersive phase control and enhanced polarization mixing, allowing efficient manipulation of phase and wavefront together with reconfigurable conversion between orthogonally polarized components. As a result, the handedness of incident circular polarization is converted into distinguishable output polarization states, enabling chirality-resolved generation in a compact single-layer metastructure.

Using the spin-dependent polarization response, we further design a practical polarimetric detection by calibrating the relative amplitudes and phases of the transmitted polarization channels. This optimization enables discrimination of left- and right-handed circular polarization and supports Stokes-parameter retrieval without bulky free-space optics. Based on this, we investigate how symmetry breaking governs the origin of chirality by comparing in-plane and out-of-plane perturbations. In-plane asymmetry primarily produces extrinsic chiral signatures that depend on illumination geometry, whereas out-of-plane symmetry breaking enables an intrinsic chiral response that remains for normal incidence. Notably, we realize an effective planar intrinsic-chiral metastructure without three-dimensional sculpting by leveraging substrate-induced out-of-plane symmetry breaking, where the resulting hybrid resonance breaks the mirror symmetry of the near-field distribution and generates helicity-dependent features analogous to those typically associated with 3D chiral systems.

Beyond polarization control and readout, we propose metastructures that produce a globally biased optical chirality density over an extended region rather than isolated hotspots. We reveal that the collective nature of the guided-mode resonance allows the chirality bias in both near- and far-field regimes. The measured and designed responses are analyzed based on a coupled-mode theory, which provides design rules that connect resonance detuning and interference to the amplitude and phase relations between co- and cross-polarized channels.

III. Conclusion

In conclusion, we propose several chiral design strategies to realize nonlocal, symmetry-broken dielectric metasurfaces as an efficient and scalable route to planar intrinsic chirality, spin-selective polarization optics, and globally biased chirality sensing for various applications such as integrated photonics and molecular-detection applications.

Acknowledgments

This work was supported by Korea Institute for Advancement of Technology (KIAT) grant funded by the

Korea Government (MOTIE) (P0020967, Advanced Training Program for Smart Sensor Engineers) and by Korea University grant.

REFERENCES

[1] M. V. Gorkunov, A. A. Antonov, and Y. S. Kivshar, "Metasurfaces with Maximum Chirality Empowered by Bound States in the Continuum." Physical Review Letters, 125, 093903 2020.

[2] K. Tanaka, D. Arslan, S. Fasold, M. Steinert, J. Sautter, M. Falkner, T. Pertsch, M. Decker, and I. Staude, "Chiral Bilayer All Dielectric Metasurfaces," ACS Nano, vol. 14, pp. 15926–15936, 2020.

[3] Y. G. Ki, B. J. Jeon, I. H. Song, S. J. Kim, S. Jeon, and S. J. Kim, "Realizing Minimally Perturbed Nonlocal Chiral Metasurfaces for Direct Stokes Parameter Detection," ACS Nano, vol. 18, no. 9, pp. 7064 –7073, 2024.

Subspace-Protected Topological Phases

Masatoshi Sato

Yukawa Institute for Theoretical Physics, Kyoto University, Japan
msato@yukawa.kyoto-u.ac.jp

***Abstract*—Symmetry is a key to controlling topological phases. In this talk, I will explain that an invariant subspace, a generalization of symmetry, protects topological phases with unconventional properties. I also discuss a possible realization of such subspace-protected topological phases in metamaterials.**

***Keywords*— metamaterials, non-Hermitian Hamiltonian, invariant subspace, topology.**

I. Introduction

Symmetry is a fundamental principle for characterizing and classifying topological phases of matter. In particular, various types of symmetry provide free-fermion systems with rich topological structure, as in topological insulators and superconductors. A unitary symmetry resolves the Hilbert space into sectors, in which topological phases are individually classified on the basis of internal symmetries or crystalline symmetries. A significant characteristic of topological phases is the bulk-boundary correspondence: the nontrivial topological phases in gapped bulk involve the presence of gapless boundary modes. Nontrivial topological insulators protected by time-reversal symmetry (TRS) exhibit helical gapless modes as the Kramers pairs, and nontrivial topological superconductors can host Majorana zero modes reflecting particle-hole symmetry. In recent years, the idea of symmetry-protected topological phases has also been applied to metamaterials with and without non-Hermiticity.

While extensive research has shown that symmetry enriches the topological phases of matter, the more general principles that protect them have yet to be explored. Here, I elucidate the roles of subspaces in free-fermionic topological phases. A subspace property for Hamiltonians enables new topological invariants. It results in peculiar topological boundary phenomena, i.e., the emergence of an unpaired zero mode or zero-winding skin modes, characterizing subspace-protected topological phases. I also propose possible platforms that possess the subspace property.

II. Subspace-protected topological phase

In this talk, I show that subspaces of Hilbert spaces provide a principle for introducing a novel type of topological phases in both Hermitian and non-Hermitian systems, beyond the conventional notion of symmetry. Specifically, we consider the following condition, which we call the subspace property, for a Bloch Hamiltonian $H(\boldsymbol{k})$ acting on a Hilbert space $\mathcal{H}$ of internal degrees of freedom,

$$H(\boldsymbol{k})\mathcal{M} \subseteq \mathcal{M}', \tag{1}$$

where $\mathcal{M}$ and $\mathcal{M}'$ are subspaces of $\mathcal{H}$ independent of the wave vector $\boldsymbol{k}$. The subspace property is not reduced to group-theoretical symmetry operations. With Kenji Shimomura, Ryo Takami, and Daich Nakamura, I propose the concept of topological phases protected by the subspace property (1), dubbed *subspace-protected topological phases*, and establish the bulk-boundary correspondence in the phases [1].

As discussed in Ref.[1], the proposed subspace-protected topological phases exhibit unusual topological properties in both Hermitian and non-Hermitian systems. In particular, they may host a topological phase transition without gap closing, which has never been seen in conventional topological phases.

The realization of systems with the subspace property is not difficult in artificial quantum systems, including metamaterials. Actually, we have recently realized such a system mechanically [2].

III. Summary

In summary, we have discovered subspace-protected topological phases and established the bulk-boundary correspondence. Our work reveals that the new principle beyond symmetry may play an essential role in topological phases.

Acknowledgments

M.S is supported by JSPS KAKENHI Grant Nos. JP24K00569 and JP25H01250.

References

[1] K. Shimomura, R. Takami, D. Nakamura, and M. Sato, "Subspace-protected topological phases and bulk-boundary correspondence", arXiv:2508.20908.

[2] Z. Li, X. Wang, R. Cai, K. Shimomura, Z. Yang, M. Sato, G. Ma, "Exceptional deficiency of non-Hermitian systems: high-dimensional coalescence and dynamics", to appear in Nat. Phys.

Fluctuation-induced Hall-like lateral forces in a chiral-gain environment

Daigo Oue[1,2,3,*], Mário G. Silveirinha[1]

[1]Instituto Superior Técnico–University of Lisbon and Instituto de Telecomunicações, Lisbon, Portugal
[2]The Blackett Laboratory, Imperial College London, United Kingdom
[3]RIKEN Centre for Advanced Photonics, Saitama, Japan
*Corresponding author: daigo.oue@gmail.com

***Abstract*—We predict a fluctuation-induced lateral force on a particle near a substrate under an electrostatic bias that induces chiral optical gain. The force arises from vacuum fluctuations in a non-Hermitian environment, is governed by the Berry-curvature dipole, and enables directional momentum transfer without a magnetic field.**

***Keywords*— non-Hermitian systems, chirality, Casimir effect**

Non-Hermitian electromagnetic media, characterised by loss and/or gain, enable wave phenomena with no direct counterpart in passive systems. In current-biased conductors, a static electric field drives carrier drift that modifies the optical response and can induce polarisation-dependent gain [1]. In low-symmetry materials possessing a finite Berry-curvature dipole, such an electrostatic bias produces *chiral optical gain*, where one circular polarisation is amplified while the opposite is dissipative. Hence, both inversion and time-reversal symmetries are broken, leading to a nonreciprocal behaviour.

We have explored fluctuation-induced forces in the chiral-gain environment [2]. We consider a small polarisable particle placed near a biased substrate (Fig. 1). Unlike conventional

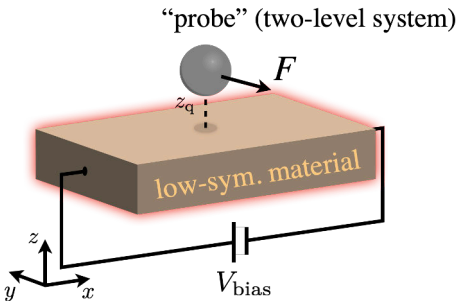

Fig. 1. A polarisable particle modelled by a two-level system placed above a low-symmetry material under an electrostatic bias.

Casimir–Polder forces, which act normal to a surface, the Hall-like lateral force arises due to the non-Hermiticity and nonreciprocity of the material. We demonstrated that the force is governed by the Berry-curvature dipole of the substrate response, establishing a link between quantum geometry and fluctuation-induced forces.

We utilised the Lindblad formalism and the Green-function-based field quantisation to obtain a reduced master equation effectively describing the dynamics of the particle. The momentum transfer between the particle and the surrounding field was evaluated at the steady state. Figure 2 depitcs the fluctuation-induced lateral force as a function of the distance z_q between the particle and the surface.

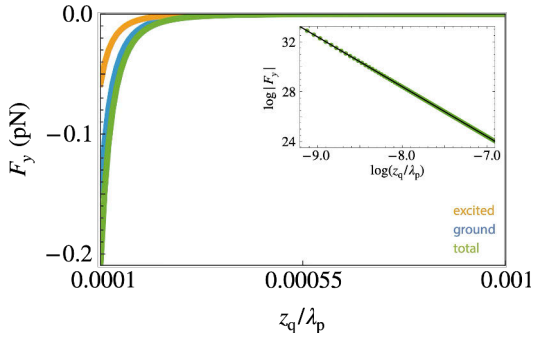

Fig. 2. Fluctuation-induced Hall-like force as a function of the distance z_q between the surface and the particle. The inset is the logarithmic plot, implying the force is proportional to $1/z_q^4$.

Our results reveal a new mechanism for engineering vacuum fluctuations using active, nonreciprocal photonic platforms.

Acknowledgments

D.O. is supported by JSPS Overseas Research Fellowship and by the RIKEN special postdoctoral researcher program. M.S. is partially supported by the Simons Foundation (award SFI-MPS-EWP-00008530-10) and by national funds through FCT – Fundação para a Ciência e a Tecnologia, I.P., and, when eligible, co-funded by EU funds under project/support UID/50008/2025 – Instituto de Telecomunicações, with DOI identifier https://doi.org/10.54499/UID/50008/2025.

References

[1] T. A. Morgado et al., *Phys. Rev. B* **109**, 245126, 2024.
[2] D. Oue and M. G. Silveirinha, *Phys. Rev. Research* **8**, 013158, 2026.

Metasurface concepts for polarisation control

Ilya V. Shadrivov

Centre of Excellence for Transformative Meta-Optical Systems
Research School of Physics, Australian National University
Canberra ACT 2601, Australia
ilya.shadrivov@anu.edu.au

***Abstract*— We develop metasurface based broadband polarisers and waveplates for controlling Terahertz radiation. We discuss effects of topology and mode interplay for achieving broadband operation of the proposed devices.**

***Keywords*— metamaterials, terahertz, gratings.**

I. Introduction

Efficient polarisation control in the terahertz frequency range is required in many applications, including material characterization, imaging, and polarimetry. Main devices that control wave polarisation are polarisers and waveplates, including quarter and half-waveplates, as well as Q-plates. There are several approaches and commercially available products with this functionality, but they have drawbacks. For example, the available quarter waveplates that convert linear polarisation into circular come in various designs, including subwavelength gratings, metamaterials, prism-type waveplates, natural birefringent material stacks, liquid crystals etc. However, these solutions still suffer from limited bandwidths, low transmission or other limitations.

II. Results and Discussions

In this work, we will present metal-based and dielectric gratings that aim to provide a full polarisation control for the Terahertz frequency range. For the metal gratings, we explore the effect of the shape of metal stripes on achievable transmission and extinction ratio of polarisers. We further demonstrate quarter-waveplates based on high-index dielectric gratings. A subwavelength linear grating is a fundamental building block for creating optical elements with tailored properties. Using high-order effective medium theory, a scattering-matrix formalism, and a particle-swarm optimization, we developed an efficient approach to predict and optimize grating parameters. Our simulations show that the relative frequency bandwidth of a single-layer grating is limited to about 40-50%, and that transmission characteristics can be improved by adjusting the grating profile.

To further increase the bandwidth, we stack multiple single-layer gratings with carefully selected dimensions and rotation angles. The resulting structure exhibits enhanced performance across a broader spectral range.

This work presents both simulation results and experimental demonstration of the proposed structures. Our fabrication techniques include lithography, laser micromachining and electrochemistry. They provide a scalable platform for the fabrication of polarisation devices. Figure 1 shows top view of dielectric micrograting, with the depth optimised so that the device acts as a quarter waveplate. The performance of the devices was characterized using terahertz time-domain spectroscopy system. The experimental results show excellent agreement with theory and numerical simulations, and they confirm the viability of the proposed approaches for achieving polarisation control in the terahertz frequency range.

III. Methods

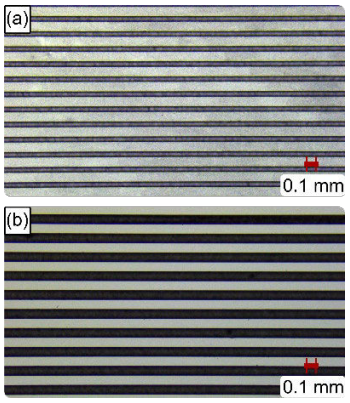

Fig. 1 Sample photographs of fabricated subwavelength gratings.

Acknowledgments

This work was supported by the Australian Research Council, through the Centre of Excellence for Transformative Meta-Optical Systems (TMOS).

References

[1] W. Withayachumnankul and M. Naftaly, “Fundamentals of Measurement in Terahertz Time-Domain Spectroscopy,” Journal of Infrared, Millimeter, and Terahertz Waves 35, 610–637 (2014).
[2] Y. Chen, J. Wang, Z. Hu, T. Gao, W. Zhu, and X. Wang, Optik **212**, 164655 (2020).
[3] Y. Yuan, J. Cheng, X. Dong, F. Fan, X. Wang, and S. Chang, Optics and Lasers in Engineering, **143**, 106636 (2021),

Numerical analysis of directional guided modes on highly anisotropic metasurface

Maxim Nikitin, Andrei V. Lavrinenko, Battulga Munkhbat, Osamu Takayama*

DTU Electro, Technical University of Denmark, Ørsteds Plads, Building 343, DK-2800, Kgs. Lyngby, Denmark
*Corresponding author: otak@dtu.dk

***Abstract*— Anisotropic materials can support directional surface waves and guided modes. Their propagation direction and its angular cone depend on the optical properties of the anisotropic materials. We numerically analyze directional surface waves on tungsten disulfide metasurface, which exhibits large effective anisotropy and transparency for near-infrared wavelengths.**

***Keywords*— surface waves, metasurfaces, transition metal dichalcogenide, anisotropy.**

I. Introduction

Photonic surface waves are supported on various nanostructured systems, such as plasmonic materials or photonic crystals [1]. In particular, directional surface waves are supported on in-plane anisotropic materials and are sometimes referred to as Dyakonov surface waves.

Here, we numerically show that nanostructured transition metal dichalcogenide (TMD) metasurface (MS) exhibits large in-plane anisotropy and can support Dyakonov surface waves and related guided modes for telecommunication wavelengths at 1550 nm due to its extreme anisotropy. The TMD MS consists of tungsten disulfide (WS_2) metasurface made of deep sub-wavelength one-dimensional gratings with air gaps. Numerical analysis is performed in combination of analytical equations and the COMSOL software based on the finite element method.

II. Results and Discussion

Numerical analysis shows:

- large propagation cone, angular existence domain, of surface waves over 20 degrees for telecom wavelengths as opposed to smaller than 1 degree of natural anisotropic material (Fig. 1), and
- the deviation between effective media and real metasurface structures, affected by the thickness and the period of deep-subwavelength gratings of the metasurface.

III. Conclusion

In this talk, we present that the significant improvement of propagation cone of the directional modes can be controlled by the design of WS_2 metasurfaces, for example, its volume fraction, and thickness. Nanostructured TMD materials can be a versatile platform with high anisotropy, low loss, and synthetic properties for some specific nanophotonic applications.

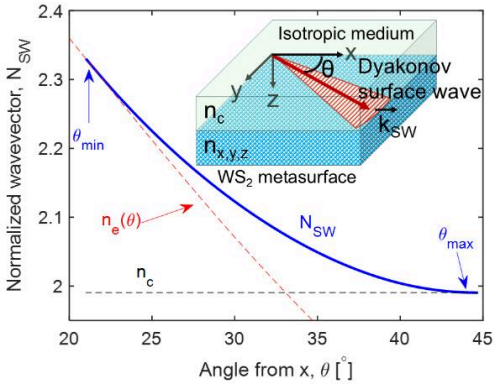

Fig. 1 Propagation direction θ from crystallographic axis x and normalized wave vector $N_{SW} = k_{SW} / k_0$, where k_{SW} and k_0 are wavenumber of Dyakonov surface wave and that in vacuum. $n_e(\theta)$ is angle dependent extraordinary refractive index of WS_2 metasurface. The inset shows the schematic illustration of WS_2 metasurface with biaxial effective refractive index components $n_x \neq n_y \neq n_z$ and isotropic layer with refractive index, n_c.

Acknowledgments

This work was supported by Novo Nordisk Fonden, Project Grant in Natural and Technical Sciences, "Extremely anisotropic nanostructures for lightwave steering" (Extra Light, grant No. 0093187). BM acknowledges support from the European Research Council (ERC-StG "TuneTMD", grant no. 101076437) and the Villum Foundation (grant no. VIL53033).

References

[1] O. Takayama, A. Bogdanov, A. V. Lavrinenko, "Photonic surface waves on metamaterial interfaces," Journal of Physics: Condensed Matter vol. 29, p. 463001, 2017.

[2] B. Munkhbat, P. Wróbel, T. J. Antosiewicz, T. O. Shegai, "Optical Constants of Several Multilayer Transition Metal Dichalcogenides Measured by Spectroscopic Ellipsometry in the 300–1700 nm Range: High Index, Anisotropy, and Hyperbolicity," ACS Photonics vol. 9, pp. 2398–2407, 2022.

Meta-optics based multidimensional imager

Fengjun Li[1], Zilan Deng[1], Xiangping Li[1,*]

[1]College of Physics & Optoelectronic Engineering, Jinan University, Guangzhou, P.R.China

*Corresponding author: xiangpingli@jnu.edu.cn

***Abstract*— Here we report the development of metasurface based integrated optics from polarization imaging to optoelectronic Stokes logic.**

***Keywords*— Metasurface, light field manipulation, polarization camera, multidimensional imaging.**

I. Introduction

Metasurfaces [1], composed of arrays of subwavelength artificial atoms, have demonstrated capability of powerful wavefront manipulation. The ultra-thin thickness metasurfaces offer a new platform for development of integrated planar optics with multifarious functionalities. In this talk, I will present our recent research progress focused on meta-optics for multidimensional light field manipulation as well as its application in multidimensional imaging.

II. Results and Discussion

Leveraging the flexible polarization control capability, we demonstrate the encryption of two images in two arbitrary nonorthogonal polarizations without crosstalks covering the full Poincare sphere [2]. This omni-potential polarization and phase manipulation capability enables the development of monolithic polarization camera. A meta-grating-lens functioning as polarization beam splitter and imaging lens allows highly compact and full stokes polarization camera [3]. The monolithic integrated polarization camera operates at the wavelength of 940 nm with a total diffraction efficiency approaching 65% and a polarization distinguish ratio close to 10 db. We applied such camera for directly imaging of internal stress inside transparent PMMA solids as well as anti-face attack. It can clearly distinguish the polarization difference between a true human face and its planar picture attack.

Additionally, we integrated this polarization camera with a graphene photocurrent detector to implement optoelectronic Stokes logic [4]. The three mutually independent Stokes components $S1$, $S2$, and $S3$ are treated as parallel logic channel. Therefore, we establish a physical device-level route from "Stokes reconstruction" to "Stokes logic", allowing information encryption as well as the edge image calculation.

Acknowledgments

This work was supported by the National Natural Science Foundation of China (62325503), the Guangdong Provincial Quantum Science Strategic Initiative (GDZX2406004, GDZX2506004).

References

[1] Rubin, N. A. et al. Matrix Fourier optics enables a compact full-Stokes polarization camera, Science 365, eaax1839 (2019).

[2] Zi-Lan, D. et al. Poincaré sphere trajectory encoding metasurfaces based on generalized Malus' law, Nature Communications. 15, 2350, (2024).

[3] FengJun, L. et al., Meta-grating-lens based monolithic polarization camera, Science Advances. 11, eadx9886, (2025).

[4] Ruoxuan, S. et al. Programmable optoelectronic Stokes logic on ultracompact meta-chip, submitted

DRUM: From Diabolic to Exceptional Point and Phase-Tunable Hysteresis toward Controllable Artificial Neurons

Stefano Biasi[1,*], Bülent Aslan[1], Davide Olivieri[1], Stefano Gretter[1] and Lorenzo Pavesi[1]

[1]Nanoscience Laboratory, Department of Physics, University of Trento, 38123 Trento, Italy
*Corresponding author: stefano.biasi@unitn.it

***Abstract*—We present the Dynamically Reconfigurable Unified Microresonator (DRUM), an integrated silicon photonic platform enabling tunable Hermitian and non-Hermitian coupling between counter-propagating modes. The DRUM exploits coupling-controlled feedback to access diabolic and exceptional points, inducing nonlinear hysteresis and memory effects. This enables controllable bifurcations and functions as a reconfigurable artificial neuron.**

***Keywords*— Microring resonator, Non-Hermitian system, integrated optics, neuromorphic hardware.**

I. Introduction

Integrated microring resonators architectures with counter-propagating modes are an ideal platform for implementing non-Hermitian systems. They enable precise control of light and demonstrate key phenomena such as unidirectional reflection [1], coherent perfect absorption [2], chiral mode control [3] and enhanced sensing [4]. When combined with optical nonlinearities, non-Hermitian systems exhibit rich dynamics, including self-oscillations, nonreciprocal transmission and multistability [5]. This offers a path towards neuromorphic photonic devices.

Here, we present the Dynamically Reconfigurable Unified Microresonator (DRUM): a fully integrated silicon photonic platform that enables on-demand tuning of the coupling between clockwise (CW) and counterclockwise (CCW) modes. As demonstrated in our recent work [6], the DRUM architecture, incorporating Mach–Zehnder interferometers (MZs) and phase shifters (PSs), enables controlled transitions between diabolic points (DPs) and exceptional points (EPs), dynamic spectral shaping, suppression of backscattering, and tunable system chirality. Moreover, we showed in [7] that intrinsic memory, arising from two-photon-absorption-induced carriers and thermal effects, supports multistability, path-dependent dynamics, and self-sustained oscillations. Here, we report that the DRUM exhibits a programmable firing threshold, highlighting its potential to mimic a controllable artificial neuron.

The DRUM thus provides a versatile testbed for fundamental studies of non-Hermitian nonlinear photonics and for neuromorphic computing, enabling the emulation of controllable neuronal behavior within a single device.

II. Methods

We experimentally investigate the linear and nonlinear response of a tunable DRUM. As shown in Fig. 1 (a), the device consists of a bus waveguide side-coupled to a microring resonator with two auxiliary side lobes. These lobes enable selective recirculation of the clockwise (α_1) and counterclockwise (α_2) modes. Electrical control of the coupling amplitudes and phases is provided by thermally tunable Mach–Zehnder interferometers (MZL and MZR for the left and right lobes, respectively) and phase shifters (PSL and PSR). This allows operation at both degeneracy points: DP or EP.

III. Results and Discussion

In the low-power (linear) regime, the transmission spectrum evolves with the current applied to the PSL, transforming the initial Lorentzian profile (black curve) into an almost balanced doublet at a phase of π (red curve) [6], as illustrated in Fig. 1(b).

As the optical power increases, the DRUM exhibits nonlinear behaviour driven by light–matter interactions, which are dominated by two-photon absorption (TPA). TPA generates free carriers, which lead to free-carrier absorption and dispersion. These carriers modify the refractive index of the microresonator via two competing mechanisms: absorption-induced heating redshifts the resonance through the thermo-optic effect, whereas plasma dispersion induces a blueshift [8]. The interplay between carrier dynamics and thermal effects can lead to self-sustained oscillations known as self-pulsing (SP), whereby a continuous-wave input is converted into a periodic output signal. Figure 1(c) shows the normalised transmission as a function of time with no current applied (0 phase), at the wavelength detuning indicated by the black square in Fig. 1(b). The measured signals are shown as solid black lines, while the red dashed lines represent sine waves at the fundamental SP frequency.

In the nonlinear regime, the DRUM can exhibit memory to PSL phase variations through the coupled dynamics of the energy of the two modes, the carrier density change ΔN, and the temperature change ΔT inside the microresonator. Because both ΔN and ΔT depend on the intracavity optical intensity,

Fig. 1. (a) Schematic of the DRUM. Red lines denote the optical waveguides, and triangles mark the grating couplers. (b) Linear transmission spectrum. (c) Time-resolved nonlinear transmission: the black trace shows the measured optical response, while the red dashed curve represents a sinusoid at the fundamental oscillation frequency. (d) Map of the SP frequency as a function of input power and laser wavelength for two values of the PSL phase. (e) Firing threshold power versus the PSL.

when the phase controlling energy exchange between counter-propagating modes varies slowly compared with carrier and thermal relaxation times, the final state strongly depends on the path in parameter space. Scanning the PSL in opposite directions, from 0 to 2π (forward) and from 2π to 0 (reverse), may yield distinct final states [7].

Controlling the SP states enables the emulation of biologically inspired neuronal behavior, as previously demonstrated in microresonators [9]. In contrast, the DRUM architecture permits the reconfiguration of fundamental characteristics, such as the firing threshold. Figure 1(d) presents SP maps as a function of the input laser wavelength and power. White regions denote non-oscillatory regimes, whereas the color scale represents the SP oscillation frequency. Upon tuning the PSL, not only the spectral response is modified (as illustrated above the maps), but the SP domain is also redistributed in both power and frequency (see dashed lines). The firing threshold, defined as the minimum optical power required to trigger SP, is shown in Fig. 1(e). The results of different SP maps are summarized in a single plot, showing two separate lines between the regions where the DRUM exhibits SP and those where it does not.

IV. Conclusion

The DRUM's versatility in emulating photonic systems at diabolic points (DPs) and exceptional points (EPs), while supporting self-pulsing (SP) regimes that reveal memory effects, enables its use as an artificial neuron. It can replicate a wide range of neuronal response behaviors within a single device, with a controllable firing threshold. Such precise control is crucial for scalable neuromorphic photonic systems. By combining nonlinear dynamics, non-Hermitian physics, and electrical tunability, the DRUM functions not just as an artificial neuron, but as a fully programmable neural element. This makes it a versatile platform for emulating diverse neuronal behaviors in a single device, representing an important step toward adaptive, hardware-based photonic neural networks.

Acknowledgments

This project has received funding from the European Research Council (ERC) under the European Union's Horizon 2020 research and innovation programme (grant agreement No. 788793, BACKUP), from the MIUR under the PRIN PELM project (20177 PSCKT) and by the European Union under NextGenerationEU project PRIN2022AEEKNC. S.B. acknowledges the co-financing from European Union - Next Generation EU, Missione 4 Componente 2 - CUP E53D23002230006.

References

[1] A. Calabrese, F. Ramiro-Manzano, H. M. Price, S. Biasi, M. Bernard, M. Ghulinyan, I. Carusotto, and L. Pavesi, "Unidirectional reflection from an integrated 'taiji' microresonator," Photonics Research, vol. 8, no. 8, pp. 1333–1341, 202

[2] S. Soleymani, Q. Zhong, M. Mokim, S. Rotter, R. El-Ganainy, and S. K. Özdemir, "Chiral and degenerate perfect absorption on exceptional surfaces," Nature Communications, vol. 13, no. 1, p. 599, 2022.

[3] Y. Chen, J. Li, K. Xu, S. Biasi, R. Franchi, C. Huang, J. Duan, X. Wang, L. Pavesi, X. Xu, et al., "Electrically reconfigurable mode chirality in integrated microring resonators," Laser & Photonics Reviews, vol. 18, no. 11, p. 2301289, 2024.

[4] R. Franchi, B. Aslan, S. Biasi, and L. Pavesi, "Controlled comparison of phase-tuned exceptional and diabolic point sensing in integrated optical microresonators," Applied Physics Letters, vol. 127, no. 20, 2025.

[5] X. Z. Hao, X. Y. Zhang, Y. H. Zhou, W. Li, S. C. Hou, and X. X. Yi, "Gain-saturation-induced self-sustained oscillations in non-Hermitian optomechanics," Physical Review A, vol. 103, no. 5, p. 053508, 2021.

[6] B. Aslan, R. Franchi, S. Biasi, S. Ali, D. Olivieri, and L. Pavesi, "Coherent control of (non-)Hermitian mode coupling: tunable chirality and exceptional point dynamics in photonic microresonators," Accepted for publication in Light: Science & Applications, 2025. DOI: 10.1038/s41377-025-02176-3.

[7] S. Biasi, S. Gretter, B. Aslan, D. Olivieri, R. Franchi, and L. Pavesi, "Phase-controlled non-Markovian hysteresis in a nonlinear, non-Hermitian silicon microresonator," Accepted for publication in Physical Review Applied, 2026. DOI: 10.1103/fcsp-jw79.

[8] J. Leuthold, C. Koos, and W. Freude, "Nonlinear silicon photonics," Nature Photonics, vol. 4, no. 8, pp. 535–544, 2010.

[9] J. Xiang, A. Torchy, X. Guo, and Y. Su, "All-optical spiking neuron based on passive microresonator," Journal of Lightwave Technology, vol. 38, no. 15, pp. 4019–4029, 2020.

Chirality in Non-Hermitian Photonic Crystals

Masaya Notomi[1,2*] Yuto Moritake[1,3] and Taiki Yoda[1]

[1]Department of Physics, Institute of Science Tokyo, Tokyo, Japan
[2]NTT Basic Research Laboratories, NTT Inc., Kanagawa, Japan
[3]Institute of Industrial Science, University of Tokyo, Tokyo, Japan
*Corresponding author: notomi@phys.isct.ac.jp

***Abstract*— We present various types of optical chirality arising from the non-Hermitian nature of photonic crystals both theoretically and experimentally. First, we reveal interesting interplay between topological singularity and 3D/2D chirality in non-Hermitian photonic crystals. Second, we show our recent results on the propagating non-Hermitian skin effect in photonic crystals, and their application to generate chiral orbital angular momentum.**

***Keywords*— non-Hermitian optics, chirality, photonic crystals, metamaterials, optical angular momentum, non-Hermitian skin effect, topological singularity, exceptional point**

I. Introduction

Optical chirality has generally been discussed and utilized in non-reciprocal (magnetic) or three-dimensional (3D) chiral media and structures. However, it has been clarified that reciprocal (non-magnetic) and planar structures can exhibit various types of optical chirality for non-Hermitian systems. As one example, planar chirality has been extensively studies in 2D metamaterials, which shows asymmetric conversion in terms of the handedness of light in transmittance and reflectance. In another direction, asymmetric reflection in PT-symmetric periodically-modulated photonic crystals has been applied to generate chiral orbital angular momentum (OAM). As such, various chiral phenomena have been observed in non-Hermitian photonics where the complex refractive index plays an essential role.

In this talk, we present two different approaches to explore novel chirality arising from non-Hermitian optical systems, especially on non-Hermitian photonic crystals (PhCs) shown in Fig. 1. First, we discuss 2D/3D chirality in non-Hermitian hybrid photonic crystals, where the real and imaginary parts of the refractive index are independently controlled. By judiciously introducing the symmetry-breaking complex index perturbation, we generate and manipulate 2D and 3D chirality in the reciprocal space. We show two examples for which singular points play an intriguing role: non-Hermitian chirality originates from exceptional points (EPs) and non-Hermitian chirality arising from topological singular points (BICs, or bound states in the continuum). These results present unique controllability in achieving exotic chiral states in optical response.

For the second topic, we investigate interesting properties of reciprocal non-Hermitian skin effect in non-Hermitian PhCs, and apply it to generate orbital angular momentum (OAM) chirality. We show that OAM appears from propagating skin modes, and its chirality is determined by the chirality of the point gap. We also present our recent result of experimental observation of the point gap in radiation-based non-Hermitian PhCs, and its application to OAM generation.

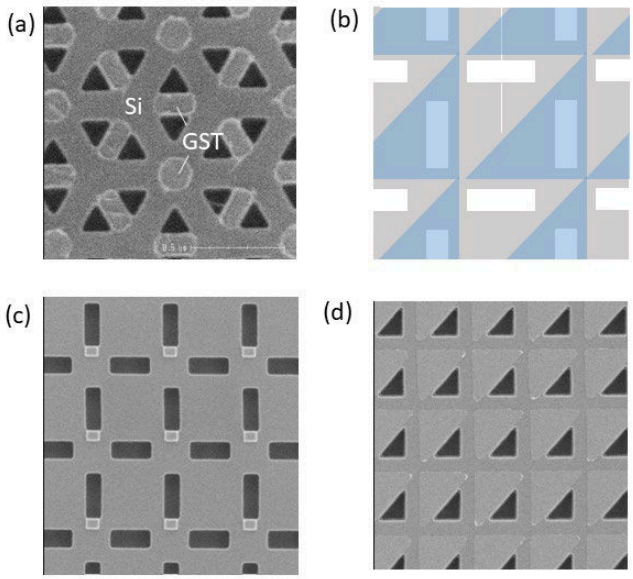

Figure 1. Hybrid photonic crystals. (a) GST-loaded PhC. (b) Graphene-loaded non-Hermitian PhC. (c) and (d) Metal-loaded non-Hermitian PhCs.

II. Chirality and Topological Singularity in Non-Hermitian Photonic Crystals

In this part, we investigate three types of optical chirality, S_3, 3D and 2D chirality in non-Hermitian systems, especially concerning the spin angular momentum, that is, polarization. First, we briefly review the S_3 chirality, which is nothing but conventional circular dichroism defined by the third Stokes parameter (S_3). It has been well clarified that the polarization chirality in far-field can be well described by the language of the singular optics. That is, the maximally-chiral point is C-point, which has a definite half-integer topological charge. In

conventional Hermitian photonic crystals, one can create various intriguing polarization states of light by manipulating topological singular points, including merging and splitting them, by breaking the crystal symmetry [1].

In this talk, we will exploit a similar scenario in non-Hermitian photonic crystals by breaking their complex symmetry. For doing so, the other two types of chirality play important roles. 3D chirality (C_{3D}) and 2D chirality (C_{2D}) are defined by the handedness-wise transmittance,

$$C_{3D} = \frac{T_{RR} - T_{LL}}{T_{RR} + T_{LL}}, \; C_{2D} = \frac{T_{RL} - T_{LR}}{T_{RL} + T_{LR}}$$

Our basic structure is a square-lattice air-hole photonic crystal, with C_{4v} symmetry, and we investigate two different approaches for manipulating polarization chirality. As is well known, the square lattice has p-like doubly-degenerate bands and two non-degenerate d-like bands for each band group. In the first approach (Fig. 1(b)), we pick up p-like degenerate bands. By applying MT-symmetric perturbation, which breaks the mirror symmetry by imaginary perturbation, one can create four EPs in the k space. Then, we break another mirror symmetry by real perturbation, leading to merging four EPs into a single 2D-chiral EP at Γ point. In the second approach (Fig. 1(c)), we pick up one of d-like bands, which is actually symmetry-protected BIC at Γ point. We split this BIC into a pair of C-points by non-Hermitian symmetry breaking perturbation. We break the mirror symmetry by real perturbation, leading to 2D chiral singular point at Γ point. For both cases, the whole processes are well explained by the topological nature of non-Hermitian singular points.

Concerning experimental demonstrations, we have recently developed a technique to fabricate so-called "hybrid PhCs", as shown in Fig. 1, where we load a patterned functional film on a host PhC to realize arbitrary symmetry breaking perturbation to a host PhC [2]. We have applied this technique to make designed non-Hermitian PhCs, and have observed some of intriguing chiral polarization properties. We will report the details at the conference.

III. Chirality in non-Hermitian skin effect

In this part, we discuss another type of chirality arising from non-Hermitian skin effect (NHSE). NHSE was first discussed in a 1D tight-binding model with non-reciprocal hopping in quantum systems based on the Hatano-Nelson Hamiltonian. This system has a so-called *point gap* in the complex frequency plane for the periodic boundary condition, and exotic localized skin modes for the open boundary condition. The existence of the point gap leads to the appearance of NHSE. These two features are strongly correlated. NHSE has attracted significant interest in various fields in physics, but experimental studies have been very limited and its application has not been clarified yet. Recently, it was found that similar NHSE can be created for a certain type of reciprocal 2D PhCs with anisotropic loss or gain. The anisotropic loss/gain plays a role of the imaginary gauge potential with the presence of finite wavevector in the direction parallel to the boundary [3].

One of the interesting aspects of this reciprocal NHSE in PhCs is the fact that this skin mode can *propagate* in the direction parallel to the boundary. This is a new degree of freedom compared to conventional 1D NHSE. We theoretically confirmed that each boundary supports unidirectional transport without backscattering, which is somewhat similar to the topological edge mode [5]. We explored various properties of this propagating skin mode, and found that one can create optical orbital angular momentum (OAM) modes when enclosing the anisotropic non-Hermitian media by open boundaries with specific directions [4]. The chirality (circulating direction) of OAM is determined by the chirality of the point gap, that is, the sign of the winding number. This means that this OAM chirality is attributed to the chiral nature of the point gap.

As for the point gap, its experimental observation has been very limited. Very recently, we have successfully observed the point gap in non-Hermitian PhCs. For this work, we first designed reciprocal and anisotropic non-Hermitian PhCs (Fig. 1(d)), which have large point gaps and exhibit NHSE. A key point is that we create anisotropic loss by managing the radiation loss, which makes experimental observation easier. We have observed point gaps in Si PhCs by the angle-resolved reflectance spectroscopy [5]. Although we could not measure the whole closed loop by the restriction of the numerical aperture, we clearly observed the existence of the point gap.

We have also designed and fabricated structures for OAM generation based on these non-Hermitian PhCs. We will report details of these studies at the conference.

Acknowledgments

We acknowledge invaluable contributions by I. Takeda, T. Uemura, S. Otsuka, S. Suzuki, T. Suzuki, T. Harada, N. Ogawa, Y. Ohinata, K. Takata, E. Kuramochi, and M. Ono.

References

[1] T. Yoda and M. Notomi, "Generation and Annihilation of Topologically Protected Bound States in the Continuum and Circularly Polarized States by Symmetry Breaking," Phys. Rev. Lett. 125, 053902 (2020).

[2] T. Uemura, Y. Moritake, T. Yoda, H. Chiba, Y. Tanaka, M. Ono, E. Kuramochi, M. Notomi, "Photonic topological phase transition induced by material phase transition", Science Advances 10, eadp7779 (2024).

[3] T. Yoda, Y. Moritake, K. Takata, K. Yokomizo, S. Murakami, and M. Notomi, "Optical non-Hermitian skin effect in uniform media", Phys. Rev. Research 7, 033214 (2025).

[4] I. Takeda, T. Yoda ,Y. Moritake, K. Takata, and M. Notomi, "Propagation and circulating modes of the reciprocal non-Hermitian skin effect," Phys. Rev. A 112, 053501 (2025).

[5] Y. Moritake, N. Ogawa, I. Takeda, Y. Ohinata, T. Uemura, T. Yoda, K. Takata, E. Kuramochi, H. Sumikura, and M. Notomi, arXiv:2512.14974

Temporal Dispersion Effects in Optical Spectra of Exciton-Plasmon Systems at Strong Coupling

Sancenia Johnson, Gabrielle Williams, Tigran V. Shahbazyan

Department of Physics, Jackson State University, Jackson, MS 39217 USA
*Corresponding author: shahbazyan@jsums.edu

***Abstract*— We show that temporal dispersion of the metal dielectric function significantly modifies the shape of scattering spectra of quantum emitters strongly coupled to surface plasmons by shifting spectral weight towards lower energy polaritonic band.**

***Keywords*— surface plasmon, strong coupling, excitons**

I. INTRODUCTION

The shape of scattering spectra of quantum emitters (QE) resonantly coupled to localized surface plasmons (LSP) in metal nanoparticles (NP) as the system transitions to the strong coupling regime has been an actively debated topic [1,2]. In general, the scattering spectrum of a hybrid system characterized by broad spectral band should be enhanced on the higher frequency side due to faster radiation rate of the upper-energy states, implying that, in the strong coupling regime, the spectral band associated with the upper-energy polaritonic state should be relatively enhanced. Such a spectral profile is consistent with the classical model of two coupled oscillators, in which one of the oscillators (LSP) couples much stronger to the electromagnetic (EM) field due to its much greater optical dipole moment as compared to the QE one [3]. However, recent experiments for excitons resonantly coupled to LSP in metal-dielectric structures [1,2] reveal the opposite asymmetry pattern characterized by enhancement of the lower polaritonic band. In this paper, we demonstrate that temporal dispersion effects in the metal dielectric function strongly affect the optical spectra of hybrid QE-LSP systems and, in the strong coupling regime, result in a pronounced shift of the spectral weight towards the lower-energy polaritonic band, consistent with the experiment

II. METHODS

We consider a hybrid system of QE located near metal NP in the external EM field $\boldsymbol{E}_0 e^{-i\omega t}$ characterized by complex metal dielectric function $\varepsilon(\omega) = \varepsilon'(\omega) + i\varepsilon''(\omega)$ and QE excitation frequency ω_e tuned to resonance with the LSP frequency ω_n. Using the LSP Green function for NP of arbitrary shape [4], we set up non-Lorentzian semiclassical Maxwell-Bloch equations which include the full complex dielectric function of the metal rather than using Lorentzian approximation for the LSP resonance:

$$\Omega_n \rho_n = g\rho_e + \boldsymbol{\mu}_n \cdot \boldsymbol{E}_0$$

$$\Omega_e \rho_e = g\rho_n + \boldsymbol{\mu}_e \cdot \boldsymbol{E}_0$$

where ρ_e and ρ_n are, respectively, the QE and LSP polarizations, which determine their induced dipole moments as $\boldsymbol{p}_e(\omega) = \boldsymbol{\mu}_e \rho_e$ and $\boldsymbol{p}_n(\omega) = \boldsymbol{\mu}_n(\omega)\rho_n$, and g is QE-LSP coupling. Here, $\Omega_e = \omega_e - \omega - i\gamma_e/2$ is QE detuning, where γ_e is the QE decay rate, $\Omega_n = [\varepsilon'(\omega_n) - \varepsilon(\omega)]/\varepsilon_n'$, with $\varepsilon_n' = \partial\varepsilon'(\omega_n)/\partial\omega_n$, is non-Lorentzian LSP detuning, and $\boldsymbol{\mu}_e$ and $\boldsymbol{\mu}_n(\omega)$ are the corresponding optical dipole moments. The latter is defined as $\boldsymbol{\mu}_n(\omega) = (1 / 4\pi) \int dV [\varepsilon(\omega) - 1] \boldsymbol{E}_n(\boldsymbol{r})$, where $\boldsymbol{E}_n(\boldsymbol{r})$ is electric field of the LSP mode. The full system induced dipole moment $\boldsymbol{p}(\omega) = \boldsymbol{p}_e(\omega) + \boldsymbol{p}_n(\omega)$ determines the system scattering spectrum near the LSP resonance.

IV. RESULTS AND DISCUSSION

In Fig. 1 we show the scattering spectra for a QE near an Au NP at two different LSP frequencies calculated using the non-Lorentzian model (left panel) compared to Lorentzian model of coupled oscillators (right panel). As the QE-LSP coupling increases relative to LSP decay rate, the system undergoes the transition to strong coupling regime signaled by the emergence of Rabi splitting between the polaritonic bands. The scattering spectra calculated using the non-Lorentzian model (left panel) exhibit pronounced enhancement of the lower energy polaritonic band [5], consistent with the experiment [1,2]. In contrast, for scattering spectra calculated in the Lorentzian approximation shown in Fig. 2, the upper energy polaritonic band is relatively enhanced, as predicted by the coupled oscillators model. This reversal of spectral asymmetry is traced to the effect of temporal dispersion of the metal dielectric function on the LSP optical dipole moment which results in a suppression of the LSP radiation efficiency for higher energies.

ACKNOWLEDGMENTS

This work was supported in part by the US National Science Foundation grants DMR- 2302088, DMR-2301350, and NSF-PREM-2423854.

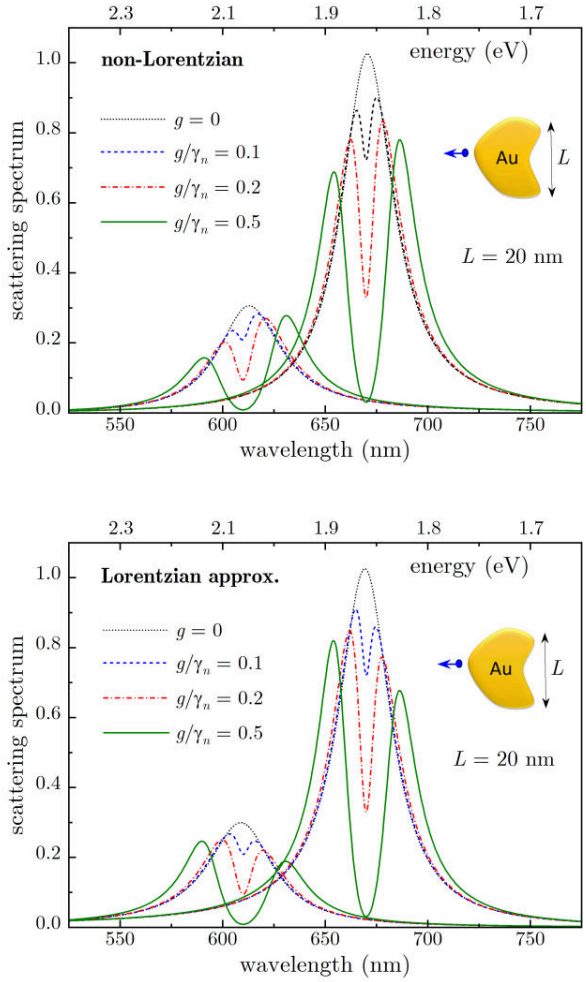

Fig. 1. Scattering spectra for a QE coupled to LSP in Au NP calculated using non-Lorentzian model (upper panel) and its Lorentzian approximation (lower panel) exhibit inversion of spectral asymmetry caused by temporal dispersion of the metal dielectric function.

REFERENCES

[1] H. Leng, B. Szychowski, M.-C. Daniel, and M. Pelton, "Strong coupling and induced transparency at room temperature with single quantum dots and gap plasmons," Nat. Commun. 9, 4012 (2018).

[2] M. Wersäll, B. Munkhbat, D. G. Baranov, F. Herrera, J. Cao, T. J. Antosiewicz, and T. Shegai, "Correlative Dark-Field and Photoluminescence Spectroscopy of Individual Plasmon–Molecule Hybrid Nanostructures in a Strong Coupling Regime," ACS Photon. 6, 2570–2576 (2019).

[3] K.-D. Park, M. A. May, H. Leng, J. Wang, J. A. Kropp, T. Gougousi, M. Pelton, and M. B. Raschke, Sci. Adv. 5, eaav5931 (2019).

[4] T. V. Shahbazyan, "Universal optical polarizability for plasmonic nanostructures", Phys. Rev. A 107, L061503, (2023).

[5] T. V. Shahbazyan, "A Non-Lorentzian Model for Strong Exciton–Plasmon Coupling," J. Phys. Chem C. 129, 19, 9026–9034 (2025).

High-Entropy Alloy-Based Metasurfaces for plasmon absorber in mid infrared wavelength

Yoshiaki Nishijima[1,2,3,4,*], Makoto Ohashi[1], Yuya Hoshimiya[1]

[1]Department of Electrical and Computer Engineering,
Graduate School of Engineering, Yokohama National University,
79-5 Tokiwadai, Hodogaya-ku, Yokohama 240-8501, Kanagawa, Japan
[2]Institute of Advanced Sciences, Yokohama National University,
79-5 Tokiwadai, Hodogaya-ku, Yokohama 240-8501, Kanagawa, Japan
[3]Institute for Multidisciplinary Sciences, Yokohama National University,
79-5 Tokiwadai, Hodogaya-ku, Yokohama 240-8501, Kanagawa, Japan
[4]PRESTO, JST, Japan
*Corresponding author: nishijima-yoshiaki-sp@ynu.ac.jp

***Abstract*—We experimentally determined the complex permittivity of a high-entropy alloy (HEA) composed of five noble metals: Au, Ag, Cu, Pd, and Pt and light metals like Al and Mg. The measurements were conducted across a broad wavelength spectrum, spanning ultraviolet, visible, and mid-infrared regions.**

***Keywords*— Metamaterials, Plsamonics, Metasurfaces, High entropy alloys**

I. Summary of the work

Optical absorbing metasurfaces are two-dimensional materials composed of metal-insulator-metal (MIM) nanostructures. By utilizing a bottom metallic layer to suppress light transmission, these structures serve as highly efficient photothermal conversion devices.Electromagnetic simulations have revealed that when metasurfaces are constructed using conventional plasmonic metals such as gold (Au), silver (Ag), or copper (Cu), the optical absorption and scattering coefficients become equivalent under impedance-matching (zero-reflection) conditions. Experimental evidence further suggests that even under perfect non-reflective conditions ($T = 0, R = 0$), the emissivity does not reach 100%, implying that perfect non-reflection does not inherently equate to perfect absorption.Previous studies have shown that by increasing the thickness of a chromium (Cr) adhesion layer between the Au and dielectric layers to approximately 50 nm, the ratio of the absorption cross-section to the scattering cross-section reaches approximately 1.2. This shift toward absorption dominance enables a state near perfect absorption. However, when used as thermal radiation materials, Au/Cr multilayer structures are thermally unstable; heating causes Cr to readily diffuse into the Au, leading to structural degradation and deterioration of optical properties. To address this, we explored metallic materials where absorption is inherently dominant while maintaining the same metal layer as the plasmonic component. We focused on High-Entropy Alloys (HEAs). In a narrow sense, an HEA is defined as a metallic material composed of five or more metallic elements in equimolar ratios, characterized by the maximization of configurational entropy. While the configurational entropy of conventional binary alloys is relatively low, leading to phase separation when alloying is enthalpically unfavorable, the high entropy in HEAs acts as a driving force for mixing, allowing for the formation of stable solid solutions. HEAs are reported to exhibit superior mechanical strength, and noble-metal-based HEAs have shown significant catalytic effects compared to pure palladium (Pd) or platinum (Pt). However, their application to optical devices, including plasmonics, has not yet been fully realized. Recently, alloys have gained attention as plasmonic materials; for instance, Au-Ag-Cu systems (categorized as medium-entropy alloys) have demonstrated utility, although X-ray diffraction (XRD) analysis indicates slight phase separation between Au-Ag and Ag-Cu. In this study, we constructed an MIM metasurface using an HEA composed of Au, Ag, Cu, Pt, Pd, Al ,Mg. While the Group 11 elements (Au, Ag, Cu) and Al, Mg are useful for plasmonics, their Drude parameters suggest that scattering remains influential. By incorporating Group 10 elements (Pt, Pd), which exhibit strong damping and high absorption loss due to their dielectric constants, we expected to increase the absorption coefficient. We report that this five-element HEA system serves as an effective metasurface material across a wide mid-infrared (MIR) range. The electric permittivity of the metallic materials were determined using spectroscopic ellipsometry. To eliminate back-surface reflections, thick films (> 200 nm) were used. Measurements were performed across a broad spectrum using both UV-Vis and MIR spectroscopic ellipsometry. The data were analyzed using a Drude-Lorentz model, where parameters were optimized via the least-squares method to merge the results into a single consistent model.

References

[1] Y Nishijima, T Sudo, Y Matsuo, S Juodkazis “A Noble Metal High-Entropy Alloy for Mid-Infrared Metasurfaces,” *Engineering*, vol. 49, pp. 81-89, 2025.

Finite-Barrier Bound States and Flat Bands Enabled by p-Orbitals

Tao Liu[1], Han-Rong Xia[1], Duanduan Wan[1], Meng Xiao[1,*]

[1]School of Physics and Technology, Wuhan University, Wuhan 430072, China

*Corresponding author: phmxiao@whu.edu.cn

Abstract— Orbital degrees of freedom provide a powerful route to engineer unconventional wave phenomena in photonic crystals. We show that p□orbital photonic lattices support finite□barrier bound states and rotation□induced flat bands. By controlling orbital orientation, multiple bands become fully degenerate and dispersionless, enabling robust mode localization and flexible photonic control.

***Keywords*— Bound states in the continue, Flat bands, p-orbitals.**

I. Introduction

Photonic crystals are commonly described using effective single□orbital models, yet realistic structures naturally host multiple orbital□like modes. By selectively enhancing p□orbital responses through material choice and structural design, orbital degrees of freedom can be isolated and exploited as an active control parameter. In this talk, we present two experimentally motivated platforms that demonstrate how p□orbitals enable qualitatively new photonic states.

II. Results and Discussion

First, we introduce a square□lattice photonic crystal with two p□orbitals per site and show that it supports boundary states trapped by a finite barrier. Despite the absence of a well□defined bulk bandgap due to finite size effect, these modes exhibit vanishing tunneling at specific wave vectors, forming finite□barrier bound states analogous to bound states in the continuum. We discuss their physical origin, tunability, and experimental observation.

Second, we study lattices hosting a single p□orbital per site, where the orbital pointing direction acts as an additional internal degree of freedom. By coherently rotating the p□orbitals within each unit cell, we induce a band□flip transition and identify critical rotation angles at which all bands become perfectly flat and degenerate across the Brillouin zone. This mechanism is robust against higher□order couplings and enables localized excitation under arbitrary sources. Together, these results establish p□orbital engineering as a versatile strategy for realizing flat bands and confined states in photonic systems.

III. Conclusion

Overall, our results establish the orbital degree of freedom as a powerful and previously underexplored mechanism for creating finite barrier bound states and flat bands in photonic systems.

Acknowledgments

This work was supported by the National Natural Science Foundation of China (Nos. 12321161645, 12334015, 12274332, 12274330).

References

[1] T. Liu, K. Bai, Y. Zhang, D. Wan, Y. Lai, C. T. Chan, and M. Xiao, "Finite barrier bound states," Light: Science & Applications, vol. 13, Art. no. 69, 2024.

[2] H.-R. Xia, Z. Wang, Y. Wang, Z. Gao, and M. Xiao, "Fully flat bands in a photonic dipolar kagome lattice," Physical Review Letters, vol. 135, no. 17, p. 176902, 2025.

Chirped Pulse Propagation and Control in Reverberant non-Hermitian Settings Enabled Through Complex Time Delay

Isabella Giovannelli[1], Thomas M. Antonsen[1,2], Steven M. Anlage[1,2]*

[1]Department of Physics, University of Maryland, College Park, MD 20742-4111 USA
[2]Department of Electrical and Computer Engineering, University of Maryland, College Park, MD 20742-3285 USA
*Corresponding author: anlage@umd.edu

***Abstract*— Complex time delay (CTD), derived from frequency domain scattering matrix data, predicts time and frequency shifts of reflected and transmitted time-domain pulses from multi-modal scattering systems. We extend these results to chirped pulses and show that the pulse time shift is a combination of real and imaginary CTD, creating new opportunities for pulse control.**

***Keywords*— metamaterials, microwave, time delay, non-Hermitian physics, chirped pulse, reflection, transmission.**

I. Introduction

It is known that transmission time delay $\tau_T = \frac{-i}{2\pi}\frac{d}{df}\ln[T]$ in non-Hermitian scattering systems is complex and encodes information about the poles and transmission zeros of the scattering matrix [1, 2]. We recently demonstrated experimentally that τ_T predicts the time shift D_t and frequency shift D_f of a transmitted Gaussian pulse with fixed center frequency [3]. Complex time delay, and its dependence on frequency, is a property of a given scattering system. However, tunable metasurfaces embedded inside the system can be utilized to modify the CTD, often quite dramatically, through the process of "cavity shaping" [4, 5]. Now the question arises, can we modify pulse propagation through complex scattering systems by means of "pulse shaping"?

II. Pulse Shaping

Chirping creates pulses whose instantaneous carrier frequency varies during the pulse, and are the basis for multiple modern technologies, and are present in various fundamental physical phenomena. This includes chirped pulse amplification, chirped pulse spectroscopy, lidar, radar, and sonar, qubit control, etc. Gaining control over the propagation of chirped pulses in reverberant scattering structures is of central importance to many scientific problems and technological applications.

We find theoretically that for narrow-bandwidth pulses interacting with a single resonance inside a reverberant scattering system, the transmitted pulse suffers a time shift given by $D_t = Re[\tau_T] - \Omega'\delta_T^2 Im[\tau_T]$, where δ_T is a measure of the duration of the pulse envelope and Ω' is the linear chirp rate. A frequency chirp effectively allows the pulse to explore the transmission properties of the system not just the center frequency, but also at neighboring frequencies, leading to a mixture of real and imaginary parts of the complex transmission time delay to contribute to the time shift of the transmitted pulse. Note that the time shift is sensitive to the sign of the chirp rate Ω' as well. Altogether, this leads to a remarkable degree of control of time shift, and to some extent the frequency shift, of the transmitted pulse, as we demonstrate experimentally.

III. Experiment and Results

Experiments are performed in transmission through microwave graphs which support a number of wide-bandwidth resonant modes. We use an arbitrary waveform generator (AWG) to synthesize the chirped pulses, and create pulses with a variety of center frequencies, pulse durations and chirp rates. The pulses are transmitted through the graphs and measured on a digital sampling oscilloscope, and the time and frequency shifts suffered by the pulses are measured.

We have explored values of the dimensionless parameter $\Omega'\delta_T^2$ between approximately -1000 and +1000 in our experiments. The results show excellent agreement with the predicted time shift D_t of the pulse and its dependence on parameters, including center frequency (which changes the real and imaginary parts of τ_T), the pulse duration δ_T, and the linear chirp rate Ω'.

IV. Conclusion

We have expanded the importance of complex time delay by showing that chirped pulses can have their propagation properties systematically varied over a considerable range through a controlled linear combination of the real and

imaginary parts of CTD. The results generally apply to all wave phenomena in multi-modal resonant settings, and serve to create new opportunities for utilization of these scientifically- and technologically-important pulses over the entire electromagnetic spectrum.

ACKNOWLEDGMENTS

This work was supported by NSF/RINGS under grant No. ECCS-2148318, ONR under grant N000142312507, and DARPA WARDEN under grant HR00112120021.

REFERENCES

[1] Lei Chen, Steven M. Anlage, and Yan V. Fyodorov, "Generalization of Wigner Time Delay to Sub-Unitary Scattering Systems," Phys. Rev. E 103, L050203 (2021).

[2] Lei Chen and Steven M. Anlage, "Use of Transmission and Reflection Complex Time Delays to Reveal Scattering Matrix Poles and Zeros: Example of the Ring Graph," Phys. Rev. E 105, 054210 (2022).

[3] Isabella L. Giovannelli and Steven M. Anlage, "Physical Interpretation of Imaginary Time Delay," Phys. Rev. Lett. 135, 043801 (2025).

[4] Jared Erb, David Shrekenhamer, Timothy Sleasman, Thomas M. Antonsen, and Steven M. Anlage, "Control of the Scattering Properties of Complex Systems By Means of Tunable Metasurfaces," Acta Physica Polonica A 144 (6), 421-428 (2023).

[5] Jared M. Erb, Nadav Shaibe, Robert Calvo, Daniel Lathrop, Thomas Antonsen, Tsampikos Kottos, Steven M. Anlage, "Topology and Manipulation of Scattering Singularities in Complex Non-Hermitian Systems: Two-channel Case," Phys. Rev. Research 7, 023090 (2025).

Plasmonic Nanostars: Engineering Optical Tunability for Enhanced Efficiency

Nicolas. Pazos-Perez

Department of Physical and Inorganic Chemistry, Universitat Rovira i Virgili, Tarragona, Spain

Corresponding author: nicolas.pazos@urv.cat

***Abstract*— We investigate the controlled epitaxial growth of silver and gold onto preformed gold nanostars, enabling precise tuning of their optical response while preserving branched morphology. Adjusting the plasmon resonance position and silver content, SERS enhancing properties can be maximized by nearly two orders of magnitude compared to conventional gold nanostars..**

***Keywords*— plasmonics, nanostars, gold nanoparticles, silver nanoparticles, SERS.**

I. Introduction

Over the last several decades, significant efforts have focused on engineering plasmonic nanoparticles that produce maximal surface-enhanced Raman scattering (SERS) signals. Although spherical gold and silver nanoparticles are widely used in SERS, their intrinsic properties typically require particle aggregation to create intense localized electromagnetic regions, or "hotspots," necessary for strong signal amplification. While such aggregation strategies can achieve very low detection limits, they often lack reproducibility, limiting their practical implementation. To overcome these drawbacks, researchers have developed controlled assembly methods that organize nanoparticles into defined architectures, including core–satellite structures.[1-4] However, in many of these systems, the electromagnetic hotspots are located within the interior of the assemblies, restricting analyte access and ultimately diminishing sensing performance.

A different strategy to circumvent these limitations involves employing single nanoparticles that inherently generate electromagnetic hotspots, such as gold nanorods and gold nanostars (NSts).[5-7] Among these nanostructures, Au nanostars stand out for their exceptional SERS performance, which arises from their numerous sharp protrusions. Each branch tip supports strongly confined and highly intensified electromagnetic fields. This distinctive morphology creates multiple readily accessible hotspots at the particle surface, promoting strong signal amplification while facilitating effective interaction with target analytes.

Although gold nanostructures are highly valued for their chemical robustness and controllable optical properties, silver nanoparticles generally exhibit stronger plasmonic responses and superior optical performance. Nevertheless, producing anisotropic silver nanostructures in a controlled and reproducible manner remains difficult, which restricts their broader implementation in SERS sensing. A widely adopted solution consists of depositing silver onto pre-synthesized gold nanoparticles.[8] This approach maintains the uniformity and defined shape of the gold templates while benefiting from the enhanced plasmonic characteristics of silver. Despite successful silver overgrowth on multiple gold nanoparticle geometries, only limited research has addressed silver deposition on gold nanostars. Furthermore, previous reports often describe silver growth occurring predominantly at the nanostar core,[9] resulting in structural modifications that diminish the branched features critical for their outstanding SERS performance.

In addition to providing stronger SERS enhancement, silver nanoparticles display plasmonic resonances at shorter wavelengths, extending into the ultraviolet (UV) range. For this reason, coating gold nanostructures with silver has become a common strategy to induce controlled blue shifts in their plasmon bands, enabling precise tuning of their optical response throughout the visible to near-infrared (Vis–NIR) region.[8]

In this work, we describe a method for the controlled epitaxial growth of gold and silver on gold nanostars (NSts), enabling accurate tuning of their optical response without compromising their branched architecture. By carefully adjusting the plasmonic response of gold nanostars, a silver shell can be grow maximizing silver content meanwhile adjusting the optical response. Notably, the process preserves the multiple sharp tips that define the nanostar morphology and sustain their intrinsic electromagnetic hotspots. SERS measurements reveal that silver-coated nanostars deliver an approximately an increase of two orders of magnitude in brightness compared standard gold nanostars.[10] Overall, these results demonstrate that silver-functionalized nanostars constitute highly effective SERS platforms with customizable optical properties, expanding their potential for advanced plasmonic sensing and molecular detection technologies.

REFERENCES

[1] Pazos-Perez, N., Fitgerald, J. M., Giannini, V., Guerrini, L., Alvarez-Puebla, R., "Modular assembly of plasmonic core–satellite structures as highly brilliant SERS-encoded nanoparticles," Nanoscale Advances, 2019, 1 (1), 122-131.

[2] Tebbe, M., Lenzt, S., Guerrini, L. Fery, A. Alvarez-Puebla, R., Pazos-Perez, N., "Fabrication and optical enhancing properties of discrete supercrystals," Nanoscale, 2016, 8 (25), 12702-12709.

[3] Blanco-Formoso, M., Pazos-Perez, N., Alvarez-Puebla, R., "Fabrication of Plasmonic Supercrystals and Their SERS Enhancing Properties," ACS omega, 2020, 5 (40), 25485-25492.

[4] Terrones-Morey, G., Xiao, X., Giannini, V., Fragoso, A., Guerrini, L., Pazos-Perez, N., "Comparative SERS Activity of Homometallic and Bimetallic Core–Satellite Assemblies," Nanomaterials, 2024, 14 (18), 1506.

[5] Tebbe, M., Maennel, M., Fery, A., Pazos-Perez, N., Alvarez-Puebla, R., "Organized Solid Thin Films of Gold Nanorods with Different Sizes for Surface-Enhanced Raman Scattering Applications," The Journal of Physical Chemistry C, 2014, 118 (48), 28095-28100.

[6] Pazos-Perez, N., Guerrini, L., Alvarez-Puebla, R., "Plasmon Tunability of Gold Nanostars at the Tip Apexes," ACS omega, 2018, 3 (12), 17173-17179.

[7] Morla-Folch, J., Guerrini, L., Pazos-Perez, N., Arenal, R., Alvarez-Puebla, R., "Synthesis and Optical Properties of Homogeneous Nanoshurikens," ACS Photonics, 2014, 1 (11), 1237-1244.

[8] Tebbe, T., Kuttner, C., Mayer, M., Maennel, M., Pazos-Perez, N., König, T.A.F., Fery, A., "Silver-Overgrowth-Induced Changes in Intrinsic Optical Properties of Gold Nanorods: From Noninvasive Monitoring of Growth Kinetics to Tailoring Internal Mirror Charges," The Journal of Physical Chemistry C, 2015, 119 (17), 9513-9523.

[9] Fales, A.M., Yuan, H., Vo-Dinh, T., "Development of Hybrid Silver-Coated Gold Nanostars for Nonaggregated Surface-Enhanced Raman Scattering," J. Phys. Chem. C 2014, 118, 7, 3708–3715.

[10] J. Peñas-Farré, X. Xiao, V. Giannini, X. Mateos, L. Guerrini,* N. Pazos-Perez*, "Synthesis and Optimization of Highly Bright Silver-Coated Au Nanostars with Tunable Plasmonic Properties," ACS Nanoscience Au, 2025, 5, 6, 469–481.

Copper-based plasmonic nanohole arrays for electromagnetic field enhancement

M. Amrani[1,*] T.Nguyet[2], G. Lévêque[2], M. El Ghafiani[1], E.H. El Boudouti[1], Y. Pennec[2], R. Boukherroub[2] and B. Djafari-Rouhani[2]

[1] LPMR, Département de Physique, Faculté des Sciences, Université Mohammed Premier, 60000 Oujda, Morocco

[2]Univ. Lille, CNRS, Univ. Polytechnique Hauts-de-France, UMR 8520 – IEMN, F-59000 Lille, France

*Corresponding author: m1.amrani@ump.ac.ma

***Abstract*— Localized surface plasmon resonance (LSPR) in copper nanoholes enhances local electromagnetic fields at the nanoscale. We investigate the effects of lattice period, hole size, and film thickness on field enhancement, analyzing both localized and propagating plasmonic modes. Optimized nanostructure designs offer potential applications in electrocatalysis and other plasmon-assisted processes.**

***Keywords*— LSPR, plasmonic structures, enhancement field.**

I. Introduction

Plasmonic nanoparticles (NPs) exhibit remarkable optical properties arising from localized surface plasmon resonance (LSPR), which corresponds to the collective oscillation of conduction-band electrons excited by incident electromagnetic radiation [1]. Under resonant conditions, LSPR can lead to strong confinement and enhancement of the electromagnetic field in the vicinity of the nanoparticle surface. This localized field enhancement plays a key role in many plasmonic phenomena, including enhanced light–matter interaction, strong optical absorption, and improved energy localization at the nanoscale. Such enhanced plasmonic fields are widely exploited in surface-enhanced spectroscopies, such as surface-enhanced Raman scattering, and are increasingly investigated for plasmon-assisted catalytic processes. The magnitude of the field enhancement strongly depends on the shape and size of the nanoparticles, as well as on the wavelength of the incident excitation.

In addition, these LSPR effects are considered promising for applications in sensing and plasmon-assisted catalytic processes. Although plasmon-driven electrochemical reactions, such as oxygen reduction, hydrogen evolution, and methanol oxidation, have been reported in recent studies [2–4], the fundamental electromagnetic mechanisms responsible for field enhancement in plasmonic nanostructures remain an active area of research.

Periodic nanohole arrays are particularly attractive plasmonic systems, because they can support both localized surface plasmons and propagating surface plasmon polaritons. In this study, we propose a triangular lattice of copper nanoholes (Cu NHs) covered with water and supported on a glass substrate. We investigate the optical response of these structures by analyzing their transmission, reflection, and absorption spectra using the finite element method implemented in COMSOL Multiphysics. A comprehensive geometrical parameter study is conducted to assess the influence of the lattice period, hole, size, and copper thickness. In addition, we examine the localized and propagating behavior of plasmonic modes as a function of these geometrical parameters in order to identify the most suitable designs for enhanced electrocatalytic applications.

II. Results and Discussion

Obviously, an enhanced plasmon mode should lead to significantly improved catalytic activity, as it is directly linked to scattering extinction (transmission, reflection, and absorption) together with the eigenfrequencies of both isolated and coupled nanoholes. An example of the Cu NH configuration is shown in Fig. 1(a), along with a corresponding experimental sample in Fig. 1(b). The structure is illuminated by a plane wave at normal incidence from the water side. Figures 1(c)–(e) display the transmission, reflection, and absorption amplitudes as functions of wavelength and lattice period. Two resonant modes are clearly observed in the visible spectral range. These modes exhibit a linear redshift with increasing period a, indicating that the plasmonic resonances can be efficiently tuned through the lattice periodicity.

An example of the optical spectra is shown in Fig. 2(a), illustrating the transmission, reflection, and absorption as a function of wavelength for a lattice period of $a = 880\ nm$. As

observed, two plasmonic modes appear as reflection maxima around 690 and 770 nm. These modes correspond to excited propagating plasmon at the water/Cu and Cu/glass interfaces, resulting from the diffraction of incident light by the nanohole (NH) array, as illustrated in the field maps of the two resonances. These resonant modes could be exploited in chemical reactions and electrocatalytic applications due to their strong field enhancement. Additionally, the proposed system may serve as a sensing platform, with its performance that could be tuned by adjusting the water height and the filling fraction

III. Conclusion

In conclusion, we analyzed the copper nanohole configuration in a triangular lattice on a glass substrate. The study revealed both localized and propagating plasmonic modes and their dependence on geometrical parameters, providing guidance for optimal design. These Cu nanostructures exhibit strong potential for plasmon-enhanced chemical reactions, electrocatalysis, and sensing applications. A detailed investigation of the properties of these plasmonic nanostructures, which demonstrate promising performance for electrocatalytic reactions, will be presented elsewhere.

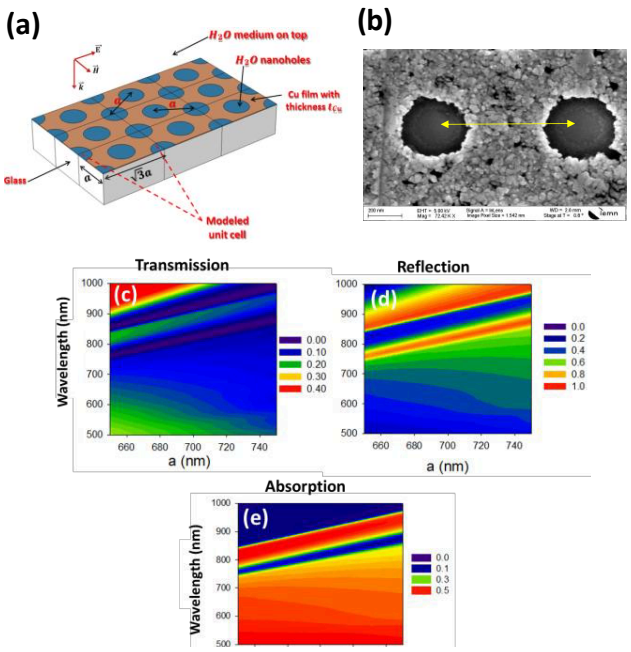

Fig. 1. (a) Schematic illustration of copper Cu NHs arranged in a triangular grating and supported on a glass substrate. The nanoholes are covered with water. (b) Experimental sample of the Cu NHs system. (c)-(e) Color-scale maps of the transmission, reflection, and absorption amplitudes, respectively, as a function of wavelength and period a for the following parameters: hole diameter of 400 nm and copper film thickness of 60 nm.

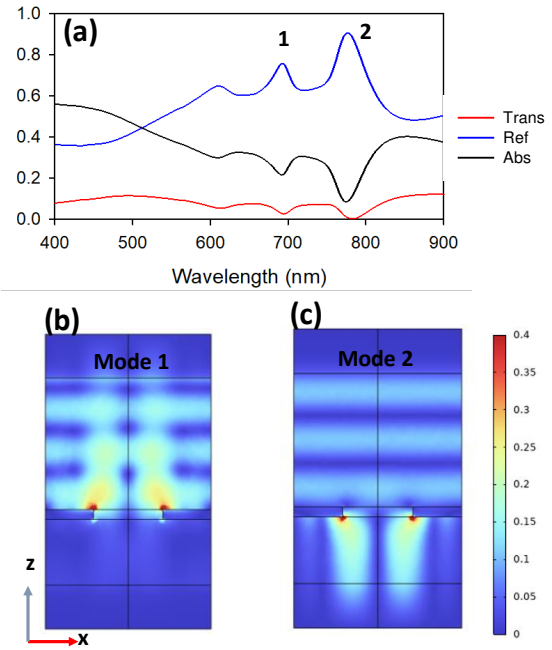

Fig. 2. (a) Transmission (red curve), reflection (blue curve) and absorption (black curve) spectra as a function of wavelength for the following parameters: hole diameter of 400 nm, grating constant a=880 nm, and copper film thickness of 60 nm. (b) and (c) 2 D cut view of the E field norm map for the two modes at 690 nm and 770 nm, respectively.

Acknowledgments

Acknowledgments: This work was funded by Agence Nationale de la Recherche (ANR) in the PEECFUEL project (ANR-23-CE05-0026)

References

1. J. Zhao et al., Localized surface plasmon resonance for enhanced electrocatalysis, Chem. Soc. Rev. 50 12070–12097 (2021)
2. N. Saada et al., Plasmon-enhanced electrocatalytic oxygen reduction in alkaline media on gold nanohole electrodes, *J. Mater. Chem. A* 8, 10395-10401, 2020
3. Pang et al., Exploring the impact of atomic lattice deformation on oxygen evolution reactions based on a sub-5 nm pure face-centred cubic high-entropy alloy electrocatalyst, *J. Mater. Chem. A* 8, 13980-13986, 2020
4. Pang et al., Plasmon-Driven Electrochemical Methanol Oxidation on Gold Nanohole Electrodes, ACS Appl. Mater. Interfaces 12, 50426-50432 2020

.

Metasurface-Driven Control of Quantum Emitters: From Visible Nanolasers to Telecom Photonics

Giovanni Mattei[1*]

[1] Department of Physics and Astronomy, University of Padova, Italy
*Corresponding author: giovanni.mattei@unipd.it

***Abstract*— Engineered optical metasurfaces enable precise control of quantum-emitter radiation at room temperature. We demonstrate three platforms: metallic nanoparticle arrays for coherent visible emission, slotted-silicon metasurfaces enhancing Er^{3+} emission at 1540 nm, and VO_2 phase-change films providing active tunability. These approaches advance scalable quantum photonic sources across visible and telecom bands.**

***Keywords*— Metasurfaces, Quantum emitters, Emission control.**

I. Introduction

Optical metasurfaces offer unprecedented control over light–matter interactions at subwavelength scales. By tailoring their geometry and materials, they reshape the emission dynamics of quantum emitters placed in the near-field. This enables enhanced, directed, or actively tunable radiation at room temperature. Such capabilities open new pathways for compact quantum photonic sources across visible and telecom wavelengths.

II. Methods

The metasurfaces were designed through electromagnetic simulations using finite-difference time-domain and rigorous coupled-wave analysis to optimize resonance modes and field enhancement. Thin-film emitters and nanostructures were fabricated by electron-beam lithography, sputtering, and controlled deposition techniques. Optical characterization involved photoluminescence spectroscopy, lifetime measurements, and angle-resolved emission analysis to quantify enhancement and directionality. Electrical excitation studies employed device stacks optimized for balanced carrier injection, enabling room-temperature electroluminescence from the embedded emitters.

III. Results and Discussion

Here we present three case studies of different metasurfaces for controlling at room temperature the emission efficiency of different emitters in the visible or telecom spectral range: (i) 2D ordered arrays of Al nanoparticles coupled with dye molecules for ultralong ($\tau_c = 29 \pm 2$ ps) temporal coherent emission in the VIS range (nanolasers)[1]; (ii) slotted Si nanodisks arrays for the 3 orders of magnitude enhancement of the emission at $\lambda = 1540$ nm from Er^{3+} ions by exploiting quasi-BIC modes with Q-factor values up to 10^5 [2]; (iii) phase-change materials thin films based on VO_2 for the active control of Er^{3+} ions, whose radiative lifetime is modulated by a factor 2 between the monoclinic (room temperature) and rutile (high-temperature) VO_2 phases [3].

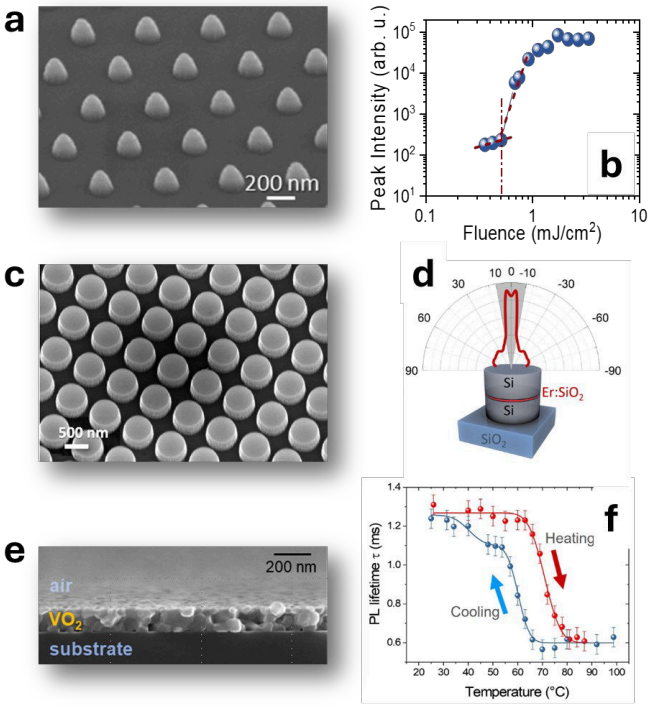

Fig. 1 (a,b) Al nanolaser: SEM image and lasing intensity; (c,d) Si nanogap array: SEM image and directional enhanced emission; (e,f) Er@VO_2: SEM image and lifetime control with temperature.

IV. Conclusion

The presented metasurface platforms demonstrate effective control of quantum-emitter radiation across visible and telecom wavelengths at room temperature. By tailoring resonant modes, field confinement, and active material responses, we achieve enhanced, directed, and tunable emission. These results highlight metasurfaces as versatile building blocks for scalable

quantum photonic devices, from nanoscale light sources to reconfigurable emitters for integrated optical technologies.

ACKNOWLEDGMENTS

This work was supported by the PNRM Project "METEORE" funded by the Italian Ministry of Defense, by the Italian MUR Departments of Excellence grant 2023−2027 "Quantum Frontiers" and by the University of Padova within the project PRDBIRD2022.

REFERENCES

[1] M. Trevisani, D. Piccotti, E. Mendoza Sandoval, G. Pirruccio, M. Ramezani, J. Gomez Rivas, T. Cesca, G. Mattei, "Ultra-long temporal coherence in a solid-state plasmonic nanolaser", ACS Photonics vol. 13, pp. 92-100, 2026.

[2] B. Kalinic, T. Cesca, I. G. Balasa, M. Trevisani, A. Jacassi, S. A. Maier, R. Sapienza, and G. Mattei, "Quasi-BIC Modes in All-Dielectric Slotted Nanoantennas for Enhanced Er^{3+} Emission", ACS Photonics vol.10, p. 534, 2023.

[3] B. Kalinic, T. Cesca, A. Lovo, C. Scian, R. Macaluso, F. Bovino, R. Li Voti, C. Sibilia, and G. Mattei, "Active Modulation of Er^{3+} Emission Lifetime by VO_2 Phase-Change Thin Films", Advanced Photonics Research vol. 5, p. 2300242, 2024.

Two Distinct Quasi-Bound States in the Continuum in an Amorphous Silicon Metasurface

Hicham Mangach[1,*], Pascal Szriftgiser[1], Gaëtan Lévêque [1], Yan Pennec [1], Bahram Djafari-Rouhani [1]

[1]Univ Lille, CNRS, UMR 8520-IEMN, F59000 Lille, France
*Corresponding author: hicham.mangach@univ-lille.fr

Abstract— **Quasi–bound states in the continuum (QBICs) enable subwavelength light confinement with long photon lifetimes. Here, we demonstrate accidental and symmetry-protected QBICs in an amorphous silicon metasurface. The quality factor of the accidental QBIC reaches 10^4, while the symmetry-protected QBIC approaches 10^5.**

***Keywords*— metasurface, quasi-bound states, photon lifetime.**

I. Introduction

Recently, bound states in the continuum (BICs) have enabled strong confinement of light within regions smaller than the wavelength scale [1]. Owing to their long photon lifetimes, these states have attracted significant interest for applications including high–coherence lasers, ultra-sensitive sensors, and optomechanical coupling [2-3]. However, these dark states are inaccessible due to symmetry protection or destructive interference [4]. Therefore, BICs remain outcoupled from all possible radiation channels. In order to make them accessible, two distinct mechanisms exist [5]. In symmetry-protected BICs, the mode is forbidden from radiating due to the incompatibility of its field profile with the symmetry of the lattice. Introducing a controlled symmetry-breaking along a certain symmetry plane, such as displacing or reshaping elements in the unit cell, allows partial coupling of the mode to free-space radiation [6]. This converts the ideal BIC into a QBIC with a finite photon lifetime, while the resonance remains sharp and well-defined. In contrast, the accidental BICs arise from the precise cancellation of multiple radiative channels. By slightly detuning structural parameters, such as the lattice spacing, element dimensions, or refractive index, this delicate interference is partially disrupted, allowing weak radiation leakage [7]. The resulting QBIC inherits a finite lifetime, determined by how closely the interference condition is preserved.

II. Accidental and Symmetry-Protected QBICs Engineering

We consider a dimerized rectangular resonator composed of amorphous silicon (a-Si) deposited on a glass substrate, arranged in a square lattice (Fig. 1A). The lattice period and the resonator aspect ratio are carefully tuned to perturb the modes' destructive interference, enabling energy exchange with external channels. The resulting accidental quasi-bound state in the continuum (A-QBIC) appears at a wavelength of 1390 nm with a photon lifetime of 10^4, as shown in Fig. 1D. To realize a second class of QBICs, here referred to as SP-QBICs, we introduce an a-Si bridge connecting the dimerized resonators at the center of the lattice (Fig. 1B). Because the bridge is placed symmetrically, the overall lattice symmetry is preserved, and the spectral position of the A-QBIC remains essentially unchanged, with only minor shifts in the resonance peak due to the modified a-Si filling factor. The SP-QBICs are obtained by breaking the horizontal mirror symmetry plane (XZ-plane) through a displacement of the bridge along the *y*-direction. This perturbation generates a SP-QBIC at a wavelength of 1450 nm with a quality factor of 10^5(see Fig.1 E). Both QBIC wavelengths lie in the near-infrared, close to the telecommunication bands, where materials such as a-Si exhibit low optical loss, facilitating on-chip integration. This spectral region offers additional advantages for sensing and optomechanical applications. The 1390 nm wavelength is highly sensitive to water vapor, which corresponds to a strong water absorption band, allowing the evaluation of water content in biological tissues, including porcine and human skin [8]. Moreover, the 1450 nm band is suitable for exploiting enhanced light-matter interactions to achieve strong optomechanical coupling [9]. The sample is fabricated from a 200-nm-thick amorphous silicon (a-Si) layer deposited on a 782-nm-thick silicon dioxide (SiO_2) substrate. A 1.5-µm-thick photoresist is spin-coated and patterned by electronic lithography, followed by the deposition of a 200-nm-thick nickel (Ni) hard mask for pattern transfer. The a-Si nanostructures are etched using reactive-ion etching (RIE, Plassys MU400) with an SF_6/O_2 gas mixture (20 sccm SF_6, 6 sccm O_2) at a chamber pressure of 5 mTorr and a temperature of 15 °C. The QBIC resonances are characterized using the setup shown in Fig. 2. A broadband telecom source is used to cover both resonances. The incident light is linearly polarized to align the polarization with the long axis of the dimerized resonators. Collimating mirrors ensure a nearly parallel beam before it enters an optical microscope with up to 20× magnification. The reflected spectrum is measured using a

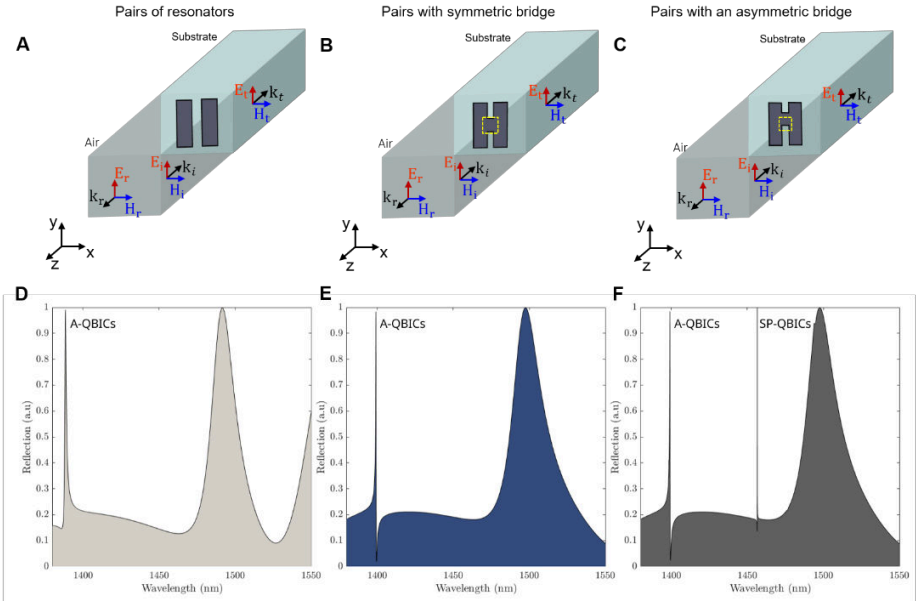

Fig 1: Illustration of QBICs formation in a-Si metasurface : (A–C) Dimerized rectangular resonators with and without a linking bridge. The A-QBIC is depicted with and without the linking bridge. The bridge is moved along the *y*-axis by 20 nm in scenario (C), for the purpose of breaking the symmetry. (D-F) Numerical simulation of the reflection spectra of the meta-designs when excited with linear polarization parallel to the resonator's long axis.

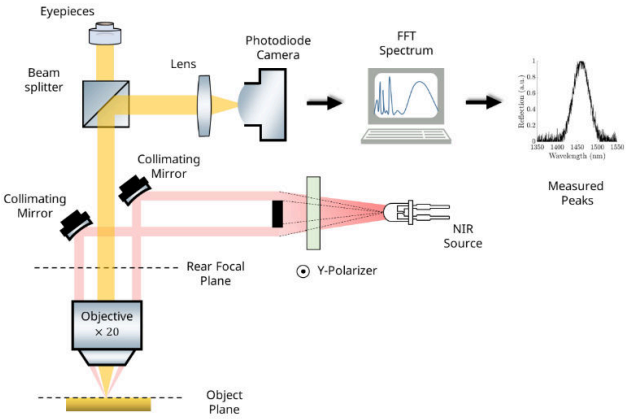

Fig 2: **Experimental Setup**: The apparatus utilizes a telecom-wavelength light source, whose output beam is first polarized, spatially filtered, and collimated using collimating mirrors to create two optical channels. The combined beam is then focused onto the sample using a 20× microscope objective (NA = 0.45), with the sample mounted on a nano-positioning stage for precise focal alignment. Reflected light is directed through a broadband beamsplitter to both a visualization eyepiece and a spectrometer equipped with a photodiode detector (600–1600 nm range).

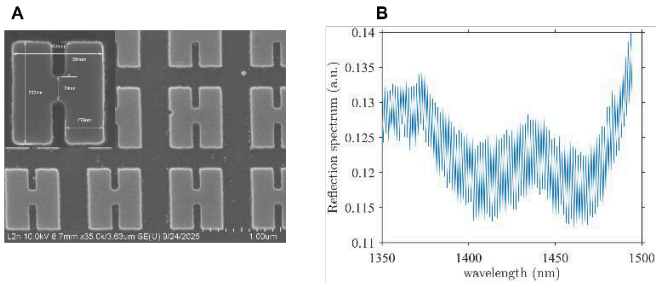

Fig 3: (A) SEM image of the fabricated sample. (B) Measured reflection spectrum indicating the existence of two resonance peaks (A- and SP-QBICs), at 1360 nm and 1440 nm, respectively.

a photodiode detector. Fig. 3(A) and (B) show the fabricated sample and the measured reflection spectra.

The spectra are not yet optimized due to the high Q of the QBIC modes and the limited spectral purity of the NIR source used. Moreover, the observed QBICs' resonance peaks shift is mainly due to manufacturing tolerance and imperfections.

ACKNOWLEDGMENTS

This work was supported by the European Union's Horizon Europe research and innovation program under grant agreement MAGNIFIC (GA No 101091968) and the CHIST-ERA Call 2021 under GA No CHIST-ERA-20-NOEMS-003.

REFERENCES

[1] M. Kang, T. Liu, C. T. Chan, M. Xiao, "Applications of bound states in the continuum in photonics," Nature Reviews Physics, vol. 5, pp. 659–678, 2023.

[2] J. Yu, W. Yao, M. Qiu, and Q. Li, " Free-space high-Q nanophotonics," Light: Science & Applications, vol. 14, pp. 174, 2025.

[3] J. M. Fitzgerald, S. K. Manjeshwar, W. Wieczorek, and P. Tassin, " Cavity optomechanics with photonic bound states in the continuum," Physical Review Research, vol. 3, pp. 013131, 2021.

[4] A. A. Kutuzova, and M. V. Rybin, " Quality factor scaling of resonances related to bound states in the continuum," Physical Review B, vol. 107, pp. 195108, 2023.

[5] S. I. Azzam, V. M. Shalaev, A. Boltasseva, and A. V. Kildishev, " Formation of bound states in the continuum in hybrid plasmonic-photonic systems," Physical Review Letters, vol. 121, pp. 253901, 2018.

[6] J. Jin, X. Yin, L. Ni, M. Soljačić, B. Zhen, and C. Peng, " Topologically enabled ultrahigh-Q guided resonances robust to out-of-plane scattering," Nature, vol. 574, pp. 501–504, 2019.

[7] M. Kang, S. Zhang, M. Xiao, and H. Xu, " Merging bound states in the continuum at off-high symmetry points," Physical Review Letters, vol. 126, pp. 117402, 2021.

[8] L. Lin, H. Lin, C. Wang, Q. Wu, Z. Yang, R. Kan, and H. Zheng, " Highly-sensitive H_2O sensor exploiting at 1.39 μm near-infrared distributed-feedback laser diode," Journal of Russian Laser Research, vol. 43, 590–594, 2022.

[9] S. Liu, H. Tong, and K. Fang, "Optomechanical crystal with bound states in the continuum," Nature Communications, vol. 13, pp. 3187, 2022.

Self enhanced generative metasurface inverse design

Mathys Le Grand[1,2,*], Pascal Urard[2], Denis Rideau[2]
Loumi Trémas[2], Damien Maitre[2], Louis-Henri Fernandez-Mouron[2],
Régis Orobtchouk[1]
[1]Institut des nanotechnologies de Lyon [2]STMicroelectronics
*Corresponding author: mathys.le-grand@insa-lyon.fr

***Abstract*—Inverse design of metasurfaces is hindered by complex structural-electromagnetic relationships and computationally expensive traditional optimization. While deep learning models offer solutions, they are limited by narrow training datasets. We propose using generative inverse design techniques to augment and diversify databases, significantly enhancing design space coverage and improving model generalization.**

***Keywords*— metasurface, inverse design, generative model, diffusion model, Schrödinger bridge.**

I. Introduction

Metasurfaces are subwavelength-patterned metamaterials capable of providing exquisite control over the phase, amplitude, and polarization of light [1], [2]. These capabilities have catalyzed breakthroughs in dielectric metalenses [1], [3], demultiplexers [4], and adaptive beam shaping [5], [6]. The central challenge of inverse design lies in identifying the specific physical geometries required to yield a target optical response. However, the high-dimensional nature of this design space makes exhaustive search computationally exhaustive when utilizing conventional solvers such as Finite-Difference Time-Domain (FDTD) [7], the Finite Element Method (FEM) [8], or Rigorous Coupled-Wave Analysis (RCWA) [9], all of which struggle with scalability and periodic constraints.

This work addresses the inherent "one-to-many" mapping problem where disparate physical architectures produce identical very similar far-field signatures by leveraging generative AI. We propose a recursive framework that utilizes generative models to iteratively refine training datasets, ultimately enhancing the model's ability to navigate complex design landscapes with high fidelity.

II. Generative method background

Diffusion models (DMs)[10], [11] have emerged as powerful generative frameworks capable of modeling complex data distributions through a gradual denoising process. DMs enable high-quality sample generation from simple noise distributions. Their iterative sampling procedure approximates the data distribution by sequentially refining noisy inputs, making them well-suited for inverse design tasks where mapping from desired properties to structural parameters is inherently ill-posed and multimodal.

Building upon this foundation, diffusion Schrödinger bridges (DSBs) [12], [13], [14] extend the classical diffusion framework by framing the generative process as a stochastic optimal transport problem. DSBs model the evolution between two probability distributions typically the data distribution and a prior via a controlled stochastic process that minimizes a Schrödinger-type entropy functional. In inverse design applications, DSBs facilitate more accurate and efficient navigation of the design space, capturing complex conditional distributions that arise from physical constraints and target specifications.

Together, DMs and DSBs offer high performance approaches to generative inverse design [15], [16], enabling the synthesis of structures that meet specified functional criteria while addressing challenges related to multimodality, nonlinearity, and data scarcity.

III. Initial Database

In the absence of an inverse design tool, constructing a database aligned with the anticipated far-field behavior was impractical. Therefore, the initial dataset was generated by sampling metasurface structural parameters from simple distributions primarily uniform across all parameters, resulting in 5,000 samples. Corresponding far-field responses were computed using FDTD simulations.

IV. Enhanced Database

Having established baseline generative models for both DMs and DSBs using the initial database, we employ these models to synthesize a refined dataset. This stage is designed to populate the design space with far-field patterns that are more representative of high-performance metasurface applications. To achieve this, we generated a diverse set of 5,000 target profiles consisting of complex polygonal shapes, including both solid and annular (hole-containing) geometries. This refined dataset allows the generative architectures to learn from a more functionally relevant distribution of optical responses, effectively bridging the gap between random structural permutations and intentional design targets.

V. Enhanced performance

The generatively enhanced database improves the performance of both generative inverse design models DMs and DSBs, as illustrated in Figure 1.

Another stakes is to scale the method to larger metasurface and as seen on Fig. 2 the generative enhanced database not only increase performance on the example with the same size of the database but also on larger metasurface. Moreover the performance metric performs relatively constantly from 23x23 pillars to 98x98 pillars.

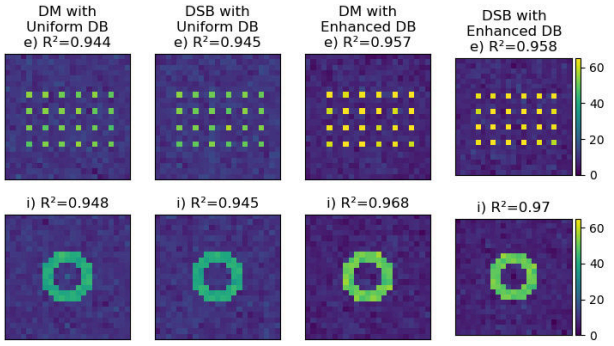

Fig. 1. Far-field distributions obtained via FDTD simulations for diffusion models (DM) and diffusion Schrödinger bridges (DSB), each trained on either the initial or the generatively enhanced database.

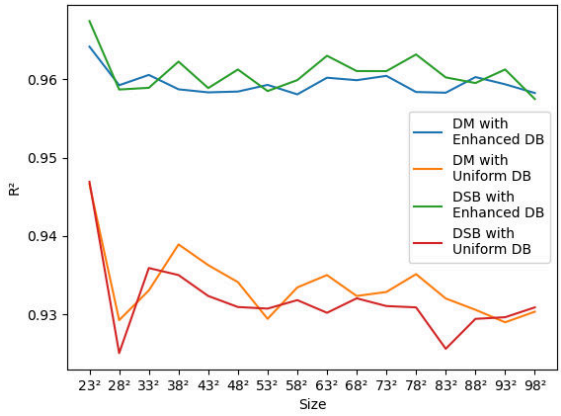

Fig. 2. R^2 metrics computed from FDTD simulations for diffusion models (DM) and diffusion Schrödinger bridges (DSB) trained on either the initial or generatively enhanced database. Inverse design was performed on metasurfaces of increasing size until simulation became computationally infeasible.

REFERENCES

[1] A. Arbabi, Y. Horie, M. Bagheri, and A. Faraon, "Dielectric metasurfaces for complete control of phase and polarization with subwavelength spatial resolution and high transmission," *Nature nanotechnology*, vol. 10, no. 11, pp. 937–943, 2015.

[2] N. Yu and F. Capasso, "Flat optics with designer metasurfaces," *Nature materials*, vol. 13, no. 2, pp. 139–150, 2014.

[3] M. Lepers, A. Ostrovsky, P. Genevet, S. Lanteri, and J. Vaillant, "Metasurface-based planar microlenses integrated on back-side illuminated cmos pixels 1 st," in *International Image Sensor Workshop (IISW)*, 2023.

[4] A. Y. Piggott, J. Lu, K. G. Lagoudakis, J. Petykiewicz, T. M. Babinec, and J. Vučković, "Inverse design and demonstration of a compact and broadband on-chip wavelength demultiplexer," *Nature photonics*, vol. 9, no. 6, pp. 374–377, 2015.

[5] S. Jafar-Zanjani, S. Inampudi, and H. Mosallaei, "Adaptive genetic algorithm for optical metasurfaces design," *Scientific reports*, vol. 8, no. 1, p. 11040, 2018.

[6] D. Rideau, M. Le Grand, L. H. F. Mouron, V. Serradeil, L. Tremas, P. Urard, D. Maitre, H. Mohamad, L. Dilhan, E. G. Carnemolla *et al.*, "Approaches to simulating meta-surfaces for flat optical devices: The transition to solutions based on neural networks," in *2024 International Conference on Simulation of Semiconductor Processes and Devices (SISPAD)*. IEEE, 2024, pp. 01–04.

[7] S. D. Gedney, *Introduction to the finite-difference time-domain (FDTD) method for electromagnetics*. Morgan & Claypool Publishers, 2011, vol. 27.

[8] B. A. Rahman and A. Agrawal, *Finite element modeling methods for photonics*. Artech House, 2013.

[9] T. K. Gaylord and M. Moharam, "Analysis and applications of optical diffraction by gratings," *Proceedings of the IEEE*, vol. 73, no. 5, pp. 894–937, 1985.

[10] J. Ho, A. Jain, and P. Abbeel, "Denoising diffusion probabilistic models," *Advances in neural information processing systems*, vol. 33, pp. 6840–6851, 2020.

[11] H. Chung, J. Kim, M. T. Mccann, M. L. Klasky, and J. C. Ye, "Diffusion posterior sampling for general noisy inverse problems," *arXiv preprint arXiv:2209.14687*, 2022.

[12] T. Chen, G.-H. Liu, and E. A. Theodorou, "Likelihood training of schrödinger bridge using forward-backward sdes theory," *arXiv preprint arXiv:2110.11291*, 2021.

[13] D. Liu, Y. Tan, E. Khoram, and Z. Yu, "Training deep neural networks for the inverse design of nanophotonic structures," *Acs Photonics*, vol. 5, no. 4, pp. 1365–1369, 2018.

[14] H. Chung, J. Kim, and J. C. Ye, "Direct diffusion bridge using data consistency for inverse problems," *Advances in Neural Information Processing Systems*, vol. 36, 2024.

[15] M. L. Grand, P. Urard, D. Rideau, L. Trémas, D. Maitre, L.-H. Fernandez-Mouron, A. Fuchs, and R. Orobtchouk, "Enhanced posterior sampling via diffusion models for efficient metasurfaces inverse design," *arXiv preprint arXiv:2601.15210*, 2026.

[16] M. L. Grand, P. Urard, D. Rideau, L. Trémas, D. Maitre, A. Fuchs, L.-H. Fernandez-Mouron, and R. Orobtchouk, "Diffusion schr\" odinger bridges with enhanced posterior sampling for metasurface inverse design," *arXiv preprint arXiv:2602.06605*, 2026.

Spatial Fourier filtering with metagratings

Mahmoud A. A. Abouelatta[1,*], Karim Achouri[1]

[1]Laboratory for Advanced Electromagnetics and Photonics, EPFL, 1015 Lausanne, Switzerland
*Corresponding author: mahmoud.abouelatta@epfl.ch

***Abstract*—Traditional 4f Fourier-optics are too bulky for integrated photonics. We present the first nanostructured metagrating providing high-fidelity angular filtering five orders of magnitude thinner than lens-based systems. By engineering dipolar resonances and Kerker-like interference, we achieve efficient spatial filtering, enabling ultra-compact, lens-free optical computing across the near-infrared.**

***Keywords*— metagratings, angular filtering, spatial Fourier filtering, optical computing.**

I. Introduction

The 4f lens configuration remains the cornerstone of Fourier-optics, facilitating essential angular filtering for applications ranging from holographic data storage to adaptive imaging. However, the inherent physical volume of these refractive systems poses a fundamental bottleneck for the evolution of on-chip integrated photonics. In this work, we transcend these spatial constraints by introducing a metagrating-based architecture [1], as shown in Fig.1, capable of replicating standard Fourier filters within a sub-wavelength footprint. By precisely tailoring the angular scattering of nanostructured arrays, we eliminate the need for traditional lens-based propagation, paving the way for ultra-compact, lens-free spatial signal processing.

II. Methods

Our experimental pipeline utilizes a combination of anisotropic wet etching and controlled material transformation. We initiated fabrication by applying KOH etching to a silicon substrate through a predefined nitride mask, resulting in a series of highly ordered periodic triangular ridges. These silicon precursors were subsequently subjected to thermal oxidation, converting the framework into high-quality silica. To achieve the desired plasmonic response, we performed dual-stage oblique gold evaporation. This technique selectively deposited gold ”hat” structures atop the dielectric ridges. The resulting architecture leverages the complex coupling between two-dimensional dipolar resonances and the Kerker-like suppression of backward scattering, allowing for sharp control over the angular transmission and diffraction profiles.

III. Results and Discussion

Characterization in the near-infrared regime confirms the robust versatility of the metagrating platform. Our measurements in full spatial Fourier space demonstrate that the device functions as an efficient low-pass filter and a controllable high-pass filter. Specifically, the system achieved power suppression exceeding 30 dB for the high-pass filter and 10 dB for the low-pass filter beyond their respective cutoff thresholds.

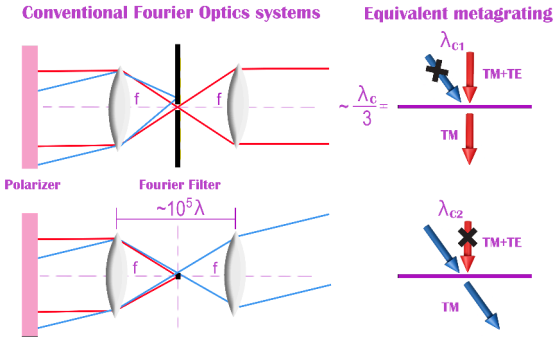

Fig. 1. Schematic representation of the nanostructured platform, providing a compact alternative to the standard 4f imaging system [1].

The gathered experimental data demonstrate excellent agreement with both our theoretical framework and full-wave electromagnetic simulations. Building on these results, we further explore the potential for a reflection-mode bandpass filter. By manipulating the diffraction cutoff conditions inherent to the periodic geometry, numerical simulations suggest the cutoff spatial frequency can be tuned based on the grating cutoff conditions, offering a pathway toward integrated reflection-domain processing that complements the experimentally verified transmission filters.

IV. Conclusion

This work demonstrates a compact metagrating alternative to the bulky 4f system, achieving extreme volume reduction while maintaining high filtering precision. The platform offers a scalable route for lens-free spatial Fourier filtering in challenging electromagnetic regimes—such as the terahertz or X-ray bands—marking a major advancement toward monolithic, high-resolution optical computing. Moreover, this architecture facilitates the simultaneous multiplexing of various spatial filtering operations at specific center wavelengths in a single step. It further broadens the scope of spatial filtering to include signals with significantly reduced coherence lengths.

Acknowledgments

We acknowledge funding from the Swiss National Science Foundation (project TMSGI2_218392).

References

[1] M. A. A. Abouelatta and K. Achouri, “Metapinhole: Planar Fourier Optics Without Lenses,” *arXiv preprint*, arXiv: 2509.05555, 2025.

Foundry-Ready Multi Laser Terahertz Bandwidth Photonic Isolator via Electro-optic Synthetic Motion

Kyunghun Han[1,2,3], Yiliang Bao[1], Junyeob Song[1,2], David Long[1], Sean Bresler[1,4], Daron Westly[1], Jason Gorman[1], Thomas LeBrun[1], Kartik Srinivasan[1], and Vladimir Aksyuk[1,*]

[1]Microsystems and Nanotechnology Division, National Institute of Standards and Technology, USA
[2]Theiss Research, USA
[3]Whiting School of Engineering, Johns Hopkins University, USA
[4]University of Maryland, USA
*Corresponding author: vladimir.aksyuk@nist.gov

***Abstract*— We demonstrate a magnet-free, intrinsically broadband photonic isolator using electro-optic traveling-wave modulation to create synthetic motion across four waveguides, realizing dynamic rotating destructive interference that continuously cancels backward-propagating light. We show ≈30 dB isolation, >24 dB isolation across a 30 nm span, and >20 dB isolation for two lasers simultaneously.**

***Keywords*— chip-scale isolator, electro-optic modulator, synthetic motion, integrated photonics**

SUMMARY

Despite recent progress, achieving nonreciprocal light propagation on chip with low-loss, high contrast and high instantaneous bandwidth remains challenging, limiting the currently available solutions for integrated isolators and circulators.

Here, we show a magnet-free, intrinsically broadband traveling-wave isolator built from foundry-compatible components. The approach, applicable from the visible to telecom, uses radio-frequency electro-optic modulation to create synthetic motion across four parallel waveguides, realizing dynamic rotating destructive interference that continuously cancels backward-propagating light while leaving forward-propagating light unaffected. We reach ≈30 dB isolation while maintaining >24 dB isolation across a 30 nm wavelength span, and show >20 dB isolation for two lasers simultaneously within 10 nm — an optical frequency range order of magnitude broader than any prior non-magnetic designs with similar isolation efficiency. Our demonstration's 770 nm to 800 nm wavelength span covers key alkali atomic transitions, enabling on-chip laser isolation for atomic spectroscopy, laser cooling, and locking applications.

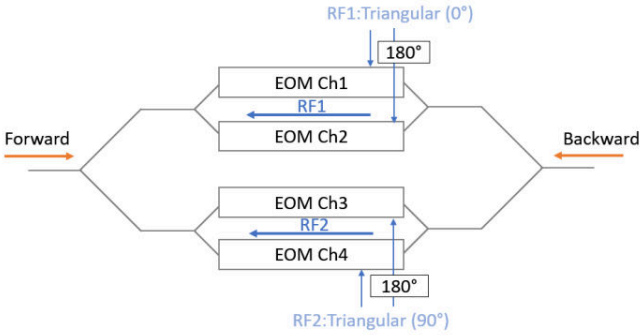

Fig. 1 Isolator schematic. Light is equally split among four channels experiencing nonreciprocal traveling wave modulation. The traveling waves shape and the relative phase offsets are engineered to apply synthetic motion resulting in continuous full destructive interference.

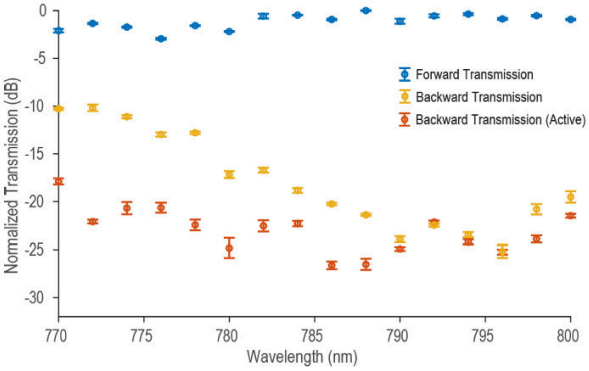

Fig. 2 Broadband isolation.

Miniaturized Full-Color Waveguide Combiner for AR Headsets: Wide Field-of-View and High Resolution via Compound Metagratings

Oksana Shramkova

Laboratoire ICube (UMR 7357), Université de Strasbourg, CNRS, France
*Corresponding author: oksana.shramkova@cnrs.fr

***Abstract*—This work presents a multi-layer metagrating design for single-waveguide near-eye displays, achieving a wide field of view (FoV) while reducing waveguide thickness. The approach enables high-resolution imaging by accommodating large lateral dimensions for the in-coupled grating, optimizing compatibility with advanced light engines.**

***Keywords*—Compound metagrating, augmented reality, high FOV, waveguide.**

I. Introduction

The demand for compact, high-performance augmented reality (AR) headsets continues to drive innovation in optical waveguide technology. Achieving a wide FoV, full-color capability, and high resolution in a miniaturized form factor remains a significant challenge. In this work, we introduce a novel multi-layer metagrating design for single-waveguide near-eye displays, enabling both ultra-thin waveguides and expanded FOV without compromising image quality.

II. Methods

Waveguide-based AR head-mounted displays (HMDs) often rely on multi-waveguide configurations to achieve full-color performance, with each waveguide dedicated to one or two specific colors [1]. However, this approach results in bulky and complex systems. Single-waveguide full-color solutions are therefore preferred for their simplicity and improved integration, but they face a critical limitation: the use of a single diffraction grating for both in- and out-coupling reduces the FOV due to dispersion effects.

Traditionally, expanding the FOV has involved employing high-refractive-index materials, which increase the internal reflection angle. Yet, these materials introduce trade-offs, such as increased waveguide thickness, added weight, and reduced efficiency. To address these challenges, diffractive metagratings offer a promising solution for achieving achromatic waveguide designs [2-5]. However, while this approach enables a wider FOV, it also necessitates larger microdisplays with higher pixel counts, which in turn requires enlarging the in-coupling grating to match the etendue. This often results in thicker waveguides to mitigate back reflection issues.

To overcome these limitations, we propose a novel approach based on polarization transformation. By enabling efficient reflection of orthogonally polarized light at the in-coupling grating, this method prevents light loss due to unintended out-coupling. This innovation allows for the use of thinner waveguides while maintaining large lateral dimensions for the in-coupling grating and accommodating the wide diameter of the in-coupled beam.

This talk introduces multilayered metasurface topologies designed for separated RGB illumination within a single high-refractive-index waveguide, achieving a diagonal FOV exceeding 70° with high uniformity and efficiency (see Fig.1). The optimized gratings transmit one polarization while reflecting the orthogonal polarization.

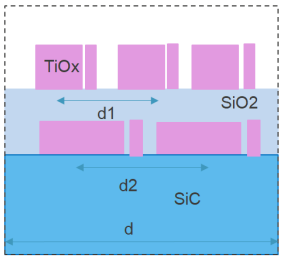

Fig. 1 Cross-sectional view of the metagrating on top of the waveguide.

III. Results and Discussion

By integrating the proposed metagratings with a sapphire retarder layer, we enable efficient light management. Sapphire layer leverages the material's birefringence to rotate the polarization of the in-coupled light (see Fig.2). When combined with a metallic mirror on the opposite side of the waveguide, this configuration further enhances performance. By integrating these gratings with retarders, we demonstrate at least a twofold reduction in waveguide thickness, enabling the development of significantly more compact AR devices.

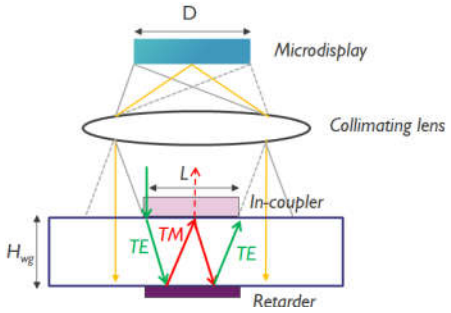

Fig. 2 Configuration of the proposed in-coupling system demonstrating polarization conversion of the in-coupled wave using a combination of an in-coupling metagrating and a retarder.

IV. Conclusion

We have demonstrated a novel approach to achieving full-color, wide-FOV AR displays using multilayered metasurface topologies within a single high-refractive-index waveguide. By leveraging polarization-selective gratings combined with a sapphire retarder and metallic mirror, we not only enhance optical efficiency and uniformity but also reduce waveguide thickness by at least half. This innovation addresses key challenges in miniaturization and performance, offering a promising pathway toward more compact, high-performance AR HMDs.

References

[1] B.C. Kress, I. Chatterjee, "Waveguide combiners for mixed reality headsets: a nanophotonics design perspective," Nanophotonics, vol. 10, pp. 41-74, 2021.

[2] Z. Tian, X. Zhu, P.A. Surman, et al. "An achromatic metasurface waveguide for augmented reality displays," Light: Sc. Appl., vol. 14, article number: 94, 2025.

[3] S. Moon, S. Kim, J. Kim, et al., "Single-layer waveguide displays using achromatic metagratings for full-colour augmented reality," Nat. Nanotechnol., vol. 20, pp. 747–754, 2025.

[4] O. Shramkova, V. Drazic, G. Bourcin, et al., "Metagrating solutions for full color single-plate waveguide combiner," EPJ Applied Metamaterials, vol. 9, p. 5, 2022.

[5] O. Shramkova, A. Shaw, F. Maudet, "Design of a full color single-plate waveguide combiner with high FOV," Proc. SPIE 13414, Optical Architectures for Displays and Sensing in Augmented, Virtual, and Mixed Reality (AR, VR, MR) VI, 134140K (21 March 2025).

Enhancing the Sensitivity of Low-cost Zero-Reflection Metasurfaces for Clinical Translation

Nurten Koc[1], Ali Belarouci[2], Serap Aksu[1,3,*]

[1] Materials Science and Engineering, Koc University, Türkiye
[2] Univ Lyon, ECL, INSA Lyon, CNRS, UCBL, CPE Lyon, INL, UMR5270, Ecully 69130, France
[3] Department of Physics, Koc University, Türkiye
*Corresponding author: saksu@ku.edu.tr

***Abstract*— Zero-reflection metasurfaces hold great promise for clinical translation. Towards this, we manufacture the metasurfaces using optimized adhesion materials with minimum optical loss. We demonstrate their large area homogenous nanofabrication using modified laser lithography and showed detection of brain metastasis relevant biomarkers in serum.**

***Keywords*— metamaterials, optical biosensing, laser interference lithography, cancer diagnostics.**

I. Introduction

Zero-reflection metasurfaces offer unmatched sensitivity but suffer from the 'adhesion-loss' trade-off. Traditional adhesion layers like Ti improve stability but kill optical performance. We identify Al as a 'best-of-both-worlds' solution. We show that Al provides near-field responses that rival adhesion-free gold films. We performed a detailed investigation determining the optimum adhesion layer. The metasurfaces are fabricated on large area using a modified laser interference lithography. The optic and metric uniformity of the nanostructures are quantified and compared against EBL fabricated ones. Finally, we demonstrate the clinical relevance of this platform through the ultrasensitive detection of proteins relevant for brain metastasis and its ability to withstand harsh environmental stress, paving the way for the next generation of robust, portable biosensors.

II. Methods

Zero-reflection metasurfaces were designed via computational modeling using Ansys Lumerical. The nanofabrication is performed using a modified laser interference lithography[1,2]. To highlight the advantages of aluminum adhesion layers in achieving perfect absorption, we utilized a narrowband metal-insulator-metal (MIM) absorber based on a nanodisc antenna architecture [1,2]. The device comprises a 100 nm Au ground plane, a 40 nm SiO_2 dielectric spacer, and a top layer of periodic Au nanodiscs (periodicity: 650 nm; diameter: 180 nm; thickness: 40 nm) on a 500 µm silicon substrate. To investigate stability and performance, 2.5 nm and 5 nm adhesion layers were integrated at the metal-insulator interfaces.

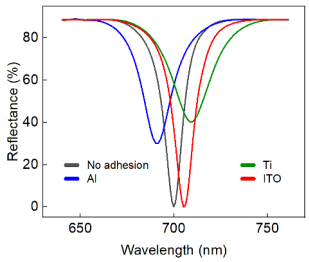

Fig. 1 The simulations showing the effect of 5 nm adhesion layer of different materials on a nanostructured perfect absorber.

III. Results and Discussion

Experimental results show that Al enhances the mechanical stability of gold nanodiscs and thin films, withstanding harsh conditions such as water flow and 40 kHz sonication. Compared to Ti, Al-based metasurfaces exhibit higher electric near-field enhancements, closely matching the performance of structures without adhesion layers. This improvement is further validated through the detection of 50 kDa proteins, where Al-based metasurfaces produce the largest refractive index-based shift, indicating superior sensing performance.

IV. Conclusion

We experimentally demonstrate that aluminum (Al) outperforms conventional adhesion material titanium for metasurface integration. Large area manufacturing enables lens free detections on metasurfaces. The relevant biomarkers as low as 1pg/ml concentrations are detected using the engineered metasurfaces.

Acknowledgments

This work was supported by TUBITAK 125F148.

References

[1] N. Koc, A. Belarouci, E. Oktem, S. Aksu, Objective-Free Ultrasensitive Biosensing on Large-Area Metamaterial Surfaces in the Near-IR. *ACS Appl Mater Interfaces* **2024,** 16(25):32516-32523.
[2] F. Ali, S. Aksu, A Narrow-Band Multi-Resonant Metamaterial in Near-IR. *Materials* **2020**, 13(22):5140. https://doi.org/10.3390/ma13225140

Plasmon Assisted Up Conversion for High Performance Photochromic Smart Windows

Ovidio Peña-Rodríguez[1], Chang Woo Kim[2], Edgardo Gabriel Santoro[3], Umapada Pal[4], Young Soo Kang[3]

[1]Instituto de Fusión Nuclear "Guillermo Velarde", Universidad Politécnica de Madrid, Spain.
[2]Department of Graphic Arts Information Engineering, College of Engineering, Pukyong National University, Republic of Korea
[3]Environmentals and Climate Technology, Korea Institute of Energy Technology, Republic of Korea
[4]Institute of Physics, Autonomous University of Puebla, Mexico
*Corresponding author: ovidio.pena@upm.es

***Abstract*— Photochromic smart windows can regulate solar radiation, but their performance is limited by the small ultraviolet fraction in sunlight. We report plasmonic yolk shell nanophosphors that convert visible light into ultraviolet emission. Integrated with tungsten oxide photochromic films, they significantly accelerate coloration kinetics and enhance optical contrast in smart windows.**

***Keywords*— smart windows, photochromic materials, plasmonic nanostructures, up conversion, nanophosphors.**

I. Introduction

Energy consumption in buildings is strongly affected by heat transfer through windows. Photochromic smart windows dynamically modulate solar radiation using light responsive materials [1,2]. However, their efficiency is limited because ultraviolet light represents only a small fraction of the solar spectrum. A promising strategy is the use of wavelength conversion materials capable of transforming visible light into ultraviolet radiation that activates photochromic layers. In this work, we develop plasmonic yolk shell nanophosphors designed to enhance up conversion efficiency through localized surface plasmon resonance [3]. These nanostructures are integrated with tungsten oxide photochromic films to fabricate fast switching smart windows with improved coloration performance (see Fig. 1).

II. Methods

Plasmonic nanophosphors with a yolk shell architecture were synthesized through a multistep wet chemical process involving:

1. Preparation of silver nanoparticles with controlled size
2. Sequential deposition of precursor shells
3. Thermal treatment to create hollow phosphor shells surrounding the plasmonic core

The resulting structures consist of a silver core inside a hollow cavity surrounded by a praseodymium doped yttrium silicate phosphor shell. The optical response of these hybrid nanostructures was analyzed experimentally and through electromagnetic simulations to understand plasmon assisted up conversion processes. For device fabrication, the optimized nanophosphors were deposited over photochromic tungsten oxide films, forming a double layer structure capable of converting visible solar light into ultraviolet radiation that activates the photochromic reaction.

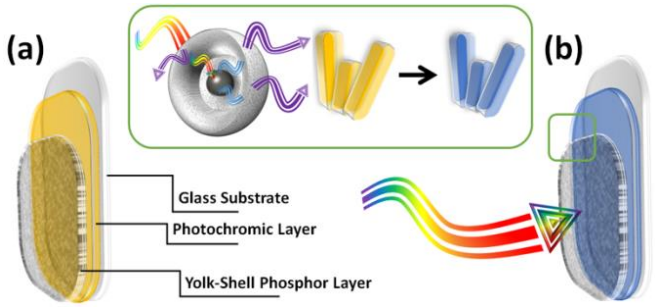

Fig. 1 Schematic illustration of up-conversion layer approach.

III. Results and Discussion

The plasmonic yolk shell geometry strongly influences the up-conversion efficiency of the nanophosphors. By optimizing the size of the metallic core, the cavity dimension and the shell thickness, the emission efficiency of the nanophosphors was significantly enhanced compared with hollow phosphor structures. The improved emission originates from plasmon assisted near field enhancement, which increases the excitation rate of the phosphor shell when the plasmon resonance of the silver core matches the excitation wavelength.

When integrated with tungsten oxide photochromic layers,

the up converted ultraviolet emission activates the photochromic reaction more efficiently. As a result, (i) the coloration rate increased by up to twenty-four times, and (ii) the kinetic constant increased by almost one order of magnitude. These improvements demonstrate that plasmon mediated up conversion can overcome the spectral limitation of conventional photochromic smart windows.

IV. Conclusion

We have demonstrated plasmonic yolk shell nanophosphors capable of enhancing up conversion through plasmon assisted electromagnetic fields. When combined with tungsten oxide photochromic films, these nanostructures dramatically accelerate the photochromic switching process. This strategy offers a promising pathway for the development of high efficiency smart windows for energy efficient buildings.

Acknowledgments

This work was supported by the Leader Project at the Sogang University, funded by the Ministry of Science and ICT, through the National Research Foundation of Korea (No. 2020R1A3B3079715) and the Brain Korea 21 Plus Project 2018. UP acknowledges CONACyT, Mexico, for funding through the grant # CB 2017-2018/A1-S-26720. OPR acknowledges the computer resources and technical assistance provided by the Centro de Supercomputación y Visualización de Madrid (CeSViMa).

References

[1] H. Khandelwal, A.P.H.J. Schenning, M.G. Debije, Infrared regulating smart window based on organic materials, Adv. Ener. Mater. 7 (2017) 1602209. https://doi.org/10.1002/aenm.201602209.

[2] B.R. Park, J. Hong, E.J. Choi, Y.J. Choi, C. Lee, J.W. Moon, Improvement in energy performance of building envelope incorporating electrochromic windows (ECWs), Energies 12 (2019) 1181. https://doi.org/10.3390/en12061181.

[3] C.W. Kim, E.G. Santoro, A.U. Pawar, D.K. Lee, O. Peña-Rodriguez, U. Pal, Y.S. Kang, Swift photochromic smart window based on plasmonic yolk-shell nanophosphors, Adv. Opt. Mater. 11 (2023) 2202171. https://doi.org/10.1002/adom.202202171.

Photonic integrated circuits on fiber tips for lab-on-fiber sensing

Arthur D. Bouamra[1,*], Pieter C. Vijn[1], René P. J. van Veldhoven[1], Jui-Hung Chen[2], Shuo-Yen Tseng[2], Andrea Fiore[1]

[1]Department of Applied Physics and Science Education, Eindhoven University of Technology, 5600 MB Eindhoven, The Netherlands; [2]Department of Photonics, National Cheng Kung University, No. 1 University Rd., Tainan City 701, Taiwan
*Corresponding author: a.d.bouamra@tue.nl

***Abstract*— We present the integration of high-Q ring resonators onto fiber tips. These sensors feature efficient coupling and high quality factors, combining the power of nanophotonics with the versatility of fiber sensing.**

***Keywords*— fiber sensors, lab-on-fiber technology, photonic integrated circuits**

I. Introduction

Integrating photonic integrated circuits (PICs) onto multicore fiber (MCF) facets bridges the gap between PIC functionality and deployable sensing. Using backside-etched grating couplers and an optimized transfer method, we achieved parallel addressing of photonic elements with −6.9 dB coupling efficiency and Q-factors up to 13,000. This scalable approach provides a robust foundation for future multi-channel, multiplexed fiber-tip sensing platforms

II. Methods

PIC design and fabrication

We used Particle Swarm Optimization (PSO) and 3D FDTD simulations to design backside couplers and ring resonators on InP membranes. PICs were patterned via electron-beam lithography and a single etch step. Alignment-controlled backside wet etching created fiber insertion apertures, ensuring membrane integrity before sacrificial layer release.

Membrane Transfer and Alignment

Membranes were integrated onto MCF tips using a transfer technique enhanced by a rotational stage. Positioning was finalized via active alignment, combining CCD monitoring with real-time transmission measurements to maximize coupling efficiency.

Temperature Compensation

To ensure stability, we integrated a reference ring resonator encapsulated in a silicon nitride (SiN) cladding. This cladding isolates the reference from the external medium, allowing the tracking of thermal fluctuations independently of the active sensing ring.

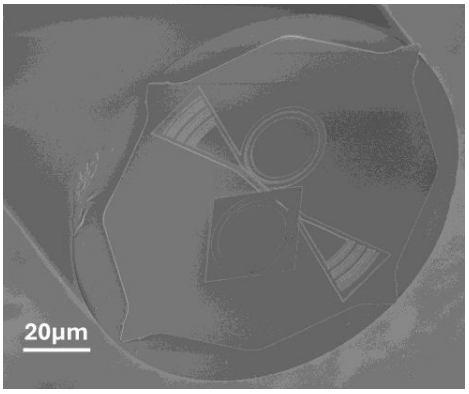

Fig. 1 SEM image of a membrane with two ring resonators, on a fiber-tip

III. Results and Discussion

Experimental results show a 20.1% (−6.9 dB) efficiency at 1478 nm for the grating couplers, a quality factor (Q) of 13,000 for the ring resonators, along with a refractive index sensitivity of 80 nm/RIU sensitivity, leading to a competitive limit of detection of 2.3×10^{-6} RIU. Additionally, temperature compensation can be achieved using the reference ring.

IV. Conclusion

We demonstrated a scalable, transfer-based method to integrate full InP PICs onto multicore fiber tips. Utilizing single-step lithography, the platform achieved high coupling efficiencies and Q-factors. Notably, the sensor reached a state-of-the-art limit of detection of 2.3×10^{-6} RIU, establishing a robust foundation for multiplexed, high-precision lab-on-fiber sensing architectures.

Acknowledgments

Funding from NWO project “PicProbe”, grant n. 19717, and the National Science and Technology Council, Taiwan (111-2923-B-006-002-MY4, 111-2221-E-006-052-MY3), is acknowledged.

Attosecond Extreme-Ultraviolet Skyrmion Pulses from High Harmonic Generation

David Marco[1,2,3,*], Luis Plaja[1,2], Carlos Hernández-García[1,2]

[1]Grupo de Investigación en Aplicaciones del Láser y Fotónica, Departamento de Física Aplicada, Universidad de Salamanca, E-37008 Salamanca, Spain
[2]Unidad de Excelencia en Luz y Materia Estructuradas (LUMES), Universidad de Salamanca, Spain
[3]Instituto de Bioingeniería, Universidad Miguel Hernández de Elche, 03202 Elche, Spain
*Corresponding author: davidmarco@usal.es

***Abstract*—We demonstrate the generation of attosecond skyrmion pulse trains via high harmonic generation driven by an infrared femtosecond vector beam carrying fractional orbital angular momentum. Consecutive far-field harmonics around 70 eV exhibit skyrmion polarization textures whose coherent superposition yields ∼500-attosecond pulses, enabling new avenues for ultrafast control, imaging, and spectroscopy.**

***Keywords*— skyrmion, structured light, attosecond science**

Skyrmions are topological field distributions in which a spatial domain maps onto a complete spherical parameter space. Such configurations have been observed across a broad range of physical platforms, including magnetic systems and structured optical fields [1]. Optical skyrmions emerge in beams whose transverse profiles contain the full set of paraxial polarization states. These fields therefore map a planar region onto the entire Poincaré sphere, where each point represents a distinct polarization state. Their potential impact is currently being investigated in complex media, topological materials, and advanced imaging schemes [1]. However, the generation of skyrmion pulses in the attosecond regime has not yet been demonstrated, with previous realizations restricted to continuous-wave illumination or long optical pulses.

The generation of attosecond pulses has been established for over two decades through high harmonic generation (HHG) in gases, where an intense infrared (IR) laser drives the emission of a plateau of high-frequency phase-locked harmonics with comparable amplitudes. The coherent superposition of selected harmonics yields attosecond pulse trains. In contrast, spatial structuring of high-energy radiation has only become feasible recently, owing to the inefficiency of conventional optical elements at extreme energies. Most approaches therefore focus on engineering the spatial profile of the driver to control the structure of the generated harmonics, enabling extreme-ultraviolet (EUV) structured beams such as attosecond vortices [2] or EUV vector beams [3].

Designing a driving field capable of producing a desired topological structure in the attosecond regime is nontrivial. In particular, HHG efficiency rapidly deteriorates with increasing polarization ellipticity, preventing a straightforward translation of optical skyrmions into the harmonic spectrum. A scheme based on a bichromatic structured driver has been proposed to induce skyrmion patterns at the gas-jet plane, where the skyrmion topology varies across consecutive harmonics [4]. Consequently, this approach does not deliver a phase-locked harmonic comb with similar skyrmion textures, which is a prerequisite for synthesizing attosecond pulses with a temporally robust skyrmion structure. Here, we show that HHG driven by a tailored linearly polarized vector beam produces a phase-locked plateau of consecutive harmonics that exhibit nearly identical skyrmion textures in the far field. Their coherent addition therefore results in attosecond skyrmion pulse trains.

Figure 1(a) illustrates the proposed scheme, where a linearly polarized IR vector driving beam interacts with a gas jet to produce an attosecond skyrmion pulse train. The local polarization state is encoded using a color representation corresponding to points on the Poincaré sphere (Fig. 1(b)). The left- and right-circular polarization (LCP and RCP) driver components carry fractional orbital angular momenta $\ell_{l,r} = -65/132$ and $67/132$, respectively, as depicted in Fig. 1(a). The choice of these parameters follows from a simplified model (see Ref. [5] for more details). The driver can be realized experimentally using metasurfaces or spatial light modulators.

We use the structured driving field in numerical HHG simulations in an argon gas jet. Our model combines a single-atom quantum response, within the strong-field approximation, with an electromagnetic propagation scheme that accounts for macroscopic phase matching and yields the far-field harmonic distribution. The driving pulse has a central wavelength of 1.2 μm, a full width at half maximum (FWHM) duration of 11.5 fs, and a peak intensity of 1.19×10^{14} W/cm^2. By applying realistic Al and Zr filters with thicknesses of 0.2 μm and 0.3 μm, respectively, we isolate five consecutive harmonics around 70 eV. The unfiltered spectrum and the selected window (purple shaded region) are shown in Fig. 2(a). The far-field spatial profiles of these five harmonics exhibit nearly identical skyrmion textures within an annular region of 0.19 mrad radius. The far-field intensity and polarization distribution for the central harmonic are displayed in Fig. 2(b).

The coherent superposition of the harmonics produces an attosecond pulse train with individual pulse durations of approximately 500 attoseconds (FWHM). The Skyrme number N_S characterizes the topology of the skyrmion by quantifying how many times the polarization texture maps the Poincaré

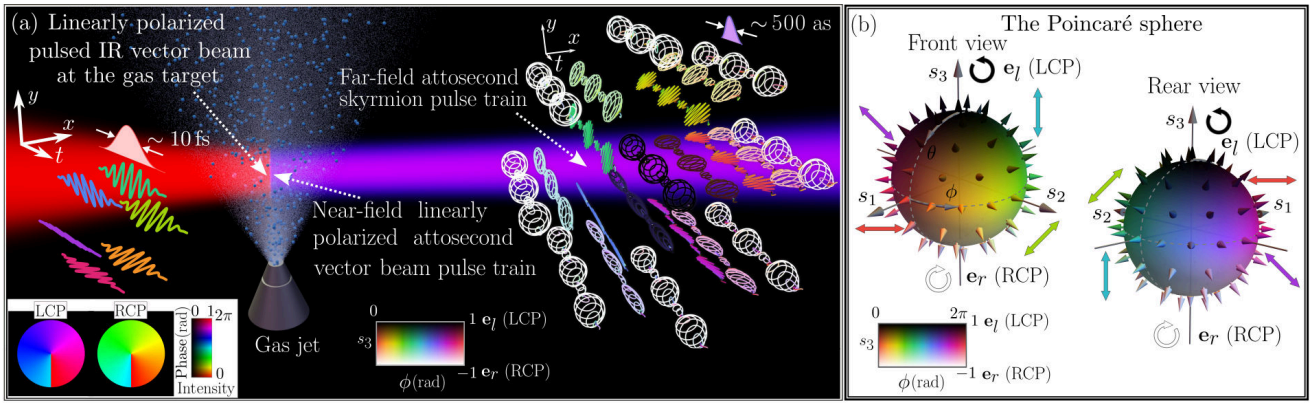

Fig. 1. (a) Illustration of attosecond EUV skyrmion pulse train generation by HHG driven by a linearly polarized femtosecond vector beam. The local polarization state of both the driver and the emitted attosecond field is represented by a color code corresponding to points on the Poincaré sphere. The driving beam consists of left- and right-circular polarization (LCP and RCP, respectively) components carrying fractional orbital angular momentum. (b) Representation of paraxial polarization states on the Poincaré sphere, where each polarization ellipse maps to a single point. The color map is defined by the azimuthal angle ϕ (twice the ellipse orientation) and the s_3 coordinate, which encodes ellipticity and handedness.

sphere [1]. Evaluated at different instants during the central pulse and within the same 0.19 mrad contour (Fig. 2(c)), N_S remains remarkably stable in time, reaching a maximum value of $N_S = 1.000$ with fluctuations limited to $\Delta N_S = 0.009$. Figure 2(d) displays the real electric-field distribution of the most intense pulse in the synthesized train, revealing a well-defined skyrmion texture that persists in time.

To sum up, we presented an experimentally viable route for generating attosecond skyrmion pulses whose topological properties are preserved in time. Such pulses open new pathways for encoding topological information into photoelectron angular and spin distributions [6], for simultaneously probing structural and anisotropic material responses in high-resolution EUV imaging [7], and for enabling ultrafast probing of magnetic helicoidal dichroism [8].

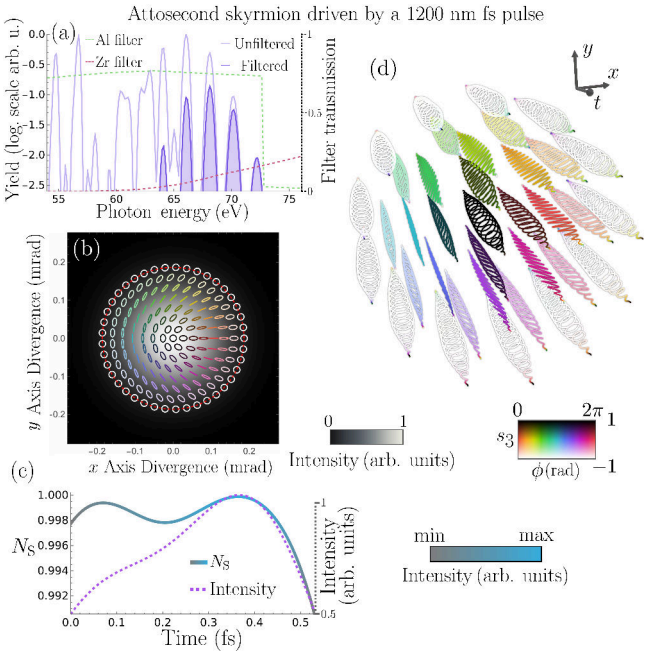

Fig. 2. Attosecond EUV skyrmion pulse train driven by a 1.2 μm driving field. (a) High-harmonic spectrum, with the purple shaded area indicating the spectral window selected by Al and Zr filters. (b) Far-field spatial profiles of intensity and polarization for the central harmonic. (c) Time-dependent evolution of the Skyrme number N_S and the field intensity evaluated inside a 0.19 mrad aperture over the FWHM temporal window of the central pulses. (d) Local temporal evolution of the real electric field corresponding to the central pulse in the train.

REFERENCES

[1] Y. Shen, Q. Zhang, P. Shi, L. Du, X. Yuan, and A. V. Zayats, "Optical skyrmions and other topological quasiparticles of light," *Nature Photonics*, vol. 18, no. 1, pp. 15–25, 2024.

[2] A. de las Heras, D. Schmidt, J. San Román, J. Serrano, J. Barolak, B. Ivanic, C. Clarke, N. Westlake, D. E. Adams, L. Plaja *et al.*, "Attosecond vortex pulse trains," *Optica*, vol. 11, no. 8, pp. 1085–1093, 2024.

[3] C. Hernández-García, A. Turpin, J. S. Román, A. Picón, R. Drevinskas, A. Cerkauskaite, P. G. Kazansky, C. G. Durfee, and Íñigo J. Sola, "Extreme ultraviolet vector beams driven by infrared lasers," *Optica*, vol. 4, no. 5, pp. 520–526, May 2017.

[4] Y. Fang and Y. Liu, "Generation and control of extreme ultraviolet free-space optical skyrmions with high harmonic generation," *Advanced Photonics Nexus*, vol. 2, no. 4, pp. 046 009–046 009, 2023.

[5] D. Marco, L. Plaja, and C. Hernández-García, "Attosecond light skyrmion pulses via high harmonic generation," *arXiv preprint arXiv:2509.19113*, 2025.

[6] D. Younis, D. F. Gordon, and B. Hafizi, "Spin-polarization control of photoelectrons using poincaré fields," *Physical Review Letters*, vol. 133, no. 4, p. 043201, 2024.

[7] M. Pancaldi, F. Guzzi, C. S. Bevis, M. Manfredda, J. Barolak, S. Bonetti, I. Bykova, D. D. Angelis, G. D. Ninno, M. Fanciulli, L. Novinec, E. Pedersoli, A. Ravindran, B. Rösner, C. David, T. Ruchon, A. Simoncig, M. Zangrando, D. E. Adams, P. Vavassori, M. Sacchi, G. Kourousias, G. F. Mancini, and F. Capotondi, "High-resolution ptychographic imaging at a seeded free-electron laser source using oam beams," *Optica*, vol. 11, no. 3, pp. 403–411, Mar 2024.

[8] M. Fanciulli, M. Pancaldi, E. Pedersoli, M. Vimal, D. Bresteau, M. Luttmann, D. De Angelis, P. c. v. R. Ribič, B. Rösner, C. David, C. Spezzani, M. Manfredda, R. Sousa, I.-L. Prejbeanu, L. Vila, B. Dieny, G. De Ninno, F. Capotondi, M. Sacchi, and T. Ruchon, "Observation of magnetic helicoidal dichroism with extreme ultraviolet light vortices," *Phys. Rev. Lett.*, vol. 128, p. 077401, Feb 2022.

Nanoscale Photonic Topological Insulators

Xiaoyong Hu[1,*]

[1]Department of Physics, Peking University, China
*Corresponding author: xiaoyonghu@pku.edu.cn

***Abstract*— Nanoscale photonic topological insulators, providing an excellent platform for information processing, are restricted by the experimental precise control of coupling strength between nanostructure lattices. We proposed new method of coupling strength controlling, and realized nanoscale plasmonic Aubry–André–Harper topological insulator and reconfigurable silicon micro-ring photonic topological insulator.**

***Keywords*— photonic topological insulators, photonic chips, photonic crystals.**

I. Introduction

Nanoscale photonic topological insulator provides an excellent platform for the light field manipulation and information processing chip. Owing to the challenge of precise control of coupling strength between photonic nanostructure lattices, it is very difficult to experimental realization of complicated photonic topological insulator. This has greatly restricted the practical applications of Nanoscale photonic topological insulator in nanophotonic devices and integrated photonic chips.

II. Methods

We propose an approach to address this challenge faced by nanoscale plasmonic topological insulators by integrating gold nanodisk lattices with connecting gold short waveguides. We found that the coupling strength between nanodisk lattices increases as the connecting gold short waveguide width increases. Therefore, precise control of coupling strength between photonic nanostructure lattices could be realized through adjusting the width of the connecting gold short waveguides. This makes the experimental realization of complicated Aubry–André–Harper configuration easily, even though the coupling strength varied between two different neighboring lattices.

We also proposed a method to precise control of coupling strength between two neighboring silicon micro-ring lattices by using a coupling nanostructure with a Mach–Zehnder interferometer configuration. Therefore, the coupling strength between two neighboring silicon micro-ring lattices could be precisely controlled by thermal adjusting the Mach–Zehnder interferometer.

III. Results and Discussion

We fabricated the plasmonic Aubry–André–Harper topological insulator sample by using electron-beam lithography method. The topological properties of the Aubry–André–Harper configuration are directly characterized by using photoemission electron microscopy. Excellent topological state near-field distribution was obtained. Moreover, polarization multiplexing control could be realized through exciting the gold nanodisks in odd or even positions of trivial staggered nanochains by using incident left- or rightcircularly polarized light, offering a promising method for further manipulating and refining plasmonic nanochains and their potential applications.

We also fabricated reconfigurable silicon micro-ring photonic topological insulator using electron-beam lithography method. Topological transition between trivial phase and topological phase was realized experimental for one- and two-dimensional photonic topological insulator.

IV. Conclusion

We have realized nanoscale plasmonic Aubry–André–Harper topological insulator and reconfigurable silicon micro-ring photonic topological insulator chip. This may be useful for the study of nanophotonic devices and integrated photonic chips.

References

[1] Qiuchen Yan, Boheng Zhao, Qinghong Lyu, Yaolong Li, Saisai Chu, Cuicui Lu, Xiaoyong Hu, C. T. Chan, and Qihuang Gong, “Near-field imaging of synthetic dimensional integrated plasmonic topological Harper nanochains”, Nature Communications, Vol. 16, pp. 2592 (2025).

[2] X. F. Smith and Y. T. Lee, “Terahertz metamaterials: design and applications,” Fictional Photonics Letters, vol. 5, pp. 50–60, 2021. Tianxiang Dai, Anqi Ma, Jun Mao, Yutian Ao, Xinyu Jia, Yun Zheng, Chonghao Zhai, Yan Yang, Zhihua Li, Bo Tang, Jun Luo, Baile Zhang, Xiaoyong Hu, Qihuang Gong, and Jianwei Wang, “A programmable topological photonic chip”, Nature Materials, Vol. 23, pp. 928-936 (2024).

[3] Yandong Li, Chongxiao Fan, Xiaoyong Hu, Yutian Ao, Cuicui Lu, C. T. Chan, Dante M. Kenne, and Qihuang Gong, “Effective Hamiltonian for Photonic Topological Insulator with Non-Hermitian Domain Walls”, Physical Review Letters, Vol. 129, 053903 (2022).

Hard and Soft: Exploiting Nanoplasmonics in Sensing Applications

Luca De Stefano[1,*], Valeria Nocerino[2], Bruno Miranda[1], Principia Dardano[1]

[1]Institute of Applied Sciences and Intelligent Systems (ISASI), National Research Council (CNR), Via Pietro Castellino 111, 80131, Naples (Italy).

[2]Department of Electrical Engineering and Information Technology, University of Naples Federico II, Via Claudio 21, 80125 Napoli, Italy

*Corresponding author: luca.destefano@cnr.it

***Abstract*— Optical (bio)sensors are based on materials that convert a (bio)molecular interaction occurring on, or near, their surface into a change in the values of the light impinging on them. Integrated optics, i.e. optical circuits on glass and silicon photonics, has been the main technology adopted in optical sensing until the advent of nanoplasmonics and metamaterials.**

***Keywords*— nanoplasmonics, nanoparticles, nanoisland.**

I. Introduction

Nanostructured plasmonic materials have revolutionized the design and fabrication of optical transducers and biosensors. Bottom-up and top-down approaches can be both be exploited to produce low cost, high sensitivity plasmonic devices that can be used in very different fields of application, from environmental monitoring to biomedical diagnostic [1-2].

In particular, the diffusion of nanomaterials, that could be easily combined with other substances in bottom-up approaches, has strongly changed the development frame and opened new routes to applications until now forbidden to traditional hard materials. The soft matter, polymers, liquid crystals, macromolecules, has been added of optical features that well compete with traditional emitters, lightguides and detectors. Moreover, their mechanical properties, flexibility and weaving, can be used to design and fabricate smart wearables, innovative sensors and much more [3].

II. Methods

Nanoislands, fabricated by sputtering a thin (less than 10 nm) gold film on glass and then annealed (at 560 °C) in rapid thermal oven, detected small molecules at very low concentration.

Diacrylate hydrogels have been photo-crosslinked together with gold nanoparticles in patches of different size and shape. Local functionalization and selective sensing have been proved.

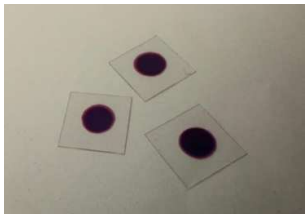

Fig. 1 Gold nanoislands (1 cm diameter) on cover slips (2x2 cm).

III. Results and Discussion

The readout of transparent devices can be simply constituted by a white light and a photodetector or a spectrum analyzer. Due to the presence of plasmonic resonances the signal no needs to be amplified and high sensitivity such as 10^{-17} M of Streptavidin in bovine serum solution in case of nanomushrooms on glass or 0.1x 10^{-12} M using a flexible hydrogel in MEF (metal enhanced fluorescence) configuration.

Acknowledgments

This work received partial financial support from CNR@Projects SAC.AD002.173.026 TIPPS (Tracking and Identification of asymptomatic Patients through engineered antibodies bioconjugated plasmonics in a Pandemic Scenario).

References

[1] R. Moretta, L. De Stefano, M. Terracciano, I. Rea, Porous silicon optical devices: recent advances in biosensing applications, Sensors 2021, 21, 1336, doi.org/10.3390/ s21041336.

[2] Nocerino, V.; Miranda, B.; Tramontano, C.; Chianese, G.; Dardano, P.; Rea, I.; De Stefano, L. Plasmonic Nanosensors: Design, Fabrication, and Applications in Biomedicine. Chemosensors 2022, 10, 150. https://doi.org/10.3390/chemosensors10050150.

[3] Miranda, B.; Moretta, R.; Dardano, P.; Rea, I.; Forestiere, C.; De Stefano, L., H^3 (Hydrogel-Based, High-Sensitivity, Hybrid) Plasmonic Transducers for Biomolecular Interactions Monitoring, Adv. Mater. Technol. 2022, 2101425.

Optical Phenomena in Time-Varying Transparent Conductors

Marcello Ferrera[1,*], Wallace Jaffray[1], Sven Stengel[1]

[1] Institute of Photonics and Quantum Sciences, Heriot-Watt University, United Kingdom
*Corresponding author: m.ferrera@hw.ac.uk

***Abstract*— Transparent conductive oxides operating near the epsilon-near-zero regime provide a powerful platform for ultrafast time-varying photonics. We outline a unified framework for extreme optical nonlinearities spanning field engineering, quantum emission control, ultrafast polarisation manipulation, and spatio-temporal metamaterials.**

***Keywords*— nonlinear optics, photonic metamaterials, polarization control, quantum optics, ultra-fast physics.**

I. Introduction

Transparent conductive oxides (TCOs) have emerged as a key platform for nonlinear and time-varying photonics due to their tunable carrier density and optical dispersion [1]. Near their crossover wavelength, they exhibit epsilon-near-zero (ENZ) behaviour where the refractive index approaches zero, strongly enhancing light–matter interaction and enabling nonlinear responses exceeding most solid-state platforms [2–5]. This is often linked to slow-light-like effects near the ENZ point [6], while preserving ultrafast femtosecond nonlinear dynamics suitable for near single-cycle index modulation [7]. These properties make near-zero-index (NZI) TCOs strong candidates for time-varying photonic systems controlling spectral and momentum properties of light, with impact across integrated nonlinear and quantum photonics [8,9].

II. Methods

The results discussed here are based on subwavelength TCO flat systems engineered to operate near their ENZ wavelength and optically driven by femtosecond pumping to induce transient carrier redistribution and strong refractive index modulation. By tailoring the optical excitation in its temporal profile and polarisation state, full control over the probe optical response can be achieved on ultrafast timescales, including its spatial and spectral distribution as well as local chiral, birefringent, and dichroic properties.

III. Results and Discussion

Recent experiments demonstrate the breadth of phenomena accessible in this platform, including modification of spontaneous emission and radiation patterns via coupling of quantum emitters to low-index ENZ environments [10]; ultrafast control of all polarization properties (i.e., transient birefringence, dichroism, and optical activity) in a single isotropic platform via optically induced plasma symmetry breaking [11]; and spatio-temporal structuring of NZI photonic metalattices with simultaneous control of photon energy and momentum through space–time modulation [12].

IV. Conclusion

NZI TCOs provide a versatile platform for ultrafast time-varying photonics, enabling nonlinear independent control over photon energy and momentum. The demonstrated capabilities across quantum emission engineering, polarisation control, and space–time metamaterials highlight the potential of these materials for next-generation integrated photonic.

Acknowledgments

M.F. acknowledges financial support from EPSRC project ID EP/X035158/1; and EPSRC/STFC/NSERC under UK-Canada Quantum for Science Research Collaborations OPP640-APP47830.

References

[1] W. Jaffray, et al., *Transparent conducting oxides: from all-dielectric plasmonics to a new paradigm in integrated photonics*, **Adv. Opt. Phot**. 14 (2), 148-208 (2022).
[2] I. Liberal, N. Engheta, *Near-zero refractive index photonics*. **Nat. Phot**. 11, 149–158 (2017).
[3] W. Jaffray, et al., *High-Order Nonlinear Frequency Conversion in Transparent Conducting Thin Films*, **Adv. Opt. Mater**., 12 2401249 (2024)
[4] W. Jaffray, et al., *Near-zero-index ultra-fast pulse characterization*, **Nat. Commun**. 13 (1), 3536 (2022).
[5] W Jaffray, et al., *Engineering waveguide nonlinear effective length via low index thin films* **Adv. Opt. Mater**. 12 (16), 2303199
[6] J.B. Khurgin, et al., *Adiabatic frequency shifting in epsilon-near-zero materials: the role of group velocity*, **Optica** 7 (3), 226 231 (2020).
[7] E. Lustig, et al., *Time-refraction optics with single cycle modulation*, **Nanophotonics**, 12, 2221 (2023)
[8] W. Jaffray, et al. *Spatio-spectral optical fission in time-varying subwavelength layers*. **Nature Photonics** 19, 558–566 (2025)
[9] I. Liberal, A. Alù, N. Engheta, *Zero-index metamaterials for classical and quantum light*, **Appl. Phys. Lett.** 120, 260401 (2022)
[10] W. Jaffray, et al. All-optical polarization control in time-varying low-index films via plasma symmetry breaking. https://doi.org/10.48550/arXiv.2510.06985
[11] S. Stengel, et al. *Quantum dots emission enhancement via coupling with an epsilon-near-zero sublayer*. https://doi.org/10.48550/arXiv.2509.09477
[12] W. Jaffray, et al. *Spatio-Temporal Photonic Metalattice*. https://doi.org/10.48550/arXiv.2510.09273

Tailoring valley polarization and optical nonlinear effect in transition-metal dichalcogenides

Mu Wang*, and Ruwen Peng

National Laboratory of Solid State Microstructures, School of Physics, and Collaborative Innovation Center of Advanced Microstructures, Nanjing University, Nanjing 210093, China
*Corresponding author: muwang@nju.edu.cn

***Abstract*— In this talk, we present the manipulation valley polarization and optical nonlinear effect in transition-metal dichalcogenides. The approaches achieve potential applications in developing low-dimensional optoelectronic materials and devices.**

***Keywords*— metasurfaces, valley polarization and optical nonlinear effect, transition-metal dichalcogenides.**

Controlling valley polarization and optical nonlinear effect in transition-metal dichalcogenides (TMDs) is essential for advancing low-dimensional devices. In this talk, we present the manipulation of valley polarization of interlayer excitons in TMD heterostructure using a dual-handedness metasurface [1]. This metasurface, composed of left- and right-handed gold nanoantenna arrays, exhibits distinct chiral optical responses. Further, we demonstrate that it enables direct and byte-invert arithmetic operations for information transmission. In addition, we show chiral second-harmonic generation in rhombohedral TMDs [2], and illustrate them as compact and multifunctional platforms for integrated photonics. The approaches achieve potential applications in developing the advanced optoelectronic materials and devices.

REFERENCES

[1] Yi Zhu, Kong-Liang Zou, Dong-Xiang Qi, Jie He, Ruwen Peng*, Mu Wang*, "Tailoring valley polarization of interlayer excitons in van der Waals heterostructure toward optical communication", Nano Letters 25, 8680-8688 (2025).

[2] Yi Zhu, Yu-Heng Hou, Ruwen Peng*, Mu Wang*, manuscript submitted (2026).

Advanced Manufacturing Tools for Data-Processing Fiber Photonics Fabrication

Marcos D. Vozer Felisberto[1], Andrey Machnev[1], Thomas W. Burkle[2], Maxwell H. Jancich[1], Babak Seradjeh[2], Phillip Richerme[2], and Alexander Gumennik[1,*]

[1]Fibers & Additive Manufacturing Enabled Systems Laboratory (FAMES Lab), Department of Intelligent Systems Engineering, Indiana University Bloomington, USA
[2]Department of Physics, Indiana University Bloomington, USA
*Corresponding author: gumennik@iu.edu

***Abstract*—By melt-shaping multimaterial fiber cores, we demonstrate building blocks of fiber-embedded photonics. Fiber photonics with data-processing capabilities could translate data on-the-fly across numerous computation platforms, including quantum and neuromorphic, each of which encodes data in a platform-specific form, thus enabling the integration of those platforms into the broader Internet.**

***Keywords*— fibers photonics, 3D printed silica preforms, fiber-integrated ion traps, mode-shaping fibers.**

I. Introduction

Optical fibers form the backbone of modern communication, sensing, and photonic computing technologies. Traditionally, fibers consist of simple cylindrical core–cladding structures fabricated through chemical vapor deposition or preform stacking techniques [1]. While these approaches have enabled tremendous technological progress, they impose strong constraints on achievable fiber geometries and integrated functionality.

Emerging photonic computing platforms, starting with quantum and neuromorphic, are frequently optimized to perform specific tasks with high fidelity, resulting in materials, computational protocols, and even physical implementations of data registers – bits or qubits – tailored for the desired tasks. As a result, however well each of those platforms may perform its isolated tasks, they cannot readily communicate with each other, especially when such communication must be quantum-coherent. To integrate those platforms into a harmonious network, an approach to translating data from a format understandable to the outbound platform into one understandable to the inbound platform is necessary for each such pair. The lack of a universal Quantum Interconnect (QuIC) has been acknowledged in recent years as a major bottleneck to the implementation of scalable quantum networks [2].

Recent advances in additive manufacturing of fiber preforms, fiber thermal drawing, and post-processing [3] enable a new paradigm for fiber design, in which complex device architectures are first fabricated at the preform scale and then translated into functional fibers through the draw and post-processing. These approaches enable the integration of electronic, optical, and quantum data-processing elements and systems directly within fiber-optic systems. As shown in **Fig. 1**, fibers with data-processing capabilities could solve the QuIC bottleneck, enabling on-the-fly, quantum-coherent data translation across the various material platforms comprising the network. Moreover, as further shown in **Fig. 1**, such fibers could provide efficient solutions for quantum routers and quantum coherent repeaters, further enhancing network scalability.

Here, we present our first practical steps toward implementing this concept. First, we demonstrate a fiber-integrated ions-to-photons quantum information converter that enables direct coupling between trapped-ion qubits and optical fiber modes. Second, we demonstrate light-shaping fibers fabricated from 3D-printed silica preforms, enabling arbitrary core geometries and beam shaping within the fiber platform. Additionally, since the 3D printed preforms don't need to be axially uniform, we can implement axially distributed classical integrated photonics elements in a fiber. For instance, we have successfully demonstrated a preform for a Y-splitter/multiplexer in a fiber, which is the first step toward photonic circuits embedded in a fiber, as demonstrated in **Fig. 1, Inset I**, required for quantum routing. Other elements of fiber photonics, including detectors and photonically resonant structures, have been demonstrated by us before and publicized elsewhere [1], [3], [4].

II. Methods And Results

Distributed quantum computing architectures rely on coherent transfer of quantum information between spatially separated nodes. However, many quantum hardware platforms encode qubits in stationary systems, such as trapped ions or solid-state defects, while communication channels use photonic qubits. Efficient interfaces between these systems, therefore, play a critical role in scalable quantum networks.

To address this challenge, we propose a fiber-integrated ions-

to-photons quantum information converter (IP-QIC). In this architecture, a Paul trap capable of confining ions is integrated directly into the cross-section of a functional fiber, as shown in **Fig. 1, Inset III**.

The device consists of a polymer cladding that encapsulates a quadrupole arrangement of RF electrodes forming a Paul trap. A central optical fiber runs through the device and includes an axial gap in the core where trapped ions can be positioned. Conductive carbon-black-filled polyethylene electrodes surrounding the optical fiber enable axial ion confinement via applied DC potentials.

Finite-element simulations were performed to co-design the electromagnetic fields and device geometry. These simulations evaluated RF confinement fields in the transverse direction and DC trapping potentials along the fiber axis, while also accounting for the frequency-dependent impedance of conductive polymer electrodes. The design ensures that the DC electrodes remain conductive at low frequencies while exhibiting minimal dielectric loss at RF trapping frequencies, allowing efficient penetration of RF fields into the trapping region.

The device is fabricated using Very-Large-Scale Integration for Fibers (VLSI-Fi), which combines additive manufacturing of fiber preforms with thermal drawing techniques. A 3D-printed polycarbonate preform containing the electrode channels is fabricated and annealed to remove porosity. During the draw process, copper wires and a conventional optical fiber are inserted into the preform and consolidated into a composite fiber structure.

This approach produces a fiber-based device that traps ions concentrically with the fiber's optical core, forming a continuous waveguide and enabling efficient coupling between trapped-ion emission and guided optical modes. Such architecture provides a promising pathway toward integrated quantum interconnects with integrated repeaters for distributed multi-processor quantum computing.

In addition to fiber-integrated fiber repeaters, additive manufacturing of preforms enables the fabrication of optical fibers with arbitrary internal geometries that cannot be produced by conventional fabrication techniques.

We demonstrate fabrication of light-shaping fibers derived from stereolithography-printed silica preforms. Using silica nanocomposite resins loaded with germanium oxide nanoparticles, we fabricate core structures with non-cylindrical geometries, beyond those shown in **Fig. 1, Inset II**, including circular, triangular, square, hexagonal, and cross-shaped cross-sectional optical core profiles.

The printed Germania-doped core structures are sleeved into

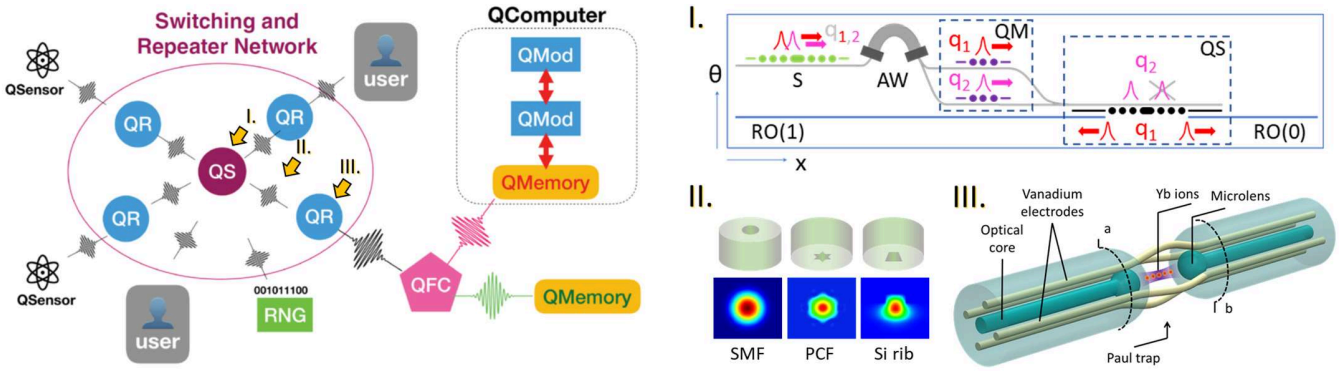

Fig. 1 Fiber photonics to address the scalability of quantum networks. Quantum computer interfacing quantum network (adapted from Awschalom *et al.* (2021) [2] and reproduced under Creative Commons Attribution 4.0. Copyright © 2021, American Physical Society. The elements of the network we aim to address at FAMES Lab using VLSI-Fi are **I.** – quantum switch (QS), **II. –** Quantum Interconnect (QuIC), **III.** – quantum repeater (QR). Other elements of the network, schematically depicted here, include a modular quantum processor (QMod), a quantum frequency converter (QFC), and a random-number generator (RNG). The QuICs are red arrows and wave packets. **Inset I** – suggested implementation of QS with photonic routing capabilities. A fiber-embedded quantum circuit is arranged circumferentially in the fiber cladding. x – longitudinal axis, θ – angular axis in cylindrical fiber coordinates. Initially continuous, cores are selectively patterned by capillary instability into a qubit source S, a quantum memory QM, a quantum all-optical switch QS, and an arrayed waveguide demultiplexer AW. Grey lines are optical cores. RO(0) and RO(1) are the single-photon readouts in superconducting nanowire cores. QS is a resonator that resonantly transmits q_1. When switched by the absorption of q_2, it gets out of resonance, and q_1 is reflected. **Inset II** – Quantum interconnect (QuIC) implemented in a fiber with adiabatic mode shapers, reshaping the long-haul communication circular mode of single-mode fiber (SMF) into a form acceptable without losses by other material platforms, such as an atomic trap in a photonic crystal fiber (PCF) with a hexagonal mode, and a quantum Si Photonics chip (Si rib) with trapezoidal mode. **Inset III** – a suggested implementation of QR with optical to ionic qubit conversion capabilities, in which a fiber-integrated Paul trap embeds an ion-array concentric with the optical mode of the fiber. It can be realized using a vanadium-quadrupole fiber, which has recently been fabricated at FAMES Lab. The Paul trap will be created by etching a gap in the fiber's silica cladding with hydrofluoric acid, which does not affect vanadium. Then the section between **a** and **b** will be heated above the softening point of SiO_2 but below the melting point of V, such that the surface tension reshapes the caps at **a** and **b** into spherical lenses. This will be done in an inert environment to prevent vanadium oxidation. Panels I, II, and III are adapted from Faccini de Lima *et al.* (2023)[5] and reproduced with permission. Copyright © 2023, Society of Photo-Optical Instrumentation Engineers (SPIE).

geometry-matched printed pure silica claddings and subsequently sintered at high temperature to produce transparent glass preforms. The sintered structures are then encased within additional silica tubing and consolidated on a glass lathe under vacuum, forming a monolithic preform suitable for fiber drawing. We have developed an improved annealing procedure to remove residual porosity introduced during 3D printing.

Thermal drawing of these preforms produces fibers with cross-sectionally scaled-down and longitudinally scaled-up versions of the original printed geometries. Electron microscopy and elemental mapping confirm that the germanium-doped cores remain well defined and compositionally uniform after drawing.

Optical characterization demonstrates effective light guidance within the engineered cores. When illuminated with a 450-nm diode source, the fibers exhibit beam profiles corresponding to the designed core geometries, confirming the ability to shape optical modes directly within the fiber. The propagation losses we measure at 1.55 µm are less than 1 dB/m. This is not on par with conventional fiber optics, yet it is more than an order of magnitude better than previously demonstrated for 3D printed silica preforms [6]. We believe that our improved preform-annealing approach enables us to further reduce propagation losses by enhancing the annealing time.

This approach provides a versatile platform for creating optical fibers with tailored modal behavior, integrated photonic components, and complex beam-shaping functionality.

III. Discussion

Together, these results demonstrate that additive manufacturing, combined with fiber thermal drawing and post-processing, enables a new class of multifunctional fibers with embedded photonic and quantum functionalities.

The light-shaping fiber platform provides unprecedented geometric freedom for engineering optical modes, while the quantum-interconnect fiber architecture demonstrates the feasibility of integrating quantum hardware components directly within fiber systems. Both approaches leverage similar fabrication principles and highlight the potential of additive manufacturing for large-scale integration of photonic and electronic structures in fibers.

Future developments will focus on reducing optical losses in printed glass fibers, refining ion-trapping architectures within fibers, and integrating additional functional elements, such as photonic cavities and single-photon sources/detectors.

IV. Conclusion

A combination of classical processing techniques, such as thermal drawing of fibers, with emerging advanced manufacturing approaches, such as additive manufacturing of preforms, is transforming the design space of optical fibers by enabling architectures that combine optical, electronic, and quantum functionality within a single microstructured glass strand. We demonstrated two complementary implementations of this paradigm: a fiber-integrated ions-to-photons quantum information converter and light-shaping fibers fabricated from 3D-printed silica preforms.

These results illustrate the potential of advanced fiber fabrication techniques to enable next-generation photonic systems for quantum communications, sensing, and computing technologies.

V. Acknowledgments

This work was supported by the US National Science Foundation (NSF), grants #CMMI-2143467 and #ECCS-2240227. The authors thank the IU NCF for its support with fiber characterization.

References

[1] A. Gumennik and C. Faccini de Lima, ‘Emerging Design Tools for Functional Architectures in Monofilament Fibers’, *Adv. Eng. Mater.*, vol. 26, p. 2400919, 2024, doi: 10.1002/ADEM.202400919.

[2] D. Awschalom *et al.*, ‘Development of Quantum Interconnects (QuICs) for Next-Generation Information Technologies’, *PRX Quantum*, vol. 2, no. 1, p. 017002, Feb. 2021, doi: 10.1103/PRXQuantum.2.017002.

[3] A. Gumennik *et al.*, ‘Very-large-scale Integration for Fibers’, in *Optical and Electronic Fibers: Emerging Applications and Technological Innovations*, John Wiley & Sons, Ltd, 2024, ch. 9, pp. 197–224. doi: 10.1002/9783527839322.CH9.

[4] C. Faccini de Lima, F. Wang, T. A. Leffel, T. Miller, S. G. Johnson, and A. Gumennik, ‘Multimaterial fiber as a physical simulator of a capillary instability’, *Nat. Commun.*, vol. 14, no. 1, pp. 1–17, Sep. 2023, doi: 10.1038/s41467-023-41216-7.

[5] C. Faccini de Lima, T. Leffel, M. Zheng, J. Coulter, A. Gumennik Camila Faccini de Lima, and A. Gumennik, ‘Creating fiber-embedded photonic circuitry by liquid-phase structuring of multi-material cores’, *https://doi.org/10.1117/12.2644870*, vol. 12433, no. 15, pp. 34–46, Mar. 2023, doi: 10.1117/12.2644870.

[6] Y. Chu *et al.*, ‘Silica optical fiber drawn from 3D printed preforms’, *Opt. Lett.*, vol. 44, no. 21, p. 5358, Nov. 2019, doi: 10.1364/ol.44.005358.

Chiral Diffraction from Quasiperiodic Monotile Lattice Based on Aperiodic Hat Tiling

Yuto Moritake[1,2,*]

[1]Institute of Industrial Science, The University of Tokyo, Japan
[2]Department of Physics, Institute of Science Tokyo, Japan
*Corresponding author: moritake@iis.u-tokyo.ac.jp

***Abstract*— We experimentally investigated optical diffraction from a newly discovered aperiodic structure, an aperiodic monotile. The monotile tessellates two-dimensional space using a single tile shape. We fabricated a quasiperiodic lattice on a nanophotonic platform based on this monotile tiling and observed interesting chiral diffraction response unique to the monotile geometry.**

***Keywords*— photonic crystals, quasicrystals, optical diffraction, aperiodic montile.**

I. Introduction

An aperiodic monotile is a newly discovered aperiodic tiling that was reported in 2023 [1]. In mathematics, minimizing the number of tiles required to aperiodic tessellation was a long-standing problem. The well-known Penrose tiling uses two tiles to tesselate the plane aperiodically, whereas a single-tile aperiodic tessellations (monotile) had not been found. In 2023, Smith discovered the first monotile, called “hat tile” after it shape (Fig. 1(a,b)).

Our motivation is explore physical phenomena enabled by this monotile on a nanophotonic platform. To generate lattice point from the hat tiling, we propose a “monotile lattice” as shown in Fig. 1(c). The lattice has C3 symmetry but lacks inversion symmetry, unlike conventional quasiperiodic lattices such as the Penrose tiling. While theoretical studies of monotile lattices have recently begun to emerge [2,3], experimental realizations remain elusive. Photonic crystals offer a promising platform to investigate this new lattice.

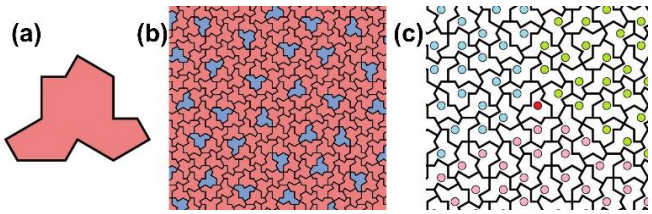

Fig. 1 (a) Geometry of the hat tile and (b) its tiling. (c) The monotile lattice generated from the hat tiling.

II. Results

We investigated diffraction from an aperiodic photonic crystal whose circular holes are positioned on the monotile lattice. The measured diffraction patterns exhibit clear, discrete peaks, indicating long-range order in the aperiodic lattice. Importantly, the patterns show sixfold rotational symmetry together with chirality. Mirror-related structures produce diffraction images with opposite handedness (Fig. 2(a,b)). We also observe an incident-helicity dependence under circularly polarized illumination [5], which is absent in conventional inversion-symmetric quasicrystals.

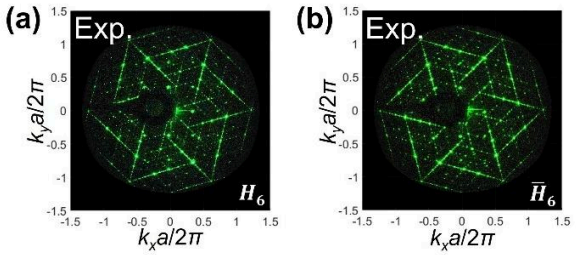

Fig. 2 Pictures of optical diffraction from the fabricated mmonotile lattice. (a) and (b) are results for the monotile lattice and its mirror-reversed structure, respectively.

III. Conclusion

Our experiments reveal unique chiral properties of monotile-based tilings. Chiral optical diffraction from quasiperiodic structures without inversion symmetry opens a new research direction in aperiodic photonics. These results also highlight the usefulness of photonic-crystal platforms for exploring the physics of newly emerging aperiodic structures.

Acknowledgments

This work is collaboration with Dr. M. Takiguchi (NTT, Japan), Dr. T. Aihara (NTT, Japan), and Prof. M. Notomi (Science Tokyo and NTT, Japan). This work was supported by KAKENHI JP20H05641, JP21K14551, 24K01377, 24H02232 and 24H00400.

REFERENCES

[1] D. Smith, J. S. Myers, C. S. Kaplan, and C. Goodman-Strauss, "An aperiodic monotile" Comb. Theory 4, 6 (2024).
[2] J. Schirmann, S. Franca, F. Flicker, and A. G. Grushinet, "Physical Properties of an Aperiodic Monotile with Graphene-like Features, Chirality, and Zero Modes," Phys, Rev. Lett. 132, 086402 (2024).
[3] C. S. Kaplan, M. O'Keeffe, and M. M. J. Treacy, "Periodic diffraction from an aperiodic monohedral tiling," Acta Cryst. A 80, 72 (2024).
[4] M. Notomi, H. Suzuki, T. Tamamura, and K. Edagawa, "Lasing Action due to the Two-Dimensional Quasiperiodicity of Photonic Quasicrystals with a Penrose Lattice." Phys, Rev. Lett. 92, 123906 (2004).
[5] Y. Moritake, M. Takiguchi. T. Aihara, and M. Notomi, arXiv:2506.07561

Silicon Nitride Photonics for High-Performance Systems

F. Y. Gardes[1]*, I. Skandalos[1], Y. Hou[1], D. Qiao[3], H. Deng[2], X. Yu[2], J. S. Park[2], C. Chen[2], M. Tang[2], M. Paparella[1], L. Bao[1], E. Sandell[1], T. D. Bucio[1], J. Moeyaert[4], T. Baron[4], P. M. Smowton[3], H. Liu[2], A. Seeds[2], S. Simos[5], T. Moschos[5], M. Moralis-Pegios[5], I. Johnson[1], T. Rangarajan[1], , J. Gates[1], and N. Pleros[5]

[1]*Optoelectronics Research Centre, University of Southampton, Southampton, SO17 1BJ, UK*
[2]*Department of Electronic and Electrical Engineering, University College London, London WC1E 7JE, UK*
[3]*School of Physics and Astronomy, Cardiff University, Cardiff CF24 3AA, UK*
[4]*LTM CNRS/UGA CEA/LETI/Minatec, 38054 Grenoble, France*
[5]*Department of Informatics, AUTH, Thessaloniki, Greece*
**Corresponding author: f.gardes@soton.ac.uk*

***Abstract*— We report the first QD SOA grown on silicon coupled to silicon nitride waveguides using a monolithic integration scheme. We also report complex photonic circuit programming using UV light trimming. These developments underscore significant strides in the field, paving the way for enhanced photonic device functionality and integration.**

***Keywords* — QD SOA, QD Laser, Silicon Nitride, Monolithic Integration**

I. Introduction

Silicon nitride photonics has emerged as a critical platform for next-generation computing and communication systems due to its exceptionally low optical losses, wide transparency window spanning visible to mid-infrared wavelengths, and full compatibility with established CMOS manufacturing processes. The platform offers propagation losses of less than 0.2 dB/cm in the O-band telecommunications window, making it ideal for complex photonic integrated circuits. However, two fundamental challenges have historically limited the capabilities of silicon nitride photonics: the integration of active gain elements for on-chip light amplification, and the development of non-volatile, zero-power optical memory elements suitable for energy-efficient computing applications. In this work, we address both challenges through breakthrough technological advances in monolithic III-V integration and UV-programmable photonic memories..

II. Results and Discussion

We demonstrate the first monolithically integrated [1-3] electrically pumped semiconductor optical amplifiers on silicon substrate coupled to silicon nitride waveguides. Our InAs/GaAs quantum dot distributed Bragg reflector lasers achieve continuous-wave operation with threshold currents below 215 mA at room temperature and maximum fiber-coupled output power exceeding 2 mW. The SOA devices demonstrate net optical gain greater than 5 dB with a 3-dB optical bandwidth of 46 nm, establishing broadband amplification capability across the O-band.

The monolithic coupling strategy between III-V gain regions and N-rich SiN passive waveguides achieves coupling losses below 1.5 dB per interface with back-reflections close to -13 dB for normal incidence.

For optical memory functionality, we exploit the intrinsic photosensitivity of nitrogen-rich Si_3N_4 with a refractive index of 1.9, deposited via plasma-enhanced chemical vapor deposition on silicon wafers with 3.2 μm of thermally grown silicon dioxide. A 244 nm frequency-doubled Argon-Ion laser with 25 mW power and 14 μm spot size permanently modifies the refractive index through controlled UV exposure at fluences of 1.5 kJ/cm² [4]. This enables non-volatile programming of Mach-Zehnder interferometer switching states without requiring continuous electrical biasing or thermal tuning, eliminating static power consumption. We experimentally validate this approach through demonstration of a 4×9 wavelength-division multiplexed ternary content addressable memory bank, representing the highest-dimension photonic memory array reported to date. The system operates at 20 Gb/s with 2-bit optical words while consuming zero electrical power during steady-state operation. Characterization reveals a 15 dB extinction ratio between ON and OFF states after 20 UV exposure cycles, with bit error rates below 10^{-9} across all stored configurations. The platform demonstrates multi-million cycle endurance with stable refractive index retention and maintains wafer-scale manufacturing compatibility.

These results establish further silicon nitride as a complete platform for high-performance photonic computing, combining monolithically integrated optical amplification with non-volatile, zero-power programmable memory. This addresses the fundamental limitation of silicon's indirect bandgap while eliminating speed-power trade-offs of electronic alternatives.

Acknowledgments

This work was supported by EPSRC under project QUDOS, and by the European Commission through Horizon Europe projects OCTAPUS (101070009) and AMBROSIA (101093166).

REFERENCES

[1] [1] I. Skandalos et al., "High Performance Monolithic Integration of Light Amplifiers in Silicon Photonic Circuits," ResearchSquare rs-7716086, 2025.

[2] [2] I. Skandalos et al., "A 100 Gb/s quantum-confined Stark effect modulator monolithically integrated with silicon nitride on Si," Commun. Eng., Nature, 2025.

[3] [3] I. Skandalos et al., "Coupling strategy between high-index and mid-index micro-metric waveguides," Sci. Rep., 2022.

[4] [4] G. De Paoli et al., "Laser trimming of silicon nitride racetrack resonators," Photon. Res. 8, 677, 2020

Spatiotemporal Metasurface for Unconventional Control of Electromagnetic Waves

Anatoly Efimov[1], Chun-Chieh Chang[1], Simo Pajovic[2,3], Wilton J. M. Kort-Kamp[2], Hou-Tong Chen[1], Diego A. R. Dalvit[2], & Abul K. Azad[1]*
[1]Center for Integrated Nanotechnologies, Los Alamos National Laboratory, New Mexico, USA
[2]Theoretical Division, Los Alamos National Laboratory, New Mexico, USA
[3]Department of Mechanical Engineering, Massachusetts Institute of Technology, Cambridge, USA
*Corresponding author: aazad@lanl.gov

***Abstract*— Lorentz reciprocity fundamentally limits the performance of photonic systems by enforcing reciprocal energy exchange between source and detector, which manifests as the symmetry of the scattering matrix. We design and fabricate a graphene-based integrated photonic structure and experimentally demonstrate nonreciprocal scattering from a metasurface modulated at gigahertz frequencies.**

***Keywords*— metamaterials, midinfrared, graphene device**

I. Introduction

In electromagnetism, the Lorentz reciprocity theorem states that a source and a detector of light can swap positions without changing the outcome of the measurement by the detector[1] . In other words, the scattering matrix is symmetric, $S_{ab} = S_{ba}$. Reciprocity assumes that light propagates in a linear, time-invariant medium with symmetric permittivity, permeability, and conductivity tensors. In reality most devices inherently operate under the regime of reciprocity, which states that the spectral directional emissivity and absorptivity of a surface are equal[2,3]: $e(\omega, \theta, \phi) = a(\omega, \theta, \phi)$, where e is emissivity, a is absorptivity, ω is (angular) frequency, and θ and ϕ are polar and azimuthal directions, respectively. In principle, a nonreciprocal system for which $S_{ab} \neq S_{ba}$, achieved by lifting one or more of the assumptions of the Lorentz reciprocity theorem. Spatiotemporal modulation has been one of the most successful approaches to nonreciprocity, having been theoretically predicted and even experimentally demonstrated in waveguides[4], antennas[5], and metasurfaces[6]. Despite the promise of mid-infrared nonreciprocity and its relevance to tailoring thermal radiation, there have been few experiments demonstrating nonreciprocal emission, absorption, or scattering in this spectral range. In this work, we experimentally demonstrate nonreciprocal frequency conversion using a spatiotemporally metamaterial (STMM) designed for operation at a wavelength of 10 μm, near the peak wavelength of room-temperature thermal radiation.

Our STMM consists of an array of 36 rectangular pixels of size 5.7 μm × 200 μm. Each pixel contains six metallic patch antennas placed on top of a graphene monolayer, which is transferred onto a dielectric stack of alumina and amorphous-germanium (a-Ge) that is backed by an optically thick metal ground plane (see Fig. 1). Monolayer graphene is used to modulate the antennas' optical response via electrically controlled charge density at 1 GHz frequency. Our metasurface is designed to generate synthetic diffraction orders in reflection around a center wavelength of about 10 μm (i.e., 30 THz) when driven with properly phase-controlled GHz RF voltage. The experiments are performed in Littrow configuration[7] using a piezo tunable mode-hop-free quantum cascade laser (QCL, Sacher Lasertechnik).

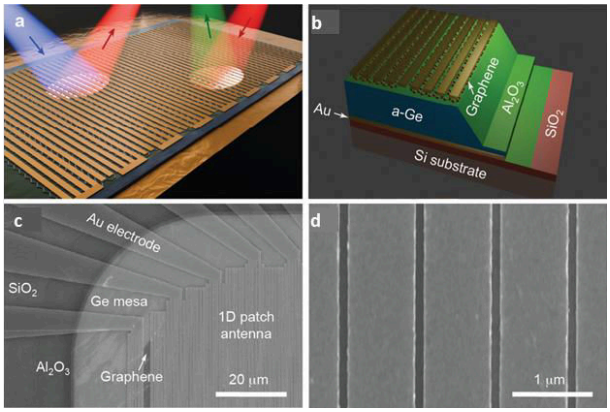

Fig. 1 . a Nonreciprocal reflection from a graphene STMM, b. Schematic layers of device, c SEM image of the fabricated device, d Expanded top-view of one-dimensional patch antenna pixels.

To perform the measurements, a 10 kHz drive voltage is applied to every third pixel of the metadevice to create a quasi-static grating for diffraction. The results of these quasi-static measurements are shown in Fig. 2 a The bright rings correspond to the transmission of a specific optical frequency at certain angles of the FPE. We then apply a spatiotemporal modulation ($\Omega/2\pi = 1$ GHz, $\Delta V = 2.5$ V) to the STMM in the 3-pixel periodic sequence $[+120°, 0, -120°]$ and obtain the 2D map in Fig. 2b. The rings are displaced to the right exactly by $\Omega/2\pi = 1$ GHz modulation frequency, demonstrating unidirectional and essentially nonreciprocal frequency conversion.

II. Results and Discussion

To understand the data, we first consider the "forward" experiment by arbitrarily choosing an input frequency of the QCL, say $\omega_{\text{in}} = \omega_0 + \Delta\omega$, where $\omega_0/2\pi \approx 31.6$ THz (wavelength 9.5 μm) and $\Delta\omega/2\pi = +0.5$ GHz. A vertical slice (solid blue line) of the map in Fig. 2b at ω_{in} cuts through one of the rings at two symmetric points (with one marked with a blue circle) located at angular positions of about $\pm 0.8°$. Following the horizontal blue dashed line, in the reference map (Fig. 2a) we find that the FPE transmission frequency is $\omega_{\text{out}}/2\pi = \omega_0/2\pi - 0.5$ GHz at these angular positions, as indicated by the yellow circle and vertical dashed line. By comparing the maps in Figs. 3a and 3b, we conclude that frequency down-conversion $\omega_{\text{out}} = \omega_{\text{in}} - \Omega$ occurred in the spatiotemporally modulated metadevice.

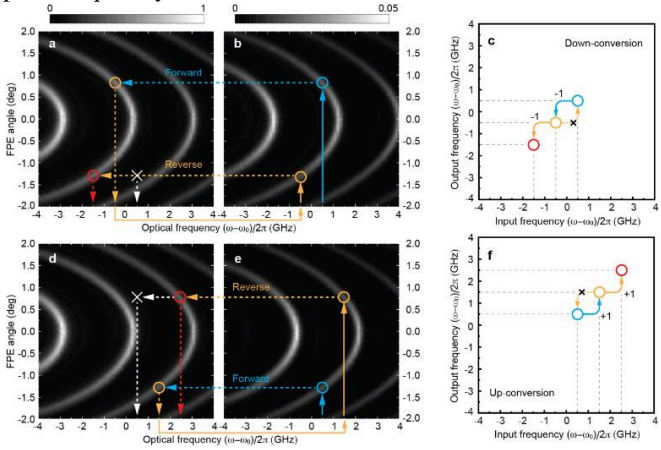

Fig. 2 The 2D maps show the transmission signal through the FPE as a function of the FPE angle and QCL frequency. Panel **(a, d)** corresponds to the case of the metasurface with no RF spatiotemporal modulation. (b) transmission for the spatiotemporally modulated metasurface for the modulation sequence [+120°,0,-120°] corresponding to frequency down-conversion (c). Panel (e, f) Same for the sequence $[-120°, 0, +120°]$ corresponding to frequency up-conversion.

We consider the "reverse" experiment while keeping the modulation protocol $[+120°, 0, -120°]$ unchanged. The Littrow configuration with colinear input and optical output modes allows us to keep the QCL laser and detector in the same positions in the reverse experiment. This leads to the same 2D optical density map depicted in Fig. 3b. We consider the previously down-converted frequency to be the new input frequency $\omega'_{\text{in}}/2\pi = \omega_{\text{out}}/2\pi = \omega_0/2\pi - 0.5$ GHz and extend a vertical slice (yellow solid line) that intersects a ring in Fig. 3b at FPE angular positions about $\pm 1.25°$ (yellow circle for the negative one). Following the horizontal yellow dashed line to the reference map in Fig. 3a we find the intersection point marked by the red circle, which corresponds to the new output frequency $\omega'_{\text{out}}/2\pi = \omega_0/2\pi - 1.5$ GHz, suggesting yet another down-conversion, $\omega'_{\text{out}} = \omega_{\text{in}} - 2\Omega$. Figure 3c schematically illustrates the two steps of the frequency down-conversion just discussed. This key observation demonstrates nonreciprocal scattering from our graphene-based spatiotemporally modulated metasurface operating at mid-infrared frequencies.

For completeness, we have also demonstrated nonreciprocal reflection in a reversed modulation sequence [-120°,0,+120°], with the 2D optical density map shown in Fig. 3e. In this case the rings are displaced to the left by the 1 GHz modulation. Following a similar procedure as above, one can show that in the forward experiment there is frequency up-conversion$\omega_{\text{out}} = \omega_{\text{in}} + \Omega$. The reverse experiment gives another up-conversion, $\omega'_{\text{out}} = \omega_{\text{in}} + 2\Omega$ and no signal at the initial input frequency is observed. Figure 3f depicts the two steps of frequency up-conversion. As before, this indicates nonreciprocal reflection from our spatiotemporally modulated metasurface. The measured efficiency of mode conversion $\omega_0 \rightarrow \omega_{\pm 1}$ is $\approx 4 \times 10^{-5}$.

III. Conclusion

In summary, we have introduced a graphene-based STMM platform modulated at GHz frequencies for experimental demonstration of breakdown of Lorentz reciprocity at mid-IR wavelengths. We have also developed a theory that relates nonreciprocal reflection with the breakdown of the spectral directional Kirchhoff's law of thermal radiation. Our work has the potential to find applications in mid-IR optical isolators, solar energy harvesting, thermophotovoltaics for waste heat recovery, active/dynamic thermal management for electronics, radiative cooling, and adaptive thermal camouflage and thermal signatures.

Acknowledgments

This work has been supported by Los Alamos National Laboratory LDRD and other programs. Part of this work was performed at the Center for Integrated Nanotechnologies, a U.S. Department of Energy, Office of Basic Energy Sciences user facility. LANL is operated by Triad National Security, LLC, for the National Nuclear Security Administration of the U.S. Department of Energy (Contract No. 89233218CNA000001). S.P. was supported by the U.S. Department of Energy, Office of Science, Office of Workforce Development for Teachers and Scientists, Office of Science Graduate Student Research (SCGSR) program.

References

[1] Lorentz HA. The theorem of Poynting concerning the energy in the electromagnetic field and two general propositions concerning the propagation of light. Amsterdammer Akademie der Wetenschappen 4, 176 (1896).

[2] Kirchhoff G. Ueber das Verhältniss zwischen dem Emissionsvermögen und dem Absorptionsvermögen der Körper für Wärme und Licht. Annalen der Physik und Chemie 185, 275-301 (1860).

[3] Howell JR, Mengüç MP, Daun K, Siegel R. Thermal Radiation Heat Transfer, 7 edn. CRC Press (2020).

[4] Yu Z, Fan S. Complete optical isolation created by indirect interband photonic transitions. Nature Photonics 3, 91-94 (2009)

[5] Hadad Y, Soric JC, Alu A. Breaking temporal symmetries for emission and absorption. *Proceedings of the National Academy of Sciences* **113**, 3471-3475 (2016).

[6] Cardin AE, *et al.* Surface-wave-assisted nonreciprocity in spatio-temporally modulated metasurfaces. *Nature Communications* **11**, 1469 (2020).

[7] Palmer C. *Diffraction Grating Handbook*, 8 edn (2020).

Symmetry-Broken q-BIC Dielectric Metasurfaces for Enhanced Linear and Nonlinear Light-Matter Interactions

Wen-Hui (Sophia) Cheng[1,*], Hung-Yi Wu[1], Tzu-Hsiang Liu[1], Hsin-Yu Shen[1]
[1] National Cheng Kung University, Taiwan
[*]corresponding author: wcheng@gs.ncku.edu.tw

Abstract: We present a dielectric metasurface supporting q-BICs induced by controlled symmetry breaking. Strong mode interference enables high-Q resonances, enhanced photoluminescence, and boosted third-harmonic generation. By balancing field confinement and radiation coupling, the design offers an efficient platform for enhancing linear and nonlinear light-matter interactions in nanophotonic devices.

Dielectric metasurfaces offer a versatile platform for manipulating light-matter interactions with low nonradiative losses and high design flexibility. In this work, we introduce a metasurface composed of biradial circular resonators that supports quasi-bound states in the continuum (q-BICs) through controlled symmetry breaking. By slightly perturbing a symmetry-protected BIC, an experimentally accessible q-BIC with a high quality factor and strong field confinement is achieved. The resonance is primarily governed by the interference between electric dipole and magnetic multipolar modes, enabling enhanced photoluminescence and robust spectral tunability. Beyond linear optical responses, we further exploit q-BIC modes to boost nonlinear light-matter interactions. By carefully balancing field confinement and radiation coupling, significant enhancement of third-harmonic generation is realized in optimized asymmetric circular array designs. Our results reveal that maximizing nonlinear conversion efficiency requires not only high-Q resonances but also appropriate radiative coupling, highlighting the critical interplay between confinement and outcoupling. This study elucidates the symmetry-driven physics of q-BIC metasurfaces and provides a practical and fabrication-friendly strategy for enhancing both linear and nonlinear optical processes, paving the way for advanced applications in frequency conversion, nanophotonics, and integrated nonlinear photonic devices.

References

1. Tzu-Hsiang Liu, Hung-Yi Wu, Wen-Hui Sophia Cheng*. *Quasi-Bound State in the Continuum of the Intracoupled All- Dielectric Coherent Metasurface.* Nano Letters 26 (1), 288-295 (**2026**).

Femtosecond Laser Direct-Written Optical Fiber Microstructure Devices for Laser Applications

Xuewen Shu[1,*] (Invited)

[1]Wuhan National Laboratory for Optoelectronics, Huazhong University of Science and Technology, Wuhan, 430074, China

*Corresponding author: xshu@hust.edu.cn

***Abstract*— We report our recent progress in the use of femtosecond lasers to fabricate various microstructures within optical fibers, including gratings and interferometric devices, and discuss their diverse applications in fiber laser systems.**

***Keywords*— fiber gratings, interferometric devices, femtosecond laser direct-writing, fiber lasers.**

I. Introduction

Femtosecond laser inscription technology has emerged as an indispensable tool for fabricating intricate microstructures in a diverse range of materials. Femtosecond laser direct writing offers several distinct advantages, such as highly localized material modification and no requirement for material photosensitivity. The strong spatial confinement of the technology, combined with laser-beam scanning or sample translation, enables the creation of geometrically complex three-dimensional structures. In recent years, we have employed this technique to fabricate various fiber-optic microstructures, including gratings and interferometric devices, and demonstrated their applications in fiber laser systems. In this presentation, we provide an overview of our research progress in this field..

II. Methods and Results

Figure 1 shows an example of using the femtosecond laser line-by-line inscription technique to fabricate a small-period long-period grating (SP-LPG) and applying it to generate ultrashort pulses in a fiber laser [1]. The SP-LPG is produced with a period of 25 μm and a length of 2.5 mm. This grating has significant polarization dependent loss (PDL) in C and L bands, making it possible to use as a mode-locking device. The laser cavity has a total length of 130 m and a net cavity dispersion of -2.738 ps^2. Figure 2 shows the output characteristics of the mode-locked laser based on the SP-LPG. The central wavelength is around 1577 nm with 3 dB spectral bandwidth of 4 nm. The signal-to-noise ratio (SNR) reaches 50 dB, demonstrating excellent stability of the mode-locked pulses.

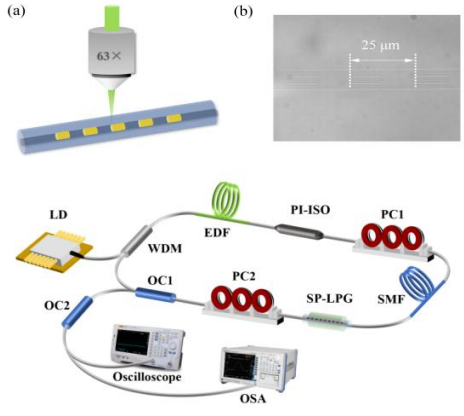

Fig. 1 (a) Schematic of the femtosecond laser inscribed process for SP-LPG; (b) CCD photograph of SP-LPG;(c) Fiber laser setup.

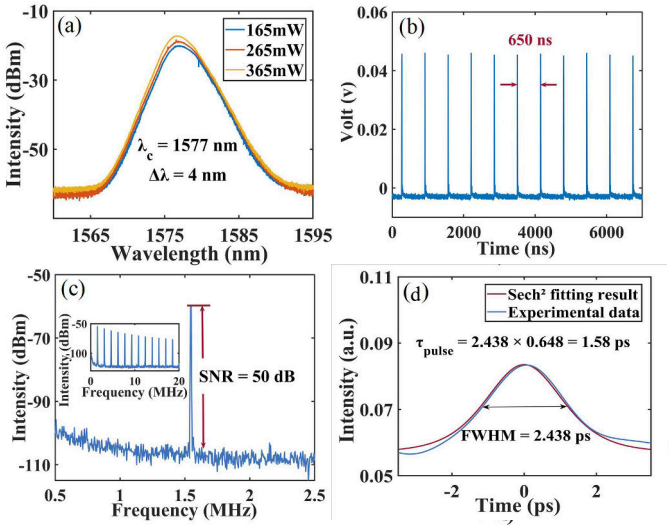

Fig. 2 Performances of the mode-locked fiber laser. (a) Optical spectrum. (b) Pulse train. (c) RF spectrum. (d) Autocorrelation trace

In another experiment, such an SP-LPG was also employed in a normal-dispersion fiber laser to generate mode-locked pulses in the L-band [2]. Other fiber grating and interferometric structures were also fabricated and applied in various laser systems, including mode-locked fiber lasers and random fiber lasers [3-6].

III. Conclusion

Femtosecond lasers can be used to fabricate various fiber gratings and interferometric devices in optical fibers, offering broad application potential in fiber laser systems.

ACKNOWLEDGMENTS

This work was supported by the National Key Research and Development Program of China (2023YFE0105800) and National Natural Science Foundation of China (62275093).

REFERENCES

[1] Q. Li, P. Cheng, R. Zhao, J. Cai, M. Shen, and X. Shu, "Mode-locked fiber laser based on a small-period long-period fiber grating inscribed by femtosecond laser," Opt. Lett., vol. 48, pp. 2241–2244, 2023.
[2] Q. Li, P. Cheng, R. Zhao, and X. Shu, "Femtosecond laser-written small-period long-period fiber grating for an L-band normal dispersion mode-locked fiber laser," Photonics, vol. 11, no. 8, p. 693, 2024.
[3] Y. Li, J. Deng, M. Shen, P. Cheng, and X. Shu, "Modeless Raman fiber laser," Optica, vol. 10, pp. 1037–1043, 2023.
[4] Q. Li, R. Zhao, M. Shen, and X. Shu, "In-fiber waveguide-based mode-locker for generating diverse ultrafast pulses," Opt. Express, vol. 32, pp. 34521–34532, 2024.
[5] M. Shen, J. Deng, Y. Li, and X. Shu, "Multi-wavelength random fiber laser based on a tilted parallel inscribed apodized fiber Bragg grating array," Opt. Lett., vol. 47, pp. 5473–5476, 2022.
[6] J. Deng, Y. Li, M. Shen, and X. Shu, "Single-frequency random distributed Bragg reflector fiber laser," J. Lightwave Technol., vol. 40, no. 13, pp. 4385–4390, 2022.
[7] J. Deng, M. Shen, Y. Li, D. V. Churkin, and X. Shu, "High-power random Raman fiber laser with an ultrashort random fiber grating," J. Lightwave Technol., vol. 40, no. 8, pp. 2535–2540, 2022.
[8] J. Deng, D. V. Churkin, Z. Xu, and X. Shu, "Random fiber laser based on a partial-reflection random fiber grating for high temperature sensing," Opt. Lett., vol. 46, pp. 957–960, 2021.

Novel Materials for UV Plasmonic Nanostructures

Michael Foltýn[1,*], Tomáš Šikola[1], Michal Horák[1]

[1]Brno University of Technology, Brno, Czech Republic
*Corresponding author: Michael.Foltyn@vutbr.cz

***Abstract*— We present a study of novel plasmonic materials, focusing on nanostructured non-noble metals at the single-particle level. We demonstrate the spectral tunability of their localized surface plasmon resonances. In particular, we investigate gallium, bismuth, lead, and tin.**

***Keywords*— non-noble metals, nanoparticles.**

I. Introduction

Localized surface plasmon resonances (LSPRs) arise from collective oscillations of free electrons in metallic nanostructures coupled to light. They enable strong, subwavelength confinement and enhancement of electromagnetic fields, allowing control of optical processes beyond the diffraction limit, consequently bringing a wide range of applications. Although gold-based plasmonics are highly promising, their broader use is limited by high fabrication costs and a restricted plasmon energy range due to interband transitions. These limitations motivate the exploration of alternative metals such as gallium, bismuth, lead, and tin, which are theoretically predicted to provide comparable performance with a wider energy range [1]. Here, we present the plasmonic properties of gallium [2], [3], bismuth [4], [5], lead, and tin.

II. Methods

To investigate all the listed metals, we employed several complementary methods to prepare the respective nanostructures. Lens-shaped gallium nanoparticles were fabricated by depositing gallium from an effusion cell directly onto silicon nitride membranes. Bismuth nanostructures were produced by focused ion beam (FIB) lithography of thin bismuth films sputtered onto silicon nitride membranes. In addition, bismuth nanoparticles were synthesized via chemical reduction of sodium bismuthate in ethylene glycol at elevated temperature. Lead nanoparticle solutions were prepared by thermal decomposition of lead acetate in tetraethylene glycol. The resulting bismuth and lead nanoparticle dispersions were subsequently drop-cast onto silicon dioxide membranes for further analysis.

The prepared nanostructures were examined by transmission electron microscopy to determine their structural and morphological characteristics. Their plasmonic properties, including the tunability of localized surface plasmon resonances, were analyzed using electron energy loss spectroscopy [6].

III. Results and Discussion

The spectral tunability of localized surface plasmon resonances in bismuth is comparable to that of gold, showing similar size-dependent behavior. This makes bismuth a significantly more cost-effective alternative for plasmonic applications. In addition, bismuth maintains its strong plasmonic performance at energies above 2 eV, extending its usefulness into the visible and near-UV range.

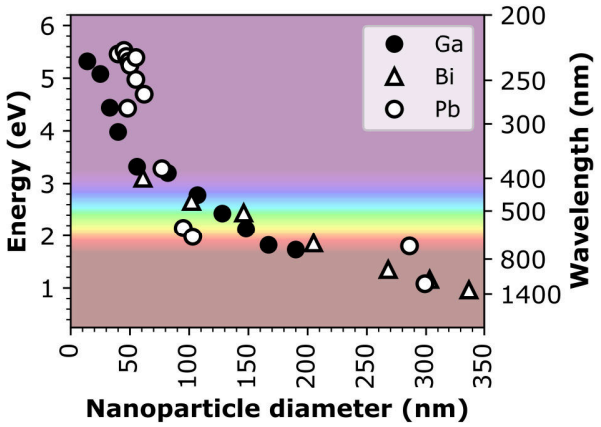

Fig. 1. Tunability of LSPR dipole mode in bismuth [5], gallium [2] and lead nanoparticles.

Lead and gallium are particularly promising for ultraviolet plasmonics. Both materials exhibit dipolar LSPR modes at energies up to 5.3 eV. Although gallium undergoes a liquid-to-solid phase transition at low temperatures, its plasmonic response remains stable, making it well suited for cryogenic surface-enhanced Raman spectroscopy and other low-temperature applications.

IV. Conclusion

We have experimentally verified the ability of lead, bismuth and gallium to support localised surface plasmon resonances, and extracted the spectral tunability of the plasmonic dipolar mode. All of the listed metals expand the spectral range to the UV spectral region, offering attractive applications, which would be inaccessible with the traditional plasmonic materials, such as gold.

Acknowledgments

This work was supported by the project QM4ST (project No. CZ.02.01.01/00/22_008/0004572) by OP JAK, call Excellent Research. M. F. acknowledges the support of the Brno Ph.D. Talent Scholarship.

REFERENCES

[1] J. M. Sanz, D. Ortiz, R. Alcaraz de la Osa, J. M. Saiz, F. González, A. S. Brown, M. Losurdo, H. O. Everitt, and F. Moreno, "UV plasmonic behavior of various metal nanoparticles in the near- and far-field regimes: Geometry and substrate effects," *J. Phys. Chem. C*, vol. 117, no. 38, pp. 19606–19615, 2013.

[2] M. Horák, V. Čalkovský, J. Mach, V. Křápek, and T. Šikola, "Plasmonic properties of individual gallium nanoparticles," *J. Phys. Chem. Lett.*, vol. 14, no. 8, pp. 2012–2019, 2013.

[3] M. Horák, M. Foltýn, V. Čalkovský, V. Mikerásek, M. Bartošík, J. Mach, and T. Šikola, "Plasmonic response to liquid–solid phase transition in individual gallium nanoparticles," *J. Phys. Chem. Lett.*, vol. 16, no. 35, pp. 8891–8896, 2025.

[4] M. Foltýn, T. Šikola, and M. Horák, "Bismuth plasmonic antennas," *ACS Nano*, vol. 19, no. 36, pp. 32299–32305, 2025.

[5] M. Foltýn, M. Kvapil, T. Šikola, and M. Horák, "Plasmonic properties of individual bismuth nanoparticles," *J. Phys. Chem. Lett.*, vol. 16, no. 38, pp. 9933–9938, 2025.

[6] M. Horák and T. Šikola, "Influence of experimental conditions on localized surface plasmon resonances measurement by electron energy loss spectroscopy," *Ultramicroscopy*, vol. 216, p. 113044, 2020.

Plasmonic Enhancement of Second Harmonic Generation from a van der Waals Crystal

Hong Liu[1,2,3*]

[1]Institute of Materials Research and Engineering, Agency for Science, Technology, and Research (A*STAR), Singapore 138634, Singapore
[2]Department of Materials Science and Engineering, National University of Singapore, Singapore 117575, Singapore
[3]School of Materials Science and Engineering, Nanyang Technological University, Singapore 639798, Singapore

*Corresponding author: liu_hong@a-star.edu.sg

***Abstract*— It has been reported that niobium oxide dichloride ($NbOCl_2$) crystal exhibits giant optical nonlinearity. We developed a plasmonic resonator insensitive to polarization to acquire strong local field amplification, which achieves fivefold enhancement of second harmonic generation (SHG) intensity. It provides a robust pathway toward high-performance, miniaturized nonlinear quantum light source.**

***Keywords*— niobium oxide dichloride ($NbOCl_2$), ferroelectrics, second harmonic generation, nonlinearity, plasmonic resonator**

I. Introduction

Layered niobium oxyhalides ($NbOX_2$, X = Cl, Br, I) have recently emerged as promising candidates for realization of efficient nonlinear light sources at nanoscale[1-2], owing to their intrinsic ferroelectricity, strong in-plane anisotropy, and large second-order susceptibility coefficients. Even though their SHG conversion is very high, which still needs to be increased remarkably to meet the requirement for practical application of quantum light sources.

II. Methods

In this work, we engineered a silver plasmonic resonator which consists of circular ring structures to amplify the local electric field upon excitation. Meanwhile, it is able to boost effective nonlinear polarization while maintaining isotropic optical response across all polarization states. Coupled with the plasmonic resonator, the van der Waals crystal of $NbOCl_2$ emits enhanced intensity of SHG.

III. Results and Discussion

Experimental results show:

- Environmental robustness of $NbOCl_2$ flakes manifested by optical property stability test
- Strong hotspot formation at the ring edges of polarization-insensitive ring resonator upon excitation at 780 nm excitation
- Fivefold enhancement of SHG intensity

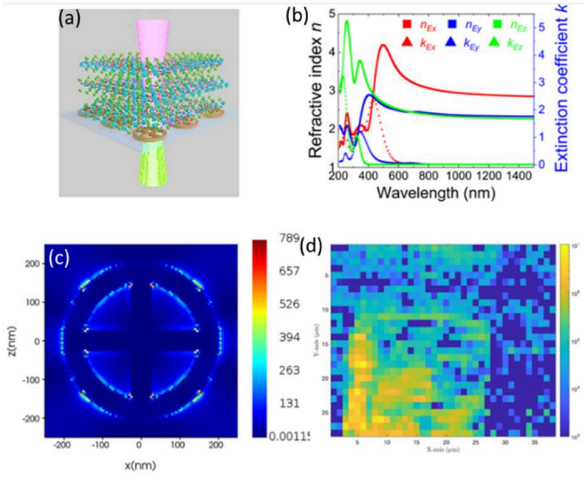

Fig. 1. The concept and experimental results. (a) Schematics of hybrid nonlinear emitter consisting of plasmonic resonator and $NbOCl_2$ flaks. (b) Optical properties measured by ellipsometer. (c) Simulated electric field of plasmonic resonator. (d) The spatial mapping of SHG intensity.

IV. Conclusion

We have demonstrated a polarization-insensitive plasmonic resonator which can significantly enhance the intrinsic SHG of $NbOCl_2$ and also validate its superior air-stability as a van der Waals ferroelectric with giant optical nonlinearity

Acknowledgments

This work was supported by National Research Foundation Competitive Research Programme (CRP) funding of Singapore (NRF-CRP31-0001), the RIE2025 Manufacturing, Trade and Connectivity (MTC) Programmatic Fund (M23M2b0056), and

RIE2025 MTC Individual Research Grants (IRG) (M24N7c0087)

REFERENCES

[1] Abdelwahab, I., Tilmann, B., Wu, Y. et al. Giant second-harmonic generation in ferroelectric $NbOI_2$. *Nat. Photon*. 16, 644–650 (2022).
[2] Guo, Q., Qi, XZ., Zhang, L. et al. Ultrathin quantum light source with van der Waals $NbOCl_2$ crystal. *Nature* 613, 53–59 (2023)

3D topological photonics: 3D Chern photonic insulators and electromagnetic axions

C. Devescovi[1], A. Morales-Perez[2], M. G. Vergniory[3], A. Garcia Etxarri[1,4,*]

[1] Institute for Theoretical Physics, ETH Zurich, 8093 Z¨urich, Switzerland

[2] Donostia International Physics Center, 20018 Donostia-San Sebastián, Spain

[3] Département de physique et Institut quantique, Université de Sherbrooke, Sherbrooke, J1K 2R1, QC, Canada

[4] IKERBASQUE, Basque Foundation for Science, Maria Diaz de Haro 3, 48013 Bilbao, Spain

[*]corresponding author: aitzolgarcia@dipc.org

***Abstract*— This work presents a method to design 3D photonic Chern and electromagnetic axion insulators with tunable topological properties. These structures support robust, unidirectional light transport via chiral edge and hinge states, enabling lossless photonic networks and offering promising applications in quantum technologies and axion dark matter detection.**

Inspired by the discoveries of topological phenomena in solid state systems, the study of topology in the propagation of light in photonic crystals has been the subject of much recent attention. Among all topological states of matter, time-reversal symmetry (TRS) broken topological materials, such as Chern insulators have been a particular focus due to their topologically protected unidirectional edge states with non-reciprocal propagation properties. In these systems, scattering processes from one boundary state into another are strongly suppressed, due to decoupling of counter-propagating 1D chiral edge channels.

In this contribution, we will firstly introduce a general strategy to design 3D Chern insulating (3D CI) cubic photonic crystals in a weakly TRS broken environment with orientable and arbitrarily large Chern vectors [1-2].

Secondly, will show how these designs can be used to build photonic axion insulators [3-4]. Such a 3D topological photonic crystal exhibits extraordinary properties such as half-quantized surface effects and unidirectional chiral hinge states that propagate exclusively along the edges. These chiral hinge states form intricate networks that enable light to travel without loss or interference, even when obstacles are present. This breakthrough offers a deeper understanding of exotic particles and paves the way for practical applications in quantum computing, advanced sensors or in the development of axion-like particle detectors such as axion dark matter particles [4].

1. Devescovi, C. et.al. Cubic 3D Chern photonic insulators with orientable large Chern vectors. Nature Comm., 12 (1), 12 (2021)
2. Devescovi, C. et. al. Vectorial Bulk-Boundary Correspondence for 3D Photonic Chern Insulators, Advanced Optical Materials, 10 (20), 2200475 (2022)
3. Devescovi, C. et. al. Axion topology in photonic crystal domain walls, Nature Communications 15, 6814 (2024)
4. Liu, Gui-Geng, et al. "Photonic axion insulator." Science387.6730 162-166 (2025)

***Keywords*— Topological Photonics, Photonic Crystals, Axions, Topology, Chern insulator**

Dirac-Polariton Bose–Einstein Condensation at Room Temperature via Bound States in the Continuum in a WS_2 Monolayer

Bruno Miranda, [1] Silvia Romano,[1] Scott Duhey,[2] Aidar Kemelbay,[2] Arian Gashi,[2] Vito Mocella,[1] Ivo Rendina,[3] Adam M. Schwartzberg,[2] Gianluigi Zito[1]*

[1]*Institute of Applied Sciences and Intelligent Systems, National Research Council, 80131, Naples, Italy*

[2]*Molecular Foundry, Lawrence Berkeley National Laboratory, Berkeley, CA 94720, United States.*

[3]*Institute of Applied Sciences and Intelligent Systems, National Research Council, 80078, Pozzuoli, Italy.*

*Corresponding author: gianluigi.zito@cnr.it

***Abstract*— Room-temperature exciton–polariton Bose–Einstein condensation is demonstrated in a WS_2 monolayer using BIC-enabled Dirac-mode confinement. Strong coupling with ~60 meV Rabi splitting persists above threshold. Topological polariton superfluids, negative-mass self-trapping, discrete Dirac-gap condensates, and pump-tunable spectra enable reconfigurable, integrable quantum photonic platforms at ambient conditions.**

***Keywords*— exciton–polaritons, bound states in the continuum, WS_2 monolayers, Bose–Einstein condensation.**

I. Introduction

Exciton–polaritons in atomically thin semiconductors offer a platform for nonlinear quantum photonics at ambient conditions. However, room-temperature polariton Bose–Einstein condensation has remained inaccessible due to strong losses. Topological bound states in the continuum [1-3] (BICs) provide a route to overcome these limitations.

II. Methods

Our methodology integrates simulation, analytical non-Hermitian Hopfield model and experimental feedback. A WS_2 monolayer is coupled to a silicon nitride photonic crystal slab supporting Dirac-point BIC modes. Strong coupling and dispersion engineering are analysed using RCWA and a polariton model, combined with a driven–dissipative Gross–Pitaevskii framework:

$$i\,\partial_t\psi = (H - i\Gamma + g\,|\,\psi\,|^2 + g_R n_R)\psi,$$

validating the experimental photoluminescence mapping of the strong coupling regime and polariton lasing.

III. Results and Discussion

Experimental observations show:

- Room-temperature polariton lasing;
- Persistent strong coupling with ~60 meV Rabi splitting above lasing threshold;
- Negative-mass polariton self-trapping and discrete Dirac-gap condensate states;
- Extended spatial coherence through first order correlation function vs pump power;
- Pump-tunable blueshifts up to ~28 meV and topological charge |2| inheritance;
- All-optical dynamical reconfiguration through pump-shape profile modulation.

IV. Conclusion

We demonstrate room-temperature polariton Bose–Einstein condensation in a WS_2 monolayer enabled by Dirac BIC confinement. The BIC dispersion supports omnidirectional negative-mass polaritons that self-trap via a reservoir-induced potential, resulting from interfering Dirac modes. A general analytical model predicts the evolving loss landscape, enabling the prediction of the condensation regime. The non-equilibrium condensate is dynamically controlled through the real-time modulation of the space-variant self-trapping potential. This open-cavity platform supports condensate arrays and integration with van der Waals heterostructures and Moiré superlattices, tracing a pathway toward emerging functionalities at ambient conditions. The resulting system establishes a new scalable platform for coherent light–matter states in low-dimensional semiconductors under ambient conditions.

Acknowledgments

EU Italian National Recovery and Resilience Plan (NRRP) of NextGenerationEU (PE0000023-NQSTI); B-PLAS grant no. PRIN-2022TXWE32, MIUR, Italy; NRRP Mission 4, Component C2 Investment 1.1, PRIN project INSPIRE, grant no. P2022LETN5. Work at the Molecular Foundry was supported by the Office of Science, Office of Basic Energy Sciences, of the U.S. Department of Energy under Contract No. DE-AC02-05CH11231.

References

[1] Hsu, C. W., et al., "Bound states in the continuum," Nat. Rev. Mater. 1, 16048 2016.

[2] Friedrich, H. & Wintgen, D. "Interfering resonances and bound states in the continuum," Phys. Rev. A 32, 3231–3242, 1985.

[3] Schiattarella, C., et al. "Directive giant upconversion by supercritical bound states in the continuum." Nature 626, 765-771, 2024.

Manipulate Multispectral 3D Polarization Structures with Optical Metasurfaces

Xianzhong Chen[1,*], Hammad Ahmed[2], Chunmei Zhang[1]

[1]School of Engineering and Physical Sciences, Heriot-Watt University, Edinburgh, UK
*Corresponding author: x.chen@hw.ac.uk

***Abstract*—3D polarization structures are garnering significant interest owing to their peculiar properties. We use optical metasurfaces to generate various multispectral polarization 3D structures and cascaded polarization cages, whose polarization profiles can be dynamically modulated.**

***Keywords*— optical metasurfaces, 3D polarization control, polarization cage, multispectral.**

I. Introduction

3D polarization distributions are garnering significant interest owing to their peculiar properties. Multi-color polarization manipulation can introduce extra degrees of freedom. It is challenging both technically and fundamentally to cascade multiple multispectral 3D polarization structures. Moreover, fuelled by system integration and miniaturization, there is considerable interest in developing compact optical devices capable of controlling polarization and color simultaneously on 3D structures.

II. Methods

To tackle these challenges, we propose a metasurface approach to generating multiple 3D polarization structures along the light propagation direction. Each polarization structure features different colors and an engineered 3D polarization profile. Our metalens design includes off-axis design, geometric phase realization, linear polarization rotation, multiple 3D structure design, introduction of color information, longitudinal control, and phase multiplexing. Different multi-colored 3D polarization knots and polarization cages are observed by changing the observation region along the longitudinal direction. We further showcase the application of the developed metalenses in realizing multiple 3D color images hidden in multiple 3D color images.

III. Results and Discussion

The light intensity distributions of the 3D polarization knots are modulated with a rotating analyzer, generating unusual features (e.g., dark gaps). Such a characteristic opens an avenue for image steganography—a technique which can hide a secret image inside a cover image. A polarization knot with the same light intensity profile can have many 3D polarization distributions and colors.

IV. Conclusion

Our approach has tackled the typical challenges of creating multiple multispectral 3D polarization structures: 3D polarization generation, multiple colors, and cascading control. The compact, flexible, and lightweight design of the metasurface provides numerous advantages over traditional polarization optics, making it highly suitable for applications across various research fields, including complex vector beam generation and optical encryption.

Acknowledgments

This was funded by the Engineering and Physical Sciences Research Council (Grant No. EP/P029892/1), the Leverhulme Trust (Grant Nos. RPG-2021-145 and RPG-2023-283).

References

[1] Y. Li, M. A. Ansari, H. Ahmed, F. Zhong, and X. Chen, "Cascading multispectral polarization cages," *npj Nanophotonics*, vol. 2, no. 1, p. 12, 2023.

[2] Y. Li, M. A. Ansari, H. Ahmed, R. Wang, G. Wang, Q. Yu, C. Zhang, S. Chen, and X. Chen, "Multiple multicolored 3D polarization knots arranged along light propagation," *ACS Photonics*, vol. 11, no. 10, pp. 4380–4389, 2024.

[3] R. Rong, Y. Li, Z. Hu, K. Li, G. Li, S. Chen, and X. Chen, "Customizing 3D polarization structures at second harmonic frequency," *Laser & Photonics Reviews*, vol. 19, no. 24, p. e01059, 2025.

[4] M. A. Ansari, H. Ahmed, Y. Li, G. Wang, J. E. Callaghan, R. Wang, J. Downing, et al., "Multifaceted control of focal points along an arbitrary 3D curved trajectory," *Light: Science & Applications*, vol. 13, no. 1, p. 224, 2024.

[5] R. Rong, Y. Li, Z. Hu, K. Li, G. Li, S. Chen, and X. Chen, "Customizing 3D polarization structures at second harmonic frequency," Laser & Photonics Reviews, vol. 19, no. 24, p. e01059.

Breakdown of the Kirchhoff's law of thermal radiation by a spatiotemporally modulated nonreciprocal metasurface

Diego A. R. Dalvit[1,*], Anatoly Efimov[2], Chun-Chieh Chang[2], Simo Pajovic[1,3], Wilton Kort-Kamp[1], Dongsung Kim[4], Hou-Tong Chen[2], Abul Azad[2]

[1]Theoretical Division, Los Alamos National Laboratory, Los Alamos NM 87545, USA
[2]Center for Integrated Nanotechnologies, Los Alamos National Laboratory, Los Alamos NM 87545, USA
[3]Department of Mechanical Engineering, Massachusetts Institute of Technology, Cambridge MA 02138, USA
[4]Accelerator Operations and Technology Division, Los Alamos National Laboratory, Los Alamos NM 87545, USA

*Corresponding author: dalvit@lanl.gov

Abstract— **Kirchhoff's law of thermal radiation fundamentally limits the efficiency of photonic systems. We report the demonstration of spatiotemporally modulated nonreciprocal mid-infrared metasurfaces enabling the violation of the Kirchhoff's law at room temperature. We develop a theoretical framework to relate nonreciprocal scattering under spatiotemporal modulation with unequal absorptivity and emissivity.**

***Keywords*— metamaterials, nonreciprocity, Kirchhoff's law of thermal radiation, mid-infrared**

I. Introduction

The Lorentz reciprocity theorem states that a source and a detector of light can swap positions without changing the outcome of the measurement by the detector. Reciprocity assumes that light propagates in a linear, time-invariant medium with symmetric permittivity, permeability, and conductivity tensors. Metamaterials have revolutionized electromagnetic wave control. Reciprocity can have undesirable effects as well. Examples include solar cells re-emitting absorbed solar energy, radiative coolers absorbing thermal radiation, and antennas hearing their own echoes.

Here, we briefly report the to demonstration of nonreciprocal scattering in free space using a spatiotemporally modulated metasurface operating at mid-IR wavelength. We describe in detail he theory that related nonreciprocal scattering from a space-time graphene-based metasurface with the breakdown of Kirchhoff's law of thermal radiation (Fig. 1).

II. Methods

Our methodology integrates theory, simulation, nanofabrication and optical experiments.

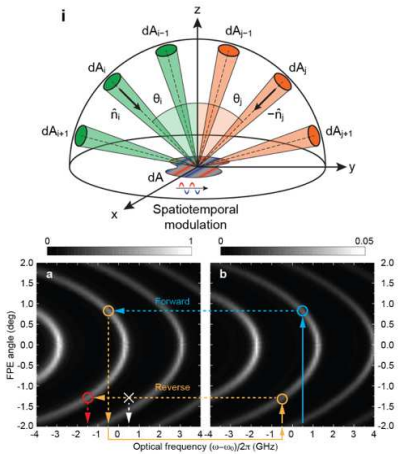

Fig. 1. (Top) Travelling-wave modulation of a metasurface; (Bottom) Frequency nonreciprocity via travelling-wave

III. Results and Discussion

We report the first demonstration of free-space non-reciprocal scattering at thermal wavelengths and connect it to the breakdown of Kirchhoff's law of thermal radiation.

IV. Conclusion

Together, our experiment and theory imply effective decoupling of absorption and emission channels by breaking time-reversal symmetry at thermal wavelengths.

References

[1] A. Efimov *et al.*," A mid-infrared spatiotemporally modulated metasurface platform for nonreciprocal scattering and implications for thermal emission control". arXiv:2509/00463. Under review in Nature Communications (2026).

Theory of Dispersive Space-Time Interfaces

Alessandra Contestabile[1*], Maria Antonietta Vincenti[2], Giuseppe Castaldi[3], Michael Scalora[2], Marcello Ferrera[4], Vincenzo Galdi[3] and Carlo Rizza[1,]

[1]Department of Physical and Chemical Sciences, University of L'Aquila, I-67100, Italy
[2]Department of Information Engineering, University of Brescia, Brescia, I-25123, Italy
[3]Fields & Waves Lab, Department of Engineering, University of Sannio, I-82100, Italy
[4]Istitute of Photonics and Quantum Sciences, Heriot-Watt University SUPA Edinburgh, EH14 4AS United Kingdom
*Corresponding author: alessandra.contestabile@graduate.univaq.it

***Abstract*— We study the scattering of waves at an interface whose properties vary in time, characterized by Lorentzian dispersion and an abrupt change in its parameters. Our work uncovers an unconventional mechanism in which novel frequency components are generated at the eigenmodes of the system. This phenomenon enables coupling between propagating and evanescent waves, allowing surface-wave modes to be directly excited from the far field without relying on spatially structured media. In addition, space-time interfaces can support unexpected optical spin effects induced by phase conjugation.**

***Keywords*— metamaterials, space-time interfaces, time-varying, linear frequency generation.**

I. Introduction

Time-modulated metasurfaces represent compact platforms capable of producing new frequencies without relying on traditional nonlinear phenomena. A representative example is a temporally modulated thin film [1], which operates through extended periodic modulation of an impedance surface. Under these conditions, the film generates additional frequencies and allows surface-wave modes to be directly excited from the far field, without requiring any supplementary spatial structuring.

In this work, we examine a temporally modulated dispersive interface characterized by Lorentz-type dispersion, whose material parameters switch abruptly in time. The system displays an unconventional linear generation of frequencies at its resonant response and, crucially, allows interaction between propagating and evanescent waves.

Our results point to a new route toward compact, high-speed photonic devices that bypasses the need for spatial patterning or prolonged temporal modulation.

II. Methods

We analyze a temporally modulated interface consisting of a dispersive dielectric slab of thickness L (with $L \ll \lambda$, where λ represents a characteristic wavelength) placed between two homogeneous, stationary, and non-dispersive half-spaces with relative permittivities ε_L and ε_R. The conceptual configuration is illustrated in Fig.1(a), which qualitatively shows the system's behavior following the temporal modulation, in the most general case of oblique incidence.

We focus both on transverse-electric (TE) and transverse megnetic (TM) modes of the form $\mathrm{Re}[E(z,t)e^{ik_x x}]\hat{\boldsymbol{e}}_y$ and $\mathrm{Re}\{e^{ik_x x}[E_x(z,t)\hat{\boldsymbol{e}}_x + E_z(z,t)\hat{\boldsymbol{e}}_z]\}$, respectively. Here k_x denotes the conserved transverse wavenumber, $\hat{\boldsymbol{e}}_\alpha$ is the unit vector oriented along the α direction, and i represents the imaginary unit. The interface is located at the plane $z = 0$, and its electromagnetic response can be described by appropriate sheet-transition conditions [2].

The dynamics of the surface polarization $\mathrm{Re}[\boldsymbol{P}(t)e^{ik_x x}]$ can be described by

$$\frac{\mathrm{d}^2\,\mathbf{P}}{\mathrm{dt}^2} + \gamma\frac{\mathrm{d}\mathbf{P}}{\mathrm{dt}} + \omega_0^2\,\mathbf{P} = \varepsilon_0\,\mathrm{L}\,\omega_\mathrm{p}^2\overline{\mathbf{E}}\,, \qquad (1)$$

where ε_0 is the vacuum permittivity, ω_0 and γ are the resonance frequency and damping parameter, respectively (constant over time), $\omega_p(t)$ is the time-varying plasma frequency, and $\overline{\mathbf{E}}(t) = \frac{1}{L}\int_{-L/2}^{L/2} dz\,\boldsymbol{E}(z,t)$.

Considering both sheet-transitions, Equation (1), one can obtain a semi-analytical theory in the case where the system features a temporal boundary (i.e., the plasma frequency experiences an abrupt change). In the stationary regime, where the plasma frequency remains constant, the interface supports both radiative and bound modes, as illustrated in Fig. 1(a). However, these modes cannot be directly excited by an incident propagating wave with a detuned frequency. Surprisingly, the temporal boundary can generate the system's eigenwaves even when the frequency of the incident field is far from the eigenfrequencies [3]. Moreover, this mechanism can be used to achieve unconventional spin/polarization conversion without the need for bi-anisotropy, chirality, or nonlinear effects [4].

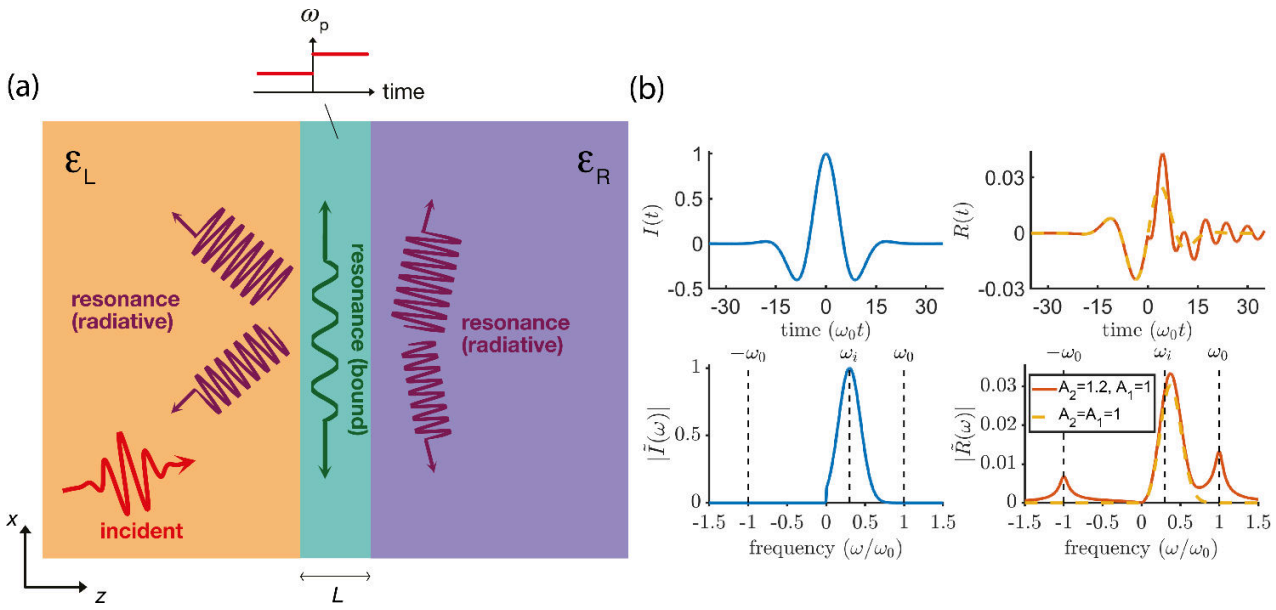

Fig. 1 (a) Schematic of the considered system: a time-varying dispersive interface implemented as a thin dielectric layer embedded between two homogeneous, stationary half-spaces with relative permittivities ε_L and ε_R. (b) Representative results for TE case, $k_x = 0$, with $\varepsilon_L = \varepsilon_R = 1$, $L = 0.16c/\omega_0$, and $\gamma = 5 \cdot 10^{-3}\omega_0$. The first row shows the temporal profiles of the incident $[I(t) = E_i(0^-, t)/E_0]$ and reflected $[R(t) = E_r(0^-, t)/E_0]$ wave packets, while the second row reports the corresponding spectra. Dashed vertical lines mark the carrier and resonance frequencies. Results obtained in the presence ($A_1 = 1$, $A_2 = 1.2$) and absence ($A_1 = A_2 = 1$) of the temporal boundary are compared. All spectra are normalized to the peak value of the incident spectrum.

III. Results and Discussion

As an illustrative example, we consider a temporally modulated Gaussian TE wave packet normally incident on the time-varying interface (i.e., $k_x = 0$), with electric – field profile $E_i(0^-, t) = E_0 e^{-t^2/\sigma^2 - i\omega_i t}$. Throughout this work, E_0 denotes a constant amplitude, ω_i the carrier angular frequency, and σ sets the temporal width of the wave packet. The temporal alignment is chosen such that the wave-packet peak reaches the metasurface exactly when the time switch occurs.

Figure 1(b) presents the system response in terms of the reflected field, for $\omega_i = 0.3\ \omega_0$, $\sigma = 10/\omega_0$, $\varepsilon_L = \varepsilon_R = 1$, $L = 0.16\ c/\omega_0$, and $\gamma = 5 \cdot 10^{-3}\ \omega_0$, where c is the speed of light in vacuum. In particular, the two panels in the first column display the temporal waveform and spectrum of the incident field, respectively, while the two in the second column show the reflected signal in the presence ($A_1 = 1$, $A_2 = 1.2$, orange solid curve) and absence ($A_2 = A_1 = 1$, yellow dashed curve) of the temporal boundary.

Notably, despite the incident wave packet not having spectral content at the resonant angular frequency ω_0, the reflected field exhibits pronounced components at $\pm\omega_0$ when a temporal boundary is introduced. As expected, this effect does not occur in the stationary case, where the plasma frequency remains constant.

IV. Conclusion

In conclusion, we introduce a semi-analytical framework for the scattering theory of dispersive space–time interfaces. These interfaces enable the generation of the system's eigenmodes, mediate the coupling between propagating and evanescent waves, exhibit unusual phase-conjugation, and spin/polarization effects. We also analyze the TM case dominated by epsilon-near-zero (ENZ) waves, with full details to be presented at the conference.

References

[1] E. Galiffi and Y.-T. Wang, Z. Lim, J. B. Pendry, A. Alù and P. A. Huidobro, Phys. Rev. Lett., Vol. 125, , No. 12, 127403, (2020).

[2] K. Achouri, M. A. Salem, and C. Caloz, "General metasurface synthesis based on susceptibility tensors", IEEE Trans. Antennas Propagat. 63, 2977 (2015).

[3] C. Rizza, M. A. Vincenti, G. Castaldi, A. Contestabile, V. Galdi and M. Scalora, "Harnessing the natural resonances of time-varying dispersive interfaces", Phys. Rev. Lett., 133(18), 186902, (2024).

[4] C. Rizza, A. Contestabile, M. A. Vincenti, G. Castaldi, M. Ferrera, A. Stroppa, M. Scalora and V. Galdi, "Optical Spin Effects Induced by Phase Conjugation at a Space-Time Interface", Small Structures, e202500359, (2025).

Exciton Polarons in 2D semiconductors

Carlos M. Escudero[1,2,*], Giuseppe Meneghini[1,2], Jamie M. Fitzgerald [1,2], Ermin Malic[1,2]

[1]Department of Physics, Philipps-Universität Marburg, Germany
[2]Marburg Center for Quantum Materials and Sustainable Technologies, Marburg, Germany
*Corresponding author: macieles@uni-marbug.de

***Abstract*— We investigate exciton polaron formation in 2D semiconductors. By solving the Dyson equation, we obtain polaron energies and identify the regime were polaronic effects, such as renormalized group velocity, effective masses and transport, become significant. Our work provides a systematic microscopy and material specific theory to investigate polaron physics.**

***Keywords*— excitons, phonons, polarons, two-dimensional materials, semiconductors.**

I. Introduction

Electron–phonon interactions in semiconductors can lead to the formation of new quasiparticles known as electron polarons. These quasiparticles emerge when an electron induces a local distortion, and thus, a polarization in the ionic lattice of the crystal [1]. This can be conceptually described as the electron being dressed by a surrounding cloud of phonons that accompanies its motion through the crystal. As a consequence of this dressing, the electron properties are modified (renormalized), including a reduced group velocity and an enhanced effective mass of the polaron compared to that of a free electron with the same crystal momentum. Although electron polaron effects have been deeply investigated in a wide range of materials [1], polaronic effects have not been extensively studied in semiconductors where electron-hole quasiparticles (excitons) dominate the optical response of the material. Semiconducting monolayers of transition metal dichalcogenides (TMDs) are of particular interest due to their ability to form excitons with large binding energies and simultaneously exhibit strong exciton–phonon coupling [2], making them a favorable platform for exploring exciton polaron physics. In this work, we present a microscopic description of exciton polarons in TMDs and show a systematic methodology to obtain their dispersion, group velocity and effective mass.

II. Methods

We consider MoS_2 monolayer as a representative two-dimensional semiconductor and compute in this material exciton polaron energies by iteratively determining the poles of Dyson equation [3]. Within this formalism, we described the self-energy of the exciton polaron using the Fan Migdal function. We further provide a systematic comparison of the contributions of optical and acoustic phonons to exciton polaron formation, considering both intra- and intervalley excitons.

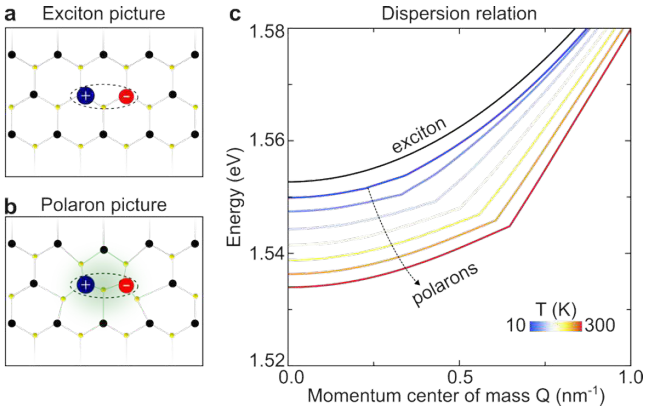

Fig. 1. **a** Schematic representation of an exciton in the hexagonal lattice of MoS_2. **b** Same as panel **a** but the lattice is distorted by the exciton. **c** Dispersion relations of 1*s* exciton (black line) in MoS_2 and acoustic exciton polarons at different temperatures (color lines).

III. Results and Discussion

Considering a single *s*-state exciton interacting with both acoustic and optical phonons in MoS_2 and WSe_2, we show that these interactions lead to the formation of exciton polarons in both materials. In particular, we find that the dispersion obtained from the Dyson equation exhibits a distinct kink at a characteristic momentum. This feature serves as a hallmark of polaron formation and emphasizes the crossover between a regime of bound exciton-polaron states and a regime dominated by exciton-phonon scattering. Below this characteristic momentum, well-defined bound polarons are formed, characterized by an energy redshift on the order of tens of meV and a mass enhancement of approximately 20% compared to that of 1*s* excitons with the same center-of-mass momentum (Fig. 1). We further show that these effects become increasingly pronounced with increasing temperature. Finally, we extend our methodology to include higher exciton states and incorporate momentum-dark excitons, thus providing a more comprehensive description of polaron formation in TMD monolayers.

IV. Conclusion

We develop a microscopic theoretical framework to investigate exciton polaron formation in two-dimensional semiconductors. Applying this framework to atomically thin semiconductors (MoS_2, WSe_2), we demonstrate that exciton-phonon interactions lead to the emergence of exciton polarons with modified group velocities, effective masses, and transport

below a specific critical momentum within the crystal. Our results provide a systematic analysis of polaronic effects in TMDs and establish a versatile methodology that can be extended to other excitonic materials, including perovskites and related TMD heterostructures.

ACKNOWLEDGMENTS

This work was supported by a Humboldt Research Fellowship from the Alexander von Humboldt Foundation to Carlos M. Escudero. Furthermore, we acknowledge support from the Deutsche Physikalische Gesellschaft (DFG) via the regular project 524612380.

REFERENCES

[1] C. Franchini, M. Reticcioli, M. Setvin and U. Diebold, "Polarons in materials," Nature Reviews Materials, vol. 6, pp. 560–586, 2021.

[2] R. Perea-Causin, D. Erkensten, J. Fitzgerald, J. J. Thompson, R. Rosati, S. Brem, E. Malic, "Exciton optics, dynamics, and transport in atomically thin semiconductors", APL Materials, vol. 10, pp. 100701, 2022.

[3] A. L. Fetter, J. D. Walecka, "Quantum theory of many-particle systems", Dover Publications, 2003.

Janus Vortex Meta-Laser

Lili Gui*, Yiyuan Xu, Hao Chen, and Kun Xu

State Key Laboratory of Information Photonics and Optical Communications, Beijing University of Posts and Telecommunications, Beijing, 100876, China
*Corresponding author: liligui@bupt.edu.cn

***Abstract*— We demonstrate a Janus vortex meta-laser, which enables simultaneous asymmetric and full 2π phase modulation of two counter-propagating beams, owing to the asymmetric–symmetric hybrid configuration of the intracavity Janus metasurface.**

***Keywords*— vortex fiber laser; Janus metasurface; bidirectional light field control.**

I. Introduction

Metasurfaces (MSs), as a potent platform for light-field modulation, have been demonstrated to integrate compactly within laser cavities, allowing intracavity spatiotemporal light-field engineering with unprecedented precision[1]. Here, we demonstrate the Janus vortex meta-laser (JVML). By integrating a Janus metasurface (JMS), which is composed of merely a single-layer metasurface and a half-wave plate (HWP), this compact system with a streamlined design enables the asymmetric generation of vortex beams in two counter-propagating directions.

II. Methods

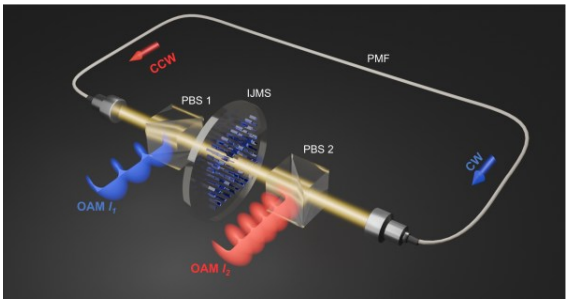

Fig. 1. The design of the Janus vortex meta-laser and the Janus metasurface. CW, clockwise; CCW, counterclockwise; PBS, polarization beam splitter; OAM, orbital angular momentum; PMF, polarization-maintaining fiber; IJMS, intracavity Janus metasurface.

The intracavity light field can be divided into two distinct categories based on its symmetry properties with respect to the wavevector (k) direction. For clockwise (CW) propagation light, the transmission matrix is given by $J_{CW} = \begin{bmatrix} a & b \\ c & a \end{bmatrix}$, while for light propagating in counterclockwise (CCW) direction, the corresponding matrix becomes $J_{CCW} = \begin{bmatrix} a & -c \\ -b & a \end{bmatrix}$. In this regime, the intracavity co-polarized component exhibits direction-independent symmetry, remaining invariant to the propagation direction. The cross-polarized component, however, displays a direction-dependent asymmetry, as it is interchanged when the k-vector direction is reversed. By harnessing this principle, our vortex laser design facilitates asymmetric structure-light emission while still fulfilling the self-consistency criterion for intracavity resonance [Fig. 1].

III. Results and Discussion

The results in Fig. 2 demonstrate that the JVML uniquely enables in-cavity, bidirectional generation of counter-propagating vortex beams (with topological charges $l_1 = -2$ and $l_2 = 8$), with different configurations achieving both high mode purity (>93%) and exceptionally large topological charges separation ($|\Delta\ell|$ up to 10).

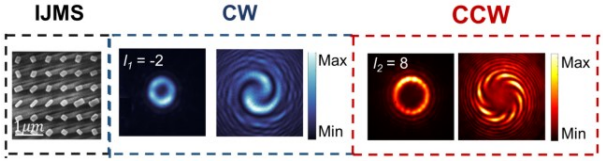

Fig. 2. Intracavity asymmetric bidirectional light-field manipulation in experiment.

IV. Conclusion

In summary, we demonstrate the first JVML, a novel architecture that enables direct intracavity generation of paired, counter-propagating vortex beams with, in principle, arbitrarily configurable topological charge separation, thereby introducing a novel degree of freedom for structured-light laser and opening up promising avenues in super-resolution microscopy, optical tweezers, precision measurement, optical communications, among others.

Acknowledgments

This work is supported in part by the National Natural Science Foundation of China under Grant 62575031, and in part by the Fundamental Research Funds for the Central Universities from China (Grant ZDYY202102).

References

1. C. Wang, C. Meng, X. Mei, L. Gui, P. C. V. Thrane, H. Chen, F. Ding, K. Xu, and S. I. Bozhevolnyi, Sci. Adv. **10**, eadq6299 (2024).

SPDC in Thin-Film LN: From Tunable Polarization Entanglement to Doubly-Resonant Metasurfaces

M. A. Weissflog[1,*], S. Shinde[1], S. Lung[1], J. Ma[2], S. Saravi[3,1], T. Pertsch[1,4], A. Sukhorukov[2], F. Setzpfandt[1,4]

[1]Institute of Applied Physics, Abbe Center of Photonics, Friedrich Schiller University Jena, Germany.
[2]ARC Centre of Excellence for Transformative Meta-Optical Systems (TMOS), Department of Electronic Materials Engineering, Research School of Physics, The Australian National University, Canberra, Australia.
[3]Heinz Nixdorf Institute, Department of Electrical Engineering and Information Technology, Institute for Photonic Quantum Systems (PhoQS), Paderborn University, Paderborn, Germany
[4]Fraunhofer Institute for Applied Optics and Precision Engineering IOF, Jena, Germany.
*Corresponding author: maximilian.weissflog@uni-jena.de

***Abstract*—We experimentally show a new mechanism for directly generating and tuning polarization entanglement for spontaneous parametric down-conversion (SPDC) in thin-film lithium niobate (TFLN), which relies on its three-fold rotational crystal symmetry. Furthermore, we demonstrate a nonlocal LN metasurface that supports frequency-tunable, degenerate and non-degenerate SPDC with doubly-resonant enhancement.**

***Keywords*— SPDC, thin-film lithium niobate, polarization-entanglement, frequency-tuning, nonlocal metasurface.**

I. Introduction

Entangled photon pairs play a pivotal role in many emerging applications including quantum communication, computing and sensing. While conventional photon-pair sources are based on spontaneous parametric down-conversion (SPDC) in bulk crystals or integrated photonic circuits, subwavelength-scale nonlinear crystals and resonant metasurfaces have emerged as a very versatile alternative [1], [2]. Here we show that leaving the track of phase-matched nonlinear bulk optics also allows the use of established nonlinear materials, such as lithium niobate (LN), in an unconventional way. We experimentally demonstrate that z-cut thin-film LN (TFLN) can directly generate photon pairs with continuously tunable polarization states. Interestingly, this does not require any specially engineered optical properties, but relies solely on LNs crystal symmetry. In the second part we demonstrate that a nonlocal metasurface consisting of TFLN combined with a nanostructured layer supports doubly-resonant and continuously frequency tunable photon-pair generation.

II. Results and Discussion

Implementations of (quasi-)phasematched SPDC in nonlinear TFLN almost exclusively relies on nonlinear interactions where pump, signal and idler wave propagate within the xy-crystal plane [3]. While this gives access to the largest nonlinear tensor component $\chi^{(2)}_{zzz}$, generation of polarization-entangled signal and idler photons is nontrivial and usually requires careful post-processing in additional optical circuitry. However, LN can actually *directly* generate polarization-entangled pairs when excited with a pump photon propagating along the z-axis – to our knowledge an approach not discussed in literature so far. The threefold rotational crystal symmetry around the z-axis enforces nonlinear tensors with equal magnitudes for polarization within the xy-plane, which can be exploited for generating polarization entanglement [4]. We experimentally demonstrate via quantum-state tomography that this tensor structure of LN enables direct generation of maximally entangled polarization Bell states for linearly polarized pump photons as well as continuous tuning of the degree of entanglement for elliptically polarized pump waves.

Next to polarization control we also demonstrate engineering of the SPDC spectrum in TFLN. For this we employ a nonlinear metasurface based on TFLN combined with a grating structure, effectively creating nonlocal guided-mode resonances in the LN layer. Momentum matching within one or multiple resonance bands provides resonant enhancement for both, signal and idler photon for any combination of energy degenerate or non-degenerate SPDC in the telecom band. Experimentally, we show SPDC with continuous tuning of the signal and idler wavelength from the degenerate case $\lambda_s = \lambda_i$ up to a wavelength difference $\Delta\lambda = 30$ nm. Both photons are always generated on resonance while their wavelength can be controlled via the incidence angle of the pump.

III. Conclusion

We demonstrate a new mechanism for generating and tuning polarization entanglement in TFLN and show doubly-resonant, spectrally tunable photon-pair generation in a nonlocal LN metasurface. These two examples highlight that LN thin films and metasurfaces offer very flexible engineering of the polarization and frequency properties of photon pairs while maintaining an extremely compact form factor.

References

[1] T. Santiago-Cruz, et al., "Photon Pairs from Resonant Metasurfaces," *Nano Lett.*, vol. 21, pp. 4423–4429, 2021.
[2] J. Zhang, et al., "Spatially entangled photon pairs from lithium niobate nonlocal metasurfaces," *Science Advances*, vol. 8, pp. eabq4240, 2022.
[3] D. Zhu, et al., "Integrated photonics on thin-film lithium niobate," *Adv. Opt. Photon.*, vol. 13, pp. 242—352, 2021.
[4] M. A. Weissflog, et al., "A tunable transition metal dichalcogenide entangled photon-pair source," *Nat. Commun.*, vol. 15, pp. 7600, 2024.

Closed-form conditions for parametric amplification in open photonic time crystals

Adrià Canós Valero[1,2,*], Sergei Gladyshev[1], David Globosits[3], Stefan Rotter[3], Egor A. Muljarov[4], Thomas Weiss[1,*]

[1]Institute of Physics, University of Graz, and NAWI Graz, 8010 Graz, Austria
[2]Riga Technical University, Institute of Telecommunications, Riga, 1048, Latvia
[3]Institute for Theoretical Physics, Vienna University of Technology (TU Wien), 1040 Vienna, Austria
[4]School of Physics and Astronomy, Cardiff University, Cardiff CF24 3AA, United Kingdom
*Corresponding author: adria.canos-valero@uni-graz.at

***Abstract*—We develop an exact theory of photonic modes in 'open photonic time crystals', radiative nanoresonators with periodically time-modulated material properties. Our framework allows deriving analytical conditions for realizing parametric amplification in systems of arbitrary shape and size. We leverage our insights to design micro- and nanoscale parametric amplifiers.**

***Keywords*— metamaterials, dielectric nanophotonics, time-varying media, quasinormal modes, resonant states, non-Hermitian physics.**

I. Introduction

Over the past decades, advances in nanofabrication and materials science have enabled engineered composites with tailored electromagnetic responses, including metamaterials, metasurfaces, and photonic crystals made from dielectric or plasmonic nanoparticles [1], [2], [3]. Their unique optical behavior arises from nanoscale resonances that confine light and control its propagation, enabling functionalities beyond natural materials. Extending this concept to the temporal domain, materials with properties modulated in time open new opportunities for manipulating light [4], [5], [6], [7], [8]. Periodic modulation gives rise to photonic time crystals, where momentum bandgaps can lead to light amplification [5], [9], [10]. Implementing PTCs in finite, radiative nanostructures introduces new challenges, as resonances and radiation dominate their dynamics. To distinguish these systems from uniform, time-modulated media, we refer to the latter as 'bulk PTCs' and the former as 'open PTCs', emphasizing their ability to exchange energy with the environment. While most theoretical work has focused on bulk PTCs [11], [12], [13], understanding the interplay of radiation and temporal modulation in open PTCs is crucial for designing these devices at the nanoscale.

We have recently developed a general formalism to describe the photonic modes of open PTCs of arbitrary shape and size [14]. Here, we present this first-principles theory, highlighting how it predicts the conditions for parametric amplification of a photonic mode in a nanoresonator of complex shape.

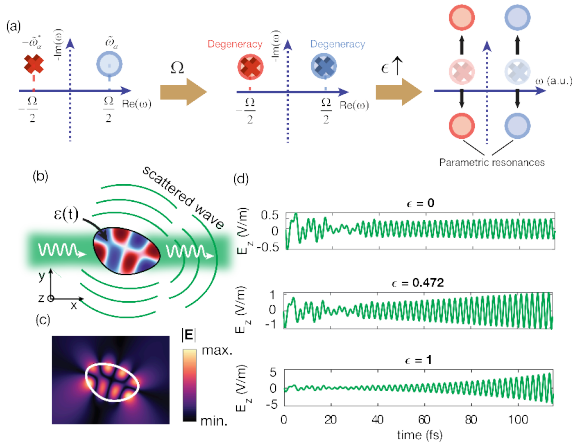

Fig. 1. (a) Sketch of the mechanism responsible for the formation of parametric resonances. Leftmost panel displays a static resonant state and its negative twin. Central panel shows the replicas from the two modes upon introducing a modulation Ω, such that $\Omega = 2\omega_\alpha$. Rightmost panel displays the modulated eigenfrequencies of the resonant states upon increasing the modulation amplitude. (b) Conceptual sketch depicting scattering of a plane wave (white arrows) by a complex-shaped cavity with periodically modulated permittivity. The static permittivity is fixed to $\varepsilon_u = 16$, emulating a high-index dielectric. (c) out-of-plane electric field of the considered unmodulated resonant state of the cavity. The resonant state has a quality factor $Q_\alpha \approx 52$. (d) Time domain simulations of the scattering by a plane wave with angular frequency $\omega = \mathrm{Re}(\tilde{\omega}_\alpha)$, when the permittivity is modulated at $\Omega = 2\mathrm{Re}(\tilde{\omega}_\alpha)$ at different modulation amplitudes ϵ. The plots show the z-component of the electric field at a point away from the scatterer along the direction of propagation of the incident plane wave.

II. Results and Discussion

We consider a sinusoidal modulation of the permittivity of an arbitrary resonator, with the following form

$$\varepsilon(t) = \varepsilon_u + \epsilon \sin(\Omega t). \tag{1}$$

As shown in our work [14], a photonic mode can amplify light when the modulation hybridizes it to a frequency-shifted replica of its negative twin. Consider a photonic mode α, whose eigenfrequency is given by $\tilde{\omega}_\alpha = \omega_\alpha - i\gamma$, where ω_α is the resonance frequency, and γ is the mode loss rate. As

sketched in Fig. 1(a), when $\Omega = 2\omega_\alpha$ a replica of the negative twin becomes degenerate with mode α.

Our theory then leads to a simple eigenvalue problem between the unmodulated photonic modes, given by

$$\begin{pmatrix} \frac{\Omega}{2} - i\gamma & 0 \\ -\Omega V & \frac{\Omega}{2} - i\gamma \end{pmatrix} \mathbf{c} = \tilde{\omega} \begin{pmatrix} 1 & V \\ -V & 1 \end{pmatrix} \mathbf{c}. \tag{2}$$

Here, the top component of $\mathbf{c}$ corresponds to the static photonic mode $\tilde{\omega}_\alpha$, while the bottom component represents the replica of its negative twin. The coupling coefficient V is obtained from the mode overlap:

$$V = \frac{\epsilon}{2i} \int |\mathbf{E}_\alpha(\mathbf{r})|^2 d\mathbf{r} \equiv \frac{\epsilon}{2i} I_\alpha. \tag{3}$$

For sinusoidal modulation, the integral is purely real since the negative twin is simply the complex conjugate of the positive-frequency mode [14].

Equation (2) can be solved exactly, but more insight is gained in the limit $V \ll 1$. With this approximation, the hybrid eigenfrequencies are:

$$\tilde{\omega}_\pm \approx \frac{\Omega}{2} - i\gamma \mp i I_\alpha \frac{\epsilon}{4} \sqrt{\Omega^2 + 4\gamma^2}. \tag{4}$$

The real parts remain $\mathrm{Re}(\tilde{\omega}_\pm) = \Omega/2$, while one of the imaginary parts increases with ϵ and the other decreases. A parametric resonance occurs when the modulation amplitude compensates the losses, bringing one eigenmode to the real axis. Beyond this threshold, further increase of ϵ can flip the sign of the imaginary part, effectively converting the mode into a lasing state, as illustrated in Fig. 1(a).

From Eq. (4), the modulation threshold ϵ_{thr} for any resonant state to become a parametric resonance can be easily found by setting the imaginary part to zero, giving:

$$\epsilon_{\text{thr}} \approx \frac{4\gamma}{I_\alpha \sqrt{\Omega^2 + 4\gamma^2}} = \frac{2\gamma}{I_\alpha |\tilde{\omega}_\alpha|}. \tag{5}$$

Equation (5) is a novel result allowing, without any fitting parameters, to estimate the required modulation amplitude to realize a parametric resonance for arbitrary open PTCs. It can be seen that the larger the imaginary part of the eigenfrequency is (the larger the decay rate), the larger will ϵ_{thr} need to be to bring it to the real axis. Therefore, it becomes clear that eigenmodes with small γ (large quality factors) can be more easily driven to the parametric regime. When $\gamma \ll |\omega_\alpha|$ and for small ϵ_{thr}, Eq. (5) simplifies to $\epsilon_{\text{thr}} \approx (Q_\alpha I_\alpha)^{-1}$, where Q_α is the quality factor of the unmodulated mode. This provides an accurate estimate of the threshold using only the mode's field and quality factor.

To illustrate that resonances govern amplification in open PTCs independent of size or geometry, we consider a complex two-dimensional high-index dielectric cavity shown in Fig. 1(b). We focus on a resonant mode in the visible range [Fig. 1(c)], which has a complex spatial profile and moderate quality factor $Q_\alpha \approx 52$, indicating significant radiation loss. Using Eq. (5), the parametric threshold is $\epsilon_{\text{thr}} \approx 0.48$.

To confirm our predictions, we perform time-domain simulations of a plane wave exciting the nanoresonator at $\omega = \omega_\alpha$ with the cavity modulated at twice the frequency. The initial time $t = 0$ is set at the start of the simulation, when the incident plane wave is turned on. We track the electric field 200 nm away from the resonator, shown in Fig. 1(d). In the unmodulated case, the field oscillates steadily at the frequency of the incident plane wave. Near the threshold, amplification emerges, and for $\epsilon > \epsilon_{\text{thr}}$, the field grows exponentially, signaling a lasing state [14], [15].

III. Conclusion

We have derived analytical conditions for parametric amplification and shown that they hold for open photonic time crystals of arbitrary shape and size. This generality confirms that our theory applies to a broad range of resonant systems, paving the way toward the rational design of time modulated nanophotonic devices, which are the natural next step in the control of light at the nanoscale.

Acknowledgments

References

[1] A. A. Basharin, M. Kafesaki, E. N. Economou, C. M. Soukoulis, V. A. Fedotov, V. Savinov, and N. I. Zheludev, "Dielectric metamaterials with toroidal dipolar response," *Physical Review X*, vol. 5, no. 1, p. 011036, 2015.

[2] D. R. Smith, J. B. Pendry, and M. C. Wiltshire, "Metamaterials and negative refractive index," *science*, vol. 305, no. 5685, pp. 788–792, 2004.

[3] M. Kim, A. M. Wong, and G. V. Eleftheriades, "Optical huygens' metasurfaces with independent control of the magnitude and phase of the local reflection coefficients," *Physical Review X*, vol. 4, no. 4, p. 041042, 2014.

[4] E. Galiffi, R. Tirole, S. Yin, H. Li, S. Vezzoli, P. A. Huidobro, M. G. Silveirinha, R. Sapienza, A. Alù, and J. B. Pendry, "Photonics of time-varying media," *Advanced Photonics*, vol. 4, no. 1, pp. 014 002–014 002, 2022.

[5] X. Wang, P. Garg, M. Mirmoosa, A. Lamprianidis, C. Rockstuhl, and V. Asadchy, "Expanding momentum bandgaps in photonic time crystals through resonances," *Nature Photonics*, pp. 1–7, 2024.

[6] D. L. Sounas and A. Alù, "Non-reciprocal photonics based on time modulation," *Nature Photonics*, vol. 11, no. 12, pp. 774–783, 2017.

[7] S. Yin, E. Galiffi, and A. Alù, "Floquet metamaterials," *ELight*, vol. 2, no. 1, p. 8, 2022.

[8] G. Ptitcyn, M. S. Mirmoosa, A. Sotoodehfar, and S. A. Tretyakov, "A tutorial on the basics of time-varying electromagnetic systems and circuits: Historic overview and basic concepts of time-modulation," *IEEE Antennas and Propagation Magazine*, vol. 65, no. 4, pp. 10–20, 2023.

[9] M. M. Asgari, P. Garg, X. Wang, M. S. Mirmoosa, C. Rockstuhl, and V. Asadchy, "Theory and applications of photonic time crystals: a tutorial," *Advances in Optics and Photonics*, vol. 16, no. 4, pp. 958–1063, 2024.

[10] S. Saha, O. Segal, C. Fruhling, E. Lustig, M. Segev, A. Boltasseva, and V. M. Shalaev, "Photonic time crystals: a materials perspective," *Optics Express*, vol. 31, no. 5, pp. 8267–8273, 2023.

[11] M. Lyubarov, Y. Lumer, A. Dikopoltsev, E. Lustig, Y. Sharabi, and M. Segev, "Amplified emission and lasing in photonic time crystals," *Science*, vol. 377, no. 6604, pp. 425–428, 2022.

[12] T. T. Koutserimpas and R. Fleury, "Nonreciprocal gain in non-Hermitian time-Floquet systems," *Physical review letters*, vol. 120, no. 8, p. 087401, 2018.

[13] X. Wang, G. Ptitcyn, V. Asadchy, A. Díaz-Rubio, M. S. Mirmoosa, S. Fan, and S. A. Tretyakov, "Nonreciprocity in bianisotropic systems with uniform time modulation," *Physical Review Letters*, vol. 125, no. 26, p. 266102, 2020.

[14] A. C. Valero, S. Gladyshev, D. Globosits, S. Rotter, E. A. Muljarov, and T. Weiss, "Resonant states of structured photonic time crystals," *arXiv preprint arXiv:2506.01472*, 2025.

[15] D. Globosits, P. Garg, J. Hüpfl, A. C. Valero, T. Weiss, C. Rockstuhl, and S. Rotter, "Exceptional points, lasing, and coherent perfect absorption in floquet scattering systems," *arXiv preprint arXiv:2510.03133*, 2025.

Cavity-Enhanced Superfluorescence and Lasing Transitions in Two-Dimensional Single-Crystal Perovskite Superlattices

Jae Yong Suh[1,*]

[1]Department of Physics, Michigan Technological University, USA
*Corresponding author: jsuh@mtu.edu

***Abstract*—We report cavity-enhanced superfluorescence in pure two-dimensional (2D) perovskite single crystals. Unlike disordered thin films, these superlattices enable clean collective emission. Using Maxwell Bloch equations, we analyze the superfluorescence lasing phase transition and Burnham Chiao ringing within a microcavity, providing a framework for room temperature quantum optoelectronic devices.**

***Keywords*—superfluorescence, perovskites, microcavity, Maxwell-Bloch, phase transition.**

I. Introduction

Superfluorescence (SF) represents a hallmark of cooperative light-matter interaction. While typically observed at cryogenic temperatures, recent advancements in quasi-two-dimensional (2D) metal halide perovskites have enabled room-temperature observations [1-2]. However, standard quasi-2D thin films often exhibit ambiguous SF signatures due to phase impurities and structural disorder. In this work, we demonstrate that single-crystal microplatelets composed of a pure 2D superlattice—free of bulk phases—enable the observation of exceptionally clean SF characteristics. By integrating these crystals into 1D distributed Bragg reflector (DBR) microcavities, we investigate the cavity-enhanced SF regime and the transition into stimulated lasing.

II. Methods

Our High-quality Ruddlesden-Popper (RP) perovskite single crystals were synthesized via a solution-growth crystallization technique, producing $(PEA)_2PbX_4$ (X=Br,I) microplatelets with a strictly periodic 2D superlattice structure [3]. These crystals were subsequently integrated into 1D DBR microcavity structures. To capture the ultrafast dynamical emergence of SF, we employed Kerr-gated time-resolved spectroscopy. This technique utilizes a femtosecond gate pulse to induce transient birefringence in a Kerr medium, allowing for sub-picosecond temporal resolution of the collective emission pulses.

To model the dynamical emergence of SF, the system Hamiltonian is reduced to a semiclassical form by deriving equations of motion for the expectation values of the collective polarization (ρ_{ab}), inverse population (w), and cavity field amplitude (E). The governing Maxwell-Bloch equations are expressed as:

$$\frac{dE}{dt} = -\kappa E + ig\rho_{ab}$$

$$\frac{d\rho_{ab}}{dt} = -(\gamma_\perp + i\Delta)\rho_{ab} + igE_w$$

$$\frac{dw}{dt} = -\gamma_\parallel(w - w_0) + 4g\mathrm{Im}(E^*)\rho_{ab}$$

where κ is the cavity decay rate, g is the coupling strength, and γ represents the respective relaxation rates.

III. Results and Discussion

The experimental results reveal distinct SF signatures in the pure 2D superlattices, including a characteristic emission delay and a quadratic dependence of intensity on excitation power. Unlike thin-film counterparts, the single crystals exhibit clear Burnham–Chiao ringing near the excitation threshold.

Key findings include:

- **SF-Lasing Transition:** We identify a clear phase transition from collective SF to stimulated lasing governed by the cavity feedback strength.
- **Superlattice Role:** Analyses indicate that the ordered superlattice structure significantly lowers the SF threshold by facilitating long-range transition dipole alignment.
- **Ringing Conditions:** Theoretical modeling provides the boundary conditions for Burnham–Chiao ringing as a function of the collective pulse area.

IV. Conclusion

We have demonstrated that pure 2D perovskite superlattices serve as an ideal platform for cavity-enhanced superfluorescence. The transition between SF and lasing regimes is well-described by our Maxwell-Bloch framework, offering a predictive tool for designing next-generation

quantum light sources that operate at ambient temperatures

ACKNOWLEDGMENTS

This material is based upon work supported by the National Science Foundation under NSF 2301580.

REFERENCES

[1] M. Biliroglu, G. Findik, J. Mendes, D. Seyitliyev, L. Lei, Q. Dong, Y. Mehta, V. V. Temnov, F. So, K. Gundogdu, Room- temperature superfluorescence in hybrid perovskites and its origins. Nat. Photonics 16 (4), 324−329, 2022.

[2] A. Wildenborg, R. Munter, F. Freire-Fernández, E. Freitas, and J. Y. Suh, Superlattice-Induced Superfluorescence in Quasi-2D Metal Halide Perovskites, ACS Photonics, 12, 3476−3483, 2025

[3] D. Ma, Y. Fu, L. Dang, J. Zhai, I. A. Guzei, and S. Jin, Single-crystal microplates of two-dimensional organic–inorganic lead halide layered perovskites for optoelectronics, Nano Research 10(6): 2117–2129, 2017

Towards Realization of Ideal Anapole Excitations

Radoslaw Kolkowski[1,*], Matti Kaivola[1], Sagar Sehrawat[1], Andriy Shevchenko[1]

[1]Department of Applied Physics, Aalto University, Finland

*Corresponding author: radoslaw.kolkowski@aalto.fi

***Abstract*—We present an alternative approach based on the scattering-current multipole expansion to describe anapole excitations in photonic nanostructures. Using the method, we derive the exact anapole condition, opening the way towards design and realization of perfect anapoles.**

***Keywords*— anapoles, toroidal dipoles, multipole expansion.**

I. Introduction

Optical anapoles are localized excitations of electromagnetic fields that do not radiate, leading to nanoscale concentration of light energy. A popular example is an anapole originating from the destructive far-field interference of an electric dipole moment ($\mathbf{p}$) and a toroidal electric dipole moment ($\mathbf{T}$), which happens at the anapole condition ($\mathbf{p} + ik\mathbf{T} = 0$) [1]. Typically, the moments $\mathbf{p}$ and $\mathbf{T}$ are calculated using multipole expansion within the small-scatterer approximation [2]. Here, we demonstrate that this common description is often not accurate, and propose an alternative method based on the exact scattering-current multipole expansion [3]. The resulting anapole condition is valid for scatterers of arbitrary size and can be used to design perfectly nonradiating anapoles.

II. Methods

The commonly used approximate expressions for the electric dipole and electric toroidal dipole moments are

$$\mathbf{p} = \frac{i}{\omega}\int_{-\infty}^{\infty}\mathbf{J}d^3\mathbf{r}, \tag{1}$$

$$\mathbf{T} = \frac{k}{10\omega}\int_{-\infty}^{\infty}[(\mathbf{r}\cdot\mathbf{J})\mathbf{r} - 2r^2\mathbf{J}]d^3\mathbf{r}, \tag{2}$$

where $\mathbf{J}(\mathbf{r}) = -i\omega\epsilon_0[\epsilon_r(\mathbf{r}) - 1]\mathbf{E}(\mathbf{r})$ is the scattering current density (for a scatterer in vacuum), and $\epsilon_r(\mathbf{r})$ is the relative electric permittivity that depends on the coordinate $\mathbf{r}$. Outside the scatterer, ϵ_r = 1 and $\mathbf{J}$ = 0. The normalized scattering cross section due to $\mathbf{p}$ and $\mathbf{T}$ is given by

$$\sigma(\mathbf{p},\mathbf{T}) = \frac{k^4}{6\pi\epsilon_0^2E_0^2S}\left|\mathbf{p} + ik\mathbf{T}\right|^2, \tag{3}$$

where E_0 is the incident field amplitude and S is the geometric cross section of the scatterer. The conventional anapole condition is derived by setting $\sigma(\mathbf{p},\mathbf{T})$ to zero.

Alternatively to Eq. (3), the total electric-dipole scattering cross section can be calculated using the exact multipole expansion [4], which is valid for scatterers of arbitrary size. Considering only the dipole moment along z, this cross section can be written as

$$\sigma(a^E_{l=1}) = \frac{3\pi}{k^2S}\left|a^E_{l=1,m=0}\right|^2, \tag{4}$$

where l and m are the spherical harmonics' indices corresponding to the subsequent multipole expansion terms. We have recently derived the expressions for $a_{l,m}$ (both electric $a^E_{l,m}$ and magnetic $a^M_{l,m}$) in terms of the scattering-current multipole moments [3]. Specifically, we have obtained

$$a^E_{l=1,m=0} = \sqrt{2}C_1p_z^{\text{exact}} + \frac{7\sqrt{2}}{3}C_3O^{\text{exact}}, \tag{5}$$

where $C_1 = -ik^3/(6\pi\epsilon_0E_0)$, $C_3 = -ik^5/(210\pi\epsilon_0E_0)$, and

$$O^{\text{exact}} = 3O_{xxz} + 3O_{yyz} + 2O_{zzz} - O_{zxx} - O_{zyy}. \tag{6}$$

Here, the superscript "exact" in the $O_{\alpha\beta\gamma}$ terms is omitted for clarity. The scattering-current dipole and octupole moments p_z^{exact} and $O_{\alpha\beta\gamma}$ are defined as

$$p_z^{\text{exact}} = \frac{i}{\omega}\int_{-\infty}^{\infty} j_0(kr)\,J_z\,d^3\mathbf{r}, \tag{7}$$

$$O_{\alpha\beta\gamma} = \frac{15i}{2\omega k^2}\int_{-\infty}^{\infty}\frac{1}{r^2}j_2(kr)\,J_\alpha r_\beta r_\gamma d^3\mathbf{r}. \tag{8}$$

Equations (4)-(8) yield correct values of the scattering cross sections for scatterers of an arbitrary size. Based on these expressions, the exact anapole condition is written as

$$p_z^{\text{exact}} + \frac{k^2}{15}O^{\text{exact}} = 0. \tag{9}$$

The above equation shows that, in fact, the anapole originates from destructive interference between the far-field radiation contributions of scattering-current dipoles and octupoles.

III. Results and Discussion

Let us consider a silicon nanodisk of radius 300 nm and thickness 60 nm in vacuum. The nanodisk's orientation with respect to the incident light is shown in Fig. 1(a). The scattering is modeled numerically using COMSOL Multiphysics. The spectral dependences of the calculated scattering cross sections are shown in Fig. 1(b). The dependences show a clear scattering dip at a frequency of 308 THz (wavelength ~974 nm). The electric field distribution at this dip, shown in Fig. 1(a), is typical for an anapole excitation.

Fulfilling the anapole condition based on the approximate expressions [Eqs. (1)-(3)] is demonstrated in Fig. 1(c) and (d). In this figure, p_z and $-ikT_z$ are plotted together, intersecting at almost the same frequency in both amplitude and phase. This near-perfect coincidence leads to an almost complete suppression of $\sigma(\mathbf{p},\mathbf{T})$, with the cross section magnitude falling down to 0.064, as can be seen in Fig. 1(b). However, Fig. 1(b) also shows that the exact electric-dipole scattering

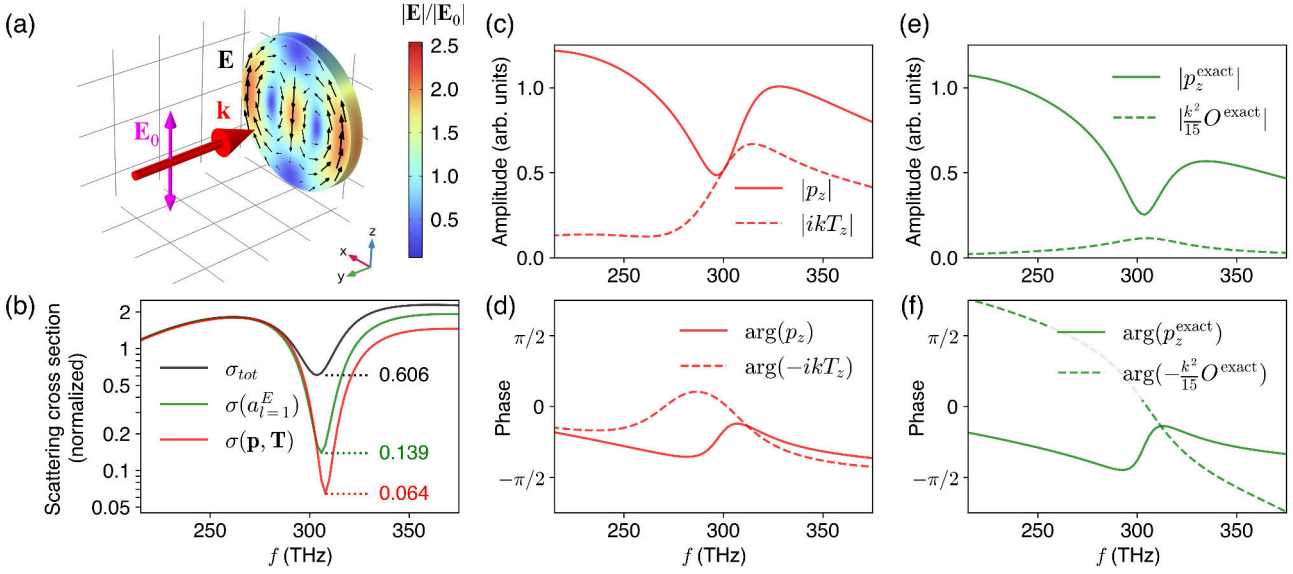

Fig. 1. (a) Excitation configuration ($\mathbf{E}_0$ and $\mathbf{k}$ - incident electric field and wave vector, respectively) and simulated electric field distribution (vector $\mathbf{E}$ and amplitude enhancement $|\mathbf{E}|/|\mathbf{E}_0|$) at the surface of a silicon nanodisk (thickness 60 nm, diameter 600 nm) at frequency 308 THz, corresponding to the anapole excitation. (b) Total scattering cross section (σ_{tot}, black curve), scattering cross section associated with the electric dipole and electric toroidal dipole moments $\sigma(\mathbf{p}, \mathbf{T})$, as defined in Eqs. (1)-(3) (red curve), and total electric-dipole scattering cross section $\sigma(a^E_{l=1})$ (green curve) obtained from the exact multipole expansion. The values at the scattering minima are shown for $\sigma(\mathbf{p}, \mathbf{T})$ and $\sigma(a^E_{l=1})$ by the corresponding red and green numbers. (c) and (d): Amplitude and phase of the electric dipole and electric toroidal dipole moments along z, calculated using Eqs. (1)-(2) (p_z and T_z, solid and dashed red curves, respectively). (e) and (f): Amplitude and phase of the exact scattering-current dipole moment p_z^{exact}, as defined in Eq. (7) (solid green curves), and the exact scattering-current octupole moments combined into $\frac{k^2}{15}O^{\text{exact}}$, i.e., the second term in Eq. (9), as defined in Eqs. (6) and (8) (dashed green curves).

$\sigma(a^E_{l=1})$ that includes scattering-current octupoles is associated with nearly twice as large a cross section at this point (0.139).

The reason for this imperfect scattering cancelation becomes clear after investigating the exact anapole condition defined by Eq. (9). Although the scattering-current dipole moment p_z^{exact} is perfectly out-of-phase with respect to the contributing octupole moments O^{exact} [see Fig. 1(f)], their amplitudes are far from identical [see Fig. 1(e)]. This reveals a room for improvement that would have been overlooked by using the approximate expressions. We also note that the total scattering cross section (σ_{tot}) is about 0.6 at the minimum due to a non-negligible contribution from unaddressed multipole moments.

IV. Conclusion and Outlook

The commonly used Eqs. (1)-(2) are valid only for deep-subwavelength scatterers, which makes them imprecise in designing nanostructures supporting anapoles, typically requiring dimensions on the order of $\lambda/2$ and larger. We present an alternative approach using a scattering-current multipole expansion, which is exact and valid for scatterers of arbitrary size. This approach opens the way to accurately design and realize perfect anapoles. For example, by using this approach, the nanodisk geometry considered here could be redesigned to enhance the octupole moments, matching the amplitudes of $\frac{k^2}{15}O^{\text{exact}}$ and p_z^{exact}. We believe that our method may unlock new capabilities of nanoscale light confinement by anapoles, which then could compete with, and possibly outperform, the recently widely explored quasi-bound states in the continuum. Experimental realization of such ideal anapole excitations on the III-V semiconductor platform is part of our ongoing work.

Acknowledgments

The authors acknowledge support of the Research Council of Finland (Grants No. 347449, 353758 and 368485). R. K. has received funding from the European Union's Horizon Europe programme for research and innovation under the Marie Skłodowska-Curie Grant Agreement No. 101060306 (NExIA). For computational resources, the authors acknowledge the Aalto University School of Science "Science-IT" project and CSC – IT Center for Science, Finland.

References

[1] A. E. Miroshnichenko, A. B. Evlyukhin, Y. F. Yu, R. M. Bakker, A. Chipouline, A. I. Kuznetsov, B. Luk'yanchuk, B. N. Chichkov, and Y. S. Kivshar, "Nonradiating anapole modes in dielectric nanoparticles," *Nature Communications*, vol. 6, pp. 8069, 2015.

[2] R. Alaee, C. Rockstuhl, and I. Fernandez-Corbaton, "An electromagnetic multipole expansion beyond the long-wavelength approximation," *Optics Communications*, vol. 407, pp. 17–21, 2018.

[3] A. Shevchenko, S. Sehrawat, and R. Kolkowski, "Exact electromagnetic multipole expansion using elementary current multipoles," *arXiv preprint*, arXiv:2508.16545, 2025.

[4] P. Grahn, A. Shevchenko, and M. Kaivola, "Electromagnetic multipole theory for optical nanomaterials," *New Journal of Physics*, vol. 14, pp. 093033, 2012.

Material and Device Optimizations for Wavelength-Selective Infrared Devices

Tadaaki Nagao[1,2,*], Keisuke Watanabe[1], Thien Duc Ngo, [1]

[1]International Center for Materials Nanoarchitectonics (MANA), National Institute for Materials Science (NIMS), Japan
[2]Department of Condensed Matter Physics, Hokkaido University, Japan
*Corresponding author: nagao.tadaaki@nims.go.jp

***Abstract*—We introduce our research on the development of infrared devices with high wavelength-selectivity. The strategy for selecting appropriate materials as well as optimizing device geometries are presented based on electronic band structure calculation and electromagnetic simulations. The devices can be applied to narrowband photothermal converters and ultrahigh Q value biosensors.**

***Keywords*—metasurfaces, Ni-based superalloy, quasi-bound state in continuum (qBIC), silicon.**

I. Introduction

Wavelength-selective light absorbers and emitters, or spectroscopic energy transducers for light, are expected to provide wide variety of applications in energy harvesting, remote and perceptive sensors for IoT devices. Especially, narrowband perfect absorption and emission in the infrared (IR) region are critical prerequisites for modern spectroscopy and energy applications such as non-dispersive infrared (NDIR) gas sensors, IR radiative heaters, and thermo photovoltaics. In this talk, we demonstrate our methodology to achieve narrowband IR absorption and thermal emission based on 2D and 3D nano architectures combined with IR plasmonic materials[1,2].

II. Results and Discussion

We investigated Ni–Al intermetallic compounds as thermally stable plasmonic building blocks for IR photothermal applications. Ni- or Al-based superalloys are thermally stable, heat-resistant materials that have been widely employed in automobile and aviation technologies. DFT calculations were employed to investigate the chemical compositions, crystal structures, and optical properties of the Ni–Al compounds. The candidates that exhibited the best optical properties were chosen for experimental characterization, including dielectric function measurements. Second, electromagnetic microdevice optimization was performed to determine the design of IR microdevices. We also examined the "material–device relationship" of the Ni–Al intermetallic compounds by benchmarking the microdevice performance and selected NiAl as the best material. Additionally, we benchmarked both the optical properties of NiAl and the performance of its microdevices against other well-known metals to highlight the potential of NiAl[1].

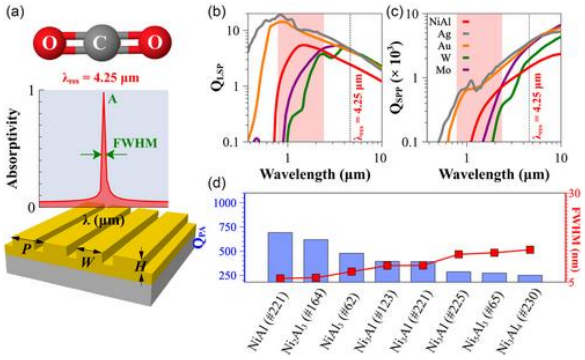

Fig. 1 a) Narrowband absorber with grating configuration. Comparison of two FOMs: b) Q_{LSP} and c) Q_{SPP} for NiAl and conventional plasmonic materials (Ag, Au, W, and Mo). The red area represents the near-IR region (0.78–2.5 μm). d) Quality factors (Q_{PA}) (blue bar plot) and FWHMs (red line plot) of all Ni–Al compounds-based grating devices constructed using the optimal structural parameters.

We have also explored the possibility of adopting low-loss semiconducting Si for ultrahigh quality (Q) factor infrared sensing applications. Quasi-bound states in the continuum (qBICs) have attracted great attention owing to their ultrahigh Q factors and strong electric field enhancement. The resulting enhancement of light–matter interactions has become among the key subjects of interest and stimulated particular interest in sensing applications in the IR region. In this study, we optimized the geometry of qBIC metasurfaces to realize resonant absorption with ultrahigh Q value for the sensing application down to single nanoparticles, or to monolayer regime[2]. Our proposed device offers promising opportunities for simple, cost-effective, and highly sensitive detection of virions and other pathogenic nanoparticles or molecules. We will also discuss the designs and possibilities of ultrahigh Q IR emitters based on our qBIC architecture.

References

[1] T. D. Ngo, H.D. Ngo, H. Harada, and T. Nagao, "Infrared Thermophotonics: Theoretical Benchmarking of Ni–Al Superalloys," *Adv.Photonics Res.* Vol. 6, pp2400093-1-10, 2025.

[2] K. Watanabe, T. Nagao, and M. Iwanaga, "Low-Contrast BIC Metasurfaces with Quality Factors Exceeding 100,000," *Nano Lett.*, vol. 25, no. 7, pp. 2777–2784, 2025.

Programmable Broadband Nonlinear Infrared Imaging with Dielectric Metasurfaces

Ze Zheng[1,*]

[1]Advanced Optics and Photonics Laboratory, Department of Engineering,
School of Science & Technology, Nottingham Trent University, Nottingham NG11 8NS, UK
*Corresponding author: ze.zheng@ntu.ac.uk

***Abstract*—We demonstrate broadband infrared imaging enabled by nonlinear wave mixing in a resonant dielectric metasurface. A pump beam at the resonant wavelength can enhance infrared-to-visible conversion, allowing detection with a conventional visible camera. Dynamic phase modulation of the pump via a spatial light modulator enables programmable, multifunctional, and reconfigurable imaging.**

***Keywords*— metasurfaces, nonlinear optics, infrared imaging.**

I. Introduction

Conventional infrared imaging techniques rely on infrared cameras that are costly, offer limited spatial resolution, lack colour information, and often require active cooling. Recent advances in metasurfaces have introduced a new pathway for infrared-to-visible conversion via nonlinear wave mixing with significantly relaxed phase-matching conditions, enabling direct visualisation of infrared images using standard visible cameras [1], [2]. However, efficient upconversion typically relies on resonant enhancement at the signal or emission wavelength, restricting the operational bandwidth to narrow resonant windows and thereby limiting practical applicability.

Here, we overcome this limitation by introducing a nonlinear imaging platform in which a pump beam, rather than the signal or generated harmonic, is tuned to couple to the metasurface resonance for enhancing wave mixing processes [3]. This strategy decouples the imaging bandwidth from the intrinsic resonance linewidth and enables broadband nonlinear imaging of arbitrary objects using a single metasurface. Furthermore, by incorporating a spatial light modulator (SLM) to engineer the phase profile of the pump beam, we realise multifunctional and programmable infrared imaging. Combined with evolutionary optimisation, the platform enables dynamic image control and tunable nonlinear focusing, establishing a reconfigurable framework for computational and multifunctional infrared imaging [4], [5].

II. Results

We first design and fabricate a Si metasurface consisting of a Si film with Si nanodisks arranged periodically on top of the film, supporting a guided-mode resonance around 1130 nm (Fig. 1(b)). A pump beam tuned to this resonance wavelength is employed to enhance the four-wave mixing (FWM) process via resonant field confinement within the nanostructures. By tuning the signal wavelength from 1350 to 4700 nm, resonantly enhanced and high-efficiency FWM emission is consistently observed across the entire spectral range, as shown in Fig. 1(c). This pump-resonant configuration establishes the foundation for broadband infrared-to-visible upconversion imaging using a metasurface and a conventional visible silicon camera. As a result, we demonstrate broadband infrared imaging spanning wavelengths over 1000 to 4000 nm for arbitrary objects, with the upconverted images directly captured by a CMOS visible camera, as illustrated in Fig. 1(a).

Furthermore, we integrate a SLM into the nonlinear imaging system to enable real-time programmable nonlinear wavefront shaping using a single silicon metasurface composed of nanodisk arrays. The SLM and CMOS camera are connected through a genetic algorithm (GA), which iteratively optimises the phase distribution imposed on the pump beam based on the captured nonlinear images. The optimisation proceeds generation by generation until the nonlinear emission pattern converges to the target image as demonstrated in Fig. 2(a). By designing a metasurface resonance at 1510 nm, efficient third-harmonic generation (THG) is achieved, allowing infrared illumination to be converted into visible light after SLM modulation. Owing to the cubic intensity dependence of the THG process, the metasurface inherently suppresses weak background fluctuations, effectively performing a nonlinear denoising operation on the wavefront. These results demonstrate a dynamically reconfigurable nonlinear metasurface platform with strong potential for real-time optical computation, adaptive information processing, and multifunctional infrared imaging as exhibited in Fig. 2(b).

Finally, we further exploit SLM-based pump phase modulation to realise multifunctional infrared imaging (Fig. 2(c)). Specifically, we utilise sum-frequency generation to convert infrared light into the visible, where the pump beam modulated by SLM constructs an optically reconfigurable virtual lens. This approach enables precise control over the phase of the generated nonlinear optical field, resulting in programmable focusing of the upconverted emission. Both theoretical and experimental results demonstrate a tunable nonlinear focusing mechanism, in which the effective focal length can be continuously adjusted by varying the pump and signal wavelengths, as well as the phase distribution. Importantly, since the focal length depends on the input signal wavelength, the imaging plane position varies accordingly, indicating a promising po-

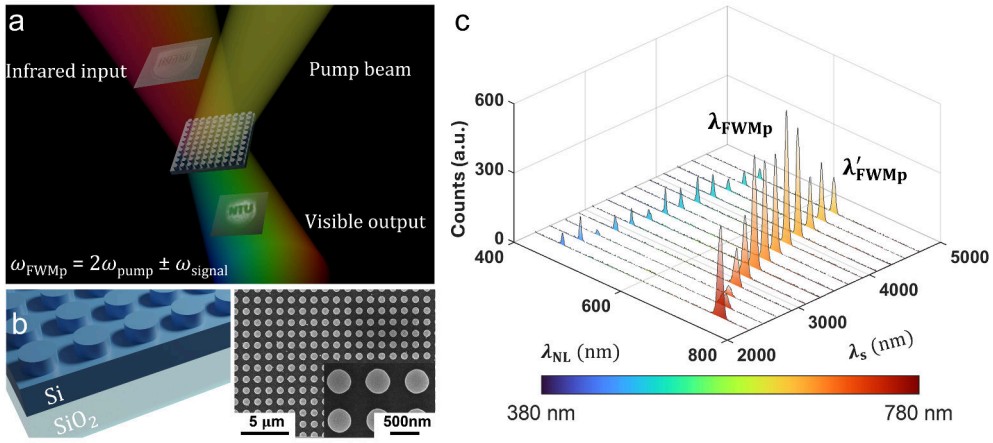

Fig. 1. (a) Schematic of the broadband nonlinear imaging process. (b) Left: schematic of the Si bi-layer metasurface. Right: top-view scanning electron microscopy images of the metasurface. (c) Measured FWM emission spectra from the Si metasurface as the signal wavelength is tuned from 2300 to 4700 nm, while the pump wavelength is fixed at 1130 nm. Adapted from [3].

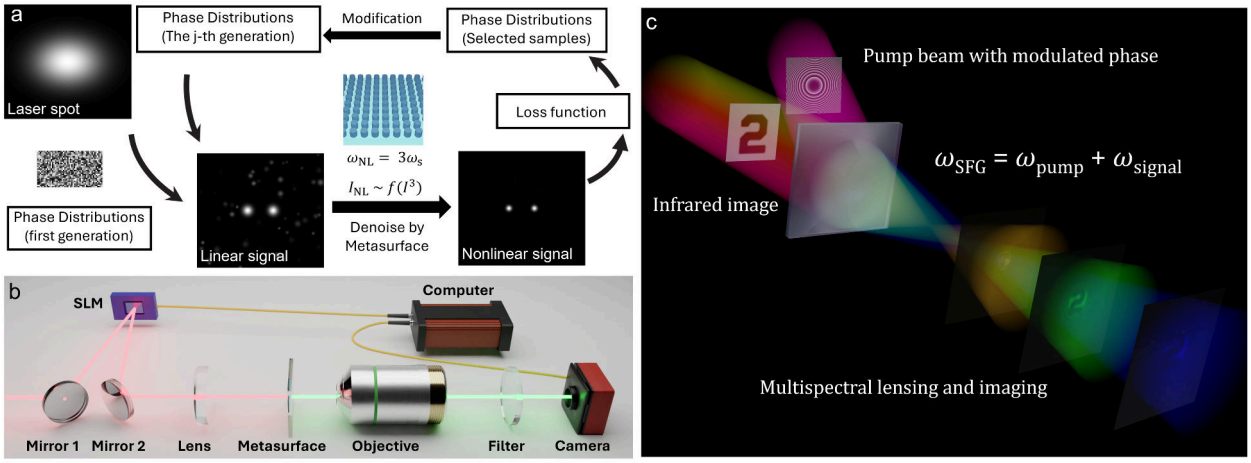

Fig. 2. (a) Schematic illustration of the proposed signal modulation process. Adapted from [4]. (b) The schematic diagram of the experimental setup for the proposed optical system. Adapted from [4]. (c) The schematic illustrates our dynamic infrared focusing and imaging technique based on sum-frequency generation with a visible camera and an SLM. Adapted from [5].

tential for multispectral infrared imaging applications.

III. Conclusion

Overall, we demonstrate a pump-resonant nonlinear metasurface platform that enables broadband infrared-to-visible upconversion imaging. By decoupling the conversion efficiency from the signal bandwidth, infrared images across a wide spectral range can be directly captured using a conventional silicon camera. Through SLM-based pump phase modulation, programmable nonlinear wavefront shaping and tunable multispectral focusing are achieved within a single static metasurface. This work establishes a dynamically reconfigurable nonlinear imaging architecture, offering a versatile framework for computational and multifunctional infrared photonics.

Acknowledgments

This work was supported by UK Research and Innovation Future Leaders Fellowship (MR/Z000270/1) and the European Union (ERC, UPIRI, 101170298). Views and opinions expressed are however those of the authors only and do not necessarily reflect those of the European Union or the European Research Council. Neither the European Union nor the granting authority can be held responsible for them. The author gratefully acknowledges the contributions of the co-authors from references [2], [3], [4], [5].

References

[1] R. Camacho-Morales, D. Rocco, L. Xu, V. F. Gili, N. Dimitrov, L. Stoyanov, Z. Ma, A. Komar, M. Lysevych, F. Karouta, A. A. Dreischuh, H. H. Tan, G. Leo, C. De Angelis, C. Jagadish, A. E. Miroshnichenko, M. Rahmani, and D. N. Neshev, "Infrared upconversion imaging in nonlinear metasurfaces," *Advanced Photonics*, vol. 3, no. 3, 036002, 2021.

[2] Z. Zheng, L. Xu, L. Huang, D. Smirnova, K. Z. Kamali, A. Yousefi, F. Deng, R. Camacho-Morales, C. Ying, A. E. Miroshnichenko, D. N. Neshev, and M. Rahmani, "Third-harmonic generation and imaging with resonant Si membrane metasurface," *Opto-Electronic Advances*, vol. 6, no. 8, 220174, 2023.

[3] Z. Zheng, D. Smirnova, G. Sanderson, C. Ying, D. C. Koutsogeorgis, L. Huang, Z. Liu, R. Oulton, A. Yousefi, A. Miroshnichenko, D. Neshev, M. O'Neill, M. Rahmani, and L. Xu, "Broadband infrared imaging governed by guided-mode resonance in dielectric metasurfaces," *Light: Science & Applications*, vol. 13, no. 1, p. 249, 2024.

[4] Z. Zheng, G. Sanderson, S. Sotoodeh, C. Clifton, C. Ying, M. Rahmani, and L. Xu, "Real-Time Programmable Nonlinear Wavefront Shaping with Si Metasurface Driven by Genetic Algorithm," *Engineering*, vol. 49, pp. 90, 2025.

[5] Z. Zheng, O. Sergaeva, D. Rocco, Y. Zhang, G. Zhang, M. Rahmani, C. De Angelis, and L. Xu, "Nonlinear virtual lens for programmable and multispectral infrared upconversion imaging," arXiv:2601.04964, 2026.

Shining light on 2D Antiferromagnets

Viktoriia Radovskaia[1,*], Mengxing Na[1], Theo H. Rasing[1],
Alexey V. Kimel[1], Dmytro Afanasiev[1]

[1] Institute for Molecules and Materials, Radboud University, The Netherlands
*Corresponding author: viktoriia.radovskaia@ru.nl

***Abstract*—Ultrafast resonant orbital excitation of transition-metal (TM) ions offers a powerful approach to drive spin dynamics in two-dimensional (2D) van der Waals (vdW) materials. In this work, we investigate mixed 2D systems containing different TM ions. Our findings demonstrate the mixing of TM species as a versatile strategy for engineering photomagnetism.**

***Keywords*— photoengineering, van der Waals materials, 2D antiferromagnetism, ultrafast magnetism, magnonics.**

I. Introduction

Ultrafast optical control of antiferromagnetic order is a key goal in spintronics and magnonics [1]. Resonant excitation of local orbital degrees of freedom, such as d–d transitions in transition-metal ions, offers a direct route to modify magnetic exchange and anisotropy on femtosecond timescales [2], [3], [4]. However, orbitally driven photomagnetism has been demonstrated in only a few materials, and the factors governing its efficiency remain unclear.

In this work, we study ultrafast spin dynamics induced by resonant pumping of d–d transitions in layered antiferromagnetic thiophosphates $Mn_{1-x}Ni_xPS_3$. First, we establish the photomagnetic response in single–magnetic-ion compounds [3], [4], where local orbital excitation triggers coherent spin precession via ultrafast anisotropy modulation. Then, we extend this approach to mixed compounds containing two distinct transition-metal ions, demonstrating that selective excitation of specific orbital resonances strongly enhances the efficiency and controllability of magnon generation.

II. Methods

Our methodology is based on the use of the ultrafast pump-probe method, where the first pulse (pump) triggers spin dynamics, which can be captured by the second pulse (probe) with time delay [5]. The pump photon energy $h\nu$ was tuned across different $d-d$ transitions of Ni and Mn ions. As a probe, we measured magnetic second harmonic generation (mSHG) and magnetic linear birefringence (mLB). These probes allow us to distinguish the antiferromagnetic order and to detect the spin dynamics.

III. Results and discussion

The main and very important observation is that $d-d$ transitions from Ni have a significantly larger photomagnetic response than from Mn, such that even at a 9:1 substitution of Mn:Ni, the spin-waves generated by photoexcitation of Ni $d-d$ transitions are nearly 15× larger than that generated by Mn. Surprisingly, the transition most effective for driving spin dynamics – one particular $d-d$ transition of Ni – is low optically active; however, it surpasses all Mn and the more optically active Ni *d-d* transitions.

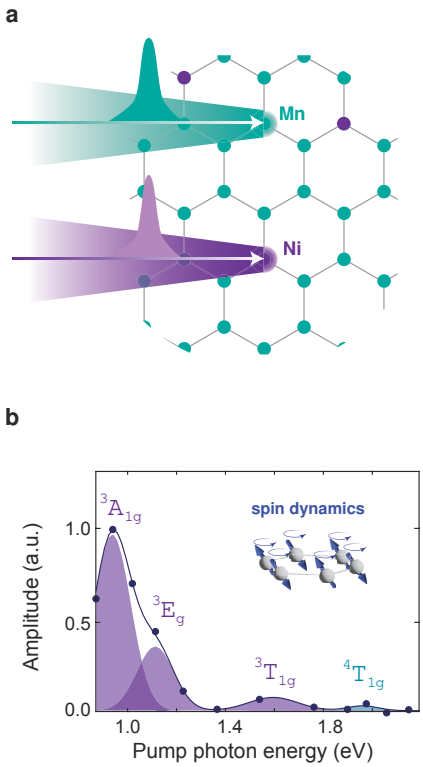

Fig. 1. (a) Schematics of the experiment. Mn (turquoise) and Ni (purple) ions form a hexagonal lattice and are randomly distributed; this image shows the fraction 9:1 of Mn:Ni. Pump photon energy was tuned across different $d-d$ transitions. (b) The amplitude of the excited spin dynamics as a function of pump photon energy. Dots are experimental data-points: solid line is a fit with four Gaussian peaks (shaded) corresponding to three Ni resonances (purple) and one Mn resonance (turquoise).

IV. Conclusions

Altogether, our results identify general design principles for orbitally driven photomagnetism in collinear antiferromagnets and establish transition-metal substitution as a powerful strategy for achieving efficient ultrafast control of antiferromagnetic spin dynamics.

Acknowledgments

This work was supported by European Research Council ERC; program “Materials for the Quantum Age” (QuMat),

which is part of the Gravitation program financed by the Dutch Ministry of Education, Culture and Science (OCW); and the European Union Horizon 2020.

REFERENCES

[1] V. Baltz, A. Manchon, M. Tsoi, T. Moriyama, T. Ono, and Y. Tserkovnyak, "Antiferromagnetic spintronics," *Rev. Mod. Phys.*, vol. 90, p. 015005, Feb 2018.

[2] R. V. Mikhaylovskiy, T. J. Huisman, V. A. Gavrichkov, S. I. Polukeev, S. G. Ovchinnikov, D. Afanasiev, R. V. Pisarev, Th. Rasing, and A. V. Kimel, "Resonant pumping of d-d crystal field electronic transitions as a mechanism of ultrafast optical control of the exchange interactions in iron oxides," *Physical Review Letters*, vol. 125, no. 15, p. 157201, 2020.

[3] D. Afanasiev, J. R. Hortensius, M. Matthiesen, S. Mañas-Valero, M. Šiškins, M. Lee, E. Lesne, H. S. J. van der Zant, P. G. Steeneken, B. A. Ivanov, E. Coronado, and A. D. Caviglia, "Controlling the anisotropy of a van der Waals antiferromagnet with light," *Science Advances*, vol. 7, no. 23, p. eabf3096, 2021.

[4] M. Matthiesen, J. R. Hortensius, S. Mañas-Valero, I. Kapon, D. Dumcenco, E. Giannini, M. Šiškins, B. A. Ivanov, H. S. J. van der Zant, E. Coronado, A. B. Kuzmenko, D. Afanasiev, and A. D. Caviglia, "Controlling magnetism with light in a zero orbital angular momentum antiferromagnet," *Physical Review Letters*, vol. 130, no. 7, p. 076702, 2023.

[5] E. Beaurepaire, J.-C. Merle, A. Daunois, and J.-Y. Bigot, "Ultrafast spin dynamics in ferromagnetic nickel," *Phys. Rev. Lett.*, vol. 76, pp. 4250–4253, May 1996.

Chiral Photonic Environments for Coherent Control of Valley Excitons

Hassan Lamsaadi[1], Aurélien Cuche[2], Hugo Lourenço Martins[2], Vincent Paillard[2,3], Sébastien Weber[2]
Jean Marie Poumirol[2*], Gonzague Agez [2,3]*

[1]LPCNO, INSA Toulouse (France)
[2]CEMES, CNRS, Toulouse (France)
[3]Université de Toulouse (France)
*Corresponding author: gonzague.agez@cemes.fr

***Abstract*—Valley coherence encodes quantum information in the relative phase of inequivalent momentum valleys, yet controlled intervalley coupling at room temperature remains challenging in monolayer semiconductors. We demonstrate that chiral liquid crystals enable near-field coupling between K and K' excitons via helicity-selective Bragg reflection accompanied by spin-flip, offering a scalable route toward valleytronic functionalities.**

***Keywords*— Valleytronics, chiral liquid crystal, monolayer semiconducting transition-metal dichalcogenides**

I. Introduction

Valley coherence in transition-metal dichalcogenide (TMD) monolayers relies on the coherent superposition of excitons residing in inequivalent K and K' valleys. However, at room temperature, rapid intervalley decoherence typically suppresses any steady-state linear polarization of the emitted photoluminescence. Here, we demonstrate that a properly engineered chiral photonic environment can instead mediate and stabilize intervalley coherence under ambient conditions.

II. Results and Discussion

By placing a WSe_2 monolayer on a chiral nematic liquid crystal supporting circular Bragg reflection, we exploit helicity-selective spin-flip reflection to induce an intrinsically unidirectional optical feedback between inequivalent valleys (Fig. 1). The optical response was investigated by polarization-resolved photoluminescence measurements, enabling both circular and linear polarization analysis of the emitted signal.

Experimentally, we observe a strong circular dichroism within the photonic band gap (Fig. 2a), associated with the emergence of a pronounced linear polarization component (Fig. 2b) revealing the existence of a coupling process responsible for the intervalley coherence. Within a Maxwell–Bloch framework, this process is captured by a coupling rate, which we estimate to exceed the excitonic decoherence rate. Numerical simulations support this picture by showing that circular Bragg reflection provides an efficient near-field feedback mechanism, consistent with a photonic spin-flip process capable of mediating intervalley coupling.

Fig. 1. Schematic representation of the coupling process for a monolayer deposited on a left-handed CLC. The emission of A ↻ and A ↺ excitons, associated with the K and K' valleys, is depicted.

Fig. 2. **a**) Photoluminescence spectra for right- (σ^-) and left-handed (σ^+) circular components. (**b**) Polar plots of the linear polarization-resolved emitted PL.

III. Conclusion

Our results establish chiral photonic spin-flip reflection as a scalable and room-temperature mechanism to mediate intervalley coupling.

References

[1] Hao, K., Moody, G., Wu, F., et al."Direct measurement of exciton valley coherence in monolayer WSe_2," *Nature Physics* 12(7), 2016
[2] Unuchek, D., Ciarrocchi, A., Avsar, et. al., "Room-temperature electrical control of exciton flux in a van der waals heterostructure". *Nature* 560(7718), 2018

Optical Properties Tuning of Quantum Emitters in WSe_2 Monolayers

Javier Martín-Sánchez[1,2]

[1]University of Oviedo, Spain
[2]Nanomaterials and Nanotechnology Research Center CINN CSIC, Spain

Abstract— We demonstrate strain control of quantum emitters in WSe_2 monolayers using piezoelectric actuators. Applied voltage enables reversible tuning of emission energy and brightness while preserving single photon purity. Strain modifies the excitonic potential landscape, enabling exciton redistribution. These results establish strain engineering as a tool for tunable photonic devices.

Keywords— quantum emitters, two dimensional materials, strain engineering, excitons, piezoelectric devices

I. Introduction

Quantum emitters in transition metal dichalcogenide monolayers, particularly WSe_2, have emerged as promising single photon sources due to their atomically thin nature, strong excitonic effects, and compatibility with nanophotonic integration [1]. Localized excitons formed by strain gradients generate discrete emission lines with single photon characteristics [2]. However, in most strain engineering approaches, the strain configuration is static, limiting the ability to dynamically control emission energy, brightness, and spectral uniformity among emitters. Achieving active and reversible control of these properties is essential for scalable quantum photonic technologies. In this work, we introduce a hybrid piezoelectric semiconductor platform that enables voltage controlled strain engineering [3]. This approach allows continuous and reversible tuning of the emission energy and intensity of individual quantum emitters by modifying the excitonic potential landscape, enabling dynamic control of single photon sources in two dimensional materials [4,5].

II. Methods

Monolayer WSe_2 flakes were mechanically exfoliated and transferred onto piezoelectric PMN-PT substrates patterned with micropillars. These pillars generate localized strain gradients that induce the formation of quantum emitters. By applying an external voltage across the piezoelectric actuator, controllable in-plane and out-of-plane strain fields were introduced, enabling dynamic modulation of the excitonic confinement potential. Optical characterization was performed using low temperature micro photoluminescence spectroscopy, allowing spatial and spectral resolution of individual emitters. Finite element simulations were used to model the strain distribution and bandgap modulation induced by the applied voltage. Additionally, drift diffusion modeling was employed to simulate exciton transport and redistribution under strain, providing insight into the mechanisms governing the observed optical modulation.

III. Results and Discussion

The application of voltage to the piezoelectric actuator induces controllable strain fields in the WSe_2 monolayer, enabling precise modulation of the optical emission of quantum emitters. We observe reversible spectral shifts of the emission lines reaching values up to several meV, and up to 18 meV in optimized configurations, demonstrating a wide tuning range without introducing degradation in the optical quality of the emitters. Time correlation measurements confirm that the single photon nature of the emission is preserved under strain, indicating that mechanical deformation does not affect photon purity or recombination dynamics.

In addition to energy tuning, strain also produces significant changes in the emission intensity of individual emitters. Some emitters become brighter while others are suppressed, indicating a redistribution of excitons across localized potential wells. Importantly, the total integrated emission remains nearly constant, demonstrating that strain does not significantly alter the total exciton population but rather modifies their spatial distribution. This behavior can be explained by strain induced changes in the band structure, which reshape the local potential landscape and influence exciton diffusion and capture processes.

Finite element simulations reveal that the strain distribution is highly non-uniform at the nanoscale, particularly near wrinkles or pillar edges, leading to both tensile and compressive strain regions. As a result, different emitters exhibit distinct spectral responses, including shifts with opposite sign depending on their position within the wrinkled monolayer. These findings demonstrate that strain engineering enables not only spectral tuning but also control of exciton localization and emission intensity, providing a versatile method for manipulating quantum emitters in two dimensional semiconductors.

IV. Conclusion

We have demonstrated a versatile piezoelectric strain engineering platform enabling dynamic control of quantum emitters in WSe_2 monolayers. Strain allows reversible tuning of emission energy over a wide spectral range while preserving single photon emission quality. Furthermore, strain induced modifications of the excitonic potential landscape enable controlled redistribution of excitons, resulting in tunable emission intensity. These combined capabilities provide a comprehensive method for controlling both spectral and intensity properties of quantum emitters. This approach represents a key step toward the realization of tunable, scalable, and integrated quantum photonic devices based on two dimensional materials.

Acknowledgments

This work was partially supported by the QuantERA project EQUAISE under the QuantERA Call 2021. Additional funding was provided by the Spanish Ministry of Science and Innovation through projects PID2023-148457NB-I00, PCI2022-132953, and CNS2024-154342, funded by MCIN/AEI and the European Union NextGenerationEU/PRTR program.

References

[1] Y.-M. He et al., "Single quantum emitters in monolayer semiconductors," Nature Nanotechnology, vol. 10, pp. 497–502, 2015; A. Srivastava, et al. "Optically active quantum dots in monolayer WSe_2," Nature Nanotechnology, vol. 10, pp. 491–496, 2015; M. Koperski et al., "Single photon emitters in exfoliated WSe_2 structures," Nature Nanotechnology, vol. 10, pp. 503–506, 2015.

[2] A. Branny et al., "Deterministic strain-induced arrays of quantum emitters in a two-dimensional semiconductor," Nature Communications, vol. 8, p. 15053, 2017; C. Palacios-Berraquero et al., "Large-scale quantum-emitter arrays in atomically thin semiconductors," Nature Communications, vol. 8, p. 15093, 2017.

[3] J. Martín-Sánchez et al., "Strain-tuning of the optical properties of semiconductor nanomaterials by integration onto piezoelectric actuators," Semiconductor Science and Technology, vol. 33, p. 013001, 2018; J. Martín-Sánchez et al., "Reversible control of in-plane elastic stress tensor in nanomembranes," Advanced Optical Materials, vol. 4, pp. 682–687, 2016; R. Trotta et al., "Wavelength-tunable sources of entangled photons interfaced with atomic vapours," Nature Communications, vol. 7, p. 10375, 2016.

[4] O. Iff, et al., "Strain-tunable single photon sources in WSe_2 monolayers," Nano Letters, vol. 19, pp. 6931–6936, 2019.

[5] G. Ronco et al., "Strain-induced exciton redistribution among quantum emitters in two-dimensional materials," npj 2D Materials and Applications, vol. 9, p. 65, 2025.

Photonic Inverse Design using Differentiable Electromagnetic Solvers for CMOS Image Sensors and Photonic Integrated Circuits

Hyunsung Park, Jaekwan Kim, Subeom Song, Junho Lee, Yongseob Yun, Sungmo Ahn,
Choonlae Cho, Sooyeon Lee, Sookyoung Roh* and Seokho Yun*
Samsung Advanced Institute of Technology, Samsung Electronics Co., Ltd.,
Republic of Korea
*Corresponding author: seok.h.yun@samsung.com or sy81.roh@samsung.com

Abstract—**We implement differentiable electromagnetic solvers for gradient-based inverse design of various optical systems. The differentiable eigenmode expansion solver is applied to photonic integrated circuits, and the differentiable RCWA solver to metasurfaces for mobile image sensors. Analytic derivatives combined with automatic differentiation enable fast and accurate large-scale optimization.**

***Keywords*— inverse design, metasurface, photonic integrated circuit, image sensor.**

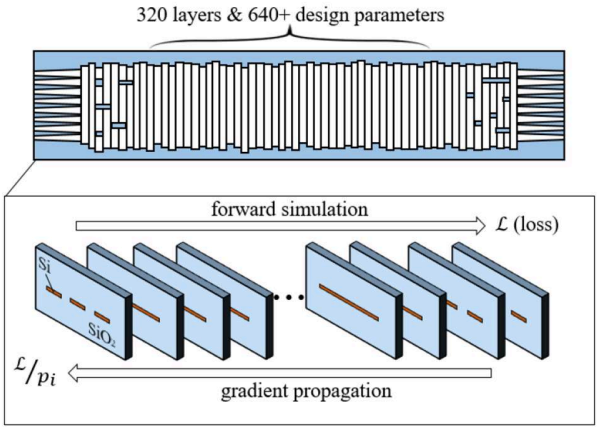

Fig. 1 Design procedure using the differentiable eigenmode expansion method (DEME).

I. Introduction

Gradient-based inverse design of large photonic structures requires efficient derivative evaluation. We implement eigenmode expansion and RCWA solvers within a framework combining analytic derivatives[1] and automatic differentiation, supporting scalable optimization of guided-wave and plane-wave devices.

II. Methods

The eigenmode expansion solver includes analytic derivatives of modal propagation and coupling operators. The RCWA solver provides analytic gradients of scattering responses. Both are embedded in an automatic differentiation pipeline to compute gradients with respect to design parameters for gradient-based optimization.

III. Results and Discussion

The mode-based solvers reduce computational cost by leveraging their scattering matrix formalism with reduced-dimensional modal representations. Matrix operations are performed in compact subspaces, and intermediate results are reused across optimization steps. This enables faster forward simulations and gradient evaluations compared to time-domain solvers such as FDTD. Large photonic structures are optimized efficiently while maintaining numerical accuracy and stable convergence.

IV. Conclusion

Differentiable eigenmode expansion and RCWA provide practical tools for large-scale photonic inverse design. The integration of analytic derivatives with automatic differentiation enables fast and accurate optimization of integrated photonic structures and metasurfaces relevant to mobile image sensors.

References

[1] Nelson, D. L. Reexamination of eigenvector derivatives. AIAA J. 14, 1201–1205 (1976).

Hybrid Photonic Crystal Platforms: Enabling High-Efficiency Photonic Devices and Novel Functionalities

Tae-Yun Lee[1,2], Hansol Lee[1,2], Lakjong Jeong[1,2], and Heonsu Jeon[1,2,3,*]

[1]Department of Physics and Astronomy, Seoul Nat'l University, Republic of Korea
[2]Inter-university Semiconductor Research Center, Seoul Nat'l University, Republic of Korea
[3]Institute of Applied Physics, Seoul Nat'l University, Republic of Korea
*Corresponding author: hsjeon@snu.ac.kr

***Abstract*— By combining passive backbones with active materials, hybrid photonic crystal (PhC) platforms facilitate devices with superior performance and novel functionalities. Planar resonant cavities provide similar physical effects but offer a simpler alternative in terms of design and manufacturing.**

***Keywords*— hybrid photonic platforms, photonic crystals, resonant cavity, colloidal quantum dots, phosphors, nanolasers.**

Photonic crystals (PhCs) play a pivotal role in exploring intriguing scientific phenomena and developing highly efficient nanophotonic devices. Our research focuses on hybrid PhC platforms that integrate passive photonic backbones—engineered to induce specific nanophotonic effects—with optically active materials capable of photon absorption and emission. These hybrid architectures enable the high efficiency, low cost, and ease of fabrication required for next-generation photonic applications. The nanophotonic structures in our platforms typically utilize two-dimensional (2D) PhCs formed on planar backbones of high-refractive-index materials such as TiO_2 or Si_3N_4.

By leveraging photonic band-edges at the Γ-point, we utilize localized electric field enhancements at periodic "hot spots" commensurate with the underlying PhC structure. Strategically placing active materials at these hot spots maximizes light-matter interaction, leading to superior device performance. When the Γ-point resonance is tuned to the emission of the active material, it facilitates vertical lasing; specifically, by employing symmetry-protected bound-states-in-the-continuum (BIC) modes, we can exploit nearly infinite quality factors to reduce lasing thresholds by orders of magnitude [1]. Conversely, when the band-edge mode is tuned to the absorption band, the platform serves as an efficient PhC phosphor, significantly improving color conversion through the enhanced absorption of excitation photons [2].

Another vital hybrid platform in our research is the resonant cavity (RC) structure, which consists of a half-wavelength-thick cavity layer sandwiched between two distributed Bragg reflectors. By incorporating optically active materials within the cavity, we can achieve enhanced emission or absorption depending on the specific resonance conditions. While vertical-cavity surface-emitting lasers represent the standard application for emission-tuned resonances, absorption-tuned cavities serve as efficient color-conversion devices. Our group has successfully demonstrated this potential by developing an RC-based phosphor platform for full-color displays [3]. Moving forward, we expect hybrid PhC platforms to continue diversifying in structure and material composition, expanding their utility across a broad spectrum of future photonic applications.

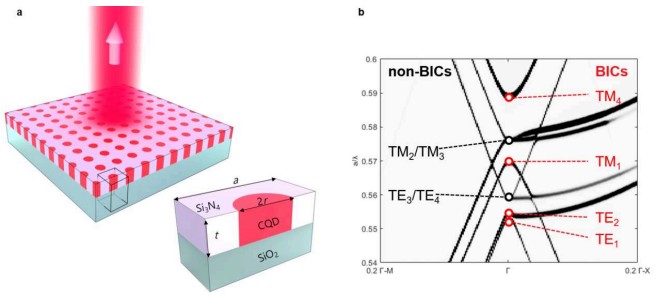

Fig. 1 Schematic of 2D PhC BIC laser platform and associated photonic band structure near Γ-point.

REFERENCES

[1] T.-Y. Lee, H. Lee, and H. Jeon, "Colloidal-quantum-dot nanolaser oscillating at a bound-state-in-the-continuum with planar surface topography for a high Q-factor," Nanophotonics, vol. 14, pp. 1645–1652, 2025.

[2] H. Lee, T.-Y. Lee, Y. Park, K.-S. Cho, Y.-G. Roh, H. Choo, and H. Jeon, "Structurally engineered colloidal quantum dot phosphor using TiO2 photonic crystal backbone," Light: Science and Applications, vol. 11:318, pp. 1–8, 2022.

[3] T.-Y. Lee, Y. Park, and H. Jeon, "Resonant cavity phosphor," Nature Communications, vol. 14:6661, pp. 1–8, 2023.

Limited Size Object Microscopy - Smaller Objects, Higher Resolution

Giorgio Adamo[1,2,*], Taeyong Chang[2], Eng Aik Chan[2], Nikolay Zheludev[1]

[1]Optoelectronics Research Centre, University of Southampton, Highfield, United Kingdom
[2]Centre for Disruptive Photonic Technologies, SPMS, TPI, Nanyang Technological University, Singapore
*Corresponding author: g.adamo@soton.ac.uk

***Abstract*— We show that the sole knowledge of an object's limited size allows to achieve far-field label-free resolution beyond the Abbe-Rayleigh diffraction limit: higher resolution is achieved for smaller objects. We experimentally image subwavelength-size nanoparticles with λ/8 resolution. Furthermore, by adopting a physics consistent learning model we can increase resolution to λ/13.**

***Keywords*— diffraction limit, superresolution microscopy, machine learning.**

I. Introduction

Label-free far-field super-resolution optical imaging is achievable by allowing sufficient prior knowledge of the object such as its sparsity or accumulated through a posteriori examination of a similar class of object. Here, we show that the sole knowledge that the object is located in a field of view of limited size is sufficient to achieve super-resolution beyond the Abbe-Rayleigh diffraction limit: a higher resolution can be achieved with smaller objects.

To prove this, we developed an imaging method that is reciprocal to generating superoscillatory fields. We first quantify the fundamental trade-off between resolution and object size and identify a photon budget for the targeted resolution using a quantum Fisher information analysis. For the experiment, we measure coefficients of the field scattered from the object based on orthonormal field-of-view-limited Slepian-Pollak functions using a variable mask. We quantify the required photon numbers for the tomographic measurement considering the distortion of the optical setup using a Fisher information analysis. We experimentally achieve λ/7 and λ/8 resolution for the two-dimensional and one-dimensional imaging of subwavelength objects. The imaging resolutions are confirmed by various quantitative criteria such as effective bandwidth, point spread function, and Siemens star test.

Furthermore, we extend the method using a learning model trained on physics-consistent examples that can exploit correlations between accurately measured low-order Slepian-Pollak modes and noise-sensitive high-order modes. This enables robust recovery of deep sub-diffraction geometric features in our nanostructures and allow us to achieve imaging resolution of λ/13.

Our limited size object microscopy (LSOM) is a far-field imaging method that requires no assumption of the shape and complexity of the object and its labelling, thus allowing a wide range of applications in nanotechnology and biological studies of nanoparticles and isolated microorganisms.

Subwavelength metamaterials for modal and thermo-optic control in silicon interferometers

Aitor V. Velasco[1,*], Irene Olivares[1], Irena Stolic[1], Raquel Fernández de Cabo[2], Alejandro Sánchez-Sánchez[3], Daniele Melati[4], Carlos Alonso-Ramos[4], David González-Andrade[3]

[1]Instituto de Óptica Consejo Superior de Investigaciones Científicas (CSIC), Spain
[2]Instituto de Ciencias Fotónicas (ICFO), Spain
[3]Telecommunication Research Institute (TELMA), Universidad de Málaga, Spain
[4]Centre de Nanosciences et de Nanotechnologies (CNRS), Université Paris-Saclay, France

*Corresponding author: a.villafranca@csic.es

***Abstract*— Subwavelength metamaterials are becoming essential building blocks for the next generation of photonic integrated circuits. In this work, we explore their potential for loss reduction and thermo-optic control in advanced interferometers for the silicon-on-insulator platform.**

***Keywords*— Integrated optics, silicon photonics, subwavelength metamaterials.**

I. Introduction

Silicon-on-insulator (SOI) microspectrometers have gathered a great interest for diverse on-chip applications such as biological analysis, environmental monitoring, and remote sensing. Spatial heterodyne Fourier-transform (SHFT) microspectrometers, implemented through arrays of linearly-increasing Mach-Zehnder interferometers (MZIs), provide high resolution and optical throughput in compact footprints [1]. However, as greater spectrometer resolutions are targeted, insertion losses and thermal dependence of the constituent MZIs become increasingly critical. In this work, we tackle both challenges through the use of subwavelength grating (SWG) metamaterials [2], providing novel SWG building blocks for modal and thermo-optic control in SOI interferometers.

II. Power Management

Firstly, we introduce a new achromatic splitter architecture [3] that uses a Y-junction with a customized SWG transition at the junction tip, achieving the broadest bandwidth reported to date for a nanophotonic silicon power splitter. The device was simultaneously optimized for the TE_0 and TE_1 modes and also showed excellent performance for the fundamental TM_0 mode. In 3D FDTD simulations, the splitter demonstrated exceptionally low excess loss—below 0.2 dB for both TE_0 and TE_1 modes—across a 700 nm wavelength span (1300–2000 nm). For the TM_0 mode, excess loss remained under 0.3 dB over a 500 nm range (1300–1800 nm). Experimental measurements, though constrained by the available setup, closely matched the simulated results and verified low excess losses for all three modes within the 1430–1680 nm window. The device also exhibited strong resilience to fabrication variations, maintaining high performance under dimensional deviations of up to ±10 nm.

III. Thermal Management

Secondly, we explore the potential of SWG metamaterials for thermo-optic control in integrated silicon-on-insulator interferometers. We previously presented a MZI incorporating a SWG section in one of the arms to compensate thermally-induced drifts [4]. We build upon this earlier work by providing both an updated interferometer architecture, and advanced SWG metamaterials with a further tailored for thermo-optic response. As a result, reduced thermal sensitivity in an extended bandwidth is achieved.

IV. Conclusions

The devices reported in this work highlight the benefits of subwavelength grating metamaterials for the development of high-performance interferometers for the silicon-on-insulator platform. The reduced losses and enhanced resilience to thermal deviations achieved through subwavelength nanotechnology offer promising prospects for SHFT microspectrometry applications.

Acknowledgments

This work was funded by the Spanish Ministry of Science, Innovation and Universities (PID2024-160056OB-C21, PID2022-139540OB-I00, PRE2022-000085); grant JDC2024-053719-I and RYC2023-045670-I (MICIU/AEI/10.13039/501100011033 and ESF+); and the European Union's Horizon Europe (Marie Skłodowska-Curie grant agreement No. 101062518; HADEA grant agreement No. 101135523). We also acknowledge project Fabrication was carried out at the C2N micro/nanotechnologies platforms, with partial support from RENATECH and the General Council of

Essonne. This study was supported by EU NextGenerationEU (PRTR-C17.I1) and Generalitat de Catalunya. Additional support came from CEX2024-001490-S (MICIU/AEI/10.13039/501100011033), Fundació Cellex, Fundació Mir-Puig, and Generalitat de Catalunya (CERCA). The views expressed are those of the authors and do not necessarily reflect those of the European Union; neither the EU nor the granting authority can be held responsible. This research work was partly funded by the European Commission – NextGenerationEU, through Momentum CSIC Programme: Develop Your Digital Talent. I.S. was hired under the Generation D initiative, promoted by Red.es, an organisation attached to the Ministry for Digital Transformation and the Civil Service, for the attraction and retention of talent through grants and training contracts, financed by the Recovery, Transformation and Resilience Plan through the European Union's Next Generation funds.

REFERENCES

[1] David González-Andrade *et al.*, "Broadband Fourier-transform silicon nitride spectrometer with wide-area multiaperture input," *Optics Letters* vol. 46, pp. 4021-4024, 2021, doi: 10.1364/OL.438361.

[2] P. Cheben *et al.*, "Subwavelength integrated photonics," *Nature*, vol. 560, no. 7720, pp. 565–572, 2018, doi: 10.1038/s41586-018-0421-7.

[3] R. Fernández de Cabo *et al.*, "Extending the spectral operation of multimode and polarization-independent power splitters through subwavelength nanotechnology", *Optics & Laser Technology*, vol. 181, 111921, 2025, doi: 10.1016/j.optlastec.2024.111921.

[4] U. A. Korai *et al.*, "Design of an Athermal Interferometer Based on Tailored Subwavelength Metamaterials for On-Chip Microspectrometry", *IEEE Photonics Journal*, vol. 11, Art 4601611, 2019, doi: 10.1109/JPHOT.2019.2943774.

Competing Lattice and Defect Dynamics Govern Terahertz-Driven Ferroelectricity in Quantum Paraelectric $SrTiO_3$

Jingbo Qi*

[1] School of Physics & State Key Laboratory of Electronic Thin Films and Integrated Devices, University of Electronic Science and Technology of China, Chengdu 610054, China

*corresponding author: jbqi@uestc.edu.cn

Abstract: Our work resolves controversies in light-induced phase transitions by revealing that intense terahertz pulses can drive transient ferroelectricity in quantum paraelectric $SrTiO_3$, but the outcome is governed by a previously unrecognized competition between lattice distortions, defect pinning, and dipolar ordering. Spatially resolved measurements reveal that coherent antiferrodistortive modes suppress symmetry breaking on picosecond scales, while defects frustrate long-range order, allowing ferroelectricity only in pristine regions. This reconciles divergent interpretations and establishes defects as key regulators of light-induced quantum phase transitions.

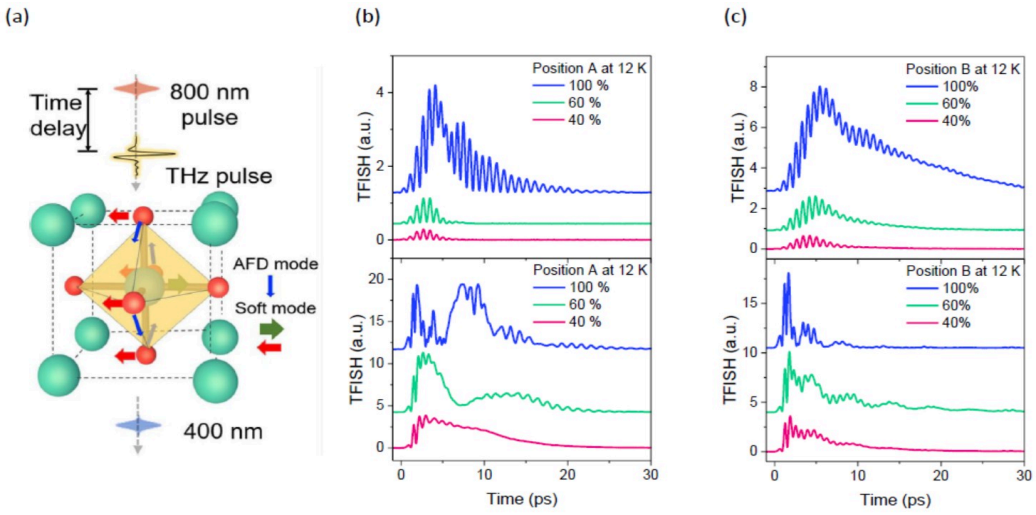

Figure1. (a) Schematic of time-resolved THz-driven SHG. Atomic displacements of soft and AFD modes are also sketched. (b-c) SHG traces at positions A (low oxygen-vacancy density) and B (high oxygen-vacancy density) at 12 K under multi-cycle resonant (center frequency of ~0.65 THz and bandwidth of 0.25~THz) and single-cycle excitation for different field strengths (100%, 60%, 40% of peak fields ~220 kV/cm (multi-cycle) and ~1.1 MV/cm (single-cycle)). Striking position dependence highlights the pivotal role of defects.

Intense terahertz (THz) pulses induce transient inversion-symmetry breaking in quantum paraelectric $SrTiO_3$, yet the underlying mechanism remains controversial [1-6]. Using fields up to ~1.1 MV/cm, we reveal spatially inhomogeneous THz-driven second harmonic generation (SHG) governed by competing lattice and defect

dynamics. Short-lived coherent antiferrodistortive (AFD) modes suppress dipole correlations within ~5 ps, while heavily damped soft/AFD modes and a defect-induced low-frequency mode (~0.1-0.3 THz) jointly prevent long-range ferroelectric coherence in oxygen-vacancy-rich regions. Collective modes manifested by oscillatory SHG components exhibit softening followed by hardening below a critical temperature $T^* \approx 28$ K, confirming transient ferroelectric order where defects are sparse. These results reconcile conflicting interpretations, establish defect-mediated competition as a central regulator of light-induced ferroelectricity, and open routes to ultrafast control of quantum materials.

Reference

[1] X. Li, T. Qiu, J. Zhang, E. Baldini, J. Lu, A. M. Rappe, and K. A. Nelson, Terahertz field-induced ferroelectricity in quantum paraelectric srtio3, Science 364, 1079 (2019),

[2] T. F. Nova, A. S. Disa, M. Fechner, and A. Cavalleri, Metastable ferroelectricity in optically strained srtio 3, Science 364, 1075 (2019).

[3] M. Basini, M. Pancaldi, B.Wehinger, M. Udina, V. Unikandanunni, T. Tadano, M. C. Hoffmann, A. V. Balatsky, and S. Bonetti, Terahertz electric-field-driven dynamical multiferroicity in srtio3, Nature 628, 534 (2024).

[4] D. Shin, S. Latini, C. Sch¨afer, S. A. Sato, E. Baldini, U. De Giovannini, H. H¨ubener, and A. Rubio, Simulating terahertz field-induced ferroelectricity in quantum paraelectric srtio3, Phys. Rev. Lett. 129, 167401 (2022).

[5] B. Cheng, P. L. Kramer, Z.-X. Shen, and M. C. Hoffmann, Terahertz-driven local dipolar correlation in a quantum paraelectric, Phys. Rev. Lett. 130, 126902 (2023).

[6] F. Yang, X. J. Li, D. Talbayev, and L. Q. Chen, Terahertz-induced second-harmonic generation in quantum paraelectrics: Hot-phonon effect, Phys. Rev. Lett. 135, 056901 (2025).

Advanced Contactless Manipulation of Micro- and Nanostructures: from Optical Forces to Acoustic Tweezers

Maria G. Donato[1,*], S. Bernatova[1], A. Foti[1], P. G. Gucciardi[1], M. A. Iatì[1], A. Magazzù[1], A. Mandanici[1,2], O. M. Maragò[1]

[1]CNR-IPCF, Istituto per i Processi Chimico-Fisici, Messina, Italy
[2] Dip. di Scienze Matematiche e Informatiche, Scienze Fisiche e Scienze della Terra, Università di Messina, Messina, Italy
*Corresponding author: maria.donato@cnr.it

***Abstract*— This work highlights CNR-IPCF group's contribution in contactless particle manipulation using optical and acoustic tweezers.**

***Keywords*— Optical tweezers, Acoustic manipulation, Nanoparticles, Raman spectroscopy, Force calibration.**

The contactless manipulation of matter at the micro- and nanoscale has emerged as a cornerstone of modern nanoscience, biophysics, and materials characterization. This abstract reviews the fundamental advancements in optical forces and optical tweezers (OT), highlighting the pioneering contributions of the CNR-IPCF group (Donato et al.) in capturing, spinning, and sensing complex nanostructures. Key developments include the spatial positioning and high-resolution structural characterization of liquid-phase exfoliated two-dimensional (2D) nanosheets [1], such as hexagonal boron nitride, where thermal fluctuation analysis allows the precise assessment of size scaling and optical trapping constants. Furthermore, by exploiting tailored polarization configurations and counter-propagating beam geometries, optical binding and the transfer of angular momentum (spin and orbital) can be effectively demonstrated in highly anisotropic systems like silicon nanowires [2] and chiral birefringent microparticles [3], inducing rich rotational and localization dynamics. Additionally, the integration of plasmon-enhanced optical trapping with surface-enhanced Raman spectroscopy (SERS) provides a robust platform for ultra-sensitive molecular detection and single-particle force transduction down to the femtonewton regime [4]. While conventional optical trapping excels at manipulating sub-micron dielectric particles and probing forces down to the femtonewton regime, it faces intrinsic limitations when scaling up to larger macroscopic volumes, or when dealing with highly absorbing, light-sensitive materials. To overcome these constraints, recent research has successfully expanded into the realm of acoustic manipulation. By transferring well-established optical tracking protocols and Brownian motion analysis frameworks to holographic acoustic tweezers, a consistent methodology for the precise force calibration of ultrasonic fields has been developed [5]. This synergistic integration bridges the gap between optical and acoustic trapping communities, enabling the stable levitation of diverse samples—ranging from cometary analogs [6] and microplastics to biological matter—far from substrate contamination. Ultimately, combining the high spatial resolution of optical forces with the extended force ranges of acoustic fields paves the way for advanced hybrid acousto-optical architectures, unlocking novel capabilities in container-less material processing, multi-scale sorting, and ultra-sensitive in-situ spectroscopy.

Acknowledgments

We acknowledge support by the Project "Space It Up" funded by ASI and MUR– Contract n. 2024-5-E.0 - CUP n. I53D24000060005 and the Joint Bilateral Agreement CNR-BioSense (Serbia), Biennal Program 2026-2027

References

[1] M. G. Donato et al., "Optical trapping and optical force positioning of two-dimensional materials", Nanoscale, vol.10, pp. 1245-1255, 2018.
[2] M. G. Donato et al., "Optical trapping, optical binding, and Rotational Dynamics of silicon nanowires in Counter-Propagating bemas", NanoLetters vol. 19, pp. 342-352, 2019.
[3] M. G. Donato et al., "Polarization-dependent optomechanics mediated by chiral microresonators", Nature Communications vol. 5, 3656, 2014.
[4] B. Fazio et al., "SERS detection of biomolecules at physiological pH via aggregation of gold nanorods mediated by optical forces and plasmonic heating", Scientific Reports vol. 6, 26952, 2016.
[5] S. Marrara et al., "Optical calibration of holographic acoustic tweezers", IEEE Transactions on Instrumentation and measurement, vol. 72, 9600808, 2023.
[6] S. Ferretti et al., "Contactless manipulation and Raman Analysis of cometary analogs and micrometeorites by acoustic levitation" , The Astrophysical Journal, vol. 974, 287, 2024.

Thermalization Speed of Highly Multimode Nonlinear Systems

Emmanouil T. Kokkinakis [1,2*], Konstantinos G. Makris [1,2], Demetrios N. Christodoulides [3,4]

[1]Department of Physics, University of Crete, 70013 Heraklion, Greece
[2]Institute of Electronic Structure and Laser (IESL), FORTH, 71110 Heraklion, Greece
[3]Ming Hsieh Department of Electrical and Computer Engineering,
University of Southern California, Los Angeles, CA 90089, USA
[4]Department of Physics and Astronomy, University of Southern California, Los Angeles, CA 90089, USA
*Corresponding author: ekokkinakis@physics.uoc.gr

***Abstract*—Within optical thermodynamics, weakly nonlinear multimode optical systems evolve toward a Rayleigh Jeans distribution. We show that identical conserved power and internal energy do not uniquely determine thermalization. Initial states with the same equilibrium distribution can thermalize at very different distances, in correlation to their short-distance chaotic response.**

***Keywords*— nonlinear optics, optical thermodynamics, thermalization, optical lattices.**

I. Introduction

In recent years, a lot of attention in nonlinear optics has been given to heavily multimode optical systems, such as a highly multimode optical fiber [1], [2], where the modes are allowed to interact though nonlinearity. Although direct numerical simulations can yield accurate results for these systems, they are often prohibitively time-consuming due to the high number of modes. Moreover, such simulations fall short in offering profound physical insights or contributing to a general theoretical framework, which has been absent. Addressing this gap, an axiomatic thermodynamic theory of light, known as *Optical Thermodynamics*, has been formulated [3], [4], [5], [6], [7]. This approach enables the prediction of the statistical behavior of weakly nonlinear multimode systems by applying principles from thermodynamics [3], [4] and classical statistical mechanics [5], [7]. Through this framework, key thermodynamic quantities such as the equation of state, entropy, and the Rayleigh-Jeans distribution for modal occupancies can be derived analytically. Importantly, apart from numerically verified, the predictions of this thermodynamic theory have been recently experimentally validated in multimode fibers and optical lattices [8], [9], offering a pathway toward innovative applications in the realm of multimode nonlinear optics.

II. Methods

We investigate the dynamics in a one-dimensional discrete waveguide lattice consisting of M waveguide channels. For such a lattice, the normalized paraxial discrete nonlinear Schrödinger equation (DNLSE) reads

$$i\frac{du_n}{dz} + u_{n+1} + u_{n-1} + |u_n|^2 u_n = 0, \tag{1}$$

where z is the propagation distance and u_n is the amplitude of the electric-field envelope at the n^{th} waveguide. The two conserved quantities, the power $\mathcal{P}$ and the internal energy U, can be expressed in terms of the projection modal coefficients c_j and the finite spectrum $\{\epsilon_j\}_{j=1}^{M}$ of the linear lattice, namely $\mathcal{P} = \sum_{j=1}^{M} |c_j|^2 \equiv \sum_{j=1}^{M} p_j$ and $U = -\sum_{j=1}^{M} \epsilon_j |c_j|^2$, from which the equilibrium temperature T and chemical potential μ can be uniquely determined [3].

Within this framework, the system can explore all accessible microstates while conserving U and $\mathcal{P}$ until it reaches thermal equilibrium, where its optical entropy $S = \sum_{j=1}^{M} \ln \overline{|c_j|^2}$ is maximized. At equilibrium, the ensemble-averaged modal occupancies follow the Rayleigh-Jeans (RJ) distribution,

$$p_j^{\text{RJ}} \equiv \overline{|c_j|^2} = -\frac{T}{\epsilon_j + \mu}. \tag{2}$$

Although any initial distribution of modal occupancies $f(\epsilon_j) = |c_{j,0}|^2$ corresponds to a unique optical temperature T and chemical potential μ, the distribution $f(\epsilon_j)$ associated with a given (T, μ) is not unique. Consequently, the propagation distance z required for thermalization—where the averaged modal occupancies converge to the RJ distribution—depends not only on T and μ, but also on the initial distribution $f(\epsilon_j)$.

To quantify the deviation of the modal occupancy distribution from thermal equilibrium, we introduce the normalized distance from the RJ distribution,

$$D_{\text{RJ}}(z) = \frac{1}{2\mathcal{P}} \sum_{j=1}^{M} \left| p_j(z) - p_j^{\text{RJ}} \right|. \tag{3}$$

This metric is bounded as $D_{\text{RJ}} \in [0, 1]$ and represents the fraction of total power that must be redistributed among eigenmodes to reach thermalization. We conventionally define the thermalization distance z_{th} as the propagation distance at which D_{RJ} falls below a prescribed threshold, $D_{\text{RJ}} < 0.03$.

III. Results and Discussion

In Fig. 1 we show that the thermalization distance is not uniquely determined by the conserved quantities $(\mathcal{P}, U)$ but

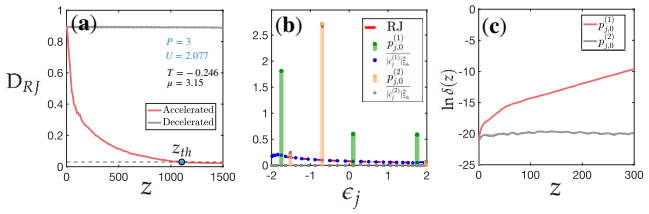

Fig. 1. (a) Evolution of $D_{\mathrm{RJ}}(z)$ for initial conditions leading to fast (red curves) and slow (gray curves) thermalization. (b) Modal occupancies $\overline{|c_j|^2}$ at z_{th} for the fast case (blue points), compared with the RJ prediction (red dashed line) and the slow case (gray square markers). Initial modal occupancies $p_{j,0} = \overline{|c_{j,0}|^2}$ are shown with green points (fast) and orange square markers (slow). (c) Short-z evolution of the occupancy-separation distance $\delta(z)$

depends sensitively on the specific initial modal distribution. For a target RJ equilibrium distribution with $T = -0.246$ and $\mu = 3.15$, we generate large ensembles of distinct initial conditions sharing identical values of (P, U) and propagate them under Eq. (1). Crucially, to isolate genuine dynamical effects from trivial proximity-to-equilibrium conditions, we restrict our analysis to initial conditions that all have the same initial distance from equilibrium. Despite this constraint, the resulting thermalization distances z_{th} exhibit pronounced variability.

In Fig. 1(b), we compare the modal occupancies at the propagation distance $z = z_{th}$ of a representative fast-thermalizing case ($z_{\mathrm{th}} \sim 10^3$) (blue points) with the corresponding theoretically predicted RJ distribution (red dashed line), while the initial modal occupancies are indicated by green points. For comparison, we also include alternative initial conditions (orange square markers) that lead to significantly slower thermalization ($z_{\mathrm{th}} \sim 10^5$), despite starting from the same initial value of $D_{\mathrm{RJ}}(z = 0)$. The latter case remains far from equilibrium at the propagation distance where the fast case have already thermalized, as reflected both in their larger values of D_{RJ} (gray curves in Fig. 1(a)) and in their modal occupancies at $z = z_{th}$, shown by gray square markers in Fig. 1(b), which exhibit significant deviations from the expected RJ distribution.

To quantify the sensitivity of the thermalization dynamics to the initial modal occupancies, we introduce a modal-occupancy-based chaos indicator defined within the manifold of fixed invariants $(\mathcal{P}, U)$. Starting from a set of modal occupancies $\{p_j^{(A)}(0)\}$ with $\mathcal{P} = \sum_j p_j^{(A)}$ and $U = \sum_j \epsilon_j p_j^{(A)}$, we construct a nearby modal-occupancy set $p_j^{(B)}(0) = p_j^{(A)}(0) + \alpha\,\delta p_j$, where α is a small fraction of $\mathcal{P}$. The perturbations δp_j are chosen to satisfy $\sum_j \delta p_j = 0$ and $\sum_j \epsilon_j\,\delta p_j = 0$, ensuring $\delta\mathcal{P} = \delta U = 0$. We then evolve both initial conditions under Eq. (1) and compute the corresponding modal occupancies $p_j^{(A)}(z)$ and $p_j^{(B)}(z)$. The occupancy-separation distance is defined as

$$\delta(z) \equiv \frac{1}{2\mathcal{P}} \sum_{j=1}^{M} \overline{\left| p_j^{(B)}(z) - p_j^{(A)}(z) \right|}, \tag{4}$$

where the overline denotes ensemble averaging over multiple random-phase realizations, taken to be common between $p_j^{(A)}(0)$ and $p_j^{(B)}(0)$. This quantity quantifies how rapidly two initially adjacent $(\mathcal{P}, U)$-conserving initial conditions develop distinct modal-occupancy trajectories.

As shown in Fig. 1(c), the short-z values of the logarithm of the occupancy-separation distance $\ln\delta(z)$ are consistently larger for the fast-thermalization initial conditions $p_{j,0}^{(1)}$ (red lines) than for the slow-thermalization initial conditions $p_{j,0}^{(2)}$. The short-z behavior of $\delta(z)$ thus provides a quantitative measure of the chaotic character of the underlying initial conditions.

IV. Conclusion

In conclusion, we have shown that thermalization distances in multimode nonlinear lattices are not uniquely determined by the conserved thermodynamic invariants but depend sensitively on the initial modal distributions. We show that fast or slow thermalization is associated with stronger or weaker short-z chaotic responses of the corresponding initial conditions, quantified through a modal-occupancy separation measure.

Acknowledgments

This work was supported by European Research Council Grant Agreement (101045135), and Stavros Niarchos Foundation (SNF) and the Hellenic Foundation for Research and Innovation (H.F.R.I.) (Project No: 11496, “PSEUDOTOPPOS”).

References

[1] L. G. Wright, D. N. Christodoulides, and F. W. Wise, Nat. Phot. **9**, 306 (2015).
[2] L. G. Wright, F. O. Wu, D. N. Christodoulides, and F. W. Wise, Nat. Phys. **18**, 1018 (2022).
[3] M. Parto, F. O. Wu, P. S. Jung, K. Makris, and D. N. Christodoulides, Opt. Lett. **44**, 3936 (2019).
[4] F. O. Wu, A. U. Hassan, and D. N. Christodoulides, Nat. Phot. **13**, 776 (2019).
[5] K. G. Makris, Fan. O. Wu, P. S. Jung, and D. N. Christodoulides, Opt. Lett. **45**, 1651 (2020).
[6] F. O. Wu, P. S. Jung, M. Parto, M. Khajavikhan, and D. N. Christodoulides, Comm. Phys. **3**, 1 (2020).
[7] F.O. Wu, Q. Zhong, H. Ren, P.S. Jung, K.G. Makris, and D.N. Christodoulides, Phys. Rev. Lett. **128**, 123901 (2022).
[8] H. Pourbeyram, P. Sidorenko, F. O. Wu, N. Bender, L. Wright, D. N. Christodoulides, and F. W. Wise Nat. Phys. **18**, 685 (2022).
[9] A.L. Marques Muniz, F.O. Wu, P.S. Jung, M. Khajavikhan, D. N. Christodoulides, and. U. Peschel, Science **379**, 1019 (2023).

Advancements in Silicon Nitride Platform

Khaled Mnaymneh*,*, Abubaker Tareki*†, Mohd Zeeshan*, Shahin Honari*, Zara Tehrani*†, and Connor Kupchak†
*Advanced Technology Fabrication Group, National Research Council Canada, Ottawa, Canada
†Department of Electronics, Carleton University, Ottawa, Canada
*Corresponding author: khaled.mnaymneh@nrc.ca

***Abstract*—Silicon nitride photonics enables low loss quantum integrated optics. We report a fabrication flow combining stoichiometric LPCVD SiN waveguides, oxide windows, and lithographically defined V g rooves t o s upport fi ber packaging and heterogeneous integration without sacrificing t he l ow loss optical platform.**

***Index Terms*—silicon nitride, integrated photonics, quantum optics, V grooves, heterogeneous integration, nanofabrication**

I. Introduction

Silicon nitride (SiN) has emerged as a leading material platform for integrated quantum photonics because it combines a wide optical transparency window, CMOS-compatible processing, and the potential for low propagation loss waveguides. These properties make SiN attractive for quantum communication, sensing, and photonic quantum information processing, where optical loss directly limits system performance and scaling.

However, a useful quantum photonic platform cannot consist only of low loss waveguides. Large scale systems also require passive fiber a lignment, r obust c hip p ackaging, a ccess to selected waveguide regions, and compatibility with hybrid or heterogeneous device integration. The key fabrication problem is therefore not merely to pattern SiN waveguides, but to add structural functionality while preserving the optical quality of the buried waveguide layer.

Here we report a fabrication approach that combines low loss stoichiometric LPCVD SiN waveguides with lithographically defined V g rooves a nd l ocalized o xide o penings above selected waveguide regions. The process is designed to maintain the integrity of the optical layer while enabling packaging and integration functions required for scalable quantum photonic circuits.

II. Fabrication Process

The process begins with a high quality silicon wafer. A 5 μm thermal oxide layer is grown to provide the lower optical cladding. Since stoichiometric LPCVD silicon nitride is intrinsically tensile stressed, a stress control step is introduced before nitride deposition. The thermal oxide is patterned using ultraviolet lithography in a damascene-like configuration to suppress crack propagation from wafer edges and within the wafer during deposition of the high stress SiN film [1].

A 400 nm stoichiometric LPCVD SiN layer is then deposited. Waveguides and photonic devices are defined using electron beam lithography with HSQ resist. A 5 μm PECVD oxide layer is deposited as the upper cladding, producing a symmetric buried-waveguide environment suitable for low scattering loss.

To define the V grooves and oxide-access windows, a thick aluminum hard mask is deposited and patterned using ultraviolet lithography. The first lithography step opens the V groove regions. The aluminum is etched using chlorine and argon plasma chemistry, followed by oxide etching using fluorocarbon inductively coupled plasma etching. This removes most of the oxide stack in the V groove openings.

A second lithography step patterns both the V groove openings and the local windows above selected waveguide sections. The exposed oxide is partially etched, leaving approximately 1.5 μm of oxide above the waveguides in the window regions while fully clearing the V groove regions down to the silicon substrate. A third lithography step protects the wafer during a timed buffered oxide etch, which removes the remaining oxide in the windows and exposes the SiN waveguide surface. Finally, anisotropic TMAH etching at 80 °C forms the silicon V grooves.

III. Results and Discussion

Figure 1 shows representative scanning electron microscope images of the fabricated structures. The local oxide windows expose selected buried waveguide regions while keeping the surrounding cladding intact. This is important for applications requiring direct access to the waveguide surface, including heterogeneous integration, sensing, post-processing, local actuation, or coupling to additional materials.

The V grooves provide passive alignment structures for fiber coupling and packaging. Their definition in the same lithographic process flow as the photonic structures improves compatibility between the optical circuit and the external fiber interface. This is critical for moving SiN quantum photonic chips from isolated test structures toward packaged, fiber-compatible modules.

The main practical advantage of this process is that the added mechanical and integration features are introduced after the low loss waveguide stack is formed. In this way, the optical layer can be optimized for propagation loss while the later processing creates the packaging and integration structures needed for deployable systems. This approach extends the fabrication-to-benchtop pathway previously developed for SiN-based quantum devices [2].

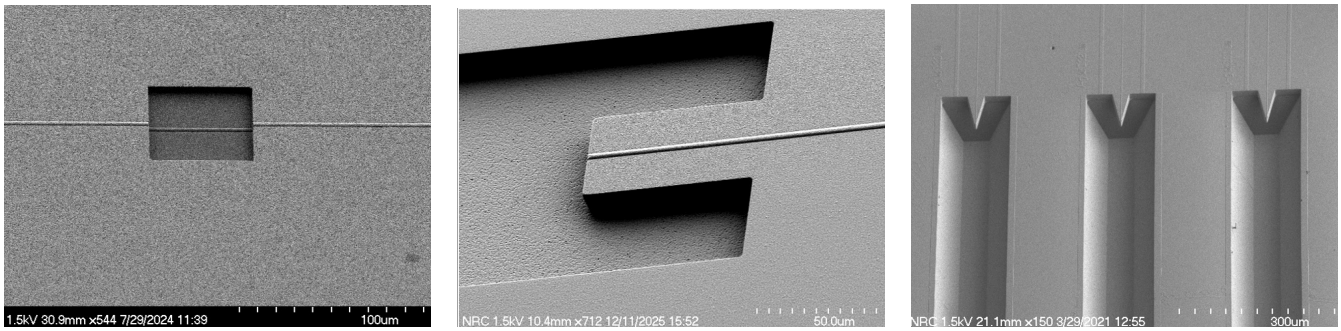

Fig. 1. Scanning electron microscope images of fabricated SiN platform features. Left: localized oxide window above a buried waveguide region. Center: window and V groove structure showing local access to the waveguide and etched alignment geometry. Right: array of anisotropically etched V grooves for passive fiber alignment.

IV. Conclusion

We have demonstrated a fabrication flow for a sovereign SiN integrated photonics platform that combines low loss stoichiometric LPCVD waveguides with structural features needed for packaging and hybrid integration. Lithographically defined V grooves enable passive fiber alignment, while localized oxide windows provide access to selected waveguide regions without removing the full cladding elsewhere on the chip. The result is a practical platform architecture for quantum integrated optics in which optical performance, fiber interfacing, and heterogeneous integration are addressed within a single process strategy.

Acknowledgments

The authors acknowledge the Advanced Technology Fabrication Group at the National Research Council Canada and collaborators at Carleton University for support in process development, fabrication, and characterization.

References

[1] A. M. Tareki, K. Mnaymneh, and C. Kupchak, "The influence of deposition temperature and material stress on low-loss silicon nitride films for integrated quantum optics," *IEEE Photonics Journal*, vol. 15, no. 4, pp. 1–7, Aug. 2023.

[2] C. Kupchak, A. Tareki, T. Moradi, P. Laferriere, N. Tait, and K. Mnaymneh, "Development of a fabrication-to-benchtop process for sin-based quantum devices," in *2024 IEEE International Conference on Quantum Computing and Engineering (QCE)*, Montreal, QC, Canada, 2024, pp. 699–705.

Electrostatic Repulsion as a Governing Mechanism in Near- and Far-Field Optical Binding of Gold Nanoparticles

Manuel I. Marqués[1,*]

[1]Departamento de Física de Materiales, IFIMAC and INC, Universidad Autónoma de Madrid, Spain

*Corresponding author: manuel.marques@uam.es

***Abstract*—. This work shows that electrostatic interactions play a key role in optically bound particle configurations in fluids. Combining experiments and modeling, it reveals that weaker electrostatic repulsion favors near-field alignment with the light polarization, while stronger repulsion leads to far-field perpendicular arrangements. Simulations quantitatively match the experimental observations.**

***Keywords*—Optical Binding, Electrostatic Repulsion, Molecular Dynamics.**

I. Introduction

The dynamics and equilibrium configurations of optically bound particles immersed in a fluid arise from the interplay of multiple physical mechanisms, including optical forces, electrostatic interactions, and hydrodynamic effects [1].

From a theoretical perspective, a key challenge lies in disentangling the relative contribution of these interactions across different length scales. In this work, we combine experiments with a theoretical and numerical framework to demonstrate that short-range electrostatic forces play a central role in determining the observed optical binding configurations.

Within our model, electrostatic repulsion between gold nanoparticles is explicitly incorporated and systematically tuned to mimic variations in salt concentration. The theoretical analysis reveals that reducing the strength of the electrostatic interaction favors near-field optical binding, leading to particle arrangements aligned along the polarization direction of the incident field. Conversely, when electrostatic repulsion is dominant, the balance of forces shifts toward far-field optical binding, resulting in equilibrium configurations oriented perpendicular to the polarization direction.

Numerical simulations based on this model quantitatively reproduce the experimentally observed particle configurations across the explored parameter space [2] (Figure 1) These results underscore the decisive influence of electrostatic interactions in shaping the energy landscape of optically bound systems, particularly in the regime of far-field optical binding, where repulsive forces critically determine both stability and orientation of the particle assemblies

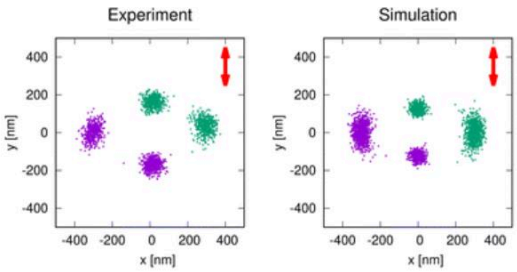

Figure 1 Particle tracking data and corresponding simulation for two trapped 230-nm-diameter Au NPs in a 750 μM NaCl solution, switching from the FF to the NF configuration

References

[1] Boris Louis, Chih-Hao Huang, Marc Melendez, Ana Sánchez-Iglesias, Jorge Olmos-Trigo, Sudipta Seth, Susana Rocha, Rafael Delgado-Buscalioni, Luis M. Liz-Marzán, Manuel I. Marqués, Hiroshi Masuhara, Johan Hofkens, and Roger Bresolí-Obach "Unconventional Optical Matter of Hybrid Metal−Dielectric Nanoparticles at Interfaces" ACS Nano , 18, 32746−32758 (2024)

[2] Jim Jui-Kai Chen, Jorge Olmos-Trigo, Boris Louis, Chih-Hao Huang, Susana Rocha, Hiroshi Masuhara, Johan Hofkens, Rafael Delgado-Buscalioni, Roger Bresolí-Obach, Manuel I. Marqués and Marc Mélendez "Tunable Optical Matter: Electrostatic Repulsion Governs Near- and Far-Field Gold Nanoparticle Arrangements" Nanoscale Advances Nanoscale Adv., 8, 1251-1259 (2026)

Foundry Enabled Chip-scale Photonics Technology and Applications

Yeshaiahu (Shaya) Fainman

Department of ECE, University of California San Diego, USA
*Corresponding author: yfainman@ucsd.edu

***Abstract*—Dense photonic integration requires miniaturization of materials, devices, circuits and systems, including passive components, active components and integrated circuits. In this talk we will discuss recent progress in developing CMOS compatible nonlinear optical materials as well as examples of foundry enabled silicon photonic circuits and systems. Specifically, we will review silicon photonics-based Fourier transform spectrometer that can bring broadband operation and fine resolution to the chip scale. Moreover, taking advantage of nanofabrication we will discuss on-chip spectrometers using stratified waveguide filters and machine learning. Moving forward, we will discuss chip-scale integrated circuit/system that will allow to realize linear algebra accelerators with superior performance in speed, energy consumption and size compared to its electronic counterpart. Such system can be manufactured using monolithic CMOS compatible manufacturing and impact such applications as 5G/6G and beyond wireless MIMO systems as well as deep learning and artificial intelligence.**

***Keywords*— nonlinear optics, Si photonics, sensors, optical interconnects, optical computing accelerators.**

Wide-angle Nonreciprocal Thermal Emitters with Strong Contrast Between Absorptivity and Emissivity

Georgios Veronis[1,*], Md T. Emrose[1], Ming Zhou[2], Gabriel Nedelea[1], Roya Ebrahimi Meymand[1], and Shanhui Fan[2]

[1]School of Electrical Engineering and Computer Science, Louisiana State University, USA
[2]Department of Electrical Engineering, Stanford University, USA
*Corresponding author: gveronis@lsu.edu

***Abstract*— We present multilayer aperiodic structures based on Weyl semimetals that maximize the nonreciprocal contrast over broad spectral and angular ranges. The strong broadband and wide-angle nonreciprocal response of the proposed structures highlights their potential in thermal photonic applications, including directional thermal emission, radiative energy control, thermophotovoltaics, and thermal management.**

***Keywords*— nonreciprocal thermal emitters, Weyl semimetals, optimization algorithms, temporal coupled-mode theory.**

I. SUMMARY

Nonreciprocal thermal emitters are photonic structures that violate Kirchhoff's law of thermal radiation, enabling asymmetric absorptivity and emissivity for waves incident from opposite directions or at symmetric angles, thereby allowing independent control of thermal absorption and emission across angles and wavelengths. This violation is achieved by breaking Lorentz reciprocity using materials such as Weyl semimetals or magneto-optical media with asymmetric permittivity tensors to decouple the rates at which thermal photons couple in and out of specific photonic channels. Weyl semimetals exhibit a large gyrotropic response in the mid-infrared, where their off-diagonal permittivity tensor components are comparable in magnitude to their diagonal elements. This allows them to achieve a near-complete violation of Kirchhoff's law, providing a level of control over thermal radiation that far exceeds the nonreciprocal effects typically observed in traditional magneto-optical materials. By strategically coupling distinct resonances, such as Fabry–Pérot, Brewster, or guided-mode resonances, the sign, magnitude, and spectral bandwidth of the contrast between emissivity and absorptivity can be precisely tuned. Such unprecedented control enables the creation of one-way thermal flows and the development of energy-harvesting technologies capable of approaching the Landsberg efficiency limit, which is impossible in conventional reciprocal systems.

However, most previously reported nonreciprocal thermal emitters achieve strong contrast between absorptivity and emissivity only under restricted conditions, such as narrow spectral windows or limited angular ranges, and are unable to maintain strong nonreciprocal contrast of opposite signs at different wavelengths over a wide angular range. Here, we present a systematic optimization framework for multilayer aperiodic structures based on Weyl semimetals that maximizes the nonreciprocal contrast over broad spectral and angular ranges. The proposed structures consist of planar thin-film stacks deposited on a semi-infinite metallic substrate, avoiding the need for complex lithographic patterning, while the use of Weyl semimetals enables strong intrinsic nonreciprocity without an external magnetic field. We use a memetic optimization algorithm combined with the transfer-matrix method to optimize both the material composition and the layer thicknesses of the structures to achieve robust wide-angle performance. We also develop a temporal coupled-mode theory formulation for the absorptivity and emissivity of the proposed structures and show that its predictions are in good agreement with the numerical results. The strong broadband and wide-angle nonreciprocal response of the proposed planar easy-to-fabricate structures highlights their potential in thermal photonic applications, including directional thermal emission, radiative energy control, thermophotovoltaics, and thermal management.

Compact High-Q Photonic Crystal Cavities with Improved Robustness to Disorder

Nicoletta Granchi[1,2,*], Camilla Gonzini[2], Matteo Lodde[3], Gabriele Calusi[1], René P. J. van Veldhoven[3], Andrea Fiore[3], Guillermo Arregui[4,5] and Francesca Intonti[1,2]

[1]Department of Physics and Astronomy, University of Florence, Italy
[2]European Laboratory for Non-Linear Spectroscopy (LENS), Italy
[3]Department of Applied Physics, Eindhoven University of Technology, The Netherlands
[4] Swiss Federal Institute of Technology Lausanne (EPFL), Switzerland
[5]Center for Quantum Science and Engineering, EPFL, Switzerland
*Corresponding author: nicoletta.granchi@unifi.it

***Abstract*— Compact photonic crystal cavities enable dense integration but typically require large footprints to achieve high Q-factors, increasing sensitivity to fabrication disorder. We present high-Q, small-footprint cavities optimized through a non-Hermitian perturbation theory framework, where periodicity breaking enhances resilience to fabrication-induced disorder as demonstrated by the near-field scanning optical microscopy experiment.**

***Keywords*— photonic-crystals, optical nanocavities, near-field scanning optical microscopy, non-Hermitian photonics.**

I. Introduction

Periodic nanostructures are widely used in photonics to engineer light–matter interaction [1-4]; however, their optical response is often strongly affected by fabrication imperfections, motivating increasing interest in design strategies that enhance robustness and reproducibility in real nanofabricated systems. Among those, photonic crystal (PhC) slab cavities [1] enabling strong light confinement within ultra small volumes, are widely used in integrated photonics and quantum optical platforms. Achieving high quality (Q) factors in these systems typically requires extended periodic mirrors surrounding the cavity defect, leading to large device footprints and enhanced sensitivity to fabrication induced disorder. Nanofabrication imperfections such as hole size variations, sidewall roughness, and positional errors introduce scattering losses and resonance detuning, limiting device reproducibility. This issue is particularly critical for applications requiring spectral alignment across multiple devices.

In this work, PhC slab cavities as small as 4 × 4 μm^2, achieving relatively high Q comparable to conventional large L3 cavities, despite occupying only a fraction of their footprint, are numerically and experimentally demonstrated. These structures are obtained through an optimization process that introduces an aperiodic, yet highly controlled, pattern of holes surrounding the cavity [4,5].

II. Methods

The investigated structures are based on L3 PhC slab cavities defined within a footprint of approximately 4 × 4 μm^2 (corresponding to 6 lattice periods). Starting from the unoptimized periodic design (R6), a gradient-based optimization framework based on non-Hermitian perturbation theory for quasinormal modes [4,6] is employed to maximize the cavity Q-factor of the fundamental L3 mode (Fig. 1a) by

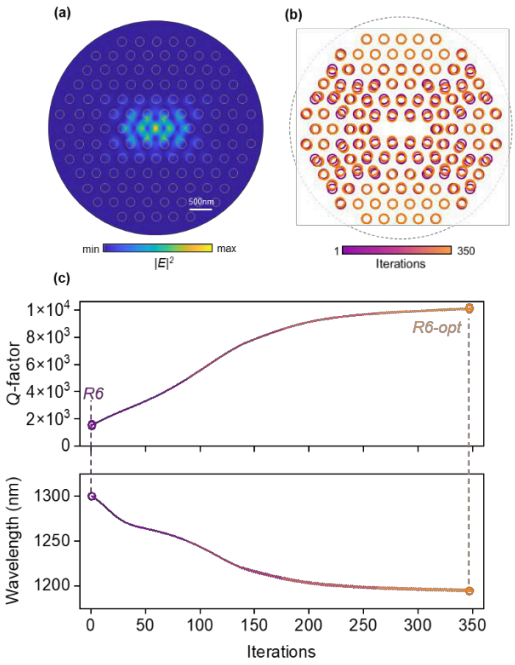

Fig. 1 (a) Simulated near-field electric field intensity maps for the fundamental mode of the original L3 cavity (R6). (b) Evolution of hole positions during the optimization process from the unperturbed reference cavity (R6, purple) to the fully optimized configuration (R6--opt, orange). (c) Simulated Q-factor (top panel) and resonant wavelength (bottom panel) as a function of optimization iteration for an L3 with lattice constant a=330nm and holes radius = 0.79a.

iteratively displacing the air holes surrounding the defect region. The optimization introduces in the final optimized design (labelled as R6-opt) correlated hole displacements that progressively break the original lattice periodicity while preserving the overall cavity symmetry [5]. Fig. 1(b) illustrates the displacement pattern of the air holes introduced during the optimization, while Fig. 1(c) summarizes the evolution of the cavity Q-factor (top panel) and resonant wavelength (bottom panel) along the optimization trajectory from R6 to R6-opt. The fabricated samples are based on GaAs heterostructures incorporating a dense layer of InAs quantum dots (QDs) emitting at 1300 nm. Optical characterization is achieved at room temperature using scanning near-field optical microscopy (SNOM).

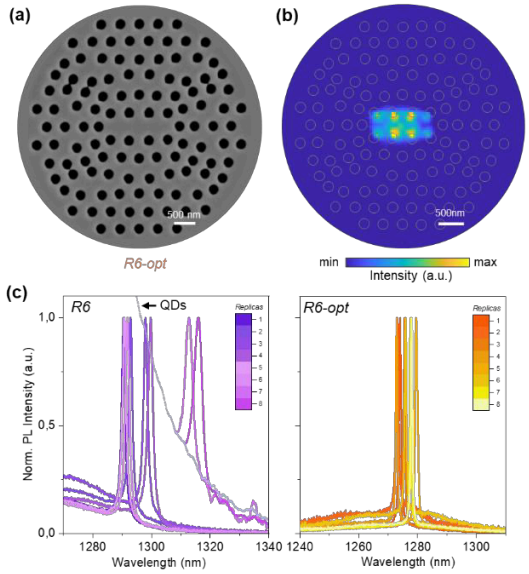

Fig. 2 (a) SEM image of the fabricated optimized R6-II cavity. (b) SNOM map of the optimized fundamental mode in the R6-II cavity. (c) Normalized SNOM PL spectra acquired at the location of maximum emission of eight nominally identical replica of R6 with a=320nm (left) and R6 II with a=350nm (right) and nominal radii. In the left graph the QD PL emission (light blue) is overlapped to the spectra.

III. Results and Discussion

In Fig. 2a we report the Scanning Electron Microscopy (SEM) image of the fabricated L3 cavity with optimized design (R6-opt), characterized by a final Q of $\sim 10^4$, that is comparable to the Q of a standard L3 cavity with 12 lattice periods (therefore extending up to $8 \times 8\ \mu m^2$ for the same lattice constant). A rigorous experimental characterization performed on R6-opt cavities with different lattice constants confirm that Q-factors follow the trend predicted by simulations, with a systematic increase from the unoptimized R6 design to the fully optimized design [4,5]. Moreover, the SNOM map acquired on the R6-opt cavity, shown in Fig. 1 (b), further demonstrates that the cavity mode remains well confined and spatially stable despite the periodicity breaking.

Beyond quality factor optimization, spectral reproducibility represents a critical and often overlooked limitation, largely arising from fabrication-induced disorder. Quantifying spectral stability provides a stringent metric to evaluate the applicability of the proposed cavities. In particular, for cavity–emitter coupling, performance is governed by the spectral alignment between the cavity mode and the emitter ensemble. Imperfections inherent to electron-beam lithography and etching processes are known to induce substantial device-to-device variations in photonic crystal cavity resonances. Here, we approach this issue by systematically investigating the spectral stability of optimized small-footprint cavities through a statistical analysis performed on multiple nominally identical replicas, directly linking engineered periodicity breaking to enhanced robustness against fabrication-induced disorder. Figure 2 (c) compares the SNOM photoluminescence (PL) spectra measured on multiple nominally identical replicas, revealing a significantly reduced spread of resonance wavelengths for the optimized cavities (right panel) with respect to the standard L3 R6 (left panel). This behavior indicates a reduced sensitivity to fabrication-induced imperfections, attributed to the correlated nature of the periodicity breaking introduced by the optimization [5].

IV. Conclusion

We have demonstrated that controlled periodicity breaking enables compact photonic crystal slab cavities combining high Q-factors with enhanced robustness to fabrication-induced disorder. By applying mode-driven optimization to small-footprint L3 cavities, we achieve improved optical performance together with significantly enhanced spectral reproducibility. In contrast to strictly periodic or fully disordered designs, PhC cavities based on engineered aperiodicity simultaneously achieve compact footprints, high optical performance, and improved reproducibility, making them suitable for dense on-chip integration.

References

[1] Y. Akahane, T. Asano, B. S. Song, S. Noda, “High-Q photonic nanocavity in a two-dimensional photonic crystal,” *Nature*, vol. 425, pp. 6961, 2003.

[2] M. Modaresialam, N. Granchi, M. Stehlik, C. Petite, S. Delegeanu, A. Gourdin, M. Bouabdellaoui, F. Intonti, B. Kerzabi, D. Grosso, L.t Gallais, and M. Abbarchi, "Nano-imprint lithography of broad-band and wide-angle antireflective structures for high-power lasers," *Optics Express*, vol. 32, pp. 12967-12981, 2024.

[3] L. Fagiani, N. Granchi, A. Zilli, C. Barri, F. Rusconi, M. Montanari, E. Mafakheri, M. Celebrano, M. Bouabdellaoui, M. Abbarchi, F. Intonti, A. Khursheed, P. Biagioni, M. Finazzi, M. A. Vincenti, M. Bollani, “Linear and nonlinear optical properties of dewetted SiGe islands”. *Optical Materials: X*, vol. 13, pp. 100116, 2022.

[4] N. Granchi, F. Intonti, M. Florescu, P. D. García, M. Gurioli, and G. Arregui, “Q-Factor Optimization of Modes in Ordered and Disordered Photonic Systems Using Non-Hermitian Perturbation Theor,” *ACS Photonics*, vol. 10 (8), pp. 2808-2815, 2023.

[5] N. Granchi, C. Gonzini, M. Lodde, G. Calusi, René P. J. Van Veldhovem, A. Fiore, G. Arregui and F. Intonti, “Improved Disorder Resilience in Small-Footprint Photonic Cavities with Periodicity Breaking”, *Advanced Optical Materials*, doi.org/10.1002/adom.202502531, 2026.

[6] P. Lalanne, W. Yan, K. Vynck, C. Sauvan, J. P. Hugonin, “Light Interaction with Photonic and Plasmonic Resonances”, *Laser & Photonics Review*, vol. 12, pp.17000113, 2018.

Graded-index metamaterials for on-chip control over mode exchange

Raquel Fernández de Cabo[1,*], Alejandro Sánchez-Sánchez[2], Daniele Melati[3], Carlos Alonso-Ramos[3], Aitor V. Velasco[4], David González-Andrade[2]

[1]Instituto de Ciencias Fotónicas (ICFO), Spain
[2]Telecommunication Research Institute (TELMA), Universidad de Málaga, E.T.S.I. Telecomunicación, Spain
[3]Centre de Nanosciences et de Nanotechnologies, CNRS, Université Paris-Saclay, France
[4]Instituto de Óptica "Daza de Valdés", Consejo Superior de Investigaciones Científicas (CSIC), Spain
*Corresponding author: raquel.fernandez@icfo.eu

***Abstract*—Conventional mode converters fully exchange optical power between two orthogonal modes, limiting multimode systems that require engineered modal power distributions. We present a passive silicon mode converter that enables geometrically defined conversion ratios using graded-index subwavelength metamaterials. Fifteen distinct and well-controlled conversion levels are demonstrated across the 1500–1600 nm bandwidth.**

***Keywords*—Silicon photonics, multimode operation, customizable mode conversion, subwavelength graded-index metamaterials.**

I. Introduction

Silicon-on-insulator (SOI) integrated photonics is increasingly leveraging multiple spatial modes to expand capacity and functionality, extending multimode platforms beyond optical communications into nonlinear, quantum, and programmable photonics[1-3]. These applications demand precise on-chip control of modal power, positioning mode converters as fundamental components in advanced multimode architectures. Customizable conversion ratios are particularly valuable for balancing modal amplitudes and compensating higher-order mode-dependent loss in intermodal four-wave mixing[1]. Moreover, spatial modes provide a high-dimensional encoding basis for integrated quantum photonics, where reproducible modal superpositions are essential for transverse mode-encoded gates and high-visibility quantum interference[3]. However, to the best of our knowledge, no fully passive structure has demonstrated geometry-defined control of the modal conversion ratio.

Here, we exploit subwavelength gratings (SWGs) and graded-index (GRIN) metamaterials to engineer modal propagation and realize broadband control of power conversion between transverse-electric (TE) modes with the same parity[4-6]. We propose a fully passive silicon mode converter comprising two back-to-back Y-junctions implemented with SWG metamaterials. The conversion ratio is set by inserting a controlled number of GRIN subwavelength (GRINS) segments between the junctions, yielding discrete, design-defined conversion levels while preserving broadband operation. Experiments demonstrate 15 TE_0–TE_2 conversion levels. The conversion fraction $CF = P_{TE2}/(P_{TE0} + P_{TE2})$ exhibits a quasi-linear dependence on the number of GRIN segments (N_{SWG}), with an average slope of (7.7 ± 0.4) % per N_{SWG} across the 1500–1600 nm wavelength range. The device occupies an ultracompact footprint of only 9.3 µm × 2.6 µm in the largest design configuration. 3D FDTD simulations indicate that the same approach can be extended to other mode pairs, such as fundamental and fourth-order TE modes, while maintaining broadband performance and compactness[7].

II. Principle of Operation and Device Design

The device implements design-customizable mode conversion by splitting and recombining the modal field using two SWG Y-junctions, as shown in Fig. 1.

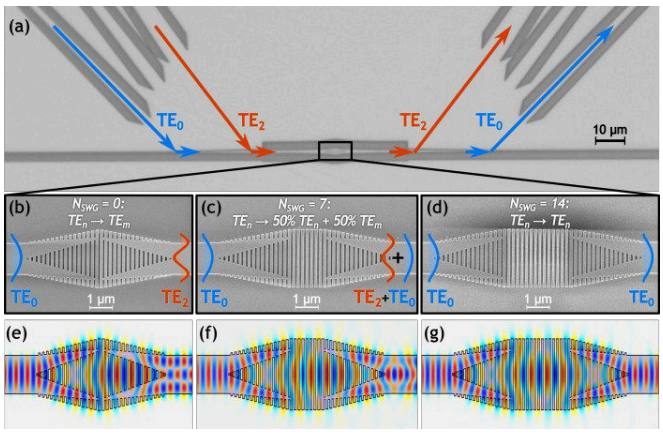

Fig. 1 (a) Optical microscope image of the characterization structure. (b–d) Scanning electron microscope images of the fabricated mode converter for N_{SWG} = 0, 7 and 14. (e-g) 3D FDTD simulations of the electric field ($\Re\{Ey\}$) propagating through the device under TE_0 mode excitation for N_{SWG} = 0, 7 and 14.

The first Y-junction excites a superposition of the two target modes. A subsequent GRINS region sets their relative optical phase and acts as a compact, broadband phase shifter. When the fields are recombined in the second Y-junction, the modal phase difference determines the interference condition and therefore the output modal distribution, enabling discrete conversion ratios between the TE_0 and TE_2 modes set by the number of GRINS segments.

The GRINS segments implement a parabolic transverse index profile through a laterally varying duty cycle. The resulting graded effective index produces mode-order-dependent propagation constants, enabling controlled TE_0–TE_2 phase accumulation with minimal dispersion by tuning the profile curvature. For $N_{SWG} = 0$ (Fig. 1(b,e)), the device operates near the full-conversion regime: injecting TE_0 (TE_2) results in in TE_2 (TE_0) at the output. For $N_{SWG} = 7$ (Fig. 1(c,f)), the converter is near the balanced point, producing an approximately equal TE_0/TE_2 power distribution at the output for either TE_0 or TE_2 excitation. Increasing N_{SWG} to 14 (Fig. 1(d,g)) suppresses mode conversion, and the injected mode remains predominantly at the output.

III. Results and Discussion

Beyond mode conversion, the proposed device enables design-defined modal weighting as a building block for multimode silicon photonics. Experimental measurements resolve 15 distinct levels of TE_0–TE_2 power conversion, as shown in Fig. 2. The conversion fraction shows an average local slope step of (7.7 ± 0.4) % per GRINS period in the entire measured wavelength range covering from 1500 nm to 1600 nm. These measurements agree closely with full three-dimensional simulations, supporting the robustness of the design for precise, broadband mode conversion in an ultracompact footprint. We further show that the same design methodology extends to higher-order mode pairs by demonstrating a second device that provides design-defined conversion ratios between fundamental and fourth-order TE modes while maintaining broadband performance and compact size.

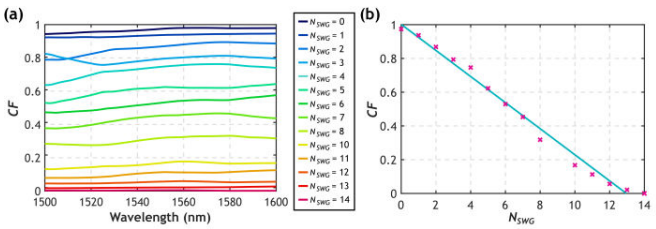

Fig. 2 (a) Measured conversion fraction for all device configurations (N_{SWG} = 0–14). (b) Linear regression of the conversion fraction at λ = 1550 nm. Results for N_{SWG} = 9 are omitted because the corresponding device was damaged during fabrication.

Acknowledgments

This work was funded by the Spanish Ministry of Science, Innovation and Universities (PID2024-160056OB-C21); grant JDC2024-053719-I (MICIU/AEI/10.13039/501100011033 and ESF+); and the European Union's Horizon Europe (Marie Skłodowska-Curie grant agreement No. 101062518; HADEA grant agreement No. 101135523). We also acknowledge project PID2022-139540OB-I00 (MCIN/AEI/10.13039/501100011033). A.S.S. acknowledges an FPI fellowship (PRE2022-000085). This publication is part of grant RYC2023-045670-I (MICIU/AEI/10.13039/501100011033 and ESF+). Fabrication was carried out at the C2N micro/nanotechnologies platforms, with partial support from RENATECH and the General Council of Essonne. This study was supported by EU NextGenerationEU (PRTR-C17.I1) and Generalitat de Catalunya. Additional support came from CEX2024-001490-S (MICIU/AEI/10.13039/501100011033), Fundació Cellex, Fundació Mir-Puig, and Generalitat de Catalunya (CERCA). The views expressed are those of the authors and do not necessarily reflect those of the European Union; neither the EU nor the granting authority can be held responsible.

References

[1] S. Signorini *et al.*, "Intermodal four-wave mixing in silicon waveguides," *Photonics Res.*, vol. 6, no. 8, p. 805, 2018, doi: 10.1364/PRJ.6.000805.

[2] L. G. Wright, W. H. Renninger, D. N. Christodoulides, and F. W. Wise, "Nonlinear multimode photonics: nonlinear optics with many degrees of freedom," *Optica*, vol. 9, no. 7, p. 824, 2022, doi: 10.1364/OPTICA.461981.

[3] L.-T. Feng *et al.*, "Transverse Mode-Encoded Quantum Gate on a Silicon Photonic Chip," *Phys. Rev. Lett.*, vol. 128, no. 6, p. 060501, 2022, doi: 10.1103/PhysRevLett.128.060501.

[4] R. Fernández de Cabo *et al.*, "Broadband mode exchanger based on subwavelength Y-junctions," *Nanophotonics*, vol. 13, no. 21, pp. 4037–4045, 2024, doi: 10.1515/nanoph-2024-0291.

[5] J. M. Luque-González *et al.*, "An Ultracompact GRIN-Lens-Based Spot Size Converter using Subwavelength Grating Metamaterials," *Laser Photon. Rev.*, vol. 13, no. 11, 2019, doi: 10.1002/lpor.201900172.

[6] P. Cheben, R. Halir, J. H. Schmid, H. A. Atwater, and D. R. Smith, "Subwavelength integrated photonics," *Nature*, vol. 560, no. 7720, pp. 565–572, 2018, doi: 10.1038/s41586-018-0421-7.

[7] R. Fernández de Cabo *et al.*, "Broadband Mode Converter With Customizable Modal Ratio Leveraging Subwavelength Engineering for Advanced Multimode Silicon Photonics," *Laser & Photonics Reviews*, Accepted (in production), 2026, doi: 10.1002/lpor.202500768.

Mechanistically Guided Plasmonic Dendrites for Selective CO_2 Reduction

Anjalie Edirisooriya[1*], Zelio Fusco, Ning Lyu[1,2], Christin David[3], Fiona Beck[1]
[1]School of Engineering, Australian National University, Canberra ACT2600, Australia
[2]IFTO, Friedrich-Schiller-Universität Jena, 07743 Jena, Germany
[3]University of Applied Sciences Landshut, Am Lurzenhof 1, 84036 Landshut, Germany
[*]corresponding author: Anjalie.Edirisooriya@anu.edu.au

Abstract - **Dendritic plasmonic catalysts enable light-driven CO_2 reduction by co-localising optical hot-spots and active surface sites. This invited contribution presents a guided strategy progressing from model systems to scalable Au and Cu dendrites. Wavelength-resolved studies reveal how optical modes and near-fields control charge transfer, enabling wavelength- and material-selective multi-electron CO_2 reduction.**

INTRODUCTION

Dendritic metal electrodes are promising platforms for plasmon-assisted CO_2 reduction because their hierarchical morphology combines high surface area, dense catalytic sites, and nanoscale optical hot-spots within a single architecture. Abundant tips and junctions naturally concentrate electromagnetic fields under illumination, making dendrites well suited to reactions requiring repeated electron transfer and stabilization of surface-bound intermediates.

Selective conversion of CO_2 into multi-carbon (C_2^+) products, however, requires more than structural complexity[1] Efficient C–C coupling demands both localized delivery of multiple electrons and catalyst surfaces that intrinsically favour bond formation. This motivates a design strategy in which plasmonic excitation and catalyst material are treated jointly: optical excitation governs energy and charge localization, while the metal defines accessible reaction pathways[2].

Our group addresses this challenge by developing mechanistic understanding of plasmon-mediated excitation and translating it into dendritic catalyst design. Controlled plasmonic structures are first used to identify how optical mode structure, near-field localization, and excitation wavelength govern interfacial charge-transfer activity, allowing wavelength to be treated as an independent control parameter[3]. These insights are mapped onto dendritic architectures, where local geometry rather than global morphology dictates optical response. Gold dendrites serve as an optically stable reference system, enabling direct correlation between plasmonic hot-spot localization and photo-assisted reaction behaviour[2].

While gold dendrites provide a platform for establishing optical design principles, copper is uniquely active for carbon-carbon coupling in CO_2 reduction[4]. Extending plasmonic concepts from gold to copper dendritic catalysts enables the integration of wavelength-guided optical excitation with material-specific chemistry. In this contribution, we present a unified framework linking wavelength-selective plasmonic excitation, dendritic architecture, and catalyst material selection, outlining a pathway toward scalable, light-driven CO_2 reduction with combined wavelength and material control.

I. Methods and Results

To connect mechanistic plasmonic insight with practical catalyst design, we employ a hierarchical approach that links simplified plasmonic model systems to complex dendritic architectures. Our methodology combines electromagnetic simulations (BEM, FEM), nanoscale optical characterization, cathodoluminescence (CL) spectroscopy, surface-enhanced Raman spectroscopy (SERS), and photo-assisted catalytic measurements[5].

Wavelength-dependent excitation behaviour is first established using well-defined plasmonic model systems, including Au nanotriangle arrays and nanoparticles. These structures support tunable optical modes, enabling systematic investigation of

how excitation wavelength, near-field localisation, and absorption influence plasmon-mediated charge-transfer activity. Electromagnetic simulations correlate geometric parameters with resonance shifts and field enhancement, while wavelength-resolved SERS using molecular probe systems provides an experimental readout of interfacial plasmonic excitation without directly probing CO_2 intermediates.

Insights from these mechanistic proof-of-concept studies are translated to self-assembled Au nano-dendrites fabricated via controlled electrodeposition. CL mapping reveals that plasmonic emission is strongly localized at high-curvature tips and branch junctions and exhibits wavelength-dependent spatial distributions, confirming that local geometry dominates optical response rather than overall morphology. Photo-assisted catalytic and electrochemical measurements demonstrate that Au dendrites provide a robust platform for plasmon-enhanced CO_2 reduction, with broadband optical modes supporting repeated interfacial electron-transfer events.

While deterministic wavelength selectivity is readily established in simplified plasmonic systems, extending precise wavelength control to dendritic architectures remains an active area of investigation due to their multi-mode optical response. Ongoing work focuses on correlating wavelength-resolved excitation with changes in reaction rate and product distribution in dendritic electrodes.

Building on this foundation, the framework is extended toward copper dendritic catalysts. Copper is intrinsically active for carbon–carbon coupling in CO_2 reduction, and coupling plasmonic excitation with Cu dendritic architectures enables the integration of wavelength-guided optical control with material-specific reaction pathways. In this context, Au dendrites serve as an optically well-defined reference, while Cu dendrites represent the chemically selective target system.

II. Conclusion

We present a mechanistically guided approach to designing plasmonic dendritic catalysts for light-driven CO_2 reduction. Wavelength-resolved studies in model plasmonic systems reveal how optical mode structure and near-field localisation govern charge-transfer activity, which is translated to scalable Au dendrites where local geometry dominates optical response. Extending these principles to Cu dendritic catalysts couples plasmonic excitation with intrinsically C–C-coupling-active surfaces, outlining a pathway toward wavelength- and material-selective CO_2 reduction

References

1. Fusco, Z. et al., *Adv. Mater. Interfaces* **10**, 2202236 (2023)
2. Fusco, Z., Catchpole, K., & Beck, F. J., *J. Mater. Chem. C* **10**, 7511–7524 (2022).
3. Fusco, Z.; Beck, F. J. Nanophotonics 2024, 13, 387–417
4. Fusco, Z.; Edirisooriya, A.; Turner, R.; Riaz, A.; Kremer, F.; Daiyan, R.; Beck, F. J. *Steering CO_2 reduction reaction pathways towards C_2^+ products with localized surface plasmon resonances*. Submitted.
5. Fusco, Z.; Catchpole, K.; Beck, F. J. J. Mater. Chem. C 2022, 10, 7511–7524

Lasers that run cool on their own

Chun-Wei Chen[1,2,*], Michel J. F. Digonnet[2], John Ballato[3],
Peter D. Dragic[4], Martin Bernier[5], Enkeleda Balliu[6]

[1]Centre for Photonics, Department of Physics, University of Bath, Bath BA2 7AY, UK
[2]Edward L. Ginzton Laboratory,Stanford University, Stanford, CA 94305, USA
[3]Department of Materials Science and Engineering, Clemson University, Clemson, SC 29631, USA
[4]Department of Electrical and Computer Engineering, University of Illinois Urbana-Champaign, Urbana, IL 61801, USA
[5]Centre d'optique, photonique et lasers (COPL), Université Laval, Québec QC G1V 0A6, Canada
[6]Cobolt AB, a HÜBNER Photonics company, 171 54 Solna, Sweden
*Corresponding author: cwc218@bath.ac.uk

[1]

***Abstract*— Almost all lasers generate heat, leading to noise and nonlinear effects that limit power-scaling. We use anti-Stokes-fluorescence cooling to offset heat generated by stimulated emission, making fibre lasers run cool without external cooling. Advances in silicate glass have enabled watt-level output and continued scaling, with promise for broader photonic systems.**

***Keywords*— Optical cooling, thermal management, silica, glass, optical fiber, fiber laser, fiber amplifier**

[1]

Perovskite Superfluorescence and High Temperature Macroscopic Quantum Effects

Kenan Gundogdu

Department of Physics, NC State University
corresponding author: kgundog@ncsu.edu

Abstract— Macroscopic quantum coherence is typically associated with low temperatures, where thermal fluctuations do not rapidly destroy phase correlations. In solids, however, electronic coherence is strongly influenced by lattice dynamics, making it unclear how collective quantum states can persist at elevated temperatures. In this talk, I will show how studies of superfluorescence provide a powerful window into the emergence of macroscopic coherence in condensed matter systems. By tracking the buildup of collective emission in lead-halide perovskites[1,2,3], we find that superfluorescence does not originate from simple radiative synchronization of independent dipoles. Instead, it reflects the formation of an underlying many-body excitonic state, shaped by strong exciton–lattice interactions.

Our results reveal a general mechanism in which lattice dynamics actively reorganize the electronic landscape, enabling the emergence of coherent excitonic order at high temperatures. This perspective establishes superfluorescence as a diagnostic of nonequilibrium phase transitions and points to a broader principle for achieving macroscopic quantum coherence in strongly interacting systems.

***Keywords*— macroscopic quantum coherence, ultrafast spectroscopy**

Funding Support: DOE, award no. DE-SC0024396 (analytical theory development), NSF-DMR-2323802 (material synthesis, optical characterization)

References:

[1] Findik. G., et.al Nature Photonics 2021
[2] Biliroglu. M., Nature Photonics, 2022
[3] Biliroglu. M., Nature, 2025

Reversible metal electrodeposition for high-contrast active optical and metamaterials

Po-Chun Hsu[1,*]

[1] Pritzker School of Molecular Engineering, University of Chicago, USA
*Corresponding author: pochunhsu@uchicago.edu

***Abstract*— Reversible metal electrodeposition (RME) can switch between plasmonic and dielectric behavior with a substantial change in refractive index, which implies a small required volume of active materials and switching energy. While conventional thin-film RME has shown great promise as color-neutral, high-efficiency smart windows, it holds even greater potential as a versatile tuning knob for accomplishing exotic functionalities when combined with nanophotonics designs and molecular engineering. In this talk, I will demonstrate these new concepts by introducing our recent RME-based active optical devices: (i) Adaptive solar heater and sub-ambient radiative cooler. We demonstrated that the RME-based solar heater can achieve high solar absorptivity via localized surface plasmon resonance (LSPR) due to temporally modulated electrodeposition and amorphous bimetallic alloy with extremely high extinction coefficient. Reversing the bias will switch the device to the radiative cooling mode, which has high solar reflectivity (for true sub-ambient cooling) due to the extreme thin device thickness. (ii) Bandwidth-optimized multispectral dynamic thermal emitter. We performed Fresnel phase-shift analysis and Bayesian optimization on a Fabry-Perot cavity to design the thermal emitter with a selective emissivity band, which can be switched by reversible metal electrodeposition and other metal-to-insulator (MIT) materials. Low-to-intermediate loss of the MIT layer and high refractive index in the dielectric layer are shown to be key to band selectivity and tunable range. (iii) High-efficiency active beam-steering metasurface. Incorporating nanoantenna with RME allows us to control the phase front and achieve active beam steering at very high signal-to-noise ratio (i.e., diffraction efficiency), thanks to the high index contrast. These RME-enabled research can bring transformative impact on active optics and thermoregulation, such as smart building envelopes, spacecraft thermal engineering, radiative cooling, and reconfigurable antenna.**

***Keywords*— active metasurface, metal electrodeposition, plasmonics**

From Simulation to Design: AI-Solvers and AI-Optimizers for Electromagnetics

Raphael Pestourie[1,*]

[1]School of Computational Science and Engineering, Georgia Tech, USA
*Corresponding author: rpestourie3[at]gatech.edu

***Abstract*—The integration of artificial intelligence with computational electromagnetics is shifting design from simulation-driven iteration toward knowledge-driven discovery. This summary categorizes AI-Solvers that accelerate physics simulation and AI-Optimizers that reduce design complexity through learned geometric representations, enabling trustworthy, scalable, and transferable electromagnetic device optimization across emerging engineering applications.**

***Keywords*— artificial intelligence, optimization, metasurfaces, approximate solvers**

I. Introduction

Electromagnetic device design increasingly requires simultaneous optimization across performance, robustness, and manufacturability constraints. Traditional workflows rely on iterative simulation-driven optimization, such as gradient-based topology optimization. Although these approaches coupled with fullwave solvers have enabled major advances in photonics and microwave engineering, they remain a computational bottleneck for many state-of-the-art electromagnetic applciations. Scientific machine learning is emerging as a transformative framework to reduce design cost while extracting transferable design knowledge across device families. We highlight how artificial intelligence can enhance both solvers and optimizers for design [1].

II. AI-Solvers: Synergistic Acceleration of Physical Simulation

A global trend in inverse design is to accelerate optimization by accelerating the underlying physical solver. Physics-informed machine learning has proposed replacing numerical solvers with neural network approximations that directly learn physical operators from data or governing equations [2]. While such approaches can significantly reduce simulation cost, they introduce approximate models in which the governing physics is implicitly relearned from data. Although this strategy appears redundant when physics is already known, the primary limitation lies in verification and generalization: these approximate models are called uncontrolled. When surrogate solvers are deployed within optimization loops, there is generally no guarantee that the resulting optimal design lies within regions where the learned model remains accurate.

An alternative paradigm consists of developing fast approximate solvers with controllable error, where approximation accuracy improves as physically meaningful parameters converge toward asymptotic limits. Data-driven approximate solvers for electromagnetics demonstrate this concept by combining physical approximation with decomposition numerical methods that preserve some theoretical guarantees asymptotically [3]. For instance, in the locally periodic approximation for metasurfaces, fast solvers become arbitrarily accurate as the rate of variation of the structure approaches zero. When the data-driven components rely on approximations with bounded error, such as Chebyshev polynomial expansions, approximation accuracy can be characterized theoretically and controllable.

However, approximate solvers face a controllability versus complexity tradeoff. Increasing geometric richness often requires introducing additional subdomain parameterizations, reintroducing the curse of dimensionality despite potential benefits from the blessing of dimensionality in high-dimensional modeling [4]. This limitation is particularly evident in parameter-intensive approximate solvers such as the overlapping-domain decomposition [5].

Hybrid approaches such as Physics-Enhanced Deep Surrogates (PEDS) provide an intermediate strategy by combining neural networks with low-fidelity solvers for interpretable machine learning models [6]. Rather than learning field responses directly, these models learn physically meaningful inputs to low-fidelity solvers, preserving interpretability while enabling accelerated evaluation. This formulation opens the black box of neural surrogates and allows direct verification of learned interpretable quantities during optimization. Recent applications to transport phenomena further demonstrate how physics-enhanced surrogates can maintain physical interpretability while achieving substantial acceleration [7].

III. AI-Optimizers: Learning Design Manifolds

The concept of learning solver inputs rather than outputs naturally leads to a second paradigm shift: accelerating design by learning a representation of high-performance solutions. Instead of attempting to reproduce physical simulations, AI-Optimizers aim to learn low-dimensional manifolds of feasible and high-performing designs. In this formulation, acceleration is achieved by reducing the number of optimization iterations rather than reducing the cost per iteration.

This paradigm fundamentally changes the relationship between machine learning and physics-based optimization. By operating in the design space rather than the physics space,

AI-Optimizers remain compatible with high-fidelity solvers embedded within optimization loops, thereby preserving reliability and addressing long-standing concerns regarding generalization in PDE-constrained optimization.

This approach raises an apparent chicken-and-egg problem: *if high-quality designs are required to learn design representations, why is optimization still necessary?* Transfer learning provides a resolution. Pretrained representation models, particularly those developed for computer vision, enable learning geometric priors from relatively limited physics-driven datasets. Because geometries resemble structured visual data they benefit from advances in generative modeling and representation learning.

Hybrid inverse-design frameworks illustrate this paradigm shift by combining representation learning with physics-based optimization [8]. These approaches demonstrate substantial reductions in simulation cost while improving state-of-the-art device performance of polychromatic beam deflectors. By leveraging latent representations and pretrained models, AI-enhanced optimizers overcome two major redundancies of traditional gradient-based topology optimization: each optimization run traditionally fails to reuse knowledge from prior solutions, and the informational return from simulation evaluations diminishes near local optima. By learning transferable design priors, AI-Optimizers enable optimization strategies that become increasingly efficient across problem instances.

IV. Conclusion

The synergy between AI-Solvers and AI-Optimizers is transforming electromagnetic design workflows into closed-loop discovery pipelines linking simulation, optimization, fabrication, and validation. Design opportunities lie both at the output and the input of electromagnetic solvers.

Acknowledgments

RP thanks Steven Johnson for fruitful discussion about controlled versus uncontrolled approximations.

References

[1] R. Marzban, A. Adibi, and R. Pestourie. ”Inverse design in nanophotonics via representation learning.” *Advanced Optical Materials*, 2026

[2] G. E. Karniadakis et al., “Physics-informed machine learning,” *Nature Reviews Physics*, 2021.

[3] R. Pestourie, ”Fast Approximate Solvers: Metamaterials design in electromagnetism,” in *IEEE Antennas and Propagation Magazine*, 2025

[4] N. A. Gershenfeld, ”The Nature of Mathematical Modeling.” *Cambridge University Press*, 1999.

[5] Z. Lin and S. G. Johnson, “Overlapping domains for topology optimization of large-area metasurfaces,” *Optics Express*, 2019.

[6] R. Pestourie et al., “Physics-enhanced deep surrogates for partial differential equations,” *Nature Machine Intelligence*, 2023.

[7] A. Varagnolo, G. Romano, and R. Pestourie, “Physics Enhanced Deep Surrogates for the Phonon Boltzmann Transport Equation,” arXiv:2512.05976, 2025.

[8] R. Marzban et al., “HiLAB: A Hybrid Inverse-Design Framework,” *Small Methods*, 2025.

Topology Optimized High-Q Photonic Crystal Resonators for the THz Band

Stephen M. Hanham[1,*]

[1]Department of Materials, Imperial College London, U. K.
*Corresponding author: s.hanham@imperial.ac.uk

***Abstract*—This work presents a topology optimization framework for designing two-dimensional slab photonic crystal resonators for the terahertz band. The method generates manufacturable resonators with high Purcell factors and sub-diffraction-limited modal volumes, while explicitly enforcing fabrication constraints through minimum feature size control and geometric filtering.**

***Keywords*— photonic crystals, terahertz, topology optimization.**

I. Introduction

Photonic crystal resonators (PCRs) have demonstrated a remarkable ability to simultaneously achieve ultra-high quality (Q) factors and extremely small modal volumes in the optical region of the electromagnetic spectrum [1]. More recently, these concepts have been successfully extended to the terahertz (THz) frequency range, where both microbeam [2], [3] and two-dimensional slab [4], [5] PCRs have been experimentally demonstrated using high-resistivity silicon and low-loss polymer platforms [6]. PCRs have also recently been employed as frequency-selective elements to stabilize low phase-noise oscillators, highlighting their growing relevance for practical millimeter-wave and THz systems [7].

Despite the high level of maturity of PCRs, the problem of systematically designing cavities that maximize the Q-factor to modal volume ratio (Q/V_m) remains an open and largely unresolved challenge. In this work, we describe an automated approach for the design of 2D silicon slab THz PCRs that attempts to maximize Q/V_m while respecting fabrication constraints.

II. Topology Optimization

Topology optimization (TO) is a computational technique that allows for the optimization of electromagnetic structures defined by free-form dielectric geometries [8]. In the present work, we apply gradient-based TO to determine the dielectric distribution ϵ_r of the silicon slab defining a THz PCR to maximize Q/V_m.

For the optimization step, a continuous density design variable $\boldsymbol{x} \in [0,1]^N$ is introduced which defines the relative permittivity according to $\epsilon_r(\boldsymbol{x}) = 1 + (\epsilon_{si} - 1)\boldsymbol{x}$ over the slab design region $D \subset \Re^2$, where $\epsilon_{si} = 11.68$ is the relative permittivity of high-resistivity silicon. The use of a continuous design variable allows for the straightforward computation of the sensitivities $\partial g(\boldsymbol{x})/\partial \boldsymbol{x}$, where $g(\boldsymbol{x})$ is the objective function defined as $g(x) = -|\psi|^2$ and ψ is the relevant field component to maximize at the center of the cavity $(x, y) = (0, 0)$. This can be set to either the electric or magnetic field depending upon the intended application of the cavity.

To encourage the optimizer to converge to a binary distribution for the relative permittivity (i.e. $\boldsymbol{x} = 0$ for air and $\boldsymbol{x} = 1$ for silicon), a projection operator is used to project $\boldsymbol{x}$ into a binary space with a gradually increasing sharpness as described in [8]. A density filter is also applied to $\boldsymbol{x}$ to impose a minimum feature size on the optimized dielectric distribution to ensure fabricability. The gradient-based optimization is performed using the Method of Moving Asymptotes (MMA) [9]. The finite element method is used to evaluate the PCR's performance at each epoch.

III. Results and Discussion

The slab area defining the PCR cavity was chosen to be $2\lambda_0$ by $2\lambda_0$. A dielectric slab waveguide was defined for exciting the cavity with its fundamental TE_0 mode.

Fig. 1(a) shows an example of an optimized cavity produced using the TO algorithm after ~400 epochs. A periodic Bragg-like structure can be observed around the central region of the cavity. The modal volume calculated was found to be significantly below the diffraction limited volume of $(0.5\lambda_0)^3$ in air.

In contrast to previous studies, TO was additionally employed to maximize the magnetic field confinement, targeting applications in which light–matter coupling is governed by the magnetic-field Purcell factor and magnetic dipole interactions. Interestingly, the optimized structures lacked the characteristic bow-tie structure demonstrated in previous works where the electric-field Purcell factor is maximized [10].

IV. Conclusion

An automated approach based on TO has been developed for the design of THz 2D slab PCRs with high Purcell factors (Q/V_m) and sub-diffraction modal volumes. Future work is to

fabricate the structures for applications in terahertz and millimeter-wave sensing and oscillators.

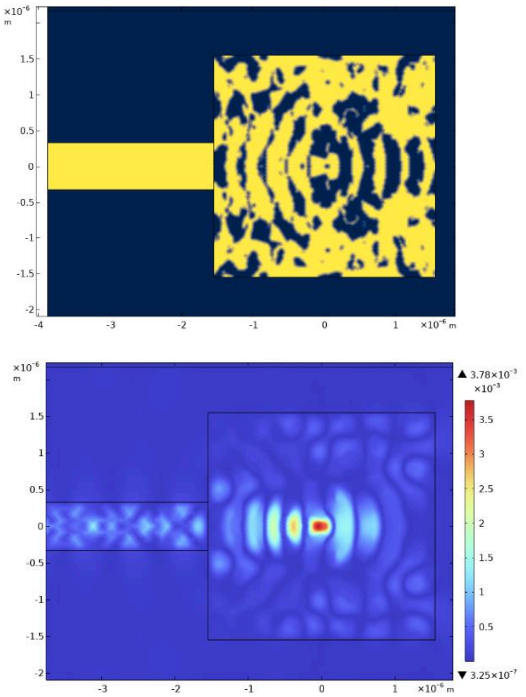

Fig. 1 (a) Example of a topology optimized PCR. In the plot yellow and navy represent silicon and air, respectively. (b) Electric field distribution of the resonant mode.

ACKNOWLEDGMENTS

The authors acknowledge the support of COMSOL.

REFERENCES

[1] Y. Akahane, T. Asano, B. S. Song, and S. Noda, "High-Q photonic nanocavity in a two-dimensional photonic crystal," *Nature*, vol. 425, no. 6961, pp. 944–947, 2003.

[2] S. M. Hanham, M. M. Ahmad, S. Lucyszyn, and N. Klein, "LED-Switchable high-Q packaged THz microbeam resonators," *IEEE Trans. Terahertz Sci. Technol.*, vol. 7, no. 2, pp. 199–208, Mar. 2017.

[3] E. Akiki *et al.*, "High-Q THz photonic crystal cavity on a low-loss suspended silicon platform," *IEEE Trans. Terahertz Sci. Technol.*, vol. 11, no. 1, pp. 42–53, Jan. 2021.

[4] S. M. Hanham *et al.*, "Low Dielectric Filling Factor Millimeter-Wave Photonic Crystal Resonator Micromachined from NTD High-Resistivity Silicon," *IEEE Trans. Microw. Theory Tech.*, vol. 72, no. 11, pp. 6601–6612, 2024.

[5] W. J. Otter, S. M. Hanham, N. M. Ridler, G. Marino, N. Klein, and S. Lucyszyn, "100 GHz ultra-high Q-factor photonic crystal resonators," *Sens. Actuators A Phys.*, vol. 217, 2014.

[6] M. Salek, S. M. Hanham, and A. P. Gregory, "High-Q 100 GHz photonic crystal resonator fabricated from a cyclic olefin copolymer," *IEEE Microw. Wirel. Technol. Lett.*, vol. 33, no. 3, pp. 279–282, Mar. 2023.

[7] E. Lia *et al.*, "Novel mm-wave oscillator based on an electromagnetic bandgap resonator," *IEEE Microw. Wirel. Technol. Lett.*, vol. 33, no. 6, pp. 863–866, Jun. 2023.

[8] J. S. Jensen and O. Sigmund, "Topology optimization for nano-photonics," *Laser Photon. Rev.*, vol. 5, no. 2, pp. 308–321, Mar. 2011.

[9] K. Svanberg, "The method of moving asymptotes—a new method for structural optimization," *Int. J. Numer. Methods Eng.*, vol. 24, no. 2, 1987.

[10] M. Albrechtsen *et al.*, "Nanometer-scale photon confinement in topology-optimized dielectric cavities," *Nat. Commun.*, vol. 13, no. 1, 2022.

Intelligent Nanofabrication for Nanophotonics: Quantifying and Understanding Process Variability

Wenhan Zhang[1,*], Ben Mills[1], and Kevin F. MacDonald[1]

[1]Optoelectronics Research Centre, University of Southampton, UK
*Corresponding author: wz2e25@soton.ac.uk

***Abstract*— Fabrication variability is an inherent challenge in nano-manufacturing. We present a bi-directional variational autoencoder – a graphical generative model – that simulates a realistic distribution of process outcomes for a given input design, enabling quantitative analysis of principal deviation modes, and thus well-informed design and process parameter optimisation.**

***Keywords*— nanofabrication, deep learning**

I. Introduction

Nanofabrication techniques underpin the development of photonic and electronic materials and devices, the performance of which is highly sensitive to nanoscale geometry. Such techniques inherently exhibit stochastic variations that lead to discrepancies between designed and realised structures. Conventional process simulation methods typically assume ideal outcomes or provide single deterministic predictions, offering little or no insight into realistic fabrication uncertainties. Here, we introduced a bi-directional conditional variational autoencoder (Bi-CVAE) neural network that models a realistic distribution of likely process outcomes for a given input mask design, generating a set of statistically plausible output sample scanning electron microscope (SEM) images that reflecting observed experimental fluctuations. In conjunction with principal component analysis, this 'one-to-many' capability enables quantitative comparisons of manufacturing variations and their occurrence probabilities. It can inform process control, material/device (inverse) design, and design tolerance and risk mitigation strategies, ultimately improving performance and yield.

II. Methods, Results, and Discussion

We consider focused ion beam (FIB) milling – a vital manufacturing and rapid prototyping technique in plasmonics, nanophotonics and metamaterials research – as a test case. The Bi-CVAE network encodes a training set of binary design masks and corresponding electron microscope (SEM) images of fabricated samples (several iterations of each design) into a latent space. By sampling this latent space, a set of plausible SEM images for new, previously unseen masks can subsequently be generated (Fig. 1a). Importantly, the bi-directional architecture of the network introduces cycle-consistency between mask-to-SEM and SEM-to-mask transformations, which is critical for stable training, and enforces physical correspondence between input and output.

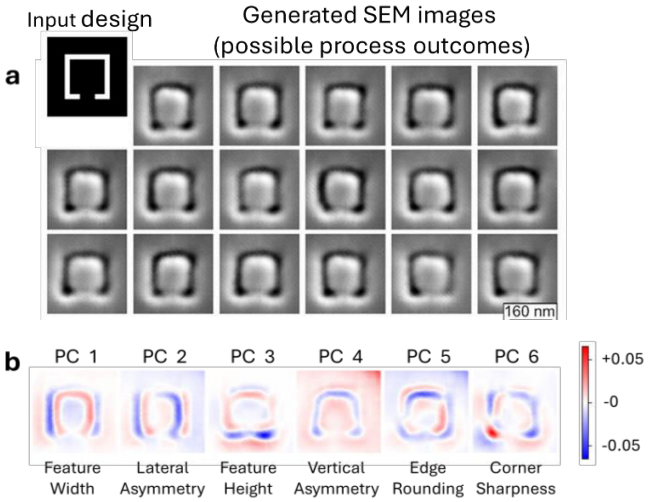

Fig. 1: Quantifying FIB milling variability for a plasmonic split-ring metamolecule: (a) Design mask [top left] and a sample set of possible SEM images for this design [milled into a gold film], generated by a trained Bi-CVAE neural network. (b) Leading principal component eigenmodes from a set of 1000 generated SEM images. Red and blue colours correspond to under- and over-milling, respectively [quantified in terms of pixel intensity].

A principal component analysis performed on the generated image set reveals the dominant modes of fabrication deviations from the intended design (Fig. 1b) and their relative statistical importance. For the plasmonic split-ring resonator case shown in Fig. 1, we find that the first three eigenmodes, corresponding to feature width, left/right asymmetry and height, together describe ~50% of variations, and 10 modes cover ~85%.

This probabilistic characterisation of fabrication variability provides a foundation for informed design adaptation and process control, enabling optimisation guided by realistic uncertainty rather than idealised assumption or trial-and-error.

Acknowledgments

This work was supported by the Engineering and Physical Sciences Research Council, UK (grant number EP/U536866/1).

Manipulating matter with vector twisted light

M. Babiker*,

School of Physics, Engineering and Technology, University of York, YO10 5DD, England
*Corresponding author: m.babiker@york.ac.uk

***Abstract*—Recent work on the influence of higher order (vector) twisted light on matter immersed in such light has led to a variety of novel effects involving dielectric and magnetic particles. This presentation describes the principles, the methodology and the results that have recently emerged in a number of interesting scenarios.**

***Keywords*— Poincaré modes, magneto-optics, optical forces.**

I. Introduction

Optical manipulation stems from the mechanical effects which laser light imparts on matter, both in the form of atoms and molecules or matter as small particles. This currently active area of research continues to be a subject of great interest, both from a fundamental point of view and for useful applications.

II. Methods

An established general framework for the description of twisted light is in terms of higher order Poincareé modes [1]. This accounts for the polarisation states of all forms of optical vortex modes, both scalar and vector and is such that any optical mode is represented by a specific point on the surface of a unit Poincaré sphere of order m. The Poincare higher order modes can possess orbital angular momentum (OAM), Spin Angular Momentum (SAM), as well as helicity and chirality.

We focus on our recent investigations on a number of topics involving twisted light and matter, namely: magneto-optic media [2]; coupling of matter to optical fiber evanescent modes [3], OAM transfer; spin-orbit coupling; dipole and quadrupole interactions optical, vortex mode mixing, atom trapping, optical forces and torques and dynamics in twisted light.

III. Results and Discussion

The interaction leads to trapping, or to matter motion in the vortex fields due to forces and torques [4]. For example, we can evaluate the trajectory and final steady state rotation of an ionic particle in the focal plane of two counter-propagating doughnut beams. In the steady state, this rotation amounts to a steady electric current and there is a corresponding magnetic field, which can be used, for instance, for switching the direction of a localized electron spin or a magnetic particle. Another example shows how the Faraday Effect can be made to change the magnitude and direction of the local polarization of an optical vortex as the beam propagates in a magneto-optic medium [2], which modifies the forces. As and example, Fig. 1 displays the distribution of the gradient torque on a particle due to reactive helicity [4].

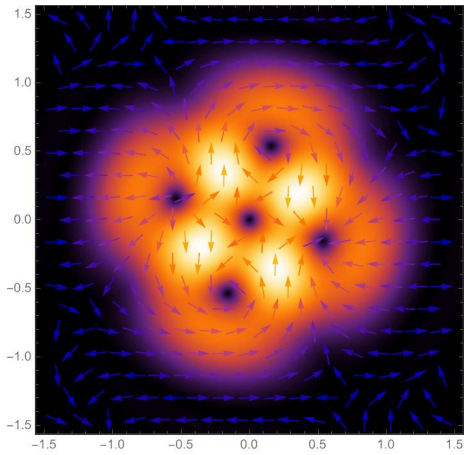

Fig. 1. Vector plot showing the (texture) distribution of the gradient torque due to the gradient of the real part of the optical helicity density for a second order ($m = 2$) radially-polarised Poincaré mode. Lengths are in units of beam waist w_0. This is one of the figures in a current article (in progress) [4]

IV. Conclusion

We have highlighted how vector twisted light leads to new different and versatile forms of matter manipulation. The versatility is enabled by the choice of any twisted light of any chosen form of wave polarizations and any of order. The useful outcomes are new types of optical forces and torques that can be used flexibly in the dynamics and trapping of matter and its use [5,6].

Acknowledgments

I am grateful to the co-investigators in this work whose names appear in the references below.

References

[1] Babiker M., K . Koksal, V. E. Lembessis and J. Yuan. “Intrinsic angular momentum, spin and helicity of higher order Poincare’ modes,” Journal of Optics, , Vol. 26, No. 11,115601 . 2024.
[2] Koksal, K., F. Tambag, J. Barakdar and M. Babiker “ Magneto-optical polarization texturing” Journal of Modern Optics, 1-9 2025.
[3] Bougouffa, S. and M. Babiker, “Absorption of hybrid fiber modes by Cs atoms in quadrupole transitions,” Journal of Physics B: Atomic, Molecular and Optical Physics, Vol. 56, No. 21, 215002, 2023.
[4] Babiker, M., and K. Koksal ”Optical torques due to higher order Poincar´e modes on a magneto-optic particle”, to be submitted.
[5] Lembessis, V. E., K. Koksal, M. Babiker and J. Yuan “ Minature atom bottle traps enabled by chiral doughnut light,” Optics Express, Vol. 32, No. 8, 13450–13466, 2025.
[6] Lembessis, V. E., J Yuan, K. Köksal, and M. Babiker” Time dilation effects in micron-size rotating optical Ferris-wheel traps” Phys. Rev. A. 112, p. 043503

Programmable Nanophotonics with the Plasmonic Phase-Change Material In_3SbTe_2

Lukas Conrads[1,*], Matthias Wuttig[1], Thomas Taubner[1]

[1]Institute of Physics (IA), RWTH Aachen University, Germany
*Corresponding author: conrads@physik.rwth-aachen.de

***Abstract*— We summarize our current research in active nanophotonics using the plasmonic phase-change material In_3SbTe_2 (IST) which exhibits a non-volatile insulator-to-metal transition upon crystallization. We highlight optical programming of functional metasurfaces for emissivity-shaping and infrared beam-shaping including holography, as well as tailoring polaritons on polar crystals and doped semiconductors.**

***Keywords*— phase-change material, metasurface, polaritons, reconfigurable.**

I. Introduction

Metasurfaces have evolved as versatile platforms for tailoring light-matter interactions. Combining metasurfaces with active materials such as phase-change materials (PCMs) [1] promises reconfigurable modifications of the metasurface functionalities. Conventional PCMs enable non-volatile resonance tuning based on a change in refractive index due to positive permittivity values in the amorphous and crystalline phases. The recently introduced plasmonic PCM In_3SbTe_2 (IST) features a plasmonic crystalline phase with negative permittivity in the entire infrared spectral range. [2,3] In contrast to conventional antenna resonance tuning based on a change in refractive index, IST allows for directly reconfiguring the shapes and sizes of the antennas to modify electromagnetic resonances accordingly.

II. Results and Discussion

Here, we now demonstrate rapid prototyping of large area metasurfaces for controlling thermal emissivity, beam steering, lensing and holography. Using a commercial direct laser writing setup, we locally switch the IST from an amorphous dielectric to a crystalline metallic phase. First, we show flexible encoding of different absorption/emission properties within a metasurface by patterning an adaptable grating absorber metasurface. [4] Moreover, we design a lithography-free narrowband and diffuse emitter based on a Fabry-Perot resonance with a switchable IST layer on top to turn on and off the emissivity of the device. [5]

Next, we exploit the geometric phase of rotated crystalline IST rod antennas in combination with circularly polarized light for designing and programming arbitrary phase profiles within the metasurface to realize a multitude of applications such as beam-steering, lensing, optical vortex beams and holography. [6] The fast writing procedure speeds up workflows and paves the way towards mass production of reconfigurable metasurfaces without cumbersome and time-consuming fabrication methods such as electron beam lithography.

Finally, we employ IST on top of the polar crystal SiC and the doped semiconductor CdO to launch and confine surface phonon polaritons and surface plasmon polaritons into laser-written resonators with the ability to modify the resonator shapes to tune the observable polariton modes. [7,8]

III. Conclusion

We have established the plasmonic PCM IST as a versatile platform in nanophotonics for direct programming and reconfiguring functional metasurfaces as well as polariton launching structures. The ability to directly program arbitrary shapes boosts fabrication of nanophotonic devices which conventionally require cumbersome and time-consuming techniques.

Acknowledgments

This work was supported by the Deutsche Forschungsgemeinschaft (DFG project 518913417 and SFB 917 Nanoswitches).

References

[1] Wuttig, M. et. al., “Phase-change materials for non-volatile photonic applications” Nat. Photon. 11, 465-476 (2017)
[2] Heßler, A. et al., “In_3SbTe_2 as a programmable nanophotonics material platform for the infrared” Nat. Commun. 12, 924 (2021)
[3] Conrads, L. et al., “Review: the plasmonic phase-change material In_3SbTe_2 for nanophotonics” Opt. Mat. Ex. 15, 2664-2687 (2025)
[4] Conrads, L. et al., “Reconfigurable and Polarization-Dependent Grating Absorber for Large-Area Emissivity Control Based on the Plasmonic Phase-Change Material In_3SbTe_2” Adv. Opt. Mat. 11, 8 (2023)
[5] Giteau, M, Conrads, L. et al., “Switchable Narrowband Diffuse Thermal Emission with an In_3SbTe_2 -Based Planar Structure” Laser Photonics Rev. 19, 2401438 (2025)
[6] Conrads, L. et al. “Infrared beam-shaping on demand via tailored geometric phase metasurfaces employing the plasmonic phase-change material In_3SbTe_2” Nat. Commun. 16, 3698 (2025)
[7] Conrads, L. et al., “Direct programming of confined surface phonon polariton resonators with the plasmonic phase-change material In_3SbTe_2” Nat. Commun. 15, 3472 (2024)
[8] Conrads, L. et al., “Real-space imaging of confined infrared surface plasmon polaritons on doped semiconductors covered with phase-change materials” Sci. Adv. 11, eadr6844 (2025)

Tailorable Light Driven Reaction with Phase-changing Material Metasurface

Ning Lyu[1,2,*], Anjalie Edirisooriya[2], Dawei Liu[3], Zelio Fusco[2], Shenyou Zhao[4], Fiona J. Beck[2], Christin David[1,5]

[1]Institute of Solid State Theory and Optics, Friedrich-Schiller-Universität Jena, Germany
[2]School of Engineering, Australian National University, Australia
[3]Department of Electronic Materials Engineering, Australian National University, Australia
[4]School of Electronic Engineering, Xi'an University of Posts and Telecommunications, China
[5]University of Applied Sciences Landshut, Germany
*Corresponding author: ning.lyu@uni-jena.de

***Abstract*— Phase-change metasurfaces are applied to manipulate light-driven reactions, enabling tunability using a Sb_2S_3 cavity. Plasmonic resonance supported by a Au nanodisk array determines the excited-electron population, and, when coupled with the tunable cavity, results in a 2.4-fold modulation of product yield, which illustrates the potential for reversible catalytic control.**

***Keywords*— Phase-changing material, tunable metasurface, light driven reactions, localized surface plasmonic resonance.**

I. Introduction

Phase-change materials (PCMs) provide a promising platform for tunable metasurfaces in energy applications[1]. In light-driven reactions, localized surface plasmonic resonance can govern reactivity by modulating the population of excited electrons in lowest unoccupied molecular orbitals[2], thereby selectively suppressing or enhancing specific products[3].

II. Methods and Results

Tunable metasurfaces exploit the phase-dependent refractive index of PCMs, which switch between amorphous and crystalline states under varying thermal conditions. Antimony sulfide (Sb_2S_3) is a promising PCM, owing to its suitable bandgap (~1.2 eV) and strong visible-light absorption. Fig. 1A illustrates the reversible phase-switching mechanism: crystallization occurs when amorphous Sb_2S_3 (a-Sb_2S_3) is heated above the activation energy, whereas amorphization is achieved by heating crystalline Sb_2S_3 (c-Sb_2S_3) above its melting point followed by rapid quenching[4].

Figure 1B shows a PCM-based tunable metasurface where the cavity material supports constructive interference in the amorphous phase. The cavity resonance hybridizes with the plasmonic resonance of a Au nanodisk array on top, enhancing plasmonic coupling and thereby increasing near-field strength and hot-electron populations[5]. In contrast, crystallization of Sb_2S_3 alters the refractive index to support destructive interference, weakening coupling to the plasmonic resonance.

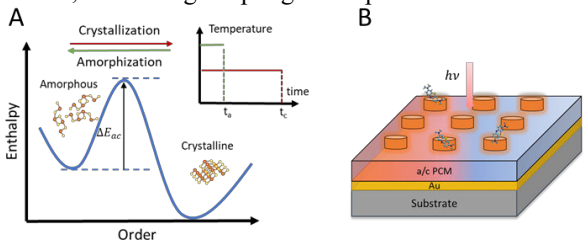

Fig. 1 A. Enthalpy–structure order diagram of Sb_2S_3. B. configuration of Au ND coupled PCM cavity.

The metasurface absorption is measured by a micro-spectrophotometer. At the effective wavelength of 633 nm of the targeted reaction, a 40% absorption difference is observed between a/c-Sb_2S_3 states. Consequently, the tailored resonance enables catalytic control, as demonstrated using methylene blue (MB) degradation as a model reaction. Surface-enhanced Raman spectroscopy reveals a 2.4-fold enhancement in reactivity upon phase switching.

III. Conclusion

A tunable PCM metasurface enables reversible control of the plasmonic resonance strength via phase transitions. Phase-induced refractive index changes drive mode hybridization with cavity resonances, allowing precise modulation of catalytic yield under identical illumination.

Acknowledgments

This work is supported by the German Research Foundation DFG through funding of the IRTG 2675 (GEPRIS 437527638).

References

1. Delaney, M., et al. *Adv Funct Materials* **30**, (2020).
2. Lyu, N. *et al. ACS Nano* **19**, 25821–25829 (2025).
3. Fusco, Z., et al. in *Semiconductors and Semimetals* vol. 115 149–179 (Elsevier, 2024).
4. Dong, W. *et al. Adv Funct Materials* **29**, 1806181 (2019).
5. Lyu, N. *et al. Advanced Optical Materials* e03650 (2026).

Hot Carriers in Balance: Molecularly Functionalised Nanogaps Resolve Wavelength-Dependent Plasmonic Charge Generation

Ishaan Lohia[1], Santiago Rodríguez-Jiménez[1,2], Charlie Readman[1,2], Christine Joy Querebillo[1,2], Rowena Davies[1], Gregory Q. Wallace[3], Duncan Graham[3], Erwin Reisner[2], Bart de Nijs[1,*]

[1]Physics for Sustainable Chemistry Group, Cavendish Laboratory, Department of Physics, University of Cambridge, Cambridge, UK

[2]Yusuf Hamied Department of Chemistry, University of Cambridge, Cambridge, UK

[3]Department of Pure and Applied Chemistry, Technology and Innovation Centre, University of Strathclyde, Glasgow, UK

*Corresponding author: bd355@cam.ac.uk

***Abstract*— Self-assembled, broadband absorbing nanoparticle films with ~1 nm plasmonic nanogaps reveal wavelength-dependent hot carrier generation. Carriers are tracked at steady-state timescales using electrochemical photovoltage spectroscopy. Molecular control over carrier extraction is demonstrated through chemical functionalisation of nanogaps. Plasmon-enhanced hot electron generation extends from visible to near-infrared wavelengths (>800 nm).**

***Keywords*— plasmonic nanogaps; hot carrier dynamics; self-assembly; electrochemical spectroscopy; solar energy conversion**

I. Introduction

Hot carrier generation in plasmonic nanostructures offers a route to extend solar-driven photocatalysis across the visible spectrum and even into the near-infrared. Extreme optical field enhancement in ~1 nm nanogaps facilitates the efficient generation and harvesting of hot carriers for photochemistry. Resolving carrier behaviour remains challenging due to their short lifetimes, but steady state analysis under extreme plasmonic confinement unveils important mechanistic insights.

II. Methods

Mono-/Multi-layer aggregate films (MLAggs) of Au nanoparticles are formed through self-assembly. Using rigid redox-active or redox-inert linker molecules, billions of highly reproducible nanogaps are formed in our large-area samples (~1 cm^2). We introduce *electrochemical photovoltage spectroscopy* (EC-PVS), a novel use of electrochemical open cell potential monitoring under monochromatic VIS-NIR illumination, to spectrally resolve plasmonic charge carrier generation and extraction on steady-state timescales.

III. Results and Discussion

Experimental results show:

- Strong, broadband absorption in ~20 nm thick MLAggs
- Distinct interband and intraband hot carrier mechanisms
- Hot carrier extraction by redox-functionalised nanogaps
- Plasmon-enhanced hot carrier generation and extraction from 450-850 nm

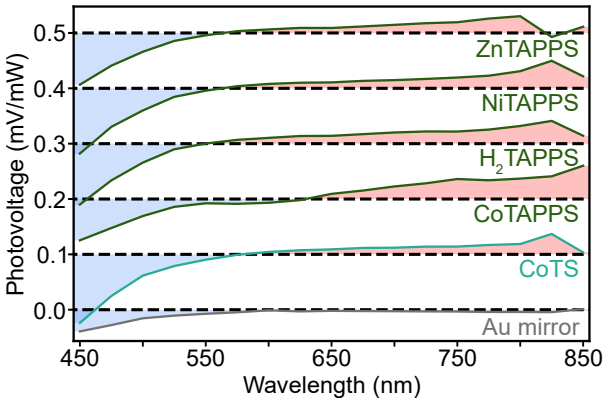

Fig. 1: Photovoltage spectra of chemically distinct MLAggs

IV. Conclusion

This work demonstrates that molecularly functionalised self-assembled plasmonic aggregates exhibit enhanced, broadband hot carrier generation and extraction, and introduces electrochemical photovoltage spectroscopy as a facile technique for tracking wavelength-dependent carrier behaviour, advancing the tools for molecular catalysis and nanoscale optical energy utilisation for full solar spectrum photocatalysis.

Acknowledgments

This work was supported by UK Research and Innovation, the Royal Society, the UK Department of Science, Innovation, & Technology, the Harding Distinguished Postgraduate Scholarship, the Winton Programme for the Physics of Sustainability, and the Royal Academy of Engineering.

References

[1] I. Lohia, S. Rodríguez-Jiménez, C. Readman, C. Joy Querebillo, R. Davies, G. Q. Wallace, D. Graham, E. Reisner, and B. de Nijs, "Hot Carriers in Balance: Molecularly Functionalized Nanogaps Resolve Wavelength-Dependent Plasmonic Charge Generation," ACS Nano, *in review*.

Solution-Processed Quantum Light Sources Spanning the Visible to the Infrared

Jennifer A. Hollingsworth,[1,*] Eric G. Bowes,[1] Han Htoon[1]

[1]Center for Integrated Nanotechnologies, Los Alamos National Laboratory, USA
*Corresponding author: jenn@lanl.gov

***Abstract*— By synthetically controlling colloidal semiconductor nanocrystal heterostructure we have made significant progress toward an ideal quantum emitter – on-demand (blinking- and bleaching-free), high-purity, room-temperature, spectrally tunable (blue-visible to telecommunications wavelengths) single-photon sources. More recently, we have engineered brightness (emission speed and directionality), chirality, polarization and photon indistinguishability through advanced nanointegration.**

***Keywords*— quantum dots, nanoantennas, single-photon source.**

I. Introduction

We synthetically control nanocrystal heterostructure to advance colloidal quantum dots (QDs) as functional, nearly ideal quantum emitters. We have further aimed to influence brightness (speed and directionality), chirality, polarization and photon indistinguishability using external environmental effects, a strategy generally outside the control of the chemist.

II. Methods

Our methodology combines precision synthesis with scanning-probe nanointegration to realize novel properties. We establish and utilize synthesis-structure-function correlations to design next-generation QD building blocks, characterized using advanced single-nanostructure optical spectroscopy and microscopy, as well as a suite of structural and chemical techniques that combine single-nanostructure and ensemble methods for a rigorous, systematic analysis of key correlations "from the inside-out" (Figure 1).[1] Lastly, we advance additive,[1] subtractive[2] and "one-pot"[3] shell-growth strategies as required by material system.

III. Results and Discussion

Through synthesis alone, we have achieved photons-on-demand. Our "giant" or thick-shell core/shell QDs (gQDs) are non-blinking and non-photobleaching.[1,2] With collaborators we take advantage of this unusual stability to construct highly directional, radially polarized and/or fiber-coupled single-photon sources by placing single gQDs into bullseye antennas using scanning probe direct-write nanolithography.[4,5] Alternatively, in a separate collaboration, we have realized ultrafast (to 65 ps) and ultrabright (to ~12.6 MHz) room-temperature single-photon emission in the O and C telecommunications bands via coupling stable PbS/CdS QDs to solution-processed plasmonic nanocavities.[6]

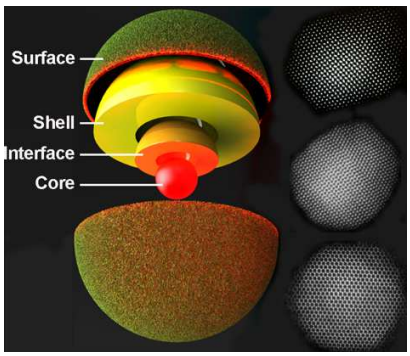

Fig. 1 Schematic illustration of the components of the core/shell QD "from the inside out." Aberration-corrected HAADF-STEM images of QDs used to study synthesis-structure-function correlations.

IV. Conclusion

Using synthesis and nanointegration, we have demonstrated new single-photon sources that provide photons-on-demand, record collection efficiencies and ultrafast photon generation.

Acknowledgments

This work was performed in part at the Center for Integrated Nanotechnologies (CINT), US DOE NSRC and User Facility, and partially supported by the US DOE OS BES *CHIME* Microelectronics Science Research Center (MSRC).

References

[1] A. Singh, et al., "From Inside Out: How the Buried Interface, Shell Defects, and Surface Chemistry Conspire to Determine Optical Performance in Nonblinking Giant Quantum Dots," Small Sci. Vol. 3, 2300092-1-14, 2023.

[2] S. Krishnamurthy, et al., "PbS/CdS Quantum Dot Room-Temperature Single-Emitter Spectroscopy Reaches the Telecom O and S Bands via an Engineered Stability," ACS Nano, Vol. 15, pp. 575-587, 2021.

[3] J. Geisenhoff, et al., "One-Pot Synthesis of HgSe/CdSe Core/Shell Heterostructures: A Fast and Stable Source of Photons in the Telecom Band," In preparation 2026.

[4] H. Abudayyeh, et al., "Single photon sources with near unity collection efficiencies by deterministic placement of quantum dots in nanoantennas," APL Photonics vol. 6, pp. 036109-1-7, 2021.

[5] B. Lubotzky, et al., "Room-Temperature Fiber-Coupled Single-Photon Sources based on Colloidal Quantum Dots and SiV Centers in Back-Excited Nanoantennas," Nano Lett. Vol. 24, pp. 640-648, 2024.

[6] S. Zhang, et al., "Solution-Processed Ultrafast, Room-Temperature Single-Photon Source at 1550 nm," ACS Nano, Vol. 19, pp. 19035-19045, 2025.

SELF-POWERED REFRACTORY NIR PLASMONIC PHOTODETECTORS WITH COMPACT, BROADBAND, AND QUANTITATIVE SPECTROSCOPY

Eslam Abubakr [1*], Shiro Saito [2], Hironori Suzuki [2], Tetsuo Kan [1]
[1] *The University of Electro-Communications, Tokyo, Japan*
[2] *IMRA JAPAN CO., LTD., Kariya, Aichi 448- 8650, Japan*
[*] abubakr_eslam@kyudai.jp

***Abstract*— This paper presents a self-powered, chip-scale near-infrared spectroscopic device with broadband, filter-free detection with high responsivity, spectral selectivity, and proportional intensity scaling. Broadband detection covering the NIR spectrum, surpassing conventional Si-bandgap limitations, operating at room temperature and zero bias, with high correlation when benchmarked against commercial FTIR measurements.**

***Keywords*— Surface plasmon resonance (SPR), NIR photodetector, Miniaturized spectrometer.**

I. Introduction

The study builds on previous efforts in NIR plasmonic photodetection, particularly the embedded grating structures [1]. Our earlier reports [2] established a solid foundation for NIR detection; however, the responsivity was limited to a few tens of μA/W, and spectroscopy beyond 1400 nm remained unproven. Additionally, device lifetime was constrained due to unstable interface properties, plasmonic shifts, and reliability concerns. This work advances these results by extending detection across a broader portion of the NIR spectrum—nearly covering the entire range—using a single tunable device. Interface modifications improved long-term stability, enabling reliable operation for over two years. Moreover, the device achieves high sensitivity and accurate spectral reconstruction at room temperature, providing a scalable, CMOS-compatible platform. These improvements represent a significant step forward, promoting device applications in gas detection and elemental identification based on absorption signatures beyond NIR-II, which are hardly achieved using conventional Si-based detectors.

II. Methods

Device geometry was optimized through extensive modeling and experimental validation to achieve wavelength-specific plasmonic photodetection, ensuring high selectivity. The diffraction grating was patterned onto the Si surface through electron beam lithography and dry etching processes. Sequential depositions of Ti/Mo interlayer and top gold (plasmonic) metals were performed using an EB evaporation system. The device is then established on a vibrating cantilever structure as shown in Fig. 1, where the device angle (incidence angle) is changed through an acoustic vibration, and a photocurrent signal is captured.

III. Results and Discussion

Combining Ti/Mo interlayer in the plasmonic structure broadened the device operation range, owing to modifying the barrier height and interface properties. This facilitates the transport of low-energy photogenerated carriers (less than 25 μW at 1900 nm), while maintaining high linearity and sensitivity as shown in Fig. 2. It further demonstrates clear SPR peaks even with parallel exposure to visible light. It maintained higher stability with neither hysteresis nor deterioration in photocurrent measurements over 700 days. The sharp and selective SPR peaks facilitated the expansion of the spectral range for reconstructive spectroscopy to longer wavelengths (Fig. 3(a)). Since the degree of surface sensitivity can be controlled by collecting photoelectrons emitted at different emission angles to the surface plane, the reconstruction of multiple parallel incident wavelengths could be successfully demonstrated (Fig. 3(b)). Making it a powerful technique for investigating the electronic and chemical structures. High sensitivity and stable responsivity even at low light intensity (Fig 4(a, b)), with fast switching capabilities of 25μs (Fig. 4 (c)), are demonstrated. Filter-free quantitative spectroscopy closely matched the performance of a commercial spectrometer (Fig. 4(d)), with long-term stability and durability testing demonstrating less than a 5% decline in responsivity with no observable plasmonic shift. Meanwhile, conventional devices exhibited a plasmonic shift in SPR peaks of 1.5° per SPR peak and a responsivity reduction exceeding 30%. This research represents a significant leap in NIR photodetection and spectroscopy, with far-reaching implications across applications for various scenarios such as gas sensing and environmental monitoring.

IV. Conclusion

We demonstrated a compact Schottky-based photodetector for reconstructive spectroscopy. The system accurately reconstructed incident spectra with high robustness, achieving over 90% correlation with a commercial FTIR spectrometer, while eliminating optical filters and multiple detectors to significantly reduce system footprint. The angle-tuning scheme is inherently compatible with MEMS actuation, providing a clear pathway toward fully miniaturized, high-precision SPR-based spectroscopic systems.

Acknowledgments

This work was supported by “Advanced ResearchInfrastructure for Materials and Nanotechnology in Japan” of the Ministry of Education, Culture, Sports, Science and Technology (MEXT).

References

[1] E. Abubakr, et al., Opt. Mater., vol. 150, 2024.
[2] Tetsuo Kan et al., Microsystems Nanoeng.,9,2023
[3] Y. Yamamoto, et al., ACS Appl. Nano Mater., vol. 4, no. 12, pp. 13405

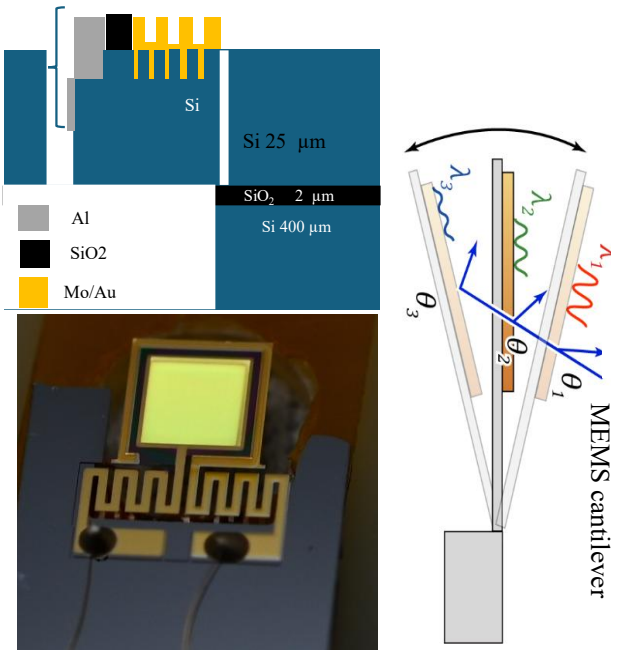

Figure 1: (a) Schematics of the fabricated device through lithography process with an image to show the final device cantilever fabricated structure.

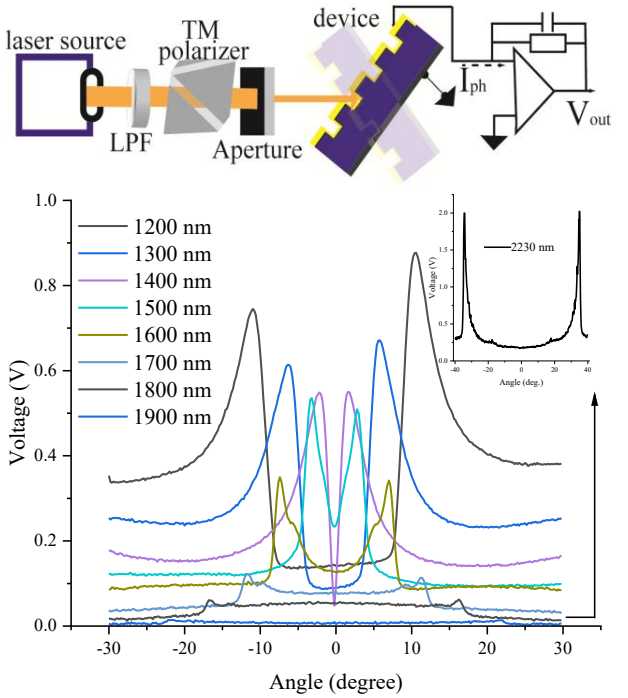

Figure 2: High linearity and selectivity of the output photocurrent signal. The upper inset shows the experimental setup.

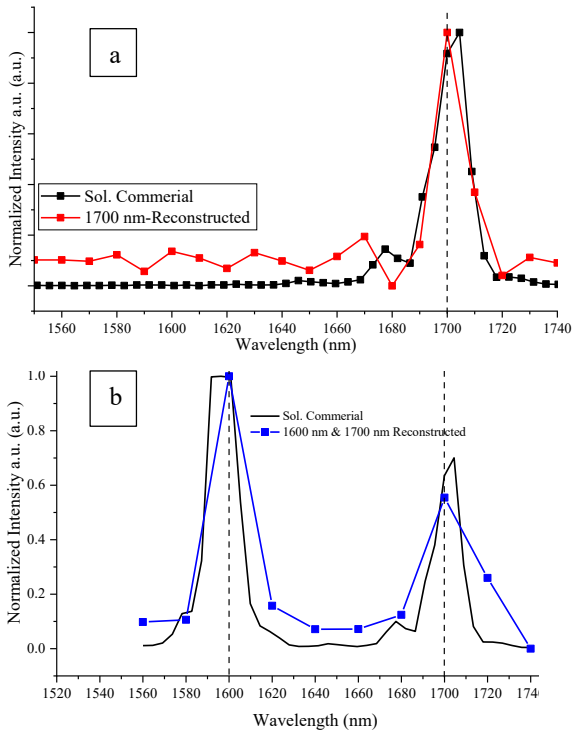

Figure 3: Accurate reconstruction of input light spectrum (vector components of the incident light intensity) through inverse calculation and compared to that captured through a commercial spectrometer.

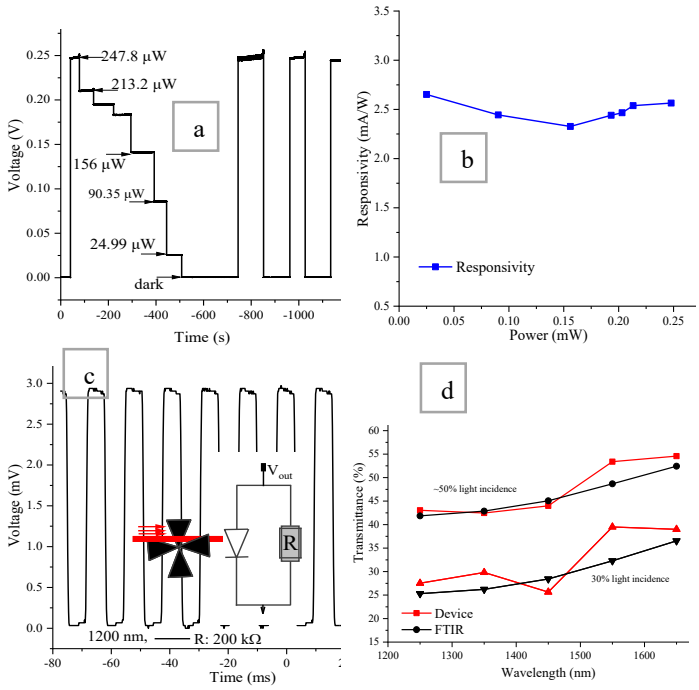

Figure 4: a) Device response following varying light intensities, and while (b) maintaining nearly the same responsivity, c) the device's transient response while chopping the incident light at high-speed using the setup shown in the inset. D)Transmittance comparison under varying incident power for commercial and proposed devices

Bound-State-in-the-Continuum Lasing Modes in InGaAs Nanowire Photonic Crystals

Bogdan-Petrin Ratiu[1], Ji Tong Wang[2], Kyle S. Netherwood[1], Nicolae C. Panoiu[2], Qiang Li[1], Sang Soon Oh[1*]

[1]School of Physics and Astronomy, Cardiff University, Cardiff, United Kingdom
[2]Department of Electronic & Electrical Engineering, University College London, London, WC1E 6BT UK
*Corresponding author: OhS2@cardiff.ac.uk

***Abstract*—We experimentally demonstrate bound-state-in-the-continuum lasing modes in deformed honeycomb-lattice nanowire photonic crystals. From the spatial distribution of local polarization, we extract and identify the associated topological charges of the lasing modes.**

***Keywords*— BIC modes, photonic crystal surface emitting lasers, photonic topological insulators.**

I. Introduction

Topological photonics allows for new designs for topological edge mode lasing, e.g., valley-Hall photonic crystal lasers [1]. Alternatively, these new designs can be used for vertically emitting lasers based on semiconductor nanowires, e.g., a deformed honeycomb lattices. Bound-states-in-the-continuum (BICs) can be used for enhancing non-linear effects with enhanced Q factors [2]. These BIC modes appear as a singular point with a topological charge in the far-field radiation pattern showing extremely high Q factors [3].

In this work, we experimentally demonstrate BIC lasing modes in epitaxially grown InGaAs nanowires. By characterizing the far-field emission patterns, we successfully identify a topological charge of -2.

II. Methods

We design the nanowire lasers by deforming the hexagons in honeycomb lattices of InGaAs nanowires. The undeformed honeycomb lattice has the periodicity a = 640 nm and the centre-to-centre distance $R = a/3$ = 213 nm. For extended honeycomb structures, we set R = 230 nm and R = 190 nm respectively. To fabricate the laser, we use the selective area epitaxy method which employs a 20 nm SiN mask with an array of air holes with the diameter of 30 to 50 nm to define the location of the InGaAs nanowires.

As reported in Ref. [4], the two band edges have different symmetries where p-orbital (d-orbital)-like are at the top (bottom) band edge. The doubly degenerate d-orbital like band edge mode is a quadrupolar mode and, importantly, is a BIC mode with a high Q factor. The radiation pattern was measured using the back-focal plane measurement.

III. Results and Discussion

As shown in Fig.1, the optically pumped lasing from the extended honeycomb lattice exhibits a characterisitic doughnut-shaped radiation pattern. Upon rotating the polarizer counterclockwise by 90°, the emission pattern of the quadrupolar modes is observed to rotate clockwise by 45°. This confirms the topological charges of the lasing modes is -2, which is consistent with the theoretical prediction in Ref. [5].

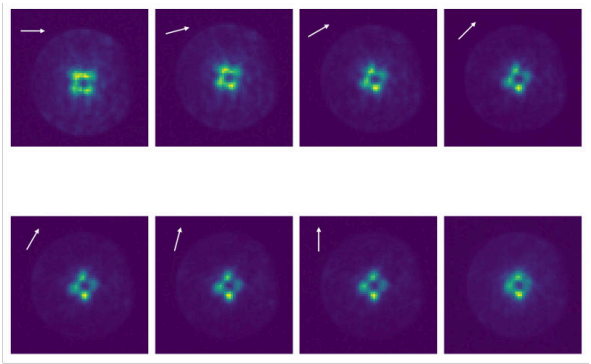

Fig. 1. Far field lasing pattern polarization dependence for an expanded lattice.

IV. Conclusion

We have demonstrated BIC lasing modes using epitaxially grown InGaAs nanowire photonic crystals. The topological charge -2 of the quadrupoloar modes has been confirmed using far-field measurement.

Acknowledgments

This work was supported by the EPSRC Manufacturing Hub (Grant No. EP/Z532848/1).

References

[1] Y. Gong, S. Wong, A. J. Bennett, D. L. Huffaker, and S. S. Oh, "Topological insulator laser using valley-Hall photonic crystals," *ACS Photonics*, vol. 7, no. 8, pp. 2089–2097, 2020.

[2] J. T. Wang *et al.*, "Giant second-harmonic generation in monolayer MoS_2 boosted by dual bound states in the continuum," *Nanophotonics*, vol. 13, no. 18, pp. 3437–3446, 2024.

[3] B.-P. Ratiu, J. T. Wang, K. Netherwood, T. Grieb, A. Rosenauer, S. S. Oh, N.-C. Panoiu, and Q. Li, "Vortex beam lasing from III–V nanowires epitaxially grown on silicon-on-insulator," *Laser & Photonics Reviews*, p. e01297, 2025.

[4] L.-H. Wu and X. Hu, "Scheme for achieving a topological photonic crystal by using dielectric material," *Physical Review Letters*, vol. 114, p. 223901, 2015.

[5] B. Zhen, C. W. Hsu, Y. Igarashi, L. Lu, I. Kaminer, and M. Soljačić, "Topological nature of optical bound states in the continuum," *Physical Review Letters*, vol. 113, p. 257401, 2014.

Circularly polarized Raman scattering for optical spin detection in silicon metasurfaces

Guillermo Serrera[1,*], Rasmus H. Godiksen[2], Lex M. Dedding[2], Tom T. C. Sistermans[3], Ershad Mohamaddi[2], T. V. Raziman[2], Søren Raza[4], Pablo Albella[1] and Alberto G. Curto[2,3]

[1] Department of Applied Physics, University of Cantabria, Spain.
[2] Department of Applied Physics, Eindhoven University of Technology, The Netherlands.
[3] Photonics Research Group & Center for Nano- and Biophotonics, Ghent University-imec, Belgium.
[4] Department of Physics, Technical University of Denmark, Denmark.

*Corresponding author: guillermo.serrera@unican.es

***Abstract*— We use polarization-resolved Raman scattering to probe optical spin in silicon metasurfaces under circular excitation. By tuning disk size and wavelength, we observe strong Raman enhancement with far field polarization losses. Simulations show that quadrupolar resonances spatially varying near fields that depolarize the emitted Raman signal.**

***Keywords*— high-index dielectric metasurfaces, Raman scattering, circular polarization, Mie resonances.**

Nanostructured dielectric metasurfaces provide a powerful platform for tailoring polarization in light–matter interactions for advanced photonic functionalities [1]. However, experimentally accessing the polarization state of optical evanescent fields remains challenging. Raman scattering in silicon, with a well-known polarization response in bulk [2], is an attractive way to address this issue. Despite Raman signal enhancements have been widely demonstrated in nanophotonic structures with strong electromagnetic confinements, its polarization response in such situations remains unexplored [3].

Here, we experimentally explore Silicon on Sapphire disk metasurfaces with polarization-resolved Raman spectroscopy (Fig. 1a). Using circularly polarized light for illumination, we relate the measured Raman enhancement and its Degree of Circular Polarization (DOCP) to Mie resonances in the metasurface, and we link these to the internal field optical spin with numerical simulations.

Our experimental results show, in different metasurfaces:
- Strong Raman enhancement with high DOCP.
- Strong Raman enhancement with strong DOCP losses.

Simulations, together with multipolar analysis, show:
- A good agreement between simulation and experiment.
- DOCP drops connected to angled collection in moderate NA objectives.
- Intrinsic loss of DOCP related to quadrupolar resonances in the metasurface (Fig. 1b).

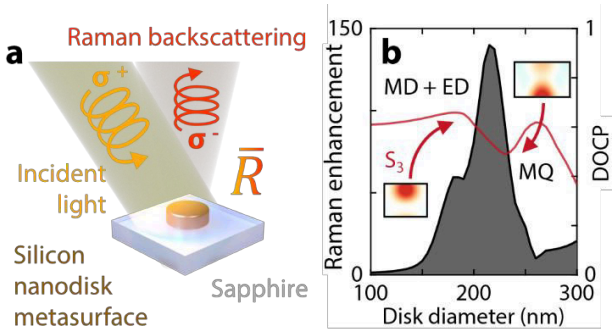

Fig 1. a) Concept art of the studied metasurface. b) Correlation of Raman enhancing resonances with DOCP in simulations.

In conclusion, quadrupolar modes produce complex near-field distributions with spatially varying optical spin, leading to polarization loss in the Raman emission. Polarization-resolved Raman scattering is a useful probe of near-field polarization and optical spin in dielectric nanophotonic systems.

Acknowledgments

This work was supported by the CHANSON European Research Council Starting Grant (ID: 948804), as well as the MOPHOSYS project (PID2022-139560NB-I00) from the Spanish Agencia Estatal de Investigación. G. S. thanks the Spanish Ministry of Education for his predoctoral contract grant (FPU21/02296).

References

[1] J. P. B. Mueller, N. A. Rubin, R. C. Devlin, B. Groever, and F. Capasso, "Metasurface Polarization Optics: Independent Phase Control of Arbitrary Orthogonal States of Polarization," Physical Review Letters, vol. 118, 113901, 2017.
[2] A. B. Talochkin, Journal of Raman Spectroscopy, vol. 5, pp. 201–206, 2021.
[3] S. Raza and A. Kristensen, "Raman scattering in high-refractive-index nanostructures," Nanophotonics, vol. 10, pp. 1197–1209, 2021.

Boosting nonlinear optical response in resonant metal-dielectric metasurfaces at visible and UV spectrum

Crina Cojocaru[1*], Shroddha Mukhopadhyay, Michael Scalora[2], Jose Trull[1]

[1]Department of Physics, Universitat Politècnica de Catalunya, Rambla Sant Nebridi 22, 08222 Terrassa, Spain
[2]Department of Information Engineering – University of Brescia, Via Branze 38, 25123 Brescia, Italy
*Corresponding author: crina.maria.cojocaru@upc.edu

***Abstract*—We present a experimental and theoretical study of plasmon-assisted harmonic generation in the visible and ultraviolet ranges. Our results are supported by a microscopic hydrodynamic model describing the nonlinear interaction at metal surfaces. This work is part of an ongoing effort to explore frequency conversion in metallic metastructures, with emphasis on efficiency, tunability and applications.**

***Keywords*— nonlinear optics, gold metasurfaces, plasmonics, harmonic generation.**

I. Introduction

Nonlinear (NL) frequency conversion in metals has been a cornerstone of nonlinear optics research since the field's inception, driven by the large third-order susceptibilities of plasmonic materials despite their inherent absorption in the visible (VIS) and near-infrared (NIR) spectral ranges. Rapid advances in nanofabrication techniques have enabled the precise design of subwavelength resonant optical metamaterials. Under resonant conditions, plasmonic nanostructures induce strong spatial confinement of the electromagnetic field in the vicinity of the metal surface, that significantly enhances light–matter interactions, leading to large surface nonlinearities and increased frequency conversion efficiencies. The resonant response is governed by both geometrical parameters and intrinsic material properties, including the dielectric functions of the metal and surrounding media at the operating wavelength [1]. Despite this fabrication progress, a comprehensive understanding of how the materials commonly used in photonic nanostructures respond to linear and nonlinear excitation by ultrashort laser pulses across different spectral ranges remains incomplete.

Recently, we have conducted systematic experimental and theoretical studies of the NL optical behavior of metals, achieving a deeper understanding of the fundamental physical mechanisms governing their response [2]. In particular, measurements of second harmonic (SH) and third-harmonic (TH) generation from 20nm and 70nm thick gold nanolayers have enabled the extraction of intrinsic material properties [3]. Studies performed on layers only a few nanometers thick eliminate common simplifying approximations and reveal additional interaction mechanisms that must be incorporated into accurate theoretical models. These insights provide a solid foundation for interpreting NL optical effects in more complex nanostructured structures.

The NL conversion efficiency of a simple metallic nanolayer is typically very low, but it can be significantly enhanced in carefully designed metasurfaces by exploiting plasmonic resonances. Under resonant conditions, plasmonic nanostructures can induce strong spatial confinement of the electromagnetic field near the metal surface. Strong plasmonic interactions substantially enhance light–matter coupling and can excite large surface nonlinearities, giving rise to efficient harmonic generation.

II. Results and Discussions

We first investigated 2D Au nanogratings exhibiting reflection resonance tunable from 700 nm to 1100 nm. We measured the SH and TH generation as a function of the input wavelength, tuned around the resonance at 800 nm. The generated SH (400 nm) and TH (266 nm) signals are shown in Fig.1. The total SH efficiency of the grating is approximately 1400 times larger than that of a planar gold nanolayer. Likewise, the total TH efficiency exhibits an enhancement factor of nearly 4000. Reflected SH efficiencies were also measured around 1000 nm and 1100 nm, yielding comparable enhancement factors. Extensive numerical simulations were performed using our theoretical model, yielding SH and TH enhancement factors in excellent agreement with the experimental results. The simulations accurately reproduce the spectral shape, bandwidth, and peak amplitude of the measured NL response, demonstrating near-perfect correspondence between theory and experiment. [4]

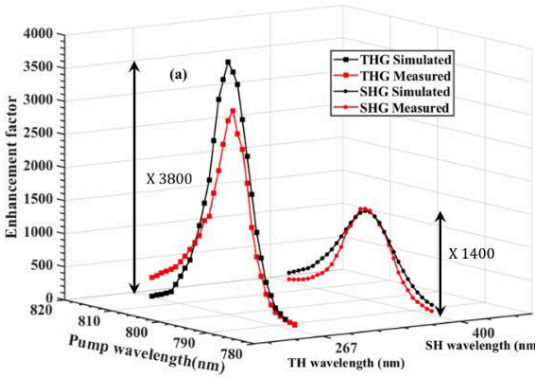

Fig. 1. SH and TH harmonic generation enhancement from a 2D gold grating.

We extend our investigation to a more sophisticated quasi-3D metasurface consisting of nanoholes patterned in gold nanolayers deposited on a structured polymer substrate (Figs. 2a and 2b). While this architecture offers increased flexibility in tuning and shaping the plasmonic resonance, our results indicate that it yields a lower NL enhancement compared to the simpler nanograting structures. Figure 2c shows a narrow plasmonic resonance cantered around 790 nm. The resonance depth and spectral position depend sensitively on the geometrical parameters of the system and the thickness of the gold layer deposited on top.

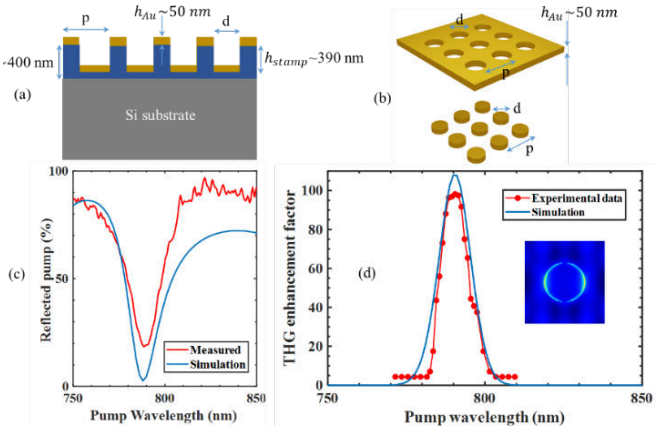

Fig. 2 (a) 2D side schematic of the crystal; (b) 3D view of the two Au layers; (c) the plasmonic resonance at normal incidence (d) Simulated and experimentally detected enhancement profile of the THG around the wavelength of resonance.

We detect and quantify the THG efficiency, and corroborate our theoretical and experimental observations of shape, spectral width, and maximum amplitude of the spectral response. The total efficiency, when scaled to the TH reference signal originating from the unpatterned portion of the gold sample, measured exactly in the same experimental conditions, gives us an enhancement factor of 100 (Fig.2(d)). [5]

III. CONCLUSIONS

We demonstrate two and three orders of magnitude enhancement of the SH and TH generation in different gold metasurface in the visible and deep-UV regime, despite their inherent absorption in these ranges. Precise engineering of metasurface and modern fabrication methods promise very well-tailored plasmonic structures and is the way to produce compact UV light sources embedded with nonlinear components, which represent a crucial step toward the realization of coherent and efficient nanoscale deep-UV light sources.

ACKNOWLEDGMENTS

This work was supported by the Spanish Agencia Estatal de Investigación from Ministerio de Ciencia, Investigación y Universidades (PID2023-148620NB-I00).

REFERENCES

[1] S. Mukhopadhyay, L. Rodriguez-Suné, C. Cojocaru, et al, "Three orders of magnitude enhancement of second and third harmonic generation in the visible and ultraviolet ranges from plasmonic gold nanogratings", APL Photonics **8**, 046108 (2023).

[2] M. Scalora, J. Trull, C. Cojocaru, et al, J. Opt. Soc. Am B 36, 2346 (2019).

[3] L. Rodriguez-Suñé, J. Trull, C. Cojocaru, Opt. Express 29, 8581 (2021).

[4] Mukhopadhyay, S. *et al.* Three orders of magnitude enhancement of second and third harmonic generation in the visible and ultraviolet ranges from plasmonic gold nanogratings. APL Photonics **8**, 046108 (2023).

[5] Mukhopadhyay, S. *et al.* Gold-polymer hybrid metasurface for polarization-independent enhanced third harmonic generation in the UV, Scientific Reports 16:8362 (2026).

Advancements in Chiral Nanophotonics via Block Copolymer Supramolecular Assembly and Plasmonic Antenna-Reactor Catalysis

Dong Ha Kim*

Department of Chemistry and Nanoscience, Ewha Womans University, Seoul 03760, Korea
*Corresponding author: dhkim@ewha.ac.kr

***Abstract*— We report chiral supramolecular assemblies from star-shaped block copolymers and chiral molecules enabling stable, full-color circularly polarized luminescence with tunable directionality for advanced optical devices. We further develop chiral plasmonic nanomaterials for optically controlled catalytic cancer therapy and spin-polarized electrocatalysts for efficient, durable acidic water electrolysis toward sustainable hydrogen production.**

***Keywords*— chirality, block copolymer, supramolecular self-assembly, plasmonic antenna-reactor, water splitting.**

I. Introduction

Chirality has emerged as a powerful design principle for controlling light–matter interactions, charge transport, and catalytic reactivity at the nanoscale. By integrating structural asymmetry with functional nanomaterials, it becomes possible to manipulate circularly polarized photons, spin-polarized electrons, and plasmon-enhanced electromagnetic fields within a unified platform.

Beyond optical functionality, chiral plasmonic nanostructures enable dynamic regulation of catalytic processes under circularly polarized light. These developments establish chirality-guided nanomaterials as a versatile framework bridging advanced optoelectronics, precision nanomedicine, and clean energy catalysis.

II. Methods

Chiral supramolecular assemblies were constructed via controlled self-assembly of star-shaped block copolymers with chiral small molecules, followed by structural and CPL characterization. Chiral plasmonic nanoparticles were synthesized through ligand-directed growth and circularly polarized light modulation, then integrated with catalytic or single-atom sites. Optical, electrochemical, and biological assays evaluated performance.

III. Results and Discussion

Hierarchical self-assembly produced well-defined chiral nanostructures exhibiting strong, tunable circularly polarized luminescence across the visible spectrum with enhanced stability, overcoming prior red-emission limitations. Under circularly polarized light, chiral plasmonic nanoparticles showed handedness-dependent field enhancement, enabling selective amplification of enzyme-mimetic catalytic cascades and significantly improved tumor cell inhibition. In electrochemical systems, integrating chiral Au nanostructures with single-atom iridium centers induced spin-polarized charge transfer, lowering overpotentials and accelerating reaction kinetics in acidic water electrolysis.

IV. Conclusion

These studies establish chirality as a unifying strategy to control photons, plasmons, and spin-polarized electrons at the nanoscale. Hierarchical supramolecular and plasmonic architectures enable advanced circularly polarized emission, optically programmable cancer therapy, and efficient acidic water electrolysis, demonstrating broad potential across photonics, biomedicine, and sustainable hydrogen energy technologies.

Acknowledgments

This work supported by National Research Foundation of Korea (NRF) funded by the Ministry of Education (RS-2021-NR060138) and by NRF grant funded by the Korea government (MSIT and MOE) (No. RS-2025-16063688).

References

[1] M. Kim,§ M. Zhang,§ Y.-L. Zhu, Y. Yan, X. Pu, W. Choi, S. Chung, K. Cho, J. Kim, V. Tsukruk, Z. Yang,* N. A. Kotov,* Z.-Y. Lu,* D. H. Kim,* Z. Lin,* "Hierarchical Chiral Supramolecular Assemblies with Strong and Invertible Chiroptical Properties", Science 2025, 389(6761), 699.

[2] K. Chae, H. Lee, W.-T. Huang, J. Son, J. Kim,* J. Moon,* R.-S. Liu,* J. Bang,* D. H. Kim,* "Spin-polarized Acidic Water Electrolysis with Antenna-Reactor Plasmonic Electrocatalysts", Adv. Mater. 2025, 37(39), 2507658.

[3] S. Yu, D. Jang, H. E. Kang, H. Lee, J. Park, H. Choi, W.-T. Huang, M. Kim, K. Chung, R.-S. Liu, J. Bang,* S. Kim,* L. P. Lee,* Dong Ha Kim,* "Photoinduced Plasmon Electron Transfer-based Bioorthogonal Cleavage Reaction for Precision Tumor Therapy", Adv. Mater. 2025, 37(47), 2418134.

Tailoring Light-Sound Interactions in Photonic Integrated Circuits

Moritz Merklein[1,2,3,*]

[1]Institute of Photonics and Optical Science (IPOS), School of Physics,
The University of Sydney, NSW 2006, Australia
[2]The University of Sydney Nano Institute (Sydney Nano),
The University of Sydney, NSW 2006, Australia
[3]ARC Centre of Excellence in Optical Microcombs for Breakthrough Science (COMBS),
Australia
*Corresponding author: moritz.merklein@sydney.edu.au

***Abstract*— Coherent coupling between light and high-frequency sound waves in integrated photonic circuits enables unique signal processing functionalities. This effect, known as Brillouin scattering, allows for frequency-selective amplification and phase shifts that are widely exploited in microwave photonics and optical signal processing applications, sensing, and the generation of low-noise microwave and optical signals. In this invited talk, I will present several approaches for tailoring Brillouin interactions on a photonic chip. On the one hand, engineering of the waveguide cross-section and the waveguide material determines both the Brillouin frequency shift and the interaction linewidth. In particular, tailoring the waveguide dimensions, especially its height, strongly influences the opto-acoustic overlap and for appropriately designed thin waveguides, Brillouin interactions can couple light to surface acoustic waves (SAWs). Exposing the acoustic wave at the surface of the waveguide provides new opportunities to manipulate light-sound interactions and to develop novel sensing schemes. On the other hand, engineering the photonic density of states in on-chip waveguides and resonators offers an additional degree of freedom for controlling Brillouin interactions. The density of states can be tailored by introducing one-dimensional photonic bandgaps into the waveguide. These bandgap structures can either enhance or inhibit the Brillouin interaction. In particular, suppressing cascaded higher-order Brillouin scattering in resonators presents a promising pathway toward improving Brillouin laser performance.**

***Keywords*— Photonic integrated circuits, Brillouin scattering, surface acoustic waves, photonic bandgaps, nonlinear optics**

Photonic cluster state Generation from a Telecom-Emitting Quantum Dot

Giora Peniakov, Reza Hekmati, Johannes Michl, Mohamed Helal, Moritz Meinecke, Jochen Kaupp, Yorick Reum, Andreas Pfenning, Sven Höfling* and Tobias Huber-Loyola

Julius-Maximilians-Universität Würzburg, Physikalisches Institut, Lehrstuhl für Technische Physik, Am Hubland, 97074 Würzburg, Deutschland
*Corresponding author: sven.hoefling@uni-wuerzburg.de

***Abstract*—An indium-arsenide quantum dot is embedded in a circular-Bragg grating microcavity to create a bright single-photon source emitting at 1.5 µm wavelength. Periodic excitation of a confined hole spin in the presence of an external magnetic field enables the sequential generation of photons entangled in a linear cluster state.**

***Keywords*— telecom wavelength, quantum dot, CBG microcavity, entanglement, photonic cluster states**

I. Introduction

Photonic cluster states are a key resource for quantum information processing. In particular, their generation at the telecom wavelength around 1.5 um enables optimal use in existing silica-fiber networks due to low photon loss. By using a semiconductor quantum dot as a matter–light interface, we generate these states deterministically, paving the way toward future scalability.

II. Methods

Emission at the telecom wavelength is achieved by growing InAs quantum dots in an InAlGaAs matrix. Compared to the traditional GaAs environment, this matrix enables the quantum dots to grow larger, relaxing the confining energies of trapped excitonic complexes. A hole-trion optical transition is then driven by externally applied laser pulses to produce photons entangled in a cluster state [1].

Harvesting the quantum dot emission is achieved by embedding it in a circular-Bragg grating ('bullseye') microcavity [2]. Its cavity mode outcouples from the material surface with a directional Gaussian profile that is efficiently collected by an optical objective. In addition, the cavity mode induces a Purcell effect of $F_p \approx 4.3$, reducing the hole-trion lifetime to $\tau_L = 240 \pm 5$ ns. This enables coherent mapping between the matter spin and the emitted photons without substantial dephasing.

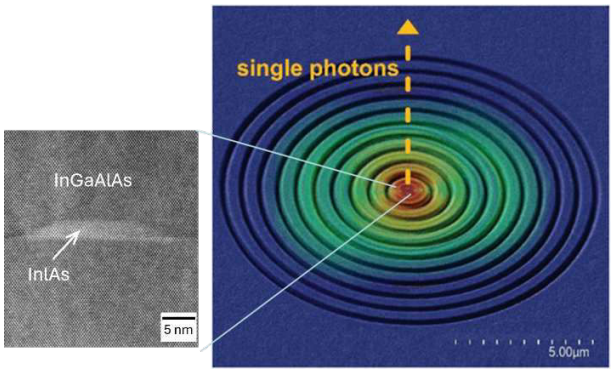

Fig. 1. A quantum dot is embedded in a circular-Bragg grating microcavity.

III. Results and Discussion

We implemented a cluster state generation protocol using a pulsed laser with a repetition rate of 80 MHz. The output spin–photon entanglement is characterized using three-photon correlation tomography.

Experimental results show:

- Hole coherence time of $T_2^* = 15.9 \pm 1.7$ ns [3]
- Spin–photon polarization entanglement with negativity $\mathcal{N} = 0.27 \pm 0.02$.
- Cluster state generation with process map fidelity of $\mathcal{F} = 0.71 \pm 0.01$ compared to the ideal case.

IV. Conclusion

We have demonstrated spin–photon-photon cluster state generation directly at the telecom C-band.

Acknowledgments

This work was supported by the PhotonQ consortium within the BMFTR.

REFERENCES

[1] D. Cogan, Z.-E. Su, O. Kenneth and D. Gershoni, "Deterministic generation of indistinguishable photons in a cluster state.", *Nature Photonics,* vol. 17, pp. 324–329, 2023.

[2] J.Kaupp, Y.Reum, et. al., "Two-Photon Interference from an InAs Quantum Dot Emitting in the Telecom C-Band." *Adv. Quantum Technologies*, e2500069, 2025.

[3] J. M. Michl, R. Hekmati, et. al., "A Spin-Photon Interface in the Telecom C-Band with Long Hole Spin Dephasing Time.", *arXiv:2512.19561 [Preprint]*, 2025.

Liquid crystalline polymer photonics for all-optical signal modulation

S. Nocentini[1,2*], D. Martellla[2,3], F. Riboli[2,4], C. Parmeggiani[2,3], D. S. Wiersma[2,5]

[1] Istituto Nazionale di Ricerca Metrologica (INRiM), Strada delle Cacce 91, Turin, 10135 Italy; [2] European Laboratory for Non-linear Spectroscopy (LENS), Via Nello Carrara 1, 50019, Sesto Fiorentino (FI), Italy; [3] University of Florence, Department of Chemistry, Via della Lastruccia 13, 50019, Sesto Fiorentino (FI), Italy; [4] Istituto Nazionale di Ottica – Centro Nazionale delle Ricerche (CNR-INO), Via Nello Carrara 1, 50019, Sesto Fiorentino (FI), Italy; [5] University of Florence, Department of Physics and Astronomy, Via G. Sansone 1, 50019, Sesto Fiorentino (FI), Italy.

*Corresponding author: s.nocentini@inrim.it; nocentini@lens.unifi.it

***Abstract*— Active, micro-scale photonic systems have been demonstrated by combining liquid crystalline polymers and 3D micro-structuration. Liquid crystalline polymers are characterized by their ability to undergo significant, reversible changes when triggered by light, enabling an all-optical reconfiguration of 3D responsive nanostructures for tunable linear and nonlinear photonics.**

***Keywords*— Liquid crystalline polymers, two-photon lithography, nonlinearity, physical unclonable function, all-optical modulation**

Polymer-based photonic platforms provide a cost-effective and versatile framework for engineering controllable optical functionalities across the micro- and nanoscale. Recent progress in advanced lithographic and additive manufacturing techniques have enabled the fabrication of complex three-dimensional architectures in functional materials, opening new opportunities for integrating stimuli-responsive systems into photonic devices.

Liquid crystalline polymers offer a unique mechanism for dynamic control, exhibiting large, reversible, and anisotropic changes under thermal or optical excitation. This responsiveness allows for the simultaneous reconfiguration of device geometry and refractive index, transforming light from a mere information carrier into a tool for the active modulation of tunable linear and nonlinear photonic components. In this way, we achieve remote and reversible modulation of optical functionalities in photonic structures, including micro-lasers, beam steering devices, microcavities, and photonic crystals [1-2]. While these structures operate in the linear regime, we are investigating nonlinear optical responses at low light intensities by thermo-optical nonlinearity of polymer-stabilized liquid crystals [3]. Furthermore, we show that the spatiotemporal control of optical responses in complex photonic materials can enhance the security of all-optical physical unclonable functions [4-5]. These photo-responsive systems can enlarge the potential of integrated polymer photonics and cybersecurity by enabling a dynamic control of light by light at low-power.

References

[1] De Bellis, I., Martella, D., et al., Adv Funct Mater (2023), 2213162.
[2] Nocentini, S., Riboli, F., et al., ACS Photonics (2018), 5 (8), 3222-3230.
[3] Massarelli, F., Wiersma, et al., Liquid Crystals (2025), 1-10.
[4] Nocentini, S., Rührmair, et al., Nature Materials (2024), 1.
[5] Salvestrini,S. Maestri, F. et al., APL Photonics (2026), 11 (2).

Part of this research project was financed by the European Union, Horizon ERC Stg 3DnanoGiant (n° 101163799).

Plasmon-Driven pn Junctions in Graphene Revealed by Raman Spectroscopy and Flexural Phonon Coupling

Maciej Wiesner[1,*], W. Strupinski[2], Jayanta Sarkar[3], Aleksandra Trzaskowska[1], Nojoon Myoung[4], Andriy Serebryannikov[1]

[1] Faculty of Physics and Astronomy, Adam Mickiewicz University, Poland
[2] Faculty of Physics, Warsaw University of Technology, Poland
[3] VTT Technical Research Centre of Finland, Finland
[4]Department of Physics Education, Chosun University, Republic of Korea

*Corresponding author: MWIESNER@AMU.EDU.PL

Abstract— **This presentation examines the formation of a lateral *pn* junction in graphene integrated with an ordered array of Au nanocylinders on a SiC substrate (fig.1a). Spatially resolved Raman spectroscopy reveals a coupled interplay between mechanical strain, plasmon-enhanced Raman response, and charge redistribution across the graphene/Au interface. The ordered nanocylinder architecture provides well-defined mechanical boundary conditions that enable separation between regions dominated by structural disorder and regions characterized by spatially correlated strain, allowing the evolution of lattice symmetry, carrier redistribution, and phonon behavior to be followed spectroscopically. A spectroscopic marker of the structural interface is provided by the appearance of a SiC-related Raman feature near 2100 cm⁻¹, observed only in the Au-covered region due to plasmon-enhanced scattering. This feature enables localization of the graphene/Au boundary independently of optical contrast. Hydrogen-intercalated graphene on SiC exhibits intrinsic *p*-type doping far from the nanocylinders, reflected in the positions of the G and 2D Raman modes and consistent with quasi-free-standing graphene formed by hydrogen intercalation [1,2]. Approaching the nanocylinder array introduces strong but spatially non-uniform strain, manifested by peak shifts and broadening of the G, G′, and 2D modes, indicating coexistence of locally distinct strain and doping environments. Deeper inside the ordered array, stabilization of Raman peak positions and intensities coincides with the emergence of a more spatially coherent strain field. Three complementary Raman signatures contribute to the physical interpretation of the graphene/Au interface. The evolution of the D band reflects enhanced Raman sensitivity to locally broken lattice symmetry and associated intervalley scattering activated by strain inhomogeneity and interfacial perturbations. The subsequent reduction of D-band intensity within the spatially ordered region indicates that the observed signal is consistent with amplification of pre-existing lattice perturbations rather than the formation of permanent structural defects. The G-band response provides an additional probe of lattice perturbation and symmetry breaking. Close to the interface, reduced G-band intensity together with increased separation of its Raman shift from the G′ mode is consistent with structural inhomogeneity and non-uniform strain. Within the ordered nanocylinder array, recovery of G-band intensity and stabilization of its spectral position coincide with the transition toward a more spatially coherent strain field and reduced disorder. In contrast, the spectral evolution of the 2D band (fig.1b) reveals lifting of phonon degeneracy in regions where strain becomes spatially correlated. The appearance of 2D-band splitting coincides with the development of coherent strain rather than with regions of strongly non-uniform strain. Simultaneously, the position of the 2D mode exhibits a maximum followed by a decrease, consistent with a gradual transition from intrinsic *p*-type to effective *n*-type carrier behavior. The lateral *pn* junction therefore forms in the region where correlated strain and plasmon-modified charge redistribution spatially overlap and is displaced from the structural interface identified by the SiC Raman feature. Finite-element simulations identify three flexural mechanical resonances of the Au nanopillars at 1.89, 2.30, and 2.32 GHz for a geometry defined by 100 nm diameter, 200 nm height, and 192 nm period. These GHz frequencies are consistent with locally resonant bending modes of the nanopillars rather than Bragg-type surface acoustic waves of the substrate. Under optical illumination, localized surface plasmons at the Au pillars generate near-field enhancement and thermo-elastic stress that provide a plausible pathway for acousto-plasmonic interaction between plasmonic excitations and GHz flexural phonons. Strain-induced modulation of graphene carrier density and screening in this regime is conceptually consistent with previously reported plasmon–phonon coupling mechanisms in graphene [3-5]. Recent experiments further demonstrate GHz acoustic modulation of plasmonic resonances in Au nanostructures [6] and describe such interactions within the framework of tunable acoustoplasmonic metasurfaces [7]. The interaction may be described phenomenologically by a strain-mediated coupling Hamiltonian :**

$$H_{int} = g\varepsilon(r,t)n(r,t)$$

where ε denotes the flexural strain field of the nanopillar resonance, n the graphene carrier density modulated within plasmonic hot spots, and g an effective strain–charge coupling constant describing energy exchange between phononic and plasmonic subsystems. Within this framework, plasmon-induced local screening can progressively compensate intrinsic *p*-type doping in hydrogen-intercalated graphene, consistent with the carrier-polarity evolution inferred from Raman spectroscopy.

Overall, the results establish a spectroscopically resolved mechanism for lateral *pn*-junction formation governed by the interplay of strain coherence, plasmon-enhanced Raman response, and charge redistribution in graphene coupled to a locally resonant metallic nanostructure. This coupled strain–plasmon–flexural-phonon behavior defines a physical platform relevant to META-scale nano-optoelectronics, where mechanical, electronic, and photonic degrees of freedom can become intrinsically linked within two-dimensional material systems.

***Keywords*— graphene, pn-junction, phonon-plasmon coupling, SiC, Raman spectroscopy, FEM calculations**

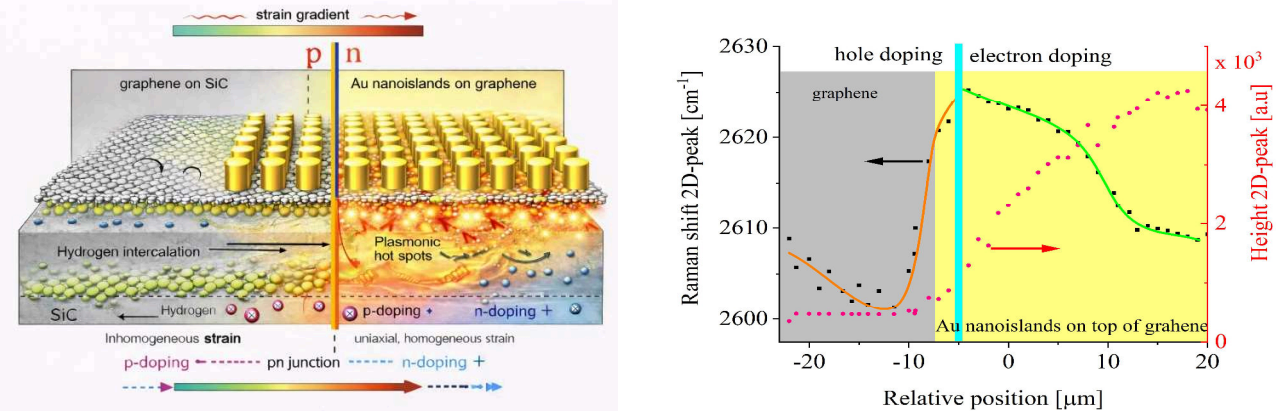

Figure 1. A schematic of investigated hybrid SiC /H2/graphene/Au nanopillars (a). Demonstration of emergence of pn junction in the hybrid structure based on 2D Raman peak behaviour (b).

REFERENCES

[1] Riedl, C. et al. Quasi-Free-Standing Epitaxial Graphene on SiC Obtained by Hydrogen Intercalation Phys. Rev. Lett. 103, 246804 (2009).

[2] Speck, F. et al. Quasi-Freestanding Graphene on SiC(0001) Mater. Sci. Forum 645–648, 629 (2010).

[3] Schiefele, J. et al. Coupling Light into Graphene Plasmons through Surface Acoustic Waves Phys. Rev. Lett. 111, 237405 (2013).

[4] Farhat, M. et al. Exciting Graphene Surface Plasmon Polaritons through Light and Sound Interplay Phys. Rev. Lett. 111, 237404 (2013).

[5] Bezares, F. J. et al. Intrinsic Plasmon–Phonon Interactions in Highly Doped Graphene: A Near-Field Imaging Study Nano Lett. 17, 5908 (2017).

[6] Imaeda K., et al Coherent acoustic vibrations of Au nanoblocks and their modulation by Al2O3 layer deposition J. Chem. Phys. 160, 144702 (2024).

[7] Holland J.E., et al. Acoustoplasmonic Metasurfaces for Tunable Acoustic Wavefront Shaping with Polarized Light ACS Photonics, 12, 2, 758 (2025)

Semiconductor Nanocrystal Optoelectronics for Classical and Quantum Light Generation

Emek Goksu Durmusoglu[1], Hilmi Volkan Demir[1,2]

NTU Singapore – Nanyang Technological University, School of Electrical and Electronic Engineering, School of Physical and Mathematical Sciences, School of Materials Science and Engineering, Singapore

Bilkent University UNAM, Department of Electrical and Electronics Engineering, Department of Physics, Institute of Materials Science and Nanotechnology, Ankara, Turkey

emek.durmusoglu@ntu.edu.sg, hvdemir@ntu.edu.sg, volkan@bilkent.edu.tr

Abstract — Here we will provide an integrated overview of our recent advances in colloidal quantum well (CQW) materials and devices, spanning their heterostructure designs and integration into metadevices. We will present examples of CQW-based photonic structures and devices for classical and quantum light generation.

Keywords — Semiconductor nanocrystals, colloidal quantum wells, optoelectronics, quantum optics

Colloidal semiconductor quantum wells (CQWs), also known as nanoplatelets, have emerged as a versatile materials platform for next-generation optoelectronics and nanophotonics owing to their atomically precise thickness control, narrow emission linewidths, giant oscillator strength, and strongly anisotropic transition dipoles. These attributes enable strong and highly tunable light–matter interactions in solution-processable media.

In this talk, we will present an integrated overview of our recent advances in CQW materials and devices, spanning heterostructure engineering, optical gain engineering, photonic integration, and quantum light generation. In particular, we will discuss atomically flat and tightly confined CQWs designed for color conversion and light-emitting applications [1–9]. By engineering advanced CQW heterostructures, we will show record-high efficiencies from CQW-based LEDs [10-12], together with record-high optical gain coefficients and ultralow lasing thresholds in colloidal laser platforms [13,14]. We will also discuss the integration of these nanocrystals with carefully designed dielectric and photonic structures to realize colloidal metadevices [15]. Finally, we will present highly engineered CQW heterostructures for room-temperature single-photon emission and high-purity quantum light generation [16].

Given their accelerating progress, these solution-processed nanocrystals offer great promise to challenge their epitaxial thin-film counterparts in semiconductor optoelectronics.

References

[1] Y. Altıntas et al., ACS Nano 13, 10662 (2019)
[2] B. Guzelturk et al., Nano Letters 19, 277 (2019)
[3] N. Taghipour et al., Nature Communications 11, 3305 (2020)
[4] F. Shabani et al., Small 18, 2106115 (2022)
[5] X. Liang et al., ACS Nano 17, 19981 (2023)
[6] H. D. Baruj et al., Small 19, 2206582 (2023)
[7] Y. Junhong, et al., Nature Communications 16, 823 (2025)
[8] O. Erdem et al., Nano Letters 19, 4297 (2019)
[9] O. Erdem et al., Nano Letters 20, 6459 (2020)
[10] B. Liu et al., Advanced Materials 32, 1905824 (2020)
[11] E. Durmusoglu et al., ACS Nano 17 (8), 7636 (2023)

[12] S. Delikanli et al., JACS 145, 12033 (2023)
[13] J. Maskoun et al., Advanced Materials 33, 2007131 (2021)
[14] F. Isik et al., Small 20, 2309494 (2024)
[15] S. T. Ha et al., Science 386, eadm7442 (2024)
[16] T. Ying, X. Liang et al., JACS (2025), DOI: 10.1021/jacs.5c08797

III-Nitrides Based Integrated Nonlinear Photonics

Changzheng Sun*, Bing Xiong, Jian Wang, Lai Wang, Zhibiao Hao, Yanjun Han, Hongtao Li, Lin Gan, and Yi Luo

Beijing National Research Centre for Information Science and Technology (BNRist),
State Key Laboratory of Space Network and Communications,
Department of Electronic Engineering, Tsinghua University, Beijing 100084, P. R. China
*Corresponding author: czsun@tsinghua.edu.cn

***Abstract*—III-nitrides, including AlN and GaN epitaxially grown on sapphire, are an attractive platform for integrated nonlinear photonics. We present our recent work on nonlinear optics in AlN/GaN microresonators and waveguides, including Kerr comb generation, optical parametric oscillation (OPO), stimulated Raman scattering (SRS), and supercontinuum generation (SCG).**

***Keywords*— AlN, GaN, microcombs, optical parametric oscillation, stimulated Raman scattering, supercontinuum.**

I. Introduction

Aluminum nitride (AlN) and gallium nitride (GaN) are wide bandgap semiconductors with both intrinsic $\chi^{(2)}$ and $\chi^{(3)}$ optical nonlinearities. AlN/GaN epitaxially grown on sapphire exhibit large refractive index contrast, making such III-nitrides on insulators an attractive platform for integrated nonlinear photonics [1,2]. In this talk, we present our recent work on nonlinear optics in AlN/GaN high-Q microrings and straight waveguides, including Kerr comb generation, optical parametric oscillation (OPO), stimulated Raman scattering (SRS), and supercontinuum generation (SCG).

II. Broadband Kerr Comb Generation

By optimizing the inductively coupled plasma dry-etching process [2,3], AlN/GaN microrings with intrinsic quality factor (Q) around 2×10^6 can be fabricated. Broadband Kerr comb generation is demonstrated at the near-infrared (NIR) regime in both AlN and GaN high-Q mircorings.

Thanks to the large nonlinear refractive index of GaN ($n_2 \sim 1.4\times10^{-18}$ m^2W^{-1}), which is several times larger than that of Si_3N_4 or $LiNbO_3$, parametric oscillation threshold power as low as 6.2 mW is demonstrated in GaN microring with an intrinsic Q factor of 1.8×10^6 [2]. In addition, single soliton comb generation in GaN microrings is implemented by an auxiliary laser pumping scheme, as shown in Fig. 1.

Being non-centrosymmetric, III-nitrides harbor intrinsic $\chi^{(2)}$ nonlinearity, which allows up-conversion of the NIR Kerr comb lines into the near-visible regime via second-harmonic (SH) and sum-frequency (SF) processes. As shown in Fig. 2, simultaneous generation of broadband NIR and near-visible combs are recorded in a 60-μm-radius AlN microring [4].

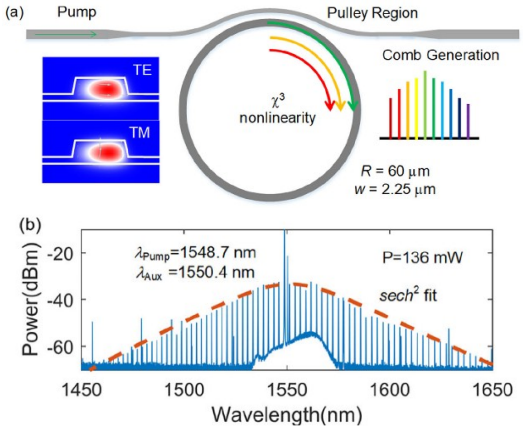

Fig. 1 Single soliton comb generation in a GaN microring.

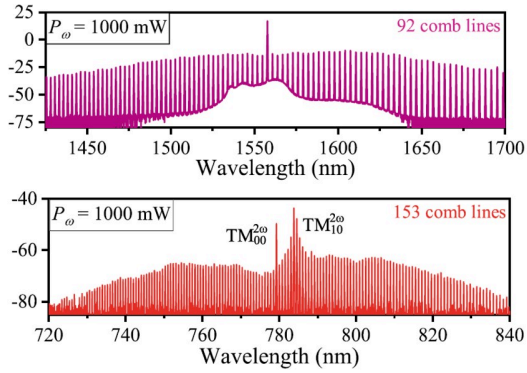

Fig. 2 Simultaneous generation of broadband NIR and near-visible combs in an AlN microring.

III. OPO in III-Nitride Microresonators

Light ranging from visible to mid-infrared wavelengths can be generated with low threshold and wide tunability via OPO based on $\chi^{(3)}$ nonlinear process. Widely separated tunable OPO is demonstrated in GaN microresonators [5]. Special care is paid to the dispersion engineering of the microring, so as to ensure phase-matching as well as to achieve normal dispersion to inhibit FWM.

As shown in Fig. 3, OPO frequency separation up to 96.6 THz is recorded in a 150-μm-radius and 2.7-μm-width GaN microring. The signal (idler) sideband can be shifted by 26.7 (21.3) THz, as the pump is tuned by 2.7 THz into different resonances.

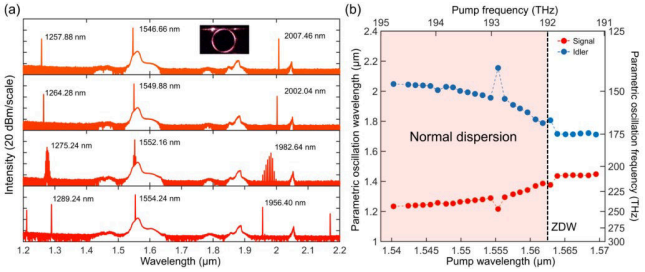

Fig. 3 Tunable OPO sidebands in a GaN microring.

IV. Microcavity Raman Lasers

Wurtzite III-nitrides boast six Raman-active optic phonons, making them appealing for Raman lasing [6,7]. As shown in Fig. 4, single-mode Raman lasing is recorded in an 80-μm-radius AlN microring with an intrinsic Q factor of 2.3×10^6. The threshold power for TM-polarized pump is as low as 8 mW. The Stokes shift is ~612 cm^{-1}, corresponding to excitation of the A_1 (TO) phonon. Furthermore, single mode Raman lasing with Stokes shift of ~657 cm^{-1} is recorded with TE pump, corresponding to the E_2 (high) phonon mode.

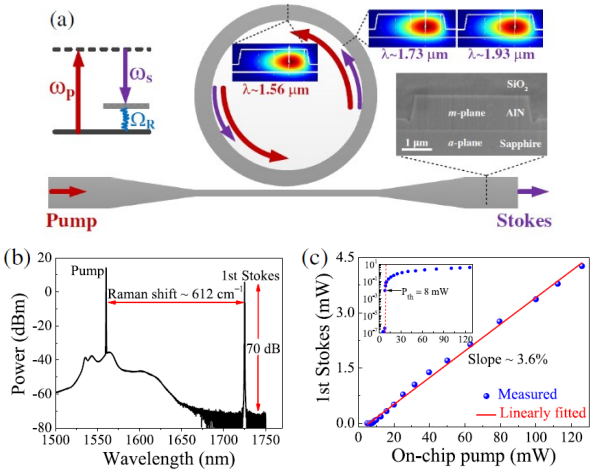

Fig. 4 Integrated AlN Raman laser with TM-polarized pump.

V. Supercontinuum Generation

Octave-spanning SCG in both AlN and GaN waveguides have been demonstrated, thanks to their wide transparency window and simultaneous $\chi^{(2)}$ and $\chi^{(3)}$ nonlinearities. The large nonlinear refractive index n_2 of GaN makes it particularly attractive for broadband SCG. As shown in Fig. 5, when pumped by erbium doped fiber laser with a pulse duration of 70 fs and a repetition rate of 100 MHz, two-octave-spanning SCG generation is obtained in a 2-mm-long dispersion engineered GaN waveguide, covering the spectral range from 600 nm to 2400 nm. Second- and third-harmonic generation are recorded simultaneously, further extending the spectral coverage [8].

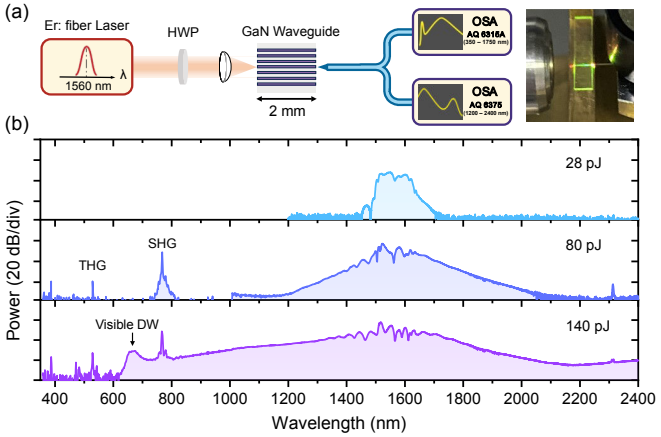

Fig. 5 Experimental setup and recorded spectra of SCG in GaN waveguides.

VI. Conclusion

A series of nonlinear optics have been implemented with AlN/GaN microresonators and waveguides, including broadband Kerr comb generation, widely separated tunable OPO, high efficiency Raman lasers, and octave-spanning SCG, confirming AlN/GaN on sapphire as an attractive platform for on-chip nonlinear photonics.

Acknowledgments

This work was supported in part by National Natural Science Foundation of China (62235005, 62127814, 62225405 and 62475130).

References

[1] X. Liu, A. W. Bruch, and H. X. Tang, "Aluminum nitride photonic integrated circuits: from piezo-optomechanics to nonlinear optics," Advances in Optics and Photonics, vol. 15, pp. 236–317, 2023.

[2] Y. Zheng, C. Sun, B. Xiong, L. Wang, Z. Hao, J. Wang, Y. Han, H. Li, J. Yu, and Y. Luo, "Integrated gallium nitride nonlinear photonics," Laser & Photonics Reviews, vol. 16, 2100071, 2022.

[3] X. Liu, C. Sun, B. Xiong, L. Wang, J. Wang, Y. Han, Z. Hao, H. Li, Y. Luo, J. Yan, T. Wei, Y. Zhang, and J. Wang, "Aluminum nitride-on-sapphire platform for integrated high-Q microresonators," vol. 25, pp. 587 –594, 2017.

[4] X. Liu, C. Sun, B. Xiong, L. Wang, J. Wang, Y. Han, Z. Hao, H. Li, Y. Luo, J. Yan, T. Wei, Y. Zhang, and J. Wang, "Generation of multiple near-visible comb lines in an AlN microring via $\chi^{(2)}$ and $\chi^{(3)}$ optical nonlinearities," Applied Physics Letters, vol. 113, 171106, 2018.

[5] Z. He, C. Sun, B. Xiong, J. Wang, Z. Hao, L. Wang, Y. Han, H. Li, L. Gan and Y. Luo, "Widely separated tunable optical parametric oscillation in GaN microresonators," Proceedings of CLEO, STu3Q.6, 2024.

[6] X. Liu, C. Sun, B. Xiong, L. Wang, J. Wang, Y. Han, Z. Hao, H. Li, Y. Luo, J. Yan, T. Wei, Y. Zhang, and J. Wang, "Integrated continuous-wave aluminum nitride Raman laser," Optica, vol. 4, 893–896, 2017.

[7] Z. He, C. Sun, B. Xiong, J. Wang, Z. Hao, L. Wang, Y. Han, H. Li, L. Gan and Y. Luo, "High efficiency Raman Lasing in integrated GaN microresonators," Proceedings of CLEO, SW3O.7, 2024.

[8] Z. He, Y. Zhang, Y. Chu, L. Yang, B. Xiong, J. Wang, Z. Hao, L. Wang, Y. Han, H. Li, L. Gan, Y. Luo, H. Guo and C. Sun, "Two-octave-spanning supercontinuum generation in gallium nitride waveguides," Proceedings of CLEO-PR, Tu1D-3, 2024.

Optics of 3D Second-Harmonic Photonic Crystals from Colloidal Self-Assembly Templating

T. Kainz[1*], Ü.-L. Talts[2], R. Grange[2], U. Steiner[1], and V. V. Vogler-Neuling[1]

[1]Adolphe Merkle Institute and NCCR Bio-inspired Materials, University of Fribourg, Switzerland
[2]Optical Nanomaterials Group, Department of Physics, ETH Zürich, Switzerland
*Corresponding author: thomas.kainz@unifr.ch

***Abstract*—We present optical measurements on inverse opals with controlled second-harmonic generation within a fabrication-tunable photonic stopband. We create scalable, 3D, second-order photonic crystals with unprecedented domain sizes (over 100 unit cells), overcoming previous limitations by combining colloidal self-assembly of polystyrene opals for templating and sol-gel barium titanate chemistry for replication.**

***Keywords*— second harmonic generation, colloidal self-assembly, 3D photonic crystals, photonic crystals, USAXS.**

I. Introduction

Three-dimensional nonlinear (second-harmonic) photonic crystals can simultaneously generate different nonlinear processes, such as second-harmonic generation, optical parametric amplification, and other sum- and difference-frequency processes, along different photonic-crystalline directions.[1] Laser-poling and laser-erasing have been utilised in materials such as lithium niobate and barium-calcium titanate.[2] With the first bottom-up fabricated 3D second-harmonic woodpile photonic crystal, we introduced the later used sol-gel chemistry in combination with soft-nanoimprint lithography.[3] However, creating large crystals in all three dimensions, mainly in the z-direction, presents a considerable challenge, primarily due to the chemical inertness of metal oxides.[4]

II. Methods

We selectively synthesised monodisperse polystyrene colloidal nanospheres with tunable unit sizes to self-assemble opal photonic crystals with different stopband wavelengths. These serve as templates for infiltration with barium titanate sol-gel. During calcination and annealing, the organic host matrix is burnt away, leaving an inverse fcc network of tetragonal barium titanate. The tetragonal phase was verified by the pumping power dependence of the higher-harmonic signal (Figure 2 a). We fabricate samples with unprecedented sizes for single domains: > 3000 unit cells in x, y directions and > 100 in the z direction (Figure 1 a, b). Due to their size, we were able to isolate individual single domains. We verified their intact internal photonic crystal structure, together with their initial growth direction normal to the substrate along the (111)-direction of the fcc crystal, using ultra-small-angle x-ray spectroscopy. One single individual domain was mounted on a rotation stage normal to the incident beam, and the resulting 2D diffraction patterns were recorded angle-dependent (Figure 1 c, d). The achieved optical reflectivity values are above 80% relative to a DBR mirror throughout all the fabrication. We can engineer the final photonic band gap over the entire optical range, matching it to both material and setup requirements.

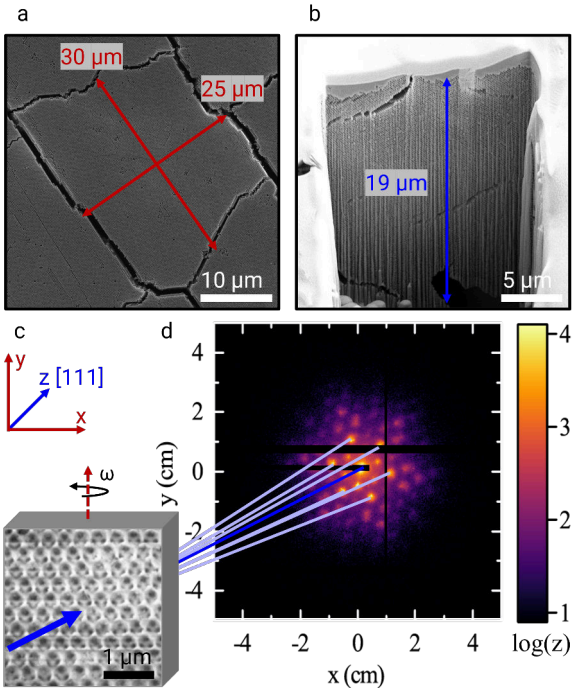

Fig. 1. Inverse barium titanate photonic crystals; Scanning electron microscopy images with domain dimensions: (a) In the (111)-plane and (b) normal to it. (c) Free-standing single domain with its rotation axis for ultra-small angle X-ray spectroscopy; (d) The corresponding 2D diffraction pattern for the (111)-direction.

III. Results and Discussion

With our approach, we overcame previous limitations, especially stacking in the z-direction, while maintaining full tunability of the initial unit cell and, consequently, the final dimensions. By reverse-engineering the final stopband centre wavelength, we can both avoid the materials' absorption regime and match the available laser setups. This allowed us to measure the SHG signal as a wavelength sweep over the stopband, where we observed band-edge enhancement,

a stopband dip, and field-localisation asymmetry. A detailed discussion on the interpretation of these experimental findings is still ongoing, but they mark important steps towards experimentally targeting inhibited spontaneous emission. [5] For this, we are taking steps to replace the colloidal fcc template with a photonically superior, larger bandgap colloidal diamond structure.[7] Configurations to investigate inhibited excitation can be fabricated using the same technique with our controlled size tunability.[6]

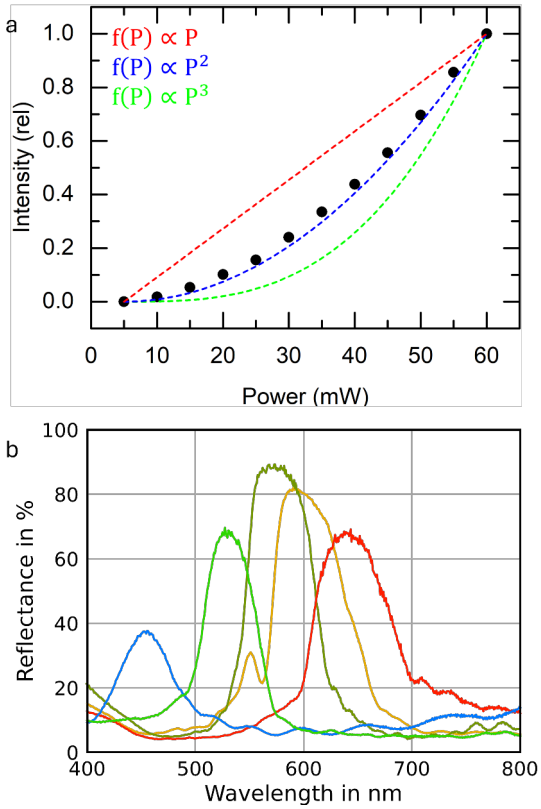

Fig. 2. Barium titanate inverse opal photonic crystals: (a) Pumping-power dependent signal intensity series showing the second-harmonic scaling; (b) Reflectance spectra for different inclinations with optical range colour coding with its most pronounced stopband in (111) direction.

IV. Conclusion

In this study, we demonstrated the use of colloidal-crystal templating for a second-order optical material. We successfully replicated the photonic network into a second-order material and demonstrated, for the first time, a stopband (linear photonic bandgap) from a fully scalable three-dimensional photonic crystal (Figure 2 b) made of a $\chi^{(2)}$ optical material (Figure 2 a).

References

[1] Slusher, R. E., and Eggleton, B. J., "Nonlinear Photonic Crystals" (*Springer Berlin Heidelberg*, Berlin, Heidelberg, 2003).

[2] Zhang, Y., Sheng, Y., Zhu, S., Xiao, M., and Krolikowski, W. "Nonlinear photonic crystals: from 2D to 3D", *Optica*, Vol.8, pp. 372-381, 2021.

[3] Vogler-Neuling, V. V., Talts, Ü.-L., Ferraro, R., Weigand, H., Finco, G., Winiger, J., Benedek, P., Kusch, J., Karvounis, A., Wood, V., Leuthold, J., and Grange, R., "Large-Scale Bottom-Up Fabricated 3D Nonlinear Photonic Crystals", *Advanced Photonics Research* , Vol. 5,Vo. 12, p. 2400058, 2024.

[4] Vogler-Neuling,V. V., Karvounis, A., Morandi, A., Weigand, H., Dénervaud, E., and Grange, R., "Photonic Assemblies of Randomly Oriented Nanocrystals for Engineered Nonlinear and Electro-Optic Effects", *ACS Photonics*, Vol. 9, 2193-2203 (2022).

[5] Yablonovitch, E., "Inhibited Spontaneous Emission in Solid-State Physics and Electronics", *Phys. Rev. Lett.*, Vol.58, No. 20, pp. 2059–2062, 1987.

[6] Soljačić, M., Johnson, S. G., Fan, S., Ibanescu, M., Ippen, E., Joannopoulos, J. D., "Photonic-crystal slow-light enhancement of nonlinear phase sensitivity", *J. Opt. Soc. Am. B*, Vol. 19, No. 9, 2002.

[7] He, M., Gales, J.P., Ducrot, É, Gong, Z., Yi, G.-R., Sacanna, S., and Pine, D. J., "Colloidal Diamond", *Nature*, Vol. 585 No. 7826, pp. 524-529, 2020.

Resolving Surface Plasmon Dispersion with Fabry–Pérot–Assisted Extraordinary Optical Transmission

Youssef El Badri[1,*], Hicham Mangach[2], Mustapha Bahich[1], Yan Pennec[2], Bahram Djafari-Rouhani[2], Younes Achaoui [1]

[1] Laboratory of Optics, Information Processing, Mechanics, Energetics and Electronics, Department of Physics, Moulay Ismail University, B.P. 11201, Zitoune, Meknes, Morocco.

[2] Univ Lille, CNRS, UMR 8520-IEMN, F59000 Lille, France

*Corresponding author: y.elbadri@edu.umi.ac.ma

***Abstract* — We present a numerical study showing the reconstruction of SPP dispersion diagram of a metal–dielectric interface from extraordinary optical transmission resonances in gratings with subwavelength Fabry–Pérot apertures. By varying periodicity, each device probes distinct momentum states, enabling reconstruction of the SPP dispersion in close agreement with eigenmode solutions.**

***Keywords* — Plasmonic Metagrating, Non-Hermitian Photonics, Quasinormal Mode Analysis, Dispersion Diagrams.**

I. Introduction

Plasmonic materials enable strong optical confinement and field enhancement, but their response is highly sensitive to the dielectric function, fabrication conditions, oxidation, and microstructure [1–3]. Consequently, small variations in optical constants can significantly alter device performance [4]. Among the most informative descriptors are the dispersion relation and plasmonic efficiency, which link frequency to momentum and determine propagation, confinement, and loss [5,6]. For periodic plasmonic lattices, dispersion diagrams are typically obtained from angle-resolved reflection measurements [7,8]. These methods probe SPP Bloch modes of the patterned interface, but the intrinsic flat-interface SPP continuum is folded into the Brillouin zone and may be obscured by Wood anomalies and geometry-dependent artifacts. As a result, extracting material-related dispersion from periodic structures remains nontrivial.

Here, we investigate an alternative approach based on extraordinary optical transmission through plasmonic gratings with subwavelength apertures acting as Fabry–Pérot (FP) resonators. Instead of scanning the incidence angle, the grating period is varied to probe different optical momenta, where each device acts as a discrete momentum probe. Because the resonances arise from hybridization between cavity-like FP modes and surface-bound plasmons, their spectral shifts encode both geometric and material dispersion. Numerical results show that, after separating these contributions, the corrected resonances reconstruct the SPP dispersion of the metal–dielectric interface.

II. Methods

The system considered is a one-dimensional plasmonic grating containing periodic subwavelength apertures. The metallic blocks are embedded in the same dielectric on both sides (Fig. 1.a). The unit-cell period and thickness are set equal (H = L). The structure is excited at normal incidence with TM polarization, so that transmission is dominated by slit-supported TM modes. Dispersion diagrams are evaluated using modal analysis based on a non-Hermitian quasi-normal mode (QNM) formulation [9,10]. Momentum-space sampling is achieved by sweeping the grating periodicity H, with each structure probing a discrete in-plane wavevector $k = 2\pi/H$.

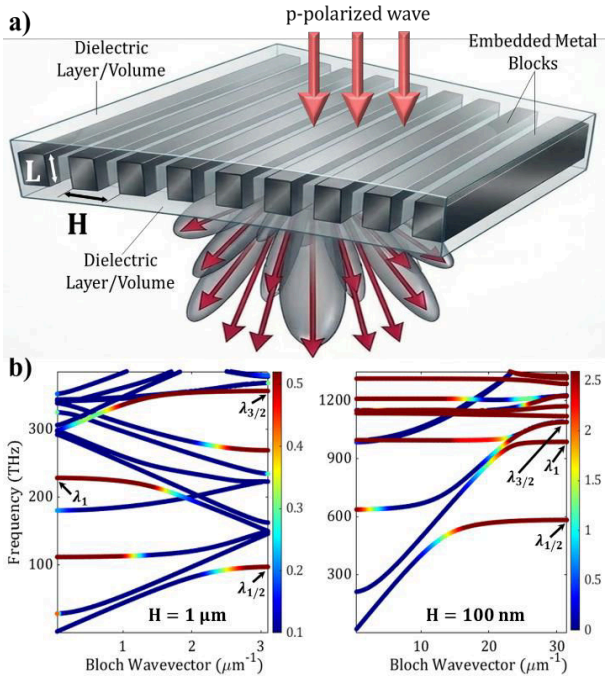

Fig. 1.a) Schematics of the structure consisting of a plasmonic slab embedded in a dielectric matrix (air). H and L are parameters of the unit cell. b) QNM-derived photonic dispersion diagrams for the plasmonic system at two sizes 1 µm and 100 nm. The colormap encodes energy leakage into the metal blocks. FP resonances at $\lambda_{1/2}, \lambda_1, \lambda_{3/2}$ are depicted.

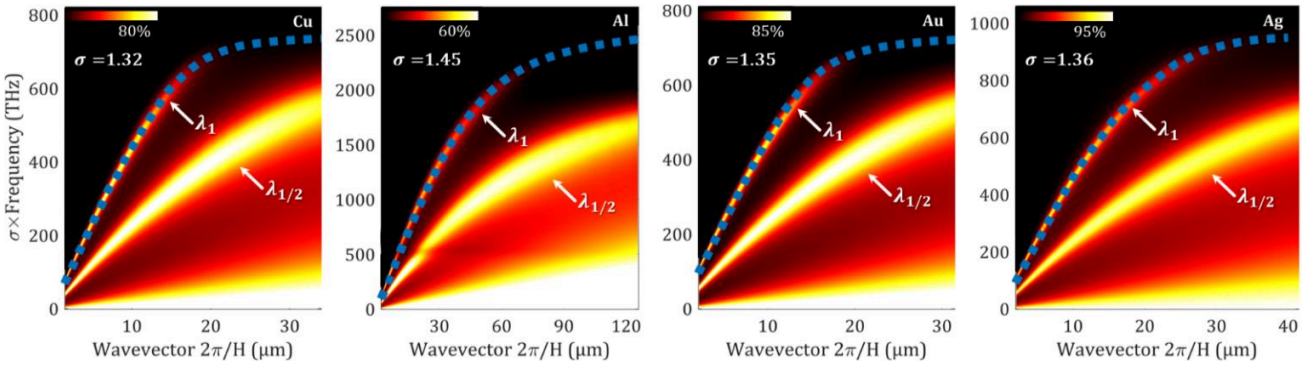

Fig. 2 Optical transmission maps through plasmonic grating composed of different materials (Cu, Al, Au, Ag) as function of the corrected frequency $\sigma(r,\varepsilon) \times f$ against the wavevector. FP resonant bands are highlighted. The colormap reflects the plasmonic efficiency. The true SPP signature, evaluated using eigenmode studies, is shown in blue.

The FP resonance frequencies extracted from transmission spectra should be corrected by a factor $\sigma(r,\varepsilon) = \sigma_{geo}(r) + \sigma_{mat}(\varepsilon)$ to recover the SPP signature. The geometric factor $\sigma_{geo}(r)$ accounts for aperture-induced field leakage and inter-cavity coupling deviating from ideal FP behavior [11]. The material factor $\sigma_{mat}(\varepsilon)$ encapsulates additional phase shifts introduced by dispersive permittivity. The total correction $\sigma(r,\varepsilon)$ is calibrated by aligning the low-frequency branch to the free-space light line, where dispersive effects are negligible [12].

III. Results and Discussion

A. Modal Hybridization and Photonic Dispersion

Fig 1.b compares the photonic dispersion diagrams obtained by QNM-FEM for two grating periodicities. The colormap encodes energy leakage into the metal blocks and reveals significant energy penetration for $H = 100$ nm. For $H = 1$ µm, the diagram exhibits classical grating-coupled SPP behavior with Bloch bands folded at the Brillouin zone boundary, modulated by FP-like resonances at half-wavelength multiples: half-wave, fundamental, and three-half-wave FP modes ($\lambda_{1/2}$, λ_1, $\lambda_{3/2}$) [13]. Above $\lambda_{3/2}$, diffraction dominated high-order modes suppress coherent optical transmission.

At H = 100 nm, the larger reciprocal lattice vector drives modes into the evanescent zone before Brillouin zone folding, producing flat bands, anti-crossings, and strong FP–SPP hybridization. The energy localization colormap clearly distinguishes delocalized photonic states from tightly bound plasmonic cavity modes, which leak optical energy into the metallic boundaries, confirming substantial field penetration into the metallic blocks at high frequencies. Above the SPP frequency (~1160 THz), additional localized modes emerge as flat bands due to hybridization between Bloch-SPP modes and aperture waveguide modes. These near-zero–group-velocity bands are a signature of strong photonic hybridization.

B. SPP Dispersion Reconstruction via FP Resonances

Fig. 2 illustrates the FP–SPP hybridization mechanism responsible for the frequency shifts as a function of the period-derived wavevector. The plasmonic response naturally appears over different frequency ranges for different metals, reflecting their distinct dielectric dispersions and plasmonic efficiencies. Overlaid in blue are the reference SPP dispersion curves obtained from eigenvalue analysis of the corresponding flat metal–air interfaces. The dispersion maps are reconstructed by tracking the second-harmonic FP resonance (λ_1) while sweeping the grating periodicity for four metals: copper (Cu), aluminum (Al), silver (Ag), and gold (Au) [14].

As shown in Fig. 2, the FP resonance bands red-shift markedly, particularly at small periods (large wavevectors), where stronger field confinement enhances interaction with the metal and dispersive effects become more pronounced in the near field. The transmission amplitude decreases accordingly, governed by the intrinsic ohmic losses of each material. These trends enable dispersion mapping, demonstrating that the second-harmonic FP modes faithfully trace the independently calculated SPP dispersion of the flat metal–air interface. Furthermore, the transmission intensity in Fig. 2 simultaneously encodes plasmonic efficiency: sharp, high-transmission resonances indicate low-loss plasmonic coupling, whereas broadened or suppressed features reflect increased ohmic dissipation and mode degradation.

IV. Acknowledgments

This work was supported by the European Union's Horizon Europe research and innovation program under grant agreement MAGNIFIC (GA No 101091968) and the CHIST-ERA Call 2021 under GA No CHIST-ERA-20-NOEMS-003.

References

[1] Oates, T. W. H., *Phys. D Appl. Phys.* **46**, 145308 (2013).
[2] Gorkunov, M. V, Artemov, V. V, Yudin, S. G. & Palto, S. P. *Photonic Nanostruct.* **12**, 122–129 (2014).
[3] Jiang, Y., Pillai, S. & Green, M. A. *Sci. Rep.* **6**, 1–7 (2016).
[4] Miller, M. & Lazarides, A. *J. Phys. Chem. B* **109**, 21556–21565 (2005).
[5] Ohad, A. *et al. Photonics Res.* **6**, 653–658 (2018).
[6] Barbara, A. *et al. Opt. Express* **18**, 14913–14925 (2010).
[7] Ghaemi, H., Thio, T., Grupp, D. & Ebbesen, T. *Phys. Rev. B* **58**, 6779 (1998).
[8] Gao, H., et al. *Proc. Natl. Acad. Sci. USA* **105**, 20146–20151 (2008).
[9] Raman, A. & Fan, S. *Phys. Rev. Lett.* **104**, 87401 (2010).
[10] Yan, W., Faggiani, R. & Lalanne, P. *Phys. Rev. B* **97**, 205422 (2018).
[11] Takakura, Y. *Phys. Rev. Lett.* **86**, 5601 (2001).
[12] El Badri, Y. *et al.* arxiv.org/abs/2508.00521 (2025).
[13] Marquier, F., *et al. Opt. Express* **13**, 70–76 (2005).
[14] Rakić, A. D., *et al. Applied Optics, Vol. 37, Issue 22, pp. 5271-5283* **37**, 5271–5283 (1998).

Tunable resonances in doubly anisotropic, high-index MoS_2 nanoplatelets

Bingying You[1,2], Tom T.C. Sistermans[1,2], Alberto G, Curto[1,2*]

[1] Photonics Research Group, Ghent University-imec, Ghent, Belgium
[2] Center for Nano- and Biophotonics, Ghent University, Ghent, Belgium
*Corresponding author: Alberto.Curto@Ugent.be

***Abstract*: Optical anisotropy plays a crucial role in the manipulation of light. Transition metal dichalcogenides possess both high refractive index and high birefringence, opening opportunities to tailor Mie resonances. Here, we investigate optical resonances in MoS_2 nanoplatelets with both geometrical and refractive index anisotropies to control light scattering.**

***Keywords*: high-refractive index, high birefringence, Mie resonances.**

Anisotropy plays a crucial role in manipulating light, underpinning optical components such as polarizers, waveplates, and modulators, as well as phenomena like phase-matching in nonlinear optics. The functionality of these devices hinges primarily on the retardance between two orthogonal linear polarizations, which is proportional to both the thickness and the birefringence (Δn) of the material. A large birefringence is thus beneficial for the performance and compactness of such components. Birefringence is also a tunability degree of freedom for nanophotonics, for example, in electro-optic modulators, waveguides with reduced cross-talk, and electro-optic polarization conversion. Beyond natural materials, metasurfaces and metamaterials can be constructed to achieve high anisotropy but suffer from losses and fabrication challenges. As a result, natural materials with higher anisotropy than conventional dielectrics or metals are in demand.

Transition metal dichalcogenides are promising birefringent materials due to their layered van der Waals structure, which naturally yields a large intrinsic birefringence exceeding unity. In particular, molybdenum disulfide (MoS_2) possesses one of the highest birefringence of all natural materials in the near infrared. Such a high birefringence is possible thanks to the presence of strong excitons. They endow MoS_2 with a high in-plane refractive index above 4, enabling a higher out-of-plane index contrast than lower-index dielectrics. A high refractive index also enables the presence of Mie-type resonances in MoS_2 nanostructures, thereby enhancing and controlling light-matter interactions.

Here, we study the optical resonances sustained by MoS_2 nanoplatelets made of high refractive index material with high optical anisotropy. These nanoplatelets have both geometrical and refractive index anisotropies. Their high refractive index

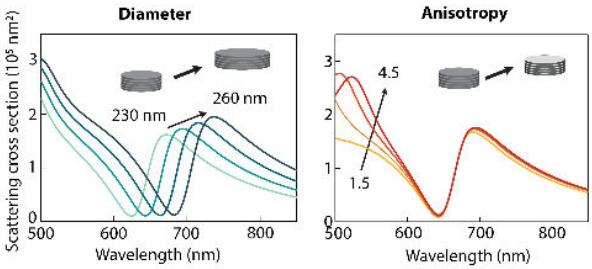

Fig. 1 - Different dependence of electric and magnetic dipole resonances on geometrical and optical anisotropy.

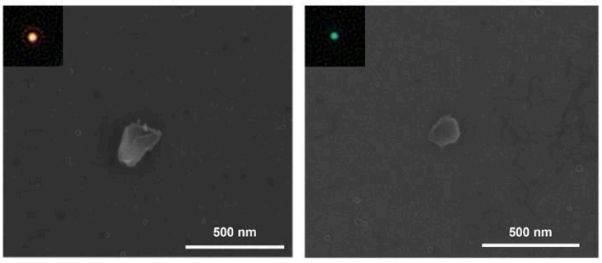

Fig. 2 - Single MoS_2 nanoplatelets: scanning electron microscopy and dark-field scattering microscopy images showing a tunable optical response.

enables them to sustain electric and magnetic resonances. We find a distinct impact of changes in geometry and birefringence on the tunability of the electric and magnetic resonances, which we explain using multipolar expansions.

Our experimental results characterize the optical response at the single MoS_2 nanoplatelet level using dark-field spectroscopy, including a variety of color changes in the visible on different substrates. We also reveal polarization-dependent resonances arising from their geometrical anisotropy. By employing chemical etching, we change the size of individual

nanoplatelets, thereby enabling controllable resonance tuning as evidenced by color changes observed in dark-field images of individual nanoplatelets.

In summary, high-refractive-index nanoplatelets with intrinsic out-of-plane anisotropy and large birefringence exhibit a wealth of electric and magnetic multipolar resonances that are sensitive to geometry and anisotropy in distinct manners. We demonstrate the diversity of optical responses of these individual MoS_2 nanoplatelets. We envision that these nanoplatelets could be used to enhance and direct light scattering and light emission, with applications in light-emitting devices and lasers.

REFERENCES

[1] Ermolaev, G. A., D. V. Grudinin, Y. V. Stebunov, et al., "Giant optical anisotropy in transition metal dichalcogenides for next-generation photonics," Nature Communications, Vol. 12, No. 854, 2021.

[2] Verre, R., D. G. Baranov, B. Munkhbat, J. Cuadra, M. Käll, and T. Shegai, "Transition metal dichalcogenide nanodisks as high-index dielectric Mie nanoresonators," Nature Nanotechnology, Vol. 14, 679-683, 2019.

Near field imaging and spectroscopy of complex stacking of semiconductors

L. Tailpied [1], C. Gureghian[2], F. Fossard[3],J.-S. Mérot[3], F. Gonzalez-Posada-Flores[4], J.-B. Rodriguez[4], G. Vincent[1], T. Taliercio [4], B. Fix [1,*]

[1]DOTA, ONERA, Université Paris Saclay, F-91123 Palaiseau, France
[3]LEM, UMR 104 CNRS-ONERA, Université Paris Saclay, F-92322 Châtillon, France
[4]IES UMR 5214, Université de Montpellier, 860 rue Saint Priest, 34095 Montpellier Cedex 5, France
[2]Sorbonne Université, CNRS, Institut des NanoSciences de Paris, 4 place Jussieu, 75005 Paris, France
*Corresponding author: baptiste.fix@onera.fr

***Abstract*—Improvement of nanostructured infrared photodetectors based on increasingly complex semiconductors epitaxies requires feedback on the optical parameters of each layer. Here, SNOM imaging and spectroscopy on a cleaved facet is used to characterize the cut-off frequency of type II superlattice, the doping level of heavily doped semiconductors and surface plasmons.**

***Keywords*— epitaxy, photodetectors, near-field, plasmons.**

I. Introduction

Sectors such as defense, medical science and chemical and bio-sensing need mid and long-wave infrared room temperature photodetectors. Commercially available technologies, as HgCdTe photodetectors, quantum well infrared detectors and more recently III-V superlattices [1], [2], face challenges to reach high sensibility at room temperature. To improve the detectivity and increase the working temperature of these photodetectors, the complexity of the epitaxy increases through the use of specific junction design or the use of nanophotonique with structured electrodes.[3], [4]. This leads to the development of complex stacking of III-V semiconductors, with the use of heavily doped semiconductor to replace traditional metals. Due to the increase in epitaxy complexity, the direct characterization of the junction function is no longer enough to answer the need of technological feedback. Moreover, classical retrieving of geometrical and composition of the layers by transmission electronic microscopy (TEM) on cross section lamella prepared by focus ion beam (FIB), is not suitable to retrieve the optical characteristics of the material in the infrared, and can be tricky to implement on some materials [5], [6].

In this context, the scattering near field optical microscope (SNOM) can be a useful tool to characterized such complex stacking. This technic can indeed be used to probe the dielectric constant of materials [7], [8] or to image plasmons and phonons in materials [9]. It has already been used to probe the doping level of thin layers [10], [11], [12], and the plasma wavelength and the dielectric constant[13], but only on bulk layer. We proposed here to investigate the use of s-SNOM characterization to analyze the layers parameters of a cleaved complex epitaxial heterostructure composed of highly doped semiconductor and type II superlattice (T2SL), design to be a long-wave infrared photodetector.

II. Methods

The sample is first cleaved with a diamond tip to characterize the sample on the lateral facets. The stacking parameters and the general optical properties of the layers are first retrieved through SNOM imaging at several infrared wavelength. The mechanical image and the optical amplitude of the stack at different wavelength are presented in Figure 1. The main layers are visible both in AFM and in optical amplitude: the heavily doped semiconductors have a mirror behavior in the infrared, and therefore the scattered optical amplitude is higher for these layers than for the other layers of the stack.

III. Results and Discussion

Combining near-field measurement and simulation, we determine the dielectric function of the T2SL heterostructure, and the plasma frequency of the heavily doped semiconductor layers. The SNOM analysis allow therefore a precise characterization of the optical properties of the layers, needed for simulation of the properties of the whole stack.

Fig. 1. A : AFM image of the stack with the mechanical phase contrast, B: Optical near field images of the stack at several wavelengths in amplitude referenced with the GaSb substrate amplitude

Finally, three bulk surface plasmon polaritons (BSPP) are studied. This phenomenon occurs at the interface of the highly

doped layer and was studied through near field and hyperspectral imaging. The nearfield imaging allows to determine the characteristic distance of the phenomenon, which are less than 100 nm, and the near field spectroscopic studied allow to precise the wavelength at which the BSPPs occurs for each interface.

IV. Conclusion

This work illustrates a new way of creating technological feedback on a more fundamental basis than the functional feedback usually available. This work paves the way to other heterostructures analysis such as T2SL bariodes, quantum well or quantum cascade photodetectors. Moreover, it paves the way to new studies of plamsons.

Acknowledgments

his work was financially supported by the Agence de l'innovation de Défense (ANR 19-ASTR-0003-01, Nanoelastir) and the Agence Nationale de la Recherche (ANR 11-EQPX-0016, EquipEx EXTRA and ANR-10-EQPX- 37, Consortium MATMECA)

References

[1] H. S. Kim et al., "Long-wave infrared nBn photodetectors based on InAs/InAsSb type-II superlattices," *Applied Physics Letters*, vol. 101, no. 16, p. 161 114, 2012. DOI: 10.1063/1.4760260.

[2] A. Rogalski, P. Martyniuk, and M. Kopytko, "Type-II superlattice photodetectors versus HgCdTe photodiodes," *Progress in Quantum Electronics*, vol. 68, p. 100 228, 2019. DOI: 10.1016/j.pquantelec.2019.100228.

[3] D. Palaferri et al., "Room-temperature nine-µm-wavelength photodetectors and GHz-frequency heterodyne receivers," *Nature*, vol. 556, no. 7699, pp. 85–88, 2018. DOI: 10.1038/nature25790.

[4] M. F. Hainey et al., "Breaking the interband detectivity limit with metasurface multi-quantum-well infrared photodetectors," *Optics Express*, vol. 29, no. 26, p. 43 598, 2021. DOI: 10.1364/OE.444223.

[5] A. Lugstein, C. Schoendorfer, M. Weil, C. Tomastik, A. Jauss, and E. Bertagnolli, "Study of focused ion beam response of GaSb," *Nuclear Instruments and Methods in Physics Research Section B: Beam Interactions with Materials and Atoms*, vol. 255, no. 2, pp. 309–313, 2007. DOI: 10.1016/j.nimb.2006.11.116.

[6] Y. Yanagida, T. Oishi, T. Miyaji, C. Watanabe, and N. Nitta, "Nanoporous Structure Formation in GaSb, InSb, and Ge by Ion Beam Irradiation under Controlled Point Defect Creation Conditions," *Nanomaterials*, vol. 7, no. 7, p. 180, 2017. DOI: 10.3390/nano7070180.

[7] A. A. Govyadinov, I. Amenabar, F. Huth, P. S. Carney, and R. Hillenbrand, "Quantitative Measurement of Local Infrared Absorption and Dielectric Function with Tip-Enhanced Near-Field Microscopy," *The Journal of Physical Chemistry Letters*, vol. 4, no. 9, pp. 1526–1531, 2013. DOI: 10.1021/jz400453r.

[8] X. Guo, K. Bertling, and A. D. Rakic, "Optical constants from scattering-type scanning near-field optical microscope Optical constants from scattering-type scanning near-field optical microscope," *Applied Phys*, vol. 041103, no. January, 2021, Publisher: AIP Publishing LLC. DOI: 10.1063/5.0036872.

[9] M. Wagner et al., "Ultrafast Dynamics of Surface Plasmons in InAs by Time-Resolved Infrared Nanospectroscopy," *Nano Letters*, vol. 14, no. 8, pp. 4529–4534, 2014. DOI: 10.1021/nl501558t.

[10] J. M. Stiegler et al., "Nanoscale Free-Carrier Profiling of Individual Semiconductor Nanowires by Infrared Near-Field Nanoscopy," *Nano Letters*, vol. 10, no. 4, pp. 1387–1392, 2010. DOI: 10.1021/nl100145d.

[11] W. Choi et al., "Direct Electrical Probing of Periodic Modulation of Zinc-Dopant Distributions in Planar Gallium Arsenide Nanowires," *ACS Nano*, vol. 11, no. 2, pp. 1530–1539, 2017. DOI: 10.1021/acsnano.6b06853.

[12] E. T. Ritchie, C. B. Casper, T. A. Lee, and J. M. Atkin, "Quantitative Local Conductivity Imaging of Semiconductors Using Near-Field Optical Microscopy," *The Journal of Physical Chemistry C*, vol. 126, no. 9, pp. 4515–4521, Mar. 2022. DOI: 10.1021/acs.jpcc.1c10498.

[13] Y. Huang et al., "Spectroscopic Nanoimaging of All-Semiconductor Plasmonic Gratings Using Photoinduced Force and Scattering Type Nanoscopy," *ACS Photonics*, vol. 5, no. 11, pp. 4352–4359, 2018. DOI: 10.1021/acsphotonics.8b00700.

All-Solid Multicore Fibre Probe for Background-Free Raman Spectroscopy

Stephanos Yerolatsitis[1,*], Thomas A. Wright[1], András Kufcsák[2,3], Alexandra C. Adams[2], Tom Quinn[2], Sohan Seth[2], Kevin Dhaliwal[2], James M. Stone[1]

[1]Centre for Photonics, Department of Physics, University of Bath, Claverton Down, BA27AY, Bath, UK

[2]Translational Healthcare Technologies Group, Centre for Inflammation Research, Institute for Regeneration and Repair, The University of Edinburgh, Edinburgh, UK

[3]Institute of Photonics and Quantum Sciences, School of Engineering and Physical Sciences, Heriot-Watt University, Edinburgh, EH14 4AS UK

*Corresponding author: sy231@bath.ac.uk

***Abstract*— We demonstrate a sub-millimetre all-solid multicore fibre probe for Raman Spectroscopy. By utilising a multicore fibre design and a differential dopant approach, we were able to suppress inter-core crosstalk and therefore reduce the generation of Silica Raman background. The monolithic all-fibre probe achieves 98 percent collection efficiency relative to direct coupling and enables fluorescence-free Raman spectra reconstruction of highly fluorescence samples.**

***Keywords*— Raman Spectroscopy, Raman Fibre Probe**

I. Introduction

Raman spectroscopy is a label-free and non-destructive optical technique capable of examining the intrinsic biochemical signatures of biological tissue. It holds strong potential for minimally invasive optical biopsy and, therefore, real-time cancer diagnostics [1]. Nevertheless, the use of Raman spectroscopy as a clinical in-vivo tool has not yet been fully realised due to various technical challenges. One such challenge is the silica background generated from the optical fibres used to remotely examine otherwise unreachable tissue regions [2]. Another significant drawback is the autofluorescence background generated from these tissue regions [3], [4].

Previous approaches have relied on hollow-core fibres and complex distal optics to suppress silica background, including negative curvature fibres such as those demonstrated in [5], [6]. While effective, such solutions require advanced fabrication and complex probe assembly, limiting scalability and disposable clinical use.

Here, we present a fully monolithic all-solid sub-millimetre single-fibre Raman probe. By engineering the refractive index contrast and dopant composition between the excitation and collection cores, we demonstrate low crosstalk, improved collection efficiency, and background suppression in a robust and manufacturable design.

II. Multicore Fibre & Fan-In/Fan-Out Design

The multicore fibre was fabricated using the stack-and-draw technique and comprises a seven-core all-solid structure: one single-mode excitation core surrounded by six graded-index multimode collection cores (Fig. 1). The excitation core consists of undoped silica with a fluorine-doped cladding, while the collection cores are germanium-doped with undoped silica cladding.

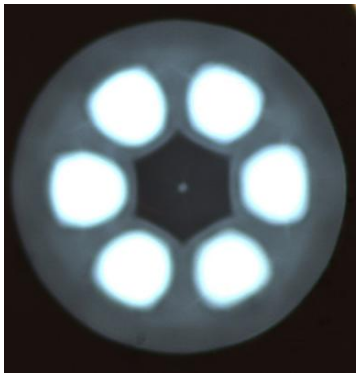

Fig. 1. Optical micrograph of our multicore fibre, which consists of a single-mode central excitation core surrounded by six multimode collection cores.

The difference in dopant composition introduces a refractive index contrast between the excitation and collection cores, resulting in distinct effective indices for the supported modes. This index difference reduces modal overlap and suppresses inter-core cross-talk, limiting the transfer of pump light from

the excitation core into the collection channels. As a result, the excitation and collection cores can be positioned in close proximity without significant optical coupling, enabling a compact probe geometry while maintaining modal isolation. The fibre has an outer diameter of 390 µm, and the complete probe diameter remains below 1 mm when enclosed in polyimide tubing, making it suitable for endoscopic use.

The probe is interfaced with the experimental system via an all-fibre fan-in/fan-out reformatter device (Fig. 2), designed to independently address each core. A single-mode fibre is aligned to the central excitation core for delivery of 785 nm pump light, while six multimode fibres are coupled to the surrounding collection cores for Raman signal retrieval. The collected signals are subsequently rearranged and directed to the spectrometer.

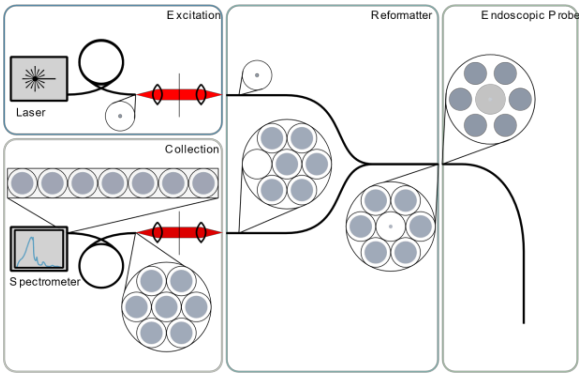

Fig. 2. Experimental setup. The central single-mode core of our probe is coupled to a 785 nm tunable single-frequency laser, and the six multimode collection cores are bundled together and fed into a portable Raman spectrometer. The central core is used to excite the distal sample, while the surrounding cores collect the Raman signal from the sample.

This fully fibre-integrated configuration eliminates the need for free-space coupling optics between the disposable probe and the benchtop system. Consequently, the assembly offers improved mechanical stability, reduced alignment sensitivity, and straightforward plug-and-play operation, which are important considerations for practical and clinical implementation.

III. Results and Discussion

To evaluate the background suppression and collection capabilities of the designed fibre probe, initial baseline measurements were conducted using ethanol. The probe's response was first recorded in air to capture any residual silica background, then submerged in ethanol to acquire the backscattered Raman spectrum of the sample. The resulting spectra, shown in Figure 3, clearly display distinct peaks within the spectral region of interest that correspond to ethanol's characteristic vibrational modes [6]. Although some residual silica background noise remains, the intrinsic response of our fibre is substantially lower than that of a conventional solid-core fibre, performing comparably to, or better than, alternative approaches such as hollow-core fibre probes.

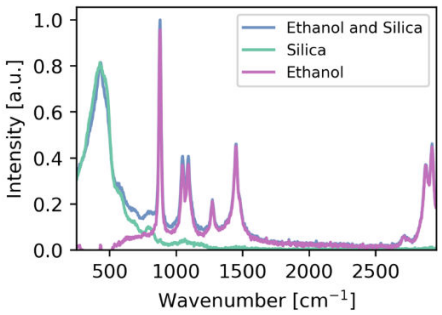

Fig. 3. The collected Raman signal when the pump light is coupled to the central single-mode core before (in air) and after the distal tip of the fibre probe was immersed in ethanol. Signal from ethanol obtained by subtracting the two plots.

We further validated the probe using sesame oil, a challenging sample for Raman spectroscopy due to being high fluorescent. Its fluorescence level is comparable to that of human lung tissue, making it a relevant benchmark for biological applications

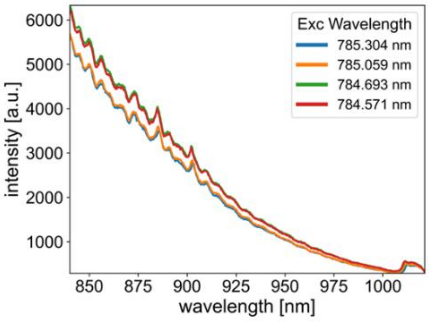

Fig. 4 Raw Raman spectra of sesame oil for four slightly shifted excitation wavelengths.

To remove background fluorescence, we applied Multi-Spectral Estimation of Regularized Spectra (MSERS) [3]. This technique exploits the fact that while fluorescence background is insensitive to small shifts in excitation wavelength, Raman peaks shift predictably with the source wavelength. MSERS uses a statistical model to simultaneously separate Raman and fluorescence contributions from a series of spectra collected at slightly shifted excitation wavelengths. To implement this, we used a temperature-tunable source (DBR-785) to acquire the shifted spectra shown in Fig. 4, from which a background-free Raman spectrum was reconstructed. The resulting fluorescence-free sesame oil spectrum is shown in Fig 5.

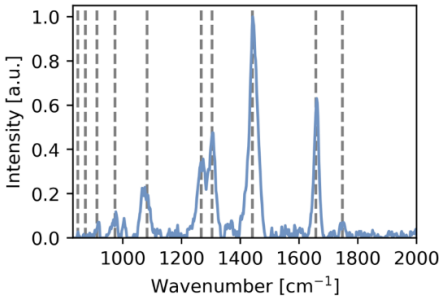

Fig. 5. Reconstructed background- and fluorescence-free spectrum of sesame oil when using the MRES technique.

IV. Conclusion

We have presented a fully monolithic all-solid sub-millimetre multicore fibre Raman probe capable of simultaneous excitation and collection through a single fibre. By engineering the refractive index contrast between cores of a multicore fibre, the probe achieves low inter-core crosstalk and effective silica background suppression without the need for complex distal optics. Validation measurements using ethanol and sesame oil demonstrate the probe's ability to recover clean Raman spectra even in highly fluorescent samples comparable to human tissue. Combined with its compact sub-millimetre diameter and plug-and-play fibre interface, this probe represents a practical and scalable step toward real-time, in-vivo Raman Endoscopy.

References

[1] M. J. Baker *et al.*, 'Clinical applications of infrared and Raman spectroscopy: state of play and future challenges', *Analyst*, vol. 143, no. 8, pp. 1735–1757, Apr. 2018, doi: 10.1039/C7AN01871A.

[2] S. Yerolatsitis *et al.*, 'Ultra-low background Raman sensing using a negative-curvature fibre and no distal optics', *J. Biophotonics*, vol. 12, no. 3, p. e201800239, 2019, doi: 10.1002/jbio.201800239.

[3] N. C. Jenkins *et al.*, 'Computational Fluorescence Suppression in Shifted Excitation Raman Spectroscopy', *IEEE Trans. Biomed. Eng.*, vol. 70, no. 8, pp. 2374–2383, Aug. 2023, doi: 10.1109/TBME.2023.3243866.

[4] E. Cordero, F. Korinth, C. Stiebing, C. Krafft, I. W. Schie, and J. Popp, 'Evaluation of Shifted Excitation Raman Difference Spectroscopy and Comparison to Computational Background Correction Methods Applied to Biochemical Raman Spectra', *Sensors*, vol. 17, no. 8, Jul. 2017, doi: 10.3390/s17081724.

[5] 'Sub millimetre flexible fibre probe for background and fluorescence free Raman spectroscopy - Yerolatsitis - 2021 - Journal of Biophotonics - Wiley Online Library'. Accessed: Mar. 03, 2026. [Online]. Available: https://onlinelibrary.wiley.com/doi/full/10.1002/jbio.202000488

[6] K. Milenko, S. Yerolatsitis, A. Aksnes, D. R. Hjelme, and J. M. Stone, 'Micro-Lensed Negative-Curvature Fibre Probe for Raman Spectroscopy', *Sensors*, vol. 21, no. 24, Dec. 2021, doi: 10.3390/s21248434.

Multilevel Spatial Programming of Photonic Devices with Phase-Change Materials

Chirine Saadi[1], Capucine Laprais[1], Fouad Bentata[1,2], Xavier Letartre[1], Guillaume Saint-Girons[1], Patrice Genevet[3], Nicolas Baboux[1], Lotfi Berguiga[1] and Sébastien Cueff[1,*]

[1]CNRS, Ecole Centrale de Lyon, INSA Lyon, Universite Claude Bernard Lyon 1, CPE Lyon, INL, UMR5270, 69130 Ecully, France
[2]STMicroelectronics, 850 Rue Jean Monnet, Crolles, 38920, France
[3]Department of Physics, Colorado School of Mines, 1523 Illinois Street, Golden, CO 80401, USA
*corresponding author: sebastien.cueff@ec-lyon.fr

***Abstract*— We exploit phase-change materials such as GST and Sb_2S_3 to propose and demonstrate original programmable and multilevel functionalities in integrated photonic devices such as photonic circuits and metasurfaces.**

***Keywords*— Nanophotonics, phase-change materials, programmable devices.**

I. Introduction

Phase change materials (PCMs) are currently revolutionizing nanophotonics by providing ways to reconfigure optical functionalities without any moving parts. Building on this phenomenon, the last decade has witnessed many exciting reports of novel devices exploiting PCMs such as for example beam-steering, tunable light emission, reflection and absorption, programmable metasurfaces and reconfigurable neural networks [1-3]. A large majority of the first studies were using standard PCMs such as GeSbTe as simple binary on-off switches. However, PCMs present another degree of freedom for tunability: multilevel non-volatile states encoded into partial change of phase. Furthermore, recently a new class of low-loss PCMs emerged (e.g. Sb_2S_3 and Sb_2Se_3), with negligible optical absorption in the near-infrared [4,6].

II. Results and Discussion

We first present a method to electrically set multilevel states of crystallization in GST and exploit it to continuously program the free-space reflection of a pixel, spanning a three-orders of magnitude modulation [7].

In a second part, we will present the concept of spatially-controlled planar crystal growth in PCMs, a novel method for programming the growth of optically homogeneous low-loss PCM, leveraging the seeded directional and progressive crystallization within confined channels. We have demonstrated the applicability of guided crystallization on the emerging PCM Sb_2S_3 in two different devices: a programmable optical phase shifter and a reconfigurable metasurface. By patterning a Sb_2S_3 patch onto a Mach-Zehnder interferometer, we successfully programmed ten distinct phase shifts. Next, the ability to precisely control the phase transition of Sb_2S_3 between amorphous and optically homogeneous states was leveraged in reconfigurable metasurfaces, enabling a 100 nm spectral modulation of a bound state in the continuum mode, while preserving the metasurface functionalities. We then conclude on the perspectives for this technology.

III. Conclusion

We have demonstrated methods to go beyond conventional phase-change modulation, by electrically-programming multilevel states in GST and by spatially programming the in-plane guided growth of optically homogeneous Sb_2S_3 crystals.

Acknowledgments

We acknowledge fundings from the French National Research Agency (ANR) under the project MetaOnDemand (ANR-20-CE24-0013) and from the IPCEI program (NCPOCOA) in the framework of France 2030.

References

[1] E. Mikheeva, et al. "Space and time modulations of light with metasurfaces: recent progress and future prospects." ACS photonics 9 (2022).
[2] S. Cueff et al. "VO_2 nanophotonics." APL Photonics 5.11 (2020).
[3] B. J. Shastri, et al. "Photonics for artificial intelligence and neuromorphic computing." Nature Photonics 15, 102 (2021).
[4] W. Dong et al. "Wide bandgap phase change material tuned visible photonics." Advanced Functional Materials 29 1806181 (2019)
[5] M. Delaney, et al. "A new family of ultralow loss reversible phase-change materials for photonic integrated circuits: Sb_2S_3 and Sb_2Se_3." Advanced Functional Materials 30, 2002447 (2020)
[6] A. Taute, et al., "Programming multilevel crystallization states in phase-change-material thin films," Optical Materials Express 13, 3113–3120 (2023).
[7] C. Saadi, et al. "Continuous Electrical Tuning of Reflectivity Using Phase-Change Materials", Applied Physics Letters, 128, 083306 (2026)
[8] F. Bentata et al., "Spatially-Controlled Planar Guided Crystallization of Low-Loss Phase Change Materials for Programmable Photonics" Advanced Materials 38 (8), e06609 (2026).

Topological Eutectic Heterostructure Plasmonic Metasurfaces for THz Lasing and Amplification

Constantine Kouderis[1,*], Anousha Khamsavi[1], Kingshuk Bandopadhyay[1], Hamid Reza Darabian[1], Dorota A. Pawlak[1], Chao Tang[2], Victor Ryzhii[2], and Taiichi Otsuji[1,3]

[1]ENSEMBLE3 Center of Excellence Ltd., Poland
[2]Frontier Research Institute for Interdisciplinary Sciences, Tohoku University, Japan
[3]Institute of High Pressure Physics of the Polish Academy of Sciences, Poland
*Corresponding author: konstantinos.kouderis@ensemble3.eu

***Abstract*— A topological Dirac semimetal/semiconductor eutectic lamellar heterostructure is introduced to a grating-gate planar transistor as a new 'striped' channel material to configure a two-dimensional active plasmonic metasurface. It effectively suppresses the oblique plasmon modes, killers for instability-driven terahertz lasing and amplification. Its novel concept, physics, and device implementation are addressed.**

***Keywords*— Dirac plasmon, topological insulator, eutectic lamellar heterostructure, instability, terahertz, metasurface.**

I. Introduction

The fundamental bottleneck to industrializing 6G and 7G terahertz (THz) communication systems is the THz technological gap [1]. We have been studying novel physics and advanced materials to overcome this challenge [2]. This paper proposes a unique laser transistor amplifier planar device structure consisting of (i) a "striped" metasurface channel that uses a topological Dirac semimetal/semiconductor eutectic lamellar heterostructure and (ii) dual- or triple grating-gate electrodes that actively control the electromagnetic responses of the metasurfaces [3]. This paper discusses the novel concept, the underlying physics, and strategy for device implementation, as well as their impact on science and technology.

II. Methods

The proposed approach integrates advanced material synthesis, theoretical modeling of plasmon instability, and device-level implementation. The conceptual framework combines Topological insulator (TI)/semiconductor eutectic lamellar heterostructures (TI-EuHetero) materials, Coulomb-drag instability, and a striped-channel transistor architecture.

A. Material synthesis and characterization [4]

The TI-EuHetero, particularly Bi_2Te_3/Te, were fabricated using controlled directional solidification. The growth process enables self-organized lamellar architectures with tunable periodicity ranging from sub-micrometer to tens of micrometers. Bi_2Te_3 is a three-dimensional topological insulator whose surface-state dispersion and hybridization gap depend on film thickness: ultrathin films exhibit a gap due to inter-surface coupling, while thicker films recover gapless Dirac surface states [5]. In bulk-like or heterostructured configurations relevant to THz device operation, however, the electrical response is predominantly governed by bulk semiconducting or semimetallic carriers, with the topological surface states contributing only weakly. Under these conditions, the material effectively behaves as a narrow-gap semimetal for high-frequency transport, while its topological surface states remain spectroscopically present but play a secondary role.

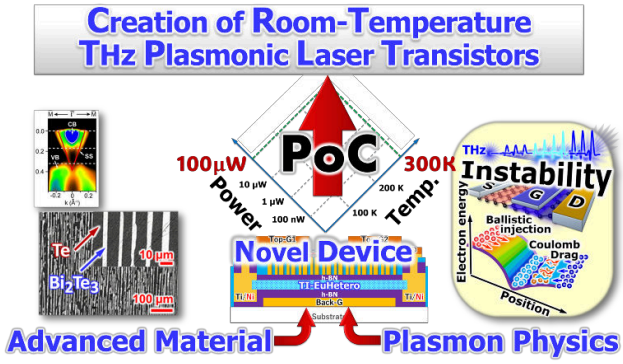

Fig. 1 Conceptual image of the proposed material/physics/devices.

B. Theoretical framework: Coulomb-drag instability [6,7]

The physical mechanism underlying THz amplification is based on the Coulomb-drag instability of Dirac plasmons, where ballistic carriers injected under drain bias interact with confined carriers in the gated channel. This interaction leads to backflow currents and negative differential conductance (NDC), enabling plasmon gain in the THz regime. Theoretical modeling incorporates carrier transport asymmetry, many-body Coulomb interactions, and hydrodynamic plasma effects, predicting instability-driven amplification even at room temperature.

C. Device architecture and metasurface design [3]

A 2.5D striped-channel plasmonic transistor is implemented by integrating TI-EuHetero into a grating-gate field-effect transistor (FET) (Figs. 2 and 3). The lamellar structure inherently forms a periodic striped channel, eliminating the need for nanoscale etching while suppressing oblique plasmon modes. Dual- or asymmetric dual-grating-gate (ADGG) electrodes are employed to:

1) electrostatically define plasmon cavities,
2) induce p–i–n junctions, and
3) enhance plasmon confinement and resonance.

Device fabrication follows a scalable top-down process including gate stack formation, heterostructure transfer, lithographic patterning, and dielectric encapsulation.

D. Simulation and experimental validation

A multiscale modeling framework combining first-principles calculations, electron–phonon-plasmon-polariton interactions, and carrier transport ensemble Monte Carlo simulations and electromagnetic simulations are used to optimize plasmon resonance conditions, effective permittivity, and damping factors, while experimental validation includes THz emission and absorption measurements under current injection. The combined methodology ensures consistency between theoretical predictions and device performance.

III. Results and Discussion

A. Material performance and electronic properties

Structural and electronic properties were characterized using micro-Raman spectroscopy, atomic force microscopy (AFM), and angle-resolved photoemission spectroscopy (ARPES), confirming high crystallinity and atomically sharp interfaces. The fabricated Bi_2Te_3/Te eutectic heterostructures exhibit excellent and tunable lamellar periodicity together with asymmetric Dirac dispersion and favorable band alignment, enabling p–i–n junction formation [4]. These properties support high carrier mobility and low plasmon damping, which are essential for efficient THz plasmonic operation.

B. Evidence of plasmonic gain and instability

Previous graphene-based devices demonstrated THz amplification up to ~9% at room temperature, confirming the feasibility of current-driven plasmon gain [8]. However, the gain remains insufficient for lasing. The proposed TI-EuHetero platform enhances this mechanism through stronger Coulomb interactions and reduced damping, enabling significantly higher instability-driven gain.

C. Suppression of plasmon damping

A critical limitation in conventional planar devices is overdamping caused by oblique plasmon modes [9]. The intrinsic lamellar “striped” geometry of TI-EuHetero channels effectively suppresses these modes, leading to improved quality factors and stronger resonant plasmon oscillations (Figs. 2 and 3). This represents a key breakthrough toward achieving coherent THz emission at room temperature.

D. Device-level performance and metasurface response

The integration of TI-EuHetero into grating-gate transistor architectures enables the realization of an active plasmonic metasurface. Experimental and simulated results demonstrate:

- strong THz absorption approaching unity at resonance,
- broadband response with significantly enhanced bandwidth compared to conventional THz absorbers, and
- good agreement between theoretical models and measured spectra.

Furthermore, cascading Coulomb-drag instability in ADGG structures enables resonant amplification and self-oscillation in the THz range. Analytical evaluation indicates an overall performance improvement exceeding two orders of magnitude compared to conventional graphene-based devices.

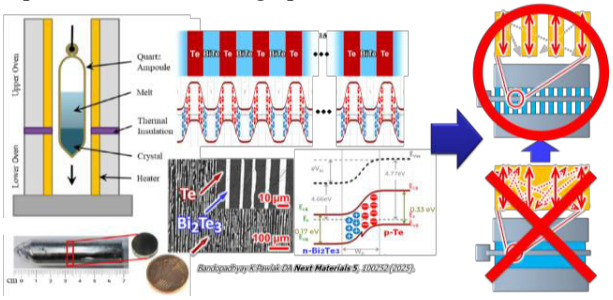

Fig. 2 Conceptual image of the TI-EuHetero lamellar structure and properties.

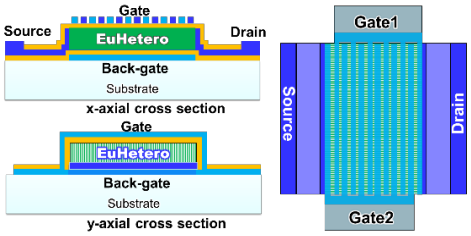

Fig. 3 Conceptual image of the striped-channel transistor architecture.

E. Implications for THz technology

The results demonstrate a viable pathway to overcome the “THz gap” by combining new materials, new physics, and novel device architectures. The proposed approach enables scalable, electrically driven, room-temperature THz sources suitable for next-generation communication systems.

IV. Conclusion

We demonstrated a pathway to room-temperature THz plasmonic laser transistors by combining advanced materials, novel physics, and scalable device architectures.

Acknowledgments

This work was supported by ENSEMBLE3 Ltd. under the International Research Agenda program of the Foundation for Polish Science (FENG.02.01-IP.05-0044/24), the European Union through the Horizon 2020 Teaming for Excellence program (GA No. 857543), the Poland Minister of Science and Higher Education Center of Excellence project under the Horizon 2020 program (No. MEiN/2023/DIR/3797), JSPS KAKENHI (Grant Nos. 21H04546, 25K22093, 25K01281), Japan, the New Energy and Industrial Technology Development Organization (Grant No. 20020912), Japan, the Murata Foundation (Grant No. AN24322), Japan, and the Iketani Foundation (Grant No. 0361181-A), Japan.

References

[1] A. Leitenstorfer et al., J. Phys. D: Appl. Phys., vol. 56, p. 223001, 2023.
[2] T. Otsuji et al., Appl. Phys. Exp., vol. 19, p. 020103, 2026.
[3] T. Otsuji et al., PL Patent P.452216, 2025.
[4] K. Bandopadhyay et al., Next Mater., vol. 5, p. 100252, 2024.
[5] Y.-Y. Li et al., Adv Mater. vol. 22(36), pp. 4002-4007, 2010.
[6] V. Ryzhii et al., Phys. Status Solidi A, vol. 219, p. 2100694, 2022.
[7] V. Ryzhii et al., Phys. Rev. Appl., vol. 16, p. 014001, 2021.
[8] S. Boubanga-Tombet et al., Phys. Rev. X, vol. 10, p. 031004, 2020.
[9] M. Dyakonov, Semiconductors, vol. 42, pp. 984-988, 2008.

Long-lived subradiance via cavity-mediated collective interaction

Kyu-Young Kim[1], JinHeeLee[1],Woong Bae Jeon[1], Dong Hyun Park[1], Suk InPark[2], Jin Dong Song[2], Changhyoup Lee[3], and Je-Hyung Kim[1,*],

[1]Department of Physics, Ulsan National Institute of Science and Technology, South Korea
[2]Center for Opto-Electronic Materials and Devices, Korea Institute of Science and Technology, South Korea

[3]Department of Physics, Hangyang University, South Korea
*Corresponding author: jehyungkim@unist.ac.kr

***Abstract*—We demonstrate strong collective emission from a cavity-mediated steady-state subradiant state. In a tailored photonic environment with balanced cavity dissipation ns emitter-field coupling strength, As a key signature of steady-state subradiance, we observe strong photon bunching with elongated decay. Our approach paves the way for generating and harnessing quantum correlations .**

***Keywords*— Collective interaction, Subradiance, quantum dots, nanophotonics.**

I. Introduction

Cooperative effects such as super(or sub)radiance in quantum systems arise from the interplay among quantum emitters. While bright superradiant states have been extensively studied and have yielded important insights into cooperative phenomena, subradiant states remain less explored due to their inherently dark state nature. However, subradiance holds significant potential as a valuable quantum resource exploiting long-lived and large-scale entanglement, which is a key for advancing quantum information technologies.

II. RESULT

We experimentally demonstrate cavity-mediated steady-state subradiance in two quantum dots (QDs) coupled to a low-Q nanophotonic cavity. The engineered cavity environment balances emitter–cavity coupling and dissipation, enabling a dominant steady-state population in a subradiant collective state.

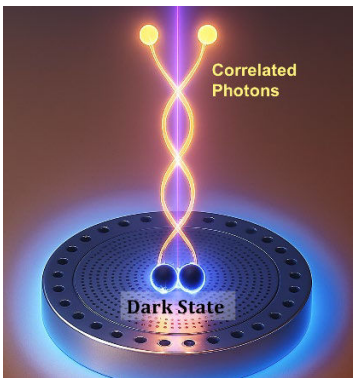

Photon correlation measurements reveal strong photon bunching, with $g^{(2)}(0)>8$ exceeding the classical limit when the QDs are spectrally coupled to the cavity.

The collective state suppresses single-photon decay while enabling a cascade two-photon emission process, resulting in an extended antibunching decay time of ~36 ns. Numerical simulations based on a Tavis–Cummings model with dissipative dynamics confirm that steady-state subradiance emerges when incoherent pumping, cavity dissipation, and emitter–cavity coupling are properly balanced.

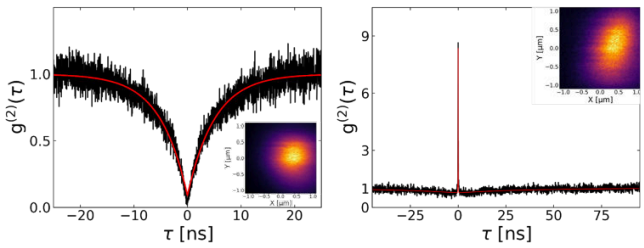

Fig. 1 Comparison of $g^{(2)}(t)$ curve with cavity-coupled single dot and two quantum dots

III. Conclusion

These results provide the first experimental demonstration of steady-state subradiance in cavity-coupled quantum dots under incoherent pumping, revealing controllable collective quantum correlations in solid-state emitters. The work establishes a platform for engineering multi-emitter cooperative phenomena and generating strongly correlated photons for quantum photonics applications.

References

[1] K.-Y. Kim, J. H. Lee, W. B. Jeon, D. H. Park, S. I. Park, J. D. Song, C. Lee, and J.-H. Kim, "Cavity-mediated collective emission from steady-state subradiance", Nature Commun. 16, 6346, 2025

Laser Processing of Metallic Surfaces for Radiative Cooling and Autonomous Dew Water Harvesting

P. Pou-Álvarez[1234]*, A. Mongruel[3], M. Fernández-Arias[12], A. Riveiro[15], D. Beysens[3], J. Pou[12]

[1] LaserON Research Group, CINTECX, Universidade de Vigo, Spain
[2] Applied Physics Department, Universidade de Vigo, Spain
[3] PMMH, CNRS, ESPCI Paris – PSL University, France
[4] School of Physics and Astronomy, Monash University, Australia
[5] Materials Engineering Department, Universidade de Vigo,
*Corresponding author: ppou@uvigo.es

Abstract **Laser micropatterning enables aluminum surfaces to achieve high infrared emissivity and superhydrophilic wetting for passive radiative cooling and autonomous dew harvesting. Laser-textured samples reach emissivity up to 0.95, promote stable filmwise condensation, and enhance capillary drainage. Outdoor experiments show up to 70 percent higher dew yield than state-of-the-art commercial condensers.**

Keywords**— laser texturing, radiative cooling, dew harvesting, infrared emissivity, superhydrophilic surfaces.**

I. Introduction

Atmospheric water harvesting through dew condensation is a promising strategy for decentralized freshwater production. Passive radiative cooling enables autonomous operation by allowing surfaces with high emissivity in the 8–13 μm atmospheric window to cool below ambient temperature and reach the dew point. However, conventional metallic surfaces suffer from low emissivity and unfavorable condensation dynamics, limiting water collection efficiency. Surface engineering via laser micro/nanofabrication provides a scalable route to tailor emissivity, wettability, and fluid transport behavior for improved dew harvesting performance.

II. Methods

Aluminum substrates were processed using nanosecond pulsed laser scanning to generate parallel microgrooves and multiscale roughness. The treatment increases surface oxidation and effective area, producing broadband infrared absorption and superhydrophilic wetting. Surface morphology was characterized by SEM and optical profilometry. Wettability was evaluated through contact angle and capillary wicking measurements. Infrared emissivity was measured by FTIR reflectivity in the atmospheric window. Condensation and water collection behavior were assessed in laboratory climatic chambers and in a one-year outdoor dew harvesting installation.

III. Results and Discussion

Laser-textured aluminum exhibits emissivity values up to 0.95 in the 8–13 μm range and transitions from moderate hydrophilicity to superhydrophilicity. The grooved topography promotes rapid capillary wicking and stable filmwise condensation, reducing retained liquid volume by approximately threefold compared with untreated dropwise-condensing surfaces. Radiative cooling experiments show temperature reductions of up to 5 °C below ambient under radiative deficit conditions. Outdoor testing demonstrates a consistent improvement of approximately 70 percent in collected dew water relative to a high-emissivity painted reference condenser [1]. The enhanced performance is attributed to earlier onset of water collection and more efficient drainage enabled by capillary-guided flow.

IV. Conclusion

Laser micropatterning transforms reflective metallic surfaces into robust radiative cooling emitters and efficient dew harvesting platforms. The combination of high infrared emissivity, superhydrophilic wetting, and capillary-driven drainage enables scalable, passive, and durable atmospheric water harvesting suitable for real-world needs.

Acknowledgments

This work was partially supported by the Government of Spain [PID2020-117900RB-I00 (MCI/AEI/FEDER, UE), EQC2018-004315-P (AEI/FEDER UE) and Margarita Salas Fellowships], and by Xunta de Galicia (ED431C 2023/25 and ED481B-2023-030).

References

[1] P. Pou-Álvarez et al. Advanced Materials, 2025. DOI: 10.1002/adma.202419472..

Metasurfaces for Laser Cooling and Trapping of Atoms and Integrated Cold-Atom Platforms

Thu H. H. Le,[1] R. Takei,[1] S. Kagami,[2] A. Takamizawa,[1] Y. Kurashima,[1] T. Motomura[1]*

[1] National Institute of Advanced Industrial Science and Technology (AIST), Japan
[2] NEC-AIST Quantum Technology Cooperative Research Laboratory, Japan
*Corresponding author: thu.le@aist.go.jp

***Abstract*— This study presents a scheme of using flat optics composed of geometric-phase metasurfaces to cool neutral atoms and assembly them into arrays of individually trapped atoms. We exploit the ability of metastructures in controlling the phase, amplitude, and polarization of light with sub-wavelength resolution to generate tailored wavefronts for cooling and optical dipole trapping of atoms.**

***Keywords*— cold atoms array, dielectric metasurfaces, magneto-optical trapping (MOT), optical dipole trapping (ODT).**

I. Introduction

Cold-atom arrays prepared by laser cooling and trapping play a central role in precision measurements and quantum technologies, enabling advances in quantum metrology, sensing, quantum computing, and quantum simulation. In conventional experiments, alkali or alkaline-earth atoms confined in an ultrahigh-vacuum chamber are first cooled near the Doppler limit using a magneto-optical trap (MOT), and then the cooled atoms are trapped and arranged into lattice configurations using optitraps (ODTs). However, these MOT and ODT implementations typically rely on complex and bulky optical assemblies, leading to large experimental footprints and high sensitivity to optical misalignment. Here, we propose and experimentally demonstrate a metasurface-based platform that enables laser cooling and optical trapping within a compact, planar architecture, by exploiting the capability of dielectric metastructures in controlling the phase, amplitude, and polarization of light at sub-wavelength resolution.

II. Methods

Our proposed metasurface-based MOT employs a metasurfaces composed of the Pancharatnam–Berry phase structures to generate the diffracted and transmitted wavefronts with tailored polarization states. Figure 1 schematically illustrates the MOT configuration employing a diffraction-engineered metasurface. The metasurface is designed such that, under normal incidence of a circularly polarized beam of a given handedness, it generates multiple diffracted beams with the opposite handedness, along with a central transmitted beam that preserves the incident polarization. The diffracted beams are directed toward the optical axis at a fixed angle θ. A second collimated circularly polarized beam is introduced from the counter-propagating direction, with the optical axes of both beams aligned along the axial direction of the quadrupole magnetic field. The transmitted axial beam and the corresponding oblique diffracted components overlap spatially, forming a region in which atoms interact with all beams. When the magnetic-field zero is adjusted to position within this overlap region, atoms are trapped and cooled.

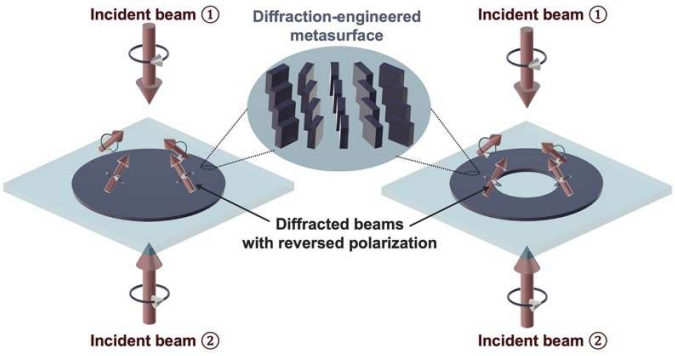

Fig.1 Schematic illustration of a magneto-optical trap (MOT) configuration employing a diffraction-engineered metasurface that enables atomic cooling under single-direction illumination.

III. Results and Discussion

In the metasurface-based MOT, the transverse restoring forces are primarily generated by the diffracted beams generated by the metasurface, whereas the axial restoring forces arise mainly from the counter-propagating axial light fields, which are essential for balancing the trapping forces along the longitudinal axis. Moreover, the independently tunable intensities of the incident and diffracted beams provide precise control over both axial and transverse restoring forces. We experimentally demonstrate successful trapping and cooling of cesium atoms, and support the trapping mechanism with numerical calculations of optical radiation forces.

After cooling in the MOT, atom ensembles are assembled into arrays of individual atoms using optical dipole trapping based on the optical tweezer principle. High-fidelity atom arrays require optical tweezers with sufficiently deep trapping

potentials, well-defined geometric configurations, and high intensity uniformity across individual traps. In this study, we demonstrate a metasurface hologram that simultaneously generates and focuses light into arrays of focal spots under collimated-beam illumination, thereby forming optical tweezer arrays. Owing to the subwavelength-scale phase modulation offered by the metastructures, which is approximately 20 times finer than that achievable with conventional spatial light modulators, the fabricated meta-hologram produces trapping potentials comparable to those of a high–numerical-aperture lens with *NA* values of up to 0.9. Furthermore, it enables the formation of dual-spot arrays with inter-spot separations approaching the diffraction limit.

IV. Conclusion

In conclusion, we have demonstrated and verified the performance of metasurfaces in magneto-optical trapping and optical dipole trapping of alkali-metal atoms. The cooling and trapping of atoms with metasurfaces, without the need for extra optical components, demonstrates high optical efficiency, and scalability potential. These characteristics highlights the potential of metasurfaces in realization of compact and lower-power quantum systems, with broad applications in quantum metrology, quantum information processing, and atomic physics.

Acknowledgments

This study was supported by PRESTO (JPMJPR235C) from The Japan Science and Technology Agency.

Polymer-Based Passive Radiative Cooling Films for Thermal Management

Emma Spotorno[1*], Paola Stagnaro[3], Lucia Conzatti[3], Roberto Utzeri[3], Simona Losio[3], Francesco Bisio[2], Michele Magnozzi[1], Maurizio Canepa[1]

[1]Department of Physics, Università degli Studi di Genova, Italy
[2]CNR-SPIN, Genoa, Italy
[3]CNR-SCITEC, Genoa, Italy
*Corresponding author: emma.spotorno@edu.unige.it

***Abstract*— Polymer based passive radiative coolers incorporating silica microspheres are investigated to enhance infrared emissivity. Films are fabricated and characterized by infrared spectroscopy. Thermal performance is evaluated through temperature dynamics measurements under controlled conditions. Compared to the pure polymer, microsphere filled samples exhibit enhanced emissivity and improved radiative cooling performance.**

Keywords - radiative cooling, polymer films, infrared emissivity, thermal characterization

I. Introduction

Passive Daytime Radiative Cooling (PDRC) has emerged as an effective strategy for reducing thermal loads without energy consumption, by exploiting selective radiative heat exchange with the cold outer space. An efficient radiative cooler must simultaneously exhibit high reflectance across the solar spectrum to minimize solar absorption and strong thermal emissivity within the mid-infrared atmospheric transparency window [1].

Polymer-based materials have recently attracted significant attention for PDRC applications due to their intrinsic infrared emissive properties [2]. In this work silica microspheres were embedded within polymer films in order to improve the emissivity and to customize the optical properties of polymer matrices [3]. The polymer-based radiative cooling films were developed and characterized to investigate the relationship between infrared emissivity and thermal cooling performance.

II. Methods

Polymer based radiative cooling films incorporating silica microspheres of different diameters are fabricated by hot pressing and laminated onto stainless steel substrates coated with an optically thick silver layer. Optical properties are characterized by infrared spectroscopic ellipsometry to assess emissivity and optical response. Thermal performance is evaluated by temperature-dynamics measurements under radiative loads in highly controlled and reproducible conditions.

III. Results and Discussion

Infrared spectroscopic measurements reveal that the incorporation of silica microspheres enhances the emissivity of the polymer films within the mid infrared atmospheric window. This is due to both the intrinsic absorbance/emissivity of silica in the mid-IR, and to the occurrence of finite-size dielectric resonances in few-micron-sized dielectric spheres.

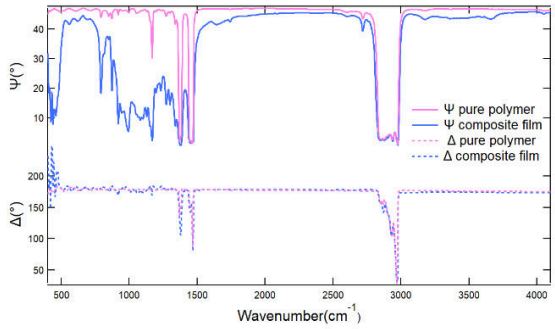

Fig. 1 Infrared spectroscopic ellipsometry response for pure polymer and silica microsphere filled composite films.

Thermal measurements were performed in a custom-built vacuum chamber, where the radiative cooler systems were exposed to a cold heat sink (liquid nitrogen source), while at the same time minimizing spurious heat losses by convection and conduction.

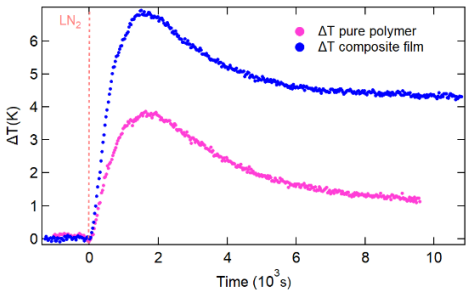

Fig. 2 Temperature difference between the radiative cooling film and a dummy reference under vacuum conditions, showing enhanced cooling for the composite sample.

The results demonstrate that polymer composite films containing silica microspheres exhibit a larger temperature reduction compared to the pure polymer reference. This enhanced cooling behavior is consistent with the increased infrared emissivity observed in the optical characterization.

IV. Conclusion

Polymer-based radiative cooling films incorporating silica microspheres demonstrate enhanced passive cooling performance compared to pure polymer samples. Infrared optical characterization and vacuum chamber thermal measurements confirm the role of increased emissivity in promoting radiative heat dissipation. These results highlight polymer composites as materials for passive thermal management.

Acknowledgments

This work was supported by the National Recovery and Resilience Plan (NRRP), Mission 4, Component 2, Investment 1.1, PRIN 2022 (Project ERACLITO, CUP B53D2300904006) and PRIN PNRR 2022 (Project ARCO, CUP B53D23027690001), funded by the European Union – NextGenerationEU.

References

[1] A. P. Raman, M. A. Anoma, L. Zhu, E. Rephaeli, and S. Fan, “Passive radiative cooling below ambient air temperature under direct sunlight,” Nature, vol. 515, pp. 540–544, 2014.

[2] T. Wang, Y. Wu, L. Shi, X. Hu, M. Chen, and L. Wu, “A structural polymer for highly efficient all-day passive radiative cooling,” Nature Communications, vol. 12, p. 365, 2021.

[3] Y. Zhai et al., “Scalable-manufactured randomized glass-polymer hybrid metamaterial for daytime radiative cooling,” Science, vol. 355, pp. 1062–1066, 2017.

Electromagnetic Wave Localisation in Aperiodic and Correlated Disorder Photonic Structures

Marian Florescu, Alex Meek and Kriss Stokkereit

Optoelectronics Research Centre, University of Southampton, United Kingdom
*Corresponding author: m.florescu@soton.ac.uk

***Abstract*— We study electromagnetic wave transport and localisation in aperiodic and correlated disordered structures in one and two dimensions. Ensemble simulations show that correlated disorder tunes transparency, localisation, and band gap formation. A minimum spacing constraint stabilises short range structure and enables controlled localisation.**

***Keywords*— hyperuniform disorder, correlated disorder, photonic structures, wave localisation.**

I. Introduction

Quasicrystalline photonic structures constitute a prime example of aperiodic structures, while hyperuniform disordered photonic systems suppress large scale density fluctuations while retaining tunable short and intermediate range correlations [1]. The one- and two-dimensional cases exhibit distinct structural behaviour compared with higher dimensions, with unusually persistent short-range correlations that strongly influence wave transport and localisation. In this context, aperiodicity and correlated disorder provides a powerful route to control light localisation, bridging regimes of extended transport and Anderson localised states without relying on perturbed periodic order or complete randomness [2-6].

II. Methods

We generate 5-fold symmetric quasicrystalline structures and stealthy hyperuniform point patterns with controlled disorder strength, optionally enforcing a minimum spacing between neighbouring points. Photonic microstructures are constructed by arranging high index scatterers along the unit cell. We compute eigenmodes and localisation metrics using band structure simulations and validate transport trends using a scattering matrix approach across ensembles and system sizes. Statistical averaging over large ensembles is used to suppress sample-specific fluctuations and isolate the role of structural correlations in governing localisation and transport behaviour.

III. Results and Discussion

Results and Discussion

• The results reveal a clear separation between distinct transport regimes governed by the degree of hyperuniformity. At low frequencies, correlated disorder gives rise to extended transparency regimes in which wave propagation is robust despite the absence of periodic order. As frequency increases, modes progressively localise, with localisation strength and spectral extent strongly modulated by the underlying structural correlations.

• Analysis of inverse participation ratios, density of states, and level spacing statistics shows that hyperuniform systems support both single parameter scaling and non-scaling transport regimes. The boundaries between these regimes shift systematically with disorder strength, reflecting the competition between long range hyperuniform correlations and short-range structural fluctuations.

• Introducing a minimum spacing between scattering elements suppresses pathological short-range clustering while preserving hyperuniformity. This modification enables the emergence of photonic band gap behaviour and produces a more controlled localisation landscape. Disorder resolved analysis demonstrates that the observed transport properties remain stable under additional perturbations, highlighting the resilience of correlated disorder engineered photonic media.

IV. Conclusion

Aperiodicity and correlated disorder provide a compact route to engineer transparency and localisation through structural correlations rather than periodicity alone. These findings establish aperiodicity and correlated disorder as a practical and robust design parameter for photonic and metamaterial systems.

Acknowledgments

This work was supported by EPSRC DTP awards EP/W524463/1 and EP/R513350/1. M. Florescu acknowledges EPSRC support under Grant EP/Y016440/

References

[1] M. Florescu, S. Torquato, and P. J. Steinhardt, Proceedings of the National Academy of Sciences, vol. 106, pp. 20658 to 20663, 2009.
[2] P. W. Anderson, Physical Review, vol. 109, pp. 1492 to 1505, 1958.
[3] S. John, Physical Review Letters, vol. 58, pp. 2486 to 2489, 1987.
[4] E. Abrahams, P. W. Anderson, D. C. Licciardello, and T. V. Ramakrishnan, Physical Review Letters, vol. 42, pp. 673 to 676, 1979.
[5] C. M. Soukoulis and E. N. Economou, Waves in Random Media, vol. 9, pp. 255 to 272, 1999.
[6] L. S. Froufe-Perez, M. Engel, J. J. Saenz, and F. Scheffold, Proceedings of the National Academy of Sciences, vol. 114, pp. 9570 to 9574, 2017.

Phase nanoengineering of complex oxides for spin-wave devices

Piero Florio[1], Matteo Vitali[1], Valerio Levati[1], Luca Ciaccarini Mavilla[2], Marco Madami[2], Silvia Tacchi[3], Daniela Petti[1], Edoardo Albisetti[1]*

[1]Dipartimento di Fisica, Politecnico di Milano, Milan, Italy
[2]Dipartimento di Fisica e Geologia, Università di Perugia, Via A. Pascoli, Perugia, Italy
[3]CNR-IOM, Sede Secondaria di Perugia c/o Dipartimento di Fisica e Geologia, Università di Perugia, Perugia, Italy
*Corresponding author: edoardo.albisetti@polimi.it

***Abstract*- Phase nanoengineering enables direct local control of the physical properties of complex oxide thin films. We create stable magnetic landscapes that define spin-wave waveguides, magnonic crystals and networks, in YIG. Such devices allow long distance spin-wave propagation and cascading, opening the way to RF signal processing using spin waves.**

***Keywords*- phase nanoengineering, yttrium iron garnet, magnonics, direct laser writing, spin waves.**

I. Introduction

Magnonics seeks to transport and process microwave information on-chip using spin waves rather than charge currents. YIG is the reference complex oxide because its exceptionally low damping supports long coherent propagation, yet conventional nanopatterning damages crystalline garnets preventing long-distance spin-wave propagation, and mostly offers two dimensional geometries. Here, we show that phase nanoengineering via direct laser writing overcomes this limitation by locally tuning the material properties after growth.

II. Methods

Phase nanoengineering [1] uses a localized energy source to write stable, grayscale property landscapes directly into a film. In particular, direct laser writing focuses ultraviolet light, producing highly localized transformations to the crystalline phase of the material, which in turn leads to changes in its magnetic properties. In crystalline YIG, a 405 nm laser is used to either recrystallize the material in a strained high anisotropy three-dimensional volume in 1 micron thick films [2], or to amorphize selected regions in 100 nanometer films [3].

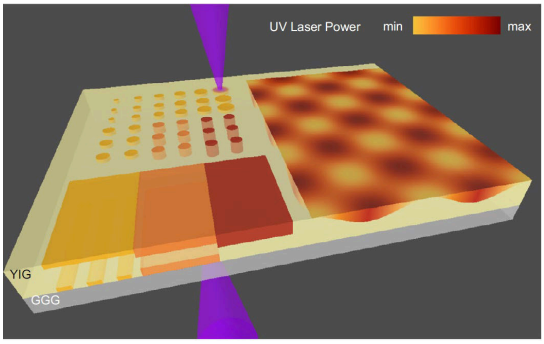

Fig. 1 Phase nanoengineering writes stable magnetic and structural landscapes that manipulate spin waves in YIG.

III. Results and Discussion

We use UV laser writing to create three-dimensional anisotropy profiles in single crystal YIG. We show that the perpendicular magnetic anisotropy rises by about thirty times, with approximately 100 nanometer-wide lateral features, continuous depth control, and the possibility to realize buried patterns written through the transparent GGG substrate. These profiles tune the spin-wave dispersion, localization and nonreciprocity, enabling direct write magnonic crystals [2].

In this second case, laser amorphization turns exposed YIG nonmagnetic while preserving crystalline channels (i.e. waveguides) for low loss propagation. The devices show spin-wave transport with low magnetic losses for hundreds of wavelengths. Using this methodology we demonstrate coherent power transfer in coupled waveguides, low-loss directional couplers, phase shifters, splitters, demultiplexers and phase controlled routers. Cascading these primitives, we realize programmable interferometric meshes with up to nineteen couplers and phase shifters in seven cascaded stages, operating without intermediate amplification [3].

IV. Conclusion

Together, these results demonstrate phase nanoengineering as a monolithic route to realize integrated low-losses magnonic platforms, overcoming the long-standing issue of scalability and cascading in magnonic platforms for classical and quantum processing.

Acknowledgments

E.A. acknowledges support from the European Union grants 948225 (B3YOND) and 101290493 (LANTERN), and from the Italian Ministry for University and Research (MUR) grant R20FC3PX8R (NAMASTE).

References

[1] V. Levati et al., "Phase Nanoengineering via Thermal Scanning Probe Lithography and Direct Laser Writing," Advanced Materials Technologies, vol. 8, 2300166, 2023.
[2] V. Levati et al., "Three-dimensional nanoscale control of magnetism in crystalline Yttrium Iron Garnet," Nature Communications, vol. 16, 9602, 2025.
[3] P. Florio et al., "Programmable Integrated Magnonic Meshes," arXiv:2605.00290v2, 2026.

Micron Scale Spontaneous Parametric Down Conversion in Periodically Poled Layered Semiconductors

Leone di Mauro Villari[1], Andrea Alessandrini[1], Benjamin Braun[2,3], Simone Paganelli[1], Chiara Trovatello[5,6], Lee A. Rozema[2], and Andrea Marini[1,4]
[1]Department of Physical and Chemical Sciences, University of L'Aquila, Italy; [2]Vienna Center for Quantum Science and Technology, University of Vienna, Austria; [3]Vienna Doctoral School in Physics, University of Vienna, Austria; [4]CNR-SPIN, c/o Department of Physical and Chemical Sciences, L'Aquila, Italy; [5]Department of Mechanical Engineering, Columbia University, New York, USA; [6]Dipartimento di Fisica, Politecnico di Milano, Italy.
*Corresponding author: leone.dimaurovillari@univaq.it

***Abstract*—We present a theoretical framework for compact photon pair generation in periodically poled layered semiconductors. The model predicts enhanced brightness, polarization tunability, and compatibility with integrated quantum photonics.**

***Keywords*– spontaneous parametric down conversion, transition metal dichalcogenides, periodic poling, entangled photons, integrated quantum photonics.**

I. Introduction

Spontaneous parametric down-conversion (SPDC) is one of the most established mechanisms for generating entangled photon pairs for quantum communication, sensing, and photonic quantum information processing. Standard SPDC sources are usually based on millimetre- or centimetre-scale bulk nonlinear crystals, because the probability of pair creation is small and must be accumulated over a long propagation length. This requirement is difficult to reconcile with integrated quantum photonics, where the desired sources should be thin, bright, stable, and directly compatible with miniaturised optical circuits.

Layered transition metal dichalcogenides (TMDs) provide an attractive alternative. In particular, the non-centrosymmetric 3R polytype of MoS_2 possesses a large second-order nonlinear response while allowing multilayer assembly at the micron scale. The central difficulty is that a short sample does not automatically guarantee efficient SPDC: the signal and idler fields must remain phase matched with the pump, and the finite stack produces reflections that cannot be ignored. The work summarised here addresses these issues by developing a full theoretical description of SPDC in periodically poled 3R-TMD slabs, with emphasis on brightness scaling, emission geometry, and polarization entanglement.

II. Methods

The proposed device is a stack of nonlinear 3R-TMD slabs in which neighbouring slabs are rotated by π around the optical axis. This rotation leaves the linear optical response essentially unchanged in the isotropic approximation, but it flips the sign of the relevant in-plane components of the second-order susceptibility tensor. The stack therefore implements quasi-phase matching, in direct analogy with periodically poled bulk crystals, but using geometric rotation of van der Waals layers rather than ferroelectric domain inversion [1], [3].

The calculation is organised in three steps. First, the linear scattering problem is solved for the finite TMD structure. In the telecom region, where absorption and dispersion are weak, the electromagnetic field can be quantized canonically in a homogeneous effective medium. Signal and idler modes are labelled by transverse momentum, propagation direction, and polarization, and the corresponding creation and annihilation operators form the basis for the perturbative treatment [2].

Second, the nonlinear interaction Hamiltonian is derived from the second-order polarization. Periodic poling is represented by a spatially alternating tensor, or equivalently by a Fourier series whose odd harmonics supply the missing longitudinal momentum. This gives an analytic coupling amplitude between pump, signal, and idler modes. In the degenerate case considered in the numerical analysis, a 780 nm pump generates signal and idler photons at 1560 nm. The phase mismatch depends on the propagation directions of the two generated photons; consequently, the model naturally includes forward-forward, backward-backward, and forward-backward pair emission.

Third, the finite-size character of the stack is retained by a transfer-matrix treatment. This step is essential because the micron-scale sample is not simply a short piece of bulk nonlinear material. Multiple reflections at the interfaces dress the quantum modes and introduce low-quality cavity resonances. The final biphoton wavefunction is obtained after rewriting the nonlinear Hamiltonian in terms of outgoing vacuum modes, allowing direct calculation of the photon-pair flux collected within a chosen numerical aperture.

The same formalism also provides direct access to the quantum state rather than only to the conversion rate. For a fixed emission direction, the biphoton state is a coherent superposition of the four polarization amplitudes HH, HV, VH, and VV. Its degree of entanglement is evaluated through the reduced-state purity, concurrence, and fidelity with respect to the target Bell state. For realistic detection, the polarization density matrix is reconstructed by integrating over the angular modes accepted by the collection numerical aperture. This step traces out spatial information and captures the dephasing that appears when photons emitted at different angles acquire different phases before being measured.

III. Results and discussion

For the parameters analysed, the optimal single-slab thickness is close to 580 nm. At this thickness, periodic poling creates a quasi-phase-matched emission cone and strongly enhances the number of detected photon pairs. The efficiency grows faster than the usual quadratic dependence on the number of coherently phased slabs. This super-quadratic behaviour is not a violation of phase-matching intuition; it arises from the combination of quasi-phase matching and finite-stack resonances.

The theory predicts that photon pairs are produced not only in the transmitted forward-forward channel, but also in backward-backward and mixed forward-backward channels. These additional channels are weaker than the forward emission, yet they are physically important because they result from the cavity-like nature of the layered system and would not be expected in the same way from a conventional long bulk crystal.

The polarization state is controlled mainly by crystal symmetry and pump polarization. Periodic poling changes brightness and angular distribution, while leaving the intrinsic entanglement structure largely intact. A linearly polarized pump can select Bell states or coherent superpositions of them, whereas circular pump polarization suppresses the polarization entanglement. This behaviour is consistent with recent demonstrations of entangled photon-pair generation in 3R-TMD materials [4], [5].

The collection aperture is a relevant design parameter. A larger aperture collects more photon pairs, increasing the useful brightness, but it also mixes angular components with different phases. The resulting polarization density matrix can therefore become less pure even when each individual emission direction is nearly maximally entangled. This trade-off is familiar from high-brightness bulk SPDC sources, but here it appears in a much thinner platform and is coupled to the finite-stack resonances. The model therefore gives a practical route for choosing the slab number, poling period, and collection geometry together, rather than optimising the pair-generation rate alone.

IV. Conclusions

The study identifies periodically poled 3R-TMDs as a promising platform for ultrathin, integrated, and polarization-programmable entangled photon sources. The next theoretical developments should include absorption near excitonic resonances, anisotropy at large emission angles, finite lateral dimensions, and realistic collection optics. Experimentally, the main challenge is precise multilayer fabrication with controlled rotation, thickness, and optical quality.

Acknowledgments

The original paper acknowledges Marco Liscidini and Alessia Stefano for useful discussions.

References

[1] J. A. Armstrong, N. Bloembergen, J. Ducuing, and P. S. Pershan, "Interactions between light waves in a nonlinear dielectric," *Phys. Rev.*, vol. 127, pp. 1918–1939, 1962.

[2] L. Mandel and E. Wolf, *Optical Coherence and Quantum Optics*. Cambridge University Press, 1995.

[3] C. Trovatello *et al.*, "Quasi-phase-matched up-and down-conversion in periodically poled layered semiconductors," *Nat. Photon.*, 2025.

[4] J. Feng *et al.*, "Polarization-entangled photon-pair source with van der Waals 3R-WS_2 crystal," *eLight*, vol. 4, p. 16, 2024.

[5] M. A. Weissflog *et al.*, "A tunable transition metal dichalcogenide entangled photon-pair source," *Nat. Commun.*, vol. 15, p. 7600, 2024.

Visible-Near Infrared Hyperbolic Polariton along Hyperbolic Metamaterials' interface

Jingbo Sun[1,*] and Ji Zhou[1]

[1] Departamento de Química Física, Universidad Complutense de Madrid, Spain
*Corresponding author: jingbosun@tsinghua.edu.cn

***Abstract*— Hyperbolic polaritons provide a powerful platform for subwavelength directional light manipulation, yet most existing systems are limited to Mid-infrared frequencies and lack rigorous analytical dispersion descriptions. Here, we realize visible-light hyperbolic polaritons in anisotropic hyperbolic metamaterial films with engineered in-plane hyperbolic anisotropy. The supported surface modes exhibit pronounced photonic spin Hall effect, which were then used to realize a multichannel spin-dependent photonic circuit based on a twinning hyperbolic metamaterial. More importantly, we derive the first closed-form analytical iso-frequency contour (IFC) for these polaritons, explicitly revealing their strict hyperbolic topology and quantitatively predicting propagation asymptotes and energy-flow directions. Near-field optical experiments and full-wave simulations show excellent agreement with the analytical model. This work establishes both a versatile visible-near infrared frequency hyperbolic polariton platform and a universal analytical framework for deterministic planar nanophotonic design.**

***Keywords*— hyperbolic polaritons, Iso-frequency contour, twinning hyperbolic metamaterials**

Quantum photonic sources based on 2D materials

Xifeng Ren[1,*]

[1] Key laboratory of quantum information, University of science and technology of China, Hefei, China, 230026
*Corresponding author: renxf@ustc.edu.cn

***Abstract*— Integrated quantum photonics has attracted intensive attention due to the compactness, scalability, and stability. Quantum photonic source, especially an on-chip entangled photon source, is a basic device for realizing quantum photonic integrated circuits (QPICs). I will introduce our recent works about quantum photonic sources based on nonlinear process of 2D materials.**

***Keywords*— quantum photonic sources, 2D materials, nonlinear optics**

Plasmonic tunnel junction electroluminescence: Effects of magnetic fields and resonant cavities

Douglas Natelson[1,2,3,4,5*] Shusen Liao[4,6], Ken W. Ssennyimba[6], Jaime Abad-Arredondo[7,8], Qian Ye[1], Alessandro Alabastri[2,4], Antonio I. Fernández-Domínguez[7,8], Francisco J García-Vidal[7,8], Kexin Xie[1]

[1] Department of Physics and Astronomy, Rice University, Houston, TX USA
[2] Department of Electrical and Computer Engineering, Rice University, Houston, TX USA
[3]Department of Materials Science and NanoEngineering, Rice University, Houston, TX USA
[4]Smalley-Curl Institute, Rice University, Houston, TX USA
[5]Rice Advanced Materials Inistitute, Rice University, Houston, TX USA
[6] Applied Physics Graduate Program, Smalley-Curl Institute, Rice University, Houston, TX USA
[7] Departamento de Física Teórica de la Materia Condensada, Universidad Autonoma de Madrid, E-28049 Madrid, Spain
[8] Condensed Matter Physics Center (IFIMAC), Universidad Autonoma de Madrid, E-28049 Madrid, Spain

*Corresponding author: natelson@rice.edu

***Abstract*— Planar tunnel junctions that host local surface plasmons are biased electrically to act as nanoscale sources of hot carrier electroluminescence. This emission is surprisingly sensitive to an external magnetic field, 100× more than expected from classical electrodynamics. We also couple such emission to a 1D photonic crystal cavity.**

***Keywords*— local surface plasmon resonance; magnetic dichroism; electroluminescence; photonic crystal cavity**

Ultra-weak force measurement with optical levitation in vacuum

Yu Zheng, Long Wang, Yuan Tian, Fang-Wen Sun*

Laboratory of Quantum Information, CAS Center for Excellence in Quantum Information and Quantum Physics, University of Science and Technology of China, China
*Corresponding author: fwsun@ustc.edu.cn

***Abstract*—Optically levitated nanoparticle in vacuum is an ideal optomechanical platform for precision measurements, particularly enabling the detection of ultraweak forces. Nevertheless, quantum backaction and inherent instabilities induced by the trapping laser fundamentally restrict further improvements in force sensitivity and resolution. To circumvent these bottlenecks, we actively drive the levitated nanoparticle's mechanical motion in a phase-locked phonon laser mode and integrate a carrier-modulation measurement architecture to enhance force sensing capabilities. The stable and high-amplitude oscillation of the phonon laser allows for the robust trapping under 1 mW-level laser power, which in turn reduces the force noise to $4.0(3) \times 10^{-22}$ N/Hz$^{1/2}$. Furthermore, by using phase-locked phonon laser, the measurement system achieves active stabilization and extended coherence time with the measured signal to 12, 500 seconds, realizing a measurement resolution of $8(4) \times 10^{-24}$ N with a sensitivity of $9.3(7) \times 10^{-22}$N/Hz$^{1/2}$ under a loaded force. These results establish the phonon laser as a low-noise, long-coherence-time, self-stabilizing platform for precision measurements, as well as in quantum and fundamental physics tests.**

***Keywords*— optical levitation in vacuum, ultra-weak force measurement, phased-locked phonon laser**

Coherent Terahertz Light Generation, Modulation, and Detection with Layered Superconducting Quantum Metamaterials

Mingqi Zhang[1], Samane Kalhor[1], Haonan He[1], Yongyu Zou[1], Maryam Allamki[1], Toshiaki Hattori[1], Takanari Kashiwagi[2], and Kaveh Delfanazari[1,*]

[1] James Watt School of Engineering, University of Glasgow, UK
[2] Institute of Pure and Applied Sciences, University of Tsukuba, Japan
*Corresponding author: Kaveh.Delfanazari@glasgow.ac.uk

***Abstract*— Coherent terahertz (THz) technologies enable ultrafast computation, communication, and sensing. We present a unified platform using layered superconducting quantum metamaterials for THz generation, modulation, and detection. Leveraging collective Josephson dynamics, this approach provides compact, tunable, phase-coherent sources, supporting integrated chip-scale THz photonic circuits with active modulation and sensitive detection capabilities.**

***Keywords*— coherent THz emitters, layered superconductors, metamaterial, Josephson junction, quantum technologies**

Topology Optimization on Weakly-confining InP Platform Enables Ultra-compact Low-loss Triplexer

Hao Jiang, Yijun Chen, Shuang Zheng*, Minming Zhang*

School of Optical and Electronic Information, Huazhong University of Science and Technology, China

*Corresponding author: mmz@hust.edu.cn

***Abstract*— We demonstrate an ultra-compact InP triplexer for combo-PON using boundary adjoint optimization. The 92-μm device achieves <0.8 dB insertion loss across three bands, overcoming weak confinement limitations. Simulations confirm high fabrication tolerance, enabling high-density monolithic integration.**

***Keywords*– integrated photonics, inverse design, topology optimization, adjoint method.**

I. Introduction

The coexistence of GPON, 10G-PON, and 50G-PON in next-generation optical networks demands compact wavelength multiplexers [1][2]. Conventional InP-based multiplexers, however, suffer from large footprints due to weak optical confinement and material dispersion over broad bandwidths. We propose an inverse-designed triplexer using boundary adjoint optimization. The device achieves an ultra-compact length of 92 μm and maintains insertion losses below 0.8 dB across all three bands, with numerical simulations further confirming its high fabrication tolerance.

II. Methods

In this study, we utilize a custom-developed adjoint-based gradient descent boundary optimization algorithm, integrated with FDTD simulation software to enable boundary topology optimization for large-scale photonic devices. The gradient calculation process is formulated as follows:

$$\left.\frac{dF(\vec{E})}{d\varepsilon}\right|_{\vec{r}} = Re\left[\frac{dF(\vec{E})}{d\vec{E}(\vec{r}_0)}\frac{d\vec{E}(\vec{r}_0)}{d\varepsilon}\right] \propto \mathrm{Re}\left[\vec{E}_{adj}(\vec{r})\cdot\vec{E}_{old}(\vec{r})\right]$$

where F denotes the objective function and ε represents the dielectric permittivity. The optimization process is illustrated in Fig. 1; the device performance is iteratively enhanced by deforming the waveguide boundaries based on the computed gradient information.

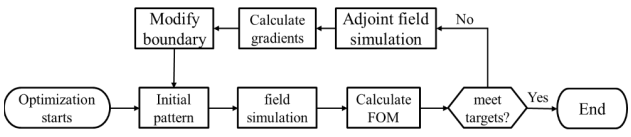

Fig. 1 Optimization algorithm process.

III. Results and Discussion

The final device model designed in this study is illustrated in Fig. 2, with the corresponding performance results shown in Fig. 3. The insertion losses at the center wavelengths of the three bands are 0.76 dB (1342 nm), 0.55 dB (1490 nm), and 0.61 dB (1577 nm), respectively. The total footprint of the device is remarkably compact, with a core length of only 92 μm.

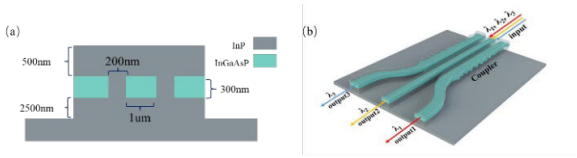

Fig. 2 (a) Device Cross-Section;(b) Device Model.

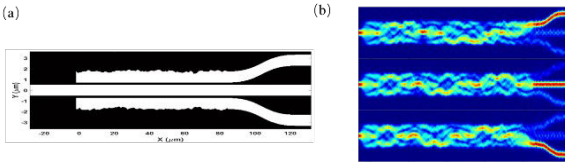

Fig. 3 (a) Structural geometry; (b) Simulated electric field distributions for the three operational wavelengths.

IV. Conclusion

In conclusion, an ultra-compact InP-based triple-wavelength multiplexer is demonstrated using boundary topology optimization. The device achieves a core length of only 92 μm, with insertion losses maintained below 0.8 dB across all three target bands. The design exhibits excellent fabrication robustness.

References

[1] Fei Guo, Dan Lu, Hao Song, Yueying Niu, Daibing Zhou and Lingjuan Zhao, "A Compact Triplexer Based on InP/InGaAsP-MMI Coupler with Channel-Shaped Core Layer for 50G PON," Photonics, vol. 11, No.3, pp. 232, 2024.

[2] Jingye Chen, Penghao Liu, Yaocheng Shi, "An on-chip silicon compact triplexer based on cascaded tilted multimode interference couplers," Optics Communications, vol. 410, pp. 483–487, 2018.

3D printed coupled micro-potentials for photonic quantum gases

J. Schulz[1], K. Karkihalli Umesh[2], S. Enns[1], F. Vewinger[2], and G. von Freymann[1,3*]

[1]Institute of Photonic Systems and Technologies, Leibniz Universität Hannover, Germany
[2]Institut für Angewandte Physik, Universität Bonn, Bonn, Germany
[3]Fraunhofer Institute for Industrial Mathematics ITWM, Kaiserslautern, Germany
*Corresponding author: georg.freymann@qtp.uni-hannover.de

***Abstract*— 3D printed micro potentials in a dye-filled micro cavity allow to study Bose Einstein condensation of photons in almost arbitrary potential landscapes. We exemplary demonstrate the influence of dimensionality on the thermodynamic properties as well as topologically protected states for these driven-dissipative quantum systems.**

***Keywords*— 3D micro printing, photonic quantum gases, dimensional cross-over, topological protection.**

I. Introduction

Photonic quantum gases explore the physics of open driven-dissipative quantum systems under ambient conditions and thus open access to thermodynamics and transport phenomena in quantum gases in the weakly interacting regime. The technology of 3D micro-printing [1], which predominantly was developed to fabricate structures for nanophotonics (e.g. photonic crystals, metamaterials) allows to create potential landscapes for photonic quantum gases in dye-filled micro cavities (see Fig. 1), which surpass the current state of the art in terms of potential size and definition, potential depth, coupling strength, and number of coupled potentials by at least an order of magnitude. We realize as demonstration of the capabilities box potentials with rectangular side walls (see Fig. 1 b), anisotropic harmonic potentials, double-well potentials with dimensions on the scale of the wavelength of light as well as potential lattices with topological non-trivial properties (see Fig. 1 c and d). [2] The high fidelity of our approach allows us to study the dimensional crossover from 2D to 1D harmonic potentials and the resulting changes in the thermodynamic properties. [3]

II. Methods and Results

We use three-dimensional micro printing [1], also known as direct laser writing, to fabricate the potential landscapes on the cavity mirrors, which are covered with a high reflectance coating. The cavity is filled with Rhodamin 6G and pumped by a cw laser running at 532 nm. To prevent bleaching of the dye, the laser is pulsed using two acousto-optical modulators. Waveplates allow to choose any polarization state of the pump light on the Poincaré sphere to study the dependence of the polarization in the quantum gas from the one of the pump laser. For linear polarization the emitted light from the condensed quantum gas follows the pump polarization while the thermal cloud emits unpolarized light.

Adding the micro potentials allows for designing the potential landscape. For example, printing a Sue-Shriefer-Heger (SSH) chain (see Fig 1 c and d) of micro potentials clearly allows for the distinction between the topological trivial and topological non-trivial variant by studying the corresponding spectra of the quantum gas (see Fig. 2).

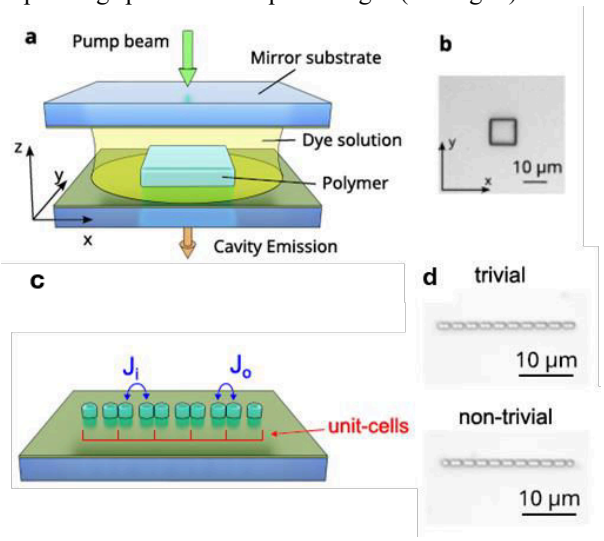

Fig. 1 a: Dye-filled micro cavity with a schematic of a printed box potential. b: light microscope image of the box potential on one of the highly reflective mirrors. c: Scheme of a non-trivial SSH chain with the two different couplings strength. d: light microscope images of a trivial and non-trivial realization of the SSH chain.

The spectra are measured by sending the light emitted from the cavity via grating onto a camera. Thus, it allows to either image the spectra over the spatial coordinate or by adding another lens into the beam path over the momentum coordinate. Plotting the spectra over the real space coordinate clearly demonstrates that the two edges states indeed appear at the two ends of the SSH chain, as expected (see Fig. 2 right hand side).

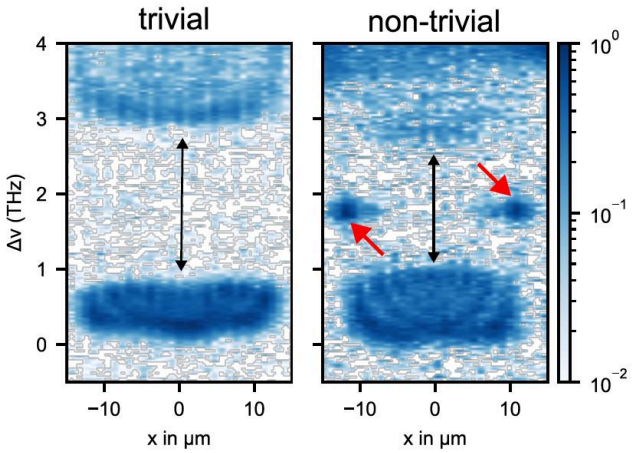

Figure 2: Spectra over the real space coordinate of the cavity. While for the trivial SSH chain only the opening of the gap can be seen (left hand side), the two characteristic edge states forming at the two ends of the chain energetically centered in the gap can be detected for the non-trivial chain (see red arrows).

III. Conclusions

We have demonstrated that combining technologies predominantly developed for the fabrication of nanopotonic structures with photonic quantum gases allows for novel investigations into the physics of open quantum systems. As proof of principle we fabricated and measure several different potential landscapes, starting from single micropotentials which we deform to study dimensional crossover, over coupled micropotentials to the topologically non-trivial SSH chain. Our approach allows in an unprecedented way defining potential landscape for photonic quantum gases and, thus, opening the way for novel studies in open driven-dissipative quantum systems.

Acknowledgments

We acknowledge valuable discussions with E. Stein, J. Kraus and A. Pelster, as well as M. Weitz, J. Schmitt, A. Redmann and L. Kleebank. This work has been supported by the Deutsche Forschungsgemeinschaft through CRC/Transregio 185 OSCAR (project No. 277625399).

References

[1] Edvinas Skliutas, Greta Merkininkaite, Shoji Maruo, Wenxin Zhang, Wenyuan Chen, Weiting Deng, Julia Greer, Georg von Freymann, and Mangirdas Malinauskas, Nature Reviews Methods Primers **5**, 15 (2025)

[2] J. Schulz, K. Karkihalli Umesh, S. Enns, F. Vewinger, and G. von Freymann, ArXiv 2510.21444 (2025)

[3] Kirankumar Karkihalli Umesh, Julian Schulz, Julian Schmitt, Martin Weitz, Georg von Freymann, and Frank Vewinger, Nature Physics **20**, 1810 (2024)

Optical Properties of Twisted Bilayer Graphene

T. Stauber[1,*], M. Sánchez Sánchez[1], I. Vasilevskiy[1], and J. González[2]

[1]Instituto de Ciencia de Materiales de Madrid, CSIC, E-28049 Madrid, Spain
[2]Instituto de Estructura de la Materia, CSIC, E-28006 Madrid, Spain
*Corresponding author: tobias.stauber@csic.es

***Abstract*— We discuss optical properties of twisted bilayer graphene (TBG) obtained from an atomistic tight-binding model including lattice relaxation. By including interaction effects within the Hartree-Fock approximation [1,2], we further accurately capture corrections to the renormalization of the Fermi velocity. Apart from the charge response, we will also calculate the magnetic and chiral response [3].**

***Keywords*— moiré materials, optical conductivity, Drude weight**

I. Introduction

There has been a lot of focus on the electronic properties of twisted bilayer graphene (TBG), but also the related optical response can be used to discuss basic phenomena. E.g., the observed superconductivity can be characterized via the Drude weight that can be measured, e.g., via scattering-type scanning near-field optical microscopy.

II. Methods

We employ a tight-binding model with Slater-Koster parametrization to model twisted bilayer graphene. Also, lattice relaxation is included, but more importantly, Coulomb interaction is approximated by a self-consistent Hartree-Fock scheme [1]. This is done using the package FORGE – Fock Optimization of Real-space Giant Environments [2]. By this, we are able to discuss the renormalization of optical properties such as the Drude weight and also the optical conductivity, shown in Fig. 1 for a twist-angle in the magic angle regime.

The interaction is parametrized by two parameters, the Hubbard interaction U and the dielectric constant ϵ respectively the related coupling constant $\alpha \sim 1/4\pi\epsilon_0\epsilon$ which is measured in units of eVa with a=0.246nm the lattice constant of graphene. Depending on the Hubbard interaction, the Hartree-Fock self-consistency procedure leads to either a valley polarized (VP) or a valley-coherent (VC) phase.

We will discuss the optical properties via the Kubo formula using the Hartree-Fock renormalized eigenfunctions and velocities/vertices. We will also discuss magnetic and chiral response as outlined in Ref. [3]. The flat-band regime is obtained for a slightly larger twist angle by increasing the interlayer hopping parameter as done in Ref. [4].

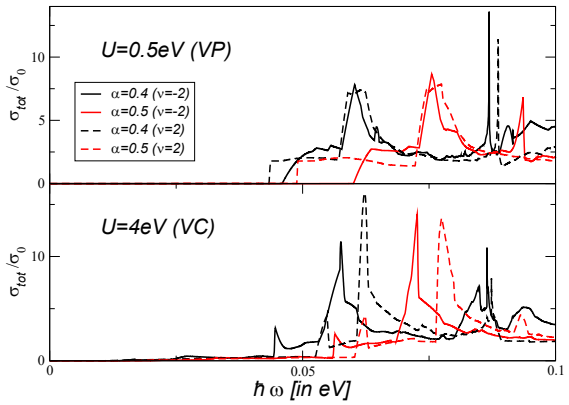

Fig. 1 The optical conductivity in units of the universal conductivity of graphene $\sigma_0 = e^2/4\hbar$ for electron ($\nu = 2$) and hole ($\nu = -2$) doping for different coupling constant α and Hubbard interaction U. Upper panel for U=0.5eV: the flat-band system is in the valley-polarized phase. Lower panel for U=4eV: the flat-band system is in the valley-coherent phase.

III. Results and Discussion

Our simulations show the following trends:

- VC bands are narrower than VP bands.
- VC Drude weights are smaller than VP Drude weights.
- VC optical gaps are soft; VP optical gaps are hard.
- VC magnetic response is 5 times smaller than VP magnetic response.
- For nematic phases, we find large in-plane magnetic dipole moments of the order of 8 Bohr magnetons.

IV. Conclusion

We have investigated the optical conductivity in twisted bilayer graphene including interactions that lead to either valley-polarized or valley-coherent phases. Our results should be relevant for future experiments in the THz-regime.

ACKNOWLEDGMENTS

The work was supported by grant PID2023-146461NB-I00 funded by Ministerio de Ciencia, Innovación y Universidades as well as by the CSIC Research Platform on Quantum Technologies PTI-001. The access to computational resources of CESGA (Centro de Supercomputación de Galicia) is also gratefully acknowledged.

REFERENCES

[1] Miguel Sánchez Sánchez, José González, and Tobias Stauber: "Nonflat bands and chiral symmetry in magic-angle twisted bilayer graphene", Phys. Rev. B 111, 205133 (2025).

[2] T. Stauber, M. Sánchez Sánchez, I. Vasilevskiy, J. González, J. C. Mouriño Gallego, M. Wackerl, P. Wenk, and J. Schliemann, Zenodo. https://doi.org/10.5281/zenodo.17368106 (2025).

[3] T. Stauber, M. Wackerl, P. Wenk, D. Margetis, J. González, G. Gómez-Santos, and J. Schliemann: "Neutral magic-angle bilayer graphene: Condon instability and chiral resonances", Small Sci. **3**, 2200080 (2023).

[4] Miguel Sánchez Sánchez, Israel Díaz, José González, and Tobias Stauber: "Nematic versus Kekulé phases in twisted bilayer graphene under hydrostatic pressure", Phys. Rev. Lett. **133**, 266603 (2024)

Artificial magnetism and passivity in plasmonic clusters with spatial dispersion

R. Dwivedi[1], K. Vynck[2], A. Baron[3], A.Aradian[3,*]

[1]Institut des Nanotechnologies de Lyon, INSA, CNRS, University Claude Bernard, France
[2]Institut Lumière Matière, University Claude Bernard, CNRS, France
[3]Centre de Recherche Paul Pascal, Université de Bordeaux, CNRS, France

*Corresponding author: ashod.aradian@crpp.cnrs.fr

***Abstract*— We show that the optical response of dense, random, spherical clusters made of plasmonic nanoparticles can be efficiently described as that of equivalent, homogeneous spheres of the same size, made of an effective, spatially dispersive medium displaying artificial magnetism. Passivity requirements for the obtained effective media will be discussed.**

***Keywords*— plasmonic nanoparticles, random clusters, effective medium, artificial magnetism, spatial dispersion, passivity.**

I. Introduction

We studied the optical properties of spherical clusters containing hundreds of 7 nm gold nanoparticles with varying volume fractions f, using high-precision T-matrix simulations. While these provide high accuracy for scattering and Mie coefficients, they are computationally expensive and lack physical intuition for dense clusters. To overcome this issue, we investigated to what extent these clusters can be equivalently described using more intuitive, effective parameters like permittivity and permeability.

II. Methods

We therefore analyzed clusters (from 50 to 80 nm radius and f=5% to 44%) using T-matrix calculations to identify their multipolar scattering response. We then set to obtain electromagnetic equivalents, by fitting these results to the scattering response of fictitious homogeneous spheres, i.e. looking for spheres made of an effective material such that their multipolar coefficients matched those of the clusters over the whole spectrum of interest.

III. Results and Discussion

For low-density clusters (f<15%), we find that equivalent spheres made of a simple medium with an effective dielectric permittivity only are sufficient to match the properties of the clusters.

For high-density clusters (f>15%, up to 44%), this simple approach fails since interparticle couplings give rise to non-local effects: we find that homogeneous spheres filled with an effective material with three physical parameters efficiently reproduce the dense clusters' Mie coefficients. This three-parameter description derives from the theory of weak spatial dispersion, and comprises an effective permittivity ε_{eff}, an effective permeability μ_{eff} (i.e., artificial magnetism) and a parameter k_L describing the presence of longitudinal waves in the medium (in addition to standard transverse waves).

Figure 1 shows the plots for ε_{eff} and μ_{eff} obtained in the homogeneous spheres equivalent to dense clusters with radii ranging from 50 to 80 nm and a fixed volume fraction f=44%.

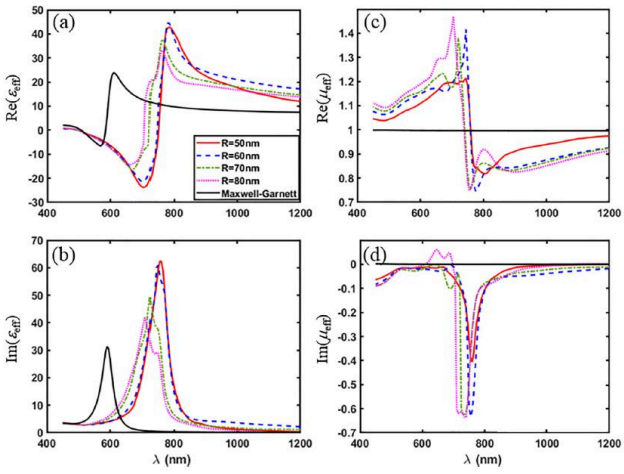

These results will be discussed during the talk, including the existence and localization of longitudinal waves in the homogeneous spheres and in the clusters. We will also discuss the fact that Im(μ_{eff}) comes out as negative, as shown in Fig.1, and whether this violates any passivity requirement.

References

[1] R. Dwivedi, A. Aradian, V. Ponsinet, K. Vynck, and A. Baron, "Effective-medium description of dense clusters of plasmonic nanoparticles with spatial dispersion," Phys. Rev. A, Vol. 109, art. 023507, 2024.

DNA origami-based photonic crystals for visible light

Gregor Posnjak*, Tim Liedl

Department of Physics and CeNS, Ludwig-Maximilians-Universität München, Germany
*Corresponding author: gregor.posnjak@lmu.de

***Abstract*— We use DNA origami to design colloidal particles which controllably assemble into intricate lattices such as the diamond structure with periodicities on the order of hundreds of nanometers. Coating the structures with high-refractive index materials leads to complete 3D photonic band gaps in the visible.**

***Keywords*— 3D photonic crystals, self-assembly, DNA origami, visible light.**

I. Introduction

Manufacturing of 3D photonic crystals in the visible is a long-standing scientific challenge. To achieve a complete photonic band gap in the visible range several conditions have to be satisfied: appropriate lattice symmetry (e.g. diamond), periodicity of about half the wavelength, a high refractive index contrast, and a suitable volume fill fraction. With most approaches it is difficult or impossible to satisfy all conditions. Recent advances in DNA origami enable us to precisely control all the relevant parameters, leading to successful formation of rod-connected diamond cubic lattices[1].

II. Methods

DNA origami is a powerful nanotechnology method which allows us to design nanoscale particles of practically arbitrary shape. The selective binding of DNA sequences enables us to program the strength and relative orientation of binding between DNA origami particles, leading to intricate lattice geometries such as the diamond cubic structure, which are otherwise difficult to achieve through self-assembly. The assembled structures have low volume fill ratios, allowing for additive modification with sol-gel chemical reactions (SiO_2) and atomic layer deposition (TiO_2 and other oxides)[2]. The freedom over DNA origami design allows us to tune the periodicity and symmetry of the assembled structures[3].

III. Results and Discussion

Our experimental results show:

- Diamond lattices with 160 and 250 nm periodicity
- Clathrate lattices with 400 and 650 nm periodicity
- Orientation dependent reflections when coated with SiO_2
- Photonic band gaps when coated with TiO_2

The DNA origami structures are modifiable in an addressable fashion, enabling precise addition of plasmonic particles and dyes, serving as nanostructured breadboards for photonics.

IV. Conclusion

DNA origami offers the versatility of design, length scale and down-steam material processing needed for manufacturing of 3D photonic crystals. The self-assembly aspect removes the need for expensive machines and makes the process massively parallel, offering a viable platform for novel photonic materials.

Acknowledgments

This work was supported by the ERC consolidator grant DNA Funs, and the DFG Cluster of Excellence e-conversion.

References

[1] G. Posnjak, X. Yin, P. Butler, O. Bienek, M. Dass, S. Lee, I. D. Sharp, and T. Liedl, "Diamond-lattice photonic crystals assembled from DNA origami," Science, vol. 384, pp. 781–785, 2024.

[2] A. Ermatov, et al., "Fabrication of Functional 3D Nanoarchitectures via Atomic Layer Deposition on DNA Origami Crystals," Journal of the American Chemical Society, vol. 147, pp. 9519–9527, 2025.

[3] X. Yin et al., "Directed assembly of tetrahedral patchy colloids," in preparation.

Fig. 1 (A) SEM image of DNA origami-based diamond cubic structure with 250 nm periodicity. (B,C) SiO_2 coated DNA origami (B) diamond cubic crystal, and (C) clathrate crystals with 650 nm periodicity, showing orientation-dependent reflections in the visible.

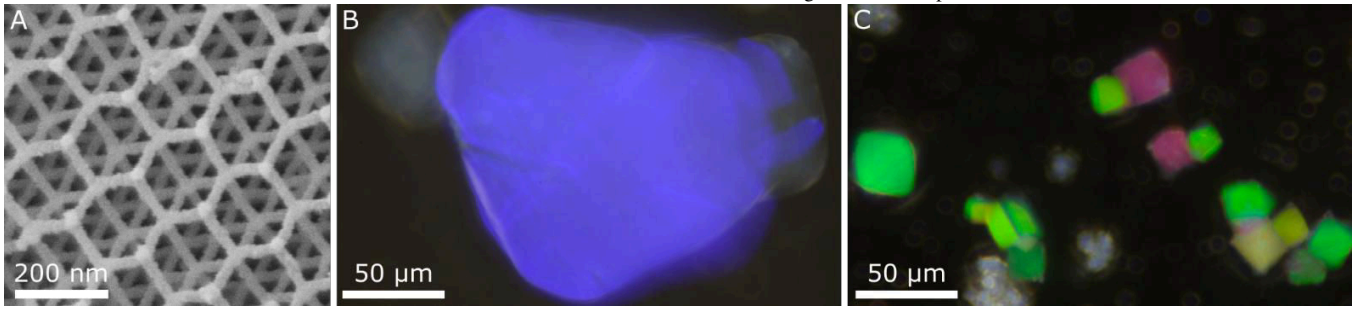

Polarization control of photons with photonic crystal devices

Xiulai Xu[1,*]

[1]School of Physics, Peking University, China
*Corresponding author: xlxu@pku.edu.cn

Abstract: We present experimental demonstration in chiral and polarization-controlled quantum photonics based on topological photonic crystal waveguides and photonic molecules. By engineering cavity–waveguide interfaces and coupled-cavity supermodes, robust chiral light–matter interaction, directional single-photon routing, and enhanced emitter–photon coupling are achieved, offering scalable routes toward integrated quantum photonic circuits.

Introduction and Methods: Precise control of photon polarization, chirality, and emitter–photon coupling at the nanoscale is a central goal of integrated quantum photonics. However, conventional nanocavities and waveguides often suffer from fixed eigenpolarizations, limited interaction regions, and sensitivity to disorder. Topological photonic crystal waveguides and photonic molecules formed by coupled cavities provide complementary routes to engineer local density of states, modal symmetry, and polarization landscapes. We combine two strategies: (i) triangular-lattice topological photonic crystal waveguides supporting high-transmittance bends and large regions of circularly polarized fields for chiral coupling to quantum emitters, and (ii) photonic molecules composed of coupled nanocavities, where hybridized supermodes enable flexible spectral and spatial control of light–matter interaction. These platforms are integrated with semiconductor quantum dots for on-chip experiments.

Results and discussion: Topological waveguides enable spin-dependent, directional photon transport and robust chiral emission, while maintaining low-loss propagation through sharp bends. Photonic molecules provide tunable mode splitting, spatially delocalized fields, and polarization-selective coupling, allowing controlled redistribution of emission among hybridized modes. Together, these effects yield enhanced and programmable emitter–photon interactions, as well as stable single-photon routing on chip. Both of them establishes a versatile toolbox for controlling polarization, chirality, and coupling strength in quantum nanophotonics. Their scalability, design flexibility, and compatibility with solid-state emitters make them promising building blocks for large-scale quantum photonic networks, spin–photon interfaces, and reconfigurable quantum information processors.

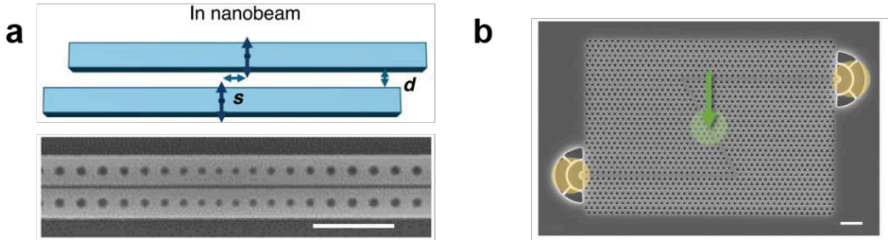

Fig. 1 Polarization control of cavity photons using (a) photonic molecules and (b) triangular-lattice photonic crystals waveguide.

References:

[1] Rui Zhu, Chenjiang Qian, Shan Xiao, et al, "Full polarization control of photons with evanescent wave coupling in the ultra subwavelength gap of photonic molecules," Light: Science & Applications, 14, 114, 2025.

[2] Hancong Li, Sai Yan, Zhikai Ma, et al, "Chiral Quantum Optics With Topological Photonic Crystal Waveguide of Triangular Lattice," Laser & Photonics Reviews, x: e01893, 2026.

Magnonic Waveguide Networks for Spin-wave Computing

Rudolf Bratschitsch[1,*]

[1]Insitute of Physics and Center for Nanotechnology (CeNTech), University of Münster, Germany

*Corresponding author: Rudolf.Bratschitsch@uni-muenster.de

***Abstract*—We demonstrate a maskless approach for fabricating spin-wave waveguides using focused silicon ion implantation. Using spatially resolved Faraday rotation microscopy, we directly image spin-wave propagation and extract dispersion relations, decay lengths, and mode profiles. To demonstrate scalability, we fabricate a large spin-wave network, paving the way for magnonic integrated circuits.**

***Keywords*— spin wave computing, waveguides, Faraday rotation, magnonic network.**

I. Introduction

The rapid growth of artificial intelligence and data-driven technologies has sparked an immense interest in alternative computing architectures, which go beyond conventional electronics. Spin waves (magnons) have emerged as a promising platform for next-generation physical computing. They are collective excitations of magnetization and offer several key advantages, such as excellent energy efficiency, broad operational frequency bandwidth and nanometer-scale wavelengths, rendering highly integrated devices possible [1]. The material of choice with the lowest known spin-wave damping is the magnetic insulator yttrium iron garnet (YIG). YIG has recently become available as high-quality single-crystal films on the wafer scale.

II. Results and Discussion

We demonstrate low-loss spin-wave waveguides in a thin YIG film using a maskless silicon ion implantation technique [2]. By using the focused ion beam, an amorphous cladding of the magnon waveguide is created, where the magnetization is drastically reduced. At the same time, the excellent magnetic properties in the YIG core of the waveguide are preserved. The spin-wave propagation is imaged via optical Faraday rotation microscopy, which enables spatially resolved measurements of spin-wave amplitude and phase throughout the engineered structures. We achieve spin-wave decay lengths exceeding 100 µm even in submicron waveguides, substantially outperforming current state-of-the-art etched devices. Furthermore, the dispersion relations of these waveguides are highly tuneable by adjusting both waveguide width and implantation dose, providing unique flexibility for integrated magnonic circuit design.

Using our new technique, we fabricate a large-scale spin-wave network, featuring 198 crossings with 34 input and output ports (Fig. 1).

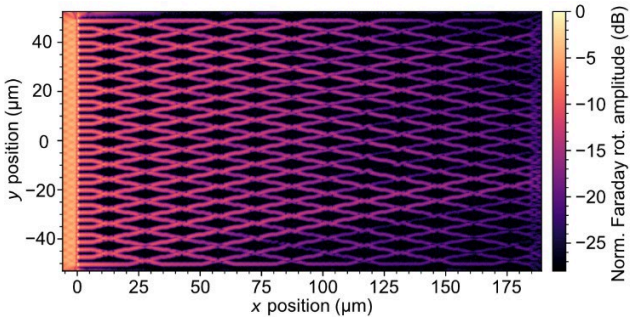

Fig. 1 Spin-wave network consisting of 198 crossings and 34 input and output ports [2].

III. Conclusion

Our etchless, scalable approach paves the way for wafer-scale, low-loss magnonic integrated circuits (MICs), enabling advanced, high-efficiency spin-wave-based computing and signal-processing architectures.

Acknowledgments

We acknowledge funding by the Deutsche Forschungsgemeinschaft (DFG, German Research Foundation), project no. 433682494, SFB 1459.

References

[1] Q. Wang et al., "Nanoscale magnonic waveguides," Physical Review Applied, vol. 21, pp. 040503, 2024.

[2] J. Bensmann et al., "Dispersion-tunable low-loss implanted spin-wave waveguides for large magnonic networks," Nature Materials, vol. 24, pp. 1920–1926, 2025.

Machine Learning for Inverse Design

Philippe Tassin

Department of Physics, Chalmers University of Technology,
SE-412 96 Göteborg, Sweden

***Abstract*—I will present an overview of our work on using machine learning for inverse design in nanophotonics, with emphasis on free-form inverse design, the use of machine learning in inverse design, physics-informed neural networks, and adaptive metamaterials.**

***Keywords*—inverse design, machine learning, nanophotonics, photonic crystals, metamaterials.**

Inverse design, i.e., fully automated design by a computer without intervention of a human, is promising to revolutionize photonics. There are currently two major ways to achieve a fully automatic free-form design of a photonic device: (1) gradient-descent optimization with the adjoint method (sometimes called topology optimization) [1] and (2) machine-learning-driven inverse design where a neural network acts as a fast surrogate model for expensive simulations [2]. Both approaches require a large number of simulations, either in the iterative optimization process or as training data for a neural network. I will first compare the advantages and disadvantages of these two methods.

I will then show two examples of the free-form design of a metamaterial, where we train a neural network as a surrogate model: a metamaterial lens [3] and a Zernike phase mask [4]. While these examples demonstrate the possibility of this method, such a brute-force approach to training a neural network as a surrogate model requires an extreme amount of training data, often in the order of tens to hundreds of thousands of simulations. This is because the network has to learn the "physics," i.e., has to learn from data that the optical response has to obey Maxwell's equations and has to respect symmetries in the physics. I will show that this knowledge can be built in into a neural network by using QNM-Net (a network containing a physics layer) [5] and/or by using equivariant networks (which have symmetries built-in) [6], and that this substantially reduces the amount of data needed to an amount that is feasible to generate.

Finally, I will show how machine learning can help to build adaptive metamaterials that respond to changes in the environment.

Acknowledgments

We acknowledge financial support from Chalmers' area of advance Nano, from the Swedish Research Council under Grant No.~2020-05284, and from the Knut och Alice Wallenberg Stiftelse under Grant No. 2022.0090. The training data generation and neural network training were performed on resources provided by the Swedish National Infrastructure for Computing (NAISS), at the Chalmers/C3SE and KTH/PDC sites, partially funded by the Swedish Research Council under Grant No. 2022-06725. The work was performed in part within the framework of the Excellence Center META-PIX (Grant No. 2022-06575).

References

[1] R. E. Christiansen and O. Sigmund, "Inverse design in photonics by topology optimization: tutorial," J. Opt. Soc. Am. B 38, 496-509 (2021)

[2] P. R. Wiecha, A. Arbouet, C. Girard, and O. L. Muskens, "Deep learning in nano-photonics: Inverse design and beyond," Photonic Res., vol. 9, p. B182, 2021.

[3] T. Gahlmann and P. Tassin, Deep neural networks for the prediction of the optical properties and the free-form inverse design of metamaterials, Phys. Rev. B 106, 085408 (2022).

[4] T. Gahlmann, T. Wenger, and P. Tassin, "Machine-learning-based inverse design of wide-band metasurfaces with interdependent unit cells," Mach. Learn.: Sci. Technol. 7, p. 015024 (2026).

[5] V. A. Lilja, A. J. Svärdsby, T. Gahlmann, and P. Tassin, "A general framework for knowledge integration in machine learning for electromagnetic scattering using quasi-normal modes, Laser Photon. Rev., in press (2026).

[6] V. A. Lilja and P. Tassin, "Symmetries in deep learning for electromagnetic scattering," under review (2026).

Wave-Based Photonic Computing: From Complexity-Driven Reservoirs to Engineered Phase Encoding

Gerard McCaul[1], Girish Tripathy[2], Luana Olivieri[2], Giulia Marcucci[3], and Juan Sebastian Totero Gongora[1,*]
[1] Department of Physics, Loughborough University, LE11 3TU, UK
[2] Emergent Photonics Research Centre, Department of Physics, Loughborough University, LE11 3TU, UK
[3] LumiAIres Ltd, Glasgow G12 0DG, UK
*Corresponding author: j.totero-gongora@lboro.ac.uk

***Abstract*— We present a unified framework for optimising photonic reservoir computing, combining nonlinear substrates and engineered encoding layers. Using gain-controlled multimode fibres, we identify structural complexity as a task-independent design metric. Complementarily, we demonstrate that deliberate phase wrapping beyond [0, 2π) dramatically enhances expressivity via synthetic Fourier mode generation and mixing.**

***Keywords*— reservoir computing, optical computing, photonic scattering, erbium-doped fibres.**

Nonlinear wave propagation provides a powerful substrate for analogue information processing. Photonic Reservoir Computing (RC) exploits these dynamics by encoding input data into optical waves interacting in a complex photonic system, and performing machine learning tasks via linear regression of intensity measurements [1,2]. Wave-based photonic reservoirs offer inherent parallelism, high bandwidth, and favourable scaling. A key challenge, however, remains how to control the degree of nonlinearity expressed by the reservoir, as required to adapt the system operating regime to different machine learning tasks.

In this invited talk, we present recent results addressing two complementary aspects of photonic RC design: the optimisation of the nonlinear photonic substrate and the engineering of the optical encoding layer. In the first part [3], we investigate a feed-forward reservoir based on Erbium-Doped Multi-Mode Fibres (ED-MMF), where input data is encoded in the wavefront of a signal beam, and the nonlinear response is controlled by a structured pump beam within the gain medium. Due to the interplay of gain saturation, mode competition, and nonlinear coupling, the system implements a tunable nonlinear transformation controlled by global parameters (pump and signal powers). We benchmark performance on regression, classification, and chaotic time-series prediction tasks, demonstrating that an intermediate nonlinear regime near the gain threshold consistently yields optimal results. The system performance is directly connected to the degree of structured information carried by the optical waves as they propagate through the system, quantified by the measurement of the Kolmogorov Complexity of the reservoir outputs. This metric provides a task-independent criterion for tuning photonic reservoirs, analogous to the spectral radius in echo-state networks. In the second part [4], we address the encoding layer in scattering-assisted photonic reservoirs, where input data is encoded in the phase front (e.g., via an SLM), propagated through a random scattering medium and detected via intensity measurement. Conventionally, phase encoding is restricted to the $[0,2\pi)$ period to preserve bijectivity. We demonstrate that deliberately wrapping the phase domain beyond the natural period yields dramatic expressivity enhancements across regression and classification benchmarks that are unattainable within a single period. The mechanism arises from the interplay of phase encoding, random scattering, and intensity detection: the SLM constructs synthetic Fourier features whose bandwidth scales with the wrapping factor α, while the scatterer and quadratic detection induce frequency-difference mixing that generates additional nonlinear features. Formally, this connects photonic RC with Random Fourier Features (RFF) methods in machine learning and with Hamiltonian-encoded quantum extreme learning machines, where eigenvalue spacings determine accessible frequencies. The enhancement is robust to finite bit depth and shot noise, confirming its experimental feasibility.

Together, these results establish that optimal photonic RC requires the co-design of the nonlinear substrate and the encoding scheme. Structured complexity, whether measured by the KC of the reservoir's output features or by the bandwidth of synthetic Fourier modes generated at the encoding stage, emerges as a unifying principle for the design of next-generation wave-based analogue computing platforms.

References

[1] G. Tanaka *et al.*, 'Recent advances in physical reservoir computing: A review', *Neural Netw.*, vol. 115, pp. 100–123, Jul. 2019
[2] D. Brunner *et al.*, 'Roadmap on Neuromorphic Photonics', Jan. 16, 2025, *arXiv*: arXiv:2501.07917.
[3] G. Marcucci, et al., 'Optimising complexity and learning for photonic reservoir computing with gain-controlled multimode fibres', *Front. Nanotechnol.*, vol. 7, Aug. 2025,
[4] G. McCaul, et al., 'Unwrapping photonic reservoirs: Enhanced expressivity via random Fourier encoding over stretched domains', *Chaos*, vol. 35, no. 9, p. 093129, Sep. 2025

Optical reconfiguration of Exceptional Points on chip

Angel Ortega-Gomez[1], Jonathan Dearlove[2], Nikolaos Farmakidis[2], Mingde Du[2], Iñigo Liberal[1], Harish Bhaskaran[2]

1-Department of Electrical, Electronic and Communications Engineering, Institute of Smart Cities, Public University of Navarre, 31006 Pamplona, Spain

2-Department of Materials, University of Oxford, Parks Road, Oxford OX1 3PH, UK.

*Corresponding author: E-mail: angel.ortega@unavarra.es

***Abstract*— We present an optically programmable photonic platform that overcomes static geometric design limitations for exceptional points. Utilizing dynamic refractive index modulation via an external pump, we successfully steer eigenvalue and eigenvector coalescence. This approach offers a tunable set of exceptional point solutions, enabling deterministic control over device directionality**

***Keywords*— photonics, non-Hermitian optics, reconfigurability.**

I. Introduction

Non-Hermitian singularities known as Exceptional Points (EPs), where eigenvalues and eigenstates coalesce, enable unprecedented light control [1]. However, exploring these degeneracies on-chip has traditionally relied on static geometric tuning, requiring the fabrication of multiple devices with different scatterer positions or configurations to tune the losses [2]. To overcome this limitation, we present a platform featuring dynamic all-optical programmability on a single chip. By applying an external optical pump, the effective refractive index of the silicon core is nonlinearly modulated. This shifts the condition for the EP activation, and, as result, this non-Hermitian effect can be tuned optically.

II. Results and Discussion

The device consists of an all-pass silicon microring loaded with two fixed nanocylinders (SEM image, Fig. 1b). Their fixed angular separation sets the asymmetric coupling between CCW and CW modes. The transformation from this static response to an optically programmable topology is schematized in Fig. 1a. Adjusting the pump power under 10 mW, a small index modulation of 0.005 is induced in the ring resonator. This variation modifies the relative optical accumulated between the scatterers. This phase shift completely changes the balance between the complex scattering strengths inducing an asymmetric divergence in CCW to CW and reverse coupling. Consequently, the coalescence conditions are swept across the probe spectrum, tracing a curved EP trajectory as a function of the power of the optical pump, that is injected at a different wavelength that the probe, eliminating any intereference possibility. As diagrammed in Fig. 1, the pump routes the system from a directional chiral state to an inverse reflection

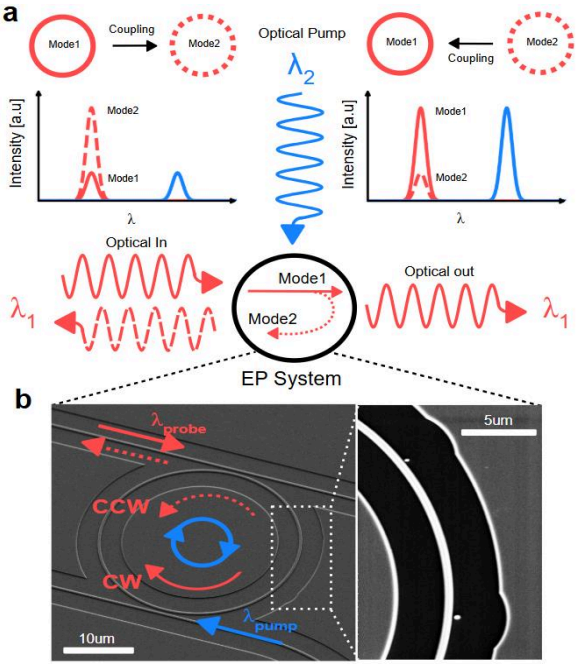

Figure 1. a) Scheme of the optical control of the EP and b) SEM image of the implementation

state, or any intermediate configuration, unlocking scalable control over the nonlinear enhancement.

III. Conclusion

We demonstrated full on-chip programmability of EPs in silicon microrings via all-optical control. Replacing physical reconfigurations with dynamic index modulation unlocks a continuous range of EP solutions on a single device, enabling reversible routing of chiral states and a scalable path to program non-Hermitian enhancements.

References

[1] H. Lee *et al.*, "Chiral exceptional point enhanced active tuning and nonreciprocity in micro-resonators," *Light Sci. Appl.*, vol. 14, no. 1, p. 25, Dec. 2025.

[2] J. Li *et al.*, "On-Chip Fabrication-Tolerant Exceptional Points Based on Dual-Scatterer Engineering," *Nano Lett.*, vol. 24, no. 13, pp. 3906–3913, Apr. 2024

Non-Reciprocal Silicon Photonic Resonators with 2D $CuCrP_2S_6$

Mahmoud S. Rasras[1,*], Ghada Dushaq.[1]

[1]Department of Electrical and Computer Engineering, NYUAD, Abu Dhabi, UAE
[2]Center for Smart Engineering Materials, NYUAD, Abu Dhabi, UAE
*Corresponding author: mrasras@nyu.edu

***Abstract*— A compact non-reciprocal photonic device is demonstrated by integrating a two-dimensional magnetic material with silicon microring resonators. Magnetic ordering induces directional asymmetry with low loss and high isolation. The device operates in the transverse electric mode and supports broadband operation relevant to short-wavelength infrared photonic systems.**

***Keywords*— 2D materials, non-reciprocal Photonic, Silicon Photonics, photonic resonators.**

I. Introduction

Non-reciprocal photonic devices are essential for integrated optical systems, enabling signal isolation and directional control in applications spanning communications and quantum technologies. Achieving optical non-reciprocity on chip remains challenging due to material and integration constraints. Two-dimensional multiferroic materials, such as $CuCrP_2S_6$, offer a promising route toward compact, efficient, and CMOS-compatible non-reciprocal photonic devices.

II. Methods

Silicon microring resonators were fabricated on silicon-on-insulator wafers with a 220 nm device layer. Multilayer CuCrP2S6 flakes were mechanically exfoliated and deterministically transferred onto the waveguide. Optical transmission was measured in the transverse electric mode under an external magnetic field applied in Voigt geometry.

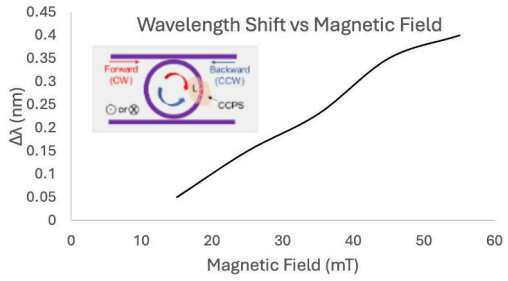

Fig. 1 Non-reciprocal transmission and resonance splitting in CCPS-integrated microring resonators.

Nonreciprocal behavior was evaluated through resonance splitting and phase shift, described by $\Delta\beta = \frac{2\pi\Delta\lambda}{FSR.L_{MO}}$ and $\Delta\lambda = \lambda\frac{\Delta n_{eff}}{n_g}$, where L_{MO} denotes the interaction length, FSR the resonator free spectral range, and n_g the group index.

III. Results and Discussion

The CCPS-integrated microring resonators exhibit clear non-reciprocal behavior under an applied magnetic field. Clockwise and counterclockwise resonances split by up to 0.4 nm, yielding isolation ratios up to 28 dB with low insertion loss. The devices operate in the transverse electric mode and maintain broadband performance across the C-band. (Fig. 1)

IV. Conclusion

We have demonstrated compact, low-loss non-reciprocal silicon photonic devices enabled by multilayer CCPS, achieving high isolation, broadband operation, and TE-mode compatibility, underscoring strong potential for short-wavelength infrared optical isolation and integrated photonic systems.

Acknowledgments

This work was supported by the Center of Smart Engineering Materials. The authors thank the Photonics PCT Platform for its support.

References

[1] L. Bi, J. Hu, P. Jiang, D. H. Kim, G. F. Dionne, L. C. Kimerling, and C. A. Ross, "On-chip optical isolation in monolithically integrated non-reciprocal optical resonators," *Nature Photonics*, vol. 5, pp. 758–762, 2011.

[2] Y. Shoji and T. Mizumoto, "Magneto-optical non-reciprocal devices in silicon photonics," *Science and Technology of Advanced Materials*, vol. 15, p. 014602, 2014.

[3] W. Yan, Y. Shoji, T. Mizumoto, R. M. Osgood Jr., and C. W. Wong, "Waveguide-integrated high-performance magneto-optical isolators and circulators on silicon nitride platforms," *Optica*, vol. 7, pp. 1555–1562, 2020.

[4] G. Dushaq, S. Serunjogi, S. R. Tamalampudi, and M. Rasras, "Non-reciprocal response in silicon photonic resonators integrated with 2D CuCrP2S6 at short-wave infrared," *Light: Science & Applications*, vol. 14, p. 157, 2025.

Light-Driven Order: Shift and Injection Raman Forces Driving Coherent Phonons

Habib Rostami[1*] and J. Luke Pimlott[1]

[1]Department of Physics, University of Bath, Bath BA2 7AY, United Kingdom
*Corresponding author: hr745@bath.ac.uk

***Abstract*—Ultrafast optical fields drive coherent lattice dynamics in quantum materials. We introduce shift and injection Raman forces as quantum-geometric mechanisms for coherent phonon generation. Arising from band geometry and interband electron-phonon asymmetry, these forces enable tunable, symmetry-selective lattice control beyond conventional Raman mechanisms.**

***Keywords*— quantum geometry, Raman forces, coherent phonons, ultrafast optics, two-dimensional materials, light-matter interaction.**

I. Introduction

Ultrafast optical excitation offers a route to control quantum materials beyond equilibrium by coupling electronic and lattice degrees of freedom on femtosecond-to-picosecond timescales. Light-induced responses can reveal hidden order, drive symmetry switching, and manipulate structural degrees of freedom in layered and low-dimensional materials. Examples include light-driven Kerr rotation in centrosymmetric bulk WSe2 [1], ultrafast symmetry switching in WTe2 [2] and MoTe2 [3], and light-induced Raman-force-driven shear motion in bilayer graphene [4]. These results motivate a microscopic theory of optical forces that goes beyond conventional descriptions of coherent phonon generation.

II. Shift and Injection Raman Forces

Coherent phonons are usually described through impulsive stimulated Raman scattering or displacive excitation. These mechanisms are commonly formulated in terms of equilibrium optical susceptibilities and do not fully expose the role of electronic band geometry, symmetry, and interband electron-phonon coupling.

Here we introduce shift and injection rectified Raman forces as generic mechanisms for coherent phonon generation [5]. These forces are phononic analogues of photogalvanic effects. They arise from quantum-geometric properties of electronic bands, including the quantum geometric tensor, a phononic shift vector, and interband asymmetries in electron-phonon coupling. The injection force produces a displacive lattice response associated with asymmetric carrier excitation, whereas the shift force generates an impulsive resonant drive that becomes prominent when time-reversal symmetry is broken.

III. Representative Example

As a prototypical platform, we consider a bilayer Haldane model and examine optically driven interlayer shear phonons. This example shows that the magnitude and direction of the Raman forces can be tuned by optical frequency and magnetic flux. The result demonstrates that coherent phonon generation can be controlled through band geometry and symmetry, rather than only through equilibrium Raman susceptibilities.

IV. Conclusion

Shift and injection Raman forces provide a quantum-geometric framework for ultrafast lattice control. The mechanism is generic and applies beyond the representative shear-phonon example. It opens a route toward symmetry-selective optical manipulation of coherent phonons and light-driven structural dynamics in layered quantum materials.

Acknowledgments

This work was supported by the Engineering and Physical Sciences Research Council (Grant No. UKRI122).

References

[1] E. Cappelluti, H. Rostami, and F. Cilento, "Hidden order revealed by light-driven Kerr rotation in centrosymmetric bulk WSe2," *npj 2D Materials and Applications*, vol. 9, p. 89, 2025.
[2] E. J. Sie *et al.*, "An ultrafast symmetry switch in a Weyl semimetal," *Nature*, vol. 565, pp. 61–66, 2019.
[3] M. Y. Zhang *et al.*, "Light-induced subpicosecond lattice symmetry switch in MoTe2," *Phys. Rev. X*, vol. 9, p. 021036, 2019.
[4] H. Rostami, "Theory for shear displacement by light-induced Raman force in bilayer graphene," *Phys. Rev. B*, vol. 106, p. 155405, 2022.
[5] J. L. Pimlott and H. Rostami, "Quantum geometric injection and shift optical forces drive coherent phonons," arXiv:2507.17814, 2025.

Infrared Silicon Metalenses through Deep-UV for Thermal Imaging

Kai Sun[1,*], Jordan Scott[1], Xingzhao Yan[2], Jun-Yu Ou[1], Otto L. Muskens[1]

[1]Physics and Astronomy, University of Southampton, UK
[2]Optoelectronics Research Centre, University of Southampton, UK
*Corresponding author: k.sun@soton.ac.uk

***Abstract*— This presentation will overview recent infrared silicon metalenses developed by our group for compact thermal imaging and telecommunications. It will cover metalenses across SWIR, MWIR and LWIR bands, scalable fabrication routes, integrated metasurface concepts and selected optical characterization results, with emphasis on practical opportunities for infrared metaoptics.**

***Keywords*— metaoptics, metalens, thermal imaging, deep-UV.**

I. Introduction

Metasurfaces consisting of subwavelength nanostructures allow for engineered optical response beyond bulk materials. Here, we demonstrate developed various silicon-based infrared metalenses for SWIR, MWIR and LWIR bands, manufactured through deep-UV lithography.

II. Methods

The metalenses were designed using Keysight RSoft Photonics Design Tools, MetaOptics Designer (MOD). The unit cell response was initially simulated through rigorous coupled wave analysis (RCWA) and then the full design was generated through multi-variable optimizations using MOD.

The designed metalenses were manufactured through Deep-UV lithography and plasma etching technique to form silicon pillars. Through our recently developed technique [1], double-sided metalenses could be manufactured in wafer-scale and on both sides of the substrates. In addition, through switching technique, metalens dimensions can be enlarged over the DUV reticle limits.

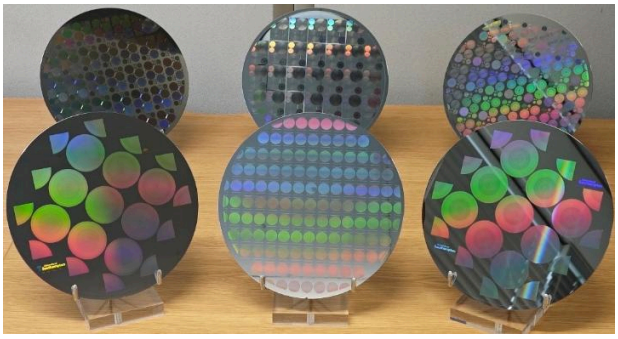

Fig. 1 Family photo 6 batches of infrared metalenses over 200 mm Si substrates.

III. Results and Discussion

Figure 1 shows the family photo of 6 metalens wafers (8-inch) using Deep UV lithography (200 nm minimal features) from serial batches, showing the progression of infrared metalens design, starting with a few millimeter diameter lenses and increasing in size to 40 mm diameter designs. These metalenses cover various infrared bands, short-wave infrared (SWIR), mid-wave infrared (MWIR) and long-wave infrared (LWIR). One set of metalenses was designed for MWIR thermal imaging with metalens and moth-eye structures on the two sides of the substrate, respectively, which is enabled by our novel manufacturing technique.

IV. Conclusion

We have demonstrated double-sided metalens with moth-eye anti-reflection coatings together with focal metalens. The fabricated metalenses were optically characterized in terms of focal performance, modulation transfer function (MTF) and thermal imaging performance. The moth-eye integrated metalens shows improved performance over single-sided metalens.

Acknowledgments

The authors acknowledge financial support by the EPSRC National Hub in High Value Photonic Manufacturing (EP/N00762X/1). J.S. acknowledges support from an EPSRC collective PhD studentship with Teledyne Qioptiq Ltd.

References

[1] K. Sun, X. Yan, J. Scott, J. Ou, J. N. Monks, and O. L. Muskens, "Production-ready Double-Sided Fabrication of Dual-Band Infrared Metaoptics using Deep-Ultraviolet Lithography," ACS Nano, vol. 19, pp. 37218–37229, 2025

Van der Waals hybrid photonic devices

Yuichiro K. Kato[1,2*]

[1]Nanoscale Quantum Photonics Laboratory, RIKEN Pioneering Research Institute, Japan
[2]Quantum Optoelectronics Research Team, RIKEN Center for Advanced Photonics, Japan
*Corresponding author: yuichiro.kato@riken.jp

***Abstract*—Two-dimensional layered materials offer unique optical properties and seamless integration with nanophotonic structures through van der Waals interactions. By hybridizing these materials with optical cavities, versatile and reconfigurable photonic devices with enhanced functionality can be realized, enabling new opportunities for nanoscale light–matter interaction and integrated photonics.**

***Keywords*— 2D materials, microcavities, hybrid photonics, van der Waals heterostructures, photonic crystals.**

I. Introduction

Two-dimensional layered materials exhibit unique optical, excitonic, and nonlinear properties arising from reduced dimensionality and strong Coulomb interactions. Their van der Waals nature enables deterministic integration onto nanophotonic structures without lattice matching constraints, making them highly attractive for hybrid device architectures. By combining atomically thin semiconductors and insulators with high-Q optical cavities, it becomes possible to engineer light–matter interaction at the nanoscale with unprecedented flexibility.

Here present our recent advances in van der Waals hybrid photonic devices, where two-dimensional materials can be used to tune, define, and reconfigure optical resonators. Across multiple cavity platforms, including air-mode silicon nanobeam cavities [1,2], self-aligned two-dimensional photonic crystal (PhC) cavities [3,4], and ultrahigh-Q silica microspheres [5], we demonstrate how atomically controlled thickness, mechanical flexibility, and optical nonlinearity of layered materials provide new mechanisms for cavity modulation, quantized resonance control, and hybrid nonlinear functionalities.

II. Air-Mode Silicon Nanobeam Cavity

Air-mode silicon photonic crystal nanobeam cavities provide strong field localization in low-index regions, maximizing overlap between the optical mode and externally integrated materials. By transferring few-layer van der Waals flakes onto these cavities, we achieve efficient and controllable modification of cavity resonances (Fig. 1).

A key feature of this platform is the quantized resonance shift induced by atomically precise layer thickness [1]. Because each additional layer introduces a well-defined perturbation to the effective refractive index, discrete mode shifts are observed, directly reflecting thickness quantization at the atomic scale. Flexible and reversible tuning of cavity properties is further enabled by stacking and removing ultrathin flakes of two-dimensional materials.

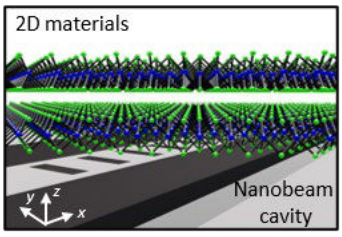

Fig. 1: A schematic of a 2D /cavity hybrid [1].

Extending this hybrid approach beyond static tuning, we have also implemented all-optical switching devices that leverage refractive index modulation in two-dimensional semiconductors integrated with air-mode silicon nanobeam cavities [2]. In these devices, a thin flake of a two-dimensional semiconductor such as molybdenum ditelluride is placed on top of the cavity and excited by an optical pump pulse. The photo-induced carriers in the flake cause a rapid shift in the cavity resonant wavelength, enabling switching operations on time scales of tens of picoseconds with low switching energies of a few hundred femtojoules.

Careful design of the nanobeam geometry ensures large mode overlap with the two-dimensional material while maintaining high cavity quality factors on the order of 10^4 even after integration. Measurements show that the quality factor remains sufficiently high for efficient low-energy switching despite modest reductions after material transfer, indicating that absorption and additional scattering introduced by the two-dimensional flake are small.

These results demonstrate that air-mode silicon nanobeam cavities not only serve as sensitive platforms for quantized mode control through van der Waals materials but also provide an efficient hybrid platform for ultrafast optical signal processing. Their performance highlights the advantages of

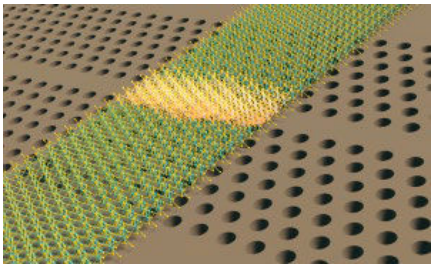

Fig. 2: A self-aligned cavity formed by an atomically thin flake [3].

integrating two-dimensional semiconductors with high-Q photonic structures for active photonic functionalities.

III. 2D Photonic Crystal Self-Aligned Cavity

Moving beyond tuning pre-fabricated nanocavities, we developed a self-aligned hybrid cavity concept in which the two-dimensional material itself locally defines the cavity within a photonic crystal waveguide (Fig. 2). When a flake is placed onto a PhC waveguide, its refractive index perturbation creates a confined defect mode at the flake position, effectively forming a cavity wherever the material is transferred [3,4].

This approach eliminates the need for lithographically predefined cavity defects and alignment steps. The cavity position and characteristics are instead determined by the geometry and thickness of the transferred flake, enabling post-fabrication cavity formation with high spatial flexibility. Arrays of hybrid cavities can therefore be realized through deterministic material placement.

Such self-aligned architectures illustrate a paradigm shift: van der Waals materials act not only as active media but also as structural elements that define photonic confinement. This concept provides a scalable route toward programmable photonic circuitry based on material placement.

IV. Ultrahigh-Q Silica Microsphere

The hybridization strategy extends beyond planar silicon photonics to three-dimensional ultrahigh-Q whispering-gallery-mode resonators [5]. Silica microspheres support extremely long photon lifetimes, providing a sensitive platform for investigating nonlinear and optomechanical effects.

By integrating two-dimensional materials onto ultrahigh-Q silica microspheres, we functionalize otherwise passive dielectric cavities. The mechanical flexibility of atomically thin layers allows conformal attachment to curved surfaces, while their strong optical nonlinearity and excitonic response introduce new interaction channels (Fig. 3). Hybrid microsphere devices demonstrate enhanced nonlinear effects and tunable optical responses without significantly degrading intrinsic cavity Q factors.

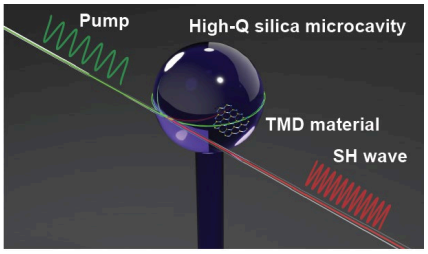

Fig. 3: Second harmonic generation with 2D-material/microsphere hybrid device.

V. Conclusion

Van der Waals hybridization offers a powerful and versatile strategy for next-generation nanophotonic devices. By integrating atomically thin materials with high-Q cavities, we demonstrate discrete and reversible resonance tuning, self-aligned cavity formation, and nonlinear functionalization across silicon nanobeams, photonic crystal waveguides, and silica microspheres.

These results highlight how layered materials transform passive photonic resonators into dynamically configurable and multifunctional devices. The convergence of ultrahigh-Q photonics and van der Waals materials opens new opportunities for hybrid nonlinear optics, reconfigurable photonic circuits, and quantum nanophotonics, establishing a flexible platform for nanoscale light–matter engineering.

Acknowledgments

This work is supported in part by JSPS (KAKENHI JP23H00262, JP25K21704) and JST (CREST JPMJCR25A1, ASPIRE JPMJAP2310). We thank the Advanced Manufacturing Support Team at RIKEN for technical assistance.

References

[1] N. Fang, D. Yamashita, S. Fujii, K. Otsuka, T. Taniguchi, K. Watanabe, K. Nagashio, Y. K. Kato, “Quantization of mode shifts in nanocavities integrated with atomically thin sheets,” Adv. Opt. Mater. 10, 2200538 (2022).

[2] D. Yamashita, N. Fang, S. Fujii, Y. K. Kato, “Hybrid silicon all-optical switching devices with 2D material,” Adv. Opt. Mater. 13, 2402531 (2025).

[3] C. F. Fong, D. Yamashita, N. Fang, S. Fujii, Y.-R. Chang, T. Taniguchi, K. Watanabe, Y. K. Kato, “Self-aligned hybrid nanocavities using atomically thin materials,” ACS Photonics 11, 2247 (2024).

[4] C. F. Fong, D. Yamashita, N. Fang, Y.-R. Chang, S. Fujii, T. Taniguchi, K. Watanabe, Y. K. Kato, “Dielectric environment engineering via 2D material heterostructure formation on hybrid photonic crystal nanocavity,” Opt. Mater. Express 16, 646 (2026).

[5] S. Fujii, N. Fang, D. Yamashita, D. Kozawa, C. F. Fong, Y. K. Kato, “Van der Waals functionalization of ultrahigh-Q silica microcavities for $\chi(2)$-$\chi(3)$ hybrid nonlinear photonics,” Nano Lett. 24, 4209 (2024).

Spatio-Temporal Metalattices in ENZ Transparent Conductors

Sven Stengel[1], Wallace Jaffray[1], Farhan Ali[2], Mustafa Goksu Ozlu[3], Colton B. Fruhling[3], Maria Antonietta Vincenti[4,5], Domenico de Ceglia[4,5], Michael Scalora[4,5], Alexandra Boltasseva[3], Vladimir M. Shalaev[3], Andrea Di Falco[2], Marcello Ferrera[1,*]

[1] Institute of Photonics and Quantum Sciences, Heriot-Watt University, United Kingdom
[2]School of Physics and Astronomy, University of St. Andrews, St Andrews, UK
[3]Elmore Family School of Electrical Computer Engineering and Birck Nanotechnology Center, Purdue University, West Lafayette, Indiana, USA
[4]Department of Information Engineering, University of Brescia, Brescia, Italy
[5]CNR - National Institute of Optics, Via Branze 45, 25123 Brescia, Italy
*Corresponding author: m.ferrera@hw.ac.uk

***Abstract*— We demonstrate a spatio-temporal photonic metalattice formed by combining a static metagrating with a transient lattice written by two-beam interference in a low-index transparent conductor. The structure is revealed via internally generated third-harmonic diffraction.**

***Keywords*— time-varying metamaterials, nonlinear optics.**

I. Introduction

Ultrafast time-varying photonics is enabled by strong nonlinearities in low-index transparent conductors, where femtosecond excitation produces large transient refractive-index modulation and control of photon energy and momentum [1–3]. This allows functionality to be written in time rather than space (nanofabrication), complementing metasurface phase-gradient approaches [4] and enabling reconfigurable diffraction and temporal lattice formation on femtosecond timescales [5,6].

II. Methods

Our experiments make use of a subwavelength AZO film, patterned into a 1D metagrating. Two phase-coherent femtosecond NIR pumps interfere to write a transient grating. The film simultaneously generates third-harmonic radiation acting as an internal probe for direct diffraction mapping [7,8].

III. Results and Discussion

Combined dual-beam excitation on the metagrating reveals a full two-dimensional spatio-temporal lattice through orthogonal diffraction signatures. The transient lattice diffracts third-harmonic radiation with efficiency comparable to the physical grating, confirming time-written periodicity as an effective diffractive structure. Pump wavelength shifts structural diffraction but leaves temporal diffraction nearly invariant due to scaling of transient pitch and the corresponding generated harmonic wavelength. Incidence angle reshapes diffraction topology, while pump delay tunes harmonic spectra through ultrafast temporal modulation [1,6].

IV. Conclusion

Combining a fabricated metagrating with an optically written transient lattice enables a spatio-temporal photonic metalattice directly visualised through self-generated third-harmonic diffraction. This approach shifts diffractive photonic design from fixed geometry toward radiation engineering, enabling ultrafast reconfigurable diffraction and full programmable control of photon momentum and spectrum [1–4].

Acknowledgments

Authors acknowledges financial support from EPSRC/STFC/NSERC under OPP640-APP47830 and from the U.S. Department of Energy, under Award DE-SC0017717 and by ACC-APG-RTP Agency grant 253 W911NF-25-2-0060.

References

[1] Jaffray, W. et al. Spatio-spectral optical fission in time-varying subwavelength layers. Nat. Photon. (2025).
[2] Jaffray, W., et al. Transparent conducting oxides: from all-dielectric plasmonics to a new paradigm in integrated photonics. Adv. Opt. Photon. 14, 148–208 (2022).
[3] Caspani, L. et al. Enhanced nonlinear refractive index in ε-near-zero materials. Phys. Rev. Lett. 116, 233901 (2016).
[4] Shaltout, A., Kildishev, A. & Shalaev, V. Time-varying metasurfaces and Lorentz non-reciprocity. Opt. Mater. Express 5, 2459–2467 (2015).
[5] Lustig, E. et al. Photonic time crystals: fundamental concepts. Opt. Express 31, 9165–9170 (2023).
[6] Lustig, E. et al. Time-refraction optics with single-cycle modulation. Nanophotonics 12, 2221–2230 (2023).
[7] Jaffray, W. et al. Near-zero-index ultra-fast pulse characterization. Nat. Commun. 13, 3536 (2022).
[8] Jaffray, Wallace, et al. "Spatio-Temporal Photonic Metalattice." arXiv preprint arXiv:2510.09273 (2025).

Spectral Design of Disordered Photonic Metamaterials

Aaron Shih[1,*], Mathias Casiulis[2], Stefano Martiniani[2], Frank Scheffold[1]

[1]Soft Matter and Photonics Group, University of Fribourg, Switzerland
[2]Center for Soft Matter Research, New York University, USA
*Corresponding author: aaron.shih@unifr.ch

***Abstract*— We create disordered structures exhibiting specific spectral features, from stealthy hyperuniformity to completely new structures, "gyromorphs", that exhibit rotational order alongside translational disorder. We evaluate their optical properties using a coupled dipoles method and show how specific optical responses may be reached by optimizing for features in the structure factor.**

***Keywords*— metamaterials, disorder, bandgap, coupled dipoles, Fourier transform.**

I. Introduction

Periodic and quasiperiodic systems are characterized by extensive peaks in their structure factors. In finite two dimensional systems, the strongest of these peaks populate the vertices of a polygon - a square in a square lattice, a triangle in a triangular lattice, and higher order polygons in quasicrystals. In contrast, disordered structures commonly only exhibit broad, smooth features in their structure factors. However, we show that it is indeed possible to create disordered structures that exhibit a ring of regularly-spaced extensive peaks in the structure factor, unifying the two seemingly contradictory qualities. These "gyromorphs" exhibit higher and better-resolved peaks than quasicrystals of the same rotational order. This specific feature of a ring of high peaks on the structure factor makes gyromorphs ideal candidates for isotropic bandgap materials. Using a coupled dipoles approximation, we show that gyromorphs indeed exhibit complete, isotropic photonic bandgaps that are deeper and wider than those formed by stealthy hyperuniformity, high-order quasicrystals, and Vogel spirals for both scalar and vector waves in 2d and 3d.

II. Methods

Disordered structures are generated via an optimization algorithm FReSCo (Fast Reciprocal Space Correlator). We use a coupled dipoles approximation to calculate transmission spectra and density of states within our structures.

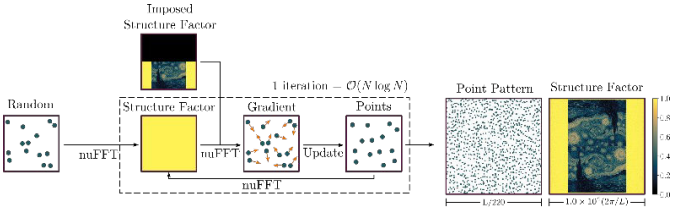

Fig. 1 Schematic diagram of the FReSCo algorithm.

Using two-photon lithography (NanoScribe), we fabricate network structures with similar structural features. We measure the transmission spectra of these networks with FTIR spectroscopy using an optical microscope with a Cassegrain objective.

III. Results and Discussion

FReSCo enables custom design of reciprocal space features in point patterns, including features that initially seem contradictory, as in the case of gyromorphs.

Using even a fairly naïve single-scattering argument, we can design spectral features (e.g. a ring of high peaks) with optical properties (e.g. an isotropic bandgap) that are preserved in the multiple scattering regime.

Network structures based on the point patterns can be shown to exhibit features of the predicted spectra.

IV. Conclusion

We have created and assembled tools to design disordered structures with specific spectral features. We are also able to utilize the relation between structure factor and single scattering to design metamaterials with specific optical properties. Future work will focus on the experimental verification of the optical properties of these structures.

References

[1] A. Shih, M. Casiulis, and S. Martiniani, "Fast Generation of Spectrally-Shaped Disorder," Physical Review E 110 (3), 034122 (2024).
[2] M. Casiulis, A. Shih, and S. Martiniani, "Gyromorphs: A New Class of Functional Disordered Materials," Physical Review Letters 135 (19), 196101, (2025).

Bulk-Radiation Correspondence in Radiative Photonic Lattices

Xinyi Yuan[1,*], Grazia Salerno [2,*]

[1]Department of Applied Physics, Aalto University, Finland
[2]Dipartimento di Fisica "E. Fermi", Università di Pisa, Italy
*Corresponding author: xinyi.yuan@aalto.fi, grazia.salerno@unipi.it

***Abstract*—We develop a non-Hermitian model to describe the guided and leaky modes of photonic crystal slabs with non-local responses. Within this framework, we investigate the concept of bulk-radiation correspondence in the vicinity of the Γ-point of the square lattice and the K-point of the honeycomb lattice. The results show that the comparability is not universal and completely breaks down around bound states in the continuum.**

Keywords — photonic crystal slab, non-hermitian, bulk-radiation correspondence, bound states in the continuum.

I. Introduction

The concept of radiation topology generalizes the photonic Berry curvature to the far-field, resulting in a curvature term defined by the unit polarization vectors in momentum space:

$$B^f = -i\left(\langle\partial_\mu E|\partial_\nu E\rangle - \langle\partial_\nu E|\partial_\mu E\rangle\right). \tag{1}$$

For two-level systems, e.g., cavity polariton system, cavity lattices, one can map the two degrees of freedom onto Bloch sphere and relate wavefunctions with observables through polarimetry [1], [2], [3]:

$$B^b = \frac{1}{2} sin\theta(\partial_x\theta\cdot\partial_y\phi - \partial_x\phi\cdot\partial_y\theta). \tag{2}$$

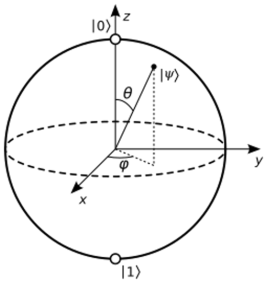

Fig. 1. A schematic showing how an effective two-level wave system is represented and mapped onto a Bloch sphere.

For photonic lattices, however, the multi-band nature makes it less legitimate to directly apply the two-level treatment. Further, the interplay between radiative modes in the far-field brings in new features, e.g., bound states in the continuum (BICs).

We develop a non-Hermitian Model to study the influence of non-locality and non-Hermiticity on the validity of the correspondence in radiative photonic lattices.

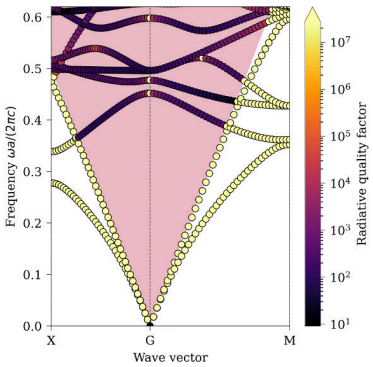

Fig. 2. Example of band structures in a PhC slab. The band structure was calculated using the Legume package [4], based on Guided Mode Expansion.

II. Modeling

Considering a photonic crystal slab made from isotropic, lossless, non-magnetic ($\mu = 1$), and nond-ispersive medium, treating the periodic change in the refractive index profile $\Delta\epsilon(\boldsymbol{r})$ as perturbation. For a time-harmonic field defined as $\boldsymbol{E}(\boldsymbol{r},t) = \boldsymbol{E}(\boldsymbol{r})e^{-i\omega t}$, the master equation for the TE mode is formulated as a *generalized eigenvalue problem*:

$$\nabla\times(\nabla\times\boldsymbol{E}) = \frac{\omega^2}{c^2}\varepsilon(\boldsymbol{r})\boldsymbol{E} \tag{3}$$

where the complex frequency $\omega = \omega_r - i\gamma$ accounts for the radiative loss through its imaginary component γ.

The band structure can be understood by considering guided modes folded at diffraction orders (m,n), where m, n are integers [4]. For a lattice with periodicity a_1 and a_2, the diffraction orders are located at multiples of the reciprocal lattice vector $\mathbf{G} = mG_1\hat{\mathbf{k}}_1 + nG_2\hat{\mathbf{k}}_2$, where $G_{1,2} = 2\pi/a_{1,2}$ defines the Brillouin zone. In the case of a rectangular lattice, for example, $a_{1,2} = a_{x,y}$, $\hat{\mathbf{k}}_{1,2} = \hat{\mathbf{k}}_{x,y}$ and $G_{1,2} = G_{x,y}$. We indicate the guided modes in the vicinity of $\mathbf{G}$ with in-plane wave vectors $(k_x,k_y) \in 1^{st}BZ$ as $|m,n\rangle$. These guided modes constitute the basis for the effective model. Here, we only consider a single "unfolded" guided mode - for instance, the fundamental TE guided mode propagating in the uncorrugated slab made of the average effective index. The thickness of the slab is chosen to ensure operation in

the single-mode regime, and all other guided TE modes lie at much higher energies.

The dispersion relation of the mode $|m,n\rangle$ in the vicinity of Γ-point corresponding to $\mathbf{G}$ with a group velocity v_g is:

$$\omega_{m,n} = \omega_0 + \frac{v_g}{\hbar}\left(|\mathbf{k_{m,n}}| - |\mathbf{G}|\right), \tag{4}$$

where ω_0 is the mode frequency at the first Γ-point. The guided modes are then coupled via a diffractive mechanism and the radiation continuum. The coefficients determining the coupling parameters can be obtained from a perturbative method based on the periodic potential profile acting on the photonic modes.

For TE modes, the unit polarization vector $\hat{\mathbf{p}}_{\mathbf{m,n}}$ associated with the guided mode $|m,n\rangle$ is perpendicular to the corresponding unit in-plane wavevector $\mathbf{k_{m,n}}$. We define the angle $\theta_{m,n}$ on the $k_x - k_y$ plane as

$$\theta_{m,n} = \arg\left[k_x + mG_x + i(k_y + nG_y)\right], \tag{5}$$

such that

$$\hat{\mathbf{k}}_{m,n} = \cos\theta_{m,n}\cdot\hat{\mathbf{k}}_x + \sin\theta_{m,n}\cdot\hat{\mathbf{k}}_y, \tag{6}$$

$$\hat{\mathbf{p}}_{m,n} = -\sin\theta_{m,n}\cdot\hat{\mathbf{k}}_x + \cos\theta_{m,n}\cdot\hat{\mathbf{k}}_y, \tag{7}$$

see Fig. **??**.

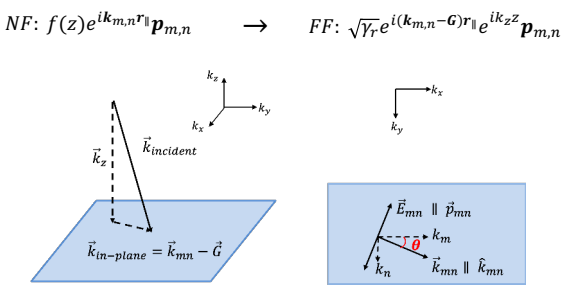

Fig. 3. The geometric representation of the basis sets $\mathbf{k_{m,n}}$ and $\mathbf{E_{m,n}}$.

The coupling via the radiation continuum is achieved through far-field interference, resulting in the loss of photons at a rate γ_r. The loss exchange depends on the product between the polarization components $\hat{\mathbf{p}}_{\mathbf{m,n}}$ and $\hat{\mathbf{p}}_{\mathbf{m',n'}}$ and the projection angle between two guided modes can be represented as

$$\varphi_{m,n,m',n'} = \theta_{m,n} - \theta_{m',n'}. \tag{8}$$

The effective Hamiltonian can thereby be written as

$$\hat{H}_{\text{rad}}(k_x,k_y) = \sum_{m,n}\left(\omega_{m,n} + i\gamma_r\right)|m,n\rangle\langle m,n| + \sum_{m,n,m',n'}\left[t_{m,n,m',n'} + i\gamma_r\cos(\varphi_{m,n,m',n'})\right]|m,n\rangle\langle m',n'|. \tag{9}$$

The unit vector that characterizes the corresponding far-field radiation can thus be written as

$$|E\rangle = \Sigma_{m,n}c_{m,n}(-\sin\theta_{m,n}\cdot\hat{\mathbf{k}}_x + \cos\theta_{m,n}\cdot\hat{\mathbf{k}}_y). \tag{10}$$

III. Results and Discussion

A. Analytical Results

Substituting Eq. (1) with Eq. (10), we get

$$\begin{aligned} B^f = &-i\sum_{j,l=1}^{N}\cos(\theta_j-\theta_l)\Big[\{\partial_\mu c_j^*\partial_\nu c_l - \partial_\nu c_j^*\partial_\mu c_l\}+ \\ &c_j^* c_l\left(\partial_\mu\theta_j\partial_\nu\theta_l - \partial_\nu\theta_j\partial_\mu\theta_l\right)\Big]+ \\ &-i\sum_{j,l=1}^{N}\sin(\theta_j-\theta_l)\Big[c_l\left(\partial_\mu c_j^*\partial_\nu\theta_l - \partial_\nu c_j^*\partial_\mu\theta_l\right)- \\ &c_j^*\left(\partial_\mu\theta_j\partial_\nu c_l - \partial_\nu\theta_j\partial_\mu c_l\right)\Big]. \end{aligned} \tag{11}$$

The term in curly brackets represents the bulk Berry curvature. Straightforwardly, the relation $B^f = B^b$ does not always hold. The establishment of the equation is subject to specific conditions, e.g., when the sum has only contributions from $j = l$. It might also hold roughly for the case where the redundant terms are sufficiently small. In real experiments, these conditions would correspond to particular choices of system settings, e.g., material properties, lattice prototypes, and site geometries. For completeness, one can analogously repeat the derivation with left eigenstates to obtain the biorthogonal curvatures B^b_{LR} and B^f_{LR}, which leads to an expression of the same form as the one in Eq. (11).

B. Numerical Results

The model is applied to the Γ-point of a square lattice and the K-point of a honeycomb lattice, respectively. Here, we present only the results for the honeycomb lattice, full numerical results can be found in [6].

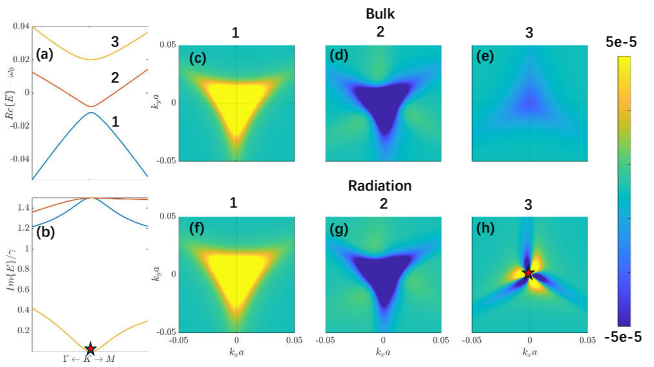

Fig. 4. Patterns showing bulk and radiation Berry curvatures around the valleys of the non-local honeycomb in a weakly asymmetric regime.

The results indicate that the concept of bulk-radiation correspondence is not universal in radiative photonic lattices. The correspondence completely breaks down in the presence of far-field singularities, while for non-BIC bands it can hold under special symmetry conditions, e.g., inversion symmetry. Besides, net Berry curvature concentration is captured at the K, K' of non-local honeycomb, corresponding to non-Hermitian AZ class A ($C_0, d = 2$) and topological invariant $\mathbb{Z}$ [7].

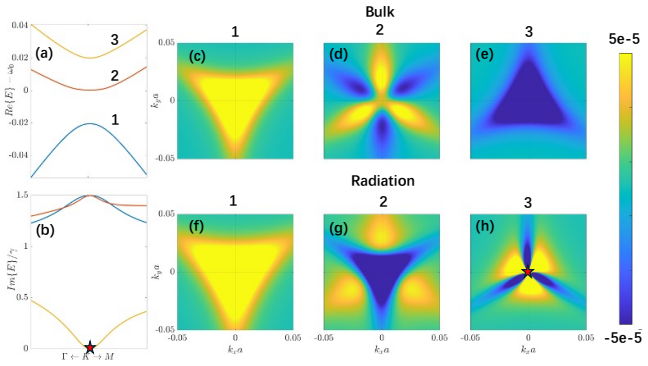

Fig. 5. Patterns showing bulk and radiation Berry curvatures around the valleys of the non-local honeycomb in a strongly asymmetric regime.

C. Discussion

The breakdown of bulk-radiation correspondence lies in two aspects: dimensional mismatch of the bulk-radiation projection and unavoidable leakage from guided resonances in the photonic crystal slab under consideration.

Firstly, it's not fully legitimate to ignore the multi-band nature of photonic lattices without any valid justification, especially for those with $a < \lambda$. The non-local nature of the photonic Hamiltonian, the vectorial aspect, and the inclusion of complex eigen-frequencies in the master equation give rise to an intrinsic dense eigenvalue problem. The full Hamiltonian is thus harder to separate into invariant subspaces with assigned dimensionality, even just locally. This results in more complicated connections between the states both within the band and among the bands, reflecting on the local geometric properties of the parameter space, e.g., the distorted Dirac cone with non-equal flattening processes as shown in Fig. 4 and Fig. 5.

Unlike the case discussed in ref.[1], the multi-band nature leads to dimensional mismatch upon projecting the bulk Hilbert space to the far-field synthetic parameter space. This dimensional mismatch results in loss, distortion, or blurring of local geometric features of the original manifolds. There are occasions when the projection is correctly done so the main features can be kept, but that's not guaranteed in general. These occasions could mostly relate to effective decoupling of the local Hamiltonian, e.g., those with block-diagonal structures accidentally formed from the wavefunction coupling, or those with inversion symmetry thus being more inherently sparse-like.

Besides, radiation loss is unavoidable in the photonic crystal slabs considered in the model built in Sec. II. The escaping photons from guided resonances interfere in the far field, and the energy redistribution resulting from far-field interference will reversely regulate the near-field photon behaviors. In our model, the far-field regulation manifests as coupling between spatially coherent modes via the radiative continuum. That is to say, the information of the bulk Bloch states carried by the leaky modes will be further deformed in the far field as a result of intensity modulation. One manifestation is that the highest degree of destructive interference happens at the BIC points, corresponding to a complete loss of all the information about the bulk Bloch states.

Thus, the bulk-radiation correspondence is not universal in radiative photonic lattices. The two-band regime is not complete, and far-field interference plays an essential role. This is consistent with the analytical results obtained in part A. Additionally, we infer that the bulk-radiation correspondence also fails in non-lattice planar photonic structures with more than two decoupled degrees of freedom, where effective two-level treatment no longer applies.

IV. Conclusion

By developing an effective model to describe the guided and leaky modes of non-local radiative photonic lattices, we construct the bulk and the radiation Berry curvatures. We analyze the comparability between bulk and radiation topology with both analytical and numerical methods. The analytical results straightforwardly convey that the bulk-radiation correspondence is not universal, and the validity depends on the particular bulk Bloch states. The numerical results further exemplify specific cases where the bulk-radiation correspondence holds and collapses.

Notably, the correspondence completely breaks down surrounding the field singularities on the BIC bands, while it can hold on non-BIC bands under special symmetry conditions, e.g., inversion symmetry. Besides, net Berry curvature concentration is captured at the valleys of the non-local honeycomb lattice, facilitating further exploration on generalized topological phases in photonic lattices beyond the regimes with localized couplings and Hermiticity.

Acknowledgments

This work was supported by the Academy of Finland under Project no. 13354165. G.S. also received support from the MUR-Italian Ministry of Research–under the Rita Levi Montalcini program.

References

[1] O. Bleu, D. D. Solnyshkov, and G. Malpuech, "Measuring the quantum geometric tensor in two-dimensional photonic and exciton-polariton systems," *Physical Review B*, vol. 97, no. 19, p. 195422, 2018.

[2] A. Gianfrate, O. Bleu, L. Dominici, V. Ardizzone, M. De Giorgi, D. Ballarini, G. Lerario, K. W. West, L. N. Pfeiffer, D. D. Solnyshkov, *et al.*, "Measurement of the quantum geometric tensor and of the anomalous Hall drift," *Nature*, vol. 578, no. 7795, pp. 381–385, 2020.

[3] M. Guillot, C. Blanchard, N. Pernet, M. Morassi, A. Lemaître, L. Le Gratiet, A. Harouri, I. Sagnes, J. Bloch, and S. Ravets, "A sublattice Stokes polarimeter for bipartite photonic lattices," *arXiv preprint arXiv:2507.16446*, 2025.

[4] J. D. Joannopoulos, S. G. Johnson, J. N. Winn, and R. D. Meade, *Photonic Crystals: Molding the Flow of Light*, 2nd ed. Princeton University Press, 2008.

[5] L. C. Andreani, "The Guided-Mode Expansion Method for Photonic Crystal Slabs," *COST P11 Training School, Univ. of Nottingham*, 2006.

[6] X. Yuan, L. Malgrey, H. Sigurðsson, H. S. Nguyen, and G. Salerno, "Breakdown of bulk-radiation correspondence in radiative photonic lattices," *Physical Review Research*, vol. 7, no. 1, p. 013084, 2025.

[7] K. Kawabata, K. Shiozaki, M. Ueda, and M. Sato, "Symmetry and topology in non-Hermitian physics," *Physical Review X*, vol. 9, no. 4, p. 041015, 2019.

Imaging-based, time-resolved detection of rare microparticles in continuous flow

Raphael Hauer[1,2,*], Christian Hill[2,3], Ulrich Hohenester[1]

[1]Institute of Physics, University of Graz, Universitätsplatz 5, 8010 Graz, Austria
[2]BRAVE Analytics GmbH, Stiftingtalstraße 14, 8010 Graz, Austria
[3]Gottfried Schatz Research Center, Division of Medical Physics and Biophysics, Medical University of Graz, Neue Stiftingtalstraße 2, 8010 Graz, Austria
*Corresponding author: raphael.hauer@edu.uni-graz.at

***Abstract*—We introduce an imaging-based microfluidic sensor for continuous, time-resolved detection and sizing of rare microparticles in flow. Incoherent illumination and an imaging geometry ensuring full-volume focus yield sharp transit images. Automated subtraction, tracking and flow-normalized counting provide calibration-free concentrations and size distributions, enabling real-time monitoring of distribution tails dynamically.**

***Keywords*— time-resolved sensing, single-particle characterization, microfluidics, imaging**

I. Introduction

Precise characterization of particle populations in liquid dispersions is a central challenge in emerging continuous processing environments across nanotechnology, biotechnology, and advanced materials manufacturing [1,2]. While established techniques provide robust access to nanoscale fractions, the statistically rare but process-critical large-diameter tail of particle distributions remains difficult to quantify in a time-resolved and calibration-independent manner. Yet, these micron-scale outliers often dominate stability, safety, and functional performance of the respective liquid [3,4].

II. Methods

Our remedy to this situation is an imaging-based sensing approach, enabling continuous, time-resolved detection and sizing of microparticles in flow. The solution combines a microfluidic platform based on the OF2i®-technology [5,6,7] with incoherent illumination and a geometry guaranteeing that each particle above the detection threshold produces a sharply resolved image during transit, enabling deterministic detection of low-concentrated, micron-sized particles. Continuous video acquisition is combined with automated background subtraction, particle tracking, and extraction of the most contrast-rich frame to extract accurate particle diameters. By correlating particle counts with flow rates during measurement and acquisition time, the method directly yields absolute number concentrations and size distributions without external calibration standards.

III. Results and Discussion

The approach enables real-time monitoring of the temporal evolution of the large-diameter tail during dynamic process adjustments. Experimentally, we demonstrate robust operation under continuous-flow conditions (cf. Fig. 1).

IV. Conclusion

Our results illustrate how tailored optical imaging geometries combined with microfluidic control can provide reliable access to low-abundance microparticles, offering a scalable platform for continuous particle characterization in both laboratory and industrial environments.

Acknowledgments

The authors acknowledge financial support from the Austrian Research Promotion Agency (FFG) (Grant No. FFG-DAVID 900612).

References

[1] S. L. Lee *et al.*, "Modernizing Pharmaceutical Manufacturing: from Batch to Continuous Production," *J. Pharm. Innov.*, vol. 10, p. 191, 2015.
[2] European Commission, "Real-time nano-characterisation technologies (RIA)," Horizon 2020 Programme, 2024. [Online]. Available: https://cordis.europa.eu/programme/id/H2020_DT-NMBP-08-2019
[3] United States Pharmacopeia (USP), "General Chapters ⟨729⟩, ⟨787⟩, ⟨788⟩, ⟨789⟩."
[4] G. B. Basim and B. M. Moudgil, "Effect of Soft Agglomerates on CMP Slurry Performance," *J. Colloid Interface Sci.*, vol. 256, no. 1, pp. 137–142, 2002.
[5] M. Šimić *et al.*, "Optofluidic Force Induction: A Workbench for Nanoparticle Characterization and Material Analytics," *Nano Lett.*, vol. 25, no. 22, pp. 8805–8813, 2025.
[6] M. Šimić *et al.*, "Real-Time Nanoparticle Characterization Through Optofluidic Force Induction," *Phys. Rev. Appl.*, vol. 18, p. 024056, 2022; *ibid.*, vol. 19, p. 034041, 2023.
[7] M. Šimić *et al.*, "Theoretical Description of Optofluidic Force Induction," *Phys. Rev. Appl.*, vol. 19, p. 034041, 2023.

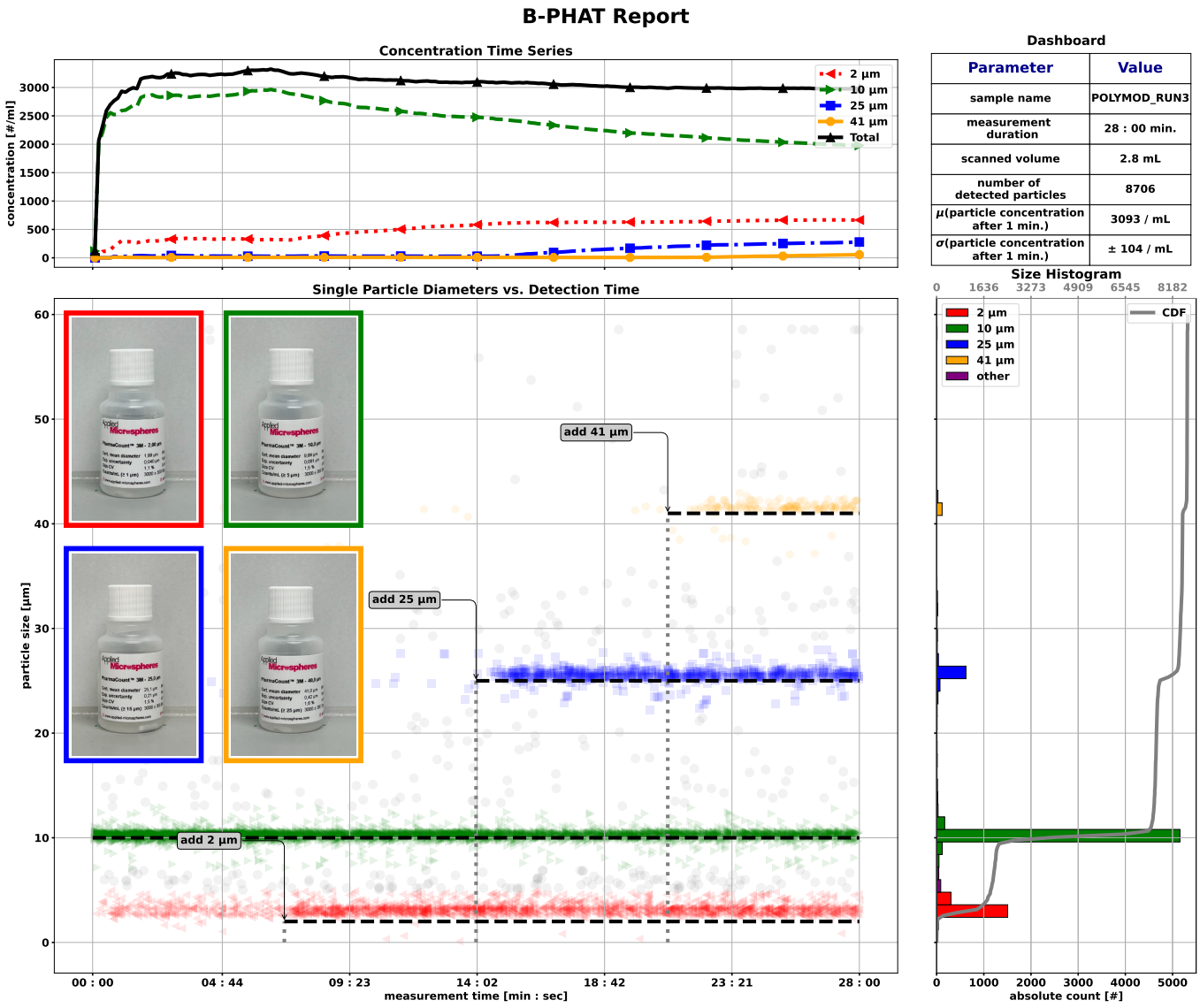

Fig. 1: Over a 28-min measurement, SI-traceable spherical polystyrene particle size and counting standards (nominal concentration: 3000 / ml each) were added sequentially to the feed reservoir supplying the device, ultimately producing a four-component mixture of 2, 10, 25, and 41 µm particles. The scatter plot shows the emergence of each population at the expected times (vertical dashed lines) and with diameters close to their nominal values (horizontal dashed lines). The concentration time series (top) demonstrates calibration-free absolute counting: the total mixture concentration (black) remains close to the expected 3000 / ml after each addition. The plot on the right gives the absolute particle size histogram over the entire measurement together with the corresponding cumulative distribution function (CDF).

Fundamental Passive Components for Topological Photonic Integrated Circuits

S. Okada[1,2], Q. Wang[1], L. Hu[1], R. Yamaji[1], X.-X. Wang[3], X. Hu[1,3], and T. Amemiya[1]

[1] Department of Electrical and Electronic Engineering, Institute of Science Tokyo, Japan
[2] The National Institute of Information and Communications Technology, Japan
[3] Department of Physics, Shanghai University, China
*Corresponding author: okada.s.ah@nict.go.jp

***Abstract*— We propose topological photonic integrated circuits (TPICs) based on topological edge states preserving spin and orbital angular momentum of light. Fundamental passive components, including topological converters, vertical couplers, and splitters, are developed for practical integration with silicon photonics. Their design principles and experimental demonstrations are presented.**

***Keywords*— topological photonic integrated circuits, silicon photonics, optical communication**

Tracing the topology of electronic systems such as topological insulators and Weyl semimetals into photonic platforms has led to the emergence of topological photonics [1]. In topological photonics, Z_2 topological phases can be realized using photonic crystal structures composed of honeycomb lattices with dielectric unit cells possessing C_{6v} symmetry [2][3]. Owing to the high degree of freedom in photonic structure design, these systems provide flexible control of photonic band structures and light propagation characteristics.

One of the most remarkable phenomena in topological photonic systems is the emergence of topological edge states at the interface between two structures with distinct topological phases. These edge states enable robust light propagation even in the presence of structural imperfections or sharp bends, while preserving the internal degrees of freedom of light, including spin angular momentum (i.e., circular polarization) and orbital angular momentum (i.e., optical vortex states). Circular polarization and optical vortices are regarded as key resources for next-generation high-capacity optical communications, and therefore topological photonic systems capable of maintaining these properties within integrated optical circuits have attracted significant attention.

Against this background, we have proposed a concept in which portions of conventional silicon photonic integrated circuits are replaced with topological photonic structures, referred to as topological photonic integrated circuits (TPICs). The objective of TPICs is not merely to introduce topological effects into optical circuits, but to establish a practical integrated photonic platform capable of leveraging the unique advantages of topological light transport while maintaining compatibility with existing silicon photonics technologies.

To realize practical TPICs, it is essential to develop a set of fundamental passive components that can efficiently interface topological photonic structures with conventional optical systems. In particular, at least the following three elements are indispensable. The first is a topological converter that enables highly efficient coupling between conventional silicon waveguides and topological photonic structures [4]. Such a converter is necessary because strong mode mismatch generally exists between ordinary waveguide modes and topological edge states. The second is a topological vertical coupler that enables efficient coupling between free-space optical beams and topological photonic systems [5][6]. This component is crucial for integrating external optical inputs with on-chip topological devices. The third is a topological splitter/switch capable of dividing optical signals into arbitrary intensity ratios while preserving the internal degrees of freedom of light, including polarization and orbital angular momentum [7][8]. Preservation of these properties during splitting operations is particularly important for advanced optical communication and information processing applications.

In conventional photonic integrated circuits, passive components for input/output coupling, routing, splitting, and signal transfer constitute the foundation of all optical functionalities. Similarly, in topological photonic systems, the realization of robust and practical integrated circuits requires a complete set of such passive building blocks. Establishing these components is therefore a key step toward the development of large-scale topological photonic integrated systems.

In this talk, we will discuss the design principles, physical mechanisms, and experimental demonstrations of these fundamental TPIC components in detail. Particular emphasis will be placed on how topological photonic structures can be utilized to preserve and manipulate the internal degrees of freedom of light within integrated optical circuits, as well as on their potential applications in future high-capacity and highly robust photonic systems.

References

[1] A. B. Khanikaev *et al.*, "Photonic topological insulators," *Nat. Mater.* **12**, 233 (2013).
[2] T. Ozawa *et al.*, "Topological photonics," *Rev. Mod. Phys.* **91**, 015006 (2019).
[3] L.-H. Wu and X. Hu, Scheme for achieving a topological photonic crystal by using dielectric material," *Phys. Rev. Lett.* **114**, 223901 (2015).
[4] H. Kagami *et al.*, "Topological converter for high-efficiency coupling between Si wire waveguide and topological waveguide," *Opt. Express* **28**, 33619 (2020).
[5] H. Kagami *et al.*, "Highly efficient vertical coupling to a topological waveguide with defect structure," *Opt. Express* **29**, 32755 (2021).
[6] S. Okada *et al.*, "Demonstration of a highly efficient topological vertical coupler," *Opt. Express* **31**, 35218 (2023).
[7] X.-X. Wang *et al.*, "Interference and switching effect of topological interfacial modes with geometric phase," *Phys. Rev. Research* **7**, 023067 (2025).
[8] T. Amemiya *et al.*, "Topological photonic integrated circuits for controlling internal degrees of freedom of light," *J. Phys. Soc. Jpn.* **94**, 101005 (2025).

Plasmon-Induced Fluorescence Enhancement in Aminoporphyrin Thin Film Coupled with Gold Nanocubes Array

Giuseppe Di Maio [1,2] , Roberto Termine[2*], Caterina Damiano[3], Emma Gallo3,Massimo La Deda[1,2]

[1] University of Calabria, Dept Chem & Chem Technol, Arcavacata Di Rende, CS, Italy
2 CNR, Institute of Nanotechnolpgy CNR Nanotec, Arcavacata Di Rende, CS, Italy

3 University of Milan, Dept Chem, Via Golgi 19, I-20133 Milan, Italy
*Corresponding author: roberto.termine@cnr.it

***Abstract*— Hybrid plasmonic–molecular architectures were fabricated by depositing a self-assembled monolayer of gold nanocubes (AuNCs) onto a previously formed aminoporphyrin (NH_2TPPH_2) thin film. The photophysical behavior of the system was investigated before and after AuNC deposition using fluorescence spectroscopy, including absorption and emission measurements as well as fluorescence lifetime analysis. The molecular fluorophore exhibits a structured absorption profile in the visible region, while the Au nanocubes display a broad extinction band spanning from the visible to the near-infrared; this spectral complementarity was deliberately selected to ensure a significant overlap with the plasmon resonance, thereby fostering strong coupling between the fluorophore and the nanostructure. Such an arrangement allowed for a systematic study of the NH_2TPPH_2 photophysical response under controlled plasmonic excitation conditions, enabling, for the first time, an investigation of the relationship between excitation wavelength and plasmon band intensity within a single platform for plasmon-enhanced fluorescence (PEF). In addition, preliminary results on the PEF performance of an AuNC monolayer-based system are presented.**

***Keywords*— aminoporphyrin, gold nanoparticle, LSPR**

A New Effective Medium Approximation for Nanostructure on a Layered Films

Kotaro Kajikawa[1]

[1]School of Engineering, Institute of Science Tokyo, Japan
*Corresponding author: kajikawa.k.1a5f@m.isct.ac.jp

***Abstract*— We present an effective medium approximation for calculating the optical response of nanostructures on layered films. Unlike conventional approaches based solely on numerical simulations such as FDTD, the proposed method enables analytical evaluation of the optical response. The calculated results show good agreement with both numerical simulations and experiments.**

***Keywords*— effective medium approximation, metal nanoparticle, LSPR**

It has been challenging to analytically evaluate the optical response of structures comprising metal nanostructures on layered films. Consequently, numerical methods such as FDTD and FEM have typically been employed; however, these approaches require substantial computational resources, and the physical interpretation of the obtained results remains limited. To address these issues, we propose a new method in which the layered film is approximated as an effective medium. This method is well-suited for use in combination with boundary value problems involving multipole expansions. Comparison with numerical simulations and experimental results demonstrates good agreement.

Harnessing Effective Medium Birefringence for Broadband Chirality Generation in Resonant Metasurfaces

Chloe F. Doiron[1,*], Andrew R. Kim[2], Lisa Hackett[2],
Sadhvikas Addamane[1], Taisuke Ohta[2], and Alexander Cerjan[1]
[1]Center for Integrated Nanotechnologies, Sandia National Laboratories, Albuquerque NM, USA
[2]Sandia National Laboratories, Albuquerque NM, USA
*Corresponding author: cfdoiro@sandia.gov

***Abstract*—Optical metasurfaces are a versatile platform for controlling chirality and enhancing chiral light–matter interactions. Rather than creating resonators with chiral geometries, we show that advances in nanofabrication enable resonant chiral metasurfaces using effective medium anisotropies arising from deeply sub-wavelength patterning, creating new avenues for harnessing chirality in resonant systems. *Keywords*— metamaterials, chiral metasurfaces, chirality.**

With advances in nanofabrication over the past two decades, our ability to realize chiral metasurfaces has grown dramatically, with recent demonstrations of chiral lasing [1], improved sensing of chiral molecules [2], and enhanced chiral light–matter interactions [3]. As geometry is often the most accessible control parameter, demonstrations of chiral metasurfaces frequently rely on chiral resonator geometries. For a lossless dielectric resonator with $\mu' = 1$, chiral structuring leads to near-field chirality generation and destruction through Eq. 1 [4].

$$-\nabla\varepsilon' \cdot \frac{1}{8}\mathrm{Im}(\mathbf{E} \times \mathbf{E}^*) \tag{1}$$

Rather than relying on chiral geometries, metasurfaces can also create or destroy chirality through the use of optically anisotropic materials for which $\nabla\varepsilon' \neq 0$ (Fig. 1a). Comparing the optical birefringence of common optical materials with their maximum refractive indices (Fig. 1b) the birefringence values range from 4×10^{-3} to 1.62, with corresponding maximum refractive indices of 2.12 and 4.16. Instead of relying on natural optical anisotropy, artificial form birefringence can be introduced through structural patterning, as is commonly done in waveplate design [5]. With the experimental realization of new optical materials possessing very large refractive indices, such as iron pyrite with $n \approx 4.6$ [6], the maximum achievable form birefringence is beginning to approach that of the best anisotropic materials (Fig. 1c). However, maintaining optical resonances in such metasurfaces requires feature dimensions below 50 nm.

Here, we experimentally demonstrate an all-dielectric metasurface composed of two length scales, with deeply sub-wavelength features producing an anisotropic effective medium response and a larger-scale feature defining the optical

Fig. 1. (a) Schematic illustrating chirality generation using either chiral structuring or an anisotropic effective medium. (b) Comparison of birefringence and maximum refractive index for common bulk optical materials and multilayer two-dimensional material flakes (MF). (c) Theoretical and computational predictions, obtained using rigorous coupled-wave analysis (RCWA), of birefringence and maximum refractive index for a grating structure with 50 nm periodicity, 200 nm thickness, and 0.5 fill fraction.

Fig. 2. (a) Scanning electron micrograph of the fabricated TiO_2 resonator, with a top-down view shown in the inset. (b) Measured transmittance spectra showing three prominent resonances for linearly polarized light with polarization angles ranging from 0° to 90°. (c) Measured S_3 Stokes parameter showing broadband chirality generation.

resonator. Using these structures, we realize visible wavelength resonances with significant chirality generation, demonstrating a promising design pathway for chiral metasurfaces.

To fabricate the metasurfaces, we used a standard damascene process in which a high aspect ratio mold was patterned by electron beam lithography into resist (SML-2000) on a fused silica substrate. After development, a low-temperature, thermal atomic layer deposition process was used to conformally coat the metasurface with TiO_2, which was then etched by reactive ion etching to remove the overgrowth. After the remaining resist was removed, the freestanding structure was obtained (Fig. 2a). For the effective medium structuring, we patterned air gaps with a width of 30 nm and a periodicity of 90 nm, corresponding to an expected effective medium birefringence of 0.37. The larger resonator structure consisted of circles with a radius of 260 nm arranged in a square lattice with a periodicity of 600 nm. A top-down scanning electron micrograph shows that the resonator profiles (Fig. 2a) slightly break two-fold rotational symmetry since the periodicity of the small-scale features is slightly mismatched with the diameter of the circles.

After fabrication, we performed transmittance measurements (Fig. 2b) for linearly polarized light with the polarization axis oriented perpendicular (0°), diagonal (45°), and parallel (90°) to the grooves that produce birefringence. Across the three orientations, three clear resonances are observed at 683 nm, 748 nm, and 790 nm, showing that the structure is capable of supporting resonances in the visible. To measure the generated chirality, we recovered the Stokes parameters for linearly polarized incident light. The spectral profile of S_3 (Fig. 2c) shows broadband chirality generation with S_3 values reaching -0.65, with the influence of the 748 nm resonance being clearly visible.

In conclusion, we demonstrated a chiral metasurface comprised of resonators with effective medium birefringence. Although the transmitted beams are elliptically polarized, these results demonstrate the potential of tailoring optical anisotropy for controlling chirality in resonant metasurfaces.

ACKNOWLEDGMENTS

CFD, LH, SA, and AC acknowledge support from the Laboratory Directed Research and Development program and Sandia National Laboratories. ARK and TO acknowledge support from the U.S. Department of Energy, Office of Basic Energy Sciences, Division of Materials Sciences and Engineering (BES 20-017574). This work was performed, in part, at the Center for Integrated Nanotechnologies, an Office of Science User Facility operated for the U.S. Department of Energy (DOE) Office of Science. Sandia National Laboratories is a multimission laboratory managed and operated by National Technology & Engineering Solutions of Sandia, LLC, a wholly owned subsidiary of Honeywell International Inc., for the U.S. Department of Energy's National Nuclear Security Administration under contract DE-NA0003525. This work describes objective technical results and analysis. Any subjective views or opinions that might be expressed in the paper do not necessarily represent the views of the U.S. Department of Energy or the United States Government.

REFERENCES

[1] X. Zhang, Y. Liu, J. Han, Y. Kivshar, and Q. Song, "Chiral emission from resonant metasurfaces," *Science*, vol. 377, no. 6611, pp. 1215–1218, 2022.

[2] J. García-Guirado, M. Svedendahl, J. Puigdollers, and R. Quidant, "Enhanced Chiral Sensing with Dielectric Nanoresonators," *Nano Letters*, vol. 20, no. 1, pp. 585–591, 2020.

[3] Q. Zhang, T. Hernandez, K. W. Smith, S. A. Hosseini Jebeli, A. X. Dai, L. Warning, R. Baiyasi, L. A. McCarthy, H. Guo, D.-H. Chen, J. A. Dionne, C. F. Landes, and S. Link, "Unraveling the origin of chirality from plasmonic nanoparticle-protein complexes," *Science*, vol. 365, no. 6460, pp. 1475–1478, 2019.

[4] L. V. Poulikakos, P. Gutsche, K. M. McPeak, S. Burger, J. Niegemann, C. Hafner, and D. J. Norris, "Optical Chirality Flux as a Useful Far-Field Probe of Chiral Near Fields," *ACS Photonics*, vol. 3, no. 9, pp. 1619–1625, 2016.

[5] A. Emoto, M. Nishi, M. Okada, S. Manabe, S. Matsui, N. Kawatsuki, and H. Ono, "Form birefringence in intrinsic birefringent media possessing a subwavelength structure," *Applied Optics*, vol. 49, no. 23, pp. 4355–4361, 2010.

[6] C. F. Doiron, J. B. Khurgin, and G. V. Naik, "Super-Mossian Dielectrics for Nanophotonics," *Advanced Optical Materials*, vol. 10, no. 22, p. 2201084, 2022.

On-chip Integrated Intelligent Photonic Computing

Kun Liao

Department of Physics, Peking University, China
Email: kunliao@pku.edu.cn

***Abstract*— We report advances in photonic neural networks that broaden functionality, increase computational complexity, and improve system-level integration for practical intelligent photonic computing, paving the way toward highly integrated and scalable next-generation intelligent photonic computing chips.**

***Keywords*— photonic neural networks, photonic computing chips, silicon photonics.**

I. Introduction

Integrated photonic chips, characterized by their high data throughput and low power consumption, have demonstrated broad application prospects in optical communications, computing, LiDAR, sensing, and imaging. Leveraging on-chip optical interconnects, integrated photonic neural networks have emerged as one of the most promising paradigms for optical computing. However, their further development remains constrained by several key challenges, including limited computational efficiency, insufficient nonlinear response, restricted network scalability, and system-level integration complexity.

II. Results and Discussion

We demonstrate a series of studies exploring new opportunities for the development of on-chip integrated photonic neural networks from multiple perspectives, including functionality expansion, computational efficiency improvement, system complexity enhancement, and high-level integration. First, we extend silicon-based integrated photonic neural networks beyond conventional inference tasks to perform complex mathematical operations, such as transcendental equation solving [1] and matrix eigenvalue solving [2]. We further design and implement a reconfigurable optical nonlinear activation layer based on a graphene/silicon heterojunction, enabling efficient and flexible on-chip nonlinear activation functions [3]. In addition, we develop an inverse-designed ultracompact photonic computing platform that supports diverse applications, including photonic simulations for topological insulator models with high measured fidelity and image classification tasks with on-chip training [4]. To enhance scalability and architectural flexibility, we propose a universal and reconfigurable on-chip neural network architecture that enables in situ switching and deployment of multiple network models within a unified photonic hardware framework, supporting both static and dynamic tasks [5]. Moreover, we demonstrate a monolithically hetero-integrated photonic computing system that integrates light sources, photonic processors, and photodetectors all on a single chip, and experimentally validate its capability in quantum simulation and computer vision tasks [6].

III. Conclusion

In summary, these studies collectively advance on-chip integrated photonic neural networks in terms of functionality, computational capability, architectural flexibility, and system-level integration. By enabling complex mathematical operations, efficient optical nonlinearity, compact inverse-designed platforms, scalable reconfigurable architectures, and monolithically integrated photonic computing systems, this body of work moves photonic neural networks closer to practical and general-purpose intelligent computing hardware. These developments not only improve the performance and versatility of photonic processors, but also highlight a viable path toward highly integrated, energy-efficient, and scalable next-generation intelligent photonic computing chips for scientific computing, artificial intelligence, and quantum technologies.

References

[1] Liao, K., Chen, Y., Yu, Z., Hu, X., Wang, X., Lu, C., Lin, H., Du, Q., Hu, J. and Gong, Q., All-optical computing based on convolutional neural networks. Opto-Electronic Advances, 4(11), p.200060, 2021.

[2] Liao, K., Li, C., Dai, T., Zhong, C., Lin, H., Hu, X. and Gong, Q., Matrix eigenvalue solver based on reconfigurable photonic neural network. Nanophotonics, 11(17), pp.4089-4099, 2022.

[3] Zhong, C., Liao, K., Dai, T., Wei, M., Ma, H., Wu, J., Zhang, Z., Ye, Y., Luo, Y., Chen, Z. and Jian, J., Graphene/silicon heterojunction for reconfigurable phase-relevant activation function in coherent optical neural networks. Nature Communications, 14(1), p.6939, 2023.

[4] Du, Z., Liao, K., Dai, T., Wang, Y., Gao, J., Huang, H., Qi, H., Li, Y., Wang, X., Su, X. and Wang, X., Ultracompact and multifunctional integrated photonic platform. Science advances, 10(25), p.eadm7569, 2024.

[5] Wang, Y., Liao, K., Zhang, K., Du, Z., Wang, Z., Ni, B., Xu, T., Feng, S., Yang, Y., Yang, Q.F. and Sun, Q., Reconfigurable versatile integrated photonic computing chip. eLight, 5(1), p.20, 2025.

[6] Liao, K., Lian, Y., Yu, M., Du, Z., Dai, T., Wang, Y., Yan, H., Wang, S., Lu, C., Chan, C.T. and Zhu, R., Hetero-integrated perovskite/Si3N4 on-chip photonic system. Nature Photonics, 19(4), pp.358-368, 2025.

Localization and diffusive transport in photonic correlated disorder materials

N. Granchi[1], G. Calusi[1], K. Stokkereit[2], M. Lodde[3], C. Gonzini[1], A. Fiore[3], M. Florescu[4] and F. Intonti*[1]

[1] Department of Physics and Astronomy and LENS, University of Florence, Italy
[2] Advanced Technology Institute and Department of Physics, University of Surrey, UK
[3] Department of Applied Physics and Institute for Photonic Integration, Eindhoven University of Technology, NL
[4] Optoelectronics Research Centre, University of Southampton, UK
*Corresponding author: intonti@lens.unifi.it

***Abstract*— We investigate a special class of disordered photonic heterostructures, hyperuniform disordered (HuD) photonic structures, that allows to deterministically tailor Anderson localization and diffusive transport.**

***Keywords*— Hyperuniformity, Scanning Near-field Microscopy.**

Disorder is traditionally regarded as a detrimental element in photonic systems, often associated with unwanted scattering losses, localization effects, and poor reproducibility. However, over the past two decades, this perspective has shifted significantly as it has become clear that disorder, when properly engineered, can serve as a powerful design parameter [1,2]. In particular, correlated disorder systems have emerged as a versatile platform for controlling light–matter interaction beyond the constraints of periodic photonic crystals and fully random media. By embedding structural correlations into otherwise disordered arrangements, it is possible to tailor optical transport, density of states, and scattering properties in ways that are inaccessible to either extreme [3].

Among correlated disordered systems, Hyperuniform Disordered (HuD) materials have attracted growing attention in photonics due to its unique statistical and physical properties. Hyperuniform structures are characterized by anomalously suppressed density fluctuations at large length scales, resulting in a vanishing structure factor in the long-wavelength limit [4]. This property places hyperuniform systems in an intermediate regime between crystalline order and complete randomness. Unlike periodic lattices, hyperuniform structures lack Bragg peaks and long-range translational symmetry, yet they retain a form of hidden order that strongly influences wave propagation. In photonic systems, disorder hyperuniformity has been shown to enable phenomena traditionally associated with periodic media, such as isotropic photonic band gaps [5,6], while preserving the robustness and fabrication tolerance of disordered architectures. This combination is particularly appealing for applications requiring omnidirectional light control, including waveguiding, light confinement, and enhanced emission control. Furthermore, the absence of long-range periodicity reduces sensitivity to defects and allows for greater flexibility in device geometry, which is advantageous for integrated photonics and three-dimensional photonic materials.

Here, Taking advantage of the combination of the HuD design in slab platforms, optically activated with embedded quantum dots, and near-field hyperspectral imaging with sub-wavelength resolution, we investigated light localization in HuD networks, and unveil different physical mechanism that lead to the formation of different kind of defects with different localization lengths and Q factors [7-10]. The possibility of detecting different regimes of light confinement in a system, whose structuring is at the junction between fully-ordered and completely random systems, open routes yet to be explored for addressing basic physics and practical applications of correlated disorder materials.

References

[1] D. Balestri et al., “Mechanical and Electric Control of Photonic Modes in Random Dielectrics,” Advanced Materials, Vol. 31, 1807274, 2019.
[2] F. Riboli et al., “Engineering of light confinement in strongly scattering disordered media,” Nature Materials, Vol. 13, 720, 2014.
[3] K. Vynck et al., “Light in correlated disordered media,” Reviews of Modern Physics, Vol. 95, 045003, 2023.
[4] S. Torquato, “Hyperuniform states of matter,” Physics Reports, Vol. 745, 1, 2018.
[5] M. Florescu et al., “Designer disordered materials with large, complete photonic band gaps” Proceedings of the National Academy of Sciences Vol. 106, 20658, 2009.
[6] L.S. Froufe-Pérez et al., “Band gap formation and Anderson localization in disordered photonic materials with structural correlations,” Proceedings of the National Academy of Sciences, Vol. 114, 9570, 2017.
[7] N. Granchi et al., “Near-Field Investigation of Luminescent Hyperuniform Disordered Materials,” Advanced Optical Materials, Vol. 10, 2102565, 2022.
[8] N. Granchi et al., “Near-field imaging of optical nanocavities in hyperuniform disordered materials,” Physical Review B, Vol. 107, 064204, 2023.
[9] N. Granchi et al., “High spatial resolution imaging of light localization in hyperuniform disordered patterns of circular air pores in a dielectric slab,” Frontiers in Photonics, Vol. 4:1199411, 2023.
[10] N. Granchi et al., “Photonic crystal-like scaling behavior of localized Anderson modes in hyperuniform disordered systems,” Journal of the European Optical Society-Rapid Publications, Vol. 21, 44, 2025.

Label-free and Label-based approaches for tapered fiber photometry in the deep brain

Massimo De Vittorio[1,2*], Ferruccio Pisanello[2]

[1]Center for Biomolecular Nanotechnologies, Istituto Italiano di Tecnologia, Italy
[2] Department of Health Technology, Technical University of Denmark, Denmark
*Corresponding author: Massimo.devittorio@iit.it, mdevit@stu.dk

***Abstract*— Tapered fiber photometry can be exploited for depth-resolved deep-brain recording using fluorescent reporters and in label-free Raman approaches to probe the intrinsic molecular composition without exogenous markers. Combined with plasmonic enhancement, these approaches offer complementary strategies to investigate neural dynamics and tissue composition in vivo.**

***Keywords*— tapered fibers, fiber photometry, deep brain recording, Raman spectroscopy, SERS, label free sensing, fluorescent reporters, plasmonic enhancement, neural activity monitoring.**

I. Introduction

Understanding neural activity in deep brain regions is fundamental for decoding brain functions and studying diseases. Optical techniques have emerged as powerful tools for interrogating neural circuits with high temporal resolution and cell-type specificity. Among these, fiber photometry has become widely adopted due to its minimal invasiveness, compatibility with freely behaving animals, and ability to access deep brain structures through implanted optical fibers.

Traditionally, fiber photometry relies on genetically encoded fluorescent indicators to monitor cellular and sub-cellular processes such as calcium and neurotransmitter dynamics. These label-based approaches provide high sensitivity and molecular specificity, enabling real-time monitoring of defined neuronal populations during behavior.

II. Discussion

Recent technological advances have expanded the capabilities of fiber-based neural interrogation. Tapered optical fibers allow improved light delivery and collection efficiency across extended brain volumes, enabling depth-resolved recordings with reduced tissue damage [1]. At the same time, the development of novel fluorescent biosensors has increased sensitivity and multiplexing capabilities for simultaneous monitoring of multiple signals.

In parallel, label-free approaches are emerging as complementary strategies. Raman spectroscopy, implemented through minimally invasive tapered fiber probes, enables detection of intrinsic molecular vibrations without the need for exogenous reporters [2]. Although inherently limited by weak scattering signals and background noise, integration with plasmonic nanostructures and surface-enhanced Raman strategies significantly improves sensitivity. When decorated with plasmonic nanostructures, these probes further enable surface-enhanced Raman detection of neurotransmitters, enabling label-free measurements of neurotransmitters in vitro with a limit of detection down to 10^{-9} molar concentration [3,4].

III. Conclusion

Together, label-based and label-free fiber photometry approaches provide a broader framework for investigating neural activity, biochemical signaling, and tissue composition in vivo.

Bare and nano-machined tapered optical fibers provide a powerful and versatile platform for multimodal neural interrogation in deep brain regions, enabling depth-resolved fiber photometry of neural activity dynamics, vibrational Raman spectroscopy for in vivo brain cancer tissue identification, and surface-enhanced Raman detection of neurotransmitter concentration.

Acknowledgments

This work was supported by the following projects: ERC project MINING (grant n. 101125498), project COMBO (CUP: E63C22002170007), project “SUPER” funded by the Novo Nordisk Foundation (grant number NNF23OC0079433).

References

[1] Pisano, F., et al. (2019). Depth resolved fiber photometry with a single tapered optical fiber implant. *Nature Methods*, ***16****, 1185–1192.*
[2] Pisano, F., et al. (2024). Vibrational fiber photometry: label-free and reporter-free minimally invasive Raman spectroscopy deep in the mouse brain. *Nature Methods*, **22**, 371–379.
[3] Zheng, D., et al., F. (2023). Toward Plasmonic Neural Probes: SERS Detection of Neurotransmitters through Gold-Nanoislands-Decorated Tapered Optical Fibers with Sub-10 nm Gaps. *Advanced Materials*, *35*(11).
[4] Zheng, D., et al. (2025). Direct Nucleation of Hierarchical Nanostructures on Plasmonic Fiber Optics Enables Enhanced SERS Performance. *Advanced Science*, *12*(42).

Self-Hybridized Exciton-Polaritons in Two-Dimensional-Perovskite Microcrystals

Martina Borreani[1,2], Alexander Schleusener[1], Sudhir K. Saini[1], Lin-Han Li[3], Miao-Ling-Lin[3], Ping-Heng Tan[3], Vincenzo Caligiuri[4], and Roman Krahne [1*]

[1] Optoelectronics Group, Istituto Italiano di Tecnologia, Genova, Italy
[2] Dipartimento di Chimica e Chimica Industriale, Università degli Studi di Genova, Italy
[3] State Key Laboratory of Superlattices and Microstructures, Institute of Semiconductors, Chinese Academy of Sciences, 100083 Beijing, China
[4] Dipartimento di Fisica, Università della Calabria, Rende, Italy
*Corresponding author: roman.krahne@iit.it

***Abstract*— We fabricate highly regular 2D perovskite microcrystals by recrystallization that function as optical cavities and sustain strong light-matter interaction. The cavity modes and polariton dispersion are governed by the non-linear wavelength dependence of the refractive index, leading to slow light propagation at the band edge.**

***Keywords*— polaritons, exciton, 2D perovskite, microcrystals.**

I. Introduction

Two-dimensional (2D) metal halide perovskites are emerging materials with bright and tunable emission that are highly attractive for light emission and lasing. Their hybrid organic-inorganic structure provides ample opportunities to tailor their optical properties and radiative recombination dynamics.[1, 2] Strong dielectric confinement results in high exciton binding energies, and their high refractive index favors strong-light matter interaction.[3, 4] In particular, highly homogeneous slabs of 2D perovskites can act themselves as optical cavities and lead to self-hybridization of the photonic cavity modes with the band edge exciton levels. One peculiar property of the architecture in which the semiconductor light emitting material itself forms the optical cavity, is the strong non-linearity of the complex refractive index. This has several interesting implications: a pronounced decrease in group velocity of the light, and an abnormal dispersion near the band edge that results in high damping and leaky optical modes.

II. Results and Discussion

We investigate the reflectance and photoluminescence of single 2D lead iodide microcrystals that act as highly efficient optical cavities. We observe an extremely large number of cavity modes in microcrystals with micrometer thickness. This allowed us to determine the complex refractive index using the interference fringes method combined with a Cauchy dispersion for the transparent low energy range of the cavity mode spectrum. We then use the obtained dispersion of the refractive index in the calculation of the exciton-polariton anticrossing based on a Lorentz oscillator model, and by fitting the experimentally obtained reflectance minima near the band gap we obtain the longitudinal optical (LO) and transversal optical (TO) exciton energies and the damping coefficient Γ.

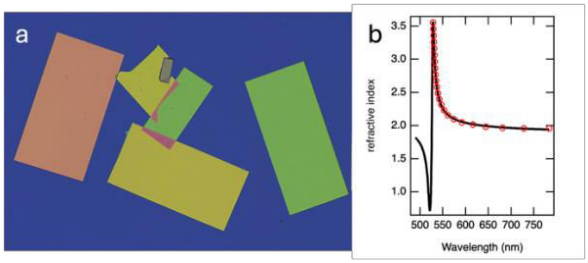

Fig.1. Optical image of 2D perovskite microcrystals (a) and the refractive index dispersion of PEA_2PbI_4 microcrystals (b).

III. Conclusion

2D perovskite microcrystals with highly regular shape and homogeneous thickness constitute a versatile platform for integrated and non-linear photonics.

Acknowledgments

R.K and A.S. acknowledge funding by the European Union under Project 101131111 – DELIGHT.

References

[1] R. Krahne, et al., Phonon Directionality Impacts Electron–Phonon Coupling and Polarization of the Band-Edge Emission in Two-Dimensional Metal Halide Perovskites. Nano Lett., 2024. **24**, 11124-11131
[2] R. Krahne, M.-L. Lin, and P.-H. Tan, Interplay of Phonon Directionality and Emission Polarization in Two-Dimensional Layered Metal Halide Perovskites. Acc. Chem. Res., 2024. **57**, 2476-2489
[3] M. Borreani, et al., Direct Growth of Rectangular 2d Layered Metal-Halide Perovskite Microcrystal Photonic Cavities on Functional Substrates. Adv. Opt. Mater., 2025. **n/a**, e01276
[4] A. Schleusener, et al., Heterostructures Via a Solution-Based Anion Exchange in Microcrystalline 2d Layered Metal-Halide Perovskites. Adv. Mater., 2024. **36**, 2402924

Flat Optics for Multispectral Grafted Vortex Beams and OAM Combs

Hammad Ahmed[1,*] and Xianzhong Chen[1]

[1]Institute of Photonics and Quantum Sciences, School of Engineering and Physical Sciences, Heriot-Watt University, Edinburgh, EH14 4AS, UK.

*Corresponding author: H.Ahmed@hw.ac.uk

Abstract: We present a compact flat-optics (metasurface) platform capable of generating and dynamically tuning multispectral grafted vortex beams together with azimuthally engineered multispectral orbital angular momentum (OAM) combs. By coherently superimposing multiple helical phase distributions, the system produces optical beams with tailored topological charges and controllable multispectral OAM spectra, creating new opportunities for applications in optical encryption, advanced communication systems, and particle manipulation.

In this work, we introduce a metasurface based strategy for the generation and manipulation of multispectral grafted vortex beams (GVBs) and azimuthally structured OAM combs, overcoming limitations of conventional bulk optical components. GVBs [1], formed through the superposition of multiple helical phase profiles, exhibit distinctive optical features and have attracted considerable interest in singular optics and quantum applications. Traditional generation techniques, however, typically require complicated and bulky optical setups. Our proposed approach employs a single metasurface to synthesize various GPVB superpositions with different topological charges, enabling asymmetric distributions of optical singularities. Moreover, the positions of these singularities can be tuned through the introduction of an initial phase offset, removing the need for complex optical alignments.

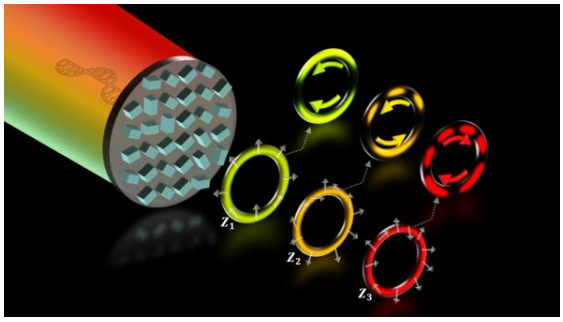

Fig. 1. Schematic of the metasurface for creating multiple longitudinally variable GPVVBs

We further demonstrate the generation of multispectral perfect vector vortex beams (GPVVBs) [2,3] using a multifunctional metasurface that combines several different colored GPVVBs (Fig. 1). These beams exhibit spatially varying polarization states and allow flexible control over multiple topological charge combinations. Dynamic modulation of these beams is achieved by incorporating a rotating half-wave plate, providing additional tunability and enabling potential applications in adaptive optical encryption and high-capacity data transmission.

Finally, the metasurface platform is extended to produce multispectral OAM combs with adjustable mode spacing, offering a compact and efficient method for generating structured OAM spectra across multiple spectral channels (Fig. 2). This capability significantly increases the information-carrying capacity of optical systems and supports emerging applications in next-generation optical communication and information processing technologies [4].

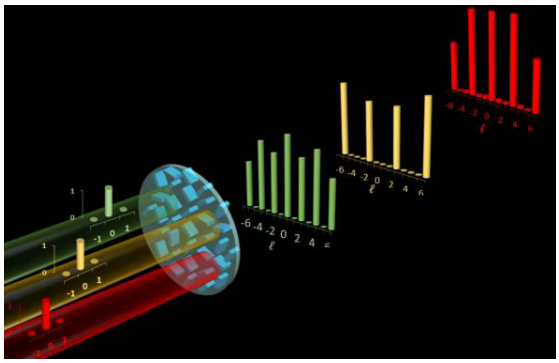

Fig. 2. Schematic of a metasurface for realizing multicolored OAM combs.

References

[1]. Ahmed, Hammad, et al. "Multichannel superposition of grafted perfect vortex beams." Advanced Materials 34.30 (2022): 2203044.

[2]. Ahmed, Hammad, et al. "Dynamic control of hybrid grafted perfect vector vortex beams." Nature Communications 14.1 (2023): 3915.

[3]. Wang, Guanchao, et al, “Creating multispectral grafted perfect vector vortex beams in a queue.” Laser & Photonics Reviews, 18.10 (2024): 2400323

[4]. Ahmed, Hammad, et al. "Customizing Multicolored Orbital Angular Momentum Combs." Nano Letters (2025).

Autonomous Agentic Systems for Metamaterial Design and Research

Willie J. Padilla,[1,*] Dary Lu,[1] and Jordan Malof[2]

[1] Department of Electrical and Computer Engineering, Duke University, Durham, North Carolina 27710, United States of America

[1] Department of Electrical Engineering and Computer Science, University of Missouri, Missouri, Columbia 65211, United States of America

*Corresponding author: willie.padilla@duke.edu

***Abstract*— The evolution from large language models (LLMs) to agentic systems has created a new frontier of scientific discovery, enabling the automation of complex research tasks that have traditionally required human expertise. We present an autonomous agentic framework that automates the complete end-to-end workflow of electromagnetic metamaterial inverse design, including the development of the forward surrogate model itself. When queried with a desired optical spectrum s^*, the agent autonomously reasons, plans, and utilizes external tools via APIs to propose a custom deep learning model and generate an optimized geometrical configuration g^* via a deep inverse method. This framework mimics the workflow of a human researcher through its ability to reason, adapt its strategy in real-time, and use internal reflection, representing a new paradigm for accelerating nanophotonic design.**

***Keywords*— artificial intelligence, metamaterials, metasurfaces, inverse design, deep learning**

Coherent Thermal Wavefront Manipulation Using Hierarchical Metasurfaces

Yungui Ma

College of Optical Science and Engineering, Zhejiang University, Hangzhou 310058, China

Conventional coherent light-field manipulation approaches are inherently incompatible with the spatiotemporal incoherence of thermal radiation sources. Although recent progress in thermophotonics has enabled directional thermal emission, arbitrary control of thermal wavefronts— essential for applications such as focusing and holography— still represents an unresolved challenge. Here, we present a universal strategy for designing meta-emitters with lossy and lossless outer boundaries, which support thermal emission with arbitrarily engineered wavefronts. The lossy and lossless interfaces are synergistically coupled via a single-mode waveguide, converting incoherent thermal photons into coherent surface waves for wavefront shaping. The designer surface mode of the meta-emitter allows independent optimization of photon lifetime and propagation length, enabling scalable spatial coherence engineering. As proof of concept, we experimentally demonstrate near-diffraction-limited self-focusing emission, high-quality speckle-free quasi-two-dimensional thermal holography, and spatially multiplexed holography. Moreover, coupling optimization indicates that spatial coherence exceeding 1000λ0 can be achieved. The proposed meta-emitter platform establishes a transformative paradigm that bridges stochastic thermodynamic emission and precise photonic engineering, paving the way for high-information-content thermal radiation technologies.

Reference:

[1] Rui Chen, Tianle Chen, Mengqi Liu, Xinqsi Liu, Sen Zhang, Faizan Raza, Honqguang Dong, Yongdi Dang, Zejie Yu, Huan Hu, Jianbing Xu, Cheng-Wei Qiu* and Yungui Ma*, Ultra-Coherent Meta-Emitter Tailors Arbitrary Thermal Wavefront, Nature Communications 2528 (2026).

Proceedings of META 2026 · Dublin, Ireland · 14–17 July 2026 · ISSN 2429-1390 · pp. 444–444

Progress in the development of efficient Quantum Dot based room temperature THz sources

E. U. Rafailov
Optoelectronics and Biomedical Photonics Group, AIPT, Aston University, Birmingham, UK
*Corresponding author: e.rafailov@aston.ac.uk

***Abstract*— Quantum-dot semiconductor structures are emerging as promising materials for compact THz sources due to their broadband gain and ultrafast carrier dynamics. We demonstrate enhanced CW and pulsed THz emission using nanoantenna-integrated photoconductive antennas, enabling efficient room-temperature operation and positioning QD-based devices for next-generation THz applications.**

***Keywords*— Quantum-Dot, THz, nanoantenna.**

I. Introduction

Quantum-dot (QD) semiconductor structures, traditionally employed in laser development, have recently emerged as promising materials for compact terahertz (THz) sources. Their unique combination of broadband gain and absorption, alongside ultrafast carrier dynamics, enables novel approaches to THz radiation generation. In this work, we present recent advances in both continuous-wave (CW) and pulsed THz emission from QD-based photoconductive antennas enhanced with optical nanoantennae. The integration of nanoantennae within the antenna gap significantly boosts efficiency, enabling room-temperature operation in an ultra-compact footprint. Furthermore, the incorporation of bandgap-engineered semiconductor materials, quantum-confined structures, and interdigitated electrodes broadens the pump absorption range and improves carrier mobility, both critical for THz performance. These developments position QD-based architectures as a highly promising platform for next-generation ultra-compact THz sources, with potential applications in spectroscopy, imaging, and high-speed wireless communications.

Single-shot polarization-resolved microscopy of nanomaterials

Julien Flamant,[1] Nathan Ullberg,[2] Baptiste Marthy,[2] Khosro Zangeneh Kamali,[3]
Patrick Ferrand,[2] Mikael Käll,[3] Guillaume Baffou[1,*]

[1]Université de Lorraine, CNRS, CRAN, F-54000 Nancy, France
[2]Institut Fresnel, CNRS, Aix Marseille Univ, Centrale Med, Marseille (France)
[3]Chalmers University, Goteborg, Sweden

*Corresponding author: guillaume.baffou@fresnel.fr

***Abstract*— We introduce an optical microscopy approach capable of retrieving the complex vectorial electromagnetic field at the image plane (that is, intensity, phase, and polarization of light) in a single acquisition. The method combines a polarization-sensitive camera with a two-dimensional diffraction grating (cross-grating) placed in close proximity to the image sensor.**

***Keywords*— microscopy, polarization, plasmonics, nanoparticles, metasurfaces, Jones, Stokes.**

Nanophotonics and optical microscopy are now tightly intertwined in modern research, as high-resolution optical characterization is essential for studying nanomaterials, such as dielectric and plasmonic nanoparticles, metasurfaces, and 2D materials. Yet, existing microscopy techniques are often complex to implement or limited to measuring light intensity, overlooking spectral, phase, and polarization features. Here, we introduce an optical microscopy approach capable of retrieving the full complex vectorial electromagnetic field at the image plane (that is, intensity, phase, and polarization of light) in a single acquisition. The method combines a polarization-sensitive camera with a two-dimensional diffraction grating (cross-grating) placed in close proximity to the image sensor. Beyond light beam characterization, this configuration enables sample characterization, through Jones matrix imaging of métasurfaces, complex optical polarizability tensor measurements of nanoparticles.

Multifunctional Optical Metasurfaces and Their On-Chip Integration

Bo, Xiong[1,*] , Minjun, Xie[1,]

[1] College of Information Science and Electronic Engineering, Zhejiang University, China
*Corresponding author: bo.xiong@zju.edu.cn

***Abstract*— Using dielectric deflective metasurfaces, we propose a novel out-of-plane modulation scheme. The metasurface is used to deflect vertical incident light to an oblique angle. This deflection introduces a lateral wave vector component. Overall, the integration of the metasurface and subwavelength grating enables a new vertical coupling scheme with high efficiency.**

***Keywords*— Metasurface, Chip Integration.**

I. Introduction

Optical micro/nanostructures enable the manipulation of light–matter interactions at subwavelength scales and serve as a key approach for optical field sensing and high-resolution detection and imaging. As a typical silicon photonics device, vertical grating couplers (VGCs) function as optical I/O interfaces that convert vertically incident light into in-plane light. They offer the advantage of not requiring angled polishing of coupling fibers, making them advantageous in wafer-level testing and multicore fiber packaging. In this paper, we propose a novel out-of-plane modulation scheme to realize vertical coupling, which combines a dielectric metasurface with an apodized binary grating to achieve high-efficient vertical coupling on the 220 nm SOI platform.

II. Methods

The overall device consists of a deflected silicon metasurface and an apodized single-etched grating coupler. The process of receiving vertically incident light into the waveguide device can be understood in two steps. Initially, TE-polarized light enters from the air and interacts with the nanopillars comprising the metasurface, resulting in deflection through the SiO2 cladding (Fig. 1 (a)). Subsequently, the obliquely incident light is captured by the SEGC and efficiently coupled into the waveguide (Fig. 1 (b)). By introducing a lateral wave vector component, the deflection prevents the vertical coupling from bi-directional transmission. This new scheme enables the straightforward realization of vertical coupling designs based on binary grating structure.

For the metasurface design, we employed a square periodic boundary with each side measuring 640 nm, and α-Si nanopillar with a height of 900 nm as the fundamental unit, as illustrated in Fig. 1 (d). The parameter "a" and "b" denote the width and length of nanopillars, respectively.

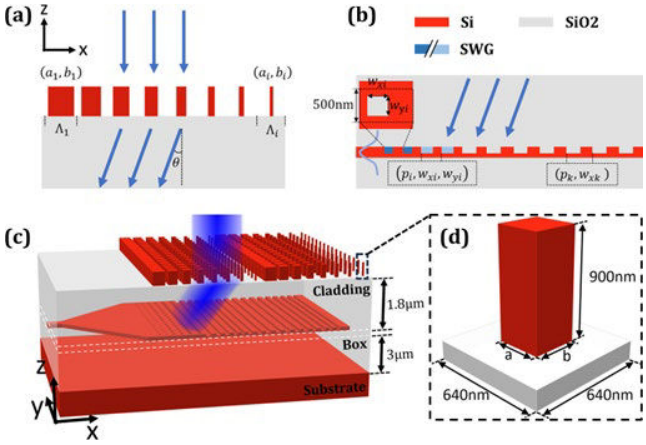

Fig. 1 (a) Operation of deflective metasurface. (b) Single-etched grating coupler. (c) Vertical grating coupler integrated with deflective metasurface. (d) Meta unit.

III. Results and Discussion

The manufacturing process of proposed VGC is illustrated in Fig.2. Fig.2 (a)-(d) shows the production process of the GC. The grating is fabricated on a 220 nm SOI wafer. After a standard Electron Beam Lithography (EBL) process a 100 nm shallow Si etch is performed. 1.8 μm SiO2 cladding and 900 nm α-Si film were grown by Plasma-Enhanced Chemical Vapor Deposition (PECVD) technology sequentially. We fixed the parabolic taper length to be 110 μm. A grating width of 12 μm were chosen for mode matching with the SMF. Fig.2 (e)-(h) show the production process of the deflective metasurface.

The sample size is adjusted to a size of 50 μm × 50 μm in order to fully cover the grating area. When the alignment error occurs, the metasurface corresponding to the grating region has a consistent phase gradient, resulting in an alignment-insensitive response. Fig. 3 (a) shows SEM images of the grating coupler while Fig. 3(b) provides more details of the SWG region. The fabricated metasurface are presented in Fig. 3 (c), from which we can clearly observe Si nanocolumns with nine different sizes. Fig.3 (d) and Fig.3 (e) show the optical images of whole VGC samples.

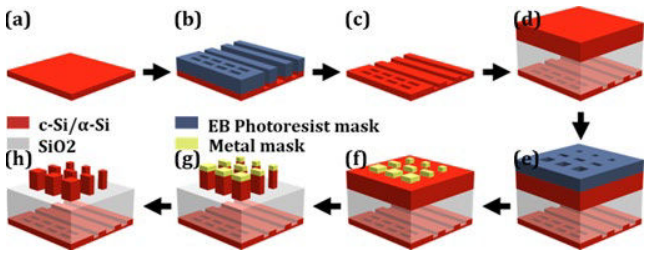

Fig. 2 Fabrication process of VGC. (a)–(c) Fabrication process of apodized single-etched grating. (d) Deposition of SiO2 and α-Si layer. (e)–(h) Fabrication process of deflective metasurface.

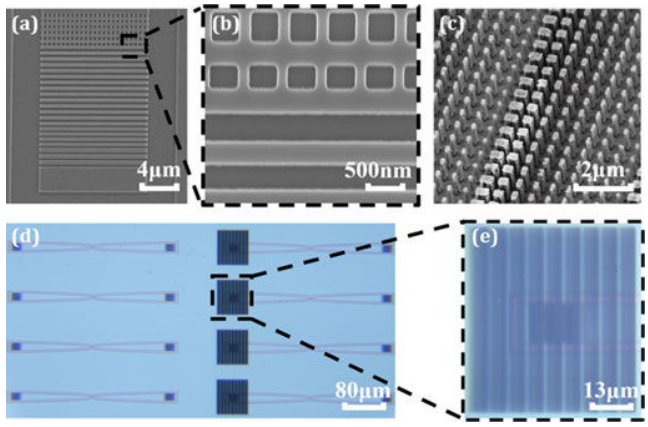

Fig. 3 (a) SEM image of single-etched GC. (b) Detailed view of the SWG area. (c) SEM image of metasurface nanopillars. (d) Mircoscopy view of VGC. (e) Detailed view of the VGC covered with metasurface.

For the measurement setup, a SANTEC TSL-550 tunable laser is utilized as the light source, and its polarization is restricted to TE mode through adjustment of the polarization controller. For the VGC sample test, the incident light is vertically coupled into the sample with the metasurface. The collected light was then measured by a YOKOGAWA AQ2200-221 optical power meter. A wavelength scan was performed from 1500 to 1600 nm with a 0.2 nm step. The grating samples with and without the metasurfaces were both evaluated under vertical incident. Compared to the reference sample without metasurface, Fig. 4 (a) shows a 45 dB significant enhancement in CE when metasurface is integrated. A more detailed test result in Fig.4 (b) shows that the VGC has a peak CE of -3.36 dB at 1549 nm with a 1-dB bandwidth of about 32 nm (blue solid line) under vertical incidence. And the reference grating under oblique incidence has a peak CE of -2.75 dB at 1550 nm with a 1-dB bandwidth of about 33 nm (orange solid line). Compared to their simulation results, the test results exhibit an extra loss of approximate 1dB, mainly owing to the fabrication error of the SEGC

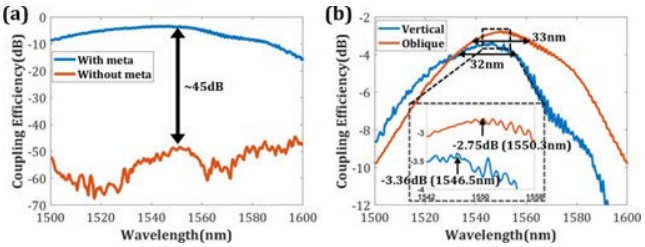

Fig. 4 (a) Experimental results of GCs with and without meta under vertical incidence. (b) Experimental results of our VGC under vertical incidence and the reference GC under oblique incident.

IV. Conclusion

In conclusion, a new vertical grating coupling scheme combined with deflective metasurfaces is experimentally demonstrated on the 220 nm SOI platform. Using dielectric metasurface, vertically incident light can be deflected to the target angle, which can be collected by the apodized single-etched grating coupler with high efficiency. The measured coupling efficiency is 3.36 dB at 1546.5 nm with a 1-dB bandwidth of 32 nm. Further characterization tests reveal the architecture's angular tolerance, with approximately 3° tolerance for angular deviations, and x-axis displacement tolerance of 6 μm. Subsequent research works will go deeper into the phase distribution and freedom of degrees of metasurface, which may develop additional functions and channels into the vertical coupler device, such as polarization splitting grating coupler and wavelength-division-multiplex receiver.

References

[1] Xiong B, Liu Y, Xu Y, et al. Breaking the limitation of polarization multiplexing in optical metasurfaces with engineered noise[J]. Science, 2023, 379(6629): 294-299.

[2] Xie M, Xiong B, Chu T. Realizing highly efficient vertical coupling with dielectric deflective metasurfaces[J]. Optics Letters, 2024, 49(11): 3182-3185.

[3] Li W, Zhou Y, Ye C, et al. Multifunctional metasurface for simultaneous light manipulation under both guided-wave and free-space incidence[J]. ACS Photonics, 2024, 11(4): 1724-1733.

Direct Nanoimprint Lithography as an Additive Full-Wafer Manufacturing Platform for All-Inorganic Metaoptics and AR Waveguides

James J. Watkins

Polymer Science and Engineering, University of Massachusetts, USA
[2]Myrias Optics, Amherst, MA, USA
watkins@umass.edu, watkins@myriasoptics.edu

***Abstract*— We fabricate all-inorganic, high-efficiency, metalenses, metasurfaces, DOEs and waveguides on full-wafer platforms with cycle times of less than 5 minutes/wafer via additive nanoimprint lithography using TiO_2 nanoparticle dispersion inks for applications in the visible and near IR. With recent advances, we achieve refractive indices up to 2.6, which further enhance device performance.**

***Keywords*— metaoptics, nanoimprint, metasurface, augmented reality**

Overview

Full wafer-scale fabrication of high-efficiency, all-inorganic optical devices, including metalenses and metasurfaces operating in the UV, visible, and IR spectra, AR/VR waveguides, IR dot projectors, and polarization-controlled metasurfaces, is demonstrated using additive nanoimprint lithography (NIL) with nanoparticle dispersion-based inks. Approximately 1,000 visible-wavelength metalenses (4 mm diameter) were fabricated per 8-inch wafer, exhibiting high optical efficiency and excellent uniformity. The absolute and relative efficiencies of the metalenses exceed 80% and 90%, respectively, reaching approximately 95% of the maximum simulated efficiencies for this design. This close agreement indicates that performance is not limited by materials or processing, but in this case by the design itself.

The use of nanoparticle dispersion inks enables the fabrication of all-inorganic, high-MTF AR waveguides with imprint cycle times significantly shorter than those of polymer/nanoparticle composites. The refractive index of these structures can be increased up to 2.3 using a short post-imprint atomic layer deposition (ALD) process. With recent advances in materials systems, we can now achieve refractive indices up to 2.6 with very low waveguide losses. Combined, these attributes offer superior performance, including an expanded field of view (FOV) in AR waveguides and reduced manufacturing costs.

Furthermore, the fabrication of polarization-sensitive, phase/amplitude-controlled holograms demonstrates that this process can replicate asymmetric nanostructures with aspect ratios >10 via direct imprinting without etching. The resulting optics are organic-free due to a post-imprint calcination step and exhibit outstanding dimensional and optical stability, as confirmed by accelerated environmental testing and laser-induced damage testing (LIDT). This work establishes a viable path for true, full-scale additive manufacturing of meta-optics across the UV-to-IR spectrum.

References

[1] Jung, D-E; Einck, V.J.; Dawicki,A.; Malgras, V.; Verrastro, L.D.; Grosso, D.; Arbabi, A; Watkins, J.J. "Full Wafer Scale Manufacturing of Directly Printed TiO2 Metalenses at Visible Wavelengths with Outstanding Focusing Efficiencies" *Advanced Materials* **2025**, *37* (30), 2500327, doi/10.1002/adma.202500327

[2] Jung, D._E.; Howell, I.R.; Einck, V.E.; Arisoy, F.D.; Verrastro, L.D.; McClung, A.; Arbbai, A.; Watkins, J.J. "Refractive Index Tuning of All-Inorganic TiO2 Nanocrystal-Based Films and High Aspect Ratio Nanostructures Using Atomic Layer Deposition: Implications for High-Throughput Fabrication of Metalenses" ACS Applied Nanomaterials 2023 6, 3, 2009–2019, doi/10.1021/acsanm.2c04982

[3] Jung, D. E.; Amann, J.; Einck, V. J.; Baltrukonis, J.; Verrastro, L. D.; Dawicki, A.; Pasdarikia, M.; Arbabi, A.; Liedl, G.; Otto, A.; Watkins, J. J., All-Inorganic TiO2 Nanoparticle-Based Metalenses Manufactured by Direct Nanoimprint Lithography for High Energy Applications: Femtosecond Laser-Induced Damage Threshold Testing. *Advanced Optical Materials* **2026,** *14* e01769, doi/10.1002/adom.202501769

[4] Einck, V. J.; Torfeh, M.; McClung, A.; Jung, D. E.; Mansouree, M.; Arbabi, A.; Watkins, J. J. Scalable Nanoimprint Lithography Process for Manufacturing Visible Metasurfaces Composed of High Aspect Ratio TiO2 Meta-Atoms. ACS Photonics 2021, 8, 2400-2409. doi/10.1021/acsphotonics.1c00609

Synthesis of Colloidal Nanoalloys by Ultrafast Laser Irradiation

Andrés Guerrero-Martínez[1,*] and Guillermo González Rubio[1]

[1] Departamento de Química Física, Universidad Complutense de Madrid, Spain
*Corresponding author: aguerrero@quim.ucm.es

***Abstract*— Colloidal nanoalloys synthesized by ultrafast laser irradiation offer tunable optical and catalytic properties driven by localized surface plasmon resonances. Femtosecond pulses enable controlled reshaping and alloying, avoiding fragmentation typical of longer pulses. This approach provides precise control over composition and structure, linking synthesis conditions with functional performance in advanced nanomaterials.**

***Keywords*— ultrafast laser irradiation, metal nanoparticle, LSPR, core-shell nanomaterial, colloidal nanoalloy**

I. Introduction

Over the past two decades, the rapid advancement of metal nanoparticles has been largely driven by their distinctive optical properties, particularly those linked to localized surface plasmon resonances (LSPRs) [1]. Significant effort has focused on the rational design and controlled assembly of these nanostructures to develop nanoplasmonic systems with tunable optical responses. A key factor in this progress has been the ability to probe light–matter interactions at the nanoscale, enabled by ultrafast laser techniques capable of resolving electron dynamics with high temporal resolution.

II. Methods

Femtosecond laser irradiation has emerged as a powerful tool for studying and tailoring plasmonic properties [2]. Following excitation, conduction electrons rapidly thermalize and transfer energy to the lattice and surrounding medium, often inducing controlled surface melting while preserving nanoparticle structure. In contrast, nanosecond pulses typically cause fragmentation or uncontrolled melting, as excitation and relaxation occur on similar timescales. These differences enable precise size tuning, including conversion of polydisperse colloids into monodisperse nanoparticles [3] and the generation of hollow nanostructures [4].

III. Results and Discussion

Applying these methodologies to multimetallic nanoparticles further expands their potential. Ultrafast laser processing enables the synthesis of nanoalloys with adjustable compositions and morphologies, leading to synergistic effects that surpass those of single-metal systems [5]. These nanoalloys exhibit improved plasmonic behavior, enhanced stability, and notable catalytic performance in areas such as sensing, energy conversion, and chemical reactions. In addition, the combination of ultrafast spectroscopy with controlled irradiation offers fundamental insight into their electronic and structural evolution, establishing a direct link between synthesis strategies and functional properties.

IV. Conclusion

The combination of pulsed laser techniques with nanoalloy engineering provides a versatile platform for both fundamental research and technological applications, opening new avenues for the development of advanced nanomaterials.

Acknowledgments

This work has been supported by the ERC Starting Grant Time4Nano (101164205), the Spanish Ministry of Science, Innovation and Universities (PID2021-123228NB-I00 and PID2024-159196NB-I00) and the International Research Network-IRN Nanoalloys. G.G-R. acknowledges the Atracción de Talento Fellowship from the Madrid Regional Government (Grant 2022-T1/IND-23908)

References

[1] K. A. Willets and R. P. Van Duyne, “Localized surface plasmon resonance spectroscopy and sensing,” Annu. Rev. Phys. Chem., vol. 58, pp. 267–297, 2007.

[2] G. González-Rubio, A. Guerrero-Martínez, and L. M. Liz-Marzán, “Reshaping, fragmentation, and assembly of gold nanoparticles assisted by pulse lasers,” Acc. Chem. Res., vol. 49, pp. 678–686, 2016.

[3] G. González-Rubio, P. Díaz-Núñez, A. Rivera, A. Prada, G. Tardajos, J. González-Izquierdo, L. Bañares, P. Llombart, L. G. Macdowell, M. A. Palafox, L. M. Liz-Marzán, O. Peña-Rodríguez, and A. Guerrero-Martínez, “Femtosecond laser reshaping yields gold nanorods with ultranarrow surface plasmon resonances,” Science, vol. 358, pp. 640–644, 2017.

[4] V. Manzaneda-González, K. Jenkinson, O. Peña-Rodríguez, O. Borrell-Grueiro, S. Triviño-Sánchez, L. Bañares, E. Junquera, A. Espinosa, G. González-Rubio, S. Bals, and A. Guerrero-Martínez, “Laser-induced transformation of nanostructures into hollow morphologies,” Chem. Mater., vol. 35, pp. 9603–9612, 2023.

[5] R. Xu, J. González-Izquierdo, L. Bañares, I. Cano, J. Pérez-Juste, A. Guerrero-Martínez, and G. González-Rubio, “Plasmonic and catalytic properties of multimetallic nanoparticles,” Nanoscale, vol. 17, pp. 8577–8587, 2025.

Polarization-Controlled Lattices of Sub-Wavelength Photonic Spin Skyrmions

Andrei Afanasev[1,*]

[1]Department of Physics, The George Washington University, USA
*Corresponding author: afanas@gwu.edu

***Abstract*— We theoretically analyze properties of topological spin textures of optical fields characterized by spin orientation in all three dimensions and described in terms of Bloch merons and skyrmions. Formation of isolated skyrmions, their lattices and their propagation in space are described.**

***Keywords*— photonic lattice, topological photonics, optical spin, optical skyrmions.**

We provide an account of newly observed three-dimensional (3D) spin skyrmions found near phase singularities of both optical and acoustic vortex beams. While beams' intensity profiles expand during propagation due to diffraction, certain polarization features near phase singularities maintain constant transverse spatial dimensions, the property noticed for optical vortices [1], and dark fringes in the interference patterns of light [2] or sound [3].

Defining a "spin alignment parameter" for the beam propagating in z-direction as

$$\chi_{TL}(\boldsymbol{s}) = |s_\perp|^2 - s_z^2,$$

where $\boldsymbol{s}$ is a unit vector along the spin direction, we analyze spin dynamics of the propagating beams, with predictions shown in Fig.1. These calculated spin textures can be identified as skyrmions of propagation-independent sub-wavelength transverse size. A detailed analysis reveals that these spin textures can be associated with Bloch-type merons (N_{sk}=1/2) and skyrmions. Such novel spin structures were recently discovered experimentally in optical [4-5] and acoustic vortices [6].

Next, we analyze formation of the lattices for the above-described topological spin textures in the intermediate field and show that in a hexagonal lattice of phase singularities formed by triplets of discrete circular polarized sources and characterized by alternating values of topological charges ($l = \pm 1$), 3D spin skyrmions form only at lattice sites which have opposite signs of circular polarization (σ) and the topological charge ($\sigma l < 0$). Flipping the sign of σ allows shifting between skyrmionics sublattices in a behavior resembling spin Hall effect of light.

Propagating of the photonic lattice into the far field, we observe that while the size of the lattice cells expands due to diffraction, the skyrmion textures remain constant in transverse size.

We present a theory of spin transfer of optical 3D spin skyrmions to the atomic matter.

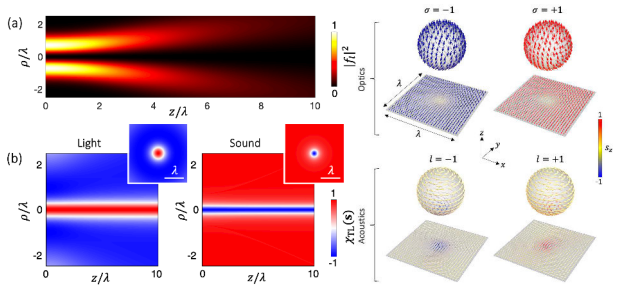

Fig. 1. (a) A diffracting intensity pattern of a vortex beam with OAM=1; (b) Calculated non-diffracting profiles of the spin alignment parameter χ_{TL} (s) for the light and sound in the longitudinal and transverse planes; (c) corresponding skyrmionic spin patterns [6].

ACKNOWLEDGMENTS

This work was supported by the US Army Research Office Award W911NF-23-1-0085.

REFERENCES

[1]. A. Afanasev, J.J. Kingsley-Smith, F.J. Rodríguez-Fortuño, and A.V. Zayats, Advanced Photonics Nexus 2, 026001 (2023).
[2]. A. Vernon, A. Kille, F. Rodríguez-Fortuño, and A. Afanasev, Optica 11, 120 (2024).
[3]. A. Kille and A. Afanasev, Phys. Rev. B109, 184305 (2024).
[4]. N. Mata-Cervera, D. K. Sharma, Y. Shen, R. Paniagua- Dominguez, and M. A. Porras,
Phys. Rev. Lett. 135, 033805 (2025).
[5]. N. Mata-Cervera, et al. arXiv preprint arXiv:2509.06555 (2025).
[6]. E. Annenkova, A. Afanasev, and E. Brasselet, arXiv preprint arXiv:2512.02964.

Fast and High efficiency photo-thermal conversion in optical nanocavity

Giuseppe Nicoletta[1,2], Giuseppe E. Lio[3], Roberto Caputo[1,2] Antonio Ferraro[2,*]

[1] Department of Physics - University of Calabria, 87036 Rende, Italy
[2]Consiglio Nazionale delle Ricerche - Istituto di Nanotecnologia, 87036 Rende, Italy
[3]Department of Physics - University of Pisa, 56126 Pisa, Italy

*Corresponding author: antonio.ferraro@cnr.it

***Abstract*—The generation of heat at the micro and nanoscale is growing research field due to their breakthrough application in nanochemistry, medical and life science. Here we investigate the photothermal conversion ability and applications of an optical nanocavity. A temperature increase higher than 550°C is obtained with an intensity of only 75 mW/mm^2.**

***Keywords*— photo-thermal conversion, ENZ metamaterials, optical nanocavity, Fano resonance.**

I. Introduction

High-efficiency photo-thermal conversion is emerging as a fundamental aspect for different applications such as nanomedicine, nanochemistry and chemical engineering. Conventional materials often struggle with spectral selectivity, but the engineering of the multilayer structure constituting the optical nanocavities provides a tunable framework for enhancing light-matter interaction. These structures localize electromagnetic energy at the nanoscale allowing to obtain high absorption at the selected wavelength. This work presents a multilayer design that maximizes heat localization, offering a scalable path for high-performance photo-thermal devices without the need for complex, high-cost nanopatterning.

II. Results and Discussion

The proposed photo-thermal converter, comprising an optimized metal-insulator multilayer architecture, was modeled using the Transfer Matrix Method (TMM) to target a resonance at $\lambda = 532$ nm. The optimized stack consists of an arrangement of metal and dielectric layers with a hundreads nanometer optical cavity between the metals. The proposed system presents a strong interaction between the metallic radiative channel and the Fabry-Perot cavity resonance producing a Fano optical response.

To elucidate the underlying physics, Finite Element Method (FEM) simulations were employed to analyze electric field localization and layer-specific absorption. The numerical results confirm the Fano behavior with an asymmetry factor of q $\approx$ -1.43. Notably, the structure maintains "flatband" absorption stability across incident angles of 20° to 40°.

Experimental validation was conducted by illuminating the structure with a 532 nm laser and monitoring the thermal response via an infrared camera. The multilayer stack demonstrated exceptional conversion efficiency, reaching temperatures exceeding 550°C at a low power intensity of only 75 mW/mm^2 within seconds.

This significant thermal enhancement was leveraged to develop a fiber-coupled optical scalpel for surgical applications. An optimized tip, designed via FEM and fabricated through 3D printing, was coated with the multilayer structure and integrated onto an optical fiber. The device achieved a localized, controlled temperature of 120°C, demonstrating high potential for precise, minimally invasive photothermal therapy.

III. Conclusion

Thermal properties of epsilon near zero(ENZ) nanocavity are experimentally and numerically demonstrated. Upon illumination at the resonance wavelength an increasing of local temperature more than 550°C is observed. The operational wavelength can be tuned by design to operate in the whole visible range. The proposed system opens the way to new applications in several field such as surgery, defrosting, nanoheaters and biotechnologies.

Acknowledgments

This work was supported by project "Proof of Concept "BiOt", CUP C28H23000270002, Unical Pathways (UP), Piano Nazionale di Ripresa e Resilienza, NextGenerationEU."

Conflict of Interest

R. Caputo, G. E: Lio and A. Ferraro, "Optical scalpel and method of operation of such scalpel", Patent Application Number: 102021000014924

Ultra-Fast Optical Response of Al:ZnO Metasurfaces in the near infrared range

Stefania Benedetti[1,*], Tersilla Virgili[2], Luca Bursi[1,3], Michele Guizzardi[2], Andrea Villa[4], Alessandro di Bona[1], Sergio D'Addato[1,3], Andrea Mescola[1], Gian Carlo Gazzadi[1], Arrigo Calzolari[1]

[1] CNR Istituto Nanoscienze, Modena, Italy
[2] CNR, Istituto Di Fotonica e Nanotecnologie, Milano, Italy
[3] Dipartimento di Scienze Fisiche, Informatiche e Matematiche, Universitàdegli Studi di Modena e Reggio Emilia, Modena, Italy
[4] Dipartimento Di Fisica, Politecnico Di Milano, Milano, Italy
*Corresponding author: stefania.benedetti@nano.cnr.it

***Abstract*— Aluminum-doped ZnO (AZO) is a promising material for photonic applications because of its tunable plasmonic response and the low optical losses in the near-infrared (NIR). We have investigated the role of nanostructuration in the ultrafast optical response and in the dynamics of electron populations of engineered AZO metasurfaces.**

***Keywords*— focused ion beam, nanostructuration, transient absorption spectroscopy, transparent conducting oxide.**

I. Introduction

Transparent conducting oxides like AZO combine high transparency and high conductivity, exhibiting epsilon-near-zero behavior in the NIR–MIR range with low losses and ultrafast switching [1]. Their optical properties are tunable via growth conditions, post-growth treatments, or external stimuli, and can be further controlled through metasurface nanostructuring. Unlike noble metals, TCOs are better suited for NIR–MIR applications due to lower, tunable charge density. However, fabricating sub-100 nm structures is challenging, requiring uniform films and optimized lithography. Combining TCOs tunability with FIB nanostructuration enables further control over local electromagnetic fields and carrier dynamics, opening the way to engineering new types of photonic components and designing new photophysical properties by using subwavelength resonant nanostructures. For this purpose ultrafast spectroscopy has revealed a powerful tool to study hot-carrier dynamics and nonlinear responses, enabling control of plasmonic excitations and supporting advanced photonic, sensing, and all-optical modulation applications.

II. Methods

Electromagnetic simulations were carried out by using the commercial software COMSOL Multiphysics, solving Maxwell's equations in the frequency-domain, using the experimental permittivity spectra measured for an AZO thin film (Al 4 at.%). AZO films were deposited at room temperature on MgO(001) substrates by magnetron sputtering and the nanostructures were fabricated by means of focused ion beam (FIB). Transient optical spectroscopy experiments were performed pumping with 1600 and 3000 nm laser and probing with two setups for the UV-VIS and the NIR range.

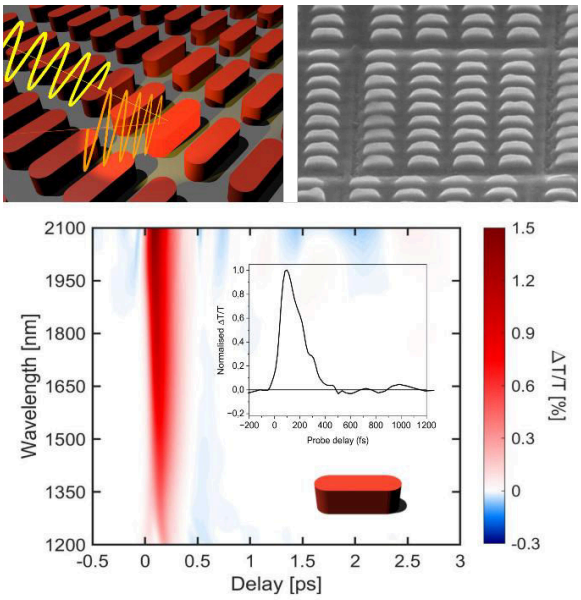

Fig. 1 AZO nanorods array by FIB (upper) and transient differential transmission map as a function of delay time and probe photon energy (lower panel).

III. Results and Discussion

We have simulated the optical static response of nanorods and nano-Ls as a function of geometrical parameters (height, lateral sizes, pitch) to maximize the absorption of the system in the NIR. We have realized the nanostructures by FIB with the parameters obtained from simulations, fabricating nanorods

with 150 nm length and 80 nm height, and nano-Ls with arm lengths of 200 and 300 nm.

We have then investigated the ultrafast response of the film and of the two arrays pumping at 1600 nm within the plasmon resonance band of the film and at 3000 nm, matching the resonance of the nanostructures, probing from 325 to 500 nm and from 1200 to 2100 nm. The transient differential transmission signal presents a negative band assigned to photoinduced absorption at time zero that decays in ∼1 ps. The NIR region is dominated by a positive band extending until 2000 nm, that after ∼ 100 fs becomes negative and then decays to zero. In the nanostructures after the excitation, a positive ΔT/T band is present in both nanostructure arrays, as for the AZO film. This bleaching signal demonstrates, as supported by our calculations, the presence of the plasmonic resonance band. However, at longer delay times, the nano-Ls behave like the film and the signal becomes negative, while in the nanorods the signal goes to zero and no negative contribution is present [2].

The pump-probe measurements indicate that the confinement induced by the small nanorod structure allows a very fast decay (100 fs) of the out of equilibrium hot carriers, while in a larger structure, such as nano-Ls or a corrugated film, the carriers relax in a thermalized population that just after 300 fs decays to the ground state [3,4]. The absence of a detectable non-thermal electrons population in the nanorods can be due to a reduction of the density of the available electronic states in the confined nanostructures, or to the extremely rapid relaxation and thermalization of these carriers, occurring on timescales shorter than the experimental resolution of this work. Alternatively, the fraction of non-thermal electrons generated under these excitation conditions may simply be too small for their contribution to produce a measurable signal.

These results indicates that it is possible to modify and control the plasmonic response of AZO metasurfaces through nanofabrication, both statically and dynamically, making them promising building blocks for infrared plasmonics and nanophotonic applications.

IV. Conclusion

We have studied the ultrafast carrier dynamics in arrays of AZO nanostructures, optimized by simulations and fabricated by FIB, by means of optical pump-probe spectroscopy. The study indicates that it is possible to modify both the static and the dynamic behavior of carriers involved in the plasmonic response through nanofabrication, making them promising building blocks for infrared plasmonics and nanophotonic applications, where metal-free and CMOS-compatible platforms are advantageous.

Acknowledgments

This work was supported by Ministero dell'Università e della Ricerca (MUR) through Piano Nazionale di Ripresa e Resilienza (PNRR) – Missione 4 Componente 2, NextGenerationEU, Investment 1.5, Project ECOSISTER ECS_00000033 – CUP E93C22001100001; Investment 1.4, National Centre for HPC, Big Data and Quantum Computing (ICSC), CN00000013; Investment 1.1, PRIN 2022 Project AMONIX – CUP B53D23004060006. This work was supported by sPATIALS3 project by Regione Lombardia.

References

[1] N. Kinsey, C. DeVault, J. Kim, M. Ferrera, V. M. Shalaev, and A. Boltasseva, "Epsilon-Near-Zero Al-doped ZnO for Ultrafast Switching at Telecom Wavelengths", Optica 2, 7, 616–622, (2015).

[2] T. Virgili, L. Bursi, R. Magrin Maffei, M. Guizzardi, A. Villa, A. di Bona, S. D'Addato, A. Mescola, G. C. Gazzadi, A. Calzolari, S. Benedetti, "Tailoring the Ultra-Fast Infrared Optical Response of Al:ZnO Through Nanostructuration", Advanced Materials Technologies, 0:e01940, 2025.

[3] A. Schirato, M. Maiuri, G. Cerullo, and G. Della Valle, "Ultrafast Hot Electron Dynamics in Plasmonic Nanostructures: Experiments, Modelling, Design,"*Nanophotonics* 12, no. 1 (2023): 1–28.

[4] L. Besteiro, X. Kong, Z. Wang, G. Hartland, and A. Govorov, "Understanding Hot-Electron Generation and Plasmon Relaxation in Metal Nanocrystals: Quantum and Classical Mechanisms,"*ACS Photonics* 4, no. 11 (2017): 2759–2781

Polarisation control in time-varying low-index films

Wallace Jaffray[1], Sven Stengel[1], Alexandra Boltasseva[2], Vladimir M. Shalaev[2], Maria Antonietta Vincenti[3], Domenico de Ceglia[3], Michael Scalora[3], Carlo Rizza[4], Marcello Ferrera[1,*],

[1] Institute of Photonics and Quantum Sciences, Heriot-Watt University, United Kingdom
[2]Elmore Family School of Electrical Computer Engineering and Birck Nanotechnology Center, Purdue University, West Lafayette, Indiana, USA.
[3]Department of Information Engineering, University of Brescia, Brescia, Italy.
[4]Department of Physical and Chemical Sciences, University of L'Aquila, L'Aquila, Italy.
*Corresponding author: m.ferrera@hw.ac.uk

***Abstract*— We present an all-optical strategy for ultrafast, reconfigurable polarisation control using subwavelength epsilon-near-zero transparent-conductor films. Femtosecond pumping transiently reshapes the carrier plasma to induce birefringence, dichroism, and pump-helicity-dependent optical activity within a single unpatterned platform, enabling broadband, sub-picosecond polarisation transformations compatible with compact integrated photonics.**

***Keywords*— Time-varying materials, nonlinear optics, ultra-fast photonics, polarization control.**

I. Introduction

Fast, compact, and programmable polarisation control is a persistent bottleneck for planar photonics, where conventional bulk components are impractical and many on-chip solutions trade speed for tunability or reconfigurability. Resonant metasurfaces and nanoantennas can deliver strong static anisotropy but their functionality is generally fixed by geometry and limited in bandwidth, while electrically or thermally tuned approaches tend to be slow and complex to implement. A complementary route is to encode functionality in time rather than structure. In this regard, time-varying photonics, enabled by extreme ultrafast nonlinearities, can in principle switch a single device between distinct polarisation transformations by changing only the excitation conditions, thus separating fabrication from functionality [1-8]. Transparent conductors operated near the epsilon-near-zero (ENZ) crossover are particularly attractive because their nonlinearity is strong, broadband, and naturally linked to ultrafast free-carrier dynamics, making them promising candidates for "temporal flat-optics" [9-11]. In this paradigm birefringence, dichroism, and optical activity can be induced on demand in the same isotropic film with sub-picosecond response and without relying on permanent geometric anisotropy or narrowband resonant design [12].

II. Methods

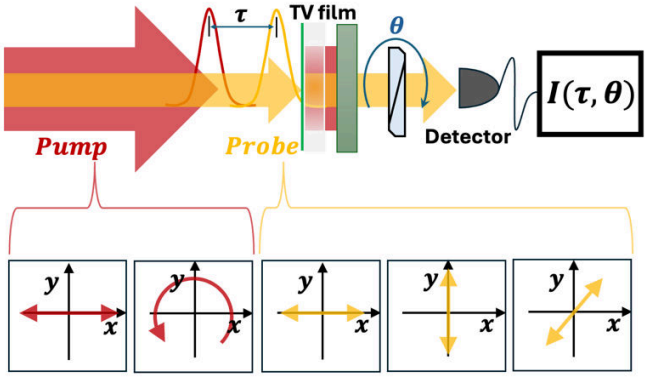

Fig. 1 Schematic of the pump–probe experimental setup used to induce and measure transient polarisation transformations in a time-varying thin film. A femtosecond pump pulse optically excites the film, generating a transient anisotropic plasma response, while a time-delayed probe pulse interrogates the induced optical properties. The transmitted probe passes through polarisation analysis optics before detection, enabling measurement of intensity as a function of pump–probe delay (τ) and analyser angle (θ). The lower panels illustrate representative pump/probe polarisation states.

Our platform employs an unpatterned, isotropic aluminium-doped zinc oxide film of subwavelength thickness operated near its ENZ crossover and driven in a pump–probe configuration, where femtosecond pumping generates a transient non-equilibrium carrier distribution and thus a time-dependent complex dielectric response. The key control dials are pump polarisation (linear or circular), intensity, and pump–probe delay, which determine whether the induced dielectric tensor is predominantly diagonal-anisotropic (supporting birefringence and dichroism) or gains antisymmetric components (supporting gyrotropic behaviour). Polarisation-resolved probe transmission is recorded as a function of analyser angle and delay to extract transient phase retardation, differential absorption, and pump-helicity-dependent rotation, while modelling treats the film as a time-varying plasma in

which pump-driven effective-mass and scattering dynamics reshape both the real and imaginary parts of the response, enabling symmetry breaking without any geometric anisotropy. Importantly, the excitation geometry is chosen so the observed effects are not contingent on Fabry-Pérot enhancement or surface-mode phase matching, keeping the mechanism rooted in intrinsic time variation rather than structural resonances.

III. Results and Discussion

Under linearly polarised pumping, the isotropic film becomes transiently anisotropic on the pump timescale, producing large polarisation coupling in transmission that manifests as a rotation of the transmitted polarisation axis together with induced ellipticity, consistent with simultaneous birefringence (phase retardation between orthogonal components) and dichroism (polarisation-dependent absorption). Retrieval of the transient complex refractive indices along orthogonal axes shows that both the real and imaginary parts are modulated in a direction-dependent manner during temporal overlap, and that the induced anisotropy is substantial over deep-subwavelength propagation distances, demonstrating that time-written anisotropy can be strong enough to compete with, and exceed, structurally written responses at comparable footprints. Beyond maximising magnitude at the ENZ crossover, wavelength detuning provides an additional degree of control over the relative weight of phase- versus absorption-driven effects, allowing partial decoupling between birefringence and dichroism through dispersion engineering of the pumped state and offering a practical route to tailoring the output state (e.g., emphasizing phase retardation while suppressing ellipticity). Switching to circularly polarised pumping produces a qualitatively different response: the probe experiences a helicity-dependent rotation whose sign reverses with pump handedness, indicating a dynamically induced, non-reciprocal optical activity in an otherwise achiral, unpatterned film. In the time-varying plasma model, this behaviour arises when the pump-imprinted symmetry of the carrier distribution generates antisymmetric tensor contributions that are algebraically equivalent to an effective transverse term acting on the probe, providing a microscopic pathway for pump-controlled gyrotropy in a planar isotropic medium. Crucially, this route does not require pre-existing chiral geometry, static magnetisation, or resonant enhancement, and therefore supports broadband operation and rapid reconfiguration among distinct polarisation functions by changing only the pump state [13-18]

IV. Conclusion

Time-varying ENZ transparent-conductor films enable a reconfigurable polarisation-control mechanism in which a single unpatterned, deep-subwavelength platform can be optically switched on sub-picosecond timescales between birefringent, dichroic, and gyrotropic behaviours by selecting pump polarisation and temporal overlap. By transferring programmability from nanofabrication to excitation design, this approach provides a scalable route to broadband ultrafast polarisation modulators and temporally reconfigurable flat-optical elements, with clear opportunities for integrated photonics where compactness, speed, and functional switching are simultaneously required .

Acknowledgments

M.F. acknowledges financial support from EPSRC project ID EP/X035158/1; AFOSR (EOARD) under award no. FA8655-23-1-7254; and EPSRC/STFC/NSERC under UK-Canada Quantum for Science Research Collaborations OPP640-APP47830. VMS and AB acknowledge support by ACC-APG-RTP Agency grant W911NF-25-2-0060.

References

[1] Nicholls, L. H. et al. Ultrafast synthesis and switching of light polarization in nonlinear anisotropic metamaterials. Nature Photonics 11, 628–633 (2017).
[2] Kildishev, A. V., Boltasseva, A. & Shalaev, V. M. Planar Photonics with Metasurfaces. Science 339, 1232009 (2013).
[3] Zhu, S. et al. Strong nonlinear optical processes with extraordinary polarization anisotropy in inversion-symmetry broken two-dimensional PdPSe. Light: Science & Applications 13, 119 (2024).
[4] Crotti, G. et al. Giant ultrafast dichroism and birefringence with active nonlocal metasurfaces. Light: Science & Applications 13, 204 (2024).
[5] Wang, H. et al. All-optical ultrafast polarization switching with nonlinear plasmonic metasurfaces. Science Advances 10, eadk3882 (2024).
[6] Zheludev, N. et al. Cubic optical nonlinearity of free electrons in bulk gold. Optics Letters 20, 1368–1370 (1995).
[7] Svirko, Y. P. & Zheludev, N. Coherent and incoherent pump–probe specular inverse Faraday effect in media with instantaneous nonlinearity. Journal of the Optical Society of America B 11, 1388–1393 (1994).
[8] Svirko, Y. P. & Zheludev, N. I. Polarization of Light in Nonlinear Optics. Wiley (2000).
[9] Kinsey, N., DeVault, C., Boltasseva, A. & Shalaev, V. M. Near-zero-index materials for photonics. Nature Reviews Materials 4, 742–760 (2019).
[10] Reshef, O., De Leon, I., Alam, M. Z. & Boyd, R. W. Nonlinear optical effects in epsilon-near-zero media. Nature Reviews Materials 4, 535–551 (2019).
[11] Jaffray, W. et al. Transparent conducting oxides: from all-dielectric plasmonics to a new paradigm in integrated photonics. Advances in Optics and Photonics 14, 148–208 (2022).
[12] Jaffray, W. et al. All-optical polarization control in time-varying low-index films via plasma symmetry breaking. arXiv:2510.06985. (2025)
[13] Rizza, C., Castaldi, G. & Galdi, V. Spin-controlled photonics via temporal anisotropy. Nanophotonics 12, 2891–2904 (2023).
[14] Jaffray, W. et al. Nonlinear loss engineering in near-zero-index bulk materials. Advanced Optical Materials 12, 2301232 (2024).
[15] Jaffray, W. et al. Near-zero-index ultra-fast pulse characterization. Nature Communications 13, 3536 (2022).
[16] Scalora, M. et al. Extreme electrodynamics in time-varying media. Physical Review A 112, 013502 (2025).
[17] Jaffray, W. et al. Spatio-spectral optical fission in time-varying subwavelength layers. Nature Photonics. 19, 558–566 (2025).
[18] Rizza, C. et al. Optical Spin Effects Induced by Phase Conjugation ata Space-Time Interface, Small Struct. 7, e202500359. (2026)

Tunable Achiral Metamaterial Substrates for Enantiomer Detection

Maryam Mirahmadi,[†,‡] Ali Douaki,[†,¥] Vincenzo Caligiuri,[¶] Denis Garoli,[†,¥] and Roman Krahne,[*,†]

[†]Optoelectronics, Istituto Italiano di Tecnologia (IIT), via Morego 30, 16163 Genova, Italy.
‡Department of Chemistry and Industrial Chemistry, University of Genoa, Italy.
¥Dipartimento di Science e Metodi per l'Ingegneria, Università degli Studi di Modena e Reggio Emilia, Viale Amendola 2, 14122, Reggio Emilia (Italy)
¶Dipartimento di Fisica, Universitá della Calabria, Rende (CS), Italy.
*Corresponding author: roman.krahne@iit.it

***Abstract*— We use tilted achiral metal-dielectric-metal nanocavities in which the top metal layer is patterned into a nanohole array as spectrally tunable metamaterial substrates for enantiomer detection. By combining circular dichroism experiments with simulations, we elucidate the different contributions to the chirality enhancement.**

***Keywords*— Circular dichroism, chirality, enantiomer, plasmonic nanohole array, photonic cavity, biosensing.**

I. Introduction

Distinguishing the chirality of biomolecules is of fundamental importance in biophysics and pharmaceutics. Circular dichroism (CD) spectroscopy provides a non-invasive approach to distinguish right- and left-handed enantiomers[1] and can offer valuable insight into the structure of the investigated molecules. However, CD spectroscopy faces a key challenge: the detection of weak chiroptical signals due to limited chirality-induced interactions with plane wave light fields. Plasmonic nanostructures and metamaterials can be designed to obtain CD enhancement across different wavelengths.

We use tilted achiral gold nanohole arrays whose resonance band could be spectrally tuned by tailoring their geometric parameters and combine them with metal-dielectric-metal optical cavities. [1] The resulting metamaterial substrates provide a flexible platform for enhancing circular dichroism signals of enantiomers through extrinsic chirality. [2]

II. Results and Discussion

We fabricate and investigate the CD response of a tilted single gold nanohole array as a substrate, and we study the CD response of L-phenylalanine as a chiral biolayer in two conditions—isolated and placed on the single gold nanohole array. We then combine plasmonic and photonic resonator effects by fabricating a metal–dielectric–metal (MDM) metamaterial structure composed of Au/Al_2O_3/Au with nanoholes in the top gold layer, and subsequently deposit an L-phenylalanine biolayer on top. This proves to be a highly promising platform for achieving strong CD signal, even compared to that obtained using a single gold nanohole layer as substrate.

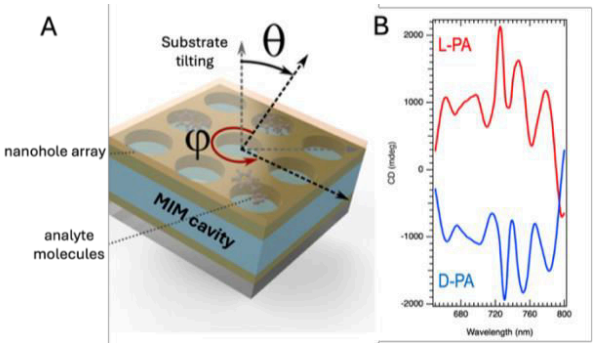

Fig. 1 A) Illustration of the achiral metamaterial substrate consisting of a metal-dielectric-metal cavity with top metal layer as nanohole array. B) Circular dichroism spectra evidencing the chirality enhancement measured in circular dichroism spectroscopy for L- and D-phenylanaline. Adapted with permission from ref. [2], copyright ACS 2025.

III. Conclusion

We establish extrinsic chirality engineering as powerful strategy for advancing chiral sensors, which paves the way for the development of next-generation nanophotonic platforms with high sensitivity and selectivity for enantiomer detection.

Acknowledgments

M.M. and R.K acknowledge funding by the European Union under Project 101131111 – DELIGHT.

References

[1] V. Caligiuri, et al., A Semi-Classical View on Epsilon-near-Zero Resonant Tunneling Modes in Metal/Insulator/Metal Nanocavities. Nano Lett., 2019. **19**, 3151-3160

[2] M. Mirahmadi, et al., Ultrasensitive and Tunable Achiral Metamaterial Substrates as Nanobiosensors for Enantiomer Detection. ACS Appl. Mater. & Interfaces, 2025, **17,** 65270

Tunable Polaritonic Topologies Generated by qBIC Metasurfaces

Connor Heimig[1], Enrico Baù[1], Jonas Biechteler[1], Florian Mangold[2], Julian Schwab[2], Manobina Karmakar[1], Leonardo Menezes[1,3], Haoran Ren[4], Stefan A. Maier[4,5], Harald Giessen[2], Andreas Tittl[1,*]

[1]Chair in Hybrid Nanosystems, Nano-Institute Munich, Department of Physics, LMU Munich, Germany
[2]4th Physics Institute, Research Center SCoPE, University of Stuttgart, Germany
[3]Departamento de Física, Universidade Federal de Pernambuco, Recife-PE, Brazil
[4]School of Physics and Astronomy, Monash University, Clayton, Victoria, Australia
[5]Department of Physics, Imperial College London, London, United Kingdom
*Corresponding author: Andreas.Tittl@physik.uni-muenchen.de

***Abstract*—We experimentally demonstrate tunable polaritonic topological textures using nonlocal photonic modes in dielectric metasurfaces supporting quasi bound states in the continuum. Hyperbolic phonon polaritons launched in hexagonal boron nitride form skyrmion lattices on individual resonators. Frequency and geometry control enable reconfigurable skyrmions, merons, and related topological textures within a single platform.**

***Keywords*—Photonic topological textures, bound states in the continuum, dielectric metasurfaces, hyperbolic phonon polaritons.**

I. Introduction

Topology provides a general framework for describing robust structures that emerge across a broad range of physical systems, including atmospheric dynamics, oceanic flows, and large-scale astrophysical phenomena. Among its key manifestations are topological defects, which cannot be removed or transformed into a different topology without fundamentally altering the system's overall configuration. A central example is the skyrmion, a topological defect formed by a three-dimensional vector field confined to a two-dimensional plane, whose configuration spans the full unit sphere in order-parameter space. [1] In condensed matter physics, skyrmions have been observed in a variety of platforms, including magnetic materials, superconductors, superfluids, and liquid crystals.

In recent years, skyrmions have been realized in photonics, both in free-space optical topologies [2], [3] and in propagating surface modes. [4], [5] These photonic skyrmions exhibit deeply subwavelength spatial features and demonstrate a degree of robustness against imperfections and environmental perturbations. [6], [7] As a result, they have attracted growing interest for applications in optical computing, nanoscale metrology, and twistronics. Beyond skyrmion configurations, photonic platforms have enabled more complex topological textures, including skyrmion bags, meron lattices, and optical vortices carrying orbital angular momentum. These structures have been generated using both surface phonon polaritons in isotropic materials [8] and hyperbolic phonon polaritons in anisotropic media [9], with potential relevance for structured thermal emission and nanoscale light control.

Despite these advances, existing approaches for generating polaritonic skyrmions rely predominantly on wavelength-specific coupling schemes, such as gratings or phase-matching structures, or on structured excitation fields including radial or circular polarization. [10] These requirements fix the resulting topological configuration for a given structure and prevent continuous tuning within the same device. In contrast to free-space skyrmions, where tunability has been experimentally demonstrated [11], this lack of reconfigurability presents a major obstacle to the integration of polaritonic skyrmions into broadband and scalable photonic architectures. Moreover, the reliance on specialized polarization states often necessitates additional optical components, increasing experimental complexity and limiting practical applicability.

II. Methods

Our approach is based on the excitation of nonlocal photonic resonances in dielectric metasurfaces to generate and control polaritonic topological textures. We employ periodic arrays of high-refractive-index dielectric resonators fabricated on a transparent substrate, designed to support quasi-bound states in the continuum (qBICs) under linearly polarized illumination and normal incidence. The nonlocal character of the qBIC resonance leads to strong mutual coupling between resonators, resulting in uniform out-of-plane electric fields across each resonator surface. This behavior is fundamentally distinct from local dipolar resonances, which produce spatially nonuniform near-field distributions.

Each resonator is covered with a thin layer of hexagonal boron nitride (hBN), and the metasurface resonance is spectrally tuned to the in-plane Reststrahlen-(RS-)band of hBN to enable efficient excitation of hyperbolic phonon polaritons (HPhPs). Due to the uniform phase and amplitude of the driving electric field, these polaritons are launched in phase from all resonator edges, leading to controlled interference at the resonator center and the formation of polaritonic skyrmion lattices.

Optical reconfigurability is achieved by tuning the excitation frequency in small steps within the linewidth of the qBIC resonance itself. Owing to the strong dispersion of HPhPs in

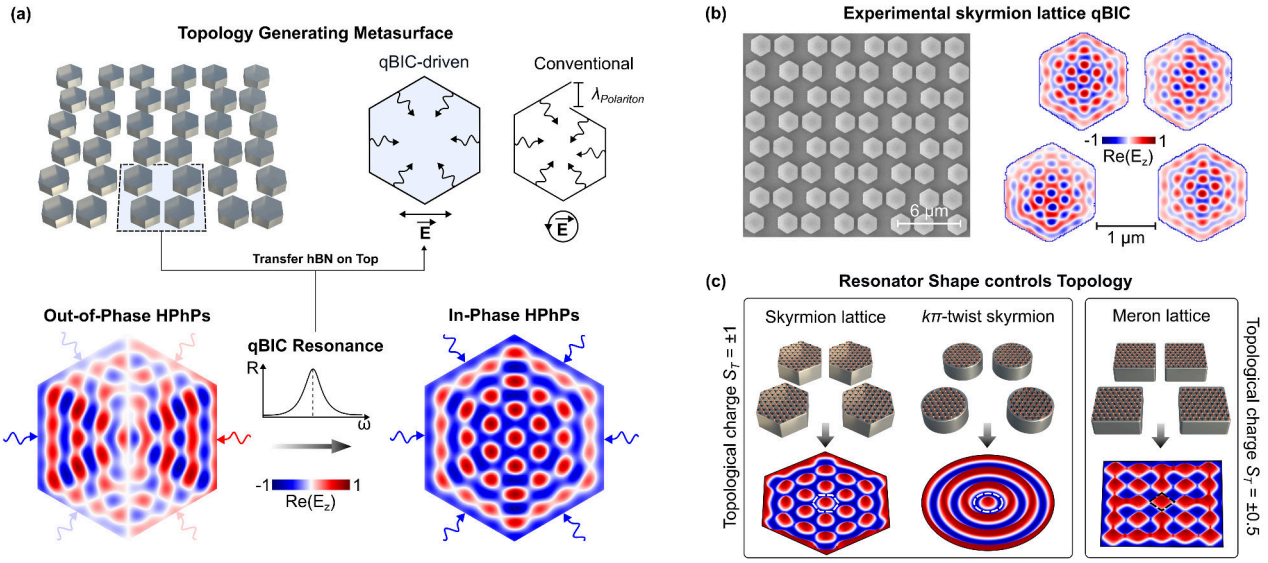

Fig. 1. qBIC-driven generation of polaritonic topological textures. **(a)** Dielectric metasurface supporting a nonlocal qBIC that provides a spatially uniform out-of-plane electric field to launch hyperbolic phonon polaritons (HPhPs) in an hBN layer placed on top. **(b)** SEM image of the metasurface and experimental near-field map of the real part of the out-of-plane electric field, $\mathrm{Re}(E_z)$ showing polaritonic skyrmion lattices on individual resonators. **(c)** Resonator geometry allows changing the resulting polaritonic topology, enabling skyrmions, $k\pi$-twist skyrmions, and meron lattices with distinct topological charge.

the RS-band of hBN, these small frequency changes induce substantial variations in the polariton wavelength, which directly modify the size and spatial arrangement of the resulting topological textures. The overall tuning range is set by the qBIC linewidth, which can be increased through controlled symmetry breaking. In addition to spectral tuning, altering the resonator geometry, enables access to distinct topological configurations such as $k\pi$-twist skyrmions and merons.

Experimental characterization is performed using scattering scanning near-field optical microscopy (s-SNOM) in transmission mode, enabling direct visualization of the deeply subwavelength polaritonic skyrmion lattices and their frequency-dependent reconfiguration.

III. Results and Discussion

Experimental results show:

- Deeply subwavelength Néel-type photonic skyrmions are experimentally resolved with polariton wavelengths ranging from approximately 451 nm down to 271 nm, corresponding to feature sizes of about $\lambda/25$.
- The photonic skyrmion lattices exhibit topological stability, confirmed by quantized winding numbers and by robustness under continuous variation of the optical phase, with the topological charge remaining invariant except at discrete transition points.
- Continuous tuning of the excitation frequency within the qBIC resonance enables dynamic control of skyrmion size on the same resonator, while the topological winding number remains close to the theoretical value of ± 1.
- Changing the resonator geometry from hexagons to disks and squares preserves the nonlocal photonic mode and enables the generation of distinct polaritonic topologies, including $k\pi$-twist skyrmions and meron lattices.

IV. Conclusion

By combining nanophotonic metasurfaces and topological polaritonic textures, our approach allows optical reconfigurability of skyrmion size and topology within the same structure through frequency tuning and resonator geometry. Future work will explore integration with actively tunable materials to extend dynamic control well as investigate more complex resonator geometries to generate higher-order and composite polaritonic topologies, enabling multiplexed and reconfigurable topological states within a single metasurface platform.

Acknowledgments

This work was supported by the Deutsche Forschungsgemeinschaft (DFG), the Australian Research Council, the European Union (ERC and EIC), and the Center for NanoScience (CeNS). S.A.M. additionally acknowledges the Lee-Lucas Chair in Physics.

References

[1] T. H. R. Skyrme, "A unified field theory of mesons and baryons," *Nuclear Physics*, vol. 31, pp. 556–569, 1962.

[2] Y. Shen, Q. Zhang, P. Shi, L. Du, X. Yuan, and A. V. Zayats, "Optical skyrmions and other topological quasiparticles of light," *Nature Photonics*, vol. 18, no. 1, pp. 15–25, 2024.

[3] Y. Shen, C. He, Z. Song, B. Chen, H. He, Y. Ma, J. A. Fells, S. J. Elston, S. M. Morris, M. J. Booth *et al.*, "Topologically controlled multiskyrmions in photonic gradient-index lenses," *Physical Review Applied*, vol. 21, no. 2, p. 024025, 2024.

[4] S. Tsesses, E. Ostrovsky, K. Cohen, B. Gjonaj, N. H. Lindner, and G. Bartal, "Optical skyrmion lattice in evanescent electromagnetic fields," *Science*, vol. 361, no. 6406, pp. 993–996, 2018.

[5] T. J. Davis, D. Janoschka, P. Dreher, B. Frank, F.-J. Meyer zu Heringdorf, and H. Giessen, "Ultrafast vector imaging of plasmonic skyrmion dynamics with deep subwavelength resolution," *Science*, vol. 368, no. 6489, p. eaba6415, 2020.
[6] L. Du, A. Yang, A. V. Zayats, and X. Yuan, "Deep-subwavelength features of photonic skyrmions in a confined electromagnetic field with orbital angular momentum," *Nature Physics*, vol. 15, no. 7, pp. 650–654, 2019.
[7] A. A. Wang, Z. Zhao, Y. Ma, Y. Cai, R. Zhang, X. Shang, Y. Zhang, J. Qin, Z.-K. Pong, T. Marozsák *et al.*, "Topological protection of optical skyrmions through complex media," *Light: Science & Applications*, vol. 13, no. 1, p. 314, 2024.
[8] A. Mancini, L. Nan, R. Berté, E. Cortés, H. Ren, and S. A. Maier, "Multiplication of the orbital angular momentum of phonon polaritons via sublinear dispersion," *Nature Photonics*, vol. 18, no. 7, pp. 677–684, 2024.
[9] M. Wang, G. Hu, S. Chand, M. Cotrufo, Y. Abate, K. Watanabe, T. Taniguchi, G. Grosso, C.-W. Qiu, and A. Alù, "Spin-orbit-locked hyperbolic polariton vortices carrying reconfigurable topological charges," *elight*, vol. 2, no. 1, p. 12, 2022.
[10] S. Tsesses, K. Cohen, E. Ostrovsky, B. Gjonaj, and G. Bartal, "Spin–orbit interaction of light in plasmonic lattices," *Nano letters*, vol. 19, no. 6, pp. 4010–4016, 2019.
[11] Y. Shen, E. C. Martínez, and C. Rosales-Guzmán, "Generation of optical skyrmions with tunable topological textures," *Acs Photonics*, vol. 9, no. 1, pp. 296–303, 2022.

SYMPOSIUM 3

Advanced passive and active metasurfaces and zero-index materials

35 contributions · pp. 462–508

META 2026 · Dublin, Ireland · ISSN 2429-1390

Plasmonic Semiconductor Laser Particles Across Surface-Supported, Metal-Coated, and Metalattice Configurations

Sangyeon Cho[1,*]

[1]Wellman Center for Photomedicine, Massachusetts General Hospital and Harvard Medical School, USA

*Corresponding author: scho9@mgh.harvard.edu

***Abstract*— We report plasmonic semiconductor laser particles across three configurations: surface-supported nanocavities enabling coherent emission from 130 nm particles, metal-coated geometries introducing hinge-localized plasmonic modes with enhanced emission, and metalattice-embedded particles supporting stable multimode lasing via internal scattering, all governed by cavity geometry and Purcell-enhanced interactions.**

***Keywords*— plasmonic nanolasers, random lasers, Purcell effect**

I. Introduction

Plasmonic nanolasers enable coherent light generation at deeply subwavelength scales by combining semiconductor gain with strong field confinement. However, metallic losses and mode competition often limit spectral coherence and stability. Here, we study surface-supported, metal-coated, and metalattice-embedded semiconductor laser particles to reveal how cavity geometry and Purcell-enhanced interactions govern coherent emission and multimode lasing.

II. Methods

Our approach combines electromagnetic simulations, nanofabrication, and hyperspectral optical characterization to study plasmonic laser particles across multiple configurations. Surface-supported nanocavities are formed by placing semiconductor particles on metallic substrates, enabling strong confinement and plasmonic resonances. Metal-coated particles support hinge-localized modes with enhanced emission at geometric features.

Metalattice systems are realized by embedding plasmonic nanoscatterers within semiconductor particles to introduce internal scattering and feedback. Optical characterization under pulsed excitation reveals emission spectra, linewidths, and spatial mode distributions, enabling systematic comparison of lasing behavior across configurations.

III. Results and Discussion

Experimental results show:

- InP particles on gold substrate down to approximately 130 nm exhibit coherent lasing on gold substrates at visible wavelengths near 730 nm.
- Metal coated perovskite microcrystals as small as 620 nm show enhanced lasing with reduced thresholds and improved stability due to plasmonic coupling.
- Metalattice embedded particles enable stable multimode lasing with multiple narrow spectral peaks arising from internal scattering.

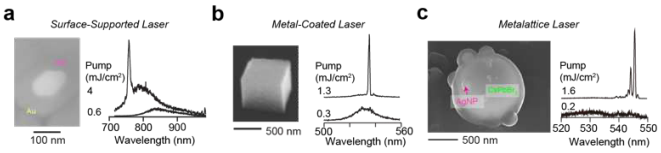

Figure 1. Surface-supported, metal-coated, and metalattice plasmonic laser particles

IV. Conclusion

We demonstrate plasmonic semiconductor laser particles across surface-supported, metal-coated, and metalattice configurations, where cavity geometry governs light–matter interaction from extreme confinement to hinge-localized enhancement and distributed feedback. These results enable programmable nanolasers with tailored emission properties, supporting standalone applications including on-chip light sources and optical communications, as well as biological cell barcoding for multiplexed single-cell tracking and real-time sensing of cellular states.

Acknowledgments

This research was supported in part by funding from the National Institutes of Health (K25CA301033, R01EB033155, and R01EB034687).

References

[1] Cho, S., Martino, N. & Yun, S.-H. Half-wave nanolasers and intracellular plasmonic lasing particles. Nat. Nanotechnol. 20, 404–410 (2025).

[2] Cho, S., Yan, H. & Yun, S. H. Noble Metal Coating on Perovskite Microcrystals for Robust and Plasmonic Lasing Applications. Adv. Opt. Mater. 13, 2403316 (2025).

[3] Cho, S., Yang, Y., Soljačić, M. & Yun, S. H. Plasmonic Hinge Modes in Metal-Coated Nanolasers. Nano Lett. 24, 13647–13652 (2024).

Nanofocusing of Orbital Angular Momentum Beams for Chirality Imaging

Zhenrong Zhang

Department of Physics, Baylor University, Waco, Texas, United States

Optical vortex beams carrying orbital angular momentum (OAM) and cylindrical vector beams (CVBs) offer unique functionalities in communication, sensing, and chiral light-matter interactions. However, their deployment at the nanoscale remains limited by inefficient coupling arising from intrinsic spatial-mode mismatch. In this talk, I present a fiber-integrated plasmonic nanostructure platform that enables subwavelength confinement of a fiber-guided vortex mode.

I will discuss the design, simulation, fabrication, and characterization of plasmonic OAM probes, as well as an integrated OAM–metasurface platform that couples a vortex laser beam into a hybrid dielectric–plasmonic helical metastructure (Si–Ag) for enhanced chirality sensing. A radial plasmonic nanorod array patterned on the facet of a polarization-maintaining ring-core vortex fiber achieves subwavelength focusing of the OAM mode. Simulations reveal symmetry-selective electric-field enhancement, efficient near-field confinement, and preservation of both polarization state and OAM phase during nanofocusing.

Experimentally, we verify stable propagation of vortex modes with preserved polarization and helicity in the far field, and we observe strong coupling of the nanofocused OAM beam into the Si–Ag helical metastructure. This coupling leads to efficient excitation of chiral molecules, demonstrating the platform's potential for highly sensitive chirality imaging and OAM-enabled nanoscale spectroscopy.

Cross-Shaped Metasurface for Advanced Spectral-Scanning LiDAR

H. Y. Fu* and Yaqi Han

[1]Tsinghua Shenzhen International Graduate School, Tsinghua University, Shenzhen, China
*Corresponding author: hyfu@sz.tsinghua.edu.cn

Abstract

Spectral scanning has emerged as a promising beam-steering technique by combining dispersive optical components with wavelength-swept laser sources for light detection and ranging (LiDAR). Based on our prior research, we have demonstrated several spectral-scanning LiDAR systems capable of high-speed 3D imaging, simultaneous velocity measurement, extended ranging distance and wide field of view detection [1-3].

Metamaterials, with their subwavelength structures and tunable electromagnetic responses, offer transformative capabilities for manipulating light beyond the limits of conventional optics. Their ability to manipulate phase, polarization, and dispersion makes them highly promising for integrated photonics, especially in compact and efficient LiDAR systems [4-6]. In frequency-modulated continuous wave (FMCW) LiDAR systems, metamaterials open new avenues for non-mechanical beam steering, spectral multiplexing, and polarization diversity—critical features for building solid-state, high-resolution 3D imaging systems.

This presentation highlights our recent progress in integrating metasurface-based components into silicon photonic platforms for LiDAR applications. We focus on the design and simulation of the metasurface with dielectric layer sandwiched between a metal ground and a metallic structured layer, specifically cross-shaped Al–SiO_2–Al structures, which enable circular polarization manipulation and broadband spectral beam steering under swept-wavelength excitation, as illustrated in Fig. 1. These metasurfaces significantly enhance the steering range while maintaining stable performance under severe environmental conditions—addressing key limitations of existing LiDAR systems.

Our results suggest that metamaterial-enabled design significantly enhances the functionality and integration level of LiDAR systems, paving the way for the next generation of intelligent sensing platforms. Future work will focus on AI-assisted inverse design of metasurfaces to further improve their performance and accelerate the optimization process, particularly for spectral-scanning LiDAR applications.

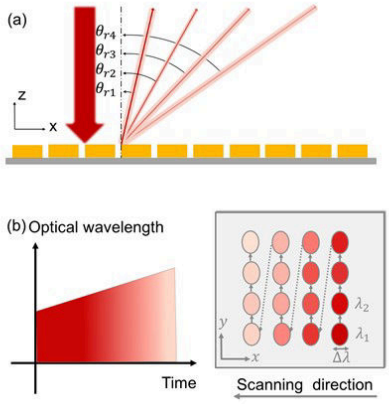

Fig. 1. (a) Designed metasurface with varying output angle under different wavelengths using a phase gradient between units. (b) Spectral scanning schematic using the metasurface under swept-wavelength input.

ACKNOWLEDGMENTS

This work was supported by Tsinghua Shenzhen International Graduate School-Shenzhen Pengrui Young Faculty Program of Shenzhen Pengrui Foundation (No. SZPR2023008). And we would like to thanks our collaborators Zijing Yang, Chenxingyu Huang, Qinghua Song fromTsinghua Shenzhen International Graduate School, Tsinghua University and Qian Li from School of Electronic and Computer Engineering, Peking University.

REFERENCES

[1] Z. Li, Y. Han, L. Wu, Z. Zang, M. Dai, S. Y. Set, S. Yamashita, Q. Li, and H. Y. Fu, "Towards an ultrafast 3D imaging scanning LiDAR system: a review," Photon. Res., vol. 12, pp. 1709–1729, 2024.

[2] Y. Han, Z. Li, L. Wu, S. Mai, X. Xing, and H. Y. Fu, "High-Speed Two-Dimensional Spectral-Scanning Coherent LiDAR System Based on Tunable VCSEL," J. Lightwave Technol., vol. 41, no. 2, pp. 412–419, Jan. 15, 2023.

[3] Y. Han, Z. Zang, L. Wu, Y. Hao, Q. Zhu, C. Chang-Hasnain, and H. Y. Fu, "Enhancing the field-of-view of spectral-scanning FMCW LiDAR by multipass configuration with an echelle grating," Opt. Lett., vol. 49, pp. 3267–3270, 2024.

[4] I. Kim, R. J. Martins, J. Jang, T. Badloe, S. Khadir, H.-Y. Jung, H. Kim, J. Kim, P. Genevet, and J. Rho, "Nanophotonics for light detection and ranging technology," Nature Nanotechnol., vol. 16, pp. 508–524, 2021.

[5] F. Ding, R. Deshpande, C. Meng, and S. I. Bozhevolnyi, "Metasurface-enabled broadband beam splitters integrated with quarter-wave plate functionality," Nanoscale, vol. 12, pp. 14106–14111, 2020.

[6] Q. Song, A. Baroni, R. Sawant, et al., "Ptychography retrieval of fully polarized holograms from geometric-phase metasurfaces," Nature Commun., vol. 11, no. 1, pp. 2651, 2020.

Broadband Metamaterial Absorbers for Highly Sensitive Molecular Detection

Takuo Tanaka[1, 2]

[1] RIKEN Center for Advanced Photonics, Japan
[2] Institute of Post-LED Photonics, Tokushima University, Japan
*Corresponding author: t-tanaka@riken.jp

***Abstract*— Broadband metamaterial absorbers were applied to ultra-sensitive molecular sensing applications. 3D coaxial metamaterial absorber was developed and applied for the multiple gas sensing with a zepto-molar sensitivity.**

***Keywords*— metamaterials, absorber, molecular sensing**

I. Introduction

Highly sensitive molecular sensing techniques, particularly for biological targets such as disease-associated biomarkers, microRNAs, and circulating tumor DNA, have become increasingly important in modern healthcare. Recently, metamaterial-based devices have been employed to enhance molecular detection sensitivity. Owing to their ability to resonantly amplify molecular signatures—including infrared (IR) absorption, Raman scattering, and refractive index changes—detection limits have reached the atto- to zeptomolar range.

II. EXPERIMENTAL RESULTS

Several years ago, we developed a metamaterial device integrated with nanofluidics to deliver analyte molecules into the hotspot region of the metamaterial, thereby maximizing the resonant interaction between the metamaterial and the molecules. When molecules whose absorption bands are overlapping the metamaterial resonance are introduced into the nanofluidic channel, strong light–matter interactions are induced, leading to enhanced reflection within the metamaterial absorption band. Using this device, we achieved a sensitivity corresponding to a molecular surface density of approximately 10^{-4} molecules/Å^2.

Recently, we proposed a vertically aligned metal–insulator–metal (v-MIM) metamaterial with a 25-nm nanogap for gas-phase molecular sensing. As proof-of-concept demonstrations, this device was applied to the detection of carbon dioxide and butane. Owing to its small footprint, the v-MIM structure enables high integration density, and the incorporation of resonators with different resonance frequencies provides broadband operation. As a result, the fabricated platform achieves zeptomolar-level detection of multiple gas species using distinct resonant elements.

To enable the detection of multiple gas species within a single device, the resonant absorption bandwidth was broadened through structural modification. Moreover, to efficiently utilize unpolarized incident light from a thermal IR source, the resonant elements were redesigned with a cylindrical geometry.

Figure 1(a) shows an SEM image of the fabricated broadband three-dimensional metamaterial absorber, and Fig. 1(b) shows its absorption spectrum, exhibiting an absorption bandwidth more than one octave.

The fabricated metamaterial absorber was placed in a gas chamber, into which a mixture of ethylene, butane, and carbon dioxide was introduced. Figure 2(a) shows the measured IR absorption spectra, where absorption signals from each gas appear as positive peaks. Figure 2(b) presents additional experimental results obtained with carbon dioxide and dimethyl ether.Based on these experimental results, the detection sensitivity of the device was estimated to be 25 zeptomoles.

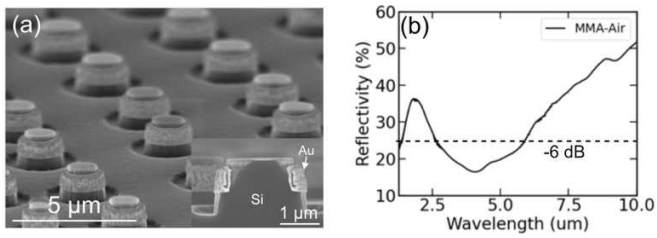

Figure 1 Broadband 3D metamaterial absorber.

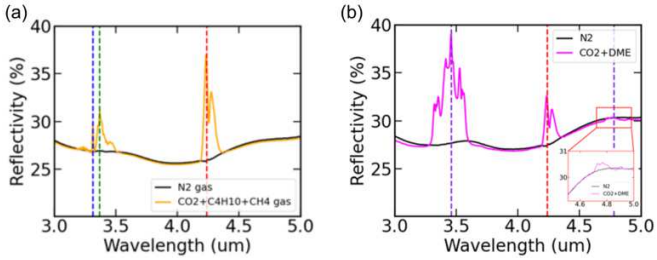

Figure 2 IR spectra of mixed gases.

In addition, a sensitivity-tunable metasurface device for label-free microRNA detection will be presented.

ACKNOWLEDGMENTS

This work was partially supported by JST CREST grant no. JPMJCR1904, Japan.

REFERENCES

[1] Atsushi Ishikawa and Takuo Tanaka, "Metamaterial Absorbers for Infrared Detection of Molecular Self-Assembled Monolayers," Scientific Reports **5**, 12570 (2015).

[2] Thu H. H Le and Takuo Tanaka, "Plasmonics - Nanofluidics Hybrid Metamaterial: An Ultra-Sensitive Platform for Infrared Absorption Spectroscopy and Quantitative Measurement of Molecules," ACS Nano **11**, 9780-9788 (2017).

[3] Thu Le, Akihiro Morita, Kazuma Mawatari, Takehiko Kitamori, and Takuo Tanaka, "Metamaterials-Enhanced Infrared Spectroscopic Study of Nanoconfined Molecules by Plasmonics-Nanofluidics Hydrid Device," ACS Photonics **5**, 3179-3188 (2018).

[4] Thu H. H. Le, Akihiro Morita, and Takuo Tanaka, "Refractive index of nanoconfined water reveals its anomalous physical properties," Nanoscale Horizons **5**, 1016-1024 (2020).

[5] Dong-Sheng Su, Din Ping Tsai, Ta-Jen Yen, and Takuo Tanaka, "Ultrasensitive and Selective Gas Sensor Based on a Channel Plasmonic Structure with an Enormous Hot-spot Region," ACS Sensors **4**, 2900-2907 (2019).

Timetronics vs Electronics

V. Raskatla [1], J. Li [2], G. Adamo [1], K. F. MacDonald [1], and N. I. Zheludev [1,3]

[1] University of Southampton, ORC, SO16 7NF, Southampton, UK
[2] Nanyang Technological University, CDPT, 67911744, Singapore
[3] Texas A&M University, Hagler Institute, Texas, TX 77843-3572, USA

*Corresponding author: zheludev@soton.ac.uk

Abstract— **Can nano-mechanical computers be scaled to the nanoscale and compete with electronic architectures? We report the timetron as a central building block for mechanical computation based on the concept of a time crystal, which can be switched with femtojoule-scale energies and sustained with only a few femtowatts of optical power.**

***Keywords*— time crystals, metamaterials, data processing.**

I. INTRODUCTION

The earliest computers, from the abacus to sophisticated clockwork calculators, were mechanical and digital. They dominated computation well into the twentieth century. Why did electronics ultimately prevail? The advantage of electronics was the transition to the nanoscale, where transistors enabled fast operation, dense integration, scalable manufacturing, and cascaded binary Boolean logic.

Can mechanical computers also be scaled to the nanoscale, and if so, could they compete with electronic architectures [1]? We examine the *timetron* as a central building block for mechanical computation that is based on the concept of a time crystal[2-4]. It is a nanomechanical element in which light switches the system between two dynamical states - rest and sustained oscillation - encoding the logical “0” and “1” of timetronics, a data-processing paradigm where information is carried by the dynamical state of nanoscale motion. Based on the timetron, key logical and memory elements can be implemented. It can be switched with femtojoule-scale energies, while the logical state can be sustained with only a few femtowatts of optical power.

REFERENCES

1. *Time crystals for photonics and timetronics.* Nikolay I. Zheludev. Nature Photonics 18, 1123 (2024)
2. *Photonic metamaterials analogue of a continuous time crystal.* Tongjun Liu, Jun-Yu Ou, Kevin F. MacDonald & Nikolay I. Zheludev. **Nature Physics** 2023. 19, 986 (2023)
3. *Continuous Space-Time Crystal State Driven by Nonreciprocal Optical Forces.* V. Raskatla, T. Liu, J. Li, K. F. MacDonald & Nikolay I. Zheludev. **PRL** 133, 136202 (2024)
4. *Time Translation Symmetry, Ergodicity and Entropy Dynamics in a Time Crystal.* Tongjun Li, Venugopal Raskat, Jinxiang Li, Kevin F. MacDonald, Nikolay I. Zheludev. **Newton,** 100206 (2025)

Generalized Lorentz Framework for Active Semiconductor Plasmonics at the Deep Nanoscale

Xue-Wen Chen*

School of Physics, Huazhong University of Science and Technology, Luoyu Road 1037, Wuhan, 430074, China

*Corresponding author: xuewen_chen@hust.edu.cn

***Abstract*— We report a generalized Lorentz framework to efficiently capture various nonclassical effects in multiscale three-dimensionally nanostructured semiconductors with arbitrary energy–momentum dispersion relations. The framework enables quantitative treatment of carrier nonlocality, surface accumulation and depletion, and Landau damping under electrical control and widely varying doping densities.**

***Keywords*— Deep nanoscale, Nonlocality, non-Parabolic dispersion, Landau damping.**

I. Introduction

Semiconductors lie at the core of modern microelectronics and, beyond electronic functionality, constitute a versatile platform for light-matter interactions across the mid-to-near infrared spectrum through surface plasmon resonances arising from collective oscillations of charge carriers. Unlike metals, semiconductors exhibit plasmonic properties actively tunable through doping and electrical gating, offering appealing opportunities for on-chip electro-optical modulation, ultrasensitive biosensors, enhanced infrared imaging, nonlinear effects, and all-optical switching. Recent advances in nanofabrication technology have enabled three-dimensional (3D) nanostructuring of semiconductor materials with single-digit-nanometer precisions. Such capability allows precise control of the interactions among light field, charge carriers, and other fields at the deep nanoscale, fostering ultrafast and efficient photonic–electronic convergence. As feature sizes shrink to deep nanoscale (~10 nm scale and below), nonclassical carrier dynamics and plasmonic responses become prominent, posing substantial challenges for a rigorous and efficient theoretical treatment.

Here we present a generalized Lorentz framework to describe the nonclassical effects in 3D nanostructured semiconductors with arbitrary energy-momentum dispersion relations. Building on the framework, we establish a QNM analysis with a consistent orthonormalization and provide accurate characterizations of the carrier dynamics and plasmonic responses of semiconductor nanostructures subject to electrostatic fields and orders-of-magnitude variation in doping density.

II. Methods

Based on a hydrodynamic description of the conduction electrons in n-doped semiconductors, we derive a generalized Lorentz model to effectively account for various nonclassical effects. It reads

$$\omega^2\mathbf{P} + i\omega\frac{\rho}{m^*}\hat{\Gamma}\mathbf{P} - \frac{\rho}{m^*}\hat{\Theta}\mathbf{P} = -\varepsilon_0\omega_p^2\rho\mathbf{E}, \quad (1)$$

where **P** is the polarization of the electrons, m* is the effective mass of the electrons, **E** is electric field, and ρ is the stationary electron density. $\hat{\Gamma}$ and $\hat{\Theta}$ are the damping and restoring (spatial differential) operators. Eq. (1) together with the curl equation of the Maxwell equations constitute the generalized Lorentz framework for effective treatment of the various nonclassical effects of the electrons in heavily doped semiconductors.

III. Conclusion

The generalized Lorentz framework constitutes a theoretical foundation for studying active semiconductor nanoplasmonics and will foster the convergence of electronics and photonics at the deep nanoscale.

Acknowledgments

We acknowledge financial support from the National Natural Science Foundation of China (62235006, 12525414, 12274160, 12404429, 12504443, 12574416), the China Postdoctoral Science Foundation (2024M760993) and the China Postdoctoral Science Foundation-Hubei Joint Support Program (2025T004HB).

References

[1] Q. Zhou, P. Zhang, and X.-W. Chen, "A general framework of canonical quasinormal mode analysis for extreme nano-optics," Physical Review Letters, vol. 127, pp. 267401, 2021.

[2] Q. Zhou, W. Li, Z. He, P. Zhang, and X.-W. Chen, "Quantum hydrodynamic model for noble metal nanoplasmonics," Physical Review B, vol. 107, pp. 205413, 2023.

[3] W. Li, Q. Zhou, P. Zhang, and X.-W. Chen, "Bright optical eigenmode of 1 nm3 mode volume," Physical Review Letters, vol. 126, pp. 257401, 2021.

Topological metasurface for wavefront manipulation

Qinghua Song[1,*]

[1]Tsinghua Shenzhen International Graduate School, Tsinghua University, Shenzhen, China
*Corresponding author: song.qinghua@sz.tsinghua.edu.cn

***Abstract*— In this talk, we will present topological metasurface based on exceptional points and their applications in wavefront manipulation. Unconventional arbitrary polarized exceptional point and zero-eigenvalue exceptional point are demonstrated.**

***Keywords*— metasurface, exceptional point, non-Hermitian, topological photonics.**

I. Introduction

Exceptional points (EPs) are spectral singularities of non-Hermitian systems that occur whenever complex eigenvalues and eigenstates coalesce, leading to a reduction of the Hilbert space dimension. Traditional photonic systems typically exhibit coalesced eigenstates that correspond to circularly polarized light of a specific handedness, thereby restricting their applicability to only two antipodal points located on top or bottom of the Poincaré sphere. Here, we introduce a continuum of EPs for which the corresponding coalesced eigenstates can access any point on the Poincaré sphere (**Fig. 1**). Our theoretical proposal and experimental implementation overcome the main practical limitation of EPs, extending the applicability of the topological phase to any arbitrarily-polarized light state. In addition, we theoretically and experimentally demonstrate a counterintuitive topological strategy based on zero-eigenvalue EP (**Fig. 2**), in which the complete suppression of the system scattering enables an effective expansion of accessible topological degrees of freedom. The emergence of these non-conventional EPs not only introduces a realm of disruptive applications in wavefront engineering and optical multiplexing, but also brings in new fundamental properties of topological systems in general.

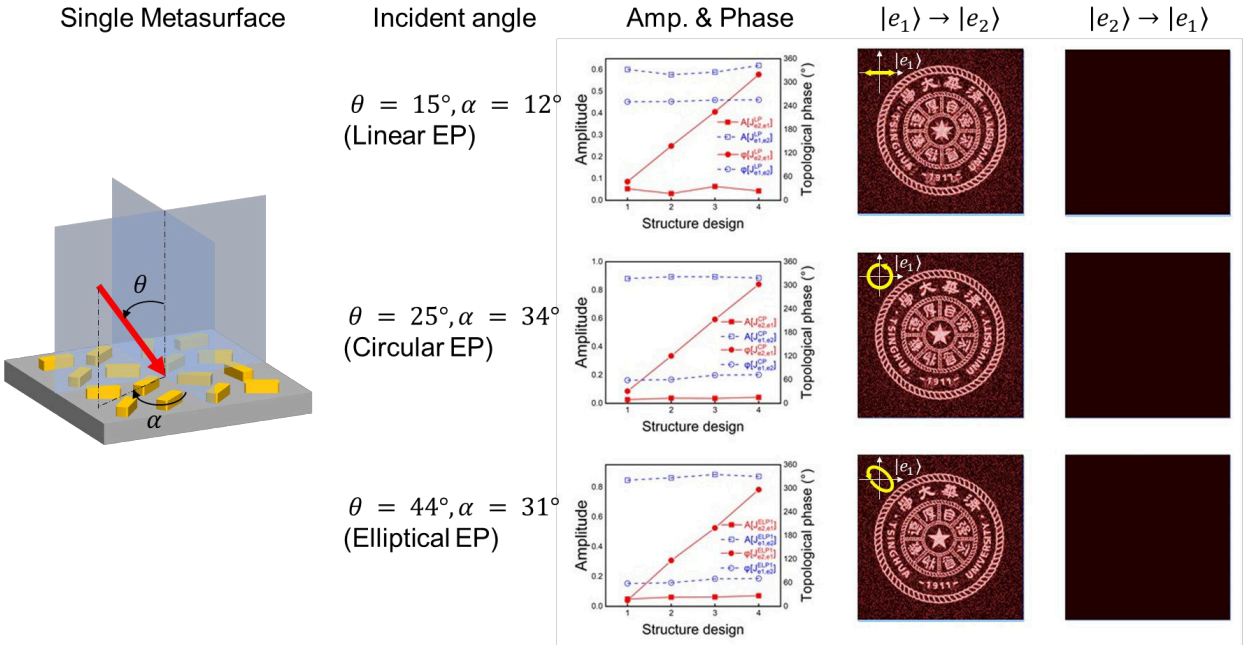

Fig. 1 Single metasurface for arbitrary polarized exceptional points.

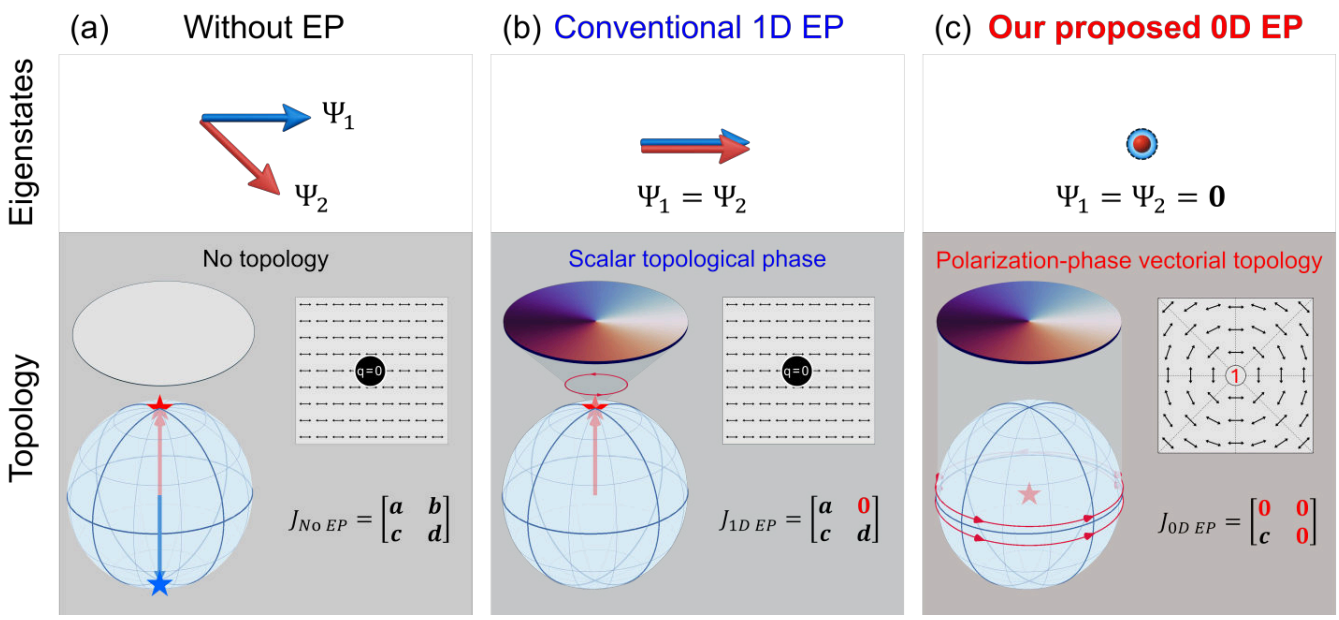

Fig. 2 Zero-eigenvalue exceptional point with vectorial topology

REFERENCES

[1] Q. Song, M. Odeh, J. Zúñiga-Pérez, B. Kanté, P. Genevet, "Plasmonic topological metasurface by encircling an exceptional point," Science, vol. 373, pp. 1133-1137, 2021.

[2] Z. Yang, P.-S. Huang, Y.-T. Lin, H. Qin, J. Zúñiga-Pérez, Y. Shi, Z. Wang, X. Cheng, M.-C. Tang, S. Han, B. Kanté, B. Li, P. C. Wu, P. Genevet, Q. Song, "Creating pairs of exceptional points for arbitrary polarization control: asymmetric vectorial wavefront modulation," Nature Communications, vol. 15, pp. 232, 2024.

[3] Z. Yang, P.-S. Huang, Y.-T. Lin, H. Qin, J. Chen, S. Han, W. Huang, Z.-L. Deng, B. Li, J Zúñiga-Pérez, P. Genevet, P. C. Wu, Q. Song, "Asymmetric Full-Color Vectorial Meta-holograms Empowered by Pairs of Exceptional Points," Nano Letters, vol. 24, pp. 844–851, 2024.

[4] H. Qin, Z. Yang, P.-S. Huang, X. Mu, S.-H. Huang, Y. Shi, W. Zhao, B. Li, J. Zhou, J. Zúñiga-Pérez, P. Genevet, P. C. Wu, Q. Song, "Sphere of arbitrarily polarized exceptional points with a single planar metasurface," Nature Communications, vol. 16, pp. 2656, 2025.

Metasurface-Enabled Solid-State Photon Sources

Fei Ding[1,2,*]

[1] Centre for Nano Optics, University of Southern Denmark, Campusvej 55, DK-5230 Odense, Denmark

[2] School of Electronic Science and Technology, Eastern Institute of Technology, Ningbo, China

*Corresponding author: feid@mci.sdu.dk

***Abstract*— We propose general approaches to designing versatile solid-state photon sources using on-chip quantum-emitter-coupled metasurfaces. This platform enables us to generate spatially propagating photon streams with arbitrary directionality, polarization, and wavefronts via designed metasurfaces.**

***Keywords*—Solod-state quantum emitters, metasurfaces, directionality, polarization, wavefronts.**

I. Introduction

Metasurfaces—ultrathin arrays of engineered meta-atoms—have revolutionized classical optics by enabling unprecedented control over the amplitude, phase, and polarization of light within compact, planar platform [1]s. By replacing bulky optical components with subwavelength nanostructures, metasurfaces have facilitated a new generation of miniaturized and multifunctional photonic devices. Beyond their transformative impact on classical light manipulation, metasurfaces are increasingly emerging as powerful interfaces for tailoring nonclassical optical fields, extending their functionality to the single-photon regime [2].

II. Methods

We introduce a conceptually new paradigm of on-chip emitter-coupled quantum metasurfaces for the room-temperature generation of nonclassical light. In this approach, quantum emitters are non-radiatively coupled to surface plasmons, which are subsequently converted—via interaction with an optical metasurface—into collimated single-photon beams with engineered quantum properties (Fig. 1).

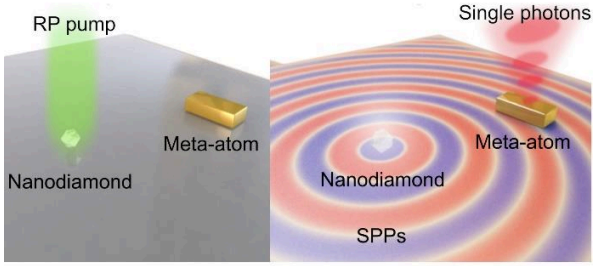

Fig. 1 Schematic of the emitter-coupled quantum metasurface.

III. Results and Discussion

This platform enables deterministic control over emission directionality, and polarization, providing a scalable and chip-compatible route toward integrated quantum light sources for advanced quantum photonic technologies. By unifying near-field light–matter interaction engineering with far-field wavefront shaping in a single metasurface architecture, it bridges the gap between quantum emitter physics and functional photonic circuitry [3-5].

IV. Conclusion

Such an approach not only enhances photon extraction efficiency and state purity at room temperature but also offers multidimensional control of single-photon states, paving the way for compact quantum communication systems, high-dimensional quantum information processing, and on-chip quantum sensing and imaging applications.

Acknowledgments

This work was supported by the Villum Fonden (37372) and Carlsberg Foundation (CF24-1777).

References

[1] F. Ding, A. Pors, and S. I. Bozhevolnyi, “Gradient metasurfaces: a review of fundamentals and applications,” Rep Prog Phys. 81,026401 (2018).

[2] F. Ding and S. I. Bozhevolnyi, “Advances in quantum meta-optics”, Mater. Today 71, 63−72 (2023).

[3] X. Liu, Y. Kan, S. Kumar, L. F. Kulikova, V. A. Davydov, V. N. Agafonov, F. Ding, and S. I. Bozhevolnyi, “Off-normal polarized single-photon emission with anisotropic holography metasurfaces”, Nano Lett. 24, 13867−13873 (2024).

[4] S. im Sande, Y. Kan, D. Komisar, C. Wu, S. Kumar, S. I. Bozhevolnyi, and F. Ding, “On-Chip Emitter-Coupled Meta-Optics for Versatile Photon Sources”, Phys. Rev. Lett. 135, 086902 (2025).

[5] X. Liu, Y. Kan, S. Kumar, F. Ding, and S. I. Bozhevolnyi, “Arbitrarily structured photoluminescence from individual nanodiamonds”, ACS Nano 19, 40416–40425 (2025).

Continuous-Wave Chiral Exciton–Polariton Lasers Across the Visible and Infrared

Siying Peng[1,*]

[1]Department of Materials Science and Engineering, Westlake University, China
*Corresponding author: pengsiying@westlake.edu.cn

***Abstract*— Chiral light-matter interactions are emerging as a key frontier in both applied photonics and fundamental optical science. Their ability to control the spin and handedness of light enables unique functionalities relevant to technologies ranging from under-display biometric recognition and stereoscopic 3D imaging to spintronic devices, quantum information processing, and molecular sensing. These diverse applications would greatly benefit from compact chiral light sources capable of emitting light with high directionality, strong polarization purity, and substantial optical power. Nevertheless, creating miniature lasers that intrinsically generate circularly polarized emission remains an outstanding materials and photonics challenge.**

Two principal design routes have been explored to achieve direct circularly polarized lasing. The first relies on chiral photonic architectures surrounding an otherwise achiral gain medium. In such systems, optical chirality arises from structural or phase asymmetry engineered into the cavity, rather than from the emitter itself. While effective, this strategy demands intricate nanofabrication or self-assembly techniques to achieve subwavelength precision. Moreover, because the active medium lacks inherent chirality, spontaneous emission couples inefficiently to the chiral optical modes, which in turn increases the lasing threshold and thermal losses.

An alternative approach introduces chemical chirality directly into the gain medium by incorporating chiral ligands or molecular building blocks. Although this strategy imparts handedness to the emitter, the magnitude of optical chirality achieved under ambient conditions is typically weak. Photoluminescence dissymmetry factors are usually in the range of 10^{-3} to 10^{-2}, leading to modest polarization purity. Consequently, neither photonic structuring nor chemical induction alone has yet produced a compact, circularly polarized laser that simultaneously exhibits strong optical chirality, low threshold operation, and high efficiency.

To overcome these limitations, we exploit strong light-matter coupling between chiral excitons and cavity photons to realize continuous-wave (CW) chiral exciton-polariton lasing spanning both the visible and infrared spectral ranges. We first demonstrate room-temperature CW circularly polarized lasing from a chiral 2D perovskite, $(MBA)_2PbI_4$, where hybrid exciton–polaritons exhibit an ultralow threshold of 0.5 $W{\cdot}cm^{-2}$ and intrinsic circular polarization with a photoluminescence dissymmetry factor of 0.30. The lasing wavelength is tunable via cavity thickness, and the device maintains >95% of its output intensity under prolonged CW operation, showing exceptional material and optical stability.

Building on this platform, we extend the concept to the infrared regime by developing chiral quasi-2D perovskite heterostructures designed through tailored organic cations and spacer layers that enhance excitonic coherence and chiroptical coupling. These engineered materials enable spin-polarized exciton–polariton condensation in the near-infrared, marking the first realization of infrared chiral polariton lasing at room temperature.

Together, these results establish a versatile photonic platform for CW, spin-polarized exciton–polariton lasing across broad spectral ranges. Beyond demonstrating record-low thresholds and high polarization purity, this work provides insights into chirality under strong coupling and paves the way toward spin-polarized quantum fluids of light and next-generation perovskite-based spintronics and photonic technologies.

***Keywords*— Exciton-polaritons, Laser, Chirality, Halide perovskites.**

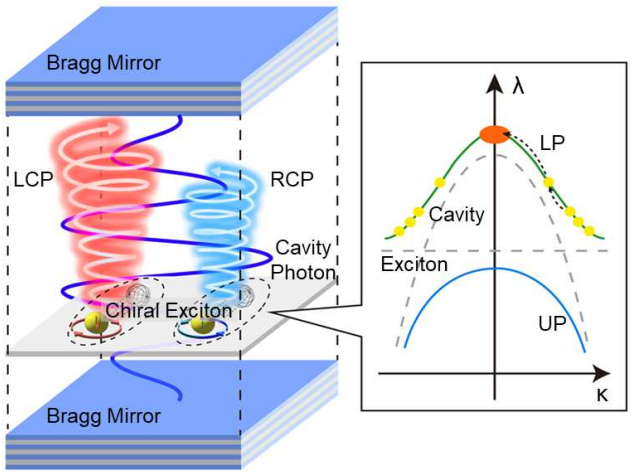

Fig. 1 Chiral exciton-polariton condensate.

Enhancing Light-Matter Coupling via Topology Optimized Cavities on 2D Excitonic Material

Brandon Triplett[1], Davide Cassara[2], Morris M. Yang[1], Karthik Pagadala[1], Federico Capasso[2], Vladimir M. Shalaev[1], Alexandra Boltasseva[1*]

[1] Elmore Family School of Electrical and Computer Engineering, Birck Nanotechnology Center and Purdue Quantum Science and Engineering Institute, Purdue University, West Lafayette, IN 47907, USA
[2] Harvard John A. Paulson School of Engineering and Applied Sciences, Harvard University, Cambridge, MA 02138, USA
Corresponding author: aeb@purdue.edu

***Abstract*— We design and fabricate dielectric cavities with extreme subwavelength transverse mode sizes of 30-40 nm and couple them to excitonic material WSe_2. We show tenfold photoluminescence enhancement, which corresponds to 10^3 normalized enhancement when accounting for deeply subwavelength mode volumes. The approach offers increased far-field collection efficiency and scalable integration.**

***Keywords*— Topology optimization, inverse design, dielectric cavity, transition metal dichalcogenides, WSe2, exciton, photoluminescence enhancement, non-exponential decay dynamics.**

Photonic inverse design and, especially, topology optimization, enable dielectric cavities with deeply sub-diffraction mode volumes and high quality factors, thus offering a powerful platform for enhanced light-matter coupling. Here, we design and fabricate arrays of CMOS-compatible silicon cavities on sapphire with extreme subwavelength transverse mode sizes of only 30-40 nm. These cavities are engineered for deterministic coupling to a monolayer (or few-layer) excitonic material WSe_2, producing strong near-field localization directly beneath the 2D material. Photoluminescence (PL) measurements show reproducible tenfold raw enhancement relative to bare silicon, which corresponds to a normalized enhancement on the order of 10^3 when accounting for the deeply subwavelength mode volume, consistent with numerical simulations that account for material absorption and fabrication tolerances. Furthermore, time-resolved PL measurements reveal pronounced lifetime shortening and non-exponential dynamics, indicating cavity-mediated exciton-exciton interactions. The optimized cavity geometry enhances the far-field collection efficiency and supports scalable integration with van der Waals semiconductors. Our results show that the arrays of topology-optimized dielectric cavities are a versatile, scalable platform for controlling excitonic emission and interactions, which creates new opportunities in nonlinear optics, optoelectronics, and quantum photonics.

Rigorous and Approximate Electromagnetic Simulators for Free-Form Light-Emitting Device Optimization

Min Seok Jang[1,*]

[1]School of Electrical Engineering, Korea Advanced Institute of Science and Technology, Korea

*Corresponding author: jang.minseok@kaist.ac.kr

***Abstract*— This presentation discusses overcoming challenges in free-form light-emitting device optimization via three methods: the diffraction matrix method, differentiable RCWA, and neural operators. These tools enable efficient, robust design of next-generation, high-performance optical technologies.**

***Keywords*— Invers design, light emitting metasurfaces, machine learning, device optimization.**

Free-form optimization of optical devices offers immense performance potential but typically involves millions of design parameters, making the search for optimal structures within these vast combinatorial spaces an intrinsically challenging task. Due to increased simulation complexity, the design problem for light-emitting devices is significantly more difficult than for standard transmission or reflection metasurfaces. In this presentation, I discuss three primary approaches to address these bottlenecks. First, the diffraction matrix method is employed to rigorously simulate periodically corrugated light-emitting devices. Second, I introduce differentiable Rigorous Coupled-Wave Analysis (RCWA) simulation software that enables the efficient back-propagation of figure-of-merit gradients for high-dimensional optimization. Finally, neural-operator-based approximate models are utilized for the rapid determination of complex optical properties. Together, these methodologies provide a robust and efficient toolkit for the design and optimization of next-generation, high-performance light-emitting technologies.

Engineering spontaneous emission with metasurfaces

Benjamin. Vest[1,*]

[1]Université Paris-Saclay, Institut d'Optique Graduate School, CNRS, Laboratoire Charles Fabry, 91127, Palaiseau, France.

*Corresponding author: benjamin.vest@institutoptique.fr

***Abstract*— Light-emitting metasurfaces enable direct control of emission from incoherent sources without bulky filtering. We design and realize photoluminescent metasurfaces where emitters couple to engineered leaky modes using a Kirchhoff-based absorptivity approach seeking critical coupling condition. Experiments demonstrate directional beams below 20° FWHM and efficient structured light generation.**

***Keywords*— spontaneous emission, metasurface, radiation engineering;**

I. Introduction

Designing a light-emitting system means shaping emission to meet requirements in radiation pattern, polarization, or spectrum. Unlike lasers, most sources such as fluorescent lamps and LEDs rely on spontaneous emission, an intrinsically random process in which photons are emitted with independent phase, polarization, and direction. Their emission is therefore typically isotropic, incoherent, and unpolarized. Wavefront control can be achieved by filtering the emitted light with polarizers, diaphragms, or spectral filters, but this approach discards a large fraction of the generated energy. Although LEDs are efficient sources, their overall efficiency is often reduced by optical shaping elements that may reject up to half of the emitted light and increase system complexity. An alternative approach is offered by Light-Emitting Metasurfaces (LEMs), where luminescent emitters couple to arrays of nanoscale resonators supporting extended electromagnetic modes. Preferential decay of incoherent emitters into a common resonant mode can induce spatial, spectral, or polarization coherence. Here we present advances in the modelling, engineering, and realization of flat structured-light sources based on emitters coupled to metallic or dielectric metasurfaces.

II. Methods

Light emission engineering is achieved by tailoring the properties of a leaky mode. We adopt a Kirchhoff-based approach in which emission properties are designed through the absorptivity of the LEM, aiming to maximize contrast between target modes and the parasitic background. Bare metasurfaces are first numerically designed and dimensioned in the overcoupled regime. Emitters are then incorporated and equalize radiative and non-radiative losses of the target mode. This enables critical coupling between emitters and metasurface, maximizing total absorption. After clean-room fabrication, emission properties are characterized using Fourier-plane imaging and spectral measurements.

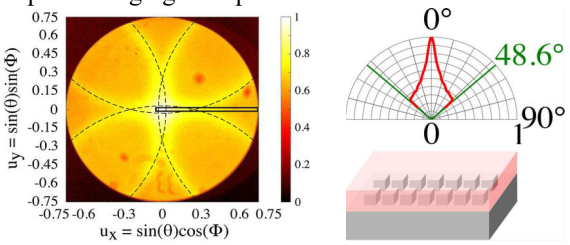

Fig. 1 Fourier plane imaging of a photoluminescent metasurface, consisting of quantum dots deposited on a silver metallic grating. [1]

III. Results and Discussion

We report the realization of directional photoluminescent metasurfaces with less than 20° FWHM emission cone, and above 60% absorptivity in the active medium. We will discuss how this approach combined with symmetry-protected bound states in the continuum (BICs) can be used to achieve other features such as the emission of circularly polarized light, and how the Kirchhoff's approach enables a quantitative modelling of energy efficiency, and how it can be related to usual figures of merit used in light source design such as light extraction efficiency, internal and external quantum efficiency.

IV. Conclusion

Directional, narrowband and polarized photoluminescent sources can be realized by coupling ensembles of incoherent emitters to a leaky mode of a metasurface. Radiation efficiency can be quantitatively modelled and optimized by maximizing absorptivity following a Kirchhoff's law approach. To maximize technological impact, this approach will be applied to design electroluminescent devices incorporating specific technological constraints.

References

[1] E. Bailly et al., "2D Silver-Nanoplatelets Metasurface for Bright Directional Photoluminescence, Designed with the Local Kirchhoff's Law," ACS Nano, 18(6) pp. 4903–4910, 2024.

Out-of-equilibrium nonlinear optical dynamics in ultraviolet epsilon-near-zero materials

M. Silvestri[1], L. Assogna[1], D. Tedeschi[1,2], C. Ferrante[2], and A. Marini[1,2,*]

[1] Department of Physical and Chemical Sciences, University of L'Aquila, Via Vetoio, 61700 L'Aquila, Italy

[2] Consiglio Nazionale delle Ricerche, CNR-SPIN, Via Vetoio 10, 67100 L'Aquila, Italy

*Corresponding author: andrea.marini@univaq.it

***Abstract*— We theoretically model out-of-equilibrium nonlinear optical dynamics due to collision-driven nonlinearity in ultraviolet epsilon-near-zero materials, particularly sodium and aluminum, exploring their potential for the development of table-top extreme ultraviolet radiation sources and integrated spectroscopy schemes.**

***Keywords*—Epsilon-near-zero media, nonlinear optics, nanophotonics.**

I. Introduction

Nonlinear (NL) radiation-matter interactions give rise to many physical phenomena particularly relevant to quantum mechanical processes, and offer a promising platform to devise compact ultraviolet (UV) radiation sources. Harmonic generation (HG) is one of the main nonlinear effects amplified by photonic materials with low dielectric permittivity, known as epsilon near zero (ENZ) materials.

ENZ materials, thanks to their natural ability to bypass phase-matching, enhance NL radiation-matter interactions and play a crucial role for advanced NL phenomena, e.g., optical switching. Currently, ENZ media are adopted to enhance NL optical effects, particularly in the near-infrared part of the spectrum, where doped semiconductors, oxides, and nitrides display ENZ behavior. Poor materials show marked ENZ features in the UV that are promising for resonant third-harmonic generation (THG) in heterogeneous nanostructures, and for manipulation and guidance of UV radiation.

II. Methods

Here, we investigate the potential of nanostructures based on sodium (Na), aluminum (Al), and sodium-aluminum (Na-Al) heterostructures for NL applications [1-4]. We study the THG due to the out-of-equilibrium (OOE) electron dynamics. In turn, to model NL electron dynamics in the heterogeneous nanostructures we consider the Fokker-Planck-Landau (FPL) theoretical framework. We analytically calculate the Landau collisional integral in the weak coupling limit [5], obtaining a set of hydrodynamical equations (HDEs). By solving perturbatively HDEs, we derive an analytical expression for the dependence of the collision-driven THG NL-susceptibility over the pump field angular frequency. Moreover, to obtain the pump field distribution within the heterogeneous nanostructures, we use the undepleted pump approximation, modeling the THG radiation process accounting for multiple reflections of forward (FW) and backward (BW) waves.

III. Results and Discussion

Due to the coupling of the pump field enhancement and the radiation of the microscopic dipoles, the THG process exhibits a double resonance for transverse magnetic (TM) pump excitation at due to dipolar emission in an ENZ environment. Conversely, for transverse electric (TE) pump excitation we observe THG enhancement due to the excitation of Fabry-Perot resonances of the considered nanostructures. Finally, we find that for specifically incidence angle conditions it is possible to excite surface plasmon polaritons (SPPs) at the Na-Al interface thanks to attenuated total internal reflection (ATIR). This enables to attain a THG enhancement factor of 7 orders to magnitude as compared to non-resonant conditions, thus suggesting that ENZ heterogeneous nanostructures offer a promising platform for the development of integrated XUV sources.

IV. Conclusion

In conclusion, we observe that ENZ nanostructures constitute a promising platform to attain efficient THG in the UV spectral domain. Both Na and Al are promising ENZ media undergoing mitigated absorption. In addition, thanks to the broadband ENZ behavior of Na, we observe that SPPs can get excited at Na-Al interfaces, contributing to the maximization of THG efficiency. Our results indicate that Al/Na ENZ nanostructures are promising for integrated nonlinear conversion platforms.

Acknowledgments

This work has been partially funded by the European Union, NextGenerationEU, under the Italian Ministry of University and Research (MUR) National Innovation Ecosystem Grant No. ECS00000041-VITALITY-CUP E13C22001060006. This work has been partially supported by the Progetti di ricerca di

Rilevante Interesse Nazionale (PRIN) of the Italian Ministry of University and Research PHOTO (PHOtonics Terahertz devices based on tOpological materials) 2020RPEPNH and TransientMeta (Light-programmed two-dimensional meta-holograms for integrated neuromorphic computing) 2022N738SA-CUP E53D23001780006.

REFERENCES

[1] M. Silvestri, A. Sahoo, L. Assogna, P. Benassi, C. Ferrante, A. Ciattoni, and A. Marini, "Resonant third-harmonic generation driven by out-of-equilibrium electron dynamics in sodium-based near-zero index thin films," Nanophotonics vol. 13, pp. 2003-2013 (2024).

[2] M. Silvestri, M. Venturi, M. Di Muzio, R. Adhikary, C. Ferrante, P. Benassi, and A. Marini, "Harnessing collisional nonlinearity for enhanced harmonic generation by ultraviolet plasmonic nanoparticles," J. Chem. Phys. vol. 161, 054111 (2024).

[3] M. Silvestri, A. Sahoo, C. Ferrante, P. Benassi, A. Ciattoni, and A. Marini, "Doubly resonant third-harmonic generation in near-zero-index heterogeneous nanostructures," Phys. Rev. A 110, 023524 (2024).

[4] C. Ferrante, E. Principi, L. Assogna, A. Sahoo, G. Batignani, G. Fumero, L. Foglia, R. Mincigrucci, L. Giannessi, T. Scopigno, C. Masciovecchio, and A. Marini, "Epsilon-near-zero nonlinearity enhancement in the extreme ultraviolet," Light Sci Appl vol. 14, 374 (2025).

[5] A. Marini, A. Ciattoni, and C. Conti, "Out-of-equilibrium electron dynamics of silver driven by ultrafast electromagnetic fields – a novel hydrodynamical approach," Faraday Discuss. vol. 214, pp. 235-243 (2019).

Octave-Spanning Terahertz Quarter-Wave Plates Based on Over-Coupled Fabry-Pérot Resonances in Reflective Metal-Dielectric-Metal Metasurfaces

Tae Gwan Park[1], Chun-Chieh Chang[1], Hou-Tong Chen[1,*]

[1]Center for Integrated Nanotechnologies, Los Alamos National Laboratory, USA
*Corresponding author: chenht@lanl.gov

***Abstract*—We demonstrate metal-dielectric-metal reflective metasurfaces for high-performance broadband THz quarter-wave plates. Four complementary designs operating at 45 degree incidence collectively span 0.25–3 THz. Each device provides near-octave bandwidth with axial ratio below 3-dB and polarization conversion efficiency above 80%. Experiments agree with simulations, confirming scalable broadband THz polarization control.**

***Keywords*— metasurfaces, terahertz, circular polarization, quarter-wave plates.**

I. Introduction

Circularly polarized terahertz (THz) radiation is indispensable for a wide range of applications, including chiral spectroscopy and molecular identification, all-optical manipulation of magnetization without external magnetic fields, and the selective probing or excitation of spin waves (magnons) and chiral phonons. These applications motivate the development of high-performance linear-to-circular polarization converters (i.e., quarter-wave plates) in the THz regime, particularly because most coherent THz sources emit linearly polarized radiation. Conventional narrowband quarter-wave plates can be realized using low-loss birefringent materials such as quartz and liquid crystals, as well as artificially engineered anisotropic effective media exhibiting form birefringence, for example, subwavelength silicon gratings [1]. A strategy widely used in the optical regime and extendable to broadband THz frequencies involves stacking multiple plates with carefully selected thicknesses and relative orientations to compensate for wavelength-dependent phase retardation, thereby forming achromatic THz wave plates [2]. Prism-based polarization elements, such as Fresnel rhombs [3], can provide truly achromatic THz quarter-wave retardation by generating polarization phase delay through total internal reflection rather than material birefringence. Nevertheless, these achromatic THz devices remain physically large and are not readily compatible with compact or integrated THz systems.

II. Results and Discussion

In this work, we present a set of reflective metal-dielectric-metal metasurfaces [4], [5] that function as quarter-wave plates and collectively span the entire THz frequency range accessible to a typical THz time-domain spectroscopy system (0.2–3 THz). Broadband spectral coverage is achieved using four complementary devices, each designed to operate within a specific subband of this range (see Fig. 1). The metal-dielectric-metal metasurfaces function as single-port cavity resonators in which reflective Fabry-Pérot resonances [6] operate in the over-coupled regime. By carefully tailoring the geometric parameters of the anisotropic subwavelength elements and the thickness of the dielectric spacer, we achieve a nearly constant relative phase delay of $\pi/2$ (or $3\pi/2$) over a broad spectral range while maintaining near-unity reflectivity for both orthogonal polarization components. We design these metasurface structures using full-wave electromagnetic simulations to target four distinct frequency windows of interest. The four devices are fabricated using standard photolithography and characterized using THz time-domain spectroscopy. Under 45° incidence and linearly polarized at 45° with respect to the plane of incidence, the results show that the incident THz waves have been converted to left-handed circular polarization, with a high conversion efficiency mostly exceeding 80%, covering an octave bandwidth for each device, and collectively spanning the 0.25–3 THz with four devices, as represented by the ≤ 3 dB axial ratio shown in Fig. 1. The experimental results show excellent agreement with numerical simulations, which also allow further structural optimization through additional simulations. This work demonstrates robust broadband reflective THz quarter-wave plates, enabling advanced THz polarimetric applications and circularly polarized THz light–matter interactions in systems such as biomolecules, chiral phonons, and magnetic materials, as well as potential applications in THz communications and imaging.

III. Conclusion

In conclusion, we have demonstrated high-performance broadband THz quarter-wave plates based on over-coupled metal-dielectric-metal reflective metasurfaces. By harnessing the phase dispersion associated with anisotropic over-coupled Fabry-Pérot cavity resonances and precisely engineering the relative phase delay between orthogonal field components, we achieve efficient linear-to-circular polarization conversion over a broad THz spectral range. Four complementary metasurface designs collectively span the 0.25–3 THz frequency range accessible to a typical THz time-domain spectroscopy system, with each device providing an approximately octave-wide

Fig. 1. Performance assessment of linear-to-circular polarization conversion for the four metasurface devices. (a) Simulated and (b) measured conversion efficiencies for devices 1–4, indicated by red, green, blue, and cyan curves, respectively. (c) Simulated and (d) measured axial ratio, quantifying the circular polarization purity across the operational bandwidth..

bandwidth characterized by an axial ratio below 3 dB and conversion efficiencies exceeding 80% across most of the operating band.

ACKNOWLEDGMENTS

We acknowledge partial support provided by the Los Alamos National Laboratory Laboratory Directed Research and Development (LDRD) program. This work was primarily performed at the Center for Integrated Nanotechnologies, an Office of Science User Facility operated for the U.S. DOE Office of Science. Los Alamos National Laboratory, an affirmative action equal opportunity employer, is managed by Triad National Security, LLC for the US DOE NNSA, under contract no. 89233218CNA000001.

REFERENCES

[1] C. Kadlec, F. Kadlec, P. Kužel, K. Blary, and P. Mounaix, "Materials with on-demand refractive indices in the terahertz range," *Optics Letters*, vol. 33, pp. 2275–2277, 2008.
[2] J.-B. Masson and G. Gallot, "Terahertz achromatic quarter-wave plate," *Optics Letters*, vol. 31, pp. 265–267, 2006.
[3] J. Shan, J. I. Dadap, and T. F. Heinz, "Circularly polarized light in the single-cycle limit: the nature of highly polychromatic radiation of defined polarization," *Optics Express*, vol. 17, pp. 7431–7439, 2009.
[4] N. K. Grady, J. E. Heyes, D. R. Chowdhury, Y. Zeng, M. T. Reiten, A. K. Azad, A. J. Taylor, D. A. R. Dalvit, and H.-T. Chen, "Terahertz metamaterials for linear polarization conversion and anomalous refraction," *Science*, vol. 340, pp. 1304–1307, 2013.
[5] C.-C. Chang, Z. Zhao, D. Li, A. J. Taylor, S. Fan, and H.-T. Chen, "Broadband linear-to-circular polarization conversion enabled by birefringent off-resonance reflective metasurfaces," *Physical Review Letters*, vol. 123, p. 237401, 2019.
[6] H.-T. Chen, "Interference theory of metamaterial perfect absorbers," *Optics Express*, vol. 20, pp. 7165–7172, 2012.

Building Uncooled Infrared Camera based on One Atom Thick Graphene

Debashis Chanda

NanoScience Technology Center, Department of Physics, CREOL-College of Optics and Photonics
University of Central Florida

Abstract: The talk will outline a novel strategy for uncooled, tunable, multispectral infrared detection. Due to the low photon energy, detection of infrared photons is challenging at room temperature. One atom thick graphene offers an alternative mechanism bypassing material bandgap restriction. Further, the ability of carrier concentration modulation on graphene via external voltage offers dynamic spectral selectivity for "color" night vision/sensing. The performance of preliminary demonstration compares favorably even with present cryogenically cooled detection schemes paving the path for commercial development of many applications from space exploration to healthcare.

Dynamic Surface-Lattice Resonance Metasurface for Time-Varying Photonics

J. Weber[1], A. Ball[1,2], D. Fomra[3,4], S. Goswami[5], B. T. Diroll[6], T. Venkatesan[5], and N. Kinsey[7,*]

[1]Department of Electrical & Computer Engineering, Virginia Commonwealth University, Richmond, VA, USA
[2]Now with Booz-Allen-Hamilton
[3]Physical Measurement Lab, National Institutes of Standards and Technology, Gaithersburg, MD, USA
[4]Now with Xanadu Inc.
[5]Department of Physics and Astronomy, University of Oklahoma, Norman, OK, USA
[6]Center for Nanoscale Materials, Argonne National Laboratory, Lemont, IL, USA
7Department of Electrical & Computer Engineering, Saint Louis University, Saint Louis, MO, USA
*Corresponding author: nathaniel.kinsey@slu.edu

***Abstract*— We realize and study the nonlinear response of a surface-lattice-resonance structure coupled to a TCO, illustrating a 30x reduction in saturation irradiance and the presence of spectral fringes of positive/negative extinction due to time varying effects.**

***Keywords*— Epsilon-near-zero, surface-lattice-resonance, nonlinear optics, time-varying photonics, metamaterials.**

I. Introduction

Time-varying processes in optical materials offer a host of unique interactions such as analog frequency control, photon trapping, sonoluminescence, non-reciprocity, and new methods of photon pair generation [1]. Despite the longstanding theoretical and experimental history studying these effects [2], a limitation has generally been the impracticality to make physical objects move an appreciable fraction of the speed of light. Early works worked toward this through the generation of plasma bubbles where the rapidly expanding plasma volume served as a moving media [1]. More recently, efforts have centered on the concept of synthetic motion which simulates physical motion and its interaction with photon velocity through the analogy between velocity and refractive index (or group index) [1,3]. This has relaxed physical constraints of the moving media, but benefits from strong and temporally fast modification of the refractive index in the media. While early works in silicon platforms counteracted this with long interaction lengths [4], the recent demonstration of nonlinearities in transparent conducting oxides (TCOs) in their epsilon-near-zero (ENZ) regime has provided a new platform where the index (and velocity) can be modified on the scale of 100% and greater [5]. This has led to the demonstration of several time-varying effects including adiabatic frequency shifting and temporal interference, while predictions suggest many more exotic phenomena are on the horizon.

Despite the advantage of TCOs in the ENZ regime, a limitation is that they require substantial irradiance levels on the scale of 0.1 – 1 TW/cm^2. Here, we seek to address this by combining an ENZ layer with an open cavity system in the form of a surface lattice resonance (SLR) structure. We show that this structure can radically reduce the required irradiance while still exhibiting time-varying interactions in the form of negative extinction bands. We develop a model for the system combining temporal coupled-mode theory and our theory of kinetic fast-slow nonlinearities in ENZ materials [5].

II. Methods

Our TCO-SLR samples were fabricated by depositing a thin film of W:In_2O_3 (IWO) on glass substrates. IWO was used due to its improved mobility (~80 cm^2/V-s) and therefore lower optical loss compared to common TCO materials ITO, AZO, and GZO (~30 cm^2/V-s) for carrier densities in the range of 10^{20} cm^{-3}.

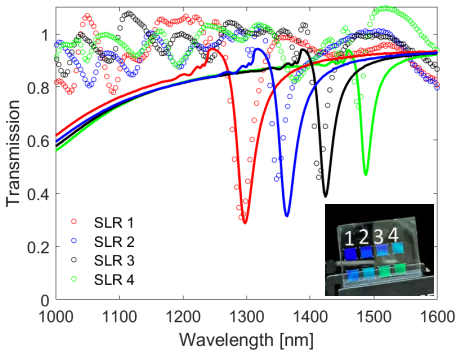

Fig. 1 Linear transmission of TCO-SLR structure. (Inset) Optical image of the TCO-SLR samples.

Following, a liftoff procedure and was used to patter an array of gold nano antennas on top of the IWO layer. The periodicity was tuned across four structures to shift the SLR resonance from ~1300 nm to ~1500 nm. The Q-factor of the SLR was intentionally kept low to match the bandwidth of the excitation beam. The sample was first characterized by linear transmission spectroscopy using a coherent supercontinuum white light

source, see Fig. 1. Subsequently, the nonlinear response of the system was studied using an excite-probe style setup (~60 fs pulses FWHM) where a strong driving pulse on resonance with the SLR was used to excite the system while a broadband supercontinuum probe, delayed from the excitation, was used to observe the spectral response and temporal response of the system. The response of the system was modeled through a three-step combination of finite element method, kinetic fast-slow-nonlinearities, and coupled mode theory techniques (CMT). Ultimately this process allows us to predict the temporal trajectory of the SLR resonance through the excitation and relaxation of the TCO layer. This is then modeled as a time-varying center frequency and damping factor of the cavity resonance in CMT.

III. Results and Discussion

Excite-probe experiments with a single beam on resonance with the SLR illustrate the introduction of the SLR reduces the saturation irradiance to 3 [GW/cm^2], Fig. 2, compared to 100's [GW/cm^2] [6,7] from literature for TCO films at ENZ - a reduction of more than 30x. Spectrally resolved measurements detail a strong nonlinearity, predominantly arising from a red shift of the center frequency of the SLR resonance. This matches phenomenological and numerical predictions wherein the excitation beam excites the intraband nonlinearity of the IWO film, resulting in an increase in the permittivity of the IWO. Of note, however, is the appearance of spectral fringes with negative extinction ratio which arise at and before time zero – when the excite and probe arrive at the sample simultaneously. These fringes were noted for excitation irradiance levels down to 2 [GW/cm^2]. Such effects have been noted in other systems including Mie resonance metasurfaces [8] and ENZ films [9]. To model this interaction, a CMT approach was used to describe the probe beam interaction with the time varying SLR resonance [8]. This was modeled as a dynamic center frequency for the SLR, whose temporal shape was matched to that of the change in linear transmission and magnitude obtained from finite element and kinetic fast slow nonlinear modeling. The result of the simulation effort is shown in Fig. 2, obtaining a good match to experimental results including the appearance of spectral fringes.

IV. Conclusion

Our efforts have demonstrated a moderate-Q SLR structure coupled to a highly nonlinear TCO material where the inherent nonlinearity of the TCO is employed to dynamically tune the resonance of the structure. The result achieved significant reduction in the irradiance necessary to reach saturation of the change in transmission as well as the introduction of negative extinction bands arising from the interaction of the probe beam with a time varying resonant structure. The work demonstrates a new platform to investigate time-varying interactions at significantly lower incident irradiance levels that is compatible with various platforms such as fiber optics.

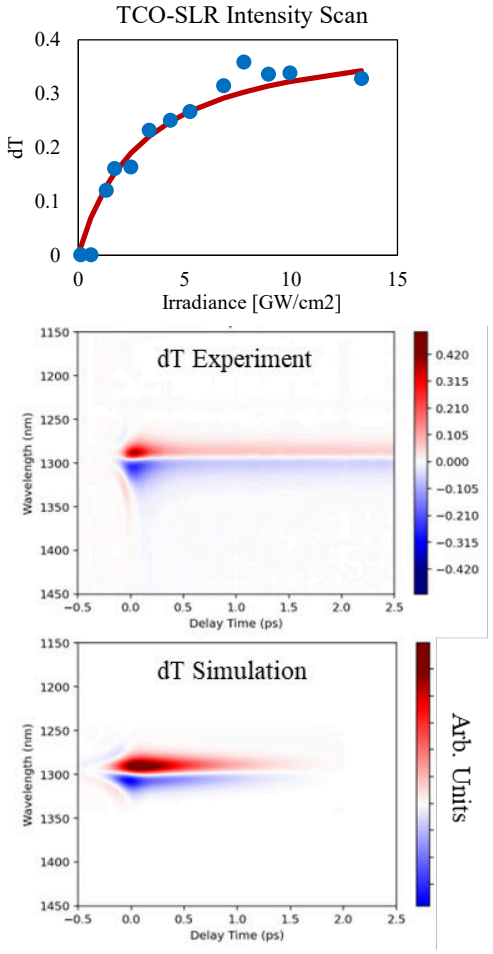

Fig. 2 (Top) Nonlinear transmission of the excitation vs incident irradiance. (Middle) Spectral and temporally resolved change in transmission of the ENZ-SLR sample under 16 GW/cm^2 excitation on resonance. (Bottom) Simulated change in transmission of probe interaction with the dynamic SLR resonance.

Acknowledgments

This work was supported by Grant FA9550-22-1-0383 from the US Air Force Office of Scientific Research.

The use of the Center for Nanoscale Materials, an Office of Science user facility, was supported by the U.S. Department of Energy, Office of Science, Office of Basic Energy Sciences under Contract No. DE-AC02-06CH11357.

[1] J. T. Mendonca, *Theory of Photon Acceleration*, CRC Press, 2000.
[2] A. Einstein, "On the electrodynamics of moving bodies," *Annalen der Physik*, vol. 17, pp. 891-021, 1905.
[3] A. C. Harwood et al, "Space-time optical diffraction from synthetic motion," *Nature Communications*, vol. 16, no. 5147, 2025.
[4] M. A. Gaafar et al, "Front-induced transitions," *Nature Photonics*, vol. 13, pp. 737-748, 2019.
[5] D. Fomra et al, "Nonlinear optics at epsilon-near-zero: From origins to new materials," *Applied Physics Reviews*, vol. 11, no. 1, 2024.
[6] L. Caspani et al, "Enhanced nonlinear refractive index in ε-near-zero materials," *Physical Review Letters*, vol. 116, no. 23, 2016.
[7] M. Z. Alam, et al, "Large optical nonlinearity of indium tin oxide in its epsilon-near-zero region," *Science*, vol. 352, no. 6287, 2016.
[8] M. R. Shcherbakov, et al, "Time-variant metasurfaces enable tunable spectral bands of negative extinction," *Optica*, vol. 6, no. 11, 2019.
[9] R. Rirole, et al, "Double-slit time diffraction at optical frequencies," *Nature Physics*, vol. 19, pp. 999-1002, 2023.

New Materials for Large Scale, Roll-to-Roll Metasurfaces

Vivian E. Ferry[1,*]

[1]Department of Chemical Engineering and Materials Science, University of Minnesota – Twin Cities, Minneapolis, MN USA

*Corresponding author: veferry@umn.edu

***Abstract*— We have developed an additive, roll-to-roll printing method for large-area metamaterial fabrication, based on a combination of nanoimprint lithography and ink delivery, which selectively infills the patterned features. We use this method to pattern light emitters, including anisotropic quantum dots, and study the polarization state of the photoluminescence.**

***Keywords*— metamaterials, nanofabrication, quantum dots**

I. Introduction

One of the central challenges facing metamaterials is the need for large-area fabrication methods with excellent control over both nanostructure shape and spacing, that also works for a diverse set of materials. While nanoimprint lithography replicates patterns well at large areas, transferring these patterns into functional materials often requires subtractive processing steps. Here we show a versatile method that combines templating and additive ink filling, produce m^2 metamaterials from a variety of different ink materials.

II. Methods

Our method uses two roll-to-roll lines. The first is roll-to-roll nanoimprint lithography, where the original lithographic pattern is translated to a stamp and imprinted into a UV-curable resin. After imprinting, the patterned resin is heated in an oven, which reduces the surface energy of the template. A second roll-to-roll line is used for ink delivery; a dispersion of ink coated onto the patterned template selectively infills the features.

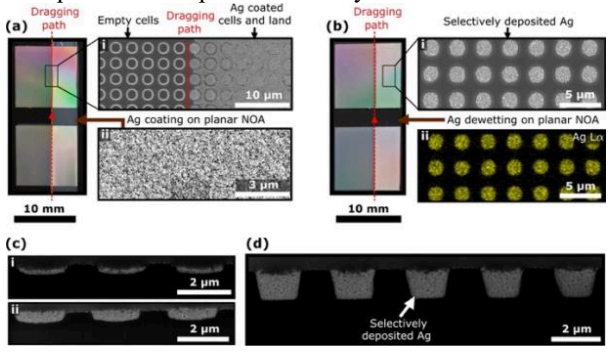

Fig. 1 (a,b) Patterning ink on a non-heat treated template (a) does not result in selective wetting, whereas patterning on a heat-treated substrate (b) facilitates topographic discontinuous dewetting.(c,d) Cross section views of infilled and cured ink into templates.

III. Results and Discussion

Our process is designed to utilize topographic discontinuous dewetting [1,2], where the coating speed and properties of the ink dispersion are tuned on a low energy substrate to enable selective infilling. We show that this process is highly versatile and works with metallic inks (both particle based and particle free), titanium dioxide, polymer blends, and semiconductor nanocrystals, provided the ink and coating conditions are correctly adapted.

To demonstrate the functionality of this system, we created metamaterials comprised of light emitters, including II-VI quantum dots, perovskite quantum dots, and nanocrystals with anisotropic shapes, materials that are challenging to pattern via other routes. We will discuss the directionality, polarization state, absorption, and photoluminescence of these patterned structures, and how the pattern can be used to manipulate the optical response.

IV. Conclusion

We have demonstrated a versatile nanofabrication process that creates large-area metamaterials based on a combination of nanoimprint lithography and additive ink infilling. This method works for a variety of ink materials. We then discuss the use of this method for directing and shaping luminescence from patterned quantum dots, including anisotropic particles.

Acknowledgments

This work was supported by the National Science Foundation under award number 2102835.

References

[1] Y. J. Donie, I. Welsch, M. Ramamurthy, C. D. Frisbie*, L. F. Francis*, V. E. Ferry*, "High resolution roll-to-roll additive patterning of functional materials on large areas via topographical discontinuous dewetting," ACS Appl. Mater. Interfaces, vol. 17, pp. 53887 - 53900, 2025.

[2] Y. J. Donie, M. Ramamurthy,R. D. Chakraborty, L. F. Francis*, C. D. Frisbie*, V. E. Ferry*, "Roll-to-roll compatible topochemical wetting control for metamaterial printing," Adv. Opt. Mater., vol. 12, 2302785, 2024.

Dual-layer metasurfaces supporting bound states in the continuum for torque sensing

Alexander Schossmann[1,3,*], Michael Töfferl[1,3], Maximilian Saiko[1], Alexander Bergmann[1,3], Peter Banzer[2,3]

[1]Institute of Electrical Measurement and Sensor Systems, Graz University of Technology, Austria
[2]Institute of Physics, University of Graz, NAWI Graz, Austria
[3]Christian Doppler Laboratory for Structured Matter Based Sensing, Austria
*Corresponding author: alexander.schossmann@tugraz.at

***Abstract*—Highly precise measurement on moving objects remains challenging, yet crucial for e-mobility, robotics, and related fields. In our work, we utilize resonant metasurfaces for telemetric torque sensing. We show that tunable dual-layer metasurfaces supporting (quasi-) bound states in the continuum offer unprecedented access to motion parameters, essential for developing robust next-generation sensors.**

***Keywords*— metamaterials.**

I. Introduction

Metamaterials have proven to be a powerful approach in the field of sensor technology [1]. Recent research has shown that tuning near-field interactions in metamaterials provides access to the detection of mechanical perturbations and deformations that are orders of magnitude smaller than their unit cell [2]. In our recent work, we exploited the electromagnetic resonance mode of millimeter-wave metasurfaces to conceptualize novel sensor systems [3], [4], [5], [6]. A central topic is metamaterial-based torque sensing. The schematic view of the sensor concept is shown in fig. 1. A picture of the test bench set up is shown in fig. 2. The metamaterial comprises two near-field-coupled metasurfaces (orange in fig. 1) distributed across two disks (green in fig. 1), each fixed separately to the rotating shaft (blue in fig. 1). Torque causes a minute twist on the shaft. Due to the separate attachment of the discs, this twist leads to a displacement of the metasurfaces that ultimately tunes the electromagnetic resonant behavior. This tuning is detectable in reflection using a mm-wave radar chip. We showed that modified Doppler radar and frequency-modulated continuous-wave (FMCW) chips are both applicable to this concept, using broadside-coupled split-ring resonators (BCSRRs) that exhibit a tunable dipole-like resonance [3], [4]. In this work, we aim to advance this sensor concept using metasurfaces supporting bound states in the continuum.

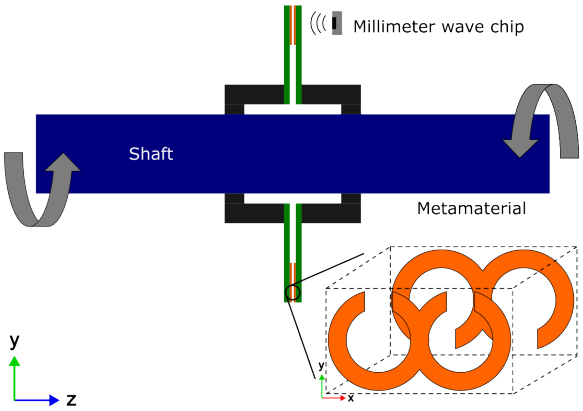

Fig. 1. Sectional view of the torques sensor system for measurement on a shaft

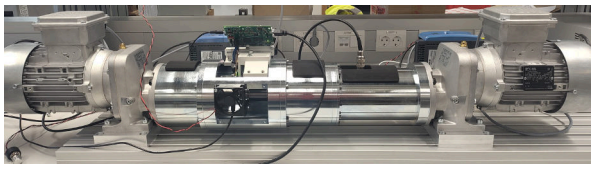

Fig. 2. Picture of the torque test bench used for the study of metamaterial-based torque sensing

II. Bound states in the continuum for torque sensing

Metasurfaces may exhibit a plethora of different resonances depending on their geometry, arrangement, and environment. A special class of metasurface resonances, particularly interesting for sensing applications, are (quasi-) bound states in the continuum (BIC). A BIC, in theory, has an infinite quality factor. However, it cannot be excited by external fields due to symmetry. When breaking the symmetry of a BIC system, for example, by introducing a minor deformation, it turns into a quasi-bound state with a finite yet extraordinarily high quality factor that can be excited from the far-field. In our sensor concept, we exploit the minute torque-induced displacement between the metasurface layers to break symmetry, thereby enabling the excitation of quasi-BICs.

III. Numerical results

The unit cell of the dual-layer metasurface supporting quasi-BICs is shown in the inset of fig. 1. It is arranged in circular arrays on the two discs such that a twist between the discs causes a transverse shift in the x-direction locally in the unit cell. We studied the resonant behavior as a function of this shift with the finite element method using COMSOL Multiphysics®. We built a 3D model of the unit cell, modeling

the conductive structures as 2D boundaries with copper's finite conductivity. The substrates were modeled using the same dielectric-layer setup as in our previous work, which is suitable for manufacturing. The Eigenfrequency analysis shows a BIC-like resonant mode at 60.6 GHz. Figure 3 shows the fields in the top plane of the unit cell, with the surface current density depicted as black arrows, the electric field as red arrows, and the absolute value of the electromagnetic field amplitude displayed in color. The result shows two counter-rotating circular currents in the split rings and two opposing electric dipoles in the gaps. The bottom plane shows the same fields, with the circular currents oriented the same way (not depicted in fig. 3). Therewith, the structure has opposing electric and magnetic dipoles that cancel each other in the far field. Thus, this mode cannot be excited by external fields, such as impinging plane waves. The torque-induced shift in the x-direction between the top and bottom planes of the unit cell breaks the symmetry of a rotation by 180° along the x-axis through the center of the unit cell. This gives small net dipole components in the x-y plane that provide a coupling channel to the far field, turning the metasurface resonance into a quasi-BIC. We analyzed this behavior by calculating scattering parameters for plane waves polarized in the x-direction. Figure 4 shows the calculated spectra of the reflection scattering parameters S_{11}. The curve for zero shift (blue in fig. 4) does not show a minimum at frequencies around 60.6 GHz. The curves for shifts other than zero exhibit distinct minima. The results in fig. 4 show the quasi-BIC behavior of the dual-layer metasurface: In the symmetric configuration, the impinging plane wave does not excite the resonance, but when breaking the symmetry, the resonance is excited by the external field. The results of the Eigenfrequency study for increasing transverse shift values are shown in table I. For the zero-shift case, the Quality factor is finite because our model includes dielectric losses in the substrates and the finite conductivity of copper. The data show that the Quality factor gradually decreases with increasing transverse shift. This is a pivotal feature of this quasi-BIC metasurface. State-of-the-art mm-wave radar chips are not built to track a resonance minimum. However, they are well-suited for detecting changes in the reflected power from a target. The quasi-BIC metasurface enables translating the torque-induced resonance shift into a gradual decrease in reflected power over a narrow bandwidth, thereby paving the way for torque detection with low-cost radar chip technology.

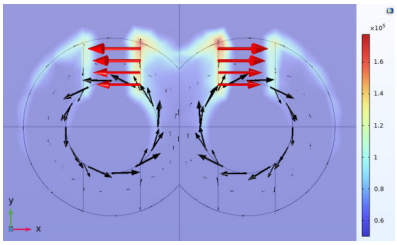

Fig. 3. Surface currents and field amplitude of the metasurface unit cell.

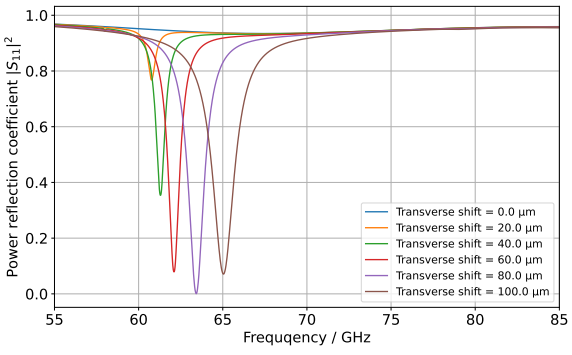

Fig. 4. BIC mode in reflection spectra.

Transverse shift / µm	Eigenfrequency	Quality factor
0	60.6	115
20	60.8	109
40	61.3	92
60	62.1	73
80	63.4	55
100	65.0	41

TABLE I
NUMERICAL RESULTS OF THE EIGNENFREQUENCIES AND THE QUALITY FACTORS OF THE DUAL-LAYER METASURFACE.

ACKNOWLEDGMENTS

The financial support by the Austrian Federal Ministry of Labour and Economy, the National Foundation for Research, Technology and Development and the Christian Doppler Research Association is gratefully acknowledged.

REFERENCES

[1] Abdelraouf, Omar AM and Wang, Ziyu and Liu, Hailong and Dong, Zhaogang and Wang, Qian and Ye, Ming and Wang, Xiao Renshaw and Wang, Qi Jie and Liu, Hong, "Recent advances in tunable metasurfaces: materials, design, and applications," *ACS nano*, vol. 16, pp. 13339–13369, 2020.

[2] Powell, David A. and Lapine, Mikhail and Gorkunov, Maxim V. and Shadrivov, Ilya V. and Kivshar, Yuri S., "Metamaterial tuning by manipulation of near-field interaction," *Phys. Rev. B*, vol. 82, 2010

[3] Schossmann, Alexander and Hammerschmidt, Dirk and Michenthaler, Christof and Bergmann, Alexander, "Torque measurement with tunable metamaterial and a modified Doppler radar," *2022 IEEE International Instrumentation and Measurement Technology Conference (I2MTC)*, 2022.

[4] Schossmann, Alexander and Hammerschmidt, Dirk and Michenthaler, Christof and Bergmann, Alexander, "Torque Sensing with Tunable Millimeter Wave Metamaterial and a FMCW Chip," *2022 Sixteenth International Congress on Artificial Materials for Novel Wave Phenomena (Metamaterials)*, 2022.

[5] Töfferl, Michael and Schossmann, Alexander and Schmidt, Christoph and Banzer, Peter and Bergmann, Alexander, "Telemetric position sensing using resonant frequency parameterization of a millimeter-wave metamaterial," *Sensors and Communication Technologies in the 1 GHz to 10 THz Band*, vol. 13203, 2024.

[6] Töfferl, Michael and Schossmann, Alexander and Saiko, Maximilian and Banzer, Peter and Bergmann, Alexander, "Towards tunable metamaterial-based torque sensing,", *The 15th International Conference on Metamaterials, Photonic Crystals and Plasmonics, META 2025*, 2025.

All-glass metasurface laser optics based on self-generation of nano-particles

Eyal Feigenbaum[1,*]

[1] The National Ignition Facility and Photon Science,
Lawrence Livermore National Laboratory, Livermore, CA USA
*Corresponding author: feigenbaum1@llnl.gov

***Abstract*— Metasurface could advance high-power laser optics, by filamentation damage mitigation, throughput enhancement, and system complexity and price reduction. We present approach based on self-generation of sacrificial nano-particle mask followed by directional etching to pattern metasurfaces on fused-silica glass. We demonstrate an ultra-broadband spectrum antireflective layer, waveplate, and optical lens elements.**

***Keywords*— metasurfaces, laser optics, waveplates.**

I. Introduction

High power and energy lasers (HPL) are becoming transformative to future technology, which encourages rapid development of its optics. Some potential applications include fusion-based clean energy, compact particle sources for medical and civil engineering, directed energy and basic science. These HPL systems, such as the National Ignition Facility (NIF), require optics with large apertures, high throughput and high durability. Conventional approaches, including multilayer dielectric coatings and bulk optical components, face significant challenges in susceptibility to laser-induced damage, optical performance and thickness. All-glass metasurfaces offer a promising alternative, provided a viable path for aperture size scale up, transmission enhancement close to unity, enhancement of laser-induced damage durability, and for some applications enabled operation at shorter wavelengths (e.g., NIF final optics are about 40 cm x 40 cm and operate at above 10 J/cm^2 of few nanoseconds laser pulse-length at 351 nm wavelength). We present here a specialized metasurface approach that is intended to provide a potential path to address these challenges. These metasurfaces are etch-engraved onto fused silica glass thus preserving the inherent robustness of fused silica. We present here implementation of several key laser optics components: broadband antireflection (AR) layer, thin optical elements (e.g., lens), and birefringent waveplates. We will discuss in this talk the manufacturing approach, the demonstrated components, and the challenges that still lay ahead.

II. Discussion

The baseline metasurface fabrication process utilizes a sacrificial metal nanoparticle (NP) mask created by thermal dewetting of a thin metal film on fused silica, followed by directional etching and mask removal to yield an all-glass nano-structured surface [1]. Thin layers of metal (e.g., Au or Pt) are deposited and dewetted either in a furnace (for uniform AR layers) or by raster-scanned continuous-wave laser (to spatially vary the mask patterning for optical elements implementation). The self-organized nanoparticle (NP) distribution determines the local fill fraction (FF) and period, which in turn set the effective refractive index of the metasurface layer after reactive ion etching (RIE) or reactive ion beam etching (RIBE). The self-generation-based approach for patterning the etching mask NP, where the properties of the NP being controlled by macroscopic properties (such as laser intensity or furnace temperature) set a path for aperture size scale-up, and for access to shorter wavelengths [1,2].

A key limitation to achieve a broad band AR metasurface layer on optical windows with this approach is the erosion of the NP mask during etching. This has previously constrained feature height and thus the AR bandwidth, and was overcome by improving mask materials and processes: Pt was found to have significantly higher etch resistance than Au, and a “seeded dewetting” approach was developed in which repeated deposition and dewetting steps grow NP height and FF while preserving a small period set in the first dewetting cycle [3]. These advancements increase metasurface depth and shape control, enabling ultra-high aspect ratio features and much wider AR bandwidth. Using these improved masks, AR metasurface have been demonstrated that surpass commercial broadband dielectric coatings, including configurations with very low reflection from the UV to the near infrared over large angles of incidence and at both polarizations [4]. Furthermore, these improvements expand the design space and control over the NP shape (e.g., cones, cylinders, flat-top cones, and their depth), providing an ability to optimize simultaneously the optical and physical properties (e.g., mechanical robustness) [3].

The same nanoparticle-based process can be adapted to fabricate metasurface lenses by spatially varying the effective index through laser-controlled dewetting [1]. Raster scanning a CW laser across the metal film with varying power tunes the

local dewetting temperature and hence the NP FF [5]. This "light-printing" approach has been used to realize mm-scale diameter optical elements with negligible reflectivity [6].

To address polarization control needs, the baseline process was modified to produce birefringent all-glass metasurfaces by breaking the in-plane symmetry of the nano-features [7]. For one of the demonstrated approaches, after NP mask formation, the etch is performed at an angle using RIBE, yielding tilted pillar structures whose effective index differs for orthogonal in-plane polarizations. Optical birefringence and controlling physical properties such as water repellency is demonstrated. Other approaches to generating all-glass metasurface waveplates will be discussed. Such robust, UV-compatible waveplates are particularly relevant for systems like NIF, where conversion to circular polarization near the final optics could increase filamentation damage thresholds.

Beyond their targeted optical functions, these all-glass metasurfaces exhibit favorable laser damage and mechanical behavior. Laser-induced damage testing shows comparable behavior to damage treated fused silica glass windows. Mechanical tests, including sonication, drag wiping, fingerprinting, and controlled indentation, show high robustness.

III. Conclusion

A self-generated-based nanoparticle-mask-based process for fabricating all-glass metasurfaces has been demonstrated and refined to meet the stringent requirements of high power and energy laser systems. The process steps of thin metal film deposition, dewetting and directional etching, can be potentially applied using equipment compatible with meter-class optics which could pave a path to large-area all-glass metasurfaces with sub-wavelength features. Enhancements such as seeded dewetting, optimized mask materials, and tailored etch chemistries enable deep, high aspect ratio structures and precise shape control. On this foundation, three key classes of optical functions have been realized: ultra-broadband, large-angle antireflective layers; thin, freeform optical elements generated by laser "light-printing" of spatially varying effective index; and birefringent metasurfaces in fused-silica glass that provide a pathway to robust waveplates. Progress as well as the remaining gaps will be discussed.

Acknowledgments

We acknowledge the support of Lawrence Livermore National Laboratory (LLNL) Laboratory Directed Research and Development grant (21-ERD-002). LLNL-CONF-2015728.

References

[1] J. H. Yoo, H. T. Nguyen, N. J. Ray, M. A. Johnson, R. Steele, J. Chesser, S. H. Baxamusa, S. Elhadj, J. T. McKeown, M. J. Matthews, and E. Feigenbaum, "Scalable light-printing of substrate-engraved free-form meta-surfaces," ACS Applied Materials & Interfaces, vol. 11, pp. 22684–22691, 2019.

[2] N. J. Ray, J. H. Yoo, H. T. Nguyen, M. A. Johnson, S. Elhadj, S. H. Baxamusa, and E. Feigenbaum, "Substrate-engraved antireflective nanostructured surfaces for high-power laser applications," Optica, vol. 7, pp. 518–526, 2020.

[3] N. J. Ray, J.-H. Yoo, S. Baxamusa, H. T. Nguyen, S. Elhadj, E. Feigenbaum, "Designer metasurfaces for antireflective applications enabled by advanced nanoparticle technology," Advanced Optical Materials, vol. 10, p. 22070037, 2022.

[4] N. J. Ray, J. H. Yoo, H. T. Nguyen, E. Feigenbaum, "All-glass metasurfaces for ultra-broadband and large acceptance angle antireflectivity: from ultraviolet to mid-infrared," Advanced Optical Materials, vol. 10, p. 20230013, 2023.

[5] J. H. Yoo, N. J. Ray, M. Johnson, H. T. Nguyen, E. Feigenbaum, "Laser-assisted tailored patterning of Au nanoparticles over inch-sized area: Implications for large aperture meta-optics," ACS Applied Nano Materials, vol. 5, pp. 10073–10080, 2022.

[6] J. H. Yoo, N. J. Ray, M. Johnson, H. T. Nguyen, E. Feigenbaum, "Low Reflectance All-Glass Metasurface Lenses Based on Laser Self-generated Nanoparticles," submitted.

[7] N. J. Ray, J.-H. Yoo, H. T. Nguyen, M. A. Johnson, E. Feigenbaum, "Birefringent glass-engraved tilted pillar metasurfaces for high power laser applications," Advanced Science, vol. 10, p. 20230013, 2023.

Harnessing Epsilon-Near-Zero Effects: Fiber Lasers, Thermo-Optic Dynamics, and Beyond

Qian Li*,†

School of Electronic and Computer Engineering, Peking University, Shenzhen 518055, China
* liqian@pkusz.edu.cn

Abstract—Epsilon-near-zero ENZ materials, with their vanishing permittivity, have emerged as a compelling platform for nanophotonics and nonlinear optics due to extreme field enhancement, phase engineering capabilities, and compatibility with complementary metal-oxide-semiconductor technology. Based on these unique features and great performance, ENZ materials can play a significant role in optical communication, data processing and laser technology. Here, a comprehensive overview of ENZ photonics is presented, revealing its fundamental principles and highlighting our research endeavors. Specifically, we show how ENZ elements can be integrated into complex photonic systems through the demonstration of a fiber laser cavity incorporating indium tin oxide nanolayers. The intra-cavity ENZ component introduces frequency-selective optical potential barriers that fundamentally reshape the mode-locking dynamics, enabling wavelength reselection and spectral redistribution through gain competition. This cavity configuration exhibits behavior analogous to radio-frequency superconducting quantum interference devices (RF-SQUID), illustrating how ENZ photonics can bridge optical phenomena with concepts from other physical domains. What's more, while substantial progress has been made in understanding their linear and Kerr nonlinear properties, the role of temperature in governing ENZ behavior has remained largely unexplored despite its critical importance for integrated photonic systems where heat generation is unavoidable. Here we present a comprehensive investigation of thermo-optic ENZ effects in indium tin oxide nanolayers, revealing that temperature systematically tunes the ENZ frequency across telecommunication bands with modulation rates reaching several gigahertz per kelvin. We demonstrate that the thermo-optic coefficient experiences an unprecedented enhancement of nearly an order of magnitude within the ENZ regime compared to conventional indium tin oxide, accompanied by fast-varying group velocity dispersion up to four orders of magnitude larger than typical optical materials. Remarkably, the thermo-optic nonlinearity exhibits enhancements exceeding 2800 percent, comparable to the renowned ENZ-enhanced Kerr nonlinearity, with an ultrafast pulse-width threshold in the femtosecond to picosecond range where thermal nonlinearities remain dominant. These findings establish that thermo-optic effects represent not merely a perturbation but rather an intrinsic and engineerable dimension of ENZ photonics. The insights provide practical design references for integrated photonic circuits where thermal management is essential, while opening new directions for ultrafast modulation, optical computing, and photonic information processing in next-generation integrated systems.

Flat Optics with Computational Imaging for Biomedical Applications

Sunil Vyas[1], Cheng Hung Chu[1,2], J. Andrew Yeh[3], Yuan Luo[1,2,4,5]
[1]*Institute of Medical Device and Imaging, NTU College of Medicine*
[2]*NTU YongLin Institute of Health*
[3]*Institute of NanoEngineering and MicroSystems, National Tsing Hua University*
[3]*Department of Biomedical Engineering, NTU College of Engineering*
[4]*Program for Precision Health and Intelligent Medicine, NTU Graduate School of Advanced technology*
[5]*Research Center for Applied Sciences, Academia Sinica*

E-mail: yuanluo@ntu.edu.tw *Web:* http://optics.mc.ntu.edu.tw/

Optical microscopy remains a cornerstone of biological research, offering indispensable insights into complex cellular processes. Recently, the strategic implementation of structured light has become pivotal in surmounting the diffraction limit and enhancing resolution. Simultaneously, the emergence of metasurfaces—engineered nanostructures capable of precise light manipulation—has revolutionized the field by enabling ultra-compact, high-performance optical functionalities.

This talk showcases recent breakthroughs in structured light and meta-optical systems for biomedical applications. We explore the development of quantitative cell imaging and high-speed optical sectioning, with a focus on integrating metalenses into light-sheet fluorescence microscopy (LSFM) for enhanced deep-tissue observation. Additionally, we discuss the synergy between flat optics and computational imaging—specifically spatially variant aberration correction—as a powerful strategy for achieving exceptional image fidelity. By merging meta-optical design with advanced computational frameworks, this presentation illustrates a transformative frontier for next-generation biomedical diagnostics.

Selected Publications:

1. “Abrupt autofocusing metasurface for high-resolution confocal fluorescence microscopy”. ***Laser Photonics Rev.***, accepted (2025)
2. "Metasurface-based Airy light-sheet fluorescence microscopy," ***Applied Physics Reviews***, 12, 031412 (2025).
3. “Metalens-based dual light-sheet fluorescence microscopy,” ***Small methods***, https://doi.org/10.1002/smtd.202402149 (2025).
4. "In vivo intelligent fluorescence endo-microscopy by varifocal meta-device and deep learning," ***Advanced Science***, doi.org/10.1002/advs.202307837
5. “Patch-based U-net model for isotropic quantitative differential phase contrast imaging,”***IEEE Transactions on Biomedical Imaging***,40, 11, 3229-3237 (2021)

Nonlocal Meta-Optics: Addressing Fundamental Scaling Constraints in Imaging Systems

Bohan Zhang[1], Yuanmu Yang[1*]

[1] Department of Precision Instrument, Tsinghua University, China

*Corresponding author: ymyang@tsinghua.edu.cn

***Abstract*—This talk explores nonlocal meta-optics to bypass traditional imaging size constraints. By engineering momentum-space (k-space), the researchers decoupled system thickness from resolution, achieved label-free super-resolution, and enabled high-dimensional sensing. These advancements pave the way for ultra-compact, wafer-scale photonic systems for 3D vision and metrology.**

***Keywords*— nonlocal, meta-optics, imaging, diffraction limit.**

Conventional imaging is governed by scaling laws where information capacity is coupled to physical dimensions. This talk will discuss an alternative approach using nonlocal meta-optics to address these constraints via momentum-space (k-space) engineering. First, we will revisit the fundamental thickness bound of an imaging system ($TTL_{min} = N\lambda_0/(4n_{max})$). Using high-Q nonlocal dielectric thin films, we show how system thickness can be decoupled from resolvable pixel count, enabling imaging within micron-scale form factors. Second, we present a nonlocal metalens for far-field label-free super-resolution based on an effect we term " k-space superoscillation", which aims to suppress parasitic sidebands and improve efficiency relative to real-space methods. Finally, we discuss applications in high-dimensional sensing, including monocular 3D vision and complex-amplitude reconstruction. These results suggest potential pathways toward integrated, wafer-scale meta-photonic systems for machine perception and metrology.

Nanophotonic Devices and Metasurfaces using High Mobility Transparent Conductive Oxides

Sudipta Biswas[1], Saika Muntaha Bari[2], Sandra Achieng[2], and Alan X. Wang[1,2,*]

[1]Department of Electrical and Computer Engineering, Baylor University, USA
[2]Materials Science and Engineering Program, Baylor University, USA
*Corresponding author: alan_wang@baylor.edu

***Abstract*— High mobility transparent conductive oxides (HMTCOs) offer exclusive advantages compared with traditional indium-tin oxide in terms of lower optical loss, stronger plasma dispersion and more prominent epsilon-near-zero effect. We demonstrate high performance nanophotonic microring resonator modulators and metasurface-based optical filters gated by hydrogen-doped indium oxide with mobility above 100 cm²/V-s.**

***Keywords*— metasurface, nanophotonic devices, microring modulators, epsilon-near-zero.**

I. Introduction

Transparent conductive oxides (TCOs) are known for their tunable optical and electrical properties, which enable advanced nanophotonic devices and metasurfaces, especially for Epsilon-near-zero (ENZ) photonics [1-2]. In the near-infrared (NIR) wavelength range, these highly doped oxide semiconductors experience a transition in the real part of their permittivity from positive to negative values and enable highly efficient electro-optic modulation. High-mobility TCO materials such as titanium-doped indium oxide (ITiO), compared with traditional indium-tin oxide (ITO), offer lower optical absorption and even stronger electro-optic effects [3]. Hydrogen-doped indium oxide (IHO) is another type of high mobility TCO that can be deposited at room temperature following a post annealing process. This refined crystalline minimizes grain boundary defects, which boosts carrier mobility and lowers electrical resistivity. We demonstrated high optical mobility polycrystalline IHO by RF-sputtering [4], which exhibits low optical loss in the NIR wavelength range. Compared with commercial ITO with a measured optical mobility of μ_opt=43 cm²/V·s, IHO demonstrates much higher mobility of 111 cm²/V·s, lower effective mass and moderate carrier density, all of which contribute to higher E-O modulation and ENZ effect.

II. Methods

In this work, we demonstrate nanophotonic devices and Metasurface optical filters based on a metal-oxide-semiconductor capacitor (MOSCAP) structure with HMTCO as the gate layer. Especially, we fabricated a silicon microring resonator (Si-MRR) with high-mobility IHO thin film. The passive device was fabricated at Intel's photonics foundry on a silicon-on-insulator (SOI) wafer with p-type doping. The silicon microring has a 300 nm-wide waveguide, chosen to enhance electro-optic efficiency. In the active region, a 10 nm HfO_2 gate dielectric was deposited using atomic layer deposition (ALD), followed by a 14 nm IHO gate layer deposited by RF sputtering and patterned through lift-off using electron-beam lithography (EBL). Ni/Au electrodes were fabricated by a combination of EBL and photolithography, followed by thermal evaporation and lift-off, providing Ohmic contacts to both the IHO and silicon layers. The device achieves extreme wavelength-tuning efficiency. In addition, we designed Metasurface optical filters with large wavelength tunability based on ENZ absorption.

III. Results and Discussion

Experimental results show:

- 175 pm/V E-O tuning efficiency
- A high Q-factor >10,000
- a $V\pi L$ of 0.09 V·cm
- ENZ wavelength tuning of optical filters across the C-band

IV. Conclusion

The demonstration confirms the potential of high-mobility IHO integration to enable highly efficient nanophotonic modulators and Metasurface optical filters and positions IHO as a promising TCO for next-generation low-power, high-speed photonic interconnects and space application.

Acknowledgments

This work was supported by by the Army Research Office (W911NF2410165), NASA ESI program (80NSSC21K0230), and the National Science Foundation (2414203 and 2240352).

References

[1] A. Anopchenko, L. Tao, C. Arndt, and H.W.H. Lee, "Field-effect tunable and broadband epsilon-near-zero perfect absorbers with deep subwavelength thickness," ACS Photonics, 5(7), pp.2631-2637, 2018.

[2] A. X. Wang, and W. C. Hsu, "Perspective on integrated photonic devices using transparent conductive oxides: Challenges and opportunities," Applied Physics Letters, 124(6), 2024

[3] W. C. Hsu, N. Nujhat, B. Kupp, J.F. Conley, H. Rong, R. Kumar, and A.

X. Wang, “Sub-volt high-speed silicon MOSCAP microring modulator driven by high-mobility conductive oxide,” *Nature Communications*, *15*(1), p.826, 2024.

[4] S. M. Bari, S. M. Rahman, K. Rong, S. Biswas, S. Achieng, and A. X. Wang, “Ultrathin high-mobility hydrogen-doped indium oxide films,” *Optical Materials Express*, *16*(4), pp.754-764, 2026.

Deciphering Chirality via Super-Resolution Near Field Chiral Absorption

Yang Zhao[1]

[1]Department of Electrical and Computer Engineering, Grainger College of Engineering, University of Illinois Urbana-Champaign, USA
*Corresponding author: yzhaoui@illinois.edu

***Abstract*—Recent advances in decoupled optical force microscopy instrumentation and signal decomposition will be discussed, highlighting improvements in measurement accuracy, the ability to resolve ultrafast thermomechanical dynamics, and enhanced spatial resolution beyond that achievable with conventional scanning probe techniques.**

***Keywords*— chirality, optical forces, photothermal, scanning probe microscopy.**

I. Introduction

Accurate temperature measurement at the nanoscale remains challenging due to rapid heat dissipation and limitations of existing thermometry techniques. While nanophotonics enables efficient light-to-heat conversion and localized thermal generation, conventional fluorescence-, Raman-, and far-field-based methods are constrained by calibration complexity, environmental sensitivity, and diffraction limits. Tip-based near-field approaches improve spatial resolution but often confound optical and photothermal effects. Here, we present a temperature quantification strategy based on decoupled optical force nanoscopy, which isolates photothermal forces and correlates them with thermally induced expansion. This platform establishes the theoretical sensitivity limits of nanoscale thermometry and enables polarization-dependent thermal analysis of chiral nanoparticles with sub-diffraction spatial resolution.

II. Methods

The decoupled optical force nanoscopy system integrates an inverted optical microscope with an atomic force microscope. A 637 nm laser was used for excitation and photothermal force measurements, with power modulation and polarization precisely controlled. The beam was focused on the back focal plane of the objective to provide wide-field illumination. AFM deflection signals were detected using lock-in amplification, and pixel-wise magnitude and phase were extracted through signal averaging. Trace and retrace signals were further averaged to minimize scanning artifacts and improve measurement reliability.

III. Results and Discussion

Figure 1 demonstrates the average photothermal force and the corresponding photothermal force maps within a chiral plasmonic nanoparticle and across the full field of view as functions of incident light intensity and polarization measured with the decoupled optical force nanoscopy. The lowest intensity (1.5×10^5 W/m^2) was used as the reference for calculating the power ratio. Figure 1(a) shows that the photothermal force within the left-handed (L-) chiral nanoparticle is higher under RCP illumination. At a power ratio of 20, the resulting contrast relative to the background is only ~2 pN, which is comparable to the noise level. In contrast, at a power ratio above 30, the measured forces yield a clear polarization-dependent difference of 10.6 pN, well above the background fluctuations, which is further corroborated by the photothermal force maps shown in Figure 1(b).

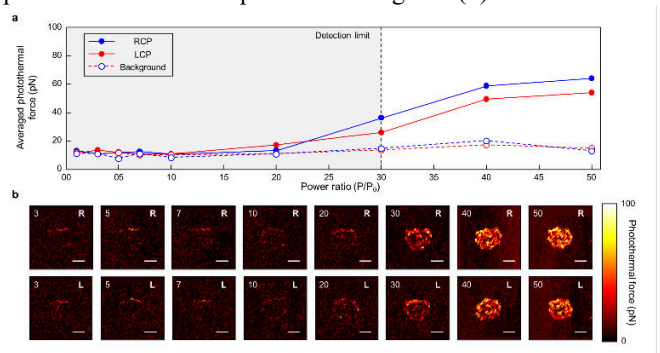

Fig. 1 Temperature mapping of chiral gold nanoparticles. (a) Average photothermal forces across one nanoparticle and background as a function of incident power. (b) Photothermal force maps at varying power ratios and circular polarizations (R/L). Scale bar: 200 nm [1].

Acknowledgments

This work was supported by NIH (R35GM157121).

References

[1] S Im, W Hong, G Chandran, X Wang, and Y Zhao, "Probing Millikelvin Temperature Sensitivity in Chiral Nanoparticles via Optical Forces," APL Materials, vol. 13, p. 101112 (2025).

Probing Molecular Dynamics in Optical Nanocavities: Decoding Ensemble Signatures

Hector Pascual Herrero,[1] Joni Spencer,[1] Alvin Yu,[2] Elizabeth M.Y. Lee,[1,2] and Regina Ragan[1,3*]

[1]Department of Material Science and Engineering, University of California, Irvine, USA
[2]Department of Physiology and Biophysics, University of California, Irvine, USA
[3]Department of Chemical and Biomolecular Engineering, University of California, Irvine, USA
*Corresponding author: rragan@uci.edu

***Abstract*— Spectral signatures from molecular ensembles in optical nanocavities are analyzed using a reaction-informed computational framework which integrates density functional theory-based Raman calculations and *ab initio* molecular dynamics. Observed vibrational spectra and simulated molecular trajectories resolve ligand dynamics in nanocavities; these systems can be used to decode signals from biological systems.**

***Keywords*— vibrational spectroscopy, *ab initio* molecular dynamics simulations, machine learning, opto-mechanics**

I. Introduction

Understanding light–matter interactions in optical nanocavities is critical for advancing plasmon-enhanced sensing, catalytic selectivity, and low-power photonic devices. Surface-enhanced Raman scattering (SERS) probes vibrational modes in confined systems yet resolving dynamic conformational behavior is challenging due to rapid time scales of molecular fluctuations and difficulty in defining nanogap chemistry. Here an integrated experimental–computational strategy provides a general framework for uncovering how nanoconfinement governs conformational dynamics and reaction pathways in chemically precise nanogaps. Experimental results further demonstrate that ensemble measurements of chemical reactions in these nanoconfined geometries can be decoded using *ab initio* molecular dynamics (AIMD) simulations and machine learning algorithms to understand biochemical network response of cellular systems for medical diagnostics [1] and environmental monitoring [2].

II. Methods

AIMD simulations sample thermally accessible ligand configurations within plasmonic nanogaps. Feedback between density functional theory (DFT) simulations of AIMD predicted structures and SERS spectra of chemical reactants and products in nanogaps is used to understand how confinement affects reactivity and molecular motion. Cosine-CaPSim similarity metrics evaluate the agreement between experimental DFT-calculated spectra.

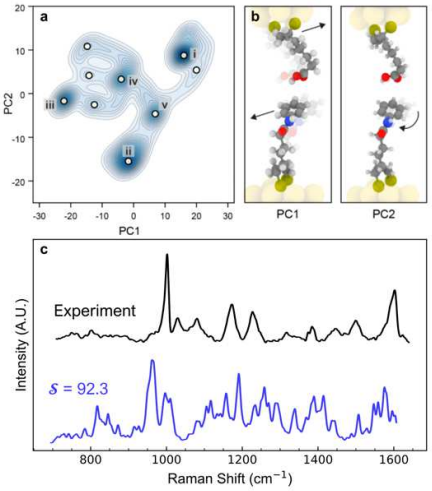

Fig. 1 (a) Two-dimensional conformational probability distributions, projected onto (b) PC1 and PC2 for nanoconfined chemical reactant. SERS experimental spectra compared to DFT simulations of AIMD predicted structures

III. Results and Discussion

Experimental results show:

- Plasmonic nanocavities reshape free-energy landscapes through steric and electrostatic interactions [3], modulating the stability of reaction intermediates and their kinetics.
- Vibrational spectra measure weighted average of high probability conformations.
- Reproducible spectra from complex systems can then be decoded to understand mechanistic chemical processes.

IV. Conclusion

A generalizable framework for elucidating molecular conformation and chemical reactions in optical nanocavities has been developed to improve our ability to design a variety of optically active and passive devices.

Acknowledgments

This work was supported by the National Science Foundation

Materials Research Science and Engineering Center program through the UC Irvine Center for Complex and Active Materials (DMR-2011967). This work used computational resources provided by Advanced Cyberinfrastructure Coordination Ecosystem: Services & Support (ACCESS), which is an advanced computing and data resource program supported by NSF under the Office of Advanced Cyberinfrastructure awards (NNT-240008: Photon-phonon interactions in optical nanocavities).

REFERENCES

[1] W. J. Thrift *et al.*, "Deep Learning Analysis of Vibrational Spectra of Bacterial Lysate for Rapid Antimicrobial Susceptibility Testing," *ACS Nano*, vol. 14, pp. 15336–15348, 2020.

[2] H. Wei *et al.*, "Decoding the metabolic response of Escherichia coli for sensing trace heavy metals in water," *Proc. Natl Acad. of Sci. USA*, vol. 120, p. e2210061120, 2023.

[3] C. E. Groome *et al.*, "Chemical Mapping of Nanoparticle–Ligand Interfaces in Optical Nanocavities," *J. Am. Chem. Soc.*, vol. 147, pp. 21319–21324, 2025.

Unconventional Semiconductors for Switchable Photonics

Marina S. Leite[1,*]

[1]Department of Materials Science and Engineering, University of California Davis, USA
*Corresponding author: mleite@ucdavis.edu

***Abstract*— We demonstrate reversible and multi-state changes in mid-infrared (MIR) transmission of inorganic halide perovskites with opposite polarity under light and heat. This opposite response results from a polaron-like lattice distortion under illumination (reducing transmission), and from the material's negative thermo-optic coefficient combined with lattice expansion from heat (increasing transmission).**

***Keywords*— switchability, halide perovskites, in situ characterization.**

I. Introduction

To date, the search for switching devices functioning in the mid-infrared (MIR) region of the electromagnetic spectrum has relied on phase-change materials. Yet, these devices usually necessitate >130 mW powered laser pulses for switching in 50 nm thick films, besides being limited to two states while presenting losses in the insulating one. Other platforms have been shown with inducing changes in material composition through metal hydrogenation metal-to-insulator temperature-dependent transitions such as in VO_2, bias-induced switching in vacancy-enriched MoS_2, polymer-dispersed liquid crystals, and mechanically strained metamaterials. However, these approaches are limited to the visible and near infrared (NIR) spectra and PCM's often degrade over several thousand cycles. Thus, there is an urgent need for the identification of materials that can enable hysteresis-free, and multi-state switchability.

II. Results and Discussion

We measure the changes in the optical transmission of bulk $CsPbBr_3$ single crystals under two different stimuli of equivalent energy [1]. First, we detect an increase in the MIR transmission ΔT of ~10% at 20 μm when the sample is heated to 80 °C. For optical visible-pump-MIR-probe measurements, we measure ΔT of the same magnitude when the crystal is excited with above-bandgap excitation (532 nm, 40 mW) at room temperature. Surprisingly, the MIR transmission in this condition shows opposite polarity. The reflectivity of the crystal remains unchanged under the same illumination conditions. The two stimuli (light and heat) embody comparable energies under the assumption that all incident photon energy (532 nm, 40 mW) is converted to thermal energy in the HP. Here, the sample is heated up to 80 °C. We note that the two stimuli, light and heat, provoke antithetical responses from the perovskite crystal suggesting that dissimilar mechanisms rule in each configuration. To confirm whether the two outcomes have conflicting or paired contributions, we perform the same optical pump-probe measurements at 80 °C and uncover that $|\Delta T|$ under illumination at 80 °C is equal to that at room temperature. Thus, the two mechanisms are independent of each other; yet the optical responses from each stimulus could effectually cancel each other. Thus, we rule out any competing influences on ΔT from laser heating and concentrate on the light and heat-induced changes independently. Our optical characterization is corroborated by in situ X-ray diffraction measurements [2].

III. Conclusion

We presented single crystal halide perovskites, a soft-lattice semiconductor material, as a promising candidate for switchable photonics in the MIR. Using above-bandgap laser illumination and heating, we detected reversible changes in transmission >10% with contrary polarities. Our findings are a consequence of the photo-induced structural distortions of the material's lattice (leading to reduced transmission), and the large thermal expansion coefficient and negative thermo-optic coefficient at elevated temperatures – which enhances transparency. These results establish halide perovskites as an alternative platform for reconfigurable photonics.

Acknowledgments

This work was supported by DARPA (awards HR00112390144 and HR00112190008), and by the NSF (award MRI-2216198).

References

[1] M. Dubey, T. J. Deppe, A. Kanak, A. R. Hering, P. Lyu, D. Kopper, P. V. Escobar, M. V. Kovalenko, J. N. Munday, and M. S. Leite, "Opposite and reversible optical switching in soft-lattice halide perovskites using light and heat," Science Advances, in review, 2026.

[2] M. Dubey, B. Turedi, A. Kanak, M. V. Kovalenko, and M. S. Leite, "Reversible, Photo-Induced Lattice Distortions in Halide Perovskites," Adv. Materials, DOI: 10.1002/adma.202521800, 2026.

Can Nanostructures and Metasurfaces Affect the Casimir Force?

Jeremy N. Munday[1,*]

[1]Department of Electrical and Computer Engineering, University of California, Davis USA
*Corresponding author: jnmunday@ucdavis.edu

***Abstract*— The Casimir force arises from quantum electromagnetic fluctuations and depends on the broadband optical response of interacting materials. This talk examines whether nanostructures—often designed for narrowband optical control—can meaningfully modify Casimir interactions. Experiments with engineered nanostructures illustrate how geometry and broadband electromagnetic response jointly determine fluctuation-induced forces.**

***Keywords*— Casimir effect, Casimir force, quantum fluctuations, zero-point energy, metamaterials, metasurfaces, nanostructures.**

I. Introduction

The Casimir force arises from quantum and thermal fluctuations of the electromagnetic field and becomes significant at sub-micrometer separations. Within Lifshitz theory, this interaction depends on the dielectric response of the interacting materials across a broad frequency range, spanning static fields through optical and ultraviolet frequencies. As a result, Casimir forces are inherently broadband phenomena that reflect the integrated electromagnetic response of a system rather than the behavior of a single resonant mode.

At the same time, advances in nanophotonics and metasurfaces have enabled unprecedented control over light–matter interactions using engineered subwavelength structures. Many metasurface concepts rely on narrowband resonant responses that tailor the phase, amplitude, or polarization of propagating optical fields. This raises an interesting question: to what extent can such nanostructures influence dispersion forces that depend on broadband electromagnetic fluctuations? While nanostructuring is often assumed to provide a route to tailoring Casimir interactions, the connection between engineered optical resonances and the broadband response relevant for vacuum forces is not always straightforward.

II. Results and Discussion

In this talk, I will discuss recent experimental and theoretical work exploring how nanoscale structuring influences the Casimir force. Measurements performed with three-dimensional nanostructures—including pillars, hollow cylinders, and periodic arrays—demonstrate that geometry alone can substantially modify the magnitude and distance dependence of the interaction. In some cases, the measured force is suppressed by an order of magnitude relative to planar geometries. These results highlight the importance of electromagnetic boundary conditions and mode confinement in determining fluctuation-induced forces.

More broadly, these studies illustrate how Casimir interactions probe the collective electromagnetic response of structured materials, making it challenging to attribute observed changes to any single optical resonance or design feature. This perspective suggests a useful framework for understanding when nanophotonic structures—whether described as nanostructures, photonic crystals, or metasurfaces—can meaningfully influence dispersion forces.

III. Conclusion

The relationship between metasurface design principles and Casimir interactions is subtle. While metasurfaces are typically engineered to manipulate light within narrow spectral bands, Casimir forces depend on broadband electromagnetic fluctuations and the global optical response of materials. As a result, nanostructuring can influence Casimir forces primarily through geometry and broadband electromagnetic response rather than through isolated optical resonances. Understanding this connection may provide new opportunities for using nanophotonic structures to tailor fluctuation-induced forces in micro- and nanoscale systems.

Acknowledgments

This work was partially supported the Defense Advanced Research Projects Agency (DARPA) QUEST program, Grant No. HR00112090084.

References

[1] C. Shelden, B. Spreng, J. L. Garrett, T. S. Rahman, J. Kim, J. N. Munday, "Casimir force control enabled by 3D nanostructures," *Nano Lett.* **25**, 9254 (2025)

[2] C. Shelden, B. Spreng, J. N. Munday, "Opportunities and challenges involving repulsive Casimir forces in nanotechnology," *Appl. Phys. Rev.* **11**, 041325 (2024)

[3] T. Gong, I. Liberal, B. Spreng, M. Camacho, N. Engheta, and J. N. Munday, "Effect of Epsilon-Near-Zero Modes on the Casimir Interaction between Ultrathin Films," Phys. Rev. Lett. 130, 196901 (2023)

[4] T. Gong, B. Spreng, M. Camacho, I. Liberal, N. Engheta, and J. N. Munday, "Electrically switchable Casimir forces using transparent conductive oxides," Phys. Rev. A 106, 062824 (2022)

Confinement-Induced Nonlocality and Optical Nonlinearity in Transdimensional Plasmonics

Igor V. Bondarev*

Department of Mathematics and Physics,
North Carolina Central University, Durham, NC 27707, USA
*Email: ibondarev@nccu.edu

***Abstract*—The latest experimental and theoretical studies are reviewed for electromagnetic (EM) properties of the new emerging plasmonic transdimensional (TD) material platform, including the optical nonlinearity enhancement due to the confinement-induced EM response nonlocality in the epsilon-near-zero region.**

***Keywords*—Transdimensional materials, Optical Nonlinearity, Confinement-Induced Nonlocality.**

Plasmonic TD materials are atomically thin metal, semimetal or doped semiconductor films of precisely controlled countable number of monolayers [1]. Due to the current progress in nanofabrication techniques [2-7], such materials can be reproducibly grown to offer high tailorability of their electronic and optical properties not only by altering their chemical and/or electronic composition (stoichiometry, doping), or strain [4], but also by varying their thickness [5,6]. While ultrathin metallic films have been quite extensively studied [2-4], the EM properties of TD plasmonic materials remain underexplored [5,6]. So far, the focus has largely been on either purely 2D structures including metal-dielectric interfaces, graphene and novel 2D semiconductors [7], or on conventional bulk materials where the dimensionality and chemical composition are the primary factors influencing the EM response. Recently, it was proposed that ultrathin TD nanostructures provide a new regime—transdimensional, in between 3D and 2D, turning into 2D as the film thickness tends to zero, challenging to study what the 3D-to-2D continuous transition has to offer to improve material functionalities [5,6,8-11]. In this regime, the strong vertical quantum confinement makes the linear EM response of the film nonlocal (spatially dispersive), and the degree of nonlocality can be controlled by the film thickness [8-12]. This makes plasmonic TD materials indispensable for research into the nonlocal light-matter interactions at the nanoscale [10-15], where they exhibit extraordinary tailorability including the capabilities of active tuning of their EM response and thus enabling new unique light-matter coupling phenomena [16,17]. The remarkable opportunities for tuning their highly confined in-plane plasma modes open access to novel quantum, nonlocal and nonlinear EM effects [10-21] in both near-infrared [14,15] and visible ranges [18]. Over the past few years, TD plasmonics has grown into a promising research direction aiming to enhance plasmonic functionalities through unparalleled tailorability of confinement-induced nonlocal and nonlinear EM response effects [11,18-21].

Acknowledgments

Work supported by U.S. ARO grant No. W911NF23-1-0206.

References

[1] A. Boltasseva and V. M. Shalaev, "Transdimensional photonics," ACS Photon., vol. 6, pp. 1-3, 2019.
[2] C. Pan, Y. Tong, H. Qian, et al., "Large area single crystal gold of single nanometer thickness for nanophotonics," Nature Commun., vol. 15, p. 2840, 2024.
[3] Z. M. Abd El-Fattah, et al., "Plasmonics in atomically thin crystalline silver films," ACS Nano, vol. 13, pp. 7771-7779, 2019.
[4] Y. Qi, et al., "Recent Progress in Strain Engineering on Van der Waals 2D Materials: Tunable Electrical, Electrochemical, Magnetic, and Optical Properties," Adv. Mater. Vol. 35, p. 2205714, 2023.
[5] D. Shah, et al., "Thickness-dependent Drude plasma frequency in transdimensional plasmonic TiN," Nano Lett., vol. 22, pp. 4622-4629, 2022.
[6] P. Das, et al., "Electron confinement-induced plasmonic breakdown in metals," Science Adv., vol. 10, p. eadr2596, 2024.
[7] K. F. Mak and J. Shan, "Photonics and optoelectronics of 2D semiconductor transition metal dichalcogenides," Nature Photon. 10, 216 (2016).
[8] I. V. Bondarev and V. M. Shalaev, "Universal features of the optical properties of ultrathin plasmonic films," Optical Mater. Express, vol. 7, pp. 3731-3740, 2017.
[9] I. V. Bondarev, H. Mousavi, and V. M. Shalaev, "Transdimensional epsilon-near-zero modes in planar plasmonic nanostructures," Phys. Rev. Research, vol. 2, p. 013070, 2020.
[10] I. V. Bondarev, "Controlling single-photon emission with ultrathin transdimensional plasmonic films," Ann. Phys. (Berlin), vol. 535, p. 2200331, 2023.
[11] I. V. Bondarev, et al., "Nonlocal effects in transdimensional plasmonics," In: Nonlocality in Photonic Materials and Metamaterials: Roadmap, Optical Mater. Express, vol. 15, pp. 1544-1709, 2025.
[12] L. Zundel, et al., "Comparative analysis of the near- and far-field optical response of thin plasmonic nanostructures," Adv. Optical Mater., vol. 10, p. 2102550, 2022.
[13] M. D. Pugh, SK. F. Islam, and I. V. Bondarev, "Anisotropic photon emission enhancement near carbon nanotube metasurfaces," Phys. Rev. B, vol. 109, p. 235430, 2024.
[14] S.-A. Biehs and I. V. Bondarev, "Far- and near-field heat transfer in transdimensional plasmonic film systems," Adv. Optical Mater., vol. 11, p. 2202712, 2023.
[15] H. Salihoglu, et al., "Nonlocal near-field radiative heat transfer by transdimensional plasmonics," Phys. Rev. Lett., vol. 131, p. 086901, 2023.
[16] I. V. Bondarev, et al., "Confinement-induced nonlocality and Casimir force in transdimensional systems," Phys. Chem. Chem. Phys., vol. 25, pp. 29257-29265, 2023.
[17] N. Rivera, et al., "Shrinking light to allow forbidden transitions on the atomic scale," Science, vol. 353, pp. 263-269, 2016.
[18] S.-A. Biehs and I. V. Bondarev, "Goos-Hänchen effect singularities in transdimensional plasmonic films," Nanophotonics, vol. 14, pp. 4513-4530, 2025.
[19] A. Boltasseva, et al., "Transdimensional materials as a new platform for strongly correlated systems," In: Roadmap for photonics with 2D materials, ACS Photon., vol. 12, pp. 3961-4095, 2025.
[20] I. V. Bondarev, A. Boltasseva, J. B. Khurgin, and V. M. Shalaev, "Crystallization of the transdimensional electron liquid," Nano Lett., DOI: 10.1021/acs.nanolett.5c03894, 2026 (arXiv:2503.05165).
[21] F.-T. Tseng, et al., "Confinement-induced nonlocality and optical nonlinearity of transdimensional titanium nitride in the epsilon-near-zero region," E-print arXiv: 2512.14035 (17 Dec 2025).

Nonlocal flat optics for frequency-angle selective light control

Jung-Hwan Song[1,2*], Qitong Li[1], Zhepeng Zhang[3,4], Fenghao Xu[1], Jorik van de Groep[1,5], Skyler Selvin[1], Andrew Mannix[3,4], and Mark L. Brongersma[1*]

[1]Geballe Laboratory for Advanced Materials, Stanford University, Stanford, CA 94305, USA.
[2]Department of Electrical and Computer Engineering, National University of Singapore, Singapore 117583, Singapore.
[3]Department of Materials Science & Engineering, Stanford University, Stanford, CA 94305, USA
[4]Stanford Institute for Materials and Energy Sciences, SLAC National Accelerator Laboratory, Menlo Park, CA 94025, USA
[5]Van der Waals-Zeeman Institute, Institute of Physics, University of Amsterdam, Amsterdam1098 XH, The Netherlands.

*Corresponding author: vsong21@nus.edu.sg, brongersma@stanford.edu

***Abstract*— Recent advances in resonant metasurfaces have enabled unprecedented control over optical fields. Deploying dense arrays of resonant optical nanostructures, typically at a subwavelength scale, this type of approach has opened spatial wavefront engineering. Such local control, however, provides functions that are hardly selective in frequency and angle domains. In this talk, a new class of metasurfaces, nonlocal flat optics, is introduced to overcome this limitation through spatially extended light-matter interactions. The translational symmetry of these resonances enables highly selective optical responses at programmed frequencies and angles. Representative examples, including a nonlocal free-space light modulator, will be presented to highlight new opportunities for such frequency- and angle-selective optical control for emerging technologies spanning communication, display, and imaging.**

***Keywords*— metamaterials, flat optics, actively tunable devices, nonlocal metasurfaces.**

Graphene-based Acive Metasurface for Mid-IR Transmission Modulation

Jinseok Kong[1,†], Heonhak Ha[1,†], Junhyung Kim[1], Jiwon Kang[1], Min Seok Jang[1,*]

[1]School of Electrical Engineering, Korea Advanced Institute of Science and Technology, Daejeon 34141, Republic of Korea

*Corresponding author: jang.minseok@kaist.ac.kr

***Abstract*—We report a graphene-based active metasurface achieving a 73.3% transmission modulation efficiency. An analytic circuit model elucidates the resonance mechanism controlled by Fermi levels. This high-efficiency platform overcomes previous limitations, enabling ultra-compact, on-chip spectroscopic systems.**

***Keywords*—active metasurface, transmission modulation, graphene, equivalent circuit model, single-chip spectrometer.**

I. Introduction

Mid-infrared (mid-IR) optoelectronics are essential for sensing and spectroscopy, serving as the key to detecting molecular fingerprints. Graphene metasurfaces have emerged as a solution for dynamic light control, yet they face a physical hurdle: atomic thinness limits light-matter interaction. To compensate, most designs rely on reflective back-mirrors like Salisbury screens [1]. But this reflection-based geometry creates a bottleneck. It prevents monolithic integration with standard transmission sources (e.g., VCSELs), effectively blocking the path to compact, on-chip optical systems.

Here, we report an electrically tunable transmission modulator designed as a graphene-gold nanograting. We specifically chose a CaF_2 substrate combined with ionic gel gating. This choice avoids the phonon absorption found in common substrates while enabling effective Fermi level tuning. As a result, our device delivers a modulation efficiency of 73.3% for TM-polarized light. This performance represents a major leap over existing transmissive devices, which typically perform below 41% [2-4]. We further clarify the mechanism behind this transparency using an analytic circuit model and validate the platform's potential as a single-chip spectrometer.

II. Results and Discussion

A. Active Transmission Modulation

The device schematic is detailed in Figure 1a. We patterned periodic gold nanogratings with 10 nm thickness on a 500 μm-thick CaF_2 substrate, specifically chosen for its mid-IR transparency. Next, we transferred monolayer graphene onto the patternd structure, followed by a 3 μm-thick ionic gel ([BMIM][PF_6]) layer for electro-optic modulation. The SEM image in Figure 1b confirms the structural quality of our optimized design, period $p = 3$ μm and gap width $g = 50$ nm. To dynamically modulate the Fermi level, we swept the gate voltage (V_g) from the charge neutrality point (~1 V) down to -3 V, driving the device deep into the hole-doped regime.

Figure 1c displays the FTIR transmission spectra collected with a numerical aperture of 0.71. We observed intrinsic ionic gel absorption bands (850, 1170, 3000 cm^{-1}) and Fabry-Perot ripples superimposed on the signal. While the TE mode remained insensitive to gating and was dominated by structural parameters, the TM mode revealed strong active modulation. At the optimal frequency of $\omega_0 = 1265$ cm^{-1}, the transmission T increased from 1.4% to 5.3% as we swept V_g from 0.75 V to -3 V. This yielded a peak efficiency of $\eta_T = 1\text{-}T_{min}/T_{max} = 73.3\%$. Notably, we sustained high performance (average efficiency of 60.1%) across a broad window from 931 to 1755 cm^{-1}.

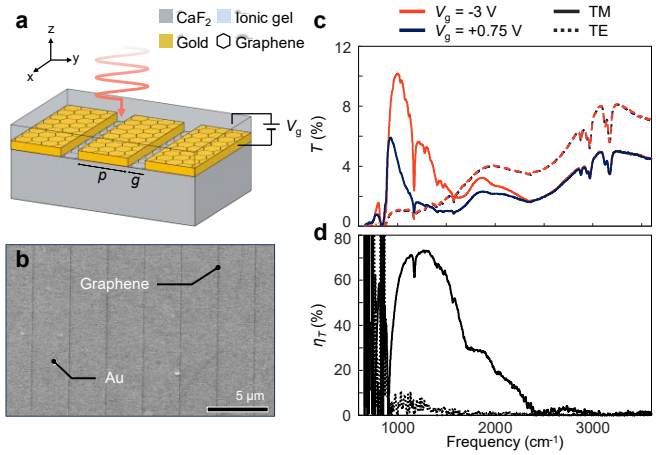

Fig. 1 Active transmission modulation metasurface. (a) Schematic of the device structure comprising a gold grating and monolayer graphene on a CaF_2 substrate, covered with ionic gel for top-gating. (b) Top-view SEM image of the fabricated device. (c) Measured transmission spectra for TM (solid lines) and TE (dashed lines) polarizations at gate voltages of V_g = -3 V (red) and +0.75 V (dark blue). (d) Transmission modulation efficiency (η_T) calculated from the spectra.

To understand the physics underlying this modulation, we employed an equivalent circuit model [5]. As shown in the

lower panels of Figures 2a and 2b, this model successfully reproduces the experimental trends. We mapped the applied gate voltages (+0.75 V to -3 V) to Fermi levels ranging from 0.16 to 0.92 eV, assuming a fixed scattering rate of $\Gamma = 0.084$ eV. These results are also consistent with full-wave RCWA simulations.

Using the equivalent circuit model, we treated our metasurface as an effective surface admittance, approximated as $Y_S \approx Y_C + Y_{Gr}$. Here, Y_C captures the capacitive nature of the metal grating, while Y_{Gr} represents the inductive contribution of the graphene. We note that this approximation is only valid for operating frequencies below $\omega_0 = 1500$ cm^{-1}, where the inductive characteristics of the metal grating can be ignored. At the charge neutrality point ($E_F = 0.16$ eV, Figure 2a), Y_{Gr} is negligible due to the low concentration of the charge carriers. Thus, the large capacitive admittance Y_C dominates, making the device opaque. Conversely, under high doping ($E_F = 0.92$ eV, Figure 2b), the inductive response of graphene increases. This inductance effectively cancels the metallic capacitance at the resonance frequency $\omega_0 = 1074$ cm^{-1}, and this impedance matching maximizes transmission.

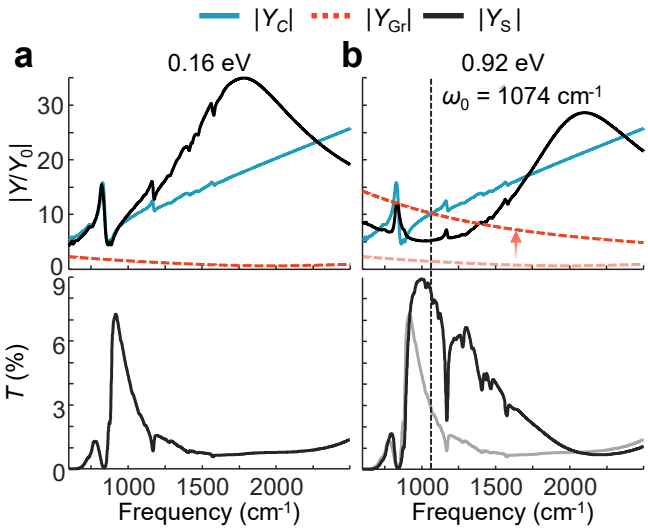

Fig. 2 Theoretical analysis of transmission modulation using an equivalent circuit model. (a, b) Calculated normalized admittance spectra ($|Y/Y_0|$, top) and corresponding transmission spectra (bottom) at Fermi levels of (a) \$0.16 eV and (b) 0.92 eV. The blue solid, red dashed, and black solid lines represent the capacitive admittance of the metal grating ($|Y_C|$), the inductive admittance of graphene ($|Y_{Gr}|$), and the total admittance ($|Y_S|$), respectively.

This transparency mechanism is further visualized by the magnetic field distributions simulated via RCWA. At 0.16 eV (Figure 3a), the incident field is strongly reflected by the metallic grating, showing low transmission. In contrast, at the resonant condition of 0.92 eV (Figure 3b), the field distribution shows minimal perturbation across the grating layer. This confirms that when the admittance is minimized, the metallic structure becomes effectively invisible to the incident wave, allowing the field to propagate through the substrate with high transmittance.

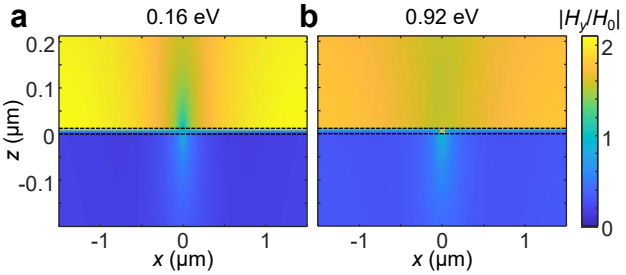

Fig. 3 Normalized magnetic field distributions ($|H_y/H_0|$) calculated using RCWA at the resonance frequency ($\omega_0 = 1074$ cm^{-1}) for (a) $E_F = 0.16$ eV and (b) 0.92 eV.

B. Single-Chip Spectrometer Application

As demonstrated in earlier sections, our metasurface has broad tunability and high modulation efficiency. By utilizing these features, we propose that our active transmission filter can be transformed into a computational single-pixel spectrometer, which reduces the footprint of the device significantly compared to conventional approaches such as spatially distributed arrays. We optimized the device geometry ($p = 800$ nm and $g = 150$ nm) and frequency band (1400–2500 cm^{-1}), to balance the modulation efficiency and operating bandwidth. By sweeping E_F from 0.1 to 1.0 eV, the generated 91 distinct transmission spectra function as a quasi-orthogonal basis set.

Since spectral reconstruction is inherently an ill-posed inverse problem, a Compressed Sensing (CS) algorithm is employed [6]. We implemented a dual-component method, where each component represents sharp peak and broadband features. To consider real-world sensing conditions, we introduced 0.5% Gaussian noise into the simulation. Figure 4a shows the reconstruction performance for narrowband inputs. The result showed high fidelity (F) for the median case, exceeding 99%. Even for broadband or complex signals (Figure 4b), our device captured the spectral features with high accuracy ($F > 99\%$) in the best case, validating the platform's potential.

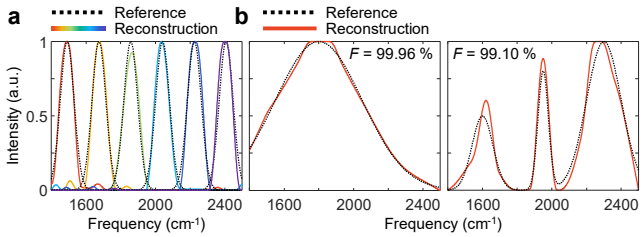

Fig. 4 Spectral reconstruction performance of the single-chip spectrometer for (a) multiple narrowband Gaussian spectra, (b) broadband (left) and complex multi-peak (right) spectra. Dotted lines indicate reference inputs, while solid colored lines represent reconstructed outputs.

III. Conclusion

In summary, we achieved a high modulation efficiency of 73.3% for TM-polarized light using a graphene-gold nanograting metasurface, surpassing previous conventional approaches. Our design employed a phonon-free CaF_2 substrate

to avoid strong absorption in the operating frequency range, and an ionic gel based top-gating method to achieve high Fermi level modulation, thereby avoiding the reflective back-gating method. While this gating method trades off switching speed, it remains the most practical route to achieve such high modulation efficiency in this spectral range.

Using equivalent circuit model analysis, we clarified the underlying LC resonance mechanism between the capacitive metal grating and the inductive graphene layer, revealing that the modulation of Fermi level results in spectral shifts. Finally, we showed that our platform, which possesses high modulating efficiency and broad tunability simultaneously, can be applied as a single-chip spectrometer with the help of CS-based reconstruction algorithm. This versatility positions our device as a key building block for future on-chip sensing and spectroscopy.

ACKNOWLEDGMENTS

This work was supported by the National Research Foundation of Korea (NRF) grants (RS-2022-NR070476, RS-2024-00416583, RS-2024-00414119) funded by the Korea government (MSIT). The authors also acknowledge the support by the Culture, Sports and Tourism R&D Program through the Korea Creative Content Agency grant funded by the Ministry of Culture, Sports and Tourism in 2024 (RS-2024-00332210).

REFERENCES

[1] M. S. Jang et al., “Tunable large resonant absorption in a midinfrared graphene Salisbury screen,” Phys. Rev. B, vol. 90, no. 16, p. 165409, 2014.

[2] S. Kim et al., “Electronically tunable extraordinary optical transmission in graphene plasmonic ribbons coupled to subwavelength metallic slit arrays,” Nat. Commun., vol. 7, p. 12323, 2016.

[3] M. D. Feinstein and E. Almeida, “Hybridization of graphene-gold plasmons for active control of mid-infrared radiation,” Sci. Rep., vol. 14, no. 1, p. 6733, 2024.

[4] G. Lan et al., “Enhanced asymmetric light-plasmon coupling in graphene nanoribbons for high-efficiency transmissive infrared modulation,” Laser Photonics Rev., vol. 18, no. 1, p. 2300469, 2024.

[5] S. Han et al., “Complete complex amplitude modulation with electronically tunable graphene plasmonic metamolecules,” ACS Nano, vol. 14, no. 1, pp. 1166–1175, 2020.

[6] C. Yao et al., “Integrated reconstructive spectrometer with programmable photonic circuits,” Nat. Commun., vol. 14, no. 1, p. 6376, 2023.

Novel Metaphotonic Structures for Enhanced Light-matter Interaction

Seyed M. Enjavi, Reza Marzban, Ashkan Zandi, Amin Khavasi, Saeed Javadizadeh, Hamed Abiri, Abhirupa Saha, and Ali Adibi
School of Electrical and Computer Engineering
Georgia Institute of Technology
Atlanta, GA 30332-0250
Phone: (404) 385-2738
Fax: (404) 894-4641
Email: ali.adibi@ece.gatech.edu

Short Abstract:
This talk is focused on using on-chip metaphotonic elements to enable a series of new integrated photonic structures that enhance light-matter interaction. Using new design techniques, it is shown how the use of metaphotonic elements increases the intensity of the optical field at the interaction region of light with matter in different classes of integrated photonic chips. In addition, metaphotonic elements can facilitate interaction by engineering the optical wavefront. Theoretical and experimental results will be used to demonstrate the unique features of these structures.

KEYWORDS
metaphotonics, metamaterials, light-matter interaction,

Biography

Ali Adibi is the director of Bio and Environmental Sensing Technologies (BEST) and a professor and Joseph M. Pettit chair in the School of Electrical and Computer Engineering, Georgia Institute of Technology. He is also a member of the Winship Cancer Research Center at the Emory University. His research group has pioneered several structures in the field of integrated nanophotonics for both information processing and sensing. He has also pioneered new sensing solutions for medical diagnosis as well as AI algorithms for diagnosis and prognosis in medicine. He is the author of more than 260 journal papers and 600 conference papers. He has served as the editor, conference chair, and technical committee members in over 30 different conferences and journals. He has also led several multidisciplinary research teams in the areas of integrated optics and metaphotonics for sensing, interconnection, and imaging. He is the recipient of several awards including Presidential Early Career Award for Scientists and Engineers, Packard Fellowship, NSF CAREER Award, and the SPIE Technology Achievement Award. He is also a fellow of OSA, SPIE, and AAAS.

Squeezing Light Fields for Ultrafast Detectors and Single Photon Sources

Maiken H. Mikkelsen[1,*]

[1]Niels Bohr Institute, University of Copenhagen, Denmark
*Corresponding author: maiken.mikkelsen@nbi.ku.dk

***Abstract*— Here, we leverage nanogap cavities—creating strongly enhanced local electromagnetic fields—to modify light-matter interactions. First, thermal detectors integrated with nanogap plasmonic structures reveal ultrafast detection speeds along with spectral and polarization sensitivity. Next, spontaneous emission rates of single solid-state emitters are enhanced up to 10,000x for quantum science applications.**

***Keywords*— plasmonics, nanogap cavity, Purcell factor, metasurface, spontaneous emission, quantum dot, photodetector**

I. Introduction

Nano- and quantum materials with unique optical properties hold the potential for breakthroughs in a wide range of areas from ultrafast optoelectronics and on-chip components for quantum information science to improved photodetection and bio-sensing. An exciting opportunity to realize such new materials lies in controlling the local electromagnetic environment on the atomic- and molecular-scale (~1-10 nm), which enables extreme local field enhancements and drastically modified local density of states. A well-controlled platform to study the emergence of extreme photonic behavior is provided by plasmonic nanogap cavities, which consist of ultrathin dielectric gaps between metals.

II. Results and Discussion

First, a room-temperature, pyroelectric photodetector will be discussed, which couples a thermally-sensitive aluminum nitride (AlN) layer with a metallic metasurface. The metasurface acts as an efficient, spectrally-selective photothermal converter [1-3] and depending on the shape of the metasurface structures, it can also be sensitive to the polarization-state of the incoming light [4]. These pyroelectric detectors exhibit record-breaking speeds, with 3 dB bandwidths up to 2.8 GHz, which corresponds to a rise time of 125 ps.

Next, using similar plasmonic nanogap structures, but now with single emitters sandwiched in the dielectric layer between the metal film and nanoparticle, strongly enhanced spontaneous emission rates are studied. We demonstrate picosecond single photon emission from SiVs in diamond [5-7] and Purcell factors greater than 10,000 for single colloidal quantum dots emitting in the telecom band at 1550 nm [8].

III. Conclusion

We have demonstrated how strongly enhanced local electromagnetic fields can modify a range of light-matter interactions. In particular to enable ultrafast detection speeds from a metasurface-coupled thermal photodetector and ultrafast single photon sources from both SiV centers in diamond and colloidal quantum dots in the telecom range.

Acknowledgments

This work was supported by the Gordon and Betty Moore Foundation and the Novo Nordisk Foundation.

References

[1] J. W. Stewart, J. H. Vella, W. Li, S. Fan, and M. H. Mikkelsen, "*Ultrafast Pyroelectric Photodetection with On-Chip Spectral Filters*", Nature Materials 19, 158-162 (2020)

[2] E. Shin, R. E. Bangle, N. C. Wilson, S. B. Nikodemski, J. H. Vella, and M. H. Mikkelsen, "*Metasurface-Enhanced Thermal Photodetector Operating at Gigahertz Frequencies*" Advanced Functional Materials (2025), DOI: 10.1002/adfm.202420953

[3] J. W. Stewart, N. C. Wilson, and M. H. Mikkelsen, "*Nanophotonic Engineering: A New Paradigm for Spectrally Sensitive Thermal Photodetectors*", ACS Photonics, 8, 1, 71-84 (2021)

[4] N. C. Wilson, E. Shin, R. E. Bangle, S. B. Nikodemski, J. H. Vella, and M. H. Mikkelsen, "*Ultrathin Pyroelectric Photodetector with Integrated Polarization-Sensing Metasurface*", Nano Letters, 23 (18), 8547-8552 (2023)

[5] H. Li, D. Acil, A. Boyce, C. Pederson, S. Chakravarthi, N. Yama, K.-M. C. Fu & M. H. Mikkelsen, "*Room-temperature Picosecond Single Photon Emission from Silicon Vacancy Center in Diamond,*" ACS Nano, 19 (20), 19310–19317 (2025)

[6] A. M. Boyce, H. Li, N. C. Wilson, D. Acil, A. Shams-Ansari, S. Chakravarthi, C. Pederson, Q. Shen, N. Yama, K.-M. C. Fu, M. Loncar & M. H. Mikkelsen, "*Plasmonic Diamond Membranes for Ultrafast Silicon Vacancy Emission*," Nano Letters 24, 12, 3575-3580 (2024)

[7] D. Acil, H. Li & M. H. Mikkelsen, "*Thin Film Interference in Diamond Membranes for Control of Silicon Vacancy Center Emission*", Advanced Optical Materials, e01609, (2025) DOI: 10.1002/adom202501609

[8] S. Zhang, A. J. Traverso, E. A. Dolgopolova, A. Singh, H. Kishida, M. Y. Livshits, C. J. Sheehan, E. G. Bowes, J. A. Hollingsworth & M. H. Mikkelsen, "*Solution-processed ultrafast, room-temperature single-photon source at 1550 nm,*" ACS Nano 19 (20), 19035–19045 (2025)

Time Reflection of Guided Light in Optically Switched Metasurfaces: Generating Magnetic Field on the Nanoscale

Shivakh Rawat[1,*], Samyobrata Mukherjee[1], Gennady Shvets[1,*]

[1]School of Applied and Engineering Physics, Cornell University Ithaca, USA
*Corresponding author: gshvets@cornell.edu

***Abstract*— Time-varying dielectric metasurfaces supporting sharp optical resonances with non-trivial electromagnetic fields distribution is used for realizing temporal interfaces for metasurface-guided waves (MGWs). We demonstrate that such time-interfaces can be used to generate large, highly localized quasi-static magnetic fields inside the metasurfaces that persist after the departure of the time-scattered MGWs.**

***Keywords*— photonic time interfaces, metasurface optics.**

I. Introduction

We propose a mechanism, backed by numerical simulations and analytic perturbation theory, for tunable red- and blue-shifting of the metasurface resonance using free carrier generation by a pump laser beam. An ultrashort high-frequency pump pulse can produce temporal reflections via localized metallization for a lower-frequency MIR mode while also red-shifting the mode. Additionally, a quasistatic magnetic field mode is also formed during a time interface.

II. Methods

I will discuss analytic expressions for the total energy density in a time-varying Drude-Lorentz medium, and how to use it to demonstrate that the optical energy decreases while the quasi-static magnetic energy and the carrier temperature increase after the TI. While time-variant lumped-element metasurfaces in the microwave frequency range have been proposed for generating the so-called "wiggler" magnetic fields, our work is the first (to our knowledge) to demonstrate how such "rectification" of the magnetic field can be carried out for optical frequencies. Because optical pulses can be many orders of magnitude more compact and intense than their microwave counterparts, the resulting quasi-static magnetization is proportionally stronger and localized to sub-micron regions – something that cannot be accomplished using conventional static magnets. To date, such ultra-short and localized magnetic fields – highly desirable for exploring ultra-fast magnetic recording – could only be produced using relativistic electron bunches at major accelerator facilities (e.g., SLAC). This work paves the way to novel approaches to generating ultra-high magnetic fields on the nanoscale.

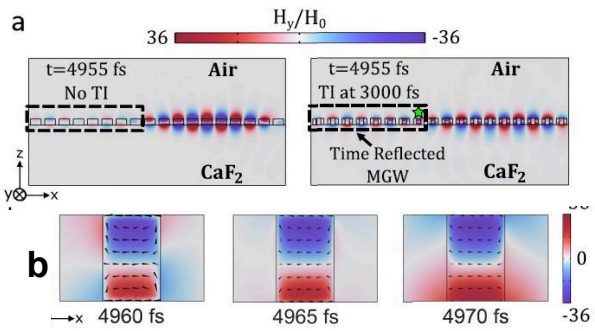

Fig. 1 **Using time interfaces (Tis) to generate dc magnetic fields**. **(a)** In the absence of a TI (left), a metasurface-guided optical wave propagates from left to right and eventually leaves the domain. With a TI (right), a time-reflected signal propagates in the backward direction. **(b)** Three sequential snapshots of the quasi-static magnetic field Hy in the x-z plane passing through the middle of a meta-atom marked by a green star. Free carriers generation at t=3,000fs inside the cylinder marked by solid lines produces a TI.

III. Results and Discussion

Our results show:

- temporal reflections from this sharp TI, including a redshift of the time-reflected waves
- after the TI, we also found a large, highly localized quasistatic magnetic field (wiggler mode) consumes a substantial part of the electromagnetic energy: see Fig.1.
- by comparing the cases with/without a TI, we validated that the total energy in a time-varying system remains unaffected by the free carriers created at rest during a TI.

Acknowledgments

This work was supported by the grants from ARO and ONR.

Chalcogenide Metamaterials for High-Speed Tunable Photonics

Jesse A. Frantz[1,*], Arash Nemati[2], Jason D. Myers[1], Robel Y. Bekele[1], Vinh Q. Nguyen[1], Yajun Gao[2], Adam Overvig[3], Andrea Alù[2]

[1]U.S. Naval Research Laboratory, Washington, DC, USA
[2]The City University of New York, Advanced Science Research Center, NY, NY, USA
[3]Stevens Institute of Technology, Hoboken, NJ, USA
*Corresponding author: jesse.a.frantz.civ@us.navy.mil

***Abstract*— We describe the design, fabrication, and testing of a leaky-wave metasurface that is tunable at femtosecond speeds. The device incorporates an arsenic sulfide thin film, leveraging its Kerr nonlinearity to achieve tuning. It is designed to focus light to a point with a position that varies with pump power.**

***Keywords*— metamaterials, high-speed tuning, leaky-wave metasurfaces, chalcogenide glass.**

I. Introduction

High-speed tuning of photonic devices is of interest for applications such as pulse shaping, rapid processing of optical data, spectroscopy of rapidly changing media, and the laboratory study of high-speed phenomena. Most existing tuning methods, however, are limited to speeds no faster than the nanosecond time scale.

This work demonstrates tunable metasurfaces incorporating arsenic sulfide (As_2S_3) glass thin films. The refractive index of As_2S_3 can be readily changed at the sub-femtosecond time scale through its high Kerr nonlinearity, enabling metamaterials with femtosecond timescale tunability.[1] Recent work has shown that leaky-wave metasurfaces (LWMs) can provide control over all four free parameters of an optical field.[2] Here, we present a LWM devices that incorporate an As_2S_3 layer, shown schematically in Fig. 1(a) and in cross section in Fig. 1(b), designed to focus light to a point with a position that varies with pump power at high speed.

II. Methods

High-purity As_2S_3 bulk material is batched, and small pieces are used as deposition sources. An As_2S_3 film is deposited via thermal evaporation onto a silicon substrate. A PMMA layer is spun on and patterned vie E-beam photolithography. Light with a wavelength of 1 μm is coupled into the waveguide. The refractive index of the As_2S_3 is modulated using a femtosecond laser, and the position of the focused spot is measured as a function of the power density of the pump.

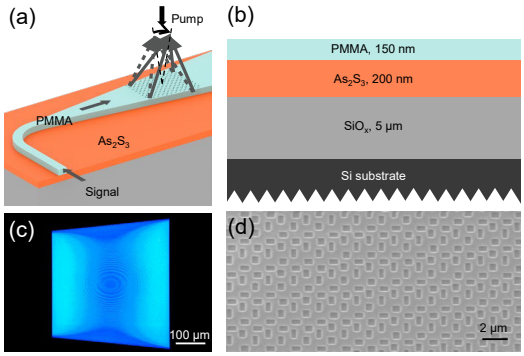

Fig. 1 (a) Schematic diagram of LWM device; (b) cross section showing device layers; (c) dark field microscope image of fabricated LWM; and (d) SEM image of patterned PMMA layer of a LWM.

III. Results and Discussion

The waveguide mode propagates in both the As_2S_3 and PMMA layers. The unit cells are optimized such that the LWM has different focal positions with different refractive indices of the As_2S_3. A dark field microscope image of a completed device is shown in Fig. 1(c), and an SEM image of multiple unit cells is shown in Fig. 1(d).

IV. Conclusion

We have designed, fabricated, and tested As_2S_3-based LWMs with the potential for femtosecond timescale tuning of the position of a focused spot.

Acknowledgments

This work was supported by a LUCI grant from the Basic Research Office, OUSD(R&E).

References

[1] J. Gao, M. Antonietta Vincenti, J. Frantz, A. Clabeau, X. Qiao, Liang Feng, M. Scalora, and N. M. Litchinitser, "All-optical tunable wavelength conversion in opaque nonlinear nanostructures," Nanophotonics, vol. 11, pp. 4027-4035, 2022.

[2] H. Huang, A. C. Overvig, Y. Xu, S. C. Malek, C. C. Tsai, A. Alù, and N. Yu, "Leaky-wave metasurfaces for integrated photonics," Nature Nanotechnology, vol. 18, pp. 580-588, 2023.

Towards dynamic metasurfaces and nanophotonics in barium titanate on insulator

David Barton*[1], Sarah Berman[1], Sina Abedini Dereshgi[1], Ethan Ray[1]

[1]Department of Materials Science and Engineering, Northwestern University, USA
*Corresponding author: dbarton@northwestern.edu

***Abstract*— Tunable subwavelength metasurfaces will enable low energy consumption and compact computing, communications, and sensing devices. Towards this, we will discuss our work fabricating subwavelength structures in thin film barium titanate on insulator and applying it for electro-optic modulators and optical metasurfaces.**

***Keywords*— nanophotonics, metasurface, barium titanate, electro-optic.**

I. Introduction

The ability to sculpt electromagnetic radiation with subwavelength optical antennas has enabled fundamental advances in small form-factor and high performance optical devices[1]. Reconfigurable metasurfaces can advance key optical technologies[2,3] including light detection and ranging[4], optical communications[5], and augmented or virtual reality. However, it remains a fundamental challenge to create dynamical optical devices that have simultaneously high efficiency, contrast, low switching voltages, and high modulation bandwidths, as either the optical properties or geometry much change by a significant amount to modify the optical transfer function.

Demonstrations of dynamic devices based on phase change materials[6], liquid crystals[7], and doped semiconductors[8] have shown promise in this space. In addition, electro-optic materials provide a platform for high speed and low-loss modulation[9-13], but are limited in the refractive index difference because of the second order nonlinearity being used. Indeed, the electro-optic coefficient of commonly available lithium niobate is approximately 31 pm/V, requiring integrated photonic modulators to be much longer (~1 cm) than metasurface devices can allow for significant optical phase shifts.

II. Results and Discussion

Here, we will show our progress in developing monolithic barium titanate-based nanophotonic structures. Barium Titanate (BTO) is a CMOS-compatible oxide that features a high electro-optic coefficient (>900 pm/V)[13] and is recently available as commercially available thin films. However, monolithic fabrication of these films is challenging[14]. We have developed an etching protocol that allows for low loss nanophotonic structures, including photonic crystals[15]. Poling protocols and electro-optic measurements demonstrate pockels coefficients over 150 pm/V and modulation efficiency greater than 10 GHz. Resonant cavities also show the possibility to use nanophotonic structures to confine light with quality factors exceeding 100,000 at telecommunications wavelengths.

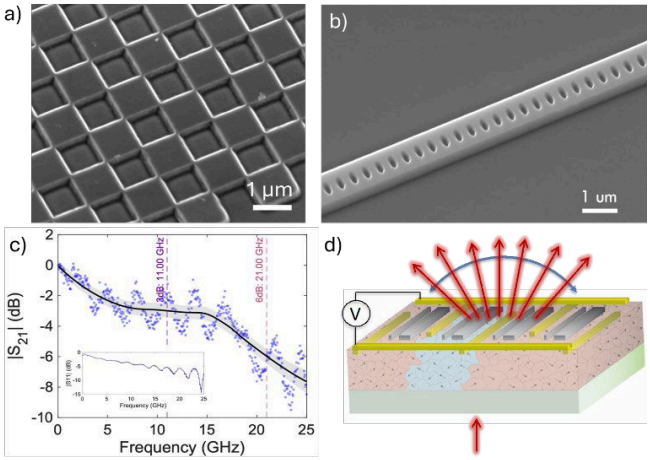

Figure 1: monolithic barium titanate on insulator nanophotonics. a) SEM image of ~1 micron scale structures etched into surface of BTO. b) SEM image of photonic crystal waveguide with subwavelength structured components. c) VNA modulation spectrum at edge of photonic crystal band gap, demonstrating greater than 10 GHz modulation bandwidth. d) future device implementation using nanoantennas interfaced with BTOI. Control of domain orientations

We will additionally discuss our progress developing reconfigurable and programmable nanophotonic devices via resonant metasurfaces. First, we will show our work understanding the ferroelectric poling and depoling dynamics in this platform using polarization-resolved confocal second harmonic generation microscopy[16]. We track the onset of poling and temporal dynamics of depoling in device-relevant geometries. Finally, we show our work developing dynamical metasurfaces using this platform.

III. Conclusion

Together this work demonstrates the value of wide bandgap nonlinear materials for electrically-controllable wavefront shaping devices, and further demonstrates that combined electronic-photonic interfaces for control of free-space light is

a meaningful platform for future photonic systems.

ACKNOWLEDGMENTS

Work was performed in part at of Northwestern University's NUANCE Center, which has received support from the IIN and Northwestern's MRSEC program (NSF DMR-2308691).

REFERENCES

[1] Kuznetsov, A.I., Brongersma, et al. Roadmap for optical metasurfaces. ACS Photonics 11, 816–865 (2024)
[2] Liu, K., Ye, C.R., Khan, S., Sorger, V.J. "Review and perspective on ultrafast wavelength-size electro-optic modulators," Laser & Photonics Reviews 9, 172–194 (2015)
[3] Jung, C., Lee, E., Rho, J.: The rise of electrically tunable metasurfaces. Science Advances 10 (2024)
[4] Kim, I., Martins, R.J., et al. Nanophotonics for light detection and ranging technology. Nature Nanotechnology (2021)
[5] Thureja, P., Sokhoyan, et al. Toward a universal metasurface for optical imaging, communication, and computation. Nanophotonics 11, 3745–3768 (2022)
[6] Li, S.-Q., Xu, X., Veetil, R.M., Valuckas, V., Paniagua-Dom´ınguez, R., Kuznetsov, A.I.: Phase-only transmissive spatial light modulator based on tunable dielectric metasurface. Science 364, 1087–1090 (2019)
[7] Zhang, Y., Fowler, et al. Electrically reconfigurable non-volatile metasurface using low-loss optical phase-change material. Nature Nanotechnology 16(6), 661–666 (2021)
[8] Huang, Y.-W., Lee, H.W.H., et al. Gate-tunable conducting oxide metasurfaces. Nano Letters 16, 5319–5325 (2016)
[9] Benea-Chelmus, I.-C., Mason, S., Meretska, M.L., Elder, D.L., Kazakov, D., Shams-Ansari, A., Dalton, L.R., Capasso, F.: Gigahertz free-space electro-optic modulators based on mie resonances. Nature Communications 13, 3170 (2022)
[10] Weigand, H., Vogler-Neuling, V.V., Escal´ e, M.R., Pohl, D., Richter, F.U., Karvounis, A., Timpu, F., Grange, R.: Enhanced electro-optic modulation in resonant metasurfaces of lithium niobate. ACS Photonics 8, 3004–3009 (2021)
[11] Weiss, A., Frydendahl, C., Bar-David, J., Zektzer, R., Edrei, E., Engelberg, J., Mazurski, N., Desiatov, B., Levy, U.: Tunable metasurface using thin-film lithium niobate in the telecom regime. ACS Photonics 9, 605–612 (2022)
[12] Damgaard-Carstensen, C., Yezekyan, T., Brongersma, M.L., Bozhevolnyi, S.I.: Highly efficient, tunable, electro-optic metasurfaces based on quasi-bound states in the continuum. ACS Photonics (2025)
[13] Abel, S., Eltes, F., Ortmann, J., et al. Large Pockels effect in micro- and nanostructured barium titanate integrated on silicon, Nature materials (2019)
[14] Kim, G., Yim, J., Bahl, G., Low loss monolithic barium titanate on insulator integrated photonics with intrinsic quality factor> 1 million, (2025) https://arxiv.org/abs/2507.17150
[15] Berman, S., Dereshgi, S., Barton, D., Barium titanate on insulator nanophotonics and electro optics, in preparation, (2026)
[16] Berman, S., Dereshgi, S., Barton, D., Visualizing poling and depoling dynamics in thin-film barium titanate nanophotonics via second harmonic generation microscopy, in preparation, (2026)

SYMPOSIUM 4

Chirality, magnetism, and magnetoelectricity: Separate phenomena and joint effects in metamaterial structures

60 contributions · pp. 510–605

Theory of Spin-Chiral Phonon Coupling in Chiral Crystals

Dapeng Yao[1], Gen Tatara[1]

[1]RIKEN Center for Emergent Matter Science (CEMS), 2-1 Hirosawa, Wako, Saitama, 351-0198, Japan
*Corresponding author: dapeng.yao@riken.jp

***Abstract*—We microscopically show spin-chiral phonon coupling in three-dimensional chiral crystals. We consider that phonons modulate the electron motions, leading to an effective magnetic field on electron spins via spin-orbital coupling. By integrating out the field of conduction electrons, we derive an effective Hamiltonian which couples the phonon and spin degrees of freedom.**

***Keywords*— chiral phonon, chiral crystal, spin-orbital coupling.**

I. Introduction

Chiral phonons accompanying rotational motions of nuclei represent circularly polarized modes, which carry phonon angular momentum [1]. Such phonons have been confirmed by recent experiments [2], [3], and the their various aspects have been revealed, such as the conversion of chiral phonons into the electric current [4], the spin excitation [5], the spin [6], [7] and orbital magnetizations [8], [9]. However, the coupling between electron spin and lattice in three-dimensional (3D) chiral crystals remain poorly understanding. Even though the so-called Raman-type spin-phonon coupling has been widely used to phenomenologically describe the coupling between the chiral lattice motion and local electron spins, the microscopic mechanism is still lacking. Furthermore, a quantitative estimate of the coupling constant was not feasible.

In this work, we microscopically derive the spin-chiral phonon coupling in 3D chiral crystals. We introduce the tight-binding model of electrons and the spring-lattice model of phonons for a 3D chiral chain. They can be simplified by a two-band model of electrons and a three-band model of phonons via the unfolding of the Brillouin zone. We then consider that phonon modulate the electron motion through the electron-phonon coupling, leading to an effective magnetic field on electron spins via spin-orbital coupling. By integrating out the field of conduction electrons, we derive an effective Hamiltonian which couples the phonon and spin degrees of freedom.

II. Methods

Here we consider a one-dimensional chiral chain with three atoms per unit cell, and we introduce the tight-binding model of electrons and spring-lattice model of phonons. Since the chiral chain has the screw symmetry, which is a combination of translation and rotation operations. By reducing the number of atoms pre unit cell from three to one, we can extend the Brillouin zone by three times. In this case, our tight-binding and spring-lattice models can be simplified by a two-band and three-band models, respectively. Then we can rewrite the electron-phonon coupling for the reduced unit cell, which is used to a two-phonon process. By integrating the field conduction electron, we can obtain the coupling between spins and lattice in chiral crystals.

III. Results and Discussion

We eventually derive the coupling between the phonon angular momentum and the electron spin, which is given by

$$H_{\text{ph-s}} = \alpha \boldsymbol{S} \cdot (\boldsymbol{Q} \times \dot{\boldsymbol{Q}}) + \beta \boldsymbol{S} \cdot (\boldsymbol{Q} \times \nabla \boldsymbol{Q}), \tag{1}$$

where $\boldsymbol{Q}$ is the phonon displacement, $\boldsymbol{S}$ is the electron spin, and α and β are their coupling constants. The first term is the so-called Raman-type spin-phonon coupling.

IV. Conclusion

We microscopically formulate the spin-chiral phonon coupling in three-dimensional chiral crystals, which requires both electron-phonon and spin-orbital couplings.

Acknowledgments

This work was supported by Japan Society for the Promotion of Science (JSPS) KAKENHI Grant No. JP25K23366, and RIKEN Special Postdoctoral Researchers Program.

References

[1] L. Zhang and Q. Niu, "Chiral phonons at hight-symmetry points in monolayer hexagonal lattices," *Physical Review Letters*, vol. 115, pp. 115502–115502, 2014.
[2] H. Zhu, J. Yi, M.-Y. Li, J. Xiao, L. Zhang, C.-W. Yang, R. A. Kaindl, L.-J. Li, Y. Wang, and X. Zhang, "Observation of chiral phonons," *Science*, vol. 359, pp. 579–582, 2018.
[3] K. Ishito, H. Mao, Y. Kousaka, Y. Togawa, S. Iwasaki, T. Zhang, S. Murakami, J.-i. Kishine, and T. Satoh, "Truly chiral phonons in α-Hgs," *Nature Physics*, vol. 19, pp. 35–39, 2023.
[4] D. Yao and S. Murakami, "Chiral-phonon-induced current in helical crystals," *Physical Review B*, vol. 105, pp. 184412–184412, 2022.
[5] D. Yao and S. Murakami, "Conversion of chiral phonons into magnons in ferromagnets and antiferromagnets," *Journal of the Physical Society of Japan*, vol. 93, pp. 034708–034708, 2024.
[6] M. Hamada and S. Murakami, "Conversion between electron spin and microscopic atomic rotation," *Physical Review Research*, vol. 2, pp. 023275–023275, 2020.
[7] D. Yao and S. Murakami, "Theory of spin magnetization driven by chiral phonons," *Physical Review B*, vol. 111, pp. 134414–134414, 2025.
[8] Y. Ren, C. Xiao, D. Saparov, and Q. Niu, "Phonon magnetic moment from electronic topological magnetization," *Physical Review Letters*, vol. 127, pp. 186403–186403, 2021.

[9] D. Yao, D. Go, Y. Mokrousov, and S. Murakami, "Dynamical orbital angular momentum induced by chiral phonons," arXiv:2511.09271.

Orbital optical chirality: Spectrally and spatially resolved measurements of multipolar chiroptical responses for optical vortex beams

Yoshito Y. Tanaka

Research Institute for Electronic Science, Hokkaido University, Japan
*Corresponding author: ytanaka@es.hokudai.ac.jp

***Abstract*— We demonstrate spatially and spectrally resolved chiral dichroism using a single twisted nanorod pair with spectrally separated plasmon resonances and rapid modulation of optical vortex handedness. At the vortex center, dichroism arises from novel optical chirality dependent on orbital angular momentum, which interacts with hybridized twisted quadrupole plasmon modes.**

***Keywords*— chiral nanostructures, optical vortex, vortex dichroism, helical dichroism, chiroptical responses, plasmon, metamaterials.**

I. Introduction

Chiral light–matter interactions are central to optical spectroscopy and nanophotonics, yet have conventionally been understood as arising from electric–magnetic dipolar interference driven by circularly polarized light with spin angular momentum ($s = \pm 1$). Recently, chiral interactions with optical vortex beams carrying orbital angular momentum (l) have attracted considerable attention from both fundamental physics and application perspectives, owing to the infinite degrees of freedom that l offers beyond s. Unlike spin angular momentum, which is determined by local polarization properties, orbital angular momentum is encoded in the spatial phase distribution of the beam. Consequently, the resulting chiroptical responses are expected to more strongly reflect the geometrical characteristics of chiral matter. However, a critical challenge arises from the size mismatch between the wavelength-scale optical vortex and nanoscale chiral structures. Here, we investigate the chiroptical response arising from interactions between plasmonic chiral nanostructures and optical vortex beams carrying both spin and orbital angular momentum, and demonstrate that this response is mediated by higher-order multipolar interactions beyond the conventional dipolar regime.

II. Sample and Methods

The subwavelength-sized twisted gold nanorod dimer (TND) shown in Fig. 1a was fabricated by three-dimensionally controlling the distance between the two rods with a spatial resolution of 10 nm or less. This chiral structure exhibits a giant chiroptical response with simple, analyzable modes through plasmonic coupling between the rods [1]. Additionally, we proposed and developed a method to achieve high-speed modulation of left- and right-handed optical vortex beams, which has been considered difficult conventionally, and to measure the difference in transmittance between left- and right-handed optical vortices (optical chiral dichroism) with high precision using a lock-in amplifier [2]. This enables spectrally and spatially resolved measurements of the chiral dichroism of a single TND (Fig. 1b).

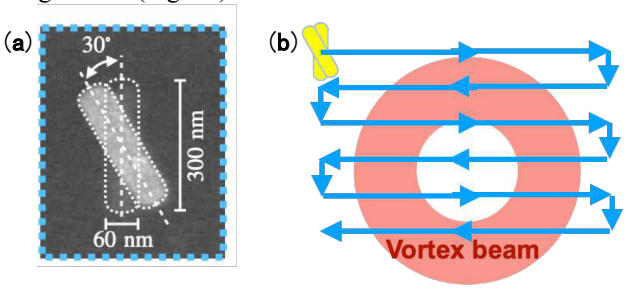

Fig. 1 (a) Twisted nanorod dimer (TND) structure. (b) Dichroism mapping of TND under left- and right-handed circularly polarized vortex beams.

III. Results and Discussion

As shown in Fig. 2a, we demonstrated that distinct dichroic responses emerge at the center and donut-shaped regions of circularly polarized optical vortex beams ($s = \pm 1, l = \pm 1$) [3]. In the donut-shaped region, no significant spectral variation was observed within the wavelength range near the quadrupole plasmon resonance. In contrast, at the beam center, the dichroic response exhibited a clear spectral dependence: negative at 800 nm, zero at 825 nm, and positive at 850 nm. Furthermore, only the sign of the dichroism at the center was reversed depending on the sign of l in the incident optical vortex ($s = \pm 1, l = \mp 1$). Reciprocity tests and angular momentum dissipation analysis [4] confirm that this response is a genuine chiral interaction dominated by orbital, rather than spin, angular momentum. Additionally, numerical simulation analysis revealed that the dichroism in the donut portion is mainly attributed to the coupling mode between dipoles (Fig. 2b), while the dichroism at the center arises from the coupling mode between

quadrupoles (Fig. 2c), which is normally forbidden. Interestingly, such dichroic response at the center cannot be explained within the framework of optical chirality as conventionally defined, and for the first time, we revealed the interaction with a novel optical chirality unique to optical vortices that depends on the order l of orbital angular momentum.

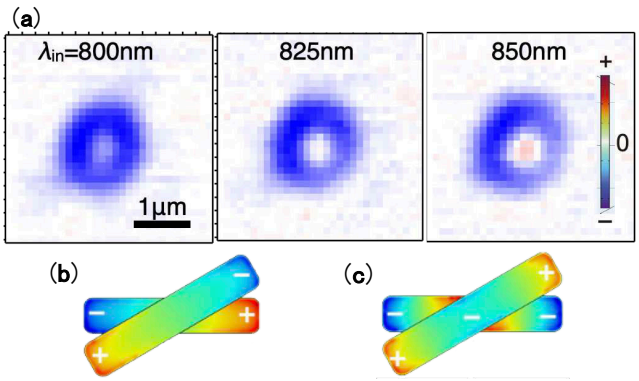

Fig. 2 (a) Measured dichroism maps at different incident wavelengths. Calculated charge distributions for (b) dipole and (c) quadrupole chiral modes excited at the donut and center positions in (a).

IV. Conclusion

We have demonstrated for the first time spatially and spectrally resolved chiral dichroism by utilizing a single twisted nanorod pair, which serves as an excellent probe due to its spectrally separated plasmon resonances, combined with rapid modulation and lock-in detection of left and right chiral light with spin and orbital angular momentum. Our key findings have revealed that the dichroism observed at the vortex center can be due to optical chirality governed by orbital angular momentum, and Its optical chirality interacts with the hybridized modes of two twisted quadrupole plasmons, resulting in a pronounced chiroptical response.

Acknowledgments

This work was conducted in collaboration with Dr. S. Hashiyada and Dr. A. Wu. This work was supported by the Japan Society for the Promotion of Science (JSPS) KAKENHI Grant Nos. JP24H00424 and JP22H05132 in Transformative Research Areas (A) "Chiral materials science pioneered by the helicity of light" (to Y.Y.T.), JP23K04669 and JP21K14594 (to S.H.); the Japan Science and Technology Agency (JST) FOREST Program, Grant No. JPMJFR213O (to Y.Y.T.); and JST PRESTO, Grant No. JPMJPR25J6 (to S.H.).

References

[1] A. Wu, Y. Y. Tanaka and T. Shimura, Giant chiroptical response of twisted metal nanorods due to strong plasmon coupling, *APL Photon.* **6,** 126104 (2021).

[2] S. Hashiyada and Y. Y. Tanaka, Rapid modulation of left- and right-handed optical vortices for precise measurements of helical dichroism, *Rev. Sci. Instrum.* **105,** 163901 (2024).

[3] S. Hashiyada, A. Wu and Y. Y. Tanaka, Unveiling orbital optical chirality through multipolar chiral light-matter interaction, *Optica* (accepted), arXiv:2508.08902.

[4] S. Hashiyada and Y. Y. Tanaka, Conservation law for angular momentum based on optical field derivatives: Analysis of optical spin-orbit conversion, *Phys. Rev. Research* **7**, L022052 (2025).

Strong coupling of chiral light with chiral matter: a macroscopic study

Sergey A. Dyakov[1,*], Natalia Salakhova[1], Ilia Smagin[1], Denis Baranov[2], Ilia Fradkin[1,2], Nikolay Gippius [1]

[1]Skolkovo Institute of Science and Technology, Moscow 121205, Russia
[2]Moscow Center for Advanced Studies, Moscow 123592, Russia
*Corresponding author: s.dyakov@skoltech.ru

***Abstract*—We consider a Fabry-Pérot resonator supporting photonic modes with non-zero handedness. By placing chiral material into such a resonator, we demonstrate chiral strong coupling. The interaction strength depends on the chiralities of both the medium and the photonic mode, enabling selective optical sensing of molecular enantiomers for pharmaceuticals and chemistry.**

***Keywords*— chirality, metasurfaces, strong coupling.**

Fundamental studies of the interaction between chiral light and chiral matter are crucial for advancing technologies that can optically distinguish different left and right enantiomers of chiral organic molecules. One promising approach in developing such technology involves creating a resonator that sustains photonic modes with non-zero electromagnetic handedness, a feature that causes these modes to interact differently with chiral molecular enantiomers. When chiral molecules are positioned in resonator hotspots, they can alter the system's characteristics due to their electric and magnetic transition dipole moments.

In this study, we explore this interaction by incorporating the Lorentz pole into the macroscopic parameters of the chiral medium: dielectric permittivity, magnetic permeability, and chirality coefficient [1]:

$$\begin{aligned}\varepsilon(\omega) &= \varepsilon_\infty + f_e \frac{\omega_0^2}{\omega_0^2 - \omega^2 - i\gamma\omega},\\ \mu(\omega) &= \mu_\infty + f_m \frac{\omega_0^2}{\omega_0^2 - \omega^2 - i\gamma\omega},\\ \kappa(\omega) &= f_{me} \frac{\omega}{\omega_0} \cdot \frac{\omega_0^2}{\omega_0^2 - \omega^2 - i\gamma\omega}.\end{aligned} \tag{1}$$

The latter, also known as the Pasteur parameter, is a dimensionless macroscopic measure indicating the medium's chirality, connecting electric and magnetic fields in the constitutive relations. Our theoretical results are the following:

- Designed a wideband handedness-preserving mirror using one-dimensional periodic gratings on a Bragg mirror [2], enabling the construction of a Fabry-Pérot resonator with chiral modes whose frequencies are tunable via grating orientation, as shown in Fig. 1(a).
- Demonstrated strong coupling between chiral cavity modes and a chiral (Pasteur) medium, showing that the Rabi splitting is directly governed by the enantiomeric compatibility of the mode and the medium [3].

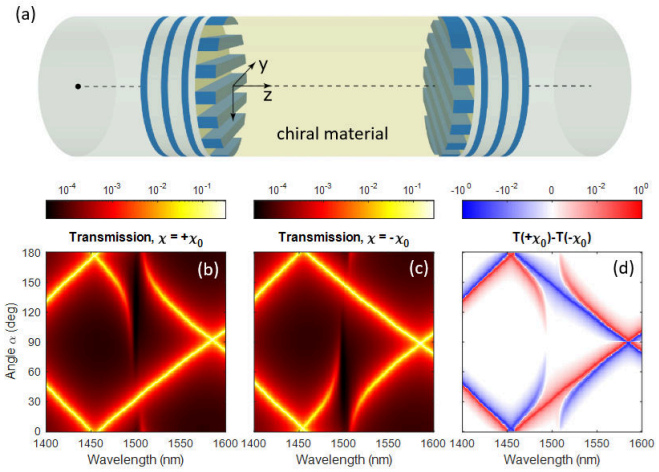

Fig. 1. (a) The sketch of a chiral Fabry-Pérot resonator. (b–d) The wavelength and twist-angle dependencies of the resonator transmission coefficient and the differential transmission coefficient.

- Validated the theoretical model by confirming Jones matrix formalism results against full-wave Fourier modal method simulations, ensuring the accuracy of the predicted light-matter interaction.
- Proposed a direct experimental method to optically distinguish left-handed and right-handed media by identifying spectral shifts of Fabry-Pérot resonances in transmission spectra near chiral transitions.

Our findings provide a foundation for designing advanced optical sensors that can selectively detect chiral molecules, with potential applications in pharmaceuticals and chemistry.

Acknowledgments

RSF (25-12-00454).

References

[1] D. G. Baranov, C. Schäfer, and M. V. Gorkunov, "Toward molecular chiral polaritons," *ACS Photonics*, vol. 10, no. 8, pp. 2440–2455, 2023.
[2] S. A. Dyakov, N. S. Salakhova, A. V. Ignatov, I. M. Fradkin, V. P. Panov, J.-K. Song, and N. A. Gippius, "Chiral light in twisted fabry–pérot cavities," *Advanced Optical Materials*, vol. 12, no. 12, p. 2302502, 2024.
[3] S. Dyakov, I. Smagin, N. Salakhova, O. Blokhin, D. G. Baranov, I. Fradkin, and N. Gippius, "Strong coupling of chiral light with chiral matter: a macroscopic study," *Optica*, vol. 12, no. 9, pp. 1406–1416, 2025.

Nonlinear magnetization dynamics as a route to nonreciprocal phases, spin superfluidity, and analogue gravity

Vincent P. Flynn[1,2,*], Benedetta Flebus[1]
[1]Department of Physics, Boston College, Chestnut Hill, MA 02467, USA
[2]Department of Physics and Astronomy, Dartmouth College, Hanover, NH 03755, USA
[*]Corresponding author: flynnvin@bc.edu

***Abstract*—Balancing dc spin torque against Gilbert damping stabilizes a self-organized spin-superfluid limit cycle in a chiral ferromagnetic multilayer. The resulting superflow is inherently nonreciprocal, enabling direction-selective magnon transport. In a comoving frame the long-wavelength dynamics map onto an effective acoustic metric, allowing sonic horizons and Hawking-like emission.**

***Keywords*—nonequilibrium dynamics, spin superfluidity, limit cycle, nonreciprocity, magnons, analogue gravity**

I. Introduction

Open, driven systems can self-organize into steady states with no equilibrium analogue [1]. Here we summarize a magnetic realization: a dc spin current counteracts intrinsic damping and stabilizes a chiral spin-superfluid limit cycle (SFLC) carrying a persistent spin supercurrent. The SFLC breaks both spatial and continuous time-translation symmetry, intertwining transport with spatiotemporal order [2].

II. Model and Methods

We consider a ferromagnetic multilayer with interlayer exchange and Dzyaloshinskii–Moriya interaction, subject to a field along $\hat{\mathbf{z}}$ and a dc spin-current-induced antidamping torque. In a continuum description, the unit magnetization $\mathbf{m}(x,t)$ obeys Landau–Lifshitz–Gilbert dynamics

$$\partial_t \mathbf{m} = -\mathbf{m}\times\mathbf{h} + \alpha\,\mathbf{m}\times\partial_t\mathbf{m} + J_s\,\mathbf{m}\times(\mathbf{m}\times\hat{\mathbf{z}}). \quad (1)$$

A uniformly precessing, current-carrying SFLC solution takes the form $\varphi_{\mathrm{LC}}(x,t) = kx + \Omega t$ with $\Omega = J_s/\alpha$, yielding a steady superflow whose chirality is set by the DMI.

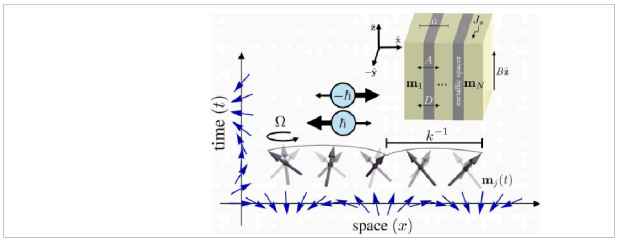

Fig. 1. Schematic SFLC background and direction-selective magnon propagation in a driven multilayer ferromagnet (adapted from Ref. [2]).

III. Results and Discussion

Our analysis demonstrates:

- Emergence of a dynamically stabilized spin superfluid limit cycle, even in parameter regimes where equilibrium superfluid states are forbidden.
- Intrinsic nonreciprocal magnon dispersion arising from flow-induced breaking of Galilean invariance.
- Regimes of fully unidirectional long-wavelength propagation.
- Exceptional-point structure at zero momentum associated with the Goldstone mode.
- Effective acoustic-metric description of long-wavelength phase dynamics.
- Formation of sonic horizons under spatial modulation of the spin torque.
- Hawking-like particle–hole pair emission from horizon interfaces.

IV. Conclusion

Driven magnetic heterostructures provide a tunable tabletop platform linking spin superfluidity, nonreciprocal transport, and analogue-gravity kinematics within a single nonequilibrium phase.

Acknowledgments

B.F. acknowledges support from DOE under Grant No. DE-SC0024090.

References

[1] P. C. Hohenberg and B. I. Halperin, "Theory of dynamic critical phenomena," Rev. Mod. Phys., vol. 49, pp. 435–479, 1977.
[2] V. P. Flynn and B. Flebus, "Emergent spatiotemporal order and nonreciprocity in driven-dissipative nonlinear magnetic systems,"arXiv:2510.21963 (2026).

Breaking of time-reversal symmetry and Onsager recirprocity in chiral molecule interfaced with an enivronment

Jonas Fransson

Department of Physics and Astronomy, Uppsala University, Uppsala, Sweden
*Corresponding author: Jonas.Fransson@physics.uu.se

***Abstract*— Molecular closed shell structures are known to form spin-singlet configurations, resulting from the spin-exchange associated with electron-electron interactions. While the vanishing total spin-moment is an immanent property of the spin-singlet, the vanishing local moments is a result of fluctuations between degenerate spin-configurations. Here, it is demonstrated that the spin-configuration of a chiral molecule is enantiospecifically locked when coupled to an electron reservoir. The coupling opens up the molecular closed shell structure, which broadens the energy levels. Together with the molecular spin-orbit coupling, this dissipative coupling generates an effective spin-splitting of the molecular energy levels and facilitates stabilization of a chirality determined spin-configuration. Simultaneously, the charge molecular charge distribution is shown to depend linearly on the magnetization of the reservoir such that no linear response regime is established with respect to the external magnetization. Accordingly, the Onsager reciprocity theorem does not apply to a chiral molecule attached to a reservoir, hence, providing a theoretical foundation for the chirality induced spin selectivity effect.**

References

[1] J. Fransson, “Breaking of time-reversal symmetry and Onsager reciprocity in chiral molecule interfaced with an environment”, APL Comput. Phys. 2, 016111 (2026).

[2] J. Fransson, “Should it really be that hard to model the chirality induced spin selectivity effect?”, APL Comput. Phys. 1, 020903 (2025).

Nonlinear terahertz magnetoelectric coupling of electromagnons in multiferroics

Youtarou Takahashi

Quantum-Phase Electronics Center (QPEC) and Department of Applied Physics, The University of Tokyo, Tokyo, Japan
*Corresponding author: youtarou-takahashi@ap.t.u-tokyo.ac.jp

***Abstract*— Multiferroics of spin-driven ferroelectricity provide strong dynamical magnetoelectric coupling, leading to versatile nonreciprocal optical responses. Here, we show the nonlinear magnetoelectric coupling of spin excitations of multiferroics, electromagnons, by using the strong terahertz field. The different nonlinear responses, anharmonic coupling of electromagnons and higher harmonic generation, have been demonstrated.**

***Keywords*— metamaterials, terahertz, machine learning, photonic crystals.**

I. Introduction

Spontaneous breaking of space inversion symmetry is often caused by the spin orderings, which is classified as type-II multiferroics, leading to spin-driven ferroelectricity and chirality (Fig. 1). The strong magnetoelectric effects, magnetization induced by electric field and electric polarization induced by magnetic field, have been discovered in multiferroics. The fluctuation of spin ordering, spin excitation, in multiferroics always exhibits the electric dipole activity, which is called as electromagnon [1]. The electromagnon resonance, which is observed in gigahertz and terahertz region, shows resonantly enhanced magnetoelectric coupling, leading to the giant nonreciprocal optical responses [2]. In the linear response regime, nonreciprocal optical absorption and gyrotropy enhanced by the electromagnons have been reported. Recently, the bulk photovoltaic effect of electromagnon, which converts the terahertz photon into charge current, has been found in type-II multiferroics [3]. In addition to the photovoltaic effect, many second order nonlinear effects are expected to appear through the large magnetoelectric coupling of electromagnon. In this talk, we demonstrate two types of nonlinear responses of electromagnons in spin-spiral magnets. The magnetoelectric effect in the strong resonant terahertz field causes higher harmonic generations with nonreciprocity. The high field excitation also drives the off-resonant creation of electromagnon through the anharmonic coupling of electromagnons.

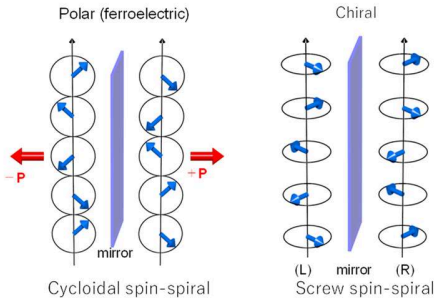

Fig. 1 Inversion breaking by spin-spiral orders.

II. Methods

Representative spin-spiral multiferroics, perovskite manganites and hexaferrites, are targeted in this work. The electromagnons in terahertz region is created by high field terahertz pulses with field strength of 600 kV/cm. To detect the anharmonic coupling, the pump-probe measurements was conducted. The terahertz emission spectroscopy was used to observe the higher harmonic generation through the magnetoelectric coupling.

III. Results and Discussion

Presence of strong anharmonic coupling among the electromagnons is found in spin-spiral phase of hexaferrite. The coherent creation of electromagnon induces off-resonant excitation of low energy electromagnon as manifested by the pump-probe measurements. The amplitude of off-resonant excitation is proportional to the square of terahertz field, indicating the second order nonlinear effect. In the centrosymmetric matter, the second order anharmonic coupling between infrared active modes is prohibited; the coupling between infrared active and Raman active modes is allowed. Although the chemical lattice of hexaferrite is centrosymmetric, the spin-spiral order breaks the space inversion symmetry and enables the anharmonic coupling of infrared active electromagnons.

References

[1] A. Pimenov, A. A. Mukhin, V. Yu. Ivanov, V. D. Travkin, A. M. Balbashov, and A. Loidl, Nat. Phys. 2, 97 (2006).
[2] Y. Takahashi and Y. Tokura, J. Phys. Soc. of Jap. 94, 052001 (2025)
[3] M. Ogino, Y. Okamura, K. Fujiwara, T. Morimoto, N. Nagaosa, Y. Kaneko, Y. Tokura, and Y. Takahashi, Nat. Commun. 15, 4699 (2024).

Zero-frequency chiral magnonic edge states protected by non-equilibrium topology

Rembert Duine[1,*], Pieter Gunnink[2], Joren Harms[3], Alexander Mook[4]

[1]Institute for Theoretical Physics and Center for Extreme Matter and Emergent Phenomena, Utrecht University, Leuvenlaan 4, 3584 CE Utrecht, The Netherlands
[2]Institute of Physics, Johannes Gutenberg University Mainz, Staudingerweg 7, Mainz 55128, Germany
[3]Fachbereich Physik, Universit¨at Konstanz, D-78457 Konstanz, Germany
[4]University of Münster, Institute of Solid State Theory, 48149 Münster, Germany
*Corresponding author: r.a.duine@uu.nl

***Abstract*—Topological bosonic excitations must, in contrast to their fermionic counterparts, appear at finite energies. This is a key challenge for magnons, as it prevents excitation and detection of topologically-protected magnonic edge states and their use in magnonic devices. We show how the edge states can be lowered to zero frequency.** ***Keywords*— magnonics, topology, chiral edge states, spintronics**

I. Summary

In this work [1] we propose a method to lower the topologically-protected chiral edge states in magnon Chern insulators to zero frequency, such that they are easily accessible by microwave techniques. This is achieved by considering magnon excitations on top of a uniform magnetization that is pointing *against* the applied external magnetic field, as opposed to considering excitations on top of a magnetization parallel to the magnetic field, as shown in Fig. 1(a-b). In such a *non-equilibrium* setup, the magnon excitations decrease the energy of the system, allowing us to tune the frequency of the edge modes to zero frequency. Since the non-equilibrium state is energetically unstable, it has to be rendered dynamically stable, which is achieved by an appropriate spin-orbit torque. Using numerical Landau-Lifshitz-Gilbert simulations we show that the edge modes can be excited at low frequencies, and are topologically protected against backscattering. Finally, we consider a propagating spin-wave spectroscopy (PSWS) experiment with two antennas, and demonstrate that the edge modes can be directly detected at gigahertz frequencies, even in the presence of disorder.

Acknowledgments

R.A.D. is member of the D-ITP consortium, a program of the Dutch Organization for Scientific Research (NWO) that is funded by the Dutch Ministry of Education, Culture and Science (OCW). This work is in part funded by the Fluid Spintronics research programme with project number 182.069, financed by the Dutch Research Council (NWO), and by the Deutsche Forschungsgemeinschaft (DFG, German Research Foundation) - Project No. 504261060 (Emmy Noether Programme).

References

[1] For more details see Pieter M. Gunnink, Joren S. Harms, Rembert A. Duine, Alexander Mook, Phys. Rev. Lett. **131**, 126601 (2023).

Fig. 1. Strategy for generating zero-frequency chiral magnonic edge states in a magnon Chern insulator ferromagnet (FM), comparing the equilibrium (a,c,e) with the non-equilibrium (b,d,f) situation, with the uniform magnetization (see arrows) and magnetic field $\boldsymbol{H}_{\pm}$ aligned parallel and anti-parallel, respectively. In the non-equilibrium case, the magnetization is stabilized by spin-orbit torques originating from the adjacent heavy metal (HM) layer. (c,d) Bulk magnon band structure with indicated Chern numbers, $\Omega_{1,2}$. (e,f) Magnon band structure of an armchair edge ribbon. The colorscale of the eigenfrequencies indicates the edge localization and dashed lines denote the bulk band gap. In equilibrium, $H_+/(JS) = 0.1$ (with J the exchange and S the spin quantum number), the edge states lie at high frequencies, but they are lowered down to zero frequency in non-equilibrium, $H_-/(JS) = -2.75$.

Gaussian quantum state preparation of ferromagnetic magnons

Marco Brühlmann[1], Monika Mycroft[1],Yunyoung Hwang[2,3], Jorge Puebla[2,4], Rostyslav O-Serha[5], Andrii V Chumak[5], Carlos Gonzalez-Ballestero[1]

[1]Institute for Theoretical Physics and Vienna Center for Quantum Science and Technology,
[2]CEMS, RIKEN, 2-1, Hirosawa, Wako 351-0198, Japan
[3]Institute for Solid State Physics, University of Tokyo, Kashiwa 277-8581, Japan
[4]Department of Electronic Science and Engineering, Kyoto University, Kyoto, Kyoto 615-8510, Japan
5 University of Vienna, A-1090 Vienna, Austria

*Corresponding author: carlos.gonzalez-ballestero@tuwien.ac.at

***Abstract*— We theoretically show how Gaussian quantum magnonic states, both propagating and confined, can be prepared using only external drives, by harnessing the intrinsic magnon nonlinearity.**

***Keywords*— magnons, quantum states, quatum magnonics.**

I. Introduction

Preparing certifiably quantum states of magnons represents a central milestone in the emerging field of quantum magnonics. Among these, Gaussian states are particularly attractive, as they can be prepared and manipulated without direct coupling to qubits, thereby allowing a wide range of current solid-state experiments to access the quantum regime.

II. Methods

We propose a method to prepare Gaussian quantum states of magnons. First, we propose to generate squeezed states and entangled states in the FMR modes of ellipsoidal magnets using parametric drive [1]. Then, we propose to prepare similar states in the continuum using phonons and magnetoelastic nonlinearity. We develop a comprehensive theory of nonlinear magnetoelasticity in thin films, quantize it, and use it to predict mean-field vacuum fluctuations of the magnetization [2]. We proceed to show that phonon-to-magnon down-conversion can result in the preparation of entangled propagating magnon states in state of the art thin film geometries.

III. Results and Discussion

- We predict vacuum squeezing up to 3dB in YIG ellipsoids.
- We predict strong entanglement between the FMR modes of two ellipsoids coupled via a cavity mode
- We propose detection methods that do not rely on single photon emitters, such as FMR and local coils.
- We analytically compute nonlinear coefficients associated with three-magnon, four-magnon, and magnon-phonon scattering in thin film geometries.
- We quantitatively predict experimental observations [3].
- We theoretically compute parametric instavility thresholds and predict that phonon-to-two magnon processes can dominate over Suhl instability process in state of the art geometries.
- We quantize our theory and provide exact nonlinear Heisenberg-Langevin equations for magnon and phonon amplitudes.
- We produce a mean-field theory of magnetization dynamics under 3-magnon Suhl instability process and compute the magnetization vacuum fluctuations across the parametric instability threshold.

IV. Conclusion

We demonstrate the possibility of preparing univocally quantum magnonic states and to detect and certify them using exclusively classical fields and classical measurements. Our work paves the way towards quantum magnonics without qubits.

Acknowledgments

These works were supported by the Austrian Science Fund FWF (Project No. PAT-1177623 and Project No. 10.55776/I6568) and by the JSPS KAKENHI No. 24K00576 from MEXT, Japan.

References

[1] M. Mycroft, Rostyslav O. Serha, Andrii V. Chumak, C. Gonzalez-Ballestero, arXiv: 2601.12833 (2026)
[2] M. Brühlmann, Y. Hwang, J. Puebla, C. Gonzalez-Ballestero, Phys. Rev. B **113**, 014430 (2026)
[3] Y. Hwang, L. Liao, J. Puebla, M. Brühlmann, C. Gonzalez-Ballestero, K.Kondou, N. Ogawa, S. Maekawa, Y. Otani, arXiv:2509.19706 (2025)

Symmetry Principles and Topology-Driven Design of Knot-Particle Metasurfaces

Nadav Goshen[1], Yarden Mazor[1*]

[1]School of Electrical and Computer Engineering, Tel-Aviv University, Tel-Aviv, Israel
*Corresponding author: yardenm2@tauex.tau.ac.il

***Abstract*—We present a topology and symmetry driven design framework, for single-layer bianisotropic metasurfaces based on knot particles. Knot topology ensures intrinsic electric–magnetic balance and strong chiral response, while controlled mirror-symmetry breaking enables hybrid chiral–omega coupling. Experiments validate efficient polarization rotation and tunable asymmetric scattering without multilayer architectures.**

Summary

Bianisotropic metasurfaces enable advanced electromagnetic wave manipulation through engineered magnetoelectric coupling. However, achieving balanced electric-magnetic responses and simultaneous control over transmission and reflection asymmetries typically requires multilayer architectures or intensive numerical optimization. Here, we introduce a unified design framework in which *topology* and *symmetry* serve as the primary control parameters for single-layer bianisotropic metasurfaces based on nontrivial knot particles. Toroidal knots, characterized by integer winding numbers (p, q) (Fig. 1(a)) are inherently chiral and support resonant closed-loop current distributions. When arranged in periodic arrays and operated near their first resonance (where the total wire length is $\approx \lambda$), we show that for specific types of knots the excited current is dominated by its first harmonic. This enables analytical multipole modeling and direct derivation of electric and magnetic dipole moments from the knot geometry which yield the scattering response.

A key result is that knots satisfying $p = q \pm 1$ naturally fulfill the dipolar balance condition required for matched polarization rotation. In particular, the trefoil exhibits near-optimal performance. Its electric and magnetic dipoles satisfy a generalized Huygens condition,

$$\tilde{p}_{x,y} = \pm \tilde{m}_{y,x}, \tag{1}$$

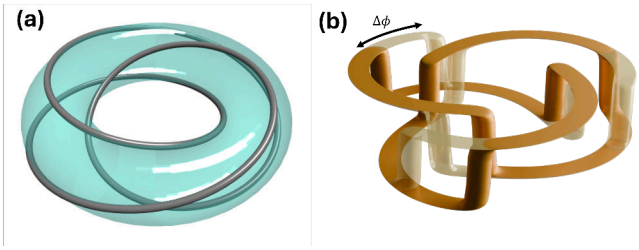

Fig. 1. (a) A toroidal trfoil knot. (b) A flattened trefoil, with controlled symmetry breaking by via offset $\Delta\phi$.

with a $\pi/2$ phase difference between orthogonal components. This balanced coupling suppresses reflection and enables efficient linear-to-linear polarization conversion. Retrieved surface susceptibilities confirm strong chiral bianisotropy originating directly from the knot topology.

While topology governs intrinsic chirality, symmetry controls the allowed coupling pathways. To extend beyond purely chiral behavior, we introduce controlled mirror-symmetry breaking in a quasi-planar trefoil implementation (Fig. 1(b)). The three-dimensional knot is projected onto a substrate and interconnected through vertical vias. When offsetting alternating vias by a geometric phase $\Delta\phi$, mirror symmetry between the two faces is broken while preserving the underlying topology. This single geometric parameter activates additional orthogonal dipole coupling, yielding a richer bi-anisotropic response.

Dipole decomposition shows that symmetric via placement ($\Delta\phi = 0$) permits only parallel electric–magnetic coupling, corresponding to pure chiral response ($\mathbf{p} \parallel \mathbf{m}$). When $\Delta\phi \neq 0$, orthogonal coupling ($\mathbf{p} \perp \mathbf{m}$) emerges, enabling omega-type bianisotropy alongside the chiral response. The resulting hybrid chiral-omega metasurface simultaneously supports cross-polarized transmission and asymmetric co-polarized reflection within a single-layer structure.

We experimentally validate these principles using both fully three-dimensional additive manufacturing and low-loss printed circuit board (PCB) implementations. Despite geometric simplification in the planar PCB realization, the essential topological and symmetry features are preserved. Measurements confirm strong polarization rotation near resonance (approaching 90° in optimized PCB samples) and demonstrate controllable hybrid behavior through symmetry engineering.

Together, these results establish a design paradigm for knot-particle metasurfaces: topology sets electric-magnetic balance and intrinsic chirality, while symmetry provides continuous control over bianisotropic coupling. This approach enables compact, single-layer realization of pure chiral or hybrid chiral–omega responses without multilayer stacking or material anisotropy, opening pathways toward advanced polarization control, asymmetric scattering, and reconfigurable electromagnetic devices.

Dynamical orbital magneto-electric response in complex materials

Yuriy Mokrousov

Peter Grünberg Institut, Forschungszentrum Jülich, Jülich, Germany
Institute of Physics, Johannes Gutenberg University Mainz, Mainz, Germany

Electrons' spin angular momentum has revolutionised magnetic technology, pushing its energy efficiency and speed to new heights. However, controlling orbital angular momentum (OAM) still remains a significant challenge, with significant advances made only very recently. OAM's origins lie in the spatio-temporal dynamics of atoms, electrons, spins and light, making it a unique force capable of igniting coupled dynamics across various order parameters and quasiparticles. This potential unlocks novel exotic properties and functionalities in hybrid magnon-phonon-electron architectures. The emerging field of orbitronics, i.e. OAM generation, manipulation and conversion, is considered one of the most promising areas within magnetism and its applications. In my talk I will explore the idea that structurally complex materials such as chiral and low-symmetry two-dimensional materials can naturally develop non-local electronic orbital response to external magnetic fields, light and lattice vibrations, which allows to transform chirality – statically or dynamically inherent either to structure, spin order or electro-magnetic field – into prominent orbital magnetism [1,2]. Moreover, I will show that in materials with non-trivial magnetic structure such as magnetic oxides [3], where the non-equilibrium magnetic properties have been traditionally interpreted in terms of spin, the strong orbital magneto-electric response can be utilized to drive strong unexpected torques and give rise to novel magnetoresistance phenomena. Overall, I will aim to identify novel avenues in engineering orbital coupling and angular momentum transfer which may resonate within the paradigm of hybrid angular-momentum-based electronics.

[1] T. Wichmann et al., arXiv:2510.26662 (2025)
[2] K. Hagiwara et al., Adv. Mater. **37**, 2418040 (2025)
[4] S. Krishna et al., under review (2026)

Pure moving optical media at microwave frequencies using magnetochiral metasurfaces

Toshiyuki Kodama

Institute for Excellence in Higher Education, and Organization for Advanced Studies, Tohoku University, Sendai, Japan
*Corresponding author: tkodama@tohoku.ac.jp

***Abstract*—We study microwave bianisotropies using magnetochiral (MCh) metasurfaces consisting of double Z-type gammadions with perpendicularly magnetized substrates. Combination of the metasurfaces with contraposition MCh metasurfaces cancels both the chiral-type bianisotropy and MO effect, resulting in pure moving optical media.**

***Keywords*— metasurface, magnetchiral effect, non-reciprocal moving-type bianisotropy.**

I. Introduction

In optics, discrete symmetries such as space-inversion (P) and time-reversal (T) govern physical restrictions. Breaking these symmetries gives rise to bianisotropy —magnetoelectric couplings categorized into four types (chiral, omega, Tellegen, and moving) based on reciprocity and polarization dependence [1]. The control of the bianisotroies is a challenge in natural materials with broken symmetries such as multiferroic materials [2]; therefore, man-made structured materials, referred to as metamaterials, are suitable to explore bianisotropies [3]. In particular, metasurfaces with two-dimensional planar structures are good playgrounds to embody a tailor-made bianisotropic medium [4].

II. Numerical simulation setup

Figure 1(a) illustrates a cell of the metasurface consisting of double Z-type gammadions with perpendicularly magnetized substrates, while (b) is a unit cell of composite metasurfaces [5]. The gammadions are made of perfect electric conductor. The unit cell is repeated in the x and y directions by a periodic boundary condition. The relative electric permittivity of the substrate is constant ($\varepsilon_{\rm r} = 3.3$). The permeability tensor $\mu_{\rm r}$ for lossless substrates is described by

$$\mu_{\rm r} = \begin{bmatrix} 1 & jm & 0 \\ -jm & 1 & 0 \\ 0 & 0 & 1 \end{bmatrix}, \qquad (1)$$

where a parameter denoted by m is related to magnetization of the substrates. The S-parameters for microwave transmission and reflection are numerically calculated using RF module of COMSOL Multiphysics. Incident microwave in $-z$ direction is linearly polarized along the x-direction as indicated by a green arrow in Fig. 1(a).

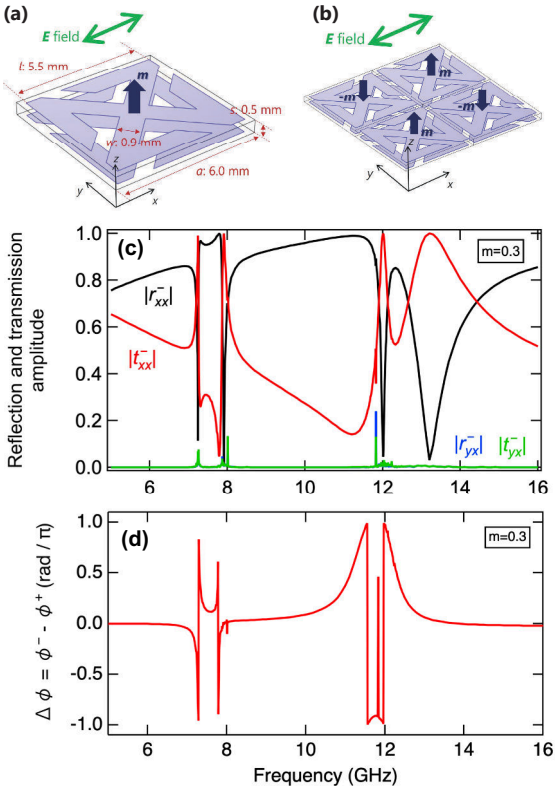

Fig. 1. (a) A calculated MCh metasurface. (b) A unit cell of a calculated composite metasurface including ordinary and contraposition MCh metasurfaces. (c) Calculated spectra and (d) directional phase difference spectra with $m = 0.3$ for the composite MCh metasurface.

III. Results and Discussion

Figure 1(c) shows the transmission and reflection coefficients spectra of the composite MCh metasurface. The subscripts denote the polarization planes of the electric field. $|r^{-}_{yx}|$ (blue) and $|t^{-}_{yx}|$ (green) accompanied by polarization rotation are almost zero, indicating that both the chiral-type bianisotropy and MO effect with polarization rotation are no longer functioning in the composite metasurface. Contrastingly, the directional phase difference spectrum plotted in Fig. 1(d) demonstrates the moving-type bianisotropy survives at approximately 7.5 GHz and 12 GHz.

Moreover, the transmission and reflection amplitude spectra in Fig. 1(c) show that perfect transmission and no reflection are achieved at 12 GHz, indicating the impedance matching. In addition, Figure 1(d) indicates that the phase difference is π at 12 GHz. This way, the ideal gyrator for arbitrary polarizations is realized using the composite metasurface with ordinary and contraposition MCh metasurfaces.

IV. Conclusion

Bianisotropies in MCh metasurfaces are studied. The chiral-type bianisotropy and MO effect are eliminated by the combining the ordinary MCh metasurfaces with the contraposition MCh metasurfaces, brings pure moving optical media. The pure moving optical media demonstrate perfect transmission with phase difference of π, which is a key to embody an ideal gyrator for arbitrary spatial and polarization modes.

Acknowledgments

This work is financially supported by KAKENHI (23K13621) and JST-CREST (JPMJCR2102). The authors are grateful to S. Tomita, T. Nakanishi, K. Sawada for fruitful discussions and comments. H. Kurosawa is also acknowledged for instructing the numerical calculation prior to this work.

References

[1] V. S. Asadchy, A. Díaz-Rubio, and S. A. Tretyakov, "Bianisotropic Metasurfaces: Physics and Applications," *Nanophotonics* 7, 1069 (2018).

[2] S. Toyoda, N. Abe, S. Kimura, Y. H. Matsuda, T. Nomura, A. Ikeda, S. Takeyama, and T. Arima, "One-Way Transparency of Light in Multiferroic CuB_2O_4," *Phys. Rev. Lett.* 115, 267207 (2015).

[3] T. Niemi, A. O. Karilainen, and S. A. Tretyakov, "Synthesis of Polarization Transformers," *IEEE Trans. Antennas Propag.* 61, 3102 (2013).

[4] C. Pfeiffer, and A. Grbic, "Bianisotropic Metasurfaces for Optimal Polarization Control: Analysis and Synthesis," *Phys. Rev. Appl.* 2, 044011 (2014).

[5] T. Kodama, T. Nakanishi, K. Sawada, and S. Tomita, "Pure moving optical media consisting of magnetochiral metasurfaces," *Opt. Mater. Express* 14, 2499 (2024).

Intrinsic Hyperbolic Anisotropy for Low-Loss Polarization Control and Chiral Light–Matter Interaction

N. Melchioni, A. Mancini, G. Venturi, L. Nan, A. Efimova, S. Chiodini, A. Ambrosio

Istituto Italiano di Tecnologia, Via Rubattino 81, 20134 – Milano, Italy

*corresponding author: nicola.melchioni@iit.it

Abstract: The ability to control light polarization at the nanoscale is central to chiral and magnetoelectric light–matter interactions, particularly in regimes combining strong field confinement with low optical losses. Here we investigate natural van der Waals hyperbolic crystals as a platform for intrinsic, lithography-free polarization control enabled by extreme in-plane optical anisotropy. Focusing on molybdenum oxychloride ($MoOCl_2$), we show that broadband hyperbolicity in the visible and near-infrared arises from a strongly anisotropic Drude response, yielding metallic and dielectric behavior along orthogonal crystal axes. This intrinsic symmetry breaking enables polarization-selective reflection and transmission with minimal dissipation, as well as highly confined hyperbolic plasmon polaritons with polarization-dependent dispersion. These results establish natural hyperbolic materials as a promising route toward low-loss polarization engineering and chiral light–matter interaction in nanophotonic and quantum platforms.

Polarization is a fundamental degree of freedom governing symmetry, selection rules, and angular momentum exchange in light–matter interaction. In chiral and magnetoelectric photonics, efficient polarization control must be achieved at deeply subwavelength scales while preserving low optical losses, a condition that remains challenging for conventional metasurfaces and metallic nanostructures. Natural hyperbolic materials provide an alternative route, where polarization selectivity emerges intrinsically from crystal symmetry rather than artificial patterning.

In this work, we focus on the van der Waals crystal $MoOCl_2$, a low-symmetry biaxial material exhibiting broadband in-plane hyperbolicity spanning the visible to the near-infrared. Owing to a strongly anisotropic Drude response, $MoOCl_2$ displays metallic behavior along one in-plane axis and dielectric behavior along the orthogonal one, resulting in record-high in-plane permittivity anisotropy. Thin flakes enable near-unity polarization extinction through simultaneous high reflectivity and high transmission along orthogonal axes, without relying on absorption-driven dichroism. This behavior enables ultrathin, low-loss polarization elements operating well below the diffraction limit.

Beyond far-field polarization control, the hyperbolic nature of $MoOCl_2$ supports highly confined plasmon polaritons with polarization-dependent dispersion and propagation direction. Near-field nano-imaging reveals hyperbolic and canalized propagation regimes governed by the interplay between polarization, momentum, and crystal anisotropy, including topological transitions between elliptic and hyperbolic dispersion. These symmetry-driven regimes provide direct access to polarization-selective electromagnetic environments.

By combining extreme spatial confinement with intrinsic polarization selectivity, natural hyperbolic crystals offer a powerful platform for chiral and symmetry-sensitive light–matter interactions. Our results pave the way toward polarization-engineered coupling to quantum emitters, chiral nanophotonics, and magnetoelectric phenomena in structured electromagnetic fields, without the need for complex nanofabrication.

References

[1] G. Venturi, A. Mancini, N. Melchioni, S. Chiodini, and A. Ambrosio, *Visible-frequency hyperbolic plasmon polaritons in a natural van der Waals crystal*, Nature Communications 15, 9727 (2024).

[2] N. Melchioni, A. Mancini, L. Nan, A. Efimova, G. Venturi, and A. Ambrosio, *Giant optical anisotropy in a natural van der Waals hyperbolic crystal for visible light low-loss polarization control*, ACS Nano (2025), DOI: 10.1021/acsnano.5c07323.

Rotation and Self-Ordering of Nanoparticles by Optical Forces Carrying Angular Momentum

H. Ishihara[1,2,*]

[1] Research Organization of Science and Technology, Ritsumeikan University, Japan
[2] SANKEN, The University of Osaka, Japan
*Corresponding author: ishi@mp.es.osaka-u.ac.jp

***Abstract*— We present optical manipulation of nanoparticles using focused beams carrying angular momentum. Generalized optical binding stabilizes rotational motion of nanoparticle assemblies and enables fusion-driven self-ordering via scattered-light interactions. We also analyze how stimulated recoil force (SRF) from resonant stimulated emission modifies optical-vortex-driven rotation, suggesting experimental signatures such as rotation reversal.**

***Keywords*— optical forces, optical vortices, nanoparticles, stimulated recoil force.**

I. Introduction

Since the invention of optical tweezers by Ashkin et al. [1], optical manipulation techniques for nano- and microparticles have advanced significantly. These techniques are now widely used across various fields of fundamental research and practical applications. A particularly promising direction is the manipulation of nanoscale materials, where precise control remains challenging.

Recently, optical forces associated with angular momentum have attracted significant interest. For instance, optical binding and rotation of metallic nanoparticle assemblies have been demonstrated under circularly polarized light [2,3], where hexagonal assemblies form beyond the focal spot and exhibit rotational motion. Optical vortices can also induce particle rotation that follows the sign of the light's orbital angular momentum, and chiral surface structures can be generated by optical vortices, reflecting their angular momentum [4]. In this paper, we introduce generalized optical binding in nanoparticle assemblies and the formation of ordered structures using two circularly polarized laser beams. We further explore, theoretically, how stimulated emission affects optical-vortex-driven rotation.

II. Results and Discussion

(1) It is known that when a focused laser beam traps gold nanoparticles, additional particles can become bound outside the focal spot, forming structures often at distances corresponding to integer multiples of the incident wavelength (in the surrounding medium). When the beam is circularly polarized, a hexagonal pattern forms and the assemblies rotate. Notably, the rotation direction does not necessarily align with the handedness of the circular polarization [2,3]. In our study [5], we analyzed this rotational motion in terms of spin–orbit coupling and angular momentum generation, and showed that the rotation direction of bound particles can be controlled by adjusting the numerical aperture of the focused beam. These results provide insights into the creation and control of large-area ordered nanoparticle assemblies using scanning laser beams.

(2) We extended the above theoretical study to the case of two laser beams and investigated generalized optical binding [6]. When particle assemblies are irradiated with two beams, two hexagonal arrays form, and their mutual interaction begins through the scattered field. Their rotations stop at specific separations and relative angles, forming distinctive standing-wave-like intensity patterns between them. This behavior differs from conventional optical binding between two individual particles, because the assemblies possess additional degrees of freedom, including collective rotation. Interestingly, when the two beams approach each other with a slight tilt, the assemblies can fuse and undergo reordering. This fusion-driven mechanism may provide a step-by-step route to large-area ordered nanoparticle structures

(3) For effective optical manipulation of nanoparticles, a promising approach is to use light resonant with electronic transitions in nanostructures [7]. Conventional resonant manipulation relies on absorption or scattering. We proposed a recoil optical force induced by stimulated emission, known as the stimulated recoil force (SRF) [8]. In relevant regimes, SRF can be less susceptible to saturation under strong driving than absorption-based forces, depending on the level structure and pumping scheme, leading to a substantially enhanced force. Experimental confirmation of SRF has been reported [9], and we proposed a scheme to sort nanodiamonds using SRF [10]. A key question is how SRF influences optical-vortex-driven rotation. We present a theoretical demonstration suggesting that SRF can be detected by monitoring changes, including possible inversion, of nanodiamond rotational motion in experiments

III. Conclusion

We reviewed our recent studies on angular-momentum

optical forces, highlighting generalized optical binding that stabilizes and reconfigures rotating nanoparticle assemblies, including fusion-driven self-ordering. We further showed that SRF can qualitatively alter optical-vortex-driven rotation, offering a practical signature for identifying SRF via rotational reversal and related changes.

ACKNOWLEDGMENTS

The author is grateful to M. Ashida, M. Tamura, T. Yokoyama, and Y. Tao for valuable collaboration and insightful discussions. This work was partially supported by JSPS KAKENHI (Grant Nos. JP21H05019 and 24K21196).

REFERENCES

[1] A. Ashkin, J. M. Dziedzic, J. E. Bjorkholm, and S. Chu, "Observation of a single-beam gradient force optical trap for dielectric particles," Opt. Lett., vol. 11, pp. 288–290, 1986.

[2] F. Han, J. A. Parker, Y. Yifat, C. Peterson, S. K. Gray, N. F. Scherer, and Z. Yan, "Crossover from positive to negative optical torque in mesoscale optical matter," Nat. Commun., vol. 9, pp. 1–8, 2018.

[3] T. Kudo, S.-J. Yang, and H. Masuhara, "A single large assembly with dynamically fluctuating swarms of gold nanoparticles formed by trapping laser," Nano Lett., vol. 18, pp. 5846–5853, 2018.

[4] K. Toyoda, K. Miyamoto, N. Aoki, R. Morita, and T. Omatsu, "Using optical vortex to control the chirality of twisted metal nanostructures," Nano Lett., vol. 12, pp. 3645–3649, 2012.

[5] Y. Tao, T. Yokoyama, and H. Ishihara, "Rotational dynamics of indirect optical bound particle assembly under a single tightly focused laser," Opt. Express, vol. 31, pp. 3804–3820, 2023.

[6] Y. Tao, T. Yokoyama, and H. Ishihara, "Generalized optical binding for multiple assemblies of nanoparticles under multiple laser beams," Nano Lett., vol. 24, pp. 11960–11967, 2024.

[7] H. Ishihara, "Optical manipulation of nanoscale materials by linear and nonlinear resonant optical responses," Adv. Phys.: X, vol. 6, Art. no. 1885991, 2021.

[8] T. Kudo and H. Ishihara, "Proposed nonlinear resonance laser technique for manipulating nanoparticles," Phys. Rev. Lett., vol. 109, Art. no. 087402, 2012.

[9] T. Kudo, B. Louis, H. Sotome, J. J. K. Chen, S. Ito, H. Miyasaka, H. Masuhara, J. Hofkens, and R. Bresolí-Obach, "Gaining control on optical force by the stimulated-emission resonance effect," Chem. Sci., vol. 14, p. 10087, 2023.

[10] T. Horai, T. Wada, Y. Saito, Y. Makino, M. Ashida, and H. Ishihara, "Proposed optical manipulation of nanoparticles to access and select emission lines," Nano Lett., vol. 25, pp. 2785–2792, 2025.

Photoinduced magnetic phase transitions in the Kondo-lattice model

Masahito Mochizuki[1,*] and Ryo Hamano[1]

[1]Department of Applied Physics, Waseda University, Japan
*Corresponding author: masa_mochizuki@waseda.jp

***Abstract*—We theoretically investigate photoinduced magnetic phase transitions in the cubic Kondo-lattice model and show that light irradiation drives a magnetic phase transition from a ferromagnetic ground state to three-dimensional antiferromagnetic nonequilibrium steady state. This transition is induced by photoinduced pseudo half-filling of the exchange-split band and is accompanied by transient antiferromagnetic correlations.**
***Keywords* photoinduced magnetic phase transition, Kondo-lattice model, nonequilibrium steady state**

I. Introduction

Light-matter interaction enables ultrafast and energy-efficient control of nonequilibrium material states, and photoinduced magnetic phase transitions have attracted great interest, especially in spin-charge coupled systems such as Kondo-lattice magnets [1]. While previous theoretical studies have mainly focused on two-dimensional systems, understanding photoinduced magnetism in three dimensions is essential for realistic materials. We thus theoretically study photoinduced phase transitions in a cubic Kondo-lattice model [2].

II. Methods

We numerically simulate spatiotemporal dynamics of itinerant electrons and localized spins in the photodriven cubic Kondo-lattice model described by the time-dependent Hamiltonian $\mathcal{H}(\tau) = \mathcal{H}_{\rm kin}(\tau) + \mathcal{H}_{\rm exc}(\tau)$ with

$$\mathcal{H}_{\rm kin}(\tau) = \sum_{\langle i,j\rangle,s} t_{ij}(\tau)\, c_{is}^{\dagger} c_{js} + \text{h.c.} \tag{1}$$

$$\mathcal{H}_{\rm exc}(\tau) = -\frac{J}{2S} \sum_{i,s,s'} \boldsymbol{S}_i(\tau) \cdot c_{is}^{\dagger} \boldsymbol{\sigma}_{ss'} c_{is'}, \tag{2}$$

where

$$t_{ij}(\tau) = \begin{cases} -t & (\tau < 0) \\ -t \exp[-i\boldsymbol{A}(\tau)\cdot(\boldsymbol{r}_i - \boldsymbol{r}_j)] & (\tau \geq 0). \end{cases} \tag{3}$$

Here $\boldsymbol{A}(\tau)$ is a time-dependent vector potential of the light electromagnetic field. The following three cases with different light polarizations are examined: (1) linearly polarized light with $\boldsymbol{E} \parallel [100]$, (2) linearly polarized light with $\boldsymbol{E} \parallel [110]$, and (3) circularly polarized light.

We study the spin-charge dynamics of this model by numerically solving the time-dependent Schrödinger equation and the Landau-Lifshitz-Gilbert equation simultaneously [3]. The equations are given, respectively, by,

$$i\frac{\partial}{\partial \tau} |\tilde{\Psi}_\alpha(\tau)\rangle = \mathcal{H}(\tau) |\tilde{\Psi}_\alpha(\tau)\rangle \tag{4}$$

and

$$\frac{\partial \boldsymbol{S}_i(\tau)}{\partial \tau} = \boldsymbol{h}_i^{\rm eff}(\tau) \times \boldsymbol{S}_i(\tau) + \frac{\alpha_{\rm G}}{S} \boldsymbol{S}_i(\tau) \times \frac{\partial \boldsymbol{S}_i(\tau)}{\partial \tau}. \tag{5}$$

III. Results and Discussion

We find that light irradiation drives a transition from a ferromagnetic ground state to three-dimensional antiferromagnetic nonequilibrium steady state in the cubic Kondo-lattice model. This photoinduced magnetic phase transition originates from pseudo half-filling of the exchange-split band and is accompanied by transient antiferromagnetic correlations.

IV. Conclusion

We theoretically investigated photoinduced magnetic phase transitions in the cubic Kondo-lattice model and demonstrated that light irradiation drives a transition from ferromagnetism to three-dimensional G-type antiferromagnetism via dynamical localization and pseudo half-filling of the exchange-split band. Transient A-type or C-type antiferromagnetic correlations emerge depending on light polarization. We have also performed a Floquet magnon analysis which reveals that polarization-dependent magnon softening underlies these nonequilibrium magnetic instabilities. Our findings provide important insights into the understanding of photoinduced magnetic phase transitions in the three-dimensional Kondo-lattice magnets.

Acknowledgments

This work was supported by JSPS KAKENHI (No. 24H02231 and No. 25H00611), JST CREST (No. JPMJCR20T1).

References

[1] M. Mochizuki, Theoretical Perspectives on Optical Control of Magnetism in Spin-charge Coupled Systems, J. Phys. Soc. Jpn. **94**, 111004 (2025).
[2] R. Hamano, and M. Mochizuki, Photoinduced magnetic phase transitions in the cubic lattice double-exchange model, Phys. Rev. B **111**, 214409 (2025). DOI: 10.1103/PhysRevB.111.214409 (arXiv:2504.12881)
[3] T. Inoue and M. Mochizuki, Photoinduced 120-degree spin order in the Kondo-lattice model on a triangular lattice, Phys. Rev. B **105**, 144422 (2022).

GHz acoustic vortex for the manipulation of orbital angular momentum of light

Alessandro Pitanti[1,2,*], Paulo V. Santos[3]

[1]Department of Physics, University of Pisa, Italy
[2]NEST Lab., CNR - NANO, Italy
[3]Paul-Drude-Institut für Forstekörperelektronik, Germany
*Corresponding author: alessandro.pitanti@unipi.it

***Abstract*—Acoustic perturbation of photonic structures enables dynamic modulation of light amplitude and phase at ultra high frequencies. By shaping acoustic fields, fast control of light angular momentum becomes possible. We report GHz acoustic vortices for advanced light modulators.**

***Keywords*— acoustic vortex, ultra-high frequency, OAM.**

I. Introduction

Light based telecommunication promises to overcome the limitations of microwave systems by enabling amplitude and phase modulation well beyond the 100s of GHz range. However, its large scale adoption is still hindered by sensitivity to atmospheric perturbations, power consumption, and the need for compact integrated devices. A promising strategy is to exploit additional degrees of freedom of light, such as spin and orbital angular momentum (OAM), to fully leverage the vectorial nature of photons [1], [2]. Encoding information in polarization or OAM improves robustness in highly scattering environments [3] and enables massive data rate increases via multiplexing [4]. Currently, accessible OAM bases are limited by quasi-static generators relying on phase masks or metasurfaces. A fast, tunable, free space OAM generator would therefore be transformative. Here we propose controlling light OAM using GHz mechanical vortices generated by bulk acoustic waves (BAW) [5].

II. Methods

BAW based devices are an established and robust technology for high frequency microwave filtering, operating in the tens of GHz range and beyond. They rely on longitudinal acoustic resonances confined between the top and bottom surfaces of a substrate and excited by a bulk acoustic wave resonator (BAWR) consisting of a piezoelectric layer between metallic electrodes.

Acoustic vortex generation is achieved by engineering the geometry of the BAWR top electrode, which shapes the transverse acoustic wavefront. An Archimedean spiral of order M, defined as $\mathrm{AS}(\theta) = R_0 + \delta R \mod (M\theta, 2\pi)/2\pi$, imposes the phase condition for an acoustic vortex with topological charge $\ell = \delta R/\lambda$, where λ is the acoustic wavelength. Using a 700 nm ZnO BAWR on sapphire operating from 0.5 to 7.5 GHz, we demonstrate tunable ℓ values from 1 to 13 and beyond, validating the device as a high frequency, tunable acoustic vortex generator.

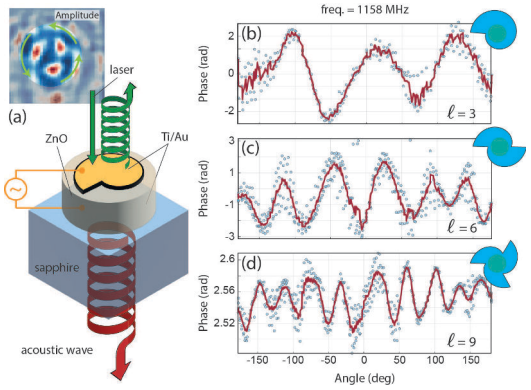

Fig. 1. (a) Device concept and acoustic map. (b) Topological charge scaling with spiral order.

III. Results and Discussion

Using laser interferometry, we mapped the acoustic vortex and demonstrated coherent phase transfer from acoustic excitations to optical fields via the moving boundary effect. Future work will focus on optimizing optomechanical coupling to achieve strong phase modulation and obtain an orthogonal angular momentum basis for light. Promising directions include copropagating schemes and the integration of tailored photonic cavities within the substrate.

Acknowledgments

This work was supported by the CNR-NANO project AUTOCUBE

References

[1] D. Ivanovich et al., "Polarization division multiplexing for optical data communications," *Opt. Interconn. XVIII*, pp. 10538, 2018.
[2] P. Martelli et al., "Free-space optical transmission with orbital angular momentum division multiplexing," *Electr. Lett.*, vol. 47, pp. 972, 2011.
[3] L. Gong et al., "Optical orbital-angular-momentum-multiplexed data transmission under high scattering," *Ligh Sci. Appl.*, vol. 8, pp. 27, 2019.
[4] J. Wang et al., "Terabit free-space data transmission employing orbital angular momentum multiplexing," *Nat. Phot.*, vol. 6, pp. 488, 2012.
[5] A. Pitanti, N. Ashurbekov, I. dePedro-Embid, M. Msall, and P. V. Santos, "GHz acousto-optic angular momentum with tunable topological charge," *Nat. Comm.*, vol. 16, pp. 8116, 2025.

Analyzing Nanoscopic Light–Matter Interactions Using Reconfigurable Photonic Integrated Circuits

Marko Šimić[1,2], Johannes Bütow[1,2], Jörg S. Eismann[1,2], Sarah Lindner[1], Peter Banzer[1,2,*]

[1]Institute of Physics, University of Graz, NAWI Graz, Universitätsplatz 5, A-8010 Graz, Austria
[2]Christian Doppler Laboratory for Structured Matter Based Sensing, Institute of Physics, Universitätsplatz 5, A-8010 Graz, Austria
*Corresponding author: peter.banzer@uni-graz.at

***Abstract*—The measurement and description of light-matter interactions at the nanoscale lie at the heart of most nano-optics applications. Here we present a combination of nano-optics experiments and reconfigurable photonic integrated circuits, establishing the basis for nanoscale particle localization and multipolar decomposition of scattered fields.**

***Keywords*— nanooptics, integrated photonics, particle metrology.**

I. Introduction

Understanding light-matter interactions at the nanoscale is central to nano-optics, with applications in high-resolution microscopy [1], sensing [2], and optical manipulation [3]. Light scattered from nanoscale structures carries detailed information encoded in intensity, phase, and polarization, which are governed by a scatterer's characteristics, such as the geometry, material composition, and the resulting multipolar contributions. However, accessing the scattered light fields at the nanoscale remains challenging, as conventional cameras are restricted to intensity-based measurements only. Over the past years, reprogrammable photonic integrated circuits (rPICs) have emerged as a versatile solution for polarization- and phase-resolved measurement [4], [5] and generation [6] of (structured) light fields, thus allowing for flexible use in nano-optics applications.

II. Methods

In this paper, we present a custom-built nano-optics setup [7], [8] combined with an rPIC for the localization and multipolar scattering decomposition of individual nanoparticles. This approach is enabled by spatially sampling and analyzing the response of a nanoparticle to excitation with a tightly focused laser beam. Our setup consists of a high numerical aperture objective (NA = 0.9) that tightly focuses a linearly polarized Gaussian beam onto a nanoparticle located on a glass substrate (see Fig. 1). A second high NA objective (NA = 1.3) index matched to the substrate collects both the incoming and scattered light fields. By imaging the back focal plane of the collection objective, we map the angular spectrum (k-space) of the scattered fields onto the free-space interface of our photonic chip. An array of circularly arranged grating couplers spatially samples and distributes light into a mesh of Mach-Zehnder interferometers of the PIC [4], [5] (see Fig. 2). By actively reconfiguring the on-chip interferometers, we guide light across the photonic circuit, enabling the analysis of scattered light fields as the particle is moved across the tightly focused laser beam.

Fig. 1. Schematics of the nano-optics free-space setup combined with a photonic integrated circuit for particle metrology. An incoming Gaussian beam is tightly focused onto a nanoparticle using a high NA objective (NA = 0.9). The scattered light is collected with another high NA objective (NA = 1.3, index matched) and imaged onto the free-space interface of the photonic chip (see also Fig. 2).

III. Results and Conclusion

We analyze the sampled light by employing our theoretical framework based on transmission-matrix theory to infer detailed information about the intensity, phase, and polarization of the scattered light field, ultimately providing the basis for particle parameter retrieval such as position and multipolar contribution to the scattering. This is supported by a calibration

of the PIC outside the imaging path, where we use a well-defined reference beam with a flat phase front and uniform intensity distribution [5].

Fig. 2. Schematics of the photonic integrated circuit for processing light fields, as obtained by sampling the back-focal plane of the collecting objective through an array of circularly arranged grating couplers. On-chip processing of the incoming light is performed by a reconfigurable mesh of Mach-Zehnder interferometers, providing information about the intensity, phase, and polarization of the scattered light by analyzing the output ports of the photonic circuit.

We discuss the basic physical principles underlying our retrieval approach and demonstrate its applicability on the example of a silicon nanoparticle featuring rich resonance spectra.

Our results prove that the combination of tightly focused light fields with a reconfigurable photonic chip provides a versatile platform for field-resolved particle localization, sensing, and future nano-optics applications [9].

ACKNOWLEDGMENTS

Financial support from the Austrian Federal Ministry of Labour and Economy, the National Foundation for Research, Technology and Development, and the Christian Doppler Research Association is gratefully acknowledged.

REFERENCES

[1] Eismann, J. S. et al., "Sub-diffraction-limit fourier-plane laser scanning microscopy", *Optica*, Vol. 9, No. 5, pp. 455–460, 2022.
[2] Šimić, M. et al., "Optofluidic Force Induction: A Workbench for Nanoparticle Characterization and Material Analytics", *Nano Letters*, Vol. 25, No. 22, pp. 8805–8813, 2025.
[3] Šimić, M. et al., "Real-time nanoparticle characterization through optofluidic force induction", *Physical Review Applied*, Vol. 18, No. 2, pp. 024056, 2022.
[4] Bütow, J. et al., "Photonic integrated processor for structured light detection and distinction", *Communication Physics*, Vol. 6, No. 1, pp. 369, 2023.
[5] Bütow, J. et al., "Spatially resolving amplitude and phase of light with a reconfigurable photonic integrated circuit", *Optica*, Vol. 9, No. 8, pp. 939–946, 2022.
[6] Bütow, J. et al., "Generating free-space structured light with programmable integrated photonics", *Nature Photonics*, Vol. 18, No. 3, pp. 243–249, 2024.
[7] Woźniak, P. et al., "Selective switching of individual multipole resonances in single dielectric nanoparticles", *Laser & Photonics Reviews*, Vol. 9, No. 2, pp. 231–240, 2015.
[8] Eismann, J. S. et al., "Nanoscale Vectorial Electric and Magnetic Field Measurement", *ACS Photonics*, Vol. 12, No. 1, pp. 522–527, 2024.
[9] Šimić, M. et al., Reconfigurable Integrated Photonics Tools for Nano-Optics Applications, In preparation.

Magnetic Multipole Dependent Dichroism Arising from Vortex Light

A. Salam

Department of Chemistry, Wake Forest University, Winston-Salem, NC 27109, USA
salama@wfu.edu

Abstract: QED theory is used to calculate circular and vortex dichroism induced by structured light in a magnetically susceptible molecule. The magnetic dipole-quadrupole cross term arising from the interference of transverse and longitudinal magnetic fields results in non-vanishing dichroic effects, explaining the recent observation of helical dichroism in artificial propeller meta-molecules.

Recently, a propeller meta-molecule was fabricated via the nano-Kirigami method [1]. On irradiation with vortex light, helical dichroism was observed and attributed to orbital angular momentum possessed by the twisted beam. A novel mechanism was proposed to explain the differential absorption in this property of light, whose wavefronts propagate as left- or right-handed helices. This involved the interference of magnetic dipole and magnetic quadrupole coupling terms induced in the stereo-twisted blades of the meta-molecule. Often the dipole approximation is sufficient to describe dichroic effects occurring in chiral species such as molecules [2], for example the differential absorption of circularly polarized light, also known as circular dichroism (CD) [3]. Lower elements of symmetry in such handed forms of matter justifies including the next higher term beyond the dominant electric dipole interaction in the multipole expansion of the charge and current density distributions, namely the magnetic dipole coupling term, with the interference of these two contributions yielding a time-even parity-odd pseudoscalar quantity that changes sign when one structural isomer is substituted by its mirror-image form. In situations where the dipole approximation needs to be relaxed, such as when the dimensions of the absorber are large relative to the wavelength of light, the electric quadrupole interaction term is also added, with CD arising from the electric dipole-quadrupole interference contribution non-vanishing for anisotropic systems [3]. Chiroptical phenomena of this type have commonly been examined when electromagnetic radiation is described as a plane wave. Higher-order magnetic multipole coupling terms are therefore rarely invoked.

We present a quantum electrodynamical theory [2,4,5] of one-photon absorption induced by a circularly polarized optical vortex beam in a molecule characterized by magnetic dipole and magnetic quadrupole moments. The structured light is described by a Laguerre-Gaussian form which is a solution of the paraxial wave equation in plane polar coordinates [6]. Such a light field possesses orbital angular momentum in addition to spin angular momentum, with the former represented by the topological charge or winding number, l, and azimuthal phase angle, φ, and the latter by left- and right-handed circularly polarized vector components, σ. This results in the possibility of not only CD occurring, but also helical or vortex dichroism (VD) taking place, as well as coupling of spin and orbital angular momentum components of light, giving rise to circular vortex dichroism (CVD) [7]. The matrix element and Fermi golden rule absorption rate is calculated, along with formulae for the various dichroic effects, for contributions that are dependent on magnetic dipole and quadrupole moments.

Proceedings of META 2026 · Dublin, Ireland · 14–17 July 2026 · ISSN 2429-1390 · pp. 532–533

To ensure that no differential spin and orbital angular momentum effects are overlooked, the longitudinal magnetic field and its gradient, as well as the usual analogous quantities involving the transverse field, are included in the development. Previously, it was shown that only accounting for transverse fields led to zero VD for oriented and isotropic dipolar systems [6], while a non-vanishing VD occurs when longitudinal fields are added [8]. Since the action of the gradient operator on both the transverse and longitudinal structured light forms of the electric displacement field introduce a linear dependence on the topological charge, l, the electric dipole-quadrupole cross-term results in VD manifesting for the anisotropic situation [8].

In the present case, in which only magnetic dipole and quadrupole coupling terms are considered, it was found that the rates for CD, VD or CVD arising from the transverse magnetic field are all zero for the isotropic purely magnetic dipole contribution, while the corresponding contribution due to the longitudinal field exhibited CD only. Furthermore, all three forms of dichroism are found to be non-vanishing when the magnetic dipole-quadrupole cross-term is extracted from the interference of the transverse and longitudinal field and field gradient components, holding for oriented species and surviving a free rotational average. This explains the observation of helical or vortex dichroism in propeller meta-molecules and allows for the possibility of CD and CVD to also be detected.

References

1. Ji, C.-Y. *et al*, “Observation of Magnetic Quadrupole Allowed Helical Dichroism in Artificial Propeller Molecules”, Adv. Opt. Mat., Vol. 12, 2302795, 2024.

2. Craig, D. P. and T. Thirunamachandran, Molecular Quantum Electrodynamics, Dover, 1998.

3. Power, E. A. and T. Thirunamachandran, “Circular Dichroism: A General Theory Based on Quantum Electrodynamics”, J. Chem. Phys., Vol. 60, 3695, 1974.

4. Salam, A., Molecular Quantum Electrodynamics, Wiley, 2010.

5. Salam, A., “Quantum Electrodynamics Effects in Atoms and Molecules”, WIREs Comput. Mol. Sci., Vol 5, 178, 2015.

6. Andrews, D. L., L. C. D. Romero and M. Babiker, “On Optical Vortex Interactions with Chiral Matter”, Opt. Comm., Vol. 237, 133, 2004.

7. Forbes, K. A. and D. L. Andrews, “Orbital Angular Momentum of Twisted Light: Chirality and Optical Activity”, J. Phys. Photonics, Vol. 3, 022007, 2021.

8. Forbes, K. A. and G. A. Jones, “Optical Vortex Dichroism in Chiral Particles”, Phys. Rev. A, Vol. 103, 053515, 2021.

Emergent Spin-Orbital Berry Curvature Fluxes in pseudo-Nodal Semimetals

Peter C. Schmitz[1,2*], Dongwook Go[3], Yuriy Mokrousov[1,4]

[1]Peter Grünberg Institute 1 Quantum Theory of Materials, Research Center Jülich, Germany
[2]Institute for Theoretical Solid State Physics, RWTH Aachen University, Germany
[3]Department of Physics, Korea University Soul, South Korea
[4]Department of Physics, Johannes-Gutenberg University Mainz, Germany

*Corresponding author: peter.christian.schmitz@rwth-aachen.de

Abstract— We investigate the relationship between crossings in Spin-Orbital-texture and the Berry-curvature-flux, in terms of divergence and vorticity, on avoided-crossing-manifolds in the Brillouin zone of analytic models and Van-der-Waals materials with Spin-Orbit coupling.

Keywords— Chirality, Spin-Orbital Texture, Spin-Hall Effect, Berry Curvature, Electrodynamics.

I. Introduction

While the topological classification of band structures has expanded rapidly, some of its foundations remained inconsistent: Could avoided crossings be the main sources of Berry curvature [1], rather than Dirac points ? Having a singularity at such, how do the textures of Spin/Orbital polarization translate to their Berry curvature counterpart ? And do these fields contain more than just scalar charges, possibly vorticity ? While Spin Weyl insulators [2], and pseudo-nodal line/ -sphere semimetals [3] have been studied by the community, it is necessary to employ Gauss+Stokes analysis of the vectorized BC to account for the chiral spin texture with a modified gauge [4] of the full perturbative spin current formula below.

II. Methods

We map the Spin texture and associated Berry curvature in momentum space, which allows to identify Bloch points at which the polarization vanishes or rotates in-plane, such that the Spinor wave-function gets twisted. We find that such SU(2) curvature is composed of 3 terms, namely an ordinary U(1) curvature within the spin channels, a twist of the channels resembling the skyrmion index, and a mixed torque of the spin texture under change of momentum.

$$\begin{aligned}\boldsymbol{\Omega}^{SU(2)}_{k_xk_y} &= -2\,\mathrm{Im}\left\langle \partial_{k_x}\begin{pmatrix}\chi_\uparrow\\ \chi_\downarrow\end{pmatrix} \middle| \partial_{k_y}\begin{pmatrix}\chi_\uparrow\\ \chi_\downarrow\end{pmatrix}\right\rangle \\ &= \nabla_{\mathbf{k}} \times \mathbf{A}_{U(1)} - i\left[\frac{\partial H}{\partial S_x},\frac{\partial H}{\partial k_y}\right] - i\left[\frac{\partial H}{\partial S_y},\frac{\partial H}{\partial k_x}\right] \\ &= \boldsymbol{\Omega}^{U(1)}_{kk} + \boldsymbol{\tau}_{sk} + \mathbf{S}\cdot\left(\partial_{k_x}\mathbf{S}\times\partial_{k_y}\mathbf{S}\right) \\ &= \sum_{n\neq m}\left[\frac{\langle n|v_{k_x}|m\rangle\langle m|v_{k_y}|n\rangle}{(E_n-E_m)^2} + \frac{\langle n|v_{S_x}|m\rangle\langle m|v_{S_y}|n\rangle}{(S_n-S_m)(E_n-E_m)} + \frac{\langle n|v_{S_x}|m\rangle\langle m|v_{S_y}|n\rangle}{(S_n-S_m)^2}\right]\end{aligned}$$

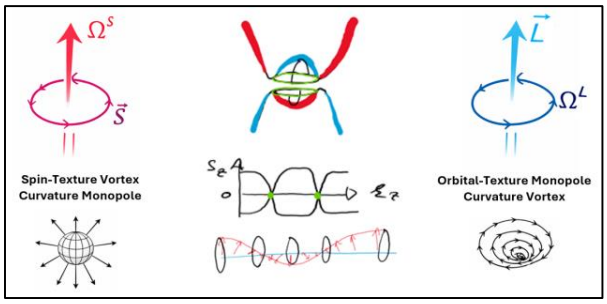

Fig. 1 Mechanism of Texture / Curvature conversion at avoided crossing.

III. Results and Discussion

We find in analytic derivation, simple models and DFT calculations of real systems that (Fig.1):

- SU2 curvature has divergence, torque and vorticity
- interaction manifolds with $S_z = 0$ are sources of Ω_S
- Rotation of Spin texture is a source of curvature
- A source of Oribtal texture rotates the Spin texture
- Spin-Orbit coupling transfers and adds curvatures

These results shed light on the curvature generating effects of Spin-Orbit coupling and similar symmetry-breaking terms which are the origin of abundant avoided crossing manifolds in the Brillouin Zone of materials.

IV. Conclusion

We show solid evidence to construct an effective Electromagnetism between Spin/Orbital texture and their Berry curvatures. Progress and limitations of these developments are discussed and connected with multiple fields in the community.

Acknowledgments

We acknowledge support by RWTH (CLAIX) and FZJ (JUREKA).

References

[1] M.A. Wilde and C. Pfleiderer, “Large curvature near a small gap”, Nature Physics 18, 731–740 (2022).
[2] R. González-Hernández and B. Uribe, “Spin Weyl Topological Insulators”, PRB, 109, 045126 (2024)
[3] J. Wang, W. Duan, F. Liu and B. Huang, “Pseudo Dirac nodal sphere semimetal”, PRB 98, 201112 (2018).
[4] F. Pientka, I. Mertig and B. L. Gyorffy, “Gauge Freedom for degenerate Bloch states”, PRB 86, 054413 (2012).

Excitonic Charge Density Waves in Moire Ladders

Paula Mellado[1,*], Javiera Cabezas[2], Francisco Muñoz[2]

[1]Facultad de Ingeniería y Ciencias, Universidad Adolfo Ibáñez, Santiago, Chile.
[2]Departamento de Física, Facultad de Ciencias,
Universidad de Chile and CEDENNA, Santiago, Chile
*Corresponding author: paula.mellado@uai.cl

***Abstract*—We analyze a half-filled four-band ladder with a relative shift between legs that generates a moiré supercell and narrows minibands near the Fermi level. Short-range interactions produce an excitonic incommensurate CDW with a gapped Higgs mode and neutral phasons, whose velocity depends on the mismatch, suggesting an excitonic origin for $HfTe_3$.**

***Keywords*— Incommensurate charge density wave, excitons, moire, phason, ladder.**

I. Introduction

Layer mismatch in real materials often arises from differences between intra- and interlayer bonding, or from twisting, pressure, and strain. Such incongruities are common in low-dimensional systems and frequently lead to charge-density-wave (CDW) instabilities. While CDWs are often associated with the Peierls mechanism driven by electron–phonon coupling, many materials display charge ordering that cannot be explained by simple Fermi-surface nesting, pointing instead to interaction-driven or excitonic scenarios. In a CDW state, the charge density forms a standing-wave pattern described by a complex order parameter with amplitude and phase components. Fluctuations of these components give rise to collective modes: a gapped amplitudon and a phason, which becomes gapless in incommensurate states. Neutral phasons are of particular interest, as they may enable dissipationless collective transport and shed light on the interplay between charge order and superconductivity.

II. Model

We study a toy model of a heterostructure consisting of a half-filled, four-band ladder with a relative shift between the legs $\delta = p/q$, which creates a moiré supercell of q composite cells and a moiré potential that compresses layer bands into flat minibands near the Fermi level. The ladder of Fig.1(a) consists of two coupled legs, each with two sites (A and B) per unit cell. The composite ladder unit cell contains a total of four sites $\{A_1, B_1, A_2, B_2\}$ (subscripts $1, 2$ label legs). Throughout, we choose a, half the legs lattice constant, as the length unit, so the composite cell has a length equal to 2, and the original reciprocal period is $G_0 = \pi$. Leg-1 is uniform, while leg-2 is dimerized by a shift δ per cell. This becomes the moiré parameter of the ladder, $\delta = p/q \in (0, 1)$, where p and q are coprime integers.

III. Results and Discussion

The relative mismatch between legs yields a moiré supercell of q composite cells with $4q$ sites in total, a moiré reciprocal vector in the reduced Brillouin zone (RBZ) $b_s = \frac{G_0}{q} = \frac{\pi}{q}$, and a real-space supercell length $L_s = 2\,q$. The intra-leg nearest neighbor hopping, t, sets the bandwidth $W \sim 4t$. Inter-leg hopping (rung tunneling) occurs between the same sublattice, and its average is t. Schrieffer–Wolff perturbation theory [1] gives rise to a first-harmonic rung tunneling of amplitude $t_1 = (1-\delta)t$ modulated by the envelope $t_\perp(n) = t + t_1 \cos\left(\frac{2\pi n}{q}\right)$. The kinetic Hamiltonian is $H = \sum_k \Psi_k^\dagger\, H(k)\, \Psi_k$, with $\Psi_k = (c_{1,A,k}, c_{1,B,k}, c_{2,A,k}, c_{2,B,k})^\top$, and

$$H(k) = \begin{pmatrix} 0 & c(k) & t_\perp(k) & 0 \\ c(k) & 0 & 0 & t_\perp(k) \\ t_\perp(k) & 0 & 0 & c_\delta(k)\, e^{+i\phi(k)} \\ 0 & t_\perp(k) & c_\delta(k)\, e^{-i\phi(k)} & 0 \end{pmatrix}, \tag{1}$$

The Hamiltonian matrix of Eq.1 is given in the extended Brillouin zone (EBZ), $\mathrm{k} \in (-\mathrm{qG}_0, \mathrm{qG}_0)$. For a given δ, the similarity transformation $\Delta = \pi q$ applied to $H(k)$ imposes constraints on p and q that determine the generic global period $2\pi q$ that gives rise to EBZ.

Including Coulomb interactions within a mean-field approach, we find an excitonic incommensurate CDW phase characterized by a rung-odd charge-density modulation, leading to long-lived neutral phason excitations. We show that the moiré phasons of our model are Goldstone modes of the effective interacting theory in which the CDW slips, with a speed controlled by δ and the inter-leg tunneling amplitude.

The moiré-based framework developed here is naturally suited to quasi-1D materials with chain-like structural motifs. As a concrete example, we examine the transition-metal trichalcogenide $HfTe_3$, whose bulk displays charge-density-wave order [2], [3]. DFPT calculations on the surface reveal a phonon instability at $q \simeq 0.06\mathbf{b}^*$ involving out-of-plane motion of the dimerized Te chains, generating a long-wavelength structural modulation. This distortion is accommodated in a $12\times1\times1$ supercell, whose relaxed geometry develops a chain-dependent phase shift—an explicit real-space moiré pattern emerging at negligible energetic cost. A Wannier analysis shows dominant intra-chain dimerization and weak inter-chain tunneling, motivating a reduced strong-coupling model with chain-dependent oscillatory hoppings. The resulting moiré

Hamiltonian reproduces the flat minibands, band reconstruction, and gap openings obtained in the DFT supercell, demonstrating that the instability-driven modulation reshapes the low-energy electronic structure in direct analogy with moiré systems. The changes in the charges due to modulation have a dipolar pattern consistent with long-range neutral excitations.These results highlight chain-dependent phase shifts and structural incongruities as a microscopic pathway to electronic instabilities in quasi-1D materials.

Fig. 1. (a) Schematic illustration of the effective moiré ladder model. The moiré modulation does not arise from a geometric lattice mismatch but from a long-wavelength modulation of the inter-leg tunneling, representing an emergent symmetry-broken state (b-d) Band spectra of the kinetic Hamiltonian $H(k)$ in the EBZ at (b) $\delta = 1$, (c) $\frac{19}{20}$ and (d) $\frac{17}{20}$.

IV. Conclusions

In this work, we demonstrate that the ordered phase of the moiré-modulated two-leg ladder realizes an excitonic charge-density wave. Microscopically, it is characterized by a particle–hole condensate formed between two flat minibands. Rung modulation produces a small indirect band gap, which permits interband particle–hole pairing, analogous to the mechanism of excitonic insulators in multiband semimetals. At the mean-field level, the resulting Hamiltonian is algebraically equivalent to a BCS Hamiltonian, except that the usual pairing sector is replaced by particle–hole coherence. Because the CDW in this electronic model does not couple to the lattice and breaks a continuous symmetry, the system hosts a neutral acoustic phason, which is the Goldstone mode of the excitonic condensate. The dispersions of the CDW collective modes, the phason and the amplitudon, appear in the two-particle spectral function computed from the retarded susceptibility, whose imaginary part also depicts the CDW continuum at higher energies.

As the effective interleg modulation amplitude is proportional to $(1-\delta)$, both the miniband width and the relevant Fermi velocity scale as $(1-\delta)t$, the phason stiffness scales as $(1-\delta)^2 t$, whereas the phason inertia maintains the $1/t$ scaling, up to weak δ-dependent corrections. Consequently, the phason velocity scales as $t(1-\delta)$.

Acknowledgments

P.M. acknowledges support from the Fondo Nacional de Desarrollo Científico y Tecnológico (Fondecyt) under Grant No. 1250122 and from the Indian Institute of Technology Madras, India, where part of this work was conducted. J.C.E acknowledges ANID for her national doctoral scholarship No. 21231429 and partial support from UAI. F.M. acknowledges support from Fondecyt grants 1231487 and 1220715, CEDENNA CIA250002, and partial support by the supercomputing infrastructure of the NLHPC (CCSS210001). This work used Bridges-2 at Pittsburgh Supercomputing Center through allocation PHY150003P from the ACCESS program.

References

[1] J. R. Schrieffer and P. A. Wolff, "Relation between the anderson and kondo hamiltonians," *Physical Review*, vol. 149, no. 2, p. 491, 1966.
[2] S. J. Denholme, A. Yukawa, K. Tsumura, M. Nagao, R. Tamura, S. Watauchi, I. Tanaka, H. Takayanagi, and N. Miyakawa, "Coexistence of superconductivity and charge-density wave in the quasi-one-dimensional material hfte3," *Scientific reports*, vol. 7, no. 1, p. 45217, 2017.
[3] Z. Liu, J. Li, J. Zhang, J. Li, P. Yang, S. Zhang, G. Chen, Y. Uwatoko, H. Yang, Y. Sui *et al.*, "Quasi-one-dimensional superconductivity in the pressurized charge-density-wave conductor hfte3," *npj Quantum Materials*, vol. 6, no. 1, p. 90, 2021.

RKKY-like interactions between two magnetic skyrmions

X. R. Wang
School of Science and Engineering, Chinese University of Hong Kong (Shenzhen),
Shenzhen 51817, China
phxwan@cuhk.edu.cn

Abstract

Interaction between two tilted skyrmions in a chiral magnetic film changes from replusion to attraction periodically with skyrmion-skyrmion distance along certain direction, akin to the Ruderman-Kittel-Kasuya-Yosida (RKKY) interaction. The essential physics is behind a previously unrecognized universal wavy tail in the skyrmion spin texture. The RKKY-like interaction is universal for all tilted skyrmions.

1 Introduction

It is well known that two isolated skyrmions in a vertically magnetized chiral film always repel each other [1–6]. However, recent studies have found that skyrmion-skyrmion interaction can be attractive under the tilted external fields [7–9], or through thermal frustration [10], or by varying sample thickness [11, 12], and or through frustrated exchange interactions [13–15]. Despite of all progress, the underlying physics of these interactions remains poorly understood, and a clear understanding of the conditions under which two skyrmions in a chiral film can attract each other is still lacking.

We demonstrate here that skyrmion–skyrmion interactions in titled (from the film perpendicular direction) chiral magnetic films, caused by either a tilted magnetic field or magnetic anisotropy, are intrinsically Ruderman-Kittel-Kasuya-Yosida-type (RKKY-type), periodically alternating between attraction and repulsion. The tail of an isolated in-plane skyrmion inherently possesses a periodic spin structure along the direction of the skyrmion's center spin, with the same period as that of the interactions. When two skyrmions are aligned along this periodic direction and separated by an integer multiple of the period, their wavy tails coincide, allowing them to share the same wavy tail, which results in a reduction in total energy and an attractive interaction. Conversely, at separations of half-integer multiples of the period, the two tails are out of phase, and significantly deformation is needed in order for two skyrmions to connect each other smoothly, leading to an increase in total energy and a repulsive force between them. These findings provide new insights into the nature of skyrmion–skyrmion interactions and open up avenues for engineering skyrmion-based devices with controllable collective behavior.

A chiral magnetic film of thickness d lying in the xy-plane is modeled by the magnetic energy E, which consists of several components: the exchange energy $E_{\rm ex} = \frac{Ad}{2}\int |\nabla \mathbf{m}|^2 \,\mathrm{d}^2\mathbf{x}$, where the exchange stiffness $A = 30\,\mathrm{pJ/m}$ is fixed and $\mathbf{m}$ is the direction of magnetization with a saturation magnetization $M_s = 1\,\mathrm{MA/m}$; the Dzyaloshinskii–Moriya interaction (DMI) $E_{\rm DM} = \frac{Dd}{2}\int [\mathbf{m}\cdot(\nabla\times\mathbf{m})]\,\mathrm{d}^2\mathbf{x}$ with DMI strength $D = 4\,\mathrm{mJ/m^2}$; the anisotropy energy $E_{\rm an} = d\int -\frac{K}{2}(m_y\sin\theta + m_z\cos\theta)^2\mathrm{d}^2\mathbf{x}$ where K is the anisotropy constant along the easy axis in the yz-plane, determined by the angle θ; the magnetic dipolar energy, which can be incorporated into the effective anisotropy term $\frac{\mu_0 M_s^2 m_z^2}{2}$, with μ_0 being the vacuum permeability; and the Zeeman energy $E_{\rm Ze} = -\mu_0 M_{\rm s} d\int \mathbf{H}\cdot\mathbf{m}, \mathrm{d}^2\mathbf{x}$, where $\mathbf{H}$ is the external magnetic field. Only K,

θ, and $\mathbf{H}$ vary to model different situations [16–18]. Two cases are considered: the first is $\mathbf{H}$ controlled anisotropy, where $\theta = 0$ and $K = 1.256\,\mathrm{MJ/m^3}$ are set to cancel the shape anisotropy, making the easy axis unsymmetrical and preferably aligning spin with $\mathbf{H}$. The second case involves setting $\mathbf{H} = 0$ and using K and θ to control the magnetic anisotropy, resulting in a symmetrical axis.

2 Skyrmion-skyrmion interaction

We fix the center of one skyrmion at the sample center $(0, 0)$ and the other at (x, y), with their center spin direction set to $\mathbf{m} = (0, 1, 0)$ in the background of spin states of $\mathbf{m} = (0, -1, 0)$ (far from two skyrmion centers). The remaining spins in the film follow the Landau-Lifshitz-Gilbert (LLG) equation and settle into a stable configuration. Figure 1(a) is the energy surface $E(x, y)$ of the two skyrmions in their stable configuration when an external field of $H = 0.164\,\mathrm{T}$ is applied along the $-y$-direction. Notably, $E(\pm x, \pm y) = E(x, y)$, so it is sufficient to plot $E(x, y)$ in just one quadrant. The energy function $E(x, y)$ is clearly anisotropic, and the interaction between the two skyrmions is also anisotropic. Along the x-axis ($y = 0$), the total energy decreases monotonically with x (black line in Fig. 1(b)), indicating that the two skyrmions repel each other. In contrast, along the y-axis ($x = 0$), the energy profile exhibits RKKY-like oscillatory behaviour with multiple energy minima at $y_{min} = 66.5, 156.5, 247.5\,\mathrm{nm}$ (red line in Fig. 1(b)), implying an alternating attractive and repulsive interactions between the two skyrmions. In other directions, oscillatory behaviour persists with the period of $\lambda/\sin\phi$, where ϕ is the angle between the skyrmion-skyrmion displacement (x, y) and y-axis, $\lambda \approx 156.5 - 66.5 \approx 247.5 - 156.5 \approx 90 \sim 91\,\mathrm{nm}$ which is not sensitive to H and ϕ. The blue curve in Fig. 1(b) is the energy variation along $y = x$ direction. According to energy surface $E(x, y)$, the skyrmion centred at (x, y) will relax to its local minimum at $(0, y_{min})$ when the skyrmion is allowed to move. Which y_{min} will end up with depends on the initial location of the skyrmion. Our simulations have confirmed this expectation.

Figure 1: (a) Energy surface $E(x, y)$ of two skyrmions for $H = 0.164\mathrm{T}$ along the y-axis. $E = 0$ is chosen for two isolated skyrmions infinitely apart. (b) $E(x, y)$ as a function of x along $y = 0$ (black line), or y along $x = 0$ (red line), or $\sqrt{x^2 + y^2}$ along $y = x$ (blue line). The vertical blue dash-lines indicate local minima.

3 Conclusion

In conclusion, skyrmions in a tilted magnetic field or in a title magnetic anisotropy with a sufficient large component in the film plane are anisotropic and have periodically wavy tails. This wavy tail leads to skyrmion–skyrmion attraction when the two tails match with each other in the overlapped region, and repulsion when their tails mismatch with each other. As a result, two tilted skyrmions exhibit RKKY-like interaction, oscillating between attraction and repulsion with a period that is determined by the period of wavy tail.

Anisotropic and oscillatory skyrmion–skyrmion interaction gives rise to new possibilities in skyrmion-based spintronics. The presence of multiple optimal skyrmion–skyrmion separations

offers an additional degree of freedom for controlling the dynamics of isolated skyrmions. Our findings thus open a promising avenue for advanced skyrmion manipulation such as creating skyrmion molecules or more complicated skyrmion superstructures.

4 Acknowledgements

This work is supported by the University Development Fund of the Chinese University of Hong Kong, Shenzhen, the NSFC Grant (No. 12374122), and Guangdong Provincial Quantum Strategy Special Project.

References

[1] X. Zhang, G. P. Zhao, H. Fangohr, J. P. Liu, W. X. Xia, J. Xia, and F. J. Morvan, Sci. Rep. **5**, 1 (2015).

[2] S. Z. Lin, C. Reichhardt, C. D. Batista, and A. Saxena, Phys. Rev. B **87**, 214419 (2013).

[3] R. Brearton, G. van der Laan, and T. Hesjedal, Phys. Rev. B **101**, 134422(2020).

[4] D. Capic, D. A. Garanin, and E. M. Chudnovsky, J. Condens. Matter Phys. **32**, 415803(2020).

[5] Y. Wang, J. Wang, T. Kitamura, H. Hirakata1, and T. Shimada, Phys. Rev. Appl. **18**, 044024 (2022).

[6] S. Z. Lin and S. Hayami, Phys. Rev. B **93**, 064430(2016).

[7] S. Z. Lin and A. Saxena, Phys. Rev. B, **92**, 180401 (2015).

[8] M. Kameda, R. Koyama, T. Nakajima, and Y. Kawaguchi, Phys. Rev. B **104**, 174446 (2021).

[9] K. L. Tiwari, J. Lavoie, T. Pereg-Barnea, and W. A. Coish, Phys. Rev. B **100**, 125414(2019).

[10] A. O. Leonov and U. K. Rößler, Nanomaterials **13**, 891 (2023).

[11] J. C. Loudon, A. O. Leonov, A. N. Bogdanov, M. C. Hatnean, and G. Balakrishnan, Phys. Rev. B **97**, 134403 (2018).

[12] H. Du, X. Zhao, F. N. Rybakov, A. B. Borisov, S. Wang, J. Tang, C. Jin, C. Wang, W. Wei, N. S. Kiselev, *et al.* Phys. Rev. Lett. **120**, 197203 (2018).

[13] L. Rózsa, A. Deák, E. Simon, R. Yanes, and L. Udvardi, Phys. Rev. Lett. **117**, 157205 (2016).

[14] L. Rózsa, A. Deák, E. Simon, R. Yanes, L. Udvardi, L. Szunyogh, and U. Nowak, Phys. Rev. Lett. **117**, 157205 (2016).

[15] A. O. Leonov and M. Mostovoy, Nat. Commun. **6**, 8275 (2015).

[16] X. C. Hu, H. T. Wu, and X. R. Wang, Nanoscale, **14**, 7516 (2022).

[17] X. R. Wang and X. C. Hu, Phys. Rev. B, **107**, 174412 (2023).

[18] X. R. Wang, X. C. Hu, and Z. Z. Sun, Nano Lett. **23**, 3954 (2023).

Microwave radiation from high chirality vortex dynamics.

Feodor Y. Ogrin

School of Physics and Astronomy, University of Exeter, UK
*Corresponding author: f.y.ogrin@exeter.ac.uk

***Abstract*— Here I present a model which uses 3D finite-difference-time-domain (FDTD) approach together with Landau-Lifshits_Gilbert (LLG) equation to find the exact solutions for electromagnetic radiation from magnetic vortex structures in cylindrical elements. Using this model I demonstrate the spectrum of radiation and explore the system in terms of geometrical parameters as well as the collective excitation properties within a macroscopic pattern.**

***Keywords*— metamaterials, magnetization dynamics, highly chiral anisotropic systems.**

I. Introduction

Vortex closure domains, such as Landau pattern, have been a focus of interest for several decades. As well as being fascinating from purely fundamental perspective (including symmetry, nonlinearity, dynamics, and coupling effects), these systems find increasing attention with respect to potential technological applications. For example, if excited by a short electromagnetic pulse the vortex core can start a gyration motion around its equilibrium position, or serve as a source of spin waves. Effectively the vortex behaves as a harmonic oscillator [1-4]. The core dynamics is however very much dependent on the structures of both the domains and the domain walls. In thin film elements, the domain walls have a Néel configuration, with purely in-plane magnetisation. However, once the thickness is increased the topology is significantly modified, and due to the increased dipolar fields, the polarisation of the moment within the domain wall gains an out-of-plane component. In our recent experiments [5] we demonstrated that this additional polarisation can lead to a range of dynamic effects, such as a change in polarisation of the magnetic singularities associated with the Landau pattern. Moreover, our subsequent micromagnetic simulation studies suggest that in thicker elements one can also create spiral spin-wave modes, propagating in the domain walls as well as the surface of the elements. These modes have shown to develop amplitudes significantly exceeding those in the bulk of the material Furthermore, their dispersion characteristics can be easily tuned by the applied magnetic field, via the manipulation of the vortex core position in the sample. Such properties are extremely interesting for spin-wave logic devices, in which the ability to control the spin-wave dynamics is one of the main challenges faced in the development of future magnonic technologies.

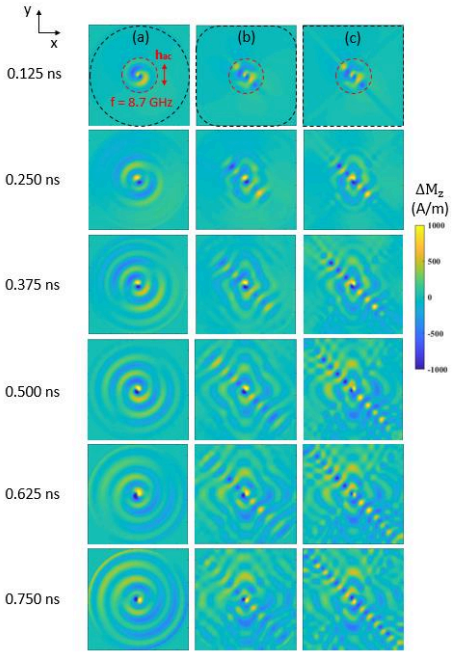

Fig. 1 . Micromagnetic simulation (using Mumax3 code) of spiral spin wave modes obtained in 80 nm thick circular (a) and square (b,c) permalloy elements. The spiral mode is initiated in the core and propagates outwards to the boundaries. In square elements, there is also a mode propagating in the domain wall (Winter's magnon) that interacts with the spiral mode and changes its topology.

II. Results and Discussion

While being a purely magnetic phenomenon vortex dynamics has also found its contribution to some electromagnetic applications. In the last two decades there have been an increased interest spin-torque oscillators, as microscopic microwave sources. A particular class of these devices relied on the vortex gyration in confined cylindrical ferromagnetic elements, where the vortex core gyration could be obtained in the microwave frequency range [6]. The main focus of the practical interest was based on the application of the devices serving as electrical sources (e.g. obtained via

magneto-resistance), however the direct radiation of microwaves from the oscillators was mainly discarded. The main difficulty is the low intensity for the direct observation of the signal, as well as the unavailability of the numerical tools to explore the effects. The 'usual' magnetostatic solvers, such as OOMMF or Mumax, while being the standard benchmark tools and usually provide a precise description of the magnetisation processes in thin-film ferromagnetic structures, are however limited in applications where full account of electric fields is required, especially when the material properties are extremely non-uniform (e.g. dielectric/metal interfaces). In such cases one needs to consider a modelling approach where a full solution of Maxwell equations is needed alongside the materialistic equations, such as e.g. Landau-Lifshits-Gilbert (LLG) providing the relation between the magnetisation and the magnetic field [7]. Here we demonstrate an application of such a model (MaxLLG ®) which uses 3D finite-difference-time-domain (FDTD) approach together with LLG to find the exact solutions for radiation effects produced by magnetisation dynamics in purely micromagnetic regime [8]. As an example we demonstrate a study of gyration effects in thin microscopic ferromagnetic discs, which exhibit vortex gyration as well as the excitation of the spiral magnetostatic waves, leading to microwave radiation. We explore the spectra of radiation from a single element and an array of elements and provide a practical assessment on potential application in practical microwave devices.

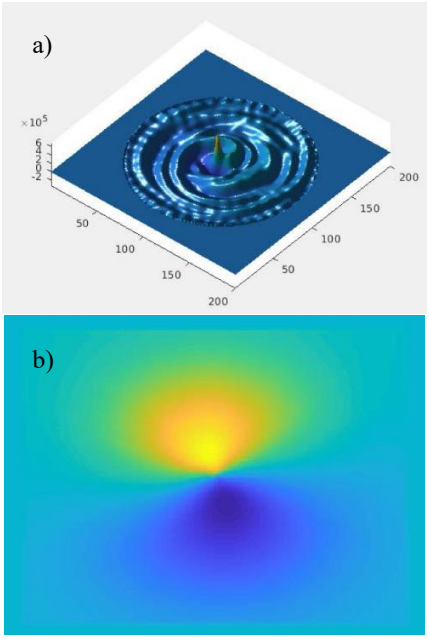

Fig. 2 . MaxLLG simulated vortex gyration in 2 µm disc. a) The core and the spiral waves, excited continuously with in-plane magnetic field. b) resulted electric field radiation pattern, spiralling clock-wise together with the core.

REFERENCES

[1] M. Madami *et al.,* Nature Nanotechnology **6** (2011) 635
[2] V.S. Pribiag *et al.,* Nature Physics **3** (2007) 498.
[3] A. Ruotolo *et al.,* Nature Nanotechnology **4** (2009) 528.
[4] A. Vogel *et al.*, Phys. Rev. Lett. **106** (2011) 137201.
[5] N. Bukin *et al.*, Scientific Reports **6** (2016) 36307.
[6] A. Dassaux et al., Nature Communications **1** (2010) 8.
[7] M. M. Aziz, Progress In Electromagnetics Research B 15, (2009) 1–29.
[8] https://www.maxllg.com/

Feedback effects of electromagnetic interactions in bianisotropic media

Kei Sawada[1,*]

[1]RIKEN SPring-8 Center, Japan
*Corresponding author: sawada@spring8.or.jp

***Abstract*— An effective theory is developed for metamaterials exhibiting bianisotropy, with particular emphasis on magnetoelectricity and chirality classified by the space-time inversion symmetry. This approach gives a framework for representing the susceptibility functions including feedback effects due to magnetoelectric couplings.**

***Keywords*— chirality, magnetoelectricity, bianisotropy**

Metamaterials exhibiting bianisotropy have been of much interest for decades [1-2]. The bianistropy arises from symmetry breakings of the space-inversion and time-reversal, and describes electromagnetic couplings in media having non-reciprocal phenomena [3-6].

Consider an effective Lagrangian density describing light, matter and light-matter interaction:

$$\mathcal{L} = \mathcal{L}_{\text{light}} + \mathcal{L}_{\text{light-matter}} + \mathcal{L}_{\text{matter}}, \quad (1)$$

$$\mathcal{L}_{\text{light}} = \frac{1}{2}\varepsilon_0 \vec{E}^2 + \frac{1}{2\mu_0}\vec{B}^2, \quad (2)$$

$$\mathcal{L}_{\text{light-matter}} = \vec{j}\cdot\vec{A}, \quad (3)$$

$$\mathcal{L}_{\text{matter}} = f\left(\partial_x, \partial_y, \partial_z, \partial_t;\ \vec{P}, \vec{M}\right), \quad (4)$$

where ε_0 and μ_0 are the electric permittivity and the magnetic permeability of vacuum. The electromagnetic fields, electric polarization and magnetization are respectively written as $\vec{E}$, $\vec{B}$, $\vec{P}$, and $\vec{M}$, with the current, $\vec{j} = \partial_t \vec{P} + \frac{1}{\mu_0}\nabla \times \vec{M}$, and the vector potential, $\vec{A}$. The first term on the right-hand side of Eq. (1), $\mathcal{L}_{\text{light}}$, gives Maxwell equations, and the second term represents light-matter interaction. The third term, $\mathcal{L}_{\text{matter}}$, is a function of the electric polarization and the magnetization with space-time derivatives, and consists of all possible terms describing interactions inside the media as partly represented and classified in Table 1. The terms which are odd for space-inversion and/or time-reversal operations are origin of bianisotropy.

From Euler-Lagrange equations for each parameter in Eq. (1), we obtain the dielectric function, the magnetic permeability, and the chiral parameter tensor, which are self-consistently determined. This result demonstrates feedback behaviors arising from magnetoelectric couplings as well as electromagnetic inductions.

Table 1 Classification of parameters and typical examples of interactions in media under space-inversion and time-reversal operations. The subscripts, i, j, k, are x, y, or z.

	space inversion	time reversal
electric polarization $\vec{P}$	odd	even
magnetization $\vec{M}$	even	odd
spatial derivatives $\partial_x, \partial_y, \partial_z$	odd	even
time derivative ∂_t	even	odd
typical interactions:		
dielectric $P_i P_j$	even	even
chiral $P_i(\partial_j P_k)$	odd	even
magnetic $M_i(\partial_t M_j)$	even	odd
magnetoelectric $P_i M_j$	odd	odd

ACKNOWLEDGMENTS

The author thanks S. Tomita, T. Kodama, T. Nakanishi, K. Konishi, M. Mochizuki, J. Ruff and J. Brock for fruitful discussions.

REFERENCES

[1] O. N. Singh and A. Lakhtakia ed., "Electromagnetic Fields in Unconventional Material and Structures," John Wiley & Sons, 2000.
[2] V. S. Asadchy, A. Díaz-Rubio and S. A. Tretyakov, "Bianisotropic metasurfaces: physics and applications," Nanophotonics, vol. 7, 1069, 2018.
[3] S. Tomita, K. Sawada, A. Porokhnyuk and T. Ueda, "Direct observation of magnetochiral effects through a single metamolecule in microwave regions," Phys. Rev. Lett., vol. 113, 2335501, 2014.
[4] M. Atzori, G. L. J. A. Rikken and C. Train, "Magneto-chiral dichroism: a playground for molecular chemists", Chem. Eur. J., vol. 26, 9784, 2020.
[5] I. Kézsmárki, D. Szaller, S. Bordács, V. Kocsis, Y. Tokunaga, Y. Taguchi, H. Murakawa, Y. Tokura, H. Engelkamp, T. Rõõm und U. Nagel, "One-way transparency of four-coloured spin-wave excitations in multiferroic materials", Nature Comm. vol 5, 3203, 2014.
[6] L. D. Laudau, E. M. Lifshitz and L. P. Pitaevskii, "Electrodynamics of Continuous Media,"

Towards compact microfluidic chips for efficient chiral recognition

David Ayuso[1,*]

[1] Department of Chemistry, Molecular Sciences Research Hub, Imperial College London, W12 0BZ London, United Kingdom

*Corresponding author: d.ayuso@imperial.ac.uk

***Abstract*— We present a route towards developing compact microfluidic platforms for efficient chiral sensing and manipulation. Our approach relies on creating synthetic chiral light inside compact microfluidic microchannels, so that the engineered light field can interact with liquid samples carrying chiral molecules in a highly enantiosensitive manner.**

***Keywords*— chirality, light-matter interaction, ultrafast science, microfluidics.**

Apart from their well-established roles in nanotechnology and drug discovery, small chiral molecules are emerging as biomarkers for early-stage diagnosis, prognosis, and personalised medicine [1]. However, unlocking the biomedical potential of small-molecule chiral detection requires being able to detect small variations in the concentration of a highly diluted biomarker (e.g. D-serine [1]) in a biological sample containing a large excess of the opposite enantiomer (L-serine). Traditional optical methods, namely polarimetry and circular dichroism, lack the sensitivity to resolve such differences, whereas chemical methods involving chromatographic columns or sophisticated analysis are not sufficiently general, rapid, and cost-effective [1].

The possibility of shaping light in 3D to shape the electronic response of chiral molecules on ultrafast timescales creates an opportunity to overcome these limitations [2]. Locally chiral light [3-6], where the tip of the electric-field vector draws a chiral Lissajous figure in time [3], can drive ultrafast electronic currents inside the molecules that interact with the chiral molecular potential in a highly enantiosensitive manner. It allows us to enhance the enantiosensitivity of traditional chiral spectroscopy from 0.1% up to 100% [3-6].

In this presentation, I will show how we can engineer compact microfluidic platforms to create locally chiral light inside their microchannels carrying liquid samples. Our ideas are supported by state-of-the-art numerical simulations showing that bringing the high chiral sensitivity from free-space optics [3-6] to confined microfluidic environments is very feasible. This creates an opportunity for designing compact microfluidic technology for efficient chiral recognition in the liquid phase, the natural environment of biological samples.

References

[1] Yaoran Liu, Zilong Wu, Daniel W. Armstrong, Herman Wolosker and Yuebing Zheng, *Nature Reviews Chemistry* **7**, 355 (2023)

[2] David Ayuso, Andrés Ordóñez and Olga Smirnova, *Physical Chemistry Chemical Physics* **24**, 26962 (2022)

[3] David Ayuso, Ofer Neufeld, Andres F. Ordonez, Piero Decleva, Gavriel Lerner, Oren Cohen, Misha Ivanov and Olga Smirnova, *Nature Photonics* **13**, 866 (2019)

[4] David Ayuso, Andres F. Ordonez, Piero Decleva, Misha Ivanov & Olga Smirnova, *Nature Communications* **12**, 3951 (2021)

[5] Joshua Vogwell, Laura Rego, Olga Smirnova and David Ayuso, *Science Advances* **9**, eadj1429 (2023)

[6] Nicola Mayer, David Ayuso, Piero Decleva, Margarita Khokhlova, Emilio Pisanty, Misha Ivanov and Olga Smirnova, *Nature Photonics* **18**, 1155–1160 (2024)

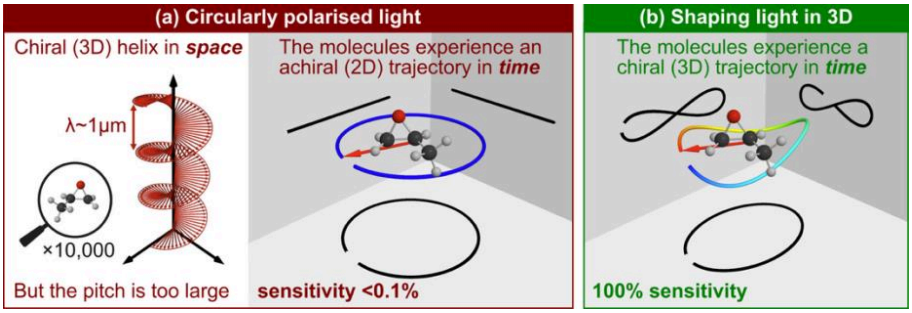

Fig. 1. a, Circularly polarized light draws a chiral helix in space, but the Lissajous figure that the tip of the electric-field vector traces in one point in space within one optical cycle (local polarisation) is a planar circle: an achiral temporal structure. **b,** Light's polarization can be shaped in 3D to realize locally chiral light inside compact microfluidic platforms for efficient chiral sensing and manipulation.

Chiral Metamaterials with Twisted Metallic Wire Structures

Ming-Li Chang[1], C. T. Chan[1,*]

[1]Department of Physics, The Hong Kong University of Science and Technology, Clear Water Bay, Hong Kong, China

*Corresponding author: phchan@ust.hk

***Abstract*— Some chiral metallic photonic crystal exhibits unusual band structures. We show that chiral metallic twisted wire bundle structures can host zero frequency solutions at off-Γ k points, which can be explained by the real space topology of structures, and the results can be modeled by circuit models.**

***Keywords*— metallic photonic crystal, chiral system, Betti number, LC circuit.**

I. Introduction

Metallic photonic crystals (MPC) can exhibit strange band dispersions including multi-degeneracies [1], off-Γ point index ellipsoid [2], and quadratic dispersion at zero frequency at the quasistatic limit [3], and the results cannot be explained using standard effective medium theories even at close to zero frequency. Here, we investigate the extent to which the low-frequency bands in these chiral metamaterials can be modeled using circuit models and how these models relate to real-space topology..

II. Methods

We can obtain the band dispersion of twisted metallic wire systems (see an example in Fig. 1) using full wave simulation. One characteristic of these chiral systems is the existence of multiple off-Γ zero frequency solutions. The emergence of zero frequency solutions away from the zone center can be explained by an effective gauge potential induced by the chirality. We also note that the quasistatic bands of chiral MPC are TEM modes and the number of modes is determined by the real space topology. If there are N metallic components piercing the periodic boundary, there are N-1 modes emerge at zero frequency. It turns out the number of zero frequency solution related to the de Rham cohomology, and N is related to the second Betti number, which measures the number of independent harmonic 2-forms on a manifold. **Error! Bookmark not defined.**

We also note that the TEM modes in chiral MPCs show in Fig. 1a (a twisted bundle of 6 metallic wires, encapsulated in a hexagonal metallic wall). The full wave band structure is shown in Fig. 1d. Fig 1b shows a LC circuit model, employing the potentials and currents (ϕ_n, I_n) of each metal components as parameters. Fig. 1e shows the band dispersion of this simple model. Fig. 1c shows an "arbitrarily connected" metal wire system, in which only the permutation is the same as Fig. 1a. Fig. 1f shows its band (full wave). We found that for twisted MPC, the number of zero frequency solutions are given by

$$Nka = 0(mod\ 2\pi) \quad , \tag{1}$$

where a is the period in the twisting direction.

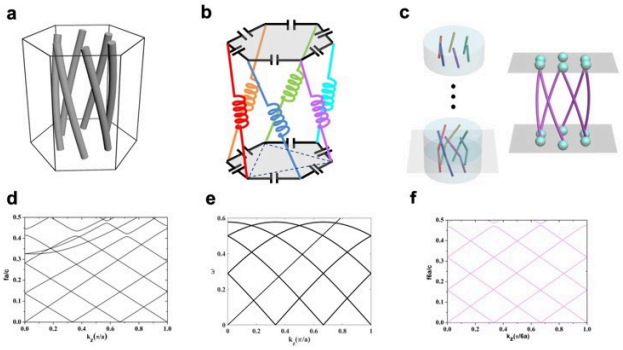

Fig. 1 Unit cells of twisted MPC and their corresponding dispersions.

III. Results and Discussion

Some salient features of the band dispersion of the twisted metal wires show in Fig 1a:

- Zero frequency solutions can be found at $k = 0, \pm\frac{1}{3}\pi, \pm\frac{2}{3}\pi, \pm\pi$ for the six twisted wires (Fig. 1a and d).
- These low frequency modes are TEM modes and their dispersion can can be captured by the LC model (Fig. 1b)
- There is good agreement of dispersions between the full wave simulation and circuit model (Fig. 1e)
- The number of zero frequency solutions is determined by the Betti number and the dispersion is primarily determined by the connectivity. Even if the wires are deformed inside the unit cell, but if they exhibit same permutation (how the wires connect from one side to another side of unit cell) as in Fig. 1a, they display essentially the same quasistatic bands (Fig. 1c and f).

When the wires are twisted in one dimension as shown in Fig.

1, the dispersion are well captured by the LC circuit and the bands are basically determined by connectivity. In higher dimension, there are modes that are not TEM modes and nonlocal effect will emerge if longitudinal component exists [4]. In these cases, their interaction by the EM waves in background medium should also be included for dispersion description.

IV. Conclusion

We have demonstrated the zero frequency solutions can be explained by topological number and their dispersions can be related to the LC circuit model. These chiral systems exhibit multiple solutions at different k values for the same frequency, and might be useful for suppressing cross talks among adjacent waveguides.

Acknowledgments

This work was supported by Hong Kong RGC.

References

[1] J. Shin, J.-T. Shen, and S. Fan, Three-dimensional electromagnetic metamaterials that homogenize to uniform non-Maxwellian media, Phys. Rev. B **76**, 113101 (2007).

[2] See, e.g., W.-J. Chen et al., Metamaterials with index ellipsoids at arbitrary k-points, Nature Communications **9**, 2086 (2018).

[3] C. R. Simovski and P. A. Belov, Low-frequency spatial dispersion in wire media, Phys. Rev. E **70**, 046616 (2004).

[4] S. I. Maslovski and M. G. Silveirinha, Nonlocal permittivity from a quasistatic model for a class of wire media, Phys. Rev. B **80**, 245101 (2009).

When Chirality Protection Fails: Bulk-Mediated Reflection of Surface Spin Waves

Alexander A. Serga[1,*]

[1]Fachbereich Physik and Landesforschungszentrum OPTIMAS,
Rheinland-Pfälzische Technische Universität Kaiserslautern-Landau, Kaiserslautern, Germany
*Corresponding author: serha@rptu.de

***Abstract*—Chirality protects Damon–Eshbach surface spin waves against direct backscattering, yet this protection breaks down in thick magnetic films. We show that reflection proceeds via bulk-mode conversion, producing localized energy deposition. Thermal imaging, Brillouin light scattering, and simulations directly resolve this bulk-mediated reflection pathway.**

***Keywords*— magnons, surface spin waves, chirality, nonreciprocal transport, Brillouin light scattering, yttrium iron garnet, magnonics.**

I. Introduction

Chiral Damon–Eshbach surface spin waves [1] exhibit intrinsically nonreciprocal transport and asymmetric localization at opposite film surfaces. This chirality has been linked to suppressed direct backscattering and robust propagation in thin films [2]. Earlier experiments in micrometer-thick yttrium iron garnet films likewise showed that surface modes are less sensitive to defects than backward-volume waves [3].

In thick films, however, bulk modes form a dense continuum that opens additional scattering channels. Here, we examine how surface waves reflect in this regime and demonstrate that reflection occurs via conversion into bulk excitations rather than direct reversal of the surface mode.

II. Methods

Experiments were performed on micrometer-thick yttrium iron garnet films supporting long-lived dipole surface spin waves. Space- and time-resolved Brillouin light scattering spectroscopy was employed to map the spatial distribution and temporal evolution of magnon populations during propagation and reflection. Infrared thermography monitored local energy dissipation associated with reflection events. Micromagnetic simulations complemented the measurements and provided microscopic insight into mode conversion between surface and bulk excitations.

III. Results and Discussion

Surface waves propagate robustly along the film boundaries while preserving their chiral localization. When encountering edges or inhomogeneities, reflection does not occur through direct reversal of the surface mode. Instead, the waves convert into bulk modes that traverse the film thickness and subsequently re-emerge at the opposite surface with reversed propagation direction.

Space- and time-resolved measurements reveal a delayed reappearance of the reflected signal, consistent with propagation through the film interior. Simultaneously, infrared thermography detects localized heating at the reflection sites, indicating accumulation and dissipation of magnon energy. Micromagnetic simulations reproduce the conversion dynamics and confirm the formation of standing bulk excitations that mediate the transfer of energy and momentum between counter-propagating surface states.

Together, these observations identify bulk-mode conversion as the dominant mechanism governing reflection in thick films. The results define the limits of chirality-based backscattering protection beyond the thin-film regime and establish bulk modes as an intrinsic reflection channel in realistic geometries.

IV. Conclusion

We demonstrate that reflection of chirality-protected surface spin waves in thick magnetic films is governed by bulk-mode conversion rather than direct backscattering. This mechanism explains localized energy deposition and clarifies the limits of protection in extended systems. The results provide a general framework for understanding and controlling magnon transport and dissipation in nonreciprocal spin-wave devices.

Acknowledgments

This research was funded by the Deutsche Forschungsgemeinschaft (DFG, German Research Foundation) in the framework of TRR 173 – Grant No. 268565370 “Spin+X” (Projects B01 and B13).

References

[1] R. W. Damon and J. R. Eshbach, “Magnetostatic modes of a ferromagnet slab,” *Journal of Physics and Chemistry of Solids*, vol. 19, pp. 308–320, 1961.

[2] M. Mohseni, R. Verba, T. Brächer, Q. Wang, D. A. Bozhko, B. Hillebrands, and P. Pirro, “Backscattering immunity of dipole-exchange magnetostatic surface spin waves,” *Physical Review Letters*, vol. 122, 197201, 2019.

[3] A. V. Chumak, A. A. Serga, S. Wolff, B. Hillebrands, and M. P. Kostylev, “Scattering of surface and volume spin waves in a magnonic crystal,” *Applied Physics Letters*, vol. 94, 172511, 2009.

Symmetry Behavior of Chiral Disordered Metamaterials

Simone Zanotto[1*]

[1]Istituto Nanoscienze – CNR, and Laboratorio NEST – SNS, Pisa, Italy
*Corresponding author: simone.zanotto@nano.cnr.it

***Abstract*—Metamaterials properties are strongly determined by symmetry. In particular, chirooptical effects are expected in systems that lack any mirror plane. Less is known about systems trat are locally asymmetric but globally symmetric, due to randomization. Here we show data about chiral metamaterials with rotational, positional, and racemic disorder.**

***Keywords*— symmetry, chirality, anisotropy, disorder.**

I. Introduction

Chirooptical effect in natural materials are typically very small, and metamaterials have proved being a key milestone towards compact, yet efficient, optical devices with a chiral response. However, the vast majority of studies on chiral metamaterials have been dealing with ordered nanoparticle (or nanohole) arrays, leaving open the question about the role of disorder in conjunction with photonic chirality.

II. Methods and Results

Our base platform is a photonic slab metamaterial made of a high-index dielectric (gallium arsenide, ε = 12) patterned with an array of L-shaped holes, as depicted in Fig. 1a. In first instance, we consider a periodic array with no disorder. The system is investigated with angle- and polarization-resolved transmission spectroscopy, where the incident polarization is either right- or left-polarized. Similarly to what reported in [1], as long as the polarization-averaged transmission is concerned (Fig. 1b), we observed a clear bandstructure, with branches originating from both TE-like and TM-like slab modes. Such branches are visible also on the transmission circular dichroism (Fig. 1c), with features of both signs that lack any symmetry upon exchange of positive with negative in-plane wavevectors.

We then investigated a sample consisting of an equal mixture of "original" and "mirrored" L-shaped holes, mimicking the composition of a chemical racemic mixture (Fig. 2a). In analogy to the previous case, we preformed angle- and polarization-resolved transmission measurements, obtaining radically different results (Fig. 2b-c). At first, the polarization-averaged transmittance shows a drastically simplified mode structure, where only a subset of the original modes have survived. Moreover, the transmission circular dichroism – which also features a minor number of dispersive structures – is very weak when the in-plane wavevector is close to zero.

In addition to the "racemic disorder", we have also

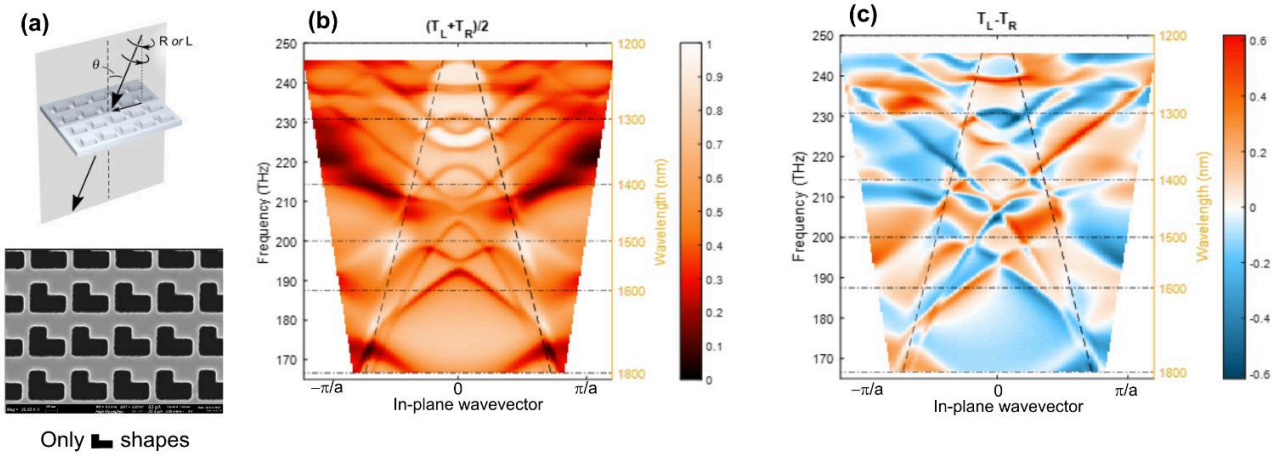

Fig. 1. Dispersive mode structure of a non-disordered chiral photonic slab metamaterial. (a), schematic of the experimental conditions and SEM image of the sample. (b), polarization-averaged transmission map, resolved in wavelength and in-plane wavevector (originating from the projection of incident wavevector un the sample plane, see (a)). Here, *a* is the pattern periodicity (approx. 1 μm). (c), transmission circular dichroism map.

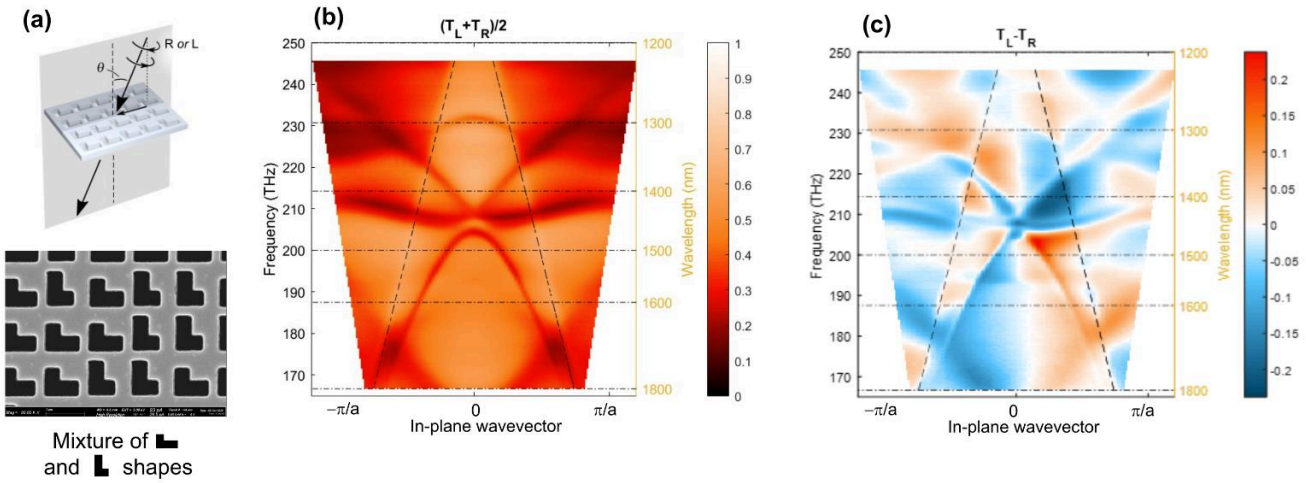

Fig. 2. Dispersive mode structure of a disordered chiral photonic slab metamaterial. The sample resembles a racemic mixture of enantiomeric chemical species. (a), schematic of the experimental conditions and SEM image of the sample. (b), polarization-averaged transmission map, resolved in wavelength and in-plane wavevector (originating from the projection of incident wavevector un the sample plane, see (a)). Here, *a* is the pattern quasi-periodicity (approx. 1 μm). (c), transmission circular dichroism map.

investigated samples with positional disorder and with orientational disorder, i.e., samples where homochiral L-shaped holes are either placed at randomly chosen positions, or with a random angle with respect to the coordinate axes. Also in these cases we have observed a selective suppression of resonant modes, as well as symmetry-driven selection rules on the transmission circular dichroism.

III. Conclusion

We have analyzed chiral dielectric metamaterial slabs with different types of disorder, and we have observed significant deviations from the resonant mode structure specific of the corresponding non-disordered structures.

References

[1] Zanotto, Simone, Mazzamuto, Giacomo, Riboli, Francesco, Biasiol, Giorgio, La Rocca, Giuseppe C., Tredicucci, Alessandro and Pitanti, Alessandro. "Photonic bands, superchirality, and inverse design of a chiral minimal metasurface" *Nanophotonics*, vol. 8, no. 12, 2019, pp. 2291-2301.

Pushing micro-focused BLS to the Nanoscale: Modeling and Nanophotonic Enhancement for Magnon Detection

Ondřej Wojewoda[1,2*], Michal Urbánek[2]

[1]DMSE, Massachusetts Institute of Technology, Cambridge, MA, Unites States of America
[2] CEITEC BUT, Brno University of Technology, Brno, Czech Republic
*Corresponding author: wojewoda@mit.edu

***Abstract*—Magnonics studies spin waves and their quasiparticles, magnons, often with use of micro-focused Brillouin light scattering (BLS). We develop a model describing BLS signal formation and use it to design dielectric nanoresonators, which enabled detection of nanoscale spin waves and allowed mapping of the dispersion relation across unprecedented ranges.**

***Keywords*— Spin-wave, magnonics, Mie resonances, Brillouin light scattering.**

Spin-wave research explores collective magnetic excitations (magnons) as a platform for energy-efficient information processing and as a probe of fundamental material properties. In mesoscopic magnonics, spin waves with relatively small wavevectors (i.e., large wavelengths) are typically investigated using magneto-optical techniques, most notably micro-focused Brillouin light scattering (μ-BLS), or electrical detection methods. These approaches enable studies of micro- and nanoscale phenomena as well as device-level concepts.

In contrast, investigations of fundamental magnetic excitations—such as chiral or high-energy spin dynamics—require access to magnons across the full Brillouin zone, corresponding to much larger wavevectors (shorter wavelengths) and higher frequencies. Such regimes are commonly addressed using neutron or X-ray scattering techniques.

However, no single experimental technique currently provides access to the entire Brillouin-zone range in both wavevector and frequency space (Fig. 1) [1]. As a consequence, a pronounced experimental blind spot exists at intermediate to large wavevectors (30–300 rad/μm). In this regime, conventional optical techniques are limited by momentum conservation and spatial resolution, whereas neutron-based techniques lack sensitivity to low frequencies and long wavelengths.

Here, we introduce a theoretical modeling framework combined with an optical approach that bridges this gap by integrating micro-focused Brillouin light scattering (μ-BLS) with Mie resonators placed on top of a magnetic thin film [1], [2], [3]. Using this concept, we demonstrate access to spin waves in a previously inaccessible k-vector regime, including incoherent magnons. The measurement can be configured either to probe a broad range of wavevectors or to selectively access specific k-vector magnitudes and directions through periodic stripe arrays. The accompanying modeling provides insight into the signal strength and spectral shape of the measured BLS response, enabling extraction of additional information about the underlying spin-wave system through detailed analysis of the resulting spectra.

Fig. 1. Schematics of a spin wave dispersion relation in a permalloy thin film spanning over the whole Brillouin zone. Various experimental techniques are highlighted with their corresponding accessible frequency and wavenumber ranges. The range achieved using Mie-enhanced μBLS in this work is emphasized.

Acknowledgments

OW acknowledge support from Horizon Europe - MSCA grant agreement No. 101211677, project FeriMag.

References

[1] J. Krčma, O. Wojewoda, M. Hrtoň, J. Holobrádek, J. A. Arregi, J. Panda, E. Pribytova, and M. Urbánek, "Mie-enhanced microfocused Brillouin light scattering for full wave vector resolution of nanoscale spin waves," *Science Advances*, vol. 11, no. 44, p. eady8833, 2025.

[2] O. Wojewoda, F. Ligmajer, M. Hrtoň, J. Klíma, M. Dhankhar, K. Davídková, M. Staňo, J. Holobrádek, J. Krčma, J. Zlámal, T. Šikola, and M. Urbánek, "Observing high-k magnons with Mie-resonance- enhanced Brillouin light scattering," *Commun. Phys.*, vol. 6, no. 1, p. 94, 2023.

[3] O. Wojewoda, M. Hrtoň, and M. Urbánek, "Modeling of microfocused Brillouin light scattering spectra", *Phys. Rev.* B 110, 224428, 2024 Phys. Rev. B 110, 224428

Momentum Space Enabled Functionalities in Chiral Metasurfaces

Alexander Antonov[1,*], Connor Heimig[1], Tao Jiang[1], Dmytro Gryb[1], Leonardo de S. Menezes[1,2], Maxim Gorkunov[3], Andreas Tittl[1]

[1] Chair in Hybrid Nanosystems, Nanoinstitute Munich, Faculty of Physics, Ludwig-Maximilians-Universität München, Munich, Germany
[2] Departamento de Fisica, Universidade Federal de Pernambuco, Recife-PE, Brazil
[3] Theoretical Physics and Quantum Technologies Department, National University of Science and Technology 'MISIS', Moscow, Russia
*Corresponding author: a.antonov@physik.uni-muenchen.de

***Abstract* —We study metasurfaces with quasi-bound state in the continuum with gutter-like dispersion remaining maximum chiral over broad areas of the momentum space. We employ them across different material platforms - van der Waals and polymer-based nanostructures - to demonstrate the formation of chiral exciton-polaritons and to engineer maximally chiral flatbands.**

***Keywords*— metasurfaces, optical chirality, momentum space, light-matter coupling, flatbands.**

I. Introduction

Metasurfaces supporting chiral photonic quasi-bound states in the continuum (qBICs) [1,2], whose polarization and Q-factor are controlled by structural asymmetry, provide a versatile platform for chiral light sources and detectors [3-6]. Typically, the qBIC's circular polarization originates from a topological singularity located at a specific point in momentum space (*k*-space) [2,3]. Small deviations in structural parameters or detuning in the *k*-space substantially degrade their circular polarization, limiting practical metasurface applications. Maintaining robust circular polarization over broad ranges of the momentum space is a recognized challenge and various approaches are being proposed based on complex geometries [6] while still remaining restricted for relatively narrow ranges of incidence angles [7].

Here we present a chiral qBIC that breaks the conventional trade-off between chirality and momentum selectivity, sustaining near-unity circular polarization over an extended k-space range: $-0.2 \leq k_i/k_0 \leq 0.2$, $i = x, y$. Furthermore, we employ the eigenstate's wavelength dispersion as an additional degree of freedom to control light-matter interaction and the formation of chiral flatbands.

II. Results and Discussion

We start from a metasurface composed of pairs of nanorods, sustaining a BIC in the form of an antiparallel dipole resonance. As demonstrated in [1], careful adjustment of the asymmetry parameters, namely the spreading angle and the vertical displacement within the singular pair, allows one to uncouple the mode from one circular polarization and form maximally chiral qBIC, whose coupling with the far-field is accompanied by a near-unity transmittance difference, defined as $\Delta T = |T_{RR} - T_{LL}| \approx 1$.

However, all previous studies considered only normally incident light, neglecting the role of in-plane momentum. Here, we address this gap and show that a maximally chiral antiparallel dipole resonance preserves stable circular polarization over a wide *k*-space range: $-0.2 \leq k_i/k_0 \leq 0.2$, $i = x, y$ (see Fig.1(a)). As for the resonance wavelength, it exhibits either parabolic dispersion along the k_x-direction ($k_y = 0$) or remains dispersionless along the k_y-direction ($k_x = 0$), forming a gutter-like landscape (see Fig.1(b)). Thus, in-plane momentum is no longer a limitation but an additional degree of freedom, enabling convenient post-fabrication control of the resonance, as discussed below.

We first discuss the advantages of parabolic dispersion for the formation of chiral exciton-polaritons. The fabrication technique for metasurfaces supporting chiral qBICs [1] is not restricted to a specific material platform and can be applied to bulk van der Waals materials such as WS_2, which hosts stable excitons at room temperature. Hybridization between achiral excitons, acting as emitters, and a chiral photonic mode, acting as a cavity, leads to the formation of chiral exciton-polaritons. To reveal the chiral strong coupling regime and estimate the Rabi splitting, the cavity wavelength must be tuned while maintaining stable polarization. In-plane momentum along the $k_y = 0$ direction provides this required degree of freedom: tilting the incident light redshifts the qBIC, allowing it to cross the excitonic resonance (629 nm in bulk WS_2) and clearly reveal the upper and lower chiral polariton branches, which we also confirm experimentally [8]. Notably, this post-fabrication tuning provides an accessible and convenient route to control hybrid polaritons, which is crucial for nonlinear optical regimes and Bose-Einstein condensation.

Next, we analyze the potential of the qBIC for realizing a chiral flatband along the $k_x = 0$ direction. The mode itself consists of dipoles, which can't radiate along their orientation axis. Although the nanorods are slightly rotated to break the required mirror symmetry, they remain predominantly oriented along the y-direction. As a result, dipole-dipole coupling between neighboring unit cells along this direction is weak. Consequently, the phase mismatch of dipole oscillations induced by oblique incidence along the $k_x = 0$ direction has a negligible effect on the resonance, leading to a stable wavelength position.

To demonstrate this in practice we employ a previously developed approach for breaking the out-of-plane symmetry using a polymethylmethacrylate (PMMA) overlayer in combination with silicon nanorods [9] to realize a metasurface supporting a chiral qBIC. This system exhibits the same *k*-space characteristics shown in Fig. 1(a) and (b) and thus supports chiral flatbands (Fig. 1(d)). Moreover, the PMMA thickness can be gradually reduced via post-fabrication low-dose reactive ion etching. By varying the overlayer thickness, the qBIC polarization (and thus the flatband polarization) can be tuned from circular to elliptical, then to linear, and finally to elliptical with opposite handedness, as demonstrated both theoretically and experimentally.

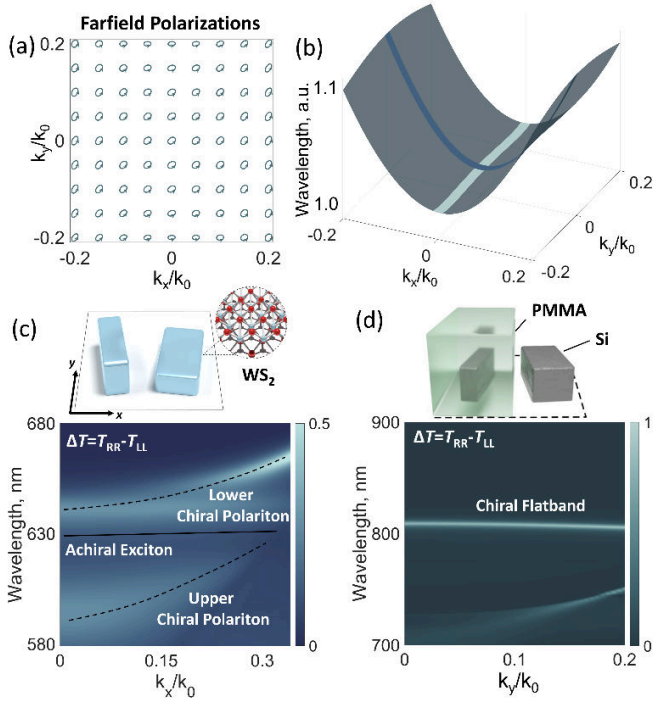

Fig.1. (a) Far-field polarization map in *k*-space of a maximally chiral antiparallel dipole qBIC and (b) its resonance position, showing parabolic dispersion (dark blue line at $k_y = 0$) and a flatband (light blue line at $k_x = 0$) in orthogonal directions. (c) Simulated transmittance difference of a metasurface made of bulk WS_2, where hybridization between an achiral exciton and a chiral qBIC with parabolic dispersion ($k_y = 0$) results in chiral polaritons. (d) Simulated transmittance difference of a silicon metasurface with a PMMA overlayer acting as an out-of-plane symmetry breaking element, exhibiting chiral flatband along the $k_x = 0$ plane.

III. Conclusion

We demonstrated that a chiral qBIC can sustain stable circular polarization over a broad region of momentum space. By exploiting the mode's gutter-like wavelength dispersion, we realize distinct regimes across different material platforms. Using parabolic resonance dispersion and bulk excitonic WS_2 we demonstrated the strong coupling regime with the formation of chiral polaritons and the corresponding Rabi-splitting. In the orthogonal direction of momentum space, a PMMA-based system enables the formation of chiral flatbands whose polarization (ranging from circular to elliptical with opposite handedness) is controlled by the overlayer thickness. All results are supported both theoretically and experimentally.

Acknowledgments

The work of A.A., C.H., T.J. and A.T. is funded by the European Union* (EIC, OMICSENS, 101129734, ERC, METANEXT, 101078018). *Views and opinions expressed are however those of the author(s) only and do not necessarily reflect those of the European Union or the European Research Council Executive Agency. Neither the European Union nor the granting authority can be held responsible for them.

References

[1] L. Kühner et al., "Unlocking the out-of-plane dimension for photonic bound states in the continuum to achieve maximum optical chirality", Light Sci. Appl, 12, 250, 2023.

[2] W. Liu, et al., "Circularly Polarized States Spawning from Bound States in the Continuum," Phys. Rev. Lett., 123, 11, 116104, 2019.

[3] X. Zhang, et al., "Chiral emission from resonant metasurfaces," Science 377, 1215-1218, 2022.

[4] Y. Lim et al., "Maximally chiral emission via chiral quasibound states in the continuum," Laser Photonics Rev. 17, 2200611, 2023.

[5] M.-H. Chen, et al. "Ultraviolet Chiral Lasing in In-Plane Photonic Crystal via Quasi-Bound State in the Continuum," Nano Letters, 25, 24, 9809–9816, 2025

[6] K. Sun, et al., "Circularly polarized thermal emission driven by chiral flatbands in monoclinic metasurfaces," Sci. Adv., 11, 31, eadw0986, 2025.

[7] M. Choi, et al., "Observation of Photonic Chiral Flatbands," Phys. Rev. Lett., 134, 10, 103801, 2025.

[8] C. Heimig et al., "Chiral nonlinear polaritonics with van der Waals metasurfaces," arXiv:2410.18760, 2024.

[9] H. Hu, et al., " Environmental permittivity-asymmetric BIC metasurfaces with electrical reconfigurability," Nat. Commun., 15, 1, 7050, 2024.

Topology Optimized Aluminum Chiral Nanogap Antennas for DUV Circular Dichroism Enhancement

Atsushi Taguchi[1,*]

[1]Research Institute for Electronic Science, Hokkaido University, Japan
*Corresponding author: taguchi@es.hokudai.ac.jp

***Abstract*—We present topology optimized aluminum chiral nanogap antennas operating at 266 nm in the deep ultraviolet. A stable inverse design scheme for metallic structures was developed. The optimized antenna exhibits strong near-field dissymmetry and high enhancement, making it a promising platform for sensitive DUV circular dichroism spectroscopy.**

***Keywords*— aluminum, deep ultraviolet (DUV), optical antenna, circular polarization, topology optimization, computational inverse design.**

I. Introduction

Topology optimization is a machine-aided design technique that enables the derivation of an optimal structure shape that meets specified physical conditions. This technique has been utilized in mechanics and has recently been applied to problems in electromagnetic fields [1]. We employed topology optimization to design a dielectric gap antenna to maximize field intensity at the nanogap when illuminated with circularly polarized light (CPL) of a specific handedness [2]. The polarization-handedness-induced dissymmetry in near-field intensity was analyzed, revealing a notably high *g*-factor of approximately 1.7 in the topology-optimized nanogap antenna. Furthermore, we demonstrated an enhanced optical chirality density within the nanogap at a nanoscale mode volume [2]. Despite the demonstrated feasibility of using topology optimization to design chiral nanophotonic structures, we have encountered a challenge in extending the technique to metal-based structures. Unlike dielectrics, metallic materials exhibit complex permittivity, which adversely affects the convergence of topology optimization algorithms, leading to stagnation during optimization.

In this study, we overcame this challenge by interpolating the refractive index rather than the permittivity as the design variable [3]. This approach effectively avoids convergence stagnation and yields a metallic chiral-gap antenna. Specifically, using aluminum, which supports surface plasmon resonance in the deep ultraviolet (DUV) range [4,5], we demonstrate a metallic chiral gap antenna optimized for 266 nm in the DUV. This development enables highly sensitive circular dichroism spectroscopy for proteins and pharmaceuticals that exhibit pronounced absorption in the DUV range.

II. Refractive Index Interpolation for Metal Structure Design

The topology optimization seeks the optimal distribution of a material region Ω and its complementary region $D\backslash\Omega$ within the design domain D. The material distribution is represented by a design variable $\rho(\mathbf{r})$, where:

$$\rho(\mathbf{r}) = \begin{cases} 1 & (\mathbf{r} \in \Omega) \\ 0 & (\mathbf{r} \in D\backslash\Omega) \end{cases} \quad (1)$$

Here, $\mathbf{r}$ is the position vector within the design domain D, and a value of $\rho(\mathbf{r}) = 1$ indicates the presence of material, while $\rho(\mathbf{r}) = 0$ indicates its absence.

In the optimization process, the design variable ρ is allowed to continuously change between 0 and 1, ultimately converging to 0 or 1. Maxwell's equations are solved by treating the permittivity ϵ as a function of ρ, which necessitates interpolation between the permittivity values of the medium (usually air) and the material. Conventionally, this interpolation is expressed as:

$$\epsilon(\rho) = \epsilon_{M1} + \rho(\epsilon_{M2} - \epsilon_{M1}) \quad (2)$$

where M_1 and M_2 are the permittivity values of the medium and the optimization material, respectively.

Figure 1 illustrates the transition of permittivity as ρ changes from 0 to 1 using Equation (2) (dashed lines). The permittivity remains positive for dielectric materials such as titanium dioxide, thereby avoiding a zero crossing. However, in metallic materials, the real part of the permittivity is negative, leading to a near-zero crossing at the origin. This causes instability in solving Maxwell's equations, making the optimization process infeasible.

To address this issue, we investigated interpolating the refractive index η and extinction coefficient κ instead of permittivity [3]:

$$\eta(\rho) = \eta_{M1} + \rho(\eta_{M2} - \eta_{M1}) \quad (3)$$

$$\kappa(\rho) = \kappa_{M1} + \rho(\kappa_{M2} - \kappa_{M1}) \quad (4)$$

$$\epsilon(\eta(\rho), \kappa(\rho)) = (\eta(\rho)^2 - \kappa(\rho)^2) - i(2\eta(\rho)\kappa(\rho)) \quad (5)$$

This method ensures that permittivity avoids zero crossings (Fig. 1, solid line), enabling the optimization process to converge even for metallic materials.

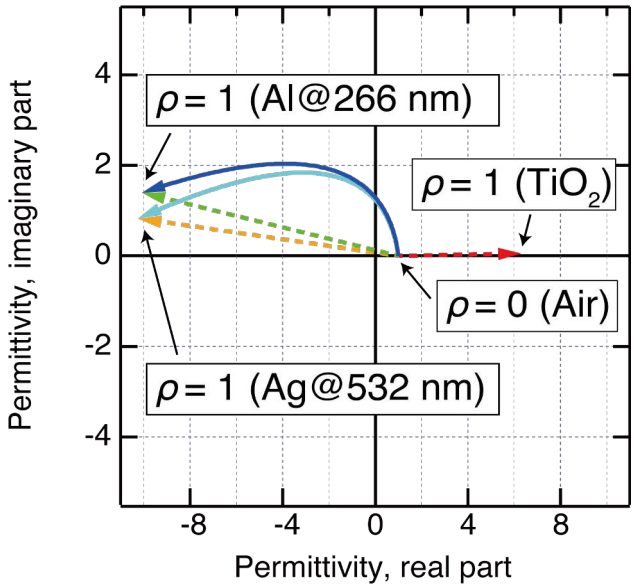

Fig. 1 The trajectories of complex permittivity as the design variables vary from 0 to 1 for dielectric (TiO_2) and metals (Ag and Al). The dashed lines represent interpolation using permittivity, while the solid lines represent interpolation using refractive index.

III. Topology Optimization of Aluminum Chiral Nanogap Antenna at the DUV Wavelength

Biomolecules such as proteins and pharmaceuticals exhibit characteristic absorption in the DUV range. Chiral spectroscopic analysis of these materials can benefit from combining DUV plasmon polaritons, which offer anticipated high enhancement and sensitivity. Among materials exhibiting metallic properties in the DUV range, aluminum is particularly promising due to its chemical stability, non-toxicity, and abundance. We apply the topology design of a chiral nanogap structure made of aluminum, using 266 nm incident light.

The topology-designed structure optimized for *r*-CPL is shown in Fig. 2(a). The cross-sectional slices of the optimized aluminum structure are shown. A gap is formed at Z = 20 nm. The electric field enhancement in the gap was calculated using finite-difference time-domain (FDTD) simulations for right- and left-handed CPLs. The volume-averaged electric field enhancement within the 4 nm×4 nm×2 nm gap region for *r*-CPL was 875-fold (Fig. 2(b)). For left-handed CPL, the same volume-averaged electric field enhancement was 34-fold. The calculated *g*-factor for the near-field intensity was 1.85, confirming the chiral nanogap antenna's highly asymmetric response to the incident CPL polarization.

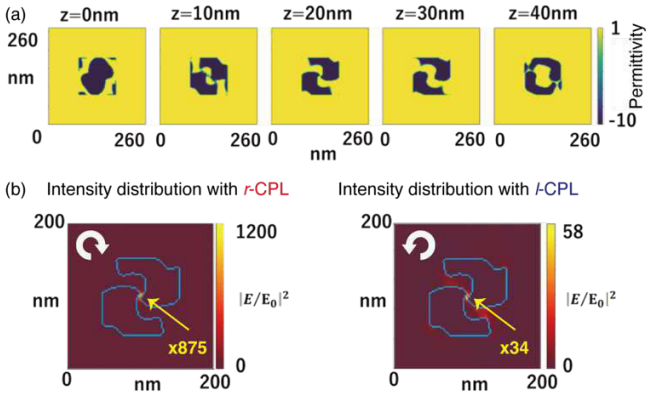

Fig. 2 (a) Z-sliced representations of the structures optimized for right-handed circularly polarized light (*r*-CPL). (b) Field intensity distributions for the structure optimized for *r*-CPL, excited by different polarizations: *r*-CPL (left) and *l*-CPL (right).

IV. Conclusions and Future Outlook

In this study, we extended topology optimization to the design of metallic chiral nanogap antennas by employing refractive-index interpolation, thereby overcoming the convergence issues traditionally associated with metallic materials. We designed a chiral gap antenna optimized for 266 nm DUV light using aluminum. Our results demonstrated significant dissymmetry in near-field intensity, achieving a g-factor of 1.85 and substantial field enhancement within the nanogap. This high dissymmetry highlights the potential of the developed structure for applications in highly sensitive circular dichroism spectroscopy, particularly for biomolecules such as proteins and pharmaceuticals that exhibit strong absorption in the DUV range. The demonstrated approach opens new possibilities for designing metallic structures in the ultraviolet and visible ranges with enhanced chiroptical responses. Future work could explore integrating these antennas into experimental setups for circular dichroism spectroscopy, potentially advancing protein analysis, pharmaceutical development, and other bioanalytical fields.

References

[1] Lu, J., and Vučković, J. "Nanophotonic computational design," Opt. Exp. 21, 13351–13367 (2013).
[2] Taguchi, A., Fukui, Y., and Sasaki, "Inverse design finds chiral nanogap antennas," Phys. Rev. Appl. (2025).
[3] Christiansen, R.E., et al., "A non-linear material interpolation for design of metallic nano-particles using topology optimization," Computer Methods in Applied Mechanics and Engineering, 343, 23-29 (2019).
[4] Taguchi, A. et al., "Deep-UV tip-enhanced Raman scattering," Journal of Raman Spectroscopy 40(9): 1324–1330 (2009).
[5] Taguchi, A. et al., "Tailoring plasmon resonances in the deep-ultraviolet by size-tunable fabrication of aluminum nanostructures," Applied Physics Letters 101(8): 081110 (2012).

On the relation between local optical chirality and circular dichroism in enantiomeric sensing

Diana Shakirova,[1] Adrià Canós Valero,[1] and Thomas Weiss[1,*]

[1]Institute of Physics and NAWI Graz, University of Graz, Austria
*Corresponding author: thomas.weiss@uni-graz.at

***Abstract*—The local optical chirality provides information on how single molecules absorb left- and right-handed circularly polarized light. It might as well seem appropriate to optimize this quantity for enhancing the circular dichroism of chiral media in the vicinity of nanoresonators. We show that this is in general not correct.**

***Keywords*— plasmonics, dielectric nanophtonics, chiral sensing.**

I. Introduction

Detecting the handedness of chiral molecules is of utmost importance for chemical, biological, and pharmaceutical applications, since the handedness of a molecule determines its interaction with the environment. This includes chemical interactions as well as the interaction with light. Hence, it is possible to determine the handedness of chiral molecules by optical measurements, but the chiroptical response of such molecules is usually rather weak. Therefore, conventional approaches require using large numbers of chiral molecules.

Nanophotonic resonators such as plasmonic and dielectric nanoantennas can enhance the chiroptical response. However, two questions naturally arise: What are the dominant mechanisms of this enhancement and how can we actually optimize a system for maximum chiral response?

II. Methods

A widespread approach to address these questions is to consider the local optical chirality $C \propto \mathrm{Im}\ \mathbf{E}^* \cdot \mathbf{H}$ (prefactor depends on unit system), which has been shown to quantify the absorption difference between left- and right-handed circularly polarized light by single molecules [1]. At a first glance, this seems quite reasonable, because the contribution of a chiral medium with Pasteur parameter κ to the absorption difference between left- and right-handed circularly polarized light, known as circular dichroism, can be shown to have a term of the form

$$\mathrm{CD}_{\mathrm{int}} \propto \kappa'' \int \mathrm{d}V\ \mathrm{Im}\ \mathbf{E}^* \cdot \mathbf{H}, \tag{1}$$

where κ'' is the imaginary part of κ, and the integration is carried out over the volume of the chiral medium. Since this expression is directly linked to the absorption in the chiral medium, we call this term *intrinsic circular dichroism*.

Assuming that the modification of the electromagnetic fields due to the chiral medium are on the order of κ, i.e., rather small, one can get a very good approximation of the intrinsic chirality by evaluating equation (1) for the fields in the absence of chirality in the medium ($\kappa = 0$). This is more straightforward and less computationally expensive than full-wave simulations for $\kappa \neq 0$.

III. Results and Discussion

When evaluating the circular dichroism for typical nanophotonic geometries, however, we find that the contribution of intrinsic circular dichroism to the total circular dichroism is often negligible, see figure 1. The dominant contribution is *induced circular dichroism*, which appears because the chiral near fields result in absorption differences in the achiral media of a given resonator. To lowest order, it is proportional to κ' as the real part of κ. Since in most spectral regions, $\kappa'' \ll \kappa'$, intrinsic circular dichroism can be often neglected.

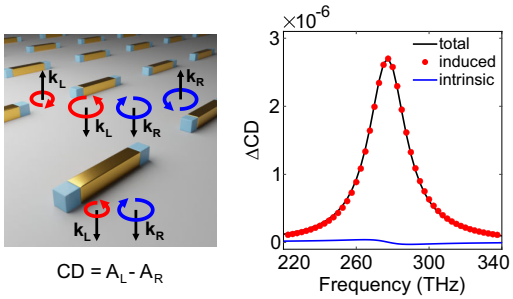

Fig. 1. Example of plasmonic rod antennas with chiral media patches [2]: Dissecting the total circular dichroism (CD) into induced and intrinsic parts, the dominant contribution turns out to be induced circular dichroism.

IV. Conclusion

We have demonstrated that the local optical chirality is often related only to a minor contribution to the circular dichroism signal. A deeper theoretical insight is provided, which opens routes for tailoring near fields to obtain circular dichroism signals that resemble the dispersion of κ'', i.e., the sole circular dichroism signal from the chiral medium.

References

[1] Y. Tang and A. E. Cohen, "Optical chirality and its interaction with matter," Phys. Rev. Lett. **104**, 163901 (2010).

[2] M. L. Nesterov, X. Yin, M. Schäferling, H. Giessen, and T. Weiss, "The role of plasmon-generated near fields for enhanced circular dichroism spectroscopy," ACS Photonics **4**, 578–583 (2016).

Spin-Wave Amplification via Phase-Transition-Driven Temporal Interfaces

Pawel Gruszecki[1,*], Krzysztof Sobucki[1]

[1]Institute of Spintronics and Quantum Information, Faculty of Physics, Adam Mickiewicz University, Poznan, Poland
*Corresponding author: gruszecki@amu.edu.pl

***Abstract*—We show that temporal modulation of magnetic field near phase transitions enables giant spin-wave amplification. Combining temporal-interface scattering with phase-transition-driven instability near an exceptional point, we achieve up to 175-fold gain. In this slow-instability regime, the growth rate scales linearly with Gilbert damping, so dissipation enhances rather than suppresses amplification.**

***Keywords*— spin waves, temporal interfaces, exceptional points.**

I. Introduction

Time-varying media have transformed photonics by enabling wave manipulation impossible with static structures: time refraction, reflection, and frequency conversion [1], [2]. Yet implementing analogous temporal control in magnonics—where Gilbert damping fundamentally limits spin-wave propagation—remains unexplored. Existing amplification schemes rely on parametric pumping or spin-torque mechanisms requiring continuous power injection, achieving gains of 10–50-fold [3], [4].

We establish a framework for magnonics of time-varying media and demonstrate that Gilbert damping, conventionally the primary obstacle to spin-wave transport, can be transformed into the engine of amplification [7]. Using ultrathin CoFeB films with perpendicular magnetic anisotropy (PMA) and interfacial Dzyaloshinskii–Moriya interaction (DMI), we show that temporal modulation of the bias magnetic field near a field-driven phase transition enables 175-fold amplitude gain without continuous pumping. In this contribution, we summarize the framework and main findings reported in Ref. [7].

II. Methods

We derive spin-wave scattering at temporal interfaces from the linearized Landau–Lifshitz–Gilbert equation. Continuity of magnetization at a temporal boundary requires wavevector conservation while frequency adjusts to the new dispersion. This yields transmission and reflection coefficients governed by the precession ellipticity ε_i, which we identify as the *magnonic impedance* $Z_i = \varepsilon_i = |m_z|/|m_x|$, where m_x and m_z are the in-plane and out-of-plane magnetization components. The coefficients take the form $T = \frac{1}{2}(1 + Z_1/Z_2)$, directly analogous to electromagnetic wave impedance matching.

For smooth temporal interfaces, we predict exponential suppression of reflections following Landau–Zener dynamics, enabling clean frequency conversion. Micromagnetic simulations using MuMax3 validate the analytical predictions for 2-nm CoFeB films with saturation magnetization $M_s = 1420$ kA/m, exchange constant $A_{\mathrm{ex}} = 13$ pJ/m, reduced perpendicular anisotropy constant $Q = 1.1$, DMI strength $D = 0.5$ mJ/m^2, and damping constant $\alpha = 0.002$.

III. Results and Discussion

Analytical model and dynamical regimes. As the bias field is lowered, the spin-wave dispersion softens until, at the critical field H_c, the frequency vanishes at a finite wavevector k_{soft}, signaling the onset of the phase transition from the uniform magnetic state to the stripe-domain pattern[6]. The spin-wave dispersion near this transition exhibits a complex dispersion relation [8] and rich non-Hermitian physics [7]. Figure 1(a,b) shows the real and imaginary parts of the complex frequency $\Omega(k)$ for several magnetic field values in the conservative case ($\alpha = 0$): instability occurs only below the exceptional point field H_{EP}. In stark contrast, finite Gilbert damping [Fig. 1(c,d)] opens a new dynamical regime: in the window $H_{\mathrm{EP}} < H < H_c$, both the real and imaginary parts of frequency change sign simultaneously—$\mathrm{Re}(\Omega_+) < 0$ and $\mathrm{Im}(\Omega_+) > 0$—enabling exponential amplification even though the system would be stable without damping. The degeneracy at the exceptional point is lifted with characteristic splitting $|\Omega_+ - \Omega_-| \propto \sqrt{\alpha}$. In this slow-instability regime, the growth rate scales linearly with Gilbert damping. For $H > H_c$, spin waves exhibit conventional behavior with $\mathrm{Re}(\Omega_+) > 0$ and $\mathrm{Im}(\Omega_+) < 0$ (oscillation with damping). This counterintuitive result—where dissipation enables amplification by opening a window with inverted signs of both frequency components—has no conservative-system analog.

Temporal interface scattering. Figure 1(e,f) demonstrates spin-wave behavior at a smooth temporal interface. When the bias field is adiabatically ramped from $\mu_0 H_1 = 300$ mT to $\mu_0 H_2 = 225$ mT, the spin-wave packet preserves its wavelength while the frequency adjusts to the new dispersion. The space-time evolution (e) shows continuous phase velocity change without back-reflection. Spectral analysis (f) confirms frequency conversion: the incident wave at $f_0 = 4.09$ GHz generates a negative-frequency component at $f_1 =$

Fig. 1. Temporal spin-wave amplification near magnetic phase transitions. **(a,b)** Complex dispersion for the conservative case ($\alpha = 0$): instability ($\mathrm{Im}(\Omega) > 0$) occurs only for $H < H_{\mathrm{EP}}$ (red curves). **(c,d)** With finite damping ($\alpha = 0.01$), a new slow-instability regime emerges for $H_{\mathrm{EP}} < H < H_c$ (black curves): both $\mathrm{Re}(\Omega_+) < 0$ and $\mathrm{Im}(\Omega_+) > 0$, enabling amplification in a field window that would be stable without damping. For $H > H_c$ (green curves), conventional damped dynamics is recovered. **(e,f)** Adiabatic temporal interface: space-time evolution shows wavelength preservation with frequency conversion (one can see reversal of the direction of the phase velocity around $t \approx 10.5$ ns); spectral analysis confirms the incident wave at 4.09 GHz generates a time-refracted component at -0.42 GHz. **(g)** Amplification via temporal slab: background shading indicates the field profile—smooth 2-ns ramps between $\mu_0 H = 300$ mT and 225 mT (low-field plateau). Larger Gilbert damping produces stronger gain ($T = 36.4$ for $\alpha = 0.01$), demonstrating dissipation-enhanced amplification.

-0.42 GHz, corresponding to the time-refracted wave on the softened dispersion branch.

Giant amplification via temporal slabs. A temporal-slab protocol (high-field → low-field → high-field) exploits the slow-instability mechanism for frequency-preserving amplification. Figure 1(g) shows the time evolution of magnetization amplitude $m_z(t)$ during passage through an optimized temporal slab for three different damping values. The amplitude grows exponentially during the low-field plateau (light green region), while smooth transitions at the temporal interfaces confirm adiabatic behavior. Crucially, the amplification scales with Gilbert damping: larger α produces stronger gain, reaching $T = 36$ for $\alpha = 0.01$ compared to $T = 1.1$ for $\alpha = 0.0003$. For extended plateau durations and $\alpha = 0.002$, we achieve transmission coefficients up to $T = 175$ [7], substantially exceeding existing parametric schemes. The amplification is wavevector-selective, peaked at $k_{\mathrm{soft}} \approx 49$ rad/μm.

IV. Conclusion

We have demonstrated that temporal modulation of the bias magnetic field near phase transitions enables giant spin-wave amplification, achieving 175-fold gain without continuous pumping—substantially exceeding existing parametric and spin-torque schemes. The key insight is that Gilbert damping becomes the engine of amplification in the slow-instability regime between the exceptional point and critical field.

Unlike photonic non-Foster approaches requiring active electronic elements [9], our mechanism exploits the intrinsic interplay between damping and magnetic phase transitions. The framework is applicable to any PMA system with field-driven stripe-domain transitions, opening pathways toward reconfigurable magnonic devices where gain, frequency conversion, and wavevector filtering are programmed dynamically rather than fixed during fabrication.

Acknowledgments

This work was supported by the Polish National Science Centre (projects 2019/35/D/ST3/03729 and 2022/45/N/ST3/01844).

References

[1] E. Galiffi *et al.*, "Photonics of time-varying media," *Adv. Photonics*, vol. 4, p. 014002, 2022.
[2] H. Moussa *et al.*, "Observation of temporal reflection and broadband frequency translation at photonic time interfaces," *Nature Phys.*, vol. 19, pp. 863–868, 2023.
[3] D. Breitbach *et al.*, "Stimulated amplification of propagating spin waves," *Phys. Rev. Lett.*, vol. 131, p. 156701, 2023.
[4] H. Merbouche *et al.*, "True amplification of spin waves in magnonic nano-waveguides," *Nature Commun.*, vol. 15, p. 1560, 2024.
[5] K. Schultheiss *et al.*, "Time refraction of spin waves," *Phys. Rev. Lett.*, vol. 126, p. 137201, 2021.
[6] J. Kisielewski *et al.*, "Between waves and patterns: Spin-wave freezing in films with Dzyaloshinskii–Moriya interaction," *Phys. Rev. B*, vol. 107, p. 134416, 2023.
[7] K. Sobucki and P. Gruszecki, "Magnonics of time-varying media: Giant amplification via phase-transition-driven temporal interfaces," *arXiv preprint*, arXiv:2512.07713, 2025.
[8] N. Leśniewski, Y. S. Dadoenkova, F. F. L. Bentivegna, and P. Gruszecki, "Perpendicular magnetic anisotropy in thin films enables extraordinary spin-wave phenomena: anti-Larmor precession, negative reflection and refraction, multi-reflection and multi-refraction," *ACS Appl. Mater. Interfaces*, 2026.
[9] V. Pacheco-Peña, Y. Kiasat, D. M. Solís, B. Edwards, and N. Engheta, "Holding and amplifying electromagnetic waves with temporal non-Foster metastructures," *Nature Commun.*, vol. 16, p. 2757, 2025.

Strong Coupling of Chiral Magnons in Altermagnets

Peng Yan
UESTC, China

***Abstract*— We show that the dipole-dipole interaction can induce the strong coupling between exchange magnons with opposite chiralities in altermagnets, manifesting as a significant level repulsion in the magnon spectrum. Crucially, the predicted magnon-magnon coupling is highly anisotropic, and observable in practical experiments. These exotic features are absent in conventional antiferromagnets.**

Relationship between Antiferromagnetic Spin Pumping and Magnetic Resonance

Masahiro Sato[1,*], and Hogara Watanabe[1]

[1]Department of Physics, Chiba University, Japan
*Corresponding author: sato.m.p2@gmail.com

***Abstract*— We develop a microscopic theory for spin pumping in antiferromagnets, by using the nonequilibrium Green's function and spin-wave theory. We find the relationship between the pumped spin current and the spin precession of magnetic resonance. It enables us to explain fundamental natures of spin pumping in different phases of antiferromagnets.**

***Keywords*—Spin pumping, spin current, THz electromagnetic wave, magnetic resonance.**

I. Introduction

Spin pumping [1,2] refers to the phenomenon that when an AC magnetic field is applied to a bilayer junction of a magnet and a metal, an DC spin current is injected from the magnet to the metal through the magnetic resonance in the magnet (see Fig. 1). In the last decades, the spintronics research has been extended from ferromagnets (or ferrimagnets) to antiferromagnets, whose resonance frequencies (typically 0.1-1.0 THz range) are generally higher compared to those (~10 GHz range) of ferromagnets. Therefore, the development and understanding of spin current generation in antiferromagnets are crucial for advancing ultrafast spintronics. Due to their low stray fields, antiferromagnets are also well-suited for integration. Furthermore, spintronic functions in more exotic magnets have been actively investigated. Despite various experimental studies of antiferromagnetic spintronics [6], the theoretical study has not progressed well. For instance, the microscopic theory for spin pumping in ferromagnets [7] has already been established, whereas such a theory for antiferromagnets has been less explored.

Given this situation, we have developed a microscopic theory [8] of spin pumping for typical three phases in antiferromagnets: The Néel and canted phases in easy-axis type antiferromagnets and the weak ferromagnetic phase accompanying another canted spin structure in antiferromagnets with a Dyzaloshinskii-Moriya (DM) interaction. Starting from a microscopic Hamiltonian, we apply the spin-wave approximation [9] and the nonequilibrium Green's function method [10] to formulate the tunneling spin current [11,12] injected from the magnetic material into the metal. We quantitatively estimate the dependence of the generated spin current on the external static magnetic field, the polarization direction of the AC magnetic field, and the AC-field frequency. From them, we show the qualitative differences among spin currents in the ferromagnetic phase, the Néel phase, the canted phase, and the weak ferromagnetic phase. From our microscopic approach, we also discover the relationship between the pumped spin current and the spin precession of magnetic resonance. Comparing our theory and recent experiments, we show that the predicted spin currents in different phases are at least qualitatively consistent with observed electric voltages driven by pumped spin currents in antiferromagnets.

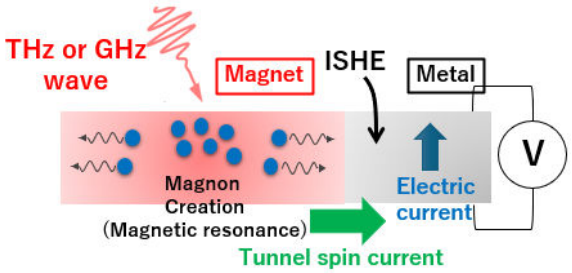

Fig. 1: Schematic image of spin pumping in an ordered magnet. When we apply frequency-tuned THz or GHz wave to a junction consisting of an ordered magnet and a normal metal with spin-orbit (SO) coupling, many magnons are resonantly created, i.e., a large spin precession occurs through magnetic resonance in the magnet. A part of the created magnons is transferred to spin current of conducting electrons in the metal through the interfacial exchange interaction and this means a spin current flows from the magnet to the metal. Finally, due to the SO coupling in metal, a part of spin current is changed into electric current via inverse spin Hall effect (ISHE) [3-5] and the current is detected as an electric voltage.

The relation between the spin current and the precession gives the fundamental insights into spin pumping in antiferromagnets: For instance, it tells us (i) the reason why the spin current in the Néel phase is generally much larger than those of the canted and weak ferromagnetic phases and (ii) that why the dependence of the AC-field polarization on pumped spin current is strong in the canted and weak ferromagnetic phases.

In the conference, we will report the essential parts of our theory, focusing on the relation between the spin current and the precession. In the remaining part of this short article, we

will explain our approach and result, focusing on the important part of our findings.

II. Theoretical Method

Our theory starts with the microscopic Hamiltonian for the junction systems of an antiferromagnet and a metal (see Fig. 1). The Hamiltonian consists of three parts:

$$H = H_{mag} + H_{metal} + H_{int} \qquad (1)$$

where H_{mag}, H_{metal}, and H_{int} are respectively the Hamiltonian of the magnet, the metal and the interfacial exchange interaction. When we consider the Néel, canted and weak ferromagnetic phases in antiferromagnets, the dominant part of H_{mag} is the Heisenberg exchange interaction between neighboring spins and the low-energy physics of H_{mag} is described by the spin-wave approximation [9]: The elementary excitations are magnons. The metal part H_{metal} can be approximated by a free electron model. By treating the interface interaction H_{int} and the external AC magnetic-field Zeeman interaction in H_{mag} as perturbations, we can derive the generic formula of AC-field driven spin current tunneling from the magnet to the metal. This calculation is based on the nonequilibrium Green's function method [10-12]. From the tunnel spin current formula, we can analytically obtain the dependence of the spin current on several parameters such as the AC-field frequency, a static magnetic field and magnetic anisotropies. The detailed calculation will be discussed in Ref. [8].

III. Results

Here, we briefly discuss three important results predicted from our theory [8] based on the model of Eq. (1). First, Fig. 2 shows the AC-field frequency and static-field dependence of computed spin currents in the Néel, canted, and weak ferromagnetic phases. We find that if we properly tune the frequency to a magnetic resonance point, spin pumping can occur. In Fig. 2, each peak position corresponds to a magnetic resonance frequency, and these peak structures are consistent with the experimental result of antiferromagnetic spin pumping. Antiferromagnets generally possess two magnon bands, and therefore two peaks of spin current exist in the Néel and weak ferromagnetic phases, which correspond to two magnon modes with wavevector $\boldsymbol{k} = \boldsymbol{0}$. However, one can also see from the panel (a) in Fig. 2 that there is only one peak in the canted phase. This is because another magnon band in the canted phase corresponds to the gapless Nambu-Goldstone mode and hence such a gapless mode cannot be excited by any AC field. These peak structures of pumped spin currents agree with the recent experiments (for example, see Refs. [13-16]) of spin pumping in antiferromagnets.

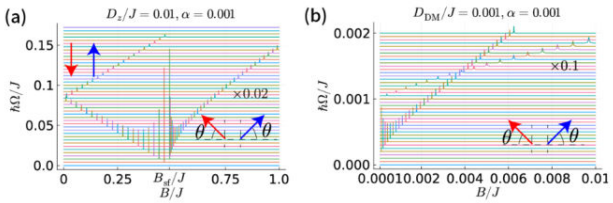

Fig. 2: AC-magnetic-field frequency (Ω) and static magnetic field (B) dependence of tunnel spin currents in (a) the Néel and canted phases and (b) weak ferromagnetic phases in spin pumping setup of Fig. 1. Peaks and their height, respectively, denotes the emergence of a finite spin current and its magnitude. In the easy-axis antiferromagnet of panel (a), weak- ($B < B_{sf}$) and strong-field ($B > B_{sf}$) regimes correspond to Néel and canted phases, respectively. In panel (b), the two spin current peaks correspond to quasi-ferromagnetic (q-FM) and quais-antiferromagnetic (q-AFM) modes of the weak ferromagnets, respectively.

Secondly, we compare the magnitudes of theoretically computed spin currents in different phases. Figure 3 shows the magnitude of pumped spin currents as a function of magnetic anisotropy (D_z) or staggered DM interaction (D_{DM}). We have

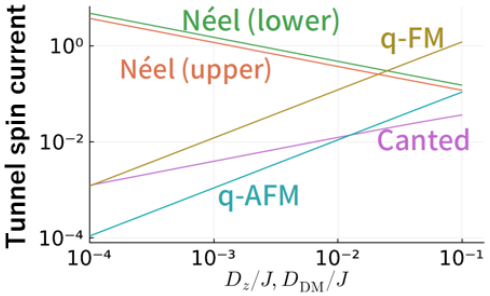

Fig. 3: Magnitudes of tunnel spin currents in spin pumping of different phases in a realistic parameter regime as a function of magnetic anisotropies (single-ion type D_z or DM interaction D_{DM}). The Hamiltonian of the magnet part H_{mag} has a magnetic single-ion anisotropy D_z, while that in the weak ferromagnets has DM interaction D_{DM} instead of D_z. Canted means the spin currents in a canted phase in easy-axis antiferromagnets. Néel (lower) and (upper) denotes two peaks of the Néel phase (see panel (a) of Fig. 2). q-FM and q-AFM means the pumped spin currents at the q-FM and q-AFM mode frequencies in the weak ferromagnets.

fixed other parameters (spin magnitude, exchange interaction, static magnetic field, etc.) at a realistic range. One sees that the spin current in the Néel phase is much larger than those of the canted and weak ferromagnetic phases in a typical range of $10^{-3}J < D_z, D_{DM} < 10^{-2}J$ (J is the strength of the Heisenberg exchange interaction). This size relationship is consistent with experimental results [13-16] of antiferromagnetic spin pumping at least in a qualitative level. These results indicate that our microscopic approach captures the essential aspects of spin pumping in antiferromagnets.

Finally, we discuss the relationship between computed pumped spin current and magnetic resonance. If we remove the attached metal in the spin pumping setup of Fig. 1, the system is equivalent to a typical experimental setup of magnetic resonance of antiferromagnets. Therefore, one can expect the

presence of a relationship between spin pumping and magnetic resonance. In fact, we can arrive at the fact that the computed spin current I_S can be described by using the language of magnetic resonance. When we apply an AC magnetic field along the α axis, whose frequency is chosen to the magnetic resonance frequency, we find that the resulting spin current satisfies the relation

$$I_S \propto A_m(\delta m^\alpha)^2 \qquad (2)$$

where A_m is the area drawn by uniform magnetic moment at the magnetic resonance, and δm^α is the amplitude of the magnetic moment oscillation driven by the AC field. The image of Eq. (2) is explained in Fig. 4. Ferromagnets have no sublattice

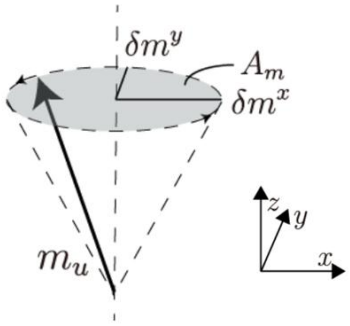

Fig. 4: Image of magnetic resonance under a static magnetic field along the z axis. The black arrow stands for macroscopic spin moment, and its precession motion is induced by an external AC magnetic field. The gray circle is the area given by the trajectory of spin precession.

structure, while antiferromagnets possess A and B sublattices. Therefore, correctly speaking, in the case of antiferromagnets, A_m and δm^α in Eq. (2) are, respectively, replaced with the mean value of areas drawn by A- and B-sublattice spins and that of A- and B-sublattice amplitude. The amplitude δm^α can be analytically estimated under the assumption that the magnon coherent state is realized for magnetic resonance.

Equation (2) gives new insights into spin pumping. For example, it tells us the reason why the pumped spin current in the Néel phase is much larger than those in the canted and weak ferromagnetic phases (see Fig. 3). The reason is as follows. It is well known that the area A_m are quite small in the canted and weak ferromagnetic phases in a weak magnetic field regime since the uniform magnetic moment is small. From this fact and Eq. (2) we can immediately see that the pumped spin current is small in these two phases. Moreover, it is also known that the precession trajectory at the magnetic resonance is an ellipse (NOT circle) in the canted and weak ferromagnetic phases. Therefore, we can predict that an AC-field polarization dependence of the pumped spin current happens in these two phases. In general, magnetic resonances in various magnetic phases have been well studied, and therefore we can extract various information about the spin pump from Eq. (2).

IV. Conclusion

In this short article, we briefly discussed our microscopic theory for spin pumping in antiferromagnets and a few important results [8]. From the theory, we can analytically obtain the dependence of the spin current on the AC-field frequency, a static magnetic field, magnetic anisotropies, etc. The results are consistent with recent experimental observations. Moreover, we discovered the relation between the spin current and magnetic resonance, which enables one to understand the spin pumping with well-established language of magnetic resonance. The detailed results will be explained in Ref. [8].

Spintronics functions of antiferromagnets have been actively investigated for more than ten years [6], whereas their microscopic theories have been less developed. Therefore, it is expected that the microscopic approach including our theory will continue to contribute to new predictions and the establishment of the foundations of antiferromagnetic spintronics.

Acknowledgments

M.S. is supported by JSPS KAKENHI (Grants No. JP25K07198, No. JP25H02112, No. JP22H05131, No. JP25H01609 and No. JP25H01251) and JST, CREST Grant No. JPMJCR24R5, Japan.

References

[1] Y. Kajiwara, K. Harii, S. Takahashi, J. Ohe, K. Uchida, M. Mizuguchi, H. Umezawa, H. Kawai, K. Ando, K. Takanashi, S. Maekawa, and E. Saitoh, Nature **464**, 262 (2010).
[2] S. Maekawa, S. O. Valenzuela, E. Saitoh, and T. Kimura, eds., *Spin Current* (Oxford University Press, 2017).
[3] E. Saitoh, M. Ueda, H. Miyajima, and G. Tatara, Appl. Phys. Lett. **88**, 182509 (2006).
[4] A. Azevedo, L. H. Vilela Le˜ao, R. L. Rodriguez-Suarez, A. B. Oliveira, and S. M. Rezende, J. Appl. Phys. **97**, 10C715 (2005).
[5] S. O. Valenzuela and M. Tinkham, Nature **442**, 176 (2006).
[6] V. Baltz, A. Manchon, M. Tsoi, T. Moriyama, T. Ono, and Y. Tserkovnyak, Rev. Mod. Phys. **90**, 015005 (2018).
[7] Y. Ohnuma, H. Adachi, E. Saitoh, and S. Maekawa, Phys. Rev. B **89**, 174417 (2014).
[8] H. Watanabe and M. Sato, in preparation.
[9] R. M. White, *Quantum Theory of Magnetism* (Springer Nature, 2007).
[10] H. Haug and A-P. Jauho, *Quantum Kinetics in Transport and Optics of Semiconductors* (Springer Nature, 2007).
[11] A.-P. Jauho, N. S. Wingreen, and Y. Meir, Phys. Rev. B **50**, 5528 (1994).
[12] K. Masuda and M. Sato, J. Phys. Soc. Jpn. **93**, 034702 (2024).
[13] P. Vaidya, S. A. Morley, J. Van Tol, Y. Liu, R. Cheng, A. Brataas, D. Lederman, and E. Del Barco, Science **368**, 160 (2020).
[14] J. Li, C. B. Wilson, R. Cheng, M. Lohmann, M. Kavand, W. Yuan, M. Aldosary, N. Agladze, P. Wei, M. S. Sherwin, and J. Shi, Nature **578**, 70 (2020).
[15] H. Wang, Y. Xiao, M. Guo, E. Lee-Wong, G. Q. Yan, R. Cheng, and C. R. Du, Phys. Rev. Lett. **127**, 117202 (2021).
[16] T. Hattori, A. Fukuoka, K. Kawagita, K. Tada, Y. Ishikawa, Y. Yamaguchi, Y. Tatematsu, Y. Fujii, M. Kimata, S. Kimura, D. Kan, J. Ohe, and T. Moriyama, Phys. Rev. Lett. **133**, 256701 (2024).

Chiral structures nanofabrication with optical skyrmions

Takashige Omatsu[1,2,3*]

[1]Molecular Chirality Research Center, Chiba University, Japan
[2]Department of Electrophysics, National Yang Ming Chiao Tung University, Taiwan
[3]Serendip Research Laboratory, Japan
*Corresponding author: takashige.omatsu@gmail.com

***Abstract*— We herein demonstrate nanofabrication of chiral surface structures in azopolymers using optical skyrmions which manifest Möbius strip shaped polarization textures with a circular polarization point defect at a focal plane.**

***Keywords*— chiral structures, structured light, nanofabrication, topology.**

I. Introduction

Helix, spiral, and vortex shaped structures possess 'chirality' (an object or phenomenon cannot be superimposed onto its mirror image), and they play an important role in materials science.

Möbius strip shaped structured materials (referred to herein as 'topological structures') are an example of an unconventional chiral structure (twisted and connected to form a ring which possesses no defined front or back). They should possess exotic physical properties (for instance, magnetic monopole, etc.), and thus, they have long been of interest.

A quasiparticle is formed from a set of particles chosen from a single group within a physical system, and it exhibits topologically protected structures in 2-D and 3-D space. For instance, a magnetic skyrmion is a most remarkable quasiparticle, which encompasses all spin vector states mapped on a Bloch sphere, and it is finding the utility in new investigations, such as high-efficiency ultrahigh capacity data storage, information encoding, and magnetic memory.

Analogous optical quasiparticles (such as optical skyrmions) involve all polarization vector states (Stokes vectors of paraxial beams) represented on a Poincaré sphere (instead of all spin vector states mapped on a Bloch sphere), and they have been theoretically predicted and experimentally demonstrated. Also, they manifest topologically protected, Möbius strip shaped polarization (Stokes vector) textures with a circular polarization point defect (C-point defect) at a focal plane under a tightly focusing condition.

Thus, they will potentially allow the development of polarization-based manipulation of chirality and topology of materials at nano and submicron scales to fabricate topological structures on a nano scale; however, in contrast to more established optical vortices, optical skyrmions are still in their infancy as a research topic. There are few reports detailing the interaction between optical skyrmions and materials at a nano scale.

We herein address the nano-manipulation of chirality and topology of materials using optical skyrmions, towards advanced topological materials science and innovative topological structures fabrication.

In particular, we demonstrate the nanofabrication of topological structures in azopolymers with tightly focused optical skyrmions with nano scale C-point defect.

Acknowledgments

This work was supported by the JSPS KAKENHI Grants-in-Aid (Nos. JP22H05131, JP22H05138, JP23H00270) and by the JST Core Re-search for Evolutional Science and Technology program (No. JPMJCR1903).

References

[1] J. Geng, S. R. Allam, Q. Sheng, T. Omatsu, "Generation of optical quasiparticles with spin–orbit conversion in a single *q*-plate," Laser and Photonics Reviews, e02439 (2025).

[2] W. Li, J. LaMountain, E. Simmons, J. Tan, H. B. Sedeh, A. Clabeau, R. Y. Bekele, J. D. Myers, T. Omatsu, J. Frantz, V. A. Podolskiy, N. M. Litchinitser, "Vortex beam nanofocusing and optical skyrmion generation via hyperbolic metamaterials," Nanophotonics, vol. 14, pp. 4545-4553 (2025).

[3] J. Zhao, K. Kizaki, A. Taguchi, M. Ono, S. Hirayama, T. Omatsu, "Surface relief formation with light possessing multiple vortices," Nanophotonics, vol. 14, pp. 4311-4322 (2024).

[4] T. Omatsu, S. R. Allam, "Structured light solid-state laser sources," Journal of Optics, vol. 27, 073001 (2025).

[5] R. Tamura, S. R. Allam, N. M. Litchinitser, T. Omatsu, "Three-dimensional projection of optical hopfion textures in a material," ACS Photonics, vol. 11, pp. 4958-4965 (2024).

[6] W. R. Kerridge-Johns, A. S. Rao, T. Omatsu, "Optical skyrmion laser using a wedged output coupler," Optica, vol. 11, pp. 769-775 (2024).

[7] R. Tamura, P. Kumar, A. S. Rao, K. Tsuda, F. Getzlaff, K. Miyamoto, N. M. Litchinitser, T. Omatsu, "Direct imprint of optical skyrmions in azopolymers as photoinduced relief structures," APL Photonics, vol. 9, 046104 (2024).

Magnetoelectric effects in truly and falsely chiral media

Omar Jesus Franca Santiago[1,*] and Stefan Yoshi Buhmann[1]

[1] Institut für Physik, Universität Kassel, Germany

*Corresponding author: uk081688@uni-kassel.de

***Abstract*—Three magnetoelectric effects are presented here. Purcell effect is studied in chiral media, quantum friction in chiral media and topological insulators, and Vavilov-Cherenkov radiation in topological insulators. How parity and time-reversal symmetry breaking allow to understand their differences in the context of true and false chirality is investigated.**

***Keywords*— Chiral media, nonreciprocal media, topological insulators, Purcell effect, quantum friction, Vavilov-Cherenkov radiation**

I. Introduction

There are different kind of materials that present a coupled electric and magnetic response. Among them, there are two important classes: chiral and nonreciprocal media. The first class breaks parity symmetry, so it is considered truly chiral and they allow to distinguish left- from right-handedness. The second class breaks time-reversal symmetry, e.g. topological insulators, so it is falsely chiral because the handedness of the medium may be inverted by either space inversion or time reversal. Although they have very similar constitutive relations, their behaviour and physical consequences are rather different.

II. Methods

Our analysis of the Purcell effect and quantum friction is based on macroscopic quantum electrodynamics [1], which allows to express the fields $\hat{\mathbf{E}}$ and $\hat{\mathbf{B}}$ through the Green's tensor and the bosonic creation $\hat{\boldsymbol{f}}^\dagger$ and annihilation operators $\hat{\boldsymbol{f}}$ as follows:

$$\hat{\mathbf{E}}(\mathbf{r}) = \int_0^\infty \mathrm{d}\omega \sum_{\lambda=e,m} \int \mathrm{d}^3 r' \mathbb{G}_\lambda(\mathbf{r},\mathbf{r}';\omega)\cdot\hat{\boldsymbol{f}}_\lambda(\mathbf{r}';\omega) + \text{ H.c.}, \tag{1}$$

$$\hat{\mathbf{B}}(\mathbf{r}) = \int_0^\infty \frac{\mathrm{d}\omega}{\mathrm{i}\omega} \sum_{\lambda=e,m} \int \mathrm{d}^3 r' \nabla\times\mathbb{G}_\lambda(\mathbf{r},\mathbf{r}';\omega)\cdot\hat{\boldsymbol{f}}_\lambda(\mathbf{r}';\omega) + \text{ H.c.}\,, \tag{2}$$

where λ denotes the polarizations and the Green's tensor $\mathbb{G}$ satisfies the corresponding Helmholtz equation. Then, by considering for the Purcell effect the interaction Hamiltonian [2] $\hat{H}_{AF} = -\hat{\mathbf{d}}\cdot\hat{\mathbf{E}}(\mathbf{r}) - \hat{\mathbf{m}}\cdot\hat{\mathbf{B}}(\mathbf{r})$, and for quantum friction the following one [3] $\hat{H}_{AF} = -\hat{\mathbf{d}}\cdot\hat{\mathbf{E}}(\mathbf{r}) + \dot{\mathbf{r}}\cdot\hat{\mathbf{d}}\times\hat{\mathbf{B}}(\mathbf{r})$, we are able to find in the weak atom-field coupling regime the decay rate for the Purcell effect in chiral environments, and the decay rate and frequency shift for the quantum friction.

On the other hand, our analysis of the Vavilov-Cherenkov radiation generated by a charged particle moving parallel to the interface of a topological insulator is purely classical. By solving the corresponding Helmholtz equation, we obtain the electric field [4]

$$\mathbf{E}(\mathbf{r};\omega) = \mathrm{i}\omega\mu_0 \int d^3 r'\, \mathbb{G}(\mathbf{r},\mathbf{r}';\omega)\cdot\mathbf{j}(\mathbf{r}';\omega)\,. \tag{3}$$

where $\mathbf{j}$ is the external current. Then, in the far-field approximation of Eq. (3) we analyse the angular distribution of the radiated energy per unit frequency at both sides of the interface given by [4]

$$\frac{d^2\mathcal{E}}{d\omega d\Omega} = \sqrt{\frac{\varepsilon_0\varepsilon}{\mu_0\mu}}\frac{r^2}{\pi}\mathbf{E}^*(\mathbf{r};\omega)\cdot\mathbf{E}(\mathbf{r};\omega)\,. \tag{4}$$

III. Results and Discussion

Our results show:

- The Purcell decay rate is enantiosensitive.
- The spectroscopical quantities of quantum friction provide two bridges between chirality and nonreciprocity.
- The radiation along the Vavilov-Cherenkov cone is inhomogeneous and asymmetric.

IV. Conclusion

We studied and fully characterized three different magnetoelectric effects gaining insight on how parity and time-reversal symmetry breaking dictamines their main properties.

Acknowledgments

O.J.F. was supported by the postdoctoral fellowships CONACYT-770691 and CONACYT- 800966. The authors gratefully acknowledge funding by the Deutsche Forschungsgemeinschaft Project No. 328961117- SFB 1319 ELCH.

References

[1] S. Y. Buhmann, D. T. Butcher, and S. Scheel, "Macroscopic quantum electrodynamics in nonlocal and nonreciprocal media" *New Journal of Physics* **14**, 083034 (2012).

[2] C. S. Rapp, Janine C. Franz, Stefan Yoshi Buhmann and O. J. Franca, "Purcell effect in chiral environments: A macroscopic QED perspective" *Physical Review A*, **112**, 013109 (2025).

[3] O. J. Franca, Fabian Spallek, Steffen M. Giesen, Robert Berger, Kilian Singer, Stefan Aull and Stefan Yoshi Buhmann, "Spectroscopic footprints of quantum friction in nonreciprocal and chiral media" *Physical Review A*, **112**, 012803 (2025).

[4] O. J. Franca and Stefan Yoshi Buhmann, "Vavilov-Cherenkov radiation for parallel motion in three-dimensional topological insulators" *Physical Review B* **110**, 195150 (2024).

Resonances and reversal in local and global chirality responses

Itamar Kimchi[1,*]

[1]Department of Physics, Georgia Institute of Technology, Atlanta, GA, USA
*Corresponding author: ikimchi3@gatech.edu

***Abstract*—We theoretically study local chirality responses and discuss several surprising results. These include a chirality reversal generated by isolated chiral or magnetic defects. We also discuss diagnosis of local chirality through extensions of local marker and relation to spectral localizer, loop current patterns, orbital magnetization, and subspace chirality.**

***Keywords*— chirality reversal, magnetic impurities, orbital magnetization, loop currents, spectral localizer, subspace chiral phases, half chiral phases, disorder, local topological markers, chiral orbital currents, resonance, defects.**

I. Introduction

In the remainder of this abstract we focus on just the first result highlighted above [1], without discussing the additional related results [2], [3], [4], [5], [6], [7] , in order to be concrete while keeping this abstract brief.

The quantum Hall effect with its topologically protected chiral edge modes has analogues in insulators with Chern bands as exemplified by Haldane's honeycomb model. The model begins with spinless fermions hopping on the honeycomb (graphene) lattice with chemical potential tuned to the two 2D Dirac cones. Time reversal breaking (TRB) is then incorporated by adding imaginary hopping on next-nearest-neighbor (NNN) bonds of the honeycomb lattice. Microscopically the imaginary hopping term is quite general and could describe orbital magnetic fields or arise via superexchange in the presence of any magnetic background. The interesting effects of the TRB term can be seen by considering its action on the gapless Dirac cones: it opens a topological gap and generates a Chern number set by the sign of the imaginary hopping. As in the Quantum Hall effect, the bulk band with nonzero Chern number has a corresponding chiral edge state whose circulating current reflects the bulk topology.

What happens to the spectral structure if time reversal is broken only by a dilute density of magnetic or chiral defects? The effects of defects on orbital magnetization, arising from the electronic bands even in the absence of spin magnetization, and therefore arising more generally for various quasiparticles in metamaterials, have not been as well explored.

II. Methods

The spinless Haldane model offers an avenue for accessing this limit. Each magnetic scatterer can be modeled as a defect hexagon. The imaginary NNN bonds are then added only within these isolated defect hexagons. Such Haldane hexagon defects provide the effective description of a magnetic impurity or any other TRB scattering, with no spin degree of freedom explicitly involved.

Thus we analyze lattice models with Dirac fermion excitations perturbed by a localized magnetic impurity that generates a Haldane type next nearest neighbor hopping pattern on a single plaquette. This perturbation produces a local topological mass and breaks time reversal symmetry in a confined region of the lattice.

To characterize the resulting chirality we compute two complementary observables. First, we evaluate orbital magnetization through real space implementations of the local Chern marker, which provides a bulk sensitive probe constructed from the occupied states of the system. Second, we calculate electronic current distributions associated with low energy states near the impurity.

In addition to these diagnostics we discuss broader real space approaches for characterizing topology in inhomogeneous systems, including spectral localizer methods and generalizations of local markers for chirality.

III. Results and Discussion

Our analysis reveals a chirality reversal as the local defect strength is tuned. For weak impurity strength the induced orbital magnetization matches the defect, while beyond a critical strength the induced magnetization flips sign. Both orbital magnetization computed from the local Chern marker and the current patterns of low energy states show a consistent reversal near the same critical impurity strength.

IV. Conclusion

Experimental implications of these results are clear: an inhomogenous TRB mass term can change its effective sign as a function of its bare TRB strength. For example, adding positive chirality defects would produce positive orbital magnetization for weak impurity scattering strength, as usually expected, but increasing the impurity scattering strength could suddenly reverse the orbital magnetization and the associated chiral currents — producing negative orbital magnetization even while the impurity chirality remains positive.

Acknowledgments

This work was supported by the U.S. Department of Energy, Office of Science, Basic Energy Sciences, under Early Career Award Number DE-SC0025478.

REFERENCES

[1] R. Xu, A. Seth, and I. Kimchi, "Chirality reversal at finite magnetic impurity strength and local signatures of a topological phase transition," *Phys. Rev. B*, vol. 113, p. 045151, 2026.

[2] A. Seth, F. Borhani, and I. Kimchi, "Chiral spin liquid instability of the Kitaev honeycomb model with crystallographic defects," *arXiv preprint arXiv:2511.19409*, 2025.

[3] A. Seth, F. Borhani, and I. Kimchi, "Generation of chirality and orbital magnetization by Stone–Wales-type lattice defects in the Kitaev spin liquid," *arXiv preprint arXiv:2512.13490*, 2025.

[4] A. Seth, J. C. Prestigiacomo, A. Xu, Z. Zeng, T. D. Ford, B. S. Shivaram, S. Li, P. A. Lee, and I. Kimchi, "Disorder-induced spin-cluster magnetism in a doped kagome spin liquid candidate," *Phys. Rev. B*, accepted 2026. DOI: 10.1103/xsp7-j8h1.

[5] G. Cao, H. Zhao, Y. Zhang, A. Fix, T. R. Cao, D. Ananth, Y. Ni, G. Schebel, R. Nandkishore, I. Kimchi, H. Chen, F. Ye, and L. E. DeLong, "Emergent inductance from chiral orbital currents in a bulk ferrimagnet," *Phys. Rev. Lett.*, vol. 135, p. 146504, 2025.

[6] F. Borhani, A. Seth, and I. Kimchi, "Real-space chirality from crystalline topological defects in the Kitaev spin liquid," *npj Quantum Materials*, vol. 10, p. 43, 2025.

[7] Y. Zhang, Y. Ni, H. Zhao, S. Hakani, F. Ye, L. DeLong, I. Kimchi, and G. Cao, "Control of chiral orbital currents in a colossal magnetoresistance material," *Nature*, vol. 611, pp. 467–472, 2022.

Topological polarization textures and emergent chirality in ferroelectric materials

Svitlana Kondovych[1,*]

[1]Institute for Theoretical Solid State Physics, Leibniz Institute for Solid State and Materials Research Dresden
Helmholzstr. 20, D-01069 Dresden, Germany
*s.kondovych@ifw-dresden.de

***Abstract*—Ferroelectric materials can host complex patterns of electric polarization, which arise from electrostatic interactions and nanoscale confinement and can exhibit switchable chirality. Understanding how these topological polar textures form and can be controlled opens new possibilities for designing functional materials and next-generation electronic devices.**

***Keywords*—ferroelectrics, polarization, chirality, topology.**

Chirality is a fundamental manifestation of broken symmetry and plays a central role in many physical phenomena. In condensed matter systems, chiral ordering of vector fields often emerges from specific microscopic interactions. For example, in magnetic materials the antisymmetric exchange known as the Dzyaloshinskii-Moriya interaction selects a preferred rotational sense of the magnetization and stabilizes chiral spin textures such as skyrmions. In contrast, ferroelectric materials provide a conceptually different platform for chirality [1]: here it can arise spontaneously from long-range electrostatic interactions and geometrical constraints, without any intrinsic microscopic interaction favoring a particular handedness.

Ferroelectrics are characterized by a vector order parameter, the electric polarization $\boldsymbol{P}$, whose spatial distribution can form complex textures resulting from the interplay of electrostatic, elastic, and anisotropy energies. In confined geometries such as nanodots, nanowires, thin films, or multilayer heterostructures, the strong depolarization fields associated with bound charges impose stringent constraints on the polarization field. To minimize electrostatic energy, the system tends to form configurations that suppress bound charges $\rho_P = -\boldsymbol{\nabla} \cdot \boldsymbol{P}$, effectively enforcing a divergence-free condition on the polarization, $\boldsymbol{\nabla} \cdot \boldsymbol{P} = 0$. Under such conditions, the polarization field behaves similarly to incompressible vector fields studied in hydrodynamics. This analogy allows one to apply mathematical concepts developed in fluid dynamics [2] to classify and understand polarization textures in ferroelectrics [3].

Within this framework, confined ferroelectrics support two main classes of topological states. Two-dimensional vortex configurations represent the simplest solutions of a divergence-free polarization field, while three-dimensional structures include knotted polarization states – hopfions [4]. The latter are topologically nontrivial and exhibit chirality arising from the twisting and linking of polarization field streamlines. In contrast to magnetic systems, where chirality is usually fixed by microscopic interactions, the handedness of chiral ferroelectric textures results from electrostatic and geometrical effects and therefore does not have a predefined orientation. Consequently, their chirality can be modified or switched by external stimuli such as electric fields [5] or mechanical strain [6], providing a platform for controlled topological polarization states in ferroic materials.

Beyond their fundamental interest, chiral polarization textures hold considerable promise for technological applications. Topological states are inherently robust against perturbations due to their global structure, which makes them appealing for information storage and processing. Ferroelectric systems further provide advantages such as low energy dissipation, electric-field control, and strong coupling to mechanical and optical degrees of freedom. These properties open prospects for novel device concepts, including high-density non-volatile memories, neuromorphic architectures, and nanoscale functional elements operating in the terahertz regime.

Acknowledgments

This work was supported by the Philipp Schwartz Initiative of the Alexander von Humboldt Foundation.

References

[1] I. Luk'yanchuk, A. Razumnaya, S. Kondovych, Y. Tikhonov, and V. M. Vinokur, "Topological ferroelectric chirality," *arXiv:2406.19728* (2024).
[2] V. I. Arnold and B. A. Khesin, *Topological methods in hydrodynamics*, Vol. 125 (Springer Science & Business Media, New York, 2021).
[3] I. A. Lukyanchuk, A. G. Razumnaya, S. Kondovych, Y. A. Tikhonov, B. Khesin, and V. M. Vinokur, "Topological foundations of ferroelectricity," *Physics Reports* 1110, 1 (2025).
[4] I. Luk'yanchuk, Y. Tikhonov, A. Razumnaya, and V. M. Vinokur, "Hopfions emerge in ferroelectrics," *Nature Communications* 11, 2433 (2020).
[5] Y. Tikhonov, S. Kondovych, J. Mangeri, *et al*. "Controllable skyrmion chirality in ferroelectrics.", *Scientific Reports* 10, 8657 (2020).
[6] M. A. Pavlenko, F. Di Rino, L. Boron, S. Kondovych, A. Sené, A., *et al*. "Phase diagram of a strained ferroelectric nanowire," *Crystals*, 12(4), 453 (2022).

From Skyrmions to Twistons to Hopfions: Topological Textures Beyond Homotopy Groups of Spheres

Maria Azhar[1,*], Sandra C. Shaju[1], Trishita Das[2], Ross Knapman[1], Alessandro Pignedoli[1], Yijie Shen[2], Karin Everschor-Sitte[1]

[1]Faculty of Physics and CENIDE, University of Duisburg-Essen, Germany
[2]Nanyang Technological University, Singapore
*Corresponding author: maria.azhar@uni-due.de

***Abstract*—Topology provides a unifying language for structured fields across optics, magnetism, and metamaterials. We demonstrate that homotopy-based classifications are incomplete when backgrounds are non-uniform, and introduce a flux-tube linking framework that captures mixed and fractional topology. The approach enables systematic classification of three-dimensional textures across physical platforms.**

***Keywords*— topology, Skyrmions, Hopfions, Twistons, screw dislocations, linking number**

Fig. 1: Topological textures in a normalized orientation field $\mathbf{v}(\mathbf{r})$: (a) Skyrmion (b) a Skyrmion string with isolines of $\mathbf{v}$ (preimages of $\mathbf{v}$) and fieldlines of emergent field $\mathbf{F}$ parallel along the z-direction, (c) a Skyrmion string with a twist along the vertical direction, (d) a Hopfion that can be imagined as a Skyrmion tube twisted and its ends connected (e) fieldlines of $\mathbf{F}$ for the Hopfion (f) any pair of fieldlines of $\mathbf{F}$ is a pair of oriented curves with Gauss linking number -1.

I. Topology Across Physical Platforms

Topological concepts play a central role in modern optics, where structured light fields host vortices, knots, and linked optical fields. Optical Skyrmions, polarization singularities, and optical Hopfions have been experimentally demonstrated and actively explored for robust information encoding and wave control [1], [2], [3]. Similar topological structures arise in magnetic systems [4], [5], liquid crystals, and acoustic or mechanical metamaterials, motivating a platform-independent topological description.

Fig. 2: (a) Skyrmion (b) meron (c) Hopfion (d) Twiston respectively with $(Q, H) = (-1, 0)$, $(-1/2, 0)$, $(0, -1)$ and $(1/2, -3/4)$. The S^2 sphere is shown as a grey sphere with the background overlayed as a black line. The degree of mapping of textures in $\mathbb{R}^2$ (a-b) or $\mathbb{R}^3$ (c-d) to an S^2 sphere can be measured in terms of topological indices Q and H. These become non-integer when the background is non-collinear, i.e., an S^1 line on the S^2 sphere [6], as in (b) and (d).

II. Skyrmions and $\pi_2(S^2)$ Topology

In two-dimensional (2D) systems with a fixed and uniform background, Skyrmions are classified by the homotopy group $\pi_2(S^2) = \mathbb{Z}$. The corresponding topological invariant, the Skyrmion number, is defined as

$$Q = \frac{1}{4\pi} \int \mathbf{F} \cdot d\mathbf{S}, \tag{1}$$

where the emergent field $\mathbf{F}$ is constructed from a normalized orientation field $\mathbf{v}(\mathbf{r}) \in S^2$ as

$$F_i = \frac{1}{2} \epsilon_{ijk}\, \mathbf{v} \cdot (\partial_j \mathbf{v} \times \partial_k \mathbf{v}) \,. \tag{2}$$

This invariant counts how many times physical space wraps around the order-parameter sphere and remains quantized under smooth deformations as long as the background at infinity ($\mathbf{r} \to \infty$) is fixed.

In magnetic systems, $\mathbf{v}$ corresponds to the local magnetization direction. In optics, analogous constructions arise when $\mathbf{v}$

Fig. 3: (a) to (f) show a continuous transformation from Hopfion to Skyrmion tube, through a change of the background [6].

represents the normalized Stokes vector, the normalized Poynting vector, or the direction of the electric or magnetic field vectors [1], [2], [3]. While Skyrmions arise from mappings of 2D space into the sphere, three-dimensional textures admit fundamentally different topology.

III. Hopfions and $\pi_3(S^2)$ Classification

In three dimensions (3D), textures such as Hopfions are classified by the homotopy group $\pi_3(S^2) = \mathbb{Z}$. The corresponding invariant is the Hopf index, traditionally computed using the Whitehead integral formula,

$$H = \int \mathbf{A} \cdot \mathbf{F}\, d^3r, \tag{3}$$

where $\mathbf{F} = \nabla \times \mathbf{A}$. This expression is gauge invariant only for compact, uniform backgrounds [7]. In systems with non-uniform backgrounds or extended textures with flux crossing the boundaries, such as $S^2 \times S^1$ configurations (shown in Fig. 1(b-c), Fig. 2(b,d) and Fig. 3(b-e)), additional boundary terms appear in H and explicit gauge fixing is required [6], limiting the practical applicability of this formula.

IV. Flux-Tube Linking Framework

To circumvent these issues, we reformulate the Hopf index in terms of linking numbers of flux tubes of $\mathbf{F}$ [6]. Decomposing the field $\mathbf{F}$ into N_Φ flux tubes yields

$$H = \sum_{i=1}^{N_\Phi} L_{ii}\Phi_i^2 + \sum_{\substack{i=1 \\ j\neq i}}^{N_\Phi} L_{ij}\Phi_i\Phi_j, \tag{4}$$

where Φ_i is the flux of tube i, L_{ii} its self-linking, and L_{ij} the mutual linking between tubes. Both linking numbers are computed using the Gauss integral formula. This formulation is gauge independent, analytically tractable, and naturally captures mixed and fractional topology: in non-collinear backgrounds, flux tubes may intersect the boundary, allowing partial flux redistribution through the boundaries and yielding continuously tunable values of Q and H. It is particularly well suited to textures such as the Twiston–that is stabilized by a screw dislocation background winding [5]–that interpolate continuously between 2D and 3D topological character (see Fig. 3).

V. Tunable Topological Textures

Distinct topological textures such as Skyrmions and Hopfions (see Fig. 1) are commonly classified by different homotopy groups under the assumption of a fixed and uniform (ferromagnetic) background. However, if the background configuration is allowed to become non-collinear (see Fig. 2), and to vary continuously, these textures can smoothly deform into one another without singularities (see Fig. 3). In this extended configuration space, the distinction between integer-valued invariants becomes less rigid and intermediate states with mixed topology naturally emerge [6].

The transformation illustrated in Fig. 3 demonstrates such a pathway: a Hopfion continuously evolves into a Skyrmion tube through intermediate configurations (screw dislocations [6], [5]) where both the Skyrmion number and Hopf index take non-integer values. Topology therefore evolves smoothly rather than changing abruptly.

This behavior reflects the dependence of topological invariants on global boundary conditions (see Fig. 2). When the constraint of a collinear background is relaxed [8], the configuration space expands, allowing continuous interpolation between textures traditionally assigned to distinct homotopy classes. Engineering the background thus provides a direct route to controlled switching between 3D particle-like states across physical platforms.

VI. Outlook and Realizations

The flux-tube picture reveals that 3D topology is far richer than suggested by conventional classification schemes using homotopy groups of spheres. Rather than isolated, discrete objects, Skyrmions, Twistons, and Hopfions form a connected landscape of textures that can continuously transform into one another when the background is allowed to vary.

Because this mechanism relies only on the geometry of oriented fields, it is not restricted to magnetism. The same principles apply to structured optical fields, liquid crystals, and engineered metamaterials.

References

[1] Y. Shen, H. Wang, and S. Fan, "Free-space topological optical textures: tutorial," *Adv. Opt. Photon.*, vol. 17, no. 2, 295–374, 2025.

[2] T. J. Davis *et al.*, "Ultrafast vector imaging of plasmonic Skyrmion dynamics with deep subwavelength resolution," *Science*, vol. 368, no. 6489, 2020.

[3] D. Sugic *et al.*, "Particle-like topologies in light," *Nat. Commun.*, vol. 12, 2021.

[4] S. Koraltan, C. Abert, M. Albrecht, M. Azhar, C. Back, H. Béa, K. Everschor-Sitte, *et al.*, "The 2026 Skyrmionics Roadmap," arXiv:2601.16575, 2026.

[5] M. Azhar *et al.*, "Screw dislocations in chiral magnets," *Phys. Rev. Lett.*, vol. 128, 2022.

[6] M. Azhar *et al.*, "3D Magnetic Textures with Mixed Topology: Unlocking the Tunable Hopf Index," arXiv:2411.06929, 2024.

[7] R. Knapman *et al.*, "Numerical calculation of the Hopf index for three-dimensional magnetic textures," *Phys. Rev. B*, vol. 111, 2025.

[8] S. C. Shaju, M. Azhar, and K. Everschor-Sitte, "Hopfions in screw chiral magnets," arXiv:2601.10853, 2026.

Local and non-local phenomena in curvilinear and 3D magnets

Oleksandr V. Pylypovskyi[1,2*]

[1]Helmholtz-Zentrum Dresden-Rossendorf e.V. 01328 Dresden, Germany
[2]Kyiv Academic University, 03142 Kyiv, Ukraine
*Corresponding author: o.pylypovskyi@hzdr.de

***Abstract*—The shape of a ferromagnet maps its geometric parameters (locally defined principal curvatures) and topologic features (connectivity and number of holes) to its magnetic state. The resulting phenomena include topological patterning and states with multiple chiral characteristics. We discuss reflections of local and nonlocal geometric features on global magnetic state.**

***Keywords*— 3D magnetism, geometry, curvature, topology, magnetostatics.**

I. Introduction

Being motivated by a potential scalability and dense packaging of electronic components beyond planar architectures, curvilinear and 3D magnetism explores the role of complex geometry in static and dynamic properties of ferro- and antiferromagnetic textures [1], [2], [3], [4]. Its theoretical foundation is based on differential geometry and topology. The language of covariant derivatives allows us to map a curvilinear magnetic shell on an effectively planar sample with the spatially varying magnetic parameters modified by such intrinsic geometric invariants as principal curvatures and reflect its chiral and anisotropic properties. The topology of a sample accounts for the number of holes and compactness of its surface. It constrains the number and type of topological solitons that can or should be available in the sample. Recent advances in fabrication provide various techniques, such as multiphoton lithography, focused electron beam induced deposition (FEBID) or glancing angle deposition, that are capable of high-quality complex-shaped nanoarchitectures and bring us an opportunity for direct verification of theoretical predictions.

The non-local phenomena in ferromagnets are under active development [5], [6], [7]. Here, we review the recent progress in understanding the role of magnetostatics and topology of the sample's geometry in equilibrium magnetic states.

II. Topological patterning

Topology of the sample with a compact (i.e., finite) surface ς is characterized by its genus, giving the number of holes. On one hand, genus determines the fixed difference between sources and drains of any vector field $\vec{m}$ defined on ς. On the other hand, it provides the degree of the normal map of $\vec{m}$. In this way, the sample's topology provides (i) an information about the balance between vortices and antivortices in soft ferromagnets [8] and (ii) a shift of the topological charge for the hard magnets with the normal easy axis [9].

The effects of topological patterning can be demonstrated with FEBID-fabricated wireframes [8]. Topologically, a magnetically soft tetrapod is equivalent to a sphere, implying that the total vorticity counted at its surface equal two. The shape anisotropy leads to the formation of four vortices at the tetrapod ends. These vortices are the surface textures similar to the flower states in nanowires. Their total vorticity is compensated with two antivortices at the junction. Depending on the asymmetry between the top and bottom "V"-shaped parts of the tetrapod, the antivortices could be either connected by a common Bloch line or also represent the textures localized in the vicinity of the surface. In a sample topologically equivalent to a torus with one hole, the number of vortices and antivortices is the same, giving zero total vorticity. With multiple holes in the geometry, it is possible to construct the topologically protected states with only antivortices.

III. Coupling between volume and surface magnetostatic charges

The leading-order contribution of surface magnetostatic charges in thin films is given by the easy-surface shape anisotropy [10]. In thick enough or highly asymmetric samples, the next-order interaction between surface and volume magnetostatic charges can lead to sizable phenomena [11].

In a wide range of radii and thicknesses, Permalloy planar nanodisks and caps support the vortex ground state. The deposition procedure commonly leads to a high asymmetry between the top and bottom surfaces in hemispherical caps. Lowering of the sample's symmetry lifts degeneracy between the opposite magnetization circulations and can even link circulation with vortex polarization. Non-planar geometry acts on the vortex Bloch line in a two-fold way. The exchange boundary conditions force it to be perpendicular to the surface, while the balance between the surface and volume magnetostatic charges at the vortex core is decisive for the vortex placement and Bloch line shape. For a low enough sample's symmetry, the Bloch line acquires a helical shape with the torsion linked to the circulation of the vortex [12].

Continuous extended films with a regular geometric pattern can be designed on the top anode aluminum oxide (AAO) templates. They can provide a hierarchy of geometric and magnetic scales from hundreds of micrometers to dozens

of nanometers within the same sample. In a squared array of nanoflowers separated by hemispherical valleys, large needle-like domains are formed by the locally uniform valley magnetization. Nanoflowers support the formation of highly asymmetric textures, including flower states and asymmetric vortices [13]. An energy landscape formed by the spatially inhomogeneous shape anisotropy assists the formation of magnonic crystals in such geometries [14].

ACKNOWLEDGMENTS

This work is supported, in part, via ERC grant 3DmultiFerro (Project No. 101141331).

REFERENCES

[1] A. Fernández-Pacheco, R. Streubel, O. Fruchart, R. Hertel, P. Fischer, and R. P. Cowburn, "Three-dimensional nanomagnetism," *Nature Communications*, vol. 8, no. 1, p. 15756, jun 2017. [Online]. Available: http://dx.doi.org/10.1038/ncomms15756

[2] D. Makarov, O. M. Volkov, A. Kákay, O. V. Pylypovskyi, B. Budinská, and O. V. Dobrovolskiy, "New dimension in magnetism and superconductivity: 3D and curvilinear nanoarchitectures," *Advanced Materials*, vol. 34, no. 3, p. 2101758, 2022. [Online]. Available: https://doi.org/10.1002/adma.202101758

[3] D. D. Sheka, *Curvilinear Magnetism*. Elsevier, 2023, pp. 760–776. [Online]. Available: https://doi.org/10.1016/b978-0-12-819728-8.00069-3

[4] G. Gubbiotti, A. Barman, S. Ladak, C. Bran, D. Grundler, M. Huth, H. Plank, G. Schmidt, S. van Dijken, R. Streubel, O. V. Dobrovolskiy, V. Scagnoli, L. J. Heyderman, C. Donnelly, O. Hellwig, L. Fallarino, M. B. Jungfleisch, A. Farhan, N. Maccaferri, P. Vavassori, P. Fischer, R. Tomasello, G. Finocchio, R. CLERAC, R. Sessoli, D. Makarov, D. Sheka, M. Krawczyk, R. A. Gallardo, P. Landeros, M. d'Aquino, R. hertel, P. Pirro, F. Ciubotaru, M. Becherer, J. Gartside, T. Ono, P. Bortolotti, and A. Fernàndez-Pacheco, "2025 roadmap on 3D nano-magnetism," *Journal of Physics: Condensed Matter*, vol. 37, no. 14, p. 143502, 2024. [Online]. Available: https://doi.org/10.1088/1361-648x/ad9655

[5] C. Donnelly, A. Hierro-Rodríguez, C. Abert, K. Witte, L. Skoric, D. Sanz-Hernández, S. Finizio, F. Meng, S. McVitie, J. Raabe, D. Suess, R. Cowburn, and A. Fernández-Pacheco, "Complex free-space magnetic field textures induced by three-dimensional magnetic nanostructures," *Nature Nanotechnology*, vol. 17, pp. 136–142, 2022. [Online]. Available: https://doi.org/10.1038/s41565-021-01027-7

[6] F. Brevis, P. Landeros, J. Lindner, A. Kákay, and L. Körber, "Curvature-induced parity loss and hybridization of magnons: Exploring the connection of flat and tubular magnetic shells," *Physical Review B*, vol. 110, no. 13, p. 134428, 2024. [Online]. Available: http://dx.doi.org/10.1103/physrevb.110.134428

[7] M. Xu, A. J. M. Deenen, H. Guo, P. Morales-Fernández, S. Wintz, E. Zhakina, M. Weigand, C. Donnelly, and D. Grundler, "Geometry-induced spin chirality in a non-chiral ferromagnet at zero field," *Nature Nanotechnology*, 2025. [Online]. Available: https://doi.org/10.1038/s41565-025-02055-3

[8] O. M. Volkov, O. V. Pylypovskyi, F. Porrati, F. Kronast, J. A. Fernandez-Roldan, A. Kákay, A. Kuprava, S. Barth, F. N. Rybakov, O. Eriksson, S. Lamb-Camarena, P. Makushko, M.-A. Mawass, S. Shakeel, O. V. Dobrovolskiy, M. Huth, and D. Makarov, "Three-dimensional magnetic nanotextures with high-order vorticity in soft magnetic wireframes," *Nature Communications*, vol. 15, no. 1, p. 2193, 2024. [Online]. Available: https://doi.org/10.1038/s41467-024-46403-8

[9] V. P. Kravchuk, U. K. Rößler, O. M. Volkov, D. D. Sheka, J. van den Brink, D. Makarov, H. Fuchs, H. Fangohr, and Y. Gaididei, "Topologically stable magnetization states on a spherical shell: Curvature-stabilized skyrmions," *Physical Review B*, vol. 94, p. 144402, oct 2016. [Online]. Available: http://link.aps.org/doi/10.1103/PhysRevB.94.144402

[10] G. D. Fratta, "Micromagnetics of curved thin films," *Zeitschrift für angewandte Mathematik und Physik*, vol. 71, no. 4, p. 111, jun 2020. [Online]. Available: https://doi.org/10.1007/s00033-020-01336-2

[11] D. D. Sheka, O. V. Pylypovskyi, P. Landeros, Y. Gaididei, A. Kákay, and D. Makarov, "Nonlocal chiral symmetry breaking in curvilinear magnetic shells," *Communications Physics*, vol. 3, no. 1, p. 128, 2020. [Online]. Available: https://doi.org/10.1038/s42005-020-0387-2

[12] O. M. Volkov, D. Wolf, O. V. Pylypovskyi, A. Kákay, D. D. Sheka, B. Büchner, J. Fassbender, A. Lubk, and D. Makarov, "Chirality coupling in topological magnetic textures with multiple magnetochiral parameters," *Nature Communications*, vol. 14, p. 1491, 2023. [Online]. Available: https://www.nature.com/articles/s41467-023-37081-z

[13] O. Bezsmertna, R. Xu, O. Pylypovskyi, D. Raftrey, A. Sorrentino, J. A. Fernandez-Roldan, I. Soldatov, D. Wolf, A. Lubk, R. Schäfer, P. Fischer, and D. Makarov, "Magnetic solitons in hierarchical 3D magnetic nanoarchitectures of nanoflower shape," *Nano Letters*, vol. 24, no. 49, p. 15774, 2024. [Online]. Available: http://dx.doi.org/10.1021/acs.nanolett.4c04584

[14] G. Gubbiotti, O. Bezsmertna, O. V. Pylypovskyi, R. Xu, S. Chiroli, F. Zighem, C. F. González, A. Sorrentino, D. Raftrey, D. Wolf, A. Lubk, P. Fischer, D. Faurie, and D. Makarov, "Curvilinear magnonic crystal based on 3D hierarchical nanotemplates," *Nano Letters*, vol. 26, no. 4, pp. 1561–1568, 2026. [Online]. Available: https://doi.org/10.1021/acs.nanolett.5c06216

Emergent Magnetoelectricity in Stacked Van der Waals (vdW) Magnets

Yong P. Chen[1,2,*]

[1]Institute for Materials Research and WPI-Advanced Institute for Materials Research, Tohoku University, Japan

[2]Institute for Physics and Astronomy, Aarhus University, Denmark

*Corresponding author: yongchen@tohoku.ac.jp

***Abstract*— We discuss our recent magneto-optical (MOKE) and magneto-transport (tunneling) experiments on stacked and/or twisted (Moire) structures (both homo and hetero) between vdW/2D layered antiferromagnets such as CrI_3 and $CrCl_3$, revealing novel magnetoelectric behaviors in new regimes of magnetism (e.g. non-collinear Moire magnetism), with potential spintronic/magnetic and optical/optoelectronic device applications.**

***Keywords*— 2D materials, 2D magnets, vdW heterostructures, twistronics, Moire, magnetism, magnetoelectric.**

I. Introduction

The past few years has witnessed the rise of a variety of van der Waals (vdW) layered magnetic "2D materials". These materials have challenged our fundamental understanding of magnetism, where the very existence of 2D magnetism has been somewhat surprising. Meanwhile, these magnetic 2D materials, which can be made down to atomic thickness, are relatively easy to transfer, deform and tune their properties, have presented exciting new opportunities for realizing novel physics and functionalities, and potential applications ranging from spintronics to quantum technologies. Recent experimental work on such magnetic 2D materials and related heterostructures and electrically gated devices have yielded many intriguing findings. In particular, as to be discussed in this talk, stacking two antiferromagnets (each with zero measured magnetization) can produce a ferromagnet-like state [1,2] or (magnetic) meta-materials-like state [2,3] (through various mechanisms such as an effective interlayer exchange bias [1] or "Moire magnetism" [2,3]), where rich behaviors tunable by a voltage and a relative "twisting" angle are observed, uncovering novel forms of magnetism and magnetoelectricity.

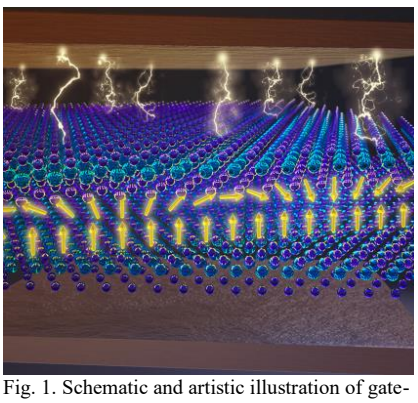

Fig. 1. Schematic and artistic illustration of gate-tunable Moire magnetism (with alternating interlayer ferromagnetic and antiferromagnetic domains) formed in twisted double bilayer CrI_3 (a layered antiferromagnet).

II. Methods

Our methodology integrates fabrication of homo/hetero vdW stacked structures (involving CrI_3 and $CrCl_3$, insulating layered antiferromagnets with out-of-plane and in-plane anisotropies respectively, and electrically gated devices and magnetic-tunnel-junctions (MTJs), magneto-optical-Kerr-effect (MOKE) measurements and electrical transport (tunneling) measurements under variable magnetic fields, temperatures and applied electrical biases, other supplemental characterizations (such as transmission electron microscopy), and DFT and micromagnetics simulations.

III. Results and Discussion

Experimental results have revealed several new forms emergent magnetism, all of which are tunable electrically:

- an out-of-plane (OP) interfacial ferromagnetism in stacked $CrCl_3/CrI_3$ (even when neither have any OP magnetizations), via an exchange-bias-like mechanism [1];
- a Moire magnetism, a metamaterial-like state for magnetism, with alternating ferromagnetic and antiferromagnetic regions, in twisted double-bilayer CrI_3, exhibiting emergent OP ferromagnetic-like behavior over a broad range of twist angles [2];
- Another Moire magnetism featuring a "twisted-S" phase with 90 degree domain walls, in twisted n-layer/n-layer (up to n=9 studied) $CrCl_3$, an in-plane XY magnet [3]

IV. Conclusion

We have demonstrated several different types of emergent magnetism in stacked vdW magnets with novel magnetoelectric couplings.

ACKNOWLEDGMENTS

Part of this work was performed at Purdue University, USA and with various collaborators. This work was supported in part by AIMR, JSPS, FRIS, DOE and DOD.

REFERENCES

[1] Guanghui Cheng, Mohammad Mushfiqur Rahman, Zhiping He, Andres Llacsahuanga Allcca, Avinash Rustagi, Kirstine Aggerbeck Stampe, Yanglin Zhu, Shaohua Yan, Shangjie Tian, Zhiqiang Mao, Hechang Lei, Kenji Watanabe, Takashi Taniguchi, Pramey Upadhyaya, Yong P. Chen, "Emergence of electric-field-tunable interfacial ferromagnetism in 2D antiferromagnet heterostructures", Nature Communications 13, 7348 (2022)

[2] Guanghui Cheng, Mohammad Mushfiqur Rahman, Andres Llacsahuanga Allcca, Avinash Rustagi, Xingtao Liu, Lina Liu, Lei Fu, Yanglin Zhu, Zhiqiang Mao, Kenji Watanabe, Takashi Taniguchi, Pramey Upadhyaya, Yong P. Chen, "Electrically tunable moiré magnetism in twisted double bilayer antiferromagnets", Nature Electronics 6, 434 (2023)

[3] G.Cheng ,…, Yong P. Chen, “Noncollinear spin textures and 90° domain walls in twisted XY magnets”, submitted (2026).

Chiral Polaritonics and Molecular Lasing: Concept, Challenges, and future Directions

Kai Müller[1], Denis Baranov[2], Christian Schäfer[3,*]

[1]Institut für Theoretische Physik, Technische Universität Dresden, D-01062 Dresden, Germany
[2]Center for Photonics and 2D Materials, Moscow Institute of Physics and Technology, Dolgoprudny 141700, Russia
[3]Institute of Applied Physics, TU Wien, Wiedner Hauptstrasse 8-10/134, Vienna, 1040, Austria
*Corresponding author: christian.schaefer@tuwien.ac.at

***Abstract*—We present a theoretical framework for molecular light–matter interactions in chiral resonators and few-emitter nanolasing. Using analytical and first-principles approaches, we reveal how strong coupling, vibrational structure, and emitter number govern enantiomer discrimination and laser performance, providing design principles for chiral control and molecular-scale photonic devices.**

***Keywords*— chirality, polaritonics, strong coupling, lasing**

I. Introduction

Fueled by an ever expanding set of metamaterials and nanocavities, new regimes have been reached for the interplay between light and matter. Here, we demonstrate the fascinating opportunities for two specific examples. First, we demonstrate that the confinement of chiral standing waves in adequately designed cavities allows to couple strongly, and especially selectively, to only one enantiomer in a racemic.[1] We discuss the current challenges of this approach and illustrate a potential path forward.[2] Second, we demonstrate that a few molecules confined in nanocavities give rise to unexpected lasing phenomena, breaking with the current paradigm for the description of molecular lasing.[3]

II. Methods

We perform analytical and numerical simulations. Our predictions for chiral polaritonics are based on the Tavis-Cummings and Hopfield model, both simplifications of the quantum electrodynamic approach to the microscopic light-matter interaction in magnetic dipolar limit

$$\hat{H}_{LM} = -\frac{1}{\varepsilon_0}\sum_n \hat{\mu}_n \cdot \hat{D}_\perp(r_n) - \sum_n \hat{m}_n \cdot \hat{B}_\perp(r_n) + \frac{1}{2\varepsilon_0}\int d^3r \hat{P}_\perp^2 + \frac{1}{8m}\sum_{n,i}(q_{ni}\hat{r}_{ni} \times \hat{B}(r_n))^2 + \mathcal{O}(\nabla D)$$

III. Results and Discussion

Our theoretical results demonstrate

- Enantiomer selective coupling with sqrt-N$_{mol}$ scaling
- A linear dependence on the molecular chirality
- Lasing for molecular few-emitter systems that shows resonant features related to vibrational structure (Fig. 1)
- The vibrational features in few-emitter lasing break the current paradigm for the description of molecular lasing

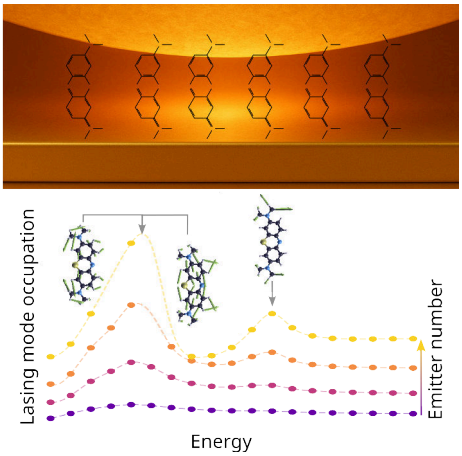

Fig. 1. Vibrational features in molecular few-emitter lasing.

IV. Conclusion

We have demonstrated that metamaterials and nanocavities promise a path to novel applications, including enantiomer selective coupling and molecular lasers. A consistent and detailed theoretical description is required. Future work will be extending the theoretical methodology as well as linking it to experimentally accessible observables and regimes.

Acknowledgments

C.S. acknowledges support from the Swedish Research Council through Grant No. 2016-06059, the FWF cluster of excellence MECS, and funding from the Horizon Europe research and innovation program of the European Union under the Marie Sklodowska-Curie grant agreement no. 101065117.

References

[1] C. Schäfer, and D. Baranov, "Chiral Polaritonics: Analytical Solutions, Intuition, and Use", J. Phys. Chem. Lett. 2023, 14, 3777-3784.
[2] D. Baranov, C. Schäfer, and M. V. Gorkunov, "Toward Molecular Chiral Polaritons", ACS Photonics 2023, 10, 8, 2440-2455.
[3] K. Müller, K. Luoma, and C. Schäfer, "A Hierarchical Approach to Quantum Many-Body Systems in Structured Environments", arXiv:2405.05093, https://doi.org/10.48550/arXiv.2405.05093

Persistent Energy Fluxes and Angular momentum in Non-reciprocal Electromagnetic Systems

Ivan Latella[1,*]

[1]Department of Condensed Matter Physics, University of Barcelona, Martí i Franquès 1, 08028 Barcelona, Spain
*Corresponding author: ilatella@ub.edu

***Abstract*—We investigate persistent energy fluxes and electromagnetic angular momentum in non-reciprocal systems at thermal equilibrium. We show that a divergence-free mean Poynting vector arises from thermal and vacuum fluctuations, with vacuum contributions dominating. This flux persists even at zero temperature, so it does not necessarily represent flow of heat.**

***Keywords*— nonreciprocal systems, electromagnetic fluctuations, angular momentum, persistent energy fluxes.**

Electromagnetic field fluctuations play a fundamental role in the transfer of energy and momentum at the nanoscale, shaping a wide spectrum of light-matter interaction phenomena. When materials exhibit non-reciprocal electromagnetic properties, such as magneto-optical media or Weyl semimetals, these fluctuations lead to behaviors that have no counterpart in reciprocal systems. In addition to enabling directional radiative heat transport in non-equilibrium conditions [1], non-reciprocity remarkably gives rise to persistent energy fluxes [2] in thermal equilibrium, where electromagnetic energy continuously flows in closed paths without net dissipation.

In this work, we examine the mean Poynting vector in thermal equilibrium and the nature of energy circulation in electromagnetic systems that are not constrained by time-reversal symmetry. Employing a theoretical framework based on Green's functions and the fluctuation-dissipation theorem, we demonstrate that the equilibrium energy flow in non-reciprocal system is inherently divergence-free [3]. This proves that the observed circulation corresponds to local redistribution of energy rather than creation or loss, thereby providing a general thermodynamic foundation for persistent fluxes in non-reciprocal systems. In close connection, we argue that persistent heat currents, while present in equilibrium, cannot be detected through conventional out-of-equilibrium heat transfer measurements.

Our results further show that equilibrium energy circulation, characterized by a non-zero mean Poynting vector, originates not only from thermal fluctuations, but also from vacuum fluctuations of the electromagnetic field. Around a single neutral non-reciprocal particle, these fluctuations generate a non-vanishing energy flux and an associated electromagnetic angular momentum. A notable finding is that the contribution of vacuum fluctuations dominate the equilibrium energy flux and angular momentum at finite temperature, implying that the effect persists even as temperature approaches zero. Importantly, such persistent flows can also exist in lossless materials, indicating that dissipation is not a necessary ingredient for their existence. This allows us to conclude that a non-vanishing mean Poynting vector can exist even in the absence of thermal fluctuations, and therefore is not necessarily a flow of heat.

Taken together, these findings establish persistent energy fluxes as a fundamental manifestation of non-reciprocal electromagnetic fluctuations. These fluxes and the associated electromagnetic angular momentum emerge as a universal equilibrium property rooted in broken time-reversal symmetry. This perspective not only advances the conceptual understanding of thermal radiation and fluctuation-induced phenomena but also suggests new opportunities for manipulating energy flow and electromagnetic angular momentum at the nanoscale through the engineering of non-reciprocal materials and structures.

References

[1] S.-A. Biehs, R. Messina, P. S. Venkataram, A. W. Rodriguez, J. C. Cuevas, and P. Ben-Abdallah, "Near-field radiative heat transfer in many-body systems," *Rev. Mod. Phys.*, vol. 93, pp. 025009, 2021.

[2] L. Zhu and S. Fan, "Persistent directional current at equilibrium in nonreciprocal many-body near field electromagnetic heat transfer," *Phys. Rev. Lett.*, vol. 117, pp. 134303, 2016.

[3] S.-A. Biehs and I. Latella, "On persistent energy currents at equilibrium in non-reciprocal systems," *J. Quant. Spectrosc. Radiat. Transf.*, vol. 347, pp. 109660, 2025.

[4] S.-A. Biehs and I. Latella, "Feynman paradox induced by vacuum and thermal fluctuations," arXiv:2509.08711, 2025.

Nonreciprocal nonlinear magneto-optical metasurfaces

Jialong Wang[1,2], Dongchen Ma[1,2], Yi Shuai[1,2], Jun Qin[1,2], Qing Zhang[1,2], Lei Bi[1,2*]

[1]National Engineering Research Center of Electromagnetic Radiation Control Materials, University of Electronic Science and Technology of China, China
[2]School of Electrical Science and Engineering, University of Electronic Science and Technology of China, China
*Corresponding author: bilei@uestc.edu.cn

***Abstract*— We report nonreciprocal second harmonic generation in a-Si/Ce:YIG based all-dielectric magneto-optical metasurfaces. Despite of negligible nonreciprocity at the fundamental frequency, large SHG intensity contrast up to 3.6 times was observed for forward and backward propagation, attributed to the nonreciprocal magneto-optical second order susceptibility of the Ce:YIG material boosted by guided mode resonance (GMR).**

***Keywords*— nonreciprocal, metasurface, magneto-optical, second harmonic generation.**

I. Introduction

Nonreciprocal metasurfaces allow on-demand bidirectional electromagnetic wave propagation can enable a variety of functionalities such as free-space electromagnetic wave isolation, circulation, nonreciprocal antennas and radomes and full-duplex communication. Despite of successful demonstration in the microwave frequency range[1,2], realizing nonreciprocal metasurfaces in the optical frequency has been challenging.[3,4] In particular, a magneto-optical nonreciprocal metasurface has not been demonstrated so far, due to the limited MO effects at optical frequencies. In this report, we show that clear optical nonreciprocity can be achieved in all-dielectric nonlinear magneto-optical metasurfaces. Up to 3.6 times intensity difference has been observed for forward and backward excitation of SHG in a magnetized a-Si/Ce:YIG all-dielectric metasurface, which can be explained by the nonreciprocal magneto-optical second order susceptibility of Ce:YIG films.

II. Methods

200 nm thick epitaxial Ce:YIG thin films were grown on gadolinium gallium garnet (GGG(111)) substrates by pulsed laser deposition. The magnetic second order susceptibility was characterized by measuring the SHG of the sample magnetized along the surface normal at 750 nm wavelength using a femtosecond pump laser at 1500 nm. The $\chi^{(2)}$ of Ce:YIG can be expressed as follows

$$\chi_{\pm}^{(2)} = \chi^{Cr} \pm \chi^{magn} \cdot M \quad (1)$$

where $\chi_{\pm}^{(2)}$ denotes the second order susceptibility, χ^{Cr} is the second order susceptibility from crystal asymmetry, $\chi^{magn} \cdot M$ is the second order susceptibility from material magnetization, and ±M stands for the magnetization of Ce:YIG. An a-Si disk on Ce:YIG all-dielectric metasurface was fabricated by chemical vapor deposition, e-beam lithography and reactive ion etch. Nonreciprocal SHG of the metasurface was measured by pumping the magnetized device along the surface normal at the GMR wavelength at 1415 nm using circular polarized light.

III. Results and Discussion

We first measured the $\chi_{\pm}^{(2)}$ of epitaxial Ce:YIG films grown on GGG. Figure 1a shows the sketch of the measurement process. Right circular polarized light at 1500 nm wavelength was incident along the surface normal direction to the sample. The sample was magnetized with 0.2 T applied magnetic field along the up or down directions, indicated as +M and -M respectively. SHG was measured at the transmission port. Figure 1b shows the measured SHG power versus the square of fundamental wavelength (FW) intensity. A linear relationship can be observed for samples at +M, -M or demagnetized states. The inset shows the fitted slope of 1.99, indicating a SHG process. A clear difference of SHG power can be observed for the two magnetization directions according to Eq. (1). By comparing the SHG intensity with a 3R-MoS_2 sample, we calculated the $\chi_{\pm}^{(2)}$ of Ce:YIG to be 4.42 pm/V and 2.49 pm/V. Correspondingly, $\chi^{magn} \cdot M = 0.96\ pm/V$ and $\chi^{Cr} = 3.46\ \ pm/V$.

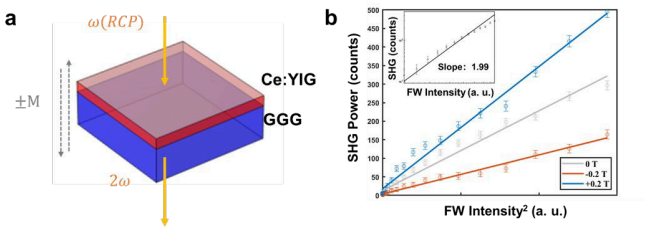

Fig. 1 (a) Sketch of the SHG measurement process on Ce:YIG films. (b) The measured SHG power versus the square of FW intensity.

Figure 2a shows the sketch of the a-Si/Ce:YIG metasurface. The magnetization was along the surface normal. The pump light was circular polarized. The nonreciprocity of SHG was measured by switching the magnetization direction. Figure 1b shows the SEM image of the fabricated sample. Figure 1c shows the reflectance of the sample near the GMR wavelength of 1415 nm. Clear reflection peak indicates the excitation of GMR mode. Notice there was almost no contrast of the reflectance for films magnetized along different directions, indicating negligible nonreciprocity at the fundamental frequency. Figure 1d shows the SHG spectrum of the metasurface. The SHG was originated from the second order susceptibility of Ce:YIG . First, the SHG was clearly boosted by over one order of magnitude at the half of the GMR mode wavelength. Second, clear nonreciprocity of the SHG is observed at the GMR resonance. The peak SHG intensity for +M magnetization is 3.6 times compared to -M magnetization. When fixing the magnetization direction and changing the chirality of the incident light, the SHG intensity also showed comparable contrast, demonstrating the nonreciprocity of the SHG process.

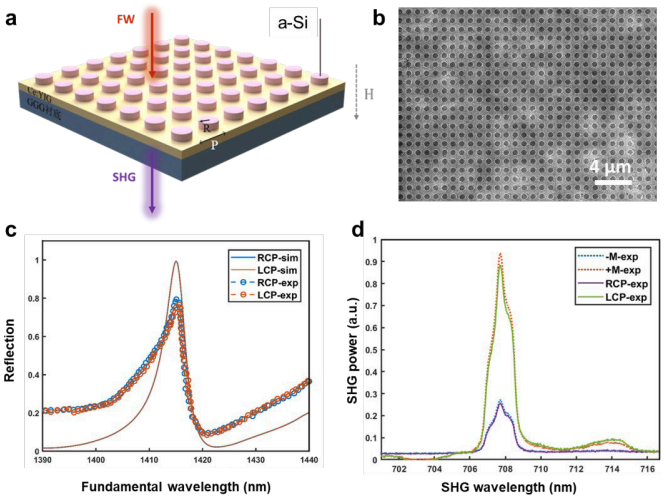

Fig. 2 Nonreciprocal SHG in nonlinear all dielectric MO metasurfaces (a) Sketch of the measurement process. (b) The sample SEM image (c) The simulated and measured reflection spectrum at the fundamental wavelength. (d) SHG power vs. SHG wavelength of the MO all dielectric metasurface

IV. Conclusion

In conclusion, we demonstrate clear optical nonreciprocity in nonlinear magneto-optical metasurfaces by utilizing the nonreciprocal $\chi^{(2)}$ of Ce:YIG thin film and GMR of a-Si/Ce:YIG metasurfaces. Our work paves the way for nonreciprocal metasurfaces in the optical frequencies for nonlinear light source, optical communication and quantum photonic applications.

Acknowledgments

The authors are grateful for the support by the National Natural Science Foundation of China (NSFC) (Grant Nos. 52450018, U22A20148, 52021001 and 52473292), Sichuan Provincial Science and Technology Department (Grant Nos. 2025ZYD0001 , 2025ZNSFSC0040, 2024NSFSC0484).

References

[1] S. Taravati, B. A. Khan, S. Gupta, K. Achouri, C. Caloz, "Nonreciprocal Nongyrotropic Magnetless Metasurface", IEEE Transactions on Antennas and Propagation, 65, 3589-3597 (2017)

[2] W. Yang, J. Qin, J. Long, W. Yan, Y. Yang, C. Li, E. Li, J. Hu, L. Deng, Q. Du & L. Bi, "A self-biased non-reciprocal magnetic metasurface for bidirectional phase modulation", Nature Electronics, 6, 225-234, 2023

[3] M. Cotrufo, A. Cordaro, D. L. Sounas, A. Polman & A. Alù, "Passive bias-free non-reciprocal metasurfaces based on thermally nonlinear quasi-bound states in the continuum," Nature Photonics, 18, 81–90 (2024)

[4] X. Guo, Y. Ding & X. Ni, "Nonreciprocal metasurface with space-time phase modulation", Light: Science & Applications, 8, 123 (2019)

On the efficiency of enantiomer separation using optical evanescent fields near waveguides

Sebastian Golat[1,*] and Francisco J. Rodríguez-Fortuño[1]
[1]Department of Physics and London Centre for Nanotechnology,
King's College London, Strand, London WC2R 2LS, UK
*Corresponding author: sebastian.1.golat@kcl.ac.uk

***Abstract*—I will present analytical estimates for sorting time, throughput, and achievable purity in all-optical enantiomer separation driven by chiral dipolar forces near waveguides. By combining a symmetry-based force decomposition with drift–diffusion dynamics in liquids, I obtain closed-form performance limits applicable to arbitrary dipolar molecules and nanoparticles under realistic experimental conditions.**

***Keywords*—chirality, enantiomer separation, optical forces, evanescent waves, waveguides.**

I. Introduction

Optical forces offer a contact-free route to enantiomer separation, yet many proposals based on propagating or evanescent waves [1, 2, 3, 4] focus primarily on demonstrating the existence of a non-zero chiral force. For applications, however, the relevant questions are: *How long does separation take? At what purity? And what throughput is physically achievable?*

In this invited contribution to the Chiral Symposium at META 2026, I address these questions analytically for dipolar chiral particles in liquids near nanophotonic waveguides, where Brownian diffusion competes directly with enantioselective drift.

II. Optical Force Framework

Within the dipolar approximation, each enantiomer labelled by the sign ($\pm$) experiences a force

$$\boldsymbol{F}_{\pm} = \boldsymbol{F}^{\pm}_{\text{gra}} + \boldsymbol{F}^{\pm}_{\text{pre}} + \boldsymbol{F}^{\pm}_{\text{rec}}. \tag{1}$$

The three contributions correspond respectively to gradient forces, which localise particles in regions of high field intensity; radiation-pressure forces, which transfer linear momentum from the optical field; and recoil forces, which arise from asymmetries in the scattered field and can generate lateral motion. Each of these contributions will have chiral and achiral parts discussed in [1].

III. Drift–Diffusion Model

In liquids, inertia is negligible and the motion of each enantiomer is overdamped. Its dynamics are therefore governed by the Langevin equation

$$\frac{\mathrm{d}\boldsymbol{r}}{\mathrm{d}t} = \boldsymbol{v}_{\pm}(\boldsymbol{r}) + \sqrt{2D}\,\boldsymbol{\xi}(t), \qquad D = \frac{k_{\mathrm{B}}T}{\gamma}, \tag{2}$$

where $\boldsymbol{v}_{\pm} = \boldsymbol{F}_{\pm}/\gamma$ is the drift velocity set by the optical force, γ is the viscous damping coefficient, T the temperature, and k_{B} the Boltzmann constant. The corresponding concentration fields $C_{\pm}$ evolve according to the drift–diffusion (Fokker–Planck) equation

$$\frac{\partial C_{\pm}}{\partial t} = -\boldsymbol{\nabla}\cdot(C_{\pm}\boldsymbol{v}_{\pm} - D\boldsymbol{\nabla}C_{\pm}), \tag{3}$$

which captures the competition between enantioselective drift and thermal diffusion. As a result, the mean positions of the two concentration profiles separate in time due to their different drift velocities, while thermal diffusion increases their variance (Fig. 1). For a chosen target enantiomeric excess, we define the separation time as the time at which the degree of separation between the two distributions reaches the corresponding threshold.

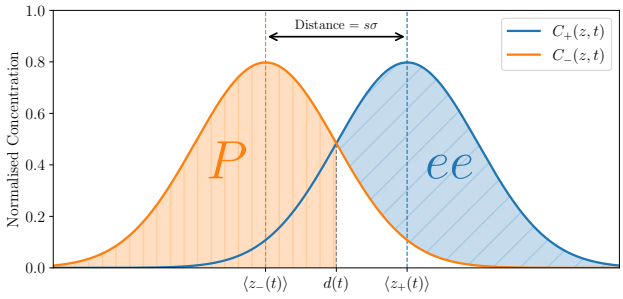

Fig. 1. Enantiomer distributions after some time t. They collectively travel a distance $d(t)$, and the separation between the peaks is $s(t)\sigma(t)$. Shaded regions represent two different measures of enantiopurity: enantiomeric fraction of the dominant enantiomer P (orange) and enantiomeric excess ee (blue). These can be related to the degree of separation $s(t) = \Delta z(t)/\sigma_z(t)$.

IV. Scope of the Talk

Using this framework, the talk will present fully analytical estimates for separation time, throughput, and achievable enantiomeric excess under realistic experimental conditions. In particular, I will compare:

- Longitudinal sorting driven by chiral radiation pressure.
- Transverse sorting arising from chiral lateral recoil forces in evanescent tails of guided modes.
- The role of trapping and confinement in modifying separation efficiency.
- The impact of the initial distribution on the separation time.

ACKNOWLEDGMENTS

SG and FJRF acknowledge support from EIC-Pathfinder-CHIRALFORCE (101046961) which is funded by Innovate UK Horizon Europe Guarantee (UKRI project 10045438).

REFERENCES

[1] S. Golat, J. J. Kingsley-Smith, I. Diez, J. Martinez-Romeu, A. Martínez, and F. J. Rodríguez-Fortuño, "Optical dipolar chiral sorting forces and their manifestation in evanescent waves and nanofibers," *Phys. Rev. Research*, vol. 6, p. 023079, 2024.

[2] J. Martínez-Romeu, I. Diez, S. Golat, F. J. Rodríguez-Fortuño, and A. Martínez, "Chiral forces in longitudinally invariant dielectric photonic waveguides," *Photonics Res.*, vol. 12, pp. 431–443, 2024.

[3] Y. Liu, W. Zhang, L. He, and X. Zhang, "All-optical separation of chiral nanoparticles on silicon-based microfluidic chips with vector exceptional points," *APL Photonics*, vol. 8, p. 036112, 2023.

[4] A. Hayat, J. P. B. Mueller, and F. Capasso, "Lateral chirality-sorting optical forces," *Proc. Natl. Acad. Sci. U.S.A.*, vol. 112, pp. 13 190–13 194, 2015.

Bottom-Up Engineered Hybrid Plasmonic Broken L-Shaped Metamaterial Platforms Reveal Broadband Enhanced Optical Chirality

Ufuk Kilic[1,#], Raymond Smith[1], Shawn Wimer[1], Yousra Traouli[1], Sema G.Kilic[1], Eva Schubert[1], Christos Argyropoulos[2] and Mathias Schubert[1,3]
[1]Department of Electrical and Computer Engineering, University of Nebraska-Lincoln, Lincoln, NE 68588, USA
Department of Electrical Engineering, The Pennsylvania State University, University Park, PA 16803, USA
[3] Solid State Physics and NanoLund, Lund University, P.O. Box 118, 22100, Lund, Sweden
*Corresponding author: ufukkilic@unl.edu

***Abstract*—We experimentally demonstrate and theoretically verify bottom-up engineered hybrid plasmonic broken L-shaped metamaterial platforms exhibiting broadband enhanced optical chirality. Two-step glancing angle deposition enables robust control of structural handedness. The resulting hybrid Si-Ag nanocolumnar architectures support strong spin-dependent plasmonic coupling and enhanced chiral near fields spanning the near-infrared to ultraviolet.**

***Keywords*— metamaterials, ellipsometry, plasmonic chirality.**

I. Introduction

Chiral light–matter interactions underpin a wide range of phenomena spanning biomolecular imaging and spectroscopy, enantioselective chemistry, spin-controlled integrated photonics, and emerging quantum optical technologies [1–3]. Chirality originates from broken mirror symmetry, whereby a structure cannot be superimposed onto its mirror image. Optically, this symmetry breaking manifests when a material interacts differently with left- and right-circularly polarized light, giving rise to circular dichroism (CD) and circular birefringence. While chirality in nature is indeed present at all scales from macro-molecules to the galaxies, the natural materials exhibit intrinsically weak chiroptical responses, typically limited to narrow spectral windows and small dissymmetry factors. This limitation arises from the intrinsic dominance of electric-dipole over magnetic-dipole interactions in natural materials, as well as the large mismatch between molecular dimensions and optical wavelengths, which suppresses higher-order multipolar contributions and results in small dissymmetry factors and narrow spectral bandwidths [4]. With the rapid development of quantum communication, spin-based information processing, and polarization-encoded photonic technologies, there is growing demand for artificial platforms capable of enhancing and controlling optical chirality across broad spectral ranges. Engineering broadband and enhanced optical chirality therefore remains a fundamental challenge in nanophotonics. Metamaterials provide a powerful route to overcome these limitations by introducing subwavelength structural asymmetry that amplifies chiral electromagnetic mode coupling [5–8]. While top-down lithographic techniques have enabled precise planar chiral geometries, scalable fabrication of ultrathin, large-area, and broadband chiral platforms at nanoscale remains difficult [9].

II. Methods

Glancing angle deposition (GLAD) offers a versatile bottom-up alternative for fabricating three-dimensional nanocolumnar architectures through oblique-angle physical vapor deposition. Under highly oblique flux conditions, self-shadowing and limited adatom surface diffusion dynamics drive the formation of self-organized spatially coherent tilted columnar structures. By dynamically controlling substrate rotation during growth, deterministic structural asymmetry and handedness can be introduced without masks or templates [8-11]. This approach enables scalable, large-area fabrication of complex chiral nanomorphologies with tunable geometric parameters. Here, we demonstrate bottom-up engineered hybrid plasmonic broken L-shaped metamaterials fabricated via a two-step GLAD process. Prior to the deposition of second segment in the proposed structure by rotating the substrate between sequential oblique depositions, hybrid Si–Ag nanocolumn architectures with controllable handedness are realized. The plasmonic–dielectric hybridization supports spin-dependent electro-magnetic mode coupling, leading to broadband enhanced optical chirality spanning the near-infrared to ultraviolet spectral range. Full-wave simulations reveal pronounced asymmetries in electric and magnetic near-field distributions under opposite circular polarizations, elucidating the physical origin of the large dissymmetry factors.

III. Results and Discussion

Figure 1*Spectrally controlled broadband enhanced chirality from Si–Ag hybrid broken L-shape twisted nanocolumnar structure design. (a) Circular dichroism (CD=$A_{LCP}-A_{RCP}$) spectra demonstrating handedness-dependent optical response of the hybrid Si–Ag nanocolumn array (blue/red correspond to opposite circular polarizations). (b) CD spectrum of a reference all-dielectric Si nanoboomerang (twisted L-shaped) structure for comparison, highlighting differences in spectral bandwidth and CD magnitude. (c–d) Finite-element simulated electric field distributions under left- and right-circularly polarized (LCP/RCP) excitation, illustrating spin-dependent near-field localization within the tilted nanocolumn geometry. (e) Polar plot of polarization-resolved far-field scattering intensity, confirming asymmetric spin-dependent radiation. (f) 3D schematic of the tilted GLAD-grown hybrid nanocolumn architecture on the substrate. (g) Differential near-field maps ($\Delta E/E_0$ and $\Delta B/B_0$) showing handedness-induced electric and magnetic field contrast above the substrate interface. (h) Cross-sectional and (i) top-view high-resolution SEM images revealing spatially coherent, axially modulated hybrid Si–Ag nanocolumn arrays (scale bar: 200 nm).*

Figure 1 summarizes the structural, spectral, and electromagnetic characteristics of the bottom-up engineered hybrid Si–Ag broken L-shaped nanocolumn metamaterials. The spectral evolution of circular dichroism shown in Fig. 1(a) clearly reveals a pronounced handedness-dependent optical response, with opposite rotation directions during the two-step GLAD process producing mirrored CD spectra. Compared to the reference silicon nanoboomerang structure, the hybrid architecture exhibits broader spectral features and enhanced CD amplitude, highlighting the role of plasmonic–dielectric coupling in strengthening the chiral response. With the visualization of near field and far field characteristics via finite element simulations (Fig. 1(c–g)) provide insight into the underlying physical mechanism. Under opposite circularly polarized excitations, the hybrid nanocolumns support asymmetric electric field localization and spin-dependent plasmonic mode coupling. The differential near-field (electric (E) and magnetic (B)) maps demonstrate pronounced field magnitude contrast ($\Delta E=E_{LCP}-E_{RCP}$) and $\Delta E=E_{LCP}-E_{RCP}$) above the substrate, indicating enhanced local optical chirality density. This asymmetric near-field distribution directly correlates with the experimentally observed broadband CD response. Cross-sectional and top-view SEM images (Fig. 1(h,i)) confirm the formation of tilted nanocolumn arrays with uniform morphology over large area. As follow up to this, ongoing experimental optical characterization using Mueller matrix generalized spectroscopic ellipsometry will further quantify the full polarization-resolved chiroptical response.

IV. Conclusion

We demonstrate a template-free and scalable approach for engineering a new class of metamaterial platform with spin-selective broadband chiral light–matter interactions. Precise control of substrate stage and particle flux dynamics enable deterministic structural handedness without lithographic patterning. The observed broadband enhanced optical chirality originates from engineered 3D plasmonic–dielectric hybridization of electromagnetic modes. This versatile platform opens new opportunities for polarization-selective photonics, chiral sensing, and integrated nanophotonic technologies.

ACKNOWLEDGMENTS

Support is acknowledged by the National Science Foundation under awards CMMI 2211858, DMR 2224456, ECCS2329940, DMR 2423277, and OIA-2044049 Emergent Quantum Materials and Technologies (EQUATE), by Air Force Office of Scientific Research under awards FA9550-21-1-0259,FA9550-23-1-0574 DEF, and FA9550-25-1-0196, and by the University of Nebraska Foundation. M. S. acknowledges support from the J. A. Woollam Foundation. U.K. and E.S. acknowledge the support from the University of Nebraska Collaboration Initiative Grant FY-2026. This work is partly supported by Knut and Alice Wallenberg Foundation funded grant 'Transforming ceramics into next generation semiconductors' (Grant No. 2024.0121) and by the Wallenberg Initiative Materials Science for Sustainability (WISE) funded by the Knut and Alice Wallenberg Foundation.

REFERENCES

[1] Qiu, J., Li, Z., Ma, J., Lu, J. and He, C., Small, p.e12675,(2026).
[2] Yuan, Z., Zhou, Y., Qiao, Z., Eng Aik, C., Tu, W.C., Wu, X. and Chen, Y.C., ACS nano, 15(5), pp.8965-8975, (2021).
[3] Rodrigues, S.P., Lan, S., Kang, L., Cui, Y. and Cai, W., Adv. Mater, 26(35), pp.6157-6162, (2014).
[4] Barron, Laurence D. Molecular light scattering and optical activity. Cambridge University Press, (2009).
[5] Petronijevic, E., Cesca, T., Scian, C., Mattei, G., Voti, R. L., Sibilia, C., & Belardini, A., Scientific Reports, 14(1), 17210, (2024).
[6] A. Kuzyk,et al., Nature 483, 311–314 (2012).
[7] Kilic, S. G., Kilic, U., Schubert, M., Schubert, E., & Argyropoulos, C. Physical Review Applied, 24(4), 044009, (2025).
[8] Olohan, Ben J., et al. "Chiroptical second-harmonic tyndall scattering from silicon nanohelices." ACS nano 18.26 (2024): 16766-16775.
[9] Kilic, U., Hilfiker, M., Ruder, A., Feder, R., Schubert, E., Schubert, M., & Argyropoulos, C., Adv. Funct. Mater., 31(20), 2010329, (2021).
[10] Kilic, U., Hilfiker, M., Wimer, S., Ruder, A., Schubert, E., Schubert, M., & Argyropoulos, C., Nature communications, 15(1), 3757, (2024).
[11] Kılıç, U., Mock, A., Feder, R., Sekora, D., Hilfiker, M., Korlacki, R., Schubert, E., Argyropoulos, C. and Schubert, M., Scientific reports, 9(1), p.71, (2019).

Theory of Electric Polarization in Inhomogeneous Crystals Based on the Quantum Transport Equation

Shuichi Murakami[1,2,3,*], Yuta Suzuki[4], Nobuhiro Arai[4], Manato Fujimoto[1], Yang Gao[5], Di Xiao[6,7]

[1] Department of Applied Physics, University of Tokyo, Tokyo, Japan
[2] CEMS, RIKEN, Wako, Japan
[3] WPI-SKCM[2], Hiroshima University, Hiroshima, Japan
[4]Department of Physics, Institute of Science Tokyo, Tokyo, Japan
[5] University of Science and Technology of China, Hefei, Anhui, China
[6] Department of Materials Science & Engineering, University of Washington, Seattle, USA
[7] Department of Physics, University of Washington, Seattle, USA
*Corresponding author: murakami@ap.t.u-tokyo.ac.jp

***Abstract*—We study the polarization in a crystal induced by a perturbation linear in the coordinates. We establish the quantum transport equation for insulators with slow modulations in space and time, and calculate the current and charge densities. From this result, we obtain the formula for the electric polarization and orbital magnetization, and compare the results with previous works.**

***Keywords*- polarization, quantum transport equation, orbital magnetization.**

I. Introduction

A formulation using Berry connections has been established for electric polarization in spatially homogeneous crystals. As an extension, an expression based on semiclassical theory has been proposed for electric polarization induced in inhomogeneous crystals [1]. This result is related to the formulation of electric quadrupoles in crystals. Meanwhile, it has been pointed out that these results are inconsistent with the expression for the electric quadrupole introduced from thermodynamic arguments [2].

II. Main Results

We point out that the previous results differ from the expression for electric polarization based on linear response theory [3], [4]. Furthermore, the topological term called the Chern-Simons 3-form, predicted by the semiclassical theory, cannot be derived from linear response theory [4]. Thus a different approach has been desired to perform a comprehensive verification.

In this talk, we address this problem from the perspective of quantum transport equations. Our focus is on the solution of the one-particle density matrix that deviates from the local equilibrium distribution due to inhomogeneity in a non-dissipative insulator. We obtain this solution up to second order in perturbation theory with respect to time and spatial gradients [5]. Furthermore, we analytically derive the expectation values of the polarization charge, polarization current, and magnetization current from the obtained density matrix solution, thereby determining the electric polarization and orbital magnetization [5]. The obtained electric polarization and orbital magnetization reproduce the known results from the modern theory. In this presentation, we also obtain the expressions for the higher-order contributions: the electric polarization induced by spatial modulation and the orbital magnetization induced by temporal modulation, and compare them with previous studies. From this result we can obtain various formulas such as charge polarizability and magnetoelectric susceptibility, and compare with the results in the previous works.

III. Conclusion

We establish the quantum transport equation for insulators with slow modulations in space and those in time, and calculate the current and charge densities due to the modulations. From this result we obtain the formula for the electric polarization and orbital magnetization.

Acknowledgments

Y.G. acknowledges the support of the Fundamental Research Funds for the Central Universities, China (Grant No. WK2340000102). D.X. is supported by DOE Award No. DE-SC0012509. S. M is supported by JSPS KAKENHI Grant Numbers JP22K18687, JP22H00108 and JP24H02231, and by MEXT Initiative to Establish Next-generation Novel Integrated Circuits Centers (X-NICS) Grant Number JPJ011438.

References

[1] Y. Zhao, Y. Gao, and D. Xiao, "Electric polarization in inhomogeneous crystals", *Phys. Rev. B* 104, 144203, 2021.
[2] A. Daido, A. Shitade, and Y. Yanase, "Thermodynamic approach to electric quadrupole moments", *Phys. Rev. B* 102, 235149, 2020.
[3] N. Arai, Y. Gao, D. Xiao, S. Murakami, Relationship between Polarization and Quadrupole in Inhomogeneous Systems, Spring meeting of the Physical Society of Japan, 2024.
[4] N. Arai, Y. Gao, D. Xiao, S. Murakami, Theory of Electric Polarization in Inhomogeneous Systems Based on the Kubo Formula, Annual Meeting of the Physical Society of Japan, 2024.
[5] Y. Suzuki, N. Arai, M. Fujimoto, Y. Gao, D. Xiao, S. Murakami, in preparation, 2026.

Magnetic Helicity of Chiral Molecules

Ivanina Ilieva[1,*], Christof Holzer[2], Carsten Rockstuhl[1,3], Ivan Fernandez-Corbaton[3]

[1]Institute of Theoretical Solid State Physics, Karlsruhe Institute of Technology, Germany
[2]Institute of Quantum Materials and Technologies, Karlsruhe Institute of Technology, Germany
[3]Institute of Nanotechnology, Karlsruhe Institute of Technology, Germany
*Corresponding author: ivanina.ilieva@kit.edu

***Abstract*—Magnetic helicity, stored in static matter, is the counterpart to the electromagnetic helicity of free radiation fields. Here, we study the magnetic helicity of different chiral molecules. We extend the current formalism, which deals with the magnetization coming from electron spin, to include the stationary currents in the system.**

***Keywords*— magnetic helicity, chirality, chiral molecules, magnetization, stationary currents, light-matter interaction**

I. Introduction

Electromagnetic helicity is the property of a free radiation field describing the sense of its twistedness. For example, for plane waves, it relates to circular polarization handedness, and the helicity is given by the difference between left- and right-handed circularly polarized parts of the field. Helicity is typically studied in dynamic fields, which are characterized by a positive frequency. However, static fields can also contain a type of helicity – magnetic helicity. The magnetic helicity is a quantity most frequently considered in scientific domains such as solar physics, astrophysics, and cosmology. Much like its electromagnetic counterpart, magnetic helicity is related to field twistedness. Namely, it can be stored in chiral magnetic field configurations.

It is natural to pose the question if these two types of helicity are actually two embodiments of the same fundamental quantity [1]. In fact, it turns out that we can use the same scalar product to describe both free fields and static matter [2], and get the correct formulas for both corresponding types of helicity. The magnetic helicity is obtained in [1] from the magnetization density of the system.

To put this framework in a more practical context, here we study the magnetic helicity of stationary chiral molecules, whose electron configurations break inversion symmetry. Chiral molecules interact differently with light of opposite helicity, as seen in their circular dichroism spectra [3], and the analysis of their magnetic helicity may help furthering our understanding these mechanisms.

II. Theoretical Results

Typically, the magnetic helicity in a spatial region D is defined as [4]

$$\int_D \mathrm{d}^3\mathbf{r}\, \mathbf{A}(\mathbf{r}) \cdot \mathrm{curl}\mathbf{A}(\mathbf{r})\,, \tag{1}$$

where $\mathbf{A}(\mathbf{r})$ is the vector potential with the magnetic field $\mathbf{B}(\mathbf{r}) = \mathrm{curl}\mathbf{A}(\mathbf{r})$. The magnetic helicity content $\langle \Lambda_{\mathrm{mag}} \rangle$ in static matter, described by an electric charge density and a magnetization distribution, can be expressed as [2]

$$\langle \Lambda_{\mathrm{mag}} \rangle = \frac{\mathrm{i}\mu_0}{c} \int_{\mathbb{R}^3} \frac{\mathrm{d}^3\,\mathbf{k}}{|\mathbf{k}|} \mathbf{M}(\mathbf{k}) \cdot \big(\mathbf{k} \times \mathbf{M}(\mathbf{k})\big)\,. \tag{2}$$

Here, μ_0 is the vacuum permeability, c the speed of light, $\mathbf{k}$ the momentum vector, and $\mathbf{M}(\mathbf{k})$ the 3-dimensional Fourier transform of the spatial distribution of the magnetization, $\mathbf{M}(\mathbf{r})$. Note that the static charge distribution has no contribution to the magnetic helicity as it produces no magnetic field. Equation (2) is proportional to expression (1) [1].

In our analysis, we extend the setting in [1], [2] by allowing for stationary currents in the system. Such currents can exist in the systems we consider as they do not change with time. We find that with the substitution

$$\mathbf{M}(\mathbf{k}) \to \mathbf{M}(\mathbf{k}) + \mathrm{i}\frac{\hat{\mathbf{k}}}{|\mathbf{k}|} \times \mathbf{J}(\mathbf{k})\,, \tag{3}$$

we can achieve the desired inclusion of the current, where $\mathbf{J}(\mathbf{k})$ the 3-dimensional Fourier transform of the spatial distribution of the current, $\mathbf{J}(\mathbf{r})$. Applying the above substitution to Eq. (2) yields different terms contributing to the magnetic helicity of a system with both a magnetization and stationary currents – pure $\mathbf{M}-\mathbf{M}$ and $\mathbf{J}-\mathbf{J}$ terms and mixed $\mathbf{M}-\mathbf{J}$ terms.

III. Numerics

We use non-collinear spin density functional theory to simulate chiral molecules and calculate the magnetization density arising from electron spin and the stationary currents arising from spin-orbit coupling [5]. Closed-shell molecules have a trivially zero magnetization in this treatment, while open-shell ones can have a non-zero $\mathbf{M}(\mathbf{r})$. As a first example, we compute $\mathbf{M}(\mathbf{r})$ and $\mathbf{J}(\mathbf{r})$ for an open-shell chiral lanthanide compound. Furthermore, we consider both 1,1'-binaphthyl-2,2'-diol (BINOL) chiral variants as well as a forced achiral configuration. BINOL is diamagnetic and has negligible spin-orbit coupling due to being composed only of light atoms, so it would have neither $\mathbf{M}(\mathbf{r})$ nor $\mathbf{J}(\mathbf{r})$ on its own. We therefore place all configurations in a static homogeneous magnetic field to induce currents. Then the magnetic field is orders of magnitude more important than the spin-orbit coupling. We vary the field strength, which changes the currents and even results in a non-zero magnetization when BINOL goes into a

triplet state. We study the variation of the different magnetic helicity contributions depending on the molecule and setting in question. Details will be presented at the conference.

IV. Discussion

Studying if and how much magnetic helicity is stored in molecules under different conditions is important for understanding this quantity in the context of the interaction of molecules with electromagnetic radiation, and in particular its helicity. The analysis has the potential to be extended to dynamical processes to investigate the possibility of helicity transfer between matter and the free field.

Acknowledgments

This work was supported by the Karlsruhe School of Optics & Photonics (KSOP) and the Ministry of Science, Research and Arts of Baden-Württemberg as part of the sustainability financing of the projects of the Excellence Initiative II.

References

[1] I. Fernandez-Corbaton, "Total helicity of electromagnetic fields and matter," *Phys. Rev. B*, vol. 103, no. 6, Feb. 2021, Art. no. 054406.
[2] I. Fernandez-Corbaton and M. Vavilin, "A Scalar Product for Computing Fundamental Quantities in Matter," *Symmetry*, vol. 15, no 10, Sep. 2023, Art. no. 1839.
[3] N. Berova, K. Nakanishi, and R. W. Woody (Eds.), "Circular Dichroism: Principles and Applications" (2nd ed.), John Wiley & Sons, 2000.
[4] A. F. Rañada, "On the magnetic helicity," *Eur. J. of Phys.*, vol 13, no. 2, pp. 70-76, Mar. 1992.
[5] C. Holzer, Y. J. Franzke, and A. Pausch, "Current density functional framework for spin–orbit coupling," *J. Chem. Phys*, vol 157, no. 20, Nov. 2022, Art. no. 204102.

Hot-Electron Generation and Photoinduced Chirality in Plasmonic Nanocrystals

Alexander Govorov

Ohio University, Athens, USA
govorov@ohio.edu

Abstract— This talk will cover the following phenomena:

1. Plasmonic hot spots efficiently generate energetic ("hot") electrons, which can be utilized in photochemistry and photodetection.

2. Nanostructures with small interparticle gaps enhance optical heat generation and can confine high photoinduced temperatures to nanoscale volumes.

3. Colloidal nanocrystal assemblies and metastructures with plasmonic resonances significantly amplify the chiroptical responses of biomolecules (e.g., circular dichroism) and can induce chiral morphologies through surface photochemical processes.

Tailoring Smith-Purcell radiation using moiré photonic crystals and chiral materials

Thomas Delplace[1], Loris Cavenaile[1], Bjorn Maes[1,*]

[1]Micro- and Nanophotonic Materials Group, Research Institute for Materials Science and Engineering, University of Mons, Place du Parc 20, 7000 Mons, Belgium
*Corresponding author: bjorn.maes@umons.ac.be

***Abstract*—Dielectric gratings provide interesting opportunities to shape Smith-Purcell radiation, which is emitted when an electron passes close by a periodic structure. We describe various designs that influence the direction, efficiency and wavelength of the emission, amongst others via moiré photonic crystals and the inclusion of chiral materials.**

***Keywords*— Smith-Purcell radiation, photonic crystals, moiré gratings, chiral materials.**

I. Introduction

When an electron beam passes in the near-field zone of a grating, the optical Bloch modes of the device can be excited and couple the evanescent electron field into far-field radiation, which is called Smith-Purcell (SP) emission [1]. Traditionally, metallic gratings, with potentially plasmonic modes, were analyzed and employed for emission into air. However, dielectric high-index gratings also offer resonances, with even higher quality factors, that can be tailored via numerous interference-based phenomena. Therefore, current research examines new types of SP-like radiation effects [2], and optimizes the dielectric resonances for increased efficiency, directionality and emission wavelength, amongst others.

In this work, we numerically evaluate a variety of high-contrast photonic crystal devices, leading to rich SP emission patterns. First, we employ longitudinal symmetry breaking, a glide translation, between two adjacent gratings, with the electron beam in-between, to direct the radiation into the upper or lower half-space, respectively [3]. Second, we employ the concept of moiré photonic crystals to position multiple resonances at desired wavelengths. Third, we introduce a chiral, Pasteur medium into the gratings, in order to couple with modes that would otherwise not be excited by the polarization of the electron source.

II. Methods

The SP phenomena can be efficiently simulated by employing only a single (super)period of the structure. We use the finite-element commercial software COMSOL, with the appropriate source term and boundary conditions, see e.g. [4]. The chiral constitutive relations for a Pasteur medium can be conveniently implemented, as explained in [5]. For physical insight, we use Coupled-Mode Theory, starting with information from the calculated Bloch dispersion relations.

III. Results and Discussion

By adjusting the glide shift between two opposing gratings, it is possible to nearly-completely direct the radiation into the upper or lower direction, respectively. With this design, no extra Bragg mirror is thus required. By coupling two gratings with a different, but commensurate, period, the resulting superperiod moiré grating leads to strong interaction between the upper and lower resonances, leading to tailored emission peaks. Finally, the chiral effects couple the transverse-magnetic electron excitation with a transverse-electric mode, which would not show up in SP spectra with only achiral materials.

IV. Conclusion

High-index-contrast coupled gratings form a versatile platform to provide new SP functionalities. Moreover, probing these dielectric structures with electron beams is a novel way to exploit advanced electromagnetic concepts, such as bound-states-in-the-continuum, moiré or twisted photonic crystals and chiral materials.

Acknowledgments

This work was supported by the FRS-FNRS.

References

[1] Y. Yang et al., “Maximal spontaneous photon emission and energy loss from free electrons,” Nature Physics, 14(9), 894, 2018.
[2] X. Zhang et al., “Electron-beam-driven anomalous Doppler effects in Smith–Purcell radiation,” Photonics Research, 12(1), 78, 2024.
[3] T. Delplace, I. Bouanati, G. Rosolen, B. Maes, “Directional Smith-Purcell radiation via coupled high-index gratings,” Optics Express, 34, 2450, 2026.
[4] A. Szczepkowicz, L. Schächter, R. Joel England, “Frequency-domain calculation of Smith–Purcell radiation for metallic and dielectric gratings,” Applied Optics, 59(35), 11146, 2020.
[5] H.-Y. Wu, F. Vollmer, “Coherent multipolar amplification of chiroptical scattering and absorption from a magnetoelectric nanoparticle,” comm. physics, 6, 2023.

Quantum materials in chiral cavities

Ceren B. Dag[1,2,*]
[1]Department of Physics, Indiana University, USA, [2]Department of Physics, Harvard University, USA
[*]Corresponding author: cbdag@iu.edu

***Abstract*—I review the recent advances in the field of *chiral* cavity quantum materials and present a perspective on the future prospects. Chiral cavities, that is the cavities that break time-reversal symmetry of the photonic cavity field, have recently been fabricated, opening the doors to test theoretical predictions given in the past years, including the chiral-vacuum-induced Quantum Anomalous Hall Effect. This perspective elaborates on some of the current challenges in the field with a focus on theory, and proposes a route to address some of those challenges.**

***Keywords*— cavity quantum electrodynamics, chiral cavities, light-matter interaction, two-dimensional quantum materials, graphene, topological edge states, quantum many-body physics.**

I. Introduction: A brief review

Engineering topological phases with light has emerged as a central theme in quantum materials research in the last decade [1]. Conventional approaches rely on periodic driving to generate Berry curvature and nontrivial band topology, but intense driving fields can introduce heating. Cavity quantum electrodynamics, on the other hand, offers an alternative route in which enhanced vacuum fluctuations of confined electromagnetic modes modify electronic structure in equilibrium [2]. Recent developments in chiral cavity architectures enable the realization of circularly polarized vacuum fields capable of breaking time–reversal (T) symmetry [3].

T symmetry is a key symmetry in graphene, as it protects the Dirac nodes, and breaking it opens a topological band gap in graphene. Inspired by the insights that are arrived in Floquet engineering of graphene with circularly polarized light, the first theoretical predictions of chiral cavities were given for graphene embedded inside a chiral cavity [4], [5]. Recently, theories on other two-dimensional quantum materials, i.e., transition metal dichalcogenides, kagome lattices, graphene stacks, 2DEG, subject to chiral vacuum fields have been developed [6].

II. Methods of the field

Quantum field theory, Schrieffer-Wolff transformation, Hartree-Fock mean field theory and exact diagonalization have been the most common techniques applied in this field to reveal the cavity mediated electronic interactions and to perturbatively solve the many-body problem of all electrons coupled to a single cavity mode [4], [6]. In the larger field of cavity-QED engineering, density matrix renormalization group has been applied to solve for the many-body ground state of one-dimensional many-body systems coupled to a single cavity mode [7].

Additionally, the problem of graphene in a chiral cavity has been solved in the single electron limit revealing topological photo-electronic, i.e., cavity polaronic, bands where photon exchange processes can introduce Berry phase to the photo-electronic wave function [5]. Recently, a transfer matrix method was developed to find the photo-electronic topological edge mode dispersions of graphene ribbons in a chiral cavity, and analytical results on these edge modes were derived, e.g., localization length in terms of light-matter coupling strength, by recognizing the connection between the Hamiltonian in single electron picture and the cornerstone model of quantum optics, the Jaynes-Cummings model [5].

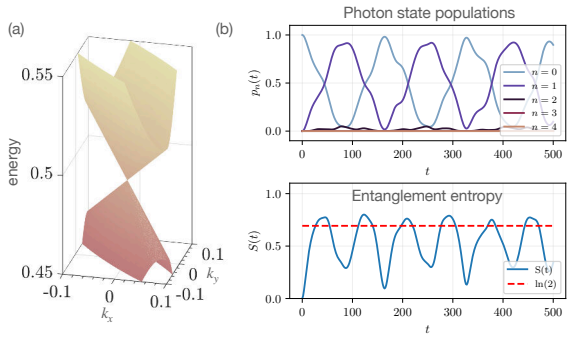

Fig. 1. (a) The band structure of a monolayer nodal superconductor minimally coupled to a chiral cavity: the nodal points are intact. (b) Photon populations (upper) and electronic entanglement entropy (lower) of edge modes in graphene ribbons after suddenly turning on light-matter coupling in a dark cavity, periodically forming bright modes. Adapted from [5].

III. Discussion

Can the T-symmetry breaking of chiral vacuum fields be imprinted in *any* 2D material embedded inside such cavities? This turns out to be not true. In particular, a $d-$wave nodal superconductor remains time-reversal symmetric even when it is subject to a chiral vacuum field that minimally couples to the electrons, shown in Fig. 1(a). This reveals that the form of electron-photon coupling, originating from minimal substitution, is significant to imprint the symmetry properties of enhanced vacuum fluctuations on the solid-state materials.

All existing chiral cavities require an external magnetic field to make the vacuum chiral, and even in the case of tHz photonic crystal cavities where the magnetic field needed is relatively low, it is not sufficiently low not to induce Landau levels in graphene [3]. This suggests that novel chiral cavity designs are in demand, where either no external magnetic field

will be needed or, the material under study will be shielded from the applied field.

Solving for the many-body ground state of strongly correlated two-dimensional systems is itself an active area of research. Here, we have even a more complicated problem of such systems coupled to a single photonic mode. We understand that in the perturbative regime where we can integrate over the photonic mode, photon mediated long-range interactions arise, i.e., all-to-all for a homogeneous field, and might compete with the intrinsic electronic interactions of the material to determine the ground state ordering. If such a competition exists, it only becomes more significant in the ultra-strong coupling regime where one cannot integrate out the photon field. These expectations are yet to be tested, and various tensor network algorithms can in fact rise to occasion. Developing tensor network methods geared particularly towards cavity quantum materials —a type of fermion-boson mixture— in higher than one dimension will be useful to answer the question whether the strong hybridization between electrons and photons, as observed in any material coupled to cavity photons, can lead to quasiparticle formation. The latter will likely be helpful to also better understand the nature of ultrastrong light-matter coupling in quantum materials, as well as deeper coupling regimes.

Ref. [5] demonstrated the presence of unidirectional edge currents carrying finite photon occupation in graphene ribbons embedded in chiral vacuum. Fig. 1(b) shows how the topological edge mode formed in graphene due to chiral cavity also acquires a photonic character and gives rise to a bright mode, i.e., 1-photon state, $n = 1$, populated, periodically in a dynamical setup. We observe that the electronic entanglement entropy maximizes at times where $n = 0$ and $n = 1$ states are equally populated, pointing to the strong hybridization between electron and photon modes. While these results constitute being a modest first step toward cavity-tunable unidirectional and hybrid channels in photonic solid-state devices, the effect of dissipation, e.g., cavity photon loss, on the hybrid edge modes needs to be understood. In fact, dissipation out of cavity can also be the way to detect such hybrid modes in the first place.

IV. Acknowledgments

C.B.D. thanks A. Vishwanath, V. Rokaj, J. Ahn, V. Karle, J. Cano, A. Baydin and J. Kono for stimulating discussions.

References

[1] J. W. McIver, B. Schulte, F.-U. Stein, T. Matsuyama, G. Jotzu, G. Meier, and A. Cavalleri, "Light-induced anomalous Hall effect in graphene," *Nature Physics*, vol. 16, pp. 38, 2020.

[2] F. Schlawin, D. M. Kennes, and M. A. Sentef, "Cavity quantum materials", *Applied Physics Reviews*, vol. 9, pp. 011312, 2022.
X. F. Smith and Y. T. Lee, "Terahertz metamaterials: design and applications," *Fictional Photonics Letters*, vol. 5, pp. 50–60, 2021.

[3] Daniel G. Suárez-Forero et al., "Chiral flat-band optical cavity with atomically thin mirrors", *Science Advances*, vol. 10, pp. eadr5904, 2024. J. Andberger, L. Graziotto, L. Sacchi, M. Beck, G. Scalari, and J. Faist, "Terahertz chiral subwavelength cavities breaking time-reversal symmetry via ultrastrong light-matter interaction", *Physical Review B*, vol. 109, pp. L161302, 2024. F. Tay, S. Sanders, A. Baydin, Z. Song, D. M. Welakuh, A. Alabastri, V. Rokaj, C. B. Dağ, and J. Kono, Terahertz chiral photonic-crystal cavities for Dirac gap engineering in graphene. *Nature Communications*, vol. 16, pp. 5270, 2025. K. M. Kulkarni, H. Xu, F. Tay, G. M. Rodriguez-Barrios, D. Kim, A. Alabastri, V. Rokaj, C. B. Dağ, A. Baydin, and J. Kono, "Realization of a chiral photonic-crystal cavity with broken time-reversal symmetry", *arXiv:2509.14366 (in press in Nature Communications)*, 2025.

[4] O. V. Kibis, O. Kyriienko, and I. A. Shelykh, "Band gap in graphene induced by vacuum fluctuations", *Phys. Rev. B* 84, 195413 (2011). X. Wang, E. Ronca, and M. A. Sentef, "Cavity quantum electrodynamical Chern insulator: Towards light-induced quantized anomalous Hall effect in graphene", *Phys. Rev. B* 99, 235156 (2019). K. Masuki and Y. Ashida, "Berry phase and topology in ultrastrongly coupled quantum light-matter systems", *Phys. Rev. B* 107, 195104 (2023). L. Yang, Q.-D. Jiang, "Emergent haldane model and photon-valley locking in chiral cavities", *Communications Physics* 8(1), 126 (2025).

[5] C. B. Dağ and V. Rokaj, "Engineering topology in graphene with chiral cavities", *Physical Review B*, vol, 110, pp. L121101, 2024. V Karle, O. K. Diessel, V Rokaj, C. B. Dağ, "Hybrid light-matter boundaries of graphene in a chiral cavity", *arXiv:2510.13373*.

[6] D.-P. Nguyen, G. Arwas, Z. Lin, W. Yao, and C. Ciuti, "Electron-Photon Chern Number in Cavity-Embedded 2D Moiré Materials", *Phys. Rev. Lett.* 131, 176602 (2023). C. Jiang, M. Baggioli, and Q.-D. Jiang, "Engineering Flat Bands in Twisted-Bilayer Graphene away from the Magic Angle with Chiral Optical Cavities", *Phys. Rev. Lett.* 132, 166901 (2024). C. Wei, L. Yang, and Q.-D. Jiang, "Cavity-vacuum induced chiral spin liquids in kagome lattices: Tuning and probing topological quantum phases via cavity quantum electrodynamics", *Phys. Rev. Lett.*, 135, 236901, (2024). L. Yang, G. Cardoso, T. H. Hansson, Q.-D. Jiang, "Quantum Hall effect in a chiral cavity", *arXiv:2503.11757*. S.A.A. Ghorashi, J. Cano, C.B. Dag, "Tunable Topological Phases in Multilayer Graphene Coupled to a Chiral Cavity", *arXiv:2504.03842*.

[7] D. Shaffer, M. Claassen, A. Srivastava and L. H. Santos, "Entanglement and topology in Su-Schrieffer-Heeger cavity quantum electrodynamics", *Phys. Rev. B*, 109, 155160, 2024. Z. Bacciconi, G. M. Andolina, C. Mora, "Topological protection of Majorana polaritons in a cavity", *Phys. Rev. B*, 109, 165434, 2024.

Geometric Phase Modulation in Circularly Birefringent Plasmonic Structures

Pasha Goz[1], Akash Das[1,2] Andre Yaroshevsky[1], Yuri Gorodetski[1,2,*]

[1]Electrical and Electronics Engineering department, Ariel University, Ariel, 407000, Israel
[2]Mechanical Engineering and Mechatronics department, Ariel University, Ariel, 407000, israel
*Corresponding author: yurig@ariel.ac.il

***Abstract*—Geometric phase in metasurfaces is conventionally realized using spatially rotated linearly birefringent meta-atoms under circularly polarized illumination. Here we demonstrate that full $\sim 2\pi$ geometric phase modulation can be achieved through circular birefringence and observed under linear polarization excitation. We introduce a plasmonic metasurface composed of spatially rotated chiral spiral unit cells designed to produce space-variant circular retardance. This generates a geometric phase ramp equivalent to a blazed grating, leading to ± 1 diffraction orders in momentum space. Using leakage radiation microscopy, we directly resolve these orders and show how their intensities depend upon the input linear polarization confirming the geometric origin of the phase. We theoretically analyze the phenomenon using a rotated Poincaré space and confirm our results by direct Stokes parameters measurement. These results establish basis-independent approach to geometric phase accumulation in circularly birefringent plasmonic metasurfaces.**

***Keywords*— metamaterials, spatio-temporal measurement, weak measurements, plasmonics, spin-orbit interaction.**

I. Introduction

Geometric phase, originating from the seminal works of Pancharatnam and Berry [1], [2], constitutes one of the most profound manifestations of gauge structure in wave physics. In optics, it arises when the polarization state undergoes cyclic evolution on the Poincaré sphere, leading to a phase shift determined solely by the geometry (enclosed solid angle) rather than optical path length [1], [2], [3], [4], [5]. This Pancharatnam-Berry (PB) phase has evolved from a conceptual curiosity into a central design principle for flat optics, singular optics, and metasurfaces [6], [7], [8], [9], [10], [11].

Conventional PB metasurfaces rely on spatially rotated linearly birefringent meta-atoms [12], [13], [6], [14]. Under circularly polarized illumination, the local optical axis orientation $\theta(x)$ imparts a helicity-dependent phase shift $\pm 2\theta$, enabling wavefront shaping via geometric phase gradients [7], [9], [10], [15]. In this widely adopted framework, geometric phase is typically described in the circular polarization basis and is intrinsically associated with spin conversion. However, geometric phase is fundamentally basis-independent: it depends only on the trajectory of the polarization state on the Poincaré sphere [2], [5], [16], [17], [18]. This raises a critical question that remains insufficiently explored [19]: can full 2π geometric phase modulation be achieved through circular birefringence instead of the conventional linear birefringence ? Establishing such complementarity would extend geometric-phase optics beyond the conventional PB paradigm and clarify the underlying gauge structure governing metasurface phase engineering.

Chiral metastructures provide a natural platform for addressing this question [19], [20]. Subwavelength spiral and twisted meta-atoms can exhibit strong circular birefringence and optical activity [21], [22], [23], with circular polarization eigenmodes as the natural basis. However, no direct experimental demonstration of spatially varying geometric phase induced by circular birefringence and its quantitative verification via solid-angle reconstruction has been reported. In such systems, spatial variation of the structural orientation induces a position-dependent geometric phase. When implemented in plasmonic platforms, the resulting phase gradient modifies the in-plane momentum of excited surface plasmon (SP) polaritons [24], [25], leading to controlled diffraction into discrete k-space channels [19]. Because SPs exhibit transverse spin and spin-momentum locking [26], [27], [28], they provide a sensitive probe of polarization-dependent geometric effects at subwavelength scales.

Here we introduce a plasmonic metasurface composed of spatially rotated chiral spiral unit cells arranged with supercell periodicity $N = 3$, engineered to produce controlled circular retardance. By rotating the effective coordinate frame on the Poincaré sphere, we formulate the transformation into a linear-eigenmode basis and show that spatial rotation of the spiral induces a geometric phase ramp analogous to a blazed grating. Crucially, this phase modulation persists for linear polarization inputs, revealing the basis independence of geometric phase accumulation.

A *leakage radiation microscopy* (LRM) [29], [30] followed by a Fourier lens is used to map the in-plane SP momentum distribution in the far field and directly resolve the geometric diffraction orders (satellites) in k-space. These orders intensities are found to be strongly dependent on the rotation of the incident linear polarization. By measuring the local Stokes parameters of the emerged field, we confirm a space-variant field ellipticity induced by the structure. This effect exemplifies the basis transformation of the Poincaré space.

Finally, we demonstrate an example of a plasmonic device based on the space-variant chirality. We fabricate a rotating spiral array with a period of $\Lambda = 1020$ nm and with $N = 3$.

Fig. 1. Optical setup for real- and k-space imaging. The beam was expanded using a beam expander (BE) and then passed through the LRM system comprising of illumination objective (O1) and the imaging oil-immersion objective (O2) attached to the substrate of the sample with an index matching oil. The imaging system included a tube lens (TL) a couple of relay lenses (L1,L2) and a camera (Cam). An aperture (A) was used to control the beam size and the wave plate (WP1) controlled the input polarization. The Stokes parameters were determined using the classical four-measurement scheme with a quarter-wave plate (WP2) followed by a linear polarizer (LP). A Fourier lens (FL) was used to image the k-space Insets show the scanning electron microscope image of the spiral array fabricated by the FIB and the schematic geometry of a single spiral slit.

Fig. 2. Plasmonic distribution measured from a rotating spiral array in the real space - (a,b) and in the k-space - (c,d) with $|\nearrow\rangle$ and $|\searrow\rangle$ input states, respectively. The yellow arrow guides the eye to the dominant satellite/plasmonic beam. The white dashed line shows the SP momentum and the k-space cross-section , taken along the blue dashed line is shown in the inset.

These parameters were chosen such that the satellites of the first diffraction order overlap with the plasmonic momentum, $k_{SP} = \frac{2\pi}{\Lambda} + \frac{2\pi}{N\Lambda}$. The inspection of the k-space (see Fig. 2a,b) reveals that a left-hand/right-hand satellite maximize for $|\nearrow\rangle$/$|\searrow\rangle$ state and provide a perfect coupling to a plasmonic unidirectional beam. This surface wave can be clearly seen in Fig. 2c,d. The yellow arrow marks the relevant geometric orders in the k-space and the resulting plasmonic beams in the real space. The white dashed line depicts the plasmonic momentum at our wavelength. The cross-section of the measured k-space along the central line is also shown, and the satellites intensity variation can be clearly observed. Similar device has been previously demonstrated with rotating rectangular plasmonic nanoapertures under circular state illumination[31]. Nevertheless, in the current system a space-variant chiral polarizer leads to the geometric phase from the linear states.

In general, our results establish a circular-birefringent analogue of PB metasurfaces and demonstrate that geometric phase modulation does not require linear birefringence nor circular polarization excitation. Our findings reveal a deeper complementarity between polarization basis and geometric phase accumulation, expanding the design space of metasurface-based phase engineering and opening opportunities for polarization-sensitive platforms in chiroptical spectroscopy and biophysical sensing. More broadly, our findings clarify the fundamental equivalence between spin-dependent and basis-independent geometric phase accumulation in structured chiral media.

REFERENCES

[1] S. Pancharatnam, "Generalized theory of interference, and its applications: Part i. coherent pencils," in *Proceedings of the Indian academy of sciences-section A*, vol. 44, no. 5. Springer, 1956, pp. 247–262.

[2] E. Cohen, H. Larocque, F. Bouchard, F. Nejadsattari, Y. Gefen, and E. Karimi, "Geometric phase from aharonov–bohm to pancharatnam–berry and beyond," *Nat. Rev. Phys.*, vol. 1, no. 7, pp. 437–449, 2019.

[3] M. V. Berry, "Quantal phase factors accompanying adiabatic changes," *Proc. of the Royal Soc. of London. A. Mathematical and Physical Sciences*, vol. 392, no. 1802, pp. 45–57, 1984.

[4] ——, "The adiabatic phase and pancharatnam's phase for polarized light," *Jour. of Mod. Opt.*, vol. 34, no. 11, pp. 1401–1407, 1987.

[5] R. Bhandari and J. Samuel, "Observation of topological phase by use of a laser interferometer," *Phys. Rev. Lett.*, vol. 60, pp. 1211–1213, Mar 1988. [Online]. Available: https://link.aps.org/doi/10.1103/PhysRevLett.60.1211

[6] N. Yu and F. Capasso, "Flat optics with designer metasurfaces," *Nat. Mat.*, vol. 13, no. 2, pp. 139–150, Feb. 2014.

[7] Z. Bomzon, V. Kleiner, and E. Hasman, "Pancharatnam–berry phase in space-variant polarization-state manipulations with subwavelength gratings," *Opt. Lett.*, vol. 26, no. 18, pp. 1424–1426, 2001.

[8] N. Yu, P. Genevet, M. A. Kats, F. Aieta, J.-P. Tetienne, F. Capasso, and Z. Gaburro, "Light propagation with phase discontinuities: generalized laws of reflection and refraction," *Science*, vol. 334, no. 6054, pp. 333–337, 2011.

[9] L. Huang, X. Chen, H. Mühlenbernd, H. Zhang, S. Chen, B. Bai, Q. Tan, G. Jin, K.-W. Cheah, C.-W. Qiu *et al.*, "Three-dimensional optical holography using a plasmonic metasurface," *Nat. Commun.*, vol. 4, no. 1, p. 2808, 2013.

[10] A. Arbabi, Y. Horie, M. Bagheri, and A. Faraon, "Dielectric metasurfaces for complete control of phase and polarization with subwavelength spatial resolution and high transmission," *Nat. Nanotech.*, vol. 10, no. 11, pp. 937–943, 2015.

[11] S. Shrestha, A. C. Overvig, M. Lu, A. Stein, and N. Yu, "Broadband achromatic dielectric metalenses," *Light: Science & Applications*, vol. 7, no. 1, p. 85, 2018.

[12] X. Xie, M. Pu, J. Jin, M. Xu, Y. Guo, X. Li, P. Gao, X. Ma, and X. Luo, "Generalized pancharatnam-berry phase in rotationally symmetric meta-atoms," *Phys. Rev. Lett.*, vol. 126, no. 18, p. 183902, 2021.

[13] J. Balthasar Mueller, N. A. Rubin, R. C. Devlin, B. Groever, and F. Capasso, "Metasurface polarization optics: independent phase control of arbitrary orthogonal states of polarization," *Phys. Rev. Lett.*, vol. 118, no. 11, p. 113901, 2017.

[14] H.-X. Xu, L. Han, Y. Li, Y. Sun, J. Zhao, S. Zhang, and C.-W. Qiu, "Completely spin-decoupled dual-phase hybrid metasurfaces for arbitrary wavefront control," *ACS Phot.*, vol. 6, no. 1, pp. 211–220, 2018.
[15] M. Khorasaninejad, W. T. Chen, R. C. Devlin, J. Oh, A. Y. Zhu, and F. Capasso, "Metalenses at visible wavelengths: Diffraction-limited focusing and subwavelength resolution imaging," *Science*, vol. 352, no. 6290, pp. 1190–1194, 2016.
[16] J. Samuel and R. Bhandari, "General setting for berry's phase," *Phys. Rev. Lett.*, vol. 60, pp. 2339–2342, Jun 1988. [Online]. Available: https://link.aps.org/doi/10.1103/PhysRevLett.60.2339
[17] T. Van Dijk, H. F. Schouten, W. Ubachs, and T. D. Visser, "The pancharatnam-berry phase for non-cyclic polarization changes," *Opt. Exp.*, vol. 18, no. 10, pp. 10 796–10 804, 2010.
[18] Y. Guo, M. Pu, F. Zhang, M. Xu, X. Li, X. Ma, and X. Luo, "Classical and generalized geometric phase in electromagnetic metasurfaces," *Photonics Insights*, vol. 1, no. 1, pp. R03–R03, 2022.
[19] L. Singh, M. Fox, S. Sternklar, and Y. Gorodetski, "Topological diffraction from grating with space variant chirality," *ACS Photonics*, vol. 9, no. 4, pp. 1395–1399, 2022.
[20] L. Singh, E. David Epstein, D. Cheskis, S. Sternklar, and Y. Gorodetski, "Experimental investigation of kramers–kronig relations in chiral metasurfaces with reduced rotational symmetry," *Jour. of Opt.*, vol. 22, no. 12, p. 12LT01, 2020.
[21] Y. Tang and A. E. Cohen, "Optical chirality and its interaction with matter," *Phys. Rev. Lett.*, vol. 104, no. 16, p. 163901, 2010.
[22] S. Zhang, J. Zhou, Y.-S. Park, J. Rho, R. Singh, S. Nam, A. K. Azad, H.-T. Chen, X. Yin, A. J. Taylor *et al.*, "Photoinduced handedness switching in terahertz chiral metamolecules," *Nat. Commun.*, vol. 3, no. 1, p. 942, 2012.
[23] C. Pfeiffer and A. Grbic, "Metamaterial huygens' surfaces: tailoring wave fronts with reflectionless sheets," *Phys. Rev. Lett*, vol. 110, no. 19, p. 197401, 2013.
[24] S. Daniel, K. Saastamoinen, T. Saastamoinen, I. Vartiainen, A. T. Friberg, and T. D. Visser, "Surface plasmons carry the pancharatnam-berry geometric phase," *Phys. Rev. Lett.*, vol. 119, no. 25, p. 253901, 2017.
[25] L. Huang, X. Chen, B. Bai, Q. Tan, G. Jin, T. Zentgraf, and S. Zhang, "Helicity dependent directional surface plasmon polariton excitation using a metasurface with interfacial phase discontinuity," *Light: Science & Applications*, vol. 2, no. 3, pp. e70–e70, 2013.
[26] K. Y. Bliokh, F. J. Rodríguez-Fortuño, F. Nori, and A. V. Zayats, "Spin–orbit interactions of light," *Nat. Phot.*, vol. 9, no. 12, pp. 796–808, 2015.
[27] K. Y. Bliokh and F. Nori, "Transverse and longitudinal angular momenta of light," *Phys. Rep.*, vol. 592, pp. 1–38, 2015.
[28] F. J. Rodríguez-Fortuño, G. Marino, P. Ginzburg, D. O'Connor, A. Martínez, G. A. Wurtz, and A. V. Zayats, "Near-field interference for the unidirectional excitation of electromagnetic guided modes," *Science*, vol. 340, no. 6130, pp. 328–330, 2013. [Online]. Available: https://www.science.org/doi/abs/10.1126/science.1233739
[29] A. Drezet, A. Hohenau, D. Koller, A. Stepanov, H. Ditlbacher, B. Steinberger, F. R. Aussenegg, A. Leitner, and J. R. Krenn, "Leakage radiation microscopy of surface plasmon polaritons," *Mat. Sci. and Eng.: B*, vol. 149, no. 3, pp. 220–229, 2008.
[30] A. Hohenau, J. Krenn, A. Drezet, O. Mollet, S. Huant, C. Genet, B. Stein, and T. Ebbesen, "Surface plasmon leakage radiation microscopy at the diffraction limit," *Opt. Exp.*, vol. 19, no. 25, pp. 25 749–25 762, 2011.
[31] M. Fox and Y. Gorodetski, "Generalized approach to plasmonic phase modulation in topological bi-gratings," *Appl. Phys. Lett.*, vol. 120, no. 3, 2022.

Giant Magneto-Impedance Effect in Magnetic Microwires: Challenges, Advances and Perspectives

Arcady Zhukov[1,,2*], Alvaro Gonzalez[1,3], Paula Corte-Leon[1,3,4], Jesus Olivera[5] and Valentina Zhukova[1,3]

[1] Dpto. de Física Aplicada, EIG, University of Basque Country (EHU), San Sebastian, Spain
[2] IKERBASQUE, Basque Foundation for Science, Spain
[3] Dept. Polym. Adv. Mater., University of the Basque Country, EHU, 20018 Donostia-San Sebastian, Spain
[4]Dept. Mater. Science & Metallurgy, Univ. Cambridge, Cambridge CB3 0FS, UK
[5]Instituto de Física, Facultad de Ciencias, Universidad Autónoma de Santo Domingo, Dominican Republic
*Corresponding author: arkadi.joukov@ehu.es

***Abstract*—We provide the overview of the state of art on development of magnetic wires with high Giant Magnetoimpedance (GMI) effect. Excellent soft magnetic properties and GMI ratio up to 750% have been observed in as-prepared low magnetostrictive amorphous Co-rich microwires. Appropriate processing, such as annealing, allows to increase further the GMI ratio value. Although less expensive Fe-rich microwires exhibit rather high magnetostriction coefficient and consequently quite low GMI effect, magnetic softness and GMI effect can be substantially improved by appropriate processing. In both Fe and Co-rich microwires the maximum GMI ratio is observed for frequencies above 100 MHz.**

***Keywords*—Giant Magnetoimpedance, Magnetoelastic anisotropy, Magnetostriction, Amorphous microwires.**

I. Introduction

Studies of Giant magnetoimpedance, GMI, effect have attracted considerable attention in the last few years owing to its suitability for technological applications [1,2]. The main features of the GMI effect have been successfully explained in terms of classical electrodynamics that consider the influence of a magnetic field on the penetration depth of AC current (MHz-GHz frequency range) flowing through the magnetically soft conductor.

The most common quantity for the characterization of the GMI effect is the GMI ratio, ΔZ/Z, defined as:

$$\Delta Z/Z = [Z(H) - Z(H_{max})] / Z(H_{max}), \quad (1)$$

where H_{max} is the axial DC-field with maximum value up to few kA/m.

Extremely high sensitivity of the GMI effect to even low magnetic field attracted great interest in the field of applied magnetism, basically for applications in magnetic sensors and smart composites. Cylindrical shape and high circumferential permeability observed in amorphous wires are quite favorable for achievement of high GMI effect [1-4].

One of the tendencies in modern GMI sensors is the size reduction [3-5]. Recently developed magnetic sensors using the GMI effect allow achieving nT and pT magnetic field sensitivity with low noise [1,3,4]

The aim of this report is to provide recent results on the optimization of soft magnetic properties and the GMI effect in magnetic microwires.

II. Methods

We measured magnetic field dependences of impedance, Z, and GMI ratio, $\Delta Z/Z$, of magnetic microwires using a specially designed micro-strip sample holder. The sample holder was placed inside a sufficiently long solenoid that creates a homogeneous magnetic field, H. The sample impedance Z was measured using vector network analyzer from reflection coefficient S_{11}, reported elsewhere [3,6].

III. Results and Discussion

As discussed elsewhere [1-4], for amorphous materials characterized by the absence of magneto-crystalline anisotropy the main sources of magnetic anisotropy are the shape and magnetoelastic anisotropy, K_{me}. The latter is determined by the magnetostriction coefficient, λ_s, and the internal stresses, σ_i, by the relation [3]:

$$K_{me} = 3/2\ \lambda_s \sigma_i, \quad (2)$$

Nearly-zero λ_s –values can be achieved in $Co_{1-x}Fe_x$ alloys at x about 0,03 – 0,08 [3]. Accordingly, Co-rich microwires can present high GMI ratio. $\Delta Z/Z(H)$ dependencies measured at different frequencies in $Co_{67}Fe_{3.9}Ni_{1.4}B_{11.5}Si_{14.5}Mo_{1.6}$ (d=10.8 μm, D= 13.8 μm) microwire are shown in Fig. 1a. This microwire presents high maximum GMI ratio, $\Delta Z/Z_m$, (~530%) at optimal frequency of about 700 MHz (see Fig. 1b).

However, from $\Delta Z/Z_m(f)$ dependence for $Co_{67.7}Fe_{4.3}Ni_{1.6}Si_{11.2}B_{12.4}C_{1.5}Mo_{1.3}$ microwires with d=10.8 μm

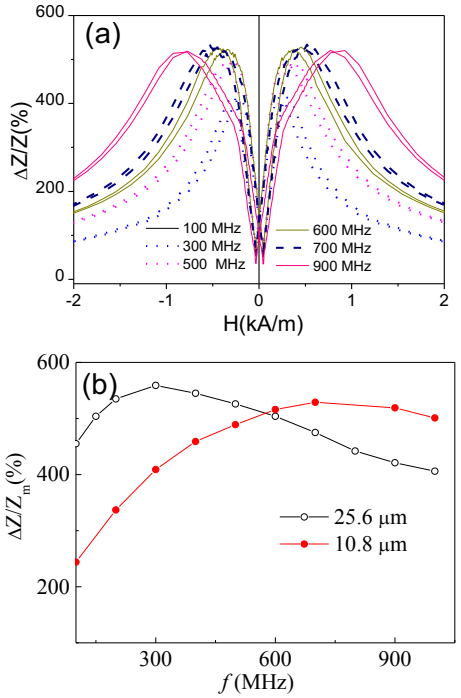

Fig. 1. *ΔZ/Z(H)* dependencies measured in $Co_{67}Fe_{3.9}Ni_{1.4}B_{11.5}Si_{14.5}Mo_{1.6}$ (d=25.6 μm, D= 26.6 μm) microwires (a) and $\Delta Z/Z_m(f)$ dependence for $Co_{67.7}Fe_{4.3}Ni_{1.6}Si_{11.2}B_{12.4}C_{1.5}Mo_{1.3}$ with d=10.8μm, D=13.8μm and d=25.6 μm, D= 26.6 μm microwires.

and d=25.6 μm we can appreciate that for $Co_{67.7}Fe_{4.3}Ni_{1.6}Si_{11.2}B_{12.4}C_{1.5}Mo_{1.3}$ microwires with d=25.6 μm the optimal frequency is about 300 MHz at which $\Delta Z/Z_m \approx 560\%$ can be achieved. The observed behaviour reflects the relationship between the optimal frequency for the GMI performance and the wire diameter: to achieve the maximum GMI effect a trade-off between wire dimensions and frequency is required [5]. The diameter reduction must be associated with the increasing of the optimal GMI frequency range [3,5].

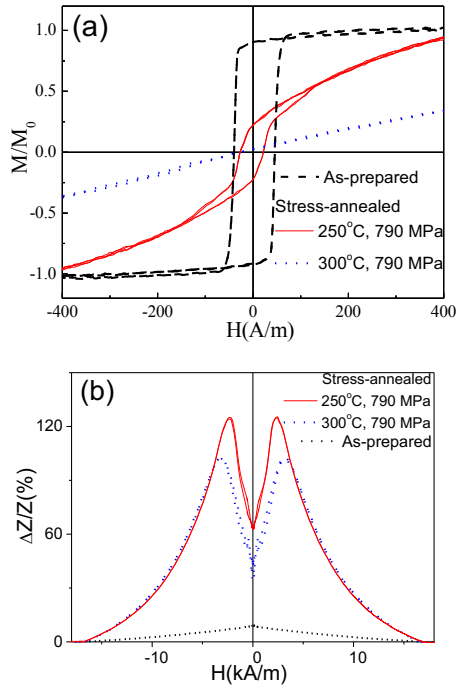

Fig. 2. Hysteresis loops (a) and *ΔZ/Z(H)* dependences measured at 300 MHz (b) of as-prepared and stress-annealed $Fe_{75}B_9Si_{12}C_4$ microwires.

Usually, highly magnetostrictive Fe-rich microwires present poor GMI effect. However, from the viewpoint of the cost Fe-rich microwires are preferable. Recently, we identified that the magnetic softness and GMI effect of Fe-rich microwires can be substantially improved by stress-annealing (see Fig. 2): an order of magnitude $\Delta Z/Z_m$ improvement (see Fig. 2b) is explained by transverse character of induced by stress-annealing magnetic anisotropy (see Fig .2a).

It is worth noting that annealing can also improve the GMI effect of Co-rich microwires. Thus, recently we reported $\Delta Z/Z_m$ up to 900% in annealed Co-rich microwires [6].

IV. Conclusion

We studied the factors allowing optimization of GMI effect of magnetic microwires. Generally, low coercivity and high GMI effect have been observed in as-prepared Co-rich microwires. We identified a relationship between the optimal frequency for the GMI performance and the wire diameter: to achieve the maximum GMI effect a trade-off between wire dimensions and frequency is required. GMI ratio of Fe-rich microwires can be substantially improved by the adequate postprocessing.

Acknowledgments

This work was supported by the Spanish MICIN, under PID2022-141373NB-I00 project, by EU (Horizon Europe) under "HARMONY", by the Government of the Basque Country, under Elkartek (MOSINCO and ATLANTIS) projects and by under the scheme of "Ayuda a Grupos Consolidados" (Ref.: IT1670-22).

References

[1] M.-H. Phan and H.-X. Peng, "Giant magnetoimpedance materials: Fundamentals and applications", Prog.Mater. Science vol. 53, pp. 323–420,2008.

[2] L.V. Panina and K. Mohri, "Magneto-impedance effect in amorphous wires" Appl. Phys. Lett. vol. 65, pp. 1189-1191,1994.

[3] A. Zhukov, M. Ipatov and V. Zhukova, "Advances in Giant Magnetoimpedance of Materials", Handbook of Magnetic Materials, ed. K.H.J. Buschow, *Elsevier*, vol. 24, ch.2., 2015, pp. 139-236.

[4] K. Mohri, T. Uchiyama, L.V. Panina, M. Yamamoto and K. Bushida, "Recent Advances of Amorphous Wire CMOS IC Magneto-Impedance Sensors: Innovative High-Performance Micromagnetic Sensor Chip" J. Sens. 2015, 718069, 2015, doi:10.1155/2015/718069

[5] D. Ménard, M. Britel, P. Ciureanu and A. Yelon, "Giant magnetoimpedance in a cylindrical conductor" J. Appl. Phys. vol. 84, pp. 2805–2814, 1998.

[6] A. Gonzalez, I. Skorvanek, M. Jakubcin, V. Zhukova, A. Zhukov, "Impact of elevated temperature on the Giant magnetoimpedance effect in Co-rich glass-coated microwires", Scr. Mater. vol.266. 116794, 2025.

An Electromagnetically Driven Vaterite-based Panacea Platform

Pavel Ginzburg[1,*] and Hani Barhom[1],
Andrey Machnev[1], Andrey Ushkov[1], Denis Kolchanov[1], Pavel Bezrukov[1]
[1]Department of Electrical Engineering, Tel Aviv University
*Corresponding author: pginzburg@taux.tau.ac.il

***Abstract*— Nano-engineered capsules for targeted drug delivery represent an essential milestone on the path to advancing precision medicine concepts. As most phenomena occur in a liquid environment in vivo, understanding cargo-fluid interaction mechanisms in vitro is an important factor that can control release rates. In this contribution, we introduce metamaterial drug-delivery capsules based on golden, gilded, and magnetized vaterite and demonstrate how electromagnetic control enables a unified light- and magnetic-based theranostic paradigm. We will demonstrate optomechanical delivery, one-photon and two-photon bioimaging, controlled release, and optothermal therapy enabled by vaterite metamaterials. Beyond optical activation, we add magnetic targeting and field-guided propulsion to address the long-standing bottleneck of precise accumulation at the site of interest. Magnetized capsules can be steered along programmed magnetic field landscapes to drive transport toward tumors or other targets, improving localization while reducing reliance on passive circulation.**

***Keywords*— Metamaterials, Biophotonics, Drug Delivery.**

I. Introduction

The presentation is based on our recent works [1], [2], [3], [4], [6], [7], [8] and on a large set of new data. In addition to our published results, we will demonstrate novel light-driven functions, including release, uptake acceleration, and cell treatment, that underline the golden', gilded', and magnetized' vaterite advantages. W*e present results from joint collaborations with leading hospitals in which our particles are under evaluation. We show that magnetic metamaterials overcome the long-standing challenge of nanoparticle targeting by propelling drug-loaded carriers toward tumors via deliberate shaping of the magnetic field landscape, thereby breaking current limitations and enabling effective delivery.*

II. Results and Discussion

The fast-changing landscape of biomedical challenges motivates the ongoing development of new functional platforms. Implantable devices made from biocompatible materials that respond to optical signals and tailor the propagation of light waves can be employed in health monitoring applications and therapeutics. The incorporation of such elements into living organisms can boost light-tissue interactions and shift conventional approaches toward precision medicine by opening new opportunities in sensing, photothermal therapy, photoacoustic tomography, and bioimaging. One of the grand challenges along those pathways is the miniaturization of biocompatible photonic structures that provide multiple functionalities, such as monitoring vital biological processes, light-responsive drug release, and local nanoscale heating with simultaneous temperature measurement.

The vaterite polymorph of calcium carbonate has a wide scope of potential applications in biology and medicine due to its outstanding combination of chemical, morphological, and physical properties. As a fully biocompatible, FDA-approved material, it possesses a sponge-like morphology that effectively entails a wide range of functional materials. As cargo release from vaterite particles is associated with structural transformations, an understanding of particle−fluid interactions is required to advance this material platform toward targeted drug delivery needs. Figure 1 is our executive summary. The panels on the left demonstrate the different shapes of fabricated particles. The shapes are not only responsible for optical properties but have a crucial impact on particle-cell interaction dynamics, as we will demonstrate. The right panel shows 'golden' vaterite – small 3nm gold nanoparticles are diffused into the mesoporous matrix, creating a new metamaterial. This structure exhibits an artificial localized plasmon resonance in the infrared spectral range, which matches the biological transparency window. The bottom part is the imaging.

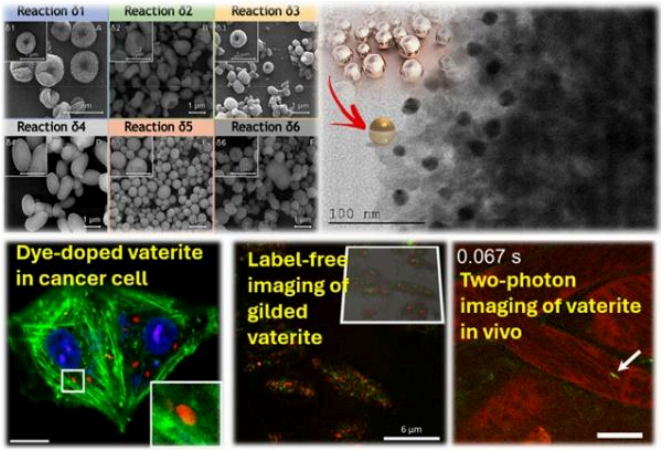

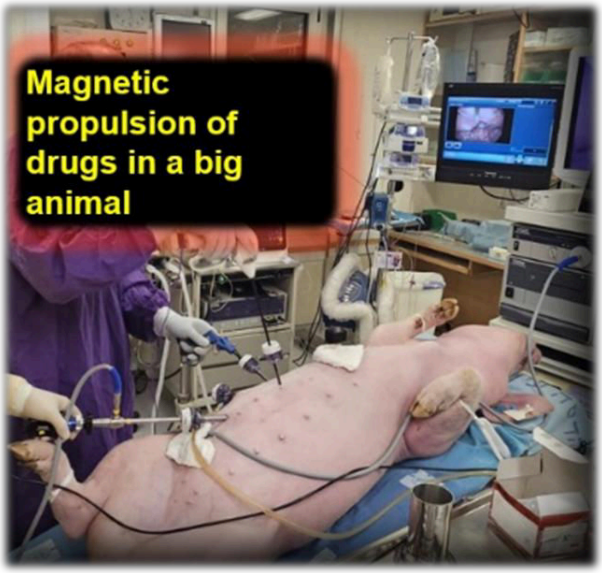

Fig. 1 Vaterite. (up) Particles of different shapes to tailor both optical properties and particle-cell interaction dynamics. (Right) 'Golden' Vaterite – TEM image of CaCO3 matrix, loaded with gold nanoparticles. Bottom: Imaging capsules in vitro and in vivo.

REFERENCES

[1] R. E. Noskov, I. I. Shishkin, H. Barhom, and P. Ginzburg, "Non-Mie optical resonances in anisotropic biomineral nanoparticles," Nanoscale, vol. 10, no. 45, pp. 21031–21040, Dec. 2018,
[2] R. E. Noskov et al., "Golden Vaterite as a Mesoscopic Metamaterial for Biophotonic Applications," Advanced Materials, 33, 2021, doi: [3] H. Barhom et al., "Biological Kerker Effect Boosts Light Collection Efficiency in Plants," Nano Lett, vol. 19, no. 10, pp. 7062–7071, 2019.
[4] H. Bahrom et al., "Controllable Synthesis of Calcium Carbonate with Different Geometry: Comprehensive Analysis of Particle Formation, Cellular Uptake, and Biocompatibility," ACS Sustain Chem Eng, vol. 7, no. 23, 19142, 2019.
[5] D. Harpaz, H. Barhom, B. Veltman, P. Ginzburg, and E. Eltzov, "Biocompatibility characterization of vaterite with a bacterial whole-cell biosensor," Colloids Surf B Biointerfaces, vol. 222, p. 113104, 2023
[6] H. Gilad et al., "Gilded vaterite optothermal transport in a bubble," Scientific Reports 2023 13:1, vol. 13, no. 1, pp. 1–11, Jul. 2023, [7] A. Ushkov, A. Machnev, and P. Ginzburg, "Controllable switch of dissolution kinetics mechanism in drug microcapsules," Apr. 2023
[8] Kislov et al., "Optothermal Needle-Free Injection of Vaterite Nanocapsules," Advanced Science, vol. 11, no. 5, p. 2305202, Feb. 2024, doi: 10.1002/ADVS.202305202.

Photonics for Thermal Management in Photovoltaics

George Perrakis[1], Anna Tasolamprou[1,2], and Maria Kafesaki[1,3]*

[1]Institute of Electronic Structure and Laser (IESL), Foundation for Research and Technology Hellas (FORTH), Heraklion, Crete, Greece
[2]Department of Materials Science and Engineering, University of Crete, Greece
[3]Department of Physics, National and Kapodistrian University of Athens, Greece
*Corresponding author: kafesaki@iesl.forth.gr

***Abstract*— Effective heat mitigation remains a central challenge for photovoltaic (PV) technologies, directly influencing conversion efficiency, operational stability, and device lifetime. In this work, by exploiting radiative cooling and spectrally engineered optical responses, we demonstrate cooling coating structures providing significant temperature reductions and measurable efficiency gains across different PV architectures.**

***Keywords*— radiative cooling, photovoltaics, solar cells**

I. Introduction

Temperature elevation in photovoltaics (PVs) constitutes a serious limiting factor for their performance and life-time. Even moderate heating degrades electrical output and accelerates material aging. Passive radiative cooling (PRC) has recently emerged as an attractive solution, capable of dissipating excess heat through engineered thermal emission, reducing thus the PV temperature. Unlike active cooling strategies, PRC operates without external power input, making it particularly appealing for scalable solar technologies.

Our work focuses on the design and demonstration of photonic structures/coatings that enhance radiative cooling in PVs and tailor spectral reflection and transmission properties, in order to reduce PV operating temperatures while preserving, or even enhancing, optical absorption in the useful spectral range.

II. Design Strategies and Key Results

Our cooling coating structures are designed as to exploit several complementary photonic mechanisms:

a) Enhancement of PRC, i.e. of thermal emission within the atmospheric transparency window (8–13 μm) and beyond ; this enables efficient heat rejection to outer space.

b) Increase of reflection of sub-bandgap radiation ; this minimizes parasitic heating.

c) Control of ultraviolet reflection (enabling reflection up to a critical wavelength, dependend on the active material); this protects sensitive photovoltaic materials (e.g. adhesion layers).

d) Preservation or even enhancement of the optical transparency (to avoid photocurrent loss).

To quantitatively evaluate these mechanisms on different PV architectures, we developed a comprehensive opto-electro-thermal simulation framework capable of predicting photovoltaic temperature and efficiency given the transmission/reflection/absorption-emission charcateristics of a cell, under realistic environmental conditions. This modeling platform allows systematic assessment of any designed cooling structure.

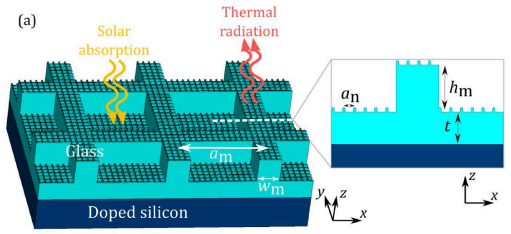

Fig. 1: A double-periodic nano-micro-structured glass coating (light-blue), able to provide a close to 6° C temperature reduction and a 3.1% solar cell efficiency increase if placed on top of Si solar cell. Inset shows a vertical cross-section of the structure

Fig. 1 shows a cooling structure that we have proposed that exploits almost all the above mechanisms. It is a double-periodic- (micro/nano) structured glass slab of micrometer thickness. This slab was placed atop a silicon solar cell, resulting to a numerical démonstration of a temperature decrease of ~ 6°C (compared to the structure without coating) and an efficiency improvement exceeding 3%. These results, among others, highlight the effectiveness of hierarchical (micro-nano) structuring in optimizing radiative heat exchange in solar cells without compromising electrical output.

The benefits of photonic cooling are even more pronounced for emerging thin-film technologies, such as organic and perovskite solar cells, which exhibit strong thermal and UV sensitivity. By incorporating ultrathin hybrid organic–inorganic radiative cooling layers in organic and perovskite cells, we demonstrated temperature reductions beyond 7°C while maintaining high photovoltaic performance.

Alternative promising approaches for “cooling” include the incorporation of cooling layers or structures in essential PV components, such as electrodes. In the framework of this work we also designed and demonstrated numerically an efficient “cooling” electrode for perovskite PV structures, resulting to ~7°C temperature reduction and more than 1.3% efficiency increase. This is a clear demostration of the high potential of smart cooling strategies for lightweight and flexible solar platforms.

III. Conclusions

This work demonstrates that carefully engineered photonic structures can substantially improve photovoltaic thermal regulation and operational efficiency. By integrating radiative cooling with spectral management techniques, it is possible to enhance device durability and performance across both conventional and next-generation PV technologies.

Our results establish a pathway toward scalable, passive thermal management solutions and provide a foundation for further developments of advanced photonic cooling architectures.

Acknowledgments

This research was supported by the Hellenic Foundation for Research and Innovation (HFRI) under the project MultiCool (ID 15117)

References

[1] G. Perrakis, A. Tasolamprou, G. Kenanakis, E. N. Economou, S. Tzortzakis, M. Kafesaki, “Passive radiative cooling and other photonic approaches for the temperature control of photovoltaics: a comparative study for crystalline silicon-based architectures,” Opt. Express, vol. 28, p. 18548, 2020.

[1] G. Perrakis, A. Tasolamprou, G. Kenanakis, E. N. Economou, S. Tzortzakis, M. Kafesaki, “Ultraviolet radiation impact on the efficiency of commercial crystalline silicon-based photovoltaics: a theoretical thermal-electrical study in realistic device architectures,” OSA Contin., vol. 3, p. 1436, 2020.

[2] G. Perrakis, A. Tasolamprou, G. Kenanakis, E. N. Economou, S. Tzortzakis, M. Kafesaki, “Combined nano and micro structuring for enhanced radiative cooling and efficiency of photovoltaic cells,” Scient. Rep., vol. 11, p. 11552, 2021.

[3] G. Perrakis, A. Tasolamprou, G. Kenanakis, E. N. Economou, S. Tzortzakis, M. Kafesaki, “Submicron organic-inorganic hybrid radiative cooling coatings for stable, ultrathin, and lightweight solar cells”, ACS Photon., vol. 9, p. 1327, 2022.

[4] G. Perrakis et. al., “Infrared-reflective ultrathin-metal-film-based transparent electrode with ultralow optical loss for high efficiency in solar cells,” Scient. Rep., vol. 14, p. 548, 2024.

Self-Polarizing Chiral Cavities for Control of Quantum Emitters

B. Semnani[1,2*], Anya Houk[1,2] , M. Soltani[1,2], Athena Xu[1,2] and M. Bajcsy[1,2]

[1]Institute for Quantum Computing (IQC), Waterloo, ON, Canada
[2]Department of Electrical & Computer Engineering, University of Waterloo, Waterloo, ON, Canada
[*]corresponding author: bsemnani@uwaterloo.ca

***Abstract*— We report experimental progress on the design, fabrication, and characterization of high-performance confocal Fabry–Pérot cavities formed by dielectric metasurfaces. These metasurfaces stabilize the cavity, optimize the mode volume, and introduce polarization birefringence, with particular emphasis on single-spin chiral cavities enabled by dielectric metasurface mirrors.**

***Keywords*— Chiral Cavities, Metasurfaces, Fabry-Perot**

I. Introduction

Free-space Fabry–Pérot cavities are powerful platforms for enhancing light–matter interactions in systems such as cold atoms and single quantum emitters. However, integrated confocal cavities with stable free-space modes have not yet been experimentally realized [1,2]. We present new design strategies and preliminary results for confocal cavities formed by (i) Pancharatnam–Berry phase reflecting metasurfaces [3] that focus a single helicity, and (ii) multilayer polarization-birefringent metasurfaces that reflect one linear polarization while transmitting the orthogonal one. The metasurface mirrors are vertically mounted with lithographically defined spacing

(I) Self-polarizing Chiral Cavity: The chiral metasurface consists of a subwavelength array of 500-nm-tall round-corner rectangular nanofins placed on a 50-nm silver back-mirror. A focusing phase profile is implemented by rotating each nanofin according to the geometric-phase relation by an angle $\theta(x,y)=2\varphi(x,y)$ where φ is the desired phase . Because subwavelength periodicity can excite lossy plasmonic modes, a thin SiO spacer is added to suppress field buildup on the silver surface, reducing depolarization and loss and enabling higher-Q performance. The design is further optimized to maintain polarization purity across all rotation angles. A second fabrication challenge is the formation of nanoislands in the silver layer during PECVD deposition of amorphous silicon, driven by thermally induced dewetting. To prevent this, the silver is magnetron-sputtered and capped with a thin SiO film before PECVD. SEM images confirm that this approach avoids dewetting compared with conventional e-beam-evaporated silver. The SiO layer therefore plays a dual role: suppressing plasmonic loss and protecting the silver film during high-temperature processing.

(II) Polarization-dichroic Fabry–Pérot cavity: A second cavity uses vertically mounted birefringent metasurfaces operating in confocal mode. Each consists of a phase-imparting layer and a dimerized high-contrast grating (DHCG) [5] providing near-unity polarization discrimination. Independent phase profiles are designed via ray tracing to ensure mode overlap. This cavity is used to implement a single-photon gate with cold Cs atoms. Figure 1 illustrates the PB-phase metasurface (a–c) and the bilayer polarization-dichroic metasurface (d–f).

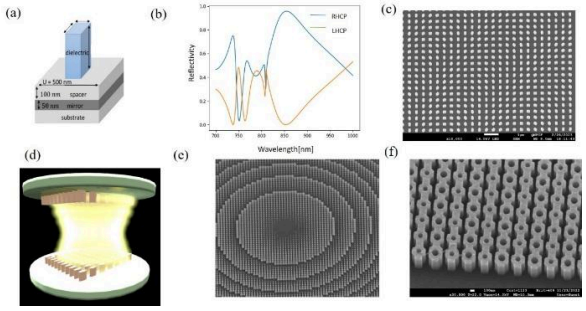

Figure 1 (a–c) depict a Pancharatnam–Berry phase reflecting metasurface made of PECVD-grown α-Si nanofins on a multilayer stack. Panels (d–f) bilayer polarization-dichroic metasurface, where one layer imparts the phase profile and the second—a dimerized HCG.

References

[1] Li, J, et al. "Strong optical confinement between nonperiodic flat dielectric gratings." Physical review letters, 106.19, 2011

[2] Liao, C, T. Hu, and D. Wang, "Optical fiber fabry-perot interferometer cavity fabricated by femtosecond laser micro-machining and fusion splicing for refractive index sensing," Optics express, vol. 20, no. 20, pp. 22813–22818, 2012.

[3] Khorasaninejad, M, W. T. Chen, R. C. Devlin, J. Oh, A. Y. Zhu, and F. Capasso, "Metalenses at visible wavelengths: Diffraction-limited focusing and subwavelength resolution imaging," Science, vol. 352, no. 6290, pp. 1190–1194, 2016.

[4] Thompson, C.V, "Solid-state dewetting of thin films," Annual Review of Materials Research, vol. 42, pp. 399–434, 2012.

[5] Overvig, AC., S. Shrestha, and N. Yu. "Dimerized high contrast gratings." *Nanophotonics* 7.6 (2018): 1157-1168.

Microscopic Hopfield Theory of Hyperbolic Phonon Polaritons in Layered Materials

Yu Zhang[1,*]
[1]Theoretical Division, Los Alamos National Laboratory, Los Alamos, NM, 87545, USA.
*Corresponding author: zhy@lanl.gov

***Abstract*—Hyperbolic phonon polaritons in biaxial van der Waals crystals (e.g., α-MoO_3) are extremely confined and anisotropic, yet usually modeled with fitted Lorentz permittivities. We present a gauge-consistent microscopic Hopfield theory linking DFPT lattice inputs to LO–TO splitting, dielectric response, slab dispersion, and twist-controlled inter-slab hybridization via Green-function coupling.**

I. Introduction

Polaritons—hybrid excitations of light and matter—enable extreme electromagnetic confinement and dispersion engineering via material resonances. In polar dielectrics, infrared-active optical phonons couple strongly to mid-IR fields, forming phonon polaritons with long lifetimes and strong near-field enhancement [1]. A particularly rich regime occurs when the dielectric response is *indefinite* (principal components of $\boldsymbol{\epsilon}(\omega)$ have opposite signs), producing hyperbolic isofrequency contours and highly directional energy flow. The biaxial van der Waals crystal α-MoO_3 hosts multiple hyperbolic Reststrahlen bands with pronounced in-plane anisotropy, making it a model platform for natural hyperbolic nanophotonics [2]. However, most existing descriptions rely on phenomenological Lorentz fits of $\epsilon_i(\omega)$, which mask the microscopic origins of oscillator strength, LO–TO splitting, and anisotropic screening and complicate extensions to multi-slab and twisted structures. This work develops a unified, gauge-consistent microscopic theory that connects *ab initio* inputs directly to macroscopic hyperbolic phonon polaritons (HPhPs) in bulk and confined geometries.

II. Methods

We construct a microscopic lattice-electrodynamics framework that bridges DFPT quantities (Born effective charges, $\boldsymbol{\epsilon}_\infty$, and phonon eigenvectors) to polariton eigenmodes. Starting from the harmonic phonon Hamiltonian, optical phonons are expressed in normal coordinates $\hat{Q}_{\mathbf{q}\nu}$, and the macroscopic polarization is written as a phonon-coordinate operator using *mode effective charges*:

$$\hat{P}_i(\mathbf{q}) = \sum_\nu Z_i^{(\nu\mathbf{q})} \hat{Q}_{\mathbf{q}\nu}, \tag{1}$$

where $Z_i^{(\nu\mathbf{q})}$ is obtained by projecting atomic Born charge tensors onto phonon eigenvectors, fixing oscillator strengths microscopically.

Long-range Coulomb interactions generate a nonanalytic correction to the dynamical matrix that produces LO–TO splitting in the $\mathbf{q}\to 0$ limit for biaxial screening:

$$D^{\mathrm{NA}}_{a\alpha,b\beta}(\mathbf{q}) = \frac{e^2}{\Omega} W_c(\mathbf{q}) \frac{\left(\mathbf{q}\cdot\mathbf{Z}^*_a\right)_\alpha \left(\mathbf{q}\cdot\mathbf{Z}^*_b\right)_\beta}{\sqrt{M_a M_b}}. \tag{2}$$

This explicitly shows that LO–TO splitting depends on propagation direction, anisotropic $\boldsymbol{\epsilon}_\infty$, and Born charges—key ingredients for hyperbolicity in biaxial crystals.

To couple phonons to photons in a gauge-consistent manner, we quantize the transverse electromagnetic field and use the multipolar Power–Zienau–Woolley (PZW) Hamiltonian, including the essential polarization self-energy term:

$$\hat{H}_{\mathrm{int}} = -\int d^3r\, \hat{\mathbf{P}}_\perp(\mathbf{r}) \cdot \hat{\mathbf{E}}_\perp(\mathbf{r}), \tag{3}$$

$$\hat{H}_{\mathrm{self}} = \frac{1}{2\epsilon_0} \int d^3r \left|\hat{\mathbf{P}}_\perp(\mathbf{r})\right|^2. \tag{4}$$

The resulting quadratic Hopfield model is diagonalized via a bosonic Bogoliubov transformation, yielding polariton eigenfrequencies and eigenmodes.

III. Results and Discussion

The theory delivers a unified microscopic explanation of hyperbolic phonon polaritons and enables predictive modeling beyond Lorentz fitting [3]: 1) Polariton eigenmodes from a gauge-consistent Hamiltonian: Including polarization self-energy ensures stability and consistency, and the Bogoliubov diagonalization yields polariton dispersions that match Maxwell-based approaches while retaining microscopic interpretability. 2) Twisted bi-slabs and controlled inter-slab hybridization: Interlayer coupling is derived from the dyadic Green function in a quasi-static limit, producing a coupled-mode splitting

$$\omega_\pm(\mathbf{q}) = \frac{\omega_1(\mathbf{q}) + \omega_2(\mathbf{q})}{2} \pm \sqrt{\left(\frac{\omega_1(\mathbf{q}) - \omega_2(\mathbf{q})}{2}\right)^2 + \kappa^2(\mathbf{q},\theta)}, \tag{5}$$

where $\kappa(\mathbf{q},\theta)$ encodes twist- and gap-dependent overlap of polarization fields and decays approximately as e^{-qg}. This provides a microscopic justification for effective block-matrix coupling models and enables predictive twist-engineered polaritonic band design.

IV. Conclusion

We develop a gauge-consistent microscopic Hopfield theory for biaxial hyperbolic phonon polaritons that directly connects DFPT quantities to polariton eigenmodes. Applied to α-MoO_3, the framework explains hyperbolic transport as a microscopic consequence of direction-dependent LO renormalization and resonant lattice polarization, and it predicts slab dispersion and thickness trends without phenomenological oscillator refitting beyond damping. By deriving inter-slab hybridization from the dyadic Green function, the approach further enables predictive modeling of twisted polaritonic heterostructures and lays a foundation for engineered hyperbolic and moiré-like phonon-polaritonic metamaterials.

Acknowledgments

We acknowledge support from the US DOE, Office of Science, Basic Energy Sciences, Chemical Sciences, Geosciences, and Biosciences Division under Triad National Security, LLC ("Triad") contract Grant 89233218CNA000001 (FWP: LANLECF7). This research used computational resources provided by the Institutional Computing (IC) Program and the Darwin testbed at Los Alamos National Laboratory (LANL), which is funded by the Computational Systems and Software Environments subprogram of LANL's Advanced Simulation and Computing program. LANL is operated by Triad National Security, LLC, for the National Nuclear Security Administration of the U.S. Department of Energy (Contract No. 89233218CNA000001).

References

[1] T. Low, A. Chaves, J. D. Caldwell, A. Kumar, N. X. Fang, P. Avouris, T. F. Heinz, F. Guinea, L. Martin-Moreno, and F. Koppens, *Nature Materials* 16, 182 (2017).
[2] M. Chen, X. Lin, T. H. Dinh, Z. Zheng, J. Shen, Q. Ma, et al., *Nature Materials*, 19, 1307 (2020).
[3] J. Williams, Y. Zhang; In preparation.

Photoelectron chiral dichroism from tailored light: symmetry and helicity

Ofer Neufeld*

[1]Technion – Israel Institute of Technology, Faculty of Chemistry, Haifa, Israel.
*Corresponding author: ofern@technion.ac.il

***Abstract*— Symmetry plays a key role in light-matter interactions, including in chiral systems. Still, a group theory for photoelectron chiral dichroism (PECD) has not been developed prior. Here I will present the first such theory, also leading to novel selection rules in PECD from tailored-light, and PECD geometries without helical driving.**

***Keywords*— chirality, PECD, ultrafast spectroscopy, optical chirality.**

Photoelectron chiral dichroism (PECD) is one of the most well-established approaches for studying gas-phase and ultrafast chirality. It provides huge chiral signals that arise from purely electric-dipolar interactions (contrarily to standard chiroptical schemes where magnetic-dipoar interactions play a role in chiral signal generation, leading to weak signals) [1] [2] [3]. Recently, PECD has been driven from polarization-tailored geometries in the strong-field regime, employing bichromatic lasers [4] [5]. The chiral signals were shown to persist even when both carrier waves were linearly-polarized, and comprised forward/backwards and up/down asymmetric spectra. Notably, it remains unclear why non-vanishing PECD can be obtained with linearly-polarized lasers (that do not carry angular momentum and have a vanishing time-average optical chirality). The fundamental origin of the PECD asymmetries are also largely unknown and have only been explained on an ad-hoc basis.

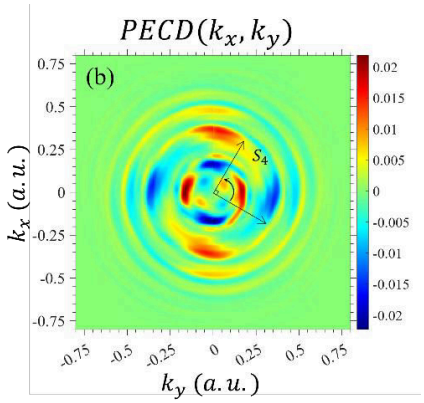

Fig. 1 Novel PECD selection rule that gives rise to 4-fold asymmetry in PECD due to a 4-fold improper rotational driving laser (comprised of three tailored laser colors).

In a related avenue, all PECD to date has been generated by helical laser beams with non-vanishing optical chirality [6]. In this mechanism the ionized photoelectron interacts with the chiral potential of the molecule left behind, and the helical laser field, as it is driven to the detector. This dual interaction permits strong chiral signals. However, chirality can also manifest in laser fields in a non-instantaneous manner [7], in which case there are no helical components in the drive on an instantaneous timescale. It remain unclear if such sources also drive a dichroic response (analytical work has proposed this to be possible for non-CEP stable longer pulses, but it has never been tested in experiments or numerically [8]).

Here we address these two issues directly. First, we develop a group theory for PECD capable of handling tailored laser fields with multiple frequency components [9]. From this theory we explain all known PECD selection rules (e.g. forwards/backwards or up/down asymmetries/symmetries), as well as predict novel selection rules in new geometries (see exemplary Fig. 1). All novel selection rules are numerically validated with *ab-initio* simulations.

Next, we directly simulate PECD driven by a train of linearly-polarized pulses, which is a non-helical light source (see Fig. 2). We show that this still leads to PECD signals that are as large as in the helical light case [10] (see Fig. 3), but the mechanism differs compared to the standard case and involves a chiral hole wave packet evolving in the molecular ensemble.

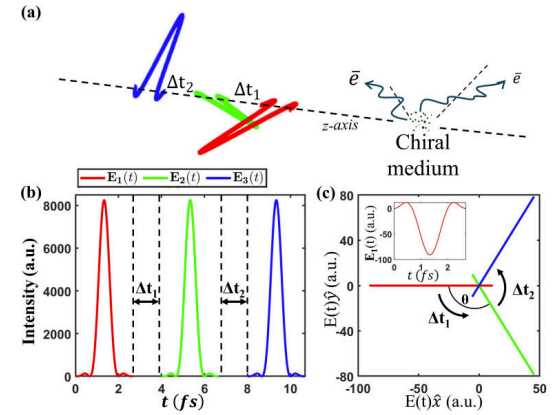

Fig. 2 PECD from non-helical light set-up. (a) pulse train comprised of three few-cycle linearly-polarized pulses, with a polarization axis rotating from pulse to pulse, drives PECD. (b) description of pulse train in time-domain. (c) description of pulse train in polarization space showing non-instantaneous chirality.

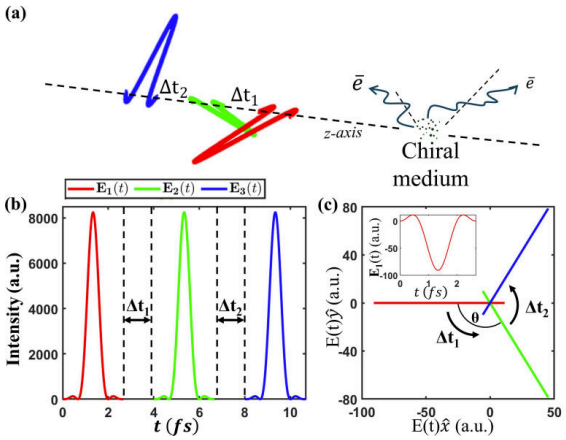

Fig. 2 PECD from non-helical light set-up. (a) pulse train comprised of three few-cycle linearly-polarized pulses, with a polarization axis rotating from pulse to pulse, drives PECD. (b) description of pulse train in time-domain. (c) description of pulse train in polarization space showing non-instantaneous chirality.

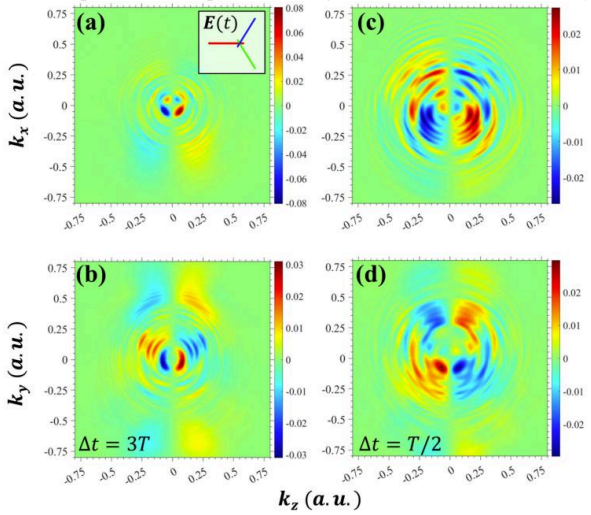

Fig. 3 PECD simulations calculated with the pulse train configuration in Fig. 2 for different inter-pulse delays (in units of T, the period of the carrier wave.

Overall, our work paves way for novel PECD geometries and analysis of PECD in unique tailored-light conditions, which could be utilized for ultrafast chirality spectroscopy.

REFERENCES

[1] D. Habibović, K. R. Hamilton, O. Neufeld, and L. Rego, Emerging tailored light sources for studying chirality and symmetry, Nat. Rev. Phys. (2024).

[2] D. Ayuso, A. F. Ordonez, and O. Smirnova, Ultrafast chirality: the road to efficient chiral measurements, Phys. Chem. Chem. Phys. **24**, 26962 (2022).

[3] O. Neufeld, M. E. Tzur, O. Kfir, A. Fleischer, and O. Cohen, Light's symmetry, asymmetry, and their role in nonlinear optics and ultrafast phenomena, ArXiv Prepr. ArXiv2503.19433 (2025).

[4] P. V Demekhin, A. N. Artemyev, A. Kastner, and T. Baumert, Photoelectron Circular Dichroism with Two Overlapping Laser Pulses of Carrier Frequencies ω and 2ω Linearly Polarized in Two Mutually Orthogonal Directions, Phys. Rev. Lett. **121**, 253201 (2018).

[5] S. Rozen et al., Controlling Subcycle Optical Chirality in the Photoionization of Chiral Molecules, Phys. Rev. X **9**, 031004 (2019).

[6] Y. Tang and A. E. Cohen, Optical chirality and its interaction with matter, Phys. Rev. Lett. **104**, 163901 (2010).

[7] O. Neufeld and O. Cohen, Optical Chirality in Nonlinear Optics: Application to High Harmonic Generation, Phys. Rev. Lett. **120**, 133206 (2018).

[8] A. F. Ordonez and O. Smirnova, Generalized perspective on chiral measurements without magnetic interactions, Phys. Rev. A **98**, 063428 (2018).

[9] O. Neufeld, Symmetries and selection rules in photoelectron chiral dichroism from tailored light, Proc. Natl. Acad. Sci. **122**, e2504816122 (2025).

[10] G. Bouskila, A. Fleischer, and O. Neufeld, Photoelectron chiral dichroism induced by lasers without helicity via chiral hole wave-packets, ArXiv Prepr. ArXiv2512.12412 (2025).

Evaluating Surface-Enhanced Chiroptical Spectroscopy on Nanostructured Aluminum Substrates in the Deep-UV

Björn M. Reinhard[1]

[1]Department of Chemistry and The Photonics Center, Boston University, Boston, Massachusetts, United States
*Corresponding author: bmr@bu.edu

***Abstract*— Scalable fabrication of aluminum nanostructures with tunable resonances in the UV provides opportunities for surface enhanced spectroscopies in which electronic transitions of molecular systems and plasmon resonances overlap. This presentation provides an overview of fabrication strategies and discusses advantages and challenges in applications for chiral molecular sensing.**

***Keywords*— nanomaterials, nanoplasmonics, nanofabrication, field-enhanced spectroscopy.**

I. Introduction

Nanostructured materials from gold and silver can provide plasmon resonances in the visible and infrared range of the electromagnetic spectrum and are widely used in sensing and surface-enhanced spectroscopy applications. The absorption lines of many molecular quantum emitters lie, however in the ultraviolet (UV) and thus outside of the range accessible with localized plasmon resonances of gold and silver. Aluminum (Al) nanostructures provide resonances in the UV and can thus extend the range for plasmon-enhanced interactions with molecular systems into a range where plasmon and molecular resonances overlap. Harnessing these interactions for the detection and characterization of chiral molecules is of great interest.

II. Methods

Our approach combines scalable fabrication of nano-structured Al surfaces with optical spectroscopy. Large areas of nanostructured Al are generated using nanosphere lithography. Choice of the NP size, etching of the NPs, and thickness of deposited Al provides control over the morphology of the array and allows for a systematic tuning of its spectral response. Alternatively, hole mask colloidal lithography was applied to generate discrete Al nanoparticles or small clusters of nanoparticles. This strategy was used to generate random arrays of Al NPs distributed over a large area. Choice of the NP size and shape as well as the aggregation state of the NPs facilitates tuning of the plasmon resonance. We chose fabrication strategies that yielded achiral plasmonic structures and arrays and then deposited chiral analyte molecules. Deep UV-Raman spectroscopy with excitation wavelengths at 266 nm and 227 nm was performed in a homebuilt microscope to characterize the substrates. Finally, circular dichroism (CD) spectra of the analyte molecules in the presence and absence of the Al nanostructures were obtained. The CD spectra were collected in a commercial CD spectrometer without adjustments.

III. Results and Discussion

Reflection measurements confirmed that Al substrates generated by scalable NP-based lithography sustain plasmon resonances throughout the deep UV down to 200 nm, the limit of our spectrometer. We also validated that the generated substrates provide electromagnetic hot-spots by Raman spectroscopy of test molecules performed at 227 and 266 nm. Although the optical response of the materials in the UV was generally broad, variation of the assembly conditions made it possible to achieve especially strong resonances at the excitation wavelengths.

The CD spectra of selected probe molecules with absorption band in the spectral range of the Al plasmons were measured and categorized. Overlap of electronic molecular resonances with plasmonic resonances resulted in an increase of the detected CD signal. The origin of the chiral CD signal enhancement through the achiral substrate are discussed and strategies for further improvements developed.

IV. Conclusion

We have implemented and tested scalable fabrication strategies for nanostructured Al substrates with plasmon resonances throughout the deep-UV. These substrates supported electromagnetic hot-spots in spectral ranges that overlap with the absorption bands of target molecules. The materials provide a rational platform to investigate resonant molecule – plasmon interactions and allows a systematic evaluation of their effect on chiroptical spectroscopy.

ACKNOWLEDGMENTS

The authors acknowledge the use of the Boston University Photonics Center shared facilities. This work was in part performed using the shared laboratories and instrumentations supported by the Boston University Photonics Center.

Nonreciprocal Neural Networks for Decoupled Bidirectional Computing via Magneto-Optical SSPP Transmission Lines

Xiaomeng Li[1,2], Enzong Wu[1,2], Hongsheng Chen[1,2], Zuojia Wang[1,2,*]

[1]International Joint Innovation Center, Zhejiang Key Laboratory of Intelligent Electromagnetic Control and Advanced Electronic Integration, Zhejiang University, China
[2]State Key Laboratory of Extreme Photonics and Instrumentation, College of Information Science and Electronic Engineering, Zhejiang University, China.
*Corresponding author: zuojiawang@zju.edu.cn

***Abstract*—We demonstrate nonreciprocal neural networks inspired by biological directionality, to achieve compact decoupled bidirectional computing. Enhanced magneto-optical effects are leveraged in TE mode spoof surface plasmon polariton (SSPP) transmission lines, providing independent forward global perception and backward localized response. We also discuss how this nonreciprocal framework enables miniaturization and reconfiguration.**

To address the burgeoning demand for computing capacity in artificial intelligence, optical neural networks have been explored for their ultrafast speed and high parallelism. However, most existing networks are restricted by Lorentz reciprocity, where forward and backward propagations are intrinsically coupled [1]. This constraint leaves the backward pathway largely unexplored and poses a critical challenge for integrated perception-response systems, which typically require bulky directional modules to prevent signal interference. Biological neural systems, which inherently exhibit nonreciprocity, offer a compelling model to address this limitation.

Here, to introduce nonreciprocity into neural networks, we first establish the physical foundation: a TE-polarized SSPP nonreciprocal phase shifter based on the transverse Faraday effect. Unlike conventional devices based on TM modes, which require scarce gyroelectric materials, our design capitalizes on the inherent magnetic transverse spin of TE surface plasmons. We show that this transverse spin enables robust resonant coupling with the Larmor precession in gyromagnetic materials. To realize this, we synthesize the required TE mode through a meticulously designed meandering SSPP structure. Our experimental results demonstrate a substantial differential phase shift of 114.07° at 10 GHz, marking a 52-fold improvement in nonreciprocal performance over conventional microstrip lines. This confirms the efficacy of the 'spin-precession' coupling mechanism for compact nonreciprocal integrated circuits.

Building upon this high-performance nonreciprocal unit, we introduce a nonreciprocal neural network to realize compact, decoupled bidirectional computing. By leveraging enhanced magneto-optical effects in SSPP transmission lines, we successfully decouple the forward and backward paths [2]. This architecture effectively emulates the unidirectional transmission of biological networks, achieving independent control within a single structure. We demonstrate broadband bidirectional decoupled image processing with tailored operator configurations: the forward propagation performs regional integration to emulate global perception, while the backward propagation executes edge detection to simulate localized response. The bidirectional functionality within a single structure eliminates the need for external directional modules and reduces the complexity of the system. As a result, this simplified design can improve resource efficiency and integration density, especially for large-scale, densely connected networks. Furthermore, matrix-solving operations can be facilitated by incorporating feedback waveguides for desired recursion paths.

Finally, extending the nonreciprocal framework, we realize physical path compression within symmetric or chiral topological structures. By exploiting the splitting of forward and backward propagation constants induced by symmetry breaking, signal pathways are effectively "folded" within a compact footprint, enabling significant miniaturization. We demonstrate that by rotating the external bias state, the system can be dynamically reconfigured to execute diverse signal processing functions.

***Keywords*— metamaterials, magneto-optical effect, spoof surface plasmon polariton, nonreciprocal.**

REFERENCES

[1] Z. Wang, H. Yang, and L. Jing, "Nonreciprocal coupling induced chiral absorption," Journal of Optics, vol. 25, no. 7, 074002, 2023.
[2] X. Li, H. Yang, E. Wu, X. Yao, Y. Li, F. Gao, H. Chen, and Z. Wang, "Nonreciprocal surface plasmonic neural network for decoupled bidirectional analogue computing," Nature Communications, vol. 16, 7703, 2025.

Spin relaxation near surfaces via gyromagnetic coupling to Rayleigh vorticity baths

Mamoru Matsuo[1], Hiroshi Funaki[2], Ryotaro Sano[3], Ai Yamakage[4], Tatsuhiko Ikeda[5]

[1]University of Chinese Academy of Sciences), China
[2]Keio University, Japan
[3]The University of Tokyo, Japan
[4]Nagoya University, Japan
[5]ZEN University, Japan
*Corresponding author: gmtsuo@gmail.com

***Abstract*— We study near-surface spin relaxation due to coupling to Rayleigh-wave vorticity set by elastic boundary conditions at a traction-free surface. This gyromagnetic spin-vorticity coupling provides a geometry-dependent channel for low-temperature longitudinal relaxation, distinct from thermally activated two-phonon processes, and shapes transverse coherence through a super-Ohmic vorticity spectrum.**

***Keywords*— 2D materials, spin relaxation, gyromagnetic effect.**

SYMPOSIUM 5

Phononics and acoustic metamaterials

43 contributions · pp. 607–674

Resonator Cascades in a 3D Lattice as a Broadband Acoustic Metamaterial

Frieder Lucklum

Centre for Acoustic-Mechanical Microsystems (CAMM), DTU Electrical and Photonics Engineering, Technical University of Denmark (DTU), 2800 Kgs. Lyngby, Denmark
Corresponding author: fluc@dtu.dk

***Abstract*— Cascading coupled resonators allows multiple frequency splitting, a common concept in electronic filters. Translating this idea to acoustic metamaterials leads to connected Helmholtz resonators in a 3D lattice, similar to elastic 3D mass-spring metamaterials. Analytical, numerical, and early experimental results demonstrate broadband sound absorption and sound insulation potential.**

***Keywords*— acoustic metamaterial, Helmholtz resonator, resonator cascade, 3D lattice, sound absorption, sound insulation.**

I. Introduction

The concept of coupled resonators is well understood in physics, e.g. for electrical or mechanical systems, leading to splitting of the original resonance into lower and higher frequencies. Cascading coupled resonators repeats this frequency split into more separate resonances and lowers the first common resonance further below the original frequency. Applying this concept to acoustic resonators offers a new design tool to optimize sound absorption and sound insulation.

Helmholtz resonators (HRs) in metamaterials allow fine tuning of resonance frequency and absorption [1]. To overcome their narrow-band limitation, one popular approach is to combine multiple differently tuned resonators that overlap their frequency response [2, 3]. In this approach, individually tuned resonators are typically treated as separate elements (Fig. 1.a). Conversely, resonance coupling has been demonstrated by near field interference of adjacent resonators [4-6]. Directly connected resonator cascades only rarely and very recently appear in literature [7-10]. In all cases, angle dependence is often ignored but this diminishes the suitability for random or diffuse wave incidence, unless explicitly optimized [3]. Multidimensional resonator cascades appear to be unexplored. This work proposes directly connecting HRs in 3D cascades, as illustrated for a cubic lattice in Fig. 1.b, similar to elastic 3D mass-spring metamaterials [11].

II. Concept and Methods

Two coupled single degree-of-freedom (DOF) resonators form a 2-DOF system with two resonances and one anti-resonance. In acoustic systems, connecting the neck (mass) of a Helmholtz resonator to another cavity (spring) effectively cascades a second acoustic mass-spring resonator to the first.

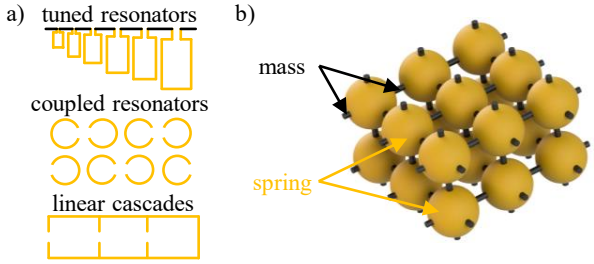

Fig. 1: a) Typical broadband approaches using multiple differently tuned resonators, coupled resonators, or simple connected cascades; b) proposed cubic lattice of connected Helmholtz resonator cascades.

The acoustic 2-DOF system exhibits two local impedance minima and one local maximum: coupled resonances below and above the original resonance frequency and an anti-resonance in between (Fig. 2). The lower resonance appears when the connected resonators are in-phase, the higher resonance when out-of-phase (see insets). The connected resonators form a resonance cascade, where the in-phase resonance does not correspond to a single resonator with twice the mass and compliance, and the out-of-phase resonance is not at twice the frequency. The neck of every layer, acting as acoustic mass, connects to the cavity of the prior layer, acting as acoustic compliance. Dampers represent primarily viscous losses in the neck due to high tangential velocities, and primarily thermal losses in the cavity. The acoustic input impedance Z_{in} at the surface cascades with the impedance of the next layer $Z_{\mathrm{i-1}}$ and the number of layers, i.e. $Z_{\mathrm{in}} = Z_{\mathrm{neck}} + Z_{\mathrm{cav}} || Z_{\mathrm{i-1}}$.

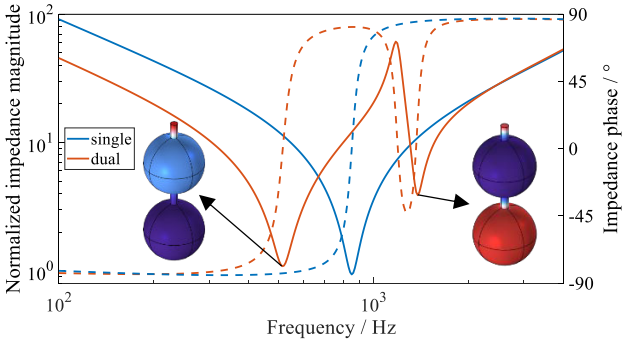

Fig. 2: Normalized input impedance of a single HR (blue) and two connected resonators (red) that show two resonances (in-phase and out-of-phase pressure, see insets) and one anti-resonance.

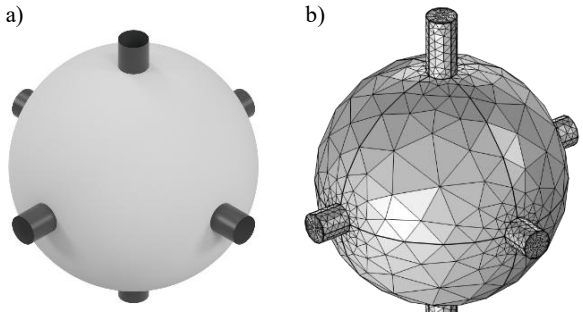

Fig. 3: a) Basic simple cubic unit cell with necks (black) of adjacent resonators connecting to cavity (gray); b) exemplary finite element boundary layer mesh for full Navier-Stokes solution.

The main studies utilized numerical finite element models built in *COMSOL Multiphysics 6.4*. Multiple layers of unit cells (Fig. 3.a) are modelled in the surface-normal direction. The infinite half-space in front (for absorption studies) and the back (for transmission) of the structure is modelled through periodic plane-wave port conditions. Lateral periodicity is achieved through Floquet boundary conditions. The boundary layer impedance (BLI) condition applies viscous and thermal losses to all solid surfaces. Reference studies with the fully linearized Navier-Stokes solution indicate very good agreement for the dimensions investigated here. The mesh for the latter is visualized in Fig. 3.b to illustrate the boundary layer thickness in the frequency range of interest compared to the neck width. The main mesh size is limited to a fifth of the wavelength in air at the highest frequency of interest. Additionally, eigen-frequency study is conducted on the unit cell to determine the dispersion relation.

III. Results and Discussion

Results are shown for a unit cell of spherical cavity and cylindrical neck with a lattice constant of 20 mm, neck diameter of 2 mm, and sphere diameter of 16 mm. These arbitrary dimensions target a single HR frequency around 1 kHz and are not optimized for any specific performance or bandwidth.

Sound absorption: A periodic 3D lattice of identical HRs is connected to a surface. Each coupled resonance leads to a maximum in absorption due to a maximum in velocity through the neck and therefore a maximum of viscous boundary losses. Figure 4 shows the absorption coefficient for a single resonator (black) as well as a cascade of two, five, ten, and twenty layers.

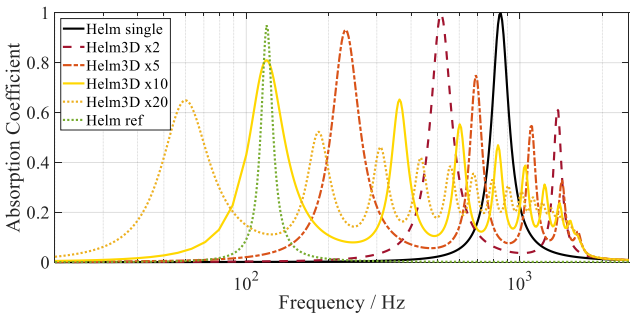

Fig. 4: Absorption coefficient for a metasurface consisting of different resonator cascades (orange colors) compared to original single Helmholtz resonator (black) and scaled single HR (green).

The first absorption peak continuously decreases in frequency for each layer, for ten layers (gold) from 850 Hz down to 120 Hz. For reference, the figure also includes a single resonator scaled to match the 10-layer cascade (dotted green). A similar first absorption peak appears, but the cascade offers larger peak bandwidths and higher order resonances.

Besides the broadband response due to multiple resonances, the cascade also displays a notably different incidence angle dependence. Figure 5 illustrates the frequency response of the single, scaled Helmholtz resonator (green) at normal incidence and near-grazing incidence in addition to a generic porous material layer (blue). In both cases, the absorption coefficient decreases drastically towards grazing incidence. On the contrary, the 10-layer cascade (gold) achieves maximum absorption around 80° incidence for multiple resonance peaks. The higher order resonances are more strongly dependent on the incidence angle. Notably, cascading does not have to extend into the depth of the surface but utilize lateral or coiling arrangements. In this case, the single HR, porous layer, and a spiraled 10-layer cascade all have similar total thickness. But only the Helmholtz resonators achieve high absorption as low as around 100 Hz and only the 10-layer cascade offers broadband absorption through multiple resonances from 100 Hz to 1.5 kHz, especially at near-grazing incidence.

Combining different cascades by connecting them to the same surface results in a similar effect as combining differently tuned single resonators. The different individual absorption peaks add up to a broadband and wide-angle absorption envelope. Considering the examples in Fig. 4 and starting with a 20-layer cascade, such an absorption envelope would extend from 50 Hz to 1.7 kHz. On top of the cascading illustrated here, each cascade and each individual resonator could also be optimized to target a specific overall absorption profile.

For validation, round cylindrical sample cascades were 3D-printed (*Epsilon W27*, BCN3D, Spain) and measured in an impedance tube with 100 mm diameter and a valid frequency range from 50 – 2000 Hz (*AcoustiTube Type II*, Acoustic Engineering Dresden, Germany) following the two-microphone method of ISO 10534-2. The printed sample as illustrated in Fig. 6 is placed at the termination and sealed to avoid leakage effects. Through the measurement of direct and flipped transfer functions, the complex reflection coefficient and subsequently the surface impedance and absorption coefficient are determined. The experimental results are in good agreement to a finite element model adapted to the actual printed dimensions.

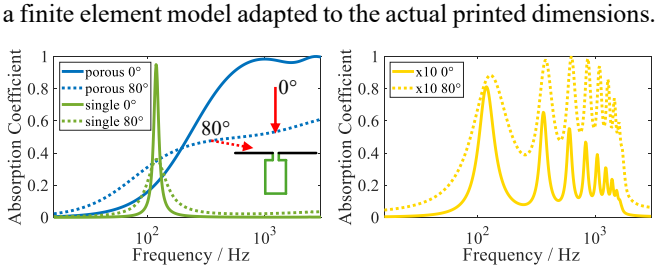

Fig. 5: Dependence of absorption on incidence angle for porous absorber and single Helmholtz resonator (left), as well as 10-layer cascade (right), all with similar total thickness around 10 cm.

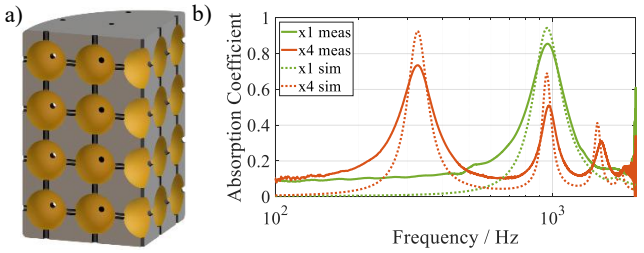

Fig. 6: a) Rendered quarter-cut of 3D-printed cascade (inverse of HR lattice with gold indicating cavities and black for necks); b) measured and simulated absorption curves for single HR and 4-layer cascade.

Sound insulation: Connecting the 3D lattice to the other side of a metamaterial slab also forms an insulator that combines the effects of a sonic or phononic crystal with local resonances. This is visualized in the full dispersion diagram shown in Fig. 7.a. The low frequency limit is determined by local resonances, including the fundamental Helmholtz resonances. Bragg scattering results in a complete band gap centered around half-wavelength in respect to the lattice constant, here at 8.6 kHz (wavelength in air 40 mm), while for the normal incidence ΓX direction the local resonances extend the gap down to 1/10th of the wavelength at 1.7 kHz (wavelength 200 mm). Further gaps form at higher frequencies (second gap at 15 – 21 kHz).

Within these gaps the transmission loss is extremely high, as high as 160 dB for a 4-layer cascade (Fig. 7.b). For comparison, a perforated plate (MPP) with the same hole dimensions as the neck of the HR and the same lattice constant and thickness offers no band gap and only limited transmission loss. The periodic pattern in the MPP response corresponds to a Fabry-Perot resonator (half-wavelength resonances starting at 2 kHz in the individual tubes). At these resonances, transmission loss is decreased but absorption increased.

Lastly, the angle dependence of power reflection, transmission, and absorption coefficients is illustrated in Fig. 8 for normal incidence and near-grazing incidence. Prior to the band gap opening frequency, transmission and absorption is increased at the cascaded resonances, with higher values for 80° incidence. Inside the first band gap, absorption also increases for grazing incidence, while transmission stays effectively zero. Transmission loss at 80° incidence decreases by approximately 10 – 15 dB, which in the case of the MPP results in up to 20% transmission at the Fabry-Perot resonance peaks.

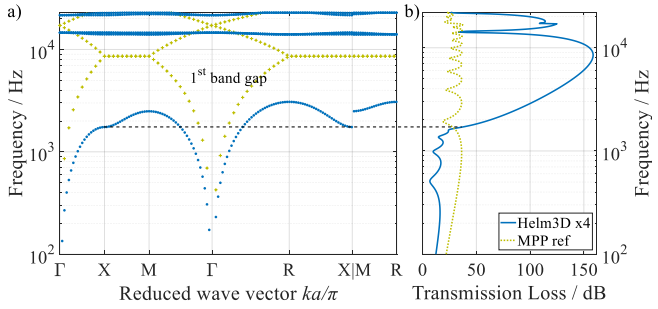

Fig. 7: a) Dispersion diagram for 3D HR unit cell (blue) with first band gap from 3 – 14 kHz (1.7 – 14 kHz for normal incidence ΓX) compared to perforated plate (beige); b) transmission loss through 4-layer cascade (blue) compared to similar perforated plate (beige).

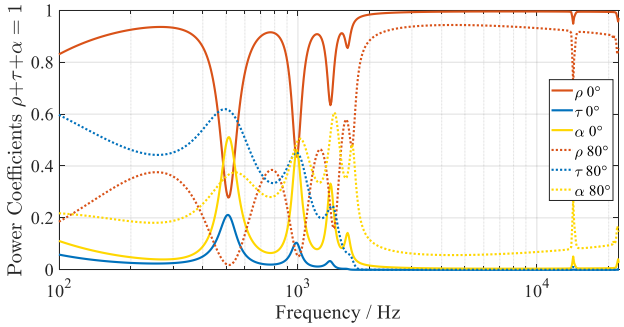

Fig. 8: Angle dependence of power reflection (ρ, red), transmission (τ, blue), and absorption (α, gold) coefficients through 4-layer 3D cascade at Helmholtz resonances (<2 kHz) and inside band gap.

IV. Conclusion

Cascading connected acoustic resonators in a metamaterial lattice leads to frequency splitting into multiple resonances with high absorption. Studies also show superior incidence angle dependence for the 3D cascades. Utilizing the coupled lattice as an insulation panel yields wide band gaps with high transmission loss superior to comparable perforated plates. Initial impedance tube experiments validate this novel conceptual design approach. In future work, the configuration and 3D lattice connections of each resonator can be optimized to achieve a desired sound absorption and sound insulation.

References

[1] C. Lagarrigue, J.-P. Groby, V. Tournat, O. Dazel, and O. Umnova, "Absorption of sound by porous layers with embedded periodic arrays of resonant inclusions," J. Acoustical Society of America 134 (2013) 4670–4680. doi: 10.1121/1.4824843

[2] N. Jiménez, V. Romero-García, V. Pagneux, and J.-P. Groby, "Rainbow-trapping absorbers: Broadband, perfect and asymmetric sound absorption by subwavelength panels for transmission problems," Scientific Reports 7 (2017) 13595. doi: 10.1038/s41598-017-13706-4

[3] D. M. Garza-Agudelo, V. Cutanda Henriquez, C.-H. Jeong, P. R. Andersen, M. Ibarias, J. Sanchez-Dehesa, and F. Lucklum, "Metasurfaces for sound absorption over a broad range of wave incidence angle," Applied Acoustics 220 (2024). doi: 10.1016/j.apacoust.2024.109965

[4] M. Krasikova *et al.* "Broadband noise-insulating periodic structures made of coupled Helmholtz resonators," APL Materials 12 (2024) 011115. doi: 10.1063/5.0175167

[5] R. Sabat, E. Cochin, M. Kalderon, G. Lévêque, I. Antoniadis, B. Djafari-Rouhani, and Y. Pennec, "Low frequency sound isolation by a metasurface of Helmholtz ping-pong ball resonators," J. Applied Physics 134 (2023). doi: 10.1063/5.0160267

[6] J. Kim, Y. Shim, and W. Jeon, "Tunable acoustic metasurface for low-frequency broadband absorption via asymmetric adjustable apertures," Applied Acoustics 246 (2026). doi: 10.1016/j.apacoust.2026.111237

[7] C. Cai and C. Ming Mak, "Acoustic performance of different Helmholtz resonator array configurations", Applied Acoustics 130 (2018). doi: 10.1016/j.apacoust.2017.09.026

[8] C. R. Liu, J. H. Wu, X. Chen, and F. Ma, "A thin low-frequency broadband metasurface with multi-order sound absorption," J. Physics D: Applied Physics 52 (2019). doi: 10.1088/1361-6463/aafaa3

[9] E. Choi and W. Jeon, "Near-perfect sound absorption using hybrid resonance between subwavelength Helmholtz resonators with non-uniformly partitioned cavities", Scientific Reports 14 (2024). doi: 10.1038/s41598-024-53595-y

[10] X.-L. Gai, X.-H. Li, X.-W. Guan, T. Xing, Z.-N. Cai, and W.-C. Hu, "Study on Acoustic Properties of Helmholtz-Type Honeycomb Sandwich Acoustic Metamaterials", Materials 18 (2025). doi: 10.3390/ma18071600

[11] F. Lucklum and M. J. Vellekoop, "Bandgap engineering of three-dimensional phononic crystals in a simple cubic lattice," Applied Physics Letters 113 (2018) 201902. doi: 10.1063/1.5049663

Practical Design of Helmholtz Resonators Considering Geometry and Acoustic Losses

Vicente Cutanda Henriquez*, Frieder lucklum

Centre for Acoustic-Mechanical Microsystems (CAMM), Department of Electrical and Photonics Engineering, Technical University of Denmark, Kgs. Lyngby, Denmark

*Corresponding author: vcuhe@dtu.dk

***Abstract*—Helmholtz resonators (HRs) are widely used as a means to achieve sub-wavelength performance in acoustic metamaterials. HRs contain compliance, mass and loss elements. The balance of the three determines resonance frequency, bandwidth and absorption. We discuss how to implement HRs for better control, robustness and performance.**

***Keywords*— Helmholtz Resonator, Acoustic Metamaterials, Viscothermal Losses.**

I. Introduction

Helmholtz resonators are based on the interplay of two fluid-filled elements: a cavity and a neck. A third element is the acoustic loss in the neck which can be assumed to be dominated by the effect of fluid viscosity. A balance of the three can provide a resonance at a given frequency with high absorption of sound. HRs resonate at frequencies corresponding to wavelengths larger than their size, making them an ideal choice for subwavelength metamaterials [1], [2].

The design of a HR for perfect absorption and wide bandwidth requires a given set of mass, compliance and resistance, which correspond to the neck, the cavity, and the acoustic losses. However, the three parameters are not independent. When the neck mass is modified, viscous losses in the neck change in a non-obvious way that depends on how its geometry is implemented [3]. Viscous losses mainly take place within a thin layer over the boundaries, with a thickness that increases as the frequency decreases [4], [5]. As the boundary layers fill the neck, losses increase, but only if the wave can propagate. Such behavior can be predicted through approximate or numerical models [2], [6]. In addition to the above, the practical construction of HRs for metamaterials is subject to fabrication tolerances. Fabrication can become cumbersome and expensive, and the result unsatisfactory if the HR is sensitive to tolerances.

This communication revises the issues associated with practical design and implementation of HRs as used in metamaterials. The goal is making the best choices for achieving good performance, manufacturability, robust geometrical tolerance and the possibility of tuning.

II. Methods and Discussion

Different HR configurations will be illustrated using a combination of lumped element models, transfer matrix method, numerical simulations and measurements. We analyze several neck geometries: i) single cylindrical tube, ii) multiple tubes or perforations, and iii) slits in different configurations.

Theory predicts that, as necks or slits get narrower, viscous and thermal boundary layers eventually merge [7]. Propagation of waves becomes heavily hindered by, mostly viscous, losses. Wide necks, on the other hand, allow propagation but losses decrease as the width becomes much larger than the boundary layers. The frequency has an inverse effect, as the boundary layer thicknesses decrease with frequency. Note that we are not considering the thermal losses in our analysis, which can be relevant for some cavity geometries at low frequencies. The choice of neck geometry controls how the viscous losses change as the acoustic mass is varied. For each neck configuration and dimensions, there is a frequency region where losses are maximized while propagation is still possible. Designing a HR with perfect or high absorption, and, at the same time, a wide bandwidth, must consider all the above factors.

III. Conclusion

We give an overview of the design choices available to the metamaterial designer and how the different geometries of HRs influence the robustness, performance and manufacturability. To this end, we study in detail the effect viscous losses for different neck geometries.

References

[1] Jiménez, N., Romero-García, V., Pagneux, V., Groby, J. P. (2017). "Rainbow-trapping absorbers: Broadband, perfect and asymmetric sound absorption by subwavelength panels for transmission problems". *Scientific Reports*, 7(1), 13595. https://doi.org/10.1038/s41598-017-13706-4

[2] Kim, J., Shim, Y., Jeon, W. (2026). "Tunable acoustic metasurface for low-frequency broadband absorption via asymmetric adjustable apertures". *Applied Acoustics*, 246, 111237. https://doi.org/10.1016/j.apacoust.2026.111237

[3] Andersen, P. R., Cutanda Henriquez, V., Aage, N. (2022). "On the validity of numerical models for viscothermal losses in structural optimization for micro-acoustics". *Journal of Sound and Vibration*, 547, 117455. https://doi.org/10.1016/j.jsv.2022.117455

[4] Morse, P. M., Ingard, K. U. (1968). "Theoretical acoustics". *McGraw-Hill*.

[5] Pierce, A. D. (2019). "Acoustics: An Introduction to Its Physical Principles and Applications, Third Edition". *Springer International Publishing*. https://doi.org/10.1007/978-3-030-11214-1

[6] Brandão, R., Schnitzer, O. (2020). "Asymptotic modeling of Helmholtz resonators including thermoviscous effects". *Wave Motion*, 97, 102583. https://doi.org/10.1016/j.wavemoti.2020.102583

[7] Bruneau, M. (2010). "Fundamentals of Acoustics". *Wiley-ISTE*. https://doi.org/10.1002/9780470612439

Transmission enhancement through a barrier induced by global and local mirror symmetries in periodic waveguides

Elie Salemeh*, Simon Félix , Vincent Pagneux

Laboratoire d'Acoustique de l'Université du Mans (LAUM),
UMR 6613, Institut d'Acoustique - Graduate School (IA-GS),
CNRS, Le Mans Université, France
*Corresponding author: elie.salemeh@univ-lemans.fr

***Abstract*—We show a broadband enhancement of transmission through an opaque barrier placed at the center of a symmetric periodic waveguide. This enhancement is sensitive to subwavelength barrier displacements and, for symmetric unit cells, recurs at half-period shifts due to local symmetries.**

***Keywords*— periodic waveguides, local symmetries, transmission enhancement.**

Multiple-wave interference in complex media can lead to striking transport phenomena when the scattering region has spatial symmetries. A notable example is the enhancement of transmission through an opaque barrier placed at the center of a mirror-symmetric complex waveguide, i.e., at the global symmetry center. In such a configuration, the transmission of the complex medium can be significantly larger than that of the barrier alone. This symmetry-induced transmission enhancement has been studied in disordered diffusive waveguides [1]–[6] and has also been reported in quantum dots [7], [8]. In this work, we investigate symmetry-induced transmission enhancement in periodic waveguides. We show that it also occurs when the barrier is placed at the symmetry center of a symmetric periodic waveguide (see Fig. 1).

Fig. 1. Enhanced transmission when a barrier is placed at the center of a symmetric periodic waveguide. (a) Opaque barrier in a uniform waveguide. (b) Opaque barrier at the center of a periodic waveguide. (c) Opaque barrier at the center of a symmetric periodic waveguide.

Unlike in disordered systems, where transmission tends to vanish due to localization, the enhancement in periodic structures persists even for long structures. We also show that, as in the disordered case, the transmission enhancement is sensitive to the barrier position. A subwavelength shift of the barrier from the symmetry center leads to a drop in transmission enhancement. For periodic structures composed of symmetric unit cells, the enhancement recurs when the barrier is shifted by half a period due to local symmetries.

References

[1] É. Chéron, S. Félix, and V. Pagneux, "Broadband-enhanced transmission through symmetric diffusive slabs," *Phys. Rev. Lett.*, vol. 122, no. 12, p. 125501, 2019.
[2] É. Chéron, S. Félix, and V. Pagneux, "Broadband subwavelength sensitivity to symmetry defects of disordered slabs," *Phys. Rev. B*, vol. 102, no. 13, p. 134201, 2020.
[3] É. Chéron, S. Félix, and V. Pagneux, "Sensitivity to losses and defects of the symmetry-induced transmission enhancement through diffusive slabs," *Sci. Rep.*, vol. 10, no. 1, p. 16635, 2020.
[4] M. Davy, C. Ferise, É. Chéron, S. Félix, and V. Pagneux, "Experimental evidence of enhanced broadband transmission in disordered systems with mirror symmetry," *Appl. Phys. Lett.*, vol. 119, no. 14, 2021.
[5] L. Borcea and J. Garnier, "Enhanced wave transmission in random media with mirror symmetry," *Proc. R. Soc. A*, vol. 480, no. 2292, 2024.
[6] A. O. Flegontov and D. B. Rogozkin, "Symmetry-induced enhancement of transmission through a disordered system," *Phys. Rev. B*, vol. 111, no. 17, p. 174205, 2025.
[7] R. S. Whitney, P. Marconcini, and M. Macucci, "Huge conductance peak caused by symmetry in double quantum dots," *Phys. Rev. Lett.*, vol. 102, no. 18, p. 186802, 2009.
[8] M. Totaro, P. Marconcini, D. Logoteta, M. Macucci, and R. S. Whitney, "Effect of imperfections on the tunneling enhancement phenomenon in symmetric double quantum dots," *J. Appl. Phys.*, vol. 107, no. 4, 2010.

Ultrafast Electronic and Acoustic Dynamics in Nanocrystalline Silicon

Tânia M. Ribeiro[1,*], Tiago E. C. Magalhães[1], Houssem Rezgui[1], Gloria Conte[1], Oili Ylivaara[2], Jouni Ahopelto[2], Clivia M. Sotomayor-Torres[1]

[1]INL - International Iberian Nanotechnology Laboratory, Av. Mestre José Veiga s/n, 4715-330, Braga, Portugal
[2]VTT Technical Research Centre of Finland Ltd, P.O. Box 1000, FI-02044 VTT, Espoo, Finland
*Corresponding author: tania.ribeiro@inl.int

***Abstract*—In this work, we report the ultrafast electronic and acoustic dynamics of nanocrystalline silicon (nc-Si) thin films and membranes, investigating how structural and morphological changes impact phonon lifetimes.**

***Keywords*— gigahertz acoustic waves, nanocrystalline silicon, phonon lifetime, photoacoustics, silicon membranes, ultrafast spectroscopy**

I. Introduction

Nanocrystalline materials provide a scalable and cost-effective alternative to single-crystal counterparts, showing advantages among several technological applications [1]. In particular, nanocrystalline silicon (nc-Si) is a versatile material for high-frequency resonators, where controlling the sample morphology enables the tailoring of mechanical damping [1], [2]. Ultrafast pump-probe spectroscopy measurements have contributed significantly to the understanding of phonon dynamics in nanoscale systems [3]. Studying these temporal oscillations is of fundamental importance, as their decay rates provide insights into phonon lifetimes and energy dissipation mechanisms. Previous pump-probe studies on single-crystal silicon membranes (c-Si) have been reported [4], [5], [6], where thickness-dependent acoustic phonon frequencies and lifetimes were measured, ranging from several nanoseconds to a few picoseconds. Our work extends this investigation to nc-Si membranes and thin films. We observe that the introduction of grains, grain boundaries, random grain orientations, and degree of crystallinity has an impact on phonon dephasing time compared to c-Si.

II. Methods

The nc-Si samples were synthesized by low pressure chemical vapor deposition (LPCVD) with different annealing and deposition temperatures. To investigate the impact of morphology on electronic dynamics, acoustic modes, and lifetimes, ultrafast pump-probe measurements were performed using the asynchronous optical sampling technique. The experiments were performed at room temperature in transmission and reflection modes. The system is driven by two Ti:Sapphire oscillators operating with a repetition rate of $\sim$ 1GHz and generating 50 fs duration pump and probe pulses. The central wavelength of the pump and probe beams is slightly shifted, corresponding to 760 nm and 830 nm, respectively. The spot size of both beams is $\sim 15\,\mu$m. The fluence of the pump is $\sim 50\,\mu$J/cm^2 and that of the probe is one order of magnitude lower.

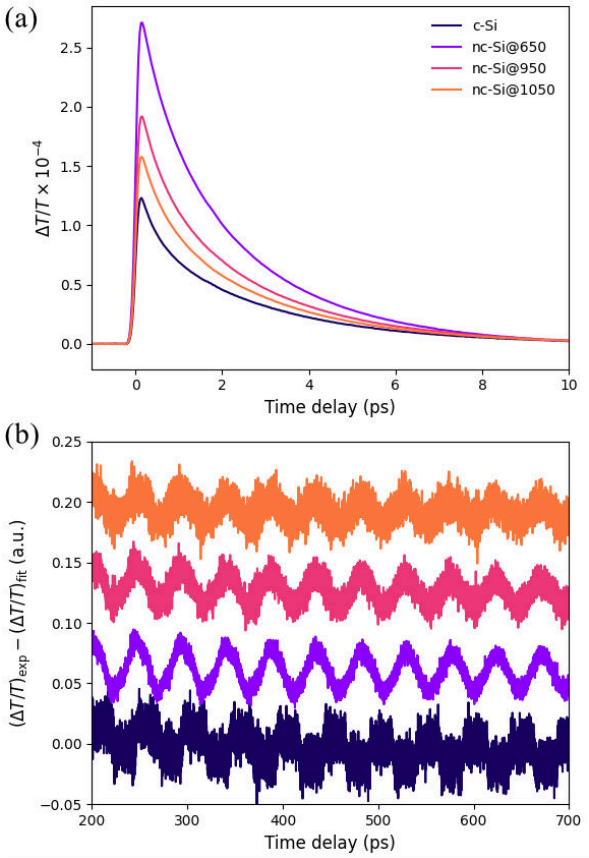

Fig. 1. Ultrafast pump-probe measurements in c-Si and nc-Si in transmision mode. (a) Time-resolved measurements within the first 10 picoseconds. (b) Time-resolved measurements with subtraction from the multiexponential fitting.

III. Results and Discussion

Ultrafast time-resolved measurements in transmission geometry are illustrated in Fig. 1, for c-Si and nc-Si membranes with different annealing temperatures (650°C, 950°C,

1050°C). A multiexponential fit was first applied to the experimental data and subsequently subtracted to isolate the underlying oscillations Fig. 1b. Then, a fast Fourier transform was performed, revealing the frequencies of the generated standing acoustic waves, which are given by [6]

$$f_n = \frac{n\, v_L}{2d}\,, \tag{1}$$

where n is an integer corresponding to the order of the mode, v_L is the longitudinal velocity, and d is the thickness. Values of around $20.5\,\mathrm{GHz}$ for c-Si and $21.3\,\mathrm{GHz}$ for nc-Si were obtained, indicating a slightly larger velocity in the nanocrystalline samples. The lifetimes of the modes for nc-Si are also observed to be smaller for nc-Si when compared to c-Si.

IV. Conclusion

We have investigated the coherent acoustic phonon dynamics of both c-Si and nc-Si samples by ultrafast pump-probe spectroscopy. We have generated and measured acoustic phonon modes, their frequency and lifetimes. From these measurements, we have retrieved the phonon velocity and lifetimes. We observe that although the phonon velocity is slightly larger for nc-Si samples when compared to that of c-Si, the phonon lifetimes are smaller. Moreover, a suppression of high acoustic modes ($n > 1$) is observed compared to c-Si.

Acknowledgments

T. M. Ribeiro, H. Rezgui, G.Conte, O. Ylivaara, J. Ahopelto and C. M. Sotomayor-Torres acknowledge funding from the MAGNIFIC project (HORIZON-CL4-2022-RESILIENCE-01, Grant Agreement No. 101091968). T. E. C. Magalhães and C. M. Sotomayor-Torres acknowledge the support from the project LEIT funded by the European Research Council, H2020 Grant, Agreement No. 885689.

References

[1] D. Navarro-Urrios, M. F. Colombano, G. Arregui, G. Madiot, A. Pitanti, A. Griol, T. Makkonen, J. Ahopelto, C. M. Sotomayor-Torres, and A. Martínez, "Room-Temperature Silicon Platform for GHz-Frequency Nanoelectro-Opto-Mechanical Systems," ACS Photonics, vol. 9, pp. 413–419, 2022.

[2] J. Maire, E. Chávez-Ángel, G. Arregui, M. F. Colombano, N. E. Capuj, A. Griol, A. Martínez, D. Navarro-Urrios, J. Ahopelto, and C. M. Sotomayor-Torres, "Thermal Properties of Nanocrystalline Silicon Nanobeams," Adv. Funct. Mater., vol. 32, pp. 2105767, 2021.

[3] R. C. Ng, A. El Sachat, F. Cespedes, M. Poblet, G. Madiot, J. Jaramillo-Fernandez, O. Florez, P. Xiao, M. Sledzinska, C. M. Sotomayor-Torres, and E. Chavez-Angel, "Excitation and detection of acoustic phonons in nanoscale systems," Nanoscale, vol. 14, pp. 13428-13451, 2022

[4] F. Hudert, A. Bruchhausen, D. Issenmann, O. Schecker, R. Waitz, A. Erbe, E. Scheer, T. Dekorsy, A. Mlayah, and J.-R. Huntzinger, "Confined longitudinal acoustic phonon modes in free-standing Si membranes coherently excited by femtosecond laser pulses," Phys. Rev. B, vol. 79, pp. 201307, 2009.

[5] A. Bruchhausen, R. Gebs, F. Hudert, D. Issenmann, G. Klatt, A. Bartels, O. Schecker, R. Waitz, A. Erbe, E. Scheer, J.-R. Huntzinger, A. Mlayah, and T. Dekorsy, "Subharmonic resonant optical excitation of confined acoustic modes in a free-standing semiconductor membrane at GHz frequencies with a high-repetition-rate femtosecond laser," Phys. Rev. Lett., vol. 106, pp. 077401, 2011.

[6] J. Cuffe, O. Ristow, E. Chávez, A. Shchepetov, P.-O. Chapuis, F. Alzina, M. Hettich, M. Prunnila, J. Ahopelto, T. Dekorsy, and C. M. Sotomayor Torres, "Lifetimes of confined acoustic phonons in ultrathin silicon membranes," Phys. Rev. Lett., vol. 110, pp. 095503, 2013

Optical probing of the vibrational and thermal dynamics of single metal nanoparticles

Nathan Berrit[1], Noelle Lascoux[1], Clément Panais[1], Sylvie Marguet[2], Natalia Del Fatti[1,3], Aurélien Crut[1,*]

[1] Université de Lyon, CNRS-UCBL, Institut Lumière Matière, 69622 Villeurbanne, France
[2] Université Paris-Saclay, CEA, CNRS, NIMBE, 91191 Gif-sur-Yvette, France
[3] Institut Universitaire de France (IUF), France
*Corresponding author: aurelien.crut@univ-lyon1.fr

***Abstract*— The resonant optical response of single plasmonic nanoparticles enables efficient probing of their vibrational and thermal dynamics. Ultrafast pump-probe experiments and numerical simulations reveal how these dynamics depend on nanodisk and substrate properties, and demonstrate that vibrations and cooling produce distinct spectral signatures, enabling their selective detection.**

***Keywords*— ultrafast dynamics, metal nanoparticles, single-particle time-resolved spectroscopy, vibrational modes.**

I. Introduction

The resonant optical response of plasmonic nanoparticles provides a powerful means for probing their electronic, vibrational and thermal dynamics via optical spectroscopy. Such experiments can now be performed at the single-particle level [1], providing access to far richer information than ensemble experiments, by revealing intrinsic dynamics otherwise obscured by averaging effects and by enabling a quantitative connection between these dynamics and the transient optical response they induce. This presentation reviews recent results on the vibrational and cooling dynamics of single gold nanodisks supported on various solid substrates.

II. Methods

Solutions of gold nanodisks with different average dimensions were produced via colloidal synthesis, allowing their deposition on a variety of solid substrates, including nanometrically thin membranes. Spatial modulation spectroscopy was employed to locate individual nanodisks on substrates and to measure their extinction spectra. The nanodisk ultrafast dynamics were probed using time-resolved single-particle pump-probe spectroscopy. These optical experiments were complemented by finite-element numerical simulations of the nanodisks' optical response, thermal and vibrational dynamics.

III. Results and Discussion

The results clarify how nanodisk dimensions and substrate properties influence the nanodisk vibrational and cooling dynamics. In particular, the cooling dynamics are significantly slowed on thin membranes compared to thick substrates, resulting in incomplete cooling between successive pump excitations [2]. While vibrational frequencies are primarily determined by nanodisk dimensions, the vibrational quality factors strongly depend on substrate properties, indicating that radiative effects play a major role in damping in our experiments. The transient responses associated with vibrations and cooling are markedly different: nanodisk temperature rise primarily manifests as a broadening of the surface plasmon resonance, whereas vibrations predominantly induce a spectral shift. This difference enables selective detection of these processes through appropriate tuning of the probe wavelength.

IV. Conclusion

This work highlights the strong influence of the environment on the ultrafast dynamics of nanoparticles following impulsive excitation, and demonstrates that distinct dynamical processes can be selectively probed using tunable light sources. Future goals include the detection of high-quality-factor vibrational modes and precise analysis of the transient optical response associated with vibrations.

Acknowledgments

This work was supported by the French National Research Agency (ANR) under the reference ANR-20-CE30-0016 (ULTRASINGLE project).

References

[1] A. Crut, P. Maioli, N. Del Fatti, and F. Vallée, "Optical absorption and scattering spectroscopies of single nano-objects" Chem. Soc. Rev., vol. 43, pp. 3921-3956, 2014.
[2] C. Panais, N. Lascoux, S. Marguet, P. Maioli, F. Banfi, F. Vallée, N. Del Fatti, and A. Crut, "Impact of supporting nanometric membranes on the thermo-optical dynamics of individual plasmonic nanodisks" Nanoscale, vol. 16, pp. 12071-12080, 2024.

Radiation Control in Fluid-Loaded Metamaterial Waveguides with Space and Time Modulation

Emanuele Riva[1,*], Alper Erturk[2]

[1]Department of Mechanical Engineering, Politecnico di Milano, Italy
[2] George W. Woodruff School of Mechanical Engineering, Georgia Institute of Technology, Georgia, US
*Corresponding author: emanuele.riva@polimi.it

***Abstract*—We investigate leaky-wave radiation in fluid-loaded elastic waveguides equipped with spatially and temporally modulated resonators. Periodic modulation induces controlled wavenumber or frequency shifts that activate radiating Floquet harmonics inside the acoustic sound cone. The resulting radiation angle is tunable and is herein engineered to steer or focus acoustic energy in the adjacent fluid. *Keywords*— leaky waves, acoustic metamaterials, space-time modulation, Floquet engineering.**

I. Introduction

When in contact with fluids, elastic waveguides naturally support leaky waves, such that guided energy continuously radiates into the surrounding medium under certain conditions. Although often regarded as a loss mechanism, leaky-wave radiation provides a powerful route toward directive emission and beam steering in submerged structures [1]. Achieving systematic and tunable control of this radiation, however, remains a central challenge. In this work, we demonstrate that spatiotemporal modulation of locally resonant metamaterials enables programmable control of leaky-wave emission. By periodically modulating the properties of resonators attached to a fluid-loaded beam, additional Floquet harmonics are generated through wavenumber or frequency conversion. These harmonics may enter the sound cone even when the underlying guided mode remains subsonic, thereby activating controllable radiation channels.

II. Dynamics of Spatially and Temporally Modulated Metamaterial

Under spatial modulation, the dispersion relation of the fluid-loaded beam with resonators becomes periodic along the wavenumber axis, and harmonic components are shifted by integer multiples of the imposed spatial periodicity, i.e. $\kappa + n\kappa_m$. Even when the fundamental guided mode remains outside the sound cone, a modulation-induced harmonic may enter it, thereby activating a radiative channel in the surrounding fluid. The resulting emission angle is directly governed by the modulation wavenumber and can be continuously tuned.

An analogous mechanism emerges under temporal modulation. In this case, frequency-shifted Floquet harmonics $\omega + n\omega_m$ are generated at fixed wavenumber [2], [3]. These harmonics also satisfy the fluid dispersion relation and radiate energy at angles controlled by the modulation frequency.

In both scenarios, the dispersion analysis, herein found through a bordered Newton-Raphson algorithm, captures the onset and direction of radiation in both configurations. The modulation parameters therefore act as programmable degrees of freedom that determine when and how guided energy is converted into leaky-wave radiation. Building on this principle, a smoothly varying spatial modulation is designed so that locally emitted wavevectors converge at a prescribed location, producing acoustic focusing in the fluid without external phased arrays or bulky gradient-index devices.

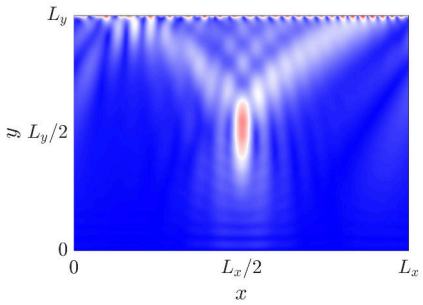

Fig. 1. RMS pressure field showing the leaky-wave-induced acoustic focusing.

III. Conclusion

Altogether, the proposed modulation strategy provides a unified way to regulate leaky-wave emission, offering direct control over radiation patterns and enabling acoustic focusing in submerged environments.

Acknowledgments

This work was supported by the European Research Council under the EU Horizon Europe programme (Grant No. 101219110, LUMEN).

References

[1] M. Mazzotti, E. Kohtanen, A. Erturk, and M. Ruzzene, "Optimizing transcranial ultrasound delivery at large incident angles by leveraging cranial leaky guided wave dispersion," *Ultrasonics*, vol. 128, Art. no. 106882, 2023.
[2] Y. Ye, C. Liu, A. Marzani, E. Riva, X. Wang, and A. Palermo, "Nonreciprocal scattering of elastic waves at time interfaces induced by spatiotemporal modulation," *Mechanical Systems and Signal Processing*, vol. 240, Art. no. 113346, 2025.
[3] C. Sugino, M. Ruzzene, and A. Erturk, "Nonreciprocal piezoelectric metamaterial framework and circuit strategies," *Physical Review B*, vol. 102, Art. no. 014304, 2020.

Coherent control of acoustic phonons in phononic waveguides

Chushuang Xiang[1,*], Edson Rafael Cardozo de Oliveira[1], Sathyan Sandeep[1], Konstantinos Papatryfonos[1], Martina Morassi[1], Luc Le Gratiet[1], Abdelmounaim Harouri[1], Isabelle Sagnes[1], Aristide Lemaitre[1], Omar Ortiz[1], Martin Esmann[1,2], and Norberto Daniel Lanzillotti-Kimura[1]

[1]Université Paris-Saclay, CNRS, Centre de Nanosciences et de Nanotechnologies, 91120 Palaiseau, France
[2]Carl von Ossietzky Universität Oldenburg, 26129 Oldenburg, Germany
*Corresponding author: chushuang.xiang@c2n.upsaclay.fr

***Abstract*—We demonstrate 20 GHz phonon transport over 20 µm in a phononic waveguide based on GaAs/AlAs multilayers. By introducing two excitation laser pulses to drive distinct phonon sources, we achieve coherent control of the propagating phonons through spatio-temporal interference.**

***Keywords*— phonon transport, coherent acoustic phonons, pump-probe spectroscopy, phononic waveguides**

Controlling high-frequency acoustic phonon propagation is essential for their use in storage, processing, and filtering applications [1-3]. Ultrafast optical excitation enables the generation and detection of coherent phonons in the gigahertz to terahertz range, while pump-probe techniques provide direct access to their frequency, amplitude, and phase. Phonon propagation can be controlled by engineering structures such as phononic crystals and microcavities.

In this work, we design a ridge waveguide based on a GaAs/AlAs superlattice. Vertically, it forms a Fabry-Perot cavity with a high quality factor, confining both photons and phonons within the spacer layer [4]. This simultaneous confinement enhances the efficiency of phonon generation and detection under ultrafast laser excitation. The planar cavity is then patterned into a ridge geometry, where the air-semiconductor sidewalls provide lateral confinement and guide phonon propagation along the waveguide.

Phonon dynamics are studied using time-resolved pump-probe measurements in two configurations. When the pump and probe beams are spatially superimposed, we observe 20 GHz phonons that decay exponentially in time, confirming the generation of propagating waves. When the beams are spatially separated, phonons can be detected at distances up to 20 µm at room temperature, demonstrating their transport in the waveguide. The phonon signal is present over the entire measurement time window. This behavior results from the high-quality-factor cavity and the periodic excitation by the laser pulse train. Successive pulses repeatedly excite the phonon field, leading to a quasi-continuous phonon source in the generation region [6].

To further investigate the coherence of propagating phonons, we introduce two pump pulses to excite two spatially separated phonon sources, allowing them to interfere at the midpoint. Since the phonon phase is determined by the excitation timing, the relative phase between the two sources can be controlled by adjusting the delay between the pump pulses [5]. By sweeping this delay, we extract the phonon amplitude, which exhibits a clear interference pattern. These results show that 20 GHz phonons remain coherent after long-distance propagation and demonstrate phase control as a basis for phonon-based information processing [6].

In the future, the number of phonon sources can be increased by implementing a spatial light modulator with independent control of their intensity and phase. This would offer a route toward phonon networks for information transfer and processing in compact nanophononic devices.

The authors acknowledge funding from European Research Council Consolidator Grant No.101045089 (T-Recs), the European Commission in the form of the H2020 FET Proactive project No. 824140 (TOCHA), and through a public grant overseen by the ANR as part of the “Investissements d’Avenir” Program (Labex NanoSaclay Grant No. ANR-10-LABX-0035).

References

[1] Stiller, B. et al. Coherently refreshing hypersonic phonons for light storage. *Optica* 7, 492 (2020).
[2] Kim, H. et al. On-Chip RF Signal Shaping by Coherent Control of Optically Driven Acoustic Wave Interference. *ACS Photonics* 9, 2938–2945 (2022).
[3] Zivari, A. et al. On-chip distribution of quantum information using traveling phonons. *Sci. Adv.* 8, eadd2811 (2022).
[4] Anguiano, S. et al. Micropillar Resonators for Optomechanics in the Extremely High 19–95-GHz Frequency Range. *Phys. Rev. Lett.* 118, 263901 (2017).
[5] Lanzillotti-Kimura, N. D. et al. Coherent control of sub-terahertz confined acoustic nanowaves: Theory and experiments. *Phys. Rev. B* 84, 115453 (2011).
[6] Xiang, C. et al. Interference of ultrahigh frequency acoustic phonons from distant quasi-continuous sources. *arXiv preprint* arXiv:2407.06821 (2024).

Wave Transport in Valley Phononic Crystals

Myung-Joon Lee[1], Il-Kwon Oh[1,*]

[1]Department of Mechanical Engineering,
Korea Advanced Institute of Science and Technology, Republic of Korea
*Corresponding author: ikoh@kaist.ac.kr

***Abstract*— We examine how interface orientation affects wave transport in valley phononic crystals. Bulk dispersion calculations, supercell models, and full field simulations are used to compare junction geometries. This work provides a conservative baseline for interpreting angle-dependent transmission variations in lattice waveguides.**

***Keywords*— valley phononic crystals, interface orientation, discrete lattices, wave transport.**

I. Introduction

Mechanical lattice metamaterials provide a convenient testbed for controlling elastic and acoustic waves through engineered geometry and coupling. A key advantage of these discrete platforms is that waveguides can be formed by simple patterning choices, including interfaces between lattice domains, and the resulting guided response can be probed directly in simulations [1].

One representative route to interface-guided modes is offered by valley phononic crystals, where momentum-space features associated with inequivalent valleys can shape how waves couple across an interface. In such systems, transport is often sensitive to interface orientation [2].

For a straight interface, the tangential component of the Bloch wave vector is conserved, so transmission depends on how this conserved momentum aligns with valley features in momentum space. Rotating the interface changes the projection of these valley features, which can make intervalley coupling more or less likely, thus modifying transmission characteristics and where the field localizes along the interface. This angle dependence matters in practice because routing networks often require oblique segments rather than only high-symmetry cuts. However, systematic studies of how interface orientation influences transmission in valley phononic crystals remain limited.

In this work, we examine interface-angle-dependent transport in valley phononic crystals based on discrete mechanical lattices. We introduce a simple projection viewpoint to interpret angle-dependent trends, and we support the discussion with unit-cell calculations, supercell analysis, and full field simulations.

II. Methods

We study how interface orientation influences wave transport in a valley phononic crystal realized in a discrete mechanical lattice. The bulk lattice is kept fixed throughout, and only the interface angle is varied. Bulk dispersion calculations provide the band structure, supercell models identify interface-guided modes for each orientation, and frequency domain full field simulations are used to compare transmission and field localization. A simple projection argument based on tangential momentum conservation is included to support the interpretation.

Bulk dispersion is computed under Bloch periodic boundary conditions to locate the frequency range where valley features are present. To connect bulk characteristics to interface behavior, we construct strip supercell models that are periodic along the interface and finite across it. The resulting band structures and mode profiles are used to confirm guided interface modes and to set a consistent baseline for comparing different interface orientations.

Transport is evaluated in finite lattices with an input section, an oblique interface segment, and an output section. A time harmonic excitation is applied at the input and the steady state response is recorded. Transmission is quantified by evaluating the same response intensity at fixed cross sections before and after the junction and applying the same normalization across all angles. Field maps are also extracted to illustrate how localization changes as the interface is rotated.

To interpret the angle dependence, we adopt a geometric projection viewpoint. Because the tangential component of the Bloch wave vector is conserved at a straight interface, bulk valley features can be projected onto the interface direction. The relative alignment of these projections is taken as a qualitative guide for when intervalley coupling is more likely. This interpretation is used only to support the discussion, while the reported comparisons are based on the supercell and full field calculations.

III. Results and Discussion

Numerical results show:

- Interface-guided transport is observed for the valley phononic crystal setting, and the guided response depends on interface orientation.
- Supercell calculations confirm interface-guided modes for multiple interface directions, providing a consistent reference for comparing orientations.
- Full field simulations indicate that transmission behavior can change noticeably as the interface angle is varied, accompanied by clear changes in where the field localizes.
- Angle-dependent trends are qualitatively consistent with a geometric projection viewpoint based on the conserved tangential momentum.

IV. Conclusion

We investigated interface-angle-dependent wave transport in a valley phononic crystal realized in a discrete mechanical lattice using bulk dispersion, supercell analysis, and full field simulations. The results highlight that interface orientation can noticeably influence transmission and field localization, and a geometric projection viewpoint provides a useful way to interpret the observed trends. Future work will extend this baseline to broader routing geometries and operating conditions.

Acknowledgments

This work was supported by the InnoCORE program of the Ministry of Science and ICT (N10250154).

References

[1] Y. Chen, X. Liu, and G. Hu, “Topological phase transition in mechanical honeycomb lattice,” Journal of the Mechanics and Physics of Solids, vol. 122, pp. 54–68, 2019.

[2] B. Orazbayev and R. Fleury, “Quantitative robustness analysis of topological edge modes in C6 and valley-Hall metamaterial waveguides,” Nanophotonics, vol. 8, pp. 1433–1441, 2019.

Numerical Study of Viscoelastic Soil Effects in Seismic Metamaterials

F. Simonetta[1], R. Zito[1], S. Laureti[1,*], and M. Miniaci[2]

[1]DIMES Dept., University of Calabria, 87036 Arcavacata di Rende (CS), Italy

[2] Dipartimento di Ingegneria Strutturale, Edile e Geotecnica, Politecnico di Torino, 10129 Torino, Italy

*Corresponding author: stefano.laureti@unical.it

***Abstract*—This work studies how a deviatoric generalized Maxwell soil response modifies seismic metamaterial dispersion. Finite-element eigenfrequency simulations show that stiffness changes and dynamic stiffening shift modal branches at higher frequency values. The results indicate that seismic metamaterial design should account for realistic soil inelasticity, since the intented functionality may change.**

***Keywords*— seismic metamaterials, viscoelasticity, band gaps, finite element modelling, eigenfrequency analysis.**

I. Introduction

Seismic metamaterials use periodic inclusions, resonators, or structured soil domains to attenuate surface waves through scattering and band-gap formation [1], [2]. Most numerical studies assume an ideal elastic soil, although realistic seismic loading can involve damping and other inelastic effects. This work enriches the non-hierarchical unit-cell model of Miniaci *et al.* [3] by adding a dissipative generalized-Maxwell soil response. It is shown that accounting for dissipative effects results in high deviation from the intended seismic metamaterial functionality, a fact that suggests that these must be designed with care for real-case scenarios.

II. Methods

The employed finite-element model follows that reported in Miniaci et al. [3]. The soil height was set to $H = \min(L_{\max}, 8\lambda)$, with $L_{\max} = 1000$ m, reducing the original computational costs while keeping the eigenfrequency problem solvable. This setup was used to isolate the effects of deviatoric viscoelasticity and increased soil stiffness.

TABLE I
Elastic material properties and reference speeds.

Case	E MPa	ρ kg/m^3	ν	c_S m/s	c_L m/s	c_R m/s
LowE	20	1800	0.30	65.4	122.3	60.6
HighE	320	1900	0.33	251.6	499.5	234.3

The c_S, c_L, and c_R references are plotted as $f = ck_x/(2\pi)$ over $k^* = k_x/(\pi/a)$ and they are reference slopes.

For the viscoelastic cases, one Maxwell branch was introduced with

$$G_0 = \frac{E}{2(1+\nu)}, \qquad G_1 = rG_0, \qquad \tau_1 = \frac{1}{2\pi f_{relax}}, \quad (1)$$

where E is the Young's modulus, ν is Poisson's ratio, G_0 is the instantaneous shear modulus, G_1 is the shear modulus of the Maxwell branch, $r = G_1/G_0$, and τ_1 is the characteristic relaxation time of that branch. In the absence of rheological data, $r = 0.3$ was chosen as a moderate contrast: a preliminary sweep showed nearly linear modal sensitivity, with a visible frequency shift already at this value. The relaxation frequency, f_{relax}, was similarly set to 12 Hz, placing the Maxwell transition within the HighE modal window, whose first mode is near 10 Hz. It must be noted that only the deviatoric response is dissipative, while the volumetric response remains elastic. The corresponding shear modulus is:

$$G^*(\omega) = G_0 + \frac{G_1 i\omega\tau_1}{1 + i\omega\tau_1}. \quad (2)$$

Thus $G^* \approx G_0$ at low frequencies, and $G^* \to G_0 + G_1$ at high frequencies, so the model introduces both damping and dynamic stiffening.

III. Results and Discussion

With respect to Miniaci et al. [3], the PML was here replaced with a low-reflecting boundary, and the use of the capped wavelength-scaled height preserves the qualitative modal structure of the reference simulation, as shown in Fig. 1(a-b). Thus, it yields the same result of the reference, though saving computational time; this is a validation step, not the main physical result.

TABLE II
Progressive modelling changes and observed trends.

Case	Main observation
Reference elastic	Baseline elastic modal structure.
No PML	Similar branches; lower computational time than Ref.
LowE viscoelastic	Modest upward shift from frequency-dependent shear stiffness.
HighE elastic	Shift from about 2.5–6 Hz to about 10–25 Hz.
HighE viscoelastic	Preserved structure with a moderate shift for $r = 0.3$, $f_{relax} = 12$ Hz.

Adding viscoelasticity to the LowE model modestly shifts the modal branches upward, consistent with the high-frequency Maxwell limit where the effective shear stiffness approaches $G_0 + G_1$. Increasing elastic stiffness has a stronger effect: the HighE elastic case shifts the spectrum from about 2.5–6 Hz to 10–25 Hz. In the viscoelastic case, $f_{relax} = 12$ Hz avoids a fully high-frequency asymptotic response, while

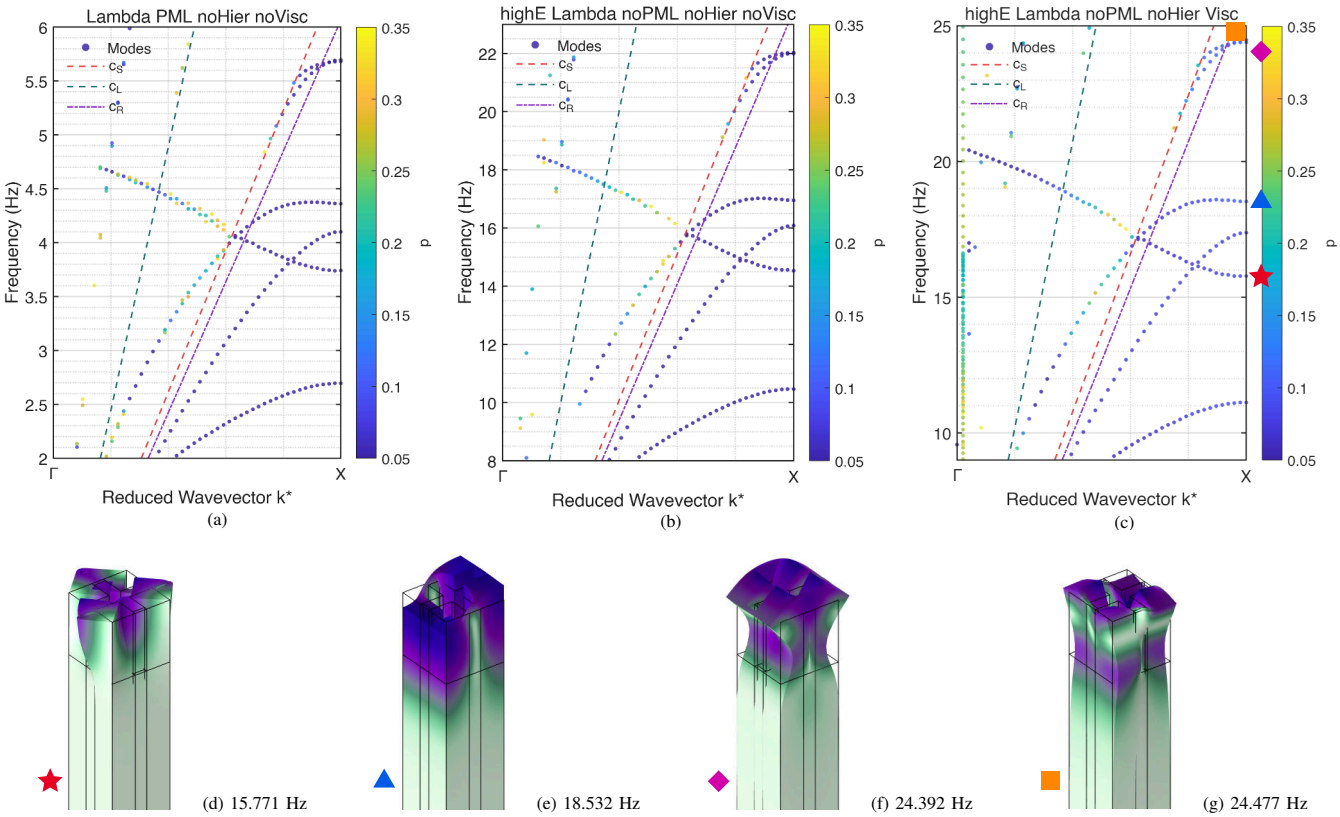

Fig. 1. Eigenfrequency results and selected HighE viscoelastic mode shapes, filtered based on the p-value. Panel (a) reports the reference elastic case; panels (b,c) use $H = \min(L_{\max}, 8\lambda)$, $L_{\max} = 1000$ m. Panel (c) uses $r = 0.3$ and $f_{relax} = 12$ Hz. Panels (d)–(g) show representative modes at X.

$r = 0.3$ gives a moderate visible deviation from the elastic diagram, Fig. 1(c). Table II separates numerical validation from stiffness and viscoelastic effects.

Stronger preliminary viscoelastic cases showed a small splitting of two modes nearly coincident in elastic simulations. This may reflect damping-induced lifting of an accidental degeneracy, although mesh/solver convergence is needed before interpreting its magnitude quantitatively.

The modal shapes in Fig. 1(d)–(g) were extracted at $k = 2$, i.e., at X along Γ–X. The deformation is localized near the surface, with out-of-plane and mixed character comparable to the surface-mode shapes reported in Miniaci *et al.* [3]. The frequency range is shifted upward by the HighE material and Maxwell-branch stiffening.

IV. Conclusion

The proposed simplified model shows the same behavior of Miniaci *et al.* [3]: the same general band-gap behavior and distinction between strongly excited, mainly out-of-plane SAW-type modes and weakly excited modes remain. In the HighE configuration, these features shift upward due to increased stiffness and Maxwell-branch dynamic stiffening. Thus, higher-order effects must be considered with due care for the faithful design of seismic metamaterials. Future works will consider plasticity and dissipative effects.

Acknowledgments

This project has received funding from the European Union's EU Framework Programme for Research and Innovation Europe Horizon (HORIZON TMA MSCA Doctoral Networks) under Grant Agreement No.101119738 "MetacMed" (www.metacmed.eu). MM is supported by the European Union's Horizon Europe programme in the framework of the ERC StG POSEIDON, Grant Agreement No. 101039576. M.M. acknowledges the DREAM project, funded by the European Union Next-GenerationEU (National Recovery and Resilience Plan–NRRP, Mission 4, Component 2, Investment 1.2). Views and opinions expressed are, however, those of the author(s) only and do not necessarily reflect those of the European Union; neither the European Union nor the granting authority can be held responsible for them.

References

[1] S. Brûlé, E. Javelaud, S. Enoch, and S. Guenneau, "Experiments on seismic metamaterials: molding surface waves," *Physical review letters*, vol. 112, no. 13, p. 133901, 2014.

[2] M. Miniaci, A. Krushynska, F. Bosia, and N. M. Pugno, "Large scale mechanical metamaterials as seismic shields," *New Journal of Physics*, vol. 18, no. 8, p. 083041, 2016.

[3] M. Miniaci, N. Kherraz, C. Cröenne, M. Mazzotti, M. Morvaridi, A. S. Gliozzi, M. Onorato, F. Bosia, and N. M. Pugno, "Hierarchical large-scale elastic metamaterials for passive seismic wave mitigation," *EPJ Applied Metamaterials*, vol. 8, p. 14, 2021.

Coupled Inertial Amplification and Local Resonance Band Gaps

Cetin Yilmaz[1,*]

[1]Department of Mechanical Engineering, Bogazici University, Istanbul, Turkey
*Corresponding author: cetin.yilmaz@bogazici.edu.tr

***Abstract*—Band gaps below the Bragg limit can be generated through local resonance and inertial amplification methods. A lever-type inertial amplification mechanism with a local resonator at its tip is analyzed. Due to their coupling, a single band gap is formed below what could be achieved by the individual mechanisms.**

***Keywords*— elastic metamaterials, local resonance, inertial amplification, coupling.**

I. Introduction

Phononic band gaps are typically generated through Bragg scattering or local resonance methods. The lowest frequency Bragg gap is centered around the ratio of the wave speed in the lattice to the lattice constant. By contrast, the local resonance approach can produce band gaps at much lower frequencies. However, achieving wide gaps at low frequencies with this method requires the use of large resonator masses [1].

An alternative band gap generation technique is inertial amplification. In this approach, amplified motion of small masses increases the effective inertia of the lattice, thereby producing low-frequency band gaps. Unlike the two conventional methods, this technique enables the formation of wide, low-frequency gaps without increasing the overall mass or reducing the stiffness of the lattice [2,3]. Bridge-type amplification mechanisms are usually utilized to generate the amplified inertial forces that result in low-frequency band gaps [2–8]. Alternatively, effective inertia of a structure can also be increased by lever-type amplification mechanisms [9–12].

Inertial amplification and local resonance methods can be used together to obtain wide band gaps at low frequencies. By using local resonators and bridge-type inertial amplification mechanisms in a periodic structure, double attenuation peaks in a band gap can be achieved [13-14].

In this study, a 1D periodic structure with a unit cell containing a lever-type inertial amplification mechanism with a local resonator at its tip will be investigated. Dispersion plot of the 1D periodic structure will be obtained to compare band gaps arising solely from inertial amplification, solely from local resonance, and from the combined effect of inertial amplification and local resonance.

II. Method

Consider the 1D periodic structure in Fig. 1. The unit cell of this periodic structure contains a lever-type inertial amplification mechanism with a local resonator at its tip.

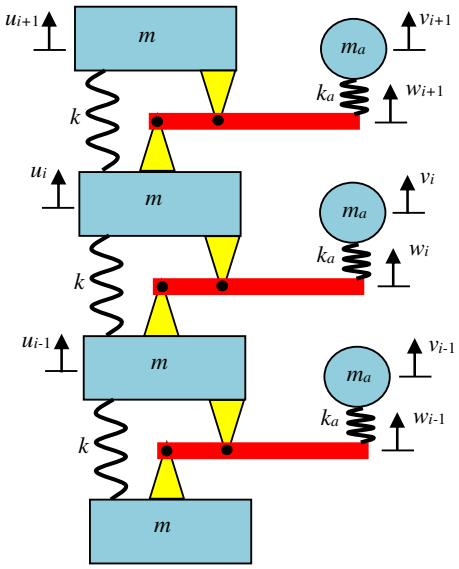

Fig 1 1D periodic structure with a unit cell containing a lever-type amplification mechanism with a local resonator at its tip.

The lever with length l_1 is assumed to be rigid and massless. Hinge spacing of the lever is l_2 and the amplification ratio is defined as $\alpha = l_1/l_2$. Assuming small amplitude motion for the lever, tip displacement of the lever (w_i) can be obtained in terms of u_i and u_{i-1} as $w_i = \alpha u_i - (\alpha - 1)u_{i-1}$. Hence, there are two independent degrees-of-freedom of the i^{th} unit cell, i.e., u_i and v_i. By applying Bloch boundary conditions, u_{i+1} and v_{i+1} can be obtained in terms of u_i and v_i as

$$u_{i+1} = u_i e^{j\gamma a} \tag{1}$$

$$v_{i+1} = v_i e^{j\gamma a} \tag{2}$$

where γ is the wave number and a is the lattice constant. Then, the equation of motion of the unit cell can be obtained as

$$M\ddot{\boldsymbol{x}} + K\boldsymbol{x} = \boldsymbol{0} \tag{3}$$

where

$$\boldsymbol{x} = \begin{bmatrix} u_i \\ v_i \end{bmatrix} \tag{4}$$

$$M = \begin{bmatrix} m & 0 \\ 0 & m_a \end{bmatrix} \tag{5}$$

$$K = \begin{bmatrix} K_{11} & K_{12} \\ K_{21} & k_a \end{bmatrix} \tag{6}$$

$$K_{11} = 2k + k_a(2\alpha^2 - 2\alpha + 1) - \left(k + k_a(\alpha^2 - \alpha)\right)(e^{j\gamma a} + e^{-j\gamma a}) \tag{7}$$

$$K_{12} = -k_a(\alpha - (\alpha - 1)e^{j\gamma a}) \tag{8}$$

$$K_{21} = -k_a(\alpha - (\alpha - 1)e^{-j\gamma a}) \tag{9}$$

Assuming harmonic motion with frequency ω, Eq. (3) can be solved to obtain the two branches of the dispersion curve.

III. Results and Discussion

The model in Fig. 1 can show an inertial amplification induced gap if $k_a \to \infty$ and $\alpha > 1$, a local resonance gap if k_a is finite and $\alpha = 1$, and a coupled inertial amplification and local resonance gap if k_a is finite and $\alpha > 1$.

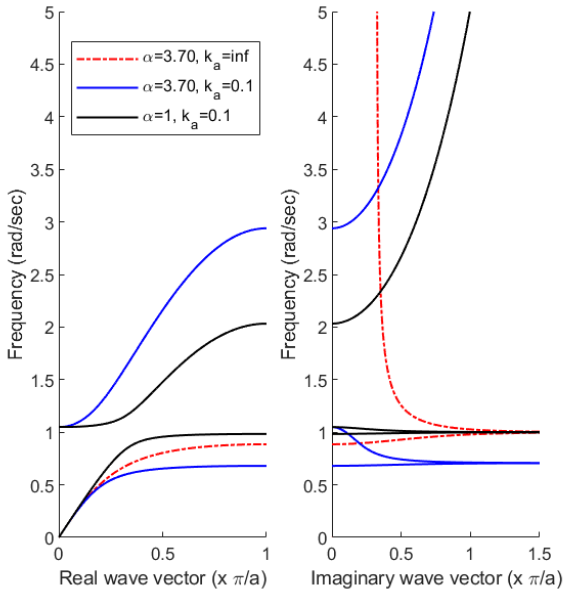

Fig 2 Complex band structure of the 1D lattice (a) Real wave vector. (b) Absolute value of the imaginary part of the complex wave vector.

Fig. 2 shows the complex band structure of this lattice for three different cases. In all cases, $m = 1$kg, $m_a = 0.1$kg and $k = 1$N/m. If $k_a \to \infty$ and $\alpha = 3.7$, a semi-infinite inertial amplification induced gap appears with a lower limit of 0.885rad/s. Peak attenuation is achieved at 1rad/s. If $k_a = 0.1$N/m and $\alpha = 1$, a narrow local resonance gap appears between 0.983-1.05rad/s. Although the peak attenuation is achieved at the same frequency (1rad/s), inertial amplification induced gap starts at a lower frequency (0.885rad/s) and extends to infinity. If $k_a = 0.1$N/m and $\alpha = 3.7$, a wide coupled gap appears between 0.68-1.05rad/s. Unlike the earlier two cases, peak attenuation is achieved at 0.707rad/s. Hence, the coupled inertial amplification and local resonance gap has the same upper limit as the local resonance gap (1.05rad/s), but its lower limit (0.68rad/s) is lower than that of the inertial amplification gap (0.885rad/s). The coupled band gap produced by the lever-type inertial amplification mechanisms and local resonators in this study shows a single attenuation peak, unlike the bridge-type amplification mechanisms combined with local resonators, which yield double attenuation peaks [13–14].

IV. Conclusion

Dispersion relation of a 1D periodic structure with a unit cell containing a lever-type inertial amplification mechanism with a local resonator at its tip is obtained. This structure displayed an inertial amplification induced gap, a local resonance gap or a coupled inertial amplification and local resonance gap depending on the parameters of the unit cell. It is shown that a wide band gap at low frequencies can be obtained due to coupling.

References

[1] Z. Liu, C. Chan, and P. Sheng, "Three-component elastic wave band-gap material", Physical Review B, vol. 65, no. 16, p. 165116, 2002.

[2] C. Yilmaz, G.M. Hulbert, and N. Kikuchi, "Phononic band gaps induced by inertial amplification in periodic media", Physical Review B, vol. 76, no. 5, p. 054309, 2007.

[3] C. Yilmaz and G.M. Hulbert, "Theory of phononic gaps induced by inertial amplification in finite structures", Physics Letters A, vol. 374, no. 34, pp. 3576–3584, 2010.

[4] S. Taniker and C. Yilmaz, "Inertial amplification induced phononic band gaps in SC and BCC lattices", In: ASME International Mechanical Engineering Congress and Exposition, p. V014T15A046, 2013.

[5] O. Yuksel and C. Yilmaz, "Size and topology optimization of inertial amplification induced phononic band gap structures", In: ASME International Mechanical Engineering Congress and Exposition, p. V013T01A007, 2017.

[6] J. Li and S. Li, "Generating ultra wide low-frequency gap for transverse wave isolation via inertial amplification effects", Physics Letters A, vol. 382, no. 5, pp. 241-247, 2018.

[7] L. Xu, R. Wu, Z. Zhang, Q. Xie, E. Li, and B. Li, "Hierarchical meta-lattice structures with inertial amplification design for broadband low-frequency vibration mitigation". Engineering Structures, vol. 346, p. 121601, 2026.

[8] B. Acar, S. N. Otlu, Z. G. Tetik, and C. Yilmaz, "Scaling Up 3D Elastic Metamaterials with Ultrawide Band Gaps: A Modular Approach with Weight Compensation", Journal of Sound and Vibration, vol. 626, p.119641, 2026.

[9] C. Yilmaz and N. Kikuchi, "Analysis and design of passive band-stop filter-type vibration isolators for low-frequency applications", Journal of Sound and Vibration, vol. 291, no. 3-5, pp. 1004-1028, 2006.

[10] K. Mizukami, R. Imanishi, H. Matsushita, and Y. Koga, "Design and additive manufacturing of elastic metamaterials with 3D lever-type inertial amplification mechanisms for mitigation of low-frequency vibration", Results in Engineering, vol. 20, p. 101389, 2023.

[11] C. Xi, H. Zheng, Y. Mi, and X. Yu, "Lever-type inertial amplification plates for low-frequency vibration reduction", Thin-Walled Structures, vol. 192, p. 111131, 2023.

[12] L. Gao, G. Xing, Y. Hao, Z. Chang, and W. Zhang, "Parallel lever-type inertial amplification for broadband low-frequency vibration control", Structures, vol. 85, p. 111188, 2026.

[13] A. Banerjee, S. Adhikari, and M. I. Hussein, "Inertial amplification band-gap generation by coupling a levered mass with a locally resonant mass", International Journal of Mechanical Sciences, vol. 207, p. 106630, 2021.

[14] A. Bhatt and A. Banerjee, "Double attenuation peaks in metamaterial with simultaneous negative mass and stiffness", Physics Letters A, vol. 443, p. 128201, 2022.

Verification of a two-fold topological phase transition ruled by third-nearest-neighbor hoppings

R. A. Méndez-Sánchez[1*], Y. Betancur-Ocampo[2], B. Manjarrez-Montañez[1], A. M. Martínez-Argüello[3], A. Franco[4], E. Flores[4], and G. Báez[4]

[1]Instituto de Ciencias Físicas, Universidad Nacional Autónoma de México, Cuernavaca, Mexico
[2]Instituto de Física, Universidad Nacional Autónoma de México, Ciudad de México, Mexico
[3]Instituto de Física, Benemérita Universidad Autónoma de Puebla, C. P. 72570 Puebla, Puebla, Mexico
[4]Departamento de Ciencias Básicas, Universidad Autónoma Metropolitana-Azcapotzalco, 02200, CDMX, México,
*corresponding author: mendez@icf.unam.mx

***Abstract*— A coupled-resonator phononic cis-polyacetylene, presenting a two-fold topological transition is studied experimentally. The artificial molecule is governed by a tight-binding model similar to that of condensed matter. The design was done through numerical simulations using finite elements. The machined molecule was characterized using acoustic resonant spectroscopy.**

***Keywords*— metamaterials, phononic crystals.**

I. Introduction

Polyacetylene is an organic polymeric molecule formed by a chain of carbon atoms with alternating double and single bonds between them; each carbon atom is also bonded to a hydrogen atom. This polymeric molecule is important due to its conductive properties. Is conductive properties yield multiple applications in microelectronics of organic compounds. This molecule can be found as the cis-polyacetylene and trans-polyacetylene isomers; the cis isomer is depicted in Fig. 1 (a). Recently, some of us found that cis-polyacetylene presents a twofold topological phase transition ruled by the third-nearest-neighbor hoppings [1].

II. Artificial molecule

This transition presents a Dirac cone and two different topological phases to each side. In this work we present experimental evidence of this transition using a coupled-resonator phononic molecule (CRPnMo) [2,3]. The artificial molecule is formed by resonators joined by finite phononic crystals (FPnCs). When a normal-mode frequency of the resonator falls within the gap of the FPnC the wave amplitude localizes in the resonator and evanescently decays along the FPnCs. When a second resonator is added, the normal modes couple evanescently emulating the quantum tunneling. This coupling gives rise to a tight-binding regime of elastic waves equivalent to that of condensed-matter physics. An image of the CRPnMo used is given in Fig. 1 (b).

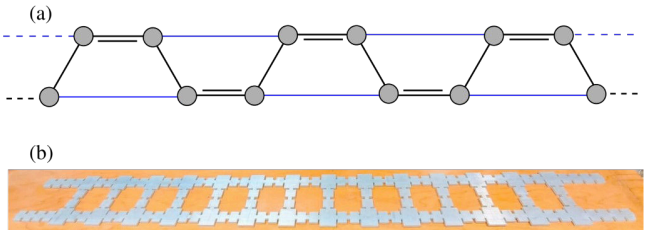

Fig. 1 Schematic representation of cis-polyacetylene with first- and third-nearest-neighbors hoppings. (b) Coupled-resonator phononic molecule of cis-polyacetylene.

III. Results and Discussion

The measured spectrum of the coupled-resonator phononic molecule of Fig. 1 is given in Fig. 2. One can observe in this figure that the level density at the center of the band is almost constant. This is in agreement with the existence of a Dirac cone. Results of the topologically protected states will be given elsewhere.

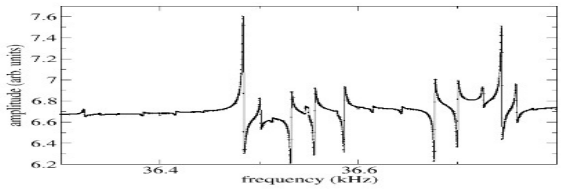

Fig. 2 Measured transmission of a coupled-resonator phononic cis-polyacetylene molecule. In this case a band is apparent. The first- and third-nearest-neighbor hoppings in the molecule are the same.

IV. Conclusion

We have measured the twofold topological phase transition predicted recently by some of use. Evidence of the Dirac cone is give. The topologicaly protected states will be shown elsewhere. The experimental results confirm the appearance of the Dirac cone as well of the topologically protected states.

Acknowledgments

This work was supported by PAPIIT-UNAM; RAMS under project IN108825 and YBO under projects IA106223 and IA102125. BMM is grateful to SECIHTI for financial support through a Ph. D. fellowship.

References

[1] Betancur-Ocampo, Y., Manjarrez-Montañez, B., Martínez-Argüello, A. M., & Méndez-Sánchez, R. A. (2024). Twofold topological phase transitions induced by third-nearest-neighbor hoppings in one-dimensional chains. Physical Review B, 109(10), 104111.

[2] Ramírez-Ramírez F., Flores-Olmedo E., Báez G., Sadurní E., and Méndez-Sánchez R.A., "Emulating tightly bound electrons in crystalline solids using mechanical waves", Sci. Rep. 10, 10229 (2020)

López-Toledo J.A., Báez G. and Méndez-Sánchez R.A, "Tight-binding model for torsional and compressional waves in high-quality coupled-resonator phononic metamaterials," Mech. Adv. Mater. Struct. (2021).

Non-reciprocal communication with signal amplification

Xinxin GUO[1,*], Zhenwei Xu[1], Ulrich Kuhl[2]. Nicolas Noiray[1,*]

[1]ETH Zürich, Department of Mechanical and Process Engineering, CAPS laboratory, 8092 Zürich, Switzerland
[2]Université Côte d'Azur, CNRS, Institut de Physique de Nice (INPHYNI), 06200, Nice, France
*Corresponding authors: guoxin@ethz.ch, noirayn@ethz.ch

***Abstract*—In this work, we present a compact acoustic circulator that enables signal-amplified non-reciprocal transmission of time-varying information via binary encoding. The nonlinear synchronization between the input wave and a spinning limit cycle is leveraged, leading to strong non-reciprocity not only in transmitted energy but also in information accuracy.**

***Keywords*— information transport, non-reciprocal transmission, dynamic synchronization, limit cycle.**

I. Introduction

Current research in metamaterials has broken the reciprocity in achieving various types of asymmetric wave manipulation. However, in the field of communications and information processing, relevant advances, such as the development of programmable and coding metamaterials, have hardly been explored at the intersection with non-reciprocity. To unlock this limitation, we design a compact acoustic circulator based on the synchronization mechanism [1] and investigate the non-reciprocal transmission of time-varying information.

II. Results and Discussion

Figure. 1 shows the experimental communication results based on the realization of a 3D-printed acoustic circulator. The information is first encoded into a binary stream (Fig. 1b), with bits 0 and 1 mapped to two frequencies ω_1 and ω_2, respectively. ω_1 and ω_2 are chosen near the frequency that yields the optimal non-reciprocal transmission. The resulting frequency-modulated input signal p_1 is sent to port 1 of the circulator. The signals transmitted to ports 2 and 3 are illustrated in Fig. 1c. The asymmetric transmission behaviors of the circulator result from the synchronization of the spinning limit cycle with the input wave p_1. As such, the time-varying information can equally be transmitted non-reciprocally. The signal p_2 received at port 2 is significantly amplified in magnitude compared to the input p_1, thanks to the energy fed by the synchronized limit cycle. Unsurprisingly, it allows the input message to be accurately decoded. However, at port 3, transmission is nearly forbidden due to the non-reciprocal responses of the circulator. The magnitude of p_3 drops to the level of stochastic noise generated by airflow. In this case, the information extraction completely fails as a result of its nonlinear coupling with noise.

III. Conclusion

In this study, we demonstrated signal-amplified non-reciprocal transmission of time-varying information through a compact acoustic circulator. We exploited the synchronization between the input acoustic wave and a flow-driven spinning limit cycle, which endows transmission with strong non-reciprocity while compensating for losses by extracting energy from the limit cycle. Based on binary encoding, our results show that the input information is transmitted with complete accuracy and signal amplification in one direction. In contrast, in the other direction, it is fully erased due to its significantly low transmission level and the nonlinear coupling with flow-induced stochastic noise. Our designed acoustic circulator not only allows steady-state transmission analysis but is also suitable for dynamic wave manipulations.

Fig. 1. Non-reciprocal communication: experimental results. **a** The designed acoustic circulator, with an inner diameter of 5 cm. **b** The time-varying input information sent to port 1. **c** Information extraction from signals transmitted to ports 2 and 3, respectively.

References

[1] T. Pedergnana, A. Faure-Beaulieu, R. Fleury and N. Noiray, "Loss-compensated non-reciprocal scattering based on synchronization," *Nature Communication*, vol. 15, pp. 7436, 2024.

From Acoustic Spin, Elastic Spin to Phonon Spin

Jie REN

Center for Phononics, School of Physics Science and Engineering,
Tongji University, Shanghai 200092, China
*Corresponding author: xonics@tongji.edu.cn

***Abstract*— Spin angular momentum was long deemed exclusive to transverse electromagnetic waves, while longitudinal acoustic waves, elastic waves and phonons were regarded as spinless. Based on a series of theoretical and experimental studies, we establish a unified framework covering acoustic spin, elastic spin and phonon spin. We prove that longitudinal and hybrid longitudinal–transverse vibrational waves carry intrinsic spin, and reveal hybrid spin, anomalous spin–momentum locking, universal geometric relations among spin, energy flux and reactive power. Experiments confirm the existence of acoustic spin and elastic spin, and realize chiral transport, symmetry-selective wave routing, topological valley–spin coupling and parity–frequency–space programmable control. We further extend spin physics to phonons, uncover chirality-induced phonon spin selectivity and collective-interference-induced circular dichroism. Our works reshape the fundamental understanding of spin in structured waves and topological metamaterials, and lays the foundation for the emerging field of spin phononics.**

***Keywords*— metamaterials, acoustic, elastic, phononic, spin.**

I. Introduction

Spin angular momentum is a core property of wave physics and quantum technology. For decades, the conventional view held that only transverse waves possess spin, excluding longitudinal acoustic, elastic and phonon systems. This paradigm limited the development of spin-based wave manipulation in acoustics, mechanics and condensed matter physics. Our group has systematically explored the spin of vibrational waves from theory to experiment, extending macroscopic acoustic and elastic spin to microscopic phonon spin, forming a complete research chain from fundamental discovery to applied mechanism. This report reviews the unified physical origin, key phenomena and applications from acoustic spin, elastic spin to phonon spin.

II. Methods

We combine theoretical derivation, numerical simulation, experimental measurement and first-principles calculation. Based on classical field theory and Noether's theorem, we derive the spin angular momentum density of elastic and acoustic waves, and extend the theory to phonons via second quantization. We design acoustic spin torque measurement, chiral elastic meta-sources and near-field acoustic structures to observe spin and directional transport. We construct metasurface waveguides, topological phononic crystals and parity–frequency–space modulated phononic circuits to realize spin-dependent chiral control. We also use quantum perturbation methods to analyze local and collective interference phonon spin.

III. Results and Discussion

We first predicted the intrinsic spin of elastic waves, breaking the traditional belief that only transverse waves have spin. Elastic waves contain both longitudinal and transverse components, producing hybrid spin from their cross coupling, which leads to the anomalous spin–momentum locking in surface elastic waves. We then experimentally observed acoustic spin by measuring spin-induced mechanical torque, and realized direct excitation and detection of elastic spin using chiral meta-sources, confirming spin–momentum locking in Rayleigh and Lamb waves.

We derived universal geometric relations linking acoustic spin, energy flux and reactive power, providing a general principle for spin-based wave control. By breaking structural symmetry, we achieved acoustic spin transport in metasurface waveguides and symmetry-selective directional excitation in near-field acoustics. Introducing topological design, we realized valley–spin locked chiral coupling in valley phononic crystals with robust anti-backscattering transport, and further established multi-dimensional programmable wave routing in parity–frequency–space phononic circuits.

We extended the spin framework to microscopic phonons and established the unified symmetry between elastic spin and phonon spin. Via elastic spin–orbit interaction, we revealed chirality-induced phonon spin selectivity for selective spin excitation. More importantly, we discovered the collective interference nature of phonon spin: phonon angular momentum includes both local atomic vibration and nonlocal collective interference between sublattices. This collective effect induces strong circular dichroism in chiral crystals, contributing over 95% in chiral quartz, linking phonon spin to optical response and multi-physical field coupling.

IV. Conclusion

This work systematically establishes the unified theory of acoustic spin, elastic spin and phonon spin, overturning the

conventional view that longitudinal waves and phonons are spinless. Key advances include intrinsic spin, hybrid spin, anomalous spin–momentum locking, universal geometric relations, topological valley–spin control, chirality-induced phonon spin selectivity and collective-interference phonon spin. These findings create the new field of spin phononics, offering new principles for topological metamaterials, chiral acoustics, topological phononics, quantum information and precision sensing.

REFERENCES

[1] Y. Long, **RJ*** and H. Chen, "Intrinsic spin of elastic waves," PNAS, Vol. **115**, No.40, 9951-9955, 2018.

[2] **RJ***, "From Elastic Spin to Phonon Spin: Symmetry and Fundamental Relations," Chin. Phys. Lett., Vol. **39**, No.12, 126301, 2022.

[3] C. Shi, R. Zhao, L. Yang, S. Yang, Y. Wang, H. Chen, **RJ*** and X. Zhang*, "Observation of acoustic spin," Nati. Sci. Rev., Vol. **6**, No.4, 707-712, 2019.

[4] Y. Long, D. Zhang, C. Yang, J. Ge, H. Chen and **RJ***, "Realization of acoustic spin transport in metasurface waveguides," Nat. Commun., Vol. **11**, No. 1, 4716, 2020.

[5] Y. Long, C. Yang, H. Chen and **RJ***, "Universal Geometric Relations of Acoustic Spin, Energy Flux, and Reactive Power," Phys. Rev. Applied, Vol. **19**, No. 6, 064053, 2023.

[6] Y. Long, H. Ge, D. Zhang, X. Xu, **RJ***, M.-H. Lu*, M. Bao, H. Chen and Y.-F. Chen, "Symmetry selective directionality in near-field acoustics," Nati. Sci. Rev., Vol.**7**, No.6, 1024-1035, 2020.

[7] C. Yang, D. Zhang, J. Zhao, … and **RJ***, "Hybrid Spin and Anomalous Spin-Momentum Locking in Surface Elastic Waves," Phys. Rev. Lett., Vol.**131**, No.13, 136102, 2023

[8] C. Yang, and **RJ*,** "Chirality-induced phonon spin selectivity by elastic spin–orbit interaction," PNAS **121**, e2411427121 (2024)

[9] Y. Huang, C. Yang, W. Yuan, Y. Zhang, Y. Pan, F. Yang, Z. Zhong, J. Zhao,* OB. Wright, and **RJ***, "Parity-Frequency-Space Elastic Spin Control of Wave Routing in Topological Phononic Circuits", Adv. Sci. 2404839, 2024.

[10] Y. Liu, Y.-T. Tan, D. Liu, and **RJ***, "Collective Interference of Phonon Spin and Dipole Moment Rotation Induced Circular Dichroism", Phys. Rev. Lett. 136, 146601 (2026).

[11] W. Yuan, C. Yang, D. Zhang, Y. Long, Y. Pan, Z. Zhong, H. Chen, J. Zhao, and **RJ***, "Observation of elastic spin with chiral meta-sources", Nature Comm. 12, 6954 (2021).

[12] J. Zhao, C. Yang, W. Yuan, D. Zhang, Y. Long, Y. Pan, H. Chen, Z. Zhong, and **RJ*** , "Elastic Valley Spin Controlled Chiral Coupling in Topological Valley Phononic Crystals", Phys, Rev. Lett. 129, 275501 (2022)

Wide-area Topological Higher-order Modes in Heterostructured Kagome Phononic Crystal

Yusuke Hata, Yuri Fukaya, Kenji Tsuruta*

Department of Electrical and Electronic Engineering
Okayama University, Japan
*Corresponding author: tsuruta@okayama-u.ac.jp

***Abstract*— We designed wide-area elastic waveguides based on higher-order topological modes in a heterostructured Kagome lattices consisting of trivial and nontrivial domains. We numerically demonstrated that interface modes as well as corner modes are broadened leading to more efficient energy storage than at the corners of the conventional structure.**

***Keywords*— elastic-wave device, phononic crystal, topological insulator.**

I. Introduction

Topological phononic crystal (TPnC), which is an artificial elastic structure to imitate a topological insulator have attracted increasing attention due to their robust boundary modes against defects, disorders, and bends with nearly zero energy dissipation even at GHz frequencies [1]. In addition to the primary boundary modes, higher-order topological state (HOTS) emerging at lower dimension in TPnCs is expected to extend the functionality of elastic devices to store elastic energy at a designated region. However, HOTS is only available at narrow boundaries, hindering its use in devices where the energy carried by phonon is converted to electrical one.

Recently, wide-area topological waveguide, which is composed of a symmetric structure surrounded by two symmetry-broken structures , has been proposed in a photonic system as a candidate of devices transporting large photonic energy [2]. Here, we proposed a heterostructured TPnC with wide-area HOTSs, which is easily excited by an external load, and applied it to an energy storage device.

II. Heterostructure Design

The unit cell of the Kagome lattice we adopted is made of aluminum alloy consisting of three hexagonal sites and intra- and inter-bonds. The topological corner modes have been shown to emerge when the intra-cell bond is smaller than the inter-cell bond [3].

III. Energy Storing With Heterostructure

The left panel of Fig. 4 shows the displacement field of the eigenmode in the conventional structure. The mode localizes at the corner of the internal domain, and decays rapidly away from the corner. In contrast, the mode profile is broadened uniformly in the corner region of the mid-domain inserted between the trivial and nontrivial regions of the heterostructure, as shown in the right-panel of Fig. 4. We calculate the ratio of the stored energy in the region surrounded by the dashed lines. The energy stored at the extended corners is 79.3% of the total energy, while only 21.6% of the total energy is concentrated at the corners of conventional structure.

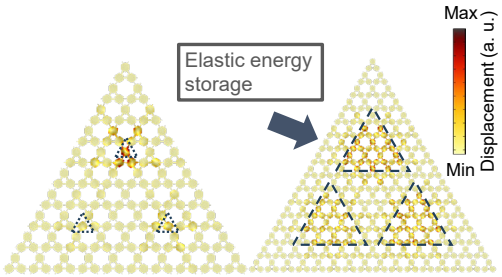

Fig. 1 The displacement field of eigenmodes calculated by finite element analysis. Triangles with dashed lines denote the corner area of conventional (left) and proposed (right) structure, respectively.

IV. Conclusion

We designed a heterostructured TPnC with Kagome lattice to broaden the area of topological corner states. By inserting the mid-domain that has a symmetric structure between the non-trivial and trivial domains, we demonstrated that the proposed structure stored significantly larger elastic energy at extended corner regions than the conventional structure. This study may open new strategies for efficient elastic energy storage and/or energy harvesting.

Acknowledgments

This research was funded in part by JSPS KAKENHI grant number JP21H05020.

References

[1] D. Hatanaka, H. Takeshita, M. Kataoka, H. Okamoto, K. Tsuruta, and H. Yamaguchi, “Valley Pseudospin Polarized Evanescent Coupling between Microwave Ring Resonator and Waveguide in Phononic Topological Insulators”, Nano Lett. **24**, 5570-5577 (2024).

[2] C. Zhang *et al.*, “Wide-mode-area slow light waveguides in valley photonic crystal heterostructures”, Opt. Mater. Express **14**, 1756-1766 (2024).

[3] Y. Hata, Y. Fukaya, K. Tsuruta, "Wide-area Topological Corner Modes in Heterostructured Kagome Phononic Crystal," Proceedings of IEEE Int'l Ultrasonics Sympo. (IEEE-IUS2025), 11201361 (2025)
.

Complex Topological Phases Driven by Beyond-Nearest-Neighbor Interactions

Amir Rajabpoor Alisepahi[1], Siddhartha Sarkar[2], Kai Sun[2], Jihong Ma[1,3*]

[1]Department of Mechanical Engineering, University of Vermont, Burlington, Vermont, USA
[2]Department of Physics, University of Michigan, Ann Arbor, Michigan, USA
[3]Department of Physics, University of Vermont, Burlington, Vermont, USA
*Corresponding author: Jihong.Ma@uvm.edu

***Abstract*—We reveal unconventional topological states driven by beyond-nearest-neighbor interactions, inaccessible to conventional winding-number methods. We introduce a local winding-number characterization derived from Berry connections and validate it experimentally using laser-assisted measurements on designed metamaterials, confirming the method's predictive power for complex topological phases.**

***Keywords*— beyond-nearest-neighbor interactions, topological states, local winding number, Berry connection, phononic crystals.**

I. Introduction

Topological mechanical metamaterials and phononic crystals enable robust wave manipulation through topologically protected boundary states (TPBS) dictated by bulk–edge correspondence. A canonical example is the one-dimensional Su–Schrieffer–Heeger (SSH) model [1], in which alternating spring stiffnesses generate distinct topological phases identified by winding numbers that quantify TPBSs [2]. While most studies consider only nearest-neighbor interactions, our recent work shows that beyond-nearest-neighbor (BNN) couplings fundamentally alter the topological landscape, producing unconventional dispersion and new boundary phenomena [3], [4]. We demonstrate that, in such systems, the number of TPBSs is governed not by global winding numbers but by *local* winding numbers extracted from the Berry connection [5], which correspond directly to the Jackiw–Rebbi (JR) indices associated with JR zero modes [6].

II. Methods

Conventional winding number n, which predicts the number of TPBSs in the SSH model can be computed directly from the stiffness matrix $C(k)$ as

$$n = \int_{-\pi/a}^{\pi/a} \frac{1}{4\pi i} \mathrm{tr}[\sigma_3 C'^{-1} \partial_k C'] dk, \tag{1}$$

where σ_3 is the third Pauli matrix, and C' is the effective Hamiltonian, defined as:

$$C'(k) = C(k) - (c_1 + c_2)\sigma_0, \tag{2}$$

with σ_0 the identity matrix, k the wave number, and c_1, c_2 the alternating interaction strengths.

However, with BNN coupling, the global winding number n no longer predicts the correct number of TPBSs. To capture the correct topological behavior, we examine the Berry connection,

$$B(k) = \frac{1}{4\pi i} \mathrm{tr}[\sigma_3 C'^{-1} \partial_k C'], \tag{3}$$

which is the integrand of n in Eqn. 1. As the BNN coupling strength c' increases, the difference in $B(k)$ between the two phases of the unit cell (i.e., when $c_1 > c_2$ and $c_1 < c_2$) generated by flipping the nearest-neighbor interactions evolves, as shown in Fig. 1. The emergence, number, and positions

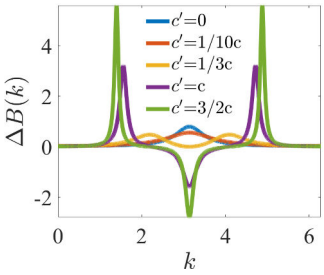

Fig. 1. (a) $\Delta B(k)$ with various c'.

of peaks and valleys in $\Delta B(k)$ correspond to local winding numbers of ± 1, and these match the predictions of the Jackiw-Rebbi theory, confirming their topological origin.

III. Results and Discussion

Although the global winding-number difference between the two topological phases remains $\Delta n = 1$, suggesting a single TPBS at the domain interface, the full supercell phonon-dispersion calculation reveals a different picture. When $c' > \frac{c_1+c_2}{6}$, three TPBSs emerge (Fig. 2). These three states correspond directly to the two peaks and one valley of $\Delta B(k)$ in Fig. 1, each carrying a local winding number of ± 1. Their spatial decay rates extracted from the eigenmodes precisely match the widths of these features in $\Delta B(k)$, confirming their topological origin. Experimental measurements obtained using a scanning laser Doppler vibrometer further verify the presence of all three TPBSs in our 3D-printed lattices.

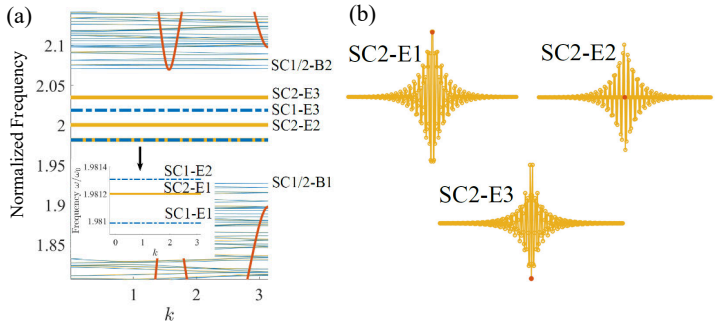

Fig. 2. (a) Phonon dispersion showing the triple topological states when $c' = \frac{c_1+c_2}{2}$. (b) Mode shapes of the three topological states.

IV. Conclusion

We have demonstrated that beyond-nearest-neighbor interactions cause the global winding number to fail in predicting the number of TPBSs in SSH lattices. To address this breakdown, we introduce a new topological characterization – local winding numbers derived from the Berry connection – which correctly captures the full set of boundary states.

References

[1] Su, W. P., Schrieffer, J. R., & Heeger, A. J., "Solitons in polyacetylene" *Physical review letters*, vol. 42, pp. 1698, 1979

[2] Pyfrom, J. R., Sun, K., & Ma, J. A., "Hierarchical topological states without dimension reduction," *Reports on Progress in Physics*, vol. 88(11), pp. 118003, 2025.

[3] Rajabpoor Alisepahi, A., & Ma, J., "In-gap edge and domain-wall states in largely perturbed phononic su–schrieffer–heeger lattices," *Crystals*, vol. 14(1), pp. 102, 2024.

[4] Alisepahi, A. R., & Ma, J., "Boundary effect on in-gap edge states in nonlocal Su-Schrieffer-Heeger model," *Health Monitoring of Structural and Biological Systems XVIII*, Vol. 12951, pp. 140-147, SPIE, 2024.

[5] Rajabpoor Alisepahi, A., Sarkar, S., Sun, K., & Ma, J., "Breakdown of conventional winding number calculation in one-dimensional lattices with interactions beyond nearest neighbors," *Communications Physics*, vol. 6(1), pp. 334, 2023.

[6] Jackiw, R., & Rebbi, C., "Solitons with fermion number 1/2," *Physical Review D*, vol. 13(12), pp. 3398, 1976.

Space-multiplexing Metalens for Multiple Ultrasonic Bessel Vortex Beams

Jie Zhu[1,2,*], Qian Cheng[1,2]

[1] Institute of Acoustics, School of Physics Science and Engineering, Tongji University, Shanghai 200092, People's Republic of China

[2] Shanghai Research Institute for Intelligent Autonomous Systems, Tongji University, Shanghai 201210, People's Republic of China

*Corresponding author: jiezhu@tongji.edu.cn

***Abstract*— The fine fabrication of metalens allows the leverage of spatial multiplexing to manipulate multi-channel ultrasonic beams independently. We experimentally demonstrate four-channel ultrasonic Bessel vortex beams as examples, showcasing great agreement with simulation results on topological charge and radiation direction. Our work offers more possibilities in designing functional ultrasound devices.**

***Keywords*— acoustic metalens, ultrasonic vortex beams, spatial multiplexings.**

I. Introduction

Acoustic vortex, with the characteristic of the helicoidal wavefront, have been widely studied due to its fascinating properties, such as orbital angular momentum (OAM) and the singularity of zero intensity [1]. Many efforts have been devoted to the generation of acoustic vortex via feasible strategies. However, the efficient generation of multi-channel and multi-directional vortex beams in water via a single, passive device remains an open challenge, primarily due to the difficulties in decoupling spatial information in each channel.

II. Methods

Our methodology relies on the precise manufacturing that allows the adjacent pixel of the metalens to be assigned independently [2]. Thus, the generate non-diffraction ultrasonic vortices can carry different topological charges and spatial orientations. For a case containing 4 channels, the phase profile for individual channels (i=1,2,3,4) can be expressed as:

$$\varphi_i = m_i\theta + k_0 \sin\alpha \sqrt{x^2+y^2} - k_0(x\cos\beta_i + y\cos\gamma_i) \quad (1)$$

where $k_0 = 2\pi f/c_0$ represents the wavenumber in water, and f, c_0 denote the ultrasonic frequency and the sound speed in water, respectively. The azimuthal angle θ is defined by $\tan\theta = y/x$. Parameter α denotes the base angle required for generating ultrasonic Bessel beams. β and γ correspond to the angles between the beam propagation axis and the positive x-axis and y-axis, respectively.

During experiments, working frequency is 2 MHz. The measured sample is designed as a 40 mm × 40 mm square. It is fabricated via 3D printing technology using a photopolymer resin (HTL resin) with a printing resolution of 10μm.

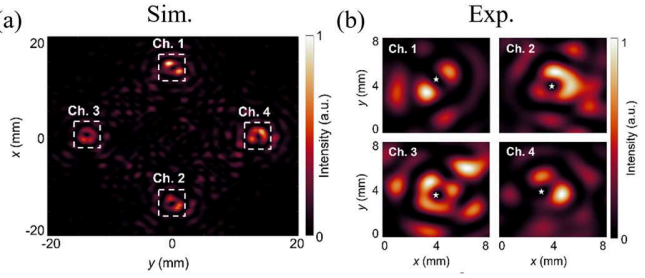

Fig. 1 The Generation of multi-channel ultrasonic Bessel vortex beams. (a) The simulation results. (b) The measured results.

III. Results and Discussion

From Fig. 1, the comparison between simulations and measurements shows that the ultrasonic beams propagate as predicted, each beam carries a donut-like pattern. Moreover, we can assign different or even higher order topological charge to the channels, which can be validated in phase distributions.

IV. Conclusion

We propose a MHz-band ultrasonic metalens that encodes four-channel phase information into a single device through spatial multiplexing, while maintaining ultrasonic field fidelity. This work may inspire more functional ultrasonic devices.

Acknowledgments

This work is supported by the National Key R&D Program of China (Grant No. 2022YFA1404403), the National Natural Science Foundation of China (Grant No. 92263208).

References

[1] S. Guo, Z. Ya, P. Wu, and M. Wan. "A review on acoustic vortices: Generation, characterization, applications and perspectives." *Journal of Applied Physics* 132, no. 21 (2022).

[2] Y. Su, D. Wang, Z. Gu, C. Liu and J. Zhu, "Multi-channel ultrasonic Bessel vortex beams by spatial multiplexing metalens." Accepted by *Communications Engineering.*

Experimental Investigation of Resonant Microdisks for the Creation of a Multiple-Scattering Acoustic Medium

Ch. Ghaisas[1], S. C. Baltogiannis[2], Y. Zhang[3], D. Garcia[1], B. Tallon[2], L. Belliard[1] and O. Boyko[1]*

[1]Institut des nanosciences de Paris, Paris, France

[2]Institut d'Alembert, Paris, France

[3]School of Aerospace Engineering and Applied Mechanics, Tongji University, China

*corresponding author: Boyko@insp.jussieu.fr

Abstract— Investigation of the interaction between elastic surface waves and nano-cylinder scatterers to identify resonant regimes and thereby extract crucial transport parameters in multiple scattering experiments aimed at exploring two-dimensional sub-diffusive Anderson localization. Using a Ti:Sapphire pump-probe setup we recorded spatial maps of the displacement on Au membranes and films.

***Keywords*— Picosecond ultrasonics, Surface acoustic waves, Lamb waves, Rayleigh waves, Resonant scattering**

In this work, we experimentally investigate the scattering properties of resonant microdisks with the objective of creating and characterizing a multiple-scattering acoustic medium. Using picosecond ultrasonics in a pump–probe configuration, we generate surface elastic waves through an opto-thermo-elastic mechanism and detect them via two interferometric techniques: a Sagnac interferometer for guided Lamb waves in membranes, and a Michelson interferometer for Rayleigh waves on bulk substrates. The microdisks consist of gold cylindrical resonators deposited either on silicon nitride membranes or on SiO_2 substrates.

We first characterize the free propagation of Lamb and Rayleigh waves, extracting dispersion relations that reveal the presence of several guided modes, including the antisymmetric A_0 and symmetric S_0 Lamb modes. We then investigate the interaction between these waves and individual gold microdisks. Although the scattered field is initially hidden within the dispersive incident wavefront, spectral filtering in the (k,ω) domain enables us to isolate a backward-scattered component. Its frequency content exhibits a set of discrete resonances, which we attribute to resonant modes of the cylindrical microresonator. The observed resonant peaks agree with theoretical predictions, confirming the excitation of transverse acoustic modes confined within the microdisk.

This study demonstrates that single microdisks act as efficient resonant scatterers for GHz surface waves. Their well-defined modal structure makes them promising building blocks for engineered multiple-scattering media, opening new perspectives for acoustic wave control, disorder-induced transport phenomena, and the realization of phononic systems operating in the gigahertz regime.

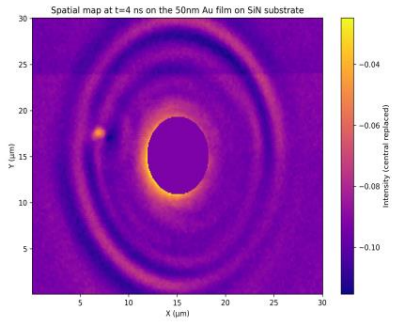

Figure 1: A (30 by 30µm) spatial scan of a Rayleigh wave with a lateral precision of 125nm at t= 4ns.

Figure 1 shows the spatial map of the out-of-plane displacement on the SiN/Si substrate. The gold cylinder appears as a bright yellow spot on the left, due to its locally enhanced reflectivity. From that point, a circular scattered wave-front propagates outward.

References

T. Tachizaki, T. Muroya "Scanning ultrafast Sagnac interferometry for imaging two dimensional surface wave propagation" Rev. Sci. Instrum. , Vol. 77, 043713, 2006.

A Tourin, A Derode, A Peyre, and M Fink. Transport parameters for an ultrasonic pulsed wave propagating in a multiple scattering medium. J. Acoust. Soc. Am., 108:503–512, 2000.

H Hu, A Strybulevych, J H Page, S E Skipetrov, and B A Van Tiggelen. Localization of ultrasound in a three-dimensional elastique network. Nature Physics, 4:945–948, 2008.

B. Perrin, Bernard, et al. "Interferometric detection in picosecond ultrasonics." *Physica B: Condensed Matter* 263 (1999)

Sub-THz electromechanics and optomechanics

Hong Tang [1]

[1] Department of Electrical and Computer Engineering, Yale University, New Haven, United States

***Abstract*— We demonstrate electromechanical and optomechanical resonator in the sub-terahertz regime. Thin film thin-film lithium is patterned and suspended to support mechanical structures oscillating at these extremely high frequencies, which are read out through elecctromechanical or cavity optomechanical coupling principles. Our hybrid platform paves the way for advancing mechanical systems in the quantum regime at elevated temperatures.**

***Keywords*— Optomechanics, electromechanics, quantum photonics, 5/6G technology**

Omnidirectional and anomalous acoustic absorption with an array of wiremeshes

Juan Pablo Escudero[1], Jean-Philippe Groby[1], Vincent Pagneux[1,*]

[1]Laboratoire d'Acoustique de l'Université du Mans (LAUM), UMR 6613, Institut d'Acoustique - Graduate School (IA-GS), CNRS, Le Mans Université, France
*Corresponding author: vincent.pagneux@univ-lemans.fr

***Abstract*— This study investigates the acoustic absorption of a rigidly-backed, periodic layer of inclined ultrathin resistive wiremeshes, aiming for strong performance across wide frequency and incidence-angle ranges. Results reveal omnidirectional absorption in subwavelength bands at high resistivity, and omnidirectional broadband absorption at medium resistivity, Anomalous scattering behaviors is also discussed.**

***Keywords*— Acoustic absorbers, wiremesh, broadband, omnidirectional.**

I. Introduction

One way to efficiently absorb acoustic waves is to combine both impedance matching and a loss mechanism to dissipate energy. Broadband angular impedance matching is generally challenging. However, for an interface between a homogeneous half-space and a periodic array of inclined thin wiremeshes, the reflection vanishes not only for waves traveling parallel to the plates, but, more remarkably, also for waves arriving at the mirror-symmetric angle, a consequence of reciprocity. In this work, our goal is to use this result to achieve broadband and omnidirectional absorption with rigid backing.

II. Methods

Our setup is depicted in Figure 1. An plane wave is incident on on array of ultra thin wiremeshes with rigid backing (Figure 1(a)). This problem can be directly solved numerically and as well through effective medium approximation Figure 1(b). It is then possible to investigate the absorption as a function of the parameters of the array (angle of the wiremeshes, resistance of the wiremeshes, thickness h versus periodicity of the array d) and of the angle of incidence [1].

III. Results and Discussion

Numerical results show:

- a resistive configuration capable of strongly absorbing acoustic energy over a wide omnidirectional broadband absorption
- a less resistive configuration capable of strongly absorbing acoustic energy at all angles of incidence for a specific subwavelength thickness

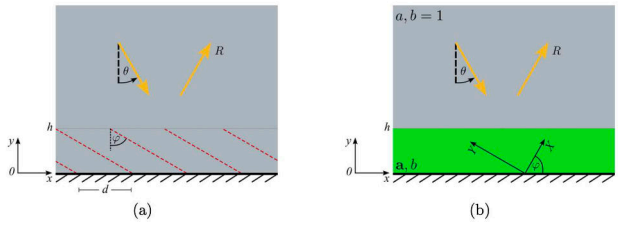

Fig. 1 (a) Reflection problem of an array of wiremeshes (in red dashed) with rigid backing. (b) Effective medium modelling of the setup

IV. Conclusion

We studied a rigidly-backed layer of inclined periodic resistive wiremeshes, analyzed numerically and via an effective medium model. Two configurations are identified: one optimized for strong all-angle absorption at a specific subwavelength thickness, and one for broadband omnidirectional absorption. Both come with large inclination angles, offering new routes toward perfect omnidirectional absorbers.

Acknowledgments

The European Commission is gratefully acknowledged for their support of the Horizon Europe DN METAVISION project (GA 101072415). Views and opinions expressed are however those of the authors only and do not necessarily reflect those of the European Union. The European Union cannot be held responsible for them.

References

1. Escudero, J. P., Groby, J. P., & Pagneux, V. (2025). Broadband-omnidirectional absorption using inclined wiremesh gratings. JASA Express Letters, 5(8).

Finite-Size Effects in Mechanical Metamaterials: The Role of Interfaces

Svenja Hermann

Technische Universität Dortmund, Germany
*Corresponding author: svenja.hermann@tu-dortmund.de

***Abstract*— C Mechanical metamaterials offer new possibilities for controlling vibrations and sound transmission through engineered band gaps. In building acoustics, they are a promising approach to improve noise insulation in lightweight wall systems, where low- and mid-frequency vibrations are difficult to mitigate with conventional materials. However, metamaterial design is typically based on infinitely periodic unit cells, while real applications involve finite structures connected to surrounding components. In this talk, we investigate how interfaces influence the vibration damping performance of finite-sized metamaterial panels. Using numerical simulations of sandwich-like assemblies, we analyze the role of material and free interfaces as well as the geometry of the connected plates. The results show that interface configuration significantly affects energy transmission and must be considered in the design of metamaterial-based structures for vibration mitigation.**

Mode conversion for elastic waves via temporal interfaces

Cong Chen [1], Zhanyu Li[1], Xiaoming Zhou [1,*], Gengkai Hu[1,2,*]

[1] School of Aerospace Engineering, Beijing Institute of Technology, Beijing 100081, China
[2] Marine Science and Technology Domain, Beijing Institute of Technology (Zhuhai), Zhuhai 519088, China
*Corresponding author: zhxming@bit.edu.cn (X.Z.), hugeng@bit.edu.cn (G.H.)

***Abstract*— We demonstrate perfect mode conversion between longitudinal and transverse elastic waves using an isotropic-anisotropic-isotropic temporal interface. This phenomenon arises from distinct phase accumulation of the two eigenmodes. For physical realization, a piezoelectric lattice with shunting circuits is proposed. These findings provide a new route for wave control via temporal interfaces.**

***Keywords*— mode conversion, temporal interface, elastic waves, anisotropy, time-varying modulation**

I. Introduction

In recent years, time-varying metamaterials have introduced an additional degree of freedom beyond spatial structuring. Temporal modulation can relax constraints imposed by time-reversal symmetry and energy conservation, thereby enabling wave phenomena and functionalities inaccessible in stationary media. Consequently, increasing attention has been devoted to time-varying systems across elasticity, acoustics, and photonics [1].

A temporal interface is formed by an abrupt change in material properties occurring on a timescale much shorter than a wave period, serving as the temporal analogue of a spatial interface. Although a variety of novel wave phenomena have been reported in electromagnetic systems [2,3], studies on temporal interfaces for elastic waves remain very limited. Moreover, the complex polarization characteristics and mode coupling inherent to elastic waves pose substantial challenges for both theoretical and experimental realization in time-varying elastic systems.

Here, perfect mode conversion between longitudinal (P) and shear (S) waves are achieved through an isotropic-anisotropic-isotropic temporal interface. We also develop a temporal transfer matrix method (TTMM) to analyze temporal multilayer structures and propose a two-dimensional piezoelectric lattice with external circuits for physical realization.

II. Methods

We consider an infinite and spatially homogeneous two-dimensional (2D) elastic medium in the plane-strain state with a constant mass density ρ. The elasticity of the medium varies in time: the elasticity tensor initially $\mathbf{C}$ takes the value $\mathbf{C}^0$, undergoes instantaneous changes to $\mathbf{C}^1$ at an instant t_1, and reverts to $\mathbf{C}^0$ at $t = t_2$, as illustrated in Fig.1. The initial and final media are assumed to be isotropic in elasticity, while the middle layer exhibits orthotropic elasticity. Without loss of generality, the principal axes of the orthotropic medium are set to align with coordinates (x, y).

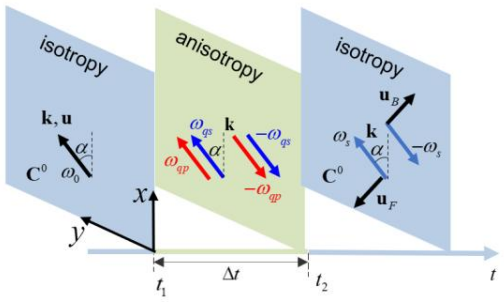

Fig. 1 Schematic of mode conversion through the temporal structure. ω_0 denotes the angular frequency for incident wave. Arrows aligned with or opposite to the wavevector $\mathbf{k}$ indicate waves with positive or negative frequencies. $\boldsymbol{u}_F$ and $\boldsymbol{u}_B$ represent the displacement vectors of the forward and backward waves in the end layer, which are perpendicular to $\mathbf{k}$.

A plane longitudinal wave with incident angle α and wavevector $\mathbf{k}$ travels in the initial layer, as shown in Fig.1. This temporal multilayer structure can be solved analytically using the temporal transfer matrix method (TTMM). For a given layer, $\mathbf{k}$ is conserved across the temporal interface due to spatial homogeneity, while the frequency changes as a result of temporal discontinuity. The converted frequencies are determined by the temporal Snell's law, while the amplitudes of the temporally scattered waves follow from the continuity of displacement $\mathbf{u}$ and momentum $\mathbf{p}$ across the temporal interface, which constitute the temporal boundary conditions.

In the final layer, there are four wave components, namely the forward and backward P and S waves. Their amplitudes can be expressed as

$$\begin{cases} F_p = M_{11}A_0, \quad F_s = M_{21}A_0 \\ B_p = M_{31}A_0, \quad B_s = M_{41}A_0 \end{cases} \tag{1}$$

where M_{ij} are the components of the temporal transfer matrix $\mathbf{M}$, and A_0 denotes the amplitude of the incident wave. Therefore, the analytical solutions for complete mode conversion from P wave to S wave can be obtained when $F_p = B_p = 0$. This condition yields

$$\begin{cases} \sin\beta_{qp} = \sin\beta_{qs} = 0 \\ \cos\beta_{qp} = -\cos\beta_{qs} \\ 2A_{12}\sin(2\alpha) + \cos(2\alpha)(A - B) = 0 \end{cases} \tag{2}$$

where α is the incident angle, $\beta_{qp} = \Delta t\omega_{qp}$ and $\beta_{qs} = \Delta t\omega_{qs}$. Here, $\Delta t = t_2 - t_1$ is the time duration of the orthotropic layer, while ω_{qp} and ω_{qs} are the angular frequencies of the quasi-longitudinal and quasi-shear waves, respectively. The coefficients A_{12}, A and B are determined by the components of $\mathbf{C}^1$ (see [4] for details). Eq. (2) provides the parameter conditions for achieving complete mode conversion at arbitrary incident angles, except for the cases $\alpha = 0$ and $\alpha = \pi/2$.

III. Results and Discussion

As a relevant example, we consider a scenario where the excitation is chosen as the 10-cycle harmonic line source modulated by a Gaussian envelope, as illustrated in Fig.2 (a). The frequency of the incident P wave is set to 0.5 kHz , and the incident angle is $\alpha = \pi/6$. The material parameters of the initial and final isotropic layers are taken as $\lambda = 1$ GPa , $\mu = 1$ GPa, $\rho = 10^3$ kg/m^3, while C_{66} is fixed at C_{66}=1 GPa for the orthotropic layer. Based on Eq. (2), it can be determined that $\Delta t = 1.861$ ms, $C_{11} = 1.053$ GPa and $C_{22} = 10.160$ GPa for the appearance of perfect mode conversion.

Wave propagation under the above parameters is simulated using the Finite-Difference Time-Domain (FDTD) method, and the results are reported in Fig.2.

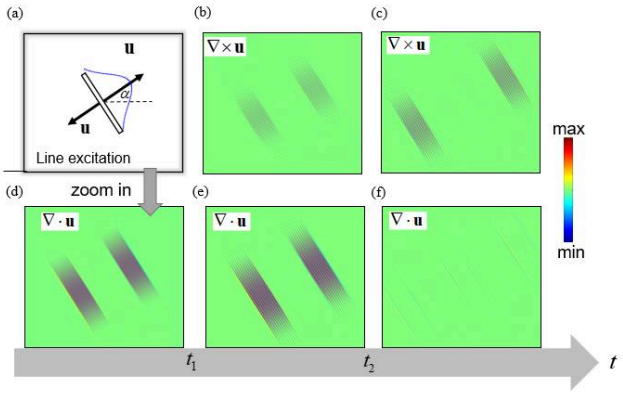

Fig. 2 FDTD results in the temporal slab: (a) the simulation model for FDTD; (b) The divergence component of displacement fields at t_1=40 ms; The curl and divergence components of displacement fields at (c,d) 40.93 ms and (e,f) 60 ms.

In Fig.2, the snapshots of the curl and divergence components of displacement field at 40 ms ($t = t_1$), 40.93 ms ($t_1 < t < t_2$) and 60 ms ($t > t_2$) are provided in Fig.2 (b-f), respectively. The incident longitudinal wave (Fig.2 (b)) undergoes the mode conversion in the orthotropic medium as shown in Fig.2 (c,d). After the sudden change at $t_2 = 41.86$ ms, the divergence component in Fig.2 (f) vanishes, signifying that the incident wave has been converted into a pure S wave. Moreover, examples of perfect S-to-P can also be found in [4].

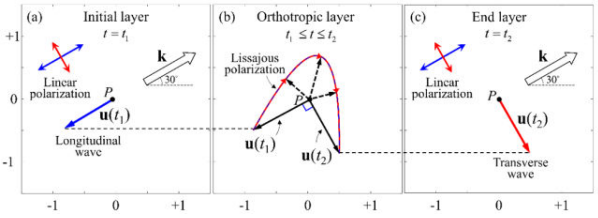

Fig. 3 The particle polarization trajectories in the regime of (a) $t \le t_1^-$, (b) $t_1^+ \le t \le t_2^-$ and (c) $t \ge t_2^+$

To elucidate the physical mechanism underlying complete mode conversion, we analyze the polarization trajectories of particles upon the sudden change of material properties. Initially, the displacement for a material point P is in align with $\mathbf{k}$, corresponding to a longitudinal polarization (Fig.3 (a)). Following the sudden transition to the anisotropic medium at $t = t_1$, both $\mathbf{k}$ and the displacement vector $\mathbf{u}(t_1)$ are preserved, while the superposition of qP and qS eigenmodes with distinct frequencies gives rise to a Lissajous-type polarization (Fig.3 (b)). After accumulating a relative phase shift over the temporal slab, $\mathbf{u}(t_2)$ becomes vertical to $\mathbf{k}$ at t_2, leading to a purely transverse polarization once isotropy is restored (Fig.3 (c)).

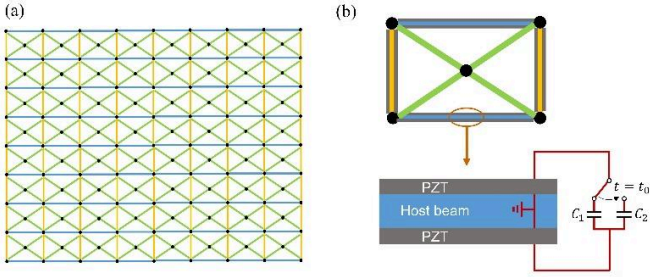

Fig. 4 (a) Schematic of a periodic square lattice structure for physical realization of medium systems with temporal interfaces, and (b) its unit cell consisting of piezoelectric composite structures shunted with the external circuit

Isotropic-anisotropic-isotropic temporal interfaces can be physically realized by two-dimensional lattice structures involving piezoelectric materials and shunting circuits, as sketched in Fig. 4. Each unit cell consists of a piezoelectric composite beam with a sandwiched configuration, where two piezoelectric patches are symmetrically bonded to both sides of a host beam and connected to an external shunting circuit containing a capacitance. By designing piezoelectric composite beams in two perpendicular directions, overall elastic properties of lattice structures can be manipulated to fulfill either isotropic or anisotropic elasticity. In addition, the modulus property can be dynamically modulated by temporally changing the circuit elements. For example, the temporal interface at time $t = t_0$ can be realized by switching the capacitance of value C_1 to a different one C_2. The structured materials presented in Fig. 4 are designed based on realistic materials, and provide a feasible platform for experimental realization of elastic temporal interfaces.

IV. Conclusion

We have demonstrated complete mode conversion between P and S waves through an isotropic-anisotropic-isotropic temporal slab, which is validated by the FDTD method. The results show that the key mechanism underlying perfect mode conversion lies in the distinct phase accumulation of two eigenmodes supported by the orthotropic material. Our findings reveal the interaction mechanism between elastic waves and time-varying materials, and provide both analytical and numerical tools for analyzing elastic waves in temporal solids. Future work will extend to the experimental validation of mode conversion via temporal interface.

Acknowledgments

This work was supported by the National Key R&D Program of China (2024YFB3408700 and 2024YFB3408702), and National Natural Science Foundation of China (Grants No. 12225203, No. 12532006, No. 11632003, No. 11972083, No. 11991030).

References

[1] E. Galiffi, R. Tirole, S. Yin, H. Li, S. Vezzoli, P.A. Huidobro, M.G. Silveirinha, R. Sapienza, A. Alú, and J.B. Pendry, Photonics of time-varying media, Advanced Photonics, 4 (2021) 014002 - 014002.

[2] C. Caloz, Z.-L. Deck-Léger, Spacetime Metamaterials—Part I: General Concepts, IEEE Transactions on Antennas and Propagation, 68 (2020) 1569-1582.

[3] N. Engheta, Four-dimensional optics using time-varying metamaterials. Science 379,1190-1191(2023)

[4] C. Chen, Z. Li, X. Zhou, and G. Hu, “Mode conversion for elastic waves via anisotropic temporal interfaces,” J. Sound Vib. 2026

Flat Band Skin Effect in Mechanical Metamaterials

Xulong Wang[1], Guancong Ma[1, 2*]

[1]Department of Physics, Hong Kong Baptist University, Kowloon Tong, Hong Kong, China
[2]Shenzhen Institute for Research and Continuing Education, Hong Kong Baptist University, Shenzhen 518000, China
*Corresponding author: phgcma@hkbu.edu.hk

***Abstract*—We report the flat-band skin effect (FBSE) in 1D non-Hermitian lattices, driven by the spectral topology of surrounding dispersive bands. The FBSE was experimentally observed in a non-Hermitian mechanical lattice. Our work reveals unique non-Hermitian localization and offers new perspectives on wave propagation.**

***Keywords*—mechanical metamaterials, non-Hermitian phononics, non-Hermitian skin effect, localized sates.**

I. Introduction

Non-Hermitian physics has fundamentally extended the study of open systems, most notably through the non-Hermitian skin effect (NHSE). In this work, we investigate one-dimensional (1D) non-Hermitian lattices hosting an ideal flat band, where we identify a distinct flat-band skin effect (FBSE) that transforms compact localized states (CLSs) into edge modes under open boundary conditions (OBCs).

Crucially, while conventional NHSE arises from a band's intrinsic topology, the FBSE is dictated by the point-gap topology of the surrounding dispersive manifold. This coupling causes the FBSE to counterintuitively vanish under high non-Hermiticity. We experimentally validate these findings using an active mechanical lattice, offering new insights into inter-band topological phenomena with broad implications for non-Hermitian metamaterials and photonics.

II. Methods

We investigate a 1D Lieb model characterized by a zero-energy flat band arising from an $(M-1)$-dimensional null space. The system is described by the Bloch Hamiltonian $H(k)$,

$$H(k)=\begin{pmatrix} 0 & t_1-\gamma_1+t_2e^{-ik} & t_2-\gamma_2 \\ t_1+\gamma_1+t_2e^{ik} & 0 & 0 \\ t_2+\gamma_2 & 0 & 0 \end{pmatrix}, \tag{1}$$

which incorporates reciprocal hopping $(t_{1,2})$ and non-reciprocal terms $(\gamma_{1,2})$, all of which are purely real.

While the Hermitian gap between the flat and dispersive bands remains robust unless the Hamiltonian itself vanishes $(t_1 = t_2 = 0)$, the introduction of non-Hermiticity facilitates line-gap closures. Specifically, these closures occur at $k = \pm\pi$ and $k = 0$ when the non-reciprocity balances the hopping parameters, satisfying critical conditions derived from $E(k) = \pm\sqrt{\Delta - (\gamma_1^2+\gamma_2^2) - 2i\gamma_1 t_2 \sin k}$ and $\Delta = t_1^2+2t_2^2+2t_1t_2cosk$. Furthermore, under OBC, the N-fold degeneracy of the flat band manifests as CLS-like wavefunctions that are localized across the bulk, enabling the engineering of diverse wavefunction profiles through linear combinations of eigenmodes.

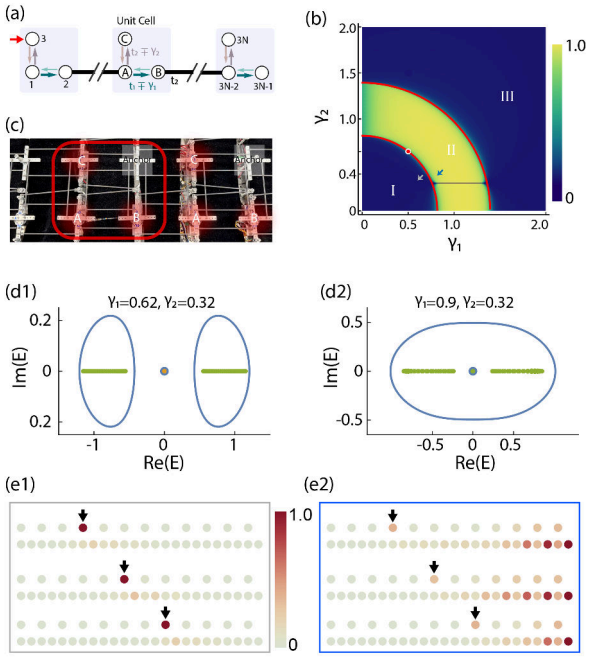

Fig. 1. (a) Schematic of 1D non-Hermitian flat-band model. (b) The averaged responses χ of the OBC flat band computed through the Green's function. (c) The active mechanical lattice realizing the non-Hermitian flat-band model. (d) and (e) Complex eigenenergy and steady-state responses of the flat band $(f = 10.9\text{Hz})$ under different parameters.

To characterize the spatial profiles of the flat-band modes, we employ the Green's function $\hat{G}(E_\eta) = (E_\eta - H_{OBC})^{-1}$ as a basis-invariant probe. Specifically, by setting the excitation energy to $E_\eta = 0 + i\eta$ with a vanishingly small imaginary part (we use $\eta = 10^{-20}$ in our numerical simulations), the source selectively targets the flat-band manifold, ensuring that the resulting response accurately reflects the characteristics of these zero-energy modes. The normalized spatial response $|R\rangle = \hat{G}(E_\eta)|s\rangle$ is generated from a source $|s\rangle$ at the first unit cell. We quantify the localization through the spatial centroid

$$\chi = \sum_n (n/3N)|R_n|^2, \tag{2}$$

where $\chi \approx 0$ indicates bulk-localized modes and $\chi \approx 1$ signifies the FBSE. The calculated $\chi(\gamma_1, \gamma_2)$ map in Fig. 1(b) reveals a well-defined regime where the response concentrates at the right boundary, providing clear evidence for the emergence of FBSE.

To elucidate the physical origin of the observed responses, we analyze the eigenvectors of zero-energy flat-band under OBC. These modes span an N-dimensional null space, $\ker(H_{OBC})$, where the right eigenvectors (REVs) typically manifest as bulk-localized, CLS-like states. The emergence of the FBSE is fundamentally understood through the Lehmann spectral representation of the Green's function:

$$G(E_\eta) \approx \sum_n \frac{|\psi^R_{0,n}\rangle\langle\psi^L_{0,n}|}{E_\eta}, \tag{3}$$

which highlights the critical role of the biorthogonal duals, or left eigenvectors (LEVs). In the FBSE-free regimes (Regions I and III), LEVs and REVs remain spatially co-localized. Conversely, within the FBSE regime (Region II), specific LEVs undergo exponential localization at the left boundary with significantly enhanced amplitudes, while their corresponding REVs still evenly in the whole bulk. This biorthogonal disparity ensures that even bulk-like excitations are projected onto boundary-dominant modes, thereby driving the non-Hermitian FBSE.

Our analysis reveals that the FBSE regime is strictly congruent with the regions where the line gaps of the dispersive bands close [Fig. 1(b)], marking a departure from standard non-Hermitian bulk-boundary correspondence. This phenomenon is rooted in an unexpected link to the point-gap topology of the surrounding manifold: the FBSE emerges only when the zero-energy flat band is enclosed within the complex spectral loops formed by the dispersive bands under periodic boundary conditions. Consequently, as further non-Hermiticity reopens the line gap, the flat band exits the spectral loop and the FBSE subsequently vanishes. This unique interplay—where the localization of a parameter-invariant flat band is dictated by the topology of its adjacent dispersive bands—constitutes a novel feature of non-Hermitian spectral topology that has been previously overlooked

III. Results and Discussion

We experimentally implement the proposed model using a versatile active mechanical lattice [Fig. 1(c)], an experimental platform engineered for the high-fidelity realization of non-Hermitian Hamiltonians. The system comprises 36 spring-coupled rotational oscillators organized into 12 unit cells, where non-reciprocal coupling is synthesized via programmable brushless DC motors driven by active feedback control. To target the flat-band manifold, all oscillators are precisely calibrated to a degenerate resonant frequency of $f_0 = 10.9$ Hz, corresponding to the zero-energy mode of the system.

The emergence of the FBSE is demonstrated by probing the steady-state spatial response under local harmonic excitation at site C. In Region I ($\gamma_1 = 0.62, \gamma_2 = 0.32$), where the FBSE is theoretically absent, the energy remains confined in the immediate vicinity of the source [Figs. 1(d1, e1)], characteristic of conventional localized modes. Conversely, upon tuning the parameters to Region II ($\gamma_1 = 0.9, \gamma_2 = 0.32$), the spatial profile undergoes a dramatic transition: the response concentrates predominantly at the right boundary. This boundary-dominant localization persists irrespective of the excitation position, providing robust experimental evidence for the non-Hermitian FBSE in the mechanical lattice.

IV. Conclusion

In summary, this work elucidates a novel FBSE that differs fundamentally from standard NHSEs in dispersive systems. Beyond theoretical insights, our findings offer significant potential for the development of advanced photonic devices and topological metamaterials.

Acknowledgments

This work was supported by supported by the National Natural Science Foundation of China (NSFC, T2525002), the National Key R&D Program (2022YFA1404400), the Hong Kong Research Grants Council (RFS2223-2S01, 12301822, 12300925), and X. W. acknowledges support from the Hong Kong RGC Junior Research Fellowship (JRFS2526-2S07).

References

[1] Wang X, Wang D, Lu C, et al. Observation of flat-band skin effect[J]. *arXiv preprint* arXiv:2512.19745, 2025.

[2] Okuma, N., Kawabata, K., Shiozaki, K. and Sato, M., "Topological origin of non-Hermitian skin effects," *Physical Review Letters*, vol. 124, p.086801, 2020

[3] Borgnia, D.S., Kruchkov, A.J. and Slager, R.J., "Non-Hermitian boundary modes and topology," *Physical Review Letters*, vol. 124, p.056802, 2020

Transient Growth Boundaries in Nonnormal Lattices

Ioannis Kiorpelidis[1,2] and Konstantinos G. Makris[1,2]

[1]Department of Physics, University of Crete, 70013 Heraklion, Greece
[2]Institute of Electronic Structure and Laser (IESL), FORTH, 71110 Heraklion, Greece
*Corresponding author: gkiorpelidis@iesl.forth.gr

***Abstract*—We investigate transient growth in the Hatano-Nelson model with uniform loss. By analyzing the nonnormality of the Hamiltonian, we identify a boundary separating the regions of transient amplification and monotonic decay. Notably, increasing only the system size N can trigger a transition between the two regions.**

***Keywords*—Lattice dynamics, Non-Hermitian skin effect, Transient growth.**

I. Introduction

Over the last few years, non-Hermitian systems have attracted significant interest due to their unique properties, such as the non-Hermitian skin effect [1]. A paradigmatic system hosting the skin effect is the Hatano-Nelson model [2], which has lately been experimentally implemented in the fields of acoustics [3] and photonics [4]. While much attention has been given to the spectral properties of the Hatano-Nelson model — particularly its extreme sensitivity to variations in the boundary conditions [1]— the transient dynamics of this model have received much less attention, even though this system offers a rich landscape for exploring amplifying effects [5], [6], [7].

In this work, we investigate the transient growth in the Hatano-Nelson model with uniform loss [Fig. 1(a)]. First, we show that different initial conditions lead to significantly different growth experiences before the eventual decay [Fig. 1(b)]. Second, we identify a boundary separating the regions of transient amplification and monotonic decay [Fig. 1(c)].

II. Model

We study wave evolution in a Hatano-Nelson (HN) lattice with N sites, with the dynamics given by

$$\dot{\boldsymbol{\psi}} = -i\mathbf{H}\boldsymbol{\psi} \tag{1}$$

where $\boldsymbol{\psi} = \begin{pmatrix}\psi_1 & \psi_2 & \cdots & \psi_N\end{pmatrix}^T$ and ψ_i is the wave field in the i^{th} site. Moreover, dot denotes differentiation with respect to time t and $\mathbf{H}$ is the non-Hermitian Hamiltonian

$$\mathbf{H} = \begin{pmatrix} -i\gamma & e^{h} & 0 & \cdots \\ e^{-h} & -i\gamma & e^{h} & \cdots \\ 0 & e^{-h} & -i\gamma & \cdots \\ \vdots & \vdots & \vdots & \ddots \end{pmatrix}. \tag{2}$$

where h is the coupling asymmetry between left and right sites and γ is the uniform loss applied to each site [Fig. 1(a)]. The solution of the wave evolution is given by

$$\boldsymbol{\psi}(t) = e^{-i\mathbf{H}t}\boldsymbol{\psi}(0) \tag{3}$$

with $\boldsymbol{\psi}(0)$ being the initial excitation in the lattice.

III. Results

A. Transient Growth and Nonnormality

Because the coupling is nonreciprocal ($e^{h} \neq e^{-h}$) , the Hamiltonian $\mathbf{H}$ is a nonnormal matrix, meaning $[\mathbf{H}, \mathbf{H}^{\dagger}] \neq 0$. This nonnormality allows for transient growth [8], [9], [10], [11], a phenomenon where the power $E(t) = \sqrt{\sum_{i=1}^{N} |\psi_i(t)|^2}$ of an initial excitation increases transiently in time before eventual decay. The maximum possible amplification is defined by the 2-norm of the propagator matrix $||e^{-i\mathbf{H}t}||$ [Fig. 1(b)–black line]. Moreover, as shown in Fig. 1(b), the system's growth experience is highly dependent on the initial conditions. Different initial states—such as a single-site excitation or a Gaussian beam—lead to distinct amplification curves. Crucially, the optimal right SVD vector, defined as the right singular vector of the propagator matrix $e^{-i\mathbf{H}t}$ associated with its largest singular value, is guaranteed to experience the highest possible amplification [11].

B. Boundary of Transient Amplification

A central focus of our study is to identify the boundary that separates regions of transient amplification from regions of monotonic decay. This transition is determined by analyzing the eigenvalues of the Hermitian matrix $\mathbf{B} = \frac{\mathbf{A}+\mathbf{A}^{\dagger}}{2}$ [11], where $\mathbf{A} = -i\mathbf{H}$. The boundary occurs when the maximum eigenvalue, λ_{max}, equals zero.We have derived an analytical expression for this boundary. By setting $\lambda_{max} = 0$, we find that for a constant loss γ, the critical coupling asymmetry h is given by

$$h = \sinh^{-1}\left[\frac{\gamma}{2\cos(\frac{\pi}{N+1})}\right]. \tag{4}$$

This result, illustrated in Fig. 1(c), demonstrates that increasing the system size N alone can trigger a transition from monotonic decay to transient growth, highlighting the sensitivity of the model to the system size.

IV. Conclusion

In this work, we demonstrated that an initial excitation in the Hatano-Nelson model with uniform loss exhibits transient growth before asymptotic decay due to the presence of coupling asymmetry. We also showed that this growth dependents on the spatial structure of the initial excitation. Finally, we identified the boundary in the (N, h) parameter space that defines the transition from a regime of transient growth to one of monotonic decay, highlighting the sensitivity of the system to its size.

Fig. 1. (a) Schematic of the Hatano-Nelson lattice with N sites, featuring nonreciprocal couplings e^{h}, e^{-h} and uniform loss γ. (b) Transient growth of the wave field norm $||\psi(t)||$ for different initial excitations: single-site (blue), Gaussian beam (green), and optimal right SVD vector (red). The black line denotes the 2-norm of the propagator $||e^{-i\mathbf{H}t}||$, representing the maximum possible amplification. Parameters: $\gamma = 1$, $N = 30$, and $h = 0.55$. Inset: Spatial profiles of the initial excitations. (c) Phase diagram in the (N, h) parameter space for $\gamma = 1$. The solid white line represents the analytical boundary given in Eq. (4), separating the regions of transient growth and monotonic decay.

ACKNOWLEDGMENTS

This work was supported from the ERC (Grant 101045135, Beyond Anderson) and the SNF/H.F.R.I. (Project 11496, PSEUDOTOPPOS).

REFERENCES

[1] N. Okuma and M. Sato. Annu. Rev. Condens. Matter Phys. **14**, 83 (2023).
[2] N. Hatano and D. R. Nelson. Phys. Rev. Lett. **77**, 570 (1996).
[3] A. Maddi, Y. Auregan, G. Penelet, V. Pagneux, and V. Achilleos. Phys. Rev. Research **6**, L012061 (2024).
[4] S. Weidemann, M. Kremer, T. Helbig, T. Hofmann, A. Stegmaier, M. Greiter, R. Thomale, and A. Szameit. Science **368**, 311 (2020).
[5] I. Kiorpelidis and K. G. Makris. Phys. Rev. Res. **7**, L032043 (2025).
[6] B. Midya. Phys. Rev. A **106**, 053513 (2022).
[7] L. Yu, C. Soci, Y. D. Chong, and B. Zhang. Nanophotonics **15**, e70039 (2026).
[8] I. Kiorpelidis, F. K. Diakonos, G. Theocharis, and V. Pagneux. Phys. Rev. B **110**, 134315 (2024).
[9] K. G. Makris, L. Ge, and H. E. Türeci. Phys. Rev. X **4**, 041044 (2014).
[10] K. G. Makris. Phys. Rev. E **104**, 054218 (2021).
[11] L. N. Trefethen and M. Embree, Spectra and Pseudospectra (Princeton University Press, Princeton, 2005).

Elastic Willis Metamaterials: Parameter Characterization and Wave Matching Application

Joo Hwan Oh[1]

[1]Department of Mechanical Engineering, Seoul National University, Republic of Korea
*Corresponding author: ojh86@snu.ac.kr

***Abstract*— This paper presents complementary studies on elastic Willis metamaterials. First, a parameter retrieval method considering mode coupling in elastic solids is proposed for analyzing complex elastic Willis metamaterials. The proposed method can characterize arbitrary Willis metamaterials with mode conversion. Then, wave matching application with Willis metamaterials is introduced.**

***Keywords*— metamaterials, Willis metamaterials, retrieval method, wave matching.**

I. Introduction

Willis metamaterials are elastic metamaterials exhibiting bianisotropic coupling between stress-velocity and momentum-strain fields [1,2]. This coupling, known as Willis coupling, gives rise to unique wave phenomena absent in conventional materials. Willis coupling in elastic media presents greater complexity due to the coexistence of longitudinal and shear wave modes and the associated mode coupling between them.

Despite growing interest, two fundamental challenges have prevented progress in this field. First, characterizing elastic Willis metamaterials through effective parameter retrieval is significantly more difficult than in acoustic or electromagnetic systems, particularly when mode coupling is present. Existing retrieval methods developed for acoustic metamaterials is not applicable when applied to general elastic cases containing mode coupling. In this presentation, a novel retrieval method with mode coupling is addressed. Additionally, the practical utility of Willis coupling in wave matching is introduced as one of the meaningful applications.

II. Methods

We propose a numerical retrieval method which can handle the full complexity of elastic Willis metamaterials including simultaneous mode coupling and Willis coupling [3]. The key strategy is to leverage eigen-decomposition on transfer matrix of Willis metamaterials. In elastic wave systems, transfer matrix is the matrix relating the state field vector at the interface of intermediate materials to the state field vector at the other interface. This matrix contains the information about wave propagation in the medium, thus it can be decomposed by the matrix composed of eigenvector of each propagating wave's mode like $T = MNM^{-1}$. For numerically retrieving effective parameters of Willis metamaterials, the numerical simulation with finite element method is conducted, then the scattering parameters such as reflection and transmission coefficients are measured. From the scattering parameters, transfer matrix can be calculated, then the effective parameters are retrieved by decomposing transfer matrix. The detailed procedures will be introduced in the presentation.

III. Results and Discussion

The process of validation is shown in the following cases

- Asymmetrically layered media with no mode coupling, but Willis coupling (Fig. 1)
- Asymmetric mass spring system with no Willis coupling, but mode coupling (Fig. 2)
- Asymmetric continuum structure with Willis coupling and mode coupling simultaneously (Fig. 3)

In two cases of layered medium and mass-spring systems, the effective parameters can be theoretically calculated, which validated the retrieving methods applied to numerical simulations. As can be seen in Figs. 1 and 2, the effective parameters can be retrieved by the proposed method. These results validate that the proposed retrieval method is effective to address the elastic metamaterials with Willis coupling and mode coupling simultaneously.

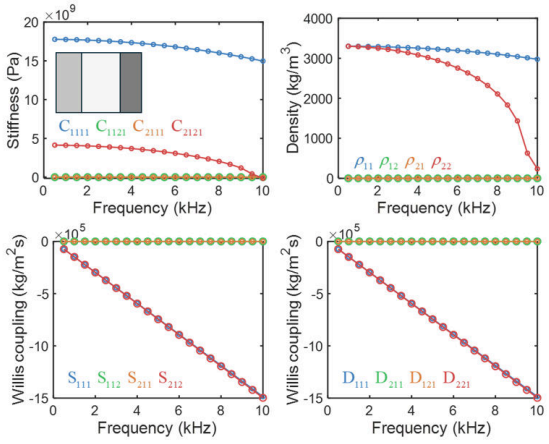

Fig. 1 The retrieved effective parameters of the layered medium.

Finally, the retrieving method was applied to complex continuum Willis metamaterials which have both Willis coupling and mode coupling simultaneously. The retrieved parameters are shown in Fig. 3. Then, the effectiveness of the proposed method was validated by comparing it with the homogenized models as described in Fig. 4. The displacement field contours are well-matched each other, which proved the validity of the proposed retrieving method.

In addition to the characterization of elastic Willis metamaterials, wave matching application will be introduced in the presentation.

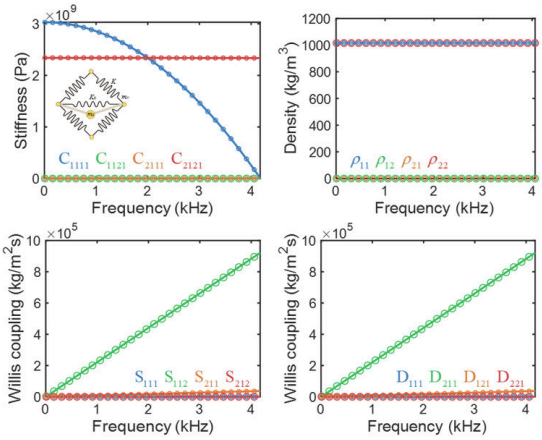

Fig. 2 The retrieved effective parameters of the mass-spring system.

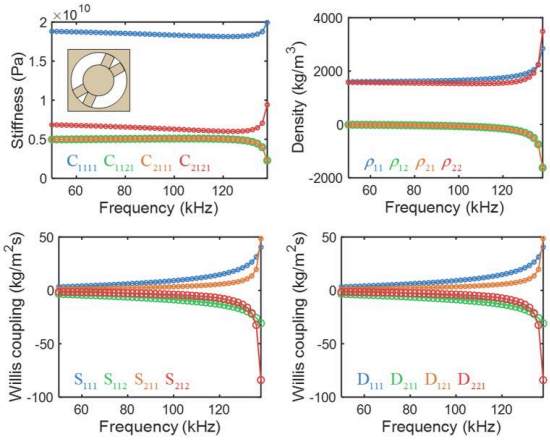

Fig. 3 The retrieved effective parameters of the continuum structure.

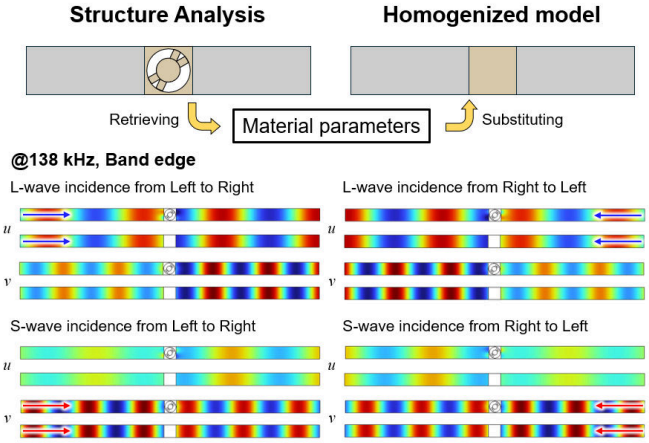

Fig. 4 The validation of the retrieving method with homogenized models.

IV. Conclusion

We have proposed a novel characterization method for retrieving the effective parameters of general elastic Willis metamaterials with Willis coupling and mode coupling simultaneously. We believe that this characterization method broadens the research area of Willis metamaterials containing mode coupling. Finally, as one of the useful applications of Willis metamaterials, wave matching application with Willis metamaterials will be introduced in the presentation.

Acknowledgments

This work was supported by the National Research Foundation of Korea (NRF) with grants funded by the Korean Government (Grants No. RS-2024-00343120, and No. RS-2024-00406514).

References

[1] J. R. Willis, "Variational principles for dynamic problems for inhomogeneous elastic media," Wave Motion, vol. 3, pp. 1–11, 1981.

[2] M. B. Muhlestein, C. F. Sieck, P. S. Wilson, and M. R. Haberman, "Experimental evidence of Willis coupling in a one-dimensional effective material element," Nature Communications, vol. 8, 15625, 2017.

[3] S. V. Jang, H. Chung, and J. H. Oh, "Retrieval method for elastic Willis metamaterials with mode coupling," Physical Review Applied, vol. 23, 044034, 2025.

Nanocrystalline Silicon for Optomechanics

Gloria Conte[1,*], Omid R. Ranjbar-Naeini[1], Manjunath Balagopalan[1], Cristiana F. Alves[1], Oliver Schraidt[1], Oili Ylivaara[2], Jouni Ahopelto[2], Clivia M. Sotomayor-Torres[1]

[1]INL - International Iberian Nanotechnology Laboratory, Braga, Portugal
[2]VTT - Technical Research Centre of Finland Ltd, Espoo, Finland
*Corresponding author: gloria.conte@inl.int

***Abstract*—Nanocrystalline silicon is a promising material for nano-opto-electro-mechanical metamaterials to be integrated into information and communication technology platform. The preparation of nanocrystalline silicon has an impact on properties associated with grain sizes and grain boundaries, which influence the mechanical quality factor of one-dimensional nanoresonators, among others.**

***Keywords*— nanocrystalline silicon, metamaterials, optomechanics, NOEMS.**

I. Introduction

Nanocrystalline silicon (nc-Si) is a novel material consisting of randomly oriented Si grains, so that it has an isotropic behavior [1]. Developed for MEMS applications in the 1980's [2], it has been recently considered as a possible material for optomechanical devices and circuits.

II. Methods

Nc-Si is produced by low pressure chemical vapour deposition (LPCVD) and consequent annealing of 220 nm of amorphous silicon on a silicon dioxide layer, which in turn is on a crystalline silicon (c-Si) substrate. The annealing temperature ranges from 650°C to 1050°C. During the annealing, nucleation and growth of nanocrystallites take place, resulting in a material as the one reported in Fig. 1.

The thermal annealing process determines the mean grain size and grain size distribution, impacting the electronic, optical and mechanical properties of nc-Si, which can be tuned by varying the annealing parameters [3]. These impact thermal transport [4] and, consequently, the performance of devices [5]. The isotropy of nc-Si has been demonstrated by an inelastic light scattering investigation [1].

The structural information is one example of characterisation needed to unravel the high mechanical quality factors of optomechanical nc-Si metamaterial devices compared to similar devices fabricated in silicon-on-insulator (SOI) [6]. The sizes of the nanocrystallites have been investigated by dark-field TEM images acquired at different diffraction areas through the hollow-cone technique [7], so that nanocrystallites with different orientations could be revealed. Complementary Raman spectroscopy characterization has provided insights about the grain size distributions at different annealing temperatures.

The devices under investigation consist of suspended nanobeams, which act as photonic-phononic one-dimensional

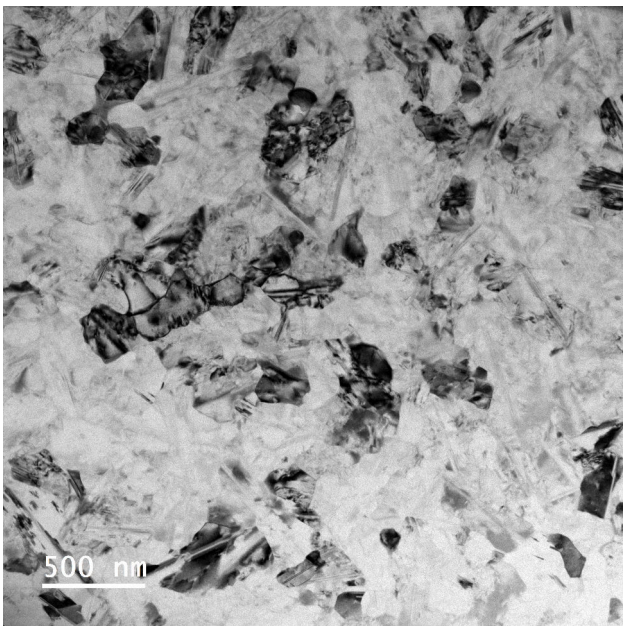

Fig. 1. TEM image of nc-Si.

structures working at hypersonic frequencies. In such devices photons and phonons are confined in a central cavity. The performance of these devices is determined not only by the material properties, but also by the device design. Two examples of nc-Si nanobeams are shown in Fig. 2.

Such devices are characterized by the fiber-loop method: the light from a tunable laser is sent into a tapered fiber which is arranged in order to have a loop, which is approached to the device so that both the photonic and phononic modes of the device are excited.

III. Results and Discussion

The resulting average grain size is larger for higher annealing temperatures (57.5 $\pm$ 2.5 nm and 53.4 $\pm$ 2.2 nm for 950°C and 1050°C, respectively) rather than the lowest annealing temperature (33.5 $\pm$ 0.7 nm for 650°C). The different average grain size determines a different volume of grain boundaries, which is crucial to understand electron and phonon transport in the material. The grain boundaries play a key role because they are expected to host a relatively high number of electronic

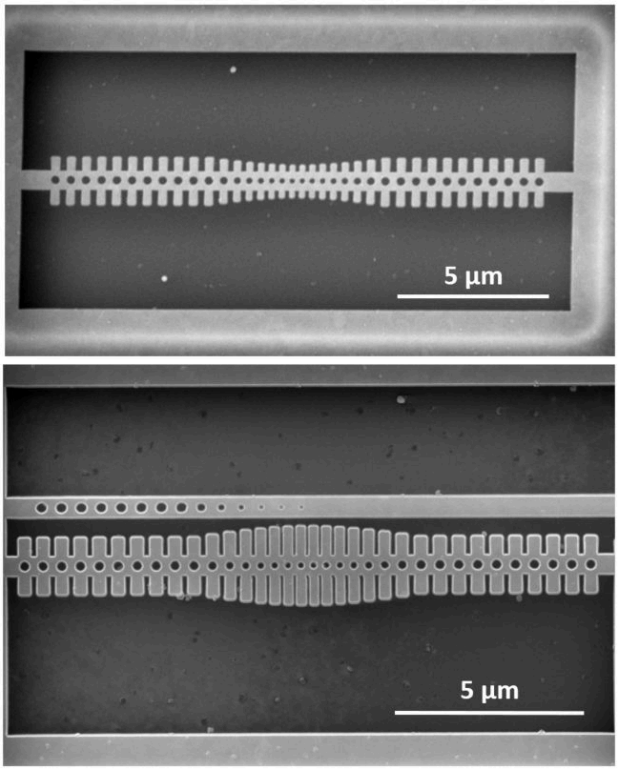

Fig. 2. SEM images of optomechanical nc-Si nanobeams. Top: device operating at a mechanical frequency of 4 GHz. Bottom: device operating at a mechanical frequency of 2 GHz and coupled to a waveguide.

gap states, which in turn affect the optical absorption, in particular the efficiency of one- versus two-photon absorption. However, the actual mid gap states densities are difficult to be determined. In some cases, the grain boundaries appear amorphous; in other cases, the grain boundaries exhibit 3-5 atomic planes.

Raman spectroscopy characterization has revealed that a reduction of the annealing temperature leads to a blueshift of the LO-TO Raman modes, accompanied by a significant broadening on the low-frequency side. Such spectral asymmetry arises from enhanced phonon confinement due to smaller grain sizes and larger grain boundary volumes [3].

The nc-Si nanobeams showed phonon lasing at MHz frequencies and, in some cases, at GHz frequencies. The typical behaviour of such devices is reported in Fig. 3.

The impact of different nc-Si fabrication parameters and of variability of critical dimensions in the performance of the devices is being assessed in both material properties and device performance.

IV. Conclusion

Further structural and optical analysis of nc-Si will shed light on the interplay among electrons, photons and phonons in the material, specifically regarding the role of nanocrystallites and grain boundaries in absorption and dissipation mechanisms at the nanoscale. This knowledge, combined with

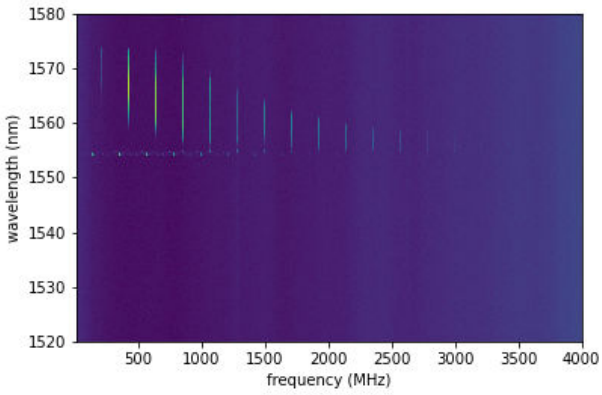

Fig. 3. Spectrogram of the light reflected from the cavity as the laser wavelength is swept from 1520 to 1580 nm at 15 mW. The bright features reveal regimes of coherent mechanical oscillations (phonon lasing) and self-pulsing in the intracavity fiels as the laser is tuned across the optical cavity resonance.

the comparison of the behaviours of devices fabricated from different nc-Si and with different deterministic fabrication variability parameters, will be crucial for a much improved understanding of losses, variability and device integration technology.

Acknowledgments

The authors acknowledge funding from the project MAGNIFIC (HORIZON-CL4-2022-RESILIENCE-01, Grant Agreement No. 101091968) and thank the Electron Microscopy and X-Rays (EMX) facility at INL.

References

[1] Y. Chen, O. M. E. Ylivaara, M. Balagopalan, O. R. Ranjbar. Naeini, G. Conte, T. Makkonen, J. Ahopelto and C. M. Sotomayor Torres, "Quasy-isotropy of nanocrystalline silicon films: an inelastic light scattering study", *Applied Physiscs Letters*, submitted.

[2] G. Harbeke, L. Krausbauer, E. F. Steigmaier, A. E. Widmer, H. F. Kappert and G. Neugebauer, "Growth and physical properties of LPCVD polycrystalline silicon films", *Journal of The Electrochemical Society*, vol. 131, pp. 675–682, 1984.

[3] D. Navarro-Urrios, M. F. Colombano, J. Maire, E. Chávez-Ángel, G. Arregui, N. E. Capuj, A. Devos, A. Griol, L. Belleries, A. Martínez, K. Grigoras, T. Häkkinen, J. Saarilahti, T. Makkonen, C. M. Sotomayor Torres and J. Ahopelto, "Properties of nanocrystalline silicon probed by optomechanics", *Nanophotonics*, vol. 9-16, pp. 4819–4829, 2020.

[4] E. Isotta, S. Jiang, R. Bueno-Villoro, R. Nagahiro, K. Maeda, D. A. Mattlat, A. R. Odufisan, A. Zevalkink, J. Shiomi, S. Zhang, C. Scheu, G. J. Snyder and O. Balogun, "Heat transport at silicon grain boundaries", *Advanced Functional Materials*, vol. 34-2405413, pp. 1–12, 2024.

[5] J. Maire, E. Chávez-Ángel, G. Arregui, M. F. Colombano, N. E. Capuj, A. Griol, A. Martínez, D. Navarro-Urrios, J. Ahopelto and C. M. Sotomayor Torres, "Thermal properties of nanocrystalline silicon nanobeams", *Advanced Functional Materials*, vol. 32-2105767, pp. 1–9, 2022.

[6] D. Navarro-Urrios, N. E. Capuj, J. Maire, M. Colombano, J. Jaramillo-Fernandez, E. Chávez-Ángel, L. L. Martin, L. Mercadé, A. Griol, A. Martínez, C. M. Sotomayor Torres and J. Ahopelto, "Nanocrystalline silicon optomechanical cavities", *Optics Express*, vol. 26-8, pp. 9829–9839, 2018.

[7] 6. B. Yao, T. Sun, A. Warren, H. Heinrich, K. Barmak and K. R. Coffey, "High contrast hollow-cone dark field transmission electron microscopy for nanocrystalline grain size quantification", *Micron*, vol. 41, pp. 177–1820, 2010.

On the Interpretation of Aeroacoustic Metadevice Performance in Terms of Spacetime Curvature

Giada Colombo[1,*] and Umberto Iemma[1],

[1]Department of Civil, Computer Science and Aeronautical Technology Engineering, Roma Tre University, Italy
*Corresponding author: giada.colombo@uniroma3.it

***Abstract*—Acoustic metamaterials enable tailored manipulation of sound waves, yet their extension to aeroacoustic environments remains challenging due to background flow effects. This work investigates spacetime curvature arising from non-uniform flows and spatially varying properties in phase-gradient metasurfaces, providing insight toward robust design of fully integrated aeroacoustic metamaterials.**

***Keywords* — metacontinua, metasurfaces, spacetime curvature, coordinate transformations**

I. Introduction

Metamaterials have revolutionised the concept of wave control, spreading across all branches of physics and engineering where manipulation of waves is desired. This rapid expansion has been enabled by the symmetries in the structure of the differential operator that governs wave propagation, which break down in the presence of a background flow. Indeed, the introduction of metamaterials in aeroacoustic environments requires, in principle, the redesign of the device, as it must account for the change in the mechanism of propagation of the perturbation. So far, the only way to do so is to embed the characteristics of the aerodynamic field directly in the metacontinua design and, thereby, tune the components derived through standard acoustic procedures [1]. The mathematical architecture allowing the manipulation of the material properties relies on the spacetime formalism, where the propagation of any scalar field can be described in a conservative form of the differential governing equation [2]. Therefore, moving in the *pseudo*-Riemannian manifold of the acoustic spacetime, it is possible to address the change in the mechanism of propagation due to convection with the generation of spacetime curvature [3]. Nonetheless, another source for deviating from flatness appears when the medium of propagation displays space-varying distributions of its mechanical properties, which is exactly what happens when metamaterials appear in the scene. This work analyses these aspects aiming to provide deeper insight into both effects toward the derivation of a more robust design for aeroacoustic metamaterials.

II. Methods

The methodology relies on the mathematical structure of the acoustic spacetime, where the notion of point is replaced by that of an *event* indicated by $\boldsymbol{\xi} = (c_0 t, x_1, x_2, x_3)$, and where the propagation of acoustic waves is governed by

$$\frac{1}{\sqrt{-g}}\partial_\mu\left(\sqrt{-g}g^{\mu\nu}\partial_\nu p\right) = 0, \tag{1}$$

being $\boldsymbol{\partial}$ the four-dimensional nabla operator, and where $g^{\mu\nu}$ are the components of the contravariant metric tensor that specify the mechanism of propagation, with g its reciprocal determinant. The shape of the metric tensor indicates the kind of propagation that we are observing. The possible scenarios could be: (i) a metric tensor with constant components, (ii) a metric tensor with event-dependent components. The case (i) results in a flat Minkowskian spacetime, whereas scenario (ii) might be associated with curved acoustic spacetime. Specifically, case (ii) can be addressed to the case of a propagation within a medium displaying non-uniform anisotropic properties or to the presence of a non-uniform background flow. However, the event-dependence of the $g^{\mu\nu}$ components is a necessary requirement but not sufficient for spacetime curvature.[4]. In fact, the local differential properties of the spacetime can be fully described by the Riemann tensor

$$R^\rho_{\sigma\mu\nu} = \partial_\mu\Gamma^\rho_{\nu\sigma} - \partial_\nu\Gamma^\rho_{\mu\sigma} + \Gamma^\rho_{\mu\lambda}\Gamma^\lambda_{\nu\sigma} - \Gamma^\rho_{\nu\lambda}\Gamma^\lambda_{\mu\sigma}, \tag{2}$$

which is a fourth-order tensor, whose interpretation is in general non-trivial. The Ricci tensor $R_{\sigma\mu} = R^\rho_{\sigma\mu\nu}$ and the Ricci scalar $R = g^{\sigma\mu}R_{\sigma\mu}$ are the first and second contraction of the Riemann tensor in Eq. (2), respectively, and can be used to have hints about the local spacetime geometry at the cost of losing some information. However, the Ricci scalar provides an overall description of the total amount of spacetime curvature that we might have, and a case where $R \neq 0$ represents the scenario in which we have some source of spacetime curvature in our domain. Specifically, anisotropic non-uniform media or non-uniform background flows generally lead to event-dependent metric components and may generate non-vanishing spacetime curvature. In such cases, the acoustic propagation path follows the geodesics of the effective metric, which may deviate from straight Euclidean paths. This aspect becomes relevant if one considers the propagation of the acoustic wave within a metamaterial: the possibility of achieving exotic wave manipulations derives from the definition of a suitable tailored spatial distribution of the material parameters. Therefore, an acoustic metamaterial can be described through an extended version of the continuum model, named *metacontinuum* [5], where the propagation of the acoustic perturbation is governed by

$$K\nabla\cdot\left(\boldsymbol{S}\boldsymbol{\rho}^{-1}\boldsymbol{S}\partial p\right) - \partial_{tt}p = 0, \tag{3}$$

where the desired distribution of parameters is embedded in the definition of an anisotropic stiffness, with an elasticity tensor provided by $\boldsymbol{C} = K\boldsymbol{S} \otimes \boldsymbol{S}$, and an anisotropic inertia $\boldsymbol{\rho}$. The key point in deriving aeroacoustic metacontinua designs is to recognise that Eq. (3) can be recast into the spacetime as Eq. (1), and, thanks to its conservative form, spacetime coordinate transformations can be used to tune the metacontinuum parameters from a static design to an aeroacoustically efficient one [1], as

$$\boldsymbol{g}_c = \boldsymbol{\Lambda}^{-1}\boldsymbol{g}\boldsymbol{\Lambda}^{-T}, \tag{4}$$

where $\boldsymbol{g}_c$ indicates the convected metric tensor obtained thanks to the spacetime mapping provided by $\boldsymbol{\Lambda}$. The Jacobian matrix in Eq. (4) enables the inclusion of the background flow characteristics directly into the metacontinuum design. Consequently, the approach for inducing convection in a region originally quiescent is limited solely by the capability of capturing the convective effects, and a transformation capable of encompassing general flow conditions is not known so far. As a consequence, deviations from the aeroacoustic benchmark will always appear, nevertheless, they could be reduced by combining together different spacetime mappings [6].

Results and Discussion

Due to the intrinsic analytical approximations of the methodology for deriving an aeroacoustic metacontinua design, efficient designs for practical aeronautical applications may be sensitive to variations of the operative conditions in which the device operates. For this reason, the present work investigates the spacetime curvature that can be generated by the presence of a metacontinuum with tailored distributions of the material properties, and by the presence of convection. A deeper understanding of spacetime curvature may provide a useful indicator for quantifying the benefit of deriving a spacetime-corrected design for each specific test case. The methodology will be assessed through its application to a phase-gradient metasurface whose design is defined to obtain extraordinary reflection. Specifically, the architecture of the metadevice will be replaced by the equivalent metafluid model with the spacetime adapted design obtained via Eq. (4). The analytical approach will ensure the computational cost saving and while enabling a direct assessment of the curvature-induced deviations from the aeroacoustic benchmark, thereby providing guidance for the development of more robust spacetime-corrected designs.

Acknowledgments

This work is supported by the European Union's Horizon Europe programme through the eVTOLUTION project, Grant Agreement ID 101138209

References

[1] U. Iemma, G. Palma, "Design of metacontinua in the aeroacustic spacetime," *Scientific Reports*, vol. 10, pp. 18192–18202, 2020.

[2] M. Visser and C. Molina-Paris, "Acoustic geometry for general relativistic barotropic irrotational fluid flow," *New Journal of Physics*, vol. 12, pp. 095014–095032, 2010.

[3] U. Iemma, "On the relationship between aerodynamic convection and acoustic spacetime curvature," *Proceeding of the International Congress of Sound and Vibration*, 2016.

[4] S. Carrol, "Spacetime and Geometry - An introduction to General Relativity," *Cambridge University Press*, 2019.

[5] A. N. Norris, "One path to acoustic cloaking," *Journal of Acousitc Society of America*, vol. 464, pp. 2411–2434, 2008.

[6] G. Colombo and U. Iemma, "Numerical assessment and comparison of spacetime convective corrections for the design of aeroacoustic metacontinua," *Journal of Sound and Vibration*, [Preprint], 2026.

Tackling the Long-Wavelength Challenge in Underwater Noise Reduction with Metabarriers

Marco Miniaci[1]

[1]*Politecnico di Torino, Corso Duca degli Abruzzi 24, 10129 Torino, Italy*

[*]*Corresponding author: marco.miniaci@polito.it*

***Abstract*—*Anthropogenic underwater noise poses a growing threat to marine ecosystems, while its mitigation remains particularly challenging at large wavelengths. Here, we propose thin anisotropic meta-barriers to achieve high sound transmission loss while maintaining thickness-to-wavelength ratios as low as 1/70. This demonstrates the potential of metamaterials for compact underwater noise control.*

***Keywords*—*elastic metamaterials, metabarriers, underwater acoustics, sound transmission loss, subwavelength control.*

Acoustic Purcell effects in phase-transitioning nanodroplets

Chengzhi Shi[1,*]

[1]Department of Mechanical Engineering, University of Michigan, Ann Arbor, MI, USA
*Corresponding author: czshi@umich.edu

Abstract— Microscale ultrasound devices are increasingly important for medical diagnostics and targeted therapies, yet achieving strong acoustic output at small scales remains challenging. Conventional strategies, including transducer arrays and MEMS components, often fail to satisfy the stringent requirements of compactness, flexibility, and power efficiency necessary for wearable applications. These challenges arise from fundamental trade-offs between miniaturization, acoustic intensity, and biological safety. We present a new strategy that leverages the acoustic Purcell effect, enabled through specially engineered perfluorocarbon nanodroplets (PFCnDs) designed to boost ultrasound emission. A theoretical framework for nanodroplet-enhanced Purcell effect is developed and experimentally confirmed through ultrasound emission measurements—the first demonstration of its kind. By tailoring the acoustic environment around the droplets, we achieve an acoustic Purcell factor normalized by droplet diameter (APF/D) of $1.6\times10^{5} \pm 2.6\times10^{2}$ m^{-1}, surpassing previous acoustic Purcell designs by two orders of magnitude. Furthermore, tunable droplet size and concentration allow precise control over Purcell-enhanced pressure radiation, mediated by the acoustic density of states. In B-mode imaging, PFCnDs operating in the Purcell-enhanced regime deliver a 42 ± 1.4 dB contrast gain relative to conventional ultrasound, arising from enhanced acoustic scattering. This work establishes a nanoscale acoustic Purcell framework for efficient ultrasound emission and marks a key advance toward integrating nanophononic design with high-contrast, ultrasound-based biomedical diagnostics and therapeutic platforms.

***Keywords*— acoustics, nanodroplets, Purcell effect, bubble dynamics, acoustic metamaterials.**

Generalization of exceptional point: high-dimensional coalescing non-Hermitian spaces

Guancong Ma

[1]Department of Physics, Hong Kong Baptist University, Kowloon Tong, Hong Kong, China
*Corresponding author: phgcma@hkbu.edu.hk

***Abstract*— We present the generalization of exceptional point, called "exceptional deficiency," characterized by the coalescence of two high-dimensional non-Hermitian linear spaces. At this condition, exceptional physics appears over a spectral continuum without fundamental limitations on bandwidths. The exceptional deficiency is experimentally realized using an active phononic crystal.**

***Keywords*—exceptional points, non-Hermitian skin effects, phononic crystals.**

Exceptional points (EPs) are spectral singularities in non-Hermitian systems, at which individual eigenvalues and eigenvectors become identical. The successful realization of EPs in diverse physical systems, such as photonics, acoustics, cold atoms, and superconducting circuits, has triggered tremendous interest in fundamental physics and inspired a vast array of novel applications. However, as the term "exceptional" suggests, EPs are usually isolated spectral points. Consequently, functionalities rooted in EPs face several inherent limitations, such as narrow bandwidth. Here, we present a generalization of the concept of EPs characterized by the coalescence of multi-dimensional Hilbert subspaces and overlapped spectra. This condition is denoted as "exceptional deficiency." When this happens, two Hilbert subspaces of identical but arbitrarily large dimensions exactly align, accompanied by the coincidence of their spectra. Consequently, the full Hilbert space is highly defective by "missing" half of its span. In the meantime, the spectrum is entirely composed of EPs. The condition of exceptional deficiency can be reached in a large variety of systems. Intriguingly, the exceptional deficiency can break the bulk-edge correspondence of non-Hermitian skin effects, which relates nontrivial point-gap topology to the existence of skin modes. As a consequence, we find that the exceptional deficiency underpins new non-Hermitian phenomena characterized by the synergy of skin effects and propagation.

The exceptional deficiency is experimentally realized using a non-Hermitian phononic lattice consisted of two unidirectionally coupled one-dimensional chains. The results also reveal new ways for flexible localization control [1].

ACKNOWLEDGMENTS

This work was supported by the National Natural Science Foundation of China (T2525002), the National Key R&D Program (2022YFA1404400), the Hong Kong Research Grants Council (RFS2223-2S01, 12301822, 12300925, JRFS2526-2S07), and the Hong Kong Baptist University (RC-RSRG/23-24/SCI/01, RC-SFCRG/23-24/R2/SCI/12).

REFERENCES

[1] Zhen Li, Xulong Wang, Rundong Cai, Kenji Shimomura, Zhesen Yang, Masatoshi Sato, Guancong Ma, "Exceptional deficiency of non-Hermitian systems: high-dimensional coalescence and dynamics," arXiv:2504.12238 (2025).

On the Quest of a Boundary Integral Formulation for Aeroacoustics of Metacontinua in Curved Spacetime

Umberto Iemma[1,*] and Giada Colombo[1]

[1]Department of Civil, Computer Science and Aeronautical Technology Engineering, Roma Tre University, Italy
*Corresponding author: umberto.iemma@uniroma3.it

***Abstract*—Boundary Integral Equation (BIE) methods represent an indispensable tool in computational aeroacoustics and acoustic metamaterial design. They basically rely on the self-adjointness (*i.e.*, Hermitianity) of the linear differential operator governing the phenomenon, which is verified when the acoustic perturbation propagates ina medium at rest or moving as a uniform stream. However, when sound propagation occurs in the presence of a non–uniform background flow or within a metacontinuum with spatially varying mechanical properties, the Hermitianity of the differential operator is lost and a pure BIE cannot be derived. This contribution focuses on the conceptual and mathematical challenges associated with the identification of an effective, design–oriented strategy to derive an integral equation formulation valid on a curved spacetime. It is shown how the non-Hermitian nature of the generalised spacetime D'Alembertian prevents the construction of a pure boundary integral formulation, and possible strategies based on boundary–field formulations or tangent spacetime approximations are discussed, outlining a path towards a general integral method for curved spacetime acoustics easily integrable with the existing integral formulations for aeroacoustic analysis.**

***Keywords*— metacontinua, aeroacoustics, boundary integral equation method, curved spacetime**

I. Introduction

Green's functions constitute the cornerstone of integral equation methods in acoustics, enabling compact formulations for scattering, radiation and metamaterial design. For homogeneous media in static condition or moving as a uniform stream, closed-form fundamental solutions exist and allow the reduction of the governing equations to boundary-only formulations.

In aeroacoustic configurations, however, sound often propagates within complex aerodynamic flows. The situation is made even more complex when the propagation domain is occupied by a non-uniform medium, such as the case of engineered metacontinua. A direct consequence of this is that the performance of metadevices designed under quiescent assumptions decays dramatically. At the same time, the non–uniform convection and the gradients of the metacontinuum properties compromise the validity of the static Green's functions and, as a consequence, prevent or limit the applicability of the BIE widely adopted in aeroacoustics. Recent developments have shown that all these effects can be consistently interpreted within a spacetime framework, where both background flow and metamaterial properties act as geometrical distortions of the acoustic spacetime. Aim of this work is to explore approaches and strategies capable to recover, at least partially, the effectiveness of boundary integral methods by reducing the contribution of field integrals (computationally critical for large domains) or relaying on the approximation of the equations on the local tangent, Minkowskian space.

II. Methods

Introducing spacetime coordinates

$$\xi_\mu = (c_0 t, x_1, x_2, x_3), \tag{1}$$

the acoustic field can be written in covariant form as

$$\frac{1}{\sqrt{-g}}\partial_\mu\left(\sqrt{-g}\, g^{\mu\nu}\partial_\nu\phi\right) = 0, \tag{2}$$

where $g^{\mu\nu}$ is an effective acoustic metric and $g = \det(g_{\mu\nu})$. For convective propagation, mixed space–time components of the metric encode the background velocity field, while anisotropic and inhomogeneous metacontinua modify the spatial part of the metric. Event–dependent variability of these quantities implies curvature of the associated acoustic spacetime.

In homogeneous isotropic media, the Green's function of the Helmholtz operator is available in closed form and forms the basis of classical boundary element methods. For anisotropic but homogeneous media, fundamental solutions can still be constructed explicitly, embedding anisotropy directly into the Green's function [3]. These anisotropic Green's functions, however, implicitly assume a flat spacetime, corresponding to a constant metric tensor. As a result, they fail to capture the effects of spatially varying flow fields or material parameters, which are responsible for acoustic spacetime curvature.

In curved acoustic spacetime, the Green's function would formally satisfy

$$\frac{1}{\sqrt{-g}}\partial_\mu\left(\sqrt{-g}\, g^{\mu\nu}\partial_\nu G\right) = \delta(\xi - \xi^*). \tag{3}$$

Closed-form solutions are available only for highly symmetric metrics[4], not relevant for realistic aeroacoustic configurations. In any such a case, G does not satisfy anymore the reciprocity condition, $G(\xi, \xi^*) \neq G(\xi^*, \xi)$. As a consequence, the presence of curvature prevents the reduction of the governing equations to a pure boundary formulation. Indeed,

the lack of a Green's function adapted to curved acoustic spacetime explains the progressive degradation of classical integral formulations in aeroacoustic metacontinuum problems. Boundary-only representations become incomplete, and equivalent source terms associated with curvature must be retained. Volume contributions associated with metric variations cannot be eliminated, inducing major numerical inconveniences that make integral formulations no longer competitive with respect to the filed methods like finite–element or finite-difference methods.

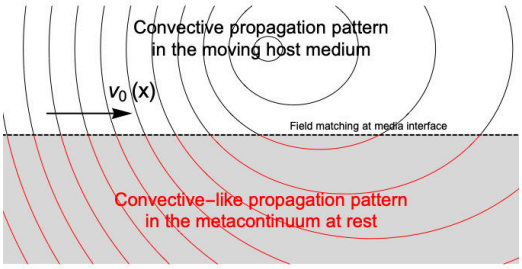

Fig. 1. A qualitative sketch of propagation patterns matching at the interface between a flowing medium and a *convective* metadevice.

III. Results and Discussion

In order to recover the potential of the integral formulations for this class of problems, two main directions appear viable: *i)* improve the numerical efficacy of boundary–field integral formulations, where volume terms are explicitly included, by enhancing the information retained in the boundary terms through the derivation of an appropriate Green's function capable to capture a general anisotropic behaviour, and, when applicable, by integration by parts of the volume terms; *ii)* explore the possibility of local approximations based on the projection of the non–Hermitian differential operator on the tangent (flat, *i.e.,* Minkowskian) spacetime. Aim of the present research is to face this challenge exploring both the approaches. In the present paper, we explore the structure of boundary–field integral equations derived from different forms of Eq. 2, rewritten by moving on the RHS all the terms inducing spacetime curvature, thus interpreting them as equivalent sources of a perturbation propagatimng on a flat equivalent spacetime. Starting from the assumption that the metric can be decomposed as $\boldsymbol{g} = \boldsymbol{g}_{\mathsf{F}} + \boldsymbol{g}_{\mathsf{C}}$, where $\boldsymbol{g}_{\mathsf{F}}$ represents the projection of $\boldsymbol{g}$ on the local tangent Minowskian spacetime, Eq. 2 can be rearranged as

$$\boldsymbol{\partial} \cdot \left(\boldsymbol{g}_{\mathsf{F}}^{-1} \boldsymbol{\partial} \varphi\right) = -\frac{1}{\sqrt{-g}} \boldsymbol{\partial} \cdot \left(\sqrt{-g}\, \boldsymbol{g}_{\mathsf{C}}^{-1} \boldsymbol{\partial} \varphi\right) - \frac{\boldsymbol{\partial}\sqrt{-g}}{\sqrt{-g}} \cdot \boldsymbol{g}_{\mathsf{F}}^{-1} \boldsymbol{\partial} \varphi, \tag{4}$$

where the spacetime–bending terms are treated as sources. Here, the operartor of Eq. 4 is reduced to the one of Stevenson's equation [3], for which a free–space Green's function exists. A similar procedure will be applied to the most general form of the convective wave equation governing the propagation within a medium in arbitrary motion. The fundamental underlying theory will be presented and discussed within the technology framework of aeronautical engineering. A preliminary numerical assessment of very simple benchmarks will be also presented.

Acknowledgments

This work is supported by the European Union's Horizon Europe programme through the eVTOLUTION project, Grant Agreement ID 101138209.

References

[1] U. Iemma and L. Burghignoli. An integral equation approach to acoustic cloaking. *Journal of Sound and Vibration*, 331(21):4731–4746, 2012.
[2] Andrew N. Norris. Acoustic metafluids. *J. Acoust. Soc. Am*, 125 (2): 839–849, 2009.
[3] R. Stevenson. Green's function for the helmholtz equation of a scalar wave in an anisotropic half-space. *SIAM Journal on Applied Mathematics*, 50(3):686–701, 1990.
[4] F. G. Friedlander. *The Wave Equation on a Curved Space-Time*. Cambridge University Press, 1976.

Band-structure calculations of phononic crystals in the hard-scatterer limit

Arkadii Krokhin*, Dmitrii Shymkiv

Department of Physics,University of North Texas, USA
*Corresponding author: arkadii.krokhin@unt.edu

***Abstract*—It is well known that the hard-scatterer limit leads to the appearance of non-physical features in the band structure of phononic crystals when calculated numerically using the plane-wave expansion method. We show that these numerical difficulties arise from a mathematical singularity in the corresponding eigenvalue problem for sound wave.**

***Keywords*— plane wave expansion, singular matrix.**

The hard-scatterer limit is not a purely mathematical abstraction. A phononic crystal composed of metal scatterers in air provides a very close physical realization of this limit, since the ratio of acoustic impedances is $Z_{metal}/Z_{air} \sim 10^5$. As shown in Fig. 1, numerical calculations of the band structure in the limit of infinite scatterer density $\rho_{sc} \to \infty$, contain flat bands that are apparently non-physical. The number of these non-physical flat bands increases drastically with the number of plane waves. Here we show that the errors observed in numerical calculations of the phononic crystal band structure originate from a singularity in the underlying eigenvalue problem.

In the plane-wave basis, the wave equation for the pressure field in a phononic crystal can be written as

$$\sum_{\mathbf{G}'} \rho^{-1}(\mathbf{G}-\mathbf{G}')(\mathbf{k}+\mathbf{G})\cdot(\mathbf{k}+\mathbf{G}')p_{\mathbf{k}}(\mathbf{G}') = \omega^2 \sum_{\mathbf{G}'} \lambda^{-1}(\mathbf{G}-\mathbf{G}')p_{\mathbf{k}}(\mathbf{G}'), \quad (1)$$

where $\rho^{-1}(\mathbf{G})$ and $\lambda^{-1}(\mathbf{G})$ are the Fourier coefficients of the inverse density and inverse elastic modulus respectively. For simplicity we consider a phononic crystal composed of fluids. The Fourier coefficients $\rho^{-1}(\mathbf{G})$ (and $\lambda^{-1}(\mathbf{G})$) are expressed through the structure factor $F(\mathbf{G}) = V_c^{-1}\int_{V_{sc}} e^{-i\mathbf{G}\cdot\mathbf{r}}d\mathbf{r}$ yielding

$$\rho^{-1}(\mathbf{G}) = (\rho_{sc}^{-1}-\rho_b^{-1})F(\mathbf{G}) \underset{\rho_{sc}\to\infty}{\to} -\frac{1}{\rho_b}F(\mathbf{G}), \quad (2)$$

$$\rho^{-1}(0) = \frac{f}{\rho_{sc}} + \frac{1-f}{\rho_b} \underset{\rho_{sc}\to\infty}{\to} \frac{1-f}{\rho_b} = \frac{1-F(0)}{\rho_b}, \quad (3)$$

where ρ_b is the density of the background fluid and f is the filling fraction of the scatterers. Equations (2) and (3) can be rewritten in matrix form as

$$\rho^{-1}(\mathbf{G}-\mathbf{G}') = \frac{1}{\rho_b}\left[\hat{I} - F(\mathbf{G}-\mathbf{G}')\right], \quad (4)$$

where $\hat{I}$ denotes the identity matrix of infinite order.

The structure factor $F(\mathbf{G})$ can be regarded as the Fourier coefficient of a piecewise function $F(\mathbf{r})$, which equals 1 inside the scatterers and 0 elsewhere within the unit cell. It is therefore clear that $F(\mathbf{r}) = F^2(\mathbf{r}) = F^3(\mathbf{r}) = \ldots$. When rewritten in Fourier space, this property implies $\det F(\mathbf{G}-\mathbf{G}') = 1$. Moreover, all eigenvalues of the matrix $F_{\mathbf{G}\mathbf{G}'}$ are equal to 1, i.e., it is a *unipotent* matrix. Notably, this is a purely geometrical property of a periodic lattice and is independent of the material properties of its constituents.

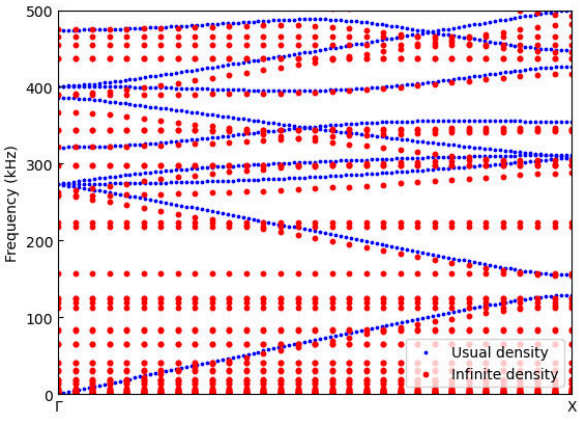

Fig. 1. Band structure of a phononic crystal of cylinders of infinite density in water.

It follows from the properties of a unipotent matrix that $\det\left[\hat{I} - F(\mathbf{G}-\mathbf{G}')\right] = 0$. Applying this result to Eq. (4), we find that $\det\rho^{-1}(\mathbf{G}-\mathbf{G}') = 0$, implying that the eigenvalue problem in Eq. (1) involves a non-invertible matrix. It is straightforward to show that the kernel matrix $\rho^{-1}(\mathbf{G}-\mathbf{G}')(\mathbf{k}+\mathbf{G})\cdot(\mathbf{k}+\mathbf{G}')$ is also singular. In numerical implementations, Eq. (1) is solved using a finite number of plane waves. In this case, the determinant of $\rho^{-1}(\mathbf{G}-\mathbf{G}')$ remains finite but small. Although the matrix is formally invertible, it becomes ill-conditioned, meaning that its output is highly sensitive to small rounding errors in the input. This sensitivity leads to numerical instability. In conclusion, the appearance of numerous spurious roots in the calculated band structure of a phononic crystal with hard scatterers can be traced to the singularity of the matrix $\rho^{-1}(\mathbf{G}-\mathbf{G}')$.

This work was supported by the Air Force Office of Scientific Research under Award No. FA9550-23-1-0630.

Optical imaging of sub-GHz acoustic waves in topological phononic crystals

Osamu Matsuda*
Division of Applied Physics, Faculty of Engineering, Hokkaido University, Japan
*Corresponding author: omatsuda@eng.hokudai.ac.jp

***Abstract*—The acoustic wave propagation in valley topological phononic crystal samples is studied using the time-resolved two-dimensional optical imaging technique. With the single frequency electronic excitation as well as the broad band optical excitation, the topologically protected robust wave-guiding is observed.**

***Keywords*— topological phononic crystals, waveguides, optical imaging, laser ultrasonics**

I. Introduction

The concept of topological insulator originally established in the quantum materials physics has been extended to various field of physics. It turns out that the concept is closely related to the wave nature of the phenomena in question, and not restricted in the quantum physics. In acoustics, even in the classical non-quantum regime, robust topologically protected robust wave propagation has been observed in topological phononic crystal waveguide structures[1].

In this paper, we study the acoustic wave propagation in two-dimensional topological phononic crystal, including topological waveguide and cavity, using our developing time-resolved two-dimensional optical imaging technique.

II. Methods

The phononic crystal structure is formed on a thin GaAs slab of thickness 1.0 μm[2] . The crystal itself is a hexagonal array of air holes. The unit cell of the crystal has the three-fold symmetry consisting of a center large circular hole with three lobe holes as shown in Fig. 1 (a). By rotating the hole structure clockwise (CW) or counter-clockwise (CCW) with respect to the axis perpendicular to the slab at the center of the hole by a small angle ($\alpha = \pm 5°$), the degeneracy at the Dirac cones at K and K' points in two-dimensional **k**-space is solved to form a phononic band gap, and the topologically non-trivial modes, so called valley topological modes, appear. At the interface between the CW and CCW rotated region, a localized interface mode (waveguide mode) appears within the opened gap by the bulk-edge correspondence. The appeared interface mode is supposed to be topologically protected and to show robust propagation of the acoustic waves. Figure 1 (b) shows an example of the structure we study. The black part consists of the CCW rotated unit cells, whereas the red part consists of the CW rotated unit cells. The whole structure has the plus shaped interfaces between CW and CCW regions.

The inter-digital transducer (IDT) is formed outside of the phononic crystal region. By applying radio frequency voltage to the IDT electrodes, the Lamb-like acoustic waves in the frequency range approximately from 475 MHz to 505 MHz are introduced into the phononic crystal region. The resulted acoustic field in the phononic crystal region is monitored by the laser pulses with picosecond temporal width using an optical interferometer which is sensitive to the surface normal displacement in picometer regime[3], [4] The typical measured area is around 100×100 μm^2.

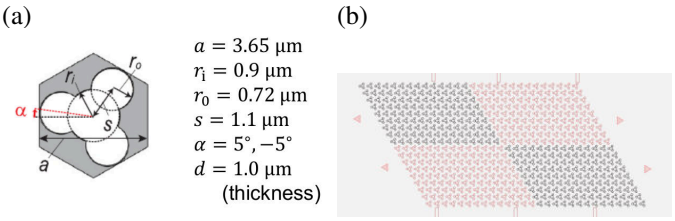

Fig. 1. (a) Unit cell geometry of the topological phononic crystal. (b) Schematic diagram of the entire structure of the phononic crystal with topological waveguide. Black part:$\alpha = -5°$ (CCW rotation), red part: $\alpha = +5°$ (CW rotation).

We also image the acoustic field with the pulse light excitation. Though the excitation efficiency is lower than above mentioned IDT excitation, the pulse excitation has an advantage of the broad band excitation (typically up to or beyond 1 GHz) comparing to the limited accessible range pre-determined by the IDT period[5].

III. Results and Discussion

Figure 2 shows an example of the measurement result, a snapshot image of the acoustic field excited by the IDT at 481.0 MHz[6]. The plane acoustic wave is incident to the phononic crystal region from the left hand side. The frequency 481.0 MHz is in the band gap of the phononic crystal, and no bulk waves penetrate into the phononic crystal. However, a localized wave propagating is clearly observed at the interface between the regions of $\alpha = \pm 5°$. It also shows a sharp turn at the corner (actuary the cross) with high efficiency > 90 %. It also shows the horizontally propagating localized wave is inhibited to to proceed across the cross because of the reversed configuration of the CW and CCW region in that part. This is another striking feature of the topologically protected mode.

IV. Conclusion

The time-resolved two-dimensional optical imaging of acoustic waves propagating on the topological phononic crystal is achieved. The excitation is done both electronically

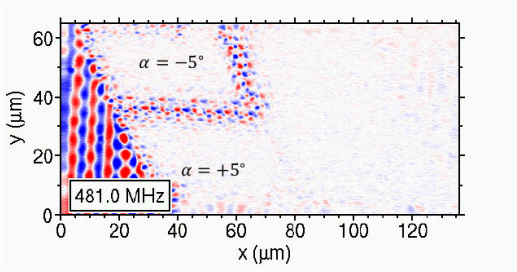

Fig. 2. A snapshot of the acoustic field on the phononic crystal waveguide. The plane wave at 481.0 MHz is incident from the left hand side.

at single frequency and optically in broad frequency band. The result shows the robust wave-guiding protected by the topological nature of the structure clearly. The method would pave a road to getting deeper understandings of the physics of acoustic waves in topological structures.

REFERENCES

[1] J. Lu, C. Qiu, L. Ye, X. Fan, M. Ke, F. Zhang, and Z. Liu, "Observation of topological valley transport of sound in sonic crystals," *Nat. Phys.*, vol. 13, pp. 369–375, April 2017.

[2] D. Hatanaka, H. Takeshita, M. Kataoka, H. Okamoto, K. Tsuruta, and H. Yamaguchi, "Valley pseudospin polarized evanescent coupling between microwave ring resonator and waveguide in phononic topological insulators," *Nano Lett.*, vol. 24, pp. 5570–5577, 2024.

[3] T. Tachizaki, T. Muroya, O. Matsuda, Y. Sugawara, D. H. Hurley, and O. B. Wright, "Scanning ultrafast Sagnac interferometry for imaging two-dimensional surface wave propagation," *Rev. Sci. Instrum.*, vol. 77, no. 4, p. 043713, 2006.

[4] O. Matsuda, S. Ueno, M. Tomoda, P. H. Otsuka, and O. B. Wright, "Time-resolved imaging of GHz acoustic vibrations at arbitrary frequencies using asynchronous periodic probe laser pulses," *Appl. Phys. Lett.*, vol. 125, p. 052201, July 2024.

[5] O. Matsuda, S. Kaneko, O. B. Wright, and M. Tomoda, "Time-resolved gigahertz acoustic wave imaging at arbitrary frequencies," *IEEE Trans. Ultrason. Ferroelectr. Freq. Control*, vol. 62, no. 3, pp. 584–595, March 2015.

[6] P. H. Otsuka, M. Tomoda, D. Hatanaka, H. Yamaguchi, K. Tsuruta, and O. Matsuda, "Imaging valley-vortex edge modes in a phononic crystal at ultrahigh frequencies," *J. Appl. Phys.*, vol. 137, no. 23, p. 235104, June 2025.

Trapping GHz Rayleigh Waves with Phononic Crystals

Daniel Torrent[1,*], Liangshu He, Fernando Soldevila[1], Yabin Jin[3], Pawel Packo[4], Agustín Mihi[5]
[1]Department of Physics, Universitat Jaume I, Spain
[2]Department of Materials Science and Engineering, Nanjing University, China
[3]Institute of Computational Mechanics × AI, Fudan University, China
[4]Department of Manufacturing Systems, AGH University of Kraków, Poland
[5]Institute of Materials Science of Barcelona (ICMAB-CSIC), Spain
*Corresponding author: dtorrent@uji.es

***Abstract*— We report optical pump probe measurements of surface acoustic waves in patterned silicon. Ordered hole arrays support long lived symmetry protected resonances, while disordered structures exhibit broadband trapping of acoustic waves in the gigahertz range. These results demonstrate complementary mechanisms for controlling phonon confinement using order and disorder.**

***Keywords*— phononic crystals, surface acoustic waves, disorder, bound states in the continuum, ultrafast acoustics.**

I. INTRODUCTION

Controlling elastic waves at the microscale is a central objective in phononics and acoustic metamaterials. Periodic structures, or phononic crystals, enable band engineering and wave confinement through Bragg scattering, while disordered systems can induce localization via multiple scattering. In parallel, bound states in the continuum (BICs), originally introduced in quantum mechanics, have recently attracted attention in acoustics as a route to achieve long-lived resonances embedded within radiative continua.

Surface acoustic waves (SAWs), and in particular Rayleigh modes in Silicon, provide an ideal platform to explore these phenomena in the GHz regime. However, experimental access to both ordered and disordered regimes within the same framework remains limited. Here we investigate the generation and confinement of SAWs in patterned silicon surfaces combining periodic and disordered hole arrays.

II. METHODS

The samples consist of arrays of circular holes with diameter 2 µm and lattice parameter 5 µm fabricated on silicon substrates. Two types of structures are studied: ordered periodic lattices and disordered arrays with controlled positional randomness.

Surface acoustic waves are generated via thermoelastic excitation using a pulsed optical pump. The resulting dynamics are probed using a time-resolved optical pump–probe setup with beam-deflection detection, providing sensitivity to local surface slope and displacement.

The temporal signals are analyzed in both time and frequency domains to extract spectral content in the 0.5–3 GHz range. The experimental configuration allows direct comparison between ordered and disordered geometries under identical excitation and detection conditions.

III. RESULTS AND DISCUSSION

In periodic structures, we observe narrow spectral features corresponding to long-lived acoustic modes. These resonances are consistent with symmetry-protected quasi-bound states in the continuum (quasi-BICs), where radiation losses are suppressed due to symmetry mismatch with the far field. The measured lifetimes and spectral selectivity indicate strong confinement despite the absence of a full bandgap.

In contrast, disordered structures exhibit broadband acoustic trapping over the 0.5–3 GHz range. The lack of translational symmetry leads to multiple scattering and spatial confinement of Rayleigh waves, resulting in extended dwell times without sharp spectral selection. The observed behavior is consistent with disorder-induced localization and does not require fine tuning of structural parameters.

These results demonstrate that both regimes can be exploited to tailor acoustic confinement depending on the desired spectral response.

ACKNOWLEDGMENTS

This work was supported by DYNAMO project (101046489), funded by the European Union.

REFERENCES

[1] Tachizaki, T., Muroya, T., Matsuda, O., Sugawara, Y., Hurley, D. H., & Wright, O. B. (2006). Scanning ultrafast Sagnac interferometry for imaging two-dimensional surface wave propagation. Review of Scientific Instruments, 77(4).

[2] He, L., Sun, S., Abraham-Ekeroth, R. M., Jin, Y., Xiang, Y., & Torrent, D. (2025). Theoretical developments and experimental Insights of acoustic and elastic bound states in the continuum. npj Acoustics, 1(1), 11.

[3] K. L. Tsakmakidis et al., "Bound states in the continuum in photonics," Nature Reviews Physics, 2020.

Color Holographic Imaging Based on an Acoustic Metasurface

Hong-Gen Chen[1], Hao-Wen Dong[2], Yue-Sheng Wang[1,3,*]

[1]Department of Mechanics, Tianjin University, Tianjin China
[2] Institute of Advanced Structure Technology, Beijing Institute of Technology, Beijing China
[3] Department of Mechanics, Beijing Jiaotong University, Beijing, China
*Corresponding author: yswang@tju.edu.cn

***Abstract*— An inverse design framework of acoustic metasurfaces for color holographic imaging is established based on the optimization method. The frequency-selective elements with the required phase-shift and transmittance are customized. The layout of the elements is optimized to achieve color holographic imaging. The design is verified through numerical simulations and experiments.**

***Keywords*— metasurface, acoustic holography, color imaging, inverse design.**

I. Introduction

An acoustic metasurface [1], a kind of two-dimensional metamaterials with microstructures of subwavelength, provides a platform for holographic imaging [1]. Although several published literatures focused on this topic [2], no color imaging has been reported. In this paper, we develop a customized inverse design of acoustic metasurfaces for color holographic imaging.

II. Methods

As shown in Fig. 1, a targeted color picture is first decomposed into a superposition of monochrome targeted imagines of three primary colors (red, green and blue) corresponding to three frequencies. Then an acoustic metasurface which can modulate the waves of three frequencies independently is designed to reconstruct three monochrome holographic imagines of three colors. Finally, the color imagine can be obtained by superimpose the three monochrome imagines. The mapping relationship from the metasurface to the holographic plane are established by using Huygens-Fresnel's principle. We obtain the distributions of phase and amplitude on the metasurface for the three frequencies. An optimization method is proposed to customize 80 types of elements with phase-shifts of $2n\pi/8$ (n=0~7) and transmission coefficients of $m/10$ (m=1~10) for each frequency. It is noted that elements are frequency-selective. That is to say, each element can transmit the wave of one frequency but block the waves of the other two frequencies. The layout of the elements with different phase shifts and transmittances is optimized to achieve holographic image.

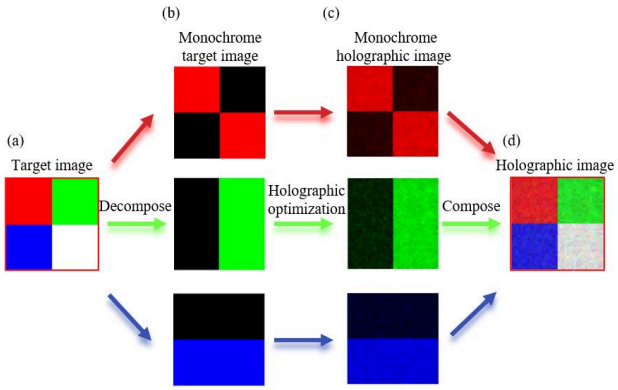

Fig. 1 Color holographic imaging.

III. Results and Discussion

As an example, the metasurface is designed for color holographic imaging of the eye part of the oil painting "Woman with a Hat and Fur Collar". Numerical simulation and experimental measurement are conducted and show agreement.

IV. Conclusion

Both numerical and experimental results show the validity of the proposed design methodology.

Acknowledgments

This work was supported by National Natural Science Foundation of China under Grant No. 12021002.

References

[1] A. L. Chen, Y. S. Wang, Y. F. Wang, H. T. Zhou, and S. M. Yuan, "Design of acoustic/elastic phase gradient metasurfaces: principles, functional elements, tunability and coding," Applied Mechanics Review, vol. 74, 020801, 2022.

[2] X. B. Miao, H. W. Dong, S. D. Zhao, S. W. Fan, G. L. Huang, C. Shen, and Y. S. Wang, "Deep-learning-aided metasurface design for megapixel acoustic hologram," Applied Physics Reviews, vol. 10, 021411, 2023..

Odd active solids

Anton Souslov[1,*],

*Corresponding author: as3546@cam.ac.uk

***Abstract*—This work focuses on novel phenomena and design principles for active materials with so-called odd elastic moduli, which are composed of non-reciprocal springs. Our results point to the design of novel soft machines at the macroscale, and guide the miniaturization of non-reciprocal metamaterials to the colloidal scale.**

I. Introduction

Active solids consume energy to allow for actuation and shape change not possible in equilibrium. As a consequence, they exhibit anomalous elasticity due to their far-from-equilibrium nature. We discover anomalies in the continuum description of non-reciprocal odd active solids, a ubiquitous class of active materials.

II. Results and Discussion

In our work on *more is less* [1], we find that as microscopic activity increases, macroscale active response can vanish below an active percolation transition. This work considers how both periodic and disordered structures exhibit this transition and discuss its microscopic origins and dynamical implications.

Another example of recent developments in this field is the formation and coarsening of dynamical patterns when active solids undergo instabilities [2]. These patterns arise in large-scale, inertial systems, and can be understood as a chiral and inertial version of so-called Type-II instabilities of pattern forming systems. Similarly to other Type-II instabilities, these patterns coarsen to system size, but uniquely in these systems, inertia, chirality, and non-linearity conspire and result in unique coarsening dynamics and steady-state phenomena associated with these solids.

III. Conclusion

Our results unveil surprising facets of active matter, offering new principles for engineering materials and locomotion far from equilibrium [3], [4].

Acknowledgments

This research was in part supported by UKRI EPSRC New Investigator Award EP/T000961/1.

References

[1] Jack Binysh, Guido Baardink, Jonas Veenstra, Corentin Coulais, Anton Souslov. More is less in unpercolated active solids. arXiv:2504.18362. Physical Review X (in press, 2026).

[2] Jonas Veenstra, Jack Binysh, Vito Seinen, Rutger Naber, Damien Robledo-Poisson, Andres Hunt, Wim van Saarloos, Anton Souslov, Corentin Coulais. Wave coarsening drives time crystallization in active solids. arXiv:2508.20052

[3] J. Veenstra, C. Scheibner, M. Brandenbourger, J. Binysh, A. Souslov, V. Vitelli, C. Coulais Adaptive locomotion of active solids. Nature 639, 935 (2025).

[4] Sami C Al-Izzi, Yao Du, Jonas Veenstra, Richard G Morris, Anton Souslov, Andreas Carlson, Corentin Coulais, Jack Binysh. Non-reciprocal buckling makes active filaments polyfunctional. arXiv:2510.14725. PNAS (in press, 2026).

Phononic Topological Waveguides for Gigahertz Applications

K. Monika Devi[1*], Y. Pennec[1], Clivia M. Sotomayor Torres[2] and B. Djafari-Rouhani[1]

[1] Institut d'Electronique, de Microélectonique et de Nanotechnologie, UMR CNRS 8520, Université de Lille, 59650 Villeneuve d'Ascq, France

[2]INL International Iberian Nanotechnology Laboratory, Avenida Mestre José Veiga s/n, 4715-330, Braga, Portugal

*Corresponding author: koijamm@univ-lille.fr

***Abstract*— We investigate topological properties of phononic waveguide interfaces, demonstrating robust propagation with negligible backscattering at gigahertz (GHz) frequencies. Forward and backward wavevector components are distinguished using Spatial Fourier transform thus, enabling the evaluation of backscattering and verification of the robustness of the excited topological mode.**

***Keywords*— topological, gigahertz, phononic crystals.**

I. Introduction

Topological waveguides have recently emerged as a powerful platform for controlling elastic waves due to their unique properties like unidirectionality, robustness, backscattering-free propagation in the presence of structural defects [1-3] thus, making them attractive for device applications [3-5]. With the ongoing device miniaturization and the push toward higher operating frequencies, the GHz regime has become increasingly important [5, 6].

II. Design of the Topological Waveguide

Motivated by this, we propose phononic topological waveguides based on a hypersonic phononic crystal structure consisting of patterned plates and exhibiting Dirac gaps ~ 13-14 GHz. The unit-cell of the phononic valley Hall crystal (PVHC) comprises two rounded triangles made of silicon (Fig.1(a)). For $\Delta r = 0$, a degeneracy exists at $f \sim 13.3$ GHz (Fig. 1(b), left), which is lifted when $r_1 \neq r_2$ as shown for Δr=0.04a in Fig. 1(b), right. The nontrivial topology of the PVHC is confirmed by calculating the Berry curvature and valley Chern numbers. Then, the waveguide is constructed by using two PVHCs of distinct topological nature: PVHC I (Δr=0.04a) and PVHC II (Δr= -0.04a). The supercell for the bridge big-big (BB) type waveguide is shown in the inset of Fig. 1(c).

III. Results and Discussion

The dispersion diagram for the bridge BB interface (Fig. 1(c)) reveals the presence of topological edge modes within the band gap. To assess the robustness of these modes, transmission is analyzed through a linear and a Z-path waveguide (Fig. 1(d)). For this, a point source is introduced near the input and the transmission is monitored along the waveguide path. The displacement field distributions (Fig. 1(f) and 1(g)), displays stronger confinement of field at the interface which is indicative of edge mode propagation.

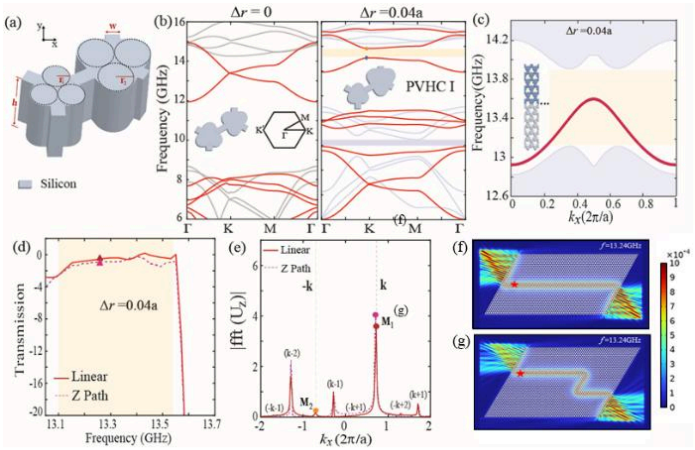

Fig. 1 (a) Unit cell for PVHC (a=381 nm, r_1=0.11a and r_2 = 0.15a). (b) Dispersion for Δr = 0, Δr = 0.04a. (c) Dispersion for Bridge BB interface (inset: Supercell). (d) Transmission for linear and Z-path waveguide. (e) Spatial Fourier spectra for linear (solid curves) and Z waveguide path (dashed curves) at f = 13.24 GHz for Δr =0.04a. (f) Comparison of forward and backward propagating wavevector magnitudes for a band of frequencies within the topological bandgap. Displacement field maps for (g) Linear and (h) Z-path waveguide. Red stars mark the position of the source.

Further insights into robustness are obtained through spatial Fourier transform (SFT) analysis (Fig. 1(e)). The Fourier spectra (Fig 1(e)) exhibits a dominant forward peak (k) along with negligible backward component (-k) for both waveguide paths confirming robust transport of the edge modes. This SFT analysis is extended across frequencies within the topological bandgap and the forward and backward magnitudes are compared. For an asymmetry of $\Delta r \approx 0.04$a, a bandwidth ~0.3 GHz of robust transport with minimal backscattering is observed. Additional studies are performed for different cases

of asymmetry as well as waveguide interface configurations. The results are significant for the design of low-loss GHz phononic device applications.

IV. Conclusion

We demonstrate robust phonon propagation with negligible backscattering using phononic topological waveguides at GHz frequencies. An asymmetry of $\Delta r \approx 0.04a$ yields a ~0.3 GHz bandwidth of robust transport with minimal backscattering. Our findings offer valuable insights for designing low-loss phononic devices at GHz frequencies.

Acknowledgments

The authors acknowledge the support from the project LEIT funded by the European Research Council (ERC) under the European Union's Horizon 2020 research and innovation programme (Grant Agreement No. 885689), and the project MAGNIFIC supported by the European Union's Horizon Europe research and innovation program under grant agreement (GA No 101091968).

References

[1] G. Ma, M. Xiao, and C.T. Chan, *Topological phases in acoustic and mechanical systems.* Nature Reviews Physics, 2019. **1**(4): p. 281–294.

[2] T. Ozawa, et al., *Topological photonics.* Reviews of Modern Physics, 2019. **91**(1): p. 015006.

[3] Y. Jin, et al., *The 2024 phononic crystals roadmap.* Journal of Physics D: Applied Physics, 2025. **58**(11): p. 113001.

[4] H. Pirie, et al., *Topological phononic logic.* Physical Review Letters, 2022. **128**(1): p. 015501.

[5] Q. Zhang, et al., *Gigahertz topological valley Hall effect in nanoelectromechanical phononic crystals.* Nature Electronics, 2022. **5**(3): p. 157–163.

[6] Y. Yao, D. Hao, and Q. Zhang, *Perspectives on Devices for Integrated Phononic Circuits.* Advanced Materials, 2025: p. 2407642

Quantum Valley Hall-Based Continuously Tunable Phononic Wave Coupler

Keita Funayama*, Kenichi Yatsugi, Hiroya Tanaka, Hideo Iizuka

Toyota Central R&D Labs., Inc., Aichi, Japan
*Corresponding author: funayama@mosk.tytlabs.co.jp

***Abstract*— We experimentally investigate a MEMS-based topological elastic wave coupler using the quantum valley Hall effect. By utilizing frequency-dependent wave localization at bridge boundaries, we achieve continuously tunable transmission coefficients within a bandgap. Furthermore, we successfully demonstrate topologically protected digital data transfer using frequency shift keying modulation within this coupler.**

***Keywords*— phononic topological insulators, wave coupler, microelectromechanical systems.**

I. Introduction

Topological insulators have significantly advanced classical wave systems by enabling unique phenomena such as robust and unidirectional wave propagation along protected interfaces [1]. These characteristics are highly promising for the development of high-efficient and robust integrated circuits across various domains, including optics, electronics, and acoustics. Active tunability in topological circuit elements such as wave couplers is significant to achieve multifunctional circuit systems. However, the topological protection, which has been considered as a unique advantage of topological wave systems, has prevented us from continuously and actively tuning the wave state at topological interface modes by external stimulus in a single structure.

In this work, we experimentally demonstrate a microelectromechanical system (MEMS)-based continuously tunable topological wave coupler utilizing the quantum valley Hall effect (QVHE). By designing the coupler consisting of two adjacent bridge boundaries with frequency-dependent wave localization, we achieve continuously tunable transmission coefficients from a single input port to two separate output ports within a single bulk bandgap. Furthermore, we demonstrate topologically protected digital signal transfer using a frequency shift keying (FSK) in the frequency dependent coupler. In our demonstration, the topological wave coupler works as a signal receiver, filter, and demodulator. The results show a data-transfer capability close to the theoretical channel capacity limit, paving the way for robust and highly efficient topological applications with high-functionality such as information communication and signal processing systems.

II. Methods

The study comprehensively implemented numerical simulations, microfabrication, and experimental evaluation of the topological MEMS coupler. Numerical models consisting of single crystal silicon structure were designed by using COMSOL Multiphysics 6.2 to follow QVH scheme. Dispersion diagrams were calculated for unit cells and supercells to identify the topological interface modes within a bandgap ranging from 305 kHz to 375 kHz.

The devices were fabricated on a silicon-on-insulator (SOI) substrate using electron beam lithography and reactive ion etching with the Bosch process. The resulting 23×23-unit cell structure features two adjacent topological waveguides with bridge boundary as shown in Fig. 1. To characterize the wave propagation, mechanical vibrations were electrostatically excited using a driving electrode in a high-vacuum chamber (2.0×10^{-5} Pa) to minimize viscosity damping. The out-of-plane displacement profiles were measured using a laser Doppler vibrometer. The detailed fabrication process and measurement setup are shown in our previous reports [4-6].

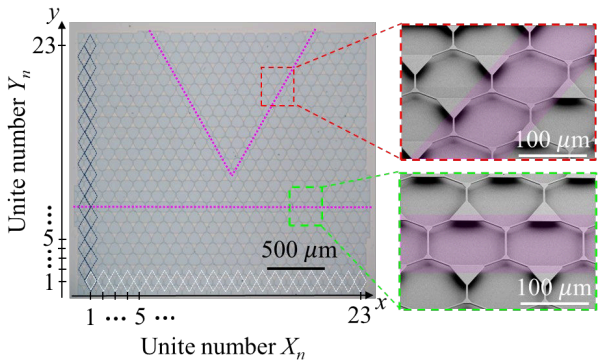

Figure 1: Top-view of the MEMS-based frequency-dependent topological wave coupler. The magenta lines represent the topological waveguides. SEM images in the right-upper and -lower panels show the enlarged views of the parts of the waveguides.

For the digital communication demonstration, binary FSK

was employed with carrier frequencies $f_1 = 315$ kHz and $f_2 = 360$ kHz. The output kinetic energy at each port was evaluated to determine the bit error rate (BER) and channel capacity, following Shannon's theorem to quantify the maximum mutual information of the topological channel.

III. Results and Discussion

Figures 2(a) and 2(b) show the experimental kinetic energy maps on the topological coupler for $f_1 = 315$ kHz and $f_2 = 360$ kHz. For the lower frequency, the elastic wave strongly localized on the V-shaped topological waveguide resulting in that the elastic wave passes through from port 1 to port 2 without coupling with the straight topological waveguide. On the other hand, when the driving frequency is high, we see the wave propagation from port 1 to port 3 by coupling with the V-shaped and straight waveguides. The coupling between the two waveguides is attributed to the frequency-dependent localization of the topological edge mode at the bridge boundaries, which enables us to continuously tune the coupling strength between them without breaking topological protection. Indeed, Fig. 2(c) shows the frequency spectrum of the output energy at ports 2 (red circles) and 3 (blue triangles) relative to the energy at port 1. As the frequency increases, the output energy at ports 2 and 3 continuously decreases and increases, respectively.

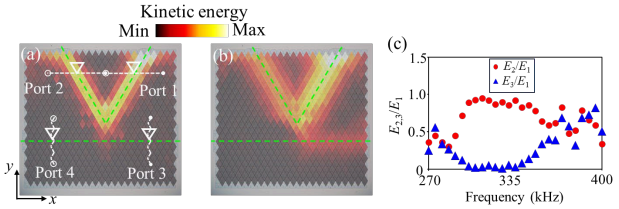

Figure 2: Two-dimensional kinetic energy maps in the topological wave coupler for (a) low and (b) high frequency. (c) Experimental frequency spectrum of the output energy at ports 2 and 3 relative to that of port 1.

Furthermore, we demonstrate digital information transfer using FSK. By assigning two frequencies ($f_1 = 315$ kHz and $f_2 = 360$ kHz) to binary states, we successfully transmitted digital signals through the coupler. Figure 3 shows the frequency response of the input signal and output kinetic energy at ports 2 and 3. The output energy at each port follows the frequency changes of input signal, indicating that the frequency-modulated digital signal is demodulated as a signal amplitude. These results indicate that the proposed coupler not only provides tunable wave routing but also serves as a robust platform for high-integrity topological communication.

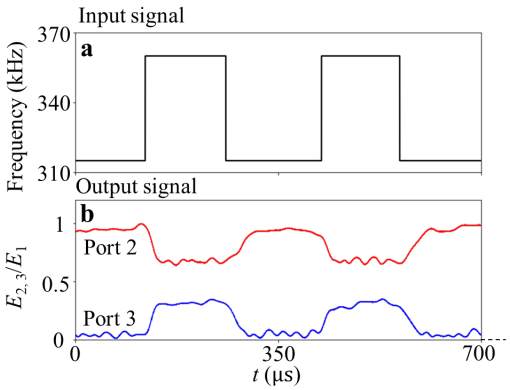

Figure 3: (a) Frequency of the input signal from port 1. (b) Output signals at ports 2 and 3. In the coupler, the frequency-modulated signal is demodulated to amplitude of mechanical vibration.

IV. Conclusion

We experimentally demonstrated a MEMS-based topological coupler with continuously tunable transmission coefficients based on the quantum valley Hall effect. By utilizing frequency-dependent wave localization at bridge boundaries, the coupler achieves tunable wave splitting within a single bandgap. Furthermore, we successfully implemented digital data transfer using frequency shift keying, achieving a channel capacity close to the theoretical limit. These results provide a robust platform for integrated topological circuits, paving the way for advanced signal processing and secure communication.

Acknowledgments

A part of this work was supported by Nagoya University microstructural characterization platform as a program of "Advanced Research Infrastructure for Materials and Nanotechnology in Japan (ARIM)" of the Ministry of Education, Culture, Sports, Science and Technology (MEXT), Japan.

References

[1] Z. Wang, Y. Chong, J. D. Joannopoulos, and M. Soljačić, "Observation of unidirectional backscattering-immune topological electromagnetic states," Nature, vol. 461, p. 772, 2009.

[2] K. Funayama, K. Yatsugi, A. Miura, and H. Iizuka, "Control of coupling between micromechanical topological waveguides," International Journal of Mechanical Sciences, vol. 236, p. 107755, 2022.

[3] K. Funayama, K. Yatsugi, and H. Iizuka, "Quantum valley Hall effect-based topological boundaries for frequency-dependent and -independent mode energy profiles," Communications Physics, vol. 7, p. 409, 2024.

[4] K. Funayama, K. Yatsugi, H. Tanaka, and H. Iizuka, "Quantum valley Hall effect-based coupler with continuously tunable transmission for topological information communication," Advanced Science, vol. 12, p. e06732, 2025.

Helmholtz Resonator-Induced All-Angle Self-Collimation in Square-Lattice Sonic Crystals

David Ramirez Solana, Muhammad Gulzari*

[1]School of Civil Engineering, University College Dublin, Ireland
*Corresponding author: muhammad.gulzari@ucd.ie

***Abstract*— Over the past three decades, phononic crystals and acoustic metamaterials have revolutionized the control of acoustic waves, enabling unprecedented sound manipulation through engineered structural periodicity and local resonances. In this work, we demonstrate that Helmholtz resonators (HRs) embedded within square-lattice sonic crystals (SCs) can induce all-angle self-collimation (AASC) of acoustic waves over broad frequency ranges—a phenomenon previously achievable only in rectangular lattices or with elliptical scatterers. Using finite element simulations and experiment, we investigate two types of locally resonant sonic crystals (LRSCs) incorporating HR-based scatterers with distinct resonant frequencies: one with a resonance in the wavelength regime (termed LRSC-Type A) and another with a lower local resonance frequency (LRSC-Type B). The LRSC-Type A configuration exhibits wideband AASC within the third band, covering 66.5% of the bandwidth (520 Hz). In contrast, LRSC-Type B demonstrates frequency-sensitive super-collimation (FSSC) and AASC in the fourth band, with a bandwidth of 22.86% (190 Hz). Frequency response analyses of finite supercell arrays confirm robust collimation performance for incident angles up to 85°. These findings underscore the unique capacity of Helmholtz resonators to enable AASC in symmetric lattices, opening new possibilities for directional sound control, low-loss acoustic waveguides, non-diffractive beam shaping, and high-resolution acoustic imaging systems.**

***Keywords*— All-Angle Self-Collimation, Acoustic metamaterials, Sonic crystals, Helmholtz resonators**

I. Introduction

Since Helmholtz first discovered the resonance phenomena in resonators and proposed an equation to describe it over 160 years ago [1], Helmholtz Resonators (HRs) have become a cornerstone in acoustic wave control [2]. They have been widely used for sound absorption [3], reflection [4], and focusing phenomena [5], [6]. However, their potential for collimating acoustic waves has remained almost unexplored, despite the extensive study of periodic HR arrangements, especially within phononic crystals [5], [7], [8]. In the broader context of periodic acoustic materials, phononic crystals (PnCs) and their air-based counterparts, Sonic Crystals (SCs) [9], have emerged as versatile platforms for controlling sound propagation. These structures, characterized by periodic arrangements of high-contrast scatterers in a host medium, exhibit Bragg bandgaps (Bragg BGs) arising from destructive interference phenomena [10], [11]. For more information, read [12].

II. Methods

We consider a two-dimensional SC composed of a periodic square-lattice arrangement of scatterers, each embedded with a HR. To analyse the acoustic wave propagation, we examine the unit cell depicted in Fig. 1a, which consists of a scatterer with an outer radiussR and a single aperture forming the HR. Periodic boundary conditions are applied along the X- and Y-directions to model an infinite periodic structure and to compute its dispersion characteristics. The lattice constant is denoted by a, and the wavevector is swept along the boundary of the irreducible Brillouin zone (BZ) in reciprocal space [13].

The resonator within each scatterer is defined by three geometric parameters: the neck length L_n (corresponding to the wall thickness, i.e., the difference between the outer and inner radii), the neck width w_n, and the inner surface area of the cavity S_c. The fundamental resonance frequency of the HR is given by [1]:

$$f_{HR} = \frac{c}{2\pi}\sqrt{\frac{\omega}{L_{eff}S}}$$

where $L_{\text{eff}} = l_n + \delta l_n$ is the effective length of the neck, and $\delta l_n = \alpha w_n$ represents the end correction. The factor α accounts for the abrupt change in cross-section at the neck–cavity interface and typically ranges between 1.3 and 1.7 for circular geometries [14]. In our two-dimensional model, however, α is found to be 2.73, which deviates from the conventional range due to the planar nature of the simulation domain.

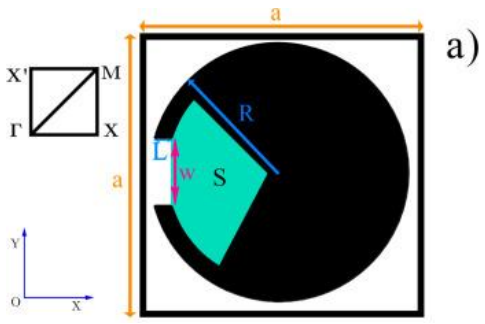

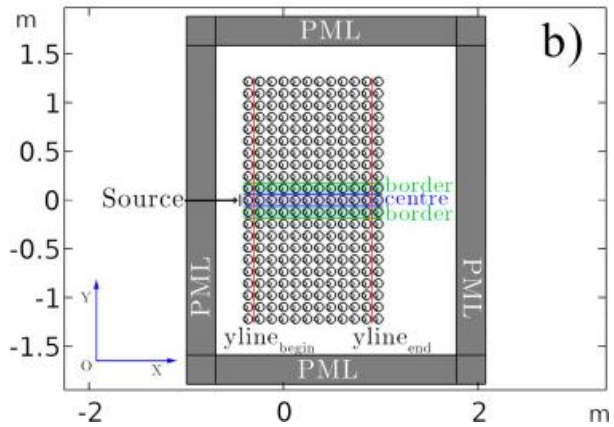

Fig. 1 (a) (a) Diagram of a unit cell comprising a cylindrical scatterer embedded with a HR, illustrating the wave propagation directions along the X and Y axes of the first Brillouin zone. Relevant geometric parameters—external radius R, neck length L, mouth width w, and cavity surface area S—are indicated. (b) Finite SC supercell array employed in numerical simulations. The blue central row marks the location where a line source, with a length equal to the lattice constant a, emits the acoustic wave. Green rows denote the lateral border regions used to evaluate the acoustic pressure relative to the collimation zone. Dashed lines P_1 (near the first column) and P_2 (near the last column) indicate the positions where the total acoustic pressure is monitored along the propagation axis. Perfectly matched layers (PMLs) of thickness 0.20 m are applied on all boundaries surrounding the LRSC to absorb outgoing waves and minimize reflections at the edges of the computational domain. This model is employed to validate all-angle self-collimation (AASC) phenomena under various excitation angles.

III. Results and Discussion

This section analyzes the band diagrams and EFCs obtained from the infinitely periodic unit cell structure of the LRSC. The vertical flat lines in the EFCs across the entire BZ correspond to eigenfrequencies that exhibit AASC. In Figs. 2a and 2b, the purple rectangles indicate the AASC frequency ranges. According to the literature, even though some frequencies in the upper part of the positive EFCs exhibit curved regions, they still support AASC [15-16]. These minor curvatures represent propagation slightly tilted toward the horizontal axis (ΓX), inducing focusing effects that help suppress wave diffraction. Furthermore, as previously reported by Rumpf et al. [63] and as will be discussed in detail in Section "*All-angle Self-Collimation* and *Frequency Sensitive Super-Collimation*", the flattest EFC region does not always yield optimal collimation.

Figs. 2-3 summarizes the EFC zones exhibiting self-collimation at specific angles (pink: LASC) and over full angular ranges (purple: AASC) for the 3rd and 4th bands of the proposed LRSCs: scatterers with $f_{HR} > f_{Bragg}$ and $f_{HR} < f_{Bragg}$. The $f_{HR} > f_{Bragg}$ case exhibits AASC in a narrow frequency region close to the origin of the BZ, while the $f_{HR} < f_{Bragg}$ case exhibits AASC over a broadband frequency region. The characteristics of AASC are analyzed by examining the shape of EFCs near the BZ origin $(0, 0)$ and as they extend toward the edge at $X(\pi/a, 0)$.

Since LASC is not the primary focus of this study, the LASC observed in the 4th band of the $f_{HR} > f_{Bragg}$ case (see Fig. 2d)—a small region near the BZ origin—will not be discussed further.

The following subsections examine two AASC cases in detail: first, a narrower yet still substantial frequency range in the $f_{HR} > f_{Bragg}$ configuration, demonstrating both AASC and FSSC phenomena; and second, the exceptionally broadband AASC observed in the $f_{HR} < f_{Bragg}$ case.

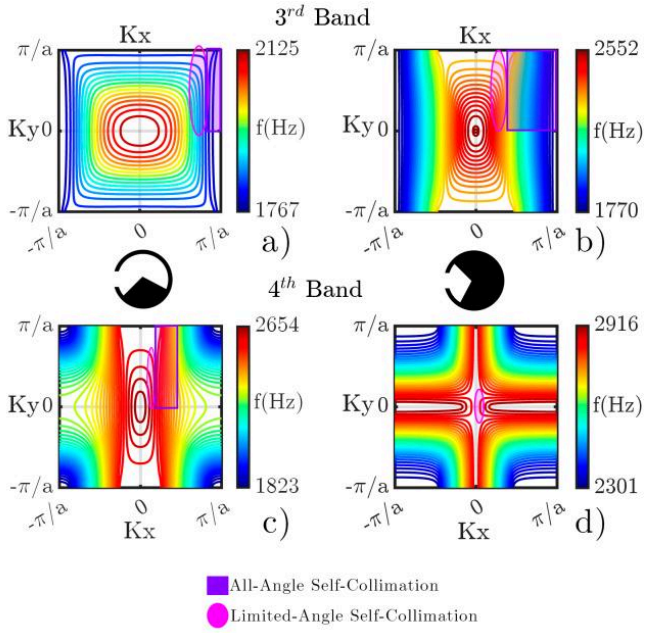

Fig. 2: Equi-frequency contours (EFCs) for the third and fourth bands of locally resonant sonic crystals (LRSCs) with Helmholtz resonator Type I ($f_{HR} > f_{Bragg}$) and Type II ($f_{HR} < f_{Bragg}$). Purple rectangles indicate all-angle self-collimation (AASC) frequency regions, while pink highlights limited-angle self-collimation (LASC) ranges. The shape and position of the EFCs are visualized, emphasizing the emergence of AASC in the Type II (broadband, third band) and Type I (narrowband, fourth band) configurations. These contours illustrate the rationale for selecting operating regimes for robust acoustic wave collimation and summarize the key findings on the band dependence of locally resonant (LR)-induced phenomena.

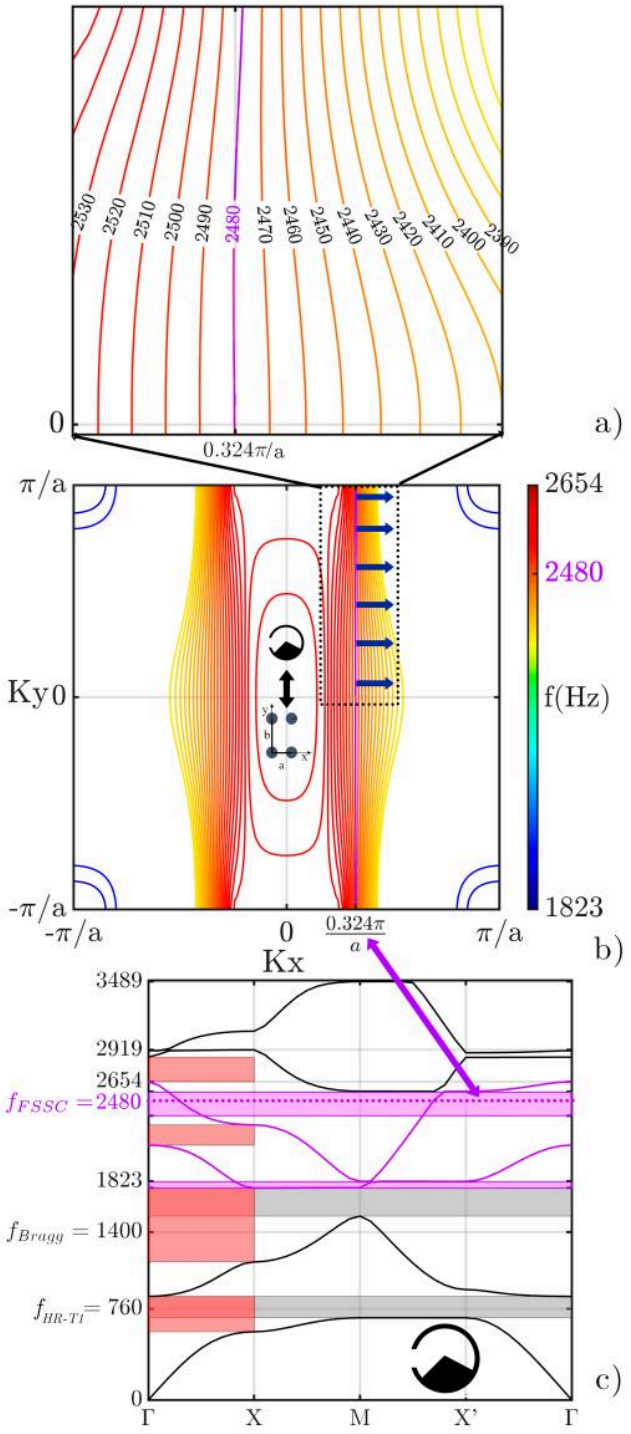

Fig. 3: (a) Magnified view of the fourth band frequency range (2290–2550 Hz) showing EFC transitions from convex to flat (at 2480 Hz) to concave geometry, with the flat EFC enabling frequency-sensitive super-collimation (FSSC). The full range supports AASC. (b) Selected EFCs of the fourth band, highlighted in blue (lower edge) and warm colors (near the FSSC frequency). (c) Band structure diagram presenting locally resonant bandgaps (LR-BGs) shaded in gray and directional Bragg bandgaps (Bragg-BGs) shaded in red. Purple highlights denote AASC regions, and the dashed purple line marks the FSSC frequency. Key frequencies—including those associated with periodicity (f_{Bragg}), local resonance ($f_{\text{HR-T1}}$), and FSSC—are explicitly annotated. Together, these panels analyze the coexistence and necessary conditions for FSSC within the fourth band, with reference to Van Hove singularities, saddle points, and relevant group velocity vectors.

IV. Conclusion

In summary, we have demonstrated that embedding Helmholtz resonators (HRs) in a square-lattice sonic crystal (SC) enables all-angle self-collimation (AASC) without requiring lattice deformation or axis elongation, and with a low filling fraction of 0.44. The emergence of AASC in locally resonant SCs (LRSCs) originates from a symmetry-breaking mechanism that induces anisotropy in the effective density and bulk modulus tensors. Specifically, the phase shift introduced by local resonance generates direction-dependent lattice constants, leading to anisotropic effective material parameters. This anisotropy modifies the dispersion relation, causing the equi-frequency contours (EFCs) to become entirely flat across the Brillouin zone (BZ). These flat EFCs sustain AASC over wide frequency ranges, representing a significant advancement over previous designs that relied on rectangular or inherently anisotropic lattices.

The physical mechanism underlying this behavior is linked to tuning the local resonance (LR) frequency above and below the first directional Bragg bandgap, creating broad frequency regions in which the group velocity remains perpendicular to the wavefronts. In addition to AASC, we report the observation of frequency-sensitive super-collimation (FSSC)—a phenomenon previously identified only in photonic systems—characterized by a flat EFC flanked by convex and concave EFCs in close proximity. The ability to control acoustic wave propagation through LRSCs without uniaxial elongation opens promising avenues for practical applications.

In defence and security, AASC structures could enable stealth communication or directed acoustic energy transfer. In telecommunications, they offer a viable route toward low-loss acoustic wave guiding in compact devices. In biomedical engineering, precise control of ultrasonic beams via self-collimating metamaterials could enhance imaging resolution or enable non-invasive therapeutic energy focusing. These findings position HR-based square lattices as a robust and versatile platform for broadband acoustic wave control, ready for integration into real-world technologies.

Although elastic wave propagation was not modelled and purely rigid scatterers were assumed, this work also expands practical applications toward tunable focusing devices. Future research will aim to establish an analytical relationship between the lattice aspect ratio η (i.e., for rectangular lattices) and the resonance frequency f_{HR} of LRSC scatterers. Additionally, experimental validation of the AASC phenomenon is planned as a key direction for subsequent work.

Acknowledgments

This work was supported by Construct Innovate, Ireland's

National Research Centre for Construction Technology and Innovation (Enterprise Ireland TC-2022-0033, Seed Fund Call CISFC1-23_002).

REFERENCES

[1] H. von Helmholtz, Die Lehre von Den Tonempfindungen Als Physiologische Grundlage Für Die Theorie Der Musik, Vieweg, Braunschweig, 1863.

[2] K. Mahesh, S. K. Ranjith, R. S. Mini, Recent Advancements in Helmholtz Resonator Based Low-Frequency Acoustic Absorbers: A Critical Review, Archives of Computational Methods in Engineering 31 (4) (2024) 2079–2107. doi:10.1007/s11831-023-10038-7.

[3] V. L. Jordan, The Application of Helmholtz Resonators to Sound-Absorbing Structures, The Journal of the Acoustical Society of America 19 (6) (1947) 972–981. doi:10.1121/1.1916649.

[4] Z. Liu, X. Zhang, Y. Mao, Y. Y. Zhu, Z. Yang, C. T. Chan, P. Sheng, Locally Resonant Sonic Materials, Science 289 (5485) (2000) 1734–1736. doi:10.1126/science.289.5485.1734.

[5] X. Yang, J. Yin, G. Yu, L. Peng, N. Wang, Acoustic superlens using Helmholtz-resonator-based metamaterials, Applied Physics Letters 107 (19) (2015) 193505. doi:10.1063/1.4935589.

[6] X. Hu, C. T. Chan, J. Zi, Two-dimensional sonic crystals with Helmholtz resonators, Physical Review E 71 (5) (2005) 055601. doi:10.1103/PhysRevE.71.055601.

[7] M. P. Peiró-Torres, S. Castiñeira-Ibáñez, J. Redondo, J. V. Sánchez-Pérez, Interferences in locally resonant sonic metamaterials formed from Helmholtz resonators, Applied Physics Letters 114 (17) (2019) 171901. doi:10.1063/1.5092375.

[8] Z. Huang, J. Wu, C. Wang, S. Yang, F. Ma, Resonant-scattering hybrid device for multiband acoustic topology valley transmission, Physical Review B 104 (9) (2021) 094110. doi:10.1103/PhysRevB.104.094110

[9] W. E. Kock, F. K. Harvey, Refracting Sound Waves, The Journal of the Acoustical Society of America 21 (5) (1949) 471–481. doi:10.1121/1.1906536.

[10] M. Sigalas, E. Economou, Elastic and acoustic wave band structure, Journal of Sound and Vibration 158 (2) (1992) 377–382. doi:10.1016/0022-460X(92)90059-7.

[11] Y.-Y. Chen, Z. Ye, Theoretical analysis of acoustic stop bands in two-dimensional periodic scattering arrays, Physical Review E 64 (3) (2001) 036616:1–036616:16. doi:10.1103/PhysRevE.64.036616.

[12] Ramírez-Solana, David, and Muhammad Gulzari. "All-angle wideband acoustic self-collimation by Helmholtz resonators." Results in Physics (2026): 108575.

[13] A. L. Vanel, M. Dubois, C. Tronche, S. Fu, Y.-T. Wang, G. Dupont, A. D. Rakic, K. Bertling, R. Abdeddaim, S. Enoch, R. V. Craster, G. Li, ´S. Guenneau, J. Perchoux, Collimated beam formation in 3D acoustic sonic crystals, New Journal of Physics 26 (7) (2024) 073021. doi:10.1088/1367-2630/ad5c94

[14] A. Bravais, Mémoire Sur Les Systèmes Formés Par Des Points Distribués Régulièrement Sur Un Plan Ou Dans l'espace, Bachelier, Paris, 1850

[15] J. Redondo, L. Godinho, K. Staliunas, J. V. Sanchez-Perez, An equivalent lattice-modified model of interfering Bragg bandgaps and Locally Resonant Stop Bands for phononic crystal made from Locally Resonant elements, Applied Acoustics 211 (2023) 109555:1–109555:6. doi:10.1016/j.apacoust.2023.109555.

[16] J.-P. Berenger, A perfectly matched layer for the absorption of electromagnetic waves, Journal of Computational Physics 114 (2) (1994) 185–200. doi:10.1006/jcph.1994.1159.

Ultrafast nanomechanics of single MoS_2 nanotubes

Alessia Colosimo[1,2], Aurélien Crut[1], Noëlle Lascoux[1], Fabien Vialla[1], Valentina Zannier[2], Valeria Demontis[3], Manjunath Krishnappa[4,5], Alla Zak[4], Lucia Sorba[2], Fabio Beltram[2], Francesco Rossella[6], Natalia Del Fatti[1], Paolo Maioli[1], Francesco Banfi[1*]

[1]Université Lyon 1, CNRS, Institut Lumière Matière, 69622, Villeurbanne, France
[2]Scuola Normale Superiore and Istituto Nanoscienze-CNR, Piazza S. Silvestro 12, I-56127 Pisa, Italy
[3]Dipartimento di Fisica, Università di Cagliari, Cittadella Universitaria di Monserrato, I-09042 Monserrato, Cagliari, Italy
[4]Department of Physics, HIT- Holon Institute of Technology, Holon 5810201, Israel
[5]Deptartment of Chemistry, Nitte Meenakshi Institute of Technology, Bangalore 560064 Karnataka, India
[6]Dipartimento di Scienze Fisiche, Informatiche e Matematiche, Università di Modena e Reggio Emilia, I-41125 Modena, Italy
*Corresponding author: francesco.banfi@univ-lyon1.fr

***Abstract*—Single MoS_2 nanotubes are examined using ultrafast, non-contact all-optical photoacoustic microscopy with picosecond temporal and submicron spatial resolution. Elastic modes in the tens of GHz are observed, and their dependence on structural features provides insight into the nanotubes' mechanical properties and internal morphology.**

***Keywords*—MoS_2 nanotube, GHz, acoustics, nano-resonator, ultrafast, microcopy, Young modulus.**

MoS_2 in its two-dimensional (2D) form has attracted significant research interest, including studies of its mechanical response at frequencies in the tens of GHz and beyond [1, 2]. Despite its technological relevance, the mechanical behavior of one-dimensional MoS_2 nanotubes remains comparatively underexplored. This is mainly due to (i) morphological variability among nominally identical nanotubes, (ii) limited knowledge of their internal radii [3], and (iii) the challenge of accessing radial eigenmodes in the tens of GHz range, corresponding to oscillation periods of tens to hundreds of picoseconds. Addressing these challenges requires an ultrafast, time-resolved, non-contact microscopy technique capable of probing both internal morphology and mechanical response at the single-nanotube level [4].

This talk reports on the nanomechanical dynamics of individual multiwalled MoS_2 nanotubes using ultrafast, all-optical photoacoustic microscopy. The method combines picosecond temporal resolution with submicron spatial precision, enabling the excitation and detection of vibrational modes in isolated nanostructures. By avoiding ensemble averaging, direct correlations between structural characteristics and vibrational response are established, revealing modes that remain undetected in bulk measurements. Elastic eigenmodes in the tens of GHz range are identified and analyzed as a function of nanotube dimensions, providing quantitative insight into their hypersonic elastic properties. Furthermore, the approach enables estimation of internal radii, which are not readily accessible through conventional techniques.

More broadly, this presentation demonstrates the effectiveness of ultrafast all-optical spectromicroscopy as a non-invasive tool for nanoscale metrology. It enables detailed characterization of both mechanical properties and morphology in individual one-dimensional nanostructures, while offering new insights into the intrinsic mechanical behavior and internal structure of MoS_2 nanotubes.

References

[1] F. Vialla and N. Del Fatti, "Time-domain investigations of coherent phonons in van der waals thin films", Nanomaterials 10, 2543 (2020).
[2] D. Soranzio, D. Puntel, M. Tuniz, P. E. Majchrzak, A. Milloch, N. M. Olsen, W. Bronsch, B. S. Jessen, D. Fainozzi, J. S. Pelli Cresi, et al., "Impact of MoS_2 monolayers on the thermoelastic response of silicon heterostructures", ACS Applied Nano Materials 7, 15317–15324 (2024).
[3] A. Colosimo, A. Crut, N. Lascoux, C. Panais, A. Casto, F. Vialla, V. Demontis, L. Martini, P. Rosi, E. Rotunno, GC Gazzadi, M. Beleggia, M. Krishnappa, A. Zak, F. Beltram, F. Rossella, F. Vallée, N. Del Fatti, F. Banfi, P. Maioli, "Single MoS2 Nanotube Experimental Optical Extinction Cross Section", J. Phys. Chem. C 129, 5086 (2025). 10.1021/acs.jpcc.4c08613
[4] A. Colosimo, M. Gandolfi, N. Lascoux, A. Crut, F. Vialla, V. Demontis, V. Zannier, L. Sorba, F. Beltram, F. Rossella, N. Del Fatti, P. Maioli and F. Banfi, "Single InAs Nanowire Hypersonic Acoustic Nanoresonator", J. Phys. Chem. Lett. 16, 11158−11166 (2025).

Self-Organized Multimode Phonon Lasing in a Silicon Optomechanical Nanobeam

David Alonso Tomás[1], Daniel Navarro-Urrios[1,*]

[1]MIND-IN2UB, Departament d'Enginyeria Electrònica i Biomèdica, Universitat de Barcelona, Spain
*Corresponding author: dnavarro@ub.edu

***Abstract*— We report self-organized multimode phonon lasing in a silicon optomechanical nanobeam driven by intrinsic optical self-pulsing. Strongly competing mechanical modes are simultaneously amplified without external modulation, producing periodic, quasi-periodic, and chaotic dynamics. The results establish self-induced coherent pumping as a compact route toward integrated multi-frequency phononic sources.**

***Keywords*— optomechanics, nonlinear dynamics, phonon lasing, silicon photonics, multimode oscillations.**

I. Introduction

Nonlinear optomechanical systems provide a powerful platform for controlling light–matter interactions and generating coherent mechanical motion. Multimode phonon lasing is particularly attractive for multi-frequency signal generation and wave-based information processing, yet it is generally hindered by strong mode competition. Existing approaches rely on external modulation or engineered frequency separation, increasing system complexity. Here we demonstrate a self-organized mechanism enabling multimode phonon lasing in a silicon nanobeam, where intrinsic optical nonlinearities generate coherent pumping capable of synchronizing multiple mechanical oscillators.

II. Methods

The platform consists of a silicon optomechanical crystal nanobeam supporting a confined optical mode coupled to several flexural mechanical resonances. Continuous-wave optical excitation is delivered via tapered-fiber coupling.

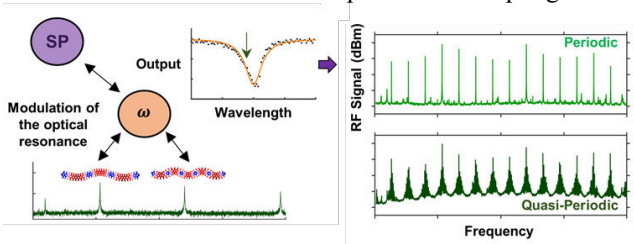

Fig. 1 A silicon optomechanical nanobeam generates self-sustained phonon lasing in multiple competing mechanical modes via self-pulsing,

Self-pulsing dynamics arise from the interplay between free-carrier dispersion and thermo-optic effects, producing a nonlinear limit cycle that modulates intracavity power. This modulation generates radiation-pressure forces that coherently drive the mechanical modes. The system is described by coupled nonlinear equations including optical, thermal, carrier, and mechanical dynamics, solved numerically to map the accessible dynamical regimes.

III. Results and Discussion

By tuning laser detuning, the system exhibits a rich nonlinear landscape including: single-mode phonon lasing, stable multimode lasing (Fig.1 top-right), quasi-periodic dynamics (Fig.1 bottom-right) and chaotic multimode states.

Remarkably, two strongly competing in-plane flexural modes simultaneously reach self-sustained oscillation under continuous-wave excitation. The adaptive self-pulsing cycle dynamically synchronizes with mechanical perturbations, enabling coherent pumping even when modal frequencies are not harmonically related. RF spectra reveal frequency-comb formation and sideband generation associated with nonlinear multimode interactions. Numerical simulations reproduce the experimental phase transitions and confirm the role of self-pulsing as an internal synchronization mechanism.

IV. Conclusion

We demonstrate a compact self-organized mechanism for multimode phonon lasing in an integrated silicon optomechanical platform. Intrinsic nonlinear dynamics enable coherent pumping that overcomes mode competition without external control, opening new opportunities for chip-scale multi-frequency phononic sources and nonlinear RF photonic systems.

Acknowledgments

This work was supported by MCINN through projects ALLEGRO (PID2021-124618NB-C21/C22), OMENS (PID2024-156058NB-I00), and an FPU fellowship (FPU23/00690).

References

[1] D. Alonso Tomás et al., "Multimode Phonon Lasing via Self-Induced Optical Coherent Pumping," Laser & Photonics Reviews, 2026.
[2] D. Navarro-Urrios et al., "A Self-Stabilized Coherent Phonon Source Driven by Optical Forces," Scientific Reports, 2015.

Localization and antilocalization of sound in a phononic crystal with symmetric disorder

José Sánchez-Dehesa[1,*], Francisco Cervera[1], Martin Ibarias[1], Dmitrii Shymkiv[2], Arkadii Krokhin[2]

[1]Wave Phenomena Group, Department of Electronic Engineering, Universitat Politècnica de Valéncia, Spain
[2]Department of Physics, University of North Texas, USA
*Corresponding author: jsdehesa@upv.es

***Abstract*—The set of eigenstates is numerically calculated for a disordered phononic crystal with an axis of mirror symmetry. The states are well localized due to strong disorder in orientation of asymmetric scatterers. However, mirror symmetry allows either symmetric or antisymmetric solutions that leads to two localized peaks for each eigenstate.**

***Keywords*— phononic crystals, disorder, symmetry.**

I. Introduction

The eigenstates in a one-dimensional disordered potential are exponentially localized. Two identical samples can form a disordered medium with mirror symmetry, for which the binary correlator of the potential, $< V(x)V(-x) >= V_0^2$ remains nonzero even as $x \to \infty$. At the same time, two neighboring points located on the same side of the symmetry axis are uncorrelated, $< V(x)V(x') >= 0$. The presence of long-range correlations in the absence of short-range correlations leads to an interesting manifestation of Anderson localization, accompanied by symmetry-induced antilocalization.

II. Results and Discussion

The solutions of a wave equation with a symmetric potential are either even or odd functions. In a 1D disordered structure, eigenstates appear as randomly centered peaks. A wave excited at any of these peaks decays exponentially with the localization length $l(\omega)$. However, in a medium with symmetric disorder, a perturbation peaked at a point x extends toward the center of the sample with an amplitude $\sim e^{-|x|/l}$. After passing through the center, the wave amplitude begins to grow, reaching its initial value at the symmetric point $-x$. This behavior of point excitations was demonstrated in a chain of LC circuits with random resonant frequencies [1]. Symmetry-induced enhancement of wave transmission through a diffusive sample was reported in Ref. [2]. Here, we report the symmetry-induced antilocalization effect in acoustics.

The sample used for numerical calculations and experiments is shown in Fig. 1. The scatterers are steel rods with circular-sector cross sections. The rods are periodically arranged in the transverse plane but randomly oriented along the length of the waveguide, producing one-dimensional disorder with a mirror-symmetry axis marked by the horizontal red line. The eigenfrequency spectrum consists of a set of doublets corresponding to even and odd eigenstates. One even eigenstate at $f = 430$ kHz is shown in Fig. 1.Two peaks separated by an exponentially weak pressure region demonstrate Anderson localization caused by random scattering in a one-dimensional structure, together with antilocalization imposed by mirror symmetry. A short pulse applied at one of the eigenstate maxima oscillates between the two peaks, mimicking the dynamics of a quantum particle in a symmetric double-well potential. In the experiment, these oscillations are strongly suppressed by thermo-viscous losses.

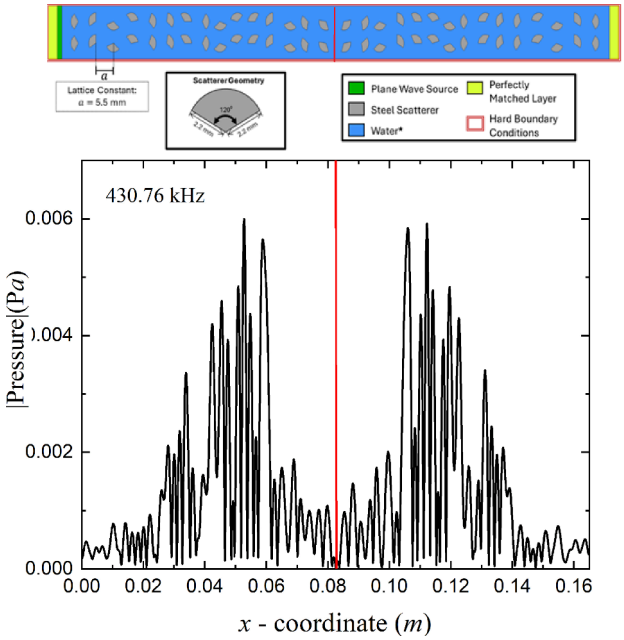

Fig. 1. Phononic crystal with symmetric disorder and distribution of pressure produced by a source with diameter 3 mm located at $x = 0.44$m.

Acknowledgment

This work was supported by the US Air Force Office of Scientific Research under Award No. FA9550-23-1-0630.

References

[1] E. Diez, F. Izrailev, A. Krokhin, A. Rodriguez, "Symmetry-induced tunneling in one-dimensional disordered potentials," *Phys. Rev. B*, vol. 78, p. 035118, 2008.

[2] Élie Chéron, Simon Félix, Vincent Pagneux, "Broadband-enhanced transmission through symmetric diffusive slabs," *Phys. Rev. Lett.*, vol. 122, p. 125501, 2019.

Nanoscale Local Electromechanical Sources for GHz Phononics

Tapani Makkonen[1], Oili Ylivaara[1], Omid R. Ranjbar-Naeni[2], Clivia M. Sotomayor Torres[2], Jouni Ahopelto[1*]

[1]Microelectronics and Quantum Technologies, VTT Technical Research Centre of Finland Ltd, Finland

[2]International Iberian Nanotechnology Laboratory, Portugal

*Corresponding author: jouni.ahopelto@vtt.fi

***Abstract*— We demonstrate an efficient and broadband nanoscale electromechanical phonon point source which can be integrated into optomechanical nanobeams or used to excite topological phononic structures. The properties have been investigated by extensive FEM simulations and verified experimentally by vibrometry and electrical measurements.**

***Keywords*— nanophononics, optoelectromechanics, topological phononics.**

I. Introduction

Compact phonon sources are essential in nanomechanical, optoelectromechanical and currently also in topological applications [1,2,3]. Here, we introduce a nanoscale broadband freestanding bulk acoustic wave (BAW) transducer that can act both as a phonon source and a detector.

II. Fabrication and Characterisation

Extensive finite element method (FEM) simulations were carried out to estimate the performance of the BeamBAW transducers. Based on the simulations, test devices were made using standard CMOS compatible cleanroom processes, The devices are 8 µm tall and 7 µm wide triangular resonators with the centre frequency at 4.5 GHz, integrated into silicon nanobeams. The devices were characterized by vibrometry and RF measurements.

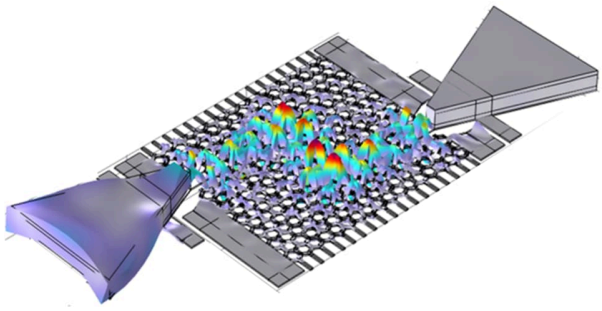

Fig. 1 FEM simulation of phonons excited by a BeamBAW transducer propagating through a topologically protected Z path.

III. Results and Discussion

Simulations show that the test transducers can generate mechanical energy flux into an integrated nanobeam up to 10 GHz frequencies. The coupling efficiency approaches 90 % with optimized supporting beams which minimise the mechanical power leaking to the substrate. In addition, simulations show that the transducers can be used to excite topologigal structures (Fig. 1).

Electrical measurements prove that the centre frequency is at 4.6 GHz. Mechanical signals generated by one transducer in the range of 4.4-4.7 GHz were detected by another transducer after travelling across a 50 µm long freestanding nanobeam. Furthermore, vibrometry shows coupling from the transducer to a nanobeam at around 2 GHz.

IV. Conclusion

We have demonstrated an efficient nanoscale phonon source which can be integrated into nanomechanical structures. FEM simulations confirm the broadband operation, supported by experimental results at around 2.0 GHz and 4.5 GHz by vibrometry and electrical measurements.

Acknowledgments

This work was supported by the European Commission through projects MAGNIFIC and LEIT and by the Academy of Finland through the project MUSICIAN.

References

[1] Priya, E. R. Cardozo de Oliveira, N. D. Lanzillotti-Kimura, "Perspectives on high-frequency nanomechanics, nanoacoustics, and nanophononics," Appl. Phys. Lett., vol. 122, 140501, 2023.

[2] D. Navarro-Urrios, M. F. Colombano, G. Arregui, G. Madiot, A. Pitanti, A. Griol, T. Makkonen, J. Ahopelto, C. M. Sotomayor-Torres, and A´. Martínez, "Room-Temperature Silicon Platform for GHz-Frequency Nanoelectro-Opto-Mechanical Systems," ASC Photonics, vol. 9, 413, 2022.

[3] Y. Liu, X. Chen, and Y. Xu, "Topological Phononics: From Fundamental Models to Real Materials," Adv. Funct. Mater., vol. 30, 1904784, 2020.

Eigenmode steering with time-varying acoustic metamaterials

Wai Chun Wong, Gregory J. Chaplain, Jensen Li*

Department of Physics and Astronomy, University of Exeter, United Kingdom

* j.li13@exeter.ac.uk

***Abstract*— We introduce a spatiotemporal gain-loss framework for eigenmode steering in coupled acoustic resonators. Cross-coupled feedback conserves total energy while directing the system toward selected modal states. Temporal modulation enables programmable transitions and energy routing, offering a route to reconfigurable metamaterials and analog information processing.**

***Keywords*— acoustic metamaterials, time-varying metamaterials, gain–loss engineering, eigenmode steering.**

I. Introduction

Time varying metamaterials provide new opportunities for controlling wave dynamics beyond passive structures. Temporal modulation can produce novel phenomena such as frequency conversion and time analogues of spatial interference, as demonstrated experimentally in optical systems [1]. These developments highlight the potential of dynamic media for manipulating wave propagation.

Here, we present a spatiotemporal gain loss framework for deterministic eigenmode steering in coupled acoustic resonators. Cross-coupled gain-loss feedback conserves total energy while guiding the system toward a selected eigenmode. Temporal modulation further enables programmable transitions between modal states and controlled redistribution of energy between resonators.

II. Methods

We consider three coupled acoustic resonators labeled a, b, and c. Their slowly varying modal amplitudes $\psi = (\psi_a, \psi_b, \psi_c)^T$ evolve according to $i\frac{d}{dt}\psi = H\psi$, where H contains resonator coupling and nonlinear gain–loss feedback. The Hamiltonian can be written as $H = H_{\text{eff}} - iGI$, where the effective linear Hamiltonian governing the modal structure is

$$H_{\text{eff}} = \frac{1}{2}\begin{pmatrix} ig_a & -\kappa/2 & -\kappa/2 \\ -\kappa/2 & ig_b & -\kappa/2 \\ -\kappa/2 & -\kappa/2 & ig_c \end{pmatrix},$$

I is the identity matrix and the nonlinear biasing diagonal matrix is GI where

$$G = \frac{1}{2E}(g_a \mid \psi_a \mid^2 + g_b \mid \psi_b \mid^2 + g_c \mid \psi_c \mid^2),$$

with $E = \mid \psi_a \mid^2 + \mid \psi_b \mid^2 + \mid \psi_c \mid^2$. The nonlinear diagonal term regulates the total amplitude but does not modify the eigenvectors of H_{eff}. Consequently, the eigenmodes of H_{eff} determine the attractor states toward which the system evolves. In theory, the system is designed to converge to the eigenvector whose associated eigenvalue has the largest imaginary part. The normalization term G ensures that the total energy E remains conserved during the evolution.

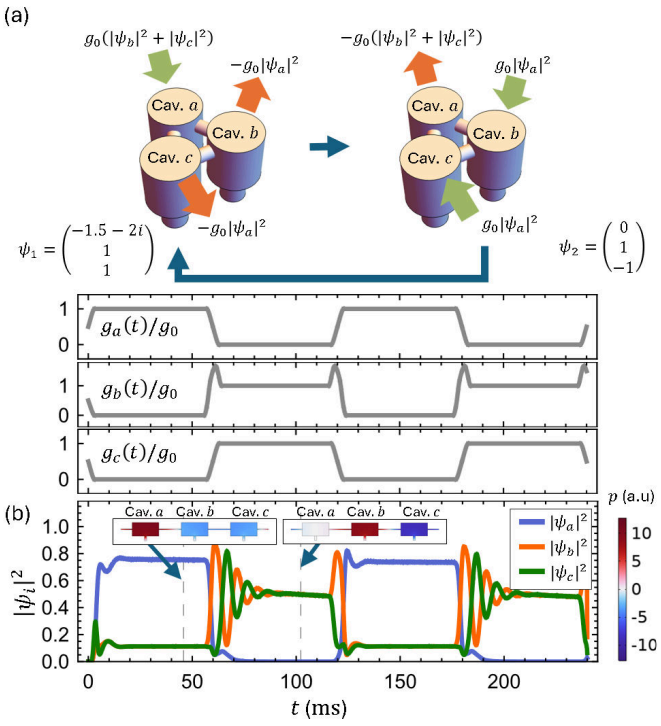

Fig. 1 Assisted eigenmode steering enabled by spatiotemporal gain modulation. (a) Time-dependent gain configuration applied to three coupled acoustic resonators. A transient perturbation breaks symmetry between cavities. (b) Simulated modal intensities showing successful transition from the initial eigenmode to the target antisymmetric mode, demonstrating symmetry-assisted energy redistribution.

III. Results and Discussion

Figure 1 demonstrates eigenmode steering using the spatiotemporal gain protocol illustrated in Fig. 1a. In the first phase, the gain configuration $(g_a, g_b, g_c) = (g_0, 0, 0)$ drives the system toward the eigenmode dominated by resonator a. The protocol then switches to $(0, g_0, g_0)$, whose effective Hamiltonian supports a target antisymmetric eigenmode with opposite phases in resonators b and c. In both phases, the selected modes correspond to the eigenvector associated with the eigenvalue having the largest imaginary part, resulting in relative amplification compared with the other eigenmodes.

Under ideal symmetry, the transition from the initial state to this target mode is inhibited because the two states have different parity with respect to the exchange of resonators b and c. To assist the transition, a transient perturbation is applied to the gain of one cavity during the switching stage, as illustrated in Fig. 1a. The resulting modal evolution is shown in Fig. 1b. After the spatiotemporal perturbation, the system converges toward the target eigenmode, with energy redistributed equally between resonators b and c (with opposite phases) while resonator a is suppressed. We note that the proposed gain–loss feedback and temporal modulation could be implemented experimentally using active acoustic resonators with digital feedback control [3].

IV. Conclusion

We have presented a spatiotemporal gain–loss framework for eigenmode steering in coupled acoustic resonators. By designing the gain distribution and temporal protocol, the system deterministically evolves toward selected eigenmodes while conserving total energy. This approach may enable programmable wave control, analog information processing, and new computation protocols in active metamaterial platforms.

Acknowledgments

This work is supported by the EPSRC META4D Programme Grant (No. EP/Y015673/1).

References

[1] R. Tirole, S. Vezzoli, E. Galiffi, I. Robertson, D. Maurice, B. Tilmann, S. A. Maier, J. B. Pendry, R. Sapienza, *Double-slit time diffraction at optical frequencies*. Nature Physics, 19, 999, 2023.

[2] W. C. Wong, G. J. Chaplain, J. Li, *Eigenmode steering in spatiotemporal gain-loss acoustic metamaterials*, Materials Horizons, 2026, in press.

[3] J. Li, "Acoustic metamaterials," in *Essential Concepts in Metamaterials*. IOP Publishing, Bristol, 2025. Ch. 6.

SYMPOSIUM 6

Advanced Techniques for Computational Electromagnetics

47 contributions · pp. 676–745

META 2026 · Dublin, Ireland · ISSN 2429-1390

Advanced electromagnetic simulations for free electrons and nanoscale optical fields

F. Javier García de Abajo[1,2,*]

[1]ICFO-Institut de Ciencies Fotoniques, The Barcelona Institute of Science and Technology, 08860 Castelldefels (Barcelona), Spain

[2]ICREA-Institució Catalana de Recerca i Estudis Avançats, Passeig Lluís Companys 23, 08010 Barcelona, Spain

*javier.garciadeabajo@nanophotonics.es

***Abstract*— Free electrons enable mapping and controlling nanoscale optical fields, advancing spatiotemporal and spectral microscopy. While analytical methods suffice for simple geometries, complex structures require numerical simulations. We discuss advanced techniques to simulate electron-light interactions illustrated through phenomena such as the generation and probing of non-classical light states.**

***Keywords*— computational electromagnetic, nonlinear optics, free electrons.**

Free electrons have emerged as a powerful tool to map and manipulate optical fields, providing exciting prospects to investigate new quantum phenomena and push the resolution of spatiotemporally and spectrally resolved microscopy. Advances in this field rely strongly on our understanding of the interaction between free electrons and nanoscale optical fields. Much progress has recently been gained by utilizing analytical methods when the electron interacts with optical fields in the presence of relatively simple material geometries. However, numerical electromagnetic simulations are generally needed for more complex structures. In this presentation, we will discuss several recent examples of applications of surface-integral techniques for simulating the interaction between free electrons and nanoscale optical fields. Furthermore, we will show that, by understanding classical optical fields and their interaction with free electrons, we can equally describe quantum interactions, whereby non-classical light states are generated or externally provided. We will discuss a general protocol to investigate the noted quantum effects based on classical electromagnetic simulations.

ACKNOWLEDGMENTS

This work was supported by the European Research Council (101141220-QUEFES), the Spanish MICIU (PID2024-157421NB-I00 and Severo Ochoa CEX2024-001490-S), the European Commission (101017720-eBEAM), and the Catalan CERCA Program.

Computational Nanophotonics for AR Optics: From Performance Targets to Artifact-Robust Designs

Christina Spaegele[1]

[1]Meta, United States
cspaegele@meta.com

Abstract: Nanophotonic optics have the potential to enable compact, lightweight AR displays by enhancing wavefront control in wearable devices. This talk links AR system requirements to nanostructure design, discusses performance and fabrication challenges, and presents examples of nanophotonic design approaches developed to overcome artifacts and meet demanding AR display standards.

Immersive AR technology aims to revolutionize digital interaction by seamlessly embedding information into our everyday surroundings. Achieving this requires display systems that are virtually invisible to the user, ensuring content integration without compromising natural vision. These goals translate into demanding optical targets, including a wide field of view, support for focus cues, a sunglasses-like form factor, and efficiency compatible with all-day wear.

Despite strong recent progress, meeting the combined requirements for compactness, visual fidelity, power efficiency, and cost will depend on continued advances in materials, optoelectronics, and photonics. Nanophotonic elements are appealing because they can enable thinner, lighter optics and more precise control of light propagation. However, their expanded degrees of freedom present significant practical challenges, including sensitivity to manufacturing tolerances and artifact pathways that can dominate perceived image quality. This talk reviews how computational nanophotonic design can translate AR system-level requirements into practical, manufacturable nanostructured optics, emphasizing artifact-robust performance under fabrication constraints and illustrating these ideas with representative design examples.

Topologically structured doughnuts: optical skyrmions, superoscillations, and axion probes

Nikitas Papasimakis[1,*]

[1]Optoelectronics Research Centre, University of Southampton, UK
*n.papasimakis@soton.ac.uk

***Abstract*— This talk will present recent developments on spatiotemporally structured toroidal pulses including their topological properties, exotic field configurations, superoscillatory behaviour, and non-trivial light-matter interactions.**

***Keywords*— toroidal pulses, superoscillations, optical skyrmions**

Toroidal light pulses, space-time nonseparable solutions to Maxwell's equations, were predicted in 1996 [1] and only recently observed [2]. A broader class of supertoroidal pulses was discovered [3] with intriguing topological structure reminiscent of skyrmions in condensed matter. Such pulses can exhibit exotic propagation properties, such as non-diffraction over arbitrary distances and energy transfer reminiscent of "vortex streets" in fluid dynamics [4]. Moreover, the spatiotemporal structure of supertoroidal pulses can lead to unusually rapid local temporal and spatial oscillations, a phenomenon termed space-time superoscillations [5]. Finally, superpositions of toroidal pulses are shown to be maximally chiral with parallel electric and magnetic field components. Finally, promising applications of toroidal pulses in telecommunications, metrology, and spectroscopy will be discussed.

References

[1] R. W. Hellwarth and P. Nouchi, "Focused one-cycle electromagnetic pulses," Physical Review E 54, 889 (1996).
[2] A. Zdagkas, C. McDonnell, J. Deng, Y. Shen. G. Li, T. Ellenbogen, N. Papasimakis, and N. I. Zheludev, "Observation of toroidal pulses of light," Nature Photonics 16, 523 (2022).
[3] Y. Shen, N. Papasimakis, and N. I. Zheludev, "Supertoroidal light pulses as electromagnetic skyrmions propagating in free-space," Nature Communications 12, 5891 (2021).
[4] Y. Shen, N. Papasimakis, and N. I. Zheludev, "Nondiffracting supertoroidal pulses and optical Karman vortex streets," Nature Communications 15, 4863 (2024).
[5] Y. Shen, N. Papasimakis, and N. I. Zheludev, "Space-time superoscillations," Nature Communications (2026). In print

A Universal Scattering Anomaly near Bound States in the Continuum

Jiaxin Zhou[1], Ya Yan Lu[1,2,*]

[1]Liu Bie Ju Centre for Mathematical Sciences, City University of Hong Kong, Hong Kong
[2]Department of Mathematics, City University of Hong Kong, Hong Kong
*Corresponding author: mayylu@cityu.edu.hk

***Abstract*—A bound state in the continuum (BIC) is an eigenmode with a frequency in the radiation continuum. When the system with a BIC is perturbed, scattering problems may exhibit unusual wave phenomena referred to as scattering anomalies. We identify a new and universal scattering anomaly associated with BICs.**

***Keywords*— bound state in the continuum, scattering anomaly, periodic structure.**

I. Introduction

In a lossless periodic structure sandwiched between two homogeneous media, a bound state in the continuum (BIC) is a special eigenmode with a frequency in the radiation continuum [1]. If the structure, with a real relative permittivity $\epsilon_*(y,z)$, is periodic in y with period L, bounded in z, and surrounded by air ($|z| > d$), a TE or TM polarized BIC is a Bloch mode $u_*(y,z) = \phi_*(y,z)e^{i\beta_* y}$ with a real Bloch wavenumber β_* satisfying $|\beta_*| < k_* = \omega_*/c$, where ω_* is the real angular frequency, ϕ_* is periodic in y and tends to 0 as $z \to \pm\infty$. For a given real pair (β,ω), there is a unitary matrix (the scattering matrix) $\boldsymbol{S}(\beta,\omega)$ satisfying $\boldsymbol{S}\boldsymbol{a} = \boldsymbol{b}$, where $\boldsymbol{a}$ and $\boldsymbol{b}$ are column vectors for the coefficients of the incoming and outgoing propagating plane waves (from and to $z = \pm\infty$, respectively). The scattering matrix is well-defined even at the BIC point (β_*,ω_*).

It is known that for β near β_*, incident waves with a special frequency ω near ω_* may give zero reflection or zero transmission [2,3]. Such scattering anomalies are interesting and useful for practical applications, but they require the structure to have some symmetry, and usually do not occur if the structure has no symmetry.

II. Results

We describe a universal scattering anomaly that does not require any symmetry. It is about special relations between $\boldsymbol{a}$ and $\boldsymbol{b}$. While they are always linearly related by the scattering matrix $\boldsymbol{S}(\beta,\omega)$, we show that it is possible to have $\boldsymbol{b} = \boldsymbol{M}\boldsymbol{a}$ for a particular nonzero $\boldsymbol{a}$, where $\boldsymbol{M}$ is *any* unitary matrix satisfying

$$\det[\boldsymbol{S}(\beta_*,\omega_*) - \boldsymbol{M}] \neq 0. \tag{1}$$

Specifically, if $e^{i\theta}$ is *not* an eigenvalue of $\boldsymbol{S}(\beta_*,\omega_*)$, then there is a particular $\boldsymbol{a}$, such that $\boldsymbol{b} = e^{i\theta}\boldsymbol{a}$. It should be emphasized that the result holds for any β sufficiently close to β_*, but only for a particular ω near ω_*.

The precise statement of our result is as follows. *For any unitary matrix $\boldsymbol{M}$ satisfying (1) and any real β near β_*, there is a real frequency $\omega_\diamond$ and a nonzero vector $\boldsymbol{a}$, such that*

$$\boldsymbol{b} = \boldsymbol{S}(\beta,\omega_\diamond)\boldsymbol{a} = \boldsymbol{M}\boldsymbol{a}. \tag{2}$$

In other words, for any β near β_*, we are able to force outgoing waves to have a special relationship with the incident waves, but only for a particular set of incident waves and only at a particular frequency. We note that $\omega_\diamond$ depends on β continuously and also depends on $\boldsymbol{M}$. For each $\boldsymbol{M}$, $\omega_\diamond(\beta;\boldsymbol{M})$ is a curve passing through (β_*,ω_*) in the β-ω plane. In addition, we can show that the curves for different $\boldsymbol{M}$ are tangential to each other at (β_*,ω_*). Since the special scattering solution satisfying (2) exists near any nondegenerate BIC, without requiring additional conditions on the structure and the BIC, we say the scattering anomaly is universal.

If (β_*,ω_*) satisfies $|\beta_*| < \omega_*/c < 2\pi/L - |\beta_*|$, then $\boldsymbol{S}$ is a 2×2 matrix. Furthermore, if $\epsilon_*(y,z)$ is even in z, the BIC is either even or odd in z, and we can also focus on scattering solutions that are even or odd in z, namely, we can choose $\boldsymbol{a} = [1;1]$ or $[1;-1]$, respectively. In that case, if $e^{i\theta}$ is not an eigenvalue of $\boldsymbol{S}(\beta_*,\omega_*)$, then for any β near β_*, there is a real $\omega_\diamond$ near ω_*, such that $\boldsymbol{b} = e^{i\theta}\boldsymbol{a}$.

III. Conclusion

We describe a special scattering anomaly near non-degenerate BICs in periodic structures. It is about the universal existence of scattering solutions with $\boldsymbol{b} = \boldsymbol{M}\boldsymbol{a}$, where $\boldsymbol{M}$ is any unitary matrix such that $\boldsymbol{S}(\beta_*,\omega_*) - \boldsymbol{M}$ is nonsingular. Applications of this anomalous wave phenomena will be explored in future works.

Acknowledgments

The work is partially support by the Research Grants Council of Hong Kong Special Administrative Region, China (Grant No. CityU 11317622).

References

[1] C. W. Hsu, B. Zhen, A. D. Stone, J. D. Joannopoulos, and M. Soljačić, "Bound states in the continuum," *Nat. Rev. Mater.* vol. 1, 16048, 2016.
[2] C. Blanchard, J.-P. Hugonin, and C. Sauvan, "Fano resonant modes in photonic crystal slabs near optical bound states in the continuum," *Phys. Rev. B*, vol 94, 155303, 2016.
[3] L. Yuan, M. Zhang, and Y. Y. Lu, "Real transmission and reflection zeros of periodic structures with a bound state in the continuum," *Phys. Rev. A*, vol. 106, 013505, 2022.

Separating partially coherent light

Charles Roques-Carmes[1, 2]

[1] Stanford University, USA
[2] Institute of Science and Technology, Austria
*Corresponding author: crc@ista.ac.at

***Abstract*— We demonstrate the automatic separation of partially coherent light into its mutually orthogonal and incoherent components by variational processing in a silicon photonic circuit. This process formally finds and measures the eigenvectors and eigenvalues of the coherency matrix, hence also completely measuring the partially coherent state, while leaving it intact after optimization.**

***Keywords*— partial coherence, photonic integrated circuits.**

Modern photonics increasingly operates with high-dimensional optical fields with partial coherence. In such settings, the relevant information is carried not only by intensity but also by statistical correlations between field components, captured by the coherency matrix. While partial coherence has often been treated as a limitation, recent work has shown that it can be engineered as a resource for imaging, sensing, communication, and optical information processing. Exploiting it at scale, however, requires practical hardware that can measure and manipulate coherence in many modes without the quadratic overhead of conventional tomographic approaches.

Here, I will present a foundry-fabricated silicon photonic platform that performs coherence tomography and coherence processing directly on chip, with a method designed to scale efficiently in dimensionality. The central result is the automatic separation of an unknown partially coherent field into its mutually orthogonal and mutually incoherent components. Operationally, the chip implements a programmable unitary transformation that is tuned *in situ* so that the output ports directly carry the principal coherence modes of the input. At convergence, the device provides the eigenvalues and eigenvectors of the input coherency matrix, and it does so in a way that physically routes the corresponding components to distinct waveguide outputs. Importantly, this separation is achieved through unitary interferometric processing prior to detection, enabling the coherence structure to be accessed without relying on destructive, basis-by-basis measurements.

Our approach casts coherence tomography as a variational optimization problem [1-4]. A self-configuring interferometric network is trained layer-by-layer to maximize measured output power, which is equivalent to learning the dominant coherence modes sequentially. To make this feasible in integrated hardware, the experiment introduces a scalable gradient readout scheme: the phases of many interferometric elements are simultaneously dithered at distinct electronic frequencies, and the photodetected signal is demodulated to recover, in parallel, the gradient of the objective with respect to every tunable parameter in a layer. These gradients drive a standard gradient-based optimizer that converges rapidly and reproducibly. Because many practical partially coherent fields are low rank, the overall procedure scales linearly with the number of supported modes up to the rank of the coherency matrix, offering an efficiency advantage over conventional techniques that require a number of measurements growing quadratically with dimension.

Our work establishes a practical route to programmable coherence analysis and control in integrated photonics. It shows that coherence-mode decomposition can be implemented physically in a compact silicon platform using scalable, gradient-driven self-configuration. Such devices could enable real-time, information-optimal optical front ends for imaging and sensing, coherence-aware receivers for communication in challenging propagation environments, and integrated photonic processors that treat partial coherence as a controllable degree of freedom alongside mode, wavelength, and polarization.

Acknowledgments

CRC was supported by a Stanford Science Fellowship and by the Institute of Science and Technology, Austria.

References

[1] Roques-Carmes, Charles, Shanhui Fan, and David AB Miller. "Measuring, processing, and generating partially coherent light with self-configuring optics." Light: Science & Applications 13.1 (2024): 260.
[2] Roques-Carmes, Charles, et al. "Automated modal analysis of entanglement with bipartite self-configuring optics." ACS Photonics 12.6 (2025): 3285-3294.
[3] Karnieli, Aviv, et al. "Variational processing of multimode squeezed light." arXiv preprint arXiv:2509.16753 (2025).
[4] Miller, David AB, et al. "Universal programmable and self-configuring optical filter." Optica 12.9 (2025): 1417-1426.

Simulation and Optimization of Large-Scale Metasurfaces

Jens Niegemann[1,*], Shin-Sung Kim[2], Thibault Leportier[1], Han-Hsiang (Michael) Cheng[3]

[1]Ansys, part of Synopsys (Canada)
[2]Ansys, part of Synopsys (UK)
[3]Ansys, part of Synopsys (Japan)
*Corresponding author: jens.niegemann@synposys.com

***Abstract*— We demonstrate efficient simulation and optimization of millimeter-scale metasurfaces using GPU-accelerated finite-difference time-domain (FDTD) methods. Additionally, we show how optimized metasurfaces can be seamlessly integrated into system-level simulations through machine learning-based surrogate models, enabling rapid evaluation without repeated full-wave analysis.**

***Keywords*— metalenses, metasurfaces, FDTD, optimization.**

I. Introduction

Metasurfaces consist of meticulously arranged sub-wavelength structures (meta-atoms) that enable precise control over the phase, amplitude, and polarization of electromagnetic waves. While these devices have demonstrated remarkable capabilities in applications ranging from beam steering to optical computation [1], their practical deployment faces significant computational challenges. The design and optimization of large-scale metasurfaces—particularly those spanning millimeter dimensions with thousands of individual elements—requires computationally intensive full-wave electromagnetic simulations, and subsequent system-level integration demands repeated evaluations that multiply this burden. In this work, we address both challenges by demonstrating that GPU-accelerated finite-difference time-domain (FDTD) methods enable efficient gradient-based optimization of mm-scale metasurfaces, while machine learning-based surrogate models provide fast, differentiable representations suitable for system-level design workflows. Together, these techniques provide a complete pathway from component optimization to system integration for large-scale metasurface devices.

II. Multi-node Multi-GPU Simulations and Discussion

The primary challenge in simulating metasurfaces stems from their multi-scale nature: while individual sub-wavelength scatterers must be accurately resolved, the overall device often extends thousands of wavelengths in each lateral dimension. Since the FDTD method typically requires at least 10 grid cells per wavelength in the material, a millimeter-scale metasurface operating in the visible range necessitates over 10,000 cells along both x- and y-directions, with approximately 100 cells in the propagation (z) direction. This corresponds to approximately 10^{11} total grid cells, with material and field data alone requiring several terabytes of memory—far exceeding the capacity of single-GPU systems.

To overcome this limitation, we employ multi-GPU distributed computing across multiple nodes. As demonstrated in Fig. 1, the FDTD method exhibits nearly ideal scaling with the number of compute nodes, maintaining high parallel efficiency even when distributed across 32 to 64 GPUs. This scalability enables routine simulation and optimization of millimeter-scale metasurfaces that would otherwise be computationally intractable.

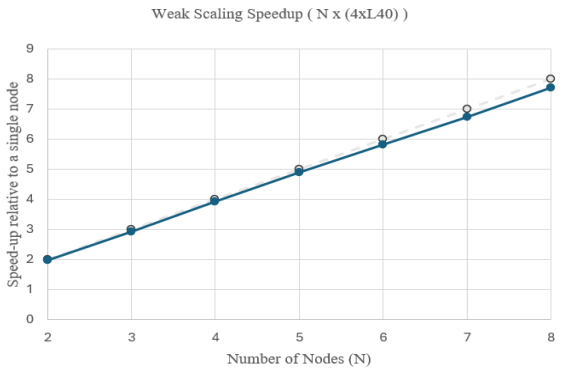

Fig. 1 Performance scaling of GPU-FDTD simulations with the number of GPU compute nodes. Each node consists of four Nvidia L40 GPUs. The dashed line shows perfect linear scaling while the solid line shows the measured speedup compared to a single node.

Since metasurfaces are typically thin (1–2 μm in the propagation direction), simulations require only approximately 10^4 time steps and complete in under 20 minutes per run. This computational efficiency not only enables millimeter-scale metasurface simulations but also makes iterative design workflows practical, including fine-grained parameter sweeps and gradient-based optimization with hundreds of iterations. Using this approach, it has been possible to design novel optical

sensors [2].

Once individual metasurface designs are finalized and verified, they must be integrated into system-level simulations that typically include combinations of traditional optical elements and metasurfaces. Ray tracing is the preferred method for such system simulations; however, accurately incorporating metasurfaces into ray-tracing frameworks without sacrificing computational efficiency remains challenging. The recently developed Windowed Fourier Transform (WFT) method [3] addresses this by maintaining ray-tracing performance while providing more accurate metasurface representation than previous approaches. However, machine learning-based surrogate models offer even greater flexibility and accuracy. By training neural networks on full-wave FDTD simulation data or on WFT results, we can create fast, differentiable representations of metasurface behavior that seamlessly integrate into ray-tracing workflows [4].

III. Conclusion

We have demonstrated that GPU-accelerated FDTD enables practical simulation and optimization of millimeter-scale metasurfaces containing thousands of sub-wavelength elements. By leveraging multi-GPU distributed computing with near-ideal parallel scaling, we achieve simulation times under 20 minutes despite handling approximately 10^{11} grid cells and terabytes of field data. This computational efficiency makes iterative design workflows feasible, including gradient-based optimization with hundreds of evaluations. Furthermore, we have shown that machine learning-based surrogate models trained on full-wave FDTD data provide accurate, efficient representations of metasurface behavior for system-level ray-tracing simulations, outperforming analytical approaches like the Windowed Fourier Transform method. Together, these advances establish a complete computational framework—from component-level optimization to system integration—that removes the computational barriers previously limiting large-scale metasurface development. This opens new opportunities for designing high-performance optical devices with unprecedented complexity and functionality.

References

[1] Y. He, B. Song and J. Tang, “Optical metalenses: fundamentals, dispersion manipulation, and applications,” Front. Optoelectron. Vol. 15, No. 24, 2022.

[2] R. Arfin, J. Son, J. Niegemann, D. McGuire, M.H. Bakr, “Adjoint-Driven Inverse Design of a Quad-Spectral Metasurface Router for RGB-NIR Sensing”. *Nanomaterials* Vol. *15*, No 21: 1671, 2025.

[3] H.-H. Cheng, T. Leportier, D. Huynh, J. Niegemann, A. Reid, W.-H. Chen, "Ray-tracing method for large-scale metalenses in multiwavelength imaging system", Proc. SPIE 13378, High Contrast Metastructures XIV, 1337809 (2025)

[4] A. Chartier, J. Niegemann, D. McGuire, S. Thibault, " Towards neural network integration of metasurfaces in optical design software," in Proceedings of SPIE Photonics West 2026, Paper 13910-6 (2026)

Photo-Excited Silicon-Based Quarter-Wave Plate for Terahertz Applications

Shohei Tsuzuki[1], Jun Shibayama[1,*]

[1]Faculty of Science and Engineering, Hosei University, Japan
*Corresponding author: shiba@hosei.ac.jp

***Abstract*—This article investigates a photo-excited silicon quarter-wave plate in the terahertz region. Using the finite-difference time-domain method, the performance of the quarter-wave plate is calculated with a focus on light emission intensity. Depending on the intensity, this device acts as either a quarter-wave plate or a blocking filter.**

***Keywords*— FDTD, photo-excited silicon, quarter-wave plate, terahertz.**

I. Introduction

Quarter-wave plates play a crucial role in communication systems. In the terahertz (THz) region, quarter-wave plates have been investigated using metal plates [1]. Meanwhile, photo-excited silicon exhibits intriguing properties in the THz range, with its dielectric properties varying according to the light emission intensity [2]. In this article, we analyze photo-excited silicon quarter-wave plates using the finite-difference time-domain (FDTD) method [3]. It is shown that the device acts as either a quarter-wave plate or a blocking filter, depending on the given light intensity.

II. Discussion

Fig. 1 shows the configuration of the quarter-wave plate made of photo-excited silicon. The configuration parameters are as follows: the period $\Lambda = 840$ μm, the thickness $t = 560$ μm, and the size of the aperture $r_x = 560$ μm and $r_y = 730$ μm. The electrical property of the silicon is represented by the simple conductivity model [2] and the conductivity is varied to simulate the carrier generation change from the light emission. A linearly polarized E_x wave is tilted $\phi_{\text{in}} = 45°$ from the x axis and excited toward the z direction. The periodic FDTD method is used to calculate one period of the quarter-wave plate.

The calculated transmittance is shown in Fig. 2, in which the results for $\sigma = 1.0 \times 10^2$ S/m as the dashed lines and those for $\sigma = 1.0 \times 10^5$ S/m as the solid lines are presented. It is shown that the transmittance for $\sigma = 1.0 \times 10^2$ S/m remains low for both E_x and E_y waves, indicating a blocking filter. This occurs because silicon acts as a dielectric, causing the electric field to be absorbed within the silicon. On the other hand, the transmittance for $\sigma = 1.0 \times 10^5$ S/m exceeds 80% for both polarizations. This is because silicon behaves as a metal, preventing the absorption of the electric field. Although not shown in the figure, the axial ratio is calculated to be less than -3 dB in the range of 0.28 to 0.34 THz, demonstrating the functionality of the quarter-wave plate in the THz band.

III. Conclusion

We have investigated a terahertz quarter-wave plate consisting of an optically excited silicon material in the terahertz region. Only one period is calculated using the periodic FDTD method. The results showed that this plate functions either as a quarter-wave plate or as a blocking filter depending on the intensity of the emitted light. This plate converts linearly polarized light into circularly polarized light in the 0.28 to 0.34 THz range.

References

[1] S. Tsuzuki and J. Shibayama, "Study of a quarter-wave plate in the THz region," *IEICE Technical Report*, vol. 124, no. 357, pp.— 91-94, 2025.
[2] N. H. Shen, M. Massaouti, M. Gokkavas, J. M. Manceau, E. Ozbay, M. Kafesaki, T. Koschny, S. Tzortzakis, and C. M. Soukoulis, "Optically implemented broadband blueshift switch in the terahertz regime," *Phys. Rev. Lett.*, vol. 106, pp. 037403-1-4, 2011.
[3] J. Shibayama, FDTD analysis of plasmonic devices, Springer, 2025.

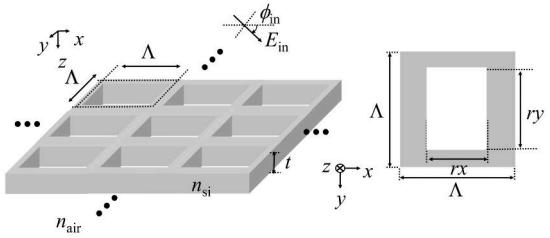

(a) Configuration (b) Unit cell

Fig. 1. Quarter-wave plate.

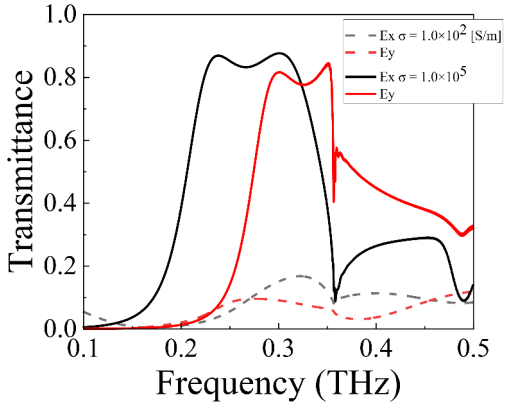

Fig. 2. Transmittance.

Near-field focusing and amplification of tip-substrate radiative heat transfer

M. Vescovo[1], P. Ben-Abdallah[1], R. Messina[1,*]

[1]Laboratoire Charles Fabry, UMR 8501, Institut d'Optique, CNRS
Université Paris-Saclay, 2 Avenue Augustin Fresnel, 91127 Palaiseau Cedex, France
*Corresponding author: riccardo.messina@institutoptique.fr

***Abstract*—By studying the spatially resolved near-field radiative heat transfer between a nanoscale probe and a substrate, we show that introducing a thin polar film atop a non-dispersive substrate leads to enhancement and lateral focusing of the heat exchange, offering a route toward the control of heat transfer at the nanoscale.**

***Keywords*— near-field radiative heat transfer, Poynting vector, heat-assisted magnetic recording.**

I. Introduction

When two bodies at different temperatures are separated by a vacuum gap, heat can be exchanged between them via the emission and absorption of thermal photons. In the far-field regime, where the separation exceeds the thermal wavelength $\lambda_{\rm th} = \hbar c/k_B T$ (on the order of a few microns at room temperature), this exchange is bounded by the Stefan–Boltzmann law. However, as first demonstrated by Rytov and later formalized by Polder and van Hove [1], [2], this limit breaks down in the near-field regime, where the separation falls below $\lambda_{\rm th}$. These pioneer works were followed by a plethora of theoretical and experimental developments (see e.g. Ref. [3] and references therein). In the near field, the radiative heat flux can be dramatically enhanced due to the tunneling of evanescent photons. This enhancement becomes especially pronounced when the interacting bodies support surface resonances such as phonon-polaritons in polar dielectrics or surface plasmons in metals [4]. These phenomena have opened promising avenues for nanoscale thermal management, solid-state cooling, infrared sensing and spectroscopy, energy conversion, and the emerging field of thermotronics.

An additional application domain is heat-assisted magnetic recording (HAMR) [5], [6], [7], where localized heating is used to transiently lower the coercivity of a magnetic substrate, enabling data writing with an external magnetic field. Achieving high information densities requires the confinement of heat to nanoscale regions, ideally approaching the superparamagnetic limit of tens of nanometers. In this context, we study the spatially resolved near-field radiative heat transfer between a nanoparticle and a substrate in the fluctuational-electrodynamics framework. Inspired by HAMR-like configurations, we address two key aspects, enhanced heat transfer and spatial localization, by investigating near-field radiative heat exchange between a nanoparticle–serving as a localized heat source–and a multilayer substrate composed of different materials. It is shown that the introduction of a thin polar film atop a non-dispersive substrate can lead to a substantial enhancement and spatial focusing of the radiative heat flux.

II. Methods

The theoretical framework employed falls within the well-established domain of dipolar near-field heat transfer, which has garnered significant interest over the past decade (see Ref. [8] and references therein). The system we consider is made of a spherical nanoparticle of radius R simulating a tip, made of silicon carbide (SiC). The nanosphere is placed at a distance d from a substrate covered by a film of thickness δ made of SiC, both assumed to be infinite along the transverse directions. The optical properties of SiC will be described by a Drude-Lorentz model [8]

$$\varepsilon(\omega) = \varepsilon_\infty \frac{\omega_L^2 - \omega^2 - i\Gamma\omega}{\omega_T^2 - \omega^2 - i\Gamma\omega}, \tag{1}$$

Concerning the underlying substrate, we explore a variety of non-dispersive materials having permittivities $\varepsilon_{\rm sub} = 2, 4, 8, 16$ and a very small imaginary part included for numerical reasons. The reason for this choice of permittivites is twofold. On one hand, sweeping over a range of possible permittivites allows us to investigate on the robustness of the effect associated with the thin film. On the other hand, the optical properties of the magnetic materials typically employed in HAMR are currently scarcely available in the far-infrared region of the spectrum, the most relevant one for radiative heat transfer close to ambient temperature. One result in this sense is the measurement of the refractive index of FePt thin films [9], resulting in a value of $n \simeq 4$ at $\lambda = 1.7\,\mu$m, motivating our choice of maximum $\varepsilon_{\rm sub}$ of 16.

III. Results and Discussion

In order to analyze the spatial distribution of the energy transferred between the nanosphere and the underlying substrate we focus on the z component S_z of the Poynting vector $\mathbf{S} = \mathbf{E} \times \mathbf{H}$, to be evaluated at the interface $z = 0$ between vacuum and substrate. This quantity can be calculated within a N-body fluctuational-electrodynamics approach complemented with the dipolar approximation [8]. In our scenario, we are going to focus on a single nanoparticle having radius

$R = 100\,\text{nm}$, temperature $T = 400\,\text{K}$, placed at distance $d = 300\,\text{nm}$ from the substrate, and assume that both the thermal bath and the substrate are at zero temperature. This allows us to focus purely on the contribution to the energy on the substrate coming from the nanoparticle thermal emission.

Our objective is to analyze the impact of the film and more specifically of its thickness on the amplification and focusing of energy transfer with respect to the reference configuration corresponding to the absence of film (substrate only). For each value of δ, the former will be quantitavely done by studying the ratio $S_z(0,0,0)/S_{\text{ref}}$ between the z component of the Poynting vector right below the particle and the reference value corresponding to the scenario in the absence of film, i.e. $\delta = 0$. As far as the focusing is concerned, it will be described by the half width at half maximum (HWHM) of the profile of $S_z(x,y,0)$, i.e. the x coordinate (in virtue of the rotational symmetry of the system) at which $S_z(x,0,0) = S_z(0,0,0)/2$.

Our main results are shown in Fig. 1, presenting these two quantites as a function of the film thickness δ for four different values of the substrate permittivity $\varepsilon_{\text{sub}} = 2, 4, 8, 16$. In Fig. 1(a), we see that for any chosen substrate permittivity, the curve starts at 1 as expected and shows a non-monotonic behavior with respect to δ, with a pronounced peak varying between 92 (for $\varepsilon_{\text{sub}} = 16$) and 183 (for $\varepsilon_{\text{sub}} = 2$). This first result already shows how a thin film having a thickness of hundreds of nanometers can induce a two-order-of-magnitude increase of the energy transferred between a nanoparticle and a substrate. Figure 1(b) shows that the presence of the thin film also has a strong impact on the width of the Poynting vector profile. These curves are also non-monotonic, with a FWHM going from the values $340, 340, 304, 260\,\text{nm}$ for $\varepsilon_{\text{sub}} = 2, 4, 8$ and 16, respectively, in the absence of film to 113, 128, 128, 128 nm in the best scenario in the presence of a film. By analyzing in detail the influence of the probe–substrate separation, film thickness and substrate permittivity, we reveal that the effect originates from near-field interactions governed by the interplay between film-induced modifications of electromagnetic mode dispersion and the distance-dependent coupling strength.

Fig. 1. (a) Ratio of the Poynting vector $S_z(0,0,0)$ below the nanoparticle and the one S_{ref} in the absence of film ($\delta = 0$) as a function of the film thickness δ. The 4 curves correspond to different values of the substrate permittivity (see legend). (b) Corresponding values of the HWHM.

IV. Conclusion

We demonstrate that the spatially resolved near-field radiative heat transfer between a polar nanoparticle and a non-dispersive substrate can be significantly controlled by introducing a thin polar film atop the substrate. By analyzing the magnitude and spatial distribution of the Poynting vector, we show that specific film thicknesses can lead to a pronounced enhancement and focusing of the local energy flux. This results from the interplay between the dispersion relations of resonant electromagnetic modes supported by the vacuum–film–substrate configuration and the nanoparticle–substrate separation. Our findings provide insights into the control of spatially resolved thermal radiation and point toward new strategies for nanoscale thermal management and may be extended to more complex scenarios, including multi-tip geometries and self-consistent treatment of heat diffusion within multilayer substrates.

References

[1] S. M. Rytov, "Theory of Electrical Fluctuations and Thermal Radiation" (Academy of Sciences Press of USSR, Moscow, 1953).

[2] D. Polder and M. van Hove, "Theory of Radiative Heat Transfer between Closely Spaced Bodies", *Phys. Rev. B*, vol. 4, p. 3303, 1971.

[3] S.-A. Biehs, R. Messina, P. S. Venkataram, A. W. Rodriguez, J. C. Cuevas, and P. Ben-Abdallah, "Near-field radiative heat transfer in many-body systems", *Rev. Mod. Phys.*, vol. 93, p. 025009, 2021.

[4] K. Joulain, J.-P. Mulet, F. Marquier, R. Carminati, and J.-J. Greffet, "Surface electromagnetic waves thermally excited: Radiative heat transfer, coherence properties and Casimir forces revisited in the near field", *Surf. Sci. Rep.*, vol. 57, p. 59, 2005.

[5] W. Srituravanich, N. Fang, C. Sun, Q. Luo, and X. Zhang, "Plasmonic Nanolithography", *Nano Lett.*, vol. 4, p. 1085, 2004.

[6] W. A. Challener et al., "Heat-assisted magnetic recording by a near-field transducer with efficient optical energy transfer", *Nat. Photonics*, vol. 3, p. 220, 2009.

[7] B. C. Stipe et al., "Magnetic recording at 1.5 Pb m^{-2} using an integrated plasmonic antenna", *Nat. Photonics*, vol. 4, p. 484, 2010.

[8] M. Vescovo, P. Ben-Abdallah, and R. Messina, "Near-field focusing and amplification of tip-substrate radiative heat transfer", *Phys. Rev. Appl.*, vol. 24, p. 064014, 2025.

[9] Z. H. Cen et al., "Optical property study of FePt-C nanocomposite thin film for heat-assisted magnetic recording", *Opt. Express*, vol. 21, p. 9906, 2013.

Time Modulation of Near-Field Radiative Heat Transfer

Mauro Antezza [1,2*]

[1]Laboratoire Charles Coulomb (L2C), UMR 5221 CNRS-Université de Montpellier, F-34095 Montpellier, France
[2]Institut Universitaire de France, 1 rue Descartes, Paris Cedex 05 F-75231, France
*Corresponding author: mauro.antezza@umontpellier.fr

***Abstract*— We develop a theory to study how a fast periodic modulation of a generic control variable affecting the near-field radiative heat coupling between two bodies produces a correction on the slow thermal dynamics.**

***Keywords*— radiative heat transfer**

The past two decades have established the foundations and experimental reality of near-field radiative heat transfer (NFRHT), where thermally excited evanescent fields enable photon tunneling across subwavelength gaps, yielding heat fluxes far exceeding the blackbody limit. Quantitative measurements down to nanometric separations have confirmed the predictions of fluctuational electrodynamics across diverse materials and geometries. These advances now allow dynamic control through electromechanical gap actuation or dispersion engineering.

In [1], we introduce a new mechanism for temperature control based on the fast modulation of parameters affecting radiative heat transfer. We analyze how rapid periodic modulation of a near-field coupling parameter influences the slow thermal dynamics of a lumped body.

References

[1] M. Antezza, submitted (2026)

Numerical advances in the computation of radiative heat transfer between nanostructures

Brahim Guizal[1,*] Omar Tada[1], Mauro Antezza[1], and Youssef Jeyar[1]

[1]Laboratoire Charles Coulomb (L2C), UMR 5221 CNRS- Université de Montpellier, F-34095 Montpellier, France

*Corresponding author: brahim.guizal@umontpellier.fr

***Abstract*— Simulating radiative heat transfer between nanostructures can be very demanding in terms of computational resources even with Fourier methods which are known to be very efficient for handling such structures, especially lamellar ones. For that case, we propose a method that leads to a further reduction of the computational load.**

***Keywords*— Fourier Modal Method, Radiative heat transfer, Computational electromagnetics.**

I. Introduction

Radiative heat transfer is a key phenomenon entering in many applications such as radiative heating-cooling or thermo-photovoltaic systems. Modelling such an effect requires efficient electromagnetic computational methods. Among these, the FMM (Fourier Modal Method) aka the RCWA (Rigorous Coupled Wave Analysis) is one of the most versatile and efficient approaches. This method can be made even more efficient when the nanostructures under study are subwavelength in height. This is possible because in such a situation, one can avoid solving the, computationally demanding, eigenvalue problem that is the heart of the FMM. Since the computation of the heat exchange is done over the entire electromagnetic spectrum, the subwavelength condition will be fulfilled over a non-negligible range of frequencies for which the computation will be greatly simplified. In this presentation, I will show how this applies, in detail, to radiative heat transfer computations. Finally, it is important to notice that such an approach can be applied in context of Casimir-Lifshitz force computations especially out of thermal equilibrium where computations over the entire electromagnetic spectrum are unavoidable.

II. Methods

The Fourier Modal Method [1] as applied to radiative heat transfer. The fields as well as the dielectric properties of the nanostructures are expanded in generalized Fourier series. When inserted into Maxwell equations this leads to an eigenvalue problem that must be solved in each periodic slice. This latter can be avoided when the height of the slice id subwavelength.

III. Conclusion

We have demonstrated a THz metamaterial with superior wavefront control and broadband absorption. Future work will extend the design to polarization-independent and reconfigurable THz devices.

References

[1] G. Granet and B. Guizal, “Efficient implementation of the coupled wave method for metallic lamellar gratings in TM polarization,” J. Opt. Soc. Am. A, Vol 13, No 5, pp 1019-1023, May 1996.

BIC-Enhanced Partial LDOS in Terahertz Metasurfaces

J. Ji, D. Peeters[2], W. Holman[1], T. X. Hoang[3], D. van Mechelen[2], J. Gómez Rivas[1], J. A. Sánchez-Gil[4,*]
[1]Department of Applied Physics and Science Education, Institute for Complex Molecular Systems, and Eindhoven Hendrik Casimir Institute, Eindhoven University of Technology, Eindhoven, the Netherlands
[2]Advanced Sensing & Quantum Materials, Department of Electrical Engineering, Eindhoven University of Technology, Eindhoven, the Netherlands
[3]Institute of High Performance Computing (IHPC), Agency for Science, Technology and Research (A*STAR), Singapore
[4]Instituto de Estructura de la Materia, CSIC, Madrid, Spain
*Corresponding author: j.sanchez@csic.es

***Abstract*— This work uses terahertz near-field microscopy to reveal how quasi–bound states in the continuum enhance the partial local density of optical states in finite metasurfaces. Experiments and simulations show strong, spatially confined PLDOS enhancement that saturates with array size, establishing practical limits and design rules for THz quasi-BIC engineering.**

***Keywords*— metasurface, bound states in the continuum, LDOS.**

I. Introduction

Near-field terahertz (THz) microscopy is used to directly probe how bound states in the continuum (BICs) enhance the partial local density of optical states (PLDOS) in nonlocal metasurfaces, revealing fundamental limits to BIC-enabled light–matter interaction. Symmetry-protected BICs supported by an infinite array of gold rod dimers remain decoupled from far-field radiation [1], but in finite arrays they manifest as quasi-BICs with finite radiative linewidths whose collective nature governs the PLDOS enhancement.

II. Methods

Here, a dual-probe THz near-field time-domain setup, enables direct excitation and detection of quasi-BIC modes and, thus, a direct experimental determination of the PLDOS at the position of the source dipole for defined dipole orientations. This technique has been previously exploited to unveil the symmetry protection of such collective modes in the near field [2], along with the strong confinement perpendicular to the metasurface plane. By comparing measurements on large-area metasurfaces to SCUFF-EM boundary-element calculations [4], a strong PLDOS enhancement is observed at the quasi-BIC frequency, highly localized at the rod edges and confined within a subwavelength mode volume [5].

III. Results and Discussion

Systematic variation of the array size from a single dimer to multi-dimer arrays shows that the quasi-BIC originates from collective modes whose number and spectral sharpness increase with metasurface size, leading to a diverging quality factor while the PLDOS enhancement saturates at moderate array sizes [5]. This saturation arises from the competition between Q-factor and mode volume, preventing an unbounded increase of PLDOS despite ever-higher Q. Spatially resolved PLDOS maps in the plane and along the out-of-plane direction demonstrate extreme confinement of the enhanced density of states to nanometric regions at the edges of the rods and an evanescent decay away from the metasurface, confirming that quasi-BICs provide both high-Q and deep subwavelength confinement. These results establish an experimental upper limits for BIC-induced LDOS enhancement in realistic finite metasurfaces and define design rules for maximizing on-chip light–matter interaction, with direct implications for THz quasi-BIC engineering.

IV. Conclusion

These results establish experimental upper limits for BIC-induced LDOS enhancement in realistic finite metasurfaces and define design rules for maximizing on-chip light–matter interaction, with direct implications for THz quasi-BIC engineering.

Acknowledgments

Financial support is acknowledged from Spanish MCIN/AEI/10.13039/501100011033/ and “ERDF A way of making Europe” (LIGHTCOMPAS, PID2022-137569NB-C41).

REFERENCES

[1] D.R. Abujetas, N. van Hoof, S.E.T. ter Huurne, J. Gómez Rivas, and J.A. Sánchez-Gil. "Spectral and temporal evidence of robust photonic bound states in the continuum on terahertz metasurfaces," Optica, vol. 6, pp. 996–1001, 2019.

[2] N.J.J. Hoof, D.R. Abujetas, S.E.T. ter Huurne, F. Verdelli, G.C.A. Timmermans, J. A. Sánchez-Gil, and J. Gómez Rivas, "Unveiling the symmetry protection of bound states in the continuum with terahertz near-field imaging," ACS Photonics, vol. 8, pp. 3010–3016, 2021.

[3] S. ter Huurne, D.R. Abujetas, N. van Hoof, J. A. Sánchez-Gil, and J. Gómez Rivas, "Direct Observation of Lateral Field Confinement in Symmetry-Protected THz Bound States in the Continuum," Adv. Opt. Mater., vol. 11, p. 2202403, 2023.

[4] M.T.H. Reid, S. G. Johnson, "Efficient computation of power, force, and torque in BEM scattering calculations," IEEE Trans. Antennas Propag., vol. 63, pp. 3588–3598, 2015.

[5] J. Ji, J.A. Sánchez-Gil, D. Peeters, W. Holman, T.X. Hoang, D. van Mechelen, and J. Gómez Rivas, "Near-field probing of the local density of optical states enhanced by bound states in the continuum in nonlocal metasurfaces," Nature Communications, vol. 16, p. 11597, 2025.

Time-Frequency Structured Light for Analog Processing of Broadband Waveforms

Majid Goodarzi, Geunweon Lim, Connor Rowe, Benjamin Crockett, Xinyi Zhu, Hao Sun, José Azaña*

Institut National de la Recherche Scientifique (INRS), Montréal, QC, Canada

*Corresponding author: Jose.Azana@inrs.ca

***Abstract*—We present time-frequency structured light for analog processing of ultrafast broadband waveforms. Using bounded Talbot array illuminator phase modulation with dispersion, phase-only optical systems redistribute coherent energy for denoising and user-defined filtering, and joint time-frequency analysis and processing of time-domain waveforms with bandwidths into the multi-THz range.**

***Keywords*— structured light, time-frequency processing, Talbot array illuminator, optical signal processing.**

Broadband waveforms encountered in microwave photonics, optical communications, sensing, spectroscopy, and ultrafast optics create a practical signal-processing problem. The relevant features may occur on picosecond or sub-picosecond time scales, while the optical or optically up-converted spectra can span hundreds of gigahertz to several terahertz. For such signals, full electronic capture followed by digital processing is often limited by the available real-time bandwidth, and in ultrafast optical measurements it may not be a realistic first step. This motivates photonic analog processing, in which selected operations are carried out directly in the optical domain before detection or lower-bandwidth electronic processing. In this work, dispersion and phase-only temporal modulation are used as the basic processing tools. The target functions include denoising, waveform reshaping, time-frequency filtering, and single-shot measurements that resolve how the spectral content of an ultrafast waveform evolves in time.

The central idea is to extend structured-light concepts from transverse spatial coordinates to the temporal and spectral coordinates of an optical waveform. In conventional structured light, one tailors the spatial amplitude, phase, polarization, or modal content of an optical beam [1]. Here, the corresponding control is applied through phase-only operations in time and optical frequency, namely temporal phase modulation and spectral phase filtering. Broadband waveform processing can therefore be formulated within a Fourier-optics framework in which the roles usually played by spatial propagation, lenses, and focusing are implemented in the time-frequency domain using dispersion and time-dependent phase modulation. The physical basis for this connection is space-time duality, where paraxial diffraction in space is mathematically analogous to dispersive pulse propagation in time, and a spatial lens is analogous to a temporal phase modulation or time lens [2], [3]. This analogy has enabled temporal imaging and temporal Fourier transformation, and more recently has supported optical wave-energy redistribution methods for analog photonic signal processing, including denoising through passive amplification and real-time, time-mapped spectrogram reconstruction, where the spectrogram is obtained through an optical implementation of the short-time Fourier transform (STFT) [4].

A practical challenge appears when the temporal-lens analogy is implemented over a large processing aperture. The ideal time lens requires a parabolic temporal phase, whose phase excursion grows with the duration of the waveform being processed. For long temporal windows or large time-bandwidth products, this can require a large and continuously varying phase swing that is poorly matched to practical electro-optic phase modulators. Talbot array illuminator (TAI) phase modulation provides a more implementable alternative. Instead of applying an unbounded parabolic phase, a TAI uses a periodic, phase-only temporal pattern designed under fractional Talbot conditions [5]. Since the phase is wrapped modulo 2π, the modulation remains bounded while still enabling controlled time-frequency energy redistribution when combined with a dispersive element.

The denoising operation provides an intuitive example of this redistribution. In a TAI followed by dispersion, coherent signal components satisfying the designed phase relation can recombine into selected temporal regions, whereas incoherent noise remains broadly distributed. The result is a passive intensity enhancement of the signal relative to the noise, which has been used for temporal passive amplification and optical signal denoising [6]. Recent theory further shows that the passive-amplification regime and the STFT regime of temporal TAIs are connected through the same underlying time-frequency mapping, analogous to the relationship between focusing and Fourier transformation in a spatial lens system [7].

The same dispersive and TAI phase elements can be configured for time-frequency analysis of broadband ultrafast optical waveforms. In this regime, dispersion and temporal phase modulation implement a time-to-frequency mapping, so that temporal features of the input waveform are transferred to resolvable positions in the output optical spectrum (see Fig. 1). The measured spectrum encodes the waveform's short-frequency Fourier transform (SFFT), allowing a time-frequency representation to be obtained from a single optical spectral acquisition. This approach has recently been demonstrated for complex optical waveforms spanning up to 11 THz over nanosecond durations, corresponding to time-bandwidth

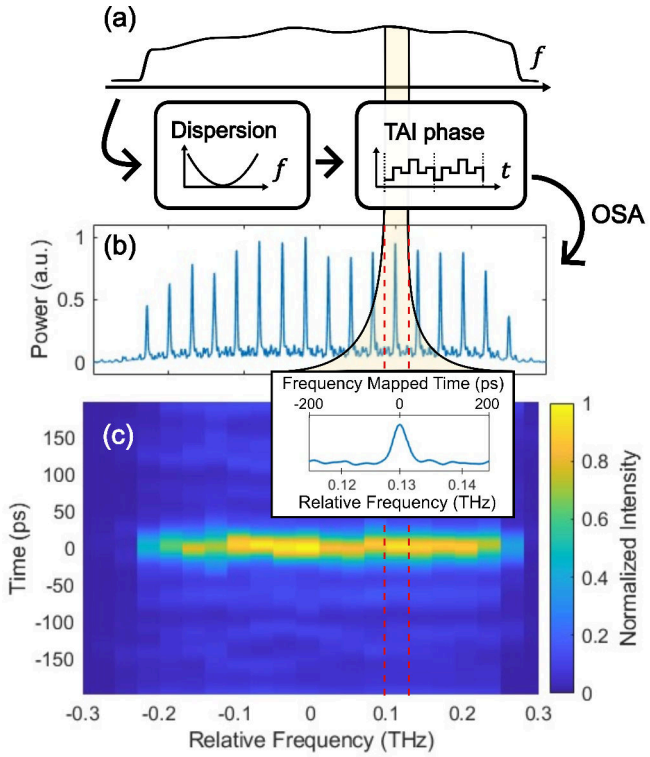

Fig. 1. Concept of the TAI-based linear optical short-frequency Fourier transform (SFFT) measurement. (a) A broadband transform-limited pulse is dispersed and then modulated with a temporal TAI phase profile. The output spectrum is measured by an optical spectrum analyzer (OSA). (b) Measured output optical spectrum after the proposed system. The selected spectral window, marked by the red dashed lines, provides the frequency-mapped temporal response shown in the inset. (c) Reconstructed time-frequency representation of the transform-limited input pulse, showing a temporally localized response across the measured bandwidth.

products above 16,000 [8]. The key point is that the optical system performs the time-frequency mapping, converting ultrafast temporal structure into a processed spectral waveform that can be measured with standard optical instrumentation.

Taken together, these results present TAI-based time-frequency structuring as a general phase-only methodology for analog photonic processing of broadband waveforms. The same physical ingredients, dispersive propagation and bounded temporal phase modulation, can support passive amplification, denoising, filtering, and single-shot time-frequency analysis, depending on the designed mapping. The approach is attractive because it does not require active optical gain or nonlinear conversion, and because its main components are compatible with practical photonic platforms. Near-term implementations can use dispersive fiber, chirped fiber Bragg gratings, electro-optic phase modulators, and optical spectrum analyzers, while integrated versions can build on dispersive waveguides, on-chip modulators, sources, and detectors [9]. More broadly, this work shows how concepts from structured light and Fourier optics can be translated from transverse beam shaping to the time-frequency processing of ultrafast waveforms.

REFERENCES

[1] A. Forbes, M. de Oliveira, and M. R. Dennis, "Structured light," *Nature Photonics*, vol. 15, pp. 253–262, 2021.
[2] B. H. Kolner and M. Nazarathy, "Temporal imaging with a time lens," *Optics Letters*, vol. 14, no. 12, pp. 630–632, 1989.
[3] B. H. Kolner, "Space-time duality and the theory of temporal imaging," *IEEE Journal of Quantum Electronics*, vol. 30, no. 8, pp. 1951–1963, 1994.
[4] C. M. L. Rowe, X. Zhu, B. Crockett, G. Lim, M. Goodarzi, M. Fernández, J. van Howe, H. Sun, S. Kaushal, A. Shoeib, and J. Azaña, "Linear optical wave energy redistribution methods for photonic signal processing," *npj Nanophotonics*, vol. 2, article 13, 2025.
[5] C. R. Fernández-Pousa, R. Maram, and J. Azaña, "CW-to-pulse conversion using temporal Talbot array illuminators," *Optics Letters*, vol. 42, no. 13, pp. 2427–2430, 2017.
[6] B. Crockett, L. Romero Cortés, R. Maram, and J. Azaña, "Optical signal denoising through temporal passive amplification," *Optica*, vol. 9, no. 1, pp. 130–138, 2022.
[7] M. Goodarzi, G. Lim, and J. Azaña, "On the link between Fourier transformation and passive amplification in temporal Talbot array illuminators," *Optics Letters*, vol. 51, no. 9, pp. 2596–2599, 2026.
[8] G. Lim, B. Crockett, M. Goodarzi, and J. Azaña, "Linear-optics time-frequency analysis of complex multi-THz-bandwidth waveforms from a single optical spectrum," *Optics Letters*, vol. 50, no. 24, pp. 7560–7563, 2025.
[9] H. Sun, X. Zhu, S. Kaushal, M. Tosi, M. Bustillos, B. Crockett, C. M. L. Rowe, and J. Azaña, "Toward on-chip integration of linear optical wave energy redistribution systems for photonic signal processing [Invited]," *Journal of the Optical Society of America B*, vol. 43, no. 5, pp. 929–942, 2026.

High-Speed Chemical Identification Enabled by Terahertz Parametric Wavelength Conversion

Kosuke Murate[1,*], Sota Mine[2, 1], Kodo Kawase[1]

[1] Department of Electronics, Nagoya University, Furocho, Chikusa, Nagoya, 464-8603, Japan
[2] RIKEN, 519-1399 Aramakiaoba, Aoba, Sendai, 980-0845, Japan
*Corresponding author: murate@nuee.nagoya-u.ac.jp

***Abstract*— We demonstrate simultaneous generation of more than ten terahertz (THz) wavelengths using parametric generation and detection. Spectroscopic information is acquired in real time as camera images, enabling instantaneous sample identification via image recognition. The system allows rapid chemical sensing with strong potential for practical THz applications.**

***Keywords*—terahertz, machine learning, parametric generation.**

I. Introduction

One of the promising applications of terahertz (THz) waves is nondestructive inspection through opaque materials. For practical implementation, a real-time spectroscopic system capable of operating in the 1–2 THz region is required, since this frequency range offers material transparency and many chemicals exhibit characteristic fingerprint spectra.

To address this need, we have been investigating simultaneous multi-wavelength THz generation and detection by optically injecting multiple near-infrared (NIR) seed beam into an injection-seeded terahertz parametric generator (is-TPG)[1-3]. However, conventional approaches required the same number of injection light sources as the number of THz wavelengths, leading to issues such as high cost, limited controllability, and increased system complexity and size.

In this study, we employed cascaded multi-wavelength Stokes beams generated under high-intensity pumping in a nonlinear optical crystal ($LiTaO_3$) as multi-wavelength injection sources[4, 5]. Using only two seed laser with pump laser, we achieved simultaneous generation and detection of more than ten wavelengths in the 1–2 THz region.

II. Results and Discussion

The experimental setup is shown in Fig. 1. Laser beam emitted from an external-cavity semiconductor laser was pulse-amplified in a $LiTaO_3$ crystal under high intensity and then injected into a second crystal ($LiNbO_3$) to generate first- to fourth-order Stokes beams. Two such high-order Stokes beam sources (each generating different wavelength groups) were prepared. After passing through relay optics composed of lenses, they were combined using a half mirror and injected into a third $LiNbO_3$ crystal.

Through parametric wavelength conversion, multi-wavelength THz waves corresponding to the difference frequencies between each pair of injected wavelengths were generated. The generated multi-wavelength THz waves were upconverted to near-infrared detection Stokes beams via terahertz parametric detection and captured with a near-infrared

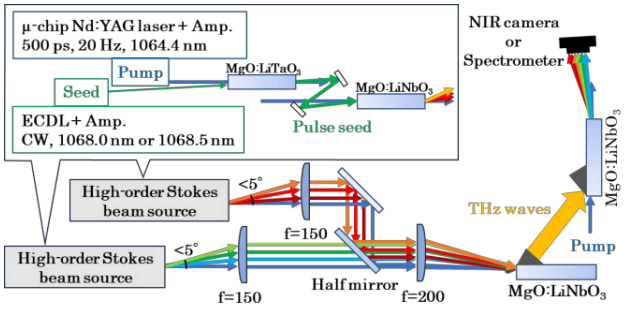

Fig. 1 Schematic diagram of multi-wavelength THz wave generation based on injection-seeded terahertz parametric generation (is-TPG) using high-order Stokes beams.

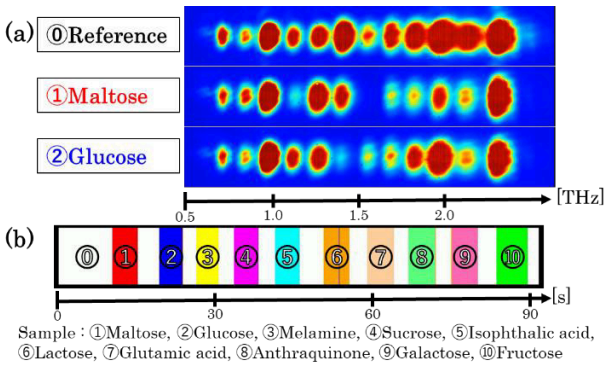

Fig. 2 Real-time identification of chemical reagents. (a) Representative detection Stokes images with and without sample insertion. (b) Time-series classification results obtained by machine learning.

camera. As shown in Reference in Fig. 2(a), simultaneous generation of 12 wavelengths was confirmed[6].

By combining this system with machine-learning-based classification[7], real-time reagent identification was demonstrated. Ten different reagents were sequentially inserted into the THz optical path, and the instantaneous changes in the detection Stokes beams were identified through image recognition. Examples of observed detection Stokes images without a sample, with maltose, and with glucose are shown in Fig. 2(a), clearly indicating differences depending on the sample.

The time-series results of machine-learning-based classification are shown in Fig. 2(b). Each color represents a different reagent. The system successfully achieved accurate real-time identification of all ten reagents.

III. Conclusion

We demonstrated simultaneous multi-wavelength terahertz generation and detection in the 1–2 THz region by using cascaded high-order Stokes beams in $LiNbO_3$ as multi-wavelength injection sources. More than ten THz wavelengths were generated and detected simultaneously with only two injection lasers.

By combining this system with machine-learning-based image recognition, real-time identification of ten different chemical reagents was achieved. The results indicate that the proposed method is effective for high-speed THz spectroscopic sensing and has strong potential for practical applications in chemical identification and nondestructive inspection.

Acknowledgments

This work was supported by JST ASPIRE (JPMJAP2340) and FOREST (JPMJFR212J), and JSPS KAKENHI (22J20963, 24K00943).

References

[1] K. Murate, S. Mine, and K. Kawase, “Terahertz Parametric Generators and Detectors for Nondestructive Testing Through High-Attenuation Packaging Materials,” *IEEE J. Sel. Top. Quantum Electron.*, vol. 29, Art. no. 8500813, 2023.

[2] K. Murate, S. Hayashi, and K. Kawase, “Multiwavelength terahertz-wave parametric generator for one-pulse spectroscopy,” *Appl. Phys. Express*, vol. 10, Art. no. 032401, 2017.

[3] K. Murate, S. Mine, and K. Kawase, “High-speed and single-shot terahertz spectroscopy using a wavelength-tunable source [Invited],” *Appl. Opt.*, vol. 64, pp. F32–F45 2025.

[4] S. Mine, K. Kawase, and K. Murate, “Cascaded Terahertz Parametric Generation Under Noncollinear Phase-Matching Condition,” *J. Infrared Millim. Terahertz Waves*, vol. 45, pp. 116-123, 2024.

[5] W. Li, F. Qi, P. Liu, Y. Wang, and Z. Liu, “Cascaded effect in a high-peak-power terahertz-wave parametric generator,” *Opt. Lett.*, vol. 47, pp. 178-181, 2022.

[6] S. Mine, K. Kawase, and K. Murate, “Multi-wavelength terahertz parametric generation using higher-order Stokes beams,” *IEEE Trans. Terahertz Sci. Technol.*, pp. 781-786, 2025.

[7] K. Murate, S. Mine, Y. Torii, H. Inoue, and K. Kawase, “Wide dynamic range and real-time reagent identification and imaging using multi-wavelength terahertz parametric generation and machine learning,” *Sci. Rep.*, vol. 13, Art. no. 12743, 2023.

Theory and experiments on GaN waveguide polariton lasers

O. Bahrova[1,2], V. Develay[3], I. Septembre[1,4], D. Bobylev[1], C. Brimont[3], L. Doyennette[3], B. Alloing[5], H. Souissi[6], E. Cambril[6], S. Bouchoule[6], T. Ackemann[7], J. Zuniga-Perez[5,8], T. Guillet[3], G. Malpuech[1], D. Solnyshkov[1,9,*]

[1]Institut Pascal, PHOTON-N2, Université Clermont Auvergne, CNRS, Clermont INP, Clermont-Ferrand, France
[2]B. Verkin Institute of the National Academy of Sciences of Ukraine, Kharkiv, Ukraine
[3]Laboratoire Charles Coulomb, Université de Montpellier, CNRS, Montpellier, France
[4]Naturwissenschaftlich-Technische Fakultät, Universität Siegen, Siegen, Germany
[5]CRHEA, Université Cote d'Azur, CNRS, Rue Bernard Gregory, Valbonne, France
[6]Centre de Nanosciences et de Nanotechnologies, CNRS, Université Paris-Saclay, France
[7]University of Strathclyde, Glasgow, UK
[8]MajuLab, International Research Laboratory, Singapore
[9]Institut Universitaire de France (IUF), Paris, France
*Corresponding author: dmitry.solnyshkov@uca.fr

***Abstract*—GaN waveguide polariton lasers are very promising for applications. We discuss recent experimental results and their theoretical description, including cw and pulsed mode-locked polariton lasing, the formation of single and multiple solitons in ridge waveguides, and also bound states in the continuum (BIC) and associated solitons in modulated waveguides.**

***Keywords*— polariton lasers, mode locking, solitons, bound states in the continuum.**

Polariton lasers are based on strong light-matter coupling of excitons and photons. They can exhibit a reduced lasing threshold thanks to the absence of the population inversion condition for Bose-Einstein condensation. GaN is one of the best materials for room-temperature polariton lasing [1] thanks to its robust excitons. Waveguide structures were suggested as best candidates for practical implementation of wide-bandgap polariton lasers, in particular in the UV, given that they provide longer photon lifetimes than planar microcavities and are much simpler to fabricate, opening the door to electrically-injected polariton lasers. Polariton amplification and lasing at room temperature have already been observed in polaritonic planar slab waveguides [2]. Here, we report several recent experiments with GaN ridge waveguides and modulated slab waveguides, focusing on the methods used for the theoretical description of these experiments.

First, *cw* monomode lasing has been observed from a ridge waveguide polariton laser under optical pumping [3]. A key feature of the polariton laser is that it does not require population inversion (or saturation of absorption), which allows lasing while pumping just a small fraction of the laser ridge. It is noteworthy that this configuration would preclude lasing in the standard electron-hole plasma regime. We used semi-classical Boltzmann equations coupled with propagation equations to describe this system and study the threshold dependence on the pumping fraction.

Next, by modifying the pumping conditions, multimode lasing was observed, with the intensity envelope exhibiting a shape characteristic for a soliton. Moreover, the modification of the free spectral range indicated the presence of mode locking [4]. We developed a model describing strong coupling of a guided photonic mode and an excitonic resonance, including spatial propagation, exciton-exciton interactions, losses, and gain due to exciton-exciton scattering from the reservoir. The model reproduces the formation of a spatiotemporal soliton, the change of the shape of the spectrum, and the mode locking due to polariton interactions. Further experiments and simulations have demonstrated the possible simultaneous presence of multiple coexisting solitons depending on the position of the pump (Fig. 1).

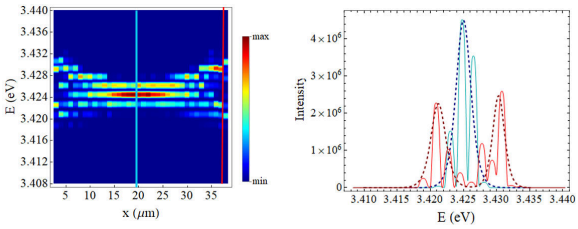

Fig. 1. Left: calculated spectrum of mode-locked polariton lasing as a function of the position of the pump along the ridge length, exhibiting a transition between a single soliton and two solitons. Right: two particular spectra for the pump positions indicated by red and blue vertical lines in the left panel.

Finally, we also studied polariton lasing in slab waveguides with a periodic modulation leading to the formation of bound states in the continuum (BICs) [5], characterized by a quenched emission rate. Computing the eigenstates with COMSOL, we demonstrate the topologically protected nature of the BIC, confirmed by polarization and momentum-resolved

experiments. Simulations of polariton condensation using a 1D time-dependent Schrödinger equation with gain, loss and interactions, demonstrate the formation of a spatial soliton at the BIC, also confirmed by experiments. The formation of this soliton is important because it affects the angular properties of emission of BIC polariton lasers, as well as their emission rate.

To conclude, we have successfully developed several theoretical models to describe different aspects of polariton condensation in GaN waveguides that reproduce qualitatively and quantitavely the experiments performed on such GaN structures.

ACKNOWLEDGMENTS

This work was supported by European Union's Horizon 2020 program, through a FET Open research and innovation action under the grant agreement No. 964770 (TopoLight), and by the European Union EIC Pathfinder Open project "Polariton Neuromorphic Accelerator" (PolArt, Id: 101130304). Additional support was provided by the ANR Labex GaNext (ANR-11-LABX-0014), the ANR program "Investissements d'Avenir" through the IDEX-ISITE initiative 16-IDEX-0001 (CAP 20-25), the ANR project MoirePlusPlus, the ANR project "NEWAVE" (ANR-21-CE24-0019), and the Région Occitanie. C2N is a member of RENATECH-CNRS, the French national network of large micro-nanofacilities.

REFERENCES

[1] G. Malpuech, A. Di Carlo, A. Kavokin, J. Baumberg, M. Zamfirescu, and P. Lugli, "Room-temperature polariton lasers based on GaN microcavities," *Appl. Phys. Lett.*, vol. 81, no. 3, pp. 412–414, Jul. 2002.

[2] O. Jamadi, F. Reveret, P. Disseix, F. Medard, J. Leymarie, A. Moreau, D. Solnyshkov, C. Deparis, M. Leroux, E. Cambril *et al.*, "Edge-emitting polariton laser and amplifier based on a ZnO waveguide," *Light: Science & Applications*, vol. 7, no. 1, p. 82, 2018.

[3] H. Souissi, M. Gromovyi, T. Gueye, C. Brimont, L. Doyennette, D. Solnyshkov, G. Malpuech, E. Cambril, S. Bouchoule, B. Alloing, S. Rennesson, F. Semond, J. Zúñiga Pérez, and T. Guillet, "Ridge polariton laser: Different from a semiconductor edge-emitting laser," *Phys. Rev. Applied*, vol. 18, p. 044029, Oct 2022.

[4] H. Souissi, M. Gromovyi, I. Septembre, V. Develay, C. Brimont, L. Doyennette, E. Cambril, S. Bouchoule, B. Alloing, E. Frayssinet *et al.*, "Mode-locked waveguide polariton laser," *Optica*, vol. 11, no. 7, pp. 962–970, 2024.

[5] V. Develay, O. Bahrova, I. Septembre, D. Bobylev, C. Brimont, L. Doyennette, B. Alloing, H. Souissi, E. Cambril, S. Bouchoule *et al.*, "Soliton formation in a bound state in the continuum gan waveguide polariton laser," *arXiv:2512.23368*, 2025.

Understanding and Designing High Harmonic Generation from Nanostructured Surfaces

Gavin Crowder[1], Jesse Thompson[1], Lora Ramunno[1*]

[1]Department of Physics and Nexus for Quantum Technologies Institute, University of Ottawa, Ottawa, Canada

*Corresponding author: lramunno@uottawa.ca

***Abstract*— High harmonic generation from solids and nanostructured surfaces is of recent interest, including to harness and control light into the XUV. I will present our progress on simulating this complex nonlinear interaction within nanostructured environments, where propagation and near field effects are crucial to device design and understanding experiments.**

***Keywords*— High harmonic generation, metasurfaces, thin films, computational electrodynamics, device design**

Inverse design frameworks towards realistic freeform flat optics (Invited)

Joao Cunha[1*], Filipe Camarneiro[1], Diogo E. Aguiam[1]

[1]INL – International Iberian Nanotechnology Laboratory, Braga, Portugal
*Corresponding author: joao.cunha@inl.int

***Abstract*— Inverse design of flat optics typically requires the simulation and optimization of systems described by over millions of parameters, which is computationally challenging. Addressing this, we introduce an open source inverse design framework and investigate its suitability in handling large parameter spaces and its most suitable optimization algorithm approaches.**

***Keywords*— inverse design, flat optics, meta-optics**

I. Introduction

Inverse design enables optimized optical elements/ optical systems reaching outstanding performance and optical functionalities beyond human intuition. Particularly, inverse design of complex shaped, i.e. freeform, flat optics has evidenced the possibilities in optimizing achromatic performance of focusing lenses [1], holograms [2], or image recognition [3], both in diffractive [4] and metasurface forms.

These advancements were enabled by the remarkable progress in computational capabilities, especially regarding gradient-based optimization strategies. In these, the calculation of the gradient is the crucial step, which has historically been performed via the Adjoint method [5]. Recently, the advent of machine learning frameworks and efficient software packages enabled the possibility to accurately calculate the gradient via automatic differentiation [6], which strongly increases design possibilities [7]. Automatic differentiation (AD) is a powerful method ultimately based on a chain rule differentiation, efficiently implemented in machine learning packages such as JAX [8]. Recent implementations show that AD is a feasible tool for inverse design of flat optics, both when employing Rigorously-Coupled Wave Analysis (RCWA) [9] or Finite-Difference Time-Domain (FDTD) [10] approaches for individual meta-element design, or when employing the thin-element approximation (TEA) with numerical diffraction propagators for amplitude and phase element design of the optical element [11]. In this line, Ref. [11] also demonstrates the appropriateness of the TEA and the local periodic approximation in design of metalenses through AD gradient-based optimization.

While AD and Adjoint method might be equivalent [12], their implementation in gradient-based optimization frameworks might differ and lead to different optimization performance (e.g. convergence, optimization time and memory usage). For large number of optimization parameters, such as the ones required in inverse design of flat optics typically with over millions of parameters, the optimization performance depends on the gradient calculation strategy, and its implementation as part of the optimization algorithm on a particular application use case [13,14]. From these, beam shaping applications are important use cases for which inverse design has demonstrated great success, both with AD [15] and Adjoint methods [16]. Yet, despite the recent success of AD approaches [15] and the historical robustness of Adjoint methods [17], their impact on the optimization performance remains unclear in the inverse design of freeform beam shaping elements within the thin element approximation.

II. Methods

Here, we introduce an optimization framework implemented into the open source package pyMOE [18] as a tool to perform inverse design of flat optics within the TEA, applied to beam shaping applications. The optimization framework flowchart is represented in Figure 1.

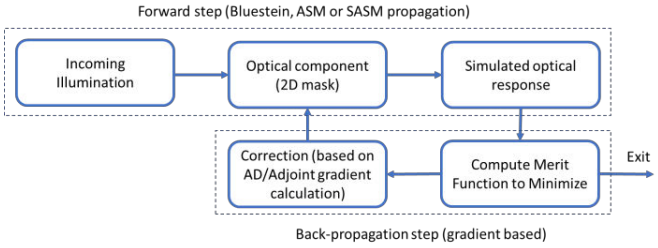

Fig. 1 Inverse design framework.

The optimization is performed such that a realistic target figure of merit is calculated for the output optical field of the element or optical system under design. The target figure of merit is a function of the system parameters, such as the number of pixels representing the optical system, which imparts a modulation of amplitude and phase to a traversing optical field. Forward simulation is employed to calculate the output field. For this purpose, efficient Bluestein [19] and (Scalable) Angular Spectrum Method (ASM) propagators [20] were implemented in Python and JAX. A loss function is constructed regarding the figure of merit quantity of the output propagated field against the desired target. The loss is iteratively minimized in a gradient-based optimizer algorithm until a convergence is reached. As such, the optimization performance depends on the gradient quality and gradient calculation efficiency.

III. Results and Discussion

To test its impact on the optimization performance, we present different inverse design runs with gradient calculations via either AD and the Adjoint method. Different optimization algorithms, such as Adam and algorithms available within SciPy optimize package, were evaluated for each of these gradient calculation methods and systematically compared. The optimization performance in terms of the figure of merit value, optimization convergence, and computation performance metrics are reported.

IV. Conclusion

This work demonstrates the merits of AD and Adjoint methods as gradient calculation strategies in gradient-based inverse design problems applied to beam shaping. The results demonstrate the suitability of the open source package pyMOE as a tool for optimization and design of realistic freeform flat optics described by a large number of parameters. The benchmarking results provide a guide for the development of appropriate inverse design numerical architectures for beam shaping applications, in terms of gradient calculation strategy and optimizer choice, as function of the number of optimized parameters. These numerical inverse design approaches generated optical elements susceptible of being physically validated in Spatial Light Modulator test setups [21], grayscale lithography [22], and/or metasurface implementations.

Acknowledgments

This work is supported by national funds, through the Operational Competitiveness and Internationalization Programme (COMPETE 2020) [Project nº 182852; Funding Reference: SIFN-01-9999-FN-182852] and co-funded by the European Union under the HORIZON-EIC Project BlueArray (grant no. 101130710).

References

[1] W.T. Chen, A.Y. Zhu, V. Sanjeev, M. Khorasaninejad, Z. Shi, E. Lee, F. Capasso, A broadband achromatic metalens for focusing and imaging in the visible, Nat. Nanotechnol. 13 (2018) 220–226. https://doi.org/10.1038/s41565-017-0034-6.

[2] S. So, J. Kim, T. Badloe, C. Lee, Y. Yang, H. Kang, J. Rho, Multicolor and 3D Holography Generated by Inverse-Designed Single-Cell Metasurfaces, Adv. Mater. 35 (2023) 1–9. https://doi.org/10.1002/adma.202208520.

[3] C.Y. Shen, P. Batoni, X. Yang, J. Li, K. Liao, J. Stack, J. Gardner, K. Welch, A. Ozcan, Broadband unidirectional visible imaging using wafer-scale nano-fabrication of multi-layer diffractive optical processors, Light Sci. Appl. 14 (2025). https://doi.org/10.1038/s41377-025-01971-2.

[4] M. Meem, S. Banerji, A. Majumder, C. Pies, T. Oberbiermann, B. Sensale-Rodriguez, R. Menon, Inverse-designed achromatic flat lens enabling imaging across the visible and near-infrared with diameter > 3 mm and NA = 0.3, Appl. Phys. Lett. 117 (2020). https://doi.org/10.1063/5.0012759.

[5] S. Molesky, Z. Lin, A.Y. Piggott, W. Jin, J. Vucković, A.W. Rodriguez, Inverse design in nanophotonics, Nat. Photonics. 12 (2018) 659–670. https://doi.org/10.1038/s41566-018-0246-9.

[6] E. Bayati, A. Wolfram, S. Colburn, L. Huang, A. Majumdar, Design of achromatic augmented reality visors based on composite metasurfaces, Appl. Opt. 60 (2021) 844. https://doi.org/10.1364/ao.410895.

[7] C. Rodríguez, S. Arlt, L. Möckl, M. Krenn, Automated discovery of experimental designs in super-resolution microscopy with XLuminA, Nat. Commun. . 15 (2024). https://doi.org/10.1038/s41467-024-54696-y.

[8] J. Bradbury, R. Frostig, P. Hawkins, M.J. Johnson, C. Leary, D. Maclaurin, G. Necula, A. Paszke, J. VanderPlas, S. Wanderman-Milne, Q. Zhang, JAX: composable transformations of Python+NumPy programs, (2018). http://github.com/jax-ml/jax.

[9] S. Colburn, A. Majumdar, Inverse design and flexible parameterization of meta-optics using algorithmic differentiation, Commun. Phys. 4 (2021). https://doi.org/10.1038/s42005-021-00568-6.

[10] S. Hooten, P. Sun, L. Gantz, M. Fiorentino, R. Beausoleil, T. Van Vaerenbergh, Automatic Differentiation Accelerated Shape Optimization Approaches to Photonic Inverse Design in FDFD/FDTD, Laser Photonics Rev. 19 (2025) 1–22. https://doi.org/10.1002/lpor.202301199.

[11] L. Huang, Z. Han, A. Wirth-Singh, V. Saragadam, S. Mukherjee, J.E. Fröch, Q.A.A. Tanguy, J. Rollag, R. Gibson, J.R. Hendrickson, P.W.C. Hon, O. Kigner, Z. Coppens, K.F. Böhringer, A. Veeraraghavan, A. Majumdar, Broadband thermal imaging using meta-optics, Nat. Commun. 15 (2024). https://doi.org/10.1038/s41467-024-45904-w.

[12] T.W. Hughes, M. Minkov, I.A.D. Williamson, S. Fan, Adjoint Method and Inverse Design for Nonlinear Nanophotonic Devices, ACS Photonics. 5 (2018) 4781–4787. https://doi.org/10.1021/acsphotonics.8b01522.

[13] C. Lee, J. Rho, Benchmarking Optimization Methods Enabling Efficient Designs for Diverse Nanophotonic Applications, Adv. Opt. Mater. 13 (2025) 1–11. https://doi.org/10.1002/adom.202500195.

[14] P. Bennet, D. Langevin, C. Essoual, A. Khaireh-Walieh, O. Teytaud, P. Wiecha, A. Moreau, Illustrated tutorial on global optimization in nanophotonics, J. Opt. Soc. Am. B. 41 (2024) A126. https://doi.org/10.1364/josab.506389.

[15] Q. Liao, H. Wang, Z. Feng, M. Li, Y. Luo, X. Mao, Differentiable design of freeform diffractive optical elements for beam shaping by representing phase distribution using multi-level B-splines, Opt. Express. 32 (2024) 41041. https://doi.org/10.1364/oe.533298.

[16] M. Mansouree, A. McClung, S. Samudrala, A. Arbabi, Large-Scale Parametrized Metasurface Design Using Adjoint Optimization, ACS Photonics. 8 (2021) 455–463. https://doi.org/10.1021/acsphotonics.0c01058.

[17] A.S. Backer, Computational inverse design for cascaded systems of metasurface optics, Opt. Express. 27 (2019) 30308. https://doi.org/10.1364/oe.27.030308.

[18] J. Cunha, J. Queiroz, C. Silva, F. Gentile, D.E. Aguiam, pyMOE : Mask design and modeling for micro optical elements and flat optics ☆, Comput. Phys. Commun. 305 (2024) 109331. https://doi.org/10.1016/j.cpc.2024.109331.

[19] Y. Hu, Z. Wang, X. Wang, S. Ji, C. Zhang, J. Li, W. Zhu, D. Wu, J. Chu, Efficient full-path optical calculation of scalar and vector diffraction using the Bluestein method, Light Sci. Appl. 9 (2020). https://doi.org/10.1038/s41377-020-00362-z.

[20] W. Zhang, H. Zhang, C.J.R. Sheppard, G. Jin, Analysis of numerical diffraction calculation methods: from the perspective of phase space optics and the sampling theorem, J. Opt. Soc. Am. A. 37 (2020) 1748. https://doi.org/10.1364/josaa.401908.

[21] F. Camarneiro, M.J.L.F. Rodrigues, J. Cunha, A. Shanker, A. Dias, F.S. Alves, D.E. Aguiam, Hardware-in-the-loop free space optical computing and optimization of polychromatic multilevel diffractive optics for imaging, Int. Conf. Transparent Opt. Networks. (2025). https://doi.org/10.1109/ICTON67126.2025.11125227.

[22] D.E. Aguiam, J.D. Santos, C. Silva, F. Gentile, C. Ferreira, I.S. Garcia, J. Cunha, J. Gaspar, Fabrication and optical characterization of large aperture diffractive lenses using greyscale lithography, Micro Nano Eng. 14 (2022). https://doi.org/10.1016/j.mne.2022.100111.

Nonreciprocal Surface Plasmons in a Metasurface Formed by Magnetically Biased Plasmonic Cylinders

Ioannis Katsantonis[1] Costas Valagiannopoulos[2], Anna C. Tasolamprou[3,*]

[1]Institute of Electronic Structure and Laser,
Foundation of Research and Technology Hellas, 71110, Heraklion, Greece
[2]School of Electrical and Computer Engineering,
National Technical University of Athens, GR-15780, Greece
[3]Department of Physics, National and Kapodistrian University of Athens, GR-15772, Greece
*Corresponding author: atasolam@phys.uoa.gr

***Abstract*— We study a metasurface formed by magnetically biased plasmonic cylinders supporting nonreciprocal magnetoplasmonic modes. Using a magnetized Drude model and cylindrical wave analysis, the electromagnetic response of the structure is investigated. The metasurface exhibits asymmetric dispersion and directional surface plasmon propagation, enabling tunable nonreciprocal behavior.**

***Keywords*— Magnetoplasmonics, Metasurfaces, Nonreciprocal wave propagation, Computational electromagnetics**

I. Introduction

Metasurfaces composed of subwavelength scatterers have emerged as powerful platforms for manipulating electromagnetic waves with unprecedented flexibility. By carefully engineering the geometry and material properties of their constituent elements, metasurfaces can control the amplitude, phase, and direction of scattered radiation, enabling applications such as beam steering, anomalous reflection, and wavefront shaping. In recent years, particular interest has been directed toward nonreciprocal metasurfaces, which break time-reversal symmetry and enable asymmetric propagation of electromagnetic waves. Nonreciprocity can be achieved through the use of magneto-optical or gyrotropic media, where the application of an external magnetic bias modifies the motion of charge carriers and introduces anisotropic electromagnetic properties. In plasmonic materials, the presence of a magnetic field affects the dynamics of free electrons through the Lorentz force, resulting in a tensorial permittivity with off-diagonal components responsible for nonreciprocal behavior. Such magnetoplasmonic systems have been shown to exhibit enhanced nonreciprocity when properly engineered [1]. Beyond conventional magneto-optical devices, nonreciprocal electromagnetic responses have also been explored in photonic topological systems, where breaking time-reversal symmetry can give rise to chiral surface states with robust propagation characteristics [2]. These developments highlight the importance of designing structured media capable of supporting asymmetric electromagnetic interactions

II. Methods

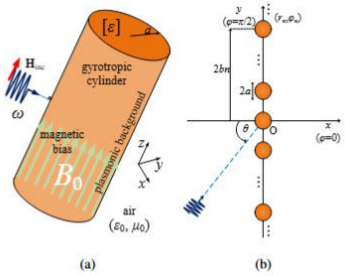

Figure 1: The building block of the considered setup. An infinitely long plasmonic cylinder biased by an axial magnetic field to inherit it with gyrotropic properties. TEz fields are assumed, able to "feel" the developed anisotropy. (b) Infinite core-shell cylinders positioned along vertical y axis to form a metasurface that gets obliquely excited by a plane TEz wave whose direction of propagation forms an angle θ with the horizontal x axis

The system under consideration consists of infinitely long plasmonic cylinders subjected to a static magnetic field applied along their axis. Under the influence of the magnetic bias, the conduction electrons within the plasmonic medium follow the magnetized Drude model, which leads to a gyrotropic permittivity tensor. The resulting medium is characterized by anisotropic electromagnetic properties, including off-diagonal permittivity components responsible for coupling orthogonal electric field components. The electromagnetic response of the structure is analyzed under transverse electric excitation, where the magnetic field is oriented parallel to the cylinder axis. The wave equation in the gyrotropic medium is solved analytically using cylindrical coordinate transformations and partial wave expansions. When the cylinder radius is significantly smaller than the operational wavelength, a dipolar approximation can be applied, allowing the scattering response to be expressed using only the lowest-order azimuthal harmonics. The metasurface configuration is formed by arranging the cylinders periodically along one spatial direction with a constant separation between adjacent rods. Each cylinder acts as a meta-atom, and the collective response of the array determines the electromagnetic behavior of the metasurface. The scattered

field from the entire structure is derived using cylindrical wave addition theorems and periodic summation techniques commonly used in the analysis of cylindrical metamaterial systems [4,5]. By applying appropriate boundary conditions at the surface of the cylinders, the scattering coefficients associated with the dominant azimuthal modes are determined. These coefficients are then used to evaluate the near-field and far-field scattering properties of both individual cylinders and the metasurface array.

III. Results and Discussion

Magnetically biased plasmonic cylinders exhibit strongly asymmetric scattering due to the difference between azimuthal modes +1 and -1. To quantify this behavior, a nonreciprocity metric is introduced based on the difference between the scattering coefficients of the two dipolar modes. In the absence of magnetic bias, the system remains reciprocal and the two modes possess identical amplitudes. However, when the cyclotron frequency associated with the magnetic field becomes nonzero, the degeneracy between these modes is lifted, producing strongly asymmetric scattering patterns. By exploring the parameter space defined by the operational frequency, cyclotron frequency, and cylinder size, operating regimes corresponding to maximally nonreciprocal scattering can be identified. In these regimes, one of the dipolar modes dominates the scattering response while the opposite mode becomes strongly suppressed. As a result, the scattered radiation exhibits highly asymmetric angular distributions. Multipolar analysis [6,7] shows that the enhanced nonreciprocity arises from the interaction between electric and magnetic dipole contributions to the scattering response. The interference between these modes produces strong directional radiation patterns and modifies the energy distribution in the near and far field. When the optimized cylinders are arranged into periodic arrays, the resulting structure behaves as a diffractive metasurface. The metasurface exhibits pronounced direction-dependent transmission and reflection properties when illuminated from opposite oblique directions. In particular, the distribution of diffracted power among the available diffraction orders changes significantly depending on the direction of incidence. This behavior demonstrates how the intrinsic nonreciprocal properties of the gyrotropic cylinders can be translated into collective metasurface responses.

IV. Conclusion

We investigated the electromagnetic response of magnetically biased plasmonic cylinders and demonstrated their use as meta-atoms for nonreciprocal metasurfaces. Analytical modeling based on cylindrical wave expansions revealed regimes where the asymmetry between azimuthal dipolar modes leads to maximally nonreciprocal scattering. Periodic arrays of these cylinders form metasurfaces exhibiting direction-dependent diffraction and asymmetric electromagnetic responses. These results highlight the potential of gyrotropic plasmonic structures for wavefront control and the development of nonreciprocal photonic devices.

Acknowledgments

This work was supported by the HorizonTech Research Initiative. The authors thank the AMBER Centre for fabrication support.

References

[1] Katsantonis, I., Tasolamprou, A. C., Koschny, T., Economou, E. N., Kafesaki, M. & Valagiannopoulos, C. Giant enhancement of nonreciprocity in gyrotropic heterostructures. Sci. Rep. 13, 21986 (2023).

[2] Tasolamprou, A. C., Mavidis, C. P., Economou, E. N., Soukoulis, C. M. & Kafesaki, M. Chiral topological surface states on a finite square photonic crystal bounded by air. Phys. Rev. Appl. 16, 044011 (2021).

[3] Valagiannopoulos, C. A. How nonreciprocal is an effective permittivity matrix? Microw. Opt. Technol. Lett. 56, 2018–2021 (2014).

[4] Mavidis, C. P., Tasolamprou, A. C., Economou, E. N., Soukoulis, C. M. & Kafesaki, M. Single scattering and effective medium description of multilayer cylinder metamaterials: Application to graphene- and metasurface-coated cylinders. Phys. Rev. B 107, 134120 (2023).

[5] Mavidis, C. P., Tasolamprou, A. C., Economou, E. N., Soukoulis, C. M. & Kafesaki, M. Polaritonic cylinders as multifunctional metamaterials: Single scattering and effective medium description. Phys. Rev. B 102, 155310 (2020).

[6] [6] Takou, E., Tasolamprou, A. C., Tsilipakos, O. & Economou, E. N. Dynamic anapole in metasurfaces made of sculptured cylinders. Phys. Rev. B 100, 085431 (2019).

[7] Tasolamprou, A. C., Tsilipakos, O., Kafesaki, M., Soukoulis, C. M. & Economou, E. N. Toroidal eigenmodes in all-dielectric metamolecules. Phys. Rev. B 94, 205433 (2016).

Nonlocal metasurfaces for Quantitative Phase Microscopy

Ann Roberts[1,*]

[1]ARC Centre of Excellence for Transformative Meta-Optical Systems, School of Physics, The University of Melbourne, Victoria, Australia[2]

*Corresponding author: ann.roberts@unimelb.edu.au

***Abstract*— Metasurfaces offer significant promise in imaging applications where operations are performed on an optical field carrying information about a sample. In particular, they can facilitate phase contrast imaging of transparent objects in a compact platform. Here we discuss the application of nonlocal metasurfaces to the quantification of phase.**

***Keywords*— metasurfaces, phase contrast imaging, quantitative phase microscopy, image processing**

I. Introduction

The visualisation of transparent samples such as biological cells remains an ongoing challenge. Stains and exogenous labels are widely used in biomedical applications and medical diagnostics, but these fundamentally change the sample. Furthermore, this is not an option for imaging of non-biological materials. When light propagates through a sample, variations in thickness and refractive index within it change both the amplitude and the phase of the transmitted field. Although the amplitude can be sensed directly with a camera or by eye, in many cases significantly more information is encoded in the phase. This has motivated the development of a wide range of methods to not only enhance the contrast of an image by converting phase information to detectable intensity, but also to quantifying the phase itself. The latter provides detailed information about cell morphology, refractive index, and/or other relevant sample parameters. Qualitative imaging methods include Zernike phase contrast [1] and widely-used Differential Interference Contrast (DIC) Microscopy. Avenues to quantification, on the other hand, include interferometric approaches such as holographic microscopy as well as non-interferometric methods that can be further subdivided into deterministic and iterative approaches [2]. The latter are potentially time-consuming and resource-intensive, counter to the drive for sensor-level processing whereas currently available deterministic methods tend to involve the complex systems typically required to acquire multiple images. Metasurfaces, however, are attracting increasing interest as potential components in next-generation, compact, phase contrast imaging systems [3]. Here we discuss the use of nonlocal metasurfaces, multiplexing wavelength and polarisation, to Quantitative Phase Microscopy (QPM).

II. Methods

Here we demonstrate the application of nonlocal metasurfaces to converting phase gradients within an optical field to intensity [4,5] and then using this information to quantitatively extract the phase. Such devices have a characteristic dependence of the plane wave transmission through the metasurface on angle of incidence which, when considering the angular spectrum decomposition of an optical field, means that the device performs direct, in plane, filtering its spatial frequency content. This modifies the field and its intensity and is the basis of object plane Fourier filtering [6].

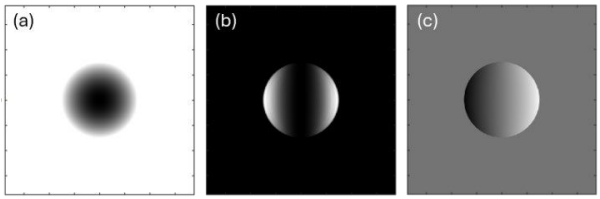

Fig. 1 (a) Phase map introduced by a spherical phase object into an optical field with zero intensity contrast; (b) resulting intensity after the field has passed through a metasurface with transfer function directly proportional to k_x; (c) intensity after the field has passed through a metasurface with transfer function of the form $H(k_x) \propto a + bk_x$.

In contrast to local metasurfaces, these Fourier processing devices are characterised in terms of their transfer function $H(k_x, k_y)$. Consider a metasurface where the transfer function is approximately linear in a component of the spatial frequency, e.g., $H(k_x) \propto k_x$. Light that has passed through a pure phase object (e.g., Fig. 1(a)) and then filtered by this metasurface results in a field that is proportional to the derivative of the phase with respect to the corresponding spatial coordinate, converting phase gradients to intensity (e.g., Fig. 1(b)). Information about the sign of the phase gradient, however, is lost. On the other hand, an offset can be introduced into the transfer function via off-normal illumination [5] or design [7,8], to produce an effective transfer function of the form $H(k_x) \propto a + bk_x$ where a and b are constants. This transfer function, asymmetric about normal incidence, generates a pseudo-3D

phase contrast image when used to image transparent objects (e.g., Fig. 1(c)) providing more information about the sample.

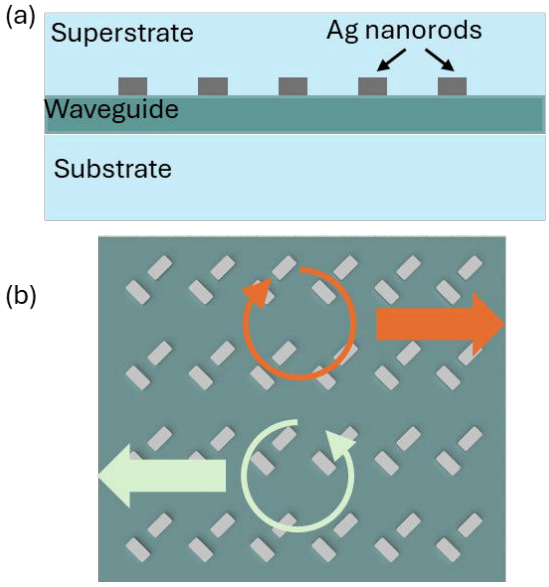

Fig. 2 Schematic showing the optical routing metasurface with (a) a side view and (b) a top view of the device highlighting the optical routing effect.

Here we generate this transfer function via the optical routing effect (Fig. 1) [7,8]. The metasurface consists of a 2D resonant waveguide grating with the waveguiding layer consisting of Si_3N_4 on a glass superstrate with a PMMA coating. Each unit cell consists of two orthogonally oriented Ag nanorods. Linearly polarised light at wavelength λ_1 illuminates a sample of interest. The transmitted field then passes through the metasurface and is then imaged with a polarisation-sensitive camera after passing through a quarter waveplate permitting discrimination of RCP and LCP images. Each of these images is formed with an asymmetric transfer function about $k_x = 0$ where changing the handedness of detection reverses the contrast of the image. This permits construction of a Differential Phase Contrast (DPC) image

$$I_{DPC} = \frac{I_{RCP} - I_{LCP}}{I_{RCP} + I_{LCP}} \quad (1)$$

highlighting horizontal phase gradients. Furthermore, the device is designed so that at a shorter wavelength λ_2, where $\lambda_1 - \lambda_2 \approx 40\,nm$, it has an asymmetric transfer function about $k_y = 0$ producing a DPC exhibiting vertical phase gradients. The DPC images generated at both wavelengths are sufficient to reconstruct the phase introduced into the field.

III. Conclusion

In this presentation the application of nonlocal metasurfaces exhibiting the optical routing effect to QPM will be discussed. The results of investigations into synthetic and biological samples will be presented.

Acknowledgments

The significant contributions of current and former members of my group, Haiwei Wang, Shaban Sulejman, Niken Priscilla, Lukas Wesemann, Wendy Lee and collaborators Shikun Ma and Elizabeth Hinde to this work are acknowledged. The research was funded by the Australian Government through the Australian Research Council Centre of Excellence grants (CE200100010) and (CE230100021). This work was performed in part at the Melbourne Centre for Nanofabrication (MCN) in the Victorian Node of the Australian National Fabrication Facility (ANFF).

References

[1] F. Zernike, “Phase contrast, a new method for the microscopic observation of transparent objects,” Physica Vol. 9, No. 7, pp. 686– 698, 1942.
[2] C. Zuo, J. Li, J. Sun, Y. Fan, J. Zhang, L. Lu, R. Zhang, B. Wang, L. Huang, and Q. Chen, “Transport of intensity equation: a tutorial,” Optics and Lasers in Engineering, Vol. 135, 106187, 2020.
[3] N. Priscilla, S. Sulejman, A. Roberts. and L. Wesemann, “New Avenues for Phase Imaging: Optical Metasurfaces,” ACS Photonics, Vol. 11, No. 8, pp. 2843-2859, 2024.
[4] S.K. Case, “Fourier processing in the object plane”, Opt. Lett. Vol. 4, No. 9, 286-288, 1979.
[5] L. Wesemann, J. Rickett, J. Song, J. Lou, E. Hinde, T.J. Davis, and A. Roberts, "Nanophotonics enhanced coverslip for phase imaging in biology" Light Sci. Appl., Vol. 10, No. 1, 98, 2021.
[6] S.K. Case, “Fourier processing in the object plane”, Opt. Lett. Vol. 4, No. 9, 286-288, 1979.
[7] T.J. Davis, F. Eftekhari, F., D.E. Gómez, and A. Roberts, “Metasurfaces with asymmetric optical transfer functions for optical signal processing,” Phys. Rev. Lett. Vol. 123, 013901, 2019.
[8] I.M. Fradkin, S.D. Dyakov, and N.A. Gippius, “Nanoparticle lattices with bases: Fourier modal method and dipole approximation,” Physical Review B, vol. 102, 045432, 2020.
[9] L. Wesemann, J. Rickett, T.J. Davis, and A. Roberts, “Real-time phase imaging with an asymmetric transfer function metasurface,”, ACS Photonics, Vol. 9, No. 5, 1803-1807, 2022.

Realization of Photonic Parallel Spaces and Overlapping Optical Devices

Yun Lai[1,*]

[1]School of Physics, Nanjing University, China
*Corresponding author: laiyun@nju.edu.cn

***Abstract*— We demonstrate the realization of photonic parallel spaces, i.e. meta-structures that behave as distinct effective media—with different refractive indices, impedances, or anisotropy—within the same physical space. This mechanism enables physically overlapping optical devices that operate independently, as if they exist in different dimensions.**

***Keywords*— metamaterials, parallel spaces, machine learning, photonic crystals.**

I. Introduction

Miniaturization and high-density integration are one of the central issues in modern science and technology. In classical physics, this is hindered by the one-to-one correspondence between a material and its unique effective parameters, making functional multiplicity inherently incompatible. Metamaterials have expanded parameter spaces beyond natural materials, yet still largely assume a one-to-one mapping between structures and their effective parameters. Here, we demonstrate a general class of meta-structures that can support multiple groups of eigenstates within the same frequency band, which are localized at distinct positions away from the Brillouin zone center in the momentum space. Each group of eigenstates correspond to a single effective medium. Depending on the boundary of excitation, different groups of eigenstates are selectively activated, causing the same structure to behave as distinct effective media—with different refractive indices, impedances, or anisotropy—within the same physical space. This phenomenon thus resembles the concept of parallel spaces existing in different dimensions, enabling functional multiplexing in space and opening a pathway toward ultra-compact, multi-functional optical systems composed of overlapping optical devices.

II. Methods

The phenomena of photonic parallel spaces and overlapping optical devices have been verified both numerically and experimentally through a series of designs.

The effective parameters of the meta-structure have been retrieved through both the transmission/reflection coefficients or the eigenfields. Both methods lead to the same results. Such parameters describe the bulk wave propagation in the meta-structure as well as the refraction/reflection behavior upon the selected boundary, but differ distinctly on different boundaries.

III. Results and Discussion

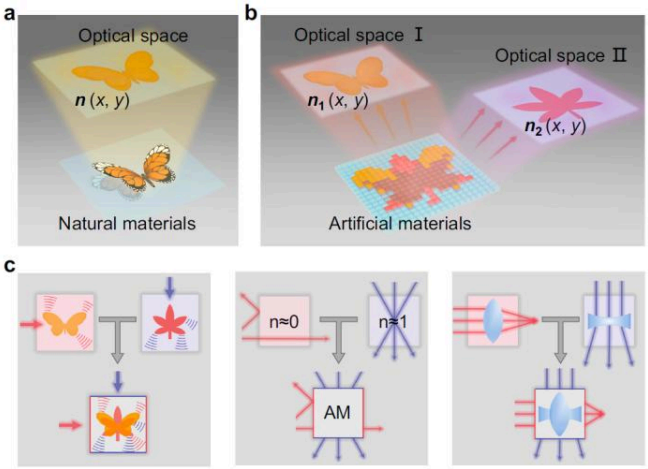

Fig. 1 The concept of photonic parallel spaces and overlapping optical devices.

Figure 1 shows the concept of photonic parallel spaces and overlapping optical devices. Unlike natural materials, meta-structures can exhibit two different distributions of refractive indices, impedances or anisotropy. For instance, such meta-structures can behave as the coexistence of a butterfly and a maple leaf, a n=0 material and a n=1 material, or a concave lens and a convex lens. They function independently for incident waves upon different boundaries. Numerical and experiments proofs will be shown in the talk.

IV. Conclusion

We have demonstrated the exciting possibility of creating photonic parallel spaces with metamaterials. This finding breaks the one-to-one correspondence between a material and its unique effective parameters for the first time.

References

[1] T.T. Song, Y.X. Jing, C.H. Shen, H.C. Chu, J. Luo, R.Q. Jia, C. Wang, M. Xiao, Z.Q. Zhang, R.W. Peng*, M. Wang*, C.T. Chan*, Y. Lai*, "Nonlocality-enabled photonic analogies of parallel spaces, wormholes and multiple realities," Nat. Commun., vol. 16, pp. 8915, 2025.

Adaptive Tapering Strategy for Waveguide Dielectric Laser Accelerators under Pulsed Operation

D. Guarnera[1], H. Y. Donkeng[2], R. Palmeri[3], G. S. Mauro[4], N. Salerno[1], A. Bacci[5], S. C. Pavone[1], G. Torrisi[4], A Locatelli[2,*], G. Sorbello[1]

[1]University of Catania, DIEEI, Italy
[2]University of Brescia, DII, Italy
[3]University Mediterranea of Reggio Calabria, DIIES, Italy
[4]National Institute for Nuclear Physics, LNS, Italy
[5]National Institute for Nuclear Physics, INFN-Milano, Italy
*Corresponding author: andrea.locatelli@unibs.it

***Abstract*— Waveguide-based dielectric laser accelerators are an emerging platform for the realization of miniaturized particle sources. In this work, we introduce a general time-domain adaptive approach that guarantees continuous synchronization between the pulsed accelerating field and particle motion in a tapered waveguide accelerator. Flexibility and accuracy of the methodology are illustrated through numerical examples with long and short pulses, as well as pulse trains.**

***Keywords*— Dielectric laser accelerators, guided-wave structures, tapered waveguides, dispersion engineering, time-domain electromagnetic modeling, optical pulse propagation.**

I. ADAPTIVE TAPERING STRATEGY

The optimal taper profile required to maintain continuous matching between the particle and phase velocity of a guided mode can be determined from the particle dynamics in the actual electromagnetic field. The taper also affects pulse propagation by modifying the envelope group velocity, higher-order dispersion coefficients and modal profile.

In this framework, it is necessary to evaluate, point by point, the relative position of the particle with respect to the pulse envelope to determine the change in particle velocity and, in turn, establish the taper. The idea behind the developed approach is to co-propagate the particle and the pulse and progressively determine the optimal waveguide profile.

Considering that the initial conditions of the problem are the velocity of the particle and the envelope of the input pulse, the optimal taper can be determined from calibration curves evaluated through mode solving. It follows that the particle time at each position, and therefore the field experienced by the particle, are calculated by applying an iterative process which continues until the particle reaches the end of the waveguide.

II. NUMERICAL EXAMPLE

The reported numerical examples focus on the longitudinal dynamics of a single electron along the axis of slot waveguides, where the transverse field components are negligible. This simplification allows for a clear treatment of the problem, while the approach can be extended to include transverse dynamics.

A relevant example of application of the algorithm is the taper for a slot waveguide driven by a pulse train. This configuration enables substantial increases in particle speed by applying short pulses in cascade. For the design example, a train of 5 pulses with $E_0 = 0.33$ GV/m and FWHM = 0.2 ps, spaced $\Delta t_0 = 0.6$ ps apart, has been considered, as illustrated in Fig. 1.

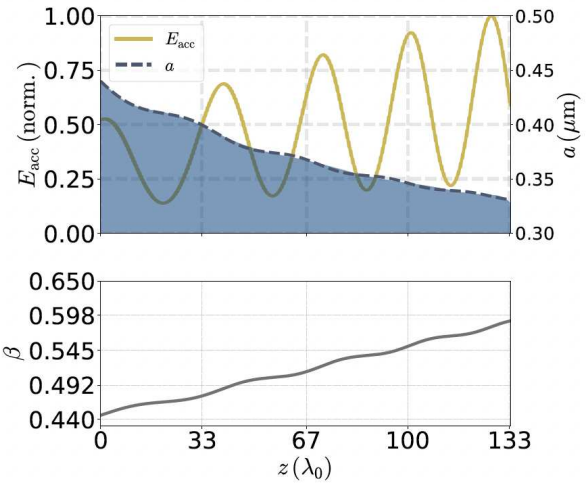

Fig. 1 Accelerating field and taper parameter a ensuring particle–field synchronization (top), and particle velocity β (bottom) along the accelerating path, induced by a train of Gaussian pulses.

ACKNOWLEDGMENTS

This work was supported in part by the Italian Ministry for University and Research and the European Union – Next Generation EU Mission 4 Component 1, as part of PRIN 2022 project DOSE (CUP D53D23001350006) and PRIN 2022 PNRR project IDEAS (CUP E53D23014520001) and from the INFN V National Committee through the CoDLAS grant.

How many channels can a photonic device support?

Paul Virally[1], Pengning Chao[2], Alessio Amaolo[3], Alejandro Rodriguez[4], Sean Molesky[1,*]

[1]Department of Engineering Physics, Polytechnique Montréal, CAN
[2]Department of Chemistry, Princeton University, USA
[3]Department of Mathematics, Massachusetts Institute of Technology, USA
[4]Department of Electrical and Computer Engineering, Princeton University, USA
*Corresponding author: sean.molesky@polymtl.ca

***Abstract*—We develop a general method to bound the ordered singular values (channel amplitudes) of the electromagnetic Green function or W-operator for arbitrarily structured linear photonic systems. The approach yields computable, quantitatively predictive, upper bounds on the n^{th} singular value that capture the complexity of multi-channel tradeoffs and competing scattering effects.**

***Keywords* limits, inverse design, photonic design, optimization.**

I. Introduction

Motivations for wanting optical devices capable of controlling as many distinct inputs as possible are simple and compelling: e.g., (1) we would like to process more information, more efficiently [1]; (2) many electromagnetic devices are essentially communication systems, and communication performance is essentially the capacity of a system to transform distinguishable inputs [2]; (3) advances realized in machine learning over the past decade have opened previously unimaginable possibilities in signal processing and inference [3], removing many former operational constraints for electromagnetic information transfer.

From this vantage, the abstraction of channels and singular value decomposition (SVD) provides as a natural language for linear system design. Conceptually, SVD expresses the action of a linear operator as completely decoupled transformations, which tends to simplify both mental and phenomenological descriptions. For example, many electromagnetic processes are (relatively) simply described in terms of the Green operator [1], re-framing phenomenological understanding as questions of why the Green operator possess certain characteristics. Via SVD, the Green function is broken down into orthogonal "channels"—mappings between input currents in some sender to output fields in some receiver—that can be analysed independently, and are quantitatively ordered in terms of relative importance by their singular values or "channel amplitudes" (top Fig. 1). Practically, the first n transformation pairs of SVD sum to give the most accurate n-rank approximation that can be made to a linear operator under the nuclear or Frobenius (Hilbert-Schmidt, or trace) norm. Due to the effective equivalence between these norms and common engineering objectives like loss functions, power transfer and energy density, SVD is innately suggested in a variety of application areas [4].

Granting the utility of SVD in design, several questions are brought forward. Principally, how can the singular values of a device be analyzed and controlled [5], [6], [7]? And the complement, how many channels can a device (of some given size, composed of some given materials) possibly support above a specified cut-off value [8], [9], [10]? Our results continue ongoing efforts to understand the (fundamental) limitations of electromagnetic devices along this second line. Specifically we will showcase the first method to generally answer the following question that beings captures the tradeoffs imposed by multiple inputs and antagonistic scattering phenomena. *Given some volumes of space that may contain arbitrarily structured materials, how large can the n^{th} singular value of an electromagnetic transfer function (Green function or W-operator) be?*

Beyond its direct implications for multi-functionality, this metric is intertwined with a number of physical quantities of interest. For example, under an additive noise model (detector dominated noise), the number of singular values above a threshold strongly dictates achievable Shannon capacity [11], and is also closely related to mutual information [12] and Fisher information. Consequently, there are a range of scenarios related to communication, imaging and classification wherein the number of singular values that can be engineered above some cut-off is of paramount importance to performance. Moreover, nearly any trace formulation can be restated as a functional sum over the singular values of some transfer function, and in this way channel counts above a cut-off value provide an interesting point of comparison for a diverse collection of physics, such as emission phenomena like fluorescence, thermal radiation, heat transfer, and Casimir forces, as well as scattering phenomena like cloaking, extinction, absorption

Building through four illustrative examples pertaining to meta-optic design, laser awareness, and near-field heat transfer, our findings indicate that by combining the Courant-Fischer-Weyl min-max principle with a "rank-removal" corollary and

[1]Defined here as the inverse of the Maxwell operator—i.e. the linear mapping between currents and fields of an electromagnetic system.

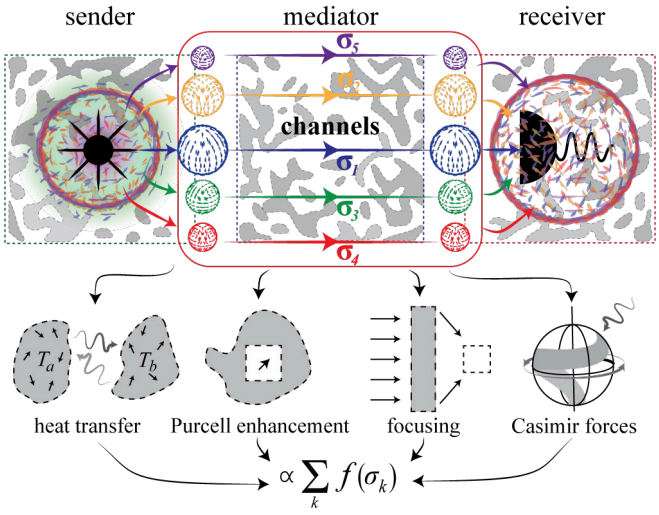

Fig. 1. **SVD, channels and channel amplitudes.** The figure illustrates the meaning of an electromagnetic channel in the sender-mediator-receiver convention. Each channel consists of a pair of connected input-output fields (one in the sender and one in the receiver) that are orthogonal to the fields of every other channel, along with a channel amplitude (the singular value σ_k) that dictates the strength of the mapping. Working in terms of channels leads to a completely decomposed description of communication. The lower part of the figure shows four physical phenomena, among many, that are described by functional sums over singular values: heat transfer, Purcell enhancement, lensing, and Casimir torques.

convex relaxation bounds [13] quantitatively accurate limits on the maximum (or minimum) of the n^{th} singular value of typical electromagnetic transfer functions are computable for moderately sized devices (up to $64\ \lambda^3$).

Acknowledgments

A.W. Rodriguez and A. Amaolo acknowledge support by a Princeton SEAS Innovation Grant and by the Cornell Center for Materials Research (MRSEC). S. Molesky and P. Virally acknowledge financial support from NSERC under Discovery Grant RGPIN-2023-05818 and the CGS-M program, as well as additional benefits provided from their affiliations to the Regroupement Qubcois sur les Matriaux de Pointes, https://doi.org/10.69777/309032, and the IVADO research consortium. The simulations presented in this article were performed on computational resources managed and supported by Calcul Qubec (calculquebec.ca) and the Digital Research Alliance of Canada (alliancecan.ca) under resource allocation RRG #5398, as well as the MIT SuperCloud and Lincoln Laboratory Supercomputing Center.

References

[1] D. T. Hai and I. Woungang, "Next-generation optical networks to sustain connectivity of the future: All roads lead to optical-computing-enabled network?" *Internet of Things*, vol. 29, p. 101445, 2025.

[2] D. A. Miller, "All linear optical devices are mode converters," *Optics express*, vol. 20, no. 21, pp. 23 985–23 993, 2012.

[3] B. Karanov, M. Chagnon, F. Thouin, T. A. Eriksson, H. Bülow, D. Lavery, P. Bayvel, and L. Schmalen, "End-to-end deep learning of optical fiber communications," *Journal of Lightwave Technology*, vol. 36, no. 20, pp. 4843–4855, 2018.

[4] S. Molesky, P. Chao, J. Mohajan, W. Reinhart, H. Chi, and A. W. Rodriguez, "$\mathbb{T}$-operator limits on optical communication: Metaoptics, computation, and input-output transformations," *Physical Review Research*, vol. 4, p. 013020, Jan 2022.

[5] D. A. Miller, "How complicated must an optical component be?" *JOSA A*, vol. 30, no. 2, pp. 238–251, 2013.

[6] ——, "Waves, modes, communications, and optics: a tutorial," *Advances in Optics and Photonics*, vol. 11, no. 3, pp. 679–825, 2019.

[7] S. SeyedinNavadeh, M. Milanizadeh, F. Zanetto, G. Ferrari, M. Sampietro, M. Sorel, D. A. Miller, A. Melloni, and F. Morichetti, "Determining the optimal communication channels of arbitrary optical systems using integrated photonic processors," *Nature Photonics*, vol. 18, no. 2, pp. 149–155, 2024.

[8] D. A. B. Miller, "Communicating with waves between volumes: evaluating orthogonal spatial channels and limits on coupling strengths," *Applied Optics*, vol. 39, no. 11, pp. 1681–1699, 2000.

[9] A. Amaolo, P. Chao, B. Strekha, S. Clarke, J. Mohajan, S. Molesky, and A. W. Rodriguez, "Maximum shannon capacity of photonic structures," *arXiv preprint arXiv:2409.02089*, 2024.

[10] Z. Kuang, D. A. Miller, and O. D. Miller, "Bounds on the coupling strengths of communication channels and their information capacities," *IEEE Transactions on Antennas and Propagation*, 2025.

[11] C. Ehrenborg and M. Gustafsson, "Physical bounds and radiation modes for mimo antennas," *IEEE Transactions on Antennas and Propagation*, vol. 68, no. 6, pp. 4302–4311, 2020.

[12] H. Pinkard, L. Kabuli, E. Markley, T. Chien, J. Jiao, and L. Waller, "Information-driven design of imaging systems," *arXiv preprint arXiv:2405.20559*, 2025.

[13] P. Chao, B. Strekha, R. Kuate Defo, S. Molesky, and A. W. Rodriguez, "Physical limits in electromagnetism," *Nature Reviews Physics*, vol. 4, no. 8, pp. 543–559, 2022.

The photonic gearbox: ultra-high local density of states via cylindrical-symmetry breaking

Alessio Amaolo[1,*]

[1]Department of Chemistry, Princeton University, Princeton, NJ, USA
*Corresponding author: alessioamaolo@princeton.edu

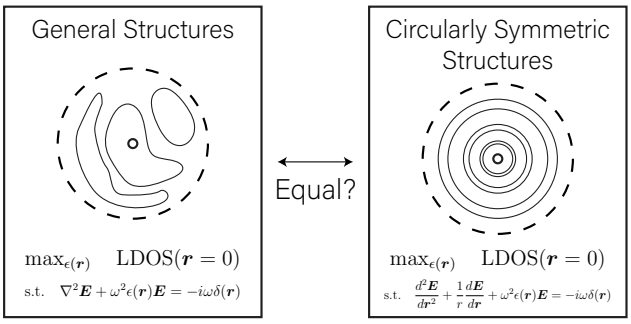

Fig. 1. Symmetry breaking in LDOS maximization. Comparison of the optimization domain for general, arbitrary dielectric structures (left) versus strictly cylindrically symmetric profiles (right). While intuition suggests that symmetric "Bragg onions" are optimal, we investigate whether the additional degrees of freedom in non-symmetric geometries can yield super-exponential scaling by coupling to higher angular momentum modes.

***Abstract*—We introduce the "Photonic Gearbox," a cavity design leveraging discrete rotational symmetry for potential super-exponential LDOS scaling. By computing fundamental limits for cylindrically symmetric structures, we empirically demonstrate the gearbox exceeds these bounds. This rigorously proves that symmetry breaking unlocks performance regimes strictly inaccessible to conventional cavity geometries.**

***Keywords*— metamaterials, inverse design, fundamental limits**

I. Summary

While traditional photonic engineering relied on assembling known physical building blocks like waveguides and resonators [1], [2], [3], the field is currently undergoing a paradigm shift toward computational inverse design. By treating the design process as a massive optimization problem, we can now discover complex, non-intuitive geometries that vastly outperform conventional devices [4], [5], [6]. However, a critical barrier remains: the "black box" nature of these gradient-based algorithms creates a fundamental ambiguity. When an optimization stalls, it is difficult to distinguish between a failure of the algorithm (trapped in a local minimum) and a failure of physics (hitting a fundamental limit). Resolving this ambiguity is essential for the next generation of optical device design. Complementing these numerical search methods is a parallel effort to quantify the ultimate physical limits of light-matter interaction. The key insight rests on a reformulation of the structural design problem to an optimization over fields (instead of geometry) subject to power conservation constraints [7], [8]. This framework has been applied to a vast array of problems, identifying scaling laws and certifying the optimality of known designs [9], [10], [11], [8], [12], [13].

In this talk, we first summarize important results in the area of photonic limits, illustrating how they can be used not only as performance metrics but useful figures for fundamental scaling behavior. We then discuss how fundamental limits are beginning to yield new paradigms of photonic design, whereupon information from fundamental limit relaxations can be leveraged to initialize inverse design problems near their global optima. We focus on one particular case study: the maximization of the Local Density of States (LDOS) in the case of a dipole surrounded by a structured cavity, a metric critical for spontaneous emission, heat transfer, and photovoltaics. In this case, standard physical intuition suggests that optimal structures resemble "Bragg onions", cylindrically symmetric quarter-wave stacks that yield exponential scaling with size via bandgap confinement. Rough arguments can be made to say that this must be optimal; for example, breaking the cylindrical symmetry could destroy the bandgap, reducing mode quality. Alternatively, we may argue that the symmetry of the problem itself requires cylindrically symmetric global optima. These structures also exhibit very favorable scaling; intuitively, each layer of the onion adds a constant factor reflectance, leading to an exponential scaling with size that is only capped by losses or by finite source bandwidth. Inverse design initialized with these structures can improve performance slightly; e.g., finite-size effects can be accounted for, yielding roughly a constant factor improvement. Yet the *scaling* remains: no structures have been found with super-exponential LDOS scaling.

Two fundamental questions arise. First, can the additional degrees of freedom available by breaking cylindrical symmetry be leveraged to exceed the performance of circularly symmetric structures? Second, can the exponential scaling of cylindrically symmetric structures be exceeded? Inspired by limits-based-design, we show an example where we answer these questions in the affirmative. These structures have discrete rotational symmetry and appear to work by coupling $m = 0$ to higher angular-momentum modes (hence the "gearbox" name). In the case of lossy structures, we demonstrate examples where gearboxes exceed the fundamental *limits* of performance

of cylindrically symmetric structures, constituting a proof of the necessity of symmetry breaking for optimal LDOS enhancement. Empirically, these structures also exhibit *super-exponential* scaling of LDOS enhancement with size up to a Q-factor of a billion, where the numerics of topology optimization begin to hinder convergence. These results suggest that improved scaling can be achieved via symmetry breaking even for a cylindrically symmetric problem, a surprising result with a multitude of potential applications.

II. Acknowledgments

This work was performed in collaboration with Pengning Chao, Sean Molesky, and Alejandro W. Rodriguez.

References

[1] A. Yariv and P. Yeh, *Photonics: Optical Electronics in Modern Communications*. Oxford University Press, Inc., 2006.

[2] J. D. Joannopoulos, J. G. Steven, J. N. Winn, and R. D. Meade, *Photonic Crystals: Molding the Flow of Light*, 2nd ed. Princeton: Princeton University Press, 2008.

[3] S. A. Maier, *Plasmonics: Fundamentals and Applications*. Springer Science & Business Media, 2007.

[4] S. Molesky, Z. Lin, A. Y. Piggott, W. Jin, J. Vučković, and A. W. Rodriguez, "Inverse design in nanophotonics," *Nature Photonics*, vol. 12, no. 11, pp. 659–670, 2018.

[5] C. M. Lalau-Keraly, S. Bhargava, O. D. Miller, and E. Yablonovitch, "Adjoint shape optimization applied to electromagnetic design," *Optics Express*, vol. 21, no. 18, p. 21693, Sep. 2013.

[6] T. W. Hughes, M. Minkov, I. A. Williamson, and S. Fan, "Adjoint method and inverse design for nonlinear nanophotonic devices," *ACS Photonics*, vol. 5, no. 12, pp. 4781–4787, 2018.

[7] G. Angeris, J. Vučković, and S. Boyd, "Heuristic methods and performance bounds for photonic design," *Optics Express*, vol. 29, no. 2, pp. 2827–2854, 2021.

[8] P. Chao, B. Strekha, R. Kuate Defo, S. Molesky, and A. W. Rodriguez, "Physical limits in electromagnetism," *Nature Reviews Physics*, vol. 4, no. 8, pp. 543–559, Aug. 2022.

[9] P. S. Venkataram, S. Molesky, W. Jin, and A. W. Rodriguez, "Fundamental limits to radiative heat transfer: The limited role of nanostructuring in the near-field," *Physical Review Letters*, vol. 124, no. 1, p. 013904, 2020.

[10] A. Amaolo, P. Chao, B. Strekha, S. Clarke, J. Mohajan, S. Molesky, and A. W. Rodriguez, "Maximum shannon capacity of photonic structures," arXiv preprint arXiv:2409.02089, oct 2024. [Online]. Available: http://arxiv.org/abs/2409.02089

[11] A. Amaolo, P. Chao, T. J. Maldonado, S. Molesky, and A. W. Rodriguez, "Physical limits on raman scattering: The critical role of pump and signal co-design," *Phys. Rev. A*, vol. 110, p. L061501, Dec 2024. [Online]. Available: https://link.aps.org/doi/10.1103/PhysRevA.110.L061501

[12] Z. Kuang and O. D. Miller, "Computational bounds to light–matter interactions via local conservation laws," *Physical Review Letters*, vol. 125, no. 26, p. 263607, Dec. 2020.

[13] S. Gertler, Z. Kuang, C. Christie, H. Li, and O. D. Miller, "Many photonic design problems are sparse QCQPs," *Science Advances*, Jan. 2025.

Multiscale simulations of electronic excitations of molecules coupled to plasmonic nanostructures

Stefano Corni[1,2*]

[1]Department of Chemical Sciences, University of Padua, Italy
[2]CNR Institute of Nanoscience, Modena, Italy
*Corresponding author: stefano.corni@unipd.it

***Abstract*— Multiscale models for coupling electronic excitations and localized surface plasmon excitations have been developed, based on boundary element methods approach for the plasmonic nanostructures. Here such approaches will be presented and the latest development discussed, particularly in relation to quantization of the nanoparticle response.**

***Keywords*— boundary element methods, localized surface plasmons, molecular electronic excitations.**

Localized surface plasmon excitations, supported by, e.g., metallic nanostructures allow very high electromagnetic coupling with nearby molecules. Accurate modeling of these effects requires using a classical electromagnetic for the nanostructures, which should be coupled to an electronic structure description of the molecules whenever its spatial extension and chemical nature are relevant.

Through the year we have developed the theoretical framework and software implementation to address such coupling, using a boundary element method approach to the electromagnetic problem.[1] We have in particular focused on the quantized description of the nanostructures,[2,3] needed to investigate the strong coupling regime between the molecular and the plasmonic excitations.[4] In this talk I will present the recent developments of such modeling approach, and examples of applications.

ACKNOWLEDGMENTS

SC thanks European Union for funding under the grant iSenseDNA (European Innovation Council under grant agreement no. 101046920)

REFERENCES

[1] E. Coccia, J. Fregoni, C.A. Guido, M. Marsili, S. Pipolo, and S. Corni, "Hybrid theoretical models for molecular nanoplasmonics," Journal of Chemical Physics, vol. 153, pp. 200901, 2020.
[2] G. Parolin, N. Peruffo, F. Mancin, E. Collini, and S. Corni "Molecularly detailed view of strong coupling in supramolecular plexcitonic nanohybrids" Nano Letters, vol. 24, pp. 2273-2281, 2024.
[3] M. Romanelli, G. Gil, and S. Corni, "Quantized plasmon modes for metallic nanoparticles of arbitrary shape with a generic dielectric function" arXiv preprint arXiv:2512.01538
[4] J. Kuttruff, M. Romanelli, E. Pedrueza-Villalmanzo, et al. "sub-picosecond collapse of molecular polaritons to pure molecular transition in plasmonic photoswitch-nanoantennas," Nature Communications, vol. 14, pp. 3875, 2023

Manipulating waves with metamaterials in multiple dimensions $(x,y,z)/(x,y,z,t)$

Victor Pacheco-Peña[1,*]

[1]School of Mathematics, Statistics and Physics, Newcastle University, Newcastle Upon Tyne, NE1 7RU, United Kingdom
*Corresponding author: victor.pachecopena@gmail.com

***Abstract*— We exploit metamaterials to control wave propagation in multiple dimensions. Studies include the calculation of mathematical operations such as partial differential equations in space as well as the emulation of time refracted waves using metamaterials that are time dependent.**

***Keywords*— metamaterials, 4D metamaterials, time interfaces, Time-Varying media.**

I. Discussion

Metamaterials enable careful engineering of waves by modifying the space (geometries and materials) along which they propagate. Since their advent, they have opened new avenues for the development of improved devices (as well as the proposal and demonstration of new structures) in applications within science and engineering [1–4].

A relevant application in the field of metamaterials is the calculation of mathematical operations [5], with examples involving vector matrix multiplication, temporal derivates as well as integration and convolution (among others) [6–10]. In addition to manipulating waves in space (x,y,z), time t can also be introduced as a new variable, giving rise to four-dimensional metamaterials (4D, x,y,z,t) [11]. Among different temporal and spacetime modulations currently being explored, time interfaces are particularly interesting as they represent the *equivalent* of spatial interfaces between two materials [12]. Time interfaces have been explored in multiple scenarios [13–22], with experimental demonstrations starting to be reported [23–25].

Inspired by the importance of metamaterials to sculpt waves, here we present our latest efforts in the field by exploring wave propagation in spatial and spacetime media. We will show how metamaterials can be used to calculate the solution of partial differential equations (PDEs) in space by carefully engineering arrays of waveguides (from microwaves up to the optical regime) [26]. Moreover, applications in time varying media will include the emulation of time refraction using slow temporal changes of the optical properties of the medium as well as mimicking photonics *temporal aiming* using isotropic spacetime effective media[27–31].

Acknowledgments

This work was supported by the Leverhulme Trust under the Leverhulme Trust Research Project Grant scheme (RPG-2023-024). The authors have applied a CC BY public copyright license to any Author Accepted Manuscript (AAM) version arising from this submission.

References

[1] A. Alù, S. Maci, and N. Engheta, Metasurfaces and Metamaterials for Electromagnetics, IEEE Transactions on Antennas and Propagation DOI 10.1109/TAP.2025.3588766 1 (2025).

[2] M. Nicolussi, J. A. Riley, and V. Pacheco-Peña, Unidirectional transparency in epsilon-near-zero based rectangular waveguides induced by parity-time symmetry, Appl. Phys. Lett. 119, 263507 (2021).

[3] C. Johnson-Richards, A. Yakovlev, and V. Pacheco-Peña, Topological Valley Photonic Waveguides: Scattering Matrix Evaluation for Linear Computing, Adv. Photonics Res. (2025).

[4] F. Puggelli, B. Biscontini, E. Martini, and S. Maci, Maximizing Independent Channels and Efficiency in BTS Array Antennas via EM Degrees of Freedom, IEEE Trans. Antennas Propag. 73, 3444 (2025).

[5] F. Zangeneh-Nejad, D. L. Sounas, A. Alù, and R. Fleury, Analogue computing with metamaterials, Nat. Rev. Mater. 6, 207 (2021).

[6] V. Nikkhah, A. Pirmoradi, F. Ashtiani, B. Edwards, F. Aflatouni, and N. Engheta, Inverse-designed low-index-contrast structures on a silicon photonics platform for vector–matrix multiplication, Nat. Photonics 1 (2024).

[7] A. Yakovlev and V. Pacheco-Peña, Enabling High-Speed Computing with Electromagnetic Pulse Switching, Adv. Mater. Technol. 5, 2000796 (2020).

[8] R. G. MacDonald, A. Yakovlev, and V. Pacheco-Peña, Amplitude-Controlled Electromagnetic Pulse Switching Using Waveguide Junctions for High-Speed Computing Processes, Advanced Intelligent Systems 4, 2200137 (2022).

[9] A. Babaee, A. Momeni, A. Abdolali, and R. Fleury, Parallel Analog Computing Based on a 2 × 2 Multiple-Input Multiple-Output Metasurface Processor With Asymmetric Response , Phys. Rev. Appl. 15, 1 (2021).

[10] T. Knightley, A. Yakovlev, and V. Pacheco-Peña, Neural Network Design of Multilayer Metamaterial for Temporal Differentiation, Adv. Opt. Mater. 11, 2202351 (2023).

[11] N. Engheta, Four-dimensional optics using time-varying metamaterials, Science (1979). 379, 1190 (2023).

[12] F. Morgenthaler, Velocity Modulation of Electromagnetic Waves, IEEE Trans. Microw. Theory Tech. 6, 167 (1958).

[13] V. Pacheco-Peña, Y. Kiasat, D. M. Solís, B. Edwards, and N. Engheta, Holding and amplifying electromagnetic waves with temporal non-foster metastructures, Nat. Commun. 16, 2757 (2025).

[14] L. Stefanini, E. Galiffi, S. Yin, S. Singh, D. M. Solís, N. Engheta, A. Toscano, D. Ramaccia, F. Bilotti, and A. Alù, Theory and

Experimental Observation of Scattering by a Space-Time Corner, Phys. Rev. Lett. 135, (2025).
[15] G. Castaldi, V. Pacheco-Peña, M. Moccia, N. Engheta, and V. Galdi, Exploiting space-time duality in the synthesis of impedance transformers via temporal metamaterials, Nanophotonics 10, 3687 (2021).
[16] E. Hendry, C. M. Hooper, W. P. Wardley, and S. A. R. Horsley, Effects due to generation of negative frequencies during temporal diffraction, ArXiv:2507.03491 (2025).
[17] J. E. Sustaeta-Osuna, F. J. García-Vidal, and P. A. Huidobro, Quantum Theory of Photon Pair Creation in Photonic Time Crystals, ACS Photonics 12, 1873 (2025).
[18] P. A. Huidobro, E. Galiffi, S. Guenneau, R. V. Craster, and J. B. Pendry, Fresnel drag in space–time-modulated metamaterials, Proceedings of the National Academy of Sciences 116, 24943 (2019).
[19] J. E. Vázquez-Lozano and I. Liberal, Incandescent temporal metamaterials, Nat. Commun. 14, 1 (2023).
[20] M. Scalora, M. A. Vincenti, D. de Ceglia, N. Akozbek, M. Ferrera, C. Rizza, A. Alù, N. Litchinitser, C. Cojocaru, and J. Trull, Extreme electrodynamics in time-varying media, Phys. Rev. A (Coll Park). 112, 013502 (2025).
[21] V. Pacheco-Peña and N. Engheta, Spatiotemporal isotropic-to-anisotropic meta-atoms, New J. Phys. 23, 095006 (2021).
[22] V. Pacheco-Peña and N. Engheta, Antireflection temporal coatings, Optica 7, 323 (2020).
[23] R. Tirole, S. Vezzoli, E. Galiffi, I. Robertson, D. Maurice, B. Tilmann, S. A. Maier, J. B. Pendry, and R. Sapienza, Double-slit time diffraction at optical frequencies, Nat. Phys. 19, 999 (2023).
[24] H. Moussa, G. Xu, S. Yin, E. Galiffi, Y. Ra'di, and A. Alù, Observation of temporal reflection and broadband frequency translation at photonic time interfaces, Nat. Phys. 19, 863 (2023).
[25] V. Bacot, M. Labousse, A. Eddi, M. Fink, and E. Fort, Time reversal and holography with spacetime transformations, Nat. Phys. 12, 972 (2016).
[26] R. G. MacDonald, A. Yakovlev, and V. Pacheco-Peña, Solving partial differential equations with waveguide-based metatronic networks, Advanced Photonics Nexus 3, (2024).
[27] M. Antyufeyeva and V. Pacheco-Peña, Emulating time refraction at photonic time interfaces via smooth temporal transitions, Phys. Rev. Appl. 24, 034004 (2025).
[28] V. Pacheco-Peña and N. Engheta, Temporal aiming, Light Sci. Appl. 9, 1 (2020).
[29] V. Pacheco-Peña and N. Engheta, Merging Effective Medium Concepts of Spatial and Temporal Media: Opening new avenues for manipulating wave-matter interaction in 4D, IEEE Antennas Propag. Mag. 65, 39 (2023).
[30] V. Pacheco-Peña and N. Engheta, Effective medium concept in temporal metamaterials, Nanophotonics 9, 379 (2020).
[31] A. M. Naylor and V. Pacheco-Peña, " Anisotropic photonic time interfaces via isotropic spacetime modulations", in preparation, 2026.

Miexciton enhanced fluorescence in monolayer WS_2 /Si Huygens metasurface

Junichi Takahara[1,2*]

[1]Dept. of Applied Physics, Graduate School of Eng., The University of Osaka, Japan
[2]Photonics Center, Graduate School of Eng., The University of Osaka, Japan
*Corresponding author: takahara@ap.eng.osaka-u.ac.jp

***Abstract*— We demonstrate Miexciton enhanced fluorescence in monolayer WS_2 coupled with Silicon Huygens metasurface. We observed 18-fold enhancement of photoluminescence from A-exciton in monolayer WS_2 in intermediate coupling regime.**

***Keywords*— Miexciton, photoluminescence, WS_2, Huygens metasurface, intermediate coupling regime**

I. INTRODUCTION

Two-dimensional (2D) nanomaterials hold promise for many photonics applications [1]. Thanks to strong confinement energy of 2D exciton within atomic layer thickness, monolayer transition metal dichalcogenides (TMDCs) are expected to be applied in nanophotonic semiconductor devices operating at room temperature. A coherent coupled system between surface plasmon and 2D exciton in TMDCs, which is named "plexiton," has been attracted much interests over the past ten years [2-4].

In recent years, coherent coupling between multipole/anapole mode in single Mie resonator and exciton in TMDCs has been achieved and the enhancement of photoluminescence (PL) has been demonstrated [5,6]. These coupled modes are so called "Miexciton". We proposed in theory Si Huygens metasurface boosts absorptivity of monolayer WS_2 further using degenerated electric dipole (ED) and magnetic dipole (MD) [7].

In this talk, we report the recent progress of our experimental study about Miexciton and enhanced fluorescence of A-exciton in monolayer WS_2 placed on Si metasurface. We obtained Rabi splitting energy of Ω =81meV and observed 18-fold enhancement of PL in intermediate coupling regime [8].

II. METHODS

We fabricated single crystalline Si (c-Si) metasurface on quartz substrate. Then, we transferred a commercially obtained monolayer WS_2 grown on a sapphire substrate to the metasurface using a surface-energy-assisted transferring process.

III. RESULTS AND DISCUSSION

We observed the total absorptivity of the Miexciton reaches ~0.84 with Rabi splitting energy of Ω =81meV. In addition, the PL intensity increased exceeding 18-fold compared to a quartz film. From absorptivity spectra, we obtained energy damping rates of Miexciton γ_1=82meV and γ_2=124.6meV (exciton and Mie mode). We confirmed that this system is in intermediate coupling regime, i.e. $|\gamma_1 - \gamma_2|/2 < \Omega < (\gamma_1 + \gamma_2)/2$.

These results suggest that Miexciton in intermediate coupling regime enables substantial enhancement of PL processes, providing a powerful strategy for boosting light–matter interactions in 2D nanomaterials.

ACKNOWLEDGMENTS

This work was supported in part by Japan Society for the Promotion of Science (KAKENHI 23H00274).

REFERENCES

[1] F. J.G. de Abajo *et al.*, "Roadmap for Photonics with 2D Materials," ACS Photonics, 12, pp. 3961–4095, 2025.
[2] J. Kern *et al.*, "Nanoantenna-Enhanced Light−Matter Interaction in Atomically Thin WS_2," ACS Photon. 2, 1260, 2015.
[3] W. Zhao *et al.*, "Exciton–Plasmon Coupling and Electromagnetically Induced Transparency in Monolayer Semiconductors Hybridized with Ag Nanoparticles," Adv. Mater., 28, 2709–2715, 2016.
[4] J. Sun *et al.*, "Light-Emitting Plexciton: Exploiting Plasmon−Exciton Interaction in the Intermediate Coupling Regime," ACS Nano 12, 10393−10402, 2018.
[5] R. Verre *et al.*, "Transition metal dichalcogenide nanodisks as high-index dielectric Mie nanoresonators," Nature Nanotech. 14, 679-684, 2019.
[6] H. Shinomiya *et al.*, "Enhanced Light Emission from Monolayer MoS_2 by Doubly Resonant Spherical Si Nanoantennas," ACS Photon. 9, 1741-1747, 2022.
[7] D. Chen, and J. Takahara, "Enhancement of excitonic absorption in WS_2 mediated by Huygens Si metasurfaces," Opt. Lett., 50(13), pp. 4246 – 4249, 2025.
[8] D. Chen, and J. Takahara, "Demonstration of Miexciton: enhancement of light–matter interaction in monolayer WS_2 on a Si metasurface," Opt. Lett., 50(24), pp. 7508 – 7511, 2025.

Radiative heat transfer measurements at small scales in systems involving several bodies

Victor Guillemot[1], Ana I. F. Tresguerres-Mata[1], Riccardo Messina[2], Valentina Krachmalnicoff[1], Rémi Carminati[1,3], Philippe Ben-Abdallah[2], Wilfrid Poirier[4], and Yannick De Wilde[1,*]

[1]Institut Langevin, ESPCI Paris, Université PSL, CNRS, 75005 Paris, France
[2]Laboratoire Charles Fabry, IOGS, CNRS, Univ. Paris-Saclay, 91127 Palaiseau, France
[3]Institut d'Optique Graduate School, Université Paris-Saclay, 91127 Palaiseau, France
[4]Laboratoire National de Métrologie et d'Essais (LNE), 78197 Trappes, France
*Corresponding author: yannick.dewilde@espci.fr

***Abstract*—We present measurements of small-scale radiative heat transfer of a glass microsphere immersed in a thermal bath facing three different planar substrates (SiO_2, SiC, and Au), or another glass microsphere, under vacuum, with different temperatures imposed within the system. We reveal many-body contributions and a subtle competition between near-field and far-field heat transfer.**

***Keywords*— thermal radiation, micro/nano scales, multi-probe measurements.**

INTRODUCTION

Several experimental demonstrations of near-field enhancement of radiative heat transfer between two bodies have been reported when a microsphere is positioned at a distance smaller than the thermal wavelength ($\lambda_{Wien} \approx 10$ µm at 25°C) from a planar substrate [1], [2]. Here, we focus on the transition regime from the far field to the near field, examining what occurs as a microsphere approaches a planar substrate [3] or as two microspheres are brought close to each other [4].

I. METHODS

We characterize the flux variations from the microscopheres in vacuum using a thermoresistive probe of platinum on a cantilever combined with a metrological Wheatstone bridge. A platform involving two such thermoresistive cantilevers has been designed for the experiments involving two microspheres, in such a way that they can be separately manipulated with nanometer precision over distances of tens of micrometers.

II. RESULTS AND DISCUSSION

The use of two independent thermal probes in our setup enables one to find where exactly radiative heat flows between the various bodies involved in the system, which also includes the bath at room temperature.

In the experiments, a non-monotonic behavior of the heat flux $\Delta Q = Q(\infty)-Q(d)$ is observed at the hottest microspheres under certain conditions. This effect results from the competition between far-field heat transfer with the environment due to the exchange of propagative waves and near-field heat transfer associated to the tunnelling of electromagnetic energy through the gap separation between the bodies when surface polaritons are thermally excited. An example of this behavior is presented in Fig. 1 in the two-microsphere configuration. Numerical simulations support our observations.

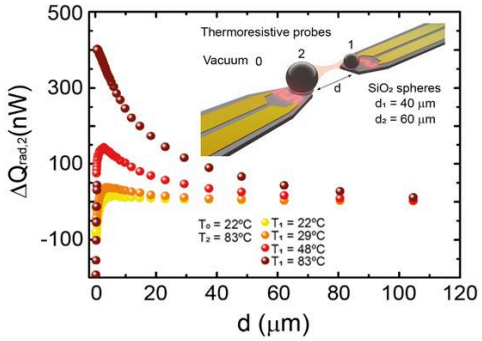

Fig. 1 Heat flux variation measured in sphere-sphere geometry with various temperatures within the system.

ACKNOWLEDGMENTS

This work was supported by the Agence Nationale de la Recherche (NBODHEAT Project No. ANR-21-CE30-0030).

REFERENCES

[1] E. Rousseau, A. Siria, G. Jourdan, S. Volz, F. Comin, J. Chevrier, J.-J. Greffet, "Radiative heat transfer at the nanoscale," Nature Photonics, vol. 3, pp 514-517, 2009.
[2] A. Narayanaswamy, S. Shen, G. Chen, "Near-field radiative heat transfer between a sphere and a substrate," Physical Review B, vol. 78, 115303, 2008.
[3] V. Guillemot, R. Messina, V. Krachmalnicoff, R. Carminati, P. Ben-Abdallah, W. Poirier, Y. De Wilde, "Nonmonotonic Radiative Heat Transfer in the Transition from Far Field to Near Field," Physical Review Letters, vol. 134, 193801, 2025.
[4] A. I. F. Tresguerres-Mata, et al., in preparation, 2026.

Scattering Symmetries in Metagratings

Karim Achouri[1,*]

[1]Institute of Electrical and Microengineering, École Polytechnique Fédérale de Lausanne (EPFL), Laboratory for Advanced Electromagnetics and Photonics, Lausanne, Switzerland
*Corresponding author: karim.achouri@epfl.ch

***Abstract*—We develop a simple formalism to connect the spatial symmetries of a metagrating unit cell and lattice to the shape of its scattering matrix. We use it to explain the emergence of extrinsic chirality in metagratings. And also to design metagratings exhibiting a step function response in momentum space.**

***Keywords*— metamaterials, metagratings, symmetries, scattering, electromagnetic theory.**

I. Introduction

Metagratings are diffraction gratings whose scattering elements are engineered to provide desired electromagnetic transformations. Note that, in this work, we are specifically interested in structures made of a single unit cell repeated periodically. In this case, metagratings are fundamentally similar to conventional metamaterials with the only difference being that they produce diffraction orders whereas metamaterials that are made of a single unit cell repeated periodically do not produced diffraction orders besides the zeroth ones in reflection and transmission [1], [2]. We therefore do not consider spatially varying metamaterials that often produce diffraction orders.

Due to the complexity of such structures and the lack of proper framework to analyze its scattering response, we have developed a formalism to connect the spatial symmetries of a metagrating to the symmetries of its angular scattering response.

II. Method and Results

The proposed methodology is based on our previous work in which we applied symmetry concepts, initially developed in [3], [4], to metasurfaces [5]. The method consists in finding representation matrices that describe how the metagrating scattering matrix transforms under a given symmetry operation, such as a reflection or a rotation. Once these representation matrices are found, it becomes trivial to compute its angular scattering properties under spatial transformations.

By using this approach, we demonstrate how achieving angular transmission asymmetry is impossible with a conventional reciprocal and lossless metasurface but possible with a metagrating [6]. This is the case because by breaking the spatial symmetries of a metagrating, we can asymmetrically direct the incident energy into a desired diffraction order, which is impossible with a conventional metasurface. At the conference, we will show the theory and experimental demonstration of this effect.

Another interesting effect is the concept of extrinsic chirality, where rotation of polarization effects akin to chiral responses are obtained with a non-chiral structure. We have already shown in [5] that such effects are impossible at normal incidence using a metasurface. However, the diffractive channels of a metagrating may be exploited to generate such extrinsic chiral responses.

III. Conclusion

The fact that metagratings exhibit open diffractive channels is an important advantage for controlling the flow of electromagnetic waves compared to conventional spatially uniform metasurfaces. These diffractive channels allow us to achieve responses that would otherwise be impossible to realize with non-diffractive reciprocal, passive and lossless structures.

Acknowledgments

We acknowledge funding from the Swiss National Science Foundation (project TMSGI2_218392).

References

[1] Y. Ra'di, D. L. Sounas, and A. Alù, "Metagratings: Beyond the Limits of Graded Metasurfaces for Wave Front Control," *Phys. Rev. Lett.*, vol. 119, p. 067404, Aug. 2017.
[2] V. Popov, F. Boust, and S. N. Burokur, "Controlling diffraction patterns with metagratings," *Physical Review Applied*, vol. 10, July 2018.
[3] V. Dmitriev, "Symmetry properties of electromagnetic planar arrays: Long-wave approximation and normal incidence," *Metamaterials*, vol. 5, pp. 141–148, June 2011.
[4] V. Dmitriev, "Symmetry Properties of Electromagnetic Planar Arrays in Transfer Matrix Description," *IEEE Trans. Antennas Propagat.*, vol. 61, pp. 185–194, Jan. 2013.
[5] K. Achouri, V. Tiukuvaara, and O. J. F. Martin, "Spatial symmetries in nonlocal multipolar metasurfaces," *Adv. Photon.*, vol. 5, June 2023.
[6] M. A. A. Abouelatta, S. Boroviks, O. J. F. Martin, and K. Achouri, "Step function in momentum space by a metagrating," *Advanced Optical Materials*, Sept. 2025.

Application of Spatial Symmetries in Plasmonic Lattice Design

Kristian Arjas[1,2,*], Grazia Salerno[3], Päivi Törmä[2],

[1]Department of Physics, Trinity College Dublin, Ireland
[2]Department of Applied Physics, School of Science, Aalto University, Finland
[3]Dipartimento di Fisica "E. Fermi",Università di Pisa, Italy
*Corresponding author: arjask@tcd.ie

***Abstract*—We utilise mathematical group theory and symmetry analysis to develop a quasicrystal design method, which is used to realise lasing from bound states in the continuum with high topological charges. Additionally, we show how these tools can be used for generating momentum space Hamiltonians with interesting topological characteristics.**

***Keywords*— plasmonics, bound states in the continuum, lasing, group theory.**

I. Introduction

Spatial symmetries act as a connecting thread across a wide variety of models and domains. In plasmonic lattices, bound states in the continuum (BICs) have been used for lasing, with the topological charge of the beam being inherently related to the rotational symmetry of the structure. By focusing on this symmetry, we develop a method for the design of quasicrystals that lase with very high topological charges. Furthermore, we show how group theoretical methods based on symmetries can be used for constructing momentum space Hamiltonians with fully controllable band-gaps and varying topological properties.

II. Methods

Our quasicrystal design method uses the symmetry properties of the desired beam to construct an approximation of the electromagnetic near-field. By targeting the nanoparticles to the nodes of this field, we can minimize ohmic losses in the desired mode, making it the most likely to lase. To build a working sample, two additional optimisation steps are required. The samples are fabricated and a produced laser beams are measured.

The momentum-space Hamiltonians consist of two components: a momentum-dependent component with degeneracies at the high-symmetry points, and a constant coupling Hamiltonian built from the symmetry-representations of the lattice.

III. Results and Discussion

We design and fabricate quasicrystals with C_8, C_{10} and C_{12} rotational symmetries and measure lasing with $q = -3, -4$ and -5 respectively. Additionally, the C_{12} lasing emission displays a rich tapestry of polarisation vortices and transitions between them, as is shown in Fig. 1.

By constructing varying momentum space Hamiltonians, we build bands carrying Chern numbers up to ± 3 and non-trivial Zak phases. Further, as the Hamiltonian is inherently built on real-space couplings, we model systems with finite sizes and directly observe topological edge states.

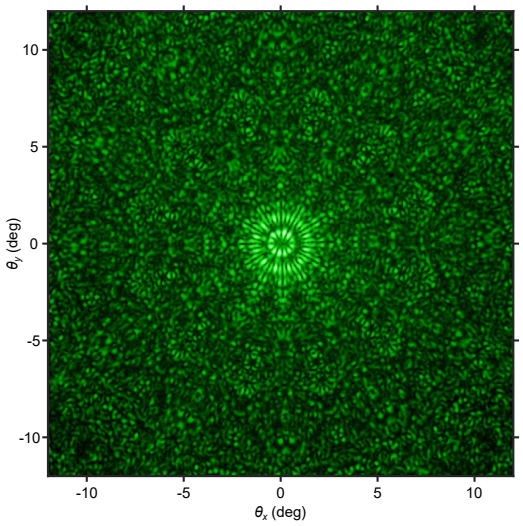

Fig. 1. Lasing emission from a C_{12v}-symmetric quasicrystal carrying high topological charges.

IV. Conclusion

We applied group theory for the design of plasmonic quasicrystals and momentum space Hamiltonians. This allowed us to reach lasing with BIC:s with high topological charges and design Hamiltonians with varying topological charactersitics.

Acknowledgments

This work was supported by the Vilho, Yrjö and Kalle Väisälä Foundation.

References

[1] Arjas, K., Taskinen, J. M., Heilmann, R., Salerno, G., & Törmä, P. (2024). High topological charge lasing in quasicrystals. *Nature Communications*, 15(1), 9544.

[2] Arjas, K., Salerno, G., & Törmä, P. (2025). Topological invariants and topological charges in photonic systems. *Physical Review B*, 112(23), 235428.

Enabling Meta-surface Design with Neural Network Technologies.

Denis RIDEAU*[1] , Mathys LE GRAND[1] , Damien MAITRE[1,2], Loumi TREMAS[1,3], Habib MOHAMAD[1] , Louis Henri FERNANDEZ MOURON[1,4], Adam FUCHS[1], Pascal URARD[1], Valerie SERRADEIL[1], James DOWNING[5]
[1] *STMicroelectronics, 850 rue J. Monnet BP16, 38926 Crolles, France*
[2] *Univ. Jean Monnet, CNRS, Institut d Optique Graduate School, Laboratoire Hubert Curien UMR 5516, F-42023, Saint-Etienne, France*
[3]*IOGS Universite Paris Saclay,2 Av. Augustin Fresnel, 91120 Palaiseau, France.*
[4] *Universite Paris Dauphine Place du Marechal de Lattre de Tassigny, 75775 Paris, France ;*
[5]*1Tanfield, Inverleigh Row, Edinburgh, UK;*
*Corresponding author: Denis.rideau@st.com

***Abstract*— Meta-surfaces, made of subwavelength nanostructures, enable ultra-thin optical components but are challenging to design at millimeter scale using conventional FDTD. Moreover, periodic-local methods can fail to capture complex electromagnetic interactions between meta-atoms and may lead to inaccurate designs. We propose an AI-driven framework based on convolutional neural network emulators that support gradient-descent and generative design, improving efficiency, accuracy, and scalability for large-scale meta-surface optics.**

***Keywords*— Meta-materials, Meta-surface, CNN, Diffusion models.**

I. Introduction

A meta-surface is made of subwavelength nanostructures that enable ultra-thin optical devices [1-3]. Using electron beam lithography, research labs have shown that lenses, spectral filters, polarization band-pass filters, and beam shapers (hereafter called meta-diffusers) can be effectively implemented with flat meta-surface optics. As the technologies mature toward large-scale production, semiconductor companies are preparing for significant growth in this field. Supporting this transition requires accurate meta-surface simulations and innovative design methods. Due to the relatively large dimensions (in mm) of these optical systems and the sub-wavelength nature of the diffraction patterns, traditional electromagnetic simulation techniques based on the Finite Difference Time Domain (FDTD) [4] method can sometimes be challenging to apply. For this reason, alternative approaches are often used by optical designers. The commonly used phase-atom mapping technique in meta-surface design relies on a local periodic approximation, where each meta-atom is assumed to reside in an effectively infinite periodic array, and its geometrical parameter (e.g. the width of a pillar) is tuned to generate the desired local phase response based on a precomputed phase–width relation obtained from a single periodic meta-atom simulation. However, this periodic-local approaches for designing meta-surfaces [5-7] face significant limitations, mainly due to the difficulty of accurately modeling the complex inter-meta-atoms interactions that are critical for achieving optimal performance.

These constraints often create bottlenecks in the design workflow and lead to a high rejection rate during verification, when many designs fail to meet optical specifications (e.g., suppression of unwanted zeroth orders in beam shapers). To overcome these challenges, we introduced a new framework for the design of large-scale meta-surfaces. The key innovation is the integration of AI-driven capabilities, in particular convolutional neural network (CNN)-based emulators. This enables AI-based designs using a gradient descent approach but also opens new design methodologies based on generative modeling.

II. CNN-Based Meta-surface Designs

A more accurate way to handle this complexity than the previously mentioned heuristic local model is to use convolutional neural networks (CNNs) [8]. We build a database of over 10,000 realistic 20×20 meta-lens and meta-diffuser patches, storing 2D electric-field images 50 nm after the meta-surface. The meta-atoms are semiconductor pillars spaced at half-wavelength intervals embedded in a surrounding oxide buffer. The simulated FDTD near field is low-pass filtered and down-sampled, reducing the network output size by over a factor 1000 and enabling smaller CNN kernels for the same physical receptive field. A resolution of one pixel per pillar is sufficient to calculate the entire far field according to the Nyquist criterion for propagating waves. Among tested architectures, CNN learns the meta-surface near-field patterns efficiently achieving R^2 (R-squared) of nearly 0.99 (the R^2 is averaged over the far field). Such high R^2 indicates that the CNN model's predictions match very well the true values obtained from the FDTD far field simulations. However, other important quantities (such as the zeroth orders and

transmission) are also accurately emulated with CNN (see later).

This AI emulation of the near fields offers two main design benefits. First, it accelerates design verification: CNN-based emulators enable fast simulation of large-scale structures, drastically shortening the design loop compared to traditional methods. The simulation time of a CNN is significantly smaller than for FDTD: typically, a 128x128 design takes only a few seconds on a single-core machine, while it requires about 10 hours on a recent 15 cores CPU system. It ought to be mentioned that FDTD simulation of larger meta-surface can be very challenging and may require state of the art GPU-based calculations or domain decomposition techniques [4].

A typical comparison between the predictions of a heuristic local model and the CNN model is shown in Figure 1. As can be seen the differences are significant. A clear zeroth order is visible in the CNN-model (leading to an undesired axial intensity peak in the far field). These results can be compared to the FDTD rigorous simulation shown in Figure 2 (top) that also exhibits a large zeroth order.

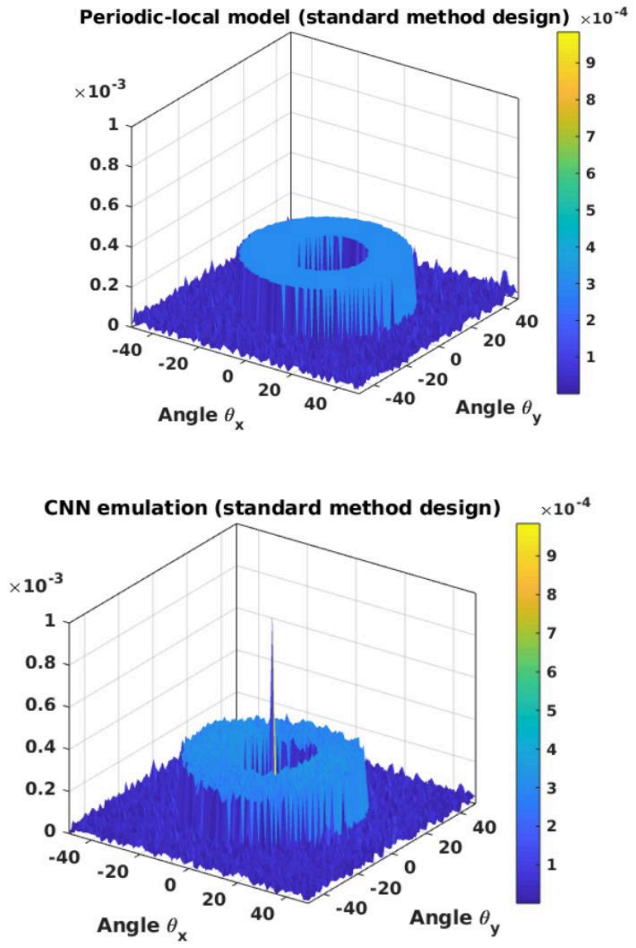

Fig. 1 Model prediction of the amplitude of the far field of a 98*98 pillars meta-surface with a heuristic local model (top) and using CNN-model (bottom).

Additionally, AI emulation of the near fields enables gradient-based performance optimization: thanks to the use of automatic differentiation, the CNN emulators can accurately compute the sensitivity of the optical response (for example, beam shape) to each structural parameter of the meta-atoms (such as pillar width). Instead of relying on brute-force verification, the framework can directly backpropagate the error between the simulated and desired performance allowing accurate optimizations based on gradient descent.

Figure 2 compares the FDTD-simulated far-field patterns of two meta-surfaces: one designed with a standard approach (relying on a periodic-local phase-pillar-width model), and one obtained using an AI-assisted gradient-descent optimization. In the case of the standard design method, a strong undesired zeroth diffraction order is clearly visible (at zero-diffracted angle), indicating poor suppression of on-axis transmission. In contrast, the AI-optimized meta-surface effectively suppresses this zeroth order, resulting in a cleaner far-field pattern that better matches the target beam profile and demonstrates the improved performance enabled by the gradient-based AI design framework. This is further emphasized in Figure 3, showing axial cuts of the previous far fields. All gradient descent-based simulation shown in this paper are obtained starting from the design obtained with a standard method (initial condition). For large meta-surfaces, composed of million pillars, we found out that such heuristic initial condition is key to achieving better results.

III. Diffusion-Based Meta-surface Designs

Beyond gradient-based optimization, recent advances in generative modeling have opened new possibilities for inverse design of complex photonic and meta-surface structures. State-of-the-art approaches such as diffusion models and Schrödinger bridges [9] offer powerful frameworks that can generate complex designs that do not depend on the relevance of the initial conditions such as with the gradient-based approaches. These methods can also generate families of high-performance candidates rather than a single locally optimized solution. They enable sampling directly from the distribution of designs conditioned on a target optical response, thereby complementing deterministic gradient-based methods and improving robustness, diversity, and exploration of the design landscape.

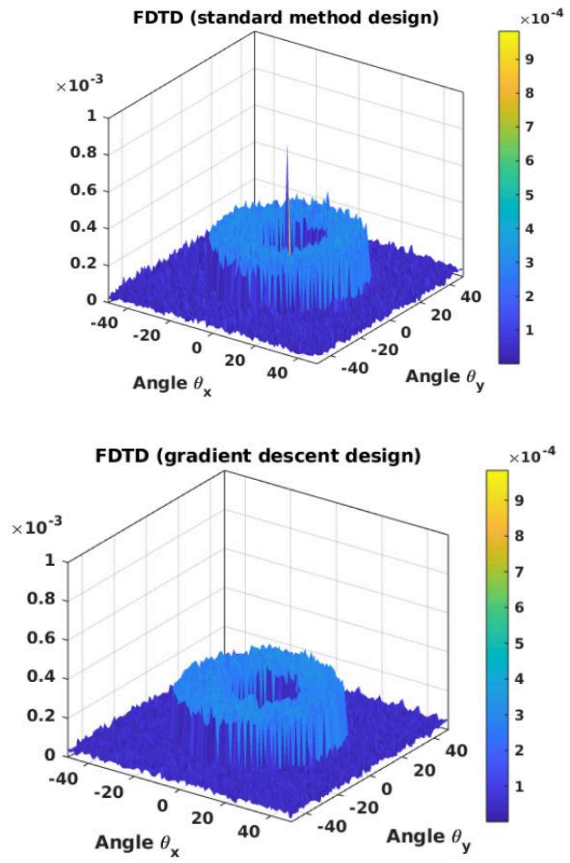

Fig. 2 FDTD simulation of the far field of a 98*98 pillars meta-surface designed with a standard method (top) and with AI-assisted design using a gradient descent (bottom).

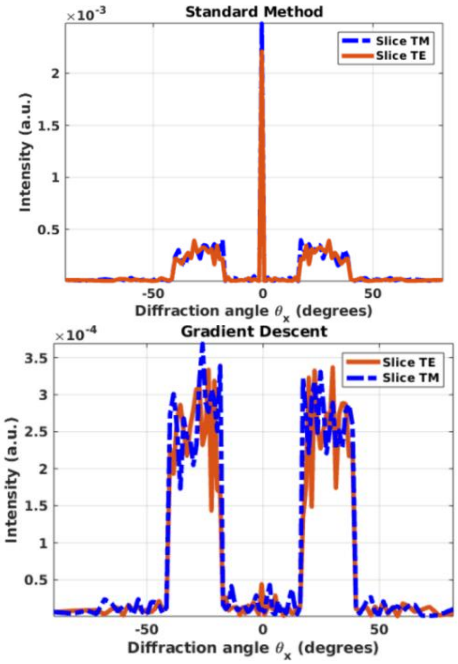

Fig. 3 Horizontal and vertical cuts of the far fields of figure 2. TE and TM refer to the two light polarization states.

We compared designs obtained with the standard method to those produced by a CNN-based gradient-descent approach, as well as by the diffusion-based method. All designs were verified using rigorous FDTD simulations. The corresponding far-field intensity patterns are shown in Figure 4 for 98×98 pillars metasurface designs obtained with the standard method, the CNN-based gradient-descent approach, and the diffusion-based method, all validated by rigorous FDTD simulations with their corresponding far-field patterns. For reference, the target design is also shown, whose far field is computed using the periodic-local-phase approximation. In that later case, the Far field exhibits a nearly perfect structure, very close to the desired far field shape.

Figure 5 report similar simulations across various design sizes. For each case, we also report the R^2 values computed with respect to the desired target far field, providing a quantitative measure of how well each design reproduces the specified optical response.

Figure 6 summarizes these results by plotting the R^2 values as a function of the meta-surface size. A clear and systematic improvement over the standard design method (based on the periodic-local approximation) is observed for both AI-based approaches. The diffusion-based generative design consistently pushes the performance closer to the target, while the CNN-driven gradient-descent method achieves slightly superior R^2 by fine-tunning the final design solution accurately. These trends highlight the scalability and effectiveness of AI-assisted design strategies for large-area meta-surfaces, especially in regimes where traditional local models fail to capture complex inter-meta-atom interactions.

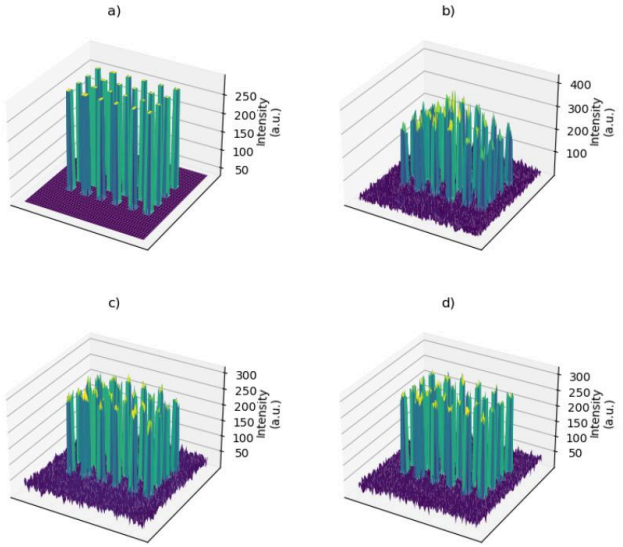

Fig. 4 Comparison of 98*98 pillars meta-surface designs obtained with the standard method (b), a CNN-based gradient descent approach (c), and the diffusion-based method (d). All designs validated using rigorous FDTD simulations, and the corresponding far-field patterns are shown. For comparison the target is also shown (a) and in that case, the far field is calculated using the periodic-local-phase approximation.

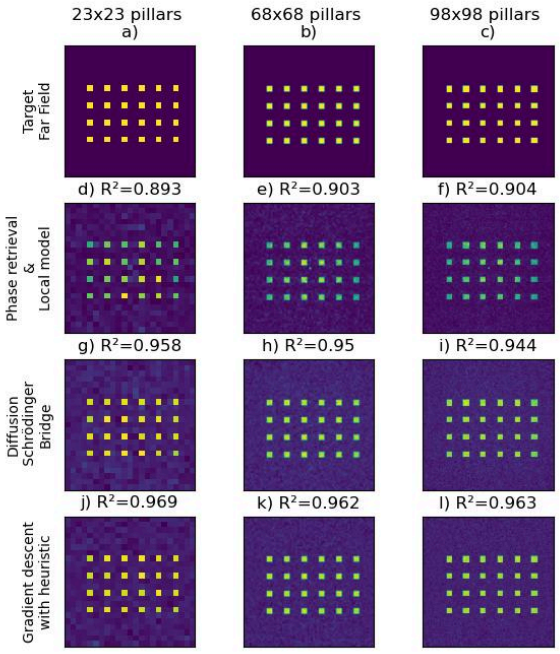

Fig. 5 Comparison of designs obtained with the standard method, a CNN-based gradient descent approach, and the diffusion-based method across various design sizes. All designs validated using rigorous FDTD simulations, and the corresponding far-field patterns are shown. The R^2 values are calculated using the target as a reference.

IV. Conclusion

We presented an AI-driven framework for large-scale meta-surface design that overcomes key limitations of both FDTD-only and periodic-local approaches. CNN-based emulators accurately reproduce FDTD responses (with averaged R^2 ≈0.99) while reducing simulation times from hours to seconds, enabling fast verification of millimeter-scale devices. Their differentiability supports gradient-based inverse design, yielding meta-surfaces with significantly improved performance—such as enhanced suppression of undesired zeroth diffraction orders—compared to standard heuristic designs.

In addition, diffusion-based generative models extend the framework to produce diverse families of high-quality designs conditioned on target optical responses, alleviating reliance on specific initial conditions. Overall, this AI-assisted methodology provides an efficient, accurate, and scalable path toward industrial-grade meta-surface optics design.

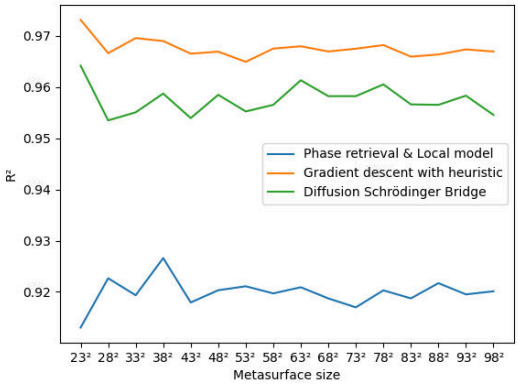

Fig. 6 Extracted R^2 as a function of the design size (see text and Figures 4-5 for details).

References

[1] S. So, J. Mun, J. Park, and J. Rho, "Revisiting the Design Strategies for Metasurfaces: Fundamental Physics, Optimization, and Beyond", Adv. Mater. 35, 2206399, 2023.

[2] C. Gigli, Q. Li, P. Chavel, G. Leo, M. L. Brongersma, and P. Lalanne, "Fundamental limitations of huygens' metasurfaces for optical beam shaping," Laser & Photonics Reviews, vol. 15, no. 8, p. 2000448, 2021.

[3] J. Hu, S. Bandyopadhyay, Y. Liu, and L. Shao, " A Review on Metasurface: From Principle to Smart Metadevices", doi: 10.3389/fphy.2020.586087, 2021.

[4] Lumerical Inc. , FDTD.

[5] S. So, J. Mun, J. Park, and J. Rho, "Revisiting the Design Strategies for Metasurfaces: Fundamental Physics, Optimization, and Beyond" , Adv. Mater. 35, 2206399, 2023.

[6] C. Gigli, Q. Li, P. Chavel, G. Leo, M. L. Brongersma, and P. Lalanne, "Fundamental limitations of huygens' metasurfaces for optical beam shaping," Laser & Photonics Reviews, vol. 15, no. 8, p. 2000448, 2021.

[7] J. Hu, S. Bandyopadhyay, Y. Liu, and L. Shao, " A Review on Metasurface: From Principle to Smart Metadevices" , doi: 10.3389/fphy.2020.586087, 2021.

[8] D. Rideau, M. Le Grand, L. H. Fernandez Mouron, V. Serradeil, L. Tremas, and P. Urard, "Approaches to Simulating Meta-surfaces for Flat Optical Devices: The Transition to Solutions Based on Neural Networks," in 2024 International Conference on Simulation of Semiconductor Processes and Devices (SISPAD), 2024.

[9] M. Le Grand, P. Urard, D. Rideau, L. Trémas, D. Maitre, L.-H. Fernandez-Mouron, and R. Orobtchouk, "Diffusion Schrödinger Bridges for Metasurface Inverse Design," submitted to *IEEE Electron Device Letters (EDL)*.

Machine-Learning Assisted Design of Tunable Metasurfaces

A. Wolff[1], L. Mueller[1], J. Krieger[1], L. Franke[1], R. Stemler[1], S. Klingel[1], and M. Rahm[1]
[1]Department of Electrical and Computer Engineering and Research Center OPTIMAS, Erwin-Schroedinger-Strasse, RPTU Kaiserslautern-Landau, 67663 Kaiserslautern, Germany

*Corresponding author: marco.rahm@rptu.de

***Abstract*— We present three machine-learning-assisted design strategies for tunable metasurfaces. We use a neural network to optimize a metasurface for dual-frequency beam steering, employ transfer learning for reduction of simulation costs for composite unit cells and use a physics-informed model to design a metasurface for independent amplitude and phase control.**

***Keywords*— metamaterials, terahertz, machine learning.**

I. Introduction

Industrial applications demand increasingly advanced designs of functional metasurfaces that meet stringent industry standards.

II. Results and Discussion

First, we optimize the bias voltages of a tunable metasurface to simultaneously steer beams at 27 GHz and 31 GHz. Ideal phase profiles from Kirchhoff diffraction theory are mapped via a neural network to feasible voltage distributions, which enables dynamic, frequency-dependent beam steering over angles from 10° to 45°.

Second, we address the computational cost of designing composite unit-cell structures. By applying transfer learning from basic to complex unit-cell configurations, we reduce simulation requirements dramatically. We show that, for the example of a dipole–dipole structure, only 29 combined simulations are needed to reach a mean squared error of 0.05, compared to 583 when training from scratch.

Third, we employ a physics-informed machine-learning framework to achieve independent amplitude and phase control in a metasurface. Using a Temporal Coupled Mode (TCM) model, the dynamic tuning behavior is captured with just four simulations per design iteration. Machine learning predicts the TCM parameters from the metasurface geometry, which enables a rapid and efficient optimization.

III. Conclusion

These studies demonstrate that integrating electromagnetic theory, physics-informed modeling, and machine learning can accelerate the design of metasurfaces and metamaterials while meeting practical performance and hardware constraints. Such an approach can pave the way for industrially viable, dynamically tunable metasurfaces that are specifically designed for demanding tasks in the industrial environment.

References

[1] [1] L. Mueller, A. Wolff, S. Klingel, J. Krieger, L. Franke, R. Stemler, and M. Rahm, “Multi user frequency selective beam steering by reconfigurable intelligent surfaces in the Ka band,” Scientific Reports 15, 10891 (2025).

[2] A. Wolff, L. Mueller, S. Klingel, and M. Rahm, “Transfer learning for data-efficient modeling of composite metasurface and FSS unit cells,” J. Mater. Sci: Mater Eng. 21, 16 (2026).

Cooperative absorption in random particulate media: achieving spectral selectivity

Cédric Blanchard[1,*], Cristina Gila[1,2], Timothée Guerra [1,3], Olivier Rozenbaum [1],

[1*]Université d'Orléans, CNRS, CEMHTI UPR 3079, Orléans, France.
[2]Departamento de Física, Facultad de Ciencias, Universidad de Oviedo, Spain
[3]Université Grenoble Alpes, CEA LETI, France
*Corresponding author: cedric.blanchard@cnrs-orleans.fr

***Abstract*—We present a predictive framework for engineering optical functionalities in disordered systems using a T-matrix multiple-scattering approach. Cooperative many-body interactions enable near-perfect absorption at a target frequency with suppressed off-resonant absorption, turning disorder into a controllable design parameter. *Keywords*— Complex media, numerical modeling, optical properties design.**

I. Introduction

Accurately modeling electromagnetic interactions in large many-particle systems remains a major challenge in computational electromagnetics, especially when particles are randomly distributed and strongly coupled through multiple scattering. In contrast to ordered nanophotonic architectures, where periodicity and symmetry simplify numerical treatments, disordered particulate media resist predictive design due to the intrinsic complexity of many-body electromagnetic interactions. Yet, these systems are highly attractive for applications requiring scalable, robust, and low-cost optical materials, including large-area absorbers, thermal emitters, and infrared photonic components. In this contribution, we establish a predictive design framework for engineering optical functionalities in disordered many-particle systems, effectively turning disorder into a controllable design parameter. We further provide an experimental realization based on this strategy, establishing a departure from conventional trial-and-error approaches to disordered nanophotonics.

II. Methods

Our approach relies on a rigorous multiple-scattering framework based on the T-matrix formalism (see for instance Mishchenko [1]), which provides an efficient and accurate description of collective scattering and absorption in ensembles of randomly distributed particles.

Rather than enforcing order or engineered correlations, we exploit the intrinsic collective interactions that naturally arise in random particulate systems. These cooperative many-body effects open new regimes for light manipulation and enable optical functionalities that are both computationally tractable and experimentally realizable.

This computational framework is illustrated through the design and fabrication of novel materials showing spectral selectivity.

III. Results and Discussion

1. Numerical design of near-perfect absorption in disordered many-particle media. We introduce a bidispersed ensemble of randomly distributed nanoparticles, where one population provides resonant absorption and the other enhances multiple scattering [2]. By tuning the electromagnetic coupling within this many-particle system, we numerically demonstrate near perfect absorption levels, achieved without periodicity, resonant cavities, or fine structural control.

2. Experimental demonstration of cooperative absorption in disordered many-particle systems. We fabricate thin, large-area layers composed of resonant and lossless particles and characterize their optical response using infrared spectroscopy. The measurements reveal a strong and spectrally selective absorption peak arising from cooperative many-body interactions, in excellent agreement with numerical predictions.

IV. Conclusion

Beyond a proof of concept, our results establish a methodological and technological rupture, demonstrating that fully disordered many-particle systems can be engineered with a level of control comparable to ordered platforms, while inherently satisfying scalability and fabrication-tolerance constraints.

Acknowledgments

This work was funded in part by the Agence Nationale de la Recherche (ANR) under the *Jeunes Chercheuses et Jeunes Chercheurs* program (Project OUTWARDS, No. ANR-19-CE05-0021).

References

[1] M. I. Mishchenko, L. D. Travis, and D. W. Mackowski, "T-matrix method and its applications to electromagnetic scattering by particles: A current perspective," *J. Quant. Spect. Radiat. Transf.*, vol. 111, pp. 1700–1703, 2010.

[2] T. Guerra *et al.*, "Generating near-perfect absorption in subwavelength slabs of nanoparticles: Towards spectral selectivity in random media," *Phys. Rev. B*, vol. 107, pp. L220202, 2023.

Deep Learning-Enhanced Dual-Comb Ghost Imaging with Minimally Invasive Probes

Myoung-Gyun Suh[1,*]

[1]NTT Research, Inc., 940 Stewart Drive, Sunnyvale, California, USA
*Corresponding author: myoung-gyun.suh@ntt-research.com

***Abstract*—We present a dual-comb ghost imaging framework enabling video-rate, high-fidelity reconstruction without spatial or spectral scanning. By combining parallel comb-generated speckle patterns via a single-core fiber with a transformer-based deep learning model, we overcome conventional speed bottlenecks, offering a minimally invasive solution for compact fiber-based endomicroscopy.**

***Keywords*— ghost imaging, single-pixel imaging, optical frequency combs, deep learning, endoscopy.**

Ghost imaging (GI) reconstructs scenes by correlating structured illumination with single-pixel detector measurements [1], circumventing the need for multi-pixel arrays. While highly advantageous for scattering media, low-light conditions, or hardware-constrained environments like endoscopy, conventional GI is bottlenecked by the sequential generation of illumination patterns via spatial light modulators or mechanical scanning. This serial acquisition severely limits imaging speed, hindering the real-time observation of dynamic scenes even when compressive sensing techniques are applied.

To overcome this limitation, we introduce ghost imaging [2], [3]. This approach leverages the intrinsic parallelism of optical frequency combs (OFCs) and dual-comb interferometry, completely eliminating the need for slow spatial modulation or wavelength tuning. Broadband dual combs propagate through a single-core fiber to generate wavelength-multiplexed hyperspectral dual-comb speckle patterns. By mapping individual spectral lines to statistically independent spatial patterns, 3D optical information (2D spatial $\times$ 1D spectral) is compressed into a single time-domain signal. This allows hyperspectral speckle measurements to be acquired in a single shot using spatially non-resolved hardware.

Notably, unlike spectral correlation–based ghost imaging that relies on swept-frequency lasers [4], [5], our dual-comb approach enables fundamentally parallel pattern generation. This parallelism is crucial for imaging moving targets, as sequential pattern projection often introduces motion artifacts. Furthermore, the inherent frequency precision and stability of OFCs ensure highly repeatable speckle patterns at each comb line. This unique combination of parallel and stable pattern generation is essential for practical, video-rate ghost imaging.

To invert this highly compressed data, we use an application-specific, transformer-based neural network [2]. This deep-learning reconstruction, paired with spectral multiplexing, accurately recovers intensity measurement data using pre-recorded speckle patterns to achieve video-rate performance. The architecture drastically simplifies the optical front end while maintaining the core benefits of GI, enabling practical deployment in space-constrained platforms.

In conclusion, we experimentally demonstrate that dual-comb ghost imaging enables video-rate imaging using only a minimal optical front end: a single-core fiber and a single-pixel photodetector. Furthermore, our transformer-based model significantly enhances image quality by minimizing information loss during compression. While challenges remain for practical deployment—such as improving compact speckle-pattern generators [4], [6], optimizing light collection, and realizing gray-scale imaging [7]—this proof-of-concept validates high-fidelity GI using minimally invasive hardware. Combining comb-based parallel processing with deep-learning reconstruction holds strong promise for next-generation biomedical and sensing applications.

References

[1] Gibson, G. M., Johnson, S. D., and Padgett, M. J., “Single-pixel imaging 12 years on: a review”, Optics express 28(19), 28190–28208, 2020.
[2] Dang, D., Suh, M.-G., Gao, M., Park, B., Hu, B., Jin, Y., Kort-Kamp, W. J., and Lee, H. W. H., “Dual-comb ghost imaging with transformer-based reconstruction for optical fiber endomicroscopy”, Thirty-ninth Annual Conference on Neural Information Processing Systems, 2025
[3] Suh, M.G., Dang, D., Gao, M., Jin, Y., Park, B.J., Hu, B., Kort-Kamp, W.J. and Lee, HW., ”Hyperspectral Dual-Comb Compressive Imaging for Minimally-Invasive Video-Rate Endomicroscopy”, arXiv preprint arXiv:2507.04157, 2025.
[4] Shin, J., Bosworth, B. T. and Foster, M. A., ”Single- pixel imaging using compressed sensing and wavelength- dependent scattering”, Optics letters 41, 886–889, 2016.
[5] Lochocki, B., Ivanina, A., Bandhoe, A., de Boer, J. F. and Amitonova, L. V.,”Swept-source multimode fiber imaging”, Scientific Reports 13, 8071, 2023.
[6] Zhu, R., Lei, Y., Wan, S., Xiong, Y., Wang, Y., Chen, Y. and Xu, F., ”Compact fiber-integrated scattering device based on mixed-phase TiO2 for speckle spectrometer”, Optics Letters, 47(7), pp.1606-1609, 2022.
[7] Chen, Y., An, H., Sun, Z., Tian, T., Chen, M., Spielmann, C. and Li, X., ”Large model enhanced computational ghost imaging”, Science China Technological Sciences, 68(11), p.2120403, 2025

Photonic driven dual-mode thermoregulation: from static to dynamic design evolution

Muluneh G. Abebe[1,*], Eva Loccufier[2], Jozefien Geltmeyer[2], Karen De Clerck[2], Bjorn Maes[1]

[1]Micro- and Nanophotonic Materials Group, Research Institute for Materials Science and Engineering, University of Mons, 20 Place du Parc, B-7000 Mons, Belgium
[2]Department of Materials, Textiles and Chemical Engineering (MaTCh), Ghent University, Tech Lane Science Park 70A, B-9052 Ghent, Belgium.
*Corresponding author: mulunehgeremew.abebe@umons.ac.be

***Abstract*— Maintaining comfort with photonic thermal-management textiles can reduce energy use for heating and cooling in residential and office buildings. Here we outline the design cycle of a passive dual-mode thermoregulation fabric based on dynamic emissivity modulation, highlighting key photonic architectures, their limitations, and the strategies used to achieve a dimensionally stable design.**

***Keywords*— metamaterials, emissivity, thermoregulation**

More than half of the energy consumed globally is used for heating and cooling of largely empty buildings, both residential and commercial. Therefore, more localized heating and cooling efforts are essential.

Research on radiative thermal textiles enabled by nanophotonic and metamaterial concepts has advanced rapidly over the last decade. A key goal is a passive, power-free textile that autonomously switches between heating and cooling (dynamic dual-mode thermoregulation), improving comfort while reducing energy demand and mitigating risks during heat waves and cold spells.

Here we summarize the design evolution of a recently introduced dynamic emissivity-modulating textile (DEST), from early architectures and numerical modeling to the final device concept (Fig. 1). Emissivity modulation is based on the Stefan–Boltzmann law, in which radiative power scales with surface emissivity and temperature to the fourth power; controlling emissivity therefore controls radiative heat exchange with the environment. An early passive dual-mode concept is a static multilayer Janus fabric with asymmetric emissivity (high/low on opposite faces) [1]. Large emissivity contrast is obtained by engineering a metal–dielectric cylindrical-fiber photonic crystal. The design provides heating or cooling, but switching requires manual flipping, motivating autonomous alternatives.

A subsequent approach uses a highly emissive carbon-fiber base paired with metal-coated, low-emissive shape-memory nanofiber islands whose apparent area changes with temperature. In cold conditions the islands expand to cover more of the high-emissivity base, reducing the effective emissivity and suppressing radiative heat loss. In hot conditions the islands retract, exposing the high-emissivity base and increasing radiative cooling. A central challenge is mechanical and dimensional stability: the islands must remain registered to their original positions during cycling while the overall textile maintains constant dimensions.

The final design, DEST addresses this by incorporating a mechanically engineered metamaterial architecture that produces reversible macropore actuation while preventing out-of-plane distortion through a tailored cut pattern. The resulting textile responds to temperature and ambient humidity, passively switching between emissive and reflective states without external energy input, and delivers an approximately 6 °C reversible thermal comfort window [2].

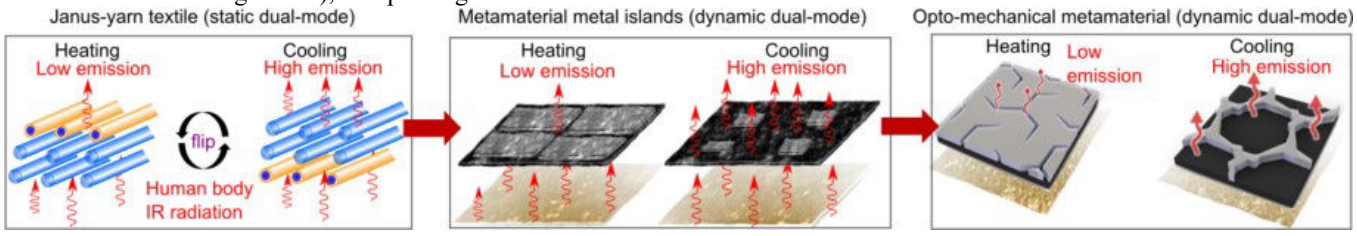

Fig. 1 From Janus Fabrics to DEST: schematic of design evolution toward passive dynamic thermoregulation

ACKNOWLEDGMENTS

This work was supported by the FRS-FNRS

REFERENCES

[1] M. G. Abebe, et al., "Janus-Yarn Fabric for Dual-Mode Radiative Heat Management," *Physical Review Applied*, vol. 16, p. 054013, 2021.
[2] E. Loccufier, M. G. Abebe, et al., "Dimensionally Stable Nanofibrous Nonwoven as a Flexible Dynamic Emissivity Switching Temperature-Regulating Material," Advanced Materials, vol. 37, p. e17161, 2025.

Photoluminescence of Pyrolytic Carbon Dots on Plasmonic Metasurfaces

Pierre Berini

School of Electrical Engineering and Computer Science, University of Ottawa, Canada
Department of Physics, University of Ottawa, Canada
Nexus for Quantum Technologies Institute, University of Ottawa, Canada
pberini@uottawa.ca

***Abstract*— The ability of surface plasmon polaritons (SPPs) to decay into energetic (non-equilibrium) carriers in metals, and the subsequent harvesting of energetic carriers at metal surfaces leads to new device applications and enhanced or new reaction pathways in photoelectrochemical or photochemical processes occurring on the surface. Here we discuss consistent, repeatable, bright and visible luminescence from pyrolytic carbon dots (CDs) on Ag gratings formed and pumped by SPPs excited at 532 nm (2.33 eV). We emphasize computational modelling aspects that capture the principal observed phenomena.**

***Keywords*— surface plasmons, metamaterials, carbon dots, Purcell factors.**

I. Introduction

Metallic metasurfaces and nanostructures such as nanoantennas, gratings and nano-resonators can be designed to couple efficiently to an incident optical beam such that surface plasmon polaritons (SPPs) are excited thereon. The fields of SPPs can be enhanced by factors of 10 to 100× with respect to the incident field due to their confinement to sub-diffraction volumes, resulting in enhanced light-matter interactions at the nanoscale. These properties are fundamental and break some of the trade-offs that apply to interactions in bulk materials.

Moreover, SPPs decay into energetic (non-equilibrium) carriers in metals through absorption. The harvesting of energetic carriers at metal surfaces leads to new device applications, and to new or enhanced reaction pathways in photoelectrochemical or photochemical processes occurring on the surface. We recently reported bright visible luminescence from carbon dots (CDs) formed photochemically from a carbonaceous seed layer on Ag gratings by SPPs excited thereon at 532 nm (2.33 eV) [1,2]. In addition to inducing their photochemical formation, SPPs also pump optically the CDs, and receive Stokes-shifted radiation therefrom, which is then outcoupled by the grating into free-space visible light [3]. Here we review recent progress on such photoluminescent gratings, bearing CDs dots formed in situ directly thereon.

II. Results

Ag gratings on a thick Ag film on a Si substrate were formed by lithography, evaporation and lift-off [4]. A Ag grating on a semiconductor substrate also operates effectively as a heat sink to minimize thermal effects. Upon illumination such gratings support Bloch SPPs. An associated periodic distribution of non-equilibrium charge carriers is created over the illuminated area by absorption of SPPs therein. CDs are created by transformation of a carbonaceous seed layer under SPP excitation in an O_2 depleted environment [2]. The seed layer consists of partially pyrolyzed carbon originating from polymethylmethacrylate (PMMA) left behind from lithographic processing of the gratings [4]. The seed layer, the formation of CDs and the growth of fluorescence were monitored in real-time in-situ using Raman spectroscopy. The structure under test was placed in a gas chamber filled with an O_2 depleted gas, such as CO_2. Measured Raman spectra reveal the growth of D and G peaks indicating the formation of sp^2 bonded carbon, suggesting that graphitized CDs have formed from the seed layer. **Error! Bookmark not defined.**

The role of SPPs in our system is fourfold, as illustrated in Fig. 1: Firstly, pump SPPs catalyse the seed layer into graphitic CDs; secondly, pump SPPs excite the CDs; thirdly, SPPs receive Stokes-shifted quanta of energy emitted by the decay of excited CDs; and fourthly, SPPs scatter from the grating into specific free-space radiation channels [3].

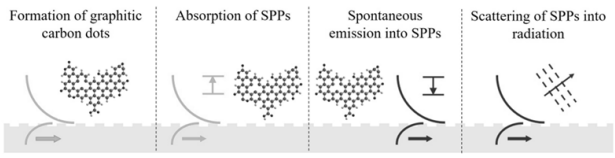

Fig. 1 The role of SPPs on photoluminescent gratings is fourfold: catalysis of carbonaceous seed layout into CDs; optical pumping of CDs; reception of Stokes-shifted emission from CDs; scattering off grating into visible free-space light.

Several aspects of the process illustrated in Fig. 1 were modelled using full-wave electromagnetic numerical techniques: i) The excitation of SPPs on Ag gratings was modelled at the pump wavelength assuming normally incident plane waves to validate the design space and arrive at theoretical enhancement factors on the surface; ii) the computed field distributions, and enhancement factors averaged over the grating surface, were then used to pump the carbon dots; iii) the Stokes-shifted emission due to the decay of the carbon dots into SPPs on the grating was then modelled to compute Purcell factors; iv) the diffraction of the SPPs from the grating into observable far field radiation was then computed. Theoretical results were compared with experiments to strong agreement.

III. Conclusion

CDs created *in situ* on a silver grating bearing a carbonaceous seed layer are shown to produce polarised photoluminescence in prescribed directions and at specific wavelengths. Photoluminescence emerges preferentially along the grating normal and in the ±1 diffraction directions, at wavelengths in the range of 560 to 700 nm when pumped at 532 nm, and with a *p*-polarisation. Photoluminescence lifetime measurements of CDs on gratings reveal a Purcell factor of about 80. These properties emerge because the CDs preferentially decay onto SPPs supported by the grating. Salient aspects of the experiments were successfully modelled via computational electromagnetics to very strong agreement. The ability to localise and form carbon dots *in situ* on nanostructured surfaces, and then control their emission characteristics, opens new possibilities for biosensing, inexpensive light sources, and quantum optics.

Acknowledgments

This work was supported by the Natural Sciences and Engineering Research Council of Canada.

References

[1] Walia, J., Rashid, S., Killaire, G., Weck, A., Berini, P., "Reconfigurable carbon quantum emitters from CO_2 gas reduced via surface plasmons," Optica 8, 708-709 (2021)

[2] Walia, J. *et al.*, "Surface plasmons on silver gratings transform pyrolytic carbon into luminescent graphitized carbon dots," J. Chem. Phys. 161, 144702 (2024)

[3] Amiri Naeini, M. S., Walia, J., Mayoral-Astorga, L.-A., Choi, H. W., Weck, A., Berini, P., "Surface plasmon enhanced photoluminescence of carbon dots formed in-situ on silver gratings," submitted

[4] Walia, J., Rashid, S., Variola, F., Berini, P., "Focussed Helium Ion Beam Exposure of Polymethylmethacrylate: Positive or Negative Tone Images, Polyenes, and Fluorescent Carbon Layers," Adv. Eng. Mat. 2201707 (2023)

Advancing Machine Learning-Assisted Quantum Photonic Device Design and Optimization

Alexander V. Kildishev[1], Vladimir M. Shalaev[1], Alexandra Boltasseva[1], Yuheng Chen[1], Vaishnavi Iyer[1], Pranshu Maan[1]
[1]Birck Nanotechnology Center,
Elmore Family School of Electrical and Computer Engineering, Purdue University, West Lafayette, IN 47906
*Corresponding author: kildishev@purdue.edu

***Abstract*—Machine learning provides a unifying framework for high-dimensional forecasting of quantum coherence and photonic design. We use anticipatory modelling to mitigate spectral diffusion in solid-state emitters, significantly reducing spectral shifts. Combined with advancements in surrogate-based inverse design for the rapid co-optimization of emitter-circuit interfaces, we pave the way for robust, multiplexed quantum networks.**

***Keywords*— deep learning; quantum sensing; nanophotonics; inverse design**

I. Methods

To mitigate environmental dephasing in quantum emitters and ensure joint optimization of emitters and circuitry under realistic fabrication constraints, we use statistical machine learning to map slowly varying environmental noise. By analyzing sparse spectral measurements, our framework finds hidden temporal correlations within decoherence channels, enabling the internal prediction of unseen spectral diffusion trajectories across diverse solid-state systems, including nitrogen vacancy centers and quantum-dot spin qubits. This rapid cooptimization effectively bypasses the high-dimensional bottlenecks of traditional full-wave simulations. This can be further corroborated with the use of surrogate-based inverse design techniques to more efficiently traverse the high-dimensional landscape associated with this problem.

II. Results and Conclusion

This feed-forward stabilization mitigates environmental decoherence, reducing spectral shifts by average factors of 2.32 to 20.19 depending on emitter stability. Ultimately, this predictive framework provides a robust, scalable pathway for multi-node synchronization in quantum communication, computation, and sensing networks.

Acknowledgments

These works are supported by the US Department of Energy, Office of Science, National Quantum Information Science Research Centers, Quantum Science Center, the Center for Nanophase Materials Sciences (CNMS), Office of Science User Facility at Oak Ridge National Laboratory, the QuPIDC, an Energy Frontier Research Center, Basic Energy Sciences (BES), under the award number DE-SC0025620, the Elmore ECE Emerging Frontiers Center 'The Crossroads of Quantum and AI', and National Science Foundation (NSF) award DMR2323910.

References

[1] P. Maan, Y. Chen et al., arXiv preprint, arXiv:2508.02638 (2025).
[2] M. Bezick et al., Adv. Opt. Mater., e00249 (2026).

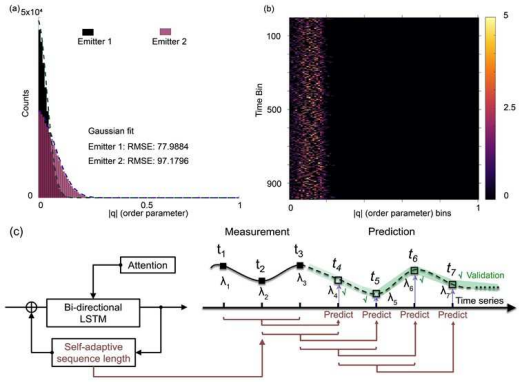

Fig. 1. Measured decoherence profiles for two distinct solid-state emitters, paired with the schematic of the statistical model used for anticipatory spectral prediction.

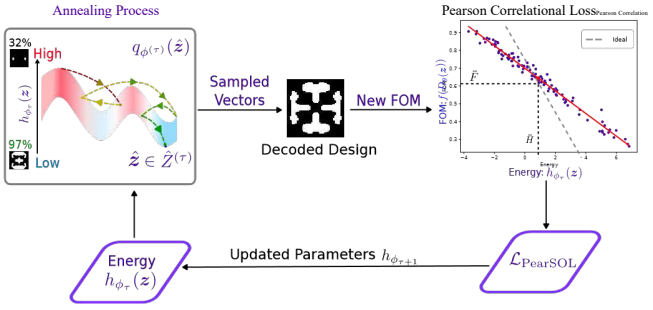

Fig. 2. Schematic of the surrogate-assisted generation process, which iteratively optimizes physical device layouts by correlating predicted and actual simulated spectral efficiencies.

From Design to Fabrication: Limits & Manufacturing Tolerances in Optical Metasurfaces and Meta-Modulators

Sonia Freddi[1], Alfonso Nardi[2], Michael Scalora[3], Agostino Di Francescantonio[2], Sofia Martins[4], Johann Osmond[4], Attilio Zilli[2], Marco Finazzi[2], Michele Celebrano[2], Maria Antonietta Vincenti[3], Monica Bollani[1*]

[1]Institute of Photonic and Nanotechnology (IFN) - Consiglio Nazionale delle Ricerche (CNR), LNESS Laboratory, Como – Italy
[2]Department of Physics, Politecnico di Milano, Piazza Leonardo da Vinci 32, 20133 Milano – Italy

[3]Department of Information Engineering, University of Brescia, Via Branze 38, 25123 Brescia – Italy
[4]ICFO-Institut de Ciencies Fotoniques, Barcelona – Spain

*Corresponding author: monica.bollani@cnr.it

***Abstract*— The study tackles making q-BIC metasurfaces reliably manufacturable, focusing on EBL and silicon ICP-RIE constraints. It compares continuous and pseudo-Bosch etching by etch rate, sidewall angle, and roughness. It also models allowable fabrication tolerances, linking geometric deviations to Q, efficiency, and uniformity, and provides practical guidelines to improve design robustness and process stability.**

***Keywords*— metamaterials, EBL, pseudo-Bosch etching, fabrication tolerance.**

I. Introduction

Planar optics is enabling a rapid miniaturization and functional integration of optical systems, with metasurfaces emerging as a key platform to replace or augment conventional bulk components. Metasurfaces exploit arrays of subwavelength nanostructures ("meta-atoms") patterned on a surface to tailor optical wavefronts and diffraction with high design freedom, offering compact and lightweight solutions for advanced beam shaping and polarization control. In particular, the ability to engineer wavelength- and polarization-selective responses within deeply subwavelength thicknesses makes dielectric metasurfaces attractive for applications ranging from high-efficiency imaging and metalenses to sensing and nonlinear and quantum nanophotonics [1,2]. Among the most compelling metasurface concepts, symmetry-protected bound states in the continuum (BICs) provide optical modes with theoretically infinite quality (Q) factors. These states are "dark" because symmetry forbids coupling to external radiation channels. By introducing a controlled, small symmetry breaking, a BIC can evolve into a quasi-BIC (q-BIC) with a finite Q factor, allowing external excitation while preserving strong field confinement. Importantly, when a broken-symmetry structure is pumped at the q-BIC wavelength, the electromagnetic energy stored in the resonator can increase dramatically, enabling significant enhancement of resonant light–matter interaction and nonlinear optical processes. Achieving and reproducing the targeted q-BIC response, however, requires tight control of the nanoscale geometry, since the Q factor and the radiative coupling strength are highly sensitive to the exact magnitude and uniformity of the asymmetry [3].

II. Results and Discussion

This work addresses the practical challenge of translating q-BIC metasurface designs into reliable nanofabrication processes. We present a fabrication-oriented study focused on the constraints introduced by electron-beam lithography (EBL) and silicon dry etching, with emphasis on process-induced deviations that directly impact metasurface performance [4]. In many dielectric metasurfaces, the local optical response (phase and often amplitude/polarization) is mapped to geometry through propagation, geometric, or resonant mechanisms. Consequently, even small departures from the nominal meta-atom cross-section (such as sidewall taper, corner rounding, or critical-dimension bias) can produce systematic phase errors and non-uniform transmission. For resonant designs (including q-BIC metasurfaces), such deviations may shift the resonance conditions, reduce Q, and degrade contrast and efficiency. Furthermore, aspect-ratio dependent etching can introduce spatially varying depth non-uniformities across dense patterns, degrading the designed optical functionality. Finally, sidewall and surface roughness contributes to parasitic scattering and loss, lowering efficiency and broadening the point-spread function in imaging applications, while also reducing reproducibility.

Within silicon nanofabrication, fluorine-based inductively coupled plasma reactive-ion etching (ICP-RIE) chemistries are widely adopted due to their high etch rates and compatibility with standard process flows. Two distinct strategies are commonly used. In continuous mixed-gas processes (e.g., SF_6/CHF_3), etching and passivation occur simultaneously: fluorine radicals promote silicon removal while fluorocarbon fragments form an inhibiting layer, and anisotropy arises from balancing chemical etching with ion-assisted inhibitor removal at the feature bottom. In Bosch-type processes, etching and passivation are time-multiplexed through alternating steps, typically an SF_6 etch step followed by fluorocarbon deposition (e.g., C_4F_8). Bosch-like approaches can enhance sidewall protection and anisotropy, especially for high aspect ratios, but may introduce cyclic artifacts and roughness (scalloping) and increased sensitivity to timing and transport effects. Despite the widespread adoption of both methods, direct benchmarking under closely matched ICP-RIE conditions remains limited for dense nanoscale patterns with pitches and lateral dimensions on the order of a few hundred nanometres—precisely the regime most relevant for state-of-the-art metasurfaces. At these scales, radical transport limitations, local depletion, and polymer build-up/removal dynamics become strongly geometry-dependent, and recipes optimized for microscale features may not translate reliably to nanostructured layouts.

Here we report a comparative study of continuous and pseudo-Bosch ICP-RIE processes for etching EBL-defined silicon nanostructures. Specifically, we compare a continuous SF_6/fluorocarbon-based strategy with a pseudo-Bosch SF_6/C_4F_8 approach. To isolate the influence of etch strategy and passivation chemistry, we keep key operating parameters comparable across the two processes, including substrate temperature and chamber pressure. We evaluate etch rate, sidewall angle, and surface/sidewall roughness as primary performance metrics, as these quantities directly determine the effective optical response and the achievable Q factor in q-BIC metasurfaces (figure 1). In addition to benchmarking process, we model the admissible fabrication tolerances required to preserve q-BIC functionality. The optical response of non-ideal metasurfaces is simulated as a function of geometrical parameters affected by fabrication errors, enabling a quantitative link between process outcomes and resonant performance. By correlating fabrication-induced deviations with changes in the resonant response, we provide practical guidelines for improving both design robustness and process stability.

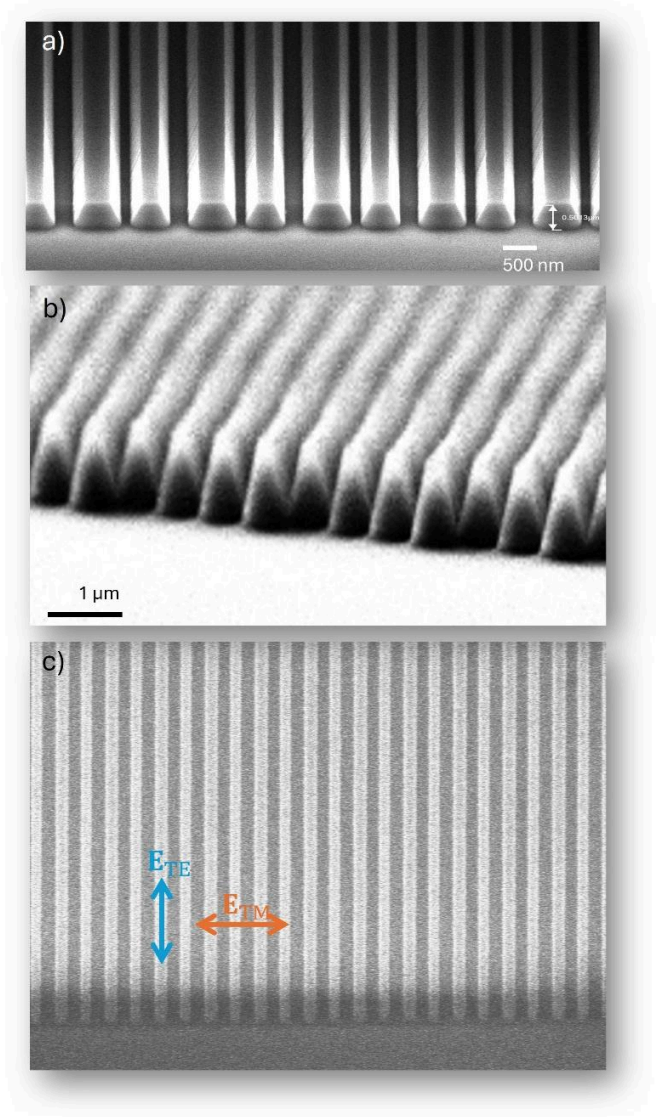

Fig. 1 (a,b) SEM images of metasurfaces fabricated with non-optimized etching processes, resulting in non-vertical sidewall profiles. (c) SEM image of the optimized asymmetric metasurfaces in amorphous silicon.

ACKNOWLEDGMENTS

This work is supported by the PRIN 2022 "PILLARS" (2022YJ5AZH).

REFERENCES

[1] W. T. Chen, A. Y. Zhu, F. Capasso, "Flat optics with dispersion-engineered metasurfaces." Nature Reviews Materials 5, 604–620 (2020).
[2] A. Arbabi, A. Faraon, "Advances in optical metalenses." Nature Photonics 17, 16–25 (2023).
[3] Fagiani, L. et al., "Dual-Mode Polarization Control with Quasi-Bound States in the Continuum", Adv. Optical Mater., 2301456, 2023.
[4] Fagiani, L. et al., "Modelling and nanofabrication of chiral dielectric metasurfaces", Micro and Nano Engineering 19,100187, 2023.

Dynamically Reconfigurable Waveguide-Fed Metasurface Apertures: From Theory to Application

David R. Smith[1,2]

[1]Department of Electrical and Computer Engineering, Duke University, USA
[2]Center for Metamaterials, Duke University, USA
*Corresponding author: drsmith@duke.edu

***Abstract*— Dynamically reconfigurable metasurfaces represent an early and ongoing commercialization success. The metasurface architecture is versatile and can be readily integrated into beam-steering systems across the electromagnetic spectrum. We describe here the fascinating electromagnetic properties of the metasurface elements and how they drive the overall aperture performance of metasurface devices.**

***Keywords*— metamaterials, metasurfaces, beam-steering, phased arrays, electromagnetics, small apertures.**

Optical Nonlinearities in Materials with Nonlocal Response

Gonzalo Álvarez-Pérez[1,*], Huatian Hu[1], Cristian Ciracì[1]

[1]Istituto Italiano di Tecnologia, Center for Biomolecular Nanotechnologies, Via Barsanti 14, 73010 Arnesano, Italy

[*]Corresponding author: gonzalo.alvarezperez@iit.it

***Abstract*— Heavily doped semiconductors and polar dielectrics enable strong mid-infrared nonlocal and nonlinear light–matter interactions. Hydrodynamic carriers and bulk plasmons enhance Kerr nonlinearities and optical bistability in tunable nanoantennas and hybrid waveguides. In polar dielectrics, anharmonic phonons generate intrinsically nonlinear phonon–polariton responses that can be strongly amplified in nanostructures.**

***Keywords*— third harmonic generation, Kerr, hydrodynamic theory, heavily doped semiconductors, phonon polaritons.**

Material platforms that support strong nonlocal and nonlinear light–matter interactions are central to the development of mid-infrared (mid-IR) photonic technologies. Among these, heavily doped semiconductors and polar dielectrics are particularly promising systems. They offer high electromagnetic confinement, relatively low optical losses, and tunability of their collective excitations, positioning them as attractive alternatives to noble metals and traditional semiconductors for nonlinear and active photonic applications. In both material classes, collective electronic or ionic excitations give rise to pronounced nonlocal and nonlinear optical responses. In heavily doped semiconductors, the high density of free carriers leads to strong spatial dispersion and nonlinearities that can be accurately described using hydrodynamic theory (HT), which extends the classical Drude model by incorporating quantum pressure, carrier convection, and carrier-density gradient effects. Within this framework, doped semiconductors are predicted to exhibit free-electron nonlinearities exceeding those typically observed in metals and conventional dielectrics [1]. These predictions have been validated by experiments on third-harmonic generation (THG) in InGaAs nanoantennas, which demonstrated that free-carrier nonlinearities can dominate over lattice-related $\chi^{(3)}$ contributions [2]. A key manifestation of nonlocality in doped semiconductors is the existence of longitudinal bulk plasmons—charge-density oscillations that propagate through the bulk and exhibit intrinsic nonlinear behavior. These modes can strongly couple to localized electromagnetic resonances. For instance, coupling longitudinal bulk plasmons to metallic gap plasmons in nanopatch antennas enables strong enhancement of Kerr nonlinearities and ultralow-threshold optical bistability (≈1 mW/μm) [3]. Integration into metal–oxide–semiconductor architectures allows dynamic control of the free-carrier density, enabling large plasma-frequency shifts (0.89 μm/V) and reducing bistability thresholds down to 10 μW [4]. Beyond resonant nanoantennas, nonlocal nonlinearities also provide opportunities for integrated photonics. In all-semiconductor platforms, hybrid waveguides incorporating doped plasmonic layers support long-range hybrid modes with record-high Kerr nonlinearities [5]. When embedded in interferometric architectures, these waveguides enable large power-dependent modulation depths, relevant for all-optical modulation. In polar dielectrics, nonlocal nonlinearities arise from the anharmonic dynamics of optical phonons, where lattice vibrations coupled through long-range Coulomb interactions produce dispersive and intrinsically nonlinear phonon–polariton responses. In nanostructures made from such polar dielectrics, phonon–polariton resonances can similarly amplify nonlinear optical effects through extreme field confinement.

Acknowledgments

G. Á.-P. acknowledges support from the European Union (Marie Skłodowska-Curie Actions, grant agreement No. 101209198). Views and opinions expressed are those of the authors only and do not necessarily reflect those of the European Union. Neither the European Union nor the granting authority can be held responsible for them.

References

[1] F. De Luca, M. Ortolani, C. Ciracì. *Phys. Rev. B* 103, 115305 (2021)

[2] A. Rossetti, H. Hu, T. Venanzi, A. Bousseksou, F. De Luca, T. Deckert, V. Giliberti, M. Pea, I. Sagnes, G. Beaudoin, P. Biagioni, E. Baù, S. A. Maier, A. Tittl, D. Brida, R. Colombelli, M. Ortolani, C. Ciracì. *Light Sci. Appl.* 14, 192 (2025)

[3] H. Hu, G. Álvarez-Pérez, T. O. Otomalo, C. Ciracì. *ACS Photonics* 11, 4812 (2024)

[4] H. Hu, G. Álvarez-Pérez, A. Valletta, M. Pea, M. Ortolani, C. Ciracì. *Phys. Rev. Appl.* 24, 044006 (2025)

[5] G. Álvarez-Pérez, H. Hu, F. Huang, T. O. Otomalo, M. Ortolani, C. Ciracì. *npj Nanophotonics* 2, 33 (2025)

Useful and detrimental thermal radiation in near-field energy-conversion devices such as thermophotovoltaics

Thomas Châtelet[1], Mathieu Thomas[1], Wissal Sghaier[1], Julien Legendre[1], Yuji Oka[2], Yusei Takai[2], Zhen Liu[2], Makoto Shimizu[2], Olivier Merchiers[1], P.-Olivier Chapuis[1]*

[1]CETHIL-CNRS, INSA Lyon, France
[2]Tohoku University, Sendai, Japan
*Corresponding author: olivier.chapuis@insa-lyon.fr

***Abstract*— We report on three different types of near-field energy-conversion devices, namely thermophotovoltaics, thermophotonics and thermal rectennae. All of them involve partial conversion of thermal radiation into electrical power above a certain energy threshold, namely the bandgap for the two first types of devices, and detrimental thermal-radiation exchange below this threshold. We discuss how to optimize the conversion and reduce the parasitic transfer by selecting an appropriate geometry and structuring the surfaces.**

***Keywords* — Thermophotovoltaics, LED, thermophotonics, thermal rectennae, phonon-polariton, multilayers, grating.**

I. Introduction

Energy-conversion devices based on light, such as photovoltaics or rectennae (see Fig. 1), can benefit from an increase of the radiative power transfer when emitter and converting device are approached at a distance below the wavelength in the photon tunneling regime. In particular, thermal-radiation based devices are not anymore bound by Planck's law and the blackbody limit in this regime. While this distance decrease provides a strong gain in potential power output, an issue is that the flux which is not converted into electrical power can lead to strong heating of the converting device and therefore to a decrease of the efficiency. We analyze the evolution of the useful and detrimental flux transfer as a function of distance for structures involving multilayers and grating-based surfaces.

II. Methods And Results

We consider first thermophotovoltaic devices, which involve a hot radiating emitter and a cold photovoltaic cell designed for conversion of mid-infrared radiation. Low-energy bandgap is required for optimum conversion [1]. Phonon-polariton have been long proposed for increased radiative exchange above bandgap, but their experimental realization seems more complex than initially thought [2]. In addition, optimizing the geometries is required in order to observe significant conversion. We then consider thermophotonic devices [3-4], which in addition to the cell include an active emitter, namely a light-emitting diode (LED) which is externally biased in order to emit light by electroluminescence in a narrow energy band just above bandgap. Very large efficiency is predicted in optimum conditions, i.e. with quantum efficiency close to unity. However, detrimental transfer below bandgap is also a severe issue, mostly due to the fact that III-V materials possess phonon-polaritons at low frequencies. Thermophotonic devices can be used as waste-heat harvesters but also as refrigerating devices [5]. Finally, we discuss thermal rectennae [6-7], the mechanism of which is based on photon-assisted electron tunneling across thin oxide layers. Whether the emitter radiative properties should be matched to the oxide layer or not is still an open question, especially in near field.

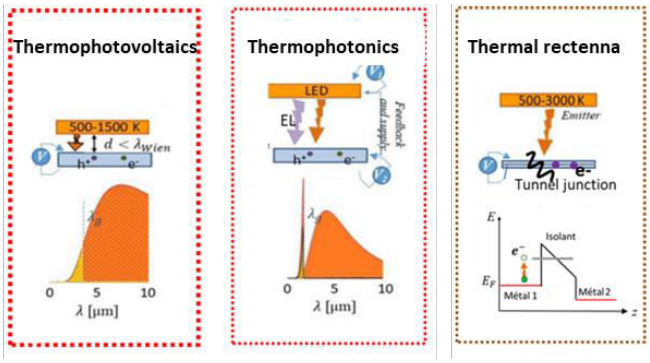

Fig. 1 Three types of radiative energy converters that can be used in near field

Fluctuational electrodynamics by means of Green's tensor and Rigourous Coupled Wave analysis (RCWA) [8] are used for the electromagnetic computations. Electrical simulations are made either in 0D (detailed balance) [4-5], by 1D analytical expressions or by using a 1D solver of the drift-diffusion equations including high carrier injection and thermionic-field emission in heterostructures [9].

III. Conclusion

We have addressed three types of near-field radiative energy converters by coupling electromagnetic and charge-carrier simulations. This allowed to study the impact of the configurations on the optical properties in the infrared and therefore their impact on power output and efficiency.

Acknowledgments

This work was supported by the EU projects TPX-Power and OPTAGON, and by ANR project STORE. We thank discussion with B. Roux and R. Vaillon.

References

[1] B. Roux, C. Lucchesi, J.-P. Perez, P.-O. Chapuis, and R. Vaillon, "Main performance metrics of thermophotovoltaic devices: analyzing the state of the art", Journal of Photonics for Energy, vol. 14, p. 042403, 2024.

[2] C. Lucchesi, D. Cakiroglu, J.-P. Perez, T. Taliercio, E. Tournié, P.-O. Chapuis, and R. Vaillon, "Near-field thermophotovoltaic conversion with high electrical power density and efficiency above 14%", Nano Letters, vol. 21, p. 4524, 2021.

[3] N.-P. Harder and M.A Green, "Thermophotonics", Semiconductor Sciance and Technology, vol.. 18, p. S270, 2003.

[4] J. Legendre and P.-O. Chapuis, "Operating conditions and thermodynamic bounds of dual radiative heat engines,", Physical Review Applied, vo. 23, p. 034023, 2025.

[5] T. Châtelet, J. Legendre, O. Merchiers, and P.-O Chapuis," Performances of far- and near-field thermophotonic refrigeration devices from the detailed-balance approach", Journal of Applied Physics, vol. 138, p. 173106, 2025.

[6] J. Shank, E.A. Kadlec, R.L. Jarecki, A. Starbuck, S. Howell, D.W. Peters, and P.S. Davids, "Power Generation from a Radiative Thermal Source Using a Large-Area Infrared Rectenna", Physical Review Applied, vol. 9, p. 054040, 2018.

[7] D. Matsuura, M. Shimizu, Z. Liu, and H. Yugami, "Optical rectenna with wide wavelength coverage from a hollow resonator coupled with a metal–insulator–metal tunnel diode", Applied Physics Express, vol. 15, p. 062001, 2022.

[8] K. Chen, B. Zhao, S. Fan, "MESH: A free electromagnetic solver for far-field and near-field radiative heat transfer for layered periodic structures", Computer Physics Communications, vol. 231, pp. 163-172, 2018.

[9] J. Legendre and P.-O. Chapuis, "CRESCENT-1D: A 1D solver of coupled charge and light transport in heterostructures for the design of near-field thermophotonic engines", IEEE Transactions on Electron Devices, vo. 72, p. 1211, 2025.

Thin-film lithium niobate channel waveguides: numerical analysis and perturbational modelling

Manfred Hammer*, Behnood Taheri, Henna Farheen, Jens Förstner

Theoretical Electrical Engineering & Institute for Photonic Quantum Systems (PhoQS), Paderborn University, Paderborn, Germany

*Corresponding author: manfred.hammer@uni-paderborn.de

***Abstract*—The crystal configuration, symmetry, and the on-chip orientation affect the modal properties of anisotropic waveguides based on TFLN / LNOI technology. Beyond the direct numerical analysis, the hybridization of guided modes and the related conversion of polarization can be understood, also fully quantitatively, in terms of coupled mode theory.**

***Keywords*—thin-film lithium niobate, lithium niobate on insulator, anisotropic waveguides, mode hybridization, numerical analysis, perturbational modelling.**

I. TFLN / LNOI PHOTONIC CIRCUITRY

Advantageous nonlinear and electrooptic properties recommend thin-film lithium niobate (TFLN, [1], [2]) or lithium niobate on insulator (LNOI, [3], [4]) as a platform for integrated optical components. Rib- or strip waveguides are prepared from TFLN slabs of standard thicknesses, often with slanted sidewalls, as illustrated in Fig. 1.

Fig. 1. X-cut TFLN strip waveguide, schematic (a) and cross section (b), crystal and channel coordinates $\{X, Y, Z\}$ and $\{x, y, z\}$; the on-chip orientation of the channel is given by the angle θ between the channel axis z and the crystal Y-axis. Parameters: core thickness $t = 0.6\,\mu$m, cover thickness $c = 1\,\mu$m, channel top width w, sidewall angle $\phi = 30°$, material parameters [5], [6] for SiO_2 (n_s, n_c) and TFLN media ($\hat{\epsilon}_f$), with air cover (n_a), at a wavelength of $1.55\,\mu$m.

In this invited contribution, we review some of our recent results on the rigorous and perturbative computational modelling of the guidance properties of TFLN waveguides [7], as well as certain analytical results [8], [9] that are instrumental for their understanding. The core anisotropy affects the waveguide properties for all crystal configurations, where the channel orientation only plays a role for X-cut samples. Hence, also with a view to the effects of mode hybridization and polarization conversion, here we pick examples of X-cut strip waveguides at a typical telecommunication wavelength, for realistic cross section shapes and material parameters [5], [6].

II. NUMERICAL ANALYSIS

In the first place, we compute effective index levels and mode profiles by rigorous numerical means on the basis of the JCMwave finite element solvers [10], for the full tensor permittivity of the LN medium. Respective reference results [7] will be briefly discussed. As an example, Figs. 2 and 3 show the dependence of modal effective indices N on the channel orientation angle θ, and on the channel width w. Largely analytical results for 1-D TFLN slab modes [8], [9] establish rigorous effective index intervals for the numerical 2-D mode analysis of the channel waveguides. For the present structures with $y \leftrightarrow -y$ mirror symmetry, the guided modes can be (roughly) sorted into one of *three* symmetry classes ("even", "odd", or "complex", [7]); these classes are distinguished by different marker symbols in Figs. 2, 3. Modal polarization is characterized through a polarization ratio Π, given by the relative TE-related contribution to the modal power [7], and indicated in the figures through the marker color.

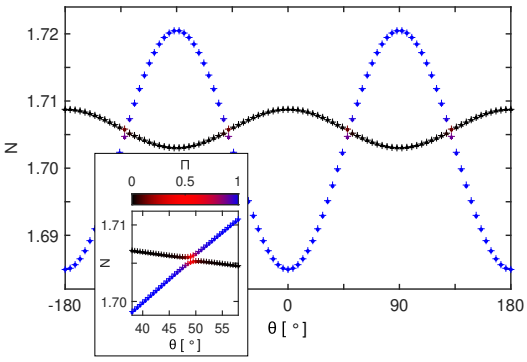

Fig. 2. Effective indices N of guided modes as a function of channel angle θ, for waveguides with a top width $w = 0.2\,\mu$m. Markers (overlapping), $+$: direct computations; other symbols: CMT approximation; marker colors indicate the polarization ratio Π, blue: TE-like, black: TM-like, red: intermediate.

III. PERTURBATIONAL MODELLING

Alternatively, the effects of the core anisotropy can be adequately modeled in terms of coupled mode theory (CMT, [11], [12], [7]). Numerical solutions for simpler channels with closeby scalar permittivity couple through the anisotropic parts of the full permittivity tensor. Fig. 2 compares respective results

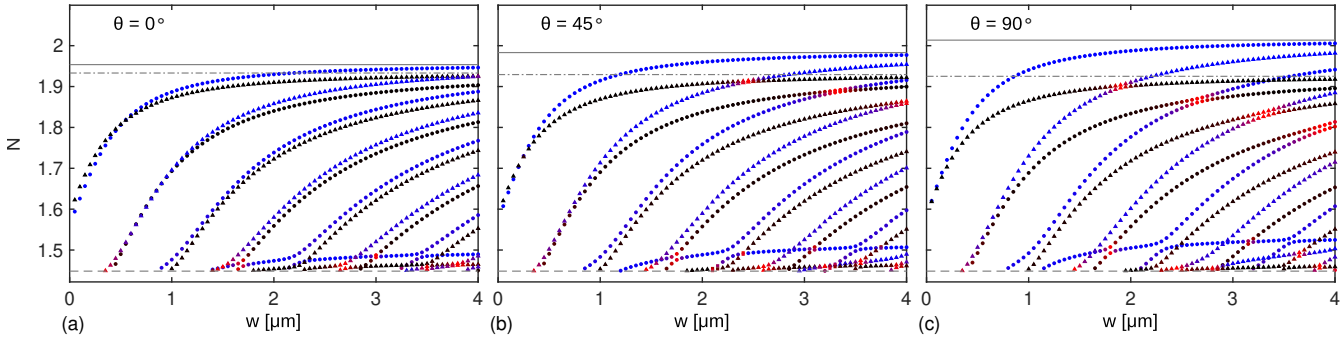

Fig. 3. Effective indices N of guided modes, as a function of channel top width w, for X-cut strip waveguides as in Fig. 1, oriented at angles $\theta = 0°$ (a), $\theta = 45°$ (b), and $\theta = 90°$ (c). Marker symbols distinguish types of $y \leftrightarrow -y$ mirror symmetry; marker colors relate to mode polarization (cf. Fig. 2, inset). Thin gray lines indicate intervals for effective indices, and their limits at large w, determined through 1-D mode analysis of related TFLN slabs.

for a scan over the waveguide orientation, for a narrow TFLN strip waveguide. Curves for effective index levels predicted by direct numerical computation, and through the CMT approximation, are in excellent agreement.

Further, good approximations of the true vectorial mode profiles are obtained in the form of CMT supermodes. Fields can become pronouncedly hybrid around avoided crossings of dispersion curves. As an example, we select parameters from the inset of Fig. 2. At $\theta = 49.25°$, the channel supports a pair of near degenerate, strongly hybrid modes with the essentially complex profiles shown in Fig. 4. Superimposing both fields with amplitudes of equal magnitude and sign leads to a TM-like field with a dominant E_x-component, while a superposition with amplitudes of opposite signs results in a TE-like profile with major E_y component. Upon balanced excitation, these modes cause full periodic TE-to-TM conversion of polarization with a half-beat length of about 1 mm.

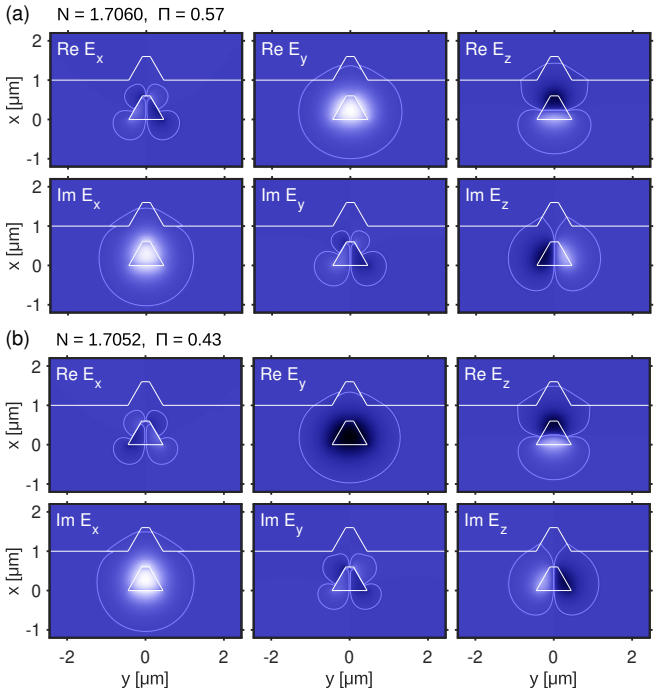

Fig. 4. Complex electric profile components of the two hybrid fundamental guided modes supported by a channel as in Fig. 1, for $w = 0.2\,\mu$m and $\theta = 49.25°$; colormap: black-negative, blue-zero, white-positive.

Acknowledgments

Financial support from the German Research Foundation (Deutsche Forschungsgemeinschaft DFG, project 231447078–TRR 142, subproject B06) and from the Ministry of Culture and Science of the state of North Rhine-Westphalia (project PhoQC) is gratefully acknowledged.

References

[1] D. Zhu, L. Shao, M. Yu, R. Cheng, B. Desiatov, C. J. Xin, Y. Hu, J. Holzgrafe, S. Ghosh, A. Shams-Ansari, E. Puma, N. Sinclair, C. Reimer, M. Zhang, and M. Lončar, "Integrated photonics on thin-film lithium niobate," *Advances in Optics and Photonics*, vol. 13, no. 2, pp. 242–352, 2021.

[2] A. Boes, L. Chang, C. Langrock, M. Yu, M. Zhang, Q. Lin, M. Lončar, M. Fejer, J. Bowers, and A. Mitchell, "Lithium niobate photonics: Unlocking the electromagnetic spectrum," *Science*, vol. 379, no. 6627, p. eabj4396, 2023.

[3] G. Poberaj, H. Hu, W. Sohler, and P. Günter, "Lithium niobate on insulator (LNOI) for micro-photonic devices," *Laser & Photonics Reviews*, vol. 6, no. 4, pp. 488–503, 2012.

[4] A. Boes, B. Corcoran, L. Chang, J. Bowers, and A. Mitchell, "Status and potential of lithium niobate on insulator (LNOI) for photonic integrated circuits," *Laser & Photonics Reviews*, vol. 12, no. 4, p. 1700256, 2018.

[5] L. Ebers, A. Ferreri, M. Hammer, M. Albert, C. Meier, J. Förstner, and P. R. Sharapova, "Flexible source of correlated photons based on LNOI rib waveguides," *Journal of Physics: Photonics*, vol. 4, no. 2, p. 025001, 2022.

[6] ——, "Corrigendum: Flexible source of correlated photons based on LNOI rib waveguides (2022 J. Phys. Photonics 4 025001)," *Journal of Physics: Photonics*, vol. 5, no. 2, p. 029501, 2023.

[7] M. Hammer, S. S. Khan, B. Taheri, H. Farheen, and J. Förstner, "TFLN channel waveguides of rib and strip type: properties of guided modes," *Optics Continuum*, vol. 4, no. 10, pp. 2356–2385, 2025.

[8] M. Hammer, H. Farheen, and J. Förstner, "Guided modes of thin-film lithium niobate slabs," *Optics Continuum*, vol. 3, no. 11, pp. 2024–2043, 2024.

[9] M. Hammer, "TFLNS — mode solver for three-layer thin film lithium niobate slab waveguides," https://www.siio.eu/tflns.html.

[10] JCMwave GmbH, Berlin, Germany; https://www.jcmwave.com.

[11] C. Vassallo, *Optical Waveguide Concepts*. Amsterdam: Elsevier, 1991.

[12] M. Lohmeyer, N. Bahlmann, O. Zhuromskyy, H. Dötsch, and P. Hertel, "Phase-matched rectangular magnetooptic waveguides for applications in integrated optics isolators: numerical assessment," *Optics Communications*, vol. 158, pp. 189–200, 1998.

Unconventional Geometric Phases in Optics

Shubo Wang[1,*]

[1]Department of Physics, City University of Hong Kong, Hong Kong, China
*Corresponding author: shubwang@cityu.edu.hk

***Abstract*—We present two advances expanding the geometric phase paradigm. We show that the Pancharatnam-Berry phase can arise from the transverse spin of surface waves and enable on-chip wavefront manipulation. Furthermore, we report a new type of geometric phase—the Riemann-Silberstein phase—induced by SU(4) evolution in 4D polarization space.**

***Keywords*— geometric phase, Berry phase, metasurfaces**

The Pancharatnam-Berry (PB) phase arises from polarization evolution on the Poincaré sphere and has transformed nanophotonics through optical metasurfaces. However, the standard narrative of the PB phase is far from complete, as the conventional framework addresses only the 2D polarization space of free-space propagating waves. In this talk, I will introduce our recent works that push the boundaries of geometric phase optics. We begin by extending the conventional PB phase to the domain of surface/guided waves carrying a transverse spin, and then proceed to fundamentally generalize the concept into a 4D polarization framework.

I will first introduce our work about on-chip optical wavefront shaping by transverse-spin-induced PB phase [1]. The conventional PB phase relies on the longitudinal spin of free-space waves. However, in the realm of integrated photonics, we deal with surface plasmon polaritons and guided waves. These waves carry an intrinsic transverse spin that is locked to their propagation direction (known as spin-momentum locking). We ask a fundamental question: Can this intrinsic transverse spin induce a geometric phase similar to the longitudinal spin? By utilizing a metasurface composed of periodic metallic nano-bars on a metal substrate, we show that rotation of these meta-atoms can give rise to a geometric phase covering the full 2π range. The physical origin is attributed to the transverse spin of the evanescent field and its SU(2) polarization evolution mediated by the meta-atoms. This transverse-spin-induced PB phase enables us to design on-chip metasurfaces that steer and focus surface plasmons with high efficiency. This work bridges the gap between free-space geometric phase and surface/guided waves, offering a new mechanism for compact light manipulation and facilitating the exploration of near-field topological phenomena [2]. The mechanism can be generalized to other classical wave systems, enabling the observation of the PB phase in acoustic waves [3] and water waves [4].

In the second part of the talk, I will introduce our work on the Riemann-Silberstein (RS) geometric phase in 4D polarization space [5]. In the conventional 2D framework, the PB phase emerges from SU(2) evolution of electric field polarization. However, electromagnetic waves comprise both electric and magnetic fields, and the complete polarization state spans a 4D space encompassing electric, magnetic, and hybrid electric-magnetic polarizations. Thus, the conventional 2D framework cannot capture all degrees of freedom in the complete electromagnetic polarization. We reveal that SU(4) polarization evolution within the 4D polarization space can give rise to a new type of geometric phase, termed the RS phase, independent of the PB phase. The RS phase is governed by the hybrid electric-magnetic polarization and can emerge in arbitrarily polarized light. We show that the complementary PB and RS phases enable a high-dimensional geometric framework for understanding and controlling phase shifts across interfaces. Leveraging this framework, we design and realize a new class of geometric-phase metasurfaces that can achieve high-dimensional wavefront manipulation.

In summary, we introduce in this talk our recent efforts in expanding the horizon of geometric phase optics, which include generalizing the PB phase to surface/guided waves carrying an intrinsic transverse spin and exploring new geometric phases in the 4D electromagnetic polarization space. These results uncover a deeper, unified geometric framework for light-matter interactions in broad physical systems.

ACKNOWLEDGMENTS

The works in this talk were supported by the Research Grants Council of the Hong Kong Special Administrative Region, China (AoE/P-502/20, CityU11301820, CityU11306019, CityU11308223) and National Natural Science Foundation of China (12322416, 11904306).

REFERENCES

[1] W. Xiao and S. Wang, "On-chip optical wavefront shaping by transverse spin induced Pancharatnam-Berry phase," Optics Letters 49, 1915 (2024).
[2] T. Fu, R.-Y. Zhang, S. Jia, C. T. Chan, and S. Wang, Near-field spin Chern number quantized by real-space topology of optical structures, Physical Review Letters 132, 233801 (2024).
[3] W. Xiao, W. Kuang, S. Huang, S. Liang, D. P. Tsai, and S. Wang, "Acoustic Pancharatnam-Berry Geometric Phase," arXiv:2408.03513 (2024).
[4] W. Xiao, S. Jia, T. Fu, and S. Wang, "Water-wave Pancharatnam-Berry phase induced by 4D spin-orbit state evolution," Advanced Science 13, e15337 (2026).
[5] Y. Cheng, Y.-S. Zeng, W. Xiao, T. Fu, J. Wu, G.-B. Wu, D. P. Tsai, and S. Wang, "Riemann-Silberstein geometric phase in 4D polarization space," arXiv:2510.09112 (2025).

Adaptive photonics with phase-change materials: multiphysics modelling and design

Dmitry N. Chigrin[1,2,*]

[1]I. Physikalisches Institut (1A), RWTH Aachen University, Aachen, Germany
[2]AMO GmbH, Aachen, Germany
*E-mail: chigrin@physik.rwth-aachen.de

Phase change materials are materials in which phase transitions can be induced rapidly and reversibly, resulting in significant changes in the physical properties of these materials. Here we report on our recent developments towards a multiphysics description of adaptive photonic components based on phase change materials.

High-Fidelity Fullwave Solvers and Reduced-Order Models for the Design of Complex Nanostructured Photonic Devices

Mahmoud Elsawy[1], Alexis Gobé[1], Stéphane Lanteri[1,*]

[1]Université Côte d'Azur, Inria, CNRS, LJAD, Sophia Antipolis, France
*Corresponding author: Stephane.Lanteri

***Abstract*—In this contribution, we review our recent works aiming at the development of high-fidelity fullwave solvers and reduced-order models for studying nanoscale light-matter interactions. Additionally, we also discuss ML-based inverse design strategies for shaping these interactions through optimization of geometrical features of nanostructures.**

***Keywords*— Discontinuous Galerkin, Proper Orthogonal Decomposition, Machine Learning, nanophotonics, plasmonics, high performance computing.**

I. Introduction

Modeling and simulation of nanoscale light-matter interactions is an important part of photonic device design. Moreover, harvesting and tailoring these interactions with the help of inverse design approaches is an increasingly considered objective of computational nanophotonics. An inverse design methodology is generally based on two ingredients: on the one hand, a numerical method for characterizing the optical performance of a given design of the photonic device at hand, which will be referred in the sequel as the numerical characterization method; on the other hand, a numerical optimization algorithm, which has to be compatible with the required number of design parameters and the computational cost of the evaluation of a single design with the numerical characterization method. In this contribution, we address this dual objective by first combining two main numerical ingredients: (1) a high-fidelity fullwave solver based on a high order Discontinuous Galerkin (DG) method for solving the system of time-domain or frequency-domain Maxwell equations in 3D coupled to appropriate differential models of physical dispersion in photonic materials and, (2) a machine learning-based (ML-based) global optimization techniques that belongs to the class of Bayesian optimization. This combined numerical methodology has been successfully applied to various problems relevant to nanophotonics and plasmonics. Yet, for the most challenging problems, the simulation cost of a high-fidelity DG-based fullwave solver can be a major drawback. Thus, in order to reduce the computational overhead when dealing with finite size structures, or when an inverse design study involves a macro-cell structures taking into account near-field coupling between nanostructures, we also explore the development of data-driven reduced-order models for time-domain electromagnetics and nanophotonics.

II. High-fidelity fullwave solvers

For the numerical modeling of nanoscale light-matter interactions with fullwave methods, popular numerical modeling approaches are either working in the time-domain regime in the framework of the FDTD (Finite Difference Time-Domain) method, or in the frequency-domain regime in the setting of the RCWA (Rigorous Coupled-Wave Analysis) or FE (Finite Element) methods. In order to deal with problems involving irregularly-shaped geometrical structures, and multiple scales in space and time (or frequency), we have extensively investigated during the last ten years the Discontinus Galerkin discretization framework [1] for developing both time-domain and frequency-domain fullwave methods tailored to differential models of nanophotonics and plasmonics. These methods, which are respectively referred as the Discontinuous Galerkin Time-Domain (DGTD) [2] and the Hybridized Discontinuous Galerkin Frency-Domain (HDGFD) [3] methods, are geometry-conforming as they are formulated on an unstructured locally refined mesh for the discretization of the computational domain, and high-order accurate by relying on a polynomial interpolation method for the approximation of the electromagnetic field components within each cell of the mesh. Moreover, our implementation of these fullwave methods for three-dimensional problems can leverage high performance computing systems, including hardware platforms with multiple GPUs.

III. Data-driver reduced-order models

A variety of physical systems occurring in nature and in engineering are usually described by partial differential equations (PDEs) whose numerical solution requires considerable computational effort, especially in the case of parameterized PDEs, which often need to be solved for a range of parameter values. Such a situation is for instance encountered when studying electromagnetic wave propagation problems in complex geometries for different input parameters including frequency, direction of the incident wave, geometric dimensions, as well as material properties, which are described by the system of time-domain Maxwell's equations. In this context, reduced-order modeling allows to construct simplifications of a high-fidelity model of a complex physical problem. The resulting lower fidelity (also referred as surrogate) model can

capture the salient features of the source model so that one can quickly study a system's dominant effects using minimal computational resources. The reduced basis (RB) method [4] is a widely used family of reduced-order modeling techniques. The Proper Orthogonal decomposition (POD) method is a poular example of RB method. The POD method begins with a set of snapshot vectors extracted from high-fidelity numerical simulations or experiments; the POD basis vectors are then obtained by an eigensystem of a correlation matrix generated by the snapshot matrix whose columns are the snapshot vectors. In the classical POD method, a ROM is created by projecting (Galerkin projection) the semi-discrete numerical scheme used for obtaining the snapshots onto a low-dimensional space spanned by the POD basis. This approach is often referred as an *intrusive* ROM technique since it requires having access to the formulatiom of the original numerical scheme. The alternative approach that avoids this constraint consists in defining an appropriate decoupling of the construction of the POD basis and the prediction of the solution in a purely data-driven workflow. As a result, one obtains a *non-intrusive* ROM technique with decoupled offline (training) and online (inference) phases. In a non-intrusive ROM, the reduced-order coefficients for a new time (and parameter) value are obtained via an approximate mapping. The high-fidelity solver is only used to generate the snapshots, i.e., the training dataset, and there is a complete decoupling between the online evaluation and the offline training. In the recent years, we haev proposed such a non-intrusive ROM for the solution of parameterized electromagnetic scattering problems [5]. In this approach, in addition to the time parameter, the dielectric permittivity is also considered as a reduction parameter.

IV. Numerical optimization algorithms

Inverse design allows to shape nanosclae lightmatter interactions driven by a performance figure of merit. Several numerical optimization methodologies including both local (gradient-based) and global search methods can be considered for this objective. In our work, we consider using a numerical optimization algorithm for tailoring the geometrical characteristics of material nanostructuring or the shape of nanostructures. In other words, we place ourselves in the setting of geometrical optimization as opposed to topology optimization. For this purpose, we investigate an optimization framework that belongs to the class of Bayesian optimization methods, and which is known as Efficient Global Optimization (EGO) [6]. Contrary to the classical common global optimization strategies like Genetic Algorithms (GAs), the EGO method is not based on an adaptive sampling, but on a surrogate model, which is built on the basis of available objective function evaluations. This surrogate model uses a statistical learning criterion related to the optimization goal (usually called merit function) in order to identify which design (set of parameters) should be tested in the next optimization iteration that would provide better results close to the stated performance target. For the evaluation of a given design, we can use of one of the two high-fidely fullwave methods, i.e., the DGTD and HDGFD methods, or a data-driver reduced-order model.

A. Applications

In the context of the Atlantis research group at the Inria center of Université Côte d'Azur, we are developing an innovative software suite dedicated to computational nanophotonics, which hosts time-domain and frequency-domain variants of the DG method specifically designed for differential systems of nanoscale light-matter interactions, data-driven reduced-order models for time-domain nanophotonics, and EGO-based inverse design workflows for mono-objective [7], multi-objective [8] and robust optimization [9] scenarios. This software suite, which is named DIOGENeS, is currently exploited in several projects in collaboration with physicists, and the involve various photonic devices such as those illustrated in figure 1. In this contribution, we will present some concrete applications for illustrating the capabilities of the proposed numerical tools.

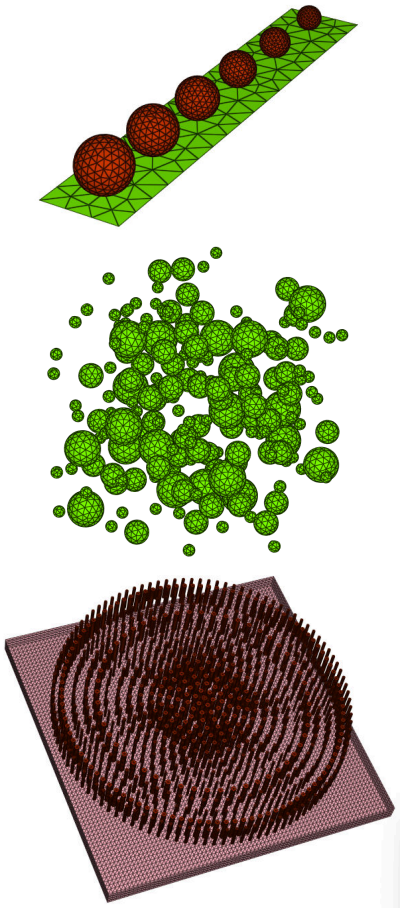

Fig. 1. Sample of photonic devices that are studied with the numerical tools of the DIOGENeS software suite. Top: a a metasurface with nanospheres. Middle: an random medium made of nanospheres with varying size. Bottom: a speherical metalens.

ACKNOWLEDGMENTS

The present work has benefited from different computational resources. On one hand, multi-CPU numerical experiments have been carried out using the Azzurra and PlaFRIM HPC clusters. As such, this work was supported by the French government through the France 2030 investment plan managed by the National Research Agency (ANR), as part of the Initiative of Excellence Université Côte d'Azur under reference number ANR-15-IDEX-01. The authors are grateful to the Université Côte d'Azur's Center for High-Performance Computing (OPAL infrastructure) for providing resources and support. PlaFRIM testbed is developed under the Inria PlaFRIM development action with support from Bordeaux INP, LABRI and IMB and other entities: Conseil Régional d'Aquitaine, Université de Bordeaux and CNRS (and ANR in accordance to the programme d'investissements d'Avenir. On the other hand, for multi-GPU numerical experiments, this work was provided with computing HPC and storage resources by GENCI at IDRIS thanks to the grant 2025-A0190616899 on the supercomputer Jean Zay's V100/A100/H100 partitions.

REFERENCES

[1] J. Hesthaven and T. Warburton, *Nodal discontinuous Galerkin methods: algorithms, analysis and applications*, ser. Springer Texts in Applied Mathematics. Springer Verlag, 2007.

[2] S. Lanteri, C. Scheid, and S. Lanteri, "Analysis of a generalized dispersive model coupled to a DGTD method with application to nanophotonics," *SIAM J. Sci. Comp.*, vol. 39, no. 3, pp. A831–A859, 2017.

[3] E. Agullo, L. Giraud, A. Gobé, M. Kuhn, S. Lanteri, and L. Moya, "High order HDG method and domain decomposition solvers for frequency-domain electromagnetics," *Int. J. Numer. Model. Electr. Netw. Dev. Fields*, vol. 33, no. 2, 2019.

[4] J. Hesthaven, G. Rozza, and B. Stamm, *Certified reduced basis methods for parametrized partial differential equations*, ser. SpringerBriefs in Mathematics. Springer, 2016.

[5] K. Li, T.-Z. Huang, L. Li, and S. Lanteri, "Non-intrusive reduced-order modeling of parameterized electromagnetic scattering problems using cubic spline interpolation," *J. Sci. Comp.*, vol. 87, no. 2, 2021.

[6] D. Jones, M. Schonlau, and W. Welch, "Efficient global optimization of expensive black-box functions," *J. Glob. Optim.*, vol. 13, no. 4, pp. 455–492, 1998.

[7] M. Elsawy, S. Lanteri, R. Duvigneau, G. Brière, M. Mohamed, and P. Genevet, "Global optimization of metasurface designs using statistical learning methods," *Sci. Rep.*, vol. 9, no. 17918, 2019.

[8] M. Elsawy, A. Gourdin, M. Binois, R. Duvigneau, D. Felbacq, S. Khadir, P. Genevet, and S. Lanteri, "Multiobjective statistical learning optimization of RGB metalens," *ACS Photon.*, vol. 8, no. 8, pp. 2498–2508, 2021.

[9] M. Elsawy, M. Binois, R. Duvigneau, S. Lanteri, and P. Genevet, "Optimization of metasurfaces under geometrical uncertainty using statistical learning," *Opt. Expr.*, vol. 29, no. 19, p. 29887, 2021.

Advanced in Topology Optimization for Metaphotonics and Integrated Optics

Antonio Calà Lesina[1,2,3,*]

[1]Hannover Centre for Optical Technologies, Leibniz University Hannover, 30167 Hannover, Germany
[2]Cluster of Excellence PhoenixD, Leibniz University Hannover, 30167 Hannover, Germany
[3]Institute for Transport and Automation Technology, Leibniz University Hannover, 30823 Garbsen, Germany
*Corresponding author: antonio.calalesina@hot.uni-hannover.de

***Abstract*—Inverse-design approaches based on topology optimization enable the discovery of fully three-dimensional nanophotonic structures with free-form geometries that transcend human intuition and achieve optical functionalities beyond the reach of conventional design strategies. This talk presents recent advances from my group in topology optimization for nanophotonics, meta-optics, and integrated optics.**

***Keywords*— inverse design, topology optimization, metasurfaces, integrated optics, nanoantennas.**

I. Introduction

Advances in computational capabilities and inverse design methodologies have enabled the discovery and engineering of novel and unconventional nanophotonic devices. In particular, topology-optimization-based inverse design can uncover fully three-dimensional, free-form nanophotonic structures that go beyond human intuition and achieve optical functionalities unattainable with conventional design approaches. By efficiently exploring vast design spaces using algorithms tailored for high-performance computing platforms, it becomes possible to identify new device concepts that can subsequently inform more conventional, physics-driven design strategies. Gradient-based topology optimization provides a robust and computationally efficient framework for navigating such large parameter spaces, enabled by efficient gradient evaluation techniques such as the adjoint method. This talk presents recent advances from my research group in computational nanophotonics and inverse design via topology optimization, with applications in meta-photonics and integrated optics, including:

- the inverse design of nanostructures made of arbitrary dispersive optical materials thanks to a formulation of the adjoint method in the time domain [1],
- the optimization of metallic and dielectric nanostructures and metasurfaces to achieve broadband absorption [2], [3],
- anapole effects in plasmonic meta-atoms that can be exploited as building blocks for transparent metasurfaces and metamaterials [4],
- integrated beam splitters designed via topology optimization to achieve arbitrary phases at the output ports [5],
- 3D free-form integrated optical circuits compatible with two-photon polymerization that outperform their 2D counterpart [6], and
- the topology optimization of nanostructures where the aim is to achieve a desired multipolar response in order to engineer the nanoantenna's scattering properties [7].

Acknowledgments

This work was supported by the Deutsche Forschungsgemeinschaft (DFG) under Germany's Excellence Strategy within the Cluster of Excellence PhoenixD (EXC 2122, Project ID 390833453), by DFG grants CA 2763/2-1 (Project ID 527470210) and CA 2763/6-1 (Project ID 544158178), and by the Volkswagen Foundation and the Lower Saxony Ministry of Science and Culture through the "zukunft.niedersachsen" funding program. Computing time was allocated by the Resource Allocation Board and provided on the supercomputers Lise and Emmy/Grete at NHR@ZIB and NHR@Göttingen within the framework of the NHR infrastructure (project nip00059).

References

[1] J. Gedeon, E. Hassan, and A. Calà Lesina, "Time-Domain Topology Optimization of Arbitrary Dispersive Materials for Broadband 3D Nanophotonics Inverse Design," *ACS Photonics*, vol. 10, no. 11, pp. 3875–3887, 2023.

[2] J. Gedeon, I. Allayarov, A. Calà Lesina, and E. Hassan, "Time-domain topology optimization of power dissipation in dispersive dielectric and plasmonic nanostructures," *IEEE Transactions on Antennas and Propagation*, vol. 73, no. 5, pp. 3079–3094, 2025.

[3] J. Gedeon, I. Allayarov, E. Hassan, and A. Calà Lesina, "Topology optimization of a superabsorbing thin-film semiconductor metasurface," *IEEE Transactions on Antennas and Propagation*, vol. 73, no. 10, pp. 7932–7942, 2025.

[4] E. Hassan, A. B. Evlyukhin, and A. Calà Lesina, "Anapole Plasmonic Meta-Atoms for Nearly Transparent Metamaterials," *Laser & Photonics Reviews*, vol. 19, no. 5, 2400118, 2025.

[5] Nanda, A., M. Kues, and A. Calà Lesina, "Exploring the fundamental limits of integrated beam splitters with arbitrary phase via topology optimization," *Optics Letters*, vol. 49, no. 5, pp. 1125–1128, 2024.

[6] A. Nanda, A. Rittmeier, A. Rüsseler, M. Hinkelmann, M. Kues, and A. Calà Lesina. "Inverse design of 3D polymer integrated optics compatible with multi-photon lithography," *Optics Letters*, 2026 [accepted].

[7] S. Bahmani, A. B. Evlyukhin, E. Hassan, and A. Calà Lesina, "Topology optimization of optical nanoantennas with desired multipoles," *Optics Express*, vol. 33, no. 9, pp. 19418–19441, 2025.

SCRIBEed GRIN-Lenses by Topology Optimization

Rasmus Ellebæk Christiansen[1,2,*] , Dajie Xie[3], Paul V. Braun[3]

[1]Department of Civil and Mechanical Engineering, Technical University of Denmark, DK-2800 Kgs. Lyngby, Denmark

[2]NanoPhoton - Center for Nanophotonics, Technical University of Denmark, DK-2800 Kgs. Lyngby, Denmark

[3]Department of Materials Science and Engineering, University of Illinois at Urbana-Champaign, 61801, United States of America

*Corresponding author: raelch@dtu.dk

***Abstract*—High-efficiency compact GRIN metalenses, tailored for fabrication by SCRIBE, are designed using density-based topology optimization. Superior performance is demonstrated experimentally compared to traditional diffractive lenses of (near) identical dimensions, revealing the potential of combining SCRIBE with inverse design to realize improved optical devices fabricated using low-index contrast materials.**

***Keywords*— metalenses, visible light, topology optimization, inverse design, SCRIBE, GRIN.**

I. Introduction

Metalenses are maturing into powerful platforms for compact, lightweight, and highly functional optical components capable of replacing or augmenting traditional refractive elements across a wide range of applications. Here we explore the integration of large-scale inverse design via topology optimization with the high-resolution, freeform fabrication capabilities of SCRIBE to engineer next-generation GRIN metalenses. This combined approach leverages unprecedented control over spatially varying refractive index profiles for increased design freedom, pushing beyond the limitations of traditional design and fabrication methods.

II. Methods

Our method integrates full-wave electromagnetic simulation and density-based topology optimization (DBTO) with the subsurface controllable refractive index via beam exposure (SCRIBE) technique [1]. Informed by fabrication constraints and an experimentally measured dispersive refractive index we extend a DBTO method [2] to the design of compact, gradient index axisymmetric metalenses for use in the visible spectrum.

The topology-optimized lenses are fabricated by SCRIBE, where two-photon direct laser writing is performed within highly transparent porous silica ($PSiO_2$). SCRIBE allows for simultaneous definition of geometry and refractive index with sub-micron accuracy in 3D.

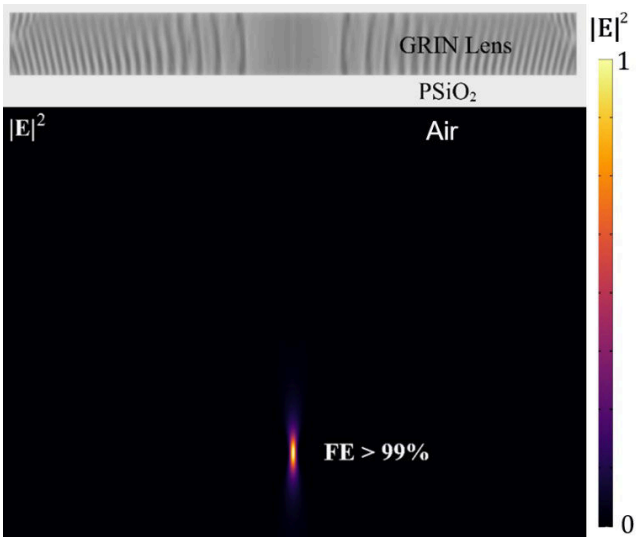

Fig. 1 Simulation data: Topology optimized GRIN metalens embedded in $PSiO_2$ (grayscale) and electromagnetic field intensity (inferno).

III. Results and Discussion

Numerically we demonstrate (near) unity focusing efficiency (FE) for all monochrome lenses (Fig 1), while above 70% focusing efficiency is demonstrated for an RGB triplet.

Experimentally, the refractive index profile and focusing efficiency of the print lens are characterized by multi-photon confocal fluorescence microscopy and custom-built setup. Monochromatic lenses with NAs of 0.3, 0.45 and 0.6 at 488nm, 542nm and 633nm respectively, are experimentally realized revealing significantly improved FE compared to traditional diffractive lenses, e.g. from FE~23% to FE~60% for 633nm light at NA=0.6. Our design and fabrication methods are extended to the design and realize a singlet achromatic lens with less than 5% chromatic focal length error. (For more details on the experimental methods see [3]).

IV. Conclusion

Leveraging density-based topology optimization, we inversely design and realize axisymmetric microlenses with NAs up to 0.6 that exhibit focusing efficiencies above 60% in the visible. We demonstrate, both numerically and experimentally, that the performance of our GRIN lenses significantly outpaces that of traditional diffractive lenses, particularly at high NAs, without compromising imaging quality. For broadband optimization across the visible spectrum, we numerically demonstrate a singlet achromatic microlens with high focusing efficiency and experimentally show a dramatic reduction in chromatic focal length error from 24.5% (for a standard diffractive lens) to 4.2%. Note that the design method may be leveraged for thin GRIN lenses with diameters in the mm-range on modern high-end desktop systems, thus our demonstrations are mainly size-limited by experimental constraints. To our knowledge, this is the first realization of singlet achromatic lens using one single lithography step and low refractive index materials.

Acknowledgments

This work was supported by the Danish National Research Foundation through grant DNRF147 NanoPhoton and the National Science Foundation through the University of Illinois at Urbana-Champaign Materials Research Science and Engineering Center DMR-2309037.

References

[1] C.R. Ocier, C.A. Richards, D.A. Bacon-Brown, et al. *Direct laser writing of volumetric gradient index lenses and waveguides*. Light & Science Applications 9, 196 (2020).

[2] R.E. Christiansen, Z. Lin, C. Roques-Carmes, et al., *Fullwave Maxwell inverse design of axisymmetric, tunable, and multi-scale multi-wavelength metalenses*, Optics Express, 28 no 23, 33854-33868, 2020.

[3] C.A. Richards, C.R. Ocier, D. Xie, et al. *Hybrid achromatic microlenses with high numerical apertures and focusing efficiencies across the visible*. Nature Communications 14, 3119 (2023).

Engineering Optical Nonlinearities Using Nanostructured Materials

L. Razzari

Institut National de la Recherche Scientifique, Centre Énergie Matériaux Télécommunications (INRS-EMT), Canada
luca.razzari@inrs.ca

Abstract: In this talk, I present nanostructuring approaches to tailor the nonlinear optical response of dielectric thin films. I discuss a phase-change platform (GSST) suitable for the mid-infrared range [1]. Finally, I show that metasurface engineering modifies the nonlinear susceptibility of amorphous silicon, controlling the polarization of the generated light [2].

References

[1] F. Yue, R. Piccoli, M.Y. Shalaginov, T. Gu, K.A. Richardson, R. Morandotti, J. Hu, L. Razzari, Nonlinear Mid-Infrared Metasurface based on a Phase-Change Material, *Laser Photonics Rev.*, 15, 2000373, 2021.

[2] F. Yue, G. Balistreri, N. Montaut, F. Riminucci, A. Toma, R. Piccoli, S. Cabrini, R. Morandotti, L. Razzari, Polarization Control via Artificial Optical Nonlinearity in Dielectric Metasurfaces, *ACS Nano*, 20, 3499, 2026.

Radiative decay of surface plasmon propagating in thin metal film

Arkadii Krokhin*, Andrey Bozhko

Department of Physics, University of North Texas, USA
*Corresponding author: arkadii.krokhin@unt.edu

***Abstract*—A narrow transition layer between metal and dielectric contains epsilon-near-zero surface (ENZ) formed by spill-out electrons and surface roughness. Electromagnetic field of surface plasmon leaks through the ENZ point leading to radiative attenuation. Here the radiative losses of surface plasmon are calculated for a thin metal film.**

***Keywords*— epsilon-near-zero, collisionless damping.**

I. Introduction

The decay of a surface plasmon propagating along a metal–dielectric interface is usually attributed to Joule losses in the metal and to wave scattering from random surface roughness. The evanescent nature of plasmonic fields in both the metal and the dielectric is a necessary condition for the existence of the surface mode and is typically assumed to arise from an ideally sharp metal–dielectric interface. However, even for atomically flat surfaces, the dielectric properties do not change discontinuously. The macroscopic dielectric function must therefore pass through zero when transitioning from its negative value in the metal to its positive value in the dielectric.

Spill-out electrons form a transition region a few angstroms thick above an atomically flat metal surface [1]. Near a rough surface, this region may become orders of magnitude thicker, depending on the mean height of the surface roughness. In any case, the thickness of the transition layer is much smaller than the optical wavelength and can therefore be safely neglected in conventional optical laws, such as Snell's law.

However, a surface plasmon carries energy distributed within the near-field zone, where the presence of even an atomically thin transition layer containing an ENZ region may strongly affect the evanescent character of the plasmonic field. At the point where the dielectric function approaches zero, plasmon energy leaks into the dielectric (or vacuum), giving rise to a radiative loss channel [2]. An analytical method for calculating radiative losses of a surface plasmon in a semi-infinite metal was proposed in Ref. [3]. It has also been demonstrated experimentally that a strong electric field applied normal to the interface shifts the ENZ point toward or away from the interface, thereby affecting the resonant conditions for surface-plasmon excitation.

Here, we analyze the effects of the transition layer on propagation of surface plasmon in a symmetric thin metallic layer and demonstrate that its energy leaks to dielectrics through the ENZ regions.

II. Dispersion and decay of surface plasmon in a metal film with two transition layers

We consider a metal slab of thickness $2d$ and dielectric function $\epsilon(\omega) < 0$ clad between two equal dielectrics with permittivities $\epsilon_d > 0$. Two metal-dielectric transition layers are formed at the both interfaces. If an external electric field is applied normal to the slab, it breaks the symmetry by decreasing the electron concentration at one interface and increasing it at the other.

A continuous dielectric function $\epsilon(z)$ approaches ϵ_d at $|z| > d$ and $\epsilon(\omega)$ for $|z| < d$. Assuming exponentially narrow transition layers, the function $\epsilon(z)$ can be written as:

$$\epsilon(z) = \epsilon_d + \frac{\epsilon(\omega) - \epsilon_d}{2}\left(\tanh\frac{z+d+l_2}{2\delta_2} - \tanh\frac{z-d+l_1}{2\delta_1}\right), \tag{1}$$

where $\delta_{1,2}$ are the widths of the transition layers on the upper and lower metal-dielectric interfaces. The parameters $l_{1,2}$ describe the asymmetry of the transition layers induced by the applied electric field. Electrical neutrality in the presence of the electric field is satisfied if $l_1 = l_2 = l$, regardless of the relation between δ_1 and δ_2. For any reasonable field strength, $l, \delta_{1,2} \ll d$. In the absence of an external field, $l_1 = l_2 = 0$ and $\delta_1 = \delta_2$. The dielectric function $\epsilon(z)$ vanishes at two points $z = z_{1,2}$ located near the metal–dielectric interfaces.

For p-polarized surface wave propagating along the x-axis, the dependence of the H_y component on the coordinate z is obtained from

$$\frac{d}{dz}\left(\frac{1}{\epsilon(z)}\frac{dH_y}{dz}\right) + \left(\frac{\omega^2}{c^2} - \frac{k^2}{\epsilon(z)}\right)H_y(z). \tag{2}$$

The differential term here exhibits a strong singularity at $z = z_{1,2}$. An analytical solution for $H_y(z)$ and the dispersion relation $\omega(k)$ can be obtained by applying a Fourier transformation over the coordinate z [3]. The Fourier transform of Eq. (1) leads to the integral eigenvalue problem for $h(p) = (2\pi)^{-1}\int_0^\infty H_y(z)e^{-ipz}dz$

$$\frac{\omega^2}{c^2}h(p) = \int_0^\infty (k^2 + pp')\eta(p-p')h(p')dp'. \tag{3}$$

In the sharp-boundary model, where $\epsilon(z)$ is a non-vanishing piecewise function, the kernel of Eq. (2) is Hermitian since $\eta(-p) = \eta^\star(p)$. The eigenvalue is then real and positive, yielding a real eigenfrequency $\omega(k)$. However, the transition layer

contains two ENZ points along the integration path. Shifting the integration contour to the lower half-plane (corresponding to $\mathrm{Im}\epsilon(z) > 0$) the function $\eta(p)$ acquires an imaginary part,

$$\eta(p) = \frac{1}{2\pi}\int_0^\infty \frac{1}{\epsilon(z)} e^{-ipz} dz - \frac{i}{2} \operatorname*{Res}_{z=z_1,z_2} \frac{e^{-ipz}}{\epsilon(z)} \tag{4}$$

which breaks the Hermiticity of the integral kernel. As a result, the dispersion relation of surface plasmon becomes complex, $\omega(k) = \omega_0(k) + \omega'(k) - i\omega''(k)$, where $\omega_0(k)$ is the surface-plasmon frequency without the transition layer. The frequency shift $\omega'(k)$ and radiative decay rate $\omega''(k)$ can be calculated from Eq. (2) using perturbation theory in a small parameter $\delta_{1,2}k$. These corrections are expressed in terms of the unperturbed magnetic-field distribution $H_0(z)$, which is an even (odd) function for the long (short)-range surface plasmon.

$$\frac{\omega'}{\omega_0} = \frac{c^2}{2\omega_0^2} \frac{\int_{-\infty}^{\infty} \left(\frac{1}{\epsilon(z)} - \frac{1}{\epsilon_0(z)}\right) \left(|kH_0|^2 + |H_0'|^2\right) dz}{\int_{-\infty}^{\infty} |H_0(z)|^2 dz} \tag{5}$$

$$\frac{\omega''}{\omega_0} = \frac{\pi c^2}{2\omega_0^2} \frac{\sum_{z=z_1,z_2} \frac{1}{|\epsilon'(z)|} \left(|kH_0(z)|^2 + |H_0'(z)|^2\right)}{\int_{-\infty}^{\infty} |H_0(z)|^2 dz} \tag{6}$$

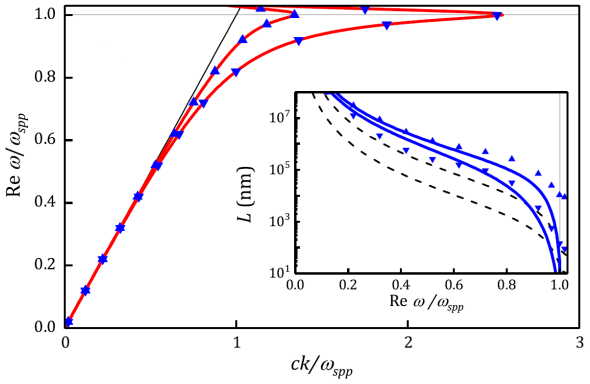

Fig. 1. Dispersion of surface plasmon for 50nm-thick silver slabs in air. The red curves and blue data points show the dispersion for the cases of sharp boundary ($\delta = 0$) and interfaces with transition layers (with $l_1 = l_2 = 0$ and $\delta_1 = \delta_2 = 2$ Å. The insets compare theoretical (blue lines) and numerical (blue data points) results for the collisionless damping rates, expressed in terms of propagation length. The rate of Joule losses is shown with dashed black lines. Dispersion with higher frequency (longer $L(\omega)$) corresponds to the long-range plasmon.

These equations were used to plot the dispersion and decay of a surface plasmon propagating in silver film of thickness 50 nm.The transition-layer widths were chosen as $\delta_1 = \delta_2 = 2$ Å and no external DC field was applied ($l_1 = l_2 = 0$). The continuous red and blue curves show the perturbative results obtained from Eqs. (5) and (6), while the blue triangles represent the numerical solution of Eq. (2).

The dispersion curves are only weakly perturbed by the presence of the transition layer. However, the radiative losses associated with the transition layer make a significant contribution to the decay length $L(\omega)$. For the short-range plasmon, radiative losses become comparable to Joule losses (dashed line) near the plasmonic resonance $0.8 < \omega/\omega_{spp} < 1$. For the long-range plasmon, radiative losses remain smaller than Joule losses. The radiative decay mechanism of the surface plasmon is, in some sense, similar to Landau collisionless damping, since neither originates from electron collisions in the metal.

These estimates were obtained for an atomically flat surface with a very narrow transition layer. Surface roughness increases the effective thickness of the transition layer by at least an order of magnitude. In this case, radiative losses can exceed Joule losses even for the long-range plasmon. Very close to resonance, the perturbation theory fails because the parameter δk is no longer small as $k \to \infty$.

Many applications of surface-plasmon resonance rely on the strength and localization of the electromagnetic fields near the metal surface. The singular behavior of the first term in Eq. (2) shifts the field maxima toward the ENZ point and enhances the discontinuities. The asymptotic solution of Eq. (2) near a point where the dielectric function vanishes yields $H_y(\xi) \sim 1 + \frac{1}{2}(k\xi)^2 \ln(k\xi)$ where $\xi = |z - z_{1,2}|$. While the magnetic field remains continuous, the electric-field components become singular: $E_x(\xi) = H_y'(\xi)/\epsilon(\xi) \sim \ln(k|\xi|)$, $E_z(\xi) = H_y(\xi)/\epsilon(\xi)$. Stronger than the sharp-boundary model predicts singularity can be considered as a "compensation" of the negative effect of radiative decay.

III. Conclusion

It is shown that due to the presence of the ENZ point within the transition layer between metal and dielectric, a surface plasmon inevitably loses energy even if the metal is lossless. The very existence of the ENZ point results in the delocalization of the plasmon energy, which therefore gradually radiates away from the interface and depletes the plasmon. The rate of radiative collisionless decay has been analytically and numerically calculated for a thin metal film sandwiched between two identical dielectrics. Even for an atomically thin transition layer a few angstroms thick, the radiative attenuation channel significantly reduces the propagation length of the short-range plasmon. A wider transition layer associated with surface roughness, with a mean height of several tens of nanometers, strongly reduces the propagation length of the long-range plasmon.

Acknowledgments

This work was supported by the US Air Force Office of Scientific Research under Award No. FA9550-23-1-0630.

References

[1] N. D. Lang and W. Kohn, "Theory of metal surfaces: Charge density and surface energy," *Phys. Rev. B*, vol. 1, p. 4555, 1970.

[2] Yu. A. Akimov and H. S. Chu, "Plasmon coupling effect on propagation of surface plasmon polaritons at a continuous metal/dielectric interface," *Phys. Rev. B*, vol. 83, p. 165412, 2011.

[3] Kevin Roccapriore, Andrey Bozhko, Gleb Nazarikov, Vladimir Drachev, Arkadii Krokhin, "Surface plasmon at a metal-dielectric interface with an epsilon-near-zero transition layer," *Phys. Rev. B*, vol. 103, p. L161404, 2021.

SPECIAL SESSION 1

Metamaterials: novel trends and applications

20 contributions · pp. 747–777

Giant Magneto-Impedance Effect in Magnetic Microwires: Challenges, Advances and Perspectives

Arcady Zhukov[1,2*], Alvaro Gonzalez[1,3], Paula Corte-Leon[1,3,4], Pablo Rodríguez Jiménez[1,], Mohamed Salaheldeen[1,3,5,], Jesus Olivera[6] and Valentina Zhukova[1,3]

[1] Dpto. de Física Aplicada, EIG, Univ. of the Basque Country (EHU), San Sebastian, Spain
[2] IKERBASQUE, Basque Foundation for Science, Spain
[3] Dept. Polym. Adv. Mater., Univ. of the Basque Country, EHU, 20018 San Sebastian, Spain
[4]Dept. Mater. Science & Metallurgy, Univ. Cambridge, Cambridge CB3 0FS, UK
[5]Physics Department, Faculty of Science, Sohag University, Sohag 82524, Egypt
[6]Instituto de Física, Facultad de Ciencias, Universidad Autónoma de Santo Domingo, Dominican Republic
*Corresponding author: arkadi.joukov@ehu.es

***Abstract*—We provide the overview of the state of art on development of magnetic wires with high Giant Magnetoimpedance (GMI) effect. Excellent soft magnetic properties and GMI ratio up to 750% have been observed in as-prepared low magnetostrictive amorphous Co-rich microwires. Appropriate processing, such as annealing, allows to increase further the GMI ratio value in both Co-rich and Fe-rich microwires. In both Fe and Co-rich microwires the maximum GMI ratio is observed for frequencies above 100 MHz.**

***Keywords*—Giant Magnetoimpedance, Magnetoelastic anisotropy, Magnetostriction, Amorphous microwires.**

I. Introduction

Studies of Giant magnetoimpedance, GMI, effect have attracted considerable attention in the last few years owing to its suitability for technological applications [1,2]. The main features of the GMI effect have been successfully explained in terms of classical electrodynamics that consider the influence of a magnetic field on the penetration depth of AC current (MHz-GHz frequency range) flowing through the magnetically soft conductor.

The most common quantity for the characterization of the GMI effect is the GMI ratio, ΔZ/Z, defined as:

$$\Delta Z/Z = [Z(H) - Z(H_{max})] / Z(H_{max}), \quad (1)$$

where H_{max} is the axial DC-field with maximum value up to few kA/m.

Extremely high sensitivity of the GMI effect to even low magnetic field attracted great interest in the field of applied magnetism, basically for applications in magnetic sensors and smart composites. Cylindrical shape and high circumferential permeability observed in amorphous wires are quite favorable for achievement of high GMI effect [1-4].

One of the tendencies in modern GMI sensors is the size reduction [3-5]. Recently developed magnetic sensors using the GMI effect allow achieving nT and pT magnetic field sensitivity with low noise [1,3,4]

The aim of this report is to provide recent results on the optimization of soft magnetic properties and the GMI effect in magnetic microwires.

II. Methods

We measured magnetic field dependences of impedance, Z, and GMI ratio, $\Delta Z/Z$, of magnetic microwires using a specially designed micro-strip sample holder. The sample holder was placed inside a sufficiently long solenoid that creates a homogeneous magnetic field, H. The sample impedance Z was measured using vector network analyzer from reflection coefficient S_{11}, reported elsewhere [3,6].

III. Results and Discussion

As discussed elsewhere [1-4], for amorphous materials characterized by the absence of magneto-crystalline anisotropy the main sources of magnetic anisotropy are the shape and magnetoelastic anisotropy, K_{me}. The latter is determined by the magnetostriction coefficient, λ_s, and the internal stresses, σ_i, by the relation [3]:

$$K_{me} = 3/2\, \lambda_s \sigma_i, \quad (2)$$

Nearly-zero λ_s –values can be achieved in $Co_{1-x}Fe_x$ alloys at x about 0,03 – 0,08 [3]. Accordingly, Co-rich microwires can present high GMI ratio. $\Delta Z/Z(H)$ dependencies measured at different frequencies in $Co_{67}Fe_{3.9}Ni_{1.4}B_{11.5}Si_{14.5}Mo_{1.6}$ (d=10.8 μm, D= 13.8 μm) microwire are shown in Fig. 1a. This microwire presents high maximum GMI ratio, $\Delta Z/Z_m$, (~530%) at optimal frequency of about 700 MHz (see Fig. 1b).

However, from $\Delta Z/Z_m(f)$ dependence for $Co_{67.7}Fe_{4.3}Ni_{1.6}Si_{11.2}B_{12.4}C_{1.5}Mo_{1.3}$ microwires with d=10.8 μm

and

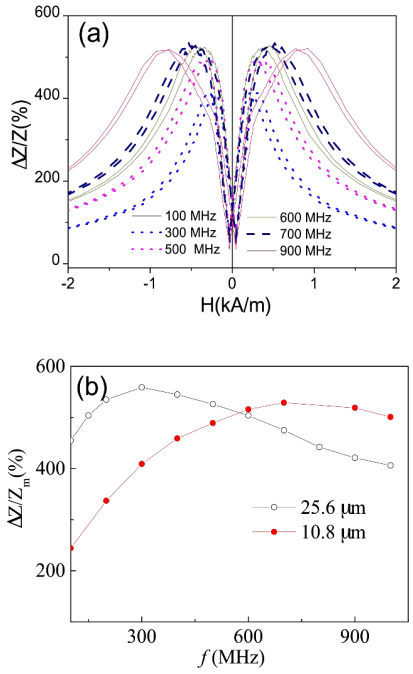

Fig. 1. *ΔZ/Z(H)* dependencies measured in $Co_{67}Fe_{3.9}Ni_{1.4}B_{11.5}Si_{14.5}Mo_{1.6}$ (d=25.6 μm, D= 26.6 μm) microwires (a) and $\Delta Z/Z_m(f)$ dependence for $Co_{67.7}Fe_{4.3}Ni_{1.6}Si_{11.2}B_{12.4}C_{1.5}Mo_{1.3}$ with d=10.8μm, D=13.8μm and d=25.6 μm, D= 26.6 μm microwires.

d=25.6 μm we can appreciate that for $Co_{67.7}Fe_{4.3}Ni_{1.6}Si_{11.2}B_{12.4}C_{1.5}Mo_{1.3}$ microwires with d=25.6 μm the optimal frequency is about 300 MHz at which $\Delta Z/Z_m \approx 560\%$ can be

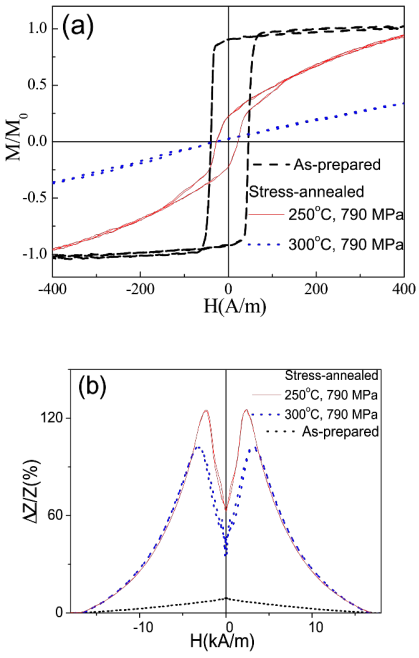

Fig. 2. Hysteresis loops (a) and *ΔZ/Z(H)* dependences measured at 300 MHz (b) of as-prepared and stress-annealed $Fe_{75}B_9Si_{12}C_4$ microwires.

achieved. The observed behaviour reflects the relationship between the optimal frequency for the GMI performance and the wire diameter: to achieve the maximum GMI effect a trade-off between wire dimensions and frequency is required [5]. The diameter reduction must be associated with the increasing of the optimal GMI frequency range [3,5].

Usually, highly magnetostrictive Fe-rich microwires present poor GMI effect. However, from the viewpoint of the cost Fe-rich microwires are preferable. Recently, we identified that the magnetic softness and GMI effect of Fe-rich microwires can be substantially improved by stress-annealing (see Fig. 2): an order of magnitude $\Delta Z/Z_m$ improvement (see Fig. 2b) is explained by transverse character of induced by stress-annealing magnetic anisotropy (see Fig .2a).

It is worth noting that annealing can also improve the GMI effect of Co-rich microwires. Thus, recently we reported $\Delta Z/Z_m$ up to 900% in annealed Co-rich microwires [6].

IV. Conclusion

We studied the factors allowing optimization of GMI effect of magnetic microwires. Generally, low coercivity and high GMI effect have been observed in as-prepared Co-rich microwires. We identified a relationship between the optimal frequency for the GMI performance and the wire diameter: to achieve the maximum GMI effect a trade-off between wire dimensions and frequency is required. GMI ratio of Fe-rich microwires can be substantially improved by the adequate postprocessing.

Acknowledgments

This work was supported by the Spanish MICIN, under PID2022-141373NB-I00 project, by EU (Horizon Europe) under "HARMONY", by the Government of the Basque Country, under Elkartek (MOSINCO and ATLANTIS) projects and by under the scheme of "Ayuda a Grupos Consolidados" (Ref.: IT1670-22).

References

[1] M.-H. Phan and H.-X. Peng, "Giant magnetoimpedance materials: Fundamentals and applications", Prog.Mater. Science vol. 53, pp. 323–420,2008.

[2] L.V. Panina and K. Mohri, "Magneto-impedance effect in amorphous wires" Appl. Phys. Lett. vol. 65, pp. 1189-1191,1994.

[3] A. Zhukov, M. Ipatov and V. Zhukova, "Advances in Giant Magnetoimpedance of Materials", Handbook of Magnetic Materials, ed. K.H.J. Buschow, *Elsevier*, vol. 24, ch.2., 2015, pp. 139-236.

[4] K. Mohri, T. Uchiyama, L.V. Panina, M. Yamamoto and K. Bushida, "Recent Advances of Amorphous Wire CMOS IC Magneto-Impedance Sensors: Innovative High-Performance Micromagnetic Sensor Chip" J. Sens. 2015, 718069, 2015, doi:10.1155/2015/718069

[5] D. Ménard, M. Britel, P. Ciureanu and A. Yelon, "Giant magnetoimpedance in a cylindrical conductor" J. Appl. Phys. vol. 84, pp. 2805–2814, 1998.

[6] A. Gonzalez, I. Skorvanek, M. Jakubcin, V. Zhukova, A. Zhukov, "Impact of elevated temperature on the Giant magnetoimpedance effect in Co-rich glass-coated microwires", Scr. Mater. vol.266. 116794, 2025.

High-Precision Nanofabrication and Characterization of Metamaterials Using ZEISS FIB-SEM Technology

Olena Vertsanova[1,2]*, Martina Schenkel[1]
[1]Carl Zeiss Microscopy GmbH, Germany
[2] National Technical University of Ukraine "KPI", Ukraine
*Corresponding author: olena.vertsanova@zeiss.com

***Abstract*— ZEISS electron microscopy is indispensable method in the discovery of materials with enhanced or novel properties, metamaterials, nanophotonic, quantum photonics, facilitating high-resolution imaging, detailed characterization, and nanofabrication. The ZEISS electron microscopy contributes significantly to the understanding and advancement of this exciting field, enabling the development of novel applications in optics, sensing, telecommunications, and beyond.**

***Keywords*—metamaterials, electron microscopy, nanofabrication, focus-ion beam, Crossbeam.**

I. Introduction

Electron microscopy plays a pivotal role in metamaterials research, providing essential capabilities for both the fabrication and characterization of these advanced materials [1]. This talk presents the contribution of the latest developments in electron microscopy for nanofabrication, characterization, and analysis of metamaterials.

II. Methods

ZEISS focused ion beam scanning electron microscopes (FIB-SEM) of Crossbeam family provide solutions for nanofabrication with high precision and high spatial resolution. They combine the powerful imaging and analytical performance of a field emission scanning electron microscope (FE-SEM) with superior next-generation focused ion beam (FIB) processing capabilities for nanofabrication of new advanced materials and devices. This talk presents the advantages of nanofabrication using a ZEISS FIB-SEM microscope and simultaneous high-resolution imaging, structural analysis, morphology examination and characterization of material properties, that define the unique properties of advanced materials, such as metamaterials, photonic crystals, and plasmonic [2].

III. Discussion

ZEISS Crossbeam FIB-SEM provides not only detailed surface morphology images, but also 3D information enabling the assessment of the shape, size, and arrangement of the metamaterial structures, which are vital for their optical and electromagnetic behavior. ZEISS Crossbeam FIB-SEM allows obtaining structural, elemental, and compositional information with integrated energy dispersive x-ray spectroscopy (EDX) and electron backscatter diffraction (EBSD) and provides an understanding of the properties of metamaterials for specific applications.

The authors show the advantages of ZEISS Crossbeam's modular platform concept with the possibility to upgrade the microscope with growing needs, e.g. with the fs-laser for massive material ablation and high throughput of sample preparation [3].

IV. Conclusion

The combination of high-resolution ZEISS Gemini optics for imaging and super stable integrated FIB-column of ZEISS FIB-SEM for nanofabrication is an ingenious solution that advances fabrication approaches in metamaterials, nanophotonic, sustainable materials, quantum photonics, and new materials for nano-optics research.

References

1. Scharf, T. "The challenges of nanophononics in modern optical technologies," Open Access Government, 2018.
2. Hentschel, M. and Koshelev K., Sterl F., S. Both S., J. Karst J., L. Shamsafar L., T. Weiss T., Y. Kivshar Y, and H. Giessen "Dielectric Mie voids: confining light in air Light," Science and Applications, Vol.12, No. 3, 2023.
3. B. Tordoff, C. Hartfield, A. Holwell, S.Hiller, M. Kaestner, S. Kelly, J. Lee, S. Müller, F. Perez-Willard, T. Volkenandt, R. White, T. Rodgers; The LaserFIB: new application opportunities combining a high-performance FIB-SEM with femtosecond laser processing in an integrated second chamber; Applied Microscopy 50 (2020), 24

The interaction of hot carriers with adsorbates

Johannes Lischner[1,*]

[1]Department of Materials, Imperial College London, United Kingdom
*Corresponding author: j.lischner@imperial.ac.uk

***Abstract*— Highly energetic or "hot" electrons and holes generated from the decay of localized surface plasmons can be harnessed for applications in photocatalysis, photovoltaics and sensing. I will discuss the interaction of these hot carriers with adsorbed molecules and connect this to experimental observations of chemical interface damping of plasmons.**

***Keywords*— hot carriers, chemical interface damping, photocatalysis.**

I. Introduction

Localized surface plasmons in metallic nanoparticles give rise to very strong light absorption. The decay of these excitations results in the generation of energetic or “hot” electrons and holes which can be harvested and harnessed for applications in photovoltaics, photocatalysis and sensing. To optimize hot carrier production in devices, a detailed theoretical understanding of the relevant microscopic processes, including light-matter interactions, plasmon decay and hot electron thermalization, is needed. In my talk, I will describe a material-specific theory of hot-carrier generation and relaxation in metallic nanoparticles which combines a classical description of the electromagnetic radiation with large-scale atomistic quantum-mechanical simulations. I will present results for hot carrier distributions in spherical nanoparticles of gold, silver and copper and discuss the relative importance of interband and intraband transitions as function of nanoparticle size. Next, I will describe how CO2 reduction performance of gold nanoparticles can be enhanced by changing the nanoparticle shape. Finally, I will present results the interaction of hot carriers with adsorbed molecules on nanoparticles surface and use this to explain recent observations of chemical interface damping.

II. Methods

Density-functional theory calculations of molecules on metallic surfaces are performed. The results of these calculations are combined with Fermi’s golden rule to evaluate the rate of chemical interface damping.

III. Results and Discussion

We calculate the contribution to the plasmon linewidth for different molecules on spherical gold nanoparticles. We are able to correlate these results with the adsorbate density of states obtained from ab initio calculations. Our results are in good qualitative agreement with recent measurements of plasmon propagation lengths in gold waveguides which are coated with different molecules.

IV. Conclusion

We have demonstrated that calculation of chemical interface damping can reliably reproduce experimental measurements.

Nanostructured GLAD optical coatings for reflectance and birefringence control

Lina Grineviciute*, Darija Astrauskyte, Lukas Ramalis

Center for Physical Sciences and Technology (FTMC), Savanoriu Ave. 231, Vilnius, Lithuania

*Corresponding author: lina.grineviciute@ftmc.lt

***Abstract* — In this work the possibilities to engineer the inner nanostructures of individual layer and applications for the formation of coating-based AR-, HR-coatings, polarizers and phase retarders were proposed.**

***Keywords* — all dielectric polarizer, waveplates, PVD technologies, high power lasers, optical elements.**

I. Introduction

During conventional physical vapor deposition (PVD), substrates are typically placed in continuously rotating holders to average the deposition angle and vapor flux intensity, resulting in homogeneous isotropic multilayer coatings. In such coatings, optical interference structures are formed by combining materials with high and low refractive indices to achieve the required variation of optical constants. In contrast, during glancing angle deposition (GLAD), the substrate is kept tilted relative to the vapor flux, allowing the formation of nanostructured anisotropic layers (Fig. 1a). This technique enables the growth of columnar thin films (Fig. 1b) with advanced optical constants and anisotropic properties (Fig. 1c).

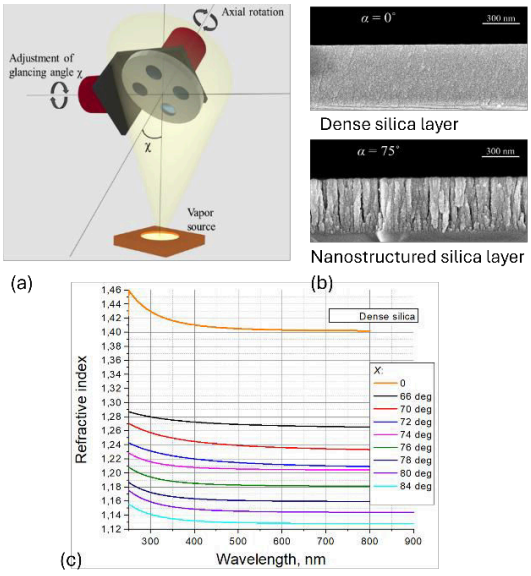

Fig, 1. a) Schematic of the GLAD deposition principle. b) Dense and nanostructured coatings. c) Effective refractive index dispersions.

II. Methods and Results

Investigations of silica-based GLAD antireflection coatings have demonstrated higher resistance to laser radiation and broader spectral performance compared with conventional two-material coatings produced by the Ion Beam Sputtering (IBS) technique. These coatings consist of porous thin films with low intrinsic stress. High-reflection all-silica mirrors have also shown improved laser resistance compared with standard dielectric mirrors [1]. However, due to the highly porous structure of GLAD films, silica-based anisotropic coatings can be sensitive to environmental conditions, as water adsorption in the pores may alter the effective refractive index and birefringence. Recent studies have therefore explored alternative materials for anisotropic coatings. In particular, GLAD-deposited LaF_3 coatings have demonstrated suitable birefringence, low optical losses, and improved environmental stability for UV polarization optics, with retardance variations below 1% under changing humidity conditions for waveplates operating at 266 nm wavelength [2,3].

In the present work, the optical and structural properties of anisotropic single-layer coatings were investigated to determine optimal deposition conditions for low-loss birefringent coatings. Transmission and phase delay (retardance) between two orthogonal polarizations - along the shadowing plane (fast axis) and perpendicular to it (slow axis) - were measured using spectrophotometry and spectroscopic ellipsometry and later analyzed to determine optical constants.

Fresnel reflections at interfaces between materials with different refractive indices are unavoidable in optical systems. Conventional antireflection or high-reflection coatings are typically formed by alternating layers of high- and low-refractive-index materials with optical thicknesses equal to a quarter or half wavelength. For a wavelength of 355 nm, the refractive index of a dense SiO_2 layer is approximately 1.41, while anisotropic porous layers exhibit refractive indices of about 1.211 and 1.231 along the fast and slow axes, respectively. Therefore, within the coating design, dense and porous anisotropic films can effectively serve as high- and low-index materials.

The waveplate design aims to minimize the number of layers while maintaining high transmission and controlled birefringence. To reduce scattering originating from the nanostructured columnar morphology, the thickness of individual anisotropic layers was kept below 400 nm. In this way, high transmittance can be achieved while the required phase delay is obtained by adjusting the total thickness of anisotropic layers. Based on these principles, a waveplate for a wavelength of 355 nm was modeled and experimentally fabricated. The resulting coating demonstrates low optical losses and high transparency ($T \approx 99\%$), while indicating the potential to withstand high laser fluence (~40 J/cm²) in the nanosecond regime.

III. Conclusion

Nanostructured optical coatings fabricated by the GLAD technique were investigated as a versatile approach for controlling both reflectance and birefringence. The optical and structural properties of anisotropic layers were analyzed to determine deposition conditions suitable for low-loss birefringent coatings. The results show that nanostructured films exhibit different effective refractive indices along the fast and slow axes, enabling controlled birefringence, while dense and porous layers of the same material can function as high- and low-refractive-index components for reflectance control.

Based on these principles, waveplate structures for the ultraviolet spectral range were modeled and experimentally fabricated. The coatings demonstrate high transparency, low optical losses, and the ability to achieve the required phase delay through controlled anisotropic layer thickness. These results highlight the potential of nanostructured GLAD coatings for multifunctional optical elements, where both reflectance and polarization properties can be tailored for high-power laser and photonic applications.

Acknowledgments

This work has received funding from the Research Council of Lithuania (LMTLT), agreement No. S-LT-TW-24-9

References

[1] L. Ramalis et al. “Near fundamental nanosecond laser damage resistance of nanostructured all-silica mirrors at 355 nm by local laser irradiation”, Results in Optics, 14, 100616 (2024)

[2] L. Grineviciute, H. Badorreck, L. Jensen, D. Ristau, M. Jupé, A. Selskis, T. Tolenis "Impact of deposition conditions on nanostructured anisotropic silica thin films in multilayer interference coatings", Applied Surface Science, 562, 150167, 2021

[3] D. Astrauskyte, M. Slipkauskas S.Tumenas A.Selskiene, L. Ramalis and L. Grineviciute, “Performance and stability evaluation of LaF3 thin-film waveplates for high-power 266 nm laser applications”, Nanoscale, 18, 4127–4134 (2026)

Lattice Resonances in Bipartite Arrays of Nanodisks

J. J. Alvarez-Serrano[1,*], V. Aglieri[2], J. R. Deop-Ruano[1], M. Sohaib[2], A. Toma[2], and A. Manjavacas[1]

[1]Instituto de Física Química "Blas Cabrera" (IQF-CSIC), Madrid, Spain
[2]Istituto Italiano di Tecnologia, Genova, Italy
*Corresponding author: juanjose.alvarez@csic.es

***Abstract*— Two-dimensional, bipartite arrays of nanostructures offer great potential for photonic technologies. By tuning the relative position of the two nanoparticles within the unit cell, we theoretically anticipate and experimentally verify lattice resonances with diverse optical properties, including super- and subradiant modes, noninteracting ones, and out-of-plane polarized resonances.**

***Keywords*— Lattice resonances, periodic arrays, bipartite arrays of nanostructures.**

I. Introduction

Periodic nanoparticle arrays sustain collective lattice resonances arising from far-field interactions [1, 2, 3, 4]. Monopartite arrays provide the simplest platform for attaining these modes but offer limited tunability, typically requiring significant changes in particle size or array period to alter their optical behavior. Bipartite arrays, however, open new possibilities for variations in the optical response due to the interactions between the lattice resonances of its two sublattices. In particular, tuning the relative positions of the two particles within the unit cell enables control of these interactions and access to a broader range of optical responses without modifying the nanostructures themselves.

II. Methods

We combine theoretical calculations, based on the coupled dipole model [2, 5] and the finite-element method, with experimental measurements of bipartite arrays of nanodisks.

III. Results and Discussion

We theoretically and experimentally show that tuning the relative positions of nanostructures within the unit cell enables:

- Excitation of lattice resonances with super- and subradiant character.
- Realization of a bipartite configuration supporting noninteracting modes.
- Access to lattice resonances with out-of-plane character under normal incidence excitation [6].

IV. Conclusion

We have demonstrated that bipartite arrays of nanodisks are versatile platforms for achieving tailored optical responses.

Acknowledgments

This work has been generously supported by Grant No. PID2022-137569NB-C42 that is funded by MICIU/AEI/10.13039/501100011033 and FEDER, EU. J.J.A-S. acknowledges support from an INPhINIT Retaining Fellowship from "La Caixa" Foundation (ID 100010434) with code LCF/BQ/DR24/12080025. He also acknowledges a postgraduate fellowship at Residencia de Estudiantes, funded by the Madrid City Council. A.T, V.A., and M.S. acknowledge support by the European Research Council under the European Union's Horizon 2020 Research and Innovation Program through the ERC Consolidator Grant REPLY (grant agreement n. 101002422).

References

[1] S. Zou, N. Janel, and G. C. Schatz, "Silver nanoparticle array structures that produce remarkably narrow plasmon lineshapes", J. Chem. Phys., vol. 120, pp. 10871–10875, 2004.

[2] F. J. García de Abajo, "Colloquium: Light Scattering by Particle and Hole Arrays", Rev. Mod. Phys., vol. 79, pp. 1267–1290, 2007.

[3] B. Auguié, and W. L. Barnes, "Collective resonances in gold nanoparticle arrays", Phys. Rev. Lett., vol. 101, pp. 143902, 2008.

[4] V. G. Kravets, A. V. Kabashin, W. L. Barnes, and A. N. Grigorenko, "Plasmonic Surface Lattice Resonances: A Review of Properties and Applications", Chem. Rev., vol. 118, pp. 5912–5951, 2018.

[5] S. Baur, S. Sanders, and A. Manjavacas, "Hybridization of lattice resonances", ACS Nano, vol. 12, pp. 1618–1629, 2018.

[6] J. J. Alvarez-Serrano, J. R. Deop-Ruano, V. Aglieri, A. Toma, and A. Manjavacas, "Normal Incidence Excitation of Out-of-Plane Lattice Resonances in Bipartite Arrays of Metallic Nanostructures", ACS Photonics, vol. 11, pp. 301–309, 2024.

Prelude to the Search for Natural Vibrations of Tensegrity-Inspired Cellular Metamaterials

Anna Al Sabouni-Zawadzka[1,*], Adam Zawadzki[2], Wojciech Gilewski[1], Maciej Kołodziejczak[1]

[1]Faculty of Civil Engineering, Warsaw University of Technology, Poland
[2]Faculty of Automotive and Construction Machinery Engineering, Warsaw University of Technology, Poland
*Corresponding author: anna.zawadzka@pw.edu.pl

***Abstract*—Two techniques for estimating the natural frequencies of tensegrity-inspired cellular metamaterials are presented and discussed. The first employs a standard frame/truss geometrically nonlinear finite element model implemented in ABAQUS™. The second uses single-degree-of-freedom modelling based on experimental results for quasi-static compression. Examples focus on a four-strut simplex tensegrity-inspired lattice.**

***Keywords*— cellular metamaterials, tensegrity, additive manufacturing, MJP, finite elements.**

I. Introduction

The final goal of the present project is to experimentally evaluate the natural frequencies of cellular metamaterials [1], [2] with uniform or graded mechanical properties [3]. Cells (or supercells) are inspired by tensegrity modules [4], [5] and lattices are printed with MultiJet Printing (MJP) additive manufacturing technology. Conducting experimental studies on a specific scale requires the selection and calibration of appropriate measuring devices. To do this, one must first estimate the order of magnitude of the measured frequencies. The goal of this paper is to determine the frequency range that can be measured. Such preliminary studies constitute a prelude to the efficient implementation of a more general task, which is to determine the effect of varying degrees of mechanical properties of the lattices on their dynamic response. Two estimation techniques are proposed, which are based on finite element (FE) formulations (frame and lattice models) [6], [7] and semi-experimental estimation based on quasi-static compression tests using a lattice continuum tensegrity model [8], [9]. A mesh consisting of 216 cells (grouped in 27 supercells) based on a four-strut simplex tensegrity module (Figure 1) was chosen as an illustrative task.

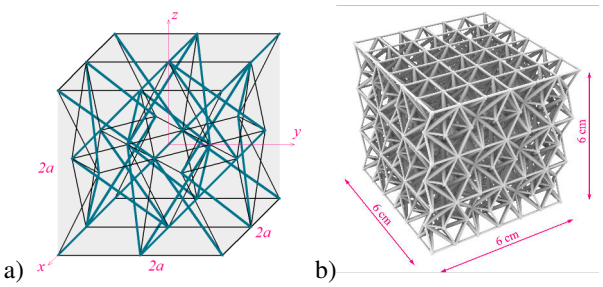

Fig. 1. Simplex-based lattice: a) Supercell; b) Metamaterial.

II. Techniques for Natural Frequency Estimation

The most widely used tool for computational modelling of structures is the FE method [6]. The first approach for estimating natural frequencies is based on the frame and truss models available in ABAQUS™ software, in the geometrically nonlinear range [7]. The FEM enables determination of the natural frequencies and corresponding eigenmodes of free vibrations. The computational data are assumed to be ideal in geometric and physical terms, consistent with the manufacturer's specifications of the printing resin. In the truss model, T3D2 finite elements are used, whereas in the frame model, B32 beam elements are applied, with three elements per each lattice member to ensure convergence.

The second approach for estimating natural frequencies is semi-experimental. Here, the effective stiffness of the lattice K is determined from the force-displacement curve obtained in a quasi-static compression test performed on additively manufactured specimens, whose mass is measured prior to testing. The system is reduced to a single-degree-of-freedom model with stiffness K and mass M, allowing the estimation of the frequency of the assumed vibration mode. Unlike the FEM-based approach, this method relies on experimentally measured properties of the printed metamaterial at the considered scale. This estimation method is motivated by the authors' observation of the uncertainty of the computational data regarding the material properties, which sometimes differ significantly from those declared by the manufacturer and depend on factors such as the time between printing and testing, humidity, and additive manufacturing technology.

Based on the continuum model of tensegrity [8], [9], the properties of the supercell can be expressed in terms of the linear theory of elasticity. In the present study, a truss model is used, which takes into account self-equilibrated normal force systems, leading to the Voight constitutive matrix $\mathbf{E}$ [10]. The effective mechanical properties of the entire structure (Figure 1b) are equivalent to those of the supercell (Figure 1a) [9]. Knowledge of the matrix $\mathbf{E}$ allows estimation of the vibration frequencies corresponding to deformation modes other than those imposed experimentally, such as shear modes.

A reliable theoretical estimation of natural frequencies at the selected scale is essential for the proper design of the experimental campaign for tensegrity-inspired metamaterials.

III. Results and Discussion

The proposed techniques are illustrated using an MJP-printed four-strut simplex lattice (Figure 1b). Each cell has dimensions of $a \times a \times a$, with $a = 1$ cm. The struts and cables have circular cross-sections with diameters of 1.46 mm and 0.65 mm, respectively. The parent material has a Young's modulus of 1612 N/mm^2 and a mass density of 0.001169 g/mm^3.

The first and second natural frequencies in the frame model are 382 Hz and correspond to shear-type vibration in vertical planes. A representative mode (XZ plane) is shown in Figure 2a. The colour scale represents the magnitude of the total displacement. The third natural frequency is 570 Hz and corresponds to a vertical (Z direction) extensional mode (Figure 2b). The natural frequencies obtained from the truss model are about 20% lower, reflecting the increased flexibility of the lattice compared to the beam-based representation.

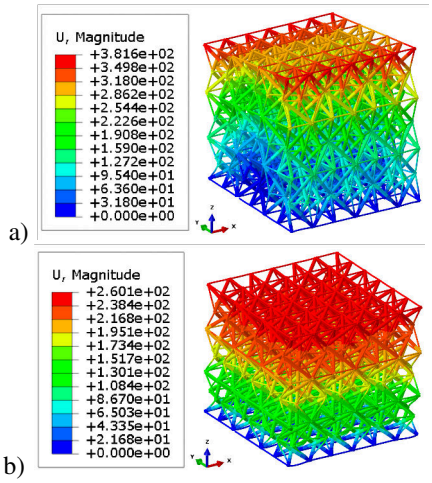

Fig. 2. Eigenmodes: a) Shear; b) Volumetric.

The semi-experimental estimation is based on a quasi-static compression test performed on the Instron 5567 testing machine (Figure 3a). The resulting force-displacement curve averaged for five specimens (with standard deviation marked) is shown in Figure 3b. The experimentally determined tangential stiffness is approximately 200 N/mm, and the average mass of the specimen is 32.84 g.

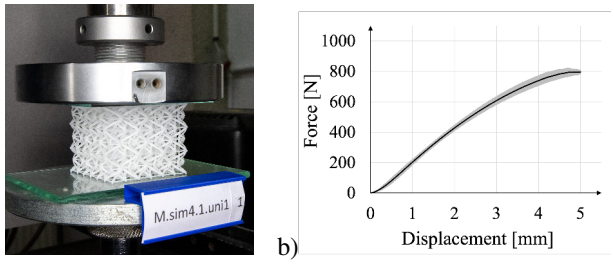

Fig. 3. Experiment: a) Compression test; b) Force-displacement graph.

The natural frequency of the single-degree-of-freedom system is estimated as 367 Hz, which is lower than the value of 570 Hz obtained from the FEM, but remains within the same order of magnitude. The quantitative discrepancy may result from uncertainty in the Young's modulus used in the FEM and the physical linearity of the computational model.

An estimate of the shear-type eigenfrequency can be obtained from the square root of the ratio of the coefficients e_{55} and e_{33} in the elasticity matrix $\mathbf{E}$ derived from the continuum model [9] for the supercell (Figure 1a):

$$e_{33} = \frac{EA}{a^2}\left(1.1851 + 2.1466k - 0.3449\sigma\right), \tag{1}$$

$$e_{55} = \frac{EA}{a^2}\left(0.7407 + 0.2683k + 0.1724\sigma\right), \tag{2}$$

where: EA— stiffness of the strut, k—cable-to-strut stiffness ratio, σ—level of self-equilibrated normal forces.

Neglecting the small influence of σ, the shear-mode vibration frequency for the single-degree-of-freedom quasi-experimental model can be estimated as $0.7 \times 367 \approx 257$ Hz.

IV. Conclusion

The two techniques presented for estimating the natural frequencies of cellular tensegrity-inspired metamaterials allow the determination of the order of magnitude of their dynamic response. The semi-experimental single-degree-of-freedom formulation leads to values slightly lower than those obtained from the FE analysis, but of the same order. The discrepancy can be attributed to uncertainties in the computational input data. For the structure fabricated using the MJP technique and inscribed in a 6 cm cube with four-strut simplex cells, the lowest natural frequency was estimated to be approximately 257 Hz.

Acknowledgments

This research was funded in whole by National Science Centre, Poland, grant no. 2024/55/B/ST8/00475. For the purpose of Open Access, the author has applied a CC BY public copyright licence to any Author Accepted Manuscript (AAM) version arising from this submission.

References

[1] T. A. Schaedler and W. B. Carter, "Architected cellular metamaterials," *Annual Review of Materials Research*, vol. 46, pp. 187–210, 2016.
[2] C. Pan, Y. Han, and J. Lu, "Design and optimization of lattice structures: A review," *Applied Sciences*, vol. 10, p. 6374, 2020.
[3] H. Niknam and A. H. Akbarzadeh, "Graded lattice structures: Simultaneous enhancement in stiffness and energy absorption," *Materials & Design*, vol. 196, p. 109129, 2020.
[4] R. Skelton and M. Oliveira, *Tensegrity Systems*. Springer, 2009.
[5] K. J. Bathe, *Finite Element Procedures in Engineering Analysis*. Prentice-Hall, 1996.
[6] J. Pełczyński, "On equivalence of algebraic and finite element formulations of prestressed bar structures," *Scientific Reports*, vol. 15, pp. 1–15, 2025.
[7] A. Al Sabouni-Zawadzka, *High Performance Tensegrity Inspired Metamaterials and Structures*. CRC Press, 2022.
[8] W. Gilewski and A. Kasprzak, "3D continuum models of tensegrity modules with the effect of self-stress," in *Proc. 11th World Congress on Computational Mechanics and 5th European Conference on Computational Mechanics*, Barcelona, Spain, 2014.
[9] W. Gilewski and A. Al Sabouni-Zawadzka, "Equivalent mechanical properties of tensegrity truss structures with self-stress included," *European Journal of Mechanics–A/Solids*, vol. 83, p. 103998, 2020.
[10] A. E. Green and W. Zerna, *Theoretical Elasticity*. Oxford University Press, 1968.

Scalable Metafibres for Advanced Imaging via On-Fibre Wavefront Engineering and Wavefront Shaping

Fei He[1], Rafael Fuentes Dominguez[1], Terry Wright[1], George S.D. Gordon[1]

[1]Optics and Photonics Research Group, Faculty of Engineering, University of Nottingham
*Corresponding author: george.gordon@nottingham.ac.uk

***Abstract*— Metasurfaces and diffractive optics integrated onto fibre tips can extend the capabilities of ultrathin imaging probes, but scalable fabrication remains a key challenge. We present transfer-fabricated metafibres and show how their combination with transmission-matrix wavefront shaping enables improved focusing, depth control, and advanced fibre-based imaging.**

Keywords—metafibres, metasurfaces, multimode fibre imaging, wavefront shaping

I. Introduction

Optical fibre endoscopes with diameters comparable to a human hair are attractive for minimally invasive imaging because they can access confined environments while supporting modalities including confocal, fluorescence, polarization-sensitive, and optical coherence tomography (OCT) imaging [1-4]. Their utility can be further expanded by incorporating on-tip optical functionality that shapes the emitted field, for example to improve lateral resolution, extend depth of field, or tailor contrast for a specific modality [3]. However, many established routes for producing fibre-tip micro-optics—including focused-ion-beam milling, direct laser writing, nanoimprinting, and serial lithographic patterning—remain difficult to scale to large numbers of low-cost devices. Transfer-based manufacturing offers a more practical path that can exploit wafer-level processing, but many existing demonstrations have been restricted to relatively simple or single-layer geometries [5,6]. Here we build on scalable transfer methods to realise single- and multi-layer metasurface devices on fibre probes, with architectures relevant to advanced imaging [8].

Multimode fibres (MMFs) are particularly compelling imaging platforms because they provide thousands of spatial degrees of freedom within an exceptionally small form factor. When the propagation through the fibre is measured through its transmission matrix (TM), wavefront shaping can be used to synthesize focused spots at the distal end and scan them to form images. TM-based approaches have already enabled high-resolution reflectance and fluorescence imaging as well as volumetric refocusing through a single MMF [1,2,7]. A key limitation, however, is that the resolution of a bare MMF is bounded by its numerical aperture (NA), which is set by the refractive-index contrast of the waveguide. For typical fibres this constrains the minimum focal width to around the micron scale at visible wavelengths, even under ideal calibration conditions. As a result, bare-fibre systems cannot fully exploit the available wavefront control to exceed the intrinsic focusing capability of the guide.

A powerful strategy is therefore to combine calibrated wavefront shaping with distal optical structures that add new spatial-frequency content or modify the phase response at the output facet. Plasmonic metasurfaces have been explored for this purpose, but scalable fabrication and system-level calibration remain significant challenges [10]. In this work we focus on transferred metasurface and diffractive elements—including Fresnel zone plates (FZPs) and axicons—that can be integrated onto fibre facets using a manufacturable process. These structures increase the effective optical functionality of the probe by supporting tighter focusing or extended-depth-of-field beams at a designed working distance from the facet. When combined with TM measurement, the fibre and on-tip element can be treated as a single composite optical system, allowing the engineered field to be scanned and exploited for imaging rather than acting as a fixed passive optic.

We therefore present a unified framework in which scalable metafibre fabrication and advanced wavefront shaping are developed together for imaging. We describe the transfer-based fabrication of single- and multi-layer devices on fibre end facets, and we discuss representative imaging behaviour from composite MMF-meta-optic systems. In particular, we show that FZP-based metafibres can produce focal spots that are smaller than those obtained with the corresponding bare fibres, while axicon-based metafibres can generate needle-like beams with substantially extended depth of field. These capabilities are directly relevant to raster-scanned MMF imaging and to hybrid modalities such as polarization-resolved imaging, where tailored distal wavefronts can improve either resolution, depth tolerance, or modality-specific contrast [11].

II. Methods

Metafibres were fabricated by defining planar diffractive and metasurface patterns on a donor substrate using wafer-compatible lithographic processing, followed by transfer of the patterned structures onto cleaved optical fibre facets (Fig. 1). The process supports both single-layer and stacked devices, enabling not only simple lenses but also more advanced multi-layer optical functions [8]. In parallel, the optical response of

selected multimode-fibre devices was characterised using transmission-matrix measurement so that the proximal input field could be optimized to generate controlled distal foci or extended beams after propagation through the combined fibre-meta-optic system [7].

To assess imaging relevance, we considered transferred Fresnel zone plates and axicons as exemplar devices. The FZP designs were chosen to provide a finite working distance and enhanced focusing strength, while the axicon designs were used to generate Bessel-like beams with extended axial invariance. Device performance was evaluated through distal beam profiling and resolution-target imaging, and preliminary compatibility with OCT instrumentation was assessed to examine the suitability of the metafibre approach for depth-resolved biomedical imaging [8].

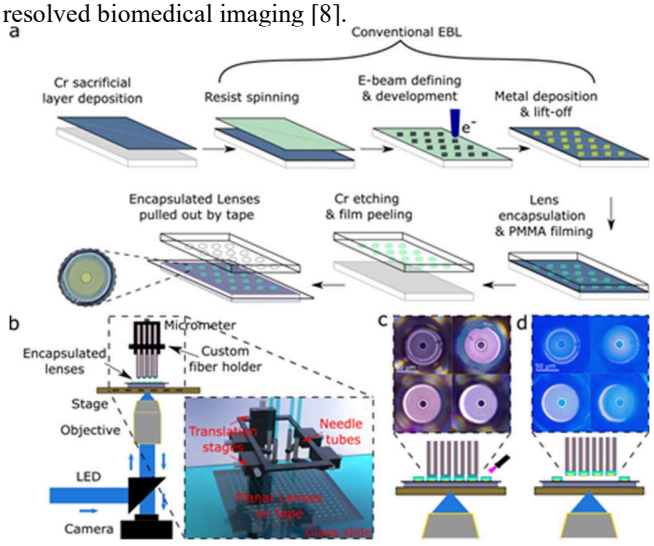

Fig. 1. Scalable fabrication process for transferring single- and multi-layer metasurface devices onto fibre facets [8].

III. Results and Discussion

The transferred devices demonstrate that wafer-scale fabrication and fibre-tip optical engineering can be combined without sacrificing imaging function. Fresnel zone plate metafibres produced compact focal spots at working distances of a few hundred micrometres from the fibre facet, allowing imaging to be performed beyond the near-contact regime of a bare fibre. In representative measurements, the zone-plate devices generated a near-Gaussian focus around 235 um from the tip with an axial extent of roughly 100 um.

To demonstrate imaging performance, we fabricated and transferred Fresnel zone plates onto fibers. The zone plate produced a tight Gaussian focus at ~235 µm with a 100 µm depth of field (DOF), enabling high-fidelity imaging at distances inaccessible to bare fibers, though with some background speckle.

Spot-size measurements as a function of imposed input NA further support the benefit of combining on-fibre diffractive elements with wavefront shaping. For FZP on both 50 um and 110 um core diameter MMFs, the composite fibre-FZP system produces smaller focal spots than the corresponding bare fibre under the same illumination constraints, with the larger FZP giving the strongest improvement. In practice, the effective NAs inferred from the measured spot widths remain below the nominal fibre NA of 0.22. This likely reflects non-ideal TM calibration, finite detector sampling, uncertainty in identifying the exact focal plane, and imperfect field synthesis at the proximal modulator. These effects also explain the residual intensity variation between nominally identical scanned spots. Even so, because the same experimental limitations apply to both bare-fibre and metafibre measurements, the observed improvement provides a conservative estimate of the enhancement enabled by the FZP.

More broadly, these results underline the value of treating the metafibre not simply as a static micro-optic but as part of an actively controlled imaging system. Scalable transfer lithography enables high-performance optical structures to be placed at the distal tip, while TM-based wavefront shaping provides the adaptive control needed to exploit those structures across the field of view. This combination is particularly promising for advanced imaging, where one wishes to tailor beam shape, working distance, and resolution in a modality-specific manner. The same platform could support future probes for OCT, multiphoton excitation, polarization-sensitive imaging, or structured illumination endoscopy.

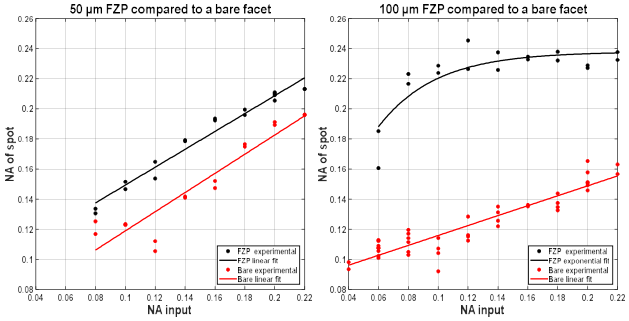

Fig. 2. Comparison of focal-spot full width at half maximum (FWHM) obtained when restricting the proximal input modes to different effective illumination NAs, for bare fibres and for fibres carrying transferred FZPs [9]

IV. Conclusion

Metafibres produced by scalable transfer lithography offer a practical route to advanced fibre-end probes that unite manufacturable nanophotonics with adaptive optical control. By integrating Fresnel zone plates, axicons, and potentially more complex multilayer metasurfaces onto fibre facets, it becomes possible to engineer the distal field for specific imaging tasks while preserving the compactness required for minimally invasive access. When these devices are combined with transmission-matrix characterisation and wavefront shaping, the resulting composite system can deliver tighter focusing, longer working distance, or extended depth of field compared with a bare fibre, all of which are highly relevant for practical endoscopic imaging.

The broader significance is that fabrication and control should be developed together: scalable metafabrication

provides the optical functionality, and wavefront shaping turns that functionality into a flexible imaging tool. This co-design perspective opens a path toward disposable or application-specific fibre probes for OCT and other advanced modalities, with scope for further gains through improved multilayer devices, better calibration fidelity, and modality-optimised meta-optic designs.

ACKNOWLEDGMENTS

GSDG acknowledges support from a UKRI Future Leaders Fellowship (MR/Y034163/1) and the Medical Research Council DPFS scheme (UKRI793).

REFERENCES

[1] Loterie, Damien, et al. "Digital confocal microscopy through a multimode fiber." *Optics express* 23.18 (2015): 23845-23858.
[2] Gataric, Milana, et al. "Reconstruction of optical vector-fields with applications in endoscopic imaging." *IEEE transactions on medical imaging* 38.4 (2018): 955-967.
[3] Pahlevaninezhad, Hamid, et al. "Nano-optic endoscope for high-resolution optical coherence tomography in vivo." *Nature photonics* 12.9 (2018): 540-547.
[4] Cao, Rui, et al. "Optical-resolution photoacoustic microscopy with a needle-shaped beam." *Nature photonics* 17.1 (2023): 89-95.
[5] Picelli, Luca, et al. "Scalable wafer-to-fiber transfer method for lab-on-fiber sensing." *Applied Physics Letters* 117.15 (2020).
[6] Sun, Xiaqing, et al. "A quasi-3D Fano resonance cavity on optical fiber end-facet for high signal-to-noise ratio dip-and-read surface plasmon sensing." *Light: Advanced Manufacturing* 3.4 (2022): 665-675.
[7] Gordon, George SD, et al. "Characterizing optical fiber transmission matrices using metasurface reflector stacks for lensless imaging without distal access." *Physical review X* 9.4 (2019): 041050.
[8] He, Fei, et al. "Scalable fabrication of single-and multi-layer planar lenses on fiber imaging probes." APL Photonics 10.5 (2025).
[9] Wright, Terry, et al. “Enhanced numerical aperture in a multimode fibre via a distal Fresnel zone plate for high-resolution imaging.” Proc. SPIE 13866, Endoscopic Microscopy XXI, 1386602 (2026)
[10] Collard, L. et al. “Holographic Manipulation of Nanostructured Fiber Optics Enables Spatially-Resolved, Reconfigurable Optical Control of Plasmonic Local Field Enhancement and SERS.” Small2022, 18, 2200975 (2022)
[11] George, George S.D. et al. “Quantitative phase and polarization imaging through an optical fiber applied to detection of early esophageal tumorigenesis”, Journal of Biomedical Optics, vol. 24, no. 12 (2019).

Nitride-based nanoparticles for metasurfaces

E. Salvaggio[1,2], J. Béal[1,2], G. Abadias[3], S. Camelio[3], D. Babonneau[3], D. Gérard[1,2], C. Couteau[1,2] and J. Plain[1,2,*]
[1]L2n, University of technology of Troyes and CNRS, Troyes, France
[2] EUTINN, European University of Technology Eut+, EU
[3] Institut Pprime, Département Physique et Mécanique des Matériaux, CNRS and Université de Poitiers, SP2MI, Poitiers, France
*Corresponding author: jerome.plain@utt.fr

***Abstract*— This work characterizes nitride-based nanoparticle arrays and shows that stoichiometry can be used to adjust their plasmonic and photothermal responses. Measurements and simulations reveal narrow, tunable, and robust plasmonic network resonances that show promise for nitride-based devices and metasurfaces.**

***Keywords*— metamaterials, nitrides, TiN, ZrN, plasmonics.**

I. Introduction

Transition metal nitrides, and in particular titanium nitride (TiN) and zirconium nitride (ZrN), are emerging as robust alternatives to noble metals for plasmonics owing to their high thermal stability, CMOS compatibility, and tuneable optical response. In this work, we provide a combined experimental and numerical study of nitride thin films and lithographically defined nitride nanoparticle arrays, and we assess their potential for near-field enhancement, photothermal conversion, and surface lattice resonance engineering from the visible to the near-infrared.

II. Methods

TiN and ZrN films are grown by DC magnetron sputtering under mixed Ar/N_2 atmospheres, with the nitrogen flow systematically varied to tune stoichiometry. A comprehensive characterization of the structural properties was conducted on the various samples. From UV–visible transmission we determine indirect optical bandgaps in the 1.2–2.4 eV range, with values and trends that differ from many literature reports due to the nature of the electronic transitions and stoichiometry.

III. Results and Discussion

Using the measured optical constants, we quantify for each film the Faraday and Joule figures of merit, which separate near-field enhancement from heat generation [1]. ZrN exhibits a pronounced plasmonic resonance around 500–600 nm with strong near-field enhancement but limited broadband photothermal response, whereas TiN shows a broader response extending into the near-IR, with a Joule number that remains significant at long wavelengths, making it attractive for broadband heat generation.

We then fabricate square arrays of nitride nanoparticles (cones and truncated cones) on fused silica by electron-beam lithography and reactive ion etching, covering diameters from 120 to 200 nm, heights from 40 to 80 nm, and periods from 200 to 700 nm. Extinction spectra are measured in a quasi-symmetric dielectric environment by index-matching glycerol, and are compared to 3D FDTD simulations using the experimentally retrieved n and k. We observe good agreement between experiment and theory, including the emergence of narrow, Fano-like lattice resonances when the localized surface plasmon of individual particles hybridizes with Rayleigh anomalies of the array. Increasing the period produces red-shifts and linewidth narrowing consistent with plasmonic surface lattice resonances, while increasing particle size induces a strong red-shift and broadening in line with Mie-type behaviour.

IV. Conclusion

Our results demonstrate that both TiN and ZrN support strong, tuneable plasmonic and lattice-mode responses, with the nitride stoichiometry offering an additional handle to engineer linewidth, resonance position, and the balance between field enhancement and photothermal conversion. These properties make nitride nanoparticle arrays promising platforms for robust, high-temperature plasmonic devices, meta surfaces, and thermoplasmonic applications where conventional noble metals are limited.

Acknowledgments

This work was supported by the French National Agency for Research ANR under contracts NATO (ANR-13-BS10-0013) and NOSE (ANR-21-CE39-0014).

References

[1] A. Lalisse, G.Tessier, J. Plain and G. Baffou, "Quantifying the efficiency of plasmonic materials for near-field enhancement and photothermal conversion," The Journal of Physical Chemistry C 119 (45), 25518-25528, 2025.

Abnormal hot carrier thermalization at van Hove singularities in twisted bilayer graphene

Nianze Shang[1], Chen Huang[2], Kaihui Liu[2], Zhipei Sun[1,*]

[1]Department of Electronics and Nanoengineering, Aalto University, Finland
[2]School of Physics, Peking University, China
*Corresponding author: zhipei.sun@aalto.fi

***Abstract*— We reveal abnormal hot carrier thermalization in twisted bilayer graphene at van Hove singularities using time-resolved ultrafast photoluminescence autocorrelation spectroscopy. A prolonged relaxation lifetime of approximately 600 femtoseconds is observed due to phonon bottleneck and interlayer charge redistribution, unveiling nonequilibrium dynamics in moiré-engineered graphene.**

***Keywords*— Twisted bilayer graphene, van Hove singularity, ultrafast spectroscopy, hot carrier dynamics, moiré photonics**

I. Introduction

Moiré engineering provides a powerful route to tailor electronic and optical properties of two-dimensional materials. Twisted bilayer graphene (TBG) exhibits angle-dependent band reconstruction, leading to van Hove singularities with enhanced density of states and strong light–matter interaction. While ground-state properties of twisted graphene systems have been extensively explored, their nonequilibrium excited-state dynamics remain largely unexplored. Understanding hot carrier thermalization at van Hove singularities is essential for developing ultrafast optoelectronic and photonic devices based on moiré materials.

II. Methods

TBG samples with controlled twist angles were fabricated via dry transfer and encapsulated with hexagonal boron nitride. Ultrafast photoluminescence (PL) measurements were performed using femtosecond pulsed laser excitation. Time-resolved ultrafast PL autocorrelation spectroscopy was employed to directly probe hot carrier relaxation dynamics with sub-30 femtosecond temporal resolution. Ground-state electronic structures were calculated using density functional theory. Real-time time-dependent density functional theory simulations were conducted to model carrier thermalization and electron–phonon coupling processes.

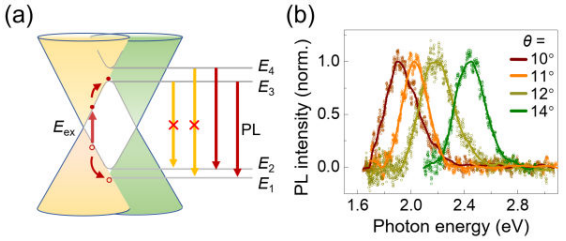

Fig. 1 Ultrafast PL of TBG. a. Schematic of optical selection rules of ultrafast PL in TBG. b. Twist angle dependent PL peaks.

III. Results and Discussion

Ultrafast PL spectra of twisted bilayer graphene exhibit distinct emission peaks associated with van Hove singularities, absent in monolayer graphene. The emission peak energy depends strongly on twist angle, confirming its moiré origin.

Time-resolved ultrafast PL autocorrelation measurements reveal two distinct relaxation channels. Carriers on linear Dirac bands relax within approximately 150 femtoseconds, comparable to monolayer graphene. In contrast, carriers associated with van Hove singularities exhibit a significantly prolonged lifetime of approximately 600 femtoseconds.

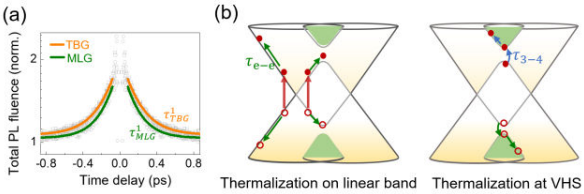

Fig. 2 Abnormal hot carrier thermalization. a. Prolonged hot carrier lifetime of TBG. b. Abnormal thermalization at VHS.

Time-dependent density functional theory simulations show that this abnormal thermalization arises from Mini-gap bottleneck effects near van Hove singularities that suppress rapid intraband scattering and interlayer charge redistribution processes that slow carrier relaxation in real space.

These findings demonstrate that moiré band engineering not only modifies static density of states but fundamentally reshapes nonequilibrium carrier dynamics.

IV. Conclusion

We experimentally and theoretically demonstrate abnormal hot carrier thermalization at van Hove singularities in twisted bilayer graphene. The prolonged relaxation lifetime originates from phonon bottlenecks and interlayer charge redistribution enabled by moiré band reconstruction. This work establishes twisted bilayer graphene as a platform for engineering ultrafast carrier dynamics and moiré-enabled photonic functionalities.

Acknowledgments

This work was supported by the MSCA Actions (ALTOS).

References

[1] Shang N, et al. Evidence of abnormal hot carrier thermalization at van Hove singularity of twisted bilayer graphene. Science Bulletin 2024, 69, 2522-2528.
[2] Lui CH, Mak KF, Shan J,Heinz TF. Ultrafast photoluminescence from graphene. Phys Rev Lett 2010, 105, 127404.
[3] Liu W-T, Wu SW, Schuck PJ, et al. Nonlinear broadband photoluminescence of graphene induced by femtosecond laser irradiation. Phys Rev B 2010, 82, 081408.
[4] Tomadin A, Brida D, Cerullo G, et al. Nonequilibrium dynamics of photoexcited electrons in graphene: Collinear scattering, Auger processes, and the impact of screening. Phys Rev B 2013, 88, 035430.

Wavelet-Fourier Modal Method for very Large-Beam Scattering in Photonics and Biophotonics

K. Edee[1]

[1]Université Clermont Auvergne, Institut Pascal, BP 10448,
F-63000 Clermont-Ferrand, France
CNRS, UMR 6602, IP, F-63171 Aubière, France
kofi.edee@uca.fr

Abstract— We present a physics-based computational framework for wide-beam electromagnetic scattering in large-scale, aperiodic, and anisotropic media. The approach combines wavelet decomposition with the Aperiodic Fourier Modal Method (AFMM), enabling scalable full-wave simulations over extended domains. A wide incident beam is represented as a superposition of localized beamlets propagated through overlapping subdomains, ensuring efficient computation and smooth field reconstruction in strongly heterogeneous and anisotropic structures. The method provides physically interpretable near-field observables, including spatial variance, kurtosis, and anisotropy indices, with applications to terahertz biophotonic imaging and, also an the efficient design of photonic metasurfaces.

ACKNOWLEDGMENT

This publication is based upon work from COST Action "The metamaterial formalism approach to recognize cancer" CA23125, supported by COST (European Cooperation in Science and Technology).

Multiphoton Luminescence and Second Harmonic Imaging in 2D Materials

Arik Ahmed[1], J. Pierce Fix[2], Sheikh Parvez[2], Jane Peabody[2], Nicholas J. Borys[2], Steve Smith[1†*]

[1]Nanoscience & Biomedical Engineering, South Dakota School of Mines and Technology, 501 East St. Joseph St, Rapid City, SD, USA 57701

[2]Department of Physics and Astronomy, University of Utah, Salt Lake City, UT, USA 84112

Corresponding author email: Steve_Smith@mailaps.org

Abstract: Two-dimensional (2D) materials show potential for compact, low-profile on-chip quantum computing and quantum communications applications. In particular, the second-order nonlinear polarizability $\chi^{(2)}$, an important materials parameter for the generation of entangled photon pairs via parametric downconversion, can be notably enhanced in monolayer 2D materials. The relationship between this nonlinear susceptibility and multi-layer stacking, orientation and material defects can be revealed by spectroscopic, polarization-resolved imaging. A spectrally-resolved multi-photon luminescence (MPL) and second harmonic generation (SHG) imaging microscope is used to examine the nonlinear optical properties of 2D materials and their heterostructures. We visualize the spectrally-resolved MPL and SHG in multi-layer two-dimensional (2D) materials WSe_2, In_2Se_3 and their heterostructures. In WSe_2, we observe the correlation between the symmetry-induced suppression of SHG for even-numbered layers, where inversion symmetry is established, and the presence of edge and localized defect states on the finite-sized 2D flakes, revealed by variations in MPL. The polarization-resolved SHG in the single and multi-layer 2D material identifies the symmetry and orientation of the layers. The application of the methods to determine $\chi^{(2)}$ in multi-layer heterostructures is also described.

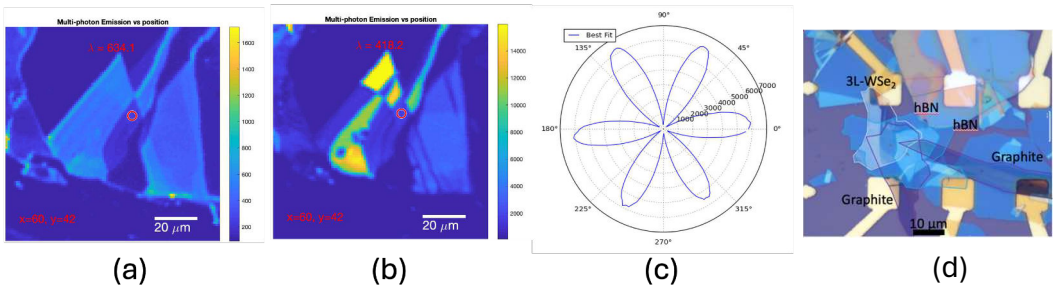

Figure: (a) Multiphoton luminescence from few-layer WSe_2 flakes; (b) second harmonic image formed at λ=418nm of sample shown in (a); (c) polarization resolved second harmonic from few-layer WSe_2 flakes; (d) heterostructure of hBN/few-layer-WSe_2.

† We acknowledge the MonArk NSF Quantum Foundry supported by the National Science Foundation Q-AMASE-i program under NSF award No. DMR-1906383 and the Quantum Materials Institute, supported by the National Science Foundation ExpandQISE program under NSF award No. 2427079.

Laser-induced formation of plasmonic nanostructures

Rodrigas Liudvinavičius, Kernius Vilkevičius, Evaldas Stankevičius*

Department of Laser Technologies, Center for Physical Sciences and Technology, Lithuania
*Corresponding author: evaldas.stankevicius@ftmc.lt

***Abstract* — Plasmonic nanostructures enable strong light matter interactions and advanced optical functionalities but are commonly fabricated using costly and low throughput lithographic techniques. We demonstrate laser induced formation of plasmonic nanostructures using direct laser writing enabling single step chemical free large area fabrication suitable for scalable and cost-effective photonic applications.**

***Keywords* — metasurfaces, plasmonic nanostructures, femtosecond laser, direct laser writing.**

Plasmonic structures are engineered systems capable of manipulating and controlling the behavior of surface plasmons, enabling strong light–matter interactions, enhanced optical absorption, and efficient light emission. These properties make plasmonic nanostructures highly attractive for applications in sensing, photonics, energy harvesting, and optical security. Conventionally, such structures are fabricated using high-resolution nanolithography techniques[1, 2], including electron-beam lithography and focused ion beam milling. While these methods provide excellent precision, they are inherently time-consuming, costly, and limited in scalability, which restricts their applicability for large-area and commercially viable production.

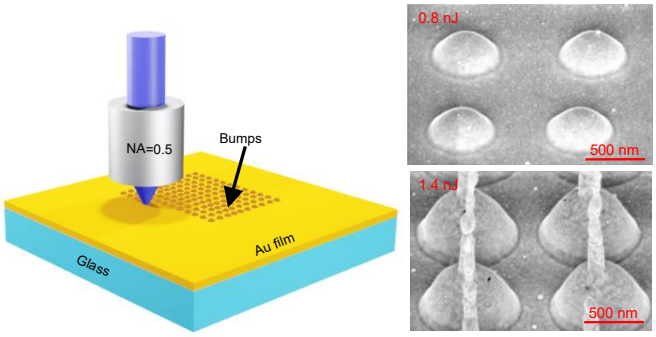

Fig. 1. Laser-induced nanostructuring on a thin Au film (left) and SEM images of structures morphologies formed at different pulse energies (right). Scale bars : 500 nm.

Laser-based fabrication techniques [3-9] have emerged as a promising alternative for the formation of plasmonic nanostructures. In contrast to conventional lithographic approaches, laser processing enables single-step, maskless patterning over large areas without the need for chemical processing or vacuum-based equipment. This significantly reduces fabrication complexity, processing time, and overall production costs. Moreover, laser-induced nanostructuring offers high flexibility in tailoring surface morphology (Fig. 1) and optical response by adjusting laser parameters such as fluence, pulse duration, and scanning strategy.

Here, the formation of plasmonic nanostructures using the direct laser writing technique will be explored. The laser–matter interaction mechanisms responsible for nanoscale structure formation, along with the resulting plasmonic properties of the fabricated surfaces, will be discussed. The demonstrated approach enables scalable fabrication of functional plasmonic structures over areas up to tens of square millimeters, making it particularly attractive for practical and industrial applications. The presented results highlight the potential of laser-based nanofabrication as a cost-effective and versatile route toward next-generation plasmonic devices.

Acknowledgments

This work was funded by the Research Council of Lithuania (LMTLT), project No S-LT-TW-25-3.

References

[1] G. Barbillon, J.L. Bijeon, J. Plain, M.L. de la Chapelle, P.M. Adam, P. Royer, "Electron beam lithography designed chemical nanosensors based on localized surface plasmon resonance," Surf. Sci., vol. 601, pp. 5057-5061, 2007.

[2] M. Horak, K. Bukvisova, V. Svarc, J. Jaskowiec, V. Krapek, T. Sikola, "Comparative study of plasmonic antennas fabricated by electron beam and focused ion beam lithography," Sci. Rep., vol. 8, pp. 9640, 2018.

[3] R. Liudvinavičius, E. Stankevičius, "Influence of gold microbump array size on the hybrid lattice plasmon resonance quality," Opt. Mater., vol. 173, pp. 117873, 2026.

[4] R. Liudvinavičius, A. Selskis, E. Stankevičius, "Titanium adhesion layer influence on the formation of hybrid lattice plasmon structures via laser-direct writing," Opt. Laser Technol., vol. 175, pp. 110807, 2024.

[5] K. Vilkevičius, I. Ignatjev, A. Selskis, G. Niaura, E. Stankevičius, "Tuning SERS performance through the laser-induced morphology changes of gold nanostructures," Appl. Surf. Sci., vol. 660, pp. 160003, 2024.

[6] K. Vilkevičius, G.D. Tsibidis, A. Selskis, E. Stratakis, E. Stankevičius, "Formation of Highly Tunable Periodic Plasmonic Structures on Gold Films Using Direct Laser Writing," Adv. Opt. Mater., vol. 12, pp. 2400172, 2024.

[7] K. Vilkevičius, K. Čepaitis, A. Selskis, E. Stankevičius, "Ultrafast laser ablation and modification of thin metal film for quasi-1D array formation," Opt. Laser Technol., vol. 183, pp. 112330, 2025.

[8] R. Liudvinavičius, K. Vilkevičius, E. Stankevičius, "High-quality grating-coupled surface plasmon resonances in silver and gold bumps arrays fabricated in thin metallic films using the third harmonic of femtosecond laser," Appl. Surf. Sci., vol. 711, pp. 164127, 2025.

[9] K. Vilkevičius, T. Rakickas, E. Stankevičius, "High-Quality Plasmonic Ag─Au Bilayer Nanobump Grating Sensor," Adv. Mater. Technol., vol. 10, pp. e01199, 2025.

Integration of metamaterial phase-shifting ICs in 3D-printed packages for wireless communication

Adam Pander[1,*], Kentaro Soeda[2], Daisuke Kitayama[1], Hibiki Kagami[1], Yoshinori Yamaguchi[2], Kuniaki Konishi[2], Junji Yumoto[2], Hiroyuki Takahashi[1]

[1]NTT Device Technology Laboratories, NTT Inc., Japan
[2]Institute for Photon Science and Technology, The University of Tokyo, Japan
*Corresponding author: adam.pander@ntt.com

***Abstract*— This study shows metamaterial phase-shifting integrated circuits with continuous 2π phase controllability operating at 300 GHz. To cope with the demand for high-density packaging in future beamforming devices, chips were mounted in hollow waveguide modules fabricated using a high-resolution 3D printer (RECILS). The phase-shifting characteristics were evaluated.**

***Keywords*— metamaterials, integrated circuits, phase shifter, terahertz, wireless communication, 3D printing.**

I. Introduction

In recent years, rapid advancements in semiconductor technology have opened many opportunities for new applications. One of these new applications that gained a lot of attention is related to terahertz waves, in particular from 100 to 500 GHz, which is a promising candidate for the development of high-capacity and high-speed wireless communication networks [1]. In wireless communication, the gradually increasing sophistication and data usage demand require larger bandwidths, higher data rates, and high-capacity systems that can support a large number of users simultaneously.

Metamaterials have revolutionized electromagnetic wave control. The growing demand for advanced terahertz technologies necessitates innovative material design approaches. However, despite very promising characteristics of terahertz waves, problems with non-line-of-sight propagation, atmospheric attenuation, or low wave wraparound are still challenging to overcome [2]. To address these issues, high-gain and highly directive antennas that can configure their radiation pattern to avoid obstacles and guide the wave in free space are necessary. In terahertz bands, the use of conventional phase arrays brings many challenges [3], including complex feed networks, large chip size compared to the wavelength, small antenna size, and resulting small gain, etc.

In this work, to tackle these issues, a metamaterial phase-shifting integrated circuit (IC) is designed to control the transmission phase of the electromagnetic (EM) wave propagating through the hollow waveguide. The design and fabrication of the chip were based on an indium phosphide (InP) semiconductor process. To cope with future development and the necessity for multichannel beamforming devices that are easy to handle and provide beam control in azimuth and elevation, a high-resolution 3D printing technology is used. 3D printing is a simple and cheap fabrication method of complex beamforming structures that can host multiple chips with various functions, providing more design freedom and flexibility than commercially used technology.

II. Methods

Fig. 1(a) shows an image of the split block module package that was designed to host metamaterial IC chips, and was fabricated using RECILS, utilizing photosensitive acrylic resin [4]. The package module includes a WR3.4 rectangular waveguide (300 GHz band) and chip mounting area in the center. To allow for guided transmission of the EM waves through the structure, the inner walls of the package were electroless plated with Cu film, as shown in the figure. The package was divided along the ***H*** plane of the waveguide, allowing for the placement of the chip along the ***E*** plane.

The inset shows a magnification of the surface of the 3D printed package with Cu plating. As can be seen, the individual passes of the printer are visible, and although, in this work, the *z*-axis (additive layer thickness) resolution of RECILS was about 20 μm (50 times smaller than the wavelength at 300 GHz), the device easily achieves the fabrication of palm-sized objects.

Fig. 1(b) shows images of fabricated metasurface IC chips [5]. An active metamaterial unit cell based on Jerusalem cross geometry was used with integrated indium phosphide high-electron mobility transistors (InP-HEMT). Transistors are used as variable capacitors and can dynamically adjust the capacitance in the gap of metamaterials, in response to negative bias voltage applied to the gate. The chip placement in 3D printed packages aligns the electric field along gaps with incorporated HEMTs, so the excited resonance can be tuned by the change of the total capacitance (C_{GS}, C_{GD}, C_{DS}) of the transistors. In this work, two types of chips were designed and fabricated, one with 39 cells (3×13 cells – 3 cell chip (3C)) and one with 72 cells (4×18 cells – 4 cell chip (4C)). The size of

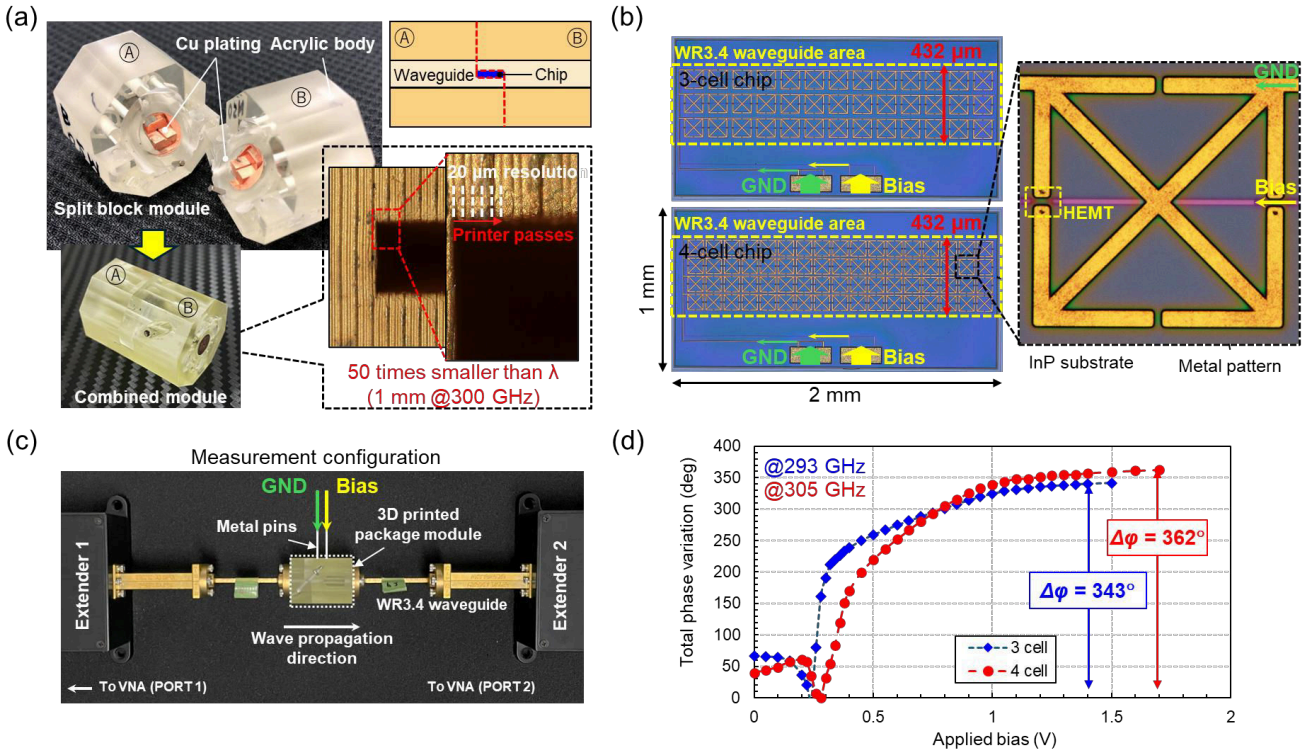

Figure 1. (a) Acrylic 3D-printed split block module for 300 GHz band fabricated with 20 µm step resolution. (b) Images of fabricated metamaterial chips and the magnification of a single cell. (c) Measurement setup and results of the total phase variation evaluation.

both chips was 1×2 mm.

III. Results and Discussion

Fig. 1(c) presents the measurement setup used in this work. The RF signal from the vector network analyzer (VNA) was applied through J-band (220-3 GHz) extenders to the device. The negative bias from an external DC power supply was applied to the metamaterial IC chips through pins and internal wiring. Fig. 1(d) shows changes of the total phase transmitted through the 3D printed package with phase phase-shifting chip. For the 3-cell metamaterial chip, the total phase variation $\Delta\varphi$ = 343° was successfully obtained for the bias change in the range from 0 V to -1.5 V. Similarly, the change of the total phase in the 4-cell chip of $\Delta\varphi$ = 362° was achieved for the bias voltage range from 0 V to -1.7 V. The differences in operation of the two chips were associated with the change of the metasurface design and associated with different numbers of cells and HEMTs.

IV. Conclusion

In this work, InP-HEMT-based metamaterial chips were implemented into a 3D printed split block module package, operating at the 300-GHz band. The controllable phase variation of over 2π (360°) was achieved, showing prospects for the replacement of conventional phase array antenna technology in higher frequency bands. The realization of a 3D-printed module package verifies the capabilities of printing technology for the fabrication of complex structures for communication in terahertz frequencies.

In the next step of this work, multiple phase shifter metamaterial IC chips will be implemented in a single 3D printed package to demonstrate the beamforming abilities of the devices in the 300 GHz band.

Acknowledgments

The authors would like to thank Syuzo Nakai for his experimental support.

References

[1] H. Hamada, T. Tsutsumi, H. Matsuzaki, T. Fujimura, I. Abdo, A. Shirane, K. Okada, G. Itami, H.-J. Song, H. Sugiyama, and H. Nosaka, "300-GHz-band 120-Gb/s wireless front-end based on InP-HEMT PAs and mixers," IEEE J. Solid-State Circuits 55(9), 2316-2335, 2020.

[2] International Telecommunication Union Recommendation ITU-R P.676-12, Attenuation by Atmospheric Gases and Related Effects, 2019.

[3] I. Abdo, T. Jyo, A. Pander, H. Wakita, Y. Shiratori, M. Muto, H. Hamada, M. Nagatani, C. da Gomez, C. Wang, K. Hatano, C. Liu, A. A. Fadila, J. Pang, A. Shirane, K. Okada, and H. Takahashi, "300-GHz-band four-element CMOS-InP hybrid phased-array transmitter with 36° steering range," IEEE Microw. Wireless Tech. Let. 33(6), 887–890, 2023.

[4] K. Soeda; K. Naganuma; K. Konishi; H. Tamaru; N. Mio; H. Ito, and J. Yumoto, "THz Low-Loss Functional Hollow Waveguide Devices Fabricated by 3D Printer and Metal Plating," Proc. of 49th Int. Conf. on Infrared, Millimeter, and Terahertz waves (IRMMW-THz), 1-2, 2024.

[5] A. Pander, K. Soeda, D. Kitayama, H. Kagami, H. Hamada, Y. Yamaguchi, K, Konishi, J. Yumoto, H. Takahashi, "300-GHz-band metamaterial-based phase shifting integrated circuit in high-resolution 3D printed waveguide packaging for future wireless communication," 2025 Nineteenth International Congress on Artificial Materials for Novel Wave Phenomena (Metamaterials 2025), X-257-X-259, 2025.

Super□Resolution Interferometric Lithography Beyond the Diffraction Limit Enabled by a Tuneable Metasurface

Mohammad Mahdi Jafarizadeh[1,*], Leila Yousefi[1,*]

[1]School of Engineering and Informatics, University of Sussex, Falmer, England, UK
*Corresponding author: l.yousefi@sussex.ac.uk

Abstract— **To overcome the diffraction limit in optical lithography and achieve resolutions beyond this fundamental barrier, we propose a multi-mask interferometric lithography technique. In this approach, a tunable metasurface is employed to engineer the light passing through the masks, enabling the formation of the desired pattern on the photoresist.**

***Keywords*— diffraction limit, interferometric lithography, metasurfaces, subwavelength patterning.**

I. Introduction

One of the major bottlenecks in nanoscale semiconductor fabrication arises from the diffraction limit, which restricts resolution to $\lambda/(2\,NA)$, where λ is the working wavelength and NA is the numerical aperture of the imaging system [1, 2]. To overcome this limitation, various methods such as interferometric lithography [3, 4] and immersion interference lithography have been developed. These techniques enable subwavelength patterning; however, their application is limited to producing only periodic structures and cannot be used to create non□periodic patterns with arbitrary shapes. Direct□write approaches, including scanning probe, dip□pen, and electron□beam lithography [5-7] eliminate the need for masks and offer super□resolution fabrication capabilities. However, they suffer from low throughput and practical fabrication constraints, which limit their suitability for mass production in the semiconductor industry.

In this work, we propose a novel interferometric lithography framework that overcomes the diffraction limit by using multiple masks with feature sizes larger than the diffraction limit and converting these features into diffraction□limited dimensions with the aid of a tuneable metasurface. Unlike conventional interference□based techniques, which are restricted to generating periodic patterns, the proposed approach enables the fabrication of non□periodic, arbitrary patterns with resolutions well beyond the diffraction limit.

II. Methods

The proposed procedure, along with the optical setup required for its implementation, is illustrated in Fig. 1. As shown in this figure, the spectrum of the desired pattern—obtained through a Fourier transform—is decomposed into spectral bands of width $2k_0$, where $k_0$denotes the propagation constant in the air. Each spectral band is then used to generate a corresponding mask following a mathematical processing step. The details of this mathematical procedure are explained in the following sections.

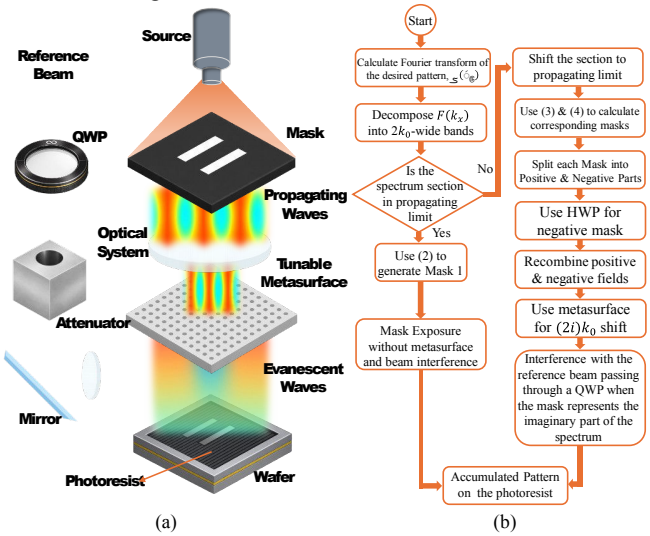

Fig. 1. (a) Workflow illustrating the mask□generation process. (b) Optical setup required to implement the proposed technique.

The intensity of the target pattern, $I(x)$ can be expressed analytically as:

$$I(x)=f_1(x)+\frac{1}{\pi}\sum_{i=2}^{m}\left[f_i^R(x)\cos(k_{sh}x)-f_i^I(x)\sin(k_{sh}x\right. \quad (1)$$

where $k_{sh}=(2i-1)k_0$, $k_0=2\pi/\lambda$, and m represents the number of sections. Here, f_1, f_i^R, and f_i^I denote the mask functions defined over the $|k|<k_0$ region and the i-th shifted spectral band, respectively. Each mask function is derived by mapping the associated spectral band $k\in[-k_0,k_0]$, yielding:

$$f_1(x)=\int_{-k_0}^{k_0}F_{\mathrm{re}}(k)\cos(kx)\,dk \quad (2)$$

$$f_i^R(x)=\int_{-k_0}^{k_0}\left[F_{\mathrm{re}}(k+k_{sh})\cos(kx)-F_{\mathrm{im}}(k+k_{sh})\sin(kx)\right]c(3)$$

$$f_i^I(x)=\int_{-k_0}^{k_0}\left[F_{\mathrm{re}}(k+k_{sh})\sin(kx)+F_{\mathrm{im}}(k+k_{sh})\cos(kx)\right]\varsigma \quad (4)$$

The mask functions shown above may contain negative values, which cannot be physically realized in transmission. To address this limitation, we propose a technique in which each pattern is decomposed into two masks representing the positive and negative components of the function. To implement the negative components optically, a half-wave plate (HWP) is incorporated into the setup (see Fig. 1b). The tunable metasurface applies a $(2i)k_0$ spectral shift to transmitted fields corresponding to each mask, thereby repositioning the spectrum to its intended location. To retrieve phase information at the photoresist, the modulated field is interfered with a coherent reference beam whose phase is set to 0 or $\pi/2$, depending on whether the real or imaginary mask set is under exposure. The accumulated intensity recorded on the photoresist can be expressed as:

$$I'(x)=\alpha_1^2 f_1^R(x)+\sum_{i=2}^{m}\left|\alpha_i e^{-jk_0x}+\alpha_{ref,i} f_i^R(x) e^{-j(2i)k_0x}\right|^2 \quad (5)$$

where $I'(x)$ denotes the reconstructed intensity pattern. The first term corresponds to the baseband contribution, while the remaining terms represent the intensity resulting from the real and imaginary masks interfering with respective reference beams. The coefficients α_i and $\alpha_{ref,i}$ determine the contribution of each mask exposure and its corresponding reference beam. These coefficients are optimized based on Rayleigh and FWHM-separation criterion to suppress the residual terms and ensure appropriate peak-to-valley contrast within the dynamic range of the photoresist.

III. Results and Discussion

To evaluate the performance of the proposed framework, we use it to reconstruct the pattern shown in Fig. 2(a). As illustrated, the pattern has an arbitrary shape with feature sizes as small as $\lambda/10$. Achieving this resolution requires a spatial spectrum extending to $|k|\le 5k_0$, which corresponds to five spectral bands, as shown in Fig. 2(b).

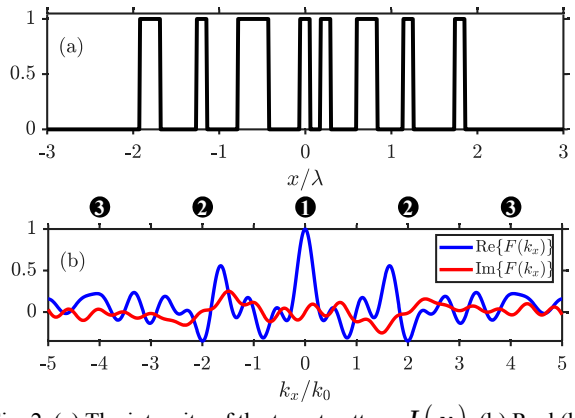

Fig. 2. (a) The intensity of the target pattern, $I(x)$. (b) Real (blue) and imaginary (red) parts of the spatial spectrum $F(k_x)$ obtained through a Fourier transform.

Using expressions (2) – (4), the real and imaginary mask patterns are computed and shown in Fig. 3. The accumulated intensity resulting from metasurface modulation and controlled interference is presented in Fig. 4. As illustrated, the reconstructed intensity closely matches the target pattern and satisfies the Rayleigh resolvability criterion for all adjacent peaks, thereby validating the accuracy and effectiveness of the proposed technique.

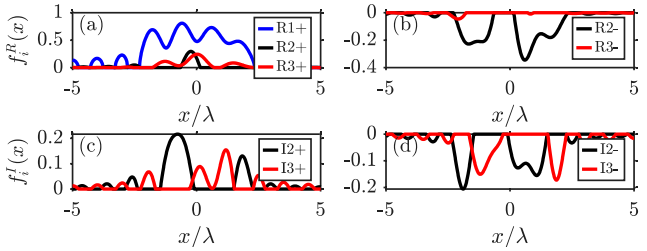

Fig. 3. Generated masks for the pattern shown in Fig. 2 representing different parts of spectrum: (a) positive real (b) negative real (c) positive imaginary (d) negative imaginary

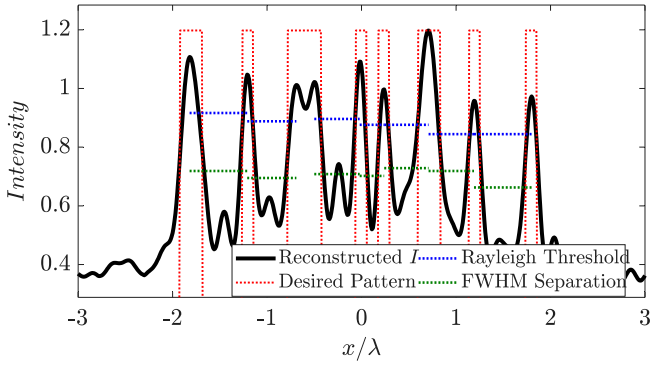

Fig 4. Reconstructed pattern (black) is compared with the desired pattern (red). Blue and green dashed lines represent the Rayleigh and FWHM criteria, respectively. The exposure coefficients obtained by optimization are $(\alpha_1,\ \alpha_{ref,1})=(0.26,0)$, $(\alpha_2,\alpha_{ref,2})=(1.2,\ 0.3)$, and $(\alpha_3,\ \alpha_{ref,3})=(1.35,0.27)$

IV. Conclusion

A super-resolution multi-mask interferometric lithography technique is proposed that overcomes the diffraction limit and achieves enhanced resolution. Unlike approaches restricted to periodic patterns, this method can generate arbitrary-shaped features. The technique leverages multiple exposures, a tuneable metasurface, and interference-based enhancement to further improve resolution. Numerical results demonstrated reconstruction of arbitrary patterns with feature sizes as small as $\lambda/10$, satisfying Rayleigh and FWHM resolvability criteria within the photoresist dynamic range.

References

[1] E. Abbe, "Beiträge zur Theorie des Mikroskops und der mikroskopischen Wahrnehmung," *Archiv für mikroskopische Anatomie,* vol. 9, no. 1, pp. 413–468, 1873.

[2] M. Born and E. Wolf, *Principles of optics: electromagnetic theory of propagation, interference and diffraction of light*. Elsevier, 2013.

[3] X. Chen and S. Brueck, "Imaging interferometric lithography: a wavelength division multiplex approach to extending optical lithography," *Journal of Vacuum Science & Technology B: Microelectronics and Nanometer Structures Processing, Measurement, and Phenomena,* vol. 16, no. 6, pp. 3392–3397, 1998.

[4] T. Bloomstein *et al*., "22-nm immersion interference lithography," *Optics Express*, vol. 14, no. 14, pp. 6434–6443, 2006.

[5] S. T. Howell *et al*., "Thermal scanning probe lithography—a review," *Microsystems & Nanoengineering*, vol. 6, no. 1, p. 21, 2020.

[6] G. Liu *et al*., "Development of Dip□Pen Nanolithography (DPN) and its derivatives," *Small*, vol. 15, no. 21, p. 1900564, 2019.

[7] R. Pease, "Electron beam lithography," *Contemporary Physics,* vol. 22, no. 3, pp. 265–290, 1981.

Constructive homogenization of dispersed random composites

Vladimir Mityushev

Faculty of Computer Science and Mathematics, Cracow University of Technology, Krakow, Poland

***Abstract*—The asymptotic analysis is applied to derive an analytical approximate formula for the macroscopic permittivity of 2D dispersed random composites. This formula extends the lower order Maxwell-Garnett approximation, revealing that many other popular formulas for dispersed media derived from effective medium approximations are asymptotically equivalent.**

***Keywords*— dispersed random composites, RVE, structural sums, macroscopic property tensor.**

I. Introduction

Consider a multi-phase composite with non-overlapping inclusions embedded in the 2D matrix. The composite is supposed to be represented by a periodicity cell Q introduced as follows. The plane coordinates $\mathbf{x} = (x_1, x_2)$ will be identified with the complex variable $z = x_1 + \mathrm{i}x_2$. Let $\boldsymbol{\omega_1} = 1, \quad \boldsymbol{\omega_2} = \mathrm{i}$ be the fundamental periods on the complex plane $\mathbb{C}$. Let Re and Im stand for the real and imaginary parts of values.

Consider N non-overlapping simply connected domains G_k in the unit periodicity cell Q with piece-wise Lyapunov's boundaries L_k and the multiply connected domain $G = Q \backslash \cup_{k=1}^{N} (G_k \cup L_k)$, the complement of all the closures of G_k to Q. Let the permittivity of the host is normalized to unity, and the permittivity of kth inclusion be a complex number ε_k.

Let complex functions u and u_k satisfy Laplace's equation. The perfect contact between the components is expressed by equations on L_k $(k = 1, 2, \dots, N)$

$$u(t) = u_k(t), \quad \frac{\partial u}{\partial \mathbf{n}}(t) = \varepsilon_k \frac{\partial u_k}{\partial \mathbf{n}}(t), \tag{1}$$

where the normal derivative $\frac{\partial}{\partial \mathbf{n}}$ on L_k is used.

II. Main formula

Introduce the contrast parameters $\varrho_k = \frac{\varepsilon_k - 1}{\varepsilon_k + 1}$ and the averaged contrast parameter over inclusions $\langle \varrho \rangle = \sum_{k=1}^{N} \varrho_k |G_k|$. Let $s_{jk}^{(0)}$ denote the normalized complex static moments of the domains G_k. Let a_k be the complex coordinate of the gravity center of G_k; $E_p(z)$ the Eisenstein functions of order p; $E_{p,mk} := E_p(a_m - a_k)$ for $m \neq k$.

Introduce the multiple structural sums

$$\mathcal{L} = \frac{1}{\pi} \sum_{k,m=1}^{N} \varrho_k \varrho_m |G_k||G_m| E_{2,mk}, \tag{2}$$

$$\begin{aligned} &\mathcal{V}_1 = \tfrac{2}{\pi} \textstyle\sum_{k,m=1}^{N} \varrho_k \varrho_m |G_k||G_m| E_{3,mk} (s_{1k}^{(0)} |G_k|^{\frac{1}{2}} \\ &- s_{1m}^{(0)} |G_m|^{\frac{1}{2}}), \end{aligned} \tag{3}$$

$$\begin{aligned} &\mathcal{V}_2 = \tfrac{3}{\pi} \textstyle\sum_{k,m=1}^{N} \varrho_k \varrho_m |G_k||G_m| E_{4,mk} \times \\ &\left(|G_k| s_{2k}^{(0)} + |G_m| s_{2m}^{(0)} - 2 \left(|G_k||G_m| \right)^{\frac{1}{2}} s_{1m}^{(0)} s_{1k}^{(0)} \right), \end{aligned} \tag{4}$$

$$\begin{aligned} &\mathcal{V}_3 = \tfrac{4}{\pi} \textstyle\sum_{k,m=1}^{N} \varrho_k \varrho_m |G_k||G_m| E_{5,mk} \times \\ &\Big[|G_k|^{\frac{3}{2}} s_{3k}^{(0)} - |G_m|^{\frac{3}{2}} s_{3m}^{(0)} \\ &+ 3 \left(|G_k|^{\frac{1}{2}} |G_m| s_{1k}^{(0)} s_{2m}^{(0)} - |G_m|^{\frac{1}{2}} |G_k| s_{2k}^{(0)} s_{1m}^{(0)} \right) \Big]. \end{aligned} \tag{5}$$

and the shape cumulative parameter

$$\mathcal{J} = \frac{1}{4\pi} \sum_{k=1}^{N} \varrho_k^2 \int_{L_k} \mathrm{d}\bar{t} \int_{L_k} \frac{\overline{\tau}}{\tau - t} \, \mathrm{d}\tau. \tag{6}$$

The above sums can be written in dimensionless form $\mathcal{J}_0 = f^{-1}\mathcal{J}$, $\mathcal{L}_0 = f^{-2}\mathcal{L}$, $\mathcal{V}_{0j} = f^{-\frac{j+4}{2}}\mathcal{V}_j$ using the total fraction f of inclusions.

The permittivity tensor can be calculated by the formula

$$\begin{aligned} \boldsymbol{\varepsilon}_\perp &= (1 + 2\langle \varrho \rangle) I + 2f \begin{pmatrix} \mathrm{Re}\, \mathcal{J}_0 & -\mathrm{Im}\, \mathcal{J}_0 \\ -\mathrm{Im}\, \mathcal{J}_0 & -\mathrm{Re}\, \mathcal{J}_0 \end{pmatrix} \\ &+ 2f^2 \begin{pmatrix} \mathrm{Re}\, \mathcal{L}_0 & -\mathrm{Im}\, \mathcal{L}_0 \\ -\mathrm{Im}\, \mathcal{L}_0 & 2 - \mathrm{Re}\, \mathcal{L}_0 \end{pmatrix} \\ &+ 2f^{5/2} \begin{pmatrix} \mathrm{Re}\, \mathcal{V}_{01} & -\mathrm{Im}\, \mathcal{V}_{01} \\ -\mathrm{Im}\, \mathcal{V}_{01} & -\mathrm{Re}\, \mathcal{V}_{01} \end{pmatrix} \\ &+ 2f^3 \begin{pmatrix} \mathrm{Re}\, \mathcal{V}_{02} & -\mathrm{Im}\, \mathcal{V}_{02} \\ -\mathrm{Im}\, \mathcal{V}_{02} & -\mathrm{Re}\, \mathcal{V}_{02} \end{pmatrix} \\ &+ 2f^{7/2} \begin{pmatrix} \mathrm{Re}\, \mathcal{V}_{03} & -\mathrm{Im}\, \mathcal{V}_{03} \\ -\mathrm{Im}\, \mathcal{V}_{03} & -\mathrm{Re}\, \mathcal{V}_{03} \end{pmatrix} + O(\varrho_0^3 f^4), \end{aligned} \tag{7}$$

III. Conclusion

The formula (7) was derived in [1]. It is the most general formula for the effective permittivity tensor for 2D dispersed random not densely packed composites. Computer simulations and applications can be found in [1] and [2].

Acknowledgments

This work was supported by the COST Action CA23125.

References

[1] V. Mityushev, N. Rylko, N. "Effective properties of two-dimensional dispersed composites. Part I. Schwarz's alternating method," *Computers & Mathematics with Applications*, vol. 111, pp. 50–60, 2022.

[2] V. Mityushev, T. Gric, R. Kycia, N. Rylko: Anisotropy of Metamaterials: Beyond Conventional Paradigms. Francis Taylor/CRC Press, 2025.

Design of an Airy-Beam-Generating Element Made with High-Refractive-Index and Low-Reflectance Metasurface in the 28 GHz Band

Yuta Tanaka[1], Mahiro Ochiai[1], Takehito Suzuki[2*]

[1]Department of Electrical Engineering and Computer Science, Graduate School of Engineering, Tokyo University of Agriculture and Technology, Japan

[2]Division of Advanced Electrical and Electronics Engineering, Institute of Engineering, Tokyo University of Agriculture and Technology, Japan

[*]Corresponding author: takehito@go.tuat.ac.jp

***Abstract*–We demonstrate an Airy-beam-generating element designed for the 28 GHz band based on our original high-refractive-index, low-reflectance metasurface. The results indicate that this metasurface is broadly applicable to electromagnetic wave manipulation.**

***Keywords*— metasurface, millimeter wave, Airy beam.**

I. INTRODUCTION

Millimeter waves play an important role in current 5G and future 6G wireless communication systems and are expected to be further utilized [1]. However, high-frequency waves often fail to reach desired locations in obstructed environments due to reduced diffraction. In this study, we designed an element to generate Airy beams [2] based on our original metasurface with a high-refractive-index and low-reflectance [3] in the millimeter-wave band. An Airy beam is a type of non-diffracting wave characterized by self-accelerating and self-healing properties [4]. Demonstrating an Airy-beam-generating element can contribute to millimeter-wave communications in obstructed environments [5].

II. DESIGN

Fig. 1 (a) and (b) show the overall view of the designed Airy-beam-generating element and its unit-cell structure, respectively. The element converts an incident plane wave at 28 GHz into an Airy beam. The structure shown in Fig.1(a) consists of cut metal wires with varying lengths l and spacings g, designed to approximate the ideal transmission phase distribution. The ideal transmission phase distribution of the Airy-beam-generating element is defined as 0° when $\mathrm{Ai}(y) > 0$ and 180° when $\mathrm{Ai}(y) < 0$ [6,7], as shown in Fig. 2. Here, $\mathrm{Ai}(y)$ denotes the Airy function given in Eq. (1), where u is a scaling constant. The Airy-beam-generating element was constructed by arranging cut metal wires with the parameters shown in Table 1.

$$Ai(y) = \frac{1}{\pi}\int_0^{\infty} \cos\left(\frac{t^3}{3} + \frac{y}{u}t\right) dt \qquad (1)$$

III. SIMULATION

Fig. 3(a) and (b) show (a) the simulation model and (b) the simulated electric-field intensity at a distance of 100 mm after the element, respectively. We investigated the self-healing property of the Airy beam by placing a PEC obstacle along the propagation path of both Airy and Gaussian beams. As shown in Fig. 3(b), the electric-field intensity of the Airy beam after transmission through the element is higher than that of the Gaussian beam in the obstacle-affected direction as highlighted in yellow. These results indicate that the beam transmitted through the Airy-beam-generating element exhibits self-healing properties.

IV. CONCLUSION

We designed the Airy-beam-generating element designed for the 28 GHz band based on our original high-refractive-index, low-reflectance metasurface. These results indicate that our original high-refractive-index, low-reflectance metasurface is broadly applicable to electromagnetic wave manipulation.

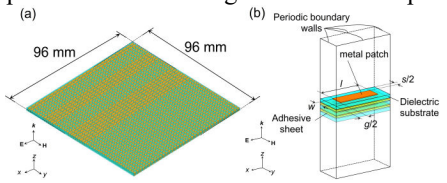

Fig. 1 (a) Overall view of the designed Airy-beam-generating element and (b) unit-cell structure used for the element.

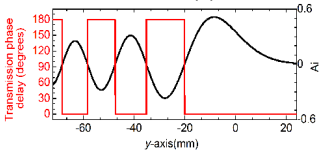

Fig. 2 Phase distribution of the Airy-beam-generating element given by Airy function.

Table 1. Parameters used for the Airy-beam-generating element.

	0 °	180 °
l (mm)	1.6	2.8
g (mm)	1.1	1.1
s (mm)	1.0	0.5
w (mm)	0.9	0.9

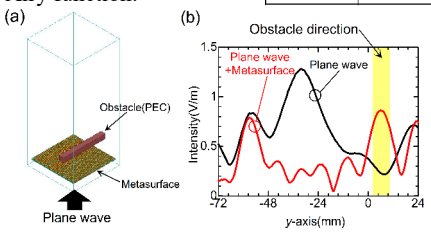

Fig. 3 (a) Simulation model and (b) simulated electric-field intensity at a distance of 100 mm after the element of Airy and Gaussian beams with a PEC obstacle.

ACKNOWLEDGMENTS

This research was supported by Fusion Oriented REsearch for disruptive Science and Technology (FOREST) from the Japan Science and Technology Agency (JST) (JPMJFR222I), Grants-in-Aid for Scientific Research (B) from the Japan Society for the Promotion of Science (JSPS) (24K01376), and Grant-in-Aid for Challenging Research (Exploratory) from the Japan Society for the Promotion of Science (JSPS) (24K21617).

REFERENCES

[1] W. Hong et al., IEEE J. Microwaves **1**(1), 101–122 (2021).
[2] G.A.Siviloglou et al., Phys. Rev. Lett., 99(312901), 312901-1–312901-2(2007).
[3] K. Ishihara and T. Suzuki, Journal of Infrared, Millimeter, and Terahertz Waves, **38**(9), 1130–1139 (2017).
[4] J. Broky et al., Optics Express, **16**(17), 12880–12891 (2008).
[5] J. Hu et al., Nat. Commun. **15**(2944), 1–9 (2023).
[6] Y. Zhuang et al., Optics Express, **32**(18), 31325–31333 (2024).
[7] J.Sheng et al., IEEE Photon. Technol. Lett., 35(5), 245–248 (2023).

Electron-Driven Photon Sources for Ramsey Interferometry with Electron Beams

Nahid Talebi[1]

[1]Institute for Experimental and Applied Physic, Kiel University, Germany
*Corresponding author: talebi@physik.uni-kiel.de

***Abstract*— Electron-driven photon sources provide compact platforms for probing decoherence dynamics of qubits in two-dimensional materials. Here, we demonstrate how both planar and 3D-printed architectures enable precise control over the properties of the emitted light.**

***Keywords*— electron-driven photon source, Ramsey interferometry, 2D materials.**

I. Introduction

Electron-driven photon sources (EDPHSs) are integrated radiation platforms inside electron microscopes that act as localized optical sources, enabling techniques such as Ramsey interferometry and pump–probe spectroscopy of material excitations at the nanoscale [1–5]. When electron beams interact with materials, they can generate light through multiple radiation mechanisms, including transition radiation, polariton excitations, Cherenkov radiation, and Smith–Purcell radiation. Engineering the electromagnetic environment of the electron beam, particularly through structured materials and metamaterials, provides a powerful route to tailoring the properties of the emitted radiation [6]. In this work, we demonstrate how both planar geometries [7] and more complex three-dimensional (3D) architectures [8] can be used to control and shape light generation within the electron microscope.

II. Results and Discussion

Planar electron-driven photon sources operate based on the generation of surface plasmon polaritons (SPPs) excited by electron beams interacting with a thin metal film, such as gold, deposited on a Si_3N_4 membrane [7]. To enable the generation of far-field radiation from SPPs, an array of nanopinholes is fabricated in the thin film using focused ion beam milling. The positions and size distribution of the pinholes are designed such that the far-field radiation pattern, as well as the emission spectrum, exhibit desired properties, such as a collimated beam [2], a focused beam [5], or a vortex beam [4] (Fig. 1). These arrays provide a flexible platform for spectral and spatial control of the emission. Moreover, multiple sources can be integrated on a single Si_3N_4 membrane, allowing fast acquisition using different sources. To control the position of the EDPHS structures with respect to the samples under investigation, a three-axis piezo stage is used.

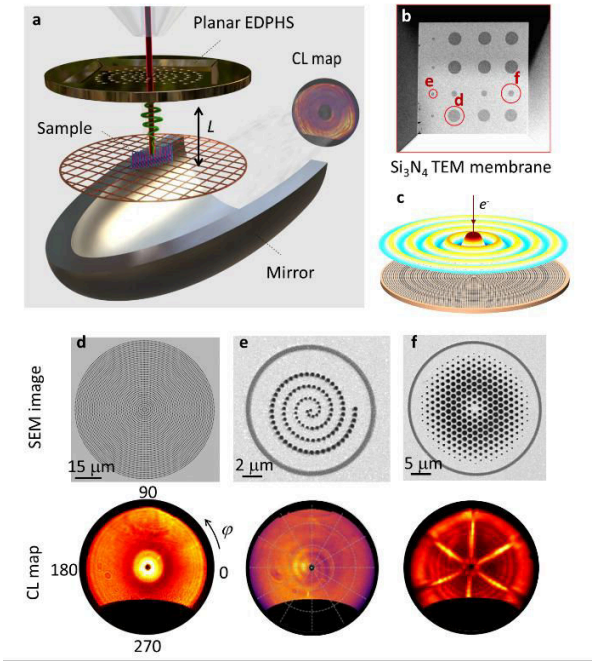

Fig. 1. (a) Ramsey interferometry setup comprising an EDPHS structure positioned above the sample and the apparatus used for collecting and analyzing the cathodoluminescence radiation. (b) SEM image of a Si_3N_4 membrane containing multiple planar EDPHS structures. (c) Radially propagating SPPs interact with the nanopinholes to generate light with tailored radiation properties. (d–e) SEM images of representative planar EDPHSs and their corresponding angle-resolved cathodoluminescence maps shown below each image, acquired at a wavelength of 800 nm.

The electron beam therefore interacts with the EDPHS, generating light with tailored radiation properties, and subsequently interacts with the sample. The radiation from the EDPHS induces a coherent polarization, such as exciting exciton polaritons [2] or creating a coherent superposition of qubit states [3]. The electron beam then interacts with the sample again after a free-evolution time, modifying the superposition. The resulting cathodoluminescence spectrum exhibits spectral and momentum-space interference fringes, whose visibility depends on the mutual coherence between the EDPHS field and the sample polarization. The visibility as a

function of time reveals quantum decoherence in the excitation scheme, such as phonon-mediated dephasing of defect excitations in hexagonal boron nitride [3].

For further enhancing the radiation intensity, we propose and realize a novel configuration for phase-matched generation of photons from electron beams, leveraging the phase-matching concept. An electron propagating parallel to a waveguide can generate light in a phase-matched configuration, when $k_g = \omega v_{el}^{-1}$, where k_g is the phase-constant of the optical modes of the waveguide, ω is the photon angular frequency and v_{el} is the electron velocity. However, in this configuration the excited optical waves remain inside the waveguide. Our principle here, utilizes a helically formed optical fiber that enables a sequential interaction of the electron beam with the waveguide in a phase-matched configuration, expressed by [8]

$$k_g = \left(\Lambda\omega/v_e - 2m\pi\right).\left(\left(2\pi r_h\right)^2 + \Lambda^2\right)^{-\frac{1}{2}}.$$

where m is an integer number specifying the diffraction modes, Λ is the helical pitch, and r_h is the radius of the helix (see Fig. 2a). In this way, the excited photons are partially guided within the waveguide and constructively interfere with the photons generated in subsequent interaction events. The cross section of the helical waveguide is designed in a way to enable the phase-matching concept by allowing optical modes with the phase

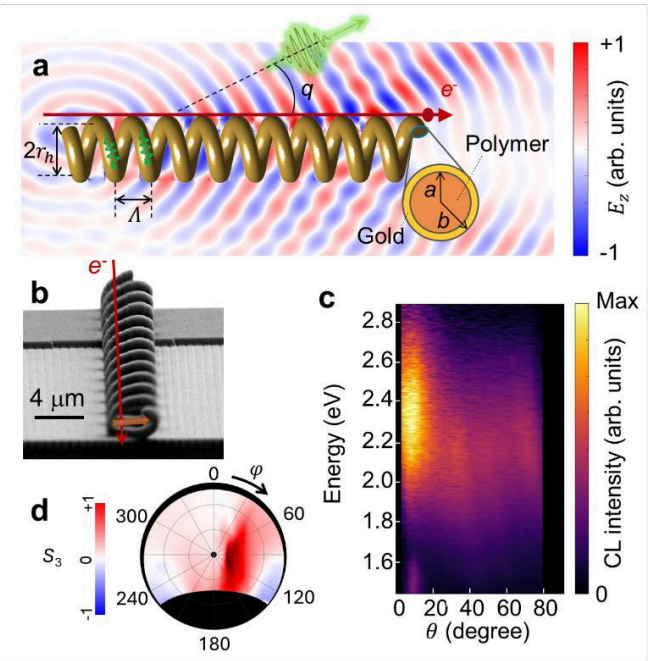

Fig. 2. (a) Sequential interaction of electron beams with a helical waveguide leading to merged waveguide and Smith-Purcell effect phase-matching concepts. (b) Secondary electron scanning electron microscopy image of such a waveguide fabricated with the NanoScribe Quantum X system. (c) Cathodoluminescence angle-resolved spectral map of the emission from the waveguide. (d) Angel-resolved S_3 Stokes parameters of the emission from the source, resolved at the photon energy of E = 2.3 eV.

constants that satisfy equation (1). The radius of the polymer fiber is therefore 400 nm. The structure is fabricated using the Quantum X series of the NanoScribe Company (Fig. 2b). We further deposit a thin layer of gold on it with the thickness of 40 nm to permit for the excitation of coherent guided plasmon polaritons that substitute the major contribution in the interaction with electron beams. The radiation from this structure was characterised using cathodoluminescence spectroscopy. The generated photons from the source exhibit two orders of magnitude higher photon yield compared to planar waveguides and demonstrate a helically-polarized and collimated radiation pattern (Fig. 2c and d).

III. Conclusion

In a summary, the realized 3D electron-driven photon source transcends the state-of-the-art via an improved photon yield and an unprecedented control on the polarization and directionality of the emitted photons. It paves the way toward phase-locked and pump-probe spectroscopy at the 1-nm spatial resolution and few-femtoseconds spatial resolution inside an electron microscope.

Acknowledgments

We acknowledge collaborations with Dr. Jochen Zimmer, Mr. Fabian Rahn and Dr. Aaron Kobler for fabricating the structures (NanoScribe Company). This project has received funding from the Volkswagen Foundation (Momentum Grant), European Research Council (ERC) under the European Union's Horizon 2020 research and innovation program under grant agreement no. 101017720 (EBEAM), from the European Research Council (ERC Consolidator Grant UltraSpecT with no. 101170341; ERC Proof-of-Concept Grant UltraCoherentCL with no. 101157312) and from Deutsche Forschungsgemeinschaft.

References

[1] N. Talebi, "Spectral interferometry with electron microscopes," Scientific Reports, vol. 6, pp. 33874, 2016.

[2] M. Taleb, M. Hentschel, K.Rossnagel, H. Giessen, and N. Talebi, "Phase-locked photon–electron interaction without a laser," Physics, vol. 19, pp. 869-876, 2023.

[3] M. Taleb, *et al.*, "Ultrafast phonon-mediated dephasing of color centers in hexagonal boron nitride probed by electron beams," Nature Communications, vol. 16, pp. 2326, 2025.

[4] N. van Nielen, M. Hentschel, N. Schilder, H. Giessen, A. Polman, and N. Talebi, "Electrons Generate Self-Complementary Broadband Vortex Light Beams Using Chiral Photon Sieves," Nano Letters, vol. 20, pp. 5975-5981, 2020.

[5] N. Talebi *et al.*, "Merging transformation optics with electron-driven photon sources," Nature Communications, vol. 10, pp. 599, 2019.

[6] N. Talebi, "Interaction of electron beams with optical nanostructures and metamaterials: from coherent photon sources towards shaping the wave function," J.Opt., vol.19, pp. 103001, 2017.

[7] J. Christopher, M. Taleb, A. Maity, M. Hentschel, H. Giessen, and N. Talebi, "Electron-driven photon sources for correlative electron-photon spectroscopy with electron microscopes," Nanophotonics, vol. 9, pp. 4381-4406, 2020.

[8] M. Taleb, M. Samadi, and N. Talebi, "Phase-matched electron-photon interactions enabled by 3D-printed helical waveguides," Nanophotonics, vol. 14, pp. 3279-3286, 2025.

Application of Metamaterials in Soft and Biodegradable Electronics

Seung-Kyun Kang

Department of Materials Science and Engineering, Seoul National University, Republic of Korea

*Corresponding author: kskg7227@snu.ac.kr

***Abstract*— Mechanical metamaterials enable new strategies for soft electronics–based implantable devices. Here, auxetic meta-architectures suppress Poisson-induced crack closure in crack-based strain sensors, achieving ultrasensitive detection of subtle biomechanical dynamics, including cerebral vascular pulsation. As an outlook, mechanically programmed meta-structures are introduced for ultrasound-driven, spatially controlled disassembly of transient implants.**

***Keywords*— metamaterials, soft electronics, mechanical sensing, auxetic structure, acoustic meta**

Summary

Metamaterials provide a powerful design framework across mechanical, optical, and acoustic domains, enabling functionalities that are inaccessible with conventional materials. In soft electronics–based implantable devices, where mechanical compliance must coexist with high functional performance, meta-structural design offers a unique opportunity to decouple material softness from device capability. In this presentation, we examine how metamaterial concepts can be applied to implantable soft electronic systems to enhance sensing performance and to introduce new modes of control over device end-of-life behavior.

The primary focus of this work is on mechanical metamaterials for ultrasensitive strain sensing, a critical function in implantable electronics for monitoring subtle biomechanical signals. Crack-based strain sensors are widely recognized for their high sensitivity, which arises from resistance modulation induced by the opening and closing of microcracks in thin conductive films. However, despite their excellent performance at relatively large strains, these sensors exhibit a fundamental limitation in the low-strain regime. At infinitesimal deformations, Poisson-induced lateral contraction of conventional substrates promotes premature crack closure, leading to a sharp loss of sensitivity and limiting their applicability to intracorporeal environments.

To overcome this intrinsic constraint, we introduce an auxetic mechanical metamaterial architecture that reprograms the crack-opening mechanism itself.[1] By engineering a substrate with a strongly negative Poisson's ratio, uniaxial tensile loading induces biaxial expansion rather than lateral contraction. This deformation mode suppresses crack-edge reconnection and enables immediate and orientation-independent crack-gap opening, even at extremely small applied strains. Finite element analysis and microscopic observations confirm that the auxetic meta-architecture fundamentally alters local strain redistribution at crack sites, activating a crack-opening regime that is inaccessible in conventional soft substrates.[2]

As a result, the mechanically programmed crack sensor exhibits dramatically enhanced sensitivity in the initial deformation regime, achieving reliable detection of strains down to the 10^{-5} level. This hypersensitive response enables the resolution of subtle biomechanical dynamics that were previously difficult to access using soft electronic sensors. In particular, we demonstrate the ability to detect pulsatile deformations associated with cerebral vasculature, highlighting the relevance of mechanical metamaterial design for implantable biointerfaces requiring extreme sensitivity and conformal contact.

Beyond sensing performance, the mechanical metamaterial framework also provides a pathway to address broader system-level challenges in soft electronics. While this presentation primarily emphasizes mechanical metamaterials, we additionally introduce an emerging concept that integrates acoustic metamaterials with transient implantable electronics as a forward-looking extension. In this approach, externally applied ultrasound is used to mechanically fragment implanted devices and accelerate their degradation. Mechanically programmed meta-structures enable more efficient localization of acoustic energy, allowing faster and more spatially controlled disassembly compared to unstructured systems. Although still at an early stage, this concept illustrates how metamaterial design can extend beyond operational performance to actively shape device behavior at the end of life.

Together, these examples demonstrate that metamaterials can serve as an enabling framework for actively governing both sensing performance and degradation pathways in implantable soft electronic systems. By shifting the design paradigm from material-centric optimization to structural and mechanical programming, this work highlights the potential of metamaterials to support next-generation bio-integrated and transient electronics that combine high sensitivity, mechanical compliance, and programmable life cycles.

REFERENCES

[1] J. H. Lee, Y. N. Kim, J. Lee, J. Jeon, J. Y. Bae, J. Y. Lee, K. S. Kim, M. Chae, H. J. Park, J. H. Kim, K. S. Lee, J. Kim, J. K. Hyun, D. H. Kang, and S. K. Kang, "Hypersensitive meta-crack strain sensor for real-time biomedical monitoring," *Science Advances*, vol. 10, p. eads9258, 2024.

[2] J. H. Lee, W. J. Lee, S. Kang, J. Y. Won, D. H. Kwon, E. Lim, U. Hwang, H. W. Cho, M. G. Lee, J. H. Kim, and S. K. Kang, "Synergistic Meta-Perforated Substrates for Hypersensitive Crack-Based Strain Sensors," *Small Structures*, 2026. (In revision)

High-efficiency nonlinear optical response of silicon based metasurfaces in the visible and UV spectrum

Shroddha Mukhopadhyay[1,*], Crina Cojocaru[1], Maria A. Vincenti[2], Michael Scalora[2], Jose Trull[1]

[1]Department of Physics, Universitat Politècnica de Catalunya, Rambla Sant Nebridi 22, 08222 Terrassa, Spain
[2]Department of Information Engineering – University of Brescia, Via Branze 38, 25123 Brescia, Italy
*Corresponding author: shroddha.mukhopadhyay@upc.edu

***Abstract*—We investigate harmonic generation in silicon-based membranes and metasurfaces operating in the visible and UV spectrum. Our combined experimental-theoretical study reveals second, third, and higher harmonic generation up to the seventh order. Resonant field confinement in corresponding metasurfaces enable enhaced efficient UV emission and predictive design of nonlinear nanophotonic devices.**

***Keywords*— nonlinear optics, silicon, silicon nitride, third-harmonic generation, ultrafast nonlinear optics, high-index dielectric metasurfaces, high harmonic generation.**

I. Introduction

Semiconductor and metallic nanostructures are now widely incorporated into photonic devices across numerous applications that harness light propagation and electromagnetic field localization at nanometer length scales. At these scales, both linear and nonlinear light–matter interactions display nonconventional behavior that cannot be adequately described by standard theoretical models. In bulk materials, harmonic generation is typically optimized in transparent, highly nonlinear media under phase-matching conditions to maximize conversion efficiency. In contrast, when dimensions are reduced to the nanoscale, phase matching loses relevance, absorption is not necessarily detrimental, and the electric-dipole approximation no longer dominates, enabling contributions from typically neglected higher-order and multipolar terms. Furthermore, the effective nonlinear susceptibilities, $\chi^{(2)}$ and $\chi^{(3)}$, can differ significantly from their bulk local values and may depend on pump depletion, pulse duration, and the underlying nonlinear mechanisms. Achieving a quantitative understanding of these nanoscale nonlinear sources is therefore crucial for the rational design and development of next-generation nonlinear nanophotonic devices.

Here, we report a series of experiments on harmonic generation in silicon(Si)-based membranes and metasurfaces. The generated harmonics are intentionally tuned to the visible and ultraviolet spectral regions, where Si-based materials are typically overlooked because of strong absorption. Despite this, our results clearly demonstrate that efficient light emission is achievable even when the harmonic wavelengths lie within the nominally opaque regime of these materials.

Beginning with simple freestanding membranes and a characterization of their intrinsic nonlinear optical response, we subsequently design and analyze resonant metasurfaces derived from the same materials. Under resonant excitation with ultrafast near-infrared pulses, these nanostructured metasurfaces strongly confine the electromagnetic field within their volume, thereby enhancing light–matter interaction and substantially increasing higher harmonics generated in the visible, UV or deep-UV wavelength ranges. Using specialized detection systems, we accurately measure THG conversion efficiencies ranging from 10^{-6} to 10^{-12}, achieving excellent agreement with theoretical predictions in terms of spectral shape, linewidth, and peak amplitude.

II. Results and Discussion

Initially we measure second harmonic generation (SHG) and third harmonic generation (THG) from Si and silicon nitride (Si_3N_4) resonant membranes. The comparison of these experimental results with the numerical predictions of our theoretical model allows the identification of the valence electrons effective mass, which determines SHG efficiency and oscillator parameters that control third order processes. With these results we can accurately predict the nonlinear optical properties of more complex structures, without artificially separating the effective $\chi^{(2)}$ into surface and volume contributions, and by simultaneously including effects of linear and nonlinear dispersions.[1] The Si sample is a single-crystal undoped $< 100 >$ Si membrane suspended over a frame(Fig.1(a). In Fig.1(b) we display linear pump transmittance vs. incident carrier wavelength for 200nm and 1340nm-thick membranes. The spectra consists of a series of Fabry-Perot resonances whose free spectral range depends on thickness. THG data are shown in Fig.1(c), where we report the spectral response for normal and oblique angles of incidence. A maximum THG efficiency of 2×10^{-9} is obtained at 466nm, with the pump tuned to 1400nm at normal incidence. Our results suggest that judicious exploitation of the nonlinear dispersion of ordinary semiconductors can provide reasonable nonlinear efficiencies well into the UV range.

We then design resonant 1D periodic gratings, etched into the abovementioned Si and Si_3N_4 membranes. Fig2 shows the Si_3N_4 membrane (Fig.2(a)) and the fully etched strips (Fig.2(d)) designed to sustain a characteristic Mie type resonance at or near 800nm (Fig.2(e)). Under TE illumination, the dip in the transmission spectra is a result of light localization in the bulk of the material (inset of 2(d)). This strong light localization corresponds to a resonant THG spectral variation

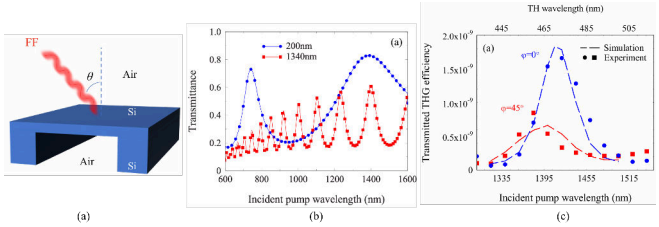

Fig. 1. (a) Si membrane Schematic diagram, (b) Transmittance vs incident pump wavelength for the 200nm- and 1340nm–thick Si membranes. Both samples display Fabry-Perot resonances according to their thicknesses. (c) Measured and simulated THG spectra for 1340nm-thick membrane. Markers exemplify the data obtained at 0° (filled blue circles) and 45° (filled red squares); corresponding simulations for 0° (dashed blue curve) and 45° (dashed red curve)[1].

as theoretically predicted, and shown in Fig.2(f), with a peak enhancement factor of $\sim$ 400 times, with respect to the THG from flat membrane(Fig.2(c). This planar architecture is fully transparent, operable at normal incidence and coan be integrated into planar Si on insulator (SOI) optical components, providing a flexible design toolbox for polarization-independent UV and deep-UV nano-light sources.

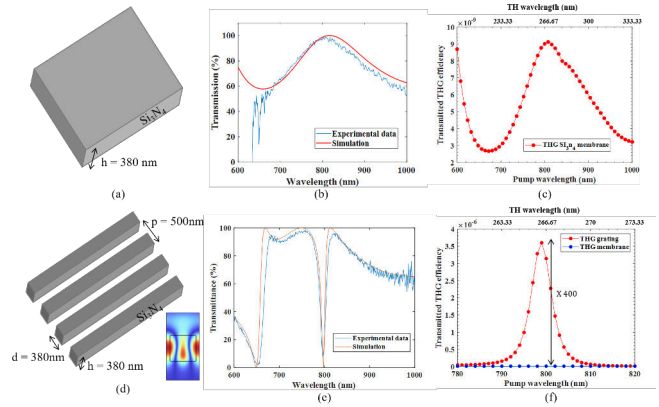

Fig. 2. Si_3N_4 membrane (a) Schematic diagram, (b) Linear transmission and (c) THG spectral response. Suspended grating in Si_3N_4 (d) Schematic diagram (e) Linear transmission and (f) Resonant THG spectral response and enhancement peak.

Finally, we report experimental observations of high harmonic generation, up to the 7th harmonic, generated from a suspended subwavelength Si film resonant in the UV range at 210 nm, the current limit of our detection system. In Fig.3 we show the measured and simulated spectra generated by a $\sim 3TW/cm^2$, 85fs pump pulse tuned to 1475 nm incident normal to the surface to temporarily suppress even harmonics. The measured conversion efficiencies are $4.2 \times 10^{-5}, 6.2 \times 10^{-7}$, and 4.57×10^{9} for 3rd, 5th, and 7th harmonic, with peak power densities of order $126MW/cm^2, 1.8MW/cm^2$ and $14kW/cm^2$, respectively, despite being tuned in the absorption and metallic ranges. We explain the experimental data with a time domain, hydrodynamic-Maxwell approach broadly applicable to most optical materials. Our approach accounts simultaneously for surface and magnetic nonlinearities that generate even optical harmonics, as well as linear and nonlinear material dispersions beyond the third order to account for odd optical harmonics, plasma formation, and a phase locking mechanism that makes the generation of high harmonics possible deep into the UV range, where semiconductors like Si start operating in a metallic regime.

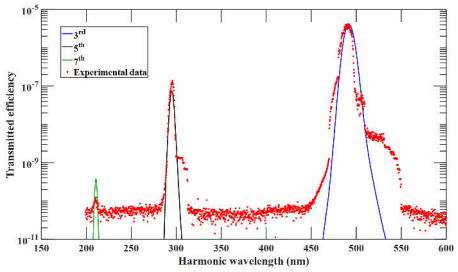

Fig. 3. Measured and simulated spectra of transmitted 3rd, 5th, and 7th harmonic conversion efficiencies for a single pulse 85 fs in duration, carrier wavelength tuned to 1475 nm, peak power density of $3TW/cm^2$, and normally incident on the Si film [3]

III. Conclusion

We demonstrate that Si and Si_3N_4 nanostructures enable efficient harmonic generation from the visible to the deep-UV, even within nominally absorbing or metallic spectral regions. Resonant metasurface engineering and strong field confinement yield orders-of-magnitude enhancement of nonlinear conversion efficiencies, including high harmonics up to the seventh order. The excellent agreement between experiments and our hydrodynamic-Maxwell model provides quantitative insight and predictive capability for designing CMOS-compatible nonlinear nanophotonic devices beyond bulk-material limitations.

Acknowledgments

SM, JT, and CC acknowledge the Spanish Agencia Estatal de Investigaci´on from Ministerio de Ciencia, Investigaci´on y Universidades (project PID2023-148620NB-I00 granted by MICIU/AEI/10.13039/501100011033 and FEDER, UE) and US Army Research Laboratory Cooperative Agreement No W911NF-22-2-0236 issued by US ARMY ACC-APG-RTP. S. M. acknowledges predoctoral grant FPI-UPC 2022, funded by Universitat Polit‘ecnica de Catalunya (Government of Catalunya). M. A. V. thanks NATO SPS Grant no. G5984 - RESPONDER for financial support.

References

[1] K. Hallman, L. Rodríguez-Suné, J. Trull, et al, "Harmonic generation from silicon membranes at visible and ultraviolet wavelengths," *Opt. Express*, vol. 31, pp. 792-801, 2023.

[2] M. Scalora, J. Trull, C. Cojocaru, et al, "Resonant, broadband, and highly efficient optical frequency conversion in semiconductor nanowire gratings at visible and UV wavelengths," J. Opt. Soc. Am. B vol. 36, pp. 2346-2351, 2019.

[3] K. Hallman, Sven Stengel, Wallace Jaffray et al, "High-harmonic generation from subwavelength silicon films," *Nanophotonics*, vol. 14, no. 23, pp. 3927-3938, 2025.

Multilayer Gap Plasmons in Periodic Perfect-Conductor–Dielectric Structures

Michael Haftel[1,2], Justin Case[1], Anatoliy Pinchuk[1,2]

[1]Department of Physics, University of Colorado at Colorado Springs, USA
[2]Center for Plasmonics, Nanophotonics, and Metamaterials, University of Colorado at Colorado Springs, USA
*Corresponding author: apinchuk@uccs.edu

***Abstract* - We demonstrate that periodic multilayer perfect-conductor dielectric structures with subwavelength slits support propagating multilayer gap plasmons with tunable wavenumber spectra and interlayer phase coherence. The number of supported modes increases with layer number, enabling controllable field localization and propagation for advanced photonic and metamaterial device applications.**

***Keywords* - gap plasmons, multilayer plasmonics, spoof plasmons, metamaterials, photonic devices**.

I. Introduction

Gap plasmons provide strong electromagnetic field confinement and enhanced propagation compared with conventional surface plasmon polaritons. While single gap plasmon modes have been extensively studied, multilayer gap plasmon systems remain largely unexplored. Theoretical and computational investigation of multilayer plasmonic systems is important because coupling between layers can enable additional control over propagation characteristics, dispersion behavior, and field localization.

This work introduces multilayer gap plasmons supported by alternating metallic and dielectric layers containing periodic subwavelength slits. The study demonstrates that collective plasmon modes can propagate through the entire multilayer stack, enabling new degrees of freedom for waveguiding, metasurface design, and metamaterial engineering.

II. Methods

The investigated structure consists of alternating perfectly conducting slabs and dielectric layers with periodic slit arrays in each conductor layer. The system is modeled using Maxwell's equations with Bloch periodic boundary conditions along the periodic direction and outgoing-wave boundary conditions normal to the multilayer stack.

Field expansions are applied separately within dielectric layers and slit regions, and boundary matching conditions are used to construct a matrix eigenvalue problem. Bound gap plasmon modes are identified by solving for wave numbers that produce near-zero eigenvalues. Numerical calculations were performed for multilayer systems ranging from three to more than fifty layers, as well as for the infinite-layer limit.

III. Results and Discussion

The results demonstrate that multilayer structures support multiple propagating gap plasmon modes across the full stack thickness. As the number of layers increases, the number of supported modes increases and approaches a continuous band structure in the infinite-layer limit.

The calculated wave number spectrum extends both below and above the free-space wave number. Modes below the free-space wave number correspond to leaky or weakly confined modes that become more confined as layer number increases, while higher wave number modes exhibit strong confinement and enhanced interlayer coherence.

Field profile analysis confirms that electromagnetic energy is localized primarily within dielectric gap regions, while metallic regions remain field-free except within slit openings. Higher-order spatial harmonics introduce only minor phase shifts without significantly distorting mode shape, confirming that the fundamental mode dominates propagation behavior.

IV. Conclusion

Multilayer periodic conductor–dielectric structures with subwavelength slits can support propagating multilayer gap plasmons with tunable spectral and coherence properties. Increasing layer number increases modal density and enables band formation. Interlayer phase behavior is governed by plasmon wave number, enabling engineering of coherent field propagation across multilayer systems. These findings provide a foundation for designing advanced plasmonic waveguides, multilayer metasurfaces, and photonic metamaterials. Future work will extend the model to real metals across the electromagnetic spectrum and explore geometry optimization for specific device applications.

Acknowledgments

AP acknowledges partial support from NATO-SPS - G6197 grant. The numerical calculations were performed using the facilities of the Department of Defense High Performance Modernization Project.

References

[1] Michael Haftel, Justin Case, and Anatoliy Pinchuk, "Multilayer gap plasmons " Optical Materials Express, Vol. 15, 9, pp. 2164-2174, (2025)
https://doi.org/10.1364/OME.568005

SPECIAL SESSION 2

Parity-Time and quasi-normal modes in Photonics, Plasmonics, Acoustics

9 contributions · pp. 779–792

Emergence of higher-order exceptional points in composite non-Hermitian quantum systems

Jan Wiersig[1,*], Weijian Chen[2]

[1]Otto-von-Guericke-Universität Magdeburg, Fakultät für Naturwissenschaften, Institut für Physik, Universitätsplatz 2, 39016 Magdeburg, Germany

[2]Department of Physics and Astronomy, North Carolina State University, Raleigh, North Carolina 27695, USA

*Corresponding author: jan.wiersig@ovgu.de

Abstract—We investigate the emergence of higher-order exceptional points (EPs) in composite quantum systems formed by the tensor product of multiple subsystems, each exhibiting an EP. We determine the resulting spectral response strength, and show that the presence of the higher-order EP causes initially entangled states to disentangle during time evolution.

Keywords— non-Hermitian physics, exceptional points, composite quantum systems.

I. Introduction

Exceptional points (EPs) are spectral degeneracies in open quantum and wave systems that produce counter-intuitive effects with potential applications. At an EP of order n, precisely n eigenenergies and the associated eigenstates of the non-Hermitian Hamiltonian $\hat{H}_0$ merge into a single state. Under a small perturbation, $\hat{H}_0 + \varepsilon\hat{H}_1$ with perturbation strength $\varepsilon > 0$, the eigenenergies E_j show a strong spectral response bound by [1]

$$|E_j - E_{\mathrm{EP}}|^n \leq \varepsilon ||\hat{H}_1||_2 \, \xi, \tag{1}$$

with spectral norm $||\cdot||_2$ and spectral response strength ξ. Clearly, EP-enhanced sensing applications prefer large ξ.

Here, we study the emergence of higher-order EPs in quantum systems composed of non-interacting subsystems, each with a completely degenerate eigenenergy spectrum exhibiting at least one EP. For instance, for a bipartite system the Hamiltonian of the full system is

$$\hat{H} = \hat{H}_{\mathrm{A}} \oplus \hat{H}_{\mathrm{B}} = \hat{H}_{\mathrm{A}} \otimes \mathbb{1}_{\mathrm{B}} + \mathbb{1}_{\mathrm{A}} \otimes \hat{H}_{\mathrm{B}} \tag{2}$$

with Kronecker sum $\oplus$, identity operators $\mathbb{1}_{\mathrm{A}}$, $\mathbb{1}_{\mathrm{B}}$, and subsystem Hamiltonians $\hat{H}_{\mathrm{A}}$, $\hat{H}_{\mathrm{B}}$ each with an EP.

II. Results and Discussion

We show that a composite system of N subsystems, each with a leading-order EP of order n_α, possesses an EP of order [2]

$$n = 1 + \sum_{\alpha=1}^{N} (n_\alpha - 1). \tag{3}$$

Crucially, $n > n_\alpha$, i.e. the EP order is increased. Moreover, Eq. (3) differs from the naive expectation $n = \prod_{\alpha=1}^{N} n_\alpha$.

Next, we prove that the spectral response strength for the full system can be calculated as

$$\xi = (n-1)! \prod_{\alpha=1}^{N} \frac{\xi_\alpha}{(n_\alpha - 1)!} \tag{4}$$

with ξ_α being the subsystem's spectral response strength.

Any generic initial state $|\psi\rangle$ of the composite system is entangled. We reveal that, in the long-time limit, such a state approaches the leading-order EP eigenstate, which is a product state. This EP-induced disentanglement is illustrated in Fig. 1 by plotting the concurrence, $\mathcal{C} := 2|\alpha\delta - \beta\zeta|$, of a normalized state $|\psi\rangle = (\alpha, \zeta, \beta, \delta)^{\mathrm{T}}$ for a composite system made of two second-order EPs. For most initial Bell states, the concurrence decays monotonically from its maximum value to zero, indicating a loss of entanglement.

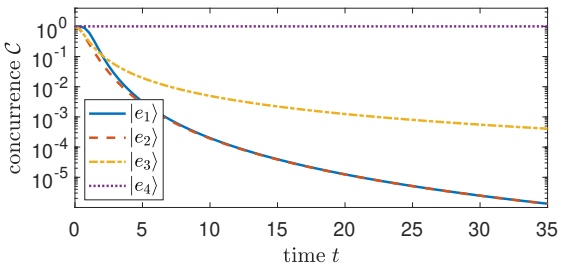

Fig. 1. Time evolution of concurrence $\mathcal{C}$ for four initial Bell states $|e_j\rangle$ in a system composed of two second-order EPs; t is dimensionless.

III. Conclusion

We have shown that composite quantum systems, each possessing an EP, can exhibit a higher-order EP whose order exceeds that of the individual components. We derived simple expressions for both the EP order and the spectral response strength, and revealed the intriguing phenomenon of EP-induced disentanglement.

References

[1] J. Wiersig, "Moving along an exceptional surface towards a higher-order exceptional point," Phys. Rev. A, vol. 108, p. 033501, 2023.

[2] J. Wiersig and W. Chen, "Higher-order exceptional points in composite non-Hermitian systems," Phys. Rev. Res., vol. 7, p. 033034, 2025.

Light Trapping by Non-Hermitian Thin Films

L. Grineviciute[1], I. Lukosiunas[2], J. Nikitina[1], I. Meskelaite[2], D. Gailevicius[2], and K. Staliunas[3,4,*]

[1]Center for Physical Sciences and Technology, Savanoriu 231, LT-02300 Vilnius, Lithuania
[2]Vilnius University, Laser Research Center, Sauletekio Ave. 10, Vilnius, Lithuania
[3]UPC, Dep. de Fisica, Rambla Sant Nebridi 22, 08222, Terrassa, Spain
[4]ICREA, Passeig Lluís Companys 23, 08010, Barcelona, Spain
*Corresponding author: kestutis.staliunas@icrea.cat

***Abstract*—One of the exceptional features of non-Hermitian systems is the unidirectional wave interactions. At a particular (exceptional) point the situation can be achieved, that the external radiation is efficiently coupled into the system, but the internal radiation cannot escape backwards. We realize this idea in non-Hermitically modulated thin films, consisting of a Hermitian part - the periodic corrugation of the surfaces of a film, and a non-Hermitian part - the modulation of losses along the film. We prove numerically and demonstrate experimentally that the incident radiation, coupled with such a non-Hermitian thin film, is unidirectionally trapped into a planar mode of the film, does not escape from the film (or escape weakly due to experimental imperfections), and is efficiently absorbed there.**

***Keywords*— metamaterials, non-Hermitian systems.**

I. Introduction

One of the exceptional features of non-Hermitian systems is unidirectional wave interactions. Simultaneous modulation of the real and the imaginary part of the interaction potentials (of the refractive index and the gain/loss in the case of optical systems) can result in unequal coupling coefficients between the fields of different parts of the system. The unidirectional coupling can be arranged between internal fields and external radiation as well. At a particular (exceptional) point, the situation can be achieved, that the external radiation is coupled into the system, but the internal radiation cannot escape backwards. In this way, the incident radiation can be trapped inside the non-Hermitian system and, eventually, can be efficiently absorbed there.

II. Results and Discussion

We design the structure by analytic estimations and numerical simulations (Fig.1); we fabricate the structure by physical vapor deposition (titanium dioxide - TiO_2) on nanostructured substrates, and nonuniformly deposit the absorber by magnetron sputtering with the glancing angle method (nickel - Ni); we record the angular transmission/reflection profiles, and we reconstruct angle – asymmetric absorption map. Asymmetric absorption (asymmetry factor 2) is mediated by the left-/right-propagating waveguiding modes of the thin film, in good correspondence with the theoretical estimations [1].

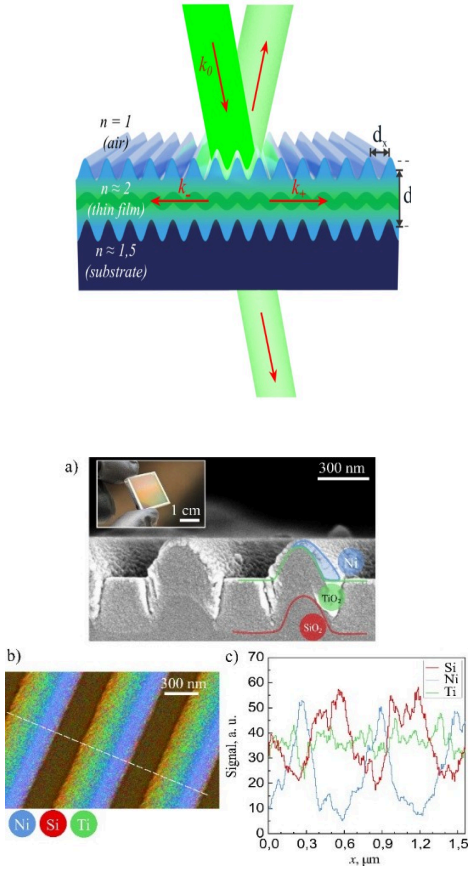

Fig. 1. Geometry, and realization.

References

[1] L. Grinevičiūtė, I. Lukosiunas, J. Nikitina, A. Selskis, I. Meskelaite, D. Gailevicius, and K. Staliunas, Light Trapping by Non-Hermitian thin films, Phys. Rev. Applied, **23**, (2025) 054014.

Photonic neuromorphic computing using non-Hermitian zero modes in coupled nanolaser arrays

Kaiwen Ji[1,*], Giulio Tirabassi[2], Cristina Masoller[3], Ge Li[4] and Alejandro M. Yacomotti[1]

[1] Le Laboratoire Photonique Numérique et Nanosciences, Talence, France
[2] Departament de Física, Universitat Politécnica de Catalunya, Terrassa, Barcelona, Spain
[3] Departament d'Informàtica, Matemàtica Aplicada i Estadística, Universitat de Girona, Girona, Spain
[4] Department of Physics and Astronomy, College of Staten Island, New York, USA
*Corresponding author: kaiwen.ji@institutoptique.fr

Abstract—We propose a photonic neuromorphic computing architecture based on symmetry-protected robust zero modes. We experimentally demonstrate that even a small set of coupled nanolasers can implement non-convex boundaries, enabling the classification of highly compressed handwritten digits.

Keywords— photonic computation, zero modes, nanolaser array.

I. Introduction

Photonic neuromorphic computing has emerged as a promising approach toward energy-efficient artificial neural networks (ANNs). Nanolasers, in particular, are attractive candidates owing to their ultralow power consumption and intrinsic nonlinearities [1], [2], [3]. In this work, we propose a photonic neuromorphic computing architecture based on symmetry-protected non-Hermitian zero modes in coupled semiconductor photonic crystal nanolaser arrays. We experimentally demonstrate that even a small set of coupled nanolasers can realize non-convex tasks, enabled by their intrinsic nonlinearities and effective multilayer features.

II. Methods

The principle of our coupled nanolasers is illustrated in Fig. 1. An input image of a handwritten '1', represented as a matrix $\mathbf{I}$, is linearly mapped onto a pump distribution $\mathbf{P}$ via a encoding matrix $\mathbf{M}$, such that $\mathbf{P} = |\mathbf{MI}|$. The resulting pump pattern is then projected onto the nanolaser array using a spatial light modulator (SLM). The coefficients of $\mathbf{M}$ are adjusted such that the optical spectrum—serving as the output layer—exhibits a lasing zero mode (interpreted as a positive response) when the digit '1' is presented. Conversely, for any other handwritten digit, the zero mode remains off, indicating a negative response [4].

III. Results and Discussion

As a proof-of-principle, we fabricate a 2×2 photonic crystal coupled nanolaser array and evaluate its performance on a highly compressed handwritten digits dataset.

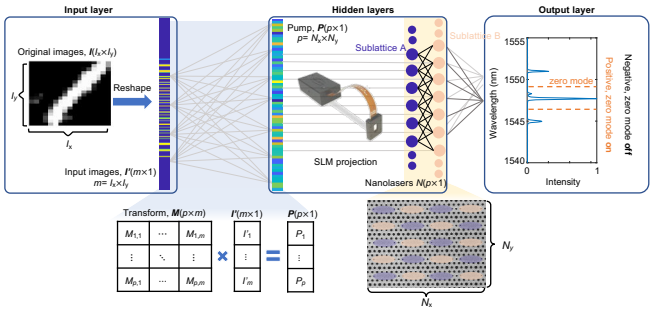

Fig. 1. Schematic of the optical computation architecture.

The dimensionality reduction induces severe information loss, resulting in substantial class overlap within the feature space (see the left panel of Fig. 2), thereby increasing the complexity of the decision boundary. We benchmark the nanolaser array against conventional nonlinear classifiers, the results are demonstrated on the right panel of Fig. 2.

At relatively high resolutions, all classifiers achieve nearly 100% accuracy as the data remain linearly separable in the high-dimensional feature space. However, as the input dimensionality decreases, classifier accuracy declines. At extremely low resolution—where the input is reduced to just 4 features—the boundaries between the two classes significantly overlap, causing single-layer linear classifiers, such as the perceptron, to fail in achieving reliable performance. In this regime, the presence of the nonlinear hidden layer with recurrent couplings becomes essential for maintaining classification accuracy. Notably, our nanolaser array performs comparably to nonlinear classifiers, particularly when the input information is highly compressed, thereby demonstrating its capability to process low-dimensional data efficiently using only four nonlinear neurons.

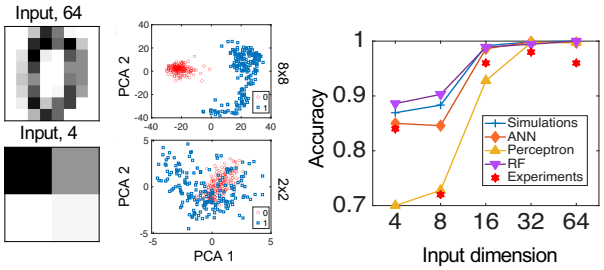

Fig. 2. Performance of different classifier as a function of the input data size.

IV. Conclusion

In this work, we propose and experimentally demonstrate a photonic neuromorphic computing architecture utilizing symmetry-protected zero modes in coupled nanolaser arrays. By engineering the optical materials to exploit exceptional point bifurcations, we could excite symmetry-protected zero modes, which serve as robust outputs for classification tasks. Moreover, the intrinsic nonlinear response—arising from gain saturation and the amplitude-phase coupling of the semiconductor nanolasers—combined with the recurrent couplings in the hidden layer, enable the array to efficiently handle nontrivial classification tasks using only a small number of neurons.

Acknowledgments

This work was partially supported by the French National Research Agency (ANR), the RENATECH network, and the Grand Programme de Recherche (GPR) LIGHT.

References

[1] M. Parto, W. E. Hayenga, A. Marandi, D. N. Christodoulides, M. Khajavikhan, Nanolaser-based emulators of spin Hamiltonians. Nanophotonics 9 (13), 4193–4198 (2020).

[2] A. Skalli, et al., Photonic neuromorphic computing using vertical cavity semiconductor lasers. Optical Materials Express 12 (6), 2395–2414 (2022).

[3] Z. Chen, et al., Deep learning with coherent VCSEL neural networks. Nature Photonics 17 (8), 723–730 (2023).

[4] G. Tirabassi, K. Ji, C. Masoller, A. M. Yacomotti, Binary image classification using collective optical modes of an array of nanolasers. APL Photonics 7 (9) (2022).

Pumped and active dissipative media with non-Hermitian periodic potentials

S. B. Ivars [1], M. Botey [1], K. Staliunas[2], and R. Herrero[1*]

[1]Departament de Fisica, Universitat Politecnica de Catalunya (UPC), Rambla Sant Nebridi 22, 08222, Terrassa, Barcelona, Catalonia, Spain

[2]Institucio Catalana de Recerca i Estudis Avancats (ICREA), Passeig Llus Companys 23, E-08010, Barcelona, Spain

*Corresponding author: ramon.herrero@upc.edu

***Abstract*—The introduction of periodic non-Hermitian potentials in damped-driven and damped-active NonLinear Schrödinger Equation permits stabilization and accessibility of solitonic structures.**

***Keywords*— Non-Hermitian metastructures, solitons, stabilization.**

I. Introduction

Many optical systems are modeled by generalizations of the Nonlinear Schrödinger Equation (NLSE). Damped-Active optical systems, such as lasers, can be well described by the Complex Ginzburg-Landau Equation (CGLE), while Damped-Driven systems like Kerr micro-resonators are modeled by the Lugiato-Lefever Equation (LLE). In both cases turbulence can be tamed by stabilizing solitonic solutions through the introduction of non-Hermitian potentials (complex modulations of the refractive index and gain/loss). While both models are generalizations of the Nonlinear Schrödinger Equation (NLSE), their stabilization mechanisms and dynamics differ according to the nature of the medium.

Non-Hemitian modulations revealed strong capabilities for the stabilization of optical systems. Introducing non-Hermitian spatiotemporal modulations in extended systems induces new phenomena and new system solutions. It permits several applications by controlling the modulation, like turbulence reduction, stabilization of eigenstates, or the generation of new stable solutions.

Aside from homogeneous solutions, other non-homogeneous stationary solutions are found in both Damped-Active and Damped-Driven systems. The most well-known are simple stable periodic solutions but also localized states although frequently showing an unstable behaviour. This is the case of solitons in Damped-Active and Damped-Driven systems modeled by the CGLE and LLE respectively.

II. Stabilization of the CGLE

The unmodulated one dimensional CGLE easily shows instability and turbulent behaviours. particularly when the self-focusing coefficient increases and diffusion decreases, leading to amplitude or phase turbulence. The system supports various stationary periodic solutions, such as Turing rolls and trains of solitons, although these states are typically highly unstable and embedded within the turbulent regime [1,2].

In this case we introduce stationary non-Hermitian potentials, consisting of complex modulations of the refractive index and gain/loss. This modulation effectively reduces or supresses turbulence by creating stable attractors from pre-existing unstable bifurcations, even with modulation amplitudes as low as 5% of the gain for particular potential configurations.

This technique is robust across different parameters, including higher spatial dimensions (2D) and fractional extensions of the model. A particular example is the emission regularization in Vertical-Cavity Surface-Emitting Lasers (VCSELs).

III. Stabilization of the LLE

Aside, systems described by Damped-Driven Nonlinear Schrödinger Equations like the LLE describes passive systems with losses where external energy is injected, such as Kerr micro-resonators. This system naturally supports dark dissipative solitons in the normal group velocity dispersion regime. These structures emerge due to the bistability between two stable homogeneous solutions. Without modulation, while single solitons are stable, trains of equidistant solitons are typically unstable due to the lack of an effective potential to pin them together [3].

Introducing non-Hermitian potentials in normal dispersion regimes uncovers a novel and hybrid formation mechanism for solitons. This mechanism blends the physics of the two canonical formation scenarios: homogeneous bistability and pattern-homogeneous state bistability. The potential induces a dual behavior in the base states, allowing the system to use wavy quasi-homogeneous states as patterns to form localized

structures. This results in a scenario where many species of stable single solitons and soliton molecules can coexist.

A particular application of this approach is the stabilization of soliton trains and the real-time manipulation of frequency combs in Kerr micro-resonators, including deterministic and reversible switching between these different types of solutions.

IV. Conclusion

In conclusion, the application of non-Hermitian potentials provides a powerful and versatile framework for stabilizing nonlinear optical systems, effectively taming the inherent turbulence in Damped-Active systems (CGLE) and enabling the deterministic control of localized states in Damped-Driven systems (LLE). By introducing complex modulations of the refractive index and gain/loss, these potentials transform unstable periodic solutions and chaotic regimes into stable attractors, such as regularized emission in VCSELs or hybrid soliton molecules in Kerr micro-resonators, offering in the last a real-time manipulation of frequency combs and the generation of diverse, stable light structures [4].

Acknowledgments

This work was supported by the Spanish government via PID2022-138321NB-C21 and Generalitat de Catalunya via 2021 SGR 00606.

References

[1] Salim B. Ivars, Muriel Botey, Ramon Herrero, and Kestutis Staliunas, ”Optical turbulence control by non-Hermitian potentials”, Physical Review A, 105(3), 033510. (2022)

[2] Salim B. Ivars, Muriel Botey, Ramon Herrero, and Kestutis Staliunas, ”Non-Hermitian control of optical turbulence in systems with fractional dispersion”, Chaos, Solitons & Fractals, 165, 112774, (2022)

[3] Salim B. Ivars, Muriel Botey, Ramon Herrero, and Kestutis Staliunas, ”Stabilisation of spatially periodic states by non-Hermitian potentials”, chaos, Solitons & Fractals, 168, 113089. (2023)

[4] Salim B. Ivars, Carles Milian, Muriel Botey, Ramon Herrero, and Kestutis Staliunas, ”Hybrid patterns and solitonic frequency combs in non-Hermitian Kerr Cavities”, Physical Review Letters, 133(9), 093802. (2024)

.

Phase conjugation and focusing in multimode non-Hermitian systems

Konstantinos G. Makris [1,2*], and Demetri Psaltis [3]
[1]Department of Physics, University of Crete, 70013, Heraklion, Greece
[2]Institute of Electronic Structure and Laser (IESL),FORTH, 71110, Heraklion, Greece
[3]Optics Laboratory, Ecole Polytechnique Federale de Lausanne (EPFL), Lausanne, Switzerland
*Corresponding author: makris@physics.uoc.gr

***Abstract*—In the framework of non-Hermitian photonics, we examine two possible ways for constructing a focused spot inside a guided wave system (photonic lattices or multimode fibers) with distributed gain-loss. The first one is that of parity-phase conjugation and the second one that of singular value decomposed transmission matrices.**

***Keywords* nonlinear optics, non-Hermitian optics, multimode waveguides, photonic lattices.**

I. Introduction

Time reversal symmetry is a fundamental concept that appears in many branches of wave physics and it is based on the underlying conservation of energy. Closely related to time reversal is the technique of phase conjugation (PC) [1], [2], [3], [4], [5]. Phase conjugation is an important method that can be experimentally realized by using four wave mixing technique of nonlinear optics or alternatively by combining digital holography with wavefront shaping by spatial light modulators. Most of the initial studies were based on applications of bulk homogeneous media, but recently phase conjugation was extended to complex media. More specifically, in a series of experiments, reverse propagation by phase conjugation was used to create tight focusing of light propagating in multimode optical fibers (MMFs).

In general the vast majority of these works on phase conjugation and reverse propagation concerns optical systems without gain or loss, in other words conservative structures. These ideas led to the area of non-Hermitian photonics [6], [7], which is the physical background of our study. Returning to our initial problem of phase conjugation, almost all studies are based on conservation of energy, in order to be able to exactly reverse the optical waves, which means that, in principle, phase conjugation works only in conservative (hermitian) systems. Once the medium contains gain or loss, problems arise. The conclusion was clearly stated in [8], where it was theoretically proven that the losses (or equivalently gain) spoil phase conjugation. More specifically, for purely lossy (or gainy) media exact reverse propagation is impossible [8]. The situation is different when we have a distributed gain and loss index spatial profile [9], [10], [11], [12].

More specifically, here we suggest two different strategies [13] in order to achieve a tight focused spot at the output of a non-Hermitian optical system. The first one [13] is based on the underlying rotational-time symmetry of the system and the second one [14] on the singular value decomposition of the propagator or the transmission matrix of the problem. Note that the second method does not require any symmetry, and can be generally applied in any non-Hermitian system.

II. Methods

Regarding the first problem of phase conjugation in complex media, we consider rotationally-time $\mathcal{RT}$-symmetric structures (where $\mathcal{R}$ stands for rotation and $\mathcal{T}$ for complex conjugation). In particular, we introduce the new concept of rotation phase conjugation ($\mathcal{R}PC$), where we apply the combination of phase conjugation and rotation-reflection symmetry operations to the wavefront in a medium that has $\mathcal{RT}$-symmetry. That way one can achieve perfect focusing via reverse propagation after the wavefront is properly rotated.

Regarding the second method, where no symmetry is required, we consider the propagator $\hat{G} \equiv e^{z\hat{M}}$ (where $\hat{M}$ is the evolution matrix of our paraxial equation of diffraction) or the transmission matrix $\hat{T}$ of the multimode system, that can be a slab waveguide or a photonic lattice or a multimode fiber. Once we have computed $\hat{G}$ or $\hat{T}$, we perform singular value decomposition (SVD) and determine the right/left singular eigenstates of the problem for a given propagation distance z. Proper superpositions of singular eigenstates result to the wavefront at $z = 0$ that will lead to a tight focused spot at the output of the system.

III. Results and Discussion

Our results are shown in Figs.1,2, where we illustrate the formation of a focused spot by the two alternative ways. First the concept of Rotation Phase conjugation ($\mathcal{R}PC$) for a multimode fiber is illustrated in Fig.1 and secondly the singular focusing for a slab waveguide in Fig. 2.

IV. Conclusion

We have examined the problem of phase conjugation-reverse propagation and focusing in media that contain gain and loss, following two different ways [13], [14] . Firstly, we showed that by properly combining gain and loss materials, we can achieve exact reverse propagation by relying on the concept of Rotation Phase conjugation ($\mathcal{R}PC$)[13] . We have

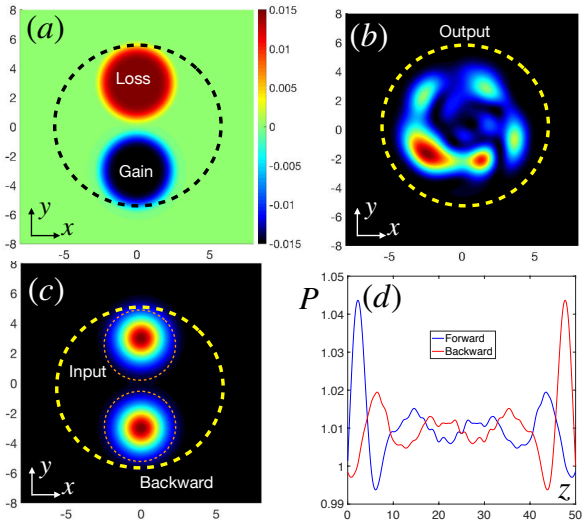

Fig. 1. Parity-phase conjugation in a multimode fiber with one core with gain and the other with loss. (a) The imaginary part of the optical potential in the transverse plane. The dotted circle is the real part of the index modulation profile. (b) Output intensity at $z = 50$ under a wide gaussian excitation localized at the lossy core. (c) Comparison of the input beam and the backward beam after $\mathcal{R}PC$ at the end facet of the fiber. (d) Power oscillations for the forward and backward evolution, in the same coordinate system.

identified the conditions under which perfect inversion of the forward propagation is possible in a single non-Hermitian $\mathcal{RT}$-symmetric complex medium. Secondly, we have performed SVD to the propagator/transmission matrix of the paraxial guided wave system, and through analytically derived formulas we identified the wavefronts at the input fact at $z = 0$ that will lead to a predetermined focused spot at the output of the system [14]. Our theoretical results may provide useful insights regarding imaging, wavefront shaping and focusing of waves in complex non-Hermitian media.

ACKNOWLEDGMENTS

This work was supported by by the European Research Council (ERC-Consolidator) under the grant agreement No. 101045135 (Beyond_Anderson) and the Hellenic Foundation for Research and Innovation (H.F.R.I.) through the 5th Call of the "Science and Society" Action, titled "Always strive for excellence-Theodoros Papazoglou" (Project Number: 11496, "PSEUDOTOPPOS").

REFERENCES

[1] A. Yariv, App. Phys. Lett. **28**, 88 (1976).
[2] Z.Yaqoob, D.Psaltis, M.S.Feld, and C.Yang, Nat. Photon. **2**, 110 (2008).
[3] C.L. Hsieh, Y. Pu, R. Grange, and D. Psaltis, Opt. Express **18**, 12283 (2010).
[4] I. N. Papadopoulos, S. Farahi, C. Moser, and D. Psaltis, Opt. Express **20**, 10583 (2012).
[5] I. N. Papadopoulos, S. Farahi, C. Moser, and D. Psaltis, Biomed. Opt. Express **4**, 260 (2013).
[6] D.F. Pile, and D. N. Christodoulides, Nat. Phot. **11**, 742 (2017).
[7] R. El-Ganainy, K.G. Makris, M. Khajavikhan, Z.H. Musslimani, S. Rotter, and D. N. Christodoulides, Nat. Phys. **14**, 11 (2018).
[8] A. Yariv, Opt. Lett. **16**, 1376, (1991).
[9] K. G. Makris, L. Ge, and H. E. Türeci, Phys Rev. X **4**, 041044 (2014).

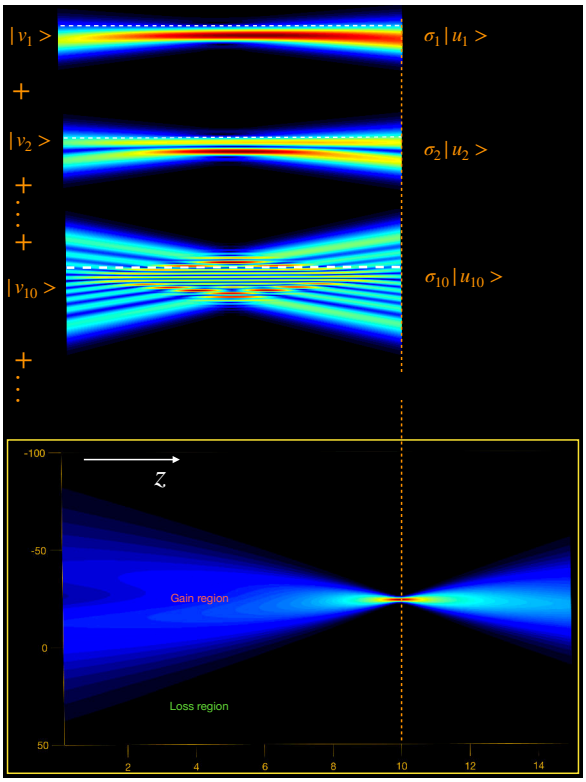

Fig. 2. Achieving focusing by SVD-modes in a slab waveguide with gain and loss. (Top panel) Intensity plots of diffraction of the first few singular eigenstates of the system. (Bottom panel) the proper superposition of many singular eigenstates lead to a predesigned focused spot at normalized distance $z = 10$.

[10] K. G. Makris, Phys. Rev. E **104**, 054218 (2021).
[11] K. G. Makris, Appl. Phys. Lett. **125**, 011102 (2024).
[12] I. Kiorpelidis, and K.G. Makris Phys. Rev. Res. **7**, L032043 (2025).
[13] K.G.Makris and D.Psaltis, accepted for publication, Phys. Rev. Res. (2026).
[14] K.G.Makris and D.Psaltis, under submission (2026).

Sensing with complex Bragg gratings over parity-time states

Tianyi Hao,[1] Pavel Cheben,[2] Jens H. Schmid,[2] Pierre Berini[1,3,4,*]

[1]School of Electrical Engineering and Computer Science, University of Ottawa, Canada
[2]National Research Council Canada, Ottawa, Canada
[3]Department of Physics, University of Ottawa, Canada
[4]Nexus for Quantum Technologies Institute, University of Ottawa, Canada
*pberini@uottawa.ca

***Abstract*— We analyze the sensitivity of non-Hermitian Hamiltonian gratings mapped onto a spherical (anti-) parity-time (PT) symmetry state space. We focus on sensing along trajectories defined by the spherical axes (r, θ, φ) of the PT sphere from initial states selected thereon.**

***Keywords*— Complex modulated gratings, Active gratings, Sensors.**

I. Introduction

Parity-time (PT) symmetry and anti-PT symmetry are general properties of non-Hermitian Hamiltonian systems that have been widely studied and developed [1,2]. Unbroken PT symmetric systems satisfy the commutation operation $[\mathcal{H}, \mathcal{PT}] = 0$, and unbroken anti-PT symmetric systems satisfy the anticommutation operation $\{\mathcal{H}, \mathcal{PT}\} = 0$, where $\mathcal{P}$ is the parity operator and $\mathcal{T}$ is the time reversal operator. The complex relationship between the non-Hermitian Hamiltonian $\mathcal{H}$ and these operators can be written [3]:

$$\mathcal{PTH} = e^{j2\theta}\mathcal{HPT} \tag{1}$$

where θ is the phase of the complex eigenvalue of the non-Hermitian Hamiltonian $\mathcal{H}$.

We consider a grating having a longitudinal perturbation satisfying [4]:

$$n(z) = n_{\text{ave}} + \Delta n_r \sin\left(\frac{2\pi}{\Lambda} z\right) + \mathrm{j}\Delta n_\mathrm{i} \cos\left(\frac{2\pi}{\Lambda} z + \theta\right) \tag{2}$$

where $n(z)$ is the complex refractive index distribution of the Bragg grating along the z (propagation) axis, n_{ave} is the average complex refractive index, Δn_r and Δn_i are the strength of the real and imaginary index perturbations, Λ is the period of the grating, and θ is the phase difference between the real and imaginary index perturbations and is equivalent to θ in Eq. 1. The grating is PT symmetric when $\theta = q\pi$, anti-PT symmetric when $\theta = q\pi \pm \pi/2$ where $q \in \mathbb{Z}$, and anyonic PT symmetric for other values of θ. Also, the system is in a PT unbroken state for $\Delta n_r > \Delta n_i$, in a PT broken state for $\Delta n_r < \Delta n_i$, and at an exceptional point (EP) for $\Delta n_r = \Delta n_i$. In previous work [4], we represented the parameter space of Eq. 2 graphically in spherical coordinates as shown in Fig. 1. We now use this representation to explore sensing along specific directions on the PT sphere representing changes in PT state from initial states. This approach provides a different perspective on the design of sensors, leading to new insights and concepts [5].

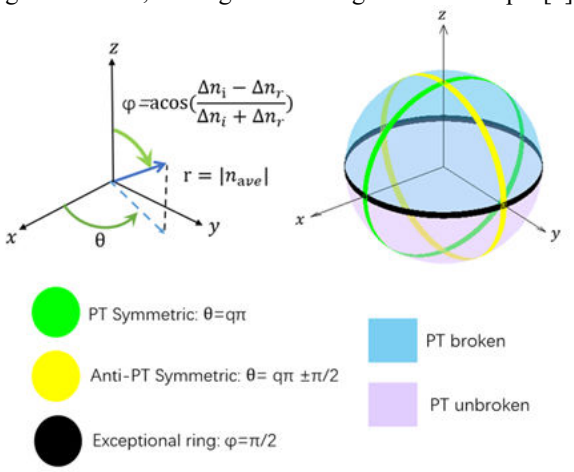

Fig. 1. Spherical representation of complex modulated Bragg gratings with the identification of special PT states.

II. Results

We analyze the sensitivity of complex-modulated gratings in specific PT states by inducing perturbations along the three spherical coordinates: Perturbation along the radius r which is directly related to average effective index n_{ave}, perturbation along the azimuthal coordinate θ which corresponds to the phase shift between the real and imaginary perturbations, and perturbation along the polar coordinate φ which is a function of the normalized differential strength between the imaginary and real perturbations (Δn_i and Δn_r).

Fig. 2 summarises example results for sensing along the anti-PT symmetry ring ($\theta = \pi/2$) about the north pole as sketched in Fig. 2(i). State evolution along the φ axis occurs by perturbing Δn_r by an additional real index perturbation Δn_c. Fig. 2(ii) shows that sensing along this ring leads to increasing

reflectance as the state evolves towards one of the EPs. The reflectance response shows slight shifts in peak wavelength around the Bragg wavelength with Δn_c. The transmittance response develops distinct extrema on either side of the Bragg wavelength, as shown in Fig. 2(iii), which can be monitored differentially (or as a ratio) as a measurand. The direction of the shifts in the reflectance response indicates the direction of state evolution with φ along the anti-PT symmetry ring, as does the side on which the transmittance maximum or minimum occurs near the Bragg wavelength. It is evident from Fig. 2 that extremely large transmittance sensitivities are possible in this scheme considering that perturbations in real index of the order of 10^{-4} can induce changes of about 0.3 in transmittance.

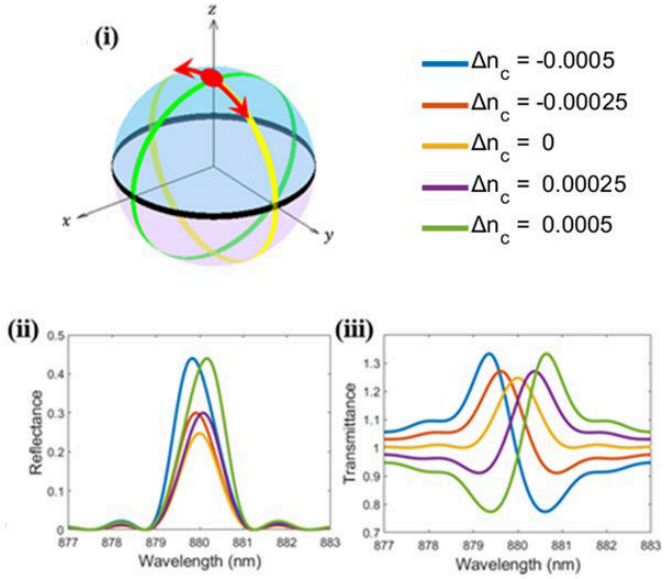

Fig. 2. Spherical representations of complex modulated Bragg gratings and sensing in the extreme PT broken state along the $\theta = \pi/2$ ring.

III. Conclusion

We introduce a PT-sphere trajectory framework for complex-modulated Bragg gratings that provides a new perspective for sensor design. By engineering evolution along the sphere's axes, the spectra exhibit controllable wavelength shifts and amplitude changes, enabling multiple practical measurands beyond conventional peak tracking. The evaluated scheme yields promising sensitivities, and the independence of the spherical axes also enables inference of responses for gratings in arbitrary (anyonic) PT states. This opens new prospects for compact, high-performance multi-parameter sensing based on PT-state engineering of Bragg gratings.

Acknowledgments

Financial support by the National Research Council of Canada and the Natural Sciences and Engineering Research Council of Canada is gratefully acknowledged.

References

[1] C. M. Bender and S. Boettcher, Phys. Rev. Lett. 80, 5243 (1998).
[2] R. El-Ganainy, K. G. Makris, M. Khajavikhan, Z. H. Musslimani, S. Rotter, and D. N. Christodoulides, Nat. Phys. 14, 11 (2018).
[3] G. Arwas, S. Gadasi, I. Gershenzon, A. Friesem, N. Davidson, and O. Raz, Sci. Adv. 8, eabm7454 (2022).
[4] T. Hao, P. Cheben, J. H. Schmid, and P. Berini, Opt. Express 32, 45521 (2024).
[5] T. Hao, P. Cheben, J. H. Schmid, and P. Berini, submitted.

Topology in space, time, and space-time

Alexander Szameit[1,*]

[1] Instituti of Physics, University of Rostock, Germany
*Corresponding author: alexander.szameit@uni-rostock.de

***Abstract*— In this invited talk, I will present our most recent experiments on topological states residing at temporal interfaces.**

***Keywords*— Topological Photonics, Quantum Simulation**

In recent years, topological phenomena in photonic systems have attracted much attention, with their striking features arising from robust states in the energy gaps of spatially periodic media. However, light waves are entities that extend in space as well as time, such that one may ask whether topological effects can also occur in the temporal domain, or even space-time. Intuitively, systems that are periodic in time may be gapped in momentum, leading to topological states localized at time interfaces. However, time - in contrast to space - exhibits a unique unidirectionality often referred to as the “arrow of time”. Inspired by these features, I will present our most recent experiments on topological states residing at temporal interfaces. Moreover, I will discuss the formation of spacetime-topological events and demonstrate unique features such as their limited collapse under disorder and causality-suppressed coupling.

Mode-cleaning in multimode fibers via chiral non-Hermitian modulations

Muriel Botey[1,*], Ramon Herrero[1], Mingshu Chen[2], Almantas Galvanauskas[2], Kestutis Staliunas[1,3]

[1]Departament de Física, Universitat Politècnica de Catalunya (UPC), Barcelona, Catalonia
[2] University of Michigan- Ann Arbor, Michigan, USA
[3] Institució Catalana de Recerca i Estudis Avancats (ICREA), Barcelona, Catalonia
*Corresponding author: muriel.botey@upc.edu

***Abstract*— We report on a spatial mode-cleaning mechanism via chiral gain/loss and index modulations in a multimode fiber. By exploiting non-Hermitian-symmetry breaking, a cascading power flow funnels energy from higher-order modes into the lowest-order mode, enabling robust, high-quality beams with fiber-standard-fabrication generation methods.**

***Keywords*— multimode fibers, non-Hermiticity, nanophotonics, exceptional point, exceptional ring**

I. Introduction

In non-Hermitian systems, exceptional points (EPs) are spectral singularities where two or more eigenvalues and their corresponding eigenvectors simultaneously coincide. Unlike degeneracies in conventional Hermitian systems—where eigenvalues are identical but eigenvectors remain orthogonal—an EP marks a collapse of the eigenbasis, rendering the underlying system matrix defective [1]. Distinctively, adiabatically encircling an EP in parameter space (e.g., in modulated non-Hermitian waveguides, photonic crystals, or nonlinear microcavities) exploits the underlying Riemann surface topology to induce a state exchange. This non-trivial evolution swaps the modes, transferring energy between them, while simultaneously accumulating a topological geometric phase.

On the other hand, light propagation in unperturbed multimode waveguides depends strictly on the core's refractive index profile; in particular, parabolic graded-index (GRIN) fibers exhibit equidistant propagation constants and periodic self-imaging, whereas arbitrary profiles yield quasi-periodic field evolution. Physical perturbations—such as bending or twisting—introduce mode coupling that triggers complex, turbulent dynamics. Crucially, conventional Hermitian perturbations (purely real refractive index modulations) always enforce symmetric, bidirectional mode coupling, manifesting as periodic Rabi oscillations governed by strictly real-valued eigenvalues.

In this paper, we propose a highly robust mode-management scheme for multimode fibers. Building upon recent demonstrations of non-Hermitian mode-cleaning in parabolic multimode waveguides [2-4].

II. Helical Waveguide

The proposed architecture implements simultaneous three-dimensional chiral modulations of both the refractive index and the gain/loss profile along the fiber, consisting of two pairs of satellite cores embedded within the main multimode fiber core, all twisted along the propagation axis, z, with a helical pitch, Λ. The trajectories tracking the centers of these modulation zones —one introducing a pure refractive-index (real, *re*) perturbation and the other an gain/loss (imaginary, *im*) perturbation —follow the helical paths in cylindrical coordinates: $(r,\phi)_{re} = (d, 2\pi z/\Lambda)$ and $(r,\phi)_{im} = (d, 2\pi z/\Lambda+\theta)$ respectively; where θ is the relative azimuthal shift. By establishing a three-dimensional non-Hermitian lattice, this helical structure represents a major advancement over earlier non-Hermitian self-cleaning methods [3,4], offering a practical and robust paradigm for regularizing modal dynamics and mitigating turbulence in high-power multimode fibers. Moreover, the proposal does not rely on high nonlinearities as other self-cleaning schemes previously reported [5]. The proposal may be realized within actual technological means, see Fig 1.

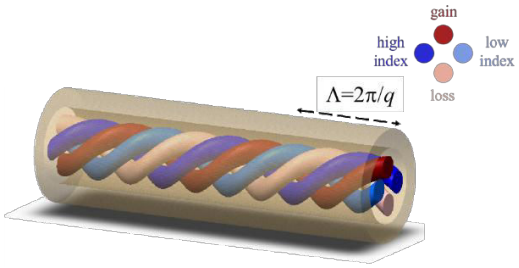

Fig. 1 Schematic representation of the proposed helical non-Hermitian fiber with four cores [6].

Numerical simulations confirm that the continuous modal cascade delivers Gaussian-shaped beams. It is important to note that, contrary to the initial proposal [2], the present modulation

scheme provides asymmetric coupling between helical modes with different orbital angular momentum.

Upon incidence of a mode with high orbital angular momentum (LG_{03}), we observe a significant energy cascading towards the lower-order mode (LG_{00}). The asymmetric mode-conversion process is shown in Fig.2.

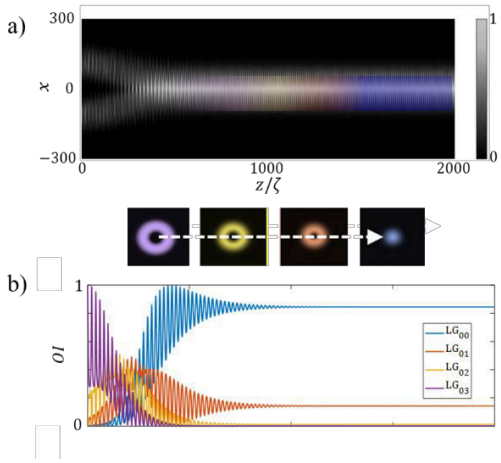

Fig. 2 a) Numerical propagation of an incident LG_{03} mode along the helical non-Hermitian fiber. b) Overlap Integral (OI) of the propagating beam on modes LG_{03}, LG_{02}, LG_{01}, and LG_{00}, showing the energy cascading.

III. Discussion

Interestingly, mapping the energy conversion in Ref. [4], we already observed that the energy transfer occurred close to resonance between the spatial modulation and propagation constant of the modes, being that the most efficient cascading does not occur exactly at the *PT*-symmetry breaking point, see Fig. 3a.

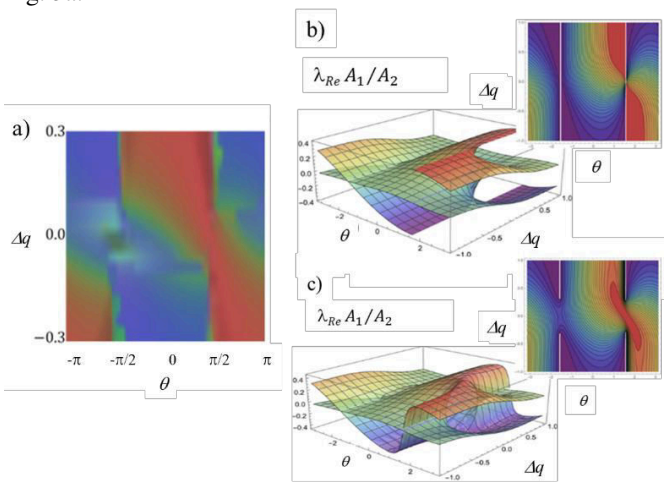

Fig. 3 a) Overlap integral, *OI,* where the lowest order mode intensity is depicted in red, the second in green, and the third in blue; depicted in the parameter space of the spatial frequency detuning, Δq, with respect to the propagation constant of the modes [4]. b)/c) Two coupled modes analysis. Ratio between the real part of the eigenvalues of both modes for an EP and an exceptional ring when the energy transfer is maximized [6].

A simplified two-mode coupled analysis—omitting non-interacting modes—fully accounts for this analytical result. In the case of balanced index/gain-loss modulation, we observe the existence of an EP. For slightly unbalanced values of the real and imaginary modulations, there exists an exception ring that efficiently funnels energy to the lower mode. In turn, a larger energy exchange area in parameter space corresponds to a more robust interaction, compare Figs. 3b and 3c.

IV. Conclusion

We propose and demonstrate a feasible non-Hermitian self-cleaning helical waveguide. The numeric simulations can be explained by a simplified two-coupled-mode analysis, which shows that the best scenario does not coincide with the PT-symmetry breaking point.

Acknowledgments

This work received funding from the Spanish Ministry of Science, Innovation, and Universities (MICINN) under Project No. PID2022-138321NB-C21.

References

[1] Li, Aodong, et al. "Exceptional points and non-Hermitian photonics at the nanoscale." Nature Nanotechnology 18, pp. 706-720, 2023.

[2] Akhter, Mohammad Nayeem, et al. "Non-Hermitian mode cleaning in periodically modulated multimode fibers." Physical Review Letters 131, 043604, 2023.

[3] Akhter, Mohammad Nayeem, et al. "Mode-cleaning in antisymmetrically modulated non-Hermitian waveguides." Nanophotonics 13, pp. 1017-1024, 2024.

[4] Akhter, Mohammad Nayeem, et al. "Non-Hermitian mode management in periodically modulated waveguide amplifiers." APL Photonics 9.10, 2024.

[5] Krupa, K. et al. “Spatial beam self-cleaning in multimode fibres” Nature Photonics, 11, pp. 237-241, 2017.

[6] Herrero, Ramon et al. Non-Hermitian Mode Cleaning in a Waveguide with a Chiral Index and Gain/Loss Modulation” In preparation.

A quantum particle in a potential well with an absorbing barrier - non-Hermitian tunneling

Eva-Maria Graefe

Department of Mathematics, Imperial College London, UK

e.m.graefe@ic.ac.uk

***Abstract*—A 1D quantum box, with a central region with negative imaginary potential, modelling absorption, is considered. For strong absorption this acts as a Zeno barrier, forming an effective double well. The resulting near-degenerate eigenstates possess complex eigenvalues, fundamentally altering superposition dynamics compared to the periodic tunneling of the Hermitian counterpart.**

***Keywords*— non-Hermitian, tunneling, spectral properties**

I. Introduction

We consider a quantum particle in a one-dimensional box, with a central region with constant imaginary potential, modelling absorption. Specifically, the Hamiltonian is given by

$$\hat{K} = \frac{1}{2m}\hat{p}^2 + V(\hat{q}), \tag{1}$$

with the complex potential

$$V(x) = \begin{cases} \infty, & x \le -L \\ 0, & -L < x \le -a, \\ -\mathrm{i}\Gamma_0, & -a < x < a, \\ 0, & a \le x < L, \\ \infty, & L \le x, \end{cases} \tag{2}$$

where $0 < a < L$, and Γ_0 is a positive real absorption constant.

II. Methods and Results

A simple textbook procedure leads to quantisation conditions for complex eigenenergies, which we solve numerically to obtain eigenvalues and eigenfunctions of the system. An example of trajectories of energy eigenvalues in the complex plane, as Γ_0 is varied from zero to nine, where $L = 3$ and $a = 1$ is depicted in Figure 1. The blue dots are eigenvalues corresponding to symmetric eigenfunctions, and the red dots correspond to anti-symmetric eigenfunctions. The nine eigenvalues with the lowest real parts of the energy are shown. Here we observe how for small values of the absorption all eigenvalues pick up negative imaginary parts corresponding to decay of the probability amplitude in the corresponding eigenstates. With larger absorption some states become increasingly shorter lived, while other states become more stable, as is common in open systems. This phenomenon is often referred to as resonance trapping or a quantum Zeno effect. For strong absorption, the absorbing region acts like a physical barrier, and the eigenstates localise either in the absorbing (very short lived states) or the non-absorbing (very long lived states) regions.

The structure of the eigenvalue trajectories depends on the relative size of the absorbing region (i.e. the ratio of a and L). For the case $a = 1$ and $L = 3$ depicted in the figure, every third state localises in the absorbing region and becomes extremely short lived for large Γ_0, while the other states form a pair of symmetric and anti-symmetric states localised in the non-absorbing regions. For other ratios of a and L other scenarios appear, including cases with exceptional points, where two states of the same symmetry type degenerate for specific values of Γ_0.

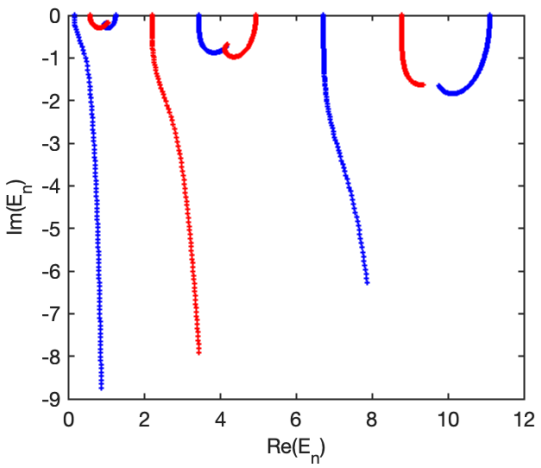

Fig. 1. Trajectories of the lowest nine complex energy eigenvalues in the complex plane in dependence of Γ_0 for 100 values of Γ_0 equidistant in the range [0 9], for $L = 3$ and $a = 1$. The eigenvalues corresponding to symmetric eigenfunctions are depicted in blue, those corresponding to anti-symmetric eigenfunctions in red.

In the case of a real potential barrier, the lowest energy pairs of symmetric and anti-symmetric states with near degenerate eigenvalues, with superpositions localised on either side of the barrier, lead to the periodic tunneling behaviour characteristic of symmetric double well potentials. In the non-Hermitian case, however, the near-degenerate energies of the symmetric and anti-symmetric pair also have (slightly different) imaginary parts. This leads to a very different phenomenon, where a superposition of the two states, initially localised on one side of the effective potential barrier, decays into the state with the longer lifetime (which is not always the symmetric state), with probability equally distributed between the two sides.

SPECIAL SESSION 3

New Advances in Metamaterials and Their Functional Applications

2 contributions · pp. 794–797

Geometric Tailoring of Anisotropic Metamaterials for Elastic Wave Steering

Jianlong Chen[1], Dong Yan[1,2], Chao Wan[1,2], Guangyan Liu[1,2], Kai Zhang[1,2,*]

[1] School of Aerospace Engineering, Beijing Institute of Technology, China
[2] Tangshan Research Institute, Beijing Institute of Technology, China
*Corresponding author: zhangkai@bit.edu.cn

***Abstract*— We propose a geometric design methodology for architected microstructures achieving highly anisotropic stiffness without altering material composition. This enables decoupled control of axial and shear moduli, facilitating directional wave control, mode conversion, and energy confinement. An annular metastructure demonstrates superior azimuthal wave trapping compared to isotropic counterparts.**

***Keywords*— elastic anisotropy, wave mode conversion, directional bandgap, vibration isolation.**

I. Introduction

Metamaterials have revolutionized the control of elastic waves, enabling applications such as acoustic insulation[1], negative refraction[2], and waveguiding[3]. However, achieving these properties often requires complex resonant elements that compromise mechanical robustness or limit operational bandwidth[4]. Anisotropic materials offer a promising alternative by utilizing direction-dependent mechanical properties to manipulate wave motion[5,6].

Current design approaches for anisotropic materials, such as fiber-reinforced composites or standard honeycombs, often face challenges regarding interface bonding or coupled stiffness properties. To address these limitations, we propose a novel design methodology for architected microstructures that achieve strong, tunable anisotropy solely through geometric configuration. By systematically varying geometric parameters, we demonstrate stiffness anisotropy exceeding three orders of magnitude. We further investigate the dynamic characteristics, revealing phenomena such as directional bandgaps and wave mode conversion, which are utilized to design an annular metastructure for efficient vibration isolation and energy localization.

II. Design and Methodology

The proposed unit cell consists of horizontal, inclined, and vertical beams arranged in a periodic lattice. The design decouples the stiffness contributions: horizontal beams primarily sustain axial forces (high stiffness), while inclined beams deform via bending under vertical loads (low stiffness).

We derived the effective elastic moduli theoretically and validated them using Finite Element Method (FEM) simulations. The normalized effective Young's modulus in the x-direction $\bar{E}_1^*$ and y-direction $\bar{E}_2^*$ are governed by the geometric parameters: horizontal beam thickness h, inclined beam angle θ, thickness t, and height d. The effective stiffness in the x-direction is approximated as:

$$\bar{E}_1^* \approx \frac{h}{l} \tag{1}$$

where l is the cell size. Conversely, the y-direction stiffness is dominated by the bending of inclined beams, allowing independent tuning of the principal moduli.

We further optimized the structure by introducing an oblique lattice configuration to enhance mode conversion efficiency and broaden directional bandgaps.

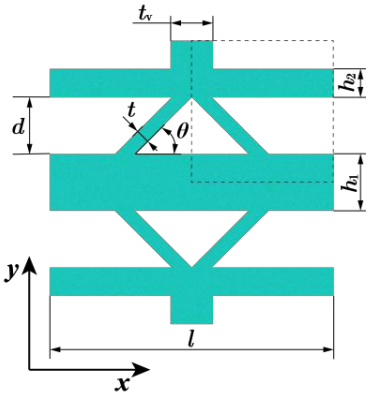

Fig. 1 Unit cell geometry of the proposed metamaterial.

III. Results and Discussion

A. Tunable Anisotropy

Systematic variation of geometric parameters reveals that the degree of anisotropy spans over three orders of magnitude. The axial stiffness ratio and shear-to-axial ratio can be tailored independently. This geometric decoupling allows for precise customization of the constitutive matrix for specific wave control requirements.

Specifically, by designing the horizontal beam thickness h to be much larger than that of the inclined beams t, we induce a transition in mechanical response. The structure behaves as a

rigid, stretching-dominated medium along the x-axis, while remaining compliant and bending-dominated along the y-axis. Consequently, the resulting anisotropy ratio can be precisely adjusted, facilitating extreme wave steering capabilities such as collimation.

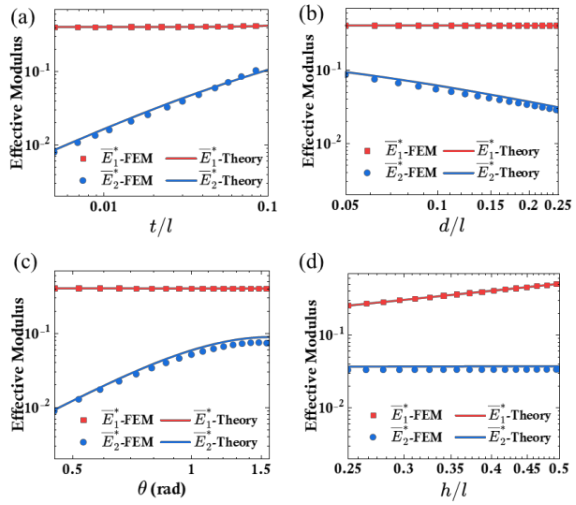

Fig. 2 Dependence of effective moduli on geometric parameters. (a-d) Variation of normalized effective Young's moduli E_1^* and E_2^* with respect to dimensionless geometric parameters.

B. Wave Propagation and Mode Conversion

Dynamic analysis reveals distinct behavior for quasi-longitudinal (Q_p) and quasi-transverse (Q_s) waves. The slowness curves indicate that energy propagation for Q_p waves is concentrated along the principal axes, while Q_s waves exhibit a butterfly-like distribution.

At high frequencies, we observed directional bandgaps where wave propagation is suppressed along the y-direction. Furthermore, a mode conversion mechanism was identified: wave vectors initially oriented in the y-direction are converted into bending waves of the horizontal beams, redirecting energy by 90 degrees into the x-direction.

C. Annular Metastructure Application

To demonstrate practical utility, we designed an annular metastructure based on the oblique lattice. The annular metastructure was constructed by mapping the Cartesian unit cells into a polar coordinate system. The radial stiffness corresponds to the soft axis, while the circumferential stiffness corresponds to the stiff axis.

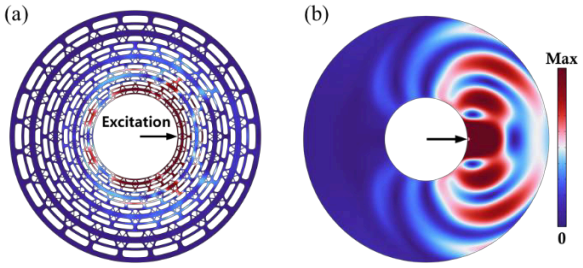

Fig. 3 Comparison of wave propagation behaviors. (a) Transient displacement field of the anisotropic annular metastructure, demonstrating effective azimuthal energy confinement under radial excitation. (b) Transient displacement field of the isotropic counterpart, showing significant outward radial energy leakage.

Under radial excitation, the structure exhibits efficient wave trapping and azimuthal energy confinement. As shown in the transient displacement fields, wave energy in the metastructure is guided circumferentially, protecting the outer boundary. In contrast, the isotropic counterpart allows energy to radiate outward. Frequency response measurements confirm that the anisotropic design suppresses radial leakage significantly compared to the isotropic case.

IV. Conclusion

This work establishes a framework for designing anisotropic architected materials with decoupled stiffness properties. We demonstrated that simple geometric tailoring can achieve pronounced anisotropy, enabling advanced wave control mechanisms such as directional bandgaps and mode conversion. The proposed annular metastructure verifies the potential for vibration isolation and acoustic steering in engineering applications.

Acknowledgments

This work was supported by the National Natural Science Foundation of China (Grant No. 12272041, Grant No. 12202054).

References

[1] Liu, Z., Zhang, X., Mao, Y., Zhu, Y. Y., Yang, Z., Chan, C. T., and Sheng, P., 2000, "Locally Resonant Sonic Materials," Science, 289(5485), pp. 1734–1736.

[2] Zhu, R., Liu, X. N., Hu, G. K., Sun, C. T., and Huang, G. L., 2014, "Negative Refraction of Elastic Waves at the Deep-Subwavelength Scale in a Single-Phase Metamaterial," Nat. Commun., 5(1), p. 5510.

[3] Wang, Z., Zhang, Q., Zhang, K., and Hu, G., 2016, "Tunable Digital Metamaterial for Broadband Vibration Isolation at Low Frequency," Adv. Mater., 28(44), pp. 9857–9861

[4] Azevedo Vasconcelos, A. C., Schott, D., and Jovanova, J., 2025, "Hybrid Mechanical Metamaterials: Advances of Multi-Functional Mechanical Metamaterials with Simultaneous Static and Dynamic Properties," Heliyon, 11(3), p. e41985.

[5] Amirkhizi, A. V., Tehranian, A., and Nemat-Nasser, S., 2010, "Stress-Wave Energy Management through Material Anisotropy," Wave Motion, 47(8), pp. 519–536.

[6] Chen, Y., Zheng, M., Liu, X., Bi, Y., Sun, Z., Xiang, P., Yang, J., and Hu, G., 2017, "Broadband Solid Cloak for Underwater Acoustics," Phys. Rev. B, 95(18), p. 180104.

Direct Tensor Processing with Coherent Light

Yufeng Zhang[1,*], Kaizhi Wang[2], Xuhan Guo[2], Zhipei Sun[1]

[1]Department of Electronics and Nanoengineering, Aalto University, Finland
[2] School of Electronic Information and Electrical Engineering, Shanghai Jiao Tong University, Shanghai, China
*Corresponding author: yufeng.zhang@aalto.fi

***Abstract*— We propose a parallel optical matrix-matrix multiplication scheme implemented using a single propagation of coherent light and extend it to tensor-matrix multiplication via wavelength multiplexing. Building on this framework, we investigate its application in different optical neural network architectures and its potential deployment in metasurface devices.**

***Keywords*— optical computing, optical neural networks.**

I. Introduction

Artificial intelligence increasingly relies on tensor processing, especially matrix-matrix multiplication (MMM), which imposes heavy bandwidth and energy demands on GPUs. Optical computing offers high bandwidth, parallelism and low power, but existing optical neural networks often trade generality for parallelism, requiring repeated propagations, multiplexing or architecture-specific designs. Here, we introduce direct parallel optical matrix-matrix multiplication, which performs MMM in a single coherent light propagation by exploiting the bosonic nature of light and spatial-frequency duality[1]. And we extend it to parallel optical tensor-matrix multiplication by wavelengths multiplexing. Simulations and experiments validate GPU-consistent processing, enabling a GPU-compatible optical neural-network framework for convolution neural networks (CNN) and vision transformers (ViT), and establishing optical computing as a scalable platform for general tensor processing.

II. Methods

Conventionally, matrix-matrix multiplication is performed by computing the Hadamard product between each row of matrix A and each column of matrix B, followed by summation to obtain each output element. In optics, the Hadamard product can be implemented by spatial amplitude modulation, while summation can be approximated by Fourier-transform-based integration using quadratic phase modulation, such as a lens[2]. The main challenge is to compute all row-column dot products in parallel and map them to distinct output positions without interference.

Our method[1] addresses this challenge by exploiting the time-shifting and frequency-shifting properties of the Fourier transform (Fig. 1a). First, the elements of matrix $\boldsymbol{A}$ are encoded into the amplitude and position of a coherent optical field, while each row is assigned a distinct linear phase gradient. A column-wise Fourier transform is then applied by imaging along the row direction and focusing along the column direction. Owing to the time-shifting property, each row after this operation contains a superposition of all rows of $\boldsymbol{A}$. Matrix $\boldsymbol{B^T}$ is subsequently encoded through amplitude modulation, producing parallel Hadamard products between this hybrid optical field and $\boldsymbol{B^T}$. Finally, a row-wise Fourier transform performs the summation. Because different rows of $\boldsymbol{A}$ carry different phase gradients, the frequency-shifting property separates their contributions into distinct spatial-frequency positions, yielding the corresponding MMM outputs without mutual interference.

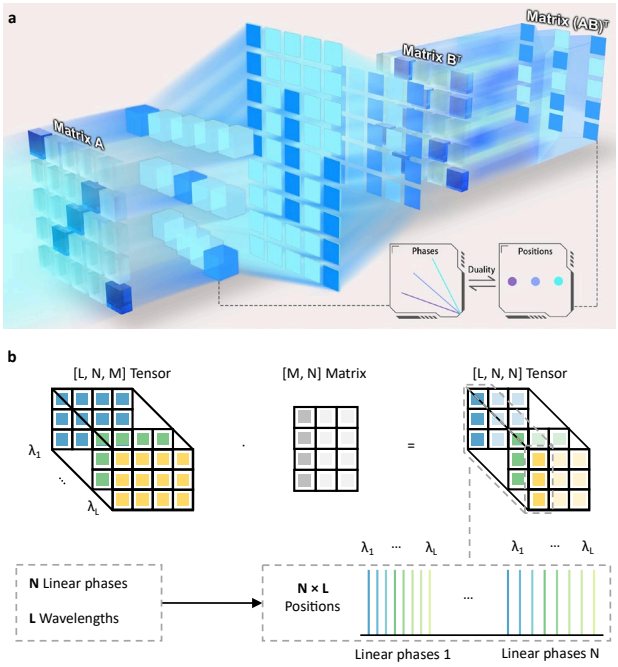

Fig. 1 Principle. a. Optical matrix-matrix multiplication with coherent light. b. Optical tensor-matrix multiplication by multiple wavelengths extension[1].

Since it relies only on coherent amplitude and phase modulation, it naturally supports wavelength multiplexing. An optical field containing L wavelengths and N phase gradients is mapped to L × N spatial-frequency positions, enabling tensor-matrix operations between an [*L, N, M*] tensor and an [*M, N*]

matrix within a single propagation process[1] (Fig. 1b).

III. Results and Discussion

To validate the reliability of our method[1], we designed an optical prototype and compared its experimental results with those obtained from GPU-based MMM across various scenarios[1]. We conducted a large sample quantitative analysis across multiple matrix sizes ([*10, 10*], [*20, 20*], [*30, 30*], [*40, 40*], [*50, 50*], with 50 random matrix pairs for each size) and evaluated the computational errors between our method[1] and GPU-based MMM (Fig. 2a). The results showed that both the mean absolute error (less than 0.15) and the normalized root-mean-square error (less than 0.1) remained low, confirming the accuracy and reliability of our method[1].

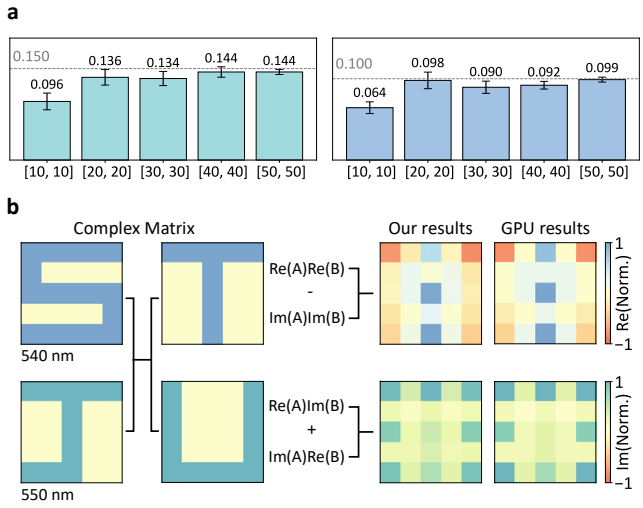

Fig. 2 Results of matrix and tensor multiplications[1]. a. Matrix-matrix multiplications. Left: average mean absolute error (MAE). Right: average normalized root-mean-square error (RMSE). The horizontal axis indicates different matrix sizes. Each bar shows the mean MAE or RMSE over 50 random samples of the corresponding size (black numbers denote the mean values; grey numbers are baselines), and the error bars represent ±1 standard deviation. b. Tensor-matrix multiplications.

In addition, we encoded the real and imaginary parts of a complex-valued matrix (with patterns 'S' and 'J') onto two distinct wavelengths and performed two rounds of two-wavelength MMM with another complex matrix (patterns 'T' and 'U') to realize full complex MMM. The results[1] show a high degree of consistency with those computed by GPU (Fig. 2b), and this process can be equivalent to the real-valued multiplication between a [*2, 5, 5*] tensor and two [*5, 5*] matrices.

Due to the high consistency between our method[1] and GPU tensor core-based MMM, this method theoretically enables the direct deployment of standard GPU-based neural network architectures. This eliminates the need to design custom network architectures tailored to the unique optical propagation constraints of conventional optical neural networks. To further validate this capability, we conducted direct inference experiments using both CNN and ViT networks on our simulation and prototype, utilizing MNIST and Fashion-MNIST (FMNIST) datasets. These architectures include three representative tensor processing steps common in modern neural networks: multi-channel convolution, multi-head self-attention and multi-sample fully connected layers. We first used four different models (CNN-MNIST, ViT-MNIST, CNN-FMNIST and ViT-FMNIST) trained on GPUs with non-negative weights and tested inference across GPU, simulation and prototype of our method[1]. Inference outputs were highly consistent across all platforms, demonstrating that our method[1] supports a wide range of tensor processing operations and enables the direct deployment of GPU-trained weights (Fig. 3a). Furthermore, we used two successive simulated optical MMM units to directly execute all linear operations with unconstrained GPU-trained weights, achieving inference accuracy highly consistent with GPU results (Fig. 3b).

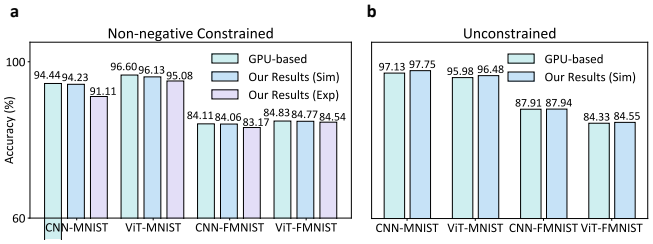

Fig. 3 Results of optical neural networks[1]. a. Tests of direct deployment of non-negative constrained GPU-trained weights across different networks and datasets on our simulation and prototype. Sim, simulation; Exp, experiment. b. Tests of direct deployment of all-step unconstrained GPU-trained weights across different datasets on our simulation.

Besides, our method[1] requires only passive phase modulation, excluding data input and output, making it broadly compatible with free-space optical computing platforms. Its high theoretical parallelism could substantially boost effective performance when combined with high-speed, large-scale photonic hardware[3]. Moreover, customized metasurfaces may replace bulky phase-modulation optics, enabling compact free-space optical accelerators compatible with advances in nanofabrication.

IV. Conclusion

In conclusion, this work[1] demonstrates that a single propagation of coherent light can realize parallel matrix-matrix multiplication and can be extended to tensor-matrix multiplication through wavelength multiplexing. We further show that this concept provides a foundation for implementing general optical neural networks.

Acknowledgments

This work was supported by the MSCA Actions (QEUST)

References

[1] Zhang, Y., Liu, X., Yang, C. et al. Direct tensor processing with coherent light. Nat. Photon. 20, 102–108 (2026).
[2] Goodman, J. W. Introduction to Fourier Optics (Roberts and Company, 2005).
[3] Chen, Z., Sludds, A., Davis, R. et al. Deep learning with coherent VCSEL neural networks. Nat. Photon. 17, 723–730 (2023).

SPECIAL SESSION 4

Chiral fields and ultrafast chiral spectroscopy

8 contributions · pp. 799–822

Manipulating chiral effects with plasmonic nanostructures

Yuanyang Xie[1]*, Alexey V. Krasavin[1], Anatoly V. Zayats[1]*

[1]Department of Physics and London Centre for Nanotechnology, King's College London, London, WC2R 2LS, UK.

*Corresponding author: yuanyang.xie@kcl.ac.uk, a.zayats@kcl.ac.uk

***Abstract*— Plasmonics offers unique opportunities to enhance and engineer optical chirality at the nanoscale. In this talk we present an overview of our recent research in chiral plasmonics, starting with discussion of how plasmonic chirality can be defined, and then presenting how it can be used to engineer chiral optical scattering and emission.**

***Keywords*— chirality, plasmonics, helicoid .**

I. Introduction

Chiral light carrying a spin or/and orbital angular momentum is of fundamental importance for controlling light-matter interactions with chiral molecules and nano-objects, paving the way for advanced applications in nanophotonics and photochemistry. Chiral plasmonic nanostructures offer unique advantages for engineering and enhancement of chiral light-matter interactions, potentially providing strong chiral responses in scattering, absorption, extinction and emission.

In this talk, we will discuss the relation between chirality and optical activity of plasmonic nano-objects, with differentiating chiral responses in extinction, absorption, scattering, and emission [1]. We will also discuss how to engineer directional chiral scattering and emission from plasmonic helicoids [2] The results are important for the design of chiral plasmonic devices for sensing, displays, and quantum technologies.

II. Methods

The circular dichroism (CD) spectrometry, optical thermometry, Fourier-plane microscopy and chiral electric luminescence were employed to analyse the chiral effects predicted in chiral plasmonic nanostructures, such as gold helicoid nanoparticles. The simulations were performed by using the finite element method (COMSOL Multiphysics software). Gold helicoids were fabricated by a L-glutathione guided growth method [1-3].

III. Results and Discussion

Molecular meso-compounds possess multiple chiral centres but do not exhibit a chiral optical signature because they have an internal plane of symmetry, In contrast to molecules, in nanostructures in addition to absorption, scattering plays an important role. We introduce a novel concept of meso-chiralilty for nanoparticles when the substantial chirality in absorption and scattering can be hidden inside a completely achiral response in extinction due to the opposite sings of these components. In this case, the essentially chiral local response of the nanoparticle remains undetected or significantly underestimated using conventional circular dichroism (CD) measurements. At the same time, while the overall chiral response of meso-chiral nanoparticles is zero, the hidden chiral behaviour can significantly affect local enantio-sensitive light-matter interactions. Notably, this property is not so uncommon in chiral plasmonic nanoparticles, which was demonstrated on the examples of multi-wound particles, helixes, and helicoids, and is experimentally verified for the latter.

In order to achieve unidirectional chiral scattering, we introduced a concept of rotating chiral dipoles. Implementing this concept by engineering multipole excitations in helicoidal plasmonic nanoparticles, we experimentally demonstrate enantio-sensitive and highly-directional forward scattering of circularly polarised light. The intensity of this highly-directional scattering is defined by the mutual relation between the handedness of the incident light and the chirality of the structure.

The chiral light emission has been explored in the chiral tunnel junctions based on gold helicoid nanoparticles. The intrinsic chirality of chiral plasmonic structures incorporating tunnel junctions, defines the spin and orbital angular momenta in tunnelling-driven light emission.

IV. Conclusion

We have demonstrated plasmonically assisted light-matter interactions affecting absorption, scattering and emission of chiral light. The diverse phenomena emerging in chiral plasmonics provide a novel framework for further design of advanced chiral nanophotonic devices.

Acknowledgments

This work was supported by the UK EPSRC projects EP/W017075/1 and UKRI3056.

REFERENCES

[1] Xie, Y., Krasavin, A. V., & Zayats, A. V. “Meso-chiral optical properties of plasmonic nanoparticles: uncovering hidden chirality. Nanophotonics,” vol. 14(25), pp. 4479-4485, 2025.
[2] Xie, Y., Krasavin, A. V., Roth, D. J., & Zayats, A. V. “Unidirectional chiral scattering from single enantiomeric plasmonic nanoparticles.,” Nature Communications, vol. 16(1), pp. 1125, 2025.
[3] Xie, Y., Krasavin, A. V., & Zayats, A. V. “Plasmonically-assisted chiral emission from tunnel junctions” in preparation.

Non-dichroic Chiral Photoelectron Spectroscopy

Letizia Fede[1], Debobrata Rajak[2], Chris Sparling[3], David Ayuso[4], Sylvain Betoule[5], Valérie Blanchet[1], Piero Decleva[6], Dominique Descamps[1], Stéphane Petit[1], Bernard Pons[1], Yann Mairesse[1], Andrés Ordóñez[7]

[1]Université de Bordeaux – CNRS – CEA, CELIA, Talence, France
[2]ELI ALPS, The Extreme Light Infrastructure ERIC, Szeged, Hungary
[3]Institute of Photonics and Quantum Sciences, Heriot-Watt University, Edinburgh, UK
[4]Department of Chemistry, Imperial College London, London, UK
[5]Sorbonne Université, CNRS, LCPMR, Paris, France
[6]Università degli Studi di Trieste, Trieste, Italy
[7]Department of Physics, Freie Universität, Berlin, Germany

*Corresponding authors: yann.mairesse@u-bordeaux.fr, andres.ordonez@fu-berlin.de

***Abstract*— We find enantiosensitive but non-dichroic signals in the 3D photoelectron angular distribution of chiral molecules upon multiphoton ionization with elliptically polarized light. The robustness of enantiosensitivity against ellipticity is an example of symmetry protection, opening unexplored opportunities for imaging ultrafast dynamics in chiral molecules with polarization-structured light.**

***Keywords*— chirality, multiphoton, symmetry, ellipticity, laser, photoelectron.**

The interaction of randomly oriented chiral molecules with circularly polarized light leads to effects that change sign upon reversal of either molecular chirality (enantiosensitivity) or light's polarization (circular dichroism). Among these effects, multiphoton ionization has provided privileged access to ultrafast electron dynamics in randomly oriented chiral molecules through the forward-backward asymmetry of photoelectron angular distributions (PADs) [1].

Here, we found that the combination of elliptical polarization, multiphoton ionization, and 3D detection reveals the presence of Non-Dichroic EnantioSensitive (NoDES) tensor observables in the PAD [2,3]. That is, upon expansion of the PAD into spherical harmonics, we found that certain expansion coefficients have opposite sign for opposite enantiomers but do not change sign upon reversal of the ellipticity, confirming recent theoretical suggestions [4]. Our experiments on camphor, fenchone, and alpha-pinene demonstrate that these NoDES contributions reach about 1% of the total ionization yield.

We found that NoDES contributions originate from the combination of two effects: (i) dichroic and enantiosensitive forward-backward asymmetry and (ii) dichroic and non-enantiosensitive angular streaking. The product of these two effects leads to a cancellation of dichroism without a cancellation of enantiosensitivity.

Our symmetry analysis reveals that the NoDES observables belong to the A_u irreducible representation of the PAD, which is antisymmetric with respect space inversion and hence enantiosensitive, but symmetric with respect to π rotations that reverse the ellipticity and hence non-dichroic. That is, the behavior of NoDES observables stems from the symmetry of a subset of (rank ≥ 3) tensors in the PAD.

Besides elliptical polarization, A_u also emerges, e.g., in bichromatic ω-2ω fields with linear polarizations perpendicular to each other. Indeed, our numerical simulations for the latter field also show NoDES contributions of the order of 1% in the two-photon, multiphoton, and strong-field regimes.

NoDES observables open new opportunities for imaging chirality when polarization is not constant throughout the interaction region, e.g., when using structured light.

Acknowledgments

Royal Society URF\R\251036. Heriot-Watt University EPSRC Doctoral Prize Fellowship. DFG-543760364. ULTRAFAST TORNADO PEPR LUMA. ANR-21-CE30-038-01, ANR-23-EXLU-0002, ANR-23-EXLU-0004, IdEx University of Bordeaux GPR LIGHT, EU Horizon 2020 871124, ELI-ALPS GINOP-2.3.6-15-2015-00001.

References

[1] C. Sparling and D. Townsend, "Two decades of imaging photoelectron circular dichroism: from first principles to future perspectives" Physical Chemistry Chemical Physics, vol. 27, pp. 2888-2907, 2025.
[2] L. Fede et al., "Non-Dichroic Enantio-Sensitive Chiroptical Spectroscopy" arXiv:2512.19062, 2025.
[3] A. Ordóñez et al., "Theory of Non-Dichroic Enantio-Sensitive Chiroptical Spectroscopy" arXiv:2512.17840, 2025.
[4] A. Ordóñez and O. Smirnova, "Disentangling enantiosensitivity from dichroism using bichromatic fields" Physical Chemistry Chemical Physics, vol. 24, pp. 7264-7273, 2022

Nonlinear Light-Matter Interactions for Ultrafast Chiral Detection in Confined Environments

Stefanos Fr. Koufidis[1,*], Jacob Edginton[1], and David Ayuso[1]

[1]Molecular Sciences Research Hub, Department of Chemistry, Imperial College London, W12 0BZ London, United Kingdom

[*]Corresponding author: steven.koufidis20@imperial.ac.uk

***Abstract*—Conventional optical methods for detecting molecular chirality rely on weak magneto-electric effects and therefore offer limited sensitivity. Here we explore an alternative approach based on locally chiral light, whose electric field follows a chiral trajectory in time and can produce strong enantio-sensitive responses within the electric-dipole approximation. We propose implementing this concept in micro-fluidic platforms for rapid optical recognition of chiral molecules in solution.**

***Keywords*—nonlinear optics, ultrafast physics, molecular chirality, enantio-sensitive detection, micro-fluids.**

Not surprisingly, the term *chirality* is not particularly informative in isolation, as it simply denotes the absence of mirror symmetry. Yet it is precisely this seemingly broad notion that underlies its physical significance. Indeed, in static media, chirality manifests itself in several distinct ways. One familiar example is circular birefringence [1], which originates from magneto-electric coupling associated with the lack of mirror symmetry at the molecular scale, whereby right- and left-circularly polarised light experience different refractive indices. Another arises in structurally chiral media, wherein the helical stacking of birefringent layers causes the principal axes of the dielectric tensor to rotate periodically along the optical axis [2]. Despite their different microscopic origins, these manifestations share a common consequence: they enable optical discrimination of chiral matter, underpinning a wide range of detection techniques—see the review in [3].

Beyond its traditional role in spectroscopy and sensing, chirality has recently emerged as a powerful mechanism for engineering light-matter interactions in structured photonic media. For instance, the interplay between circular birefringence and structural chirality has been shown to give rise to unconventional Bragg-type phenomena, such as the so-called *reverse* circular Bragg resonance, which occurs in regimes of extreme optical activity where negative refraction leads to a 'reversal' of the medium's handedness [4]. It has further been demonstrated that sufficiently strong chirality can fundamentally alter modal dispersion in wave-guiding systems, whence enabling the emergence of exceptional points through contra-directional coupling between modes without the need for gain–loss modulation or indeed spatial periodicity [5]. Chirality has also been exploited as a design parameter for optical analog computing: indeed, by combining circular and linear birefringence in cascaded uniform slabs, it becomes possible to engineer spectral holes that enable broadband spatial differentiation and edge detection without relying on conventional Bragg gratings or resonant nano-structures [6].

The aforementioned applications of chirality, whether arising from molecular handedness or from the chiral meta-atoms of artificial meta-materials, rely on magneto-electric coupling. In practice, however, this coupling is intrinsically weak. Nature's optically active media, such as sugar solutions, produce only minute optical rotations (order of 10^{-5}), which ultimately limits any sensitivity capabilities. Recent advances in ultrafast photonics have opened new prospects for the detection of small chiral molecules, which are increasingly recognised as important biomarkers in diagnostics. Traditional chemical approaches, e.g. mass spectrometry, can offer greater sensitivity, yet they typically do so at the expense of speed and experimental simplicity.

In the nonlinear regime of light-matter interactions, chiral effects are symmetry allowed already within the electric-dipole approximation [7]. This creates an opportunity to circumvent the intrinsically weak magneto-electric coupling responsible for conventional optical activity. Indeed, locally chiral electromagnetic fields [8-10], whose electric field vector itself traces a chiral trajectory in time, can drive ultrafast electronic currents in molecules with a strongly enantio-sensitive response, whence enabling chiral discrimination that can approach unity [8-10].

Building on these recent proposals [8-10], we have developed analytical and numerical approaches to model the generation of locally chiral fields within *micro-fluidic* environments, wherein tailored optical waveforms interact with liquid-phase samples confined within micro-channels. In this talk, I will discuss how the high enantio-sensitivity demonstrated in free-space strong-field experiments can be transferred to such compact platforms, thereby opening the possibility of integrated photonic devices for efficient chiral sensing in biological media.

References

1. Barron, L. D., Molecular Light Scattering and Optical Activity, *Cambridge University Press* (2009)
2. Robbie, K., Brett, M. J., and Lakhtakia, A., *Nature* **384,** 616 (1996)
3. You, S. and Park, Q.-H., *Nanophotonics* **8,** 249 (2019)
4. McCall, M. W. and Koufidis, S. F., *Physical Review Research* **4**, 043154 (2022)
5. DeCorte, A., Koufidis, S. F., McCall, M. W., and Maes, B., *Physical Review A* **110**, 053513 (2024)
6. Koufidis, S. F., Hayran, Z., Monticone, F., Pendry, J. B., and McCall, M.W., *Nanophotonics* **14,** 5449 (2025)
7. Belkin, M. A. and Shen, Y. R., *International Reviews in Physical Chemistry* **24**, 257 (2005)
8. Ayuso, D., Neufeld, O., Ordonez, A. F., Decleva, P., Lerner, G., Cohen, O., Ivanov, M., and Smirnova, O., *Nature Photonics* **13**, 866 (2019)
9. Ayuso, D., Ordonez, A. F., Decleva, P., Ivanov, M., and Smirnova, O., *Nature Communications* **12**, 3951 (2021)
10. Vogwell, J., Rego, L., Smirnova, O., and Ayuso, D., *Science Advances* **9**, eadj1429 (2023)

Twisted light generates robust many-body states for practical quantum computing

F. J. Rodríguez[1], L. Quiroga[1], N. F. Johnson[2,*]

[1]Departamento de Física, Universidad de Los Andes, Bogotá D.C., Colombia
[2]Physics Department, George Washington University, Washington, DC 20052, USA
[*]neiljohnson@gwu.edu

***Abstract*—Twisted light carries orbital angular momentum and can drive interaction-enabled excitations of confined electrons that are dark to uniform dipolar probes. We show how this "beyond-Kohn" channel becomes a concrete control primitive for quantum computing: correlation sectors in few-electron quantum dots form a tunable ladder of robust many-body states (robust here in the limited sense of symmetry-protected selection rules and persistent chiral fingerprints; topological gap protection requires $N \geq 3$), and a twisted-light pulse provides fast optical write, read, and scalable addressing. The analytically solvable Calogero limit provides closed-form spectra and matrix elements that translate directly into gate parameters, while screened and Coulomb interactions preserve the same qualitative chiral fingerprints.**

***Index Terms*—twisted light, orbital angular momentum, chiral spectroscopy, quantum dots, correlations, fractional quantum Hall physics, Calogero model, quantum computing**

I. Introduction

Ultrafast chiral spectroscopy is often formulated through polarization and dipole selection rules. Twisted light adds chirality via orbital angular momentum (OAM) and can address internal (relative-motion) excitations that remain dark to spatially uniform dipolar driving. [1]–[3] In magnetized quantum dots, these internal excitations are precisely where strong correlations live: they organize the "magic-number" angular-momentum spectrum and (for larger particle number N) they connect continuously to fractional quantum Hall effect (FQHE) states. [7], [8], [11]

The motivation for quantum computing is twofold.

First, topological many-body states offer a route to hardware-level robustness: a gap and symmetry structure can suppress certain local error channels. [9], [10] Even before true topological order sets in (which requires $N \geq 3$), few-electron "Laughlin-like" correlation sectors provide sharply distinct wavefunctions with different correlation holes and different spatial structure.

Second, twisted light provides an *optical* control layer: the same OAM selection rules that make certain transitions visible also make them *addressable*. This suggests a "photonic control bus" concept in which a spatial light modulator (SLM) steers and sets the beam's OAM so that (i) beam position selects the dot, while (ii) vorticity selects the transition. This optical addressing can, in principle, scale without dense on-chip wiring.

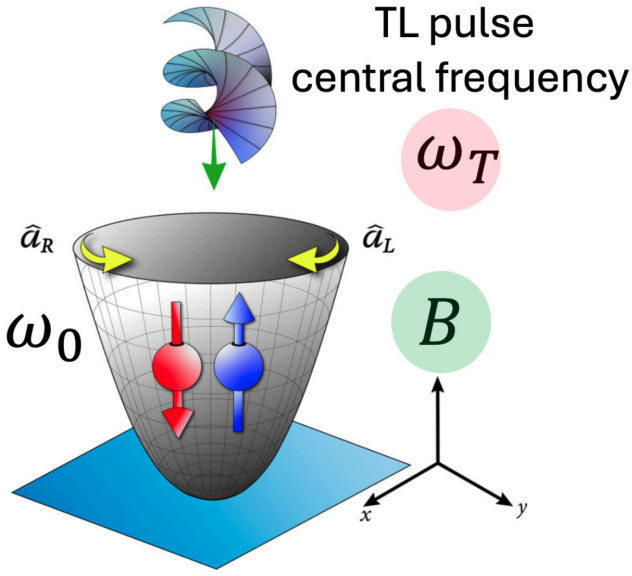

Fig. 1. Schematic representation of the system. A twisted-light (TL) pulse is incident on two interacting charged electrons confined in a two-dimensional harmonic quantum dot, under a perpendicular magnetic field B. The chiral operators $\hat{a}_R$ and $\hat{a}_L$ destroy right- and left-circular orbital quanta of the relative motion, respectively.

The underlying physics channel is established in our recent work on twisted-light chiral spectroscopy of interacting electrons in nanostructures under magnetic field. [4] In that setting, twisted light breaks the (generalized) Kohn theorem by coupling to the *relative* coordinate, opening interaction-enabled "dark" lines that are absent for uniform dipole probes. [4] Here we recast those exact selection rules and matrix elements in the language of quantum information: they define a natural qubit encoding, a universal single-qubit gate set, and a concrete path toward entangling two-qubit gates.

II. Two-electron quantum dot under magnetic field: why $N = 2$ matters

A. Center-of-mass vs. relative motion and Kohn Theorem protection

Two electrons of effective mass m^* in a 2D parabolic confinement (frequency ω_0) under perpendicular magnetic

field B are described by a Hamiltonian that separates exactly into center-of-mass (CM) and relative parts. Defining complex coordinates $z_j = x_j + iy_j$, and

$$Z = \frac{z_1 + z_2}{2}, \qquad z = z_1 - z_2, \tag{1}$$

the non-interacting problem becomes two independent Fock–Darwin oscillators with frequencies

$$\omega = \sqrt{\omega_0^2 + \omega_c^2/4}, \qquad \omega_c = \frac{eB}{m^*}, \tag{2}$$

and (in ladder-operator form) right/left circular modes with $\omega_R = \omega + \omega_c/2$ and $\omega_L = \omega - \omega_c/2$.

The **generalized Kohn theorem** states that a spatially uniform dipolar probe ($l = 0$) excites only the CM degree of freedom in a parabolic dot, independent of interactions. [11] Hence, dipole absorption cannot diagnose the internal correlated spectrum.

Twisted light changes this: because its field has spatial structure (nonzero OAM index l), it can carry multipole components that couple directly to the *relative* coordinate. The resulting absorption therefore fingerprints correlations rather than just the CM mode. [4]

B. Correlation sectors as "Laughlin-like" states at finite N

In the lowest Landau level (LLL) language, the two-electron antisymmetric polynomial is $(z_1 - z_2)$, and the Laughlin-like family is

$$\Psi_q^{(N=2)}(z_1, z_2) = (z_1 - z_2)^q \, e^{-(|z_1|^2 + |z_2|^2)/(4\ell_B^2)}, \qquad q \text{ odd}. \tag{3}$$

For $N = 2$, calling $q = 3$ a "$\nu = 1/3$ Laughlin state" is algebraically correct but physically thin: it has the correct correlation hole but not the topological features (anyon statistics, edge theory, degeneracy) that require $N \geq 3$. [8] Nevertheless, the *ladder* $q = 1 \to 3 \to 5 \to \cdots$ is a sharp, exactly defined set of correlation sectors. This is precisely the structure that twisted light can address selectively.

III. Twisted Light Coupling and Selection Rules

A twisted-light mode is characterized by OAM index l and helicity $\sigma = \pm 1$ (circular polarization). The *total* angular momentum transferred per absorbed photon is $s = l + \sigma$. For the parabolic-dot geometry, the internal (relative-motion) coupling takes a compact ladder-operator form. [4] For example, for the quadrupole-like case ($l = 1$ with $\sigma = +1$, hence $s = 2$) one obtains

$$\hat{H}_{2e}^{(l=1)} = \hbar\omega_R \hat{a}_R^\dagger \hat{a}_R + \hbar\omega_L \hat{a}_L^\dagger \hat{a}_L + V_{e-e}(|\hat{\vec{r}}|) + i\mathcal{E}_0 f(t) \left[e^{-i\omega_T t} \left(\hat{a}_R^\dagger + \hat{a}_L \right)^2 - e^{i\omega_T t} \left(\hat{a}_R + \hat{a}_L^\dagger \right)^2 \right], \tag{4}$$

with a coupling amplitude $\mathcal{E}_0$ (an energy scale) set by the beam amplitude and waist, and $f(t)$ the pulse envelope. This dimensionless light-matter coupling strength is $\mathcal{E}_0 = \frac{q_e A_0 k_r \ell_0^2 \omega_T}{2}$ using the notation of Ref. [4] to which we refer for definition of the parameters. The key point is the selection rule:

$$\Delta|m| = \pm s, \qquad s = l + \sigma, \tag{5}$$

so that, for $l = 1, \sigma = +1$, twisted light drives $\Delta|m| = \pm 2$ transitions between odd-$|m|$ correlation sectors. In the left-chiral convention appropriate to the LLL branch for $B > 0$, the physical states have $m \leq 0$ and we use $|m| = -m$ as a nonnegative sector label; then absorption that *increases* $|m|$ corresponds to $m \to m - s$.

IV. Exactly Solvable Calogero Limit: Closed-Form Spectrum and Matrix Elements

A. Why the Calogero interaction is useful

A generic screened interaction can be modeled as $V(r) \propto 1/r^\eta$ with $1 \leq \eta \leq 2$. [4] The inverse-square limit $\eta = 2$ is special: it yields the Calogero interaction

$$V_{\text{Cal}}(r) = \frac{\hbar^2}{2\mu} \frac{\alpha}{r^2}, \qquad \mu = m^*/2, \tag{6}$$

for which the relative-coordinate eigenstates are analytic. [6], [12] This solvable limit provides a symmetry "skeleton" for the spectroscopy, and the qualitative chiral fingerprints persist for Coulomb-like interactions. [4]

B. Exact eigenstates and energies

For the relative coordinate (r, ϕ), the Calogero ground state at fixed angular momentum m (radial quantum number $n = 0$) is [6], [12]

$$\psi_{0,m}^{(\alpha)}(r, \phi) = \frac{e^{im\phi}}{2\sqrt{\pi}\,\ell_0 \sqrt{\Gamma(\alpha_m + 1)}} \left(\frac{r}{2\ell_0} \right)^{\alpha_m} e^{-r^2/(8\ell_0^2)}, \qquad \alpha_m = \sqrt{m^2 + \alpha}. \tag{7}$$

Here ℓ_0 is the single-particle Fock–Darwin length, $\ell_0 = \sqrt{\hbar/(2m^*\omega)}$ with $\omega = \sqrt{\omega_0^2 + \omega_c^2/4}$, so that a product of single-particle Gaussians $e^{-\sum_i |z_i|^2/(4\ell_0^2)}$ produces the relative Gaussian $e^{-r^2/(8\ell_0^2)}$. The corresponding relative energy spectrum is

$$E_{n,m}^{\text{rel}} = \hbar\omega \, (2n + 1 + \alpha_m) + \frac{m\hbar\omega_c}{2}, \tag{8}$$

with $\omega = \sqrt{\omega_0^2 + \omega_c^2/4}$. For the physically relevant left-chiral branch at $B > 0$ we take $m \leq 0$ and label sectors by $|m| = -m$; since α_m depends on m^2, only the linear cyclotron term distinguishes the two chiralities.

These closed-form expressions are rare in correlated quantum systems. They imply that energy splittings between correlation sectors (e.g. $|m| = 3$ vs. $|m| = 5$) are analytic functions of the interaction parameter α.

C. Exact twisted-light matrix elements

For transitions between $n = 0$ Calogero states labelled by the nonnegative sector index $|m|$ (so we write $m \geq 0$ below) driven by twisted light carrying total angular momentum $s = l + \sigma$, the reduced matrix element takes the closed form [5]

$$\mathcal{M}_{m \to m+s}^{(\alpha)} = \frac{\Gamma\left(\frac{\alpha_m + \alpha_{m+s} + s + 2}{2} \right)}{\sqrt{\Gamma(\alpha_m + 1)\,\Gamma(\alpha_{m+s} + 1)}}. \tag{9}$$

This analytic dependence is not a mathematical luxury: it directly sets the Rabi frequency of a driven qubit and therefore the gate time and fidelity (Section V).

V. Quantum computing mapping: correlation-sector qubit and gates

A. Qubit encoding in correlation sectors

We define a computational basis from two odd-$|m|$ relative-motion sectors. A concrete choice is

$$\begin{aligned} |0\rangle &\equiv |m=-3\rangle \quad (\text{sector } |m|=3), \\ |1\rangle &\equiv |m=-5\rangle \quad (\text{sector } |m|=5). \end{aligned} \tag{10}$$

which are adjacent under the $s=2$ selection rule. Throughout, we make the reasonable assumption that the spin-polarized triplet manifold is selected by magnetic field and Zeeman splitting, so the qubit is encoded purely in the orbital correlation sector. Physically, $|1\rangle$ has a larger correlation hole than $|0\rangle$ and a larger typical relative separation.

This encoding is not (yet) topological: at $N=2$ there is no anyonic braiding, no edge conformal field theory, and no topological degeneracy. The value is instead that these are *interaction-defined* wavefunctions with distinct correlations, and twisted light addresses them selectively.

B. Single-qubit X rotations: twisted-light Rabi oscillations

Near resonance with the $|0\rangle \leftrightarrow |1\rangle$ transition and within the rotating-wave approximation, the driven two-level subspace has an effective Hamiltonian of the form

$$H_{\text{eff}} = \frac{\hbar\delta}{2}\sigma_z + \frac{\hbar\Omega_R}{2}\sigma_x, \tag{11}$$

where δ is the detuning and Ω_R is the Rabi frequency. Up to known geometric prefactors from the optical field, Ω_R is proportional to the Calogero matrix element in Eq. (9):

$$\Omega_R \propto \mathcal{E}_0 \left|\mathcal{M}^{(\alpha)}_{3\to 5}\right|. \tag{12}$$

A resonant pulse of duration t implements

$$R_x(\theta) = \exp\left(-i\frac{\theta}{2}\sigma_x\right), \qquad \theta = \Omega_R t, \tag{13}$$

i.e. an X rotation with angle set by pulse area.

C. Single-qubit Z rotations: phase accumulation

Free evolution for a time τ between pulses produces a Z rotation through the energy splitting between the two chosen sectors:

$$\hbar\omega_{\text{qubit}} = E^{\text{rel}}_{0,-5} - E^{\text{rel}}_{0,-3} = \hbar\omega\left(\alpha_5 - \alpha_3\right) - \hbar\omega_c, \tag{14}$$

i.e.

$$\omega_{\text{qubit}} = \omega\left(\sqrt{25+\alpha} - \sqrt{9+\alpha}\right) - \omega_c. \tag{15}$$

The corresponding phase gate is

$$R_z(\phi) = \exp\left(-i\frac{\phi}{2}\sigma_z\right), \qquad \phi = \omega_{\text{qubit}}\tau. \tag{16}$$

Because Eq. (8) is analytic in α, the qubit frequency is known in closed form.

D. Universality: compiling arbitrary single-qubit unitaries from Rx and Rz

In circuit-model language, a *universal* single-qubit gate set is one from which any unitary $U \in SU(2)$ can be synthesized to arbitrary accuracy. The pair $\{R_x(\theta), R_z(\phi)\}$ is universal: any single-qubit unitary admits an Euler-angle decomposition

$$U = R_z(\phi_3)\, R_x(\theta)\, R_z(\phi_1), \tag{17}$$

so in practice a pulse–wait–pulse sequence suffices to implement an arbitrary rotation. The significance of the $N=2$ TL–Calogero system is that both the pulse-driven angle $\theta = \Omega_R t$ and the free-evolution phase $\phi = \omega_{\text{qubit}}\tau$ are controlled by *analytic* functions of the interaction parameter α (Eqs. (12) and (8)).

E. Readout: twisted-light spectroscopy as a correlation diagnostic

A key conceptual point is that twisted light provides a natural *state-discrimination channel*: the same selection rules that enable writing excitations also yield correlation-sensitive absorption lines. [4] Spectroscopy is a route toward readout by resolving transitions that originate predominantly from $|0\rangle$ or from $|1\rangle$ (e.g. by driving to a higher $|m|$ sector with distinct resonance). A true projective, single-shot measurement still requires a device-specific detector architecture and signal-to-noise analysis. This gives the platform a useful write–diagnose symmetry: prepare with one pulse family, interrogate with the same optical channel.

F. Why the Calogero parameter matters for gate design

The interaction parameter α enters both the spectrum (Eq. (8)) and the matrix element (Eq. (9)). Hence, it acts as a continuous "knob" that tunes:

- the qubit frequency ω_{qubit} (phase gate rate),
- the Rabi frequency Ω_R (pulse time),
- leakage and selectivity, by controlling level spacings to nearby sectors.

In realistic dots, α is not literally an inverse-square coupling, but it can be viewed as an effective parameter capturing screening and confinement; the analytically solvable point provides guidance for robust operating regimes. [4]

G. Leakage and anharmonicity: why an interacting ladder can help gate fidelity

A practical qubit must behave approximately as a two-level system under the applied drive. Here the relevant leakage channels are transitions from $|0\rangle \equiv |m|=3$ and $|1\rangle \equiv |m|=5$ into neighboring sectors such as $|m|=1$ or $|m|=7$. A helpful feature of the Calogero spectrum is that it is *anharmonic* in m because $\alpha_m = \sqrt{m^2+\alpha}$. For a TL mode carrying s units of angular momentum, the transition frequency between $n=0$ sectors is

$$\begin{aligned} \omega_{|m|\to|m|+s} &= \frac{E^{\text{rel}}_{0,-(|m|+s)} - E^{\text{rel}}_{0,-|m|}}{\hbar} \\ &= \omega\left(\alpha_{|m|+s} - \alpha_{|m|}\right) - \frac{s\omega_c}{2}. \end{aligned} \tag{18}$$

TABLE I
TWISTED LIGHT AS A CONTROL LAYER FOR CORRELATION-SECTOR QUBITS.

Role	Physical action	Quantum-information meaning
WRITE	Resonant TL pulse (choose l, σ, pulse area)	Implements $R_x(\theta)$ between correlation sectors.
READ	TL spectroscopy of correlation-sensitive lines	Distinguishes correlation sectors; projects onto $\|0\rangle$ or $\|1\rangle$.
SCALE	SLM steering + vorticity selection	Optical addressing of many dots without dense wiring; mode selectivity sets $\Delta\|m\|$.

For the qubit choice in Eq. (10) with $s = 2$, the *anharmonicity* that controls off-resonant leakage to $|m| = 7$ is

$$\mathcal{A} \equiv \omega_{5\to7} - \omega_{3\to5} = \omega\left[(\alpha_7 - \alpha_5) - (\alpha_5 - \alpha_3)\right]. \quad (19)$$

Because $\mathcal{A}$ is an analytic function of α, the solvable limit provides a direct way to identify parameter regimes where $\mathcal{A}$ is large compared to the Rabi rate Ω_R, suppressing leakage. This is the same "anharmonicity engineering" logic used in transmons, but here it arises from *correlations* rather than Josephson physics.

VI. TOWARD A PHOTONIC CONTROL BUS AND MULTI-QUBIT OPERATIONS

A. Write, read, scale: a minimal control narrative

Table I summarizes the operational viewpoint suggested by the physics above.

B. Addressability: diffraction limit and near-field requirements at THz frequencies

The "SCALE" line in Table I intentionally highlights an attractive idea: a spatial light modulator (SLM) can steer a beam to select a dot, while the OAM/polarization choice selects $\Delta|m|$ and therefore the internal transition. However, for the intraband orbital transitions emphasized here, the natural frequencies are typically in the THz range (Sec. IX), corresponding to free-space wavelengths $\lambda \sim 0.3$–3 mm. A diffraction-limited far-field spot size is therefore orders of magnitude larger than typical lithographic dot spacings (tens to hundreds of nm, or $\sim \mu$m-scale pitches in larger arrays). This mismatch is the central scalability challenge for the "photonic control bus" vision and should be stated explicitly.

There are several physically plausible routes forward, all of which fit naturally into the META (metamaterials/photonics) scope: (i) *Proof-of-principle sparse arrays*: begin with isolated dots separated by tens–hundreds of μm so that a THz focus can address them individually. (ii) *On-chip near-field localization*: integrate each dot with a local THz antenna, resonator, or metasurface element that converts an incident beam into a tightly confined near field at the dot location (subwavelength confinement is routine in resonant near-field structures even when λ is macroscopic). (iii) *Waveguide delivery*: route THz/mid-IR power on chip to selected sites, using the optical beam mainly as a global clock or for frequency selectivity. (iv) *Frequency-upshifted designs*: use stronger confinement and/or different materials to push the relevant orbital splittings into the mid-IR, where λ is ~ 10 μm and far-field addressing becomes less extreme.

In short: mode selectivity via OAM is a genuine asset, but *spatial* selectivity at THz wavelengths will likely require near-field or structured-photonic engineering rather than simple far-field focusing.

C. A concrete two-qubit entangling gate mechanism

A scalable architecture requires at least one entangling two-qubit gate. For two nearby dots A and B, the inter-dot Coulomb interaction depends on the charge distribution in each dot. Because different correlation sectors have different spatial extent, the interaction energy is state dependent. A clean analytic diagnostic of this size difference is the exact Calogero expectation value [5]

$$\langle r^2\rangle_{m,\alpha} = 4\ell_0^2(\alpha_m + 1), \qquad \alpha_m = \sqrt{m^2 + \alpha}. \quad (20)$$

This motivates an effective ZZ coupling model:

$$H_{ZZ} = \frac{\hbar J}{4}\,\sigma_z^{(A)}\sigma_z^{(B)}, \qquad J \equiv \frac{U_{11} + U_{00} - U_{10} - U_{01}}{\hbar}, \quad (21)$$

where U_{ij} is the electrostatic energy when dot A is in $|i\rangle$ and dot B in $|j\rangle$.

1) Closed-form estimate of J from a long-distance multipole expansion: Equation (21) defines the entangling rate J, but it is useful to have an explicit estimate. Assume two *non-overlapping* dots whose centers are separated by an in-plane distance D (typically $D \sim 200$–500 nm in gated devices [15]). Let the electron positions in dot A be $\mathbf{r}_{A,1} = \mathbf{R}_A + \mathbf{r}_A/2$ and $\mathbf{r}_{A,2} = \mathbf{R}_A - \mathbf{r}_A/2$, where $\mathbf{r}_A$ is the internal (relative) coordinate; similarly for dot B. The inter-dot interaction is then

$$V_{AB} = \frac{e^2}{4\pi\varepsilon}\sum_{a=1}^{2}\sum_{b=1}^{2}\frac{1}{|\mathbf{D} + \mathbf{r}_{A,a} - \mathbf{r}_{B,b}|}, \qquad \mathbf{D} \equiv \mathbf{R}_B - \mathbf{R}_A. \quad (22)$$

For $D \gg \sqrt{\langle r^2\rangle}$ one may expand $1/|\mathbf{D} + \boldsymbol{\delta}|$ in powers of $\boldsymbol{\delta}/D$ and then average over the rotationally symmetric internal states (for which $\langle\mathbf{r}\rangle = \mathbf{0}$). A derivation can be obtained by Taylor expanding $1/|\mathbf{D} + \boldsymbol{\delta}|$ and using isotropic angular averages; equivalently, it is the leading quadrupole–quadrupole contribution for planar charge distributions. The result is:

$$U_{ij} \approx \frac{e^2}{4\pi\varepsilon}\left[\frac{4}{D} + \frac{\langle r^2\rangle_i + \langle r^2\rangle_j}{4D^3} + \frac{9}{64}\frac{\langle r^2\rangle_i\,\langle r^2\rangle_j}{D^5} + \cdots\right], \quad (23)$$

where $\langle r^2\rangle_i$ denotes the internal size in dot A when it is in $|i\rangle$, and $\langle r^2\rangle_j$ is the corresponding size in dot B. The D^{-3} term produces only *single-qubit* frequency shifts (it is additive in i and j and cancels in $U_{11} + U_{00} - U_{10} - U_{01}$). The leading *entangling* contribution is the D^{-5} cross-term, giving

$$J \approx \frac{1}{\hbar}\frac{e^2}{4\pi\varepsilon}\frac{9}{64}\frac{\left(\Delta\langle r^2\rangle\right)^2}{D^5}, \qquad \Delta\langle r^2\rangle \equiv \langle r^2\rangle_1 - \langle r^2\rangle_0. \quad (24)$$

Using the exact Calogero size formula in Eq. (20), $\Delta\langle r^2\rangle = 4\ell_0^2(\alpha_5 - \alpha_3)$, this becomes

$$J \approx \frac{1}{\hbar}\frac{e^2}{4\pi\varepsilon}\frac{9}{4}\frac{\ell_0^4(\alpha_5-\alpha_3)^2}{D^5}. \tag{25}$$

For representative GaAs parameters ($\varepsilon = \kappa\varepsilon_0$ with $\kappa \simeq 12.9$ and $\ell_0 \simeq 10$ nm; Sec. IX) and $\alpha_5 - \alpha_3 \simeq 2$ (noninteracting limit), Eq. (24) gives $J/(2\pi) \sim 0.08$–8 MHz for $D = 500$–200 nm, corresponding to a controlled-phase time $t_{\rm CZ} = \pi/J \sim 6$ μs–70 ns. The steep D^{-5} scaling makes this gate *highly tunable*: bringing dots closer or using a larger effective size difference (larger $\Delta\langle r^2\rangle$) rapidly enhances J.

Free evolution for time $t = \pi/J$ implements a controlled-phase (CZ-equivalent) gate up to single-qubit Z rotations.

This mechanism is not topological—it is analogous to capacitive ZZ coupling in other platforms—but it is concrete and testable, and its distinctive feature is that the basis states are *correlation sectors* written and read optically by twisted light.

D. Coupled $N = 2$ dots as a two-qubit module: analytic interdot entanglement and an XY gate channel

a) Connecting single-dot and coupled-dot "magic-number" transitions.: In an isolated, spin-polarized $N = 2$ parabolic dot, the low-energy branch is organized by odd relative angular momenta $|m| = 1, 3, 5, \ldots$; as the magnetic field is increased the ground state typically steps through this odd-$|m|$ ladder (the $N = 2$ analogue of the well-known $N = 3$ magic-number sequence $L = 3k$). For two dots, the uncoupled spectrum is the direct product $|m_A, m_B\rangle$ of the *same* single-dot ladders. Coulomb-range interdot interactions then reshape these inherited "magic" sectors by creating resonant anticrossings and entangled eigenstates when two product states become nearly degenerate. The Benjamin–Johnson selection rule makes this concrete: the dominant mixing occurs between $|m, m+2\rangle$ and $|m+2, m\rangle$, i.e. the same $\Delta|m| = 2$ step that twisted light addresses within a single dot. In this sense, coupled-dot "magic-number transitions" are not a separate phenomenon: they are the single-dot magic ladder *promoted* to a two-site module, where interdot interactions convert near-degeneracies into exchange-like (XY) entangling dynamics.

The capacitive ZZ mechanism in Sec. VI-C1 is the simplest entangling interaction to model, but it is not the only one available when two dots are brought into Coulomb range. In fact, a qualitatively different entangling channel—a resonant, exchange-like XY *coupling* between $|01\rangle$ and $|10\rangle$—appears already in early analytic work on coupled few-electron dots with $N = 2$ electrons *per dot*. This is directly relevant to the present proposal because our qubit basis states $|0\rangle \equiv ||m| = 3\rangle$ and $|1\rangle \equiv ||m| = 5\rangle$ differ by $\Delta|m| = 2$, exactly the "quantum" transferred between dots in those analytic coupled-dot solutions.

1) Benjamin–Johnson multiple-dot model: entanglement without tunneling: Benjamin and Johnson introduced an analytically solvable model of P colinear, two-dimensional quantum dots, each containing two electrons, arranged vertically with interdot separation s. [22] Interdot tunneling is neglected; adjacent dots are coupled purely by the two-body electron–electron interaction, an "optical wiring" channel that can exist even in the absence of any single-particle tunneling term. [22] They take an inverse-square interaction (Calogero form) both within each dot and between adjacent dots,

$$V_{\rm intra} = \sum_{a=1}^{P} \frac{\beta}{\left|\mathbf{r}_{a,1} - \mathbf{r}_{a,2}\right|^2}, \tag{26}$$

$$V_{\rm inter} = \sum_{a=2}^{P}\sum_{i,j=1}^{2} \frac{\beta}{\left|\mathbf{r}_{a,i} - \mathbf{r}_{a-1,j}\right|^2 + s^2}, \tag{27}$$

and then Taylor-expand $V_{\rm inter}$ under the physically transparent assumption that typical in-plane separations are smaller than s. [22] To order Pr^2/s^4 the coupled-dot problem remains exactly solvable; higher-order terms (schematically Pr^4/s^6) are then treated by analytic perturbation theory. [22]

For $P = 2$ identical dots, the low-lying eigenstates can be labeled as direct products $|m_1, m_2\rangle$, where m_a is the relative angular momentum quantum number of the two-electron state in dot a. [22] At the exactly solvable order ($\propto r^2/s^4$), the pair $|m, m+2\rangle$ is degenerate with $|m+2, m\rangle$. The next-order interdot perturbation then mixes these states *selectively*: in the nearly-degenerate subspace, the perturbation only connects $|m_a, m_b\rangle$ to $|m_c, m_d\rangle$ if $m_a - m_c = m_d - m_b = 0$ or ± 2. [22] As a result, the relevant eigenstates are entangled superpositions of the form

$$|\Psi_\pm\rangle = \frac{1}{\sqrt{2}}\Big(\,|m+2, m\rangle \pm |m, m+2\rangle\,\Big) \tag{28}$$

(identical dots, on resonance) and for unequal dot sizes (weakly nondegenerate case) they become $(p\,|m+2, m\rangle + q\,|m, m+2\rangle)$ with $p \neq q$ set by the detuning. [22] Benjamin and Johnson show that these entangled states can become *ground states* over finite B-field windows, and interpret their formation as a resonance phenomenon closely analogous to Förster energy transfer; in an array, the corresponding "Frenkel exciton" can propagate and form an exciton band. [22]

2) Mapping to the correlation-sector qubit: an iSWAP/$\sqrt{i\text{SWAP}}$ entangler: This structure maps almost one-to-one onto the present qubit encoding. Take two dots A, B with local basis $|0\rangle \equiv ||m| = 3\rangle$ and $|1\rangle \equiv ||m| = 5\rangle$. Then the two-qubit states

$$|01\rangle \equiv |3, 5\rangle\,, \qquad |10\rangle \equiv |5, 3\rangle \tag{29}$$

are precisely the $(m, m+2)$ and $(m+2, m)$ pair with $m = 3$ in Eq. (28). The coupled-dot perturbation therefore generates an effective *exchange* Hamiltonian in the $\{|01\rangle\,, |10\rangle\}$ subspace:

$$\begin{aligned} H_{XY} &= \hbar J_{\rm ex}\Big(\,|01\rangle\langle 10| + |10\rangle\langle 01|\,\Big) \\ &= \frac{\hbar J_{\rm ex}}{2}\Big(\sigma_x^{(A)}\sigma_x^{(B)} + \sigma_y^{(A)}\sigma_y^{(B)}\Big), \end{aligned} \tag{30}$$

with $J_{\rm ex}$ set by the relevant interdot matrix element (the same perturbative order that produces the entangled eigenstates). On exact resonance (identical dots), the eigenstates are the Bell

states $|\Psi_\pm\rangle = (|01\rangle \pm |10\rangle)/\sqrt{2}$ with splitting $2\hbar J_{\rm ex}$. Free evolution under H_{XY} implements an entangling gate:

$$U(t)\,|01\rangle = \cos(J_{\rm ex}t)\,|01\rangle - i\sin(J_{\rm ex}t)\,|10\rangle\,, \tag{31}$$
$$U(t)\,|10\rangle = \cos(J_{\rm ex}t)\,|10\rangle - i\sin(J_{\rm ex}t)\,|01\rangle\,. \tag{32}$$

Thus $t = \pi/(2J_{\rm ex})$ yields an iSWAP (up to single-qubit phases), and $t = \pi/(4J_{\rm ex})$ yields a $\sqrt{i\rm SWAP}$ which is maximally entangling. Crucially, the same coupled-dot analysis provides a *control knob*: detuning the dots (e.g. via slightly different confinement strengths) moves the $|01\rangle$ and $|10\rangle$ energies apart, suppressing the mixing (the "quadratic Stark" analog in Ref. [22]). In quantum-information language, this is an on/off switch for the XY entangler, complementary to the always-on but tunable ZZ coupling of Sec. VI-C1.

3) Johnson–Benjamin double-layer model: analytic four-electron precursor to bilayer FQHE: A closely related analytic benchmark is provided by Johnson and Benjamin's exactly solvable *double-layer* (vertical) model with two electrons per layer. [23] They consider electrons confined in each layer by a 2D parabolic potential in a perpendicular magnetic field, neglect inter-layer tunneling, and include both intra- and inter-layer inverse-square interactions. By introducing center-of-mass and relative coordinates within each layer and between the layer centers of mass, and then Taylor-expanding the inter-layer interaction under the assumption that the typical in-plane separation is less than the layer separation s, the Hamiltonian becomes exactly solvable once the expansion is truncated at quadratic order. [23] In particular, truncation at the second term yields an additive constant plus a sum of four decoupled solvable Hamiltonians,

$$\begin{aligned} H &= \frac{4\beta}{s^2} + \sum_{i=1}^{4} H_i(u_i, q_i), \\ \omega_1 &= \omega_0, \quad \omega_2 = \omega_3 = \left(\omega_0^2 - \frac{4\beta}{m^* s^4}\right)^{1/2}, \\ \omega_4 &= \left(\omega_0^2 - \frac{8\beta}{m^* s^4}\right)^{1/2}. \end{aligned} \tag{33}$$

where H_1 and H_4 are single-particle Fock–Darwin problems and H_2, H_3 are two-body (Calogero) problems for the intra-layer relative coordinates. [23] The resulting ground-state sequence in magnetic field is $|m_2, m_3\rangle = |1,1\rangle, |3,3\rangle, |5,5\rangle, \ldots$ with odd $m_{2,3}$ set by antisymmetry within each layer. [23] Johnson and Benjamin further define an effective small-N filling factor per layer $\nu_a \simeq 1/m_a$, giving a total sequence $\nu = \nu_1 + \nu_2 = 2, 2/3, 2/5, \ldots$ that is consistent with the observed bilayer fractions for sufficiently separated layers. [23] They also emphasize that the analytically obtained correlated wavefunctions differ fundamentally from the standard Jastrow/Greek–Roman (mmn) forms used in bilayer FQHE modeling. [23]

For the present proposal, Eq. (33) is useful in two ways. First, it provides a closed-form dependence of mode frequencies on the geometric separation s, making it an analytic "calibration model" for how vertical coupling renormalizes energy scales (and hence how interdot coupling shifts qubit splittings and detunings). Second, it highlights a genuinely multi-dot feature absent in the single-dot problem: an additional collective coordinate (the relative coordinate between layer centers of mass) with its own tunable frequency $\omega_4(s)$. In an engineered device, this degree of freedom can be viewed as a candidate mediator mode for coupling qubits beyond pure static ZZ shifts.

4) How this strengthens the twisted-light quantum-computing proposal: Taken together, these two analytic coupled-dot benchmarks strengthen and extend the QC narrative in three concrete ways:

(a) **They provide an explicit, symmetry-selective XY entangler for the same $\Delta|m| = 2$ qubit ladder.** The $|3,5\rangle \leftrightarrow |5,3\rangle$ mixing predicted for coupled $N = 2$ dots is precisely the exchange channel needed for iSWAP-type two-qubit gates, complementing the capacitive ZZ gate in Sec. VI-C1.

(b) **They suggest an "exciton transport" architecture for dot arrays.** In the Benjamin–Johnson picture, a localized change of m on one dot can resonantly propagate as a Frenkel exciton band in a chain. [22] In our language, this is propagation of a local correlation-sector excitation. Twisted light provides the natural way to *write* such an excitation on a selected dot and *read* it out spectroscopically at another location.

(c) **They supply analytic s-dependence and mode structure for vertically coupled modules.** The Johnson–Benjamin decomposition makes clear which collective coordinates are activated by vertical coupling and how their frequencies scale with s. [23] This is exactly the kind of analytic handle needed to design detuning-based on/off control of interdot exchange and to anticipate extra spectator modes that may need to be dynamically decoupled.

In short: the coupled-dot literature already contains an analytic demonstration that two $N = 2$ dots can generate strong, interaction-mediated *entangled* eigenstates without tunneling. Twisted light adds the missing ingredient for quantum information: a structured, sector-selective optical handle to coherently address the internal ladders and thereby turn those coupled-dot correlations into a programmable gate set.

E. Comparison with established qubit platforms

The correlation-sector qubit shares features with several established platforms while introducing genuinely new elements: (i) an interacting many-body basis, and (ii) structured-light control of internal motion. Table II provides a compact comparison.

VII. Noise channels and robustness considerations

Because the encoding in Eq. (10) uses different *charge-correlation* sectors, the dominant decoherence mechanisms are expected to resemble those of "charge-like" qubits rather than pure spin qubits. This does not invalidate the platform; it clarifies what must be engineered and what "robustness" realistically means at the $N = 2$ stage.

TABLE II
CONTEXT: CORRELATION-SECTOR QUBIT COMPARED TO COMMON PLATFORMS (QUALITATIVE).

Feature	$N = 2$ **correlation-sector qubit**	**Superconducting transmon**	**Trapped ion**
Basis states	Relative-motion sectors $\|m\| = 3, 5$ (correlations)	Weakly anharmonic oscillator levels	Hyperfine/optical atomic levels
Single-qubit drive	Twisted light pulse (l, σ)	Microwave pulse	Laser pulse
Native X gate	TL Rabi oscillation (Eq. (13))	Microwave Rabi	Raman/direct Rabi
Native Z gate	Free evolution (Eq. (16))	Detuning/flux bias	Free evolution
Anharmonicity	Correlation-induced $\alpha_m = \sqrt{m^2 + \alpha}$	Josephson nonlinearity	Atomic structure
Analytic gate parameters	**Exact** in Calogero limit (Eqs. (8), (9))	Typically calibrated numerically	Exact (atomic theory)
Two-qubit coupling idea	State-dependent Coulomb ZZ (Eq. (21))	Capacitive/inductive coupling	Shared motional modes
Topological upgrade path	$N \geq 3$ FQHE droplets and quasiholes	None intrinsic	None intrinsic

A. Control errors: pulse area, detuning, and mode purity

Twisted-light gates rely on resonant driving, so standard coherent-control considerations apply: (i) pulse area errors ($\theta \neq \Omega_R t$), (ii) detuning errors ($\delta \neq 0$ in Eq. (11)), and (iii) imperfect OAM/helicity mode purity (admixture of unwanted s values). The advantage of the analytic framework is that these errors can be propagated through closed-form expressions for the gate unitary and (in principle) optimized using composite pulses and robust control sequences, without relying purely on black-box calibration.

B. Environmental decoherence: phonons and electrostatic noise

In a semiconductor dot, coupling to acoustic phonons and to charge noise in nearby gates and impurities will induce relaxation and dephasing between correlation sectors. Since $|0\rangle$ and $|1\rangle$ differ in spatial extent, they couple differently to fluctuating electrostatic potentials, producing dephasing analogous to that of charge qubits. A practical strategy is therefore to operate in regimes where: (i) the energy splitting $\hbar\omega_{\text{qubit}}$ is large compared to $k_B T$ (suppressing thermal mixing), and (ii) the relevant transitions are well separated from leakage channels (large anharmonicity $\mathcal{A}$ in Eq. (19)).

C. What "robust" can mean in this context

At $N = 2$, "robust" should not be interpreted as topological fault tolerance. Instead, it refers to two experimentally useful features already demonstrated in the spectroscopy setting: (i) twisted light targets internal excitations that are symmetry forbidden to dipole probes (a clean signal channel), and (ii) the qualitative chiral fingerprints persist for a range of interaction forms from screened to Coulomb. [4] These properties motivate the $N = 2$ dot as a *calibration-grade* gate primitive and as a stepping stone to $N \geq 3$ droplets where true topological protection may be approached.

D. Decoherence: a quantitative dephasing estimate and the key engineering challenge

A realistic assessment must confront decoherence. Our encoding uses *orbital correlation sectors* ($|m| = 3$ and $|m| = 5$), so it is "charge-like" in the sense that the energy depends on the spatial distribution. However, a definite-m state in an ideal circular dot is *rotationally symmetric* and satisfies $\langle \mathbf{r} \rangle = \mathbf{0}$, so it carries *no permanent in-plane dipole moment*. As a result, spatially uniform electric-field noise couples primarily to the center-of-mass (Kohn) mode rather than directly dephasing the internal qubit. The leading internal sensitivity is instead *quadrupolar*: fluctuations of the confining curvature (or equivalently, field gradients) shift the two qubit levels differently because $\langle r^2 \rangle$ differs.

A simple analytic estimate follows from a "curvature-noise" model in which gate-voltage noise induces a small fluctuation $\delta\omega_0$ of the bare harmonic confinement. Since $\omega^2 = \omega_0^2 + \omega_c^2/4$, the relative Hamiltonian contains a term $(\mu\omega^2/2)\, r^2$ with $\partial H/\partial\omega_0 = \mu\omega_0 r^2$. By the Hellmann–Feynman theorem,

$$\frac{\partial E_m}{\partial \omega_0} = \mu\omega_0 \langle r^2 \rangle_{m,\alpha}, \qquad \Rightarrow \qquad \frac{\partial \omega_{\text{qubit}}}{\partial \omega_0} = \frac{\mu\omega_0}{\hbar} \Delta\langle r^2 \rangle, \tag{34}$$

with $\Delta\langle r^2 \rangle \equiv \langle r^2 \rangle_{|m|=5} - \langle r^2 \rangle_{|m|=3} = 4\ell_0^2(\alpha_5 - \alpha_3)$ from Eq. (20). For quasi-static Gaussian noise with rms amplitude σ_{ω_0}, the rms fluctuation of the qubit splitting is

$$\sigma_{\omega_{\text{qubit}}} = \left| \frac{\partial \omega_{\text{qubit}}}{\partial \omega_0} \right| \sigma_{\omega_0} = \frac{\mu\omega_0}{\hbar} \Delta\langle r^2 \rangle\, \sigma_{\omega_0}, \qquad T_2^* \sim \sigma_{\omega_{\text{qubit}}}^{-1}. \tag{35}$$

Equation (35) cleanly identifies the levers that improve dephasing: suppress curvature noise (σ_{ω_0}), reduce sensitivity via large magnetic field ($\omega_0/\omega \ll 1$ so gate voltages weakly perturb ω), or engineer a smaller $\Delta\langle r^2 \rangle$ (at the cost of reduced J in Sec. VI-C1).

To connect with experiment, charge qubits in semiconductor double quantum dots typically exhibit T_2^* in the ns range

when operated away from optimized "sweet spots" (e.g., a decoherence time $\sim$ 1 ns in early GaAs charge-qubit oscillations [19], and a maximum coherence time $\sim$ 7 ns at the charge-degeneracy point consistent with a $1/f$ noise model [20]). An important mitigating feature of our *single-dot, circular* encoding is that the internal qubit is not a dipole qubit; in an ideal harmonic dot the leading charge-noise coupling can be strongly suppressed [21]. Nevertheless, the message for feasibility is clear: unless the device is engineered to reduce effective curvature noise (material choice, screening, symmetric operation, and/or dynamical decoupling enabled by fast optical control), decoherence is likely to be the dominant constraint for gate fidelity.

Finally, it is useful to express a minimal "coherent-control" requirement in terms of the Rabi frequency. From Eqs. (11) and (12), a resonant pulse drives oscillations at $\Omega_R = 2\mathcal{E}_0|M^{(\alpha)}_{3\to5}|/\hbar$ (up to envelope factors). A necessary condition for high-contrast Rabi oscillations is therefore

$$\Omega_R T_2^* \gg 1, \tag{36}$$

while two-qubit gates require $J T_2^* \gg 1$. Equations (24)–(36) provide a compact quantitative checklist: *fast optical control is available in principle*, but turning the correlation-sector qubit into a high-fidelity quantum-computing primitive hinges on suppressing (or refocusing) the remaining quadrupolar charge-noise channels.

VIII. Roadmap: from N=2 gate primitives to topological FQHE control

The $N = 2$ system is simultaneously (i) a fully analytic gate primitive and (ii) a stepping stone toward genuinely topological FQHE degrees of freedom at $N \geq 3$.

A. What carries over robustly to larger N

Three qualitative features are expected to generalize:

1) **OAM selection rules are symmetry-protected.** The angular-momentum transfer $s = l + \sigma$ implies $\Delta L = \pm s$ for the many-body state, providing a tunable ladder between total-angular-momentum sectors.
2) **Kohn protection remains the baseline.** Spatially uniform dipole probes ($l = 0$) excite only CM motion, remaining blind to correlations in a parabolic dot. Twisted light is therefore the minimal optical route to correlation spectroscopy.
3) **Line strengths are correlation diagnostics.** The intensity of a TL-driven transition depends on interaction-defined eigenstates (pseudopotentials), so spectroscopy directly probes correlation content. [4]

B. Quantitative $N = 3$ Calogero scaffold: $1/N$ expansion and the magic-number ladder

For $N = 3$ the pairwise inverse-square interaction

$$V^{(N=3)}_{\rm Cal} = \frac{\hbar^2\beta^2}{m^*}\sum_{i<j}\frac{1}{r_{ij}^2}, \tag{37}$$

admits a semi-analytic spectrum in a magnetic field via the resummed $1/N$ expansion of Ref. [12] (see also Ref. [6]). The center-of-mass still decouples exactly in a parabolic dot, so the relevant spectrum organizes by the *internal* total angular momentum. To avoid confusion with the optical OAM index l, we denote the many-body angular-momentum sector by $L \geq 0$ (standard FQHE convention); for $B > 0$ this corresponds to the low-energy left-chiral branch of the dot spectrum.

In the notation of Ref. [12], the internal energies can be written in the compact form

$$E_{L;\,n_u,n_\triangle,m_\triangle} \approx \hbar\omega\Big[\sqrt{L^2+6\beta^2}+\delta(L;n_\triangle,m_\triangle) + 2n_u + 1\Big] - \frac{\hbar\omega_c}{2}L, \tag{38}$$

where $\omega = \sqrt{\omega_0^2+\omega_c^2/4}$, n_u counts the symmetric "breathing" mode, and $(n_\triangle, m_\triangle)$ label an effective 2D "shape" mode of the triangle. The shift $\delta(L; n_\triangle, m_\triangle)$ is an $\mathcal{O}(1)$ quantity fixed by a simple transcendental equation (given explicitly in Ref. [12]) and is easily obtained numerically. Ref. [12] also provides explicit approximate eigenfunctions in the normal-mode coordinates, so TL matrix elements reduce to standard oscillator integrals. Equation (38) is therefore a *design-level* scaffold for $N = 3$: it gives transition frequencies, anharmonicities, and parameter trends without full diagonalization.

a) Magic-number ladder and the $L = 3k$ sequence.: For three *spin-polarized* fermions, Ref. [12] finds that the ground state progresses through the "magic" angular momenta

$$L_{\rm gs}(B) \in \{3, 6, 9, 12, \dots\}, \tag{39}$$

as the magnetic field is increased, reproducing the well-known incompressible/magic-number phenomenology of three-electron dots and agreeing qualitatively with Coulomb calculations. [13] In particular, the $q = 3$ Laughlin precursor sits at $L = 9$, and the adjacent $L = 12$ manifold is precisely where the single-quasihole and the $\Delta L = 3$ edge excitations live.

b) Why an $s = 3$ twisted-light pulse is special at $N = 3$.: A quasihole at the origin is created by

$$\hat{Q}_{\rm qh} = \prod_{i=1}^{3} z_i \equiv e_3(z_1, z_2, z_3), \tag{40}$$

which raises total angular momentum by $\Delta L = +3$. A twisted-light mode with $s = l + \sigma = 3$ therefore targets the correct sector *directly* ($L = 9 \to 12$). In the LLL-projected language, the simplest $s = 3$ optical multipole is the power-sum symmetric polynomial

$$p_3(z) \equiv \sum_{i=1}^{3} z_i^3. \tag{41}$$

Newton's identity for three variables,

$$p_3 = e_1^3 - 3e_1e_2 + 3e_3, \tag{42}$$

makes the physics transparent: an $s = 3$ drive necessarily contains a *direct quasihole component* ($\propto e_3$) plus components

TABLE III
KEY GATE-LEVEL QUANTITIES AND HOW TO OBTAIN THEM IN THE ANALYTIC CALOGERO MODEL VS. A REALISTIC COULOMB/SCREENED DOT. THE POINT IS NOT THAT CALOGERO MUST BE QUANTITATIVELY EXACT, BUT THAT ALL REQUIRED PARAMETERS ARE EITHER CLOSED-FORM (CALOGERO) OR DIRECTLY CALIBRATABLE (DEVICE).

Quantity	Calogero ($1/r^2$)	Coulomb/screened ($1/r$)
ω_{qubit}	Eq. (14)	TL spectroscopy (line positions)
$\mathcal{A}$	Eq. (19)	ED / radial solve + spectroscopy
$M_{3\to5}$	Eq. (9)	ED / radial solve (wavefunctions)
Ω_R	Eqs. (11) and (12)	Rabi calibration (pulse area)
$\langle r^2\rangle_m$	Eq. (20)	ED / radial solve
J	Eq. (24)	multipole + ED / calibration

in the other $\Delta L = 3$ basis states (e_1^3 and e_1e_2). Interactions select the eigenbasis within the $L \to L+3$ manifold, so the experimentally relevant question becomes quantitative: what is the overlap of the TL-driven superposition with the quasihole eigenstate, and can it be enhanced by spectral selectivity and pulse shaping?

C. Realistic interactions vs. Calogero: what must be validated quantitatively

The Calogero model is powerful because it yields exact closed-form energies and matrix elements, but a quantum-computing proposal ultimately lives or dies on quantitative device-level parameters: the qubit splitting ω_{qubit}, the Rabi rates Ω_R and leakage rates set by the anharmonicity $\mathcal{A}$, and the two-qubit coupling J. For generic Coulomb or screened interactions, the *qualitative* chiral fingerprints and selection rules can persist [4], but high-fidelity pulses require that the key quantities be either (i) close enough to Calogero predictions, or (ii) experimentally calibratable.

A practical viewpoint is that the Calogero analytics should be used as an *initial design model* and as a way to identify which transitions are symmetry-allowed/forbidden and which sectors are targeted by a given (l,σ). Then, for a given device with a realistic interaction, one performs a short spectroscopic calibration using the same TL control channel: the transition frequencies directly determine ω_{qubit} and $\mathcal{A}$, while Rabi oscillations determine Ω_R for the chosen pulse shape. This is completely standard in other qubit modalities (superconducting circuits, trapped ions), and it reduces the burden on the Calogero-to-Coulomb *quantitative* match.

To make this explicit, Table III lists the minimal set of quantities that must be known (or measured) to run gates, together with the closed-form Calogero expressions already derived in this paper and the corresponding "how to obtain" route for a Coulomb/screened dot. For $N = 2$, the Coulomb/screened problem is still one-dimensional in the relative radius r for each m, so all entries can be produced numerically by straightforward radial diagonalization (or by exact diagonalization in a truncated Fock–Darwin basis) without the exponential complexity of many-body FQHE.

The remaining quantitative question is *fidelity transfer*: how close must the Calogero-designed pulse be to the Coulomb-optimized pulse to achieve high fidelity? Because our protocol is intrinsically spectroscopic, the most conservative answer is: it need not be close at all, provided the device is stable enough that ω_{qubit} and Ω_R can be calibrated and remain stationary over the experiment. The more optimistic possibility—to be tested numerically for representative device geometries—is that the relevant quantities (especially the selection-rule structure and relative strengths of the dominant matrix elements) vary smoothly across repulsive central interactions, so that Calogero provides not just qualitative guidance but a quantitatively good first guess.

D. How the Gambardella $\mathrm{SU}(1,1)$ machinery can be leveraged for this project

A central practical obstacle in scaling beyond the analytically solvable $N = 2$ case is to retain an operator-level understanding of *which* many-body sectors are bright/dark under twisted light and how the relevant transition frequencies and anharmonicities scale with interaction strength. A powerful (and underused in the quantum-dot literature) route is to exploit the fact that inverse-square interactions belong to a broad class of Hamiltonians whose *dynamical group* is $\mathrm{SU}(1,1)$.

Gambardella showed that for N interacting particles in any spatial dimension, after eliminating the center of mass, the internal Hamiltonian with a quadratic (harmonic) term plus an additional translation-invariant potential that is homogeneous of degree -2 has $\mathrm{SU}(1,1)$ as a spectrum-generating algebra: the Casimir eigenvalue fixes the ladder spectrum, and a family of eigenfunctions can be generated algebraically by raising operators acting on the ground state. [14] This includes (as special cases) Calogero–Sutherland-type inverse-square forces and also certain three-body and higher-body homogeneous interactions. [14]

a) Why this is directly relevant to parabolic quantum dots.: Even though quantum dots are defined by a *one-body* parabolic confinement $V_{\mathrm{dot}} = \frac{1}{2}m^*\omega_0^2\sum_i r_i^2$ rather than an explicit pair potential, the identity

$$\sum_{i=1}^{N} r_i^2 = NR^2 + \frac{1}{N}\sum_{i<j} r_{ij}^2, \qquad R \equiv \frac{1}{N}\sum_{i=1}^{N} r_i, \tag{43}$$

implies that *after* center-of-mass separation the internal confinement is proportional to $\sum_{i<j} r_{ij}^2$. Thus, the internal problem in a parabolic dot fits naturally into the "quadratic pair + homogeneous -2" class treated in Ref. [14] once the CM degree of freedom is removed. The magnetic field adds the standard Fock–Darwin L_z term; it lifts chiral degeneracies but does not eliminate the internal ladder structure (Sec. IV already illustrates this explicitly for $N = 2$).

b) $\mathrm{SU}(1,1)$ *generators and ladder structure.:* In Jacobi coordinates $\{X_a\}_{a=1}^{N-1}$ for the internal motion (with conjugate momenta $\{P_a\}$), define the quadratic "size" operator, dilation

operator, and scale-invariant Hamiltonian,

$$\hat{C} = \frac{m^*}{2}\sum_{a=1}^{N-1} X_a^2, \qquad \hat{D} = \frac{1}{2}\sum_{a=1}^{N-1}(X_a\cdot P_a + P_a\cdot X_a)\,, \\ \hat{H}_0 = \frac{1}{2m^*}\sum_{a=1}^{N-1} P_a^2 + V_{\rm hom}(\{X_a\}), \tag{44}$$

where $V_{\rm hom}$ is translation invariant and homogeneous of degree -2 (e.g. Calogero $1/r_{ij}^2$). Then (under the homogeneity condition) these operators close an $\mathfrak{su}(1,1) \cong \mathfrak{so}(2,1)$ Lie algebra, [14]

$$[\hat{C},\hat{D}] = 2i\hbar\hat{C}, \qquad [\hat{C},\hat{H}_0] = i\hbar\hat{D}, \\ [\hat{H}_0,\hat{D}] = -2i\hbar\hat{H}_0. \tag{45}$$

The trapped internal Hamiltonian is $\hat{H}_{\rm int} = \hat{H}_0 + \omega^2\hat{C}$ (with an appropriate effective ω set by ω_0 and B). Standard linear combinations of $(\hat{H}_0, \hat{C}, \hat{D})$ define $\mathrm{SU}(1,1)$ ladder operators $\hat{K}_\pm$ and a Cartan generator $\hat{K}_0$ such that $\hat{K}_+$ raises the "breathing" quantum number by one step. [14] Consequently, within each $\mathrm{SU}(1,1)$ tower the spectrum is a near-harmonic ladder with step $\simeq 2\hbar\omega$ (exact in the solvable class), while the tower label is set by the Casimir (equivalently, by the interaction-determined "angular" sector on the $(N-1)$-dimensional shape sphere).

c) How this helps twisted-light control design.: For the purposes of this proposal, the Gambardella viewpoint supplies three concrete project tools:

1) **State construction beyond brute force.** Ref. [14] gives a constructive scheme in which a family of excited states is generated by an energy-raising operator acting on the ground state. This mirrors our $N = 2$ Laguerre–tower structure (Sec. IV) and provides an analytic scaffold for $N \geq 3$ breathing-mode ladders.
2) **Selection-rule bookkeeping.** Twisted-light operators are low-order polynomials in the coordinates (LLL-projected multipoles). Decomposing them into irreducible pieces with respect to $\mathrm{U}(1)$ rotations ($\Delta L = \pm s$) and the $\mathrm{SU}(1,1)$ ladder structure predicts, *a priori*, which internal towers are addressable at given s and which matrix elements are symmetry-forbidden.
3) **A bridge to realistic Coulomb dots.** Even when the true Coulomb interaction breaks exact solvability, $\mathrm{SU}(1,1)$ remains a useful organizing principle for near-harmonic internal ladders. The program is then to (i) use the $\mathrm{SU}(1,1)$ scaffold to design pulses and expected spectral patterns, and (ii) calibrate the remaining interaction-specific mixing by exact diagonalization in the LLL basis.

d) Worked example: $N = 3$ and the $s = 3$ TL operator selects a finite set *of SU(1,1) towers.:* To make the "tower selectivity" concrete, consider the lowest-Landau-level polynomial language for $N = 3$. The Laughlin state at filling $\nu = 1/3$ has polynomial $\mathcal{V}^3 = \prod_{i<j}(z_i - z_j)^3$ and total angular momentum $L = 3N(N-1)/2 = 9$. A TL pulse with $s = l + \sigma = 3$ (e.g. $l = 2$, $\sigma = +1$) injects $\Delta L = +3$. In the LLL-projected long-wavelength limit, the corresponding internal driving operator reduces to the symmetric power-sum polynomial

$$\hat{O}^{\rm LLL}_{s=3} \propto \sum_{j=1}^{3} z_j^3 \equiv p_3(z_1, z_2, z_3), \tag{46}$$

which maps the $L = 9$ Laughlin state into the $L = 12$ manifold. For $N = 3$ this manifold is three-dimensional, and a natural basis is given by multiplying $\mathcal{V}^3$ by the degree-3 symmetric polynomials $\{e_3,\ e_1e_2,\ e_1^3\}$. Using Newton's identity (Eq. (42)),

$$p_3 = e_1^3 - 3e_1e_2 + 3e_3, \tag{47}$$

we immediately see that a *single* $s = 3$ TL pulse does not create a pure quasihole state $e_3\mathcal{V}^3$; rather, it creates a specific superposition across *three* candidate towers.

This is exactly where the SU(1,1) language earns its keep. After separating the center of mass, e_1 is proportional to the CM coordinate ($e_1 = 3Z_{\rm CM}$), so the e_1^3 and e_1e_2 pieces contain CM excitation content, while e_3 is the quasihole factor. In Gambardella's terms, each linearly independent homogeneous polynomial that solves the "angular" problem is a lowest-weight vector of some SU(1,1) representation; the internal breathing ladder is generated by K_+ acting on it. Equation above therefore *decomposes the TL drive into reduced matrix elements* connecting the Laughlin tower to a *finite, explicitly identified set* of target towers. All other towers in the same $L = 12$ sector (if present at larger N) are "dark" in the idealized limit because their lowest-weight vectors are orthogonal to the polynomial content of p_3. Interactions and non-idealities can mix these towers, but the polynomial decomposition provides a controlled starting point for which modes are expected to be bright/dark and why.

In short, Gambardella's dynamical-group framework turns "$N \geq 3$ is hard" into a structured workflow: identify the relevant $\mathrm{SU}(1,1)$ towers (breathing vs. shape), compute the twisted-light selection rules and dominant overlaps, and then layer Coulomb realism on top.

E. What becomes genuinely new at $N \geq 3$

At $N \geq 3$, Laughlin-like droplets support quasiholes with fractional charge and anyonic exchange phases. [8], [9] Optically addressing the $\Delta L = N$ quasihole sector is therefore the first step from "correlation spectroscopy" toward preparation of topological excitations. For $N = 3$, the preceding subsection makes this concrete: an $s = 3$ twisted-light drive targets the $L = 9 \to 12$ manifold where the single-quasihole and the $\Delta L = 3$ edge excitations reside.

To connect explicitly to standard FQHE wavefunction language, recall that a quasihole at the origin is created by multiplying the many-body polynomial by $\prod_{i=1}^{N} z_i$, which increases total angular momentum by N and inserts one quantum of vorticity (one unit of flux) through the droplet. Hence, for $N = 3$ the operator $\hat{Q}_{\rm qh} = \prod_{i=1}^{3} z_i$ raises L by $+3$, and a twisted-light mode with $s = 3$ (e.g. $l = 2, \sigma = +1$) is the minimal optical multipole that can populate that sector

in a single pulse. If the relevant matrix element is sizable *and* the $L = 12$ eigenbasis is spectroscopically resolvable, this becomes an optical "write" primitive for a quasihole *sector* (with selectivity set by interaction-defined overlaps, cf. Sec. VIII-B).

a) Abelian anyons as a phase resource.: Laughlin quasiholes are *Abelian* anyons: exchanging two quasiholes yields statistical angle $\theta = \pi/q$ (a full braid gives $2\theta = 2\pi/q$) but (on simply connected geometries with fixed quasihole positions) no fusion-space degeneracy, so braiding alone is not universal. [9], [10] Nevertheless, such phases can provide robust, geometry-insensitive conditional phases when combined with non-topological control. In this sense, Abelian anyons provide a *protected phase resource* even when they do not supply a universal gate set by braiding alone. [9]

b) How twisted light might participate in braiding protocols.: If twisted light can (i) create quasihole sectors and (ii) be spatially steered by a spatial light modulator, a natural speculative direction is to use structured light not only as a spectroscopy tool but as a way to *move* localized charge deficits (quasiholes) in time. In macroscopic FQHE samples, quasihole motion is typically controlled by electrostatic gates or local potentials; an optical route would be faster (pulse timescales) and potentially more flexible in geometry. A key open question for this program is whether sufficiently localized optical potentials can be engineered without heating the electronic system out of the LLL.

c) Long-term direction.: The "photonic control bus" viewpoint motivates extending the same TL-selective spectroscopy/state-preparation ideas to engineered dot states whose excitations are non-Abelian. [9], [10]

d) Non-Abelian targets.: Ultimately, universal topological quantum computation requires non-Abelian anyons. [9], [10] While the present work focuses on Laughlin-like correlations and their Calogero limits, the broader program is clear: identify correlated dot states (possibly in higher Landau levels or in engineered interactions) whose excitations support non-Abelian statistics, and test whether twisted light can selectively prepare and interrogate those sectors.

F. Proposed conference-scale research program

A concrete near-term experimental roadmap is:

1) **Spectroscopy in a single dot ($N = 2$).** Verify TL-only internal transitions and extract $\Delta m = \pm 2$ selection rules. [4]
2) **Coherent control.** Demonstrate Rabi oscillations between $|m| = 3$ and $|m| = 5$ sectors and Ramsey interferometry for phase control.
3) **Two-dot conditional phase.** Engineer state-dependent Coulomb coupling and test a ZZ-type entangling phase gate.
4) **Scale-up.** Extend to $N = 3$ dots and test $s = 3$ pumping into the quasihole sector as an optical state-preparation primitive.

Even if the long-term target is topological quantum computing, the $N = 2$ stage already yields a complete, analytically characterized, optically driven single-qubit gate module—a rare benchmark system for bridging correlated-electron physics and quantum information science.

TABLE IV
REPRESENTATIVE NUMBERS SUPPORTING TL CONTROL OF CORRELATED SECTORS IN FEW-ELECTRON QUANTUM DOTS.

Quantity	Typical value	Comment / source
Dot confinement energy	$\hbar\omega_0 \sim 3$ meV	Harmonic estimate used to model GaAs dots with $d_{\mathrm{eff}} \approx 100$ nm [15].
Charging energy	$E_c \sim 1$–4 meV	Screened vs. unscreened estimates for $d_{\mathrm{eff}} \approx 100$ nm (and a commonly used intermediate value $E_c \simeq 2$ meV in model spectra) [15].
Magnetic field	$B \lesssim 16$ T	Field range routinely applied in few-electron dot spectroscopy [15].
Cyclotron energy (GaAs)	$\hbar\omega_c \simeq (1.73\,\mathrm{meV/T})\,B$	Set by the effective mass $m^* = 0.067m_e$ [15].
Zeeman scale (GaAs)	$\lvert g\rvert\mu_B B \simeq (0.025\,\mathrm{meV/T})\,B$	With $g_{\mathrm{GaAs}} = -0.44$ [15].
Base temperature	$T \sim 100$–200 mK	Typical measurement temperatures in few-electron dot transport spectroscopy [15].
THz-TDS waveform	pulse $\lesssim 1$ ps, bandwidth around 1 THz	Single-cycle THz pulses used in time-domain spectroscopy (photoconductive or optical-rectification based) [16].
Strong-field THz example	$E_{\mathrm{pk}} = 236$–819 kV/cm	High-repetition-rate DSTMS optical-rectification source (1–10 kHz) [17].
THz vortex-beam components	0.3–0.45 THz ($\lvert L\rvert = 1, 2$); 0.62–1.3 THz ($\lvert L\rvert = 1$)	Survey of demonstrated THz vortex shapers and mode converters (including reports of $\lvert L\rvert \le 3$ at 1.8–2.8 THz) [18].

IX. REPRESENTATIVE EXPERIMENTAL NUMBERS AND FEASIBILITY

To make the proposal concrete, we collect representative parameter values from the few-electron quantum-dot and ultrafast/THz literature. The goal is not to lock in a single device design, but to show that the *energy scales, magnetic fields, temperatures, and pulse bandwidths* required to drive the twisted-light (TL) selection rules are already standard in nanostructure experiments.

A useful conversion is $1\ \mathrm{meV}/h \simeq 0.242$ THz, so a typical confinement $\hbar\omega_0 \sim 3$ meV corresponds to a natural scale $f_0 \sim 0.73$ THz. In the quantum Hall (Fock–Darwin) regime, the low-energy ladder spacing between successive lowest-Landau-level orbitals is

$$\hbar\omega_- = \hbar\sqrt{\omega_0^2 + \omega_c^2/4} - \frac{\hbar\omega_c}{2}, \tag{48}$$

so for $\hbar\omega_0 = 3$ meV and $B = 3$ T (i.e. $\hbar\omega_c \simeq 5.2$ meV) one finds $\hbar\omega_- \approx 1.36$ meV ($f_- \approx 0.33$ THz), while at $B = 5$ T one finds $\hbar\omega_- \approx 0.93$ meV ($f_- \approx 0.22$ THz), all within standard far-infrared/THz bandwidths [16], [17]. These are precisely the frequencies relevant for the $|m| \to |m| + s$ internal ladders that TL addresses.

For spatial scales, $\hbar\omega_0 = 3$ meV and $m^* \approx 0.067m_e$ imply a single-particle Fock–Darwin length $\ell_0 = \sqrt{\hbar/(2m^*\omega_0)} \approx 14$ nm at $B = 0$. In a magnetic field the relevant Gaussian length uses $\omega = \sqrt{\omega_0^2 + \omega_c^2/4}$, giving $\ell_0(B = 5\ \mathrm{T}) \approx 10$ nm,

comparable to the magnetic length $\ell_B = \sqrt{\hbar/(eB)} \approx 11.5$ nm at $B = 5$ T. Hence the relevant internal-coordinate matrix elements are set by tens-of-nanometre length scales, consistent with few-electron dots in the $d_{\text{eff}} \sim 100$ nm class [15].

Finally, the optics side is compatible with the selection rules: the protocol requires only modest OAM charges ($l = 1, 2$ in most of the worked examples), and THz vortex converters with $|L| = 1$ (and in some cases $|L| = 2$) have been demonstrated in the 0.3–1.3 THz range, with reports of $|L| \leq 3$ at a few THz [18].

A. How the González–Quiroga–Rodríguez $N = 3$ theory can scaffold the topological roadmap

A main bottleneck in moving from the fully analytic $N = 2$ case to genuinely topological droplets ($N \geq 3$) is that the correlated spectrum becomes multi-dimensional and brute-force exact diagonalization scales rapidly with Hilbert-space size. A particularly useful intermediate step already exists in the few-body literature: González, Quiroga, and Rodríguez developed a resummed $1/N$ expansion (with N essentially set by the internal angular momentum scale) for three particles in a 2D parabolic dot under magnetic field with a Calogero ($1/r^2$) repulsion. [12] For our purposes, the value is practical: their method yields a design-level semi-analytic spectrum *and* explicit normal-mode wavefunctions (breathing vs. shape) that reduce twisted-light matrix elements to oscillator integrals, while reproducing the correct "magic-number" ground-state ladder and its magnetic-field-driven transitions in good qualitative agreement with Coulomb benchmarks. [12], [13]

X. Conclusion

Twisted light provides an optical handle on correlation physics in magnetized quantum dots by accessing relative-motion excitations that are dark to uniform dipolar probes. In the analytically solvable Calogero limit, both the spectrum and the twisted-light matrix elements are closed-form functions of the interaction strength, allowing gate parameters to be written down explicitly. This makes the $N = 2$ system a concrete single-qubit gate primitive (with a plausible two-qubit extension via state-dependent Coulomb coupling) and a controlled stepping stone toward $N \geq 3$ FQHE droplets where quasiholes become genuinely topological excitations. The central message for quantum computing audiences is operational: twisted light enables *WRITE* (pulse-create a correlation sector), *READ* (spectroscopically diagnose correlations), and *SCALE* (optical addressing via SLM) in a unified photonic control layer.

References

[1] L. Allen, M. W. Beijersbergen, R. J. C. Spreeuw, and J. P. Woerdman, "Orbital angular momentum of light and the transformation of Laguerre–Gaussian laser modes," *Phys. Rev. A*, vol. 45, pp. 8185–8189, 1992.

[2] A. Afanasev, C. E. Carlson, and A. Mukherjee, "Two properties of twisted-light absorption," *J. Opt. Soc. Am. B*, vol. 31, pp. 2721–2727, 2014, doi: 10.1364/JOSAB.31.002721.

[3] G. F. Quinteiro and J. Berakdar, "Electric currents induced by twisted light in quantum rings," *Opt. Express*, vol. 17, no. 22, pp. 20465–20475, 2009.

[4] F. J. Rodríguez, L. Quiroga, and N. F. Johnson, "Twisted light drives chiral excitations of interacting electrons in nanostructures with magnetic field," *Phys. Rev. B*, vol. 112, p. 115115, 2025.

[5] N. F. Johnson, F. J. Rodríguez, and L. Quiroga, *Laughlin States, Vandermonde Determinants, and Quasihole Excitations in Few-Electron Systems: A Pedagogical Tutorial with Explicit $N = 2, 3$ Calculations*, Tutorial document (2025–2026).

[6] N. F. Johnson and L. Quiroga, "Analytic results for N particles with $1/r^2$ interaction in two dimensions and an external magnetic field," *Phys. Rev. Lett.*, vol. 74, p. 4277, 1995.

[7] N. F. Johnson, "Quantum-dot excitation spectrum: Laughlin-like states," *Phys. Rev. B*, vol. 46, p. 2636(R), 1992.

[8] R. B. Laughlin, "Anomalous quantum Hall effect: an incompressible quantum fluid with fractionally charged excitations," *Phys. Rev. Lett.*, vol. 50, p. 1395, 1983.

[9] C. Nayak, S. H. Simon, A. Stern, M. Freedman, and S. Das Sarma, "Non-Abelian anyons and topological quantum computation," *Rev. Mod. Phys.*, vol. 80, p. 1083, 2008.

[10] A. Yu. Kitaev, "Fault-tolerant quantum computation by anyons," *Ann. Phys.*, vol. 303, p. 2, 2003.

[11] S. M. Reimann and M. Manninen, "Electronic structure of quantum dots," *Rev. Mod. Phys.*, vol. 74, p. 1283, 2002.

[12] A. González, L. Quiroga, and B. A. Rodríguez, "Planar three-body problem with Calogero interactions and a magnetic field," *Few-Body Systems*, vol. 21, p. 47, 1996.

[13] P. Hawrylak and D. Pfannkuche, "Magnetoluminescence from correlated electrons in quantum dots," *Phys. Rev. Lett.*, vol. 70, p. 485, 1993.

[14] P. J. Gambardella, "Exact results in quantum many-body systems of interacting particles in many dimensions with $\mathrm{SU}(1,1)$ as the dynamical group," *J. Math. Phys.*, vol. 16, pp. 1172–1187, 1975, doi: 10.1063/1.522651.

[15] L. P. Kouwenhoven, D. G. Austing, and S. Tarucha, "Few-electron quantum dots," *Rep. Prog. Phys.*, vol. 64, pp. 701–736, 2001.

[16] M. Koch, D. M. Mittleman, J. Ornik, and E. Castro-Camus, "Terahertz time-domain spectroscopy," *Nature Reviews Methods Primers*, vol. 3, p. 48, 2023, doi: 10.1038/s43586-023-00232-z.

[17] Z. Zheng, K. Wang, H. Li, X. Meng, Y. Tian, and L. Song, "High-repetition-rate strong-field terahertz source by optical rectification in DSTMS crystals," *High Power Laser Science and Engineering*, vol. 12, e61, 2024, doi: 10.1017/hpl.2024.50.

[18] N. V. Petrov, B. Sokolenko, M. S. Kulya, A. Gorodetsky, and A. V. Chernykh, "Design of broadband terahertz vector and vortex beams: I. Review of materials and components," *Light: Advanced Manufacturing*, vol. 3, p. 43, 2022, doi: 10.37188/lam.2022.043.

[19] T. Hayashi, T. Fujisawa, H. D. Cheong, Y. H. Jeong, and Y. Hirayama, "Coherent manipulation of electronic states in a double quantum dot," *Phys. Rev. Lett.*, vol. 91, p. 226804, 2003, doi: 10.1103/PhysRevLett.91.226804; arXiv:cond-mat/0308362.

[20] K. D. Petersson, J. R. Petta, H. Lu, and A. C. Gossard, "Quantum coherence in a one-electron semiconductor charge qubit," *Phys. Rev. Lett.*, vol. 105, p. 246804, 2010, doi: 10.1103/PhysRevLett.105.246804; arXiv:1008.3089.

[21] J. K. Gamble, M. Friesen, S. N. Coppersmith, and X. Hu, "Two-electron dephasing in single Si and GaAs quantum dots," *Phys. Rev. B*, vol. 86, p. 035302, 2012, doi: 10.1103/PhysRevB.86.035302; arXiv:1203.6332.

[22] S. C. Benjamin and N. F. Johnson, "Entangled electronic states in multiple-quantum-dot systems," *Phys. Rev. B*, vol. 51, no. 20, pp. 14733–14736, 1995.

[23] N. F. Johnson and S. C. Benjamin, "Electron correlations and fractional quantum Hall states in a double-layer electron system," *J. Phys.: Condens. Matter*, vol. 7, pp. L159–L164, 1995.

Dynamically Tuneable Helicity in Twisted Electromagnetic Resonators

E. C. I. Paterson[1,*], J. Bourhill[1], M. E. Tobar[1], M. Goryachev[1]
[1]Quantum Technologies and Dark Matter Labs
University of Western Australia, Australia
*Corresponding author: emma.paterson@research.uwa.edu.au

***Abstract*—We demonstrate real-time macroscopic control of electromagnetic helicity and resonant frequency in a rectangular cross-section microwave cavity resonator by dynamically twisting its conducting boundaries. The resulting mirror asymmetry induces magnetoelectric coupling between near-degenerate transverse electric and magnetic modes, generating helical hybrid eigenmodes with resonant frequencies proportional to their electromagnetic helicity.**

***Keywords*— electromagnetic helicity, chirality, microwave cavity resonators, mode hybridisation.**

I. Introduction

Electromagnetic radiation that is chiral in nature is distinguished by its left- or right-handed polarization and underpins a broad range of phenomena in nanophotonics [1], [2], metamaterials [3], quantum information, and precision sensing [4], [5], [6]. A fundamental measure of this chirality is electromagnetic helicity [7], [8], which quantifies the spatial overlap of electric and magnetic fields.

It has traditionally been assumed that hollow metallic cavity resonators cannot sustain bulk electromagnetic helicity in free space [9]. However, recent work has demonstrated the existence of helical resonant eigenmodes in vacuo [5], [4]. Here, we extend this concept by experimentally demonstrating continuous, real-time modulation of electromagnetic helicity in a mechanically twisted rectangular microwave cavity resonator.

II. Methods

Electromagnetic helicity may be expressed by projecting the complex electromagnetic state vector's spin onto its linear momentum [10], [11], [12], [13], [14]. For a monochromatic resonant mode i, the global electromagnetic helicity is defined as

$$\mathscr{H}_i = \frac{2\,\mathrm{Im}\left[\int \vec{\mathbf{E}}_i(\vec{r}) \cdot \vec{\mathbf{H}}_i^*(\vec{r}) dV\right]}{\sqrt{\int \vec{\mathbf{E}}_i(\vec{r}) \cdot \vec{\mathbf{E}}_i^*(\vec{r}) dV \int \vec{\mathbf{H}}_i(\vec{r}) \cdot \vec{\mathbf{H}}_i^*(\vec{r}) dV}}, \quad (1)$$

where $\vec{\mathbf{E}}_i(\vec{r})$ and $\vec{\mathbf{H}}_i(\vec{r})$ denote the electric and magnetic field distributions of the mode.

Introducing a geometric twist angle ϕ breaks the mirror symmetry of the rectangular cavity boundaries. This perturbation induces magnetoelectric coupling between near-degenerate transverse electric (TE) and transverse magnetic (TM) modes of the untwisted resonator. Finite-element simulations of the transverse electric ($\vec{E}_\perp$) and magnetic ($\vec{H}_\perp$) fields for the $\mathrm{TM}_{2,1,0}$ and $\mathrm{TE}_{2,0,1}$ eigenmodes of a WR-137 cavity are shown in Fig. 1(a) and (b), respectively. The twist lifts the modal degeneracy, producing hybrid eigenstates $\psi^{\pm}_{2,1,0}$ corresponding to in-phase and out-of-phase TE-TM superpositions. The resulting hybrid modes are shown in Fig. 1(c,d). This behaviour can be understood through the dual symmetry of Maxwell's equations: the geometric twist effectively rotates the electric and magnetic fields together, generating helical resonant eigenmodes.

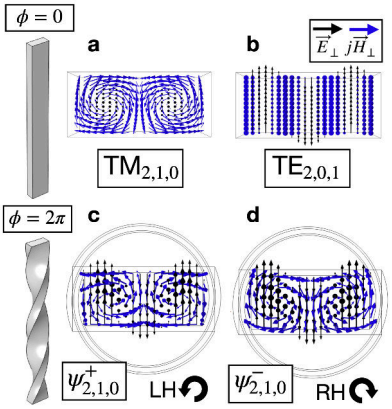

Fig. 1. The $\vec{E}_\perp$ (magenta) and $j\vec{H}_\perp$ (black) field distributions for FEM eigenmode simulations of the WR-137 rectangular cross-section cavity resonator are shown for $\phi = 0$ ((a) $\mathrm{TM}_{2,1,0}$ and (b) $\mathrm{TE}_{2,0,1}$ modes) and $\phi = 2\pi$ ((c) $\psi^+_{2,1,0}$ and (d) $\psi^-_{2,1,0}$ modes).

The hybrid states $\psi^{\pm}_{2,1,0}$ not only acquire non-zero $\mathscr{H}_i$ under twist but also exhibit symmetric frequency splitting relative to their untwisted counterparts, $\mathrm{TM}_{2,1,0}$ and $\mathrm{TE}_{2,0,1}$.

III. Results

Geometric twisting is analogous to filling the cavity with an isotropic chiral medium characterised by a chirality parameter κ. An empirical mapping between twist angle and effective chirality for the $\psi^{\pm}_{2,1,0}$ modes is given by

$$\kappa_{\mathrm{eff}} \approx -\frac{\phi}{88.55}. \quad (2)$$

The corresponding resonant frequency shift follows the perturbative relation

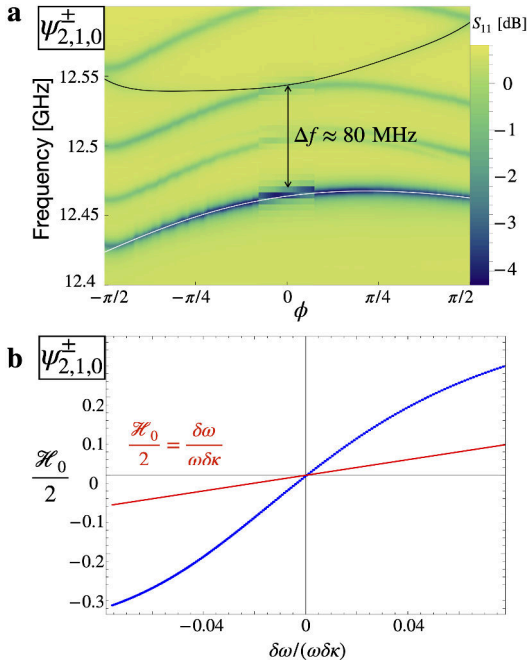

Fig. 2. (a) Measured reflection (S_{11}) response of the helically corrugated WR-137 rectangular cavity. The resonance of the hybrid mode $\psi^{\pm}_{2,1,0}$, arising from coupling between the $\mathrm{TE}_{2,0,1}$ and $\mathrm{TM}_{2,1,0}$ modes, is highlighted by cyan and black dashed markers. The experimentally extracted $\psi^{\pm}_{2,1,0}$ frequencies (black trace) are then used in (b) to compare the left-hand side of Eq. (3) with the right-hand side derived from finite-element eigenmode simulations of the untwisted cavity, where an effective chirality parameter κ_{eff} is introduced into the medium. The blue line denotes the theoretical prediction given by Eq. (3).

$$\left(\frac{\delta\omega}{\delta\kappa\,\omega_0}\right)_{\kappa_0 \ll 1} = \frac{\mathscr{H}_0}{2\mu_r\epsilon_r}, \tag{3}$$

where $\mathscr{H}_0$ denotes the helicity of the untwisted mode. Here $\delta\omega = \omega_1 - \omega_0$ corresponds to a small perturbation $\delta\kappa$. This proportionality establishes a direct link between helicity and resonant frequency tuning, enabling mechanical control of both quantities.

Experimentally, a commercially available helically corrugated WR-137 waveguide was enclosed with metallic endcaps to form a twistable resonator. One endcap was mounted on a motorised rotation stage, enabling continuous variation of ϕ while monitoring the reflection response.

The measured S_{11} spectra (Fig. 2) show clear twist-induced frequency shifts of the $\psi^{\pm}_{2,1,0}$ hybrid modes. The frequency maximum occurs at a small positive twist angle, attributed to intrinsic right-handed corrugation that introduces effective surface chirality.

The experimentally extracted frequency shifts exhibit an approximately linear dependence between $\frac{\delta\omega}{\omega_0\delta\kappa}$ and $\mathscr{H}_0$, consistent with the perturbative model of Eq. (3). The experimental gradient is steeper than the theoretical prediction, likely due to corrugation effects and geometric changes arising from waveguide buckling during twisting. Despite this, the rate of change of both $\mathscr{H}_0$ and $\frac{\delta\omega}{\delta\kappa\omega_0}$ is consistent.

IV. Conclusion

We experimentally demonstrate dynamically tunable electromagnetic helicity in twisted microwave cavity resonators. Geometric mirror asymmetry induces magnetoelectric mode coupling, generating bulk chiral eigenmodes in free space. The proportional relationship between helicity and resonant frequency enables real-time mechanical tuning, establishing a reconfigurable platform for chiral cavity engineering and helicity-based device applications.

Acknowledgments

This work was supported by the Centre of Excellence for Dark Matter Particle Physics and the Defence Science Centre Research Higher Degree Student Grant.

References

[1] Y. Tang and A. E. Cohen, "Optical chirality and its interaction with matter," *Phys. Rev. Lett.*, vol. 104, no. 16, p. 163901, Apr. 2010. doi: 10.1103/PhysRevLett.104.163901.

[2] T. Zhao, D. Meng, Z. Hu, W. Sun, Y. Ji, J. Han, X. Jin, X. Wu, and P. Duan, "Enhanced chiroptical properties of nanocomposites of achiral plasmonic nanoparticles decorated with chiral dye-loaded micelles," *Nat. Commun.*, vol. 14, p. 81, Jan. 2023. doi: 10.1038/s41467-022-35699-z.

[3] Z. Li, M. Mutlu, and E. Ozbay, "Chiral metamaterials: from optical activity and negative refractive index to asymmetric transmission," *J. Opt.*, vol. 15, no. 2, p. 023001, Feb. 2013. doi: 10.1088/2040-8978/15/2/023001.

[4] J. F. Bourhill, E. C. I. Paterson, M. Goryachev, and M. E. Tobar, "Searching for ultralight axions with twisted cavity resonators of anyon rotational symmetry with bulk modes of nonzero helicity," *Phys. Rev. D*, vol. 108, no. 5, p. 052014, Sep. 2023. doi: 10.1103/PhysRevD.108.052014.

[5] E. C. I. Paterson, J. Bourhill, M. E. Tobar, and M. Goryachev, "Electromagnetic helicity in twisted cavity resonators," *Phys. Rev. A*, vol. 112, no. 1, p. 013530, Jul. 2025. doi: 10.1103/6gp4-76td.

[6] M. E. Tobar, C. A. Thomson, W. M. Campbell, A. Quiskamp, J. F. Bourhill, B. T. McAllister, E. N. Ivanov, and M. Goryachev, "Comparing instrument spectral sensitivity of dissimilar electromagnetic haloscopes to axion dark matter and high frequency gravitational waves," *Symmetry*, vol. 14, no. 10, art. no. 2165, 2022. doi: 10.3390/sym14102165.

[7] A. Bottarelli, M. Frigerio, and M. G. A. Paris, "Quantum routing of information using chiral quantum walks," *AVS Quantum Sci.*, vol. 5, no. 2, p. 025001, Jun. 2023. doi: 10.1116/5.0146805.

[8] Y. You, Y. Hu, G. Lin, Y. Qi, Y. Niu, and S. Gong, "Quantum nonreciprocity based on electromagnetically induced transparency in chiral quantum-optical systems," *Phys. Rev. A*, vol. 103, no. 6, p. 063706, Jun. 2021. doi: 10.1103/PhysRevA.103.063706.

[9] S. A. Tretyakov and A. J. Viitanen, "Waveguide and resonator perturbation techniques measuring chirality and nonreciprocity parameters of biisotropic materials," *IEEE Trans. Microw. Theory Tech.*, vol. 43, no. 1, pp. 222–225, Jan. 1995. doi: 10.1109/22.362985.

[10] F. Alpeggiani, K. Y. Bliokh, F. Nori, and L. Kuipers, "Electromagnetic helicity in complex media," *Phys. Rev. Lett.*, vol. 120, no. 24, p. 243605, Jun. 2018. doi: 10.1103/PhysRevLett.120.243605.

[11] K. Y. Bliokh, Y. S. Kivshar, and F. Nori, "Magnetoelectric effects in local light-matter interactions," *Phys. Rev. Lett.*, vol. 113, no. 3, p. 033601, Jul. 2014. doi: 10.1103/PhysRevLett.113.033601.

[12] J. Martínez-Romeu, I. Diez, S. Golat, F. J. Rodríguez-Fortuño, and A. Martínez, "Chiral forces in longitudinally invariant dielectric photonic waveguides," *Photon. Res.*, vol. 12, no. 3, pp. 431–443, Mar. 2024. doi: 10.1364/PRJ.509634.

[13] K. Y. Bliokh, A. Y. Bekshaev, and F. Nori, "Dual electromagnetism: helicity, spin, momentum, and angular momentum," *New J. Phys.*, vol. 15, p. 033026, 2013. doi: 10.1088/1367-2630/15/3/033026.

[14] E. C. I. Paterson, M. E. Tobar, M. Goryachev, and J. Bourhill, "Dynamically tuneable helicity in twisted electromagnetic resonators," arXiv:2506.07320 [physics.class-ph], 2026.

Attosecond Chiral Interferometry with Free Electron Lasers

D. Facciala[1,*], J. Terentjevas[3], A. Senftleben[4], J. Mikosch[4], M. Ruberti[2], A. Schneider[3], M. Padovani[3], A. G. Löhr[3], A. Roos[3], P. Martin Maier[3], P. C. Flores[3], R. Heilemann[3], E. A. Christou[3], J. Ghosh[4], L. Oberti[7], L. Germeroth[4], M. Mirahmadi[3], C. Vozzi[1], K. Prince[5], M. Di Fraia[8], S. Patchkovskii[3], O. Plekan[5], T. Baumert[4], K. Ueda[6], P. Kolorenc[9] , V. Averbukh[2], C. Callegari[5], D. Ayuso[2], O. Smirnova[3]

[1]CNR - Istituto di Fotonica e Nanotecnologie (CNR-IFN), Milano, Italy
[2] Department of Physics, Imperial College London, London, United Kingdom
[3] Max Born Institute for Nonlinear Optics and Short Pulse Spectroscopy, Berlin, Germany
[4] University of Kassel, Kassel, Germany
[5] Elettra Sincrotrone Trieste, Basovizza, Trieste, Italy
[6] Tohoku University, Sendai, Japan
[7] Dipartimento di Fisica, Politecnico di Milano, Milano, Italy
[8] CNR – Istituto Officina dei Materiali (CNR-IOM), Basovizza, Trieste, Italy
[9] Faculty of Mathematics and Physics, Charles University, Prague, Czech Republic
*Corresponding author: davide.facciala@cnr.it

***Abstract*— We show that two color phase-locked free-electron laser pulses induce interferometric and enantio-sensitive photoemission in propylene oxide. Our method isolates coherent chiral contributions, resolving individual multi-electron states. This provides direct access to chiral electronic currents on sub-femtosecond timescales.**

***Keywords*— chirality, free electron laser, attosecond science, interferometry**

Electron dynamics in chiral molecules unfold on attosecond timescales and often involve correlated multi-electron motions that are difficult to isolate from single-electron signals and rapid decoherence. A probe combining attosecond temporal resolution with inherent sensitivity to molecular handedness is required to access these fundamental many-body effects. Here we demonstrate such a probe using two-color phase-locked pulses from the free-electron laser (FEL) FERMI, which provides the necessary spectral resolution (<40 meV) and phase stability (<10 as) for addressing these dynamics [1,2].

We employ phase-locked, orthogonally polarized ω and 2ω pulses from the FERMI FEL to ionize propylene oxide. Photoelectrons are detected by VMI as function of two-color delay. The interference of ω+ω and 2ω quantum pathways to the same final ionic state is controlled by the phase between the two colors and produces an enantio-sensitive rotation of the photoelectron angular distribution that encodes a characteristic chiral molecular phase [3,4]. In our experiment, we identified in the photoelectron spectrum of propylene oxide a specific interference pathway. The 2ω *reference* pathway produces a 2h1p (2-holes 1-particle) ionic state via shake-up process. The ω+ω *signal* pathway involves the photoexcitation by the first ω photon to a state with an inner-valence hole, which then undergoes a prompt, laser-assisted Auger-Meitner decay, a multi-electron process stimulated by the absorption of a second ω photon. By performing the Fourier transform of the rotation of the photoelectron angular distribution with respect to two-color phase delay, we extracted the enantio-sensitive molecular phase associated to this interference, with a temporal resolution of ~40 as, across the photoelectron energy region of 2h1p final states. This phase exhibits a clear π-shift between opposite enantiomers, which confirms the enantiosensitivity of the measurement. Its complete characterization as a function of the energy provides a direct signature of the internal helical currents and sub-femtosecond charge redistribution of a chiral system.

With this experiment, we demonstrate attosecond enantio-sensitive interferometry of correlated multi-electron dynamics. The method is particularly sensitive to coherent pathways, providing a robust way to trace attosecond multi-electron correlations that precede rapid decoherence and fragmentation, and opening new avenues for observing ultrafast charge redistribution in chiral systems.

References

[1] E. Allaria et al., Nat. Photon. 6, 699–704 (2012).
[2] K. C. Prince et al., Nat. Photon. 10, 176–179 (2016).
[3] P. V. Demekhin et al., Phys. Rev. Lett. 121, 253201 (2018)..
[4] A. F. Ordonez and O. Smirnova, Phys. Chem. Chem. Phys. 24, 7264 (2022).

Tailored laser fields for driving nonlinear interactions with chiral molecules

A. Rodriguez[1], J. Edginton[2], A. Löhr[3], J. Terentjevas[3], P. Vindel-Zandbergen[4], A. Ordóñez[5], J. Vogwell[2], O. Smirnova[3,6], D. Ayuso[2], and L. Rego[1,*]

[1]Instituto de Ciencia de Materiales de Madrid (ICMM-CSIC), Madrid, 28049, Spain
[2]Department of Chemistry, MSRH, Imperial College London, London, SW7 2AZ, UK
[3]Max-Born-Institut, Berlin, 12489, Germany
[4]Department of Chemistry, New York University, New York 10003, USA
[5]Department of Physics, Freie Universität Berlin, 14195 Berlin
[6]Technische Universität Berlin, 10623 Berlin, Germany
*Corresponding author: laura.rego@csic.es

***Abstract*—Tailored laser fields are a powerful tool to investigate chirality. We show that the interaction of vector beams with chiral molecules results in topological chiral rings, where the handedness of the molecules is imprinted in the divergence of their light emission.**

***Keywords*— chirality, tailored laser fields, structured light, nonlinear optics, vector beams**

I. Introduction

Laser light can be tailored in a wide variety of ways. From standard temporal and spectral shaping, which led to the generation of ultrashort laser pulses, to harnessing light's polarization or creating beams with properties associated to their spatial structure. Interestingly, the capability of shaping light's symmetries and structure can be used to investigate matter's symmetries and structure. Chirality, a universal property of objects that are not superimposable to their mirror image, is especially relevant in this context. Tailored fields allow us to probe chiral matter and ultrafast chiral dynamics in unprecedent ways. The merging of these two ingredients, tailored light and chirality, has led to new methods for studying chiral molecules [1].

II. Methods

Microscopic tailoring includes shaping the electric field's polarization by mixing frequencies, which results in a collection of Lissajous curves. If the resulting polarization at one point in space is 3-dimensional in time (Fig. 1A), the field is locally chiral [2]. Macroscopic tailoring includes topological light, such as vortex beams, which carry orbital angular momentum due to its azimuthally-varying phase (Fig. 1B), and which have proven to be a valuable tool to obtain enantio-sensitive observables [3]. Another noteworthy type of topological light are vector beams, which possess a Poincaré index associated to its azimuthally-rotating polarization (Fig. 1C).

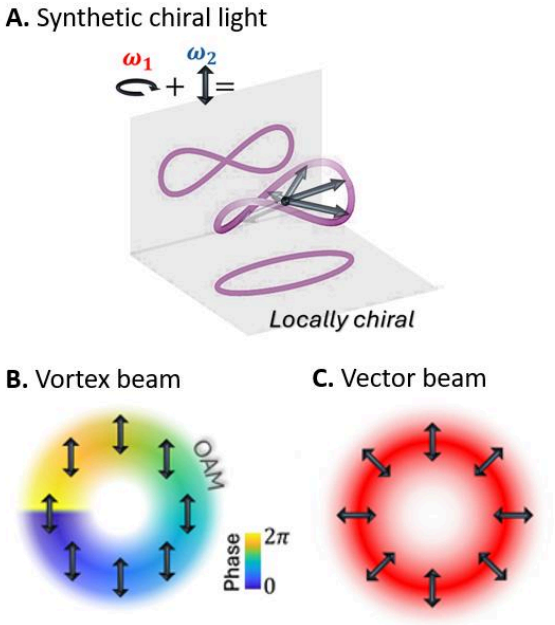

Fig. 1 Examples of tailored laser fields for studying chirality (the arrows indicate polarization). Synthetic chiral light presents a locally chiral (3-dimensional) polarization (A). Vortex beams (B) and vector beams (C) carry topological charges linked to their spatial structure. Figure adapted from [1].

III. Results and Discussion

Here, we present the first topological imaging technique that uses vector beams for enantiomeric discrimination. We shape a vector beam's polarization in 3D, creating topological locally chiral light. Then, we drive low-order nonlinear interactions, a combination of sum-frequency generation and third harmonic generation, in a sample of randomly oriented chiral molecules. This results in the handedness of chiral molecules being imprinted in the divergence of the emitted light, leading to

topological chiral rings.

IV. Conclusion

We propose an all-optical for enantiomer discrimination where, by shaping the light's polarization in 3D and driving nonlinear interactions, the handedness of the sample can be determined by measuring the divergence of the light emission. Our configuration is robust, requires gentle intensities, and results in chiral rings: spatially different rings for each enantiomer.

Acknowledgments

L. R acknowledges that the project leading to these results have received funding from "la Caixa" Foundation (ID 100010434), under the agreement "LCF/BQ/PR24/12050018", the Spanish Ministry of Science, Innovation and Universities & the State Research Agency through the project ref. PID2024-163024NA-I00 (MICIU/AEI/10.13039/501100011033/ FEDER, UE) and from the Severo Ochoa Centers of Excellence program through Grant CEX2024-001445-S.

References

[1] D. Habibović, K.R. Hamilton, O. Neufeld, and L. Rego, "Emerging tailored light sources for studying chirality and symmetry," Nat. Rev. Phys. 6, 663–675, 2024.
[2] D. Ayuso, et al. "Synthetic chiral light for efficient control of chiral light–matter interaction". Nat. Photonics 13, 866–871, 2019.
[3] N. Mayer, et al. "Chiral topological light for detection of robust enantiosensitive observables," Nat. Photon. 18, 1155–1160, 2024.

Controlling Intensity and Polarization at Deep Subwavelength Scale with Plasmonic Metastructures

Viktor A Podolskiy[1,*], Brandon Gomes[1], Jiaren Tan[2], Hooman Barati Sedeh[2], Yuruo Zheng[2], Jacob LaMountain[1], Sean Morrison[1], Anatoly Zayats[3], and Natalia Litchinitser[2]

[1]Department of Physics and Applied Physics, University of Massachusetts Lowell, USA
[2]School of Electrical Engineering, Duke University, USA
[3]Department of Physics, King's College London, UK
*Corresponding author: viktor_podolskiy@uml.edu

***Abstract*— Recently, plasmonic multilayered structures have been utilized to generate skyrmionic distributions of optical spin fields with deep subwavelength scale. We explore relationship between the details of such distributions and the structural properties of the multilayer/metasurface systems.**

***Keywords*— metamaterials, plasmonics, hyperbolic dispersion, metasurface, optical skyrmion.**

I. Introduction

Plasmonic structures have been known to enable focusing of light to deep subwavelength areas[1]. Recent results demonstrate that in addition to generating tight focusing, multi-layer structures yield non-trivial distributions of optical spin density that can be mapped to topologically-protected skyrmionics profiles[2]. The structure of field and spin distributions can be controlled by the interplay between the incident beam and the metasurfaces embedded into multilayer stack[3]. Here we demonstrate that complex metasurface-metamaterials structures can be utilize to engineer subwavelength distributions of both intensity and spin profiles.

II. Methods

Numerically, we investigate light propagation and interaction with metastructures via both finite-element solvers and analytical tools that assess the dispersion of the modes in the composites.

Experimentally, metastructures are fabricated using a combination of layer deposition and milling techniques, and their optical response is analyzed with microscopy and spectroscopy.

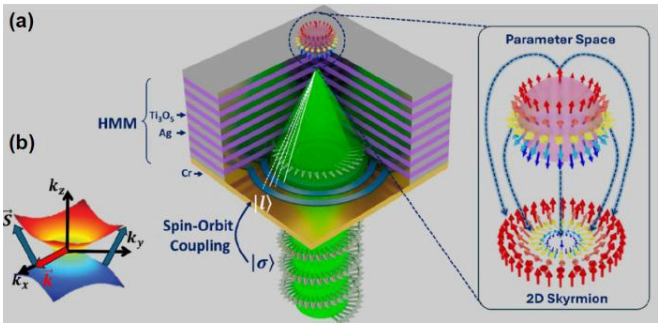

Fig. 1 Schematic of the plasmonic multilayer/metasurface structure generating the optical skyrmion [3]

III. Results and Discussion

The typical distributions of electric field achievable with metastructures are shown in Fig.2. It is seen that by adjusting the parameters of multilayer stack and the parameters of the circular metasurface the intensity can be engineered along the focal line, designing hot-spots across the multilayer thickness. Adding chirality to the metasurface breaks the rotational symmetry and introduces chiral response to the overall structure.

IV. Conclusion

We have developed a metastructure platform that combine the benefits of the bulk planar metamaterials and the ultra-thin metasurfaces to engineer field and spin distributions at deep subwavelength scales.

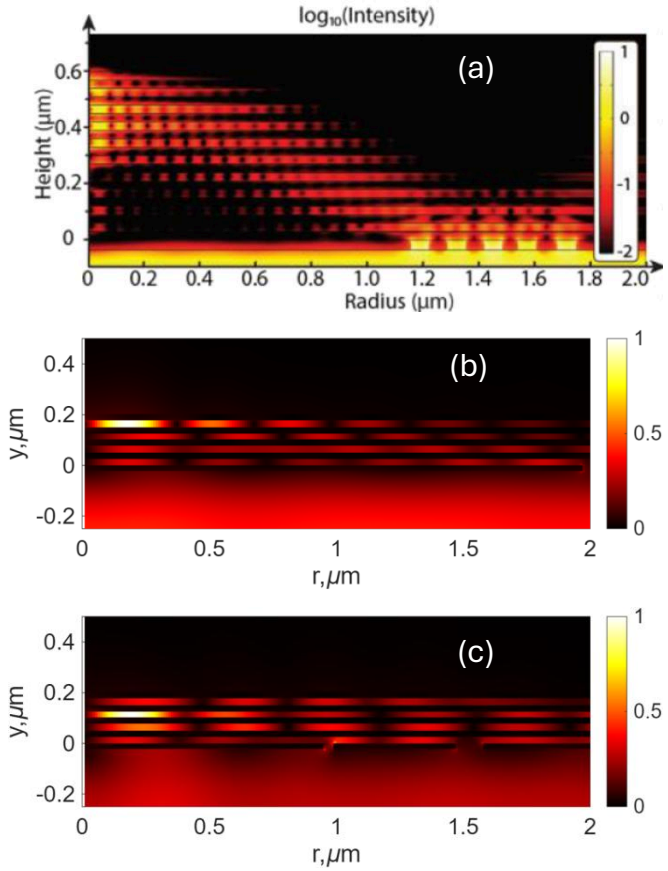

Fig. 2 Typical intensity distributions in plasmonic metastructures operating at free space wavelength of $\lambda_0 = 532\ nm$ (a) and $\lambda_0 = 1550\ nm$ (b,c)

ACKNOWLEDGMENTS

This work was supported by the National Science Foundation (Awards 2525896 [VP] and 2525895 [NL]), Intel [VP and NL], and EPSRC [AZ].

REFERENCES

[1] Z. Jacob, L. V. Alekseyev, and E. Narimanov. Opt. Express, 14(18):8247–8256, Sep 2006; A. Salandrino and N. Engheta Phys. Rev. B, 74:075103, Aug 2006.; S. Thongrattanasiri and V. A. Podolskiy, *Opt. Lett.*, vol. 34, no. 7, pp. 890−892, 2009; A. Poddubny, I. Iorsh, P. Belov, and Y. Kivshar, *Nat. Photonics*, vol. 7, no. 12, pp. 948−957, 2013

[2] Y. Shen, Q. Zhang, P. Shi, L. Du, X. Yuan, and A. V. Zayats, *Nat. Photonics*, vol. 18, no. 1, pp. 15−25, 2024; L. Du, A. Yang, A. V. Zayats, and X. Yuan, *Nat. Phys.*, vol. 15, no. 7, p. 650, 2019.

[3] W. Li, J. LaMountain, E. Simmons, J. Tan, H.B. Sedeh, A. Clabeau, R.Y. Bekele, J.D. Myers, T. Omatsu, J. Frantz, V.A. Podolskiy, N.M. Litchinitser, Nanophotonics DOI:10.1515/nanoph-2025-0315 (2025)

SPECIAL SESSION 5

Functional materials for tunable and reconfigurable photonics

18 contributions · pp. 824–855

Polymer plasmons and gating for active metaoptics

Magnus P. Jonsson[1,*]

Laboratory of Organic Electronics, Linköping University, Norrköping, SE-60174, Sweden

*Corresponding author: magnus.jonsson@liu.se

***Abstract*— We will present our latest findings related to dynamic tuning of optical metasurfaces and nanophotonic devices based on redox-tunable conducting polymers.**

***Keywords*— conducting polymers, metasurfaces, tunability, plasmonics, lattice resonances.**

In 2020, our group demonstrated the first switchable plasmonic nanoantennas made from a conducting polymer, enabling chemically and electrically controlled nanooptics and metasurfaces.[1-3] I will discuss challenges and advances in this emerging area of metamaterials and metasurfaces, including exploration of different polymers,[4,5] narrowing of resonances through nonlocal coupling,[6] possibilities based on anisotropic hyperbolic polymers[7,8], nearfield coupling to epsilon-near-zero materials,[9] and spectral tuning including to the mid-IR[10] and to the visible through the concept of "conducting polymer gating".[11]

Acknowledgments

We acknowledge support from the European Research Council (Consolidator Grant, 101086683), the Knut and Alice Wallenberg Foundation (Wallenberg Academy Fellow, KAW 2019.0163, 2020.0301), the Swedish Research Council (VR, Consolidator Grant, 2020-00287), and the Swedish Government Strategic Research Area in Materials Science on Functional Materials at Linköping University (Faculty Grant SFO-Mat-LiU No. 2009 00971).

References

[1] S. Chen *et al.* "Conductive polymer nanoantennas for dynamic organic plasmonics", *Nature Nanotech.* 15, 35-40 (2020)
[2] Karki *et al.* "Electrical Tuning of Plasmonic Conducting Polymer Nanoantennas", *Adv. Mater.* 34, 2107172, (2022)
[3] Chen et al. "Dynamic conducting polymer plasmonics and metasurfaces", *ACS Phot.* 10, 3, 571–581, (2023)
[4] Karki et al. "Doped Semiconducting Polymer Nanoantennas for Tunable Organic Plasmonics", *Comm. Mat.* 3, 48 (2022)
[5] Kazi et al. "n-Type redox-tuneable conducting polymer optical nanoantennas", *JMCC* 12, 17469–17474 (2024)
[6] Lin et al. "Switchable Narrow Nonlocal Conducting Polymer Plasmonics", *Nature Communications*, 16, 4484 (2025)
[7] Duan et al. "Tuneable anisotropic plasmonics with shape-symmetric conducting polymer nanoantennas", *Advanced Materials* 35, 51, 2303949 (2023)
[8] Duan et al. "Broadband chiroptics with twist-stacked hyperbolic conducting polymer thin films", *Advanced Materials, 37, 16, 2417024* (2025)
[9] Duan et al. "Electrotunable coupling between epsilon-near-zero thin film and conducting polymer nanoantennas", *PNAS* , in press (2026)
[10] Bandaru et al. "Switchable thermal mid-IR conducting polymer antenna arrays", *Advanced Functional Materials*, early view, e25508 (2025)
[11] Lin et al. "Dynamic Optical Lattices through Conducting Polymer-Gated Confinement", *Advanced Materials*, e20674, early view (2025)

Metamaterial devices and metalenses for optical beam steering

Daniele Melati[1,*], Sarra Salhi[1], Jian Cao[1], Gervasio D'Anzieri[1], Zindine Mokeddem[1], Hachim Lahbib[1], Warren Kut King Kan[1], Sandeep-Yadav Golla[1], Constantine Papakonstantinou[1], Amir Hossein Masominia[1], Laurent Vivien[1], Carlos Alonso-Ramos[1], Eric Cassan[1], Pavel Cheben[2], Jens H. Schmid[2], Xiaochen Xin[3], Winnie N. Ye[3]

[1]Centre de Nanosciences et de Nanotechnologies, Université Paris-Saclay, CNRS, 91120 Palaiseau, France
[2]Advanced Photonics and Electronics Research Centre, National Research Council Canada, K1A 0R6 Ottawa, Canada
[3]Department of Electronics, Carleton University, Ottawa, ON K1S 5B6, Canada
*Corresponding author: daniele.melati@universite-paris-saclay.fr

***Abstract*— We present our work on metamaterial-integrated photonic devices for optical beam steering, including polarization-insensitive grating antennas and optical phased arrays. Moreover we discuss our work on singlet metalenses achieving broadband achromatic focusing and a large field of view.**

***Keywords*— metamaterials, metamaterials, metasurfaces, subwavelength gratings, optical beam steering, metalens, silicon photonics, optical phased arrays**

I. Introduction

Optical beam steering underpins key technologies including free-space optical communications, light detection and ranging (LiDAR), and 3D imaging. Photonic integration enables compact, scalable, and low-cost implementations of beam steering systems. For example. optical phased arrays (OPAs), exploiting arrays of integrated antennas, allow steering and shaping beams without bulky mechanical components [1,2]. Metalenses, based on arrays of subwavelength nanoscatterers, offer a complementary approach to achieve beam focusing and steering with ultra-thin devices [3]. The use of metamaterial and metasurface engineering, combined with innovative design approaches, provide powerful additional tools to overcome the limitations of current integrated solutions [4]. In this work, we present our recent results on metamaterial-integrated grating antennas, OPAs,, as well as singlet metalenses combining achromatic focusing with wide-angle beam steering.

II. Metamaterial based antennas

Surface gratings are commonly used as antenna elements in OPAs. However, their strong polarization dependence in radiation angle and efficiency can represent a major drawback, especially when the OPA is used for reception. We developed a polarization-insensitive grating antenna on a 500 nm SOI platform [5]. The grating unit cell combines an L-shaped structure, partially etched to 250 nm for high upward diffraction efficiency, with a subwavelength metamaterial section enabling independent tuning of the TE and TM Bloch mode effective indices. By adjusting the metamaterial duty cycle, the Bloch indices for the two polarizations are equalized, yielding polarization-insensitive operation. Experiemental results demonstrate a diffraction angle of 10° at λ = 1550 nm for both TE and TM inputs, with upward diffraction efficiencies of -4 dB for both polarizations, offering a very promising path for polarization insensitive phased arrays.

III. Optical metalenses

Metalenses demonstrated in the literature often achieve either achromatic focusing or a wide field of view, but rarely both simultaneously [3,6]. We designed and experimentally demonstrated a singlet metalens that combines these two properties [8]. A quadratic phase profile is adopted, which maintains a constant focal distance under wide-angle illumination. For each position in the metalens, the meta-atom dimensions are selected to minimize dispersion. The fabricated achromatic metalens exhibits a relative focal shift of only 1.1% over the 100 nm bandwidth, compared to more than 14% for a single-wavelength reference design. Experimentally, the illumination angle can be tilted up to ±43° while preserving achromatic focusing performance.

IV. Conclusion

We presented metamaterial-engineered photonic devices addressing key challenges in optical beam steering. These results highlight the effectiveness of metamaterial integration for advancing compact beam steering systems.

Acknowledgments

This work was partially funded by the European Union

through the European Research Council (ERC) project BEAMS (Grant agreement No. 101041131).Views and opinions expressed are however those of the author(s) only and do not necessarily reflect those of the European Union or the European Research Council Executive Agency. Neither the European Union nor the granting authority can be held responsible for them. The device fabrication was performed within the C2N technological platforms and partly supported by the RENATECH network and the General Council of Essonne.

REFERENCES

[1] R. Fatemi et al., IEEE J. Solid-State Circuits, vol. 54, pp. 1200–1215, 2019.
[2] C. Poulton et al., Opt. Lett., vol. 42, pp. 4091–4094, 2017.
[3] N. Yu and F. Capasso, Nat. Mater., vol. 13, pp. 139–150, 2014.
[4] P. Cheben et al., Adv. Opt. Photon., vol. 15, no. 4, pp. 1033–1105, 2023.
[5] S. Salhi et al., Sci. Rep., vol. 15, no. 1, p. 13276, 2025.
[6] Y. Liu et al., Opt. Express, vol. 30, no. 22, pp. 39860–39867, 2022.
[7] W. K. K. Kan et al., Opt. Express, vol. 33, no. 2, pp. 3554–3561, 2025.
[8] J. Cao et al., Sci. Rep., vol. 15, no. 1, p. 43343, 2025.

Integrated Optical Phased Arrays for AR Displays, Biophotonics, Trapped Ions, & Beyond

Jelena Notaros[1,*]

[1]Research Laboratory of Electronics, Massachusetts Institute of Technology, Cambridge, MA 02139, USA
*Corresponding author: notaros@mit.edu

***Abstract*— This talk will review our work on developing integrated optical-phased-array-based platforms, devices, and systems for applications in LiDAR sensing, augmented-reality displays, 3D printing, optical trapping for biophotonics, and trapped-ion quantum engineering.**

***Keywords*— silicon photonics, integrated optical phased arrays, LiDAR sensing, augmented-reality displays, optical trapping, trapped ions.**

I. Review of OPA-Based Platforms, Devices, Systems, and Applications

By enabling the integration of millions of micro-scale optical components on compact millimeter-scale chips, silicon photonics is positioned to enable next-generation optical technologies that facilitate revolutionary advances for numerous fields spanning science and engineering.

An emerging class of silicon-photonics systems is integrated optical phased arrays (OPAs), which enable manipulation and dynamic control of free-space light in a compact form factor, at low costs, and in a non-mechanical way.

This talk will highlight our work on developing novel integrated-OPA-based platforms, devices, and systems that enable chip-based solutions to high-impact problems in areas including light-detection-and-ranging (LiDAR) sensing for autonomous vehicles [1-12], free-space optical communications [13-14], three-dimensional (3D) holography for augmented-reality (AR) displays [14-28], laser-based 3D printing [29-33], optical trapping for biophotonics [34-44], and trapped-ion quantum engineering [45-53].

Acknowledgments

This work was supported by the National Science Foundation (NSF) Faculty Early Career Development (CAREER) Program (Grant No. 2239525), the Semiconductor Research Corporation (SRC) JUMP 2.0 CogniSense Center (Grant No. 034021), and the MIT Center for Quantum Engineering (CQE), the Air Force Research Laboratory (AFRL) AIM Photonics Institute (FA8650-21-2-1000), the Defense Advanced Research Projects Agency (DARPA) Visible Integrated Photonics Enhanced Reality (VIPER) program (Grant No. FA8650-17-1-7713), and the Defense Advanced Research Projects Agency (DARPA) Electronic-Photonic Heterogeneous Integration (E-PHI) program (Grant No. HR0011-12-2-0007).

The author thanks Milica Notaros, Sabrina M. Corsetti, Tal Sneh, Andres Garcia Coleto, Henry Crawford-Eng, Daniel M. DeSantis, Ashton Hattori, Benjamin M. Mazur, Michael Torres, Manan Raval, Christopher V. Poulton, Matthew J. Byrd, Nanxi Li, Zhan Su, Emir Salih Magden, Erman Timurdogan, Michael R. Watts, Thomas Dyer, Christopher Baiocco, Alin Antohe, Nick M. Fahrenkopf, Lewis Carpenter, Soumen Kar, Kevin Fealey, Seth Kruger, Gerald Leake, Mark Wagner, Chris Striemer, Daniel Coleman, David Harame, Ethan R. Clements, Felix W. Knollmann, John Chiaverini, Isaac L. Chuang, Reuel Swint, Patrick T. Callahan, Gavin N. West, Dave Kharas, Thomas Mahony, Colin D. Bruzewicz, Cheryl Sorace-Agaskar, Robert McConnell, Alex Stafford, Zachariah A. Page, Kruthika Kikkeri, Joel Voldman, Taehwan Kim, Pavan Bhargava, Vladimir Stojanovic, Yuan Liu, Chongxin Tyler Zhang, Diya Hu, Thomas Meissner, and Jonathan Klamkin for their contributions to the work discussed in this talk.

References

[1] DeSantis, D.M., Mazur, B.M., Notaros, M., and Notaros, J., "Multi-beam solid-state LiDAR using star-coupler-based optical phased arrays," *Optics Express* 32(21), 36656–36673 (2024).

[2] Crawford-Eng, H., Garcia Coleto, A., Mazur, B. M., DeSantis, D. M., and Notaros, J., "Reduced-Crosstalk Grating-Based Antennas for Wide-Field-of-View Integrated Optical Phased Arrays," in *Proceedings of Frontiers in Optics (FiO)* (OSA, 2025), paper FM3D.7.

[3] Liu, Y., Zhang, C., DeSantis, D.M., Hu, D., Meissner, T., Notaros, J., and Klamkin, J., "High-Resolution Arrayed Waveguide Grating-Assisted Passive Optical Phased Array for 2D Beam Steering," *Optics Express* 33(4), 7714–7722 (2025).

[4] Liu, Y., Zhang, C., DeSantis, D.M., Hu, D., Meissner, T., Coleto, A.G., Mazur, B., Notaros, J., and Klamkin, J., "High-Resolution Arrayed-Waveguide-Grating-Assisted Passive Integrated Optical Phased Array for 2-D Beam Steering," in *CLEO: Science and Innovations,* STu4N.1, Optica Publishing Group (2024).

[5] Zhang, Z., Notaros, M., Gao, Z., Chakraborty, U., Notaros, J., and Boning, D., "Impact of process variations on splitter-tree-based integrated optical phased arrays," *Optics Express* 31(8), 12912–12921 (2023).

[6] Zhang, Z., Notaros, M., Gao, Z., Chakraborty, U., Notaros, J., and Boning, D., "Impact of Spatial Variations on Splitter-Tree-Based Integrated

Optical Phased Arrays," in *Optical Fiber Communication Conference (OFC)*, W2A.35, Optica Publishing Group (2023).

[7] Notaros, J., Li, N., Poulton, C.V., Su, Z., Byrd, M.J., Magden, E.S., Timurdogan, E., Baiocco, C., Fahrenkopf, N.M., and Watts, M.R., "CMOS-compatible optical phased array powered by a monolithically-integrated erbium laser," *Journal of Lightwave Technology* 37(24), 5982–5987 (2019).

[8] Notaros, J., Li, N., Poulton, C.V., Su, Z., Byrd, M.J., Magden, and Watts, M.R., "CMOS-compatible optical phased arrays with monolithically-integrated erbium lasers," in *CLEO: Science and Innovations*, STu4B.2, Optical Society of America (2018).

[9] Li, N., Vermeulen, D., Su, Z., Magden, E.S., Xin, M., Singh, N., Ruocco, A., Notaros, J., Poulton, C.V., Timurdogan, E., Baiocco, C., and Watts, M.R., "Monolithically integrated erbium-doped tunable laser on a CMOS-compatible silicon photonics platform," *Optics Express* 26(13), 16200–16211 (2018).

[10] Kim, T., Bhargava, P., Poulton, C.V., Notaros, J., Yaacobi, A., Timurdogan, E., Baiocco, C., Fahrenkopf, N., Kruger, S., Ngai, T., Timalsina, Y., Watts, M.R., and Stojanovic, V., "A single-chip optical phased array in a wafer-scale silicon photonics/CMOS 3D-integration platform," *IEEE Journal of Solid-State Circuits* 54(11), 3061–3074 (2019).

[11] Kim, T., Bhargava, P., Poulton, C.V., Notaros, J., Yaacobi, A., Timurdogan, E., Baiocco, C., Fahrenkopf, N., Kruger, S., Ngai, T., Timalsina, Y., Watts, M.R., and Stojanovic, V., "A single-chip optical phased array in a 3D-integrated silicon photonics/65nm CMOS technology," in *2019 IEEE International Solid-State Circuits Conference (ISSCC)*, 464–466, IEEE (2019).

[12] Bhargava, P., Kim, T., Poulton, C.V., Notaros, J., Yaacobi, A., Timurdogan, E., Baiocco, C., Fahrenkopf, N., Kruger, S., Ngai, T., Timalsina, Y., Watts, M.R., and Stojanovic, V., "Fully integrated coherent LiDAR in 3D-integrated silicon photonics/65nm CMOS," in *2019 Symposium on VLSI Circuits*, C262–C263, IEEE (2019).

[13] DeSantis, D.M., Notaros, M., Torres, M.R., and Notaros, J., "Underwater Wireless Optical Communications Using Integrated Optical Phased Arrays," in *2023 IEEE Photonics Conference (IPC)*, 1–2, IEEE (2023).

[14] Notaros, M., DeSantis, D.M., Raval, M., and Notaros, J., "Liquid-Crystal-Based Visible-Light Integrated Optical Phased Arrays and Application to Underwater Communications," *Optics Letters* 48(20), 5269-5272 (2023).

[15] Notaros, J., Notaros, M., Raval, M., and Watts, M.R., "Liquid-crystal-based visible-light integrated optical phased arrays," in *CLEO: Science and Innovations*, STu3O.3, Optical Society of America (2019).

[16] Crawford-Eng, H., Garcia Coleto, A., and Notaros, J., "Visible-Spectrum-Spanning Integrated Optical-Phased-Array-Based Systems," *Optics Letters* 50(19), 6065-6068 (2025).

[17] Crawford-Eng, H., Garcia Coleto, A., and Notaros, J., "Demonstration of Visible-Spectrum-Spanning Integrated Optical-Phased-Array-Based Systems," in *Proceedings of the Conference on Lasers and Electro Optics (CLEO)* (OSA, 2025), paper SS174_6.

[18] Garcia Coleto, A., Notaros, M., and Notaros, J., "Visible-light uniform and unidirectional grating-based antennas for integrated optical phased arrays," *Optics Express* 32(26), 46447–46466 (2024).

[19] Garcia Coleto, A., Notaros, M., and Notaros, J., "Design and Demonstration of Grating-Based Antennas for Visible-Light Integrated Optical Phased Arrays," in *Proceedings of the Conference on Lasers and Electro Optics (CLEO)* (OSA, 2025), paper SS186_3.

[20] Sneh, T., Garcia Coleto, A., Dyer, T., Notaros, M., Fealey, K., and Notaros, J., "Transparent and Flexible Wafer-Scale Silicon-Photonics Fabrication Platform," in Proceedings of Frontiers in Optics (FiO) (OSA, 2025), paper JTu7A.3.

[21] Notaros, M., Coleto, A.G., Raval, M., and Notaros, J., "Integrated liquid-crystal-based variable-tap devices for visible-light amplitude modulation," *Optics Letters* 49(4), 1041-1044 (2024).

[22] Notaros, M., Notaros, J., Raval, M., and Watts, M.R., "Integrated visible-light liquid-crystal variable-tap amplitude modulator," in *Integrated Photonics Research, Silicon and Nanophotonics*, ITh2C.6, Optical Society of America (2019).

[23] Notaros, M., Dyer, T., Raval, M., Baiocco, C., Notaros, J., and Watts, M.R., "Integrated visible-light liquid-crystal-based phase modulators," *Optics Express* 30(8), 13790-13801 (2022).

[24] Notaros, M., Raval, M., Notaros, J., and Watts, M.R., "Integrated visible-light liquid-crystal phase modulator," in *Frontiers in Optics*, FW6B.5, Optical Society of America (2018).

[25] Garcia Coleto, A., Notaros, M., and Notaros, J., "Packaging Considerations and Evaluation Techniques for Integrated Liquid-Crystal-Based Modulators," *IEEE Photonics Journal* 17(5), 1-6 (2025).

[26] Coleto, A.G., Notaros, M., and Notaros, J., "Integrated Liquid-Crystal-Based Modulators: Packaging Processes and Evaluation Techniques," in *2023 IEEE Photonics Conference (IPC)*, 1–2, IEEE (2023).

[27] Park, S., Notaros, M., Mohanty, A., Kim, D., Notaros, J., and Mouradian, S., "Technologies for modulation of visible light and their applications," *Progress in Quantum Electronics*, 100534 (2024).

[28] Notaros, J., Raval, M., Notaros, M., and Watts, M.R., "Integrated-phased-array-based visible-light near-eye holographic projector," in *CLEO: Science and Innovations*, STu3O.4, Optical Society of America (2019).

[29] Corsetti, S., Notaros, M., Sneh, T., Stafford, A., Page, Z.A., and Notaros, J., "Silicon-Photonics-Enabled Chip-Based 3D Printer," *Light: Science and Applications* 13, 132 (2024).

[30] Corsetti, S., Notaros, M., Sneh, T., Stafford, A., Page, Z.A., and Notaros, J., "Visible-Light Integrated Optical Phased Arrays for Chip-Based 3D Printing," in *Optica Advanced Photonics Congress*, IM2B.4, Optica Publishing Group (2022).

[31] DeSantis, D.M., Torres, M.R., Garcia Coleto, A., Mazur, B.M., Corsetti, S., Notaros, M., and Notaros, J., "Spiral integrated optical phased arrays for tunable near-field-focusing emission," *Optics Express* 32(25), 44567–44580 (2024).

[32] DeSantis, D.M., Torres, M.R., Garcia Coleto, A., Mazur, B.M., Corsetti, S., Notaros, M., and Notaros, J., "Spiral Integrated Optical Phased Arrays for Variable Near-Field Focusing Emission," in *Proceedings of the Conference on Lasers and Electro Optics (CLEO)* (OSA, 2025), paper SS117_1.

[33] Notaros, J., Byrd, M.J., Raval, M., and Watts, M.R., "Integrated optical phased array butterfly architecture for independent amplitude and phase control," in *Integrated Photonics Research, Silicon and Nanophotonics*, IM4A.4, Optical Society of America (2019).

[34] Sneh, T., Corsetti, S., Notaros, M., Kikkeri, K., Voldman, J., and Notaros, J., "Optical tweezing of microparticles and cells using silicon-photonics-based optical phased arrays," *Nature Communications* 15, 8493 (2024).

[35] Sneh, T., Corsetti, S., Notaros, M., and Notaros, J., "Focusing Integrated Optical Phased Arrays for Chip-Based Optical Trapping," in *CLEO: Science and Innovations*, STh4G-4, Optica Publishing Group (2022).

[36] Sneh, T., Corsetti, S., Notaros, M., Kikkeri, K., Voldman, J., and Notaros, J., "Optical Tweezing of Microspheres and Cells Using Integrated Optical Phased Arrays," in *2023 IEEE Photonics Conference (IPC)*, 1–2, IEEE (2013).

[37] Notaros, M., Dyer, T., Garcia Coleto, A., Hattori, A., Fealey, K., Kruger, S., and Notaros, J., "Mechanically-flexible wafer-scale integrated-photonics fabrication platform," *Scientific Reports* 14, 10623 (2024).

[38] Notaros, M., Dyer, T., Hattori, A., Fealey, K., Kruger, S., and Notaros, J., "Flexible Wafer-Scale Silicon-Photonics Fabrication Platform," in *Frontiers in Optics + Laser Science 2022 (FIO, LS)*, FW1E.3, Optica Publishing Group (2022).

[39] Notaros, J., Poulton, C.V., Raval, M., and Watts, M.R., "Near-field-focusing integrated optical phased arrays," *Journal of Lightwave Technology* 36(24), 5912–5920 (2018).

[40] Notaros, J., Poulton, C.V., Raval, M., Byrd, M.J., Coolbaugh, D., and Watts, M.R., "Fresnel-lens-inspired focusing phased arrays for optical trapping applications," in *CLEO: Science and Innovations*, STh1M.3, Optical Society of America (2017).

[41] Notaros, J., Poulton, C.V., Byrd, M.J., Raval, M., and Watts, M.R., "Integrated optical phased arrays for quasi-bessel-beam generation," *Optics Letters* 42(17), 3510–3513 (2017).

[42] Notaros, J., Poulton, C.V., Byrd, M.J., Raval, M., and Watts, M.R., "Bessel-beam-generating integrated optical phased arrays," in *CLEO: Science and Innovations*, SM3I.5, Optical Society of America (2018).

[43] Garcia Coleto, A., Crawford-Eng, H., Tyndall, N., Antohe, A., Kar, S., Carpenter, L., Stievater, T., and Notaros, J., "Extracting the Core and Cladding Contributions to Fluorescence and Raman Emission in Integrated Photonic Waveguides," *Optics Express* 33(22), 45631-45643 (2025).

[44] Garcia Coleto, A., Crawford-Eng, H., Tyndall, N., Antohe, A., Kar, S., Carpenter, L., Stievater, T., and Notaros, J., "Extracting the Core and Cladding Contributions to Fluorescence and Raman Emission in Integrated Photonic Waveguides," in *Proceedings of Frontiers in Optics (FiO)* (OSA, 2025), paper FM1D.3.

[45] Corsetti, S.M., Hattori, A., Clements, E.R., Knollmann, F.W., Notaros, M., Swint, R., Sneh, T., Callahan, P.T., West, G.N., Kharas, D., Mahony, T., Bruzewicz, C.D., Sorace-Agaskar, C., McConnell, R., Chuang, I.L., Chiaverini, J., and Notaros, J., "Integrated-Photonics-Based Systems for Polarization-Gradient Cooling of Trapped Ions," *Light: Science & Applications* 15, 57 (2026).

[46] Corsetti, S.M., Clements, E.R., Knollmann, F.W., Hattori, A., Notaros, M., Swint, R., Sneh, T., Callahan, P.T., West, G.N., Kharas, D., Mahony, T., Bruzewicz, C.D., Sorace-Agaskar, C., McConnell, R., Chuang, I.L., Chiaverini, J., and Notaros, J., "Integrated-Photonics-Based Devices and Systems for Polarization-Gradient Cooling of Trapped Ions," in *Proceedings of the Conference on Lasers and Electro Optics (CLEO)* (OSA, 2025), paper SS117_1.

[47] Clements, E.R., Knollmann, F.W., Corsetti, S.M., Li, Z., Hattori, A., Notaros, M., Swint, R., Sneh, T., Kim, M.E., Leu, A.D., Callahan, P.T., Mahony, T., West, G.N., Sorace-Agaskar, C., Kharas, D., McConnell, R., Bruzewicz, C.D., Chuang, I.L., Notaros, J., and Chiaverini, J., "Sub-Doppler cooling of a trapped ion in a phase-stable polarization gradient," *Physical Review Letters* 136, 023201 (2026).

[48] Knollmann, F.W., Corsetti, S.M., Clements, E.R., Swint, R., Leu, A.D., Kim, M.E., Callahan, P.T., Kharas, D., Mahony, T., Sorace-Agaskar, C., McConnell, R., Bruzewicz, C. D., Chuang, I. L., Notaros, J., and Chiaverini, J., "Collection of fluorescence from an ion using trap-integrated photonics," *Light: Science & Applications* 15, 95 (2026).

[49] Knollmann, F.W., Corsetti, S.M., Clements, E.R., Swint, R., Leu, A.D., Kim, M.E., Callahan, P.T., Kharas, D., Mahony, T., Sorace-Agaskar, C., McConnell, R., Bruzewicz, C. D., Chuang, I. L., Notaros, J., and Chiaverini, J., "Collecting Fluorescence from a Trapped Ion Using Trap-Integrated Photonics," in *Proceedings of the Conference on Lasers and Electro Optics (CLEO)* (OSA, 2025), paper SS117_2.

[50] Hattori, A., Corsetti, S., Sneh, T., Notaros, M., Swint, R., Callahan, P.T., Bruzewicz, C.D., Knollmann, F., McConnell, R., Chiaverini, J., and Notaros, J., "Integrated-Photonics-Based Architectures for Polarization-Gradient and EIT Cooling of Trapped Ions," in *Frontiers in Optics + Laser Science 2022 (FIO, LS)*, FM4B.3, Optica Publishing Group (2022).

[51] Hattori, A., Sneh, T., Notaros, M., Corsetti, S., Callahan, P.T., Chiaverini, J., and Notaros, J., "Integrated Visible-Light Polarization Rotators and Splitters for Atomic Quantum Systems," *Optics Letters* (2024).

[52] Sneh, T., Hattori, A., Notaros, M., Corsetti, S., and Notaros, J., "Design of Integrated Visible-Light Polarization Rotators and Splitters," in *Frontiers in Optics + Laser Science 2022 (FIO, LS)*, JTu5A.48, Optica Publishing Group (2022).

[53] Corsetti, S., Hattori, A., Swint, R., Notaros, M., West, G.N., Sneh, T., Knollmann, F., Callahan, P.T., Mahony, T., Clements, E.R., Kharas, D., Sorace-Agaskar, C., McConnell, R., Chiaverini, J., and Notaros, J., "Integrated Polarization-Diverse Grating Emitters for Trapped-Ion Quantum Systems," in *Frontiers in Optics and Laser Science (FiO, LS)*, JTu7A.3, Optica Publishing Group (2023).

Active and Reconfigurable Free-Space Photonics using Phase-Change Metamaterials

C. David Wright[1]*, Joe Shields[1], Guoce Yang[2], Carlota Ruiz de Galarreta[1], Mengyun Wang[2], Stuart Kendall[1], Joe Pady[1], Nikolaos Farmakidis[1,2], David B. Phillips[1], Jacopo Bertolotti[1], Andrea Alù[3], Harish Bhaskaran[2], C. David Wright[1*]

[1] Centre for Metamaterial Research and Innovation, University of Exeter, EX4 4QF, UK
[2] Department of Materials, University of Oxford, Oxford OX1 3PH, UK
[3] Advanced Science Research Center, The City College of New York, NY 10031, USA
*Corresponding author: david.wright@exeter.ac.uk

***Abstract*— The design, simulation and experimental realisation of various phase-change metasurface devices for the active and reconfigurable control of light is described. Particular emphasis is placed on metasurfaces for free-space implementations of optical image processing, optical mode conversion and optical orbital angular momentum control.**

***Keywords*— Phase-change metasurfaces, optical mode control, optical image processing.**

I. Introduction

Chalcogenide phase-change materials (PCMs), such as $Ge_2Sb_2Te_5$, Sb_2Se_3 and $Ge_2Sb_2Se_4Te$, exhibit huge differences in refractive index (real and imaginary parts) between their crystalline and amorphous states. They can be switched billions of times between such states (and to fractionally crystallised states) [1] on the (tens of) nanosecond time scales [2], and are stable in such states for years at room temperature (as opposed volatile reconfigurable materials such as VO_2). The inclusion of PCMs into metasufaces allows for both a dynamically active optical response, i.e. one that is changed frequently on relatively fast timescales such as in modulation and beam steering [3] and display applications [4], and to reconfigurability, where the functionality is switched from time to time for specific needs, e.g. in optical computing [5] and reconfigurable lensing [6]. In this paper we present some of our recent work in the area of the design, simulation and fabrication and testing of phase-change metasurface devices for free-space photonics applications, with special emphasis on PCM metasurfaces for free-space optical computing showing potential for applications ranging from analog image processing to optical telecommunications and more.

II. Results and Discussion

The design of typical unit cells – or meta-atoms – used in our PCM metasurfaces for active and reconfigurable photonics applications is given in Fig. 1, with Fig. 1a showing a design suitable for transmission type optical systems and Fig. 1b an example of a reflective design. The resonant frequency of the unit cell depends on the size of the meta-atom and the material properties. For a given material, we can control the resonant frequency by selecting appropriate feature sizes, in particular the radius of the resonator. For example, in Fig. 2a we show the transmission (intensity) and phase response at 1550 nm for a metasuface consisting of the unit cell shown in Fig. 1a and with a pitch of 1000 nm and height of 225 nm. Clearly, by controlling the meta-atom radius we can, when the Sb_2Se_3 is in its crystalline form, achieve dramatic changes in optical transmission (Fig. 2a) and optical phase (Fig. 2b). Upon switching the Sb_2Se_3 to its amorphous state, the transmission and phase responses demonstrate minimal dependence on meta-atom radius. This leads to the possibility of an ON-OFF type functionality in which the metasurface performs a targeted function with the PCM in one phase state (crystalline in this case), but interacts very little with incident light when the PCM is switched to its other state.

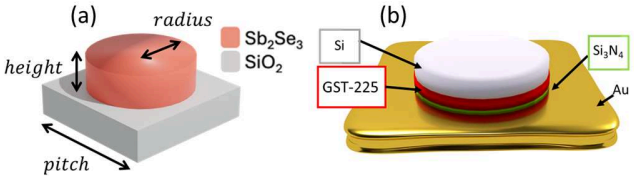

Fig. 1 Schematic of example PCM metasurface unit cells. (a) Shows a design suitable for use in transmission and uses the PCM composition Sb_2Se_3, whereas (b) shows a reflective design using the archetypal PCM composition $Ge_2Sb_2Te_5$.

We have exploited the ON-OFF capabilities of various PCM metasurfaces with device designs similar to those shown in Fig. 1, and optical responses as in Fig. 2, to deliver a range of interesting functionalities, including switchable image

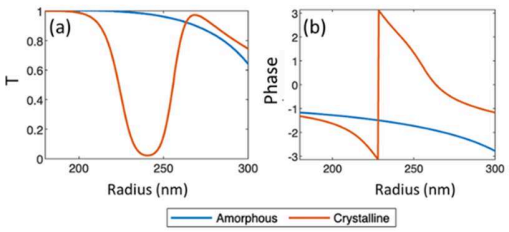

Fig. 2 Transmission (a) and phase response (b) at 1550 nm as a function of meta-atom radius for a PCM metasurface designed using the unit cell of Fig. 1a.

processing [7, 8], optical mode conversion and optical orbital angular momentum control. Examples of all of these applications will be showcased at the conference, but here, for brevity, we concentrate on optical mode conversion functionality.

The ability to manipulate optical modes is crucial for a variety of important applications in modern photonics, ranging from classical and quantum communication to advanced imaging and information processing, beam shaping and even nanoparticle manipulation via optical tweezing. Traditional approaches to optical mode control include the use of axicons, physical phase-plates, computer-generated holograms and multi-plane light converters [9, 10]. Metasurface optical mode converters have also recently been demonstrated [11]. However, conventional metasurfaces are static - that is to say their optical response is fixed at the point of fabrication – whereas the use of PCM metasurfaces introduces the opportunity for active and/or reconfigurable operation. An example of the latter is shown in Fig. 3, where a PCM metasurface (of the type shown in Fig. 1a) is designed to switch ON and OFF a mode conversion capability, here converting a fundamental Gaussian beam into a higher-order Hermite-Gaussian mode (here for concept demonstration, TEM_{00} to HG_{10} mode conversion). With the PCM meta-atoms in their crystalline state, the mode conversion proceeds as desired, but switching the PCM to its amorphous state allows the beam to pass through unaltered.

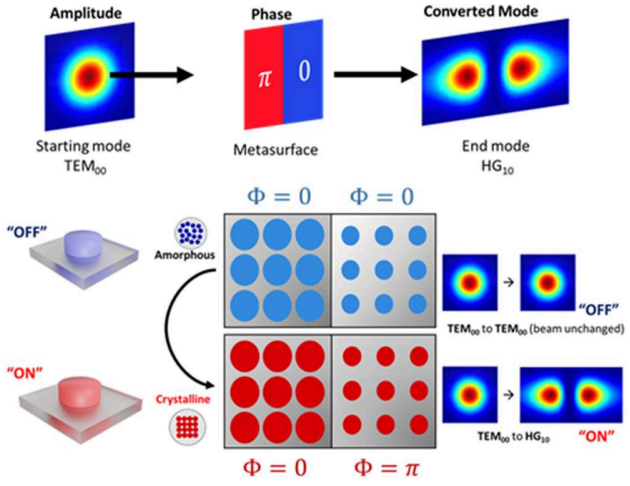

Fig. 3 Concept of an ON-OFF optical mode converter implemented using a phase-change metasurface.

Mode converter metasurfaces of the type shown in Fig. 3 and using unit-cells of the type shown in Fig. 1a were fabricated via magnetron sputtering and e-beam lithography. Exemplar as-fabricated structures are shown in Fig. 4a, and experimental mode conversion results are given in Fig. 4b. As predicted by simulation, the target mode conversion from TEM_{00} to HG_{10} modes is obtained with the PCM metasurface in its crystalline state, whereas with it in the amorphous state the TEM_{00} mode propagates essentially undisturbed.

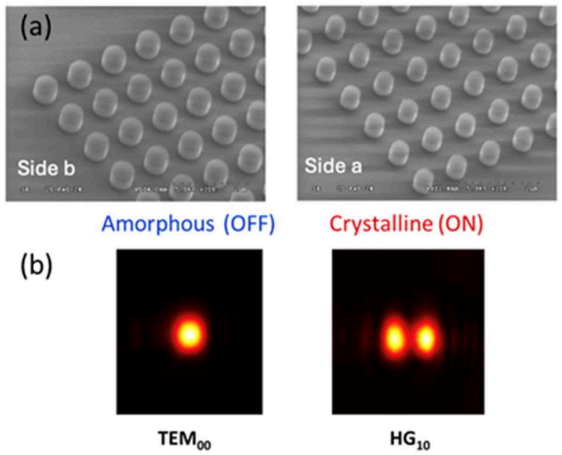

Fig. 4 (a) As-fabricated PCM (Sb_2Se_3) mode converting metasurface and (b) the optical response for an incident TEM_{00} mode when the metasurface is amorphous (left) and crystalline (right).

III. Conclusion

Phase-change metasurfaces provide a powerful platform for active and reconfigurable control of light. In the above we concentrated on optical mode conversion, but other functionalities also addressed at the conference include optical image processing, optical computing and optical orbital angular momentum control.

Acknowledgements

Funding is acknowledged from the EPSRC's AMETA (EP/W003341/1), APT-NuCOM (EP/W022931/1) and MetaHUB (UKRI1255) grants.

References

[1] C. Ruiz de Galarreta et al., Optica, vol. 7, no. 5, p. 476, 5 2020.
[2] G. W. Burr et al., IEEE Journal on Emerging and Selected Topics in Circuits and Systems, vol. 6, no. 2, pp. 146–162, 6 2016.
[3] C. Ruiz de Galarreta et al., Advanced Functional Materials, vol. 28, no. 10, p. 1704993, 3 2018.
[4] P. Hosseini, C. D. Wright, and H. Bhaskaran, Nature, vol. 511, no. 7508, pp. 206–211, 7 2014.
[5] M. Cotrufo et al., Nature Communications, vol. 15, no. 1, p. 4483, 5 2024.
[6] M. Wang et al., Advanced science, vol. 10, no. 6, 2204899, 2023.
[7] G. Yang et al., Light Sci Appl, vol. 14, art. no. 182, 2025.
[8] S. Kendall et al., Opt. Express, vol. 33, pp. 8971-8982, 2025.
[9] J. Demas et al., Optics Express, vol. 23, no. 22, pp. 28531-28545, 2015.
[10] J.C.A. Rocha, U.G. Būtaitė, J. Carpenter and D.B. Phillips Nature Communications, vol. **17**, art. no. 73, 2026.
[11] G. Soma et al., Nature Communications, vol. 16, art. no. 7744, 2025.

Broadband Optical Properties and Thermal Stability of Thermal Evaporated GST and GSST Thin Films for Reconfigurable Metalens Applications

J. M. Borlido[1,3*], R. Machado[1], B. S. Dores[1], J. A. Rodrigues[1,2], Filipa C. Mota[1,3], E. M. F. Vieira[1], Julien Legendre[4], Ioannis Draganidis[4], Georgia T. Papadakis[4], Diogo E. Aguiam[3], J.H. Correia[1,2]

[1]CMEMS – UMinho, University of Minho, 4800-058, Guimarães, Portugal
[2]LABBELS – Associate Laboratory, Braga, Guimarães, Portugal
[3]INL - International Iberian Nanotechnology Laboratory, Avenida Mestre José Veiga s/n, 4715-330 Braga, Portugal

[4]ICFO-Institut de Ciencies Fotoniques, The Barcelona Institute of Science and Technology, Castelldefels, Barcelona 08860, Spain
*Corresponding author: joao.borlido@cmems.uminho.pt

***Abstract*—GST and GSST enable tunable photonics but exhibit severe chemical and structural instability when uncapped at elevated temperatures. We quantify the magnitude of thickness, stoichiometry, crystallization, optical degradation in thermal evaporated GST and GSST films using EDX, XRD, topology, transmittance, and broadband ellipsometry, and discuss the implications for reconfigurable metalenses.**

***Keywords*— GSST, Phase-change materials, Ellipsometry**

I. Introduction

Phase-change materials such as Ge–Sb–Te (GST) and Se-doped GST (GSST) are central to tunable and reconfigurable photonic platforms due to their large refractive index contrast, reversible crystallization, and compatibility with thin-film processing. GSST, in particular, has emerged as a low-loss alternative to GST, offering improved transparency and broadband optical performance, making it highly attractive for metasurfaces, metalenses, and actively reconfigurable optical components.[1][2]

Despite these advantages, the chemical and structural stability of uncapped, thermal evaporated GST and GSST films at elevated temperatures remains insufficiently quantified. While encapsulation is commonly employed in device implementations, understanding the intrinsic environmental sensitivity of these alloys is critical for interpreting annealing-induced changes and for benchmarking material robustness. In particular, the magnitude of thickness loss, stoichiometry drift, often dominated by tellurium depletion, and crystallization pathway disruption at temperatures around 350 °C has not been systematically assessed for GSST compositions. [3][4]

Since photonic functionality depends critically on precise refractive index control across a broad spectral range, even moderate chemical instability can significantly impact device performance.

In this work, we investigate the environmental sensitivity of GST and GSST films by decoupling intrinsic thermal effects from oxygen-assisted degradation mechanisms. By correlating thickness evolution, chemical composition, crystallographic phase transitions, broadband transmittance, and spectroscopic ellipsometry, we assess how structural instability translates into changes in complex refractive index and ultimately affects the reliability of reconfigurable photonic and metalens platforms.

II. Methods

Thermal evaporated GST and GSST thin films with varying selenium content were deposited on optical substrates and subjected to post-deposition annealing at 200 °C and 350 °C under low-vacuum (LV) (10^{-2} mbar) and high-vacuum (HV) (10^{-5} mbar) conditions to decouple intrinsic thermal effects from oxygen-assisted degradation. Film thickness evolution was monitored to distinguish densification from material loss. Chemical composition changes were evaluated using energy-dispersive X-ray spectroscopy (EDX), while crystallographic phase transitions were characterized by X-ray diffraction (XRD). Optical performance was assessed through spectroscopic transmittance measurements. To directly quantify the broadband optical response, variable-angle spectroscopic ellipsometry was performed from 0.2 µm to 14 µm wavelength, enabling extraction of the complex refractive index (n and k) for both amorphous and crystalline states. Simulation of a metalens was done with FDTD and RCWA by

discretizing the phase map of a spherical lens into subwavelength lattices with GST/GSST nanostructures from a meta-atom library capable of 2π phase range. The nanostructures and their arrangement were tuned in order to allow for focusing performance in the amorphous and crystalline state, and therefore adaptive focus.

This comprehensive approach allows correlation of environmental stability, phase evolution, and broadband optical properties, providing a unified understanding of how chemical instability impacts reconfigurable photonic functionality.

III. Results and Discussion

Experimental results show:

- Up to ~66% thickness loss at 350 °C under LV (vs. ≤13% under HV)
- Degradation at 350 °C is oxygen-driven, not temperature-driven.
- Preferential Te depletion dominates chemical instability in low vacuum.
- HV allows for better hexagonal crystallization in GST and GSST
- Broadband ellipsometry show a 1.5 refractive index contrast for HV GST (Fig. 1).
- LV samples exhibit significant spatial and compositional heterogeneity, complicating reliable optical constant extraction.
- HV GST/GSST metalens simulation show a near diffraction limit performance.

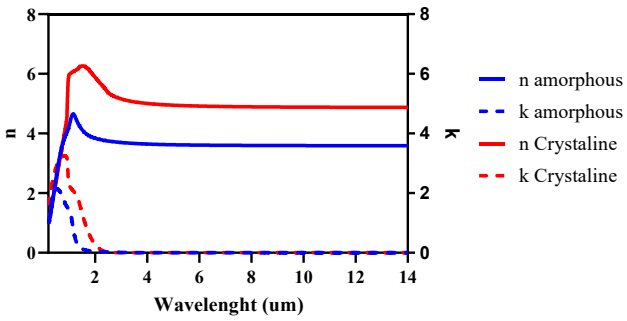

Fig. 1 Refractive index (n) and extinction coefficient (k) for HV GST

IV. Conclusion

We demonstrate that severe instability in uncapped, thermal evaporated GST and GSST films at 350 °C is predominantly oxygen-driven rather than thermally intrinsic. HV annealing preserves intrinsic crystallization behavior and enables reliable broadband refractive index extraction, directly impacting metalens performance. These findings establish quantitative stability limits for GST/GSST thin films and emphasize the necessity of environmental control for reconfigurable photonic applications operating at elevated temperatures.

Acknowledgments

This work was funded by the HORIZON-EIC Project BlueArray (grant 101130710),by the project 101217446 – POEMS supported by the Chips Joint Undertaking and its members, including top-up funding by FCT – Fundação para a Ciência e a Tecnologia, I.P, by CEX2024-001490-S (MICIU/AEI/10.13039/501100011033), the Spanish MICINN (PID2021-125441OA-I00, PID2020-112625GB-I00, and CEX2019-000910-S), the European Union (Fellowship No. LCF/BQ/PI21/11830019 under Marie Skłodowska-Curie Grant Agreement No. 847648 and CATHERINA, 101168064), and the Generalitat de Catalunya (2021 SGR 01443) through the CERCA program, Fundació Cellex, and Fundació Mir-Puig. I. D. was supported by Fundació "la Caixa" (Fellowship Code LCF/BQ/DFI25/130000, ID 100010434), J. M. Borlido thanks FCT for the PhD grant 2023.00645.BDANA.(https://doi.org/10.54499/2023.00645.BDANA) J. A. Rodrigues thanks FCT for his contract with reference2023.06261.CEECIND/CP2841/CT0011(https://doi.org/10.54499/2023.06261.CEECIND/CP2841/CT0011). E.M.F Vieira thanks FCT for her contract under the FCT Tenure program 1st edition.

References

[1] D. Sahoo and R. Naik, “GSST phase change materials and its utilization in optoelectronic devices: A review,” Mater. Res. Bull., vol. 148, p. 111679, Apr. 2022, doi: 10.1016/J.MATERRESBULL.2021.111679.

[2] M. Y. Shalaginov et al., “Reconfigurable all-dielectric metalens with diffraction-limited performance,” Nat. Commun. 2021 121, vol. 12, no. 1, pp. 1–8, Feb. 2021, doi: 10.1038/s41467-021-21440-9.

[3] Q. Gong, H. Jiang, M. Peterlechner, S. V. Divinski, and G. Wilde, “Tellurium self-diffusion in crystalline Ge2Sb2Te5 phase change material,” Acta Mater., vol. 289, no. 9, p. 120929, May 2025, doi: 10.1016/j.actamat.2025.120929.

[4] R. Golovchak et al., “Oxygen incorporation into GST phase-change memory matrix,” Appl. Surf. Sci., vol. 332, pp. 533–541, Mar. 2015, doi: 10.1016/J.APSUSC.2015.01.203.

Analysis of the fast dynamics of optical properties in phase change materials

Sebastian Walfort[1], Nils Holle[1], Julia Vehndel[1], Niklas Vollmar[1], Nils Weber[1], Joel Billermann[1], Martin Salinga[1,*]

[1]Institute of Materials Physics, University of Münster, Germany
*Corresponding author: martin.salinga@uni-muenster.de

***Abstract*— We resolved the entire switching cycle of a single-element phase change material (PCM) in optical pump-probe measurements with femtosecond resolution. Based on ab-initio simulations we revealed a complex multi-step process, where the intermediate transient states exhibit distinct optical properties with even larger contrasts than those observed between crystal and glass.**

***Keywords*— phase change materials, permittivity analysis, femtosecond resolution, density functional theory.**

I. Introduction

Where metamaterials or integrated photonics are based on phase change materials for their remanent permittivity contrast between amorphous and crystalline configurations, the transient path from one to the other deserves attention. Pure antimony is an attractive material choice due its extreme compositional simplicity.

II. Methods

Optical pump-probe measurements with femtosecond resolution are quantitatively described with a phenomenological model including thermalization of the hot electron–hole plasma, the formation of a quasi-equilibrium atomic structure with a lower distortion, coherent vibrational modes, strain waves due to thermal expansion, and heat dissipation into the surrounding. Atomistic simulations based on density functional theory are used to calculate structures, energy landscapes and optical spectra.

III. Results and Discussion

On ultrafast timescales, the excitation of charge carriers to antibonding states results in a shift in the quasi-equilibrium atomic structure towards a smaller Peierls distortion. Density functional theory calculations show that a small shift in distortion strongly influences the optical properties across the entire interband absorption region, from the visible to IR. As energy is transferred from the hot electron-hole system to the lattice, it melts after few picoseconds, initially transitioning to an undistorted, metallic liquid. Upon quenching, starting at around 600 K, it is again the formation of Peierls-like distortions that contributes decisively to the optical contrast that is observed on long timescales between crystal and glass.

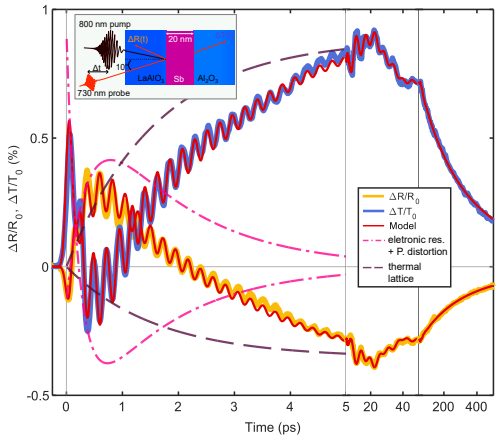

Fig. 1 The fast optical response to photo excitation resolved by pump-probe spectroscopy.

IV. Conclusion

It is evident that the switching of antimony involves multiple intricate processes through intermediate transient states. These states are characterized by distinct optical properties, with larger optical contrasts than the one usually exploited between the non-volatile crystalline and amorphous states of PCMs. For the application of PCMs as optical memory in tunable or reconfigurable photonics, setting a certain memory state is therefore inevitably accompanied by these orders of magnitude in time spanning dynamics. The provided quantitative understanding forms the basis for exploitation in high bandwidth photonic applications.

Acknowledgments

This work was partially funded by the Deutsche Forschungsgemeinschaft (DFG, German Research Foundation) – 566292984; 433682494.

References

[1] S. Walfort, et al., “The Photoinduced Response of Antimony from Femtoseconds to Minutes” *Adv. Mater.* 2025, *37*, 2414687.

A Fabrication-Friendly All-optical Integrated Photonic Phase-change Memory with Plasmonic Enhancement

Joe Pady[1*], Junchao Song[1], Emanuele Gemo[2], Joe Shields[1], Stuart Kendall[1], Nikolaos Farmakidis[1], Harish Bhaskaran[3], Ivonne Bente[4], Wolfram H. P. Pernice[4,5], C. David Wright[1]

[1] Department of Engineering, University of Exeter, Exeter, UK
[2] Department of Electronics and Telecommunications, Politecnico di Torino, Torino, Italy
[3] Department of Materials, University of Oxford, Oxford, UK
[4] Institute of Physics, University of Münster, Münster, Germany
[5] Kirchhoff-Institute for Physics, University of Heidelberg, Heidelberg, Germany
*Corresponding author: j.pady@exeter.ac.uk

***Abstract*— The optical characteristics and device switching properties of a fabrication-friendly all-optical, plasmonically-enhanced phase-change memory are investigated through both finite-element modelling and a bespoke phase-change computational model. Rapid and low-energy (16 pJ to 50 pJ) optical switching is numerically demonstrated, and device optical contrast is enhanced through cascading multiple plasmonic nanoantennas.**

***Keywords*— All-optical Memory, Plasmonic-enhancement, Phase-change Integrated Photonics, In-memory Computation.**

I. Introduction

It has previously been demonstrated that the use of electric field enhancing plasmonic resonant structures can improve the switching energies and speeds of all-optical integrated-photonic phase-change memories [1]. However, such designs required the precise fabrication of a pair of plasmonic dimer nanoantennas on top of a Si_3N_4 waveguide with a nanoscale region of $Ge_2Sb_2Te_5$ (GST) phase-change material deposited into the antenna gap region [1]. In this work, we present a simpler, more fabrication-friendly plasmonically enhanced phase-change memory cell, substantially relaxing fabrication constraints. In contrast to the prior dimer-gap design which requires nanoscale GST alignment, this configuration relies on the use of a comparatively large 500 x 500 nm patch of GST with thickness 10 nm deposited directly on the (1200 x 334 nm) waveguide, upon which Au plasmonic nanoantennas are fabricated (here with a width of 40 nm and thickness of 30 nm).

A schematic of the conventional (non-plasmonically enhanced) integrated phase-change photonic memory/computing cell is shown in Fig. 1a, while the original plasmonically enhanced version is shown in Fig. 1b. A schematic of the modified fabrication-friendly design is shown in Fig 1c: here, the gap region between the nanoantennas is 40 nm in size; also included is a 5 nm thick ITO barrier layer between the GST and Au bars to prevent interdiffusion.

Phase-change materials such as GST can exist in two distinct structural phases based on atomic ordering – the amorphous and crystalline states – which exhibit dramatically different optical properties: most notably here, the crystalline phase is significantly more absorbing at 1550 nm. Reversible switching between the two phases can be triggered by heating, therefore, optical switching and also reading of the device state can be carried out by optical pulses sent through the waveguide where the plasmonic resonance enhances the interaction between the GST and the propagating optical mode.

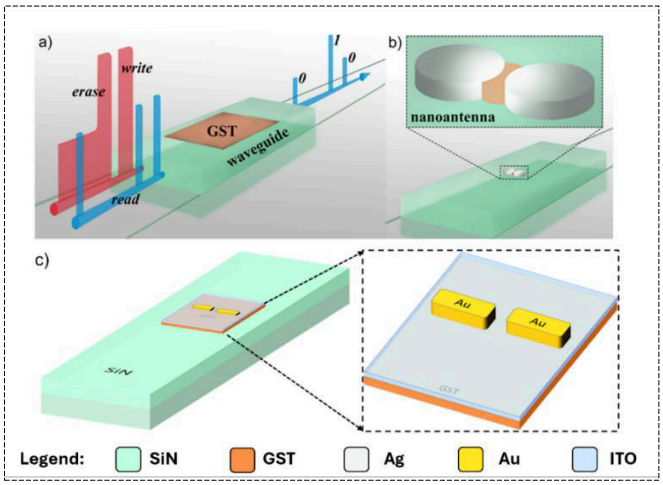

Fig. 1 Schematic of (a) the conventional integrated phase-change photonic memory/computing device, (b) the original all-optical plasmonically enhanced cell design (from [1]) and (c) the simplified fabrication-friendly all-optical plasmonically-enhanced device.

II. Methods

The optical performance and the switching characteristics of the cells are investigated through combined use of thermo-optic finite-element (FE) simulations [2] and a bespoke Gillespie algorithm-based phase-change model, already shown to accurately reproduce crystallisation dynamics in GST [3,4]. In the latter, the rates for crystal nucleation, growth and dissociation are taken from classical nucleation and growth theory and are applied across a computationally constructed grid of GST 'monomers' which represents the entire GST patch region within the device.

III. Results and Discussion

Using FE simulations, a very strong enhancement of the electric field can be observed between the Au nanoantennas for both GST phases when an optical pulse is sent through the waveguide (see Fig. 2a). When compared to the maximum electric field at the input, the central 50 x 50 nm region between the nanoantennas sees an electric field enhancement of up to 15–20 times for the amorphous phase and 4-5 times for the crystalline. This plasmonic enhancement triggers temperatures significant enough for crystallisation and amorphisation of the GST layer lying beneath the gap region of the nanoantennas. As the increase in temperature is very localised, only the GST within the gap region undergoes switching. Fig. 2b shows the device optical transmission contrast as a function of Au nanoantenna length assuming a central 50 x 50 nm region of GST between the bars switches. A maximum contrast of ~ 4.5% is achieved at bar length 185 nm.

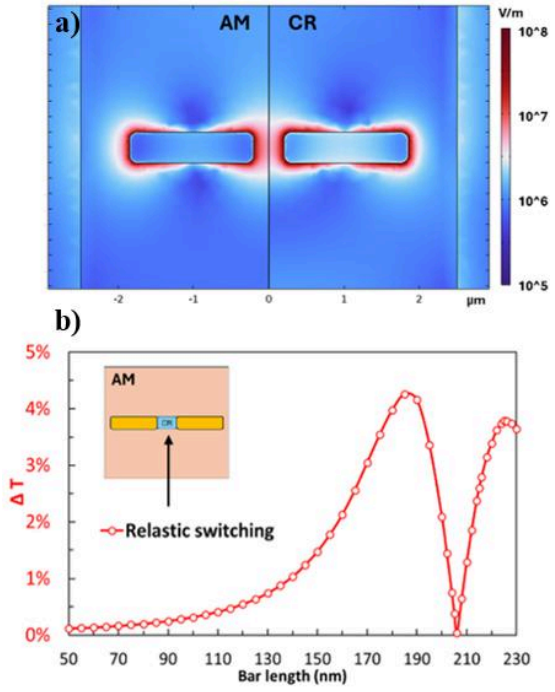

Fig. 2 a) Normalised E-field distributions within amorphous and crystalline GST. b) Optical contrast as a function of Au bar length assuming realistic switching (as seen in inset).

Using the previously described phase-change modelling techniques, reversible switching of the device is demonstrated. Starting in the fully amorphous phase, a train of 8 ns pulses with powers 2.8, 1.3, 1.2 and 0.95 mW at 1550 nm wavelength are applied to crystallise the GST in the gap region (multiple pulses are used to prevent unwanted melting of the GST as it crystallises). Re-amorphisation is achieved using a single 2.0 mW, 8 ns, 1550 nm pulse to melt and quench the material. Both crystallisation and amorphisation operations are shown in Fig. 3a,b respectively, here an optical contrast of ~4.5 % is achieved. The switching energies for the crystallisation and amorphisation are 50 pJ and 16 pJ respectively. These values are one order of magnitude smaller than those associated with conventional integrated photonic phase-change memory cell designs [5], and only slightly larger than the original - yet significantly more difficult to fabricate - plasmonically enhanced cell [1].

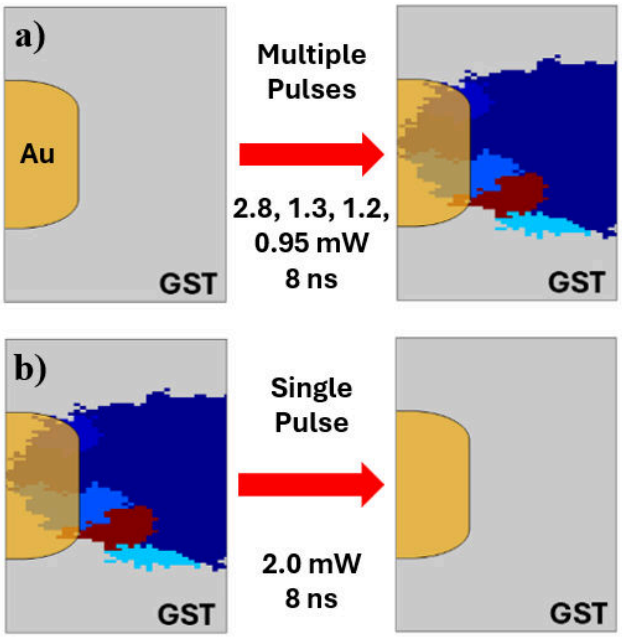

Fig. 3 a) Crystallisation and b) re-amorphisation of the phase-change cell (Coloured regions represent crystallite grains of different orientations, whereas grey is amorphous).

Finally, we look to enhance the relatively modest optical transmission contrast achieved in these devices. To do so the cascading of two pairs of plasmonic nanoantennas is investigated. Using FE simulations it was found that a maximum optical transmission contrast was seen at bar lengths of 185 nm (see inset of Fig. 4). An optimum separation between the two pairs of bars of 410 nm was determined. At this separation, both the maximum temperature and the temperature distributions in the GST are essentially identical in both gap regions, indicating that the switching behaviour should in turn be the same for both regions. For this thermally-optimum choice of antenna separation, the optical contrast is reduced slightly for the maximum achievable contrast, but still approaches a sizeable value of around 10%, as shown in Fig. 4.

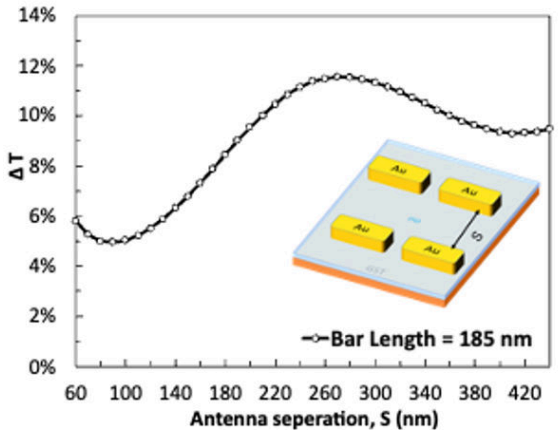

Fig. 4 Optical transmission contrast when two pairs of Au nanoantennas are cascaded on the GST patch.

IV. Conclusion

Simulations combining FE and phase-change models have demonstrated a fully rewriteable, simple-to-fabricate, all-optical, plasmonically enhanced phase-change memory cell with much improved switching properties as compared to conventional cells. Furthermore, the optical contrast can be enhanced through the cascading of plasmonic nanoantennas.

Acknowledgements

Funding is acknowledged from the EU Phoenics Project (101017237) and EPSRC's APT-NuCOM (EP/W022931/1) and MetaHUB (UKRI1255) grants

References

[1] E. Gemo, S. G.-C. Carillo, C. R. de Galarreta et al, "Plasmonically-enhanced all-optical integrated phase-change memory" Opt. Express, Vol. 27, No. 17, pp. 24724-24738, 2019.

[2] Z. Cheng, C. Ríos, N. Youngblood et al, "Device-Level Photonic Memories and Logic Applications Using Phase-Change Materials" Adv. Mater. Vol. 30, pp. 1802435, 2018.

[3] P. Ashwin, B. S. V. Patnaik and C. D. Wright "Fast simulation of phase-change processes in chalcogenide alloys using a Gillespie-type cellular automata approach" J. Appl. Phys. Vol. 104, No. 8, pp 084901, 2008.

[4] Y. Wang, J. Ning, L. Lu et al, "A scheme for simulating multi-level phase change photonics materials" npj Comput. Mater. Vol. 7, No. 183, 2021.

[5] C. Ríos, M. Stegmaier, P. Hosseini et al, "Integrated all-photonic non-volatile multi-level memory" Nat. Photonics, Vol. 9, pp. 725-732, 2015.

Self-Consistent Optical-Thermal Modeling of VO2 Nanoparticles for Tunable Photonic Applications

Peter Kepič[1,*], Jiří Kabát[1,2], Tereza Bačová[2], Filip Ligmajer[1,2]

[1]Brno University of Technology, Central European Institute of Technology, Brno, Czech Republic

[2] Brno University of Technology, Faculty of Mechanical Engineering, Brno, Czech Republic

*Corresponding author: peter.kepic@ceitec.vutbr.cz

***Abstract*— This study investigates the photothermal dynamics of VO2 nanostructures through numerical simulations. We identify "nonlinear ignition," where plasmonic resonance triggers a positive feedback loop, causing abrupt temperature and optical jumps at specific intensity thresholds. Additionally, we optimize VO2-integrated SiN waveguides, demonstrating high-performance on-chip modulation for energy-efficient photonic applications.**

***Keywords*— phase-change materials, vanadium dioxide, photonic integrated circuits.**

I. Introduction

Vanadium dioxide (VO2) is a phase-change material exhibiting an insulator-to-metal transition near 68 °C, accompanied by pronounced changes in refractive index and absorption. These properties make VO2 attractive for tunable and nonlinear photonic devices. In this work, we present results of numerical simulations of the optical properties of VO2 nanostructures, specifically accounting for the coupled dynamics of heat propagation and temperature-induced electromagnetic effects. We utilize an iterative convergence algorithm to solve for the steady-state temperature of VO2 nanospheres and nanodiscs. Our results reveal a phenomenon termed "nonlinear ignition": the onset of a localized surface plasmon resonance in the metallic phase creates a positive feedback loop between absorption and photothermal heating. This leads to an abrupt, step-like jump in temperature and optical state once a critical threshold intensity is reached. We demonstrate that this threshold is highly sensitive to the thermal bias and refractive index of the substrate. Furthermore, we analyze the integration of VO2 into hybrid silicon nitride (SiN) waveguides for on-chip amplitude modulation. Contrary to intuition, we find that a direct-contact configuration can be superior to designs utilizing low-index buffer layers. By optimizing the VO2 patch thickness, high extinction ratios can be achieved with manageable loss. This work establishes a robust framework for designing scalable, energy-efficient photonic devices based on the intrinsic thermodynamics of VO2.

II. Methods

Optical cross sections were calculated using the commercial software COMSOL Multiphysics, using the radio-frequency and heat transfer toolboxes. The electromagnetic wave geometry is embedded within a larger geometry to facilitate convergence in heat propagation. The nanoparticle is illuminated by a background wave, taking the Fresnel coefficients into account. Heat transfer simulation is performed in all domains. We solve the heat diffusion equation to obtain the temperature. We then couple the radio-frequency and heat-transfer toolboxes via Multiphysics coupling, with the dissipated electromagnetic power serving as a heat source. The simulation iterates until the steady-state temperature converges.

Semimetallic nanostructures as multifunctional materials for nanophotonics

Fernando Chacon-Sanchez[1*], J. Toudert[1] and R. Serna[1]

[1]Laser Processing Group, Instituto de Optica (IO-CSIC), Madrid, Spain
*Corresponding author: fernando.chacon@csic.es

***Abstract*— Bismuth and Antimony are semimetallic materials, that displays a versatility unmatched by most widespread materials for nanophotonics. It behaves as a plasmonic, high refractive index and phase change material simultaneously on different wavelengths. We will show the potential of Bi metasurfaces for structural coloring, sensing and photonics.**

***Keywords*— Bismuth, antimony, plasmonics, phase change materials, structural color.**

I. Introduction

Nanophotonics is an emergent field that has a constant need for new materials in order to access novel functionalities. On the field of plasmonics, gold and silver are widespread, on the high-refractive index in the infrared silicon is the standard, and for tunable metasurfaces GeSbTe and similar compounds are very extended. Bismuth (Bi) and Antimony (Sb) emerge as promising materials towards multifunctional metasurfaces, as they show a unique combination of optical and structural-thermodynamical properties. In particular they behave as ultra-high refractive index (n up to 10) materials in the IR, as plasmonic materials in the VIS-UV and as phase change materials (crystalline-amorphous for Sb and solid-liquid for Bi).

II. Results and Discussion

On this invited contribution, we will explore how these advantageous properties are originated due to their intense interband transitions in the NIR, and how their dielectric response (refractive index and absorption) is successfully manipulated by modifying the film morphology at the ultrathin regime.

We will review our recent results and show the applications on nanophotonics for semimetallic thin films and nanostructures. They are exceptionally suitable for structural coloring, by using either plasmonic or interferential approaches [1], and extending this interferential approach they enable sustainable and efficient coloring of industrial materials [2]. We will show their capabilities to display subwavelength perfect absorption, both on the IR [3] and in the VIS, and we will evaluate their sensing potential. Finally, we will focus on the solid-liquid phase transition of Bi, designing metasurfaces where we tune the fraction of molten Bi to control the polarization of reflected light [4]. These metasurfaces can also display sub-ns melting upon laser irradiation, displaying great potential for optical switching [5].

Acknowledgments

This work was supported by the projects ALPHOMENA (PID2021-123190OB-I00f), SLIM-2P (PID2024-156974OB-C21), funded by MCIN/AEI/10.13039/501100011033 and by the European Union NextGenerationEU/PRTR and the European Regional Development Fund (ERDF), and the MaXCSIC Excellence Award (SYNERGY-IO/03 project)

References

[1] F. Chacon-Sanchez, C.R. de Galarreta, E. Nieto-Pinero, M. Garcia-Pardo, E. Garcia-Tabares, N. Ramos, M. Castillo, M. Lopez-Garcia, J. Siegel, J. Toudert, C.D. Wright, and R. Serna, Adv Opt Mater 12(10), 2302130 (2024).

[2] F. Chacon-Sanchez, and R. Serna, ACS Applied Optical Materials 3(3), 727–736 (2025).

[3] J. Toudert, R. Serna, M.G. Pardo, N. Ramos, R.J. Peláez, and B. Maté, Opt Express 26(26), 34043 (2018).

[4] M. Garcia-Pardo, E. Nieto-Pinero, A. K. Petford-Long, R. Serna and J. Toudert Nanophotonics 9 (2020) 885–896.

[5] M. Alvarez-Alegria, J. Siegel, M. Garcia-Pardo, F. Cabello, J. Toudert, E. Haro-Poniatowski, and R. Serna, Adv Opt Mater 10(3), (2022).

Phase transitions for tunable nanophononics

Sandeep Sathyan[1*], Ornella Colmegna[1], Helmut Karl[2], Sébastien Cueff [3], Norberto Daniel Lanzillotti-Kimura[1]

[1]Université Paris-Saclay, CNRS, Centre de Nanosciences et de Nanotechnologies, 10 Boulevard Thomas Gobert, 91120 Palaiseau, France
[2]Lehrstuhl für Experimentalphysik IV, Universität Augsburg, 86159 Augsburg, Germany
[3]CNRS, Ecole Centrale de Lyon, INSA Lyon, Universite Claude Bernard Lyon 1, CPE Lyon, INL, UMR5270, 69130 Ecully, France
*Corresponding author: sandeep.sathyan@c2n.upsaclay.fr

Keywords -acoustic phonons, nanophononic platform, phase-transition materials; tunable nanoacoustics

Acoustic phonons govern fundamental solid-state properties through their direct coupling to atomic displacements, strain fields, and elastic energy transport. Recent advances in nanophononics have enabled the confinement and manipulation of GHz–THz acoustic modes in semiconductor and oxide multilayers, including acoustic nanocavities and opto-phononic micropillars[1]. However, most demonstrated nanoacoustic devices rely on static architectures with predetermined functionality. Introducing tunability into nanoacoustic systems remains a central challenge. A promising strategy consists in integrating responsive phase-transition materials whose elastic properties can be modified by external stimuli. Among such materials, vanadium dioxide (VO_2) is particularly attractive due to the significant structural reorganization occurring during its reversible transition between monoclinic and rutile crystalline phases, accompanied by the well-known insulator–metal transition.

Here, we experimentally investigate the dynamics of coherent GHz acoustic phonons in thin VO_2 films using ultrafast pump–probe transient reflectivity measurements. By thermally driving the material across the phase transition, we systematically compare the acoustic response in the insulating and metallic phases. The time-domain measurements, together with their Fourier analysis, reveal clear changes in both the temporal dynamics and the acoustic frequencies, indicating phase-dependent modifications of the interaction mechanisms governing the coherent acoustic response. Simple theoretical simulations further identify the origins of these differences and support the experimental observations. These results motivate the design of advanced hybrid nanoacoustic heterostructures integrating phase-transition materials within distributed Bragg reflector cavities and micropillar resonators. Such systems can enable tunable acoustic resonators through dynamic cavity switching, as well as reconfigurable phononic networks operating in the GHz regime. Beyond fundamental studies, this approach paves the way toward nanoacoustic sensing technologies and programmable optoacoustic nanodevices.

[1] Priya, E.R. Cardozo de Oliveira, N.D. Lanzillotti-Kimura, Perspectives on high-frequency nanomechanics, nanoacoustics, and nanophononics, Appl Phys Lett. 122 (2023).

Nanoresonators and metasurfaces for nonreciprocal photonics

Sergey Kruk

[1]Faculty of Engineering and Natural Sciences, Tampere University, Finland
[2]School of Mathematical and Physical Sciences, University of Technology Sydney, Australia
*sergey.kruk@outlook.com

***Abstract*— Nonreciprocity underpins signal routing in modern technology. While nonreciprocal electronic components – diodes, transistors – have been miniaturized to the nanoscale, nonreciprocal photonics remains bulky. We develop pathways to nonreciprocal control of light at the nanoscale, enabling compact manipulation of amplitude, phase, and polarization, and opening new opportunities for integrated photonic systems.**

***Keywords*— metasurfaces, nonreciprocity, nonlinear photonics, phase change materials, epsilon-near-zero materials.**

I. Introduction

Contemporary optics is experiencing rapid advancements driven by nanotechnology. We can now mass-produce optical components that are hundreds of times thinner than a human hair, yet these components outperform conventional, bulky optical devices [1]. One crucial unresolved challenge in modern optics is how to achieve nonreciprocity at the nanoscale [2].

Nonreciprocity in a system means that the transmission of signals differs when the positions of the sources and detectors are swapped. This phenomenon is essential for controlling signal traffic and is vital in both optics and electronics. In electronics, tiny nonreciprocal components like diodes and transistors are common and indispensable. In optics, nonreciprocal components, like isolators and circulators, are much larger than their electronic counterparts, and much more expensive.

II. Results and Discussion

We present several approaches to achieving optical nonreciprocity at the nanoscale [3,4]. The building blocks are dielectric Mie-type nanoresonators hybridized with strongly nonlinear materials such as epsilon-near-zero materials [3] and phase-change materials [4].

Nonreciprocity achieved with this approach is passive, requiring no external bias. We demonstrated broadband nonreciprocal transmission covering over 100 nm in the telecommunication range (around $\lambda = 1.5$ μm). Moreover, nonreciprocity was observed down to modest light intensities of about 150 W/cm², comparable to the power density of a laser pointer. The first-generation nonreciprocal nanoresonators designed to work as isolators demonstrated

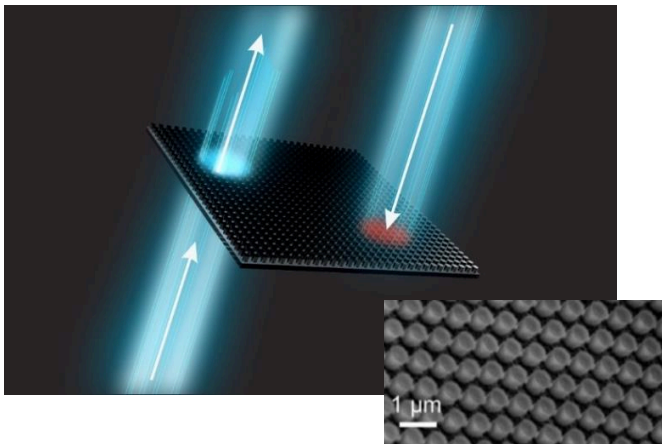

Optical isolation by a metasurface. Inset – electron microscope image of the nano-resonators.

15 dB isolation in simulations and approximately 5× isolation in experimental tests with estimated transmission fall time of 100 ps and a transmission rise time on the order of 100 ns.

We will discuss expansion of nonreciprocal nanophotonics from control of transmission amplitudes (like in isolators and circulators) to nonreciprocal control over phase and wavefront, polarization and other parameters of light.

Bias-free nanoscale nonreciprocal optics controlling forward-to-backward ratios of amplitude, phase and polarization will enable conceptually new optical components with independent pairs of on-demand functionalities for forward vs backward directions of light propagation.

Acknowledgments

This work was supported by the Australian Research Council (grant DE210100679), the EU Horizon 2020 Research and Innovation Program (grant 896735) and the Australia-Germany Joint Research Cooperation Scheme (Grant 57692192)..

References

[1] Kruk, S. S. et al., ACS Photon. 4, 2638 (2017)
[2] Asadchy, V. S. et al., Proc. IEEE 108, 1684 (2020)
[3] Tripathi, A. et al., Nat Commun. 15, 5077 (2024)
[4] Mathew, A. et al., Nano Lett. 25, 8, 3259–3264 (2025)

Canalization-based super-resolution imaging using an individual van der Waals thin layer

Jiahua Duan[1,2,3,4*†], Aitana Tarazaga Martín-Luengo[3*†], Christian Lanza[3†], Stefan Partel[5], Kirill Voronin[6], Ana Isabel F. Tresguerres-Mata[3], Gonzalo Álvarez-Pérez[3,4,7], Alexey Y. Nikitin[6,8], Javier Martín-Sánchez[3,4], Pablo Alonso-González[3,4*] † These authors contributed

[1] Centre for Quantum Physics, Key Laboratory of Advanced Optoelectronic Quantum Architecture and Measurement (MOE), School of Physics, Beijing Institute of Technology, Beijing, China / [2] Beijing Key Laboratory of Nanophotonics and Ultrafine Optoelectronic Systems, Beijing Institute of Technology, Beijing, China / [3] Department of Physics, University of Oviedo, Oviedo, Spain / [4] Center of Research on Nanomaterials and Nanotechnology, CINN (CSIC–Universidad de Oviedo), El Entrego, Spain / [5] Vorarlberg University of Applied Sciences, Research Center of Microtechnology, Dornbirn, Austria / [6] Donostia International Physics Center (DIPC), Donostia–San Sebastian, Spain [7] Computational Nanoplasmonics group, Center for Biomolecular Nanotechnologies, Istituto Italiano di Tecnologia, Arnesano (LE), Italy / [8] IKERBASQUE, Basque Foundation for Science, Bilbao, Spain

*Corresponding authors: duanjiahua@bit.edu.cn, aitanatarazaga@uniovi.es, pabloalonso@uniovi.es

***Keywords*— canalization, phonon polaritons, α-MoO$_3$, super-resolution imaging, s-SNOM.**

I. Introduction

Phonon-polariton (PhP) canalization is diffractionless transport enabled by flattened isofrequency contours (IFC), previously realized with twisted multilayers at selected angles [1–5]. We show [6] that stacks are unnecessary, engineering the substrate permittivity to an optimal negative value that flattens α-MoO$_3$ PhPs in a single layer on SiC, enabling shiftable $\sim\lambda_0/220$ imaging.

II. Methods

Design metric and variables. At a fixed optical frequency ω (cm^{-1}), the in-plane PhP wavevector $q(\omega,\varphi)$, where φ is the propagation angle in the flake plane with respect to a chosen laboratory axis x (the [100] α-MoO$_3$ crystal direction). The IFC is the curve in q-space containing all allowed q at fixed ω. Canalization corresponds to a locally flat IFC, meaning that the longitudinal wavevector component $q_x(\omega,\varphi)$, varies weakly with φ. We quantify this with the flatness factor $F(\omega) = dq_x/d\varphi$. Canalization corresponds to $|F| \approx 0$ over the relevant angular range.

Substrate-permittivity engineering. The α-MoO$_3$ layer is described by its anisotropic permittivity tensor components $\varepsilon_x, \varepsilon_y, \varepsilon_z$ along the crystallographic axes [100], [001], [010], respectively. The substrate is described by a complex permittivity $\varepsilon_{sub}(\omega) = \varepsilon'_{sub}(\omega) + i\varepsilon''_{sub}(\omega)$. From the analytical dispersion of the relevant polaritonic mode, we obtain an "optimal" substrate permittivity $\varepsilon_{optimal}$, with $\varepsilon'_{optimal} < 0$, that minimizes $|F|$, then we select a practical substrate whose ε_{sub} best matches this value across the target band (SiC in this work).

Modeling and extracted quantities. Full-wave simulations are used to compute near-field maps for realistic excitations (dipole and antenna launchers), for a given α-MoO$_3$ thickness d, substrate $\varepsilon_{sub}(\omega)$, and the in-plane azimuthal orientation angle θ of the crystal with respect to the laboratory axis or object/antenna axis. From simulated and measured interference fringes we extract $Re(q_x)$, the PhP wavelength $\lambda_{PhP} = 2\pi/Re(q_x)$, and the free-space wavelength $\lambda_0 = 2\pi c/\omega$. The propagation length L_p is defined as the 1/e decay length of the near-field amplitude envelope along x. The group velocity is obtained from the dispersion as $v_g = \partial\omega/\partial Re(q_x)$, and the PhP lifetime is estimated as $\tau \approx L_p/v_g$.

Experiments and imaging. α-MoO$_3$ flakes (thickness d from AFM) are transferred onto SiC and control substrates, Au nanoantennas launch phonon polaritons, and s-SNOM maps amplitude and phase. For nanoimaging, buried Au nanodisks are covered by α-MoO$_3$/SiC, and the reconstructed top-surface near field is analyzed as a super-resolved image whose lateral displacement Δ from the object's vertical projection is tuned by ω, d and θ.

III. Results and Discussion

1- **Substrate-engineered single-layer canalization**. Matching $\varepsilon_{sub}(\omega)$ to an analytically identified $\varepsilon_{optimal}(\omega)$, with negative $\varepsilon'_{optimal}(\omega)$, tlattens the α-MoO$_3$ IFC, making q_x nearly invariant with φ, this produces diffractionaless, strongly collimated propagation in a single unpatterned layer, avoiding twisted stacks and angle-specific "magic" conditions.

2- **Practical realization with SiC, broadband and low**

loss. SiC provides $\varepsilon_{sub}(\omega)$ close to $\varepsilon_{optimal}(\omega)$ in the relevant Reststrahlen band, yielding a canalization window of about 50 cm^{-1} (~850-900 cm^{-1}). From near-field dispersion measurements, $v_g \cong 10^{-3}c$ at 877 cm^{-1}, and combining v_g with the measured L_p gives PhP lifetimes of about 2 ps.

3- **Super-resolution imaging of buried nanostructures.** In the canalization regime, high-spatial-frequency (evanescent) information is transported with minimal diffraction, enabling imaging of buried Au disks. At ω_0= 885 cm^{-1}, disks separated by 50 nm (edge-to-edge) are resolved, corresponding to $\sim\lambda_0/220$.

4- **Shiftable imaging controlled by ω, d and θ** . The super-resolved image is laterally displaced from the vertical projection and can be repositioned by tuning ω_0, using different layer thickness d, and choosing a different azimuthal orientation θ. The frequency dependence is demonstrated for two devices with $d_1 =$ 415 nm and $d_2 = 340$ nm, showing tunable separation between image replicas as ω_0 varies.

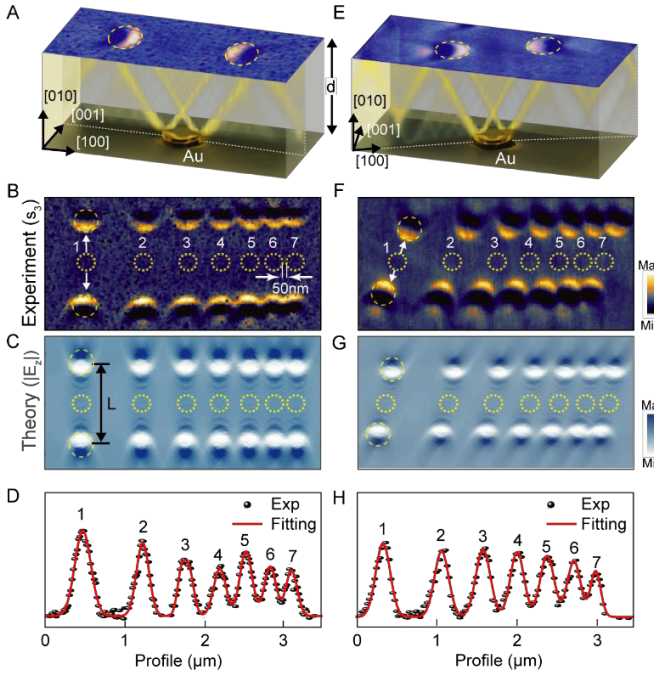

Fig. 1 Shiftable canalization-based super-resolution imaging through a single α-MoO_3 layer on SiC. Schematics (A,E), experimental and simulated s-SNOM near-field maps of buried Au nanodisks resolving 50-nm gaps (B,C,F,G), and corresponding line profiles with fits (D,H).

IV. Conclusion

Canalization is achieved in a single α-MoO_3 van der Waals layer by engineering the substrate permittivity to a suitable negative value, removing the need for complex twisted multilayers and finely selected twist angles. The resulting canalized PhPs are broadband (~50 cm^{-1}), slow ($v_g \cong 10^{-3}c$), and low-loss ($\tau \cong 2$ ps), enabling a shiftable superlens that resolves buried features down to $\sim\lambda_0/220$, with image placement controlled by ω, d and θ.

Acknowledgments

Funding: J.D. acknowledges Beijing Natural Science Foundation (Z240005) and NSFC (12474027). A.I.F.T.-M. and G.Á.-P. acknowledge the Severo Ochoa program of the Government of the Principality of Asturias (PA-21-PF-BP20-117 and PA-20-PF-BP19-053). J.M.-S. acknowledges PID2023-148457NB-I00 (MCIU/AEI/FEDER) and PCI2022-132953 (MCIN/AEI and EU NextGenerationEU/PRTR). P.A.-G. acknowledges ERC Starting Grant 101044461 (TWISTOPTICS) and PID2022-141304NB-I00. A.Y.N. acknowledges PID2020-115221GB-C42, PID2023-147676NB-I00, and Basque Government grants PIBA-2020-1-0014 and PIBA-2023-1-0007. K.V. acknowledges "la Caixa" Foundation fellowship LCF/BQ/DI21/11860026..

References

[1] G. Hu, Q. Ou, G. Si, Y. Wu, J. Wu, Z. Dai, A. Krasnok, Y. Mazor, Q. Zhang, Q. Bao, C. W. Qiu, and A. Alù, "Topological polaritons and photonic magic angles in twisted α-MoO_3 bilayers," Nature, vol. 582, no. 7811, pp. 209–213, 2020.

[2] J. Duan, N. Capote-Robayna, J. Taboada-Gutiérrez, G. Álvarez-Pérez, I. Prieto, J. Martín-Sánchez, A. Y. Nikitin, and P. Alonso-González, "Twisted Nano-Optics: Manipulating Light at the Nanoscale with Twisted Phonon Polaritonic Slabs," Nano Letters, vol. 20, no. 7, pp. 5323–5329, 2020.

[3] Z. Zheng, F. Sun, W. Huang, J. Jiang, R. Zhan, Y. Ke, H. Chen, and S. Deng, "Phonon Polaritons in Twisted Double-Layers of Hyperbolic van der Waals Crystals," Nano Letters, vol. 20, no. 7, pp. 5301–5308, 2020.

[4] M. Chen, X. Lin, T. H. Dinh, Z. Zheng, J. Shen, Q. Ma, H. Chen, P. Jarillo-Herrero, and S. Dai, "Configurable phonon polaritons in twisted α-MoO_3" Nature Materials, vol. 19, no. 12, pp. 1307–1311, 2020.

[5] J. Duan, G. Álvarez-Pérez, C. Lanza, K. Voronin, A. I. F. Tresguerres-Mata, N. Capote-Robayna, J. Álvarez-Cuervo, A. Tarazaga Martín-Luengo, J. Martín-Sánchez, V. S. Volkov, A. Y. Nikitin, and P. Alonso-González, "Multiple and spectrally robust photonic magic angles in reconfigurable α-MoO_3 trilayers," Nature Materials, vol. 22, no. 7, pp. 867–872, 2023.

[6] J. Duan, A. Tarazaga Martín-Luengo, C. Lanza, S. Partel, K. Voronin, A. I. F. Tresguerres-Mata, G. Álvarez-Pérez, A. Y. Nikitin, J. Martín-Sánchez, and P. Alonso-González, "Canalization-based super-resolution imaging using an individual van der Waals thin layer," Science Advances, vol. 11, Art. no. eads0569, 2025

Room-temperature zero differential thermal emitters enabled by the controllable metal-insulator transition in rare-earth perovskite nickelates

Luigi Matera[1], Laurent Divay[2], Luis Moreno Vicente-Arche[1], Manuel Bibes[1], Paolo Bortolotti[1], Julian Peiro[1,*], Lucía Iglesias[1,*]

[1]Laboratoire Albert Fert, CNRS, Thales, Université Paris-Saclay, 91767 Palaiseau, France
[2]Thales Research and Technology, Campus Polytech, 1 Avenue Augustin Fresnel, 91767 Palaiseau, France
*Corresponding author: julian.peiro@cnrs-thales.fr, lucia.iglesias@cnrs-thales.fr

***Abstract*—In this work, we present room temperature zero differential thermal emitters based on strained Sm 1-x Nd x NiO3 thin films. By engineering the metal insulator transition, we obtain nearly constant long wavelength infrared emission over about 15 degrees Celsius, confirmed by outdoor thermal imaging experiments.**

***Keywords*— camouflage, infrared, LWIR, nickelates.**

I. Introduction

All objects at temperatures above absolute zero emit thermal radiation. For an ideal black body, the emitted spectral radiance is described by Planck's law, and the total radiated power follows the Stefan–Boltzmann relation, scaling as T^4. Real materials deviate from this ideal behavior through their emissivity, which depends on wavelength, angle, and temperature. While emissivity is often weakly temperature dependent, materials undergoing phase transitions can exhibit strong and abrupt variations in their optical properties, enabling control of thermal radiation. Such control is attractive for applications including spacecraft thermal management, energy harvesting, and thermal camouflage. An appealing concept for thermal camouflage is that of zero-differential thermal emitters (ZDTEs), whose radiated power remains nearly constant over a finite temperature range. This condition requires compensating the intrinsic T^4 increase of blackbody emission with a temperature-dependent emissivity. In practice, this can be achieved in materials displaying metal–insulator transitions (MITs), where large and reversible changes in optical properties occur. To date, most ZDTE demonstrations rely on VO_2 [1], whose sharp transition and pronounced hysteresis require careful compositional and structural engineering to achieve gradual emissivity modulation, motivating the search for alternative material platforms. Rare-earth perovskite nickelates, $RNiO_3$, offer a compelling alternative due to their chemically tunable MIT spanning a wide temperature range [2]. Their reversible changes in optical properties have already enabled ZDTE demonstrations in $SmNiO_3$ [3], [4]. Furthermore, alloying with $NdNiO_3$ allows continuous tuning of the transition temperature [5]. In this work, we investigate the MIT in $Sm_{1-x}Nd_xNiO_3$ thin films and demonstrate how compositional engineering enables ZDTE behavior in the long-wave infrared (8–14 μm), a spectral range relevant to atmospheric transmission and uncooled thermal imaging systems.

II. Methods

Perovskite nickelate thin films were synthesized using Pulsed Laser Deposition, allowing precise control over composition and thickness. To ensure optimal structural properties, X-Ray Diffraction pattern were measured. The electrical behavior of the films was characterized using transport measurements, revealing the temperature-dependent metal-insulator transition. Optical properties were investigated through Fourier-transform infrared spectroscopy, providing insight into the films' temperature-dependent optical response. In addition, outdoor thermal imaging measurements were performed to directly visualize the films' infrared emission and assess their thermal behavior under controlled heating, **Fig.1**.

III. Results and Discussion

In this work, we fabricated two ZDTE: ZDTE-1, a film of $Sm_{0.85}Nd_{0.15}NiO_3$ and ZDTE-2, a film of $Sm_{0.75}Nd_{0.25}NiO_3$; both grown on (001)-oriented $LaAlO_3$ substrates. During the MIT, the films undergo large changes in infrared reflectivity, which compensates for the temperature-dependent increase in blackbody emission, resulting in a nearly constant radiated power in the LWIR range. Infrared imaging under outdoor conditions demonstrates that the ZDTE films significantly reduce the apparent thermal contrast compared to the bare substrate, effectively masking temperature variations, **Fig.1**. These results illustrate that rare-earth nickelate films can act as single-layer thermal camouflage coatings, with their optical and electronic properties tuned via composition to achieve near-constant LWIR emission under ambient conditions.

IV. Conclusion

In this work, we demonstrated room-temperature zero differential thermal emitters based on the metal-insulator transition of rare-earth perovskite nickelates. Exploiting the modulation of infrared optical properties, we realized ZDTEs operating in

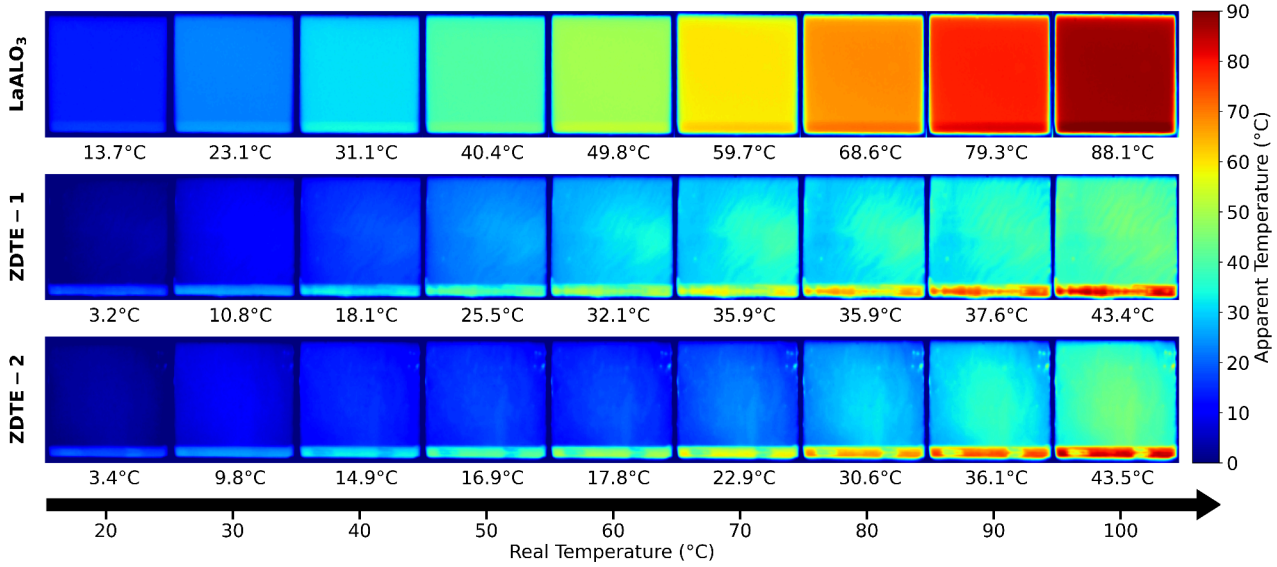

Fig. 1. Long-wavelength infrared (LWIR) images of nickelate samples held at temperatures from 20 to 100 °C (real temperature indicated by the bottom black arrow). The thermal camera was calibrated by using a black body (not shown here). To reduce reflections from surrounding objects, the experiments were conducted outdoors under a clear sky. The first row shows thermal camera images of the bare (001)-oriented $LaAlO_3$ substrate. The second and third rows show two different ZDTEs: ZDTE-1, a film of $Sm_{0.85}Nd_{0.15}NiO_3$ and ZDTE-2, a film of $Sm_{0.75}Nd_{0.25}NiO_3$; both grown on (001)-oriented $LaAlO_3$ substrates. The emissivity of the ZDTEs films decreases with increasing temperature, effectively masking variations in the real temperature as seen by the thermal camera (apparent temperature is indicated below each image). The lower part of each ZDTE image corresponds to the exposed substrate, which exhibits a higher apparent temperature, consistent with the bare substrate.

the long-wavelength infrared band, whose emissivity decreases as T^{-4}, compensating the intrinsic T^4 increase of blackbody radiated power. As a result, the LWIR radiated power remains nearly constant over a temperature range of approximately $15\,^{\circ}\mathrm{C}$, effectively masking real temperature variations, as confirmed by outdoor thermal imaging experiments. Beyond demonstrating room-temperature ZDTEs, this study establishes rare-earth nickelates as a versatile material platform for adaptive thermal emission control. More generally, the strong coupling between electronic correlations, lattice structure and optical properties in nickelates offers promising opportunities for next-generation dynamic thermal photonic devices, including tunable coatings for thermal management, infrared camouflage, and adaptive photonic applications.

References

[1] K. Tang, X. Wang, K. Dong, Y. Li, J. Li, B. Sun, X. Zhang, C. Dames, C. Qiu, J. Yao, and J. Wu, A Thermal Radiation Modulation Platform by Emissivity Engineering with Graded Metal–Insulator Transition, Advanced Materials 32, 1907071 (2020).

[2] S. Catalano, M. Gibert, J. Fowlie, J. Iniguez, J.-M. Triscone, and J. Kreisel, Rare-earth nickelates R NiO3 : Thin films and heterostructures, Reports on Progress in Physics 81, 046501 (2018).

[3] A. Shahsafi, P. Roney, Y. Zhou, Z. Zhang, Y. Xiao, C. Wan, R. Wambold, J. Salman, Z. Yu, J. Li, J. T. Sadowski, R. Comin, S. Ramanathan, and M. A. Kats, Temperature-independent thermal radiation, Proceedings of the National Academy of Sciences 116, 26402 (2019).

[4] J. L. King, A. Shahsafi, Z. Zhang, C. Wan, Y. Xiao, C. Huang, Y. Sun, P. J. Roney, S. Ramanathan, and M. A. Kats, Wavelength-by-Wavelength Temperature-Independent Thermal Radiation Utilizing an Insulator–Metal Transition, ACS Photonics 9, 2742 (2022).

[5] A. Ambrosini and J.-F. Hamet, Sm x Nd 1-x NiO 3 thin-film solid solutions with tunable metal–insulator transition synthesized by alternate-target pulsed-laser deposition, Applied Physics Letters 82, 727 (2003).

Coherent Spin–Photon Interfaces based on Molecular Rare-Earth Systems

Diana Serrano

[1]Institut de Recherche de Chimie Paris, Chimie ParisTech, CNRS, PSL University, 75005 Paris, France

*Corresponding author: diana.serrano@chimieparistech.psl.eu

***Abstract*—Rare-earth ions (REIs) are promising candidates for quantum hardware owing to their optically addressable, highly coherent spin states. Integrating these properties into scalable quantum architectures, however, remains challenging. Here, we introduce REI-based molecular materials that combine long optical and spin coherence with the synthetic versatility of coordination chemistry.**

***Keywords*— rare-earth ions, molecular materials, spin-photon interfaces, coherent spectroscopy.**

I. Introduction

Molecular systems that combine electron and/or nuclear spin states with optical transitions constitute a promising platform for quantum spin–photon interfaces. Their appeal lies in the atomically precise structure of molecules and the virtually unlimited diversity of accessible chemical compositions. By exploiting rational molecular design, both optical and spin properties can be finely tuned, enabling the development of optically addressable spin qubits, quantum transducers, optical quantum memories, and sensors [1].

Among optically active molecular systems, rare-earth ion (REI) complexes are particularly attractive, exhibiting record-narrow optical linewidths together with well-defined spin degrees of freedom. In this contribution, we review the major results reported for Eu(III) complexes [2,3] and present recent advances achieved through improved sample fabrication and coherent spectroscopic investigations. These studies allow us to elucidate the microscopic mechanisms that determine the Eu^{3+} homogeneous optical linewidth, including the roles of structural disorder and spin–environment interactions, which ultimately limit optical coherence in molecular REI materials.

II. Methods

A key figure of merit for quantum photonic applications is the homogeneous optical linewidth (Γ_h), which determines the optical coherence time (T_2) and ultimately sets the performance of spin–photon interfaces and quantum memories.

We have developed dedicated high-resolution spectroscopic methods to accurately determine Γ_h in challenging sample formats, including crystalline powders and thin films. These approaches enable reliable extraction of optical coherence properties beyond conventional bulk single-crystal measurements. We apply these techniques to a series of molecular crystals incorporating Eu^{3+} ions (Figure 1), allowing us to directly evaluate the impact of molecular design, local coordination symmetry, and solid-state organization on optical coherence.

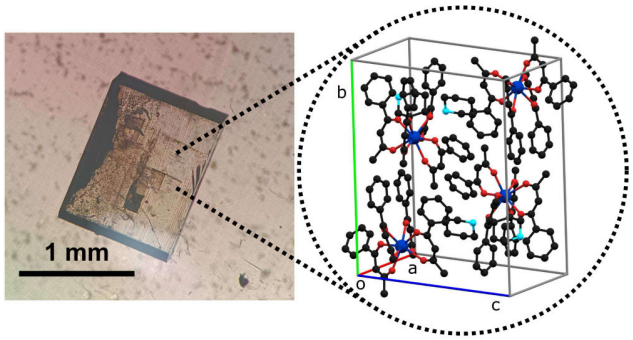

Fig. 1 High-quality molecular crystal of $Eu(BA)_4(pip)$

III. Results and Discussion

The optical homogeneous linewidth of Eu^{3+} has been investigated in two molecular crystals, $Eu(BA)_4(pip)$ and Eu(TMHD)(phen), as a function of temperature, waiting time, and average Eu–Eu distance. Detailed spectroscopic analysis reveals that, in the zero-temperature limit, Γ_h is not fundamentally limited by ion–ion interactions or magnetic noise. Instead, it remains strongly dependent on crystalline quality, highlighting the critical role of structural disorder and defects.

Nevertheless, the measured Γ_h values—reaching the tens of kHz range—are sufficiently narrow to enable optical addressing of nuclear spin levels and the demonstration of optical quantum storage. These results establish quantitative benchmarks for molecular REI systems in the context of quantum photonics.

Ongoing efforts toward robust and reproducible fabrication protocols for defect-minimized molecular REI materials, as well as controlled sample shaping for photonic integration, will also be discussed.

IV. Conclusion

REI-based molecular materials constitute an emerging platform for coherent spin-photon interfaces. In particular, Eu^{3+} complexes stand out for their exceptionally narrow optical linewidths in the tens of kHz range, enabling optical spin polarization and optical quantum storage. Continued advances in material quality and device integration are expected to further position molecular REI systems as scalable building blocks for quantum technologies.

Acknowledgments

This work received government funding managed by the French National Research Agency under grants ANR-20-CE09-0022-01 (UltraNanoSpec), and ANR-23-CE47-0011 (MoleQuBe) as well as under France 2030, reference ANR-23-PETQ-0007.

References

[1] S.K. Kuppusamy, D. Hunger, M. Ruben, P. Goldner, D. Serrano, "Spin-bearing molecules as optically addressable platforms for quantum technologies," Nanophotonics, vol. 13, pp. 4357–4379, 2024.

[2] K. S. Kumar, D. Serrano, A. M. Nonat, B. Heinrich, L. Karmazin, L. J. Charbonnière, P. Goldner, M. Ruben, "Optical spin-state polarization in a binuclear europium complex towards molecule-based coherent light-spin interfaces," Nat. Commun, vol. 12, pp. 2152, 2021.

[3] D. Serrano, S. K. Kuppusamy, B. Heinrich, O. Fuhr, O., D. Hunger, M. Ruben, P. Goldner, "Ultra-narrow optical linewidths in rare-earth molecular crystals," Nature, vol. 603, pp. 241–246, 2022.

The Old Brewster Effect Meets New Phase-Change Materials for Optical Switching

G. Santos[1,†], D. Pérez-Francés[1,†], J. Resl[2], M. Losurdo[3], Y. Gutiérrez[1] and F. Moreno[1,*]

[1]Department of Applied Physics, University of Cantabria, 39005 Santander, Spain
[2]Center for Surface and Nanoanalytics (ZONA), Johannes Kepler Universität, A- 4040 Linz, Austria
[3]CNR ICMATE, Corso Stati Uniti 4, I- 35127 Padova, Italy
[†]Both authors contributed equally to this work.
[*]Corresponding author: morenof@unican.es

***Abstract*— Phase-change materials enable optical switching devices with highly tunable optical behavior, ultrafast modulation speeds, and low energy requirements. In this work, we introduce a new optical amplitude switch that employs the phase-change material antimony trisulfide (Sb_2S_3) and exploits the Brewster-angle effect to achieve efficient, controllable modulation.**

***Keywords*— phase change materials, optical switching, Brewster effect.**

I. Introduction

The increasing importance of high-speed data processing with minimal energy consumption has spurred the utilization of light for signal transmission and processing. By employing nanostructures, the energy requirements and interaction timescales can be greatly reduced, enabling the integration of multiple devices that possess the ability to control, modulate, and process light signals with high speed and energy efficiency in the same chip [1]. The pursuit of more versatile nanophotonic devices has led to the exploration of phase-change materials (PCMs), offering the potential to create tunable and switchable nanophotonic systems through the modulation of their optical properties via external stimuli [2]. Reconfigurability offers significant advantages over conventional fixed-function devices by allowing dynamic adjustments in real-time, thus meeting the evolving demands of many photonic applications [3].

II. Results and Conclusion

Amorphous and crystalline samples of Sb_2S_3 are optically and structurally characterized to explore their potential in the design of an optical amplitude switch based on the Brewster angle phenomenon [4]. The Brewster angle value depends on the refractive index of both materials at the reflective interface. Thus, the Brewster angle is strongly affected by the phase of the PCM. When the non-reflection condition is met for one of the Sb_2S_3 phases (i.e., at the Brewster angle), upon phase-change the Brewster condition is broken, leading to light reflection at the interface and producing an optical contrast in reflection that can be harnessed for optical switching applications. Sb_2S_3 is the alternative low-loss PCM with larger transparency window. i.e. spectral range beyond which neither of the material's phases experience optical losses. This is important for the optical switch based on Brewster angle, as this phenomenon only takes place if the material is transparent to light (negligeable extinction coefficient, $k \simeq 0$). With this optical switch configuration, we experimentally demonstrate an optical contrast of 22 dB [5]. Noteworthy, we theoretically predict that this contrast could be further enhanced by tailoring the incident angle and the wavelength of the beam. These findings highlight the potential of using the old Brewster angle effect in developing new efficient optical switch devices based on low-loss wide band gap PCMs such as Sb_2S_3.

Acknowledgments

H2020 Future and Emerging Technologies (899598 – PHEMTRONICS). Y.G. acknowledge funding from funding from a Ramón y Cajal Fellowship (RYC2022-037828-I).

References

[1] S. Zhu, P. Qiu, X. Shan, et al, "High-speed long-distance visible light communication based on multicolor series connection micro-leds and wavelength division multiplexing," Photonics Res. 10(8), 1892–1899, 2022.
[2] M. Wuttig, H. Bhaskaran, and T. Taubner, "Phase-change materials for non-volatile photonic applications," Nat. Photonics 11(8), 465–476, 2017.
[3] S. Abdollahramezani, O. Hemmatyar, H. Taghinejad, et al, "Tunable nanophotonics enabled by chalcogenide phase-change materials," Nanophotonics 9(5), 1189–1241, 2020.
[4] R. M. A. Azzam, "Fresnel's interface reflection coefficients for the parallel and perpendicular polarizations: global properties and facts not found in your textbook," in Polarization Analysis and Measurement II, vol. 2265 D. H. Goldstein and D. B. Chenault, eds., International Society for Optics and Photonics (SPIE, 1994), pp. 120–140.
[5] D. Pérez-Francés, et al, "Sb_2S_3-based optical switch exploiting the Brewster angle phenomenon [Invited]". Optical Materials Express, 13(12), 3677–3687, 2023.

SP5

Scalable Tunable Phase-Change Metasurfaces by soft Nanoimprint Lithography: from dielectric/PCM hybrid architectures to volatile VO_2 photonics

M. Putero[1*], O. Meskini[1,2], R. Mamberti[1], L. Weber[2], N. Weber[3], S. Walfort[3], M. Salinga[3], M. Abbarchi[2], B. Kerzabi[2], D. Grosso[2]

[1] Aix Marseille Univ, CNRS, IM2NP, Marseille, France

[2] Solnil, Marseille, France

[3] University of Münster, Institute of Materials Physics, Wilhelm-Klemm-Str. 10, Münster, Germany

[*]corresponding author: magali.putero@univ-amu.fr

Abstract: Scalable phase-change metasurfaces combining soft nanoimprint lithography with GeTe, Sb_2S_3 and VO_2 are demonstrated for tunable visible and near-infrared photonics. Large-area hybrid dielectric/PCM architectures exhibit reversible optical switching, resonance modulation and strong electrical contrast. The approach enables low-cost, scalable fabrication of reconfigurable photonic devices compatible with industrial-scale manufacturing.

Metasurfaces composed of subwavelength nanostructures provide exceptional control of light propagation, but most demonstrated devices remain static and rely on costly nanofabrication methods. Integrating Phase Change Materials (PCMs) into metasurfaces enables dynamically tunable photonic systems through reversible structural or electronic transitions. However, scalable fabrication compatible with large-area manufacturing remains a major challenge.

Here, we present scalable approaches combining soft Nano Imprint Lithography (soft-NIL), sol-gel processing and PCMs to fabricate tunable metasurfaces operating from the visible to the near infrared. Three complementary strategies are demonstrated: (i) dielectric nanostructures fabricated by etch-free soft-NIL and used as templates for PCM conformal deposition, (ii) NIL-patterned dielectric masks enabling direct etching of PCM layers, and (iii) direct imprinting of PCM-based inks. These methods enable centimeter-scale metasurfaces with strongly reduced fabrication complexity compared with conventional electron-beam lithography.

Different PCMs were investigated, including GeTe, Sb_2S_3 and volatile VO_2. VO_2 thin films and metasurfaces were developed from a sol-gel route based on $VO(acac)_2$ precursors and optimized to achieve efficient and reproducible metal-insulator transition (MIT) switching near 53 °C. We show that crystallographic texture, particularly preferential M1(011) orientation, strongly influences optical and electrical switching performances. Optimized VO_2 films exhibit electrical resistance switching over more than two orders of magnitude together with refractive index modulation exceeding one unit in the near infrared.

The optimized PCM layers were integrated onto dielectric SiO_2 metasurfaces composed of submicronic periodic pillar arrays fabricated by soft-NIL. Upon thermal or laser-induced switching, the resulting hybrid metasurfaces exhibit reversible spectral modulation in reflection and transmission, with resonance shifts up to 70 nm in the visible and modulation depths reaching 7. These performances are comparable to state-of-the-art PCM metasurfaces despite the absence of advanced design optimization.

Finally, in situ synchrotron X-ray diffraction combined with simultaneous electrical measurements was used to investigate switching stability, phase-transition dynamics and structure–property relationships governing the optical response. The proposed approaches provide a versatile and scalable platform

compatible with flexible substrates, solution processing and large-area manufacturing for practical reconfigurable photonics and tunable meta-devices.

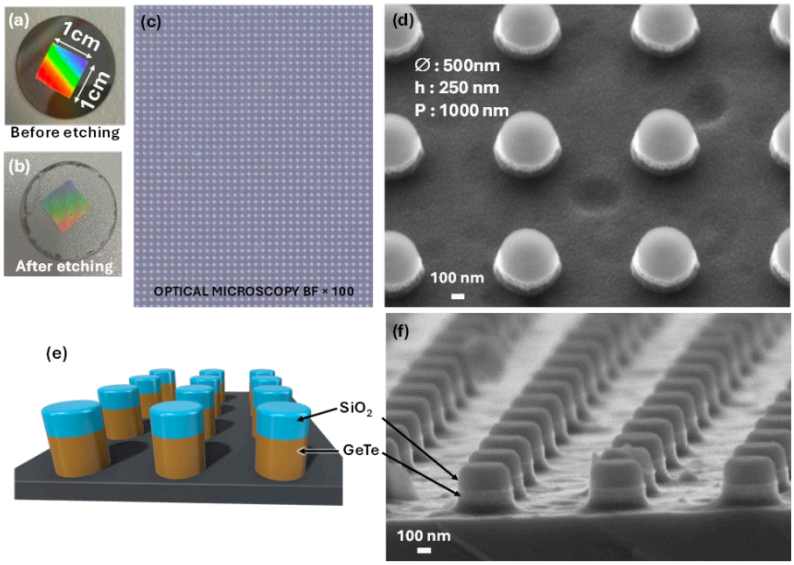

Fig. 1. GeTe metasurface obtained using SiO_2 NIL as a mask. (a) and (b) Photographs of the obtained 1 cm^2 sample with GeTe in the amorphous (a) and crystalline (b) states. (c) Optical microscope image (bright field × 100); (d) and (f) SEM images of the GeTe metasurface with the corresponding scheme of material distributions (e).

References

1. Hosseini, P., Wright, C. D. and Bhaskaran, H. "An optoelectronic framework enabled by low-dimensional phase-change films." Nature 511, 206–211 (2014).
2. Conrads, L. et al. "Infrared Resonance Tuning of Nanoslit Antennas with Phase-Change Materials." ACS Nano 17, 25721–25730 (2023).
3. Laprais, C. et al. "Reversible Single-Pulse Laser-Induced Phase Change of Sb_2S_3 Thin Films: Multi-Physics Modeling and Experimental Demonstrations." Adv. Opt. Mater. 2401214, 1–13 (2024).
4. Checcucci, S. et al. "Multifunctional Metasurfaces Based on Direct Nanoimprint of Titania Sol–Gel Coatings." Adv. Opt. Mater. 7, 1801406 (2019).
5. Modaresialam, M., Chehadi, Z., Bottein, T., Abbarchi, M. and Grosso, D. "Nanoimprint lithography processing of inorganic-based materials." Chem. Mater. 33, 5464–5482 (2021).

Near-Unity Optical Switching by Sb_2S_3/Si Hybrid Metasurfaces

Amin Zamani[1*], Gabriel Sanderson[1,2], Meibao Qin[3], Lu Zhang[4], Qiwei Miao[4], Sara Moujdi[1], Ze Zheng[1], Mohammadhossein Momtazpour[1], Christopher J. Mellor[5], Wending Zhang[4], Ting Mei[4], Zakaria Mansouri[1], Lei Xu[1], Mohsen Rahmani[1]
[1]Department of Engineering, School of Science & Technology, Nottingham Trent University, UK
[2]Faculty of Engineering, University of Nottingham, UK
[3]School of Education, Nanchang Institute of Science and Technology, China
[4]School of Physical Science and Technology, Northwestern Polytechnical University, China
[5]School of Physics & Astronomy, Faculty of Science, University of Nottingham, UK
*Corresponding author: amin.zamani2023@my.ntu.ac.uk

***Abstract*— We demonstrate high-throughput optical modulation in monolithic and hybrid Sb_2S_3/Si metasurfaces, where silicon-enhanced resonances enable 99% transmission modulation at telecom wavelengths using only ~3% optically induced crystallization in Sb_2S_3. This phase transition also allows large-scale tuning of nonlinear emission, offering a versatile platform for reconfigurable linear and nonlinear nanophotonics.**

***Keywords*— metasurfaces, optical switching, phase change materials, high-Q resonance, third-harmonic generation.**

I. Introduction

Dielectric metasurfaces, consisting of arrays of dielectric nanoresonators, have attracted growing interest in recent years, due to their potential for high-throughput optical switching in flat optical systems [1]. By supporting low-loss electric and magnetic resonances with strong field enhancement, these structures offer efficient light-matter interaction while maintaining high transmission, making them highly attractive for compact and energy-efficient photonic devices. However, traditional metasurface functionalities remain intrinsically static, limiting their integration into dynamic photonics systems. Enabling active and reversible control over the optical response of metasurfaces is therefore essential for realizing reconfigurable and programmable flat optics systems. Among various electrical, mechanical, and optical techniques for switching metasurfaces, contact-less switching via phase change materials (PCMs) has been proposed as a promising candidate due to their large refractive index contrast between the amorphous and crystalline phases and their low optical loss across the visible-to-near-infrared spectral window [2]. A key challenge, however, is to maximize optical modulation while minimizing the PCM's phase transition.

II. Methods

Our methodology is based on electromagnetic modeling, parametric optimization, nanofabrication, and linear and nonlinear optical characterization.

Among the multipolar responses supported by dielectric nanostructures, the conventional magnetic dipole resonance is well known for its strong near-field enhancement within the nanostructure and relatively larger mode volume compared to other multipoles [3]. Therefore, we first designed a Sb_2S_3 nanopillar metasurface on a silica substrate supporting a magnetic dipole resonance at the telecom wavelength region. To further enhance the light-matter interaction, we deposited a silicon layer with an optimized thickness on top of the metasurface to form a hybrid structure supporting Fano-like high-Q resonances. Intermediate phase change states were modeled to enable optical switching and tunable third-harmonic generation (THG). We performed experimental transmission measurements together with THG characterization on the selectively fabricated metasurfaces to validate the proposed concept.

III. Results and Discussion

Owing to the strong near-field enhancement associated with the magnetic dipole resonance, the monolithic Sb_2S_3 metasurface enables a broadband spectral tunability with only a partial phase transition. Specifically, a modulation depth of 92% at 1560 nm is achieved both numerically and experimentally, with only 53% crystallization of the phase change material induced by external laser illumination. As can be seen from Figure 1a, a pronounced resonance shift is observed from the amorphous to the poly-crystalline state, which is in excellent agreement with the experimental

measurements shown in Figure 1b. Furthermore, the integration of a thin silicon layer dramatically enhances the modulation performance, enabling a hybrid metasurface achieving 99% modulation depth with only 3% crystallization [4]. Figure 2b gives the simulated transmission spectra where the Fano-like high-Q resonance near 1457 nm, suggesting that a minimal crystallization of only 3% is sufficient to achieve complete optical switching with the designed hybrid metasurface. Subsequently, the experimentally measured modulation performance is shown in Figure 2b, where a modulation depth exceeding 90% is demonstrated with a twofold reduction in the required switching laser power as compared to the monolithic metasurface for switching.

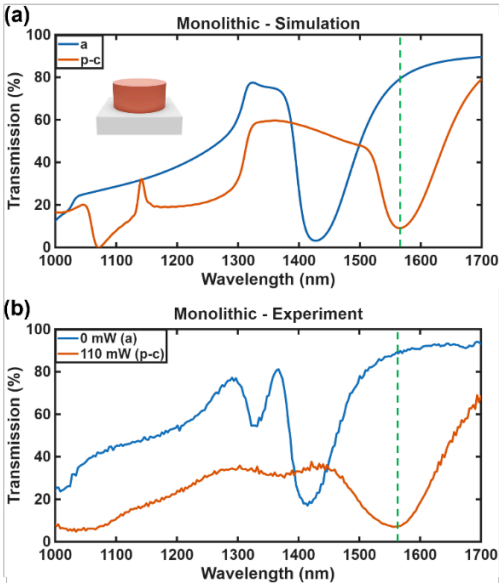

Fig. 1. Monolithic Sb_2S_3 metasurface optical switching. (a) Simulated and (b) experimental transmission spectra showing 92% modulation depth at 1560 nm with 53% crystallization. Adapted from Ref [4].

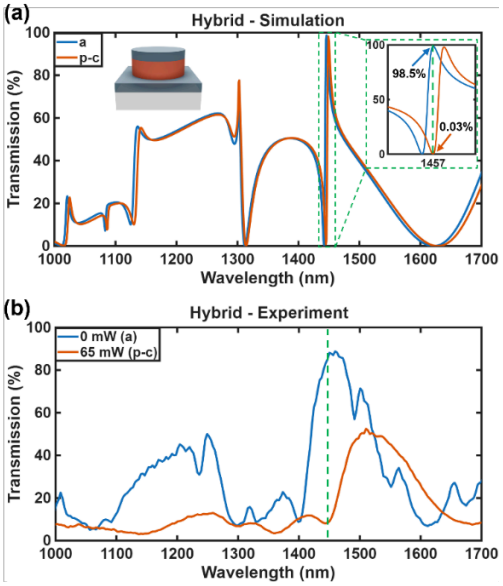

Fig. 2. Hybrid Sb_2S_3/Si metasurface optical switching. (a) Simulated transmission with 99% modulation (inset: Transmission conversion achieved with 3% crystallization). (b) Experimental validation showing over 90% modulation depth. Adapted from Ref [4].

This hybrid metasurface platform for optical switching can be further extended to the nonlinear regime [5]. The strong near-field enhancement associated with the designed high-Q resonance facilitates the nonlinear optical processes, leading to enhanced nonlinear generation. Moreover, the tunable resonant response allows large-scale, spectrally controllable nonlinear emission. We experimentally obtain efficient THG tuning with 20 nm spectral shift through partial crystallization, enabling switchable harmonic generation across different visible wavelengths (Fig. 3).

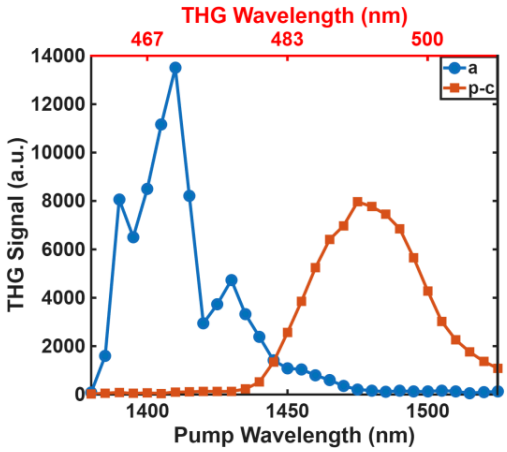

Fig. 3. Experimental THG signals from the hybrid design in amorphous and poly-crystalline states, demonstrating large-scale nonlinear tunability.

IV. Conclusion

We have demonstrated ultra-efficient optical switching through hybrid Sb_2S_3/Si metasurfaces, achieving 99% transmission modulation at telecom wavelengths with only 3% crystallization. This exceptional performance is enabled by high-Q resonances that amplify sensitivity to minimal refractive index changes ($\Delta n = 0.02$) in the phase change material. Furthermore, we demonstrated that the resonance-supported field enhancement in this hybrid system provides a powerful route for large-scale tuning of THG from the designed hybrid metasurfaces. These results suggest Sb_2S_3-based hybrid metasurfaces as a versatile platform for highly efficient tunable linear and nonlinear nanophotonic functionalities in integrated photonic devices.

Acknowledgments

This study was kindly supported by The Royal Society, The Wolfson Foundation (RSWF\FT\191022) and the United Kingdom Research and Innovation (MR/T040513/1).

References

[1] S. A. Schulz, R. Oulton, M. Kenney, A. Alù, I. Staude, et al., "Roadmap on photonic metasurfaces," *Applied Physics Letters*, vol. 124, no. 26, 2024.

[2] P. Prabhathan, K. V. Sreekanth, J. Teng, J. H. Ko, Y. J. Yoo, et al., "Roadmap for phase change materials in photonics and beyond," *iScience*, vol. 26, no. 10, 2023.
[3] V. E. Babicheva and A. B. Evlyukhin, "Mie-resonant metaphotonics," *Advances in Optics and Photonics*, vol. 16, no. 3, pp. 539–658, 2024.
[4] A. Zamani, G. Sanderson, L. Zhang, Q. Miao, S. Moujdi, Z. Zheng, M. Momtazpour, C. J. Mellor, W. Zhang, T. Mei, Z. Mansouri, L. Xu, and M. Rahmani, "High throughput optical switching in telecommunication band via hybrid phase change metasurfaces," *arXiv preprint*, arXiv:2510.11881, 2025.
[5] A. Zamani, G. Sanderson, M. Qin, L. Zhang, Q. Miao, C. J. Mellor, W. Zhang, T. Mei, L. Xu, and M. Rahmani, "Tunable third harmonic generation in monolithic and hybrid Sb_2S_3/Si metasurfaces," in preparation.

Reproducible 2D Structural Color Platforms for Reliable pH Sensing Applications

Jing Qian[1], Yekaterina Tskhe[1], Luke A. Madden[2], Enrique Azuaje-Hualde[1], David A. Hoey[2,3], A. Louise Bradley[4], Larisa Florea[1], Colm Delaney[1,*]

[1]School of Chemistry & AMBER, Trinity College Dublin, Dublin, Ireland
[2]School of Mechanical, Manufacturing and Biomedical Engineering & AMBER, Trinity College Dublin, Dublin, Ireland
[3]Department of Anatomy and Regenerative Medicine, Royal College of Surgeons in Ireland (RCSI), Dublin, Ireland
[4]School of Physics & AMBER, Trinity College Dublin, Dublin, Ireland
*Corresponding author: cdelane5@tcd.ie

***Abstract*— A well-designed 2D cube-array structural color platform was combined with a pH-responsive polymer to achieve sensitive optical pH sensing. The resulting color shift provides a reliable sensing element, offering a practical route toward integrating structural color architectures into real-world pH sensor devices.**

***Keywords*— photonic structures, pH sensing, two photon polymerization, digital analysis.**

I. Introduction

Photonic structures have drawn wide interest in recent years because their periodic micro- and nanoscale architectures provide an effective way to control light. Such structures can produce vivid structural colors through optical interference and diffraction, offering a simple colorimetric signal without the need for traditional pigments or dyes. Since these colors are highly dependent on geometry and local refractive index, photonic platforms have become an attractive choice for compact and reliable optical sensing.

By introducing stimuli-responsive polymers into photonic architectures, structural color systems can be further developed into practical sensing devices. Responsive polymers can swell or shrink under external conditions such as pH or chemical changes, which in turn alters the photonic geometry and leads to visible color shifts. This coupling between structural variation and optical response enables sensitive detection in a straightforward and intuitive manner [1-3].

Among these applications, pH-responsive photonic sensors are particularly promising for biomedical analysis, environmental monitoring, and microfluidic platforms. With the increasing demand for miniaturized and integrated lab-on-chip systems, reliable on-chip pH sensing remains an important challenge. Structural color-based photonic sensors provide a useful approach toward label-free, visually readable, and easily integrable pH detection at the microscale.

II. Methods

In this work, two-photon polymerization was employed to fabricate the designed cube-array photonic structures. The samples were produced using a commercial system (Photonic Professional, Nanoscribe GmbH, Germany), enabling high-precision microfabrication. A 63X oil-immersion objective (Zeiss, NA = 1.4) was used during the writing process. The structural design and optical response were modeled using Lumerical FDTD; detailed simulation results are not included in this short abstract.

For pH sensing measurements, a microfluidic chamber was constructed to deliver buffered solutions with five different pH values. The dynamic optical response of the samples under continuous flow was recorded using a 4X objective (Olympus, NA = 0.1) coupled with a CCD camera. The resulting dynamic structural color variations were subsequently analyzed using imageJ software.

III. Results and Discussion

The samples were fabricated using an acrylic acid-based pH-responsive polymer together with the commercial non-responsive IP-L resin. The schematic in Fig. 1a illustrates the dual-photoresist design, which significantly improves the mechanical stability of the structures.

The structural colors of the cube arrays are shown in Fig. 1b. A clear and pronounced color change is observed when the samples are immersed in pH 2.17 buffered solution, resulting from both the increase in the surrounding medium's refractive index and the swelling of the photonic structures. This vivid color response in solution forms the basis for pH detection.

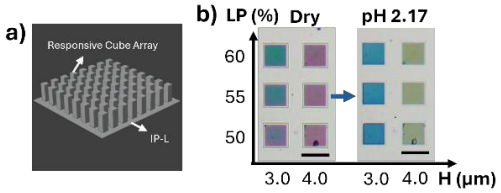

Fig. 1 a) Schematic of the cube array fabricated using a dual-photoresist approach. b) Structural colors of the cube arrays in dry state and in pH 2.17 buffered solution. The arrays have heights of 3.0 and 4.0 μm and were fabricated under laser powers of 50%, 55%, and 60%. The scale bars are 100 μm.

Fig. 2a compares the structural colors of the samples in five different buffered pH solutions. As the pH increases, the colors gradually shift toward blue in a clear and noticeable manner. Trainable Weka Segmentation, a machine-learning plugin in imageJ, was used to isolate the sensor regions in the images and quantify their structural color changes. Large image datasets were then processed in batch using custom imageJ macros. After processing, the RGB values were converted to CIE Lab coordinates and subsequently transformed into XYZ and chromaticity (x, y) values for representation on the CIE color space diagram. The color pixel data extracted from Fig. 2a i) using imageJ are presented in Fig. 2a ii) as a CIE chromaticity map. From the CIE plot, the samples show clear separation under different pH conditions, providing a potential basis for establishing standard colorimetric rules to quantify structural color variations across varying pH environments.

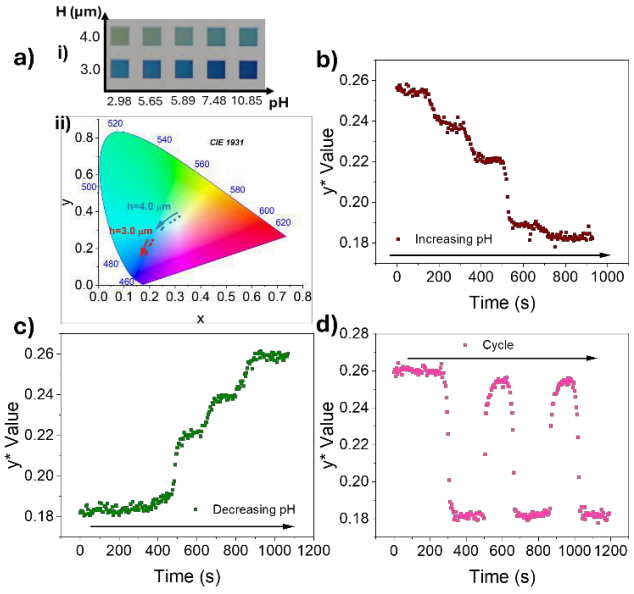

Fig. 1 a) i) Optical images showing the structural colors of the samples (h = 3.0 - 4.0 μm, LP = 60%) in buffered solutions with different pH values. ii) CIE chromaticity diagrams of the samples shown in i), plotted using imageJ digital image analysis. b) and c) "y" values of sample (H = 3.0 μm) extracted from the CIE diagram under increasing and decreasing pH conditions as a function of time, respectively. d) "y" values for the sample with height of 3.0 μm in acidic (pH = 2.98) and basic (pH = 10.85) solutions.

The sample was sealed in a microfluidic flow-in and flow-out chamber and driven by a syringe pump. Multiple dynamic pH response tests were performed to verify its effectiveness. The "y" values were extracted for quantitative analysis. During the experiment, buffered pH solutions were gradually introduced into the microfluidic chamber while the structural color response was recorded on video. Individual frames were then collected for processing. As the pH increased (2.98, 5.65, 5.89, 7.48, and 10.85), the extracted "y" values decreased consistently, as shown in Fig. 2b. The opposite trend was observed when the pH was lowered (Fig. 2c). The "y" values remained stable at each pH step, highlighting the pH responsive cube array's reliability as a pH sensing platform.

The repeatability and reproducibility of the sensor response are demonstrated in Fig. 2d. An acidic buffer (pH = 2.98) and a basic buffer (pH = 10.85) were selected as the two main solutions for three consecutive pH cycling tests. The extracted "y" values are plotted in Fig. 2d, showing consistent and repeatable behavior across all cycles. The signal returns reliably to its original level when switching between acidic and basic conditions, indicating good reversibility of the structural color response.

IV. Conclusion

The cube-array photonic structures provide stable and reproducible optical readouts under repeated pH variations. This repeatable step-like behavior highlights their potential as robust structural color platforms for practical on-chip pH sensing applications. In addition, the combination of digital image-based analysis with direct, label-free optical readout makes the pH detection approach more flexible and accessible for integration into compact sensing systems.

Acknowledgments

This work was supported by the European Research Council (ERC) Starting Grant (No. 101077430 - BIO4D). The authors acknowledge the AMBER Centre for fabrication support, funded by Taighde Éireann - Research Ireland and the European Regional Development Fund (ERDF) under grant 12/RC/2278_P2.

References

[1] C. Delaney, J. Qian, X. Zhang, R. Potyrailo, A. L. Bradley, and L. Florea. "Direct laser writing of vapour-responsive photonic arrays." Journal of Materials Chemistry C 9.35 (2021): 11674-11678.

[2] J. Qian, S. Kolagatla, A. Pacalovas, X. Zhang, L. Florea, A. L. Bradley, and C. Delaney. "Responsive spiral photonic structures for visible vapour sensing, pattern transformation and encryption." Advanced Functional Materials (2023): 2211735.

[3] T. Faraone, J. Qian, S. Kolagatla, A. L. Bradley, L. Florea, C. Delaney. "Direct Laser Writing of Polymer Nanocomposites for Tunable Structural Color." Advanced Materials 37, no. 43 (2025): 2504116.

SPECIAL SESSION 6

Quantum metaphotonics

4 contributions · pp. 857–861

Integrated Single-Photon Emitters with Plasmonic Nanostructure

Keyu Jin[1,2,*], and Lian Shen[1,2]

[1] College of Information Science and Electronic Engineering Zhejiang University, Hangzhou 310027, China

[2] ZJU-Hangzhou Global Scientific and Technological Innovation Center Zhejiang University, Hangzhou 310058, China

*Corresponding author: keyujin@zju.edu.cn

***Abstract*— Integrated single-photon emitters (SPEs) are pivotal for advancing quantum technologies, including quantum communication, computing, sensing, and simulation, as they serve as reliable carriers of quantum information within quantum systems. A promising strategy to enhance the capabilities of SPEs is to leverage plasmonic nanostructures, which can dramatically improve light-matter interactions. However, despite the potential, the use of plasmonic nanostructures for SPEs has encountered significant bottlenecks. We have made considerable progress in overcoming these challenges by incorporating techniques for efficient emission and extraction. Nevertheless, we have found that, beyond achieving efficient emission and extraction, substantial hurdles remain in realizing scalable quantum systems. The primary issue lies in the intrinsic randomness and uncertainty associated with practical SPEs. This unpredictability restricts precise control over photon emission, extraction, emitter orientation, and spatial positioning, ultimately limiting both integration density and device performance. To address these challenges, we propose a viable solution based on V-shaped plasmonic nanoantennas that enhance both photon emission and extraction for multiple SPEs, viewed through the framework of transformation optics. This innovation not only improves the performance of individual emitters but also enables their deterministic integration, thus facilitating the reusable, large-scale integration of SPEs into future quantum systems.**

***Keywords*— Single-photon emitters, Plasmonic nanoantennas, Transformation optics.**

Non-Reciprocal Photon-Pair Generation from Nonlinear Metasurfaces

Jinyong Ma[1,2,*], Xiwen Qiu[1], Tongmiao Fan[1], Tuomas Haggren[1], Hark Hoe Tan[1], Chennupati Jagadish[1], Andrey A. Sukhorukov[1]

[1]ARC Centre of Excellence for Transformative Meta-Optical Systems (TMOS), Department of Electronic Materials Engineering, Research School of Physics, The Australian National University, Canberra ACT 2601, Australia

[2]Institute of Quantum Precision Measurement, State Key Laboratory of Radio Frequency Heterogeneous Integration, College of Physics and Optoelectronic Engineering, Shenzhen University, Shenzhen 518060, P. R. China

*Corresponding authors: jinyong.ma@szu.edu.cn, andrey.sukhorukov@anu.edu.au

***Abstract*—Photon-pair generation from ultra-thin nonlinear metasurfaces opens new possibilities for quantum technologies. We reveal that the quantum photon states can exhibit a strongly non-reciprocal behaviour, where the generation rate and quantum entanglement can dramatically vary depending on which side of the metasurface the pump light is incident from.**

***Keywords*— non-reciprocity; metasurface; biphoton entanglement**

I. Introduction

Optical metasurfaces incorporating nonlinear materials are emerging as new platforms for generating photon pairs through spontaneous parametric down-conversion (SPDC) at the nanoscale with tunable frequency [1] and polarization [2], [3], [4] entanglement. However, the directional control of quantum states was limited to nonreciprocal structures with a thickness of multiple wavelengths [5]. We reveal, for the first time to our knowledge, that photon generation from metasurfaces with sub-wavelength-thin nonlinear nanostructures can exhibit strong non-reciprocity. Specifically, we predict theoretically and establish experimentally that the rate and quantum state of the signal and idler photons can dramatically depend on their emission and the pump incidence directions, as schematically illustrated in Fig. 1.

II. Results and Discussion

We demonstrate nonreciprocity for a semiconductor metasurface incorporating [110] InGaP nano-resonators with approximately cylindrical shapes [4]. Whereas the presence of the substrate makes the whole metasurface asymmetric, the linear transmission and reflection remain independent of the pump direction.

Most remarkably, we find that the nonlinear process of SPDC can feature big differences in the generation of entanglement between various polarization components depending on the incidence direction, as sketched in Fig. 1. Our numerical simulations identify optimal metasurface designs that resonantly enhance nonreciprocity, enabling a generation rate contrast up to 20 dB and the creation of totally distinct quantum states. We further confirm these principles experimentally by fully characterizing the quantum states.

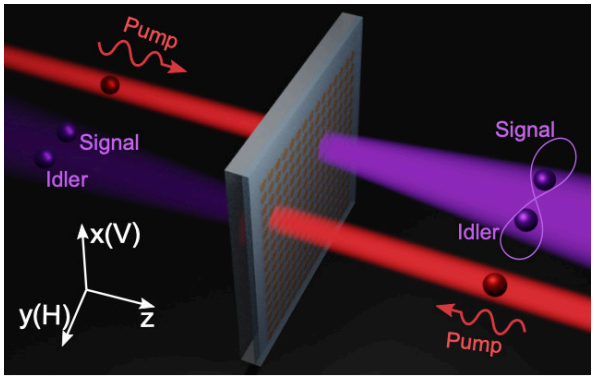

Fig. 1. Concept of non-reciprocal generation of quantum-entangled pairs of signal and idler photons from a nonlinear metasurface. The process efficiency and emerging quantum state can dramatically depend on the pump incidence and the corresponding photon emission directions.

III. Conclusion

In conclusion, we report the first prediction and experimental observation of quantum nonreciprocity in the generation of entangled photons from ultra-thin nonlinear metasurfaces, revealing new possibilities for multi-functional and reconfigurable operation of quantum nanophotonic devices.

References

[1] T. Santiago-Cruz *et al.*, "Resonant metasurfaces for generating complex quantum states," *Science*, vol. 377, pp. 991–995, 2022.

[2] J. Noh *et al.*, "Quantum pair generation in nonlinear metasurfaces with mixed and pure photon polarizations," *Nano Lett.*, vol. 24, pp. 15 356–15 362, 2024.

[3] W. H. Jia *et al.*, "Polarization-entangled Bell state generation from an epsilon-near-zero metasurface," *Sci. Adv.*, vol. 11, p. eads3576, 2025.

[4] J. Y. Ma *et al.*, "Nonlinearity symmetry breaking for generating tunable quantum entanglement in semiconductor metasurfaces," *Sci. Adv.*, vol. 11, p. eadu4133, 2025.

[5] J.-T. Pan *et al.*, "Nonreciprocal quantum photon-pair source with chiral ferroelectric nematics," *arXiv*, p. 2503.11399, 2025.

Metamaterials with Varactors: Manipulating Spoof Surface Plasmon Polaritons

Jinhui Shi[1*], Zhaoqi Jiang[1], Zheng Zhu[1], Wenjia Li[1], Chunying Guan[1]

[1] Key Laboratory of In-Fiber Integrated Optics of Ministry of Education,College of Physics and Optoelectronic Engineering, Harbin Engineering University, Harbin 150001, China
*Corresponding author: shijinhui@hrbeu.edu.cn

***Abstract*—We experimentally demonstrate that a spin-dependent programmable plasmonic metamaterial can manipulate the propagation of surface spoof surface plasmon polaritons (SSPP) wave. The spin and coding information are used to independently control frequency and space routing, respectively. Our findings provide a surface EM wave platform for multi-channel signal communication systems.**

***Keywords*— metamaterials, spoof surface plasmon polaritons.**

I. Introduction

Spin is an intrinsic property of electromagnetic wave. There is a locking relationship between the spin and momentum of EM waves, which is called the spin-momentum locking.[1,2] The spin-momentum locking is that when the direction of spin is flipped, the direction of momentum is also flipped. In the SSPP wave platform, the momentum of the SSPP wave can be controlled by the spin of the incident source, so that the propagation direction of the SSPP wave can be changed and the information can be distributed to users at different locations. In previous literatures, seldom attempts have been made to achieve the manipulation of SSPP wave in the frequency and spatial domains simultaneously. In this work, we demonstrate a spin-controlled plasmonic metamaterial with varactors to manipulate the propagation of the SSPP wave.

II. Methods

We design a programmable metamaterial that realizes a four-channel SSPP wave transmission system via space and frequency routing. Firstly, the four raw datas are mapped to the spin information and coding information. Then, the spin information and coding information are used as the input of the programmable SSPP metamaterial. Spin information is the spin of the source and the coding information is the voltage value of the varactor in the SSPP unit. The information is transmitted to four users at different frequency bands or different positions in the form of SSPP wave. Among them, different coding information controls the frequency bands of information transmission, thereby determining frequency routing of metamaterials. Different spin information controls the direction of information transmission, thereby determining the spatial routing of metamaterials.

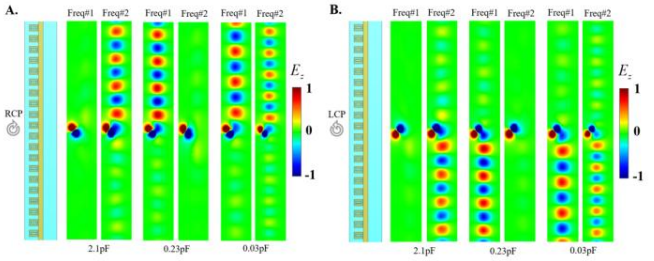

Fig. 1 Simulated results of the metamaterial with four-channel SSPP routing.

Figure 1 shows simulated results of the metamaterial with four-channel SSPP routing, in which three capacitance values are considered. The experimental results agree well with the simulated ones (not shown here). Obviously, the spin freedom controls the spatial routing and the coding freedom controls the frequency routing.

III. Conclusion

We have demonstrated a space- and frequency-routing device based on spin-controlled plasmonic metamaterial. Our findings provide a way for multi-channel signal communication systems.

Acknowledgments

This work was supported by National Natural Science Foundation of China (NSFC) (U2541207, 62275061).

References

[1] X. Ling, Z. Zhang, Z. Dai, Z. Wang, H. Luo, L. Zhou, "Photonic Spin-Hall Effect at Generic Interfaces," Laser Photonics Rev. vol. 17, pp. 2200783, 2023.

[2] J. Liu, J. Wu, X. Fu, W. Tang, T. Cui, "Arbitrary Polarization Syntheses Based on Spin-Momentum Locking in Spoof Surface Plasmon Polaritons," Adv. Opt. Mater. Vol. 11, pp. 2202618, 2023.

Diffractive Optical Elements Empowered Spectropolarimetry via Single-Shot Imaging

Bing Lei[1,2,*], Jianyu Weng[1,2], Xiaoyu Cao[1,2], Zong Xiang[1,2], Xinyu Ma[1,2], Jie Li[1,2], Zhe Xie[1,2], Wei Wang[1,2], Jianhua Shi[1,2]

[1] College of Advanced Interdisciplinary Studies, National University of Defense Technology, Changsha, 410073, China

[2] Nanhu Laser Laboratory, National University of Defense Technology, Changsha, 410073, China

*Corresponding author: leibing_2000@nudt.edu.cn

***Abstract*— We propose a novel broadband polarimeter by employing a metasurface-based diffractive optical element and a vortex retarder to convert polychromatic waves into structured vector beams. Experimental validation demonstrates exceptional measurement accuracy, with RMS errors below 1% for each Stokes component across the visible range (400-700 nm).**

***Keywords*— metasurfaces, diffractive optical elements, vortex retarder, spectropolarimetry, broadband polarimeter.**

I. Introduction

Broadband polarization measurement plays a crucial role in numerous fields, spanning from fundamental physics to a wide range of practical applications [1-2]. However, traditional approaches typically rely on combinations of various dispersive optical elements, requiring bulky systems and complicated time-consuming multiple procedures [3-4]. As an emerging class of planar diffractive optical elements (DOEs), meta-surfaces can function as an ultracompact platform for polarization measurement[5]. In this paper, we have achieved broadband spectropolarimetry based on single-shot images for spatial intensity distributions of polychromatic vector beams. A custom-designed diffractive optical element and a vortex retarder convert the incident polychromatic waves into structured vector beams: the former diffracts light of different wavelengths into concentric circles of different radii while the latter codes their polarization information into intensity distributions along the azimuthal direction [6].

II. Methods

The incident broadband beam with unknown polarizations can be described by a wavelength-dependent Stokes vector $S(\lambda) = [S_0(\lambda) \quad S_1(\lambda) \quad S_2(\lambda) \quad S_3(\lambda)]^T$. To measure $S(\lambda)$, the incident light is firstly dispersed into a rainbow donut beam with different wavelength at different radii through a specially designed DOE. Therefore, the wavelength-dependent Stokes vector $S(\lambda)$ is mapped into a radius-dependent $S(r)$. The relation between wavelengths and the radii can be established by the dispersive regularities of DOE. Then a vortex retarder is employed to encode the donut beam into a polychromatic vector beam (PVB), whose Stokes vector can be described by $S(\varphi, r)$, where φ is the azimuth angle. The linearly polarizer is added between the vortex retarder and camera to analyze the PVB into a spatially varying intensity distribution. The recorded intensity $I(\varphi, r)$ is a function of the radius r and the azimuthal angle φ, which can be described by the Mueller-Stokes formula as $I(\varphi, r) = \vec{a}(\varphi, r) \cdot S(\lambda)$, where $\vec{a}(\varphi, r)$ is the first row of the total Mueller matrix of the PVB based spectropolarimeter.

The effective dispersion of broadband light into circular rainbow rings is realized through the DOE. The operational wavelength range of the DOE was designed to be 400-700 nm. The effective optical area of 4 mm × 4 mm was subdivided into 8000 × 8000 square cells, each with a side length of 500 nm. Within each cell, regular quadrilateral *SiNx* nanopillars (see Fig. 1(a)) with varying sizes (a) and a fixed height (H=1000 nm) were arranged. These *SiNx* nanopillars introduce spatially distributed phase shifts that cause beam diffraction and achieve the desired annular dispersion effect. Further, the phase shift profile for the annular dispersion function was calculated and shown in Fig. 1(b). Then the sizes a of the *SiNx* nanopillars with different phase shift between 0-2π were calculated by using finite difference time domain method, which are shown in Fig.1(c). As shown in Fig. 1(d), the DOE was then fabricated by using the photolithography technique.

The feasibility of the PVB based spectropolarimeter is demonstrated by using the configuration shown in Fig. 2. A broadband light, a polarizer (P), and a quarter wave plate (Q) are utilized to generate different incident spectral polarization states. The incident beam is then dispersed into a rainbow donut by the DOE, and an achromatic plano-convex lens (L) is utilized to collimate the divergent rainbow donut beam. A liquid crystal polymer vortex retarder (V) is utilized to convert the rainbow donut beam into PVBs. Then the PVBs are mapped into a unique spatially varying intensity pattern by an analyzer (A). Finally, the intensity image is recorded by a scientific CMOS camera (sCMOS) for further analysis.

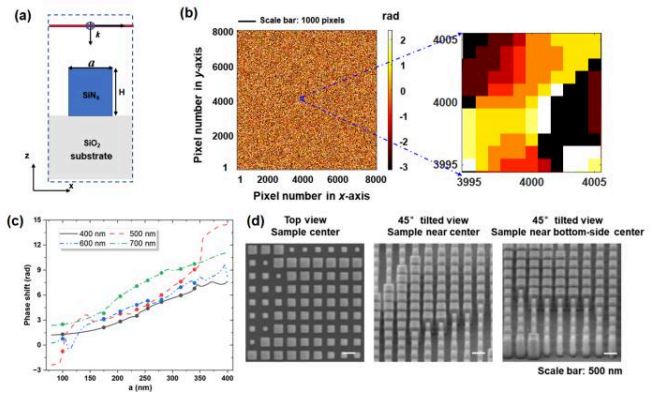

Fig. 1 Design and fabrication of DOE. (a) The schematic of one *SiNx* nanopillar; (b) The calculated phase profile and zooming in; (c) The phase shift of the 8 selected *SiNx* nanopillars at 4 representative wavelengths; (d) The SEM results of the fabricated DOE.

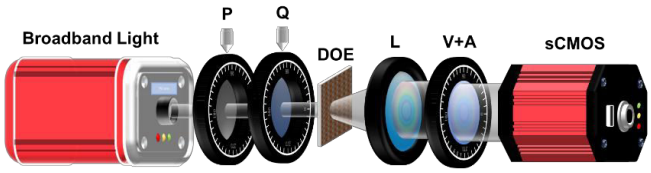

Fig. 2 Demonstration configuration of PVB based spectropolarimeter.

III. Results and Discussion

To validate the performance of the PVB based spectro-polarimeter, incident beams with various broadband polarization states are generated using different azimuthal combinations of P and Q, and subsequently measured by the spectropolarimeter. Fig. 3(a) shows the intensity images of a spectrally uniform linearly polarized beam generated by a 30° P, while Fig. 3(b) displays a spectrally varying polarized beam generated by a 40° P and a 5° Q. For the actual calculations, we employed the sCMOS camera, which provides superior image quality and allows for better computational accuracy. The measurement results and measured errors are shown in Fig. 4. The RMS errors of the measured Stokes parameters in VIS range (400-700 nm) are calculated, and an error of <1% for each vector component is obtained. In our experiment, the intensity image processing time is 9.895 ms (using an i7-10700F CPU @ 2.90GHz and Matlab R2021a software), yielding an output rate of 100 Hz. The measurement accuracy we obtained is comparable to the excellent full Poincaré polarimeter and is much better than the well-established traditional polarimeter and the modern light-matter interactions based polarimeters[7].

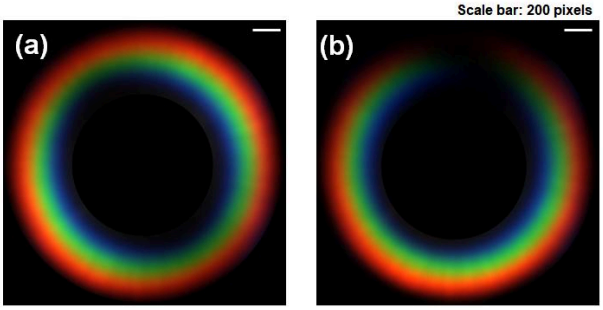

Fig. 3 Captured RGB intensity images. (a) 30° P, (b) 40° P and 5° Q.

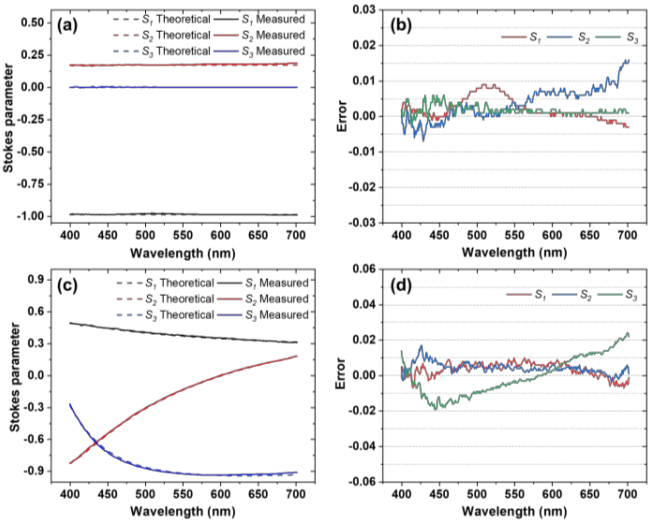

Fig. 3 Measured results and measured error for normalized Stokes vector. (a) and (b) Spectrally uniform linearly polarized beam generated by a 30° P; (c) and (d) Spectrally varying polarized beam generated by a 40° P and a 5° Q.

IV. Conclusion

We have demonstrated a single shot, accurate and simple approach for broadband polarization measurement. The concept relies on the mapping of any input broadband polarization into a polychromatic structured vector beams by using a specifically designed DOE with axisymmetric dispersion and a vortex retarder. Some broadband polarization states are experimentally measured to demonstrate the feasibility of the PVB based spectropolarimeter. The measured Stokes parameters in visible light range (400-700 nm) show excellent RMS errors of <1%, and its output rate can reach about 100 Hz. However, the system also faces some limitations, such as the lack of imaging capability and the unoptimized condition number, which will be considered in future work.

Acknowledgments

This work was supported by the National Natural Science Foundation of China (Grant NO. 62475285 and 61975235).

References

[1] J. Mun, M. Kim, Y. Yang, et al., "Electromagnetic chirality: from fundamentals to nontraditional chiroptical phenomena," Light: Sci. Appl. 9, 139, 2020.
[2] L. Rossi, J. Berzosa-Molina, J. M. Desert, et al., "Spectropolarimetry as a tool for understanding the diversity of planetary atmospheres," Exp. Astron. 54, 1187-1196, 2022.
[3] W. Liu, J. Liao, Y. Yu, and X. Zhang, "High-efficient and high-accurate integrated division-of-time polarimeter," APL Photonics, 6, 071302, 2021.
[4] Y. Ni, C. Chen, S. Wen, et al., "Computational spectropolarimetry with a tunable liquid crystal metasurface," eLight, 2, 23, 2022.
[5] J. P. Balthasar Mueller, K. Leosson, and F. Capasso, "Ultracompact metasurface in-line polarimeter," Optica, 3, 42-47, 2016.
[6] C. Gao, X. Cao, J. Weng, et al., " Broadband spectropolarimetry based on single-shot intensity images of polychromatic structured vector beams," Photonics Research, 13, 781-790, 2025.
[7] C. He, J. Lin, J. Chang, et al., "Full Poincaré polarimetry enabled through physical inference," Optica, 9, 1109-1114, 2022.

SPECIAL SESSION 7

Enhanced light-matter interactions: fundamentals and sensing applications

18 contributions · pp. 863–895

Nanomaterials and Nanostructures for Semi-Transparent and Color Photovoltaics

Ilya Sychugov

Department of Applied Physics, KTH Royal Institute of Technology, Stockholm
ilyas@kth.se

***Abstract*— Large-area luminescence solar concentrators with metal nanoclusters and Si quantum dots feature high visible light transparency (~ 70-80%) and generate ~ 1 W of electrical power under 1 sun. A sub-monolayer of silicon nanospheres, as selective Mie scatterers, improves device efficiency and color-neutrality, and can be used for color photovoltaics.**

***Keywords*— metal nanoclusters, silicon nanoparticles, Mie scatterers, luminescence solar concentrator.**

I. Introduction

As photovoltaic (PV) technology reaches industrial maturity, some niche applications remain less explored. Those include semi-transparent and color PV towards building-integrated photovoltaics, agrivoltaics and li-fi [1-2]. Control of transparency and color are crucial for his purpose. In his paper we demonstrate how selective Mie scatterers together with luminescent metal nanoclusters and silicon quantum dots can be used for such large-area PV devices.

II. Methods

Luminescent gold-silver metal nanoclusters (~ 1-2 nm size) were synthesized by metal salt reduction in a control environment [3]. Silicon quantum dots (5-10 nm) and Mie nanospheres (100-200 nm) were fabricated by annealing (disproportionation reaction) of silicon-rich silica pre-cursors [4]. Nanomaterials for LSC were dispersed in thiol-ene polymer layer sandwiched between two glass plates in a triplex geometry (Fig1). Quantum yield and photon budget were measured in an integrating sphere, and I-V curves were recorded under 1 sun.

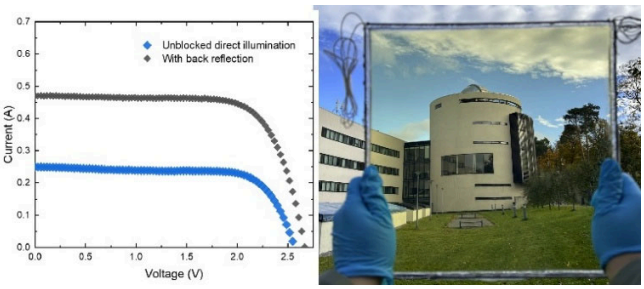

Fig. 1 (left) I-V curve of the 30x30 cm^2 LSC device with Si QDs, generating up to ~ 1W of electrical peak power under one sun illumination; (right) device photo shows high transparency.

III. Results and Discussion

Nanomaterial properties feature a large Stokes shift and a high luminescent quantum yield (up to 70-80%) [1-3]. LSC device has visible light transparency 70-80% and generates up to 1 W of electrical peak power under one sun.

Silicon nanosphere sub-monolayer selectively back-reflects incoming radiation, increasing optical path of the photons through the active layer [4]. This results in increase in LSC photocurrent by 10-15% and makes LSC devices more color neutral. Color coordinates (a*, b*) become (0, 4) from the original device (-1, 13) after the application of Mie scatterers.

IV. Conclusion

We have demonstrated how luminescent light converting nanomaterials (nanoclusters and quantum dots) in combination with dielectric Mie resonators in the form of silicon nanospheres can be utilized for transparent photovoltaics. Further applications of Si nanospheres will be in color PV to improve aesthetics of traditionally opaque black solar cells.

Acknowledgments

This work was supported by the Swedish Energy Agency (P2022-00859). It was also funded by CETPartnership, the Clean Energy Transition Partnership under the 2023 joint call for research proposals, co-funded by the European Commission (GA No. 101069750) and with the funding organizations Swedish Energy Agency, Agencia Estatal de Investigacion, and Ministero dell'Università e della Ricerca.

References

[1] J. Huang, J. Zhou, E. Jungstedt, A. Samanta, J. Linnros, L. Berglund, and I. Sychugov, "Large-area Transparent "Quantum Dots Glass" for Building Integrated Photovoltaics" ACS Photonics 9, 2499 (2022).

[2] Y. Wu *et al.*, "Enlarging Stokes Shift of $CuInS_2$ Quantum Dots by Thiol-Ene Polymers for Efficient Large-area Luminescent Solar Concentrators" Energy Environ. Sci. 17, 6338 (2024).

[3] M. Jash, X. Lu, M. S. Toprak, J. Zhou, and I. Sychugov, "In Situ Transformation of Electrum Nanoclusters Embedded in Polymer Matrices Exhibit Near-Infrared Emission with Quantum Yield Exceeding 70%" Adv. Opt. Mater. e01158 (2025).

[4] Z. Song, X. Lu, O. Vu, J. Song, H. Sugimoto, M. Fujii, L. Berglund, and l. Sychugov, "Selective Scatterers Improve Efficiency and Color Neutrality of Semi-Transparent Photovoltaics" ACS Photonics 12, 6458 (2025).

AI-driven Design and Synthesis of Plasmonic Nanoparticles

José Luis Montaño-Priede[1], Ana Sánchez-Iglesias[1], Anish Rao[1], Marek Grzelczak[1,*]

[1]Centro de Física de Materiales (CFM-MPC), CSIC-EHU, Donostia – San Sebastián, Spain

*Corresponding author: marek.g@csic.es

***Abstract*—Here, we report the use of open- and closed-loop pipelines for the synthesis and in silico design of gold nanoparticles, using global optimization algorithms (Bayesian optimization) to identify optimal experimental conditions for nanoparticle synthesis and to determine optimal dimensions for enhanced plasmonic performance.**

***Keywords*— gold nanoparticles, plasmonics, optimization algorithms**

I. Introduction

Plasmonic performance is inherently tied to nanoparticle (NP) geometry. The design and synthesis of NPs with optimal plasmonic performance are typically intuition-driven processes, in which a single parameter is adjusted at a time to evaluate performance through the so-called Edisonian approach. Finding the optimal dimensions for targeted performance is time-consuming and requires a trial-and-error approach. As a result, the field of plasmonics, both experimental and theoretical, is fragmented into multiple specialized areas, each optimized for specific applications.

Global optimization algorithms are increasingly important in materials design and synthesis.[1] For example, Bayesian optimization (BO) allows exploration and exploitation of the multidimensional parameter space to find a solution with fewer iterations, thereby accelerating the process. Despite recent progress, there is a lack of methods that integrate global optimization with numerical and experimental tools to design and synthesize NPs with desired optical properties and dimensions, thereby achieving desired plasmonic performance. Here, we discuss the development of pipelines that use a Bayesian optimizer to orchestrate electrodynamics simulations to find the optimal dimensions of gold bipyramids for a range of plasmonic applications, and to assist human experimenters in identifying experimental conditions to obtain gold nanorods.

II. Methods

To design nanoparticles in a closed-loop fashion, we developed a pipeline using an experimentally determined parameter space based on the recipe recently published by our group.[4] The BO process uses a random search sequence to generate priors from initial evaluations, then constructs a surrogate model using Gaussian processes to predict outcomes for unobserved parameter sets and quantify their uncertainty. At each iteration, the orchestrator executes numerical simulations of the electromagnetic response of nanoparticles by using MNPBEM toolbox. The simulation results were used to estimate the objective functions that optimize AuBP dimensions. To synthesize nanoparticles, we used an open-loop model in which the algorithms proposed the experimental conditions, followed by human-based execution. As an objective of the synthesis, we used numerical spectra featuring the position of the plasmon band at a given wavelength.

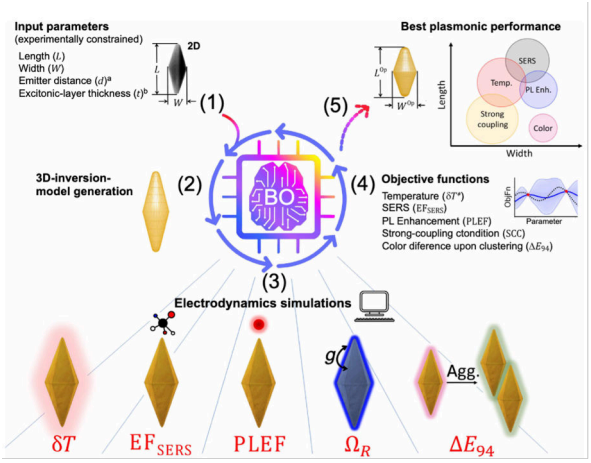

Fig. 1. An example of closed-loop design of nanoparticles. The algorithm suggests structural parameters for gold bipyramids that maximize targeted plasmonic performance. The workflow comprises (1) sampling a set of input parameters within experimentally constrained parameter space, (2) generating a 3D model, (3) calculating properties, (4) updating the surrogate model, and (5) selecting the next set of parameters to reach the highest objective function value.

III. Results and Discussion

In the computational design of gold bipyramids, BO achieves a 600-fold acceleration over traditional "human-in-the-loop" trial-and-error, enabling the precise identification of dimensions that maximize performance in applications such as SERS, photothermal heating, and strong plexcitonic coupling.[2] Key results include the identification of optimal dimensions for gold bipyramids (137 nm by 27 nm) for use in photothermal therapies or neuronal photo-modulation. In addition, we found that multi-objective optimization can successfully balance competing requirements, such as maximizing the photoluminescence enhancement factor while minimizing temperature increase to protect the thermal stability of the hybrid plasmonic system.

In open-loop synthesis, we found that BO-based protocols can uncover ”missed knowledge” by exploring a broader parameter space than intuition-guided methods. We identified viable synthesis conditions at elevated temperatures (up to 40 ºC), enabling high-quality nanoparticles 4.7 times faster than standard protocols.[3] An interpretative ML of the resulting dataset allowed us to establish a hierarchy of parameters, confirming that silver ions are the most critical factor for achieving specific spectroscopic features.

IV. Conclusion

The implementation of Bayesian optimization has emerged as a transformative strategy for designing superior plasmonic nanoparticles by providing a universal pipeline that bridges global optimization and numerical simulations. These algorithms are becoming critical in computational and experimental plasmonics for navigating the complex, nonlinear relationships in multidimensional parameter spaces and escaping the ”knowledge traps” inherent in intuition-guided methods. By utilizing multiobjective optimization, one can effectively balance competing requirements, thereby streamlining the transition from proof-of-concept research to real-world nanophotonic applications.

Acknowledgments

J.l.M.-P. and A.S.-i. acknowledge the financial support received from the iKUR Strategy under the collaboration agreement between the ikerbasque Foundation and Materials Physics center on behalf of the department of Science, Universities and innovation of the Basque Government. A.R. acknowledges funding from the Spanish MiciU for the Juan de la cierva (FJc2021-047710-i) fellowship. M.G. acknowledges the grant Pid2022141017OB-i00 funded by Mcin/Aei/10.13039/501100011033 and by “eRdF A way of making europe.”

References

[1] R. Pollice, G. dos Passos Gomes, M. Aldeghi, R. J. Hickman, M. Krenn, C. Lavigne, M. Lindner-D’Addario, A. Nigam, C. T. Ser, Z. Yao, A. Aspuru-Guzik, Data-driven strategies for accelerated materials design. *Acc. Chem. Res.* 2021, 54, 849–860

[2] Montaño-Priede, J. L.; Rao, A.; Sánchez-Iglesias, A.; Grzelczak, M. Accelerated Design of Gold Nanoparticles with Enhanced Plasmonic Performance. *Sci. Adv.* 2025, 11 (33), eadx2299.

[3] Rao, A.; Grzelczak, M. Revisiting El-Sayed Synthesis: Bayesian Optimization for Revealing New Insights during the Growth of Gold Nanorods. *Chem. Mater.* 2024, 36, 2577–2587

[4] Sánchez-Iglesias, A.; Grzelczak, M. Expanding Chemical Space in the Synthesis of Gold Bipyramids. *Small* 2025, 21, 2407735.

Engineering Optical Sensitivity in Plasmonic Metasurfaces: from LSPR to high-Q Surface Lattice Resonances

Kartikey Pandey,[1] Mathias Dolci,[1*] Yun Luo,[2] Stéphanie Lau-Truong,[1] Sarra Gam-Derouich,[1]
Alexandre Chevillot-Biraud,[1] Nordin Félidj[1] and Claire Mangeney[2]
[1] Université Paris Cité, ITODYS, Paris, France
[2]Université Paris Cité, LCBPT, Paris, France
*Corresponding author: mathias.dolci@u-paris.fr

***Abstract*— In this work, we design plasmonic metasurfaces supporting surface lattice resonances (SLRs) and tailor their design to control optical modes and achieve high quality factors. Refractive index sensing measurements are performed to assess the sensitivity associated with different resonance modes, highlighting the potential of engineered SLRs for efficient plasmonic detection.**

***Keywords*— metasurfaces, plasmonics, lithography, sensing.**

I. Introduction

The confinement of light at the scale of metallic nanostructures has enabled numerous applications in nano-optics, molecular detection, and surface-enhanced spectroscopy. Metasurfaces, such as periodic arrays of metallic nanostructures, allow efficient coupling between localized surface plasmon resonances (LSPRs) and diffractive modes arising from lattice periodicity. This coupling leads to the formation of collective optical modes known as surface lattice resonances (SLRs), which have attracted increasing interest due to their highly tunable optical properties and exceptionally high quality factors.[1], [2] The spatial distribution of the electromagnetic field near these lattices makes them particularly suitable for biosensing applications.[3] In this work, we demonstrate the crucial role of the grating period in governing the refractive-index sensitivity of plasmonic lattice resonances. To highlight this dependence, we exploit diffractive coupling in square arrays of gold nanodisks deposited on an indium tin oxide (ITO) layer on a glass substrate.

II. Methods

Plasmonic metasurfaces were fabricated by electron-beam lithography in order to achieve large-area arrays with precise control over the geometrical parameters. Square lattices of gold nanodisks with a diameter of 100 nm and a thickness of 50 nm were patterned on glass substrates coated with a thin ITO layer. The lattice period was systematically varied from 300 to 600 nm to tune the diffractive coupling conditions and the resulting surface lattice resonances.

Optical characterization was carried out by extinction spectroscopy under normal incidence using linearly polarized light. Extinction spectra were recorded to identify resonance features, from which the spectral positions and quality factors of the SLR modes were extracted. Refractive index sensitivity measurements were performed by gradually increasing the refractive index of the surrounding medium using controlled water–ethanol solvent mixtures, enabling a quantitative evaluation of the resonance shifts induced by changes in the dielectric environment (Fig. 1).

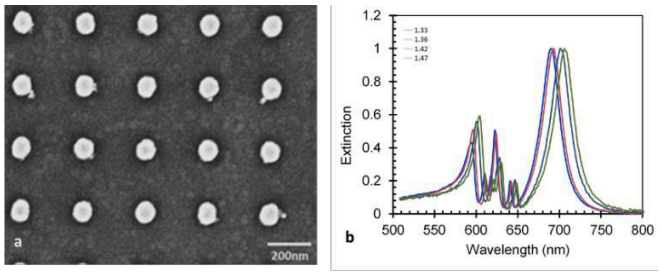

Fig. 1 (a) SEM image of the periodic array of gold nanodisks deposited on a glass substrate. (b) Extinction spectra of the periodic array, demonstrating a red shift in resonance response with an increasing refractive index of the surrounding medium.

III. Results and Discussion

The refractive index sensitivities of different plasmonic modes were systematically compared, including the localized surface plasmon resonance (LSPR) and two surface lattice resonance modes associated with the (1,0) and (1,1) diffractive orders of the array. Distinct spectral shifts were observed upon variation of the surrounding refractive index, revealing mode-dependent sensing responses. For certain lattice parameters, the resonances exhibit hybrid character arising from the coupling between LSPR and SLR modes, combining localized and collective plasmonic features. This hybridization was further confirmed by numerical simulations, which reproduce the experimentally observed resonance positions and dispersions.

Notably, SLR modes exhibit significantly enhanced refractive index sensitivities, reaching values up to 250 nm/RIU, substantially exceeding typical sensitivities associated with LSPR modes.

IV. Conclusion

We experimentally and numerically investigated the role of interparticle spacing in modulating resonance coupling in plasmonic metasurfaces. Increasing the interparticle distance enhances diffractive coupling, leading to resonances with reduced radiative and non-radiative losses, as evidenced by higher quality factors. We further demonstrate that the refractive index sensitivity of surface lattice resonances is strongly dependent on the coupling strength between localized plasmons and lattice diffraction modes. This coupling, governed by the lattice period, plays a key role in determining both the resonance quality factor and the sensing performance. Furthermore, the detection performance of SLRs is demonstrated to surpass that of localized surface plasmon resonances in terms of both sensitivity and figure of merit, confirming their strong potential for sensing applications.

Acknowledgments

This work was supported by the HorizonTech Research Initiative. The authors thank the AMBER Centre for fabrication support.

References

[1] V. G. Kravets, A. V. Kabashin, W. L. Barnes, et A. N. Grigorenko, « Plasmonic Surface Lattice Resonances: A Review of Properties and Applications », *Chem. Rev.*, vol. 118, nº 12, p. 5912-5951, juin 2018, doi: 10.1021/acs.chemrev.8b00243.

[2] M. S. Bin-Alam *et al.*, « Ultra-high-Q resonances in plasmonic metasurfaces », *Nat. Commun.*, vol. 12, nº 1, p. 974, févr. 2021, doi: 10.1038/s41467-021-21196-2.

[3] D. Men *et al.*, « Multi-mode detection of iodine based on Au@Ag nanoparticle array with highly sensibility and stability using plasmonic surface lattice resonances », *Sens. Actuators B Chem.*, vol. 398, p. 134743, janv. 2024, doi: 10.1016/j.snb.2023.134743.

Engineering High-Q Dielectric Metasurfaces for Enhanced Light-Matter Interaction and Multimodal Biosensing

J. F. Algorri [1,2,3,*], D.C. Zografopoulos[4,5], L. Rodríguez-Cobo[1,2,3], A. Cobo[1,2,3], M. Janneh[6], P. Vaiano[6], M. Pisco[6], A. Cusano[6]

[1]Photonics Engineering Group, Universidad de Cantabria, 39005 Santander, Spain.
[2]Instituto de Investigación Sanitaria Valdecilla, 39011 Santander, Spain.
[3]CIBER-BBN, Instituto de Salud Carlos III, 28029 Madrid, Spain
[4]School of Electrical and Computer Engineering, Aristotle University of Thessaloniki, GR-54124 Thessaloniki, Greece.
[5]CNR, IMM, Via del Fosso del Cavaliere 100, 00133 Roma, Italy
[6]Department of Engineering, University of Sannio, Benevento, 82100, Italy
*Corresponding author: algorrijf@unican.es

***Abstract*— To overcome fabrication vulnerabilities of traditional BICs in dielectric metasurfaces, we analyze robust high-Q resonances within fully symmetric unit cells. By comparing localized multipolar states in hollow nanocuboids against delocalized Surface Lattice Resonances in solid cuboids, we delineate fundamental fabrication and performance trade-offs to optimize real-world nanophotonic sensors.**

***Keywords*— dielectric metasurfaces, bound states in the continuum, surface lattice resonances, multipolar resonances.**

I. Introduction

In recent years, all-dielectric metasurfaces have emerged as a highly versatile platform for engineering light-matter interactions at the nanoscale. By leveraging high-refractive-index materials such as silicon, these structures overcome the severe ohmic damping inherent to plasmonic devices, enabling operation with minimal absorption losses in the visible and near-infrared spectra. Furthermore, the strong electromagnetic confinement within subwavelength dielectric resonators allows for the excitation of both electric and magnetic multipolar Mie resonances.

A prominent mechanism for achieving extreme electromagnetic field enhancement and ultra-high-quality factors (Q-factors) in these architectures is the excitation of Bound States in the Continuum (BICs) [1,2]. True BICs are perfectly confined, non-radiating states that exist within the radiation continuum but possess theoretically infinite Q-factors and zero resonance linewidth. By introducing controlled structural perturbations, these "dark" states can be coupled to free-space radiation, transforming into accessible quasi-BICs (qBICs) characterized by sharp, asymmetric Fano lineshapes [3].

Historically, the design of qBICs has relied heavily on symmetry-protected mechanisms, wherein the radiative lifetime of the mode is dictated by the degree of structural asymmetry introduced into the metasurface unit cell. While architectures such as asymmetric silicon slots have demonstrated tremendous theoretical potential for ultra-sensitive refractometric sensing [4], translating these designs into robust experimental platforms remains a critical challenge. Experimental realizations consistently reveal that measured Q-factors are orders of magnitude lower than their theoretical predictions [5]. This performance degradation is primarily driven by resonance damping caused by statistical variations in nanoscale features during electron-beam lithography, etching roughness, and the angular spread of the probing beam [6].

To overcome the physical vulnerabilities associated with symmetry-breaking, current research is pivoting toward robust high-Q mechanisms that do not rely on structural asymmetry [7,8]. In this regime, radiative decay is suppressed not by altering the geometry, but through mechanisms such as the destructive interference of competing resonant channels (Friedrich-Wintgen BICs) or collective diffractive coupling (Lattice Resonances) within fully symmetric unit cells.

In this contribution, we present a comprehensive study on the evolution of radiative loss engineering by comparing two distinct robust mechanisms in silicon-based metasurfaces: localized single-particle multipolar interference and delocalized Surface Lattice Resonances (SLRs). We first demonstrate how the precise geometric tuning of hollow silicon nanocuboids induces the cancellation of electric and toroidal dipoles (anapole state), yielding an ultra-high-Q resonance that is highly resilient to environmental impedance mismatch and ideally suited for novel Surface-Enhanced Raman Scattering (SERS) applications. Subsequently, we introduce an alternative, highly simplified architecture utilizing solid nanocuboids to excite SLRs by coupling Mie resonances with the diffractive Rayleigh anomaly. By analyzing the inherent trade-offs between the highly localized fields of toroidal dipoles

and the loss-tolerant, delocalized fields of SLRs, we provide a unified design framework for optimizing all-dielectric platforms across a variety of advanced sensing applications.

II. Methods

We employ the Finite Element Method (FEM) via COMSOL Multiphysics and Rigorous Coupled-Wave Analysis (RCWA) to conduct both full-wave scattering and eigenfrequency analyses of the metasurface unit cells. To accurately account for material dispersion during eigenvalue extraction, we utilize an auxiliary-fields formulation that explicitly incorporates the dispersive optical properties of the constituent materials across the near-infrared spectrum. To unravel the physical mechanisms driving both symmetry-protected BICs and toroidal states, we apply the Cartesian Multipole Decomposition Technique (CMDT) to the polarization currents of the evaluated eigenvectors. This decomposition allows us to quantify the dominant radiating and non-radiating (dark) moments, such as Cartesian electric/magnetic dipoles and toroidal quadrupoles, and systematically observe how they couple to the radiation continuum upon symmetry reduction or geometric tuning.

III. Beyond Symmetry-Breaking

To overcome the stringent fabrication limitations inherent to symmetry-protected modes, we pivot toward robust high-Q mechanisms that do not rely on structural asymmetry. In this paradigm, radiative decay is suppressed through interference phenomena within fully symmetric unit cells, fundamentally improving resilience to fabrication tolerances. Within this framework, we highlight two distinct design trends, localized multipolar interference and delocalized SLRs, illustrating a critical trade-off between environmental index matching and fabrication complexity.

The first mechanism leverages the multipolar interference within symmetric, hollow silicon nanocuboids. We demonstrate that precise geometric tuning of the cuboid's aspect ratio and central hole size induces the exact cancellation of broad Cartesian electric dipoles and toroidal dipole moments. This configuration yields a highly confined, non-radiating dark mode. By engineering the metasurface array to couple this dark state with broader "bright" background modes, the anapole state evolves into an ultra-high-Q Fano resonance. Numerical analyses confirm high Q-factors with a near-field enhancement localized tightly within the central void and gaps. From an application standpoint, this extreme localization provides distinct advantages. Most notably, this resonance is remarkably robust against environmental impedance mismatch. It remains highly functional even with significant refractive index contrast between the substrate and superstrate (e.g., a glass substrate paired with an air or water superstrate), entirely eliminating the need for symmetric index-matching. Furthermore, this architecture allows for a double-resonance condition, aligning a sharp resonance with a broader mode, making it an exceptionally powerful and novel all-dielectric platform for Surface-Enhanced Raman Scattering (SERS). However, this exceptional near-field performance comes with a fabrication caveat: etching the precise nanoscale central void required to support the toroidal mode presents scalable manufacturing challenges.

To circumvent the fabrication complexity of hollow structures, we introduce an alternative architecture based on SLRs utilizing simple, solid nanocuboids. Moving beyond single-particle interference, this mechanism relies on collective, diffractive coupling across the metasurface array. By engineering the array pitch, we couple localized, broadband Mie resonances with the diffractive Rayleigh Anomaly (RA) to generate a high-Q collective radiative mode accessible at normal incidence. The physics of the SLR represent a fundamental shift toward delocalized field manipulation. Unlike the internally confined multipoles, the electromagnetic energy of an SLR is distributed across the metasurface interface via evanescent decay. This delocalized nature severely limits the interaction of the field with the bulk volume of the superstrate, making the SLR mode extraordinarily robust to absorption losses within the fluidic analyte, a major advantage for bulk sensing applications. While the use of solid cuboids vastly simplifies the lithographic and etching processes, the SLR mechanism imposes strict environmental constraints. Being a diffractive effect, the SLR is highly sensitive to the array pitch and, crucially, requires a homogeneous refractive index environment (a symmetric substrate and superstrate) to properly support the delocalized resonance.

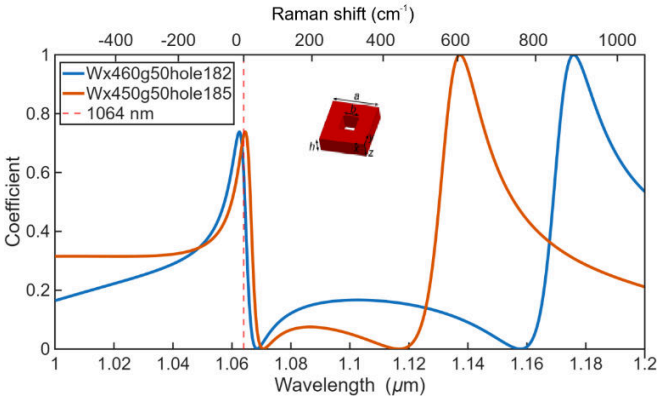

Fig. 1 Coefficient spectra of the fully symmetric hollow nanocuboid metasurface, highlighting a double-resonance condition. A sharp resonance is successfully tuned to the 1064 nm excitation line (red dashed line), alongside a broader localized mode. The inset depicts the 3D structural parameters of the unit cell.

In summary, these robust symmetric architectures provide a compelling alternative to symmetry-protected modes, but require a strategic choice based on the target application. Hollow metasurfaces offer unparalleled, localized near-field enhancement and immunity to index mismatch, ideal for SERS, but require complex fabrication. Conversely, solid SLR metasurfaces offer simplified fabrication and remarkable tolerance to analyte absorption losses, but demand strict refractive index matching to function.

IV. Conclusion

In conclusion, the successful translation of BICs from theoretical constructs into viable, real-world nanophotonic platforms necessitates a rigorous re-evaluation of radiative loss engineering. While our experimental implementations of

symmetry-protected quasi-BICs in silicon slot metasurfaces demonstrated competitive refractometric sensitivities and strong internal field confinement, they also revealed the inherent fragility of this physical mechanism. The reliance on nanoscale structural asymmetry makes these platforms highly vulnerable to fabrication tolerances, sidewall roughness, and angular dispersion, severely limiting their experimental quality factors. To address these vulnerabilities, we have demonstrated that pivoting toward robust high-Q mechanisms in fully symmetric unit cells offers a significantly more viable path.

Ultimately, there is no single "perfect" metasurface architecture. By understanding the distinct physical mechanisms driving both localized multipoles and delocalized SLRs, we can intelligently tailor all-dielectric silicon platforms to meet the specific fabrication and environmental demands of next-generation optical sensors and surface-enhanced spectroscopies.

ACKNOWLEDGMENTS

This work was supported by the R+D projects: INNVAL23/10, INNVAL24-28, and PREVAL23/05, funded by Instituto de Investigación Marqués de Valdecilla (IDIVAL); RYC2022-035279-I, funded by MCIN/AEI/10.13039/501100011033 and FSE+; TED2021-130378BC21, funded by MCIN/AEI/10.13039/501100011033 and European Union NextGenerationEU/PRTR; PID2022-137269OB-C22, funded by MCIN/AEI/10.13039/501100011033 and FEDER, UE. D.C.Z. acknowledges the support by the project PRIN-2022 ALPHA "ALl-dielectric resonant metasurfaces enhancing Photon emission phenomenA" (CUP:D53D23001060006) funded by the Italian Ministry of University and Research.

REFERENCES

[1] J. F. Algorri; F Dell'Olio, P. Roldán-Varona, L. Rodríguez-Cobo, J. M. López-Higuera, J. M. Sánchez-Pena, D. C. Zografopoulos. "Strongly resonant silicon slot metasurfaces with symmetry-protected bound states in the continuum," Optics Express. 29 (7), pp. 10374 - 10385. 2021. DOI: 10.1364/OE.415377

[2] J. F. Algorri, F. Dell Olio, P. Roldán-Varona, L. Rodriguez-Cobo, J. M. Lopez-Higuera, J. Sanchez-Pena, V. Dmitriev, and D. Zografopoulos, "Analogue of electromagnetically induced transparency in square slotted silicon metasurfaces supporting bound states in the continuum," Optics Express 30, 4615-4630 (2022) DOI:10.1364/OE.446720

[3] J.F. Algorri, V. Dmitriev, H.E. Hernández-Figueroa, L. Rodríguez-Cobo, F. Dell'Olio, A. Cusano, J.M. López-Higuera, D.C. Zografopoulos, Polarization-independent hollow nanocuboid metasurfaces with robust quasi-bound states in the continuum, Optical Materials 147, 114631, (2024) DOI: 10.1016/j.optmat.2023.114631

[4] M. Samadi, F. Abshari, J. F. Algorri, P. Roldán-Varona, L. Rodríguez-Cobo, J. M. López-Higuera, J. M. Sánchez-Pena, D. C. Zografopoulos and F. Dell'Olio, "All-Dielectric Metasurface Based on Complementary Split-Ring Resonators for Refractive Index Sensing," Photonics 9(3), 130 (2022) DOI: 10.3390/photonics9030130

[5] G. Nousios, J.F. Algorr , W. Fuscaldo, F. Dell'Olio , S. Romano , G. Zito, B. Miranda,Y. Ding,V. Dmitriev, L.C. Andreani, M. Galli, O. Tsilipakos, E.E. Kriezis, D.C. Zografopoulos "Silicon slot metasurface supporting a multitude of bound states in the continuum: theoretical and experimental studies," Optics and Laser Technology, 192, art. no. 113398 (2025) DOI: 10.1016/j.optlastec.2025.113398.

[6] J. F. Algorri, F. Dell'olio, Y. Ding, V. Dmitriev, J. M. López-Higuera, J. M. Sánchez-Pena, L. C. Andreani, M. Galli, and D. C. Zografopoulos, "Experimental demonstration of a silicon-slot near-infrared quasi-bound state in the continuum in resonant dielectric metasurfaces," Optics & Laser Technology 161(109199) (2023) DOI: 10.1016/j.optlastec.2023.109199.

[7] J. F. Algorri, D. C. Zografopoulos, A. Ferraro, B. García-Cámara, R. Beccherelli and J. M. Sánchez-Pena, "Ultrahigh-quality factor resonant dielectric metasurfaces based on hollow nanocuboids," Opt. Express 27, 6320-6330 (2019). DOI: 10.1364/OE.27.006320

[8] J. F. Algorri, D. C. Zografopoulos, A. Ferraro, B. García-Cámara, R. Vergaz, R. Beccherelli and J. M. Sánchez-Pena, "Anapole modes in hollow nanocuboid dielectric metasurfaces for refractometric sensing," Nanomaterials, 9(1), 1-13 (2019). DOI: 10.3390/nano9010030

Nanoimprinted Chiral Photonic Architectures for Circularly Polarized Photoluminescence

Agustín Mihi*, Jose Mendoza-Carreño, Xiaoyu Qi, Luis A. Pérez, Miquel Garriga, Isabel Alonso
Institute of Materials Science of Barcelona (ICMAB-CSIC),
Campus de la UAB, 08193 Bellaterra, Spain
corresponding author: amihi@icmab.es

***Abstract*—Soft nanoimprint lithography enables the scalable fabrication of nanophotonic architectures with high-resolution and over large areas. Here we demonstrate how the technique can be extended to create chiral metasurfaces (dielectric and metallic) exhibiting strong circular dichroism which can be transferred to nearby emitters to produce circularly polarized photoluminescence.**

***Keywords*— nanoimprinting, chirality, photoluminescence, lattice resonances.**

I. Introduction

Nanophotonic architectures enable advanced optical phenomena that can enhance optoelectronic device performance. However, large-scale integration requires fabrication methods that are cost-effective, scalable, and compatible with established device processing techniques. This is even more challenging in the are of chiral nanophotonics.

II. Methods

Soft nanoimprint lithography (s-NIL) relies in the use of pre-patterned elastomeric stamps to fabricate photonic structures from resists, biopolymers, colloids, and nanomaterials. This approach enables sub-50 nm resolution over large areas. In our variation of s-NIL we used elastomeric molds pre-patterned with chiral motifs to induce the order of different metal colloids (Fig 1) resulting in chiral plasmonic lattices. We also can pattern thin films which coated with titanium dioxide exhibit a broad set of chiroptical properties over the visible range.

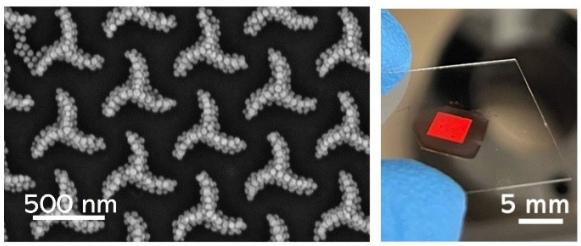

Fig. 1 SEM and photograph of a chiral plasmonic array made with silver colloids.

III. Results and Discussion

Chiral plasmonic gratings made with non-chiral metal colloids exhibit strong circular dichroism ($g \approx 0.4$) which can be transferred to an organic dye placed on top. The high refractive index counterparts made with titanium dioxide become a single chiral platform supporting broadband visible chiroptical resonances which are used to transfer chirality to multiple emitters, achieving glum > 1.

IV. Conclusion

Soft nanoimprint lithography provides a scalable route to high-performance nanophotonic and chiral architectures. The demonstrated structures offer strong optical activity, efficient chirality transfer, and compatibility with diverse materials, supporting practical integration into advanced optoelectronic and photonic applications.

Acknowledgments

This work has received funding from the Spanish Agencia Estatal de Investigación (MCIN/AEI/10.13039/501100011033) through grants, PID2022-141956NB-I00 (OUTLIGHT), and CEX2023-001263-S (Spanish Severo Ochoa Centre of Excellence program). This research was also supported by the EIC PATHFINDER CHALLENGES project 101162112 (RADIANT), funded by the European Union.

References

[1] **[1]** J. Mendoza-Carreño et al., "A single nanophotonic platform for producing circularly polarized white light from non-chiral emitters," *Nature Communications*, vol. 15, Art. no. 10443, 2024, doi:10.1038/s41467-024-54792-z.

[2] **[2]** X. Qi et al., "Chiral plasmonic superlattices from template-assisted assembly of achiral nanoparticles," *Nature Communications*, vol. 16, Art. no. 1687, 2025, doi:10.1038/s41467-025-56999-0.

[3] **[3]** X. Qi, L. A. Pérez, M. I. Alonso, and A. Mihi, "High Q-Factor plasmonic surface lattice resonances in colloidal nanoparticle arrays," *ACS Applied Materials & Interfaces*, vol. 16, no. 1, pp. 1259–1267, 2024, doi:10.1021/acsami.3c08617.

Photoelectrochemical Chiral Nanofabrication by Circularly Polarized Light

Takuya Ishida[1,2,*], Tetsu Tatsuma[3]

[1]Center for Optical Research and Education, Utsunomiya University, Japan
[2]JST PRESTO
[3]Institute of Industrial Science, The University of Tokyo
*Corresponding author: t-ishida@a.utsunomiya-u.ac.jp

***Abstract*— We demonstrate bottom-up chiral nanofabrication driven by circularly polarized light (CPL). CPL-induced chiral near-field distribution around plasmonic nanoparticles enables site-selective growth via photoelectrochemical reactions, leading to chiral nanostructures. Extending this concept to magneto-chiral nanocomposites yields directional dichroism under static magnetic fields, providing a scalable route to nonreciprocal metamaterials.**

***Keywords*— circularly polarized light, chiral near-field distribution, nanofabrication, magneto-chiral metamaterials.**

I. Introduction

Chiral nanostructures, a representative form of bianisotropic metamaterials, exhibit magnetoelectric coupling in which the magnetic field component of light can induce electric polarization even in the visible to near-infrared region, leading to strong chiroptical responses and optical nonreciprocity. However, the fabrication of chiral nanostructures remains challenging. Here, we present a bottom-up approach to chiral nanofabrication. A key feature of our method is that, whereas conventional bottom-up strategies typically rely on chiral molecules as the chiral source, we use CPL to induce the chiral shaping of nanoparticles (Fig. 1).[1-4]

II. Methods

As a representative example, Au nanocubes exhibiting localized surface plasmon resonance (LSPR) were immobilized on a TiO_2 film and irradiated with CPL in the presence of Pb^{2+} ions.[2] Electric field distributions and optical responses were calculated using finite-difference time-domain simulations.[1-5]

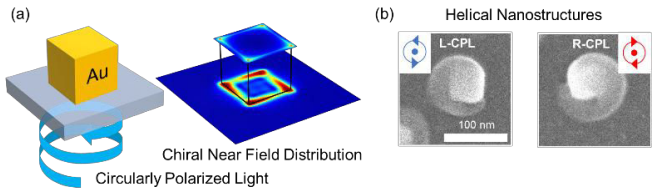

Fig. 1 (a) CPL induces a chiral near-field distribution. (b) Chiral Au–PbO_2 nanocomposites.

III. Results and Discussion

Under left- and right-handed CPL, the near-field distributions around a Au nanocube become mirror images of each other (Fig. 1a).[5] In regions where the near field is strongly enhanced, plasmon-induced electron–hole pairs are generated. In the presence of Pb^{2+} ions, its oxidation driven by the holes leads to site-selective deposition of PbO_2 and the formation of chiral Au–PbO_2 nanocomposites (Fig. 1b). As a result, the fabricated nanostructures exhibit clear circular dichroism at the LSPR wavelengths, with opposite signs depending on the handedness of the incident CPL.

Furthermore, we extend this concept to magneto-chiral nanocomposites, where superparamagnetic Fe_3O_4 nanoparticles serve as magnetic cores. CPL-induced reduction of Ag^+ ions and deposition of Ag, driven by photocatalytic reduction on Fe_3O_4 and plasmon-assisted reduction on deposited Ag[3,4], produced chiral Fe_3O_4–Ag nanocomposites, thereby breaking spatial inversion and time-reversal symmetries. Under an external static magnetic field, these nanocomposites exhibit directional dichroism in the visible range, demonstrating a feasible pathway toward magneto-chiral metamaterials with nonreciprocal optical responses. This light-driven shaping mechanism provides a scalable route toward chiral and magneto-chiral nanostructures.

IV. Conclusion

We have established CPL-driven chiral near-field engineering as a powerful strategy for constructing chiral and magneto-chiral nanomaterials. Future work will extend this approach to other classes of bianisotropic metamaterials, including omega- and Tellegen-type systems.

Acknowledgments

This work was supported by a Grant-in-Aid for Scientific Research (C) (No. JP24K08359), and JST PRESTO (No. JPMJPR24L3).

REFERENCES

[1]. K. Saito and T. Tatsuma, “Chiral Plasmonic Nanostructures Fabricated by Circularly Polarized Light,” Nano Letters, vol. 18, pp. 3209–3212, 2018.

[2]. K. Shimomura, Y. Nakane, T. Ishida, and T. Tatsuma, “Photofabrication of Chiral Plasmonic Nanospiroids,” Applied Physics Letters, vol. 122, 151109, 2023.

[3]. T. Ishida, A. Isawa, S. Kuroki, Y. Kameoka, and T. Tatsuma, “All-Plasmonic-Metal Chiral Nanostructures Fabricated by Circularly Polarized Light,” Applied Physics Letters, vol. 123, 061111, 2023.

[4]. Y. Kameoka, T. Ishida, S. H. Lee, and T. Tatsuma, "Symmetry Breaking and Chiral Shaping of Au Nanodisks by Plasmon-Induced Ag Deposition under Circularly Polarized Light," Electrochemistry, vol. 93, 094006, 2025.

[5]. N. Ichiji, T. Ishida, I. Morichika, T. Tatsuma, and S. Ashihara, “Rotationally Displaced Electric Field Intensity Distribution around Square Nanoantennas Induced by Circularly Polarized Light,” Physical Review B, vol. 109, 035428, 2024.

Mie Voids for Refractive Index Measurement of Unknown Water under High-Pressure

Hiromasa Niinomi[1,2,*], Hiroki Nada[3], Tetsuya Hama[4], Kazuhiro Gotoh[5], Yumiko Kodama[6], Tomoya Oshikiri[1,2], Masaru Nakagawa[1,2,7], Yuki Kimura[8]

[1]Institute of Multidisciplinary Research for Advanced Materials, Tohoku University, Japan
[2]S-Hub, Tohoku University, Japan
[3]Graduate School of Engineering, Tottori University, Japan
[4]Komaba Institute for Science, The University of Tokyo, Japan
[5]Graduate School of Science and Technology, Niigata University, Japan
[6]Institute for Materials Research, Tohoku University, Japan
[7]Photonic Meta Sensing Co-creation Research Center, Tohoku University, Japan
[8]Institute of Low Temperature Science, Hokkaido University, Japan
*Corresponding author: hiromasa.niinomi.b2@tohoku.ac.jp

***Abstract*— We developed a novel method for refractive index (RI) sensing of materials under high-pressure using Mie voids fabricated on a 4H-SiC anvil in an anvil cell, enabling *in-situ* local measurement of RI in materials under high-pressure inaccessible by conventional methods including unknown water at interfaces between water and high-pressure ices.**

***Keywords*— Mie void, Refractive index sensing, High-pressure, Anvil cell, Homoimmiscible water.**

I. Introduction

Measurement of refractive index (RI) of materials under high-pressures is important in materials science for the clarification of dielectric properties of unique states of condensed matters under high-pressure such as unknown water, which macroscopically separates from bulk water, at non-equilibrium interfaces water and high-pressure ices (homoimmiscible water).[1] Conventional methods such as interferometry in conjunction with an anvil cell generally require technically challenging optical setups, complex analyses, and homogeneity of the target sample. Novel insights would be provided by the development of a simple method for *in-situ* measurement of local RI of materials under confinement by anvil cell. Here, we developed simple, *in-situ* and local RI measurement method by applying Mie-void-resonance-based RI sensing[2] to RI sensing under high-pressure by using Mie voids fabricated on a 4H-SiC anvil in an anvil cell.[3]

II. Methods

Reflection spectra of a Mie void array fabricated on a 4H-SiC anvil were obtained using a reflection-optical microscope connected to a hyperspectral camera in the process of depressurization of ultrapure water.

III. Results and Discussion

Figure 1 shows the optical micrographs and the reflection spectra of the Mie void array in the process of depressurization. The spectrum of the void array showed 25 nm blue-shift by depressurization. This suggests that the sensitivity was approximately 290 nm/RIU, which is comparable to that of plasmon-based RI sensing. Since Mie-void-based RI sensing can detect local RI change of materials inside of the void,[2] our method can measure RI of homoimmiscible water, which locally forms at water/high-pressure ices interfaces, in principle.

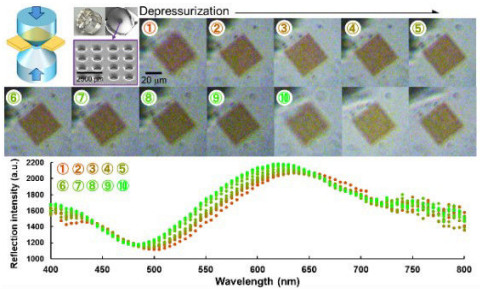

Fig. 1 Reflection optical micrographs and their reflection spectra in the process of depressurization. The figures were adopted from ref. 3 under the CC-BY-4.0 license.

IV. Conclusion

We first demonstrated Mie-void-based RI sensing of a high-pressure material under confinement by anvil cell as a novel, simple, *in-situ* and local RI sensing method.

References

[1] H. Niinomi et al., "Low-and high-density unknown waters at ice–water Interfaces," *J. Phys. Chem. Lett.*, vol. 13(19), pp. 4251–4256, 2022.
[2] S. Arslan et al., "Attoliter Mie Void Sensing," *ACS Photonics*, vol. 12(7), pp. 3950–3958, 2025.

[3] H. Niinomi et al., “Mie Voids for High-Pressure Refractive Index Sensing,” *J. Phys. Chem. C*, vol. 129(46), pp. 20676–20683, 2025.

Exploring the Origins of Circular Dichroic Optical Forces at the Nanoscale

Junsuke Yamanishi[1,*]

[1]Graduate School of Engineering Science, The University of Osaka, Japan
*Corresponding author: yamanishi.es@osaka-u.ac.jp

***Abstract*—We investigate the microscopic origin of circular dichroic optical forces at the nanoscale using photoinduced force microscopy. We reveal three distinct contributions: intrinsic material chirality, local chirality in achiral assemblies, and probe-induced symmetry breaking. Our results establish a unified framework for interpreting circular dichroic optical forces in near-field measurements.**

***Keywords*— circular dichroism, optical force, near-field optics.**

I. Introduction

Circular dichroism (CD) is a fundamental signature of structural chirality and plays a central role in chemistry, nanophotonics, and metamaterials. While conventional CD spectroscopy provides ensemble-averaged information, many artificial and natural nanostructures exhibit spatially localized or emergent chirality that cannot be resolved in the far-field [1].

Recent advances in photoinduced force microscopy enable nanoscale visualization of optical forces generated by light-matter interactions [2]. When circularly polarized illumination is applied, enantio-selective optical forces can emerge [3, 4]. However, the physical origin of circular dichroic (CD-) force signals remains unclear. It is not evident whether these forces arise solely from intrinsic material chirality or whether geometrical and probe-induced effects also contribute.

In this work, we systematically investigate the origins of CD-forces at the nanoscale and establish a unified framework for interpreting CD-forces in near field measurements.

II. Methods

CD-force measurements were performed using a heterodyne frequency modulation photoinduced force microscopy system combined with frequency modulation atomic force microscopy. This configuration enables selective detection of optical gradient forces while suppressing photothermal background contributions [5, 6].

Left and right circularly polarized laser light was introduced through the substrate to illuminate both the nanostructure and the probe apex. The modulation scheme allowed differential detection of forces under opposite circular polarizations, directly isolating the CD-force component.

To disentangle the physical origin of the observed signals, we investigated three representative systems: three-dimensional chiral gold nanoparticles, achiral gold nanoparticle dimers, and single spherical gold nanoparticles. All measurements were performed in the non-contact regime to minimize thermal and mechanical artifacts.

III. Results and Discussion

CD-force signals were clearly resolved at the nanoscale under circularly polarized illumination. For intrinsically chiral gold nanoparticles, the measured force contrast reverses sign with handedness, consistent with enantioselective light-matter interaction. The spatial distribution of the force signal follows the local CD of the near-field around the particle.

In achiral gold nanoparticle dimers, finite CD-force signals were observed despite the absence of intrinsic structural chirality. The signal magnitude and sign depend strongly on the position relative to the dimers, indicating that the locally induced chirality generates near-field CD responses.

For single spherical gold nanoparticles, CD-force signals were also detected. Since the particle itself is fully achiral, this observation reveals the contribution of probe-induced symmetry breaking inherent to photoinduced force microscopy. The interaction between the probe apex and the nanoparticle forms a chiral measurement configuration, generating a measurable force contrast.

These results demonstrate that CD-forces at the nanoscale arise from three fundamentally distinct mechanisms: intrinsic material chirality, local chirality, and probe induced symmetry breaking. The coexistence of these contributions explains previous ambiguities in interpreting near field CD signals and highlights the importance of carefully separating measurement-induced effects from genuine material chirality.

IV. Conclusion

We have demonstrated that CD-forces at the nanoscale originate from three distinct physical mechanisms: intrinsic structural chirality, local chirality in achiral assemblies, and probe induced symmetry breaking inherent to near field measurements. By systematically separating these contributions, we establish a unified physical framework for interpreting CD-force signals.

This work clarifies ambiguities in nanoscale CD measurements and provides a foundation for quantitative

analysis of chiral light matter interactions beyond conventional far field spectroscopy. The results open new possibilities for exploring structured light interactions and symmetry-controlled nanophotonic systems.

Acknowledgments

This work was supported by JSPS KAKENHI (grant nos. JP22H05131, JP22H05135, JP21H04641, and JP22H01901). This work was also supported by the Frontier Photonic Sciences Project of the National Institutes of Natural Sciences (NINS) (Grant Numbers 01212403, and 01212201), the NINS program for cross-disciplinary study (Grant Number 01312103), and the grant of OML Project by the National Institutes of Natural Sciences (NINS program No. JPMXP1223MS5027). We would like to express our gratitude to Equipment Development Center of the Institute for Molecular Science for assistance with the experimental setup.

References

[1] L. D. Barron, *Molecular Light Scattering and Optical Activity*, Cambridge University Press, 2009.
[2] I. Rajapaksa, K. Uenal, and H. K. Wickramasinghe, "Image force microscopy of molecular resonance: A microscope principle," *Appl. Phys. Lett.*, vol. 97, 073121, 2010.
[3] M. Kamandi, et al., "Enantiospecific detection of chiral nanosamples using photoinduced force," *Phys. Rev. Appl.*, vol. 8, 064010, 2017.
[4] J. Yamanishi, H. Y. Ahn, and H. Okamoto, "Nanoscopic observation of chiro optical force," *Nano Lett.*, vol. 23, pp. 9347–9352, 2023.
[5] J. Yamanishi, et al., "Heterodyne frequency modulation in photoinduced force microscopy," *Phys. Rev. Appl.*, vol. 9, 024031, 2018.
[6] J. Yamanishi, et al., "Optical force mapping at the single nanometre scale," *Nat. Commun.*, vol. 12, 3865, 2021.

Ultimate Magneto-Optical Bounds at the Nanoscale

Jorge Olmos Trigo
[1]Departamento de Fısica de Materiales, Universidad Autonoma de Madrid, 28049 Madrid, Spain.
*Corresponding author: jolmostrigo@gmail.com

***Abstract*—Controlling light–matter interactions with external static magnetic fields is a central goal of non-reciprocal photonics. Despite the field's maturity, it remains unknown whether an upper bound on the magneto-optical activity of nanoparticles exists—and, if so, what its ultimate limit might be. In this work, we demonstrate that such an upper bound does exist. We derive a simple expression for this fundamental limit and show that it an be reached only by non-absorbing nanoparticles. This bound, rooted in energy conservation, constrains all observables derived from the polarizability tensor of magneto-optically active nanoparticles. As illustrative examples, we show how it limits the maximum attainable signals in Magnetic Circular Dichroism and the Faraday effect, two cornerstone techniques to detect magneto-optical activity at the nanoscale.**

***Keywords*— magneto-optics, nanoparticles, external magnetic fields.**

I. Introduction

An object is said to be magneto-optically active if its electromagnetic properties are modified under the action of an externally applied static magnetic field. Since the discovery of magneto-optical activity by Michael Faraday in 1845 [1], researchers have sought to enhance the intrinsically weak magneto-optical response of non-reciprocal nanoparticles (NPs) by optimizing the conditions under which light fields interact with them. At the material level, both metallic and dielectric NPs have been widely employed to strengthen magneto-optical interactions by leveraging their plasmonic and Mie resonances, respectively. Beyond controlling the response of magneto-optical NPs at the single particle level, arranging them into ordered lattices enables collective resonances that can further augment the magneto-optical activity.

Despite the ongoing interest in all these nanophotonic strategies, a fundamental understanding of the ultimate limit of magneto-optical activity at the nanoscale is lacking in the field. So far, no general framework exists to answer a deceptively simple but profound question: How large can the magneto-optical activity of a NP be? In particular, it remains unknown whether a upper bound exists and, if so, what determines its value, including possible dependencies on material composition, illumination conditions, and the strength and direction of the externally applied static magnetic field.

In this work, we analytically demonstrate that the magneto-optical activity of NPs is subject to an ultimate upper bound. We obtain a simple, explicit expression for its value and show that it can be reached if and only if the NPs are lossless. Importantly, this upper bound follows from an exact energy conservation law in magneto-optics and depends exclusively on scalar polarizabilities [2]; it therefore constitutes an inherent limit for any magneto-optical NP, independent of both illumination conditions and magnetic-field strength.

Moreover, this upper bound constrains all observables that are derived from the polarizability tensor of magneto-optical NPs. As examples, we show how the Magnetic Circular Dichroism and Faraday effect, two of the most widely employed techniques for probing magneto-optical activity at the nanoscale, are strictly constrained by this ultimate limit [3].

II. Methods

- To describe the optical response of magneto-optically active Nps we employ the widely used linear dipolar approximation.
- To find the energy-bounds we use the hermitian properties of a semipositive defined absorbance matrix. In particular, we use the Sylverter's criteria.
- To describe the polarizability of the system we use the widely used magneto-optical Drude model.

III. Conclusion

We have demonstrated that the magneto-optical activity of NPs has an ultimate upper bound. We have found its exact value and showed that this can be attained I and only if the NP is lossless. This limitation underscores the importance of selecting nonabsorbing NPs when seeking extreme magneto-optical responses at the single-particle level.

References

[1] M. Faraday, Philosophical transactions of the Royal Society of London , 145 (1857).
[2] J. Olmos-Trigo. arXiv preprint arXiv:2601.10255
[3] J. Olmos-Trigo. Magneto-optical activity of nanoparticles reaches an ultimate upper bound. Submitted to PRL on 9 February.

A single photon source for the THz regime

Diego Martín Cano[1,2,3*], Caspar Groiseau[4],
Antonio Fernández-Domínguez[1,2,3], Miguel Ángel Martínez-García[1,2,3,]
Carlos Sánchez Muñoz[5]

[1] Departamento de Física Teórica de la Materia Condensada,

[2] Condensed Matter Physics Center (IFIMAC) and

[3] Instituto Nicolas Cabrera (INC), Universidad Autónoma de Madrid, E-28049 Madrid, Spain.

[4] Department of Microtechnology and Nanoscience, Chalmers University of Technology, 41296 Gothenburg, Sweden.

[5] Institute of Fundamental Physics, IFF-CSIC, Madrid, Spain.

*Corresponding author: diego.martin.cano@uam.es

***Abstract*— We propose a feasible single-photon source that performs over the THz frequency regime based on a single quantum polar emitter coupled to a nanocavity. We demonstrate nonclassical photon correlations showing the single photon nature of its emission as well as the nonlinear production of multiphoton pairs.**

***Keywords*— Single photon sources, terahertz, quantum emitters,.**

I. Introduction

Terahertz (THz) radiation, spanning frequencies from 0.1 THz to 70 THz, is one of the latest explored gaps in the electromagnetic spectrum, with diverse applications in communications, biology and medicine, vibrational spectroscopy, and materials characterization [1]. The historical lag in the advancement of classical THz technology, combined with the lack of bright and efficient photonic transitions at THz frequencies—typically found in molecules, superconducting junctions, or semiconductors— has hindered the experimental discovery of THz single-photon emitters (SPEs). Developing such THz SPEs would establish an alternative quantum optical platform, bridging the challenges of the visible and microwave spectra while paving the way for innovative quantum optics sources and experiments in this frequency range. In this work, we present a design strategy for a tunable single-photon source operating in the THz regime [2].

II. Methods

Our methodology integrates quantum optical simulations and analytical calculations based on feasible electromagnetic calculations and experimental parameters [2].

III. Results and Discussion

- Our approach converts incident visible photons into THz output photons using three key components: an optical laser, a nanophotonic THz cavity, and a single polar quantum emitter. The interaction between the emitter and the laser fields induces THz transitions via the emitter's permanent dipole moment, which couples to the THz nanocavity (see Fig.1). We demonstrate that this setup can generate strongly antibunched THz radiation with significant brightness, while enabling optical tunability of key properties, such as emission frequency and quantum statistics [2]. Finally we also perform time domain excitations to demonstrate deterministic and heralded emission in THz hybrid nanocavity scenarios [3].

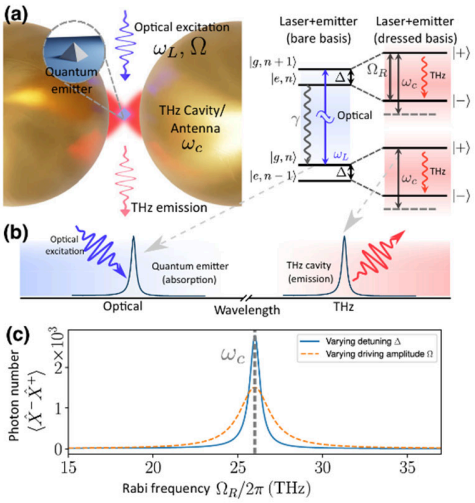

Fig. 1 (a) Sketch of the implementation (left) and energy levels (right): the left side represents the bare states basis while the right one represents the dressed-state basis highlighting THz transitions (red). (b) Absorption and emission properties in the THz and the optical domain. (c) Resonance in the cavity population as the Rabi frequency crosses the cavity frequency.

IV. Conclusion

We have demonstrated the design of CW and deterministic single photon sources for the THz regime based on polar quantum emitters coupled to a THz nanocavity. We show that this scheme is feasible with current state-of-the-art nanophotonic technology, providing a new pathway for exploring quantum optics in the THz regime [4,5].

Acknowledgments

This work makes use of the Quantum Toolbox in Python (QuTiP) [6]. We acknowledge financial support from the Proyecto Sinergico CAM 2020 Y2020/TCS- 6545 (NanoQuCoCM), and MCINN projects PID2021-126964OBI00 (QENIGMA), (ADIQUNANO) and TED2021-130552B-C21 PID2024-156077OB-I00 (DQUOTE). C. S. M. acknowledges support by the project PID2023-149969NA-100 funded by the Spanish Agencia Estatal de Investigación MICIU/AEI/10.13039/501100011033, and by a 2025 Leonardo Grant for Scientific Research and Cultural Creation from the BBVA Foundation. C. S. M. and D. M. C. also acknowledge the support of a fellowship from la Caixa Foundation (ID 100010434), from the European Union's Horizon 2020 Research and Innovation Programme under the Marie Sklodowska-Curie Grant Agreement No. 847648, with fellowship codes LCF/BQ/PI20/11760026 and LCF/BQ/PI20/11760018. D. M. C. also acknowledges support from the Ramon y Cajal program (RYC2020-029730-I). C. G. acknowledges support from the Knut and Alice Wallenberg Foundation through the Wallenberg Centre for Quantum Technology (WACQT).

References

[1] M. Tonouchi,"Cutting-edge terahertz technology", Nature Photonics, vol. 1, pp. 97–105 ,2007.

[2] C. Groiseau, A. Fernández-Domínguez, D. Martín-Cano and C.S. Muñoz," Single-photon source over the terahertz regime", PRX Quantum, vol. 5, pp. 010312, 2024.

[3] C Groiseau, MÁ Martínez-García, D Martín-Cano, CS Muñoz, "Deterministic single-photon source over the terahertz regime" arXiv preprint, arXiv:2509.26486, 2025.

[4] W. Chen, et al.,"Continuous-wave frequency upconversion with a molecular optomechanical nanocavity", Science, vol. 374, pp. 1264–1267, 2021.

[5] R. Chikkaraddy, R. Arul, L. Jakob, and J.J. Baumberg," Single-molecule mid-infrared spectroscopy and detection through vibrationally assisted luminescence", Nature Photonics, vol. 17, pp. 865–871, 2023.

[6] J. R. Johansson, P. D. Nation, and F. Nori, "QuTiP 2: A Python framework for the dynamics of open quantum systems", Computer Physics Communications, vol. 184, pp. 1234, 2013.

Optically Enhancing or Detecting Single Molecules on DNA Origamis

Sebastien Bidault

Institut Langevin, CNRS, ESPCI Paris, PSL University, Paris, France
sebastien.bidault@espci.fr

***Abstract*— We demonstrate how plasmonic dimers on DNA origamis are a versatile platform to sense or detect single molecules. In particular, we develop a colorimetric biosensor for single DNA strands with femtomolar sensitivity and single-mutation specificity. We also demonstrate bright single photon sources with picosecond lifetimes at room temperature.**

***Keywords*— Plasmonics, DNA origamis, biosensing, enhanced fluorescence, single molecules.**

The ability to monitor single molecules or biomolecules with light is at the heart of numerous technologies ranging from diagnostic tools in biotechnology to single-photon sources in quantum technologies. However, single molecules interact extremely weakly with optical electromagnetic fields at room temperature: a fluorescent molecule resonantly interacts with less than one in a million photons that are focused on it, while, for a typical biomolecule, this value drops by a further 6 orders of magnitude. Using DNA origamis in conjunction with gold nanoparticles, we craft complex hybrid nanostructures that are capable of translating the detection of single short DNA strands into macroscopic color changes (Figure 1, left) or of enhancing the fluorescence of single molecules by several orders of magnitude (Figure 1, right). These architectures open exciting perspectives for the development of new biosensing strategies with single molecule sensitivity, as well as for the study of coherent interactions between light and single quantum emitters at room temperature.

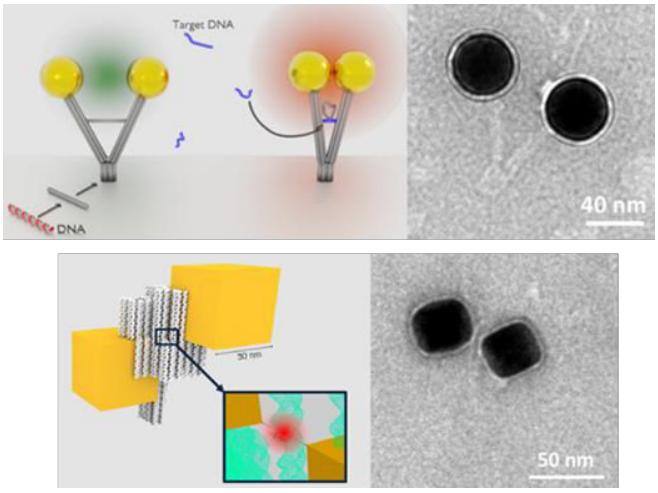

Fig. 1 (left) Scheme and TEM image of a hybrid gold-DNA origami nanostructure, which changes color when interacting with a specific DNA single-strand. (right) Scheme and TEM image of a plasmonic nanocube dimer capable of enhancing the fluorescence of a single molecule.

Modelling the Purcell Enhancement on Nonlocal Metasurfaces

Joshua T. Y. Tse[1,*], Taisuke Enomoto[2], Shunsuke Murai[1], Katsuhisa Tanaka[2]

[1]Department of Physics and Electronics, Osaka Metropolitan University, Japan
[2]Department of Material Chemistry, Kyoto University, Japan
*Corresponding author: jtytse@omu.ac.jp

***Abstract*— Spontaneous emission of photons can be enhanced with metasurfaces. Yet, accurately predicting the enhancement factor has presented a challenge for empirical systems. We proposed a versatile analytical model that describes the Purcell effect of metasurfaces coupled with a photoluminescence thin film with spectral parameters.**

***Keywords*— Purcell effect, nonlocal metasurfaces, analytical modelling.**

I. Introduction

Metasurfaces supporting optical resonances have been widely utilized to enhance the Purcell effect, through both increased local density of states (LDOS) for enhanced spontaneous emission rate and redirecting the emitted photons to specific out-coupling channels.[1,2] Theoretically, we know that the Purcell enhancement is proportional to Q/V, where the quality factor Q is divided by the effective modal volume V. This represents the temporal and spatial confinement of the metasurface respectively. However, while Q is straightforward to define and measure, V was known to be difficult to determine experimentally or analytically.

II. Methods

We recently reported about our new analytical model that predicted the Purcell enhancement factor of nonlocal metasurfaces through parameters fitted from spectral measurements.[3,4] In particular, our model predicts the photoluminescence enhancement (PLE) to follow:

$$\mathrm{PLE}(\omega_0) = \frac{c\Gamma_{\mathrm{rad}}}{\omega_0 t \Gamma_{\mathrm{tot}}{}^2} \frac{\Gamma_{\mathrm{abs,dye}}}{\kappa}$$

where ω_0 is the resonant frequency, t is the dye layer thickness, κ is the extinction coefficient of the dye layer, and c is the speed of light in vacuum. $\Gamma_{\mathrm{tot}} = \Gamma_{\mathrm{rad}} + \Gamma_{\mathrm{abs,dye}} + \Gamma_{\mathrm{abs,NP}}$ is the total decay rate where Γ_{rad} is the radiative decay rate, $\Gamma_{\mathrm{abs,dye}}$ and $\Gamma_{\mathrm{abs,NP}}$ are the absorptive decay rates contributed by the dye layer and the nanoparticles. This model dissects the underlying mechanisms of the Purcell effect into the contributions from the quality factor, the spatial confinement and the out-coupling efficiency of emitted photons.

III. Results and Discussion

We then verify our analytical model with numerical and experimental metasurfaces. We analyzed the Purcell effect and the out-coupling of the enhanced luminescence on metasurfaces supporting *quasi*-bound states in the continuum (q-BIC) and surface lattice resonances (SLR). As illustrated in Fig. 1, the analytical model accurately predicted the numerical and experimental PLE of a variety of metasurfaces.

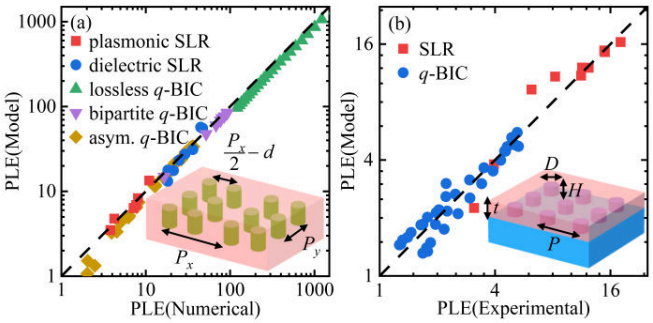

Fig. 1. The analytical PLE accurately predicts the (a) numerical and (b) experimental PLE. Insets: Metasurfaces supporting (a) q-BIC and (b) SLR.

IV. Conclusion

In conclusion, we developed an analytical model that describes the Purcell effect on metasurfaces and predicted the PLE that can be observed from resonant modes. This result presents a useful analytical framework for optimizing metasurfaces for luminescence applications.

Acknowledgments

This work was partly supported by Kakenhi, MEXT, Japan.

References

[1] C. Sauvan, J. P. Hugonin, I. S. Maksymov, and P. Lalanne, *Phys. Rev. Lett.* **110**, 237401 (2013).
[2] M. Ramezani, G. Lozano, M. A. Verschuuren, and J. Gómez-Rivas, *Phys. Rev. B* **94**, 125406 (2016).
[3] J. T. Y. Tse, S. Murai, and K. Tanaka, *Phys. Rev. A* **111**, 013511 (2025).
[4] J. T. Y. Tse, T. Enomoto, S. Murai, and K. Tanaka, *Nanophotonics* **14**, 5407 (2025).

Structural colours using transition metal dichalcogenide nanostructures

Ida Juliane Bundgaard[1,*], Yonas Lebsir[1], Catarina Ferreira[1,2], Christos Tserkezis[1]

[1] POLIMA — Center for Polariton-driven Light–Matter Interactions, University of Southern Denmark
[2] SCC — SDU Climate Cluster, University of Southern Denmark
*Corresponding author: bundgaard@mci.sdu.dk

***Abstract*—We introduce transiton metal-dichalcogenide (TMD) nanostructures as a promising platform for the realization of structural colours. Processing of semianalytically calculated reflectance spectra of TMD nanosphere arrays shows a wide range of colours, which are obtained simply through tailoring the radius and separation of spheres in the array. *Keywords*— structural colours, nanostructures, TMDs, light-matter interactions.**

I. Introduction

The continuous interest in structural colours as a route towards sustainable and recyclable products [1], or for efficient anti-counterfeiting tools [2] has been driving advances in material science and nanoengineering. One avenue of progress is expanding our arsenal of materials and architectures for producing colours. Here, we propose transition metal dichalcogenides (TMDs), which have the advantage of being high-index materials and important components in the research of optoelectronics. In this work we theoretically explore the possibility of structural colours stemming from TMD nanostructures in the form of arrays of spherical nanoparticles (NPs).

II. Methods

All results were obtained using semi analytical methods, specifically using the T-matrix-based software Treams [3]. The permittivity for WS_2, used for the computation of the data in Fig. 1, comes from the experimental results of [4].

III. Results and Discussion

As can be seen in Fig. 1c and Fig. 1e, our investigation [5] has shown that it is possible to create a range of colours utilising arrays of spherical NPs made from one of the most commonly used TMDs (WS_2). NP arrays present a superior platform for structural colours compared to slabs of the same materials, as shown in [5], due to the tailoring possibilities and the effect of multiple scattering as opposed to cavity resonances. Additionally, the interaction of the NP Mie modes with TMD excitons presents itself as an additional mechanism for controlling spectral features. Further tuneability, and experimental feasibility, can be achieved through TMD nanodiscs.

IV. Conclusion

Arrays of spherical NPs made from TMDs provide a good platform for the realization of structural colours, especially due to their many tailorable parameters allowing to reproduce much of the colour spectrum.

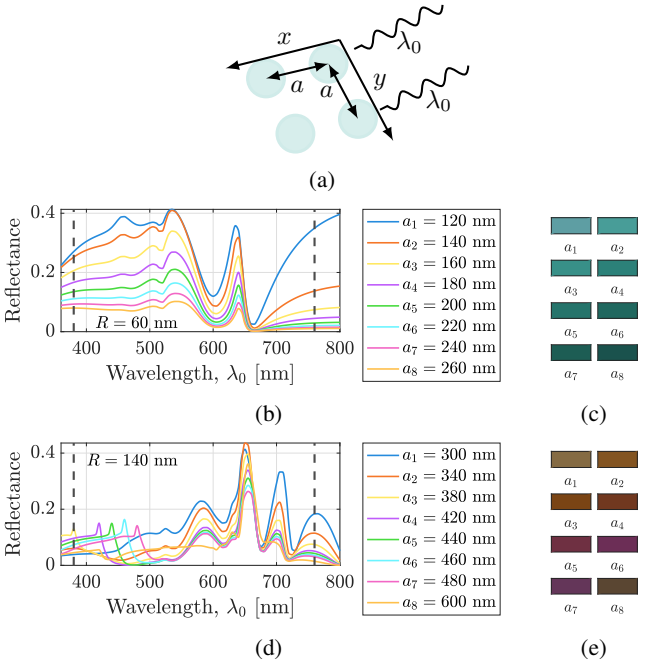

Fig. 1: Reflectance spectra and resulting colours for square arrays of spherical WS_2 NPs, see sketch in (a), with radii of (b),(c) 60 nm and (d),(e) 140 nm and variable separation a_i.

Acknowledgments

We acknowledge support from the Independent Research Fund Denmark (Grant No. 5281-00155B) and Danish National Research Foundation (Project No. DNRF165, POLIMA)

References

[1] J. S. Clausen et al., "Plasmonic metasurfaces for coloration of plastic consumer products", Nano Letters, vol. 14, pp. 4499–4504, 2014.
[2] W. Hong, Z. Yuan and X. Chen, "Structural color materials for optical anticounterfeiting", Small, vol. 16, pp. e1907626, 2020.
[3] D. Beutel, I. Fernandez-Corbaton and C. Rockstuhl, "treams – a T-matrix-based scattering code for nanophotonics", Computer Physics Communications, vol. 297, pp. 109076, 2024.
[4] A. A. Vyshnevyy et al., "Van der Waals materials for overcoming fundamental limitations in photonic integrated circuitry", Nano Letters, vol. 23, pp. 8057–8064, 2023.
[5] I. J. Bundgaard et al., "Structural colours with transition metal dichalcogenide nanostructures", submitted.

Few-molecule nonlinear vibrational spectroscopy with dual-resonant plasmonic nanocavities

Christophe Galland[1,*], Zhiyuan Xie[1], Nobuaki Oyamada[1], Francesco Ciccarello[1], Wen Chen[2]

[1]Institute of Physics, Ecole Polytechnique Fédérale de Lausanne (EPFL), CH-1015 Lausanne, Switzerland
[2]State Key Laboratory of Precision Spectroscopy, East China Normal University
*Corresponding author: chris.galland@epfl.ch

***Abstract*—We implement high-resolution (< 1 cm^{-1}), coherent nonlinear vibrational sum- and difference-frequency spectroscopy from 860 to 1670 cm^{-1} on dual-resonant antennas under ambient conditions, with commercial continuous-wave lasers. The spectra exhibit interference between resonant (vibrational) and nonresonant (electronic) contributions to the second-order nonlinear response, previously accessible only under pulsed excitation.**

***Keywords*— Nanocavities, nanoplasmonics, molecular vibrations, nonlinear spectroscopy, sum frequency generation**

I. Introduction

Vibrational absorption spectroscopy in the mid-infrared (MIR, 400–4,000 cm^{-1}) and vibrational Raman spectroscopy in the visible (VIS) wavelength domain underpin label-free molecular identification across chemistry, materials, and biology. Field-enhanced implementations, namely, surface-enhanced Raman scattering (SERS) and surface-enhanced infrared absorption (SEIRA), have expanded their sensitivity down to molecular monolayers and nanomolar concentrations in liquids.

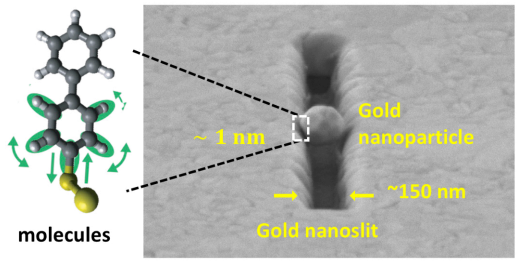

Fig. 1. Scanning electron micrograph on a dual-particle Nanoparticle-in-Slit cavity. The chosen molecule is introduced as a spacer between the gold nanoparticle and the slit etched in the gold film.

Beyond these single-frequency excitation schemes, simultaneous driving of molecular vibrations with MIR and VIS fields coherently interrogates modes that are both IR- and Raman-active through nonlinear frequency mixing. Here, we show that self-assembled plasmonic nanocavities allow ultra-broadband photonic engineering and illustrate this opportunity with a nanocavity supporting colocalized mid-infrared and visible resonances. This is realized using the "nanoparticle-on-slit" (NPoS) concept (see Fig. 1) and is used for vibrational sum- and difference frequency (SFG, DFG) spectroscopy on a small ensemble of molecules.

II. Methods

We design and fabricate nanoparticle-on-slit (NPoS) cavities as first demonstrated in [1] and theoretically analysed in [2]. The experimental setup in sketched in Fig. 2a. We are able to resolve all the nonlinear processes described in Fig. 2b under simultaneous illumination with weak continuous wave lasers at MIR and VIS frequencies.

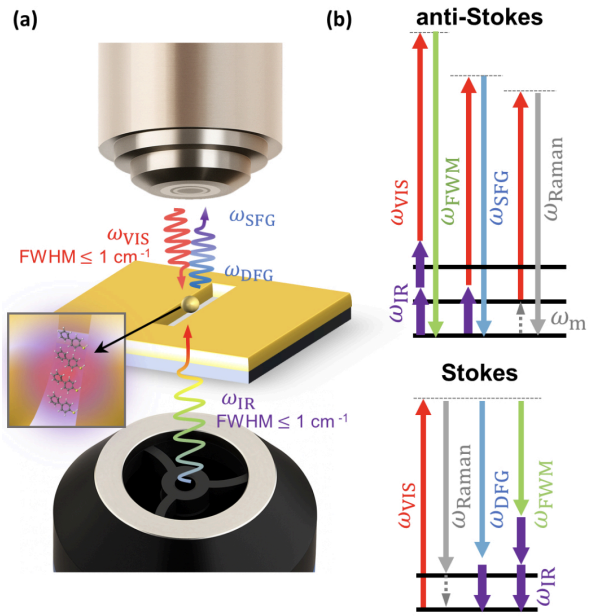

Fig. 2. **(a)** Experimental scheme. A 780 nm laser and a tunable MIR laser are co-focused onto an NPoS nanocavity. The analyte layer resides in the nanometer gap between the gold nanoparticle and the slit walls (inset). **(b)** Energy-diagram representation of photon scattering pathways under simultaneous VIS (ω_{VIS}) and MIR (ω_{IR}) excitation. *Adapted from Ref. [3]*

III. Results and Discussion

Compared to previous results [1], I will show data covering an extended spectral range from 860 to 1670 cm^{-1}, giving access to the full IR vibrational fingerprint of the molecules and revealing coherent interference between resonant (vibrational)

and nonresonant (electronic) contributions to the effective $\chi^{(2)}$ response [3]. To test the versatility of our platform, we measured single–NPoS spectra for biphenyl-thiol (BPhT), 4'-cyanobiphenyl-4-thiol (cn-BPhT) and 4-nitrothiophenol (4-NTP) molecules embedded in the gap. We could measure reproducible spectra by either functionalising the nanoparticles our forming a self-assembled monolayer on the gold substrate. Some illustrative spectra are shown in Fig. 3.

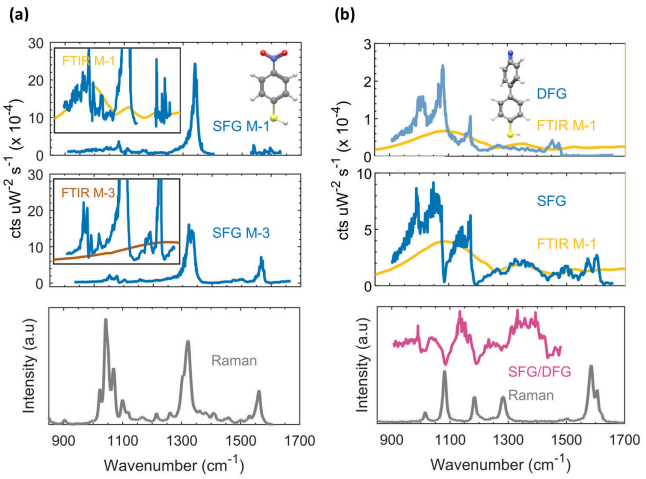

Fig. 3. **(a) 4-NTP on two metasurfaces.** Top: SFG spectrum from a single NPoS on a nanoslit metasurface having its main resonance around 1100 cm^{-1} (see FTIR spectrum in the inset, yellow line). Middle: SFG spectrum from a single NPoS on another metasurface having its main resonance around 1600 cm^{-1} (see FTIR spectrum in the inset, orange line). Bottom: corresponding SERS spectrum. The visible laser power was limited to 1 µW to avoid triggering photochemical reactions with 4-NTP. **(b) cn-BPhT on a metasurface resonant at 1100 cm^{-1}.** Power-normalized DFG (top) and SFG (middle) from a single NPoS, overlaid with the metasurface FTIR spectrum (yellow); bottom: SFG/DFG ratio and co-recorded SERS. *Adapted from Ref. [3]*

The SFG and DFG spectra obtained for the two molecules featured in Fig. 3 illustrate two qualitative regimes of nonlinear polarization interference. For 4-NTP, the vibrational mode involving the electron-withdrawing nitro- group exhibits large IR and Raman dipoles. Consequently, its resonant second-order (SFG and DFG) response is much stronger than the off-resonance response and it dominates the overall spectrum. In contrast, cn-BPhT exhibits pronounced interference between the resonant response of its IR+Raman active vibrational modes and the broad non-resonant nonlinear electronic response. The latter is assigned to the molecule-metal interface, where inversion symmetry is broken, and can be possible enhanced by charge-transfer resonances.

IV. Conclusion

Our work establishes a robust platform for nonlinear molecular spectroscopy under weak continuous-wave drive. Its extended optical bandwith is useful for disentangling resonant and non-resonant contributions, probing charge-transfer–assisted nonlinearities, and characterizing surface nonlinearities of the nanostructure. Compared to conventional SFG spectroscopy, our approach bridges coherent nonlinear spectroscopy with chip-integrated chemical analysis. It offers high spectral resolution, much lower molecular detection limits, compact implementation, and direct compatibility with commercial MIR-Raman microscopes. I will conclude with some prospects for using this system in the single-molecule regime for physical chemistry and quantum optics. [4].

Acknowledgments

This research received funding from the Swiss National Science Foundation (SNSF project No. 214993) and the European Union's Horizon 2020 research and innovation program under Grant Agreement No. 820196 (ERC CoG 'QTONE')

References

[1] Chen, W. *et al.* "Continuous-wave frequency upconversion with a molecular optomechanical nanocavity." *Science* **374**, 1264-1267 (2021)
[2] Hu, H. *et al.* "Plasmonic Nanoparticle-on-Nanoslit Antenna as Independently Tunable Dual-Resonant Systems for Efficient Frequency Upconversion", *Adv. Opt. Mat.* **13**, e01674 (2025)
[3] Xie, Z *et al.* "Continuous-wave, high-resolution, ultra-broadband mid-infrared nonlinear spectroscopy with tunable plasmonic nanocavities" arXiv:2508.12097
[4] Moradi Kalarde, F. *et al.* "Photon antibunching in single-molecule vibrational sum-frequency generation" *Nanophotonics* **14**, 59-73 (2025)

Tip-Enhanced Sum Frequency Generation: Nonlinear Molecular Responses and Electrophotonic Effects Observed beyond the Diffraction Limit

Atsunori Sakurai[1,2*], Shota Takahashi[1], Tatsuto Mochizuki[1,2], and Toshiki Sugimoto[1,2]

[1]Institute for Molecular Science, Japan
[2]Graduate Institute for Advanced Sciences, SOKENDAI, Japan
*Corresponding author: asakurai@ims.ac.jp

***Abstract*— Tip-enhanced sum-frequency generation (TE-SFG) beyond the diffraction limit is achieved using a scanning tunneling microscope (STM), enabling nanoscale vibrational detection with spatial resolution smaller than 30 nm, molecular orientation analysis, and >10^7 signal enhancement. Furthermore, giant signal enhancement was observed under an applied bias between the STM tip and substrate.**

***Keywords*— tip-enhanced spectroscopy, sum-frequency generation, vibrational spectroscopy, electrophotonic effect, near-field scanning optical microscopy.**

I. Introduction

Vibrational sum frequency generation (SFG) is a nonlinear spectroscopic technique widely used to study molecular structures, orientations, and dynamics at surfaces and interfaces [1]. However, the spatial resolution achieved by far-field observations is constrained by the diffraction limit, obscuring molecular details in inhomogeneous structures smaller than the wavelength of light. To overcome this limitation, we developed a system for tip-enhanced SFG (TE-SFG) spectroscopy based on a scanning tunneling microscope (STM) (Fig. 1) [2] and successfully observed signals from molecular vibrations [3].

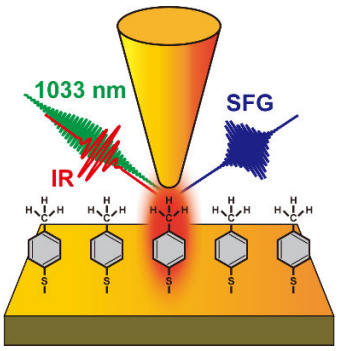

Fig. 1 Schematic of TE-SFG spectroscopy. Tunable IR and 1033 nm laser beams were collinearly focused onto the nanojunction formed between a STM tip and a sample substrate.

II. Methods

The experimental setup of the TE-SFG system is schematically illustrated in Fig. 2. The output from an Yb-fiber laser (1033 nm, 280 fs, 40 W, 50 MHz) was divided into two arms by a beam splitter. The first arm served to pump an optical parametric oscillator (OPO), which generated two output beams: a signal (1.3–2 μm) and an idler (2.1–5 μm). The second arm was directed through an air-spaced Fabry–Pérot etalon to narrow the spectral bandwidth and make the pulses temporally asymmetric. The idler and spectrally narrowed beams were combined collinearly at a dichroic mirror and simultaneously focused onto the nanojunction between a gold tip and a sample substrate in an STM system at an incident angle of 55°. The beams were linearly polarized along the tip axis (*p*-polarization) to effectively excite the gap-mode plasmon. Two identical CaF_2 aspherical lenses were employed to focus the incident beams and collect the emitted signals. The emitted signals were passed through a short-pass filter (transmissive over the 500–900 nm range) and then coupled into an optical fiber. The fiber-coupled signals were spectrally dispersed by a spectrometer and detected using an electronically cooled CCD camera. The sample was a self-assembled monolayer (SAM) of 4-methylbenzenthiol (4-MBT, CH_3–C_6H_4-SH) on a Au(111) substrate.

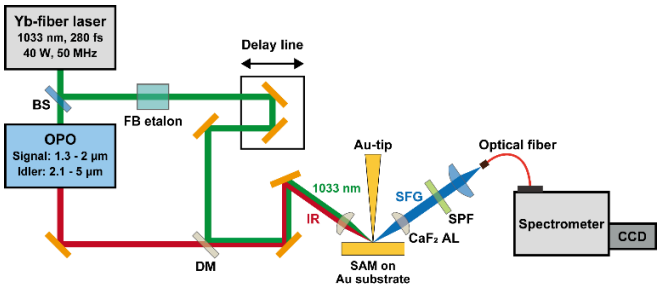

Fig. 2 Experimental setup of the TE-SFG system. BS: beam splitter, FB etalon: air-spaced Fabry–Pérot etalon, CaF_2 AL: CaF_2 aspherical lens, SPF: short-pass filter. The delay line was used to adjust the delay between the idler and the 1033 nm pulses.

III. Results and Discussion

The observed TE-SFG spectra are shown in Fig. 3. The idler central wavenumber was varied from 2800 to 3150 cm^{-1}, and eight spectra were recorded. The broad spectral shape of each spectrum originates from the spectrum of the incident idler pulse, resulting from the vibrational non-resonant contribution. Furthermore, dip structures are observed at the three positions indicated by the red arrows. These features are attributed to the interference between the vibrational resonant signal and the non-resonant signal.

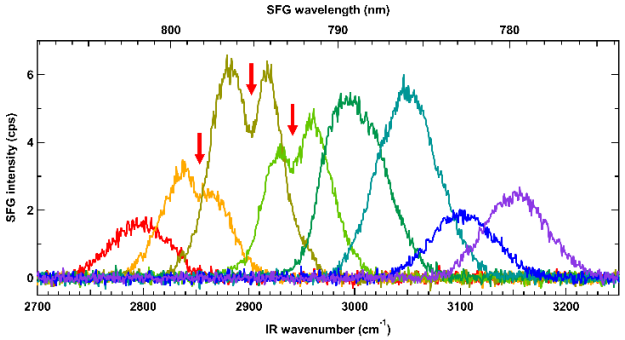

Fig. 3 TE-SFG spectra for different IR central wavenumbers ranging from 2800 to 3150 cm^{-1}. The spectra obtained at a tip-sample distance of 50 nm were subtracted as background for each dataset. Dip structures are observed at the three positions indicated by the red arrows. Intensities are normalized to counts per second (cps) [3].

To extract the molecular vibrational information, we performed a fit using the following equation,

$$I(\omega_{\mathrm{IR}}) = \exp\left[-\frac{(\omega_{\mathrm{IR}}-\omega_0)^2}{\sigma_{\mathrm{IR}}^2}\right]\left|A_{\mathrm{NR}}e^{i\theta_{\mathrm{NR}}} + \frac{A_q}{\omega_q-\omega_{IR}-i\Gamma_{\mathrm{q}}}\right|^2, \quad (1)$$

where ω_0 and σ_{IR} are the central wavenumber and spectral width of the incident idler pulse, respectively. The resonant term is expressed as a vibrational mode with amplitude A_q, resonant frequency ω_q, and damping constant Γ_q, while the non-resonant term is characterized by a constant amplitude A_{NR} and the phase factor θ_{NR}. In addition, we calculated the imaginary part of the resonant contribution to the second-order susceptibility ($\mathrm{Im}\left[\chi_{\mathrm{R}}^{(2)}(\omega_{\mathrm{IR}})\right]$), using the same parameters as those used in the fitting, which corresponds to the purely absorptive response of the vibrational mode, given by

$$\mathrm{Im}\left[\chi_{\mathrm{R}}^{(2)}(\omega_{\mathrm{IR}})\right] = \mathrm{Im}\left[\frac{A_q}{\omega_q-\omega_{IR}-i\Gamma_q}\right]. \quad (2)$$

The fitting results using Eq. (1) are shown in Fig. 4(a) as black curves, which agree well with the experimental results. The light red curves in Fig. 4(b) represent $\mathrm{Im}\left[\chi_{\mathrm{R}}^{(2)}(\omega_{\mathrm{IR}})\right]$, calculated using Eq. (2), and the sum of these contributions is plotted as the red line. The extracted three vibrational modes are assigned to (1) methyl stretching (CH_3–SS) vibration, (2) Fermi resonance (CH_3–FR) between CH_3–SS and an overtone of a methyl bending vibration, and (3) degenerate methyl stretching (CH_3–DS) vibration. The negative sign of $\mathrm{Im}\left[\chi_{\mathrm{R}}^{(2)}(\omega_{\mathrm{IR}})\right]$ indicates that the terminal methyl group is oriented with its hydrogen atoms pointing away from the substrate. This result show that TE-SFG can determine absolute molecular orientation at the nanoscale with high precision.

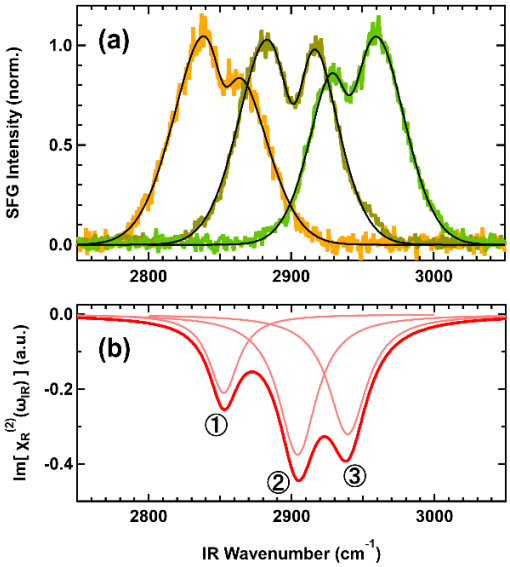

Fig. 4 (a) Three TE-SFG spectra in Fig. 4 were fitted using Eq. (1). The fitting results are shown as black curves. (b) The light red curves represent the respective imaginary parts of the resonant contribution to the second-order susceptibility ($\mathrm{Im}\left[\chi_{\mathrm{R}}^{(2)}(\omega_{\mathrm{IR}})\right]$), which correspond to the purely absorptive responses given by Eq. (2). The extracted peaks are assigned to (1) CH_3–SS, (2) CH_3–FR, and (3) CH_3–DS. The red curve is the sum of these three contributions [3].

Moreover, by introducing a controlled delay between the first idler pulse and the second 1033 nm pulse, the non-resonant background was effectively suppressed, which led to an optimized ratio between the resonant and non-resonant signals, thereby maximizing the contrast of the interferometric signal and improving the detectability of weak vibrational signals, enabling the detection of an aromatic CH mode that had not been observed previously [4]. The signal enhancement factor was also estimated to be $6.3 \times 10^6 - 1.3 \times 10^7$ based on the experimental data [4].

Furthermore, we measured TE-SFG spectra across the boundary between different SAM domains while scanning the sample. The observed TE-SFG spectra showed a rapid change at the boundary, and this change was confirmed to occur over a spatial range of 30 nm around the boundary [5].

In addition, we investigated the effects of a bias voltage applied to the STM nanojunction on the intensity of the second harmonic generation (SHG) and SFG signals. The results revealed a significant enhancement of the signals as the applied bias increased [6]. This signal enhancement is attributed to so-called electric-field-induced SHG and SFG processes. Unlike typical cases, the signal exhibited a quadratic dependence on the applied voltage rather than a linear one due to the very strong electric field generated across the STM nanojunction ($\sim 10^9$ V/m).

IV. Conclusion

We have demonstrated TE-SFG measurements on a SAM of 4-MBT adsorbed on a Au surface. The observed signals

exhibited dips arising from vibrational modes within the broadband non-resonant background spectrum. These three dips are assigned to vibrational modes of the terminal methyl group of 4-MBT molecules. By introducing a delay between the two pulses, the ratio between the resonant and non-resonant signals was optimized, and the vibrational signal arising from an aromatic CH mode was additionally detected. The spatial resolution was confirmed to be within 30 nm. Furthermore, a giant signal enhancement due to the applied voltage between the STM tip and the substrate was observed.

ACKNOWLEDGMENTS

This work was supported by JST-PRESTO (JPMJPR1907), JST-CREST (JPMJCR22L2), and JSPS KAKENHI Grants-in-Aid for Scientific Research (A) (19H00865 and 22H00296), Transformative Research Areas (A) (24H02205), Scientific Research (B) (23K26548), Challenging Research (Exploratory) (24K21759), and JSPS Fellows (22KJ3099).

REFERENCES

[1] Y. R. Shen, *Fundamentals of Sum-Frequency Spectroscopy* (Cambridge University Press, Cambridge, 2016).

[2] S. Takahashi, A. Sakurai, T. Mochizuki, and T. Sugimoto, "Broadband Tip-Enhanced Nonlinear Optical Response in a Plasmonic Nanocavity," *The Journal of Physical Chemistry Letters*, vol. 14, pp. 6919–6926, 2023.

[3] A. Sakurai, S. Takahashi, T. Mochizuki, and T. Sugimoto, "Tip-Enhanced Sum Frequency Generation for Molecular Vibrational Nanospectroscopy," *Nano Letters*, vol. 14, pp. 6390–6398, 2025.

[4] A. Sakurai, S. Takahashi, T. Mochizuki, T. Hirano, A. Morita, and T. Sugimoto, "Tip-Enhanced sum frequency generation spectroscopy using temporally asymmetric pulse for detecting weak vibrational signals," *The Journal of Chemical Physics*, 2026. DOI: 10.1063/5.0310824

[5] S. Takahashi, K. Kumagai, A. Sakurai, T. Mochizuki, T. Hirano, A. Morita, and T. Sugimoto, "Tip-Enhanced Sum-Frequency Vibrational Nanoscopy beyond the Diffraction Limit," *The Journal of Physical Chemical C*, vol. 130, pp. 373–385, 2026.

[6] S. Takahashi, A. Sakurai, T. Mochizuki, and T. Sugimoto, "Giant near-field nonlinear electrophotonic effects in an angstrom-scale plasmonic junction," *Nature Communications*, 2026. DOI: 10.1038/s41467-026-68823-4.

Optical Fields with Spatially Modulated Chirality Toward Chiral Trapping and Separation

Atsushi Kamegaya[1], Shun Hashiyada[1,2,*], Yoshito Y. Tanaka[1]

[1]Research Institute of Electronic Science, Hokkaido University, Japan
[2]PRESTO, Japan Science and Technology Agency, Japan
*Corresponding author: shun.hashiyada@es.hokudai.ac.jp

***Abstract*—We experimentally realize an optical field with spatially uniform energy density and periodically sign-reversing optical chirality using two orthogonally polarized beams. Polarimetric imaging confirms chirality fringes without intensity modulation. Circular dichroism mapping of chiral gold nanoparticles reveals position dependent enantioselective interaction, evidencing optical chirality gradients toward chiral selective trapping.**

***Keywords*—optical chirality, chiral gradient force, circular dichroism, enantioselective interaction, nanophotonics.**

I. Introduction

Chirality plays a central role in chemistry, biology, and materials science. Although opposite enantiomers share identical bulk physical properties, their interaction with chiral environments differs fundamentally. Circularly polarized light represents the simplest form of optical chirality, with left and right circular polarization corresponding to opposite signs of optical chirality density. This quantity governs enantioselective light–matter interaction and forms the physical basis of circular dichroism (CD).

Beyond spectroscopy, it has been theoretically predicted that spatial gradients of optical chirality density can generate chiral optical forces acting in opposite directions on opposite enantiomers [1]. Interferometric schemes capable of producing spatially alternating optical chirality have been proposed theoretically [2,3] and later demonstrated experimentally [4]. These studies established the feasibility of structuring optical chirality in free space. However, direct verification that spatially structured optical chirality couples enantioselectively to nanoscale chiral objects has not yet been directly demonstrated. Moreover, previously demonstrated chirality patterns were realized on spatial scales much larger than the optical wavelength [4].

In this work, we experimentally realize wavelength-scale modulation of optical chirality under spatially uniform energy density conditions and directly confirm enantioselective interaction with chiral nanoparticles through position-resolved CD mapping. This architecture provides a physically consistent platform for isolating genuine chiral optical forces toward future chiral trapping and separation.

II. Field Design and Experimental Approach

The optical field is constructed by coherently superposing two orthogonally polarized beams propagating in a common plane. Due to their polarization orthogonality, the superposition produces no intensity interference, resulting in a spatially uniform optical energy density. At the same time, the relative phase between the two field components varies along one spatial direction, leading to periodic conversion between linear and circular polarization states. As a result, the optical chirality density undergoes periodic sign reversal while the total intensity remains invariant.

The generated field is experimentally visualized using polarization selective imaging. Intensity measurements confirm the absence of spatial interference fringes, whereas circular polarization resolved detection reveals clear periodic modulation consistent with theoretical expectations.

To probe enantioselective interaction, individual nanoparticles are scanned across the structured field. The local optical chirality is inverted through controlled manipulation of the incident polarization state, enabling differential transmission measurements corresponding to CD at each spatial position.

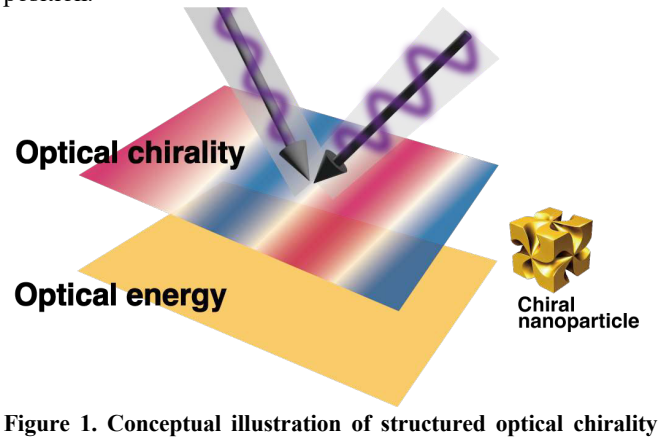

Figure 1. Conceptual illustration of structured optical chirality under uniform energy density. Two orthogonally polarized beams incident at ±θ create spatially uniform energy density while generating alternating regions of opposite optical chirality. A nearby chiral nanoparticle experiences position-dependent enantioselective interaction governed by the local chirality distribution.

III. Results and Discussion

Achiral nanoparticles exhibit negligible differential transmission throughout the field, confirming effective suppression of conventional gradient contributions.

In contrast, chiral nanoparticles display position dependent CD signals that follow the periodic modulation of optical chirality. The sign of the response reverses upon inversion of the optical chirality distribution, demonstrating enantioselective interaction governed by the local optical chirality density.

Importantly, the absence of correlated intensity modulation indicates that the observed effect does not originate from conventional interference or energy density gradients. These results provide experimental evidence that spatially structured optical chirality selectively couples to chiral nanoparticles under suppressed achiral force conditions.

The demonstrated architecture therefore constitutes a viable platform for future realization of chiral gradient force driven trapping, spatial separation, and ordered assembly of enantiomeric particles.

IV. Conclusion

We have experimentally realized optical fields with spatially modulated chirality and uniform energy density and demonstrated enantioselective interaction with chiral nanoparticles. By suppressing achiral gradient contributions, this approach establishes a practical platform for isolating chiral optical forces and advancing optical enantioseparation strategies.

Acknowledgments

This work was supported by Grants-in-Aid for Scientific Research (KAKENHI) (Nos. JP24H00424, JP22H05132 in Transformative Research Areas (A) “Chiral materials science pioneered by the helicity of light” to Y.Y.T., and Nos. JP23K04669, JP21K14594 to S.H.) from the Japan Society for the Promotion of Science (JSPS), and JST FOREST Program (No. JPMJFR213O to Y.Y.T.) and PRESTO (Grant No. JPMJPR25J6 to S.H.), and Ministry of Education, Culture, Sports, Science and Technology (MEXT), Japan, Crossover Alliance to Create the Future with People, Intelligence and Materials (Grant No. 2025Y002 to S.H.).

References

[1] A. Canaguier-Durand et al., New J. Phys. 15, 123037 (2013).
[2] R. P. Cameron et al., J. Mod. Opt. 61, 25–31 (2014).
[3] R. P. Cameron et al., New J. Phys. 16, 013020 (2014).
[4] N. Kravets et al., Phys. Rev. Lett. 122, 024301 (2019).

Ultrasensitive label-free miRNA sensing realized by a Q-tunable plasmonic metasurface

Daiki Kawasaki[1], Takuo Tanaka[1,*]

[1]RIKEN Center for Advanced Photonics, Saitama., 351-0198, Japan
*Corresponding author: t-tanaka@riken.jp

In this report, we developed a plasmonic metasurface biosensor of which sensitivity is tunable to match the required limit of detection and dynamic range in miRNA detection in human serum. Our metasurface biosensor is promising as reliable and highly sensitive biosensing platform for simple and rapid diagnostic technologies.

***Keywords*— miRNA, biosensor, plasmonics, Bound states in the continuum**

I. Introduction

Minimally invasive biomarkers are essential for early diagnosis. Circulating microRNAs (miRNAs) are short (~22 nt) noncoding RNAs that remain stable in biofluids and are linked to diverse diseases.[1] Practical miRNA testing requires assays that work in complex samples with femtomolar sensitivity, sequence specificity, rapid readout, simple protocols, and multiplexing.[2] Label-free transducers that directly report nucleic-acid hybridization at a surface offer an alternative; optical refractometric sensing can monitor binding-induced refractive-index changes in real time and readily supports parallelized measurements.[3] In particular, resonant metasurfaces—periodic nanostructures supporting optical resonances—convert molecular adsorption into measurable resonant shifts, with performance governed by the resonance quality factor (Q) for resolutions and enhanced near-field hot spots at the interface for responsivites.[4] Balancing high-Q resonances with strong surface overlap between enhanced near-field and molecules is therefore critical for detecting miRNA-scale small molecular targets. Dielectric metasurfaces can provide ultrahigh Q via (quasi-)bound states in the continuum (q-BICs), but diffraction-limited mode volumes and internal field localization reduce interaction with nm-scale analytes. Plasmonic metasurfaces provide strong surface near-fields yet often suffer reduced Q due to ohmic loss.[5] Here we propose a symmetry-broken plasmonic lattice that couples localized surface plasmons (LSPs) to surface lattice resonances (SLRs) to jointly tune radiative and absorptive losses, enabling high-Q resonances with dense and intense hot spots on gold nanostructured surfaces; symmetry breaking in unit-cell offers the radiative loss tunability supported by q-BICs based LPSs while hybridizing with SLRs yields the absorptive loss tunability. Therefore, critical coupling condition, at which the electric-field enhancement factor (EF) is maximized, can be achieved with desirable Q. Joint parametric tuning provides the tunability of Q, EF, and hot spot density on the metasurface. In this work, we experimentally and numerically investigated the tunability of bulk and surface refractive index sensitivity via parametric tunning in our metasurface to realize sub-femtomolar limit of detection and sub-femtomolar-to-picomolar dynamic range in label-free detection of miRNA in human serum. Our metasurface sensor provided the required dynamic range in sub-femtomolar-to-picomolar with sub-femtomolar limit of detection in miR-29c-3p sensing, which is known to implicate to neurodegenerative diseases.

II. Methods

1. Optical characterization. Metasurface spectra were recorded with a custom microscope–spectrometer setup. The reflectance spectrum $R(\lambda)$ was obtained by normalizing the measured intensity from the metasurface to that from a flat gold reference. Absorptance was calculated as $A(\lambda) = 1 - R(\lambda)$. Resonance parameters were extracted by Lorentzian fitting to the absorptance peak; the quality factor was computed as $Q = \frac{\lambda_{peak}}{FWHM}$ Finite-difference time-domain simulations (Ansys Lumerical) reproduced the fabricated geometry and measurement configuration. Periodic boundary conditions were applied in the in-plane directions (x,y) and perfectly matched layers along z. Gold was modeled with Palik optical constants; the MgF_2 spacer was treated as a dielectric with $n = 1.37$.

2. Theory for refractive index sensitivity. In electromagnetic perturbation theory, the plasmonic resonance is treated as an eigenmode of Maxwell's equations. A small permittivity perturbation Δε(r) produces a first-order eigenwavelength shift.

$$\Delta\lambda = \frac{\lambda}{2} \cdot \frac{\int \Delta\varepsilon(r)|E(r)|^2 dV}{\int \varepsilon(r)|E(r)|^2 dV}. \quad (1)$$

Bulk refractive index sensitivity (BRIS) is defined by a uniform index change in the sensing region, $n_{bg} \rightarrow n_{bg} + \Delta n$. With spatially constant $\Delta\varepsilon \approx 2\, n_{bg} \Delta n$, the response is linear, $\lambda_{bulk} = BRIS\, \Delta n$. For non-uniform perturbations we write $\Delta\lambda = BRIS\, \Delta n_{eff}$, where Δn_{eff} is obtained by weighting the local index change $\delta n(z)$ with the normalized normal-direction intensity profile $W(z) \propto |E(z)|^2$. For a thin overlayer of index n_s and thickness t on a background n_{bg} (z = 0 at the metal–dielectric interface, z > 0 into the dielectric), the perturbation is $\delta n(z) = n_s - n_{bg}$ for $0 \le z \le t$ and $\delta n(z) = 0$ for $z > t$. Assuming an exponential near-field decay $|E(z)|^2 \propto$

$\exp\left(\frac{-2z}{l_d}\right)$, we use $W(z) = \left(\frac{2}{l_d}\right)\exp\left(\frac{-2z}{l_d}\right)$. The effective index change becomes

$$\Delta n_{eff(t)} = (n_s - n_{bg})\int_0^t W(z)dz = (n_s - n_{bg})\left[1 - \exp\left(\frac{-2t}{l_d}\right)\right] \quad (2)$$

and the corresponding resonance shift is

$$\Delta\lambda(t) = BRIS\,(n_s - n_{bg})\left[1 - \exp\left(\frac{-2t}{l_d}\right)\right]. \quad (3)$$

The surface refractive index sensitivity is defined as

$$SRIS(t) \equiv \frac{\partial^2\Delta\lambda}{\partial t\,\partial n_s} = \left(\frac{2\,BRIS}{l_d}\right) \quad (4)$$

For a homogeneous film (index n_s, thickness t_{anal}) that fully covers the responsive metal area, integrating SRIS yields

$$\frac{\partial\Delta\lambda}{\partial n_s}\Big|_{t\,=\,t_{anal}} = \int_0^{t_{anal}} SRIS(t)dt\,. \quad (5)$$

In the dilute-coverage regime, a finite number of analyte objects (cross-sectional area s_{anal}, height t_{anal}) covering only a fraction f of the responsive surface scales the response linearly:

$$\frac{\partial\Delta\lambda}{\partial n} = f\int_0^{t_{anal}} SRIS(t)dt\,. \quad (6)$$

Relating f to the metasurface geometry using the unit-cell area A_{cell}, the responsive gold area per cell A_{gold}, and analyte number density ρ (per total metasurface area), we have $f = \frac{\rho\, s_{anal} A_{cell}}{A_{gold}}$.

3. MiRNA sensing protocol. Disulfide-modified probe DNA (22 nt with a C6 spacer) and miRNAs (miR-29c-3p and miR-19) were purchased commercially. Thiolated probes (1 μM) were immobilized on gold by overnight incubation at 37 °C in PBS (pH 7.4) containing EDTA (0.04 wt%) and Tween-20 (0.5 wt%), followed by sequential rinses to remove weakly adsorbed species. For quantitative assays, sensors were exposed to miRNA-spiked 10% plasma (1 fM–1 μM, 10 μL) containing RNase inhibitor (500 U/mL). After hybridization (37 °C, 20 min) and rinsing, spectral shifts were again analyzed in air (N = 5 independent sensors).

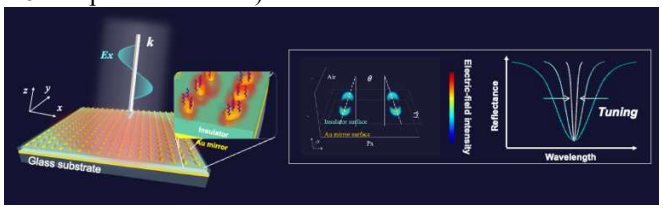

Fig. 1 The schematis for plasmonic metasurface sensor.

III. Results and Discussion

The sensor is a periodic array of gold elliptical nanopillar dimers on a 150-nm dielectric spacer backed by a gold mirror. The mirror suppresses transmission, producing a high-contrast absorptance resonance in the near infrared, and the gold surface supports robust thiol probe chemistry. We tune the unit cell using the long-axis period *Px* and the in-plane orientation angle θ (Fig. 1a). The resonance is a mirror-coupled plasmonic quasi–bound state in the continuum (q-BIC), where radiative leakage follows $\gamma_{rad} \propto sin^2\theta$ thus θ provides a direct "radiation knob" to satisfy critical coupling ($\gamma_{rad} = \gamma_{abs}$) and maximize absorptance. Independently, sweeping Px through the Rayleigh-anomaly region tunes the linewidth over ~1–2 orders of magnitude. Temporal coupled-mode theory predicts $EF = \left|\frac{E_{max}}{E_0}\right|^2$ peaks at critical coupling. Numerical simulation over *Px* = 400–900 nm and θ = 5°–40° reveal a critical-coupling locus (near-unity absorptance for each *Px*) along which *EF* increases with Q, reaching $EF > 10^4$ with $Q > 150$.

We benchmarked refractometric performance using bulk refractive-index sensitivity ($BRIS = \frac{\Delta\lambda}{\Delta n_B}$) and $FOM = BRIS/FWHM$. For *Px* = 400–800 nm at θ = 20°, both BRIS and FOM increase with *Px* because lattice assistance boosts bulk responsivity while narrowing the resonance. The best experimental values reached BRIS = 1270 nm/RIU and FOM = 205 RIU^{-1}. For biosensing, the relevant metric is surface refractive-index sensitivity (SRIS). Using a thin-film perturbation model with exponential field decay, $SRIS(t) = \left(2\cdot\frac{BRIS}{l_d}\right)\cdot\exp\left(-\frac{2t}{l_d}\right)$, so SRIS(0) highlights the trade-off between large BRIS and tight confinement (small l_d). Numerical simulation fits show that increasing Px lengthens l_d, so SRIS(0) decreases with *Px* even though BRIS rises—smaller *Px* favors interfacial sensitivity for nm-scale layers (Fig. 2a). Partially perturbed refractive index sensitivity, which is defined by $\Delta\lambda \approx f\cdot SRIS$ (f is a partial coverage factor) for effective sensitivity to finite number molecules, was reached its maximum around Px = 700–800 nm, agreed between experimental results with miRNA detection and simulated values.

By using metasurface which provided the highest partially perturbed sensitivity (Px = 800 nm), we quantified miR-29c-3p in 10% diluted serum (10-μL aliquots) from 1 fM to 1 μM and fitted Hill–Langmuir curves to extract LOD (blank + 3σ), and dynamic range (C10–C90). As a result, we achieved the LOD of 0.110 fM with dynamic range from 0.4 fM to 0.5 nM, meeting the demands for label-free miRNA sensing (Fig. 2b).

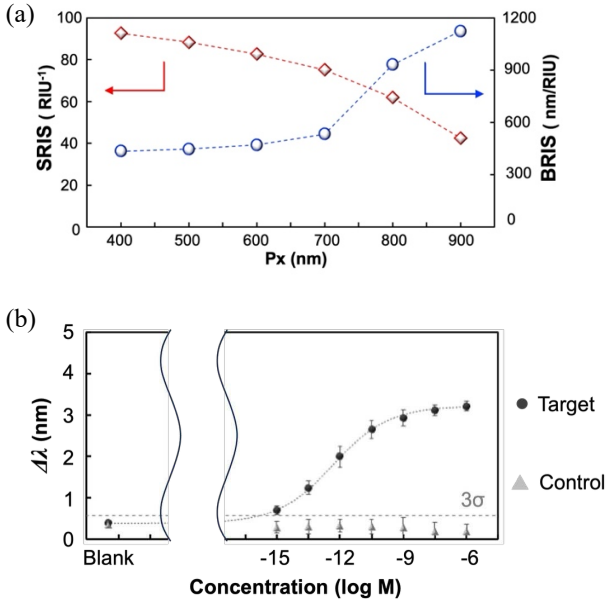

Fig. 2 (a) The plots of BRIS (Blue) and SRIS (Red) across Px. (b) Response curves in miRNA sensing by metasurface with Px 800 nm.

IV. Conclusion

In this report, we developed a plasmonic metasurface biosensor of which sensitivity is tunable to match the required limit of detection and dynamic range in miRNA detection in human serum. Q and EF of our metasurface are tunable by jointly engineering radiative and absorptive loss via symmetry breaking-induced q-BICs coupled to SLRs. Cooperative parametric tuning provides critical coupling condition with wide-range Q to control density and intensity of hot-spots. We experimentally and numerically evaluated BRIS and SRIS to reveal that they are in tread-off to strength of the coupling between LSPs and SLRs which was controlled via lattice pitch. In addition, SRIS per responsive surface, i.e., the sensitivity to molecules, was also tuned to maximize the sensitivity to miRNAs and minimized the limit of detection to sub-femtomolar in 10 μL human serum with suitable dynamic range from sub-femtomolar-to-picomolar. We achieved 0.110 fM (1.10 zmol) limit of detection of miR-29c-3p in human serum. Our metasurface biosensor is promising as reliable and highly sensitive biosensing platform for next-generation simple and rapid diagnostic technologies.

Acknowledgments

This work was supported in part by the JSPS Grants-in-Aid for Scientific Research (KAKENHI) under no. 23KJ2181 (DK), 25K21568 (DK), 24KJ01377 (DK) and JST CREST grant no. JPMJCR1904, Japan (TT).

References

[1] Williams, Z., Ben-Dov, I. Z., Elias, R., Mihailovic, A., Brown, M., Rosenwaks, Z. and Tuschl, T., "Comprehensive profiling of circulating microRNA via small RNA sequencing of cDNA libraries reveals biomarker potential and limitations," Proc Natl Acad Sci U S A 110(11), 4255–4260 (2013).

[2] Metcalf, G. A. D., "MicroRNAs : circulating biomarkers for the early detection of imperceptible cancers via biosensor and machine-learning advances," Oncogene(June) (2024).

[3] Altug, H., Oh, S. H., Maier, S. A. and Homola, J., "Advances and applications of nanophotonic biosensors," Nat Nanotechnol 17(1), 5–16 (2022).

[4] Barulin, A., Nguyen, D. Du, Kim, Y., Ko, C. and Kim, I., "Metasurfaces for Quantitative Biosciences of Molecules, Cells, and Tissues: Sensing and Diagnostics," ACS Photonics 11(3), 904–916 (2024).

[5] El-Helou, A. J., Liu, Y., Chen, C., Wang, F., Altug, H., Reece, P. J. and Zhu, Y., "Optical Metasurfaces for the Next-Generation Biosensing and Bioimaging," Laser Photon Rev 19(10) (2025).

Single-molecule mass distribution sensing of proteins with high-Q silicon nitride microresonators

Koji Masuda[1,2], Abdullah Alabbadi[3], Linda Kasiarova[4], Pascal Del'Haye[3], Tobias Herr[5], Jiri Damborsky[4], Martin Marek[4], Stanislav Mazurenko[4], Josef Sivic[5], Frank Vollmer[1,2]

[1] Living Systems Institute, University of Exeter, UK
[2] Department of Physics and Astronomy, University of Exeter, UK
[3] Max Planck Institute for the Science of Light, Erlangen, Germany
[4] Loschmidt Laboratories, Masaryk University and FNUSA-ICRC, Brno, Czech Republic
[5]Deutsches Elektronen-Synchrotron DESY, Hamburg, Germany
[6]Czech Technical University, CIIRC, ELLIS Unit Prague

***Abstract*— We demonstrate label-free single-molecule detection of proteins using high-Q silicon nitride microring resonators. Immunoglobulin M (~970 kDa) and thyroglobulin (~660 kDa) are measured, revealing multimodal mass distributions. Results are compared against iSCAT, DLS, and gel electrophoresis. Plasmonic enhancement enables the detection of proteins with 100× lower molecular weight.**

***Keywords*— single-molecule sensing, microresonators, plasmonics, Immunoglobulin M, thyroglobulin.**

I. Introduction

Label-free single-molecule sensing enables analysis of protein mass distributions in solution. We investigate Immunoglobulin M (IgM, ~970 kDa) and thyroglobulin (Tg, ~660 kDa) using integrated photonic microresonators, and compare results with established techniques including iSCAT, dynamic light scattering (DLS), and gel electrophoresis.

II. Methods

Silicon nitride microring resonators (20–150 µm) were fabricated and optically interrogated using a 950 nm laser. Protein samples were introduced via microfluidics. Binding events were detected via resonance shifts. Comparative measurements were performed using iSCAT, DLS, and gel-based assays.

III. Results and Discussion

IgM and Tg show discrete binding events with multimodal step-height distributions corresponding to different oligomeric states. Measured distributions agree with benchmark techniques (iSCAT, DLS, gels). Plasmonic enhancement (via attaching resonant Au nanorods to the SiN resonator) significantly increases sensitivity, enabling detection of proteins with ~100× lower molecular weight.

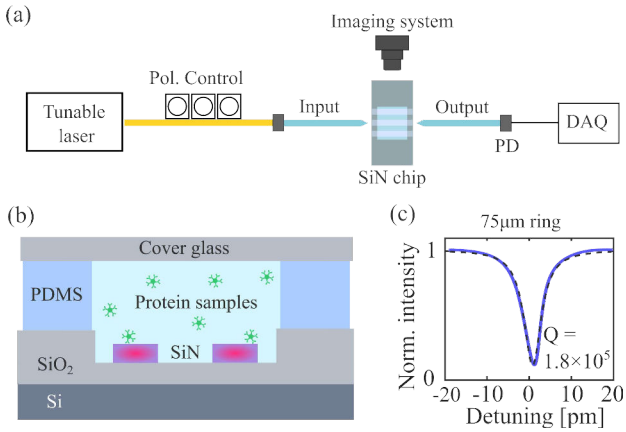

Fig. 1 Experimental Setup. (a) Optical measurement setup. (b) Cross-section of the sensing chamber. (c) Representative resonance dip in the transmission of the 75 µm ring measured in PBS buffer with Lorentzian fit: $Q = 1.8\times10^5$.

IV. Conclusions

The platform enables label-free determination of protein mass distributions in solution. With plasmonic enhancement, detection extends to much smaller biomolecules, providing a

scalable tool for biochemical sensing.

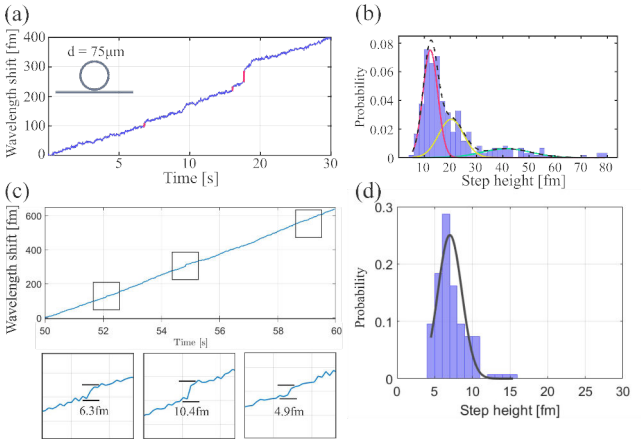

Fig. 2 Single-molecule detection with SiN microring resonators. Representative resonance wavelength trace discrete binding events of (a) IgM with three events highlighted in red, and (c) Tg with zoomed insets. Step-height histograms with Gaussian fits showing multiple peaks from IgM data, suggesting distinct molecular mass species (b), and a single dominant peak from Tg data (d).

ACKNOWLEDGMENTS

This work was supported by EPSRC – EP/W013770/1 and by EU Horizon Europe – 101136607 CLARA.

REFERENCES

[1] Masuda, K. *et al*., "Future directions in all-optical label-free single-molecule sensing,". npj Biosensing ***3***, 3 (2026).

[2] Zhan, S. *et al*., "Low-temperature sputtered ultralow-loss silicon nitride for hybrid photonic integration,". Laser & Photonics Rev. ***18***, 2300642 (2024).

SPECIAL SESSION 8

Bio-Inspired Nanophotonics

9 contributions · pp. 897–908

Strategies for Infrared Management and Thermal Insulation Inspired from Biological Organisms

Amandine Marchand[1], Kevin Delmote[2], Olivier Deparis[2], Sébastien R. Mouchet[1,2,3,*]

[1]Micro- and Nanophotonic Materials Group, Research Institute for Materials Science and Engineering, University of Mons, Belgium
[2]Department of Physics and Namur Institute of Structured Matter (NISM), University of Namur, Belgium
[3]Department of Physics and Astronomy, University of Exeter, UK
*Corresponding author: sebastien.mouchet@umons.ac.be

***Abstract*—Nature provides advanced strategies for managing infrared radiation through micro- and nanostructures. By studying biological examples, from insects to mammals, we derive principles for engineered materials enabling efficient insulation, passive cooling, and selective IR management. This work highlights how bioinspired designs support sustainable thermal technologies.**

***Keywords*— Bioinspired materials, infrared control, thermal management, thermal insulation, photonic structures, energy efficiency, bioinspiration.**

I. Introduction

Many organisms rely on finely tuned thermal-radiation control to survive, especially species exposed to extreme climates or lacking internal thermoregulation, so-called "ectotherms" or "cold-blooded animal". Over millions of years, evolution has produced sophisticated natural structures capable of absorbing, emitting, or redirecting infrared radiation. Examples such as nanostructured butterfly scales or the specialised fur of Arctic mammals reveal exceptional biological strategies for modulating heat transfer [1].

II. Methods and Results

This work examines several biological systems that demonstrate highly optimised forms of thermal regulation. Cold blooded insects, which depend heavily on environmental temperatures, use precise infrared interactions (Fig. 1), while desert adapted mammals like dromedaries employ structural features that enable efficient heat control. These micro- and nanoscale architectures often serve multiple roles, integrating thermal management with functions like camouflage or communication [1].

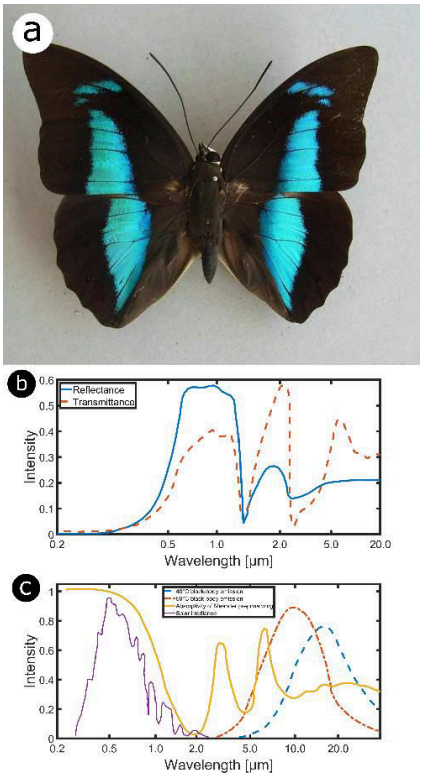

Fig. 1 Radiative cooling contributes significantly to the thermal regulation of some butterfly species, such as *Archaeoprepona meander* (a). This effect stems from the specific structure of the scales forming the dark wing regions. Measurements show a pronounced contrast between visible and near infrared reflectance and transmittance (b). By comparing black body emission curves at 40°C and 50°C with solar irradiance and the wing's absorptance (c), Berthier [23] demonstrated that the thermoregulation mechanism is linked to the chitin C=O absorption band near 6 µm. Fig. (a) and (b,c) were reproduced from Notafly, https://commons.wikimedia.org/wiki/File:Archaeoprepona_meander_(Cramer,_-1775-).JPG, License CC-BY-SA-3.0 and ref. [1], License CC-4.0, respectively. Data in fig. (b,c) are from [2].

Recent progress in bioinspired materials science has enabled the reproduction of such natural designs. By analysing photonic structures and thermal strategies observed in nature [3], we extract design guidelines that support the development of multifunctional materials capable of selective IR absorption and enhanced insulation.

Our findings highlight the interdisciplinary potential of bioinspiration, linking biological insight with physics and materials engineering. The resulting concepts show promise for applications requiring passive and energy efficient thermal regulation. Ultimately, the study underscores how nature's innovations, when carefully studied and adapted, can lead to sustainable and high-performance solutions for modern engineering challenges.

III. Conclusion

Biological systems offer many strategies for managing infrared radiation, and translating these mechanisms into engineered materials opens pathways to sustainable thermal technologies. By integrating principles derived from evolution with modern fabrication techniques, we can develop versatile, energy efficient solutions that address growing needs in thermal management across diverse engineering sectors.

Acknowledgments

This research used resources of the "Plateforme Technologique de Calcul Intensif (PTCI)" (https://platforms.unamur.be/ptci) of UNamur, which is supported by the Belgian National Fund for Scientific Research (FRS-FNRS)-"Fonds de la Recherche Fondamentale Collective" (FRFC), the Walloon Region, and UNamur (Conventions No. 2.5020.11, GEQ U.G006.15, 1610468, RW/GEQ2016 and U.G011.22). PTCI is a member of the "Consortium des Équipements de Calcul Intensif (CÉCI)" (http://www.ceci-hpc.be). SRM is an FRS-FNRS Research Associate and was supported by a BEWARE Fellowship (Convention n°2110034) of the Walloon Region (COFUND Marie Skłodowska-Curie Actions of the European Union #847587).

References

[1] S. R. Mouchet, "Infrared absorbers inspired by nature", Journal of the Royal Society Interface, vol. 22(223), 20240284, 2025.

[2] S; Berthier, "Thermoregulation and spectral selectivity of the tropical butterfly *Prepona meander*: a remarkable example of temperature auto-regulation", Applied Physics A, vol. 80, pp. 1397-1400, 2005.

[3] S. R. Mouchet, and O. Deparis, "Natural Photonics and Bioinspiration", Artech House: Boston, MA, USA; London, UK, 2021.

Switchable Nonlocal Organic Metasurfaces

Dongqing Lin[1], Yulong Duan[1], Magnus Jonsson[1*]

[1] Laboratory of Organic Electronics, Department of Science and Technology (ITN), Linköping University, Norrköping, SE-60174, Sweden
*Corresponding author: magnus.jonsson@liu.se

***Abstract*—We present two types of tunable collective lattice resonances (CLRs) through conducting polymer metasurfaces, with resonance wavelengths ranging from 4500 to 640 nm. Poly(3,4-ethylenedioxythiophene) nanoantenna arrays either form plasmonic CLRs by themselves or serve as "optical gate" to switch light confinement and Mie CLRs in low-index organic dielectrics.**

***Keywords*— Active Organic Metasurfaces, Collective Lattice Resonances, Conducting Polymers**

I. Introduction

Conducting polymers, with tunable refractive index (or permittivity) induced by redox reactions, have been exploited as active materials for optical metasurfaces. Since 2020, conducting polymer metasurfaces have been applied for switchable surface plasmon resonances, beam steering and tunable lensing. However, conducting polymer plasmonics suffer from low resonance intensities and low quality factors ($Q < 2$), which are detrimental to metasurfaces' performances such as high-resolution and high-contrast switching. Meanwhile, due to the low charge carrier density in conducting polymer films, it is rather difficult to induce dynamic organic plasmonics within visible/NIR-I wavelength ranges (<960 nm). Here, we address these problems by inducing collective lattice resonances (CLRs) based on poly(3,4-ethylenedioxythiophene) (PEDOT) nanoantennas. Within the IR range (2-4.5 μm), PEDOT nanoantenna units in metallic state can fulfill the matching conditions between their isolated polarizability and the array factor of lattice [1]. This realizes the narrow plasmonic resonances (linewidth up to 300-400 nm) with Q-factors reaching 12. On this basis, the isolated polarizability of PEDOT nanoantenna units is tuned by redox reactions, enabling the dynamic control of CLR-matching states and the switching of surface plasmon resonances with a large extinction contrast (30-40%). Apart from the switching of plasmonic CLRs, PEDOT nanoantennas can also serve as the "optical gate" when combining with organic low-index nanocylinders (refractive index < 1.7). In the metallic state, PEDOT nanoantennas work as the "closed gate" to block the optical leakage between dielectric nanocylinders and substrate, and thus enhance the electric dipole resonance within dielectric nanocylinders [2]. By utilizing a dielectric nanocylinder array, this enables Mie CLRs within a wavelength range of visible-NIR-I region (< 950 nm). The Q-factors of these Mie CLRs reach 25, as 16 times higher than previous works of organic metasurfaces near this wavelength range. When performing reduction reactions, PEDOT nanoantennas in dielectric states behave as the "opened gate" to allow the light leakage into the substrate and eliminate the light confinement and Mie CLRs.

We believe our studies put forward important steps for active conducting polymer metasurfaces by breaking through key limitations of both low Q-factors and IR wavelength regimes. This provides potential feasibility for more extensive practical applications, such as in photonic circuits and biosensors.

II. Conclusion

We developed tunable nonlocal organic metasurfaces by inducing plasmonic and Mie CLRs through PEDOT nanoantennas. The nonlocal resonance wavelengths range from mid-infrared to visible regimes, and the Q-factors are improved up to 25. Future work will include the practical applications of these active metasurfaces in nano-optic systems and sensors.

Acknowledgments

These works were supported by the European Research Council (Consolidator Grant, 101086683); Knut and Alice Wallenberg Foundation (Wallenberg Academy Fellow, 2019. 0163); Swedish Research Council (VR, Consolidator Grant, 2020-00287); Swedish Government Strategic Research Area in Materials Science on Functional Materials at Linköping University (Faculty Grant SFO-Mat-LiU No. 2009 00971).

References

[1] D. Lin, Y. Duan, P. Bandaru, P. Li, M. S. Ansari, A. Y. Polyakov, J. Wilhelmsen, M. P. Jonsson, Nat. Commun. 2025, 16, 4484.
[2] D. Lin, Y. Duan, S. Kazi, M. P. Jonsson, Adv. Mater. 2025, e20674.

Bio-inspired photonic devices as a platform for quantum photonics

Oliver Trojak[1], Sean Gorsky[2], Fabrizio Sgrignuoli[2], Felipe Pinheiro[3], JinDong Song[4], Luca DalNegro[2], Luca Sapienza[1,*]

[1]Department of Engineering, University of Cambridge, Cambridge, United Kingdom
[2]Department of Electrical and Computer Engineering, Boston University, USA
[3]Instituto de Fisica, Universidade Federal do Rio de Janeiro, Rio de Janeiro, Brazil
[4]Korea Institute of Science and Technology, Seoul 136-791, South Korea
*Corresponding author: LS2052@cam.ac.uk

***Abstract*— Enhancing light-matter interactions on a chip is important for classical and quantum photonics, sensing, and energy harvesting applications. We demonstrate that bio-inspired aperiodic arrangements of air holes in suspended membranes represent a platform for enhancing the light-matter interaction in active on-chip nanophotonic devices embedding light emitters.**

***Keywords*— photoluminescence spectroscopy, quantum dots, photonic crystals, cavity quantum electrodynamics**

We report on the demonstration of enhanced light-matter interaction and Purcell effects on a chip, based on bio-inspired aperiodic photonic devices fabricated in silicon nitride and gallium arsenide. We fabricate silicon nitride [1] and gallium arsenide [2] devices where aperiodic patterns of air holes, are written by electron-beam lithography, followed by dry-etching and chemical undercut of a sacrificial layer to create free-standing membranes (see Fig.1a). By using defects in silicon nitride and indium arsenide single quantum dots as internal light sources, we image, by means of micro-photoluminescence [3], the optical modes supported by photonic devices with aperiodic patterns of air holes (Fig.1b).

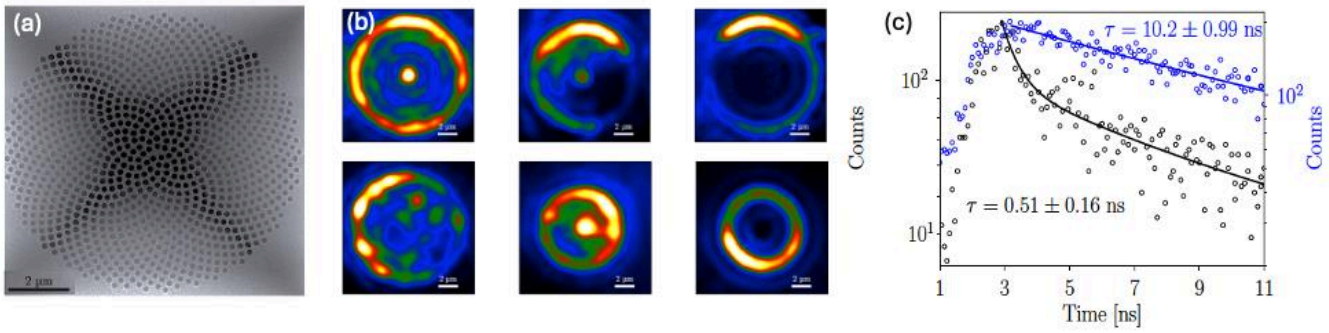

Fig.1: (a) Scanning electron micrograph of a suspended silicon nitride membrane with an etched aperiodic pattern of air holes. (b) Photo-luminescence images of the optical modes confined by an aperiodic nano-photonic devices (c) Time-resolved measurement of the intensity of the light emitted by quantum dots emitting at different wavelengths, collected by an avalanche photo-diode. Solid lines are exponential fits to the data (symbols) and decay time characteristics (lifetimes τ) are shown.

Our results show cavity quantum electrodynamic effects, providing strong modifications of the spontaneous emission dynamics of single quantum dots (see Fig.1c). In particular, thanks to the significant modification of the density of optical states due to the aperiodic structure, we show control of the decay lifetime of single quantum dots, with reduction of the lifetimes of up to a factor 2 and increase in the lifetimes by up to a factor 10.
Our results show that aperiodic nano-photonic devices based on bio-inspired aperiodic geometries are a novel and effective platform for efficient light confinement on a chip and for cavity quantum electrodynamics experiments with single emitters.

[1] O.J. Trojak, S. Gorsky, C. Murray, F. Sgrignuoli, F.A. Pinheiro, L. Dal Negro, L. Sapienza, *Cavity-enhanced light–matter interaction in Vogel-spiral devices as a platform for quantum photonics*, Applied Physics Letters **118**, 011103 (2021).
[2] O.J. Trojak, S. Gorsky, F. Sgrignuoli, F.A. Pinheiro, S.-I. Park, J.D. Song, L. Dal Negro, L. Sapienza, *Cavity quantum electro-dynamics with solid-state emitters in aperiodic nano-photonic spiral devices*, Appl.Physics Letters **117**, 124006 (2020).
[3] L. Sapienza, et al, *Nanoscale optical positioning of single quantum dots for bright and pure single-photon emission*, Nature Communications **6**, 7833 (2015).

Spatial Memory of Hot Carriers in Disordered Plasmonic Structural Colors

Manobina Karmakar[1], Ayon Jyoti Karmakar[2], Aritra Biswas[1,3], Mahdi Soudi[1,4], Tianyi Guo[1,4], Pablo Cencillo-Abad[1], Prasanta Kumar Datta[2], and Debashis Chanda[1,3,4]

2 Department of Physics, Indian Institute of Technology Kharagpur, Kharagpur, West Bengal 721302, India.

3 CREOL, The College of Optics and Photonics, University of Central Florida, Orlando, Florida 32816, USA.

4 Department of Physics, University of Central Florida, Orlando, Florida 32816, USA.
*Corresponding author: Debashis.Chanda@ucf.edu, Manobina.Karmakar@ucf.edu

***Abstract*— We investigate disordered aluminum nanoparticle ensembles generating structural colors via localized gap plasmons. Combining near-field imaging and ultrafast spectroscopy, we reveal that plasmon-induced hot carriers retain partial spatial localization for hundreds of picoseconds. This unexpected spatial memory links disorder, confinement, and energy dynamics, offering new bio-inspired design principles for nanophotonic and hot-carrier devices.**

***Keywords*— Gap plasmons, Hot carrier localization, Near-field imaging, Ultrafast spectroscopy.**

I. Introduction

Structural colors in nature arise from complex nanoscale architectures that combine order and disorder to achieve robust optical functionalities. Inspired by such bio-photonic systems, disordered plasmonic nanoparticle ensembles provide a powerful platform to explore how nanoscale localization and ultrafast energy dynamics govern optical responses. Here, we investigate aluminum nanoparticle-based structural colors and reveal that plasmon-generated hot carriers partially retain spatial localization memory long after plasmon dephasing, introducing a new spatiotemporal dimension to hot-carrier physics and bio-inspired nanophotonics.

II. Methods

We study self-assembled aluminum nanoparticles coupled to a metal–dielectric–metal cavity that display strong, yet broadband plasmonic response from 450-800 nm. Scattering-type scanning near-field optical microscopy (s-SNOM) is used to visualize nanoscale gap plasmon modes with ~20 nm spatial resolution. Ultrafast transient reflection spectroscopy with narrowband, tunable pump and broadband (450-800 nm) probe investigates the temporal evolution of plasmonic and electronic dynamics with 150 fs temporal resolution. By comparing resonant (630 nm and 700 nm) and non-resonant (415 nm) excitation, we distinguish global and spatially localized plasmon responses and extract key parameters such as dephasing time, spectral shifts, and effective linewidths. Resonant excitation "activates" a homogeneously broadened sub-ensemble through spectral-hole-burning and eventually diphase and generate hot carriers. We track the temporal evolution of the hot carriers and correlate how the LGP-assisted hot carriers affect the broadband, resonant probe.

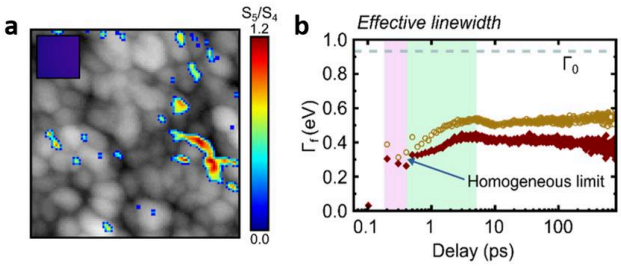

Fig. 1 (a) Overlay of the high near-field scattering amplitude corresponding to gap plasmons with the AFM height profile. LGPs can be observed as brighter intensities within nanoparticle gaps. (b) Ultrafast spectroscopy reveals pump-induced linewidth dynamics of the selective LGP modes upon 630 nm (yellow) and 700 nm (brown) excitation, representing their spatial localization.

III. Results and Discussion

Near-field imaging reveals randomly distributed, strongly localized gap plasmon (LGP) modes concentrated in interparticle gaps, forming wavelength-dependent hot-spot landscapes analogous to biological photonic structures (see Fig. 1(a)). Ultrafast spectroscopy shows that resonant excitation selectively addresses a homogeneously broadened sub-ensemble of plasmon modes, leading to spectral hole burning and a plasmon dephasing time of ~4 fs. Following dephasing, plasmon energy is transferred to hot carriers that exhibit only partial spatial delocalization. Remarkably, the effective plasmon linewidth does not recover to its steady-state value even after hundreds of picoseconds (Fig. 1(b)), demonstrating that hot carriers preserve a memory of the original plasmonic localization. This behavior highlights the critical role of disorder in controlling nanoscale energy flow.

IV. Conclusion

Our results uncover an unexpected spatial memory in plasmon-assisted hot carriers within disordered nanoparticle-based structural colors. By linking disorder, localization, and ultrafast dynamics, this work provides new design principles for bio-inspired nanophotonic materials and devices, with implications for plasmonic memory, sensing, and hot-carrier-based energy harvesting.

Acknowledgments

This work at the University of Central Florida was supported by the National Science Foundation (Grant no. ECCS 1920840).

Metasurface Tongues as Universal Liquid Sensors

Justin R Sperling[1], Finlay Walton[1], Daniel D Osborne[3], Badri Aekbote[1], Anthony E Perri[2], Rebecca A Setford[1], Hanyu Gao[1], Liam T Wilson[3], Chad M Sipperley[2], Rudolf J Schick[2], Baptiste Poursat[1], Caroline Gauchotte-Lindsay[1], William J. Peveler[3], Alasdair W. Clark[1]

[1]James Watt School of Engineering, University of Glasgow, Glasgow, United Kingdom
[2] Spraying Systems Co., Glendale Heights, IL 60139, United States
[3] School of Chemistry, University of Glasgow, Glasgow, United Kingdom

*Corresponding author: Alasdair.clark@glasgow.ac.uk

***Abstract*— We present a reusable plasmonic metasurface "tongue" that generates distinctive hyperspectral patterns for complex liquid mixtures through cross-reactive sensing. Simple machine learning enables both holistic quality assessment and targeted event detection. A single 24-element metasurface architecture supports universal deployment across diverse liquid-sensing tasks without bespoke receptors.**

***Keywords*— Plasmonics; sensor array; chemical sensor; nanophotonics; metasurface; taste; cross reactive sensing; food; beverage; environmental sensing.**

Industries centred on liquid products, from beverage manufacturers to drinking water providers, must manage chemically complex, dynamically evolving systems. Yet these sectors still rely heavily on centralised laboratory testing or sensory panels to track the quality of their product. These approaches are slow, episodic, and poorly suited to real-time decision-making, leaving operators unable to detect quality drift, emerging faults, or contamination events as they occur. This talk will describe the development of new bio-inspired metasurface sensors designed to address this gap.

We have developed a cross-reactive plasmonic metasurface platform that functions as an artificial "tongue" for liquids. A single 24-element metasurface chip, engineered with distinct non-binding surface chemistries, is interrogated using hyperspectral imaging to generate rich, multidimensional optical response patterns when exposed to a liquid sample. Rather than targeting individual analytes, the metasurface architecture amplifies subtle, collective interactions with the surrounding chemical environment, producing reproducible patterns that reflect overall composition. The device is fully reusable and requires no bespoke receptors or reconfiguration between applications.

In this presentation, I will survey our work applying this platform across two challenging and economically important domains: high-value beverages and drinking-water treatment. In both contexts, simple machine-learning models enable the chip's output to be interpreted either holistically (as continuous measures of quality and process stability) or in a targeted manner, flagging specific events or threshold exceedances.

Taken together, these studies demonstrate how a single metasurface "tongue" can be deployed as a universal liquid sensor, capable of supporting diverse sensing tasks without redesign. More broadly, this work illustrates how bio-inspired sensing principles, implemented through nanophotonic metasurfaces, can shift liquid analysis from retrospective laboratory testing to real-time, point-of-need insight.

Structural Dyes by Design: Physics-Guided Photonic Color Modules on Commodity Substrates

Hannah Sanford-Crane[1,*]
[1]MAAD Scientist Technologies Inc., Vancouver, BC, Canada
*Corresponding author: drhannah@maadscientisttech.com

Abstract—Structural color arises from nanoscale scattering architectures rather than molecular absorption, but translating optical design targets into chemically realizable materials remains difficult. Here we introduce structural dyes: modular molecular shells on commodity particle cores that function as programmable optical layers, whose refractive index and absorption define chromaticity. Designed from first-principles Mie scattering, Percus-Yevick structure factors, and CIE colorimetry, these modules attach to diverse substrates via silane and click chemistry without specialized infrastructure.
Keywords— structural color, structural dyes, inverse design, photonic glass, Mie scattering, click chemistry, colloidal assembly.

1 Introduction

Structural color in nature—beetle cuticles, bird feathers, *Morpho* wings—arises from scattering geometry rather than pigments. While the forward physics is well understood [1], translating optical predictions into chemically deployable materials remains an open problem. Vacuum-deposited multilayers, lithographic metasurfaces, and proprietary block copolymers all produce structural color, but require infrastructure that limits deployment to specialized facilities.

We propose *structural dyes*: modular photonic color units in which the target color is specified from first-principles scattering physics and implemented using molecular shells on commodity particle scaffolds. The shell acts as a programmable optical layer—its refractive index n and absorption k define the chromaticity of the assembled film—while its chemical handles (silane coupling, click tags) enable attachment to SiO_2, FeO_x, TiO_2, polymer, and textile surfaces. Color-bearing photonic modules can thus be designed computationally and deployed on arbitrary substrates using solution-phase chemistry at ambient conditions.

2 Physics-Guided Design

The inverse design engine (MABE) chains four modules with zero parameters fitted to structural color data. **Mie scattering** provides single-particle form factors $|F(q)|^2$. **Percus-Yevick structure factors** $S(q)$ provide the interference peak for disordered films. **Bragg diffraction** ($\lambda_{\text{peak}} = 1.633 D n_{\text{eff}}$) handles ordered assemblies [2]. **CIE colorimetry** converts predicted $R(\lambda) \propto S(q)|F(q)|^2$ to perceptual color using the Maxwell-Garnett effective index [1].

As a consistency check, predicted peaks for PMMA photonic glasses ($\phi = 0.55$) match Magkiriadou *et al.* [1] with MAE = 15 nm and zero fitted parameters. The model also reproduces the red problem (Fig. 1): for $D = 330$ nm, Mie backscattering from cavity-like modes floods the blue channel, producing purple rather than red—exactly as reported experimentally. The engine identifies reduced-index shells (e.g. porous silica, 30% porosity) as extending the accessible gamut toward red by suppressing this Mie bias.

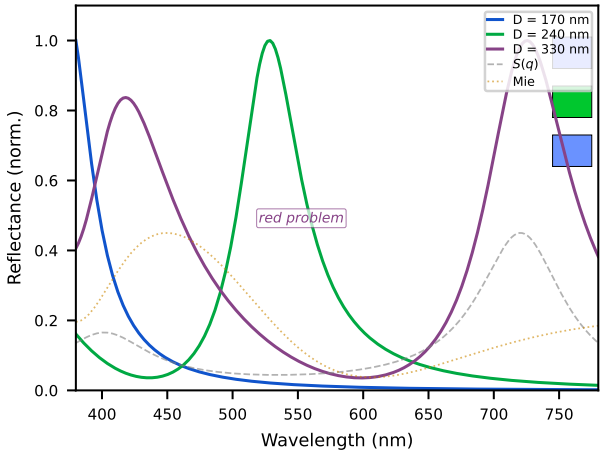

Figure 1: Predicted reflectance for PMMA photonic glasses, reproducing the red problem of [1]. The $D = 330$ nm spectrum shows competing Mie (dotted) and structural $S(q)$ (dashed) resonances. MAE = 15 nm vs. experiment, zero fitted parameters.

3 Shell Programmability: Bridging Binding to Optics

The molecular shell is the design variable. On a common SiO_2 core, different shells produce different optical responses—each a distinct structural dye (Fig. 2). Rather than inserting Δn and Δk as free parameters, the binding engine derives them from coordination chemistry.

Absorption (Δk): The donor set determines ligand field splitting Δ via the spectrochemical series. A tetradentate nitrogen chelator (2 pyridyl + 2 amine) coordinating Cu^{2+} produces $\Delta \approx 15{,}200$ cm^{-1}, placing the d-d band at $\sim$680 nm. Since d-d transitions are Laporte-forbidden ($\varepsilon \approx$ 50–100 M^{-1}cm^{-1}), k remains small ($\sim$0.01). A bidentate bipyridyl shell produces a weaker field ($\Delta \approx 13{,}800$ cm^{-1}, d-d at $\sim$750 nm). Pb^{2+} ($d^{10}s^2$) has no d-d transitions: $\Delta k = 0$.

Refractive index (Δn): Metal coordination replaces six water molecules (combined $\alpha \approx 8.8$ Å^3) with a metal-ligand complex of higher total polarizability. The net $\Delta\alpha$ enters the Lorentz-Lorenz relation to give Δn. Pb^{2+} produces the largest $\Delta n \approx 0.12$ despite weaker binding than Cu^{2+}, because its $6s^2$ lone pair makes it 5.6× more polarizable ($\alpha \approx 6.8$ vs. 1.2 Å^3). The binding engine ranks Cu^{2+} as the stronger binder; the optical engine ranks Pb^{2+} as the stronger color shifter. Different rankings for different

functions—from the same platform.

All three shell–metal combinations produce chromaticity shifts exceeding the perceptual threshold ($\Delta E_{xy} > 0.03$): $+5$ nm for the nitrogen chelator, $+10$ nm for the thiolate-amine, $+5$ nm for bipyridyl.

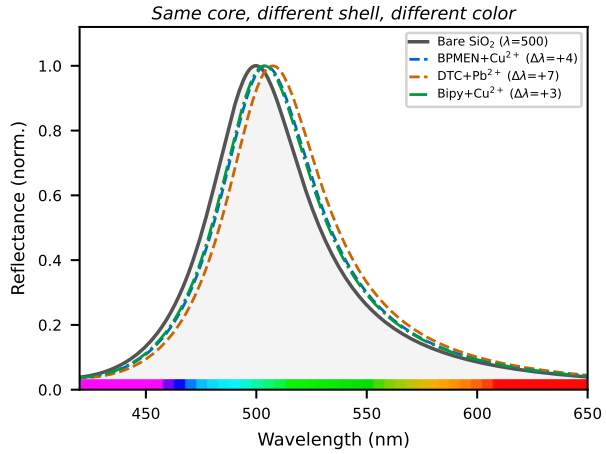

Figure 2: Three molecular shells on the same SiO_2 core produce distinct chromaticity shifts via $\Delta n + \Delta k$ (nitrogen chelator, bipyridyl) or pure Δn (thiolate-amine). Same core, different shell, different color.

4 Assembly and Deployment

Given a target chromaticity, the engine returns a complete layer specification: Fe_2O_3 hematite primer silane-coupled to the substrate and DBCO-functionalized, onto which azide-bearing structural dye particles are click-assembled via SPAAC into a disordered photonic glass. The primer provides both adhesion and spectral shaping—its wavelength-dependent reflectance selectively recycles transmitted light [3], producing a predicted chromaticity displacement $|\Delta E_{xy}| = 0.12$ relative to a flat absorber. Each layer is chemically locked to its neighbors through orthogonal click handles.

5 Outlook

Structural dyes establish a path from physics-first optical design to chemically deployable structural color. The same modular pattern—computed function, commodity scaffold, click-attached surface—already achieves $R^2 = 0.89$ for molecular binding prediction across 500 NIST metal-ligand complexes, suggesting the architecture generalizes beyond photonics. Experimental validation of the predicted shell chromaticity shifts on fabricated films is in progress.

References

[1] S. Magkiriadou, J.-G. Park, Y.-S. Kim, and V. N. Manoharan, "Absence of red structural color in photonic glasses, bird feathers, and certain beetles," *Phys. Rev. E*, vol. 90, p. 062302, 2014.

[2] G. I. N. Waterhouse and M. R. Waterland, "Opal and inverse opal photonic crystals," *Polyhedron*, vol. 26, pp. 356–368, 2007.

[3] M. Iwata *et al.*, "Bio-inspired bright structurally colored colloidal amorphous array enhanced by controlling thickness and black background," *Adv. Mater.*, vol. 29, p. 1605050, 2017.

Dynamically Tunable Structural Colors

Aritra Biswas, Debashis Chanda

Abstract: Structural coloration offers many advantages over conventionally used pigment-based colors due to their non-toxic, fade-resistant, and environmentally friendly nature. These colors arise from the structural arrangements of colorless materials at the nanoscale, which create optical resonances and vibrant hues. Over the last decade, dynamic color generation has been the subject of extensive research across various scientific disciplines. However, commercial adoption has been limited by the absence of effective tuning mechanisms, structural complexities and fabrication challenges. In this work, we demonstrate active color tuning based on phase modulation of a multilayer stack composed of a phase-changing material (PCM) and a high-index material on a reflective surface. We elucidate the underlying interfacial and cavity phase modulation mechanisms responsible for the dynamic color changes, highlighting the potential for tailoring the optical properties of this thin-film stack for a wide range of practical applications. Furthermore, we showcase the lithography-free implementation of this concept for large-area, color-tunable textiles, complex surfaces, and temperature sensitive consumer product labeling, highlighting its efficacy in tunable, scalable, and sustainable coloration. Leveraging dynamic phase modulation, this concept holds immense promise for applications in thermal sensing, advanced textile engineering, camouflage, and reconfigurable displays.

Reversible and Dynamic Photonic Bandgap Modulation via Chemical Reactions in Liquid Crystalline Polysaccharides

Cécile A. C. Chazot[1,*], Simona G. Fine[1], Nina Hildenhagen[2], Bart Jan Ravoo[2]

[1]Department of Materials Science and Engineering, Northwestern University, USA
[2]Organisch-Chemisches Institut and Center for Soft Nanoscience, Universität Münster, Münster, Germany
*Corresponding author: cchazot@northwestern.edu

***Abstract*— We develop chemically responsive liquid crystalline polysaccharides whose hierarchical organization enables reversible modulation of photonic bandgaps. By coupling molecular transformations with chiral self-assembly, we create dynamic photonic materials in which optical function is encoded at multiple length scales and tunable through targeted chemical reactivity, expanding design rules for adaptive soft matter.**

***Keywords*— liquid crystals, structural color, photoswitches, cellulose**

I. Introduction

Structural colors in non-living natural materials, particularly those derived from liquid crystalline polysaccharides,[1] are remarkable yet fundamentally constrained. Their photonic responses are typically static, or they react only to global stimuli such as temperature, mechanical stress, or humidity, triggers that are difficult to localize and challenging to modulate with spatial or temporal precision.[2], [3] As a result, while these chiral biopolymer mesophases offer sustainable, self-assembled photonic architectures, their functional tunability remains limited by the nature of the stimuli that affect their photonic crystal structure.

Here, we will discuss how targeted chemical modification of polysaccharides can overcome these limitations. By incorporating moieties that undergo molecular transformations (such as light-responsive photoswitches or groups activated by other localized chemical reactions)[4] we directly couple chemical reactivity to liquid crystalline order. Embedding reactive units into the mesogen itself enables local modulation of chain conformation, hydration, and twisting power, unlocking reversible and spatially programmable control over the photonic bandgap. This strategy shifts the design paradigm of liquid crystalline biopolymers: instead of relying on external physical fields to perturb the mesophase, we engineer materials in which molecular-scale chemistry drives mesoscale optical function.

II. Methods

Our methodology relies on the functionalization of cellulose ethers and esters with reactive moieties that undergo reversible transformations, such as isomerization or oxidation state, to locally alter sterics, polarity and interchain interaction. These reactions, in turn, modify the mesogens geometry or their packing. Concentrated aqueous mesophases are prepared to probe how small chemical modifications propagate up length scales, from molecular conformation to cholesteric pitch and domain organization. We combine reflection spectroscopy, angle-resolved scattering, circular dichroism, X-ray scattering, and solution-state and solid-state NMR to map these changes across hierarchical structure. Time-resolved optical experiments allow us to disentangle the fast kinetics of the chemical reaction from the slower evolution of cholesteric order and resulting photonic bandgap shifts.

III. Results and Discussion

Chemical reactivity within the mesogen produces reversible and dynamic photonic responses that diverge significantly from traditional stimulus-responsive polysaccharides. Molecular transformations (such as photoswitching) are completed on short time scales, yet the cholesteric rearrangement they initiate unfolds more slowly, revealing the multistep pathway through which molecular events reconfigure mesoscale order. We observe spectral shifts in the selective reflection wavelength that depend sensitively on the density and placement of reactive groups, demonstrating that even subtle modifications to mesogen geometry control the twisting power, hydration, and unfolding of the polysaccharide chain.

Importantly, we observe that the photonic bandgap response does not always stem from large-scale domain reorientation or changes in inter-mesogen spacing. Instead, chemical reactivity induces local changes in chain conformation that propagate upward, expanding the cholesteric pitch and producing

dynamic optical states, including reversible bimodal bandgaps in highly substituted systems. These findings clarify how chemical transformations reshape hierarchical self-assembly in polysaccharides and establish new structure-reactivity-function relationships for chiral soft matter.

IV. Conclusion

By embedding reversible molecular chemistry directly into the mesogenic unit, we access a new modality for dynamically reconfiguring photonic behavior in liquid crystalline polysaccharides. This approach yields materials with tunable bandgap shifts, reversible color changes, and distinct optical states inaccessible by conventional stimuli. More broadly, it demonstrates how chemical reactivity can act as a molecular lever for programming adaptive function across hierarchical biopolymer assemblies. These insights open new pathways for designing sustainable, stimuli-responsive photonic materials and lay foundational principles for reactivity-driven control of self-assembled structure.

Acknowledgments

This work was funded by the Army Research Laboratory Early Career Program Award to C. A. C. C. (Contract No. W911NF2510082), and additional partial funding from the NU MRSEC seed funds awarded to C. A. C. C. (NSF Award Number DMR-2308691). This work was also funded by the Deutsche Forschungsgemeinschaft (IRTG 2678 – Project ID 437785492 and CRC 1459 – Project ID 433682494) awarded to B. J. R.

References

[1] S. G. Fine and C. A. C. Chazot, "Unraveling the Governing Mechanisms Behind the Chiral Nematic Self-Assembly of Cellulose-Based Polymers," *Chemistry of Materials*, vol. 35, no. 21, pp. 8774–8787, Nov. 2023, doi: 10.1021/ACS.CHEMMATER.3C01904/ASSET/IMAGES/LARGE/CM3C01904_0005.JPEG.

[2] S. G. Fine, C. Guo, and C. A. C. Chazot, "Dynamic Structural Colors in Cholesteric Cellulose Composites: Achieving Spatial and Temporal Control," *Adv. Opt. Mater.*, vol. 13, no. 19, p. 2500521, Jul. 2025, doi: 10.1002/ADOM.202500521.

[3] S. G. Fine, S. E. Branovsky, and C. A. C. Chazot, "Structural Color Out of the Blue: A Quantitative Framework for the Self-Assembly Kinetics of Cholesteric Cellulosic Mesophases," *Biomacromolecules*, vol. 25, no. 8, pp. 4977–4990, Aug. 2024, doi: 10.1021/ACS.BIOMAC.4C00411/ASSET/IMAGES/MEDIUM/BM4C00411_0015.GIF.

[4] S. G. Fine, N. Hildenhagen, W. R. Linke, M. R. Hansen, B. J. Ravoo, and C. A. C. Chazot, "Photochromic Cholesteric Liquid Crystals via Arylazopyrazole Functionalization of Hydroxy-propyl Cellulose," *Under Review*.

Tunable "Meta"-Optical Fibers for Ultrawide-Field Bio-Imaging

Ho Wai Howard Lee[1,2,3*], Andrew Palmer, [1,2,3] Yucheng Jin, [1,2,3] Jin Yan, [1,2,3] Harvey Lin,[1,2] Albert Teoh [1,2,] Emma Wallace-Wilmot,[1,2] Sophia Turean[1,2]

[1] Department of Physics & Astronomy, University of California, Irvine, United States

[2] Beckman Laser Institute and Medical Clinic, University of California, Irvine, United States

[3] Eddleman Quantum Institute, University of California, Irvine, United States

*Corresponding author: Howardhw.lee@uci.edu

***Abstract*—** Optical endoscopes are critical for surgical and diagnostic applications, allowing for direct, real-time, and non-invasive imaging of internal biological structures. However, conventional optical fiber endoscopes are bulky, which increases procedural complexity and restricts their operation largely to the interior of hollow organs. Here, we demonstrate the first implementation of optical fiber tip-integrated metasurfaces combined with wavefront shaping of a multimode fiber output to realize tunable "meta"-optical fibers capable of active, continuous beam steering, achieving an ultrawide field of view of up to 140°. We further apply these devices for fluorescent bio-imaging and observe significantly enhanced imaging fidelity, with a minimum detectable feature size below 1 μm. This approach extends endoscopic imaging access to deep and previously inaccessible tissue regions, while the versatility of the underlying platform enables compact, multifunctional, and highly miniaturized fiber-based imaging technologies.

Acknowledgments

This work was supported in part by the National Science Foundation (grant numbers 2345825 and 2145235), Gordon and Betty Moore Foundation (GBMF ID #13829), and UCI Beall Innovation Award in Physical Sciences.

SPECIAL SESSION 9

When ‘meta' meets ‘materials': innovative materials, fabrication, functionalities

21 contributions · pp. 910–935

Exploiting strong confinement of light in hybrid self-assembled metamaterials

Anton Yu. Bykov[1,*], Nicolas Spiesshofer[1], Charalambos Louca[1], Tabitha Jones[1], Lille Borresen[1], Nima Taghipour[1], Jeremy J. Baumberg [1]

[1]Nanophotonics centre, Cavendish laboratory, Department of Physics, University of Cambridge, CB3 0US, UK

***Abstract*— Plasmonic nanocavities can realise extreme confinement of light. Here we discuss hybrid metamaterials, produced by self assembly of quantum dots, metal nanocrystals, and plasmonic particles, stabilized by robust molecular scaffolds. These artificial structures harness plasmonic confinement to enable infrared sensing, control of emission, and hot carrier physics on the nanoscale.**

***Keywords*— Plasmonics, quantum materials, chemical self-assembly, nanoparticle aggregates.**

I. Introduction

Using ultrathin gaps between noble metals allows confinement of light to ultra-small volumes, realizing extreme regimes of light-matter interaction. This has enabled many intriguing demonstrations including strong coupling to individual quantum emitters[1], nanoscale sensing[2], and few-molecule optomechanics[3]. An archetypal plasmonic nanocavity – the gold nanoparticle-on-mirror (NPoM), allows one to trap light to unprecedented volumes below 1 nm^3, and can be engineered to host a variety of gap materials, including self-assembled molecular monolayers, quantum dots, and 2D materials, realizing hybrid structures. Building upon the rich physics of NPoM nanocavities, and robust machinery of chemical self-assembly, we realize a hybrid metamaterial approach to harness strong confinement of light in extended plasmonic systems.

II. Results and Discussion

Our approach utilizes chemical self assembly of hybrid structures, with the help of selected scaffolding molecules. We demonstrate how the assembly of gold nanoparticles allows one to effectively create three-dimensional metamaterials in the mid-infrared spectral range, featuring high effective refractive indices (even $n > 10$) with surprisingly low loss. We show that optical Fabry-Perot modes in such structures confine mid-IR light into sub-1 nm gaps and realize efficient surface-enhanced IR absorption (SEIRA), enabling real-time IR sensing. We show extended tuneability of the optical properties of the IR metamaterials through selective electrochemical growth, and use selective dissolution[4] in co-assembled bimetallic Au:Ag structures, to tune fill fractions and nanogap area and control resonance positions. We demonstrate applicability of such metamaterials for real world sensing applications.

We further discuss the emission properties of hybrid structures featuring self-assembled layers of quantum dots and metal nanocrystals, in this plasmonic environment. We show that construction of nanoparticle-on-nanocrystal-on-mirror structures increases the efficiency of usually very weak hot-carrier-driven light emission from noble metals by several orders of magnitude compared to the state of the art. This allows us to study nonequilibrium features of the emission in great detail. We discuss the origin of this emission within two existing paradigms - hot carrier photoluminescence and electronic Raman scattering and experimentally compare the emission of Au, Au:Ag nanocrystals and quantum dots in the same plasmonic environment. We further discuss hot electron-induced birefringence on ultrafast time scales in such self-assembled plasmonic metamaterials in the near-IR spectral domain, and its connection to light localization, disorder, and heat dissipation.

Finally, we discuss the control of collective emission in such self-assembled plasmonic metamaterials incorporating light-emitting dyes in the plasmonic nanogaps. We demonstrate the emergence of a long-range power-dependent superradiant state in the structure, enabled by dipole-dipole coupling between emitters in plasmonic gaps[5].

References

[1] R. Chikkaraddy, et al., “Single-molecule strong coupling at room temperature in plasmonic nanocavities,” Nature, vol. 535, pp. 127–130, 2016.

[2] A. W. Powell et al., “Plasmonic gas sensing using nanocube patch antennas” Advanced Optical Materials, vol. 4, pp. 634–642, 2016.

[3] J. Griffiths, et al., “Resolving sub-angstrom ambient motion through reconstruction from vibrational spectra” Nature Comm., vol. 12, pp. 6759, 2021.

[4] N. Spiesshofer et al., “Tailoring ultrahigh index plasmonic combinatorial metamaterials for SEIRA and SERS by tuning the fill fraction” Optica 12, 1357-1366 (2025)

[5] R Arul et al.,; “Coherent room-temperature dipole synchronization in nanocavity sheets”, under review (2025)

Light and Molecules at the Nanoscale

Pablo Alonso-González [1,2]

[1]Department of Physics, University of Oviedo, Spain
[2] Center of Research on Nanomaterials and Nanotechnology, CINN (CSIC-Universidad de Oviedo), El Entrego 33940, Spain
*Corresponding author: pabloalonso@uniovi.es

***Abstract*— Recent experiments have discovered light at the nanoscale (polaritons) exhibiting strongly anisotropic propagation (hyperbolic) and extreme field confinement in 2D materials, such as α-phase molybdenum trioxide (α-MoO_3) [1]. In this talk, we will demonstrate that this exotic nanolight enables, for the first time, the visualization of directional-dependent strong coupling phenomena with organic molecules (pentacene) (Fig.1). To support this claim, we will show near-field images taken by scattering-type scanning near-field optical microscopy (s-SNOM), which allow to directly corroborate the strong coupling variation as a function of in-plane angle. This result opens the door to several new applications such as directional sensing or directional local control of chemical properties at the nanoscale [2].**

***Keywords*—2D materials, Mid-IR, strong coupling, s-SNOM.**

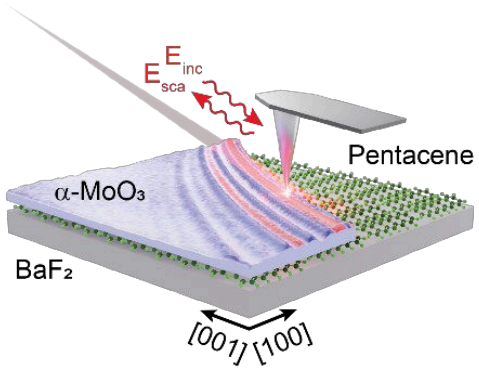

Fig. 1 Schematic of the visualization by s-SNOM of strong coupling between polaritons and pentacene molecules.

ACKNOWLEDGMENTS

The author acknowledges support from the Spanish Ministry of Science and Innovation under grant PID2022-141304NBI00, and the European Research Council under Consolidator grant No.101044461, TWISTOPTICS.

REFERENCES

[1] W. Ma, P. Alonso-González, et al. "In-plane anisotropic and ultra-low-loss polaritons in a natural van der Waals crystal" Nature, vol. 562, pp. 557–562, 2018.
[2] AI F. Tresguerres-Mata, O. G. Matveeva, C. Lanza, et al. "Directional strong coupling at the nanoscale between hyperbolic polaritons and organic molecules" Nature Photonics, vol. 19, pp. 1196–1202, 2025.

Publishing in Nature Portfolio

Rachel Won

Nature Reviews Electrical Engineering
Springer Nature Limited, 4 Crinan Street, London N1 9XW, United Kingdom
r.won@nature.com

***Abstract*—This talk will give you an overview of Nature Portfolio, with emphasis on *Nature Reviews Electrical Engineering*, before detailing the editorial and peer review processes for its research and review journals. The editorial criteria and editorial policies of these journals will also be presented.**

***Keywords*— publishing, Open Access, AI, metamaterials, electrical engineering.**

I. Nature Portfolio Journals

Nature Portfolio journals[1] can be categorized into Communications journals, npj Series, Scientific Reports, Scientific Data and Nature journals that include Nature, Nature Research journals, Nature Reviews journals, Nature Communications and Nature Protocols.

II. Why Publishing with Nature Portfolio

Nature Portfolio publishes high-quality, independently peer-reviewed research and reviews, as well as comment and news, for the scientific and clinical research communities. Nature Portfolio uses pioneering technologies, innovative formats and first-class editing to provide cutting-edge, timely yet readable information for researchers in the public and private sectors, government agencies, educators, clinicians and the general public. Nature Portfolio has a close relationship with the scientific community. By working with scientists, listening to what they say, and always placing emphasis on quality, it is the leading publisher for innovative solutions to scientists' information needs. Publishing with the Nature Portfolio family provides an author with a wide range of benefits.

III. Nature Research Journals vs Nature Reviews Journals

Nature Research journals publish selected research of the highest quality and impact in their specific disciplines. They publish papers online weekly, with an issue compiled monthly. Besides original research, these journals include informal material and reviews.

With the expanding volume of data generated by the research community, it is becoming increasingly difficult for researchers to find the information they need in a format that is reliable and immediately useful. Nature Reviews journals address these needs, publishing high-quality content that highlights and reviews the latest information for a broad range of disciplines, n a way that addresses the inter- and multi-disciplinary nature of research today.

IV. Nature Reviews Electrical Engineering

Nature Reviews Electrical Engineering[2] is an online-only journal aiming to cover the breadth and depth of modern electrical engineering by publishing timely and accessible top-quality Reviews, Perspectives and Comments encompassing every aspect of electronics, photonics, power and energy, control systems, signal processing and telecommunication engineering. The journal also aims to bring to the attention of its readers topics beyond engineering research with particular focus on societal, ethical, environmental and commercial aspects of electrical engineering.

It publishes a range of content types, including Reviews, Perspectives, Roadmaps, Comments, News & Views, Lab to Fab, Viewpoints, Research Highlights, Q&As, Journal Club and Correspondences, that elaborate on significant advances in the field and cover topical issues.

V. Editorial and Peer Review Processes

What are Nature Research journals' editors looking for? What are Nature Reviews journals' editors looking for? They are editorially independent and have their own editorial criteria and processes. General information can be found in the "How to publish your paper" site[3].

VI. Editorial Policies

Although the journals are broadly similar and share editorial policies[4], all authors should consult the author information pages of the specific journal before submitting, to obtain detailed information on criteria for publication and manuscript preparation for that journal, as some differences exist.

References

[1] https://www.nature.com/nature-portfolio/for-authors/nature-research-journals
[2] https://www.nature.com/natrevelectreng
[3] https://www.nature.com/nature-portfolio/for-authors/publish#editorial-process
[4] https://www.nature.com/nature-portfolio/editorial-policies

Interband plasmonic elemental materials for sustainable nanophotonics: widening the spectral range

Johann Toudert[1], Fernando Chacón-Sánchez[1] and Rosalia Serna[1]

[1] Laser Processing Group, Instituto de Optica, IO-CSIC, Serrano 121, 28006 Madrid, Spain

*Corresponding author: rosalia.serna@csic.es

***Abstract*— We will show how interband transitions in semimetals and semiconductor nanostructures enable an alternative plasmonic response that expands from far-UV to the IR, therefore allowing the development of sustainable and reliable platforms for nanophotonics that will support advanced functionalities such as perfect absorption, structural coloration, and tunable optical response.**

***Keywords*— Plasmonics, nanophotonics, metamaterials, semimetals, semiconductors, Bi, Sb, Si**

I. Introduction

Conventional plasmonic platforms based on noble metal nanostructures, Au and Ag, offer a unique strong field enhancement but rely on scarce and expensive materials whose integration into large-scale photonic technologies remains limited. In this invited talk, we will review and critically discuss recent advances that point toward an alternative paradigm based on the interband plasmonic response exhibited by sustainable elemental materials, including semimetals and amorphous semiconductors. These findings open the path towards the development of alternative nanophotonics platforms for next-generation optoelectronics.

II. Results and Discussion

Studies of the optical response of semimetal nanostructures of the p-block (such as Bi and Sb) have demonstrated to be crucial to unveil the existence of unconventional plasmonic phenomena based on interband transtitions. The optical response of these semimetal is dominated by strong interband transitions that provide a plasmonic behaviour in the UV-visible, and enable an extraordinary high refractive index in the infrared [1-3]. These complementary features have facilitated the design of both narrowband, spectrally selective components and broadband light-trapping architectures [4-6]. Moreover, a final advantage of Bi is the ability of modulation of its optical response through phase change thanks to its low melting temperature, opening routes to dynamically reconfigurable devices [7-8]. Their spectral tunability and compatibility with thin-film deposition methods have allowed to demonstrate their successful application from structural coloring to optical switching [5-7].

In this context of sustainable elements for photonics, more recently we have unveiled the plasmonics properties of amorphous silicon (a-Si) nanostructures. Experimental results and simulations show that they can sustain plasmonic-like resonances extending deep into the far-UV [9]. This finding is remarkable because it shows that crystalline order is not a necessary condition for sustaining strong plasmonic resonances: the response is once again governed by interband transitions, which in a-Si produce strong absorption plasmonic peaks. It is noteworthy that these results significantly expand the spectral reach of sustainable plasmonics, covering wavelengths inaccessible to most conventional plasmonic materials and suggesting new opportunities for UV photonics, and high-energy photodetectors.

Acknowledgments

This work has been partly funded by the national research grants ALPHOMENA (PID2021-123190OB-I00f) and SLIM-2P (PID2024-156974OB-C21) funded by MCIN/AEI/ 10.13039/501100011033 and by the European Union NextGenerationEU/PRTR and the European Regional Development Fund (ERDF).

References

References

[1] J. Toudert, R. Serna, I. Camps, J. Wojcik, P. Mascher, E. Rebollar, T. A. Ezquerra, J. Phys. Chem. C 121 (2017) 3511.

[2] J. Toudert and R. Serna, Opt Mater Express 7 (2017) 2299.

[3] J. Toudert, R. Serna, C. Deeb, E. Rebollar, Opt Mater Express 9 (2019) 2924.

[4] J. Toudert, R. Serna, M. G. Pardo, N. Ramos, R. J. Peláez, B. Maté, Opt. Express. 26 (2018) 34043.

[5] F. Chacon-Sanchez, et al., Adv Opt Mater 12 (2024) 2302130.

[6] F. Chacon-Sanchez and R. Serna, ACS Appl. Opt. Mater. (2025).

[7] M. Alvarez-Alegria, J. Siegel, M. Garcia-Pardo, F. Cabello, J. Toudert, E. Haro-Poniatowski, R. Serna, Adv. Opt. Mater. 10 (2022) 2101405.
[8] M. Garcia-Pardo, E. Nieto-Pinero, A. K. Petford-Long, R. Serna, J.Toudert, Nanophotonics 9 (2020) 885.
[9] J. Toudert, R. Serna, J. Martín-Sánchez, J.I. Larruquert, and L. Calvo-Barrio, J. Physics: Photonics, 7 (2025), 045019.
[10] J. Toudert, R. Serna, L. López-Conesa, J.M. Rebled, F. Peiró, S. Estradé and L. Calvo-Barrio, J. Phys. Chem. C 119 (2015) 10899.

Chiroptical Emergence in Disordered Plasmonic Assemblies

Aso Rahimzadegan[1,*], Zihao Lu[2,*], Thomas G. Parton[1,2], Sinuhé Perea-Puente[1], Antonio Carone[1], Jessica Ma[3], Emeline Raguin[1], Bruno Frka-Petesic[2,4], Aurimas Narkevicius[2,5], Junyoung Kwon[6], Heather F. Greer[2], Nicholas A. Kotov[3], Kevin Vynck[7,†], & Silvia Vignolini[1,2,†]

[1] Max Planck Institute of Colloids and Interfaces, Potsdam, Germany.
[2] Department of Chemistry, University of Cambridge, Cambridge, UK.
[3] Department of Chemical Engineering, University of Michigan, Ann Arbor, MI, USA.
[4] International Institute for Sustainability with Knotted Chiral Meta Matter (WPI-SKCM2), 1-3-1 Kagamiyama, Hiroshima University, Higashi-Hiroshima, Hiroshima, 739-8526, Japan.
[5] B CUBE Center for Molecular Bioengineering, Technische Universität Dresden, Dresden, Germany.
[6] Department of Nanotechnology Engineering, Pukyong National University, Busan, Republic of Korea.
[7] Institute of Light and Matter, Claude Bernard University Lyon 1, CNRS, Villeurbanne, France.

* These authors contributed equally to this work.
† Corresponding author. Email: kevin.vynck@univ-lyon1.fr, sv@mpikg.mpg.de.

***Abstract*— We demonstrate chiroptical activity in disordered ensembles of plasmonic nanospheres despite showing no chirality in their retrieved coordinates. Optical simulations verify the experimental results and reveal that the observed circular dichroism emerges from mesoscopic electromagnetic correlations rather than local chiral coupling, establishing a new paradigm for scalable self-assembled chiral metamaterials.**

***Keywords*— plasmonics, disorder, mesoscopic correlations, metamaterials, chirality.**

I. Introduction

Optical activity such as circular dichroism and circular birefringence are traditionally associated with geometrically chiral architectures, including helices, twisted assemblies, or intrinsically chiral nanoparticles. In plasmonic systems made from achiral components, strong optical activity typically arises from engineered near-field coupling in well-defined chiral arrangements.

Here we report a counterintuitive result: a statistically isotropic and homogeneous ensemble of spherical silver nanoparticles exhibits reproducible and significant chiroptical activity. The particles themselves are achiral and sparsely distributed, with densities on the order of one particle per cubic wavelength at resonance. Several structural chirality metrics fail to detect any dominant handedness in the spatial distribution. Nevertheless, both experiment and theory reveal a robust electromagnetic chirality emerging at mesoscopic scales.

II. Methods

Silver nanoparticles were nucleated within a chiral nematic template formed by self-assembled chitin nanocrystals. The template pitch lies in the micrometer range and is optically inactive.

Three-dimensional particle coordinates were retrieved using FIB-SEM tomography, yielding spatial information for more than 30,000 nanoparticles in a volume of approximately 1,800 cubic micrometers. Multiple conventional and also proposed structural chirality measures were evaluated, including pseudoscalar and Hausdorff-distance-based metrics. None showed statistically significant deviation from random point distributions that show no dominant handedness.

To analyze the optical response, we employed a coupled-dipole formalism treating each nanoparticle as an isotropic point dipole. Circular dichroism and circular birefringence cross sections were computed and combined into a complex-valued chiroptical index. The chiroptical index capture both absorptive and dispersive components of electromagnetic chirality in a unified representation.

Statistical significance was assessed by subdividing the reconstructed volume into independent voxels and applying both univariate and multivariate tests.

III. Results and Discussion

Experimentally, the composite Ag-Chitin films exhibit a bisignate circular dichroism spectrum centered at the plasmonic resonance, with dissymmetry g-factors in the order of 10^{-3}.

Conventional and a proposed structural analysis confirms the absence of structural chirality. However, coupled-dipole simulations reproduce the measured spectra and reveal that the ensemble-averaged chiroptical index is much larger than that of purely random particle configurations of identical density.

Importantly, statistical significance emerges only when electromagnetic interactions are considered over length scales comparable to the micrometer-scale pitch of the original template. Short-range particle clusters do not produce

distinguishable electromagnetic chirality. This demonstrates that the effect is intrinsically non-local and mesoscopic in origin.

Together, these results establish that electromagnetic chirality can arise without measurable structural chirality.

IV. Conclusion

We demonstrate that macroscopic disordered ensembles of achiral plasmonic nanospheres can exhibit statistically significant chiroptical activity. Structural chirality measures fail to detect dominant handedness, yet mesoscopic electromagnetic correlations generate a robust optical response.

This work challenges the conventional paradigm that evident structural chirality is a prerequisite for optical chirality. Instead, it reveals disorder-enabled mesoscopic correlations as a new route toward scalable chiral plasmonic metamaterials. The findings open opportunities for disorder engineering in chiral metamaterials and complex photonic media.

Acknowledgments

H.F.G. acknowledges funding from EPSRC (EP/P030467/1). Z.L. acknowledges support by the Cambridge Trust. S.P.P. acknowledges support from the SALTO program (MPG/CNRS, No. 57142201151). S.V. acknowledges support from the Max Planck Society, the European Research Council, the Philip Leverhulme Prize, and EPSRC grants.

Disorder silica microsphere coating for efficient sub-ambient radiative cooling

Jorge Burgos[1,*], Ares Llados[2], Sara Núñez-Sánchez[1], Ceferino López[1], Juliana Jaramillo[2], Pedro David Garcia[1]

[1] Material Science Institute of Madrid (ICMM), CSIC, Campus UAM, Madrid 08193, Spain.
[2] Departament de Màquines i Motors Tèrmics, UPC, Barcelona 08222, Spain.
*Corresponding author: jorge.burgos@csic.es

***Abstract*— Passive radiative cooling rejects heat to outer space through the 8–13 µm window, enabling sub-ambient temperatures without power. We develop disordered SiO_2-microsphere coatings combining >93% solar reflectance with strong mid-IR emissivity. Their microstructure, optical response, and outdoor thermal behavior are experimentally validated, confirming effective cooling under direct sunlight.**

***Keywords*— radiative cooling, atmospheric transparency window, disorder, silica.**

I. Introduction

Sustainable thermal management technologies have driven renewed interest in passive radiative cooling (RC). By reflecting incident solar radiation while emitting thermal radiation toward cold outer space, RC devices can achieve net cooling even under solar illumination [1]. Over the past decade, these technologies have gained prominence as a complementary mechanism for heat dissipation alongside conduction and convection. Their potential was first experimentally confirmed in 2014, when Raman et al. [2] demonstrated cooling below ambient temperature.

Achieving daytime radiative cooling requires minimizing solar absorption while maximizing mid-IR emission. Silica (SiO_2) enables this because its particles support surface phonon-polaritons (SPhPs) near the Si–O vibrational resonances (8–10 µm), which fall within the atmospheric window. When arranged as microspheres or shells, these modes couple efficiently to the far field, boosting mid-IR emissivity. As a result, SiO_2 acts as a selective emitter that reflects sunlight and radiates strongly in the mid-IR, making it highly effective for sub-ambient daytime cooling. Randomly packed silica microparticle coatings, or SiO_2-based disordered photonic structures, have emerged as a cost-effective pathway to obtain high solar reflectance and strong selective mid-IR emission.

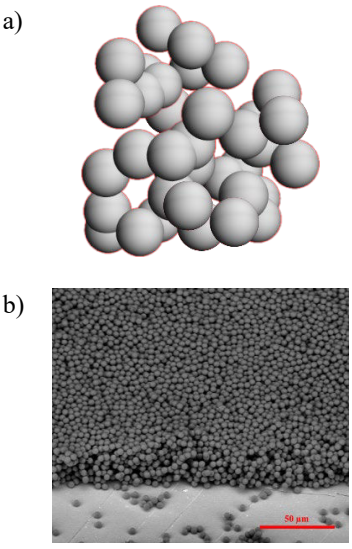

Fig. 1 *Structural characterization of randomly packed silica microsphere coatings: (a) Schematic of the disordered photonic structure. (b) Cross-sectional SEM image of ~25 µm thick coating (scale bar: 50 µm).*

II. Methods

Photonic-glass coatings were produced by depositing polydisperse suspensions of commercial SiO_2 microspheres (2–8 µm) onto highly reflective substrates (Fig 1a-b). A 15 mL dispersion (0.4–0.5 wt%) was allowed to settle under controlled temperature and humidity, and drying at 45 °C yielded uniform, mechanically stable coatings ~25 µm thick.

Optical characterization used UV–Vis spectroscopy with an integrating sphere to measure broadband solar reflectance, and FTIR spectroscopy with a gold-coated integrating sphere to determine mid-infrared emissivity within the atmospheric window. Coherent-backscattering measurements employed a TEM_{00} He–Ne laser; the backscattered light was polarization-

filtered, recorded with a CCD camera, and the cone's angular profile was analysed to obtain the transport mean free path.

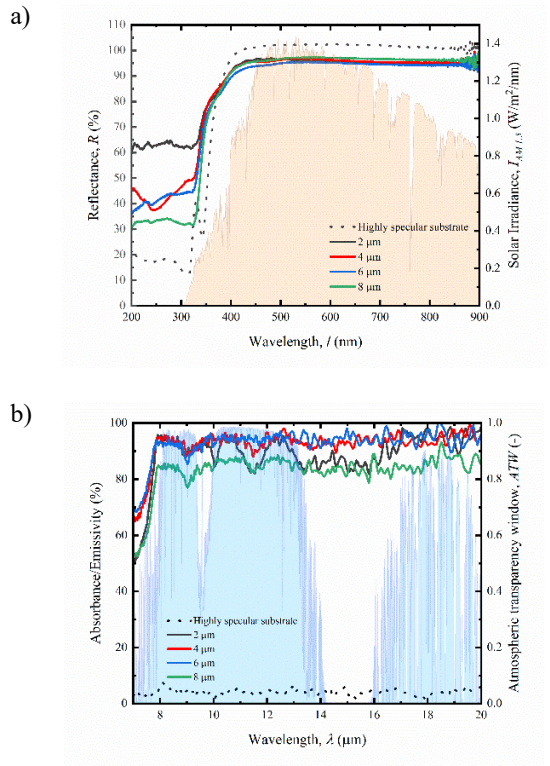

Fig. 2 *Optical characterization of randomly packed silica microsphere coatings: (a) Solar reflectance >93%. (b) Mid-IR emissivity in the 8–13 µm atmospheric window.*

Thermal performance was tested outdoors under clear skies in Barcelona. Samples were placed on an elevated reflective platform inside a non-emissive enclosure to reduce parasitic heat exchange. Sample and ambient temperatures were measured with calibrated PT100 sensors, while irradiance and meteorological data were recorded continuously. Cooling power was determined using a PID-controlled resistive heater that maintained a fixed temperature offset above ambient; the electrical power required at steady state quantified radiative heat dissipation.

III. Results and Discussion

All coatings exhibit excellent radiative properties, with solar reflectance between 93.6–95.3% and mid-infrared emissivity of 0.85–0.93 in the 8–13 µm atmospheric window (Fig 2a-b). Coherent-backscattering measurements confirm operation deep in the multiple-scattering regime, with transport mean free paths of 2–7 µm, always far below the 25 µm coating thickness. Despite this variation in scattering strength, the optical response remains essentially invariant with particle size, as both reflectance and emissivity vary by less than 10% across all samples. Under outdoor conditions with peak irradiance around 800 W m^{-2}, all silica-coated surfaces remain at or slightly below ambient temperature, while reference substrates heat up by more than 5 °C compared to those with silica microspheres. Sub-ambient cooling appears as irradiance decreases, reaching up to 4.8 °C relative to references in the late afternoon and 3.7 °C below ambient at night. Night-time cooling powers of 44–61 W m^{-2} and low integrated solar absorption (5–8%) confirm efficient radiative performance with no measurable dependence on microsphere diameter.

IV. Conclusion

In summary, we demonstrate that silica-microsphere coatings can provide effective passive radiative cooling, achieving temperature drops below ambient under direct sunlight and delivering net cooling powers on par with leading radiative-cooling materials. By systematically tuning the microsphere diameter and combining spectral, thermal, and power-based analyses, we show that the cooling performance remains essentially unchanged across the full particle-size range examined. This size-independent behaviour stems from the dominance of collective multiple-scattering processes in these optically thick layers, which makes the overall response insensitive to the specifics of individual particle resonances. Consequently, precise size control is not required, easing fabrication demands and enabling integration with the broader design flexibility offered by colloidal chemistry. This opens opportunities for scalable, multifunctional cooling coatings that can incorporate surface treatments, chemical functionalization, or other modifications without compromising thermal performance.

Acknowledgments

This work was supported by the Spanish Ministry of Science, Innovation and Universities via the national project PID2024-158832NB-C21 (PSYNC), by the HORIZON-EIC-2022 Pathfinder project ADAPTATION (Grant No.~101129661), and by the Spanish MICIU Severo Ochoa program for Centres of Excellence through Grant CEX2024-001445-S.

References

[1] M. M. Hossain and M. Gu, "Radiative cooling: Principles, progress, and potentials," Jul. 01, 2016, Wiley-VCH Verlag. doi: 10.1002/advs.201500360.

[2] A. P. Raman, M. A. Anoma, L. Zhu, E. Rephaeli, and S. Fan, "Passive radiative cooling below ambient air temperature under direct sunlight," Nature, vol. 515, no. 7528, pp. 540–544, Nov. 2014, doi: 10.1038/nature13883.

[3] Z. Ding et al., "Designer SiO_2 Metasurfaces for Efficient Passive Radiative Cooling," Adv Mater Interfaces, vol. 11, no. 3, p. 2300603, 2024, doi: 10.1002/admi.202300603.

Silicon metasurfaces for thermal control of classical and quantum light

Agostino Di Francescantonio[1,*], Omer Can Karaman[1], Giulia Tagliabue[1]

[1]École Polytechnique fédérale de Lausanne, Laboratory of Nanoscience for Energy Technologies, STI, 1015, Lausanne, Switzerland
*Corresponding author: agostino.difrancescantonio@epfl.ch

***Abstract*— We investigate resonant, thermo-optically reconfigurable silicon metasurfaces modulating light in the classical and quantum regime. Thermo-optic effect enables dynamic modulation of photon pairs and efficient control of the transmittance via engineering of heat and optical time scales, opening interesting avenues for optical modulation and computing.**

***Keywords*— metasurfaces, thermo-optic effect, optical computing.**

I. Introduction

Optical metasurfaces, consisting in 2D artificial arrangements of subwavelength nanostructures (i.e., meta-atoms) with sub-micrometer thickness, are a unique platform to tailor light-matter interactions and modulate freely-propagating light in small-footprint optical devices [1]. In recent years, actively reconfigurable metasurfaces have attracted a growing interest, driven by the quest for fast, efficient, and miniaturized components capable of dynamically controlling the various properties of light. Different physical mechanisms are exploited to modulate light properties [2,3], like amplitude, phase, and polarization. Here, we leverage thermo-optic (TO) nonlinearity in semiconducting materials, like silicon, to produce a change in the refractive index Δn upon a variation in material's temperature; this last can be induced either *via* a direct heat stimuls or by light absorption through photo-thermal (PT) heating. Although limited in speed by the heat dynamics, TO effect brings about a strong nonlinearity in the optical response of the system, which can be further enhanced and tailored by leveraging optical resonances. Moreover, the different time scale of heat and optical dynamics is a feature with interesting perspectives in metasurface-based optical modulation optical computing.

II. Results and Discussion

We investigate optical metasurfaces fabricated by nanostructuring a thin layer of amorphous silicon (aSi), deposited by chemical vapour deposition on an insulating, low index, SiO_2 substrate. We leverage the high refractive index contrast between aSi and SiO_2 to engineer electromagnetic resonances in the visible and near infrared, to enhance the TO nonlinearity. We exploited TO effect to manipulate entangled photons pairs generated by spontaneous four-wave mixing in aSi metasurfaces[4]. Here, electric- and magnetic-dipole resonances hosted by the meta-atoms enhance the rate of photon pairs up to 3.6 kHz. Moreover, the shift of the resonant modes spectral position induced by the heating from same laser pump modulates photon pairs generation, opening the way for dynamic tuning of thermally reconfigurable quantum light sources. The same platform served to demonstrate a dynamic modulation of the transmittance[5]. Here, the thermal and optical response is engineered, allowing a modulation of more than 30% at 100 kHz through an optimization of the heat diffusion process and PT heating area. In addition, the resonant nature of the system allows encoding different optical states in the same modulation cycle, with interesting perspectives in free-space optical computing.

III. Conclusion

The presented studies report engineered nanoscale platforms exploiting TO effect to achieve an efficient control of light in the classical and quantum regime. In perspective, the modulation efficiency can be further enhanced by exploiting high-quality-factor resonances like quasi-bound-states-in-the-continuum. Moreover, the complex interplay of PT heating and TO effect, eventually leading to peculiar phenomena like optical bistability, is of great interest for optical computing and for the rapidly growing field of optical neural networks.

References

[1] S. A. Shulz, R. F. Oulton, M. Kenney et al., "Roadmap on photonic metasurfaces", *Appl. Phys. Lett.* 124, 260701, 2024.
[2] A. Di Francescantonio et al., "All-optical free-space routing of upconverted light by metasurfaces via nonlinear interferometry", *Nat. Nanotechnol.* 19, 298–305, 2024
[3] A. Di Francescantonio *et al.* "Efficient GHz electro-optical modulation with a nonlocal lithium niobate metasurface in the linear and nonlinear regime", *Nat Commun* 16, 7000, 2025.
[4] O. C. Karaman et al., "Photo-Thermally Tunable Photon-Pair Generation in Dielectric Metasurfaces" *ACS Nano*, 2026
[5] O. C. Karaman et al., "Decoupling Optical and Thermal Dynamics in Dielectric Metasurfaces for Self-Encoded Photonic Control", *Laser Photonics Rev*. e01014, 2025.

Designer metasurfaces from the bottom-up

Beniamino Sciacca*[1]

[1]CNRS, Aix-Marseille University, CINaM, Marseille
*Corresponding author: beniamino.sciacca@cnrs.fr

***Abstract*— The development of cost-effective approaches to fabricate metasurfaces at a macroscopic scale is essential for their spread in industrially-relevant products. We show how templated assembly of colloidal building blocs, such as nanocubes, can be employed to fabricate functional metasurfaces with an arbitrary design.**

***Keywords*— metasurfaces, templated assembly, epitaxy, nanocubes.**

I. Introduction

High-quality monocrystalline materials and nanostructures are key to high-efficiency optoelectronic devices, plasmonic materials and metasurfaces. A large variety of materials can be synthesized at low temperature in solution as colloidal single crystals, combining the advantages of high-quality material and low-cost fabrication, but the potential for large area integration into nanophotonic and plasmonic devices via nanoparticle assembly techniques still remain elusive. The two major bottleneck are:

-Difficulty to achieve defect-free colloids self-assembly in truly arbitrary patterns;

-Poor optical and electronic properties resulting from the discreetness of individual building blocks.

II. Results and Discussion

In this invited talk I will present recent breakthroughs from our team tackling both challenges with a new approach that we have introduced based on nanocube epitaxy. In the first part I will focus on advances on templated-assembly with detailed insight into the mechanisms. I will show the fabrication of complex and truly arbitrary organisation of nanocubes on a large surface, with a single nanocube resolution. Examples includes 1D linear assembly[1], 2D nanocube grid arrays for transparent electrodes[2,3], highly dense split-ring resonator absorbers and Pancharatnam–Berry metasurfaces[4].

In the second part I will focus on advances on nanocube epitaxy, showing a general methodology to transform an arbitrary assembly of nanocubes into defect-free continuous nanostructures and operando mechanistic insights[5,6]. This approach enables to obtain monocrystalline plasmonic and nanophotonic surfaces that can be readily printed on any substrate (flat, microstructured), but also to make nanocrystals with unconventional (à la carte) geometries, that can be used as colloids to go beyond Platonic solids.

Finally, I will show optical characterisation of the resulting large area metasurfaces, supported by numerical simulations.

IV. Conclusion

I believe that this constitute a major breakthrough in the field, can inspire many scientists and lead the way for a new generation of bottom-up functional nanocomposites and their spread in industrially-relevant products.

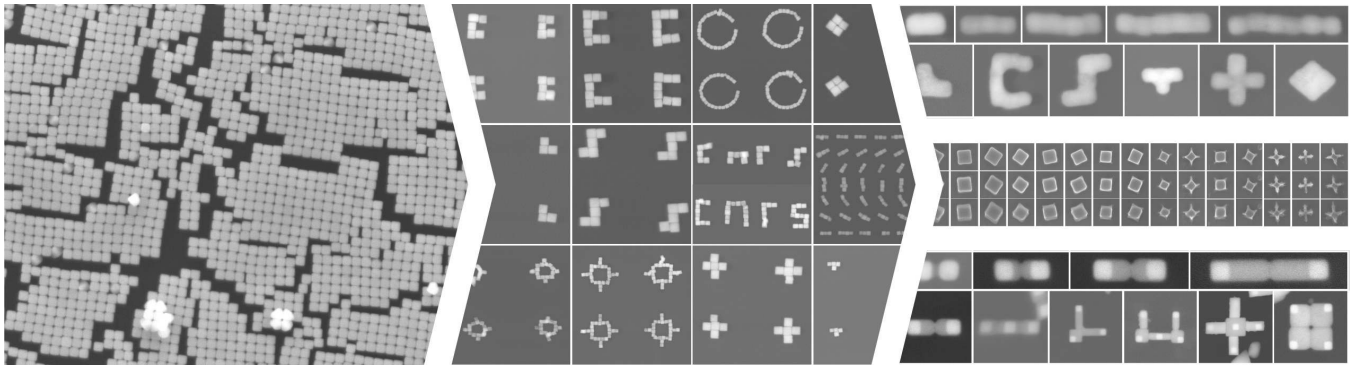

References

1. A. Capitaine et al., Small Methods 2023
2. A. Capitaine et al. ACS Nano 2024
3. L. Fenzi et al,. Under review.
4. M. Fajri et al., ACS Nano 2024
5. M. Fajri et al., Small Methods 2025
6. A. Capitaine et al., Adv. Mat. 2022

Directed Self-Assembly of Block Copolymers for Ultra-High-Resolution Gold Metasurfaces and Photonic Crystals

Achmad F. Putranto[1], Hong Li[2], Martin Kogelschatz[1], Guillaume Fleury[3], Sébastien Cavalaglio[1], Badreddine Smiri[1], David Fuard[1], Camille Petit-Etienne[1], Raphael Ramos[4], Redouane Borsali[2], Marc Zelsmann[1,*]

[1]Univ. Grenoble Alpes, CNRS, CEA/LETI-Minatec, Grenoble INP, LTM, Grenoble, France
[2]Univ. Grenoble Alpes, CNRS, CERMAV, Grenoble, France
[3]Univ. Bordeaux, CNRS, Bordeaux INP, LCPO, Pessac, France
[4]Univ. Grenoble Alpes, CEA, LITEN, Grenoble, France
*Corresponding author: marc.zelsmann@cea.fr

***Abstract*— The self-assembly of block copolymers is used here to fabricate sub-10 nm gold nanocrevices metasurfaces (that are used as sensitive and polarization-dependent SERS substrates) as well as 1D responsive photonic crystals.**

***Keywords*— block copolymers, self-assembly, metasurfaces, SERS, photonic crystals.**

In various plasmonic and photonic applications, generating high-density large-area, and high-resolution features remains a bottleneck for conventional lithography due to throughput and cost constraints. Block copolymer (BCP) self-assembly offers a highly effective bottom-up route for generating a rich variety of nanoscale geometries, including lamellae, cylinders, spheres, and gyroids, simply by tuning the polymer block composition. This versatility allows for the selection of an optimal morphology for a specific function. Indeed, leveraging BCP nanostructurations as templates for metasurface fabrication is highly desirable.

In a first part, we demonstrate here a scalable fabrication route for dense arrays of gold (Au) nanocrevices using the directed self-assembly (DSA) of a high-χ poly(1,1-dimethylsilacyclobutane)-block-polystyrene (PDMSB-b-PS) block copolymer with a 9 nm half-pitch. This approach produces periodic, anisotropic Au nanocrevice metasurfaces with ultrasmall gap features. Comprehensive optical characterization and finite-difference time-domain (FDTD) simulations reveal a robust, tunable plasmonic resonance across the visible spectrum (550–635 nm). We show that these resonant properties are exquisitely sensitive to Au film morphology. The platform delivers exceptional SERS sensitivity, with signal enhancements significantly surpassing those of reference planar Au films and conventional Au gratings. Optimal SERS performance is achieved at a specific Au thickness using 638 nm excitation, a condition that aligns with both the simulated resonance and experimental reflectance, thereby maximizing plasmonic enhancement. Furthermore, we demonstrate precise control over the SERS response by showing that the polarization anisotropy ratio can be tuned simply by varying the metal thickness. This work establishes DSA as a scalable route to designer plasmonic metasurfaces, providing a versatile platform for advanced plasmonics and quantitative surface-enhanced spectroscopy.

In a second part, a new series of well-defined and novel carbohydrate-based bottlebrush BCPs are introduced, that self-assemble into 1D photonic crystals (1D-PCs), and their self-assembly in lamellae structures is investigated using a wide range of techniques. The 1D-PCs formed from different bottlebrushes display a full spectrum of colors, ranging from colorless to rainbow colors, including blue, green, orange, and red, effectively spanning the entire UV–vis range. Remarkably, a very fast (a few seconds) change in the color is obtained simply by different solvent, a consequence of the lamellae domain swelling. Furthermore, by mixing the bottlebrushes with small carbohydrates, their optical properties can be further modified, achieving a red shift in reflective colors from orange to red. This approach provides a flexible strategy for tailoring the optical characteristics of photonic crystals without the need for synthesizing new carbohydrate-based bottlebrushes, thus offering a versatile platform for controlling their properties.

Acknowledgments

This work was supported by the French RENATECH network, the ANR project BONSAI n°ANR-21-CE09-0009 and the ANR project SUGARCOLORS n°ANR-23-CE06-0004. The authors want to thank the FMNT – Fédération MicroNanoTechnologies - for its support. Part of this work was carried out on the Platform for Nanocharacterization (PFNC) of CEA Grenoble.

Engineered 3D Topological Eutectics: Tailoring Dirac-Rashba Interfaces via Directional Solidification for Advanced Spin-Orbitronics

Kingshuk Bandopadhyay[1,*], Krzysztof Markus[1], Andrzej Materna[1], Federico Mazzola[2], Dorota A. Pawlak[1]

[1] ENSEMBLE[3] Centre of Excellence, Wolczynska 133, 01-919 Warsaw, Poland
[2] CNR – SPIN, University of Napoli, Federico II, 21 - 80126 Napoli, Italy
*Corresponding author: kingshuk.bandopadhyay@ensemble3.eu

***Abstract*— We report the fabrication of Topological Insulator heterostructures using a scalable solidification method, achieving atomically smooth interfaces. ARPES data confirms that topological surface states coexist with giant-Rashba states. Observed charge transfer and robust electronic features establish this system as a premier platform for advancing spintronics, quantum computing, and next-generation optoelectronics.**

***Keywords*— topological insulators, eutectics, heterostructure, metamaterials.**

I. Introduction

Three-dimensional topological insulators (TIs) have attracted considerable attention due to their topologically protected, gapless surface states, which arise from strong spin–orbit coupling and time-reversal symmetry. These surface states host Dirac-like fermions with suppressed backscattering from nonmagnetic impurities, making TIs promising candidates for topological spintronics and quantum information technologies [1].

One promising strategy to expand the application paradigm, is the deliberate engineering of TI heterostructures, where interfaces are used as an additional degree of freedom to tailor electronic states [2]. In this context, heterostructured and composite materials can be viewed from a metamaterial perspective, in which macroscopic functionalities emerge from the periodic arrangement of distinct quantum materials and their interfaces. Ordered TI-based composites provide enhanced interfacial area, improved robustness, and new pathways for engineering spin-orbit-coupled electronic structures beyond those available in single-phase crystals.

II. Methods

The TI heterostructures were prepared by directional eutectic solidification methods [3]. The sample quality and crystallinity were verified by different characterization methods. ARPES measurements were performed at CASSIOPEE beamline of SOLEIL Synchrotron.

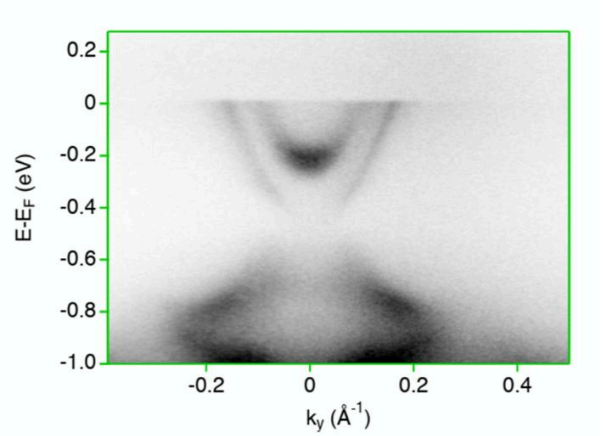

Fig. 1 ARPES intensity map of the Bi_2Te_3-BiTeI heterostructure.

III. Results and Discussion

Figure 1 shows an ARPES cut along the k_y direction. A V-shaped dispersion centered at $k_y = 0$ is observed, characteristic of the topological surface state of Bi_2Te_3.

At higher binding energies, additional dispersive features with a broad parabolic character are observed. Their momentum offset and energy scale are consistent with Rashba-split states previously reported in BiTeI [4].

Importantly, the Dirac-like and Rashba-like states overlap in both momentum and energy, in contrast to conventional band-bending-induced 2DEGs where these states are typically well separated.

IV. Conclusion

We have demonstrated the coexistence of a Dirac-like topological surface state and Rashba-type dispersions within the same momentum-energy window. These findings demonstrate the robustness of the Bi_2Te_3 topological surface state at the interface with an intrinsic giant-Rashba

semiconductor and highlight the potential of such heterostructures for studying interface-driven spin-orbit physics.

ACKNOWLEDGMENTS

The authors thank ENSEMBLE^3 Project (MAB/2020/14) which is carried out within the International Research Agendas Programme (IRAP) of the Foundation for Polish Science co-financed by the European Union under the European Regional Development Fund and Teaming Horizon 2020 programme (GA. No. 857543) of the European Commission and the project of the Minister of Science and Higher Education "Support for the activities of Centers of Excellence established in Poland under the Horizon 2020 program" under contract No. MEiN/2023/DIR/3797.

REFERENCES

1. Pesin, D. and A.H. MacDonald, *Spintronics and pseudospintronics in graphene and topological insulators.* Nat Mater, 2012. **11**(5): p. 409–16.
2. Murakami, F., et al., *Probing photocarrier dynamics in a Bi2Te3–Te eutectic p–n junction with a laser terahertz emission microscope.* APL Materials, 2023. **11**(3): p. 031102.
3. Bandopadhyay, K., et al., *Self-organized topological insulator heterostructures via eutectic solidification of Bi2Te3-Te.* Next Materials, 2024. **5**: p. 100252.
4. Ishizaka, K., et al., *Giant Rashba-type spin splitting in bulk BiTeI.* Nat Mater, 2011. **10**(7): p. 521–6.

Tamm plasmon laser diodes

J. Bellessa[1,*], M. Laupretre[1], C. Symonds[1], J.M. Benoit[1], A. Lemaitre [2]

[1]Institute of Light and Matter, Université Claude Bernard Lyon 1, Lyon, France
[2]Université Paris-Saclay, Centre de Nanosciences et de Nanotechnologies, Palaiseau, France
*Corresponding author: joel.bellessa@univ-lyon1.fr

***Abstract*—The realization of an electrically driven Tamm laser diode, a new type of laser diode based on surface-confined Tamm plasmon modes, will be presented. The device is based on the integration of a silver microdisk with a quantum-well-embedded distributed Bragg reflector (GaAs/AlAs) presenting Tamm surface resonances. In a second part, the integration of metasurfaces in Tamm structures will be described.**

I. Introduction

The integration of metallic components into semiconductor laser architectures has proven to be a highly effective strategy for enhancing device efficiency through optical confinement at the micro- and nanoscale. Tamm plasmons, which are optical modes occurring at the interface between a distributed Bragg reflector (DBR) and a metallic layer, lie between metal-semiconductor cavities and spasers. A Tamm mode can be interpreted either as a cavity mode in a zero-thickness cavity or as a surface mode, since its field amplitude decays away from the metal/semiconductor interface. Owing to their surface-bound nature, microscale optical confinement in Tamm plasmon structures is achieved through straightforward patterning of the thin metallic layer, which defines the modal geometry[1]. This approach enables the realization of complex confinement geometries that would be extremely challenging to fabricate by etching several hundreds of nanometers into a semiconductor medium within a vertical cavity structure. Furthermore, the metallic patch responsible for optical confinement can simultaneously serve as an electrical contact for current injection.

For Tamm lasers, subwavelength structures, engraved in the metal part of Tamm devices, can significantly modify the laser properties. Indeed, due to the Tamm surface mode character, the nanostructure is inserted within the cavity, thereby directly influencing the laser emission behavior.

II. Results and Discussion

Based on these principles, we demonstrate an electrically injected Tamm plasmon laser obtained by integrating a silver microdisk with a GaAs/AlAs DBR incorporating InGaAs quantum wells positioned at the antinodes of the electric field. Under electrical injection and cryogenic operation (95 K), the device exhibits clear lasing behavior, with a maximum emitted power of 200 µW at 906 nm. Spectral measurements reveal the onset of optical gain and strong mode confinement, ultimately leading to lasing characterized by pronounced spectral and angular narrowing[2]. Dispersion imaging further confirms these observations, evidencing lasing from the fundamental confined Tamm mode. These results establish Tamm plasmon lasers as a promising platform for compact, integrable, and potentially reconfigurable coherent light sources.

In addition to demonstrating a Tamm laser diode, we investigate the incorporation of nanostructuring within the metallic film to tailor the emission properties. In particular, unconventional polarization behaviors are observed. The polarization characteristics and spatial intensity distributions are presented and discussed.

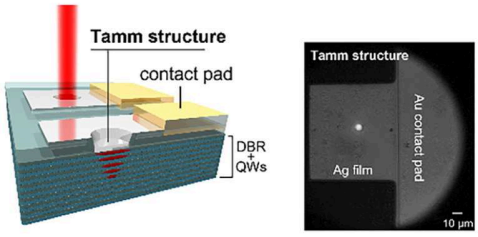

Fig. 1 Left: Schematic of the Tamm laser diode structure. Right: Top-view optical image of the fabricated device.

III. Conclusion

These results establish Tamm plasmon lasers as a promising platform for compact, integrable, and potentially reconfigurable light sources. First experiments on the integration of nanostructuration in Tamm devices show the capability of this approach to engineer novel emission properties and expand the functionality of semiconductor lasers.

Acknowledgments

This work was supported by the French ANR Altar (AAPG2025-PRC).

References

[1] C. Symonds, G. Lheureux, J.P. Hugonin, J.J. Greffet, J. Laverdant, G. Brucoli, A. Lemaitre, P. Senellart and J. Bellessa, Nano Lett. 13, 3179, 2013

[2] M. Laupretre, C. Symonds, J.-M. Benoit, Ł. Duda, K. Czyż, M. Guzik, E. Cleyet-Merle, M. Morassi, F. Bessueille, A. Pereira, A. Lemaître, J. Bellessa, Appl. Phys. Lett. 127, 151104, 2025.

Photoluminescence Modulation in Self-Coupled Molecular Cavities

Evan S. H. Kang[1,*]

[1]Department of Physics, Chungbuk National University, Republic of Korea
*Corresponding author: eshkang@chungbuk.ac.kr

***Abstract*— Self-coupled molecular cavities, formed by organic dye nanostructures without external resonators, enable tunable photoluminescence through geometry-controlled resonances. By combining experiments and FDTD simulations, we show that emission modulation arises from excitation-dependent nearfield enhancement and cavity-modified radiative quantum efficiency.**

***Keywords*— photoluminescence modulation, self-coupling, metasurfaces, organic nanophotonics**

I. Introduction

Organic dye molecules with large oscillator strengths can support strong light–matter interactions and are promising building blocks for compact photonic and optoelectronic devices. In particular, nanostructures composed of such molecules may sustain cavity-like optical resonances within the molecular assembly itself, without requiring a separate external cavity. In these systems, molecular excitons interact with the internally supported resonant modes, forming what can be described as self-coupled molecular cavities.

This concept provides a route toward highly compact and structurally simple nanophotonic platforms, where optical emission can be modulated directly through the molecular cavity geometry. Despite growing interest in light–matter interactions in organic nanostructures, the mechanisms governing photoluminescence (PL) modulation in self-coupled molecular cavity systems remain insufficiently understood. In this work, we investigate how cavity geometry influences PL peak position and intensity, and clarify the physical origins of this modulation by combining optical measurements with numerical simulations.

II. Methods

Self-coupled molecular cavity structures were prepared using organic dye-based nanostructures designed to support cavity-like resonances. Photoluminescence spectra were measured as a function of excitation and emission wavelength. To interpret the experimental observations, finite-difference time-domain (FDTD) simulations were performed. From the simulated optical fields, an enhancement factor was calculated to evaluate the effect of cavity resonance on the excitation and emission processes.

III. Results and Discussion

The experiments reveal that the PL response of self-coupled molecular cavities can be systematically modulated by tuning the cavity geometry. As the resonance condition shifts with geometry, both the absorption and PL spectra change in a controllable manner. This demonstrates that the internal cavity mode of the molecular structure plays an active role in shaping the emission spectra. The FDTD simulations successfully reproduce the measured PL by calculating enhancement factors. The PL modulation does not arise from a single mechanism, but rather from the interplay of multiple cavity-mediated effects. First, the spatial distribution of the nearfield depends strongly on the excitation wavelength, which affects how efficiently excitons are generated within the molecular structure. Second, the cavity resonance modifies the radiative quantum efficiency, thereby altering the probability that excited states contribute to far-field emission. The results, therefore, establish that self-coupled molecular cavities provide a platform for controlling light emission, even in the absence of an external resonator.

IV. Conclusion

We have demonstrated photoluminescence modulation in self-coupled molecular cavity systems formed by organic dye nanostructures. By tuning cavity geometry, the resonance condition can be controlled, leading to systematic changes in PL spectra. FDTD simulations show that the modulation originates from excitation-dependent nearfield distributions and cavity-modified radiative quantum efficiency. These findings can enable tunable organic emitters and nanophotonic devices based on controlled cavity geometry and self-coupling.

Acknowledgments

This work was supported by the National Research Foundation of Korea(NRF) grant (RS-2024-00458225), the Korea Basic Science Institute(National research Facilities and Equipment Center) grant (RS-2024-00403096) funded by the Korea government(MSIT), and Global - Learning & Academic research institution for Master's·PhD students, and Postdocs(LAMP) Program of the National Research Foundation of Korea(NRF) grant funded by the Ministry of Education (RS-2024-00445180).

US Defense Perspective on Past and Future of Metamaterials

Mark S. Spector

Office of Naval Research, USA
*Corresponding author: mark.spector.civ@us.navy.mil

***Abstract*— The field of metamaterials began through initiatives sponsored by the US Department of Defense (DoD). The first comprehensive metamaterials program was a 2001 Multidisciplinary University Research Initiatives (MURI) effort sponsored by the Office of Naval Research (ONR) in collaboration with the Defense Advanced Research Projects Agency (DARPA). Research programs at ONR and other DoD agencies continue to support fundamental and applied research with the aim of mapping out the potential of metamaterials for a variety of applications. These programs are pursuing optical, RF and acoustic materials for applications across the electromagnetic spectrum, from novel RF antennas to devices utilizing optical magnetism. Acoustic metamaterials are of unique interest to the Navy for underwater applications. In recognition of the 25th anniversary of the ONR MURI program, this talk will provide a historical perspective of significant US Defense contributions to this field and future areas of interest. Common challenges associated with loss, bandwidth, and scalability will be discussed along with the needs for innovative designs, materials, and fabrication approaches.**

***Keywords*—metamaterials, defense, ONR**

Geometry Matrix: From Physical Model to Computational Framework

Alonso Moreta[1], Mateo Perez[1], Karen Caicedo[3], Ashod Aradian[4], Alessandro Veltri[2,1,*]

[1]Universidad San Francisco de Quito, Quito, Ecuador
[2]Università della Calabria, Cosenza, Italy
[3]Institute of Applied Sciences and Intelligent Systems (ISASI-CNR), Napoli, Italy
[4]Université de Bordeaux, CNRS, CRPP, UMR5031, Pessac, France
*Corresponding author: aveltri@unical.it

***Abstract*—The Geometry Matrix formalism provides a unified framework for modeling active plasmonic nanoparticles across quasi static and Mie regimes. It enables prediction of emission thresholds, spectra, and modal instabilities in gain assisted nanostructures. We present its implementation as a modular open library for reproducible nanophotonics modeling.**

***Keywords*— active plasmonics, nanophotonics modeling, Mie scattering, computational electromagnetics.**

I. Introduction

Metamaterials and metasurfaces derive their optical properties from the response of fundamental building blocks. Among these, active plasmonic nanoparticles have repeatedly emerged as promising elements for nanoscale light sources, spasers, and gain assisted nanophotonic devices. Understanding their emission dynamics and stability therefore remains an important problem in nanophotonics.

II. Geometry Matrix Formalism

In previous work we introduced the Geometry Matrix formalism, an analytical framework describing the electrodynamic behavior of gain assisted plasmonic nanoparticles by solving a self consistent eigenvalue problem. The approach establishes a direct connection between nanoparticle geometry, multipolar plasmonic modes, and stimulated emission dynamics.

The system evolution can be expressed in compact matrix form

$$\frac{d\mathbf{q}}{dt} = \mathbf{A}\mathbf{q} + \mathbf{b} \tag{1}$$

where the vector $\mathbf{q}$ contains the electromagnetic mode amplitudes. The matrix $\mathbf{A}$ encapsulates both structural and gain dependent properties of the system and is therefore referred to as the geometry matrix. This formulation enables direct prediction of emission thresholds, spectral properties, and dynamical instabilities in gain assisted plasmonic nanostructures.

The time dependent formulation of the model also enables the investigation of transient emission dynamics. In particular, it allows the study of phenomena such as gain switching, relaxation oscillations, and other time resolved processes in active plasmonic nanoresonators.

This framework applies both in the quasi static approximation and in the full Mie regime. In the quasi static limit compact analytical expressions can be derived for dipolar nanoshell systems, while the Mie formulation incorporates full electrodynamic effects, enabling accurate modeling of subwavelength plasmonic resonators and their emission spectra.

III. From Model to Computational Framework

In this work we present the transition of the Geometry Matrix formalism from a theoretical model to a reusable computational framework. The method has been implemented as a modular open source library named

https://github.com/lexwolf/nano_geo_matrix

released under the MIT license.

The library provides reusable tools for constructing geometry matrices, solving emission eigenvalue problems, and analyzing modal instabilities in gain assisted nanostructures. By separating the physical formalism from specific implementations, this framework facilitates reproducible simulations and simplifies the development of new models for active nanophotonic systems.

IV. Conclusion

The Geometry Matrix formalism provides a unified approach for modeling active plasmonic nanoparticles across different electrodynamic regimes. Its implementation as an open computational library enables reproducible modeling and supports the development of new theoretical and numerical studies of active nanophotonic structures.

References

[1] A. Veltri, A. Chipouline, and A. Aradian, "Multipolar, time dynamical model for plasmonic nanoparticle spasers," *Scientific Reports*, vol. 6, 33018, 2016.
[2] A. Aradian, K. Caicedo, A. Cathey, M. Infusino, and A. Veltri, "Emission dynamics and spectrum of a nanoshell based plasmonic nanolaser spaser," *Nanophotonics*, 2024.
[3] N. Recalde, D. Bustamante, M. Infusino, and A. Veltri, "Dynamic multi mode Mie model for gain assisted metal nano spheres," *Materials*, vol. 16, no. 5, 2023.
[4] K. Caicedo *et al.*, "Mode dependent emission thresholds and frequencies in metal nanoparticles within gain enhanced media," *Physical Review B*, vol. 112, 195412, 2025.

Silicon Nanoparticle Monolayer Coating for Glossy, Non-Iridescent and Tunable Reflective Colors

Hiroshi Sugimoto*, Jialu Song, Keisuke Moriasa, Mojtaba Karimi Habil, Minoru Fujii

Department of Electrical and Electronic Engineering, Graduate School of Engineering, Kobe University, Kobe, Japan
*Corresponding author: sugimoto@eedept.kobe-u.ac.jp

***Abstract*— We report a core–shell architecture composed of Mie-resonant Si core and SiO_2 shell for nanocoating that enhances both structural color reflectance and surface gloss. By optimizing the SiO_2 shell thickness, we achieved the total reflectance >70% experimentally. By leveraging this coating strategy, uniform color coatings on 3D objects, enabling diverse visual appearances, are demonstrated. This work establishes a new design strategy for lightweight, durable and tunable structural color coatings suitable for practical applications.**

***Keywords*— Mie resonances, nanoparticles, structural color, core-shell particles.**

I. Introduction

Color coatings are widely used across industries, where not only hue but also brightness, saturation, and surface gloss critically determine visual quality. However, conventional coloration strategies face intrinsic trade-offs among gloss, durability, thickness, and angle dependence. Here, we introduce a Si@SiO_2 core–shell nanosphere (NS) architecture that simultaneously enhances structural color brightness and surface gloss in a single-particle monolayer. The low-index SiO_2 shell introduces refractive-index contrast, enabling total reflectance exceeding 70% experimentally. The Mie-resonant coloration offers a practical route toward bright, high-gloss, non-iridescent color coatings.

II. Results and Discussion

Monodisperse Si NSs are developed in our group using a density-gradient centrifugation process.[1,2] Figure 1a presents photographs of the size-separated colloidal suspensions, displaying vivid and distinct structural colors ranging from pink to orange as the average diameter increases from 109 to 207 nm. The corresponding normalized extinction spectra confirm a redshift of the resonance peaks with increasing Si NS size.

Figures 1b display TEM images of Si@SiO_2 NSs prepared using a modified Stöber method. A clear core-shell contrast is clearly observed in all samples, indicating the successful formation of SiO_2 shells.

We then fabricated large-area (>1 cm^2) densely packed NS monolayers on 3D objects using the modified Langmuir-Schaefer method. In contrast to the original black surface, the coated cars exhibit brilliant, metallic-like structural colors ranging from purple to reddish, and the coloration remains highly uniform even over the steep curved surfaces of the car bodies. These confirm that Si@SiO_2 NS monolayers can achieve conformal and continuous coverage on 3D objects. The SEM images in Fig. 1d show the monolayer formed on a flat substrate. This capability addresses a key limitation of many lithography-based structural color approaches, which are typically restricted to small-area and flat substrates.

In the presentation we will discuss the mechanism of the high reflectance and the other applications using Si@SiO_2 NS monolayers.

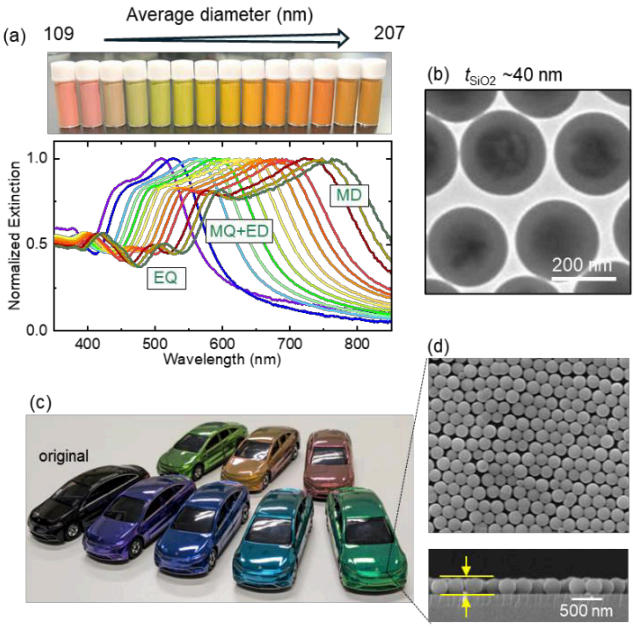

Fig. 1 (a) Photos and extinction spectra of Si NS suspensions after a size-separation process with different average diameters from 109 to 207 nm. (b) TEM image of Si@SiO_2 NS with shell thickness of 40 nm. (c) Photograph comparing an original black toy car with those coated by Si@SiO_2 NS monolayer. (d) Top-view and cross-sectional SEM images of fabricated Si@SiO_2 NS monolayers.

References

[1] H. Sugimoto, T. Okazaki, M. Fujii, *Adv. Opt. Mater.* **2020**, *8*, 2000033.

[2] H. Tanaka, S. Hotta, T. Hinamoto, H. Sugimoto, M. Fujii, *ACS Appl. Nano Mater.* **2024**, *7*, 2605.

Nanometer-Precision Optical Metrology of Large Area Nanoimprinted Metasurfaces

Jaime Gómez Rivas[1*], Masoumeh Goudarzi[1], Sunghwan Jo[2], Maira Perez Sosa[3], Yu-Chen Wei[1], Matthijs Berghuis[1], Mohammad Ramezani[4], Agustín Mihi[2]

[1]Department of Applied Physics, Eindhoven University of Technology, The Netherlands
[2]Institute of Materials Science of Barcelona (ICMAB-CSIC), Spain
[3]Department of Electrical Engineering, Eindhoven University of Technology
[4]TeraNova B.V., Eindhoven, The Netherlands
*Corresponding author: j.gomez.rivas@tue.nl

***Abstract*— We present a non-destructive optical metrology method for wafer scale inspection of large area plasmonic metasurfaces. Angle resolved scatterometry implemented in a Fourier microscope enables nanometer sensitive mapping of structural uniformity. Comparison with simulations and microscopy links optical signatures to nanoscale variations in nanoparticle geometry.**

***Keywords*— Metasurfaces, Optical Scatterometry, Fourier Microscopy, Wafer-Scale Metrology, Nanoimprint Lithography.**

I. Introduction

Scaling metasurfaces toward practical optical devices demands fabrication methods that deliver high uniformity over large areas, as well as metrology tools capable of detecting nanometer-scale deviations. Even small variations in feature size or height can significantly modify diffraction efficiency, angular response, and resonant behavior, particularly in plasmonic systems. Conventional techniques such as scanning electron microscopy and atomic force microscopy offer high spatial resolution but are limited in throughput, field of view, and suitability for inline inspection.

II. Methods

We employ Fourier-microscope-based scatterometry using collimated, angle-controlled illumination to probe periodic plasmonic nanopillar arrays. Gold nanopillars on indium phosphide and aluminum nanopillars on ITO-coated glass are fabricated by nanoimprint lithography over areas exceeding tens of square millimeters. Angle-resolved reflectance and diffraction intensities are measured at a fixed wavelength and compared with finite-difference time-domain simulations. A variation index is introduced to quantify deviations from a reference optical response and to map structural uniformity across the metasurface.

III. Results and Discussion

The measurements reveal a strong correlation between the angular scattering profile and nanoscale variations in nanopillar geometry. Regions with increased variation index exhibit reduced specular reflection and enhanced diffraction, consistent with simulations incorporating small changes in height and diameter. Independent verification by dark-field microscopy and atomic force microscopy confirms that nanometer-scale morphological deviations, rather than changes in lattice periodicity, dominate the observed optical variations. This approach enables rapid, spatially resolved inspection of large-area metasurfaces with sensitivity beyond the diffraction limit.

IV. Conclusion

Fourier-microscope scatterometry provides a powerful, non-destructive metrology platform for quantitative quality inspection of large-area plasmonic metasurfaces. By linking angle-resolved optical signatures to nanoscale structural variations, this method enables wafer-scale uniformity mapping with nanometer precision. The technique is well-suited to inline quality control during the fabrication of metasurface-enabled devices, including (O)LEDs and optical sensors.

Acknowledgments

This work was funded by NWO-STW through the NanoWicom project (Grant Agreement No. 13551), and by the European Union through the SCOLED project (Grant Agreement No. 101098813). Views and opinions expressed are, however, those of the authors only and do not necessarily reflect those of the European Union or the European Innovation Council and SMEs Executive Agency (EISMEA). Neither the European Union nor the granting authority can be held responsible for them. It has been also funded from the Spanish Agencia Estatal de Investigación through grants, PID2022-141956NB-I00 (OUTLIGHT), and CEX2023-001263-S (Spanish Severo Ochoa Centre of Excellence program).

Metasurface Stickers for Tailoring Photoluminescence and Inducing Chirality

Shunsuke Murai[1,*], Koichi Okamoto[1]

[1]Department of Physics and Electronics, Graduate School of Engineering, Osaka Metropolitan University, Japan
*Corresponding author: murai@omu.ac.jp

***Abstract*— Metasurface stickers—flexible, transferable nanoantenna arrays—enable post-fabrication control of light–matter interactions on diverse substrates. By stacking and twisting layers, photoluminescence can be enhanced, redirected, and spectrally tuned, while moiré coupling induces controllable chirality for reconfigurable optical functionalities.**

***Keywords*—Metasurface stickers; Directional emission; Polymer-embedded nanostructures**

I. Introduction

Metasurfaces enable compact and versatile control of light using subwavelength nanostructures; however, most realizations remain confined to rigid, planar platforms. Extending their functionality toward three-dimensional architectures while preserving fabrication simplicity and post-assembly reconfigurability is highly desirable, particularly for tailoring emission from incoherent light sources. Here, we introduce flexible and stackable metasurface stickers as a practical approach to quasi-3D metasurface design, enabling directional emission and tunable light–matter interactions through layer-by-layer integration.

II. Methods

The metasurface was designed as a periodic nanoantenna array to tailor angular radiation through collective lattice effects. The nanostructures were first fabricated on a sacrificial substrate and subsequently embedded in a flexible polymer, yielding a freestanding metasurface sticker [1,2].

The resulting stickers can be laminated onto light-emitting substrates or vertically stacked to form quasi-3D configurations [3]. Optical characterization was carried out by measuring far-field emission patterns under incoherent illumination, enabling direct evaluation of angular radiation distributions and emission directionality. For same stickers stacked in twisted geometry, circular dichroism (CD) was evaluated [4].

III. Results and Discussion

A single metasurface sticker markedly reshaped the emission profile of an incoherent light source, producing pronounced intensity enhancement in selected angular directions (Fig. 1, top panel)[5]. Stacking multiple stickers provided additional degrees of control over the radiation distribution, evidencing effective out-of-plane structuring through vertical layer integration [3].

For the bilayer twist moiré metasurfaces, the magnitude and spectral position of CD signal are tunable via twist angle and interlayer spacing (Fig. 1, bottom) [4].

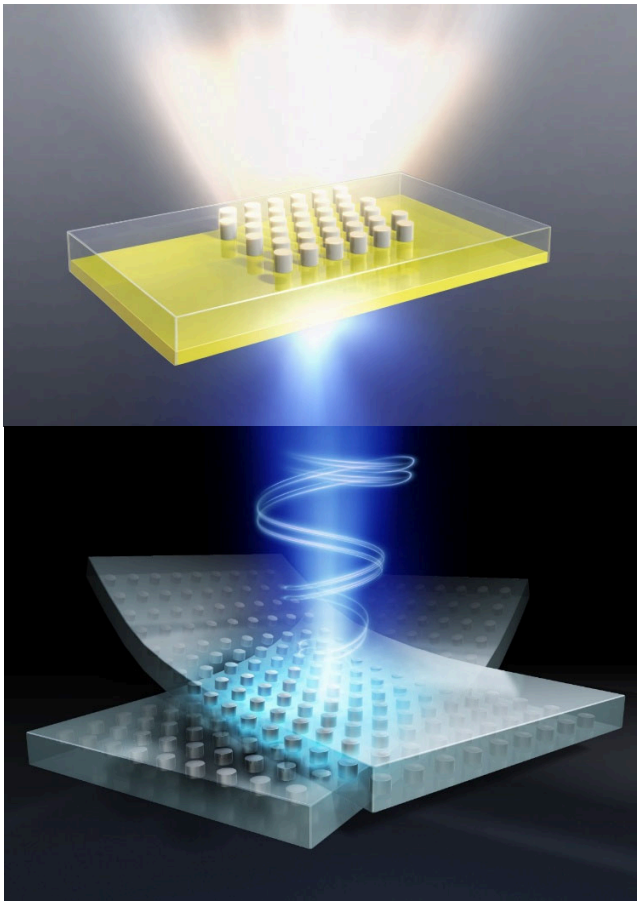

Fig. 1: Sketches of the stickers; (top) Monolayer sticker on the phosphor plate [5], (bottom) Bilayer Moire Metasurface made from stack of metasurfaces [4].

IV. Conclusion

Metasurface stickers provide a simple yet powerful route for tailoring emission from incoherent light sources. Even a single sticker markedly reshapes the emission profile, while stacking multiple layers enables additional control over radiation distribution through effective out-of-plane structuring.

This approach achieves angular emission engineering without complex fabrication or stringent alignment, while maintaining mechanical flexibility and post-fabrication reconfigurability. Metasurface stickers therefore represent a scalable platform for quasi-3D photonic architectures and adaptive control of light–matter interactions.

Acknowledgments

This work was partly supported by the Nanotechnology Hub, Kyoto University. We gratefully acknowledge financial support from Kakenhi (25K01501, 25K21709), provided by JSPS, Japan, and the Futaba foundation.

References

[1] T. Takashima, et al., *Jpn.J. Appl. Phys.* 64, 03SP66 (2025)
[2] S Murai, et al., *J. Appl. Phys.* 129 183101 (2021)
[3] TY Lo, et al., *Adv. Opt. Mater.*, e02518 (2025)
[4] J He et al., *ACS Photonics* 12, 4608-4615 (2025).
[5] H Gao et al., *Nanophotonics* 14, 4627 (2025)

Phase Transition Driven Nanoparticle Assembly in Multicomponent Systems based on Liquid Crystals

Piotr Lesiak[1,*], Natalia Kasian[1,2], Anna Kozanecka-Szmigiel[1], Jan Bolek[1], Karol Kakarenko[1], Natalia Kowalska[3], Wiktor Lewandowski[3], Tomasz R. Woliński[1]

[1]Faculty of Physics, Warsaw Univ. of Technology, Koszykowa 75, 00-662 Warszawa, Poland
[2]Institute for Scintillation Materials NAS of Ukraine, 60 Nauky Ave., 61072 Kharkiv, Ukraine
[2]Faculty of Chemistry, University of Warsaw, ul. Pasteura 1, 02-093 Warszawa, Poland
*Corresponding author: piotr.lesiak@pw.edu.pl

***Abstract*— This work demonstrates the potential for creating patterns of nanoparticle groups formed in a liquid crystal base material. Nanoparticles coated with a carefully selected ratio of two types of ligands are used. This selection of materials allows for the control of the preferential positioning of nanoparticles within the liquid crystal.**

***Keywords*— nanoparticles, self-assembly, liquid crystals, .**

I. Introduction

If a composite material consisting of a liquid crystal doped with gold nanoparticles (LC/NP) is heated to the phase transition temperature, the phase transition will disrupt the uniform spatial distribution of gold nanoparticles, leading to a distribution characterized by areas of high and low concentration (Fig. 1), and thus areas of increased and decreased light absorption. This phenomenon results directly from the fact that gold nanoparticles are surrounded by pro-messogenic ligands to prevent nanoparticle aggregation on the one hand and to achieve homogeneous mixing with the nematic liquid crystal on the other [1]. At the phase transition temperature, the nanoparticles are pushed, and the direction of this movement depends on the ratio of pro-mesogenic ligands to non-mesogenic ligands surrounding the nanoparticle. A properly selected ratio of both types of ligands allows control over the preferential positioning of the nanoparticles — depending on the proportion, they can cluster in either the nematic or isotropic phase. This concentration of nanoparticles can be distributed in a more or less orderly manner in space.

In this paper, we will demonstrate that individual parameters, such as heating or cooling rates and the type of dopant, can influence the resulting pattern. As seen in Fig. 1, both the transition to the isotropic phase (heating) and the return to the nematic phase (cooling) influence the positioning of nanoparticles. Furthermore, if the process is repeated, groups of nanoparticles can either group or split. However, using only the temperature changes, we cannot control the positioning of nanoparticle groups. A solution could be to heat the liquid crystal to a temperature close to the phase transition temperature (while still maintaining the nematic phase) and then illuminate the system with a light beam. This approach allows for a more deterministic arrangement of nanoparticle groups.

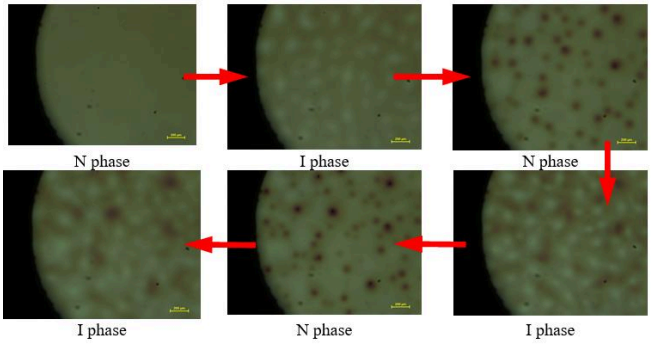

Fig. 1 Unit cell geometry of the proposed metamaterial.

Acknowledgments

The work was supported by the National Science Centre, Poland, under research project no UMO-2020/39/B/ST7/02356 and partially by Marie Skłodowska-Curie Actions for Ukraine (MSCA4Ukraine), under research project no 1245451.

References

[1] P. Lesiak, et al. „Self-Organized, One-Dimensional Periodic Structures in a Gold Nanoparticle- Doped Nematic Liquid Crystal Composite”, ACS Nano, 13(9):10154-10160, 2019.

Optical Metrology of Chiral and Strain Engineered Metasurfaces

Fabian Haake[1,*], Marcello Pozzi[1], Theresa Stecher[1], Henning Galinski[1]
[1]Laboratory for Nanometallurgy, Department of Materials, ETH Zurich, Switzerland
*Corresponding author: fabian.haake@mat.ethz.ch

***Abstract*—Controlling local optical anisotropy is central to functional metasurfaces. This talk presents scanning reflectance anisotropy microscopy (SRAM) as a powerful, non-destructive tool for probing anisotropies with sub-degree phase sensitivity and diffraction-limited resolution. We demonstrate local amplitude and phase mapping of chiral and symmetry broken metasurfaces and showcase detection of strain-induced symmetry breaking in metasurfaces and conventional materials. [1], [2]**

Keywords— metasurfaces, metamaterials, chiral resonators, scanning reflectance anisotropy microscopy

References

[1] J. Sendra, F. Haake, M. Calvo, H. Galinski, and R. Spolenak, "Multi-Material Strain Mapping with Scanning Reflectance Anisotropy Microscopy," *Advanced Functional Materials*, vol. 33, 2302179, 2023, doi: 10.1002/adfm.202302179.

[2] F. Haake, J. Sendra, M. Calvo, H. Galinski, and R. Spolenak, "Strain mapping in amorphous germanium thin films with scanning reflectance anisotropy microscopy," *Applied Physics Letters*, vol. 125, no. 4, p. 041602, 2024, doi: 10.1063/5.0218645

Engineering Silicon Optical Properties *via* Metal-Assisted Chemical Etching

Gilles R. Bourret[1,*]

[1]Department of Chemistry and Physics of Materials, University of Salzburg, Austria
*Corresponding author: gilles.bourret@plus.ac.at

***Abstract*— Metal-assisted chemical etching (MACE) enables scalable, solution-based nanostructuring of silicon with precise control over its optical response. This talk highlights key parameters to achieve homogeneous MACE and optimize field enhancement in silicon nanowire arrays, for SERS, photocatalysis, solar hydrogen generation, and microchip authenticaton.**

***Keywords*— silicon, nanowires, metal-assisted chemical etching, SERS, photocatalysis**

I. Introduction

Nanostructuring silicon provides unique properties with potential applications in electronics, photonics, sensing, photocatalysis, and photovoltaics. When structured into vertically aligned Si nanowires (VA-SiNW) arrays, Si can sustain a variety of optical resonances, such as Fabry-Pérot and Mie resonances, and leaky waveguide modes.[1] Despite this potential, structuring silicon with nanoscale precision is synthetically demanding. Metal-assisted chemical etching (MACE) provides a solution-based, benchtop and versatile alternative, compatible with the high-resolution structuring of silicon (Fig. 1a), which can be used to finely tune the optical properties of silicon (Fig. 1b-e).[2]

II. Methods

During MACE, a metal catalytic mask etches through silicon in presence of an oxidant and HF. [2] The oxidizing agent, usually H_2O_2, is preferentially reduced at the surface of the metal catalyst, generating holes (eq. 1) that are injected through the metal/silicon Schottky barrier, which, in the presence of HF, oxidizes silicon into a soluble product and generates hydrogen gas as a byproduct (eq. 2).

$$H_2O_2 + 2H^+ \rightarrow 2H_2O + 2h^+ \quad (1)$$

$$Si + 4HF_2^- + 2h^+_2 \rightarrow SiF_6^{2-} + 2HF + H_2(g) \quad (2)$$

where h^+ is a hole. As a result, the silicon in contact with the metal catalyst dissolves, leading to a highly anisotropic etching: during MACE, isolated metal catalyst particles sink into the silicon, forming vertical and straight pores, while continuous metal nanomeshes can be used to produce VA-SiNW arrays. Achieving large-scale homogeneity can be challenging because of the instability of the metal catalyst when the experimental parameters are not set appropriately.

III. Results and Discussion

I will discuss the critical parameters that influence the stability of the metal catalyst layer for achieving homogeneous MACE.[2] I will present how optically active metal nanostructures can be interfaced within VA-SiNW arrays using (electro-)chemical approaches,[3] used for surface-enhanced Raman spectroscopy,[4] water-splitting,[5] and photocatalysis. The use of nanoscale silicon fingerprints prepared *via* MACE for counterfeit prevention in microchips will also be discussed (Fig. 1f).[6]

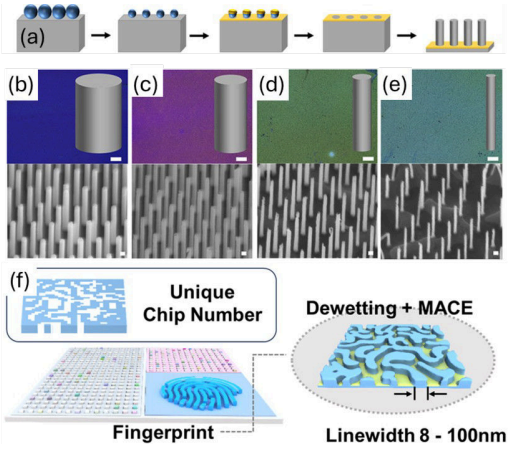

Fig. 1 (a-e) Colored VA-SiNW arrays. (f) Nanoscale Si fingerprints.

References

[1] Wendisch, F. J. et al. "Morphology-Graded Silicon Nanowire Arrays via Chemical Etching: Engineering Optical Properties at the Nanoscale and Macroscale" ACS AMI, 12 (11), 13140-13147, 2020

[2] Wendisch, F. J.; Rey, M.; Vogel, N.; Bourret, G. R., Large-Scale Synthesis of Highly Uniform Silicon Nanowire Arrays Using Metal-Assisted Chemical Etching. Chem. Mater., 32 (21), 9425-9434, 2020

[3] Wendisch, F. J.; Saller, M. S.; Eadie, A.; Reyer, A.; Musso, M.; Rey, M.; Vogel, N.; Diwald, O.; Bourret, G. R., Three-Dimensional Electrochemical Axial Lithography on Si Micro- and Nanowire Arrays. Nano Letters, 18 (11), 7343-7349, 2018

[4] Bartschmid, T.; Menath, J.; Roemling, L.; Vogel, N.; Atalay, F.; Farhadi, A.; Bourret, G. R., Au Nanoparticles@Si Nanowire Oligomer Arrays for SERS: Dimers Are Best. ACS Applied Materials & Interfaces, 16 (31), 41379-41389, 2024

[5] Farhadi, A.; Bartschmid, T.; Menath, J.; Vogel, N.; Bourret, G. R., Optimizing Catalyst Location within Nanostructured Photoelectrodes. ACS Applied Materials & Interfaces, 17, 48670−48679, 2025,

[6] Liu, B.; Farhadi, A.; Bartschmid, T.; Zhang, Y.; Guo, C.; Feng, S.; Bourret, G. R., Nanoscale Silicon Fingerprints for Counterfeit Prevention in Microchips. Small, 21 (10), 2500878, 2025

Nondestructive testing of metamaterials by Photoacoustic and Photothermal Techniques

R. Li Voti, G. Leahu, E. Petronijevic, C. Skubisz, A. Maurizi, G. Lalle, G. Cesarini, M.C. Larciprete, M. Centini, A. Belardini, C. Sibilia

Department of Basic and Applied Science for Engineering,
Sapienza Università di Roma, Italy
*Corresponding author: roberto.livoti@uniroma1.it

***Abstract*—Recent advancement in experimental Photoacoustic and Photothermal techniques has enabled a large number of interesting observations and understanding of heat transfer processes on metamaterials at the nanoscale**

***Keywords*— Metamaterials, Eutectics, Nanoscale Optics, Heat Transfer, Photothermal and Photoacoustic Technique.**

I. Introduction

We review recent advances in the methodology of Photoacoustic and Photothermal techniques. In particular we applied photoacoustic spectroscopy (PAS) to detect circular dichroism of intrinsic chiral materials [1] as well as extrinsic chiral metasurfaces [2-4].

In disordered media PAS is confirmed to be the most appropriate technique to determine separately the absorption and the scattering coefficients allowing to determine the size of both metallic (AgNP) [5], or semiconductor nanospheres (ZnO) [6, 7], or clusters of nanospheres bridged by the ligands [8], in contrast to nanolayered samples [9] or self-organized eutectic composites [10, 11].

On the other hand photothermal deflection spectroscopy (PDS) may be used as a complementary technique to measure the absorbance spectrum in nanostructures so to detect absorption lines, or photonic band gap in photonic crystals [12, 13], or to measure the out-of/in-plane thermal diffusivity in 2D materials [14].

We also underline some applications of photothermal radiometry (PTR) used to localize the internal heat sources where the pump light is absorbed, and to measure the effective thermal diffusivity. The modulation frequency obtained by an acousto-optical modulator ranges from 1 Hz up to 100 kHz, allowing the improvement of the thermal resolution till submicron range. We have applied PTR and IR Thermography techniques to PCM-VO_2 nanolayered samples [15-17], nanodisks [18] and W-doped VO_2 thin films [19, 20]. Such a technique has been applied also to carbon nanotube film deposited onto a silicon substrate: in this case PTR allows to detect the thermal wave interference in the film and to measure the effective thermal diffusivity of the CNT, and the thermal resistance with the substrate [21]. Photothermal radiometry and thermography can be also used to measure the emissivity of nanostructured materials, nanoantennas and metasurfaces designed so to have specific directional emittance properties [22, 23]. The invited talk summarizes several research topics and recent works done in collaboration with many partners (Universities, Research Centres and the European Centre of Excellence Ensamble3).

References

[1] A. Benedetti et al. Scientific Reports, 7, 5257 (2017).
[2] Petronijevic, E.; Cesca T.; Scian C.; Mattei G.; Li Voti, R.; Sibilia C.; Belardini A., Scientific Reports 14, 17210 (2024)
[3] Petronijevic E.; Cesca, T; Scian, C; Mattei, G; Li Voti, R; Sibilia, C; Belardini, A, Nanoscale 16, 16477 (2024)
[4] Petronijević, E., Belardini, A., Leahu, G., Li Voti, R., Sibilia, C, Optical Materials Express 12, 2724, (2022)
[5] R. Li Voti, et al. Int J Thermophys, 36, 342 (2015).
[6] F.R. Lamastra et al., Nanotechnology 28, 375704 (2017).
[7] F.R. Lamastra et al, Int J Thermophys, 39, 110, (2018).
[8] R. Li Voti et al., Nanoscale Advances 3, 4692 (2021).
[9] Cesarini, G., Leahu, G., Grilli, M.L., Sytchkova, A., Sibilia, C., Li Voti, R., Physica Status Solidi (C) 13, 998 (2016).
[10] P. Osewski et al. Adv. Optical Mater. 1901617 (2020).
[11] E. Petronijevic, et al. Advanced Materials, 35, 2206005 (2023)
[12] R. Li Voti, G. Leahu, E. Petronijevic, A. Belardini, T. Cesca, C. Scian, G. Mattei, C. Sibilia, Applied Sciences, 12, 1109, (2022).
[13] G. Leahu et al., Adv. Optical Mater. 2100670 (2021).
[14] C. Yao, et al., Advanced Functional Materials (2024) DOI 10.1002/adfm.202405235
[15] T. Cesca, et al., Nanoscale 12, 851 (2020).
[16] R. Li Voti, G. L. Leahu, M. C. Larciprete, C. Sibilia, M. Bertolotti, Int J Thermophys, 36, 1004 (2015).
[17] R. Li Voti et al. International Journal of Thermal Sciences 197, 108832 (2024)
[18] Emlija Petronijevic et al. Scientific Reports 14, 25324 (2024)
[19] A.Bile et al. Optical Materials 154, 115732 (2024)
[20] Maria Cristina Larciprete et al., APL Mater. 11, 091107 (2023)
[21] G. Leahu, R. Li Voti, M. C. Larciprete, C. Sibilia, M. Bertolotti, I. Nefedov, I. V. Anoshkin, Int J Thermophys, 36, 1349 (2015).
[22] M. Centini, M.C. Larciprete, R. Li Voti, M.Bertolotti, C.Sibilia, and M.Antezza, Opt. Express 28, 19334 (2020).
[23] M. Centini, A. Benedetti, M. C. Larciprete, A. Belardini, R. Li Voti, M. Bertolotti, and C. Sibilia, Phys. Rev. B, 92, 205411 (2015).

SPECIAL SESSION 10

Non-Hermitian Photonics - Topological, Disordered and Quantum systems

9 contributions · pp. 937–952

Non-Ergodic Extended Phase for Electromagnetic Waves in 3D Non-Hermitian Disordered Media

Marcus Prado[1,2], Romain Bachelard[3], Robin Kaiser[4], Felipe A. Pinheiro[1,*]

[1] Instituto de Física, Universidade Federal do Rio de Janeiro, Brazil
[2] Institut Langevin, ESPCI Paris, France
[3] Universidade Federal de São Carlos, Brazil
[4] Institut de Physique de Nice, Université Côte d'Azur, France
*Corresponding author: fpinheiro@if.ufrj.br

***Abstract*—We demonstrate a Non-Ergodic Extended phase with fractal states for electromagnetic waves in 3D non-Hermitian disordered systems. Unlike scalar waves that localize, electromagnetic waves remain in the fractal phase due to their vector nature, enabling anomalous light transport without spatial correlations.**

I. Introduction

Wave transport in complex media exhibits a wide range of regimes, from conventional diffusion to Anderson localization. While scalar waves in three dimensions undergo a localization transition, Anderson localization is absent for electromagnetic (EM) waves in ensembles of dielectric scatterers due to their vectorial character [1], [2], [3]. Recent advances in many-body localization and random matrix theory predict the emergence of a Non-Ergodic Extended (NEE) phase, in which states are spatially extended but occupy a vanishing fraction of the available volume in the thermodynamic limit [4], [5], [6]. In this work, we demonstrate the existence of such a NEE phase for three-dimensional optical systems composed ensembles of randomly distributed point-like scatterers.

II. Microscopic Model

Collective excitations are described by an effective non-Hermitian Hamiltonian [7]

$$\mathcal{H} = (\omega_0 - i\Gamma_0/2)\mathbb{1} - (\Gamma_0/2)\mathbb{G},$$

where ω_0 and Γ_0 denote the resonance frequency and natural linewidth, respectively [8], [9]. For electromagnetic waves, $\mathbb{G}$ corresponds to the dyadic Green's function coupling dipoles at positions $\mathbf{r}_i$ and $\mathbf{r}_j$ [9],

$$\mathbb{G}_{ij} \propto \frac{e^{ikr_{ij}}}{kr_{ij}} \left[P(ikr_{ij})\mathbb{1}_3 + Q(ikr_{ij}) \frac{\mathbf{r}_{ij} \otimes \mathbf{r}_{ij}}{r_{ij}^2} \right], \quad (1)$$

where $r_{ij} = |\mathbf{r}_i - \mathbf{r}_j|$. The scalar-wave case is obtained by replacing $\mathbb{G}$ with the scalar Helmholtz Green's function [8]. Anderson and Ergodic transitions are investigated through the Ioffe-Regel parameter $k\ell$ as a function of the dimensionless density $\rho\lambda^3$ [7].

III. Results and Discussion

To characterize the spatial structure of the eigenstates, we analyze the scaling of the inverse participation ratio (IPR), defined as $\mathrm{IPR}_n = \sum_{i=1}^{N} |\psi_n(\mathbf{r}_i)|^4$. A scaling behavior $\langle \mathrm{IPR} \rangle \sim N^{-D_F}$ defines the fractal dimension D_F of the eigenstates, normalized by the Euclidean dimension [4], [5], [6]. The value of D_F provides a criterion for ergodicity, as it determines whether the occupied fraction of space remains finite or vanishes in the thermodynamic limit $N \to \infty$ [4].

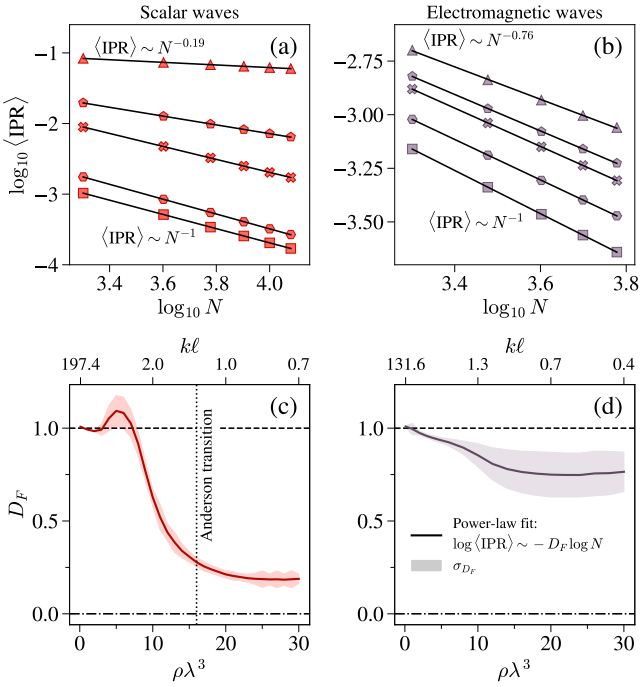

Fig. 1. (a),(b) Scaling of the inverse participation ratio (IPR) with system size N for scalar and electromagnetic waves, respectively. Symbols correspond to $\rho\lambda^3 = 0.1, 4, 8, 10, 30$, increasing from bottom to top. Solid black lines are power-law fits. Panels (c) and (d) present the normalized fractal dimension D_F for the whole range of density. Solid lines show the result of the fitting analysis and the shaded region corresponds to standard deviation. Horizontal dashed (dash-dotted) lines are the predictions for the extended (localized) regime. The vertical line in (a) shows the Anderson transition.

As shown in Fig. 1(a–b), a clear power-law scaling $\langle \mathrm{IPR} \rangle \sim N^{-D_F}$ is observed for all densities. At low densities ($\rho\lambda^3 \lesssim 8$), both scalar and electromagnetic waves exhibit $D_F \approx 1$, corresponding to an ergodic, fully extended phase. At higher densities ($\rho\lambda^3 \gtrsim 20$), scalar waves display a reduced fractal dimension $D_F \approx 0.2$, approaching the expected value $D_F = 0$ of the Anderson-localized regime. In contrast, electromagnetic waves retain a significantly larger value, $D_F \approx 0.8 < 1$, indicating the presence of the extended phase.

While the analysis of the Thouless number signals the absence of an Anderson transition in the vectorial case [1], [3], the fractal-dimension analysis reveals a qualitative change in the nature of the eigenstates responsible for wave transport. Interestingly, both scalar and vectorial models exhibit the onset of fractality at comparable densities $\rho\lambda^3 \approx 8$, below the localization threshold $\rho_{\mathrm{AT}} \approx 16/\lambda^3$ for scalar waves, corresponding to the Ioffe–Regel criterion $k\ell \sim 1$. This crossover regime suggests that near-field interactions play a limited role before the Ioffe-Regel limit is reached.

To further confirm the existence of a NEE phase in the thermodynamic limit, we perform a finite-size scaling analysis based on the participation entropy [10]

$$\mathcal{S} = \left\langle \sum_{i=1}^{N} |\psi(\mathbf{r}_i)|^2 \log |\psi(\mathbf{r}_i)|^2 \right\rangle,$$

and its normalized derivative $\tilde{\mathcal{S}}' = \partial_{\rho\lambda^3}\mathcal{S}/\log N$ [10]. This quantity is known to capture both ergodic and Anderson transitions in the Rosenzweig-Porter model, where a NEE phase has been analytically established [4]. As shown in Fig. 2, for scalar waves a size-independent crossing point appears at $\rho\lambda^3 \approx 3$, signaling the transition from an ergodic to a NEE phase. A similar transition is found for electromagnetic waves at $\rho\lambda^3 \approx 4$, further supporting the existence of a NEE phase despite the absence of Anderson localization.

IV. Conclusions

We demonstrate a transition to a non-ergodic extended phase of fractal quasimodes for both scalar and electromagnetic waves in randomly distributed point-like scatterers in 3D, beyond the conventional diffusive-to-localized scenario. A direct determination of the fractal dimension shows that, for scalar waves, this fractal phase emerges at densities below the Anderson localization threshold. As fractal states are expected to support anomalous diffusion, such transport may occur even where Thouless-number scaling predicts conventional diffusion [7]. To our knowledge, this constitutes the first prediction of a non-ergodic extended phase in a realistic 3D optical system, featuring a crossover between different degrees of ergodicity with increasing disorder. Our results provide a framework for interpreting observations of subdiffusive light transport [11], [12] and suggest new routes for engineering light transport in non-hermitian random media without relying on spatial correlations.

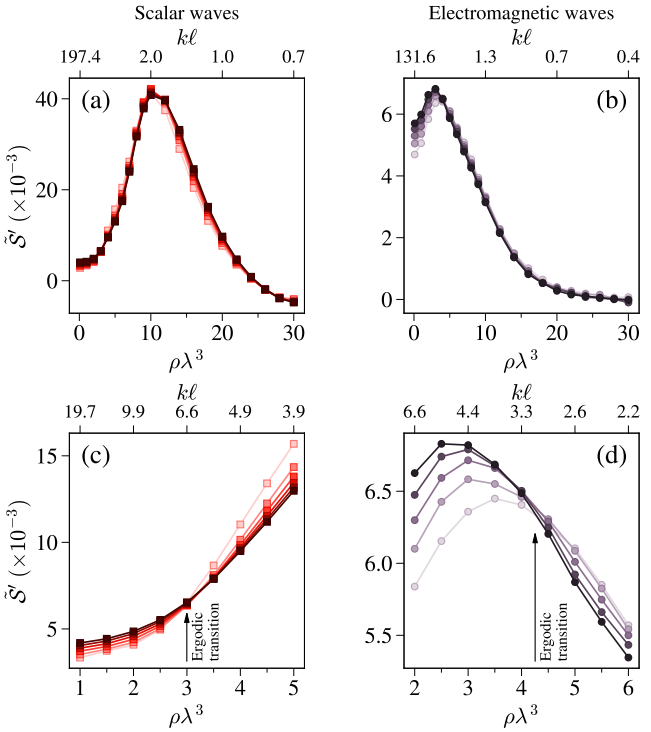

Fig. 2. Derivative of the normalized participation entropy $\tilde{S}'$ as a function of the scatterer density $\rho\lambda^3$ for (a) scalar and (b) electromagnetic waves. Darker colors correspond to larger system sizes N. Panels (c) and (d) show an enlarged view of the curves from (a) and (b) around the crossing points corresponding to the ergodic transition, whose location is indicated by the arrows.

V. Acknowledgments

M.P. and F.A.P. acknowledge CNPq, CAPES, and FAPERJ for financial support. F.A.P. acknowledges CAPES-COFECUB (Ph 997/23, CAPES 88887.711967/2022-00). R.B. acknowledges support from FAPESP (Grants No. 2023/03300-7 and 2022/00209-6) and CNPq (Grants No. 313632/2023-5 and 403653/2024-0). R.K. acknowledges funding from ERC Advanced Grant No. 832219 (ANDLICA). R.B. and R.K. received support from STIC-AmSud, CAPES-COFECUB, and ANR LiLoA (ANR-23-CE30-0035). M.P. acknowledges support from the French “Investissements d’Avenir” program.

References

[1] S. E. Skipetrov and I. M. Sokolov, Phys. Rev. Lett. **112**, 023905 (2014).
[2] A. Yamilov *et al.*, Nat. Phys. **19**, 1308 (2023).
[3] B. A. van Tiggelen and S. E. Skipetrov, Phys. Rev. B **103**, 174204 (2021).
[4] V. E. Kravtsov *et al.*, New J. Phys. **17**, 122002 (2015).
[5] I. M. Khaymovich and V. E. Kravtsov, SciPost Phys. **11**, 045 (2021).
[6] P. A. Nosov, I. M. Khaymovich, and V. E. Kravtsov, Phys. Rev. B **99**, 104203 (2019).
[7] M. Prado, R. Bachelard, R. Kaiser, F. A. Pinheiro arXiv:2510.20346.
[8] F. A. Pinheiro, M. Rusek, A. Orlowski, and B. A. van Tiggelen, Phys. Rev. E **69**, 026605 (2004).
[9] F. A. Pinheiro, Phys. Rev. A **78**, 023812 (2008).
[10] T. Cadez *et al.* New J. Phys. **26** 083018 (2024).
[11] L. A. Cobus, G. Maret, and A. Aubry, Phys. Rev. B **106**, 014208 (2022).
[12] R. Rezvani Naraghi and A. Dogariu, Phys. Rev. Lett. **117**, 263901 (2016).

Anomalous surface response in a non-Hermitian Weyl semimetal

Y. D. Chong[1,*], Shuxin Lin[1], Rimi Banerjee[1], Zheyu Cheng[1], Kohei Kawabata[2], and Baile Zhang[1]

[1]School of Physical and Mathematical Sciences, Nanyang Technological University, Singapore
[2]Institute for Solid State Physics, University of Tokyo, Japan
*Corresponding author: yidong@ntu.edu.sg

***Abstract*—The profound connection between band topology and field theoretic anomalies has recently been generalized to a non-Hermitian (NH) Weyl semimetal. We show that the NH anomaly is mediated by exotic states called continuum Landau modes (CLMs), giving rise to a dramatically higher density of surface states scaling with the volume, not surface area.**
***Keywords*— Non-Hermitian physics.**

I. Introduction

The bulk and edge states of various topological materials can serve as manifestations of field theoretic anomalies (violations of classical symmetries by quantum fields [1]), such as quantum Hall edge states and Weyl semimetal states with the chiral anomaly [2]. Recently, this link between topological states and anomalies was generalized to non-Hermitian (NH) topological phases [3], [4].

In this work [5], we show that the manifestation of an NH anomaly in a three-dimensional (3D) Weyl semimetal occurs via unusual surface states called continuum Landau modes (CLMs) [6]: eigenstates that form a continuous spectrum but are spatially localized, in violation of the usual dichotomy between bound and free states exhibited by Hermitian wavefunctions. CLMs were originally discovered in models with no evident connection to NH band topology [6], but here they emerge as surface states of a 3D NH Weyl semimetal (WSM) under an applied magnetic field. Strikingly, we find that the density of surface states is proportional to the sample volume $V = L_x L_y L_z$. By contrast, in the usual Hermitian anomaly inflow mechanism, this scales with surface area $A = L_x L_y$ [1], and this had been expected to be the case in the NH system [4]. This previously unaccounted-for feature seems to be tied to the unusual properties of CLMs.

Fig. 1. (a) Complex spectrum for a NH Weyl semimetal under an applied magnetic field $\mathbf{B} = 2\pi/30\,\hat{z}$, with lattice size $L_x = L_z = 11$, $L_y = 22$. The states in $|E| < 1$ are CLMs on the $-z$ surface. (b) Plot of $d\Delta n/dB \cdot (L_x L_y L_z)^{-1}$ versus B. Here, $\Delta n = n_- - n_+$ is the difference in the number of in-gap modes ($|E| < 1$) localized on the bottom and top surfaces, and the derivative is estimated using $\delta B = 0.02$. Results are plotted using $L_x = L_y = 11$, with different values of L_z. Excerpted from [5].

Acknowledgments

This work was supported by the Singapore National Research Foundation (NRF) under the NRF Investigatorship NRF-NRFI08-2022-0001, and Competitive Research Program (CRP) Nos. NRF-CRP23-2019-0005, NRF-CRP23-2019-0007, and NRF-CRP29-2022-0003. K. K. is supported by MEXT KAKENHI Grant-in-Aid for Transformative Research Areas A "Extreme Universe" No. JP24H00945.

References

[1] R. Bertlmann, "Anomalies in Quantum Field Theory," *International Series of Monographs on Physics*, 2000.
[2] X.-L. Qi, T. L. Hughes, and S.-C. Zhang, "Topological field theory of time-reversal invariant insulators," Physical Review B—Condensed Matter and Materials Physics 78, 195424 (2008).
[3] T. Bessho and M. Sato, "Nielsen-ninomiya theorem with bulk topology: duality in floquet and non-hermitian systems," Physical Review Letters 127, 196404 (2021).
[4] K. Kawabata, K. Shiozaki, and S. Ryu, "Topological field theory of non-hermitian systems," Physical Review Letters 126, 216405 (2021).
[5] S. Lin, R. Banerjee, Z. Cheng, K. Kawabata, B. Zhang, and Y. D. Chong, "Continuum Landau surface states in a non-Hermitian Weyl semimetal," arXiv:2509.05138.
[6] Q. Wang, C. Zhu, X. Zheng, H. Xue, B. Zhang, and Y. D. Chong, "Continuum of bound states in a non-hermitian model," Physical Review Letters 130, 103602 (2023).

Solitons Mediated by Skin-Mode Localization and Band Nonreciprocity

Kun Ding

Department of Physics, State Key Laboratory of Surface Physics, and Key Laboratory of Micro and Nano Photonic Structures (Ministry of Education), Fudan University, Shanghai 200438, China

*Corresponding author: kunding@fudan.edu.cn

***Abstract*— By clarifying a classification criterion intrinsic to the non-Hermitian skin effect, we distinguish two soliton families supported in non-Hermitian lattices and further construct the soliton threshold diagram as a function of nonreciprocity and dimensionality.**

***Keywords*—Non-Hermitian skin effect, nonreciprocity, solitons.**

I. Introduction

Solitons, typically arising from a competition between band dispersion and nonlinearity, occur in lattices featuring the non-Hermitian skin effect as nonlinearity increases, accompanied by a transition in localization from linear skin modes to solitons. However, localization does not disentangle the role of skin modes in soliton formation from that of band dispersion, nor does it clarify their impacts on soliton classifications. By mapping out a soliton diagram, we here establish a universal framework for characterizing solitons in nonreciprocal lattices with non-Hermitian skin effect [1,2].

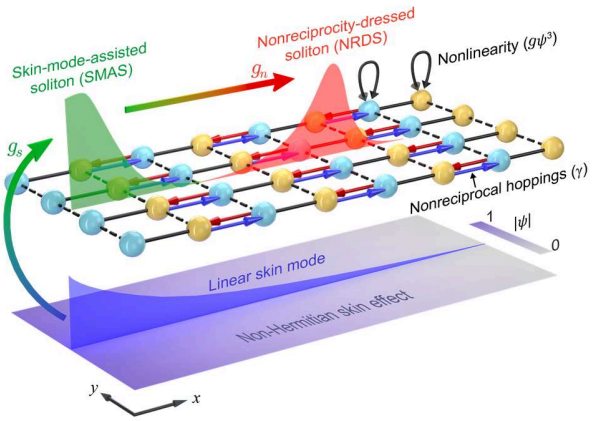

Fig. 1 Schematic illustration of transitions among skin modes and various solitons. The upper panel shows a two-dimensional lattice featuring nonreciprocal hoppings and nonlinearity, with their respective strengths characterized by γ and g. Two arrows with gradient color sketch the sequential transitions from non-Hermitian skin modes (blue) to skin-mode-assisted solitons (SMASs, green), and subsequently to nonreciprocity-dressed solitons (NRDSs, red), driven by variations in g. .

II. Results and Discussion

We uncover two distinct soliton phases, skin-mode-assisted solitons (SMASs) and nonreciprocity-dressed solitons (NRDSs). Rooted in fundamentally different mechanisms, SMASs originate from skin effect, while NRDSs stem from band nonreciprocity, each exhibiting unique spatial profiles. Using a stacked Su-Schrieffer-Heeger-like model as a prototype (Fig. 1), we delineate the phase diagram of SMASs and NRDSs, each having clear phase boundaries.

To interpret them, we formulate a Wannier-function-based nonlinear Hamiltonian, showing that soliton formation depends critically on how skin-mode localization and band nonreciprocity suppress or enhance wave dispersion. For SMASs, skin-mode localization reduces wave broadening at the localization sites, thereby lowering the formation threshold. This soliton phase is observable from edge dynamics and accompanied by a dynamical stability reentrance when transitioning from linear skin modes. In contrast, NRDSs, as well as their thresholds, arise from bulk-band nonreciprocity and persist under periodic boundary conditions.

With such a framework, we further demonstrate that soliton classifications in nonreciprocal lattices, independent of dimension and lattice types, are determined by skin-mode localizations rather than geometry. Therefore, our framework offers predictive tools for characterizing and engineering solitons in experimentally realizable non-Hermitian systems, spanning optics to mechanics.

III. Conclusion

We identify two soliton families from numerically obtained nonlinear eigenstates in non-Hermitian lattices, dubbed SMAS and NRDS, which respectively arise from skin-mode localization and band nonreciprocity. Using this classification, we construct the soliton threshold diagram as a function of nonreciprocity and dimensionality. To interpret and predict these thresholds, we develop a Wannier-projected effective nonlinear Hamiltonian that captures the threshold values and

reveals the dominant mechanisms for each soliton family. We further demonstrate that, regardless of dimensionality and lattice intricacy, SMASs (NRDSs) emerge at the lattice sites where skin modes are localized (or not), highlighting the generality of our framework.

ACKNOWLEDGMENTS

This work is supported by the National Key R&D Program of China (No. 2022YFA1404701, No. 2022YFA1404500).

REFERENCES

[1] Kun Ding, Chen Fang, and Guancong Ma, "Non-Hermitian topology and exceptional-point geometries," Nature Reviews Physics 4 (12), 745-760, 2022.

[2] Shanyue Li, Mengying Hu, Jing Lin, Chen Fang, Zhensheng Tao, and Kun Ding, "Soliton transitions mediated by skin-mode localization and band nonreciprocity," arXiv:2508.02311.

Machine Learning for Drawing Phase Diagrams of Nonlinear Optical Resonators with 1D Su-Schrieffer-Heeger Lattice

Chukwunaedum Patrick Izediuno[1], Ghada Alharbi[1,2], Zeeshan Ahmad[4], Stephan Wong[3], Sang Soon Oh[1*]

[1]School of Physics and Astronomy, Cardiff University, Cardiff, United Kingdom
[2]University of Tabuk, Tabuk 741, Kingdom of Saudi Arabia
[3]Center for Integrated Nanotechnologies, Sandia National Laboratories, Albuquerque, New Mexico 87185, USA
[4]Bentham Instruments Ltd. 2 Boulton Rd, Reading, RG2 0NH, United Kingdom
*Corresponding author: OhS2@cardiff.ac.uk

***Abstract*—Identifying dynamical phases in nonlinear systems is a central challenge in nonlinear dynamics, particularly for complex nonlinear optical systems. Here, we propose two machine-learning approaches—augmented dynamic mode decomposition and a convolutional neural network—to construct phase diagrams of the Su–Schrieffer–Heeger model with Kerr nonlinearity.**

***Keywords*— phase diagram, photonic topological insulator, optical nonlinearity, machine learning**

I. Introduction

The topology of photonic bands enables the design of novel photonic devices supporting unique modes known as topological modes. For example, topological edge and corner modes that are robust against local perturbations can be realized in two-dimensional photonic crystals and metamaterials by appropriately tailoring their geometries [1], [2]. Moreover, topological design principles can be applied to semiconductor microlasers [3]. On the other hand, combining optical nonlinearities with topological designs opens new opportunities for achieving diverse optical functionalities, ranging from bistable states in Kerr nonlinear ring resonators to novel thermodynamic behavior in multimode waveguides [4]. Understanding the dynamics of nonlinear optical systems requires constructing phase diagrams. However, most existing approaches rely on numerical simulations combined with heuristic identification of phases. Recently, a machine-learning approach based on augmented dynamic mode decomposition (aDMD) has been successfully applied to coupled topological lasers in one-dimensional SSH and two-dimensional kagome lattices with saturable gain [5], [6].

In this work, we apply both aDMD and convolutional neural networks (CNNs) to construct phase diagrams for one-dimensional SSH ring resonator arrays with Kerr nonlinearity.

II. Methods

A. Phase diagram using aDMD

The unsupervised aDMD method builds a library of time-augmented DMD bases from representative trajectories. A bottom-up step adds bases when the reconstruction error exceeds $\epsilon_{\text{add}} = 0.20$, and a top-down step merges equivalent bases when their subspace alignment $\gamma_{ij} > \gamma_{\text{merge}} = 0.50$ [6].

B. Phase diagram using CNN

The supervised CNN method involves training on heuristically labelled trajectories from 70% of the parameter grid, with labels assigned from steady-state intensity statistics, spectral peak ratios, and counter-propagating mode switching. The remaining 30% of grid points are classified solely by the trained network without further simulation.

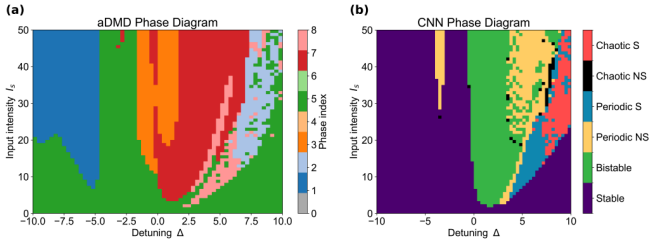

Fig. 1. (a) Phase diagram obtained using the aDMD method, with colours indicating distinct, unlabelled phases identified through bottom-up library construction and top-down merging. (b) Phase diagram obtained using a CNN trained on heuristic labels, showing stable, bistable, periodic, and chaotic regions with switching (S) and non-switching (NS) sub-phases

III. Results and Discussion

Figure 1 shows the phase diagrams obtained from both methods over the detuning Δ and input intensity I_s parameter space. The aDMD result [Fig. 1(a)] successfully identifies the periodic and chaotic switching phases (pink, light blue) and clearly separates the stable behaviours. However, the bistable phase is incorrectly split across two clusters (red, orange), and the periodic non-switching phase (blue) is greatly overestimated at negative Δ and missing at positive Δ. Furthermore, the total amount of phases is overestimated. The CNN result [Fig. 1(b)] identifies regions consistent with the six expected phases across the parameter space, though a few grid points are falsely classified as chaotic non-switching.

IV. Conclusion

We have demonstrated that the phase diagrams of nonlinear optical systems can be obtained using machine learning approaches. The aDMD method, an unsupervised learning technique, was able to identify the different dynamical phases despite ambiguous phase boundaries and occasional misclassification. In contrast, the CNN method, based on supervised learning, clearly distinguished and identified all phases with fewer misclassification.

Acknowledgments

This work was supported by the EPSRC Manufacturing Hub (Grant No. EP/Z532848/1).

References

[1] S. Wong, M. Saba, O. Hess, and S. S. Oh, "Gapless unidirectional photonic transport using all-dielectric kagome lattices," *Phys. Rev. Research*, vol. 2, no. 1, p. 012011, 2020.

[2] M. Saba, S. Wong, M. Elman, S. S. Oh, and O. Hess, "Nature of topological protection in photonic spin and valley Hall insulators," *Phys. Rev. B*, vol. 101, no. 5, p. 054307, 2020.

[3] Y. Gong, S. Wong, A. J. Bennett, D. L. Huffaker, and S. S. Oh, "Topological insulator laser using valley-Hall photonic crystals," *ACS Photonics*, vol. 7, no. 8, pp. 2089–2097, 2020.

[4] S. Wong, A. Cerjan, K. G. Makris, M. Khajavikhan, D. Christodoulides, and S. S. Oh, "Nonlinear topological photonics: Capturing nonlinear dynamics and optical thermodynamics," *ACS Photonics*, vol. 12 no. 5 , pp. 2291-2303, 2025.

[5] S. Wong, J. Olthaus, T. K. Bracht, D. E. Reiter, and S. S. Oh, "A machine learning approach to drawing phase diagrams of topological lasing modes," *Communications Physics*, vol. 6, p. 1, 2023.

[6] S. Wong, D. E. Reiter, and S. S. Oh, "Machine learning for identifying dynamical phases in topological lasers," in M. te Vrugt, (eds) *Artificial Intelligence and Intelligent Matter. Machine Intelligence for Materials Science. Springer, Cham*, 2026.

Measurement-Induced Crossover of Quantum Jump Statistics in Postselection-Free Many-Body Dynamics

Kazuki Yamamoto[1], Ryusuke Hamazaki[2,3*]

[1]Department of Physics, Institute of Science Tokyo, Tokyo, Japan
[2]RIKEN Pioneering Research Institute (PRI), RIKEN, Saitama, Japan
[3]RIKEN Center for Interdisciplinary Theoretical and Mathematical Sciences (iTHEMS), RIKEN, Saitama, Japan
*Corresponding author: ryusuke.hamazaki@riken.jp

***Abstract*—We find a nontrivial crossover of subsystem fluctuations of quantum jumps in many-body systems under continuous measurement [1]. Whereas the fluctuations exhibit the conventional volume law following Poissonian statistics for sufficiently weak measurement strength, anomalous yet universal scaling law exhibiting super-Poissonian statistics appears for strong measurement strength.**

***Keywords*— measurement, quantum jumps, many-body systems.**

I. Summary

Open quantum systems under measurement have now been extensively studied because they exhibit interesting nonequilibrium dynamics absent in isolated quantum systems [2]. Of particular interest is the physics of quantum trajectories, where one tracks the monitored dynamics with the measurement outcomes (i.e., quantum jumps) retained. Indeed, such quantum trajectories concerning many-body systems can exhibit interesting phenomena represented as measurement-induced phase transitions (MIPT) [3], which cannot be obtained by the dynamics where measurement outcomes are averaged. However, the MIPT generally requires the postselection of the same quantum measurement outcomes, which causes experimentally unfriendly exponential cost.

Our work [1] shows that a nontrivial crossover of subsystem fluctuations of quantum jumps in many-body dynamics, which does not require the aforementioned postselection problem because quantum jumps are directly obtained in a single quantum trajectory. Whereas the fluctuations show the conventional volume law ($\sim L$) following Poissonian statistics for sufficiently weak measurement strength, anomalous universal scaling law ($\sim L^{2.7}$) exhibiting super-Poissonian statistics appears for strong measurement strength. We also discuss that this crossover significantly affects the precision of estimating the rate of quantum jumps. That is, for strong (weak) measurement, the estimation uncertainty is enhanced (suppressed) as the system size increases. Moreover, we demonstrate that the obtained anomalous scaling of the subsystem fluctuation results from an integrated many-body autocorrelation function. We can access the measurement-induced crossover only through the postselection-free information, i.e., the time and the position of quantum jumps, which can be tested in ultracold atom experiments.

Acknowledgments

This work was supported by JST ERATO Grant No. JPMJER2302, and KAKENHI Grants No. JP24K16982, and No. JP25K17327. K.Y. was also supported by Murata Science and Education Foundation, Hirose Foundation, the Precise Measurement Technology Promotion Foundation, and the Fujikura Foundation. The numerical calculations were partly carried out with the help of QuSpin [4]. The simulations were performed in part with the help of the supercomputing system in ISSP, the University of Tokyo.

References

[1] K. Yamamoto and R. Hamazaki, "Measurement-Induced Crossover of Quantum Jump Statistics in Postselection-Free Many-Body Dynamics," *arXiv*, arXiv:2503.02418, 2025.
[2] R. Hamazaki, K. Mochizuki, H. Oshima, and Y. Fuji, "An introduction to monitored quantum systems and quantum trajectories: spectrum, typicality, and phases," *arXiv*, arXiv:2512.19922, 2025.
[3] B. Skinner, J. Ruhman, and A. Nahum, "Measurement-Induced Phase Transitions in the Dynamics of Entanglement," *Phys. Rev. X* 9, 031009, 2019
[4] P. Weinberg and M. Bukov, "QuSpin: a Python package for dynamics and exact diagonalisation of quantum many body systems part I: spin chains," *SciPost Phys.* 2, 003, 2019.

Topological insulator-based quantum optical sensor arrays

H. Zheng[1], A. Banerjee[1], and P. Bermel[2,*]

[1]Department of Physics, Purdue University, West Lafayette, IN 47907, USA
[2]Birck Nanotechnology Center, Purdue University, West Lafayette, IN 47907, USA
[*]corresponding author: pbermel@purdue.edu

***Abstract*— Topological insulator (TI) materials like $InBi_2Se_3$ are highly sensitive to external electrical & magnetic fields, both at RF and optical frequencies, making for an emerging quantum sensing platform. In this work, we calculate the optical conductivity of TIs using Quantum Espresso, and design optical sensing devices and arrays.**

***Keywords*— topological insulators, Density Functional Theory, quantum sensing, optical conductivity.**

I. Introduction

The growing desire to achieve improved sensitivity and speed in sensing applications has given rise to the field of quantum sensors. This includes sensing optical, electric & magnetic fields, applied strain, and other approaches [1]. While the most common platforms are spins, trapped ions, and quantized fluxes, many of these approaches require cryogenic temperatures or other complex support mechanisms for use in many applications. This gives rise to interest in specifically quantum photonic platforms. While color centers like NV centers have received a great deal of interest, they can also be limited by complex fabrication techniques. Another emerging approach utilizes topological materials that exhibit topological phase transitions [2]. The transition is of first order, which leads to emergence of *helical states*. In this approach, we can envision an array of detectors, in which the quantum spin Hall helical states will entangle. Coupling these edge states to the interior regions of the detectors results in magnetochiral anisotropy (MCA) and potential topological-trivial phase transitions. Both phenomena can result in heightened sensitivity to electric and magnetic fields, including optical frequencies. In this work, we aim to explore the potential of this approach to provide the basis for a distinct type of quantum optical sensing platform.

II. Methods

Our first-principles simulations of topological insulator materials use Quantum Espresso and WannierTools to compute the electronic structures of topological materials in both bulk and nanosheet structures. From these calculations, we derive optical conductance, using the following expression [3]:

$$\sigma_{\alpha,\beta}(\omega) = i\frac{e^2\hbar}{V}\int \frac{d^2\mathbf{k}}{(2\pi)^2}\sum_{m,n}\frac{n_F(\varepsilon_{n,\mathbf{k}}) - n_F(\varepsilon_{m,\mathbf{k}})}{\varepsilon_{m,\mathbf{k}} - \varepsilon_{n,\mathbf{k}}}\frac{\langle n,\mathbf{k}|j_\alpha|m,\mathbf{k}\rangle\langle m,\mathbf{k}|j_\beta|n,\mathbf{k}\rangle}{\hbar(\omega+i\eta) - (\varepsilon_{m,\mathbf{k}} - \varepsilon_{n,\mathbf{k}})}$$

where n_F denotes the Fermi occupation, $|m,\mathbf{k}>$ and $\varepsilon_{m,\mathbf{k}}$ are the eigenvectors and eigenvalues for band m at momentum $\mathbf{k}$, $\hbar\eta$ is the lifetime broadening, and j_α is the current operator.

Special attention is given to understanding how strain and electrostatic gating can modulate the topological phase transitions essential for sensing mechanisms.

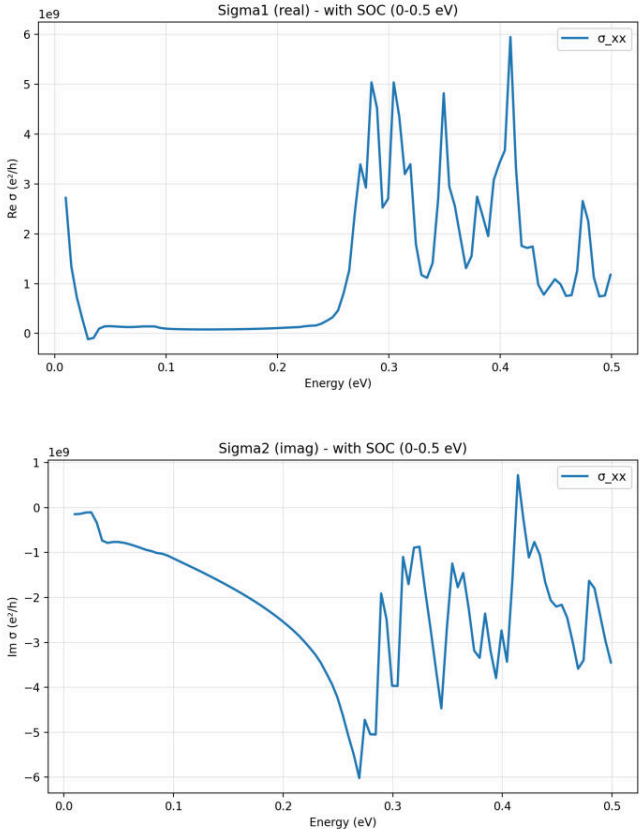

Fig. 1 (a) Real and (b) imaginary components of optical conductivity for $InBi_2Se_3$ topological insulators, calculated using Quantum Espresso, Wannier Tools, and an analytical formula [3].

III. Results and Discussion

As shown in Figure 1, we are able to calculate the optical conductivity for topological insulator materials such as $InBi_2Se_3$. Similar to previous related work [3], we find that the optical conductivity has a large DC (Drude-like) component, as well as a significant number of higher frequency components in the infrared. Furthermore, we are able to verify that the real components of the diagonal components exhibit sharp jumps that are sensitive to the Fermi level (doping) or quasi-Fermi

level (photon detection rate).

IV. Conclusion

We have demonstrated that topological insulators have strong and highly sensitive response as measured in optical conductivity. Ongoing work to be included in this presentation will incorporate these calculated properties into semiclassical device simulations to estimate the degree of sensitivity under various conditions.

Acknowledgments

This work was supported by the Center for Quantum Technologies (Award #2224960).

References

[1] Degen, Christian L., Friedemann Reinhard, and Paola Cappellaro. "Quantum sensing." *Reviews of modern physics* 89, no. 3 (2017): 035002.

[2] Li, Xin, Hua Lu, Runze Li, Zhengfen Wan, Xiaolin Wang, Salvatore Macis, Stefano Lupi, Min Gu, Hongxia Wang, and Zengji Yue. "Topological insulator materials for optics: Research progress and prospects." *Applied Physics Reviews* 13, no. 1 (2026).

[3] Lasia, Martha, and Luis Brey. "Optical properties of magnetically doped ultrathin topological insulator slabs." Physical Review B 90, no. 7 (2014): 075417.

Scattering Properties of non-Hermitian Resonant Systems Explored Through the Generalized Wigner-Smith Operator

Nadav Shaibe[1], Jared Erb[1], Thomas M. Antonsen[1,2], Steven M. Anlage[1,2]*

[1]Physics Department, University of Maryland, College Park, MD 20742-4111 USA
[2]Department of Electrical and Computer Engineering, University of Maryland, College Park, MD 20742-3285 USA
*Corresponding author: anlage@umd.edu

***Abstract*— We explore uses of the generalized Wigner-Smith operator in understanding the scattering properties of non-Hermitian systems with many embedded parametric perturbers. We focus on the statistical properties of complex parametric derivatives of the scattering matrix and compare them to those of the Wigner-Smith time delay, both obtained from experiments.**

***Keywords*— metamaterials, microwave, time delay, non-Hermitian physics, scattering matrix, generalized Winger-Smith operator.**

I. Introduction

The Wigner-Smith operator has a long history since it was first introduced in the context of nuclear scattering, and has found varied applications such as wavefront shaping [1] and identifying complex poles and zeros of the scattering matrix [2]. However, the operator is still mainly used today as it was decades ago, whereas more can be learned from the Wigner-Smith operator with just a few simple generalizations. In this talk, we generalize the Wigner-Smith operator in the following three ways: (a) from operating on unitary to sub-unitary scattering matrices which results in the complex Wigner-Smith time delay $\tau_{WS} = \frac{-i}{M}\frac{\partial}{\partial f}\ln[\det[S]]$ [3], where $S(f)$ is the $M \times M$ frequency-dependent scattering matrix, (b) from the complete scattering matrix to subblocks and functions of the elements of the scattering matrix, which results in a myriad of complex time delays such as transmission time delay $\tau_T = -i\frac{\partial}{\partial f}\ln[T]$ (where T is an off-diagonal element of S) [2], and (c) from a derivative with respect to frequency to a derivative with respect to other parameters p which results in another multitude of complex *generalized* delays, such as Wigner-Smith generalized delay $g_{WS}^{p} = \frac{-i}{M}\frac{\partial}{\partial p}\ln[\det[S(f,p)]]$ [4].

Experiments

Our experimental work is done in one-dimensional microwave graphs, two-dimensional billiards, and three-dimensional cavities, all with embedded analog tunable perturbers, such as reflective metasurfaces on the walls of a cavity [5], which endow the measurements with multiple parameters p. Because the systems used have a dense set of modes, we are able to see a large variety of phenomena, including extreme events such as scattering singularities [6], allowing us to studying the statistical properties of the generalized Wigner-Smith operator.

II. Results

In the experiments we utilize the parameters to alter the locations of poles and zeros of the scattering matrix in the complex frequency plane. In a graph we vary the length of a bond as the parameter p of interest. We have previously found that complex g_{WS}^{p} diverges at scattering singularities (see Appendix G of [7]), such as g_{WS}^{p} diverging at Coherent Perfect Absorption, and transmission generalized delay g_{T}^{p} diverging at transmission nulls. Because the divergence of g^{p} has the form of a simple pole, we expect the PDFs of any complex generalized delay g^{p} to have -3 power-law tails [7, 8]. It should also be noted that since both the real and imaginary components of the complex generalized delay independently diverge at singularities, it can be used as a method to more accurately determine the existence and location of singularities, as compared to linear-response measurements.

In our graph experiments we recover very clear -3 power-law tails for both the positive and negative tails of both the $Re[g_{WS}^{p}]$ and $Im[g_{WS}^{p}]$ distributions, extending the range of validity of our observed super-universality of delay statistics [7, 8]. An interesting question that arises is whether or not the mean of the real part of the distribution $\langle Re[g_{WS}^{p}]\rangle$ can be used to count the number of poles in the lower half of the complex plane, as we previously demonstrated for τ_{WS} [9].

III. Conclusion

The generalized Wigner-Smith operator shows potential for extracting more information about the scattering matrix of

complicated non-Hermitian systems, with the advantage that it does not require multi-frequency measurements. We have shown that densely-moded microwave cavities with multiple *in-situ* continuously-tunable parametric perturbers serve as ideal platforms for studying the statistical properties of generalized Wigner-Smith operators.

ACKNOWLEDGMENTS

This work was supported by NSF/RINGS under grant No. ECCS-2148318, ONR under grant N000142312507, and DARPA WARDEN under grant HR00112120021.

REFERENCES

[1] H. Cao, A.P. Mosk and S. Rotter, "Shaping the propagation of light in complex media," *Nature Phys*., vol. 18, p. 994–1007, September 2022.

[2] Lei Chen and Steven M. Anlage, "Use of Transmission and Reflection Complex Time Delays to Reveal Scattering Matrix Poles and Zeros: Example of the Ring Graph," *Phys. Rev. E* 105, 054210 (2022).

[3] Lei Chen, Steven M. Anlage, and Yan V. Fyodorov, "Generalization of Wigner Time Delay to Sub-Unitary Scattering Systems," *Phys. Rev. E* 103, L050203 (2021).

[4] P. Ambichl, A. Brandstötter, J. Böhm, M. Kühmayer, U. Kuhl and S. Rotter, "Focusing inside disordered media with the generalized Wigner-Smith operator," *Phys. Rev. Lett*., vol. 119, p. 033903, July 2017.

[5] Jared Erb, David Shrekenhamer, Timothy Sleasman, Thomas M. Antonsen, and Steven M. Anlage, "Control of the Scattering Properties of Complex Systems By Means of Tunable Metasurfaces," *Acta Physica Polonica A* 144 (6), 421-428 (2023).

[6] Jared M. Erb, Nadav Shaibe, Robert Calvo, Daniel Lathrop, Thomas Antonsen, Tsampikos Kottos, Steven M. Anlage, "Topology and Manipulation of Scattering Singularities in Complex Non-Hermitian Systems: Two-channel Case," *Phys. Rev. Research* 7, 023090 (2025).

[7] N. Shaibe, J. M. Erb and S. M. Anlage, "Superuniversal statistics with topological origins for non-Hermitian scattering singularities," *Phys. Rev. Research*, vol. 7, p. 043185, November 2025.

[8] N. Shaibe, J. M. Erb and S. M. Anlage, "Superuniversal statistics of complex time delays in non-Hermitian scattering systems," *Phys. Rev. Lett.*, vol. 134, p. 147203, April 2025.

[9] Lei Chen, Steven M. Anlage, Yan V. Fyodorov, "Statistics of Complex Wigner Time Delays as a counter of S-matrix poles: Theory and Experiment," *Phys. Rev. Lett*. 127, 204101 (2021).

Topological perfect transition in one-dimensional multi-orbital photonic lattices

Polette Parra-Palavecino[1,2], Diego Román-Cortés[1,2], Rodrigo A. Vicencio[1,2*]

[1]Departamento de Física, Facultad de Ciencias Físicas y Matemáticas, Universidad de Chile, Chile
[2]Millenium Institute for Research in Optics - MIRO, Chile
*Corresponding author: rvicencio@uchile.cl

***Abstract*—We study one-dimensional (1D) photonic lattices on a topologically trivial phase for S mode excitation. We demonstrate how the excitation of dipolar P states together with the engineering of the coupling angle induce a zero dimerization regime on a SSH-like model, including the emergence of an all flat band regime.**

***Keywords*— photonic lattices, topological lattices, evanescent coupling, femtosecond laser writing.**

I. Introduction

The ability to freely varying the coupling constants on a given lattice geometry is one of the key of success for light manipulation on photonic systems [1]. This could be achieved by different means; however, the constraint on the waveguide distance for evanescent coupling finally determines the experimental possibilities and concrete dimensions of the system. For example, the SSH 1D lattice model [2] is very well known for showing a topological phase transition depending on a lattice dimerization. This lattice possesses intra C_1 and inter C_2 coupling constants, which determines the respective regime. At $C_1 = C_2$ the lattice is a simple 1D dispersive lattice. For $C_1 < C_2$ the lattice enters into a topologically non-trivial phase, and the bulk-edge correspondence allows the emergence of a non-trivial exponentially localized edge state. At zero dimerization C_1, the lattice transforms into a set of uncoupled dimers with frequencies $\pm C_2$ forming two flat bands (FB), plus two isolated single-site states at zero frequency. These perfectly localized states are the origin of the edge modes, which acquire an exponential tail as soon as $C_1 > 0$. To achieve a zero coupling, on evanescently coupled systems, implies an abrupt increment of the waveguide separation, as the coupling constant decreases exponentially with the inter-site distance [3]. This limit is therefore not available in standard configurations [4] and constitutes a mathematical dream.

II. Methods

We fabricate different photonic structures by means of the fs laser writing technique [1], [3]. We tightly focus a pulse of $\sim$ 200 fs, with a wavelength of 1030 nm, inside a borosilicate glass wafer. The laser induces a weak modification of the refractive index contrast, estimated as $\Delta n \sim 10^{-3}$ over $n_0 = 1.48$ (wafer). A full waveguide is fabricated after translating the glass along its length (coordinate z), at a given writing velocity and power. By carefully selecting these parameters, we can transit from single-mode waveguides having only S-like modes into multi-mode waveguides having multi-orbital states [1]. The performance of the waveguides not only depends on the fabrication parameters, but also on the excitation wavelength: for shorter λ's a larger number of modes are available in the same photonic structure.

III. Results and Discussion

Multi-orbital interactions [1] allow the control of the coupling constants depending on the specific orbital states as well as on their orientation. Figs.1(a)–(c) show pictorially this interaction picture for S and P states. Fig.1(d) describes how the couplings vary depending on the rotation angle θ. Interestingly, we can achieve a zero coupling interaction for P-P and S-P interactions, independently of the distance in between waveguides. Focusing on a dipolar coupling C_p only, we find an invisibility angle at around $\theta_i \approx 32$ degrees [5] for 730 nm, as shown in Fig.1(e).

We fabricate new photonic couplers and perform a full characterization of C_p versus θ and versus excitation wavelength. Fig.1(f) shows the extracted data for the respective coupling constants, where red and blue data indicate positive and negative values, while a white fringe implies a zero value. We notice how this transition region shifts to larger angles for larger wavelengths, as the guided modes become broader as well. The black line indicates the position for which $C_p(\theta, \lambda) = -C_p(0, \lambda)$.

Now, we implement these findings on a lattice geometry, where the intersite distance is kept constant and the dimerization is inserted by modifying the lattice angle. Fig.2(a) shows a 1D dipolar lattice, for which all horizontal couplings ($C_p(0)$) are positive and $C_p(\theta)$ varies according to Fig.1. Therefore, by sweeping on the angle θ we can transform the lattice geometrically, but also topologically. If we apply the SSH model to this configuration $C_1 = C_p(\theta)$ and $C_2 = C_p(0)$. Therefore, in the region defined by $\theta = 0$ and the black line of Fig.1(f), $|C_1| < C_2$ and the lattice is in a topologically non-trivial phase. However, this is only true if the system size is infinite. For finite lattices the topological transition is shifted into smaller values of $|C_1|$. We fabricate several lattices with different angles θ and excite them at the bulk and the edges. Fig.2(b) top and bottom shows the respective output

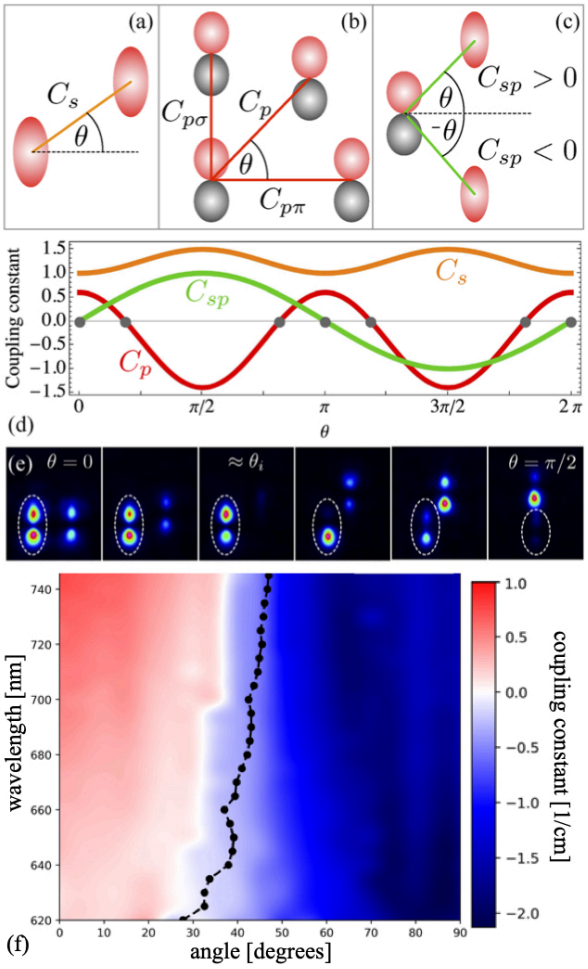

Fig. 1. (a)–(c) Coupling diagram for S-S, P-P, and S-P interaction cases, respectively. (d) Coupling constant vs θ for C_s (orange), C_p (red), and (d) C_{sp} (green). Dots show the angles for zero coupling. (e) Experimental output profiles for P-P photonic couplers at different values of θ, after exciting the encircled waveguide. (f) Experimentally obtained coupling constant C_p versus θ and versus excitation wavelength.

profiles, obtained for 730 nm. We clearly observe the transition into localization for both excitations at the invisibility angle (see dashed area). There, the two bands transform into two FBs, and the edge topological state collapses to a single-site mode. Around this collapse, a well-defined SSH edge state is observed with the respective staggered phase at a given lattice polarization [5].

Fig.2(c) shows the extracted output participation ratio as a measure of the wavepacket size, where the black (yellow) color indicates a value close to 1 (9) implying localization (delocalization). The data describes quite clearly the transition into localization around the invisibility angle. This is very well defined for bulk excitation, implying an all FB lattice regime which interestingly coincides with the highest topological regime for this lattice.

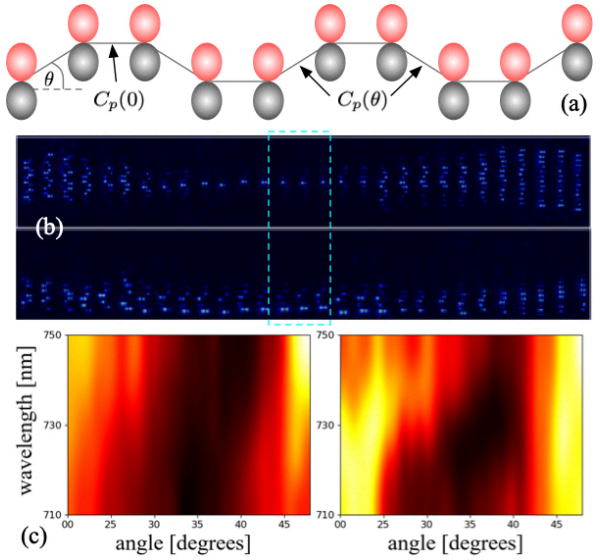

Fig. 2. (a) Dipolar lattice configuration. (b) Output profiles at $\lambda = 730$ nm for different angles θ from 0 (left) to 50 (right) degrees, and for bulk (top) and edge (bottom) excitations. (c) Averaged output participation ratio for bulk (left) and edge (right) excitations.

IV. Conclusion

We have discussed how we can switch the dipolar coupling by varying the rotation angle among P waveguides. The obtained degree of control is very high, allowing to transit from positive to negative values, including zero at the invisibility angle. We study a 1D zig-zag-like geometry as a dipolar realization of an SSH lattice. By varying the lattice angle θ, we observe an abrupt and clear transition into localization for bulk localization as a manifestation of an all FB regime. Edge localization is also very sharp around the invisibility angle and a perfect zero dimerization is clearly evidenced. This is a remarkable result as it constitutes the first experimental demonstration of a physically inaccessible regime when considering standard S modes.

Acknowledgments

This work was supported by ANID FONDECYT Grant 1231313 and Millennium Science Initiative Program ICN17_012.

References

[1] R.A. Vicencio, "Multi-orbital photonic lattices," *APL Photonics*, vol. 10, pp. 071101, 2025.
[2] P. Delplace, D. Ullmo, and G. Montambaux, "Zak phase and the existence of edge states in graphene," *Physical Review B*, vol. 84, pp. 195452, 2011).
[3] A. Szameit, et al., "Discrete nonlinear localization in femtosecond laser written waveguides in fused silica," *Optics Express*, vol. 13, pp. 10552, 2005.
[4] G. Cáceres-Aravena, et al., "Experimental observation of edge states in SSH-Stub photonic lattice," *Physical Review Research*, vol. 4, pp. 013185, 2022.
[5] D. Román-Cortés, et al, "Observation of invisibility angle and flat band physics in dipolar photonic lattices," *Nano Letters*, vol. 25, pp. 4291, 2025.

Programmable Anisotropic Exceptional Points in Passive Multiport Scattering Networks

Kaiyuan Wang[1,2], Niall Byrnes[1], Matthew R. Foreman[1,2,*]

[1]School of Electrical and Electronic Engineering, Nanyang Technological University, Singapore
[2]Institute for Digital Molecular Analytics and Science, Nanyang Technological University, Singapore
*Corresponding author: matthew.foreman@ntu.edu.sg

***Abstract*—Exceptional points are spectral degeneracies of non-Hermitian operators. We show that a passive multiport network can be programmed to exhibit exceptional-point behaviour in a measured-port subspace, even though the full scattering matrix is unitary. By tuning internal phases, we engineer anisotropic eigenvalue splitting and prescribe sensitivity directions in parameter space.**

***Index Terms*—exceptional points, non-Hermitian physics, scattering networks, metamaterials, programmability**

I. Introduction

Exceptional points (EPs) represent spectral singularities in non-Hermitian operators where the eigenvalues and their corresponding eigenvectors coalesce, giving rise to non-analytic responses and unique topological features [1], [2], [3]. Whilst early studies focused primarily on gain-loss engineering, recent attention has shifted toward *anisotropic* EP behaviour, wherein the spectral scaling is dictated by the direction of approach in parameter space [4]. Such directionality offers attractive capabilities for sensing and reconfigurable wave devices, however, current demonstrations predominantly rely on limited mode spaces and active, non-passive constituents [5]. In this work, we address this limitation by targeting a complementary regime: a strictly *passive* multiport scattering network. Whilst the full scattering matrix of the network is assumed unitary, a measured port subspace can nevertheless exhibit effective non-unitary behaviour arising from controlled leakage into unobserved ports. Utilising such a complex optical network as a platform to achieve a programmable scattering matrix [6], [7], we show that internal phase control alone is sufficient to facilitate the formation of scattering EPs and shape their anisotropic response along a user-defined direction in parameter space.

II. Concept and design principle

We consider an M-port lossless network operating at a fixed frequency. The full scattering matrix $\mathbf{S}$ is strictly unitary and cannot host an EP. A sub-scattering block $\mathbf{A}$, however, obtained by restricting attention to a specific subset of ports, is generally non-unitary and thus potentially defective. Restricting to, for example, a 2-port subsystem, an EP within the 2×2 matrix $\mathbf{A}$ can be achieved by tailoring the propagation phases along a subset of the network's internal links so that the discriminant of the characteristic polynomial of $\mathbf{A}$ vanishes (corresponding to two real parametric constraints that the system must satisfy). A conventional EP would exhibit a square root dependence for perturbations in any direction in parameter space. Imposition of an anisotropic response along a specific direction in parameter space, however, imposes further conditions, thereby necessitating tuning of additional propagation phases. Realisation of anisotropic EP behaviour therefore can be formulated as a programmable objective function which then can be used for system design. The wealth of links in a complex network affords increased degrees of freedom, providing us with the ability to achieve customisable EP responses tailored to, for example, specific sensing requirements.

III. Anisotropic response and EP verification

We validate our theoretical framework using a four-port cross network equipped with multiple tunable internal phases (Figure 1), which can be realistically adjusted through the refractive index (we assume a wavelength of $\lambda = 600$ nm in our simulations). By systematically scanning the phase

Fig. 1. **Passive programmable multiport network.** The full scattering matrix is unitary, but the measured two-port subsystem (top and right ports) is non-unitary due to leakage into unobserved ports (bottom and left ports). Tunable internal phases provide a high dimensional control space for programming EP behaviour.

Fig. 2. **Anisotropic exceptional-point response and verification.** (a) Eigenvalue splitting $|\lambda_+ - \lambda_-|$ of the measured-port sub-scattering matrix $\mathbf{A}$ versus perturbation magnitude $|\delta\phi|$ for a generic direction (orange) and the programmed design direction (purple). The generic perturbation exhibits the conventional square-root scaling (slope ≈ 0.5 on the log–log plot), whereas the design direction exhibits a linear scaling (slope ≈ 1.0), demonstrating anisotropic sensitivity. (b) Phase rigidity of the eigenmodes of $\mathbf{A}$ as a function of $\delta\phi$ for the same two perturbation directions. The rigidity vanishes at the operating point ($\delta\phi = 0$), confirming eigenvector coalescence and thereby the exceptional-point character.

of four individual network links (as indicated in Figure 1), we locate a network configuration that achieves the specified constraints. In this case the system was programmed such that the EP exhibited a linear response to refractive index variations of one specific network link, whereas other perturbations gave rise to the conventional square-root type dependence. To verify the anisotropic nature of the singularity, we compared the perturbations along (i) the specified anisotropic response direction and (ii) a generic direction. As shown in Figure 2(a), the eigenvalue gap exhibits distinct local scalings depending on the perturbation trajectory. Specifically, the purple curve, corresponding to perturbation of the design link, exhibits a linear dependence, while the orange curve, corresponding to a generic perturbation scales as $|\delta\phi|^{1/2}$, thereby demonstrating the desired anisotropy. Furthermore, in Figure 2(b) we observe that the phase rigidity vanishes at the nominal operating point, confirming the coalescence of the eigenvectors of $\mathbf{A}$. This combination of metrics explicitly precludes the possibility that the observed behaviour arises from a diabolic point (DP) type degeneracy, confirming the genuine EP character of the system.

IV. Conclusion

In conclusion, we have presented a passive route to achieve programmable anisotropic EP responses in multiport scattering networks. Our results underscore that unitary scattering at the global device level is fully compatible with realisation of non-Hermitian degeneracies in a measured subspace. Moreover, we have demonstrated that phase-only control is sufficient to both place and shape the EP response in parameter space. This architecture is particularly relevant for reconfigurable metamaterial and photonic network platforms where phase shifters are easily realisable.

References

[1] W. D. Heiss, "The physics of exceptional points," *J. Phys. A: Math. Theor.*, vol. 45, p. 444016, 2012.

[2] R. El-Ganainy *et al.*, "Non-Hermitian physics and PT symmetry," *Nat. Phys.*, vol. 14, pp. 11–19, 2018.

[3] M.-A. Miri and A. Alù, "Exceptional points in optics and photonics," *Science*, vol. 363, p. eaar7709, 2019.

[4] J. Chen, Z. Zhou, Y. Xiao, N. Wang, X. Wang, and Y. Li, "Observation of Hybrid Degenerate Point in Projected Non-Hermitian Metasurfaces," *Phys. Rev. Lett.*, vol. 135, p. 116601, 2025.

[5] K. Ding, G. Ma, Z. Q. Zhang, and C. T. Chan, "Experimental Demonstration of an Anisotropic Exceptional Point," *Phys. Rev. Lett.*, vol. 121, p. 085702, 2018.

[6] T. Kottos and U. Smilansky, "Periodic orbit theory and spectral statistics for quantum graphs," *Ann. Phys.*, vol. 274, pp. 76–124, 1999.

[7] S. Gnutzmann and U. Smilansky, "Quantum graphs: Applications to quantum chaos and universal spectral statistics," *Adv. Phys.*, vol. 55, pp. 527–625, 2006.

SPECIAL SESSION 11

Nano-Lasers, Spasers, and Nanostructures with Quantum Elements

9 contributions · pp. 954–971

Temporal coherence properties of an aluminum nanocone lattice laser

Tiziana Cesca[1,*], Elizabeth Mendoza-Sandoval[1], Giuseppe Pirruccio[2], Giovanni Mattei[1]

[1]Department of Physics and Astronomy, University of Padova, Italy
[2]Instituto de Física, Universidad Nacional Autónoma de México, México
*Corresponding author: tiziana.cesca@unipd.it

***Abstract*— This work investigates the room-temperature temporal coherence properties of a solid-state plasmonic nanolaser made of a hexagonal array of tapered aluminum nanocones coupled to a dye-doped polymer film. The device shows exceptionally long coherence, with a measured coherence time of ~30 ps and a corresponding coherence length of ~8.8 mm.**

***Keywords*— plasmonic lattice lasers, nanoarrays, temporal coherence.**

I. Introduction

In recent years, plasmonic lattice lasers have emerged as a promising platform, drawing growing interest for their potential as compact, coherent light sources integrated at the nanoscale [1]. In these systems, lasing emerges from the interaction between a gain medium and the collective modes supported by periodic arrays of plasmonic nanostructures, namely surface lattice resonances (SLRs). Extensive studies have examined the lasing behavior of these devices by analyzing key parameters such as lasing threshold, temporal dynamics, emission polarization, and the influence of structural disorder [2]. Coherence is a defining feature of lasers, yet at present only a limited number of studies have investigated the coherence properties of plasmonic nanolasers. In the present work, we experimentally investigated the lasing emission properties in the visible range and at room temperature of a fully solid-state plasmonic array nanolaser consisting of a hexagonal array of Al nanocones coupled to a dye-doped polymeric film [3]. The temporal coherence properties of the lasing mode are characterized by interference measurements.

II. Methods

The plasmonic lattice laser consists of a hexagonal array of tapered aluminum nanocones (a_0 = 475 nm) coupled with an organic dye (Lumogen Red 305) in a 300 nm-thick PMMA matrix. Lasing emission is optically excited at 532 nm by pumping with a picosecond laser and is characterized by a wavevector-resolved photoluminescence (PL) setup as a function of the excitation fluence. Room temperature PL spectra are recorded by an optical fiber-coupled spectrometer (Ocean Optics HR4000). Temporal coherence measurements of the lasing emission are performed with a tilted-mirror Michelson interferometer [4].

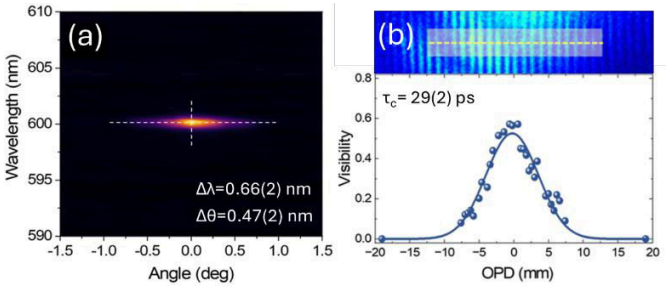

Fig. 1 (a) Map of the lasing emission. (b) Top: interference image at the optical path difference OPD = 1.8 mm; bottom: visibility as a function of the OPD.

III. Results and Discussion

Efficient mono-modal lasing emission at λ_{em} = 600 nm was measured at the Γ-point by pumping at the incidence angle θ_{exc} = 18.1°. This corresponds to the (1,0) Rayleigh anomaly of the nanoarray, which enables optimal in-plane coupling and confinement of the pumping field within the PMMA layer, resulting in the highest excitation energy density in the active layer volume. The lasing threshold results F_{th} = 0.51 ± 0.02 mJ/cm^2 and, above threshold, the emission has a spectral bandwidth (limited by the spectral resolution of the spectrometer) $\Delta\lambda$ = 0.66 ± 0.02 nm and an angular divergence $\Delta\theta$ = 0.47 ± 0.02 deg (Fig 1a). The lasing mode exhibits an ultralong temporal coherence (Fig. 1b), with a coherence time of τ_c = 29 ± 2 ps, (corresponding to a coherence length of L_c = 8.8 ± 0.5 mm and to an actual spectral line width of 0.04 nm). Such a long coherence can be related to a reduced scattering dephasing by the nanoparticles promoted by high Q-factor modes in the nanoarray and by the small thickness of the active layer, both of which contribute to the coherent feedback throughout the entire nanoarray.

IV. Conclusion

We have investigated the room temperature lasing emission properties of a solid-state plasmonic lattice laser, consisting of

a hexagonal array of Al nanocones coupled with a dye-doped polymeric layer. A record-long temporal coherence of the lasing mode was measured, which exceeds the state-of-the-art values reported for plasmonic lattice nanolasers by more than an order of magnitude, highlighting the remarkable potential of this system for the development of coherent nanoscale sources operating at room temperature.

ACKNOWLEDGMENTS

This work was supported by the Department of Physics and Astronomy of the University of Padova with the project PRD-BIRD22-Cesca, and in part by the Italian MUR Departments of Excellence grant 2023-2027 “Quantum Frontiers” and the Consejo Nacional de Ciencia y Tecnología (México) through projects 1564464 and 1098652, UNAMPAPIIT IN104522, IN104325 and PIIF 2024.

REFERENCES

[1] F. Freire-Fernández, S.-M. Park, M. J. H. Tan, T. W. Odom, Plasmonic lattice lasers. Nat. Rev. Mater. vol. 10, pp. 604−616, 2025.

[2] D. Wang, W. Wang, M. P. Knudson, G. C. Schatz, T. W. Odom, Structural Engineering in Plasmon Nanolasers. Chem. Rev. vol. 118, pp. 2865−2881, 2018.

[3] M. Trevisani, D. Piccotti, E. Mendoza Sandoval, G. Pirruccio, M. Ramezani, J. Gomez Rivas, T. Cesca, G. Mattei, Ultra-long temporal coherence in a solid-state plasmonic nanolaser, ACS Photonics vol. 13, pp. 92-100, 2026.

[4] D. Piccotti, M. Trevisani, G. Pirruccio, B. Kalinic, T. Cesca, G. Mattei, Polarized coherent emission outside high-symmetry points of dye-coupled plasmonic lattices, Phys. Chem. Chem. Phys. vol. 25, pp. 8641-8650, 2023.

.

Quantum Nonlinear Response of Emitter Lattices

Blas Durá-Azorín[1,2,3*], Antonio I. Fernández-Domínguez[1,2], Alejandro Manjavacas[3]

[1]Departamento de Física Teórica de la Materia Condensada,
Universidad Autónoma de Madrid, E-28049 Madrid, Spain
[2]Condensed Matter Physics Center (IFIMAC),
Universidad Autónoma de Madrid, E-28049 Madrid, Spain.
[3]Instituto de Química Física Blas Cabrera (IQF), CSIC, E-28006 Madrid, Spain
*Corresponding author: blas.dura@uam.es

We theoretically study [1] the optical response of a coherently driven periodic lattice of quantum emitters. Unlike lattices of classical resonators, we find that a resonant plane wave can populate excitonic Bloch states with parallel wavevectors different from that of the incident field, including states lying outside the light cone.

***Keywords*—quantum emitters, nonlinearities, subradiant states.**

Recently, advances in the creation and manipulation of quantum emitter (QE) ensembles [2] have sparked an intense research into the optical response of these systems. Many studies have focused on the single excitation limit, which allows for a linearization of the emitters. Within this approximation, it has been shown that QE lattices and metasurfaces can implement strong magnetic responses or deeply subradiant modes. In our work, we go beyond the single excitation limit, revealing the impact of quantum nonlinearities in the optical response of coherently driven QE lattices by a laser. We find that, in contrast to the classical (bosonic) case, the incident plane wave populates not only the excitonic Bloch states with the same parallel wavevector as the driving laser, but a continuum of states with different parallel wavevectors, including those lying outside the light cone. Therefore, we provide an alternative approach to excite subradiant states in atomic arrays, which currently rely on more complicated mechanisms [3]. Moreover, for periods approaching the driving wavelength, the emitter lattice enters in a bistable regime due to the renormalization of the driving rate [4]. We show how this bistable behavior enables the selective activation and deactivation of the optical quantum nonlinearities of the system.

References

[1] B. Durá-Azorín, A. I. Fernández-Domínguez, and A. Manjavacas, "Quantum Nonlinear Response of Emitter Lattices," *arXiv preprint* arXiv:2510.19992, 2025.

[2] K. Srakaew, P. Weckesser, S. Hollerith, D. Wei, D. Adler, I. Bloch, and J. Zeiher, "A subwavelength atomic array switched by a single Rydberg atom," *Nature Physics*, vol. 19, pp. 714–720, 2023.

[3] P.-O. Guimond, A. Grankin, D. V. Vasilyev, B. Vermersch, and P. Zoller, "Subradiant Bell states in distant atomic arrays," Phys. Rev. Lett., vol. 122, p. 093601, 2019.

[4] C. D. Parmee and J. Ruostekoski, "Bistable optical transmission through arrays of atoms in free space," *Phys. Rev. A*, vol. 103, p. 033706, 2021.
.

Chiral light from exceptional points in a coupled nanolaser ring array

Kaiwen Ji[1,*], Melissa Hedir[2], Ramy El-Ganainy[3], Li Ge[4], Alejandro M. Yacomotti[1]

[1]Laboratoire Photonique Numérique et Nanosciences, Université Bordeaux, CNRS, 33405 Talence, France
[2]Laboratoire des technologies de la microelectronique, CNRS, Grenoble, 38054, France
[3]Department of Electrical and Computer Engineering, Saint Louis University, Saint Louis, MO, USA
[4]Department of Physics and Astronomy, College of Staten Island, New York 10314, USA
*Corresponding author: alejandro.giacomotti@institutoptique.fr

***Abstract*—We propose and experimentally demonstrate an orbital angular momentum nanolaser array arranged in a ring geometry on an InP-based photonic crystal membrane. Our approach leverages exceptional-point singularities with net phase circulation. These results demonstrate a robust and scalable strategy for engineering compact, phase-locked laser arrays with controllable angular momentum output.**

***Keywords*— nanolasers, non-Hermitian photonics, photonic crystals.**

I. Introduction

Thanks to the increasing flexibility of parameter tuning in photonic designs, micro and nanophotonic coupled cavity arrays —such as coupled micropillars, microrings and photonic crystal nanocavities— are ideal platforms to investigate topological photonics [1, 2]. Symmetry and/or topologically protected modes may arise in such lattices, which prove robust against some kind of disorder. Importantly, III-V semiconductor materials enable non-zero imaginary parts of the electrical susceptibility, leveraging active —e.g. lasing— regimes, and also nonlinear and non-Hermitian operation in the form of gain/loss spatial modulations.

In the context of topological lasers [2,3], devices able to generate vortex beams from modes with nonzero orbital angular momentum (OAM) have attracted considerable attention. In Ref. [4] a six-coupled micropillar laser in a ring with uniform couplings —or photonic "benzene" molecule— has been utilized to generate non-zero OAM laser beams. In this case, the pump is uniformly distributed in the system, therefore the ring can be mapped to a Hermitian system in which clockwise (CW) and counter clockwise (CCW) modes are degenerated. This can be seen as a consequence of the eigenmodes of a symmetric real matrix: these can always be rescaled to be purely real functions, i.e. standing waves. Hence, chiral modes $e^{im\pi}$, where m is an integer, are linear superpositions of pairwise degenerated standing waves. In Ref. [4] mode selection is realized using pump beams with circularly polarized light (nonzero spin). Noticeably, pure chiral modes are no longer possible for arbitrary Hermitian couplings because degeneracies become lifted in general. In such a case, (non-Hermitian) gain/loss distributions can restore OAM. In this work, we show that $e^{im\pi}$ chiral modes and phase singularities can be generated at the exceptional points (EPs) of a four coupled nanolaser ring with alternating couplings and sublattice pump imbalance. Such a nanocavity ring can be seen as a non-Hermitian version of the Rice-Mele model, where the on-site potentials are originally real.

II. Methods

We first performed finite-element simulations (COMSOL Multiphysics®) to identify chiral EPs (CEPs) in a photonic crystal nanocavity ring (Fig. 1a). The coupled cavity geometry imposes a detuning between the two sublattices: the two cavities featuring gain in Fig. 1a on the top belong to sublattice A (cavity 1, top, and cavity 3, bottom), while the two others belong to sublattice B (cavities 2 and 4 at the left and right sides, respectively), verifying $\omega_A - \omega_B \approx 50$ GHz. Additionally, in order to produce an EP, the couplings between cavities 1 and 2, and cavities 3 and 4 (t_1) is designed to be slightly larger than the one between 1 and 4, and cavities 2 and 3 (t_2), such that $t_1 - t_2 \approx 7$ GHz. In this design, the CEP can be restored provided $\omega_A - \omega_B \approx 2\alpha(t_1 - t_2)$, where α is the Henry parameter of the semiconductor quantum wells ($\alpha \sim 3$), pumping sublattice B with a higher intensity (Fig. 1a, bottom), leading to a CCW chiral mode.

Experiments are implemented on a III-V semiconductor photonic crystal (PhC) platform. PhCs enable extreme device miniaturization and, at the same time, a large control over the system parameters. Here we realize a ring nanocavity array with tailored couplings by employing photonic barrier engineering [5], [6]; furthermore, quantum well (QW) InGaAs/InGaAsP materials provide optical gain that can be locally induced by means of spatial light modulation of the pump beam, eventually leading to the imaginary detunings. We fabricated four coupled PhC nanolasers in an InP suspended membrane (Fig. 1a) and used PhC L3 nanocavities as the building blocks. The leading evanescent coupling takes place along the $\pm 60°$ direction, whereas horizontal and vertical coupling can be neglected, therefore forming a four-coupled nanocavity ring. The different coupling coefficients t_1 and t_2 are designed using a photonic barrier engineering technique, which consists in modifying the size of the nanoholes between the cavities.

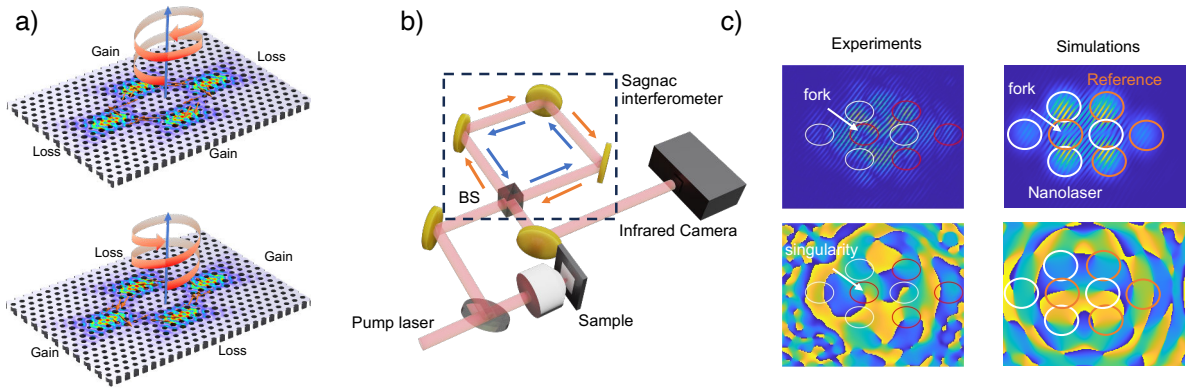

Fig. 1. a) Schematic of the chiral mode operating at the EP in a complex Rice-Mele photonic crystal coupled nanolaser array, with arrows indicating the Poynting vector, under nonuniform (sublattice) pump distribution. (b) Experimental setup for the near-field interference measurements. (c) Near-field interference pattern near the EP (left). The circles mark the positions of the cavities, and a fork-shaped feature appears at the center of the structure. The lower panel shows the corresponding phase distribution, revealing a clear phase singularity. The right panel presents the corresponding simulation results.

III. Results and Discussion

The nonzero OAM in our system is enabled by the consecutive $\pi/2$ phase change along the PhC nanolaser array. This guiding principle is largely model independent, and we only require a tight-binding description of our nanolaser array, where each nanolaser is represented by a lattice site and coupled to its nearest neighbors. Denoting ψ_n, θ_n as the complex light amplitude and its phase at the nth site, it can be demonstrated that the flux $J_{n+1,n}$ from cavity n to its neighbor cavity $n+1$ is maximized when

$$\delta\theta = \theta_{n+1} - \theta_n = \mp\pi/2, \tag{1}$$

where the sign determines the *local* chirality of wave propagation, i.e., whether the flux is in the CW or CCW direction. Furthermore, it can be shown that the dimensionless OAM number is directly related to the optical flux with the normalization $\sum_n |\psi_n|^2 = 1$:

$$\langle L_z \rangle = \frac{1}{2} \sum_n \frac{J_{n+1,n}}{t_{n+1,n}} = \sum_n |\psi_{n+1}\psi_n| \sin\delta\theta. \tag{2}$$

where t_n are the Hermitian couplings in the ring. To achieve a chiral state and a nonzero OAM, we unbalance the pump in the sublattice. With sufficient gain (loss) in the left cavity, we find $\delta\theta = \pi/2$ $(-\pi/2)$ in a non-Hermitian zero mode.

Figure 1(a) shows that two chiral modes with opposite OAM are generated at the EPs by inverting the sublattice pump imbalance. Using both COMSOL and a tight-binding model, we calculated the OAM perpendicular to the PhC $\langle L_z \rangle$ using the near field distribution, and obtained $\langle L_z \rangle \sim 1$ for a sublattice pump imbalance of nearly $r = (P_B - P_A)/(P_B + P_A) \approx 0.5$.

Experimentally, a Sagnac interferometer [Fig. 1(b)] enables robust near-field interference measurements with spatially shifted patterns to determine the phase distribution of these chiral modes. When operated close to the EP, a fork-shaped feature appears at the center of the structure [Fig. 1(c), left panel]. Furthermore, off-diagonal Fourier filtering [4] provides direct evidence of the formation of the phase singularity.

IV. Conclusion

This work presents a flexible approach to achieving nonzero OAM via non-Hermiticity in a coupled semiconductor nanolaser array, potentially benefiting various applications in fields such as optical communications.

Acknowledgments

This work was supported by the National Science Foundation (NSF) under Grants No. PHY-1847240 and No. DMR-2326698, the French National Research Agency (ANR), Grant No ANR-22-CE24-0012-01, by the RENATECH network, and by the "Grand Programme de Recherche" (GPR) LIGHT. We also acknowledge support from the AFOSR Multidisciplinary University Research Initiative Award on Programmable Systems with Non- Hermitian Quantum Dynamics (Grant No.FA9550-21-1-0202), Army Research Office (W911NF-23-1-0312).

References

[1] L. Lu, J. D. Joannopoulos, and M. Soljacic, "Topological photonics," *Nat. Photon.*, vol. 8, pp. 821–829, 2014.
[2] Y. Ota, et al. "Active topological photonics," *Nanophoton.*, vol. 9, pp. 547-567, 2020.
[3] P. Miao, et al. "Orbital angular momentum microlaser," *Science*, vol. 353, pp. 464–467 (2016).
[4] N. Carlon Zambon, P. St-Jean, M. Milićević, et al. "Optically controlling the emission chirality of microlasers", *Nat. Photonics*, vol. 13, pp. 283–288, 2019.
[5] S. Haddadi, P. Hamel, G. Beaudoin, I. Sagnes, C. Sauvan, P. Lalanne, J. A. Levenson, and A. M. Yacomotti, "Photonic molecules: tailoring the coupling strength and sign", *Optics Express*, vol. 22, pp. 12359–12368, 2014.
[6] P. Hamel, S. Haddadi, F. Raineri, P. Monnier, G. Beaudoin, I. Sagnes, A. Levenson, and A. M. Yacomotti, "Spontaneous mirror-symmetry breaking in coupled photonic-crystal nanolasers", *Nature Photonics*, vol. 9, pp. 311–315, 2015.

Assembled Nanocrystal Lattice Nanolasers

Mindaugas Juodėnas[1,*], Nadzeya Khinevich[1], Gvidas Klyvis[1], Domantas Peckus[1], Joel Henzie[2], Tomas Tamulevičius[1], Sigitas Tamulevičius[1]

[1]Institute of Materials Science, Kaunas University of Technology, Lithuania
[2]Research Center for Materials Nanoarchitectonics, National Institute for Materials Science, Japan
*Corresponding author: mindaugas.juodenas@ktu.lt

***Abstract*— We demonstrate a surface lattice resonance (SLR)-based plasmonic nanolaser that leverages the bulk production of colloidal nanoparticles and their organization via template-assisted assembly. Unlike conventional top-down fabrication methods, this approach utilizes monocrystalline silver nanocubes to reduce absorptive losses associated with grain boundaries. Using capillary-assisted particle assembly, we created periodic arrays of silver nanocubes that support high-quality SLRs. Furthermore, utilizing transient absorption spectroscopy, we discuss the impact of ultrafast photophysical processes on these systems. Specifically, we analyze how coherent optomechanical vibrations of the nanocubes modulate the localized surface plasmon resonance (LSPR) and, consequently, the lattice resonance on picosecond timescales. When combined with the gain medium Pyrromethene-597, these arrays demonstrate lasing at 574 nm with competitive characteristics despite the assembly-related disorder. Our results indicate that eliminating ohmic losses via monocrystallinity is more critical for nanolasing than achieving perfect geometric periodicity, validating low-cost assembly as a superior fabrication route.**

***Keywords*— nanolaser, lattice resonance, self-assembly, plasmonics.**

I. Introduction

Plasmonic metal nanoparticles support localized surface plasmon resonances (LSPRs), which are collective oscillations of conduction electrons. While individual LSPRs often suffer from broad extinction peaks due to radiative damping, arranging these particles into periodic arrays can generate surface lattice resonances (SLRs). SLRs arise from the diffractive coupling between neighbors (Rayleigh anomalies) when the scattering spectrum of the constituent particles overlaps it. This hybridization results in high quality factors (Q-factors) and delocalized electromagnetic fields. These properties make SLRs good candidates for feedback mechanisms in nanoscale coherent light sources.[1]

However, a significant challenge in the field has been the fabrication of these arrays. Most SLR-based nanolasers are produced using top-down techniques like electron-beam lithography and physical vapor deposition. These methods result in polycrystalline nanoparticles with rough facets and grain boundaries, leading to diminished scattering properties and increased absorptive losses compared to theoretical models. To address this, we propose the use of chemically synthesized colloidal nanoparticles. Colloidal synthesis yields monocrystalline particles with smooth facets, offering superior scattering-to-absorbance ratios.[2]

The primary challenge lies in organizing these colloids into the precise geometries required for lasing. By utilizing capillary-force-assisted particle assembly (CAPA), we can achieve single-particle resolution on large scales, bridging the gap between high-quality colloidal materials and functional nanophotonic devices.[3]

II. Methods

Monodisperse silver nanocubes were synthesized using a modified polyol method, producing single-crystal particles coated with a thin layer of polyvinylpyrrolidone (PVP) surfactant. The assembly templates were fabricated by molding a polydimethylsiloxane (PDMS) replica from a silicon master stamp patterned with periodic pillars. This soft-lithography approach allows for the repeated reproduction of templates without continuous reliance on expensive lithography steps.

The assembly was performed using a custom setup where a droplet of colloidal solution is confined between the PDMS template and a glass slide. Dimethylformamide (DMF) was selected as the solvent because it acts as a theta-solvent for the PVP coating, preventing aggregation and ensuring the particles behave as hard spheres. By controlling the temperature and the translation speed of the meniscus across the template, convective currents and capillary forces trap individual nanocubes into the template voids. This method achieved high yield (>99%) over areas larger than 1 cm².

Transient absorption spectroscopy (TAS) was employed to probe the ultrafast dynamics of the nanocrystal lattices, using a variable pump-probe delay to monitor the evolution of the plasmonic response. For the nanolaser device, assembled Ag nanocube arrays (periodicity Λ = 400 nm) were soaked in a solution of Pyrromethene-597 (P597) dye. P597 was selected for its high quantum yield and spectral overlap with the lattice resonance. The device was pumped with a 515 nm femtosecond pulsed laser (270 fs pulses, 50 Hz) to drive the gain medium.

III. Results and Discussion

The fabricated nanolaser device was designed such that the lattice periodicity (400 nm) in the PDMS environment (n = 1.42) created a flat band at the Γ point near 562 nm, overlapping with the emission of the P597 dye. Upon optical pumping, the device exhibited clear lasing behavior. We observed a nonlinear increase in emission intensity with a distinct threshold at approximately 80 μJ/cm^{-2}. This transition was accompanied by a dramatic spectral narrowing, where the emission linewidth collapsed from ~45 nm (spontaneous emission) to <1.2 nm above the threshold (limited by spectrograph resolution).

The emitted beam profile displayed a fan-like pattern characteristic of 1D distributed feedback lasers, suggesting that the 2D array functions as a collection of 1D feedback channels aligned with the lattice directions. The emission was linearly polarized, following the resonator geometry. Crucially, the superior scattering-to-absorbance ratio of the monocrystalline silver compensates for the minor positional disorder inherent to self-assembly. We demonstrate that perfect periodic order is less critical for low-threshold lasing than the elimination of grain-boundary losses found in top-down fabricated structures.[4]

While the static design of the lattice is critical for lasing, the ultrafast dynamics of the gain and the resonator also play a vital role. Nanoparticles are not static structures; following photon absorption, they undergo rapid heating and expansion via electron-phonon coupling, exciting coherent optomechanical breathing modes. Transient absorption spectroscopy (TAS) of our arrays reveals that silver nanocubes support two primary breathing modes: a tip mode (approx. 27 GHz) involving deformation of the corners, and a face mode (approx. 38 GHz) involving the facets. These vibrational modes dynamically alter the shape of the nanocubes on picosecond timescales. Because the SLR depends on the spectral overlap between the localized surface plasmon resonance (LSPR) and the Rayleigh anomaly, modulations in the particle shape—which shift the LSPR—consequently modulate the SLR.[5]

Our analysis shows that these optomechanical modes cause the SLR to oscillate and transiently red-shift. In the context of a nanolaser, where the feedback mechanism relies on a precise spectral match between the gain bandwidth and the high-Q lattice mode, these ultrafast fluctuations are non-negligible. While this does not prevent lasing, it introduces a dynamic detuning between the gain medium and the cavity mode, potentially broadening the linewidth or destabilizing the output intensity during long-pulse operation. Specifically, the modulation depth is sufficient to alter the optical density of the array. This suggests that future designs of SLR-based active devices must account for these optomechanical effects, particularly for applications requiring ultrafast switching or high-stability pulsed emission.

IV. Conclusion

We have successfully demonstrated a scalable, cost-effective route to fabricating plasmonic nanolasers using template-assisted colloidal assembly. The resulting devices utilize monocrystalline silver nanocubes to achieve low-threshold lasing with high coherence, challenging the necessity of perfectly ordered, lithographically produced lattices. Furthermore, we highlight that the stability and performance of such devices are intricately linked to the intrinsic optomechanical vibrations of the constituent nanoparticles. By understanding the interplay between the mechanical breathing modes of the nanocubes and the photonic modes of the lattice, we can better design robust plasmonic devices for applications in on-chip optical communications and sensing.

Acknowledgments

This research was performed within project “LaSensA” under the M-ERA.NET scheme and was funded by the Research Council of Lithuania (LMTLT), agreement No. S-M-ERA.NET-21-2.

References

[1] F. Freire-Fernández, S.-M. Park, M. J. H. Tan and T. W. Odom, “Plasmonic lattice lasers,” Nature Reviews Materials, vol. 10, pp. 604–616, 2025.

[2] Khinevich, N. *et al.*, “Size and crystallinity effect on the ultrafast optical response of chemically synthesized silver nanoparticles,” Journal of Materiomics, vol. 10, pp. 594–600, 2024.

[3] Juodėnas, M., Tamulevičius, T., Henzie, J., Erts, D. & Tamulevičius, S., “Surface Lattice Resonances in Self-Assembled Arrays of Monodisperse Ag Cuboctahedra,” ACS Nano, vol. 13, pp. 9038–9047, 2019.

[4] Juodėnas, M. *et al.*, “Lasing in an assembled array of silver nanocubes,” Nanoscale Horizons, vol. 10, pp. 142–149, 2024.

[5] Juodėnas, M. *et al.*, “Effect of Ag Nanocube Optomechanical Modes on Plasmonic Surface Lattice Resonances,” ACS Photonics, vol. 7, pp. 3130–3140, 2020.

Vortex nanolaser based on a photonic disclination cavity

Hong-Gyu Park[1,*]

[1]Department of Physics and Astronomy, Seoul National University, Republic of Korea
*Corresponding author: hgpark@snu.ac.kr

***Abstract*—Photonic topological insulators that exploit topological defects of disclinations provide a robust solution for light manipulation to form compact optical vortices and on-chip integration with reduced scattering loss and energy consumption. In this work, we demonstrate wavelength-scale, low-threshold, vortex and anti-vortex nanolasers in an optical cavity formed by a topological disclination. Various photonic disclination cavities are designed and analyzed using the similarities between tight-binding models and optical simulations. Unique resonant modes are strongly confined in these cavities, which exhibit wavelength-scale mode volumes and retain topological charges in the disclination geometries. In the experiment, the optical vortices of the lasing modes are clearly identified by measuring polarization-resolved images, Stokes parameters and self-interference patterns. Specifically, we measure topological charges of 1 and 2 in C_5 and C_6 disclination cavities, respectively. This work paves the way for the application of advanced nanophotonic devices in laser technology and high-precision optical communications.**

***Keywords*—Nanolaser, disclination, topological charge, optical vortex**

I. Introduction

Optical vortices [1, 2], which manifest as singularities in either the phase or polarization of light, are categorized as phase vortices and polarization vortices, respectively. Phase vortex beams, characterized by their helical wavefronts and orbital angular momentum (OAM), have found widespread application in fields like optical trapping, tweezers, spanners, and high-resolution microscopy. Their ability makes them valuable in quantum information technologies, where precise OAM control supports innovative quantum computing strategies. Recent developments have realized vortex microlasers through novel microstructures, including microring resonators and spiral nanostructures.

Polarization vortex beams, defined by spatially varying polarization states, are employed to manipulate atomic spin and light polarization, aiding in the development of hybrid quantum memories that store both polarization and OAM information. These beams also contribute to secure and high-capacity communication systems through quantum encryption. Meanwhile, topological photonics offers a robust platform for guiding and confining light, with topological photonic insulators enabling disorder-resistant waveguides and lasers. By exploiting topological defects, researchers can generate novel optical vortex states and engineer light-matter interactions that lead to compact, efficient photonic devices.

Developing compact vortex lasers involves several fundamental challenges, including achieving strong optical confinement within wavelength-scale cavities, minimizing scattering losses, and lowering the lasing threshold. Conventional approaches for generating optical vortices, such as spiral phase plates and metasurfaces, are inherently bulky and unsuitable for chip-scale integration. As device sizes are further reduced, these issues become more critical, threatening both performance and reliability. Ensuring that vortex modes remain robust under varying environmental and operational conditions—and making them compatible with existing photonic platforms—is essential for real-world implementation.

Although considerable progress has been made in the design and nanofabrication of photonic devices, a major bottleneck in realizing highly compact and efficient vortex lasers lies in the lack of mechanisms that allow for strong light confinement without degrading the vortex nature of the modes. Current designs often depend on iterative, trial-and-error approaches that require tuning of cavity geometry and material parameters to achieve desired performance. Moreover, achieving versatile and precise control over vortex properties such as OAM, wavelength, and spatial distribution remains a major challenge. Managing multiple singularities simultaneously and tuning them flexibly calls for advanced material platforms and design strategies beyond what conventional photonic architectures can provide.

II. Results

In response to the above challenges, a promising new strategy based on the concept of photonic disclination cavities has been introduced [3]. Drawing inspiration from topological defects in structured matter, this approach enables the formation of ultra-compact optical cavities capable of generating and confining vortex modes with well-defined topological properties. Specifically, the design mimics atomic disclinations by replacing lattice sites with air holes in a photonic crystal structure, allowing electromagnetic modes to localize in the disclination core. By applying tight-binding (TB) theory—particularly the 2D Su–Schrieffer–Heeger (SSH) model—researchers can identify interface states of higher-order topological insulators (HOTIs) and map them to optical analogues. A bulk lattice with C4 symmetry can be transformed into a C_5 disclination cavity, featuring tunable intra-cell, inter-cell, and next-nearest-neighbor couplings. The TB model solutions reveal spatially confined resonant modes whose topological characteristics inform the design of the actual photonic cavity. Comparing the tight-binding charge distributions with the electromagnetic field profiles in full-wave optical simulations helps optimize these cavities for strong confinement and desired vortex characteristics.

Experimentally, nanolasers based on C_5-symmetric photonic disclination cavities have been demonstrated, successfully generating vortex and anti-vortex modes with topological charges of ±1 [3]. These lasers operate under room-temperature optical pumping and display hallmark lasing features, such as sharp spectral peaks and super-linear intensity increase beyond the threshold. The threshold pump power was notably low—an order of magnitude smaller than prior vortex laser demonstrations—thanks to the effective confinement and symmetry-engineered mode structure. Polarization-resolved imaging further confirms the unique vortex characteristics of the emitted light. Without a polarizer, the far-field patterns appear doughnut-shaped, while inserting a polarizer reveals azimuthal and hybrid polarization states, depending on whether the cavity structure is expanded or shrunken.

Furthermore, we successfully demonstrated a wavelength-scale photonic disclination nanolaser with a topological charge of 2 [4]. A C_6 disclination structure formed by the Volterra's process supports a variety of bound states with angular momenta of 0, 1, 2, and 3, and the energy levels of these in-gap states can be tuned by adjusting the position of the atoms in the core region and the coupling strength. In the photonic disclination cavity corresponding to this TB model, a vortex mode with a topological charge of 2 was excited, and by adjusting the position of the air holes in the core region, only this single mode was located inside the photonic band gap, resulting in a relatively high Q and a small mode volume on the wavelength scale. The designed cavity was experimentally fabricated, and clear lasing action was measured. In particular, the polarization-resolved mode images showed excellent agreement between calculation and measurement: when the polarization direction rotates twice, the mode image rotates once, indicating a winding number of 2.

III. Conclusion

The disclination-based design framework offers a robust path forward for overcoming longstanding obstacles in vortex nanolaser development. It enables the realization of stable, low-threshold, and highly compact OAM light sources that are suitable for integration into photonic chips. Ultimately, this advancement opens the door to scalable on-chip implementations of vortex-based devices, potentially transforming high-bandwidth optical communications through enhanced data transmission rates and improved compatibility with modern photonic infrastructure.

Acknowledgments

This work was supported by the Samsung Science and Technology Foundation (project no. SSTF-BA2401-02).

References

[1] Andrew Forbes, "On-chip lasers with twisted light," Nature Photonics 18, 209–210 (2024).

[2] Min-Soo Hwang, Yuri Kivshar, and Hong-Gyu Park, "Vortex lasing from photonic disclinations," Optics & Photonics News (2024); https://www.optica-opn.org/home/articles/volume_35/december_2024/extras/vortex_lasing_from_photonic_disclinations/

[3] Min-Soo Hwang, Ha-Reem Kim, Jungkil Kim, Bohm-Jung Yang, Yuri Kivshar, and Hong-Gyu Park, "Vortex nanolaser based on a photonic disclination cavity," Nature Photonics 18, 286–293 (2024).

[4] Chiwon Shin, Ha-Reem Kim, Donghwee Kim, and Hong-Gyu Park, "Photonic disclination nanolaser with a high topological charge of 2," ACS Photonics 12, 2530–2537 (2025).

Optical Response of Active Plasmonic Nanoshells with Retardation and Gain Saturation Effects

Luis Cerdán[1,*]

[1]Instituto de Química Física "Blas Cabrera", Consejo Superior de Investigaciones Científicas, Spain
*Corresponding author: l.cerdan@csic.es

***Abstract*—In this communication, we report a semianalytical model to analyze plasmonic nanoshells with gain including retardation (radiative and dynamic depolarization corrections), that is valid for any strength of the pump and probe fields. We analyze the retardation effects on both in its laser performance and its nonlinear optical response.**

***Keywords*— plasmonics, spasers, nanolasers, Mie resonances, simulation.**

I. Introduction

The incorporation of optical gain into metallic nanostructures not only mitigates their inherent nonradiative losses, but also enables the development of active nanophotonic devices with enhanced optical responses, suitable for advanced sensing and nanoscale light-emission applications [1]. However, a rigorous theoretical description of these systems remains challenging. Their complexity often forces researchers to adopt simplified gain models –whose range of validity is not always clear– or to rely on fully numerical approaches, which may obscure the underlying physical mechanisms. Most semianalytical treatments of the laser and optical response of active nanoparticles or core-shell structures rely on the quasistatic (QS) approximation [2,3], implicitly neglecting retardation effects such as radiative damping and dynamic depolarization. Yet spasers (plasmonic nanolasers) are inherently radiative systems, and this approximation can therefore constitute an excessive oversimplification.

To address this issue from first principles, we have developed an intuitive yet accurate semianalytical model that replicates the dipolar Mie response, incorporating both radiative and depolarization corrections, as well as the inherently nonlinear behavior of the gain medium. This framework allows us to analyze the optical and lasing characteristics of small-to-medium active metallic nanoshells under arbitrary pump and probe strengths, and to quantitatively assess the limits of validity of the quasistatic approximation.

II. Methods

The system under study consists of a spherical nanoshell with a radius a and inner-to-outter radii ratio ρ embedded in a dielectric medium (Fig. 1a). The nanoshell has a plasmonic nature arising from the presence of a metallic shell and an active character resulting from a dielectric core doped with a gain medium. We consider the nanoshell to be incoherently excited by a pump field with rate $\mathcal{P}$ and analyze its optical responses with a probe field of amplitude E_0 and frequency ω. To study the response of the active nanoshell, we resort to a conventional time-domain approach to capture the nonlinear nature of the gain and then look for the steady-state (SS) solutions. There are two contributions to the total polarization of the active nanoshell: one from the polarization of the free electrons and another from the gain medium. The dynamics of the former is described by a modified Drude model with plasma frequency ω_{m} and non-radiative damping $2\Gamma_{\mathrm{m}}$. This model incorporates second and third derivatives to account for dynamic depolarization and radiative damping corrections [4], respectively, which allow us to obtain an exact dipolar Mie-like response. To model the gain medium, we assume a conventional 4-level system (Fig. 1a), whose polarizability is described with a forced Lorentz oscillator with frequency ω_{g} and linewidth $2\Gamma_{\mathrm{g}}$ [2]. By virtue of the small size of the nanoshell, the fields and polarizations inside its different regions are analytical [3]. Under these conditions, and assuming a continuous wave excitation, the time harmonic dependency can be removed, and a SS solution can be found. The resulting system of coupled equations, that correlates the metallic and gain polarizations with the population inversion (gain) and the parameters accounting for radiative damping and depolarization effects, can be readily solved by converting it into a multidimensional root-finding problem similar to the one reported in [2].

III. Results and Discussion

The optical response of the active nanoshell under probe excitation is fully characterized by its polarizability, α, which in the far field is directly reflected in the extinction cross section, σ_{ext}. Figure 1b shows σ_{ext} for an active silver nanoshell pumped at a rate $\mathcal{P}$ just below threshold, $\mathcal{P}_{\mathrm{th}}$, as computed either with the QS model adapted from Ref. [3] (left) or with our Mie-based approach (right), for different probe field amplitudes E_0. In the small-signal regime, where the probe is too weak to significantly deplete the excited-state population, both models predict progressive narrowing of the plasmon linewidth and up to a 40-fold enhancement of the peak extinction relative to the passive case (gray dashed curves). These effects, consistent with previous observations [2,3], arise from the reduction of metallic nonradiative losses produced by the gain medium. However, the QS model predicts a more energetic resonance and a narrower, higher peak than the Mie

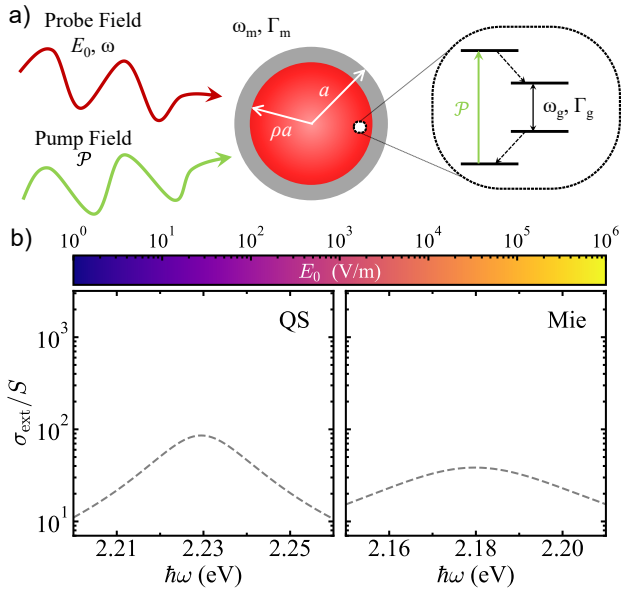

Fig. 1. (a) Schematics of the system under consideration, consisting of a silver nanoshell of $a = 20$ nm and $\rho = 0.8$ with a dielectric core doped with a gain medium described by a 4-level energy diagram. (b) Extinction cross-section normalized by the nanoparticle geometric cross-sectional area $S = 4\pi a^2$ of an active (solid coloured curves) and a passive (dashed gray curves) nanoshell as a function of the probe field frequency, ω, for different values of the probe field amplitude, E_0 (see the colour bar), for a quasi-static model (left panel) and that computed with our methodology (right panel). In both cases, the gain frequency ω_g is tuned to the passive nanoshell resonance and the pump rate is $\mathcal{P} = 0.95\mathcal{P}_{\rm th}$, with $\mathcal{P}_{\rm th}$ the threshold pump rate.

model. This discrepancy is expected: dynamic depolarization shifts the plasmon resonance to lower frequencies, while radiative corrections increase the total damping, both of which reduce the achievable response. Importantly, even for such a small nanoshell, retardation effects already produce substantial deviations from the QS prediction. This highlights important limitations of the QS approximation and highlights the need to incorporate these corrections, especially when modeling lasing behavior.

The response of active nanoshells changes drastically when the probe-field amplitude exceeds the small-signal regime. As E_0 increases, the polarization of both the free electrons and the gain medium grows accordingly. This enhanced polarization accelerates the depletion of the upper laser level, reducing the population inversion and therefore diminishing the effective gain. As shown in Fig. 1b, both models predict that the plasmonic resonance broadens and the overall magnitude of $\sigma_{\rm ext}$ decreases as the probe-field amplitude becomes larger. In fact, for $E_0 \geq 10^5$ V/m, the extinction cross section of the active nanoshell becomes indistinguishable from that of the passive system, irrespective of the pump level. This behavior is fully consistent with gain saturation, originating from the intrinsic nonlinear response of the gain medium and the depletion of the population inversion induced by the probe field [2].

IV. Conclusion

In summary, we have developed an intuitive yet accurate semianalytical model that combines the semiclassical laser equations for a four-level gain medium with the fully retarded electromagnetic response of a nanoshell. We have verified that, under weak probe excitation, the optical response of an active plasmonic nanoparticle is strongly enhanced as the pump rate approaches threshold. However, the QS approximation systematically predicts narrower resonances and larger enhancements than our Mie-based model, highlighting the importance of including retardation effects. Furthermore, both approaches reveal that increasing the probe-field strength leads to saturation behavior that progressively suppresses the influence of the gain, rendering the nanoshell effectively passive regardless of the pump level. These results highlight the need to account for both retardation and saturation effects when modeling loss-compensated or gain-assisted plasmonic systems, from both theoretical and practical perspectives.

Acknowledgments

This work was supported by a Ramón y Cajal Research Fellowship, Grant RYC2022-038362-I, funded by MICIU/AEI/10.13039/501100011033 and by the ESF+.

References

[1] S. I. Azzam, A. V. Kildishev, R. -M. Ma, C.-Z Ning, R. Oulton, V. M. Shalaev, M. I. Stockman, J.-L. Xu, X. Zhang, "Ten years of spasers and plasmonic nanolasers" *Light Sci. Appl.* 9, 90 2020.

[2] L. Cerdán and A. Manjavacas, "Analysis of the Limits of the Optical Response of a Metallic Nanoparticle with Gain," *J. Phys. Chem. C* 127, 5, 2371–2378, 2023.

[3] A. Aradian, K. Caicedo, A. Cathey, M. Mora, N. Recalde, M. Infusino, and A. Veltri, "Emission dynamics and spectrum of a nanoshell-based plasmonic nanolaser spaser," *Nanophotonics*,13, 26, 4817–4837, 2024.

[4] M. Januar, B. Liu, J.-C. Cheng, K. Hatanaka, H. Misawa, H.-H. Hsiao, and K.-C. Liu, "Role of Depolarization Factors in the Evolution of a Dipolar Plasmonic Spectral Line in the Far- and Near-Field Regimes," *J. Phys. Chem. C*, 124, 5, 3250–3259, 2020.

Controlling light–matter interactions with engineered nanolaser patterns

D. Vass[1], M. Waldhauser[1], V. Szünstein[1], A. Szenes[1], B. Bánhelyi[2], M. Csete[1]

[1]Department of Optics and Quantum Electronics, University of Szeged, Hungary
[2]Department of Computational Optimization, University of Szeged, Hungary
*Corresponding author: mcsete@physx.u-szeged.hu

***Abstract*— Control of light-matter interaction is demonstrated in 3D arrays of nanoresonators (i) filled with, (ii) randomly arranged and embedded into, (iii) composing multilayer complex metamaterials and coated by appropriate gain medium. Spectral engineering of passive nanoresonator configurations and optimization of dye-concentration – pump-E-field parameters enables to tailor complete lasing characteristics.**

***Keywords*— nanoresonator arrays, metamaterials, lasing, spasing, optimization.**

I. Introduction

Active plasmonic metamaterials are intriguing quantum optical systems with inherently large degrees of freedom in amplification, lasing and spasing [1]. Exploration of the key nanophotonical phenomena enables to control near-field modes and far-field characteristics [2], while exploitation of critical parameter regions opens novel avenues in light-matter interactions [3]. In our previous steady-state and time-domain studies distinctly different operation regions were demonstrated for various plasmonic active nanoresonators [4] and the dynamics of energy deposition and near-field enhancement (NFE) in random plasmonic nanoantenna arrays was controlled via distribution and pump-parameters [5].

II. Methods

The method of plasmonic spectral engineering was generalized, and the active medium and illumination parameters were added to the configuration optimization realized with GLOBAL algorithm implemented into COMSOL Multiphysics software. First the passive nanoresonators were tuned to enhance lasing, thereafter the coupled Maxwell and rate equations were solved numerically in pump-and-probe scheme, and the active metamaterial was evaluated via retrieval method. In steady-state computation the active metamaterial responses were mapped above the dye-concentration and E_{pump}-field strength parameter plane, in addition the time-domain response was also inspected to uncover the nanophotonical phenomena. Parameter regions resulting in (i and ii) large and uniform NFE, (ii) as well as uniform phase distribution and epsilon-near-zero (ENZ) characteristic, (iii) enhanced and direction specifically polarized emission, were determined.

III. Results and Discussion

Hybridization of plasmonic resonances on multilayers of spherical nanoresonators results in multiple peaks, a broader (narrower) one is capable of resulting in homogeneous field inside core (dipolar distribution on outer layer), with maximal NFE~50. It is possible to enter into spasing operation region at smaller pump through large concentration region. When a quad-layer is created from periodic nanoresonator patterns, similar NFE with good FOM=NFE/δ_{NFE} is achievable at perpendicular incidence, but tilting enables to reach even larger NFE values. Optimization of quad-layers constructed with sub-wavelength patterns of spherical nanoresonators with gain-metal-dielectric core-shell composition using ENZ operation as objective function allows for achieving NFE~10 uniformly at small tilting.

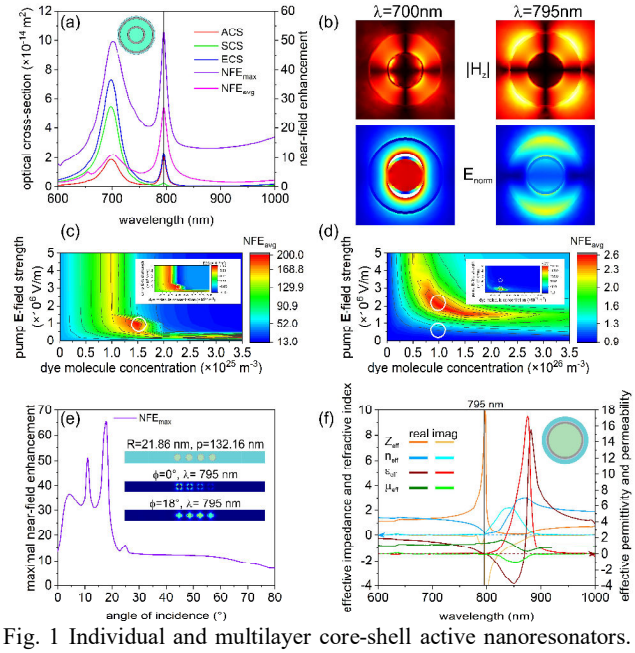

Fig. 1 Individual and multilayer core-shell active nanoresonators. (a, b) Optical cross-sections and NFE of a multishell; (c, d) maps of NFE_{avg} and ECS (FOM) of individual (periodic) multishell; (d, e) NFE and effective properties of active ENZ-like core-shell quad-layers.

Plasmonic nanoantennas of different, e.g triangular, shapes distributed even randomly, enable to enhance the NFE, absorbed power (PL) and deposited energy (E), when the target is illuminated with counter-propagating laser pulses (120 fs, 795 nm). Besides the nanoantennas number density distribution which was pre-optimized in passive targets, dye concentration distribution was also adjusted in active targets, while the average concentration corresponded to the maximum in NFE map. Active targets turned to be better in the standard deviation of the monitored quantities (δNFE, δPL, δE), moreover allowed to reach larger $FOM_x = X/\delta_X$. Also the temporal dynamics was different, namely the minimal standard deviation /it's delay compared to pulses overlap, was smaller compared to the passive target for NFE/E&PL in case of silver triangles.

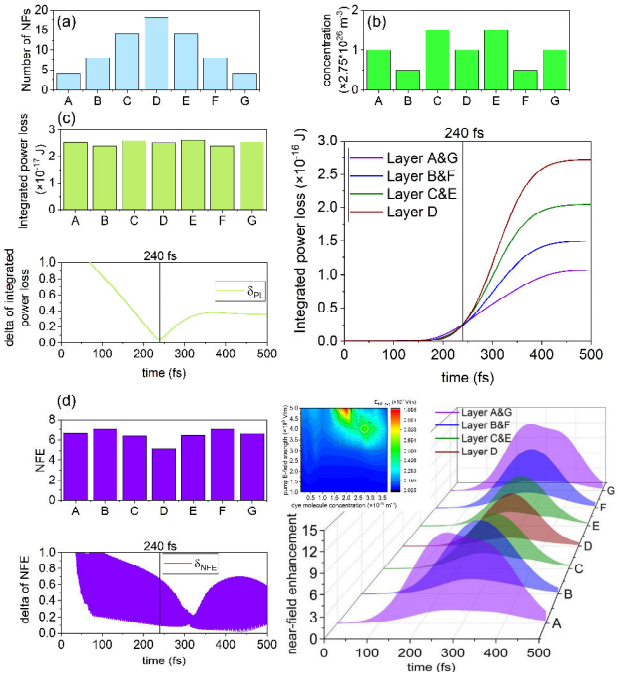

Fig. 2 Silver triangular nanoantenna seeded active targets, 120 fs pulsed illumination. (a, b) Number density and dye concentration distribution; (c, d) Power loss and NFE distribution with the temporal evolution of quantities and their standard deviations in different layers.

Tri-layers of complex patterns constructed with Babinet complementary miniarrays allows for asymmetric transmission (AT) due to bianisotropy. However, the achievable AT is limited by the loss in the layers of convex-concave-convex plasmonic components, therefore an active layer was positioned in close proximity of the multilayer to ensure gain. Appropriate spacing and layer thickness of the active medium, as well as E_{pump} and concentration parameters enable two /one order of magnitude enhancement of AT computed in the mixed bases corresponding the Generalized Faraday Rotation (GFR), in case of the inspected Pattern-I/II. GFR occurs, when nonreciprocal rotation approximates 90° in propagation direction dependent azimuthal orientations, while the forward leaving polarization is entering in backward direction. The ellipticity of emitted light polarization is slightly increased /decreased in forward /backward direction in both inspected multilayers.

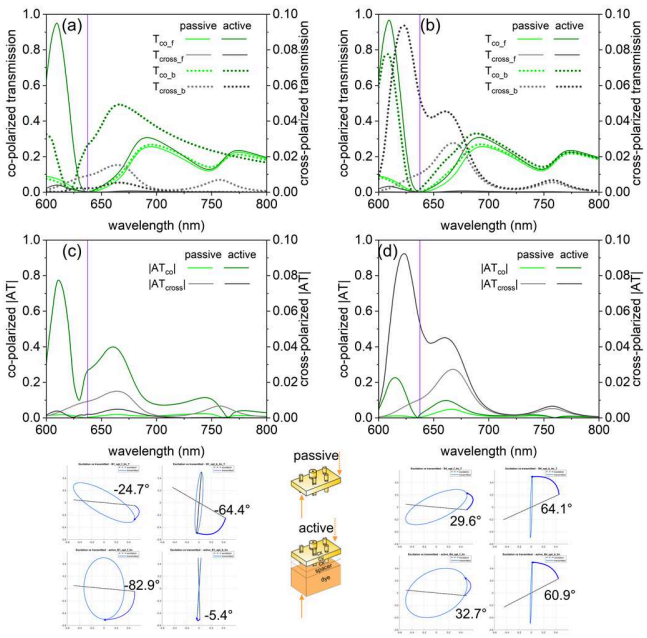

Fig. 3 Tri-layers of Babinet complementary (convex, concave-convex) patterns in GFR configuration with loss compensation and enhanced AT. (a, c) Pattern-I, (b, d) Pattern-II, with transmission and AT in mixed bases as well as entering and leaving polarization ellipses in forward and backward propagation directions.

IV. Conclusion

Optimized active plasmonic metamaterial configurations were demonstrated with potential to achieve resonant gain phenomenon, ENZ medium, uniform and enhanced energy deposition and improved NFE, as well as more efficient unidirectional enhanced optical signal transfer.

Acknowledgments

This work was supported by the National Research, Development and Innovation Office (NKFIH) of Hungary, projects: "Nanoplasmonic Laser Inertial Fusion Research Laboratory" (NKFIH-2022-2.1.1-NL-2022-00002) and "National Laboratory for Cooperative Technologies" (NKFIH-2022-2.1.1-NL-2022-00012) in the framework of the Hungarian National Laboratory program, as well as the Hu-rizont METAOPTQIP.

References

[1] O. Hess, J. B. Pendry, S. A. Maier, R. F. Oulton, J. M. Hamm, and K. L. Tsakmakidis, "Active nanoplasmonic metamaterials," Nature Materials vol. 11, pp. 573-84, 2012.

[2] V. Caligiuri, L. Pezzi, A. Veltri, and A. De Luca, "Resonant Gain Singularities in 1D and 3D Metal/Dielectric Multilayered Nanostructures," ACS Nano, vol. 11, pp. 1012-1025, 2017.

[3] A. Aradian, K. Caicedo, A. Cathey, M. Mora, N. Recalde, M. Infusino, and A. Veltri, "Emission dynamics and spectrum of a nanoshell-based plasmonic nanolaser spaser," Nanophotonics, Vol. 13, pp. 4817-4837, 2024.

[4] D. Vass, A. Szenes, P. Z. Nagy, B. Bánhelyi, and M. Csete, "Lasing and spasing with active individual core-shell plasmonic nanoresonators," Optics and Laser Technology, vol. 193, p. 114251, 2026.

[5] D. Vass, E. Tóth, A. Szenes, B. Bánhelyi, I. Papp, T. S. Bíró, L. P. Csernai, N. Kroó, and M. Csete, "Plasmonic nanoprism distributions to promote enhanced and uniform energy deposition in passive and active targets," Nanomaterials, vol. 15(23), p. 1801, 2025.

Design for a qBIC laser based on a TiO_2 metasurface

Justin Schulz[1,*], Jack Dobie[1,2], Yongliang Zhang[1], A. Louise Bradley[1,2,*]

[1]School of Physics, Trinity College Dublin, Dublin 2, Ireland
[2]IPIC, Tyndall, University College Cork, Cork, Ireland
*Corresponding author: juschulz@tcd.ie and bradlel@tcd.ie

***Abstract*—We propose a design for a linear polarizable laser in the visible wavelength range. Consisting of a TiO_2 metasurface with a pronounced quasi-bound state in the continuum (qBIC) and utilising high quantum yield colloidal quantum dots as a gain material.**

***Keywords*— Dielectric metasurface, Quasi-Bound States in Continuum, Laser, TiO_2, Enhanced light-matter interaction.**

I. Introduction

Dielectric metasurfaces, engineered to manipulate light primarily by controlling the phase and amplitude of the scattered light have garnered significant interest in recent years, particularly because they can support quasi-Bound States in the Continuum (qBIC-modes) [1]. This resonance can be either created by breaking the inversion symmetry in the unit cell of the metasurface or by breaking the symmetry with the incoming or outgoing light. The qBIC has really high Q-factors and is therefore a perfect candidate to build 2D-lasing devices. Most qBIC lasers used dyes [2] as the gain material, with pervoskites [3] also being used. Both gain materials lag in photostability and tunability. Therefore, quantum dots with high quantum yields are the material of choice. has been tuned to have the qBIC resonance at 655 nm, corresponding to the emission wavelength of the quantum dots.

II. Design and Fabrication

A tilted ellipse metasurface [4] has been tuned to have the qBIC resonance at 655 nm corresponding to the emission wavelength of the quantum dots. A direct etch process produces the 50 µm×50 µm metasurface. The mode verification is done via a normal transmission measurement. Afterwards, the colloidal quantum dots are spin-coated onto the metasurface and photoluminescence and the interaction between the emitters and the cavity are investigated.

A high quality 120 nm thick TiO_2 layer is deposited on a SiO_2 using low-pressure chemical vapour deposition (LPCVD). Ellipsometry measurements have confirmed insignificant optical losses in the visible wavelength range between 400 and 800 nm. With the height fixed due to fabrication processes, this leaves three design parameters: the periodicity a and the length of the long (r_l) and short axes (r_s) of the ellipses. The dependencies of the transmission on these can be found in the figure 1 (a-c). Further, the dependence on the asymmetry parameter, the tilting angle θ, and the scaling behaviour s and the polarisation dependency of the angle φ are also shown in figure 1 (d-f).

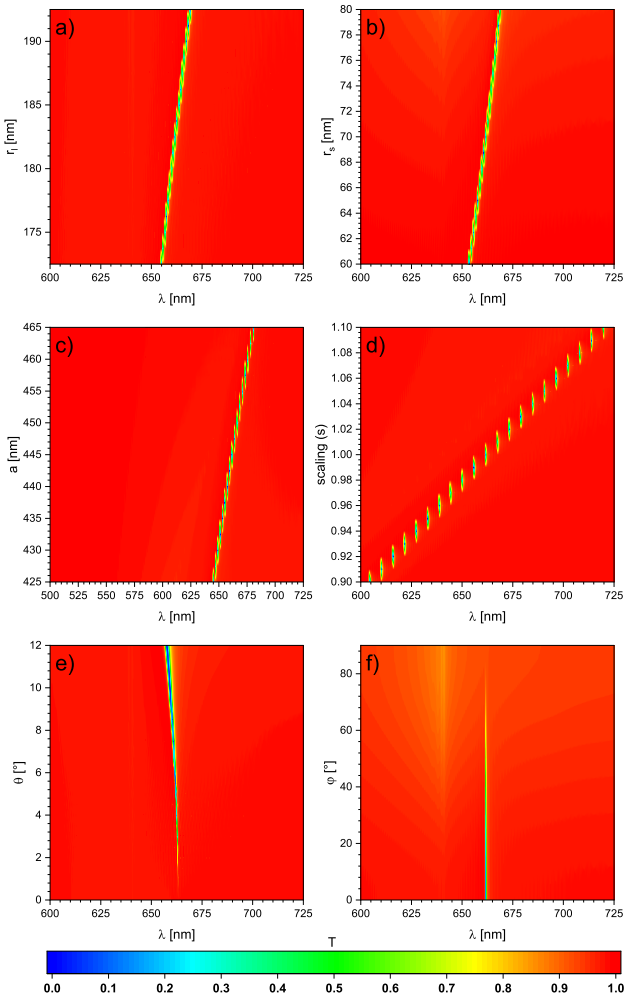

Fig. 1. Simulated transmission spectra for different design parameters. The optimal parameters that are kept constant are a height of $h = 120\,\text{nm}$, a periodicity $a = 445\,\text{nm}$, a short radius of $r_s = 70\,\text{nm}$, a long radius of $r_l = 182.5\,\text{nm}$, a tilting angle of $\theta = 6°$ and a polarization in x-direction with $\varphi = 0°$.

One can generally observe the trend that if one size parameter increase the qBIC mode red shifts. Further, it is noticeable that

there is no other mode for this polarisation spectrally close by. As expected for a qBIC mode, it blue shifts with increasing asymmetry parameter, and the Q factor decreases as it couples more with the continuum.

In addition to the Q factor, the electric field enhancement and its accesibilty, is important for the Purcell factor, which describes the interaction between the gain material and the mode. The electric field enhancement of the qBIC mode is shown in figure 2. The left-hand side shows the enhancement in the x-y plane at z=10 nm, and the right-hand side shows the slice through the centre of the ellipse in the y-z plane. One

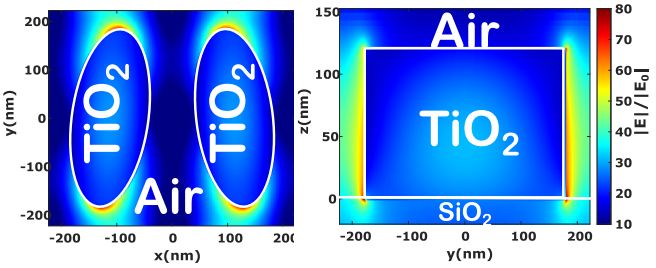

Fig. 2. Electric field enhancement $|E|/|E_0|$ of the qBIC mode on the left in the x-y plane at $z = 10$ nm. On the right-hand side, a cut through the ellipse in the y-z plane is shown.

can see in the field maps an enhancement factor of 80 and that the field is well localised outside the TiO_2 structures. This, in combination with the high Q-factor, makes the tilted ellipse design an ideal candidate for a qBIC lasing device.

To reduce the steps of the top-down fabrication process and achieve higher fidelity structures, no etching hard mask is used, instead the negative resist is used directly as a mask. This eliminates one evaporation step and one lift-off step, leaving the following fabrication procedure:

- Negative resist lithography, utilising a high precision He-ion microscope.
- Reactive ion etching (RIE) of the TiO_2 using the negative resist as a mask.
- Wet chemical removal of the remaining negative resist.

A SEM image of the produced structures can be seen in the inset of figure 4. This shows the high quality of the produced structures achiving high Q-factors up to 700.

III. Experimental evidence

After fabricating the TiO_2 metasurface, normal transmission measurements are performed to characterise the qBIC mode. The polarisation dependent transmission measurements are shown in figure 3 as well as measurements for different tilting angles of the ellipses. The experimental results show the same behaviour as predicted by the simulations. On the one hand, the high extinction of the qBIC mode with the change of polarisation, and on the other hand, the broadening of the qBIC mode with increasing asymmetry parameter. Further, the blue shift with increasing asymmetry parameter can also be observed.

After the spin coating of colloidal quantum dots on the sample,

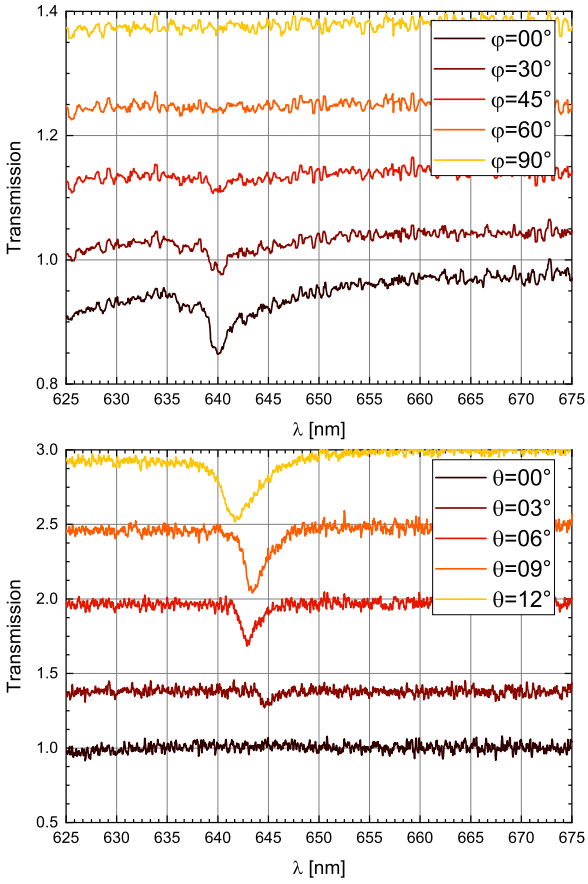

Fig. 3. Normal transmission measurements in dependence on the polarisation of the light displayed in the upper graph. In the bottom graph, the transmission for different tilting angles of the ellipses is shown.

the photoluminescence intensity is measured. This shows a coupling between the emitters and the cavity and is also highly polarised, as can be seen in the figure 4. One can also see that the photoluminescence enhancement aligns perfectly with the qBIC mode. Further lifetime measurements indicate a reduction in emitter lifetime by one nanosecond, indicating the possibility of achieving qBIC lasing with higher pump powers.

IV. Conclusion

We designed an all-dielectric metasurface of TiO_2 supporting a quasi bound sate in the continuum. It is tuned to the QD emission wavelength and the mode properties were investigated using FDTD simulations. With a novel reactive ion etching process using the photoresist directly as a mask, a high Q-factor metasurface is fabricated. Normal transmission measurements confirm the highly polarised qBIC mode and its dependence on the asymmetry parameter. Further, the coupling between colloidal quantum dots and the qBIC mode is observed, paving the way for a low-threshold qBIC lasing device.

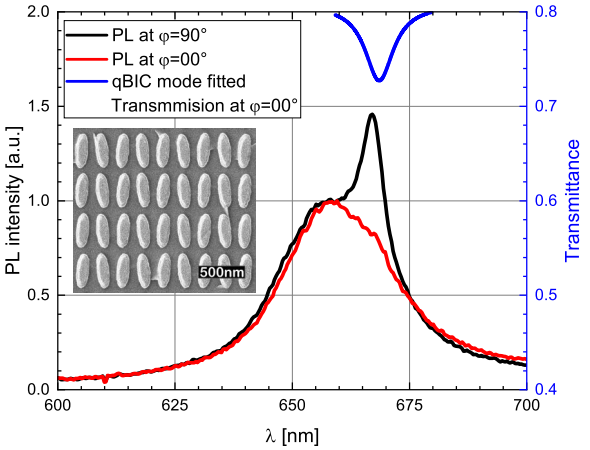

Fig. 4. The polarisation-dependent photoluminescence emitted from the metasurface pumped with a 532 nm continuous wave laser. For reference, the corresponding transmission measurement of the qBIC mode is shown on the right-hand side axis. In the inset, an SEM image of a TiO_2 metasurface is shown, the scale bar corresponds to 500 nm.

ACKNOWLEDGMENTS

This project is funded through: Taighde Éireann/Research Ireland Frontiers for the Future Award - SFI-21/FFP-P/10187, 12/RC/2278_2, and 12/RC/2276_P2. The authors thank Riley Gatensby, CRANN and the AML for fabrication support. We also thank Brian Corbett and Owen Moynihan at the Tyndall National Institute in Cork for providing the TiO_2.

REFERENCES

[1] K. Watanabe, T. Nagao, and M. Iwanaga, "Low-Contrast BIC Metasurfaces with Quality Factors Exceeding 100,000," *Nano Lett.*, vol. 25, no. 7, pp. 2777–2784, Feb. 2025.

[2] X. Zhang, Y. Liu, J. Han, Y. Kivshar, and Q. Song, "Chiral emission from resonant metasurfaces," *Science*, vol. 377, no. 6611, pp. 1215–1218, Sep. 2022.

[3] C.-C. Liu, H.-H. Hsiao, and Y.-C. Chang, "Nonlinear two-photon pumped vortex lasing based on quasi-bound states in the continuum from perovskite metasurface," *Science Advances*, vol. 9, no. 22, p. eadf6649, May 2023.

[4] H. Hajian et al., "Quasi-bound states in the continuum for electromagnetic induced transparency and strong excitonic coupling," *Opt. Express*, OE, vol. 32, no. 11, pp. 19163–19174, May 2024, doi: 10.1364/OE.525535.

Robust Perovskite Quantum Dots for Microcavity Photonics

Yu-Hsun Chou [1,2*]

[1] Department of Photonics, National Cheng Kung University, Tainan 701, Taiwan
[2] Program on Key Materials, Academy of Innovative Semiconductor and Sustainable Manufacturing, National Cheng Kung University, Tainan 701, Taiwan
*Corresponding author: tnc@gs.ncku.edu.tw

***Abstract*— Quantum confined perovskite quantum dots integrated with optical microcavities exhibit remarkable environmental stability and versatile emission behavior at room temperature. We report sustained luminescence in water, temperature dependent excitonic responses, cavity enhanced emission, and strong light matter interactions, establishing a robust platform for nanoscale photonics and stable quantum light emitters.**

***Keywords*— Perovskite quantum dots; optical microcavities; quantum confinement; cavity enhanced emission; light matter interaction.**

I. Introduction

Perovskite quantum dots are promising light-emitting materials because of their high photoluminescence efficiency, strong excitonic effects, and spectral tunability[1-5]. Their practical use in microcavity photonics, however, remains limited by poor environmental stability, particularly under moisture exposure. Spatial confinement in a porous host offers an attractive route to simultaneously improve stability and preserve nanoscale optical properties. In this work, we study quantum-confined perovskite quantum dots embedded in a Metal Organic Framework and integrated with optical microcavities. We highlight their sustained luminescence in water, temperature-dependent excitonic responses, cavity-enhanced emission, and the broader implications of this platform for stable nanophotonic emitters and light-matter interaction studies.

II. Methods

Quantum-confined perovskite quantum dots were prepared within defective UiO-66 hosts through a two-step conversion route[5]. Lead species were first immobilized in the porous framework, and subsequent treatment with a cesium bromide precursor generated the emissive perovskite phase inside the host matrix[5]. The resulting composites were examined by structural and optical characterization to verify confined formation and environmental durability. For photonic studies, the composite was incorporated as the active medium in planar optical microcavities formed by two distributed Bragg reflectors. Room-temperature and temperature-dependent photoluminescence measurements were then used to evaluate emission stability, excitonic response, and cavity-modified optical behavior.

III. Results and Discussion

The porous host provides nanoscale confinement while preserving the structural integrity of the composite. Nitrogen sorption and diffraction results support successful incorporation of perovskite quantum dots into pores on the order of one to two nanometers, which is consistent with a confined emitter configuration rather than a conventional bulk-like phase. This confined architecture also leads to remarkable environmental robustness: the composite maintains nearly unchanged photoluminescence over extended ambient storage and still preserves substantial emission after prolonged immersion in water[5]. The median emission wavelength remains around 530 nm, which was used as a practical reference for subsequent cavity design. Temperature-dependent photoluminescence further reveals pronounced excitonic behavior and a confinement-modified thermal response, indicating that the optical properties of the embedded dots remain well defined over a broad temperature range[5]. When the material is integrated into a distributed Bragg reflector microcavity, the emission evolves from a broad spontaneous band into a much narrower cavity-dominated feature near 532 nm as the pump density increases. The linewidth contracts from about 16 nm to 0.5 nm, accompanied by a clear nonlinear rise in output intensity with a threshold near 2 kW/cm^2, as shown in Figure 1. Together, these results show that the confined perovskite quantum dots function as a stable active medium for cavity-enhanced emission and provide a versatile platform for discussing broader microcavity light-matter phenomena in the invited presentation.

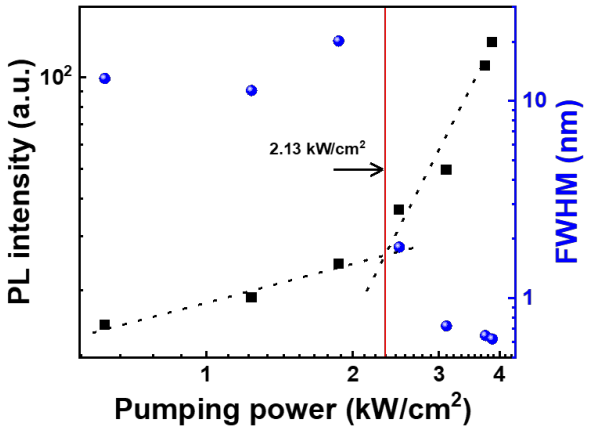

Figure 1. Light-in/light-out (L-L) characteristics of the $CsPbBr^3$@UiO-66 device. The left axis (black) depicts the PL intensity as a function of increasing pump power, and the right axis (blue) shows the corresponding FWHM of the emission peak. The nonlinear trend in the light-in/light-out curve confirms the achievement of lasing at a threshold power density of 2 kW/cm².

IV. Conclusion

In summary, this work demonstrates that quantum-confined perovskite quantum dots can combine environmental durability with rich optical functionality in resonant microcavities. Their sustained emission in water, excitonic optical response, and cavity-enhanced spectral evolution highlight their promise as stable building blocks for compact light sources, nanophotonic devices, and future studies of light-matter interaction in confined photonic systems.

Acknowledgments

The authors gratefully acknowledge financial support from the National Science and Technology Council, Taiwan, under Grant No. NSTC 114-2923-M-006-002-MY2. The authors also sincerely thank Prof. Chung-Wei Kung of the Department of Chemical Engineering, National Cheng Kung University, for providing the synthesized materials used in this work.

References

[1] S. A. Veldhuis, et al., "Perovskite materials for light-emitting diodes and lasers," Adv. Mater., vol. 28, no. 32, pp. 6804–6834, 2016.

[2] Y. Wei, Z. Cheng, and J. Lin, "An overview on enhancing the stability of lead halide perovskite quantum dots and their applications in phosphor-converted LEDs," Chem. Soc. Rev., vol. 48, no. 1, pp. 310–350, 2019.

[3] M. Baranowski and P. Plochocka, "Excitons in metal-halide perovskites," Adv. Energy Mater., vol. 10, no. 26, p. 1903659, 2020.

[4] M.-C. Yen, et al., "Tamm-plasmon exciton-polaritons in single-monolayered $CsPbBr_3$ quantum dots at room temperature," Adv. Opt. Mater., vol. 11, no. 4, p. 2202326, 2023.

[5] C.-C. Lin, S.-C. Wan, C.-H. Shen, Z.-L. Liao, Y. Liu, Z. Y. Wu, S.-C. Wu, C.-K. Lin, C.-W. Kung, H.-C. Hsu, and Y.-H. Chou, "Achieving long-term water stability and strong exciton–photon coupling in $CsPbBr_3$ quantum dots via MOF encapsulation," Nanophotonics, 2025. DOI: 10.1515/nanoph-2025-0059.

SPECIAL SESSION 12

Plasmonics and Nanophotonics: Fundamentals and Applications

10 contributions · pp. 973–987

Twist photonics in 2D materials

Yunyun Dai[1]
[1]*State Key Laboratory of Chips and Systems for Advanced Light Field Display, Advanced Research Institute of Multidisciplinary Sciences, Beijing Institute of Technology, Beijing 100081, China*
*Corresponding author: yunyundai@bit.edu.cn

***Abstract*—Twist photonics exploits interlayer rotation in two-dimensional stacks to create moiré superlattices with programmable symmetry and electronic structure. By engineering the structural chirality, linear and nonlinear circular dichroism is modulated, offering a versatile platform for tunable light–matter interactions and chiral optoelectronic devices.**

***Keywords*— nonlinear optics, twist photonics, two-dimensional materials.**

I. Introduction

Twist photonics exploits interlayer rotation in two-dimensional stacks to create moiré superlattices with programmable symmetry and electronic structure. By engineering the structural chirality, linear and nonlinear circular dichroism is modulated, offering a versatile platform for tunable light–matter interactions and chiral optoelectronic devices.

II. Methods

Twist photonics, defined by the interlayer twisting in two-dimensional material stacks, creates a new paradigm for engineering optical phenomena[1]. Precise control of the twist angle creates a moiré superlattice, a long-wavelength periodic potential that reconstructs electronic bands and gives rise to moiré excitons, flat bands, and correlated quantum states, thereby offering unprecedented control over optical absorption and emission. Concurrently, this engineered lattice symmetry breaking induces and dramatically enhances intrinsic chiral optical activity, such as strong circular dichroism (Fig. 1).

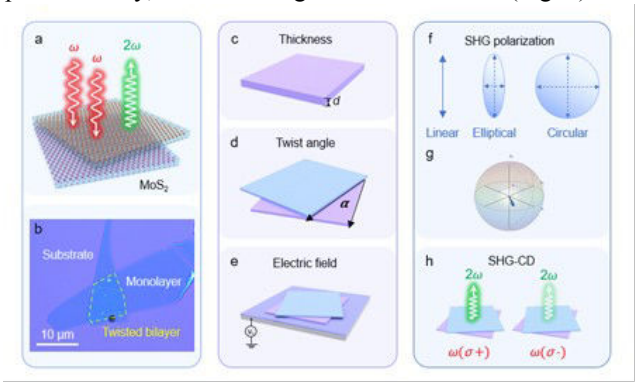

Fig. 1 Chiral optical nonlinearity in van der Waals materials.

III. Results and Discussion

By engineering the twist angle, layer thickness and the incident polarization, the ellipticity and the chirality of the nonlinear optical response can be precisely modulated. The synergistic interplay between the tailored moiré landscape and the engineered chirality defines a new paradigm for controlling light-matter interactions.

IV. Conclusion

This field of twist photonics provides a powerful platform for programming novel photonic functionalities, paving the way for advanced applications including twist-tunable polaritonic devices, quantum light emitters, and chiral optoelectronic sensors.

Acknowledgments

The authors thank funding from the National Key Research and Development Program of China.

References

[1] Luojun Du, Maciej R. Molas, Zhiheng Huang, Guangyu Zhang, Feng Wang, Zhipei Sun, Moiré photonics and optoelectronics, Science 379, 1313 (2023)

Universal detection of layer-breathing modes in two-dimensional materials enabled by plasmonic nanocavity

Miao-Ling Lin[1,*], Heng Wu[1], Ping-Heng Tan[1,*]

[1] State Key Laboratory of Semiconductor Physics and Chip Technologies, Institute of Semiconductors, Chinese Academy of Sciences, Beijing 100083, China
*Corresponding authors: linmiaoling@semi.ac.cn, phtan@semi.ac.cn

***Abstract*—We demonstrate a universal plasmon-enhanced Raman spectroscopy strategy using gold/silver nanocavities to detect layer-breathing modes in multilayer graphene, hBN, and their heterostructures. By developing an electric-field-modulated interlayer bond polarizability model, we quantitatively explain the observed intensity profiles with synergistic roles of localized plasmonic field enhancement and interfacial polarizability modulation.**

***Keywords*— plasmonic cavities, layer-breathing modes, two-dimensional materials, electric-field-modulated interlayer bond polarizability.**

I. Introduction

The metallic nanocavities enables localized surface plasmon resonance to confine the optical field into sub-wavelength volumes, providing unprecedented opportunities for plasmon-enhanced Raman spectroscopy (PERS) to uncover light-matter interactions at the nanoscale. A promising application of PERS lies in the investigation of low-frequency interlayer modes in two-dimensional materials, where the inherent Raman inactivity or inherently weak electron-phonon coupling (EPC) of some interlayer modes prevents their observation via conventional Raman spectroscopy.

II. Methods

We fabricated Au or Ag nanocavities by thermally evaporated an 8 nm-thick Au or Ag films on two-dimensional materials and related heterostructures. The different morphologies and densities of Au or Ag nanocavities were obtained by changing annealing temperature and time.

To understand the observed PERS of layer-breathing modes, we established the electric-field-modulated interlayer bond polarizability model, integrating simulation, optimization algorithms:

$$I_j \propto \frac{n_j+1}{\omega_j}\left|\sum_l (\eta_{l,x}-\eta_{l+1,x})\Delta z_{j,l} E^2_{Loc,l,x}\right|^2,$$

Where $\eta_{l,x}$ is interlayer bond parameter related to the x component of the interlayer bond, $E_{Loc,l,z}$ is the z-component of plasmonic field obtained by finite-difference time-domain method, $\Delta z_{j,l}$ is the layer displacement of the l-th layer in $LB_{N,N-j}$ mode, ω_j is the frequency of $LB_{N,N-j}$ mode and n_j is its corresponding Bose-Einstein factor.

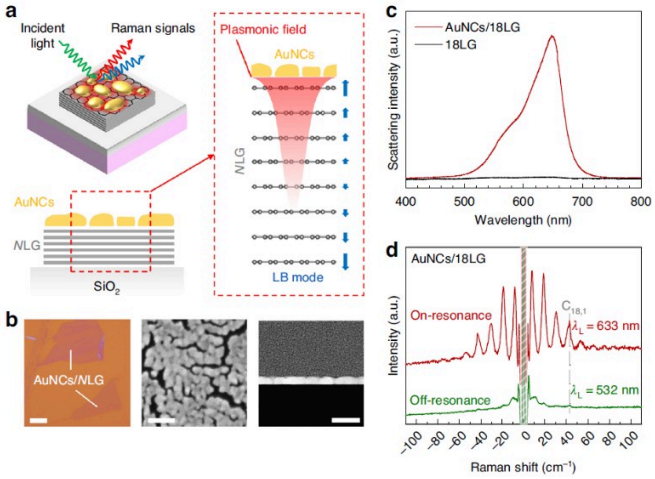

Fig. 1 Enhanced layer-breathing modes by PERS.

III. Results and Discussion

Experimental results show:

- upon resonant excitation of plasmonic cavities, a series of layer-number-dependent Raman features emerged below 130 cm^{-1}, which should be assigned as layer-breathing modes (Fig. 1).
- Strong interfacial coupling between Au/Ag nanocavities and two-dimensional materials, which modulated the interfacial polarizability modulation
- Strong agreement between simulated and measured spectra (Fig. 2)

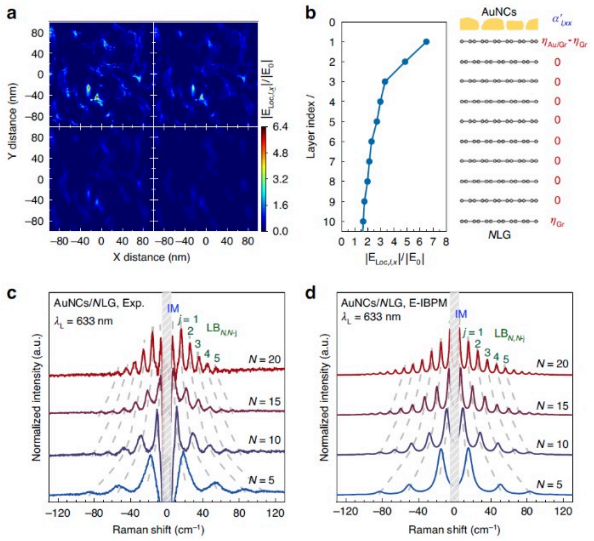

Fig. 2 Electric-field-modulated interlayer bond polarizability model for plasmon-enhanced LB modes in Au(Ag)NCs/NLG.

IV. Conclusion

We have developed a PERS approach using Au or Ag nanocavites to characterize LB modes in multilayer graphene, hBN and related heterostructures. This work opens avenues for precise characterization of interlayer interactions in emerging two-dimensional devices while providing fundamental insights into plasmon-phonon coupling phenomena.

Acknowledgments

This work was supported by the National Key Research and Development Program of China (Grant No. 2023YFA1407000), the Strategic Priority Research Program of Chinese Academy of Sciences (CAS) (Grant No. XDB0460000), National Natural Science Foundation of China (Grants No. 12322401, No. 12127807, and No. 12393832), Beijing Nova Program (Grant No. 20230484301), Youth Innovation Promotion Association, Chinese Academy of Sciences (No. 2023125), Science Foundation of the Chinese Academy of Sciences (Grant No. JCPYJJ-22), CAS Project for Young Scientists in Basic Research (YSBR-026).

References

[1] Jon A. Schuller, Edward S. Barnard, Wenshan Cai, Young Chul Jun, Justin S. White & Mark L. Brongersma, Plasmonics for extreme light concentration and manipulation. Nat. Mater., vol. 9, pp. 193–204, 2010

[2] Xiang Wang, Sheng-Chao Huang, Shu Hu, Sen Yan, Bin Ren, Fundamental understanding and applications of Plasmon-enhanced Raman spectroscopy, Nat. Rev. Phys. vol. 2, pp. 253–271, 2020.

[3] P. H. Tan, W. P. Han,; W. J. Zhao, Z. H. Wu, K.Chang, H.Wang, Y. F. Wang, N. Bonini, N. Marzari, N. Pugno, G. Savini, A. Lombardo, A. C. Ferrari, The shear mode of multilayer graphene. Nat. Mater. vol. 11, pp. 294–300, 2012

[4] Heng Wu, Miao-Ling Lin, Sen Yan, Lin-Shang Chen, Zhong-Jie Wang, Yi-Fei Zhang, Ti-Ying Zhu, Zheng-Yu Su, Jun Wang, Xue-Lu Liu, Zhong-Ming Wei, Yan-Meng Shi, Xiang Wang, Bin Ren and Ping-Heng Tan, Plasmonic nanocavity-enabled universal detection of layer-breathing vibrations in two-dimensional materials, vol. 15, 109, 2026

Chiral Plasmonic Nanoparticles

Jianfang Wang*

Department of Physics, The Chinese University of Hong Kong, Shatin, Hong Kong SAR, China

*Corresponding author: jfwang@phy.cuhk.edu.hk

***Abstract*— Chiral plasmonic Au nanoparticles are synthesized and demonstrated for chiral optical switching, chiral fluorescence emissions, circularly polarized organic light-emitting devices (CP-OLEDs), and photonic spin-Hall effect.**

***Keywords*— chiral plasmonic nanoparticles, circularly polarized light-emitting diodes, photonic spin-Hall effect, plasmon resonance, seed-mediated growth.**

Chirality is a fundamentally important concept in chemistry and physics. Chiral molecules exhibit chiroptical responses, which, however, are usually small. In this regard, the synthesis of plasmonic metal nanoparticles that possess chiral features on their surfaces has recently received much attention. Such chiral plasmonic nanoparticles exhibit much stronger chiroptical responses than molecules because of their larger sizes and localized surface plasmon resonance.

We have developed recipes for using seed-mediated growth to synthesize chiral Au nanoparticles in the presence of small peptide enantiomers. Different Au nanocrystals are employed as the starting seeds. The growth with Au nanodisks gives chiral Au nanotriskelions and helicoid Au nanocrystals. Halide ions are added to adjust the growth rates along different lattice directions of Au. The averaged scattering dissymmetry factors of the L- and D-nanotriskelions are as large as +0.57 and −0.49 at 650 nm, respectively. Moreover, the extinction dissymmetry factor of the chiral Au nanoparticles can be adjusted to change the sign using the chiral directing molecules of the same handedness. The growth with Au nanodecahedrons gives chiral Au nanorods, with five concave grooves inscribed on the side surface along the length axis. The length of the chiral Au nanorods can be varied by use of Au nanodecahedrons with different elongations.

We have further demonstrated the use of the chiral Au nanoparticles in chiral optical switching, chiral fluorescence emissions, circularly polarized organic light-emitting devices (CP-OLEDs), and photonic spin-Hall effect. The chiral optical switching device is fabricated by depositing the chiral nanoparticles randomly and densely on a substrate and coating them with an active electrochromic polymer layer that can be chemically and electrochemically switched between different redox states that have different dielectric functions. The chiral nano-emitters that preferentially emit left- or right-handed circularly polarized photons are prepared by coating mesostructured silica onto the individual chiral Au nanoparticles with fluorophores embedded in the silica shell. Efficient CP-OLEDs are realized through the assembly of chiral plasmonic Au nanoparticles and supramolecular aggregates. The chiral plasmonic nanoparticles serve as the chiral scaffold and chiral optical nanoantenna to modulate the circularly polarized absorption and emission of the supramolecular chromophores. The emissions of the OLEDs are dominated by either chiral excitons or chiral plasmons, dependning on the type of chiral plasmonic nanoparticle. The CP-OLED showing a high external quantum efficiency of 2.5% and a large dis-symmetry factor of 0.31 is achieved, as a result of multiscale chirality transfer, plasmonic enhancement, and the suppression of the overshoot effect. Previously reported CP-OLEDs generally exhibit an inverse relationship between the external quantum efficiency and the dis-symmetry factor. The CP-OLEDs fabricated in our work can achieve both high external quantum efficiencies and high dis-symmetry factors. The external quantum efficiencies of our devices are about two orders of magnitude higher than those of lanthanide-complex-based devices and the dis-symmetry factors are about two orders of magnitude larger than those of chiral cluster-based devices. When a chiral Au nanoparticle is attached on a silver nanowire, the linearly polarized incident light can be routed to the two ends of the nanowire. The direction of the routed light is determined by the handedness of the chiral nanoparticle.

Acknowledgments

This work was supported by the Research Grants Council of Hong Kong (ANR/RGC, A-CUHK404/21; GRF, 14303124).

References

[1] Zheng, J. P.; Boukouvala, C.; Lewis, G. R.; Ma, Y. C.; Chen, Y.; Ringe, E.; Shao, L.; Huang, Z. F.; Wang, J. F. *Nat. Commun.* 2023, 14: 3783.

[2] Zhang, L. L.; Chen, Y. L.; Zheng, J. P.; Lewis, G. R.; Xia, X. Y.; Ringe, E.; Zhang, W.; Wang, J. F. *Angew. Chem. Int. Ed.* 2023, 62: e202312615.

[3] Chen, Y. L.; Zheng, J. P.; Zhang, L. L.; Li, S. S.; Chen, Y.; Chui, K. K.; Zhang, W.; Shao, L.; Wang, J. F. *ACS Nano* 2024, 18: 383.

[4] Zheng, J. P.; Fu, Y. A.; Wang, J.; Zhang, W.; Lu, X. H.; Lin, H.-Q.; Shao, L.; Wang, J. F. *Nat. Commun.* 2025, 16: 1658.

Controllable Self-Assembly of Gold Nanoparticles with Concave Geometries

Limin Qi*

College of Chemistry and Molecular Engineering, Peking University, Beijing, China
*Corresponding author: liminqi@pku.edu.cn

***Abstract*— The nanoparticles with concave geometries emerge as unique nanoscale building blocks for the construction of nanoparticle assemblies with novel structures and unique photonic properties. This presentation summarizes our recent work on controllable self-assembly of concave gold nanoparticles, such as supercrystal engineering of gold nanoarrows and chiral self-assembly of gold nanodumbbells.**

***Keywords*— self-assembly of nanoparticles, concave nanoparticles, gold, nanoarrows, nanodumbbells.**

I. Introduction

Precise self-assembly of nanoparticles provides a facile and efficient bottom-up route towards ordered nanoparticle assemblies with novel properties and nanodevices with superior performance. In this regard, the plasmonic nanoparticles with concave geometries emerge as a unique kind of nanoscale building blocks for the construction of nanoparticle assemblies with novel structures and unique photonic properties.

II. Results and Discussion

First, shallowly concave gold nanoarrows (GNAs) with a delicately controlled concave-convex geometry are synthesized and employed for shape-directed self-assembly of a wealth of unprecedented, complex supercrystals. The concavity-enabled supercrystal engineering offers a promising route toward unconventional nanoparticle superstructures with expanded complexity and tunability in configuration.

Second, ligand-mediated self-assembly of gold nanoarrows into macroscopic monolayer films with tunable orientations is achieved at the oil-water interface, with the particle orientation readily modulated by adjusting the relative adsorbed amounts of the hydrophilic and hydrophobic ligands. After transferred onto a transparent polydimethylsiloxane substrate, the monolayer GNA films with type II orientation exhibits switchable color response toward the ethanol solvent.

Third, gold nanodumbbells (GNDs) are employed as achiral building blocks for controllable self-assembly into stable homochiral assemblies exhibiting strong chiroptical activity (Fig. 1). The formation of helically stacked side-by-side assemblies (SSAs) with a right handedness is triggered by introducing bovine serum albumin as the chiral additive. Remarkably, an asymmetry factor as high as 0.23 is obtained.

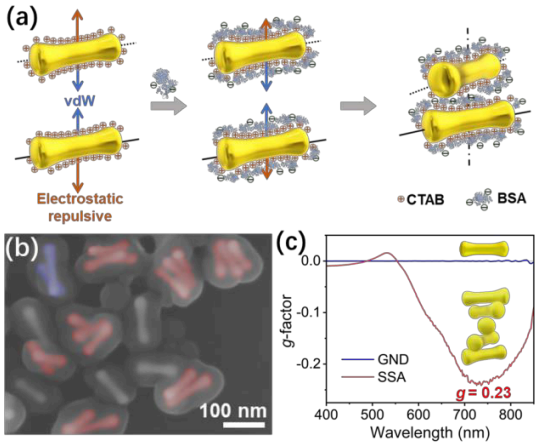

Fig. 1 Chiral self-assembly of gold nanodumbbells.

III. Conclusion

Controllable self-assembly of concave gold nanoparticles including supercrystal engineering of GNAs, interfacial self-assembly of GNAs, and chiral self-assembly of GNDs has been achieved. This work may advance the structural design of nanoscale plasmonic building blocks for supercrystal engineering and chiral assembly useful in nanophotonics.

Acknowledgments

This work was supported by the National Natural Science Foundation of China (Grant No. 22132001).

References

[1] Q. Wang, Z. Wang, Z. Li, J. Xiao, H. Shan, Z. Fang, L Qi, Controlled growth and shape-directed self-assembly of gold nanoarrows. *Sci. Adv.* **2017**, *3*, e1701183.

[2] C. Chen, Q. Wang, P. Wang, M. Dai, X. Jiang, J. Zhou, L. Qi, Supercrystal engineering of nanoarrows enabled by tailored concavity. *Small* **2024**, *20*, 2403970.

[3] M. Dai, C. Chen, Y. Lu, P. Wang, L. Qi, Interfacial self-assembly of gold nanoarrows into macroscopic monolayer films with tunable orientations and reversible color switching. *Adv. Funct. Mater.* **2026**, *36*, e18223.

[4] J. Zhou, Y. Gao, D. Zhang, K. Ren, M. Dai, H. Wang, L. Qi, Concavity-enhanced chiral self-assembly of anisotropic nanoparticles toward strong chiroptical activity. *Nat. Commun.* **2025**, *16*, 6897.

Transition Metal–CO Bond: σ-bonding or π-bonding?

Zhen-Chao Dong*

Hefei National Research Center for Physical Sciences at the Microscale,
University of Science and Technology of China, China
*Corresponding author: zcdong@ustc.edu.cn

***Abstract*— By exploiting sub-nanometer resolved tip enhanced Raman spectroscopy (TERS), we identify the bonding type between transition metal (M) and CO molecule (namely, σ-donation or π-back donation) at the single-bond level through vibrational Stark effects under an external electric field, an issue theoretically well understood but experimentally very hard to achieve.**

***Keywords*— tip enhanced Raman spectroscopy, CO, coordinate bond, molecule-substrate interaction.**

Precise control over molecule-surface interactions is a cornerstone of surface chemistry, dictating the efficiency and selectivity of catalytic processes that underpin our industrial world. In particular, the interaction of carbon monoxide (CO) molecules with transition metals (M), which often serves as model catalytic systems, playes a pivotal role in facilitating chemical transformations such as carbonylation and reduction–oxidation reactions. Theoretically, based on the Dewar-Chatt-Duncanson model or Blyholder model (Fig. 1), the CO molecule can either serve as an acceptor to receive electrons from the metal atom through 2π*←d orbitals (known as the π back-donation, the classical regime called π bonding), or as a donor to give electrons to the metal atom through 5σ→d orbitals (known as the σ donation, the non-classical regime called σ bonding). Generally, the σ donation and the π back-donation would coexist and act synergistically. In the classical regime, π back-donation plays a more significant role and weakens the C−O bonding strength, while in the non-classical regime, the σ donation strengthens the C−O bond. Therefore, experimentally identifying these two bonding contributions is of fundamental importance, as it can not only determine and confirm the electronic structure of metal–-CO complexes, but also enable to gain insights into the mechanism that governs their catalytic reactivity and selectivity.

Various experimental approaches have been employed to investigate such a bonding interaction issue, including Raman, IR and single-crystal x-ray diffraction, largely performed on ensemble systems. However, experimental methods to unambiguously identify the bonding nature in this system is still out of reach. One natural and attractive approach is to chemically identify the bonding types of M−CO bonds at single-molecule single-bond scales, free of any ensemble averaging complication.

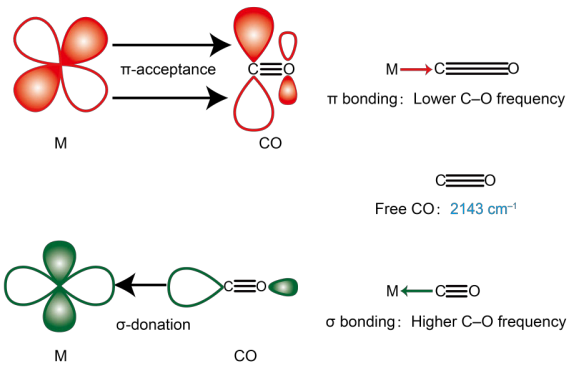

Fig. 1 Schematic representation of the σ donation and π back-donation.

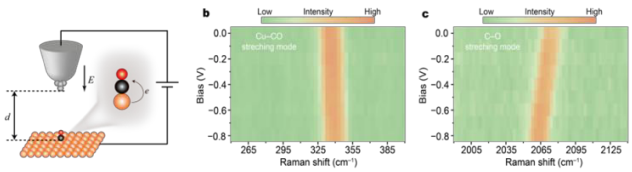

Fig. 2 Vibrational Stark effects in TERS.

In this work, by combining sub-nanometer resolved TERS [1-4] with vibrational Stark effects [5], we demonstrate a novel approach that can monitor the evolution of both the M−CO and C−O bond strengths through the shift of vibrational frequencies of these bonds in situ at the single-bond level (Fig. 2). Two model systems are selected, Cu-CO system for the classical regime and Ag-CO for the non-classical regime. By modulating the charge transfer between the transition metal and CO through the application of an electric field, the Cu−CO coordinate bond can be identified to be dominated by π back-donation while the Ag−CO bond is dominated by the σ donation due to their different evolution of the bonding strengths for the M−CO and C−O bonds along with the increase of electric fields.

References

[1] R. Zhang, et al., Nature 498, 82–85 (2013).
[2] J. Lee, et al., Nature 568, 78-82 (2019).
[3] Y. Zhang, et al., Natl. Sci. Rev. 6, 1169–1175 (2019).
[4] J. Y. Xu, et al., Science 371, 818 (2021).
[5] X. R. Dong, et al., Light: Adv. Manuf. 3, 52 (2022).

Rational Design and Applications of Intrinsically Chiral Plasmonic Nanoparticles

Xiaolu Zhuo[1,], Yilin Chen[1,2], Shengyan Wang[1], Zhongyi Chen[1], Ruiqian Zhang[1,2], and Jianfang Wang[2]*

[1]Guangdong Basic Research Center of Excellence for Aggregate Science, School of Science and Engineering, The Chinese University of Hong Kong, Shenzhen, Guangdong, 518172, China.

[2]Department of Physics, The Chinese University of Hong Kong, Hong Kong SAR, China.

*Corresponding author: zhuoxiaolu@cuhk.edu.cn

***Abstract*— Chiral plasmonics has emerged as a frontier in nanophotonics, offering unprecedented opportunities to manipulate light at the nanoscale through handedness-dependent optical responses. However, unlocking its full potential demands precise synthetic control over chiral plasmonic nanostructures and rational strategies for dynamically tuning their optical properties.**

In recent years, we have initiated our research with the colloidal synthesis of intrinsically chiral plasmonic nanoparticles, including diverse morphologies such as chiral gold nanorods and Janus nanoparticles. Through systematic investigation, we have elucidated the growth mechanisms underlying chirality emergence and identified key synthetic parameters that govern morphological control. We further demonstrate how these nanostructures respond to external stimuli, including polymer encapsulation and shell engineering, to modulate their far-field and near-field chiroptical characteristics. These studies establish design principles for achieving dynamic switching, spectral tunability, and localized superchiral hotspot generation in plasmonic systems. On this basis, we demonstrate preliminary applications of these chiral plasmonic nanoparticles in circularly polarized luminescence, enantioselective sensing, and valleytronic devices. These explorations collectively advance chiral plasmonics toward practical implementation in next-generation photonic and optoelectronic technologies.

Plasmonic Control of Dark Excitons and Valley Coherence in TMDC Monolayers under Ambient Conditions

Lei Shao[1,*]

[1]State Key Laboratory of Optoelectronic Materials and Technologies, Guangdong Province Key Laboratory of Display Materials and Technologies, School of Electronics and Information Technology, Sun Yat-sen University, Guangzhou 510275, China
*Corresponding author: shaolei5@mail.sysu.edu.cn

***Abstract*—We demonstrate the use of plasmonic nanocavities to enable control of dark excitons and valley coherence in monolayer WSe_2 under ambient conditions. With the help of a Au nanodisk-based nanocavity, the dark exciton emission is switched on with 22-fold enhancement and valley coherence is achieved through strong plasmon-exciton coupling.**

***Keywords*—transition metal dichalcogenides, dark excitons, valley coherence, plasmonic nanocavities.**

I. Results

Transition metal dichalcogenide (TMDC) monolayers are at the forefront of research in atomically thin optoelectronics and quantum technologies due to their direct bandgap and unique spin-valley locking properties. Harnessing their full potential requires the ability to control both long-lived, optically inactive (dark) excitons for quantum information processing and valley coherence for valleytronic applications. Traditionally, accessing these phenomena has necessitated complex photonic structures or extreme experimental conditions, such as cryogenic temperatures and high magnetic fields. Here, we introduce our recent results on using plasmonic nanostructures to overcome these limitations, enabling the control of both dark excitons and valley coherence in monolayer WSe_2 under ambient conditions. First, we demonstrate the switching-on of dark exciton emission using a simple, highly reproducible plasmonic nanodisk-on-mirror cavity. By sandwiching the WSe_2 monolayer within this structure and tuning the nanodisk diameter, we achieve a 22-fold enhancement in the dark-to-bright exciton emission ratio. This control is mediated by two orthogonal plasmon modes that generate strongly confined out-of-plane electric fields, coupling efficiently to the otherwise dark states. Second, we show that strong coupling between excitons and plasmons in a similar plasmonic architecture gives rise to distinct Rabi splitting in the polarization-resolved photoluminescence spectra. This strong coupling regime facilitates the addressing of valley coherence at room temperature within a sub-145 nm wide area, circumventing the need for bulky magnets or cryogenic cooling. Together, these findings establish that precisely engineered plasmonic nanocavities provide a versatile and practical platform for controlling the fundamental excitonic properties of TMDC monolayers. This work paves the way for the development of integrated nanophotonic and optoelectronic devices, including sources for quantum information processing and room-temperature valleytronic logic, by bringing the control of dark excitons and valley coherence from extreme conditions to readily accessible, chip-scale environments.

Acknowledgments

This work was supported by the National Natural Science Foundation of China (62375290, 2024YFA1209003, 12088101), the Pearl River Talent Recruitment Program (2019QN01C216) and the Science and Technology Planning Project of Guangdong Province (2023B1212060025).

References

[1] H. Huang, B. Tian, Y. Chen, X. Y. Xia, X. M. Cui, L. Shao, H. J. Chen, J. F. Wang, "Coherent polaritons in WSe_2-monolayer-sandwiched Au-nanodisk-on-mirror structures," ACS Nano, vol. 19, pp. 25284–25294, 2025.

[2] X. Y. Xia, H. Huang, S. S. Li, R. Q. Ai, Z. Y. Tian, F. Yan, L. Shao, J. F. Wang, "Switching on dark excitons in WSe_2 monolayer at room temperature with plasmonic Au nanodisk-on-mirror cavities," Laser Photonics Rev. vol. 19, e02012, 2025.

[3] X. Zhen, H. Z. Wu, W. Y. Feng, H. W. Chen, J. Wang, H. J. Chen, N. S. Xu, L. Shao, S.-Z. Deng, "Single-particle plasmon spectroscopy revealing the local strain-induced band structure change in two-dimensional semiconductors," Advanced Optical Materials, vol. 13, 2500158, 2025.

[4] S. S. Li, H. Wang, J. Wang, H. J. Chen, L. Shao, "Control of light–valley interactions in 2D transition metal dichalcogenides with nanophotonic structures," Nanoscale vol. 13, pp. 6357–6372, 2021.

Interaction between Plasmonic Nanostructures and 2D Semiconductor Materials

Hong Wei*

Institute of Physics, Chinese Academy of Sciences, Beijing 100190, China
*Corresponding author: weihong@iphy.ac.cn

***Abstract*— In this presentation, I will introduce our research on the coupling systems of plasmonic nanostructures and monolayer or few-layer transition metal dichalcogenides.**

***Keywords*— surface plasmons, excitons, strong coupling, photoluminescence**

Metal nanostructures supporting surface plasmons can concentrate light into nanoscale volumes, enabling the manipulation of light beyond the diffraction limit. Two-dimensional semiconductor materials such as monolayer transition metal dichalcogenides possess unique optical properties, making them promising for nanophotonic applications. The combination of plasmonic nanostructures and two-dimensional semiconductor materials provides a versatile platform for investigating light-matter interaction at the nanoscale. In this talk, I will present our research on the coupling systems of plasmonic nanostructures and monolayer or few-layer transition metal dichalcogenides, focusing on photoluminescence and chiroptical properties.

Controlling Activity and Selectivity through Charge-Flow Engineering in Plasmonic Catalysis

Yicui Kang[1,2*], Bart de Nijs[1], Emiliano Cortés[2]

[1]Department of Physics, University of Cambridge, UK
[2]Department of Physics, LMU Munich, Germany
*Corresponding author: yk475@cam.ac.uk

***Abstract*—Plasmonic catalysis offers new opportunities to improve photocatalytic activity and selectivity. By comparing carbon dioxide reduction and hydrogen peroxide synthesis systems, we identify charge-flow engineering as a common mechanism governing carrier utilization. These findings establish a general design strategy for efficient and selective solar-to-chemical conversion.**

***Keywords*—Plasmonic Catalysis, Charge-Flow Engineering, Morphology-Controlled Nanostructures, Solar-to-Chemical Conversion.**

I. Introduction

Solar-driven chemical conversion offers a promising route toward sustainable fuel and chemical production. However, the efficiency of conventional photocatalytic systems remains limited by rapid charge recombination, inefficient carrier utilization, and poor reaction selectivity. Plasmonic photocatalysis has emerged as a promising strategy to address these challenges[1].

Upon light irradiation, plasmonic nanostructures strongly interact with light through localized surface plasmon resonance (LSPR). LSPR can generate energetic charge carriers, localized electromagnetic fields, and photothermal effects that enhance catalytic reactions, attracting considerable attention in recent years[2,3].

Understanding how plasmonic structures influence charge-carrier behavior is essential for the rational design of efficient photocatalysts. In this work, two representative plasmonic systems are examined: morphology-dependent Au nanocrystals for CO_2 reduction and Au@TiO_2 core-shell structures for H_2O_2 synthesis. Although these systems involve different reactions, both reveal a common role of plasmonic excitation in regulating charge-carrier generation, transport, and utilization. Through a comparative analysis of these systems, charge-flow engineering is proposed as a general framework for controlling activity and selectivity in plasmonic catalysis.

II. Methods

2.1 Plasmon-assisted electrocatalytic CO_2 Reduction System

The first system consists of Au nanocrystals with controlled morphologies, including cubic (NC), rhombic dodecahedral (RD) and octahedral (OC) structures, as shown in Fig. 1(a). These nanocrystals expose different crystallographic facets and exhibit distinct plasmonic responses. Electrocatalytic CO_2 reduction performance was evaluated under both dark and illuminated conditions. Spectroscopic characterization together with numerical simulations was employed to investigate plasmonic behavior and charge-carrier dynamics[4].

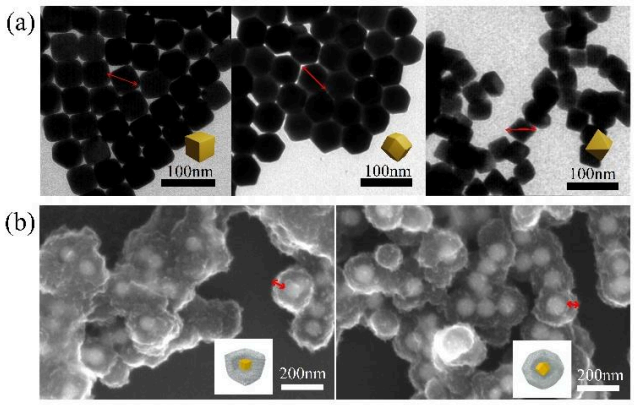

Fig. 1 Images of the plasmonic catalytic systems. (a) TEM images of morphology-controlled Au nanocrystals, including nanocubes (NC), rhombic dodecahedra (RD), and octahedra (OC), used for plasmon-assisted CO_2 reduction. (b) SEM image of Au@TiO_2 core–shell structures with NC and RD Au cores used for photocatalytic H_2O_2 synthesis.

2.2 Au@TiO_2 H_2O_2 Synthesis System

The second system consisted of Au@TiO_2 core-shell photocatalysts with morphology-controlled Au cores. Nanocubic and rhombic dodecahedral Au nanocrystals were encapsulated within porous anatase TiO_2 shells (NC@TiO_2 and RD@TiO_2), as depicted in Fig. 1(b). H_2O_2 production was quantified by iodometric analysis under full-spectrum irradiation and selected wavelength ranges. Electrochemical measurements, spectroscopic characterization, and electromagnetic simulations were performed to investigate the LSPR effect in carrier generation and transfer processes in Au@TiO_2 systems[5].

III. Results and Discussion

3.1 Morphology-Dependent Catalytic Performance

Both systems exhibit strong morphology-dependent photocatalytic performance.

In the CO_2 reduction system, Au nanocrystals showed distinct responses to light depending on their morphology. Under illumination, Au OCs exhibited approximately twofold higher CO Faradaic efficiency and threefold higher CO partial current density compared with dark conditions. Au NCs also showed noticeable performance enhancement under illumination, whereas Au RDs displayed little change. The observed enhancement could not be fully explained by conventional facet-dependent catalytic activity alone, indicating an additional contribution from plasmonic effects[4].

A similar morphology dependence was observed in the H_2O_2 synthesis system. NC@TiO_2 photocatalysts achieved substantially higher H_2O_2 production rates than their RD@TiO_2 counterparts. Moreover, H_2O_2 decomposition was more effectively suppressed in the NC@TiO_2 system, resulting in a significantly higher net H_2O_2 accumulation[5].

Although the two systems involve different catalyst architectures and reaction pathways, both exhibit a strong correlation between nanoparticle morphology and photocatalytic performance. These observations suggest that catalyst geometry influences photocatalytic behavior beyond conventional surface-structure effects and point toward a common plasmon-involved mechanism.

3.2 Photocarrier Dynamics as the Governing Factor

To understand the origin of the morphology-dependent catalytic behavior, mechanistic investigations including spectroscopy, numerical simulations, and electrochemical analyses were performed in the original studies. Although the experimental approaches differed between the two systems, both investigations consistently identified plasmon-induced charge-carrier dynamics as the key factor governing catalytic performance.

For plasmon-assisted electrocatalytic CO_2 reduction, the superior performance of Au OC was associated with stronger plasmonic excitation and more efficient utilization of photogenerated carriers. Electromagnetic simulations revealed enhanced electric-field distributions at low-coordinated surface sites, while atomistic simulations suggested morphology-dependent hot-carrier generation[4]. In contrast to conventional electrocatalytic systems, where catalytic activity is often governed by adsorption energetics on specific facets, plasmon-involved systems appear to be strongly influenced by low-coordinated sites. These findings indicate that plasmon-generated carriers actively participate in catalytic processes, allowing LSPR to modify the contributions of different active sites and activate the same material differently from conventional catalytic processes.

The Au@TiO_2 system provided further insight into the role of carrier transport. Spectroscopic analyses and simulations revealed that plasmon excitation in the Au core enhances charge separation across the Au-TiO_2 interface. Upon plasmon excitation, electrons generated within TiO_2 were preferentially transferred to Au sites, where oxygen reduction occurs, while plasmon-generated hot electrons mitigated hole-driven pathways responsible for H_2O_2 decomposition. As a result, plasmonic excitation simultaneously enhanced H_2O_2 formation and suppressed undesired product degradation. The stronger LSPR response of NC@TiO_2 further amplified these effects, leading to higher overall H_2O_2 yields[5].

Despite the differences in reaction chemistry, both systems reveal a common phenomenon in which plasmonic excitation influences charge-carrier behavior. Rather than simply increasing carrier populations, plasmonic nanostructures regulate the generation, transport, and utilization of photogenerated carriers. This ability to control charge-carrier flow provides a common explanation for the morphology-dependent catalytic behavior observed in both systems.

3.3 Design Principles and Future Perspectives

The common charge-flow control observed in both systems suggests that the primary advantage of plasmonic nanostructures lies in their ability to regulate carrier utilization during catalysis. In both CO_2 reduction and H_2O_2 synthesis, the observed performance improvements arise from more effective use of photogenerated carriers rather than merely increased carrier production. This perspective provides a useful framework for designing plasmonic photocatalysts with improved activity and selectivity.

Based on these observations, several design principles for plasmonic photocatalysts can be proposed. First, nanoparticle morphology should be carefully engineered to maximize localized plasmonic responses and promote favorable carrier distributions. The strong morphology dependence observed in both systems demonstrates that catalyst geometry directly influences photocatalytic performance through its impact on charge-carrier dynamics.

Second, catalyst architectures should be designed to facilitate directional charge transport and efficient carrier utilization. Rather than functioning solely as active catalytic components, plasmonic nanostructures can serve as regulators of charge flow, guiding charge-carriers toward desired reaction pathways while suppressing competing processes. This capability provides a unique opportunity to simultaneously improve catalytic activity and selectivity.

More broadly, plasmonic photocatalysis should be viewed as a platform for charge-flow engineering rather than solely light-harvesting enhancement. While plasmon excitation may not directly drive chemical reactions with high efficiency, it can strongly influence the transport and utilization of photogenerated carriers, thereby enhancing catalytic performance and controlling reaction pathways.

Despite the promise of plasmonic catalysis, the underlying

physical mechanisms remain incompletely understood. Key processes, including hot-carrier generation, interfacial charge transfer, and energy dissipation, occur on ultrafast timescales and nanometre length scales, making them challenging to observe directly. As a result, many fundamental questions regarding the relationship between plasmon excitation and catalytic activity remain unresolved[3].

Future studies should combine precisely engineered plasmonic nanostructures with advanced operando spectroscopic techniques, such as surface-enhanced Raman spectroscopy (SERS), surface-enhanced infrared absorption spectroscopy (SEIRAS), and ultrafast optical measurements[6,7]. In particular, self-assembled multilayer gold nanoparticle architectures with precisely controlled interparticle separations provide promising platforms for generating reproducible plasmonic hotspots and probing carrier dynamics under realistic reaction conditions[8]. Such approaches will enable direct observation of charge and energy transfer processes during catalysis and provide deeper insight into the mechanisms governing plasmon-mediated photocatalytic reactions. A more complete understanding of photocarrier generation, transport, and utilization will not only advance the fundamental understanding of plasmonic catalysis but also guide the rational design of highly efficient and selective light-driven systems for future energy conversion and chemical production[3,7].

IV. Conclusion

A comparative analysis of plasmon-assisted CO_2 reduction and plasmon-enhanced H_2O_2 synthesis reveals a common role of plasmonic excitation in regulating charge-carrier behavior. In both systems, LSPR influences the generation, transport, and utilization of photogenerated carriers, resulting in enhanced catalytic performance and selectivity. The strong morphology dependence observed across both systems further highlights the importance of charge-carrier dynamics in plasmonic catalysis.

These findings suggest that the role of LSPR extends beyond enhanced light harvesting, providing a means to control charge-carrier flow and reaction pathways. This perspective establishes charge-flow engineering as a promising strategy for the design of next-generation plasmonic catalysts.

Despite recent progress, a deeper understanding of hot-carrier generation, transfer, and dissipation remains necessary. Future operando and ultrafast spectroscopic studies will be crucial for revealing these processes and advancing the rational design of efficient light-driven catalytic systems.

Acknowledgments

This work was supported by the Engineering and Physical Sciences Research Council (EPSRC), grant number EP/Y008294/1. We acknowledge funding and support from the Deutsche Forschungsgemeinschaft (DFG) under Germany´s Excellence Strategy-EXC 2089/2-390776260, the Bavarian Program Solar Technologies Go Hybrid (SolTech) and the Center for NanoScience (CeNS).

References

[1] S. Ezendam, et al., “Hybrid plasmonic nanomaterials for hydrogen generation and carbon dioxide reduction,” ACS Energy Letters, vol. 7, pp. 778–815, 2022.

[2] B. de Nijs, et al., “Plasmonic tunnel junctions for single-molecule redox chemistry,” Nature Communications, vol. 8, 994, 2017.

[3] P. H. C. Camargo and E. Cortés (eds.), “Plasmonic catalysis: from fundamentals to applications,” John Wiley & Sons, 2021.

[4] Y. Kang, S. M. João, et al., “Effect of crystal facets in plasmonic catalysis,” Nature Communications, vol. 15, 3923, 2024.

[5] Y. Kang, Y. Tan, et al., “Promoting formation and suppressing decomposition of H_2O_2 via photocarrier flow at Au@TiO_2 interfaces,” Journal of the American Chemical Society, vol. 147, pp. 47244–47254, 2025.

[6] J. J. Baumberg, et al., “Extreme nanophotonics from ultrathin metallic gaps,” Nature Materials, vol. 18, pp. 668–678, 2019.

[7] A. Stefancu, et al., “Impact of surface enhanced Raman spectroscopy in catalysis,” ACS Nano, vol. 18, pp. 29337–29379, 2024.

[8] S. M. Sibug-Torres, et al., “In situ electrochemical regeneration of nanogap hotspots for continuously reusable ultrathin SERS sensors,” Nature Communications, vol. 15, 2022, 2024.

.

Quantum Quasinormal Mode Theory for Spatio-Temporally Resolved Magnetodielectric Cavity Quantum Electrodynamics

Lars Meschede[1], Daniel D. A. Clarke[1,*], Ortwin Hess[1,*]

[1]School of Physics and CRANN Institute, Trinity College Dublin, The University of Dublin, College Green, Dublin 2, Ireland

*Corresponding authors: clarked5@tcd.ie, ortwin.hess@tcd.ie

***Abstract*—The rapidly evolving ability to harness quantum effects in various cavity quantum electrodynamics (cQED) architectures demands a rigorous theory for the investigation of inherently non-Hermitian systems. We present a quasinormal mode quantization scheme for electromagnetic resonators and demonstrate its capabilities for spatio-temporal studies and characterization of non-trivial cQED systems.**

***Keywords*— quasinormal modes, quantum electrodynamics, nanophotonics, plasmonics, magnonics.**

I. Introduction

Cavity-mediated control and enhancement of light-matter interaction has become a pervasive paradigm in modern quantum science and technology, enabling applications in quantum computation, memory and sensing, nano-lasing and quantum light sources. The rich nexus of nanotechnologies based on cQED systems stems from the vast diversity of architectures available to realize and harness quantum optical effects in evermore robust and reproducible ways, ranging from plasmonic systems able to confine light at deeply sub-wavelength scales and operate in an ultrafast temporal regime at ambient temperatures [1], through silicon-based photonic systems suitable for low-loss and scalable, on-chip operation [2], to magnonic systems able to elevate quantum effects to a macroscopic spatial scale [3].

In all these platforms, confined electromagnetic resonances can become inextricably intertwined with the excitonic or spin-related excitations of matter, giving rise to diverse light-matter dynamics whose richness and technological potential can only be truly unlocked with the aid of spatially and temporally resolved, fully quantum mechanical treatments. In particular, hybrid cQED platforms that are promising for nascent quantum device protocols often feature strongly coupled and dissipative resonances of photonic, plasmonic or magnonic character, giving rise to a panorama of polaritons, and where perturbative approaches for describing the dressing of matter by cavity electric and magnetic fields quickly become inadequate for the rigorous calculation of quantum optical figures of merit. Towards an improved understanding of both the near- and far-field properties of these systems, a unified theoretical framework is called for which captures the quantum properties of these myriad excitations, the coupling between them, as well as their interaction with embedded matter supporting electric and magnetic transition moments.

In this light, we present a quantum quasinormal mode (QNM) formalism for addressing problems in dissipative cQED [4], offering a unified, rigorous and practical simulation methodology for photonic, plasmonic and magnonic cavities interacting with quantum emitters (QEs) and spin qubits. We demonstrate its predictive power via the characterization of non-trivial, hybrid cavity systems and their interaction with QEs, paving the way towards a fully quantum mechanical description of phenomena such as quantum nanoplasmonic coherent perfect absorption [5], lasing in $\mathcal{PT}$-symmetric photonic systems, magnonic strong coupling and cavity-mediated spin-photon interfaces at the nanoscale.

II. Methods

a) Quasinormal modes: QNMs are used to describe the response of open and lossy, resonant electromagnetic systems and are defined as the eigensolutions of the macroscopic Maxwell's equations with complex frequencies:

$$\begin{pmatrix} 0 & -\mathrm{i}\mu^{-1}(\mathbf{r},\tilde{\omega}_n)\nabla\times \\ \mathrm{i}\varepsilon^{-1}(\mathbf{r},\tilde{\omega}_n)\nabla\times & 0 \end{pmatrix} \begin{pmatrix} \tilde{\mathbf{H}}_n \\ \tilde{\mathbf{E}}_n \end{pmatrix} = \tilde{\omega}_n \begin{pmatrix} \tilde{\mathbf{H}}_n \\ \tilde{\mathbf{E}}_n \end{pmatrix} \tag{1}$$

They can be used to expand the electromagnetic field within the resonator for scattering or radiation problems. By leveraging perfectly matched layers (PMLs) and an auxiliary-field method for both numerical computations and analytical considerations, efficient finite-element-based QNM solvers have been implemented and simple analytical formulae for the excitation coefficients in the QNM expansion of the scattered electromagnetic field, $\mathbf{E}_{\mathrm{sca}} = \sum_n \alpha_n \tilde{\mathbf{E}}_n$, in both frequency and time domain have been derived [6] and applied for many different types of resonators [7]. By appropriately modeling the material parameters ε and μ, it is possible to describe photonic, plasmonic, magnonic or any kind of hybrid system. The QNM methodology thus provides a practical computational technique for solving scattering and radiation problems, while simultaneously allowing a much deeper physical insight into these processes as opposed to a brute-force numerical solution of Maxwell's equations in the frequency or time domain. In

the case of non-trivial backgrounds such as waveguides or substrates, the PML modes resulting from the introduction of a truncated, PML-transformed space also ensure the completeness of the set of modal solutions, which is otherwise not guaranteed by the QNMs alone.

b) Macroscopic QED and QNM quantization: Macroscopic QED provides a unified theory for the quantization of the electromagnetic field in the presence of arbitrary, 3D, dispersive and lossy, linear media characterized by the permittivity ε and permeability μ. The frequency components of the E-field operator satisfy the equation

$$\nabla \times \mu^{-1} \nabla \times \hat{\mathbf{E}}(\mathbf{r},\omega) - \varepsilon \frac{\omega^2}{c^2} \hat{\mathbf{E}}(\mathbf{r},\omega) = \mathrm{i}\mu_0 \omega \hat{\mathbf{j}}_{\mathrm{N}}(\mathbf{r},\omega) \ , \quad (2)$$

with an additional noise current density

$$\hat{\mathbf{j}}_{\mathrm{N}}(\mathbf{r},\omega) = \omega \sqrt{\frac{\hbar\varepsilon_0}{\pi}} \sqrt{\Im(\varepsilon(\mathbf{r},\omega))}\, \hat{\mathbf{f}}_{\mathrm{e}}(\mathbf{r},\omega) + \sqrt{\frac{\hbar}{\mu_0 \pi}} \nabla \times \left(\sqrt{-\Im(\mu^{-1}(\mathbf{r},\omega))}\, \hat{\mathbf{f}}_{\mathrm{m}}(\mathbf{r},\omega) \right) \ , \quad (3)$$

in accordance with the fluctuation-dissipation theorem and which ensures the preservation of the fundamental commutation relations. The bosonic operators $\hat{\mathbf{f}}_{\mathrm{e}}(\mathbf{r},\omega)$, $\hat{\mathbf{f}}_{\mathrm{m}}(\mathbf{r},\omega)$ correspond to the joint excitations of the electromagnetic-field-dressed media (polaritons) and diagonalize the Hamiltonian of the system. Utilizing the dyadic E-field Green's function of the system leads to an expansion of the E-field operator in terms of the continuum of bosonic modes:

$$\hat{\mathbf{E}}(\mathbf{r}) = \mathrm{i}\mu_0 \int_0^\infty \mathrm{d}\omega\, \omega \int \mathrm{d}^3 r\, G(\mathbf{r},\mathbf{r}',\omega) \hat{\mathbf{j}}_{\mathrm{N}}(\mathbf{r}',\omega) \ . \quad (4)$$

These formulae can be generalized for materials that exhibit amplification in certain spectral and spatial domains, in which creation and annihilation operators switch roles [8]. As the system is described by a very large continuum of bosonic modes in this formulation, an alternative treatment in terms of a small number of discrete modes is desirable. By incorporating PMLs into the quantum description and leveraging the QNM/PML mode expansion of the Green's function, such an alternative bosonic modal expansion of the E-field operator $\hat{\mathbf{E}}(\mathbf{r}) = \sum_n \hat{a}_n \tilde{\mathbf{E}}_n^{\mathrm{sym}}(\mathbf{r}) + \mathrm{h.c.}$ in terms of symmetrized QNMs $\tilde{\mathbf{E}}_n^{\mathrm{sym}}(\mathbf{r}) = P_{n'n}^{+\frac{1}{2}} \tilde{\mathbf{E}}_{n'}(\mathbf{r})$ can be derived. The temporal evolution of the modal operators is governed by Heisenberg-Langevin equations

$$\frac{\mathrm{d}\hat{a}_n}{\mathrm{d}t} = \frac{\mathrm{i}}{\hbar} \left[\hat{H}_{\mathrm{eff}}, \hat{a}_n \right] - \gamma_{nn'} \hat{a}_{n'} + \hat{F}_n(t) \ , \quad (5)$$

with some quantum noise term $\hat{F}_n(t)$. Practically, these equations can be solved approximately by solving the corresponding master equation [9] or by using the quantum cumulant expansion to obtain approximate truncated equations of the expectation values of the operators and their products. All quantities involved in these equations can be directly calculated from classical PML-based QNM computations and in the presence of amplification, the equations can be adjusted accordingly.

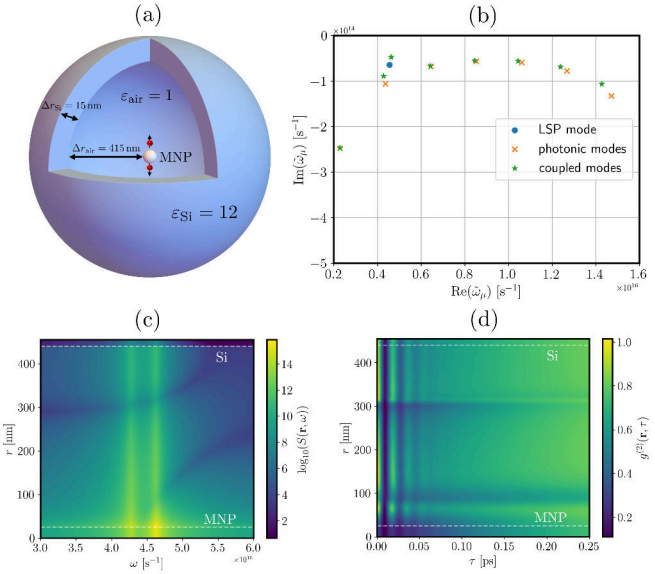

Fig. 1. Example metallodielectric cQED system. (a) Schematic of the hybrid system. (b) $\mathrm{TM}_{l=1}$ QNM frequencies of the system compared to the QNM frequencies of the bare dielectric cavity and the MNP. (c) Position-dependent, steady-state E-field spectrum $S(\mathbf{r},\omega)$ along the QE axis. (d) Position-dependent, steady-state second-order E-field coherence function $g^{(2)}(\mathbf{r},\tau)$ along the QE axis.

III. Results and Discussion

The presented quantum QNM theory can be used to rigorously investigate non-trivial cQED systems in a fully spatially and temporally resolved manner. To demonstrate the necessity of a more thorough investigation of such systems, we briefly discuss some results for a spherical, metallodielectric cavity consisting of a metal nanoparticle (MNP) (described by a Drude model $\varepsilon_{\mathrm{MNP}}(\omega) = \varepsilon_\infty[1 - \omega_{\mathrm{p}}^2/(\omega^2 - \omega_0^2 + \mathrm{i}\gamma\omega)]$ with the parameters typically used for the Drude pole of gold [7], $r_{\mathrm{MNP}} = 25\,\mathrm{nm}$), in the center of a hollow dielectric cavity ($\varepsilon_{\mathrm{air}} = 1$, $\Delta r_{\mathrm{air}} = 415\,\mathrm{nm}$) made out of a thin Si shell ($\varepsilon_{\mathrm{Si}} = 12$, $\Delta r_{\mathrm{Si}} = 15\,\mathrm{nm}$). The parameters are tuned so that a photonic mode of the cavity is strongly coupled to a localized surface plasmon mode (LSP) of the MNP, resulting in two hybrid modes in the QNM spectrum, as shown in Fig. 1(b). These QNMs were quantized and two quantum emitters (QEs) with radially oriented transition dipole moments $d = 30\,\mathrm{D}$, pure dephasing rates $\gamma_{\mathrm{d}} = 4 \times 10^{13}\,\mathrm{s}^{-1}$ and pumping rates $\gamma_{\mathrm{pump}} = 2 \times 10^{12}\,\mathrm{s}^{-1}$ were asymmetrically placed on opposite sides of the MNP ($r_{\mathrm{QE},1} = 32\,\mathrm{nm}$, $r_{\mathrm{QE},2} = 26\,\mathrm{nm}$) and tuned to the first and second hybrid QNM frequencies, respectively. In Fig. 1(c), the radially mapped, steady-state E-field spectrum (along the QE axis) was plotted. It is apparent that the form and the relative heights of the two QNM peaks are dependent on position. The consequences of the position-dependence become even clearer in the steady-state, second-order E-field coherence function in Fig. 1(d). Inside the MNP and in close proximity to its surface, we find $g^{(2)}(\mathbf{r},0) < 0.5$, corresponding to photon antibunching and the single-photon emission regime. Within the cavity, the $g^{(2)}(\mathbf{r},0)$ values are

modified due to multi-mode excitation and the hybridized photonic and LSP character of the modes, even reaching values of $g^{(2)}(\mathbf{r}, 0) > 1.0$, corresponding to photon bunching. This example illustrates that the experimentally accessible far-field quantities cannot be inferred directly from the dynamics of the modal operators, owing to their inherent position dependence within the cavity system. Instead, a near-field-to-far-field transformation is required to rigorously determine the emitted far-field characteristics from the internal dynamics. Analogous studies can be envisaged for cavity magnonic systems as well.

Such spatio-temporally resolved simulations of non-trivial cQED systems, which embrace diverse excitation types along with the rigorous calculation of near- and far-field properties, offer a deeper understanding of the relationships between them. Moreover, the proposed methodology facilitates optimized system design towards targeted performance metrics for quantum technological applications. Notably, architectures incorporating multiple excitation types enable platforms that are switchable across distinct quantum optical regimes, leveraging the spatial dispersion of key quantum optical figures of merit arising from the entanglement and coexistence of these excitations.

IV. Conclusion

We have presented a quantum QNM theory that enables spatio-temporally resolved studies of the dynamics of general magnetodielectric cQED systems. We demonstrate its capabilities with studies of hybrid systems in which different types of excitations lead to a spatial dispersion of typical quantum optical figures of merit.

Acknowledgments

The authors gratefully acknowledge funding from Research Ireland (formerly Science Foundation Ireland) via Grants No. 18/RP/6236 and 22/QERA/3821.

References

[1] D. D. A. Clarke, O. Hess, “Near-field strong coupling and entanglement of quantum emitters for room-temperature quantum technologies,” *PhotoniX*, vol. 5, pp. 33–41, 2024.
[2] L. Feng et al., “Silicon photonic devices for scalable quantum information applications,” *Photonics Research*, vol. 10, pp. A135–A153, 2022.
[3] B. Z. Rameshti et al., “Cavity magnonics,” *Physics Reports*, vol. 979, pp. 1–61, 2022.
[4] L. Meschede, D. D. A. Clarke, and O. Hess, “Quantum quasinormal mode theory for dissipative nano-optics and magnetodielectric cavity quantum electrodynamics,” *APL Quantum*, vol. 3, pp. 016103, 2026.
[5] Y. Lai et al., ”Room-temperature quantum nanoplasmonic coherent perfect absorption,” *Nature Communications*, Vol. 15, pp. 6324, 2024.
[6] W. Yan, R. Faggiani, and P. Lalanne, “Rigorous modal analysis of plasmonic nanoresonators,” *Physical Review B*, vol. 97, pp. 205422-1–10, 2018.
[7] T. Wu et al., ”Modal analysis of electromagnetic resonators: user guide for the MAN program,” *Computer Physics Communications*, Vol. 284, pp. 108627, 2023.
[8] C. Raabe, D. G. Welsch, ”QED in arbitrary linear media: Amplifying media,” *Eur. Phys. J.: Spec. Top.*, Vol. 160, pp. 371–381, 2008.
[9] S. Franke et al., ”Quantization of quasinormal modes for open cavities and plasmonic cavity quantum electrodynamics,” *Physical Review Letters*, Vol. 122, pp. 213901-1–6, 2019.

SPECIAL SESSION 13

Commercialization of Metasurface and Nanophotonic Devices

13 contributions · pp. 989–1007

Building the Innovation Pipeline: Leveraging Princeton Core Facilities and Statewide Resources for Photonics Commercialization

Alexander Norman
Princeton University, USA

***Abstract*— Princeton Materials Institute is the home to two large core facilities: the Micro/nanofabrication center (MNFC) and the Imaging and Analysis Center (IAC). Core facilities are used across the community to accelerate research and help steer ultimate product development. The broader innovation ecosystem in this area will also be highlighted.**

Azopolymer photomorphing as holographic lithography for reconfigurable structured surfaces

Marcella Salvatore[1] and Stefano Luigi Oscurato[1,*]

[1]Physics Department "E. Pancini", University of Naples Federico II, Complesso Universitario di Monte Sant'Angelo, via Cinthia, 80126, Naples, Italy.

*Corresponding author: stefanoluigi.oscurato@unina.it

***Abstract*— Azopolymers capture the inherent vectorial nature of the light in the form of reversible surface reliefs. Tailored intensity and polarization patterns directly map into operating surfaces, without requiring development or etching. We outline here the general phenomenology of azopolymer photomorphing and its potential routes for scalable photonic manufacturing.**

***Keywords*— holographic lithography, azopolymers, structured light, multiple degrees of freedom, diffractive optical elements.**

I. Introduction

Scalable fabrication remains a bottleneck for translating flat-optics concepts into accessible devices. Azopolymer offer a fundamentally different route to structured surfaces that fully leverages the spatio-temporal degrees of freedom of structured light, to propose an alternative lithographic approach based on direct, directional, and reversible material transport, rather than development and etching of conventional workflows. The material at the film surface moves following the local polarization direction and/or the local intensity gradient, originating a surface relief pattern that encodes the geometry of the vector light field (Fig. 1) [1].

Furthermore, wavefront, wavelength, time evolution of the optical field, and even the exposure history directly translate into the final surface morphology. The result are unique patterning capabilities that only require light to fabricate microstructured surfaces ranging from diffraction gratings and Fourier surfaces to anisotropic and chiral micropillars [2,3].

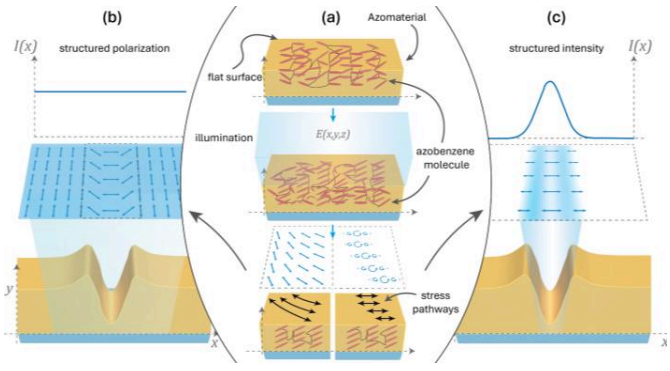

Fig. 1. All-optical vectorial holographic lithography in azopolymers.

II. Results and Discussion

We present the phenomenology of the light-induced mass transport of azobenzene-containing polymers (azopolymers) in several experimental configurations, moving from multi-beam interference to digital holographic configurations, up to tightly focused regimes, where the resolution is pushed down to the diffraction limit and the optical field acquires full 3D vectorial nature. We frame the capabilities of the azopolymer holographic lithography within our current shift toward the adoption of in-situ metrology and feedback during writing. Real-time, non-contact monitoring (e.g., holographic microscopy and diffractive models) can reconstruct evolving 3D topography without perturbing the surface, potentially enabling target morphologies or surface functionalities (e.g. diffraction efficiency) to be dynamically and automatically corrected in real-time.

III. Conclusion

Our work establishes a spatiotemporal strategy for on-demand, all-optical microfabrication and reprogramming of structured surfaces, where spatial and temporal degrees of freedom of structured light intermix to produce advanced patterning capabilities, to be directly exploited as flat optical elements or as reprogrammable templates for replication.

Acknowledgments

This work was supported by the ERC grant HyperMaSH, (GA.101164874), funded by the European Union. The authors thank Prof. David McGee (The College of New Jersey) for insightful discussion.

References

[1] S. L.Oscurato, M. Salvatore, P. Maddalena, and A. Ambrosio, "From nanoscopic to macroscopic photo-driven motion in azobenzene-containing materials" Nanophotonics, vol. 7, no. 8, 2018, pp. 1387-1422.

[2] S. L. Oscurato, F. Reda, M. Salvatore, F. Borbone, P. Maddalena, A. Ambrosio, Shapeshifting Diffractive Optical Devices. Laser & Photonics Reviews 2022, 16, 2100514.

[3] I.K. Januariyasa & al. Stress-driven photo-reconfiguration of surface microstructures with vectorial light fields. Light: Science and Applications 2026, DOI:10.1038/s41377-025-02174-5.

A Scalable Structural-Color Nanocavity Platform for Stain-Free Digital Pathology

Qizhe Chen[1], Qiaoqiang Gan[1, *]

[1]Materials Science and Applied Physics, Physical Science and Engineering Division, King Abdullah University of Science and Technology, Saudi Arabia
*Corresponding author: qiaoqiang.gan@kaust.edu.sa

***Abstract*— We introduce a scalable structural-color nanocavity platform for stain-free digital pathology. The planar nanocavities-on-silicon design avoids nanopatterning, enables wafer-scale manufacturing, and operates with standard optical microscopes. By minimizing system modification and cost, this platform supports large-scale deployment and AI-compatible histological imaging.**

***Keywords*— Structural color, Nanocavity platform, Stain-free pathology.**

I. Introduction

Pathology increasingly demands imaging technologies that are scalable, cost-effective, and compatible with existing clinical infrastructure. While advanced nanophotonic and label-free imaging techniques can provide rich contrast, their adoption is often limited by complex fabrication, expensive instrumentation, and substantial workflow disruption [1-2]. For broad clinical and industrial deployment, stain-free imaging platforms must balance optical functionality with manufacturability and system-level compatibility.

Structural-color nanocavities offer a promising route to achieve this balance. By encoding intrinsic tissue properties into visible color contrast, they enable stain-free visualization without reliance on chemical reagents or complex optical systems. In this work, we introduce a scalable structural-color nanocavity platform designed specifically for stain-free digital pathology, emphasizing simplicity, manufacturability, and seamless integration with existing imaging workflows.

II. Methods

The platform is based on planar nanocavities-on-silicon (NOS), formed by a single dielectric layer on a silicon substrate. This pattern-free architecture enables wafer-scale fabrication using established semiconductor processes. As illustrated in the workflow of Fig. 1a, tissue sections are directly mounted on the nanocavity slide, imaged using standard reflection-mode bright-field microscopy, and subsequently available for either visual assessment or downstream digital analysis. Structural-color imaging is performed without specialized illumination sources or major modifications to existing imaging instrumentation. The design prioritizes robustness, reproducibility, and seamless compatibility with standard digital pathology and AI-enabled analysis pipelines.

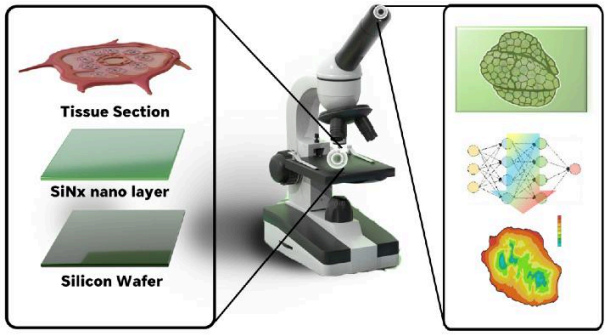

Fig. 1 Schematic of smart histological diagnosis on NOS slides.

III. Results and Discussion

Experimental results show:

- The structural-color nanocavity platform produces vivid, spatially resolved color contrast that translates intrinsic optical variations of tissue into diagnostically relevant visual information without staining. As shown in Fig. 2, its planar design ensures a uniform optical response across large areas and stable color contrast for tissue sections under routine imaging conditions.
-

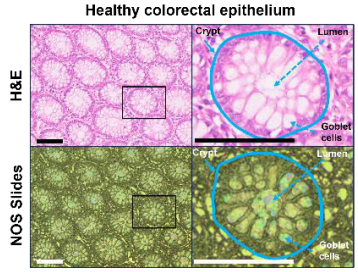

Fig. 2 Comparison of pathological serial sections of organs and tissues imaged using H&E staining and NOS slides, showing healthy colorectal epithelium with a zoomed-in epithelial cell.

- Compared with many advanced imaging modalities, the platform operates without substantial changes to optical hardware or imaging systems, significantly reducing system-level cost and deployment barriers. As demonstrated in Fig. 3, the resulting low manufacturing cost enables large-scale image acquisition, creating favorable conditions for downstream artificial-intelligence-based analysis and automated tissue assessment. These features position the platform as a practical bridge between nanophotonic innovation and real-world digital pathology.

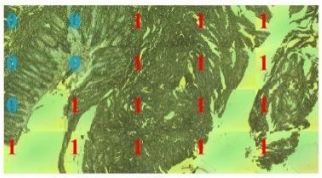

Fig. 3 Results of an AI classification model using the dataset from NOS slides.

IV. Conclusion

We have demonstrated a scalable structural-color nanocavity platform that enables stain-free digital pathology while addressing key barriers to commercialization. By combining planar nanocavity design, wafer-scale manufacturability, and compatibility with standard optical microscopes, this platform offers a realistic pathway for large-scale deployment and AI-enabled histological imaging. The approach illustrates how simplified nanophotonic architectures can accelerate translation from laboratory research to clinical and industrial applications.

Acknowledgments

This work was supported by King Abdullah University of Science and Technology (KAUST), the KAUST Center of Excellence for Smart Health.

References

[1] J Balaur, Eugeniu, et al. "Colorimetric histology using plasmonically active microscope slides." Nature 598.7879 (2021): 65-71.

[2] Balaur, Eugeniu, et al. "Plasmon-induced enhancement of ptychographic phase microscopy via sub-surface nanoaperture arrays." Nature Photonics 15.3 (2021): 222-229.

Twenty Years of Research in Subwavelength Grating Metamaterial Integrated Photonics: From Fundamentals to Real-World Impact

J.G. Wangüemert-Pérez[1,*], A. Ortega-Moñux[1], R. Halir[1], P. Cheben[2], J.H. Schmid[2], J.D. Sarmiento-Merenguel[3], A. Maese-Novo[3], P. Ginel-Moreno[3], I. Molina-Fernández[1]

[1]Telecommunication Research Institute (TELMA), Universidad de Málaga, CEI AndalucíaTECH, Louis Pasteur 35, Málaga 29010, Spain
[2]National Research Council Canada, 1200 Montreal Road, Ottawa, ON, K1A 0R6, Canada
[3]AGPhotonics, Edf. Bioinnovación UMA, C. Severo Ochoa, 34, Campanillas, 29590 Málaga
*Corresponding author: jgwanguemert@uma.es

***Abstract*— Subwavelength grating metamaterials have become a key tool in silicon photonics, enabling integrated optical devices with unprecedented performance. This invited talk reviews some of the main contributions made by the University of Málaga, in close collaboration with the National Research Council of Canada (NRC), to the development of this field. Particular emphasis will be placed on practical considerations in the design, fabrication, scaling, and qualification of these devices, as well as on how this line of research ultimately led to the creation of AGPhotonics, a university spin-off focused on integrated-photonics solutions for free-space optical wireless communications.**

***Keywords*— integrated photonics, silicon photonics, subwavelength gratings, metamaterials, optical antennas, free-space optical communications.**

Integrated photonics is rapidly emerging as a foundational technology for next-generation communications, sensing, signal processing, and AI-oriented computing hardware. Within this landscape, silicon photonics has become particularly attractive thanks to its scalability and compatibility with mature CMOS manufacturing techniques. One of the developments that most profoundly expanded its design space was the advent of subwavelength grating (SWG) metamaterials, which enabled precise lithographic control of effective index, dispersion, anisotropy, and radiation, converting periodic structures into essential building blocks for high-performance photonic integrated circuits [1].

This invited talk reviews the contributions that shaped our group's twenty-year trajectory in subwavelength grating integrated photonics [2]. From early SWG-based fiber-chip couplers [3] and dispersion-engineered broadband directional couplers [4], our work developed the theoretical, numerical, and technological basis needed to exploit periodic structures across their subwavelength, Bragg, and radiative regimes, while also clarifying practical issues such as substrate leakage in SWG waveguides through experimentally validated design rules [5]. This enabled a broad portfolio of high-performance devices, including ultra-broadband compact 3-dB/90° couplers based on anisotropy engineering [6], polarization-insensitive components in standard 220-nm SOI [7], narrowband and arbitrary-response Bragg filters [8], distributed Bragg deflectors for controlled on-chip beam shaping [9], and, more recently, directive, steerable integrated optical phased-array antennas for free-space optics [10].

Beyond the scientific and technological advances, this work also had a strong educational and technology-transfer impact. Over two decades, the group has trained numerous undergraduate, MSc, and PhD students, many of whom produced award-winning research, high-impact publications, and patents. This accumulated know-how in periodic integrated photonics, together with the sustained formation of talent, enabled the creation of AGPhotonics, a spin-off focused on integrated transceivers for future optical wireless communications [11].

Acknowledgments

Agencia Estatal de Investigación, Ministerio de Ciencia, Innovación y Universidades (PID2023-151178OB-I00); Universidad de Málaga. The authors gratefully acknowledge all current and former members of the Photonics and RF Research Lab for their dedication and effort over the past twenty years.

References

[1] P. Cheben et al., "Recent advances in metamaterial integrated photonics," Adv. Opt. Photon., vol. 15, 2023.
[2] Photonics & RF Research Lab. https://www.photonics-rf.uma.es/
[3] R. Halir et al., "Continuously apodized fiber-to-chip surface grating coupler with refractive index engineered subwavelength structure," Opt. Lett., vol. 35, 2010.
[4] R. Halir et al., "Colorless directional coupler with dispersion engineered sub-wavelength structure," Opt. Express, vol. 20, 2012.
[5] J.D. Sarmiento-Merenguel et al., "Controlling leakage losses in subwavelength grating silicon metamaterial waveguides," Opt. Lett., vol. 41, 2016.
[6] A. Maese-Novo et al., "Wavelength independent multimode interference coupler," Opt. Express, vol. 21, 2013.
[7] D. Pereira-Martín et al., "Complex spectral filters in silicon waveguides based on cladding-modulated Bragg gratings," Opt. Express, vol. 29, 2021.
[8] C. Pérez-Armenta et al., "Polarization insensitive metamaterial engineered multimode interference coupler in a 220 nm silicon-on-insulator platform," Optics & Laser Technology, vol. 164, 2023.
[9] A. Hadij-ElHouati et al., "High-efficiency conversion from waveguide mode to an on-chip beam using a metamaterial engineered Bragg deflector," Opt. Lett., vol. 46, 2021.
[10] P. Ginel-Moreno et al., "On-chip metamaterial antenna array with distributed Bragg deflector for generation of collimated steerable beams," Laser Photon. Rev., vol. 16, 2022.
[11] AGPhotonics. https://ag-photonics.com/

Photonic Band Gap Robustness of Stealthy Hyperuniform Metamaterials

Manuel Gallego[1,*], Uzair Malik[1,2], Yezhezi Zhang[1,3],Michael A. Klatt[4,5,6], Claire F. Gmachl[1]

[1]Department of Electrical and Computer Engineering, Princeton University, Princeton, NJ, 08544, USA
[2]Current Address: Accenture PLC, 323 Congress Avenue, Austin, TX, 78701
[3]Current address: Cruise LLC, 333 Brannan St, San Francisco, CA 94107, USA
[4]German Aerospace Center, Institute for AI Safety and Security, Wilhelm-Runge-Str. 10, 89081 Ulm, Germany
[5]German Aerospace Center, Institute of Frontier Materials on Earth and in Space, 51170 Cologne, German
[6]Department of Physics, Ludwig-Maximilians-Universität München, Schellingstr. 4, 80799 Munich, Germany
*Corresponding author: mg6693@princeton.edu

***Abstract*—We design, simulate, and fabricate stealthy hyperuniform metasurfaces of variably shaped silicon pillars for the mid-IR. Simulations reveal large photonic band-gaps (PBG) approximately 37% in width. Measurements show enhanced reflection regions around 950-1020 cm^{-1} corresponding to the PBG location for all geometries, confirming band-gap robustness to variations in pillar cross-section.**

***Keywords*— metamaterials, metasurfaces, disordered media, photonic gap, stealthy hyperuniform, fabrication, silicon, FTIR**

I. Introduction

Hyperuniform structures are metamaterials that exhibit an exotic state of matter [1], [2], [3] by blending crystal and liquid like characteristics. Characterizing these novel heterostructures using order metrics, such as pair correlation or structure factor, reveals long range order in inherently disordered media. For a point distribution to be *hyperuniform*, the structure factor $S(k)$ must vanish in the neighborhood of small k [1]:

$$\lim_{|k|\to 0} S(k) = 0 \tag{1}$$

Stealthy hyperuniform (SHU) structures are a special subclass of hyperuniformity; "Stealthiness" requires the structure factor $S(k)$ to vanish for a finite range of wavenumbers smaller than a critical wavenumber $k < K_c$. Studies have demonstrated SHU structures exhibiting crystal and liquid like behavior, such as photonic band gaps (PBGs) and spatial isotropy in the microwave [4] and mid-IR range [5]. Applications of hyperuniformity include silicon photonic waveguides [6], and hyperuniform THz quantum cascade lasers [7].

In this work, we design, simulate, fabricate, and characterize a SHU pattern of shaped pillars on a low doped silicon substrate to maximize transparency. The pattern is realized through a collective coordinate optimization algorithm with a targeted structure factor condition [8]. The generated SHU pattern forms a 30 X 30 μm square unit cell with periodic boundary conditions that can be tiled. We simulate the SHU structure as infinitely long semiconductor pillars embedded in air, and the transverse magnetic (TM) band diagram is computed along the irreducible Brillouin zone. Various regular geometric shaped pillars were generated to examine the robustness of the PBG size and location. Patterns of circles, triangles, squares and crosses were found to have large PBGs of widths about 37%, 37%, 40%, and 14%, and PBG center frequencies around 1065 cm^{-1}, 1065 cm^{-1}, 1165 cm^{-1}, and 1288 cm^{-1}, respectively.

II. Fabrication

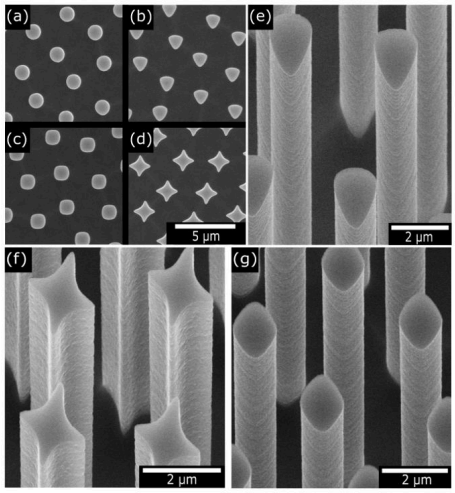

Fig. 1. Scanning Electron Microscopy (SEM) top view images of (a),(b),(c),(d) the shaped silicon pillars, and (e), (f), (g) the tilted view showing silicon pillars approximately 8.5 μm tall. Scalloping from the Bosch process is noticeable on the sidewalls.

Once the size and location of the PBG is confirmed via simulations, the SHU designs are then fabricated in two major steps; lithography and dry etch. The low doped silicon is spin coated with AZ 5214 image reversal photoresist for its thickness and feature resolution. The SHU pattern is then tiled to cover an area of approximately 1 cm^2, and the exposure conducted via direct write. An optimized recipe using this method of photolithography allows for writing of sub micrometer features necessary for our shaped pillars. The sample is then dry etched using the Bosch process using the photoresist

as a mask. Shown in Fig. 1 are top, and side view, electron microscopy images of the fabricated samples; sharper angles can be achieved by switching to electron beam lithography. The shaped silicon pillars were etched to approximately 8.5 μm deep and cleaned in piranha/HF solutions. Scalloping from the Bosch process is present on the sidewalls of all structures, however, these features are about 100 nm wide and do not interfere with IR spectrum measurements from the FTIR.

III. Characterization

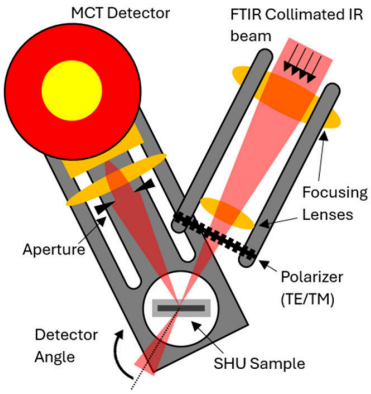

Fig. 2. Experimental setup for transmission and reflection spectra measurement for the SHU metasurfaces. Broadband IR light is TM polarized and focused onto the surface of the SHU structure. The sample and detector can freely rotate to measure various incidence angles.

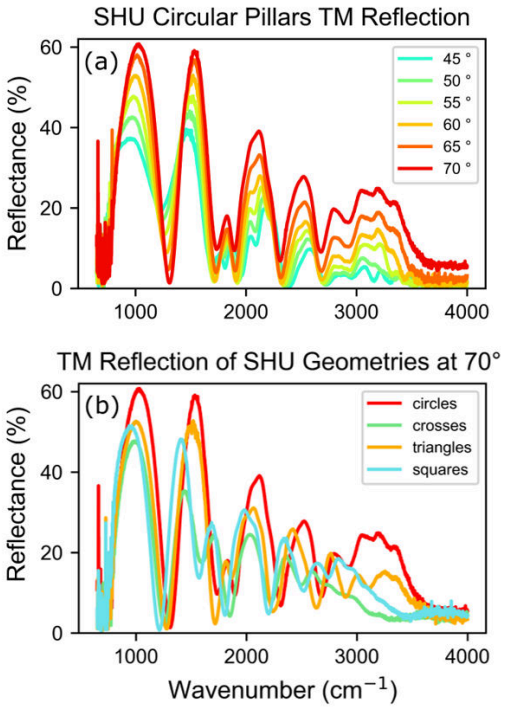

Fig. 3. FTIR TM spectra of (a) the circular pillars, and (b) the 70° reflection of all shapes. The circle spectra shows enhanced reflection with increasing incidence near 1020 cm^{-1} corresponding to the PBG from simulation at 1065 cm^{-1}. All geometrical shapes display an enhanced reflection region around 950-1020 cm^{-1}, and fringing associated with thin film interference from the metasurface.

The shaped pillar SHU samples are characterized by using a broadband IR light from a FTIR. Fig. 2 shows light passing through a polarizer and focused by ZnSe lenses onto the sample surface. The SHU sample and photodetector are both placed in independent rotational stages; allowing for fine adjustment of the incidence angle onto the metasurface. Fig. 3 (a) shows the TM reflection of the circular pattern SHU metasurface for various incidence angles (45°-70°) with an enhanced reflection region around 1020 cm^{-1}. This increased reflection corresponds closely to the simulated PBG around 1065 cm^{-1}, and is most notable with increasing incidence angles. Moreover, the oscillating peaks at 1020 cm^{-1}, 1530 cm^{-1}, 2120 cm^{-1}, ..., correspond to interference fringes from the SHU metasurface acting as a thin film on the bulk silicon substrate. Fig. 2 (b) shows the TM 70° incidence reflection of all four geometries, where an enhanced reflection region near 950-1020 cm^{-1} appears; confirming that SHU structures are indeed robust to changes in geometric shape.

IV. Applications and Conclusion

Studies have demonstrated that metamaterials with PBGs are capable of image differentiation [9], [10], Additionally, SHU metasurfaces function as tunable IR low pass filters by adjusting the target structure factor [5], [9]. In this study, we have simulated and realized a SHU metasurface and observed increased reflection associated with the designed PBG in all four geometries, cementing the fact that changes in the pillar geometry does not cause the PBG to shrink or be destroyed. SHU metasurface manufacturing can be scaled up via UV stepper photolithography, and large diameter automatic wafer processing to increase yield. Moreover, the robustness of the PBG to changes in geometry make it resilient to fabrication defects, such as sidewall roughness from dry etching.

This work was performed in part at the Micro/Nano Fabrication Center (MNFC), a core shared-use facility of the Princeton Materials Institute (PMI). We acknowledge Salvatore Torquato for valuable discussions. M.A.K. acknowledges funding and support by the Deutsche Forschungsgemeinschaft through the SPP2265, under grant numbers KL 3391/2-2, WI 5527/1-1 and LO 418/25-1, and by the Initiative and Networking Fund of the Helmholtz Association through the Project “DataMat”.

References

[1] Torquato, Stillinger, Phys. Rev. E 68(4), 041113 (2003).
[2] Torquato, “Hyperuniform states of matter,” Phys. Rep. 745, 1–95 (2018).
[3] Florescu, Torquato, Steinhardt, Proc. Natl. Acad. Sci. USA 106(49), 20658–20663 (2009).
[4] Man, Florescu, Matsuyama, Opt. Express 21(17), 19972–19981 (2013).
[5] Gallego, Kacmoli, Zhang, Klatt, Gmachl, Opt. Express 33, 31701-31712 (2025)
[6] Milošević, Man, Nahal, Sci. Rep. 9(1), 20338 (2019).
[7] Degl’Innocenti, Shah, Masini, Sci. Rep. 6(1), 19325 (2016).
[8] Uche, Stillinger, Torquato, Phys. Rev. E 70(4), 046122 (2004).
[9] Zhang, Ph.D. Thesis, Princeton University, 2022
[10] Guo, Xiao, Minkov, Shi, Fan, Optica 5, 251-256 (2018)

Application focused meta-surface design: workflow, methods & examples

L. Penninck[1,*], C. Beckerleg[1], B. Robben[1]

[1]PlanOpSim NV, Gent, Belgium

*Corresponding author: lieven.penninck@planopsim.com

***Abstract*—Large volume metasurface applications are now a commercial reality. In this contribution we outline the engineering methods and workflows that enable design of metasurface products not demonstrators. This includes efficient design cycles, design-for-manufacture and system integration. Popularization of these methods will allow broad adaptation of metasurfaces in the optical industry.**

***Keywords*— metasurfaces, sensitivity analysis, design-for-manufacture.**

I. Introduction

Metasurface sensors are now applied in smartphone sensors. This marks a milestone for the metasurface field., that what once was an curious lab experiment is now a competitive mass market application. While many research groups have demonstrated metasurfaces for various applications on a lab scale. The know-how to develop metasurfaces for products and volume manufacturing is limited to a few specialized companies. The next step needed for a broad scale application of metasurface is for these methods to become known and available to the field as a whole.

II. Manufacturability

A critical concept is design-for-manufacture. Designing nanostructures, components not just for optimal performance in the idealized nominal situation but for robust performance given realistic manufacturing variability.

The field of electronics and photonic integrated circuits extensively used foundry provided design rules and process development kits (PDKs). Adhering to design rules ensures that a design meets the foundries processes. While PDKs ensure that structure are not only manufacturable but that their process has been optimized. An additional benefit is that designs made with the same PDK can share a lithograpy/imprint mask in a multi-project wafer (MPW). MPWs significantly reduce the prototyping cost making metasurface design accessible for more designers. First meta-atom PDKs have been released and integrated in commercial software tools [1].

In addition to process optimization, sensitivity and Monte Carlo analysis are needed to identify sensitive parameters and designs with higher tolerance to inevitable variability across wafers and between batches [2].

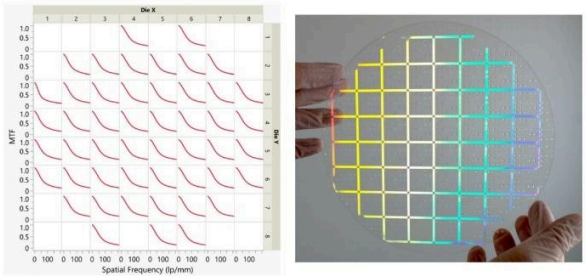

Fig. 1 MTF variability across dies in a wafer via PDK process. PDKs are integrated into design software [1].

III. System integration

Manufacturability is not limited to individual metasurfaces. Their integration and alignment with other sensors, lenses, and metasurfaces also can make or break product performance.

Integration methods for co-optimization of meta-surfaces have been developed. These allow combining traditional refractive and reflective designs with metasurfaces. These methods generally rely on continuous phase approximations. An important future development will be extending these methods to take into account higher order diffraction and stray light. As well as mitigating the system impact of nanostructure variability.

IV. Conclusion

Metasurfaces have reached the stage of mass manufacturing. Broad availability of design-for-manufacture methods and system design can enable a new range of applications for metasurfaces..

References

[1] Commercial software by PlanOpSim NV (www.planopsim.com).

[2] Penninck, L., & Woestenborghs, W. (2021). Sensitivity analysis and tolerancing of Mid Wave IR metalenses. OSA Optical Design and Fabrication 2021 (Flat Optics, Freeform, IODC, OFT), FTu4A.4. https://doi.org/10.1364/FLATOPTICS.2021.FTu4A.4

Metal oxide metasurfaces elaborated by nanoimprint and derived methods

D. Grosso[1*], B. Kerzabi,[1] M. Abbarchi,[1] M. Putero,[2] A. Gourdin,[1] M. bouabdellaoui,[1] E. Daher, and L. Weber[1]

[1] Solnil SAS, 95 rue de la république, 13002, Marseille, France
[2] Institut of Materials Microelectronics and Nanosciences of Provence, IM2NP, Avenue escadrille Normandie Niemen 13 397, UMR 7334, Marseille, France
[*]corresponding author: david.grosso@univ-amu.fr

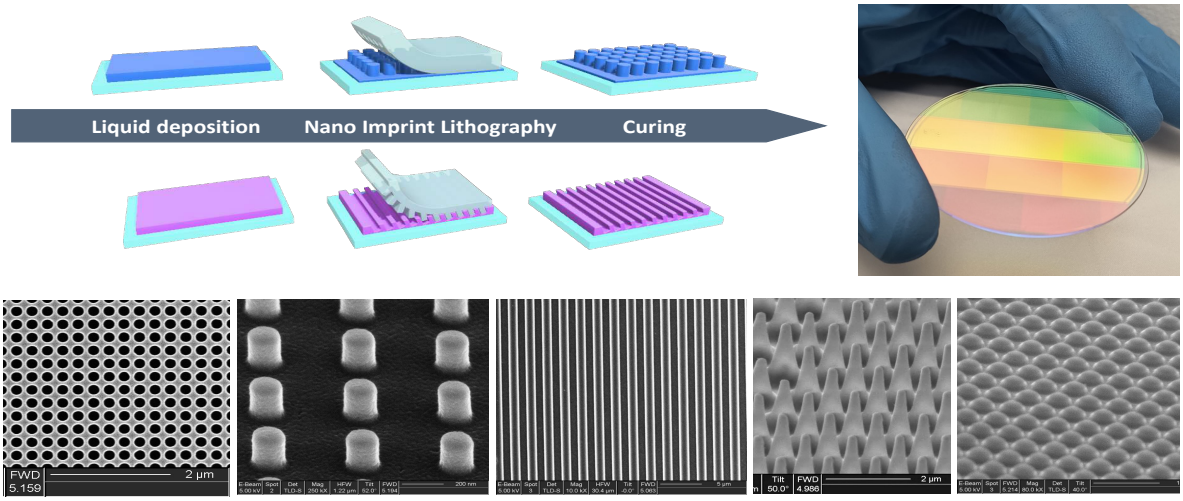

Figure 1 : Schemes of the NIL method and SEM images of different metaatom arrays composed of metal oxides.

***Abstract*: Sol-gel chemistry combined to direct nanoimprint lithography was developed to elaborate robust metal-oxide meta-surfaces. This presentation shows that such a combination enables the facile production of various types of metasurfaces with materials specifically developed to cover a wide span of refractive index and an exceptional transparency.**

***Keywords* - Extreme refractive index (meta)materials, high transparency, direct NIL processing,**

Conventional top-down fabrication methods for metasurfaces are often cumbersome and expensive (both CapEx and production costs). Here, we showcase the use of Soft-Nano-Imprint-Lithography (soft-NIL) as a scalable, cost-effective, and CMOS-compatible method for directly imprinting sol-gel precursor resins into metasurfaces of metal oxides (e.g. SiO_2, TiO_2, VO_2, see Fig. 1). Photonic metasurfaces can be prepared with vertical aspect ratios up to 7, on diverse substrates such as glass, fused silica, sapphire, and silicon wafers. A precise adjustment of the chemical precursors and nano-imprint conditions ensure faithful replicas over large areas: the method is scalable up to 200 mm wafers, limited only by the plate-to-plate machinery employed. The resulting materials offer controlled, on-demand refractive indices ranging from 1.12 to 2.6@520 nm with near-zero extinction for passive photonic devices and extremely low haze. Various metasurface designs addressing diverse functionalities,[1-7] such as (i) light in- and out-coupling and transport for Augmented Reality and PICs using ultra high index materials, (ii) broadband and broad-angle anti-reflection coatings with high LIDT for high power laser optics, (iii) air-gap alternatives and cladding layers using ultra-low index materials, together with (iv) reconfigurable metasurfaces using the Metal to Insulator Transition of VO_2 metaatoms, have been developed and are discussed. This work highlights the potential of soft-NIL in advancing the field of optical metasurfaces and paves the way for their widespread applications in next-generation devices.

References

1. Yudha Ramanda, Jacopo Remondina, Magali Putero, Olivier Soppera, Marco Abbarchi, Victor Malgras, and David Grosso*. Tailoring the Visible Spectral Response of Phase-Change VO_2 Sol–Gel Coatings with Large Resistivity Contrast Using Nanoimprinted Metasurfaces. **ACS Applied Materials and Interfaces**, 2025, doi.org/10.1021/acsami.5c14988.
2. Zeinab Chehadi, Michele Montanari, Nicoletta Granchi, Mehrnaz Modaresialam, Mathieu Koudia, Mathieu Abel, Magali Putero, David

Grosso, Francesca Intonti, and Marco Abbarchi. Soft Nano-Imprint Lithography of Rare-Earth-Doped Light-Emitting Photonic Metasurface**, Advanced Optical Materials,** 10, 21, 2022, 2201618, DOI 10.1002/adom.202201618.

3. Modaresialam, M.; Bordelet, G.; Chehadi, Z.; O'Byrne, M.; Favre, L.; Putero, M.; Abbarchi, M.; Grosso, D. Enhanced Refractive Index Sensitivity through Combining a Sol-Gel Adsorbate with a TiO_2 Nanoimprinted Metasurface for Gas Sensing. 2021, **ACS Applied materials & interfaces**. DOI:10.1021/acsami.1c13248
4. M; Chehadi, Z; Bottein, T; Abbarchi,; Grosso, D. Nanoimprint Lithography Processing of Inorganic-Based Materials (review). Modaresialam, 2021, **Chemistry of Materials**. DOI: 10.1021/acs.chemmater.1c00693
5. Bochet-Modaresialam, Mehrnaz; Claude, Jean-Benoit ; Grosso, David ; Abbarchi, Marco. Methylated Silica Surfaces Having Tapered Nipple-Dimple Nanopillar Morphologies as Robust Broad-Angle and Broadband Antireflection Coatings. **ACS Appl. Mater. Inter. 2020**, 3, 5231-5239, DOI: 10.1021/acsanm.0c00646.
6. S. Checcucci, T. Bottein, M. Gurioli, L. Favre, D. Grosso, M. Abbarchi. Multifunctional metasurfaces based on direct nanoimprint of titania sol-gel coatings. **Adv. Opt. Mater.** 2019 7, 10, AN 1801406. DOI: 10.1002/adom.201801406
7. Faustini, Marco, Cattoni, Andrea, Peron, Jennifer, Boissiere, Cedric, Ebrard, Paul, Malchere, Annie, Steyer, Philippe, and Grosso, David.Dynamic Shaping of Femtoliter Dew Droplets. **ACS NANO**, 12, **2018**, 3243-3252. **DOI:** 10.1021/acsnano.7b07699

Applications of azopolymers in planar diffractive optics and dynamic microstructure lithography

David J. McGee[1,*], Christopher Baker[2], Coleman Huetz[2], Brielle Zemer[2]

[1]Department of Physics, College of New Jersey, Ewing, NJ USA
[2]Department of Mechanical Engineering, College of New Jersey, Ewing, NJ USA
*Corresponding author: mcgeed@tcnj.edu

***Abstract*— Structured light from a spatial light modulator can programmably drive a real-time photomechanical response in azopolymer films. This new platform can print a variety of planar diffractive optics, including linear, circular and chirped gratings, dynamic diffractive elements, and structured color elements.**

***Keywords*— holographic, azopolymer, diffractive optical elements, microstructure, grating.**

I. Introduction

Spatially structured optical intensity or polarization drives a photomechanical response in azopolymer films, resulting in the formation of surface relief microstructures. The writing light is conventionally generated via multibeam laser interference, which is limited to fabricating structures of fixed period and orientation. Here we report that a spatial light modulator (SLM) configured as an intensity or polarization modulator is an alternative writing technique with several key advantages. The SLM can project structured light that is spatially addressable, enabling the facile fabrication of microscale planar optics in real-time and with no post-exposure chemical processing. Structures can be replicated immediately after exposure and in many cases can be dynamically reconfigured.

II. Experiment

Figure 1 shows the experimental setup. The laser is a 488 nm DPSS and the SLM is a liquid crystal on silicon, phase-only device.

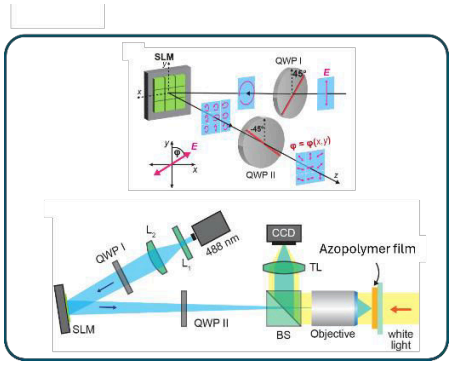

Fig. 1 SLM-based setup for dynamic photofabrication

III. Results and Discussion

When configured as a polarization modulator, the SLM maps grayscale images directly to the orientation of linearly polarized light on the film surface, resulting in a photomechanical stress that drives surface deformation. Single exposures of order 0.01 mm^2 in area can be stitched or raster-scanned for larger area structures. Structures such as linear gratings, sin-phase plates, and computer-generated holograms are readily implemented. First order diffraction efficiencies for typical holographic gratings are 33% at 633 nm. Currently, the lateral resolution is 600 nm, with z-resolution 2 nm.

One appealing application is in structured color. Here, the SLM is addressed to write spatially-multiplexed gratings with periodicities that generate RGB color-additive diffraction modes, with custom color generation based on grating area and amplitude.

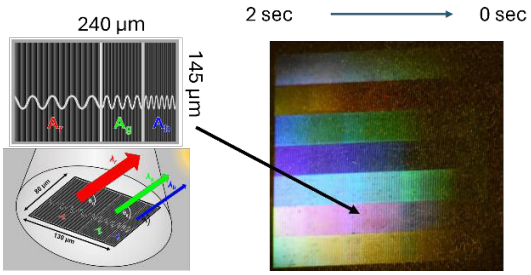

Fig. 2 100 x 100 array (right) of area-tuned RGB microgratings

IV. Acknowledgments

US National Science Foundation award numbers 2024118 and 2515653. We also acknowledge collaborative discussions with Prof. Stefano Oscurato (University of Naples Federico II).

References

[1] J. Strobelt, S. Santer, H. Abourahma, M. Music, Z. Farzan, P. Nezamis, R. Leon, and D.J. McGee, "Photomechanical azopolymers and digital polarization optics: A versatile platform for surface microstructure fabrication," ACS Applied Optical Materials, 3(7), 1461-1476, (2025).

[2] F. Reda, M. Salvatore, M. Astarita, F. Borbone, and S. L. Oscurato, "Reprogrammable Holograms from Maskless Surface Photomorphing," Adv. Opt. Mater. 11(21) 2300823, (2023).

Plasmonically powered organic light emitting devices for advanced display applications

Haridas Mundoor[1], Michael A. Fusella[1], Gearht VanVoorhis[1], Mathew Philippou[1], Renata Saramak[1], Vinod M. Menon[1], Nicholas J. Thompson[1*], Michael S. Weaver[1], Julia J. Brown[1]

[1] Universal Display Corporation, Ewing, New Jersey, USA,
*Corresponding author: nthompson@oled.com

***Abstract*— Plasmonic OLEDs, which utilize plasmonic effects to control light emission, demonstrate enhanced performance compared to traditional devices. Here, we present our recent results and discuss their potential applications in both current and future display technologies.**

***Keywords*— Plasmonics, OLED, displays, metasurface.**

I. Introduction

Organic light emitting devices (OLEDs) offer superior color saturation, unconventional form factors and reduced power consumption compared to conventional display architectures leading to their widespread adoption in displays. Plasmonic OLEDs further improve the properties of OLEDs by enhancing device stability, setting new limits on efficiency, and enabling tunable emission via device design. The decay rate enhancement caused by the coupling of excited states to the surface plasmon modes of metal contact enhances the device stability by minimizing the likelihood of destabilizing excited state interactions. Metallic structures with plasmonic material extracts energy from the surface plasmon mode and convert it to light, thereby enhancing the device efficiency, while providing the emission control needed for advanced display applications. Here, we present our recent results on plasmonic PHOLED research, highlighting emission tunability and device stability enhancements which may be leveraged for future display technologies.

References

[1] M. A. Fusella et al, Nature, 585, 379–382 (2020)

Metasurface Electrodes for Enhanced Light-Matter Interactions in Organic Light-Emitting Materials and Devices

Deirdre O'Carroll[1,2*], Sneha Sreekumar[2], Keshan Perera,[2] Haydee Pacheco[1]

[1]Department of Materials Science and Engineering, Rutgers University, Piscataway, New Jersey 08854, USA

[2]Department of Chemistry and Chemical Biology, Rutgers University, Piscataway, New Jersey 08854, USA

*Corresponding author: ocarroll@rutgers.edu

***Abstract*—Manipulation of light below the diffraction limit in a two-dimensional plane is possible using patterned surfaces called metasurfaces. For light-emitting applications, metasurfaces can be coupled to semiconductor films to increase luminescence quantum-yield, rate, and directionality of photon emission. In this presentation, our research on improving light extraction efficiency and photostability of organic semiconductor thin films using plasmonic metasurfaces will be presented.**

***Keywords*—metasurface, light-emission, Purcell Effect, light-extraction, OLEDs**

I. Introduction

Plasmonic metasurfaces can be used to modify the light-extraction efficiency, emission rate and photostability of light-emitting materials placed with their near-field. In this presentation, we report on our investigations of interactions between plasmonic modes of the metasurface and the excitonic transitions of fluorescence and phosphorescent organic semiconductors used in blue organic light-emitting diode (OLEDs). Optimization of the Purcell effect enables greater photostability of the OLED emitter at the expense of quantum efficiency. However, the light-extraction ability of the metasurface can be used to compensate for non-radiative pathways introduced by the metasurface. The work is relevant to addressing the poor stability and low efficiency of blue OLED pixels using in portable display applications.

II. Methods

Silver nanoparticles are introduced at different device interfaces and within different layers from the anode to the cathode of blue OLEDs to combat the various optical losses that reduce light-extraction efficiency and to study the impact of changes in recombination rate on operational stability. We chose a blend of PFO:F8BT to study fluorescent OLEDs, and a blend of PVK: FIr6 to study blue phosphorescent OLEDs as a function of different nanoparticle additions. Studies of photostability used grating, nanoparticle and nanoporous silver metasurfaces fabricated by thermal dewetting and nanoimprint lithography. Additionally, for device studies, both colloidal silver nanoparticles and discrete thermally dewetted silver nanoparticles were integrated within OLED layers. We measured photoluminescence (PL) lifetime, PL quantum yield and PL stability of the emissive layers on the different silver metasurfaces and characterized the current-density, luminance, electroluminescence, and external quantum efficiency of the OLEDs to investigate how positioning of the plasmonic structures affects the efficiency and operational stability of the OLEDs.

III. Results and Discussion

Initial proof-of-concept studies of the use of silver metasurfaces to improve the photoluminescence stability of blue OLED phosphors show that the increased recombination rate improves the photostability of the phosphor due to the reduction in triplet quenching pathways [1]. The lifetime of phosphorescence is decreased significantly by nanoparticle-based plasmonic surfaces, which improves the photostability of the blue organometallic phosphor by up to a factor of 3.6. Other plasmonic surfaces are also tested and exhibit less significant photostability improvements due to a reduced spectral overlap of the plasmonic modes with the emitter and lower mode confinement. The use of plasmonic surfaces to improve phosphor photostability at blue wavelengths is distinct from other approaches because it involves modification to the local electromagnetic environment of the phosphor rather than modifications to the phosphor molecular structure or the emitting material composition.

In electroluminescent devices that integrate discrete silver nanoparticles into a bottom-emitting OLED device stack, we study several factors like quantum efficiency, PL lifetime and operational stability and find that although the silver nanoparticles can influence the radiative rate as well as the light outcoupling efficiency in OLEDs, they can also cause new photonic and electronic effects, particularly near the anode side

of the device, that need further study and optimization. In particular, we need a deeper understanding of the different mechanisms happening at the anode/hole-transport layer interface and the hole-transport layer/emissive layer interface to fully understand what needs to be done further increase Purcell enhancement, so as to improve the device stability [2]. Future work will focus on integrating the silver metasurfaces into top-emitting OLEDs, which are more amenable to the integration to metasurfaces into the back silver electrode. Additionally, the need for planarization layers and rapid nanofabrication to aid in the commercialization of metasurface-integrated OLEDs will be discussed.

IV. Conclusion

This work aims to contribute to solving the issue of low-performance blue OLEDs by improving the stability and efficiency of the devices, as well as achieving the "true blue" color that is required by the display industry, by manipulating interactions between plasmonic silver nanoparticles and metasurfaces, and OLED emissive layers.

Acknowledgments

This work was supported by the U. S. National Science Foundation, grant TI-2314068. The authors acknowledge helpful discussions and insights from collaborators Dr. Catrice Carter, Ms. Kelsey Gwynne, Ms. Rahma Leil, and Mr. Boyuan Huang.

References

[1] C. M. Carter, K. M. Gwynne, R. Leil, Z. Shen, Z. Cheng, N. Javed, C. Kumah, E. Bethur, D. Santa, C. D. Wang, D. M. O'Carroll, Photostability of blue phosphorescent films on plasmonic surfaces. J. Chem. Phys. 158, 174704 (2023).

[2] S. Sreekumar, "Controlling Metal-Polymer Interfaces for Optoelectronic Devices." PhD Thesis, Rutgers University, January 2025.

Agentic Photonic Simulation with Tidy3D

Zongfu Yu and Yannick Augenstein

Flexcompute Inc.

zongfu@flexcompute.com

Abstract

The design and simulation of photonic devices traditionally demands deep domain expertise, manual scripting of simulation parameters, and iterative debugging — a workflow that creates steep barriers for new researchers and limits throughput even for experienced practitioners. In this work, we present an agentic framework for photonic simulation built on Tidy3D, a GPU-accelerated finite-difference time-domain (FDTD) platform, that leverages large language model (LLM) agents to automate the end-to-end simulation lifecycle. Our framework, powered by FlexAgent and the Model Context Protocol (MCP), transforms the conventional simulation workflow into a natural-language-driven, context-aware process in which an AI agent can autonomously construct electromagnetic models, configure simulation parameters, launch cloud-based GPU computations, and interpret results — all without requiring users to write a single line of code.

Central to our approach is the integration of physics-informed tool use within the agentic paradigm. Rather than relying on generic code generation, our agent is equipped with structured access to Tidy3D's full API surface, up-to-date documentation, and a 3D visualization interface through the MCP framework. This enables the agent to reason about electromagnetic simulation concepts — such as boundary conditions, mesh refinement, source placement, and monitor configuration — with domain-specific accuracy, substantially reducing the error rates commonly observed when general-purpose LLMs attempt simulation scripting. The agent can also iteratively refine simulations by analyzing intermediate outputs and adjusting parameters in a closed-loop fashion, mimicking the expert-level workflow of an experienced photonic engineer.

We demonstrate the capabilities of this agentic framework across a range of representative photonic devices, including waveguide couplers, grating structures, and metasurface elements, showing that the agent can reliably produce simulation setups that converge to physically meaningful results. We further discuss the implications of agentic simulation for accelerating photonic design cycles, democratizing access to high-fidelity electromagnetic modeling, and enabling new paradigms such as agent-driven inverse design and autonomous design-space exploration. Our results suggest that the combination of GPU-accelerated solvers with LLM-based agents represents a transformative step toward fully autonomous photonic design workflows.

Keywords: photonic simulation, large language models, agentic AI, FDTD, Tidy3D, Model Context Protocol, inverse design, GPU-accelerated computing

Inverse Designed Flat Optics for Extended Depth of Focus Laser Beam Shaping

Rajesh Menon[1,2,*], Apratim Majumder[1], Tina M. Hayward[1], Nicole Brimhall[2], Vishwa Pal[3], Kamal P. Singh[4]

[1]Department of Electrical and Computer Engineering, University of Utah, Salt Lake City, Utah 84112, USA
[2]Oblate Optics, Inc., San Diego, California 92130, USA
[3]Department of Physics, Indian Institute of Technology Ropar, Rupnagar 140001, Punjab, India
[4]Indian Institute of Science Education and Research Mohali, SAS Nagar, Mohali 140306, Punjab, India
*Corresponding author: rmenon@eng.utah.edu

Abstract- Inverse designed flat optics enable compact generation of long depth of focus laser beams for micromachining and structured light. We report multilevel diffractive lenses that maintain focused femtosecond spots over twenty millimeters, extend plasma channels to fifty five millimeters, and generate nondiffracting bottle beams over more than five centimeters.

Keywords- flat optics, inverse design, multilevel diffractive lens, beam shaping, micromachining, meta optics.

I. INTRODUCTION

Inverse designed multilevel diffractive lenses provide a compact route to three dimensional laser focus control with a single surface optical element. By optimizing the transmitted phase directly for a target axial intensity distribution, these flat optics can generate extended depth of focus, structured focal volumes, and application specific beam profiles that are difficult to realize with conventional refractive lenses. This direction is especially timely for the META community because recent rigorous comparisons at high numerical aperture show that conventional diffractive optics can remain highly competitive with, and in some cases outperform, metalenses when evaluated on equal footing [1-4].

II. METHODS

We use inverse design to determine the radial height profile of multilevel diffractive lenses for a prescribed three dimensional intensity distribution. The devices are fabricated by grayscale lithography as concentric multilevel structures. For bottle beam generation, a binary axicon first produces a Bessel input beam with suppressed sidelobes, which is then transformed by the multilevel diffractive lens. For femtosecond micromachining, the designed lens is illuminated by 800 nm pulses with 25 fs duration and pulse energies up to about 2 mJ [2,3].

III. RESULTS AND DISCUSSION

In this presentation, we will show several experimentally validated beam shaping regimes. First, a 1064 nm multilevel diffractive lens produced an extended depth of focus exceeding 15 mm with an approximately 32 μm focal width, while maintaining nearly constant beam size over propagation distances up to about 70 mm [1]. Second, for femtosecond pulses, a 10 mm diameter lens designed for a 200 mm working distance achieved an extended depth of focus of 20 mm, with focused spot sizes of about 24 to 35 μm across z = 18 to 22.5 cm and about 90% intensity transmission [2]. A second design provided an average spot size of about 60 μm over z = 27 to 37 cm [2].

In air, the same approach increased plasma channel length from 15 mm for a conventional lens to 55 mm for the flat optic, while laser marking on glass retained widths on the order of tens of microns over the extended focal region [2]. Third, when a Bessel beam illuminates the flat lens, the output becomes a sharply defined nondiffracting bottle beam with visibility about 0.86, period ranging from 0.2 to 1.36 mm, and propagation invariant behavior over more than 5 cm, reaching about 75 mm in our experiments [3]. Finally, recent high NA comparisons show that a Fresnel zone plate can reach 30 percent focusing efficiency at NA = 0.98, compared with 12 percent for a metalens of identical specification, reinforcing the performance relevance of carefully designed conventional diffractive optics within meta optics [4].

IV. CONCLUSION

These results position inverse designed diffractive flat optics as a practical platform for compact high performance laser beam shaping. The combination of long depth of focus, structured bottle beams, high transmission, and manufacturable multilevel profiles makes this approach promising for micromachining, filamentation, imaging, and broader meta optics applications.

ACKNOWLEDGMENTS

Funding: Office of Naval Research (N00014-22-1-2014).

REFERENCES

[1] R. Menon, A. Majumder, T. Hayward, N. Brimhall, V. Pal, and K. Singh, “3D laser focus shaping using inverse designed flat optics,” SPIE Optics & Photonics, 2025.

[2] A. N. Jena, T. M. Hayward, A. Kumari, A. Majumder, J. S. Devara, R. Menon, K. P. Singh, and V. Pal, “Extended depth of focus femtosecond

laser pulses for flexible micromachining," Optics Letters 50, 4670-4673, 2025.

[3] A. N. K. Reddy, S. R. Allam, A. Tiwari, V. Pal, T. M. Hayward, R. Menon, and T. Omatsu, "Generating nondiffracting bottle beams with a flat multilevel diffractive lens," ACS Photonics, 2026.

[4] A. Majumder, J. A. Doughty, T. M. Hayward, H. I. Smith, and R. Menon, "Fresnel zone plate outperforms the metalens at high NA," Optics Express 33, 23313-23321, 2025.

Metaoptics metrology using a wave front sensor

Matthieu Ansquer, Nolan Chan, Benoit Wattellier

PHASICS, Parc Technologique, 91190 Saint Aubin, FRANCE
*Corresponding author: bw@phasics.com

***Abstract*— We present a solution for the metrology of metasurface optical properties based on wave front sensing. For this purpose, we use quadriwave lateral shearing interferometry, on which all PHASICS products are based. This commercial solution is easily integrated in academic laboratories for upstream studies but also in industrial metrology labs or in production lines.**

***Keywords*— metasurfaces, wave front sensing, quadriwave lateral shearing interferometer, singular beams, non-hermitian beams**

I. Introduction

Metasurfaces can be used to modulate the intensity and phase of a light beam. Polarization modulation is also often implemented with such optics. In theory, their behavior is well known but in real-life environments the optical function may differ from what is expected. Therefore, metrology of their transmittance is of great interest.

Errors on manufactured metasurfaces originate from their design (the theoritical optical function may not be perfect and often neglects coupling between meta-atoms), manufacturing technology (machines are limited in terms of spatial resolution or aspect ratio), manufacturing processes (exposure time calibration, mask alignment) and finally defects (punctual defects, incidents during manipulation).

At each step, metrology can help validating simulation models, understand technology and machine limits, tune exposure times, and other parameters, or detect manufacturing drifts. Finally, metrology is used for quality control of finished products.

Control means [1] include electron microscopy (SEM), which is very accurate but lengthy and can be destructive for the sample. People check the focusing quality of metalenses with intensity measurements in the focal volume. This is an indirect diagnosis and no feedback is usually possible with the design.

Optical transmittance measurement (intensity AND phase) is fast and applicable to any of the above requirements. It is often done with interferometers, which are limited in terms of available wavelengths and do not authorize multispectral characterization.

At PHASICS, we propose using a wave front sensor based on quadriwave lateral shearing interferometry (QLSI) [2] to characterize the transmittance of metasurfaces. It measures the optical ray directions which are proportional to the phase spatial derivatives. These are integrated to obtain the beam wave front (phase or equivalently optical path difference). This wave front sensor is compatible with any wavelength and unsensitive to polarization. The latter is important if one wants to check polarization sensitive MS such as Pancharatmann-Berry (PB) MS (see Fig. 1).

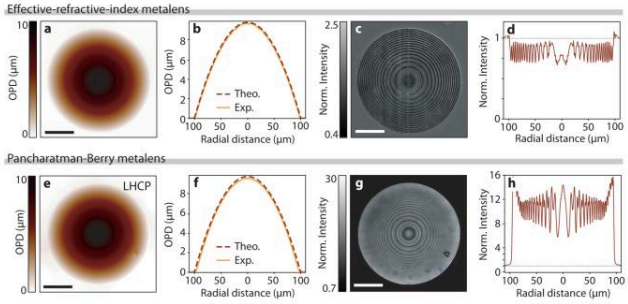

Fig. 1 – Examples of metasurface transmittance measurement with a QLSI of two metalenses using ERI or PB technologies. Extracted from [3]

II. Metrology for metasurface optimization

The set-up to measure the transmittance of any kind of metasurface is quite simple and easily implemented with a standard microscope. An optical source illuminates the metasurface with a plane wave (see Fig. 2). The MS is imaged onto the wave front sensor thanks to a microscope objective. If necessary, circular polarizers are placed before and/or after the sample. The transmittance is obtained by subtracting the wave front measured without the sample in the beam path to the wave front measured with the sample.

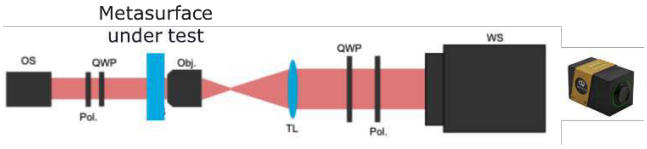

Fig. 2 – Experimental set-up to measure the transmittance of a metasurface in a microscope configuration. The Polarizer (Pol.)/Quarter wave plate (QWP) couples are used as circular polarizers for the characterization of PB MS. OS : optical source, namely a LED. Obj : microscope objective. TL : tube lens. WS : Wave Front Sensor.

Defects in the metasurface are easily and quickly observed without the need to use a scanning electron microscope (see Fig. 3). In this example, the thinnest pillars of an ERI metasurface were washed out during the development step. From the phase image, we could easily feedback with the manufacturing laboratory to further avoid this removal.

The transmittance can be decomposed into the transmission (the square of its modulus) and the phase-shift introduced by the MS optics. The transmission is used to assess the conversion or diffraction efficiency of a metasurface (see Fig. 4).

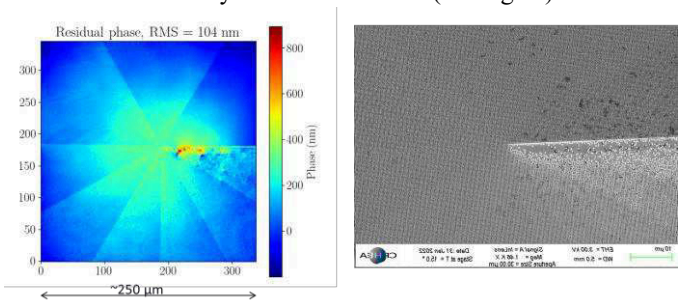

Fig. 3 – ERI metasurface defect as seen from the transmittance map (left) and a scanning electron microscope (right)

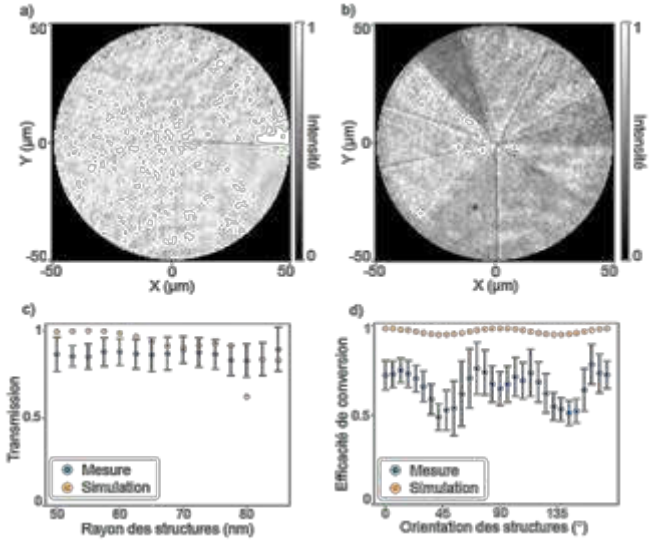

Fig. 4 – Efficiency study for an ERI (left) and PB (right) metasurfaces. The transmission is extracted from the intensity map and compared to the one obtained without a sample. For the ERI MS, we plot the transmission as a function of the pillar radius, which corresponds to the phase levels. For the MS, the phase variation is obtained by rotating a base pattern, generating a so-call geometrical phase. Due to coupling between different orientations, the conversion efficiency may be lower.

III. Singular and non-Hermitian metasurfaces

We got interested into the characterization of singular metasurfaces, which generate optical vortices for instance. Here the challenge is that the transmitted phase is not continuous and its derivatives are not a conservative vector field. Standard numerical integration algorithms cannot recover such functions. However, the information is still there and singularities are visible as peaks when one computes the curl of the derivatives [4,5].

Using this method, we were able to characterize MS generating beams containing multiple vortices (see Fig. 5) or a combination of irrotational and rotational patterns.

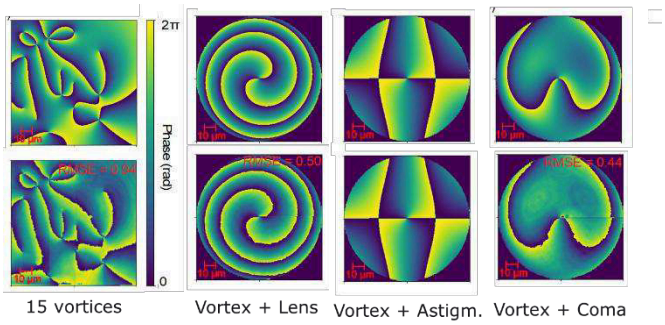

Fig. 5 – Examples of transmitted phase measurement of PB metasurfaces containing one of more singularities combined with other "irrotational" patterns

IV. Conclusion

In this presentation, we show how a wave front sensor is a powerful tool to characterize the transmission of any kind of metasurface. We focus on the use of QLSI, a wave front sensing technique well suited for this purpose thanks to its dense spatial resolution, low phase resolution (below 1 nm) and insensitivity to wavelength and polarization.

References

[1] Jérôme Primot and Nicolas Guérineau, "Extended Hartmann test based on the pseudoguiding property of a Hartmann mask completed by a phase chessboard," Appl. Opt. 39, 5715-5720 (2000)

[2] Samira Khadir, Daniel Andrén, Ruggero Verre, Qinghua Song, Serge Monneret, Patrice Genevet, Mikael Käll, and Guillaume Baffou, "Metasurface Optical Characterization Using Quadriwave Lateral Shearing Interferometry", ACS Photonics, 8, 603 (2021)

[3] Nicolas Kossowski, Yanel Tahmi, Amir Loucif, Martin Lepers, Benoit Wattellier, Guillaume Vienne, Samira Khadir, and Patrice Genevet, "Metrology of metasurfaces: optical properties", *npj Nanophoton.* **2**, 5 (2025)

[4] Wu, T.; Berto, P.; Guillon, M. "Reference-less complex wavefields characterization with a high-resolution wavefront sensor". Appl. Phys. Lett. 2021, 118-25 (2021)

[5] Yanel Tahmi, Matthieu Ansquer, Pierre-Marie Coulon, Sébastien Chenot, Virginie Brändli, Clément Majorel, Adelin Patoux, Rémi Colom, Benoit Wattellier, Patrice Genevet, and Samira Khadir, "Phase characterization of singular metasurfaces", ACS Photonics 2025, 12, 11, 6081–6090

SPECIAL SESSION 14

Towards chiral and magnetoelectric quantum electrodynamics

18 contributions · pp. 1009–1037

Mechanisms of noise immunity in quantum nonlinear and nonreciprocal dynamics

Nicholas Rivera[1]

[1]School of Applied and Engineering Physics, Cornell University, USA
*Corresponding author: nrivera@cornell.edu

***Abstract*— Noise immunity: observables weakly sensitive to dominant noise channels, can extend photonic devices to ultimate quantum limits of sensitivity and performance. We present a new mechanism of noise immunity based on nonlinear nonreciprocal Kerr lattices that directionally route injected noise, preserving squeezing via a non-Hermitian skin effect.**

***Keywords*— quantum noise, nonlinear optics, non-reciprocity, quantum optics**

I. Introduction

Noise often sets limits on the performance of photonic devices such as high-power lasers, quantum sources of light, and sensing and metrology systems. In this context, the existence of observables that are weakly sensitive (or insensitive) to the dominant noise sources, which we call *noise immunity*, is desirable. This is particularly important also in the context of intriguing effects such as chirality, non-Hermiticity, and non-reciprocity, that are known for adding fundamental noise which can preclude sensitive measurement applications.

II. Results

One approach to noise-immunity, which our group has been developing, is based on exploiting nonlinear multimode dynamics which generate anticorrelations between different modes that mutually cancel the effect of excess noise. For example, in [1], we demonstrate that intense femtosecond fields are converted into outputs with shot-noise-level (and below-shot-noise) intensity fluctuations despite large excess noise at the input, with reported overall noise reduction by a factor of ~30 while retaining extreme intensities (approaching 0.1 TW cm^{-2}). The mechanism is the creation of multimode quantum correlations by conservative nonlinear mixing (e.g., four-wave mixing), followed by *mode-selective filtering* that "down-selects" correlated degrees of freedom whose responses to dominant input-noise channels cancel in the measured observable. In a second approach [2], we show how combining programmable wavefront shaping (via a spatial light modulator) with *spatiotemporally* multimode Kerr dynamics can induce noise-immunity, steering a complex nonlinear system into output states whose intensity noise is dramatically reduced—down to the shot-noise level, even when the incident light carries very large excess fluctuations.

Motivated by these nonlinear-correlation routes to noise immunity, in this talk we highlight a new approach we have developed [3] based on nonlinear, nonreciprocal systems, where symmetry breaking manifests in the spatial transport of fluctuations. A nonreciprocal driven–dissipative lattice of Kerr resonators can route externally injected excess noise predominantly in one direction, thereby isolating a region of the device from excess noise such as intensity noise. In a representative example, injecting phase-insensitive excess noise into a central port degrades squeezing throughout a reciprocal chain, but in the nonreciprocal case the noise is funneled to one side and the other side remains essentially unaffected by the noise, preserving even a small amount of squeezing over a wide (~40 dB) range of injected noise levels. This behavior can be understood through the topology of an effective "noise Hamiltonian" and its associated non-Hermitian skin effect, which produces boundary-sensitive, edge-localized noise eigenmodes and strongly asymmetric steady-state noise profiles.

III. conclusions

Our results illustrate that by combining ideas in non-reciprocal systems with controlled nonlinearity, seemingly fundamental noise generation in non-reciprocal systems can be mitigated, potentially enabling the incorporation of these effects in practical photonic devices and sensors.

References

[1] Shiekh Zia Uddin*, **Nicholas Rivera***, Devin Seyler, Yannick Salamin, Jamison Sloan, Charles Roques-Carmes, Shutao Xu, Michelle Sander, and Marin Soljačić. "Noise-immune quantum correlations of intense light." *Nature Photonics* (2025).

[2] Jamison Sloan, Michael Horodynski, Shiekh Zia Uddin, Yannick Salamin, Michael Birk, Pavel Sidorenko, Ido Kaminer, Marin Soljačić, and **Nicholas Rivera**. "Programmable control of the spatiotemporal quantum noise of light." *arXiv preprint arXiv:2509.03482* (2025).

[3] Jamison Sloan, Sachin Vaidya, **Nicholas Rivera**, and Marin Soljačić. "Noise immunity in quantum optical systems through non-Hermitian topology." *arXiv preprint arXiv:2503.11620* (2025).

Triangular cross-section Möbius resonators: electromagnetic helicity and experimental observation of mode-dependent Berry phases

Jeremy Bourhill[1,*], Emma C. I. Paterson[1], Maxim Goryachev[1], Michael E. Tobar[1]

[1]Quantum Technologies and Dark Matter Research Labs, The University of Western Australia, Australia
*Corresponding author: jeremy.bourhill@uwa.edu.au

***Abstract*—We experimentally demonstrate two distinct spin redirection Berry phases in a single triangular Möbius microwave resonator. Fractional azimuthal mode numbers and frequency shifts relative to symmetric cavities confirm geometric phase accumulation linked to electromagnetic helicity.**

***Keywords*— Berry phase, Möbius resonator, microwave cavity, electromagnetic helicity, topological photonics.**

I. Introduction

The Berry phase, Π, is a geometric phase acquired during cyclic adiabatic evolution and appears across quantum and classical systems. In photonics, spin redirection Berry phases arise when polarised waves follow non-planar trajectories in momentum space [1]. Recent optical experiments [2] demonstrated a single Berry phase in rectangular dielectric Möbius resonators. Here, we extend this concept to microwave frequencies in a free-space resonator, using a triangular cross section electrically conducting boundary with D_3 symmetry. Unlike previous studies, this geometry supports two distinct Berry phases of equal magnitude but opposite sign within a single device. The resonator geometry supports electromagnetic modes with nonzero helicity, $\mathscr{H}$ [3], found to relate to the sign of Π, enabling direct observation of geometric phase accumulation through spectral measurements.

II. Methods

Three geometries were studied: asymmetric twisted Möbius resonators; untwisted toroidal resonators; and mirror-symmetric curved resonators, in which the cross section is twisted in one direction across π-radians and then twisted back the opposite direction for the remaining π-radians. These geometries are presented in Fig. 1 and are denoted by the nomenclature D^r_{sx}, where D_s specifies the s-fold dihedral symmetry of the resonator cross-section, r indicates the absolute number of full rotations of the cross-section in 2π-radians, and x identifies the global symmetry of the resonator, with A denoting mirror asymmetric Möbius-type geometries and S denoting mirror-symmetric. It can be shown that the two symmetric systems in Fig. 1 are topologically identical and therefore produce the identical resonant frequency spectra.

The twisted triangular resonator enforces a discrete rotational twist of integer multiples of $2\pi/3$ per circulation of the resonator. Finite element modelling was used to compute eigenfrequencies and field distributions for the lowest order Transverse Electric resonant mode family, $\mathrm{TE}_{1,0,n}$. The azimuthal mode number was extracted by counting surface current density antinodes over a complete loop. Twisted resonators require three windings for closure, leading to fractional mode numbers of the form: $n = \mathbb{Z} \pm 1/3$. Fractional values indicate accumulated Berry phase, a result of the $\mathrm{TE}_{1,0,n}$ modes' lack of rotational symmetry and hence exhibiting a $2\pi r/3$ phase offset with themselves after completing a full circuit of the resonator. Mirror symmetric geometries yield integer mode numbers only.

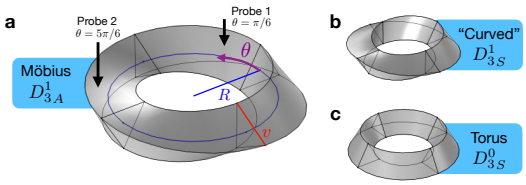

Fig. 1. Examples of the geometries considered; (a) the D^1_{3A} resonator, (b) the D^1_{3S} resonator and (c) the D^0_{3S} resonator. Shown are the free-space volume of the devices, with boundary conditions simulated as perfect electric conductors.

The Berry phase was extracted from measured frequency shifts between twisted and symmetric resonators. The phase is proportional to the frequency difference between $n = \pm 1/3$ modes in the former and $n = \mathbb{Z}$ modes in the latter. Separate internal eigenchannels corresponding to positive and negative electromagnetic helicity [3], which is proportional to the degree that electric and magnetic field vectors are parallel or anti-parallel, respectively, acquire distinct geometric phases, specifically $\Pi = \pm 2\pi/3$.

The D^1_{3S} and D^1_{3A} systems were then 3D-printed in aluminium and the frequency difference between resonant modes used to determine the experimentally confirm the simulated estimates of Berry phase in the Möbius resonators.

III. Results and Discussion

Simulated results confirm the appearance of fractional azimuthal mode numbers in the D^1_{3A} resonators, which are frequency shifted from their symmetric counterparts in opposite directions corresponding to the mode's electromagnetic

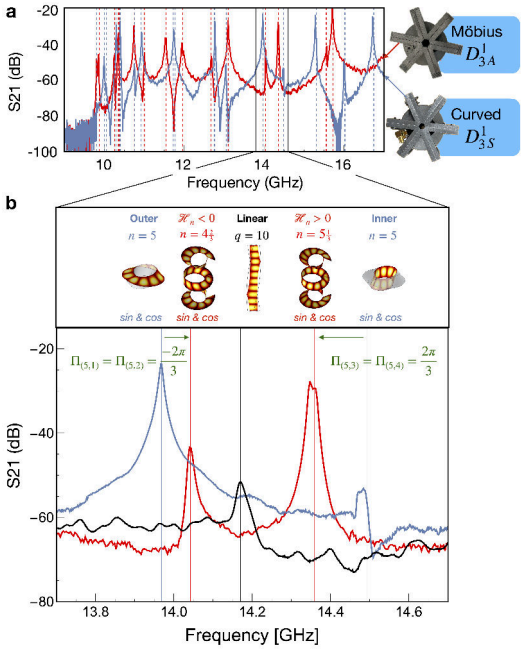

Fig. 2. (a) Experimental S_{21} transmission measurements of the D^1_{3S} (blue) and the D^1_{3A} (red) resonators. The gridlines, colour-coded to match the respective measurements, mark the simulated resonant frequencies of the $\mathrm{TE}_{1,0,n}$ modes for each resonator. These 3D-printed cavities are shown on the right.(b) A magnified view of the transmission spectra highlighting the $\mathrm{TE}_{1,0,5}$ mode of the D^1_{3S} resonator and the $\mathrm{TE}_{1,0,4\frac{2}{3}}$ and $\mathrm{TE}_{1,0,5\frac{1}{3}}$ modes of the D^1_{3A} resonator. For comparison, the transmission of a linear cavity with identical dimensions is also shown for the $\mathrm{TE}_{1,0,10}$ mode.

helicity, $\mathscr{H}_n$. Simulations are conducted for a much larger resonator with radius $R = 79.58$ mm as it gives access to a greater range of n before the onset of higher order modes, whilst a smaller $R = 23.67$ mm was also simulated to match the dimension of the 3D-printed cavities, chosen such that the device was printable.

The 3D-printed resonators demonstrate strong agreement with simulated results, as demonstrated in Fig. 2. The fractional modes appear spectrally between the split doublets of the symmetric resonator. Positive helicity modes shift upward in frequency, while negative helicity modes shift downward. These frequency shifts are directly linked to the Berry phase, which accounts for the adjustment needed to align the fractional $n = \mathbb{Z} \pm \frac{1}{3}$ modes in the D^1_{3A} resonator with the integer modes of the D^0_{3S} resonator. This relationship is expressed as [4]:

$$\Pi_n = \Delta \mathrm{f}_n \frac{4\pi^2 R}{c\sqrt{1 - \left(\frac{2c}{3v f^S_{(n,j)}}\right)^2}}, \tag{1}$$

where $\Delta \mathrm{f}_n$ denotes the frequency difference between companion modes in the two resonators, and c is the speed of light in vacuum.

Using (1), we can relate the difference in frequency spectra between symmetric and asymmetric resonators to the Berry phase for both experimental and simulated devices. In both

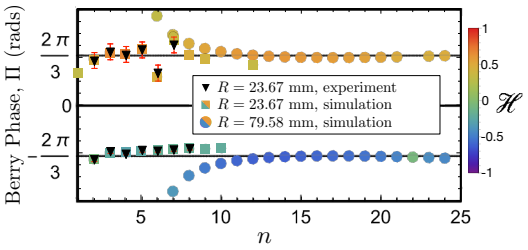

Fig. 3. Π_n as a function of n for the $\mathrm{TE}_{1,0,n}$ modes in the D^1_{3A} resonator for $R = 23.67$ mm (simulated and experimental) and $R = 79.58$ mm (simulated), with associated $\mathscr{H}_n$ depicted by colour. Asymptotic limits of $\pm 2\pi/3$ are shown as black lines. Error bars on the experimental results represent systematic errors.

cases, for both sizes of resonator, as the azimuthal number increases, the Berry phase asymptotically approaches $\pm 2\pi/3$, as demonstrated by Fig. 3. Simulations reveal that reversing the twist direction reverses the sign of the phase for the corresponding helicity, confirming its geometric origin.

The next mode family in these systems, the $\mathrm{TE}_{1,1,n}$ and $\mathrm{TM}_{1,1,n}$, have field profiles that share the rotational symmetry of the D_3 cross-section, and therefore meet up with themselves in-phase after one circulation of the cavity. As a result, these modes do not accumulate any Berry phase and no difference in resonant frequencies observed between the D^1_{3S} and D^1_{3A} resonators.

IV. Conclusion

We have demonstrated the first observation of two distinct Berry phases within a single triangular Möbius microwave resonator. Fractional azimuthal mode numbers and helicity-dependent frequency shifts confirm geometric phase accumulation of $+2\pi/3$ and $-2\pi/3$. This work extends geometric phase engineering to microwave cavity platforms and provides a route toward topologically robust photonic and quantum sensing devices.

Acknowledgments

This work was funded by the Australian Research Council Centre of Excellence for Dark Matter Particle Physics, CE200100008 and used the NCRIS and Government of South Australia enabled Australian National Fabrication Facility - South Australian Node (ANFF-SA).

References

[1] M. V. Berry, "Quantal Phase Factors Accompanying Adiabatic Changes," *Proceedings of the Royal Society of London*, Series A, 392(1802):45–57, 1984.

[2] J. Wang, S. Valligatla, Y. Yin, L. Schwarz, M. Medina-Sánchez, S. Baunack, C. H. Lee, R. Thomale, S. Li, V. M. Fomin, L. Ma, O. G. Schmidt, "Experimental observation of Berry phases in optical Möbius-strip microcavities", *Nature Photonics*, vol. 17(1), pp. 120–125, 2023.

[3] E. C. I. Paterson, J. Bourhill, M. E. Tobar, M. Goryachev, "Electromagnetic helicity in twisted cavity resonators," *Phys. Rev. A*, vol. 112, 013530, 2025.

[4] E. C. I. Paterson, M. E. Tobar, M. Goryachev, J. Bourhill, "Distinct Berry Phases in a Single Triangular Möbius Microwave Resonator." arXiv:2506.07320, 2026.

Spin-selective Structural Phase Transitions in Chiral Crystals Driven by Chiral Phonon Condensation

Shun Asano*, Youichi Yanase

Department of Physics, Kyoto University, Japan
*Corresponding author: asano.shun.57x@st.kyoto-u.ac.jp

***Abstract*— We predict novel structural phase transitions unique to chiral crystals, where the renormalization of chiral phonon frequency by the electron-phonon coupling depends on their handedness. Consequently, soft mode encoding phonon angular momentum induces spin-selective Peierls gaps in the electronic band, entailing a helical spin density wave and chiral lattice distortion.**

***Keywords*— chiral crystal, Peierls transition, chiral phonon, helical spin density wave.**

I. Introduction

Structural chirality manifests across material classes ranging from inorganic solids to molecular and biological architecture. Chiral materials have attracted interest due to their distinctive functionalities such as chirality-induced spin selectivity (CISS) and chiral phonons. In parallel, artificial strategies to engineer desirable chiral structures have advanced, with biological systems providing blueprints for elaborated chiral architectures.

However, existing design strategies are primarily chemical or symmetry-based, leaving open whether functionality can stabilize chiral structure and be active drivers of self-organization of materials. Addressing this question demands elucidating how structures and functional electronic or lattice responses mutually shape one another, ultimately determining ordering principles in chiral materials. Here, we address this issue by unveiling a spontaneous phase transition unique to chiral crystals with screw symmetry. Inspired by the Peierls transition [1], we predict a structural phase transition driven by condensation of chiral phonons, which we term chirality-induced spin-selective Peierls transition (CISSPT).

II. Methods

This presentation is based on our work in Ref [2]. In this work, we focus on the case where the parent phase is a chiral metal as shown in Figure 1, and we first formulate the electron–phonon couplings constrained by screw symmetry [3]. We thereby elucidate the handedness-selective softening of chiral phonons and the resultant phase transition by the qualitative calculation and theoretical analyses.

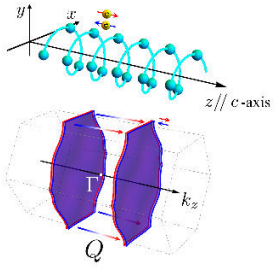

Element	Requirement		Consequences
Material Structure	Inversion ($\hat{\mathcal{P}}$)	✗	Existence of chiral phonon
	Mirror ($\hat{\mathcal{M}}$)	✗	
	Screw/ Helix ($\hat{\mathcal{S}}_{n,\zeta}$)	✓	Pseudo-angular momentum
Electronic States	Metallic/ Conductive		Fermi surface instability
	Nesting along c-axis		Softening of chiral phonon
Phase Control	External field	–	Spontaneous phase transition
	Thermal cooling	✓	

Fig1. (left) An illustration of the target material class in this work: chiral crystals with screw or helical structure and the well-nested electronic bands along c-axis in the Brillouin zone. (right) Minimal requirements and their physical consequences.

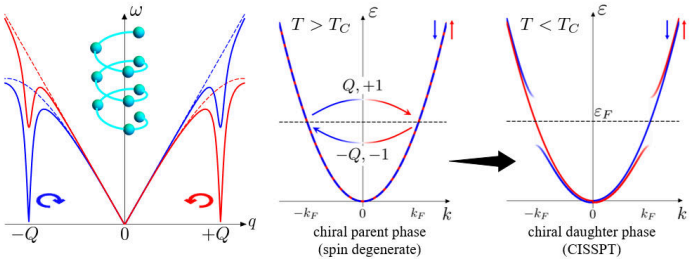

Fig.2 Schematic illustrations of the handedness-selective softening of chiral phonon and resultant spin-selective Peierls transition, in left-handed parent crystals.

III. Results and Discussion

When the high-temperature phase is chiral crystal, the phonon frequency is energetically splitting depending on circular polarization. Therefore, the renormalized frequencies of chiral phonons are handedness-selective, which reveals in the nesting vector involving not merely the linear momentum but also the phonon angular momentum. As a result, a spin-selective Peierls gap is introduced in the electronic band, accompanied by a helical spin density wave and a macroscopic chiral lattice distortion, regardless of whether the original band is spin-degenerate or not (Figure 2). Moreover, due to the coupling between the electronic and lattice sectors, the sliding mode carries mechanical phonon angular momentum and can be electrically actuated.

We have also identified minimal requirements to explore target material classes via symmetry and physical-property criteria. The CISSPT constitutes a family of the transverse Peierls transition which is recently experimentally recognized [4,5]. Furthermore, our mechanism—helical spin density waves stabilized by chiral lattice dynamics—offers a new possibility for the emergence of itinerant helimagnets in structurally chiral materials such as MnSi [6], providing an alternative to conventional scenarios.

IV. Conclusion

We have demonstrated a spontaneous structural phase transition unique to chiral crystals, driven by the mutual coupling between electrons and chiral phonons. While CISSPT is a fundamentally different phenomenon from CISS, our results unveil novel functionalities hosted by chiral materials. Leveraging functionality to shape structures introduces an additional axis for materials design principles, providing strategies for the synthesis and engineering of chiral materials.

From a broader perspective, we offer a novel perspective that bridges various viewpoints—from structure to function and from function to structure—within chirality research. Our findings may thus represent a key missing piece of the puzzle in chirality-driven phenomena in physics and beyond.

Acknowledgments

This work was supported by JSPS KAKENHI (Grant Numbers 25KJ1482, JP22H01181, JP22H04933, JP23K22452, JP23K17353, JP24K21530, JP24H00007, JP25H01249).

References

[1] G. Grüner, “The dynamics of charge-density waves,” Reviews of Modern Physics, vol. 60, pp. 1129–1181, 1988.
[2] S. Asano and Y. Yanase, “Chirality-induced spin-selective Peierls transition,” arXiv:2512.11417, 2025.
[3] T. Tateishi, A. Kato, and J. Kishine, “Electron–Chiral Phonon Coupling, Crystal Angular Momentum, and Phonon Chirality,” Journal of the Physical Society of Japan, vol. 94, p. 053601, 2025.
[4] K. Luo and X. Dai, “Transverse Peierls Transition,” Physical Review X, vol. 13, p. 011027, 2023.
[5] F. Z. Yang *et al.*, “Incommensurate Transverse Peierls Transition and Signature of Chiral Charge Density Wave in $EuAl_4$,” Nature Communications, vol. 16, p. 10401, 2025.
[6] S. M. Stishov and A. E. Petrova, “Itinerant helimagnet MnSi,” Physics-Uspekhi, vol. 54, p. 1117, 2011.

Deterministic generation of a large-scale multi-photon GHZ state

Zu-En Su[1,3*],Dan Cogan[1], Oded Kenneth[1] and David Gershoni[1,2,3]

[1]The Physics Department and the Solid State Institute, Technion-Israel Institute of Technology, Haifa, Israel
[2]Guangdong-Technion-Israel Institute of Technology, Shantou, Guangdong, China
[3]Quantum Science Center of Guangdong-Hong Kong-Macao Greater Bay Area, Shenzhen 518045, China
*Corresponding author: suzuen@technion.ac.il

***Abstract*—We present a novel device based on a semiconductor quantum dot embedded in a photonic microcavity, which deterministically generate at gigahertz rate, strings of indistinguishable single photons in a Greenberger-Horn-Zeilinger (GHZ) multiphoton entangled state with entanglement length surpassing a dozen photons, providing valuable resources for quantum communication and computing.**

***Keywords*— quantum light sources, entangled multiphoton states.**

I. Introduction

Quantum technologies witness rapid contemporary developments transforming abstract scientific ideas and fundamental proof of principle demonstrations into systems of sufficient quality, enabling real applications in quantum information processing. Photonics quantum technologies, in particular, are playing pivotal role in these developments, since photons are quite robust, easy to detect, control and measure and thus to be used as flying quantum bits for carrying quantum information and distributing entanglement. The efforts invested in developing photonics-based quantum technologies stem also from the maturity of the relevant classical technologies. Most relevant to our work is the conceptual proof that a quantum light source of 3 entangled photons is sufficient for building a large-scale quantum computer using otherwise classical optical elements [1]

We present a novel device which deterministically generate at above a GHz rate, strings of entangled and indistinguishable single photons with entanglement robustness exceeding dozen photons. Our device is based on a semiconductor quantum dot embedded in an optical microcavity. The QD confines a spin, precessing in a very weak, externally applied magnetic field in Voigt configuration [2], [3]. The spin is resonantly excited periodically at an optimized rate of about 1.5 GHz, deterministically emitting a long string of single photons in a robust Greenberger- Horn-Zeilinger (GHZ) multi qubit entangled state [4].

The novelty in our device is in its natural spin echo, provided by the opposite precession-directions of the electron spin in the excited state before the photon emission and the hole spin in the ground state after the emission. The magnetic field independent optimized excitation rate is tuned to exactly nullify the acquired phase during both spin precessions.

II. Results

Our results can be summarized as follows:

- The optimized field independent excitation rate is 1.45 ± 0.01 GHz
- The maximal field dependent entanglement length achieved at external field of 50 milliTesla is 13 ± 1
- The field dependent indistinguishability between 2 sequential photons in the string at 50 milliTesla is 0.94 ± 0.02

These values are in good agreement with the model that we developed[5].

III. Conclusion

This deterministic, high-rate and robust quantum light source of more than a dozen of entangled photons, significantly reduces the overhead requirements for photonic measurement-based quantum computation [6] and communication [7], thereby bringing advanced photonic quantum technologies, closer to reality

References

[1] T. Rudolph , "Why I am optimistic about the silicon-photonic route to quantum computing" *APL Photonics* 2, 030901 (2017)
[2] D. Cogan, Z.-E. Su, O. Kenneth, and D. Gershoni "Deterministic generation of indistinguishable photons in a cluster state". *Nat. Photon.* 17, 324, (2023).
[3] Z.E. Su, I. Schwartz, D. Cogan, I. Nassar, O. Kenneth, N. H. Lindner, and D. Gershoni, "Continuous and deterministic all-photonic cluster state of indistinguishable photons". *Rep. Prog. Phys.* 87 077601 (2024)
[4] G. Peniakov, Z.E. Su, A. Beck, D. Cogan, O. Amar, and D. Gershoni "Towards supersensitive optical phase measurement using a deterministic source of entangled multiphoton states". *Phys. Rev. B* 101, 245406 (2020)
[5] D. Cogan , Z.-E. Su, O. Kenneth, and D. Gershoni, "Spin purity of the quantum dot confined electron and hole in an external magnetic field". *Phys. Rev. B* 105, L041407 (2022).
[6] R. Raussendorf, D. E. Browne, and H. J. Briegel, "Measurement-based quantum computation on cluster states," *Phys. Rev. A* , 68, 32,(2003).
[7] K. Azuma, K. Tamaki, and H. K. Lo, "All-photonic quantum repeaters," *Nat. Commun.*, 6, 1, (2015).

Exponentially-enhanced sensing with a frequency-encoded bosonic Kitaev chain

Paul-Édouard Blanchard[1], Alexandre McDonald[2], and Philippe St-Jean[1,2,*]

[1]Department of Physics, Université de Montréal, Canada
[2] Institut quantique, Université de Sherbrooke, Canada
*Corresponding author: philippe.st-jean@umontreal.ca

***Abstract*—We experimentally realize a bosonic Kitaev chain by encoding the corresponding Hamiltonian in the resonant modes of a frequency comb. We harness the inherent nonreciprocal propagation of light in frequency space to detect a small microwave tone with a signal-to-noise ratio that scales exponentially with system size.**

***Keywords*— optical sensors, nonreciprocity, non-Hermitian physics, frequency combs.**

I. Introduction

The ability to optically detect faint perturbations through a noisy background underpins a wide range of important applications. Yet photonic systems, which are intrinsically open quantum systems, are unavoidably susceptible to environmental electromagnetic noise that couples into the apparatus. This unwanted noise mixes with the probe signal and ultimately degrades the signal-to-noise ratio (SNR) at the output.

Here we overcome this fundamental challenge by demonstrating a novel approach, based on a bosonic analogue of the Kitaev model, to realizing optical sensors in which environmental noise and input signal do not scale similarly with the system size, leading to an exponential enhancement of the signal-to-noise ratio.

II. BKC encoding in frequency space

A bosonic Kitaev chain (BKC) is described by the following lattice Hamiltonian with single-particle hopping (ω) and two-mode squeezing (Δ) processes (see Fig. 1a) :

$$H_{\mathrm{BKC}} = \sum_{n=1}^{N} \left[i\omega a_{n+1}^{\dagger} a_n + i\Delta a_{n+1}^{\dagger} a_n^{\dagger} + \mathrm{h.c.} \right]. \qquad (1)$$

The perturbation corresponds to a slight detuning of the last lattice site and the probe signal is weakly coupled to the first site and monitored with a homodyne detection [1].

This hamiltonian equivalently describes the chiral transport of the field's quadrature with $x_n = (a_n^{\dagger} + a_n)/\sqrt{2}$ and $x_n = i(a_n^{\dagger} - a_n)/\sqrt{2}$ respectively propagating to the left and right. In this equivalent picture, the perturbation now becomes a $x - p$ coupling term on the last site. We have encoded this chiral propagation using an electro-optic frequency comb where the nonreciprocal propagation is tailored through simultaneous phase and amplitude modulation (see Fig. 1b).

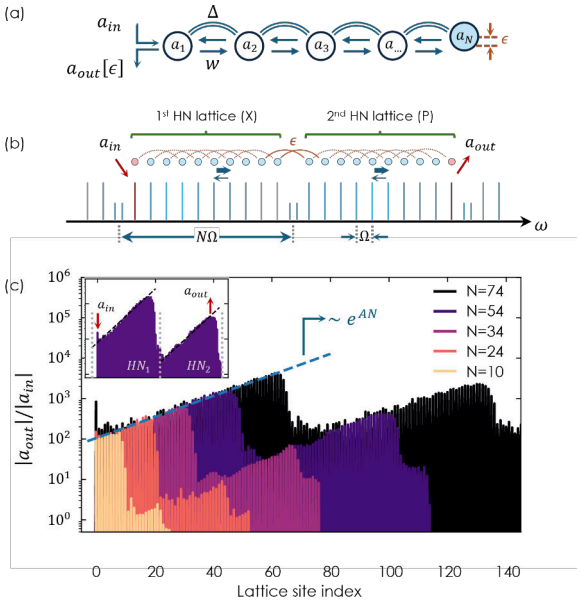

Fig. 1. (a) Bosonic Kitaev chain. (b) Encoding of a BKC in frequency space. (c) Exponential enhancement of the signal.

III. Results

Driving the frequency comb at the first resonant mode of one lattice allows measuring the transmitted light and extracting all its Fourier components through a heterodyne scheme. We observe an occupation of multiple combs as the perturbation couples neighbouring lattices (see Fig. 1c). The non-Hermitian skin effect in each lattice gives rise to an e^{2AN} scaling of the signal, whereas (not shown here) the noise scales as e^{AN} [2].

IV. Conclusion

We have observed an exponential scaling of the SNR in an optical sensor. This has potential applications in remote sensing, notably the optical readout of superconducting circuits.

References

[1] A. McDonald, and A. A. Clerk, "Exponentially-enhanced quantum sensing with non-Hermitian lattice dynamics," *Nature Communications*, vol. 11, no. 5382, 2020.

[2] P.-É. Blanchard, A. McDonald and P. St-Jean, "Exponentially enhanced sensing through nonreciprocal light propagation ," *arXiv*:2511.16895v1

Enhanced Microwave-to-Optical Quantum Transduction with Optomechanical Nanobeam Heterostructures

Akihiko Sekine[1,*], Ryo Murakami[1], Yoshiyasu Doi[1]

[1]Fujitsu Research, Fujitsu Limited, Kawasaki, Japan
*Corresponding author: akihiko.sekine@fujitsu.com

***Abstract*—Achieving a high transduction efficiency and a low added noise simultaneously is essential for the realization of quantum state transfer between distant superconducting qubits. We show theoretically that introducing optomechanical nanobeam heterostructures can improve the transduction efficiency and lower the added noise of the microwave-to-optical quantum transduction in optomechanical systems.**

***Keywords*—quantum transduction, quantum frequency conversion, optomechanical effect, nanobeam, quantum computing, superconducting qubit.**

I. Introduction

The quantum transduction, or equivalently quantum frequency conversion, between microwave and optical photons is an essential quantum technology for the realization of scalable quantum computers with superconducting qubits [1,2,3]. Due to the large frequency difference between microwave and optical ranges, the microwave-to-optical quantum transduction needs to be done via intermediate bosonic mode(s) or via nonlinear interaction process between photons. Theoretically, in the context of the quantum capacity, it has been known that the condition such that the transduction efficiency $\eta > 1/2$ and the added noise $N_{\mathrm{add}} \ll 1$ is required for quantum state transfer [3].

So far, the microwave-to-optical quantum transduction via the optomechanical effect, i.e., mediated by phonons, has attracted much attention as a promising method toward the practical quantum transduction including superconducting qubits [4]. However, achieving a high transduction efficiency of $\eta > 1/2$ and a low added noise of $N_{\mathrm{add}} \ll 1$ simultaneously still requires tremendous effects. It is well known that one of the ways for improving the transduction efficiency is to increase the optical input pump power. As a trade-off, however, there will be an increase in the environmental temperature, which can affect the nearby superconducting qubits.

II. Results

In this work, we show theoretically that introducing optomechanical nanobeam heterostructures can lead to a simultaneous improvement of the transduction efficiency η and lowering of the added noise N_{add} of the microwave-to-optical quantum transduction in optomechanical systems [5]. Such a heterostructure consists of N_{L} layers of an optomechanical crystal nanobeam and N_{L} layers of an insulator. We show that, in the ideal and simplest case where each nanobeam has the same geometrical structure, the electromechanical and optomechanical coupling strengths in the heterostructures are both enhanced by the factor $\sqrt{N_{\mathrm{L}}}$ compared to the single-layer case. As a result, the electromechanical and optomechanical cooperativities are also enhanced by the factor N_{L} compared to the single-layer case, giving rise to the enhanced microwave-to-optical transduction efficiency η. We also find that the added noise N_{add} in the heterostructures is suppressed by the factor $1/N_{\mathrm{L}}$ compared to the single-layer case. Our study opens up a new pathway for a high-efficiency and low-added-noise quantum transduction between microwave and optical photons.

Acknowledgments

We would like to thank Shintaro Sato and Norinao Kouma for their advice and support.

References

[1] X. Han, W. Fu, C.-L. Zou, L. Jiang, and H. X. Tang, *Microwave-optical quantum frequency conversion*, Optica **8**, 1050 (2021).
[2] D. Awschalom *et al*., *Development of Quantum Interconnects (QuICs) for Next-Generation Information Technologies*, PRX Quantum **2**, 017002 (2021).
[3] A. Sekine, R. Murakami, and Y. Doi, *Microwave-to-Optical Quantum Transduction of Photons for Quantum Interconnects*, arXiv:2509.26349.
[4] M. Mirhosseini, A. Sipahigil, M. Kalaee, and O. Painter, *Superconducting qubit to optical photon transduction*, Nature **588**, 599 (2020).
[5] A. Sekine, R. Murakami, and Y. Doi, in preparation.

Cavity control of Kondo physics in two-dimensional materials

Jun Mochida[1,*], Yuto Ashida[1,2]

[1]Department of Physics, University of Tokyo, Japan
[2]Institute for Physics of Intelligence, University of Tokyo, Japan
*Corresponding author: jun-mochida@g.ecc.u-tokyo.ac.jp

***Abstract*—We theoretically investigate a cavity control of magnetic materials, including the Kondo effect in quantum impurities and heavy-fermion systems realized in two-dimensional materials. We show the possibility of enhancing Kondo effect and controlling quantum phases using vacuum fluctuations of quantized electromagnetic fields.**

***Keywords*— cavity QED, Kondo effect, 2D materials, strongly correlated systems**

I. Introduction

Cavity quantum electrodynamics (QED) provides a powerful platform to manipulate light-matter interactions that can effectively control electronic structure of materials at terahertz frequencies. In particular, vacuum fluctuations in cavity QED can offer a novel route to controlling quantum phases in a stable manner.

Such control has been mainly achieved through coupling electromagnetic fields to collective electronic excitations. However, using cavities based on van der Waals materials can provide a more precise control over the electromagnetic environment, enabling enhanced coupling between photons and electrons in two-dimensional systems at the level of single-electron excitations. This implies that the planar cavity consisting of van der Waals materials are particularly suitable for studying cavity-induced effects in two-dimensional correlated electron systems [1].

On the other hand, the interaction between localized magnetic moments and conduction electrons gives rise to the Kondo physics, a fundamental phenomenon in strongly correlated electron systems. At the low temperatures, the Kondo effect leads to the formation of a many-body singlet state, known as the Kondo singlet. In the Kondo lattice system, which consists of a periodic array of magnetic moments, the competition between the Kondo effect and magnetically ordered phases leads to quantum phase transitions and quantum criticality.

Recent advances in two-dimensional materials have enabled the realization of Kondo lattice physics in reduced dimensions. In particular, moiré-engineered structures provide effective realizations of two-dimensional Kondo lattice models with tunable parameters.

Motivated by these developments, we investigate how cavity QED can be employed to control Kondo physics in two-dimensional systems, ranging from impurity problems to Kondo lattice models (Fig. 1). Our study highlights van der Waals cavities as a versatile and well-matched platform for engineering quantum phases in strongly correlated two-dimensional materials.

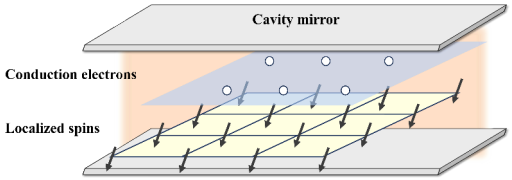

Fig. 1. Schematic of Kondo-lattice systems embedded in a cavity.

II. Methods

Our starting point is the Anderson model coupled to quantum electromagnetic fields in the Coulomb gauge represented as follows:

$$H = H_{\mathrm{PA}} + \sum_{\boldsymbol{k},\sigma} \frac{(\boldsymbol{p} + e\boldsymbol{A})^2}{2m} c^\dagger_{\boldsymbol{k}\sigma} c_{\boldsymbol{k}\sigma} + \sum_{\boldsymbol{q}} \hbar\omega_{\boldsymbol{q}} a^\dagger_{\boldsymbol{q}} a_{\boldsymbol{q}}, \quad (1)$$

where $c_{\boldsymbol{k}\sigma}$ is the annihilation operator for conduction electrons with momentum $\boldsymbol{k}$ and spin σ. H_{PA} is the standard Anderson model, which includes the hybridization between the localized and conduction electrons, the energy of the localized electrons, and the Coulomb interaction for the localized electrons. Here we consider that conduction electrons are affected by quantum electromagnetic fields. We consider the vector potential for multi-mode electromagnetic fields, given by

$$\boldsymbol{A} = \sum_{\boldsymbol{q}} A_{\boldsymbol{q}} (a^\dagger_{\boldsymbol{q}} + a_{\boldsymbol{q}}) \boldsymbol{e}_{\boldsymbol{q}}, \quad (2)$$

where $A_{\boldsymbol{q}}$ is proportional to $1/\sqrt{V_0}$, with V_0 being the mode volume of the cavity. $a_{\boldsymbol{q}}$ is the annihilation operators of bosonic mode with momentum $\boldsymbol{q}$ and frequency $\omega_{\boldsymbol{q}}$..

In the impurity problem, the single-impurity Anderson model coupled to a single-mode cavity photon provides a minimal setup for manipulating the Kondo state at the ground state level, owing to the broken translational symmetry introduced by the impurity. For this simplified model, we used a non-perturbative variational approach by applying a unitary transformation.

On the other hand, in the Kondo lattice model, where translational symmetry is preserved due to the periodic arrangement of local spins, more complex modes of electromagnetic fields are introduced to control the ground-state phase diagram. We analyze this model using controlled perturbative approaches and mean-field approximations.

III. Results and Discussion

We theoretically show the possibility of using cavity confinement to modify the electronic band structures through quantum electromagnetic fields. The characteristic energy scale of the Kondo effect is determined by a physical quantity called the Kondo temperature T_{K}. Variational calculations of the impurity system show that the Kondo state is enhanced by the cavity confinement [2]. Physically, this originates from an effective enhancement of the electron mass due to dressing by cavity photons. We also confirmed a similar mechanism by using the perturbative renormalization group analysis, which shows that the Kondo temperature is enhanced by the light-matter interaction g (Fig. 2).

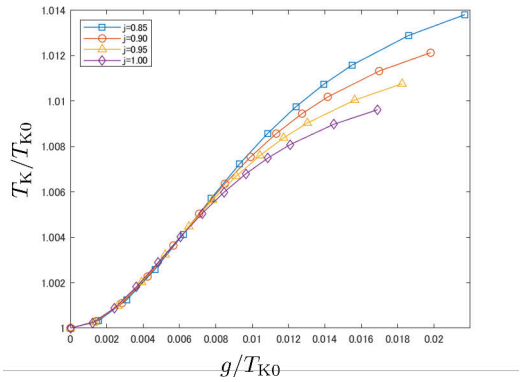

Fig. 2. Enhancement of Kondo temperature T_K as a function of light-matter coupling strength g.

In the two-dimensional Kondo lattice model incorporating interactions that mimic the Ruderman-Kittel-Kasuya-Yosida (RKKY) interaction, we demonstrate that the energies of both the Kondo-dominated (heavy-fermion) phase and the antiferromagnetic phase are lowered by the cavity-induced effects. Our analysis suggests that the antiferromagnetic phase can be stabilized more efficiently than the Kondo phase under cavity confinement.

IV. Conclusion

In conclusion, we have theoretically demonstrated that cavity QED can potentially provide an alternative and versatile tool for controlling Kondo physics in two-dimensional materials. By coupling correlated electron systems to quantum electromagnetic fields, both the impurity Kondo effect and quantum phases in Kondo lattice systems can be modified. Specifically, our results show that cavity-induced effects can enhance Kondo correlations and lower the energies of competing quantum phases, including the heavy-fermion and antiferromagnetic phases. These findings highlight the potential of cavity-based approaches for engineering quantum phases in strongly correlated systems and open new possibilities for stable control of quantum many-body states in low-dimensional materials.

References

[1] Y. Ashida, A. I.mamogl̆u, and E. Demler, "Cavity quantum electrodynamics with hyperbolic van der Waals materials," *Phys. Rev. Lett.*, vol. 130, p. 216901, 2023.

[2] J. Mochida and Y. Ashida, "Cavity-enhanced Kondo effect," *Phys. Rev. B*, vol. 110, p. 035158, 2024.

Induced angular momentum from axion electrodynamics of metals and insulators

Flavio S. Nogueira[1,*], Anastasiia Chyzhykova[1], Vira Shyta[1]

[1]Institute for Theoretical Solid State Physics, IFW Dresden, Helmholtzstr. 20, 01069 Dresden, Germany
[2]Max-Planck Institute for Physics of Complex Systems, 01187 Dresden, Germany
*Corresponding author: f.de.souza.nogueira@ifw-dresden.de

***Abstract*—Axion electrodynamics describes the electromagnetic response of certain topological materials, including three-dimensional topological insulators and Weyl semimetals. Here we discuss the application to Weyl semimetals and a mechanical effect induced by the axion response in topological insulators.**

***Keywords*— axion, topological insulators, Weyl semimetals, plasmonics**

I. Introduction

Broadly, axion electrodynamics is a theory of electromagnetic interactions whose action contains the following term,

$$S_a = \frac{\alpha}{4\pi^2}\int dt \int d^3r a(t,\boldsymbol{r})\boldsymbol{E}\cdot\boldsymbol{B}, \tag{1}$$

where $\alpha = e^2/(\hbar c)$ is the fine structure constant, and $a(t,\boldsymbol{r})$ is the so-called axion scalar field [1]. Quite generally, the above contribution to the action modifies the Maxwell equations. For a nonzero uniform axion field inside a sample, the Maxwell equations are not modified, but the boundary conditions change, like for example in the case of topological insulators [2], [3].

Even within a static setting, electric fields may induce magnetic fields and vice-versa. As a result, a nonzero angular momentum of the electromagnetic field arises [3], [4].

II. Induced angular momentum in Weyl semimetals

Recently we have obtained that a Weyl semimetal with broken time-reversal (TR) symmetry features an angular momentum per unit area of the form [5],

$$\boldsymbol{L}_{\rm EM} = \frac{B_{\rm ap}^2 L\sqrt{\epsilon}}{8\pi g\coth\left(\frac{gL}{2\sqrt{\epsilon}}\right)}\left[\coth\left(\frac{gL}{\sqrt{\epsilon}}\right)-\frac{\sqrt{\epsilon}}{gL}\right]\hat{\boldsymbol{z}}, \tag{2}$$

in a system of thickness L. Here ϵ is the dielectric constant and $g = 2e^2b/\pi$ is related to the axion coupling, with e being the elementary electric charge and b the distance between the Weyl cones.

III. The Feynman paradox in axion insulators

The Feynman paradox highlights that static electromagnetic fields can store angular momentum. Recently, we have demonstrated [6] that axion electrodynamics in a spherical topological insulator provides a topological realization of this effect. Varying the distance of a nearby charged probe q induces Hall currents on the surface that convert electromagnetic angular momentum into mechanical rotation of the sphere, with a frequency derived from the topological response.

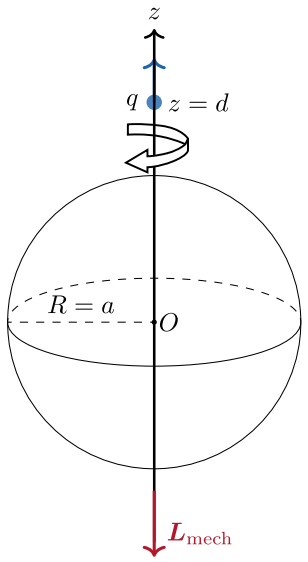

References

[1] F. Wilczek, "Two applications of axion electrodynamics," *Phys. Rev. Lett.*, vol. 58, no. 18, pp. 1799–1802, May 1987. [Online]. Available: https://link.aps.org/doi/10.1103/PhysRevLett.58.1799

[2] X.-L. Qi, E. Witten, and S.-C. Zhang, "Axion topological field theory of topological superconductors," *Phys. Rev. B*, vol. 87, p. 134519, Apr 2013. [Online]. Available: https://link.aps.org/doi/10.1103/PhysRevB.87.134519

[3] F. S. Nogueira and J. van den Brink, "Absence of induced magnetic monopoles in maxwellian magnetoelectrics," *Phys. Rev. Res.*, vol. 4, p. 013074, Jan 2022. [Online]. Available: https://link.aps.org/doi/10.1103/PhysRevResearch.4.013074

[4] F. S. Nogueira, Z. Nussinov, and J. van den Brink, "Fractional angular momentum at topological insulator interfaces," *Phys. Rev. Lett.*, vol. 121, p. 227001, Nov 2018. [Online]. Available: https://link.aps.org/doi/10.1103/PhysRevLett.121.227001

[5] V. Shyta, J. van den Brink, and F. S. Nogueira, "Axion electrodynamics of weyl superconductors with broken time-reversal symmetry," *Phys. Rev. B*, vol. 112, p. 104517, Sep 2025. [Online]. Available: https://link.aps.org/doi/10.1103/5fpw-gc9g

[6] A. Chyzhykova, J. van den Brink, and F. S. Nogueira, "The feynman paradox in a spherical axion insulator," 2025. [Online]. Available: https://arxiv.org/abs/2512.10436

Large topological magneto-optical effect from atomic-scale skyrmion-like texture

Yoshihiro Okamura[1,*]

[1]Department of Applied Physics & Research Center for Advanced Science and Technology, University of Tokyo, Japan

*Corresponding author: okamura @ap.t.u-tokyo.ac.jp

***Abstract*— We report the large spontaneous magneto-optical Kerr effect solely from scalar spin chirality of all-in-all-out state in quasi-two-dimensional triangular-lattice compound $CoNb_3S_6$. Over the entire measured energy region from 55 to 2000 meV, the topological effect dominates the optical response, whose figure of merit largely exceeds other magnets.**

***Keywords*— Skyrmion, topological magneto-optical effect, spin chirality.**

I. Introduction

Electrodynamics rooted in the topology and geometry of quantum states is a cornerstone of modern physics. When a conduction electron undergoes adiabatic transport through a topological spin texture, it acquires a nontrivial Berry phase that acts as an emergent electromagnetic vector potential, giving rise to novel quantum phenomena. In skyrmion magnets such as MnSi, the corresponding emergent magnetic field is typically predicted to reach several tens of tesla [1]. Nevertheless, the resulting electromagnetic responses do not markedly surpass those realized in archetypal ferromagnets. Recently, extensive materials exploration has uncovered the so-called all-in–all-out (AIAO) spin configuration, which breaks time-reversal symmetry while retaining an almost vanishing net magnetization [2]. The AIAO order can be viewed as the small-size limit of a magnetic skyrmion and inherently hosts much larger emergent fields (see figure). Such a state is therefore expected to produce gigantic topological electromagnetic responses, far exceeding those in conventional skyrmion magnets. Yet, this intriguing possibility remains largely unexplored.

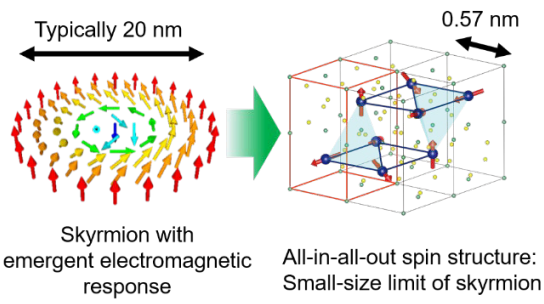

II. Methods

We perform ultrabroadband spectroscopic measurement from 55 meV to 2000 meV and real-space imaging. Combined with numerical Kramers Kronig analysis, we obtain the Hall conductivity spectra down to zero frequency,

III. Results and Discussion

We observe a gigantic spontaneous magneto-optical Kerr effect (MOKE) arising solely from scalar spin chirality of the AIAO order in $CoNb_3S_6$. Ultra-broadband spectroscopy reveals that MOKE is overwhelmingly dominated by spin chirality, whose contribution is so large that any conventional magnetization-induced component is hardly visible. Spectral analysis further shows that the momentum-space Berry curvature generated by the AIAO structure governs the topological Hall responses including the optical regime. Remarkably, the figure of merit of this topological MOKE exceeds that of conventional magnets, including Mn_3Sn, by more than two orders of magnitude [3]. These results demonstrate exceptionally strong light–spin coupling mediated by Berry flux concentrated in the atomic-scale skyrmion-like texture, opening new avenues for antiferromagnetic spintronics and optospintronic applications.

IV. Conclusion

We have demonstrated the large topological MOKE induced by the intense Berry curvature arising from the atomic-scale skyrmion-like texture. Our findings demonstrate the spin-light coupling through the spin chirality, paving the way for future topological optospintronic devices.

References

[1] C. Back, C. *et al.,* J. Phys. D: Appl. Phys. **53**, 363001 (2020).
[2] H. Takagi, *et al*. Nat. Phys. **19,** 961 (2023).
[3] T. Higo, *et al*. *Nat. Photon.* **12,** 73 (2018).

Room-Temperature Orbital Angular Momentum Detection via Degree of Valley Polarization Tuning

Jiang Hao, Yan Zhang, Weibo Gao

Abstract

Excitons in transition metal dichalcogenides possess a valley degree of freedom, and tuning degree of valley polarization (DoP) is pivotal for advancing valleytronics, quantum communication, and quantum sensing. To date, most studies have focused on the influence of circularly polarized light on valley polarization, offering relatively limited tunability. Here, we report the interaction between the orbital angular momentum of twisted light (LG_0^l beam) with the valley degree of freedom in monolayer WSe_2. Through detecting the DoP of 1L-WSe_2 under the excitation of circularly polarized twisted light with different OAM number *l*, we find that the DoP of 1L-WSe_2 can be tuned directly by the OAM number *l*. The result shows that the DoP increases from 9% to 55% with the *l* changed from 0 to 10, and also increases from 9% to 58% when negative *l* changed from 0 to -10. This is consistent with the theoretical model we proposed for xxx. Leveraging this tunability, we fabricated 1L-MoS_2/1L-WSe_2 valleytronic transistor. For variations of OAM topological charge *l* from ±1 to ±10, the device exhibited a steadily increasing valley Hall voltage that enabled successful discrimination. This direct DoP-tuning scheme successfully enables on-chip OAM detection, offering a pathway towards high-capacity optical communication and quantum sensing.

Introduction

In monolayer transition metal dichalcogenide (TMDs), strong spin-orbit coupling and the time-reversal symmetry dictate the spin splitting to have opposite signs at the K and K' valleys in the Brillouin zone, which gives rise to an effective coupling between spin and valley pseudospin. An exciton, as a bound electron-hole pair, inherits the valley pseudospin as well (*1-3*). Meanwhile, the broken inversion symmetry in monolayer TMDs leads to a valley-dependent optical selection rule (*4*) (Fig. 1a). Excitons in the K valley couple to left-circularly polarized photons (σ^+), while excitons in K' valley couple to right-circularly polarized photons (σ^-), thus enabling the control of specific valley excitation through corresponding circularly polarized light (*5*). Therefore, it provides a promising platform for using the valley degree of freedom to carry and modulate information, known as valleytronics (*6, 7*).

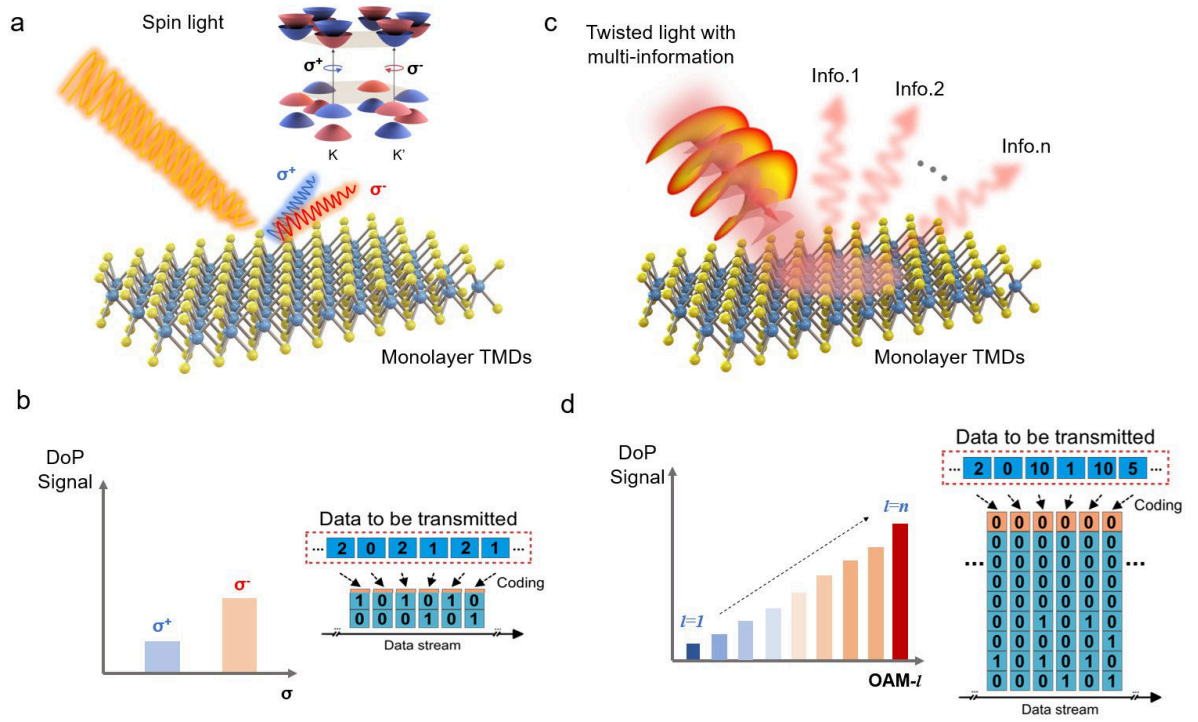

Figure 1. **Valley degrees of freedom carrying information. a**, Schematic of the band structure and optical selection rules in monolayer TMDs. Left-circularly (right-circularly) polarized light, σ^+ (σ^-), couples the valence and conduction bands at the K (K') valley. **b,** The degrees of freedom in DoP modulation by CPL and their applications. The modulation of DoP by CPL offers two degrees of freedom (σ±), which imposes limitations in encoding and communication. **c**, The combination of twisted light possessing boundless OAM $l\hbar$ per photon and the valley degrees of freedom makes monolayer TMDs a promising platform for information technologies. **d,** The degrees of freedom in DoP modulation by OAM and their applications. The modulation of DoP by OAM offers unlimited degrees of freedom (l = 1…n), showing great potential for encoding and communication.

In the experiment, circularly polarized light is used to preferentially excite just one valley (K or K'), which generates a difference in the population of the two valley excitons (*8, 9*). This degree of valley polarization (DoP), ρ, can be read out through measuring the circularly polarized components of the emitted photoluminescence (PL) intensity, which is expressed as $\rho = \left(I_{\sigma^+} - I_{\sigma^-}\right) / \left(I_{\sigma^+} + I_{\sigma^-}\right)$, where $I_{\sigma^{+(-)}}$ is the intensity of $\sigma^{+(-)}$-polarized emission. Accordingly, how to manipulate and tune the valley pseudospins, especially the DoP, is the key to realising practical valleytronic devices. Many efforts have been made to develop abilities to tune the DoP, such as applying an external magnetic field (*10, 11*), electrical field (*12-14*), and strain engineering (*15*). Nevertheless, all of them focus on the circular polarization degree of freedom (*16*), which exists in only two states $\sigma^{+(-)}$, thereby resulting in highly limited communication capacity (Fig. 1b). To increase the communication bandwidth, it is desirable to explore other degrees of freedom and make the DoP tuning rely on the light itself rather than the external control (*17*).

Twisted light (TL) exhibits this possibility. Apart from spin angular momentum (SAM), light can also carry orbital angular momentum (OAM), which is also referred to as twisted light. Whereas SAM of light decides its polarization state with only $\hbar$ or $-\hbar$ per photon, OAM of light involves its helical wavefront shape with a quantized but boundless value $l\hbar$ per photon

(*18, 19*), as shown in Fig. 1c, where *l* is the helical mode number. This unbounded OAM number *l* in twisted light apparently provides the possibility of carrying more information than nonstructured light carrying the SAM only (*20, 21*). Therefore, the successful manipulation of the DoP via OAM is expected to greatly expand the communication dimensionality, as shown in Fig. 1d. Up to now, many theoretical researches on the twisted light have exceptionally pushed its huge development (*18, 42*), as well as the theoretical (*38, 43-45*) and experimental (*36, 46-48*) twisted light matter interaction. However, the experimental investigation on twisted light interacting with DoP has not been systematically carried out, which is important to make TL-valleytronics realized.

Here, we report the interaction between the twisted light and the degree of valley polarization in monolayer WSe_2 (1L-WSe_2). The Laguerre-Gaussian (LG_p^l) beam, one of the typical twisted light, was used to excite the 1L-WSe_2. We find that the DoP of 1L-WSe_2 can be tuned directly by the OAM number *l*. The DoP increases from 9% to 55% with the *l* changed from 0 to 10, and also increases from 9% to 58% when negative *l* changed from 0 to -10. This phenomenon is associated with the out-of-pane magnetic field induced by twisted light, which directly affects the Zeeman splitting. Together with the transfer of momentum from photons with OAM to excitons, the intervalley electron-hole exchange interaction can be largely tuned. The realization of using twisted light to directly tune the degree of valley polarization in 1L-WSe_2, without any external field assisting, will certainly open a new avenue for valleytronics-based information technology. As an important validation and application, we designed and fabricated a 1L-MoS_2/1L-WSe_2 valleytronic transistor based on this mechanism. For variations of OAM topological charge *l* from ±1 to ±10, the device exhibited a steadily increasing valley Hall voltage that enabled successful discrimination, consistent with its tuning behavior to the valley DoP. This work proposes a method to directly tune the valley DoP using twisted light, without the need for any auxiliary external fields, and uniquely applies valleytronic devices to room-temperature OAM detection. The approach offers a pathway towards high-capacity optical communication, quantum sensing, and optical anti-counterfeiting.

Extraction of Circularly Polarized Single Photons from Linearly Polarized Emitters

Sarah Lindner[1,*], Peter Banzer[1]
[1] Department of Physics, University of Graz, Austria
*Corresponding author: sarah.lindner@uni-graz.at

***Abstract*—We target direct extraction of single photons with controlled circular polarization from linearly polarized emitters. We exploit the near-field features of linear dipole emitters to couple the emitters to waveguides, establishing a foundation for efficient, orientation-controlled extraction of circularly polarized single photons at the nanoscale applications.**

***Keywords*— single-photon emission, circular polarization, nanodiamonds, photonic integrated circuits.**

I. Introduction

The polarization state of single photons is a vital resource for quantum information encoding and secure communication protocols. Photonic integrated circuits (PICs) enhance quantum applications by enabling precise control over light-matter interactions through the manipulation of phase and polarization states. Solid-state emitters, such as defect centers in diamond, are ideal candidates for integration within these circuits, serving as the cornerstone for future on-chip light processing.

II. Methods

A key challenge for scalable quantum circuits is efficient, on-chip control of single-photon polarization, often relying on complex or inefficient external filtering. Our novel approach based on near-field coupling of quantum emitters and photonic integrated waveguide architectures will enable the direct on-chip extraction of circularly polarized single photons with defined handedness, significantly enhancing the integration and efficiency for quantum applications.

We aim to couple single photons from silicon-vacancy centers (SiV centers) in nanodiamonds to waveguide modes. We use the fact that linearly polarized dipoles feature partially circularly polarized near-fields. These non-zero near-field spin density components can be converted into circularly polarized waveguidemodes if waveguide and emitter are placed in close proximity. By positioning the SiV center on top of the intersection of waveguides which are tailored to match the near-field spin density distributions, we aim to extract circularly polarized single photons, emitted by a linear dipole-like single photon source, in different orientations propagating as waveguide modes along pre-defined directions (Fig. 1) [1].

III. Results and Discussion

Silicon-vacancy (SiV) centers in nanodiamonds serve as the ideal foundation for this architecture due to their robust and narrow-band fluorescence at room temperature [2], [3], paired with an almost fully linearly polarized zero-phonon line emission [4]. Their short lifetimes support high-rate quantum communication , while compatibility with pick-and-place techniques enables the precise spatial integration required for our waveguide design [5], [6]. FDTD simulations confirm that our cross-shaped geometry successfully exploits the longitudinal spin density of the evanescent field to convert linear dipole emission into circularly polarized light [1]. To maximize performance, we optimized the waveguide dimensions to match the specific spectral range of the SiV emission, ensuring efficient photon extraction.

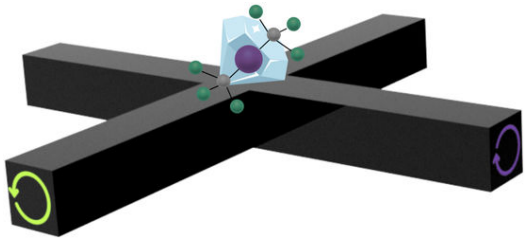

Fig. 1. Sketch of the proposed design for the waveguide structure with a nanodiamond hosting a SiV center positioned at the intersection of two orthogonally crossed waveguides.

IV. Conclusion

Our optimized waveguide geometry enables the direct extraction of circularly polarized single photons from solid-state emitters. By exploiting evanescent field characteristics, this architecture bridges the gap between linearly polarized quantum emitters and the requirements for integrated, polarization-encoded quantum applications.

References

[1] M. Neugebauer *et al.*, "Emission of circularly polarized light by a linear dipole," *Science Advances*, vol. 5, no. 6, 2019.
[2] S. Lindner *et al.*, "Strongly Inhomogeneous Distribution of Spectral Properties of Silicon-Vacancy Color Centers in Nanodiamonds," *New Journal of Physics*, vol. 20, 115002, 2018.
[3] C. Hepp *et al.*, "Electronic structure of the silicon vacancy color center in diamond," *Physical Review Letters*, vol. 112, 036405, 2014
[4] P. Siyushev *et al.*, "Low-temperature optical characterization of a near-infrared single-photon emitter in nanodiamonds," *New Journal of Physics*, vol. 11, 113029, 2009.
[5] A. W. Schell *et al.*, "A scanning probe-based pick-and-place procedure for assembly of integrated quantum optical hybrid devices," *Review of Scientific Instruments*, vol. 82, no. 7, 2011.
[6] S. Lindner *et al.*, "Coupling of a nanodiamond to a plasmonic antenna," *Nanotechnology*, vol. 36, 135001, 2025.

Bulk-Edge Correspondence in Photonic Spacetime Insulators

João C. Serra[1,2,*], Rudin Kraja[3], Foster Sabatino[3], Alexander B. Khanikaev[3], Mário G. Silveirinha[1,2]

[1]University of Lisbon – Instituto Superior Técnico, Lisboa, Portugal
[2]Instituto de Telecomunicações, Lisboa, Portugal
[3]College of Optics and Photonics – CREOL, University of Central Florida, Orlando, USA
*Corresponding author: joao.serra@lx.it.pt

***Abstract*— Unlike general space-time crystals, periodic travelling-wave modulations possess a continuous translation symmetry and exhibit a truly insulating bulk response. This work analyzes the bulk-edge correspondence in such systems and reveals some unusual properties of the topological edge channels, such as a geometry-dependent Doppler effect and codirectional reflection mechanisms.**

***Keywords*— topological insulators, photonic crystals, time-variant modulations, bulk-edge correspondence.**

I. Introduction

Since their proposal in 1987, photonic crystals have revolutionised light-based technologies by allowing unprecedented control over the band structure and laid the foundations for future integrated platforms fully operated with light waves. In particular, two-dimensional periodic structures can be used as Bragg reflectors where light does not penetrate the bulk region but may propagate along the boundaries in the form of edge states. Notably, the net number of modes circulating in these edge-type channels is dictated by the bulk topology through the bulk-edge correspondence [1]. Edge waveguides are largely insensitive to path deformations and small fabrication defects.

The recent ability to control a system's response in time at an electrically small scale has opened an exciting degree of freedom to break Lorentz's reciprocity [2] and to explore exotic wave phenomena like temporal scattering [3]. For this reason, understanding how topology shapes the flow of light in time-variant systems is crucial to design compact waveguides that are simultaneously robust against deformations and exhibit frequency conversion mechanisms that may not conserve the wave's energy. Within this context, different topological aspects of systems periodically driven in time [4] and in space-time [5,6] have been discussed in the literature.

In this work, we argue that realistic Floquet-Bloch crystals do not behave as true insulators for light due to the unbounded photonic spectrum, and present travelling-wave modulations as a natural alternative. Additionally, we examine how trivial and nontrivial Chern phases in such platforms lead to unusual edge-like channels in moving-type boundaries.

II. Photonic Spacetime Insulators

Photonic insulators are platforms characterised by gaps in the spectral domain within which light cannot propagate. These spectral gaps, i.e., the absence of bulk modes for specific wavevectors and/or frequencies, are typically found in continuous systems with material dispersion or periodic man-made structures. Topological protection ensures that edge waves cannot be backscattered at the boundary between two inequivalent crystals. As space/time crystals conserve the wave's frequency/wavevector due to their invariance in time/space, their frequency/wavevector gaps make them true insulators only for spatial/temporal boundaries, respectively.

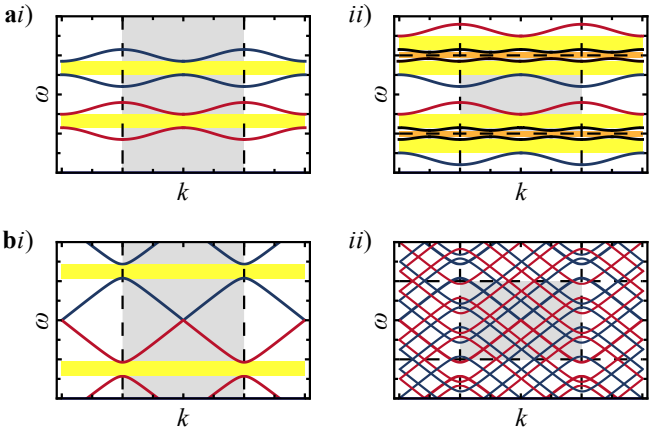

Fig. 1 Band structures for (a) a lattice of two-mode resonators and (b) a photonic crystal before (i) and after (ii) being periodically driven in time. The yellow strips represent the static frequency gaps, while the new Floquet gaps are coloured in orange.

Conventional space-time-variant insulators are engineered by periodically driving a crystalline structure in time [5,6]. Such Floquet-Bloch crystals lack a continuous time symmetry, but their discrete temporal translation symmetry conserves the Floquet frequency. This approach is suitable for systems with a bounded spectrum (e.g., a lattice of resonators), since the modulation frequency can be commensurable with the largest frequency of the bulk spectrum in the time-invariant case and open Floquet gaps [see Fig. 1a]. However, photonic space

crystals possess an infinite set of bands with a frequency accumulation point at infinity as illustrated in Fig. 1bi. Thus, due to the interaction of the different bands, the temporal modulation yields a very intricate dispersion without spectral gaps (Fig. 1bii).

To overcome this fundamental limitation, we introduced in Ref. [7] a new class of topological insulators characterised by periodic travelling-wave modulations of the material response $\bar{M} = \bar{M}(\mathbf{r} - \mathbf{v}t)$. Different from Floquet-Bloch insulators, these systems exhibit a continuous spacetime translation symmetry and conserve the Doppler-shifted frequency $\omega - \mathbf{v}\cdot\mathbf{k}$. Accordingly, the band structure in Fig. 2a presents spectral gaps within which the bulk region behaves as a true insulator since light cannot excite bulk modes.

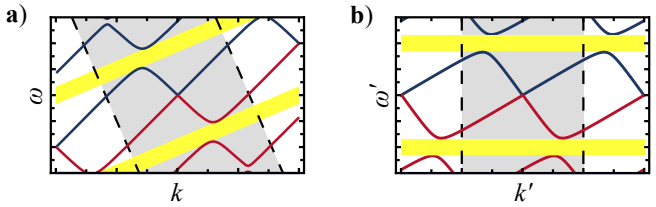

Fig. 2 Band structure in the laboratory frame (a) and in the comoving frame (b) for a photonic spacetime crystal with a travelling-wave modulation. The yellow strips highlight the spectral gaps.

These systems can be conveniently analysed in a reference frame

$$\begin{aligned} \mathbf{r}' &= \mathbf{r} - \mathbf{v}t, \\ t' &= t \end{aligned} \tag{1}$$

that moves with the synthetic velocity $\mathbf{v}$. In this Galilean comoving frame, the crystal becomes time-invariant and supports regular frequency gaps [see Fig. 2b] that can be topologically classified using conventional tools like the Green's function method [8]. Moreover, since the bulk-edge correspondence [1] is valid over static boundaries in this primed frame $(\mathbf{r}', t')$, it is only natural that the bulk topology ensures the existence of robust edge-type channels over boundaries that follow the travelling-wave perturbation in the original laboratory frame $(\mathbf{r}, t)$.

III. Bulk-Edge Correspondence

To better understand this novel bulk-edge correspondence, we consider the two-dimensional spacetime crystal represented in Fig. 3a with a synthetic velocity $\mathbf{v}$ inside the plane of propagation $x0y$. It comprises a honeycomb lattice of red rods isorefractive with vacuum and a green ring with a broken inversion symmetry characterised by the inhomogeneous refractive index

$$n_{\mathrm{G}}^2(\varphi) = 1 + \delta\cos(\varphi), \tag{2}$$

where φ denotes the angular coordinate around the ring's centre. In-plane travelling-wave modulations of this central inclusion implement a rotating vector field $\mathbf{A}'$ in the comoving frame for photons with a transverse electric polarisation $\mathbf{E}' \sim \hat{\mathbf{z}}$ that is analogous to the magnetic vector potential for electrons [9]. Notably, this photonic angular momentum bias $\langle \nabla' \times \mathbf{A}' \rangle \cdot \hat{\mathbf{z}} \sim \delta \mathbf{v} \cdot \hat{\mathbf{y}}$ splits the Dirac cones of the honeycomb lattice and opens a spectral gap [see Fig. 3b] characterised by the topological Chern $\mathcal{C}_{\mathrm{gap}}$ phase diagram shown in Fig. 3c.

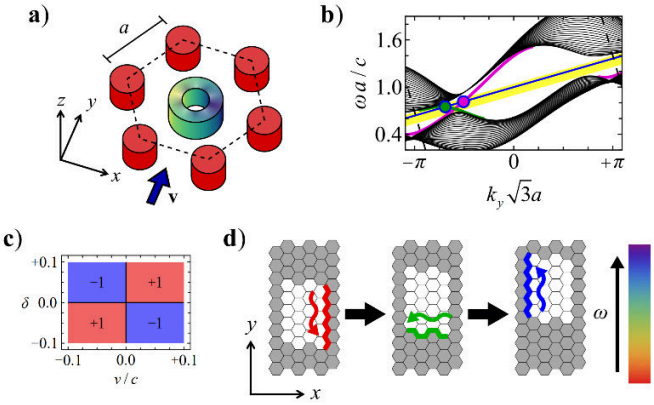

Fig. 3 (a) Unit cell of the spacetime Chern insulator with an in-plane travelling-wave modulation. (b) Band structure in the laboratory frame for the Chern insulator enclosed by two zigzag boundaries parallel to the synthetic velocity $\mathbf{v} = v\hat{\mathbf{y}}$: bulk modes are represented by black curves, while the green and purple solutions denote edge states localised near different boundaries. (c) Chern phase diagram. (d) Qualitative representation of a topological edge state propagating inside a spacetime cavity: the oscillation frequency varies along the propagation path due to a geometry-dependent Doppler effect.

To characterise the edge dispersion over moving opaque boundaries, we developed a simplified tight-binding description. Specifically, we considered zigzag terminations parallel to the modulation velocity $\mathbf{v} = v\hat{\mathbf{y}}$ and armchair terminations with the orthogonal orientation. In both scenarios, we found $\mathcal{C}_{\mathrm{gap}}$ unidirectional clockwise edge states that cross the spectral gap [see Fig. 3b for the zigzag termination], in agreement with the conventional bulk-edge correspondence in the comoving frame.

Remarkably, due to the conservation of the spectral parameter $\omega' = \omega - \mathbf{v}\cdot\mathbf{k}$, one may control the oscillation frequency ω in the laboratory frame of these edge modes by tailoring the shape of the moving frontier. For instance, in the spacetime cavity represented in Fig. 3d, the edge state experiences a Doppler effect determined by the local orientation of its cycloid-like path. This exotic behaviour may find applications in compact frequency conversion devices resilient against backscattering interference.

It is worth noting that the direction of propagation of these boundary modes does not need to coincide in the comoving and laboratory frames. Indeed, the velocities of edge states in the two frames differ by a relativistic velocity addition determined by the modulation velocity. For this reason, topologically trivial systems may exhibit unidirectional

channels in the laboratory frame for sufficiently fast (but subluminal) modulations. In the comoving frame the edge channels remain bidirectional, as required by the bulk-edge correspondence. At the conference, we will show that such edge-type waveguides exhibit a spacetime scattering mechanism, where light is constantly being "reflected" into the same direction.

IV. Conclusion

In summary, unlike tight-binding models, the unbounded spectrum of realistic photonic systems poses fundamental restrictions on the topology of space-time-variant platforms. To circumvent this challenge, we propose travelling-wave modulations as a simple and powerful scheme to achieve genuine insulation in topological systems. The proposed periodic structures can host topological Chern phases that control the flow of light over moving-like boundaries through a well-defined bulk-edge correspondence in a comoving frame. Finally, we argued that these novel topological channels may exhibit unusual properties in the laboratory frame, such as a geometry-dependent Doppler effect and codirectional reflection mechanisms.

Acknowledgments

This work was partially funded by the Simons Foundation (Award SFI-MPS-EWP-00008530-10) and by national funds through FCT – Fundação para a Ciência e a Tecnologia, I.P., and, when eligible, co-funded by EU funds under project/support UID/50008/2025 – Instituto de Telecomunicações, with DOI identifier <https://doi.org/10.54499/UID/50008/2025>.

References

[1] M. G. Silveirinha, "Proof of the bulk-edge correspondence through a link between topological photonics and fluctuation-electrodynamics," Phys. Rev. X, vol. 9, 011037, 2019.

[2] P. A. Huidobro, E. Galiffi, S. Guenneau, R. V. Craster, and J. B. Pendry, "Fresnel drag in space-time-modulated metamaterials," Proc. Natl. Acad. Sci. U.S.A., vol. 116 (50), pp. 24943-24948, 2019.

[3] E. Galiffi, D. M. Solís, S. Yin, N. Engheta, and A. Alù, "Electrodynamics of photonic temporal interfaces," Light: Science and Applications, vol. 14, no. 338, 2025.

[4] E. Lustig, Y. Sharabi, and M. Segev, "Topological aspects of photonic time crystals," Optica, vol. 5, no. 11, 2018.

[5] M. S. Rudner, N. H. Lindner, E. Berg, and M. Levi, "Anomalous edge states and the bulk-edge correspondence for periodically driven two-dimensional systems," Phys. Rev. X, vol. 3, 031005, 2013.

[6] B. Höckendorf, A. Alvermann, and H. Fehske, "Topological invariants for Floquet-Bloch systems with chiral, time-reversal, or particle-hole symmetry," Phys. Rev. B, vol. 97, 045140, 2018.

[7] J. C. Serra and M. G. Silveirinha, "Engineering topological phases with a traveling-wave spacetime modulation," Laser Photonics Rev., e00560, 2025.

[8] M. G. Silveirinha, "Topological classification of Chern-type insulators by means of the photonic Green function," Phys. Rev. B, vol. 97, 115146, 2018.

[9] J. C. Serra, M. G. Silveirinha, "Rotating spacetime modulation: Topological phases and spacetime Haldane model," Phys. Rev. B, vol. 107, 035133, 2023.

Time-Varying Metamaterials for Synthetic Motion

Satoshi Tomita
Institute for Excellence in Higher Education, and Department of Physics, Tohoku University, Sendai, Japan
tomita@tohoku.ac.jp

***Abstract*—We demonstrate time-varying magnetic metamaterials at GHz frequencies using ferromagnetic permalloy ($Ni_{80}Fe_{20}$). The experimental results are reproduced via numerical simulation, verifying that frequency conversion observed is caused by time modulation of magnetic permeability. The present study opens a door to magnetoelectric metamaterials with synthetic motion for probing quantum vacuum effects.**

***Keywords*— time-varying metamaterials, magnetoelectric effects, moving media, quantum vacuum effects.**

I. Introduction

Metamaterials are man-made structured materials exhibiting intriguing optical properties unavailable in natural materials. The most typical examples are metamaterials for negative refractive indices and for invisible cloaks. These are referred to as space-varying metamaterials because of the spatially modulated refractive indices.

Very recently, a new paradigm for light generation and steering using metamaterials has emerged – time-varying metamaterials, in which refractive indices are temporally modulated. Time-varying metamaterials bring about exotic phenomena, for example, time refraction, time reflection, and analogue of a continuous time crystal as well as promising applications to frequency converters, nonreciprocal devices, and antireflection temporal coatings. Furthermore, time-varying metamaterials mimic magnetoelectric interaction in equivalent moving media [1].

In particular, the space-time modulation of both electric permittivity (ε) and magnetic permeability (μ) is indispensable for investigating Fresnel drag for light in the synthetically moving media. However, experimental demonstration of time modulation in μ is still lacking [2], [3] while time-varying ε has been achieved. Therefore, time-varying μ metamaterials are highly desired.

II. Methods

We prepare magnetic metamaterials including a ferromagnetic-metal (permalloy (Py), Ni80Fe20) layer together with modulation and carrier lines. Temporal modulation of μ is realized by altering an effective magnetic field for ferromagnetic resonance of the Py layer using time-periodic Oersted magnetic field generated by modulation microwaves of frequency $f_{\rm m}$. Output carrier microwaves of $f_{\rm c}$ = 4.0 GHz are measured under $\mu_0 H_{\rm dc}$ = 24.4 mT at various $f_{\rm m}$.

III. Results and Discussion

Figure 1 shows experimetal results [4]. We observe frequency up- and down-conversions of the carrier microwave of $f_{\rm c}$ = 4.0 GHz, which are caused by the temporal μ modulation with $f_{\rm m}$. These experimental results are reproduced via numerical calculation, verifying that the frequency conversion is traced back to time-varying μ. Moreover, numerical calculation indicates that the nonlinear magnetization dynamics and microwave response through nonlinear susceptibility are keys of the predominant frequency up-conversion observed in the experiments.

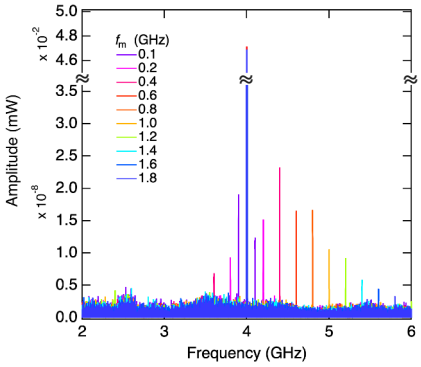

Fig. 1. Output carrier microwaves spectra of $f_{\rm c}$ = 4.0 GHz under $\mu_0 H_{\rm dc}$ = 24.4 mT at various modulation frequency $f_{\rm m}$..

IV. Conclusion

We demonstrate time-varying μ metamaterials at GHz frequencies using ferromagnetic Py. The present study opens a door to magnetoelectric metamaterials with synthetic motion [5], [6], [7] for probing quantum vacuum effects, for example, dynamical Casimir effects.

Acknowledgments

This work is financially supported by JST-CREST (JPMJCR2102) and JSPS-KAKENHI (A24H022320, 25K00929).

References

[1] P. A. Huidobro et al., *PNAS* 116, 24943 (2019).
[2] T. Kodama et al., *Physical Review Applied* 19, 044080 (2023).
[3] T. Kodama et al., *Physical Review B* 109, 214419, (2024).
[4] T. Kodama et al., arXiv:2503.04571.
[5] T. Kodama et al., *Optical Materials Express* 14, 2499 (2024).
[6] K. Mita et al., *Physical Review Applied* 23, L011004 (2025).
[7] K. Mita et al., arXiv:2503.22279.

Inverse Design in Nanophotonics: From Diffusion Models to Time-Domain Adjoint Optimizations

Mingyu Park[1,*], Seunghyun Lee[1,*], Jinseong Bae[1,*], Donghyun Kim[1,*], Chanik Kang[2,*], Kyungmin Kim[3,*], Donghyun Park[3,*], Dongjin Seo[4,*], Soobin Um[5], and Haejun Chung[1,2,3,†]
[1]Department of Electronic Engineering, Hanyang University, Seoul, Korea
[2]Department of Artificial Intelligence, Hanyang University, Seoul, Korea
[3]Department of Artificial Intelligence Semiconductor Engineering, Hanyang University, Seoul, Korea
[4]Department of Applied Physics, Yale University, New Haven, Connecticut, United States
[5]Department of Artificial Intelligence, Kookmin University, Seoul, Korea
[†]haejun@hanyang.ac.kr (corresponding author)

***Abstract*—This talk presents nanophotonic inverse design methods, ranging from physics-guided diffusion models to time-domain adjoint optimization. We demonstrate broadband metalenses, multi-functional AR waveguide couplers, and angle-robust CMOS color routers. Emphasis is placed on scalable, fabrication-aware optimization methods for nanophotonic inverse design.**
***Keywords*— Metasurface, Inverse Design, Diffusion Model, Time-Domain Adjoint Optimization.**

I. Introduction

Inverse design has emerged as a pivotal approach in nanophotonics, enabling the discovery of freeform device geometries that can achieve performance far beyond traditional intuitive designs. Modern optical systems demand multi-functional components, for example, metasurface lenses that operate across broad bandwidths, or couplers that perform simultaneous display and imaging tasks, which greatly expands the design parameter space. Adjoint-based topology optimization [1] provides efficient gradients to navigate these high-dimensional spaces, but it often requires cumbersome filtering to enforce fabrication constraints and can stagnate in suboptimal local minima. Conversely, data-driven strategies (e.g., generative models and reinforcement learning) explore vast design spaces but typically require prohibitive training data or simulation budgets. Additionally, designing for multiple objectives or broadband operation has been challenging: frequency-domain methods require separate simulations for each wavelength, while naive time-domain approaches blur multi-band goals into a single response. In this talk, we demonstrate recent advances [1], [2], [3], [4], [5] that address these challenges by tightly integrating physics into machine-learning models and extending adjoint optimization into the time domain. We summarize two methodological innovations, a physics-guided diffusion model and a multi-objective time-domain adjoint technique, and demonstrate their impact on complex nanophotonic devices for augmented reality and imaging sensors.

II. Methods

Physics-Guided Diffusion Models [3]: We developed an inverse design framework that embeds first-principles physics into a generative diffusion model, yielding a fabrication-aware and simulation-efficient optimization tool. In our approach (dubbed AdjointDiffusion), a diffusion neural network is first trained on a library of manufacturable device patterns, and during generation its iterative denoising process is guided by adjoint electromagnetic gradients. At each step, the physics-based gradient nudges the design toward higher performance (greater figure-of-merit) while inherently respecting fabrication constraints. This closed-loop integration of adjoint feedback allows the algorithm to avoid the complex binarization filters that brute-force optimizers require, directly producing physically realizable nanostructures. Notably, the diffusion-driven optimizer achieved 15% higher performance at equal simulation cost compared to state-of-the-art gradient-based methods, or required only about one-third the simulations to reach the same performance. It also showed a three-orders-of-magnitude reduction in required simulations versus purely data-driven generative approaches, highlighting the benefit of physics guidance. By eliminating tedious parameter tuning and reducing computational overhead, the physics-informed diffusion model offers a powerful new paradigm for photonic inverse design.

Multi-Objective Time-Domain Adjoint Optimization [4], [2]: To efficiently handle broadband and multi-criteria design targets, we extended adjoint optimization into the time domain with novel spectral control techniques. Traditional frequency-domain adjoint methods become computationally expensive when optimizing multiple wavelengths or functions, as they require independent gradient computations for each frequency or objective. Our approach leverages finite-difference time-domain (FDTD) simulation of the device to capture a wide bandwidth in a single simulation, then isolates individual objective responses via temporal signal processing. In one strategy, we apply temporal convolution filtering to the recorded fields, using band-pass filters to extract frequency-specific gradients from a single time-domain simulation. By invoking the convolution theorem, this method yields band-selective adjoint gradients without needing separate simulations for each spectral band, thus restoring the efficiency advantage of

time-domain optimization for multi-band problems. In another complementary strategy, we introduce dynamic pulse shaping during iterative optimization: the incident pulse (or other waveform parameters) is adaptively adjusted in each iteration to emphasize underperforming wavelength ranges, balancing broadband efficiency and uniformity. These enhancements enable true multi-objective optimization in one framework, as demonstrated by our designs of complex photonic components that meet several performance goals simultaneously. For example, using a convolution-enabled time-domain adjoint, we inverse-designed a wavelength demultiplexer with over 90% efficiency at each output channel, achieving this in a fraction of the runtime required by conventional multi-frequency optimizations. Likewise, dynamic pulse shaping was key to our achromatic metalens design, discussed below, enabling simultaneous improvements in efficiency and spectral consistency across the visible spectrum. Together, these time-domain adjoint innovations dramatically broaden the scope of inverse design, making it feasible to optimize broadband, multi-functional nanophotonic devices without incurring multiplicative simulation costs.

III. Conclusion

In this talk, we demonstrate that combining advanced optimization algorithms with physical-domain knowledge can substantially improve the design of multifunctional nanophotonic devices. Physics-guided diffusion models allow us to traverse the enormous solution space of topology optimization with unprecedented efficiency, yielding manufacturable designs that were previously impractical to discover. Time-domain adjoint methods equipped with spectral filtering and adaptive sources restore computational tractability for broadband, multi-objective problems, enabling devices that operate over wide frequency and angular ranges simultaneously. The application case studies, from AR waveguide couplers and wide-FOV color routers to high-efficiency achromatic metalenses, demonstrate the real-world impact of these methodologies in enabling compact optical systems with performance near theoretical limits. Looking forward, several open challenges and opportunities remain. Integrating the strengths of generative models and adjoint optimization (for example, by using hybrid approaches that refine AI-generated designs through adjoint fine-tuning) is a promising way to further improve design quality and reduce costs. Scaling these inverse design techniques to fully three-dimensional, large-area metastructures while accounting for fabrication imperfections and tolerances will be crucial for practical deployment. Additionally, expanding the design frameworks to incorporate active or nonlinear materials could unlock dynamically reconfigurable photonics optimized via similar principles. By addressing these challenges, the community can continue to push the frontier of optical device functionality. This talk will conclude by discussing how the presented innovations in physics-aware inverse design can be extended to meet future needs, and by identifying the key avenues where theory, computation, and fabrication must converge to realize the next generation of nanophotonic technologies.

Acknowledgments

This work was supported by the National Research Foundation of Korea (NRF) grant funded by the Korean government (MSIT) (RS-2024-00338048)(RS-2024-00414119), (RS-2025-25463760), and also supported by the Republic of Korea's MSIT, under the Global Research Support Program in the Digital Field program) (RS-2024-00412644) supervised by the IITP (Institute of Information and Communications Technology Planning & Evaluation) and also supported by Culture, Sports and Tourism R&D Program through the Korea Creative Content Agency grant funded by the Ministry of Culture, Sports and Tourism in 2024(RS-2024-00332210) and also Artificial Intelligence Graduate School Program (No. RS-2020-II201373, Hanyang University) supervised by the IITP, and under the artificial intelligence semiconductor support program to nurture the best talents ((IITP-(2025)-RS-2023-00253914) grant funded by the Korea government, and by the MSIT (RS-2025-02283217, RS-2025-25441264).

References

[1] S. Lee, B. Lee, and H. Chung, "Optical see-through augmented reality via inverse-designed waveguide couplers," *Nanophotonics*, vol. 14, no. 27, pp. 5555–5576, 2025.

[2] M. Park, H. Chung, and K.-Y. Jung, "Time-domain adjoint optimization for metalens design toward enhanced broadband efficiency and uniformity," *iScience*, 2025.

[3] D. Seo, S. Um, S. Lee, J. C. Ye, and H. Chung, "Physics-guided and fabrication-aware inverse design of photonic devices using diffusion models," *ACS Photonics*, 2025.

[4] M. Park, H. Chung, and S. V. Boriskina, "Multi-objective time-domain adjoint via temporal convolution for band-selective electromagnetic topology optimization," *Available at SSRN 5734344*, 2025.

[5] J. Seo, J. Jo, J. Kim, J. Kang, C. Kang, S.-W. Moon, E. Lee, J. Hong, J. Rho, and H. Chung, "Deep-learning-driven end-to-end metalens imaging," *Advanced Photonics*, vol. 6, no. 6, pp. 066 002–066 002, 2024.

Theoretical prediction and experimental testing of photon emission directionality in spontaneous and stimulated emission

Valerica Raicu[1,2,*] Michael Stoneman[1]

[1]Department of Physics and Astronomy, University of Wisconsin-Milwaukee, USA
[2]Department of Electrical Engineering, University of Wisconsin-Milwaukee, USA
*Corresponding author: vraicu@uwm.edu

***Abstract*— A mathematical framework for quantization of the electromagnetic fields emitted by single dipole radiators is presented. The theory predicts directionality of photon emission probability and light-induced electromagnetic wave collapse, which will be tested using an experimental setup currently under development.**

***Keywords*— spontaneous emission, stimulated emission, photon emission probability, angular dependence of photon emission.**

I. Introduction

The advent of single-molecule fluorescence imaging techniques [1, 2] has made it necessary to relate photon emission statistics to the orientation of the emitting dipoles. While classical electrodynamics (ED) does predict a dependence of the dipole radiation pattern on the polar angle, the standard approach to the quantization of the free electromagnetic field [3] has not revealed any such dependence. In this presentation, we first outline a recently proposed theoretical framework [4] for a classical ED derivation of the electromagnetic fields of single dipoles and their subsequent quantization [5], and then present the design and preliminary results of an experimental setup for testing the angular dependence of the photon emission probability predicted by the aforementioned theoretical work.

II. Methods

In the first successful attempt to quantize the electromagnetic field, Dirac considered a "free field" arising from the vector potential only. When traced back to the source of the field and potentials – a transition dipole –, Dirac's approximation turns out to be equivalent [5] to a zero-order small dipole approximation in which the scalar potentials related to the opposite ends of the emitting dipole cancel each other out exactly. Using the general quantization protocol introduced by Heisenberg, Dirac expanded the vector potential into a series of plane waves with arbitrary amplitudes and replaced the latter with quantum mechanical creation and annihilation operators, which obey usual commutation relations. This approach has been essential for understanding quantum optics with free electromagnetic fields and led to numerous practical applications. In the recent generalization of Dirac's approach by one of us [5], contributions to the electric field of velocity-dependent terms in the scalar potential, neglected in the standard approach, also have been incorporated. These led to the following Hamiltonian ($\hat{H}$) and electromagnetic momentum ($\hat{G}$) operators and their eigenvalues:

$$\hat{H} = \sum_k \hbar\omega_k \sin^2\varkappa_k \left(\hat{N}_k + \frac{1}{2}\right) \rightarrow E = \sum_{\vec{k}} \hbar\omega_k \sin^2\varkappa_k \left(n_k + \frac{1}{2}\right), \quad (1)$$

$$\hat{G} = \sum_k \hbar\,\vec{k}\ \sin^2\varkappa_k \left(\hat{N}_k + \frac{1}{2}\right) \rightarrow \vec{G} = \sum_k \hbar\,\vec{k}\ \sin^2\varkappa_k \left(n_k + \frac{1}{2}\right), \quad (2)$$

where the other symbols have their usual meaning. The additional trigonometric function depends on the angle, $\varkappa_k$, between the mode vector $\vec{k}$ and the direction of the emitting dipole for each field mode and indicates that spontaneous emission is maximal for directions perpendicular to the emitting dipole and zero along its direction, in agreement with classical electromagnetism. This is the first testable experimental prediction of the theory.

When used to describe single-radiator emission stimulated by collimated single photons, this approach gives the eigenvalues of the Hamiltonian ($\hat{H}_{SE}$) and momentum ($\hat{G}_{SE}$) operators and their eigenvalues:

$$\hat{H}_{SE} = 2\hbar\omega_s \sin^2\varkappa_{kS} \left(\hat{N}_{kS} + \frac{1}{2}\right) \rightarrow E_{SE} = 2\hbar\omega_S \sin^2\varkappa_{kS} \left(1 + \frac{1}{2}\right), \quad (3)$$

$$\hat{G}_{SE} = 2\hbar\vec{k}_s \sin^2\varkappa_{kS} \left(\hat{N}_{kS} + \frac{1}{2}\right) \rightarrow \overrightarrow{G_{SE}} = 2\hbar\vec{k}_S \sin^2\varkappa_{kS} \left(1 + \frac{1}{2}\right). \quad (4)$$

The last equations indicate that (**i**) the dipole and stimulating fields carry away, in the direction of propagation of the stimulating field (given by angle $\varkappa_{kS}$), all the energy and momentum which, when compared to Eqns. (1) and (2) are equivalent to those of two photons plus twice the vacuum, and that (**ii**) the stimulating field *collapses the electromagnetic radiation* emitted by the dipole into a single mode.

Experimental tests of these predictions may include defocused imaging of single fluorescent molecules, which allows for determination of transition dipole orientation [6], as well as cavity QED experiments with Rydberg atoms or fluorescent molecule monolayers [7, 8], in which the emitters

have differing orientation angles relative to cavity walls.

In my lab, an experimental setup is being developed to determine the emission probability of fluorescent molecules whose dipole orientation is optically selected by choosing the linear polarization orientation of the excitation light, while emission is detected in a direction perpendicular to the optical axis of the excitation. The setup (Fig. 1) consists of a tunable Ti:Sapphire laser (680-1040 nm) for two-photon excitation of the sample, two optical micro-spectroscopes (OptiMiS) [9] with optical axes perpendicular to one another, and a computer-controlled half-wave plate for selective excitation of the molecules whose transition dipoles are oriented under a set angle ($\varkappa_k$) relative to the horizontal OptiMiS optic axis. The sample consists of fluorescent (mEGFP) molecules whose rotational diffusion was reduced by fusion to a large macromolecule (that increased total molecular size) and suspension in a viscous 50/50 glycerol/water mixture.

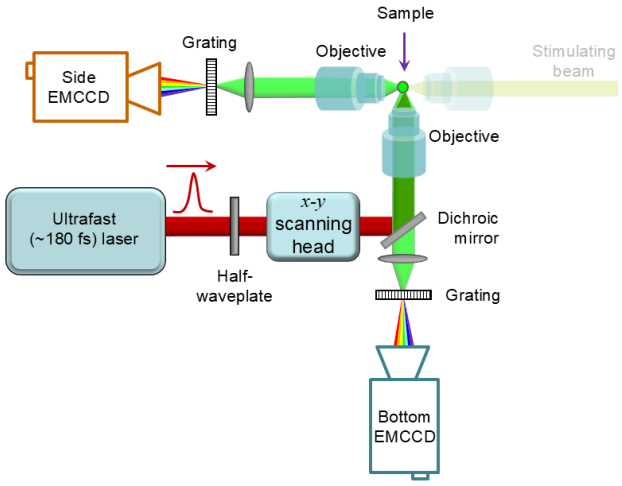

Fig. 1 Experimental setup for testing photon emission probability on the dipole orientation angle which is optically selected through polarization control.

III. Results and Discussion

The preliminary results shown in Fig. 2 show agreement with the $\sin^2 \varkappa_k$ prediction for the case of spontaneous emission. The intensity does not vanish at its minimum both because (1) rotational diffusion of the excited molecules causes rapid thermalization of the orientations of the transition dipoles, and (2) the relatively large numerical aperture objective (NA=0.5) integrates emission over a wide range of angles. These measurements will be refined by testing the effects of microscope objectives with various numerical apertures, further increasing the viscosity of the medium (e.g., by immobilization of the fluorophores within gels), and extending the study to investigate the dependence of the stimulated emission photon probability on the angular orientation of the transition dipoles. In addition, we will probe for the existence of an anticorrelation between the spontaneous emission rate detected by the Bottom EMCCD (as a function of the stimulation angle $\varkappa_{kS}$) and the stimulated emission rate detected by the Side EMCCD; observing such an anticorrelation would support stimulated wave collapse.

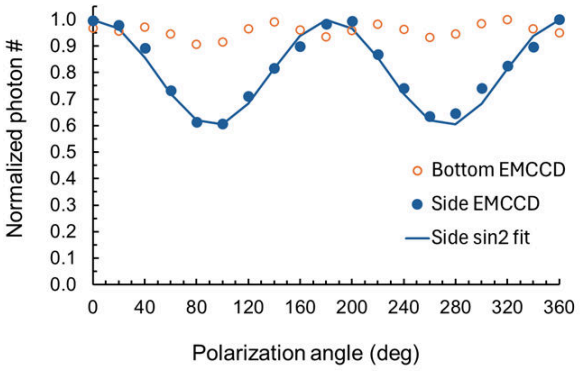

Fig. 2 Preliminary results on spontaneous emission from fluorescent molecules whose transition dipole is optically selected using the experimental setup shown in Fig 1.

IV. Conclusion

The proposed theoretical approach may lead to a better understanding of the processes accompanying radiation emission from excited atoms and molecules in the presence and absence of vacuum fluctuations or stimulating light [10]. It also opens a path for rigorous yet intuitive interpretations of the results of single molecular dipole imaging experiments [6] and quantum mechanics experiments with single photons [11].

Acknowledgments

This work was partly supported by a Discovery and Innovation Grant from the University of Wisconsin-Milwaukee (DIG 101X453). VR is grateful to Prof. Peter Milonni for stimulating discussions.

References

[1] A. von Diezmann, Y. Shechtman, W.E. Moerner, Three-Dimensional Localization of Single Molecules for Super Resolution Imaging and Single-Particle Tracking, Chem Rev, 117 (2017) 7244-7275.
[2] M.R. Stoneman, V. Raicu, Fluorescence-Based Detection of Proteins and Their Interactions in Live Cells, J Phys Chem B, 127 (2023) 4708-4721.
[3] P.A.M. Dirac, The quantum theory of the emission and absorption of radiation, Proceedings of the Royal Society of London A, 114 (1927) 23.
[4] V. Raicu, Derivation and Physical Interpretation of the General Solutions to the Wave Equations for Electromagnetic Potentials, Ann Phys-Berlin, 537 (2025).
[5] V. Raicu, Quantization of the Electromagnetic Fields From Single Atomic or Molecular Radiators, Ann Phys-Berlin, 537 (2026).
[6] E. Toprak, J. Enderlein, S. Syed, S.A. McKinney, R.G. Petschek, T. Ha, Y.E. Goldman, P.R. Selvin, Defocused orientation and position imaging (DOPI) of myosin V, P Natl Acad Sci USA, 103 (2006) 6495-6499.
[7] H. Walther, B.T.H. Varcoe, B.G. Englert, T. Becker, Cavity quantum electrodynamics, Rep Prog Phys, 69 (2006) 1325-1382.
[8] K. Drexhage, Interaction of light with monomolecular layers, in: E. Wolf (Ed.) Progress in Optics, North-Holand, 1974, pp. 163-232.
[9] V. Raicu, M.R. Stoneman, R. Fung, M. Melnichuk, D.B. Jansma, L.F. Pisterzi, S. Rath, M. Fox, J.W. Wells, D.K. Saldin, Determination of supramolecular structure and spatial distribution of protein complexes in living cells, Nat Photonics, 3 (2009) 107-113.
[10] P.W. Milonni, The Quantum Vacuum: An Introduction to Quantum Electrodynamics, Academic Press, San Diego, 1994.
[11] C.C. Gerry, P.L. Knight, Introductory quantum optics, Second edition ed., Cambridge University Press,, Cambridge, United Kingdom ; New York, NY, 2024.

Landau polaritons and cavity-driven attractive interactions in single and bilayer graphene

G. Scalari[1,*], E. Jöchl[1], F. Helmrich[1], L. Hale[1], L. Graziotto[1], A. Imamoglu[1], T. Nova[1], J. Faist[1]

[1] Institute for Quantum Electronics, ETH Zürich, Zürich 8093, Switzerland
*Corresponding author: gscalari@ethz.ch

***Abstract*— We demonstrate ultrastrong coupling between highly subwavelength THz resonators and high quality, HBN encapsulated single and bilayer graphene. The presence of gates allows the study of coupling strength as a function of carrier density and , in the case of bilayer, bandgap tuned in the 0-7 THz range.**

***Keywords*— van der Waals, terahertz, near field, strong coupling, cavity driven**

I. Introduction

Strong light-matter coupling has been recently successfully explored in the GHz and THz range with on-chip platforms, where metallic resonators with small cavity volumes are combined with high electron density materials to exploit the collective enhancement of the coupling **Ω**. New and intriguing quantum optical phenomena have been predicted in the ultrastrong coupling regime, when the coupling strength **Ω** becomes comparable to the unperturbed frequency of the system ω [1], [2]. The use of extremely small cavity volumes ($V/\lambda^3 \simeq 10^{-6}$), attainable with circuit-like resonators, has allowed the study of ultrastrong light-matter coupling at THz frequencies[3], [4], [5] While sub-wavelength localization of terahertz fields can be efficiently achieved using micro-structured metallic resonators, conventional approaches rely on metamaterials of repeating resonators placed atop the material of interest.[4] [6] This method is incompatible with exfoliated 2D materials, which are usually limited to in-plane dimensions of just a few microns, and with the study of few-electron systems requiring an active mode surface of a few micrometer squared.

II. Results and Discussion

We will discuss experimental results where a *single strongly subwavelength resonator* is coupled to a single graphene flake and, in a second experiment, to a dual-gated Bernal stacked bilayer graphene.

In the first experiment, we use the Landau polariton platform that has been extensively exploited to investigate the physics of ultrastrong light-matter coupling both in optical and transport experiments [4], [7]. We employ a system of immersion lenses [8] to spectroscopically investigate a graphene flake encapsulated in hexagonal Boron Nitride and embedded in single resonator operating at 1.2 THz. The resonator features an electrical gate in order to modulate the graphene's electron density ρ_{2deg} and, as a consequence, the Rabi frequency **Ω**. The normalized coupling ratio **Ω**/ ω scales with the expected fourth root of the density reaching a maximum value of 0.3, well within the ultrastrong coupling range.

In the second experiment, we couple a Bernal stacked bilayer graphene (BLG) to a bow-tie antenna resonator, operating at 2.3 THz. The presence of a dual gate system allows to independently tune the carrier density and the displacement field, with which we tune the BLG gap in the range 1-6 THz[9]. The immersion lens assembly allows the measurement of the field-tunable bandgap of bilayer graphene as a function of the displacement field. With such a setting we demonstrate that terahertz cavity photons can mediate attractive interactions in a tunable van der Waals material and reorganize a continuum of electron–hole transitions into an exciton-like state [10] [11]. Spectral measurements in the 1- 6 THz range reveals an anticrossing behavior of such an exciton-like state, and the estimated coupling strength, $\eta = \Omega/\omega \approx 0.43$, which places our system well into the ultrastrong coupling regime.

References

[1] P. Forn-Díaz, L. Lamata, E. Rico, J. Kono, and E. Solano, "Ultrastrong coupling regimes of light-matter interaction," *Reviews Of Modern Physics*, vol. 91, no. 2, p. 025005, Jun. 2019.

[2] C. Ciuti, G. Bastard, and I. Carusotto, "Quantum vacuum properties of the intersubband cavity polariton field," vol. 72, no. 11, p. 115303, Sep. 2005.

[3] A. Bayer *et al.*, "Terahertz Light–Matter Interaction beyond Unity Coupling Strength," *Nano Letters*, p. acs.nanolett.7b03103-5, Sep. 2017.

[4] G. Scalari *et al.*, "Ultrastrong Coupling of the Cyclotron Transition of a 2D Electron Gas to a THz Metamaterial," *Science*, vol. 335, no. 6074, pp. 1323–1326, Mar. 2012.

[5] Y. Todorov *et al.*, "Ultrastrong Light-Matter Coupling Regime with Polariton Dots," *Physical Review Letters*, vol. 105, no. 19, p. 196402, Nov. 2010.
[6] X. Jin *et al.*, "Enhanced Terahertz Spectroscopy of a Monolayer Transition Metal Dichalcogenide," *Advanced Functional Materials*, vol. n/a, no. n/a, p. 2419841, Jan. 2025, doi: 10.1002/adfm.202419841.
[7] F. Appugliese *et al.*, "Breakdown of topological protection by cavity vacuum fields in the integer quantum Hall effect," *Science*, vol. 375, no. 6584, pp. 1030–1034, Mar. 2022, doi: 10.1126/science.abl5818.
[8] S. Rajabali *et al.*, "An ultrastrongly coupled single terahertz meta-atom," *Nature Communications*, vol. 13, no. 1, p. 2528, May 2022, doi: 10.1038/s41467-022-29974-2.
[9] F. Helmrich *et al.*, "Cavity-Driven Attractive Interactions in Quantum Materials." Nature (in press), 2026.
[10] E. Cortese, I. Carusotto, R. Colombelli, and S. De Liberato, "Strong coupling of ionizing transitions," *Optica*, vol. 6, no. 3, pp. 354–8, 2019.
[11] J. B. Khurgin, "Excitonic radius in the cavity polariton in the regime of very strong coupling," *Solid State Communications*, vol. 117, no. 5, pp. 307–310, Jan. 2001, doi: 10.1016/S0038-1098(00)00469-5.

MEQED and Bianisotropy

Eugene Kamenetskii*

School of Electrical and Computer Engineering, Ben Gurion University of the Negev, Israel
*Corresponding author: kmntsk@bgu.ac.il

***Abstract*— Near field bianisotropy and chirality are associated with violations of local P and T symmetry and the problem of cross polarization coupling energy – the ME energy. The quantum behavior of bianisotropic metamaterials arises from quantum effects in ME meta atoms. These fundamental challenges lead to the development of ME quantum electrodynamics (MEQED).**

***Keywords*— metamaterials, magnetoelectric energy, symmetry breakings, quantum electrodynamics.**

The interplay between light and matter is fundamentally shaped by concepts such as bianisotropy and chirality. It is assumed that due to the cross-coupling dyadics in constitutive relations, magnetoelectric (ME) interactions in bianisotropic media occur. The problem of local bianistropy and local chirality (in other words, near-field bianistropy and near-field chirality) is the problem of cross-polarization coupling energy – the ME energy. This mesoscopic problem of quasi-static oscillations contradicts classical electrodynamics. The intense near-fields – ME near fields – are enantioselective fields. The additional (with respect to macroscopic Maxwell equations) coupling introduces fundamental challenges that have led to the development of ME quantum electrodynamics (MEQED). MEQED is an extension of standard QED that describes the quantum behavior of light-matter systems characterized by strong ME coupling. It provides a theoretical framework for studying systems where spatial inversion P and temporal reversal symmetries T are broken, often using engineered meta-atoms to observe these effects in subwavelength regions. MEQED advances the study of ME interactions into the quantum realm, treating coupled electric and magnetic responses not just as material parameters, but as fundamental quantized excitations in structured materials and the nearby vacuum.

Quantum Noise Spectroscopy of Chiral Quantum States

Benjamin J Lawrie[1]

[1]Materials Science and Technology Division, Oak Ridge National Laboratory, Oak Ridge TN, 37830, USA

*Corresponding author: lawriebj@ornl.gov

***Abstract*— We explore critical dynamics in the presence of competing ferromagnetic and antiferromagnetic interactions with all-optical spin-based quantum sensing protocols in variable temperature and variable magnetic-field environments.**

***Keywords*— quantum sensing, quantum noise spectroscopy, chiral quantum materials.**

I. Introduction

We recently used all-optical relaxometry measurements with a scanning nitrogen vacancy (NV) center probe to measure the spin fluctuations in a magnetic thin film near criticality[1]. This approach proved to be a valuable tool for extracting the universality class for the thin film in question, but scanning NV probes are challenging to deploy in low temperature, high-magnetic field environments, as field components orthogonal to the NV spin axis can suppress the spin contrast. Spin defects in hexagonal boron nitride (hBN) like the boron vacancy (V_B^-) are aligned out-of-plane and exhibit no loss of contrast in out-of-plane fields of up to 7 T[2,3]. Here, we use 2D spin-based quantum sensors for quantum noise spectroscopy of chiral quantum materials.

II. Methods

We initially focus on $LuMn_6Sn_6$, an antiferromagnetic material with a rich phase diagram of field-induced phases, including a canted antiferromagnetic phase that exhibits an anomalous Hall effect[4]. In order to better understand the interplay between magnetic phases in $LuMn_6Sn_6$, we leverage all-optical quantum noise spectroscopies of V_B^- spin defects in an exfoliated hBN flake transferred onto a bulk $LuMn_6Sn_6$ crystal. Measurements are performed at 2-300K and 0-7 T. Initial measurements have focused on the spin fluctuations near a phase transition between collinear and incommensurate spiral antiferromagnetic phases, but we are now extending to lower temperatures and higher fields in order to explore spin-interactions in additional commensurate antiferromagnetic phases, and a transverse conical spiral phase that may exhibit the topological Hall effect with associated scalar spin chirality.

III. Results and Discussion

The results shown in Fig. 1 highlight the measured spin noise near one phase transition in $LuMn_6Sn_6$ acquired at zero field and near room temperature. While conventional pulse sequences for measuring spin lifetime and spin coherence time can be applied at small magnetic fields, it becomes very challenging to deliver pi pulses in cryogenic environments at fields greater than 0.7T as the relevant frequencies exceed 20GHz. Thus, we use all-optical relaxometry schemes to extend these spectroscopies to fields of up to 7T.

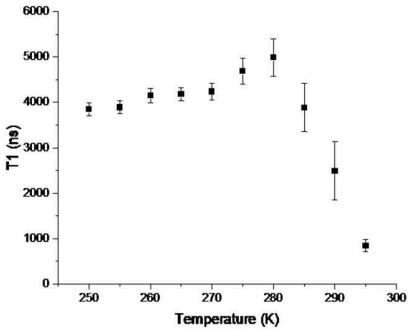

Fig. 1: Initial quantum noise spectroscopy of a phase transition between collinear and incommensurate spiral antiferromagnetic phases in $LuMn_6Sn_6$.

IV. Conclusion

All optical quantum noise spectroscopies of chiral quantum materials offer key understanding of critical spin dynamics and may help to unlock new understanding of chiral interactions in condensed matter.

Acknowledgments

This research was sponsored by the U. S. Department of Energy, Office of Science, Basic Energy Sciences, Materials Sciences and Engineering Division.

References

1. Wu, Y.-C. *et al.* Nanoscale Magnetic Ordering Dynamics in a High Curie Temperature Ferromagnet. *Nano Lett.* **25**, 1473–1479 (2025).

2. Solanki, A. B. *et al.* Broadband Relaxation Dynamics of Boron-Vacancy Centers in Hexagonal Boron Nitride. Preprint at https://doi.org/10.48550/arXiv.2507.16786 (2025).
3. Vlassiouk, I. V. *et al.* Defect Engineering in Large-Scale CVD-Grown Hexagonal Boron Nitride: Formation, Spectroscopy, and Spin Relaxation Dynamics. *Small* **n/a**, e06874.
4. Mozaffari, S. *et al.* Diverse magnetic phase diagram and anomalous Hall effect in antiferromagnetic ${\mathrm{LuMn}}_{6}{\mathrm{Sn}}_{6}$. *Phys. Rev. B* **112**, 115147 (2025).

SPECIAL SESSION 15

Plasmonic Nanomaterials for Bio-diagnostics, Environmental Monitoring and Food Safety

27 contributions · pp. 1039–1086

Vanadium Dioxide Nanoparticles: A Platform for Tuning Localized Surface Plasmons

Michal Horák[1,*], Jiří Kabát[1], Rostislav Řepa[1], Jordan A. Hachtel[2], Peter Kepič[1], Vlastimil Křápek[1], Andrea Konečná[1], Tomáš Šikola[1]

[1]Institute of Physical Engineering and CEITEC BUT, Brno University of Technology, Brno, Czech Republic
[2]Center for Nanophase Materials Sciences, Oak Ridge National Laboratory, Oak Ridge, USA
*Corresponding author: michal.horak2@ceitec.vutbr.cz

***Abstract*—We present a comprehensive modal analysis of single-phase and multi-phase vanadium dioxide nanoparticles using in-situ high-resolution electron energy loss spectroscopy. In addition to identifying individual plasmonic modes and bulk losses as a function of nanoparticle size, our focus is on capturing the dynamic nanoscale optical response throughout the metal-insulator transition.**

***Keywords*—vanadium dioxide, insulator-metal transition, tunable devices, EELS.**

I. Introduction

Vanadium dioxide (VO_2) has been identified as a promising phase-changing material for use in tunable plasmonic devices due to its insulator-metal phase transition, which occurs at a convenient temperature of around 67 °C [1]. It was shown that VO_2 is biocompatible [2] and that its metallic phase supports near-infrared plasmonic resonances [3]. These findings open a way to design a temperature-driven plasmonic biosensor. However, localized surface plasmon resonances have been so far investigated in detail only in VO_2 nanostructure arrays using optical microscopy techniques, which did not provide comprehensive information about individual plasmonic modes and their tunability. In our recent studies of individual VO_2 nanoparticles using transmission electron microscopy techniques [4], [5], the transition and hysteresis were also probed by tracking plasmonic resonances that appear when VO_2 undergoes a transition from an insulator to a metal. Despite being able to link those results directly to optical properties, these plasmonic resonances and their modes have been discussed sparsely. Here, we present a spatial modal analysis of excitations within individual VO_2 nanoparticles in both the low-temperature insulating and high-temperature metallic phases using in-situ scanning transmission electron microscopy (STEM) with high-resolution electron energy-loss spectroscopy (EELS) [6].

II. Methods

VO_2 nanoparticles were manufactured on a heating chip (Protochips) with a 30 nm thick silicon nitride membrane in a two-step process introduced in [2]. STEM EELS measurements were performed on a TEM FEI Titan equipped with a monochromator, a GIF Quantum spectrometer for EELS, and an in-situ Fusion Select system (Protochips) for heating experiments at CEITEC Nano and on the Nion aberration-corrected high energy resolution monochromated EELS-STEM (HERMES^{TM}) equipped with a prototype Nion spectrometer possessing a Hamamatsu ORCA high-speed CMOS detector and an in-situ Fusion Select system (Protochips) for heating experiments at Oak Ridge National Laboratory.

Fig. 1. Tuning of the dipole plasmon mode in a vanadium dioxide nanoparticle via partial insulator-metal transition. The schematic depiction of the thermally tunable NP followed by measured EEL spectra for the fully dielectric state, four transition states, and the fully metallic state of the nanoparticle. HAADF STEM image with marked area for the EEL spectra integration and EEL maps (1.0–1.5 eV) of a partially switched NP at different temperatures. The green arrows indicate the approximate size of the metallic part (brighter area).

III. Results and Discussion

We have studied an ensemble of VO_2 nanoparticles of hemispherical shape using STEM-EELS in order to experimentally resolve the dipole plasmon peak, in addition to potentially higher-order and breathing plasmonic modes and

bulk losses. As a result, we introduce a full modal analysis of both insulating and metallic VO_2 NPs with an experimental observation of the energy of the dipole plasmon mode and its other parameters (amplitude and quality factor) as a function of the size of the metallic VO_2 NPs. The energy tunability of the dipole mode reads $0.1\,\mathrm{eV}$ for the size of NPs from 50 to $220\,\mathrm{nm}$. The quality factor of the VO_2 resonances was found to be significantly lower than that of traditional plasmonic materials, with values ranging from 1 to 1.5.

Furthermore, we have focused on transitional states within the insulator-to-metal transition. The tuning of the dipole plasmon mode in a $120\,\mathrm{nm}$ VO_2 nanoparticle via partial insulator-metal transition is shown in Figure 1. One can clearly see that it represents a system that can be switched on and off and tuned to the extent of $0.18\,\mathrm{eV}$. As a result, the dynamics of the phase transition facilitated the specific particle's ability to establish a correlation between the local temperature and the relative switched volume. This correlation was achieved by employing the dipole plasmon mode in the metallic region as the linking variable, with the peak position serving as the indicator.

IV. Conclusion

To summarize, we have introduced a comprehensive modal analysis of single-phase and multi-phase vanadium dioxide nanoparticles using in-situ high-resolution electron energy loss spectroscopy. We have shown that an individual vanadium dioxide nanoparticle represents a nanophotonic system that can be gradually switched on and off in terms of the emergence of near-infrared plasmonic absorption. The switching is accompanied by a gradual spectral shift of the absorption peak. It is envisioned that this phenomenon can be generalized to larger nanostructures with a higher aspect ratio, thereby introducing a wider tunability of the system, which is essential for functional nanodevices based on vanadium dioxide.

Acknowledgments

This work has been supported by the Czech Science Foundation (grants No. 22-04859S and 23-05119M), the OP JAK Excellent Research program (project QM4ST, No. CZ.02.01.01/ 00/22_008/0004572), MEYS CR (project Czech-NanoLab, No. LM2023051) and Brno University of Technology (grants No. FSI-S-23-8336 and CEITEC VUT-J-25-8860). Ultrahigh energy resolution monochromated EELS was performed at the Center for Nanophase Materials Sciences (CNMS), which is a US Department of Energy, Office of Science, User Facility, using instrumentation within ORNL's Materials Characterization Core provided by UT-Battelle, LLC, under Contract No. DE-AC05-00OR22725 with the DOE and sponsored by the Laboratory Directed Research and Development Program of Oak Ridge National Laboratory, managed by UT-Battelle, LLC, for the U.S. Department of Energy. J.K. acknowledges the Brno Ph.D. Talent Scholarship – Funded by the Brno City Municipality.

References

[1] S. Cueff, J. John, Z. Zhang, J. Parra, J. Sun, R. Orobtchouk, S. Ramanathan and P. Sanchis, VO_2 nanophotonics," *APL Photonics*, vol. 5, pp. 110901, 2020.

[2] J. Guo, H. Zhou, J. Wang, W. Liu, M. Cheng, X. Peng, H. Qin, J. Wei, P. Jin, J. Li and X. Zhang, "Nano vanadium dioxide films deposited on biomedical titanium: a novel approach for simultaneously enhanced osteogenic and antibacterial effects," *Artificial Cells, Nanomedicine, and Biotechnology*, vol. 46, pp. 58–74, 2018.

[3] P. Kepič, F. Ligmajer, M. Hrtoň, H. Ren, L. S. Menezes, S. A. Maier and T. Šikola, "Optically Tunable Mie Resonance VO2 Nanoantennas for Metasurfaces in the Visible," *ACS Photonics*, vol. 8, pp. 1048–1057, 2021.

[4] M. Horák, P. Kepič, J. Kabát, M. Hájek, F. Ligmajer, A. Konečná, T. Šikola and V. Křápek, "Efficient nanoscale imaging of solid-state phase transitions by transmission electron microscopy demonstrated on vanadium dioxide nanoparticles," *arXiv*, arXiv:2408.11972, 2024.

[5] P. Kepič, M. Horák, J. Kabát, M. Hájek, A. Konečná, T. Šikola and F. Ligmajer, "Coexisting Phases of Individual VO_2 Nanoparticles for Multilevel Nanoscale Memory," *ACS Nano*, vol. 19, pp. 1167–1176, 2025.

[6] J. Kabát, R. Řepa, J. A. Hachtel, P. Kepič, V. Křápek, A. Konečná, T. Šikola and M. Horák, "Tuning of Localized Surface Plasmons in Vanadium Dioxide Nanoparticles via Size and Insulator-Metal Transition," *arXiv*, arXiv:2602.00673, 2026.

Correlation Spectroscopy based Nanobiosensor: Application for Cu-Zn Superoxyde Dismutase detection

Mohand Chalal[1], Abdelhak Dhibi[2], Nordin Felidj[2], and Nadia Djaker[1,2*]

[1]Université Sorbonne Paris Nord, UFR SMBH, 74 rue Marcel Cachin, F-93017 Bobigny, France, France

[2]Univ Paris Cite, CNRS, ITODYS, F-75013 Paris, France

*Corresponding author: nadia.djaker@univ-paris13.fr

***Abstract*— Gold nanoparticles (GNP) are widely used in many fields, such chemistry and nanomedicine. Recently, scattering correlation spectroscopy (SCS) is one of the most used techniques for GNP surface and biomolecules interaction characterization. The SCS correlation curve is very sensitive to Parameters such as molecules orientation, binding affinity and cooperativity regarding the GNP surface.**

***Keywords*— Gold nanoparticles, biomolecules, correlation spectroscopy, biosensors, Superoxyde Dismutase (SOD).**

I. Introduction

In recent years, aptamer-based biosensors (aptasensors) have emerged as powerful alternatives to antibody-based detection systems due to their high affinity, strong specificity, chemical stability, and cost-effectiveness. Aptamers are short, single-stranded nucleic acid sequences, which enables them to fold into unique three-dimensional structures capable of binding molecular targets with high selectivity [1]. Although a broad body of literature addresses aptamer-based biosensors for various analytes, there are relatively few reports specifically describing the application of aptamers for SOD detection. Among them, studies have demonstrated the conjugation of SOD-specific aptamers on metallic nanoparticles to enable sensitive protein recognition via optical or SERS-based readouts, with detection limits in the nanomolar to picomolar range [2].

Scattering Correlation Spectroscopy (SCS) has emerged as a sensitive analytical technique for characterizing the dynamic and structural properties of nanoscale systems, particularly gold nanoparticles (GNP) in colloidal solutions. Unlike traditional light-scattering methods, SCS analyzes the temporal fluctuations of scattered intensity within a confined optical volume, enabling the determination of particle diffusion coefficients, hydrodynamic radii, and concentration without the need for external labels. This confocal autocorrelation approach, analogous in concept to fluorescence correlation spectroscopy, exploits the statistical analysis of intensity fluctuations to extract detailed information about particle motion and interaction dynamics over time.

In recent years, SCS has been increasingly applied to the study of GNP, whose morphology, surface chemistry, and interaction with biological molecules critically influence their behavior in sensing, biomedical, and catalytic applications. Djaker and co-workers have significantly contributed to this field by demonstrating the utility of SCS for distinguishing subtle differences in nanoparticle shapes and surface functionalities. They employed SCS to measure hydrodynamic sizes and biomolecules interactions of various GNPs, highlighting enhanced sensitivity to structural features such as surface branches and anisotropy in gold nanoflowers and nanourchins [3,4].

In this work, we present an SOD biosensor based on GNP-aptamer by using SCS. The results shows that this technique can provide many information such as binding affinity constant, binding cooperativity and number of interacted molecules on GNP.

II. Methods

SCS was previously described by the authors [3,4]. The set-up is based on an inverted microscope (Nikon) with an excitation wavelength at 633nm (He-Ne laser, Thorlabs) and an excitation power of 10 µW. A water immersion objective (Olympus, 40, NA = 1.2) was used for both excitation and collection signal. The confocal volume is selected by a 50µm pinhole and recorded by two avalanche photodetectors (PerkinElmer). The cross-correlation was performed by a correlator (ALV-7004). SCS curves were obtained by averaging at minimum five runs, each of 60 s duration.

III. Results and Discussion

Fig. 1 shows the extinction spectra of GNS before and after aptamer grafting and incubation with SOD1 (10 µM) at saturation. The results show that the LSPR maximum wavelength of pegylated GNS is around 533 nm with a FWHM around 30 nm, which reveals a good monodispersity of the

nanoparticles as already demonstrated by the authors.

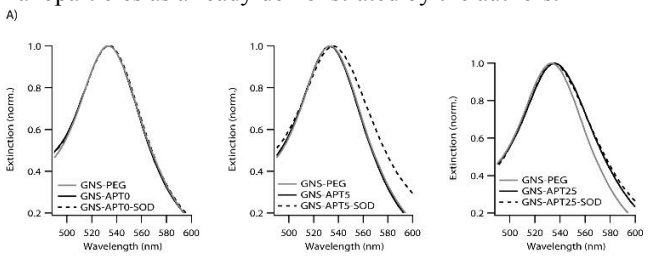

Fig. 1 Normalized extinction spectra of GNP before and after interaction with SOD (A).

In general, the aptamer and SOD grafting at the GNS surface leads to a red-shift of the LSPR position and an increase of the FWHM of the extinction spectrum. By considering the error bars, the LSPR red-shift and FWHM variations are not visible in each case, especially in the case of GNS-APT0 (without thymine-spacer). While, for GNS-APT25, the FWHM increases gradually. For all GNS-APT, the functionalization with SOD1 gives a higher LSPR and a larger FWHM, which demonstrates the SOD-APT interaction. This interaction is also revealed by DLS and zeta-potential measurement. The synthesized pegylated GNS have a hydrodynamic size about (78±6) nm and a ζ-potential of (-47±5) mV. The functionalization with the different aptamers and after interaction with SOD1 proteins (10 μM) gave generally a higher hydrodynamic size and ζ-potential. In the case of GNS-APT0, without thymine spacer, the hydrodynamic size decreases after interaction with SOD1, which reveals that the aptamers orientation and immobilization in GNS-APT0 is different than the GNS functionalized with thymine-spacer aptamers. Note that, the hydrodynamic radius doesn't reflect only the size of the particle but also its shape and surface chemistry, which affect its mobility in the solvent. This mobility seems to be different in the presence or not of the thymine-spacer. The error-bars given by the DLS method are too large to make a precise observation in this case, so that, the aim of this work is to use the scattering correlation spectroscopy as a powerful tool to precisely measure the variations of the hydrodynamic size at different SOD1 concentrations and to see the effect of the different thymine-spacer lengths on SOD1 sensing.

Fig 3 shows normalized SCS curves of gold nanoparticles at each step of functionalization. Pegylated gold nanoparticles showed a diffusion time of 9.85 ms corresponding to a hydrodynamic radius of 38.3 nm (hydrodynamic size of 76.6 nm). After interaction with the aptamer (without thymine spacer, GNS-APT0), the diffusion time increased to 11.4 ms corresponding to a hydrodynamic radius of 45.0 nm (hydrodynamic size of 90.0 nm), this gave an increase of the hydrodynamic radius of about 6.7 nm due to the aptamer (0T) interaction (typical size for an aptamer of 72 bases).

Hydrodynamic radius R_H calculated from SCS curves of gold nanoparticles after interaction with different concentrations of SOD (dots).

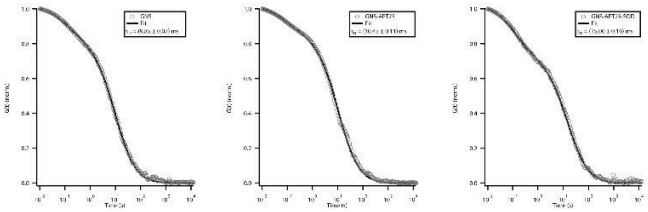

Fig. 3 Normalized cross-correlation curves (grey circles) and their fits (solid lines) of gold nanoparticles before and after interaction with SOD.

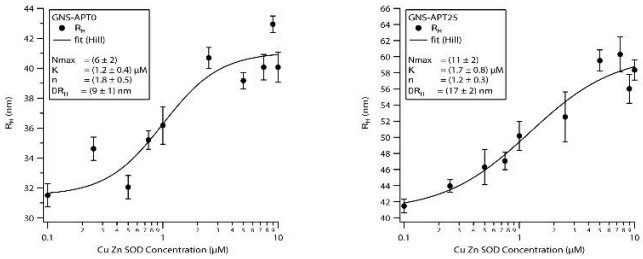

Fig. 4 GNP hydrodynamic radius after interaction with different concentrations of SOD (dots). The curves were fitted (solid lines) by using Hill equation.

IV. Conclusion

In this work, we have demonstrated an aptamer-GNP biosensor for SOD detection based on correlation spectroscopy. The SCS technique enables highly precise quantitative analysis, providing an exceptional level of accuracy in nanoparticle characterization. It is the only method capable of determining the exact number of molecules bound to a single nanoparticle. This study was performed using only microliter sample volumes and picomolar nanoparticle concentrations, making it both highly sensitive and resource-efficient.

Acknowledgments

This work was supported by the Federative research structure Nano Sciences and Applications of Sorbonne Paris Nord University (NapMosaic).

References

[1] W. Wang, Y. He, S. He, L. Deng, H. Wang, Z. Cao, Z. Feng, B. Xiong and Y. Yin, "A Brief Review of Aptamer-Based Biosensors in Recent Years" Biosensors 2025, Biosensors, 15, 120, 2025.

[2] A. Kanioura, G. Geka, I. Kochylas, V. Likodimos, S. Gardelis, A. Dimitriou, N. Papanikolaou, S. Kakabakos and P. Petrou, "Superoxide Dismutase Detection on Silver Nanostructured Substrates through Surface-Enhanced Spectroscopic Techniques", Chemosensors,12, 89, 2024.

[3] H. Moustaoui, J. Saber, I. Djeddi, Q. Liu, D. Movia, A. Prina-Mello, J. Spadavecchia, M. Lamy de la Chapelle and N. Djaker, "In situ protein corona study by scattering correlation spectroscopy: a comparative study between spherical and urchin-shaped gold nanoparticles", Nanoscale, 11, 8, pp 3665-3673, 2019.

[4] D. Issaad, H. Moustaoui, L. Lalaoui, J. Spadavecchia, A. Medjahed, M. Bouafia, M. Lamy de la Chapelle, N. Djaker, "Scattering Correlation and SERS Spectroscopy of Thiophenol on Gold Nanoparticles: Comparative Study between Nano-Spheres and Nano-Urchins". Journal of Physical Chemistry C, 121,33, 2017.

Decoding Intracellular Microenvironment by SERS

Aleksandra Szaniawska[1,*], Agnieszka Girstun[2], Katarzyna Bogusz[1], Justyna Grzęda[1], Aleksandra Miszczak[1], Hubert Sobiech[1], Katarzyna Wleciał[1], Andrzej Kudelski[1],

[1]Faculty of Chemistry, University of Warsaw, Pasteura 1 Str., 02-093 Warsaw, Poland
[2] Faculty of Biology, University of Warsaw, Miecznikowa 1 Str., 02-096 Warsaw, Poland
*Corresponding author: aleksandra.szaniawska@uw.edu.pl

***Abstract*— Surface enhanced Raman spectroscopy is employed to probe intracellular pH and local chemical microenvironments using plasmonic gold nanostructures functionalized with pH sensitive Raman reporters. Systematic comparison of reporter molecules and nanoparticle architectures reveals how cellular environment nanoparticle morphology and reporter chemistry jointly determine sensor response inside living cells.**

***Keywords*— surface enhanced Raman spectroscopy, intracellular pH, gold nanoparticles, nanopopcorn, cellular microenvironment.**

I. Introduction

Intracellular pH is a key regulator of cellular processes including metabolism protein activity endocytosis and cell fate decisions. While average cytosolic pH is relatively well characterized much less is known about local pH heterogeneity at the nanoscale and its dynamic changes within organelles. Conventional fluorescence based probes face limitations related to photobleaching spectral overlap and restricted multiplexing. Surface enhanced Raman spectroscopy offers molecular specificity high photostability and the ability to probe highly localized environments near plasmonic nanostructures.

II. Methods

Gold nanoparticles with controlled morphology including spherical particles and anisotropic nanopopcorn structures were synthesized using seeded growth approaches. Nanoparticles were functionalized with thiolated pH sensitive Raman reporters including mercaptobenzoic acid mercaptopyridine and aminothiophenol derivatives. SERS calibration curves were established in buffer solutions and cell culture media over physiologically relevant pH ranges. Nanoparticle uptake intracellular localization and biocompatibility were assessed using transmission electron microscopy confocal microscopy and viability assays. Intracellular SERS measurements were performed in living cells to extract local pH information.

III. Results and Discussion

Distinct Raman reporters exhibit different pH sensitivities dynamic ranges and stability depending on their chemical structure and orientation on the gold surface. Nanopopcorn architectures provide enhanced electromagnetic hot spots leading to increased SERS signal and improved intracellular detectability compared to spherical nanoparticles. Calibration curves obtained in buffer solutions differ substantially from those measured in cell culture media and inside cells highlighting the influence of protein corona formation ionic strength and confinement effects. The results demonstrate that intracellular SERS based pH sensing reflects not only proton concentration but also the complex physicochemical microenvironment surrounding the nanosensor.

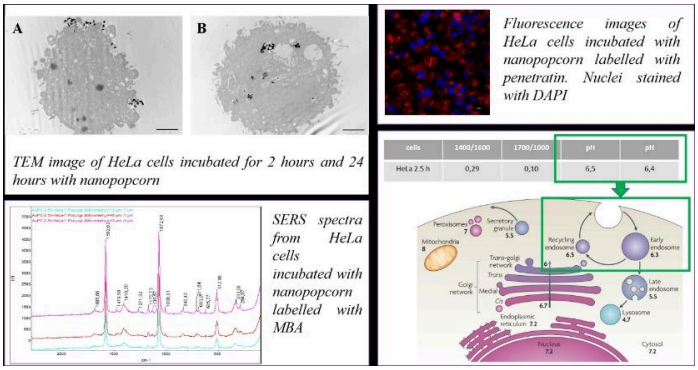

Fig. 1 Multi-Technical Approach for Intracellular pH Measurements: Integration of SERS, Fluorescence, and TEM.

IV. Conclusion

This study demonstrates that SERS based nanosensors enable probing of intracellular microenvironments with high chemical specificity. Understanding how nanoparticle morphology reporter chemistry and cellular context affect sensor response is essential for reliable intracellular pH measurements. These insights provide a framework for designing next generation SERS probes for studying dynamic processes inside living cells.

Acknowledgments

This work was supported by the National Science Centre, Poland, grant SONATA, No. UMO-2020/39/D/ST4/01973.

REFERENCES

[1] A. Jaworska, K. Malek, A. Kudelski, Spectrochimica Acta Part A: Molecular and Biomolecular Spectroscopy 251 (2021) 119410

Multimetallic plasmonic nanoparticles for colorimetric sensing

Vincenzo Amendola[1,*]

[1]Department of Chemical Sciences, University of Padova, via Marzolo, 1, 35131, Padova, Italy

*Corresponding author: vincenzo.amendola@unipd.it

***Abstract*—**

Colorimetric sensors based on a color change in the presence of an analyte represent one of the most extensively investigated applications of plasmonic nanoparticles, particularly gold nanoparticles. In a colloidal system of surface-functionalized gold nanoparticles, aggregation can occur upon interaction with an analyte, producing a spectral shift that can be quantitatively analyzed by UV–visible spectroscopy [1,2] and qualitatively detected by the naked eye.

A similar behavior has been observed in silver nanoparticles and, more recently, in rhodium nanoparticles [3], although their plasmonic and physicochemical properties make these materials generally less attractive for this specific application.

In this contribution, we discuss the potential of these three types of plasmonic nanomaterials and highlight the still unexplored opportunities they may offer to the field of plasmonic colorimetric sensing.

***Keywords*— gold nanoparticles, silver nanoparticles, rhodium nanoparticles, colorimetric sensors, colloids.**

References

[1] V. Amendola, R. Pilot, M. Frasconi, O. M. Maragò, and M. A. Iatì, "Surface plasmon resonance in gold nanoparticles: a review," *Journal of Physics: Condensed Matter*, vol. 29, no. 20, 203002.

[2] D. Revignas and V. Amendola, "Artificial Neural Networks Applied to Colorimetric Nanosensors: An Undergraduate Experience Tailorable from Gold Nanoparticles Synthesis to Optical Spectroscopy and Machine Learning," *Journal of Chemical Education*, vol. 99, no. 5, pp. 2112–2120.

[3] D. M. Arboleda, V. Coviello, A. Palumbo, R. Pilot, and V. Amendola, "Rhodium nanospheres for ultraviolet and visible plasmonics," *Nanoscale Horizons*, vol. 10, no. 2, pp. 336–348.

Low-Power Plasmonic Strategies for Nanoscale Analyte Transport and Trapping

Aliaksandra Rakovich[1,*], Marciano Palma do Carmo[1], David Mack[2], Diane J. Roth[1], Miao Zhao[1], Ancin Maria Devis[1], Francisco Rodríguez-Fortuño[1], Stefan A. Maier[2,3], Paloma A. Huidobro[4,5]

[1]Department of Physics, King's College London, United Kingdom
[2]Department of Physics, Imperial College London, United Kingdom
[3]School of Physics and Astronomy, Monash University, Australia
[4]Departamento de Física Teórica de la Materia Condensada, Universidad Autónoma de Madrid, Spain
[5]Condensed Matter Physics Center (IFIMAC), Universidad Autónoma de Madrid, Spain
*Corresponding author: aliaksandra.rakovic@kcl.ac.uk

***Abstract*—This work reports a low-power hybrid plasmonic platform for nanoscale analyte transport and trapping aimed at plasmonic biosensing applications. The platform integrates asymmetric nanoantenna arrays that enable rectified Brownian transport under modulated illumination with plasmonic bowtie electrodes that provide frequency controlled dielectrophoretic trapping and release, enabling spatially resolved analyte delivery.**

***Keywords*— plasmonics, dielectrophoresis, optical trapping, nanoparticle transport, biosensing**

I. Introduction

Efficient manipulation of nanoscale analytes is a key requirement for plasmonic sensing and lab on chip technologies. Conventional optical trapping techniques typically rely on high optical intensities [1], which can induce heating, photodamage, and degradation of sensitive biological samples. These limitations motivate the development of alternative low power strategies capable of enhancing analyte localization and transport without compromising sample integrity.

In this work, two complementary plasmonic approaches are investigated to address analyte manipulation across different spatial regimes. First, plasmonic Brownian ratchets based on asymmetric nanoantenna arrays are employed to generate directed, long range transport of nanoparticles under temporally modulated illumination. Second, hybrid plasmo dielectrophoretic traps combine localized plasmonic field enhancement with electrically driven dielectrophoretic forces to achieve stable, frequency dependent trapping and controlled release. Together, these systems provide versatile routes for analyte delivery and confinement in integrated plasmonic platforms.

II. Methods

Plasmonic nanostructures were investigated using finite-element frequency-domain simulations performed in COMSOL Multiphysics to model their electromagnetic response under optical (RF module) and electrical (AC/DC module) excitations. Simulations were used to calculate near-field distributions, optical forces, trapping potentials, and electric-field gradients generated by asymmetric nanoantenna geometries. For the plasmonic Brownian ratchet structures, a range of asymmetric gold nanoantenna unit-cell geometries was examined to assess how structural asymmetry influenced the optical force landscape along a defined transport axis. For the dielectrophoretic structures, bowtie-shaped nanoantennas integrated with in-plane electrodes were examined to evaluate optical near-field confinement and electrically induced field gradients relevant for dielectrophoretic manipulation. In all cases, the nanostructures were modelled as 40 nm high gold features fabricated on a quartz substrate with a 5 nm chromium adhesion layer and immersed in water.

Optical forces acting on dielectric nanoparticles were calculated using the Maxwell stress tensor (MST) formalism:

$$\mathbf{T} = \frac{1}{2}\mathrm{Re}\left[\varepsilon_0\varepsilon\left(\mathbf{E}\mathbf{E}^* - \frac{1}{2}|\mathbf{E}|^2\mathbf{I}\right) + \mu_0\mu\left(\mathbf{H}\mathbf{H}^* - \frac{1}{2}|\mathbf{H}|^2\mathbf{I}\right)\right], \tag{1}$$

The force acting on the analyte particle was then obtained by integrating $\mathbf{T}$ over a closed surface enclosing the particle. Trapping potentials were obtained by spatial integration of the force along the transport axis.

Arrays were fabricated by electron-beam lithography followed by metal deposition (Cr/Au) and lift-off (Fig. 1(a) and (Fig. 2(b)). Experiments were carried out on an inverted microscope (Nikon Eclipse Ti2) equipped with a 40× objective and an sCMOS camera. Nanoparticles were illuminated using dark-field or angled bright-field white-light illumination (Fig. 1(d)). Optical excitation was provided by a normally incident continuous-wave laser at 980 nm. For ratcheting experiments, directional transport was induced by periodically modulating the laser intensity using a mechanical chopper with a 50% duty cycle. Videos were acquired for subsequent trajectory analysis. Particle positions were extracted frame-by-frame to obtain (x, y, t) trajectories for large ensembles. Tracks were filtered by minimum duration, and net displacements were computed over defined time windows. Mean particle velocities were obtained from linear fits of displacement versus time. Trap stiffness was estimated using equipartition-based analysis.

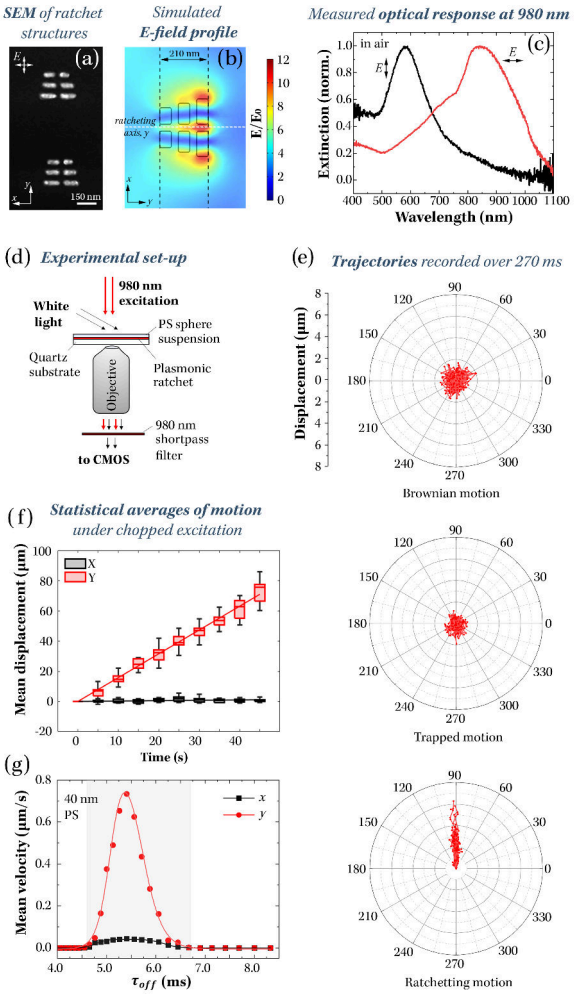

Fig. 1. Plasmonic Brownian ratchet structures and nanoparticle transport under temporally modulated excitation. (a) SEM image of an asymmetric plasmonic ratchet unit cell; arrows indicate the excitation polarization and ratchet axis. (b) Simulated near-field intensity profile under 980 nm illumination, showing an asymmetric optical potential along the transport direction. (c) Measured extinction spectra for orthogonal polarizations, confirming resonant excitation near 980 nm. (d) Schematic of the experimental configuration for particle tracking above the ratchet arrays. (e) Representative particle trajectories recorded over 270 ms in the absence of optical excitation (top), under continuous-wave illumination (middle), and under temporally modulated illumination (bottom). (f) Mean particle displacement as a function of time under chopped excitation, showing directed motion along the ratchet axis. (g) Mean particle velocity as a function of modulation off-time for 40 nm polystyrene particles, exhibiting a finite operating window for rectified transport.

For dielectrophoretic experiments, bowtie-electrode antenna arrays were mounted on a custom holder providing electrical contacts. An alternating-current voltage generated by a function generator (Agilent 33120A) was applied across the integrated electrodes, with frequencies swept in the kilohertz to megahertz range at fixed peak-to-peak voltage to switch between positive and negative dielectrophoretic regimes. Trapping and release dynamics were recorded optically. Particle accumulation at individual bowtie sites was quantified by integrating scattering intensity over regions of interest around the antennas and normalizing by background signals measured in adjacent regions.

III. Results and Discussion

Nanoparticle trajectories above the plasmonic Brownian ratchet arrays exhibited distinct regimes depending on the optical excitation used (Fig. 1(e)). In the absence of the 980 nm illumination, particle motion was consistent with free Brownian diffusion, while continuous-wave illumination resulted in localization at optical potential minima without net transport. When the excitation was temporally modulated, Brownian motion was rectified, producing net particle displacement along the direction defined by the ratchet asymmetry, with trajectories extending over several tens of micrometers during the recorded 40 ms time window (Fig. 1(f)).

Statistical analysis of large particle ensembles revealed that the rectified transport depended on the modulation parameters (Fig. 1(g)). For 40 nm polystyrene particles, directed motion was observed only within a finite range of modulation frequencies, consistent with diffusion times set by the ratchet unit-cell dimensions and the asymmetry of the potential established within. Outside of this regime, rectified transport diminished when the modulation off-time was either shorter than the characteristic diffusion time between adjacent potential minima or sufficiently long that particles explored multiple unit cells before re-trapping, resulting in negligible net displacement.

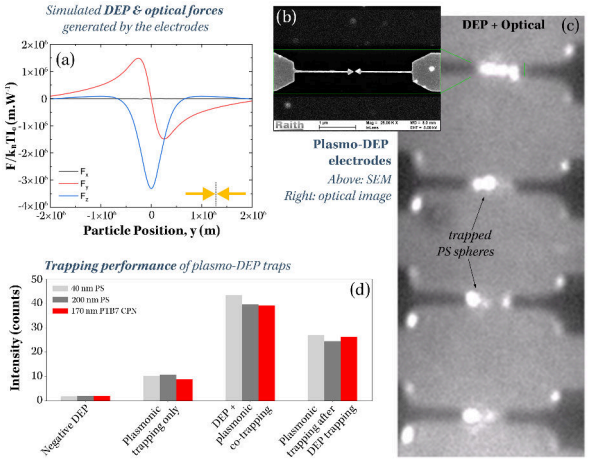

Fig. 2. Plasmonic bowtie-electrode antennas for dielectrophoretic trapping and optical confinement. (a) Simulated dielectrophoretic and optical force components acting on a nanoparticle along the bowtie axis under combined electrical and optical excitation. (b) SEM image of a bowtie-electrode antenna with integrated in-plane electrodes. (c) Optical image showing nanoparticle accumulation at the bowtie gap under simultaneous dielectrophoretic and optical excitation. (d) Trapping performance quantified by scattering intensity for different particle sizes and materials under negative DEP, optical trapping only, combined DEP and optical co-trapping, and optical trapping following DEP pre-concentration.

Dielectrophoretic manipulation using plasmonic bowtie-electrode antennas exhibited a distinct frequency-dependent response. When an AC voltage was applied across the integrated electrodes, nanoparticles accumulated above the bowtie gaps

under conditions corresponding to positive dielectrophoresis. Increasing the excitation frequency resulted in a transition to particle repulsion, defining a well-resolved crossover between trapping and release (Fig. 2(c)). For 40 nm polystyrene particles, this crossover occurred in the megahertz range, consistent with the frequency dependence of the Clausius–Mossotti factor of the particle–medium system. Concurrent optical excitation at 980 nm enhanced particle confinement at the bowtie gaps by increasing local field gradients at the plasmonic hotspot, while the sign of the dielectrophoretic force remained governed by the electrical excitation. Quantitative analysis of scattering intensity confirmed increased particle accumulation under combined optical and electrical excitation compared to electrical excitation alone (Fig. 2(d)).

IV. Conclusion

Plasmonic Brownian ratchet arrays were shown to rectify Brownian motion and drive directional nanoparticle transport under temporally modulated optical excitation. For 40 nm particles, net displacements over tens of micrometers and mean transport velocities of up to $\sim$2–3 μm s^{-1} were achieved at incident intensities below 1 kW cm^{-2}, well below those typically required for conventional optical trapping [2]. The transport was governed by the relation between the modulation off-time and the particle diffusion time between adjacent potential minima, defining a finite operating regime for rectification.

Plasmonic bowtie-electrode antennas enabled localized nanoparticle manipulation through frequency-dependent dielectrophoresis. Application of an alternating-current voltage produced reversible switching between trapping and release, with confinement occurring at the bowtie gaps below a well-defined crossover frequency in the megahertz range for 40 nm particles. Optical excitation at 980 nm enhanced confinement through increased near-field gradients, while the sign of the dielectrophoretic force remained controlled by the electrical excitation.

Together, these results demonstrate low-power plasmonic approaches for nanoparticle transport and localization operating over distinct spatial and temporal regimes relevant to micro- and nanoscale analyte manipulation.

Acknowledgments

This work was supported by Royal Society (RGF\R1\180068, UF150542, URF\R\211023); EPSRC (EP/W017075/1); Lee-Lucas Chair in Physics (ICL, UK); MICIU and AEI (RYC2021-031568-I and "María de Maeztu" Programme for Units of Excellence in R&D CEX2023-001316-M); ERC iCOMM 789340.

References

[1] M. L. Juan, M. Righini, and R. Quidant,"Plasmon nano-optical tweezers," *Nature Photonics*, vol. 5, pp. 349–356, 2011.

[2] M. P. do Carmo, D. Mack, D. J. Roth, M. Zhao, A. M. Devis, F. J. Rodríguez-Fortuño, S. A. Maier, P. A. Huidobro, A. Rakovich, "Plasmonic Brownian Ratchets for Directed Transport of Analytes," *Nano Letters*, vol. 26, pp. 181–187, 2026.

Fluorescence-based chiral sensing with silicon metasurfaces

Tom T.C. Sistermans[1], Artemijs Krimovs[2], Robert Pal[2], Alberto G. Curto[1*]

[1]Photonics Research Group, Ghent University-imec, Ghent, Belgium
[2]Department of Chemistry, Durham University, Durham, UK
*Corresponding author: Alberto.Curto@UGent.be

***Abstract*— Chiral molecules with opposite handedness can have strongly differing biological properties. Identifying chirality is, however, limited by low sensitivity, restricting detection to high concentrations and large sample volumes. To overcome this, we propose a silicon nanophotonics-based sensing technique to enhance the sensitivity of chiral molecular detection.**

***Keywords*— metasurface, chirality, sensing, nanophotonics.**

Detecting the handedness of chiral molecules is essential in biochemistry, as the biological behavior of proteins, amino acids, and carbohydrates can differ dramatically between enantiomers. Circularly polarized light is commonly used to distinguish enantiomers by their differential absorption of left- and right-handed circularly polarized light, a technique known as circular dichroism (CD). However, this transmission-based technique relies on detecting small absorption differences, which becomes challenging at low concentrations where the overall absorption is negligible. Consequently, the weak signal becomes buried in background noise, severely limiting sensitivity and requiring high molecular concentrations and long measurement times. These limitations make conventional CD unsuitable for critical applications such as the early detection of protein aggregates associated with various diseases.

Using circularly polarized luminescence (CPL), some of the limitations of CD can be bypassed. The luminescence is shifted in wavelength, allowing separation from the excitation beam and strongly reducing background noise. The chirality is now detected by analyzing the circular polarization of the luminescence. Nonetheless, CPL contrasts are typically small because fluorescence is weak and the polarization asymmetry is low. To address this, we employ a metasurface composed of an array of silicon nanodisks, which act as optical resonators to enhance light–matter interaction [1-3]. The periodic arrangement introduces collective resonances that further enhance fields and scattering [4]. In addition, the resonators can increase the radiative decay rate via the Purcell effect and improve emission directionality, enabling more efficient detection. Together, these mechanisms can substantially boost the detected fluorescence intensity.

For chiral discrimination, the emission polarization properties are equally critical. High-index dielectric nanodisks allow tuning of electric and magnetic resonances to control the local optical chirality density, potentially enabling super-chiral near fields to enhance the CPL.

The metasurface is fabricated by electron-beam lithography from crystalline silicon, providing high refractive-index contrast and low optical losses in the visible range. Deposited on a glass substrate, the structures are compatible with transmission-mode measurements in our custom-built polarization microscope. The setup integrates dual single-photon counting detectors and dual photoelastic modulators to enable full Stokes polarimetry of the photoluminescence, allowing reliable CPL quantification with a spatial resolution of a few micrometers.
To evaluate performance, we deposit a chiral lanthanide complex embedded in a PMMA layer on the metasurface. Depending on the nanodisk radius, the fluorescence intensity increases by up to 2.5 times compared to the bare thin film. Importantly, by carefully tuning the electric and magnetic resonances of the silicon disks, this enhancement is achieved while largely preserving the emitters' intrinsic circular polarization. This combination of simultaneous enhancement of fluorescence while preserving circular polarization is a key advantage over other enhancement approaches and highlights the strength of high-index dielectric metasurfaces for chiral sensing. Overall, the metasurface more than doubles the total CPL sensitivity, demonstrating that silicon nanophotonics can substantially boost fluorescence-based chiral readout.

Acknowledgements. This work was financially supported by the European Research Council (ERC) under the European Union's Horizon 2020 research and innovation program (grant agreement 948804, CHANSON).

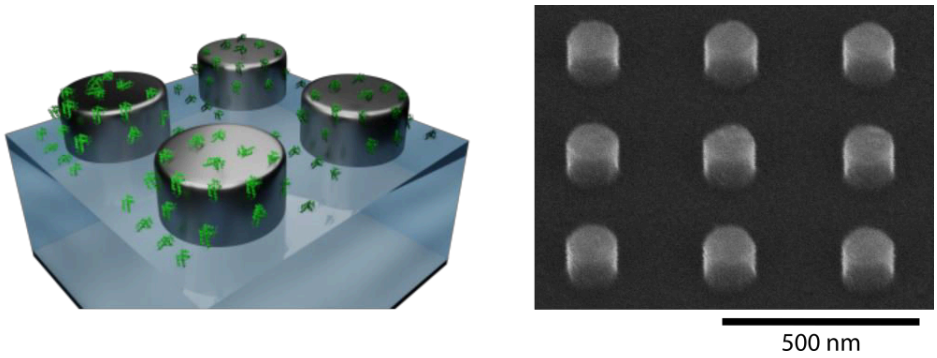

Figure 1: (left) Chiral molecules on a silicon metasurface. (right) SEM micrograph of a silicon metasurface

REFERENCES

[1] E. Mohammadi, A. Tittl, K. L. Tsakmakidis, T. V. Raziman, and A. G. Curto, "Dual Nanoresonators for Ultrasensitive Chiral Detection," ACS Photonics, vol. 8, no. 6, 2021, doi: 10.1021/acsphotonics.1c00311.

[2] T. V. Raziman, R. H. Godiksen, M. A. Müller, and A. G. Curto, "Conditions for Enhancing Chiral Nanophotonics near Achiral Nanoparticles," ACS Photonics, vol. 6, no. 10, 2019, doi: 10.1021/acsphotonics.9b01200.

[3] E. Mohammadi, T. V. Raziman, and A. G. Curto, "Nanophotonic Chirality Transfer to Dielectric Mie Resonators," Nano Lett, vol. 23, no. 9, 2023, doi: 10.1021/acs.nanolett.3c00739.

[4] S. Murai, G. W. Castellanos, T. V. Raziman, A. G. Curto, and J. G. Rivas, "Enhanced Light Emission by Magnetic and Electric Resonances in Dielectric Metasurfaces," Adv Opt Mater, vol. 8, no. 16, 2020, doi: 10.1002/adom.201902024.

Smart materials for thermal management by utilizing environmental sensing

D. S. Sutherland[1,*] and X. B. González[1]

[1]NANO Center Aarhus University, Aarhus, Denmark

*Corresponding author: duncan@inano.au.dk

***Abstract*— Solar conversion to heat in building interiors causes significant energy use through air-conditioning, contributing massively to global CO_2 emission. A smart windows solutions based on plasmonics makes use of environmental sensing to dynamically modulate near infrared light entry as a function of solar intensity.**

***Keywords*— Thermoplasmonics, dynamic blocking, NIR**

INTRODUCTION

Plasmonic metamaterials provide multiple functional applications including sensing and photo-thermal conversion. These two capabilities can be combined to provide a smart nanoscale material solution for windows applications.

I. METHODS

Nanofabrication of plasmonic nanostructures via self-assembly approaches such as colloidal lithographies open for applications were larger areas of plasmonic materials are required. Here we developed Hole mask Colloidal Lithography (HCL) for the fabrication of nanoscale rings of arbitrary materials [1-2]. Silver nanorings arrays on glass were characterized spectroscopically and by FDTD then integrated into double-glazed window designs where small amounts of solvents were injected into the interior cavity of the windows to build a responsive system where the plasmon resonance shifted in response to the intensity of light shone on it. The complete window was tested under natural solar illumination and showed dynamic response as the sun intensity changed across a day[3].

II. RESULTS AND DISCUSSION

Silver nanoring arrays with major plasmon resonance around 950nm showed light blocking in the near infrared by absorption of photons. For windows without solvent in the interior space the NIR blocking effect reduced the temperature of black objects behind the window by up to 4 degrees C. By placing solvent in the interior space a thin solvent layer formed on the plasmon arrays shifting the plasmon resonance 80-100nm to longer wavelength through refractive index effects. Solvent covered plasmonic surfaces showed photothermal conversion and bulk heating and evaporation of the solvent which in turn shift the plasmon resonance to shorter wavelength. When integrated into a double-glazed window the effect was reversible so that turning off the illumination and subsequent cooling lead to resonance shift to longer wavelength. The combined system was a dynamically responding photothermal switch which reduced NIR transmission as light intensity increased. Solar testing dynamic response where NIR transparency was controlled by the solar intensity over the course of the day.

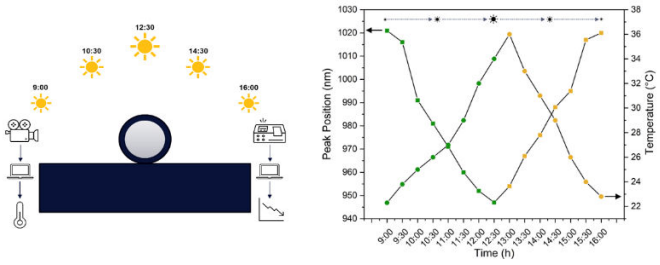

Figure1 Left: Schematic of solar illumination during the day. Right: Glass temperature and plasmon peak position shift in response to altered solar intensity. Reproduced from [3]

III. CONCLUSION

Plasmonic materials integrated into windows can utilize environmental sensing and photothermal conversion to provide passive technology for dynamic solar blocking while retaining visible transparency.

ACKNOWLEDGMENTS

This work was supported by DFF and NNF funding sources

REFERENCES

[1] X. B. González, J. Duc Tran, D. S.Sutherland "Versatile nanoring fabrication assisted by hole-mask colloidal lithography" ACS Appl. Mater. Interf. Vol 16 pp 35361-35371 2024.

[2] X. B. González, P. M. Leidinger, B. Rente, R. Bower, J. V. Lauritsen, P. K. Petrov, D. S.Sutherland "Thermally Robust Plasmonic Nanorings from Titanium Nitride" ACS Omega Vol 10 pp 46176-46187 2025

[3] X. B. González, D. S.Sutherland "Thermoplasmonic nanorings for passive solar-responsive smart windows in energy-efficient building applications" Ad. Funct. Mater. Vol 36 e18295 2025.

Resonant Heat Transfer for Efficient Off Grid Photothermal Desalination

William Schmid[1], Qian Ye[1,2], Aleida Machorro-Ortiz[1], Peter Nordlander[1,2,4,5], Naomi J. Halas[1,2,3,4,5], and Alessandro Alabastri[1,4,5]*

[1]Department of Electrical and Computer Engineering, Rice University, Houston TX, USA
[2]Department of Physics and Astronomy, Rice University, Houston TX, USA
[3]Department of Chemistry, Rice University, Houston TX, USA
[4]Laboratory for Nanophotonics, Rice University, Houston TX, USA
[5]The Smalley-Curl Institute, Rice University, Houston TX, USA
*Corresponding author: alessandro.alabastri@rice.edu

***Abstract*- Solar photothermal desalination is limited by latent heat. We demonstrate resonant heat transfer that recycles condensation heat back to the feed when counterflows are dynamically matched. With nanophotonic or plasmonic absorbers for high light to heat conversion, resonance increases fresh water output and enables off grid desalination.**

***Keywords*- solar desalination, resonant energy transfer, photothermal, plasmonics, heat recovery.**

I. Introduction

Sunlight is an abundant electromagnetic energy source for decentralized thermal desalination when efficiently absorbed and converted into localized heat[1]. However, evaporation is intrinsically energy intensive, so practical systems must recover and reuse latent heat while remaining scalable and resistant to fouling[2].

II. Methods

We couple photothermal evaporation modules with countercurrent heat exchange so that condensation heat is circulated back to preheat the feed. Resonant Energy Transfer (RET) occurs when the interacting flow rates satisfy a resonance condition that maximizes internal heat circulation, analogous to coupled oscillators[3]. RET can be implemented in membrane distillation and in membrane free humidification dehumidification architectures, with dynamic flow control under variable solar input.

III. Results and Discussion

Key results include:

- Up to five-fold increase in collected distillate in a photothermal membrane system at the RET resonance condition by matching feed and distillate flows[4].
- Membrane free architecture extends RET to humidification dehumidification, predicting weeklong productivity gains of about 77 percent and average gained output ratio near 1.9 at seawater salinity under realistic solar profiles[5]
- Broadband nanophotonic and plasmonic absorbers localize solar heating at the evaporation interface, improving scalability and enabling compact off grid modules (Refs. 1 and 5).

IV. Conclusion

Resonant heat transfer provides a unifying physics framework for optimizing solar thermal desalination beyond component level absorber design. By combining engineered electromagnetic absorption with flow tuned heat recovery, RET enables higher efficiency, continuous production under time varying sunlight, and architectures that avoid fragile membranes.

Acknowledgments

This work was supported by Rice University, the Nanotechnology Enabled Water Treatment Center and the Department of Energy Solar Desalination Prize We thank our collaborators for contributions to the underlying studies.

References

[1] P. D. Dongare, A. Alabastri et al., *Nanophotonics enabled solar membrane distillation for off grid water purification*, **Proc. Natl. Acad. Sci.** U.S.A., 114, 6936-6941, 2017.

[2] W. Schmid et al., *Decentralized solar driven photothermal desalination*, **ACS Photonics**, 9, 3764-3776, 2022.

[3] Q. Ye, S. Sanders, and A. Alabastri, Resonant energy transfer and storage in coupled flow driven heat oscillators, **PRX Energy**, 2, 023007, 2023.

[4] A. Alabastri et al., *Resonant energy transfer enhances solar thermal desalination*, **Energy Environ. Sci.**, 13, 968-976, 2020.

[5] W. Schmid et al., *Resonant energy transfer for membrane free off grid solar thermal humidification dehumidification desalination*, **Nature Water**,5, 2025.

[6] L. Mascaretti et al., *Solar steam generation on scalable ultrathin thermoplasmonic TiN*, **Nano Energy**, 83, 2021

Micro- and Nanolasers for Biomolecular detection

Soraya Caixeiro[1, *]

[1]Department of Physics, University of Bath, UK
*Corresponding author: scc201@bath.ac.uk

***Abstract*— Micro- and nanolasers exhibit sharp optical resonances that make them powerful platforms for sensitive biomolecular detection. We demonstrate spectral-shift sensing using surface-functionalised whispering-gallery-mode microlasers, with gold-nanoparticle coupling providing enhanced, label-free sensitivity. This approach enables the detection of subtle molecular interactions and offers a versatile route toward compact, high-precision biosensing devices.**

***Keywords*— microlasers; whispering-gallery modes; biosensing; nanoparticles; label-free.**

REFERENCES

[1] S. Caixeiro, R. Dorrenhaus, A. Popczyk, M. Schubert, S. Kath-Schorr, M. C. Gather, "DNA sensing with whispering gallery mode microlasers", Nanoletters, vol. 25, pp. 4467–4475, 2025.

[2] S. Caixeiro, P. Rodríguez-Sevilla, K. Dholakia, M. C. Gather "Optical Manipulation of Whispering Gallery Mode Microlasers for Precision Controlled Cellular Delivery" arXiv preprint arXiv:2409.01485, 2024.

[3] V. M. Titze, S. Caixeiro, V. S. Dinh, M. König, M. Rübsam, N. Pathak, A S., M. Germer, C. Kukat, C. M. Niessen, M. Schubert, M. C. Gather, "Hyperspectral confocal imaging for high-throughput readout and analysis of bio-integrated microlasers" Nature Protocols, vol. 19, pp. 928–959, 2024.

[4] S. Caixeiro, R. Dorrenhaus, A. Popczyk, M. Schubert, S. Kath-Schorr, M. C. Gather, "Local sensing of absolute refractive index during protein-binding using microlasers with spectral encoding", Advanced Optical Materials, vol. 11, pp. 2300530, 2023.

Hybrid Photonic–Electronic Tapered Optical Fibers for Multimodal Neural Interfacing

Ferruccio Pisanello[1,*], L. Piscopo[1,2], B. Spagnolo.[1], A. Balena[1,6], S. Pottekad[1,2], C. Lattebovio[1], Giulio Mastrototaro[1,2], M. F. Kashif[1,4], C. Montinaro[1], S. Aslanoglou[1], M. Kazemzadeh[1], A. Qualtieri[1], M. De Vittorio[1,2,7],

[1] Istituto Italiano di Tecnologia, Center for Biomolecular Nanotechnologies, 73010 Arnesano, Italy
[2] Dipartimento di Ingegneria dell'Innovazione, Università del Salento, 73100 Lecce, Italy
[3] State Key Laboratory of Radio Frequency Heterogeneous Integration, Shenzhen University, Shenzhen 518060, China
[4] Dipartimento di Ingegneria Elettrica e delle Tecnologie dell'Informazione, Università Degli Studi di Napoli Federico II, 80125 Napoli,Italy
[5] Comprehensive Cancer Centre, School of Cancer and Pharmaceutical Sciences, King' s College London, London, UK
[6] Laboratoire Kastler Brossel, Sorbonne University, CNRS, ENS-PSL University, Collège de France, Paris, 75005, France
[7] IDUN section, Department of Health Technology, Technical University of Denmark, DK-2800 Kgs. Lyngby, Denmark
*Corresponding author: ferruccio.pisanello@iit.it

Abstract— Optical interfaces for deep brain regions are enabling new opportunities for multimodal investigation of neural activity. Here we present a multifunctional tapered optical fiber platform that integrates plasmonic nanostructures and microelectronic elements on a non-planar implantable waveguide. By exploiting radiative and evanescent field components along the taper surface, we achieve enhanced light–matter interaction for highly sensitive surface-enhanced Raman spectroscopy of neurotransmitters such as dopamine and serotonin. The engineered plasmonic structures also enable localized photothermal stimulation through wavelength-selective excitation. In parallel, a custom two-photon lithography approach allows the integration of active and passive electronic components for extracellular recording and sensing. This hybrid photonic–electronic system provides an integrated and versatile tool for multimodal neural interfacing.

***Keywords*— plasmonics, neurophotonics, implantable photonic devices, neural interfaces, hybrid photonic-electronic systems, nanophotonics**

I. Introduction

The adoption of optical methods for accessing deep brain regions has empowered the neurophotonics community to explore new frontiers in photonic interfaces with the mammalian brain [1]. These advances enhance optical control and monitoring of neural activity while integrating multiple functionalities —such as electrophysiological and neurochemical detection—within a single device.

In this presentation we describe our tapered optical fibers technology, capable of providing multifunctional photonic interaction with the brain tissue [2,3,4]. This is achieved by the integration of plasmonic nanostructures on the wide surface area of the implantable waveguide together with passive and active electronic elements.

II. Results and Discussion

Our approach exploits the coexistence of radiative and evanescent field on the wide surface of the narrowing waveguide to enhance the coupling between the electromagnetic field and photonic structures fabrication on the taper. We have investigated multiple methods to overcome the challenge of fabricating nanophotonic structures on the non-planar highly-curve implantable waveguide, including focused ion beam milling, repeated dewetting, wet-chemical overgrowth and sputtering deposition [5,6,7,8]. This enabled to achieve very low detection limit with surface-enahnced Raman spectroscopy for neurotransmitter molecules, including serotonin and dopamine. In addition to sensing capabilities, the implemented plasmonic nanostructures design allows to generate local heat with a simple wavelength switch, resulting in all-photonic integrated multifunctionality for neural interfaces.

Together with nanoparticles, the same implantable system can host microelectronic elements, fabricated with a custom approach to two-photon lithography [9]. We have indeed developed a method to adapt planar microfabrication to the non-planar tapered surface, achieving the integration of active and passive electronic elements. These can provide extracellular recording of neural activity, temperature sensing as well as neurochemical detection.

III. Conclusion

In conclusion, we will present a hybrid photonic–electronic approach expanding the functional capabilities of implantable

devices and represents a promising step toward fully integrated, multimodal tools for neuroscience research and future neurotechnological applications.

ACKNOWLEDGMENTS

M.D.V. and F.P. acknowledge funding by European Union's Horizon Europe under grant agreement 101125498, project MINING "Multifunctional nano-bio interfaces with deep brain regions". D.Z., M.F.K., Li.C., M.D.V., and F.P. acknowledge funding from the European Union's Horizon 2020 Research and Innovation Program under Grant Agreement No. 828972. Li.C., C.M., M.D.V., and F.P. acknowledge funding from the Project "RAISE (Robotics and AI for Socio-economic Empowerment)" code ECS00000035 funded by European Union – NextGenerationEU PNRR MUR - M4C2 – Investimento 1.5 - Avviso "Ecosistemi dell'Innovazione" CUP J33C22001220001. M.D.V. and F.P. acknowledge funding from the European Union's Horizon 2020 Research and Innovation Program under Grant Agreement No. 101016787. M.D.V and F.P acknowledge financial support under the National Recovery and Resilience Plan (NRRP), Mission 4 "Education and Research" – Component 2 "From Research to Business" Investment 1.3, funded by the European Union NextGenerationEU, within the framework of the cascade funding call of Spoke 3 – Extended Partnerships among Universities, Research Centers, and Enterprises for Research Project Funding, "Mnesys" (PE00000006).

REFERENCES

[1] M. Mohammadiaria *et al.* "Emerging technologies toward the integration of multiple functionalities on non-planar implantable neurophotonics probes", Neurophotonics 11, S11514 (2024)
[2] F. Pisano *et al.*, "Depth-resolved fiber photometry with a single tapered optical fiber implant" Nature Methods 16, 1185 (2019)
[3] B. Spagnolo *et al.*, "Depth-resolved fiber photometry with a single tapered optical fiber implant" Nature Materials 16, 1185 (2019)
[4] F. Pisano *et al.*, "Vibrational fiber photometry: label-free and reporter-free minimally invasive Raman spectroscopy deep in the mouse brain" Nature Methods 22, 371 (2025)
[5] F. Pisano *et al.*, "Plasmonics on a Neural Implant: Engineering Light–Matter Interactions on the Nonplanar Surface of Tapered Optical Fibers», *Advanced Optical Materials*, vol. 10, fasc. 2, p. 2101649, gen. 2022, doi: 10.1002/adom.202101649.
[6] D. Zheng *et al.* "Toward Plasmonic Neural Probes: SERS Detection of Neurotransmitters through Gold-Nanoislands-Decorated Tapered Optical Fibers with Sub-10 nm Gaps", Advanced Materials 16, 2200902 (2023)
[7] D. Zheng *et al.* "Tunable Nanoislands Decorated Tapered Optical Fibers Reveal Concurrent Contributions in Through-Fiber SERS Detection" ACS Photonics 11, 3774 (2024)
[8] D. Zheng *et al.* "Direct Nucleation of Hierarchical Nanostructures on Plasmonic Fiber Optics Enables Enhanced SERS Performance" Advanced Science 12, e09947 (2025)
[9] A. Balena *et al.* "Fabrication of nonplanar tapered fibers to integrate optical and electrical signals for neural interfaces in vivo", Nature Protocols 20, 1768 (2025)

Disordered Plasmonic Metasurfaces: From Scalable Fabrication to Imaging Applications

Doeun Kim[1], Juhwan Kim[2], Gyurin Kim[2], Youn Ju Na[3], Hyeon-Ho Jeong[1,2,3,*]

[1]GIST InnoCORE AI-Nano Convergence Institute for Early Detection of Neurodegenerative Diseases, Gwangju Institute of Science and Technology (GIST), Republic of Korea
[2]Department of Electrical Engineering & Computer Science, GIST, Republic of Korea
[2]Department of Semiconductor Engineering, GIST, Republic of Korea
*Corresponding author: jeong323@gist.ac.kr

***Abstract*— Disordered plasmonic metasurfaces provide scalable alternatives to lithographic nanophotonics, creating dense hotspots and robust structural colors. We overview rapid wafer-scale electrostatic nanoparticle assembly and highlight imaging-oriented functions including imaging-based molecular sensing, optical security authentication, and emerging opportunities toward label-free bioimaging.**

***Keywords*— disordered plasmonics, plasmonic metasurface, scalable assembly, imaging, sensing**

I. Introduction

Disorder has emerged as a practical design degree of freedom in plasmonics because it relaxes nanofabrication constraints and can spontaneously produce dense electromagnetic hotspots. In this work, we present a wafer-scale, rapid electrostatic assembly strategy to construct disordered plasmonic metasurfaces within minutes [1]. By integrating colloidal nanoparticle coatings with metal–dielectric mirrors, the platform provides (i) reproducible far-field structural colors and (ii) strong near-field enhancement. We then summarize how these features can be exploited for imaging-oriented functions, including imaging-based molecular sensing [2], optical secure identification [3], and recent directions toward label-free cellular contrast enhancement.

II. Methods

Disordered plasmonic metasurfaces are fabricated by electrostatically assembling colloidal metal nanoparticles onto dielectric-spaced metallic mirrors (Fig. 1), forming a nanoparticle-on-mirror architecture. A proton-assisted process accelerates adsorption in aqueous media and enables rapid, uniform, and surface-selective coating over wafer-scale substrates [1]. Optical hotspots are formed both in interparticle nanogaps and between nanoparticles and the underlying mirror, providing strong local field confinement that is advantageous for sensing and imaging modalities.

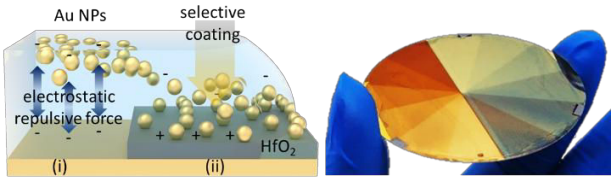

Fig. 1 Disordered plasmonic metasurface fabricated via rapid electrostatic assembly.

III. Results and Discussion

Representative results and applications include:

- Rapid wafer-scale fabrication: Proton-assisted electrostatic assembly yields uniform nanoparticle-on-mirror constructs with consistent structural colors, enabling lithography-free, scalable production [1].
- Imaging-based molecular sensing: Droplet-array projection imaging translates physicochemical properties (e.g., refractive index and surface tension changes) into intuitive optical signatures (color/size features), enabling binding-free taste visualization [2].
- Secure optical identification: The metasurfaces can maintain uniform far-field colors while exhibiting unclonable, stochastic scattering fingerprints, enabling robust authentication and anti-counterfeiting [3].
- Toward label-free cellular contrast: The disordered metasurfaces suggest a route to enhance optical contrast associated with refractive-index variations in biological samples, offering an emerging direction for imaging applications.

IV. Conclusion

Disordered plasmonic metasurfaces enabled by rapid electrostatic assembly provide a scalable route from nanoscale light confinement to system-level imaging functions. By combining wafer-scale manufacturability, uniform structural color, and strong near-field enhancement, this platform supports low-cost sensing and imaging concepts as well as optical security labels. Beyond established demonstrations, the approach also motivates future extensions toward compact,

label-free imaging components.

ACKNOWLEDGMENTS

This work was supported by the National Research Foundation of Korea (NRF) grant funded by the Korea government (MSIT) (Grant No. RS-2024-00352033), the Regional Innovation System & Education (RISE) program (2025-RISE-05-001) through the Gwangju RISE Center, funded by the Ministry of Education (MOE) and the Gwangju Metropolitan City, Republic of Korea, and the InnoCORE program of the Ministry of Science and ICT (GIST InnoCORE KH0860).

REFERENCES

[1] D. Kim, J. Lee, G Kim, J Ma, HM Kim, J.-H. Han, H.-H. Jeong, "Proton-assisted assembly of colloidal nanoparticles into wafer-scale monolayers in seconds," Advanced Materials, vol. 36, p. 2313299, 2024.

[2] J. Lee, D Kim, G Kim, J.-H. Han, H.-H. Jeong, "Binding-free taste visualization with plasmonic metasurfaces." ACS Applied Materials & Interfaces, vol. 16, p. 16622, 2024.

[3] G. Kim, D. Kim, J. Lee, J. Kim, S.-Y. Heo, Y.M. Song, H.-H. Jeong, "Quasi-ordered plasmonic metasurfaces with unclonable stochastic scattering for secure authentication," Nature Communications, vol. 16, p. 6269, 2025.

Silver Bullet – Vaterite-Based Metamaterials for Controllable ROS Generation in Biomedicine

P. Bezrukov[1,*], H. Barhum[2], P. Ginzburg[1,3]

[1]School of Electrical and Computer Engineering, Tel Aviv University, Israel
[2]Triangle Research and Development Center, Israel
[3]Light-Matter Interaction Centre, Tel Aviv University, Israel
*Corresponding author: bezrukov1@mail.tau.ac.il

***Abstract*— Light-activated vaterite–silver nanoparticle metamaterials enable precise, localized ROS production for photodynamic therapy. Silver plasmonic effects extend visible-light absorption (400–700 nm), enhancing oxygen activation under mild irradiation, while the porous vaterite host stabilizes and uniformly distributes AgNPs, ensuring controlled radical generation and biocompatibility.**

***Keywords*— metamaterials, reactive oxygen species, silver nanoparticles, vaterite cargo.**

I. Introduction

Reactive oxygen species (ROS) are chemically reactive molecules containing oxygen that induce oxidative stress, damaging cellular components such as DNA, proteins, and lipids. This property makes ROS powerful therapeutic agents for selectively eliminating diseased cells or pathogens in cancer therapy, antimicrobial treatments, and wound healing. Photodynamic therapy (PDT) utilizes light-activated photosensitizers to produce ROS precisely at the target site, demonstrating remarkable success in treating early-stage cancers with minimal side effects. [1]. However, conventional photosensitizers suffer from low stability, unpredictable degradation in biological environments, and limited tissue penetration due to UV activation requirements. Nanotechnology addresses these challenges by enabling stimuli-responsive nanoparticles that generate ROS only under specific triggers like visible light, which offers deeper tissue penetration and reduced photodamage to healthy tissues.

Vaterite, a metastable polycrystalline form of $CaCO_3$, serves as an ideal carrier due to its biocompatibility, high porosity, biodegradability, and pH sensitivity. These properties enable controlled drug release and surface functionalization with plasmonic silver nanoparticles. Vaterite-AgNP metamaterials integrate plasmonic enhancement through localized surface plasmon resonance (LSPR), shifting activation to therapeutic visible wavelengths (400-700 nm). The porous vaterite matrix prevents nanoparticle aggregation while enabling tunable loading for reproducible dosing. This platform combines plasmonic "optical antenna" effect amplifying local electromagnetic fields for enhanced ROS production with SERS capability for molecular fingerprinting and biosensing (10^4-10^6 enhancement). This multifunctional system enables Raman-guided cell differentiation followed by selective light-activated cell death, bridging diagnostics and therapy in precision nanomedicine.

II. Methods

Vaterite microparticles were synthesized via controlled co-precipitation of $CaCl_2$ and Na_2CO_3 in ethylene glycol:water mixture and stabilized in ethanol. PVP-capped AgNPs were prepared by chemical reduction of $AgNO_3$ with $NaBH_4$. Composites with different loading cycles were formed by iterative impregnation of vaterite suspension with AgNP colloid, followed by ultrasonication, vortexing, and centrifugation [2]. Loading efficiency was quantified from supernatant UV-Vis spectra (SPR ~440 nm). Samples were characterized by SEM/EDS, FTIR spectroscopy, and ROS generation via fluorescence and absorbance probes (Fig. 1a,b).

The general catalytic efficiency of ROS generation was performed using the L-ascorbic acid (LAA) reaction leading the direct oxidation of LAA following the decreasing its absorbance in UV region. The diving deeper study of detection specific ROS types (hydroxyl radicals - ·OH, singlet oxygen radicals - $^1O_2$) was performed using selective fluorescence and absorbance probes, which showed qualify and quantify ROS types of generation rates (Fig. 2a,b,c.) [3].

III. Results and Discussion

• FTIR, SEM and EDS confirmed the successful injection of 2-6 nm in diameter AgNPs into vaterites pores (fig. 2a.). Broadband absorption verifies intra-particle AgNP distribution. UV-Vis analysis revealed broadband absorption for Ag-vaterite hybrids confirming intra-particle AgNP distribution, while supernatant spectra quantified loading efficiencies: VAg1 (LE=28%), VAg2 (47%), VAg3 (62%), VAg4 (74%), VAg5 (85%) based on 440 nm plasmon peak depletion. ROS generation, measured by 7-hydroxycoumarin (7HC) fluorescence (λex. 350 nm, λem. 440 nm), showed strong dependence on AgNP loading and irradiation dose: increasing the AgNPs concentration within vaterite increases the ROS

generation efficacy, but prolonged irradiation negatively effects on it

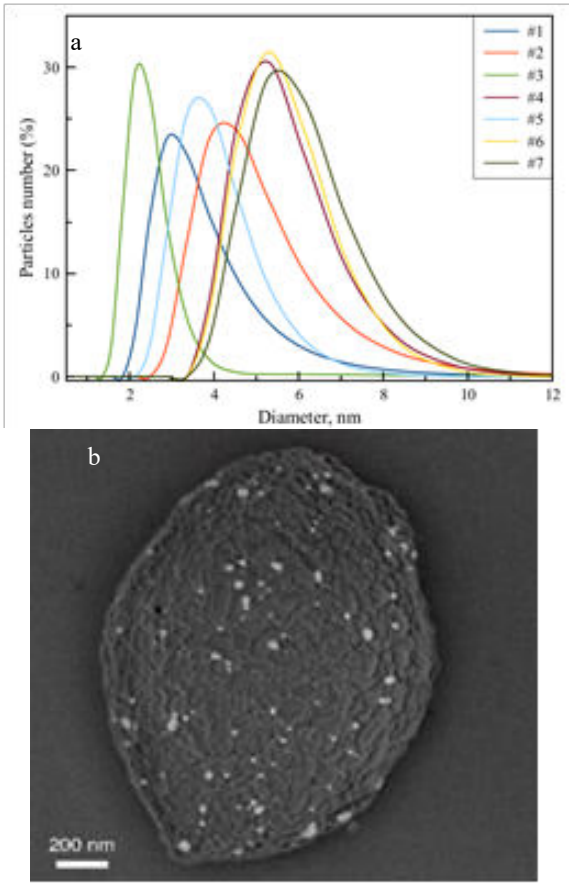

Fig 1. (a) AgNPs sizes measures via DLS; (b) SEM image of silvered vaterite.VAg

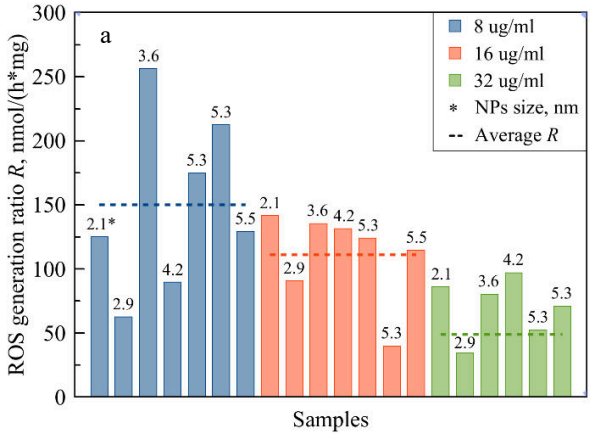

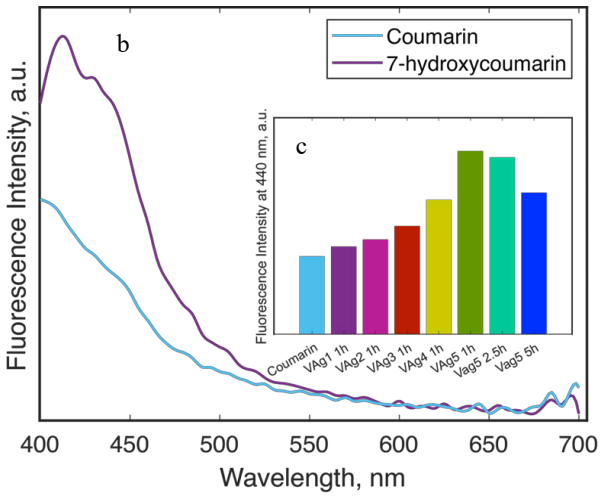

Fig 2. (a) General ROS generation efficacy by various AgNPs sizes; (b) Hydroxyl radicals generation by silvered vaterite and (c) the effect of AgNPs concentration and prolonged irradiation on hydroxyl radicals formation.

IV. Conclusion

Vaterite-AgNP metamaterials deliver efficient, visible-light ROS generation with proven biocompatibility, tunable loading (28–85% LE), and superior antimicrobial performance. The platform shows potential for antibacterial action, compatibility with cellular models, and applicability in targeted therapy, accelerated wound healing, and photocatalytic purification of water and air, while remaining technologically scalable and compatible with widely used optical diagnostic methods.

References

[1] S. Alfei, G. Piatti, D. Caviglia, G. C. Schito, G. Zuccari and A. M. Schito, “Biocidal Cationic Mactomolecules Irrespective of Bacterials Resistance: Our Best Achievements” Int. J. Mol. Sci., vol. 25(13), p. 7182,2024.

[2] A. Ushkov, P. Bezrukov, D. Kolchanov, A. Machnev and P. Ginzburg, “Golden Vaterite and a Thermo-Optical Agent” Laser Photonics Rev., vol. 19, p. 2500461,2025 .

[3] S. Nonell and C. Flos, Singlet Oxygen: Application in Biosciences and Nanosciences, 1st ed., The Royal Society of Chemistry, 2016.

Free-Electron-Driven Chip-Scale Mercury-Free Broadband UV Light Sources with Ultrahigh Germicidal Efficiency

Vijay Kumar Sharma[1,2]* and Hilmi Volkan Demir[1,2]*
[1]LUMINOUS! Centre of Excellence for Semiconductor Lighting and Displays, School of Electrical and Electronic Engineering, Nanyang Technological University, Singapore
[2]Department of Electrical and Electronics Engineering and Department of Physics, Bilkent University, Ankara, Turkey

*Corresponding author: vksharma@ntu.edu.sg, hvdemir@ntu.edu.sg

***Keywords*: Chip-scale, Mercury-free, Cathodoluminescence, Cold field-emission, Broadband UV emission, 9-log reduction**

Summary:
We report free-electron-driven, compact, chip-scale, mercury-free ultraviolet (UV) light sources enabled by cathodoluminescence and cold field-emission.[1] The devices deliver spectrally engineered broadband emission spanning the UVC, UVB, and UVA regions, with peak intensity precisely aligned near the DNA absorption maximum (~262 nm). Owing to strong spectral overlap with germicidal effectiveness curves, the UV chip provides, to our knowledge, the first single-source chip-scale platform capable of achieving log-9 microbial reduction — a performance level traditionally requiring multiple discrete emitters.[2]

Experimental validation demonstrates a 9-log reduction of *Escherichia coli* within 6 minutes at a delivered dose of ~45 mJ/cm², enabled by synergistic activation of DNA damage, protein oxidation, membrane disruption, and oxidative stress pathways.[2] Beyond germicidal efficacy, the devices offer decisive practical advantages, including intrinsically mercury-free operation, compact architecture, and instant ON/OFF capability. Long-term stability testing confirms robust operation up to ~2000 hours, while thermal characterization across –20 °C to 80 °C demonstrates consistent optical output and strong environmental tolerance. The sources operate at ≈4% efficiency with optical power ≥20 mW, underscoring their viability for energy-efficient deep-UV generation.[1]

Unlike conventional UV technologies limited by material constraints, efficiency droop, thermal management requirements, or bulky vacuum hardware, our approach employs high-integrity vacuum microcavities integrating ZnO nanostructured cold cathodes and spectrally tuned high-efficiency phosphor anodes, enabling stable, energy-efficient free-electron-driven UV generation without active thermal management.[3] The demonstrated performance establishes chip-scale cathodoluminescent UV sources as a scalable, high-impact platform for disinfection, food safety, healthcare, environmental monitoring, and advanced sterilization applications.

Acknowledgements
The authors acknowledge financial support from a collaborative project titled "Next-Generation Ultralow-Cost High-Efficiency Eco-Friendly Lamps" between NTU Singapore and PureFize Technologies AB (previously LightLab Sweden AB).

References

1. V. K. Sharma *et al.,* On-Chip Mercury-Free Deep-UV Light-Emitting Sources with Ultrahigh Germicidal Efficiency. *Adv. Opt. Mater.* **9**, (2021).
2. V. K. Sharma *et al.,* Chip-scale mercury-free UV light sources enabling Log-9 reduction of E. coli. *J. Environ. Chem. Eng.* **13**, 119855 (2025).
3. V. K. Sharma & H. V. Demir, Bright Future of Deep-Ultraviolet Photonics: Emerging UVC Chip-Scale Light-Source Technology Platforms, Benchmarking, Challenges, and Outlook for UV Disinfection. *ACS Photonics* **9**, 1513–1521 (2022).

Engineering FRET mechanism via plasmonic systems for ultra-sensitive biosensing

Vincenzo Caligiuri[1,2], Olga Favale[1,2], Ferdinanda Annesi[2], Angela Candreva[3,2], Massimo La Deda [3,2], Marco Filice[4], Marzia Marciello[4], Antonio De Luca[1,2,*]

[1]Department of Physics, University of Calabria, via P. Bucci 31c, 87036, Rende (CS), Italy
[2]CNR Nanotec UOS Rende, via P. Bucci, 33c, 87036, Rende (CS), Italy.
[3]Department of Chemistry and Chemical Technologies, University of Calabria, via P. Bucci 12c, 87036, Rende (CS), Italy
[4]Chemistry in Pharmaceutical Sciences Department, Pl. de Ramón y Cajal, s/n, Moncloa - Aravaca, 28040 Madrid, Spain
*Corresponding author: antonio.deluca@unical.it

***Abstract*—We report a biological FRET platform based on engineered bacteria enabling direct spectro temporal mapping of donor and acceptor dynamics. By tuning protein spacing and coupling to different plasmonic systems, we modulate energy transfer efficiency and excited state kinetics, establishing a route toward plasmon assisted biointegrated optical sensing.**

***Keywords*— FRET, plasmonic systems, fluorescent proteins, biosensing.**

I. Introduction

Fluorescence Resonant Energy Transfer in the Förster regime is a widely studied photodynamic process based on a non-radiative dipole-dipole interaction between an excited donor molecule and a ground-state acceptor molecule [1]. Due to its strong dependence on the distance and relative orientation of the interacting dipoles, as well as the electromagnetic properties of the surrounding environment, FRET has emerged as a powerful tool for biosensing applications. While FRET inhibition can be achieved by increasing the donor-acceptor distance, its enhancement can be realized through interaction with resonant photonic environments, such as plasmonic structures or optical cavities [2].

In this work we report on the electromagnetic interaction between multi-resonant plasmonic systems and a biological FRET platform. By tailoring plasmonic resonances to match the absorption and/or emission spectra of the donor-acceptor pair (DAP), we aim to selectively modulate the acceptor fluorescence, enabling precise control over FRET efficiency [3]. Beyond fundamental insights into energy transfer mechanisms, this approach holds great potential for developing highly sensitive biosensors. Compared to conventional sensing platforms, plasmon-assisted FRET offers superior specificity, rapid response, and the ability to detect biomarkers at ultralow concentrations, making it a promising candidate for next-generation diagnostic tools.

II. Methods

We engineered Escherichia coli (*E. coli*) bacteria to express a fusion protein composed of enhanced cyan fluorescent protein (eCFP) as donor and enhanced yellow fluorescent protein (eYFP) as acceptor.

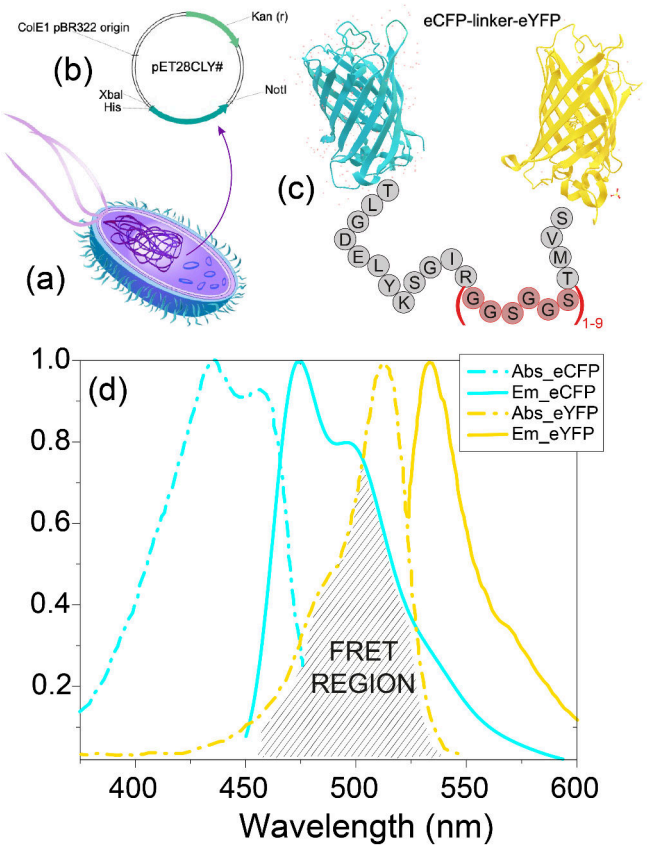

Fig. 1. Schematic representation of the biological FRET system: (a) sketch of the bacterium (*E. coli*); (b) vector map of pET28-CLY#, indicating the open reading frame of fusion protein between the Xba I and Not I sites, antibiotic resistance gene (Kan(r)), and its origin of replication; (c) sketch of fusion protein: eCFP-peptide-eYFP. (d) Absorption (dashed) and emission (solid) curves both for donor (cyan) and acceptor (yellow).

The two fluorophores are connected by a peptide linker

with variable length, depending on the number of (GGSGGS) repeats, ranging from 1 to 9 (see highlighted red area in Figure 1c). The resulting fusion proteins are indicated as CLY#, where # represents the number of (GGSGGS) repeats. In this study, the optical properties of bacterial strains expressing CLY1, CLY3, CLY6, and CLY9 have been investigated. Absorption (dashed) and emission (solid) curves both for donor (cyan) and acceptor (yellow) are reported in Figure 1d, including the FRET region. Excitation at 405 nm selectively pumps eCFP while avoiding direct excitation of eYFP. This configuration ensures that acceptor emission arises predominantly from FRET. Time wavelength resolved photoluminescence was measured using a streak camera system, providing two dimensional intensity maps $I(t, \lambda)$. This approach enables simultaneous extraction of donor bi-exponential decay components and acceptor population dynamics. FRET bacteria were mixed with 50 nm gold nanoparticles supporting a plasmon resonance centered near 530 nm, overlapping mainly with the acceptor emission band. This configuration allows investigation of Purcell enhanced donor emission and metal enhanced fluorescence effects. Two other plasmonic structures have been investigated to enable a controlled manipulation of the local density of optical states (LDOS), offering a direct route to modulate spontaneous emission rates, non-radiative channels, and energy transfer efficiency. This demonstrates how morphology, emitter–metal distance, and spectral overlap determine the balance between emission enhancement, quenching, and energy transfer.

III. Results and Discussion

Steady state spectra show two emission bands corresponding to eCFP and eYFP. The ratio between acceptor and donor emission decreases monotonically with linker length, confirming reduced FRET efficiency at larger separations. Streak camera maps (see Figure 2a and 2b referred to CLY3 and CLY6, respectively) reveal a clear temporal delay between donor emission maximum and acceptor emission maximum (see black dashed curves on the colored maps). This delay increases systematically from CLY1 to CLY9, providing a direct visualization of excited state energy transfer (see the sigmoidal behavior reported in the curves of Figure 2c). Bi-exponential analysis of donor decay allows extraction of FRET efficiency and estimation of donor acceptor distance, in excellent agreement with nominal linker lengths.

Unlike conventional time correlated single photon counting, this approach directly resolves acceptor build up dynamics, offering experimental access to excited state reaction signatures described by Joseph R. Lakowicz [1].

When coupled to 50 nm gold nanoparticles, two distinct regimes emerge. For intermediate spacing (CLY6), donor lifetime shortens and donor emission increases, consistent with Purcell enhanced radiative decay. This additional channel competes with FRET, slightly reducing transfer efficiency while simultaneously boosting acceptor fluorescence through metal enhanced fluorescence.

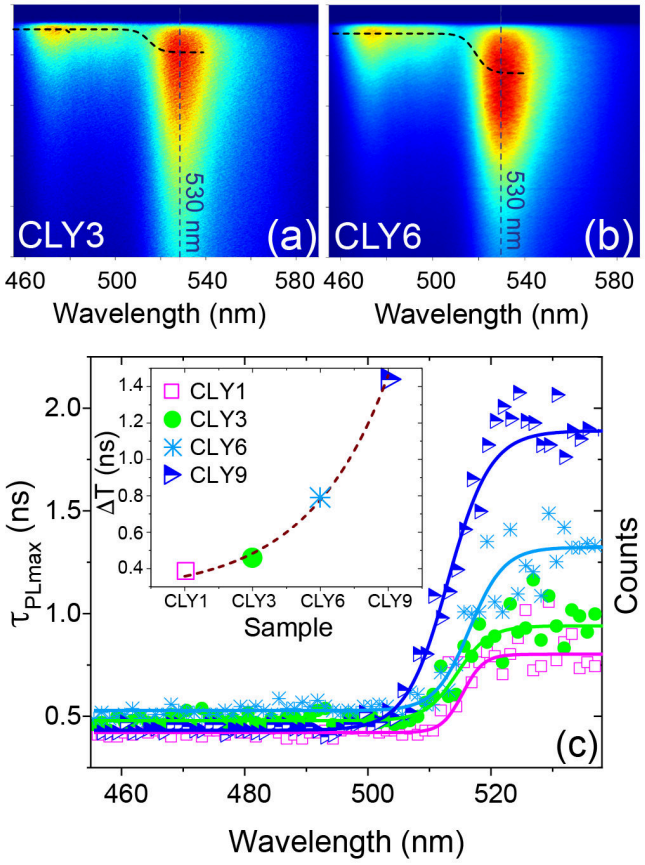

Fig. 2. Time/wavelength maps for (a) CLY3 and (b) CLY6 system. (c) Wavelength/delay-time graph showing the time points at which the emission maxima were recorded for each wavelength within the investigation range, for the CLY1 and CLY2 systems. The inset shows the Δt calculated for each biological FRET system.

For large spacing (CLY9), where intrinsic FRET is weak, plasmon induced radiative pathways dominate. The donor lifetime increases and FRET contribution is suppressed, demonstrating that plasmonic environments can either enhance or inhibit biological energy transfer depending on the initial coupling regime.

These results prove that FRET in intact bacteria can be externally engineered without protein extraction or membrane disruption, bridging nanophotonics and living systems.

IV. Conclusion

We demonstrated a living bacterial FRET platform enabling direct spectro-temporal visualization of donor-acceptor coupling. Controlled linker length allows quantitative distance extraction, while plasmonic structures modulate decay pathways through Purcell and metal enhanced fluorescence effects. This work establishes a foundation for plasmon assisted bio-integrated sensing and engineered nano-bio energy transfer systems.

REFERENCES

[1] J. R. Lakowicz, *Principles of Fluorescence Spectroscopy*, 3rd ed. New York, NY: Springer, 2006.
[2] H. Zong, X. Wang, X. Mu, J. Wang, and M. Sun, "Plasmon-enhanced fluorescence resonance energy transfer," *Chemical Record*, vol. 19, pp. 818–842, 2019.
[3] L.-Y. Hsu, W. Ding, and G. C. Schatz, "Plasmon-coupled resonance energy transfer," *Journal of Physical Chemistry Letters*, vol. 8, no. 10, pp. 2357–2367, 2017.

Towards Point-of-Care and Food Safety Applications of SERS for Shiga Toxin Detection

Alessia Milano[1*], Amalia D'Avino[1,2], Valentina Marchesano[1], Domenico Sagnelli[1], Massimo Rippa[1], Bryan Guilcapi[1], Lu Zhou[3], Maurizio Brigotti[4], Gianluigi Ardissino[5], Stefano Morabito[6], and Lucia Petti[1]

[1] Institute of Applied Sciences and Intelligent Systems "E. Caianiello" CNR, Pozzuoli, 80078, Italy
[2] Department of Engineering, University of Naples "Parthenope", Centro Direzionale Isola C4, Napoli, 80143, Italy
[3] Shandong First Medical University & Shandong Academy of Medical Sciences, Jinan, 271016, China
[4] Dipartimento di Scienze Mediche e Chirurgiche, Sede di Patologia Generale, Università di Bologna, Bologna, 40126, Italy
[5] Fondazione IRCCS Ca' Granda Ospedale Maggiore Policlinico, Milano, 20122, Italy
[6] Department of Food Safety, Nutrition and Veterinary Public Health, Istituto Superiore di Sanità, Rome, 00161, Italy

*Corresponding author: alessia.milano@isasi.cnr.it

***Abstract*— We present a low-cost SERS-based sensing platform for the detection and discrimination of Shiga toxins in clinical and food-related matrices. The approach enables label-free toxin typing with clinically relevant sensitivity and shows potential for translational applications ranging from patient diagnostics to food safety monitoring.**

***Keywords*— Nanoparticles, Shiga toxin, SERS, Clinical diagnostics, Food safety.**

I. Introduction

Shiga toxin–producing Escherichia coli (STEC) represents a major threat to public health, causing severe gastrointestinal infections that may progress to life-threatening complications such as hemolytic uremic syndrome (HUS). Among STEC virulence factors, Shiga toxins (Stxs) play a central role in disease severity, with Stx2 being strongly associated with an increased risk of systemic complications. Beyond the clinical setting, STEC infections are closely linked to food contamination, making food safety a critical component of Shiga toxin surveillance. Conventional detection methods, including culture-based assays, immunoassays, and RT-PCR, offer high sensitivity and specificity but rely on specialized laboratories and relatively long turnaround times. These constraints limit their suitability for rapid decision-making in both clinical diagnostics and food monitoring, where fast screening tools are essential to enable prompt intervention and outbreak prevention.

Surface-enhanced Raman spectroscopy (SERS) has emerged as a powerful bioanalytical technique, combining molecular fingerprinting with ultra-high sensitivity and enabling label-free detection of biomolecules. SERS can offer strong signal enhancement through simple and low-cost fabrication strategies, making it particularly attractive for real-life applications. Nevertheless, the direct detection and discrimination of Stxs by SERS, especially in complex biological and food-related matrices, remains largely unexplored.

In this context, we present a SERS-based sensing platform based on low-cost gold nanoparticle substrates for the detection and discrimination of Stxs. Building on a validated clinical proof of concept, we outline ongoing translational studies. These include the application of the platform to fecal samples for rapid toxin typing in a broader patient cohort and its extension to food safety, through the analysis of enriched media obtained from STEC-contaminated food matrices. By integrating clinical and food-related applications within a single SERS-based framework, this work highlights the potential of SERS to address urgent challenges in infectious disease detection.

II. Methods

SERS substrates were fabricated using a bottom-up approach based on the self-assembly of gold nanoparticles into plasmonic monolayers on silicon supports. This strategy enables the production of low-cost, reproducible substrates suitable for real-life applications.

In the clinical proof of concept, the platform was validated using human serum samples, where Stxs were selectively

captured on the SERS substrates through antibody-based functionalization and physical adsorption. Spectral data were analyzed using PCA to discriminate between samples containing Stx1, Stx2, and cleaved Stx2. The SERS-based classification was compared with RT-PCR results obtained for the same samples.

Ongoing investigations aim to extend the SERS platform to more complex matrices, including fecal samples and food-related environments. For fecal samples, supervised learning approaches are being explored to train classification models that can discriminate between toxin profiles and large spectral datasets. In the food safety context, preliminary experiments were performed on enriched media obtained from food matrices contaminated with Stx2-producing *E. coli* to assess sensitivity and feasibility. These studies are currently under development.

III. Results and Discussion

The SERS-based platform was first validated using human serum samples spiked with Shiga toxins. As shown in Figure 1a, the SERS fingerprints of Stx1, Stx2a, and cleaved Stx2a exhibit distinct spectral features that remain detectable despite the complexity of the serum matrix, demonstrating the capability of the substrates to preserve toxin-specific vibrational signatures.

Multivariate analysis was employed to evaluate toxin discrimination. PCA of SERS spectra acquired from antibody-functionalized substrates enabled the separation of Stx1, Stx2a, and cleaved Stx2a (Figure 1b), indicating that subtle spectral differences can be effectively captured through data-driven approaches for accurate toxin typing.

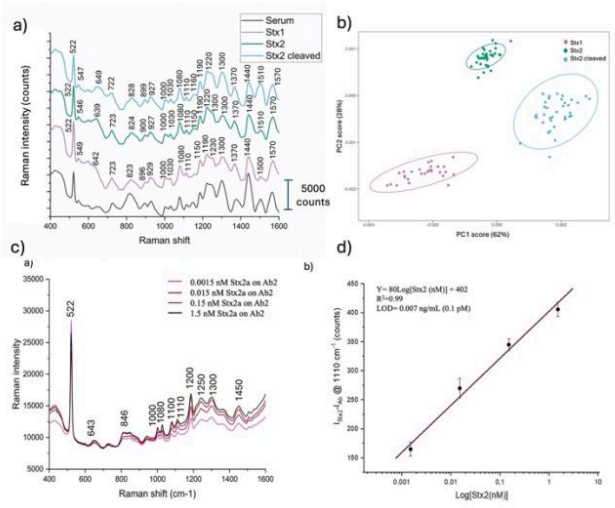

Figure 1. Results obtained in human serum. a) Fingerprint of the three Stxs in serum and serum itself; b) PCA discriminating the three toxins in serum on antibody; c) Stx2 on antibody spectra at increasing concentrations; d) calibration curve for LOD of Stx2.

Sensor sensitivity was assessed by measuring Stx2a at increasing concentrations. A progressive reduction in Raman intensity was observed while maintaining characteristic spectral features (Figure 1c). Quantitative analysis revealed a linear response on a semi-logarithmic scale (Figure 1d), allowing the estimation of a limit of detection of 0.007 ng/mL (0.1 pM), within the clinically relevant range.

In addition to controlled spiking experiments, the platform was evaluated in a blinded proof-of-concept study using sera from HUS patients with STEC infection confirmed by RT-PCR. PCA analysis of spectra acquired with toxin-specific antibodies showed overlap between clinical samples and their corresponding spiked controls in early-collected sera, indicating the presence of Stx2 and, where expected, Stx1 at low concentrations. These results demonstrate the ability of the SERS-based approach to detect and discriminate Shiga toxins directly in real patient-derived matrices despite inter-individual serum variability.

Building on these validated results, ongoing studies aim to extend the SERS-based approach to more complex and application-oriented matrices. In the clinical context, current efforts focus on fecal samples, where increased matrix complexity and variability require the acquisition of large spectral datasets and the implementation of supervised learning strategies to enable robust toxin classification. In parallel, preliminary investigations in the food safety domain explore the detection of Stx2 in enriched media derived from artificially contaminated food matrices. These studies are intended to assess feasibility across different foods and to define appropriate data analysis strategies for reliable screening applications.

IV. Conclusion

Overall, this work demonstrates the potential of SERS combined with data-driven analysis to support rapid and flexible Shiga toxin monitoring across clinical and food-related contexts.

Acknowledgments

The authors gratefully acknowledge the support for this work from the European Union - NextGenerationEU Call PRIN2022 Development of a plasmonic nanobiosensor for the rapid diagnosis of Shiga toxin-producing E. coli human infections at the point of care - SENSOSTEC (CUP B53D23019990006).

References

[1] A. Milano, A. D'Avino, V. Marchesano, D. Sagnelli, M. Rippa, B. Guilcapi, L. Zhou, E. Varrone, G. Rossi, M. Brigotti, G. Ardissino, S. Morabito, L. Petti, "Advancing Medical Diagnostics: Rapid, Label-Free Detection and Differentiation of Shiga Toxin Variants in Human Serum Using a Cost-Effective PCA-Assisted SERS Platform", ACS Appl Mater Interfaces, 2025 doi: 10.1021/acsami.5c18171.

[2] A. D'Avino, A. Milano, V. Marchesano, B. Guilcapi, D. Sagnelli, M. Rippa, L. Zhou, G. Rossi, L. Consagra, M. Brigotti, S. Morabito, L. Petti, "Flexible gold nanoparticle SERS tape for rapid, label-free and ultrasensitive detection and differentiation of Shiga toxin variants", Biosensors and Bioelectronics: X,

Volume 27, 2025, 100696, ISSN 2590-1370, https://doi.org/10.1016/j.biosx.2025.100696.

[3] M. Rippa, A. Milano, V. Marchesano, D. Sagnelli, B. Guilcapi, A. D'Avino, G. Palermo, G. Strangi, L. Consagra, M. Brigotti, S. Morabito, J. Zyss, L. Petti, "Diagnostic oriented discrimination of different Shiga toxins via PCA-assisted SERS-based plasmonic metasurface" *Nanophotonics*, vol. 14, no. 23, 2025, pp. 4005-4018. https://doi.org/10.1515/nanoph-2024-0696

[4] M. Rippa, D. Sagnelli, A. Vestri, V. Marchesano, B. Munari, D. Carnicelli, E. Varrone, M. Brigotti, R. Tozzoli, M. Montalbano, S. Morabito, J. Zhou, J. Zyss, L. Petti, "Plasmonic Metasurfaces for Specific SERS Detection of Shiga Toxins", ACS Appl Mater Interfaces 2022, 14 (4), 4969–4979. https://doi.org/10.1021/ACSAMI.1C21553.

On-chip biosensing by Surface Plasmon Resonance of antibiotic and insecticide residues in real samples

Salvatore Moschetto[1], Kelment Zahoaliaj[1], Mario Prosa[1], Andrea Lorenzoni[1], Jeroen Peters[2], Stefano Toffanin[1], Erik Beji[2], Margherita Bolognesi[1,*]

[1]Institute for the Study of Nanostructured Materials, National Research Council, Italy
[2]Wageningen Food Safety Research, Wageningen University and Research, Wageningen, The Netherlands
*Corresponding author: margherita.bolognesi@cnr.it

***Abstract*— We demonstrate a Surface Plasmon Resonance biosensor chip, based on organic optoelectronics and a biofunctionalized nanoplasmonic grating, capable of being used as a reusable, semi-automated and semi-quantitative screening test for sulfonamide antibiotics in milk and neonicotinoid-class insecticides in soil, at concentrations down to the maximum residue levels.**

***Keywords*— Surface Plasmon Resonance, plasmonic biosensors, organic photonics, food safety, environmental sensing, photonic chips.**

I. Introduction

Miniaturized optical plasmonic-based sensors are demonstrating the largest potential for Lab-on-a-chip systems to perform label-free sensitive, quantitative, and fast sensing for healthcare and environmental monitoring. While complete miniaturization of Surface Plasmon Resonance (SPR) biosensors integrating on the same chip an organic light source/light detector and a plasmonic sensing surface has been fully assessed, [1] main challenges for real world applications are still related to biofunctionalization and regeneration issues, and to automatized data analysis, which both correlate with sensor's specificity, reusability and reliability. We addressed those issues in our SPR biosensor chip, demonstrating semi-quantitative detection, below 10 ppb, of small-molecular contaminants in real matrices. Targets selected from crops and agrifood production chains included sulfonamide-class antibiotics in milk and neonicotinoid-class insecticides in soil.[2]

II. Methods

The full characterization of the SPR biosensor chip is carried out. The antibody-based competitive immunoassays, including cross-reactivity and optimization of regeneration protocols of the sensing surface, are developed through benchmark instrumentation. Simple sample preparation protocols include filtration, centrifugation, and dilution. Optimization of the SPR biosensor chip response to antibody injections in absence or presence of competition from targets is carried out, and matrix effects for real sample measurements are evaluated. Finally, an algorithm for automatic analytical signal extrapolation from SPR sensorgrams is implemented, with experimental feedback.

III. Results and Discussion

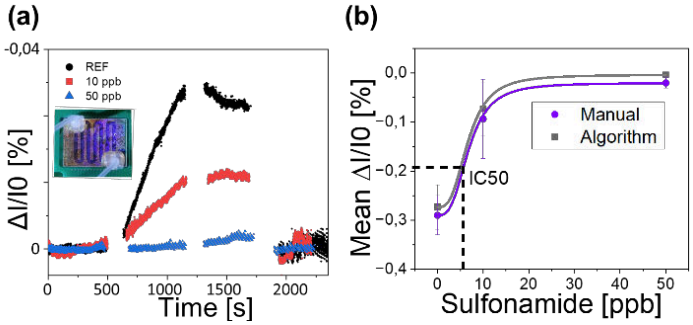

Fig. 1 (a) SPR sensograms from the proposed miniaturized SPR biosensor for injections of 0, 10 or 50 ppb of a sulfonamide-class antibiotic. Inset: picture of the sensor chip. (b) Dose-response curves extrapolated from the manual or algorithm-based analysis.

Experimental results show:

- Sensograms (Fig. 1a) and dose-response curves (Fig. 1b) matching with competitive immunoassay mechanisms
- Effective regeneration of the biofunctionalized sensing surface, which allows running triplicates
- Strong agreement between manual and algorithm-based data analysis (Fig. 1b)
- Half-maximal Inhibitory Concentration (IC50) below 10 ppb for both small-molecular target contaminants.

IV. Conclusion

We have demonstrated a new SPR biosensor chip with multiplex and semi-quantitative analytical capability of detecting small-molecular contaminants in real matrices, which can be applied in the future by operators in the crops and agrifood production value chains at the point of need.

ACKNOWLEDGMENTS

This work was supported by the European Union's Horizon Europe research and innovation programme under grant agreement 101157922 (E-SPFdigit) and by the PNRR MUR ECS_00000033_ECOSISTER project under the FARM project.

REFERENCES

[1] Bolognesi, M., Prosa, M., Toerker, M., Lopez Sanchez, L., Wieczorek, M., Giacomelli, C., Benvenuti, E., Pellacani, P., Elferink, A., Morschhauser, A., Sola, L., Damin, F., Chiari, M., Whatton, M., Haenni, E., Kallweit, D., Marabelli, F., Peters, J. and Toffanin, S. (2023), A Fully Integrated Miniaturized Optical Biosensor for Fast and Multiplexing Plasmonic Detection of High- and Low-Molecular-Weight Analytes. Adv. Mater., 35: 2208719.

[2] Manuscript in preparation.

Hybrid Plasmonic–Photonic Platforms for Enhanced Biosensing and Optical Information Processing

Alessio Buzzin[1], Nicolas Hanine[2], Lorenzo Giannini[2], Michela Baiocchi[2], Angelica Focardi[2], Ahmadreza Alaeddini[2], Badrul Alam[2], and Rita Asquini[2*]

[1] Interdisciplinary Department of Wellbeing, Health and Environmental Sustainability (BeSSA), Sapienza University of Rome, Italy
[2] Department of Information Engineering, Electronics and Telecommunications (DIET), Sapienza University of Rome, Italy
*Corresponding author: rita.asquini@uniroma1.it

***Abstract*— Plasmonic nanomaterials, metasurfaces and integrated photonic circuits enable compact biosensing platforms. Recent advances in waveguide-integrated sensors, plasmonic nanoarrays and metasurface-based architectures are discussed, highlighting their potential for lab-on-chip diagnostics and sensing applications in environmental monitoring, food safety and biomedical analysis.**

***Keywords*— plasmonics, biosensing, SERS, metasurfaces, integrated photonics, lab-on-chip sensing.**

I. Introduction

The development of compact optical biosensors is attracting increasing interest as rapid analytical tools become essential for environmental monitoring, food safety and biomedical diagnostics. Nanophotonics and plasmonics are playing a key role in this technological evolution, enabling highly sensitive detection mechanisms through enhanced light–matter interaction [1], [2].

Plasmonic nanostructures support surface plasmon resonances that confine electromagnetic fields at subwavelength scales, generating intense localized fields that enhance optical sensing mechanisms and spectroscopic signals [3–5]. Such properties make plasmonic nanomaterials highly attractive for biosensing applications.

Among the techniques benefiting from plasmonic enhancement, Raman spectroscopy has received considerable attention due to its ability to provide molecular fingerprints of chemical and biological species. In particular, surface-enhanced Raman spectroscopy (SERS) enables dramatic amplification of Raman signals through the localized electromagnetic fields generated by plasmonic nanostructures [6–8]. Recent advances have demonstrated flexible SERS sensors based on plasmonic nanoparticles capable of detecting biological toxins at extremely low concentrations, with limits of detection in the picomolar range [9]. Such technologies open new perspectives for rapid detection of pathogens and contaminants in environmental monitoring and food safety.

In parallel with plasmonic sensing technologies, integrated photonics provides compact platforms for guiding and manipulating optical signals. Optical waveguides enable precise control of light propagation in miniaturized systems and allow multiple optical functions on the same chip [10].

The integration of plasmonic nanostructures with photonic waveguides therefore represents a promising strategy for the development of compact sensing devices for environmental monitoring, food safety, and biomedical sensing [11–14]. Hybrid plasmonic–photonic architectures can exploit both the field enhancement provided by metallic nanostructures and the scalability of photonic integration.

Photonic waveguides can be implemented using a wide variety of material platforms, including dielectric, polymeric, and hybrid systems, enabling operation across a broad spectral range from the visible to the infrared. Among these approaches, ion-exchanged glass waveguides, polymer-based structures such as SU-8, and liquid-crystal-integrated photonic devices have attracted considerable attention for sensing and integrated photonics applications [15–19].

This work reviews some recent developments in integrated photonic biosensors, plasmonic nanoarrays and metasurface-based sensing platforms. Perspectives toward future photonic sensing systems capable of integrating optical signal processing functionalities are also discussed.

II. Integrated Photonic Biosensing Platforms

Integrated optical waveguide sensors represent an important class of compact biosensing devices. These sensors exploit the interaction between the evanescent field of a guided optical mode and the surrounding medium, enabling detection of refractive index variations or optical absorption changes associated with biomolecular binding events [20], [21], [22].

Compared with conventional free-space optical systems, waveguide-based sensors provide several advantages. They ensure stable optical alignment, reduced system complexity and

compatibility with microfabrication technologies, making them suitable for portable diagnostic devices and lab-on-chip platforms.

Recent developments have demonstrated integrated sensing architectures in which both the interaction region and the detection module are fabricated on the same substrate. In these devices, light propagates through an optical waveguide and interacts with the analyte through the evanescent field, while the resulting optical variations are detected by integrated photodiodes.

Integrated biosensors based on this principle have been demonstrated for several applications including biochemical sensing and beverage quality monitoring [23], [24]. These platforms highlight the potential of integrated photonics for developing compact and cost-effective sensing technologies suitable for real-world environments.

III. Plasmonic Nanoarrays for Enhanced Light–Matter Interaction

The sensitivity of integrated photonic sensors can be significantly improved by incorporating plasmonic nanostructures. Metallic nanoarrays placed near optical waveguides interact with the evanescent field of guided light and produce strong electromagnetic field localization.

Periodic arrays of plasmonic nanostructures such as nanocylinders or nanogratings can efficiently couple guided optical modes to radiated fields. Numerical studies have shown that waveguide-fed plasmonic nanoarrays can produce highly directional scattering patterns and enhanced optical emission signals [25]. These effects are particularly relevant for spectroscopic sensing applications where enhanced scattering and field localization improve light–analyte interaction. Further improvements in the coupling between waveguides and plasmonic nanostructures can be obtained by introducing intermediate optical layers. Transparent conductive materials acting as optical buffer layers can enhance the interaction between guided modes and metallic nanoarrays, leading to improved scattering efficiency [26].

These hybrid structures illustrate how nanomaterials can be integrated with photonic waveguides to develop highly sensitive optical sensing platforms.

IV. Plasmonic Metasurfaces for Advanced Biosensing Applications

Beyond periodic nanoarrays, plasmonic metasurfaces offer additional possibilities for engineering the optical response of nanostructured materials. Metasurfaces consist of planar arrays of subwavelength resonators capable of tailoring amplitude, phase and polarization of light with high precision [27–29].

In biosensing applications, metasurfaces can be designed to enhance specific optical interactions with analytes. Metasurface geometries can generate strong polarization-dependent responses or concentrate electromagnetic fields in selected regions of the structure [30]. Planar plasmonic metamaterials composed of engineered nanostructures have demonstrated strong optical activity and circular dichroism in the visible spectral range [31–34]. These effects can be exploited to enhance optical detection of chiral molecules and improve the sensitivity of spectroscopic sensing techniques.

The integration of metasurfaces with optical waveguides therefore represents a promising direction for future biosensing platforms, combining plasmonic field enhancement with the signal routing capabilities of photonic integrated circuits.

V. From Plasmonic Sensing to Quantum Plasmonics and Photonic Information Processing

Recent research has explored the integration of quantum nanoplasmonics with biosensing technologies. In such systems, plasmon–polariton modes strongly interact with quantum emitters, enabling coupling effects that enhance sensing sensitivity. Quantum plasmonic immunoassays based on plasmonic cavities can produce characteristic spectral signatures for ultrasensitive detection [35]. Nanoplasmonic waveguides supporting slow-wave plasmon–polariton modes have also been proposed as platforms for collective quantum dynamics of spatially separated quantum emitters [36].

While plasmonic nanostructures enhance light–matter interactions with analytes, integrated photonic circuits provide compact platforms for guiding and manipulating light. Reconfigurable photonic elements capable of dynamically controlling light propagation enable programmable interferometric architectures and adaptive sensing configurations [37].

Photonic circuits can also implement optical information processing through all-optical logic elements. Optical logic gates based on semiconductor optical amplifiers have been proposed as building blocks for photonic computing architectures performing logical operations entirely in the optical domain [38].

The convergence of plasmonic sensing, nanophotonic integration and photonic information processing may therefore enable intelligent lab-on-chip systems capable of combining analyte detection with real-time optical signal analysis.

VI. Conclusions

Plasmonic nanomaterials, metasurfaces and integrated photonic circuits are rapidly converging toward a new generation of compact optical sensing technologies. Plasmonic nanostructures provide strong electromagnetic field enhancement, while metasurfaces enable advanced control of the optical response of nanostructured materials. When integrated with photonic waveguides, these elements allow the development of compact sensing platforms capable of guiding and manipulating optical signals.

Future developments are expected to further integrate plasmonic nanostructures, metasurfaces and photonic information processing elements within the same platform, enabling intelligent sensing devices capable of combining

enhanced detection, spectroscopy and on-chip signal processing. Such hybrid technologies hold strong potential for future diagnostic systems addressing challenges in environmental monitoring, food safety and biomedical sensing.

ACKNOWLEDGMENTS

This work was partially supported by the European Union under the Italian National Recovery and Resilience Plan (NRRP) of Next Generation EU, PNRR MUR project PE00000023-NQSTI (the National Quantum Science and Technology Institute), by the European Union under the Italian National Recovery and Resilience Plan (NRRP) of Next Generation EU, partnership on "Telecommunications of the Future" (PE00000001—Program "RESTART"); by the Sapienza University Major Project RG12419112B8DBA3 "Water Cookie"; and by the European Union - Next Generation EU under the Italian National Recovery and Resilience Plan (NRRP), M4C2, Investment 1.1, PRIN PNRR MUR Project Title "BioEMC" - Biochips for Emerging Micro-Contaminants – CUP B53D23024060001 – MUR Project Code: P2022R85AA.

REFERENCES

[1] S. A. Maier, Plasmonics: Fundamentals and Applications, Springer, 2007.
[2] J. Homola, S. S. Yee, and G. Gauglitz, "Surface plasmon resonance sensors: Review," Sens. Actuators B Chem., vol. 54, pp. 3–15, 1999.
[3] J. N. Anker, W. P. Hall, O. Lyandres, N. C. Shah, J. Zhao, and R. P. Van Duyne, "Biosensing with plasmonic nanosensors," Nature Materials, vol. 7, pp. 442–453, 2008.
[4] A. G. Brolo, "Plasmonics for future biosensors," Nature Photonics, vol. 6, pp. 709–713, 2012.
[5] A. Minopoli, A. Acunzo, B. Della Ventura, and R. Velotta, "Nanostructured surfaces as plasmonic biosensors: a review," Advanced Materials Interfaces, vol. 9, no. 2, Art. no. 2101133, 2022.
[6] K. Kneipp, Y. Wang, H. Kneipp, L. T. Perelman, I. Itzkan, R. R. Dasari, and M. S. Feld, "Single molecule detection using surface-enhanced Raman scattering (SERS)," Physical Review Letters, vol. 78, no. 9, pp. 1667–1670, 1997.
[7] S. Nie and S. R. Emory, "Probing single molecules and single nanoparticles by surface-enhanced Raman scattering," Science, vol. 275, no. 5303, pp. 1102–1106, 1997.
[8] E. C. Le Ru and P. G. Etchegoin, Principles of Surface-Enhanced Raman Spectroscopy and Related Plasmonic Effects. Amsterdam, Netherlands: Elsevier, 2009.
[9] A. D'Avino, A. Milano, V. Marchesano, B. Guilcapi, D. Sagnelli, M. Rippa, L. Zhou, G. Rossi, L. Consagra, M. Brigotti, S. Morabito, and L. Petti, "Flexible gold nanoparticle SERS tape for rapid ultrasensitive detection of Shiga toxins," Biosensors and Bioelectronics X, vol. 27, Art. no. 100696, 2025.
[10] B. Jalali and S. Fathpour, "Silicon photonics," Journal of Lightwave Technology, vol. 24, no. 12, pp. 4600–4615, 2006.
[11] Y.F. Chou Chau, "Plasmonics in environmental sensing, pollution monitoring, and sustainable applications," Materials Today Physics, vol. 60, Art. no. 101984, 2026.
[12] S. Bilal, A. Tariq, S. I. Khan, M. Liaqat, S. Andreescu, H. Zhang, and A. Hayat, "A review of nanophotonic structures in optofluidic biosensors for food safety and analysis," Trends in Food Science & Technology, vol. 147, Art. no. 104428, 2024.
[13] H. Kim, H.Yun, S. Jeong, S. Lee, E. Cho, and J. Rho, "Optical metasurfaces for biomedical imaging and sensing," ACS Nano, vol. 19, no. 3, pp. 3085–3114, 2025.
[14] M.A. Butt, "A review on novel materials in optical waveguide sensors: opportunities and challenges for the next decade," Materials Today, vol. 93, Art. no. 103226, 2026.
[15] R. Asquini, A. Buzzin, D. Caputo and G. de Cesare, "Integrated Evanescent Waveguide Detector for Optical Sensing," in IEEE Transactions on Components, Packaging and Manufacturing Technology, vol. 8, no. 7, pp. 1180–1186, 2018.
[16] A. Buzzin, R. Asquini, D. Caputo, G. de Cesare, "On-Glass Integrated SU-8 Waveguide and Amorphous Silicon Photosensor for On-Chip Detection of Biomolecules: Feasibility Study on Hemoglobin Sensing", Sensors, vol. 21, no. 2, 415, 2021.
[17] R. Asquini, C. Chiccoli, P. Pasini, L. Civita, and A. d'Alessandro, "Low power photonic devices based on electrically controlled nematic liquid crystals embedded in poly(dimethylsiloxane)," Liquid Crystals, vol. 45, no. 13–15, pp. 2174–2183, 2018.
[18] R. Asquini, A. Fratalocchi, A. d'Alessandro, and G. Assanto, "Electro-optic routing in a nematic liquid-crystal waveguide," Applied Optics, vol. 44, no. 19, pp. 4136–4143, 2005.
[19] R. Asquini and, A. D'Alessandro, "BPM analysis of an integrated optical switch using polymeric optical waveguides and SSFLC at 1.55 μm," Mol. Cryst. Liq. Cryst., vol. 375, no. 1, pp. 243–251, 2002.
[20] X. Fan, I. M. White, S. I. Shopova, H. Zhu, J. D. Suter, and Y. Sun, "Sensitive optical biosensors for unlabeled targets: A review," Anal. Chim. Acta, vol. 620, no. 1–2, pp. 8–26, 2008.
[21] H. Altug, S. H. Oh, S. A. Maier, and J. Homola, "Advances and applications of nanophotonic biosensors," Nature Nanotechnology, vol. 17, pp. 5–16, 2022.
[22] S. Berneschi, F. Baldini, A. Cosci, D. Farnesi, G. Nunzi Conti, S. Tombelli, C. Trono, S. Pelli, and A. Giannetti, "Fluorescence biosensing in selectively photo-activated microbubble resonators," Sensors and Actuators B: Chemical, vol. 242, pp. 1057–1064, 2017.
[23] A. Buzzin, R. Asquini, D. Caputo, and G. De Cesare, "Evanescent waveguide lab-on-chip for optical biosensing in food quality control," Photonics Research, vol. 10, no. 6, pp. 1453–1461, 2022.
[24] A. Buzzin, R. Asquini, D. Caputo, and G. De Cesare, "Sensitive and compact evanescent-waveguide optical detector for sugar sensing in commercial beverages," Sensors, vol. 23, no. 19, Art. no. 8184, 2023.
[25] B. Alam, A. Ferraro, R. Caputo and R. Asquini, "Optical properties and far-field radiation of periodic nanostructures fed by an optical waveguide," Optical and Quantum Electronics, vol. 54, Art no. 497, 2022.
[26] R. Asquini, A. Buzzin, N. Hanine, A. Mannetta, B. Alam and V. Ferrara, "Enhancing the scattering induced by gold periodic arrays over optical waveguides through indium tin oxide buffer layers," IEEE Photonics Journal, vol. 16, no. 2, Art. no. 0600606, 2024.
[27] N. Yu and F. Capasso, "Flat optics with designer metasurfaces," Nature Materials, vol. 13, pp. 139–150, 2014.
[28] A. V. Kildishev, A. Boltasseva, and V. M. Shalaev, "Planar photonics with metasurfaces," Science, vol. 339, Art. no. 1232009, 2013.
[29] T. J. Cui, S. Zhang, A. Alù, M. Wegener, J. B. Pendry, et al., "Roadmap on electromagnetic metamaterials and metasurfaces." J. Phys. Photonics, vol. 6, no. 3, Art. no. 032502, 2024.
[30] E. Negri, W. Fuscaldo, P. Burghignoli, and A. Galli, "Reconfigurable THz leaky-wave antennas based on innovative metal–graphene metasurfaces." J. Phys. D: Appl. Phys., vol. 57, no. 48, Art. no. 485102, 2024.
[31] G. Palermo, B. Guilcapi, R. Kolkowski, A. Guglielmelli, D. M. Aceti, L. Valente, J. Zyss, L. Petti, and G. Strangi, "Plasmonic Metasurfaces with Structural Chirality and Pseudo-Chirality for Enhanced Circular Dichroism and Enantiomeric Recognition." Advanced Optical Materials, vol. 14, no. 1, Art. no. e02488, 2026.
[32] B. Alam, R. Asquini, A. Veroli, L. Maiolo, F. Todisco, L. Dominici, M. De Giorgi, G. Pettinari, and A. M. Gerardino, "Potentialities and key design challenges in titanium-based plasmonic metasurfaces for biosensing applications," In: Di Francia, G., Di Natale, C. (eds) Sensors and Microsystems. AISEM 2021. Lecture Notes in Electrical Engineering, vol 918, pp. 59–64, Springer, Cham.
[33] A. Veroli, B. Alam, L. Maiolo, F. Todisco, L. Dominici, M. De Giorgi, G. Pettinari, et al., "High circular dichroism and robust performance in planar plasmonic metamaterial made of nano-comma-shaped resonators," J. Opt. Soc. Am. B, vol. 36, pp. 3079–3084, 2019.
[34] G. Palermo, M. Rippa, D. M. Aceti, A. Guglielmelli, L. Valente, D. Sagnelli, A. D'Avino, B. Guilcapi, N. Maccaferri, L. Petti, and G. Strangi, "Intrinsic superchirality in planar plasmonic metasurfaces," Nano Letters, vol. 24, no. 33, pp. 10202–10209, 2024.
[35] N. Kongsuwan, X. Xiong, P. Bai, J.-B. You, C. E. Png, L. Wu, and O. Hess, "Quantum plasmonic immunoassay sensing," Nano Letters, vol. 19, no. 9, pp. 5853–5861, 2019.
[36] Z. Jalali-Mola, S. Asgarnezhad-Zorgabad, and O. Hess, "Collective quantum dynamics with distant quantum emitters in slow-wave nanoplasmonic waveguides," APL Quantum, vol. 1, no. 4, Art. no. 046104, 2024.
[37] N. Hanine, A. Buzzin, L. Giannini, A. Alaeddini, N. P. Belfiore, and R. Asquini, "Tunable MOEMS microring resonator based on in-plane bending through rotary comb drives," in Proc. Conf. Lasers Electro-Optics Europe Eur. Quantum Electron. Conf. (CLEO/Europe-EQEC), Munich, Germany, 2025.
[38] R. Asquini, A. Buzzin, B. Alam, A. Ceschini, A. Rosato and M. Panella, "All-optical AND logic gate with high extinction ratio for neural network hardware implementation," in IEEE Journal on Emerging and Selected Topics in Circuits and Systems, vol. 16, no. 1, pp. 106–114, 2026.

DNA identification using surface-enhanced Raman spectroscopy and surface plasmon resonance

Andrzej Kudelski*

Faculty of Chemistry, University of Warsaw, Poland
*Corresponding author: akudel@chem.uw.edu.pl

***Abstract*— Surface plasmon resonance and surface-enhanced Raman scattering spectroscopy are promising methods for detection of specific DNA fragments. Example applications of these two techniques in DNA analysis is presented. Sensitivity of both methods in the identification of six the most popular in Poland variants of *BRCA1* gene mutations is compared.**

***Keywords*— surface plasmon resonance, surface-enhanced Raman scattering, SPR, SERS, DNA.**

I. Introduction

The deoxyribonucleic acid (DNA) is the carrier of genetic information for all living organisms. Detection of DNA which is characteristic of a given organism allows, for example, for identification of various dangerous microorganisms or for detection of counterfeit food products. Detection of mutations of DNA is also very important in medical diagnostics. Therefore, developing sensitive, fast and precise methods for detection of specific DNA fragments is very important.

II. Methods

Surface-enhanced Raman scattering (SERS) and surface plasmon resonance (SPR) sensors for identifying various fragments of DNA were constructed and tested. Both sensors were based on a selective hybridization of the target DNA with capture DNA immobilized on various plasmonic substrates (see Figure 1).

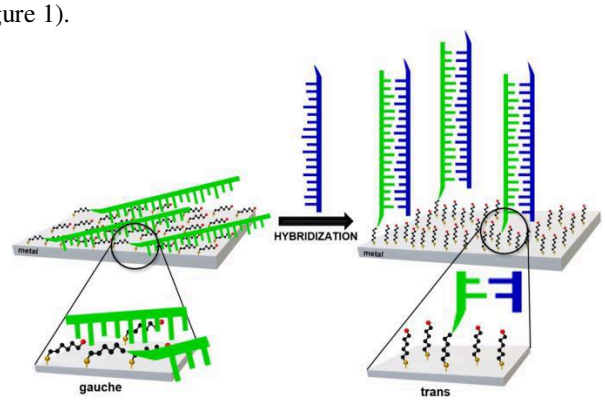

Fig. 1. Scheme of the SERS DNA sensor based on DNA hybridization-induced rearrangement of the alkanethiol chains (alkanethiolate linking moiety of single stranded DNA and 6–mercaptohexan–1–ol). Reprinted from ref. [1]. CC BY-NC-ND license.

The SPR sensor relied on the shape of the SPR sensorgrams, whereas the intensity of the Raman band at about 715–735 cm^{-1} (this band is mainly due to the superimposition of the band due to the ν(C–S) vibration of the alkanethiol chain in the *trans* conformation and the band due to the breathing vibration of adenine [2]) was the analytical signal for the SERS sensors.

III. Results and Discussion

The constructed SERS and SPR DNA biosensors are characterized by a low detection limit at a level of $fg \cdot \mu L^{-1}$, a wide analytical range, and high selectivity [2]. For the first time, the sensitivity of SERS and SPR methods was compared when hybridizing DNA chains that had not been labeled before hybridization [2].

IV. Conclusion

SPR and SERS techniques have great potential in DNA analysis (including detection of gene mutations). Our results indicate that SPR and SERS methods are much more sensitive at detecting mutations in clinical samples than standard genetic methods such as PCR-HRM. For different DNA sequences, either the SPR or the SERS sensor displayed greater detection sensitivity, which means that the selection of the optimal sensor type depends on the sequence of the target DNA.

Acknowledgments

The author thanks: A. Kowalczyk, A. M. Nowicka, A. Michałowska, M. Duszczyk, M. Sikorska, J. L. Weyher, S. Zięba, and A. Kowalik for their participation in this research.

References

[1] A. Michałowska, A. Gajda, A. Kowalczyk, J. L. Weyher, A. M. Nowicka, and A. Kudelski, "Surface enhanced Raman scattering used to study the structure of layers formed on metal surfaces from single stranded DNA and 6-mercaptohexan-1-ol: influence of hybridization with the complementary DNA and influence of the metal substrate," *RSC Advances*, vol. 12, pp. 35192–35198, 2022.

[2] A. Kowalczyk, A. Michałowska, M. Duszczyk, M. Sikorska, J. L. Weyher, S. Zięba, A. Kowalik, A. Kudelski, and A. M. Nowicka, "Identification of *BRCA1* gene mutation variants in clinical samples without a labeling step - A comparison of the functionality and sensitivity of SPR and SERS sensors," *The Journal of Physical Chemistry C*, vol. 129, pp. 8239–8251, 2025.

Thermal management of plasmonic nanoparticles using 2D materials for single-molecule biosensing

Peter Zijlstra[1,*]

[1]Eindhoven University of Technology, Eindhoven, The Netherlands
*Corresponding author: p.zijlstra@tue.nl

***Abstract* — Plasmonic structures are widely used for biomolecular detection, down to the single-molecule level. However, non-radiative decay of surface plasmon resonances causes photothermal heating which mitigates real-world applications in sensing and beyond. Conventional cooling strategies fail at these scales due to limited heat transport and high interfacial thermal resistance, motivating the integration of advanced materials for thermal management. I will discuss simulations and experiments on the use of hexagonal boron nitride (hBN) thin flakes as a new class of nanoscale heat spreaders to efficiently mitigate plasmonic heating of single gold structures in aqueous environments.**

***Keywords*— single-particle spectroscopy, 2d materials, nanoscale thermometry, biosensing**

I. Introduction

In this presentation I will show our recent work on biomolecular sensing using single plasmonic particles. I will discuss the mechanisms by which plasmon-enhanced fluorescence can be employed for single-molecule biosensing at picomolar levels [1] and in complex biological fluids [2].

I will then discuss strategies to mitigate optical heating [3,4]. Although plasmonic effects enable enhanced optical functionalities, the associated temperature rise can degrade performance in heat sensitive applications such as biosensing, nanophotonics, and microelectronics. Conventional cooling strategies fail at these scales due to limited heat transport and high interfacial thermal resistance, motivating the integration of advanced materials for thermal management. I will discuss the use of hexagonal boron nitride (hBN) thin flakes as nanoscale heat spreaders to mitigate plasmonic heating of gold nanospheres surrounded by water. Using finite-element simulations, we quantify the influence of hBN thickness, in-plane thermal conductivity, and interfacial thermal conductance on cooling efficiency. Complementary experiments employ cross-grating wavefront microscopy (CGM) for nanothermometry to map temperature distributions around optically heated gold nanoparticles and quantify the cooling effect of hBN flakes. Our results reveal a strong thickness dependence, where heat dissipation in thin flakes is limited by the heat capacity of hBN and in thick flakes by interfacial thermal conductance. We obtain a reduction in the steady-state temperature rise by up to ~60 % compared to glass by including hBN. In addition, the presence of two main heat dissipation pathways emerges: a direct one from the nanoparticle to the hBN and an indirect one from the particle via water to the hBN. This combined simulation–experiment framework offers a versatile approach to improve thermal management in plasmonic systems and beyond, establishing design guidelines for integrating 2D materials into thermally sensitive platforms such as biosensors, integrated circuits, and energy conversion.

Acknowledgments

This project has received funding from the European Research Council (ERC) under the European Union's Horizon 2020 Research and Innovation Program (Grant Agreement No. 864772).

References

[1] V. Lamberti, M. Dolci, P. Zijlstra, ACS Nano 18, 5805-5813 (2024).
[2] L. Oliveira de Miranda, M. Dolci, K. Sergelen, C. Scarpellini, A. Dillen, A. Saateh, J. Yan, J. Lammertyn, H. Altug, P. Zijlstra, ChemRxiv (2025).
[3] S.W. Nooteboom, Y. Wang, S. Dey, P. Zijlstra, Small 18, 2201602 (2022)
[4] M. Russo, R. van der Vegt, B. Liu, S. Beijers, S. Salera, G. Baffou, K.-J. Tielrooij, P. Zijlstra, *submitted* (2026)

Electronic precursors to bond formation and controller reaction pathways in single-molecule junctions

Kristina R. Rusimova[1,2]

[1]Department of Physics, University of Bath, Bath, UK
[2]Centre for Photonics, University of Bath, Bath, UK
*Corresponding author: k.r.rusimova@bath.ac.uk

***Abstract*— We investigate how probe proximity modifies interfacial electronic structure in single-molecule junctions on Si(111)-(7×7). Building on equilibrium interface-state measurements and controlled single-molecule reactivity, we integrate optical and electronic probes to examine how hybridized junction states influence energy redistribution and competing reaction pathways at room temperature.**

***Keywords*— STM-induced luminescence, single molecule junctions, atomic manipulation.**

Understanding how atomic-scale contacts influence molecular electronic structure is crucial for molecular and quantum devices, as well as nanoscale chemical control. The proximity of a probe can fundamentally alter junction electronic structure through structural relaxation, orbital hybridization, and emergent interface states, which in turn can govern transport and reaction dynamics [1]. While scanning probe studies have long highlighted these phenomena, direct experimental observation of interface states at equilibrium - and their impact on reaction selectivity - remains largely unexplored.

In our recent investigations, we identified equilibrium electronic states emerging from molecule-surface proximity that act as precursors to covalent bonding. These states are robust across different local environments and do not depend on specific orbital symmetries or probe-induced effects. Computational modelling links the formation of these interface states to subtle nuclear motion preceding bond formation or desorption, revealing a direct connection between evolving electronic structure and nascent reaction pathways.

We further observed that single-molecule excitations can lead to competing reaction outcomes [2], with branching ratios that depend on the energy delivered to the system rather than simple geometric considerations. This demonstrates the potential to control reaction selectivity through the local electronic environment, offering a pathway toward targeted single-molecule reactivity.

Building on these findings, we have begun combining simultaneous optical and electronic measurements to correlate the emergence of interface states with energy redistribution and reaction probabilities [3]. This approach provides a new window into how equilibrium junction states govern energy flow and selectivity in single-molecule reactions, establishing a conceptual framework for state-engineered control of chemical outcomes.

References

[1] K. R. Rusimova, R. M. Purkiss, R. Howes, F. Lee, S. Crampin, and P. A. Sloan, *Regulating the Femtosecond Excited-State Lifetime of a Single Molecule*, Science (80-.). **361**, 1012 (2018).

[2] P. J. Keenan, R. M. Purkiss, T. Klamroth, P. A. Sloan, and K. R. Rusimova, *Measuring Competing Outcomes of a Single-Molecule Reaction Reveals Classical Arrhenius Chemical Kinetics*, Nat. Commun. **15**, 10322 (2024).

[3] R. M. Purkiss, H. G. Etheridge, P. A. Sloan, and K. R. Rusimova, *Common Source of Light Emission and Nonlocal Molecular Manipulation on the Si(111)−7 × 7 Surface*, J. Phys. Commun. **3**, 095010 (2019).

Plasmonic nanofibers for neurochemical monitoring

Jean-Francois Masson[1,*], Maryam Hojjat Jodaylami[1], Ailsa Geddis[1]

[1]Department of Chemistry, Université de Montréal, Canada
*Corresponding author: jf.masson@umontreal.ca

***Abstract*— The use of plasmonic optical fibers allows to design sensors for many neurochemicals and neuroproteins. These fibers combine enhancement from the fiber acting as an optical element (resonator and microlens) and from the plasmonic materials. The presentation will show their application for the detection of neuroproteins and neurotransmitters**

***Keywords*— Plasmonic sensing, nanomaterials, metamaterials, neurochemistry.**

I. Introduction

Plasmonic nanomaterials offer a suite of opportunities for the design of nanosensors for proteins and other metabolites. In this presentation, we will focus on plasmonic nanofibers harvesting the sensitivity benefits of optoplasmonic architectures for the detection of brain protein S100b in animal models.

II. Neuroproteins

The quantification of proteins involved in the complex neurobiochemistry of the brain remains a frontier in analytical sensing. The challenge is even greater if the monitoring of proteins requires high spatial resolution and minimal invasiveness to be compatible with monitoring directly in the brain of a living organism. We have developed an optical fiber-based surface-enhanced Raman scattering (SERS) nanoendocope for the quantitative detection of S100β, an astrocytic protein, with high regiospecificity and minimal invasiveness. The concentration of S100β protein released in specific regions of mouse brain slices was measured under various stimulation conditions, including N-methyl-D-aspartate, electrical, and optogenetic stimulation. SERS nanoendoscopes were also used to investigate the in vivo release of S100β protein in the brainstem and the primary somatosensory cortex of mouse models following the rhythmic jaw movements induced by optogenetic stimulation of the cortical masticatory area and the tactile stimulation of the hindlimb, respectively. This presentation will show the ability of SERS nanoendoscopes for ex vivo and in vivo quantification of proteins in the complex biological matrix of the brain, which is important for understanding the molecular mechanisms underlying neuronal activity and brain function.

III. Neurochemistry

For neurotransmitters, unfunctionalized Au nanoraspberries or gold nanostars were synthesized and immobilized on a pulled fiber functionalized with a block copolymer. The sensors were tested for sensing neurochemicals and a convolutional neural network (CNN) was trained for spectral classification. Dynamic SERS will be shown to detect neurotransmitters secreted upon neuronal stimulation and in the presence of therapeutic compounds. Different levels of neurotransmitters were seen for cultured neurons from different regions of mouse brain tissue.

IV. Conclusion

We will show the use of plasmonic fibers for the detection of various chemicals and biochemicals important for neuroscience studies.

Acknowledgments

This work was supported by the Natural Science and Engineering Research Council of Canada (NSERC), the Fonds de Recherche du Québec and by the Canadian Foundation for Innovation.

Self-Assembly Nanostructures for Highly Sensitive SERS Platforms

Maria Alessandra Cutolo[1,*], Francesco Galeotti[2], Sara Spaziani[3], Giuseppe Quero[4], Mohammed Janneh[3], Alberto Micco[1], Andrea Irace[5], Giovanni Breglio[5], Marco Pisco[3], Andrea Cusano[3]

[1]Centro Regionale Information Communication Technology (CeRICT Scrl), BN, Italy

[2]Istituto di Scienze e Tecnologie Chimiche "G. Natta" (SCITEC) (CNR)

[3]Optoelectronic Division-Engineering DepartmentUniversity of SannioBenevento 82100, Italy

[4]Biosciences and Territory DepartmentUniversity of Molise

[5]Department of Electrical Engineering and Information Technology, University of Naples Federico II ,NA, Italy

*Corresponding author: mariaalessandra.cutolo@unina.it

***Abstract*— Self-assembly Plasmonic nanostructures provide a scalable bottom-up approach for engineering surfaces with controlled localized surface plasmon resonances. Techniques such as nanosphere lithography and hierarchical sphere assembly enable ordered arrays and dense nanogaps, generating intense and reproducible electromagnetic hot spots for SERS and biosensing applications.**

***Keywords*— Plasmonics, Self-assembly, SERS, Nanosphere lithography, Biosensing**

I. Introduction

Self-assembly is a promising technique for creating SERS-active surfaces, characterized by technological simplicity, scalability and cost-effectiveness. Self-assembled nanosphere-based architectures have been extensively studied due to their formation of homogeneous and reproducible ordered matrices. However, these systems have limitations due to their uniform morphology and low dimensionality, which limit the localization of the electromagnetic field and accessibility to hot spots. To address these challenges, new self-assembled platforms based on hierarchical nanostructures have been developed. Specifically, colloidal plasmonic arrays (CPAs) with binary hierarchical designs offer improved multiscale roughness [1]. These systems increase the density of accessible hot spots and optimize light–matter interactions, while maintaining the scalability and low-cost advantages inherent in self-assembly methods. On the other hand, nanopillar-based structures represent an alternative due to their three-dimensional architecture and larger surface area. This study will also present preliminary results on the fabrication of self-assembled structures based on nanopillars.

II. Methods

The fabricated planar SERS substrates were carefully characterized to evaluate both their structural and sensing performance. In particular, the morphology of the nanostructures was analyzed using microscopy SEM and AFM. Subsequently, Raman measurements were performed to evaluate SERS activity in terms of increased signal intensity and to identify the presence and distribution of electromagnetic hot spots in the substrate.

III. Results and Conclusion

Self-assembly enables planar SERS substrates ranging from highly ordered nanosphere arrays to structurally complex architectures, realized through different bottom-up strategies. Numerical and experimental results, supported by SEM, AFM and Raman measurements, confirm improved Raman signals compared to simpler configurations, highlighting the potential for further optimization and improved fabrication strategies.

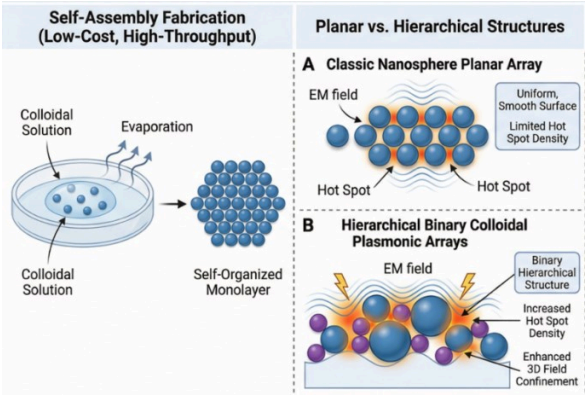

Figure 1: schematic representation of self-assembly technique, showing hot spot's accessibility for a) CPA and b) hierarchical nanostructures.

References

[1] Cutolo, M. A., Galeotti, F., Spaziani, S., Quero, G., Calcagno, V., Micco, A., ... & Cusano, A. (2024). Self-Assembled Hierarchical Nanostructures: Toward Engineered SERS-Active Platforms. Laser & Photonics Reviews, 18(10), 2301056.

Pesticide Recognition in Water Using Silver Plasmonic SERS Nanostructures Assisted by PCA

Massimo Rippa[1,*], Alessia Milano[1], Valentina Marchesano[1], Domenico Sagnelli[1], Bryan Guilcapi[1], Amalia D'Avino[1], Anna De Girolamo Del Mauro[2] and Lucia Petti[1]

[1]Institute of Applied Sciences and Intelligent Systems "E. Caianiello" CNR, Pozzuoli, Italy

[2]Energy and Sustainable Economic Development, ENEA, Italian National Agency for New Technologies, Portici Research Centre, Portici, Naples 80055, Italy

*Corresponding author: massimo.rippa@isasi.cnr.it

***Abstract*—A silver plasmonic SERS nanostructure is presented for the recognition of pesticides in water. Fingerprint spectra of fipronil, imidacloprid, and thiram are acquired and analyzed using principal component analysis, enabling clear label-free discrimination and demonstrating the potential of the platform for water quality monitoring.**

***Keywords*— Silver nanostructure, pesticide, SERS, PCA, sensing, electron beam lithography.**

I. Introduction

The widespread use of pesticides in agriculture has led to increasing contamination of surface and groundwater, raising serious concerns for environmental safety and human health [1,2]. Insecticides such as fipronil and imidacloprid, as well as fungicides like thiram, are among the most frequently detected compounds in aquatic environments, even at trace concentrations. Prolonged exposure to these substances has been associated with toxic and ecotoxic effects, making their rapid and reliable detection in water a critical challenge.

Conventional analytical techniques, including gas and liquid chromatography coupled with mass spectrometry, provide high sensitivity and selectivity but often require complex sample preparation, expensive instrumentation, and laboratory-based analysis. In this context, Surface-Enhanced Raman Spectroscopy (SERS) has emerged as a powerful alternative, offering molecular fingerprint specificity, label-free detection, and the potential for rapid analysis [2,3]. The effectiveness of SERS strongly depends on the design of the plasmonic substrate, particularly its ability to generate intense and reproducible electromagnetic hot spots.

In this work, we present an engineered silver plasmonic SERS nanostructure used for efficient and sensitive pesticide recognition in water. By combining SERS measurements with principal component analysis (PCA), we demonstrate the ability to distinguish between different classes of pesticides based on their vibrational fingerprints.

II. Methods

The SERS substrate consists of a periodic array of nanocavities fabricated on a silver thin film using a top-down electron beam lithography process. Each unit cell is formed by three equilateral triangles with a side length of 200 nm, arranged such that their midpoints lie on the vertices of a virtual equilateral triangle with a side length of 230 nm. The overall patterned area has dimensions of approximately 450 × 430 μm². This geometry was designed to promote strong localized surface plasmon resonances and a high density of electromagnetic hot spots.

Three pesticides were investigated: fipronil, imidacloprid (both insecticides), and thiram (a fungicide). All analytes were prepared in water and deposited onto identical silver nanostructured substrates by direct adsorption. SERS measurements were performed under identical experimental conditions to ensure spectral reproducibility. For each pesticide, multiple spectra using a laser wavelength of 785 nm were acquired and averaged. PCA was applied to the normalized SERS spectra to extract the most relevant spectral features and enable multivariate discrimination.

III. Results and Discussion

The average, normalized SERS spectra of fipronil, imidacloprid, and thiram are reported in Figure 1a. Each pesticide exhibits a characteristic vibrational fingerprint associated with its molecular structure. While some Raman bands partially overlap, clear differences in peak positions and relative intensities can be observed, particularly between the insecticides and the fungicide.

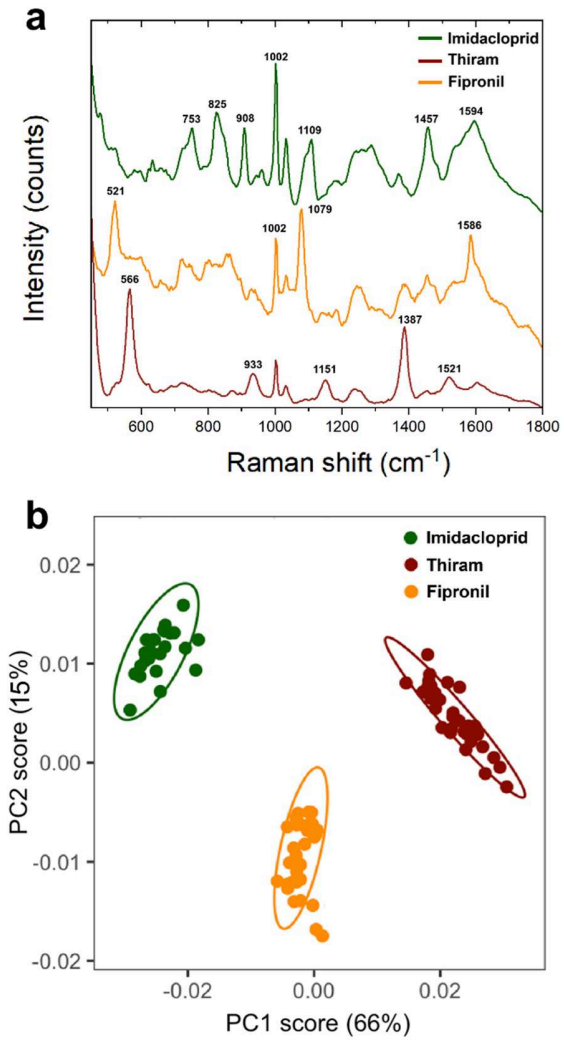

Fig. 1 SERS recognition of pesticides: a) average normalized SERS spectra of imidacloprid (green line), thiram (red line), and fipronil (yellow line); b) PCA analysis associated with the SERS measurements of the imidacloprid (green points), thiram (red points), and fipronil (yellow points).

To enhance analyte discrimination and objectively assess spectral differences, PCA was applied to the SERS datasets. The PCA score plot shown in Figure 1b reveals a clear separation of the three pesticides into distinct clusters. Fipronil, imidacloprid, and thiram occupy well-defined regions in the PC1–PC2 space, indicating that the SERS nanostructure provides sufficient sensitivity to capture subtle chemical differences.

The successful separation can be attributed to the variance explained by the first two principal components, with PC1 accounting for 15% and PC2 for 66% of the total variance. Together, they explain more than 80% of the overall variance, a commonly accepted threshold for reliable analyte discrimination. These results demonstrate that the combination of a silver plasmonic SERS nanostructure and PCA enables robust, label-free recognition of pesticides in water.

IV. Conclusion

A silver plasmonic SERS nanostructure has been demonstrated as an effective platform for pesticide recognition in water. The combination of SERS fingerprinting and principal component analysis enables clear discrimination between fipronil, imidacloprid, and thiram without the use of labels or selective probes. This approach shows strong potential for rapid and reliable water quality monitoring and environmental sensing applications.

Acknowledgments

The authors gratefully acknowledge the support for this work from Prof. Giulia Rusciano of University of Naples "Federico II" for plasma activation of the silver nanostructures.

References

[1] A. Birah, “Pesticide contamination in groundwater: processes, risks, and mitigation strategies,” Discov Agric 3, 152 (2025).

[2] M. Syafrudin, R. A. Kristanti, A. Yuniarto, T. Hadibarata, J. Rhee, W. A. Al-onazi, T. S. Algarni, A. H. Almarri, A. M. Al-Mohaimeed, “Pesticides in Drinking Water—A Review,” Int. J. Environ. Res. Public Health, 18, 468, 2021.

[3] M. Rippa, A. Milano, V. Marchesano, D. Sagnelli, B. Guilcapi, A. D'Avino, G. Palermo, G. Strangi, L. Consagra, M. Brigotti, S. Morabito, J. Zyss, L. Petti, “Diagnostic oriented discrimination of different Shiga toxins via PCA-assisted SERS-based plasmonic metasurface,” Nanophotonics. Apr 17;14(23):4005-4018, 2025.

[4] H. Altug, S. H. Oh, S. A. Maier, J. and Homola, “Advances and applications of nanophotonic biosensors,” Nat. Nanotechnol., Vol. 17, 5–16, 2022.

Low-Cost Flexible SERS Platforms for On-Site Detection of Bacterial and Viral Pathogens in Wastewater

Amalia D'Avino[1,2*], Alessia Milano[1], Valentina Marchesano[1], Bryan Guilcapi[1], Domenico Sagnelli[1], Massimo Rippa[1] and Lucia Petti[1]

[1]Institute of Applied Sciences and Intelligent Systems "E. Caianiello" CNR, Pozzuoli, Italy
[2]Department of Engineering, University of Naples "Parthenope", Centro Direzionale Isola C4, 80143, Napoli, Italy
*Corresponding author: amalia.davino@isasi.cnr.it - amalia.davino001@studenti.uniparthenope.it

***Abstract*— We present low-cost flexible SERS platforms for label-free detection of *Escherichia coli* and *rotavirus* in wastewater. The platforms combine high plasmonic performance with mechanical conformability and system integrability, enabling portable and on-site pathogen monitoring. The approach offers a scalable alternative to rigid and highly engineered sensors for environmental surveillance applications.**

***Keywords*— SERS, gold nanoparticles, paper tape, wastewater monitoring, pathogens biosensing.**

I. Introduction

Bacterial and viral contamination of water represents a major concern for public health and environmental safety. Among fecal indicators, *Escherichia coli* is one of the most widely used markers of microbiological water quality, as pathogenic strains can cause severe gastrointestinal diseases and serious clinical complications. Similarly, Rotavirus is a leading cause of acute gastroenteritis worldwide and is frequently detected in wastewater due to its high environmental stability and resistance to conventional treatment processes. [1-4]

Conventional detection techniques, including culture-based methods, PCR, ELISA, and sequencing, provide high specificity but rely on complex laboratory workflows, expensive instrumentation, and long analysis times, limiting their applicability for rapid and decentralized environmental monitoring. [5]

Surface-Enhanced Raman Scattering (SERS) has emerged as a powerful label-free technique for pathogen detection, offering high sensitivity, molecular specificity, and minimal sample preparation. Most SERS platforms are based on rigid substrates, such as silicon or glass, which are costly, fragile, and poorly suited for in-field applications. In this context, flexible SERS substrates represent a promising alternative, enabling mechanical conformability, low fabrication costs, and straightforward integration into portable sensing systems for real-world environmental surveillance. [6-8]

II. Methods

Flexible SERS substrates were fabricated through bottom-up self-assembly of gold nanostructures onto commercial adhesive paper tape, forming a plasmonically active and mechanically compliant platform [9]. The fabrication relies on simple and scalable procedures, avoiding complex lithographic steps and costly cleanroom technologies. Wastewater samples were spiked with inactivated *Escherichia coli* and Rotavirus. SERS measurements were performed directly on the contaminated samples without labeling or extensive preprocessing. The collected spectra were analyzed using multivariate statistical methods, including Principal Component Analysis (PCA), to enable pathogen discrimination.

III. Results and Discussion

The developed SERS substrate exhibited an enhancement factor on the order of 10^7 and enabled the acquisition of reproducible Raman fingerprints of both bacterial and viral targets in wastewater. Distinct spectral features associated with inactivated *Escherichia coli* and inactivated Rotavirus allowed their reliable differentiation despite the complexity of the environmental matrix [10–11], as shown in Fig. 1. Compared to conventional rigid and engineered SERS substrates, the proposed platform offers advantages in terms of cost-effectiveness, scalability, and ease of system integration. Its mechanical conformability supports coupling with portable optical systems and in-field devices while preserving sensing performance. For inactivated *Escherichia coli*, a detection limit of 26 CFU/mL in water was achieved. Compared to existing flexible SERS substrates, the sensor demonstrates competitive sensitivity together with straightforward fabrication and

suitability for on-site environmental monitoring [12–13].

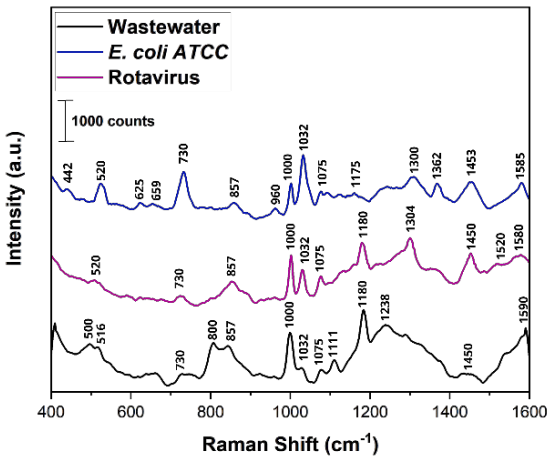

Fig. 1 SERS spectral fingerprints of inactivated *Escherichia coli* (10^8 CFU/mL) and Rotavirus (10^5 $TCID_{50}$/mL) in wastewater acquired using the flexible paper tape SERS sensor. Each spectrum is the average of acquisitions collected at different points of the same droplet.

IV. Conclusion

This study shows the potential of low-cost flexible SERS platforms for real-world monitoring of pathogenic microorganisms in wastewater. By combining very good sensing performance with mechanical conformability and easy system integration, these substrates provide a practical and scalable solution for on-site surveillance, representing a valid alternative to rigid and laboratory-based biosensing technologies.

Acknowledgments

This work was supported by OPUS AUTOMAZIONE SpA and project EMDAS - “Environment Mobile Data Acquisition System” funded by PR Campania FESR 21/27. The authors thank Dr. Ivan Perrotta from OPUS for his support, Dr. Giovanna Fusco of Istituto Zooprofilattico Sperimentale del Mezzogiorno, Dr. Rosa Ambrosio from Veterinary Dept. of University of Naples Federico II.

References

[1] Bell, R. L., Kase, J. A., Harrison, L. M., Balan, K. V., Babu, U., Chen, Y., Macarisin, D., Kwon, H. J., Zheng, J., Stevens, E. L., Meng, J., & Brown, E. W. (2021). The persistence of bacterial pathogens in surface water and its impact on global food safety. In Pathogens (Vol. 10, Issue 11). MDPI. https://doi.org/10.3390/pathogens10111391

[2] Kristanti, R. A., Hadibarata, T., Syafrudin, M., Yılmaz, M., & Abdullah, S. (2022). Microbiological Contaminants in Drinking Water: Current Status and Challenges. In Water, Air, and Soil Pollution (Vol. 233, Issue 8). Springer Science and Business Media Deutschland GmbH. https://doi.org/10.1007/s11270-022-05698-3

[3] Du, Y.; Chen, C.; Zhang, X.; Yan, D.; Jiang, D.; Liu, X.; Yang, M.; Ding, C.; Lan, L.; Hecht, R.; Zhu, C.; Yang, S. Global Burden and Trends of Rotavirus Infection-Associated Deaths from 1990 to 2019: An Observational Trend Study. Virol J 2022, 19 (1), 166. https://doi.org/10.1186/s12985-022-01898-9.

[4] Adriaenssens, E. M.; Farkas, K.; Harrison, C.; Jones, D. L.; Allison, H. E.; McCarthy, A. J. Viromic Analysis of Wastewater Input to a River Catchment Reveals a Diverse Assemblage of RNA Viruses. mSystems 2018, 3 (3). https://doi.org/10.1128/mSystems.00025-18.

[5] Amani, J., Ahmadpour, A., Fooladi, A. A. I., & Nazarian, S. (2015). Detection of E. coli O157: H7 and Shigella dysenteriae toxins in clinical samples by PCR-ELISA. Brazilian Journal of Infectious Diseases, 19(3), 278–284. https://doi.org/10.1016/j.bjid.2015.02.008

[6] D’Avino, A., Milano, A., Marchesano, V., Guilcapi, B., Sagnelli, D., Rippa, M., Zhou, L., Rossi, G., Consagra, L., Brigotti, M., Morabito, S., & Petti, L. (2025). Flexible Gold Nanoparticle SERS Tape for Rapid, Label-Free and Ultrasensitive Detection and Differentiation of Shiga Toxin Variants. Biosensors and Bioelectronics: X, 100696. https://doi.org/10.1016/j.biosx.2025.100696

[7] Haque Chowdhury, M. A., Tasnim, N., Hossain, M., & Habib, A. (2023). Flexible, stretchable, and single-molecule-sensitive SERS-active sensor for wearable biosensing applications. RSC Advances, 13(30), 20787–20798. https://doi.org/10.1039/d3ra03050d

[8] Pan, Y., Xu, S., Wang, Z., Jiang, C., & Ma, X. (2024). Sensitive SERS aptasensor for histamine detection based on Au/Ag nanorods and IRMOF-3@Au based flexible PDMS membrane. Analytica Chimica Acta, 1288. https://doi.org/10.1016/j.aca.2023.342147

[9] Zhou, L., Vestri, A., Marchesano, V., Rippa, M., Sagnelli, D., Picazio, G., Fusco, G., Han, J., Zhou, J., & Petti, L. (2023). The Label-Free Detection and Identification of SARS-CoV-2 Using Surface-Enhanced Raman Spectroscopy and Principal Component Analysis. Biosensors, 13(12). https://doi.org/10.3390/bios13121014

[10] Lemma, T., Saliniemi, A., Hynninen, V., Hytönen, V. P., & Toppari, J. J. (2016). SERS detection of cell surface and intracellular components of microorganisms using nano-aggregated Ag substrate. Vibrational Spectroscopy, 83, 36–45. https://doi.org/10.1016/j.vibspec.2016.01.006

[11] Biswas, S., Devi, Y. D., Sarma, D., Hatiboruah, D., Chamuah, N., Namsa, N. D., & Nath, P. (2023). Detection and analysis of rotavirus in clinical stool samples using silver nanoparticle functionalized paper as SERS substrate. Spectrochimica Acta Part A: Molecular and Biomolecular Spectroscopy, 295, 122610.

[12] Hameed, S. M., Ali, N. H., Rostaminia, A., Abed, S. H., Khojasteh, H., Kadhim, S. A., Aspoukeh, P., & Eskandari, V. (2024). Development and Evaluation of Surface-Enhanced Raman Spectroscopy (SERS) Filter Paper Substrates Coated with Antibacterial Silver Nanoparticles for the Identification of Trace Escherichia coli. Chemistry Africa, 7(8), 4541–4553. https://doi.org/10.1007/s42250-024-01064-4

[13] Muthukumar, D., & Shtenberg, G. (2023b). SERS-based immunosensor for E. coli contaminants detection in milk using silver-coated nanoporous silicon substrates. Talanta, 254. https://doi.org/10.1016/j.talanta.2022.124132

Photonics on multimode optical fibers

Linda Piscopo[1,2,*], D. Zheng[1,3], M. F. Kashif[1,4], A. La Grasta[1], T. O. Otomalo[1], L. Collard[1,5], A. Corrado[1,2], A. Balena[1,6], C. Montinaro[1], M. De Vittorio[1,2,7], F. Pisanello[1]

[1] Istituto Italiano di Tecnologia, Center for Biomolecular Nanotechnologies, 73010 Arnesano, Italy
[2] Dipartimento di Ingegneria dell'Innovazione, Università del Salento, 73100 Lecce, Italy
[3] State Key Laboratory of Radio Frequency Heterogeneous Integration, Shenzhen University, Shenzhen 518060, China
[4] Dipartimento di Ingegneria Elettrica e delle Tecnologie dell'Informazione, Università Degli Studi di Napoli Federico II, 80125 Napoli,Italy
[5] Comprehensive Cancer Centre, School of Cancer and Pharmaceutical Sciences, King' s College London, London, UK
[6] Laboratoire Kastler Brossel, Sorbonne University, CNRS, ENS-PSL University, Collège de France, Paris, 75005, France
[7] IDUN section, Department of Health Technology, Technical University of Denmark, DK-2800 Kgs. Lyngby, Denmark
*Corresponding author: linda.piscopo@iit.it

***Abstract*— We describe a platform that optimizes coupling between guided modes in multimode fibers and photonic structures on the facet, eighter metalenses or plasmonic nanoparticles. Using wavefront shaping, we control light propagation to enhance imaging, SERS, and thermoplasmonic heating, demonstrating the potential of compact fiber-based probes for minimally invasive biological interfacing.**

***Keywords*— plasmonics, endoscopes, wavefront shaping, SERS, thermal heating, metalenses**

I. Introduction

Plasmonic platforms offer versatile routes to enhance light–matter interactions, enabling both advanced sensing modalities and highly localized photothermal effects across a range of applications.[1], [2] Although translating these concepts into in vivo environments remains challenging, they offer compelling opportunities for minimally invasive optical interfacing with neural tissue. On the other hand, dielectric metalenses have the potential to revolutionize endoscopy, enabling complex shaping of the wavefront at the output of optical fibers. A key requirement for unlocking full potential of this approach is the ability to tailor the excitation conditions both in the near and in the far-field. In this context, wavefront-shaping techniques offer a promising route to improve the coupling between guided modes and the integrated photonics structures.

II. Methods

Our approach entails the integration of plasmonic and dielectric photonic structures on flat multimode fibers (MMFs), exploiting different fabrication strategies. For the fabrication of plasmonic surfaces of the fiber facet, we employed solid-state dewetting, enabling high-throughput formation of nano-islands with diameters of approximately 50 nm and gaps of 20 nm. While MMFs represent a promising substrate thanks to the small cross-section to sustained mode ratio, they also entail a challenge due to the scrambling of light into a speckle pattern.[3] To enhance the performance of our probes, we have implemented a wavefront shaping method that allows controlling the coupling between guided modes in MMFs and plasmonic resonances both in the near field and the far field of metallic nanostructures fabricated on the distal fiber facet.[4] A phase-modulation algorithm tailors key excitation parameters, controlling spatial confinement on the plasmonic facet and the angular distribution in the far field (kx, ky).

Another promising direction is to combine wavefront-shaping algorithms with dielectric metalenses fabricated on the multimode fiber facet. The integration of the metalens can be achieved through two-photon lithography, which allows direct printing on the MMF.

Together, these two approaches could overcome the intrinsic limitations of multimode optical fibers.

III. Results and Discussion

We will describe how wavefront shaping can successfully control the near and far field emitted from MMFs decorated with plasmonic structures or with metalenses. Moreover, by functionalizing the nanostructures with benzenethiol molecules, spatially resolved SERS can be achieved. Dewetted nanoparticles are also able to detect neurotransmitters dispersed in aqueous solutions.

The use of metalenses allows improved resolution in the near field and expanded angular control over the far field.

Lastly, plasmonic heating can be also explored, opening the possibility to employ fiber-based endoscopes not only for diagnostic purposes but also for thermal treatments.

IV. Conclusion

In conclusion, combining MMFs with plasmonic structures or metalenses with wavefront-shaping strategies has the potential to achieve precise control over light–matter

interactions, enabling both sensitive optical readout, improved imaging capabilities, and localized photothermal functionality within compact endoscopic platforms.

ACKNOWLEDGMENTS

M.D.V. and F.P. acknowledge funding by European Union's Horizon Europe under grant agreement 101125498, project MINING "Multifunctional nano-bio interfaces with deep brain regions". D.Z., M.F.K., Li.C., M.D.V., and F.P. acknowledge funding from the European Union's Horizon 2020 Research and Innovation Program under Grant Agreement No. 828972. Li.C., C.M., M.D.V., and F.P. acknowledge funding from the Project "RAISE (Robotics and AI for Socio-economic Empowerment)" code ECS00000035 funded by European Union – NextGenerationEU PNRR MUR - M4C2 – Investimento 1.5 - Avviso "Ecosistemi dell'Innovazione" CUP J33C22001220001. M.D.V. and F.P. acknowledge funding from the European Union's Horizon 2020 Research and Innovation
Program under Grant Agreement No. 101016787. M.D.V and F.P acknowledge financial support under the National Recovery and Resilience Plan (NRRP), Mission 4 "Education and Research" – Component 2 "From Research to Business" Investment 1.3, funded by the European Union NextGenerationEU, within the framework of the cascade funding call of Spoke 3 – Extended Partnerships among Universities, Research Centers, and Enterprises for Research Project Funding, "Mnesys" (PE00000006).

References

[1] F. Pisano *et al.*, «Plasmonics on a Neural Implant: Engineering Light–Matter Interactions on the Nonplanar Surface of Tapered Optical Fibers», *Advanced Optical Materials*, vol. 10, fasc. 2, p. 2101649, gen. 2022, doi: 10.1002/adom.202101649.

[2] D. Zheng *et al.*, «Toward Plasmonic Neural Probes: SERS Detection of Neurotransmitters through Gold-Nanoislands-Decorated Tapered Optical Fibers with Sub-10 nm Gaps», *Advanced Materials*, vol. 35, fasc. 11, p. 2200902, mar. 2023, doi: 10.1002/adma.202200902.

[3] M. Plöschner, T. Tyc, e T. Čižmár, «Seeing through chaos in multimode fibres», *Nature Photon*, vol. 9, fasc. 8, pp. 529–535, ago. 2015, doi: 10.1038/nphoton.2015.112.

[4] L. Collard *et al.*, «Holographic Manipulation of Nanostructured Fiber Optics Enables Spatially-Resolved, Reconfigurable Optical Control of Plasmonic Local Field Enhancement and SERS», *Small*, vol. 18, fasc. 23, p. 2200975, giu. 2022, doi: 10.1002/smll.202200975.

Topological Bound States in the Continuum in Photonic Crystal Slabs for Label-Free Biosensing

Karen Caicedo[1], Silvia Romano[1], Gianluigi Zito[1], Ivo Rendina[1] and Vito Mocella[1,*]

[1]Institute of Applied Sciences and Intelligent Systems (ISASI), National Research Council (CNR), Naples, Italy

*Corresponding author: vito.mocella@cnr.it

***Abstract*— We report the first experimental observation of broadband bound states in the continuum (BICs) in simple photonic crystal slabs: continuous lines of vanishing radiation loss extending over approximately 15 nm along high-symmetry directions. This new class of high-Q states opens transformative perspectives for label-free sensing, including biodiagnostics and food safety applications.**

***Keywords*- bound states in the continuum, broadband BIC, photonic crystal slabs, biosensing, food safety, ochratoxin A.**

I. Introduction

Bound states in the continuum (BICs) are localized photonic modes embedded in the radiation continuum that exhibit theoretically infinite quality factors and giant field enhancement [1]. In photonic crystal slabs (PhCS), BICs have been conventionally realized at isolated points in momentum space, typically at the high-symmetry point. Our group has exploited these isolated BICs to develop a powerful sensing platform in silicon nitride PhCS, demonstrating record-level detection of ochratoxin A for food safety [3] and selective trace-detection of cancer biomarkers for clinical diagnostics [5,6]. However, isolated BICs inherently limit the operational bandwidth available for sensing. Here, we present a fundamentally new result: broadband BICs, i.e. continuous lines of BICs extending along high-symmetry directions in momentum space, can be realized in simple, vertically asymmetric PhC slabs. Unlike isolated BICs, broadband BICs maintain vanishing radiative losses over an extended spectral range, offering a paradigm shift for high-Q photonic devices with direct implications for enhanced, multiplexed biosensing.

II. Methods

We fabricate silicon nitride photonic crystal slabs on silicon and characterize them using Photonic Angle-Resolved Transmission Spectroscopy (PARTS), a far-field technique that maps the full dispersion surfaces with angular accuracy of 3 x 10^{-4} rad and spectral resolution of 0.2 nm. PARTS enables the precise identification of symmetry-protected and accidental BICs, Friedrich–Wintgen BICs arising from avoided band crossings, and - crucially - broadband BICs that appear as continuous lines of vanishing radiative linewidth along the high-symmetry direction. The underlying topological structure is revealed by tracking polarization vortices and C-points carrying well-defined topological charges. A non-Hermitian two-level Hamiltonian model predicts that broadband BICs emerge when a frequency-degenerate and radiatively balanced doublet of modes interferes destructively along a mirror line. Vertical asymmetry of the slab is essential: it forces both modes to radiate into the same physical channels, enabling the interferometric cancellation that converts ordinary isolated BICs into a continuous BIC line.

III. Results and Discussion

Using PARTS, we achieve the first direct experimental observation of broadband BICs in simple PhC: continuous lines of vanishing radiation loss spanning approximately 15 nm in wavelength along the high-symmetry direction, in excellent agreement with the non-Hermitian theoretical model and full numerical simulations. The Q-factor diverges as the BIC line is approached from any direction in momentum space, confirming the genuine BIC character of the extended dark state. This result fundamentally expands the BIC paradigm from isolated points to continuous lines in a minimal, technologically relevant platform. The implications for sensing are far-reaching. Our group has already demonstrated that isolated BICs in the same silicon nitride PhCS platform deliver record-level performance: trace detection of ochratoxin A (OTA) with a limit of detection of 2.3 pg/mL for food safety [3], selective detection of cancer biomarkers such as TGF-beta [5], and resolution of protein binding kinetics for clinical diagnostics [6]. Broadband BICs are expected to substantially enhance these capabilities by extending the high-Q interaction region over a wider spectral window, enabling simultaneous multi-analyte detection and more robust signal acquisition in complex biological matrices.

IV. Conclusion

We present the first experimental demonstration of broadband BICs in a photonic crystal slabs, a discovery that extends the BIC concept from isolated points to continuous high-Q lines in momentum space. Combined with the already

proven sensing capabilities of our silicon nitride BIC platform - including record detection of ochratoxin A and cancer biomarkers - broadband BICs open a clear pathway toward next-generation integrated, multiplexed lab-on-chip devices with broadband sensitivity for biodiagnostics, environmental monitoring, and food safety.

REFERENCES

[1] V. Mocella and S. Romano, "Giant field enhancement in photonic resonant lattices," Phys. Rev. B, vol. 92, p. 155117, 2015.

[2] S. Romano, G. Zito, S. N. Lara Yépez, S. Cabrini, E. Penzo, G. Coppola, I. Rendina, and V. Mocella, "Tuning the exponential sensitivity of a bound-state-in-continuum optical sensor," Opt. Express, vol. 27, pp. 18776–18786, 2019.

[3] G. Zito, S. Romano, S. Cabrini, and V. Mocella, "High-Q photonic aptasensor based on avoided crossing bound states in the continuum and trace detection of ochratoxin A," Results Phys., vol. 42, p. 105987, 2022.

[4] S. Romano, A. Lamberti, M. Masullo, E. Penzo, S. Cabrini, I. Rendina, and V. Mocella, "Optical biosensors based on photonic crystals supporting bound states in the continuum," Materials, vol. 11, p. 526, 2018.

[5] G. Zito et al, " Molecularly Imprinted Polymer Sensor Empowered by Bound States in the Continuum for Selective Trace-Detection of TGF-beta" 11-41, 2401843, 2024

[6] B. Miranda et al, "Resolving SPARC–HSA binding kinetics with an ultrasensitive photonic sensor based on bound states in the continuum" Biosensors and Bioelectronics, 288, 117754, 2025.

Flowthrough Raman readout in plasmonic nanopores for sequencing applications

Francesco De Angelis

Istituto Italiano di Tecnologia, Via Morego 30, 16163, Genova, Italy

*Corresponding author: francesco.deangelis@iit.it

***Abstract*— Inspired by nanopore sequencing, we developed a Raman sequential readout strategy based on plasmonic nanopores. Molecules are delivered electrophoretically while real-time Raman spectra are recorded. We identified four DNA nucleotides and multiple amino acids at single-monomer level, achieving 89% nucleotide discrimination accuracy and angstrom-scale spatial resolution, corresponding to only 4 nucleotides.**

***Keywords*— plasmonic nanopores, sequencing, Raman, SPAD camera.**

I. Introduction

Surface-Enhanced Raman Scattering has been studied for decades as a recognition technique due to its high sensitivity and discriminative power, particularly in biological applications. Inspired by nanopore sequencing technology, we developed a plasmonic device capable of operating in a flow-through configuration to detect individual molecules as they pass through the plasmonic hotspot [1-5]. Among different kinds of nanopores, a scalable device consists of permeable plasmonic films [2], through which single molecules are sequentially delivered via electrophoresis, while Raman spectra are recorded in real time. A very effective light matter coupling, combined with the ultrasmall size of plasmonic spots enabled to access spatial and temporal scales compatible with polymer sequencing, namely few angstroms and few µs [1-2].

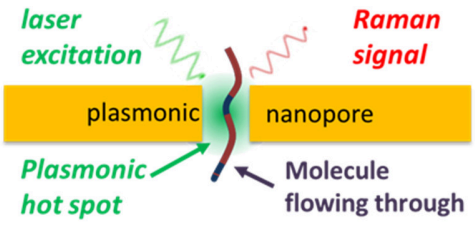

Fig. 1: Scheme representing the concept of Raman sequential readout in nanopores. SPAD camera and effective plasmonic nanopore enables sequential readout at a speed comparable to the translocation time of molecular subunits such as nucleotides in DNA or Amino Acids in protein.

II. Methods

The key point of the presented approach is based on innovative plasmonic membranes and solid state nanopores, combined with latest generation SPAD camera [1-2].

III. Results and Discussion

We successfully captured the Raman spectra of the four DNA nucleotides as well as multiple amino acids at a frame rate fast enough to detect the translocation of individual monomers. Leveraging SPAD cameras, we achieved an acquisition time of just 10 microseconds, maintaining a continuous frame rate of 100 kHz. By analyzing the sequential Raman spectra, it becomes possible to determine the precise sequence of the polymeric molecule, whether it be DNA, RNA, or proteins. For nucleotides we achieved a discrimination accuracy of 89% at single molecule level. Also, we demonstrated a spatial resolution on the order of a few angstroms, suggesting clear potential for Raman based identification and sequencing of nucleic acids (DNA/RNA) and proteins including post translational and transcriptional modifications.

IV. Conclusion

We demonstrated a spatial resolution comparable to single units in biopolymers, suggesting clear potential for Raman based identification and sequencing of nucleic acids (DNA/RNA) and proteins including post translational and transcriptional modifications.

References

[1] F. Khozeymeh Sarbishe et al., “High-Speed Raman Readout of Single Polypeptides via Plasmonic Nanopores”, Adv. Mater. 2025, 37, 2504436.

[2] K. Khabarov et al., “Raman identification of single nucleotides flowing through permeable plasmonic films”, Nat Commun 16, 9113 (2025).

[3] Y. Zhao et al., “Single-Molecule SERS Discrimination of Proline from Hydroxyproline Assisted by a Deep Learning Model”, Nano Lett. 2025, 25, 18, 7499–7506.

[4] M. Iarossi et al., “High-Density Plasmonic Nanopores for DNA Sensing at Ultra-Low Concentrations by Plasmon-Enhanced Raman Spectroscopy”, Adv. Funct. Mater. 2023, 33, 2301934.

[5] Y. Zhao et al., “Plasmonic Bowl-Shaped Nanopore for Raman Detection of Single DNA Molecules in Flow-Through”, Nano Lett. 2023, 23, 11, 4830–4836.

SPECIAL SESSION 16

Metamaterials and Metasurfaces as Platforms for Next-Generation Electromagnetics: Fundamentals, Applications and Future Trends

8 contributions · pp. 1088–1099

Communicating and Computing with Microwave Networks

Matteo Nerini[1,*], Bruno Clerckx[1]

[1]Department of Electrical and Electronic Engineering, Imperial College London, UK
*Corresponding author: m.nerini20@imperial.ac.uk

***Abstract*—Future wireless systems will communicate and process extremely high-dimensional signals under stringent latency constraints. As antenna arrays scale toward massive and gigantic multiple-input multiple-output (MIMO), conventional digital signal processing becomes prohibitive, motivating paradigm shifts where both communication and computation are partially offloaded from the digital to the analog domain.**

***Keywords*— Beyond-diagonal reconfigurable intelligent surface (BD-RIS), microwave linear analog computer (MiLAC).**

Reconfigurable intelligent surfaces (RIS) were introduced to make the wireless channel programmable by adjusting the reflection or transmission properties of a surface (see Fig. 1(a)) [1]. Conventional RIS architectures are typically restricted to diagonal scattering matrices, meaning that each surface element independently applies a tunable phase to the incident wave. While attractive for their simplicity, such diagonal constraints limit the channel shaping capabilities. Beyond-diagonal RISs (BD-RISs) overcome this limitation by enabling controlled coupling among surface elements through tunable interconnections [2]. A BD-RIS is a microwave network whose scattering matrix is fully programmable and not limited to being diagonal. This additional freedom allows the surface not only to reflect energy individually at each element, but also to reflect the energy absorbed by an element from other elements, enhancing the impact on the wireless channel [3].

While the microwave networks used in BD-RIS are used to shape the wireless channels, they can also be exploited to perform computations (see Fig. 1(b)). Microwave (linear) networks used for computations have been denoted as microwave linear analog computers (MiLACs) [4]. In a MiLAC, the multiport microwave network is reconfigured such that its response implements a desired transformation. By programming their admittance matrix, MiLACs can realize operations such as matrix–vector multiplication, matrix inversion, linear minimum mean square error (LMMSE) estimation, and least squares estimator directly in the analog domain. For example, matrix inversion, LMMSE, and the least squares estimator can be computed with a complexity growing with the square of the matrix size rather than the cube.

The relevance of MiLAC becomes particularly evident in gigantic MIMO systems, where electromagnetic (EM) signals at hundreds or thousands of antennas must be jointly processed. The least squares estimator is commonly used in MIMO communications to perform zero-forcing beamforming. Therefore, a MiLAC can be used to efficiently precode

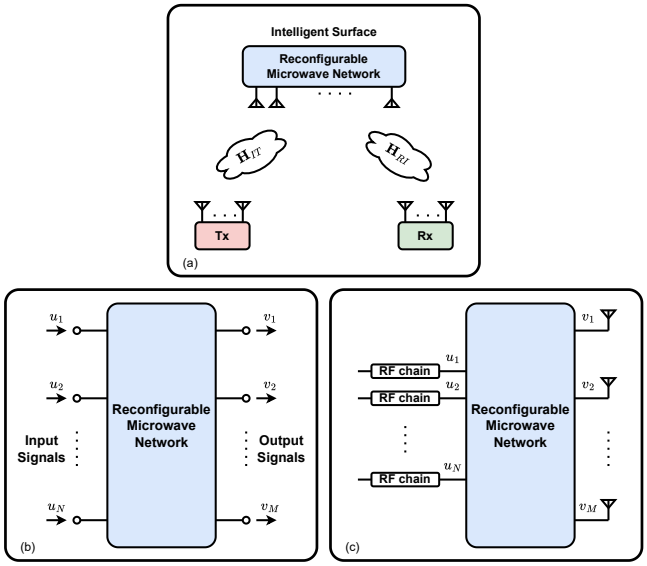

Fig. 1. (a) a reconfigurable microwave network implementing an intelligent surface to improve the wireless channel, (b) a reconfigurable microwave network processing EM signals in the analog domain, and (c) a transmitter with a reconfigurable microwave network that processes the transmitted symbols.

symbols intended for multiple users in a gigantic MIMO base station (see Fig. 1(c)) [5], offering several benefits in terms of hardware and computational complexity.

References

[1] Q. Wu, S. Zhang, B. Zheng, C. You, and R. Zhang, "Intelligent reflecting surface-aided wireless communications: A tutorial," *IEEE Trans. Commun.*, vol. 69, no. 5, pp. 3313–3351, 2021.

[2] S. Shen, B. Clerckx, and R. Murch, "Modeling and architecture design of reconfigurable intelligent surfaces using scattering parameter network analysis," *IEEE Trans. Wireless Commun.*, vol. 21, no. 2, pp. 1229–1243, 2022.

[3] H. Li, M. Nerini, S. Shen, and B. Clerckx, "A tutorial on beyond-diagonal reconfigurable intelligent surfaces: Modeling, architectures, system design and optimization, and applications," *IEEE Commun. Surv. Tutor.*, vol. 28, pp. 4086–4126, 2026.

[4] M. Nerini and B. Clerckx, "Analog computing for signal processing and communications — Part I: Computing with microwave networks," *IEEE Trans. Signal Process.*, 2025.

[5] M. Nerini and B. Clerckx, "Analog computing for signal processing and communications — Part II: Toward gigantic MIMO beamforming," *IEEE Trans. Signal Process.*, 2025.

Universal Wave-Control Framework for Reconfigurable Microwave Systems

Philipp del Hougne[1,2,*]

[1]Univ Rennes, CNRS, IETR - UMR 6164, F-35000, Rennes, France
[2]Department of Electronics and Nanoengineering, Aalto University, 00076 Espoo, Finland
*Corresponding author: philipp.del-hougne@univ-rennes.fr

***Abstract*—Reconfigurable microwave systems, including contemporary examples involving programmable metasurfaces (e.g., dynamic metasurface antennas, reconfigurable intelligent surfaces), can be abstracted in terms of a multiport-network representation. This abstraction enables a universal framework for formulating the model, experimentally estimating its parameters to avoid model-reality mismatch, and leveraging the model for optimization and determining fundamental bounds. In addition, the model structure reveals fundamental insights into principles for maximizing wave-domain flexibility. Altogether, this universal wave-control framework for reconfigurable microwave systems paves the way to a prototype-aware electromagnetic information theory for programmable wave systems.**

***Keywords*—electromagnetic information theory, multiport-network theory, programmable metasurface.**

I. Introduction

Programmable metasurfaces such as dynamic metasurface antennas (DMAs) and reconfigurable intelligent surfaces (RISs) are technological enablers for the next generation of systems in wireless communications, sensing, and wave-domain computing. Despite many theoretical studies and some antenna-level experiments, system-level experimental demonstrations remain challenging. The fundamental crux is the availability of an accurate forward model mapping the configuration of the tunable parameters to the resulting transfer function. On the one hand, intricate electromagnetic coupling effects intertwine the effects of the tunable parameters. On the other hand, due to fabrication inaccuracies and/or unknown system details, the model parameters are generally neither known in closed form nor accessible via numerical simulation.

Because tunable lumped elements are the predominant mechanism for reconfigurability in programmable metasurfaces, a universal representation in terms of multiport network theory exists. Techniques developed for estimating its parameters, as well as leveraging it for optimization, and determining fundamental bounds are thus broadly applicable.

II. Results

To minimize model-reality mismatch, the model parameters should be estimated experimentally. However, they cannot be measured directly because the tunable lumped elements are not connectorized and too numerous. Various techniques enable the estimation of a set of proxy model parameters that accurately map the chosen configuration to the physically observable scattering parameters [1], [2], [3], [4], [5]. However, ambiguities in these proxy parameters are usually inevitable, unless the loads have specific and known characteristics [6], [7], [8]. Fortunately, these ambiguities do not influence model-based optimization and bounding.

Once a calibrated forward model is available, standard techniques for discrete optimization (e.g., genetic algorithm, coordinate descent, etc.) can be used for model-based optimization of the prototype's configuration. In addition, we can derive fundamental bounds on achievable functionalities with a given prototype [9], [10], [11]. Such bounds can inform us, for instance, about the quality of our optimization outcomes.

Finally, we can explore principles for designing reconfigurable wave systems with maximal wave-domain flexibility. In particular, the model structure reveals benefits of strong mutual coupling between tunable elements. The latter is typically treated as a vexing nuisance to be mitigated, instead of reaping it as a resource for maximizing wave-domain flexibility [12], [13].

III. Conclusion

We review recent efforts toward establishing a universal wave-control framework for reconfigurable microwave systems.

Acknowledgments

This work was supported in part by the Nokia Foundation (project 20260028), the ANR PRCI program (project ANR-22-CE93-0010), and the ANR France 2030 program (project ANR-22-PEFT-0005).

REFERENCES

[1] J. Sol, H. Prod'homme, L. Le Magoarou, and P. del Hougne, "Experimentally realized physical-model-based frugal wave control in metasurface-programmable complex media," *Nat. Commun.*, vol. 15, no. 1, p. 2841, Apr. 2024.

[2] P. del Hougne, "Experimental Multiport-Network Parameter Estimation and Optimization for Multi-Bit RIS," *IEEE Wirel. Commun. Lett.*, 2025.

[3] P. del Hougne, "Ambiguity-Aware Segmented Estimation of Mutual Coupling in Large RIS: Algorithm and Experimental Validation," *IEEE Trans. Commun.*, 2026, doi: 10.1109/TCOMM.2026.3653083.

[4] P. del Hougne, "Reduced-Rank Mutual Coupling Representation and Experimental Estimation for Large RIS," *IEEE Wireless Commun. Lett.*, vol. 15, pp. 1836–1840, 2026.

[5] J. Tapie and P. del Hougne, "Experimental Multiport-Network Parameter Estimation for a Dynamic Metasurface Antenna," Dec. 27, 2025, *arXiv*: 2512.22607.

[6] P. del Hougne, "Virtual VNA 2.0: Ambiguity-Free Scattering Matrix Estimation by Terminating Not-Directly-Accessible Ports With Tunable and Coupled Loads," *IEEE Trans. Antennas Propagat.*, vol. 73, no. 7, pp. 4903–4908, Jul. 2025.

[7] P. del Hougne, "Virtual VNA 3.0: Unambiguous Scattering Matrix Estimation for Nonreciprocal Systems by Leveraging Tunable and Coupled Loads," *IEEE Trans. Instrum. Meas.*, vol. 74, 2025, doi: 10.1109/TIM.2025.3598388.

[8] P. del Hougne, "Wireless Multi-Port Sensing: Virtual-VNA-Enabled De-Embedding of an Over-the-Air Fixture," *IEEE Trans. Antennas Propagat.*, 2025, doi: 10.1109/TAP.2025.3639951.

[9] A. Salmi, V. Viikari, and P. del Hougne, "Electromagnetically Consistent Bounds on Information Transfer in Real-World RIS-Parametrized Wireless Channels," Jan. 27, 2026, *arXiv*:2601.20017.

[10] P. del Hougne, "Electromagnetic Bounds on Realizing Targeted MIMO Transfer Functions in Real-World Systems with Wave-Domain Programmability," Feb. 15, 2026, *arXiv*:2602.14152.

[11] P. del Hougne, "Effective Electromagnetic Degrees of Freedom in Backscatter MIMO Systems," Dec. 07, 2025, *arXiv*::2512.06799.

[12] H. Prod'homme and P. del Hougne, "Mutual Coupling in Dynamic Metasurface Antennas: Foe, but also Friend," *IEEE Wirel. Commun.*, vol. 32, no. 4, pp. 30–36, 2025.

[13] H. Prod'homme, J. Tapie, L. Le Magoarou, and P. del Hougne, "Benefits of Mutual Coupling in Dynamic Metasurface Antennas," *IEEE Trans. Antennas Propag.*, Sep. 2025.

Compressive Metasurfaces for Communications and Imaging Applications

Okan Yurduseven[1,*], David R. Smith[2],

[1]Centre for Wireless Innovation, Queen's University Belfast, BT9 5BN, Belfast, UK
[2]Department of Electrical and Computer Engineering, Duke University, Durham, NC 27708 USA
*Corresponding author: okan.yurduseven@qub.ac.uk

***Abstract*—In this work, we present a physical layer compression framework for communications and imaging applications. The system makes use of wave-chaotic metasurface antennas, generating spatio-temporally varying quasi-random radiated field patterns. This mechanism enables wireless channels to be characterized using a single-pixel hardware architecture while operating as a single-pixel microwave camera to image a region of interest. We show different examples of compressive coded-aperture-driven electromagnetic use case scenarios, from direction of arrival estimation to through-wall imaging and ground penetrating radar.**

***Keywords*— computational imaging, compressive sensing, direction of arrival estimation, microwave imaging, metasurface.**

Self-Organized Photonic Metasurface Synthesis Inspired by Morphogenesis

Thomas Fromentèze[1,*], Marco Gandolfi[2], Andrea Locatelli[2], Costantino De Angelis[2], Emebet Woldu Hadgu[1], Raphaël Pestourie[3]

[1]University of Limoges, XLIM, UMR 7252, F-87000 Limoges, France
[2]Dipartimento di Ingegneria dell'Informazione, Università degli Studi di Brescia and CNR-INO, Via Branze 38, 25123 Brescia, Italy
[3]Georgia Institute of Technology, Atlanta, USA
*Corresponding author: thomas.fromenteze@unilim.fr

***Abstract*—We introduce a bio-inspired generative model that serves as a parametrization of photonic metasurfaces. This approach, inspired by morphogenesis, has proved successful in the microwave range. This framework utilizes reaction-diffusion patterns to self-organize dielectric structures. We demonstrate a functional 50 µm silicon lens operating at λ = 1550 nm.**

***Keywords*— metasurfaces, self-organization, reaction-diffusion.**

I. Introduction

Metasurfaces have emerged as a powerful paradigm for wavefront manipulation, yet their synthesis relies on the juxtaposition of discrete unit cells. This method often fails at synthesizing metasurfaces with large phase gradients. Our decentralized synthesis framework inspired by morphogenesis addresses this limitation [1], [2], generating structures that adapt to the constraints of photonic metasurface fabrication through the use of non-uniform unit cells.

II. Generative Model and Mapping

Our approach utilizes the Gray-Scott reaction-diffusion model, which mimics chemical pattern formation. The evolution of species u and v is governed by:

$$\frac{\partial u}{\partial t} = D_u(x)\nabla^2 u - uv^2 + F(1-u) \quad (1)$$

$$\frac{\partial v}{\partial t} = D_v(x)\nabla^2 v + uv^2 - (F+k)v \quad (2)$$

with feed rate $F = 0.04$, kill rate $k = 0.0605$, and a fixed diffusion ratio $D_v = 0.5\,D_u$, parameters chosen to support pattern self-organization. The diffusion coefficient $D_u(x)$ acts as the local control parameter for the pattern's period, while a binarization threshold σ applied to the concentration of v adjusts the fill factor (silicon/air ratio). To link geometries to electromagnetic responses, we compute the transmission of a database of periodic supercells. A path is identified in the (D_u, σ) generative space that maximizes transmission while providing 2π phase coverage. This defines a mapping function Φ encompassing the complex relationship between the generative parameters and the electromagnetic response.

III. Lens Synthesis and Results

We synthesize a metalens with a holographic approach, combining an incident plane wave and a spherical wave to maximize constructive interference at a focal point. The target local transmission is translated into a spatial distribution of generative parameters via the inverse mapping Φ^{-1}, allowing for the growth of a self-organized structure following local rules in a few seconds (Fig. 1).

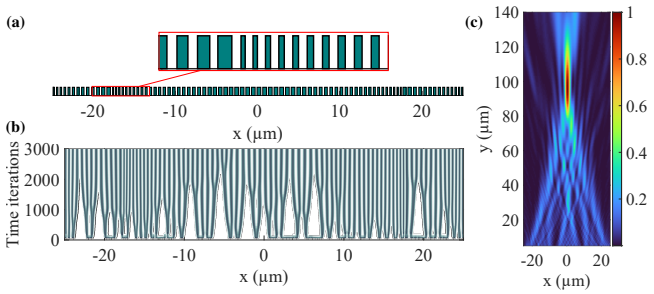

Fig. 1. (a) Generated metalens. (b) Generative growth of the lens where Φ^{-1} translates the target transmission into growth dynamics $D_u(x)$. High concentration of v results in pillar formation, later binarized by $\sigma(x)$. (c) Simulated electromagnetic field intensity showing lens behavior.

The resulting metasurface and focused field (Fig. 1) demonstrate the capability of the proposed method. The structure evolves seamlessly, avoiding the abrupt discontinuities inherent to unit-cell discretization. Full-wave simulations confirm the formation of a sharp focal spot, validating that the bio-inspired approach successfully meets the trade-off between scattering efficiency and phase control in a non-uniform, self-organized metalens. This method bridges local generative computations to large-scale structures. Future works will extend this method to the synthesis of two-dimensional, polarization-constrained metalenses.

References

[1] A. M. Turing, "The chemical basis of morphogenesis," *Philos. Trans. R. Soc. Lond. B*, vol. 237, no. 641, pp. 37–72, 1952.
[2] T. Fromenteze, O. Yurduseven, C. Uche, E. Arnaud, D. R. Smith, and C. Decroze, "Morphogenetic metasurfaces: Unlocking the potential of Turing patterns," *Nat. Commun.*, vol. 14, no. 1, p. 6249, 2023.

Physical Neural Networks for Wireless Communications

Marco Di Renzo

Université Paris-Saclay, CNRS, CentraleSupélec, Laboratoire des Signaux et Systèmes, 3 Rue Joliot-Curie, 91192 Gif-sur-Yvette, France
King's College London, Department of Engineering - Centre for Telecommun. Research, WC2R 2LS London, United Kingdom
*Corresponding author: marco.direnzo@centralesupelec.fr, marco.di_renzo@kcl.ac.uk

***Abstract*— In this talk, we introduce wave-domain processing enabled by reconfigurable metasurfaces with the aim to redesign the physical layer of wireless communications. We will discuss the motivations, enabling technologies and our recent contributions in this emerging field of research.**

***Keywords*—Metasurface, wireless communications.**

I. Introduction

We introduce wave-domain processing enabled by reconfigurable metasurfaces with the aim of redesigning the physical layer of wireless communications. We will discuss motivations, enabling technologies and our recent contributions in this emerging field of research, with a focus on the emerging concepts of physical neural networks and stacked intelligent metasurfaces.

Acknowledgment

The work of M. Di Renzo was supported in part by the European Union through the Horizon Europe project COVER under grant agreement number 101086228, the Horizon Europe project UNITE under grant agreement number 101129618, the Horizon Europe project INSTINCT under grant agreement number 101139161, and the Horizon Europe project TWIN6G under grant agreement number 101182794, as well as by the Agence Nationale de la Recherche (ANR) through the France 2030 project ANR-PEPR Networks of the Future under grant agreements NF-PERSEUS 22-PEFT-004, NF-YACARI 22-PEFT-0005, NF-SYSTERA 22-PEFT-0006, NF-Founds 22-PEFT-0010, and by the CHIST-ERA project PASSIONATE under grant agreements CHIST-ERA-22-WAI-04 and ANR-23-CHR4-0003-01. Also, the work of M. Di Renzo was supported in part by the Engineering and Physical Sciences Research Council (EPSRC), part of UK Research and Innovation, and the UK Department of Science, Innovation and Technology through the CHEDDAR Telecom Hub under grant EP/X040518/1 and grant EP/Y037421/1, and through the HASC Telecom Hub under grant EP/X040569/1.

Analysis and Simulation of Intrinsic Response Time of Time-Varying Metasurfaces

Sheng Lei[1], Alex M. H. Wong[1,2,*]

[1]Department of Electrical Engineering, City University of Hong Kong, Hong Kong, China
[2]State Key Laboratory of Terahertz and Millimeter Waves, City University of Hong Kong, Hong Kong, China
*Corresponding author: alex.mh.wong@cityu.edu.hk

***Abstract*— We investigate the causes of time delays for varactor-driven meta-atoms. Particularly, through theory, simulation and experiment, we study the electromagnetic response time of the meta-atom given fast switching signals. Our results pave way to designing fast time-varying metasurfaces whose modulation approaches or exceeds the frequency of the illumination wave.**

***Keywords*—Intrinsic response time, time-varying metasurface, frequency conversion**

I. Introduction

Time-varying metasurfaces are two-dimensional artificial active structures whose electromagnetic properties can be modulated in real time by external signals. It exhibits extraordinary capabilities to freely control electromagnetic waves in both the spatial and temporal domains, with a low profile and high efficiency [1]. Over the past few years, time-varying metasurfaces have been applied to harmonic wave control [2], time-varying orbital angular momentum (OAM) wave generation [3], nonreciprocal communication [4], and Doppler cloaking [5], demonstrating their potential. However, the performance of existing time-varying metasurfaces is constrained by their modulation speeds, which are typically much slower than their design frequencies, resulting in a narrow harmonic frequency conversion range, limited nonreciprocal performance, and slowly varying OAM waves. For a realistic meta-atom, there are three main limitations on its modulation speed, including the control network, the switching element, and the electromagnetic response of its structure. While the former two limitations can be overcome with advanced electronics and component technology, the intrinsic response time remains a fundamental limitation on meta-atom design. To overcome this constraint, we conduct a comprehensive investigation of the intrinsic response time and its influence on the performance of time-varying metasurfaces. In this work, we investigate the response speed of time-varying meta-atoms inside a rectangular waveguide. An equivalent circuit analysis is performed to find the cause of the intrinsic response time, which is further validated by finite-difference time-domain (FDTD) simulations. To visualize the effect of the intrinsic response time on the performance of the time-varying metasurface, frequency conversion experiments are conducted using the fabricated waveguide model.

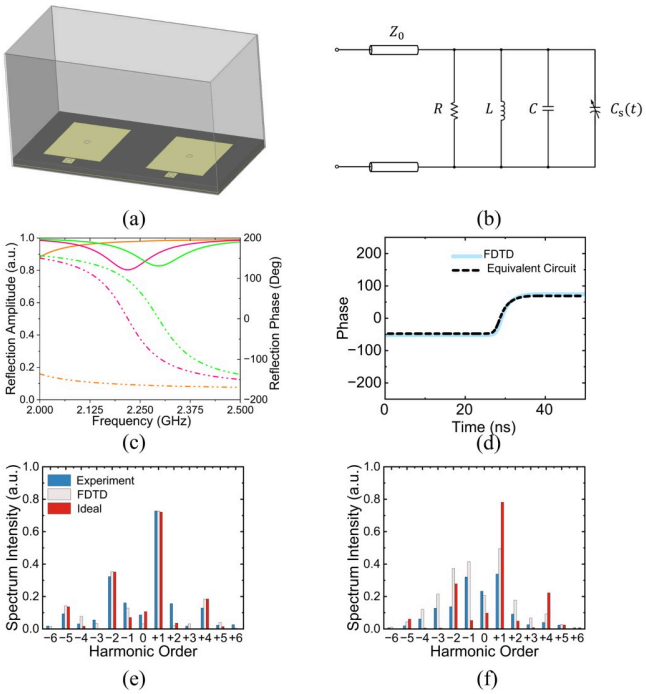

Fig. 1 (a) Schematic of the proposed waveguide model associated with time-varying meta-atoms. (b) Equivalent circuit of the waveguide model. (c) Reflection coefficients of the waveguide model under different reverse-bias voltages. (d) The equivalent circuit analysis and FDTD simulation results for the intrinsic phase response time. (e-f) The reflected wave spectrum from the FDTD simulation, experimental results, and the ideal case with modulation speeds of (e) 10 MHz and (f) 120 MHz.

II. Methods

Fig. 1(a) shows the structure of the waveguide model. The meta-atom comprises a radiation patch and a varactor diode for tunability. The wave propagating along the waveguide will be reflected and modulated by the meta-atom. Therefore, as shown in Fig. 1(b), the equivalent circuit of the waveguide structure can be modelled as a terminated transmission line. The meta-atoms studied here is similar to the type we used in two previous works [3, 6]. can be divided into two parts. The radiation patch can be modelled as a parallel RLC circuit, and the varactor can be regarded as a time-varying capacitance in parallel with the

radiation patch. By changing the reverse-bias voltage applied to the varactor, the capacitance of the varactor can be changed accordingly, which further leads to the variation of the meta-atom's property. As shown in Fig. 1(c), the structure has three states whose reflection coefficients have nearly unit amplitudes and a 120° phase difference. By analyzing the voltage and circuit relationship of the equivalent circuit model, we find that the response times required by the meta-atom to change within these three states are limited by a coefficient

$$\tau = -\frac{2RZ_0(C+C_s)}{R+Z_0} \approx -2Z_0(C+C_s) \quad (1)$$

Therefore, it can be clearly observed that the intrinsic response time of this meta-atom is induced by charging the equivalent capacitor. Furthermore, to validate the equivalent-circuit analysis results, we also conduct full-wave FDTD simulations of the time-varying meta-atom. The varactors are modelled as time-varying lumped elements whose capacitance is updated at each time step based on the applied modulation signal. As shown in Fig. 1(d), it is obvious that the phase of the reflected wave requires some time to gradually change from the previous state to the target state, even with an ideal modulation signal. Additionally, the FDTD simulation results agree well with the equivalent circuit analysis results.

III. Results and Discussion

Finally, we fabricate the waveguide model and perform several frequency-conversion experiments to demonstrate the limitation imposed by the intrinsic response time. The modulation signal is provided by an arbitrary waveform generator, which is a periodic signal that equally contains the aforementioned three states. A spectrum analyzer is used to capture and analyze the reflected wave from the time-varying meta-atoms at different modulation frequencies. As shown in Fig. 1(e), at a low modulation speed, the response time is negligible. Therefore, both the simulation and experimental results exhibit a frequency spectrum similar to that of the ideal case, in which we assume the meta-atom's property changes instantaneously with the modulation signal, so the +1st and -2nd harmonics dominate the spectrum. However, as shown in Fig. 1(f), when the modulation speed is sufficiently high, the intrinsic response time will destroy the modulation, resulting in a nonideal frequency spectrum. Therefore, to further improve performance and overcome the limitations of time-varying metasurfaces, the intrinsic response time should be considered a significant parameter in the design of time-varying meta-atoms, which can be analyzed and simulated using the aforementioned methods.

IV. Conclusion

In this work, we have proposed an equivalent circuit analysis method and an FDTD simulation method to determine the intrinsic response time of meta-atoms to transition between states. Using a waveguide model, we experimentally demonstrated the existence of the intrinsic response time and its limitation on the time-varying metasurface's performance via frequency conversion experiments. The proposed method can simulate the intrinsic response time of an arbitrary meta-atom, enabling the design of time-varying metasurfaces with a short response time and a fast modulation speed. Besides, our method enables ultrafast modulations that may exceed the incident frequency, such as parametric amplification and oscillation, providing a powerful tool to explore the limits and expand the potential of time-varying metasurfaces.

Acknowledgments

This work was supported by the Research Grants Council of the Hong Kong SAR, China, under Project CityU 11215125.

References

[1] A. M. Shaltout, V. M. Shalaev, and M. L. Brongersma, "Spatiotemporal light control with active metasurfaces," Science, vol. 364, no. 6441, p. eaat3100, May 2019.

[2] L. Zhang et al., "Space-time-coding digital metasurfaces," Nat. Commun., vol. 9, no. 1, p. 4334, Oct. 2018.

[3] J. Zhang, P. Li, R. C. C. Cheung, A. M. H. Wong, and J. Li, "Generation of time-varying orbital angular momentum beams with space-time-coding digital metasurface," Adv. Photonics, vol. 5, no. 03, Apr. 2023.

[4] L. Zhang et al., "Breaking reciprocity with space-time-coding digital metasurfaces," Adv. Mater., vol. 31, no. 41, p. 1904069, Oct. 2019.

[5] B. Liu, Y. He, S.-W. Wong, and Y. Li, "Experimental demonstration of a time-domain digital-coding metasurface for a Doppler cloak," Opt. Express, vol. 29, no. 2, p. 740, Jan. 2021.

[6] J. Zhang et al., "Experiment-based deep learning approach for power allocation with a programmable metasurface," APL Mach. Learn., vol. 1, no. 4, 046122, Dec. 2023.

Transformer-based Neural Network Enabled Subpixel-Resolution in Wide-Field Meta-Microscope

Shanshan Hu, Tao Li*

School of Physics, College of Engineering and Applied Sciences, Nanjing University, China
*Corresponding author: taoli@nju.edu.cn

***Abstract*— We propose and experimentally demonstrate a synergistic computational imaging framework that integrates a compact metalens microscope with a transformer-based neural network, which enables wide-field and subpixel resolution imaging without added optical complexity, illustrating a scalable and cost-effective approach to miniaturized and intelligent microscopy.**

***Keywords*— metalens, deep learning, microscope, subpixel-resolution, wide-field imaging.**

I. Introduction

Metalenses have revolutionized ultracompact imaging systems, benefiting from their ultra-thin, lightweight, and flat design that facilitates assembly onto image sensors. While the integration of metalens and sensor eliminents the bulky optical elements, the resolution remains limited by pixel-induced undersampling, and a fundamental trade-off exists between resolution and field of view (FOV). These challenges are especially pronounced in microscopy, motivating the development of innovative strategies for compact microscopy systems.

II. Methods

We have proposed a computational imaging strategy that utilizes a unit-magnification meta-microscope equipped with a transformer-based neural network, overcoming the inherent sensor pixel size limitation through data-driven reconstruction. To bridge the gap between simulation and experimental implementation, the first experimental dataset of metalens-acquired thyroid pathological sections images was constructed. The Hybrid Attention Transformer model was employed to reconstruct high-resolution images by learning the mapping from unit-magnification and three-fold magnification imaging. After training, the model demonstrates computational subpixel-resolution reconstruction, producing high-fidelity, high-resolution images from a single-frame input.

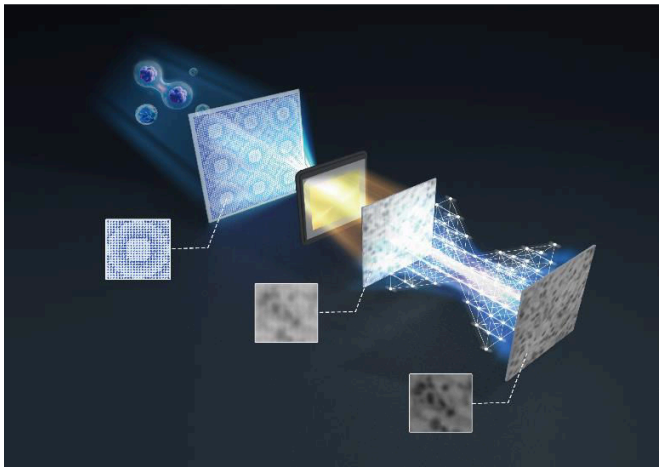

Fig. 1 Schematic diagram of the proposed intelligent meta-microscope

III. Results and Discussion

The trained model enables rapid (~0.2s for 110 μm × 110 μm FOV), high-fidelity (structural similarity up to 91%) reconstruction from single-frame inputs, achieving 3× spatial sampling density and computational subpixel-resolution (close to 0.87 μm, pixel size is 1.67 μm). A cross-tissue generalization experiment also showed that the model maintained good performance on other tissues with similar morphology.

We further incorporate the metalens array-based integrated microscope with the trained model, achieving wide-field (4 mm × 6 mm) and high-resolution (comparable with the Olympus 10×/0.25NA objective) imaging, providing a FOV approximately 14.5 times that of the Olympus objective with similar resolution.

IV. Conclusion

We have demonstrated a synergistic computational imaging scheme that provides wide-field, subpixel resolution imaging without added optical complexity via a metalens-transformer design, demonstrate experimentally validated performance on real thyroid pathology sections with reasonable cross-tissue generalizability, and feature a compact, low-cost configuration suitable for portable diagnostic applications.

ACKNOWLEDGMENTS

This work was supported by the National Key Research and Development Program of China, the National Natural Science Foundation of China, and Dengfeng Project B of Nanjing University. The authors acknowledge the micro-fabrication center of the National Laboratory of Solid State Microstructures (NLSSM) for technique support.

REFERENCES

[1] Shan, Hu. et al, "Transformer-based neural network enabled subpixel-resolution in wide-field meta-microscope," PhotoniX, vol. 6, 52, 2025.

A Machine-Learning-Enabled Metasurface Adapting to the Environment

Thijs A. van Rossum,[1,*] Thomas Koschny,[2] and Philippe Tassin[1]

[1]Department of Physics, Chalmers University of Technology, SE-41296 Göteborg, Sweden
[2]Ames Laboratory-U.S. DOE, and Department of Physics and Astronomy,
Iowa State University, Ames, Iowa 50011, USA
*Corresponding author: thijs.vanrossum@chalmers.se

***Abstract*—We propose a machine-learning-based adaptive algorithm for tunable metasurfaces in a changing environment. We use a neural network processing information from the metasurface to predict the environment, followed by another neural network to reconfigure it. We demonstrate this for a metasurface adapting to a beam with unkown angle of incidence.**

***Keywords*— metamaterials, machine learning, adaptive metasurfaces.**

Tunable metasurfaces are ultrathin engineered surfaces made of subwavelength ”meta-atoms” that can precisely control light (or other waves) in terms of phase, amplitude, polarization, and direction [1]. By incorporating active materials or external controls such as electrical bias, heat, mechanical strain, or optical pumping, they enable tunable and reconfigurable functions such as beam steering, adaptive lenses, and programmable holography [1–3]. However, when a metasurface has to adapt to the environment, one needs a way to reconfigure the tunable elements in response to a changing environment. This not only requires calculating the state of the environment, but also an inverse design step during every update.

Inverse design of a metasurface is a rather slow process that normally requires multiple full-wave simulations. Recently, machine-learning has been used to achieve inverse design of metasurfaces [4]. Although it requires time to generate training data from simulations, once trained, neural networks can generate metasurface designs fast, with typical inference times of the order of milliseconds.

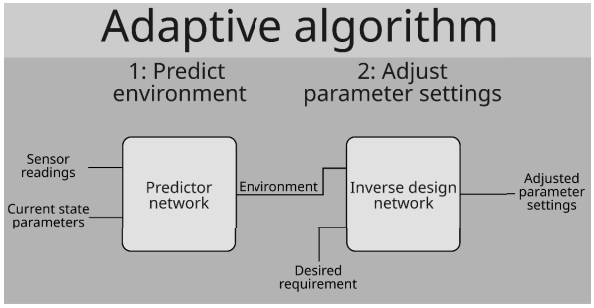

Fig. 1: Overview of the adaptive algorithm. The first step of the algorithm is a *predictor network* that predicts the environment, which is subsequently used in the second step by an *inverse-design network* in order to adjust the tunable element in order to correctly adapt to the environment.

In this contribution, we will present a machine-learning-based algorithm to adapt a tunable metasurface to the environment. Such an algorithm needs two components: a detection component, which takes physical quantities in the metasurface as input (e.g., a current in a capacitor) and uses that information to predict the environment, and an action component, which performs an inverse design of the metasurface under the condition of the current environment.

To achieve this, we implement the adaptive algorithm using two neural networks [4], as illustrated in Fig. 1. First, the detection step is performed by a predictor network that predicts the state of the environment from the current state of the metasurface, obtained from sensor readings from the metasurface (e.g., current through a capacitor) and the settings the tunable parameters. Second, the action step is performed by an inverse design network that does inverse design, i.e., calculates the tunable elements’ values (e.g., capacitances) from a desired output state (e.g., reflectance), but with the predicted environment as an extension of its input.

The neural networks are trained on a data set that is constructed from full-wave simulations of a meta-atom proposed in Ref. [3]. These simulations are carried out for random input values of the angle of incidence and the capacitor values. This allows us to train a forward network that maps the capacitances of the metasurface onto the reflection phase. Constructing both the predictor and inverse design networks are two ill-posed problems [4], which, however, can be solved using a so-called tandem network. We use our pre-trained forward network and freeze it, meaning we no longer change its weights. The predictor and inverse design networks are then connected separately to the input of a forward network, where the objective function of the forward model is to reproduce the original inputs to the respective neural network. After training, the forward networks can be removed.

Finally, we show the performance of the entire adaptive algorithm in Fig. 1 by running an experiment where we randomly change the angle of incidence of the incident beam and let the adaptive algorithm adjust the tuneable parameter on the meta-atom, such that the reflection phase stays constant.

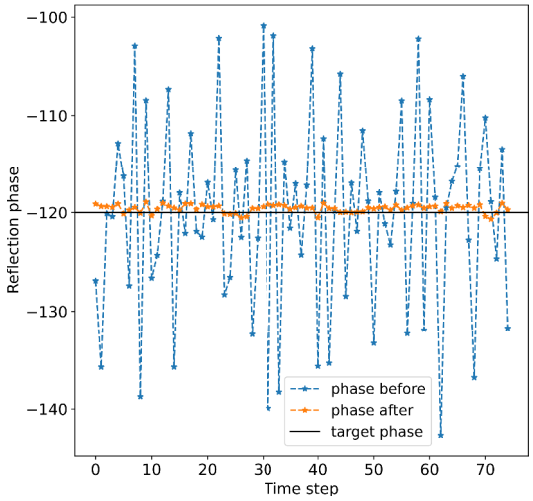

Fig. 2: Results from the experiment, from both before and after the correction from the adaptive algorithm. The adaptive metasurface is able to adjust its tunable parameter to maintain a constant -120 degrees phase output for 75 random angles of incidence

The result is shown in Fig. 2. In every time step, the angle of incidence is changed between between 20 and 40 degrees. This causes the reflection phase to alter significantly (blue line). However, after correction of the capacitances by the adaptive algorithm, the reflection phase is almost constant around our target phase (orange line). The inference times of the adaptive algorithm are of the order of milliseconds, which allows for an update frequency of the order of kilohertz, which makes it useful for application in communications systems, holograms, and other optical applications where the system needs to be corrected for changes in the environment.

Our work paves the way for adaptive metasurfaces that change in response of environments of increasing complexity. This is due to the flexibility neural network design and the rapid detection of the environment and the rapid inverse design by machine learning.

Acknowledgments

We acknowledge financial support from Chalmers' area of advance Nano and from the Swedish Research Council under Grant No. 2020-05284. Work at Ames National Laboratory was supported by the Department of Energy (Basic Energy Sciences, Division of Materials Sciences and Engineering) under Contract No. DE-AC02-07CH11358. The training data generation and neural network training were performed on resources provided by the Swedish National Infrastructure for Computing (NAISS), at the Chalmers/C3SE and KTH/PDC sites, partially funded by the Swedish Research Council under Grant No. 2022-06725.

References

[1] O. A. Abdelraouf, Z. Wang, H. Liu, Z. Dong, Q. Wang, M. Ye, X. R. Wang, Q. J. Wang, and H. Liu, "Recent Advances in Tunable Metasurfaces: Materials, Design, and Applications," *ACS Nano*, vol. 16, pp. 13 339–13 369, 2022.

[2] L. Li, T. Jun Cui, W. Ji, S. Liu, J. Ding, X. Wan, Y. Bo Li, M. Jiang, C.-W. Qiu, and S. Zhang, "Electromagnetic reprogrammable coding-metasurface holograms," *Nature Communications 2017 8:1*, vol. 8, p. 197, 2017.

[3] F. Liu, O. Tsilipakos, A. Pitilakis, A. C. Tasolamprou, M. S. Mirmoosa, N. V. Kantartzis, D.-H. Kwon, J. Georgiou, K. Kossifos, M. A. Antoniades, M. Kafesaki, C. M. Soukoulis, and S. A. Tretyakov, "Intelligent Metasurfaces with Continuously Tunable Local Surface Impedance for Multiple Reconfigurable Functions," *Physical Review Applied*, vol. 11, p. 044024, 2019.

[4] A. Khaireh-Walieh, D. Langevin, P. Bennet, O. Teytaud, A. Moreau, and P. R. Wiecha, "A newcomer's guide to deep learning for inverse design in nano-photonics," *Nanophotonics*, vol. 12, pp. 4387–4414, 2023.

SPECIAL SESSION 17

Topological Insulator Metamaterials

9 contributions · pp. 1101–1110

Attosecond Extreme-Ultraviolet Skyrmion Pulses from High Harmonic Generation

David Marco[1,2,3,*], Luis Plaja[1,2], Carlos Hernández-García[1,2]

[1]Grupo de Investigación en Aplicaciones del Láser y Fotónica, Departamento de Física Aplicada, Universidad de Salamanca, E-37008 Salamanca, Spain
[2]Unidad de Excelencia en Luz y Materia Estructuradas (LUMES), Universidad de Salamanca, Spain
[3]Instituto de Bioingeniería, Universidad Miguel Hernández de Elche, 03202 Elche, Spain
*Corresponding author: davidmarco@usal.es

***Abstract*—We demonstrate the generation of attosecond skyrmion pulse trains via high harmonic generation driven by an infrared femtosecond vector beam carrying fractional orbital angular momentum. Consecutive far-field harmonics around 70 eV exhibit skyrmion polarization textures whose coherent superposition yields ∼500-attosecond pulses, enabling new avenues for ultrafast control, imaging, and spectroscopy.**

***Keywords*— skyrmion, structured light, attosecond science**

Skyrmions are topological field distributions in which a spatial domain maps onto a complete spherical parameter space. Such configurations have been observed across a broad range of physical platforms, including magnetic systems and structured optical fields [1]. Optical skyrmions emerge in beams whose transverse profiles contain the full set of paraxial polarization states. These fields therefore map a planar region onto the entire Poincaré sphere, where each point represents a distinct polarization state. Their potential impact is currently being investigated in complex media, topological materials, and advanced imaging schemes [1]. However, the generation of skyrmion pulses in the attosecond regime has not yet been demonstrated, with previous realizations restricted to continuous-wave illumination or long optical pulses.

The generation of attosecond pulses has been established for over two decades through high harmonic generation (HHG) in gases, where an intense infrared (IR) laser drives the emission of a plateau of high-frequency phase-locked harmonics with comparable amplitudes. The coherent superposition of selected harmonics yields attosecond pulse trains. In contrast, spatial structuring of high-energy radiation has only become feasible recently, owing to the inefficiency of conventional optical elements at extreme energies. Most approaches therefore focus on engineering the spatial profile of the driver to control the structure of the generated harmonics, enabling extreme-ultraviolet (EUV) structured beams such as attosecond vortices [2] or EUV vector beams [3].

Designing a driving field capable of producing a desired topological structure in the attosecond regime is nontrivial. In particular, HHG efficiency rapidly deteriorates with increasing polarization ellipticity, preventing a straightforward translation of optical skyrmions into the harmonic spectrum. A scheme based on a bichromatic structured driver has been proposed to induce skyrmion patterns at the gas-jet plane, where the skyrmion topology varies across consecutive harmonics [4]. Consequently, this approach does not deliver a phase-locked harmonic comb with similar skyrmion textures, which is a prerequisite for synthesizing attosecond pulses with a temporally robust skyrmion structure. Here, we show that HHG driven by a tailored linearly polarized vector beam produces a phase-locked plateau of consecutive harmonics that exhibit nearly identical skyrmion textures in the far field. Their coherent addition therefore results in attosecond skyrmion pulse trains.

Figure 1(a) illustrates the proposed scheme, where a linearly polarized IR vector driving beam interacts with a gas jet to produce an attosecond skyrmion pulse train. The local polarization state is encoded using a color representation corresponding to points on the Poincaré sphere (Fig. 1(b)). The left- and right-circular polarization (LCP and RCP) driver components carry fractional orbital angular momenta $\ell_{l,r} = -65/132$ and $67/132$, respectively, as depicted in Fig. 1(a). The choice of these parameters follows from a simplified model (see Ref. [5] for more details). The driver can be realized experimentally using metasurfaces or spatial light modulators.

We use the structured driving field in numerical HHG simulations in an argon gas jet. Our model combines a single-atom quantum response, within the strong-field approximation, with an electromagnetic propagation scheme that accounts for macroscopic phase matching and yields the far-field harmonic distribution. The driving pulse has a central wavelength of 1.2 μm, a full width at half maximum (FWHM) duration of 11.5 fs, and a peak intensity of 1.19×10^{14} W/cm^2. By applying realistic Al and Zr filters with thicknesses of 0.2 μm and 0.3 μm, respectively, we isolate five consecutive harmonics around 70 eV. The unfiltered spectrum and the selected window (purple shaded region) are shown in Fig. 2(a). The far-field spatial profiles of these five harmonics exhibit nearly identical skyrmion textures within an annular region of 0.19 mrad radius. The far-field intensity and polarization distribution for the central harmonic are displayed in Fig. 2(b).

The coherent superposition of the harmonics produces an attosecond pulse train with individual pulse durations of approximately 500 attoseconds (FWHM). The Skyrme number N_S characterizes the topology of the skyrmion by quantifying how many times the polarization texture maps the Poincaré

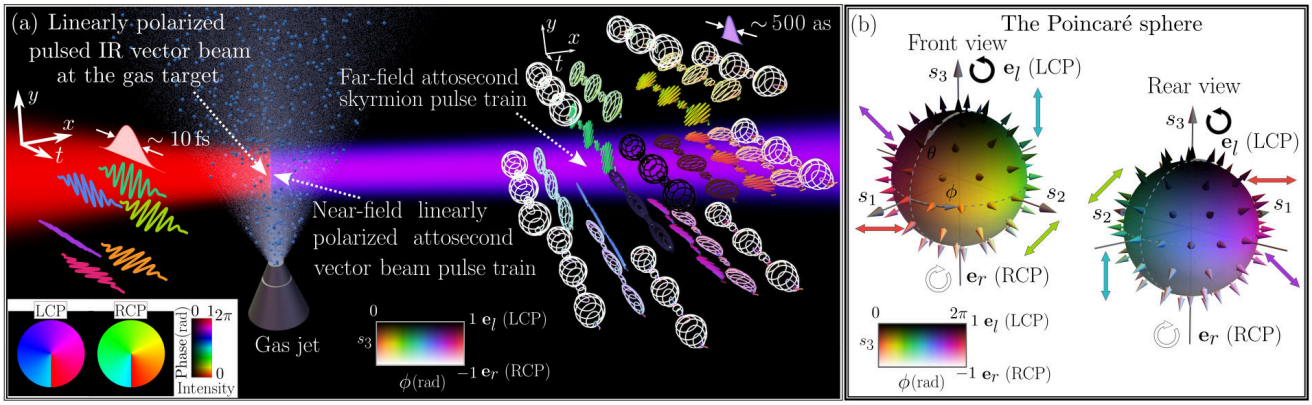

Fig. 1. (a) Illustration of attosecond EUV skyrmion pulse train generation by HHG driven by a linearly polarized femtosecond vector beam. The local polarization state of both the driver and the emitted attosecond field is represented by a color code corresponding to points on the Poincaré sphere. The driving beam consists of left- and right-circular polarization (LCP and RCP, respectively) components carrying fractional orbital angular momentum. (b) Representation of paraxial polarization states on the Poincaré sphere, where each polarization ellipse maps to a single point. The color map is defined by the azimuthal angle ϕ (twice the ellipse orientation) and the s_3 coordinate, which encodes ellipticity and handedness.

sphere [1]. Evaluated at different instants during the central pulse and within the same 0.19 mrad contour (Fig. 2(c)), N_S remains remarkably stable in time, reaching a maximum value of $N_S = 1.000$ with fluctuations limited to $\Delta N_S = 0.009$. Figure 2(d) displays the real electric-field distribution of the most intense pulse in the synthesized train, revealing a well-defined skyrmion texture that persists in time.

To sum up, we presented an experimentally viable route for generating attosecond skyrmion pulses whose topological properties are preserved in time. Such pulses open new pathways for encoding topological information into photoelectron angular and spin distributions [6], for simultaneously probing structural and anisotropic material responses in high-resolution EUV imaging [7], and for enabling ultrafast probing of magnetic helicoidal dichroism [8].

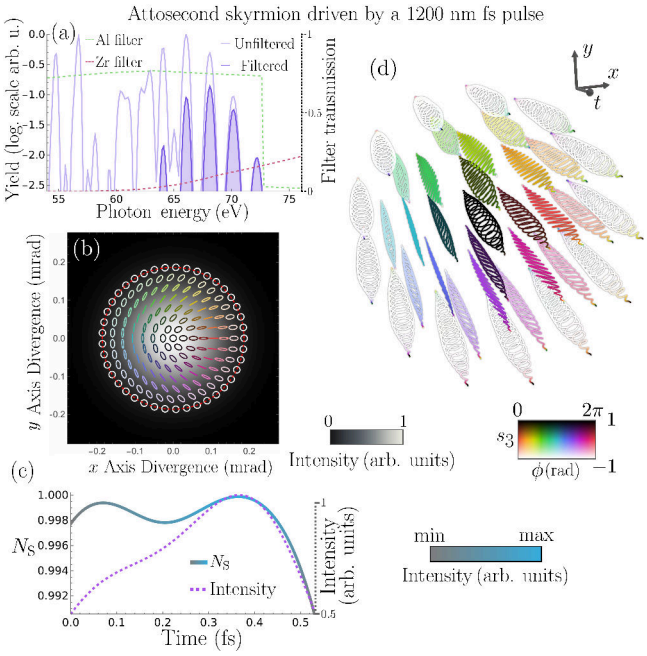

Fig. 2. Attosecond EUV skyrmion pulse train driven by a 1.2 μm driving field. (a) High-harmonic spectrum, with the purple shaded area indicating the spectral window selected by Al and Zr filters. (b) Far-field spatial profiles of intensity and polarization for the central harmonic. (c) Time-dependent evolution of the Skyrme number N_S and the field intensity evaluated inside a 0.19 mrad aperture over the FWHM temporal window of the central pulses. (d) Local temporal evolution of the real electric field corresponding to the central pulse in the train.

REFERENCES

[1] Y. Shen, Q. Zhang, P. Shi, L. Du, X. Yuan, and A. V. Zayats, "Optical skyrmions and other topological quasiparticles of light," *Nature Photonics*, vol. 18, no. 1, pp. 15–25, 2024.

[2] A. de las Heras, D. Schmidt, J. San Román, J. Serrano, J. Barolak, B. Ivanic, C. Clarke, N. Westlake, D. E. Adams, L. Plaja *et al.*, "Attosecond vortex pulse trains," *Optica*, vol. 11, no. 8, pp. 1085–1093, 2024.

[3] C. Hernández-García, A. Turpin, J. S. Román, A. Picón, R. Drevinskas, A. Cerkauskaite, P. G. Kazansky, C. G. Durfee, and Íñigo J. Sola, "Extreme ultraviolet vector beams driven by infrared lasers," *Optica*, vol. 4, no. 5, pp. 520–526, May 2017.

[4] Y. Fang and Y. Liu, "Generation and control of extreme ultraviolet free-space optical skyrmions with high harmonic generation," *Advanced Photonics Nexus*, vol. 2, no. 4, pp. 046 009–046 009, 2023.

[5] D. Marco, L. Plaja, and C. Hernández-García, "Attosecond light skyrmion pulses via high harmonic generation," *arXiv preprint arXiv:2509.19113*, 2025.

[6] D. Younis, D. F. Gordon, and B. Hafizi, "Spin-polarization control of photoelectrons using poincaré fields," *Physical Review Letters*, vol. 133, no. 4, p. 043201, 2024.

[7] M. Pancaldi, F. Guzzi, C. S. Bevis, M. Manfredda, J. Barolak, S. Bonetti, I. Bykova, D. D. Angelis, G. D. Ninno, M. Fanciulli, L. Novinec, E. Pedersoli, A. Ravindran, B. Rösner, C. David, T. Ruchon, A. Simoncig, M. Zangrando, D. E. Adams, P. Vavassori, M. Sacchi, G. Kourousias, G. F. Mancini, and F. Capotondi, "High-resolution ptychographic imaging at a seeded free-electron laser source using oam beams," *Optica*, vol. 11, no. 3, pp. 403–411, Mar 2024.

[8] M. Fanciulli, M. Pancaldi, E. Pedersoli, M. Vimal, D. Bresteau, M. Luttmann, D. De Angelis, P. c. v. R. Ribič, B. Rösner, C. David, C. Spezzani, M. Manfredda, R. Sousa, I.-L. Prejbeanu, L. Vila, B. Dieny, G. De Ninno, F. Capotondi, M. Sacchi, and T. Ruchon, "Observation of magnetic helicoidal dichroism with extreme ultraviolet light vortices," *Phys. Rev. Lett.*, vol. 128, p. 077401, Feb 2022.

A spectral localizer approach for Floquet insulators

Stephan Wong [1], Alexander Cerjan[1], Justin T. Cole [2,*]

[1]Center for Integrated Nanotechnologies, Sandia National Laboratories, USA
[2]Department of Mathematics, University of Colorado Colorado Springs, USA
*Corresponding author: jcole13@uccs.edu

***Abstract*—A spectral localizer methodology for diagnosing topology in Floquet insulators will be presented. This approach leverages local topological markers to probe topology in periodically driven lattice systems without time-reversal symmetry. Quantitative bounds on the range of topological protection can be proved.**

***Keywords*— Floquet insulator, local Chern number**

I. Summary

A well-known challenge in periodically driven (Floquet) systems is the characterization of Chern topology and its relationship to topologically protected chiral states. In the anomalous insulator regime, the presence of gapless edge states in both the zero and π gaps results in trivial Chern numbers, defying the typical intuition of Chern insulators.

In [1] we developed a spectral localizer technique for diagnosing topology in periodically driven waveguide systems. A local Chern number, defined in terms of the Floquet Hamiltonian, directly characterizes the presence of chiral edge states without having to resort to a bulk-edge correspondence. To test the method, we apply it to the Floquet tight-binding model given in [2]. The Floquet localizer is able to correctly identify space-energy values that support topologically protected states.

An additional benefit of the spectral localizer framework is the ability to derive quantitative bounds on topological states. That is, when the instantaneous Hamiltonian is perturbed, a sufficient condition for guaranteeing the topological state is derived. Said differently, how much disorder can be tolerated before we lose our topological state? A set of bounds in terms of the Floquet Hamiltonian and the instantaneous Hamiltonian are obtained.

References

[1] S. Wong, A. Cerjan, and J. T. Cole, "Quantitative measure of topological protection in Floquet systems through the spectral localizer," *Phs. Rev. B*, vol. 112, 224306, 2025.

[2] M. S. Rudner, N. H. Lindner, E. Berg, and M. Levin, "Anomalous edge states and the bulk-edge correspondence for periodically driven two-dimensional systems," *Phs. Rev. X*, vol. 3, 031005, 2013.

CVD-Synthesized $PtTe_2$ Nanoribbon Arrays for Tunable Mid-IR Polarized Photocurrent via SPP Control

Christian Martella[1,*], Alessandro Molle[1]

[1] CNR-IMM, Unit of Agrate Brianza, Via C. Olivetti 2, Agrate Brianza 20864, Italy

*Corresponding author: christian.martella@cnr.it

***Abstract*— Here, we investigate experimental parameters for synthesizing engineered $PtTe_2$ microribbon arrays, enabling precise control of surface plasmon polariton excitation. This design selectively enhances mid-infrared polarization-sensitive photocurrent, with spectral tunability via ribbon array geometry**

***Keywords*— Dirac semimetal, MIR, Surface Plasmon Polaritons, $PtTe_2$, topological Schottky junction.**

I. Introduction

Platinum ditelluride ($PtTe_2$) is a type-II topological Dirac semimetal allowing for broadband optical absorption within its tilted Dirac cones. Given its robust topological nature persisting up to room temperature, $PtTe_2$ represents an ideal candidate for uncooled Mid-infrared (MIR) photodetection.[1] Moreover, the high carrier mobility and low scattering rate of Dirac semimetal results in a very low loss for surface plasmon polaritons (SPPs) propagation in these materials in comparison to the normal metals and make them suitable for application in optical devices. [2]

II. Methods

Large area $PtTe_2$ microribbons array are synthetized in a two-step process consisting of sputtering deposition of few nm thick Pt microribbons (typically in a range of 4 – 8 nm) and subsequent tellurization at 400 – 450 °C in a tubular furnace. [3] By combining the Pt deposition with maskless optical lithography, arbitrarily patterned $PtTe_2$ microstructures are then fabricated over large areas (~cm^2). The main advantage of this growth technique is the material homogeneity, which is a critical requirement for scalable integration in any device configuration. Material characterization is carried out by Raman spectroscopy, atomic force microscopy, X-ray photoelectron spectroscopies and FTIR absorbance and reflectance. Electrical characterizations are carried out with magneto-transport measurements, and under illumination with optical excitation in the MIR range.

III. Results and Discussion

Experimental results show that when the $PtTe_2$ microribbons are directly in contact with a n-type Si substrate a topological Schottky junctions (TSJ) is formed. The TSJ tested under MIR laser illumination (9 μm wavelength) shows photocurrent response with responsivity up to 10^{-4} A/W and a detectivity of 10^4 Jones. More importantly, we observed a polarization-sensitive response of the TSJ driven by the selective excitation of the SPP resonances at both the $PtTe_2$/air and $PtTe_2$/substrate interfaces.

IV. Conclusion

We have realized $PtTe_2$ microribbon arrays on doped silicon as a versatile platform that addresses multiple critical challenges in MIR photodetection: achieving room-temperature operation, enabling polarization sensitivity, and providing tunable spectral response through geometric design. The fundamental insights gained from this investigation of SPP-mediated photodetection mechanisms are expected to inspire new directions in topological photonics and advance the development of next-generation infrared sensing technologies

Acknowledgments

This work was supported by the EU under the Italian National Recovery and Resilience Plan (NRRP) of Next Generation EU partnership “Telecommunications of the Future” (PE00000001 - program “RESTART”, Structural Project DREAMS) and by Leonardo S.p.a. under the research grant “Graph-IR”, contract no.LDO/CTI/P/0003059/23.

References

[1] Zeng, L. et al.,”Van Der Waals Epitaxial Growth of Mosaic-Like 2D Platinum Ditelluride Layers for Room-Temperature Mid-Infrared Photodetection up to 10.6 micron”. Advanced Materials 2020, 32 (52), 2004412

[2] S. Macis, et al. “Terahertz and Infrared Plasmon Polaritons in PtTe2 Type-II Dirac Topological Semimetal”, Adv. Mater. 2024, 36, 2400554.

[3] M. Gardella et al. “Substrate-Versatile and Stress-Free Tellurization of PtTe2 Films” *Phys. Status Solidi RRL*. 2025; 000, e202500305.

Magnetic Response Enhancement in Topological Insulator Metamaterial Hybrid Layers

Qiang Sun[1,*], Eitan Dvorquez[2], Felipe A Pinto[2], Mohan C Mathpal[2], Jeronimo R Maze[2], Brant C Gibson[1] and Andrew D Greentree[1]

[1]Department of Physics, School of Science, RMIT University, Australia
[2]Department of Physics, Pontificia Universidad Catolica de Chile, Chile
*Corresponding author: qiang.sun@rmit.edu.au

***Abstract*—We demonstrate that combining a topological insulator layer with an active metamaterial substrate strongly enhances the magnetic field induced by an electric point source. Optimized substrate parameters increase the response by over four orders of magnitude and extend the magnetic field into free space.**

***Keywords*—topological insulators, metamaterials, magnetic field enhancement, hybrid layered structures.**

I. Introduction

Topological insulators are materials with insulating bulk states and conductive surfaces. Their electromagnetic response includes coupling between electric and magnetic fields. A well-known example is that an electric charge near a topological insulator surface induces a weak magnetic field response [1].

In practice, this magnetic signal is extremely small, typically in the pT range. This limits experimental detection and reduces the potential for device applications. Enhancing this response is therefore important for both fundamental studies and engineering use.

In this work, we propose a hybrid platform where a topological insulator layer is placed on an active metamaterial substrate [2]. We show that the substrate can be designed to strongly amplify the induced magnetic field.

II. Methods

We model a layered structure consisting of free space, a finite-thickness topological insulator film, and an infinitely thick substrate. A static electric point source is positioned above the top surface.

The electromagnetic fields are obtained using the constitutive relations of topological insulators, which include a magneto-electric coupling term. We solve the resulting boundary value problem using a Hankel transform approach, which is efficient for cylindrical symmetry.

The substrate is treated as either a conventional insulator or an active metamaterial with tunable effective permittivity and permeability. We perform parameter sweeps to identify conditions that maximize the magnetic field response in free space.

III. Results and Discussion

Our simulations show that conventional dielectric substrates produce only weak induced magnetic fields, which decay rapidly away from the topological insulator surface.

In contrast, active metamaterial substrates can generate resonant enhancement when their effective permittivity and permeability take specific negative values. Under optimized conditions, the induced magnetic field increases by more than four orders of magnitude, reaching the mT range.

The enhanced field is strongest at the interface between the topological insulator and metamaterial substrate, and it extends into free space over a much larger distance than in standard configurations.

We also find that thicker topological insulator layers broaden the enhancement region, making the design more tolerant to substrate variations.

IV. Conclusion

We have demonstrated that topological insulator metamaterial hybrid structures provide a practical route to amplify the static magnetic response induced by electric charges. By selecting suitable metamaterial substrate parameters, the magnetic field enhancement can exceed four orders of magnitude and become accessible for experimental detection. This approach opens new opportunities for magnetic sensing, spintronic devices, and engineered platforms for studying topological electromagnetic phenomena.

Acknowledgments

This work was supported by the Air Force Office of Scientific Research (FA2386-21-1-4125) and ANID Fondecyt Grant (1221512).

References

[1] X. L. Qi, R. Li, J. Zang and S. C. Zhang., “Inducing a magnetic monopole with topological surface states,” Science, vol. 323, pp. 1184-1187, 2009.

[2] Q. Sun, E. Dvorquez, F. A. Pinto, M. C. Mathpal, J. R. Maze, B. C. Gibson and A. D. Greentree, “Magnetic response of topological insulator layer with metamaterial substrate induced by an electric point source,” New Journal of Physics, vol. 27, pp. 033021, 2025.

Terahertz non-linear optics in van der Waals topological insulator metamaterials

Miriam Serena Vitiello[1*]

[1] NEST, CNR-NANO and Scuola Normale Superiore, Pisa (Italy)
*Corresponding author: miriam.vitiello@sns.it

***Abstract* — High-order harmonic generation (HHG) in solids—the frequency up-conversion of an optical signal—is governed by symmetries. Here, we demonstrate frequency up-conversion in the 6.4 (even-order)–9.7 (odd-order) THz frequency range. This results from bulk centro-symmetry (odd states) and symmetry breaking in the topological surface states (odd and even).**

***Keywords*— metamaterials, terahertz, harmonic generation**

INTRODUCTION

Optical nonlinearity in the terahertz (THz) range represents a key technology to access high frequency spectral windows that are usually difficult to cover using conventional solid state laser technologies.

Over the past decade, the non-linear optical properties of graphene have been extensively investigated, and a wide range of related applications demonstrated, ranging from optical modulators [1] to saturable absorbers [2]. High harmonic generation (HHG) – the frequency up-conversion of an optical signal – in materials systems is governed by symmetries. This effect has been exploited in graphene [3], where HHG has been demonstrated, albeit only at odd multiples of the driving frequency owing to its inherent centro-symmetry. In topological insulators (TIs), unconventional HHG has been predicted [4], supported by the bulk and topological surface states, which are usually difficult to distinguish, relying on the ultrafast intraband dynamics, and the inversion symmetry-breaking even-order nonlinearity in the topological phase.

Here, we exploit innovative technological approaches in large area topological insulator metamaterials and heterostructures to device high efficient non-linear micro-devices, optically pumped by quantum cascade lasers (QCLs) delivering 2W optical power, and electrically-driven integrated plasmonic lasers comprising integrated QCL heterostructures, targeting HHG in the technologically relevant *Reststrahlen* gap (6-12 THz) at both odd or even orders, via symmetry breaking [5], [6], [7].

This talk will provide future perspectives in the fascinating field of topological photonics and non-linear THz photonics.

ACKNOWLEDGMENTS

This work was supported by the European Union through the FET Open project EXTREME IR (944735),

REFERENCES

[1] A. Di Gaspare et al., *Electrically Tunable Nonlinearity at 3.2 Terahertz in Single-Layer Graphene,* **ACS Photonics**, 10, 3171−3180 (2023)

[2] A. Di Gaspare et al., *All in one-chip, electrolyte-gated graphene amplitude modulator, saturable absorber mirror and metrological frequency-tuner in the 2-5 THz range*, **Adv. Optical Mater.,** 10, 2200819 (2024)

[3] H. A. Hafez et al., *Extremely efficient terahertz high-harmonic generation in graphene by hot Dirac fermions*, **Nature,** vol. 561, no. 7724, pp. 507–511, (2018)

[4] J. Stensberg et al., *Observation of terahertz second harmonic generation from Dirac surface states in the topological insulator Bi2Se3*, **Phys. Rev. B,** vol. 109, no. 24, p. 245112, (2024)

[5] A. Di Gaspare et al., *Compact terahertz harmonic generation in the Reststrahlenband using a graphene-embedded metallic split ring resonator array*, **Nature Commun.**, vol. 15, no. 1, p. 2312, (2024)

[6] A. Di Gaspare et al., *Second and third harmonic generation in topological insulator-based van der Waals metamaterials*, **Nature Light Science&Applications** 14, 337 (2025)

[7] A. Di Gaspare et al. *Electrically-driven heterostructured wire lasers with integrated graphene plasmons,* **Nature Nanotechnology** 20, 1611–1617 (2025)

Graphene and Topological Insulator Metamaterials for Terahertz Applications

Klaas-Jan Tielrooij[1,2,*]

[1]Department of Applied Physics, Eindhoven University of Technology, the Netherlands
[2]Catalan Institute of Nanoscience and Nanotechnology (ICN2), BIST and CSIC, Spain
*Corresponding author: k.j.tielrooij@tue.nl

***Abstract*— Graphene and topological insulators have in common that photoexcitation with virtually any wavelength, including gigahertz (GHz) and terahertz (THz) light, can lead to highly efficient carrier heating. This carrier heat can be exploited to create novel metamaterial devices with applications in terahertz nonlinear photonics and terahertz photodetection for quality inspection.**

***Keywords*— metamaterials, terahertz, graphene, topological insulators**

I. Introduction

The THz region of the electromagnetic spectrum is still lacking behind in terms of available techniques for the creation, detection and conversion of radiation, compared to the regimes on either side of the THz spectrum. For lower frequencies, electronic techniques are effective, while for higher frequencies, optical techniques provide solutions. While the THz regime has thus far strongly relied on optoelectronic techniques, strategies exploiting electronic heat in quantum materials, in particular graphene and topological insulators, are highly promising.

The electronic heat that is generated in graphene and topological insulators is the result of efficient electron-electron thermalization after photoexcitation and their relatively low carrier densities [1]. Importantly, electronic heating occurs both after interband excitation and intraband excitation, and therefore also for light with low photon energy, such as GHz and THz radiation. By designing suitable (metamaterial) devices, it is possible to exploit electronic heat for different GHz/THz applications, as we will show here. In particular, we will discuss i) efficient nonlinear conversion of (sub-)THz light using metamaterials that consist of graphene or a topological insulator, combined with a metallic grating for field enhancement; ii) highly sensitive detection of (sub-)THz light using graphene-metal-antenna metamaterials.

II. Methods

For part (i) on THz nonlinear photonics, our approach consists of shining (sub-)THz multicycle pulses onto graphene- and topological-insulator-based metamaterials and detecting upconverted signals, such as harmonics up to the 9th harmonic, using electro-optic sampling. This up-conversion is the result of the ultrafast heating-cooling dynamics of electronic heat.

For part (ii) on THz photodetection, we use continuous wave (sub-)THz light sources to shine light onto graphene-based metamaterial photodetector devices and measuring the directly generated photocurrent via the photo-thermoelectric effect.

III. Results and Discussion

For part (i), notable results have been the observation of highly efficient THz harmonic generation in graphene-grating metamaterials [2] and almost a milliwatt of output power from a topological-insulator-grating metamaterial [3].

For part (ii), we have very recent results [4] that demonstrate that graphene-based THz detectors can function as an integrated detector-interferometer that allows for the coherent detection of (sub-)THz light, with applications in quality control and wireless communication.

IV. Conclusion

These results demonstrate that exploiting electronic heat in graphene- and topological-insulator-based metamaterials indeed forms a promising alternative to conventional, purely optoelectronic approaches.

Acknowledgments

This work is the result of collaborations with scientists at TELBE (Germany), Bielefeld University (Germany), ICFO (Spain), ICN2 (Spain), and the University of Manchester.

References

[1] M. Massicotte, G. Soavi, A. Principi, and K.J. Tielrooij, "Hot carriers in graphene – fundamentals and applications," Nanoscale, vol. 13, pp. 8376–8411, 2021.
[2] J.C. Deinert et al., "Grating-graphene metamaterial as a platform for terahertz nonlinear photonics," ACS Nano, vol. 15, pp. 1145–1154, 2021.
[3] K.J. Tielrooij et al., "Milliwatt terahertz harmonic generation topological insulator metamaterials," Light: Sci. and Appl, vol. 11, pp. 315 (2022)
[4] R. De La Bastida et al., "Graphene-enabled coherent terahertz wave detection and thickness determination" Arxiv:2511.03308 (2025)

Exceptional points can enable lower-Q modes to lase first

J. Kullig[1], Q. Zhong[2,3], J. Wiersig[1], and R. El-Ganainy[2]
[1]Institut für Physik, Otto-von-Guericke-Universität Magdeburg, Germany
[2]Department of Electrical and Computer Engineering, Saint Louis University, USA
[3]Department of Physics, Michigan Technological University, USA

Abstract

Laser systems are commonly expected to lase first in the cavity mode with the highest quality factor Q under uniform pumping. We show that this intuitive rule can fail in the presence of non-Hermitian degeneracies known as exceptional points (EPs). As the pump strength increases, two initially lower-Q modes may coalesce at an EP, after which one of the resulting hybrid modes exhibits a faster increase in modal gain and reaches the lasing threshold before a competing higher-Q mode. We illustrate this mechanism using a coupled-cavity toy model and confirm it in a uniformly pumped polygonal microcavity. These results reveal a previously overlooked pathway for lasing mode selection in non-Hermitian laser systems.

Introduction— Laser systems are essential in many modern technologies. Although laser implementations vary widely in materials and cavity geometries, their operation generally follows a simple principle: under uniform gain, the cavity mode with the highest quality factor Q is expected to reach the lasing threshold first.

Because lasers inherently involve both gain and loss, they naturally form non-Hermitian systems. Recent advances in non-Hermitian photonics have revealed a variety of counter-intuitive effects in laser dynamics, including gain-induced suppression of lasing and the closely related phenomenon of loss-induced lasing [1, 2].

Despite these developments, one fundamental rule of lasing mode selection has remained largely unquestioned: under uniform pumping and weakly dispersive gain, the mode with the highest Q factor and the largest modal gain increase rate is expected to reach threshold first as the pump power increases. In this work [3], however, we demonstrate a mechanism that violates this rule. Specifically, we show that in certain systems two initially lower-Q modes can coalesce at an exceptional point (EP) [4] as the pump is increased from zero. Beyond the EP, one of the resulting hybrid modes acquires a larger gain increase rate and ultimately reaches the lasing threshold before the initially dominant higher-Q mode.

We illustrate the underlying mechanism using two complementary approaches. First, we analyze a simplified model in which coupled-mode theory provides physical insight into the effect. We then demonstrate the phenomenon in a single uniformly pumped cavity by solving the full-wave Maxwell equations.

Conclusion— Exceptional points below threshold can fundamentally modify laser mode competition. The usual rule that the highest-Q mode lases first can fail because EP-induced mode coalescence changes the gain evolution of competing modes. These results show that non-Hermitian degeneracies must be taken into account when predicting lasing order in multimode systems.

References

[1] M. Liertzer, L. Ge, A. Cerjan, A. D. Stone, H. E. Türeci, and S. Rotter, "Pump-induced exceptional points in lasers," *Phys. Rev. Lett.* **108**, 173901 (2012).

[2] B. Peng, S. K. Özdemir, S. Rotter, H. Yılmaz, M. Liertzer, F. Monifi, C. M. Bender, F. Nori, and L. Yang, "Loss-induced suppression and revival of lasing," *Science* **346**, 328 (2014).

[3] J. Kullig, Q. Zhong, J. Wiersig, and R. El-Ganainy, "Exceptional points and lasing thresholds: When lower-Q modes win," *Phys. Rev. Lett.* **135**, 173802 (2025).

[4] M.-A. Miri and A. Alù, "Exceptional points in optics and photonics," *Science* **363**, eaar7709 (2019).

Proceedings of META 2026 · Dublin, Ireland · 14–17 July 2026 · ISSN 2429-1390 · pp. 1108–1108
1108

Directional Solidification as a Platform for Bulk Plasmonic and Metamaterial Composites

Dorota Anna Pawlak[1*], Kingshuk Bandopadhay[1], Krzysztof Markus[1], Andrzej Materna[1], Ali Abbas[1], Hamid Reza-Darabian[1], Piotr Piotrowski[1], Monika Tomczyk[1], Katarzyna Sadecka[1], Nada Aghad[1]

[1] Centre of Excellence ENSEMBLE3 sp. z o. o.

Wólczynska 133, 01-919 Warsaw, Poland
*Corresponding author: dorota.anna.pawlak@ensemble3.eu

***Abstract*— This study explores directional solidification to fabricate bulk metamaterials and topological-insulator-based eutectic heterostructures. By engineering complex interfaces, these self-organized composites exhibit unique light-matter interactions, offering promising avenues for advancements in ultrafast photonics and energy-efficient optoelectronics.**

***Keywords*— Directional solidification; Bulk metamaterials; Topological insulators; Eutectic heterostructures; Ultrafast photonics; Crystal growth.**

Directional solidification provides a versatile route for fabrication of bulk metamaterials and photonic composites with engineered electromagnetic properties. In this work, we present recent advances in self-organized eutectic structures and nanoparticle-doped composites designed for plasmonic, photonic, and topological functionalities.

Particular attention is devoted to topological-insulator-based heterostructures integrated with self-assembled metamaterial-like architectures. We demonstrate that directionally solidified eutectic systems combining topological insulators with semiconducting and magnetic phases exhibit distinctive light-matter interactions arising from their complex lateral heterostructures and high density of interfaces. These materials provide a versatile platform for studying optical and ultrafast carrier dynamics, including terahertz emission, interface-driven photocurrent generation, and polarization-dependent electromagnetic responses.

These results highlight the potential of crystal-growth-based metamaterial platforms for applications in ultrafast photonics, sensing, and energy-efficient optoelectronic devices.

Topological Metamaterials Driven Study of the Dielectric Response of the Cancerous Biological Tissue

Tatjana Gric[1,*]

[1] Department of Electronic Systems, Vilnius Gediminas Technical University, Vilnius, Lithuania

*Corresponding author: tatjana.gric@vilniustech.lt

***Abstract*— Cancerous tissues are treated as the disordered anisotropic media. The classical Maxwell-Garnett technique is utilized to evaluate an effective medium of the sample with no needs of human intervention. In this relation, the presented technique allows for the creation of the phantom tissue models for the usage in clinical applications.**

***Keywords*— metamaterials, cancer, effective medium theory.**

I. Introduction

This work aims to refine fundamental ideas used in electrodynamics and some optical problems and to apply them for biological systems. We aim to correct a common practice if effective medium models for biological systems. An analytical approach to calculate the macroscopic complex dielectric properties of materials is possible due to the effective medium theory models. The former is performed by employing the dielectric properties of their constituents and their volume fractions [1]. It is well-known that early cancer detection is of substantial importance to increase the chances of survival. To address this grand societal challenges, this work aims at introducing a paradigm shift in the study of the dielectric response of the cancerous biological tissues.

II. Methods

Effective medium theories stand for as a perfect toll aiming to identify an effective dielectric function for a composite material taking into account the dielectric function of its components and their geometrical distribution [2]. Let us now assume that inclusions are embedded into the host medium. Moreover, the implants are prepared by utilizing different materials with permittivities ε_n (n=1, 2, … , N). Then Maxwell-Garnett equation is generalized as

$$\frac{\varepsilon_{MG}-\varepsilon_h}{\varepsilon_{MG}+2\varepsilon_h}=\sum_{n=1}^{N} f_n \frac{\varepsilon_n-\varepsilon_h}{\varepsilon_n+2\varepsilon_h}, \qquad (1)$$

where f_n is the volume fraction of the n-th component.

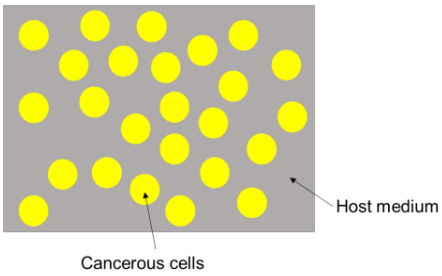

Fig. 1 Biological tissue with the embedded cancerous cells.

III. Results and Discussion

The phantom tissue models are created based on the topological metamaterial formalism methodology. It is assumed, that brain (grey matter) forms the host medium and cancerous cells are implanted in it. Following the former approach one may construct an anisotropic metamaterial (Fig. 1) with the host material being grey matter of the brain and the nanocylinders embedded in it possessing permittivity of the cancerous cells.

IV. Conclusion

It was concluded that cancerous tissues can be treated from the perspectives of the highly disordered topological metamaterial medium. In this relation, effective permittivity of the biological tissue under consideration can be considered. The presented approach may serve as a perfect tool aiming to create phantom tissue models for the clinical applications.

Acknowledgments

This article/publication is based upon work from COST Action CA23125, supported by COST (European Cooperation in Science and Technology).

References

[1] X. C. Zeng, D. J. Bergman, P. M. Hui, and D. Stroud, “Effective-medium theory for weakly nonlinear composites,” Phys. Rev. B, vol. 38, pp. 10970– 10973, 1988.

[2] T. Gric, S. G. Sokolovski, N. Navolokin, O. Semyachkina-Glushkovskaya, and Ed. U. Rafailov, "Metamaterial formalism approach for advancing the recognition of glioma areas in brain tissue biopsies," Opt. Mater. Express, vol. 10, pp. 1607-1615, 2020.

SPECIAL SESSION 18

Inverse design, topology optimization, and machine learning

6 contributions · pp. 1112–1122

Algorithm-driven Design for Functionally Multiplexed Metasurfaces

Wei Ma[1,*], Yuhang Wang[1]

1 Zhejiang Key Laboratory of Advanced Micro-nano Transducers Technology, State Key Laboratory of Extreme Photonics and Instrumentation, College of Information Science and Electronic Engineering, Zhejiang University, Hangzhou, 310027, China.

*Corresponding author: ma_wei@zju.edu.cn

***Abstract*— We present an algorithm-driven strategy to automatically design metasurfaces for functionally multiplexed light manipulation. Our metasurface design pipeline comprises iterative optimization steps, integrating gradient-based optimization or heuristic algorithms enhanced by machine learning models. This approach has been experimentally validated using multi-channel holograms, focusing lenses, and wavelength routers.**

***Keywords*— Machine Learning, optimization algorithms, metasurface, multiplexed functions.**

I. Introduction

Recently, with the aid of intelligent algorithms, the nanophotonic community has witnessed tremendous development in the design, measurement and application of nanophotonic devices and systems. The core impetus is the prevalence of inverse design methods, which convert a design problem into an optimization problem, and solve it with various algorithms automatically[1-3].

II. Methods

In this talk, we conceptually propose and experimentally demonstrate an end-to-end design pipeline with embedded statistical machine learning models for automatic design of metasurfaces. Instead of a two-step design routine including designing each meta-atom through a parameter sweep and then arrange them periodically, we resort to statistical machine learning as the bridge that directly links the structural parameters of each single meta-atom and the target metasurface performance. The machine learning model is composed of several probabilistic inverse retrieving models and a deterministic predicting model, which accurately capture and faithfully reproduce the statistical features of the high-dimensional joint distribution of meta-atom structures and their optical responses. Consequently, instead of artificially decoupling the complex optical response into independent sub-targets, a system-level multi-object optimization can be implemented to fully exploit the design space to push the design capacity to its physical limit. Under this design scheme, we experimentally demonstrated several design examples of metasurfaces including multi-channel holograms, wavelength-multiplexed light focusing and optical wavelength router.

III. Results and Discussion

Experimental results show:

- Through algorithm-driven optimization, multifunctional metasurface holograms achieve generation of up to 8 independent holographic images using combinations of 4 wavelengths and 2 polarizations (Fig 1).
- Algorithm-optimized wavelength routers deliver a 50% energy utilization efficiency, significantly surpassing the 25% theoretical upper bound of traditional 2×2 filter-array architectures (Fig 2).
-

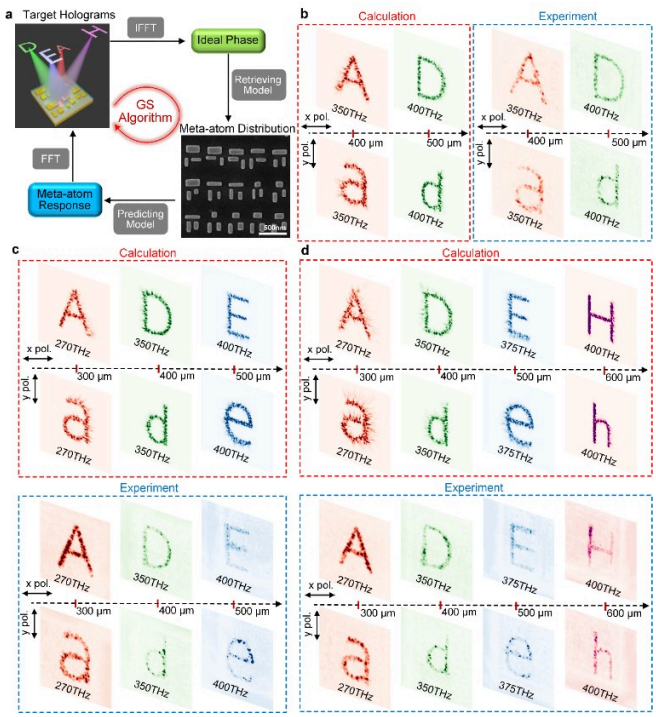

Figure 1 Embedding the statistical learning model in GS algorithm for multifunctional metasurface holograms.

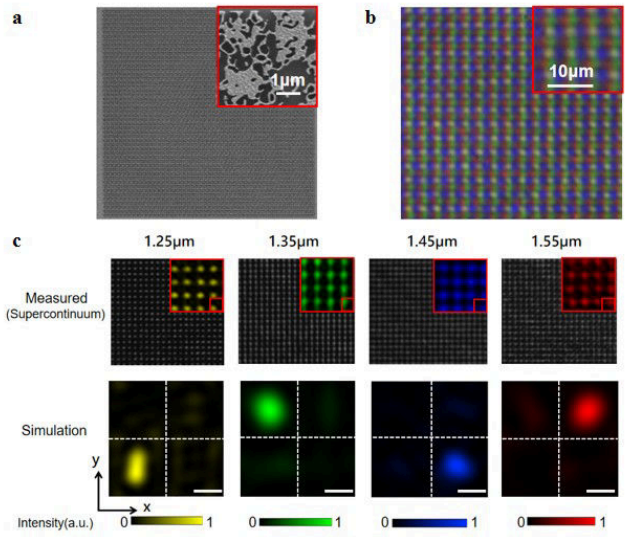

Figure 2 Focal-plane characterization of a four-wavelength router device

IV. Conclusion

We have demonstrated multi-channel holograms, focusing lenses, and wavelength routers using algorithm-driven metasurface design.

Acknowledgments

This work was supported by NSFC.

References

[1] Yihao Xu, Bo Xiong, Wei Ma*, Yongmin Liu*, “Software-defined nanophotonic devices and systems empowered by machine learning”, Progress in Quantum Electronics, Vol. 89, 100469, 2023.

[2] Wei Ma*, Yihao Xu, Bo Xiong, Lin Deng, Ruwen Peng*, Mu Wang, and Yongmin Liu*, “Pushing the Limits of Functionality-multiplexing Capability in Metasurface Design based on Statistical Machine Learning”, Advanced Materials, Vol. 34, No. 16, 2110022, 2022.

[3] Bo Xiong, Yihao Xu, Wenwen Li, Wei Ma,* Tao Chu,* and Yongmin Liu*, “Deep Learning Design for Multiwavelength Infrared Image Sensors Based on Dielectric Freeform Metasurface”, Advanced Optical Materials, online, (2024). https://doi.org/10.1002/adom.202302200

Adjoint-Based Characterization of Anisotropic and Bianisotropic Metamaterials Guided by Group Theory

Edgar Bustamante[1,*] Denis Ridzal[1] , Ihab Fathy El-Kady[1]

[1]Sandia National Laboratories, USA
*Corresponding author: ebustam@sandia.gov

***Abstract*— Group theory and adjoint optimization are combined to characterize anisotropic and bianisotropic metamaterials. Using MIRaGE, a target constitutive tensor is mapped to compatible metamaterial symmetries. Adjoint optimization is then used to determine the effective tensor values of a homogenized material model whose effective electromagnetic response approximates an explicitly modeled metamaterial unit cell.**

***Keywords*— adjoint optimization, anisotropy, bianisotropy, group theory, homogenization, metamaterials.**

I. Introduction

Metamaterials are engineered materials whose electromagnetic properties arise from the arrangement of subwavelength structures rather than from the intrinsic properties of the base materials alone. Depending on the symmetry of the unit cell, their effective response may require anisotropic permittivity and permeability tensors, as well as bianisotropic magnetoelectric coupling terms. Accurately characterizing this response enables homogenized simulations of periodic devices without explicitly meshing the detailed subwavelength metamaterial structures. Conventional S-parameter retrieval methods that use reflection and transmission data are useful for extracting homogenized effective parameters [1], but a full tensorial constitutive description requires identifying which parameters are physically admissible and which independent excitations are needed to determine them [2]. This presentation considers a workflow that combines group-theory constraints with adjoint-based parameter extraction.

II. Symmetry Constrained Constitutive Model

Multiscale inverse rapid group-theory for engineered-metamaterials (MIRaGE) maps prescribed constitutive tensor forms to compatible metamaterial symmetry groups [3]. Once the entries of the effective permittivity, permeability, and magnetoelectric coupling tensors are selected, compatible symmetry groups are identified. This step determines which tensor components are allowed by symmetry [4]. The resulting symmetry-constrained tensor form is then used in an adjoint-based parameter extraction procedure, where electromagnetic simulation data are used to recover numerical values for the independent tensor components.

III. Adjoint Parameter Extraction

The resolved metamaterial geometry is first simulated for a set of incident angles, polarizations, and frequencies chosen to test the independent tensor components. These simulations provide the reference electromagnetic response used in the parameter extraction. In the homogenized model, the metamaterial is replaced by a homogeneous block occupying the same region, with its constitutive tensors constrained by MIRaGE. The independent anisotropic or bianisotropic tensor entries are then treated as the unknowns in the adjoint-based optimization.

The objective function measures the mismatch between the resolved and homogenized responses over the selected excitations. Forward simulations are used to evaluate this mismatch, while the corresponding adjoint simulations provide gradients with respect to the active constitutive parameters [5]. The optimization updates the effective tensor values rather than the unit-cell geometry, producing a homogenized anisotropic or bianisotropic material model that best matches the metamaterial response while preserving the symmetry constraints.

IV. Discussion And Outlook

This work combines group-theory-based symmetry classification with numerical extraction of effective material tensors. MIRaGE is used to reduce the number of tensor components that need to be fitted and to enforce symmetry constraints. Adjoint sensitivities are then used to fit the material response across multiple excitations simultaneously. The presentation will discuss how the excitations are chosen, which response quantities are used in the fitting, and how the extracted tensors are validated by comparing full-wave simulations of the resolved metamaterial with simulations of the homogenized model. The goal is to obtain effective tensor descriptions that can make metamaterial analysis faster while preserving the relevant electromagnetic response.

REFERENCES

[1] D. R. Smith, S. Schultz, P. Markoš, and C. M. Soukoulis, "Determination of effective permittivity and permeability of metamaterials from reflection and transmission coefficients," Physical Review B, vol. 65, p. 195104, 2002.

[2] X. Chen, B. I. Wu, J. A. Kong, and T. M. Grzegorczyk, "Retrieval of the effective constitutive parameters of bianisotropic metamaterials," Physical Review E, vol. 71, p. 046610, 2005.

[3] MIRaGE Software, "MIRaGE Software: Multiscale Inverse Rapid Group-Theory for Engineered-Metamaterials." Website: https://mirage-software.com/

[4] J. F. Nye, Physical Properties of Crystals: Their Representation by Tensors and Matrices. Oxford: Oxford University Press, 1985.

[5] S. Molesky, Z. Lin, A. Y. Piggott, W. Jin, J. Vučković, and A. W. Rodriguez, "Inverse design in nanophotonics," Nature Photonics, vol. 12, pp. 659–670, 2018.

Large-Scale Photonic Inverse Design for Co-Optimized Photonic Systems

Geun Ho Ahn[1,*]

[1]Department of Electrical Engineering and Ginzton Laboratory, Stanford University, USA
*Corresponding author: gahn@stanford.edu

***Abstract*— Scaling photonic inverse design from isolated components to deployable systems requires optimization frameworks that capture multi-block interactions, enforce foundry manufacturability, and remain computationally tractable at large design scale. I will describe a co-optimized inverse design methodology that leads to performance improvements, and highlight inverse designs in foundry photonic systems.**

***Keywords*— photonic inverse design, silicon photonics, foundry-photonics.**

SUMMARY

Scaling photonic inverse design from isolated components to deployable systems requires optimization frameworks that capture multi-block interactions, enforce foundry manufacturability, and remain computationally tractable at large design scales. I will describe a co-optimized inverse-design methodology that treats a photonic system as a coupled optimization problem, jointly optimizing multiple subsystems under shared constraints and system-level figures of merit, while co-designing around pre-existing foundry-qualified building blocks. As a representative demonstration, I present a co-optimized inverse-designed WDM in which the wavelength-routing element is optimized together with Bragg filters, rather than cascading independently optimized blocks. Finally, I show how foundry photonics enables these inverse-designed components to transition rapidly into scalable photonic solutions, supporting system-level demonstrations that highlight a practical path to manufacturable, high-yield photonic systems.

ACKNOWLEDGMENTS

This work was supported by DARPA under the PIPES program, AMD through the System X Alliance at Stanford University, and Department of Energy under MEERCAT/ESTEEM program through SLAC National Accelerator Laboratory.

REFERENCES

[1] S. Mason, G. H. Ahn, J. Grzesik, S. Eun, and J. Vučković, "High-Performance Wavelength Division Multiplexers Enabled by Co-Optimized Inverse Design". *arXiv preprint arXiv:2509.07233*, 2025

[2] K. Omirzakhov, A. Pirmoradi, G. H. Ahn, A. Shoobi, H. Hao, J. Vučković, and F. Aflatouni, "Single chip 1 Tb/s optical transmitter with inverse designed input and output couplers". arXiv preprint arXiv:2510.12163, 2025.

Resolution and Robustness Bounds for Reconstructive Spectrometers

Y. D. Chong[1,*], Changyan Zhu[1], Hsuan Lo[2] Jianbo Yu[3] Qijie Wang[3]

[1]School of Physical and Mathematical Sciences, Nanyang Technological University, Singapore 637371
[2]Department of Physics, Massachusetts Institute of Technology, Cambridge, Massachusetts 02139
[3]School of Electrical and Electronic Engineering, Nanyang Technological University, Singapore 637371
*Corresponding author: yidong@ntu.edu.sg

***Abstract*—Reconstructive spectrometers are devices that combine complex scattering with inference. We argue that their reconstruction error is governed by Fisher information, and can be expressed via the spectral correlation length, mean transmittance, and the number of frequency and measurement channels. This numerically-validated theory also predicts the conditions for superresolution.**

***Keywords*—enhanced spectroscopy, disorder**

I. Introduction

Spectrometers are devices that decompose light into its spectral constituents for analysis. Traditional designs—dispersive spectrometers and interferometric spectrometers—benefit from increased device size, and so face limits in miniaturization. An emerging family of spectrometers, called reconstructive spectrometers [1], [2], [3], [4], [5], may be able to overcome such limits. Broadly speaking, they encode the input light into a complex interference pattern, which is used to infer the spectrum via prior knowledge (e.g., a one-time calibration). Although we have a sound understanding of the limitations of conventional spectrometers (e.g., the pixel-limited spectral resolution of a dispersive spectrometer scales inversely with the optical path length), the physical determinants of performance for reconstructive spectrometers remain unclear.

Recently [6], we have developed a broadly-applicable figure of merit for the performance of reconstructive spectrometers. Under the assumptions that (i) the spectrum is inferred from light intensity measurements on a fixed set of output channels; (ii) each intensity measurement is subject to independent Gaussian noise; and (iii) there are no additional relevant priors about the spectrum (e.g., sparsity), the theory of Fisher information [7] states that the reconstruction error is bounded below by $\sigma_\epsilon^2 \,\mathrm{Tr}[(\mathbf{A}^T\mathbf{A})^+]$, where σ_ϵ is the noise level, $\mathbf{A}$ is the normalized spectral transmission matrix, and $(\cdots)^+$ denotes the Moore–Penrose pseudoinverse. Using empirically-grounded features of generic $\mathbf{A}$ matrices [8], [9], we derive the noise-induced reconstruction error and effective resolution in terms of the spectral correlation length Γ_{corr}, the average transmittance, and the number of frequency and measurement channels. These results clarify the necessary conditions for a reconstructive spectrometer to achieve "super-resolution" below the scale set by Γ_{corr}. We have also validated the theory using random matrix theory (RMT) simulations and full-wave simulations.

II. Theory

A schematic of a reconstructive spectrometer is shown in Fig. 1(a). Light enters an input port (0), is scattered, and partly exits through output ports 1 to M. The scattering matrix is $\mathbf{S}(\omega)$. We sample N equally-spaced frequencies $\{\omega_n\}$, hence defining the $M \times N$ spectral transmission matrix $\mathbf{A}$, where $A_{mn} = |S_{m0}(\omega_n)|^2 \in \mathbb{R}_0^+$. For input spectrum $\mathbf{x}$, we assume the output intensities are $\mathbf{y} = \mathbf{A}\mathbf{x} + \boldsymbol{\epsilon}$ (i.e., additive Gaussian noise $\boldsymbol{\epsilon} \sim \mathcal{N}(\mathbf{0}, \sigma_\epsilon^2 \mathbf{1}_M)$). By the Cramér–Rao lower bound [7], the estimator variance is bounded below by

$$\sigma_\epsilon^2 \,\mathrm{Tr}(\mathbf{G}^+), \quad \mathbf{G} = \mathbf{A}^T\mathbf{A}. \tag{1}$$

We analyze this bound under a set of broadly-applicable physical constraints, including speckle statistics typical of chaotic scattering media, with Lorentzian correlations. In the under-determined regime $M < N$, we obtain [6]

$$\mathbb{E}\left[\,\mathrm{Tr}(\mathbf{G}^+)\,\right] \approx \frac{MN}{|M-N|}\frac{\tilde{J}(a)}{T_0^2}, \tag{2}$$

$$\tilde{J}(a) = \frac{2\sinh\left(\sqrt{2}\frac{M}{N}\pi a\right)}{\pi a^2}\tan^{-1}\left[\tanh\left(\frac{\pi a}{2}\right)\right]. \tag{3}$$

where $a \equiv \Gamma_{\mathrm{corr}}/\Delta\omega$ is the normalized correlation length.

From this result, we can proceed to derive various performance characteristics of the spectrometer. For instance, Fig. 1(b) shows the results of numerical simulations based on random matrix theory (RMT)—specifically, the Mahaux-Weidenmüller model of a scatterer [10]. We plot the effective resolution $\Delta\omega_{\mathrm{min}}$, defined as the minimum frequency spacing to keep the reconstruction mean squared error (MSE) below a stated threshold, versus the outcoupling constant γ of the RMT model. The theory predicts, and the numerical results confirm, that it is possible for a reconstructive spectrometer to achieve "superresolution" regime where $\Delta\omega_{\mathrm{min}}$ is smaller than the spectral correlation length Γ_{corr}.

We have also validated our theory against finite-difference time-domain (FDTD) simulations of an exemplary reconstructive spectrometer [3], shown in Fig. 1(c). The resulting plot of $\mathrm{Tr}[\mathbf{G}^+]$ versus cavity size L is shown in Fig. 1(d): the simulation results (stars) agree well with the predictions from

Fig. 1. (a) Schematic of a reconstructive spectrometer with M output ports. (b) Effective resolution $\Delta\omega_{\text{min}}$ versus coupling strength γ (orange dots), obtained from a Mahaux-Weidenmüller random matrix theory (RMT) model [10] with 500 cavity modes, using $M = 50$, $N = 100$ and averaging over 200 samples per data point. The effective resolution is defined as the minimum frequency spacing to keep the reconstruction MSE below a threshold $\delta_{\text{th}}^2 = 4 \times 10^{-4}$. Over a range of γ, the device exhibits super-resolution ($\Delta\omega_{\text{min}} < \Gamma_{\text{corr}}$. (c) Schematic of an on-chip reconstructive spectrometer with a $L \times L$ scattering region. (d) Reconstruction error metric $\text{Tr}[\mathbf{G}^+]$ versus L. The results obtained directly from the simulated $\mathbf{A}$ matrices (blue stars) are close to the theoretical predictions (blue line). The minimum of the latter matches the optimal cavity size L_{opt} derived by combining the theory with diffusive scattering scaling laws (vertical dashes).

our theory (solid line). By combining the scaling laws of diffusive transport [11], we can also predict the optimal cavity size, which closely matches the numerical minimum (vertical dashes).

III. Conclusions

The performance of a reconstructive spectrometer is largely determined by the variance bound $\text{Tr}[\mathbf{G}^+]$, derived from its spectral transmission matrix. When noise is present but non-dominant, this quantity accurately describes the noise-induced error for not only pseudoinverse-based reconstruction, but also inference using a neural network, implying that the criterion is reasonably algorithm-independent. We have derived expressions for $\text{Tr}[\mathbf{G}^+]$, and hence the effective frequency resolution, in terms of physically meaningful variables: the spectral correlation length Γ_{corr}, mean transmittance T_0, the number of intensity measurement channels, etc. The theory yields successful predictions for both RMT models and a full-wave simulation of an on-chip device. The tests confirm that Γ_{corr} is not the sole determinant of performance for a reconstructive spectrometer; notably, T_0 also plays a role and can lead to a trade-off.

Acknowledgments

We thank A. Nussupbekov, B. Zhu, F. J. N. Jorgensen, and S. G. Johnson for helpful discussions. This work was supported by the Singapore National Research Foundation (NRF) under the NRF Investigatorship NRF-NRFI08-2022-0001, and Competitive Research Program (CRP) Nos. NRF-CRP23-2019-0005, NRF-CRP23-2019-0007, and NRF-CRP29-2022-0003.

References

[1] B. Momeni, E. S. Hosseini, M. Askari, M. Soltani, and A. Adibi, "Integrated photonic crystal spectrometers for sensing applications", *Optics Communications* 282, pp. 3168 (2009).
[2] Z. Xia, A. A. Eftekhar, M. Soltani, B. Momeni, Q. Li, M. Chamanzar, S. Yegnanarayanan, and A. Adibi, "High resolution on-chip spectroscopy based on miniaturized microdonut resonators", *Optics express* 19, pp. 12356 (2011).
[3] B. Redding, S. F. Liew, R. Sarma, and H. Cao, "Compact spectrometer based on a disordered photonic chip", *Nature Photonics* 7, pp. 746 (2013).
[4] Z. Yang, T Albrow-Owen, W. Cai, and T. Hasan, "Miniaturization of optical spectrometers", *Science* 371, pp. eabe0722 (2021).
[5] L. Zhang, J. Chen, C. Ma, W. Li, Z. Qi, and N. Xue, "Research progress on on-chip fourier transform spectrometer", *Laser & Photonics Reviews* 15, pp. 2100016 (2021).
[6] C. Zhu, H. Lo, J. Yu, Q. Wang, and Y. D. Chong, "Resolution and Robustness Bounds for Reconstructive Spectrometers", arXiv:2512.20415.
[7] B. R. Frieden, *Physics from Fisher information: a unification* (Cambridge University Press, 1998).
[8] N. Lehmann, D. Saher, V. Sokolov, and H.-J. Sommers, "Chaotic scattering: the supersymmetry method for large number of channels", *Nuclear Physics A* 582, pp. 223 (1995).
[9] Y. V. Fyodorov and H.-J. Sommers, "Statistics of resonance poles, phase shifts and time delays in quantum chaotic scattering: Random matrix approach for systems with broken time-reversal invariance", *Journal of Mathematical Physics* 38, pp. 1918 (1997).
[10] Y. V. Fyodorov, "Random matrix theory of resonances: An overview", in *2016 URSI International Symposium on Electromagnetic Theory (EMTS)*, pp. 666-669 (2016).
[11] E. Akkermans and G. Montambaux, *Mesoscopic physics of electrons and photons* (Cambridge University Press, 2007).

Symmetry-Informed Deep Learning for Scattering Parameter Prediction

Viktor A. Lilja and Philippe Tassin

Department of Physics, Chalmers University of Technology, SE-41296 Göteborg, Sweden

***Abstract*—Deep learning surrogate models can accelerate modeling of electromagnetic devices by several orders of magnitude, but usually require very large amounts of training data. We show that neural networks can be made more data efficient by utilizing symmetries of Maxwell's equations.**

***Keywords*— machine learning, symmetries, scattering, metasurfaces, diffraction gratings, inverse design.**

I. Introduction

Physics-informed machine learning has recently gathered significant attention in the field of artificial electromagnetic materials. While traditional neural networks are applicable to a wide range of problems, they typically require very large amounts of data to train, generalize poorly, and make predictions that are not consistent with the governing physics [1]. Physics-informed machine learning aims to alleviate these issues by incorporating prior knowledge about the physics into neural network architecture or training procedure. Previous works in physics-informed machine learning for artificial electromagnetic materials have primarily focused on feature engineering, building algebraic expressions into the neural network architecture, or adding extra loss functions to promote consistency with governing physical laws [2].

In this contribution, we propose symmetries as a new direction in physics-informed machine learning for electromagnetic scattering. Our approach is applicable to any supervised learning problem where the label is a set of parameters $\mathbf{d}$ describing a material distribution in space (ε, μ), and the target is a set of scattering parameters S describing the relation between the amplitudes $\mathbf{s}^+$ and $\mathbf{s}^-$ of incoming and outgoing electromagnetic waves through $\mathbf{s}^- = S\mathbf{s}^+$. The training data for such problems is typically generated by a numerical simulator, here represented by a function $F : \mathbf{d} \mapsto S$. The simulator can calculate the scattering parameters of any design but is expensive to evaluate. However, given a sample $(\mathbf{d}, S)$, the scattering parameters $\hat{S}$ of a new design $\hat{\mathbf{d}}$ can often be inferred from symmetry without any additional evaluations of F, as illustrated in Fig. 1. In the language of group theory, F is said to be an *equivariant map*, commuting with the action $\triangleright$ of the transformation g, i.e.,

$$F(g \triangleright \mathbf{d}) = g \triangleright F(\mathbf{d}),$$

where the action is defined such that $g \triangleright \mathbf{d} = \hat{\mathbf{d}}$ and $g \triangleright F(\mathbf{d}) = g \triangleright S = \hat{S}$. This equivariance is not automatically respected by standard neural networks, and can therefore be exploited to improve data efficiency.

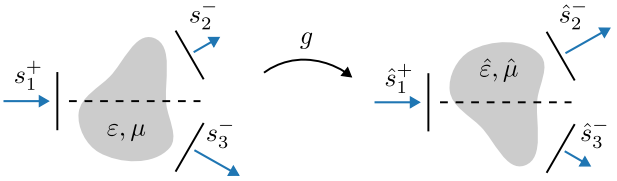

Fig. 1. Reflecting the electromagnetic geometry on the left yields the new geometry on the right. The scattering parameters of the new geometry can be inferred from the scattering parameters of the original geometry without any additional simulations.

II. Method

The most straight-forward way to exploit the equivariance of F is to use it to generate more training samples, a strategy referred to as data augmentation. A more sophisticated approach is to construct the neural network such that it has the same symmetry as F. This is possible using openly available software libraries for equivariant deep learning [3, 4].

We compare these two methods on a dataset of 24 000 randomly generated one-dimensional diffraction gratings. In this case, the goal is to predict the scattering parameters

$$S = \begin{pmatrix} S_{-1} \\ S_0 \\ S_{+1} \end{pmatrix}$$

from a binary vector $\mathbf{d} = (d_1, d_2, \ldots, d_{32})$ describing the geometry of the grating as shown in Fig. 2(a). Translating the grating by a distance t corresponds to a cyclic permutation of the design vector and transforms the scattering parameters as

$$t \triangleright S = \begin{pmatrix} e^{\frac{2\pi i t}{a}} & 0 & 0 \\ 0 & 1 & 0 \\ 0 & 0 & e^{-\frac{2\pi i t}{a}} \end{pmatrix} \begin{pmatrix} S_{-1} \\ S_0 \\ S_{+1} \end{pmatrix}, \tag{1}$$

where a is the lattice parameter. Mirroring the grating reverses the order of the design vector and transforms the scattering matrix as

$$m \triangleright S = \begin{pmatrix} 0 & 0 & -1 \\ 0 & 1 & 0 \\ -1 & 0 & 0 \end{pmatrix} \begin{pmatrix} S_{-1} \\ S_0 \\ S_{+1} \end{pmatrix}.$$

These actions on the scattering parameters have to be calculated analytically for each new problem. We have derived a systematic procedure for this purpose that is applicable to a wide range of geometries and transformations.

Fig. 2. Diffraction grating example. (a) Illustration of the unit cell, parameterized by a vector of zeros and ones. (b) The action of translation and mirroring on the grating geometry. (c) Test error as a function of the number of training samples for five models trained to predict the scattering parameters of the grating. (d) Illustration of the model-predicted paths of S_{-1} through the complex plane as the grating in the top-right is translated through its periodicity. Markers (circle, diamond, square, cross) correspond to the un-translated grating, black dashed lines are the ground-truth path.

III. Results and Discussion

We compare three different neural networks architectures on the grating dataset. The first is a standard multilayer perceptron (MLP), the second a standard convolutional neural network that partially satisfies translation equivariance (CNN), and the third is a carefully constructed CNN with a custom readout layer that ensures exact equivariance to both translations and reflections (ECNN). We also train MLPs and CNNs with data augmentation (MLP-A and CNN-A).

The test error of all models as a function of the number of training samples is shown in Fig. 2(c). Applying data augmentation to the MLP and CNN yields an improvement in test loss that corresponds to increasing the dataset size by a factor of approximately 20. The ECNN preforms even better than the models using augmentation, especially for large dataset sizes. This improvement is partially due to the equivariant model converging faster during training, which is favoured by our fixed-epoch evaluation scheme.

To test the translation equivariance of the models, we select a sample grating $\mathbf{d}$, generate the set of all possible translated versions of this grating, and feed this set through the neural networks. The resulting predictions of S_{-1} are plotted in Fig. 2(d), together with S_{-1} from the ground-truth simulator. According to the transformation rule (1), translating the grating adds a complex phase to S_{-1}, meaning that S_{-1} should trace out a circle in the complex plane. This symmetry is respected by the exactly equivariant ECNN, but not by the MLP or CNN, even when trained with augmentation. This highlights another benefit of building equivariance directly into the model architecture.

IV. Conclusion

In conclusion, we have shown that symmetries in the underlying physics can be exploited to improve data efficiency in deep learning for electromagnetic scattering parameter prediction through data augmentation and equivariant neural networks. This approach is applicable to a wide range of problems and can be combined with other physics-informed techniques. Although only spatial symmetries and basic neural network architectures were used in the example shown here, the same methods could be applied to more exotic symmetries and advanced architectures using tools from geometric deep learning [5]. We hope this work will spark an interest in equivariant deep learning in the field of metamaterials and enable more data efficient and consistent surrogate models for a wide range of applications.

Acknowledgments

We acknowledge partial financial support from Chalmers' area of advance Nano (Excellence Grant), from the Swedish Research Council under Grant No. 2020-05284, and from the Knut och Alice Wallenberg Stiftelse under Grant No. 2022.0090. Training data generation and NN training were performed on resources provided by the Swedish National Infrastructure for Computing (NAISS), at the Chalmers/C3SE and KTH/PDC sites, partially funded by the Swedish Research Council under Grant No. 2022-06725. The work was performed in part within the framework of the Excellence Center META-PIX.

References

[1] P. R. Wiecha, A. Arbouet, C. Girard, and O. L. Muskens, "Deep learning in nano-photonics: Inverse design and beyond," *Photonic Res.*, vol. 9, p. B182, 2021.

[2] Y. Deng, K. Fan, B. Jin, J. Malof, and W. J. Padilla, "Physics-informed learning in artificial electromagnetic materials," *Appl. Phys. Rev.*, vol. 12, p. 011331, 2025.

[3] T. S. Cohen and M. Welling, "Group Equivariant Convolutional Networks," 2016.

[4] G. Cesa, L. Lang, and M. Weiler, "A Program to Build E(N)-Equivariant Steerable CNNs," in *International Conference on Learning Representations*, 2022.

[5] M. M. Bronstein, J. Bruna, T. Cohen, and P. Veličković, "Geometric Deep Learning: Grids, Groups, Graphs, Geodesics, and Gauges," 2021.

Inverse design of OPA beam shaping corrective meta optics

Joao Cunha[1], Filipe Camarneiro[1], J. M. Borlido[1,2], Patrícia C. Sousa[1], Diogo E. Aguiam[1*]

[1]INL – International Iberian Nanotechnology Laboratory, Braga, Portugal
[2]CMEMS – UMinho, University of Minho, 4800-058, Guimarães, Portugal
*Corresponding author: diogo.aguiam@inl.int

***Abstract*— Optical phased arrays (OPA) are promising solid-state integrated photonic technologies for compact beam steering targeting free-space optical telecommunication and sensing applications. In this work we present an inverse design framework to optimize correction silicon nitride meta optics to straighten the curved OPA radiation pattern and expand the field of view coverage.**

***Keywords*— inverse design, OPAs, beam correction, meta optics**

I. Introduction

Optical phased arrays (OPA) are compact solid-state photonic integrated devices that enable large angle beam steering without moving parts, with enormous potential for applications such as free space optical telecommunication and LIDAR sensing. OPAs consist of arrays of optical emitters with fixed spacing between them [1]. By introducing a phase difference between consecutive emitters, using integrated phase shifters, the wavefront normal, or beam direction, can be electronically steered. A two-dimensional beam steering OPA photonic integrated circuit (PIC) has been demonstrated with large azimuthal 180° field of view (FoV), combining a slab output grating as a single emitter, allowing the elevation angle, or second axis, to be altered by tuning the laser wavelength [2]. Here, however, the output grating pitch, beam direction, and varying wavelength, result in a curved radiation field of view that lead to coverage blind spots, as illustrated in Figure 1. A new fully integrated blue spectrum 2D OPA transceiver PIC module based on a similar architecture is under development, targeting underwater optical wireless communications. To correct the curved FoV and eliminate blind spots, a novel corrective meta optics will be integrated at the package level, enabling optical links to be established between two or more transceivers without rotating the modules.

In this work, we present a versatile inverse design framework to optimize beam shaping metasurfaces, or corrective meta optics, and demonstrate its application in designing corrective silicon nitride meta optics targeting blue light OPAs.

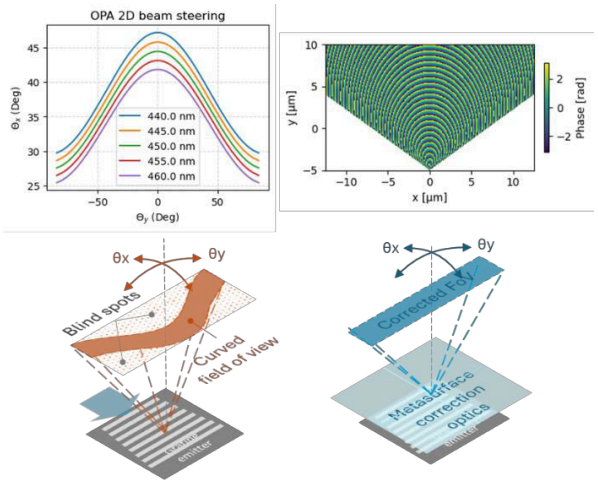

Figure 1 – Top: Expected directions (left) and vectorial field phase (right) of the radiation pattern of the blue light OPA. Illustration of the curved field of view and coverage blind spots(center); and straightened field of view by the meta surface correction optics (right).

II. Methods

The inverse design method for optimization of corrective meta optics is implemented into the open-source Python library pyMOE [3], which was recently expanded to include accurate and efficient Bluestein, and non-paraxial Scalable Angular Spectrum Method propagators, with automatic differentiation enabled by the JAX machine learning package [4]. A model of the OPA emitter was developed to describe its output vectorial field and its spatial distribution incident on the metasurface (see Figure 1 top right), dependent on the grating dimensions, laser wavelength, and tuning phase. Taking these input vectorial fields and the target desired output radiation pattern (e.g. regular FoV), the phase distribution of the metasurface is iteratively optimized.

III. Results and Discussion

We employed the developed method to optimize beam shaping metasurfaces towards arbitrary non-paraxial far field distributions, from distorted input fields, such as the curved

large angle OPA radiation pattern. The figures of merit are defined as the smallest orthogonal deviations of the far field pattern from an ideal azimuth cut, when sweeping the OPA phase, or from the elevation cut, when sweeping the laser wavelength, reducing the cross-dependence between steering inputs. We introduce boundaries to the optimization to discourage solutions outside fabrication feasibility of silicon nitride blue-light metasurfaces, such as too small critical dimensions, low transmission amplitudes, or sub-2π phase modulation ranges.

IV. Conclusion

We have demonstrated that inverse design can provide correction optics for large field of view beam steering of OPAs in wavelengths compatible with underwater communications. The reported designs are suitable for fabrication using nanofabrication techniques, specifically e-beam lithography, with the meta optics device being integrated at the package level with the OPA PIC.

Acknowledgments

This work is funded by the European Union under the HORIZON-EIC Project BlueArray (grant 101130710).

References

[1] M. Z. Alam, "Metasurface phased arrays for conventional and quantum optics," *J. Opt.*, vol. 27, no. 1, p. 013001, Jan. 2025, doi: 10.1088/2040-8986/ad9288.

[2] Y. Liu and H. Hu, "Silicon optical phased array with a 180-degree field of view for 2D optical beam steering," *Optica*, vol. 9, no. 8, p. 903, Aug. 2022, doi: 10.1364/OPTICA.458642.

[3] J. Cunha, J. Queiroz, C. Silva, F. Gentile, and D. E. Aguiam, "pyMOE: Mask design and modeling for micro optical elements and flat optics," *Computer Physics Communications*, 305, August, 109331, 2024, doi: 10.1016/j.cpc.2024.109331. https://doi.org/10.1016/j.cpc.2024.109

[4] J. Bradbury, R. Frostig, P. Hawkins, M.J. Johnson, C. Leary, D. Maclaurin, G. Necula, A. Paszke, J. VanderPlas, S. Wanderman-Milne, Q. Zhang, "JAX: composable transformations of Python+NumPy programs", (2018). http://github.com/jax-ml/jax.

SPECIAL SESSION 19

Quantum Matter and Dynamics in Hybrid Metamaterial Platforms

2 contributions · pp. 1124–1126

Engineering van der Waals Materials for Quantum Optical Emission

Shengxi Huang

Department of Electrical and Computer Engineering & Department of Materials Science and NanoEngineering, Rice University, Houston, TX 77005

shengxi.huang@rice.edu

Abstract: We report new atomic engineering approaches on van der Waals materials to generate high quality single photon emitters. Our approaches include atomic substitution through plasma treatment, in-situ doping, and manipulating layer thickness and polarization. Such approaches have led to single photon emission with high purity, high brightness, and high stability.

Key words: single photon purity, Debye-Waller factor, atomic substitution, transition metal dichalcogenide, hexagonal boron nitride

Designer van der Waals (vdW) materials offers enormous opportunities to tune material properties for various applications. Isolated, optically-active defects generated in vdW materials could lead to single photon emission. 2D vdW materials as host materials for single photon emission hold various advantages, such as high optical extraction efficiency from the atomically-thin layered materials, and readiness to integrate with on-chip photonic and electronic devices. However, single photon emission from 2D vdW materials typically suffers from low purity and lack of controllability, due to the sensitivity of these atomically-thin materials to external dielectric environments, surface defects and adsorbents, and strains and wrinkles introduced during material processing. This talk introduces our recent efforts to improve the single photon purity and controllability in vdW materials. We developed novel defect structures that can overcome several current issues, and explored their electronic structure and tunability in optical emission. Through a combination of approaches, including strain engineering, heterostacking, employing optical selection rules for excitation and detection, optimization of material synthesis and handling, we were able to achieve high purity (> 98%) for single photons emitted from 2D transition metal dichalcogenides (TMDs) at cryogenic temperature and in hBN at room temperature. This work provides deep insights into the electronic, spin, and valley properties of TMDs and hBN. It also paves the way towards the

application of 2D vdW materials for quantum optical applications. The materials engineering approaches developed here can be applied to the optimization of other optical and quantum materials.

References:

[1] A. Chatterjee, A. Biswas, A.S. Fuhr, T. Terlier, B.G. Sumpter, P.M. Ajayan, I. Aharonovich, S. Huang, "Room-Temperature High-Purity Single Photon Emission from Carbon-Doped Boron Nitride Thin Films," *Science Advances*, 11, eadv2899 (2025)

[2] W. Wu, A. Strasser, Z. Xiu, K. Ngan, T. D. Hoang, S. Liu, H. Shen, L. Holtzman, J. H. Edgar, J. C. Hone, V. Perebeinos, S. Sun, J. Kono, X. Qian, S. Huang, "Ultrahigh-Purity Single-Photon Emission from 2D WSe2 via Effective Suppression of Classical Emission," *Nano Letters*, 25, 29, 11226–11233 (2025)

[3] Q. Qian, W. Wu, L. Peng, Y. Wang, A. M. Z. Tan, L. Liang, S. M. Hus, K. Wang, T. H. Choudhury, J. M. Redwing, A. A. Puretzky, D. B. Geohegan, R. G. Hennig, X. Ma, S. Huang, "Photoluminescence Induced by Substitutional Nitrogen in Single-Layer Tungsten Disulfide," *ACS Nano*, 16, 5, 7428 (2022)

Topological plasmonics: A study of a non-Hermitian Su-Schrieffer-Heeger chain

Flore K. Kunst[1,2,*]

[1]Max Planck Institute for the Science of Light, Staudtstraße 2, 91058 Erlangen, Germany
[2]Department of Physics, Friedrich-Alexander-Universität Erlangen-Nürnberg, Staudtstraße 7, 91058 Erlangen, Germany
*Corresponding author: flore.kunst@mpl.mpg.de

***Abstract*—I will present a framework to study the topology of coupled metallic nanoresonantors arranged in a Su-Schrieffer-Heeger geometry embedded in a dielectric. To correctly account for Ohmic losses, we use a non-Hermitian description allowing us to uncover boundary states, and compare our results to existing literature and full-wave numerics.**

***Keywords*— plasmonics, topology, non-Hermitian physics.**

Plasmonics is the study of the interaction between light and free electrons at metal-dielectric interfaces at a nanoscale level. In this context, we are interested in coupled metallic nanoresonators, MNRs, embedded in a dielectric material. Such MNRs can be used to construct metasurfaces for, e.g., sensing applications. Topology provides a route towards novel functionalities to the already rich physics of these structures. To analyze and design the topological properties of these systems, we employ a non-Hermitian treatment to accurately account for Ohmic losses.

In my talk, I will present a framework to analyze the topology of coupled MNRs. In particular, the properties of the coupled MNRs are encoded in the solutions of a non-Hermitian eigenvalue problem. Using this method, we analyze a plasmonic analogue of the Su-Schrieffer-Heeger chain, and compare our results with the existing literature and full-wave numerics.

Acknowledgments

I acknowledge support from the Max Planck Society Lise Meitner Excellence Program 2.0. I also acknowledge support from the European Union's ERC Starting Grant "NTopQuant" (101116680). The views expressed are those of the authors and do not necessarily reflect those of the European Union or the European Research Council. I also acknowledge support from the Max Planck-uOttawa Centre for Extreme and Quantum Photonics.

SPECIAL SESSION 20

Nonlocal and nonlinear nanophotonics

32 contributions · pp. 1128–1177

Integrated Nonlinear Photonics for Compact Terahertz and Quantum Devices

Shima Rajabali[1,2,*]

[1]Quantum and Computer Engineering Department, Delft University of Technology
[2]School of John A. Paulson School of Engineering and Applied Sciences, Harvard University, USA
*Corresponding author: s.rajabali@tudelft.nl

***Abstract*— In this talk, I will highlight our recent advancement in realizing terahertz photonic devices and electro-optic quantum transducers on a nonlinear integrated photonic platform.**

***Keywords*— nonlinear optics, integrated photonics, terahertz, thin film lithium niobate, electro optic.**

SUMMARY

Real-world use of terahertz communications and broadband terahertz spectroscopy requires compact, energy-efficient devices capable of high-speed performance and high sensitivity. Integrated photonics offers a promising chip-scale platform for addressing these needs [1]. Among emerging technologies, thin-film lithium niobate (TFLN) stands out as an ideal wafer-scale solution for high-speed devices and systems [2,3]. Its strong optical nonlinearity, broad transparency window, low propagation loss, high electro-optic coefficient, and wide modulation bandwidth make it particularly well-suited for optical-to-terahertz transduction and the development of compact THz devices. However, researchers are actively working to overcome challenges such as integrating active components and minimizing device footprints, further advancing the capabilities of the TFLN platform.

In this talk, I will showcase the recent development of hybrid photonic-THz TFLN chips for compact THz resonators [4], broadband integrated generation/detection up to multi-THz bandwidths [4,5], frequency combs with millimeter wave Spacing [6], and dual-tone source for compact THz transmitters [7]. Current challenges, and future opportunities in integrated nonlinear photonic devices for optical-terahertz applications will be discussed to explore how integration and miniaturization can enable complex terahertz photonic functionalities on a single chip.

Beyond classical use cases, I will also present the potential of TFLN platform for quantum networks, including on-chip microwave-to-optical transduction [8, 9] and other nonlinear functions [10].

ACKNOWLEDGMENTS

The works presented here are mainly done in a collaboration between HYLAB (EPF Lausanne, Switzerland), NanoOptics Lab (Harvard University, United states), and QuIN Photonics (Delft University of Technology, the Netherlands).

REFERENCES

[1] S. Rajabali and I.-C. Benea Chelmus, "Present and future of terahertz integrated photonic devices," in APL Photonics 8, 080901, 2023.

[2] D. Zhu, et al. "Integrated photonics on thin-film lithium niobate," in Advances in Optics and Photonics 13, pp 242–352, 2021.

[3] Y. Hu, et al. "Integrated electro-optics on thin-film lithium niobate," in Nat. Rev. Phys. 7, pp 237–254, 2025.

[4] Y. Lampert et al. "Photonics-integrated terahertz transmission lines," in Nature Communications, 16, 2025.

[5] A. Tomasino et al. "Large-area photonic circuits for terahertz detection and beam profiling," in Light: Science & Applications 15, 9, 2026.

[6] A. Gaier et al "Wireless millimeter wave electro-optics on thin film lithium niobate", in arXiv:2505.04585v2, 2025.

[7] S. Rajabali et al. "An On-Chip Dual-Tone Source for Photonic-Based Terahertz Transmitters," in European Conference on Optical Communications (ECOC), Copenhagen, Denmark, pp. 1-3, 2025. doi: 10.1109/ECOC66593.2025.11263279.

[8] H.K. Warner et al., "Coherent control of a superconducting qubit using light", in Nat. Phys. 21, 831–838, 2025.

[9] H. K. Warner et al., "Tunable Microwave Resonators for Superconducting Electro-optic Devices", in CLEO Conference, 2025.

[10] D. Assumpcao et al., "A thin film lithium niobate near-infrared platform for multiplexing quantum nodes," in Nat. Comm. 15, 10459, 2024.

GaAs nanowires as a tunable source of polarization-entangled photons

Elise Bailly-Rioufreyt[1], Zoya Polshchykova[1], Grégoire Saerens[1], Wenhe Jia[1,2], Helena Weigand[1], Thomas Dursap[3], Andreas Maeder[1], Philippe Regreny[3], Robert Chapman[1], Alexandre Danescu[3], Nicolas Chauvin[3], José Penuelas[3], Rachel Grange[1]

[1.] ETH Zurich, Department of Physics, Institute for Quantum Electronics, Optical Nanomaterial Group, Auguste-Piccard-Hof 1, 8093 Zurich, Switzerland

[2.] State Key Laboratory for Precision Measurement Technology and Instruments, Department of Precision Instrument, Tsinghua University, Beijing 100084, China

[3.] CNRS, ECL, INSA Lyon, UCBL, CPE Lyon, INL, UMR 5270, 69130 Ecully, France

*Corresponding author: ebailly@phys.ethz.ch

This work introduces a novel approach for realizing a tunable nanoscale source of polarization-entangled photon pairs in the near-infrared, using orthogonal GaAs nanowires. Photon pairs arise from type-0 spontaneous parametric down-conversion (SPDC) and the quantum state is adjustable via pump polarization, enabling a continuous transition from entangled to separable states.

***Keywords*— SPDC, GaAs nanowires, polarization-entanglement, quantum nanophotonics.**

As fundamental building blocks of quantum technologies, entangled photon-pair sources enable applications such as quantum communication and quantum imaging [1,2]. Spontaneous parametric down-conversion (SPDC) has been the prevalent process to generate polarization entanglement. While the use of bulk non-centrosymmetric crystals in most of the realizations prevents chip-scale integration, emerging nanoscale platforms provide a route to miniaturization. Among them, GaAs nanowires (NWs) stand out as a new promising solution for quantum application at the nanoscale. GaAs NWs not only exhibit an intrinsically large second-order nonlinear susceptibility $\chi^{(2)}$, reaching values as high as 370 pm/V [3], but also offer significant advantages over conventional top-down fabrication techniques thanks to their bottom-up growth. In particular, they exhibit a high crystalline quality with minimal defects, and their diameter and length can be precisely controlled through the adjustment of growth parameters.

Here, we show that we can exploit the emission of photon pairs from GaAs NWs via type-0 SPDC [4] to generate polarization entangled states, by pumping two orthogonal GaAs NWs with a linearly polarized laser. In type-0 SPDC, the pump, signal, and idler photons all share the same polarization. Rotating the pump polarization then enables to tune the quantum state from separable to entangled [5].

I. Methods

The schematic of the tunable nanosource of polarization-entangled is shown in Fig. 1, together with the SEM image shown in the inset. It consists of two orthogonal Zinc Blende GaAs NWs (≈ 400 nm diameter, ≈ 5 µm long), grown in the (111) direction and laid on a transparent SiO_2 substrate. The two nanowires are pumped at the same time by a continuous-wave (cw) linearly polarized laser at 778 nm, with a power of 12 mW.

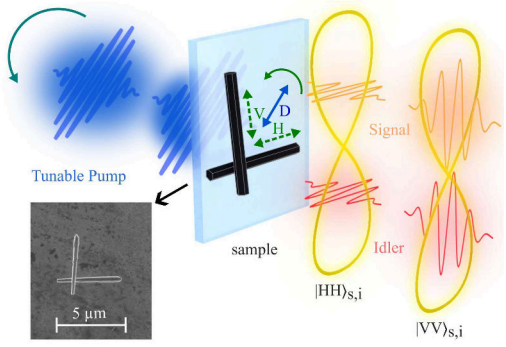

Fig. 1 : Schematic of the tunable nanosource of polarization-entangled photons from orthogonal GaAs nanowires (NWs) and SEM image of the GaAs NWs.

The pump polarization can be rotated to be aligned with either one of the NWs (referred as horizontal H or vertical V pump

polarizations), or at ±45° of the NWs' axis (referred as diagonal D and antidiagonal A pump polarizations). The quantum state is then measured as a function of the pump polarization by performing quantum state tomography and the density matrices are retrieved via the maximum likelihood estimation method [6].

II. Results and Discussion

The real parts of the experimental density matrices are plotted in Fig. 2, as a function of the pump polarization. When the pump is aligned at ±45° of the nanowires long axis, two entangled Bell's states are generated with $|\Psi^{D,A}\rangle = \frac{1}{\sqrt{2}}(|HH\rangle \mp |VV\rangle)$ (Fig. 2a,b) with high fidelities reaching 90% for both cases. However, when the pump is aligned along the long axis of one NW, the photon pair is generated exclusively by that NW. In this configuration, the quantum state is either $|\Psi^{H}\rangle = |HH\rangle$ for H-polarized pumping (Fig. 2c), or $|\Psi^{V}\rangle = |VV\rangle$ for V-polarized pumping (Fig. 2d), with fidelities reaching 88% and 89% respectively.

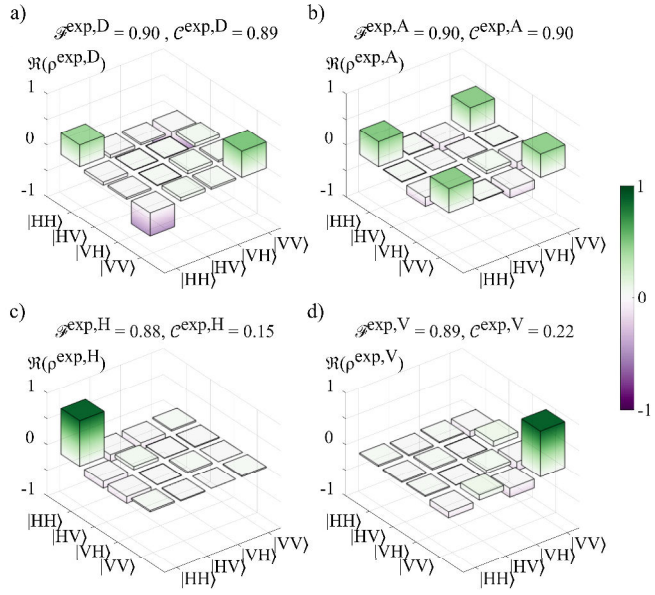

Fig. 2 : Real parts of the experimental density matrices ρ^{exp} for a) diagonal (D), b) antidiagonal (A), c) horizontal (H) and d) vertical (V) pump polarizations.

The degree of entanglement can be evaluated by computing the concurrence C as a figure of merit [7], ranging from 0 (for fully separable states) to 1 (for fully entangled states). Here, we obtained an experimental concurrence of 0.15 and 0.22 for H and V pump polarizations respectively. Conversely, the concurrence reaches 0.89 and 0.90 for D and A pump polarization respectively. These experimental results confirm that changing the polarization of the pump enables to tune the degree of polarization entanglement without post selection or without any additional optical components.

III. Conclusion

In this work, we have demonstrated a tunable nanosource of polarization entangled photons from bottom-up GaAs nanowires via spontaneous parametric down-conversion. Rotating the pump polarization enables to tune the degree of entanglement of the state, from separable to entangled, without the need of additional optical components. Besides its versatility, it is among the most compact polarization-entangled photon pair sources ever obtained.

Acknowledgments

The authors thank the Scientific Center for Optical and Electron Microscopy (ScopeM), the Binning and Rohrer Nanotechnology Center (BRNC), the FIRST cleanroom and D-MATL X-ray service platform at ETH Zurich for technical assistance. This work was supported by the Swiss National Science Foundation SNSF (Consolidator Grant 213713 and Grant 179099). The authors also thank the Nanolyon platform, a member of the CNRS-RENATECH+ French national network, for access to equipment and J. B. Goure for technical assistance.

References

[1] Z.-S. Yuan, X.-H. Bao, C.-Y. Lu, J. Zhang, C.-Z. Peng, J.-W, Pan, "Entangled photons and quantum communication", Physics Reports, 497, 1–40, 2010.

[2] H. Defienne, B. Ndagano, A. Lyons, D, Faccio, "Polarization entanglement-enabled quantum holography", Nature Physics, 17, 591–597, 2021.

[3] R. W., Boyd, "Nonlinear Optics", 3rd edn. Academic Press, Burlington, MA, 2008.

[4] G. Saerens, T. Dursap, I. Hesner, N.M.H. Duong, A.S. Solntsev, A. Morandi, A. Maeder, A. Karvounis, P. Regreny, R.J. Chapman, A. Danescu, N. Chauvin, J. Penuelas, R. Grange, "Background-free near-infrared biphoton emission from single GaAs nanowires", Nano Letters 23, 3245–3250, 2023.

[5] E. Bailly-Rioufreyt, Z. Polshchykova, G. Saernes, W. Jia, T. Dursap, A. Maeder, P. Regreny, R. J. Champman, H. Weigand, A. Danescu, N. Chauvin, J. Penuelas, R. Grange, "Tunable polarization-entangled near-infrared photons from orthogonal GaAs nanowires, arXiv:2512.02980, 2025 (*submitted*).

[6] D.F.V., James, P.G., Kwiat, W.J., Munro, A.G., White, "Measurement of qubits", Physical Review A 64, 052312, 2001.

[7] W.K., Wootters, "Entanglement of formation of an arbitrary state of two qubits", Phys. Rev. Lett. 80, 2245–2248, 1998.

Metasurface-controlled external cavity tunable lasers

Zahra Basiri[1], Alessandro Tomasino[1], Gabriel Juelg[1], Andrea Lanfranchi[2], Ileana-Cristina Benea-Chelmus[*]

[1]Hybrid Photonics Laboratory, École Polytechnique Fédérale de Lausanne (EPFL), Switzerland

[2] Department of Chemistry and Industrial Chemistry, University of Genoa, 16146, Genova, Italy

*Corresponding author: cristina.benea@epfl.ch

***Abstract*— Tunable lasers are essential for optical communication, spectroscopy, and precision sensing. Many tunable laser systems rely on mechanical components, limiting speed and stability. Here, we demonstrate an external cavity semiconductor laser capable of achieving ultrafast frequency and amplitude modulation within a compact footprint without any moving parts.**

***Keywords*— external cavity lasers, metasurfaces, electro-optics.**

I. Introduction

Tunable single-mode lasers are essential in applications such as spectroscopy, metrology, ranging and communications. Since their invention in the mid-1960s, external cavity diode laser (ECDL) designs have evolved significantly, often improving wavelength tunability and spectral purity. Among the simplest and most widely used is the Littrow configuration, where light emitted from an anti-reflection (AR) coated laser diode facet is collimated and directed onto a diffraction grating. The first-order diffracted beam is reflected back into the diode to provide optical feedback. This configuration depends on mechanical tuning for wavelength adjustments, limiting speed and tuning range. To overcome this, electro-optic modulators have been inserted into the laser's cavity, but their bulk footprint limited the development of compact laser diodes [1].

II. Methods

In this work, we integrate a compact, frequency-selective electro-optic metasurface into the cavity as its external mirror (Fig. 1), replacing both the bulk EO crystal and the diffraction grating. The electro-optic metasurface is made from an array of interdigitated electrodes covered by a layer of electro-optic polymer JRD1 and supports guided-mode resonances [2] which occur when the diffraction angles from the gold stripes coincide with the total internal reflection angle of the polymer slab. The metasurface is electro-optically active and the refractive index of the entire external mirror can be tuned electro-optically through the Pockels effect.

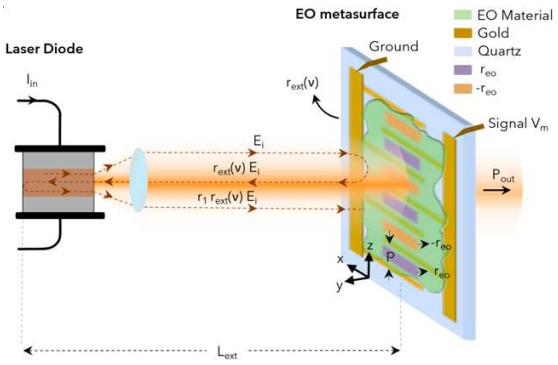

Fig. 1 Concept of metasurface-controlled external cavity tunable laser.

III. Results and Discussion

By opting for a resonant electro-optic metasurface as the external mirror, we simultaneously achieve single-mode and voltage-tunable frequency response. We demonstrate linear frequency tuning rates of up to 180 THz/s, with frequency excursions reaching 110 MHz under a 10 V peak RF drive, clearly surpassing rates attainable through piezoelectric actuation. When biasing the laser close to its threshold, our method also provides intensity modulation, exceeding 100% modulation efficiency at a peak RF voltage of 4 V.

IV. Conclusion

We have demonstrated a high-speed tunable external cavity laser in the telecom C-band, enabled by a single ultrathin electro-optic metasurface employed as the external cavity mirror. Further cavity [3,4] and resonance designs [5,6,7] can be considered in the future to improve the frequency excursion and stability of the devices proposed here.

Acknowledgments

Z.B. and I.C.B.C. acknowledge support from the Swiss National Science Foundation (PRIMA, grant number 201547). A.T. acknowledges funding from the Swiss National Science

Foundation (SPARK, grant number 221119). G.J. acknowledges funding from the Swiss National Science Foundation - National Science Foundation (SNSF-NSF) Lead Agency program (grant number 219409)

REFERENCES

[1] A. Schremer, C. Tang, Single-frequency tunable external-cavity semiconductor laser using an electro-optic birefringent modulator. Applied physics letters 55 (1), 19–21 (1989).
[2] I.-C. Benea-Chelmus, et al., Electro-optic spatial light modulator from an engineered organic layer. Nature communications 12 (1), 5928 (2021)
[3] C. Spaegele, et al., Multifunctional wide-angle optics and lasing based on supercell metasurfaces, Nature communications 12 (1), 3787 (2021)
[4] M. Ossiander, et al., Metasurface-stabilized optical microcavities. Nature Communications 14 (1), 1114 (2023)
[5] G. Soma, K. Ariu, S. Karakida, Y. Tsubai, T. Tanemura, Subvolt high-speed free-space modulator with electro-optic metasurface. Nature Nanotechnology pp. 1–8 (2025),
[6] E. Klopfer, S. Dagli, D. I. Barton, M. Lawrence, J. A. Dionne, High-Quality-Factor Siliconon-Lithium Niobate Metasurfaces for Electro-optically Reconfigurable Wavefront Shaping. Nano Letters 22 (4), 1703–1709 (2022)
[7] Y. Zhang, et al., Electrically reconfigurable non-volatile metasurface using low-loss optical phase-change material. Nature Nanotechnology 16 (6), 661–666 (2021)

Enhancing the Kerr-effect in nonlinear media for mid-IR single-photon detection at room temperature

Richarda Niemann[1,*], Ke-Sean J. Peter[1], Maxwell J. Tolchin[2], Jon-Paul Maria[2], Sahin Ozdemir[3], Nathaniel Kinsey[3], Durdu Guney[4], and Joshua D. Caldwell[1]

[1]Department of Mechanical Engineering, Vanderbilt University, USA
[2]Department of Materials Science and Engineering, The Pennsylvania State University, USA
[3]Department of Electrical and Computer Engineering, Saint Louis University, USA
[4]Department of Electrical and Computer Engineering, Michigan Technological University, USA
*Corresponding author: richarda.niemann@vanderbilt.edu

***Abstract*—We present our work on maximizing the nonlinearity in CdO at its ENZ frequency to enhance the phase shift occuring due to the effective optical Kerr-effect tracing the ultimate goal of mid-IR single photon detection at room temperature. We discuss the nonlinear refractive index response to wavelength and angular tuning.**

***Keywords*— single photons, mid-infrared, optical Kerr effect, epsilon-near-zero material, nonlinear refractive index.**

I. Introduction

The generation and detection of single photons is a crucial part of the progress in quantum technology. The detection of light in the atmospheric transmission window in the mid-infrared (mid-IR) plays a crucial role in a variety of research fields such as materials characterization[1], quantum communication[2], and medical imaging[3]. Within this frequency regime, however, single photon detection has so far only been realized with cryogenic temperatures around 1K [4,5] due to the lower energy of mid-IR photons. Detector operation at room temperature comes at the cost of increased thermal background noise and a limited detector sensitivity as well as increased absorption and scattering.

We here present our scheme to circumvent these problems in a setup exploiting the benefits of cross-phase modulation. Our approach as shown in Fig. 1 is based on the effective optical Kerr-effect: A mid-IR signal beam travelling through a highly nonlinear medium can induce a phase shift in a second probe beam that is travelling through the medium simultaneously [6]. This phase shift is proportional to the signal beam photon population. A material with stronger nonlinearity leads to an increased phase shift induced by each photon and is thus highly desirable for mid-IR detection.

We use the well-established z-scan technique [7] to measure the nonlinearity of CdO at its epsilon-near-zero (ENZ) frequency. At the ENZ frequency, the complex dielectric permittivity ε is close to zero, leading to a maximized shift Δn in the nonlinear refractive index n_2:

$$\Delta n = \frac{\Delta \varepsilon}{2\sqrt{\varepsilon}}$$

.

We will discuss the influence of different parameters on the nonlinear refractive index, starting with the excitation wavelength. By changing the thickness of the CdO layer, we can actively tune the response of the nonlinear refractive index as the influence of the ENZ character owned by our sample changes. This will be further analyzed with angular sample rotation measurements, where we will discuss the influence of the ENZ condition vs. active coupling to ENZ modes.

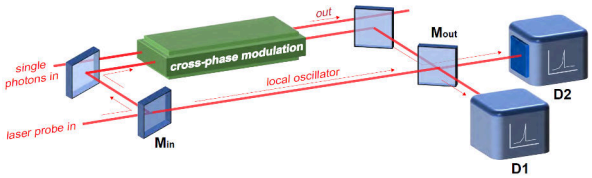

Fig. 1. Schematic of the single photon detection scheme. A laser beam at a probe frequency ω_{probe} is split into two beams, one at lower intensity guided through a strongly nonlinear medium and and a second higher intensity local-oscillator beam propagating in free space. Due to the effective optical Kerr effect, the electric field of a mid-IR signal travelling through the nonlinear medium simultaneously with the probe induces a phase shift in the probe beam. This phase shift is proportional to the signal beam photon population. The phase-shifted probe beam is then recombined with the local-oscillator beam in a Mach-Zehnder configuration, and the intensity difference recorded by the balanced detector is related to the phase shift induced on the probe beam by the signal beam.

Acknowledgments

This work was supported by the United States Army Research Office (ARO) under MURI grant (W911NF2420195).

References

[1] Cai et al., "Mid-infrared single-photon upconversion spectroscopy enabled by nonlocal wavelength-to-time mapping," *Sci. Adv.* 10, eadl3503, 2024.
[2] Shields et al., "Mid-infrared Quantum Interference and Polarization Entanglement." In Proceedings of the OSA High-Brightness Sources and Light-Driven Interactions Congress 2020 (EUVXRAY, HILAS, MICS), Washington, DC, USA, 16–20 November 2020
[3] Fang et al., "Mid-infrared single-photon 3D imaging." *Light Sci Appl* 12, 144, 2023.
[4] Chang et al., "Efficient mid-infrared single-photon detection using superconducting NbTiN nanowires with high time resolution in a Gifford-McMahon cryocooler," *Photon. Res.* 10, 1063-1070 (2022) .

[5] Verma et al., "Single-photon detection in the mid-infrared up to 10 μm wavelength using tungsten silicide superconducting nanowire detectors." *APL Photonics* 6 (5): 056101, 2021
[6] Newell. Nonlinear Optics (1st ed.). CRC Press. 2004.
[7] Sheik-Bahae et al., "Sensitive measurement of optical nonlinearities using a single beam", *IEEE J. Quantum Electron.* 26 (4), 1990

Phonon-Enhanced Sum-Frequency Generation Spectro-Microscopy of Hexagonal Boron Nitride

Niclas S. Mueller[1,2,*], Alexander P. Fellows[2], Nasim Mirzajani[2], Purbita Kole[1], Mira Kreßler[1], Kyoungpyo Lee[3], Ben John[2], Andrew E. Naclerio[4], Tao Yang[2], Christian Carbogno[5], Katayoun Gharagozloo-Hubmann[1], Damián Baláž[5], Ryan A. Kowalski[4], Hendrik H. Heenen[5], Christoph Scheurer[5], Karsten Reuter[5], Joshua D. Caldwell[4], Martin Wolf[2], Patryk Kusch[1], Xiaoqin Li[3], Piran R. Kidambi[4], Martin Thämer[2], and Alexander Paarmann[2]

[1]Department of Physics, Freie Universität Berlin, Germany
[2]Department of Physical Chemistry, Fritz Haber Institute of the Max Planck Society, Germany
[3]Department of Physics, University of Texas at Austin, USA
[4]Department of Electrical and Mechanical Engineering, Vanderbilt University, USA
[5]Theory Department, Fritz Haber Institute of the Max Planck Society, Germany
*Corresponding author: niclas.mueller@fu-berlin.de

***Abstract*— We demonstrate 800-fold enhancement of the second-order nonlinear response of hexagonal boron nitride (hBN) monolayers by a mid-IR phonon. This enables rapid imaging of the usually invisible monolayers with sum-frequency generation microscopy, revealing their crystal orientation. Furthermore, we characterize the nonlinear response of buried hBN interfaces with artificial stacking.**

***Keywords*— sum-frequency generation, hexagonal boron nitride, mid-infrared, 2D materials, nonlinear.**

I. Introduction

Hexagonal boron nitride (hBN) is an important material for infrared nanophotonics, quantum light emission and van der Waals heterostructures. The second-order nonlinear optical response of hBN is however typically much lower than that of other 2D materials, such as transition metal dichalcogenides, because the material has no optical resonances across the VIS and near-IR spectral ranges. This limits the applicability of hBN for nonlinear nanophotonics and makes monolayers optically almost invisible.

II. Methods

We employ phase-resolved sum-frequency generation (SFG) microscopy combining mid-IR and VIS femtosecond laser pulses to characterize the second-order nonlinear optical response of hBN.[1] The microscope provides combined spatial, spectral and crystallographic information, as described in previous works.[2-3]

hBN monolayers were grown by chemical vapor deposition (CVD) and subsequently transferred to a transparent fused silica substrate.[1,4] Thicker hBN slabs (~5-10 nm) were folded resulting in near-180° twist angles to realize stacking configurations with sliding ferroelectricity.[5]

III. Results and Discussion

We observe a strong enhancement of the nonlinear optical response when matching the mid-IR laser wavelength with the transverse optical (TO) phonon of CVD-grown hBN monolayers (Fig. 1b). The measured second-order nonlinear susceptibility exhibits a pronounced resonance at the TO phonon frequency with imaginary part $\chi^{(2)}_{\mathrm{eff}}(\omega_{\mathrm{TO}}) = 1.9 \cdot 10^{-19}\ \mathrm{m^2/V}$, which corresponds to an exceptionally large bulk susceptibility of $\chi^{(2)}_{\mathrm{eff}}(\omega_{\mathrm{TO}}) = 580\ \mathrm{pm/V}$ when assuming a thickness of 0.33 nm of the hBN monolayer. This is much larger than the off-resonant susceptibility $\chi^{(2)}_{\mathrm{eff}}(\omega_{\mathrm{VIS}}) \approx 20\ \mathrm{pm/V}$ and makes SFG of hBN monolayers equally efficient as second-harmonic generation in transition metal dichalcogenide monolayers. The TO phonon resonance therefore causes an ~800-fold enhancement of the SFG intensity.

The enhanced SFG response makes it possible to record nonlinear images of hBN across large 100×100 μm² sample areas in less than 1 s, enabling rapid screening of usually optically invisible monolayers. Furthermore, the polarization selection rules of SFG enable us to determine the full crystal orientation of the hBN monolayers. We analyze SFG images for various azimuthal sample orientations and obtain an image of the crystal orientation from a Fourier analysis of the rotation dependent signal (Fig. 1c). Comparison to DFT calculations reveals that the CVD-grown hBN monolayer flakes have nitrogen terminated zigzag edges, which could so far only be probed locally with atomic resolution microscopy techniques.

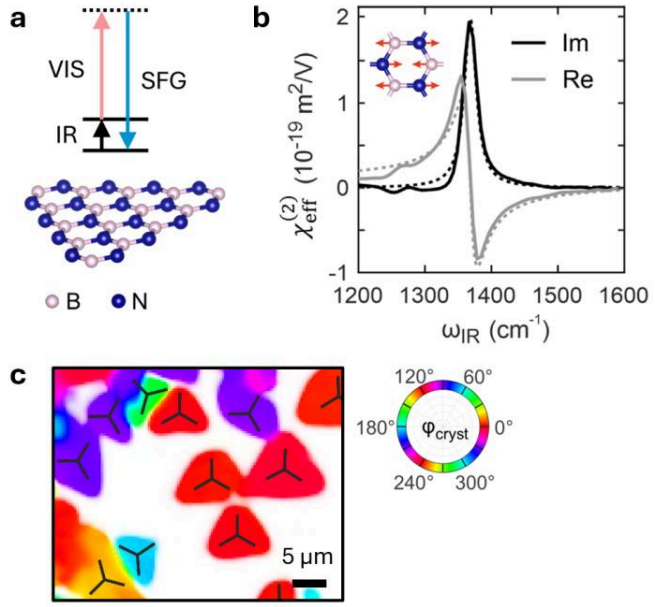

Fig. 1 SFG Spectro-Microscopy of hBN. (a) Scheme of SFG from fs mid-IR and VIS laser pulses (top) and crystal structure of hBN monolayer (bottom). (b) Spectrum of second-order nonlinear susceptibility enhanced by phonon resonance, with experimental data (solid) and fit (dashed). (c) Crystal orientation of hBN monolayers from phase-resolved nonlinear images. Colors show angles between B-N arm-chair directions (black lines) and *x* axis. Figure panels adapted from Ref. 1, Wiley-VCH, published under a Creative Commons Attribution (CC BY) license.

The second-order nonlinear response of hBN can be tailored by stacking and twisting several hBN layers. We find that CVD-grown hBN bi- and few-layers exhibit non-standard stacking configurations with an increased SFG signal. Furthermore, we characterize the SFG response of thin exfoliated hBN slabs that were stacked with near-180° twist angles. Kelvin probe force microscopy (KPFM) measurements reveal the formation of domains with out-of-plane static dipoles, a phenomenon known as sliding ferroelectricity.[5] SFG spectro-microscopy enables selective microscopy and spectroscopy of these buried interfaces, which break inversion symmetry. We observe a modified nonlinear optical response that depends on the twist angle. Furthermore, preliminary data reveal spectral shifts and broadening of the nonlinear phonon-spectra, which could arise from to the formation of domains walls with large uniaxial strain.

IV. Conclusion

We showed that the second-order nonlinear optical response of hBN is strongly enhanced by a phonon resonance in the mid-IR, which enables rapid imaging the usually optically invisible monolayers. Furthermore, we show that the nonlinear response can be tuned by artificial stacking and twisting of hBN. This enables efficient spectral conversion of mid-IR to visible light on the nanoscale and opens a toolbox for nonlinear mid-IR nanophotonics.

Acknowledgments

N.S.M. acknowledges funding from the Deutsche Forschungsgemeinschaft (DFG, German Research Foundation) - Projektnummer 551280726.

References

[1] N.S. Mueller, A.P. Fellows, B. John, A.E. Naclerio, C. Carbogno, K. Gharagozloo-Hubmann, D. Baláž, R.A. Kowalski, H.H. Heenen, C. Scheurer, K. Reuter, J.D. Caldwell, M. Wolf, P.R. Kidambi, M. Thämer, and A. Paarmann, "Full Crystallographic Imaging of Hexagonal Boron Nitride Monolayers with Phonon-Enhanced Sum-Frequency Microscopy". Advanced Materials, vol. 38, pp. e10124, 2026.

[2] A. P. Fellows, B. John, M. Wolf, and M. Thämer, "Spiral packing and chiral selectivity in model membranes probed by phase-resolved sum-frequency generation microscopy". Nature Communications, vol. 15, pp. 3161, 2024.

[3] T. Khan, B. John, R. Niemann, A. Paarmann, M. Wolf, and M. Thämer, „Compact oblique-incidence nonlinear widefield microscopy with paired-pixel balanced imaging". Optics Express, vol. 31, pp. 28792, 2023.

[4] P. Chaturvedi, A.E. Naclerio, S.M. Hus, I.V. Vlassiouk, N. Lavrik, M. Checa, L. Collins, A.-P. Li, and P.R. Kidambi, "Sieving Hydrogen Isotopes via Machine Learning Assisted Chemical Vapor Deposition (CVD) of High-Quality Monolayer Hexagonal Boron Nitride (h-BN) on Iron Foils". Advanced Materials, vol. 38, pp. e11868, 2026.

[5] D.S. Kim, R.C. Dominguez, R. Mayorga-Luna, D. Ye, J. Embley, T. Tan, Y. Ni, Z. Liu, M. Ford, F.Y. Gao, S. Arash, K. Watanabe, T. Taniguchi, S. Kim, C.-K. Shih, K. Lai, W. Yao, L. Yang, X. Li, and Y. Miyahara, "Electrostatic moiré potential from twisted hexagonal boron nitride layers". Nature Materials, vol. 23, pp. 65–70, 2024.

Probing Low-Frequency Excitations with Visible Light and Electron Beams

Leila R. Prelat[1,*], Eduardo J.C. Dias[2], F. Javier García de Abajo[1,3]

[1] ICFO–Institut de Ciencies Fotoniques, The Barcelona Institute of Science and Technology, Barcelona, Spain
[2] POLIMA–Center for Polariton-driven Light–Matter Interactions, University of Southern Denmark, Odense, Denmark
[3] ICREA–Institució Catalana de Recerca i Estudis Avançats, Barcelona, Spain
*Corresponding author: leilaprelat@gmail.com

***Abstract*—We introduce wave mixing cathodoluminescence, combining visible light and focused electron beams to probe low-frequency excitations with nanoscale resolution. Calculations for a retinal-coated silver nanorod show that far-infrared vibrational fingerprints are up-converted to visible sidebands, enabling electron microscopy in electron microscopes without low-frequency detectors.**

***Keywords*— wave-mixing cathodoluminescence, electron-light wave mixing, sum- and difference-frequency generation, low-frequency excitations, nanoscale spectroscopy, cathodoluminescence, vibrational mode detection.**

I. Introduction

Nonlinear optics describes processes whose description requires going beyond the linear response of a given system. A particularly important example of such processes is wave mixing, whereby two or more input waves combine in nonlinear materials to generate output waves with new frequencies, with widespread applications in communication, imaging, sensing, and quantum optics. However, such applications are hindered by challenges like complex experimental setups, low nonlinear susceptibilities, and limited frequency generation, which cap the nonlinear conversion efficiency. While nonlinear processes are traditionally driven by intense laser fields, we present electron beams as an alternative source for wave mixing. Specifically, we introduce Wave-Mixing Cathodoluminescence (WMCL), in which a specimen is simultaneously illuminated by monochromatic visible light and a focused electron beam. We leverage the broadband and highly localized nature of the electron field to probe low-frequency excitations with nanoscale resolution.

II. Methods

We model wave-mixing cathodoluminescence (WMCL) by combining the self-consistent linear fields generated by a monochromatic optical pump and a swift electron beam with the second-order nonlinear response of the specimen. For a pump field $\mathbf{E}_{\rm pump}(\mathbf{r})\mathrm{e}^{-\mathrm{i}\omega_{\rm pump}t}$ and a frequency-resolved electron field $\mathbf{E}_{\rm electron}(\mathbf{r},\omega)$, the nonlinear polarization density at the emitted frequency $\omega_{\rm WM}$ is written as [1]

$$\mathbf{P}^{\nu}_{\rm WMCL}(\mathbf{r},\omega_{\rm WM}) = \chi^{(2)} : \mathbf{E}_{\rm pump}(\mathbf{r})\mathbf{E}_{\rm electron}(\mathbf{r},\omega), \quad (1)$$

where $\chi^{(2)}$ is the position- and frequency-dependent second-order susceptibility tensor corresponding to the three different WMCL channels under consideration, indexed by ν, with the appropriate frequency arguments [2]. The emitted field is then obtained from the electromagnetic Green tensor,

$$\mathbf{E}^{\nu}_{\rm WM}(\mathbf{r},\omega_{\rm WM}) = \int_V d^3\mathbf{r}'\, \mathcal{G}(\mathbf{r},\mathbf{r}',\omega_{\rm WM})\cdot\mathbf{P}^{\nu}_{\rm WMCL}(\mathbf{r}',\omega_{\rm WM}), \quad (2)$$

where V denotes the nonlinear material volume. From here, we obtain the far-field WMCL amplitude

$$\mathbf{f}^{\nu}_{\rm WM}(\Omega_{\hat{\mathbf{r}}}) = \int_V d^3\mathbf{r}'\, g(\Omega_{\hat{\mathbf{r}}},\mathbf{r}',\omega_{\rm WM})\cdot\mathbf{P}^{\nu}_{\rm WM}(\mathbf{r}',\omega_{\rm WM}) \quad (3)$$

where $\Omega_{\hat{\mathbf{r}}}$ denotes the emission direction $\hat{\mathbf{r}}$, and we implicitly defined the far-field Green tensor as $\mathcal{G}(\mathbf{r},\mathbf{r}',\omega_{\rm WM}) \approx g(\Omega_{\hat{\mathbf{r}}},\mathbf{r}',\omega_{\rm WM})\mathrm{e}^{\mathrm{i}k_{\rm WM}r}/r$. The far-field kernel is obtained from reciprocity by calculating the self-consistent near field produced inside the structure by plane-wave illumination incident from the opposite emission direction, following the procedure described in Methods of Ref. [2].

We start by addressing the case of small cavities (compared with all relevant wavelengths), which can be treated analytically in the electrostatic limit. The optical and electron fields inside the particle are uniform and approximately given by the external fields at the sphere center times a factor $3/(\epsilon+2)$ evaluated at the frequencies $\omega_{\rm pump}$ and ω, respectively. We use a Drude–Lorentz permittivity given by $\epsilon(\omega) = 1 + f\omega_{\rm r}^2/[\omega_{\rm r}^2 - \omega(\omega+\mathrm{i}\eta)]$, where f is a dimensionless factor, $\omega_{\rm r}$ is an intrinsic resonance frequency, and η is an inelastic damping rate. We calculate the corresponding output frequency emission rate out in a generic Drude metal spherical cavity for all different allowed outcomes of SFG and DFG in this limit and find that it is boosted when the incident light and/or electron beam resonates with the natural modes supported by the cavity, following $\omega_0 = \omega_{\rm r}\sqrt{1+f/3}$.

We extend the study to a retinal-coated silver nanorod, for which we calculate the optical and electron-induced fields with an axisymmetric boundary-element method [3]. Since silver is a centrosymmetric material, its second-order nonlinear response only arises from the nanorod surface, and is quantified by a nonlinear surface susceptibility $\chi^{(2)}$ for which we

Fig. 1. **Probing low-energy excitations through WMCL. (a)** Scheme of the structure under consideration, consisting of a silver nanorod (length $L = 100$ nm, radius $a = 10$ nm) coated by a retinal layer (thickness t). The structure is irradiated by a light plane wave of frequency $\omega_{\rm pump}$ and polarization along the rod. The electron moves with a velocity $v = 0.45\,c$ and passes at a distance $b = 3$ nm from one end of the coated rod. SFG and DFG produce output photon energies $\omega_{\rm WM} = \omega_{\rm pump} \pm \omega$ through the second-order susceptibility $\chi^{(2)}_{\perp\perp\perp}(\omega_{\rm pump}, \pm\omega, \omega_{\rm WM})$ at the silver surface. **(b)** CL spectra for bare ($t = 0$) and coated ($t = 5$ nm) silver nanorods under the geometry depicted in (a). **(c)** Normalized probability of SFG and DFG photon emission as a function of electron energy change. We plot the quantity $\mathcal{R}(\omega)/\xi^2$ for bare and retinal-coated nanorods, with $\mathcal{R}(\omega) = \Gamma_{\rm SFG/DFG}(\omega_{\rm WM})/\Gamma_{\rm CL}(\omega_{\rm WM})$, $\omega = \pm(\omega_{\rm WM} - \omega_{\rm pump})$, and $\xi^2 = \left|\chi^{(2)}_{\perp\perp\perp} E_{\rm pump}\right|^2/A$ combining the surface area of the nanorod $A = 2\pi a L$ and the incident light-field amplitude $E_{\rm pump}$. The upper horizontal scale indicates the output photon energy for the retinal-coated nanorod (blue curve), with the bare-nanorod counterpart (green curve) shifted by $+184.5$ meV. **(d)** Comparison of $\partial_\omega \mathcal{R}(\omega)$ to the imaginary part of the permittivity of retinal as a function of absolute electron frequency change $\omega = |\omega_{\rm WM} - \omega_{\rm pump}|$.

only retain the dominant $\perp\perp\perp$ component. Silver is described using tabulated experimental permittivity [4], whereas retinal is modeled as a sum of Lorentz oscillators fitted to its far-infrared vibrational response [5].

III. Results and Discussion

We first analyze a small nonlinear cavity in the electrostatic limit and find that the WMCL signal is maximized when either the optical pump or the electron spectral component is resonant with the cavity mode, confirming that plasmonic confinement can strongly enhance electron–light wave mixing (shown in Fig. 2 of Ref. [2]).

We then consider a retinal-coated silver nanorod, as schematized in Fig. 1a. The visible pump is tuned to the nanorod plasmon resonance, shown in Fig. 1b, for the bare (green curve) and coated (blue curve) nanorod. The resulting WMCL spectra are shown in Fig. 1c as a function of the change in electron energy, with the SFG and DFG spectra shown as filled and dashed curves, respectively. Compared with the bare nanorod, the coated structure exhibits features associated with retinal far-infrared vibrations. The top axis shows the detected energy for the coated case, which lies in the visible. The retinal vibration features are absent in the bare structure and become more evident in Fig. 1d, where we take the derivative of the normalized WMCL response with respect to $\omega = |\omega_{\rm WM} - \omega_{\rm pump}|$ (shown in blue), which closely follows the imaginary part of the retinal permittivity (dashed red). Therefore, the low-frequency molecular resonances are encoded in visible-frequency sidebands, while the CL background remains comparatively featureless. This comparison indicates that WMCL can identify analytes through their low-energy fingerprints using visible optical readout and nanometer-scale electron-beam localization.

IV. Conclusion

In summary, WMCL provides a practical route to probe low-frequency excitations by mixing monochromatic visible light with the broadband near field of swift electrons via the second-order response of a specimen. Our calculations show that this mechanism can up-convert far-infrared vibrational fingerprints to visible photon energies and recover the spectral signature of retinal in a plasmonic nanorod geometry. Beyond molecular vibrations, the same concept should apply to other low-energy modes, including phonon-polaritons, low-frequency plasmons, and magnetic excitations, offering a promising strategy for nanoscale spectroscopy in electron microscopes without relying on low-frequency detectors.

Acknowledgments

This work was supported by the European Research Council (Adv. Grant 101141220-QUEFES), the European Commission (FET-Proactive 101017720-eBEAM), the Spanish MICIU (PID2024-157421NB-I00 and Severo Ochoa CEX2024-001490-S), and the CERCA program.

References

[1] Robert W. Boyd, *Nonlinear Optics*, 3rd ed., Academic Press, Amsterdam, 2008.

[2] L. Prelat, E.J.C. Dias, and F.J. García de Abajo, "Wave-mixing cathodoluminescence microscopy of low-frequency excitations", *Nature Communications*, vol. 16, pp. 11551, 2025.

[3] F. J. García de Abajo, and A. Howie, "Retarded field calculation of electron energy loss in inhomogeneous dielectrics", *Physical Review B*, vol. 65, pp. 115418, 2002.

[4] P. B. Johnson, and R. W. Christy, "Optical constants of the noble metals", *Physical Review B*, vol. 6, pp. 4370–4379, 1972.

[5] M. Walther, B. Fischer, M. Schall, H. Helm, and P. Uhd Jepsen, "Far-infrared vibrational spectra of all-trans, 9-cis and 13-cis retinal measured by Thz time-domain spectroscopy", *Chemical Physics Letter* vol. 332, pp. 389–395, 2000.

Limitations and Opportunities in Second Order Nonlinear Optical Materials: The Role of the Penn Gap

Jacob B. Khurgin
Department of ECE , Johns Hopkins University, Baltimore, USA

***Abstract*— This study investigates the limitations and potential of second order nonlinear optical (NLO) materials, focusing on the Penn gap as a critical parameter for predicting upper limits of nonlinear susceptibility, $\chi^{(2)}$. Results indicate that while substantial improvements in $\chi(2)$ are unlikely in the mid-infrared range, there is significant room for enhancement in the ultraviolet region. The goal is to combine a wide Penn gap with reduced bond polarity to facilitate the discovery of new materials with improved nonlinear optical properties.**

***Keywords*—nonlinearity, Penn gap, band gap, polarity**

Second-order nonlinear optical materials play a vital role in many photonic applications, but the range of materials used has not changed significantly over the last few decades. Despite improvements in material quality and processing methods, much of the field still relies on traditional compounds. This paper reassesses the achievable second-order nonlinear susceptibility ($\chi^{(2)}$) by focusing on the Penn gap, a parameter that has not been widely emphasized in the context of NLO materials but is instrumental for predicting the upper limits of $\chi(2)$.

The basis for $\chi^{(2)}$ is grounded in the absence of inversion symmetry within materials. Miller's Empirical Rule provides an important framework, illustrating the correlation between $\chi(2)$ and various macroscopic properties related to bond characteristics. While prior studies have examined the relationship between bond polarity and $\chi^{(2)}$ this research deepens the exploration of how these factors connect to the Penn gap, which represents the energy difference between bonding and antibonding states within a material.

The analysis highlights a notable relationship between fundamental bandgap energies and the Penn gap, emphasizing its influence on nonlinear optical responses. The results indicate that while current materials in the mid to far infrared range exhibit $\chi^{(2)}$ values close to theoretical limits, there remains significant potential for enhancing $\chi^{(2)}$ in the ultraviolet region.

This work specifically aims to establish upper limits for $\chi(2)$ rather than providing precise estimates, guiding researchers in their pursuit of materials that meet optimal conditions defined by the Penn gap. The findings show that exploring materials with wide bandgaps and favorable bond polarities in the ultraviolet range can offer opportunities to improve nonlinear optical performance.

In conclusion, the study suggests that future research should concentrate on identifying new inorganic materials characterized by advantageous bonding properties in relation to the Penn gap. This targeted approach could pave the way for advancements in second-order nonlinear optical properties crucial for the next generation of photonic technologies.

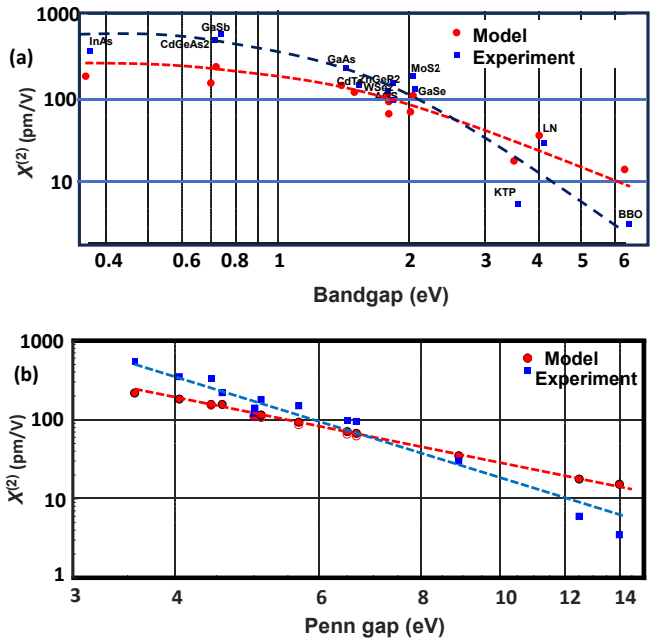

Fig. 1 Second order susceptibility vs (a).fundamental bandgap and (b) Penn gap according to our model (red circles) and experimental data (blue squares).

Using material and structural resonances to shape photon pair emission by four-wave mixing

Hua Li[1], Omer Can Karaman[1], Valeria Vento[1], Giulia Tagliabue [1], Christophe Galland[1,*]

[1]Institute of Physics, Ecole Polytechnique Fédérale de Lausanne (EPFL), CH-1015 Lausanne, Switzerland
*Corresponding author: chris.galland@epfl.ch

***Abstract*—Four-wave mixing (FWM) is a universal nonlinear process that can take place in any material under sufficiently strong optical excitation. We show how the polarization and spectra of quantum-correlated photon pairs produced by FWM can be tailored through the use of material resonances (phonon modes) and structural resonances (Mie-type modes and qBIC).**

***Keywords*— Photon pairs, Nonlinear optics, Four-wave mixing, Entangled photons, quantum optics**

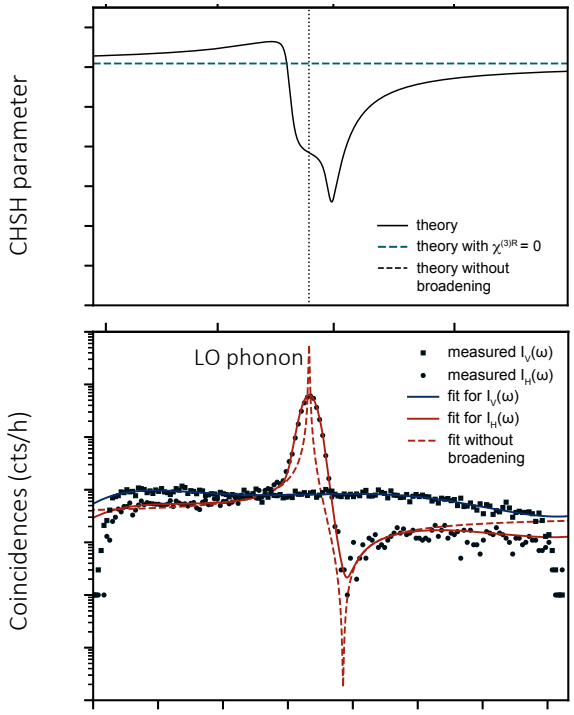

Fig. 1. **Polarization entangled photon pairs from bulk single-crystal diamond** The lower panel shows the raw photon pair coincidence detection rate under pumping with sub-ps laser pulses at 780 nm, as a function of the photon energy (expressed as detuning from the pump). The top panel is the measured polarization entanglement witness (CHSH parameter): a Bell inequality is violated in the blue-shaded area, demonstrating broadband polarization entangled photons generated by four-wave mixing. *Adapted from Ref. [1]*

I. Introduction

In the process of degenerate spontaneous FWM, two incident photons from the pump laser generate a pair of photons with respective energies symmetrically spaced around that of the pump. Compared to parametric down-conversion, FWM is not restricted by crystal symmetries and can occur in all crystalline and amorphous materials. Moreover, because the frequencies of the emitted photons can remain close to that of the pump, FWM is typically easier to phase-match, and working in a relatively narrow frequency band simplifies photonic design.

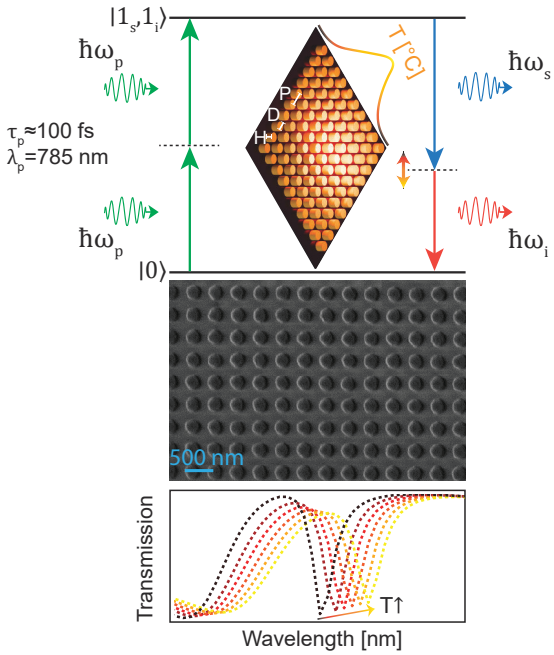

Fig. 2. **Photo-thermal tuning of photon pair generation in dielectric metasurfaces** Top panel: concept of the experiment, where spontaneous FWM converts two photons from the pump at 785 nm into a quantum-correlated photon pair at symmetrically detuned frequencies. The pump also causes local heating of the metasurface, thereby altering the nonlinear mode overlap and resonance frequencies and, consequently, the photon pair spectrum. Middle panel: scanning electron micrograph of a silicon metasurface on glass. Lower panel: shift of the resonance with temperature. *Adapted from Ref. [2]*

II. Methods

Experiments are performed under pulsed laser excitation (pulse duration varying between 200 and 800 fs, wavelength

centered around 785 nm). The diamond sample was a single-crystal plate cut along the [100] plane. The photon coincidence spectrum is measured by fiber spectroscopy (the dispersion translated frequency to time domain). The amorphous silicon metasurfaces were fabricated in EPFL Cmi clean room using electron beam lithography.

III. Results and Discussion

In this talk, I will address the challenges of polarization and frequency engineering of photon pairs produced by FWM. First, I will show how phonon resonances in a crystal like diamond can be used to tailor the biphoton polarization quantum state as a function of the detuning from the pump. [1], [3], [4] As shown in see Fig. 1, under appropriate geometrical conditions, polarization entangled photons violating a Bell inequality are produced out of the pumped diamond thin film without further optical engineering nor phase-matching constraints. I will also briefly explain how single-photon counting can be used to reveal quantum coherence among a macroscopic number of independently vibrating molecules [5], prepare nonclassical phonon states [6] and generate light-vibration entanglement [7].

Second, switching to amorphous silicon thin films, I will present an approach based on a Mie-mode metasurface to actively tuned the FWM spectral efficiency by the photothermal effect, as sketched in Fig. 2. [2]

IV. Conclusion

Our results motivate the further development of diamond photonic integrated circuits tailored to produce broadband polarization-entangled photons around any center wavelength in the material's transparency window. Our findings also link photothermally driven optical dynamics to quantum light generation, revealing a route to compact, reprogrammable photon-pair sources with wavelength trimming, fabrication-tolerance compensation, and fast power-controlled switching between brightness and purity regimes, features absent in static integrated devices.

Acknowledgments

G.T. acknowledges the support of the Swiss National Science Foundation (Starting Grant No. 211695). E.N.D. and G.T. acknowledge the support of the Swiss National Science Foundation (Eccellenza Grant 194181). C.G. acknowledges the support of the Swiss National Science Foundation (SNSF project No. 214993) and the European Union's Horizon 2020 research and innovation program under Grant Agreement No. 820196 (ERC CoG 'QTONE'). H.L. acknowledges the support of the National Natural Science Foundation of China (No. 22203042). The authors also acknowledge the support of the Center of MicroNanoTechnology (CMi) at EPFL.

References

[1] Vento, Valeria. *et al.* "How to use the dispersion in the $\chi^{(3)}$ tensor for broadband generation of polarization-entangled photons." *Phys. Rev. Res.* **7**, L022017 (2025)

[2] Karaman, O. C. *et al*. "Photo-Thermally Tunable Photon-Pair Generation in Dielectric Metasurfaces", *ACS Nano* https://doi.org/10.1021/acsnano.5c14740 (2026)

[3] Freitas, T. A. *et al*. "Microscopic origin of polarization-entangled Stokes–anti-Stokes photons in diamond", *Phys. Rev. A* **108** L051501 (2023)

[4] Sier, D. *et al.* "Emergent broadband polarization entanglement from electronic and phononic Stokes–anti-Stokes indistinguishability" *Phys. Rev. A* **112**, 033702 (2025)

[5] Vento, V. *et al.* "Measurement-induced collective vibrational quantum coherence under spontaneous Raman scattering in a liquid", *Nature Communications* **14**, 2818 (2025)

[6] Tarrago Velez, S. *et al.* "Preparation and decay of a single quantum of vibration at ambient conditions" *Physical Review X* **9**, 041007 (2019)

[7] Tarrago Velez, S. "Bell correlations between light and vibration at ambient conditions" *Science Advances* **6**, eabb0260 (2020)

Nonlinear Self-Action Driven by Quasi-Bound States in the Continuum

Alfonso Nardi[1], Sonia Freddi[2], Michael Scalora[3], Agostino Di Francescantonio[1], Johann Osmond[4], Attilio Zilli[1], Marco Finazzi[1], Michele Celebrano[1], Monica Bollani[2], Maria Antonietta Vincenti[3,*]
Corresponding Author: maria.vincenti@unibs.it

[1]Department of Physics, Politecnico di Milano, Piazza Leonardo 32, 20133 Milano – Italy
[2]Institute of Photonic and Nanotechnology (IFN) - Consiglio Nazionale delle Ricerche (CNR), LNESS Laboratory, Como – Italy
[3]Department of Information Engineering, University of Brescia, Via Branze 38, 25123 Brescia – Italy
[4]ICFO-Institut de Ciencies Fotoniques, Barcelona – Spain

***Abstract*— We experimentally investigate nonlinear self-action in a nonlocal metasurfaces supporting quasi-bound states in the continuum. By comparing picosecond and femtosecond excitation, we directly observe resonance-enhanced third-harmonic generation, saturation of cubic power scaling, and power-dependent spectral reshaping. Full-wave simulations link these effects to ultrafast resonance shifts driven by nonlinear refractive index modulation, revealing how high-Q field confinement governs nonlinear dynamics across different excitation regimes.**

***Keywords*— Quasi-bound states in the continuum, Nonlinear metasurfaces, Ultrafast nonlinear optics, nonlocal metasurfaces, Third-harmonic generation**

I. Introduction

Nonlinear light–matter interactions are central to frequency conversion, ultrafast control, and all-optical signal processing, yet their practical implementation is often limited by the weak nonlinear response of optical materials [1-6]. Dielectric nanostructures supporting high-Q resonances offer a compelling route to overcoming these limitations by providing strong field confinement with low losses and high damage thresholds [7]. Metasurfaces supporting bound states in the continuum (BICs), and their experimentally accessible counterparts, quasi-bound states in the continuum (qBICs), are among the most promising realizations of this concept [8, 9]. These resonances combine extreme field enhancement with long photon lifetimes, enabling efficient nonlinear processes in compact geometries [10-14]. However, the same properties that enhance nonlinear efficiency also render qBIC resonances highly sensitive to nonlinear self-action. Intensity-dependent refractive-index changes dynamically modify the resonance condition itself, leading to resonance shifts, saturation of harmonic generation, and deviations from simple power-law scaling. Such behavior places nonlinear qBIC metasurfaces within the broader context of time-dependent photonics, where ultrafast modulation gives rise to rich dynamical phenomena [15-17]. In resonant nonlinear nanostructures, however, this time dependence emerges intrinsically from strong field confinement and ultrafast material response, without the need for externally imposed modulation. Despite growing interest, nonlinear self-action in qBIC metasurfaces has largely been explored within isolated excitation regimes. In particular, how pulse duration and excitation bandwidth govern the coupling to high-Q resonances and the resulting nonlinear dynamics remains poorly understood. Here, we address this question by experimentally probing nonlinear self-action in a nonlocal dielectric metasurface using third-harmonic generation, directly comparing narrowband picosecond and broadband femtosecond excitation to reveal a unified mechanism governing nonlinear saturation, scaling, and spectral dynamics.

II. Results and Discussion

We probe nonlinear self-action in the qBIC metasurface via third-harmonic (TH) generation under two complementary excitation regimes, spectrally matched picosecond pulses and broadband femtosecond pulses, and find two distinct, experimentally robust manifestations of the same underlying mechanism. With a narrowband excitation tuned across the qBIC, the TH excitation spectrum shows a strong, resonance-peaked enhancement: TH conversion is maximized when the pump overlaps the qBIC wavelength. As input intensity is increased from 1 to ~10 MW cm^{-2} the resonant TH profile broadens, and the power dependence departs from the expected cubic law. More specifically we found that the TH signal follows cubic scaling away from the resonances, but near the resonance the fitted power exponent steadily decreases, approaching nearly linear scaling at the highest intensities (not shown). These observations indicate that intense, resonantly confined fields modify the effective optical response of the metasurface during the pulse, limiting conversion efficiency as the mode itself is reshaped by the pump field. On the other hand, when femtosecond excitation pulses are used, the pump inevitably couples less efficiently to the narrow qBIC mode due to its limited spectral overlap. In this regime, when the pump is detuned from the qBIC the TH spectra closely follow the pump spectrum and remain essentially power-invariant. In contrast, for pump wavelengths overlapping the qBIC we observe a pronounced spectral reshaping and broadening of the TH emission. The spectral changes include a narrow component that remains pinned to the resonant feature and a broader

component that tracks the pump spectrum, whose relative weights evolve with power. Full-wave time-domain simulations reproduce both the picosecond and femtosecond trends and attribute them to an ultrafast, intensity-driven modulation of the effective refractive index that dynamically shifts the qBIC during the excitation pulse. In the picosecond limit the pulse effectively drives the resonance over its lifetime, so a dynamically shifted resonance reduces field enhancement and produces saturation of conversion efficiency. In the femtosecond limit the pulse contains many spectral components that sample different instantaneous resonance conditions: the qBIC acts as a dynamic, intensity-dependent spectral filter, imprinting a transient spectral structure onto the TH emission. Thus, narrowband and broadband excitation reveal complementary facets of the same self-action physics, efficiency and power-law modification in the former, spectral reshaping in the latter.

III. Conclusion

We have experimentally demonstrated nonlinear self-action in dielectric metasurfaces supporting quasi-bound states in the continuum by directly comparing narrowband picosecond and broadband femtosecond excitation. Although these regimes couple to the same high-Q resonance in fundamentally different ways, both reveal the same underlying mechanism: ultrafast, intensity-driven modification of the resonant response. Our results establish qBIC metasurfaces as versatile nonlinear systems and provide practical guidance for controlling efficiency, scaling, and spectral dynamics in ultrafast nanophotonics.

Acknowledgments

This work is supported by the PRIN 2022 “PILLARS” (2022YJ5AZH).

References

[1] R. W. Boyd and D. Prato, *Nonlinear Optics*. Elsevier Science, 2008.

[2] Y.-R. Shen, "Principles of nonlinear optics," 1983.

[3] G. Li, S. Zhang, and T. Zentgraf, "Nonlinear photonic metasurfaces," *Nature Reviews Materials,* vol. 2, no. 5, pp. 1-14, 2017.

[4] A. M. Weiner, *Ultrafast optics*. John Wiley & Sons, 2011.

[5] M. Maiuri, A. Schirato, G. Cerullo, and G. Della Valle, "Ultrafast all-optical metasurfaces: Challenges and new frontiers," *ACS Photonics,* vol. 11, no. 8, pp. 2888-2905, 2024.

[6] A. E. Willner, S. Khaleghi, M. R. Chitgarha, and O. F. Yilmaz, "All-optical signal processing," *Journal of Lightwave Technology,* vol. 32, no. 4, pp. 660-680, 2013.

[7] Z. Liu *et al.*, "High-Q quasibound states in the continuum for nonlinear metasurfaces," *Physical review letters,* vol. 123, no. 25, p. 253901, 2019.

[8] C. W. Hsu, B. Zhen, A. D. Stone, J. D. Joannopoulos, and M. Soljačić, "Bound states in the continuum," *Nature Reviews Materials,* vol. 1, no. 9, p. 16048, 2016/07/19 2016, doi: 10.1038/natrevmats.2016.48.

[9] D. C. Marinica, A. G. Borisov, and S. V. Shabanov, "Bound States in the Continuum in Photonics," *Physical Review Letters,* vol. 100, no. 18, p. 183902, 05/08/ 2008, doi: 10.1103/PhysRevLett.100.183902.

[10] L. Carletti, K. Koshelev, C. De Angelis, and Y. Kivshar, "Giant Nonlinear Response at the Nanoscale Driven by Bound States in the Continuum," *Physical Review Letters,* vol. 121, no. 3, p. 033903, 07/19/ 2018, doi: 10.1103/PhysRevLett.121.033903.

[11] K. I. Okhlopkov *et al.*, "Tailoring third-harmonic diffraction efficiency by hybrid modes in high-Q metasurfaces," *Nano Letters,* vol. 21, no. 24, pp. 10438-10445, 2021.

[12] L. Carletti, S. S. Kruk, A. A. Bogdanov, C. De Angelis, and Y. Kivshar, "High-harmonic generation at the nanoscale boosted by bound states in the continuum," *Physical Review Research,* vol. 1, no. 2, p. 023016, 2019.

[13] G. Zograf *et al.*, "High-harmonic generation from resonant dielectric metasurfaces empowered by bound states in the continuum," *Acs Photonics,* vol. 9, no. 2, pp. 567-574, 2022.

[14] P. Tonkaev *et al.*, "Unconventional high-harmonic generation in resonant membrane metasurfaces," *Nature Communications,* vol. 16, no. 1, p. 11571, 2025/12/22 2025, doi: 10.1038/s41467-025-67871-6.

[15] M. Scalora *et al.*, "Extreme electrodynamics in time-varying media," *Physical Review A,* vol. 112, no. 1, p. 013502, 07/02/ 2025, doi: 10.1103/5cjl-ltvg.

[16] E. Galiffi *et al.*, "Photonics of time-varying media," *Advanced Photonics,* vol. 4, no. 1, pp. 014002-014002, 2022.

[17] V. Bruno *et al.*, "Broad frequency shift of parametric processes in epsilon-near-zero time-varying media," *Applied Sciences,* vol. 10, no. 4, p. 1318, 2020.

A Boundary Element Method Solver for Dispersive Feibelman Parameters in Plasmonics

Ulrich Hohenester[1,*], Lorrenz Huber[1]

[1]Department of Physics, University of Graz, Austria
*Corresponding author: ulrich.hohenester@uni-graz.at

***Abstract*—We develop a computational Maxwell solver based on the boundary element method incorporating frequency dependent and dispersive Feibelman parameters, which accounts for nonlocal effects in plasmonic nanoparticles. Typical runtimes are comparable to those of normal simulations, and we discuss how to obtain the pertinent Feibelman parameters for realistic metals.**
***Keywords*— nanophotonics, nonlocality, Feibelman parameters.**

Optical excitation of plasmonic nanoparticles enables light confinement in subwavelength volumes and strong field enhancements [1]. When dealing with sharp particle features, narrow gap regions, or quantum emitters in close proximity to structures, quantum surface effects start to play an important role. Recently, it has been suggested to account for such quantum effects through mesoscopic boundary conditions [2] that incorporate frequency-dependent Feibelman parameters [3]. The question of how to describe and exploit nonlocal photonic materials and metamaterials has attracted in the past years considerably interest [4].

In this paper, we develop the methodology and implement mesoscopic boundary conditions into a computational Maxwell solver based on the boundary element method (BEM) [5]. Contrary to previous work [6], we additionally account for dispersive Feibelman parameters that are nonlocal in the directions parallel to the metal surface. It has recently been demonstrated from supplementary time-dependent density functional theory (TDDFT) simulations that the consideration of nonlocal parameters is imperative for the accurate description of situations where the electromagnetic fields vary on a nanometer range. We discuss the critical implementation details for a Galerkin BEM scheme with Raviart-Thomas basis elements.

We have additionally developed a modified Mie theory incorporating nonlocal Feibelman parameters, and show for sodium spheres that the results of Mie theory agree well with those of our BEM simulations. The simulation results converge perfectly to the analytic predictions when refining the mesh discretization in our BEM approach. Additionally, the computational cost for the novel scheme is shown to not differ significantly from normal BEM simulations, thus rendering our approach ideal for future investigations of different particle geometries and materials. We also discuss how the pertinent Feibelman parameters can be obtained for realistic metals from supplementary calculation schemes, either based on ab-initio TDDFT simulations or hydrodynamic model description schemes [4]. Altogether, we believe that our simulation platform makes Feibelman parameters accessible to a broader community, and could establish mesoscopic boundary conditions as an integral part of plasmonics simulations.

Acknowledgments

We acknowledge Tomáš Neuman, Antton Babaze, Andrei Borisov, Vyacheslav Silkin, and Javier Aizpurua for providing nonlocal Feibelman parameters obtained from ab-initio calculations and for their valuable discussions This work was supported by Austrian Science Fund FWF under project P 37150.

References

[1] U. Hohenester, “Nano and Quantum Optics”, Springer Cham, Switzerland, 2020.
[2] P. J. Feibelman, “Surface electromagnetic fields”, Prog. Surface Science. vol. 12, pp 287, 1982.
[3] 3. Y. Yang, D. Zhu, W. Yan, A. Agarwal, M. Zheng, J. D. Joannopoulos, P. Lalanne, T. Christensen, K. K. Berggren, and M. Soljacic, “A general theoretical and experimental framework for nanoscale electromagnetism”, Nature vol. 576, pp. 248, 2019.
[4] F. Monticone, A. Mortensen, et al.. “Roadmap on Nonlocality in Photonic Materials and Metamaterials”, Optical Materials Express vol. 15, pp. 1544, 2025.
[5] L. Huber and U. Hohenester, “A computational Maxwell solver for nonlocal Feibelman parameters on plasmonics”, J. Phys. Chem. C vol. 129, pp. 2590, 2025.
[6] U. Hohenester and G. Unger, “Nanoscale electromagnetism with the boundary element method”, Phys. Rev. B vol. 105, pp. 075428, 2022.

Mapping Nonlocal Bulk Continuum to Few Surface Modes

Runzhi Zou[1], Qiang Zhou[1,*], Pu Zhang[1,#], Xue-Wen Chen[1,†]

[1]School of Physics, Huazhong University of Science of Technology, Wuhan, China

*Corresponding author: q_zhou@hust.edu.cn

#Corresponding author: puzhang0702@hust.edu.cn

† Corresponding author: xuewen_chen@hust.edu.cn

***Abstract*—The quasi-continuum of nonlocal bulk modes greatly complicates the optical responses of nanostructures and modal analysis. We establish a general framework to effectively map the nonlocal bulk continuum to few modes of an equivalent system, which admits the classical description and helps reveal physical insights from the complicated responses.**

***Keywords*— nonlocality, bulk modes, surface response, polar dielectrics**

I. Introduction

Photonic structures and devices with deep nanoscale geometric features have been experimentally feasible with advanced nanofabrication techniques and hold promise for improving performances in nanophotonic applications. Material nonlocality becomes indispensable for characterizing the localized fields in these multiscale systems, as it exerts significant influences through the induced longitudinal field interactions. The latter particularly complicate the responses by generating a quasi-continuum of bulk modes apart from perturbing surface modes. The typically subnanometer resolved mode patterns of the numerous bulk modes are almost fully confined inside nanostructures and thus often of limited interest, but pose grand challenges for theoretical description [1], [2]. Surface response models such as local analog and Feibelman's d-parameter models are specially appealing for studying the nonlocal responses due to their elegance and numerical efficiency [3], [4]. However, they are apparently incompatible with the description of the bulk modes. In this talk we report on a general framework that allows for accurate account of the bulk mode contribution to nonlocal responses with surface response models (SRMs), and more importantly effectively maps the nonlocal bulk continuum to few surface modes. Applicable to general nonlocal materials our theory provides a valuable asset for the nanophotonics community.

II. Theoretical Framework

The optical field scattered from a nanostructure is concerned in most situations. Making use of the dyadic Green's function, we prove that under certain conditions the nonlocal responses of the nanostructure can be accurately approximated with a volume-surface separated formulation of the scattered field

$$\mathbf{E}_{\text{sca}}(\mathbf{r};\omega) \approx \frac{k_0^2}{\varepsilon_0}\Bigg[\int_{\mathcal{V}} \bar{\bar{\mathbf{G}}}_0(\mathbf{r},\mathbf{r}';\omega)\mathbf{P}_{\text{LRA}}(\mathbf{r}';\omega)\,d^3\mathbf{r}' + \int_{\mathcal{L}} \bar{\bar{\mathbf{G}}}_0(\mathbf{r},\mathbf{r}';\omega)\mathbf{P}_{\text{ENL}}(\mathbf{r}';\omega)\,d^3\mathbf{r}'\Bigg]. \tag{1}$$

In essence, the scattered field results via the free-space Green's function $\bar{\bar{\mathbf{G}}}_0(\mathbf{r},\mathbf{r}',\omega)$ from a local response approximation (LRA) of volume polarization and an effective nonlocal (ENL) polarization in a surface layer of practically infinitesimal thickness. We emphasize that the latter surface contribution encompasses the bulk nonlocal effects. Based on this formulation, we are able to develop SRMs *e.g.* in vein of a preferred existing SRM to describe the nonlocal bulk modes. In the spirits of the LAM we demonstrate the surface layer is characterized with a permittivity ε_{ENL}. Then nanostructure is equivalently described with a system fully characterized with local permittivities, and seems to be readily prepared for modal analysis. Yet a physically meaningful quasinormal mode (QNM) analysis turns out only possible by further recognizing that ε_{ENL} in general should comprise of multiple Lorentzians

$$\varepsilon_{\text{ENL}}(\omega) = \varepsilon_{\infty,\text{ENL}} - \sum_{n=1}^{N} \frac{f_n \omega_{p,n}^2}{\omega^2 + i\omega\gamma_n - \omega_{0,n}^2}. \tag{2}$$

III. Results and Discussion

To exemplify the above theoretical framework we examine the nonlocal optical response of a 30 nm radius silicon carbide nanosphere dimer. Both our theory and the nonlocal theory for polar dielectrics [2] are deployed to calculate the extinction spectra of the dimer under a plane wave excitation and perform the QNM analysis for the extinction. The results are summarized in Fig. 1. As shown in Fig. 1(a), the QNM spectra of the dimer by the two theories manifest starkly contrasting features. The nonlocal theory leads to a quasi-continuum of QNMs, making the corresponding QNM analysis and reconstruction tedious and meaningless. Contrarily, our surface response model based QNM theory gives only few modes in the concerned spectral range. Thereby the QNM analysis becomes efficient and helps provide physical insights into the optical response of the dimer. In Fig. 1(b) the spectrum

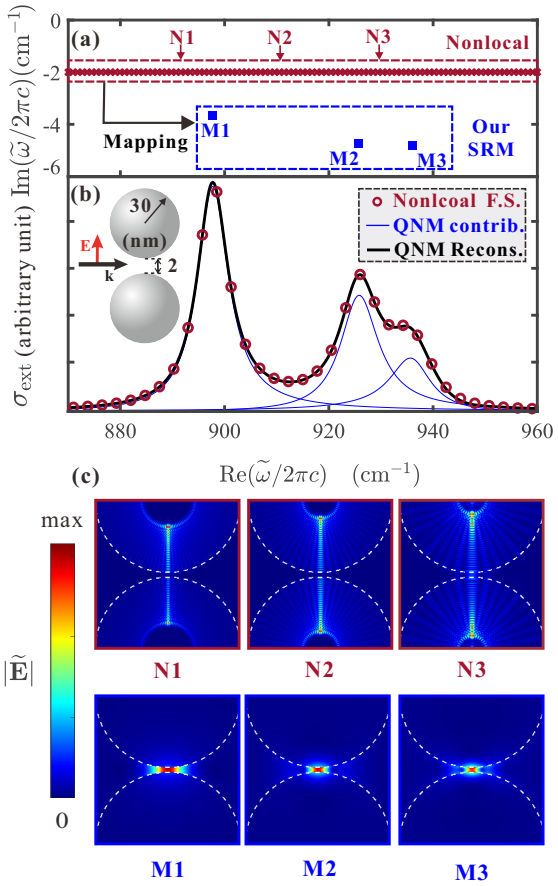

Fig. 1. Mode mapping from the nonlocal bulk mode continuum to few surface modes for a silicon carbide nanosphere dimer. (a) The QNM spectra on the complex wavenumber plane of the dimer according to the nonlocal theory and our SRM. N1, N2 and N3 are three randomly sampled QNMs from the quasi-continuum spectrum. (b) The extinction spectra of the dimer under a plane wave excitation calculated by nonlocal fullwave simulation (FS, red circles) and QNM reconstruction based on our SRM (black trace). The individual QNM contributions are depicted with blue traces. (c) The modal field pattern comparison between the sampled QNMs by the nonlocal theory and the dominant QNMs by the SRM.

reconstruction by the few QNMs successfully reproduces the extinction spectrum according to the nonlocal theory. The individual QNM contributions clearly reveal that three dominant modes are responsible for the optical response, instead of the numerous modes otherwise required in the nonlocal theory. The contrasting QNMs due to the two theories are furthermore illustrated with their modal field patterns in Fig. 1(c). All the three QNMs by the nonlocal theory have subnanometer scale standing wave patterns, which are computationally demanding to resolve and unnecessary for in most scenarios. In comparison, the dominant QNMs in our theory show rather clean patterns with vanishing field inside the nanospheres and enhanced field in the gap.

IV. Conclusion

In summary, we have established a theoretical framework which enables the description of nonlocal optical effects including bulk modes in multiscale nanostructures with convenient surface response models. More importantly its QNM theory effectively maps the quasi-continuum of bulk modes in a traditional nonlocal theory to few surface modes. Besides the application to polar dielectrics, we remark that the framework is built upon some general assumptions and is thus equally relevant in nanoplasmonics.

Acknowledgments

We acknowledge financial support from the National Natural Science Foundation of China (Grant No. 12274160 and 12574416).

References

[1] Søren Raza, Sergey I. Bozhevolnyi, Martijn Wubs and N. Asger Mortensen, "Nonlocal Optical Response in Metallic Nanostructures," *Journal of Physics: Condensed Matter*, vol. 27, pp. 183204, 2015.

[2] Christopher R. Gubbin and Simone De Liberato, "Optical Nonlocality in Polar Dielectrics," *Physical Review X*, vol. 10, pp. 021027, 2020.

[3] Yu Luo, A. I. Fernandez-Dominguez, Stefan A. Maier and J. B. Pendry, "Surface Plasmons and Nonlocality: A Simple Model," *Physical Review Letters*, vol. 111, pp. 093901, 2013.

[4] N. Asger Mortensen, "Mesoscopic electrodynamics at metal surfaces: — From quantum-corrected hydrodynamics to microscopic surface-response formalism," *Nanophotonics*, vol. 10, pp. 2563–2616, 2021.

On An Integral-Equation Method in Quantum Hydrodynamics: Efficiency and Convergence Issues

Christos Mystilidis[1,*], Xuezhi Zheng[2], Christos Tserkezis[1]

[1]POLIMA – Center for Polariton-driven Light–Matter Interactions, University of Southern Denmark, Odense, Denmark
[2]College of Electronics and Information Engineering, Nanjing University of Aeronautics and Astronautics, Nanjing, China
*Corresponding author: chrmys@mci.sdu.dk

***Abstract*— We present a Volume Integral Equation (VIE) method for the analysis of scattering from spherical nanoparticles (NPs) described by the Quantum Hydrodynamic Theory (QHT). Exploiting the inherent symmetries, we overcome significant computational bottlenecks and explore convergence issues by investigating the asymptotic behaviour of matrix elements.**

***Keywords*— hydrodynamic models, quantum plasmonics, integral-equation methods**

I. Introduction

Semiclassical hydrodynamic models emerged during the first decades of the 21st century as an essential and popular framework for quantum plasmonics [1]. QHT [1, 2] is a very promising model, reconciling nonlocal electron dynamics with electron spill-out. Despite its strong predictive powers, it has been marred by performance [1] and convergence [2] issues, showing significant dependence on the computational domain, and in particular on the spill-out length. Here, we address both issues through a VIE lens [3].

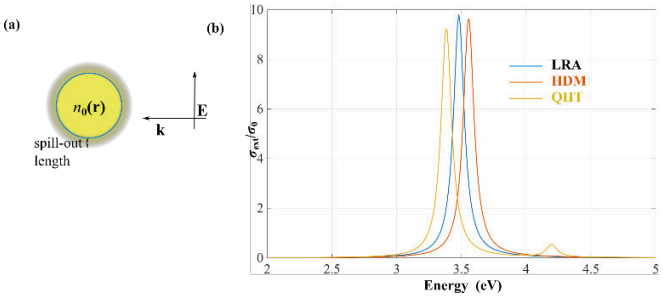

Fig. 1: (a) Scattering problem. (b) Normalised extinction cross-section for the Local Response Approximation (LRA), the Hydrodynamic Drude Model (HDM), and QHT.

II. Methods

The core element of the VIE perspective is to replace the scattering problem (see Fig. 1) with an equivalent current that induces the EM field everywhere in space. The dyadic Green's function becomes the mediator of the interaction between observation and source points and enables the introduction of IE formalism to the coupled system of QHT and Maxwell's equations. We then employ Method of Moments and Galerkin testing to acquire the linear system. The advantageous formalism together with exploiting spherical symmetries lead to computational performance on par with classical approaches.

To explore the notorious convergence issues of QHT, we investigate the asymptotic behaviour of matrix elements due to material contributions far from the origin of the NPs.

III. Results and Discussion

Our method can probe hundreds of frequency points for spherical NPs in a matter of seconds on a personal laptop. In Fig. 1, we show the extinction cross-section of a 4 nm sodium NP using three material models of progressive sophistication. QHT accurately predicts redshift with respect to the classical localized plasmon as well as the so-called Bennett resonance.

We find that the material kernels of the matrix elements involved grow exponentially the further we move away from the origin. This leads to large differences in the amplitudes of different matrix elements, and as such to severe ill-conditioning and eventual collapse of the method.

IV. Conclusion

We have demonstrated an efficient VIE method able to treat spherical NPs described by the advanced QHT. We have further analysed the asymptotic behaviour of the matrix elements and deduced that the method becomes progressively ill-conditioned as the spill-out length is increased.

Acknowledgments

This work was supported by the Independent Research Fund of Denmark (Grant No. 5281-00155B) and the Danish National Research Foundation (Project No. DNRF165).

References

[1] G. Toscano *et al.*, "Resonance shifts and spill-out effects in self-consistent hydrodynamic nanoplasmonics," *Nature Communications*, vol. 6, no. 1, May 2015.
[2] C. Ciracì and F. Della Sala, "Quantum hydrodynamic theory for plasmonics: Impact of the electron density tail," *Physical Review B*, vol. 93, no. 20, May 2016.
[3] C. Mystilidis *et al.*, Overcoming Computational Bottlenecks in Quantum Hydrodynamics: A Volume-Based Integral Formalism, https://arxiv.org/abs/2512.22920, 2025.

Probing the extreme optical field around plasmonic nanocavities

Hongli Zhou[1], Shunping Zhang[1,*]

[1]School of Physics and Technology, Wuhan University, China
*Corresponding author: spzhang@whu.edu.cn

***Abstract*— Near field enhancement is the base for a wide range of plasmonic applications. Probing fundamental limit of plasmonic field enhancement is technically challenging. Using atomic layer material as probe, we show that the averaged electric field enhancement in a resonant Ag nanocavity reach > 1200 times, extrapolating to > 1600 times for the maximum position. Using a single QD, we show that the vacuum field of a plasmonic mode is highly localized around a tip.**

***Keywords*— field enhancement, quantum tunneling, plasmon-exciton coupling, SERS.**

Correlated dark-field scattering spectra and transmission electron microscope reveals that there is always a dip in the scattering spectrum if a QD is attached around the tip of a Au nanotriangle. If it attaches to the side edge of the triangle, the dip is less pronounced or even disappear (see Figure 1). There is a clear correlation between the plasmon-exciton coupling strength and the precise position of the QD (Figure 2), reflecting the highly localized vacuum field of the plasmon.

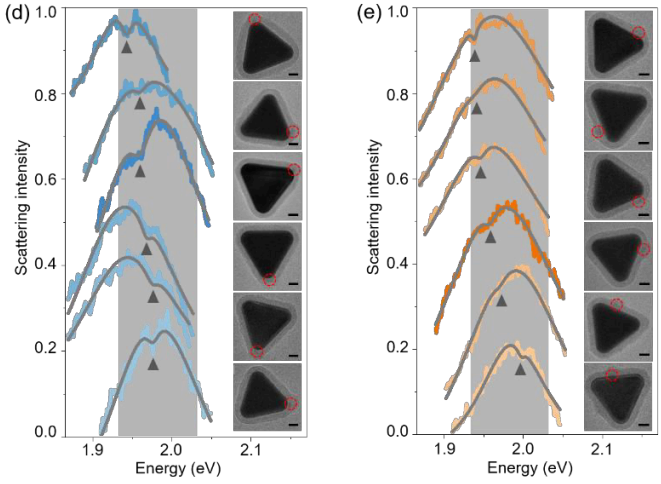

Figure 1. Scattering spectra of a Au nanotriangle-QD hybrid, correlated with transmission electron microscope image on the right. Scale bars are 20 nm.

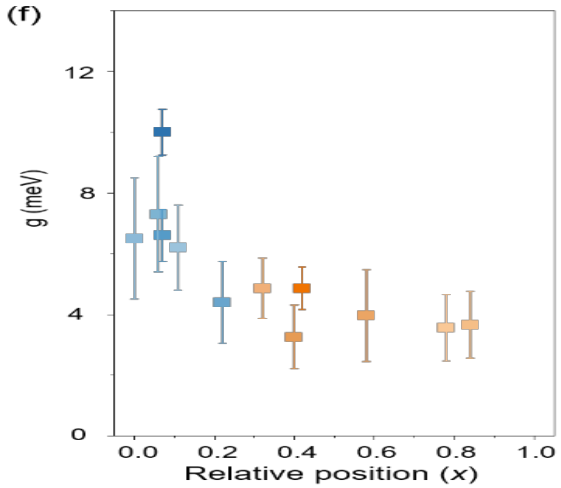

Figure 2. Distributions of the coupling strength g as a function of relative position of the QD.

REFERENCES

[1] Chen, W.; Zhang, S.; Kang, M.; Liu, W.; Ou, Z.; Li, Y.; Zhang, Y.; Guan, Z.; Xu, H. Light: Science & Applications 2018, 7, 56.

[2] Lu, Z.; Ji, J.; Ye, H.; Zhang, H.; Zhang, S.; Xu, H. "Quantifying the Ultimate Limit of Plasmonic near-Field Enhancement," Nat. Commun. 2024, 15, 8803.

[3] Lu, Z.; Song, D.; Lin, C.; Zhang, H.; Zhang, S.; Xu, H. ACS Nano 2025, 19, 5637-5648.

Lattice Resonances in Periodic Arrays of Time-Modulated Scatterers

Juan R. Deop-Ruano[1,*], María Blanco de Paz[1], Diego M. Solís[2], A. Manjavacas[1]

[1]Instituto de Química Física Blas Cabrera (IQF), CSIC, 28006 Madrid, Spain
[2]Departamento de Teoría de la Señal y Comunicaciones, University of Vigo, 36301 Vigo, Spain
*Corresponding author: juan.deop@csic.es

***Abstract*— In this work, we investigate lattice resonances in periodic arrays of time-modulated scatterers by modelling each scatterer as a harmonic oscillator with periodically varying optical properties. Our work establishes a simple theoretical framework for understanding collective lattice resonances in time-modulated arrays, enabling dynamic control and amplification of these modes.**

***Keywords*— time-varying, lattice resonances, periodic arrays, amplification, nanolasing.**

I. Introduction

Lattice resonances are collective modes emerging from coherent multiple scattering in periodic arrays of scatterers [1]. These resonances, owing to their collective nature, are characterized by an inherent nonlocal behavior and exhibit enhanced lifetimes and optical responses compared to those of individual scatterers. Despite extensive theoretical and experimental studies in passive systems, their behavior and potential applications when supported by time-modulated arrays remain largely unexplored.

II. Methods

We model each scatterer as an electric dipole whose temporal dynamics follow a harmonic oscillator equation with periodically modulated properties [2]. We include radiative losses through an Abraham-Lorentz term. This framework covers a wide range of systems that display dipolar resonances, regardless of their physical nature. We exploit the periodic nature of the modulation, and we expand both the dipole moment and the external field in Floquet series. This procedure allows us to define a polarizability tensor that relates the Floquet coefficients of the dipole to those of the external field. We then analyze the response of the system through its absorption. Absorption takes positive values when dissipation dominates, and it becomes negative when the system radiates more energy than it absorbs, a condition that signals amplification.

III. Results and Discussion

Our calculations show

- Amplification in time-modulated individual scatterers for sufficiently large modulation amplitudes.
- An intuitive picture to understand the amplification mechanism based on the evolution of eigenfrequencies with modulation amplitude and frequency.
- Amplification enabled by lattice resonances in periodic arrays, requiring significantly smaller modulation amplitudes than isolated scatterers.
- Nonlinear scattering at frequencies generated by the mixing of the excitation and modulation frequencies.

IV. Conclusion

We predict that lattice resonances in periodic arrays of time-modulated scatterers enable amplification at reduced modulation amplitudes. Thanks to our general framework, these results apply to a wide range of systems regardless of the nature of the scatterers.

Acknowledgments

This work has been supported by Grant No. PID2022-137569NB-C42 funded by MICIU/AEI/ 10.13039/501100011033 and FEDER, EU. M.B.dP. acknowledges support from a Juan de la Cierva fellowship (Grant No. JDC2023-050683-I) funded by MICIU/AEI/10.13039/501100011033 and the ESF+. J.R.D-R. acknowledges support from a predoctoral fellowship (Grant No. PRE2020- 095025) funded by MICIU/AEI/10.13039/501100011033 and ESF. D. M. S acknowledges support from a Ramón y Cajal fellowship (Grant No. RYC2023-045265-I) funded by MICIU/AEI/10.13039/501100011033 and by the ESF+, as well as from Xunta de Galicia Regional Government (Consolidation of Competitive Research Units type C: Grant No. ED431F 2025/22).

References

[1] J. J. Alvarez-Serrano, V. Aglieri, J. R. Deop-Ruano, M. Sohaib, J. Olmos-Trigo, A. Toma, A. Manjavacas, "Conceptualizing collectivity in lattice resonances of periodic arrays of nanostructures," J. Phys. Photonics, vol. 8, pp. 015069, 2026.

[2] María Blanco de Paz, Juan R. Deop-Ruano, Diego M. Solís, A. Manjavacas. "Lattice Resonances in Periodic Arrays of Time-Modulated Scatterers," arXiv preprint: arXiv:2511.11454.

Nonlocal metasurfaces controlling the geometric phase and direction of light

Adam C. Overvig[1,*]

[1]Department of Physics, Stevens Institute of Technology, USA
*Corresponding author: aovervig@stevens.edu

***Keywords*— nonlocal metasurface, geometric phase, photonic crystals.**

Summary:

We discuss progress in the field of nonlocal metasurfaces to control the direction of light scattering within a narrow bandwidth. Most notably, we engineer the local scattering properties of nonlocal modes called quasi-bound states in the continuum via symmetry-breaking design concepts. We clarify how geometric phases arise in this process, both based on polarization properties for resonant polarization-dependent reflection, and a scalar geometric phase representing a novel manifestation of the "detour phase", previously associated with the computer generated holography community. We overview the application of these ideas to several new areas, including reflectarrays overcoming previous efficiency limits of single-layer devices; multipolar nonlocal metasurfaces supporting rationally designed unidirectional modes; topological cavities controlled by the scalar geometric phase; and nonlinear metasurfaces with narrowband control of the harmonic generation.

Single-cycle optical nonlinearity of transparent conducting oxides explained

Ieng-Wai Un[1], Subhajit Sarkar[2], Yonatan Sivan[3]
[1]*Physics Department, South China Normal University, Guangzhou, China.*
[2]*Physics Department, Shiv Nadar University, Delhi, India.*
[3]*School of Electrical and Computer Engineering, Ben-Gurion University of the Negev, Beer-Sheva, Israel.*
sivanyon@bgu.ac.il

Abstract: We provide a quantitative model for the electro-optic response of transparent conducting oxides to single cycle intense pulses. We show that the interplay between spatio-temporal aspects of absorption, stimulated emission and multi-photon absorption can explain the weaker-than-before nonlinear response observed in experiments, as well as on the unexplained relaxation dynamics.
© 2023 The Authors

Time-reversal (sometimes referred to as time-reflection), time refraction and temporal photonic crystals are exotic nonlinear optical effects that attracted a lot of interest and debates in recent years. The challenge associated with realizing these effects in experiment is the need for a strong and rapid changes to the material permittivity. Transparent conducting oxides were identified as the most promising candidate materials to enable these manipulations due to their associated extremely large optical nonlinearity, reaching 100's of percent of the refractive index/permittivity [1].

After a decade of extensive experiments, a comprehensive quantitative theoretical (Boltzmann-based) description of their electronic, thermal and optical response was obtained in [2]; it revealed the cumulative (absorptive) thermal nature of their optical nonlinearity, and quantified its strength correctly in terms of the total energy in the electron sub-system. Yet, the model in [2] was capable of explaining experiments done with pulse durations of a few picosecond down to 50-100 femtosecond, but is unsuitable to describe the dynamics due to intense *single-cycle* illumination. Such extremely short illumination is needed to probe the claims of instantaneous turn-on of the optical response [1] as well as the femtosecond scale turn-off dynamics required for the realization of temporal photonic crystals. In particular, the formulation of [2] is not suitable to model the unexpectedly-short 50-100 femtosecond decay rate of the transmission observed in [3].

To meet this challenge, we have extended the formulation of [2] by switching to the density matrix formulation. This approach treats (previously-ignored) coherent aspects of the photon-electron interactions and allows accounting for coherent control schemes via phase manipulations of the incoming pulses. We find that stimulated emission approaches absorption levels at high intensities, yet, the system only reaches partial transparency (see Fig. 1(a)) due to the absence of population inversion in the remainder of the conduction band. In that regard, stimulated emission gives rise to a weaker nonlinearity (see Fig. 1(b)), but cannot invert its sign.

We then characterize the thermalization occurring under the extreme non-equilibrium conditions in the non-parabolic and narrow conduction band, and provide a simple theory that captures its new features (see Fig. 1(c)). Finally, we show that electron-phonon interactions are too weak to explain the observed fast transmission relaxation, but that a (multi-photon) absorption of valence band electrons (modelled via DFT), and spatial dynamics and substrate effects can explain experimental findings. Our approach paves the way for quantitative modelling of time-varying photonics and coherent wave control on few-femtosecond timescales in these systems.

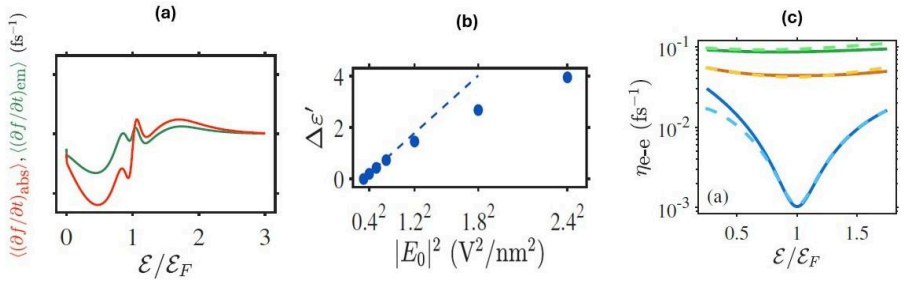

Fig. 1. (a) A comparison of the strengths of absorption and stimulated emission of an ITO particle under illumination by strong single cycle pulse. (b) The associated changes of the ITO permittivity as a function of illumination strength. (c) The e-e relaxation rate (solid) and its analytic approximated form (dashed) for various time cross-sections.

References

[1] R. Tirole *et al.*, Nature Physics 19, 999 (2023).
[2] S. Sarkar, I.W. Un, Y. Sivan, Phys. Rev. Appl. 19, 014005 (2023). I.W. Un, S. Sarkar, Y. Sivan, Phys. Rev. Appl., 19, 044043 (2023).
[3] Lustig *et al.*, Nanophotonics 12, 2221-2230 (2023).

Hydrodynamic model for nonlocal electrodynamics effects in ultra-confined plasmons.

A. J. Chaves[1,2*], T. C. Barbosa[3], L. Jelver[4], S. S. Cardoso[1], D. R. da Costa[5], L-. C. Campos[3], I. D. Barcelos [6], N. A. Mortensen [4,7], N. Peres[1,4,8]

[1] Centro de Física (CF-UM-UP) and Departamento de Física, Universidade do Minho, Braga, Portugal
[2] Department of Physics, Aeronautics Institute of Technology, São José dos Campos, SP, Brazil
[3] Centro de Tecnologia em Nanomateriais e Grafeno, Universidade Federal de Minas Gerais, Belo Horizonte, MG Brasil and Departamento de Física, Universidade Federal de Minas Gerais, Belo Horizonte, MG, Brasil
[4] POLIMA—Center for Polariton-driven Light-Matter Interactions, University of Southern Denmark, Odense, Denmark
[5] Departamento de Física, Universidade Federal do Ceará, Campus do Pici, Fortaleza, Ceará, Brazil
[6] Laboratório Nacional de Luz Síncrotron, Centro Nacional de Pesquisa em Energia e Materiais, Campinas, SP, Brasil
[7] Danish Institute for Advanced Study, University of Southern Denmark,Odense M, Denmark
[8]International Iberian Nanotechnology Laboratory (INL), Av Mestre José Veiga, Braga, Portugal
*Corresponding author: d14891@uminho.pt

***Abstract*—Using a quantum hydrodynamic model, we show that hyperbolic plasmon–polaritons in few-layer black phosphorus are strongly renormalized by nonlocal effects. We further demonstrate that nonlocal electrodynamics is essential to describe plasmon–phonon–polariton dispersion in twisted bilayer graphene on talc obtained from SNOM measuraments.**

***Keywords*— plasmons, anisotropic, quantum hydrodynamic model, graphene, twisted bilayer graphene, two-dimensional materials, snom**

I. Introduction

The hydrodynamic model has emerged as a versatile and robust framework for studying the light-matter interaction in condensed matter. It was successfully applied in various systems: metals, heavy-doped semiconductors, and two-dimensional (2D) materials. Here, we will focus on surface plasmon-polaritons in 2D materials, including, as examples, graphene and phosphorene.

II. Hydrodynamic model in graphene

For the semimetal graphene, we derive a hydrodynamic model from the Boltzmann equation considering a Drude mass for graphene electrons, which links the Fermi momentum with the Fermi velocity. We study the formation of plasmonic wakes when transverse fast electrons move parallel to the graphene sheet, obtaining simple expressions for the electrostatic potential. We demonstrate a transition from Mach-type wakes at high speeds to Kelvin-type wakes at lower speeds, obtaining the plasmonic parameters to calculate the Froude number. The electron-energy loss spectrum was calculated, which shows the effect of resonances caused by graphene surface plasmons [1].

III. Nonlinear and nonlocal properties of plasmons in two-dimensional materials

We study a 2D electron gas using the Madelung equations for quantum mechanics in conjunction with Poisson's equation; we calculate the spectrum of magnetoplasmons and the magneto-optical conductivity in the electrostatic regime, incorporating nonlocal corrections due to the Fermi pressure and the Bohm potential. We analyze nonlinear and nonlocal second-harmonic generation, demonstrating how plasmon excitation enhances this process. We further discuss the self-modulation that renormalizes the plasmon dispersion, driven by nonlinearity. For both cases, we obtain simple analytical expressions [2].

IV. Nonlocal electrodynamics in anisotropic plasmons

Using the Madelung formalism, we apply it to anisotropic systems. As a case study for an anisotropic two-dimensional electron gas, we applied our model to electrons in monolayer black phosphorus, i.e., phosphorene. The plasmon dispersion obtained with the hydrodynamic model is in excellent agreement with ab initio calculations. We then focus on the study of surface plasmon-polaritons, which can be hyperbolic in the case of phosphorene when the contributions from interband transitions are included in the optical conductivity. Our findings demonstrate that including nonlocal effects in the optical conductivity inhibits phosphorene to host hyperbolic surface plasmon-polaritons, which shows the importance of going beyond Drude or other local models to describe plasmon-polaritons in hyperbolic media [3].

V. Plasmon-phonon-polaritons in twisted bilayer graphene

Recently IR s-SNOM measurements of twisted bilayar graphene over talc [4] revealed strongly confined plasmon-phonon polaritons. Talc, a van der Waals phyllosilicate, induces p-type doping in graphene, and its phonon modes hybridize with graphene plasmons, giving rise to ultra-confined surface plasmon–phonon–polariton (SP^3) modes. We demonstrate that a local electromagnetic description of graphene's conductivity is fails to reproduce the measured dispersion relation of the SP^3 modes, whereas a nonlocal hydrodynamic model correctly quantitatively captures the experimental results.

References

[1] Chaves, A. J., Peres, N. M. R., Mortensen, N. A., 2017. Phys. Rev. B., Hydrodynamic model approach to the formation of plasmonic wakes in graphene, 96, 195438.

[2] Cardoso, S. S., Chaves, A. J., Mortensen, N. A. Peres, 2024. Arxiv, Quantum Hydrodynamics Meets Plasmonics and Nonlinear Optics in Two-Dimensional Materials.

[3] Chaves, A. J., Jelver, L., da Costa, D. R., Cox, J. D., Mortensen, N. A., Peres, N. M. (2025). Nonlocal electrodynamics of two-dimensional anisotropic magnetoplasmons. Nanophotonics, 14(25), 4495-4511.

[4] Barbosa, T. C., Chaves, A. J., Freitas, R. O., Campos, L. C., Barcelos, I. D. (2025). Ultra-confined plasmons reveal moiré patterns in a twisted bilayer graphene–talc heterostructure. Nanoscale, 17(15), 9205-9212.

Nonlocal and Nonlinear Effects in Plasmonics from a Time-Dependent Density Functional Theory Perspective

Antton Babaze [1,2,*], Javier Aizpurua[3,4,5], Andrei G. Borisov[6]

[1]Department of Applied Physics, School of Architecture, UPV/EHU, Spain
[2]Centro de Física de Materiales CSIC-UPV/EHU, Spain
[3]Donostia International Physics Center DIPC, Spain
[4]Department of Electricity and Electronics, FCT-ZTF, UPV/EHU, Spain
[5]IKERBASQUE, Basque Foundation for Science, Spain
[6]Institut des Sciences Moléculaires d'Orsay ISMO, CNRS, Université Paris-Saclay, France
*Corresponding author: antton.babaze@ehu.eus

***Abstract*—Using time-dependent density functional theory, we study electron dynamics in metallic nanostructures under different excitation conditions, including continuous-wave illumination, ultrashort pulses, quantum emitters, and fast electron beams, and investigate the role of nonlocality, nonlinearity, and other quantum phenomena in the excitation of plasmonic resonances, harmonic generation and nanoscale electron transport.**

***Keywords*— TDDFT, Feibelman parameter, Landau damping, EELS, harmonic generation, ultrafast dynamics, photoemission.**

I. Introduction

Plasmonic nanostructures enable the manipulation of light at the nanoscale, giving rise to confined and enhanced optical fields within volumes on the order of nm^3. As a result, quantum effects such as nonlocal dynamical screening and strong-field nonlinearities gain importance in optical and electronic responses, challenging classical or semiclassical descriptions. Such effects manifest, for example, in energy shift and broadening of localized surface plasmon resonances (LSPRs) of metallic nanoparticles (MNPs) and in optical field emission from MNPs.

In this context, time-dependent density functional theory (TDDFT) provides a fully quantum-mechanical framework that captures these effects in a unified manner without fitting parameters. Here, we employ TDDFT to investigate nonlocal and nonlinear response of MNPs, as well as electron tunneling and photoemission, under a variety of excitation conditions, including cw illumination, ultrashort and intense optical pulses, interactions with quantum emitters (QEs), and fast electron beams.

II. Methods

Our approach is based on the direct solution of the Kohn–Sham equations within TDDFT,

$$i\frac{\partial}{\partial t}\Psi_j(\mathbf{r},t) = \hat{H}[n(\mathbf{r},t)]\,\Psi_j(\mathbf{r},t),$$

where the time-dependent Kohn–Sham Hamiltonian is given by

$$\hat{H}[n(\mathbf{r},t)] = \hat{T} + V_{\text{eff}}[n(\mathbf{r},t)] + V_{\text{ext}}(\mathbf{r},t),$$

with $\hat{T}$ being the kinetic-energy operator, $V_{\text{ext}}(\mathbf{r},t)$ the external potential driving the excitation, and $V_{\text{eff}}[n(\mathbf{r},t)] = V_{\text{H}}[n(\mathbf{r},t)] + V_{\text{xc}}[n(\mathbf{r},t)]$ the effective potential, including Hartree and exchange–correlation contributions. The electronic density is computed as $n(\mathbf{r},t) = \sum_{j\in\text{occ}} \chi_j |\Psi_j(\mathbf{r},t)|^2$, where the sum runs over all initially occupied Kohn–Sham orbitals $\Psi_j(\mathbf{r},t=0)$, with degeneracy factors χ_j. The initial ground-state orbitals are obtained from the static Kohn–Sham equations.

Numerical implementation of the time-dependent Kohn–Sham equations is performed using wave-packet propagation on a real-space mesh. In our real-time TDDFT calculations, the metal is treated within the jellium model, where the ionic charge density is represented as a uniform positive background. This framework allows us to address plasmonic systems of sufficiently large size to be directly comparable with experiments. Complementary atomistic calculations are performed within the linear-response frequency-domain framework using the PyNAO package [1].

III. Results and Discussion

First, we analyze nonlocal effects in coupled MNP–QE systems, where LSPRs in simple MNPs (such as, e.g. alkali metals) are found to redshift and broaden as the nanoparticle size decreases. These trends originate from nonlocal dynamical screening and the finite potential barrier at the metal surface, which give rise to spill-out of the induced electron density and to surface-enabled Landau damping. For QEs positioned within nanometric plasmonic cavities, the TDDFT description of the nonlocal metallic response can, in many situations, be accurately reproduced by the surface-response formalism (SRF) [2], particularly when employing *dispersive* Feibelman

parameters $d_\perp(\omega, k_\parallel)$ that depend on both frequency and parallel momentum transfer [3]. This extension is essential for properly describing higher-order LSPRs involving large in-plane wavevectors and extreme field localization. However, when the cavity size is reduced to subnanometric MNP–QE separations, the TDDFT results show the emergence of charge-transfer processes [4], [5]. Consequently, the SRF breaks down because it cannot account for electronic-state hybridization and tunneling across the junction.

Next, we turn to the influence of nonlocal effects on plasmonic modes confined within the nanoparticle volume. The nonlocal response of the electron cloud in MNPs affects not only LSPRs but also confined bulk plasmons (CBPs), which correspond to longitudinal collective oscillations of the electron density. Since CBPs cannot be efficiently excited by light, we employ penetrating electron beams to analyze their modal structure [6]. Our TDDFT calculations show that, for electron trajectories passing through the MNP center, the electron-energy loss spectrum is dominated by a pronounced CBP peak near the plasma frequency ω_p, corresponding primarily to the angularly symmetric (monopolar) mode, and is accompanied by weaker higher-energy multipolar bulk modes. As the electron-beam impact parameter increases, the excitation strength of the higher-order multipolar modes increases, and additional CBP resonances appear, resulting in a blueshift of the main CBP peak. The robustness of these trends is further corroborated by complementary calculations based on a classical hydrodynamic model.

We then consider nonlinear optical processes in plasmonics, which become relevant when the system is driven by intense electromagnetic fields and are strongly determined by the geometry and symmetry of both the nanostructure and the driving field. For an axially symmetric metallic nanowire driven by light linearly polarized perpendicular to the nanowire axis, our TDDFT calculations show that far-field scattering occurs exclusively at odd harmonics of the fundamental frequency, consistent with axial symmetry. When the nanowire is excited by circularly polarized light (in the plane perpendicular to the nanowire axis), the nonlinear optical response is clearly distinct [7]: i) any harmonic emission into the far field is suppressed and ii) multipolar near fields are induced at the harmonic frequencies carrying spin angular momentum opposite to that of the incident field. Furthermore, our TDDFT results show that coupling QEs to centrosymmetric MNPs activates second-harmonic generation in the far field and enables control of this otherwise symmetry-forbidden process [8].

Finally, we explore a different class of nonlinear processes, namely electron transport across (sub)nanometric metallic junctions induced by ultrashort single-cycle or few-cycle optical pulses. Real-time TDDFT calculations allow us to track the ultrafast electron dynamics and identify distinct transport regimes. In particular, we identify photon-assisted tunneling and over-the-barrier transitions associated with multiphoton absorption at low optical fields, and adiabatic optical-field emission at high optical fields [9]. Additionally, we investigate how these transport regimes evolve as the junction size is further reduced and a dc bias is applied [10].

IV. Conclusion

We have presented a TDDFT-based study of quantum effects in nanoplasmonics, with a focus on nonlocal and nonlinear responses, as well as electron tunneling and photoemission, under excitation by continuous illumination, ultrashort single-cycle pulses, and fast electron beams. Our work provides a fully quantum-mechanical picture of nanoscale light–matter interaction and electron dynamics, revealing rich phenomena under extreme conditions. These insights advance our understanding of photonic and optoelectronic systems and suggest strategies for controlling spectroscopy, high-harmonic generation, and ultrafast electron transport in next-generation nanoscale devices.

Acknowledgments

The authors gratefully acknowledge all collaborators who contributed to this work, and in particular the members of the "Theory of Nanophotonics Group" in San Sebastian. This work was supported by grant PID2022-139579NB-I00 funded by MICINN/AEI/10.13039/501100011033 and by ERDF/EU, and by grant IT-1526-22 funded by the Department of Science, Universities and Innovation of the Basque Government.

References

[1] P. Koval, M. Barbry, and D. Sánchez-Portal, "PySCF-NAO: An efficient and flexible implementation of linear response time-dependent density functional theory with numerical atomic orbitals," *Comput. Phys. Commun.*, vol. 236, pp. 188–204, 2019.

[2] A. Babaze, E. Ogando, P. E. Stamatopoulou, C. Tserkezis, N. A. Mortensen, J. Aizpurua, A. G. Borisov, and R. Esteban, "Quantum surface effects in the electromagnetic coupling between a quantum emitter and a plasmonic nanoantenna: Time-dependent density functional theory vs. semiclassical Feibelman approach," *Opt. Express*, vol. 30, pp. 21159–21183, 2022.

[3] A. Babaze, T. Neuman, R. Esteban, J. Aizpurua, and A. G. Borisov, "Dispersive surface-response formalism to address nonlocality in extreme plasmonic field confinement," *Nanophotonics*, vol. 12, pp. 3277–3289, 2023.

[4] A. Babaze, R. Esteban, A. G. Borisov, and J. Aizpurua, "Electronic exciton–plasmon coupling in a nanocavity beyond the electromagnetic interaction picture," *Nano Lett.*, vol. 21, pp. 8466–8473, 2021.

[5] B. Candelas, N. Zabala, P. Koval, A. Babaze, D. Sánchez-Portal, and J. Aizpurua, "Influence of atomistic features in plasmon–exciton coupling and charge transfer driven by a single molecule in a metallic nanocavity," *J. Chem. Phys.*, vol. 161, p. 044707, 2024.

[6] B. Candelas, M. Urbieta, A. Babaze, E. Ogando, A. G. Borisov, N. Zabala, and J. Aizpurua, "Ab initio atomistic characterization of confined bulk and Bennett plasmons in metallic nanoparticles as probed by penetrating electrons," *J. Phys. Chem. Lett.*, vol. 16, pp. 2965–2971, 2025.

[7] M. Quijada, A. Babaze, J. Aizpurua, and A. G. Borisov, "Nonlinear optical response of a plasmonic nanoantenna to circularly polarized light: Rotation of multipolar charge density and near-field spin angular momentum inversion," *ACS Photonics*, vol. 10, pp. 3963–3975, 2023.

[8] A. Babaze, R. Esteban, J. Aizpurua, and A. G. Borisov, "Second-harmonic generation from a quantum emitter coupled to a metallic nanoantenna," *ACS Photonics*, vol. 7, pp. 701–713, 2020.

[9] A. G. Borisov, B. Ma, M. Zapata-Herrera, A. Babaze, M. Krüger, and J. Aizpurua, "Femtosecond optical-field-driven currents in few-nanometer-size gaps with hot electron injection into metallic leads," *ACS Photonics*, vol. 12, pp. 2137–2150, 2025.

[10] B. Ma, A. Babaze, M. Krüger, J. Aizpurua, and A. G. Borisov, "Ultrafast optically induced tunneling in narrow metallic gaps from the time-dependent density functional perspective," *arXiv:2509.14802*, 2025.

Controlling the optical response of 2D semiconductors with THz pulses

Tommaso Venanzi[1], Marzia Cuccu[1], Edith Wietek[1], Xiaoxiao Sun[2], Raul Perea-Causin[3], Samuel Brem[4], Daniel Erkensten[4], Takeshi Taniguchi[5], Kenji Watanabe[5], Ermin Malic[4], Manfred Helm[1,2], Stephan Winnerl[2] and Alexey Chernikov[1]

[1]TUD Dresden University of Technology, Dresden, Germany
[2]Helmholtz-Zentrum Dresden-Rossendorf (HZDR), Dresden, Germany
[3]Department of Physics, Stockholm University, Stockholm, Sweden
[4]Department of Physics, Philipps-Universität Marburg, Marburg, Germany
[5]National Institute for Materials Science (NIMS), Tsukuba, Japan

*Corresponding author: tommaso.venanzi@tu-dresden.de

***Abstract* – We use THz pulses to manipulate the optical response of $MoSe_2$ and WSe_2 monolayers, and $MoSe_2/WSe_2$ heterostructures. This method can be used to control excitonic populations on ultrafast time-scales, to access optical-driven nonlinear properties of matter and to design photonic devices with THz switches.**

***Keywords* - terahertz, 2D materials, optical control of matter**

I. Introduction

An important avenue of research is to find means for external control of light-matter interaction by tailoring on-demand the optical response of materials. In this way, it is possible to realize reconfigurable photonic devices.

2D semiconductors offer a promising and versatile platform to reach this goal. In fact, they feature high exciton binding energies that lead to a strong light-matter coupling [1] and their optical response is easily reconfigurable by the application of voltages, strain fields, and by patterning the dielectric environment [2]. However, there are major limitations to how fast the optical response of these materials can be tuned, restricting the majority of applications to an essentially static regime. Here, we use short THz pulses to manipulate the optical response of 2D semiconductors on an ultrafast time scale, showing a fascinating route for optically-controlled photonic devices and optically-triggered nonlinear properties of matter.

II. Methods

A sketch of the introduced experimental approach is shown in Fig. 1a. The picosecond, spectrally narrow THz pulses are generated at the infrared Free-Electron Laser facility (FELBE) at 13 MHz repetition rate with tunable photon energies [3]. Visible pulses (λ = 400 nm) are obtained from a frequency-doubled Titanium:Sapphire laser to excite populations of electron-hole pairs into the 2D semiconductors, that then form complex excitonic quasiparticles, such as excitons, trions, and

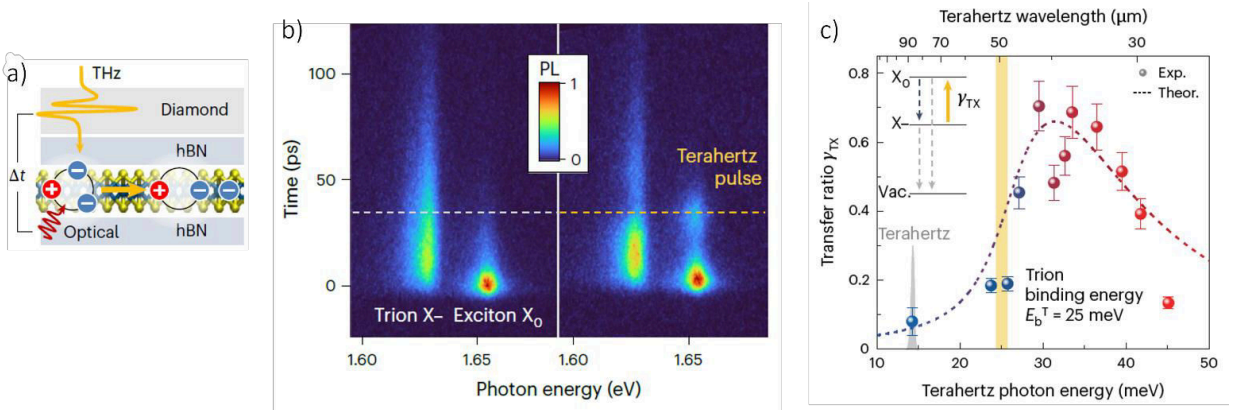

***Figure 1**: (a) Sketch of the experiment. (b) Time-resolved PL spectra of $MoSe_2$ monolayer with and without THz pulses. (c) Fraction of trions transferred to excitons as a function of THz photon energy.*

biexcitons [1]. The exciton dynamics is subsequently monitored by recording time-resolved photoluminescence (trPL) spectra with a streak camera. The arrival of the THz pulse is controlled by an externally tunable delay. We study different Transition Metal Dichalcogenide monolayers and heterostructures, such as $MoSe_2$, WSe_2, and $WSe_2/MoSe_2$. All the samples are encapsulated in hBN and deposited on a diamond substrate.

III. Results and Discussion

Figure 1b shows the trion and exciton dynamics in MoSe2 monolayer after optical excitation [4]. By adding THz pulses after about 30 picosecond delay with respect to the visible excitation (Fig 1b, right panel), we observe a strong quenching of the trion emission and a temporary brightening of the exciton emission. Furthermore, by tuning the frequency of the THz pulses, we record the THz deionization spectrum of trions (Fig. 1c). Importantly, efficient trion-to-exciton conversion is observed when the THz photon energy is equal or higher than the trion binding energy.

Recently, we observed similar impact of THz radiation in other materials such as WSe_2 monolayers [5] and $MoSe_2/WSe_2$ heterostructures [unpublished], that host more complex excitonic species such as charged biexcitons and interlayer excitons, respectively. In particular, we show that beyond manipulation of charged excitonic complexes, THz can induce both triplet-to-singlet and inter-to-intralayer exciton transitions in heterobilayers.

IV. Conclusion

Altogether, the results open promising pathways towards external optical control of many-particle excitonic states in 2D semiconductors. This method can be employed to access non-equilibrium nonlinear properties of matter and to tailor the optical response of low-dimensional materials for reconfigurable photonic devices with ultrafast THz switches.

Acknowledgments

Funding by the BMBF / DESY grant “ultraTELEQ” (05K25OD1) is gratefully acknowledged. We thank M. M. Glazov, M. Ortolani and L. Baldassarre for helpful discussions. Financial support by the DFG via Emmy Noether Initiative (CH 1672/1, project ID 287022282, A.C.), SFB 1277 (project B05, project ID: 314695032, A.C.) and SFB1083 (project B09, project ID 223848855, E.M.), DFG project ‘Propagation dynamics of exciton-electron complexes in atomically-thin semiconductors’ (project ID542873285, E.M., A.C.), the Würzburg-Dresden Cluster of Excellence on Complexity and Topology in Quantum Matter (ct.qmat) (EXC2147, project ID 390858490, A.C.) is gratefully acknowledged. Parts of this research were carried out at ELBE at the Helmholtz-Zentrum Dresden-Rossendorf e.V., a member of the Helmholtz Association. We thank P. Michel and the ELBE team for support. A.C. acknowledges funding from ERC through CoG CoulENGINE (GA number 101001764). K.W. and T.T. acknowledge support from the JSPS KAKENHI (grant numbers 20H00354, 21H05233 and 23H02052) and World Premier International Research Center Initiative (WPI), MEXT, Japan.

References

[1] G. Wang et al., “Colloquium: Excitons in atomically thin transition metal dichalcogenides”, *Reviews of Modern Physics*, *90*(2), 021001, 2018.

[2] F. de Abajo et al., “Roadmap for photonics with 2D materials”, ACS Photonics 12, 8, 3961–4095, 2025.

[3] M. Helm et al., “The ELBE infrared and THz facility at Helmholtz-Zentrum Dresden-Rossendorf”, The European Physical Journal Plus, 138(2), 158, 2023.

[4] T. Venanzi, et al., “Ultrafast switching of trions in 2D materials by terahertz photons”, Nature Photonics, 18(12), 1344-1349, 2024.

[5] M. Cuccu, et al., “Terahertz-induced population transfer between exciton complexes in monolayer WSe_2”, Physical Review B, 112(20), 205302, 2025.

Mid-infrared Nonlinearity in Heavily-doped Semiconductor Nanoantennas and Waveguides

Michele Ortolani[1,*], Raffaella Polito[2], Maria Gambelli[1,2], Enrico Bau[3], Andreas Tittl[3], Luca Lucia[4], Adel Bousseksou[4], Raffaele Colombelli[4], G. Beaudoin[4], I. Sagnes[4], Huatian Hu[5], Gonzalo Alvarez-Perez[5], Cristian Ciraci[5], Enrico Talamas-Simola[6], Monica De Seta[6], Sara Cibella[2], Francesco Mattioli[2] Andrea Notargiacomo[2], Marialilia Pea[2], Tommaso Venanzi[7] and Valeria Giliberti[1,7]

[1]Department of Physics, Sapienza University of Rome, Italy
[2] Institute for Photonics and Nanotechnologies, CNR, Rome, Italy
[3] Faculty of Physics, Ludwig-Maximilian University, Munich, Germany
[4] Centre de Nanosciences et de Nanotechnologies, CNRS, Palaiseau, France
[5] Center for Biomolecular Nanotechnologies, IIT, Arnesano, Italy
[6]Department of Science, Roma Tre University, Rome, Italy
Center for Life Nano and Neuro Sciences, IIT, Rome, Italy
*Corresponding author: michele.ortolani@roma1.infn.it

***Abstract*— The hydrodynamic behaviour of free electrons generates strong nonlinear optical response when the effective mass is small, as in the n-type doped semiconductors InGaAs and Ge. We show nanoantennas and waveguides where the nonlinear response depends on carrier density, is resonant with antenna geometry, and tunable with a field-effect voltage.**

***Keywords*— nanoantennas, mid-infrared, doped semiconductors, hydrodynamics.**

I. Introduction

Two fundamental mechanisms exist in a plasmonic structure for the enhancement of the instantaneous nonlinear optical response. The first mechanism is the well-known dielectric nonlinear susceptibility of bulk materials hosting or surrounding the free electrons, which can be enhanced by the local plasmonic field enhancement. The second mechanism is due to the collective motion of free electrons under an external driving field, which can be modeled by a set of hydrodynamic equations of motion in analogy with a classical fluid. While there is a physical limit to the maximum dielectric nonlinearity, related to the form of anharmonic potential that sets upper bounds for $\chi^{(2)}$ and $\chi^{(3)}$ [1], there is no such a limitation to free-electron nonlinearities that increase in strength when the electron effective mass is small, as it is the case in many n-type doped semiconductors such as (In,Ga)As and Ge, which are extremely relevant for the development of integrated photonic technology [2]. Even though the response of a homogeneous electron gas is intrinsically nonlinear, coupling the free-electron nonlinear field to the far-field requires the patterning of the free-electron host medium into well-designed nanostructures, which can also resonantly enhance the local fields and field gradients [3], and therefore the nonlinear effects.

If the semiconductor is very heavily doped at the solubility limit, its plasma frequency can reach the mid-infrared here defined as the wavelength range between 5 and 12 μm, short enough for the development of on-chip photonic integrated circuits (PICs), but long enough for the fabrication of lithographic plasmonic cavities and nanoantenna arrays illuminated at normal incidence. In addition, in doped semiconductors the free electron density (and, with it, the optical nonlinearity) can be voltage-tuned with a metal gate electrode separated from the semiconductor by a dielectric (oxide) layer. In this work, we show several experiments conducted on doped semiconductor nanostructures in the last years on nanoantennas and integrated waveguides that support the above picture of hydrodynamic enhancement of optical nonlinearities in the mid-infrared, and, more generally, of nonlocal effects that shift the resonance frequency of deeply sub-wavelength cavities.

II. Methods

The nonlinear and nonlocal dynamics of a free-electron fluid under external electric and magnetic fields, $\mathbf{E}(r, t)$ and $\mathbf{H}(r, t)$, is described by the following equation for the electron density $n(r, t)$ and current $\mathbf{J}(r, t)$:

$$m^*\left(\frac{\partial}{\partial t}-\frac{\mathbf{J}}{en}\cdot\nabla+\gamma\right)\frac{\mathbf{J}}{en}=e\mathbf{E}-\frac{\mathbf{J}}{n}\times\mu_0\mathbf{H}+\nabla\frac{\delta G[n]}{\delta n} \quad (1)$$

where μ_0 denotes the magnetic permeability, e the electron charge, γ a suitable damping rate of free-carrier oscillations, and $G[n]$ is the free-energy functional whose derivative vs. n gives the *quantum pressure* of the fluid, related to Thomas-Fermi

screening and Pauli exclusion principle. We use this equation in combination with Maxwell's equations to simulate and predict the linear and nonlinear behavior of the investigated semiconductor nanostructures.

Fabrication is carried out at CNRS and CNR facilities mainly with electron-beam lithography, lift-off of metal layers and dry etching of semiconductor layers. Notably, ridge waveguides with vertical walls are obtained by inductively-coupled plasma etching. HfO_x deposited by atomic layer deposition is employed as the gate oxide for the field-effect devices.

Linear and nonlinear optical measurements are performed, respectively, by Fourier-transform infrared spectroscopy and by optical pumping of the semiconductors with short mid-IR pulses (duration of the order of 100 fs) generated by optical parametric amplifiers (OPA).

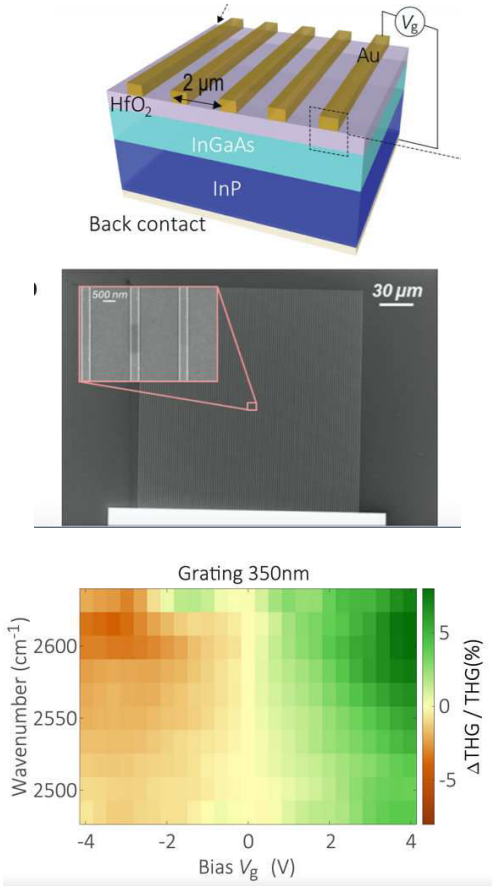

Fig. 1 Field-effect tuning of the nonlinear coefficient for third harmonic generation (THG) in a heavily doped InGaAs layer under a metal grating antenna, also acting as the gate electrode. The OPA pump spectrum extended from 11.5 to 12 µm, while the antenna resonance measured by FTIR was at 10.7 µm for this specific grating.

III. Results

Experimental results show:

- Enhancement of the nonlinearity of free electrons by two orders of magnitude above the dielectric susceptibility of the undoped host material in InGaAs dipole nanoantennas [4].
- Plus/minus 5 percent tunability of the nonlinear coefficient with a field-effect voltage of plus/minus 4 V in grating-coupled layers (Fig. 1).
- Blueshift of plus 10 percent of metal-Ge-metal cavity resonances due to increasing nonlocal effects with decreasing temperature hence decreasing free-electron oscillation damping rate (Fig. 2a).
- Onset of supercontinuum generation in integrated hybrid waveguides with a dielectric core and a thin plasmonic cap layer (Fig. 2b).

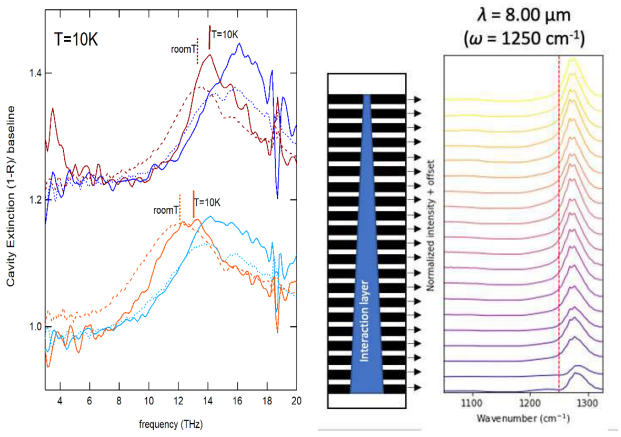

Fig. 2 (a) Resonance blueshift with decreasing T in a metal-Ge-metal cavity. (b) Transmitted spectrum for a 8 µm pump pulse trough integrated hybrid waveguides with increasing interaction length.

IV. Conclusion

Nonlinear and nonlocal effects define the linear and nonlinear optical response of doped semiconductors, with clear technological opportunities.

Acknowledgments

This work was supported by the European Union under the European Innovation Council (EIC) project NEHO (Grant No.101046329). Views and opinions expressed are those of the authors only and do not necessarily reflect those of the European Union or the EIC and SMEs Executive Agency (EISMEA). Neither the European Union nor the granting authority can be held responsible for them.

This work received funding from the Italian Ministry of Research program PRIN 2022 "Strong light-matter coupling manipulation in SiGe quantum wells at terahertz frequencies" CUP F53D23001190006.

References

[1] M. G. Kuzyk, "Physical limits on electronic nonlinear molecular susceptibilities." Physical Review Letters 85, 1218 (2000).

[2] F. De Luca, M. Ortolani, and C. Ciracì "Free electron nonlinearities in heavily doped semiconductors plasmonics." Physical Review B 103, 115305 (2021).

[3] J. R. Maack, N. A. Mortensen, and M. Wubs. "Two-fluid hydrodynamic model for semiconductors." Physical Review B 97, 115415 (2018).

[4] A. Rossetti, T. Venanzi, H. Hu et al. "Control and enhancement of optical nonlinearities in plasmonic semiconductor nanostructures." Light: Science & Applications 14, 192 (2025).

Remote Nonlinear Imaging of Hyperbolic Phonon Polaritons using Sum-Frequency Microscopy

Richarda Niemann[1,2], Gonzalo Álvarez-Pérez[3], Ana Isabel F. Tresguerres-Mata[4], Enrique Teran-Garcia[4], Dorotheé Mader[1], Niclas Sven Mueller[1,5], Sören Wasserroth[1], Martin Wolf[1], Aitana Tarazaga Martín-Luengo[4], Javier Martín-Sánchez[4], Pablo Alonso-Gonzáles[4], Alexander Paarmann[1]

[1]Fritz-Haber Institut der Max-Planck-Gesellschaft, Berlin, Germany
[2]Vanderbilt University, Nashville, TN, USA
[3]IIT, Istituto Italiano di Tecnologia, Arnesano, Italy
[4]University of Oviodo, Oviedo, Spain
[5]Freie Universität Berlin, Berlin, Germany
*Corresponding author: alexander.paarmann@fhi-berlin.mpg.de

***Abstract*— Sum-frequency generation (SFG) wide-field spectro-microscopy of thin flakes of the biaxial van der Waals crystal α-MoO_3 placed on an AlN substrate is used to remotely image hyperbolic phonon polaritons propagating within SFG-inactive α-MoO_3, through their fields leaking into the inversion-broken AlN substrate.**

***Keywords*— nonlinear, infrared, microscopy, polaritons, hyperbolic.**

I. Introduction

Hyperbolic phonon polaritons supported in strongly anisotropic polar crystals due to ultrastrong light-matter coupling between infrared light and directional phonon resonances have emerged as a workhorse of modern nanophotonics[1]. They provide extreme spatial confinement and highly directional propagation at low material losses[1,2]. The excitation and detection of such deeply subdiffractional modes is typically achieved using a sharp metallic tips in scattering-type near-field optimal microscopy (s-SNOM)[3]. While being very useful for studying such systems, s-SNOM – as a scanning probe technique – typically requires long acquisition times as well as high laser stability for high-quality images.

Recently, infrared-visible sum-frequency generation (SFG) spectro-microscopy has been introduced as an alternative method, also providing infrared sub-diffractional resolution[4-6]. Markedly, SFG microscopy was introduced in a wide-field imaging mode providing mega-pixel images within a few seconds[5]. When combined with a tunable infrared laser, SFG spectro-microscopy thus enables full spatio-spectral polariton mapping with a large field-of-view, as well as high spatial and spectral resolution[4,6]. Notably, quite similarly to s-SNOM, travelling polariton waves can be imaged as fringe patterns also in SFG microscopy through spatial interferometry[4]. This methodology has, for instance, enabled comprehensive studies of the strong coupling between propagating and localized phonon polaritons, simultaneously in the dispersion and in real space for a SiC metasurface[4].

Thus far, however, these SFG microscopy studies have been limited to imaging materials with broken inversion symmetry of their crystal structure, such as SiC or AlN, to provide sufficient photon yield of the nonlinear SFG process[6]. Inversion-symmetric materials such as hexagonal boron nitride, α-MoO_3, or β-Ga_2O_3, however, remained inaccessible for SFG studies. In this work, we demonstrate indirect, remote SFG imaging of in-plane hyperbolic phonon polaritons in α-MoO_3 by placing thin flakes of α-MoO_3 onto inversion-broken AlN as a substrate.

Polaritonic near-fields from hyperbolic polaritons confined within α-MoO_3 evanescently decay into the substrate. We show here that these evanescent fields can act as source for SFG, and how this mechanism enables remote SFG imaging of hyperbolic modes confined to volumes that themselves cannot generate SFG. We confirm the nature of the polaritons by mapping the dispersion through spatial interferometry. Notably, we show that these hyperbolic modes emerge in a frequency range where no surface polaritons are supported at the surface of the AlN substrate. The methodology introduced here enables wide-field, high-throughput screening of polaritonic nanostructures, metasurfaces, or even optoelectronic devices by SFG microcroscopy without the materials constraints of broken inversion symmetry.

II. Methods

The SFG spectro-microscopy employs the infrared (IR) free-electron laser (IR-FEL) at the Fritz Haber Institute in combination with a synchronized femtosecond visible laser, as

described in detail elsewhere[4-6]. Samples were produced by placing mechanically exfoliated α-MoO_3 flakes onto an *a*-cut single crystal AlN. SFG wide-field images were acquired over a large IR spectral range from 600-1000 cm^{-1}(wavelength 16.6 – 10 µm), each image providing a spatial resolution of ~1.4 µm (~λ/10) to allow resolving subdiffractional modes[5].

The edges of the ~200 nm thick α-MoO_3 flakes can scatter the incident IR light to excite subdiffractional phonon polaritons. Notably, despite of these modes being evanescent in the IR, the large momentum of the visible upconversion results in SFG emitted from these polaritons that is not evanescent and can thus radiate into the far-field to be collected by the microscope objective and camera. Furthermore, the propagating polariton waves interfere with the incident IR beam. Since both IR source terms for the SFG – edge-launched polariton fields and direct beam – propagate with different velocities across the image, there form an stationary interference pattern similar to a standing wave, enabling direct access to the polariton wavelength.

III. Results and Discussion

We observe different spectral regimes of polariton propagation within our data. All across the AlN Reststrahl region (~670-850 cm-1), the MoO3 flake edges acts as a non-resonant antenna to launch AlN surface phonon polaritons, as confirmed by analyzing their dispersion. These modes spatially only emerge outside the MoO3 flake. In the lower-frequency range of the AlN surface polariton band, we further observe faint fringes also with the MoO3 flake area, indicative of hybridization of AlN surface and MoO3 hyperbolic modes.

Markedly, just above the surface polariton cutoff frequency (~850 cm^{-1}, $\varepsilon_{AlN} = -1$), AlN no longer supports surface polaritons, and no more fringes are observed from the AlN surface. Yet, our data reveals pronounced fringes solely within the MoO3 flake up there, and up to frequencies of ~900 cm-1. We confirm that indeed strongly anisotropic, hyperbolic phonon polaritons are predicted for the AlN/MoO_3 heterostructure in this frequency range, with their predicted dispersion in excellent agreement with experiment. We further confirm the volume-confined hyperbolic nature of these modes by mapping their dispersion for various MoO3 flake thicknesses showing excellent agreement with theory. Additionally, polariton fringes are observed only when launched from the [001] MoO_3 crystal edges, *i.e.*, propagating along the [100] direction. No polaritons are observed for perpendicular [001] direction as expected for MoO_3.

In our experiments, the AlN substrate acts as a nonlinear transducer to remotely facilitate the upconversion from hyperbolic phonon polaritons. However, since AlN is also a polar crystal supporting surface polaritons in partially overlapping spectral range, the hyperbolic modes hybridize at the interface, and thus the remote nonlinear probe is not completely decoupled from the polaritons in this specific case. Future experiments will instead employ more neutral nonlinear transducer crystals such as GaP or GaAs, in order to enable imaging hyperbolic modes in their native state. More generally, our results demonstrate the power of nonlinear microscopy of hybrid photonic systems where nanophotonic functionality and nonlinear efficiency do not necessarily have to be provided by the same constituents.

IV. Conclusion

We have demonstrated remote nonlinear imaging of propagating hyperbolic phonon polaritons. We employed wide-field SFG spectro-microscopy and spatial interferometry to image volume-confined in-plane hyperbolic polaritons in MoO_3, an inversion-symmetric material which does not itself provide SFG yield. Instead, we use evanescent polaritonic fields leaking into the inversion-broken AlN substrate, which provides high-yield SFG, acting as a remote nonlinear probe. We map the dispersion of these modes for different flake thicknesses and along different crystal directions, confirming their in-plane hyperbolic nature. Our results demonstrate how remote nonlinearity can be used in hybrid photonic systems to expand the materials base for nonlinear photonics.

Acknowledgments

This work was supported by the HorizonTech Research Initiative. The authors thank the AMBER Centre for fabrication support.

References

[1] Galiffi et al., “Extreme light confinement and control in low-symmetry phonon-polaritonic crystals”, Nat. Rev. Mat. 9, 9-28, 2024.
[2] Hillenbrand et al, “Visible-to-THz near-field nanoscopy”, Nat. Rev. Mat. 10, 285–310,2025.
[3] Zhou et al., “Fundamental optical phenomena of strongly anisotropic polaritons at the nanoscale”, Nat. Nano. 21, 23-38, 2025.
[4] Niemann et al., “Spectroscopic and interferometric sum-frequency imaging of strongly coupled phonon polaritons in SiC metasurfaces”, Adv. Mat. 36, 2312507, 2024.
[5] Niemann et al., “Long-wave infrared super-resolution wide-field microscopy using sum-frequency generation”, Appl. Phys. Lett. 120, 131102, 2022.
[6] Mader at al., “Sum-frequency generation spectro-microscopy in the reststrahlen band of wurtzite-type aluminum nitride”, J. Chem. Phys. 161, 094706, 2024.

Prospects to bypass metal nonlocal phenomena using phonon-polaritons

Jacob T. Heiden[1,2,*], Eduardo J. C. Dias[2], Minhyuk Kim[3], Martin Nørgaard[2], Vladimir A. Zenin[4], Sergey G. Menabde[1], Hu Young Jeong[3], N. Asger Mortensen[2,5], Min Seok Jang[1]

[1] School of Electrical Engineering, Korea Advanced Institute of Science and Technology (KAIST), Korea
[2] POLIMA—Center for Polariton-driven Light–Matter Interactions, University of Southern Denmark (SDU), Denmark
[3] Graduate School of Semiconductor Materials and Devices Engineering, Ulsan National Institute of Science and Technology (UNIST), Korea
[4] Center for Nano Optics, University of Southern Denmark (SDU), Denmark
[5] Danish Institute for Advanced Study, University of Southern Denmark (SDU), Denmark
*Corresponding author: jahe@mci.sdu.dk

***Abstract*—Under extreme confinement of light, omission of nonclassical response often yields big discrepancies between classical predictions and measurements. Here, we show that phonon-polaritons in hexagonal boron nitride screened by gold can be confined unobstructed by nonlocal phenomena, even for phase velocities approaching the Fermi velocities of electrons in gold.**

***Keywords*—nonlocality, nanophotonics, polaritonics, van der Waals materials, near-field optical microscopy.**

State-of-the-art nanophotonic systems rely increasingly on mesoscopic features [1]; hence, it is desirable to verify that Maxwell's equations are still appliable for these systems. So-called acoustic graphene plasmons can confine light into atomically thin spacers by screening with metallic substrates like Au [2]. This extreme confinement reduces the plasmon velocity to approach the Fermi velocities of graphene (1.0×10^6 m/s) and Au (1.4×10^6 m/s), where nonlocal effects emerge and fundamentally limit further reduction (Fig. 1a).

Phonon-polaritons in hexagonal boron nitride (hBN) are compressible into a single atomic layer [3], which suggest that a heterostructure with thin hBN on Au could probe nonlocality by slowing polariton propagation speed to the Fermi velocity of Au – notably, this can theoretically be realised with upwards of 20 atomic layers of hBN in the middle of the upper Reststrahlen band (Fig. 1a). Yet, nonlocal theory predicts minimal Fermi velocity-induced perturbation, raising the question.

We use thin crystals of hBN on monocrystalline Au flakes to near-field probe phonon-polaritons with effective indices exceeding 90. Significant deviations (>20%) from analytical dispersion (Fig. 1b) were measured in thin hBN (>20 nm) due to native Au surface layers, as confirmed by transmission electron microscopy (Fig. 1c). These interfacial layers, consisting primarily of carbon containing compounds, fully account for the observed deviations (Fig. 1d-f). Unlike acoustic graphene plasmons, which exhibit nonlocal saturation, phonon-polaritons remain purely local [4], clearing the path towards record-breaking field confinement.

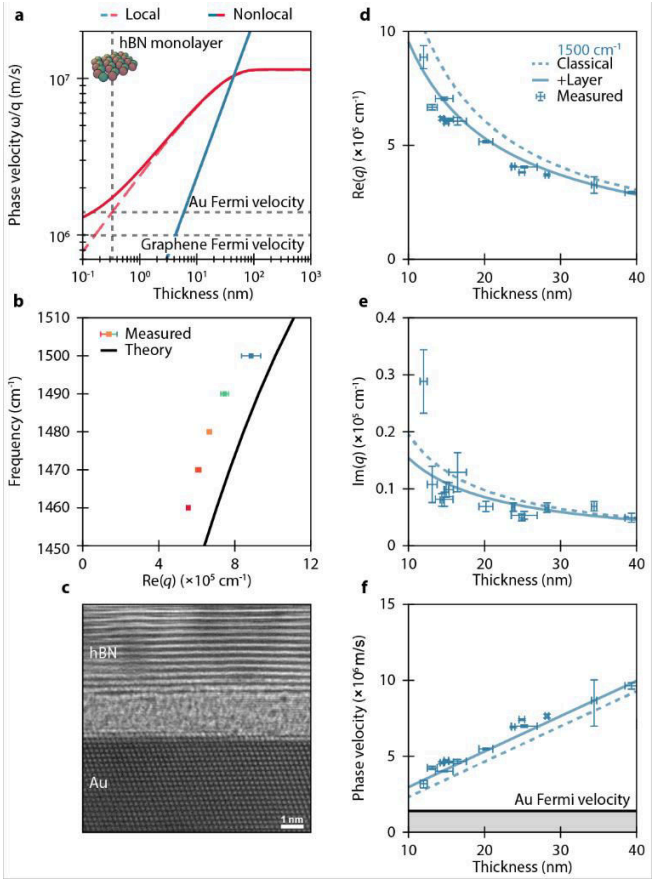

Fig. 1 a, Effect of hBN thickness on HIP phase velocity (blue lines) and spacer thickness on AGP phase velocity (red lines). **b**, Experimental and theoretical dispersion relation. **c**, Cross-sectional bright-field TEM image of the hBN/Au interface. **d-f**, Measured (markers) dispersion of Re(q) (**d**), Im(q) (**e**), and the phase velocity (**f**) as a function of hBN thickness. Classical theory (dashed lines) deviates considerably from our observations but fits well when adding a 2 nm interfacial layer with a refractive index of 1.2 in the classical theory (solid lines).

ACKNOWLEDGMENTS

This work was supported by the National Research Foundation of Korea (NRF) grants (RS-2022-NR070476, RS-2024-00340639, 2022R1A2C2011109) and the Institute of Information & communications Technology Planning & Evaluation (IITP) grant (RS-2024-00412644) funded by the Korea government (MSIT). This work also received support from the Culture, Sports and Tourism R&D Program through the Korea Cre-ative Content Agency grant funded by the Ministry of Culture, Sports and Tourism (RS-2024-00332210). The Center for Polariton-driven Light−Matter Interactions (POLIMA) is sponsored by the Danish National Research Foundation (Project No. DNRF165). E.J.C.D. acknowledges support from the European Union (Marie Skłodowska-Curie Actions, grant agreement No. 101209876). V.A.Z. acknowledges financial support from VILLUM FONDEN (Grant No. 40707).

REFERENCES

[1] Lee, I.-H., *et. al*. *Nat. Nanotechnol*., **14**, 313-319 (2019).
[2] Iranzo, D. A., *et. al*. *Science*, **360**, 291-295 (2018).
[3] Dai, S., *et. al*. *Adv. Mater*., **31**, 1806603 (2019).
[4] Heiden, J. T., *et. al*. *ACS Nano*., **19**, 42719- 42728 (2025).

Nonreciprocal plasmons in nanostructured graphene

Joel D. Cox[1,2]

[1]POLIMA—Center for Polariton-driven Light-Matter Interactions, University of Southern Denmark, DK-5230 Odense M, Denmark

[2]Danish Institute for Advanced Study, University of Southern Denmark, DK-5230 Odense M, Denmark

*Corresponding author: cox@mci.sdu.dk

***Abstract*— We investigate nonreciprocal plasmon polaritons in electrically and magnetically biased graphene nanoribbons and carbon nanotubes. Quantum confinement and edge-termination effects strongly modify drift-induced nonreciprocity, while magnetoplasmons enable propagation-dependent coupling to circularly polarized emitters. These results establish one-dimensional graphene platforms for actively controlled and chiral nanoscale light-matter interactions.**

***Keywords*— nonreciprocity, graphene, plasmon polaritons, magnetoplasmons, graphene nanoribbons, carbon nanotubes.**

Nonreciprocal nanophotonic systems enable unidirectional wave propagation, underpinning key functionalities such as optical isolation, directional signal routing, and controlled energy transport. Graphene plasmons, characterized by extreme electromagnetic confinement and electrical tunability, offer powerful opportunities to manipulate electromagnetic energy flow at the nanoscale via static electric and magnetic biasing. In particular, drift-biased graphene supports nonreciprocal plasmons exhibiting pronounced Fizeau (Doppler-like) wavelength shifts [1,2], while magnetically biased graphene sustains magnetoplasmons capable of inducing strong Faraday rotation [3,4]. In parallel, one-dimensional carbon nanostructures—including graphene nanoribbons (GNRs) and carbon nanotubes (CNTs)—have emerged as versatile plasmonic waveguides, tunable both with respect to geometry and charge carrier doping.

Here, we investigate nonreciprocal plasmon polaritons in electrically and magnetically biased GNRs and CNTs, with particular emphasis on their near field interactions with quantum emitters. We first demonstrate active, which way control of propagating plasmons in drift-biased 1D nanostructures with lateral dimensions below ~10 nm, where quantum confinement and edge-induced modifications of the electronic and structure substantially alter the nonreciprocal response [5]. We then examine graphene magnetoplasmons, whose gyrotropic character and hybridization with Landau levels lead to strong asymmetric light-matter interactions [6]. In particular, magnetoplasmons in GNRs enable propagation-direction-dependent emission from nearby circularly polarized dipoles [7], highlighting their potential for chiral quantum photonic platforms.

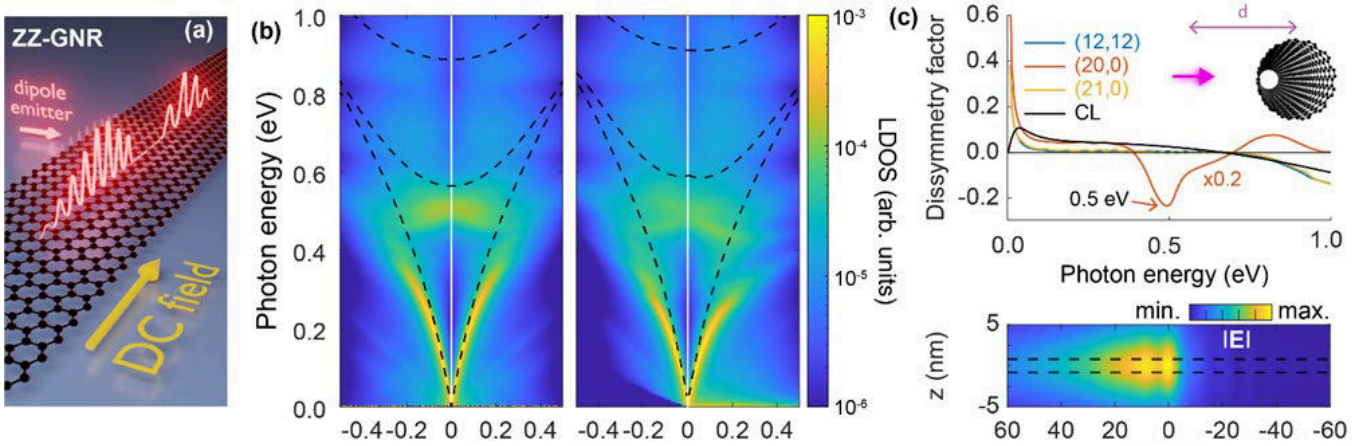

Fig. 1 (a) Schematic of nonreciprocal surface plasmons in a biased zigzag graphene nanoribbon (ZZ-GNR) excited by a dipole emitter. (b) Local photonic density of states (LDOS) for a dipole located near to and in the plane of an unbiased (left) and biased (right) 10 nm wide ZZ-GNR at Fermi energy 0.5 eV subjected to a static electric field of 5.2 MV/m. (c) Top: Dissymmetry factor (relative difference between the contribution from left- and right-propagating modes in the local photonic density of states) in carbon nanotubes (CNTs) with different structural chirality indices (m, n). (c) Bottom: Electric near-field produced by a (20,0)-CNT excited by a nearby dipole emitting photons with energy 0.5 eV.

ACKNOWLEDGMENTS

This work was supported by Independent Research Fund Denmark (grant no. 0165-00051B). The Center for Polariton-driven Light-Matter Interactions (POLIMA) is funded by the Danish National Research Foundation (Project No. DNR165).

REFERENCES

[1] Y. Dong et al., “Fizeau drag in graphene plasmonics,” Nature, vol. 594, pp 513, 2021.
[2] W. Zhao et al., ”Efficient Fizeau drag from Dirac electrons in monolayer graphene,” Nature, vol. 594, pp. 517, 2021.
[3] M. Tymchenko, A. Y. Nikitin, and L. Martín-Moreno, “Faraday rotation due to excitation of magnetoplasmons in graphene microribbons,” ACS Nano, vol. 7, pp. 9780, 2013.
[4] J. W. Han, et al., “Strong transient magnetic fields induced by THz-driven plasmons in graphene disks,” Nat. Commun., vol. 14, pp 7493, 2023.
[5] A. Rodríguez Echarri, F. J. García de Abajo, and J. D. Cox, “Nonreciprocal plasmons in one-dimensional carbon nanostructures,” Nat. Commun., vol. 17, pp 1114, 2026.
[6] M. H. Eriksen, J. R. Deop-Ruano, J. D. Cox, and A. Manjavacas, “Chiral light-matter interactions with thermal magnetoplasmons in graphene nanodisks,” Nano Lett., vol. 25, pp. 313, 2025.
[7] M. H. Eriksen and J. D. Cox, “Chiral near-field control of quantum light generation using magneto-optical graphene,” Phys. Rev. B, vol. 112, pp. 125429, 2025.

Quantum Plasmonics in Metals and Emerging Applications of Graphene Plasmons

P. André D. Gonçalves[1,*]

[1]POLIMA – Center for Polariton-driven Light-Matter Interactions, University of Southern Denmark, Denmark

*Corresponding author: padgo@mci.sdu.dk

***Abstract* — We review progress in quantum plasmonics and present analytical expressions for mesoscopic scattering coefficients of metallic cylinders, discussing how quantum nonlocal effects influence plasmon resonances and light–matter interactions. We then show that graphene plasmons can be leveraged to probe ultrafast thermoelectric phenomena and control donor–acceptor energy-transfer rates in nanoribbon structures.**

***Keywords*— quantum plasmonics, graphene plasmons, nonlocal effects, light–matter interactions.**

The optical response of metallic nanostructures can deviate strongly from classical predictions when their characteristic dimensions reach the nanometer scale ($\lesssim$10 nm) and/or when plasmon-mediated light–matter interactions processes involve near-fields characterized by large wavevector components [1–3]. The surface-response formalism based on Feibelman's *d*-parameters provides a practical and scalable framework for incorporating quantum nonlocal effects in nanoplasmonic systems [1–3]. After reviewing recent progress in this area, we present closed-form, analytical expressions for the *d*-parameter-corrected scattering coefficients of metallic cylinders, thereby completing the set of highly symmetric canonical geometries—the planar interface and the sphere having been derived previously in Refs. [3] and [1], respectively. We further analyze the impact of quantum surface response on plasmon resonances, plasmon-mediated Purcell enhancement, and electron energy-loss spectra for both single metallic cylinders and the dimer configuration.

In the second part, we present two applications of graphene plasmons. First, we show how plasmon-enhanced absorption in graphene can be used to probe ultrafast thermoelectric phenomena through the generation of transient electric fields on the picosecond timescale. Second, we demonstrate how plasmons in graphene nanoribbons can be exploited to control the energy-transfer rate between a donor–acceptor dipole pair.

REFERENCES

[1]P. A. D. Gonçalves, et al., "Plasmon–Emitter Interactions at the Nanoscale", Nat. Commun. **11**, 366 (2020)

[2]P. A. D. Gonçalves, *Plasmonics and Light–Matter Interactions in Two-Dimensional Materials and in Metal Nanostructures: Classical and Quantum Considerations* (Springer Nature, 2020).

[3]P. J. Feibelman, "Surface electromagnetic fields", Prog. Surf. Sci. **12**, 287–407 (1982).

Quantum Hydrodynamic Theory with a frequency-dependent kinetic-energy kernel in real-space

Lucian A. Constatin[1], F. Della Sala [1,2,*]

[1]Institute for Microelectronics and Microsystems (CNR-IMM), Via Monteroni, Campus Unisalento, 73100 Lecce, Italy
[2]Center for Biomolecular Nanotechnologies, Istituto Italiano di Tecnologia, Via Barsanti 14, 73010 Arnesano, LE, Italy
*Corresponding author: fabio.dellasala@unisalento.it

***Abstract*—We have developed a frequency-dependent kinetic-energy functional for the Quantum Hydrodynamic Theory (QHT), which is non-empirical and can be implemented in a real-space framework. We show results for metallic nanoparticles and compare to full Time-Dependent Density Functional Theory (TD-DFT).**

***Keywords*— Quantum hydrodynamic theory, Density functional theory, plasmonic nanoparticles**

I. Introduction

The Quantum Hydrodynamic Theory (QHT), which can be considered a reformulation of the Time-Dependent Orbital-Free Density Functional Theory[1], [2], have been successfully applied to model optical properties of metallic nanoparticles[1]

The accuracy of the QHT absorption spectrum depends on the approximation of the kinetic energy (KE) functional. Conventional KE approximations are based on gradient-corrected KE functionals, such as the Thomas-Fermi-von Weiszäcker (TFvW), which can reproduce accurately the main plasmon peak or including higher-order corrections [3].

Most of the KE functionals for QHT are, however, static or defined within a different theoretical background[4] or in the reciprocal space[2]

II. Method and Results

The Lindhard response function has been fitted with the TFvW kinetic energy functional using complex-valued frequency-dependent coefficients. In this way the broadening is included in the functional without any empirical fit. As an example, in Fig. 1 we report the normalized absorption spectra for a jellium nanosphere comparing the reference Time-Dependent Density Functional Theory (TDDFT) and with our QHT theory. The position and the brodening of the main plasmon peak is well described, without any empirical input.

III. Conclusion

We have extended the QHT theory using complex-valued kinetic energy functionals. The method can be ready implemented in any real-space code, to model absorption spectra of plasmonic systems including the broadening without empirical inputs.

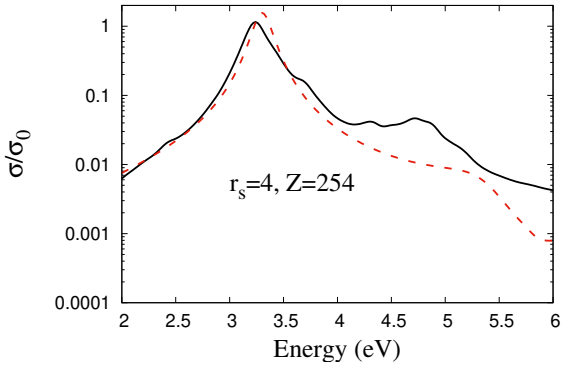

Fig. 1. Normalized absorption spectra for a jellium nanosphere with $r_s = 4$, i.e. sodium, with N=254 electrons. Black line is the reference TDDFT, dashed-red line is QHT.

Acknowledgments

We acknowledge the financial support from ICSC - Centro Nazionale di Ricerca in High Per- formance Computing, Big Data and Quantum Comput- ing, funded by European Union - NextGenerationEU.

References

[1] F. Della Sala, "Orbital-Free Methods for Plasmonics: Linear Response", *J. Chem. Phys.* vol. 157, 104101 (2022).
[2] K. Jiang, and M. Pavanello, "Time-dependent orbital-free density functional theory: Background and Pauli kernel approximations" *Phys. Rev. B* vol. 103, 245102 (2021).
[3] H. M. Baghramyan, F. Della Sala, C. Ciracì, "Laplacian-level quantum hydrodynamic theory for plasmonics", *Phys. Rev. X* vol. 11, 011049 (2021).
[4] C. Ciracì, "Current-dependent potential for nonlocal absorption in quantum hydrodynamic theory", *Phys. Rev. B* vol 95, 245434 (2017).

Shaping Light and Matter in Non-Perturbative Light-Matter Coupling Regimes

Erika Cortese[1,*], Johannes Bürger [2], Simone Di Muzio[3,*], Dario Ballarini[2], Simone De Liberato[2,3]

[1]School of Physics and Astronomy, University of Southampton, Southampton SO17 1BJ, UK
[2]CNR Nanotec, Institute of Nanotechnology, Via Monteroni, 73100 Lecce, Italy

[3] Istituto di Fotonica e Nanotecnologie, CNR, Piazza Leonardo da Vinci 32, Milano, Italy

*Corresponding author: e.cortese@soton.ac.uk

***Abstract*—Non-perturbative multi-mode light–matter coupling modifies physical properties beyond those set by geometry. We demonstrate this across three platforms: resonant laser fields stabilize ionizing atomic transitions against continuum decay; cavity coupling suppresses photodissociation in molecular cations; and co-localized superstrong coupling in visible nanophotonic waveguides enables in-situ spatial control of electromagnetic field distributions.**

***Keywords*— polaritons, ultrastrong coupling, photostabilization, nanophotonics, photodissociation, super strong coupling.**

I. Introduction

Non-perturbative light–matter coupling involving multiple modes modifies intrinsic properties of both material and photonic systems beyond what geometry alone determines. We present three realizations spanning atomic, molecular, and solid-state platforms: (i) resonant laser driving stabilizes ionizing electronic transitions via AC Stark level repulsion [1]; (ii) multi-mode cavity coupling to the dissociative vibrational continuum suppresses photodissociation in diatomic molecular cations; and (iii) co-localized superstrong coupling (SSC) between an exciton and multiple photonic modes in visible nanophotonic waveguides gives real-space control over the electromagnetic field distribution [2].

II. Results and Discussion

Laser-stabilized ionizing transitions

Resonant pumping of an ionizing transition above a critical intensity creates a metastable discrete resonance via AC Stark level repulsion—a semiclassical counterpart of the photon-bound exciton (PBE) observed in microcavity-embedded doped quantum wells [3]. Unlike the Mollow triplet of a bound-to-bound transition, only two of the four emission channels survive, their spectral weights probing the hybridization with the continuum, and the state decays via two-photon (photon–polariton) ionization [1].

Multi-mode photostabilization of molecular photodissociation

Extending the Lee–Friedrichs framework to diatomic cations (H_2^+, K_2^+), multi-mode cavity coupling to the dissociative vibrational continuum reshapes polaritonic potential energy surfaces. Franck–Condon overlaps with continuum modes together with the coupling-strength dependence of the lower polariton energy define a threshold above which cavity-induced stabilization suppresses photodissociation, opening a route to optically controlled molecular reactivity.

Co-localized superstrong coupling in visible nanophotonic waveguides

Co-localized SSC is the photonic counterpart of multi-mode matter coupling: rather than one photon hybridizing with multiple matter excitations, one exciton hybridizes simultaneously with multiple photonic modes [2], whose distinct transverse field profiles make exciton-energy tuning a direct handle on the spatial electromagnetic energy distribution. Planar grating-coupled waveguides realize this in the visible range: restricting a 2D hybrid organic-inorganic perovskite active layer to 30% of the waveguide core yields a full modal overlap between TE_0 and TE_1, producing multi-mode polaritons. RCWA simulations fitted with a generalized Hopfield model [2] confirm a characteristic S-shaped dispersion; coupling the lowest-order modes yields up to 44% higher coupling strength than higher-order pairs, and exciton-energy tuning continuously switches the electromagnetic energy distribution between the bulk and surface of the waveguide.

III. Conclusion

Non-perturbative coupling to a structured continuum of modes opens degrees of freedom that geometry alone cannot provide: a coupling-induced threshold separating stabilized from ionizing or dissociating dynamics in atomic and molecular systems, and coherent mixing of spatially distinct field profiles in nanophotonic waveguides. Both directions point toward a unified design language for polaritonic devices, from decay-rate engineering to field-distribution control in integrated visible-wavelength photonics.

References

[1] E. Cortese and S. De Liberato, "Laser-stabilized ionizing transitions," *Optica*, vol. 13, pp. 101–108, 2026.
[2] E. Cortese *et al.*, "Real-space nanophotonic field manipulation using non-perturbative light–matter coupling," *Optica*, vol. 10, p. 11, 2023.
[3] E. Cortese *et al.*, "Excitons bound by photon exchange," *Nature Physics*, vol. 17, pp. 31–35, 2021.

Geometric Phase Wavefront Shaping in Nonlinear Meta-Optics: From Tensor-Driven Phase to Nonlocal Metasurfaces

Luca Carletti[1,*]

[1] Department of Information Engineering, University of Brescia, Via Branze 38, 25123 Brescia, Italy
*Corresponding author: luca.carletti@unibs.it

Abstract—Nonlinear metasurfaces enable compact frequency conversion while shaping the generated wavefront. We outline two complementary routes: tensor driven phase control in AlGaAs metasurfaces for second-harmonic beam steering and structured light, and nonlocal resonant Silicon metasurfaces for third-harmonic generation that combine high quality factors with efficient beam steering.

Keywords— nonlinear metasurfaces, wavefront shaping, geometric phase, AlGaAs, silicon, nonlocal resonances.

I. INTRODUCTION

Metasurfaces provide subwavelength control of phase, polarization, and amplitude in ultrathin optical elements. Extending these concepts to nonlinear harmonic generation enables ultra-thin nonlinear light sources whose output can be structured without bulk optics [1]. Key challenges are simultaneously achieving strong nonlinear conversion and full wavefront control under realistic fabrication constraints.

II. METHODS

We consider two design paradigms, both based on geometric rotation of the unit elements of the metasurface to control the phase of the generated harmonic. First, in zincblende semiconductors the effective second-order susceptibility changes under in-plane rotations, introducing a nonlinear tensor-driven phase term that adds to the familiar rotation induced phase [2,3]. Rotated AlGaAs meta-atoms can therefore encode a desired phase profile directly onto the second-harmonic field. Second, nonlocal silicon metasurfaces are designed to support extended resonant modes with large quality-factors beyond single meta-atoms; by locally tailoring the unit-cell geometry or orientation, a spatially varying geometric phase can be imposed on the generated third-harmonic while benefiting from resonant enhancement [4].

III. RESULTS AND DISCUSSION

Both approaches are demonstrated experimentally:

- Second harmonic beam steering from AlGaAs metasurfaces that routes opposite circular polarizations into opposite diffraction orders.
- Generation of structured second harmonic light with unit topological charge by quadrant phase encoding, verified via fork-like interferograms and helical phase retrieval.
- Third harmonic beam steering in the visible from nonlinear nonlocal silicon metasurfaces combining high-Q resonances with spatially varying geometric phase.

IV. CONCLUSION

Tensor sensitive nonlinear phases and nonlocal resonant enhancement address complementary limitations of conventional nonlinear metasurfaces. Together they enable efficient harmonic generation with tailored wavefront control, supporting applications in compact beam steering, structured light sources, and nonlinear holography.

REFERENCES

[1] G. Grinblat, “Nonlinear Dielectric Nanoantennas and Metasurfaces: Frequency Conversion and Wavefront Control,” ACS Photonics 8, 3406–3432, 2021

[2] L. Carletti, et al. “Intrinsic nonlinear geometric phase in SHG from zincblende crystal symmetry media,” Nanophotonics 13, 3321-3326, 2024.

[3] G. Guercio et al., "Tensor-driven geometric phase in nonlinear AlGaAs metasurfaces," arXiv:2601.18246, 2026.

[4] M. Cotrufo, L. Carletti, A. Overvig, and A. Alù, "Nonlinear nonlocal metasurfaces," eLight 6, 5, 2026.

Quantum and emitter-size effects in emitter-plasmon interactions

Tadele O. Otomalo[1,*], Gabriel Gil[2], Gonzalo Á-Pérez[1], Huatian Hu[1], Ferruccio Pisanello[1], Stefano Corni[2], Fabio Della Sala[1,3], Cristian Ciracì[1,4]

[1]Istituto Italiano di Tecnologia, Center for Biomolecular Nanotechnologies, Lecce, Italy
[2]Università degli Studi di Padova, Padova, Italy
[3]Institute for Microelectronics and Microsystems (CNR-IMM), Via Monteroni, Campus Unisalento, Lecce, Italy
[4]Neurophos Inc., 4120 Freidrich Ln, Austin, TX 78744, United States
*Corresponding author: tadele.otomalo@iit.it

***Abstract*—We combine density functional and quantum hydrodynamic theories to study how molecular size and quantum tunnelling jointly affect the emitter-plasmon interaction in a plasmonic dimer. Compared with a point-dipole-based model, pronounced deviations arise at sub-nanometer separations, and the onset gap for tunnelling-induced quenching is over three times larger.**

***Keywords*— Quantum hydrodynamic theory, Density functional theory, Nonlocality, tunnelling, Plasmon-emitter interactions, emitter's spatial extent.**

I. Summary

The computationally demanding nature of purely quantum-mechanical methods to simulate fabrication-feasible plasmonic systems has made it indispensable to use either a semi-classical or a classical approximation to study emitter-plasmon coupling. Even though classical techniques, like the point dipole approximation (PDA), accurately predict long-range effects, they fail to account for important phenomena when the emitter-plasmon separation decreases to scales where the emitter size and plasmonic quantum effects become relevant. Semi-classical theories, including the Feibelman d-parameter scheme and the quantum hydrodynamic theory (QHT), have been advanced to address this issue by solving Maxwell's equations while systematically embedding the quantum effects. These extended classical models can be combined with quantum-mechanical treatment of the emitters, owing to their small size, offering a computationally feasible hybrid approach that addresses the emitter's finite-size effects as well as the critical quantum plasmonic effects.

In this talk, we present such a hybrid scheme by combining QHT [1] and time-dependent density functional theory (TDDFT) [2]. We utilize TDDFT to calculate the dipolar transition charge density of a p-nitroaniline (PNA) molecule, which then serves as a realistic excitation source for the QHT-treated plasmonic systems. We begin by examining how the emitter's finite spatial extent influences its interaction with a plasmonic nanoparticle within a classical framework. Emission rates of the molecule-based system are compared with those based on a point dipole (PD) [3] whose moment is determined from the same molecule. At large emitter-plasmon distances, the molecular and corresponding PD emission rates converge, as anticipated, confirming that they characterize the same underlying emitter response. However, at sub-nanometer distances, large differences appear in both the weak and strong coupling regimes.

Implementing the hybrid model in a plasmonic dimer and comparing it with its PD-based counterpart reveals substantial discrepancies for dimer gaps below 3.2 nm (i.e., sub-nanometer emitter-plasmon separations), affecting both the oscillator strength of the emission rates and the spectral positions of prominent modes. Interestingly, the maxima of the highest order mode analyzed in this work for the molecule-dimer system exhibit a non-monotonic dependence on the dimer gap, characterized by increasing and decreasing parts, where the quenching part is due to the effect of the tunneling electrons that start to emerge after a gap size of 1.64 nm. This exceeds the onset gap reported for the PD-based QHT-treated system in Ref. [4] by more than a factor of three.

We further analyse PD- and molecule-based emitter-plasmon coupling by progressively increasing the order of quantum effects, from local response approximation (LRA) to nonlocal Thomas-Fermi hydrodynamic theory (TFHT) up to full QHT. This hybrid approach interpolates between fully quantum and semi-classical methods, enabling systematic analysis of nanoscale emitter-plasmon interactions, with the potential to advance the design of quantum plasmonic devices.

References

[1] C. Ciracì and F. Della Sala, 'Quantum hydrodynamic theory for plasmonics: Impact of the electron density tail," *Physical Review B*, vol. 93, pp. 205405, 2016.
[2] G. Gil, G. Dall'Osto and S. Corni, "Continuum models for metal nanoparticles coupled to real-space real-time time-dependent DFT treatments of molecules," *The Journal of Chemical Physics*, vol. 162, pp. 234107, 2025.
[3] T. O. Otomalo, H. Hu, G. Álvarez-Pérez, J. Rho and C. Ciracì, "Computation of emitter-plasmon interactions using an axis-symmetric model for off-axis dipoles," *Optics Express*, vol. 32, pp. 37668–37677, 2024.
[4] M. H. Baghramyan, and C. Ciracì, "Fluorescence quenching in plasmonic dimers due to electron tunneling," *Nanophotonics*, vol. 11, pp. 2473–2482, 2022.

Tunability of nonlinear plasmonics in nanostructured 2D materials

Line Jelver[1,*], Joel D. Cox[1,2]

[1] POLIMA Center for Polariton-driven LightMatter Interactions, University of Southern Denmark, DK-5230 Odense M, Denmark.

[2]Danish Institute for Advanced Study, University of Southern Denmark, DK-5230 Odense M, Denmark.

*Corresponding author: lije@mci.sdu.dk

***Abstract*—We employ first-principles simulations to investigate how localized plasmons in nanostructured 2D materials can be leveraged to drive strong nonlinear optical processes, spanning both perturbative frequency conversion and high-harmonic generation. We identify multiple pathways to enhance nonlinear light–matter interactions through either electrostatic doping, heterostructure engineering, or ultrafast photothermal activation.**

***Keywords*— nonlinear optics, nanophotonics, thermoplasmons, first-principles modelling.**

Nonlinear optics enables all-optical temporal and spectral control, central to future integrated photonic and quantum optical devices. [1], [2]. Extreme light–matter interactions under intense optical driving produce nonlinear electron dynamics that enable strong photon–photon coupling. A prime example is high-harmonic generation (HHG), in which radiation is emitted at integer multiples of the drive frequency, terminating at a sharp cutoff energy.

Using ab initio modelling and self-consistent perturbation theory, we have developed a framework based on Maximally Localized Wannier Functions (MLWFs) that captures both quantum finite-size effects and nonlocal electrodynamics in the nonlinear optical response of nanostructured 2D materials [3], [4]. Applying this framework, we characterize the highly adjustable plasmonic resonances in electrostatically doped in phosphorene nanoribbons (PNRs) that can be brought into resonance with the driving field to yield pronounced nonlinear emission and efficient HHG, see Figure 1 (a-b).

Beside the active control afforded by electrostatic doping, passive control of the nonlinearities can be achieved though heterostructuring. Our recent results demonstrate how the nonlinear response of graphene and phosphorene nanoribbon dimers, can be actively and passively tuned by independently controlling each constituent ribbon (geometry and carrier density) [5]. Notably, inter-ribbon coupling and symmetry breaking enable large, highly tunable even-order responses in these materials that would otherwise appear inversion-symmetric, see Figure 1 (c-d). Our finding additionally illustrated that the same design knobs extend into the extreme nonlinear regime to yield rich HHG spectra with tunable even-order harmonic content.

Finally, we address transient thermoplasmonics in narrow graphene nanoribbons (GNRs), where intense photoexcitation can convert absorbed energy into electronic heat on ultrafast timescales, producing hot-carrier distributions that support mid- and near-IR plasmonic features without requiring static doping. Because graphene's electronic heat capacity is low, modest absorbed energy densities accessible in ultrafast experiments can raise electron temperatures dramatically. Our simulations reveal how these induced thermoplasmons leads to pronounced changes in both linear absorption and third-order nonlinearities, including strong third-harmonic generation and Kerr-type responses, see Figure 2 [6]. This photothermal route offers a robust, non-invasive mechanism to switch on transient nonlinear plasmonic behaviour at infrared frequencies.

Fig. 1. **a** Schematic of a PNR illuminated with confinement-direction polarization. **b** Dipole acceleration from a $W \approx 5$,nm hole-doped zigzag (ZZ) PNR driven by an ultrashort pulse, shown versus input carrier energy $\hbar\omega_{\mathrm{in}}$ and emitted photon energy $\hbar\omega_{\mathrm{out}}$. Top: linear absorption at the indicated doping. Right: output spectra for resonant excitation of the plasmon ($\hbar\omega_{\mathrm{in}} = \hbar\omega_{\mathrm{p}}$) marked by vertical white line. **c** Schematic of second-harmonic generation (SHG) in a co-planar GNR dimer with two independently doped ribbons of width $W_{\mathrm{a}} \approx 10$,nm. **d** SHG susceptibilities $\chi_2^{(2)}$ under normally incident plane-wave excitation polarized along the confinement direction, for a co-planar AC-edge GNR dimer with 2,nm separation. Ribbon a is fixed at $n_{\mathrm{a}} = 1.2 \times 10^{14}$,cm^2 (isolated plasmon at $\hbar\omega = 0.75$,eV; horizontal dashed line), while ribbon b is tuned from hole ($n_{\mathrm{b}} < 0$) to electron ($n_{\mathrm{b}} > 0$) doping, with its isolated plasmon given by dashed curves. SHG is fully quenched at $n_{\mathrm{a}} = n_{\mathrm{b}}$.

Fig. 2. **a** Linear absorption cross-section (top) and third-harmonic susceptibility (bottom) of an AC-terminated GNR with $W \approx 5$,nm. Electronic occupations follow Fermi-Dirac statistics at the indicated electron temperatures and corresponding chemical potentials, obtained from particle and energy conservation for an undoped GNR (solid) and a hole-doped GNR with $p = 10^{14}$,cm^{-2} (dashed). **b** Electronic temperature and chemical potential versus added thermal energy per area Q for the same $W \approx 5$,nm AC GNR: undoped (solid) compared with high electron (dotted) and high hole (dashed) doping.

ACKNOWLEDGMENTS

The authors thank C. Wolff and Eduardo J. C. Dias for insightful and enjoyable discussions. L.J. is supported by a career grant from the Novo Nordisk Foundation (grant no. NNF25OC0105410). J.D.C. is a Sapere Aude research leader supported by Independent Research Fund Denmark (grant no. 0165-00051B). The Center for Polariton-driven Light-Matter Interactions (POLIMA) is funded by the Danish National Research Foundation (Project No. DNRF165). Part of the computation in this project was performed on the DeiC Large Memory HPC system managed by the eScience Center at the University of Southern Denmark.

REFERENCES

[1] D. E. Chang, V. Vuletić, and M. D. Lukin, "Quantum nonlinear optics — photon by photon," *Nature Photonics*, vol. 8, pp. 685–694, 2014.
[2] A. Dutt, A. Mohanty, A. L. Gaeta, and M. Lipson, "Nonlinear and quantum photonics using integrated optical materials," *Nature Reviews Materials*, vol. 9, pp. 321–346, 2024.
[3] J. D. Cox, I. Silveiro, and F. J. G. de Abajo, "Quantum effects in the nonlinear response of graphene plasmons," *ACS Nano*, vol. 10, pp. 1995–2003, 2016.
[4] L. Jelver and J. D. Cox, "Nonlinear plasmonics in nanostructured phosphorene," *ACS Nano*, vol. 17, pp. 20 043–20 052, 10 2023.
[5] ——, "Nonlocal and nonlinear plasmonics in atomically thin heterostructures," *arXiv:2512.18339*, 2025.
[6] ——, "Nonlinear thermoplasmonics in graphene nanostructures," *Nano Letters*, vol. 24, pp. 13 775–13 782, 2024.

Excitation of Dark Modes and Multipole Plasmons via Surface-Response Function

Fan Yang[1,*]

[1]College of Physics, Sichuan University, Chengdu, Sichuan 610065, China
*Corresponding author: fyang@scu.edu.cn

***Abstract*—The dark mode can be excited by far-field illumination when surface electronic quantum effects are considered, which are modeled by the Feibelman d-parameter. On the other hand, multipole plasmons can be excited and engineered via surface nonlinearity.**

***Keywords*— dark mode, multipole plasmon, Feibelman d-parameter, surface nonlinearity**

I. Introduction

Dark modes are featured with a vanishing net dipole momentum, resulting minimum coupling with far-field illumination. It is conventionally believed that these modes cannot be excited by plane waves. However, we challenge this conventional view and propose that classical dark modes can be accessed by far-field illumination when surface electronic quantum effects are considered.

Multipole plasmons are characterized by high angular momentum. They cannot be accessed by the far field in strongly sub-wavelength nanoparticles and they are therefore dark. Localized sources, structured light, and electron beams have been proposed to excite these multipole plasmons. We find that these multipole plasmon can also be excited and engineered by surface nonlinearity, offering an alternative approach for their excitation.

II. Results and Discussion

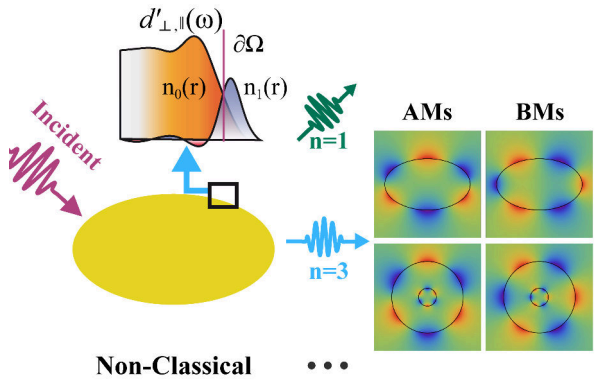

Fig. 1. Nonclassical effects at the metallic surface excite dark modes in an ellipical nanoparticle.

In Fig. 1, we present our result on dark mode excitation in an elliptical nanoparticle. The sub-wavelength elliptical nanoparticle features many non-degenerate eigenmodes with different angular quantum number m, where only dipolar mode with $m = 1$ can be excited by the plane wave according to the classical electrodynamics. However, we show in Fig. 1 that modes with higher quantum numbers can be excited if surface electronic quantum effects are taken into account.

To explore dark mode excitation, we employ the surface-response function—Feibelman d-parameter—to compute the dispersion of these dark modes. It is found the scattering matrix exhibits off-diagonal terms purely due to the non-zero d-parameter. These terms couple modes with different angular momenta, enabling dark modes to be excited via coupling with the dipolar mode.

Similarly, multipole plasmons can be excited by the nonlinear surface-response function, i.e. the nonlinear surface susceptibility. For an elliptical nanoparticle, the eigenfrequency can be engineered by varying the particle's elongation. By overlapping the dispersion lines of different harmonics, a desired multipole mode can be enhanced.

III. Conclusion

We have theoretically demonstrated that the classical dark mode becomes bright when electronic quantum effects are considered. Furthermore, the excitation and enhancement of multipole plasmons can be well controlled via surface nonlinearity.

Acknowledgments

F.Y. acknowledges the financial support from the National Natural Science Foundation of China (Grant No. 12204328), Sichuan Science and Technology Program (Grant No. 2024NSFSC1351).

References

[1] B. Ren, F Gao, and F. Yang, "Is dark mode really dark?" *under review*.
[2] Y. Zhang, Z. Li, B. Ren, F. Gao, and F. Yang, "Engineering Multipole Plasmons via Surface Nonlinearity," *manuscript in preparation*.

Electro-Optic Phonon Polaritons

Michael S. Spencer[1,*], Olga Minakova[1], Maximilian Frenzel[1], Joanna M. Urban[1], Martin Wolf[1], Sebastian F. Maehrlein[1,2,3*]

[1]Department of Physical Chemistry, Fritz Haber Institute of the Max Planck Society, Germany
[2]Institute of Radiation Physics, Helmholtz-Zentrum Dresden-Rossendorf, Germany
[3]Institute of Applied Physics, Dresden University of Technology, Germany
*Corresponding author: spencer@fhi-berlin.mpg.de, maehrlein@fhi-berlin.mpg.de

***Abstract*— We report on local electro-optic sampling of phase-resolved phonon-polariton electrodynamics inside of cryogenically cooled, high-quality terahertz (THz) quartz cavities. With our novel detection scheme, we isolate the light and matter components of the polariton signal, thereby measuring the full eigenvector of the phonon-polariton, in contrast to conventional THz transmission measurements.**

***Keywords*— Terahertz Cavity Electrodynamics, Strong Light-Matter Coupling, Nonlinear Field Sensing**

I. Introduction

Terahertz cavity electrodynamics has received increasing attention recently, with much excitement focused on the renormalization of ground-state properties in correlated materials[1] and on modifications of phase transition temperatures. In the context of strong-field terahertz (THz) excitation, there is also significant interest in using cavities to modify the nonlinear excitation pathways by way of modification of the IR-active resonances, which mediate several nonlinear excitation routes.[2] It is within this context, where knowledge of the precise field structure inside the cavity is crucial to understanding field-driven effects, that we recently made the critical first step of applying the standard THz spectroscopic tool of electro-optic sampling[3] to trace electric-field dynamics inside a Fabry-Pérot cavity for the first time.[4]

Cavity electro-optic sampling is a powerful technique that enables measurement not only of the electric field inside the cavity but also of IR-active excitations that can be driven resonantly and selectively with a broadband THz pulse. We aim to take full advantage of this capability by measuring electro-optic sampling signals from z-cut α-Quartz embedded within a THz Fabry-Pérot cavity, which we demonstrate reaches strong coupling with the ~4 THz phonon at cryogenic temperatures and high cavity quality factors (Q>20). Furthermore, we take advantage of the sub-cycle, or phase-resolved, capabilities of THz spectroscopy to separate the light and matter components of the polariton signal. We note that this is only possible because of the phase-resolved spectral information, which allows the inclusion of effects such as the phonon inertial delay.

II. Methods

We measure electro-optic sampling traces by co-focusing a broadband, single-cycle THz pulse from a spintronic emitter along with a short near-IR probing pulse, accessing the electro-optic signal stroboscopically by employing a variable time delay for the probe pulse. The signal is generated nonlinearly using a $\chi^{(2)}$ process which is linear with respect to the probe field and THz field and read out using a balanced detection scheme. [4] The nonlinear susceptibility within our THz spectral bandwidth can be decomposed into a spectrally-flat, i.e. instantaneous, component, which responds instantaneously to the local electric field, and a Lorentzian component which reflects the signal corresponding to the local amplitude of the coherently-driven IR-active phonon within quartz. Therefore, the nonlinear susceptibility is written as follows:

$$\chi^{(2)} = \chi^{(2)}_{\text{light}} + \chi^{(2)}_{\text{matter}} = \chi^{(2)}_{\infty} + \frac{SR}{\omega_o^2 - \omega^2 - i\Gamma\omega}, \qquad (1)$$

where $\chi^{(2)}_{\infty}$ is the amplitude of the non-resonant susceptibility term, S is the phonon oscillator strength, and R is the Raman tensor for the mode in the near-IR, where the probe laser is spectroscopically situated.

III. Results and Discussion

We experimentally demonstrate the disentanglement of the light and matter components of the polariton signal, thereby retrieving the complex polariton eigenvector. This contrasts with conventional spectroscopic measurements, which measure transmitted light intensity and therefore the norm-squared of only the light character. Our novel method, in contrast, measures both the light and matter components and retains their true, complex nature, owing to the measurement of fields rather than intensities.

Furthermore, we utilize a wedged cavity structure to perform highly detailed investigations of light-matter interactions as a function of the resonant detuning between the participating cavity mode and the IR-active phonon, which can undergo

strong coupling at the highest cavity quality factors. This is enabled directly by the wedge structure, where translation of the wedge allows sampling of polariton propagation at variable thicknesses, thereby changing the cavity mode frequencies. In this way, we investigate the avoided crossing between the responsible cavity mode and the optical phonon, visualized for both the phonon and the electric-field components of the phonon polariton.

IV. Conclusion

We have demonstrated a novel experimental platform for measuring phonon-polaritons, enabling simultaneous measurement of the light and matter components of the polariton signal. We also implement a wedge cavity structure, which allows unprecedentedly detailed investigations of THz light-matter coupling as a function of resonance detuning, in conjunction with the light-matter decoupling principles.

Acknowledgments

We thank Sven Kubala for depositing the gold films, which serve as the cavity end mirrors of the quartz cavities.

References

[1] F. Schlawin, D. M. Kennes, M. A. Sentef, “Cavity quantum materials,” Applied Physics Reviews, vol. 9, 011312, 2022.

[2] D. M. Juraschek, T. Neuman, J. Flick, P. Narang, “Cavity control of nonlinear phononics,” Physical Review Research, vol. 3, L032046, 2021.

[3] M. Frenzel, J. M. Urban, L. Nest, T. Kampfrath, M. S. Spencer, S. F. Maehrlein, “Quartz as an accurate high-field low-cost THz helicity detector,” Optica, vol. 11, pp. 362–370, 2014.

[4] M. S. Spencer, J. M. Urban, M. Frenzel. N. S. Mueller, O. Minakova, M. Wolf, A. Paarmann, S. F. Maehrlein, “Electro-optic cavities for in-situ measurement of cavity fields,” Light: Science & Applications, vol. 14, 2025.

Nonlocal Optical Response of Phonon-Polaritonic Nanoparticles

Yina Wu[1], Fadil Iyikanat[1], Vahagn Mkhitaryan[2], Eduardo J. C. Dias[1], Andrea Konečná[3,4], Jordan A. Hachtel[5], and F. Javier García de Abajo[1,6]

1. ICFO-Institut de Ciencies Fotoniques, The Barcelona Institute of Science and Technology, 08860 Castelldefels (Barcelona), Spain

2. School of Electrical and Computer Engineering, Purdue University, 465 Northwestern Ave, West Lafayette, 47907 Indiana, United States of America

3. Institute of Physical Engineering, Brno University of Technology, 61669 Brno, Czech Republic

4. Central European Institute of Technology, Brno University of Technology, 61200 Brno, Czech Republic

5. Center for Nanophase Materials Sciences, Oak Ridge National Laboratory, Bethel Valley Road, Oak Ridge, 37831 Tennessee, United States of America

6, ICREA-Institució Catalana de Recerca i Estudis Avançats, Passeig Lluís Companys 23, 08010 Barcelona, Spain
E-mail: yina.wu@icfo.eu

***Abstract*— We report dramatic nonlocal optical effects in hexagonal boron nitride nanoparticles using electron energy-loss spectroscopy. Local dielectric theories fail to describe observed bulk modes and surface-mode splitting. Atomistic simulations incorporating long-range dipole-dipole interactions successfully reproduce experimental spectra, highlighting the critical role of nonlocality at the nanoscale.**

***Keywords*— phonon polaritons, hBN, nonlocality, EELS, atomistic simulations.**

I. Introduction

Mid-infrared phonon polaritons in polar van der Waals materials, such as hexagonal boron nitride (hBN), have attracted significant interest due to their ability to confine electromagnetic energy deep below the diffraction limit and their long lifetimes [1,2]. While the optical response of extended bulk hBN is well-described by local Drude-Lorentz models, these local approximations become insufficient for nanostructured materials. In the nanoscale regime, the optical response is often dominated by nonlocal effects, where the electric displacement depends on the field at other spatial locations.

In this work, we investigate these nonlocal effects in hBN nanoparticles using monochromated electron energy-loss spectroscopy (EELS). We observe spectral features, specifically bulk modes and surface-mode splitting, that cannot be explained by standard local dielectric theory. By employing atomistic calculations that account for long-range dipole-dipole interactions, we provide a microscopic explanation for the particle-size-dependent separation between longitudinal and transverse modes.

II. Methods

Experimental Setup: We prepared hBN nanoparticles via mechanical exfoliation and dry etching on silicon nitride membranes. The vibrational excitations were probed using a Nion high-energy-resolution monochromated EELS system in a scanning transmission electron microscope (STEM) at 30 kV. We focused on a representative semi-ellipsoidal nanoparticle with a radius R=33 nm and height H=64 nm, as attached Fig. 1 (a).

Theoretical Modeling: We compared two theoretical approaches. First, a continuum model using the finite-element method (FEM) where hBN is described by an anisotropic local dielectric tensor. The components are given by:

$$\epsilon_s(\omega) = \epsilon_{\infty,s}\left[1 - \frac{\omega_{\mathrm{LO},s}^2 - \omega_{\mathrm{TO},s}^2}{\omega(\omega + \mathrm{i}\gamma_s) - \omega_{\mathrm{TO},s}^2}\right]$$

where s denotes directions parallel or perpendicular to the atomic planes. Second, we performed atomistic simulations solving the equations of motion for atomic vibrations. This model utilizes dynamical matrices constructed from density functional theory (DFT) force constants and explicitly includes long-range dipole-dipole interactions.

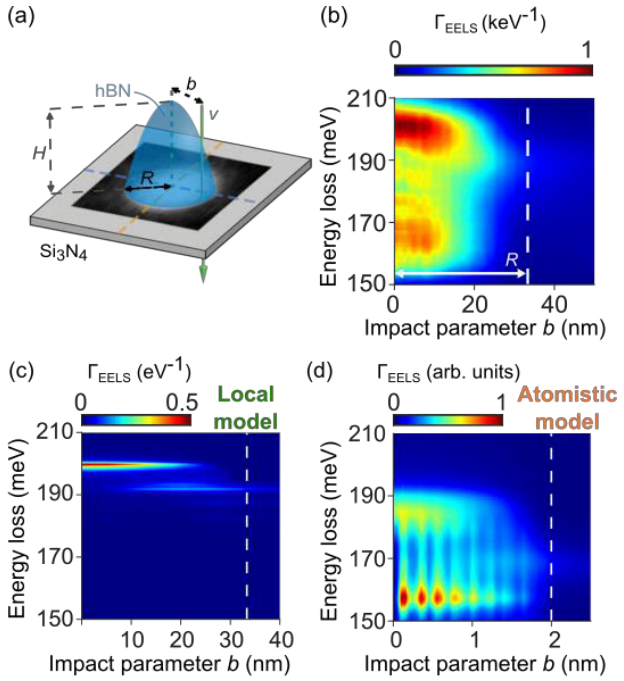

Fig. 1 (a) Schematic representation of an electron beam interacting with a hBN ellipsoid nanostructure positioned on a silicon nitride membrane. (b) Experimentally measured EELS probability distribution. (c) Simulated EELS probability using a local dielectric model via COMSOL. (d) DFT-based atomistic simulation of the EELS probability distribution incorporating dipole-dipole interactions.

III. Results and Discussion

The experimental EELS probability maps reveal two distinct spectral features: a low-energy mode near 158 meV and a high-energy mode near 200 meV (see Fig. 1 (b)). The intensity of these modes is strongest near the particle center and decays toward the edges.

Failure of Local Theory: The continuum FEM simulation based on the local permittivity reproduces the high-energy feature associated with longitudinal optical (LO) modes. However, it completely fails to capture the low-energy mode. This failure arises because the low-energy feature corresponds to transverse optical (TO) phonons, which require finite momentum transfers (a nonlocal effect) to be excited by the electron beam (see Fig. 1 (c)).

Success of Atomistic Theory: The atomistic simulations successfully reproduce both spectral features (see Fig. 1 (d)). Our analysis identifies the low-energy peak as a bulk-like TO mode, where atomic displacements are perpendicular to the propagation direction. This mode is insensitive to long-range dipole-dipole interactions. Conversely, the high-energy peak is identified as a surface-localized LO mode. Crucially, the spectral position of this LO mode is strongly dependent on dipole-dipole interactions.

IV. Conclusion

We have demonstrated that the optical response of sub-100 nm hBN particles is governed by nonlocal effects that escape conventional local dielectric descriptions. The excitation of bulk TO modes and the splitting of LO-TO modes are driven by finite momentum transfers and long-range Coulomb interactions, respectively. These findings establish that atomistic descriptions are essential for designing future phonon-polaritonic nanodevices.

Acknowledgments

This work was supported by the European Research Council (Adv. Grant 101141220-QUEFES) and the Spanish MICIU. Vibrational EELS research was supported by the Center for Nanophase Materials Sciences (CNMS) at ORNL.

References

[1] Basov, D.N., Fogler, M.M. and García de Abajo, F.J., 2016. Polaritons in van der Waals materials. Science, 354(6309), p.aag1992.

[2] X Low, T., Chaves, A., Caldwell, J.D., Kumar, A., Fang, N.X., Avouris, P., Heinz, T.F., Guinea, F., Martin-Moreno, L. and Koppens, F., 2017. Polaritons in layered two-dimensional materials. Nature Materials, 16(2), pp.182-194.

SPECIAL SESSION 21

New trends in light-matter interaction at the nanoscale

22 contributions · pp. 1179–1217

The Impact of Dark Excitons on Polariton Spatiotemporal Dynamics in 2D Semiconductors

Jamie M. Fitzgerald[1,*], Roberto Rosati[1], Ermin Malic[1]
[1]Fachbereich Physik, Philipps-Universität, Marburg, 35032, Germany
*Corresponding author: jamie.fitzgerald@physik.uni-marburg.de

***Abstract*—We investigate phonon-driven exciton polariton transport in monolayer $MoSe_2$ at ambient temperatures. Three distinct regimes are identified: initial sub-ps ballistic-like expansion, few-ps transient superdiffusion, and a slow exciton-limited diffusion after thermalization. This work will help trigger and guide future experimental studies on phonon-mediated polariton transport in 2D semiconductors. *Keywords*— spatiotemporal dynamics, exciton polaritons, 2D materials, transition metal dichalcogenides**

I. Introduction

Exciton transport plays a key role in light-energy conversion technologies and has potential for ultrafast and energy-efficient excitonic circuits that bridge nano-scale electronics and micrometer-scale photonics. Particularly promising are transition metal dichalcogenides (TMD) monolayers, which support tightly bound Wannier excitons that are stable at room temperature and interact strongly with light [1]. At ambient temperatures and low excitation power, excitons propagate via phonon-driven diffusion, resulting in short propagation distances and small diffusion coefficients (on the order 1-10 cm^2/s in TMD monolayers [2]). The hybridization of excitons with cavity photons to form exciton polaritons enhances the propagation by orders of magnitude, enabling long-range ballistic transport suitable for quantum applications (Fig. 1(a)). The rich exciton landscape of TMDs provides intervalley scattering pathways via momentum-indirect excitons. These dark states have been extensively studied in the case of bare TMD monolayers, where they facilitate rapid energy relaxation on sub-ps timescales, and have recently been demonstrated to play a key role in both polariton absorption [3] and relaxation [4]. In the latter, it was shown that the KK' exciton reservoir can efficiently populate the polariton groundstate for certain detunings, circumventing the notorious polariton bottleneck effect. To date, the role of momentum-dark excitons in polariton transport has not been explored. This has become especially relevant, as recent experiments have reported a detuning-dependent crossover between ballistic and diffusive transport regimes [5]; however, the microscopic origins of this crossover are still not well understood. Focusing on a representative hBN-encapsulated $MoSe_2$ monolayer integrated within a Fabry-Pérot microcavity that is initialized with a localized non-resonant distribution, we provide a microscopic description of the phonon-driven spatiotemporal relaxation for different temperatures and detunings [6]. Crucially, we include momentum-resolved, real-space dynamics of polaritons and dark intra- and intervalley reservoir excitons.

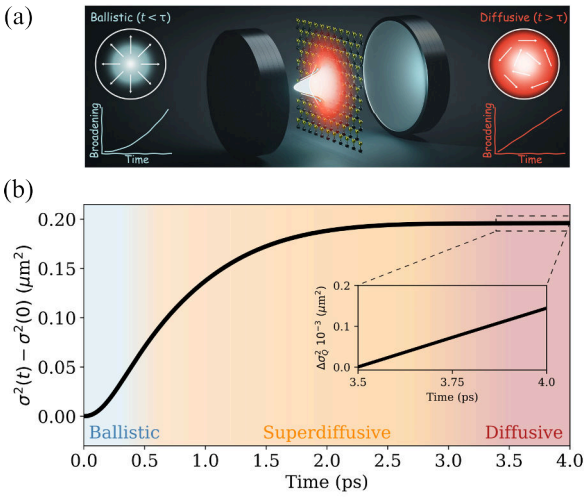

Fig. 1. (a) Schematic of a $MoSe_2$ monolayer integrated within a microcavity where the system is in the strong coupling regime. In this case, transport behavior is strongly modified because of the large group velocities of exciton-polaritons. Both the ballistic (left, blue) and diffusive (right, red) regimes are depicted, with the corresponding real-space broadening in time shown. The timescale τ represents a typical thermalization time that dictates the crossover from rapid ballistic-like expansion (quadratic) to a slower diffusive regime (linear). (b) Broadening of the momentum-integrated polariton density, illustrating a crossover from an ultrafast ballistic-like regime (blue shading), to a transient superdiffusive regime from $\sim 0.5 - 3$ ps (orange), and finally exciton-like diffusion (red) characterized by a linear slope.

II. Methods

The spatiotemporal dynamics are described by a Boltzmann transport equation within the polariton basis

$$\partial_t N_{n\mathbf{Q}}(\mathbf{R},t) = (-\mathbf{v}_{n\mathbf{Q}}\cdot\nabla - 2\Gamma_{n\mathbf{Q}} - 2\gamma_{n\mathbf{Q}})N_{n\mathbf{Q}}(\mathbf{R},t) + \sum_{m\mathbf{Q}'}\Gamma_{m\mathbf{Q}',n\mathbf{Q}}N_{m\mathbf{Q}'}(\mathbf{R},t) \quad (1)$$

where $N_{n\mathbf{Q}}(\mathbf{R},t)$ is the Wigner function, $v_{n\mathbf{Q}} = \partial_Q E_{n\mathbf{Q}}/\hbar$ is the group velocity, $\gamma_{n\mathbf{Q}}$ the radiative decay rate, $\Gamma_{n\mathbf{Q}}$ the exciton/polariton-phonon dephasing rate, and $\Gamma_{m\mathbf{Q}',n\mathbf{Q}}$ the in-scattering rate from the state $|m,\mathbf{Q}'\rangle$ into $|n,\mathbf{Q}\rangle$ via emission or absorption of phonons. The index n denotes both the polariton branch and the exciton valley, while $\mathbf{Q}$ is the centre-of-mass momentum and $\mathbf{R}$ the spatial coordinate. Our focus is re-

stricted to the low-excitation regime, where exciton/polariton-phonon scattering dominates. Exciton/polariton-phonon scattering is treated at the level of the second-order Born-Markov approximation [3], [4].

III. Results and Discussion

Figure 1(b) shows the time-dependent broadening of the momentum-integrated polariton cloud (i.e., $\sigma^2(t) - \sigma^2(0)$, where $\sigma^2(t) = \int N(\mathbf{R}, t) R^2 d^2R / \int N(\mathbf{R}, t) d^2R$ and $\sigma^2(0)$ is determined by the initial spatial profile). This is a directly extractable observable from time- and spatially resolved PL and pump-probe measurements commonly used in transport studies of excitons and polaritons [2]. Three distinct transport regimes can be identified:

- Below $\sim$ 300 fs, there is a rapid ballistic-like expansion characterized by a quadratic time dependence (blue shaded region). In this regime, the polariton occupation grows quickly as it is fed efficiently from the non-thermalized KK and KK' exciton reservoirs via intervalley phonon scattering. As a consequence, the polariton cloud expands rapidly as any radiative or scattering losses are compensated by the strong in-scattering.
- As the initial growth in the polariton occupation slows and the system approaches a characteristic timescale where the majority of polaritons will have radiatively decayed or scattered with a phonon, the rate of expansion drops and the system smoothly evolves into the transient superdiffusive regime (orange region). The time dependence of the broadening is now no longer quadratic but the polariton cloud still expands at a much larger rate than bare excitons (the peak diffusion coefficient is $\sim$ 1000 cm^2/s).
- Lastly, as the system tends toward the steady state, the expansion rate decreases by orders of magnitude and appears flat on the scale of Fig. 1(b) (red region). Closer inspection reveals a linear slope (see inset), characteristic of conventional Fickian diffusion. The rate of expansion is now about three orders of magnitude smaller than in the earlier transient ballistic-like and superdiffusive regimes, with an associated diffusion coefficient close (but still enhanced via the cavity) to typical excitonic values of around 1 cm^2/s. At these timescales, the polariton subsystem has reached thermal equilibrium with the exciton reservoir due to the strong scattering with phonons at room temperature.

In addition to the results shown in Fig. 1(b), we have also shown that in the ballistic regime there is a phonon-induced velocity renormalization. We also establish that polariton transport is strongly dependent on temperature, cavity detuning, and nonresonant excitation conditions [6]. These key experimental parameters act as effective levers to manipulate the transport dynamics of both polaritons and reservoir excitons, providing a framework for future experiments to probe the fundamental role of phonons.

IV. Conclusion

We have provided microscopic insights into ultrafast transport phenomena of exciton-polaritons in 2D semiconductors, crucially taking into account scattering with phonons and the full exciton energy landscape. The approach detailed here can be applied to a wide range of excitonic 2D materials, such as metal-halide perovskites, TMD bilayers, as well as to spatially structured cavities that host, for example, trapped and lattice polaritons.

Acknowledgments

We acknowledge funding from the Deutsche Forschungsgemeinschaft (DFG) via the regular project 524612380.

References

[1] Perea-Causin, R., Erkensten, D., Fitzgerald, J., Thompson, J., Rosati, R., Brem, S. & Malic, E. Exciton optics, dynamics, and transport in atomically thin semiconductors. *APL Materials*. **10** (2022)

[2] Kulig, M., Zipfel, J., Nagler, P., Blanter, S., Schüller, C., Korn, T., Paradiso, N., Glazov, M. & Chernikov, A. Exciton diffusion and halo effects in monolayer semiconductors. *Physical Review Letters*. **120**, 207401 (2018)

[3] Ferreira, B., Rosati, R., Fitzgerald, J. & Malic, E. Signatures of dark excitons in exciton–polariton optics of transition metal dichalcogenides. *2D Materials*. **10**, 015012 (2022)

[4] Fitzgerald, J., Rosati, R., Ferreira, B., Shan, H., Schneider, C. & Malic, E. Circumventing the polariton bottleneck via dark excitons in 2D semiconductors. *Optica*. **11**, 1346-1351 (2024)

[5] Xu, D., Mandal, A., Baxter, J., Cheng, S., Lee, I., Su, H., Liu, S., Reichman, D. & Delor, M. Ultrafast imaging of polariton propagation and interactions. *Nature Communications*. **14**, 3881 (2023)

[6] Fitzgerald, J., Rosati, R. & Malic, E. Polariton transport in 2D semiconductors: Phonon-mediated transitions between ballistic, superdiffusive, and exciton-limited regimes. *Science Advances*. **11**, eaea3495 (2025)

Electrical excitation of surface plasmons and light

Elizabeth Boer-Duchemin

Institut des Sciences Moléculaires d'Orsay (ISMO),
Université Paris-Saclay, Orsay, France
Elizabeth.Boer-Duchemin@universite-paris-saclay.fr

***Abstract*— We use the inelastic tunneling current from a biased tunneling junction to locally and electrically excited surface plasmons on gold nanostructures.**

***Keywords*— surface plasmons, plasmonics, electrical excitation, scanning tunneling microscopy.**

I. Introduction

In today's information society, smaller, faster and more efficient devices with new functionalities for information transfer and storage are continually being sought after. In this context, we investigate the local, electrical excitation of surface plasmons on metallic nanostructures using a nanoscale tunneling junction. This tunneling junction may be the one found naturally between the tip of a scanning tunneling microscope (STM) and a conducting sample [1]; or, such a tunneling junction may also be intentionally engineered and incorporated into the sample [2].

II. Methods

Our main set-up consists of a commercial STM/AFM head operating in air, combined with an inverted optical microscope (see Fig. 1). When the biased STM tip is less than 1 nm from the metallic sample, tunneling current will flow. While most of this tunneling current is *elastic,* a small portion is *inelastic,* and may be used to excite the optical modes of the sample, including surface plasmons. The light emitted from the radiative decay of the excited optical modes is then collected through the transparent substrate by the oil immersion objective lens (NA=1.45). One of the main advantages of this technique is that wide-field images may be realized: when the *real plane* is projected on the CCD camera, information about the *spatial distribution* of the emitted light is obtained; when the *Fourier plane* or *back focal plane* is imaged on the CCD, we obtain information about the *angular distribution* of the emitted light. In particular, this information is key for the interpretation of the physical phenomena at play[3]. In order to further understand our results, we use simple models and sophisticated simulations (COMSOL Multiphysics) [4-5].

III. Results and Discussion

Using these techniques we have shown that:

- Propagating surface plasmon polaritons may be excited by inelastic tunneling current [1],
- The STM nanosource may be used to probe the radiative electromagnetic density of states of a sample[4],
- Near-field excitation of the plasmonic resonances of a nanoparticle will cause spectral shifts[5] and
- A biased cubic nanoantenna separated from a gold film by a thin insulating layer may be used to excite surface plasmons and to tailor the spectrum of the emitted light[2].

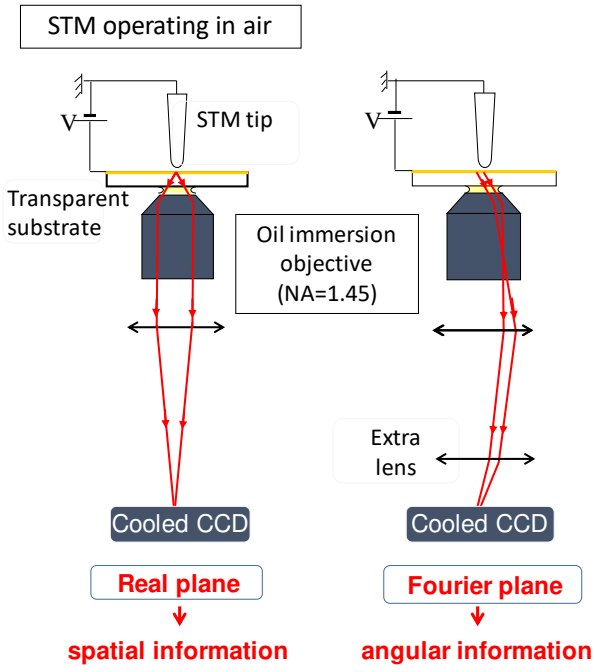

Fig. 1 Experimental set-up for the electrical excitation of surface plasmons and light.

IV. Conclusion

We have demonstrated that a scanning tunneling microscope coupled to an inverted optical microscope is a versatile tool for studying the local, electrical excitation of surface plasmons and light.

References

[1] T. Wang et al., Nanotechnology, 22, 175201 (2011).
[2] D. Pommier et al., ACS Photonics 10, 2641 (2023).
[3] D. Pommier et al., Phys. Rev. Lett., 123, 027402 (2019).
[4] S. Cao et al., ACS Photonics 7, 1280 (2020).
[5] M. Zapata-Herrera et al., Phys. Rev. B 109, 155433 (2024)

Organic Hyperbolic Metamaterials and Nanostructures for Light-Matter Interactions

Sara Núñez Sánchez*

[1]Instituto de Ciencia de Materiales de Madrid (ICMM), Consejo Superior de Investigaciones Científicas (CSIC), Sor Juana Ines de la Cruz, 3 Cantoblanco, Madrid 28049, Spain
*Corresponding author: s.nunez.sanchez@csic.es

***Abstract*— We present all-organic excitonic nanostructures and hyperbolic metamaterials based on J-aggregates, enabling tunable permittivity, ENZ behaviour, and polaritonic coupling. These organic platforms and nanostructures can establish the playground for flexible, metal-free photonics and metamaterials.**

***Keywords*— organic metamaterials, organic photonics, exciton polaritons, J-aggregates**

Organic excitonic materials based on J-aggregates are emerging as versatile building blocks for next-generation photonics and nanophotonic metamaterials. Their delocalised Frenkel excitons and narrowband resonances enable optical responses that mimic plasmonic behaviour in selected spectral regions, including epsilon-near-zero (ENZ) conditions. [1] By tailoring molecular aggregation and supramolecular order, we achieve unprecedented refractive-index contrasts and tunable permittivity in fully organic systems. When integrated into photonic architectures, these properties unlock new optical modes and reshape absorption [2], emission, and dispersion [3], providing opportunities for enhanced nanoscale light–matter interaction, field confinement, and metamaterial-like dispersion engineering.

Our initial work in the area has shown that excitonic thin films composed of J-aggregates can exhibit metal-like reflectance and strong dispersive behaviour. By combining these films with distributed Bragg reflectors (DBRs), we demonstrated how compositional control and photonic design converge to modulate light–matter interactions in soft matter [3]. Building on this concept, we developed all-organic 1D-photonic crystals inspired by photosynthetic architectures [2]. These structures exploit near-zero refractive index properties to provoke slow-light effects to enhance absorption and tailor photoluminescence, achieving narrowband reflectance and directional emission without metals or complex nanofabrication. Such results highlight how tuning composition and supramolecular order enables new functionalities in organic photonic systems.

In this invited talk, I will present our latest advances toward exploiting the polaritonic properties of these organic platforms for all-organic metamaterials, following two complementary approaches:

(ii) **Organic Hyperbolic Metamaterials**. We demonstrate anisotropic multilayer architectures based on J-aggregates that achieve controlled dispersion regimes, including hyperbolic and epsilon-near-zero conditions. We further show that this hyperbolic dispersion can be achieved by a complete materials library from the visible to the infrared. Opening new routes to engineer polaritonic transport and directional optical states in ultrathin organic films. [5]

(i) **Colloidal nanoparticles.** We developed J-aggregate flakes that preserve supramolecular order in aqueous media and display robust colloidal stability. Optical characterization reveals sharp excitonic bands and angular-dependent reflectance consistent with plasmonic-like excitonic resonances at room temperature [4]. The flakes exhibit size-dependent scattering, which broadens extinction and induces photoluminescence redshifts, enabling tunable local photonic environments and controllable nanoscale field distributions.

Together, these two new approaches establish the transition from planar photonic stacks to nanostructured excitonic matter, enabling unprecedented control over morphology, anisotropy, and optical functionality. By creating materials composed by supramolecular structures as J-aggregates is possible to achieve ENZ regimes and engineered hyperbolic dispersion. These materials can define a roadmap toward an all-organic photonic metamaterial for light harvesting, emission control, and reconfigurable nanophotonic structures. Future work will extend these concepts to telecom wavelengths through molecular engineering and validate device-level gains via photonic integration.

ACKNOWLEDGMENTS

This work was supported by the European Union under Grant Agreement #101129661 - ADAPTATION. S.N.-S. acknowledges the Severo Ochoa Centres of Excellence program through Grant CEX2024-001445-S.

REFERENCES

[1] S. Holder, et al. Nanophotonics, 2023
[2] M.A. Castillo, et al., Adv. Funct. Mater., 2022.
[3] S. Núñez-Sánchez, et al., ACS Photonics, 2016.
[4] C. Estévez-Varela, et al., Adv. Optical Mater., 2025.
[5] J. Gama, et al., arXiv:2512.20411.

Brewster Quasi-BICs in Out-of-Plane Symmetry Broken Nanodisk Metasurfaces

Beatriz Castillo López de Larrinzar[1,2], Lucía Hidalgo-Arteaga[1], Antonio García-Martín[2], Diego R. Abujetas[3], José A. Sánchez-Gil[1]

[1] Instituto de Estructura de la Materia (IEM, CSIC). Serrano 121, 28006 Madrid, Spain

[2] Instituto de Micro y Nanotecnología (IMN-CNM, CSIC). Isaac Newton 8, Tres Cantos, 28760 Madrid, Spain

[3] Departamento de Matemáticas Universidad de Castilla-La Mancha Avenida Carlos III s/n, 45071 Toledo, Spain
*Corresponding author: j.sanchez@csic.es

***Abstract*— Bound states in the continuum (BICs) have attracted significant interest in nanophotonics for their ability to confine light with formally infinite quality factors. While traditional BICs are symmetry-protected at normal incidence, breaking out-of-plane symmetry by tilting meta-atoms gives rise to Brewster quasi-BICs (qBICs). Initially observed in the microwave regime using high-index ceramic disks, these states are characterized by large but finite Q-factors and a distinctive "dark" behavior at specific angles. In this work, we demonstrate that Brewster qBICs can be realized in the optical domain using Silicon metasurfaces. Using a coupled electric/magnetic dipole (CEMD) model, we reveal that these optical qBICs occur at modified Brewster angles that can deviate significantly from the physical tilt angle due to resonance hybridization [1].**
A key feature of these states is their profound mirror asymmetry. At one angle the qBIC is uncoupled and the metasurface is transparent. Conversely, at the symmetric angle the qBIC is strongly excited but remains cloaked, as symmetry forbids far-field reflection. The diverse phenomena associated with these asymmetric states offer a wide variety of applications in tunable/reconfigurable photonics.

***Keywords*— Bound states in the continuum, cloaking, Brewster q-BICS, symmetry breaking**

I. Introduction

Bound States in the Continuum (BICs) have transformed nanophotonics by enabling light confinement with theoretically infinite lifetimes. While traditional symmetry-protected BICs are well-understood, recent advances in out-of-plane symmetry breaking have revealed a richer landscape of "cloaked" and "uncoupled" quasi-BICs (qBICs). This work explores the emergence of cloaked qBICs in semiconductor metasurfaces composed of tilted nanostructures, where the spectral overlap of in-plane and out-of-plane dipolar resonances leads to a complex hybridization of the optical response.

II. Methods

We use silicon nanodisks with height h = 80 nm and diameter D = 200 nm, and Si nanopillars with height h = 250 nm and diameter D = 100 nm, both in a square array with a period a = 400 nm. Our methodology combines analytical modeling with advanced numerical simulations. We employ a Coupled Electric and Magnetic Dipole (CEMD) model to describe the metasurface response, accounting for the interaction between in-plane and out-of-plane dipoles. The effective polarizability and the condition for Brewster qBICs are validated using FDTD (Finite-Difference Time-Domain). For rigorous calculation of the electromagnetic coupling in periodic structures, we have used the T-matrix method (SMUTHI).

III. Results and Discussion

The results demonstrate that optical Brewster qBICs occur at specific angles ϕ_B that depend on the nanodisk tilt φ and the spectral overlap of resonances. Key findings include:

- Asymmetric Response: For an incident angle $\theta = \phi_B$, qBIC is uncoupled (transparency). For $\theta = -\phi_B$, the qBIC is excited but "cloaked" because the far-field reflection is cancelled by symmetry.
- Resonance Hybridization: Optical qBICs are driven by the interference of multiple dipolar modes, causing ϕ_B

to deviate from the geometric tilt φ.

- Near-Field Localization: Such asymmetric response is shown to have a strong impact in the case of the cloaked qBIC. Despite being undetected by the incoming plane wave, it exhibits largely enhanced near-field intensities.

IV. Conclusion

We have demonstrated that tilting the nanodisk meta-atom in a metasurfaces with out-of-plane symmetry breaking support dark asymmetric qBICs in the optical domain, either cloaked or uncoupled, resulting from various dipolar resonances of the meta-atoms that combine non-trivially. Moreover, the interplay between geometric tilt and tunable material properties offers a promising path toward high-efficiency devices where both the excitation state and the polarization of transmitted light can be precisely controlled.

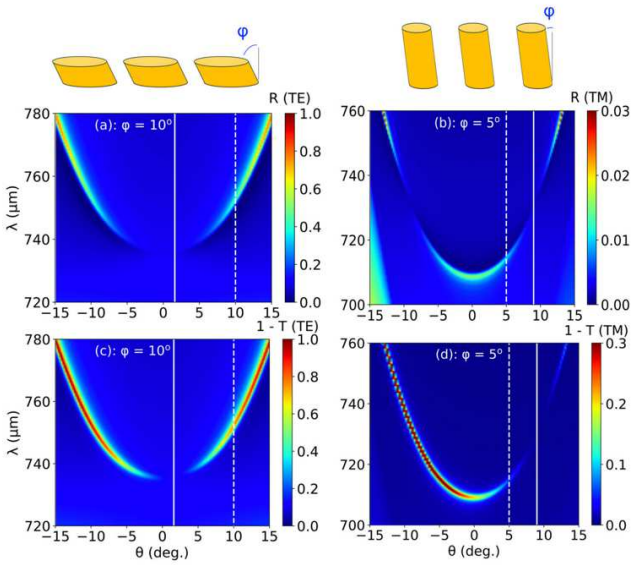

Fig. 1 Color maps of the reflectance and extinction calculated through FDTD for the two qBIC bands emerging in the two metasurfaces. Dashed lines represent again angles at which $\theta = \varphi$, whereas solid lines denote angles matching the uncoupled (dark) qBIC condition for the effective Brewster angles $\theta = \phi_B$.

Acknowledgments

This work was supported by the Spanish Ministry of Science and Innovation (MCIN/AEI) through projects BICPLAN6G and LIGHTCOMPAS, and the European Social Fund.

References

[1] Hidalgo-Arteaga, Lucía & Larrinzar, Beatriz & García-Martín, Antonio & Abujetas, D. & Sánchez-Gil, Jose. (2025). Cloaked Quasi Bound States in the Continuum in Semiconductor Metasurfaces with Out-of-Plane Symmetry Breaking. Laser & Photonics Reviews. 19. 10.1002/lpor.202500799.

Electron-beam spectroscopy simulations using the T-matrix method

P. Elli Stamatopoulou[1,2,*], Carsten Rockstuhl[1,3,4]

[1]Institute of Nanotechnology, Karlsruhe Institute of Technology, Germany
[2]POLIMA–Center for Polariton-driven Light—Matter Interactions,University of Southern Denmark, Denmark
[3]Institute of Theoretical Solid State Physics, Karlsruhe Institute of Technology, Germany
[4]Center for Integrated Quantum Science and Technology, Karlsruhe Institute of Technology, Germany
*Corresponding author: elli.stamatopoulou@kit.edu

***Abstract*—Advanced computational tools describing electron interactions with nanostructured materials are crucial for designing and interpreting experiments. Here, we report the extension of a generalized T-matrix scattering formalism to study observables in electron-beam spectroscopy. This method is implemented in the Python package *treams_ebeam*, and demonstrated while studying different nanophotonic materials of contemporary interest.**

***Keywords*— T-matrix method, cathodoluminescence, electron energy-loss spectroscopy.**

I. Introduction

In recent years, electron-beam spectroscopy has proven indispensable for exploring the optical properties of matter. Fast electrons passing by a sample transfer energy to the optical modes sustained therein, which can then be detected in two complementary techniques: cathodoluminescence (CL) and electron energy-loss spectroscopy (EELS) [1]. However, the systematic exploration of free-electron and matter interactions requires robust and versatile numerical tools.

The T-matrix method constitutes a highly efficient method for modeling such interactions [2], especially for systems comprising many scatterers, and for studies involving multiple length scales or requiring extensive parameter sweeps.

II. Methods

In a system consisting of one or more scatterers excited by an external illumination, the incident and scatterer field can be expressed on the basis of spherical or cylindrical waves. In a linear response theory these fields are related via a T-matrix as

$$\mathbf{p} = \mathbf{T}\mathbf{a}, \tag{1}$$

where $\mathbf{a}$ and $\mathbf{p}$ are vectors containing the expansion coefficients of the respective incident and scattered field in the chosen basis, and $\mathbf{T}$ is the T-matrix, which encodes all material and geometrical parameters of the entire structure, including interactions between scatterers.

Given the spherical or cylindrical T-matrix characterizing the system under study, the field of a fast electron can be readily expanded in the same basis, and then scattered field coefficients can be computed using Eq. (1). Once obtained, these coefficients are employed to simulate the CL and EELS spectra of the system.

Fig. 1. (a) Sketch of an infinite periodic array of amorphous silicon elliptical nanodisks excited by an electron beam. (b) Simulated EELS and (c) CL spectra per scatterer, considering a single nanodisk ($N = 1$), a finite cluster of equidinstant nanodisks of different sizes ($N = 3, 5, 9, 15$), and the infinite periodic array ($N = \infty$) shown in panel (a). Consecutive curves are vertically offset by $3 \cdot 10^{-3}$ eV^{-1} for readability.

The method is implemented as an extension of the in-house developed Python toolbox *treams*, designed for electromagnetic scattering computations [3]. The extended module *treams_ebeam* includes all functionalities of the original software, while adding electron beams as sources of illumination, and functions computing the relevant observable quantities [4]. The code is open-source and available online at https://github.com/tfp-photonics/treams_ebeam.

III. Results and Discussion

We demonstrate the capabilities of our approach and the *treams_ebeam* code through three representative examples: single scatterers of various shapes, a periodic chain of elliptical nanodisks (Fig. 1), and a finite cluster of nanospheres arranged in a two-dimensional (2D) lattice.

In all examples, we provide a detailed description of how to calculate the individual T-matrices for scatterers of different shapes, within *treams* or other numerical methods, as well as how to use the functions related to the electron-beam illumination provided in *treams_ebeam*. We show that the method can describe a wide range of optical modes, such as Mie resonances, and surface plasmon polaritons, as well as

collective phenomena, including lattice resonances and Smith-Purcell radiation.

IV. Conclusion

We have presented a T-matrix-based scattering formulation for modeling the interaction of fast electrons with single or multiple periodically and aperiodically arranged scatterers, and implemented it within the Python package *treams_ebeam*. To demonstrate both the method and the software, we have explored various representative examples. We envision this tool serving as a user-friendly resource for CL and EELS simulations.

Acknowledgments

P. E. S. is supported by a research grant (VIL71383) from VILLUM FONDEN.

References

[1] F. J. García de Abajo and V. Di Giulio, "Optical excitations with electron beams: Challenges and opportunities," *ACS Photonics*, vol. 8, pp. 945–974, 2021.

[2] P. C. Waterman, "Matrix formulation of electromagnetic scattering", *Proceedings of the IEEE*, vol. 53, pp. 805-812, 1965.

[3] D. Beutel, I. Fernandez-Corbaton, and C. Rockstuhl, "*treams* – a T-matrix-based scattering code for nanophotonics," *Compututer Physics Communications*, vol. 297, pp. 109076, 2024.

[4] P. E. Stamatopoulou and C. Rockstuhl, "A T-matrix scattering formalism for electron-beam spectroscopy", arXiv preprint (submitted).

Within and Beyond the Photon Beam: 3D Electrokinetic Mapping-to-Manipulation of Optical Matter

R. Bresolí-Obach[1,*], B. Louis[2], J. Hofkens,[2] H. Masuhara,[3] M.I. Marques,[4] J. Olmos,[4] R. Delgado-Buscalioni,[4] COODY Network partners.

[1]Institut Químic de Sarrià, Universitat Ramon Llull, Barcelona, Spain
[2]Department of Chemistry, KU Leuven, Leuven, Belgium
[3]Department of Chemistry, NYCU, Hsinchu, Taiwan
[4]Department of Physics, Universidad Autonoma de Madrid, Madrid, Spain
*Corresponding author: roger.bresoli@iqs.url.edu

***Abstract*— We present a mapping-to-manipulation framework for optical matter that couples fast 3D imaging with electrokinetic control. Using dielectrophoresis and tailored electrodes, we map particle trajectories, quantify flows, and then program selective assembly, transport, and sorting beyond the photon beam. The approach enables species-selective patterning, sequence writing, and reconfigurable colloidal devices.**

***Keywords*— metamaterials, optical matter, dielectrophoresis.**

I. Introduction

Optical matter sits at the crossroads of photonics, nanotechnology, and materials science: light not only traps single particles but also assembles, binds, and reconfigures them into ordered structures with emergent properties. From the early demonstrations of optical trapping and optical binding, the field has evolved to encompass complex nanoparticle assemblies, dynamically reconfigurable colloids, and light-induced forces in structured environments. These capabilities underpin advances in nanofabrication, sensing, optoelectronics, and reconfigurable materials, where sub-wavelength architectures yield functionalities unattainable in conventional matter.

One compelling frontier links optical matter to colloidal memory, where information is encoded as sequences of nanoparticles inside nano-/micro-capillaries. This vision demands sub-micrometer positional control and species selectivity, requirements naturally met by dielectrophoresis (DEP), which tunes particle attraction/repulsion through the frequency-dependent response of polarizable particles and the solvent. Equally crucial is fast 3D imaging (~100 fps over micrometer volumes) to visualize writing and diagnose limits. We present a multiplane microscopy toolbox that tracks 200-nm polystyrene particles over quadrupolar electrodes, resolving both positive and negative DEP, and quantifying electrokinetic flows in all three dimensions. By exposing regime-dependent dynamics and flow fields, this approach clarifies how to program spatiotemporal particle control, paving the way for selective sequence writing in colloidal memory and for chemically/optically reconfigurable optical-matter architectures.

II. Methods

Our methodology integrates theory and experiment. On the theoretical side, we collaborate with Profs. Delgado-Buscalioni and Marques (UAM, Madrid), Prof. Ishihara (Osaka University, Japan), and Prof. Hannah (University of Bristol, UK). Experimentally, we work with Prof. Hofkens (KU Leuven, Belgium) and Prof. Masuhara (NYCU, Hsinchu, Taiwan). When needed, we employ tailored nanoparticles prepared by Prof. Liz-Marzán (UVigo, Vigo; CIC biomaGUNE, San Sebastián, Spain) and Prof. Klymchenko (University of Strasbourg, France). This collaborative network emerged from the COODY research initiative, currently funded by the Flemish Government (FWO, W002221N).

III. Results and Discussion

We probed how surface-plasmon resonances govern swarming by tuning the trapping-laser wavelength with respect to the dipolar mode of gold nanoparticles of different sizes.[1] Swarming was maximized when the laser operated near the dipole resonance, which enlarged the active swarming region. We also found that the quadrupolar scattering mode supports optical binding, yet its scattered field remains confined to the focal volume and does not propagate efficiently beyond it.[2] This interpretation is consistent with single-particle simulations, scattering spectra and spatial light-scattering maps, showing that resonant matching of the first trapped particle to

the trapping beam is a key prerequisite for swarming to develop.

In a separate set of measurements, we demonstrated optical binding outside a single, tightly focused spot.[3] By trapping at an interface, up to three gold nanoparticles assembled linearly within the focus, in line with the state of the art. Crucially, light scattered by this in-focus chain seeded discrete, arc-shaped potential wells at half-wavelength intervals outside the focus. Particles entering these arcs moved in a correlated fashion with the in-focus chain and with each other, forming a dynamic binding network mediated by back-scattering and multichannel light scattering.

Finally, we linked these swarming architectures to optical matter, i.e., transient structures formed by light–object interactions at the micro/nanoscale. Using silica-shelled gold nanoparticles, we showed that the shell thickness tunes binding pathways and thus the resulting optical-matter phases.[4] For shells ≥50 nm, assemblies transitioned from linear chains to hexagonal lattices exhibiting circular motion, with the swarming morphology evolving from dumbbell-like to lobe-like patterns. A combined experimental–numerical model for metal–dielectric core–shell particles accounts for these behaviors; by incorporating non-optical interactions (e.g., electrostatic repulsion), the model provides a route to designing tunable optical matter.[5]

IV. Conclusion

We have established a mapping-to-manipulation framework for optical matter that couples fast 3D imaging with field- and resonance-guided control. By tuning the trapping wavelength to the dipolar plasmon of Au nanoparticles, we showed that resonance of the first trapped particle is a prerequisite for swarming, while quadrupolar scattering supports binding but remains localized at the focus. We further demonstrated optical binding outside the focal spot: a linear in-focus chain seeds half-wavelength, arc-shaped potential wells that recruit external particles into a correlated, many-body network via back- and multichannel scattering. Using silica-shelled Au nanoparticles, we mapped a shell-thickness–driven transition from linear chains to hexagonal, circulating lattices and rationalized these phases with an experiment-informed model that also incorporates non-optical interactions (e.g., electrostatics). Together, these results provide design rules for tunable, reconfigurable optical matter and, when combined with dielectrophoretic selectivity and multiplane microscopy, open a realistic route to species-selective sequence writing for colloidal memory and to adaptive photonic materials operating in fluid environments.

Acknowledgments

This work was funded by the Flemish Government through long term structural funding Methusalem (CASAS2, Meth/15/04), by the Fonds voor Wetenschappelijk Onderzoek-Vlaanderen (FWO, W002221N), by a bilateral agreement between FWO and MOST (VS00721N), by the internal funds of KU Leuven (C14/22/085), by the Departament de Recerca i Universitats de la Generalitat de Catalunya for the support given to the research groups (2021 SGR 01023, 2021 SGR 00357), by the Spanish Agencia Estatal de Investigación and FEDER (PID2022-137569NA-C44, PID2023-149483NB-C22, CNS2025-166106) and by the European Union under the Horizon Europe grant 101130615 (FASTCOMET). R.B.-O. thanks the Spanish Agencia Estatal de Investigación for a Ramon y Cajal contract (RYC2021-032773-I).

References

[1] C.-H. Huang et al., “Surface plasmon resonance effect on laser trapping and swarming of gold nanoparticles at an interface,” Opt. Exp., 28(19), 27727 (2020).

[2] C.-H. Huang et al., “Plasmonic dipole and quadrupole scattering modes determine optical trapping, optical binding, and swarming of gold nanoparticles,” J. Phys. Chem. C, 128, 5731−5740 (2024).

[3] C.-H. Huang et al., “The primeval optical evolving matter by optical binding inside and outside the photon beam,” Nat. Commun., 13, 5325 (2022).

[4] B. Louis et al., “Unconventional optical matter of hybrid metal−dielectric nanoparticles at interfaces,” ACS Nano, 18, 32746-32758 (2024).

[5] Jim J.-K. Chen et al., “Tunable optical matter: electrostatic repulsion modulates near-and far-field gold nanoparticle arrangements,” Nanoscale Adv., 8, 1251-1259 (2026).

Quantitative Analytical Model for Scattering-type Scanning Near-field Optical Spectroscopy

Kirill V. Voronin[1,*], Rainer Hillenbrand[2,3], Alexey Y. Nikitin[1,3]

[1]Donostia International Physics Center (DIPC), Donostia-San Sebastián 20018, Spain
[2]CIC nanoGUNE BRTA, Tolosa Hiribidea 76, 20018 Donostia-San Sebastian, Spain
[3]IKERBASQUE, Basque Foundation for Science, Bilbao 48013, Spain

*Corresponding author: kirill.voronin@dipc.org

***Abstract* — We present an accurate analytical solution for the prolate spheroid model of the scattering-type scanning near-field optical microscopy in the quasi-electrostatic limit. The model is developed and experimentally validated for calculating near-field spectra of bulk and layered samples, and can be extended to more complex nanostructures.**

***Keywords* — field-enhanced spectroscopy; infrared nanospectroscopy; Laplace equation; prolate spheroidal coordinates.**

I. Introduction

Scattering-type scanning near-field optical microscopy (s-SNOM) is a versatile technique in nanooptics, enabling local probing of optical responses beyond the diffraction limit from vis to THz frequencies. Its theoretical modeling based on tip-sample interactions typically relies on computationally intensive numerical methods or phenomenological models with empirically fitted parameters, complicating spectral analysis and interpretation. Developing a rigorous quantitative analytical model remains a significant challenge in near-field microscopy. Here, we introduce an accurate analytical solution for the prolate spheroid model of s-SNOM in the quasi-electrostatic limit. We validate our solution through comparisons with numerical simulations and experimental spectra.

II. Methods

Our methodology integrates analytical approaches for electrostatic problems, finite-element numerical simulation, and s-SNOM measurements using a commercial nano-FTIR setup.

III. Results and Discussion

We analytically solve the electrostatic problem of charge distribution on the surface of a spheroid placed above the sample surface, as shown in Figure 1. This solution determines the dipole moment of the tip and, therefore, the expected near-field signal. As shown in Figure 1, the analytical solution matches the numerical simulation result perfectly.

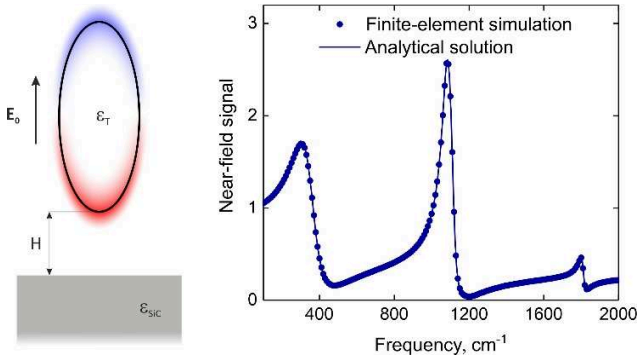

Fig. 1. Left: schematic of the spheroid over the sample surface in a uniform electric field. Right: Comparison of the numerically simulated and analytically calculated amplitude of the near-field signal second harmonic.

IV. Conclusion

We have developed a quantitative analytical model for scattering-type scanning near-field optical microscopy (s-SNOM). Due to its higher computational efficiency compared to numerical simulation and higher accuracy compared to phenomenological solutions, our solution for the spheroid model facilitates spectrum prediction and interpretation for bulk and layered samples. To promote further research and broader adoption, we have implemented the model in an open-source numerical tool available on GitHub [1].

Acknowledgments

This work was supported by "la Caixa" Foundation (ID 100010434, fellowship code LCF/BQ/DI21/11860026), the Spanish Ministry of Science and Innovation (grant PID2023-147676NB-I00) and the Basque Department of Education (grant PIBA-2023-1-0007).

References

[1] K. V. Voronin, I. Herrero León, R. Hillenbrand, A. Y. Nikitin, "Quantitative Analytical Spheroid Model for Scattering-Type Scanning Near-Field Optical Spectroscopy", Adv. Optical Mater. 13, no. 31 (2025): e01539.

Tailoring the Optical Properties of Random Metasurfaces for Multifunctional Applications

Alejandro Reyes-Coronado[1,*], Jonathan A. Urrutia-Anguiano[1], Isabel Y. Rojas-Martinez[1]

[1]Departamento de Física, Facultad de Ciencias, Universidad Nacional Autónoma de México, Ciudad de México, México
*Corresponding author: coronado@ciencias.unam.mx

***Abstract*—We demonstrate versatile light control using random metasurfaces modeled via the Coherent Scattering Model. By exploiting multipolar interference in disordered metallic and dielectric nanostructures, we achieve angle-independent structural colors, broadband reflection suppression, and phase-sensitive sensing. Our results establish random metasurfaces as robust, scalable alternatives to periodic systems.**

***Keywords* random metasurfaces, plasmonics, high-refractive index metasurfaces.**

I. Introduction

Metasurfaces have emerged as transformative platforms for photonic engineering due to their ability to manipulate light at subwavelength scales. Comprised of ultrathin layers of nanoscale elements—arranged in either periodic or disordered patterns—these planar, artificially structured materials circumvent the limitations of conventional bulk optics by providing tailored electromagnetic responses. While ordered metasurfaces have been extensively documented, random metasurfaces offer a unique paradigm for light-matter interaction, often providing advantages in fabrication scalability and spectral robustness. By precision-engineering these disordered subwavelength features, we have unlocked a diverse suite of applications: the generation of structural color via light transmission [1], the development of broadband antireflection coatings [2], the realization of the generalized Brewster effect for both polarizations [3], and the enhancement of light absorption through leaky lossy guided modes [4]. Furthermore, the high sensitivity of these disordered systems to environmental changes has positioned them as leading candidates for advanced sensing and biosensing technologies [5].

II. Methods

The description of the optical properties of disordered metasurfaces consisting of either dielectric or plasmonic nanospheres has been approached with effective medium theories (EMTs) such as the Bruggeman mixing formula, van der Hulst model, the erroneously used Maxwell-Garnett theory and the Dipolar Model. However, these models do not capture the complex light-matter interactions. Thus, we employ the Coherent Scattering Model (CSM), an approximate solution to Maxwell equations obtained by truncating the hierarchical LippmannSchwinger equations within the quasi-crystalline approximation [6]. This approach is particularly robust as it accounts for all multipolar orders induced within the nanospheres composing the metasurface and encompasses multiple-scattering effects, provided the system maintains a relatively low surface coverage and avoids grazing incidence angles.

As shown in Ref. [6], the reflection and transmission amplitude coefficients for a free-standing random monolayer are given by

$$r_{\mathrm{CSM}}(\theta_i) = \frac{-\alpha S_n(\pi - 2\theta_i)}{1 + \alpha S(0) + \frac{1}{4}\alpha^2\left[S^2(0) - S_{s,p}^2(\pi - 2\theta_i)\right]} \quad (1)$$

and

$$t_{\mathrm{CSM}}(\theta_i) = \frac{1 - \frac{1}{4}\alpha^2\left[S^2(0) - S_{s,p}^2(\pi - 2\theta_i)\right]}{1 + \alpha S(0) + \frac{1}{4}\alpha^2\left[S^2(0) - S_{s,p}^2(\pi - 2\theta_i)\right]}, \quad (2)$$

with

$$\alpha = \frac{2\Theta}{x_m^2 \cos\theta_i}, \quad (3)$$

where Θ represents the surface coverage, θ_i is the angle of incidence, and $x_m = ka$ is the size parameter (where k is the wavenumber in the matrix and a is the particle radius). The terms $S(0)$ and $S_{s,p}(\pi - 2\theta_i)$ denote the amplitude scattering coefficients at the scattering angles 0 and $\pi - 2\theta_i$, respectively, with subindices s and p specifying the incident polarization. These coefficients allow for the subsequent calculation of the reflectance and transmittance of a supported metasurface on a substrate.

In Fig. 1 we show a typically reflectance map for a metasurface made of identical gold spherical nanoparticles, as a function of the wavelength of the incident light λ_0 and the angle of incidence θ_i.

III. Results and Discussion

By employing all-dielectric random metasurfaces composed of polydisperse silicon nanoparticles onto a glass substrate, we demonstrate the generation of angle-independent transmission colors. As a proof of concept, we show that it is possible to generate a palette of colors with a combination of nanospheres with different radii and surface coverages. In this regard, we present a glimpse for a potential application that can be useful to design metasurfaces that display from warm to cold whites, as the typically emitted by light bulbs [1].

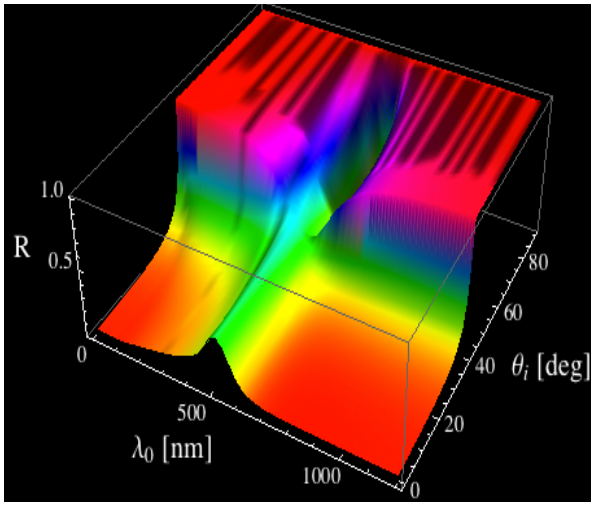

Fig. 1. Reflectance of a metasurface made of identical spherical gold nanoparticles of 5 nm radius and surface coverage of 5%, as a function of the wavelength of the incident light λ_0 and the angle of incidence θ_i .

The interplay between different multipolar contributions provides a powerful degree of freedom for controlling reflection. For metallic random metasurfaces, we observed a broadband suppression of reflection across a wide range of incident angles, independent of polarization. This phenomenon is rooted in the constructive interference between the radiation fields of the induced electric dipole and electric quadrupole within the subwavelength gold and bismuth spheres [2].

In contrast, high-refractive-index silicon metasurfaces exhibit a generalized Brewster effect for both s and p polarizations [3]. This behavior is dictated by the Kerker-like interference between induced electric and magnetic dipoles, which leads to total angle-selective scattering suppression.

Under internal reflection configurations, gold nanoparticle metasurfaces significantly enhance light absorption through the excitation of leaky lossy guided modes [4]. These modes arise from a balanced interplay between near-field coupling and the scattering properties of the individual particles.

Furthermore, we explored the application of these random metasurfaces in high-sensitivity sensing [5]. By operating at the near-zero reflectance point—a region characterized by a phase singularity in ellipsometric measurements—the system becomes hyper-sensitive to minute changes in the local refractive index. This topological feature in the phase response offers a significantly higher detection limit compared to traditional intensity-based plasmonic sensors.

IV. Conclusion

In conclusion, we have demonstrated that random metasurfaces, described by the Coherent Scattering Model, provide a versatile and robust platform for advanced light manipulation. By leveraging the interplay between electric and magnetic multipolar resonances in both plasmonic and dielectric nanospheres, we successfully engineered a diverse suite of optical responses, ranging from angle-independent structural colors and broadband reflection suppression to phase-sensitive sensing. These results highlight the advantages of random arrangements in achieving spectral stability and polarization independence, offering a scalable and efficient alternative to periodic photonic architectures for next-generation optoelectronic and biophotonic applications.

Acknowledgments

This work was partially supported by DGAPA-UNAM PAPIIT project IN101825.

References

[1] A. K. González-Alcalde and A. Reyes-Coronado, "Large angle-independent structural colors based on all-dielectric random metasurfaces," *Optics Communications*, vol. 475, 126289, 2020.

[2] A. K. González-Alcalde, I. Y. Rojas-Martinez, and A. Reyes-Coronado, "Broadband antireflective random metasurfaces," *Journal of the Optical Society of America B*, vol. 38, pp. 1974–1983, 2021.

[3] A. K. González-Alcalde, I. Y. Rojas-Martinez, and A. Reyes-Coronado, "Brewster effect in random and periodic high-refractive-index metasurfaces," *Optics Communications*, vol. 521, 128597, 2022.

[4] A. Reyes-Coronado, G. Pirruccio, A. K. González-Alcalde, J. A. Urrutia-Anguiano, A. J. Polanco-Mendoza, G. Morales-Luna, O. Vázquez-Estrada, A. Rodríguez-Gómez, A. Issa, S. Jradi, A. García-Valenzuela, and R. G. Barrera, "Enhancement of Light Absorption by Leaky Modes in a Random Plasmonic Metasurface," *The Journal of Physical Chemistry C*, vol. 126, pp. 3163–3170, 2022.

[5] J. P. Cuanalo-Fernández, N. Korneev, I. Cosme, M. B. de la Mora, J. A. Urrutia-Anguiano, A. Reyes-Coronado, R. Ramos-García, and S. Mansurova, "Phase Singularity in Random Gold Metasurface for Refractive Index Sensing: Experimental Demonstration and Theoretical Analysis," *The Journal of Physical Chemistry C*, vol. 128, pp. 11372–11381, 2024.

[6] A. Reyes-Coronado, G. Morales-Luna, O. Vázquez-Estrada, A. García-Valenzuela, and R. G. Barrera, "Analytical modeling of optical reflectivity of random plasmonic nano-monolayers," *Optics Express*, vol. 26, pp. 12660–12683, 2018.

Active light steering with electron beams

Eduardo J. C. Dias[1,*], Á. Rodríguez-Echarri[2], T. Rasmussen[1], J. García de Abajo[3,4], J. D. Cox[1,5]

[1]POLIMA – Center for Polariton-driven Light-Matter Interactions, University of Southern Denmark, Odense, Denmark
[2]AMOLF – Center for Nanophotonics, NWO-Institute AMOLF, Amsterdam, The Netherlands
[3]ICFO – Institut de Ciencies Fotoniques, Castelldefels (Barcelona), Spain
[4]ICREA-Institució Catalana de Recerca i Estudis Avançats, Barcelona, Spain
[5]DIAS – Danish Institute for Advanced Study, University of Southern Denmark, Odense, Denmark

*Corresponding author: dias@mci.sdu.dk

***Abstract*— By engineering a periodic non-uniform 1D array, we are able to steer the cathodoluminesce generated by a passing electron beam. We further demonstrate how to control such emission actively using disks of fluence-controlled phase-changing materials or electrostatically tunable graphene ribbons.**

***Keywords*— electron microscopy, 2D materials, Smith-Purcell.**

I. Introduction

Smith-Purcell (S-P) effect [1] consists of the constructive interference of cathodoluminescence (CL) arising from the interaction between moving charged particles and periodic structures, and it has traditionally been exploited for various applications, namely for the generation of broadband radiation sources.

In typical configurations, S-P effect is realized with perfectly periodic arrays where all elements are equivalent and thus are uniformly polarized up to a phase delay due to the finite velocity of the electron. Under such conditions, the resulting radiation at wavelength λ_0 follows a well-known geometric pattern resonating at angles obeying $\cos\theta_n = c/v - n\lambda_0/a$ [1], where n is an integer, a is the lattice period, and v is the electron velocity. Nevertheless, if the array is periodic but non-uniform, the induced dipole moment $\mathbf{p}_j$ in each array element j is in general different, and the far-field pattern is constructive according to the modified "generalized Smith-Purcell" (GSP) condition [2] $\cos\theta_n = c/v - [n - \ell/(N+1)]\,\lambda_0/a$, where $\ell = 0, \cdots, N-1$ denotes the normal modes of the dipole moment distribution according to the Fourier transform $\tilde{\mathbf{p}}_\ell = \sum_j \mathbf{p}_j e^{2\pi i j \ell/N}$.

II. Results and Discussion

In Fig. 1(a), we show the first few GSP channels for $n = 1$ and for parameters $v/c = 0.1$ and $a/\lambda = 0.09$. Although mode $\ell = 0$ is not viable (i.e., $\sin\theta_{1,0} < -1$) and therefore regular S-P emission is kinematically prohibited in a uniform array, modes $\ell = 1 - 9$ are viable channels for emission into the far-field that can be accessed through an adequate design of the array elements. To target such modes, we devise an induced dipole density with the harmonic form $\mathbf{p}_j(\xi)/p_0 = 1 + 2\sin(2\pi j\xi/N)$ whose Fourier transform directly yields modes $\ell = 0$ and $\ell = \pm\xi$. The far-field angular profile of GSP emission for a given modulation frequency ξ is shown in Fig. 1(b), with light emission accurately following the predicted GSP angles for each different ξ.

In practice, one can design the dipole moment imprinted in each element either passively (by controlling, for example, the

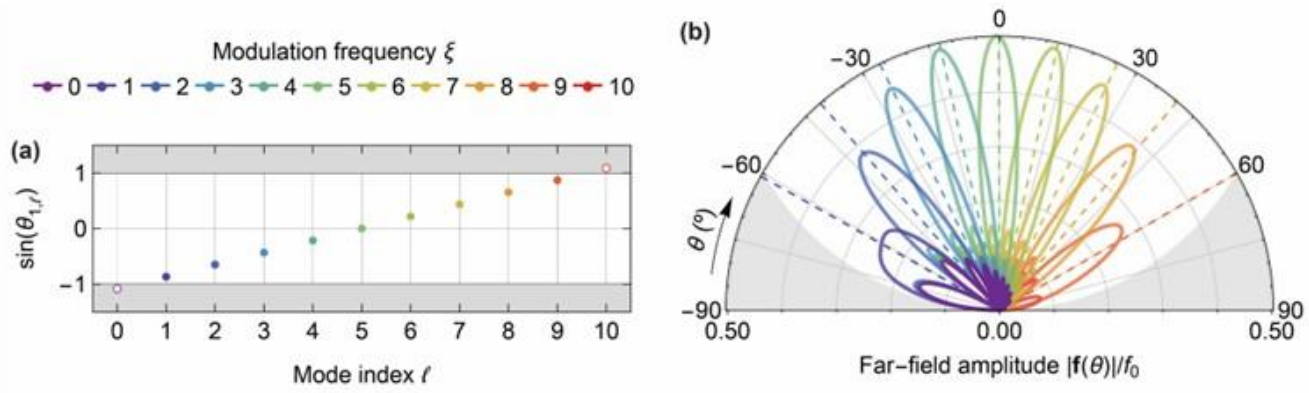

Fig. 1 (a) GSP channels emission angle for $n = 1$ and for an array/electron system with $v/c = 0.1$ and $a/\lambda = 0.09$. (b) Far-field emission angular profile of an array designed to target each modulation frequency ξ.

size and/or material of each array element), or actively (by controlling tunable physical or chemical properties of the individual array elements). We demonstrate this principle by exploring arrays composed by disks of VO_2 (a phase-change material) or graphene ribbons. In the former (latter) case, we inverse design the necessary fluence dosage (electrostatic gating) necessary to rigorously produce the designed dipole moment distribution $\mathbf{p}_j(\xi)$ (including intra-array interactions) and show that the reconstructed far-field profile matches perfectly the target angle for each ξ.

III. Conclusion

Our findings pave the way for the development of advanced S-P radiation sources with tailored and actively-controllable emission properties. By mapping a chosen angle to an implementable pattern on a compact finite array, the same device can be reprogrammed to steer, split, or modulate the beam without mechanical motion.

Acknowledgments

E. J. C. D. acknowledges support from the European Union (Marie Skłodowska-Curie Actions, grant agreement No. 101209876). A. R. E. and F. J. G. A. acknowledge support from ERC (Advanced Grant 789104-eNANO), the Spanish MINECO (MAT2017-88492-R and SEV2015-0522), the Catalan CERCA Program, and Fundació Privada Cellex. J. D. C. acknowledges support from Independent Research Fund Denmark (grant no. 0165-00051B). The Center for Polariton-driven Light–Matter Interactions (POLIMA) is funded by the Danish National Research Foundation (Project No. DNRF165).

References

[1] S. J. Smith and E. M. Purcell, Phys Rev 92, 1069 (1953).
[2] E. J. C. Dias, A. Rodríguez-Echarri, T. Rasmussen, F. J. García de Abajo, J. D. Cox, arXiv:2512.11422 (2025).

Multi-Electron Effects in Free-Electron Beams: Light Generation and Electron-Electron Correlations

Valerio Di Giulio[1,2*], Rudolf Haindl[1,2], Armin Feist[1,2], and Claus Ropers[1,2]

[1] Department of Ultrafast Dynamics, Max Planck Institute for Multidisciplinary Sciences, Göttingen, Germany.

[2] 4th Physical Institute - Solids and Nanostructures, University of Göttingen, Göttingen, Germany.

*Corresponding author: valerio.digiulio@mpinat.mpg.de

Abstract **- We predict and experimentally demonstrate Coulomb-driven crystallization in few-electron pulses and explore how discrete symmetry can emerge even in continuous beams. This reveals crystal-like ordering and enables new regimes for electron microscopy. We further study the quantum statistics of light emitted by such beams also modulated by an external laser field.**

Keywords **- electron microscopy, strong light-matter interaction, quantum-light generation, electron-electron correlations.**

I. Introduction

Under suitable conditions, particles with the same charge sign confined in a potential can form ordered structures stabilized by Coulomb repulsion, known as Coulomb crystals. This phase of matter has been extensively explored and observed in various systems, ranging from cooled ions in storage rings [1] to electrons in two-dimensional materials [2]. The formation of a Coulomb crystal is primarily determined by strong Coulomb coupling, i.e., a large ratio between the average interparticle Coulomb energy and the average kinetic energy associated with temperature in classical systems and with the energy level spacing in quantum systems.

In the context of electron microscopy, Coulomb repulsion between electrons in a high-current beam is typically regarded as detrimental. Known as the Boersch effect [3], intrabeam Coulomb scattering leads to an increase in emittance and, consequently, to a degradation of beam quality. Interestingly, it has recently been shown that electron-electron interactions can be exploited to generate a phase-space distribution with well-defined energy-time correlations, as observed in few-electron pulses photoemitted from a metallic nanotip and imaged in a transmission electron microscope [4].

In contrast to ions, whose spatial density can be measured via fluorescence, free electrons lack addressable internal energy transitions. Nevertheless, the electron phase-space density can be reconstructed using inelastic electron-light scattering (IELS) [5]. In this process, the electron couples to the evanescent fields generated by the scattering of a laser pulse at a material surface, resulting in the exchange of multiple light quanta that is imprinted onto the final electron spectrum. Since the strength

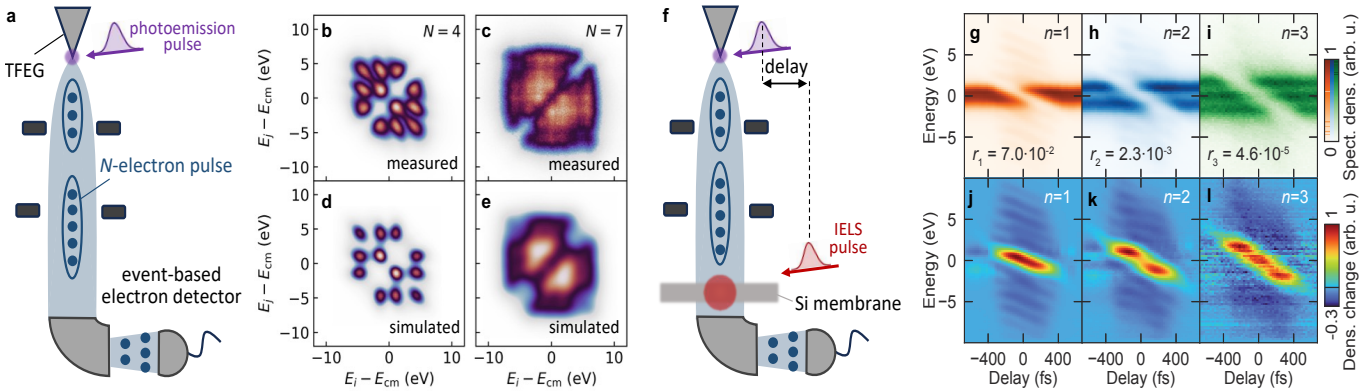

Figure 1. (a) Electron pulses are generated via photoemission from a thermal-field emission gun (TFEG) and then resolved in number and in energy using an event-based electron detector (Timepix3). Measured energy-energy correlations of expanded 4- (b) and 7-electron (c) Wigner crystallites, together with corresponding Monte-Carlo simulations (d,e) reproducing the data. (f) Coulomb-correlated electron pulses traverse a time-delayed optical near field at a silicon membrane, undergoing inelastic electron-light scattering. (g-i) Pump-probe delay scans of pulse charge-resolved components from 1 to 3 electrons. (j-l) Delay-dependent spectral change reveals the temporal separation of electrons within a pulse. Adapted from Ref. [7] under a CC BY 4.0 license.

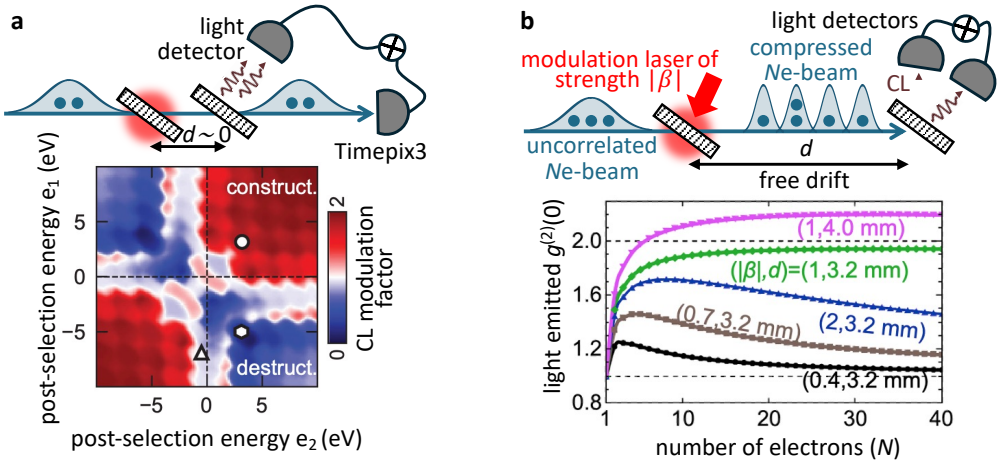

Figure 2. (a) A laser-modulated but uncompressed two-electron pulse interacts with a second structure; energy-time correlations still tailor CL emission via two-electron energy post-selection using an electron-resolved camera. (b) A multi-electron beam, laser-modulated and drifted over length *d*, forms density bunches; the CL two-photon correlation from a second sample is analyzed for various light modulations.

of this interaction depends on the light intensity, femtosecond laser pulses can be employed to capture snapshots of the electron density at a given time.

At the quantum level, due to the strong dependence between the input electron wave function and the output light state, IELS has been used for energy-time tailoring of free electrons, inspiring several works where electrons act not only as probes but as active elements capable of controlling the quantum state of light emitted into photonic structures [6].

II. Methods

We use Monte Carlo simulations, including charge-charge interaction between the electrons in the beam, to predict the phase-space evolution of the electrons in the column. We use quantum optics methods combined with the simulations to obtain the properties of the electron-triggered emission in cavities and in cathodoluminescence (CL) radiation.

Experiments were performed using the Göttingen Ultrafast Transmission Electron Microscope (UTEM), a platform based on a modified JEOL JEM-F200. Few-particle electron pulses have been generated via near-threshold photoemission from a W(100)/ZrO Schottky emitter.

III. Results and Discussion

In this work, we challenge the paradigm that associates Coulomb crystals exclusively with trapped particles by using Monte Carlo simulations to investigate the conditions under which Coulomb repulsion yields ordered one-dimensional chains of electrons, supported by experimental data. For finite particle numbers, we show how a photoemitted beam transitions from a stochastic state to a few-electron Coulomb crystal, enabled by the one-dimensional structure arising from the combined action of acceleration and time-dependent photoemission. Before expanding deterministically under Coulomb repulsion, thereby developing a phase space with well-defined energy and time peaks, the electron pulse evolves from a stochastic state to a transient state that is time-ordered but energy-disordered. Based on this observation, we interpret the well-defined energy-energy correlations measured in few-electron pulses photoemitted from a thermal-field emission gun in a transmission electron microscope (Fig. 1a), containing 4 to 8 particles (with only 4 and 7 shown in Fig. 1b,e), as evidence of transient ordered Coulomb crystallites formed during propagation in the column.

Furthermore, we report results from a related work [7], in which the energy-time distributions of two- and three-electron pulses are measured via an IELS interaction at a silicon membrane (see Fig. 1f). Delay scans, sorted according to the number of electrons in each pulse, are presented in Figs. 1g-i. At long time delays, distinct single-, double-, and triple-lobed spectral features appear. When the laser and electron pulses temporally overlap, the electrons undergo inelastic scattering to both higher and lower energy states, resulting in depletion of the zero-loss peak. This behavior becomes evident in the delay-dependent spectral difference plots (Fig. 1j-l), obtained by subtracting the large-delay spectra from those measured at varying delays. The electron pulse distributions are multimodal, with different regions exhibiting multiple-lobe structures arising from strong Coulomb-induced correlations.

Such two-electron Coulomb-IELS-modulated pulses can then be used to enhance or suppress the CL emission by post-selecting their energies alone, without the use of dispersive bunching (see Fig. 2a). Furthermore, by increasing the number of electrons and adjusting the IELS modulation parameters while allowing for free drift of the beam, the generated light can exhibit statistics ranging from thermal to Poissonian (see Fig. 2b).

IV. Conclusion

These results represent a fundamental step toward exploring correlated phases in free-electron systems and developing high-brightness beams for electron microscopy, as well as creating quantum light sources driven by correlated electron beams.

Acknowledgments

We acknowledge the continued support from the Göttingen UTEM team. We thank Thomas Rittmann for insightful discussions on phase-space density reconstruction. The

experiments were conducted at the Göttingen UTEM Lab, funded by the Deutsche Forschungsgemeinschaft (German Research Foundation) through Project-ID 432680300 (SFB 1456, project C01 to C.R.), the Gottfried Wilhelm Leibniz program (RO 3936/4-1 to C.R.) and the European Union's Horizon 2020 research and innovation programme under grant agreement no. 101017720 (FET-Proactive EBEAM), and we acknowledge fruitful discussions with the authors.

REFERENCES

[1] G. Birkl, K. Kassner, and H. Walther, Nature 357, 310-313 (1992).
[2] H. Li1, Z. Xiang, A. P. Reddy, T. Devakul, R. Sailus, R. Banerjee, T. Taniguchi, K. Watanabe, S. Tongay, A. Zettl, L. Fu, M. F. Crommie, F. Wang, Science 285, 86-91 (2024).
[3] H. Boersch, Zeitschrift für Physik 139, 115 (1954).
[4] R. Haindl, A. Feist, T. Domröse, M. Möller, J. H. Gaida, S. V. Yalunin, C. Ropers, Nat. Phys. 19, 1410-1417 (2023).
[5] A. Feist, K. E. Echternkamp, J. Schauss, S. V. Yalunin, S. Schäfer, C. Ropers, Nature 521, 200-203 (2015).
[7] V. Di Giulio, R. Haindl, C. Ropers, Nanophotonics 14, 1865-1878 (2025).
[6] R. Haindl, V. Di Giulio (CA), A. Feist, and C. Ropers (CA), Phys. Rev. Lett. 135, 165002 (2025).

Free electrons shape light, light shapes free electrons

Álvaro Rodríguez Echarri

Center for Nanophotonics, NWO Institute AMOLF, 1098 XG Amsterdam, The Netherlands
*Corresponding author: a.rodriguezecharri@amolf.nl

***Abstract*— Swift electrons enable nanoscale light–matter interaction beyond optical diffraction. In electron energy-loss spectroscopy and cathodoluminescence, electrons generate optical excitations, whereas in photon-induced near-field electron microscopy incoming light reshapes electronic states. We present a wave-based perspective highlighting the reciprocal roles of light and free electrons in nanophotonic systems.**

***Keywords*— free electrons, nanophotonics, PINEM, near-field spectroscopy, light–matter interaction, electron microscopy.**

I. Introduction

Achieving control over light–matter interaction at the nanoscale is fundamentally limited by optical diffraction. Swift electrons provide nanometer spatial resolution and ultrafast temporal sensitivity, enabling access to electromagnetic excitations beyond the reach of conventional optical techniques. Electron-based approaches have therefore emerged as powerful tools for nanoscale nanophotonics.

II. Methods

We employ a semiclassical theoretical framework combining Maxwell's equations with quantum descriptions of free-electron wave packets. The approach captures electron-driven and light-driven processes, enabling the analysis of Smith-Purcell radiation, electron energy-loss spectroscopy, and photon-induced near-field electron microscopy. We further contextualize the theory by examining and comparing recent experimental and theoretical results in the field of swift electrons and near-field optics.

III. Results and Discussion

Electron–induced plasmonic excitations in spherical and cylindrical nanostructures:
We study electron–photon coupling in nanostructures with high symmetry, focusing on spherical and cylindrical geometries. For spherical particles, we revisit Mie theory with particular emphasis on penetrating electron trajectories, which access additional coupling channels to plasmonic modes that are forbidden for purely external trajectories. This perspective enables a complete modal decomposition of electron-induced electromagnetic excitations and clarifies the role of internal fields in plasmon excitation [1].
Extending these ideas to cylindrical geometries, we discuss recent analytical solutions for electron–photon interactions in systems with translational symmetry. These results go beyond numerical approaches, providing deeper physical insight into mode excitation, dispersion relations, and radiation processes, and highlighting both parallels and key differences with the spherical case [2].

Generalized Smith–Purcell radiation:
We present generalized Smith–Purcell frameworks that extend classical formulations to complex nanostructures and near-field regimes. This approach enables active, on-demand steering of Smith–Purcell radiation, providing full control over the emitted light [3]. The model applies to a diverse set of photonic devises.

Multiple PINEM interactions:
We analyze regimes of coherent photon-induced near-field electron microscopy interactions, where electrons undergo multiple energy exchanges with optical near fields. This leads to structured electron wave packets and highlights the active role of light in shaping electronic quantum states [4]. We also analyse the effect of the coherence in their interaction.

IV. Conclusion

The reciprocal interaction between light and free electrons establishes a unifying platform for nanoscale nanophotonics, where electrons act not only as high-resolution probes but also as controllable sources and manipulators of optical fields. By combining electron-driven light emission and light-driven electron-state engineering within a semiclassical framework, a physical playground emerges across EELS, Smith–Purcell radiation, and PINEM. This reciprocity enables unprecedented access to spatial, spectral, and temporal degrees of freedom, extending from classical near-field optics to coherent and quantum regimes. Such concepts point toward the development of hybrid electron–light devices, including electron-controlled light sources, optically shaped electron beams, and integrated platforms for ultrafast and quantum nanophotonics.

Acknowledgments

The European Commission (project no. 101017720-EBEAM).

References

[1] P.E. Stamatopoulou, et al,, PRR **6**, 013239 (2024)
[2] A. Rodríguez Echarri, et al., PRB **111**, 205436 (2025)
[3] E. Días, et al., submitted (arXiv:2512.11422)
[4] A. Rodríguez Echarri, in preparation (2026)

Scaling Up Light-Matter Interactions - Challenges in Fabrication

Rijil Thomas[1]

[1]AMO GmbH, Aachen, Germany
*Corresponding author: thomas@amo.de

***Abstract*— Rapid advances in microscale-to-nanoscale light–matter interactions are redefining the limits of photonics, leading to a paradigm shift in photonic technologies. However, bridging the gap between laboratory breakthroughs and scalable real-world systems remains a central challenge. At AMO GmbH, we progress to address these challenges by developing fabrication processes that enable scalable realization of these emerging technologies.**

***Keywords* — photonic integrated circuits, PICs, nanofabrication, integrated photonics**

SUMMARY

Rapid advances in microscale-to-nanoscale light–matter interactions are continuously redefining the limits of photonics and leading to a paradigm shift in integrated photonic technologies. However, bridging the gap between laboratory breakthroughs and scalable, real-world systems remains a central fabrication challenge. Since their first conceptual demonstration in the early 1970s, photonic integrated circuits (PICs) have evolved into robust and scalable platforms that underpin increasingly sophisticated technologies, including terabit-scale data-center engines [1], programmable photonic processors [2], high-speed plasmonic modulators [3], ultra-low-loss waveguide platforms [4], and much more. Continuing the trend, we have now emerging challenges at hand like photonic designs that rely on extreme nanoscale light interactions at the expense of extremely tiny feature sizes and integration of diverse material platforms – such as 2D materials, polymers, plasmonic metals (eg: Ag, Au), etc - pushing the limits of fabrication capabilities. As a research foundry, AMO GmbH plays a critical role in developing fabrication processes to realize and scale up these next-generation technologies as illustrated by the examples highlighted in this summary.

Designing photonic components that push performance boundaries from ultralow-loss couplers to inverse design and machine-learning-inspired metasurfaces, inevitably tightens fabrication tolerances and drives process innovation. For eg: continuing advances in ultralow-loss silicon-nitride platforms have forced designers to trade waveguide loss for out-of-plane coupling strength - a trade that our grating-coupler work addresses by adding an amorphous-Si overlay and extremely controlled thickness/etch of the amorphous-Si and a 100 nm Si_3N_4 core. Such designs demand <10 nm nanometer film-thickness uniformity on a wafer scale, highly repeatable overlay deposition and etch recipes, and very low sidewall and surface roughness to avoid spoiling the platform's <0.1 dB/cm propagation loss. Overlay pattern alignment and lithography are also critical to achieve the coupling efficiency and directionality [4]. In parallel, chip-integrated inverse design and binary metasurfaces for beam-shaping and polarization control shift the burden to high-resolution pattern fidelity: such designs require lithographic feature sizes at, or below, the sub-100 nm scale, extremely low pattern placement error, and tight control of fabrication variability so that the simulated phase/amplitude response maps to the fabricated device performance across the chip (Figure *1*a,b) [5]. Such designs also add another layer complexity during SEM inspection to correlate and characterize the mismatch between the designed target vs on-wafer fabricated structures.

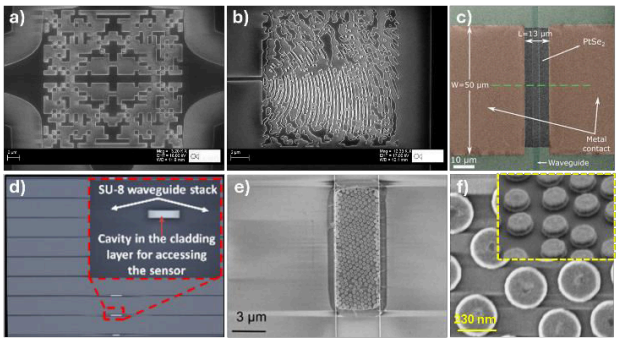

Figure 1: Photonic structures fabricated on advanced integrated platforms: a) and b) Advanced grating couplers for chip-Integrated quantum applications [5], c) Waveguide-integrated 2D $PtSe_2$ photodetectors [6], Bimodal plasmonic refractive index sensors [7], e) and f) Integrated plasmonic light sources [8].

The integration of emerging materials introduces additional fabrication challenges centered on heterogeneous processing and interface control. Our $PtSe_2$ photodetector (Figure *1*c) work highlights the need for scalable, low-temperature synthesis or transfer methods that provide precise layer-thickness control, uniform crystallinity, and clean interfaces compatible with photonic substrates. Reliable performance further depends on optimized contact engineering and encapsulation to suppress

dark current and enable reproducible integration of 2D materials into scalable photonic platforms [6]. Polymer-based bimodal plasmonic sensors (Figure *1*d) and plasmonic and nanopatch devices that enhance emitter radiation (disc-on-disc (DoD) nanoantennas with controlled openings) (Figure *1*e,f) introduce a second class of challenges: nanometer-scale gap control, reproducible antenna geometry, and deterministic placement/encapsulation of colloidal quantum dots into hotspots without degrading their emission. Achieving the emission enhancements and accessible hotspots reported requires lithography with tight critical-dimension control, robust lift-off or etch processes for very small gaps, and surface/chemical treatments that maintain QD optical properties during assembly and encapsulation [8]. For the polymer-clad bimodal plasmo-photonic sensors, integrating an aluminum plasmonic stripe with a bilayer SU-8 waveguide and a specialized optical cladding poses additional issues: metal patterning on polymer (adhesion, thermal budget, edge roughness), achieving high refractive-index contrast while avoiding scattering from rough interfaces, and encapsulation to provide opto-mechanical isolation and long-term stability - all of which addressed tailored process flows that emphasize CMOS-compatible steps, polymer curing control, and careful metal/polymer interface engineering. Collectively, these examples highlight both the addressed and ongoing challenges faced in cleanroom fabrication environments striving to realize exotic light–matter interactions within scalable technological platforms.

REFERENCES

1. S. Bernabé, Q. Wilmart, K. Hasharoni, K. Hassan, Y. Thonnart, P. Tissier, Y. Désières, S. Olivier, T. Tekin, and B. Szelag, "Silicon photonics for terabit/s communication in data centers and exascale computers," Solid. State. Electron. **179**, 107928 (2021).

2. W. Bogaerts, D. Pérez, J. Capmany, D. A. B. Miller, J. Poon, D. Englund, F. Morichetti, and A. Melloni, "Programmable photonic circuits," Nature **586**, 207–216 (2020).

3. A. Melikyan, L. Alloatti, A. Muslija, D. Hillerkuss, P. C. Schindler, J. Li, R. Palmer, D. Korn, S. Muehlbrandt, D. Van Thourhout, B. Chen, R. Dinu, M. Sommer, C. Koos, M. Kohl, W. Freude, and J. Leuthold, "High-speed plasmonic phase modulators," Nat. Photonics **8**, 229–233 (2014).

4. B. Chmielak, S. Suckow, J. Parra, V. C. Duarte, T. Mengual, M. A. Piqueras, A. L. Giesecke, M. C. Lemme, and P. Sanchis, "High-efficiency grating coupler for an ultralow-loss Si 3 N 4 -based platform," Opt. Lett. **47**, 2498 (2022).

5. A. Sorokina, L. Shelling Neto, A. Alcape Meyer, C.-F. Grimpe, G. Du, S. Sauer, E. Jordan, P. Sah, R. Thomas, S. Suckow, T. E. Mehlstäubler, and S. Kroker, "QR-Code Structure for Beam Shaping and Polarization Control via Machine Learning for Chip-Integrated Quantum Applications," EPJ Web Conf. **335**, 05013 (2025).

6. S. Parhizkar, M. Prechtl, A. L. Giesecke, S. Suckow, S. Lukas, O. Hartwig, A. Quellmalz, K. B. Gylfason, D. Schall, G. S. Duesberg, and M. C. Lemme, "Waveguide-Integrated Photodetectors based on 2D Platinum Diselenide," in *2021 Device Research Conference (DRC)* (IEEE, 2021), pp. 1–2.

7. O. Bhalerao, S. Suckow, H. Windgassen, H. Biller, K. Fotiadis, S. Simos, E. Chatzianagnostou, D. Spasopoulos, P. Das, L. Markey, J.-C. Weeber, N. Pleros, M. Schirmer, and M. C. Lemme, "Bimodal Plasmonic Refractive Index Sensors Based on SU-8 Waveguides," (2024).

8. V. Gupta, J. L. Montaño-Priede, S. Hu, E. S. A. Goerlitzer, M. Zapata-Herrera, R. Esteban, N. Zabala, J. J. Baumberg, J. Aizpurua, and N. Vogel, "Emission enhancement of colloidal quantum dots confined in double disc nano-antennas with controlled opening," Nanoscale **18**, 1576–1588 (2026).

Directional Energy Delivery at the Nanoscale: The Iris-Gated Approach for Photothermal Applications

Javier González-Colsa[1], Jose M. Saiz[1], Alfredo Franco[1], Dolores Ortiz[1], Francisco González[1], Fernando Bresme[2], Pablo Albella[1,*]

[1]Department of Applied Physics (Group of Optics), University of Cantabria, Spain
[2]Department of Chemistry, Molecular Sciences Research Hub, Imperial College London, UK
*Corresponding author: pablo.albella@unican.es

***Abstract*— The rational control of nanoscale heat transport is essential for advancing photothermal therapies. We introduced the Iris-Gated Core–Double–Shell (ICDS) nanoparticle as a minimalistic strategy to induce thermal asymmetry while preserving geometric symmetry. By introducing a conical aperture into a spherical glass/gold/polymer overshell, we enable directional heat redistribution without perturbing the underlying plasmonic response. We identified an optimal configuration resonant within the first biological window that redirects up to 67% of the conductive heat flux and enhances local surface power density by 50% ($\Delta T \approx 20-23$ °C). Transient analysis under pulsed excitation confirms that this thermal asymmetry persists during the considered pulse intervals. The ICDS framework provides an efficient route for tailoring anisotropic heat transport, offering a promising platform for controlled photothermal therapies.**

***Keywords*— Thermoplasmonics, Plasmonics, Nanophotonics.**

I. Introduction

Plasmonic nanoparticles have revolutionized photothermal applications by acting as efficient light-to-heat converters. However, most conventional designs generate isotropic thermal envelopes, limiting their effectiveness in therapies requiring precise spatial control [1]. While Janus-like particles can break this symmetry, they often require complex fabrication or sacrifice optical efficiency [2,3]. We propose the ICDS architecture, which utilizes a strategic "iris" aperture in a dielectric overshell. This design allows for "thermal gating," where the gold core provides the heat source via Localized Surface Plasmon Resonance (LSPR), and the modified shell dictates the direction of the resulting heat flux [4]. This study explores the trade-offs between optical absorption and thermal anisotropy in both stationary and transient regimes.

II. Methods

To evaluate the ICDS architecture, we employed a hybrid analytical–numerical approach combining electromagnetic absorption and heat diffusion. Optical properties were characterized using generalized Mie theory to optimize the nanoparticle geometry for maximum absorption within the first biological window. Heat transport was modeled through the stationary heat diffusion equation to quantify the steady-state thermal bias. For transient regimes under pulsed excitation, we implemented a generalized heat-source formulation accounting for electron–phonon relaxation and pulse duration. Finally, a thermal focusing gain parameter was introduced to quantify the performance of the iris gate relative to a symmetric counterpart

III. Results and Discussion

Our optimization yields an ideal configuration at $(r_c, \delta_{Au}, \delta_p, \theta) = (36\,nm, 5\,nm, 40\,nm, 70°)$. In the steady state, the ICDS redirects 67% of the conductive heat flux toward the aperture-side hemispace, achieving temperature rises of 20–23 °C under reference illumination. This directional redistribution corresponds to a 50% increase in local surface power density, effectively "focusing" the heat. Under pulsed excitation, while the directional effect is most efficient in the stationary regime, the ICDS architecture retains measurable thermal asymmetry during the pulse interval. This confirms that the thermal bias is fundamentally rooted in the structural design and persists even under fast transient dynamics.

IV. Conclusion

The ICDS nanoparticle represents a significant step towards "programmable" nanothermal sources. By using a symmetric core-shell structure with a conical aperture, we achieve high-impact directional heat delivery without compromising the stability of the optical resonance. This framework is not only computationally efficient but also offers a scalable design rule for the next generation of anisotropic photothermal agents and advanced thermoplasmonic applications.

Acknowledgments

This project was supported by the Spanish Ministerio de Ciencia e Innovación under project MOPHOSYS (grant no. PID2022-139560NB-I00).

References

[1] J. González-Colsa et al. Opt. Express 30, 125–137 (2021).
[2] J. González-Colsa et al. Sci Rep 12, 14222 (2022).
[3] V. Barbieri et al. ACS Nano 19, 16, 15331–15344 (2025).
[4] J. González-Colsa, F. Bresme and P. Albella. arXiv:2601.19646. https://arxiv.org/abs/2601.19646 (2026)

Chiral Cavities Made from Lattices of Highly Electromagnetically-Chiral Scatterers

Lukas Rebholz[1,*], Carsten Rockstuhl[1,2], Ivan Fernandez-Corbaton[2]

[1]Institute of Theoretical Solid State Physics, Karlsruhe Institute of Technology, Germany
[2]Institute of Nanotechnology, Karlsruhe Institute of Technology, Germany
*Corresponding author: lukas.rebholz@kit.edu

***Abstract*—Chiral cavities are required to harness light–matter interactions for the optical control of chirality, especially in molecular processes. We computationally study chiral cavities assembled from metasurface mirrors featuring optimized electromagnetically-chiral scatterers. Our aim is to provide the necessary environment for applications such as maximizing enantioselective effects for chiral molecules.**

***Keywords*—chiral cavities, electromagnetic chirality, light–matter interaction, metasurfaces, transition matrix formalism.**

I. Introduction

Chirality – the geometric property of an object that cannot be brought to coincide with its mirror image through translations and rotations – is ubiquitous in nature, and its detection and control are crucial. For instance, most biologically relevant molecules are chiral, and organic processes are vitally sensitive to the handedness of the enantiomers involved. Therefore, advancing our abilities to detect and manipulate chemicals in a handedness-selective manner is an extremely relevant task, not least for drug synthesis.

Light promises to be a useful tool for this purpose, as it can interact with matter in a handedness-selective manner. The exemplary system to capitalize on the interaction of light and matter is an optical cavity due to the resonant enhancement it provides. Importantly, application in a chiral context requires the cavity to be selective with regards to the light's circular polarization handedness, i.e., more generally, helicity-selective [1]. This is not the case with ordinary Fabry–Perot cavities, for instance, since each reflection from a typical mirror or surface at normal incidence results in a reversal of the circular polarization handedness.

In our work [2], we approach the design of chiral cavities, focusing on metasurfaces consisting of periodic arrangements of optimized electromagnetically-chiral scatterers.

II. Methods

The proposed design of the chiral cavity follows a bottom-up scheme, starting from the optimization of a chiral unit and its assembly into a periodic structure yielding a collective chiral optical response. In the optimization, we make use of the electromagnetic chirality (em-chirality) [3] which quantifies the chirality of an object's response to light. Similar to Garcia-Santiago et al. [4], we use em-chirality as an objective function to optimize the response of nanohelical metallic scatterers.

We use the transition matrix (T-matrix) formalism to represent the scatterers' linear optical response. The in-house developed open-source code *treams* [5] allows us to efficiently study the optical properties of single as well as periodically arranged scatterers.

III. Results and Discussion

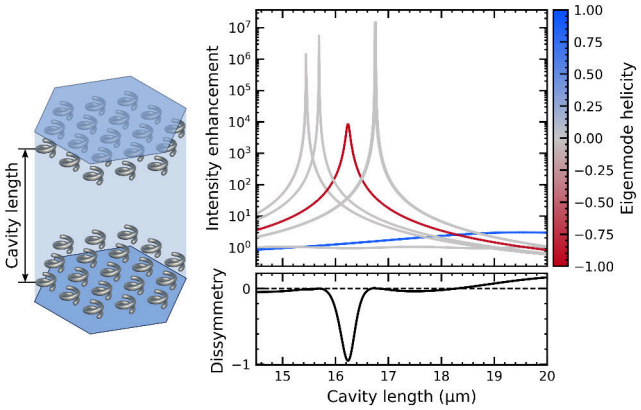

Fig. 1. Internal intensity enhancement of cavity eigenmodes colored according to their helicity content (top), and total dissymmetry (bottom). By varying the cavity length, different eigenmodes are brought into and out of resonance. On resonance, the contrast in the intensity enhancement between the negative helicity and positive helicity modes is nearly four orders of magnitude. Taking all modes into account, negative helicity dominates the cavity with a total dissymmetry reaching $95.3\,\%$ of its absolute bound at a cavity length of $16.23\,\mu\mathrm{m}$.

We consider a chiral cavity formed by two facing planar mirrors featuring hexagonal lattices of optimized em-chiral scatterers, schematically shown on the left of Fig. 1. The lattice spacing is chosen to be barely diffracting in the embedding material at the considered operating frequency of $44.21\,\mathrm{THz}$. This follows a similar approach to the one used by Feis et al. [6]. Consequently, we consider not only normally incident modes but also modes with large in-plane, or transverse, momenta, constituted by the six first diffraction orders. Our approach combines the high degree of helicity preservation exhibited by grazing angle reflection with the strong helicity selectivity introduced by the optimized em-chiral scatterers. As a result, the cavity supports modes of nearly pure helicity

(98.8 %). Figure 1 shows the internal intensity enhancements of the eigenmodes of the cavity for a varied cavity length. Importantly, the cavity exhibits a contrast of almost four orders of magnitude between the maximal (on resonance) intensity enhancement of the negative helicity eigenmode and its positive helicity counterpart. Expressed as a dissymmetry by normalizing the helicity-weighted sum of all intensity enhancements to the total sum of all intensity enhancements, this contrast reaches 95.3 % of its upper bound (corresponding to a cavity with a modal landscape of pure helicity).

IV. Conclusion

We have demonstrated a chiral optical cavity featuring eigenmodes with nearly pure helicity and a strong dissymmetry between the resonant intensity enhancements of modes of opposite helicity. On resonance, the enhancement of the negative helicity eigenmode exceeds that of its positive helicity counterpart by nearly four orders of magnitude. These values signify the cavity's ability to provide the strongly helicity-selective electromagnetic environment for potential applications such as the enhancement of enantioselectivity in cavity-aided chiral molecular chemistry.

Acknowledgments

L.R. acknowledges support by the Karlsruhe School of Optics & Photonics (KSOP). I.F.C. and C.R. acknowledge support by the Helmholtz Association via the Helmholtz program "Materials Systems Engineering" (MSE). This work was partially funded by the Deutsche Forschungsgemeinschaft (DFG, German Research Foundation) – Project-ID 258734477 – SFB 1173. We are grateful to the company JCMwave for their free provision of the FEM Maxwell solver JCMsuite.

References

[1] K. Voronin, A. S. Taradin, M. V. Gorkunov, and D. G. Baranov, "Single-handedness chiral optical cavities," *ACS Photonics*, vol. 9, no. 8, pp. 2652–2659, May 2022.

[2] L. Rebholz, C. Rockstuhl, and I. Fernandez-Corbaton, "Chiral cavities made from lattices of highly electromagnetically-chiral scatterers," 2025, *arXiv:2507.10481 [physics.optics]*.

[3] I. Fernandez-Corbaton, M. Fruhnert, and C. Rockstuhl, "Objects of maximum electromagnetic chirality," *Phys. Rev. X*, vol. 6, no. 3, Jul. 2016, Art. no. 031013.

[4] X. Garcia-Santiago, M. Hammerschmidt, J. Sachs, S. Burger, H. Kwon, M. Knöller, T. Arens, P. Fischer, I. Fernandez-Corbaton, and C. Rockstuhl, "Toward maximally electromagnetically chiral scatterers at optical frequencies," *ACS Photonics*, vol. 9, no. 6, pp. 1954–1964, May 2022.

[5] D. Beutel, I. Fernandez-Corbaton, and C. Rockstuhl, "treams – a T-matrix-based scattering code for nanophotonics," *Comput. Phys. Commun.*, vol. 297, Apr. 2024, Art. no. 109076.

[6] J. Feis, D. Beutel, J. Köpfler, X. Garcia-Santiago, C. Rockstuhl, M. Wegener, and I. Fernandez-Corbaton, "Helicity-preserving optical cavity modes for enhanced sensing of chiral molecules," *Phys. Rev. Lett.*, vol. 124, no. 3, Jan. 2020, Art. no. 033201.

Novel quantum effects in (Surface-Enhanced) Raman Scattering from molecular systems

Adrián Juan-Delgado[1,2,3*], Ruben Esteban [1,4], Lukas A. Jakob[5], Jean-Baptiste Trebbia[6,7], Shu Hu[5], Rakesh Arul[5], Roberto A. Boto[4], Quentin Deplano[6,7], Philippe Tamarat[6,7], Rémi Avriller[8,9], Niclas S. Mueller[5,10], Diego Martín-Cano[3], Paloma A. Huidobro [3], Jeremy J. Baumberg[5], Brahim Lounis[6,7], Javier Aizpurua[2,4,11]

[1]Centro de Física de Materiales, CSIC-UPV/EHU, Donostia-San Sebastián, Spain
[2]Departament of Electricity and Electronics, University of the Basque Country (UPV/EHU), Leioa, Spain.
[3]Departamento de Física Teórica de la Materia Condensada and Condensed Matter Physics Center (IFIMAC), Universidad Autónoma de Madrid, 28049 Madrid, Spain.
[4]Donostia International Physics Center (DIPC), Donostia-San Sebastián, Spain.
[5]Nanophotonics Centre, Cavendish Laboratory, University of Cambridge, Cambridge, U.K.
[6]Université de Bordeaux, Talence, France
[7] Institut d'Optique and CNRS, LP2N,Talence, France
[8] Université de Bordeaux, CNRS, LOMA, Talence, France
[9] Université de Strasbourg, CNRS, Institut de Physique et Chimie des Matériaux de Strasbourg, Strasbourg, France
[10] Department of Physical Chemistry, Fritz-Haber-Institute of the Max-Planck-Society, Berlin, Germany
[11] Ikerbasque, Basque Foundation for Science, 48009 Bilbao, Spain
*Corresponding author: adrianjuand1996@gmail.com

***Abstract*—We discuss novel effects in molecular Raman scattering unveiled using quantum-mechanical frameworks. For example, we demonstrate that quantum coherence can influence Stokes emission from two molecules interacting via dipole–dipole coupling. We also identify collective effects in the Raman signal generated by many molecules confined within a plasmonic nanocavity.**

***Keywords*— molecules, Raman scattering, molecular optomechanics, photon correlations, collective effects, quantum coherence.**

I. Introduction

The electronic degrees of freedom of organic molecules can interact with internal vibrational modes, as well as with phonon modes of the surrounding environment. As a consequence, when a laser is used to excite the molecules, they can emit photons inelastically due to energy exchange between light and vibrations, a process known as Raman scattering. For example, photons that are red-shifted with respect to the excitation laser are emitted when the final vibrational state has a higher energy than the initial one; these lower-energy photons are referred to as Stokes photons. In the opposite case, when the emitted photons have a higher energy than the excitation laser, they are called anti-Stokes photons. Here, we discuss recent advances in Raman scattering obtained by using quantum-mechanical models and that contrast with often-invoked assumptions. We first consider the Stokes-shifted emission from two molecules embedded in a solid-state matrix that interact electromagnetically with each other due to their short separation distance [1], [2]. In this case, we analyze the correlation of Stokes photons and show that it can be affected by quantum coherence [3]. Next, we consider Surface-Enhanced Raman Scattering (SERS) from many molecules in a plasmonic nanocavity, showing that the cavity optical modes can mediate molecular interactions and give rise to collective effects in the Raman signal [4]. Moreover, we explore the possible connection between Raman scattering and time-varying media, which are material whose electromagnetic properties are modulated on time [5].

II. Methods

We describe the molecular dynamics using a master-equation formalism, with the corresponding numerical simulations performed using the QuTiP Python package [6]. Further, to describe the interaction between molecules and the plasmonic nanocavity, we use a molecular optomechanics framework [7], [8], where the molecular vibrations play the role of the mechanical degrees of freedom in standard cavity optomechanics. The finite element method solver COMSOL Multiphysics [9] is used to characterize the electromagnetic response of the nanocavity.

III. Results and Discussion

We first consider the Stokes-shifted emission from organic molecules embedded in a solid-state matrix at cryogenic temperatures, in the absence of any plasmonic cavity. The molecules are excited by a laser resonantly tuned to the electronic transition. In this context, recent experiments have been able to analyze the optical response of pairs of molecules

at sufficiently short separation distances such that they can interact electromagnetically [1], [2], leading to the formation of hybrid superradiant and subradiant states [10]. In these experiments, the molecules are resonantly driven to the electronic excited state, and the detected light is spectrally filtered to eliminate the laser contribution, so that only Stokes photons (i.e., the Raman signal) are collected.

We develop a master-equation framework to describe the intensity correlations of the Stokes photons emitted from these interacting molecules. Importantly, we show that the resulting expression for the Stokes correlation can be decomposed into a contribution that is unaffected by quantum coherence (neither molecular coherence nor electromagnetic-field coherence) and additional contributions that explicitly depend on coherence effects. By comparing the different contributions with experimental observations, we demonstrate that quantum coherence can indeed play a significant role in the correlation of Stokes photons, in contrast to the often assumption that Raman scattering is an incoherent process.

Next, we consider many molecules at room temperature in an extreme plasmonic nanocavity known as a Nanoparticle-on-a-Mirror (NPoM). The NPoM nanocavity consists of an Au nanosphere and an Au substrate, which are separated by a $\sim$1 nm gap, in which the molecules are located. We use a molecular optomechanics framework that accounts for the intermolecular interactions mediated by the NPoM nanocavity [11], [12]. In this way, we study the dependence on the laser intensity of the Stokes signal, of the anti-Stokes signal (corresponding to the emission of higher-energy photons due to the exchange of energy between light and a molecular vibration), as well as of the anti-Stokes-to-Stokes ratio. By varying the separation distance between the molecules in the nanogap, which modifies the strength of the nanocavity-mediated interaction between the molecules, we show that the behavior of the anti-Stokes-to-Stokes ratio is modified, constituting a strong signature of many-molecule collective effects in SERS. These results are in good agreement with experiments, challenging the typical assumptions that collective effects can be ignored in SERS and thus that the Raman signal scales with the number of molecules.

Finally, we address effective macroscopic quantities of optically driven molecules, with the aim of exploring possible connections between the fields of molecular optomechanics and time-varying media.

IV. Conclusion

We show that quantum coherence can affect the Stokes-shifted emission from two interacting molecules, and that collective effects can impact the SERS signal from many molecules in a plasmonic nanocavity. These results challenge typical assumptions in classical models of Raman scattering, thus unveiling new quantum effects in molecular Raman scattering.

Acknowledgments

We acknowledge support from the European Union through the ERC grant TIMELIGHT under GA101115792, from grant no. PID2022-139579NB-I00 funded by MICIU/AEI/10.13039/501100011033 and by ERDF/EU and grant no. IT 1526-22, from the Dpt. of Education of the Basque Government, from grant PRE2020-095013 funded by MICIU/AEI/10.13039/501100011033 and by "ESF Investing in your future", from the Elkartek Project u4Smart from the Dept. of Economy Development of the Basque Country, from the CSIC Research Platform PTI-001 (Project No. 20219PT023), from the French National Agency for Research (Grant No. ANR-22-CE47-0015), from Région Nouvelle-Aquitaine, Idex Bordeaux (Research Program GPR Light), from the EUR Light S&T (PIA3 Program, Grant No. ANR-17-EURE-0027), from the EUR Light S&T Graduate Program (PIA3 Program "Investment for the Future", Grant No. ANR-17-EURE-0027), from IdEx of the University of Bordeaux/Grand Research Program GPR LIGHT, from Euskampus Transnational Common Laboratory QuantumChemPhys, from Quantum Matter Bordeaux, from the Laboratory for Transborder Cooperation LTC TRANS-LIGHT from the University of Bordeaux and the University of the Basque Country, from the Gipuzkoa Quantum project QSEIRA (grant no. 2024- QUAN-000011-01) funded by the Dept. of Economic Development and Strategic Projects of the Provincial Council of Gipuzkoa, from European Research Council (ERC) under Horizon 2020 research and innovation programme THOR (grant agreement no. 829067), and PICOFORCE (grant agreement no. 883703), and UK EPSRC grants EP/L027151/1 and EP/R020965/1, from the Cambridge Trust and EPSRC award 2275079, from the Rutherford Foundation of the Royal Society Te Aparangi of New Zealand, from the Winton Programme for the Physics of Sustainability, and Trinity College, University of Cambridge, and from the German National Academy of Sciences Leopoldina.

References

[1] J. B. Trebbia, Q. Deplano, P. Tamarat, B. Lounis, "Tailoring the superradiant and subradiant nature of two coherently coupled quantum emitters", *Nature Communications*, vol. 13, 2962, 2022.

[2] C. M. Lange, E. Daggett, V. Walther, L. Huang, J. D. Hood, "Superradiant and subradiant states in lifetime-limited organic molecules through laser-induced tuning", *Nature Physics*, vol. 20, pp. 836-842, 2024.

[3] A. Juan-Delgado, J.-B. Trebbia, R. Esteban, Q. Deplano, P. Tamarat, R. Avriller, B. Lounis, J. Aizpurua, "Addressing the correlation of Stokes-shifted photons emitted from two quantum emitters", *Physical Review Letters*, vol. 135, 163602, 2025.

[4] L. A. Jakob, A. Juan-Delgado, N. S. Mueller, S. Hu, R. Arul, R. A. Boto, R. Esteban, J. Aizpurua, J. J. Baumberg, "Optomechanical Pumping of Collective Molecular Vibrations in Plasmonic Nanocavities", *ACS Nano*, vol 19, pp. 10977-10988, 2025.

[5] E. Galiffi, R. Tirole, S. Yin, H. Li, S. Vezzoli, P. A. Huidobro, P. A., M. G. Silveirinha, R. Sapienza, A. Alù, J. B. Pendry, "Photonics of time-varying media", *Advanced Photonics*, 4, 014002-014002, 2022.

[6] J. R. Johansson, P. D. Nation, F. Nori, "QuTiP: An open-source Python framework for the dynamics of open quantum systems", *Computer physics communications*, vol. 183, pp. 1760-1772, 2012.

[7] P. Roelli, C. Galland, N. Piro, T. J. Kippenberg, "Molecular Cavity Optomechanics as a Theory of Plasmon-Enhanced Raman Scattering", *Nature Nanotechnology*, vol. 11, pp. 164-169, 2016.

[8] M. K. Schmidt, R. Esteban, A. González-Tudela, G. Giedke, J. Aizpurua, "Quantum Mechanical Description of Raman Scattering from Molecules in Plasmonic Cavities", *ACS Nano*, vol. 10, pp. 6291-6298, 2016.
[9] Comsol Multiphysics, version. 5.5, COMSOL AB, Stockholm, Sweden.
[10] A. Juan-Delgado, R. Esteban, Á. Nodar, J. -B. Trebbia, B. Lounis, J. Aizpurua, "Tailoring the statistics of light emitted from two interacting quantum emitters", *Physical Review Research*, vol. 6, 023207, 2024.
[11] Y. Zhang, J. Aizpurua, R. Esteban, "Optomechanical collective effects in surface-enhanced Raman scattering from many molecules", *ACS Photonics*, vol. 7, pp. 1676-1688, 2020.
[12] L. A. Jakob, W. M. Deacon, Y. Zhang, B. de Nijs, E. Pavlenko, S. Hu, C. Carnegie, T, Neuman, R. Esteban, J. Aizpurua, J. J. Baumberg, "Giant optomechanical spring effect in plasmonic nano-and picocavities probed by surface-enhanced Raman scattering", *Nature Communications*, vol. 14, 3291, 2023.

Light management in high-refractive index semiconductor nanowires

Nicklas Anttu[1,*]

[1] Physics, Faculty of Science and Engineering, Åbo Akademi University, FI-20500 Turku, Finland

*Corresponding author: nicklas.anttu@abo.fi

***Abstract*— High refractive index nanowires find use for example for fluorescence-based biosensors and solar cells. In such biosensors, both excitation and emission properties can be enhanced, while in nanowire solar cells, different types of light-trapping can enhance absorption. We present recent results from both types of applications.**

Photonic time crystals assisted by high-Q resonances

Puneet Garg[1,*], Viktar Asadchy[2], Carsten Rockstuhl[1,3]

[1]Institute of Theoretical Solid State Physics, Karlsruhe Institute of Technology, Kaiserstr. 12, Karlsruhe, Germany
[2]Department of Electronics and Nanoengineering, Aalto University, Maarintie 8, Espoo, Finland
[3]Institute of Nanotechnology, Karlsruhe Institute of Technology, Kaiserstr. 12, Karlsruhe, Germany
*Corresponding author: puneet.garg@kit.edu

***Abstract*—Photonic time crystals generally require a high modulation amplitude of the time-varying permittivity to show detectable momentum bandgaps. We demonstrate that by efficiently trapping light in time-varying metasurfaces using their high-Q resonances, even with weak permittivity modulation, noticeable bandgaps can be achieved.**

***Keywords*— photonic time crystals, bound states in the continuum, Mie theory.**

I. Introduction

Photonic time crystals (PTCs) are formed by rapidly modulating the permittivity of the underlying medium as a function of time in a periodic fashion. The frequency of such a modulation compares with the oscillation frequency of light. PTCs exhibit momentum bandgaps as their characteristic feature. Inside these gaps, complex frequency modes exist that can amplify light that couples to them (see Fig. 1). However, to show detectable momentum bandgaps, bulk PTCs generally require relative permittivity changes of the order of unity. To overcome this limitation, we utilize the high-Q resonances of the time-varying metasurfaces. In particular, we show that by using Mie and quasi-bound states in the continuum (qBIC) resonances, the large modulation amplitude requirement of the PTCs to open detectable momentum bandgaps can be considerably relaxed [1–3].

II. Methods

The proposed metasurface-based PTC is made from a periodic arrangement of finite nanoresonators in two dimensions (2D) (see Fig. 1). The permittivity $\Delta\varepsilon(t)$ of each nanoresonator varies as a function of time as

$$\Delta\varepsilon(t) = \varepsilon_\infty \left[1 + m\cos(\omega_\mathrm{m} t)\right] , \tag{1}$$

where ε_∞ denotes the background permittivity of the underlying static medium, m is the modulation amplitude, and ω_m is the modulation frequency. We use the Mie theory-based T-matrix method to computationally model the metasurfaces [1].

III. Results and Discussion

Our numerical simulations show:

- Noticeable momentum bandgaps corresponding to an incident angle range of $\Delta\theta = 4^\circ$ for modulation amplitudes as small as $m = 10^{-4}$ can be achieved using the resonant metasurface-based PTCs [3].
- Four orders of magnitude reduction in the required modulation amplitude is theoretically realized as compared to the bulk PTCs while simultaneously expanding the momentum bandgap approximately 60 times [3].

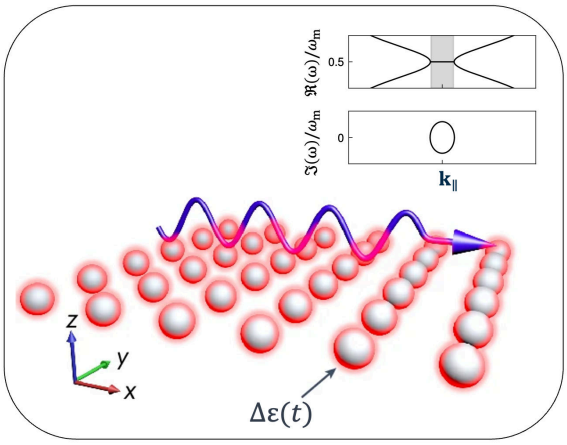

Fig. 1. A metasurface-based photonic time crystal (PTC). The PTC is formed by a periodic arrangement of nanoresonators in two dimensions (2D). The momentum bandgap is shown in the inset. Here, ω is the eigenfrequency, and $\mathbf{k}_\parallel$ is the in-plane wave vector of an eigenmode.

IV. Conclusion

We have discussed that using the high-Q resonances such as the Mie and qBIC resonances of metasurfaces, the modulation amplitudes required to attain noticeable momentum bandgaps can be considerably reduced. Future theoretical work will involve investigating the designs made from multilayered time-varying metasurfaces.

Acknowledgments

We would like to thank Dr. Aristeidis Lamprianidis, Prof. Xuchen Wang, Dr. Evangelos Almpanis, Dr. Nikolaos Papanikolaou, Prof. Nikolaos Stefanou, Dr. Mohammad S. Mirmoosa, Dr. Dominik Beutel, Prof. Theodosios Karamanos, Mr.

Leander Zimmer, Mr. Jan David Fischbach, Dr. Markus Nyman, and Prof. Barbara Verfürth who have been contributing to some of the presented findings.

V.A. acknowledges the Finnish Foundation for Technology Promotion, and Research Council of Finland Flagship Programme, Photonics Research and Innovation (PREIN), decision number 346529, Aalto University. P.G. and C.R. are part of the Max Planck School of Photonics, supported by the Bundesministerium für Bildung und Forschung, the Max Planck Society, and the Fraunhofer Society. P.G. and C.R. acknowledge support by the German Research Foundation within the SFB 1173 (project ID no. 258734477).

REFERENCES

[1] P. Garg, A.G. Lamprianidis, D. Beutel, T. Karamanos, B. Verfürth, C. Rockstuhl, "Modeling four-dimensional metamaterials: a T-matrix approach to describe time-varying metasurfaces", Optics Express **30**, 45832 (2022).

[2] X. Wang, P. Garg, M. S. Mirmoosa, A. G. Lamprianidis, C. Rockstuhl, V. S. Asadchy, "Expanding momentum bandgaps in photonic time crystals through resonances", Nature Photonics **19**, 149 (2025).

[3] P. Garg, E. Almpanis, L. Zimmer, J. D. Fischbach, X. Wang, M. S. Mirmoosa, M. Nyman, N. Stefanou, N. Papanikolaou, V. Asadchy, and C. Rockstuhl, "Photonic time crystals assisted by quasi-bound states in the continuum," arXiv preprint, arXiv:2507.15644 (2025).

Color Routing and Beam Steering of Single-Molecule Emission with a Spherical Silicon Nanoantenna

M. Sanz-Paz[1,2*], N. Siegel[1], G. Serrera[3], J. González-Colsa[3], F. Zhu[1], K. Kolataj[1], M. Fujii[4], H. Sugimoto[4], P. Albella[3], and G. P. Acuna[1]

[1]Department of Physics, University of Fribourg, Chemin du Musée 3, Fribourg CH-1700, Switzerland
[2]Sorbonne Université, CNRS, Institut des NanoSciences de Paris, INSP, F-75005 Paris, France
[3]Group of Optics, Department of Applied Physics, University of Cantabria, 39005, Santander, Spain.
[4]Department of Electrical and Electronic Engineering, Graduate School of Engineering, Kobe University, Rokkodai Nada, Kobe 657-8501, Japan
*corresponding author: maria.sanz-paz@insp.upmc.fr

Abstract: Nanoscale photon sources exhibit a dipole-like emission pattern, limiting their incorporation into on-chip devices. Nanoantennas can control their radiation pattern, but often involve lossy plasmonic nanoparticles. Here, we show that a single dielectric nanoparticle can direct the emitted light of a nearby nanoemitter, allowing for geometrical and spectral light routing.

Summary: Nanoscale photon sources such as fluorescent molecules exhibit a dipole-like emission pattern, significantly limiting the amount of light that can be collected and hampering their incorporation into flat photonic devices. Developing nanophotonic structures capable of directing photon emission with tunable angular distributions in the visible spectrum has been pursued for applications ranging from integrated optical systems to discrimination of molecular species. To date, such directional control has been achieved using optical antennas whose overall footprint is larger than the emission wavelength and often rely on lossy plasmonic components. Researches attempts to design compact directional plasmonic antennas rely on achieving unidirectional emission through interference between electric multipoles. Alternatively, interference between electric and magnetic resonances have recently been explored as an alternative to enhance nanoantenna directivity based on the Kerker condition. Although metal-based multiparticle geometries can deliver high directivity following this effect, their performance is often narrow band and sensitive to small variations in element size or emitter position.

Individual low-loss high-index dielectric nanoparticles (HID NPs) offer a low-loss alternative that supports strong electric and magnetic Mie resonances and flexible scattering-pattern engineering in the visible range.[1] Numerical studies indicate that a single HRID NP can effectively direct emission from a nearby dipolar emitter,[2,3] drastically reducing the footprint of previous demonstrations. Moreover, a single HID NP promises to have more advantages, as it has been proposed to be able to reverse this directionality depending on the emission wavelength,[2] and to be able to either collect or reflect the emitted light by tuning the particle-emitter distance.[3] However, those effects have never been demonstrated experimentally, mainly due to the difficulties of placing an individual dipole emitter in the proximity of the NPs with high accuracy.

Here, we experimentally demonstrate that a single SiNP with a footprint $< 0.05\ \lambda^2$ can serve not only as an optical antenna capable of directing light from a nearby emitter, but also as a versatile element for color routing and beam-steering. Using DNA origami assembly, we position single emitters adjacent to one SiNP with

nanometric accuracy and map the resulting far-field emission patterns. Using a 120 nm SiNP, we achieve robust broadband directionality in the visible range, with F/B values as high as 7 dB, for emitter-NP separations ranging from 8 to 85 nm. Furthermore, the emission direction follows the displacement of the emitter around the NP, realizing a beam-steering effect previously predicted theoretically.[4]

For 170 nm SiNPs and specific emitter positions, the emission direction becomes wavelength-dependent, routing green and red emission into nearly opposite directions, i.e., color routing,[2] (see shematic figure below). These results are in good agreement with previous theoretical works. Moreover, specific simulations of the experiments elucidate the underlying modal interference mechanisms responsible for directionality, beam steering, and color routing, opening the way for further designs of HRID nanophotonic directional devices.

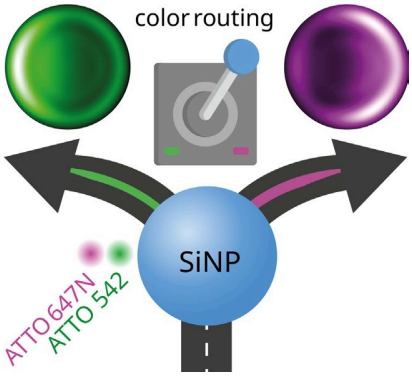

Figure: *Spectral fluorescence routing of single molecule emission with a spherical silicon nanoparticle.*

References

1. Fu, Y. ; Kuznetsov, A. ; Miroshnichenko, A. ; Yu, H. F. ; and Luk'yanchuk, B. "Directional visible light scattering by silicon nanoparticles," Nat Commun 2013, 4 (1527)
2. Krasnok, A. E.; Miroshnichenko, A. E.; Belov, P. A.; and Kivshar, Y. S. "All-Dielectric Optical Nanoantennas," Opt. Express 2012, 20 (18), 20599.
3. Rolly, B.; Stout, B.; and Bonod, N. "Boosting the Directivity of Optical Antennas with Magnetic and Electric Dipolar Resonant Particles," Opt. Express 2012, 20 (18), 20376.
4. Krasnok, A. E.; Simovski, C. R.; Belov, P. A.; and Kivshar, Y. S. "Superdirective Dielectric Nanoantennas," Nanoscale 2014, 6 (13), 7354–7361.

Theoretical characterization of tip-enhanced nanocavities for active control of vibrational signals

I. Pascual Robledo[1,2*], P. Roelli[2], I. Niehues[3], J. Aizpurua[4,5,6] and R. Hillenbrand[2,4,5]

[1]Material Physics Center, CSIC-UPV/EHU, 20018 Donostia-San Sebastián, Spain
[2]CIC nanoGUNE BRTA, 20018 Donostia-San Sebastián, Spain
[3]Institute of Physics, University of Münster, 48149 Münster, Germany
[4]IKERBASQUE, Basque Foundation for Science, 48013 Bilbao, Spain
[5]Department of Electricity and Electronics, University of the Basque Country (EHU), 48490 Leioa, Spain
[6]Donostia International Physics Center (DIPC), 20018 Donostia-San Sebastian, Spain
*Corresponding author: i.pascual@nanogune.eu

***Abstract*— We present an in-operando controllable platform for vibrational upconversion using tip-enhanced nanoparticle-on-mirror nanocavities. Simulations and experiments show that combining a s-SNOM tip with a visible-resonant NPoM form a cascaded nanolens system that enables the enhancement of sum-frequency generation signals from molecule-filled nanogaps up to 14 orders of magnitude.**

***Keywords*— Infrared spectroscopy, Nanocavities, Nonlinear optics, Vibrational Upconversion.**

I. Introduction

Vibrationally-assisted sum-frequency generation (SFG) in plasmonic nanoantennas enables the coherent upconversion of near- and mid-infrared photons into visible light [1]. This upconversion happens via molecular vibrations acting as optomechanical transducers placed nearby nanogaps formed by dually IR- and VIS-resonant plasmonic nanostructures [2]. While recent dual nanoantenna designs have demonstrated to be useful for SFG, yet they often lack the flexibility to selectively target different molecular vibrational modes [3, 4]. Efficient upconversion further requires precise spatial overlap of strong infrared and visible near fields inside the plasmonic nanogaps, as well as an efficient far field radiation from plasmonic nanocavities in the IR. These challenges prevent previously presented approaches from reaching the upconversion efficiencies of other optomechanical devices operating in different frequency ranges [5].

II. Methods

We present an innovative approach for vibrational upconversion based on scattering-type Scanning Near-field Optical Microscopy (s-SNOM) coupled to individual visible-resonant gold nanoparticle-on-mirror (NPoM) cavities filled with BPT molecules (Fig 1a). The metallic s-SNOM tip acts as a broadband infrared and visible antenna, locally illuminating the NPoM cavity forming a cascaded nanolens (Fig 1b). Finite-element electromagnetic simulations (COMSOL) are used to model the optical response of the multiscale system, which consists of a micron-sized metallic tip positioned above a faceted gold nanoparticle separated from a gold substrate by a thin dielectric spacer, forming a nanometer-sized gap. Field enhancement distributions are calculated as a function of the lateral and vertical tip position relative to the nanoparticle, enabling for quantitative evaluation of the enhancement on linear (SERS) and nonlinear (SFG, DFG) vibrational upconversion mechanisms.

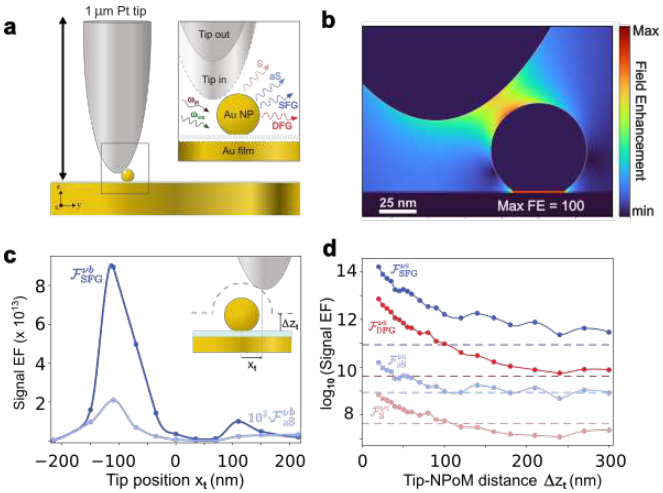

Fig. 1 **a** Illustration of the simulated tip-enhanced nanocavity. A 1 µm Pt ellipsoid is placed nearby an Au NPoM, in whose nanogap SFG, DFG, and SERS processes take place. **b** Near Field Enhancement (FE) distribution for a tip-enhanced NPoM in the IR. **c** Simulated SFG and anti-Stokes SERS signals Enhancement Factor (EF) for different tip-NPoM lateral distances. **f** Simulated SFG, DFG, anti-Stokes and Stokes SERS signals EF for different tip-NPoM vertical distances.

III. Results and Discussion

Numerical simulations reveal that the s-SNOM tip plays a critical role in activating and modulating the NPoM plasmonic resonances, resulting in cascaded near-field enhancement across both the IR and VIS spectral ranges. As a consequence, SFG signals are enhanced by up to 14 orders of magnitude (Fig 1c). The tip concentrates non-resonant infrared fields at its apex, which subsequently drive intense localized fields within the NPoM gap, enabling efficient coherent IR to VIS light upconversion. We experimentally demonstrate the efficient generation of SFG and DFG signals from individual molecule-filled NPoM cavities upon continuous wave illumination. The enhancement of SFG and DFG signals is actively controlled by the 3D nanopositioning of the tip. Numerical simulations reproduce the experimentally observed spatial dependence of SFG signals on the tip position (Fig 1c,d), confirming in-operando control of linear and nonlinear vibrational signals.

IV. Conclusion

We present tip-enhanced NPoM nanocavities as a versatile and efficient platform for vibrational upconversion under low-power continuous-wave excitation. Our approach circumvents limitations of previous approaches, such as the need for pulsed lasers and complex doubly resonant nanostructures. We demonstrate sensitivity down to individual molecule-filled nanocavities and active control of nonlinear signals. These capabilities open new opportunities for nanoscale vibrational spectroscopy, nonlinear nanoimaging, and the study of molecular dynamics at deeply subwavelength length scales.

Acknowledgments

This work was supported by from Grant CEX2020-001038-M funded by MICIU/AEI/10.13039/501100011033 and Grant PID2021-123949OB-I00 (NANOSPEC) funded by MICIU/AEI/10.13039/501100011033 and by ERDF/EU. P. R. acknowledges financial support from the Swiss National Science Foundation (Grant No. 206926) and from the European Union's Horizon 2020 research and innovation program under the Marie Skłodowska-Curie grant agreement No. 101065661. I. N. acknowledges financial support from the Ministerium für Kultur und Wissenschaft des Landes Nordrhein-Westfalen as well as from the Deutsche Forschungsgemeinschaft (project number 467576442). JA and IP acknowledge funding from project IT1526-22 from the Department of Education of the Basque Government, from Elkartek project "u4smart" from the Dept. of Industry of the Basque Government, and from grant PID2022-139579NB-I00 funded by MCIN/AEI/10.13039/501100011033 and by "ERDF A way of making Europe".

References

[1] Y. R. Shen, *Fundamentals of Sum-Frequency Spectroscopy,* 1st edition, Vol. 316 (Cambridge: Cambridge University Press, 2016).

[2] P. Roelli, D. Martin-Cano, T. J. Kippenberg, and C. Galland, "Molecular platform for frequency upconversion at the single-photon level". *Phys. Rev. X* 10, 031057 (2020).

[3] W. Chen, P. Roelli, H. Hu, S. Verlekar, S. P. Amirtharaj, A. I. Barreda, T. J. Kippenberg, M. Kovylina, E. Verhagen, A. Martinez and C. Galland, "Continuous-wave frequency upconversion with a molecular optomechanical nanocavity", *Science* 374, pp. 1264–1267, 2021.

[4] A. Xomalis, X. Zheng, R. Chikkaraddy, Z. Koczor-Benda, E. Miele, E. Rosta, G. A. E. Vandenbosch, A. Martínez and J. J. Baumberg "Detecting mid-infrared light by molecular frequency upconversion in dual-wavelength nanoantennas". *Science* 374, 1268–1271 (2021).

[5] Y. W. Chu and S. Gröblacher, "A perspective on hybrid quantum opto- and electromechanical systems". *Appl. Phys. Lett*. 117, 150503 (2020).

Imaging the spatial distribution of tunneling-induced luminescence beyond the diffraction limit of light

Elysé Laurent[1], Ricardo Javier Peña Román[2], Sarah Miller[1], Aditi Raman Moghe[3], Etienne Lorchat[4], Séverine Le Moal[1], Elizabeth Boer-Duchemin[1], Luiz Fernando Zagonel[2], Stéphane Berciaud[3], Eric Le Moal[1,*]

[1]Université Paris-Saclay, CNRS, Institut des Sciences Moléculaires d'Orsay, Orsay, France
[2]Institute of Physics "Gleb Wataghin", State University of Campinas-UNICAMP, Campinas, Brazil
[3]Institut de Physique et de Chimie des Matériaux de Strasbourg, Université de Strasbourg, CNRS, Strasbourg, France
[4]NTT Research, Inc., Physics & Informatics (PHI) Laboratories, Sunnyvale, CA 94085, USA
*Corresponding author: eric.le-moal@universite-paris-saclay.fr

***Abstract*—An iterative deconvolution algorithm is used to resolve, beyond the diffraction limit of light, the spatial distribution of radiatively recombining excitons excited in a transition metal dichalcogenide monolayer by current tunneling under the tip of a scanning tunneling microscope.**

***Keywords*— 2D materials, excitons, scanning probe microscopy, superresolution.**

I. Introduction

Two-dimensional (2D) semiconductors such as transition metal dichalcogenide monolayers are the building blocks of a future generation of optoelectronic devices, and in particular, of ultrathin electroluminescent devices. The diffusion of charge carriers and excitons (bound electron-hole pairs) and their interactions with defects play a key role in the electroluminescence properties of these materials. Understanding and controlling these processes is crucial for the performance of future devices based on these materials. Unfortunately, exciton diffusion occurs at scales (20 - 200 nm) that are smaller than the spatial resolution of far-field optical microscopes (200 - 500 nm), which are limited by the diffraction of light. There are nanoscopy techniques coupling light and scanning near-field probes that overcome this diffraction limit. Recently, the electroluminescence properties of 2D semiconductors have been mapped at the nanoscale by recording light induced by tunneling current under the tip of a scanning tunneling microscope (STM) scanned over the sample [1], [2], [3], [4]. However, such techniques provide no information on the diffusion of charge carriers and excitons, as they are not sensitive to the spatial distribution of emission around the excitation source. At each tip position, the signal emitted by the entire sample, regardless of its source, is integrated. In this work, we demonstrate a solution to this problem: we combine tunneling-current excitation under the tip of an STM (for extremely local excitation), wide-field optical microscopy (to image the spatial distribution of the emission), and deconvolution of optical microscopy images using an iterative Richardson-Lucy algorithm (to achieve spatial resolution beyond the diffraction limit) [5].

II. Methods

The excitonic luminescence of monolayer tungsten diselenide (WSe_2) and tungsten disulfide (WS_2) is locally and electrically excited using the tunneling current of a scanning tunneling microscope (STM). The spatial distribution of emitters is resolved beyond the diffraction limit of light by deconvolving real-space optical microscopy images of the emitted light using an iterative algorithm, i.e., Richardson-Lucy (RL) deconvolution. The point spread function of the optical microscope is calculated using an analytical dipole model, where the polarization and spectral dependence of the emitted light are taken into account.

III. Results and Discussion

In this way, we reconstruct spatial emission distributions around the excitation point that have full widths at half maximum as small as $\lambda_0/(9.4 \pm 0.7)$ (λ_0 is the emission wavelength), where the resolution of the optical microscope is at best $\lambda_0/2.98$ (Abbe criterion) or $\lambda_0/2.44$ (Rayleigh criterion). This result corresponds to an improvement in spatial resolution of at least a factor of 3. One reason why this has never been done before is that this type of deconvolution requires knowledge of the point spread function (PSF), which is generally very difficult to define for this type of combination of optical microscopy and scanning probes. Here, we overcome this difficulty by using known exciton properties to simulate the PSF as the image of an emitting exciton.

IV. Conclusion

We show that the information extracted from the deconvolved images about the spatial distribution of emitters around and away from the excitation source is valuable for understanding the mechanisms of STM-induced luminescence and, more broadly, the elementary electronic and excitonic processes involved in the operation of TMD-based electroluminescent devices. We anticipate that this type of information will be used in future studies for the development of models that better integrate the spatial aspect of these mechanisms and elementary processes.

ACKNOWLEDGMENTS

This work was supported by the META 2026 organizing committee. This work is supported by public grants from the Agence Nationale de la Recherche (ATOEMS ANR-20-CE24-0010, TEXTURES ANR-22-CE09-0008, INFERNO ANR-22-CE42-0015, and EXODUS ANR-23-QUAC-0004). We are grateful to the STnano cleanroom staff for technical support. This work of the Interdisciplinary Thematic Institute QMat, as part of the ITI 2021–2028 program of the University of Strasbourg, CNRS and Inserm, was supported by IdEx Unistra (ANR 10 IDEX 0002), and by the SFRI STRAT'US project (ANR 20 SFRI 0012) and EUR QMAT ANR-17-EURE-0024 under the framework of the French "Investments for the Future" program. S.B. and A.R.M. acknowledge support from the Indo-French Centre for the Promotion of Advanced Research (CEFIPRA). This work has received financial support from the Fundação de Amparo à Pesquisa do Estado de São Paulo (FAPESP), through projects 18/08543-7, 20/12480-0 and 14/23399-9. S.M. acknowledges support through the 2023 "Optics in the City of Light" NSF-REU program.

REFERENCES

[1] D. Pommier, R. Bretel, L. E. Parra López, F. Fabre, A. Mayne, E. Boer-Duchemin, G. Dujardin, G. Schull, S. Berciaud, and E. Le Moal, "Scanning Tunneling Microscope-Induced Excitonic Luminescence of a Two-Dimensional Semiconductor," *Physical Review Letters*, vol. 123, 027402, 2019.

[2] B. Schuler, K. A. Cochrane, C. Kastl, E. S. Barnard, E. Wong, N. J. Borys, A. M. Schwartzberg, D. F. Ogletree, F. J. García de Abajo, and A. Weber-Bargioni, "Electrically driven photon emission from individual atomic defects in monolayer WS_2," *Science Advances*, vol. 6, no. 38, eabb5988, 2020.

[3] L. E. Parra López, A. Rosłlawska, F. Scheurer, S. Berciaud, and G. Schull, "Tip-induced excitonic luminescence nanoscopy of an atomically resolved van der Waals heterostructure," *Nature Materials*, vol. 22, no. 4, pp. 482–488, 2023.

[4] H. Geng, J. Tang, Y. Wu, Y. Yu, J. R. Guest, and R. Zhang, "Imaging Valley Excitons in a 2D Semiconductor with Scanning Tunneling Microscope-Induced Luminescence", *ACS Nano*, vol. 18, no. 12, pp. 8961-8970, 2024.

[5] E. Laurent, R. J. Peña Román, S. Miller, A. Raman Moghe, E. Lorchat, S. Le Moal, E. Boer-Duchemin, L. F. Zagonel, S. Berciaud, and E. Le Moal, "Sub-diffraction-resolved spatial distribution of emitting excitons in STM-induced luminescence of 2D semiconductors via Richardson-Lucy deconvolution," *arXiv*, cond-mat.mes-hall, 2512.08401, 2025.

Nanoscale heat flow in laser-heated silicon nanospheres probed by pump-probe cathodoluminescence

Saskia Fiedler[1,*], Evelijn Akerboom[1], Théo Soler[1], Loriane Monin[1], Hiroshi Sugimoto[2], Minoru Fujii[2] Wiebke Albrecht[1], and Albert Polman[1]

[1]Department of Sustainable Energy Materials, NWO-Institute AMOLF, Science Park 104, 1098 XG Amsterdam, the Netherlands
[2]Department of Electrical and Electronic Engineering, Graduate School of Engineering, Kobe University, Rokkodai, Nada, Kobe 657-8501, Japan
*Corresponding author: s.fiedler@amolf.nl

***Abstract*— Cathodoluminescence (CL) spectroscopy in a scanning electron microscope enables optical characterization of nanostructures with nanometer spatial resolution. Here we investigate optical Mie resonances in individual crystalline silicon nanospheres using hyperspectral CL mapping and time-resolved pump-probe CL spectroscopy. By coupling a laser into the SEM, we locally heat single nanoparticles and observe thermo-optic spectral shifts of the Mie modes. Synchronizing pulsed laser excitation with nanosecond electron pulses allows us to probe the temporal evolution of these shifts and monitor nanoscale heating dynamics. These results demonstrate that dielectric Mie resonances can serve as sensitive probes for nanoscale thermometry and highlight the potential of pump–probe CL for studying ultrafast electron–light–matter interactions.**

***Keywords*— cathodoluminescence, Mie resonance, dielectric nanoparticles, pump-probe spectroscopy.**

I. Introduction

Cathodoluminescence (CL) spectroscopy in a scanning electron microscope enables optical characterization of nanostructures with nanometer spatial resolution. Dielectric nanoparticles such as silicon nanospheres[1] support well-defined optical Mie resonances that can be efficiently excited by fast electrons[2]. In addition to mapping these modes, understanding thermal effects in nanostructures is important for nanophotonic applications. Here we combine CL spectroscopy with optical excitation inside the SEM to study thermo-optic shifts of Mie resonances and implement pump–probe CL spectroscopy to probe nanoscale heating dynamics.

II. Results and Discussion

Hyperspectral cathodoluminescence (CL) measurements of individual silicon nanospheres reveal distinct spectral signatures of their optical Mie resonances. The excitation efficiency of these modes varies with the electron beam position, reflecting the spatial distribution of the associated optical near fields[3].

By coupling a continuous-wave laser (λ = 442 nm) into the SEM, we locally heat individual nanoparticles and observe thermo-optic red-shifts of the Mie resonances[4]. As shown in Fig. 1, the electric quadrupole (EQ) mode exhibits spectral shifts of up to ~100 meV under optical excitation, demonstrating its sensitivity to temperature changes. Complementary heat-flow simulations show that the temperature rise strongly depends on the thermal contact between the nanoparticle and the supporting SiN membrane, with contact areas ranging from 3 nm^2 at low laser power to ~100 nm^2 at highest applied power.

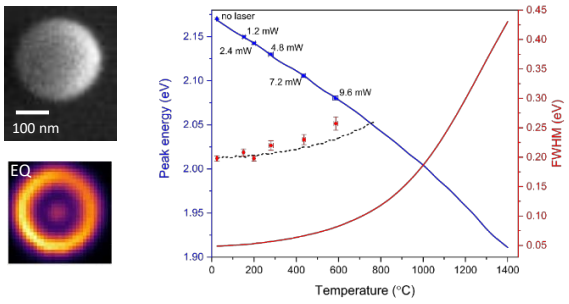

Fig. 1 Left: SEM image of 250 nm-sized Si nanosphere (top) and corresponding 30 keV-CL map of electric quadrupolar (EQ) Mie mode (bottom). Right: Peak energy (blue) and linewidth (red) of EQ Mie mode in Si nanosphere vs. temperature calculated using Mie model with temperature-dependent optical constants (solid lines). Experimental data for all laser powers are displayed at squares.

Finally, pump–probe CL spectroscopy is implemented by synchronizing nanosecond electron pulses with pulsed laser excitation. By varying the delay between laser and electron pulses, we probe the transient spectral response of the Mie

resonances and monitor the heating dynamics of a single silicon nanoparticle.

III. Conclusion

Experimental results show:

- Hyperspectral cathodoluminescence spectroscopy enables nanoscale mapping of optical Mie resonances in individual silicon nanospheres and their directional far-field emission.
- Optical heating inside the SEM induces thermo-optic red-shifts of the resonances, allowing the electric quadrupole mode to be used as a sensitive nanoscale temperature probe.
- Heat-flow simulations reveal that the temperature rise strongly depends on the thermal contact between the nanoparticle and the supporting SiN membrane.
- Pump–probe cathodoluminescence with synchronized laser and electron pulses enables time-resolved measurements of heating dynamics in a single nanoparticle.
- These results demonstrate the potential of pump–probe CL for studying nanoscale thermometry and electron–light–matter interactions in nanophotonic systems.

Acknowledgments

This work was financed by the Dutch Research Council (NWO) and has received funding from the European Research Council (ERC) under Grant Agreement No. 101019932 (QEWS), the European Innovation Counsel (EIC) under Grant Agreements No. 101017720 (EBEAM) and No. 101151994 (EXPLEIN) under the European Union's Horizon 2020 Research and Innovation Program. This work was partly supported by JSPS KAKENHI Grant No. 24K01287 and Kobe University Strategic International Collaborative Research Grant.

References

[1] H. Sugimoto, T. Okazaki, and M. Fujii, "Mie Resonator Color Inks of Monodispersed and Perfectly Spherical Crystalline Silicon Nanoparticles," Adv. Optical Mater., 8, 2000033, 2020.

[2] S. Fiedler, P. E. Stamatopoulou, A. Assadillayev, C. Wolff, H. Sugimoto, M. Fujii, N. A. Mortensen, S. Raza, and C. Tserkezis, "Disentangling Cathodoluminescence Spectra in Nanophotonics: Particle Eigenmodes vs Transition Radiation," Nano Lett., 22, 6, 2320-2327, 2022.

[3] T. Soler, E. Akerboom, P. E. Stamatopoulou, H. Sugimoto, M. Fujii, S. Fiedler, and A. Polman, "Electron-Energy Dependent Excitation and Directional Far-Field Radiation of Resonant Mie Modes in Single Si Nanospheres," ACS Photonics, 12, 4161−4170, 2025.

[4] S. Fiedler, L. Monin, H. Sugimoto, M. Fujii, W. Albrecht, and A. Polman, "Nanoscale Heat Flow and Thermometry in Laser-Heated Resonant Silicon Mie Nanospheres Probed with Spatially Resolved Cathodoluminescence Spectroscopy," ACS Photonics,12, 5668−5674, 2025.

Infrared Magnetoplasmonics in Transparent Conductive Oxide Nanocrystals

Alessio Gabbani[1,*]

[1]Department of Chemistry and Industrial Chemistry, University of Pisa, Italy

*Corresponding author: alessio.gabbani@unipi.it

***Abstract*— Magnetoplasmonics is a promising strategy for active nanophotonics. Here, we demonstrate that transparent conductive oxide nanocrystals (NCs) enable superior tunability of carrier parameters through defect engineering. Exploiting these NCs, we achieve enhanced magnetic circular dichroism and Faraday rotation in the near infrared, and further demonstrate their photochemical modulation.**

***Keywords*— magnetoplasmonics; magneto-optics; nanocrystals; active plasmonics.**

I. Introduction

Infrared (IR) light is attractive for nano-optics, as the low loss windows of optical fibers for telecommunications fall in the near IR, and vibrational modes of molecules have absorption fingerprints in the medium IR. Transparent Conductive Oxide (TCO) nanocrystals (NCs) represent a unique platform for infrared plasmonics, as they provide tuneable carrier density, covering a wide spectral range, from 1.5 to 10 μm.[1,2] Magnetic tunability of surface plasmon is also extremely interesting for nanophotonics, enabling to remotely tune the plasmonic response for optical isolators or improving the sensitivity of plasmon resonance tracking.[3] Here, we demonstrate how TCO NCs can provide a promising platform for infrared magnetoplasmonics.

II. Methods

We exploit colloidal chemistry synthetic approaches to prepare different TCO NCs with different dopants type and content. Their plasmonic response was studied through UV-vis-NIR spectroscopy. Magnetoplasmonic response was measured on colloidal dispersion of such NCs in transmission geometry through Magnetic Circular Dichroism and Faraday rotation at room temperature. Post synthetic photo-chemical simulation was performed in situ through illumination with a 365 nm light emitting diode, while measuring the optical and magneto-optical response. Optical and magneto-optical spectra were fitted with an analytical model to extract carrier parameters, namely carrier density and mass.

III. Results and Discussion

Our results demonstrate that:

- Magneto-optical response of TCO in the infrared challenges state-of-the-art metallic nanostructures;
- Magneto-optical spectroscopy can be used to extract carrier parameters in TCO NCs, and in particular carrier density and mass;
- Large post-synthetic modulation of Faraday rotation and Magnetic Circular Dichroism is achievable.

IV. Conclusion

We demonstrated the outstanding magnetoplasmonic response of TCO NCs, challenging state-of-the-art metallic nanostructures. We further demonstrate the possibility of switching the sign of Faraday rotation at fixed wavelength through photo-chemical post synthetic modulation of the plasmonic response.

Acknowledgments

This work was supported by European Union through the EIC grant agreement No. 101161583.

References

[1] A. Gabbani, E. Della Latta, A. Mohan, A. Scarperi, X. Li, M. Ruggeri, F.Martini, F. Biccari, M. Kociak, M. Geppi, S. Borsacchi, F. Pineider, “Direct determination of Carrier Parameters in Indium Tin Oxide Nanocrystals”, ACS Nano, 2024, Vol. 18, 23, 15139–15153. https://doi.org/10.1021/acsnano.4c02875.

[2] A. Agrawal, S. H. Cho, O. Zandi,S. Ghosh, R. W. Johns, D. J. Milliron*, “Surface Plasmon Resonance in Semiconductor Nanocrystals”, Chem. Rev. 2018, 118, 6, 3121–3207.

[3] N. Maccaferri, A. Gabbani, F. Pineider, T. Kaihara, T. Tapani, P. Vavassori, “Magnetoplasmonics in confined geometries: Current challenges and future opportunities”, Applied Physics Letters, 2023, Vol. 122, 120502; doi: 10.1063/5.0136941.

SPECIAL SESSION 22

Surface-Enhanced Raman Scattering: Integrating Theoretical and Experimental Perspectives

10 contributions · pp. 1219–1236

SERS Chemosensing of Metal Ions: Transduction Strategies and Interface Design

Luca Guerrini[1,*]

[1] Department of Physical and Inorganic Chemistry. Universitat Rovira i Virgili, Spain.
*Corresponding author: luca.guerrini@urv.cat

***Abstract*—Due to the intrinsic Raman silence of monoatomic species, SERS-based detection of metal ions necessarily relies on indirect strategies that translate coordination chemistry into a measurable spectroscopic response. This contribution presents a concise overview of key transduction mechanisms and interface design principles enabling effective SERS chemosensing of metal ions.**

***Keywords*—plasmonic, metal ions, sensing, SERS**

Transition metal contamination represents a major environmental and public health concern. Although many transition metals are naturally occurring and biologically essential, anthropogenic activities have significantly increased human exposure [1]. Their toxicity depends critically on chemical identity, oxidation state, speciation, dose, and exposure time, making selective and ultrasensitive detection a central analytical challenge [1]. Over the past decades, SERS has evolved into a powerful strategy for metal ion sensing in aqueous environments [2]. Because monoatomic ions are intrinsically Raman silent, detection relies on indirect approaches in which molecular receptors immobilized on plasmonic substrates selectively bind the target ion. Measurable metal-dependent SERS read-outs commonly originate from: (i) conformational changes of surface-bound receptors, such as DNA-based systems [3]; (ii) electronic modifications of molecular chemosensors upon metal coordination [2,4–7]; and (iii) specific chemical reactions between receptor and analyte [2,8]. In the latter two cases, receptors act simultaneously as recognition elements and SERS transducers, enabling speciation analysis and ratiometric quantification. More recently, we addressed a central bottleneck in SERS metal-ion sensing: the limited availability of surface receptors capable of translating selective binding of vibrationless analytes into measurable spectroscopic signals. To overcome this constraint, we developed hybrid substrates combining highly SERS-active plasmonic cores with ZIF-8 metal–organic framework (MOF) shells (Fig. 1) [6,7]. The MOF layer captures aromatic ion-selective receptors in close proximity to the plasmonic surface regardless of their intrinsic metal affinity, while preserving their coordination chemistry. At the same time, the porous framework provides molecular sieving and preconcentration effects, enabling direct operation in complex media. Using different classes of chromogenic ligands, this architecture allowed ultrasensitive detection of transition and alkaline earth metal ions, including Cu^{2+} quantification in untreated biological fluids. These multifunctional MOF–plasmon platforms significantly expand the practical applicability of SERS in real-life environmental and biomedical metal-ion analysis.

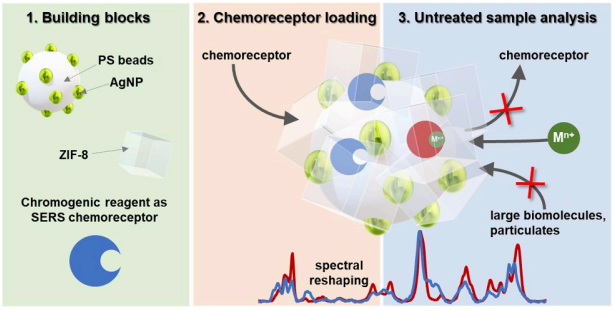

Fig. 1 Hybrid plasmonic/MOF particles and their application in metal ion detection in complex aqueous media

ACKNOWLEDGMENTS

Grant PID2022-141499OB-100, funded by FEDER/UE and MICIU/AEI/10.13039/501100011033/.

REFERENCES

[1] P. B. Tchounwou, *et al.*, "Heavy metal toxicity and the environment," *Exp Suppl*, vol. 101, pp. 133–164, 2012.

[2] L. Guerrini *et al.*, "Surface-Enhanced Raman Scattering Sensing of Transition Metal Ions in Waters," *ACS Omega*, vol. 6, pp. 1054–1063, 2021.

[3] Y. Shi, *et al.*, "Silicon nanohybrid-based SERS chips armed with an internal standard for broad-range, sensitive and reproducible simultaneous quantification of lead(II) and mercury(II) in real systems," *Nanoscale*, vol. 10, pp. 4010–4018, 2018.

[4] L. Guerrini *et al.*, "Chemical speciation of heavy metals by surface-enhanced Raman scattering spectroscopy: identification and quantification of inorganic- and methyl-mercury in water," *Nanoscale*, vol. 6, pp. 8368–8375, 2014.

[5] L. Guerrini *et al.*, "Multiplex SERS Chemosensing of Metal Ions via DNA-Mediated Recognition," *Anal. Chem.*, vol. 91, pp. 11778−11784, 2019.

[6] N. Pazos-Perez and L. Guerrini, "Extending the range of metal ions SERS detection using hybrid plasmonic/ZIF-8 particles," Talanta, p. 124941, 2023.

[7] T. Zorlu et al., "Optical Quantification of Metal Ions Using Plasmonic Nanostructured Microbeads Coated with Metal–Organic Frameworks and Ion-Selective Dyes," ACS Nanoscience Au, vol. 3, pp. 222–229, 2023.

[8] Q. Zhao, *et al.*, "Raman reporter-assisted Au nanorod arrays SERS nanoprobe for ultrasensitive detection of mercuric ion (Hg^{2+}) with superior anti-interference performances," J. Hazard. Mater., 122890, vol. 398, 2020.

Time-Dependent Surface Enhanced Raman Scattering Simulations

Giulia Dall'Osto[1] and Stefano Corni[2]

[1] Elettra Sincrotrone Trieste, SS 14 Km 163.5 in AREA Science Park, Basovizza, Trieste, Italy;
[2] Dipartimento di Scienze Chimiche, Università di Padova, via F. Marzolo 1, 35131, Padova, Italy.
*Corresponding author: giulia.dallosto@elettra.eu

***Abstract*— We present a time-dependent theoretical approach to simulate plasmon-enhanced Raman spectra. By propagating the vibronic wave function of a molecule coupled to a plasmonic nanoparticle, we capture the real-time Raman response and field interactions, enabling quantitative modeling aligned with experimental setups.** ***Keywords*— SERS, time-dependent, theory**

I. Introduction

Surface-enhanced Raman scattering (SERS) is a powerful spectroscopic technique that provides detailed insight into the vibrational and electronic (vibronic) properties of molecules.[1] SERS relies on the enhancement of the local electromagnetic field induced by surface plasmon resonances on metal nanoparticles (NPs), resulting in a stronger Raman response. The scientific community widely agrees that the enhancement of the molecular signal arises from two primary mechanisms: electromagnetic and chemical interactions. In particular, the electromagnetic contribution is generally assumed to dominate the SERS signal, especially when electric fields resonant with the plasmonic peak are used. Theoretical modeling of the Raman signal has greatly advanced our understanding of the underlying mechanisms. Our work focuses on developing a new theoretical strategy to simulate plasmon-enhanced Raman spectra in the time domain,[2] inspired by the pioneering theory of Lee and Heller.[3] This approach uniquely provides insights into the time evolution of the molecular Raman signal, capturing the dynamics of the incident electric field and its interaction with a plasmonic nanoparticle. Its flexibility allows the use of various incident electric field shapes, enabling closer alignment with experimental setups.[4]

II. Methods

Time-dependent SERS simulations are based on the real-time propagation of the system wave function, mutually with the polarization charges on the NP surface. The electronic properties of the molecule are equilibrated with the electromagnetic field of a nearby NP. The vibronic wave function is then constructed by dressing the electronic states with vibrational levels computed at the TDDFT level, incorporating the Franck–Condon and Herzberg–Teller expansions of the transition dipole moments.[5] During the real-time dynamics, coupling with the plasmonic NP is treated within a multiscale framework that combines a quantum mechanical description of the molecule with a polarizable continuum model for the NP.[6,7] Propagation of the vibronic wave function under a light pulse yields the time evolution of the vibronic coefficients, from which the Raman signal is obtained via an inverse Fourier transform of these dynamics.

III. Results and Discussion

We present numerical examples on a realistic organic molecule to demonstrate the approach. Calculations have been performed on Porphine molecule close to a gold nanoellipsoid considering different polarization for the incident electric field. Time-dependent raman scattering is computed providing insight into the timescale and the dynamics involved into the Raman scattering process.

IV. Conclusion

We have proposed a method able to compute the time-dependent surface-enhanced Raman scattering of molecules, which gives information on the Raman signal accumulated during the molecule-NP electrodynamics. This method combines multiscale approach for molecule-NP interaction in time-domain with a time-dependent approach for Raman scattering, which paves the way for simulation of time-resolved plasmon enhanced Raman scattering.

Acknowledgments

This work was supported by the European Union under the H2020-FET project ProID (Grant Agreement No. 964363).

References

[1] A. I. P.rez-Jim.nez, D. Lyu, Z. Lu, G. Liu, and B. Ren, Chem. Sci. 11, 4563–4577 (2020).
[2] G. Dall'Osto and S. Corni, J. Chem. Phys. 161, 044103 (2024).
[3] S.-Y. Lee and E. J. Heller, J. Chem. Phys 71, 4777–4788 (1979).
[4] G. Dall'Osto and S. Corni, J. Phys. Chem. A 126, 8088–8100 (2022).
[5] J. Cerezo and F. Santoro, J. Comput. Chem. 44, 626–643 (2023).
[6] S. Pipolo, and S. Corni, J. Phys. Chem. C, 120(50), 28774-28781 (2016).
[7] G. Dall'Osto, G. Gil, S. Pipolo, and S. Corni, J. Chem. Phys 153, 184114 (2020).

Operando SERS: From Molecular Spectroscopy to Plasmon-Driven Photochemistry

Shashank K. Gahlaut*, Ilko Bald, Radwan M.Sarhan, Biswajit Bhattacharyya

[1] Institute of Chemistry, University of Potsdam, Germany
*Corresponding author: gahlaut@uni-potsdam.de

***Abstract*— Light-driven chemical transformations on plasmonic metal nanostructures offer promising opportunities for sustainable synthesis and photocatalysis. The interaction of light with plasmonic nanoparticles generates enhanced electromagnetic fields, energetic charge carriers, and localized heating, which collectively drive chemical reactions at the nanoscale. Surface-enhanced Raman spectroscopy (SERS), enabled by near-field enhancement at plasmonic interfaces, provides a unique platform to both initiate and monitor these reactions in real time.**

We employ operando SERS to investigate bond cleavage and bond formation processes occurring on plasmonic nanostructures. Time-resolved SERS measurements are used to follow model plasmon-driven reactions, including the dehalogenation of 8-Bromoadenine, the dimerization of 4-nitrothiophenol to 4,4′-dimercaptoazobenzene (DMAB). These reactions serve as well-established probes for understanding plasmon-mediated chemistry. More recently, plasmon-assisted cross-coupling reactions have also emerged as an exciting class of transformations, demonstrating the potential of plasmonic nanostructures to drive complex catalytic processes under light excitation.

We further explore how the geometry and composition of plasmonic nanostructures influence reaction dynamics. Hybrid nanostructures based on noble metals such as Ag and Au are investigated to reveal structure-dependent catalytic behavior. In particular, chiral plasmonic gold helicoids allow efficient control of reaction rates using circularly polarized light. The generation of chiral hot carriers in these structures amplifies the photochemical g-factor, which can be reconfigured through nanoparticle assembly on substrates.

Beyond noble metals, the development of earth-abundant alternative plasmonic materials is essential for scalable photocatalysis. In this context, $CuFeS_2$ nanocrystal exhibiting plasmon-like resonances in the visible region is investigated as emerging plasmonic photocatalyst. Using operando SERS, we demonstrate previously unexplored plasmon-driven chemical transformations on this material system.

These results highlight the power of operando SERS as a versatile tool for understanding and controlling plasmon-driven chemistry, opening new opportunities for designing light-driven catalytic processes and chiral photochemistry at the nanoscale.

***Keywords*—Plasmon chemistry, SERS, chiral plasmonics, Alternative Plasmonic materials.**

REFERENCES

[1] Bald, Ilko. "An Introduction to Plasmonic Chemistry." Advances in Atomic and Molecular Physics at the Interfaces with the Natural Sciences, Technology and Medicine. 165-190 (2026).

[2] Dutta, Anushree, et al. "Plasmon-driven chemical transformation of a secondary amide probed by surface enhanced Raman scattering." Communications chemistry 7.1, 188 (2024).

[3] Gahlaut, Shashank K., et al. "Amplification of photochemical chiroptical activity of chiral gold nanocubes." *Small* 21.36, 2505093 (2025).

[4] Stefancu, Andrei, et al. "Impact of surface enhanced Raman spectroscopy in catalysis." *ACS nano* 18.43, 29337-29379 (2024)

[5] Kanehira, Yuya, et al. "The Effect of Nanoparticle Composition on the Surface-Enhanced Raman Scattering Performance of Plasmonic DNA Origami Nanoantennas." *ACS Nano* 17.21, 21227-21239 (2023).

Plasmonic Nanopore Geometry Effects in Flow-Through Single-Molecule SERS

Kirill Khabarov[1,*], Xinxin Liu[2], Ilaria Micol Baldi[1,3], Frank Niklaus[2], Francesco De Angelis[1]

[1]Italian Institute of Technology, Genova, Italy
[2]KTH Royal Institute of Technology, Stockholm, Sweden
[3]University of Genova, Genova, Italy

*Corresponding author: kirill.khabarov@iit.it

We investigate the influence of plasmonic nanopores geometry on flow-through single-molecule SERS during electrophoretic molecular delivery. Using microsecond-resolved SPAD detection, we compare circular, slit, and V-shaped nanopores. Experiments and simulations show enhanced SERS efficiency for the slit and V-shaped pores, highlighting geometry as a key parameter for SERS-based molecular sensing.

Keywords: **Single-molecule SERS, plasmonic membrane, nanopores, electrical translocations.**

I. Introduction

Surface-Enhanced Raman Spectroscopy (SERS) is a powerful technique for biosensing due to its single-molecule sensitivity, molecular specificity, and rapid response. Despite significant progress in recent years, reliable high-throughput detection and sequencing of biopolymers remain major challenges [1]. Fast and accurate identification of DNA and proteins would enable transformative diagnostic, therapeutic, and analytical applications.

In our previous works, we established an approach combining SERS with a solid-state nanopore for identification and sequencing, and demonstrated the feasibility of discriminating individual nucleotides and amino acids during their translocation through plasmonic nanopores [2,3]. However, further progress toward robust SERS-based sequencing requires nanopore geometries capable of providing stronger and more reproducible electromagnetic enhancement. Here, we systematically investigate the influence of nanopore geometry on SERS signal strength and detection efficiency in a flow-through translocation regime, which defines **the central novelty of the current research**.

II. Methods

We employ our previously developed approach for single-molecule identification and sequencing based on permeable plasmonic membranes combined with real-time microsecond SERS detection [2]. This platform enables an ultrafast acquisition of spectral data during molecular translocation with high spatial and temporal resolution.

To evaluate the impact of different nanopore geometries on SERS signal strength and detection efficiency, we fabricated nanopores with different geometries fabricated on 5 nm thick HfO membranes. We studied three pore types: Circular (O), slit-shaped (I), and V-shaped (V), all with characteristic lateral dimensions of approximately 15 nm. To further reduce the effective pore size and enable plasmonic enhancement, we sputtered a 20 nm Ag layer on top of the HfO membranes, preceded by a 2 nm Ti adhesion layer.

We validated the SERS behavior of these pores using poly-L-arginine (polyArg) molecules with an average length of approximately 100 amino acids. The molecules were prepared at a concentration of 1 nM in a 150 mM NaCl buffer, diluted in deionized water (>18.2 MΩ·cm, Milli-Q system), and additionally filtered through a 0.22 µm membrane before use. Molecular translocation was driven by an applied bias voltage of 50 mV across a single nanopore in a membrane. These conditions are close to physiological and are commonly used in related nanopore studies.

SERS spectra were collected in a flow-through geometry using a Single-Photon Avalanche Diode (SPAD) camera set to 100 µs temporal resolution for a single-event detection.

III. Results and Discussion

Our results demonstrate that nanopore geometry plays a critical role in determining the efficiency of SERS signal enhancement during molecular translocation.

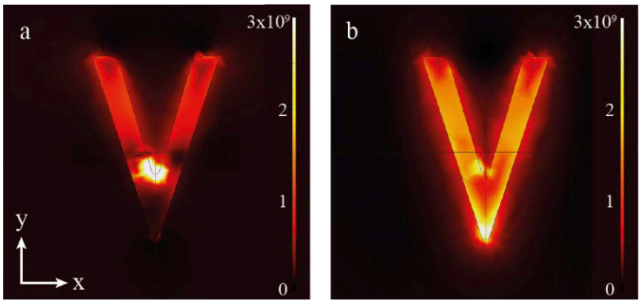

Fig. 1 Simulated electromagnetic field intensity distribution in a V-shaped nanopore excited at 532 nm with incident polarization along the y-axis (a) and x-axis (b).

Figure 1 shows simulated electromagnetic field distributions for a V-shaped nanopore excited at 532 nm with different polarizations, oriented parallel and perpendicular to the pore axis. The simulations show the hot spot distribution inside the pore and reveal a strong dependence of the local field enhancement on the incident polarization. These results indicate that both pore geometry and excitation conditions critically affect the SERS performance.

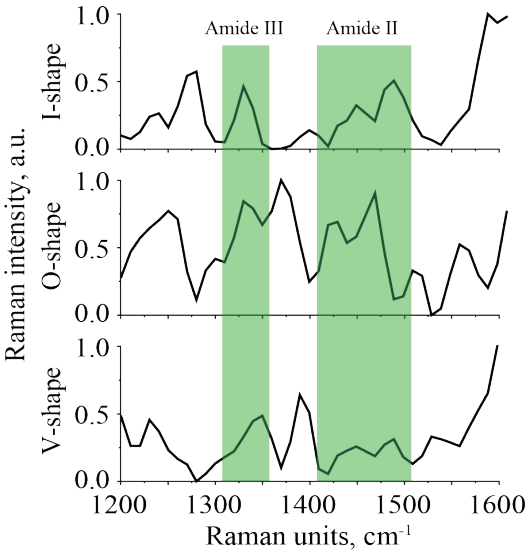

Fig. 2 Averaged SERS spectra of polyArg molecules acquired during single-molecule translocation through V-, I-, and O-shaped plasmonic nanopores for 532 nm laser excitation with laser polarization oriented perpendicular to the pore (x-axis, Fig. 1a).

We further analyzed experimentally acquired SERS spectra of polyArg molecules by averaging ~100 individual single-molecule translocation events. The resulting spectra for V-, I-, and O-shaped pores are shown in Figure 2. While the relative peak intensities may vary between pore types, the spectral peak positions are consistent with minimal fluctuations, normal for single-molecule SERS. This demonstrates a reliable molecular identification across different nanopore geometries.

To quantitatively assess nanopore performance, we analyzed photons detected for each individual translocation. Event selection was performed using a threshold based on the total number of detected photons per frame. The threshold was defined as a 3σ deviation of the distribution of photons per acquired frame during the experiment, corresponding to a 99% confidence level. The resulting histograms of photon counts are shown in Figure 3, highlighting differences in overall detection efficiency for the three different pore geometries.

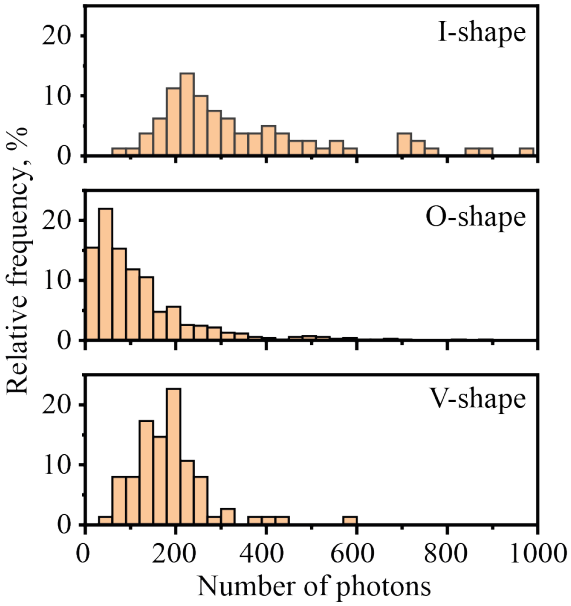

Fig. 3 Histograms of detected photons per each individual molecular translocation for each nanopore geometry, excited with 532 nm laser and polarization oriented perpendicular to the pore (x-axis, Fig. 1a).

Owing to the enhanced performance of the non-circular nanopores, these plasmonic nanopores represent a promising platform for high-throughput SERS-based molecular sensing.

IV. Conclusion

We demonstrated a strong dependence of a flow-through SERS enhancement on nanopore geometry and excitation polarization during single-molecule translocation, using polyArg molecules as a model system. Regular circular pores exhibited the weakest enhancement, limiting their applicability for SERS-based translocation studies. In contrast, I-shaped and V-shaped nanopores provided significantly stronger enhancement due to their geometry, with additional sensitivity to excitation polarization. These results show the importance of nanopore design for emerging SERS sequencing and single-molecule sensing applications.

References

[1] M. M. Schmidt, A. G. Brolo, and N. C. Lindquist, "Single-molecule surface-enhanced Raman spectroscopy: challenges, opportunities, and future directions," *ACS Nano*, vol. 18, no. 38, pp. 25930–25938, 2024.

[2] K. Khabarov, M. Blanco Formoso, I. M. Baldi, F. Khozeymeh Sarbishe, R. Marongiu, G. Bruno, **et al.**, "Raman identification of single nucleotides flowing through permeable plasmonic films," *Nature Communications*, vol. 16, no. 1, p. 9113, 2025.

[3] F. Khozeymeh Sarbishe **et al.**, "High-speed Raman readout of single polypeptides via plasmonic nanopores," *Advanced Materials*, vol. 37, no. 39, p. 2504436, 2025.

Materials for Surface-Enhanced Raman Spectroscopy Detection of Per- and Poly-fluoroalkyl Substances in Aqueous Film-Forming Foams

Chuntao Wang,[1] Kushal Biswas,[2] Sangmin Jeong,[1] Anila Bello,[2] Dhimiter Bello,[2] Michael B. Ross[1]

[1]Department of Chemistry, University of Massachusetts Lowell, USA
[2]Department of Biomedical and Nutritional Science, University of Massachusetts Lowell, USA
*Corresponding author: Michael_ross@uml.edu

***Abstract*— Rapid identification of PFAS in complex mixtures is critical for environmental monitoring and remediation. We use concave cubic gold nanoparticles for SERS detection of six MassDEP-regulated PFAS at ppm levels. The platform enables quantitative analysis, chain-length differentiation, and identification in real AFFFs, validated by mass spectrometry for field-deployable screening applications.**

***Keywords*— SERS, PFAS, AFFFs, gold nanoparticles**

I. Introduction

Per- and polyfluoroalkyl substances (PFAS) comprise a large class of synthetic fluorinated compounds widely used in industrial processes and consumer products due to their thermal stability and surfactant properties. Their environmental persistence, resistance to degradation, and documented associations with adverse human health outcomes have driven increasingly stringent regulatory limits, often at parts-per-trillion levels. Analytical detection is complicated by the extensive structural diversity of PFAS, their occurrence in complex multicomponent matrices such as aqueous film-forming foams (AFFFs), and interference from coexisting surfactants, organic constituents, and variable pH conditions.

Liquid chromatography–tandem mass spectrometry (LC-MS/MS) remains the gold standard for PFAS quantification due to its sensitivity and specificity; however, it requires laboratory-based instrumentation, extensive sample preparation, and still captures only a fraction of the thousands of PFAS in commercial use. These limitations motivate the development of rapid, field-deployable screening tools capable of selective detection in chemically complex environments.

Surface-enhanced Raman spectroscopy (SERS) offers a promising alternative by leveraging plasmonic nanostructures to amplify Raman scattering signals and enable trace-level detection. With rationally designed nanoparticle substrates, SERS has demonstrated the potential for sensitive and selective PFAS identification across environmentally relevant concentration ranges, providing a pathway toward portable, high-throughput monitoring of contaminated water sources and AFFF-impacted sites.

II. Methods

Concave Cubic Gold Nanoparticle Synthesis

Synthesis of Au seeds: 0.250 mL of 10 mM $HAuCl_4$ and 0.02 mL of 1 M HCl were added sequentially to 10.0 mL of 100 mM CTAC with vigorous stirring, resulting in a light-yellow solution. Next, 0.60 mL of freshly prepared 10 mM $NaBH_4$ was rapidly injected into the vigorously stirring solution, which led to the formation of an orange-brown seed solution. The seed solution was allowed to stir for an additional minute to ensure uniform dispersion of the reducing agent. The solution was allowed to age at room temperature for 2 h. Next, 0.20 mL of 1 M HCl, 0.50 mL of 10 mM $HAuCl_4$, and 100 µL of 10 mM $AgNO_3$ were added sequentially into 10.0 mL of 100 mM CTAC with gentle swirling. Then 0.10 mL of 100 mM ascorbic acid was introduced, causing a noticeable color change from light yellow to clear. 0.10 mL of an aliquot of seeds, which had been diluted 1000× in 100 mM CTAC, was then added to initiate the growth of particles.

SERS Scan of PFAS

SERS data were collected from a Bruker Senterra Dispersive Raman microscope, Serial number R200.0238, Detector model DU420A-OE-152, at a laser 785 nm. To avoid damage due to laser-induced heating, all measurements were performed at a low laser power of 50 mW. The integration time was set to 10 s, with an averaging of 4 scans to improve the signal-to-noise ratio. Concave cube Au nanoparticles were synthesized by following the method above, transferred to a 2 mL centrifuge tube, and concentrated to 50 µL. The concentrated nanoparticle solution was drop-cast onto a silicon wafer and dried at room temperature. SERS PFAS samples were prepared by diluting 6-MA-regulated PFAS stock solutions to different low concentrations down to 0.1 ppm. A silicon wafer with a concave cube Au nanoparticle was placed on a glass slide, a drop-cast-diluted PFAS solution was placed on the silicon wafer surface, and dried at room temperature.

The frequency gap (Δ) was calculated from Raman spectra as the difference between the C–C alkyl chain stretching, located near 250 cm^{-1}, and the C–C symmetric stretching modes, located near 1150 cm^{-1}, referenced to an internal silicon standard, located at 520 cm^{-1}, and normalized to the characteristic C–F stretching vibration, located near 750 cm^{-1}.

III. Results and Discussion

Concave cubic nanoparticles clearly result in enhanced SERS of PFAS down to ppm concentrations. The talk will detail how this was performed for 6 PFAS relevant for environmental regulation, in addition to comparing with bulk and calculated spectra.

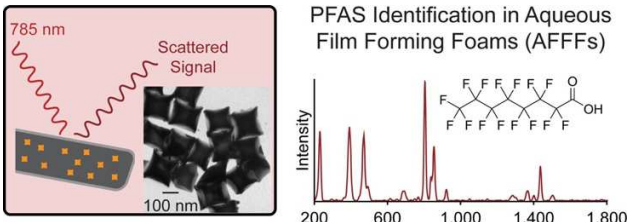

Fig 1. Scheme and typical SERS result.

Separately, experimental results highlight the ability to detect PFAS, specifically PFOS and PFOA, in real firefighting foams. This is supported by ^{19}F nuclear magnetic resonance (NMR) spectroscopy).

IV. Conclusion

We demonstrate that concave cubic gold nanoparticle SERS substrates (785 nm excitation) enable rapid, nondestructive identification of the six MassDEP-regulated PFAS at ppm levels and detect PFOS directly within complex commercial AFFF mixtures, with key spectral assignments supported by spontaneous Raman, DFT calculations, 19F NMR, and LC-MS/MS. Ongoing efforts focus on improving substrate durability, lowering detection limits, and expanding analysis to structurally diverse PFAS analogues to strengthen quantitative capability and real-world applicability in complex environmental matrices.

Acknowledgments

This work was funded by the Federal Emergency Management Agency (FEMA) Assistance to Firefighters Grant Program (#EMW-2020-FP-00078). We are grateful to the UMass Lowell Core Research Facilities and Fire Protection Research Foundation for their guidance and support of this work.

References

Wang, C., et al. Environ. Sci. and Technol. **2026**, *1*, 1153-1160.

From AI Design to SERS Spectral Shaping and Nanoplastics Detection with Metal Film over Nanospheres

Cosmin Farcău[1,2*], Ioana Cârdan[1], Ana M. M. Gherman[1], Fran Nekvapil[1]

[1]National Institute for Research and Development of Isotopic and Molecular Technologies INCDTIM, Cluj-Napoca, Romania

[2]Institute for Interdisciplinary Research in Bio-Nano-Sciences, Babeș-Bolyai University, Cluj-Napoca, Romania

*Corresponding author: cfarcau@itim-cj.ro

***Abstract*— Here, we present our recent results concerning the investigation and exploitation of metal film over nanosphere (MFoN) SERS substrates, spanning from rational, AI-driven plasmonic design to fundamental studies on spectral shaping induced by focusing / defocusing, and issues related to real-world analytical applications in nanoplastic detection.**

***Keywords*— localized plasmons, colloidal-based SERS substrates, machine learning, nanoplastics.**

The first part of this work discusses our approach to combine finite-difference time-domain (FDTD) simulations with artificial neural networks (ANN) to achieve rational optimization of metal film over nanosphere (MFoN) SERS substrates. FDTD simulations are used to systematically map the influence of key geometrical parameters on the localized surface plasmon resonance (LSPR) properties and the electromagnetic SERS enhancement [1]. The resulting dataset trains an ANN capable of accurately predicting the average electromagnetic field at the substrate surface. This predictive model is subsequently employed as a surrogate for optimization, identifying substrate geometries that maximize electric field intensity at 785 nm. The excellent agreement between ANN predictions and FDTD-calculated values validates the reliability and efficiency of this machine learning-guided design framework.

Next, we address a subtle yet critical factor affecting SERS measurements on solid planar nanostructured SERS substrates: the role of laser focus positioning along the optical axis (Z direction) [2]. Axial scans reveal that the SERS signal intensity follows a Lorentzian profile, with the maximum consistently occurring above the physical substrate surface. More significantly, the intensity ratios between different spectral features, including SERS bands and the broad background, vary non-monotonically along the Z axis. FDTD simulations attribute these spectral shape variations to the plasmonic near-field response of the substrate under focused and defocused illumination conditions. These findings underscore the importance of precise focus control in quantitative SERS analyses, particularly in band-ratio-based assays performed on nanostructured solid substrates.

Finally, we extend the investigation of MFoN substrates to the analytically challenging problem of nanoplastic detection. Using wavelength-scanned SERS in the near-infrared range, we first characterize the performance of various substrates with benzenethiol as a molecular probe analyte. We then assess the same substrates for the detection of individual polystyrene nanoplastic particles. The results reveal an important insight: while a substrate optimized for molecular detection may exhibit excellent sensitivity towards small-molecule analytes, separate and distinct optimization is required for effective detection of nanoscale particulate matter such as nanoplastics [3].

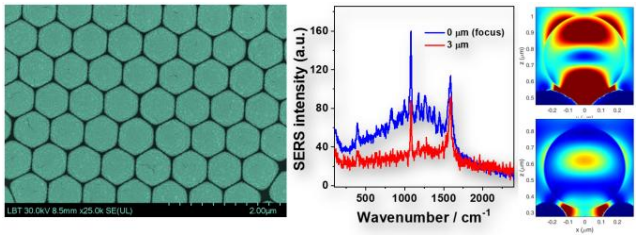

Fig. 1 (left) SEM image of metal film over nanosphere; (centre) SERS spectra of 4-aminobenzenethiol upon focusing/ defocusing; (right) FDTD simulations of spherical nanoplastic on the SERS substrate.

Taken together, these interconnected studies on the MFoN platform provide a unified perspective spanning computational substrate design, fundamental understanding of SERS spectral shape, and emerging environmental sensing applications, contribution to the rational development and application of SERS substrates.

ACKNOWLEDGMENTS

This work was supported through the “Nucleu” Program

within the National Research Development and Innovation Plan 2022–2027, Romania, carried out with the support of MEC, project no. 27N/03.01.2023, component project code PN 23 24 01 02. C.F. acknowledges support from the Babes-Bolyai University through internal grants AGC32054, AGC32055, AGC32056 /27.05.2025.

REFERENCES

[1] N. Nechita and C. Farcau, "Tuning plasmons of metal-coated microsphere arrays towards optimized surface-enhanced spectroscopy," Optics Express, vol. 29, pp. 42238-42250, 2021.

[2] F. Nekvapil and C. Farcau, "The role of focused laser plasmonics in shaping SERS spectra of molecules on nanostructured surfaces," Nanoscale Advances, vol. 7, pp. 3008-3017, 2025.

[3] I. Cardan, V. Zani, A. M. M. Gherman, R. Signorini, R. Pilot, and C. Farcau, "From molecular to nanoplastic SERS detection: insights into the role of analytes in plasmonic substrate design," Nanoscale, vol. 17, pp. 25680-25690, 2025.

Simulating Surface-Enhanced Spectroscopies: The ωFQFμ Model

P. Grobas Illobre[1], T. Giovannini[2,*], C. Cappelli[1,*]
[1]Scuola Normale Superiore di Pisa, Italy
[2]Department of Physics, University of Rome Tor Vergata, Italy
*Corresponding author: tommaso.giovannini@uniroma2.it , chiara.cappelli@sns.it

***Abstract*— We present a multiscale quantum and classical framework for simulating surface enhanced spectroscopies of molecules near plasmonic substrates. The method combines quantum molecular response with an atomistic classical electromagnetic description of metals. We demonstrate accurate and efficient prediction of surface enhanced Raman signals of molecules on realistic plasmonic substrates.**

***Keywords*— QM/MM, SERS, plasmonics, atomistic.**

I. Introduction

Surface-enhanced spectroscopies arise from the coupled response of a molecule and a plasmonic substrate, requiring a balanced description of (i) the substrate electromagnetic response and (ii) molecule–substrate coupling. We address this problem with an atomistic, frequency-dependent classical model for the metal response and its coupling to a quantum description of the molecule, enabling realistic simulations at low computational cost.

II. Methods

The plasmonic substrate is modeled through the frequency-dependent Fluctuating Charges and Fluctuating Dipoles (ωFQFμ) approach, which provides a fully atomistic description of the metal electromagnetic response. Under a monochromatic external field at frequency ω, the ωFQFμ unknowns q and μ are obtained from the linear system:

$$\begin{pmatrix} \mathbf{A}^{qq} & \mathbf{A}^{q\mu} \\ \mathbf{T}^{\mu q} & \mathbf{T}^{\mu\mu} \end{pmatrix} \begin{pmatrix} \mathbf{q} \\ \boldsymbol{\mu} \end{pmatrix} = \begin{pmatrix} \mathbf{f}^{q} \\ \mathbf{f}^{\mu} \end{pmatrix} \qquad (1)$$

where $\mathbf{A}^{qq}$ and $\mathbf{A}^{q\mu}$ collect charge–charge and charge–dipole couplings (including Drude-like terms), $\mathbf{T}^{\mu\mu}$ and $\mathbf{T}^{\mu q}$ are the dipole–dipole and dipole–charge interaction kernels, and $\mathbf{f}^{q}$ and $\mathbf{f}^{\mu}$ account for the driving electric potential and field at the atomic positions. Molecular properties are computed with TDDFT, while the ωFQFμ environment enters as a frequency-dependent embedding contribution. From the coupled response we obtain the frequency-dependent polarizability and compute SERS intensities within Placzek's approximation.

III. Results and Discussion

Figure 1 compares computed SERS spectra of pyridine adsorbed at distinct sites (vertex, edge, and face) on an icosahedral gold nanoparticle (10 179 atoms) with the corresponding experimental spectrum. The simulations reproduce the main experimental features, and the average over site-resolved signals provides a practical estimate of the measured response, indicating that realistic nanoparticle sizes and heterogeneous adsorption environments can be treated within a fully atomistic framework at a computational cost compatible with routine simulations.

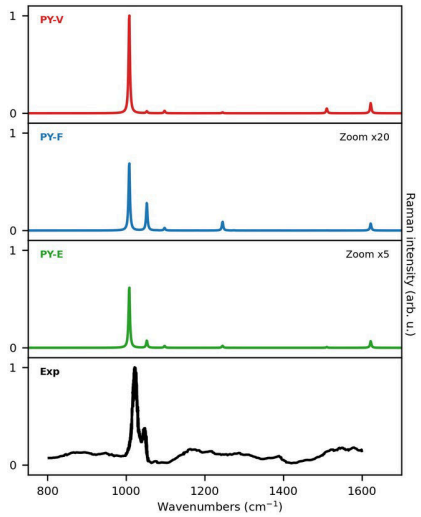

Fig. 1 QM/ωFQFμ SERS spectra of pyridine at different adsorption sites on an icosahedral gold nanoparticle (10 179 atoms), compared with experiment.

IV. Conclusion

We have presented the multiscale QM/ωFQFμ framework for the efficient simulation of SERS signals of molecules adsorbed on plasmonic substrates (e.g., silver, gold, graphene). The approach combines a quantum-mechanical description of the molecule with an atomistic electromagnetic model of the substrate, delivering results in good agreement with experimental benchmarks at a substantially reduced computational cost. We also introduced further developments aimed at improving the overall efficiency of the method, and extended the same multiscale strategy to access additional surface-enhanced spectroscopies, including SEIRA and SEF.

Acknowledgments

This work has received funding from the European Research Council (ERC) under the European Union's Horizon

2020 research and innovation programme (Grant Agreement No. 818064).

References

[1] T. Giovannini, M. Rosa, S. Corni, and C. Cappelli, "A classical picture of subnanometer junctions: An atomistic Drude approach to nanoplasmonics," *Nanoscale*, vol. 11, pp. 6004–6015, 2019.

[2] T. Giovannini, L. Bonatti, P. Lafiosca, L. Nicoli, M. Castagnola, P. Grobas Illobre, S. Corni, and C. Cappelli, "Do we really need quantum mechanics to describe plasmonic properties of metal nanostructures?" *ACS Photonics*, vol. 9, pp. 3025–3034, 2022.

[3] T. Giovannini, L. Bonatti, P. Lafiosca, L. Nicoli, M. Castagnola, P. Grobas Illobre, S. Corni, and C. Cappelli, "Do we really need quantum mechanics to describe plasmonic properties of metal nanostructures?" *ACS Photonics*, vol. 9, pp. 3025–3034, 2022.

[4] T. Giovannini, P. Grobas Illobre, P. Lafiosca, L. Nicoli, L. Bonatti, S. Corni, and C. Cappelli, "plasmonX: an open-source code for nanoplasmonics," *Computer Physics Communications*, vol. 322, art. 110035, 2026.

[5] P. Lafiosca, L. Nicoli, L. Bonatti, T. Giovannini, S. Corni, and C. Cappelli, "QM/Classical Modeling of Surface Enhanced Raman Scattering Based on Atomistic Electromagnetic Models," *Journal of Chemical Theory and Computation*, vol. 19, no. 12, pp. 3616–3633, 2023.

[6] P. Grobas Illobre, P. Lafiosca, L. Bonatti, T. Giovannini, and C. Cappelli, "Mixed atomistic-implicit quantum/classical approach to molecular nanoplasmonics," *The Journal of Chemical Physics*, vol. 162, no. 4, art. 044103, 2025.

[7] P. Grobas Illobre, P. Lafiosca, T. Guidone, F. Mazza, T. Giovannini, and C. Cappelli, "Multiscale modeling of surface enhanced fluorescence," *Nanoscale Advances*, vol. 6, pp. 3410–3425, 2024.

[8] S. Sodomaco, P. Lafiosca, T. Giovannini, and C. Cappelli, "Atomistic QM/Classical Modeling of Surface-Enhanced Infrared Absorption," *The Journal of Physical Chemistry C*, 2025.

Theoretical Investigation of Vibrational Imaging Induced by Electronically Forbidden Transitions in Tip-Enhanced Raman Scattering

Mamoru Tamura[1,2,3,4*], Hiroyuki Ikagawa[2], Hajime Ishihara[2,3,5,6]

[1]School of Science, Kwansei Gakuin University, Hyogo, Japan
[2]Department of Materials Engineering Science, The University of Osaka, Osaka, Japan
[3]Research Organization of Science and Technology, Ritsumeikan University, Shiga, Japan
[4]Research Institute for Light-induced Acceleration System (RILACS), Osaka Metropolitan University, Osaka, Japan
[5]SANKEN, The University of Osaka, Osaka, Japan
[6]Ritsumeikan Semiconductor Application research center (RISA), Ritsumeikan University, Shiga, Japan
*Corresponding author: mamoru.tamura@kwansei.ac.jp

***Abstract*— We developed a theoretical framework for visualizing vibrational modes in tip-enhanced Raman scattering based on resonance Raman processes. In particular, by exploiting electronically forbidden excitations, we showed that the resulting spatial distribution of vibrational signals can differ fundamentally from that obtained via conventional allowed transitions.**

***Keywords*— Raman scattering, nonlocal response theory, quantum electrodynamics, plasmon.**

I. Introduction

Raman scattering enables access to vibrational information intrinsic to matter. Recent advances in tip-enhanced microscopy, both experimentally [1–3] and theoretically [4–8], now enable visualization of vibrational states at the single-molecule level. Although Raman scattering originating from electronically forbidden excitations has been reported [9], its observation in tip-enhanced Raman scattering (TERS) has not yet been demonstrated.

In this work, we develop a theoretical framework for single-molecule TERS imaging in which not only the incident field but also scattering processes are treated self-consistently with the optical near field generated by the metallic tip–substrate nanostructure. Furthermore, by incorporating a spatially distributed molecular dipole response, we construct a nonlocal description of light–matter interaction. Using this formulation, we investigate how Raman processes mediated by electronically allowed and forbidden excitations give rise to distinct mode-resolved TERS imaging patterns, revealing that forbidden pathways can enhance Herzberg–Teller (HT)–related symmetry components in the spatial contrast, thereby enabling discrimination of vibrational modes with similar energies.

II. Methods

We formulate tip-enhanced Raman scattering (TERS) within a nonlocal quantum–electrodynamical framework. The total Hamiltonian is written as,

$$\hat{H} = \hat{H}_{\mathrm{mol}} + \hat{H}_{\mathrm{rad}} + \hat{V}, \tag{1}$$

where $\hat{H}_{\mathrm{mol}}$ describes the electronic and vibrational states of the molecule and $\hat{H}_{\mathrm{rad}}$ represents the quantized electromagnetic field in the plasmonic nanostructure. The light–matter interaction is given by,

$$\hat{V} = -\int d\boldsymbol{r}\, \hat{\boldsymbol{P}}(\boldsymbol{r}) \cdot \hat{\boldsymbol{E}}(\boldsymbol{r}), \tag{2}$$

with the polarization operator expressed in terms of transition dipole densities $\boldsymbol{\mathcal{P}}_{nm}(\boldsymbol{r})$, expanded into Franck–Condon (FC) and HT components, allowing us to evaluate their interference.

Starting from the quantum master equation under the Born–Markov approximation, we evaluate the expectation value of the polarization to first order in the interaction. This yields a spatially nonlocal response of the form [10-12],

$$\boldsymbol{P}(\boldsymbol{r},\omega) = \varepsilon_0 \int d\boldsymbol{r}'\, \boldsymbol{\chi}(\boldsymbol{r},\boldsymbol{r}',\omega)\boldsymbol{E}(\boldsymbol{r}',\omega), \tag{3}$$

where, in the present TERS formulation, the nonlocal susceptibility is derived as,

$$\boldsymbol{\chi}(\boldsymbol{r},\boldsymbol{r}',\omega) = \frac{1}{\varepsilon_0}\sum_{n,m}(\langle\hat{\sigma}_{nn}(0)\rangle - \langle\hat{\sigma}_{mm}(0)\rangle) g_{mn}(\omega)\boldsymbol{\mathcal{P}}_{nm}(\boldsymbol{r})\boldsymbol{\mathcal{P}}_{mn}(\boldsymbol{r}'). \tag{4}$$

Here $g_{mn}(\omega)$ denotes the molecular energy denominator including relaxation. Because the transition dipole density is spatially distributed, the response is intrinsically nonlocal and naturally incorporates multipolar coupling to spatially varying near fields. The plasmonic environment is incorporated through a renormalized Green's function obtained from Maxwell's equations including the metal dielectric response. This Green's function incorporates the full set of plasmonic modes and consistently modifies both excitation and the subsequent spontaneous emission.

The Raman scattering intensity is evaluated from the time derivative of the photon number operator. After solving the coupled operator equations under steady-state conditions, the scattered intensity at frequency ω_s can be written in the form,

$$S(\omega_s) = \frac{1}{\pi}\sum_{n,m} \mathrm{Re}\left[\sum_{p=1}^{4} D_{n,m}^{(p)}(\omega_i, \omega_s)\, Y_{n,m}^{(p)}(\omega_s)\, I_{n,m}^{(p)}(\omega_i)\right]. \quad (5)$$

Here $I_{n,m}^{(p)}$ contains the near-field–dependent excitation process, $Y_{n,m}^{(p)}$ represents the Green-function–mediated spontaneous emission process, and $D_{n,m}^{(p)}$ corresponds to molecular energy denominators. Under appropriate approximations, and in the absence of metallic structures, the four terms reduce to the conventional Kramers–Heisenberg–Dirac dispersion formula. This formulation enables mode-resolved analysis of electronically forbidden Raman processes under tip-enhanced conditions.

The simulation model is shown in Fig. 1(a) and (b). For computational simplicity, the gold tip is modeled as a sphere with an atomically small protrusion at its apex. A pentacene molecule is placed between the tip and a gold substrate, oriented parallel to the substrate surface.

III. Results and Discussion

The electronic structure and vibrational modes of the pentacene molecule were calculated using Gaussian. The spatial distributions of the vibrational mode corresponding to the Raman shift at 1027 cm^{-1}, visualized via electronically allowed and forbidden transitions, are shown in Fig. 2. When mediated by an allowed excitation, the signal appears at the upper and lower regions along the short molecular axis of pentacene. In contrast, excitation via a forbidden transition yields four spatially separated signal regions.

For the allowed transition, the HT–induced contribution produces a transition dipole at both molecular termini oriented along the same direction of the short axis, resulting in the distribution shown in Fig. 2(a). By contrast, in the electronically forbidden case, the transition dipole densities at the two molecular ends are oppositely oriented, leading to the four-lobed distribution shown in Fig. 2(b). This contrast can be understood as arising from a phase reversal of the HT-related polarization between the two termini in the forbidden pathway, which makes the intrinsic two-end character of the HT distribution more explicit in the spatial imaging pattern.

IV. Conclusion

In conclusion, we have developed a nonlocal quantum–electrodynamical framework for single-molecule TERS imaging that consistently incorporates plasmonic renormalization and spatially distributed molecular dipole responses. The formulation enables mode-resolved analysis of FC and HT contributions, including electronically forbidden excitations. Our results demonstrate that vibrational imaging patterns can differ qualitatively depending on whether the Raman process is mediated by electronically allowed or forbidden transitions. In particular, the reversal of transition dipole moment densities at the molecular termini in the forbidden case gives rise to a distinct four-lobed spatial distribution. These results suggest that electronically forbidden excitations provide a symmetry-sensitive pathway for contrast formation, enabling discrimination of vibrational modes with similar energies.

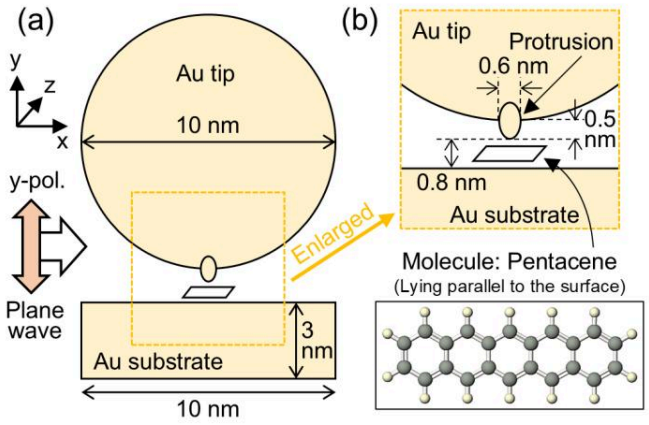

Fig. 1. (a) Schematic of the overall simulation model. (b) Enlarged view of the tip region with the pentacene molecule.

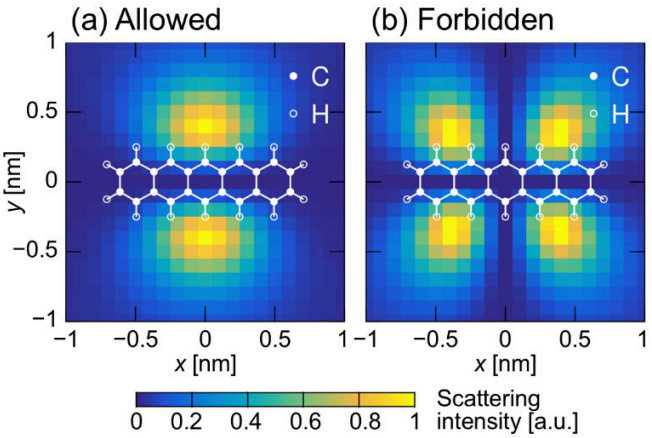

Fig. 2. Calculated spatial distributions of the TERS scattering intensity for the 1027 cm^{-1} vibrational mode obtained via (a) electronically allowed and (b) electronically forbidden transitions.

ACKNOWLEDGMENTS

This work was supported by JST, the establishment of university fellowships towards the creation of science technology innovation (Grant Number JPMJSP2138) and JSPS KAKENHI (Grant Numbers JP21H05019, JP24K21196, JP24K08282, and JP25H01627).

REFERENCES

[1] J. Lee, K.T. Crampton, N. Tallarida, and V.A. Apkarian, "Visualizing vibrational normal modes of a single molecule with atomically confined light," Nature, vol. 568, pp. 78–82, 2019.

[2] R.B. Jaculbia, H. Imada, K. Miwa, T. Iwasa, M. Takenaka, B. Yang, E. Kazuma, N. Hayazawa, T. Taketsugu, and Y. Kim, "Single-molecule resonance Raman effect in a plasmonic nanocavity," Nature Nanotechnology, vol. 15, pp. 105–110, 2020.

[3] J. Xu, X. Zhu, S. Tan, Y. Zhang, B. Li, Y. Tian, H. Shan, X. Cui, A. Zhao, Z. Dong, J. Yang, Y. Luo, B. Wang, and J.G. Hou, "Determining structural and chemical heterogeneities of surface species at the single-bond limit," Science, vol. 371, pp. 818–822, 2021.

[4] S. Duan, G. Tian, Y. Ji, J. Shao, Z. Dong, and Y. Luo, "Theoretical modeling of plasmon-enhanced Raman images of a single molecule with subnanometer resolution," Journal of the American Chemical Society, vol. 137, pp. 9515–9518, 2015.

[5] Z. Xie, S. Duan, G. Tian, C.-K. Wang, and Y. Luo, "Theoretical modeling of tip-enhanced resonance Raman images of switchable azobenzene molecules on Au(111)," Nanoscale, vol. 10, pp. 11850–11860, 2018.

[6] P. Liu, D.V. Chulhai, and L. Jensen, "Single-molecule imaging using atomistic near-field tip-enhanced Raman spectroscopy," ACS Nano, vol. 11, pp. 5094–5102, 2017.

[7] X. Chen, P. Liu, Z. Hu, and L. Jensen, "High-resolution tip-enhanced Raman scattering probes sub-molecular density changes," Nature Communications, vol. 10, p. 2567, 2019.

[8] Y. Zhang, Z.-C. Dong, and J. Aizpurua, "Theoretical treatment of single-molecule scanning Raman picoscopy in strongly inhomogeneous near fields," Journal of Raman Spectroscopy, vol. 52, pp. 296–309, 2021.

[9] M. Takase, H. Ajiki, Y. Mizumoto, K. Komeda, M. Nara, H. Nabika, S. Yasuda, H. Ishihara, and K. Murakoshi, "Selection-rule breakdown in plasmon-induced electronic excitation of an isolated single-walled carbon nanotube," Nature Photonics, vol. 7, pp. 550–554, 2013.

[10] H. Yamane, N. Yokoshi, H. Oka, Y. Sugawara, and H. Ishihara, "Near-field circular dichroism of single molecules," Optics Express, vol. 31, pp. 3415–3426, 2023.

[11] Y. Tomoshige, M. Tamura, T. Yokoyama, and H. Ishihara, "Enhanced photoluminescence of strongly coupled single molecule-plasmonic nanocavity: analysis of spectral modifications using nonlocal response theory," Nanophotonics, vol. 14, pp. 1157–1169, 2025.

[12] Y. Tomoshige, M. Tamura, and H. Ishihara, "Tip-enhanced photoluminescence imaging of porphyrin tapes: exploring the nonlocality of molecular orbitals," Applied Physics Express, vol. 18, p. 022004, 2025.

Zwitterionic polymeric coacervates as plasmonic boxes for one-pot SERS biomarkers detection in biofluids

Caterina Dallari[1,2] and Francesca Torrini[1,2], Luisa Ponticelli[2,3], Silvia Bagnoli[4], Benedetta Nacmias[4], Valentina Bessi[4], Francesco Saverio Pavone[1,2,3], Paolo Arosio[5], Caterina Credi[1,2]

[1]National Research Council, National Institute of Optics, Florence, Italy
[2]European Laboratory for Non-Linear Spectroscopy (LENS), Florence, Italy
[3]Department of Physics, University of Florence, Italy
[4]Department of Neurological and Psychiatric Sciences, University of Florence, Italy
[5]Department of Chemistry and Applied Biosciences, ETH Zürich, Switzerland
*Corresponding author: caterina.dallari@ino.cnr.it; dallari@lens.unifi.it

***Abstract*— We develop zwitterionic polymeric coacervates as antifouling plasmonic boxes for one-pot SERS sensing in complex biofluids. Local enrichment of selected targets and Raman-active gold nanoparticles increase signal to noise ratio of at least 10-fold compared with free gold nanoparticles in solution, enabling limits of detection below nM range in plasma and cerebrospinal fluid, as demonstrated here with the amyloid beta 1-42.**

***Keywords*— zwitterionic coacervates, Raman-SERS spectroscopy, biofluids, plasmonic boxes, amyloid beta.**

I. Introduction

Direct biomarker detection in plasma and cerebrospinal fluid is hindered by low analyte abundance, matrix interference, and biofouling on sensing interfaces. While surface enhanced Raman spectroscopy (SERS) can provide chemically specific readout, its use in complex biofluids is often limited by uncontrolled hotspot formation, nonspecific adsorption, and poor signal to background. Liquid-liquid phase separated associative coacervates offer a complementary route to preconcentrate targets under mild conditions. Zwitterionic coacervates are characterized by interesting antifouling features suppressing nonspecific binding, engineered to uptake specific biomolecules in complex biofluids [1,2]. When integrated with biophotonics technologies such as SERS-active nanostructures [3], these engineered droplets create confined plasmonic systems that enhance molecular signatures. Here we combine antifouling zwitterionic coacervates with programmed affinity capture and Raman active plasmonic probes to create tunable liquid plasmonic boxes for one pot sensing in biofluids.

II. Methods

A zwitterionic copolymer was prepared starting from sulfobetaine based monomers and further functionalized via EDC NHS coupling with capturing probes to increase selectivity. Phase separation into polymer rich droplets was induced by reducing ionic strength to 100 mM NaCl across a broad pH window. Gold nanoparticles were synthesized as multilayer core shell structures embedding a Raman reporter with a 2235 cm^{-1} band in the biological silent region. Droplet recruitment was quantified by fluorescence microscopy and SERS spectra were acquired by confocal micro-Raman microscopy.

III. Results and Discussion

Engineered zwitterionic coacervates form stable, liquid-like droplets that act as confined microenvironments and intrinsically enrich molecular clients. The droplets show robust phase behavior under mild conditions and provide a low-fouling compartment where biomolecules can be concentrated without extensive sample processing. By programming the droplet phase with affinity ligands, we achieve selective uptake of biomolecules and concomitant recruitment of plasmonic probes. Plasmonic multilayer gold nanoparticles provide a strong Raman band in the biologically silent region and once compartmentalized inside droplets, generate confined hotspots that markedly improve signal to background compared with bulk measurements. Streptavidin is first used as a model system to validate specific and controllable partitioning: biotin-based affinity drives droplet loading, while the zwitterionic matrix minimizes nonspecific adsorption, demonstrating effective discrimination against background components, with sensitivity down to 0.8 pM (Fig.1 a-c). Building on this modular strategy, antibody functionalization enables selective capture of amyloid beta 1-42 and its enrichment in complex media. This plasmonic box configuration enables one-pot quantification of amyloid beta 1-42 with a 0.1 to 10 nM working range and a 0.24 nM limit of detection. Importantly, the assay maintains performance in clinically relevant matrices, allowing direct

readout in plasma and cerebrospinal fluid (CSF) with good reproducibility and low coefficient of variation (Fig. d-f).

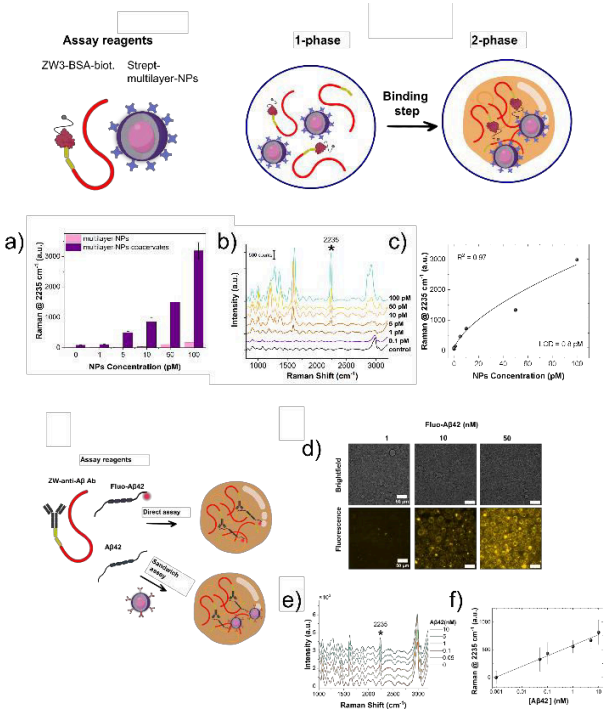

Fig. 1 Zwitterionic coacervate “plasmonic box” for one pot SERS in biofluids: selective recruitment of reporter encoded gold nanoparticles into liquid droplets creates confined hotspots in the silent region. Plots and images show nanoparticle enrichment, Raman spectra, for streptavidin as gold-standard and amyloid beta 1-42 quantification in plasma and CSF.

IV. Conclusion

Zwitterionic coacervates act as programmable, antifouling liquid compartments that concentrate biomarkers and plasmonic probes to generate confined hotspots for Raman readout. This plasmonic box strategy enables streamlined, one pot quantification of amyloid beta 1-42 directly in clinically relevant biofluids and can be adapted to other targets by changing the affinity ligands.

Acknowledgments

This work was supported by I-PHOQS” project financed by the EU next generation PNRR action (CUP B53C22001750006); “SENSOR project” (Agyr 2024 – Airalzh Foundation); BioQantSense Project within the “Twinning for excellence of the Serbian Research Center for quantum biophotonics”; PNRR Tuscany Health Ecosystem (THE). The authors thank the Advance Lightsheet Microscopy Italian Mode of Euro-bioimaging ERIC.

References

[1] U. Capasso Palmiero, et al., Adv. Mater. 34 (2022) 2104837.
[2] F. Torrini, et al., Adv. Sci. 12 (2025) 2411653.
[3] C. Dallari, et al., ACS Sens. 8 (2023) 3693-3700.

SERS behavior of the antiepileptic drug cenobamate

L. F. Gervasini[1], A. D'Urso[2], E. Ciusani[2], A. Cutri[1], S. Trusso[3], P. M. Ossi[3,4,5], A. Lucotti[1], M. Tommasini[1,3,*]

[1]Dip. di Chimica, Materiali e Ing. Chimica, Politecnico di Milano, Milano, Italy;
[2]Lab. di Patologia Clinica e Genetica Medica, Fondazione IRCCS Istituto Neurologico C. Besta, Milano, Italy;
[3]Istituto per i Processi Chimico-Fisici (IPCF), CNR, Messina, Italy;
[4]Dip. Chimica, Farmacia, Scienze Ambientali, Università di Messina, Messina, Italy;
[5]Dip. di Energia, Politecnico di Milano, Milano, Italy.
*Corresponding author: matteo.tommasini@polimi.it

***Abstract*—Surface-Enhanced Raman Spectroscopy (SERS) is a sensitive technique that has the potential to be implemented in Therapeutic Drug Monitoring protocols for anti-epileptic drugs, reducing the time and cost of High-Performance Liquid Chromatography (HPLC) methods.**

***Keywords*— Raman, Cenobamate, gold nanoparticles.**

I. Introduction

Epilepsy is a neurological disease affecting 1% of the population worldwide. Nowadays, antiepileptic drugs can help people suffering from epilepsy to guarantee up to 100% seizure control. To do so, it is important to monitor the concentration of these types of drugs in blood to ensure they are below a certain threshold, which can lead to toxicity, especially in children, the elderly, and people suffering from other pathologies. It is also important to ensure that drug concentrations are high enough to control seizures. Therapeutic Drug Monitoring (TDM) is the process of assessing drug concentrations in body fluids for medical purposes [1]. In this context, HPLC coupled with mass spectrometry is a powerful detection method for quantifying drug concentrations in human plasma and is currently used in hospitals [2]. The possibility of complementing this costly and time-consuming technique with a quicker and sensitive spectroscopic technique, such as SERS, is of interest to speed up the analyses and improve the quality of life of patients, reducing the blood sample volumes used for the analyses [3]. SERS is a sensing technique based on Raman spectroscopy in which, thanks to the interaction of the analyte molecule with a nanostructured metal substrate, Raman signals can be intensified by several orders of magnitude. Here, we investigate the SERS behavior of the recently approved anti-epileptic drug Cenobamate [2], for which, to the best of our knowledge, such spectroscopic data are lacking in the literature. To this end, we use both gold nanoparticles obtained from colloidal phases and gold thin films prepared by Pulsed Laser Deposition (PLD), which have demonstrated appealing SERS capabilities [4] and tunable plasmon resonances [5,6].

II. Methods

Cenobamate (CNB) has been purchased by Alsachim®. It appears as a white powder, poorly soluble in pure water. A stock solution of CNB (10^{-3} M) has been prepared by dissolving 1 mg of CNB in 0.3 ml of methanol and adding 1.2 ml of water. Successive dilutions of this stock solution (down to 10^{-6} M) were prepared to study the SERS behavior as a function of drug concentration.

Gold nanoparticle colloids have been prepared following the Turkevich approach [7], which involves preparing a 10^{-3} M solution of $HAuCl_4$ in water (75 ml), and mixing it under stirring with a 1 wt% water solution (7.5 ml) of trisodium citrate (TSC) after both solutions have reached the boiling point. In about 20 minutes, the mixed solution reaches a stable, red wine-like color, indicating the formation of gold nanoparticles about 20 nm in diameter. After cooling, the colloidal suspension is ready for use. SERS samples were prepared by mixing 200 µl of CNB solution with 50 µl of Au colloidal solution, then centrifuging for 10 minutes at 10000 RPM. After removing the supernatant, the concentrated colloidal mixture was drop-cast onto an aluminum foil and dried, forming a film of aggregated nanoparticles suitable for SERS measurements.

Thin-layer gold substrates produced by the PLD technique [5], with a plasmon resonance peak around 720 nm, were tested by directly depositing on the films a 10 µl drop of the CNB aqueous solution (5×10^{-5} M).

Micro-Raman spectra were recorded using a 785 nm excitation wavelength, with a laser power of 1 mW focused through a 50× objective. The spectra were acquired with a 30-second exposure time, averaging 2 accumulations. To obtain clear SERS signals from colloids, five spectra were recorded on the edge of each dried drop, where the nanoparticle film is denser. For each of the five repeats, we selected the spectrum with the best-resolved and intense spectral features. The spectra were compared with both a blank spectrum (the dried colloid without the drug) and a reference Raman spectrum of the CNB molecule in aqueous solution (10^{-3} M).

III. Results and Discussion

The plasmon resonance of the gold colloids shown in Fig. 1 matches the expected optical properties of the Turkevich colloid [7]. Upon aggregation, the original plasmon resonance broadens and red-shifts, and additional light absorption in the 700–850 nm region arises from interactions among the

nanoparticles. This feature enables the use of 785 nm excitation for SERS experiments with both aggregated Au colloids and SERS substrates produced by PLD, which are known to exhibit tunable plasmon resonances in the 650–800 nm range [5,6].

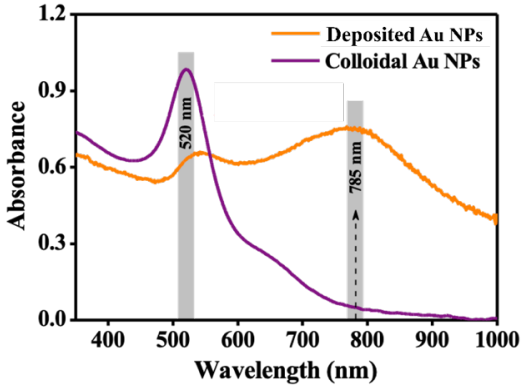

Fig. 1. UV-Vis extinction of the as-prepared gold colloids and a film formed by aggregated colloids deposited on glass.

Fig. 2 compares the reference Raman spectrum of CNB in aqueous solution and representative SERS spectra of CNB collected using the gold colloids and the PLD gold substrates. We observe a good match between the SERS spectra and the reference Raman spectrum of CNB. In the context of TDM, such correspondence supports the use of the strongest SERS peaks (424, 1040, 1212 cm^{-1}) as markers of the drug's presence. Interestingly, by comparing the SERS signal obtained from the colloids with that from the PLD gold substrates, we observe that the latter show lower band intensities. This is due to the shift of the plasmon resonance peak of the PLD substrates relative to the laser excitation wavelength (720 nm *vs*. 785 nm). This point highlights the importance of carefully tuning the optical properties of PLD-produced films, which will be addressed in future work.

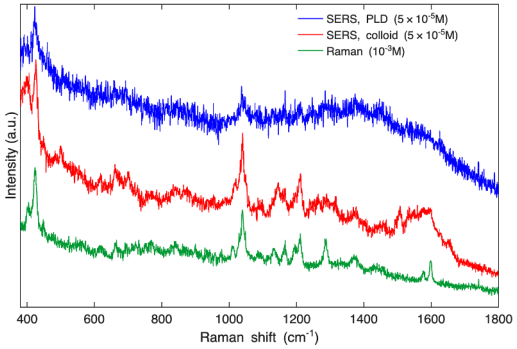

Fig. 2. Raman and SERS spectra of CNB (see text). For clarity, the SERS intensity from PLD has been doubled.

Fig. 3 shows the SERS spectra recorded with gold colloids exposed to decreasing concentrations of CNB, ranging from 5×10^{-5} to 5×10^{-6} M. Notably, this range of concentrations overlaps with the one considered in the HPLC investigation of CNB [2]. Due to the uneven distribution of hotspots in the dried film formed by gold colloids, a robust linear correlation between band intensity and concentration has not yet been established. However, we observe good reproducibility in the overall shape of the SERS spectra across different spots on a single sample and a monotonic increase in SERS intensity with CNB concentration. This is appealing for setups in which the SERS signal is spatially averaged using a spinning device [8].

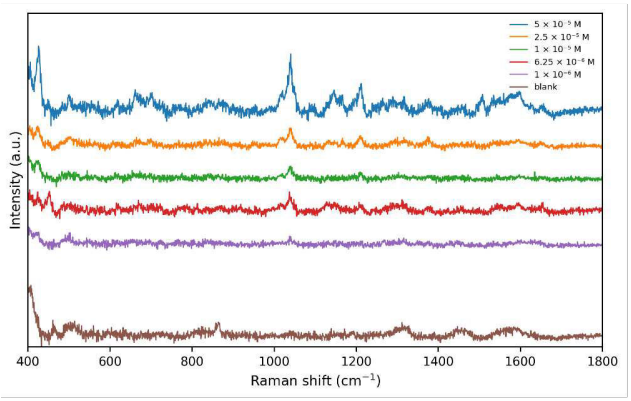

Fig. 3. Baseline-corrected SERS spectra of CNB from gold colloids (see text).

IV. Conclusion

The results presented here show that SERS is a promising sensing technique for the antiepileptic drug Cenobamate. Being quick and sensitive, SERS might speed up procedures, reduce clinic workload, and improve the quality of life for people with neurological diseases.

Acknowledgments

L.F. Gervasini gratefully acknowledges Prof. N.R. Agarwal for a visiting period at Ontario Tech University (Oshawa, Canada) and financial support from the European Union (NextGenerationEU, PNRR grant).

References

[1] C. Johannessen Landmark, S. I. Johannessen, and P. N. Patsalos, "Therapeutic drug monitoring of antiepileptic drugs: current status and future prospects," *Expert Opin. Drug Metab. Toxicol.*, vol. 16, 227, 2020.

[2] L. Molteni, B. Charlier, A. Coglianese, V. Izzo, G. Assenza, P. Menna, U. de Grazia, and A. D'Urso, "Quantitative Analysis of Cenobamate and Concomitant Anti-Seizure Medications in Human Plasma via Ultra-High Performance Liquid Chromatography–Tandem Mass Spectrometry," *Molecules*, vol. 29, no. 4, 2024

[3] A. Jaworska, S. Fornasaro, V. Sergo, and A. Bonifacio, "Potential of Surface Enhanced Raman Spectroscopy (SERS) in Therapeutic Drug Monitoring (TDM). A critical review," *Biosensors*, vol. 6, no. 47, 2016.

[4] C. Zanchi, L. Giuliani, A. Lucotti, M. Pistaffa, S. Trusso, F. Neri, M. Tommasini, and P.M. Ossi, "On the performance of laser-synthesized, SERS-based sensors for drug detection," *Appl. Surf. Sci.*, vol. 507, no. 145109, 2020.

[5] C. Zanchi, A. Lucotti, M. Tommasini, M. Pistaffa, L. Giuliani, S. Trusso, and P. M. Ossi, "Pulsed laser deposition of gold thin films with long-range spatial uniform SERS activity," *Appl. Phys. A Mater. Sci. Process.*, vol. 125, no. 311, 2019.

[6] N. R. Agarwal, P. M. Ossi, and S. Trusso, "Driving electromagnetic field enhancements in tailored gold surface nanostructures: Optical properties and macroscale simulations," *Appl. Surf. Sci.*, vol. 466, pp. 19–27, 2019.

[7] B. J. Turkevich, P. Cooper Stevenson, J. Hillier, "A study of the nucleation and growth processes in the synthesis of colloidal gold," *Discuss. Faraday Soc.*, vol. 11, pp. 55-75, 1951.

[8] A. Macrelli, N. S. Villa, A. Lucotti, D. Dellasega, P. M. Ossi, and M. Tommasini, "Sensing the anti-epileptic drug Perampanel with paper-based spinning SERS substrates," *Molecules*, vol. 27, no. 30, 2022.

SPECIAL SESSION 23

Nanoscale Phononics : Energy Transport, Light-Matter Coupling, and Emerging Applications

19 contributions · pp. 1238–1271

Inelastic light scattering by metallic nanocrystals: symmetry, shape and chirality

Lucien Saviot[1,*]

[1]Université Bourgogne Europe, CNRS, Laboratoire Interdisciplinaire Carnot de Bourgogne ICB UMR 6303, 21000 Dijon, France

[*]Corresponding author: lucien.saviot@cnrs.fr

***Abstract*—Inelastic light scattering spectra of metallic nanocrystals depend strongly on shape, elasticity, and environment. To assign the observed features, numerical approaches are presented to calculate the vibrations by taking advantage of the symmetries including for core-shell nanocrystals and to calculate the spectra with application to chiral shapes.**

***Keywords*— metallic nanocrystals, inelastic light scattering, Rayleigh-Ritz approximation, finite element method**

I. Introduction

Acoustic vibrations of nano-objects can be observed using inelastic light scattering (ILS) measurements and provide information about the size, the shape, the material the nano-objects are made of and also their environment[1]. Complex Brillouin or low-frequency Raman spectra have been obtained recently for core-shell nanocrystals[2]. Numerical approaches to interpret such spectra are presented. The first one improves the convergence of the Rayleigh-Ritz (RR) method to calculate the vibrations of core-shell nanocrystals. The second one relies on the finite element method (FEM) to calculate the scattered intensities for nanocrystals having arbitrary shapes. They are validated by comparison with analytic calculations obtained for spherically symmetric systems.

II. Methods, Results and Discussion

The shape of the nanocrystals considered in this work are shown in Fig. 1.

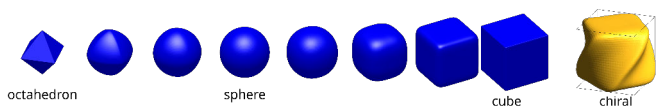

Fig. 1. Shapes modeled with superellipsoids allow variations from a tetrahedron to a sphere and to a cube. A twisted rounded cube is used as a model for a chiral gold nanocrystal (right).

Vibrations are calculated using the RR method by expanding the displacement on the $x^l y^m z^n$ basis of functions. It is very efficient provided volume integrals of the basis functions have analytic expressions and enables to take into account the symmetry of the nanocrystals and classify the vibrations according to their irreducible representations[3]. The convergence is poor for core-shell objects because the slope of the displacement changes at the inner interface. This is challenging to approximate with the power functions basis. To overcome this issue, functions suitable for the vibrations of the clamped core were added to the basis. Such functions vanish at the core-shell interface and in the shell. Calculations using this extended basis for a simple isotropic core-shell sphere for which an analytic solution exists show a significantly improved convergence[4].

ILS spectra were calculated using FEM by adapting an analytic approach developed for isotropic gold spheres[5]. We first reproduced these results with FEM. Then the shape of the gold nanocrystal was varied and revealed that nanospheres are very particular in this context. In the quasistatic approximation, the electric field inside the spherical gold nanocrystal is constant resulting in a vanishing ILS intensity. The non-zero intensity is due to deviations from the quasistatic approximation coming from the retardation effect[5]. For non-spherical shapes, the electric field inside the nanocrystal is not constant anymore even in the quasistatic approximation resulting in a quick increase of the ILS intensity as the shape deviate from a sphere[6]. Calculations for chiral shapes reveal a significant difference in the scattered intensities for right versus left incident circular polarizations.

Acknowledgments

This work has been supported by the EIPHI Graduate School (ANR-17-EURE-0002), CHIRNATIO (ANR-22-CE09-0007) and the HPC resources from DNUM CCUB (Centre de Calcul de l'Université de Bourgogne).

References

[1] H. Portalès, N. Goubet, S. Casale, X. Z. Xu, M. Ariane, A. Mermet, J. Margueritat, and L. Saviot, "Inelastic light scattering by long narrow gold nanocrystals: When size, shape, crystallinity, and assembly matter," *ACS Nano*, vol. 14, pp. 4395–4404, 2020.

[2] C. Vernier, "Étude de nanocristaux métalliques anisotropes par spectroscopies optique et vibrationnelle," Ph.D. dissertation, Sorbonne Université, 2024. [Online]. Available: https://theses.fr/2024SORUS300

[3] L. Saviot, "Free vibrations of anisotropic nano-objects with rounded or sharp corners," *Nanomaterials*, vol. 11, p. 1838, 2021.

[4] Sajana S., M. C. Marco de Lucas, and L. Saviot, "Rayleigh-Ritz approximation of the acoustic vibrations of clamped superquadrics – application to free core-shell objects," *Nanomaterials*, vol. 15, p. 1865, 2025.

[5] A. Girard, J. Lermé, H. Gehan, J. Margueritat, and A. Mermet, "Mechanisms of resonant low frequency raman scattering from metallic nanoparticle lamb modes," *The Journal of Chemical Physics*, vol. 146, 2017.

[6] L. Saviot and V. Laude, "Strong shape-dependent intensity of inelastic light scattering by gold nanocrystals," *Phys. Rev. B*, vol. 111, p. 205431, 2025.

Driving giant monochromatic THz strain waves in metal heterostructures by electronic pressure

Matias Bargheer [1,2]

[1] Institute of Physics and Astronomy, University of Potsdam, Potsdam, Germany
[2] Helmholtz-Zentrum Berlin, HZB, Berlin, Germany
*Corresponding author: bargheer@uni-potsdam.de

***Abstract*— Nanolayered metal superlattices are thermoacoustic metamaterials, in which we drive giant THz strain waves by ultrafast optical excitation across the visible spectrum. Electronic stress at metal-metal interfaces actuates the coherent phonons faster than the electron-phonon coupling time. Ultrafast x-ray diffraction probes the phonons beyond the optical skin depth.**

***Keywords*— metamaterials, terahertz strain, ultrafast x-ray diffraction, metal heterostructures.**

I. Introduction

High-frequency strain engineering is a central challenge for phononics at the nanoscale with broad application potential. Coherent strain control at terahertz (THz) frequencies in metal heterostructures has remained elusive because free electrons are expected to delocalize energy beyond the optical penetration depth, preventing rapid and efficient stress generation.

This presentation discusses robust and cost-effective metal–metal superlattices (SLs), where periodic repetitions of bilayers — each layer a few atoms thick — are deposited by sputtering, as thermoacoustic metamaterials that overcome this limitation.

II. Methods

Ultrafast x-ray diffraction (UXRD) is our key to material-specific nanoscale sensing of strain even in optically opaque metal heterostructures.[1-3]

For modeling we rely on density-functional theory for electron-phonon coupling within each material and two-temperature modelling (2TM) [4] coupled to the elastic wave equation for the spatio-temporal dynamics. We utilize the modular Python library udkm1Dsim that supports N-temperature models in layered structures - coupled to the one-dimensional wave equation. [5] Optical excitation is included via a matrix formalism and dynamical X-ray diffraction models include a temperature-dependent structure factor (Debye-Waller factor) to simulate the UXRD experiments.

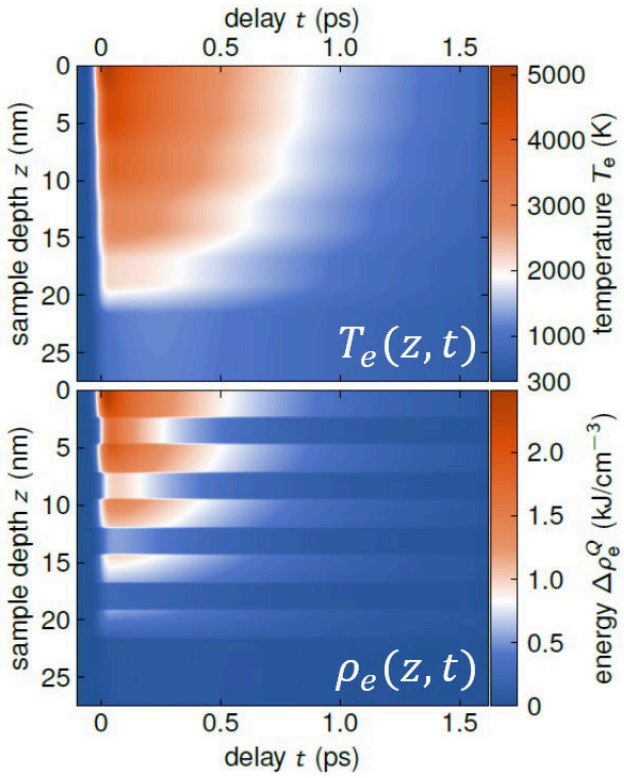

Fig. 1 Spatiotemporal temperature and energy density in a Pt/Cu superlattice with about 5 nm period. The electron temperature essentially shows rapid thermalization which leads to sharp localized features of the energy density in the electron system.

III. Results and Discussion

Our model fits UXRD data on various metal-metal superlattices (PtAu, FeAu and PtCu) at different pump wavelengths and fluences. The 2TM shows that after a nearly homogenous optical excitation, the energy deposited in the electron system spontaneously localizes in thin layers with a periodicity significantly below the skin depth (Fig. 1). While the electrons are significantly hotter than the phonons, electronic pressure acts on metal-metal interfaces, although the latter are transparent to electronic energy transport. Once

electron-phonon coupling sets in, very large temperature gradients can persist across the metallic interface for several tens of picoseconds.[6] Within the 2TM we rationalize heat transport without heating [2] and dominant energy transport via phonons at the nanoscale in noble metals [3].

The main ingredient for these observations is that metals with d-orbitals at the Fermi level (Pt, Pd, Ni, Fe, Co…) have a significantly larger thermally accessible electronic density of states, which increases the electronic heat capacity and the electron phonon coupling. It is the combination of such materials with nobler metals such as Au and Cu, which leads to the counterintuitive phenomena, which we uniquely cross-check via the material specific ultrafast X-ray diffraction.

We explain how monochromatic THz phonons can be actuated by electronic pressure, although the electron-phonon coupling time is longer than the period of the generated THz phonon. The presentation reports 1 THz strain waves with a 1% strain amplitude.

IV. Conclusion

We establish electron pressure as an engineerable, dominant actuation mechanism in metallic metamaterials, in which THz strain can be tailored by the pitch and the constituent materials of the superlattice structure. This will enable new applications such as ultrafast strain-mediated control of functional materials.

Acknowledgments

We acknowledge funding by the Deutsche Forschungsgemeinschaft (DFG, German Research Foundation) – CRC/SFB 1636 – Project ID 510943930 - Project No. A01 and Z02 and TRR 227 – Project-No. 328545488, projects A10 and MF.

References

[1] M. Mattern, A. von Reppert, S. P. Zeuschner, M. Her-zog, J.-E. Pudell, and M. Bargheer, Photoacoustics 31, 100503 (2023).
[2] J. Pudell, M. Mattern, M. Hehn, G. Malinowski, M. Her-zog, and M. Bargheer, Advanced Functional Materials 30, 2004555 (2020)
[3] M. Herzog, A. von Reppert, J.-E. Pudell, C. Henkel, M. Kronseder, C. H. Back, A. A. Maznev, and M. Bargheer, Advanced Functional Materials 32, 2206179 (2022)
[4] S. I. Anisimov, B. L. Kapeliovich, and T. L. Perelâ€™man, Journal of Experimental and Theoretical Physics 39, 375 (1974).
[5] D. Schick, Computer Physics Communications 266, 108031 (2021)
[6] F. Stete, S. Kesarwani, C. Ruhmlieb, S. H. C. Askes, F. Schulz, M. Bargheer, and H. Lange, Nature Commu-nications 16, 8168 (2025).

Modeling the Acousto-Plasmonic Coupling: Raman Energy Density Framework

Nicolas Large[1,*]

[1]Department of Physics and Astronomy, University of Texas at San Antonio, United States

*Corresponding author: nicolas.large@utsa.edu

***Abstract*— We present a theoretical study of the interactions between confined acoustic vibrations and localized surface plasmons in metallic nanoparticles. We introduce a new physical quantity, the Raman energy density, which is a local quantity that serves as a tool for the study of Raman scattering mediated by plasmons in nanoparticles.**

***Keywords*— plasmonic nanoparticles, localized surface plasmons, acoustic vibrations, acoustic Raman scattering, Raman energy density, computational modeling.**

I. Introduction

Multifunctional nanomaterials are of high interest to a wide range of technological applications in optoelectronics, biomedicine, energy, sustainability, optics, photonic devices, quantum sensing, quantum computing, and applied chemistry. The development of such materials relies critically on a deep understanding of the relationships between structure, interfaces, and physical properties at the nanoscale, where collective excitations, confinement, and non-equilibrium effects dominate the response of matter. The interesting properties of LSPs and their coupling to phonons also offer a unique platform for unconventional light manipulation pathways. LSPs can be temporally modulated by acoustic phonons naturally present in nanomaterials and their environment [1]. Such modulation can be used to increase detection and sensing accuracy of plasmonic-based nanosensors. Acoustic Raman scattering, which directly probes acoustic phonons in nanomaterials, is a very effective, high precision, non-invasive technique for nanometrology.

II. Methods

Here, the transition rate associated with the Raman scattering by acoustic phonons is calculated using a Fermi golden rule where we introduce a new physical quantity: the Raman energy density (RED; Fig. 1) [2]:

$$U_R(r,\omega_i,k_i,\omega_f,k_f) = -\varepsilon_0\chi(r)\left[\frac{V_{DP}}{\hbar\omega_{ex}-\hbar\omega_{ib}}\nabla\cdot u(r)\right] \times E_f(r)\cdot E_i(r) - \varepsilon_0\chi(r)E_f(r)\cdot\left[E_f(r)\cdot E_i(r)\right] \quad (1)$$

where $E_i(r)$ and $E_f(r)$ are the local electric fields associated to the LSP before and after the interaction with the acoustic phonons, respectively. $\chi(r)$ is the electric susceptibility of the metallic NP and is defined using a size-corrected Drude model, $\hbar\omega_{ib}$ is the interband transition threshold, V_{DP} is the deformation potential, and $\nabla\cdot u$ is the divergence of the displacement field obtained from elastodynamic simulations.

The first term in eq. (1) is called the deformation potential coupling mechanism or volume mechanism. It describes the modulation of the electric susceptibility by the acoustic phonons. A change in a NP volume results in a change in the electronic band structure *via* the deformation potential. The effect of the electric susceptibility modulation on the intraband transitions is negligible in the visible range because their excitations are in the infrared range. Nevertheless, the interband transition modulation contributes to the volume mechanism because the interband transitions lay in the UV range, close to the LSP. Therefore, this term could be negligible in metals but not in semiconductors. The second term in eq. (1) is the surface orientation coupling mechanism. Contrary to the volume mechanism, the surface mechanism is the dominant contribution to the Raman scattering in metals [1].

This framework allows for rigorously calculate the acoustic Raman scattering spectra of any nanostructured material:

$$\sum_{vib}\frac{2\pi}{\hbar^2}\left|\int U_R^{vib}(r)\,dV\right|^2\frac{\Gamma_{vib}}{\left(\hbar\omega_{ex}-\hbar\omega_{vib}\right)^2+\left(\Gamma_{vib}/2\right)^2}\cdot\frac{1}{e^{\left(\hbar\omega_{ex}/k_BT\right)}} \quad (2)$$

III. Results and Discussion

Here, we present a theoretical investigation of the interactions between confined acoustic vibrations and LSPs (Fig. 1, left) in the framework of resonant acoustic Raman scattering. We express the Raman scattering process in the framework of the Raman energy density (Fig. 1, center). Similarly to the Raman-Brillouin electronic density (RBED) introduced for semiconductors [3–4], this new physical quantity is used as a theoretical tool for the interpretation of resonant Raman scattering mediated by LSPs in metallic nanoparticles. The RED represents the electromagnetic energy density excited by the Raman probe and modulated by the acoustic vibrations of the nanoparticle. We show that,

similarly to the local density of optical states (LDOS) and the RBED, the RED is a local physical quantity that can be mapped in the near-field region. It provides a clear picture of the interaction between LSPs and acoustic vibrations which give rise to inelastic Raman scattering measurable in the far-field. Here, we use the newly introduced RED concept to investigate elastic (an)isotropy effects and calculate the Raman selection rules of spherical nanoparticles in a dielectric environment (Fig. 1, right).

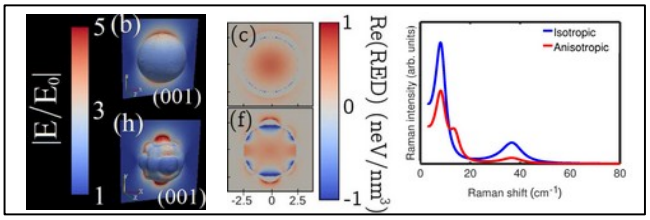

Fig. 1 Left: Isotropic (l=0) and Anisotropic (A1g) breathing acoustic mode of a AuNP modulating the near electric field induced par the dipolar localized surface plasmon (LSP). Center: Raman energy density (RED) resulting from the interaction of the l=0 and A1g vibration mode with the dipole LSP. Right: Calculated acoustic Raman spectra for the isotropic and anisotropic nanoparticles.

Lastly, the RED formalism is applied to nanoparticle-on-mirror (NPoM) nanocavities, which represent extreme cases of electromagnetic confinement [5]. In these systems, molecules confined within sub-nanometer gaps experience enormous field enhancement and strong optomechanical coupling. Using combined electrodynamic and elastodynamic simulations in the RED framework, we demonstrated that the dominant low-frequency Raman background arises from Lamb-type shear modes confined within the molecular layer (Fig. 2). These terahertz vibrational modes were previously unidentified and are comparable in strength to conventional molecular SERS peaks.

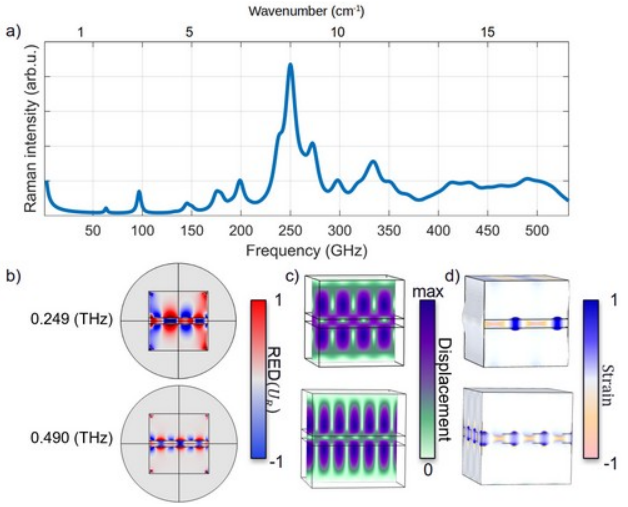

Fig. 1 Modelling of surface acoustic waves in nanogaps. (a) Raman spectrum computed from over 800 vibrational modes in the Au-BPT-Au system. (b) RED calculated for the two Lamb modes at 0.249 and 0.490 THz . Normalized displacement fields and strain are shown in (c,d) respectively. In (d) FEM model consists of a 1.1 nm BPT layer sandwiched between two gold slabs, each of side 5nm.

IV. Conclusion

Similar to the RBED previously introduced for semiconductors, the RED is used as a theoretical tool for the interpretation of resonant Raman scattering mediated by LSPs in metallic nanostructures. Analogous to the LDOS, it represents the electromagnetic energy density excited by the Raman probe and modulated by acoustic phonons. It is a local quantity mapped in the near-field which provides a clear picture of the acousto-plasmonic interaction involved in the far-field Raman scattering. It can predict the Raman (in)active modes, thus providing the Raman selection rules and open the door to study effects such as vibrational transfer, acouto-plasmonic hot-spots, acoustic SERS, and symmetry breaking will be investigated.

Acknowledgments

This work received partial financial support from the U.S. Office of Naval Research (ONR) under Grant No. N00014-21-1-2729 and computational support from UTSA's HPC cluster ARC operated by University Tech Solutions.

References

[1] Large, N.; Saviot, L.; Margueritat, J.; Gonzalo, J.; Afonso, C. N.; Arbouet, A.; Langot, P.; Mlayah, A.; Aizpurua, J. "Acousto-Plasmonic Hot Spots in Metallic Nano-Objects". Nano Lett. 2009, 9 (11), 3732–3738.

[2] Montaño-Priede, J. L.; Mlayah, A.; Large, N. "Raman Energy Density in the Context of Acoustoplasmonics". Phys. Rev. B 2022, 106 (16), 165425.

[3] Mlayah, A.; Huntzinger, J.-R.; Large, N. "Raman-Brillouin Light Scattering in Low-Dimensional Systems: Photoelastic Model versus Quantum Model". Phys. Rev. B 2007, 75 (24), 245303.

[4] Large, N.; Huntzinger, J. R.; Aizpurua, J.; Jusserand, B.; Mlayah, A. "Raman-Brillouin Electronic Density in Short Period Superlattices." Phys. Rev. B 2010, 82, 75310–75318.

[5] Boehmke, A.; Bar-David, J.; Sibug-Torres, S.; de Nijs, B.; Ferere, A. B.; Large, N.; Baumberg, J. J. Tracking Molecular Shear at Metal Surfaces Using Enhanced Lamb Wave Scattering in Plasmonic Nanocavities. Nano Lett. 2025, 25 (44), 15817–15823.

Energy transfer from hot holes to phonons in photoexcited Germanium: ultrafast heating of Raman-active modes

Jelena Sjakste[1,*], Raja Sen[1], Nathalie Vast[1]

[1] Laboratoire des Solides Irradiés, CNRS, CEA, Ecole Polytechnique, IP Paris, F-91128 Palaiseau, France

*Corresponding author: jelena.sjakste@polytechnique.edu

***Abstract*— We present our recent collaborative work on coupled hole and phonon dynamics in photoexcited germanium, which was studied by time-resolved Raman spectroscopy as well as by DFT calculations. Our time-dependent model based on DFT data can describe the observed changes in temperature of Raman-active optical modes on picosecond time scale.**

***Keywords*— electron-phonon interaction, DFT, Raman, semiconductors, phonon-phonon interaction, ultrafast**

I. Introduction

In recent years, progress in time-dependent computational approaches which couple density functional theory (DFT) – based description of the electron-phonon and phonon-phonon scattering rates with the time-dependent Boltzmann transport equations (t-BTEs) as well as progress in time-resolved spectroscopy experiments allowed unprecedented insight into coupled dynamics of hot carriers and phonons [1]. In this paper, we discuss our recent collaborative work on coupled hole and phonon dynamics in photoexcited germanium, which was studied by time-resolved Raman spectroscopy as well as by DFT calculations coupled with t-BTEs in two-temperature approximation.

II. Methods

From the experimental side, novel developments by the team of University of Basel [2] allowed to observe the temperature dynamics of Raman-active optical phonon modes in photoexcited Ge with unprecedented accuracy, and to quantitatively describe the phonon temperature rise due to the transfer of energy from photoexcited carriers, as well as subsequent temperature decay. From the theoretical side, in order to explain the observed dynamics, we have coupled DFT-based description of the carrier-phonon and phonon-phonon interactions with the t-BTEs for carriers and phonons [2].

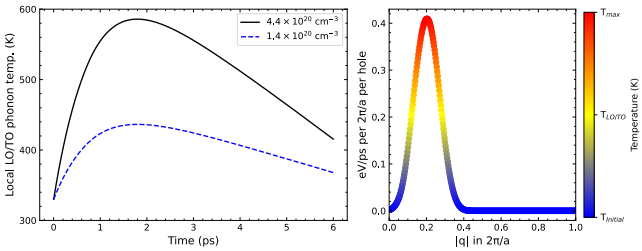

Fig. 1 From [2]. Dynamics of temperature rise of TO/LO modes calculated with time-dependent two-temperature model for carriers and phonons, coupled with DFT-based description of the hole-phonon and phonon-phonon coupling in Ge. Right: Hole-phonon energy transfer rate calculated with DFT as a function of phonon wavevector, which illustrates the localization in the Brillouin zone of the overheated optical modes. Left: Calculated local temperature rise of Raman optical modes due to hole-phonon interaction, for two values of hole densities. Subsequent decay into acoustical phonons is modeled with a calculated phonon-phonon decay rate of 2.5 ps.

III. Results and Discussion

According to the results of our calculations, the temperature rise of Raman optical phonons is attributed to the photoexcited hole dynamics: the dominant scattering process for photoexcited holes is intravalley scattering with optical phonons, that leads to the heating of Raman-active optical modes. In contrast, the dynamics of photoexcited electrons are mostly determined by the intervalley scattering [1], which explains why photoexcited electrons do not influence the dynamics of Raman-active optical modes. As seen in the right panel of Fig. 1, photoexcited holes transfer their energy only to phonons localized close to the Brillouin zone center, producing a strong rise in the local phonon temperature. The left panel of Fig. 1 shows our calculated phonon temperature dynamics. The calculated rise is found to occur on ps scale in agreement with experiments. The subsequent temperature decay with 2.5 ps rate is due to the decay of optical phonons into acoustic ones, also in very good agreement with experiments.

ACKNOWLEDGMENTS

. We acknowledge financial support from the ANR DragHunt project ANR-24-CE50-3505. Computer time has been granted by the national centers GENCI-CINES and GENCI-TGCC (Project 2210) and GENCI-IDRIS (Project 7320) and by Ecole Polytechnique through the 3Lab computing cluster.

REFERENCES

[1] J. Sjakste, R. Sen, N. Vast, J. Saint-Martin, M. Ghanem, P. Dollfus, F. Murphy-Armando, J. Kanasaki, J. Chem. Phys 162, 061002 (2025)
[2] G. Raciti, B. Abad, R. Dettori, et al. " Unraveling Energy Flow Mechanisms in Semiconductors by Ultrafast Spectroscopy: Germanium as a Case Study." *Adv. Sci.* (2026): e15470.

Unveiling Acoustic Phonon Dynamics via Time-Resolved Brillouin Spectroscopy of optophononic Resonators

Carlos Montenegro[1*], Elham Mehdi[1], Sandeep Sathyan[1], Edson Rafael Cardozo de Oliveira[1], Isabelle Sagnes[1], Martina Morassi[1], Aristide Lemaître[1], Norberto Daniel Lanzillotti-Kimura[1]

[1]Université Paris-Saclay, CNRS, Centre de Nanosciences et de Nanotechnologies, 10 Boulevard Thomas Gobert, 91120 Palaiseau, France
*Corresponding author: carlos.montenegro@c2n.upsaclay.fr

Keywords -acoustic phonons, nanophononic platform, Brillouin scattering

Abstract: The growing interest in acoustic phonon engineering in microstructures is driven by applications in optoelectronics, solid-state simulations, and quantum technologies [1]. In these platforms, the physical properties are governed by the coupled dynamics of charge and heat carriers. Therefore, for the manipulation of confined sub-THz acoustic phonons, it is crucial to understand the mechanisms governing the energy relaxation of photoexcited charge carriers. Brillouin spectroscopy is a powerful tool for probing acoustic phonon dynamics; however, it faces significant experimental challenges in ultrafast pump–probe configurations. In particular, detecting scattered signals spectrally close to the excitation laser is limited by the finite spectral bandwidth of ultrafast laser pulses, while the measurable signal corresponds to minute variations at extremely low photon fluxes.

In this work, we present advancements in an experimental scheme for time-resolved Brillouin spectroscopy in GaAs/AlAs-based Fabry–Perot optophononic resonators using single-photon detectors (SPDs). Our approach exploits a double optical resonance condition [2,3] in semiconductor planar cavities to simultaneously enhance Brillouin scattering excited by two pulsed laser sources. This scheme enables efficient spectral filtering of both Brillouin signals, making it compatible with single-photon detection experiments. The proposed setup provides a versatile platform for exploring the dynamics of confined phonons in engineered optophononic microresonators.

[1] Priya, E.R. Cardozo de Oliveira, N.D. Lanzillotti-Kimura, Perspectives on high-frequency nanomechanics, nanoacoustics, and nanophononics, Appl Phys Lett. 122 (2023).

[2] M. Trigo, A. Bruchhausen, A. Fainstein, B. Jusserand, and V. Thierry-Mieg, "Confinement of Acoustical Vibrations in a Semiconductor Planar Phonon Cavity", Physical Review Letters 89(22), (2002).

[3] A. Rodriguez, P. Priya, O. Ortiz, P. Senellart, C. Gomez-Carbonell, A. Lemaître, M. Esmann, and N. D. Lanzillotti-Kimura, "Fiber-based angular filtering for high-resolution Brillouin spectroscopy in the 20-300 GHz frequency range," Opt. Express 29, 2637-2646 (2021)

Plasmon-Enhanced Brillouin Light Scattering Investigations of Acoustoplasmonic Metasurfaces

Thomas Vasileiadis

Faculty of Physics and Astronomy, Adam Mickiewicz University,
Uniwersytetu Poznańskiego 2, Poznan, 61-614, Poland.
thomas.vasileiadis@amu.edu.pl

***Abstract*— Acoustoplasmonic metasurfaces (APMs) combine plasmonic and phononic resonances to enhance optomechanical interactions. This talk will present APMs offering plasmon-enhanced Brillouin light scattering (BLS) and optomechanics for propagating surface acoustic waves. Plasmon-enhanced BLS can result from plasmonic coupling between adjacent nanostructures or colocalization of plasmonic and acoustic fields on nanostructured surfaces.**

***Keywords*— metasurfaces, plasmonics, phononics, Brillouin light scattering.**

I. Introduction

Plasmons enhance Raman scattering by molecular vibrations, and enable molecular optomechanics in nanocavities. However, less emphasis has been given to plasmon-enhanced optomechanics for GHz acoustic phonons. For confined GHz vibrations, plasmon-enhanced Brillouin light scattering (BLS) and optomechanics can arise from plasmonic coupling between metallic nanoparticles [1]. Plasmon-enhanced BLS from surface acoustic waves (SAWs) requires nanostructured surfaces with plasmonic and phononic resonances, *i.e.*, acoustoplasmonic metasurfaces (APMs).

II. Methods

Plasmons, SAWs, and optomechanics were studied with finite element method calculations. The measured BLS intensity (I) depends on the optomechanical coupling constant, g_{OM}, according to $I \propto |g_{\mathrm{OM}}|^2$. The momentum-resolved, backscattering BLS spectra were recorded on- and off-resonance with the plasmons, using 660 and 532 nm wavelength of light (λ), respectively. The probed phonon wavenumber parallel to the APM surface ($k_{||}$) was $k_{||} = 4\pi \sin\theta/\lambda$, where θ is the angle of incidence.

III. Results and Discussion

Bottom-up synthesized APMs consisted of self-assembled Au nanoparticles (**Fig. 1a**, Ref. [2]). Top-down synthesized APMs consisted of 30 nm-thick Au, grown on a thermal SiO_2-on-Si wafer, and patterned with a square lattice of holes (**Fig. 1b**, Ref. [3]). The phonon-mode specific enhancement was captured with momentum-resolved BLS on- and off-resonance with the plasmons. Plasmonic coupling of nanoparticles enhanced low-frequency vibrational coupling modes, while colocalization of plasmons and SAWs near nanohole edges enhanced high-frequency modes (**Fig. 1c**) due to the moving interface effect.

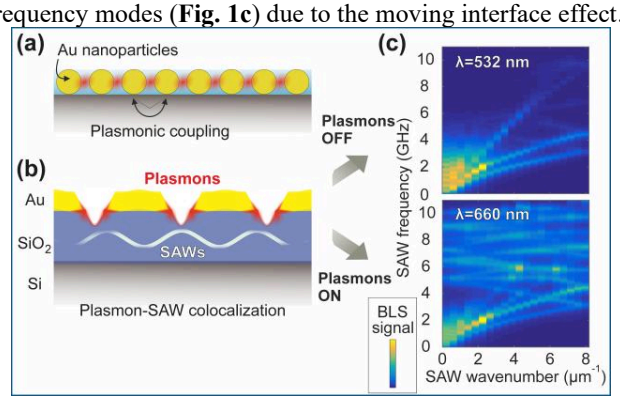

Fig. 1 Metasurfaces were synthesized with self-assembled plasmonic nanoparticles (a) or by perforating a Au/SiO_2/Si surface with nanoholes (b). In the latter case, the mode-resolved BLS (c) revealed enhanced optomechanical coupling of high-frequency SAWs.

IV. Conclusion

Electromagnetic field confinement on APMs enables the control of optical beams with mechanical vibrations [2],[3]. Our work paves the way for developing plasmon-enhanced optomechanical sensors and modulators operating at GHz frequencies.

Acknowledgments

This project was supported by the National Science Center (NCN) of Poland with the SONATA grant no. UMO-2021/43/D/ST3/02526. The speaker acknowledges the collaboration with B. Graczykowski and G. Fytas (AMU, MPG), R. J. Macfarlane (MIT) and B. D. Rouhani (ULille).

References

[1] A. Girard, H. Gehan, A. Mermet, C. Bonnet, J. Lermé, A. Berthelot, E. Cottancin, A. Crut, and J. Margueritat, "Acoustic Mode Hybridization in a Single Dimer of Gold Nanoparticles," Nano Letters vol. 18, pp. 3800–3806, 2018.

[2] T. Vasileiadis, A. K. Dhiman, A. Noual, N. Sbalbi, M. Ye, R. J. Macfarlane, B. Graczykowski, and G. Fytas, "Acoustoplasmonic Metasurfaces Based on Polymer-Grafted Nanoparticles," Nano Letters vol. 25, pp. 12351–12359, 2025.

[3] A. K. Dhiman, P. Graczyk, H. Dongre, K. Zaleski, B. D. Rouhani, B. Graczykowski, and T. Vasileiadis, "Metasurfaces with Enhanced Optomechanical Coupling through the Co-localization of Plasmonic and Acoustic Fields," ACS Nano 2026 (accepted).

Nanostructuration for Ultra-High Frequency Acoustic Wave Emission and Detection using Femtosecond Laser Pulses

Arnaud Devos*

1IEMN, UMR 8520 CNRS, Avenue Poincaré BP 69, 59652 Villeneuve d'Ascq, France
*Corresponding author: Arnaud.Devos@iemn.fr

***Abstract*— Picosecond acoustics uses ultrafast lasers to generate and detect ultra-high-frequency acoustic waves, which are ideal for thin-film characterization, but is inherently limited to longitudinal modes. To overcome this limitation, we have developed two distinct nano-structuring approaches that enable transverse wave generation, along with adapted optical detection schemes.**

***Keywords*—picosecond acoustics, transverse waves, phononic crystals.**

I. Introduction

Picosecond acoustics has been widely used to study thin film elasticity, hypersound attenuation, and adhesion of thin films to substrates[1-3]. A major limitation of the technique is its restriction to only longitudinal waves. And this is a problem for accessing to elasticity since it is governed by several constants that require the measurement of speed of sound of several types of waves. Previous work has shown that it is sometimes possible to get around this limitation[4], but always in specific sample configurations. In particular, it was impossible to generalize to thin-film samples on silicon, the basic geometry for applications.

In recent years, we have explored two approaches to overcoming this difficulty. One approach involves using a 2D phononic crystal deposited on top of the sample to be characterized, which acts as a surface acoustic wave (SAW) transducer[5]. The other approach is based on using a thin, nanostructured metal film made of tilted columns, which allow for the direct emission of bulk transverse waves[6]. We examine both approaches in the following, discussing the particular optical detection needed in each case.

II. 2D Phononic Crystals as SAW Transducers

Our initial motivation was to study the elastic properties of artificial crystals made of 2D ensemble of nanocubes. When illuminated by a laser pulse, two types of acoustic mode are expected: individual modes of the cubes which originate from the eigenmodes of the isolated cube. As the cubes are organized in a lattice, each of these modes becomes a band that is more or less flat depending on the coupling between dots [7]. A second class of modes is also expected, with a much more lower frequency. We elaborated such crystals made with 200 nm cubes with different lattice symmetries and parameters (see Fig. 1), and studied the acoustic modes in the time-domain. In particular, we demonstrated that these phononic crystals act as SAW transducers: the low-frequency or collective modes are SAWs emitted in various directions, as determined by the crystal symmetry. In the time domain, several frequencies are detected and we show that they correspond to the same SAW mode but propagating in different directions. This is illustrated in Fig. 1, in which we plot the measured frequencies for several lattice parameters a. As these frequencies correspond to the same mode, but are emitted in different directions, remarkable ratios exist between them. By measuring the response of the sample for different lattice parameters, it is possible to build the dispersion curve from which the speed of sound of the Rayleigh mode can be deduced in case of an infinitely extended lattice, in other words, the Rayleigh of the sample without cubes. By performing an usual longitudinal measurements on the same layer, we obtain two sound velocities from which we deduce the Young modulus and Poisson ratio of the film[5].

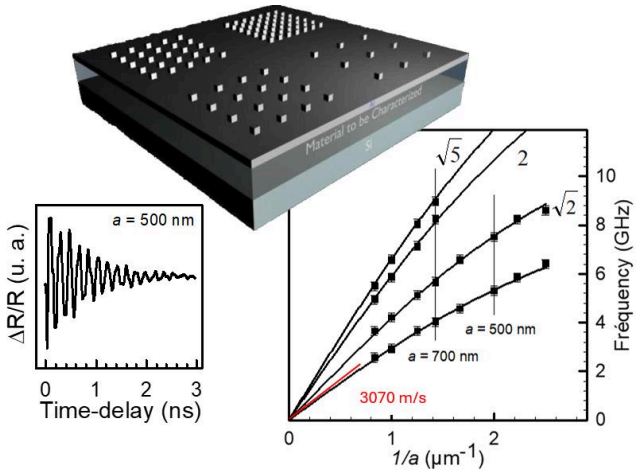

Fig. 1 Artificial crystals made of 200 nm Al nanocubes with various lattice parameters a deposited on top of a silica layer. Such a nanostructuration allows the emission/detection of very high

frequency surface acoustic waves.

This protocol requires extensive and costly sample preparation, as it uses electronic beam lithography. Indeed, the lattice parameter must be as small as possible in order to confine the SAW in the layer to be characterized, thus avoiding the need for simulation to eliminate the substrate contribution. Despite this, the technique has known quite a great success as measuring the Young modulus and Poisson ratio on layer as thin as 150 nm is very challenging.

To extend the process to thinner and thinner films, crystals with smaller and smaller lattice parameters are required. If the same technology can be used to prepare smaller dots (typically 50 nm) and arranged in a more denser lattice (typically spaced by 100 nm), the usual optical setup cannot detect a signal. Indeed, optical detection of SAWs is limited by the probe wavelength, which must be smaller than or comparable to the lattice step. One way to characterize thinner films is therefore to use shorter wavelengths. This is what we did by exploring the capabilities of picosecond acoustics in the middle UV using a probe beam obtained by tripling the femtosecond laser source (around 266 nm)[8]. Then, we demonstrated that it is possible to overcome the limitation related to the diffraction of the probe light by the lattice, by using an interferometric detection[9]. In that case, SAW as high as 25 GHz have been measured in a 50 nm AlN film.

III. Nanostructured Metal Transducer

In a second approach, a thin, nano-structured metal film consisting of tilted columns is deposited on top of the layer to be characterized. Originally, our goal was to focus on the characterization of a thin, transparent film deposited on silicon.

Thanks to its columnar geometry, the laser light excites longitudinal and bulk transverse waves in the metal film. Both types of wave are detected in the transparent layer using the Brillouin oscillation mechanism. Several conditions are required for this to happen. Firstly, the nanostructured metal film must be thin enough to allow the probe light to penetrate the sample. Secondly, in order to detect transverse wave, an optical setup must be modified to be sensitive to any change in the probe polarization. Fig. 2 illustrates this in the case of a 3 µm thick SiC layer grown on Si(100).

After t=0, acoustic waves are emitted from the top metal film and penetrate the transparent layer. As the metal film is sufficiently thin, the propagation can be detected by the probe light through an acousto-optic mechanism, known as the Brillouin oscillation. At around 300 ps, the longitudinal pulse reaches the Si substrate and the typical Si signature is detected[9]. The Fourier transform of the signal between 0 and 300 ps reveals two peaks: the peak around 150 GHz corresponds to the longitudinal mode and the one below 120 GHz corresponds to the transverse frequency.

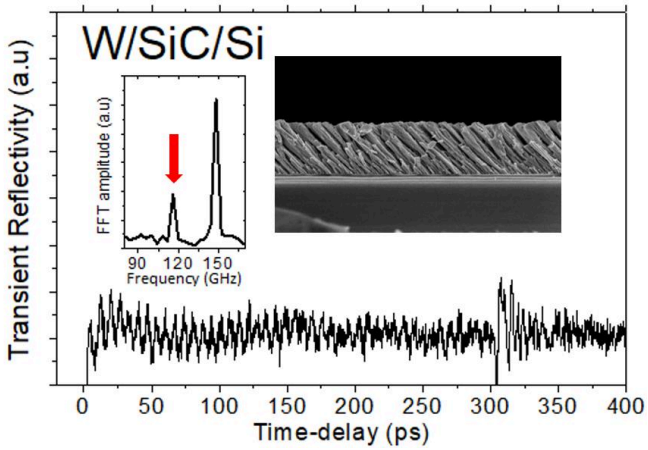

Fig. 2 Time-resolved reflectivity measured on a W/SiC/Si sample, where W is a thin nano-structured Tungsten film The texture of such a metal film is illustrated in the SEM image (400 nm thick W).

We have demonstrated this capability in a wide variety of transparent materials, using different metals, such as Ti, Mo, and W. One major advantage of this approach is that the sample preparation can be made using a standard deposition tool. Although the protocol was originally developed for thin transparent film, it can be easily extended to opaque films, in which no Brillouin oscillation can be detected. In that case, the transverse time of flight in the layer is measured by detecting a returning transverse echo in the nanostructured film itself.

IV. Conclusion

We have developed two approaches to extend picosecond acoustic characterization to transverse waves, combining specific sample preparations with modifications of the optical detection. Using 2D artificial crystals as SAW transducers. Optical detection in this case requires a short wavelength or an interferometric detection. Using a nanostructured metal film composed of tilted columns, which is capable of emitting both longitudinal and transverse bulk waves. Detection must be adapted to be sensitive to change in light polarization.

References

[1] C. Thomsen, J. Strait, Z. Vardeny, H. J. Maris, J. Tauc, and J. J. Hauser, Phys. Rev Lett. 53, 989–992 (1984).
[2] A. Devos, Ultrasonics 56, 90 (2015).
[3] J. Costa Dantas Faria, P. Garnier, and A. Devos, Appl. Phys. Lett. 111, 243105 (2017).
[4] T. Pezeril, Opt. Laser Technol. 83, 177 (2016).
[5] P.A. Mante, J.F. Robillard, and A. Devos, Appl. Phys. Lett. 93, 071909 (2008). DOI: 10.1063/1.2975171.
[6] A. Chargui, N. Martin, G. Ferro, and A. Devos, Appl. Phys. Lett. 125, 192202 (2024) https://doi.org/10.1063/5.0228331.
[7] A. Devos, Chapter 7 in Handbook of Nanophysics, Volume 1, Principles and Methods, edited by Klaus D. Sattler, CRC Press, Taylor& Francis Group.
[8] S. Ayrinhac, A. Devos, A. Le Louarn, P.-A. Mante, and P. Emery, Optics Letters 35, 20, 3510 (2010).
[9] A. Devos, S. Sadtler, P.-A. Mante, A. Le Louarn, and P. Emery, Applied Physics Letters 105, 231905 (2014).
[10] A. Devos and R. Cote, Physical Review B, 70, 12, 125208 (2004).

Thermal Metamaterial Design for Phonon Heat Management at Low Temperature

Boris Brisuda[1], Jon Canosa Diaz[2], Thierry Crozes[1], Jean-François Robillard[2], Olivier Bourgeois[1,*]

[1]Institut NEEL, CNRS and UGA, 25 avenue des Martyrs, 38042 Grenoble, France
[2]IEMN and JUNIA, avenue Henri Poincaré, 59650 Villeneuve d'Ascq, France
*Corresponding author: olivier.bourgeois@neel.cnrs.fr

Abstract **This study explores nanoscale phonon (heat) flux control—critical for quantum tech and thermal management. Using a nanostructured SiN ribbon with staggered triangles, we demonstrated thermal rectification at 900 mK; the heat flow being favored toward triangle tips which seems to be related to ballistic phonon flow in anisotropic structures.**

Keywords**- thermal metamaterials, phonons, thermal bridge method, nanostructuration, phononic crystal, thermal rectification.**

I. Introduction

The manipulation of phonon fluxes (or heat management) is becoming essential in many important situations like energy harvesting using thermoelectric materials, evacuation of heat flows, thermal balance in qubits etc… In all these cases, controlling the flux heat through phonon flow is mandatory, especially at the nanoscale. Here, we will illustrate this through many experiments where the transport of phonons is measured at the nanoscale. Indeed, using advanced nanostructuration, thermal transport is studied in nanowires, nanomembranes, 2D materials or thermal metamaterials, one of the major challenges of the current nanoscale energy management from room temperature to very low temperature (down to 50 mK).

II. Sample design

The studied systems are designed in such a way that temperature gradients can be applied across a nanostructured sample in both directions. The idea of the thermal bridge experiment is to allow establishing temperature differences across a nanostructured sample. As shown in the Fig. 1, the suspended thermal bridge is shown with the sample connecting the two platforms. The major advantage of the two symmetric platforms is to ensure the ability to establish identical temperature difference across the sample but with an opposite sign to probe thermal rectification [1]. The sample is an array of staggered triangles of the following edge dimension of 300 nm.

In order to perform very sensitive measurement of temperature, highly sensitive niobium nitride thermometry is used with two NbN transducers installed on each membrane [2]; this will help to precisely control the temperature profile over each platform [3].

III. Thermal bridge methods

Our methodology for measuring the heat rectification consists in comparing the two heat fluxes in forward (a->b) and reverse (b->a) directions for identical amplitude of temperature difference across the sample (see Fig. 2). The rectification ratio is given by this equation:

$$\eta = \frac{\Phi_{sample}^{a\to b} - \Phi_{sample}^{b\to a}}{\Phi_{sample}^{a\to b}}$$

Where $\Phi_{sample}^{a\to b}$ the larger flux and $\Phi_{sample}^{b\to a}$ the smaller flux to ensure that η will be between 0 and 1. The determination of the heat flux through the nanostructured sample requires precise measurement of the thermal conductance to heat bath.

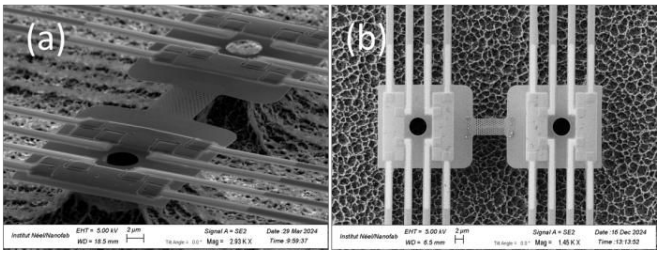

Fig. 1 Suspended double platform and nanostructured sample. On each platform two transducers allow the fine control of temperature over a broad temperature range from 50 mK to 5 K.

These measurements have been done at very low temperature where thermal properties of (nano)materials become of significant interest [3,4]. The ratio between the thermal flux flowing through the sample and the one flowing to the heat bath

is on the same order of magnitude, the ideal range for optimized sensitivity.

IV. Results and Discussion

The experimental results obtained at 900 mK are presented in Fig. 2 where the heat flux is represented as a function of the temperature difference between the two membrane temperatures T_1 and T_2. In the case of the red squares, the temperature gradient has been established from a to b. As for the measurement of black dots the temperature gradient has been reversed for b to a. When comparing the two heat fluxes with opposite directions, we can clearly see the differences; the flux in the a to b direction being much larger than the one from b to a direction. The flux pointing to the tip of the triangle is favored, demonstrating thermal rectification in such dissymmetric phononic crystal. The rectification factor η is between 0.1 and 0.2.

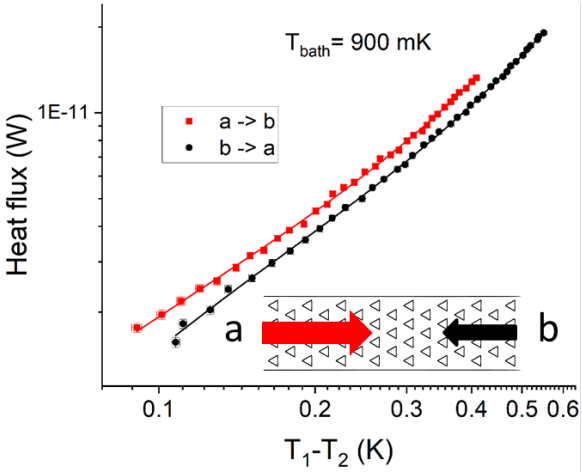

Fig. 2 Heat flux measured as a function of the direction of temperature difference at 900 mK bath temperature.

The rectification effect may arise not only from the asymmetry of the sample but also from inherent non-linearities in the systems, like the temperature variation of all the thermal properties of the sample (heat capacity and thermal conductance).

V. Conclusion

We have set-up a thermal bridge experiment to probe potential thermal rectification effect in nanostructured ribbons of SiN. We have demonstrated thermal rectification at 900 mK in a thermal metamaterial in the limit of phonon ballistic limit. The sample is a nanostructured SiN ribbon with an array of staggered triangles. The phonon flow is favored in the a to b direction pointing to the tip of the triangles. More investigations are required to clearly demonstrate the origin of the phenomena, especially by measuring over a broader temperature range. We also plan to investigate theoretically this effect by modelling the phonon transport is such nanostructure at very low temperature in the ballistic regime.

Mastering thermal management at the nanoscale and at cryogenic temperature is of major importance for all the enabling quantum technologies to ensure proper thermalization process [5-7].

Acknowledgments

The authors acknowledge support from ANR (Agence Nationale de la Recherche) through project HANIBAL ANR-20-CE42-0019-01. We acknowledge also technical supports from Institut NEEL and IEMN especially from the technical pools of electronics, cryogeny and mechanics, nanofabrication facilities.

References

[1] A. Tavakoli, J. Maire, B. Brisuda, T. Crozes, J.F. Motte, L. Saminadayar, E. Collin and O. Bourgeois, *Experimental evaluation of thermal rectification in a ballistic nanobeam with asymmetric mass gradient*, Sci. Rep. **12**, 7788 (2022).

[2] T.D. Nguyen, A. Tavakoli, S. Triqueneaux, R. Swami, A. Ruhtinas, K. Hasselbach, A. Frydman, B. Piot, M. Gibert, E. Collin, O. Bourgeois, *Niobium nitride thin films for very low temperature resistive thermometry*, J. Low Temp. Phys. 197, 348–356 (2019).

[3] C.A. Polanco, A. van Roekeghem, B. Brisuda, L. Saminadayar, O. Bourgeois, and N. Mingo, *The phonon quantum of thermal conductance: are simulations and measurements estimating the same quantity?* Sci. Adv. **9**, eadi7439 (2023).

[4] E. Collin, I. Golokolenov, O. Maillet, L. Saminadayar, and O. Bourgeois, *On the link between mechanics and thermal properties: mechanothermics,* New J. of Physics 25, 043008 (2023)

[5] G. Ridgard, J. Prance, M. Thompson, L. Schreckenberg, N. Deshpande, C. Degenhardt, A. Cabrera-Galicia, O. Bourgeois, and V. Doebele, *Voltage Noise Thermometry in Integrated Circuits at Millikelvin Temperatures*, J. Appl. Phys. **137**, 245901 (2025).

[6] Boris Brisuda, PhD thesis, *Thermal rectification of phonon heat flux at very low temperatures in nanostructured asymmetric systems*, July 2025.

[7] Jon Canosa Diaz, PhD thesis, *Nanophononics at low temperature: towards heat manipulation at the nanoscale*, December 2025.

Acoustic Phonons, Vibronic Coupling, and Room-Temperature Super-Radiance in Engineered, Icosahedral Virus Capsids

Bogdan Dragnea[1,*]

[1]Department of Chemistry, Indiana University – Bloomington, USA
*Corresponding author: dragnea@iu.edu

***Abstract*—Molecular dyes covalently bonded to the confines of a symmetric viral capsid can spontaneously synchronize after simultaneous excitation, producing a burst of super-radiant fluorescence, at room temperature, in solution. The underlying mechanisms enabling the accelerated, collective emission at room temperature—despite the presence of collisional dephasing and inhomogeneous broadening—remains unresolved. In other low-dimensional condensed matter systems where room-temperature superradiance has been observed, vibronic coupling between phonons and electronic states is thought to be crucial. Guided by this observation, we investigated experimentally the presence of underdamped phonon modes in virus capsids. Our results suggest that the electronic state responsible for super-radiant emission is coupled to long-lived, acoustic modes of the capsid. The frequencies of these global modes suggest significantly greater stiffness at high frequencies than one might expect from quasi-static mechanical measurements. Building on these insights, we propose a vibronic coupling model that outlines key design parameters for future implementations of super-radiant bioengineered nanoparticles in applications.**

***Keywords*— virus symmetry, acoustic modes, vibronic coupling, super-radiance**

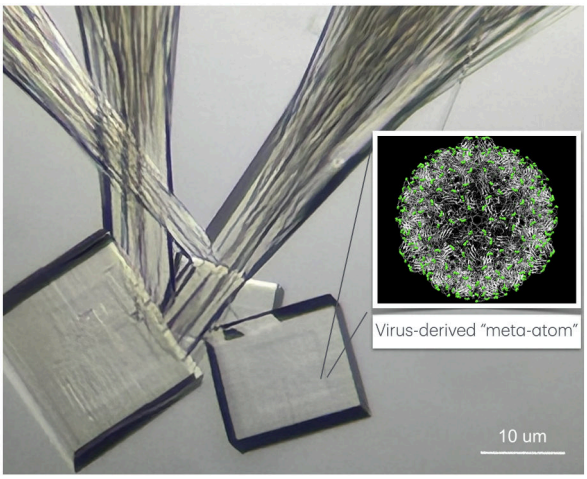

Fig. 1. Virus shells were repurposed as templates for symmetric arrays of hundreds of coupled quantum light emitters per particle. Light-emission from such bio-architected particles has non-classical characteristics. Crystals of virus-derived meta-atoms can be grown to macroscopic scales.

ACKNOWLEDGMENTS

This work was supported by the US National Science Foundation, CBET Awards #: 2232717 and 2232718, and by the Army Research Office, the Materials Design Program, through Award #: W911NF2410225.

REFERENCES

[1] J. Holmes, A. A. Sushma, I. B. Tsvetkova, W. L. Schaich, R. D. Schaller, and B. Dragnea. (2022) Ultrafast Collective Excited-State Dynamics of a Virus-Supported Fluorophore Antenna. J. Phys. Chem. Lett., 13(14):3237–3243.

[2] M. G. Benedict (Ed.). (1996). Super-radiance: Multiatomic Coherent Emission (1st ed.). CRC Press. https://doi.org/10.1201/9780203737880

Approaching Ultimate Quality Factors in Nanomechanical Resonators Made of Silicon Carbide

Eva M. Weig[1,2,3*]

[1] School of Computation, Information and Technology, Technical University of Munich, Germany
[2] TUM Zentrum für QuantumEngineering (ZQE), Technical University of Munich, Germany
[3] Munich Center for Quantum Science and Technology (MCQST), Germany
*Corresponding author: eva.weig@tum.de

***Abstract*—Silicon carbide (SiC) is an outstanding platform for high-quality nanomechanical resonators, combining intrinsic material quality with the possibility of dissipation dilution engineering. We compare resonators made of 4H-SiC and 3C-SiC, demonstrating routes to ultrahigh Q-factors, suitable for spin-mechanics and spin-cavity optomechanics applications.**

***Keywords*— nanomechanical resonators, silicon carbide, quality factor, dissipation dilution.**

I. Introduction

Nanomechanical resonators with ultrahigh quality factor (Q) are at the forefront of quantum sensing, quantum transduction, and hybrid quantum systems. The quality factor, a dimensionless measure of energy storage relative to dissipation, determines both the coherence time and the force sensitivity of a mechanical oscillator. Silicon carbide (SiC) is an exceptionally attractive material for such resonators, combining extraordinary mechanical stiffness and low intrinsic damping with a rich set of functionalities including integrated spin defects. SiC exists in multiple polytypes, most notably the hexagonal 4H-SiC and the cubic 3C-SiC, each offering distinct pathways towards high quality factors.

II. Intrinsic Quality Factors in 4H-SIC

Hexagonal 4H-SiC is a well-established material in nanophotonics and power electronics, and is considered an emerging material platform for nanomechanical systems. This is a consequence of its large Young's modulus (~450 GPa) and its high intrinsic quality factor. Nanomechanical resonators monolithically fabricated from high-purity semi-insulating 4H-SiC wafers yield intrinsic quality factors exceeding 10^5 at room temperature. Crucially, 4H-SiC hosts highly coherent spin defects, such as the silicon vacancy and the divacancy, whose spin states can be initialized and read out optically. The co-integration of these atomic-scale qubits with high-Q mechanical resonators in a monolithic platform is a key asset for realizing spin-mechanics experiments and spin-cavity optomechanics [1].

III. Dissipation Dilution Engineering in 3C-SIC

Cubic 3C-SiC, grown epitaxially as a thin film on silicon substrates, offers a complementary route to ultrahigh Q-factors through the mechanism of dissipation dilution [2]. Epitaxial growth of 3C-SiC on Si(111) substrates naturally incorporates strong biaxial tensile pre-stress, in the SiC film. Nanomechanical string resonators fabricated from this material exhibit a tensile stress of several GPa [3,4]. This results in significant dissipation dilution, boosting the measured Q-factor beyond its intrinsic value [5,6] and enabling Q x frequency products approaching 10^{13} Hz at room temperature. The thin-film geometry is furthermore amenable to hierarchical clamping designs and soft-clamped phononic crystal patterning, techniques that have proven highly successful in silicon nitride membranes [6] and which we now translate to the SiC material platform.

IV. Results and Discussion

We present a systematic comparison of nanomechanical resonators fabricated from both 4H-SiC and 3C-SiC, with device geometries ranging from singly-clamped cantilevers over doubly-clamped nanobeam and -strings to optomechanical crystals, a combined photonic and phononic crystal slab with a co-localized defect cavity. We perform a thorough material characterization, enabled by the high-throughput characterization and statistical analysis of many modes. For both materials, we discuss the Young's modulus, residual tensile stress and intrinsic quality factor, and identify the limiting dissipation mechanisms. For 3C-SiC, we experimentally determine the dissipation dilution factor. This comprehensive analysis allows to point out pathways towards the mitigation of the dominant loss channels, paving the way towards further enhanced quality factors.

V. Conclusion

Silicon carbide represents a uniquely versatile material platform for approaching ultimate quality factors in nanomechanical resonators. The hexagonal 4H polytype enables monolithic, defect-integrated devices with high intrinsic Q, while the cubic 3C polytype harnesses dissipation dilution from epitaxial tensile stress to surpass intrinsic limits. Together, these two material routes

establish SiC as a leading contender for the realization of macroscopic quantum states of mechanical motion and for next-generation hybrid quantum devices combining mechanical, spin, and photonic degrees of freedom.

ACKNOWLEDGMENTS

This work was supported by the Deutsche Forschungsgemeinschaft (DFG, German Research Foundation).

REFERENCES

[1] A. Hochreiter, P. Bredol, F. David, B. Demiralp, H. B. Weber, and E. M. Weig, Phys. Rev. Appl. 24, 034005 (2025)
[2] P. Bredol, F. David, N. S. Jagtap, Y. S. Klass, G. V. Astakhov, A. Erbe, and E. M. Weig, Phys. Rev. Appl. 22, 034036 (2024)
[3] Y. Klaß, J. Doster, M. Bückle, R. Braive, and E. M. Weig, Appl. Phys. Lett. 121, 083501 (2022)
[4] M. Bückle, Y. S. Klaß, F. B. Nägele, R. Braive, and E. M. Weig, Phys. Rev. Appl. 15, 034063 (2021)
[5] L. Sementilli, E. Romero, and W. P. Bowen, Adv. Funct. Mater. 32, 2105247 (2021)
[6] N. J. Engelsen, A. Beccari, and T. J. Kippenberg, Nat. Nano 19, 725 (2024)

Energy transport and switching in finite disordered networks

Yann Chalopin[1,*]

[1]CNRS, Laboratoire SPMS, CentraleSupelec, Universite Paris-Saclay, Gif-sur-Yvette, France
*Corresponding author: yann.chalopin@centralesupelec.fr

***Abstract*—We examine how disorder and localization shape vibrational energy transport in finite networks. A multiterminal conductance framework reveals sparse communication backbones whose reorganization under small perturbations produces switch like responses without thermodynamic criticality. The same physical picture connects disordered solids, metamaterials, and allosteric proteins.**

***Keywords*— phonons, localization, disorder, energy transport, allostery.**

I. Introduction

Wave transport in disordered matter is intrinsically heterogeneous. Disorder, interference, and mode mixing generate broad distributions of amplitudes, relaxation times, and mean free paths, blurring the distinction between propagating, diffusive, and localized vibrations [1], [2]. The central issue is therefore not only how much transport survives disorder, but how the surviving transport is organized in space.

This question is especially acute in finite systems. Macroscopic switch-like responses are usually associated with symmetry breaking or critical thresholds, yet finite heterogeneous networks cannot access such singular limits. Still, many display abrupt and cooperative behavior. We argue that this regime can be understood by viewing transport not as a bulk coefficient, but as a structured network process.

II. Multiterminal transport and sparse vibrational backbones

A natural description is provided by a multiterminal framework, in which transport is resolved into pairwise energy-exchange channels between nodes or functional units. In the harmonic or near-equilibrium regime, this leads to effective couplings

$$Q_{ij} = \int_0^\infty \frac{g_i(\omega)\, g_j(\omega)}{\sum_k g_k(\omega)}\, d\omega, \qquad . \tag{1}$$

where $g_i(\omega) = \sum_\mu |\psi_\mu(i)|^2\, \delta(\omega - \omega_\mu)$ is the power spectral density of of atomic sites at i and j. Rather than a single effective conductivity, one obtains a transport map that reveals where energy exchange concentrates and which links dominate communication. Recent work showed that this mode-resolved quantum–Langevin formalism provides a transparent multiterminal theory of coherent phonon transport in complex networks [3].

Its main implication is conceptual: in heterogeneous structures, transport is typically sparse and anisotropic. A small subset of channels carries a disproportionate fraction of the total flux, much as force chains dominate granular load transmission or marginal backbones dominate response near connectivity thresholds. Localization should therefore not be viewed only as transport suppression, but as a mechanism that organizes transport into a structured backbone.

III. Switching without thermodynamic criticality

Once transport is backbone-dominated, weak local perturbations can produce large system-level effects. It is not necessary to modify the whole network uniformly; altering a bottleneck or bridge is sufficient to reroute energy flow globally. Finite switch-like behavior can then emerge without singularity, diverging correlation length, or genuine phase transition. The mechanism is instead a finite-size crossover sharpened by heterogeneity and by the sparsity of dominant transport paths.

This viewpoint suggests an alternative strategy for wave-based metamaterials: rather than relying solely on global spectral gaps or resonant selection, one may engineer architectures whose function is controlled by selective rewiring of internal energy routes.

IV. From disordered solids to proteins

Biological macromolecules offer a striking realization of this physics. Proteins are finite, anisotropic, and disordered elastic networks with broad vibrational spectra, making them natural candidates for backbone-dominated transport [4], [5]. In this language, allostery becomes a transport problem: the relevant question is how a local perturbation reorganizes the network of vibrational exchange linking distant functional sites.

Hemoglobin provides a paradigmatic example. Successive ligation events do not merely populate effective conformational states [6]; they also reweight intersubunit communication pathways. The resulting cooperative response can be interpreted as the cumulative rewiring of a sparse vibrational backbone, producing a marked yet rounded switch in a system far too small to exhibit conventional criticality.

V. Conclusion

Disorder does more than degrade transport. By generating heterogeneous vibrational landscapes, it creates sparse communication backbones that can be exploited for control. A

multiterminal description makes these backbones visible and provides a general framework for understanding strong switch-like responses in finite disordered networks, from phononic structures to biological macromolecules.

REFERENCES

[1] P. W. Anderson, "Absence of diffusion in certain random lattices," *Phys. Rev.*, vol. 109, pp. 1492–1505, 1958.

[2] P. B. Allen and J. L. Feldman, "Thermal conductivity of disordered harmonic solids," *Phys. Rev. B*, vol. 48, pp. 12581–12588, 1993.

[3] Y. Chalopin, "Mode-resolved quantum Langevin theory of multiterminal coherent phonon transport," *Phys. Rev. B*, vol. 113, p. 024202, 2026.

[4] T. Tlusty, A. Libchaber, and J.-P. Eckmann, "Physical model of the genotype-to-phenotype map of proteins," *Phys. Rev. X*, vol. 7, p. 021037, 2017.

[5] Q. Cui and M. Karplus, "Allostery and cooperativity revisited," *Protein Sci.*, vol. 17, pp. 1295–1307, 2008.

[6] J. Monod, J. Wyman, and J.-P. Changeux, "On the nature of allosteric transitions: A plausible model," *J. Mol. Biol.*, vol. 12, pp. 88–118, 1965.

Non-Diffusive Nanoscale Phonon Heat Transport in 2D Materials

Sebin Varghese[1,2], Jordi Tur Prats[3], Albert Beardo[3], Francesc Xavier Alvarez[3], Klaas-Jan Tielrooij[1,2,*]

[1]Department of Applied Physics, Eindhoven University of Technology, the Netherlands
[2]Catalan Institute of Nanoscience and Nanotechnology (ICN2), BIST and CSIC, Spain
[3]Department of Physics, Autonomous University of Barcelona, Spain
*Corresponding author: k.j.tielrooij@tue.nl

***Abstract*— Heat transport at the nanoscale and in nanoscale materials can differ from conventional, diffusive heat transport. Here we use spatiotemporal microscopy to follow heat in space and time and observe highly viscous heat transport in two-dimensional semiconductors toward the monolayer limit, which we attribute to combined hydrodynamic and thermoelastic effects.**

***Keywords*— 2D materials, heat transport, nanoscale, hydrodynamic, thermoelastic.**

I. Introduction

Understanding and – ideally – controlling heat transport in materials is important both from a fundamental and an applied standpoint. This is particularly true at the nanoscale, where novel fundamental heat transport phenomena can occur and where hotspots can emerge that can lead to device failure.

Two-dimensional (2D) semiconducting materials, such as MoS_2, are also interesting both from a fundamental and an applied standpoint. They have several fundamentally different properties compared two their three-dimensional counterparts, such as extremely high exciton binding energies, which dictate many of their optical properties. And for applications, there are several leading roadmaps that project that they will be used in transistors for future logic.

We studied heat transport in $MoSe_2$ and MoS_2 and observed highly non-diffusive transport. We identified the origin of this non-diffusive behavior as a combination of hydrodynamic and thermoelastic effects, thus unravelling a novel "hydro-thermoelastic" heat transport regime [1]. Whereas hydrodynamic transport in MoS_2 had been predicted [2], this had so far not been observed. Moreover the interplay between hydrodynamic and thermoelastic effects had so far not been addressed in any material. Importantly, the observed non-diffusive "hydro-thermoelastic" heat transport regime is controllable via material thickness and heating mode – pulsed *vs.* continuous.

II. Methods

The technique that we used to observe heat transport is spatiotemporal pump-probe microscopy [3,4], which makes it possible to follow heat spreading directly in space and time with ~100 femtosecond temporal and ~10 nanometer spatial accuracy. In particular, we probed near the exciton absorption peak, whose linewidth depends on temperature [5], thus giving us a high temperature sensitivity with a thermoreflectance coefficient on the order of 10^{-4} K^{-1}, which means that we can observe sub-Kelvin changes in temperature [6].

We used suspended single-crystalline flakes of $MoSe_2$ and MoS_2 of varying thickness, prepared via exfoliation and PDMS-assisted transfer, following Ref. [7]. The suspended region had a diameter of 15 μm.

III. Results and Discussion

The experimental results showed that upon decreasing the thickness of the 2D semiconducting materials, the effective diffusivity decreased by an order of magnitude. This only occurs under pulsed heating, as probed using spatiotemporal pump-probe microscopy, and not under continuous heating, as probed using Raman thermometry. Indeed, our earlier Raman thermometry study showed very little change in the thermal conductivity of $MoSe_2$ even in the monolayer limit [8].

In order to understand these results, we developed a mesoscopic model that extends the Guyer-Krumhansl description of hydrodynamic heat transport [9] to include out-of-equilibrium thermoelastic effects. As input parameters for the model, we used values from *ab initio* calculations. This model accurately predicts the observed experimental results without any freely adjustable fit parameters.

IV. Conclusion

We have demonstrated a novel non-diffusive "hydro-thermoelastic" heat transport regime, where hydrodynamic and thermoelastic effects jointly lead to highly viscous heat transport, which is controllable via material thickness and heating mode. These results pave the way for unprecedented control over heat transport pathways in the industrially promising material platform of 2D semiconductors and beyond.

REFERENCES

[1] S. Varghese et al., "Controllable hydro-thermoelastic heat transport in ultrathin $MoSe_2$ and MoS_2 at room temperature," *under review.*

[2] A. Cepelotti et al., and Y. T. Lee, "Phonon hydrodynamics in two-dimensional materials," Nat. Commun., vol. 6, pp. 6400, 2015.

[3] S. Varghese et al., "A pre-time-zero spatiotemporal microscopy technique for the ultrasensitive determination of the thermal diffusivity of thin films," Rev. Sci. Instr. vol. 94, pp 034903, 2023.

[4] G.D. Brinatti Vazquez et al., "Spatiotemporal microscopy: shining light on transport phenomena," Adv. Electron. Mater. vol. 10, pp. 2300584, 2024.

[5] M. Selig et al., "Excitonic linewidth and coherence lifetime in monolayer transition metal dichalcogenides," Nat. Commun. vol. 7, pp. 13279, 2016.

[6] L. Moczko et al., "Seeing heat flow with two novel time-resolved optothermal techniques" *in preparation.*

[7] S. Varghese et al., "Fabrication and characterization of large-area suspended $MoSe_2$ crystals down to the monolayer," J. Phys. Mater. vol. 4, pp. 046001, 2021

[8] D. Saleta et al., "Unraveling heat transport and dissipation in suspended $MoSe_2$ from bulk to monolayer," Adv. Mater. vol. 34, pp. 2108352, 2022.

[9] R.A. Guyer and J.A. Krumhansl, "Thermal conductivity, second sound, and phonon hydrodynamic phenomena in non-metallic crystals," Phys. Rev. vol. 148, pp. 778-788, 1966.

Anisotropic phonon dynamics at the nanoscale in a nanophononic SiN membrane

V. M. Giordano[1,*], S. Mazzoleni[1,2], S. Pailhès[1], F. Bencivenga[3]

[1]Universite Claude Bernard Lyon 1, CNRS, Institut Lumière Matière, UMR5306, F-69100, Villeurbanne, France

[2]Department of Materials Science, University of Milano-Bicocca, Via Roberto Cozzi 55, 20125 Milano
[3]Elettra Sincrotrone Trieste S.c.P.A., Strada Statale 14, km 163.5, AREA Science Park, I-34149 Basovizza, Trieste, Italy
*Corresponding author: valentina.giordano@univ-lyon1.fr

We report the investigation of phonon dynamics in nanophononic membranes with square and rectangular lattices of holes, at phonons wavelengths comparable with the nanostructure lengthscale. We unveil the signature of lattice anisotropy both on phonon energies and lifetimes, and identify its microscopic origin at the light of finite element simulations.

***Keywords*— nanophononic materials, extreme ultraviolet transient grating, phonon lifetime, phonon coherence**

I. Introduction

Nanophononic materials are characterized by a periodic nanostructuration,which may lead to coherent scattering of phonons, enabling interference and resulting in modified phonon dispersions. Recently, we have invetsigated phonon frequencies and lifetimes in a low-roughness nanoporous phononic membrane of SiN at wavelengths between 50 and 100 nm, comparable to the nanostructure lengthscale. We have revealed a drastic phonon lifetime reduction upon nanostructuration, which has been explained as due to a strong interference of the phonon with its own reflections at periodic interfaces. This mechanism becomes dominant for phonon wavelengths comparable to the holes lattice period and neck (inter-holes distance) [1]. In this work, we pursue our understanding of interference effects on phonon dynamics by investigating the orientation dependence of phonon energy and lifetime in SiN membranes with a square and a rectangular lattice of holes.

II. Methods

The study has been performed on commercially available suspended membranes of LPCVD amorphous SiN, provided by Norcada Inc. (Edmonton, Canada). The membranes were 55nm thick. For the square lattice, the period was 377 nm, and the hole diameter 124 nm, averaged along the thickness. For the rectangular lattice, the long period was 377 nm, the short one 179.6 nm, and the average hole diameter 105 nm. We used the extreme ultraviolet transient grating (EUV TG) technique at the TIMER beamline of the FERMI free electron laser (Trieste, Italy).

III. Results and Discussion

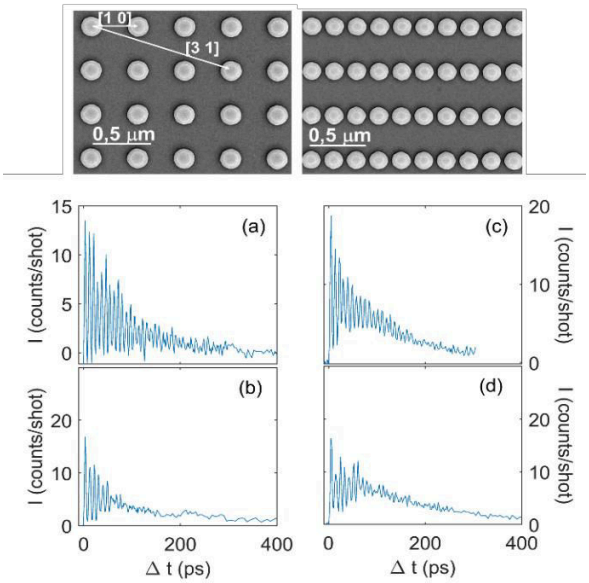

Fig. 1 Transient grating signal for a phonon wavelength 84 nm in the two nanostructures on the top. Left column: square lattice. (a): [1 0] direction; (b): [3 1] direction. Right column: rectangular lattice. (a): long period direction; (b): short period direction

We have measured phonon dynamics in the two membranes, as a function of orientation, including low symmetry directions, such as the [3 1] in the square lattice (see Figure). We observe a strong dependence of both phonon energy and lifetime on the orientation in both lattices. This anisotropy may be understood in terms of a modification of coherent phonon interference with the geometry.

Acknowledgments

This work was supported by the IdexLyon (ANR-16-IDEX-0005), ANR (project MAPSANR-20-CE05-0046). This project has received funding from the European Union's Horizon 2020 research and innovation program under grant agreement no. 654148 and 871124 Laserlab-Europe

References

[1] M. Hadi et al., , Nat. Comm. 15, 1317 (2024)

Surface Acoustic Waves and Spin Waves interaction in iron thin film

Pauline Rovillain[1*], Anupam Sharma[1], Florian Millo[1], Louis Christienne[1], Jean-Yves Duquesne[1], Mahmoud Eddrief[1], Franck Fortuna[2], Laura Thévenard[1], Catherine Gourdon[1] and Massimiliano Marangolo[1]

[1] Sorbonne Université, CNRS, Institut des NanoSciences de Paris, UMR7588, F-75005 Paris,
[2] ISMO, CNRS, Université Paris-Saclay, Orsay, France
*Corresponding author: pauline.rovillain@sorbonne-universite.fr

***Abstract*—We investigate surface acoustic wave–induced ferromagnetic resonance in magnetic thin films. By measuring the magnetic-field and angular dependence of Rayleigh SAW velocity variations, extract the magnetoelastic coupling. A non-reciprocal acoustic response is also observed at resonance, highlighting the potential of tunable magnetoelastic devices.**

***Keywords*— magnetoacoustic, magnonic.**

I. Introduction

Magnon straintronics enables voltage control of spin-wave (SW) amplitude and phase through strain-mediated magnon–phonon coupling, offering promising perspectives for beyond-CMOS technologies. Surface acoustic wave–induced ferromagnetic resonance (SAW-FMR) provides a powerful platform to probe this interaction.

II. Methods

We investigate SAW-FMR in epitaxial Fe thin films grown on GaAs(001) [1,2], forming a magnetoelastic/piezoelectric heterostructure compatible with spintronic and magnonic devices (Fig. 1). We introduce an original method to tune and quantitatively determine the magnetoelastic coupling constant in pristine and nitrogen-implanted Fe films. After determining the magnetocrystalline anisotropy by standard magnetic characterization, we extract the magnetoelastic constant from the magnetic-field and angular dependence of Rayleigh SAW velocity variations.

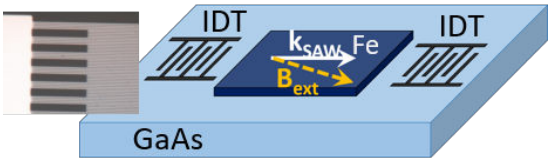

Fig. 1 Sketch of the sample: The Fe mesa is 54 nm thick on GaAs(001). The wave vector $\mathbf{k}_{SAW}$ is parallel to [110], the Fe magnetic hard axis, $\mathbf{B}_{ext}$ is the in-plane applied magnetic field.

III. Results and Discussion

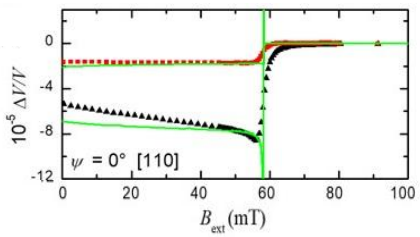

Fig. 2 Relative variation of the SAW velocity V measured versus decreasing amplitude of the external field. The magnetic field $\mathbf{B}_{ext}$ is applied in the film plane, parallel to the [110] direction (hard axis, ψ = 0◦)

Experimental results show: resonant coupling, SAW-FMR for a particular configuration when the magnetic field $\mathbf{B}_{ext}$ is applied in the film plane, parallel to the [110] direction and $\mathbf{k}_{SAW}$ propagation (Fig. 2). A phenomenological model derived from the Landau–Lifshitz–Gilbert formalism, including calculated SW dispersion relations, accurately reproduces the field dependence of SAW velocity vs angles between SAW propagation direction and $\mathbf{B}_{ext}$ in both pristine and implanted samples. From this calculation the magnetoelastic constant B_2 was extracted (Fig. 3) [3].

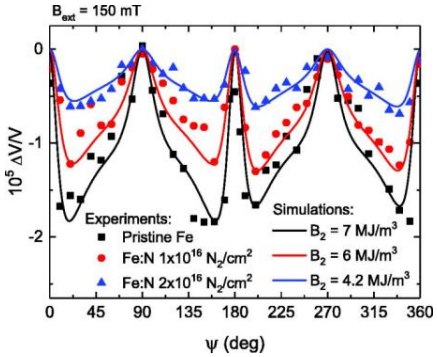

Fig. 3 SAW relative velocity variation as function of the angle between $\mathbf{k}_{SAW}$ and $\mathbf{B}_{ext}$ for pristine Fe, intermediate and highest doped Fe:N at = 150 mT.

IV. Conclusion

We have observed an almost twofold reduction of the magnetoelastic coupling constant at a nitrogen dose of 2×10^{16} N_2/cm^2, as well as a non-reciprocal acoustic response at resonance, highlighting the potential for tunable and non-reciprocal magnetoelastic devices.

Acknowledgments

This work was supported by the French National Research Agency, ANR-22-CE24-0015 SACOUMAD and the France 2030 program PEPR SPIN, under Contract Nos. ANR-22-EXSP-0008 and ANR-22-EXSP-0004.

References

[1] J-Y Duquesne, et al., Phys. Rev Applied Phys. Rev. Applied 12 024042, 2019
[2] P. Rovillain, et al., Phys. Rev. Applied 18 064043, 2022.
[3] A. Sharma et al. Appl. Phys. Lett. 128, 062404, 2026.

Experimental realization of Algorithm-designed Nanophononic Metasurfaces

Michele Diego[1,*], Matteo Pirro[1], Jade Hardouin[1], Gabrielle Mazevet-Schargrod[1], Junior Rognon[1], Byunggi Kim[1,2], Roman Anufriev[3] and Masahiro Nomura[1]

[1]Institute of Industrial Science, The University of Tokyo, Japan
[2]Institute of Science Tokyo, Japan
[3]LIMMS CNRS-IIS, Japan
*Corresponding author: diego@iis.u-tokyo.ac.jp

***Abstract*— Nanophononic metamaterials are key components for controlling acoustic signals in nanotechnology. Here, we present automated, algorithm-driven strategies for realizing phononic metasurfaces based on inverse-design and hyperuniform architectures. The resulting designs are fabricated and experimentally characterized, validating the predicted phononic properties and demonstrating the effectiveness of algorithm-designed metastructures.**

***Keywords*— metamaterials, nanophononics, inverse design, phononic crystals**

I. Introduction

Controlling acoustic properties at the nanoscale is crucial across a wide range of fields, from thermal transport and mechanical resonators to nanosensing and quantum technologies. In this context, phononic crystals have emerged as efficient metamaterials for tailoring the propagation of acoustic waves [1]. These structures are typically implemented by patterning a membrane or depositing pillars on the surface of a substrate. However, the design of such structures still largely relies on conventional geometries and simple rules guided by human intuition. To overcome this limitation, algorithm-based design strategies have been proposed and explored theoretically [2]. To translate these approaches into real-world devices, the fabrication feasibility must be explicitly incorporated into the optimization process. Here, we present the results of two studies investigating nanophononic metasurfaces for controlling acoustic wave propagation designed using different algorithmic approaches. The resulting designs are fabricated into experimental devices, whose characterization demonstrates the effectiveness of algorithm-designed phononic structures.

II. Methods

The design algorithms presented in this talk are based on two strategies. First, we employ a genetic algorithm that mimics Darwinian evolution to optimize a quasi–two-dimensional silicon phononic metasurface over successive generations (Fig.1) [3]. The optimization follows the principle of survival of the fittest with respect to a selected property – in this work, the chosen property corresponds to the anisotropy of acoustic wave propagation. At each generation of phononic structures, only those that maximize the acoustic anisotropy are allowed to transmit their genes, i.e., their design parameters, to the next generation.

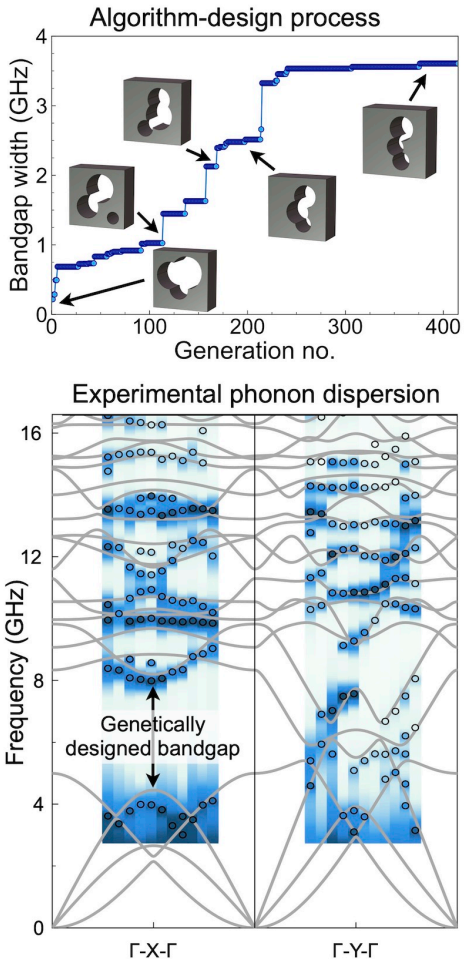

Fig.1 Top: Optimization of the unit cell of the algorithm-designed phononic metasurface. Bottom: Experimental phonon dispersion (color and circles) vs theoretical prediction (solid lines).

The second metasurface is obtained by depositing gold nanopillars on a piezoelectric substrate [4]. The position of the pillars is driven by an algorithm to achieve a hyperuniform distribution, while their shape is defined by a Voronoi tessellation (Fig.2). The interest in hyperuniform structures stems from their unique nature as systems with properties in between ordered and disordered systems, allowing them to combine characteristics of both, such as the presence of bandgaps and resilience to defects.

For both the genetically-designed and the hyperuniform metasurfaces, fabrication constraints are taken into account within the automated design process, allowing us to fabricate the devices by nanoscale cleanroom techniques. Finally, the two structures are characterized using, respectively, Brillouin light scattering spectroscopy and interdigital transducer techniques.

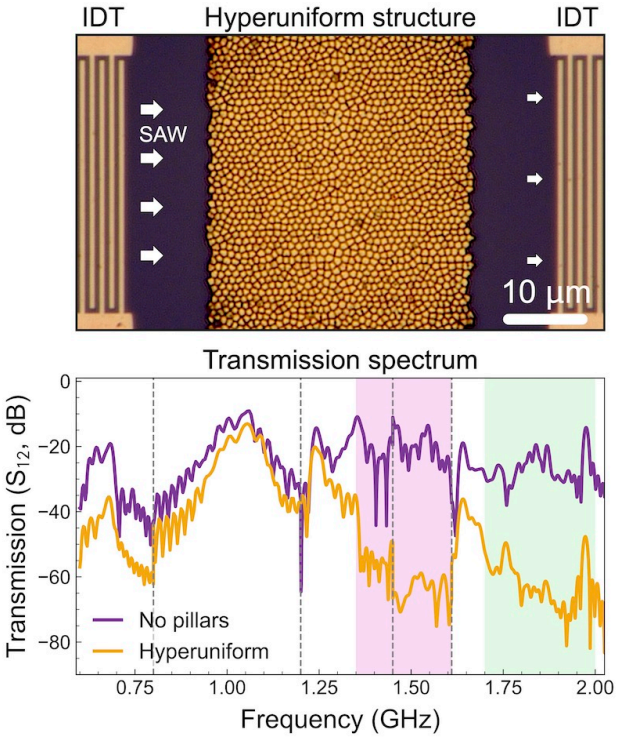

Fig. 2. Top: Hyperuniform metasurface with interdigital transducers (IDTs) on the side for generation/detection of acoustic waves (SAW). Bottom: Experimental acoustic transmission in the presence and absence of the hyperuniformly distributed pillars.

III. Results and Discussion

For the genetically designed phononic metasurface, we measured its phonon dispersion relation and compared it with the prediction obtained from finite-element simulations. The good agreement between experiment and theory confirms the optimized strong anisotropy of the structure, characterized by a large unidirectional bandgap (Fig.1).

For the hyperuniform structure, we observe a broader attenuation of surface acoustic wave transport compared to conventional pillar-based phononic crystals, which typically suppress acoustic waves only within narrow frequency ranges (Fig.2). This behavior is explained by calculating the phononic mode density of states, which shows that the hyperuniform distribution, together with the Voronoi tessellation, broadens the density-of-states peaks and results in broadband acoustic wave attenuation. Finally, we further investigate waveguiding effects for different waveguide shapes by removing pillars from the hyperuniform metasurface. The waveguide structures exhibit high-transmission acoustic modes, demonstrating the effectiveness of hyperuniform devices in supporting acoustic waveguides.

IV. Conclusion

We experimentally realized two examples of phononic metasurfaces for acoustic wave control designed using automated algorithms. The first device is based on genetically designed nanopatterning of a quasi-two-dimensional membrane, while the second relies on hyperuniform nanopillars on a piezoelectric substrate. Both devices exhibit good agreement with the expected phononic properties, showing the effectiveness of the algorithm-based design approach.

Acknowledgments

This work was supported by Japan Science and Technology Agency Moonshot R&D grant (JPMJMS2062), and by the JSPS KAKENHI Grants (JP23K19196, JP23KF0203, and 25K17905).

References

1. M.Diego, R.Anufriev, R.Yanagisawa and M.Nomura, “Phonon dispersion of nanoscale honeycomb phononic crystal: gigahertz and terahertz spectroscopy comparison”, Eur. Phys. J. Plus 139, 1032, 2024
2. M. Diego, B.Kim, M.Pirro, S.Volz, and M.Nomura, “Piezoelectrically driven diamond phononic nanocavity by phonon-matching scheme for quantum applications”, Phys. Rev. Applied 21, 064064, 2024
3. M. Diego, M.Pirro, B.Kim, R.Anufriev and M.Nomura, “Tailoring Phonon Dispersion of Genetically Designed Nanophononic Metasurface”, ACS Nano 18, 28, 18307–18313, 2024
4. M. Diego, J. Hardouin, G. Mazevet-Schargrod, M. Pirro, B. Kim, R. Anufriev and M. Nomura, “Hypersonic acoustic wave control via stealthy hyperuniform phononic nanostructures”, Sci. Adv., 11, 32 eadw7205, 2025

Acoustic vibrations of single gold nanodisks supported on solid substrates

Nathan Berrit[1,*], Clément Panais[1], Noëlle Lascoux[1], Sylvie Marguet[2], Natalia Del Fatti[1,3], Aurélien Crut[1]

[1]Université de Lyon, CNRS, Université Claude Bernard Lyon 1, Institut Lumière Matière, F-69622 Villeurbanne, France
[2]Université Paris-Saclay, CEA, CNRS, NIMBE, 91191 Gif-sur-Yvette, France
[2]Institut Universitaire de France (IUF), 1 rue Descartes, F-75231 Paris cedex 05, France
*Corresponding author: nathan.berrit@univ-lyon1.fr

***Abstract*—Metallic mechanical nanoresonators' performances are often limited by their strong acoustic damping. Here, we conduct optical pump-probe time-resolved spectroscopy to study the vibrational dynamics of single gold nanodisks supported on different solid substrates. We study the impact of the nanoresonators' morphology, the substrate composition and thickness on these dynamics.**

***Keywords*— Time-resolved spectroscopy, Plasmonic nanoparticles, Vibrations, Quality factor, Finite-element simulations.**

I. Introduction

Mechanical nano-resonators are useful for a variety of applications, including quantum phononics experiments at room temperature or micro-mass sensing [1]. Their performance can be quantified with the fQ product of their oscillation frequencies f and quality factor Q.

Metallic nanoparticles are an interesting system for such applications, thanks to their inherently high oscillation frequencies (in the GHz-THz range). However, it has been observed that they undergo strong acoustic damping, leading to Q factors of the order of a few tens [2]. It is therefore important to better understand and minimize acoustic damping mechanisms in these systems, which are associated with two processes: radiative damping caused by the emission of acoustic waves within the environment, and intrinsic damping, linked to internal phonon attenuation.

In this context, we present an optical investigation of the vibrational dynamics of individual supported gold nanodisks. These experiments were done at the single-particle level using the combination of two single-particle techniques (namely SMS and pump-probe spectroscopy), thus avoiding the spurious statistical effects linked to ensemble measurements.

The nanodisks (NDs) present a simple geometry characterized by two parameters, the diameter D and the thickness h. Our previous work, conducted on a thick sapphire substrate, showed that a significant reduction of radiative damping could be achieved for specific aspect ratios $\eta = \mathrm{D/h}$ of such resonators [2]. This effect is linked to the radiative coupling of two close-frequency acoustic modes, leading to the creation of a Bound State in the Continuum [3]. Here, we propose to extend this study by also exploring the influence of both the substrate composition and thickness on acoustic damping.

II. Methods

The gold NDs were chemically synthesized in a two-step process involving the growth of hexagonal gold plates, later chemically etched, leading to a smooth cylindrical shape. They were later deposited at a low concentration on three distinct substrates: ∼1 mm thick sapphire, ∼1 mm thick silica, and a 40 nm thick silica membrane.

Optical experiments were conducted with a Ti:sapphire pulsed oscillator associated with a frequency-doubling BBO crystal and an Optical Parametric Oscillator, eventually leading to an optical source tunable within a 400-1040 nm range, with an 80 MHz repetition rate and a ∼150 fs pulse duration.

The detection and linear extinction measurement of single NDs was performed using Spatial Modulation Spectroscopy (SMS). This far-field technique is based on a mechanical oscillation of the sample, leading to a temporal modulation of the transmitted beam power when a ND is present in the beam [5]. A displacement amplitude of 300 nm at a 1.5 kHz frequency was used. Light was focused on the sample using a x100 objective microscope, leading to a spot size close to the diffraction limit (about 0.7 times the wavelength). A second-harmonic lock-in detection enables a quantitative measurement of the extinction spectra σ_{ext} as a function of the wavelength (Figure 1a).

For each ND, the extinction spectra exhibit a quasi-Lorentzian Plasmon Surface Resonance, as expected for metal nanoparticles. Since the resonance spectral position and area are strongly linked to the nano-object morphology (D and h), these dimensions could be estimated for each ND by comparing its extinction spectrum with finite-element modeling (FEM) simulations of the ND optical response.

The acoustic dynamics of the NDs were subsequently measured using pump-probe time-resolved spectroscopy. In this technique, the nano-object is illuminated by two light beams separated by a tunable delay t. The first beam (pump-beam) is used to excite the nano-object, with a wavelength set at 410 nm and a fluence of ~ 0.3 J/cm^2. The pump power is modulated through a mechanical chopper at 30 kHz for additional noise reduction.

By measuring the relative transmission $\Delta\frac{\mathrm{T}}{\mathrm{T}}(t)$ of the second

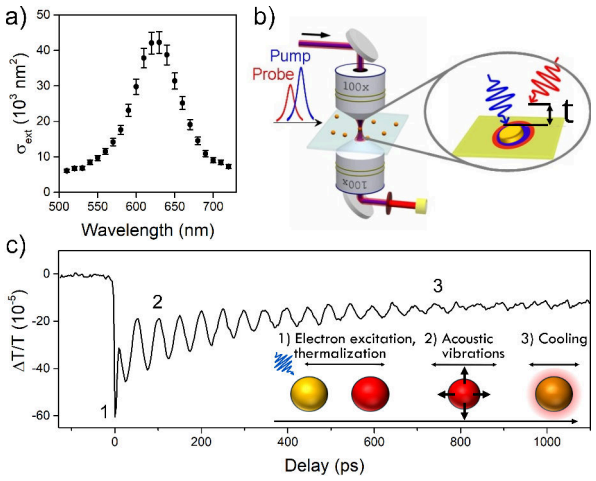

Fig. 1. (a) Linear extinction spectrum of a single gold nanodisk deposited on thick silica. This nano-object exhibits a quasi-Lorentzian plasmonic resonance at a 625 nm central wavelength. (b) Pump-probe experiment setup. (c) Ultrafast dynamics of the same nanodisk for a 410 nm pump wavelength and a 660 nm probe wavelength.

beam (probe-beam), the ND transient optical response can eventually be reconstructed, containing the signature of three ultrafast processes (Figure 1b,c): the initial electron heating and thermalization (few ps), the nano-object's acoustic oscillations (few hundreds of ps) and its cooling in the environment (few ns).

The thermal signal was fitted using either one or two decaying exponentials. The acoustic dynamics are then fitted with one damped oscillation:

$$\left(\frac{\Delta T}{T}\right)_{\text{acoustic}}(t) = A \exp\left(\frac{-t}{\tau}\right) \sin\left(\frac{2\pi}{T}t + \phi\right) \qquad (1)$$

where the acoustic mode frequency f and quality factor Q= $\frac{\pi\tau}{T}$ can be extracted. Following this protocol, a systematic study was conducted on all substrates. Experimental frequencies and quality factors were compared with those obtained with acoustic FEM simulations.

III. Results and Discussion

Pump-probe experiments were conducted on over 50 NDs, with diameters ranging from 50 nm to 120 nm, and an average thickness of h = 24 ± 3 nm (as determined through AFM measurements).

A strong dependence of acoustic dynamics on the substrate is observed: NDs of similar aspect ratio show similar oscillation frequencies but markedly different quality factors. For instance, two nanoresonators with $\eta = 3$ on thick sapphire and silica membrane exhibit a quality factor of 19 and 45 respectively (Figure 2). Since intrinsic acoustic damping is expected to be almost independent of the nanodisks' environment, these results confirm that radiative damping plays a crucial role in acoustic mode attenuation.

Both thick sapphire and thick silica samples show a low dependence of the quality factor on η, with an average , Q = 15±3 and Q = 27±3 respectively. However, on silica membrane, a strong η-dependence is observed, with quality factors ranging from 13 (for $\eta = 5.4$) to 51 (for $\eta = 2.2$).

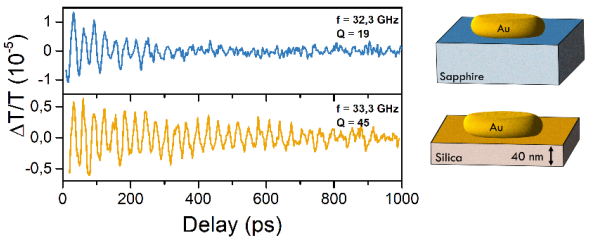

Fig. 2. Acoustic dynamics of two nanodisks with the same aspect ratio ($\eta = 3$).

FEM simulations reveal the existence of two close-frequency acoustic modes within the range experimentally detected. The first mode was the one experimentally detected and shows a relatively low Q modification with η. The second mode (mode 2) consistently presents an important radiative Q-factor exaltation over a broad range of ND aspect ratios, while its excitation amplitude is significantly lower than that of the first mode, thus making its experimental detection challenging. Nevertheless, by increasing the pump-beam fluence, focusing on long-delay dynamics, and increasing the signal averaging, we were able to detect mode 2 on one resonator on the thick sapphire substrate, with an estimated quality factor of 45.

IV. Conclusion

Through this work, we conducted a systematic optical study of both substrate geometry and composition in the design of high-quality factor metallic nanoresonators.

Firstly, we showed that for similar NDs geometries, changing either the substrate composition or thickness has a significant impact on the resonator's quality factor, indicating the dominant role of radiative damping in acoustic dynamics. Moreover, we highlighted the influence of the nanoresonators' aspect ratio on damping processes. In particular, on a silica membrane substrate, the quality factor was improved by more than a factor of 4 for low aspect ratios with respect to higher ones. Finally, we experimentally demonstrated the existence of a second acoustic mode which exhibits lower radiative damping as well as low excitation amplitude.

Acknowledgments

This work was supported by the ANR ULTRASINGLE project.

References

[1] C. Yiwen, and S Gröblacher, "A perspective on hybrid quantum opto- and electromechanical systems," *Applied Physics Letters*, vol. 117, 2020.
[2] H. D. Boggiano et al., "Coherent Acoustic Phonons in Plasmonic Nanoparticles: Elastic Properties and Dissipation at Low Temperatures," *ACS Nano*, vol. 18, 2024.
[3] F. Medeghini et al., "Controlling the Quality Factor of a Single Acoustic Nanoresonator by Tuning its Morphology," *ACS Nanoletters*, 2018.
[4] A. Crut, "Substrate-supported nano-objects with high vibrational quality factors," *Journal of Applied Physics*, vol. 131, 2022.
[5] A. Arbouet et al., "Direct Measurement of the Single-Metal-Cluster Optical Absorption," *Physical Review Letters*, vol. 93, 2004.

The optomechanics way to probe a single living cell

Hilario Boggiano [1], Louis Waquier [1], Cherif Belacel [1], Ivan Favero [1,*]

[1]Matériaux et Phénomènes Quantiques, Université Paris Cité, CNRS, France
*Corresponding author: ivan.favero@u-paris.fr

Optomechanical resonators, where the motion of a solid-state body couples to light trapped in a cavity, form a new class of elementary quantum systems on their own. Operated at the quantum limit, they are pushing our capability to probe forces with higher sensitivity and time resolution. Here we will show how to employ an optomechanical resonator to open a new experimental window in the measurement of a single living cell. Results cover the investigation of cell rheology at high frequencies unexplored so far, as well as the resolution in the membrane region of fluctuating processes at the sub-microsecond scale, two decades faster than allowed by prior techniques.

Keywords **— Optomechanics, Sensing, Single living cell, Nanomechanics, Fluctuations**

Mapping electrostatic and Casimir forces above metallic nanostructures using suspended nanowires

L. Judéaux[1,*], P. Heringlake[1], H. Weltz[1], C. Dousset[1], B. Pigeau[1], O. Arcizet[1]

[1]Institut Néel, CNRS, France

*Corresponding author: lucas.judeaux@neel.cnrs.fr

***Abstract*—We optically probe the vibrations of an ultrasensitive force sensor, a suspended silicon carbide nanowire to map the lateral electrostatic and proximity forces experienced above a metallic nanostructure. We probe and compensate the electrostatic forces at each position above the sample and spatially map the lateral Casimir force field.**

***Keywords*— nanomechanics, electrostatic, force measurements, Casimir forces.**

I. Methods

The lateral vibrations of the SiC nanowire are readout using the reflexion of a laser beam focused on the nanowire vibrating extremity and collected back into a high numerical aperture objective. Exploiting the two quasi-degenerated fundamental mechanical modes of the nanowire, which oscillate along the transverse directions above a sample of interest, the nanowire can be used as a lateral force sensor. As in an atomic force microscope, the force gradients are modifying the eigenmodes properties, causing here both mechanical frequency shifts and rotations of the eigenvectors' orientations, whose measurement allows extracting the four components of the local lateral force field gradients experienced by the nanowire[1], [2]. Furthermore, the static deflexions of the nanowire in the transverse plane are separately recorded to evaluate the static forces produced by the sample.

We developed force and force field gradient sensing protocols of the 2D lateral force fields experienced by the nanowire, featuring a vectorial character with sensitivities in at the $\mathrm{aN}/\sqrt{\mathrm{Hz}}$ level at room temperature (10 $\mathrm{zN}/\sqrt{\mathrm{Hz}}$ at dilution temperatures [3]) operating at a quasi real-time measurement rate (10 Hz), limited by the mechanical coherence time of the nanowire. To do so, we use a reference radiation pressure force produced by a time-modulated pump laser to simultaneously drive both mechanical resonances of the nanowire, and activate two phase lock loops to track the mechanical frequency shifts produced by the force field gradients. By scanning the nanowire above the sample, for different bias voltages, it is possible to map the electrostatic force field and its voltage dependence, which first allow to separate the contribution of the voltage dependent electrostatic fields, and the residual contributions produced by the sample imperfections- electrostatic patches, contaminants- which do not depend on the bias voltages.

By simultaneously modulating the electrostatic potentials applied on the sample, at frequencies close to each mechanical resonance tone, it is possible to also measure the electrostatic force field produced by the sample and compare it to the force field gradients determined independently. This real-time measurement of the electrostatic forces also allows to efficiently determine at each position above the sample, the set of bias voltages that must be applied to compensate the electrostatic force at which the Casimir force field gradients must be measured to operate in the electrostatic vacuum.

The samples are made of a gold layer deposited on top of an insulating SiO_2/Si wafer, and the sub-micron nanostructures are realized with a focused ion beam. Most of the results are obtained on a 400 nm trench drilled in a 150 nm

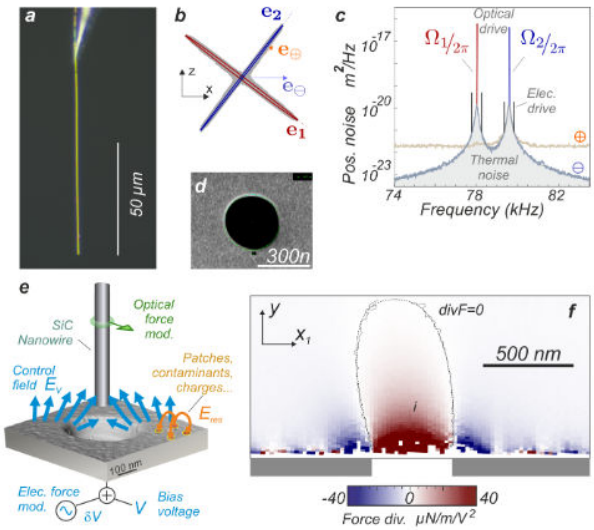

Fig. 1. **a** optical images of a 240 nmn thick nanowire. **b,c** Gray: optically readout thermal noise spectrum of the vibrations of the nanowire extremity, revealing the two transverse mechanical eigenmodes, whose orientations in the transverse horizontal plane can be identified by resonantly driving each eigenmode, here with a radiation pressure force produced by a time-modulated pump laser. Applying a voltage modulation on the sample of interest at frequencies close to the mechanical resonances allow to measure the local electrostatic force experienced by the nanowire. **d** SEM image of a 300 nm hole drilled in a 100 nm gold layer whose AFM image is used to build the image of panel **e**. The local electrostatic field can be controlled and modulated by external gate voltages, aiming at compensating the residual electrostatic fields produced by surface imperfections (patches, contaminants, charges..). Scanning probe image obtained by scanning the nanowire above a hole. The patch structure is visible at low altitude.

thick gold layer, which separates two electrodes which can be independently voltage biased to control the vertical and horizontal components of the electrostatic field above the trench. The measured electrostatic patches are produced by the 50 nm grains of gold. The inhomogeneity of the residual field they produce vanishes with the altitude above the sample and become sufficiently smooth for altitudes above 100 nm to be compensated by the electrodes.

The nanowire force probes are specifically adapted to this experiment. We chose rather large diameters, above 350 nm to enhance the Casimir forces (and adapt the trench diameter accordingly). We artificially enhance their relative mechanical frequency splitting, up to 10 percents, by adding a smaller nanowire at their base, to break their rotational symmetry in the region of large dynamical strain and we orientate the eigenmodes and the trench orientation at 45 degrees of the laser axis. We control the perpendicularity between the nanowire axis and the sample with an approx. 1° precision, which allows to get rid of the vertical forces produced by the sample. Finally, the laser wavelength- and the nanowire diameter- are chosen not to be resonant, to minimize the optical absorption, which can cause unwanted photothermal effects [6].

II. Results and Discussion

The Casimir repulsion of a needle above a hole in vacuum was theoretically predicted in [4] but the faintness of the forces have for the moment precluded from experimental observation. The elongated character of the nanowire deviates from the proposed needle geometry, so that the vertical repulsion does not exist with a nanowire, but the lateral Casimir repulsion persists. Beyond this aspect, our measurement also allows to map the Casimir force field above nanostructures, with sub-micron dimensions and approx. 50 nm lateral resolution. For small nanowire diameters, this measurement method can also be viewed as a mapping of the spatial density of vacuum fluctuations above nanostructures. This dual electrode scheme allows to map and cancel both the horizontal and vertical components of the electrostatic field, and enables the measurement of the lateral Casimir forces which persist at zero field. In a first step, we measured the force and force gradients above the nanostructure, while varying the different bias voltages over a wide range in each position. We extracted the set of bias voltages which allow cancelling the electrostatic force- and thus the electrostatic field components and evaluated the Casimir force divergence in each position. Those measurements allowed a complete analysis of the force and force gradients and provided a good force/divergence comparison and Casimir divergence reconstruction but was time consuming and sensitive to low-frequency drifts in the experiment. Implementing the real-time measurement of the electrostatic forces, based on electrostatic force sidebands, we demonstrated the possibility to use a dual feedback loop on the two bias voltages to cancel the demodulated electrostatic force at each position above the sample. This method provided similar results to the previous method but helped significantly reducing the measurement time and thus the sensitivity to the experimental drifts.

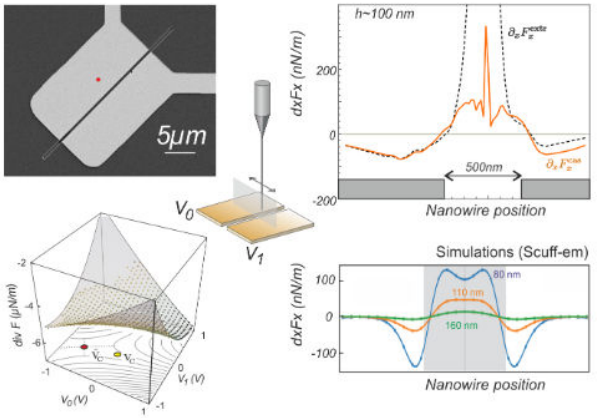

Fig. 2. **a** SEM image of the samples employed for the Casimir measurements: a 400 nm wide trench is drilled in a gold layer, and a separate bias voltage can be applied on each side of the trench. **b** measurement of the force field divergence at a fixed nanowire position above the trench, while varying the two bias voltages. The obtained quadratic form serves to determine the electrostatic force properties, while the simultaneously measured electrostatic force serves to identify which set of bias voltages allow compensating the electrostatic force, revealing the Casimir force field gradient. **c** Reproducing similar measurements at different positions above the trench (see inset) serves to measure the lateral gradients of the lateral Casimir force (orange curve, preliminary measurements), revealing a laterally repulsive character (positive values) above the trench. Those measurement are in agreement with the original prediction [4], and in qualitative agreement with numerical simulations [5] realized on Scuff-em.

Our measurements demonstrate a laterally repulsive structure above the trench, the nanowire being attracted towards the edges of the trench, as expected from the original theoretical predictions [4] and in agreement with our numerical simulations[5] based on the open-source Scuff-em software. The lateral Casimir force field gradients range from a few $\mu\mathrm{N/m}$ at an altitude of approx. 100 nm, and rapidly decay down to the $\mathrm{nN/m}$ at an altitude of approx. 600 nm above the trench, corresponding to nanowire sensitivity limit in those fast measurement protocols, at room temperature. A clear transition from the near-field to the far field regime is observed, when the nanowire altitude is smaller/larger than the trench width (equal to the nanowire diameter). The corresponding lateral Casimir forces are of a few 100 fN at short distances. Our measurement also allow to map the electrostatic force field above the trench, which dominate the force landscape, especially at large distances due to their weaker decrease with the nanowire elevation, and here again our results are found in good agreement with numerical simulations. Furthermore, these measurements provide information about the electrostatic imperfections of the sample, which are valuable when investigating nano-fabrication processes.

III. Conclusion

With the real-time measurement protocols, we measured the Casimir and electrostatic force fields above metallic nanostructures, achieving a good qualitative agreement with numerical

simulations. The prospects of the work aim at exploring Casimir force fields above more complex nanostructures, at different temperatures [3] and opening connections towards cavity nano-optomechanical experiments realized at small photon numbers realized in the group. [7]

ACKNOWLEDGMENTS

L.J. and C.D.acknowledge PhD funding from the Program QuanTEdu-France ANR-22-CMAS-0001 France 2030. This work was supported by the French National Research Agency (SinPhoCOM project) and by the European Research Council under the EU's Horizon 2020 research and innovation program, grant agreements No 820033 (AttoZepto).

REFERENCES

[1] Mercier de Lépinay, L., Pigeau, B., Besga, B. et al. A universal and ultrasensitive vectorial nanomechanical sensor for imaging 2D force fields. Nature Nanotech **12**, 156–162 (2017). https://doi.org/10.1038/nnano.2016.193

[2] Mercier de Lépinay, L., Pigeau, B., Besga, B. et al. Eigenmode orthogonality breaking and anomalous dynamics in multimode nano-optomechanical systems under non-reciprocal coupling. Nat Commun **9**, 1401 (2018). https://doi.org/10.1038/s41467-018-03741-8

[3] Fogliano, F., Besga, B., Reigue, A. et al. Ultrasensitive nano-optomechanical force sensor operated at dilution temperatures. Nat Commun **12**, 4124 (2021). https://doi.org/10.1038/s41467-021-24318-y

[4] Levin, M., McCauley, A., Rodriguez, A., et al. Casimir repulsion between metallic objects in vacuum. Phys. Rev. Lett. **105**, 2010

[5] Johnson, S. Numerical methods for computing Casimir interactions. Casimir Physics **834**, 175-218 (2011) https://doi.org/10.1007/978-3-642-20288-9

[6] Gouriou, C. *et al.*, Nano-optomechanical exploration of the dynamical photothermal response of suspended nanowires to laser-induced thermal waves, arXiv:2507.02017 (2025)

[7] Fogliano, *et al.*, Mapping the cavity optomechanical interaction with subwavelength-sized ultrasensitive nanomechanical force sensors, Phys Rev. X **11**, 021009 (2021)

Vibrational dynamics of self-assembled nanoparticles

Shaik Mohammad Imran[1,*], Nicholas Blanchard[1], Benoit Mahler[1], Jeremie Margueritat[1]

[1]Institut Lumière Matière (ILM), UMR5306
Université Lyon 1 – CNRS, 69622 Villeurbanne, France

[*]Corresponding author: Mohammad-imran.shaik@univ-lyon1.fr

***Abstract*—** We measure interaction-induced vibrational modes in nanoparticle assemblies down to 20 nm and show that the Johnson–Kendall–Roberts (JKR) contact-mechanics model breaks down below ∼100 nm, coinciding with emergence of disordered, weakly connected networks and transition to percolation scaling that establishes mechanical connectivity as the governing mechanism in this regime.

***Keywords*—** nanoparticle assemblies, vibrational dynamics, Brillouin spectroscopy, mechanical coupling.

Introduction

Colloidal nanoparticles can self-assemble into ordered or partially ordered structures whose physical properties are tunable through particle size, interparticle interactions, and fabrication conditions. [1, 2] Such assemblies enable a wide range of applications, including plasmonics [3], biosensing platforms [4], and photonic and phononic materials whose functionality is governed by collective mechanical and vibrational responses. [5, 6] A central challenge is to understand how interparticle interactions control the mechanical and vibrational behavior of nanoparticle assemblies.

Brillouin light scattering (BLS) is a non-contact optical technique that probes gigahertz-frequency acoustic excitations and elastic properties in condensed and nanostructured materials.[7, 8] For isolated, homogeneous spherical nanoparticles, the vibrational response measured by BLS is well described by Lamb theory and dominated by intrinsic spheroidal modes. [9, 10, 11, 12] In dense assemblies, mechanical coupling between neighboring particles modifies the single-particle response and gives rise to additional low-frequency spectral features associated with collective motion. [13, 14, 15]

In particular, interparticle contacts lift the degeneracy of the rigid-body translational $f(s,1,1)$ mode, leading to a finite-frequency interaction-induced collective mode [13], as schematically illustrated in (Fig. 1).

Figure 1. Conceptual schematic of the interaction-induced translational $(s,1,1)$ mode. **Top:** Isolated nanoparticles exhibit rigid-body translation. **Bottom:** Interparticle contacts introduce a restoring force, yielding a finite-frequency collective mode. M_{eff} and K_{eff} denote the effective mass and interparticle stiffness.

Such interaction-induced modes have been reported in polymer nanoparticle assemblies [13, 15], as well as in silica [14], semiconductor [16], and metals. [17] For ordered or partially ordered assemblies with well-defined contacts, their frequency scaling has been successfully described using classical contact-mechanics frameworks, most notably the Johnson–Kendall–Roberts (JKR) model, yielding a characteristic size dependence $f \propto d^{-7/6}$. [18, 13] These studies have predominantly focused on assemblies composed of particles larger than approximately 100 nm, where contacts are relatively uniform and structural order is preserved.

As a result, it remains unclear whether contact-mechanics descriptions developed for ordered assemblies remain applicable as particle size decreases, where even minor absolute size variations result in larger relative polydispersity that can hinder long-range ordering and periodicity. In this study, we therefore investigate self-assembled polystyrene nanoparticle assemblies in the sub-100 nm regime, where structural disorder and heterogeneous connectivity are expected.

Methods

Monodisperse polystyrene (PS) nanoparticles (20–200 nm) were used as received. The particles consist of plain polystyrene cores with polydispersity $\leq 2\,\%$, verified by TEM. Films were prepared by drop-casting 10 µL of a 1 wt % suspension onto cleaned glass substrates and drying at room temperature, producing coffee-ring patterns and multilayer assemblies with micrometre-scale thickness, as confirmed by SEM. Brillouin measurements targeted regions of high particle coverage.

Brillouin spectra were acquired using a home-built VIPA-based confocal backscattering spectrometer. A 640 nm continuous-wave diode laser delivered ∼45 mW at the sample and was focused with a 0.80 NA objective, yielding a spot size of ∼1 µm. Backscattered light was collected through the same objective, filtered to suppress elastic scattering, and dispersed by a VIPA etalon with a free spectral range of ∼30 GHz. Spectra were recorded on an sCMOS camera with 1 s exposure time. Brillouin peaks were extracted using Lorentzian fits. The interaction-induced mode was identified by its low-frequency spectral position and separation from intrinsic Lamb modes.

Interaction-induced translational modes were analyzed using two complementary descriptions. For assemblies with homogeneous contacts, nanoparticles were modeled as rigid masses coupled by JKR model springs, predicting the classical scaling $f \propto d^{-7/6}$.

For disordered assemblies, a percolation-based elastic network model was considered, in which rigidity is governed by a fractal load-bearing backbone ($D_f \approx 2.5$) and

effective stiffness scales as $K_{\text{eff}} \propto d^{\alpha}$ ($\alpha \approx 1.7$), leading to:

$$f(d) \propto d^{(\alpha - D_f)/2}. \quad (1)$$

Results and Discussion

Brillouin measurements were performed using the VIPA-spectrometer setup described in the Methods. The central experimental findings are summarized in (Fig. 2), which combines frequency scaling, mechanical schematics, and structural characterization to capture the collective vibrational dynamics of polystyrene nanoparticle assemblies across the investigated size range.

The Brillouin data (Fig. 2b) reveal an interaction-induced translational mode whose frequency decreases monotonically with increasing particle diameter, consistent with previous reports on polymer nanoparticle assemblies.[13, 15] For larger particles, the measured frequencies approach the JKR contact-mechanics scaling $f \propto d^{-7/6}$, as expected for assemblies with homogeneous elastic contacts.[13, 15] For diameters above 100 nm, the mode shifts to lower frequencies, increasing overlap with elastic scattering in the VIPA; tandem Fabry–Perot interferometer was used to resolve the Brillouin peak.

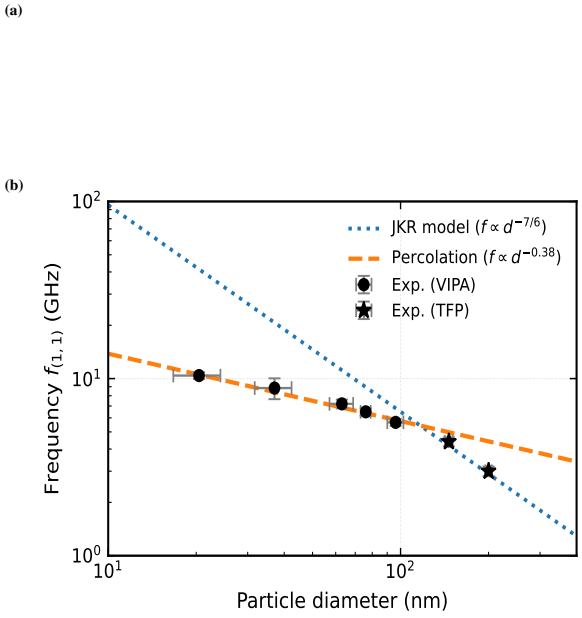

Figure 2 — Crossover from contact-limited to connectivity-limited vibrational mechanics in nanoparticle assemblies. **a** Schematics illustrating connectivity-limited coupling in disordered assemblies (percolation regime) and contact-limited coupling in ordered assemblies described by Johnson–Kendall–Roberts (JKR) mechanics. **b** Log–log scaling of the interaction-induced translational mode $f_{(s,1,1)}$ with particle diameter, showing a shallow percolation-based scaling $f \propto d^{-0.38}$ at small sizes and convergence toward the JKR prediction $f \propto d^{-7/6}$ as assemblies become ordered and fully connected.

At smaller particle sizes, however, the experimental data deviate strongly from JKR predictions and instead follow a much shallower size dependence, $f \propto d^{-0.38}$. This deviation suggests a change in the underlying mechanical coupling as particle size decreases.

Complementary structural characterization provides insight into this crossover. As particle size increases, SEM reveals a progressive evolution in structural organization: assemblies formed from 40 nm particles are strongly disordered, 100 nm particles exhibit mixed or partially ordered domains, and 200 nm particles form extended, close-packed structures with continuous interparticle contacts (Fig. 3). The increasing structural order with particle size is consistent with the assumptions of classical contact mechanics.

In contrast, assemblies composed of 40 nm particles exhibit disordered packing with heterogeneous and incomplete contacts, consistent with previous observations in disordered nanoparticle systems.[14, 13] This structural evolution coincides with the observed crossover in vibrational scaling.

The transition therefore reflects a change in mechanical connectivity. In ordered assemblies, elastic coupling is governed by well-defined particle–particle contacts, yielding contact-limited mechanics described by JKR theory. In disordered assemblies, however, elastic coupling is governed by a weakly connected elastic network rather than pairwise contacts.

Figure 3 — Structural evolution of nanoparticle assemblies with particle size. SEM images of assemblies formed from 40 nm, 100 nm, and 200 nm particles showing the transition from disordered packing to progressively ordered, close-packed structures as particle diameter increases.

As illustrated schematically (Fig. 2a), this connectivity-limited regime is captured by a percolation-based description, in which rigidity emerges from a load-bearing backbone with fractal mass dimension $D_f \simeq 2.5$ and effective stiffness scaling $K_{\text{eff}} \propto d^{\alpha}$ with $\alpha \simeq 1.7$[19, 20], yielding $f(d) \propto d^{(\alpha - D_f)/2} \approx d^{-0.38}$.

Together, (Fig. 2) establishes a clear crossover from contact-limited to connectivity-limited vibrational mechanics as particle size decreases, identifying mechanical connectivity—not contact geometry alone—as the dominant control parameter governing collective vibrational dynamics in nanoparticle assemblies.

Conclusion

This study demonstrates that interaction-induced vibrational modes provide a sensitive probe of mechanical connectivity in nanoparticle assemblies. By combining Brillouin spectroscopy with structural characterization, we access collective dynamics that are invisible at the single-particle level and directly reflect interparticle mechanical coupling. Beyond polystyrene nanoparticles, these results highlight the importance of connectivity-controlled mechanics in disordered nanostructured materials, where classical contact-based descriptions are limited. More broadly, direct access to interaction-driven vibrational modes establishes Brillouin spectroscopy as an effective approach for probing collective mechanical behavior in heterogeneous nanoscale systems.

Acknowledgements

This work was supported by the European Union through the VIRUSONG project. Views and opinions expressed are those of the author(s) only and do not necessarily reflect those of the European Union or the granting authority.

References

[1] W. Cheng, J. J. Wang, U. Jonas, W. Steffen, G. Fytas, R. S. Penciu, and E. N. Economou. The spectrum of vibration modes in soft opals. *The Journal of Chemical Physics*, 123(12):121104, 2005.

[2] Bartlomiej Graczykowski, Nicolas Vogel, Karina Bley, Hans-Jürgen Butt, and George Fytas. Multiband hypersound filtering in two-dimensional colloidal crystals: Adhesion, resonances, and periodicity. *Nano Letters*, 20(3):1883–1889, 2020.

[3] Anna Klinkova, Rachelle M. Choueiri, and Eugenia Kumacheva. Self-assembled plasmonic nanostructures. *Chemical Society Reviews*, 43(11):3976–3991, 2014.

[4] Borja Sepúlveda, Paula C. Angelomé, Laura M. Lechuga, and Luis M. Liz-Marzán. Lspr-based nanobiosensors. *Nano Today*, 4(3):244–251, 2009.

[5] C. Bourdillon, S. Gam Derouich, W. Daney de Marcillac, L. Coolen, A. Maître, C. Mangeney, and C. Schwob. Self-assembled photonic crystals for a chemical sensing. In *Photonic and Phononic Properties of Engineered Nanostructures VI*, volume 9756 of *Proceedings of SPIE*, page 97561L, 2016.

[6] Jason D. Forster, Jin-Gyu Park, Manish Mittal, Heeso Noh, Carl F. Schreck, Corey S. O'Hern, Hui Cao, Eric M. Furst, and Eric R. Dufresne. Assembly of optical-scale dumbbells into dense photonic crystals. *ACS Nano*, 5(8):6695–6700, 2011.

[7] J. G. Dil. Brillouin scattering in condensed matter. *Reports on Progress in Physics*, 45:285–334, 1982.

[8] Pierre Bouvet et al. Consensus statement on brillouin light scattering microscopy of biological materials. *Nature Photonics*, 19:681–691, 2025.

[9] Horace Lamb. On the vibrations of an elastic sphere. *Proceedings of the London Mathematical Society*, 13(1):189–212, 1882.

[10] Augustus Edward Hough Love. *A Treatise on the Mathematical Theory of Elasticity*, volume 1. Cambridge University Press, Cambridge, 1892.

[11] Yi Li, Hock Siah Lim, Zhi Kui Wang, Ser Choon Ng, and Meng Hau Kuok. Micro-brillouin study of the eigenvibrations of single isolated polymer nanospheres. *Journal of Nanoscience and Nanotechnology*, 8(11):5869–5872, 2008.

[12] Maurizio Montagna. Brillouin and raman scattering from the acoustic vibrations of spherical particles with a size comparable to the wavelength of the light. *Physical Review B*, 77(4):045418, 2008.

[13] Maurizio Mattarelli, Maurizio Montagna, Tim Still, Dirk Schneider, and George Fytas. Vibration spectroscopy of weakly interacting mesoscopic colloids. *Soft Matter*, 8(15):4235–4243, 2012.

[14] Adil Ayouch, Xavier Dieudonné, Gwenaëlle Vaudel, Hervé Piombini, Karine Vallé, Vitalyi Gusev, Philippe Belleville, and Pascal Ruello. Elasticity of an assembly of disordered nanoparticles interacting via either van der waals-bonded or covalent-bonded coating layers. *ACS Nano*, 6(12):10614–10621, 2012.

[15] Hojin Kim, Yu Cang, Eunsoo Kang, Bartlomiej Graczykowski, Maria Secchi, Maurizio Montagna, Rodney D. Priestley, Eric M. Furst, and George Fytas. Direct observation of polymer surface mobility via nanoparticle vibrations. *Nature Communications*, 9(1):2918, 2018.

[16] Caroline L. Poyser, Thomas Czerniuk, Andrey Akimov, Benjamin T. Diroll, E. Ashley Gaulding, Alexey S. Salasyuk, Anthony J. Kent, Dmitri R. Yakovlev, Manfred Bayer, and Christopher B. Murray. Coherent acoustic phonons in colloidal semiconductor nanocrystal superlattices. *ACS Nano*, 10(1):1163–1169, 2016.

[17] Jean Lermé, Jérémie Margueritat, and Aurélien Crut. Vibrations of dimers of mechanically coupled nanostructures: Analytical and numerical modeling. *The Journal of Physical Chemistry C*, 125(15):8339–8348, 2021.

[18] K. L. Johnson, K. Kendall, and A. D. Roberts. Surface energy and the contact of elastic solids. *Proceedings of the Royal Society of London. Series A, Mathematical and Physical Sciences*, 324(1558):301–313, 1971.

[19] Ariel Amir, Jacob J. Krich, Vincenzo Vitelli, Yuval Oreg, and Yoseph Imry. Emergent percolation length and localization in random elastic networks. *Physical Review X*, 3(2):021017, 2013.

[20] M. B. Isichenko. Percolation, statistical topography, and transport in random media. *Reviews of Modern Physics*, 64(4):961–1043, 1992.

SPECIAL SESSION 24

Cavity Quantum Materials and Polaritonic Devices: From Microscopic Theory to Functionality

3 contributions · pp. 1273–1279

Probing Cavity Polaritons via Scattering of Frequency-Entangled Biphoton States

Andrei Piryatinski[1,*], Nishaant Jacobus[1,2], Sameer Dambal[1,3], Eric R. Bittner[3], Yu Zhang[1], Ajay R. S. Kandada[4]

[1]Theoretical Division, Los Alamos National Laboratory, United States
[2] Department of Chemistry, Center for Quantum Information and Quantum Control, University of Toronto, Canada
[3] Department of Physics, University of Houston, Houston, United States
[4] Department of Physics and Center for Functional Materials, Wake Forest University, United States
*Corresponding author: apiryat@lanl.gov

***Abstract*—We have developed scattering theory for frequency-entangled photon pairs interacting with cavity polariton and bipolariton states. Within the Tavis–Cummings framework, we elucidate biphoton scattering signatures in the joint spectral amplitude and entanglement entropy, demonstrating the technique's potential as a probe of polaritonic states in semiconductor and molecular nanostructures.**

***Keywords*— biphoton scattering, cavity polaritons, frequency-entanglement.**

I. Introduction

Quantum light has recently been shown to be a powerful probe of electronic and vibrational dynamics in condensed phase molecular systems. This sensitivity arises from the unique characteristics of quantum photon states, such as entanglement and squeezing, and from the ability to detect changes in nonclassical photon statistics induced by the material response [1].

Optical microcavities enable strong light–matter interactions that are particularly useful platforms for low-intensity quantum-photon spectroscopies. Such interactions give rise to hybrid light–matter quasiparticles known as polaritons, formed via the coupling between cavity photons and elementary material excitations. Given recent advances in polariton chemistry, quantum-light spectroscopy offers promising opportunities for probing molecular cavity polaritons. At the same time, emerging studies on the unique properties of cavity quantum materials open new perspectives for applying quantum-light techniques as sensitive probes of strongly correlated electronic, vibrational, orbital, and spin degrees of freedom. Advancing the use of quantum-light techniques in this context calls for the development of theoretical frameworks capable of describing the scattering of entangled photon states by cavity polaritons in strongly correlated condensed-matter systems.

In this work [2], we develop a generalized scattering-matrix framework that directly relates input and output biphoton states, while consistently incorporating both coherent and dissipative polariton dynamics. This methodology provides a unified and systematic approach to modeling biphoton scattering in quantum cavity materials and molecular condensed-phase systems.

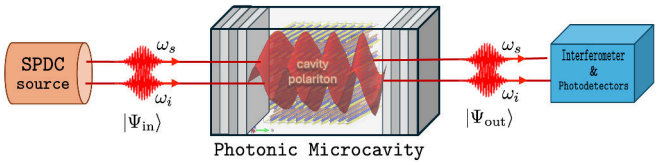

Fig. 1. Schematics of a photonic microcavity containing quantum emitter, e.g., semiconductor nanostructure, where the interaction between a cavity photon mode and nanostructured material excitons forms a hybrid light–matter quasiparticle — the cavity polariton. The polariton steady state can be prepared by applying a weak incoherent pump to the quantum emitters (not shown in the plot), which also results in a steady-state cavity photon population. The polariton state is further probed by scattering an input entangled photon pair, $|\Psi_{\text{in}}\rangle$, generated via spontaneous parametric down-conversion (SPDC), with the output state, $|\Psi_{\text{out}}\rangle$, detected after transmission through the interferometric setup.

II. Methods

As illustrated in Fig. 1, we consider the scattering of a frequency-entangled photon pair by a photonic cavity containing a material system, such e.g., a semiconductor nanostructure. The electronic excitations of the material system are assumed to be in resonance with the confined cavity photon mode, leading to the formation of polaritons. Both the input and output entangled photon pairs can be described as quantum wave packets, $|\Psi_{\text{in/out}}\rangle = \iint d\omega_s d\omega_i \mathcal{F}_{\text{in/out}}(\omega_s,\omega_i)|\omega_s\rangle\omega_i\rangle$, where $|\omega_s\rangle$ and $|\omega_i\rangle$ denote the signal and idler photon states, respectively. All information about signal-idler entanglement is encoded in the two-photon joint spectral amplitude (JSA) $\mathcal{F}_{\text{in/out}}(\omega_s,\omega_i)$, which can be measured experimentally and analyzed by calculating the entanglement entropy [2].

The relation between the input and output JSAs is given by

$$\mathcal{F}_{\text{out}}(\omega_s,\omega_i) = \iint d\omega_s' d\omega_i' \mathcal{S}(\omega_s,\omega_i;\omega_s',\omega_i')\mathcal{F}_{\text{in}}(\omega_s',\omega_i'). \quad (1)$$

where $\mathcal{S}(\omega_s,\omega_i;\omega_s',\omega_i')$ is the polariton scattering matrix that accounts for both single-polariton and correlated bi-polariton structure. Using the Tavis-Cummings model for cavity (bi-)polaritons together with a Feynman diagrammatic expansion shown in Fig. 2, we calculated the scattering matrix amplitudes and analyzed the resulting output JSA.

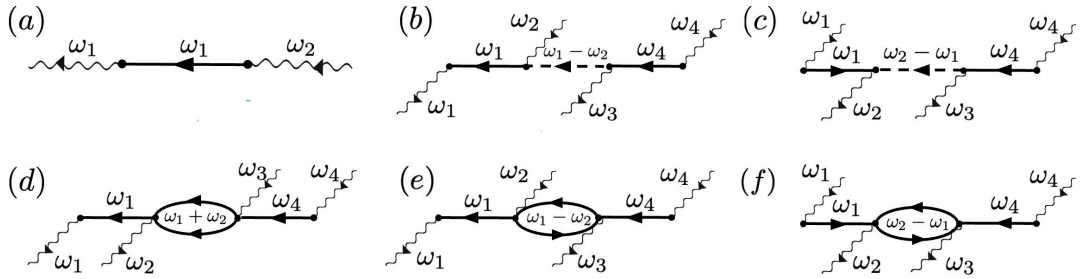

Fig. 2. Feynman diagrams describing (a) single-photon scattering by polariton mode, (b, c) bi-photon scattering involving the steady/ground state polariton propagation. The other diagrams describe the bi-photon scattering events that involve (d) the bipolariton coherence and (e,f) the polariton-polariton excited state coherences and populations. Adopted from Ref. [2].

III. Results and Discussion

Figure 2 shows the output JSA (panel c) obtained from the scattering of the input SPDC JSA (panel b) by the polariton branches indicated by the red dashed line in panel a where strong light-matter coupling occurs. The observed in Fig. 2 d increase in entanglement entropy after scattering is attributed to bi-polariton dynamics, providing their quantitative signatures. Such signatures could be measured experimentally, offering a means to probe correlated bi-polariton fluctuations over the quantum vacuum. Our analysis demonstrated that the entanglement entropy of the outgoing biphoton state arises not only from the interplay between decoherence processes and bipolariton correlations that lead to entropy production, but also depends on the input photon entanglement entropy encoded in the biphoton JSA. This distinction must be taken into account when employing entangled biphoton states to probe bipolariton correlations. Furthermore, isolating these correlations requires subtracting the contribution from coherent biphoton scattering. Since our analytical formulation explicitly separates these terms, the present theory provides a clear prescription for modeling and subsequently removing the coherent component while analyzing experimental data.

IV. Conclusion

In conclusion, we have developed a tractable scattering theory framework for describing the scattering of a biphoton wavepacket through a photonic cavity supporting polariton and bipolariton quasiparticles. The adopted Green function representation provides a versatile approach for modeling quasiparticle dynamics in molecular and semiconductor materials coupled to a cavity mode. Our model calculations based on the TC model revealed that the output JSA is a result of an interplay between polariton and bipolariton Fano-type resonance and the input JSA. Moreover, we identified the limitations imposed by the structure of the input JSA and demonstrated the sensitivity of the technique for probing polaritons supported by a cavity in the vacuum state.

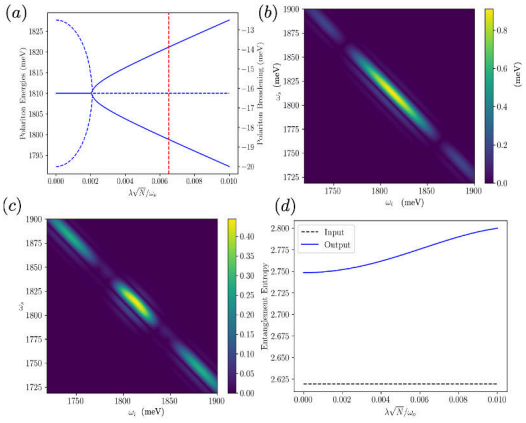

Fig. 3. Calculated (a) polariton dispersion relation, i.e., the energy spectrum and decay rates as a function of light-matter coupling strength, (b) input two-photon joint spectral amplitude (JSA), $\mathcal{F}_{\mathtt{in}}(\omega_s\omega_i)$ produced by SPDC source and (c) output two-photon joint spectral amplitude $\mathcal{F}_{\mathtt{out}}(\omega_s\omega_i)$ (d) entanglement entropy of the input (dash) and output (solid) photon pair.

Acknowledgments

A.P. and N.J. work at LANL was supported by the U.S. Department of Energy Office of Science as part of the CHIME, a Microelectronics Science Research Center (MSRC). The work at the University of Houston, E.R.B, was supported by the National Science Foundation under CHE-2404788 and S.D. by the Robert A. Welch Foundation (E-1337). Y.Z. acknowledges the support from the US DOE, Office of Science, Basic Energy Sciences, Chemical Sciences, Geosciences, and Biosciences Division under Triad National Security, LLC ("Triad") contract Grant 89233218CNA000001 (FWP: LANLECF7). ARSK acknowledges funding from the National Science Foundation CAREER grant (CHE-2338663), This work was performed, in part, at the Center for Integrated Nanotechnologies, an Office of Science User Facility operated for the U.S. Department of Energy (DOE) Office of Science. Los Alamos National Laboratory, an affirmative action equal opportunity employer, is managed by Triad National Security, LLC for the U.S. Department of Energy's NNSA, under contract 89233218CNA000001.

References

[1] S. Mukamel, et al., "Roadmap on quantum light spectroscopy", *J. Phys. B: At. Mol. Opt. Phys.* **53**, 072002 (2020).

[2] A. Piryatinski, N. Jacobus, S. Dambal, E. R. Bittner, Y. Zhang, A. R. S. Kandada, "Scattering theory of frequency-entangled biphoton states facilitated by cavity polaritons," *Phys Rev. A*, Accepted (2026);

Cavity coupling of van der Waals heterostructures

Gunda Kipp[1,2*], Hope M Bretscher[2,3], Gaetan Membrez[1], Ethan Koskas[1], Lorenzo Graziotto[1], Felix Helmrich[1], Luca Somboli[1], Benedikt Schulte[2,3], Dorothee Herrmann[2], Kateryna Kusyak[2,3], Matthew W Day[2,3], Sivasruthi Kesavan[2], Toru Matsuyama[2], Xinyu Li[2], Sara Maria Langner[2], Jesse Hagelstein[2], Felix Sturm[3], Alexander M Potts[2,3], Christian J Eckhardt[2,4], Yunfei Huang[3], Kenji Watanabe[5], Takashi Taniguchi[6], Angel Rubio[2,7,8], Dante M Kennes[2,4], Michael Sentef[9,2], Emmanuel Baudin[10,11], Guido Meier[2], Christian Reichl[13], Giacomo Scalari[1], Werner Wegscheider[13], Marios H Michael[2], James McIver[2,3], Jérôme Faist[1]

[1]Institute for Quantum Electronics, ETH Zürich, CH-8003 Zürich, Switzerland.
[2]Max Planck Institute for the Structure and Dynamics of Matter, Hamburg, Germany.
[3]Department of Physics, Columbia University, New York, NY, USA.
[4]Institut für Theorie der Statistischen Physik, RWTH Aachen University ana JARA-Fundamentals of Future Information Technology, Aachen, Germany.
[5]Research Center for Electronic and Optical Materials, National Institute for Materials Science, Tsukuba, Japan.
[6]Research Center for Materials Nanoarchitectonics, National Institute for Materials Science, Tsukuba, Japan.
[7]Center for Computational Quantum Physics, Simons Foundation Flatiron Institute, New York, NY, USA.
[8]CNano-BioSpectroscopy Group, Departamento de Fisica de Materiales, Universidad del País Vasco, San Sebastián, Spain.
[9]Institute for Theoretical Physics and Bremen Center for Computational Materials Science, University of Bremen, Bremen, Germany.
[10]Laboratoire de Physique de l'Ecole Normale Supérieure, Université PSL, CNRS, Sorbonne Université, Université Paris-Citéo, Paris, France.
[11]Institut Universitaire de France, France.
[13]Laboratory for Solid State Physics, ETH Zürich, 8093 Zürich, Switzerland.
*Corresponding author: gukipp@phys.ethz.ch

***Abstract*— Van der Waals heterostructures host strongly correlated phases tunable *in situ* via electrostatic gates. Their conductive layers, including the gates themselves, can form plasmonic self-cavities for terahertz light due to finite-size effects. Here we investigate how these effects enable cavity engineering in the ultrastrong coupling regime, with and without light.**

***Keywords*— van der Waals heterostructures, graphene plasmons, cavity engineering, on-chip THz spectroscopy, ultrastrong coupling.**

I. Introduction

Van der Waals heterostructures, formed by stacking two-dimensional crystals, host a wide range of quantum phenomena that can be tuned *in situ* with electrostatic gates. Each 2D material including the gates, which are most commonly made from graphite, can inherently act as plasmonic self-cavities, where finite-size effects confine the light into standing wave patterns of current density. As the plasmonic resonances of typical graphite gates fall in the GHz-THz range that corresponds to the same μeV-meV energy scale as the quantum phenomena they electrostatically control, it is possible that the self-cavity modes of graphite gates could also dynamically shape these emergent quantum phases.

However, probing such cavity-mediated electrodynamics has remained challenging. Device dimensions are deeply sub-wavelength compared to the relevant wavelengths of THz light, limiting the reach of conventional far-field spectroscopy.

II. Methods I

To overcome the size mismatch, we employed on-chip THz spectroscopy to investigate the intrinsic cavity conductivity of gate-tunable graphene heterostructures. As the carrier density is tuned, we observed spectral weight transfer and an avoided crossing between graphene and graphite plasmonic modes (see Fig. 1), demonstrating their ultrastrong coupling [1].

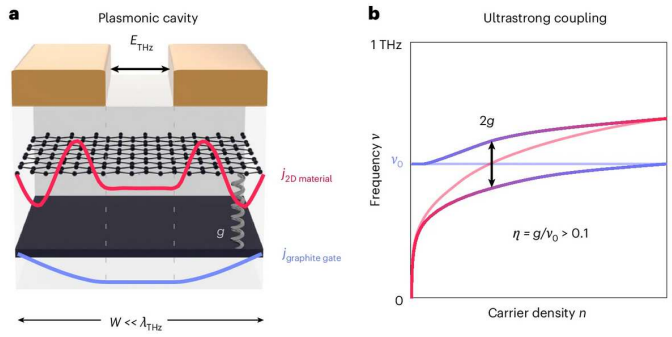

Fig. 1 **a**: Schematic of a subwavelength vdW heterostructure: a 2D material (in this work graphene) and a graphite gate embedded in a micropatterned dielectric created from the metallic transmission line of the on-chip THz spectroscope. Plasmonic self-cavity modes of a 2D material (red) and a graphite gate (blue) can couple. **b**: The 2D material's screened plasmon frequency (light red) is tuned via carrier density into resonance with the graphite mode, ν0 (light blue). The self-cavity modes of the 2D material and the graphite couple of different momenta couple due to resonant enhancement of unscreened currents in the transmission line gap, leading to an avoided crossing with energy splitting 2g. For $\eta = \frac{g}{\nu 0} > 0.1$, the system reaches the ultrastrong coupling regime. Figure adapted from [1] under a CC BY 4.0 license.

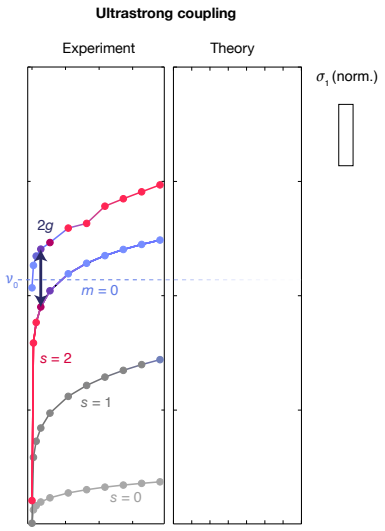

Fig. 2: The frequencies of the screened plasmonic modes in graphene can be tuned with carrier density into resonance with the screened graphite mode, ν0. The resonance condition can be achieved between the s = 2 (magenta) and m = 0 (blue) mode within the explored carrier density range. Both experimental data (left panel) and simulated data from the analytical theory (right panel) reveal that the coupling of graphene and graphite modes of different momenta exceed $\eta > 0.1$, marking the entry to the ultrastrong coupling regime. Figure adapted from [1] under a CC BY 4.0 license.

We developed an analytical theory [2] to capture these effects and provide design principles [3] for engineering cavity responses including guidelines to maximize or minimize the self-cavity coupling strength. Specifically, the coupling strength can be tuned through the geometry of the metallic transmission lines in the on-chip THz spectroscope. Wide transmission lines separated by a narrow nanogap yield negligible self-cavity coupling ($\eta = \frac{g}{\nu 0} \approx 0$), whereas narrow lines with a wide gap can reach the ultrastrong coupling regime, defined by $\eta > 0.1$, where cavity engineering of the thermodynamic ground state is expected to emerge [4].

III. Results and Discussion

Experimental results show:

- Multimodal plasmonic coupling between a graphene layer and its graphite gate across a measurement bandwidth of 0.05 – 1 THz.
- A normalized coupling strength of $\eta = 0.12$, indicating entry into the ultrastrong coupling regime.
- Strong agreement between measured and calculated spectra (see Fig. 2).

Calculations with the developed analytical theory show:

- A tunable self-cavity coupling mechanism governed by the sample and metallic transmission-line geometry, enabling coupling strengths in the range $0 \lesssim \eta \lesssim 0.2$ by design.

IV. Methods II

A remaining key question is whether THz illumination is required to activate these self-cavity effects, or whether vacuum fluctuations themselves can be reshaped by finite-size effects and a deliberately microstructured dielectric environment. Even in the absence of real photons, the electromagnetic vacuum at absolute zero exhibits quantum fluctuations that profoundly influence physical systems, giving rise to phenomena such as spontaneous emission, the Lamb shift [5], and the Casimir force [6]. Engineering these fluctuations through a (self-)cavity therefore offers a compelling route to tailor material properties.

In this context, we have recently demonstrated that a hovering complementary split-ring resonator (CSSR), operating in the absence of external illumination, can strongly influence a high-mobility GaAs heterostructure subjected to a magnetic field at millikelvin temperatures. These experiments revealed a breakdown of the topological protection of edge states in the integer quantum Hall regime [7], an enhancement of the quantum Hall energy gap at several fractional filling factors [8], and the cavity-QED stabilization of thermally disordered quantum Hall stripe phases [9].

Here we now extend this hovering-cavity concept to the much smaller length scales of van der Waals heterostructures to

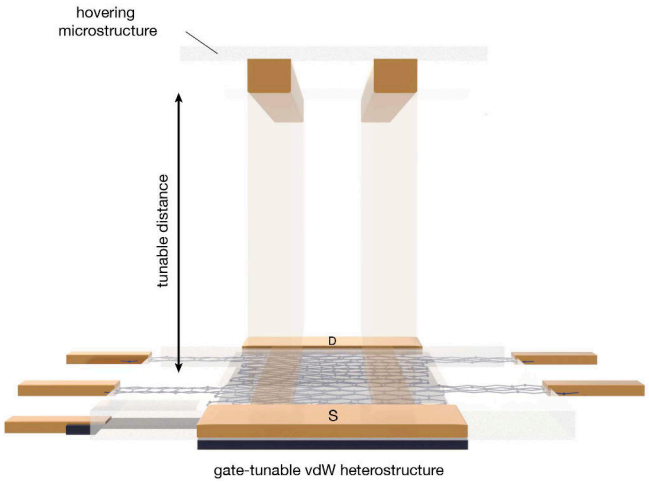

Fig. 3: Schematic of the hovering microstructure platform to explore the impact of the microstructure on the DC transport properties of a gate-tunable vdW heterostructure.

explore whether both intrinsic and externally engineered cavity vacuum fields can reshape the thermodynamic ground states of their emergent phases (see Fig. 3). The resulting platform enables systematic studies of cavity-modified vacuum fluctuations, with *in situ* referencing provided by a movable hovering microstructure architecture. By comparing DC transport measurements taken with the microstructure positioned in close proximity to the sample to those obtained when it is retracted far above it, we can directly determine the influence of the microstructure on the material's properties.

V. Conclusion

We have shown through on-chip THz spectroscopy that cavity engineering in van der Waals heterostructures is not only feasible but can arise intrinsically. Owing to finite-size effects, many of the constituent materials naturally form plasmonic self-cavities, enabling coupling strengths that reach the ultrastrong coupling regime. As experimental evidence for ground-state modification in these systems is scarce, we are now developing a hovering microstructure platform for van der Waals heterostructures that operates in the dark at millikelvin temperatures and strong magnetic fields.

Acknowledgments

We acknowledge support from the Max Planck-New York City Center for Non-Equilibrium Quantum Phenomena. G.K. and A.R. acknowledge support by the German Research Foundation through the Cluster of Excellence CUI: Advanced Imaging of Matter (EXC 2056, project ID 390715994). H.M.B., M.H.M. and M.W.D. acknowledge support from the Alexander von Humboldt Foundation. H.M.B. acknowledges financial support from the European Union under the Marie Sklodowska-Curie grant agreement no. 101062921 (Twist-TOC). The fabrication of terahertz circuitry optimization devices was supported by the US Department of Energy, Office of Science, Basic Energy Sciences, under Early Career Award DE-SC0024334. Development of the cavity coupling theory was supported by the Center on Programmable Quantum Materials, an Energy Frontier Research Center funded by the US Department of Energy (DOE), Office of Science, Basic Energy Sciences (BES), under award DE-SC0019443. K.W. and T.T. acknowledge support from the JSPS KAKENHI (grant numbers 21H05233 and 23H02052), the CREST (JPMJCR24A5), JST and World Premier International Research Center Initiative (WPI), MEXT, Japan. A.R. acknowledges support from the Grupos Consolidados (IT1453-22). The Flatiron Institute is a division of the Simons Foundation. At the early stages of the project, G.K. and K.K. were supported by SFB 925 – project 170620586/Deutsche Forschungsgemeinschaft (German Research Foundation). D.M.K. acknowledges funding by the Deutsche Forschungsgemeinschaft (DFG, German Research Foundation) within the Priority Program SPP 2244 '2DMP' – 443274199 and under Germany's Excellence Strategy – Cluster of Excellence Matter and Light for Quantum Computing (ML4Q) EXC 2004/1 – 390534769. A.M.P. was supported by the Defense Advanced Research Projects Agency (DARPA) under the QUAMELEON Advanced Research Concept. The views, opinions and/or findings expressed are those of the authors and should not be interpreted as representing the official views or policies of the Department of Defense or the US Government. D.M.K., M.A.S. and J.W.M. acknowledge funding by the Deutsche Forschungsgemeinschaft (DFG, German Research Foundation), 508440990 and 531215165 (Research Unit 'OPTIMAL'). M.A.S. was funded by the European Union (ERC, CAVMAT, project no. 101124492).

References

[1] G. Kipp et al. Nature Physics 21, 1926-1933 (2025) .

[2] M. H. Michael et al. (2025) arXiv:2505.12799.

[3] G. Kipp et al. (2025) arXiv:2511.23365.

[4] C. J. R. Duncan et al. Nature 647, 619-624 (2025).

[5] P. W. Milonni, *The Quantum Vacuum*. Elsevier, (1993).

[6] W. E. Lamb and R. C. Retherford. *Phys. Rev.*, vol. 72, no. 3, pp. 241–243 (1947).

[7] F. Appugliese et al. Science, 375(6584), 1030–1034 (2022).

[8] J. Enkner et.al. Nature 641, 884-889 (2025).

[9] L. Graziotto et al. arXiv:2502.15490 (2025).

Restoring Bloch's Theorem for Cavity Exciton Polaron-Polaritons

Michael AD Taylor[1,*] and Yu Zhang[1,†]

[1]Theoretical Division, Los Alamos National Laboratory, Los Alamos, NM, USA
*Corresponding author: mike_tay@lanl.gov
†Corresponding author: zhy@lanl.gov

***Abstract*—We introduce a hybrid photon–exciton–phonon quantum electrodynamics Hamiltonian to restore Bloch's theorem. The interchange of momenta between fermions and bosons breaks crystalline excitons' translational symmetry. Restoring said symmetry, we efficiently compute experimentally accessible observables, enabling investigations that elucidate material properties in strong coupling.**

***Keywords*— quantum electrodynamics, 2D materials, polarons**

In recent years, cavity and polariton physics have advanced dramatically, both experimentally and theoretically. We are now able to reach and probe the strong- and ultrastrong-coupling regimes for a wide variety of materials and cavity structures. Hybrid light-matter states created in these platforms offer powerful tools for engineering electronic structure and elementary excitations, with far-reaching implications for quantum materials, quantum information science, and micro- and optoelectronics. However, as theoretical studies seek to explain increasingly more complicated physical systems, the computational cost grows exponentially, necessitating approximations to make the calculations computationally tractable.

In condensed matter physics, Bloch's theorem drastically simplifies the complexity of calculating periodic systems by allowing each wavevector of the total Hamiltonian to be treated independently. However, this structure can break down upon interactions with other systems such photonic and phononic fields. In minimal-coupling cavity QED the transverse vector potential does not commute with the crystal momentum unless long-wavelength or single-mode approximations are imposed, and Fröhlich-type electron-phonon couplings similarly exchange momentum with the lattice. The resulting light-matter-phonon Hamiltonian is no longer block-diagonal in Bloch momentum, forcing many recent studies to resort to the site-basis under harsh approximations, removing any advantages gained by the periodic symmetry of the fermionic system.

In this work, we restore Bloch's theorem for an exciton model strongly coupled to both photonic and phononic modes, so-called exciton polaron-polaritons. This is done by performing a gauge-like transformation on the total system that changes the momentum frame from the exciton momentum to the polaron-polariton momentum. We demonstrate on a 2D exciton model how to formulate such a Hamiltonian, and demonstrate how the new framework drastically simplifies calculations of experimentally accessible observables like the dielectric function. By treating all degrees of freedom on the same footing while conserving translational symmetry, this theory opens the door to quantitatively accurate and symmetry-efficient simulations of cavity-modified quantum materials. This is particularly timely for Moiré superlattices and other van der Waals heterostructures, whose very large real-space unit cells make existing polaron-polariton simulations that rely on site bases and broken translational symmetry prohibitively costly. The theory presented here, however, does not suffer from the same shortcoming, and can be applied to existing inter-layer exciton models for Moiré superlattice structures, incorporating strong exciton-boson coupling without breaking the translational symmetry.

By taking advantage of the symmetries of the interactions between these degrees of freedom, we can create new quantum number, a so-called polaron-polariton wavevector, which turns our Hamiltonian block-diagonal in wavevector without using the long-wavelength approximation. While we demonstrate the advantages of this for static calculations such as band structures and dielectric functions, this method will drastically improve that computational speed of dynamics simulations, allowing each individual k-point to have its own independent dynamics. We expect this representation has far-reaching implications for strongly coupled fermion-boson systems due to its fundamental nature, opening the door to more investigations that elucidate materials properties in strong coupling with applications in tuning electronic/optical properties, and enhancing coherent transport. These have the potential enable research in very impactful fields like quantum transduction for quantum information science and quantum transport for microelectronics, whose systems can capitalize on this dynamic interplay between photons, phonons, and fermions.

Acknowledgments

We acknowledge support from the US DOE, Office of Science, Basic Energy Sciences, Chemical Sciences, Geosciences, and Biosciences Division under Triad National Security, LLC ("Triad") contract Grant 89233218CNA000001 (FWP: LANLECF7). This research used computational resources provided by the Institutional Computing (IC) Program and the Darwin testbed at Los Alamos National Laboratory (LANL), funded by the Computational Systems and Software Environments subprogram of LANL's Advanced Simulation and Computing

program. LANL is operated by Triad National Security, LLC, for the National Nuclear Security Administration of the US Department of Energy (Contract No. 89233218CNA000001).

PRE-CONFERENCE WORKSHOP

META Quantum Nanophotonics Workshop

7 contributions · pp. 1281–1291

Engineering Quantum Light with Perovskite Quantum Dots

Yury Rakovich[1,2,3,4*], Alexey Y Nikitin[2,4], Virginia Martínez-Martínez[5], Andrey Rogach[6], Igor Aharonovich[7]

[1]Centro de Física de Materiales (MPC), Donostia-San Sebastián, Spain
[2]Donostia International Physics Center, Spain
[3]Polymers and Materials, University of the Basque Country, Spain
[4]IKERBASQUE, Basque Foundation for Science, Spain
[5]Departamento de Química, Física, Universidad del País Vasco, Spain
[6]Department of Materials Science and Engineering, City University of Hong Kong, P.R. China
[7]School of Mathematical and Physical Sciences, University of Technology Sydney, Australia

*Corresponding author: yury.rakovich@ehu.eus

***Abstract*— Perovskite quantum dots (PCDs) have emerged as efficient room-temperature quantum light sources. This invited talk presents recent advances in controlling single- and multiphoton emission using plasmonic metasurfaces, doping, and van der Waals encapsulation, enabling reversible emission switching and enhanced photostability for practical quantum photonic applications.**

***Keywords*— quantum emitters, perovskite quantum dots, metasurfaces, nanophotonics, plasmonics.**

I. Introduction

Room-temperature quantum emitters are key enablers of scalable quantum communication and integrated quantum photonics. PQDs combine high radiative efficiency, short lifetimes, and solution-processable fabrication, making them attractive candidates for practical quantum light sources. However, challenges related to deterministic emission control, environmental stability, and the realization of advanced functionalities - such as tunable photon statistics and on-demand reconfigurability - at the single-emitter level remain.

II. Methods

We address these challenges through photonic and materials engineering. Plasmonic metasurfaces are employed to tailor the local density of optical states and actively control emission dynamics, including reversible switching between single-photon and multiphoton regimes. Complementary strategies such as transition-metal doping and van der Waals encapsulation are used to suppress photodegradation, blinking, and spectral diffusion at ambient conditions.

III. Results and Discussion

Coupling individual PQDs to plasmonic metasurfaces enables strong modification of their radiative properties through Purcell enhancement and tailored local electromagnetic environments. [1] By controllably varying the emitter-metasurface separation, we demonstrate reversible switching of photon statistics from antibunched single-photon emission to multiphoton emission, without altering the chemical composition or structural integrity of the PQDs. This metasurface-mediated control provides an active and noninvasive route to engineer quantum emission dynamics at the level of individual nanoemitters.

To address the intrinsic instability of PQDs under ambient conditions, complementary materials-engineering strategies are employed. Transition-metal (nickel) doping leads to exciton localization and substantially suppressed photodegradation, enabling highly pure and stable single-photon emission with narrow linewidths at room temperature.[2] In parallel, van der Waals encapsulation using hexagonal boron nitride creates an effective diffusion barrier against moisture and oxygen, strongly reducing blinking, spectral diffusion, and photobleaching while preserving the intrinsic emission characteristics.[3]

Together, plasmonic control and materials stabilization form a versatile platform for quantum light engineering. The combination of on-demand control over photon statistics, room-temperature operation, and enhanced environmental robustness establishes PQDs as reconfigurable building blocks for hybrid metasurface-quantum photonic systems.[4]

IV. Conclusion

The presented results demonstrate that PQDs, combined with metasurface and materials engineering, offer a powerful and scalable route toward practical quantum light sources. Active control, room-temperature operation, and enhanced stability position these systems for future integrated quantum photonic technologies.

Acknowledgments

This work was supported by the IKUR Strategy under the collaboration agreement between the Ikerbasque Foundation and MPC on behalf of the Department of Education of the Basque Government.

References

[1] A. Olejniczak, Z. Lawera, M. Zapata-Herrera, A. Chuvilin, P. Samokhvalov, I. Nabiev, M. Grzelczak, Y. Rakovich, V. Krivenkov, "On-demand reversible switching of the emission mode of individual semiconductor quantum emitters using plasmonic metasurfaces," APL Photonics, vol. 9, pp. 016107, 2024.

[2] J. Ryu, V. Krivenkov V., A. Olejniczak A., M. Arruabarrena, J. Janovec, A. Leonardo, V. Martínez-Martínez, A. Ayuela, A.Y. Nikitin, Y. Rakovich, „Nickel Doping Unlocks Ambient-condition Photostability in Individual Cesium Lead Bromide Perovskite Quantum Dots", Nano Letters, vol. 25, pp.16630–16636, 2025.

[3] J. Kim, K. Yamamura, J. Horder, J. Ryu, I. Zhigulin, N. Coste, A.Y. Nikitin, Y. Rakovich, I. Aharonovich, "Facile Van der Waals hBN Encapsulation and Stabilization of Perovskite Quantum Dots Emission", Advanced Functional Materials, 2026. https://doi.org/10.1002/adfm.202527591

[4] J. Ryu, V. Krivenkov, A. Olejniczak, A.Y. Nikitin, Y. Rakovich, Perovskite Nanocrystals as Emerging Single-Photon Emitters: Progress, Challenges, and Opportunities, Applied Physics Reviews, vol. 12, pp. 041323, 2025

Telecom-wavelength quantum nanophotonics with self-assembled quantum dots

Nir Rotenberg[1,*]

[1]Centre for Nanophotonics, Department of Physics, Engineering Physics & Astronomy, Queen's University, Canada
*Corresponding author: nir.rotenberg@queensu.ca

***Abstract*— This talk introduces novel telecom-wavelength quantum dots, grown by chemical beam epitaxy in indium phosphide. These bright emitters generate photons in both the telecom O- and C-bands and whose transitions approach the transform limit (i.e. are highly coherent). Nanophotonic structures are fabricated about these quantum dots, controlling and enhancing their interaction with photons.**

***Keywords*— quantum nanophotonics, quantum dots, photonic engineering, telecom-wavelength quantum optics.**

I. Telecom-Wavelength Quantum Dots

Telecommunication quantum light sources will be key components of emerging large-scale quantum technologies, and especially of any future quantum network. Such sources must be efficient, providing high quality – and in particular noiseless, photons in the telecom C-band where ultralow loss fibers are available. Here, we introduce a new platform for the generation and control of telecom-wavelength quantum light, based on self-assembled indium arsenide quantum dots (QDs) grown in an indium phosphide matrix. These QDs, grown in an ultrapure environment, are capable of supporting near noiseless light-matter interactions with no enhancement or charge control. We then present an integrated photonic platform based on these quantum dots, discussing how this enables highly directional light-matter interactions needed for scalable and on-demand quantum technologies.

Acknowledgments

This work was supported by the Canadian Fund for Innovation (CFI), the National Science and Engineering Research Council (NSERC), Queen's University, the Ontario Ministry of Universities and Colleges and funding from the National Research Council of Canada (NRC).

Subradiant entangled states in plasmonics and the quantization of radiative systems

Angela Demetriadou[1,*]

[1]School of Physics and Astronomy, University of Birmingham, Birmingham, B15 2TT, uk
*Corresponding author: a.demetriadou@bham.ac.uk

***Abstract*—Significant advances have been achieved in quantum nanoplasmonics in recent years. We demonstrate that, under appropriate conditions, plasmonic nanocavities can support the formation of subradiant entangled states between quantum emitters. In addition, we introduce an exact and complete second-quantization framework for open photonic systems with intrinsic radiative losses.**

***Keywords*— quantum plasmonics, nanoplasmonics, quantization, subradiant entanglement.**

I. Introduction

Since the demonstration of room-temperature strong coupling in nanoplasmonic systems, the field has progressed rapidly, enabling unprecedented control of light–matter interactions at the nanoscale. These advances have translated into a broad range of successful applications, including plasmon-enhanced photocatalysis and emergent ultrasensitive spectroscopies, alongside experiments achieving detailed control of polariton-exciton interactions in complex nanostructures. Despite this maturity, nanoplasmonic platforms are still widely viewed as incompatible with genuinely quantum operations and functionalities. Strong Ohmic and radiative losses in metallic nanostructures, together with rapid molecular decoherence at room temperature, are commonly believed to fundamentally limit coherence, thereby preventing the generation of entanglement, the preparation of nonclassical quantum states, or the execution of coherent quantum operations with meaningful fidelity.

In this talk, I show that plasmonic losses—traditionally regarded as a fundamental limitation for quantum plasmonics—can instead be exploited to facilitate the formation of persistent sub-radiant entangled states [1]. I will further discuss how the presence of multiple multipolar modes in plasmonic systems impact the formation of such entangled states [2] and how this understanding can be used to design new plasmonic devices that enahnce and stabilize sub-radiant entanglement [3]. Beyond the physical insights, I will introduce a new second quantization scheme for open, non-Hermitian nanophotonic systems [4] that incorporates radiative losses, without relying on an external bath or other phenomenological assumptions. This approach reveals intrisically non-Markovian dynamics in the interaction between open nanophotonic structures and quantum emitters, uncovering memory effects that are often not captured by other descriptions.

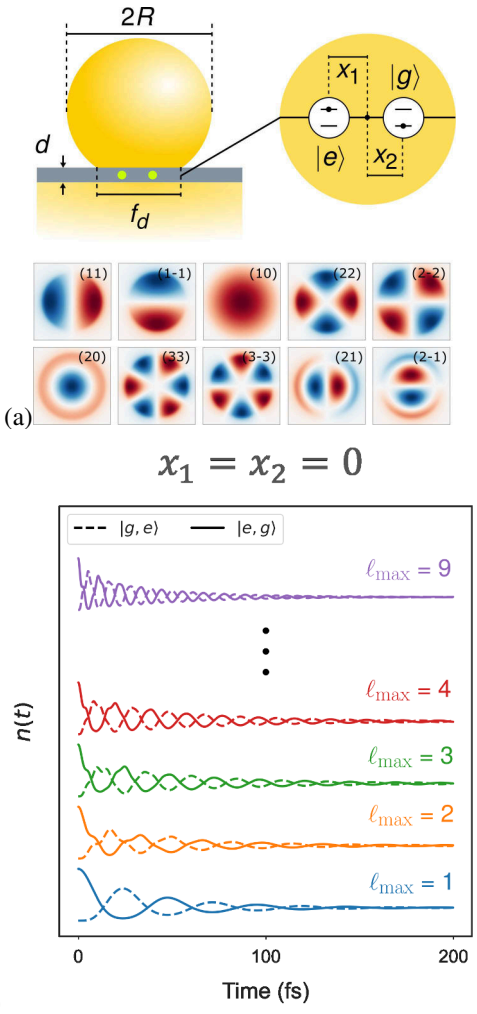

Fig. 1. (a)Nanoparticle on mirror geometry hosting multiple emitters in the gap and supports multiple multipolar modes. (b) The quantum dynamics of the two quantum emitters as they are increasingly coupled to higher-order modes.

II. Results and Discussion

We start with a phenomenological cavity Quantum Electrodynamics description for a system of multiple quantum emitters j in a plasmonic cavity with multiple multipolar

modes ξ (see Figure 1) [1], [2], [3]:

$$\mathcal{H} = \sum_{\xi=1}^{N} \omega_\xi \, a_\xi^\dagger a_\xi + \sum_{j=1}^{M} \frac{\omega_e}{2} \, \sigma_z^j + \\ + \sum_{\xi,j}^{N,M} \left[g_\xi(\mathbf{r}_j) \, a_\xi^\dagger \sigma_j + g_\xi^*(\mathbf{r}_j) \, a_\xi \sigma_j^\dagger \right], \tag{1}$$

where $a_\xi^\dagger$, a_ξ are the creation/annihilation operators of the plasmonic mode ξ with frequency ω_ξ and $\sigma_j^\dagger$, σ_j are the raising and lowering operators of the jth quantum emitter with transition frequency ω_e. The position-dependent coupling strength $g_\xi(\mathbf{r}_j)$ between mode ξ and quantum emitter j at position $\mathbf{r}_j$) is a complex quantity given by $g_\xi(\mathbf{r}_j) = g_\xi e^{i\phi_{\xi j}}$, with g_ξ its magnitude and phase $\phi_{\xi j}$ defined by the phase of the mode [2].

For such multimode systems, the population trapping mechanism is satisfied when a dark state $|\psi_D\rangle = \cos\theta \, |e,g\rangle + e^{i\chi} \sin\theta \, |g,e\rangle$ is decoupled from the cavity, while the corresponding bright state $|\psi_B\rangle = -e^{-i\chi} \sin\theta \, |e,g\rangle + \cos\theta \, |g,e\rangle$ decays rapidly. Here, $\theta \in [-\pi/2, \pi/2]$ and $\chi \in [0, 2\pi]$. So in general, the state $|\psi_D\rangle$ is dark (and therefore persistent) under the conditions $\left(\frac{g_{\xi 1}}{g_{\xi 2}}\right) e^{i(\phi_{\xi 1} - \phi_{\xi 2})} = -e^{i\chi} \tan\theta$, which is valid for any dissipative multimode cavity [3]. For plasmonic nanocavities, this condition is satisfied when the emitters are only coupled to either the even modes (see Figure 1(b)) or only the odd modes of the system, and hence only in these two cases persistent sub-radiant entangled states are formed. When both types of modes are simultaneously coupled to the quantum emitters (even if off detuned from the quantum emitter transition frequency), the sub-radiant entanglement is either rapidly decaying or cannot be formed. Based on these new findings, we design new plasmonic nanocavities that allow us to spatially separate the even and odd modes, and hence allow for the persistent formation of subradiant entangled states.

However, the aforementioned method phenomenologically accounts for radiative losses in the system by coupling the closed system into a reservoir bath, which effectively dissipates the energy in the system. Most methods use similar or equivalent techniques to model the radiative losses. Recently, we developed an exact and complete second quantization scheme for radiative, open and non-Hermitian systems that intrinsically accounts for the radiative losses of the photonic environment [4]. We start by enclosing the photonic system with a putative surface S whose shape matches the geometry of the nanophotonic device on which we apply the boundary condition $(\mathbf{E} \times \mathbf{H}) \cdot d\mathbf{S} = 0$ (Figure 2). This boundary is subsequently taken to infinity, which leads to a continuous set of Helmholtz solutions $\mathbf{u}_\xi(k, \mathbf{r})$. These mode functions are then transformed into a set of discreet set of pseudomodes

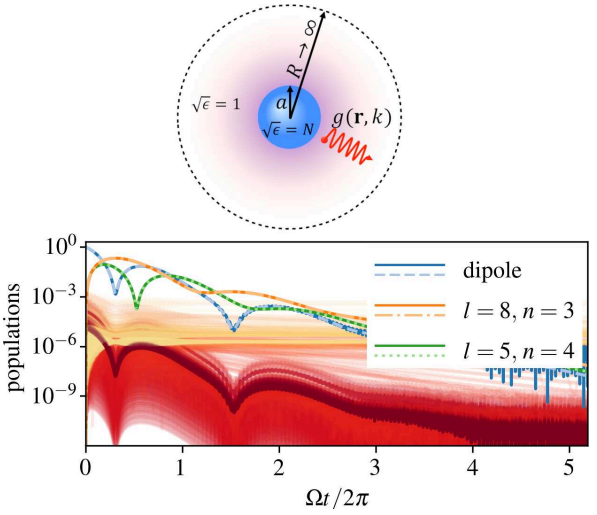

Fig. 2. The pseudomode picture by enclosing a scatterer with a surface, which is then taken to infinity, and the quantum dynamics of a spherical silicon particle coupled to a quantum emitter (dipole).

$\mathbf{v}_\xi(\mathbf{r})$, determined by the transformation [4]:

$$\int_0^\infty k \mathrm{d}k \rho(k) \mathbf{u}_\xi(k, \mathbf{r}) \mathbf{u}_\xi(k, \mathbf{r}') e^{-ick\tau} = \\ = \sum_n z_{\xi n} \mathbf{v}_{\xi n}(\mathbf{r}) \mathbf{v}_{\xi n}(\mathbf{r}') \Theta(\tau - \Delta_t(\mathbf{r}, \mathbf{r}')) \, e^{-icz_{\xi n}\tau}, \tag{2}$$

where $c_0 z_{\xi n}$ are the complex frequencies of the pseudomodes corresponding to the n^{th} resonance of mode ξ, and $\Theta(\tau - \Delta_t(\mathbf{r}, \mathbf{r}'))$ is a Heavyside-step function that physically accounts for the finite time delay for light to propagate from $\mathbf{r}'$ to $\mathbf{r}$. Now the electromagnetic fields can be expressed exactly by a time-dependent superposition of pseudomodes, with the intensity found from the field quadrature acting on $|\psi(t)\rangle$ [4]:

$$\mathbf{E}^+ |\psi(t)\rangle = i \sum_{\xi,n} \sqrt{\frac{\hbar c z_{\xi n}}{2\varepsilon_0 \varepsilon(\mathbf{r})}} \mathbf{v}_{\xi n}(\mathbf{r}) \tilde{b}_{\xi n}(t - \Delta t) \, e^{-icz_{\xi n} t}, \tag{3}$$

where $\tilde{b}_{\xi n}(t - \Delta t)$ is the pseudomode population.

We apply this method for a spherical silicon particle of radius $1\mu m$, and show the quantum dynamics of the system (Figure 2). The quantum emitter is on resonance with the two photonic modes $(8, 3)$ and $(5, 4)$, while all the other detuned modes give rise to many more dynamics of which some demonstrate non-Markovian (memory) effects, often ignored in quantum nanophotonics [4].

III. Conclusion

We have shown that subradiant entangled states can be formed in plasmonic nanocavities, given the right conditions, and introduce a new second quantization scheme that provides an exact and complete description for open, non-Hermitian photonic systems.

ACKNOWLEDGMENTS

This work was supported by Royal Society University Research Fellowship Grant Nos. URF\R1\180097 and URF \R \231024, Royal Society Research Grant No. RGS\R1\211093, Royal Society Research Fellows Enhancement Award No. RGF\EA\181038 and funding from EPSRC Grant Nos. EP\Y008774\1, EP\X012689\1 and the CDT in Topological Design Grant No. EP\S02297X\1.

REFERENCES

[1] K. Bedingfield, B. Yuen, and A. Demetriadou, "Subradiant entanglement in plasmonic nanocavities," *Physical Review B*, vol. 111, pp. 075420, 2025.

[2] A. Crookes, B. Yuen and A. Demetriadou, "Collective multimode strong coupling in plasmonic nanocavities," *Nanophotonics*, vol. 14, pp. 2065–2073, 2025.

[3] A. Crookes, B. Yuen and A. Demetriadou, "Taming plasmonic nanocavities for persistent entanglement," *Physical Review B*, vol. 112, pp. 085427, 2025.

[4] B. Yuen and A. Demetriadou, "Exact Quantum Electrodynamics of Radiative Photonic Environments," *Physical Review Letters*, vol. 133, pp. 203604, 2024.

Quantum optical metasurfaces for photon pair generation

Igal Brener

Center for Integrated Nanotechnologies, Sandia National Laboratories, USA
ibrener@sandia.gov

***Abstract*—Resonant dielectric metasurfaces with multiple engineered modes, especially high-Q qBICs, enable efficient nonlinear conversion and quantum-light generation without bulk phase matching. They provide control of biphoton polarization, allow two-photon interference between overlapping SPDC channels, and, via symmetry-designed nonlocal quadromer lattices, yield orders-of-magnitude enhancement of four-wave mixing.**

***Keywords*— metasurfaces, SPDC, photon-pairs, quantum, nonlinear optics**

I. Introduction

Resonant dielectric metasurfaces are emerging as a single platform where nonlinear frequency conversion and quantum-light generation can be engineered by design rather than by bulk phase matching. [1] In subwavelength nonlinear media, metasurface resonances effectively define which nonlinear pathways are accessed and how the generated light is structured in spectrum, directionality, and polarization. By incorporating multiple resonances—particularly high-Q quasi-bound states in the continuum (qBICs)—metasurfaces move beyond "field enhancement" toward devices that can shape both classical and quantum states of light.

A key capability enabled by qBIC-based metasurfaces is polarization engineering of spontaneously generated photon pairs. Polarization tomography of nondegenerate SPDC shows that the polarization state of a resonant photon can closely follow the far-field polarization of the driving qBIC mode, making polarization an intrinsic design parameter set by symmetry breaking and the chosen resonances. [2] Furthermore, controlling the Q-factors of the resonances associated with the signal and idler photons can enable separable two-photon polarization states that are attractive for heralded single-photon generation with programmable polarization.

With sufficient efficiency, multichannel SPDC in a single metasurface becomes accessible and allows quantum interference effects to appear directly in the biphoton spectrum. Using a favorable crystal orientation in GaAs to improve overlap with $\chi^{(2)}$ boosts SPDC rates enough that photon pairs generated through a high-Q qBIC channel and a low-Q Mie-like channel can contribute simultaneously over the same spectral region. When a polarization analyzer erases the distinguishability between these two pathways, the biphoton spectrum exhibits a Fano lineshape, providing evidence of biphoton interference. [3]

Further improving parametric processes to include $\chi^{(3)}$ nonlinearities requires a different paradigm for designing multiresonant nonlocal metasurfaces. A symmetry-based rational framework built around "quadromer" lattices (four elements per unit cell) uses double band folding and selection rules to realize several qBIC resonances whose free-space polarizations, Q-factors, mode profiles, and spectral separations can be chosen in a predictable and fabrication-robust way. Applying this design paradigm to $\chi^{(3)}$ processes enabled several-orders-of-magnitude enhancement of four-wave mixing compared to unpatterned films. [4, 5]

Overall, these results point to a coherent route toward compact meta-optics where symmetry, nonlocality, resonance engineering, and material orientation jointly enable efficient nonlinear conversion and programmable quantum-light generation, including controlled interference between resonant channels.

Acknowledgments

This work was supported by the U.S. Department of Energy, Office of Basic Energy Sciences, Division of Materials Sciences and Engineering and performed performed, in part, at the Center for Integrated Nanotechnologies, an Office of Science User Facility operated for the U.S. Department of Energy (DOE) Office of Science.

References

1. T. Santiago-Cruz, S. D. Gennaro, *et al.*, "Resonant metasurfaces for generating complex quantum states", Science **377**, 991 (2022).
2. J. Noh, T. Santiago-Cruz, *et al.*, "Quantum Pair Generation in Nonlinear Metasurfaces with Mixed and Pure Photon Polarizations", Nano Lett. **24**, 15356 (2024).
3. J. Noh, T. Santiago-Cruz, *et al.*, "Fano interference of photon pairs from a metasurface", Light: Science & Applications **14**, 371 (2025).
4. S. C. Malek, C. F. Doiron, *et al.*, "Robust multiresonant nonlocal metasurfaces by rational design", Nanophotonics **14**, 449 (2025).
5. S. C. Malek, T. Norden, *et al.*, "Giant Enhancement of Four-Wave Mixing by Doubly Zone-Folded Nonlocal Metasurfaces", ACS Nano **19**, 35609 (2025).

Ultrasensitive nanothermometry with single organic dye molecules

M. Musavinezhad[1], J. Renger[1], S. Götzinger[1,2], A. Shkarin[1,*], V. Sandoghdar[1,2]

[1]Max Plank Institute for the Science of Light, 91052 Erlangen, Germany
[2]Department of Physics, Friedrich Alexander University Erlangen-Nuremberg, 91058 Erlangen, Germany
*Corresponding author: alexey.shkarin@mpl.mpg.de

***Abstract*—We use single organic dye molecule at cryogenic temperatures as a readout of the state of a nearby two-level system (TLS). The temperature dependence of the TLS behavior allows us to perform nanoscale thermometry with sub-millikelvin sensitivity. We report on the detection of sub-picowatt heat generation from a single molecule.**

***Keywords*— quantum emitters, dye molecules, single-molecule spectroscopy, nanothermometry.**

Single organic dye molecules at cryogenic temperatures serve as high-quality quantum emitters, demonstrating large light-matter interaction cross-section, negligible dephasing, high photon count, and narrow transition lines[1]. Importantly, their transition frequency and linewidth are sensitive to the properties of the environment such as electric field, strain, and temperatures. This lets them function as an optical interface to the local excitations, an important capability for realizing hybrid quantum systems.

In our work, we use dibenzoterrylene (DBT) dye molecules inside nano-printed anthracene crystals, which has been demonstrated as a versatile platform for quantum optical experiments[2]. We investigate in detail a molecule which is dispersively coupled to a nearby two-level system (TLS). Due to the narrow optical linewidth, different TLS states lead to resolved peaks (see Fig. 1a) in the molecule absorption spectrum, which lets us investigate the TLS dynamics by observing the molecule's spectral jumps. We find that the transition rate between the two TLS states obeys the Arrhenius activation law and is, therefore, extremely sensitive to the local temperature. Thus, combined with the molecular readout, it implements an optically-addressable nanometer-scale cryogenic thermometer with mK-level temperature sensitivity[3].

We first showcase this sensitivity by detecting temperature changes caused by laser-induced heating with a power of about $5\,\mathrm{nW}$ induced about $10\,\mu\mathrm{m}$ away, resulting in a temperature change of $1.5\,\mathrm{mK}$. After that, we use another "heater" molecule at a distance of about $100\,\mathrm{nm}$ as a localized optically-induced point heat source. Surprisingly, despite estimated heating power of about $1\,\mathrm{pW}$, such molecular heater induces a much larger temperature change of about $50\,\mathrm{mK}$ (see Fig. 1b). This is about three orders of magnitude larger than the expectations from the standard Fourier heat transport suggesting $\Delta T \propto 1/r$, which highlights qualitatively different heat behavior at these short length scales and cryogenic temperatures.

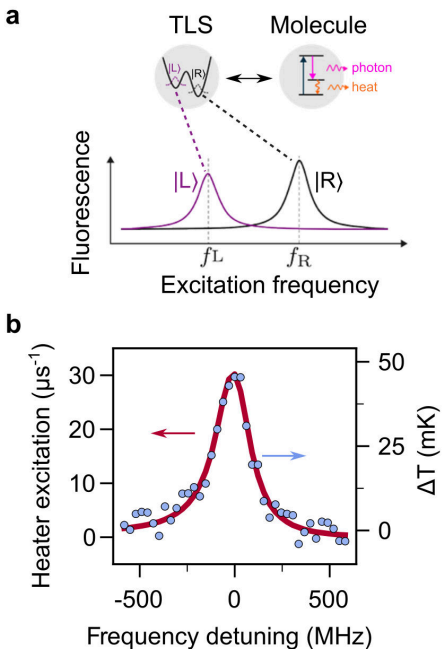

Fig. 1. (a) Illustration of dispersive coupling of a TLS to a single molecular emitter. (b) Excitation rate of a heater molecule (red line, left axis), and the corresponding change in the detected temperature (blue dots, right axis).

Our work demonstrates the utility of dye molecules for detecting and manipulating their environment, serving both as optical interfaces for detection of the nearby TLS state, and as a local optically controlled heat source. In the future, we plan to extend the TLS thermometry approach to different kinds of heaters and environment geometries to explore the intricacies of nanoscale heat transport.

References

[1] C. Toninelli, I. Gerhardt, A. S. Clark, A. Reserbat-Plantey, S. Götzinger, Z. Ristanović, M. Colautti, P. Lombardi, K. D. Major, I. Deperasińska, W. H. Pernice, F. H. L. Koppens, B. Kozankiewicz, A. Gourdon, V. Sandoghdar, and M. Orrit, "Single organic molecules for photonic quantum technologies", *Nature Materials*, **20**, 1615–1628 (2021)

[2] M. Musavinezhad, J. Renger, J. Zirkelbach, T. Utikal, C. U. Hail, T. Basché, D. Poulikakos, S. Götzinger, and V. Sandoghdar, "High-Resolution Cryogenic Spectroscopy of Single Molecules in Nanoprinted Crystals", *ACS Nano*, **18**, 21886–21893 (2024)

[3] M. Musavinezhad et al., *in prep* (2026)

Thermalization of photons in disordered scattering media

V. Krachmalnicoff [1,*], L. Soncin[1], Y. De Wilde[1], R. Pierrat [1], R. Carminati[1]

[1]Institut Langevin, ESPCI Paris, CNRS, PSL University, Paris, France

*Corresponding author: valentina.krachmalnicoff@espci.fr

***Abstract*—We show the first demonstration of photon thermalization in a scattering medium interacting with Rhodamine molecules. Scattering and fluorophores' absorption and emission cycles drive dramatic changes of the emission spectrum. A delicate balance between these phenomena leads to an emission spectrum following a Bose-Einstein distribution with a non-vanishing chemical potential.**

***Keywords*— Thermalized radiation, Scattering, Fluorescence, Blackbody**

I. Introduction

A blackbody is a source whose emission depends only on its temperature. The number of emitted photons and their wavelength is described by the Planck's law. In such source, photons exhibit a vanishing chemical potential, meaning that their number is not conserved when the temperature of the blackbody is varied.

It has been shown that a different behaviour can be observed for photons emitted by laser-pumped Rhodamine fluorescent molecules in a cavity [1]. In such a system, multiple absorption-emission cycles generate an equilibrium photon gas characterised by the temperature of the dye solution, and by a chemical potential that depends on the population of the excited and fundamental electronic molecular levels. The chemical potential is therefore controlled by the external pumping, independently of temperature.

Multiple scattering of light in a disordered medium can be used to increase the time that photons spend in the medium. Therefore multiple scattering can replace the role of a cavity in an apparently simple and efficient way and can be used to promote absorption-emission cycles by an ensemble of emitters immersed within the medium. Replacing the cavity by a multiple scattering medium is at the heart of the generation of random laser emission [2].

II. Results and Discussion

In this talk we will show the first demonstration of photon thermalisation in a scattering medium interacting with Rhodamine molecules [3], in a regime which is far from the one of random lasers that require both multiple scattering and large pump power. Studied samples with a fixed density of Rhodamine and increasing densities of scatterers are shown in fig.1. We will show a dramatic change of the Rhodamine emission spectrum driven by both scattering and fluorophores' absorption and emission cycles. Such modification strongly depends on the density of scatterers and fluorophores. A delicate balance between these phenomena leads to photon thermalisation in which the emission spectrum follows a Bose-Einstein distribution with a non-vanishing chemical potential. We demonstrate that the number of emitted photons is driven by the chemical potential, set by the external pumping, and that the spectrum is thermalised at the temperature of the sample.

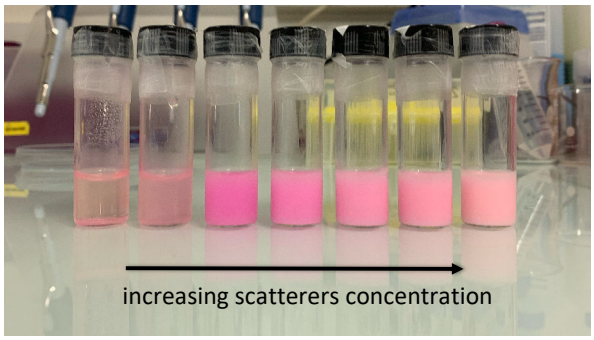

Fig. 1. Samples containing an aqueous solution of Rhodamine and increasing densities of scatterers.

III. Conclusion

We have demonstrated thermalisation of photons in an active scattering random medium. This work opens interesting outlooks for the study of thermalisation and of Bose-Einstein condensation in simple disordered scattering media and its difference from the random laser regime.

Acknowledgments

This work was supported by ANR FLUOSCATT.

References

[1] J. Klaers, F. Vewinger, and M. Weitz, "Thermalization of a two-dimensional photonic gas in a 'white wall' photon box," *Nature Physics*, vol. 6, 512–515, 2010

[2] H. Cao, *Opt. Photon. News*, vol. 16, 24, 2005

[3] L. Soncin et al., in preparation (2026).

Enhanced Plasmon-Emitter Coupling and Emission at the Single-Molecule Level

R. Margoth Córdova-Castro[1,*]

[1]Department of Physics, University of Ottawa, Canada
*Corresponding author: rcordova@uottawa.ca

***Abstract*— We show that using Purcell enhanced emitters coupled to high LDOS metamaterials and detected at the single-molecule level, can serve to translate very minute changes in the electromagnetic environment and in nanopositions impossible to detected, to measurable signals such as bright point sources.**

***Keywords*— bright single-emitter, Purcell factor, dispersive metamaterials, plasmonic, single-molecule super localization microscopy.**

I. Introduction

Controlling emitter-matter interaction beyond the nanoscale resolution and at the single-emitter level is a key challenge for on-chip emerging quantum applications. The rate at which an emitter can convert its excited-state energy into a photon increases as more photonic states are available to radiate into, which is quantified by the local density of states (LDOS) and the Purcell factor. The efficiency with which a single quantum emitter can generate photons in a prescribed optical mode depends on a number of factors: efficiency of excitation (absorption cross-section of the system), the quantum yield of emitted fluorescence and overall collection efficiency.

Coupling single emitters to nanostructures that support very small mode volumes can enhance the interaction. Using the Purcell enhanced emitters can serve to translate very minute changes in environment and nanopositions impossible to detected to measurable signals such as bright point spread functions (PSFs) in an imagine system and the spontaneous emission lifetime via single-photon avalange diodes.
Achieving experimentally systems composed of single quantum emitters coupled to metasurfaces and plasmonic nanoantennas that presents high density of photonic states raises several difficulties, namely: the difficulty of fabricating nanodevices at such small dimensions where high localization and enhancement of electromagnetic fields can be achieved, fabricating the nanomaterial in a controllable and scalable way, coupling the emitters to it (in particular to the regions featuring high LDOS), and observing where these light-matter interactions occur at the nanometer scale. Yet, controlling and measuring these effects at super resolution opens new possibilities for non-invasive quantum nanometrology for sensing small electromagnetic fields and a small density of viruses and viral fragments. In this work, we aim to overcome these challenges by coupling single emitters to a unique plasmonic nanomaterial platform that supports a very rich spectrum of optical modes with extremely high field enhancement and photonic density of states.

II. Methods

We apply super-resolved measurements which unveil unprecedented non-averaged high Purcell factors, giving us access to observe the fine details of quantum light-matter interaction at the nanoscale; simultaneously mapping the position of single emitters and its spontaneous emission decay rate modified by the enhanced density of photonic states in unique engineered material platforms. Far-Field Single-Molecule Super Localization Microscopy (SMLM) allows the detection of single- emitter position and emission rate modification without disrupting the local environment with metallic probes. The single-photon emission lifetime is measured by a single-photon avalanche diode connected to a time correlating single photon counter (TCSPC) with picoseconds resolution and correlated with SMLM to image the Purcell factor enhancement below the diffraction limit. technologies. To compare our measured single-emitter interactions at the nanoscale, we numerically solved Maxwell's equations to analyze the interaction of single electric dipoles with the 3D plasmonic nanorod and hollow nanocone metamaterials, we carried out total and radiated contributions at various positions $\boldsymbol{r}_i$, considering two distinct dipole orientations (in-plane and out-of-plane), across the visible spectrum. To assess the enhanced radiated power, we simulated finite square arrays of increasing size, monitoring the convergence of the results.

III. Results and Discussion

The strong variation of the single emitter properties when coupled to the truncated plasmonic cones placed in a square array with 250nm lattice constant, makes this approach ideal for molecular sensing at the nanoscale resolution, inferring the nano-position and orientation of molecules, or electromagnetic variations inside the 3D nanomaterial.
Hyperbolic nanorod metamaterials represent a cutting-edge approach to manipulating light at the nanoscale, we used plasmonic nanorod metamaterial with 100 nm lattice constant, for spontaneous emission enhancement in the hyperbolic

dispersion region observed significant enhance from nanosecond to picosecond lifetime at the single-molecule level. Both 3D plasmonic metamaterials can be manufactured with centimeter scalable fabrication technique. In addition to their unique anisotropic dispersion, spectral tunability, and fabrication versatility offer promising routes toward scalable quantum photonic devices, ultrasensitive sensors, and light sources with unprecedented efficiency.

Non only for photoactivatable organic single-molecules but for blinking CdS quantum dots and quantum platelets we observe significant improvement of the photophysical properties when coupled to the plasmonic metamaterials in the visible spectra range.
By acceleration of the spontaneous emission process the number of photons per second can significantly increase achieving a bright single photon, yielding quantum light behavior at room temperature. In addition, this makes the single-photon emission rate a precise measure of location, far more accurate than the optical resolution from the same photon. The calculated total decay rate enhancement values vary depending on the emitter position and dipolar moment orientation. For the hollow nanocones the highest values are observed for dipoles placed on the top ring of the truncated cone while for the nanorod metamaterial the coupling effect between nanostructures is more pronounced, showing the highest enhanced emitter-plasmon interaction in the middle of the metamaterial along the rod axis.

IV. Conclusion

We apply super-resolved measurements on coupled plasmon-emitter system with enhanced LDOs, which unveil unprecedented non-averaged high Purcell factors, giving us access to observe the fine details of quantum light-matter interaction at the nanoscale; simultaneously mapping the position of single emitters and its spontaneous emission decay rate modified by the enhanced density of photonic states in unique engineered material platforms. Our findings demonstrate the promise of single-molecule emitters in nanoscale devices to developing quantum nanophononics technologies.

References

1. Córdova-Castro, R. M., van Dam, B., Lauri, A., Maier, S. A., Sapienza, R., De Wilde, Y., Izeddin, I., Krachmalnicoff, V.. “Single- emitter super resolved imaging of radiative decay rate enhancement in dielectric gap nanoantennas”, *Light: Science & Applications*, 13, 2024.

2. Jonker, D., Jafari, Z., Winczewski, J., Eyovge, C., Berenschot, J. W., Tas N. R., Gardeniers J. G. E., De Leon, I., and Susarrey-Arce, A., “A wafer-scale fabrication method for three dimensional plasmonic hollow nanopillars,” Nanoscale Adv., 3, 2021.

GENERAL SESSION

Plasmonics and Nano-Optics

4 contributions · pp. 1293–1303

Epsilon-near-zero mode in highly doped GaN thin films

Julia Inglés-Cerrillo[1,*], Maria Villanueva-Blanco[1], Benjamin Damilano[2], Stéphane Vézian[2], Miguel Montes Bajo[1], Adrian Hierro[1].

[1]ISOM, Universidad Politécnica de Madrid, Spain
[2]Univeristé Côte d'Azur, CNRS, CRHEA, Valbonne, France
*Corresponding author: julia.ingles@upm.es

***Abstract* — We analyze the plasmonic properties of highly doped GaN thin films on Si, and show that they exhibit low optical losses and frequencies up to 3 µm. We identify the epsilon-near-zero (ENZ) and near-zero-index (NZI) regions and demonstrate the ENZ character of the polaritonic mode near the plasma frequency.**

***Keywords* — GaN, epsilon-near-zero, near-zero-index, hybrid plasmon-phonon polaritons, thin layers.**

I. Introduction

Epsilon-near-zero (ENZ) materials, defined by $|\mathrm{Re}(\varepsilon)| < 1$, enable the confinement of light within sub-wavelength regions, along with other unique light propagation characteristics. [1,2] To reduce losses in this regime, materials with both near-zero permittivity and $n < 1$ refractive index, known as near-zero-index (NZI) materials, are desired. When both conditions are satisfied, the resulting region is classified as a low-loss ENZ medium combining strong light confinement with reduced optical losses. [2] To achieve this behavior in the mid-IR, heavily doped semiconductors are required, and those compatible with current technologies are most desirable. [3]

Although gallium nitride (GaN) is one of the key semiconductors in industry today, it has not been widely investigated within the plasmonic field or for ENZ-related applications. The present work addresses this gap by providing the first comprehensive study of the plasmonic properties of GaN over Si, including the experimental demonstration of a plasmonic low-loss ENZ mode in the mid-IR. We report highly doped GaN thin films and by analyzing its optical behavior, we establish GaN as a viable low-loss plasmonic ENZ material in the mid-IR.

II. Methods

All the samples employed in this work were grown by molecular beam epitaxy (MBE) on resistive Si (111) substrates. Each sample consists of a highly doped, 100 nm-thick GaN layer deposited on a 100 nm-thick AlN layer, grown on a 2-inch substrate.

Reflectance measurements were carried out in a Fourier Transform Infrared (FTIR) Spectrometer, using p-polarized incident light. Additionally, to match the light in-plane momentum to the polariton momentum and excite the SPPs and SPhPs, the attenuated total reflectance (ATR) technique was used in Otto configuration, using a ZnSe prism with a value of the refractive index of 2.37. The angle of incidence at the prism−air gap interface was controlled from 39° to 59°.

Simulations of the reflectance spectra and the dispersion curves of our structures were made employing the Transfer Matrix Method (TMM), defining the full layer structure of our samples by defining each material by its individual dielectric function and thickness.

Calculations of the band structure and charge distribution were performed using the simulation software *BandEng*. [4]

III. Results and Discussion

Five samples of highly doped GaN thin layers are analyzed in terms of their plasmonic response. **Fig. 1 (a)** shows the measured reflectance spectra of all samples in the region where the minimum corresponding to their plasma frequency is observed in each case. By fitting the measured spectra with the TMM model, we extract the values of plasma frequency (ω_p), which ranges from 2500 cm^{-1} (4 µm) to 3350 cm^{-1} (3 µm), and the optical losses, showing values of 25-30% of the plasma frequency in all cases. The dielectric function of GaN for each sample is then calculated using these extracted parameters, in addition to those related to the phonon resonances of GaN, which are likewise measured and fitted using the TMM model, following the same procedure as for the plasma frequency. **Fig. 1 (b)** shows the case of the most heavily doped sample, showing a zoomed-in version of the spectral region near the plasma frequency, where the ENZ and NZI conditions are satisfied and indicated in dark and light blue bands, respectively. It is important to note that a spectral band exists where these two regimes overlap, resulting in a low-loss ENZ behavior of the material at those frequencies. In the case represented in **Fig. 1 (b)**, the low-loss ENZ regime is found from 2990 to 3540 cm^{-1}.

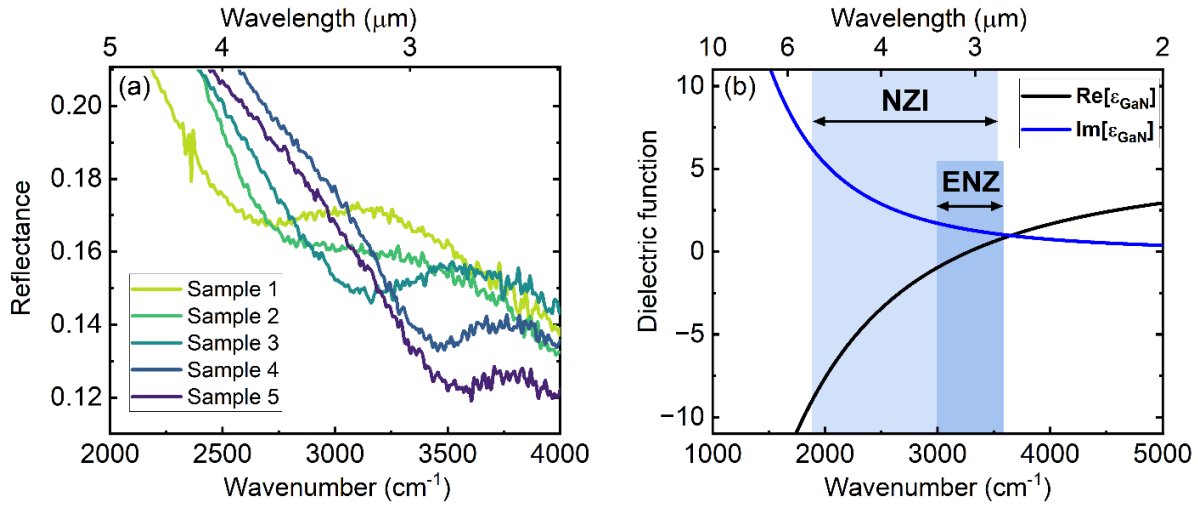

Fig. 1: (a) Reflectance measurements of the series of five samples used in this work, showing the region where the minima corresponding to the plasma frequency are found. (b) Calculated dielectric function of GaN of the most heavily doped sample in the spectral region near the crossover wavelength, including the regions where the material satisfies the ENZ and NZI conditions

Due to the fact that the GaN thin layers in our structures have a thickness of only 100 nm, we anticipate observing a resonance associated with the polaritonic mode near the plasma frequency which is non-dispersive with the incidence angle, a defining feature of ENZ modes in thin films. [2,5] **Fig. 2 (a)** shows the ATR data for the case of the most heavily doped sample. The measurements were made to demonstrate the non-dispersive character of the reflectance minima, which can be deduced from the figure. However, in order to improve visibility, the inset shows the data after a straight baseline has been subtracted, making it evident that the position of the minimum remains pinned when changing the incidence angle. This serves as the experimental demonstration of ENZ nature of the polaritonic mode near the plasma frequency in GaN thin films.

To further validate the ENZ character of the observed non-dispersive mode, we construct the dispersion curves of such sample, shown in **Fig. 2 (b)**. The cone limited by the grey lines represents the measurable range of our experimental ATR setup, and the circular dots are the experimentally resonance frequencies. It can be observed that the high-energy mode is pinned very close to wp, as observed experimentally in **Fig. 2 (a)**, showing a flat dispersion at higher k_x that confirms its ENZ character. On the other hand, the calculation of the dispersion curves allows us to analyze the behavior of all the other polariton modes present in the thin-film structures, at lower frequencies. In particular, it can be observed that the low-energy surface plasmon polariton (SPP) mode couples to the

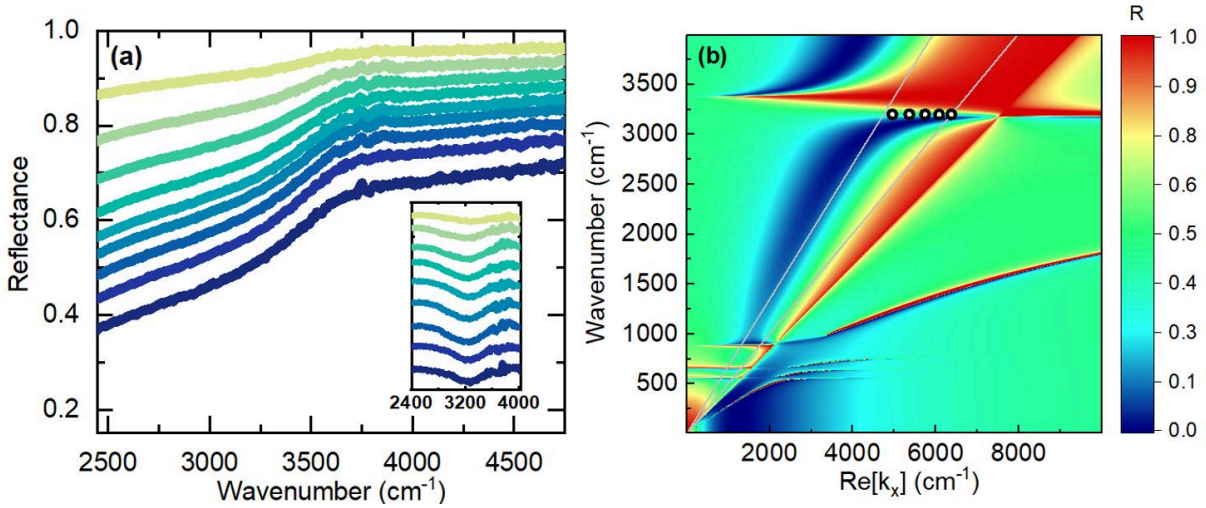

Fig. 2: (a) ATR angle-resolved measurements of the most heavily doped sample. Inset shows the measurements after subtracting a straight baseline, to improve visibility of the minima. The angle of incidence was varied from 41° to 57° in steps of 2°. (b) Simulated dispersion curves assuming low optical losses for the most heavily doped sample. The cone limited by the grey lines represents the measurable range of our experimental ATR setup and the circular dots are the experimentally determined resonance frequencies.

multiple surface phonon polariton (SPhP) modes it encounters in its way up in frequency. This coupling indicates the hybrid nature of all surface polariton modes present in the thin film structures.

IV. CONCLUSION

This work provides the first demonstration of a plasmonic ENZ mode in GaN thin films, highlighting GaN as a promising platform for mid-IR ENZ plasmonics and enabling its future integration into infrared photonic technologies.

ACKNOWLEDGMENTS

This work was partly supported by Projects PID2024-156706OB-C2 funded by MICIU/AEI/10.13039/501100011033/FEDER,UE and PDC2023-145827-C2 funded by MICIU/AEI/10.13039/501100011033 and by European Union Next Generation EU/ PRTR

REFERENCES

[1] J. Wu, Z. T. Xie, Y. Sha, H. Y. Fu, Q. Li, "Epsilon-near-zero photonics: infinite potentials", *Photon. Res.* **2021**, *9*, 1616.
[2] N. Kinsey, C. DeVault, A. Boltasseva, V. M. Shalaev, "Near-zero-index materials for photonics", Nat Rev Mater 2019, 4, 742.
[3] G. V. Naik, V. M. Shalaev, A. Boltasseva, "Alternative Plasmonic Materials: Beyond Gold and Silver", *Advanced Materials* 2013, *25*, 3264.
[4] M. Grundmann, BandEng Software, 2005. Available at: https://my.ece.ucsb.edu/mgrundmann/bandeng/
[5] S. Campione, I. Brener, F. Marquier, "Theory of epsilon-near-zero modes in ultrathin films", Phys. Rev. B 2015, 91, 121408.

Symmetry enhanced modal design for magnetic emission from plasmonic core-satellite resonators

Joshua Davis[1], Sébastien Bidault[2], Mathieu Mivelle[3], Mona Tréguer-Delapierre[4], and Alexandre Baron[1, 5, *]

[1]Centre de Recherche Paul Pascal, Université de Bordeaux, F-33600, Pessac, France
[2]Institut Langevin, ESPCI Paris, Université PSL, CNRS, F-75005 Paris, France
[3]Sorbonne Université, CNRS, Institut des NanoSciences de Paris, INSP, F-75005 Paris, France
[4]Université Bordeaux, CNRS, ICMCB, UMR 5026, F-33600 Pessac, France
[5]Institut Universitaire de France, 1 rue Descartes, F-75231 Paris Cedex 05, France
*Corresponding author: alexandre.baron@u-bordeaux.fr

***Abstract*—Realistic highly symmetric dielectric-metal core-satellite particles are proposed as promising structures to enhance magnetic dipole emission. Magnetic Purcell factors in excess of 200, low losses, robustness to emitter orientation and placement, are all achieved. Quasi-normal modes enhance the optimization, while mode volumes reveal the physics behind the exceptional structure properties.**

***Keywords*— metamaterials, Purcell factor, optics, quasi-normal modes, magnetic emission.**

I. Introduction

Interactions between light and matter are typically dominated by the electric dipole (ED) transitions interaction with the electric field. Nevertheless, the interaction Hamiltonian contains other terms, $H_{int} = -\mathbf{p}\cdot\mathbf{E} - \mathbf{m}\cdot\mathbf{H} - ...$ [1]. In some lanthanide ions, such as Eu^{3+}, which contain a magnetic dipole (MD) transition, ED transitions are parity forbidden. In practice, second order effects, cause the ED transition to become dominant. This motivates the search for other strategies to boost the MD transition over the ED transition. Famously, Purcell showed that the transition rate of an emitter in a cavity can be altered by modifying the photonic density of states in its environment, a phenomenon known as the Purcell effect [2]. Careful resonator design can enhance the MD transition while simultaneously suppressing the ED transition, with a plethora of structures having been proposed to this end [3]. Regardless, challenges still persist, for example, many designs only yield significant enhancements for emitters oriented along a single axis, a factor which is difficult to control experimentally [3]. Plasmonic resonators, are usually associated with large non-radiative losses, while dielectric resonators typically only have large Purcell factors (PF)s for resonators at the micro-scale, with specific emitter locations and orientations, and fabrication remains challenging. More generally, the design of these resonators also remains a challenge due to the large parameter space, which includes the emitters location and orientation, the source wavelength, and any geometrical degrees of freedom for the resonator. We solve both of these problems by designing efficient, isotropic MD emitters with large quantum efficiencies, using existing structures with a known fabrication route. We do so by leveraging a modal design philosophy and exploiting the symmetries of core-satellite nanostructures.

Highly symmetric dielectric-metal core-satellite structures with N satellites (N-pods) have recently emerged as promising candidates for enhancing the magnetic PF. Silica-silver N-pods in particular, are nano-scale structures that have both a large MD moment at optical frequencies and a clear fabrication route for $N \leq 12$ [5], [6]. Modal design is enabled via the use of quasi-normal modes (QNMs) [7], [8], which removes much of the computation expense for the wavelength and emitter locations and orientations while providing significant physical insight into the mechanism of the magnetic PF enhancement. The QNMs are calculated once for a structure, after which nearly any quantity of interest may rapidly be obtained by projecting the QNM fields onto an exciting dipole moment.

We consider these plasmonic N-pods, with Eu^{3+} emitters in the dielectric core, which have a MD transition at 590 nm and an MD transition at 610 nm. We show that for N-pods which can already be fabricated, orientation and location independent magnetic PFs in excess of 40, with magnetic purity and quantum efficiency greater than 90% can be obtained. For an optimized particle, magnetic PFs exceeding 200 can be achieved for a structure smaller than 75 nm in diameter. We further show that structures with tetrahedral symmetry are highly desirable for orientation independence of an emitting magnetic dipole enhanced via the Purcell effect.

II. Theory

QNMs are solutions to the source free Maxwell's equations. The field at the real frequency ω is expanded in the QNM basis as $\mathbf{E}(\omega) = \sum_j \alpha_j(\omega, \widetilde{\omega}_j)\widetilde{\mathbf{E}}_j(\widetilde{\omega}_j)$, where α_j is the excitation coefficient of the j'th QNM $\widetilde{\mathbf{E}}$ with complex frequency $\widetilde{\omega}_j$. The magnetic PF for an emitter at $\mathbf{r}_0$ is,

$$\frac{\gamma_m(\mathbf{r}_0)}{\gamma_{0,m}} = -\frac{2}{\hbar\gamma_{0,m}}\sum_j \Im\left(\alpha_j \mathbf{m}^* \cdot \widetilde{\mathbf{B}}_j(\mathbf{r}_0)\right) \qquad (1)$$

where, $\gamma_{0,m}$ is the MD decay rate of the undressed emitter, γ_m the decay rate of the dressed emitter, $\widetilde{\mathbf{B}}$ the magnetic field of the j'th QNM. The electric PF (γ_p) can be similarly defined in terms of the QNMs [8].

The total decay rate γ_m can be decomposed into its radiative, and non-radiative parts, γ=γ^{rad}+γ^{nrad}, where $\gamma^{nrad} = \int \Im(\varepsilon(\mathbf{r}))|\mathbf{E}(\mathbf{r})|^2 \mathrm{d}^3\mathbf{r}$. The quantum efficiency may then be defined as $QE = \gamma^{rad}/\gamma$, and magnetic branching ratio defined as $\beta_m = \gamma_m/(\gamma_m + \gamma_p)$. We further define the orientation and volume averaged PF as $\bar{\gamma}$, the polydispersity factor ψ and the orientation factor φ, (see Figure 1 (a) for a definition of ψ and φ). This allows the definition of a figure of merit (FOM), which completely encompasses the important optical properties of any resonator.

$$\mathrm{FOM} = \frac{\bar{\gamma}_m}{\varphi}\beta_m QE\frac{\psi}{r_s}, \tag{2}$$

where r_s is the radius of the satellites.

An attractive element of the modal method is the ability to calculate the complex mode volumes $\widetilde{V}_\mathrm{A}$, which can be defined for both electric $A = E$ and magnetic $A = H$ fields. In photonics, the mode volume is loosely analogous with the probability density function in quantum mechanics. For the complex mode volume associated with QNMs, $|\widetilde{V}_A^{-1}|$ indicates the interaction strength, while $\arg(\widetilde{V}_A^{-1})$ is indicates the non-Hermitian character of the mode, and importantly, encompasses the retardation of the radiation back action of a perturber on the mode. The complex modal volume is defined as,

$$\widetilde{V}_\mathrm{A}(\mathbf{r},\mathbf{u}_i) = \frac{\int\left[\widetilde{\mathbf{E}}\cdot\frac{\partial\omega\varepsilon}{\partial\omega}\widetilde{\mathbf{E}} - \widetilde{\mathbf{H}}\cdot\frac{\partial\omega\mu}{\partial\omega}\widetilde{\mathbf{H}}\right]\mathrm{d}^3\mathbf{r}}{2\left[\tilde{\mathbf{A}}(\mathbf{r})\cdot\mathbf{u}_i\right]^2}, \tag{3}$$

where $\mathbf{u}_i$ is the orientation of a smaller perturber, such as a quantum emitter.

We consider N-pods with N between 4 and 30, the placement of the satellites is determined via the solution to the Thompson problem [9], exact solutions exist for $\mathrm{N} = 4, 6, 12$, otherwise we use numerically optimized solutions. Examples for $\mathrm{N} = 7$ and $\mathrm{N} = 12$ are shown in the insets of Figure 1 (a) and (b) respectively. Each of these solutions has an equivalent polyhedron, whose face centers correspond to the locations of the satellites. The symmetries of these equivalent polyhedra are crucial in determining the orientation invariance for an emitter. We initially calculate the magnetic PFs at the MD transition wavelength of $\lambda = 590$ nm for each particle with an emitter at the center of the core and oriented along each axis, for the core radius of $r_c = 42.5$ nm, (which corresponds to the experimental realization of these structures), and vary the satellite radii (r_s). These results, along with the average of the orientations, for $\mathrm{N} = 7$ and $\mathrm{N} = 12$ are shown in Figure 1 (a) and (b) respectively. The importance of the symmetries are immediately made clear, $N = 12$ (along with all Platonic solids) have at least tetrahedral symmetry, while $N = 7$ has dihedral symmetry, the result being that $N = 7$ has a large orientation variance along a single axis, while the $N = 12$ particle is completely invariant to the emitter orientation. We call this variance φ. The maximum mean magnetic PFs for all particles, along with the particles symmetry order are summarized in Figure 1 (c), where φ corresponds to the error bars.

Fig. 1. (a-b) The Magnetic PF calculated at $\lambda = 590$ nm as a function of satellite radius for the $N = 7$ and $N = 12$ structures. The insets show the structures, the red circles denote the orientation averaged PF, while the blue diamonds, black inverted triangles and green triangles show the x, y, and z orientations respectively. The orientation and polydispersity factors, φ and ψ respectively, are shown in (a). (c) The left hand axis and blue circles show the maximum of the mean magnetic PF for each N, the error bars show φ, while the right hand side and red diamonds show the symmetry order of the equivalent polyhedra. (d) The blue dots and left axis show the optimal radius size for $r_c = 42.5$ nm while the right axis and red diamonds shows the normalized polydisersity factor. (e) The left hand side and blue dots show the FOM, the P indicates the structures with platonic equivalent polyhedra, the left side and red inverted triangles, red diamonds, show the magnetic branching ratio and quantum efficiency respectively. (f) Shows Pfs of the fully optimized dodecapod for wavelengths between 300 and 500 nm with $r_c = 24.8$ nm and $r_s = 24.5$ nm, the left axis and solid blue, dashed blue curves show the total and radiated magnetic PF respectively, while the right axis and solid red, dashed red curves show the total and radiated electric PF respectively. (g-j) show the mode volumes of the dominant magnetic mode at the wavelength $\lambda_j = 580+41$ nm for the dodecapod with $r_c = 42.5$ nm and $r_s = 32.5$ nm, (g) shows $|\widetilde{V}_H^{-1}|$, (h) shows $\arg(\widetilde{V}_H^{-1})$, (i) shows $|\widetilde{V}_E^{-1}|$, while (j) shows $\arg(\widetilde{V}_E^{-1})$.

Another experimentally important parameter is the robustness of the optical properties to structural polydispersity, this is characterized by the full width half maximum of the mean PF, and is summarized in Figure 1 (d). It is desirable for ψ to be large and Figure 1 (d) shows a rapid decrease in ψ with increasing N, for example, when $N = 20$ a deviation in r_s of only 1 nm results in a PF decrease of 50%.

Next, we investigate the radiative properties of the optimized particles with $r_c = 42.5$ nm, by calculating γ^{nrad}, β_m, QE and the FOM. These results are summarized in Figure 1 (e), and show that the radiative properties of all particles is exceptional. The branching ratio rapidly asymptotes to above 95% with increasing N, while the QE slowly decreasing to a minimum of $\approx 90\%$ at $N = 30$. The FOM shows very clearly that structures with a platonic equivalent polyhedra are always preferable, and that the dodecapod ($N = 12$), is the most desirable particle. As such we perform a downhill simplex optimization [10] to maximize the cost function $f = \gamma_m^{rad}\beta_m QE$ at the MD transition wavelength of 590 nm, where we vary both r_c and r_s. The structure obtained has remarkable properties, shown in Figure 1 (f), these properties include, a total magnetic PF of nearly 250, a magnetic branching ratio approaching unity and a quantum efficiency of $\approx 72\%$. The QE's associated with the structures here, are surprisingly high for plasmonic based resonators, particularly for structure with the larger core where $QE > 90\%$ for nearly all structures.

To determine the reason for these exceptional properties, we calculate the mode volumes of the dominant magnetic mode. For the optimized dodecapod, the magnetic emission is dominated by a single QNM with the complex wavelength of the mode at $\lambda_j = 582 + 41i$ nm, which is close to the MD emission frequency. The plots of $|\widetilde{V}_A^{-1}|$ and $\arg(\widetilde{V}_A^{-1})$, for $A = E$ and H are shown in Figure 1 for the optimized dodecapod with $r_c = 42.5$ nm. Figure 1 (g) and (h) show a large and spatially uniform interaction strength with a MD in the core of the structure indicated by $|\widetilde{V}_H^{-}1|$, there is also minimal dephasing in the core as $\arg(\widetilde{V}_H^{-1}) \approx 0$. On the other hand, Figure 1 (i) and (j) show a weak interaction with an ED in the core with significant dephasing. Additionally, Figure 1 (i) shows that the electric field is almost entirely confined outside of the metal satellites, which explains the large QE's of the structure.

III. Conclusion

We have explored the use of dielectric-metal core-satellite resonators, which can already be fabricated, as candidates for enhancing MD emissions. An analysis technique, using quasi-normal modes was employed, which enhances the optimization speed while providing significant insight into the physical mechanisms behind the exceptional properties of the structures. The proposed structures have a large magnetic Purcell factor, large quantum efficiencies and branching ratios, and are insensitive to dipole orientation and location. These properties are explained with the aid of symmetries of the structures equivalent polyhedra and the complex mode volumes of the dominant magnetic mode.

References

[1] M. Sanz-Paz, C. Ernandes, J. Ur. Esparza, G. W. Burr, N. F. van Hulst, A. Maitre, L. Aigou, T. Gacoin, N. Bonod, M. F. Garcia-Parajo, S. Bidault and M. Mivelle, "Enhancing Magnetic Light Emission with All-Dielectric Optical Nanoantennas," *Nano Letters*, vol. 18, pp. 3481–3487, 2018.

[2] E. M. Purcell, "Spontaneous Emission Probabilities at Radio Frequencies," *Physcial Review*, vol. 69, 1946.

[3] H. W. Wu, "Tailoring Magnetic Dipole Emission with Plasmonic Split-Ring Resonators," *Physical Review Letters*, vol. 111, p. 026803, 2013

[4] H. W. Wu, Y. Li, H. J. Chen, Z. Q. Sheng, H. Jing, R. H. Fan and R. W. Peng, "Strong Purcell effect for terahertz magnetic dipole emission with spoof plasmonic structure," *ACS Applied Nano Materials*, vol. 2, p. 1045-1052, 2019

[5] V. Many, R. Dézert, E. Duguet, A. Baron, V. Jangid, V. Ponsinet, S. Ravaine, P. Richetti, P. Barois and M.Tréguer-Delapierre, "High optical magnetism of dodecahedral plasmonic meta-atoms," *Nanophotonics*, vol. 8, p. 549-558, 2018

[6] L. Lermusiaux, V. Many, P. Barois, V. Ponsinet, S. Ravaine, E. Duguet, M. Tréguer-Delapierre, A. Baron, "Toward Huygens' Sources with Dodecahedral Plasmonic Clusters," *Nano Letters*, vol. 21, pp. 2046-2052, 2021

[7] P. Lalanne, W. Yan, K. Vynck, C. Sauvan and J. Hugonin, "Light Interaction with Photonic and Plasmonic Resonances," *Laser Photonics Reviews*, vol. 12, p. 1700113, 2018

[8] T. Wu, D. Arrivault, W. Yan and P. Lalanne, "Modal analysis of electromagnetic resonators: User guide for the MAN program," *Computer Physics Communications*, vol. 284, p. 108627, 2023

[9] J. J. Thomson, "On the structure of the atom: an investigation of the stability and periods of osciletion of a number of corpuscles arranged at equal intervals around the circumference of a circle; with application of the results to the theory atomic structure," *The London, Edinburgh, and Dublin Philosophical Magazine and Journal of Science,* vol. 7, p. 237–265, 1946.

[10] J. A. Nelder, R. Mead, "A simplex method for function minimization," *Computer Journal*, vol. 7, pp. 308-313, 1965

Nanostructured Cd(Zn)O for mid-infrared, near-field enhancement

Miguel Montes Bajo[1], Pablo Ibañez-Romero[1], Javier Yeste[2], Eduardo Martínez Castellano[1], María Villanueva-Blanco[1], Andrea C. Illana[1], Fernando Gonzalez-Posada[3], Thierry Taliercio[3], Vicente Muñoz-Sanjosé[2], Adrian Hierro[1]

[1] ISOM, ETSI Telecomunicación, Universidad Politécnica de Madrid, Madrid, Spain
[2] Departament de Física Aplicada i Electromagnetisme, Universitat de València, Spain
3 IES, University of Montpellier, CNRS, Montpellier, F-34095, France
*Corresponding author: miguel.montes@upm.es

***Abstract*— Cd(Zn)O alloys have arguably the best figure of merit for plasmonics in the mid-infrared. However, reports on Cd(Zn)O nanostructures are scarce. This works presents our results on Cd(Zn)O self-assembled nanoparticles and top-down processing of nanostructures with a focus on the near field enhancement.**

***Keywords*— CdO, mid-infrared, self-assembly, dry etching, near-field enhancement, nanoparticles**

I. Introduction

The mid infrared (IR) is a region of the electromagnetic spectrum receiving a great deal of research attention for the development of plasmonic materials and devices. This is in part due to the interest of this region for molecular detection and identification, since many molecules have bonds with vibrational resonances in this, so-called molecular fingerprint region. Thermal imaging and emission, taking advantage of the atmosphere's transparency windows in this region, are also of great interest [1].

Traditionally, the materials of choice for plasmonic structures in the mid-IR have been noble metals, but they suffer from losses that sparked the search for new, better-suited materials. Among these, doped semiconductors and conducting oxides have received a great deal of attention [2]. The latter group include CdO and its related alloys, with arguably the best figures of merit in the mid-IR range due to the large plasma frequency (~4000 cm^{-1}, screened) and low losses (around 15% of the plasma frequency) [3].

Many reports on the plasmonic properties of CdO have been published in the last decade, but mostly focused on thin films; reports on CdO nanostructures have been scarce. Some of these dealt with the synthesis of CdO and related nanoparticles [4], [5], [6]. Our group has also reported self-assembled Cd(Zn)O nanoparticles on GaAs substrates [7], [8]. However, it has not been until very recently that we have reported the first ever top-down approaches for Cd(Zn)O processing by electron beam lithography and dry etching [9].

This work focuses on the results about near-field enhancement by Cd(Zn)O nanostructures from our groups. This will be split in two approaches: self-assembled Cd(Zn)O nanoparticles on GaAs substrates, on the one hand, and nanostructures fabricated on CdO thin films on sapphire substrates, on the other.

II. Methods

The Cd(Zn)O materials presented in this work were deposited by metal-organic chemical vapour deposition (MOCVD) using tertiary butanol, dimethylcadmium, and diethylzinc as O, Cd, and Zn precursors, respectively, with N_2 as the carrier gas. Two different substrates were employed. On the one hand, *r*-plane sapphire, which has a good lattice match with respect to Cd(Zn)O. Thin films (~100 nm thickness) grown on these substrates have shown good crystalline quality and excellent plasmonic properties in the past [10], [11]. Currently, we can fabricate nanostructures on these thin films via electron beam lithography and inductively coupled plasma (ICP) etching. On the other hand, GaAs is employed as a substrate as well. In this case, due to the lattice mismatch between Cd(Zn)O and the substrate, self-assembled Cd(Zn)O nanoparticles (NPs) with very good crystalline quality can be formed [7].

The top down approach to process nanostructures on Cd(Zn)O/*r*-sapphire films consists on standard electron beam lithography with poly(methyl methacrylate) (PMMA) photoresist followed by a novel dry etching protocol we have developed using BCl_3 and Ar in an ICP reactive ion etching chamber [9].

The morphology of the Cd(Zn)O nanostructures is assessed by means of scanning electron microscopy (SEM) and atomic force microscopy (AFM). Fourier transform infrared spectroscopy (FTIR) is used to probe the optical properties of

the structures. COMSOL Multiphysics with the waveoptics module is employed to calculate the electric field distribution around the nanostructures in the near field.

III. Results and Discussion

Figure 1(a) shows a set of representative fabricated CdO stripes on *r*-sapphire. The stripes are 1600 nm wide with a 400 nm gap between them. From Figure (b) it is apparent that the vertical walls of the CdO stripe are actually slanted at an angle of approximately 45º. This is due to the initial shape of the PMMA photoresist [9].

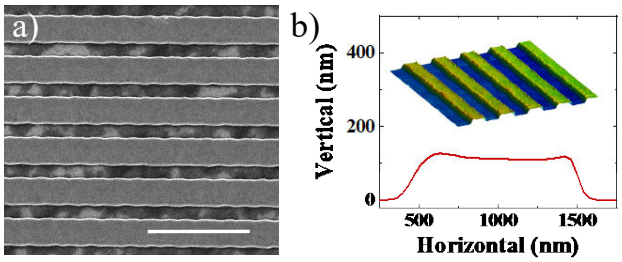

Figure 1. (a) Top-view SEM image of representative CdO stripes on an *r*-plane sapphire substrate. The white scale bar is 5 µm long. (b) AFM profile of a single stripe. The inset shows a 3D AFM reconstruction of a set of stripes.

Figure 2(a) shows the FTIR reflectance of a set of CdO stripes, featuring a reflectance band due to the formation of a localized surface plasmon in the stripes. The figure also includes a calculated reflectance spectrum. The spectra feature several bumps at higher energies than the main peak which calculations show correspond to different modes and field distribution around the edges and corners of the stripes.

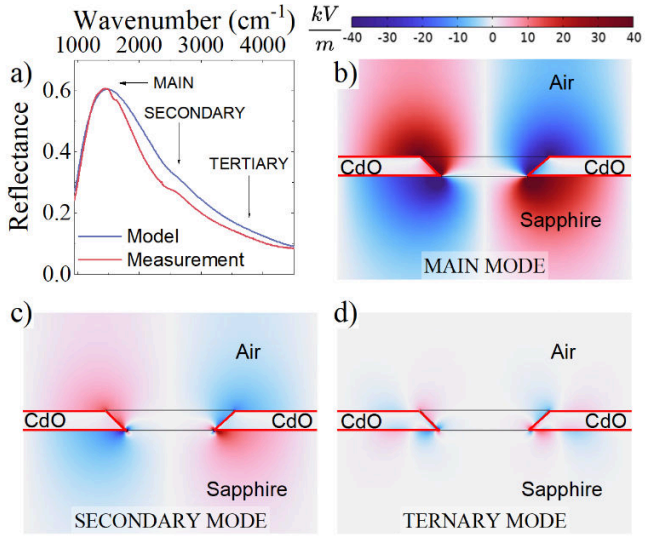

Figure 2. (a) Experimental (red) and calculated (blue) reflectance of a set of CdO stripes. (b) to (d) Calculated electric field around the edges of the stripes at different frequencies in the spectra in (a).

Coupling of these modes to both the phonons of the substrate and also to the resonances of substances deposited on top of the stripes will be discussed. Also, the feasibility of applying this processing protocol to Cd(Zn)O on substrates different from sapphire, such as GaAs and SiC will be discussed.

With regard to the self-assembled Cd(Zn)O NPs, we have produced ensembles of particles with varying radius, which correlates inversely to the surface particle density. It will be shown how the size distribution and surface coverage homogeneity have improved a great deal compared to previous reports from our group (Figure 3(a), compared to references [7], [8]).

Figure 3(b) shows the reflectance spectrum of the NPs. Two modes are apparent, one at lower energy (high reflectance) attributed to electron oscillations along the substrate plane, and another at higher energy (lower reflectance) attributed to electron oscillations perpendicular to the substrate. The low-energy (LE) mode features a large divergence of the electric field at the edges of the hemispherical NPs [7].

It is found from finite element modelling (FEM) that the volume in the substrate in which the electric field is enhanced is much larger for larger nanoparticles (Figure 3(c) and (d)), reaching as deep as 400 nm for NPs of 240 nm radius. This is really attractive from the point of view of e.g. increasing the intersubband absorption by quantum wells located underneath the particles. The implications of this on the performance of quantum well infrared photodetectors (QWIPs) will be discussed and the integration of the NPs on the photodetectors will be shown.

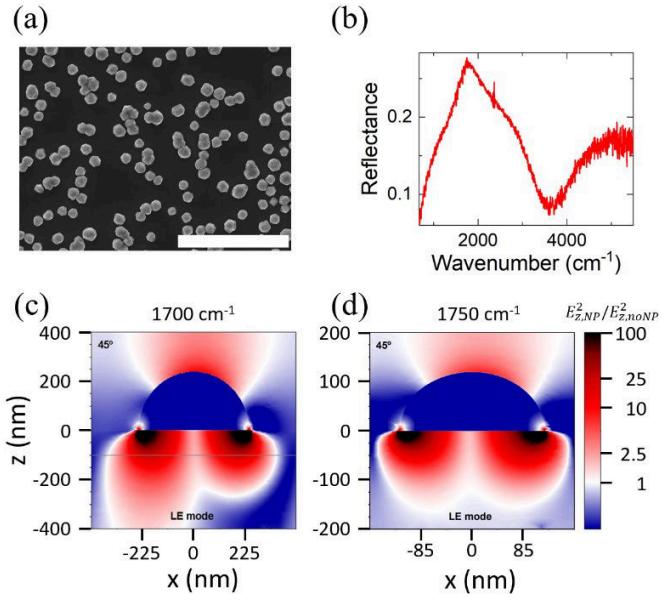

Figure 3. (a) Top view SEM image of a sample with 240 nm-radius NPs. (b) Reflectance spectra of the sample in (a). (c) and (d) Electric field enhancement FEM calculation for a 140 nm-radius NP (c) and for a 240 nm-radius NP (d). Calculations in (c) and (d) are normalized to the case with no NP and performed at the respective low energy-mode frequency. The angle of incidence is 45º. Note the different x and z scale in both cases.

Also, the near-field enhancement atop the NPs is attractive for applications such as surface-enhanced IR absorption (SEIRA). Results in terms of vibrational signal enhancement for several molecular species will be shown as well. Notably, a vibrational signal enhancement from vanillin of around × 4 has been achieved [8].

IV. Conclusion

A novel dry etching protocol to generate nanostructures on Cd(Zn)O thin films grown on *r*-sapphire substrates is presented. Details about the processing and discussion of the field enhancement due to plasmonic (from Cd(Zn)O) and phononic (from the substrate) effects induced by the stripes will be discussed. Currently, this etching protocol is being developed for Cd(Zn)O films grown on other substrates such as GaAs and SiC.

Self-assembled Cd(Zn)O NPs have been demonstrated on GaAs substrates, with two plasmonic modes corresponding mainly to in-plane and out-of-plane electron oscillations. Good control of NP size, with a very good homogeneity of NP size and distribution over the substrate has been achieved. NPs as large as 240 nm in average radius have been deposited, capable of concentrating the electromagnetic field up to 400 nm into the substrate. Applications to SEIRA and QWIP enhancement will be shown.

Acknowledgments

This work was partly supported by project PID2024-156706OB-C2, funded by MICIU/AEI/10.13039/501100011033/FEDER, UE; project PDC2023-145827-C2 funded by MICIU/AEI/10.13039/501100011033 and by European Union Next Generation EU/ PRTR; Generalitat Valenciana under Project No. PROMETEU/2021/066; SEA (Occitanie French Region – ESR-PREMAT-238); EXTRA (ANR 11-EQPX-0016); NanoElastir (ASTRID 2020–2023); ENVIRODISORDERS (MUSE UM 2021–2023).

References

[1] S. Law, V. Podolskiy, and D. Wasserman, "Towards nano-scale photonics with micro-scale photons: the opportunities and challenges of mid-infrared plasmonics," *Nanophotonics*, vol. 2, no. 2, pp. 103–130, Apr. 2013, doi: 10.1515/nanoph-2012-0027.

[2] P. R. West, S. Ishii, G. V. Naik, N. K. Emani, V. M. Shalaev, and A. Boltasseva, "Searching for better plasmonic materials," *Laser & Photon. Rev.*, vol. 4, no. 6, pp. 795–808, Nov. 2010, doi: 10.1002/lpor.200900055.

[3] J. D. Caldwell *et al.*, "Low-Loss, Extreme Subdiffraction Photon Confinement via Silicon Carbide Localized Surface Phonon Polariton Resonators," *Nano Lett.*, vol. 13, no. 8, pp. 3690–3697, Aug. 2013.

[4] A. Tadjarodi and M. Imani, "A novel nanostructure of cadmium oxide synthesized by mechanochemical method," *Materials Research Bulletin*, vol. 46, no. 11, pp. 1949–1954, Nov. 2011, doi: 10.1016/j.materresbull.2011.07.016.

[5] D. Z. Husein, R. Hassanien, and M. Khamis, "Cadmium oxide nanoparticles/graphene composite: synthesis, theoretical insights into reactivity and adsorption study," *RSC Adv.*, vol. 11, no. 43, pp. 27027–27041, 2021, doi: 10.1039/D1RA04754J.

[6] T. Ghoshal, S. Biswas, P. M. G. Nambissan, G. Majumdar, and S. K. De, "Cadmium Oxide Octahedrons and Nanowires on the Micro-Octahedrons: A Simple Solvothermal Synthesis," *Crystal Growth & Design*, vol. 9, no. 3, pp. 1287–1292, Mar. 2009, doi: 10.1021/cg800203y.

[7] E. Martínez Castellano *et al.*, "Self-assembled metal-oxide nanoparticles on GaAs: infrared absorption enabled by localized surface plasmons," *Nanophotonics*, vol. 10, no. 9, pp. 2509–2518, Jul. 2021, doi: 10.1515/nanoph-2021-0167.

[8] P. Ibañez-Romero *et al.*, "Large-area sensors using Cd(Zn)O plasmonic nanoparticles for surface-enhanced infrared absorption," *Nanophotonics*, May 2025, doi: 10.1515/nanoph-2025-0020.

[9] P. Ibañez-Romero *et al.*, "Near-Field Enhancement via Plasmon–Phonon Polariton Coupling with CdO Stripes," *Advanced Optical Materials*, Jan. 2026, doi: 10.1002/adom.202502974.

[10] J. Tamayo-Arriola, A. Huerta-Barberà, M. Montes Bajo, E. Muñoz, V. Muñoz-Sanjosé, and A. Hierro, "Rock-salt CdZnO as a transparent conductive oxide," *Applied Physics Letters*, vol. 113, no. 22, p. 222101, Nov. 2018, doi: 10.1063/1.5048771.

[11] J. Tamayo-Arriola *et al.*, "Controllable and Highly Propagative Hybrid Surface Plasmon–Phonon Polariton in a CdZnO-Based Two-Interface System," *ACS Photonics*, vol. 6, no. 11, pp. 2816–2822, Nov. 2019, doi: 10.1021/acsphotonics.9b00912.

Tunable coupling between conducting polymer nanoantennas and epsilon-near-zero thin films

Suraya Kazi, Yulong Duan, Magnus Jonsson*

Laboratory of Organic Electronics, Department of Science and Technology,
Linköping University, Norrköping, SE-60174, Sweden
*Corresponding author: magnus.jonsson@liu.se

***Abstract*— Epsilon-near-zero thin films offer unconventional for optics including nonlinear applications. While metal nanostructures can enhance these effects through strong coupling, their fixed permittivity restricts tunability. By replacing metal with a conducting polymer, we can reversibly tune this coupling. Such hybrid system allows for on-demand optical functionalities for reconfigurable nanophotonics.**

***Keywords*— epsilon-near-zero mode, conducting polymers, plasmonic nanoantennas, dynamic coupling, tunable nanophotonics.**

I. Introduction

Materials whose real permittivity approaches zero within a specific wavelength range while maintaining a low imaginary component are known as epsilon near zero (ENZ) media. Thin films of indium tin oxide (ITO) have been employed as a platform for exploring ENZ phenomena that can funnel obliquely incident near-infrared light into highly confined modes and exhibit strong nonlinear optical behavior.[1] Stronger ENZ responses was achieved under normal incidence by integrating metallic nanoantennas on top of the ITO layer.[2] In these hybrid architectures, the localized surface plasmon resonance (LSPR) of the metal antennas couples to the ENZ mode in the ITO. However, this coupling is typically static due to the fixed permittivity of metals. In this work, we demonstrate dynamically tunable coupling to ENZ modes based on conducting polymer nanoantennas.

II. Methods

Finite-difference time-domain method was employed for numerical simulations, using the commercial software Ansys Lumerical. As experiments, we fabricated thin films of poly(3,4 ethylenedioxythiophene) (PEDOT) through vapor phase polymerization of its monomer and employed electron beam lithography to create nanostructures. Sulfuric acid solution and polyethylenimine vapor were used for chemical doping and dedoping of the samples, respectively. For electrical switching, a two-electrode electrochemical setup with ion gel electrolyte was used.

III. Results and Discussion

Conducting polymers offer electrically and chemically tunable permittivity: they act metallic when doped and dielectric when dedoped. [3] This enables adjustable LSPR modes in conducting polymer nanostructures, as demonstrated in our recent studies.[4]–[6] By placing PEDOT nanoantennas on ITO thin film, we realized a hybrid ENZ-plasmonic nanosystem and the results show:

- >90% modulation of the electric field intensity inside the ENZ layer upon doping/dedoping of the nanoantennas (see simulations in Fig. 1a)
- Extinction peak splitting in the spectroscopic measurements, a characteristic of coupling and polariton formation.
- Reversible control of coupling strength applying very low voltages or simple chemical treatments. (see spectra in Fig. 1b)

This work [7] also clarifies the dual role of ITO in many other dynamic conducting polymer nanosystems where ITO thin films are used as electrodes and provides guidelines for electrically switchable plasmonic–ENZ devices.

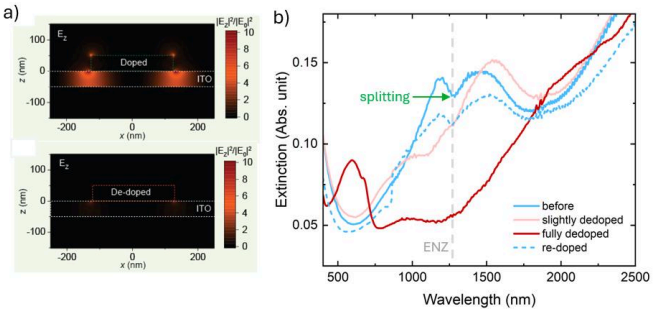

Fig. 1 a) Simulated electric field distribution for doped PEDOT (upper panel) vs de-doped PEDOT (lower panel) antenna on top of ITO thin film. b) Experimental spectra of hybrid ENZ-plasmonic system at varying chemical redox state of PEDOT showing reversible peak-splitting due to coupling.

IV. Conclusion

We demonstrated coupling between the LSPR of conducting polymer nanoantennas and the ENZ mode of an ITO thin film. [7] By leveraging the reversible charge carrier density changes in the polymer through chemical or electrochemical stimuli, the coupling strength was dynamically tuned. Future work can enable local control of the polymer charge density which can further allow spatially programmable ENZ field patterns, offering new capabilities for reconfigurable photonics.

Acknowledgments

This work was supported by the European Research Council, the Swedish Research Council, the Knut and Alice Wallenberg Foundation, and the Swedish Government Strategic Research Area in Materials Science on Functional Materials at Linköping University.

References

[1] M. Z. Alam, I. De Leon, and R. W. Boyd, "Large optical nonlinearity of indium tin oxide in its epsilon-near-zero region," *Science (80-.).*, vol. 352, no. 6287, pp. 795–797, May 2016, doi: 10.1126/science.aae0330.

[2] M. Z. Alam, S. A. Schulz, J. Upham, I. De Leon, and R. W. Boyd, "Large optical nonlinearity of nanoantennas coupled to an epsilon-near-zero material," *Nat. Photonics*, vol. 12, no. February, pp. 79–83, 2018, doi: 10.1038/s41566-017-0089-9.

[3] S. Chen *et al.*, "On the anomalous optical conductivity dispersion of electrically conducting polymers: Ultra-wide spectral range ellipsometry combined with a Drude-Lorentz model," *J. Mater. Chem. C*, vol. 7, no. 15, pp. 4350–4362, 2019, doi: 10.1039/c8tc06302h.

[4] S. Chen *et al.*, "Conductive polymer nanoantennas for dynamic organic plasmonics," *Nat. Nanotechnol.*, vol. 15, no. 1, pp. 35–40, 2020, doi: 10.1038/s41565-019-0583-y.

[5] A. Karki *et al.*, "Electrical Tuning of Plasmonic Conducting Polymer Nanoantennas," *Adv. Mater.*, vol. 34, p. 2107172, 2022, doi: 10.1002/adma.202107172.

[6] S. Kazi *et al.*, "n-Type redox-tuneable conducting polymer optical nanoantennas," *J. Mater. Chem. C*, vol. 12, no. 43, pp. 17469–17474, 2024, doi: 10.1039/D4TC03038A.

[7] Y. Duan, S. Kazi, D. Lin, L. Liu, and M. P. Jonsson, "Electrotunable coupling between an epsilon-near-zero thin film and conducting polymer nanoantennas," *Proc. Natl. Acad. Sci.*, vol. 123, no. 7, pp. 1–7, Feb. 2026, doi: 10.1073/pnas.2517549123.

GENERAL SESSION

Nanophotonics and Plasmonics Applications: Optical Antennas, Quantum Photonic Devices, and Beyond

3 contributions · pp. 1305–1313

Switching Quantum Dot Microresonators by Ultrafast Laser Pulses

Pietro Castronovo[1], Marco Reale[1], Susan A. Rigter[2,3], Cherie R. Kagan[4], Christopher B. Murray[4], Salvatore Lorenzo[1], Erik C. Garnett[2,3], Peter Schall[3], Emanuele Marino[1], Alice Sciortino[1], Fabrizio Messina[1,*]

[1]Department of Physics and Chemistry, University of Palermo, Italy
[2]Center for Nanophotonics, AMOLF, Amsterdam, The Netherlands
[3]Van der Waals-Zeeman Institute, University of Amsterdam, The Netherlands
[4]Department of Chemistry, University of Pennsylvania, USA

*Corresponding author: fabrizio.messina@unipa.it

***Abstract*—The ultrafast optical control of microresonators remains underexplored despite many prospective applications in nanophotonics. We demonstrate that ultrafast optical pulses can reversibly modulate whispering-gallery resonances in quantum-dot superparticle microresonators due to combined electronic and thermal effects. The results suggest quantum dot superparticles as metamaterials for photonic switching and optoelectronic nanotechnologies.**

***Keywords*—superparticles, ultrafast, microresonators, quantum dots**

I. Introduction

The self-assembly of nanoscale building blocks such as semiconductor quantum dots (QDs) into ordered superstructures enables the realization of artificial metamaterials with emerging collective properties. Depending on their degree of organization, such assemblies may exhibit phenomena such as exciton delocalization and transport [1], superfluorescence [2], collective plasmonic response [3]. Among the various realizations, superstructures based on fluorescent semiconductor QDs are particularly attractive for photonic and optoelectronic applications. Spherical QD superparticles (SPs) with micrometric dimensions can sustain, so-called, whispering-gallery modes, giving rise to sharp optical resonances that coexist with intense photoluminescence. This combination has recently enabled their use as active microresonators and microlasers [4]. While the steady-state optical properties of these metamaterials have been widely investigated, the ultrafast dynamical response remains far less explored. In particular, the possibility of controlling whispering-gallery mode SP microresonators using ultrashort optical pulses has hardly been addressed, despite representing an appealing route toward all-optical photonic circuits.

Addressing such problems requires experimental techniques capable of simultaneously achieving micrometer-scale spatial resolution and femtosecond temporal resolutions, as required to resolve the fundamental relaxation processes at the nano- and micro-scale. Following our recent work [5], here we report the use of ultrafast optical microscopy to investigate and manipulate the transient optical response of individual SP microresonators under femtosecond excitation. Specifically, we employ ultrafast optical microscopy to probe and manipulate the relaxation dynamics of whispering-gallery-mode microresonators consisting in SPs self-assembled from fluorescent QDs. We show that femtosecond optical excitation can induce reversible modifications of the resonant photonic modes over a wide spectral window, originating from ultrafast variations of the refractive index associated with both electronic excitation and subsequent thermal processes. These findings provide new insight into the picosecond- and femtosecond-scale optical dynamics of active microresonators and suggest potential applications in photonic technologies, including all-optical ultrafast circuitry and optical switching.

II. Methods

We started from CdSe core/CdS shell QDs (10.3 nm size, core diameter 3.5 nm, Figure 1b) to assemble quasi-monodisperse spherical SPs (10.8 μm size) through an approach recently demonstrated by some of the authors [6]. Each SP (Figure 1c), with a clearly defined spherical shape, contains more than 10^8 individual QDs assembled in a regular supercrystalline structure.

As a preliminary study, we investigated the optical properties of SPs individually and at the ensemble level, by steady-state photoluminescence and micro-photoluminescence. Then we carried out micro-pump-probe experiments on individual SPs, in a home-built setup [5] where the spatial resolution is dictated by the probe beam size (2.5 μm) and the temporal resolution is dictated from the pump pulse duration (50 fs). Individual SPs are pumped by light pulses at 400 nm with 50 fs duration, produced by second-harmonic generation of the fundamental beam from an amplified Ti:Sapphire laser, and probed by a

white-light continuum produced by focusing a fraction of the same beam through a water cell. The pump and probe pulses are tightly focused on the sample by a short focal length parabolic mirror, and the transmitted probe is collected by a microscope objective and sent to a spectrometer for analysis.

III. Results and Discussion

Individual SPs assembled from CdSe/CdS QDs exhibit intense photoluminescence accompanied by a distinct comb of narrow spectral features (Figure 1f), confirming their behavior as whispering-gallery mode microresonators. The emission quantum yield exceeds 90% and shows a slight spectral shift relative to that of isolated QDs (compare Figure 1d with Figure 1e and 1f), indicating significant electronic coupling within the assembled structure.

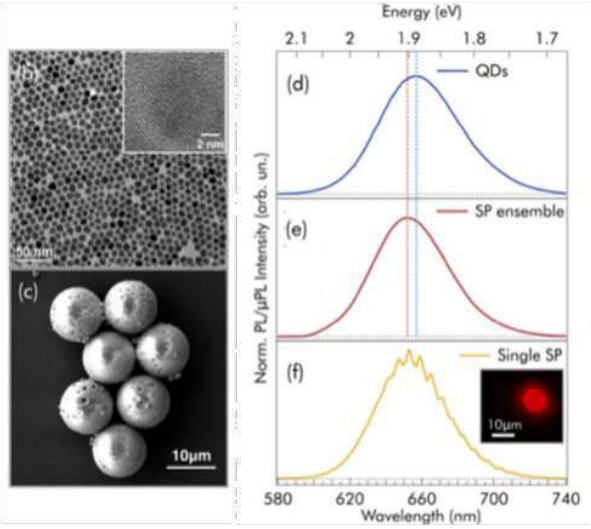

Fig. 1 The self-assembly of nanometrically-sized CdSe/CdS quantum dots (b) leads to the formation of spherical whispering-gallery mode SPs (c). Photoluminescence spectra of quantum dots (d), of SPs at ensemble level (e) and of individual SPs (f). Figure adapted from ref. [5]

A typical result of micro pump-probe measurements on individual SPs is summarized in Figure 2. Ultrafast pump–probe measurements (Figure 2a, 2b) reveal a transient differential absorption signal dominated by a negative contribution associated with so-called state-filling effects [7] in the QDs. While the temporal dynamics of this signal provide information on the electron-electron and electron-phonon relaxation pathways, this will not be discussed here. Superimposed on this broad response, a fine modulation pattern is observed (Figure 2c, 2d), which is the main focus of this work. The modulation pattern can be isolated from the signal envelope by subtracting a smoothed version of the signal (see Figure 2c-2d), yielding the residuals shown in Figure 2e. We attribute these modulations to a photo-induced shift of the whispering-gallery mode structure. In particular, the effect arises from transient changes in the refractive index of the SP following photoexcitation. Small variations in SPs size lead to distinct modulation patterns in different SPs (Figure 2e).

The photo-induced modulation pattern appears as a succession of positive and negative lobes in close succession: because of the differential nature of the transient absorption signal, the negative lobes represent the original spectral positions of microresonator modes, that is, the modes before photo-excitation, while the positive lobes represent the spectral positions of the new modes shifted by photo-excitation. Therefore, from this measurement we infer that photo-excitation induces a transient shift of the mode structure of the SP microresonator. This effect can be used in principle to "switch" the resonance modes of the metamaterial by purely optical means.

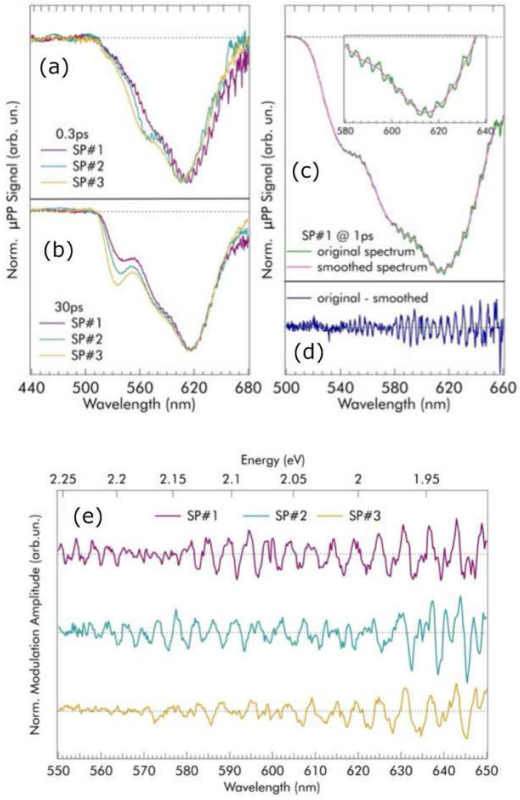

Fig. 2 Differential absorption spectra at two different delays from photoexcitation(a,b), as detected from three different SPs. Isolation of the modulation pattern appearing on top of the broad differential absorption signal (c)(d). Modulation pattern as observed on three different SPs (e). Figure adapted from ref. [5]

Time-resolved analysis of these signals (not shown) shows that the modulation amplitude rises within the pump–probe cross-correlation time, indicating an almost instantaneous electronic contribution. A further increase on the picosecond timescale reflects lattice heating mediated by electron–phonon interactions, followed by a gradual recovery over hundreds of picoseconds as the system returns to equilibrium.

IV. Conclusion

In summary, we showed that femtosecond optical excitation can induce reversible modifications in the modal structure of

whispering-gallery-mode SP microresonators based on fluorescent QDs, through the combined action of electronically- and thermally-driven modifications of the refractive index. Quantum-dot SPs can be seen as a class of metamaterials with considerable potential for photonic applications, including microlasers and micro-scale communication devices. In this context, the ability to reversibly tune their resonator properties using ultrashort light pulses offers new opportunities for all-optical control in advanced quantum-dot-based photonic technologies.

ACKNOWLEDGMENTS

M.R. and F.M. acknowledge Project PRIN 2022-2022H8LE9P. C.R.K. and C.B.M. acknowledge the U.S. National Science Foundation Science and Technology Center for the Integration of Modern Optoelectronic Materials on Demand, under GrantDMR-2019444. A.S. acknowledges Project PRIN 2022-20223CWFZT. E.C.G. acknowledges funding received from the EU through ERC Grant 101043783.

REFERENCES

[1] X. Lan, M. Chen, M. H. Hudson, V. Kamysbayev, Y. Wang, P. Guyot-Sionnest, D. V. Talapin, “Quantum Dot Solids Showing State-Resolved Band-like Transport”. Nat. Mater. 19, 323, 2020.

[2] X. Li, L. Chen, D. Mao, J. Li, W. Xie, H. Dong, L. Zhang, “Low-Threshold Cavity-Enhanced Superfluorescence in Polyhedral Quantum Dot superparticles”, Nanoscale Adv. 6, 3220, 2024

[3] Y.-H. Lee, C. L. Lay, W. Shi, H. K. Lee, Y. Yang, S. Li, X. Y. Ling, “Creating Two Self-Assembly Micro-Environments to Achieve Supercrystals with Dual Structures using polyhedral nanoparticles”, Nat. Commun. 9, 2769, 2018

[4] M. Reale, P. Castronovo, M. Cannas, E. Marino, A. Sciortino, F. Messina, “Excitation-Wavelength-Tunable Lasing in Individual Quantum Dot Superparticles”, Advanced Optical Materials 2500838, 2025

[5] P. Castronovo, M. Reale, S. A. Rigter,C. R. Kagan, C. B. Murray, S. Lorenzo, E. C. Garnett, P. Schall, E. Marino, A. Sciortino, F. Messina, “Ultrafast Switching of Whispering Gallery modes in Quantum Dot Superparticles”, Nano Letters 25, 5828, 2025

[6] E. Marino, S. van Dongen, S. J. Neuhaus, W. Li, A. Keller, C. R. Kagan, T. E. Kodgerm C. B. Murray, “Monodisperse Nanocrystal Superparticles through a Source−Sink Emulsion System”, Chem. Mater. 34, 2779, 2022

[7] Chem. Mater. 2022, 34 (6), 2779−2789.V. I Klimov, D. W. McBranch, “Electron and hole relaxation pathways in semiconductor quantum dots”, Phys. Rev. B 60, 13740, 1999

Coupling-Controlled Exceptional Points in Intersubband Polaritonic Metasurfaces

Beomjoon Kim[1], Hyeongju Chung[1], Gerhard Boehm[2], Mikhail A. Belkin[2] and Jongwon Lee[1,*]

[1]Department of Electrical Engineering, Ulsan National Institute of Science and Technology (UNIST), Ulsan 44919, Republic of Korea

[2]Walter Schottky Institute, Technical University of Munich, Am Coulombwall 4, Garching 85748, Germany

*Corresponding author: jongwonlee@unist.ac.kr

***Abstract*— We present non-Hermitian degeneracies, specifically exceptional points (EPs), in geometry-controlled intersubband polaritonic metasurfaces consisting of two plasmonic resonators strongly coupled to intersubband transitions. By varying the resonator gap, we precisely control the coupling coefficient and demonstrate EP emergence near 9.74 μm through numerical simulations in the mid-infrared regime.**

***Keywords*— Exceptional Points, Non-Hermitian, Metasurfaces**

I. Introduction

Metasurfaces enable precise control over the local phase, amplitude, and polarization of scattered light. Over the past decade, passive flat optical platforms such as metalenses and waveplates have attracted significant attention. In the mid-infrared (MIR) region, polaritonic metasurfaces combining plasmonic ridge resonators with intersubband transitions (ISTs) in multiple quantum wells (MQWs) have demonstrated strong coupling. This strong coupling supports the formation of intersubband polaritonic modes, providing a robust passive platform for polarization control and beam manipulation in the MIR regime.[1]

The non-Hermiticity inherent to metasurfaces originates from their open-system nature, where continuous energy exchange occurs between incident radiation and resonant nanostructures through radiation and dissipative losses. Such non-Hermitian frameworks allow engineered control of coupling strength and loss imbalance, giving rise to unconventional spectral responses and modal behavior beyond conventional Hermitian systems. Exceptional points (EPs) are non-Hermitian degeneracies where eigenvalues and eigenvectors merge, resulting in parity–time symmetry breaking, increased sensitivity, non-orthogonal states, and optical scattering singularities.[2] These unique features have attracted considerable interest across photonics and physics. However, despite extensive studies in other spectral regimes, the realization of exceptional points in the mid-infrared regime has not yet been reported.

In this work, we realize EPs by systematically tuning the coupling coefficient between two plasmonic resonators via precise control of their gap separation. By exploring multiple coupling regimes defined by different gap sizes, we map the parameter space to the condition where the coupling rate balances the loss contrast, leading to eigenmode coalescence at the EP.

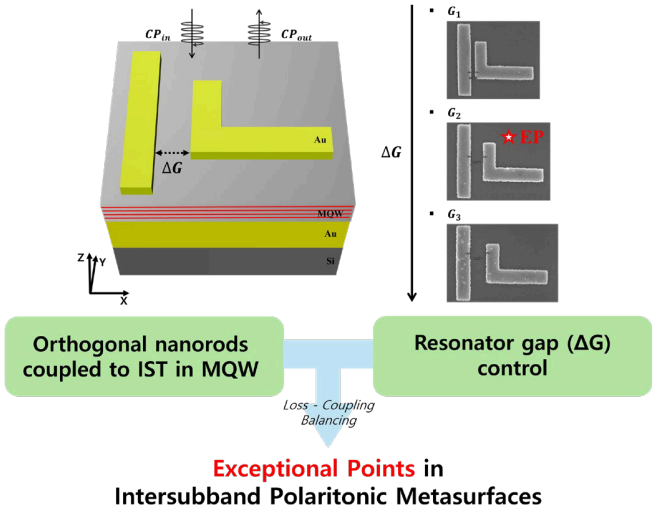

Fig. 1. Concept of the Non-Hermitian Metasurfaces.

II. Device Design

We designed a 300nm-thick MQW layer comprising 16 repetitions of double quantum wells, composed of $In_{0.52}Al_{0.48}As/In_{0.53}Ga_{0.47}As$ heterostructures. The absorption energy of IST between the 1st and 2nd states in the conduction band of the MQW is 122 meV (λ ~ 10.3 μm) at 0 V as shown in Fig. 2(a). Fig. 2(b) displays the unit cell structure, consisting of x- ("L" shape) and y- ("I" shape) polarized plasmonic resonators, supporting two orthogonal modes with different dissipative loss rates. The coupling rate is controlled by the coupling length (ΔG) between the two resonators. As shown in Fig. 2(c)-(d), each resonator can induce plasmonic resonances for x- and y- polarized incident light. These resonances generate enhanced E_z fields inside the MQW layer, which can be strongly coupled to the IST.

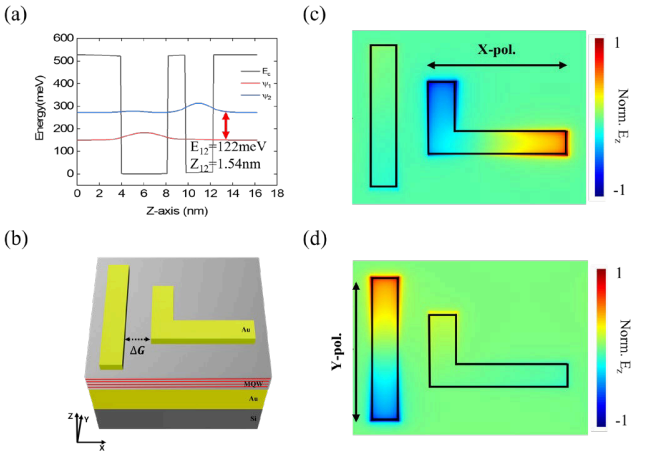

Fig. 2. Design of Non-Hermitian metasurfaces. (a) Conduction band diagram of one period of a MQW at 0 V. The layer sequence (unit: nm) is 4/4.2/1.6/2.5/4 where InGaAs wells are marked in red. (b) Schematic of one unit cell of the metasurface. Top metal(yellow) is gold. (c, d) Top-view cross sections of the normalized E_z field in the MQW layer at $\lambda = 9.74\mu m$ for x- and y-polarized incident light.

III. RESULTS AND DISCUSSION

First, we numerically investigate the evolution of the non-Hermitian eigenvalues and eigenpolarization states by sweeping the ΔG between the two resonators. Fig. 3(a) shows the eigenpolarization states plotted on the Poincaré sphere as the ΔG is swept. As ΔG is gradually tuned, the two eigenpolarization states approach each other and eventually coalesce at a single point, indicating the formation of an EP. Fig. 3(c)-(d) present the simulated eigenvalue magnitude and phase, respectively, mapped as functions of ΔG and wavelength. At ΔG =303 nm and λ =9.74 μm, both the magnitude and phase of the two eigenvalues simultaneously merge, confirming the coalescence of the non-Hermitian eigenmodes at the EP. Fig. 3(b) shows the corresponding eigenpolarization states projected onto the two-dimensional polarization plane. Near the EP, the two states converge to left circular polarization (LCP). As ΔG is further varied beyond this condition, the eigenpolarization states separate again, indicating the transition away from the EP regime.[3]

As discussed in the previous section, the coalescence of eigenpolarization states into the LCP state at the EP prohibits polarization conversion from RCP to LCP. Consequently, the reflection coefficient corresponding to the $R \rightarrow L$ channel approaches zero at the EP condition. Fig. 4(b) presents the circular-basis reflection spectra, where the evolution of the resonances can be observed as the system approaches the EP. By performing a basis transformation from the linear basis to the circular basis, the corresponding circular reflection components are obtained. Notably, the R_{RL} component converges toward zero near the EP, indicating the suppression of cross-circular polarization conversion. To further highlight this effect, Fig. 4 (c) shows the same circular-basis reflection expressed in the dB scale. The contrast between the R_{LR} and R_{RL} channels become significantly enhanced, demonstrating a pronounced circular dichroism with a high extinction ratio. These results confirm that the EP-induced eigenstate coalescence directly leads to unidirectional circular polarization selectivity in the reflected field.

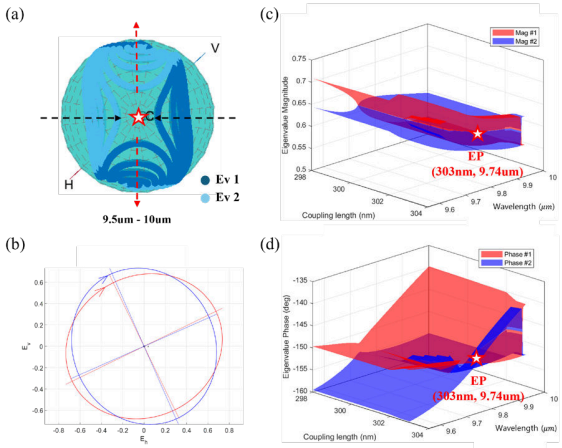

Fig. 3. (a) Poincaré sphere representation of eigenpolarization evolution during a coupling-length sweep, culminating in LCP state coalescence. (b) Near the exceptional point, both eigenpolarization states collapse into a single LCP eigenstate, evidencing polarization-state degeneracy. (c,d) Eigenvalue amplitude and phase dispersions versus coupling length and wavelength, revealing degeneracy and the characteristic branch-point topology of the EP.

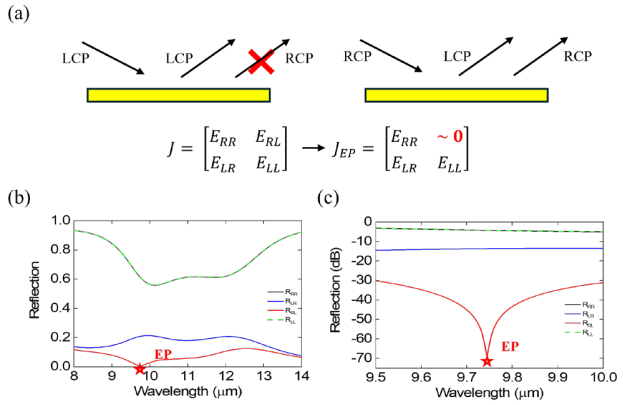

Fig. 4. (a) Chiral degeneracy at the exceptional point, where eigenstate coalescence occurs toward the LCP state. (b,c) Reflection responses in the circular polarization basis near the EP; (b) is shown in linear scale, and (c) is presented in dB scale.

Based on the theoretical predictions presented earlier, we are carrying out fabrication and measurements to experimentally realize the Exceptional Point. Fig. 5(a) shows scanning electron microscope (SEM) images of the fabricated samples with intentionally varied ΔG (or gap). The structures with different gap sizes (e.g., 350 nm, 290 nm, 160 nm, and 80 nm) are well defined, confirming that the geometric parameters were accurately implemented as designed. Using these fabricated samples, we measured the reflection spectra under linearly polarized incidence with an FTIR (Fourier-transform infrared) system, as shown in Fig. (b)–(d). The co-polarized reflection components (R_{xx} and R_{yy}) exhibit resonance features consistent across different gap conditions, while the cross-polarized

component (R_{xy}), shown in Fig. (d), reveals a clear gap-dependent behavior. As the gap decreases, the coupling strength between the two nanorods increases, leading to a significant enhancement of the cross-polarized reflection. This trend confirms that the coupling coefficient can be effectively and systematically controlled through geometric gap variation, providing an experimental pathway toward accessing the Exceptional Point regime.

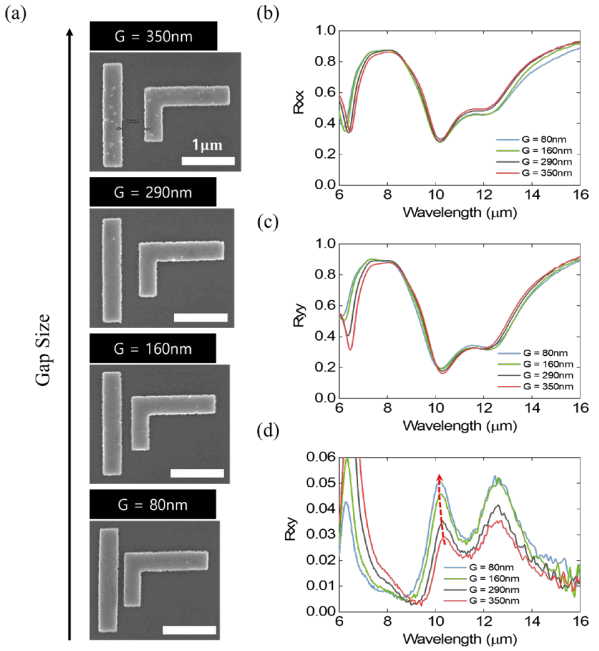

Fig. 5. (a) SEM images of the fabricated metasurfaces with different gap sizes (G = 350 nm, 290 nm, 160 nm, and 80 nm), confirming the controlled geometric variation of the proposed structure. (b–d) Measured reflection spectra under linear polarization basis: (b) $\boldsymbol{R_{xx}}$, (c) $\boldsymbol{R_{yy}}$, and (d) $\boldsymbol{R_{xy}}$. In (d), the cross-polarized reflection increases as the gap decreases, indicating enhanced coupling strength between the two resonators at smaller separations.

IV. Conclusion

In this work, we numerically demonstrated the emergence of an Exceptional Point (EP) by systematically mapping the coupling–loss parameter space and observing the coalescence of both eigenvalues and eigenpolarization states. Based on the fabrication results and measured linear-basis reflection spectra, we experimentally verified that the coupling strength is effectively controlled through geometric gap variation, confirming that the loss–coupling balance required for the realization of the EP can be achieved via coupling engineering.

Having confirmed the controllability of the coupling coefficient toward the EP condition, we are now extending the measurements to the circular polarization basis to directly probe the EP behavior and the associated chiral response.

Acknowledgments

This work was partly supported by Institute of Information & Communications Technology Planning & Evaluation (IITP) grant funded by the Korea government (MSIT) (RS-2023-00227854, RS-2023-00259676) and by the National Research Foundation of Korea (NRF) (2022R1A2C301189812, 2022M3H4A1A04096465).

References

[1] Chung, H. et al., “Electrical Phase Modulation Based on Mid-Infrared Intersubband Polaritonic Metasurfaces,” Advanced Science, 10, 2207520 (2023)

[2] Ergoktas, M. S. et al., "Topological engineering of terahertz light using electrically tunable exceptional point singularities," Science, 376, 184-188 (2022)

[3] Lawrence, M. et al., “Manifestation of PT Symmetry Breaking in Polarization Space with Terahertz Metasurfaces,” Phys. Rev. Lett. 113, 093901 (2014)

Solving the Helmholtz equation with analog systems at telecommunications wavelengths

Ross G. MacDonald[1], Andrew M. Naylor[1], Victor Pacheco-Peña[1,*]

[1]School of Mathematics, Statistics and Physics, Newcastle University, Newcastle Upon Tyne, NE1 7RU, United Kingdom

*Corresponding author: victor.pachecopena@gmail.com

***Abstract*— Solutions to PDEs in the form of the Helmholtz equation are produced at 193.41 THz by exploiting a network of dielectric waveguides with wave splitters and Bragg gratings. Numerical simulation results will be presented demonstrating the potential for this technique to produce accurate solutions to Dirichlet boundary value problems.**

***Keywords*— Analog computing, PDE solving.**

I. Introduction

Optical analog computing has emerged as an interesting paradigm [1, 2] owing to the advantages of exploiting light as an information carrier [3-7]. Platforms such as plasmonics [8, 9], photonic integrated circuits [4, 10-13] and gratings [11, 14] have proved promising candidates for realizing optical computing. Additionally, the introduction of metamaterials and metasurfaces also has enabled new opportunities in optical analog computing [1, 2, 15], due to the near arbitrary control they enable over propagation in both space and time [16-19]. Various analogue processors have been proposed to solve a range of computing tasks [4, 8, 13, 20-26].

While modern analog computing harnesses light to perform calculations, early examples exploited mechanical [27] and later electrical [28, 29] systems. For instance, analog PDE solutions could be produced by exploiting a grid-like network of electrical lumped elements [28, 29]. Similar approaches have also been applied at higher frequencies. For instance, metatronic circuits embedded in an epsilon-near-zero medium [25] and photonic circuits PICs [4, 13] have been used to produce solutions to the Poisson equation at optical frequencies. It has also been shown how waveguide-based metatronic circuits may be used to produce solutions to the Helmholtz equation at microwave frequencies [26].

In this work, we demonstrate a structure capable of calculating solutions to the Helmholtz equation at optical frequencies ($f = 193.41$ THz). This is done by exploiting a network of dielectric waveguides with wave splitters and Bragg gratings. During the conference, the design process behind the PDE solving network will be presented alongside a full theoretical analysis of the structure. Numerical simulation results will also be presented demonstrating the capabilities of this structure to calculate accurate solutions to Dirichlet boundary value problems.

II. Methods

A schematic representation of the proposed dielectric waveguide-base PDE solving structure is presented in Fig. 1a (right). As can be seen, the network consists of an array of dielectric waveguides, forming a grid, with wave splitters and Bragg gratings. Each wave splitter is constructed from a hollowed dielectric cylinder placed at the crossing point between waveguides [30]. As will be explained in detail during the conference, the geometry of these wave splitters is optimized to ensure that the signals are equally spread throughout the network [31-33], as a requirement of the PDE solving technique [26, 34]. Between each splitter, a Bragg grating is placed. During the conference, a full mathematical study of this structure will be presented, demonstrating how it can emulate the behavior of a quadrilateral finite difference mesh (shown in Fig. 1a, left). When doing so, one should consider the waveguide junctions as analogous to the sampling points of the finite difference mesh, while the Bragg gratings, which control the coupling between splitters, determine the PDE parameters h and k to be solved. Here h is the separation between sampling points in the finite difference analogy and k is the wavenumber of the PDE.

Furthermore, this work exploits a simple waveguide splitting structure which, even after optimization, exhibits non-ideal behavior (scattering losses and non-ideal phase relation). During the conference it will be explained how this non-ideal behavior is considered when producing a mapping between the reflection and transmission coefficient of the Bragg grating and the parameters of the PDE to be solved. In doing so we demonstrate that a wide range of PDE solutions are attainable when exploiting simple non-ideal splitting structures.

III. Results and Discussion

To demonstrate the potential of this PDE solving technique, numerical simulation results of two example solutions are presented in Fig. 1c,d. Here a 5×5 grid is used to solve a Dirichlet boundary value problem in which the boundaries are

all set to $H = 1$. For the 5×5 example, the PDE solution may be extracted from the 9 central junctions (labeled 1-9 in Fig. 1c). Numerical simulation results for the magnetic field sampled at the center of these 9 junctions are presented in Fig. 1d alongside theoretical values corresponding to an ideal PDE solutions. These examples are for networks designed to solve the Dirichlet boundary value problem when $h^2k^2 = 0.05 + 2.54i$ (top panel) and $h^2k^2 = -0.248 - 0.193i$, respectively. As can be seen, the numerical simulation results are in agreement with the theoretical results in both scenarios indicating that the network is indeed producing accurate PDE solutions

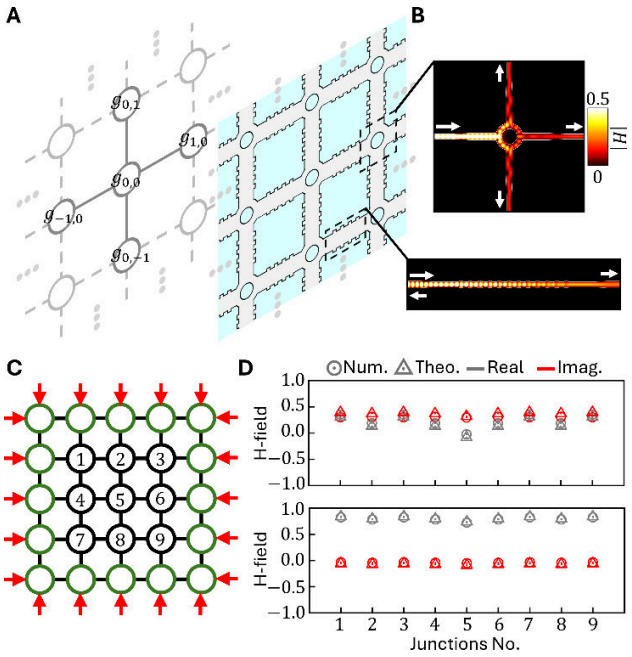

Fig. 1 **a**. Schematic representation of the PDE solving network. **B**. Numerical results of network components: (Top) wave splitter and (bottom) Bragg grating **c**. Schematic representation of a 5×5 network. **d**. Numerical simulation results of the scenario presented in **c** when (top) $h^2k^2 = 0.05 + 2.54i$ and (bottom) $h^2k^2 = -0.248 - 0.193i$, respectively.

IV. Conclusion

A method of producing discretized solutions to PDEs in the form of the Helmholtz wave equation using analog systems at 193.41 THz has been presented. Similar to circuit-based PDE solving techniques, this method exploits a network designed to emulate the performance of a finite difference mesh. During the conference, numerical simulation results will be presented showing networks of various sizes producing accurate solutions to Dirichlet boundary value problems. This demonstrates the potential of this PDE solving approach even when exploiting relatively simple wave splitter designed with non-ideal behavior.

Acknowledgments

This work was supported by the Leverhulme Trust under the Leverhulme Trust Research Project Grant scheme (No. RPG-2023-024).

References

[1] K. Cheng, Y. Fan, W. Zhang, Y. Gong, S. Fei, and H. Li, "Optical Realization of Wave-Based Analog Computing with Metamaterials," *Applied Sciences*, vol. 11, no. 1, p. 141, Dec. 2020.

[2] F. Zangeneh-Nejad, D. L. Sounas, A. Alù, and R. Fleury, "Analogue computing with metamaterials," *Nat. Rev. Mater.*, vol. 6, no. 3, pp. 207–225, Oct. 2020.

[3] H. Yang *et al.*, "Vector analog computing via on-demand metasurface dispersive polarization transformation," *Sci. Adv.*, vol. 11, no. 42, p. 5123, Oct. 2025.

[4] J. Anderson *et al.*, "Virtualizing a Post-Moore's Law Analog Mesh Processor: The Case of a Photonic PDE Accelerator," *ACM Transactions on Embedded Computing Systems*, vol. 22, no. 2, pp. 1–26, Mar. 2023.

[5] H. Rajabalipanah, A. Momeni, M. Rahmanzadeh, A. Abdolali, and R. Fleury, "Parallel wave-based analog computing using metagratings," *Nanophotonics*, vol. 11, no. 8, pp. 1561–1571, May 2022.

[6] A. Babaee, A. Momeni, A. Abdolali, and R. Fleury, "Parallel Analog Computing Based on a 2 ×2 Multiple-Input Multiple-Output Metasurface Processor With Asymmetric Response," *Phys. Rev. Appl.*, vol. 15, no. 4, p. 044015, Apr. 2021.

[7] A. Momeni, K. Rouhi, and R. Fleury, "Switchable and simultaneous spatiotemporal analog computing with computational graphene-based multilayers," *Carbon N. Y.*, vol. 186, pp. 599–611, Jan. 2022.

[8] T. Zhu *et al.*, "Plasmonic computing of spatial differentiation," *Nat. Commun.*, vol. 8, no. 1, p. 15391, Aug. 2017.

[9] J. Zhang, Q. Ying, and Z. Ruan, "Time response of plasmonic spatial differentiators," *Opt. Lett.*, vol. 44, no. 18, p. 4511, Sep. 2019.

[10] J. Dong, A. Zheng, D. Gao, L. Lei, D. Huang, and X. Zhang, "Compact, flexible and versatile photonic differentiator using silicon Mach-Zehnder interferometers," *Opt. Express*, vol. 21, no. 6, p. 7014, Mar. 2013.

[11] J. Azana, R. Slavik, Y. Park, and M. Kulishov, "Ultrafast All-Optical Differentiators Based on Fiber Gratings," in *2007 9th International Conference on Transparent Optical Networks*, IEEE, Jul. 2007, pp. 101–104.

[12] N. K. Berger, B. Levit, B. Fischer, M. Kulishov, D. V. Plant, and J. Azaña, "Temporal differentiation of optical signals using a phase-shifted fiber Bragg grating," *Opt. Express*, vol. 15, no. 2, p. 371, Jan. 2007.

[13] S. Sun *et al.*, "Induced homomorphism: Kirchhoff's law in photonics," *Nanophotonics*, vol. 10, no. 6, pp. 1711–1721, Apr. 2021.

[14] Z. Dong, J. Si, X. Yu, and X. Deng, "Optical spatial differentiator based on subwavelength high-contrast gratings," *Appl. Phys. Lett.*, vol. 112, no. 18, Apr. 2018.

[15] A. Silva, F. Monticone, G. Castaldi, V. Galdi, A. Alù, and N. Engheta, "Performing Mathematical Operations with Metamaterials," *Science (1979).*, vol. 343, no. 6167, pp. 160–163, Jan. 2014.

[16] V. Pacheco-Peña and N. Engheta, "Temporal aiming," *Light Sci. Appl.*, vol. 9, no. 1, p. 129, Dec. 2020, doi: 10.1038/s41377-020-00360-1.

[17] V. Pacheco-Peña and N. Engheta, "Antireflection temporal coatings," *Optica*, vol. 7, no. 4, p. 323, 2020.

[18] V. Pacheco-Peña and N. Engheta, "Temporal equivalent of the Brewster angle," *Phys. Rev. B*, vol. 104, no. 21, p. 214308, Dec. 2021.

[19] V. Pacheco-Peña and N. Engheta, "Effective medium concept in temporal metamaterials," *Nanophotonics*, vol. 9, no. 2, pp. 379–391, Feb. 2020.

[20] S. Abdollahramezani, O. Hemmatyar, and A. Adibi, "Meta-optics for spatial optical analog computing," *Nanophotonics*, vol. 9, no. 13, pp. 4075–4095, Sep. 2020.

[21] R. G. MacDonald, A. Yakovlev, and V. Pacheco-Peña, "Time derivatives via interconnected waveguides," *Sci. Rep.*, vol. 13, no. 1, p. 13126, Aug. 2023.

[22] T. Knightley, A. Yakovlev, and V. Pacheco-Peña, "Neural Network Design of Multilayer Metamaterial for Temporal Differentiation," *Adv. Opt. Mater.*, vol. 11, no. 5, p. 2202351, Mar. 2023.

[23] V. Nikkhah, A. Pirmoradi, F. Ashtiani, B. Edwards, F. Aflatouni, and N. Engheta, "Inverse-designed low-index-contrast structures on a silicon photonics platform for vector–matrix multiplication," *Nat. Photonics*, vol. 18, no. 5, pp. 501–508, May 2024.

[24] M. Park and Y. Park, "Metasurface-Based Imagers Enabled Arbitrary Optical Convolution Processing," *Light Sci. Appl.*, vol. 11, no. 1, p. 98, Apr. 2022.
[25] M. Miscuglio *et al.*, "Approximate analog computing with metatronic circuits," *Commun. Phys.*, vol. 4, no. 1, p. 196, Aug. 2021.
[26] R. G. MacDonald, A. Yakovlev, and V. Pacheco-Peña, "Solving partial differential equations with waveguide-based metatronic networks," *Advanced Photonics Nexus*, vol. 3, no. 05, p. 056007, Oct. 2024.
[27] D. R. HARTREE, "The Differential Analyser," *Nature*, vol. 135, no. 3423, pp. 940–943, Jun. 1935.
[28] Y. D. Save, H. Narayanan, and S. B. Patkar, "Solution of Partial Differential Equations by electrical analogy," *J. Comput. Sci.*, vol. 2, no. 1, pp. 18–30, Mar. 2011.
[29] G. Kron, "Electric circuit models of partial differential equations," *Electrical Engineering*, vol. 67, no. 7, pp. 672–684, Jul. 1948.
[30] E. Feigenbaum and H. A. Atwater, "Dielectric based resonant guided wave networks," *Opt. Express*, vol. 20, no. 10, p. 10674, May 2012.
[31] A. Yakovlev and V. Pacheco-Peña, "Enabling High-Speed Computing with Electromagnetic Pulse Switching," *Adv. Mater. Technol.*, vol. 5, no. 12, p. 2000796, Dec. 2020.
[32] V. Pacheco-Peña and A. Yakovlev, "Computing with Square Electromagnetic Pulses," in *Handbook of Unconventional Computing,* 1st ed., A. Adamatzky, Ed., London: World Scientific, 2021, pp. 465–492.
[33] R. G. MacDonald, A. Yakovlev, and V. Pacheco-Peña, "Amplitude-Controlled Electromagnetic Pulse Switching Using Waveguide Junctions for High-Speed Computing Processes," *Advanced Intelligent Systems*, vol. 4, no. 12, p. 2200137, Dec. 2022.
[34] R. G. Macdonald and V. Pacheco-Peña, *In Prep*.

GENERAL SESSION

Chiral and Hyperbolic Metamaterials

2 contributions · pp. 1315–1319

Inverse Faraday Effect and Gyrotropy in Time-Varying ENZ Films

Domenico de Ceglia[1,*], Carlo Rizza[2], Michael Scalora[1], Maria Antonietta Vincenti[1], Wallace Jaffray[3], Sven Stengel[3], Marcello Ferrera[3]

[1]Department of Information Engineering, University of Brescia, Brescia, Italy
[2]Department of Physical and Chemical Sciences, University of L'Aquila, L'Aquila, Italy
[3]Institute of Photonics and Quantum Sciences, Heriot-Watt University, United Kingdom
*Corresponding author: domenico.deceglia@unibs.it

***Abstract*—We investigate the origin of inverse Faraday effect and gyrotropy in epsilon-near-zero films under circularly polarized excitation. We compare four theoretical frameworks: (a) isotropic third-order nonlinearity, (b) Hertel's plasma model with time-averaged charge–velocity interaction, (c) nonlinear free-electron hydrodynamics, and (d) mass-varying Drude theory. Common mechanisms and key differences are discussed.**

***Keywords*— Epsilon-near-zero materials, gyrotropy, inverse Faraday effect, ultrafast photonics, nonlinear optics, plasmonics.**

I. Introduction

Gyrotropic optical effects are typically associated with magnetized or chiral media and manifest as antisymmetric off-diagonal terms in the permittivity tensor. In magneto-optical systems, the constitutive relation is commonly written as

$$\bar{\varepsilon} = \begin{pmatrix} \varepsilon & ig & 0 \\ -ig & \varepsilon & 0 \\ 0 & 0 & \varepsilon \end{pmatrix}, \tag{1}$$

where g is the gyrotropic coefficient responsible for circular birefringence and Faraday rotation. In linear magneto-optics, the gyrotropic coefficient is proportional to the magnetic field applied in the longitudinal direction. In nonlinear optics, for example in a pump-probe setup, the magnetic field may be induced and controlled by an intense pump.

Epsilon-near-zero (ENZ) materials provide an exceptional platform for all-optical symmetry breaking due to their extreme dispersion and field enhancement. Under intense pumping, even small perturbations of the electronic plasma can strongly modify the optical response. In particular, circularly polarized (CP) excitation carries spin angular momentum (SAM), which may be transferred to the electron gas, inducing a quasi-static axial response. This phenomenon can be interpreted in terms of the inverse Faraday effect (IFE), i.e., the conversion of optical SAM into electronic orbital motion and therefore magnetization.

Despite long-standing interest in the IFE [1], [2], [3], the microscopic origin and magnitude of gyrotropy in ENZ plasmonic films, and, more generally, in plasmonic systems, remains debated, especially in ultrafast regimes where time-varying conductivity, effective mass, and carrier density may play a major role. This work compares four theoretical models predicting light-induced gyrotropic responses in ENZ films, highlighting common physical foundations and critical differences.

II. Models and Physical Mechanisms

A. $\chi^{(3)}$ Inverse Faraday Effect

The classical approach to the IFE assumes an isotropic, instantaneous, third-order response and links the light-induced gyrotropy to a cubic nonlinear polarization term. The analogy of IFE to degenerate four-wave mixing has been discussed in [4] and [5]. For a monochromatic pump field $\mathbf{E}$, one obtains an antisymmetric nonlinear polarization contribution proportional to [1], [2], [3]

$$\mathbf{P}_0^{(3)} \propto \chi^{(3)}\, i\,(\mathbf{E}\times\mathbf{E}^*)\times\mathbf{E}. \tag{2}$$

In particular, the vector $i(\mathbf{E}\times\mathbf{E}^*)$ is proportional to the optical spin density and points along the propagation direction for CP pumping, and it may be interpreted as an effective, light-induced magnetization in the longitudinal direction. This model has the great advantage of compactness and applicability to a variety of materials, both opaque and transparent. However, the approach is inherently perturbative and fails to elucidate the physical origin of the nonlinear effects in ENZ structures, where the contribution of free electrons is generally dominant.

B. Hertel's model

Hertel [6] derived an IFE model for conducting plasmas where longitudinal magnetization emerges from charge continuity. A CP pump induces transverse electron velocity oscillations, while the continuity equation enforces a correlated density modulation. Their nonlinear mixing yields a nonzero time-averaged current circulation with a solenoidal component that may be associated with a longitudinal magnetization:

$$\mathbf{M}_0 = i\frac{ne^3}{4m^2\omega^3}\mathbf{E}\times\mathbf{E}^* \tag{3}$$

where m and n are the electron effective mass and density, respecitvely, e the elementary charge, and ω the angular frequency of the pump. This model explicitly ties gyrotropy to plasma dynamics and predicts strong dependence on plasma

frequency ($\varepsilon_0\omega_p^2 = ne^2/m$), and it has been invoked to explain the experimental observation of light-induced magnetism in gold nanoparticles pumped with CP light [7]. The appearance of this magnetization leads to symmetry breaking, i.e., to a pump-controlled gyrotropy mediated by the Lorentz force $\mu_0\sigma\mathbf{E}\times\mathbf{M}_0$. Recently, the linear magneto-optic effect in ENZ films has been investigated in the static configuration in which a magnetic field externally applied in the longitudinal direction induces a gyrotropic effect [8], [9]. The Faraday rotation is significantly enhanced near the ENZ wavelength. Here we will assess the ability of this model to quantitatively predict the amount of light-induced Faraday rotation in ENZ films.

C. Hydrodynamic Nonlinearities

Hydrodynamic approaches provide a more complete classical description of nonlinear electron motion in plasmonic media, incorporating convective, Coulomb, and Lorentz second-order nonlinear contributions, as well as the impact of losses [10], [11]. In such models, the coupled current-density equations generate a DC effective magnetic field arising from quadratic mixing of the pump-induced oscillating velocity (or current):

$$\mathbf{B}_{\text{eff}} \sim \langle \mathbf{v} \times \mathbf{v}^* \rangle \propto i\,(\mathbf{J} \times \mathbf{J}^*)\,. \tag{4}$$

The quasi-static field breaks time-reversal symmetry and modifies the effective permittivity experienced by a probe via magnetic Lorentz force. According to this model, the amount of gyrotropy associated with the IFE effect is mediated by the following effective magnetization:

$$\mathbf{M} = i\frac{|\sigma(\omega)|^2}{2n_0 e\omega}\mathbf{E}\times\mathbf{E}^* \tag{5}$$

in which $\sigma(\omega) = \frac{ne^2}{m(\gamma - i\omega)}$ is the complex conductivity. This represents an extension of the Hertel model to the case of a lossy plasma ($\gamma \neq 0$). The hydrodynamic model also predicts IFE from the orbital angular momentum of light [11], as well as surface nonlinear IFE whose role in light-induced gyrotropic effects has not been yet assessed.

D. Mass-varying Drude model

A further mechanism is associated with ultrafast carrier heating. In ENZ and plasmonic materials, strong pumping generates hot-electrons. The rate of change of the effective mass of these carriers introduces an additional damping term in the hydrodynamic model with anisotropic features. Recently, ultrafast polarization control has been observed in ENZ films [12]. The mass-varying Drude model provides a complete explanation of all the observed anisotropic effects, including the appearance of a handedness-dependent, time-varying gyrotropic conductivity [12]. This model suggests that gyrotropy can arise not only from applied or induced magnetization static fields, but also from pump-induced modulation of transport parameters.lin

III. Results and Discussion

All investigated models share a unifying physical picture: CP pumping produces an axial DC quantity proportional to the optical spin density

$$\mathbf{S} \propto i(\mathbf{E}_p \times \mathbf{E}_p^*), \tag{6}$$

which induces either a quasi-static magnetization $\mathbf{M}_0$, an effective field $\mathbf{B}_{\text{eff}}$, or an antisymmetric correction to the conductivity tensor. In each case, the probe experiences a permittivity tensor producing polarization rotation and circular birefringence.

However, the models differ in predictive scaling laws. The $\chi^{(3)}$ model provides a perturbative Kerr-like dependence but lacks explicit plasma transport physics. Hertel's approach captures charge continuity but predicts polarization rotation angles much smaller than those observed in the experiments. Hydrodynamic models with second-order multipolar nonlinearities incorporate interface effects, making them particularly suitable for nanometric ENZ films, but their bulk contribution is on the same order of the Hertel's model. Hot-electron models, such as the mass-varying Drude model, provide an additional contribution associated with ultrafast modification of the effective mass m and γ. This mechanism can be the most relevant in pump-probe experiments in ENZ films [12], and its contribution becomes increasingly significant for few-cycle and subcycle pulses.

IV. Conclusion

We compared four theoretical models predicting gyrotropic responses in plasmonic and ENZ films driven by circularly polarized pumping: isotropic $\chi^{(3)}$ IFE, Hertel plasma magnetization, nonlinear hydrodynamic models, and hot-electron effective mass anisotropy. All approaches rely on the conversion of optical SAM into electronic angular momentum, generating antisymmetric permittivity terms. Hydrodynamic and plasma-based models appear most consistent with ENZ thin-film physics, especially when interfaces and ultrafast parameter renormalization are significant.

References

[1] J. P. van der Ziel, P. S. Pershan, and L. D. Malmstrom, "Optically-induced magnetization resulting from the inverse Faraday effect," *Physical Review Letters*, vol. 15, p. 190, 1965.

[2] Y. R. Shen, *The Principles of Nonlinear Optics*. Wiley, 1984.

[3] R. W. Boyd, *Nonlinear Optics*, 3rd ed. Academic Press, 2008.

[4] Y. P. Svirko and N. Zheludev, "Coherent and incoherent pump–probe specular inverse Faraday effect in media with instantaneous nonlinearity," *Journal of the Optical Society of America B*, vol. 11, pp. 1388–1393, 1994.

[5] Y. P. Svirko and N. I. Zheludev, *Polarization of Light in Nonlinear Optics*. Wiley, 2000.

[6] R. Hertel, "Theory of the inverse Faraday effect in metals," *Journal of Magnetism and Magnetic Materials*, vol. 303, no. 1, pp. L1–L4, 2006.

[7] O. H.-C. Cheng, D. H. Son, and M. Sheldon, "Light-induced magnetism in plasmonic gold nanoparticles," *Nature Photonics*, vol. 14, pp. 365–368, 2020.

[8] K. Ikeda, T. Liu, Y. Ota, N. Kobayashi, and S. Iwamoto, "Enhanced magneto-optical effects in epsilon-near-zero indium tin oxide at telecommunication wavelengths," *Advanced Optical Materials*, p. 2301320, 2023, doi: 10.1002/adom.202301320.

[9] J. R. Schrecengost, A. J. Cleri, M. J. Tolchin, R. Mohan, J. P. Murphy, S. Adamkovic, A. J. Grede, M. V. Imperatore, P. E. Hopkins, J.-P. Maria, and N. C. Giebink, "Large mid-infrared magneto-optic response from doped cadmium oxide at its epsilon-near-zero frequency," *Advanced Optical Materials*, p. 2400803, 2024, doi: 10.1002/adom.202400803.

[10] M. Scalora, M. A. Vincenti, D. de Ceglia, V. Roppo, M. Centini, N. Akozbek, and M. J. Bloemer, "Second- and third-harmonic generation in metal-based structures: hydrodynamic model," *Physical Review A*, vol. 82, p. 043828, 2010.

[11] V. Karakhanyan, C. Eustache, Y. Lefier, and T. Grosjean, "Inverse Faraday effect from the orbital angular momentum of light," *Physical Review B*, vol. 105, p. 045406, 2022.

[12] W. Jaffray, S. Stengel, A. Boltasseva, V. M. Shalaev, M. A. Vincenti, D. de Ceglia, M. Scalora, C. Rizza, and M. Ferrera, "All-optical polarization control in time-varying low-index films via plasma symmetry breaking," arXiv:2510.06985 [physics.optics], 2025.

Carrier Drift Modulation and Hyperbolic Time Crystals

Evgenii Narimanov[1,*] and Boris Shapiro[2]

[1]Purdue University, West Lafayette, IN 47907, USA
[2]Technion - Israel Institute of Technology, Haifa 32000, Israel
*Corresponding author: evgenii@purdue.edu

***Abstract*—Carrier Drift Modulation imparts a transient drift momentum to free carriers using few-cycle optical excitation, producing strong anisotropy in nominally isotropic conductors. This ultrafast mechanism enables hyperbolic dispersion and supports time-periodic amplification, offering a practical route to low-loss hyperbolic media in standard semiconductor platforms.**

***Keywords*— hyperbolic media; photonic time crystals.**

I. Introduction

Temporal modulation of optical media has emerged as a powerful tool for reshaping electromagnetic response in ways that static materials cannot achieve [1]. By altering material parameters on timescales comparable to or shorter than the optical period [2], one can access regimes where the usual constraints of causality, dispersion, and spatial symmetry are fundamentally modified [1]. Such temporal control has enabled concepts ranging from time refraction and time reflection to photonic time crystals with engineered Floquet band structures [3], [4], [5].

Despite this promise, most approaches to ultrafast temporal modulation face significant limitations [6]. Mechanisms based on carrier density modulation require high fluence and suffer from slow relaxation. Nonlinear optical methods demand extreme intensities and often introduce unwanted heating. Electro-optic modulation is fundamentally bandwidth-limited. As a result, achieving strong, reversible modulation at optical frequencies has remained a central challenge.

Carrier Drift Modulation (CDM) [7] offers a fundamentally different route. Instead of modifying the number of carriers or their temperature, CDM uses a few-cycle optical pulse to impart a net drift momentum to the electron gas. This directional shift of the carrier distribution is extremely fast – limited only by the duration of the optical pump pulse – and naturally reversible on the carrier relaxation timescale. Because real electronic bands are non-parabolic, the drift modifies the effective mass tensor and produces a transient anisotropy that can be surprisingly large even for a moderate drift.

This anisotropy is strong enough to induce a topological transition to hyperbolic dispersion in an initially isotropic conductor. When the drift is applied periodically, the system becomes a hyperbolic photonic time crystal (HTC), combining the high-wavenumber support of hyperbolic media with the parametric amplification inherent to time-periodic systems. The resulting platform supports tunable dispersion, ultrafast reconfigurability, and intrinsic gain – all using standard semiconductor materials and commercially available ultrafast sources.

II. Carrier Drift Modulation

A sub-cycle pump pulse $E_M(t)$ transfers a net impulse

$$p_0 = e\int_{-\infty}^{\infty} E_M(t)\,dt, \tag{1}$$

shifting the carrier distribution to

$$f_M(\mathbf{p},t) \simeq f_0(\mathbf{p}-\mathbf{p}_0), \tag{2}$$

for $\tau_M \ll t \ll \tau_0$. This shift is conceptually simple but physically profound. The electron gas is then displaced in momentum space. Because the effective mass depends on the magnitude of the momentum, this displacement changes the inertia of the carriers in a direction-dependent manner, producing an anisotropic dielectric response.

For a moderate drift when the transferred impulse is less than the Fermi momentum ($p_0 < p_F$), the non-parabolicity of the band yields

$$\Omega_{\parallel}^2 \simeq 3\frac{\alpha_*\omega_p^2}{m_0}p_0^2, \tag{3}$$

$$\Omega_{\perp}^2 \simeq \frac{\alpha_*\omega_p^2}{m_0}p_0^2, \tag{4}$$

leading to the permittivity tensor

$$\epsilon_{\parallel,\perp} = \epsilon_\infty\left(1-\frac{\omega_p^2-\Omega_{\parallel,\perp}^2}{\omega^2}\right). \tag{5}$$

The resulting anisotropy is not a small perturbation: even a modest drift can shift the plasma frequency in the directions parallel and perpendicular to the free carriers drift, opening the hyperbolic dispersion window for

$$\sqrt{\omega_p^2-\Omega_{\parallel}^2} < \omega < \sqrt{\omega_p^2-\Omega_{\perp}^2}. \tag{6}$$

This transition occurs on a timescale much shorter than τ_0, making it effectively instantaneous from the perspective of the probe field. The medium abruptly switches from isotropic to hyperbolic, enabling ultrafast control of high-wavenumber modes and directional propagation.

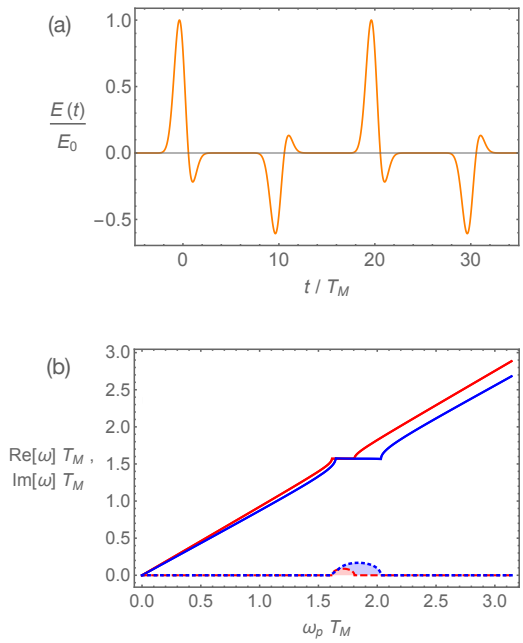

Fig. 1. (a) Modulation pulse sequence and resulting drift-momentum pattern defining the temporal unit cell. (b) Floquet–Bloch quasi-frequency versus the scaled modulation interval $\omega_p T_M$, showing its real and imaginary components for different modulation strengths (red and blue color). Solid and dashed lines represent the real and imaginary parts of the Floquet–Bloch frequency, respectively. Complex quasifrequencies indicate the onset of parametric gain.

III. Hyperbolic Time Crystal

Periodic drift modulation produces a temporal photonic crystal whose Floquet bands depend sensitively on the modulation period. For short periods, the system behaves as a temporal metamaterial with effective parameters given by the time-averaged permittivity. In this regime, the medium behaves like a conventional hyperbolic material, but with tunable anisotropy and ultrafast switching capability.

As the modulation period increases and approaches a significant fraction of the optical cycle, the full Floquet structure becomes important. The system develops bandgaps in the temporal domain, analogous to spatial photonic crystals. However, because the modulation is strong and anisotropic, these bandgaps occur in a regime where the medium is already hyperbolic. This leads to a hyperbolic time crystal, a new class of photonic structure that combines the unbounded-k support of hyperbolic media with the temporal band engineering of time crystals.

Figure 1 illustrates the corresponding modulation protocol in panel (a), and the resulting quasifrequency spectrum (panel (b)) – which highlights the emergence of complex quasifrequencies, marking the transition to an amplifying regime. These features arise directly from the strong, ultrafast anisotropy produced by CDM.

The Floquet dispersion reveals a rich structure, including avoided crossings, band folding, and regions of complex quasifrequency. The latter correspond to parametric amplification, where the modulation pumps energy into the probe field. The interplay between hyperbolic dispersion and temporal periodicity produces a landscape of modes that have no analogue in either static hyperbolic media or conventional time crystals.

IV. Parametric Gain and Loss Compensation

One of the most important consequences of CDM is that the same mechanism that creates hyperbolic dispersion, also provides parametric gain. When the modulation period satisfies a simple resonance condition, the Floquet bands acquire a positive imaginary component. This corresponds to the exponential amplification of the probe field.

In realistic materials such as crystalline semiconductors GaAs or InGaAs, the gain can reach or exceed the intrinsic absorption of the medium. This directly addresses a long-standing challenge in hyperbolic photonics, where substantial intrinsic losses have consistently restricted the performance and applicability of such materials. CDM provides a route to low-loss hyperbolic media, something that has been sought for more than a decade. The ability to compensate losses without introducing external gain media or complex architectures represents a significant step toward practical nanophotonics.

V. Practical Feasibility

A key advantage of CDM is that it requires no exotic materials or extreme fields. The required pump impulses correspond to peak fields on the order of a few hundred kV/cm – well within the capabilities of commercial few-cycle IR sources. The materials themselves are standard: heavily doped semiconductors and transparent conducting oxides, both widely used in photonics and electronics.

The modulation is ultrafast, reversible, and compatible with high-repetition-rate operation. Because the drift momentum decays only on the carrier relaxation timescale, the modulation can be applied at tens of terahertz without requiring continuous high-power pumping. This makes CDM suitable for integration into on-chip photonic platforms, where compactness and compatibility with existing fabrication processes are essential.

VI. Conclusion

Carrier Drift Modulation provides an ultrafast route to inducing hyperbolic dispersion in isotropic conductors. Periodic modulation forms a hyperbolic time crystal with intrinsic parametric gain, enabling low-loss hyperbolic media using standard semiconductor materials and readily available ultrafast sources.

References

[1] E. Lustig *et al*, Opt. Express **31**, 9165 (2023).
[2] E. Lustig *et al.*, Nanophotonics **12** (12), 2221 (2023).
[3] R. Morgenthaler, IRE Trans. Microw. Theory Tech. **6**, 167 (1958).
[4] J. T. Mendonça and P. K. Shukla, Phys. Scr. **65**, 160 (2002).
[5] E. Lustig *et al.*, Optica **5**, 1390 (2018).
[6] J. B. Khurgin, Laser & Photonics Reviews **18** (4), 2300836 (2024).
[7] E. Narimanov and B. Shapiro, preprint arXiv:2601.00547

GENERAL SESSION

Metasurfaces: Flat Optics, FSS, HIS, and Beyond

8 contributions · pp. 1321–1339

Reconfigurable Optical Imaging via a Wavelength-Driven Multifunctional Metasurface

Hongliang Li[1,*], Yang Xiao[1], Yuning Ye[2], Jisen Wen[2], Xuechao Yu[1]

[1] Suzhou Institute of Nano-Tech and Nano-Bionics, Key Laboratory of Multifunctional Nanomaterials and Smart Systems, Chinese Academy of Sciences, Suzhou, 215123, China
[2] State Key Laboratory of Extreme Photonics and Instrumentation, College of Optical Science & Engineering, Zhejiang University, Hangzhou, 310027, China
*Corresponding author: hlli2025@sinano.ac.cn

***Abstract*—Wavelength-multiplexed metasurfaces offer a compact platform for multifunctional optical imaging, yet achieving reconfigurable operation with low crosstalk remains challenging. Here, we present a wavelength-driven multifunctional metasurface that enables reconfigurable optical imaging within a single device. The metasurface selectively generates a focused beam at 450 nm for bright-field imaging and a vortex beam at 532 nm for edge-enhanced imaging. Experimental results demonstrate robust, crosstalk-suppressed mode switching across geometric, resolution, and biological samples, validating the proposed approach as a versatile platform for adaptive compact optical systems.**

***Keywords*— Wavelength-multiplexing, reconfigurable imaging, metasurface.**

I. Introduction

Optical imaging provides access to fine spatial and morphological details, underpinning diverse applications from biological observation and machine vision to industrial inspection.[1-3] Comprehensive sample characterization often necessitates multiple imaging modalities. In particular, bright-field imaging captures subwavelength structural details, while edge-enhanced imaging emphasizes object boundaries by filtering high-frequency components. Integrating both functions into a single system remains challenging due to inter-channel crosstalk arising from competing phase and amplitude requirements.[4-7]

Wavelength multiplexing offers a promising route to channel isolation, yet its implementation with conventional refractive optics is hindered by limited design freedom and bulky configurations.[8-9] Optical metasurfaces-ultrathin arrays of subwavelength scatterers-enable precise, wavelength-dependent wavefront control within a compact platform.[10] Although recent metasurface designs have realized single or dual functionalities under fixed illumination, a robust strategy for fully independent, switchable multi-wavelength operation is still needed.

Here, we demonstrate a wavelength-multiplexed metasurface that supports reconfigurable bright-field and edge-enhanced imaging in a single device. Under linearly polarized light, the metasurface generates a focused beam at 450 nm and a vortex beam at 532 nm, corresponding to the two imaging modes. Through complex-transmission-coefficient optimization and superimposed phase engineering, crosstalk is suppressed while maintaining high efficiency. Experimental characterization and imaging of geometric, resolution, and biological samples confirm reliable mode switching and functional versatility, establishing a practical platform for multifunctional compact optical systems.

II. Methods

Our methodology integrates simulation, optimization algorithms, and experimental feedback: Current optical imaging techniques face a trade-off between spatial resolution and edge contrast. Conventional wide-field microscopy is straightforward but diffraction-limited; confocal methods enhance resolution at the cost of complexity; and edge-detection systems typically rely on bulky 4f setups with limited functional versatility. To overcome these limitations, we propose a wavelength-multiplexed metasurface that integrates bright-field and edge-enhanced imaging within a single planar device.

As illustrated in Fig. 1a, the metasurface comprises periodic rectangular TiO_2 nanoposts on a silica substrate (period: 0.35 μm, height: 0.5 μm). A meta-atom library was constructed via FDTD simulations by varying nanopost dimensions, providing full 2π phase coverage with high transmission under both x- and y-polarizations at the two target wavelengths: 450 nm and 532 nm. The design encodes two independent phase profiles: a focusing phase for 450 nm TE polarization (Eq. 1) and a vortex phase carrying topological charge $\ell = 1$ for 532 nm TM polarization (Eq. 2). These profiles are spatially combined into a single metasurface layout through a phase-superposition strategy, enabling dual-wavelength and dual-polarization operation without crosstalk. Figure 1b illustrates the operational principle: under 450 nm x-polarized light, the device focuses the beam for bright-field imaging; under 532 nm y-polarized light, it generates a focused vortex for edge-enhanced imaging. The fabricated metasurface (diameter:

90.3 μm) is shown in the SEM images in Fig. 1c and 1d, confirming uniform nanopost arrangement and geometric variation.

$$\varphi_{TE}(x,y) = \frac{2\pi n}{\lambda_1}\left(f - \sqrt{x^2+y^2+f^2}\right) \quad (1)$$

$$\varphi_{TM}(x,y) = \frac{2\pi n}{\lambda_2}\left(f - \sqrt{x^2+y^2+f^2}\right) + \ell \tan^{-1}\frac{y}{x} \quad (2)$$

where x, y are the in-plane coordinates of the metasurface. The wavelengths λ_1 and λ_2 are 450 nm and 532 nm, serving as the beams for bright-field and edge-enhanced imaging, respectively. The refractive index of air is denoted by n, f represents the focal length, and ℓ symbolizes a topological charge.

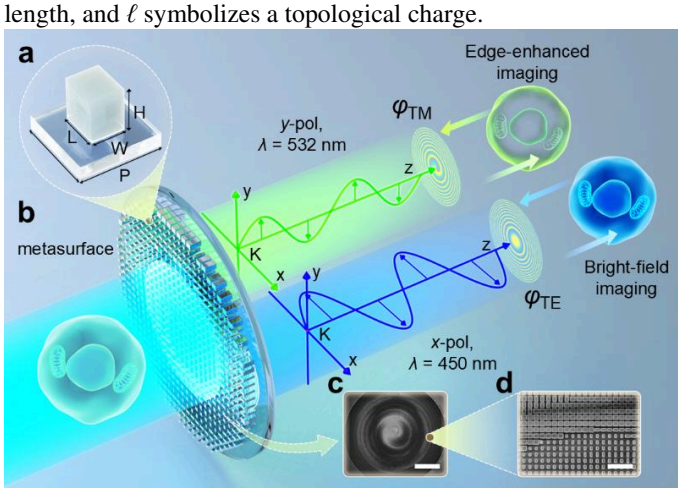

Fig. 1 Unit cell geometry of the proposed metamaterial. Dual-wavelength and dual-polarization metasurface design and characterization. (a) Unit cell consisting of a TiO_2 nanopost on a silica substrate. (b) Operating principle: under 450 nm x-polarized light, the metasurface produces a focused beam for bright-field imaging; under 532 nm y-polarized light, it generates a vortex beam for edge-enhanced imaging. (c) Scanning electron microscopy (SEM) image of the fabricated metasurface (90.3 μm × 90.3 μm; scale bar, 30 μm). (d) Zoomed-in top-view SEM showing rectangular TiO_2 nanoposts with varying aspect ratios (scale bar, 2 μm).

III. Results and Discussion

To assess practical imaging performance, we next evaluated the metasurface on real samples with complex structures. Figure 2a illustrates the experimental setup, which employs linearly polarized illumination for enhanced stability and alignment robustness compared to circular polarization[41]. As schematized in Fig. 2b–c, the metasurface operates as a high-pass spatial filter: it suppresses low-frequency background while selectively enhancing high-frequency edge components in the spatial-frequency domain, thereby achieving optical edge enhancement.

Figure 2d–e presents images of four 3D-printed geometric patterns under 450 nm (bright-field) and 532 nm (edge-enhanced) illumination. In bright-field mode, overall shapes and internal details are clearly resolved. In edge-enhancement mode, boundaries are accentuated with a relief-like appearance, while uniform regions are suppressed—consistent with the high-pass filtering behavior. Intensity profiles across these images (Fig. 2f–g) show distinct peaks at object edges, confirming effective edge extraction.

Further validation was performed using a USAF resolution target (Fig. 3a–b). The 450-nm channel faithfully reproduces fine structural details, whereas the 532-nm channel emphasizes intensity transitions at edges, improving boundary contrast. Quantitative line profiles (Fig. 3c–d) exhibit sharp peaks corresponding precisely to physical edges, confirming background suppression and edge resolution. Consistent performance across different magnifications underscores the reliability of the wavelength-multiplexed design.

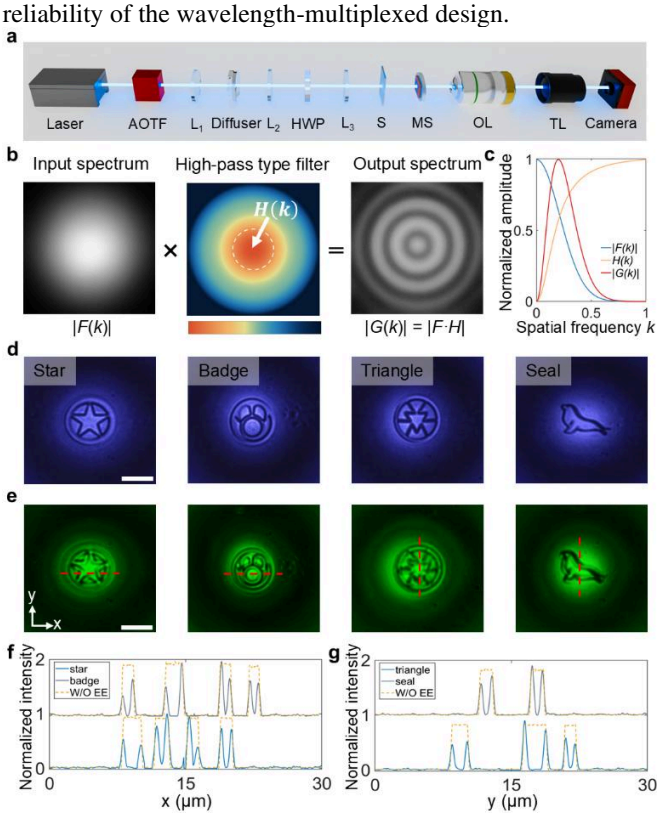

Fig. 2 | Experimental demonstration of dual-wavelength imaging via metasurface beam shaping. (a) Schematic of the optical imaging setup. (b) Conceptual diagram of edge-enhanced imaging: the metasurface acts as a high-pass filter, attenuating low-frequency background and amplifying high-frequency edge components in the spatial-frequency domain. (c) Normalized frequency-response curves illustrating the high-pass filtering mechanism. (d) Bright-field images of 3D-printed test patterns obtained under 450 nm illumination. (e) Corresponding edge-enhanced images of the same patterns under 532 nm illumination. Scale bars: 20 μm. (f, g) Intensity profiles along the dashed lines in (e), showing enhanced edge signals compared to the ideal profiles without edge enhancement (labeled "W/O EE").

The metasurface was further applied to biological imaging using transverse stem cells from a monocot plant. Under 450 nm illumination, bright-field imaging clearly resolved intracellular structures, including the nucleus and cytoplasmic strands (Fig. 3e). In contrast, under 532 nm illumination, the vortex-based edge-enhancement mode suppressed low-frequency background—characteristic of weakly scattering cells—resulting in diminished internal details while emphasizing high-frequency features such as the cell wall (Fig. 3f).

Quantitative spatial-frequency analysis (Fig. 3g) showed that the bright-field channel retained spectral power across a broad frequency range, whereas the edge-enhanced channel exhibited steeper decay at higher spatial frequencies. Edge-gradient statistics (Fig. 3h) further indicated stronger local intensity variations in bright-field images (median gradient ≈ 0.34, P90 ≈ 0.65) compared to edge-enhanced images (median ≈ 0.25, P90 ≈ 0.54), consistent with the preservation of fine intracellular textures in the former.

In multicellular samples, bright-field imaging at the cell-wall plane captured continuous cellular contours and overall tissue organization (Fig. 3i). Edge-enhanced imaging under the same condition accentuated inter-cellular boundaries, improving individual cell delineation (Fig. 3j). When focused on the nucleus plane (Fig. 3k–l), the 532 nm channel revealed subtle intra-nuclear intensity variations, suggesting sub-nuclear heterogeneity that was less apparent in bright-field mode.

These results demonstrate that the metasurface supports reliable switching between two complementary imaging modes within a single device: bright-field imaging for holistic structural morphology and edge-enhanced imaging for boundary-specific contrast enhancement, confirming its versatility across varied imaging scenarios.

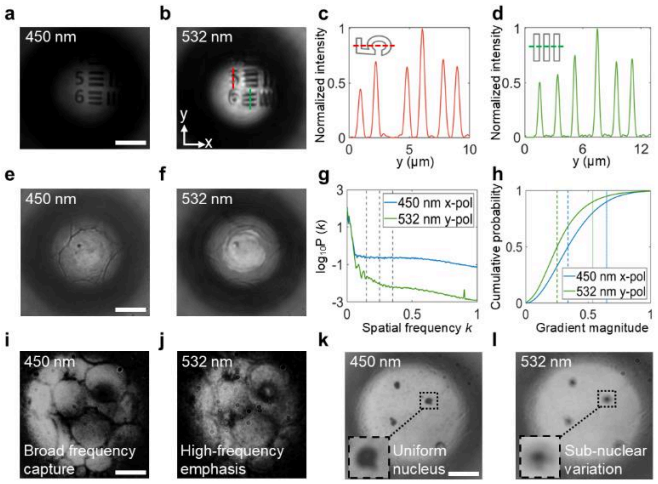

Fig.3 | Experimental imaging performance of the dual-wavelength metasurface. (a, b) USAF resolution target images under 450 nm (bright-field) and 532 nm (edge-enhanced) illumination. (c, d) Intensity profiles along the dashed lines in (b), showing clear edge-enhanced peaks. (e, f) Single-cell images captured at 450 nm and 532 nm, respectively. (g, h) Corresponding log-scale radial power spectra (dashed lines mark spatial frequencies k = 0.15, 0.25, 0.35) and edge-gradient cumulative distribution functions (CDFs). Median and 90th-percentile (P90) gradient levels are indicated. (i–l) Multi-cell images focused on the cell-wall plane (i, j) and the cell-nucleus plane (k, l) under the two wavelengths. Scale bars: 20 μm.

IV. Conclusion

In summary, we have developed a wavelength-multiplexed metasurface that enables independent wavefront control at two visible wavelengths (450 nm and 532 nm), supporting switchable bright-field and edge-enhanced imaging within a single planar device. Using propagation-phase modulation and a complex-transmission-coefficient-based design strategy, the metasurface achieves high-efficiency amplitude and phase control with suppressed inter-channel crosstalk. Operation under linear polarization ensures alignment robustness and system compatibility. Experimental imaging across geometric, resolution, and biological samples confirms reliable mode switching and dual-function performance. This work establishes a practical route toward compact, multifunctional optical systems and paves the way for extending wavelength-multiplexed metasurfaces to broader spectral ranges and more complex imaging modalities.

Acknowledgments

This work was financially supported by the National Natural Science Foundation of China (Grant No. 62505351), the Basic Research Program of Jiangsu (Grant No. BK20250501), the Jiangsu Funding Program for Excellent Postdoctoral Talent (Grant No. 2025ZB653), and the Wuxi Science and Technology Development Fund Project (K20241026).

References

[1] Yoon, S. et al. Deep optical imaging within complex scattering media. Nat. Rev. Phys. 2, 141-158 (2020).
[2] Meng, X. et al. Recent advances in optical imaging of biomarkers in vivo. Nano Today 38, 101156 (2021).
[3] Hu, X. et al. Metasurface-based computational imaging: a review. Adv. Photonics 6, 014002-014002 (2024).
[4] Zhao, W. et al. Sparse deconvolution improves the resolution of live-cell super-resolution fluorescence microscopy. Nat. Biotechnol. 40, 606-617 (2022).
[5] Ji, Z. et al. Multidimensional multiplexing metalens for STED microscopy. Sci. Adv. 11, eadt2807 (2025).
[6] Zhou, C. et al. Metasurface enabled broadband, high numerical aperture Laplace differentiator under multiple polarization illumination. PhotoniX 6, 10 (2025).
[7] Zhou, J. et al. Metasurface enabled quantum edge detection. Sci. Adv. 6, eabc4385 (2020).
[8] Chen, H.-T. et al. A review of metasurfaces: physics and applications. Rep. Prog. Phys. 79, 076401 (2016).
[9] Li, A. et al. Metasurfaces and their applications. Nanophotonics 7, 989-1011 (2018).
[10] Xingdong, F. et al. Single-layer, cascaded and broadband-heat-dissipation metasurface for multi-wavelength lasers and infrared camouflage. Opto-Electron. Adv. 8, 240280 (2025).

SuperLattice Plasmon Mode in a Grating of 2D Electron Strips

A. Shuvaev[1,*], A. R. Khisameeva[1], V. M. Muravev[2], K. R. Dzhikirba[2], A. A. Zabolotnykh[3], P. A. Gusikhin[2], M. S. Ryzhkov[1], D. A. Khudaiberdiev[1], A. S. Astrakhantseva[2], I. V. Kukushkin[2], A. Pimenov[1]

[1]Institute of Solid State Physics, Vienna University of Technology, 1040 Vienna, Austria
[2]Institute of Solid State Physics, RAS, Chernogolovka, 142432 Russia
[3]Kotelnikov Institute of Radio-engineering and Electronics of the RAS, Moscow, 125009 Russia
*Corresponding author: shuvaev@ifp.tuwien.ac.at

***Abstract*—We report an experimental observation of a new plasmon mode in the metasurface made up of two-dimensional electron system strips. A collective effect from the superlattice, along with lateral screening between the strips are the key properties of the novel resonance. The developed analytical approach accurately describes the observed behavior.**

***Keywords*— metasurfaces, plasmons, terahertz.**

I. Introduction

Plasma excitations in two-dimensional electron systems (2DES) have been the focus of active research for the past 50 years. The metasurface made up of a grating of 2DES strips shows great potential for terahertz applications. Predictions suggest that such a tunable metasurface could function as an effective THz amplitude and phase modulator, enabling beam steering and wavefront shaping [1]. The tunability of the 2DESs is achieved by changing the electron density or applying an external magnetic field, allowing for continuous tuning of the properties of the plasmonic metasurface.

In the present talk, we report on terahertz spectroscopy experiments on the GaAs membranes with a grating of strips formed lithographically in a high-mobility 2DES. The developed metasurface demonstrates a strong plasmonic response when the incident radiation polarization is perpendicular to the strips.

II. Methods

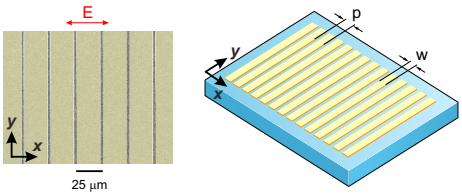

Fig. 1. (Left) E-beam photo of the sample comprising a grating of isolated 2DES strips. The area of the 2DES is highlighted in yellow. Each 2DES strip has a width of $w = 23$ μm, and the period is $p = 25$ μm. (Right) Schematic of the plasmonic metasurface device. The two-dimensional electron system is represented in yellow, while the GaAs substrate is shown in blue.

The samples were made from the industrial GaAs heterostructures with a 20 nm wide quantum well grown at a distance of 210 nm below the crystal surface. The quantum well hosts the 2DES with the density $n_s = 9.3 \times 10^{11}$ cm^{-2} and electron mobility $\mu = 10^5$ cm^2/Vs at $T = 5$ K. The effective mass of electrons is $m^* = 0.071\, m_0$. A grating of 2DES isolated strips (Fig. 1) is lithographically fabricated on the 1×1 cm^2 samples. For eight of them, the metasurface period is fixed $p = 25$ μm and the strip width varies from $w = 13$ μm to 23.7 μm. The phase/intensity of the electromagnetic wave that passed through the sample was investigated using a Mach-Zehnder interferometer. All experiments were conducted at a base sample temperature of 5 K.

III. Results and Discussion

The inset to Fig. 2 shows the transmission spectrum recorded for a metasurface period of $p = 25$ μm and a strip width of $w = 21.5$ μm. A clear plasmon resonance is observed at $f_p = 0.2$ THz, superimposed on the Fabry-Pérot transmission function of the bare dielectric membrane. To eliminate the Fabry-Pérot background and spurious resonances of the quasi-optical path, we divide the transmission at $B = 0$ T by the transmission through the sample at $B = 7$ T. At such a strong magnetic field, the motion of the 2D electrons in the quantum well plane is quenched in cyclotron orbits. As a consequence, the 2DES does not affect the transmittance. The resultant normalized transmission spectra recorded for three samples with different 2DES strip widths $w = 13, 21.5$ and 23.7 μm but fixed metasurface period $p = 25$ μm are shown in Fig. 2. The plasmon resonance moves to a higher frequency as the gap between the strips is increased.

However, the experimentally obtained values of the plasmon frequency differ significantly from those predicted by the standard dispersion equation:

$$\omega_p(q) = \sqrt{\frac{n_s e^2}{2\, m^* \varepsilon_0 \varepsilon_{\text{eff}}} q} \qquad (q \gg \omega/c). \tag{1}$$

Here, q is the wave vector of the plasmon excitation, n_s and m^* are the density and the effective mass of the 2DES electrons, while ε_0 and ε_{eff} denote the vacuum permittivity and the effective permittivity of the surrounding medium. For the 2DES strip with a width of w, the wave vector is typically assumed to be $q \approx 3\pi/4w$ [2].

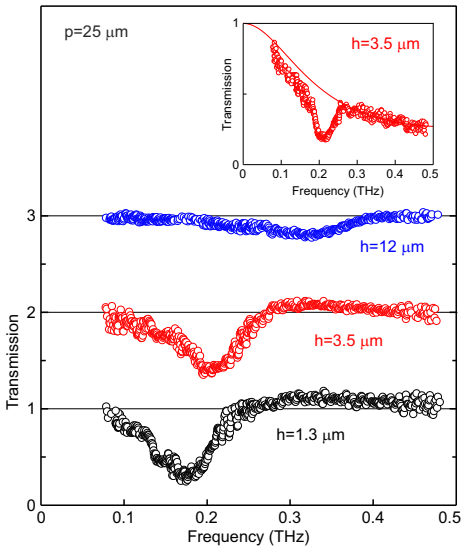

Fig. 2. The normalized transmission spectra of three samples with different strip spacings, specifically $h = 12$, 3.5, and 1.3 μm. All three samples share the same period, $p = 25$ μm. For clarity, the curves have been vertically shifted by 1 unit. The inset shows the transmission spectrum of the $h = 3.5$ μm sample without normalization. The solid red line represents the Fabry-Pérot function for the bare dielectric membrane with no 2DES.

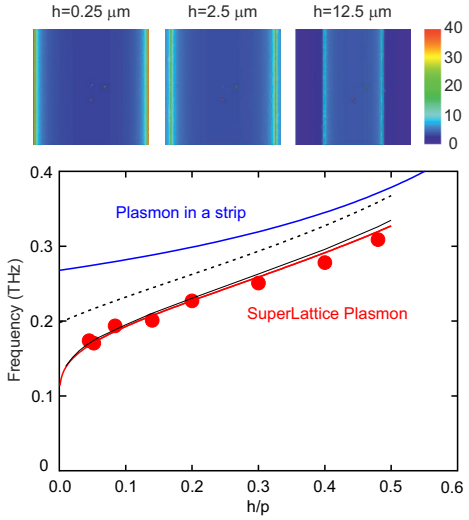

Fig. 3. Dependence of the plasmon frequency on the h/p. The period of the plasmonic metasurface was maintained at a fixed value of $p = 25$ μm. The solid red line represents a theoretical prediction (2), while the blue line presents the standard 2D plasmon frequency (1) in a single strip with wave vector $q = 3\pi/4w$. The solid black line shows the result of simulation in the HFSS 3D high-frequency simulation software. The dotted curve in Fig. 3 depicts the result for the analytical prediction from [2]. Top inset displays the color maps of field-$|E|$ distribution at the plasmon resonance for $h = 0.25$, 2.5, and 12.5 μm ($p = 25$ μm). The 2DES strip is located at the center of each color map.

Indeed, Fig. 3 shows how the plasmon frequency depends on the gap between the 2DES strips $h/p = (p - w)/p$. This dependence was measured across eight samples, all with the same period of $p = 25$ μm. The solid blue line in the Figure represents the theoretical prediction based on equation (1) with $q = 3\pi/4w$. It is clear that there is a significant discrepancy between this theoretical prediction and the experimental results, even with significant spacing between the individual strips. To better understand the situation underway, we have developed a theoretical framework to describe the behavior of the plasmonic metasurface under consideration.

The theoretical analysis follows to that applied in Refs. [3], [4] devoted to the electromagnetic response of plasmonic crystals. Under a number of reasonable assumptions [5] we arrive at the final expression for the frequency of the fundamental superlattice plasmon mode:

$$\omega_{sp} = \sqrt{\frac{n_s e^2}{2\, m^* \varepsilon_0 \varepsilon_{\text{eff}}} \frac{\pi}{p} \frac{1}{\ln\left(\dfrac{p}{2\pi h}\right) + 2}}, \qquad (2)$$

where p is the metasurface period, $h = p - w$ is the gap between the 2DES strips, and $\varepsilon_{\text{eff}} = (1 + \varepsilon_{\text{GaAs}})/2$ is the effective dielectric permittivity. It is the logarithmic factor that represents the mutual capacitance between the strips leading to zero frequency of the superlattice plasmon mode as the gap h closes. There is a remarkable agreement between the analytical formula (2) displayed in Fig. 3 by a solid red curve and the experimental data.

IV. Conclusion

In conclusion, we discovered that a collective effect from the superlattice, combined with lateral screening between the strips, gives rise to the emergence of a new superlattice plasmon mode. This mode arises from the superposition of standing plasma waves across all wave-vectors of the metasurface's reciprocal lattice [5]. We developed an analytical expression for the frequency of the mode, which shows remarkable agreement with experimental results. The distinguishing feature of the novel mode is that its frequency approaches zero as the gap between the strips closes.

Acknowledgments

The authors gratefully acknowledge the financial support of the TU Wien Bibliothek through its Open Access Funding Program.

References

[1] Z. Li, K. Yao, F. Xia, S. Shen, J. Tian, and Y. Liu, "Graphene plasmonic metasurfaces to steer infrared light," *Scientific Reports*, vol. 5, no. 1, p. 12423, 2015. [Online]. Available: https://doi.org/10.1038/srep12423

[2] K. A. Velizhanin, "Geometric universality of plasmon modes in graphene nanoribbon arrays," *Phys. Rev. B*, vol. 91, p. 125429, Mar 2015. [Online]. Available: https://link.aps.org/doi/10.1103/PhysRevB.91.125429

[3] S. A. Mikhailov and N. A. Savostianova, "Microwave response of a two-dimensional electron stripe," *Phys. Rev. B*, vol. 71, p. 035320, Jan 2005. [Online]. Available: https://link.aps.org/doi/10.1103/PhysRevB.71.035320

[4] A. R. Khisameeva, A. Shuvaev, A. A. Zabolotnykh, A. S. Astrakhantseva, D. A. Khudaiberdiev, A. Pimenov, I. V. Kukushkin, and V. M. Muravev, "Spectrum of plasma excitations in a plasmonic crystal fabricated in an AlGaAs/GaAs heterostructure," *Phys. Rev. Res.*, vol. 7, p. 033224, Sep 2025. [Online]. Available: https://link.aps.org/doi/10.1103/3gnt-w1zj

[5] V. M. Muravev, K. R. Dzhikirba, A. A. Zabolotnykh, P. A. Gusikhin, A. Shuvaev, M. S. Ryzhkov, D. A. Khudaiberdiev, A. S. Astrakhantseva, I. V. Kukushkin, and A. Pimenov, "Superlattice plasmon mode in a grating of two-dimensional electron strips," *Phys. Rev. Res.*, vol. 8, p. 013066, Jan 2026. [Online]. Available: https://link.aps.org/doi/10.1103/vp8j-ws4g

Strong Coupling between quasi-bound states in the continuum and monolayer WS_2 on a Si_3N_4 metasurface

Yongliang Zhang[1,*], Oisin McCormack[1,2], Na Jia[1,3], Hodjat Hajian[1,3], Jack Dobie[1,2], Justin Schulz[1], Xia Zhang[4], Owen Moynihan[2], Brian Corbett[2] and A. Louise Bradley[1,2,3*]
[1]School of Physics, Trinity College Dublin, College Green, Dublin 2, Ireland
[2]IPIC, Tyndall National Institute, Cork T12R5CP, Ireland
[3]Advanced Materials and BioEngineering Research, Trinity College Dublin, College Green, Dublin 2, Ireland
[4]College of Sciences, Northeastern University, Shenyang 110819, China
*Corresponding author: yonzhg@tcd.ie, bradlel@tcd.ie

***Abstract*—We designed a tunable quasi-BIC metasurface using machine learning. Strong coupling with monolayer WS_2 achieved 29.3 meV Rabi splitting, increased to 35.64 meV *via* a PMMA layer. The PMMA enhanced transmission and the electric field. The PL and Raman intensities increased 5.9-fold and 2.4-fold respectively, confirming metasurface-enhanced light–matter interactions.**

***Keywords*— metasurfaces, strong coupling, WS_2 monolayer, quasi-bound states in the continuum.**

I. Introduction

All-dielectric metasurfaces supported quasi-bound states in the continuum (q-BICs) provide a pathway to develop a new paradigm for trapping and confining resonant optical modes with high quality factors (Q-factors) in q-BIC , as well as broad spectral tunability and strongly enhanced near-fields for boosting both surface-driven and material-intrinsic processes in the field of nanophotonics [1-3]. Q-BIC can be obtained by breaking the in-plane symmetry of the structure, and the ultrahigh Q-factor resonance modes in the q-BIC can be readily tuned by the degree of asymmetry [4, 5]. Herein, slotted disk metasurface designs are used to obtain strong light-matter interaction between the metasurface q-BIC and the excitons in a WS_2 monolayer. To further increase the Rabi splitting energy, a PMMA overlayer was introduced. The PMMA overlayer increases the refractive index around metasuraface, inducing a redshift of the q-BIC resonance and enhancement of the field confinement by reducing top□bottom index asymmetry [6]. It also protects the WS□ monolayer from environmental degradation, ensuring stable optoelectronic properties.

II. Methods

The Si_3N_4 metasurfaces were designed using machine learning algorithms implemented in Python. Full-wave electromagnetic simulations were performed using the finite-difference time-domain method (Lumerical). The structures were modeled with experimentally determined dimensions. The Si_3N_4 metasurfaces were fabricated on fused silica substrates via Helium Ion Lithography (Raith) followed by reactive ion etching (RIE, CHF_3/O_2 plasma). Key parameters are period (P P_x = 400 nm, P_y = 420 nm), disk radius (r = 170 nm), height (h = 120 nm), and slot width (varied from 70 to 90 nm). A PMMA layer (100 nm thick) was spin-coated at 6000 rpm for 60 s and cured at 120°C for 2 min, forming a PMMA/WS_2 stack. Finally, the stack was transferred onto the slotted disk metasurface with alignment under an optical microscope.

III. Results and Discussion

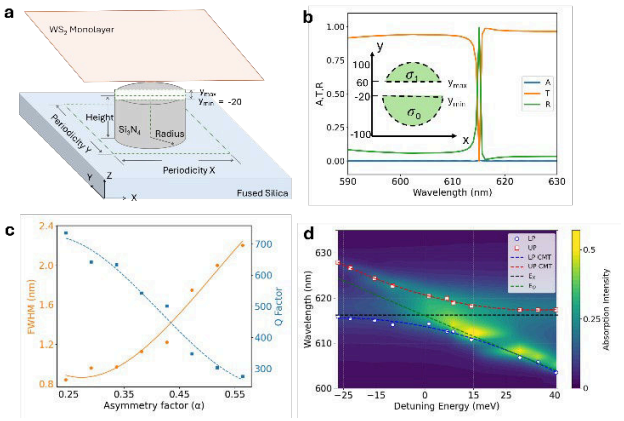

Fig. 1 (a) Three-dimensional schematic of a single period of the hybrid system consisting of monolayer WS_2 and a Si_3N_4 all-dielectric metasurface. (b) Reflection (R), transmittance (T), and absorption (A) spectra of a lossless bare metasurface in air, calculated using the ML-assisted structural design parameters. the dimension parameters are P_x = 400 nm, P_y = 420 nm, y_{min} = −20 nm, y_{max} = 70 nm, r = 170 nm, h = 120 nm. (c) Quality factor Q as a function of the asymmetry parameter (α), showing an inverse square relationship. (d) A color map of the absorptance spectra of the WS_2/Si_3N_4 metasurface/fused

silica hybrid structure as a function of detuning energy of $\Delta = E_Q - E_X$. The black dashed line represents the exciton energy E_X, the dashed green line represents the tuned q-BIC mode resonance E_Q, and the red and blue dashed curves (UP CMT and LP CMT) are the fitted polariton dispersion of the lower polariton (LP) and upper polariton (UP) branches using coupled-mode theory (CMT).

The goal is to realize strong coupling between monolayer WS_2 and a silicon nitride metasurface featuring asymmetric slotted disks that support quasi-bound states in the continuum, as illustrated in Fig 1(a). The q-BIC resonance is tuned by optimizing the unit cell period, disk thickness (H), radius (r), and slot width (G). Initial simulations were performed using Lumerical's Finite-Difference Time-Domain (FDTD) solver. Machine learning (ML) was subsequently employed to accelerate the design process. Artificial Neural Network (ANN) achieves the lowest Mean Squared Error (MSE, 0.0043) compared to Extreme Gradient Boosting (XG Boost) and Support Vector Regression (SVR). Fig 1(b) shows the simulated reflectance, transmittance and absorbance spectra with the q-BIC resonance at 616 nm. The q-BIC mode is confirmed in Fig 1(c). Fig 1(d) shows the simulated absorption spectra as a function of detuning energy with varying the slot width. An anticrossing behavior is clearly visible in the colour map, indicating strong coherent interaction between q-BIC mode and the excitonic mode. where the two peaks correspond to the upper polariton (UP) branch and lower polariton (LP) branch. The Rabi-splitting energy difference between the UP and LP branches at zero detuning is 29.43 meV. The simulated spectra were fitted using coupled-mode theory (CMT) with Eq. (1) [1]

$$E_{\pm} = \hbar\omega_{\pm} = \frac{\hbar}{2}\left[\omega_X + \omega_Q + i\left(\gamma_Q + \gamma_X\right)\right] \pm \frac{\hbar}{2}\sqrt{4\Omega^2 + \left[\left(\omega_X - \omega_Q\right) + i\left(\gamma_X - \gamma_Q\right)\right]^2} \quad (1)$$

The corresponding resonant frequency and damping rate are ω_Q (ω_X) and γ_Q (γ_X), respectively, and they coherently exchange energy with coupling constant, Ω. The vacuum Rabi splitting, defined as the minimum energy spacing between the two branches, is $\hbar\Omega_R = \mathrm{Re}(E_+ - E_-)_{\min}$. When $\omega_X = \omega_Q$ it yields $\hbar\Omega_R = \sqrt{4\Omega^2 - \left(\gamma_Q - \gamma_X\right)^2}$. To observe the characteristic anticrossing of strong coupling, the Rabi splitting must exceed the total dissipation of the hybrid system: $\hbar\Omega_R > \hbar(\gamma_Q + \gamma_X)$. Thne criteria of strong coupling or polaritonic coupling are:

$$\hbar\Omega > \hbar/2\,|\gamma_Q - \gamma_X|, \quad \hbar\Omega = \sqrt{\frac{1}{2\left(\gamma_Q - \gamma_X\right)^2}} \quad (2)$$

The extracted values of $\hbar\Omega_R$ =29.43meV, $\hbar\gamma_Q$ = 31.33meV, and $\hbar\gamma_X$ =27meV clearly meet the criterion in Eq. (2).

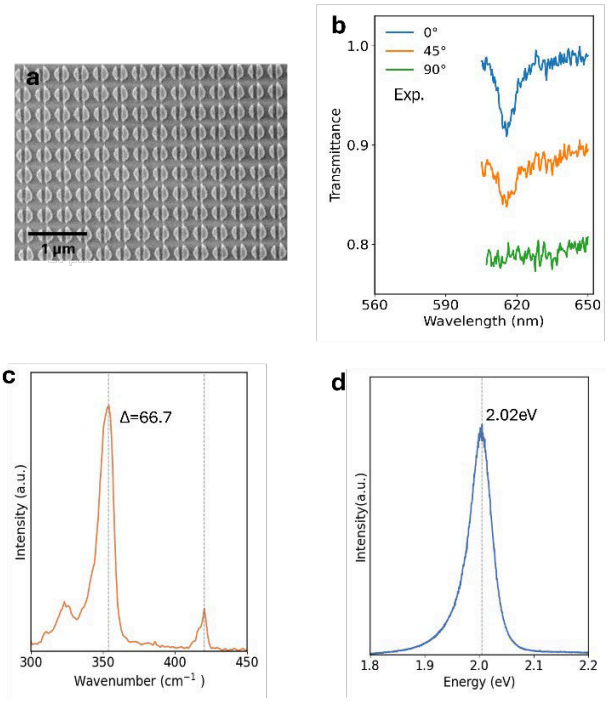

Fig. 2 (a) SEM image of the Si_3N_4 disk array on the fused silica substrate. (b) Polarization dependent transmittance spectra of the experimental Si_3N_4 metasurface. (c,d) Raman and PL characterization of the monolayer WS_2.

The slotted Si_3N_4 disk metasurface was fabricated by helium ion beam lithography followed by reactive ion etching as shown in Fig 2(a). At 0° polarization, a distinct transmittance resonance is observed experimentally, while its amplitude decreases continuously and eventually disappears at 90° as shown in Fig 2(b). A monolayer WS_2 film was transferred onto the metasurface the characteristic $E_{2g}{}^1$and A_{1g} vibrational modes of monolayer WS_2 appear at approximately 352.3 cm^{-1} and 419 cm^{-1}, respectively, yielding a frequency separation Δ≈ 66.7 cm^{-1} (Fig 2(c)) in line with expectations for monolayer WS_2. Room-temperature photoluminescence (PL) measurements reveal strong excitonic emission at 2.02 eV in agreement with values reported for monolayer WS_2.[7, 8] (Fig 2(c)).

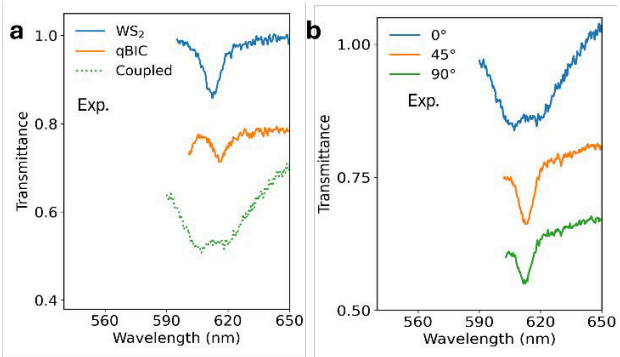

Fig. 3 (a) Transmittance spectra of the bare WS_2, the Si_3N_4 metasurface and the coupled WS_2/Si_3N_4 metasurface under x-polarized illumination (b) Polarization dependent transmittance spectra of the WS_2/Si_3N_4 metasurface coupled system.

For the hybrid WS_2-Si_3N_4 metasurface a clear mode splitting emerges, giving rise to two well-resolved peaks at 617.8 nm and 608.9 nm (Fig 3(a)), corresponding to a Rabi splitting of 29.3 meV. Polarization-dependent transmission measurements were performed on the coupled system in Fig 3(b), As the polarization angle increases from 0° to 90°, the spectral splitting gradually diminishes due to the weakened excitation of the qBIC mode.

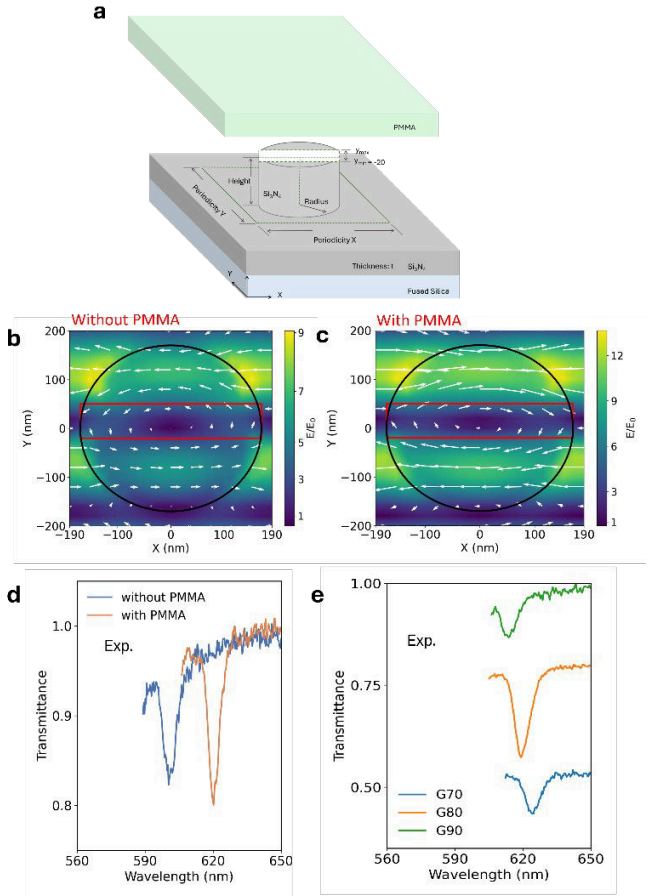

Fig. 4 (a) Schematic of PMMA/Si_3N_4 metasurface hybrid system. (b, c) Electric field distribution maps in the X-Y plane at the top surface of the disk without and with the PMMA layer. (d) Experimental transmittance spectra with and without PMMA. Structural parameters: P_x = 380 nm, P_y = 400 nm, y_{min} = −20 nm, y_{max} = 70 nm, r = 170 nm, h = 90 nm, and bottom- layer thickness t = 30 nm. (e) Experimental transmittance spectra of the Si_3N_4 metasurface with different slot widths (70 nm, 80 nm, and 90 nm).

To further increase the Rabi splitting energy, a PMMA overlayer was introduced onto the Si_3N_4/Fused silica metasurface as the schematic shown in Fig. 4(a). In the first instance the impact of the PMMA layer on the q-BIC resonance is explored. The simulations indicate that the in-plane electric field intensity increases from 9 to 13.7 when a 100 nm-thick PMMA film is added on top of the metasurface (Fig 4(b)). In the experiment, the PMMA-coated metasurface (slot width = 80 nm) exhibits a 12 nm redshift of the q-BIC resonance, accompanied by a noticeable increase in the amplitude q-BIC mode (Fig 4(d)). Fabricated samples with slot widths of 70 nm, 80 nm and 90 nm, each coated with a 100 nm− thick PMMA layer, are shown in Fig 4(e), with the q-BIC mode redshifting from 607 nm to 623 nm with increasing slot width.

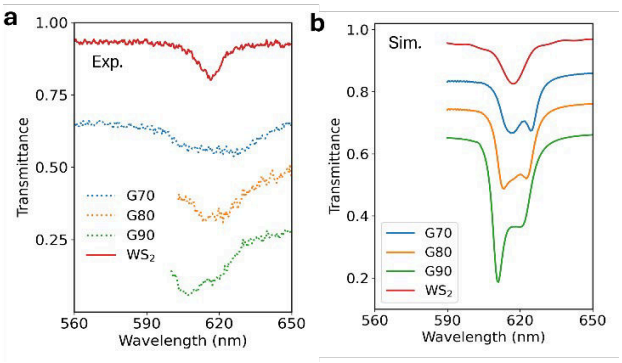

Fig. 5 (a, b) Experimental and simulated transmittance spectra of the PMMA/WS_2/Si_3N_4 metasurface with varying slot width (70 nm, 80 nm and 90 nm).

The transmittance spectra of the PMMA/WS_2/Si_3N_4/fused-silica system exhibit spectral splitting (Fig 5(a)), where the q-BIC resonance splits into upper and lower polariton branches around the excitonic transition. The extracted Rabi splitting energy is 35.64 meV. The experimental results show excellent agreement with the simulated results, which predict a Rabi splitting energy of 36.56 meV (Fig 5(b)).

IV. Conclusion

We have demonstrated a metasurface supporting a quasi-BIC resonance. Utilizing a machine-learning-assisted design the structural parameters for the 590–650 nm range were determined. Experimentally, strong coupling with a WS_2 monolayer yields a Rabi splitting of 29.3 meV, which increases to 35.64 meV after introducing a PMMA layer on the top. The 100 nm PMMA layer increases the transmission peak intensity and enhances the field. Simulations reveal an increase in the in□plane electric field from 9 to 13.7, attributed to suppressed radiation loss in the PMMA− glass symmetric sandwich structure.

Acknowledgments

Y. Z, A. L. B., J. D., J. S., O. McC., H. H., O. M. and B. C. acknowledge financial support by Research Ireland under awards SFI-21/FFP-P/10187, 12/RC/2276_P2 and 12/RC/2278_2. O. McC. acknowledges funding from the Marie Sklodowska Curie SPARKLE fellowship and N. J. acknowledges funding under ACM: 18/EPSRC-CDT/3581_26.

References

[1] X. Zhang, and A. L. Bradley, "Polaritonic critical coupling in a hybrid quasibound states in the continuum cavity–WS 2 monolayer system," *Physical Review B,* vol. 105, no. 16, pp. 165424, 2022.

[2] H. Hajian, X. Zhang, O. McCormack, Y. Zhang, J. Dobie, I. D. Rukhlenko, E. Ozbay, and A. Louise Bradley, "Quasi-bound states

in the continuum for electromagnetic induced transparency and strong excitonic coupling," *Optics Express,* vol. 32, no. 11, pp. 19163-19174, 2024.

[3] C. Zhou, L. Huang, R. Jin, L. Xu, G. Li, M. Rahmani, X. Chen, W. Lu, and A. E. Miroshnichenko, "Bound states in the continuum in asymmetric dielectric metasurfaces," *Laser & Photonics Reviews,* vol. 17, no. 3, pp. 2200564, 2023.

[4] O. McCormack, J. Dobie, X. Zhang, O. Moynihan, J. Qian, K. Mamaeva, H. Hajian, Y. Zhang, B. Corbett, and A. L. Bradley, "Silicon nitride slotted-disk metasurfaces for refractive index sensing based on quasi-bound states in the continuum," *Optics Express,* vol. 33, no. 23, pp. 49845-49859, 2025.

[5] M. Luo, Y. Zhou, X. Zhao, Z. Guo, Y. Li, Q. Wang, J. Liu, W. Luo, Y. Shi, and A. Q. Liu, "High-sensitivity optical sensors empowered by quasi-bound states in the continuum in a hybrid metal–dielectric metasurface," *ACS nano,* vol. 18, no. 8, pp. 6477-6486, 2024.

[6] Z. He, X. Han, L. Zhang, J. Yang, S. Chen, S. Xiao, S. Ji, K. Wang, and P. Lu, "Strong Coupling in Monolayer WS2 Integrated All-Dielectric Metasurfaces with Electric-Quadrupole Modes," *Nano Letters*, 2025.

[7] B. Zhu, X. Chen, and X. Cui, "Exciton binding energy of monolayer WS2," *Scientific reports,* vol. 5, no. 1, pp. 9218, 2015.

[8] K. M. McCreary, A. T. Hanbicki, S. Singh, R. K. Kawakami, G. G. Jernigan, M. Ishigami, A. Ng, T. H. Brintlinger, R. M. Stroud, and B. T. Jonker, "The effect of preparation conditions on Raman and photoluminescence of monolayer WS2," *Scientific reports,* vol. 6, no. 1, pp. 35154, 2016.

Wafer-scale fabrication of quartz-monolithic metalenses for the ultraviolet

Jaewon Jang[1,2*], Hui Jae Cho[3], Yeonsang Park[1,2*]

[1]Department of Physics, Chungnam National University, Daejeon, Korea
[2]Institute of Quantum Systems, Chungnam National University, Daejeon, Korea
[3]Office of Nano Convergence Technology, National NanoFab Center, Daejeon, Korea
*Corresponding author: yeonsang.park@cnu.ac.kr

***Abstract*—We fabricated 8-inch wafer-scale, quartz-monolithic ultraviolet metalenses operating at 325 nm using ArF photolithography. This platform circumvents the scarcity of high-index dielectrics that are CMOS-compatible and transparent in ultraviolet, while maintaining high optical efficiency. This work presents a cost-effective pathway for scalable manufacturing of highly compact ultraviolet optical systems.**

***Keywords*— wafer-scale, quartz-monolithic, ultraviolet, metalenses, ArF photolithography, CMOS-compatible**

I. Introduction

Ultraviolet (UV) optical components are essential in photolithography and high-resolution spectroscopy, but face significant hurdles in fabrication due to the limited selection of UV-transparent materials and the requirement of stringent fabrication tolerances [1]. While metasurfaces offer a compact alternative, their adoption in the UV regime has been stifled by the non-negligible absorption of high-index materials (e.g., Si, TiO_2, Nb_2O_5, and Ta_2O_5) necessary for sustaining their performance [2]. Even for transparent candidates such as HfO_2, wafer-scale fabrication is hindered by low throughput due to the slow atomic layer deposition (ALD) process. Crucially, regardless of the material choice, heterogeneous integration creates fragile interfaces prone to delamination caused by thermal expansion mismatches.

To address these challenges, we present quartz-monolithic UV metalenses fabricated using ArF photolithography on an 8-inch wafer, eliminating the need for heterogeneous high-index materials and slow electron-beam writing.

II. Methods

We designed a metalens with a diameter of 2 mm and a numerical aperture (NA) of 0.3, corresponding to a focal length of approximately 3.18 mm at an operating wavelength of 325 nm. The unit cells consist of fused quartz cylinders with a height of 1020 nm on a square lattice with a period of 430 nm.

We specifically selected cylindrical geometry to prevent pattern bridging issues during ArF photolithography. Furthermore, the 1020 nm height overcomes the relatively low refractive index of fused quartz. This tall structure provides the required phase modulation without excessively enlarging the cylinder diameters, effectively securing an ample gap between adjacent structures. Although the lattice constant of 430 nm deviates from the strict sub-wavelength regime, we leveraged the property that low-index platforms suppress higher-order Bloch modes, enabling high efficiency even with increased lattice constants [3]. Ultimately, the strategic configuration of high-aspect-ratio cylindrical nanopillars with a widened lattice constant effectively alleviates the stringent resolution requirements of the lithographic process while maintaining robust optical performance.

III. Results and Discussion

To rigorously validate the wafer-scale uniformity and optical performance of the mass-produced metalenses, we characterized 20 metalenses sampled across the fabricated 8-inch wafer at a wavelength of 325 nm (Fig. 1). Quantitative analysis revealed high optical efficiency for the fused quartz UV metalenses. The best-performing metalens achieved a focusing efficiency of 51.92% and a diffraction efficiency of 59.87%, along with a transmittance of 86.72% and a focal length of 3.173 mm. Furthermore, statistical analysis across the 20 metalenses demonstrated manufacturing consistency, yielding an average focusing efficiency of $47.65 \pm 2.47\%$ and a diffraction efficiency of $54.20 \pm 3.20\%$. The measured focal lengths showed precise agreement with the design value, averaging 3.178 ± 0.004 mm, which confirms the high fidelity between the fabricated structures and the original design (Fig. 2).

These results experimentally verify that our monolithic fused quartz platform is highly effective for the UV regime. Moreover, this consistent performance demonstrates the feasibility of uniform wafer-scale manufacturing of metalenses, overcoming the scalability limits of conventional nanofabrication. Ultimately, this work provides a robust and scalable foundation for the mass production of high-performance UV meta-optics.

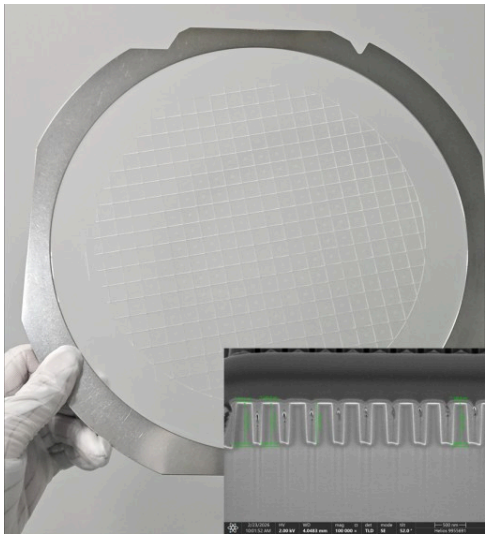

Fig. 1 Fabricated metalenses on an 8-inch fused quartz wafer. Inset: Cross-sectional SEM image of the fabricated metalens.

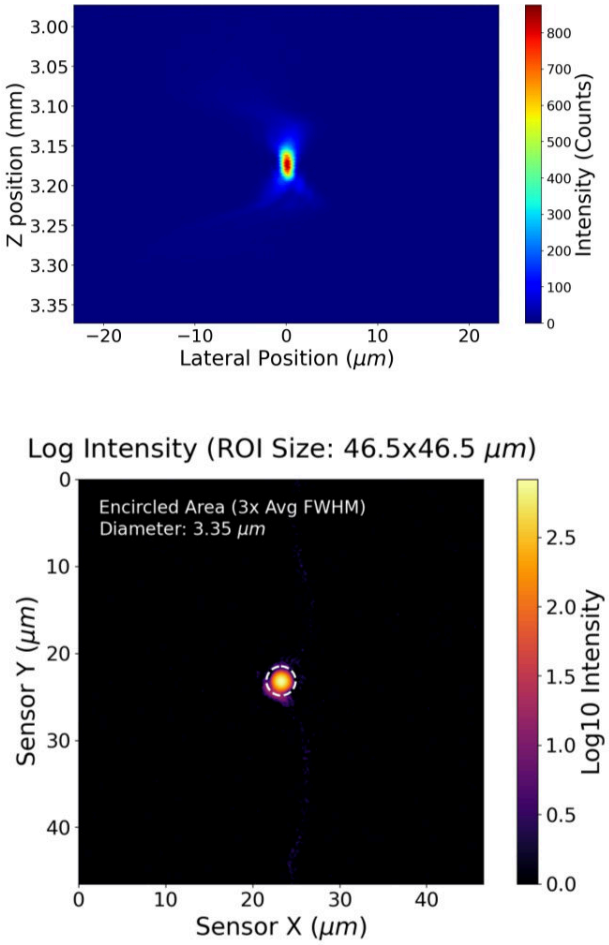

Fig 2. Measured beam profile along the optical axis (Top) and point spread function (PSF) at the focal plane (Bottom).

IV. Conclusion

We have successfully demonstrated the wafer-scale realization of quartz-monolithic metalenses for the UV regime using high-throughput ArF photolithography. By adopting the strategic configuration of high-aspect-ratio cylindrical nanopillars with a relaxed lattice constant, we ensured a sufficient fabrication margin that prevented pattern bridging and enabled the precise transfer of 2 mm diameter metalenses across an 8-inch wafer. Our results confirm that the monolithic, low-index fused quartz platform eliminates the absorption losses and interfacial instabilities associated with traditional heterogeneous high-index UV platforms, while maintaining high optical efficiency.

The experimental validation, showing high fabrication uniformity and optical performance, proves that this approach effectively overcomes the longstanding material and fabrication bottlenecks inherent in conventional UV optics. This work establishes a robust and scalable framework for the mass-production of high-performance UV meta-optics, offering a new pathway for compact UV optical systems in semiconductor manufacturing and high-resolution spectroscopy.

Acknowledgments

This work was supported by the Basic Science Research Program through the National Research Foundation of Korea (NRF) funded by the Ministry of Education (RS-2020-NR049597), the Technology Innovation Program (or Industrial Strategic Technology Development Program) (RS-2023-00235080) funded by the Ministry of Trade, Industry & Energy (MOTIE, Korea), and the National Research Foundation of Korea (NRF) grant funded by the Korea government (Ministry of Science and ICT) (RS-2025-24533176).

References

[1] D. Zhao *et al.*, "Recent advances in ultraviolet nanophotonics: from plasmonics and metamaterials to metasurfaces," *Nanophotonics,* vol. 10, no. 9, pp. 2283-2308, 2021.

[2] Y. Deng *et al.*, "All-silicon broadband ultraviolet metasurfaces," *Advanced Materials,* vol. 30, no. 38, p. 1802632, 2018.

[3] L. Sacchi, A. Palmieri, V. Mishra, J.-S. Park, M. Piccardo, and F. Capasso, "Silica Meta-Optics: When High Performance Does Not Need a High Index," *Nano Letters,* vol. 25, no. 50, pp. 17448-17457, 2025.

Colorimetric thermography by a long-infrared dual-band metalens

Zhendong LUO[1,2], Peng ZHANG[2], Yang ZHAO[2], Mu Ku CHEN[1,*]

[1]Department of Electrical Engineering, City University of Hong Kong, Kowloon, Hong Kong SAR, China

[2]CAS Key Laboratory of Mechanical Behavior and Design of Materials, Department of Precision Machinery and Instrumentation, University of Science and Technology of China, Hefei 230026, China

*Corresponding author: mkchen@cityu.edu.hk

***Abstract*— Colorimetric thermography enables emissivity-independent temperature measurement but requires bulky optics. We present a compact dual-band metalens for LWIR colorimetric thermography at 9.5 and 12.5 μm. It images low-emissivity objects and measures temperature without presetting emissivity, reducing errors by 50.16% (60–180°C), enabling compact multi-target IR systems.**

***Keywords*— Infrared detection; Colorimetric thermography; Emissivity; Dual-band metalens.**

I. Introduction

Infrared (IR) thermography is widely used but its accuracy is compromised by unknown emissivity variations of objects. Colorimetric thermography determines temperature from the ratio of radiances in two spectral bands, theoretically eliminating emissivity effects. However, conventional implementations require bulky filters, spectrometers, or complex sensor structures. Metalenses offer a compact, customizable alternative for spectral manipulation. Here we demonstrate a dual-band metalens that performs IR colorimetric thermography with a simple optical setup, achieving accurate temperature measurement of low-emissivity targets without prior knowledge of emissivity.

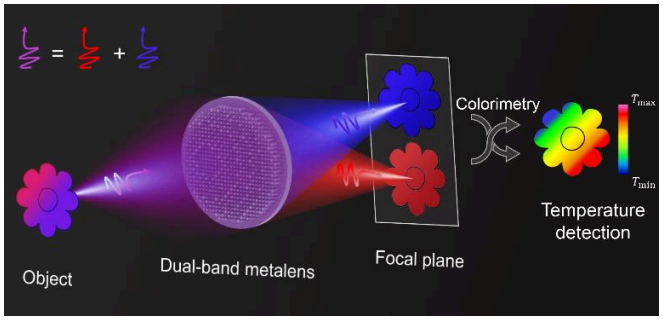

Fig. 1 Schematic of dual-band metalens imaging principle.

II. Methods

Principle. For a gray body with emissivity ε(T), the intensity ratio in two spectral bands is

$$R(T) = \frac{M_1(T)}{M_2(T)} == \frac{\int_{\lambda_{start}}^{\lambda_{end}} M_b(\lambda, T) * F_1(\lambda) d\lambda}{\int_{\lambda_{start}}^{\lambda_{end}} M_b(\lambda, T) * F_2(\lambda) d\lambda} \quad (1)$$

, which is independent of ε(T). The function T = f(R) is obtained by calibration.

Metalens design. The metalens (diameter 2 cm, focal length 1 cm) is designed to focus 9.5 μm and 12.5 μm light at laterally separated spots (offset ±0.5 cm). Phase profiles are

$$\Phi_1(x,y) = -2\pi n(\sqrt{(x+x_0)^2 + y^2 + f^2} - f)/\lambda_1 \quad (2)$$

$$\Phi_2(x,y) = -2\pi n(\sqrt{(x-x_0)^2 + y^2 + f^2} - f)/\lambda_2 \quad (3)$$

The metasurface consists of cylindrical silicon pillars (height 7 μm, radius 0.6–2 μm, period 5 μm) on a silicon substrate, providing full 2π phase coverage and high transmission at both wavelengths. Fabrication used maskless lithography and deep reactive-ion etching.

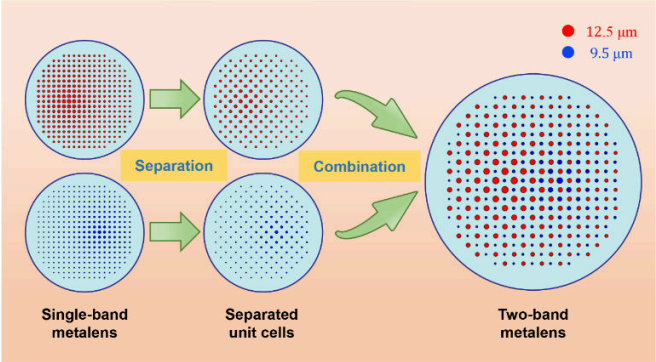

Fig. 2 Schematic of a dual-band metalens constructing process.

III. Results and Discussion

Experimental results show:

Dual-band imaging. The fabricated metalens produces two distinct focal spots separated by 1.03 cm on the sensor plane (Fig. 3a). When illuminated by a broadband IR source, it forms two images corresponding to the two spectral channels. Imaging of test patterns confirms wavelength-selective focusing (Fig. 3b).

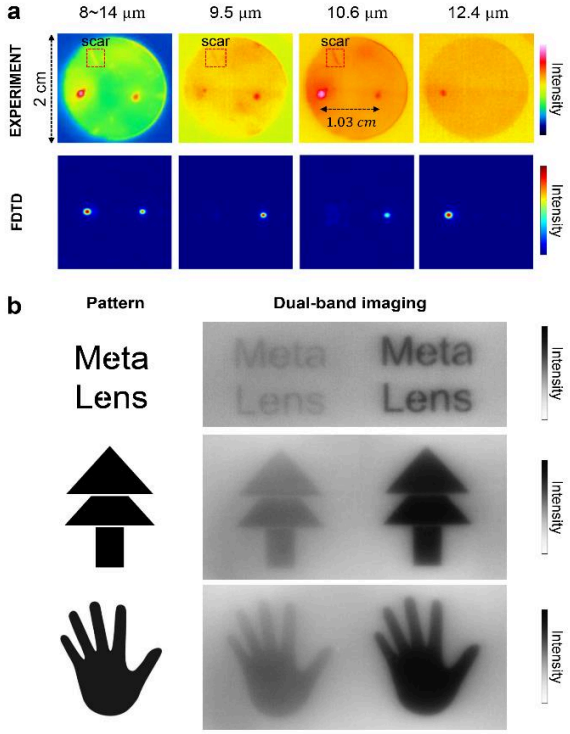

Fig. 3. Bi-focusing and dual-band imaging.

Colorimetric thermography. The ratio–temperature calibration curve was obtained using a glass plate ($\varepsilon \approx 0.9$) heated from 60°C to 180°C, yielding a linear fit $R = -1.7\times10^{-4}T + 1.006\times10^{-4}$ (R^2=0.9992). A CuO plate ($\varepsilon \approx 0.51$) was then measured. Conventional thermography without emissivity input gave errors up to ~50°C, while our colorimetric method reduced the average error by 50.16% (Fig. 2). Temperature maps derived from the two images show excellent agreement with the actual temperature.

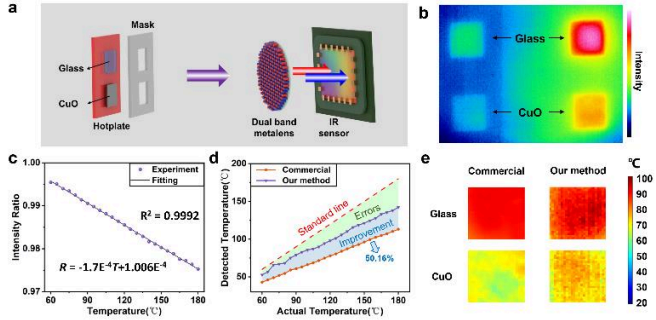

Fig. 4. Experimental setup and results of colorimetric thermography.

These results confirm that the dual-band metalens enables accurate emissivity-free thermography in a compact format.

IV. Conclusion

We have demonstrated a long-infrared dual-band metalens for colorimetric thermography. The approach eliminates the need for bulky optical components and prior emissivity knowledge, reducing measurement errors by half. It opens new possibilities for compact, multi-target IR thermography in dynamic environments.

Acknowledgments

This work was supported by the National Natural Science Foundation of China (12302251, 12172348), the National Key R&D Program of China (2022YFA1203604), and the Hong Kong RGC (CRF C5031-22G, GRF CityU11310522, CityU11300123). Fabrication was performed at the USTC Center for Micro and Nanoscale Research and Fabrication.

References

[1] Z. Luo et al., "Colorimetric Thermography by a Long‐Infrared Dual‐Band Metalens," Adv. Sci., vol. 12, no. 2, p. 2408683, Jan. 2025.

[2] Z. Luo et al., "Optomechanical Infrared Detector Monolithically Integrated with Micro-Metalens Array," ACS Photonics, vol. 11, no. 11, pp. 4597–4605, Nov. 2024.

[3] H. Hou et al., "Design and fabrication of monolithically integrated metalens for higher effective fill factor in long-wave infrared detectors," Opt. Lasers Eng., vol. 150, 106849, 2022.

Passive and Reconfigurable Terahertz Logic Metasurfaces via Frequency and Orientation Multiplexing

Mohammadhossein Momtazpour[1,*], Lei Xu[1], Dou Feng[2], Anjali Chaudhary[3,4], Dominic Craske[5], Costas Tsakonas[6], Cuifeng Ying[1], Demosthenes Koutsogeorgis[5], Miguel Navarro-Cía[2,4] and Mohsen Rahmani[1]

[1]Advanced Optics and Photonics Laboratory, Department of Engineering, Nottingham Trent University, Nottingham, UK
[2]Department of Electronic, Electrical and Systems Engineering, University of Birmingham, Birmingham, UK
[3]Department of Physics, Indian Institute of Technology Delhi, New Delhi, India
[4]School of Physics and Astronomy, University of Birmingham, Birmingham, UK
[5]School of Science and Technology, Nottingham Trent University, Nottingham, UK
[6]Medical Technologies Innovation Facility (MTIF), Nottingham Trent University, Nottingham, UK
*Corresponding author: mohammadhossein.momtazpour2023@my.ntu.ac.uk

***Abstract*— We demonstrate a terahertz metasurface platform capable of implementing up to five distinct logic operations within a single passive architecture, representing a record level of multifunctionality. The system enables low-power operation and scalable THz signal processing, advancing the transition from electronic to optical logical decision-making.**

***Keywords*— All-optical Boolean operations, terahertz metasurfaces, photonic computing, polarization-encoding, mechanical reconfigurability.**

I. Introduction

Terahertz (THz) metasurfaces have emerged as promising candidates for ultrafast and compact optical logic platforms due to their subwavelength control of amplitude, phase, and polarization. Most reported THz logic metasurfaces, however, rely on active materials, electrical biasing, or complex multilayer architectures, which increase system complexity and power consumption. Furthermore, many designs are restricted to a single logic function or require structural modification to switch between operations [1,2].

To overcome these limitations, passive metasurface logic platforms that exploit intrinsic electromagnetic responses are highly desirable. In this work, we present two complementary approaches for realizing multifunctional, passive THz logic metasurfaces: (i) a frequency-multiplexed fractal metasurface and (ii) a mechanically reconfigurable L-shaped metasurface. In both platforms, logical inputs are encoded in the polarization state of the incident THz wave, and the logic output is retrieved using fixed transmission-intensity thresholds.

II. Methods

The first platform consists of a fractal H-shaped metasurface designed to support multiple resonant modes across a broad THz spectral range [3]. The fractal geometry introduces self-similar resonant paths, enabling several polarization-dependent resonances at distinct frequencies. Full-wave simulations were performed using frequency-domain solvers, i.e. COMSOL Multiphysics to obtain polarization-resolved transmission spectra (Fig. 2a-b).

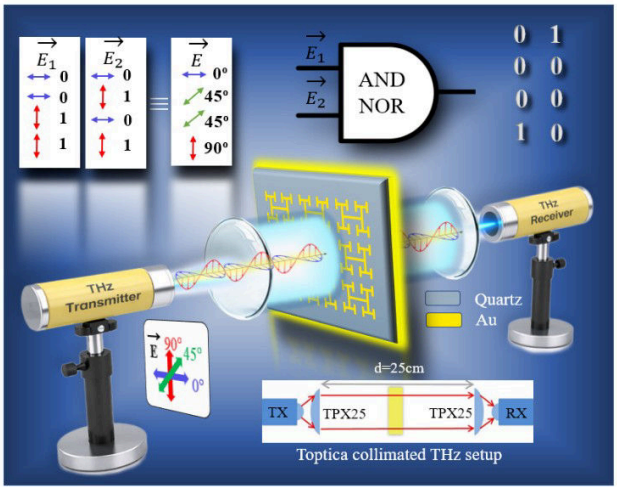

Fig. 1. Frequency-multiplexed logic operation in the fractal H-shaped metasurface, showing logic states realized at multiple resonant frequencies within a single passive structure.

The second platform employs an array of asymmetric L-shaped gold resonators fabricated on a 25 µm polyimide substrate [4]. The unit cell dimensions were chosen to support two electric-dipole-dominated resonances near 0.9 THz and

1.66 THz. The metausrface was designed to be mechanically reconfigurable through in-plane rotation and mirror-flip operations, which effectively reshape its induced polarization response. This further allows flexible control over co- and cross-polarized transmission channels without altering the physical structure, offering a robust way for realizing programmable flat-photonic systems.

In both platforms, logical inputs were encoded using three polarization states: 0°, 45°, and 90°, representing the Boolean combinations (0,0), (0,1)/(1,0), and (1,1), respectively. Output logic states were determined using fixed transmission-intensity thresholds.

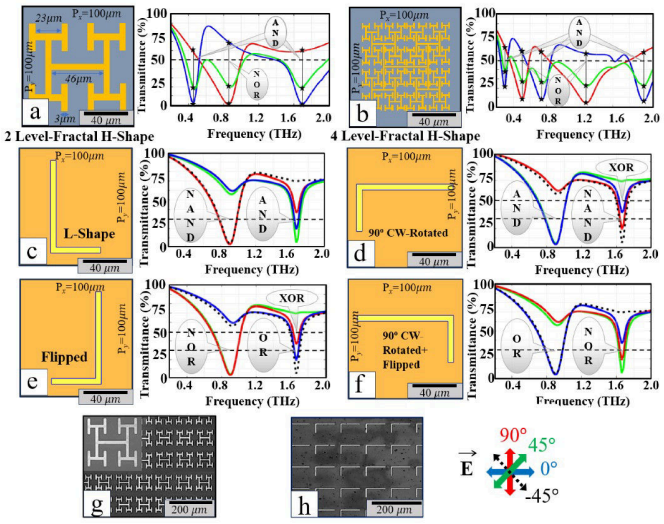

Fig. 2. Polarization-dependent transmittance characteristics of THz metasurfaces with varying geometries and logic functionalities. (a–b) 2-level and 4-level fractal H-shaped metasurfaces with corresponding spectra demonstrating multi-frequency responses. (c–f) L-shaped metasurface and its rotated/flipped variants showing distinct logical behavior under different polarization angles (0°, 45°, 90°, −45°), including AND, OR, NAND, NOR and XOR operations. (g–h) Optical microscopy images of fabricated 2-level fractal H-shaped and L-shaped metasurface arrays.

III. Results and Discussion

The fractal H-shaped metasurface exhibits multiple polarization-dependent resonances across the 0.2–2.0 THz range. At each resonance, different input polarizations produce distinct transmission levels, enabling simultaneous implementation of multiple logic functions at separate frequencies. This frequency-multiplexed behavior allows a single passive structure to perform parallel logic operations without mechanical or electrical tuning (Fig. 1).

The L-shaped metasurface demonstrates a complementary form of reconfigurability. Due to its anisotropic geometry, the structure exhibits a fully populated Jones matrix with unequal diagonal and nonzero off-diagonal terms, enabling strong polarization-dependent coupling. Two dominant resonances are observed at approximately 0.9 THz and 1.66 THz (Fig. 2c-d).

By applying in-plane rotation or mirror-flip transformations, the Jones matrix elements are deterministically redistributed. As a result, the polarization-dependent transmission spectra are reconfigured without changing the physical structure or excitation conditions. Depending on the metasurface orientation and operating frequency, different Boolean logic gates—including AND, OR, NAND, NOR, and XOR—are obtained using fixed intensity thresholds.

Experimental THz time-domain spectroscopy measurements show good agreement with simulations, with consistent resonance positions and logic-state transitions across all configurations. Minor discrepancies are attributed to fabrication tolerances, finite conductivity of gold at THz frequencies, and beam-profile effects.

Together, the two platforms demonstrate two distinct but complementary passive logic mechanisms:

- Frequency multiplexing: multiple logic functions realized simultaneously at different resonant frequencies using a fractal geometry.
- Orientation reconfiguration: dynamic switching between logic gates via simple mechanical transformations of an anisotropic metasurface.

Both approaches eliminate the need for active materials, electrical biasing, or nonlinear effects, significantly reducing system complexity and energy consumption.

IV. Conclusion

We have demonstrated two passive metasurface platforms for multifunctional THz logic operations: a frequency-multiplexed fractal H-shaped metasurface and a mechanically reconfigurable L-shaped metasurface. The first enables parallel logic processing across multiple spectral channels, while the second allows dynamic switching among logic gates through geometric transformations. These complementary strategies provide scalable, energy-efficient solutions for future THz photonic computing and signal-processing systems.

Acknowledgments

MR acknowledges support from the UK Research and Innovation Future Leaders Fellowship (MR/T040513/1). MN-C acknowledges the kind support of The Royal Society (IES\R1\241009). AC appreciates funding from the Commonwealth Scholarship Commission in the UK (INCN-2024-2).

References

[1] M. Manjappa, Y. K. Srivastava, and R. Singh, “Reconfigurable MEMS Fano metasurfaces with multiple-input–output states for logic operations at terahertz frequencies,” Nature Communications, vol. 9, p. 4056, 2018.

[2] Y. Wang, J. Cheng, F. Fan, Y. Peng, and S. Zhuang, “All-in-one cascadable dynamic terahertz logic gates enabled by polarization encoding and multiplexing,” Laser & Photonics Reviews, vol. 19, p. 2200072, 2025.

[3] M. H. Momtazpour *et al.*, “Generating all-optical frequency-multiplexed THz logic operations via fractal metasurfaces,” submitted, 2025.

[4] M. H. Momtazpour *et al.*, “Mechanically reconfigurable terahertz logic metasurface based on orientation-dependent Jones-matrix transformations,” in preparation, 2026.

Deep-UV Photonic-Crystal Surface-Emitting Lasers with Sub-Degree Beam Divergence

Philippe Tassin*

Dogukan Apaydin, Hjalmar Andersson, Lukas Uhlig, Sarina Graupeter, Joachim Ciers, Giulia Cardinali, Erik Strandberg, Tim Wernicke, Michael Kneissl, Ulrich Theodor Schwarz, and Åsa Haglund

*Department of Physics, Chalmers University of Technology, SE-412 96 Göteborg, Sweden

***Abstract*— We demonstrate the first optically pumped deep-ultraviolet photonic-crystal surface-emitting lasers operating below 280 nm. By optimizing the photonic crystal's filling factor, single-mode emission at 279 nm with sub-degree beam divergence is achieved. These results establish PCSELs as a promising platform for high-beam-quality, high-power deep-UV semiconductor lasers.**

***Keywords*— Deep-ultraviolet (UV-C) lasers, Photonic crystal surface-emitting lasers (PCSELs), Photonic band engineering.**

Semiconductor lasers have become the light source of choice for many applications in optical communication, metrology, and spectroscopy, especially in the infrared and visible parts of the electromagnetic spectrum. Ultraviolet-C (UV-C, $\lambda < 280$ nm) semiconductor lasers, on the other hand, remain limited by low efficiency and poor beam quality. While edge-emitting lasers have recently achieved electrically injected deep-UV operation [1], they inherently suffer from multi-mode emission and large divergence. Photonic crystal surface-emitting lasers (PCSELs), first demonstrated in 1999 [2], offer a pathway to simultaneously achieve high output power and excellent beam quality, as shown in infrared devices exceeding 50 W in single-mode operation [3], and recent blue PCSEL advances.

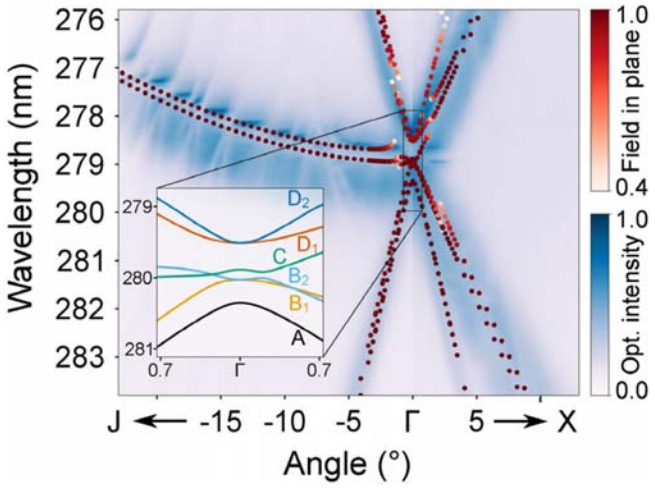

Comparison of experimentally and numerically obtained band structure.

Here, we report the first optically pumped deep-UV PCSELs operating below 280 nm [4]. The devices are based on an AlGaN multiple-quantum-well heterostructure incorporating a hexagonal photonic crystal (period 140 nm) etched into the top AlN cladding. Achieving two-dimensional (2D) optical feedback in AlGaN is challenging due to its low refractive index contrast and enhanced scattering at short wavelengths. By carefully engineering the photonic crystal geometry—particularly the hole filling factor—we are able to engineer the photonic bands and allow for sufficiently large local field enhancement to enable lasing.

Under 266 nm pulsed optical pumping at room temperature, the devices exhibit single-mode lasing at 279 nm with a linewidth of 17 pm (spectrometer-limited) and a clear threshold around 17 MW/cm². Optimized devices show a characteristic doughnut-shaped far-field light distribution with beam divergence below 1°, representing a major improvement over conventional deep-UV edge-emitting lasers

These findings establish PCSELs as a viable architecture for high-beam-quality deep-UV sources and mark an important step toward electrically injected Watt-class UV-C PCSELs.

Acknowledgments

This work was partially supported by the Knut and Alice Wallenberg Foundation (Grant No. 2020.0119) and the Leibniz Society within the SAW "UV SimTech" project (Contract No. K415/2021). The authors acknowledge Myfab for support and access to the nanofabrication laboratories at Chalmers University of Technology. Simulations were performed on resources provided by the Swedish National Infrastructure for Computing (NAISS), at the Chalmers/C3SE and KTH/PDC sites, partially funded by the Swedish Research Council under

Grant No. 2022-06725. The authors thank Niclas Lindvall and Marcus Rommel for help and support with the e-beam lithography system and the process, and Sylvia Hagedorn (FBH) and Markus Weyers (FBH) for providing AlN/sapphire substrates.

REFERENCES

[1] Z. Zhang, M. Kushimoto, A. Yoshikawa, K. Aoto, L. J. Schowalter, C. Sasaoka, and H. Amano, "Continuous-wave lasing of AlGaN-based ultraviolet laser diode at 274.8 nm by current injection," Appl. Phys. Express, vol. 15, 041007 (2022).

[2] M. Imada, S. Noda, A. Chutinan, T. Tokuda, M. Murata, and G. Sasaki, "Coherent two-dimensional lasing action in surface-emitting laser with triangular-lattice photonic crystal structure," Appl. Phys. Lett., vol. 75, p. 316 (1999).

[3] M. Yoshida, S. Katsuno, T. Inoue, J. Gelleta, K. Izumi, M. D. Zoysa, K. Ishizaki, and S. Noda, "High-brightness scalable continuous-wave single-mode photonic-crystal laser," Nature, vol. 618, p. 727.(2023).

[4] D. Apaydın, H. Andersson, L. Uhlig, S. Graupeter, J. Ciers, G. Cardinali, E. Strandberg, T. Wernicke, M. Kneissl, U. T. Schwarz, P Tassin, and Å. Haglund, "Deep-UV Photonic Crystal Surface-Emitting Lasers," Laser Photonics Rev., vol. 2025, e00271 (2025).

Tunable Emission Enhancement in Ge Films through All-Dielectric Metasurfaces

Jon Schlipf[1,*], Diana Ryzhak[1], Giovanni Capellini[1], Paul Oleynik[2], Yuji Yamamoto[1], Inga A. Fischer[1,2]

[1]IHP - Leibniz Institute for High Performance Microelectronics, Frankfurt (Oder), Germany
[2]Chair of Experimental Physics and Functional Materials, BTU Cottbus-Senftenberg, Cottbus, Germany
*Corresponding author: schlipf@ihp-microelectronics.com

***Abstract*—We show photoluminescence enhancement up to a factor of 43 with respect to unetched layers in Ge all-dielectric metasurfaces. Our results point to band-to-band recombination as the dominant emission mechanism. Emission peaks correspond to multipole modes of coupled Mie resonators, and are controlled by lateral nanostructuring.**

***Keywords*— all-dielectric metasurface, photoluminescence, RCWA, germanium.**

I. Introduction

For decades, silicon photonics has been the leading platform for integrated optics, primarily geared towards optical data transmission. Recently, the field has diversified considerably, towards applications in optical sensing, quantum technologies, and computing. While coherent sources are essential to optical communications, light-emitting diodes have been proposed for photonic computing[1]. Monolithic integration of the required emissive materials into silicon technologies remains a challenge, due to band structures of silicon and germanium favoring nonradiative transitions. Nanostructuring can be used to engineer radiative lifetimes through the Purcell effect, particularly using all-dielectric metasurfaces[2], [3]. This can boost light emission, potentially up to the point of practical applicability in light emission devices.

Here, we present photoluminescence (PL) results in Ge metasurfaces etched from material grown in an industrial chemical vapour deposition system on 200 mm wafers, with the ultimate goal of process-integrated vertical light emitting diodes. We achieve considerable, structurally tunable PL enhancement even in thin Ge layers.

II. Methods

We grew epitaxial Ge (150 nm) and Si (45 nm) on a silicon-on-insulator (SOI) substrates with a buried oxide thickness of 2 μm and a Si layer of 65 nm using chemical vapour deposition. After photolithography, the stack was down to the SOI substrate, creating periodic arrays of nanopillars with various pitches. As the samples were originally intended for electrical contacting, etch stopped within the SOI Si layer. Finally, the samples were covered in silicon dioxide using plasma-enhanced chemical vapour deposition for passivation. We created six periodic arrays of metasurface nanopillars with diameters of 300 nm pitches increasing from 850 nm to 1200 nm. Schematic layer stacks can be found in figure 1, the fabrication flow has been published in more detail elsewhere[4].

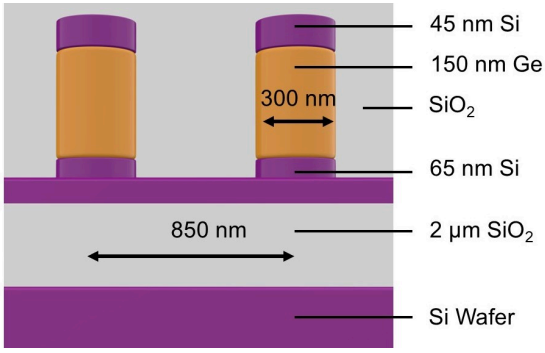

Fig. 1. Schematic layer stack.

We performed micro-photoluminescence spectroscopy measurements at 80 K and room temperature under excitation by an 1064 nm Nd:YAG laser source. The pump power was 34.4 mW, spectra were recorded using HORIBA iHR320 spectrometer and a SYNAPSE/SYMPHONY InGaAs detector. A low-magnification (5X) objective was used, in order to achieve near-vertical incidence at the sample surface.

Optical simulations were carried out using an own implementation[5] of the rigorous coupled-wave analysis (RCWA)[6]. We considered Fourier orders up to $N = 5$ and relied on literature values for the relative permittivity of materials[7], [8], [9].

III. Results and Discussion

We observe distinct PL peaks in the metasurfaces. The signal exceeds that of an unetched reference area with the same layer stack, and a bulk Ge wafer reference. Increased PL, despite smaller material volume, points to a spontaneous emission increase in the resonant metasurface cavity through the Purcell factor[2], as well as enhanced absorption of the 1064 nm pump. We report PL enhancement up to a factor of 43 with respect to unetched material. Based on simulation, pump absorption enhancement is < 3 as the metasurface is not matched to the pump wavelength, so the effect we observe is mostly due to emission enhancement.

With increasing array pitch, resonances and their related emission peaks shift to lower wavelength. Generally, emission

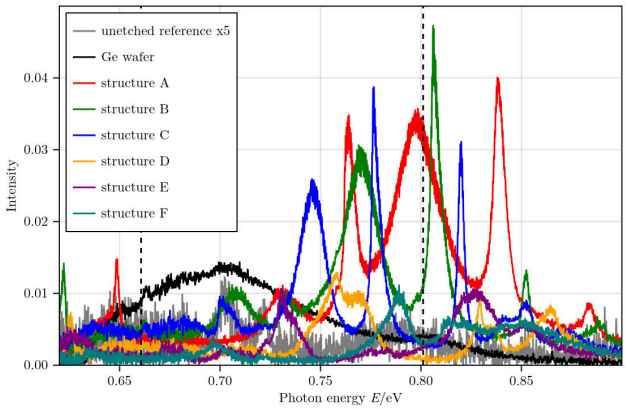

Fig. 2. PL spectra of all-dielectric metasurfaces, compared to an unetched reference area on the same sample (multiplied by 5 for visibility) and a bulk Ge wafer. Dashed black lines indicated the direct and indirect bandgap of Ge at 0.8 and 0.66 eV.

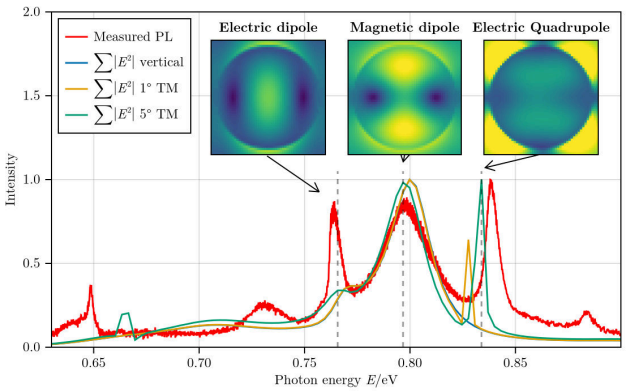

Fig. 3. Measured PL compared to simulated field enhancement under plane-wave excitation for the sample with a pitch of 850 nm. The insets show the absolute electric field along a lateral cross-section through the center of the Ge pillars.

peaks are highest when their geometry-dependent resonances are close to the direct gap. Comparing peak intensities I for different excitation powers P_0 yields a power-law dependence $I \propto P_0^k$, with k between 1.52 and 1.74, this indicates direct band-to-band transitions[10]. This confirms that our metasurfaces boost direct bandgap emission through a reduction in radiative lifetime.

Changing the sample temperature only slightly affects the resonance peaks, as it modifies the refractive index. However, the change in bandgap with temperature modifies the relative amplitudes of the peaks with respect to each other.

We conducted RCWA simulations to understand the resonant modes leading to enhanced emission. While direct simulation of emission is difficult, we rely on reciprocity in Maxwell's equations, as plane waves excited due to local fields are equivalent to local fields excited by plane waves[3]. Notably, we achieve better agreement for simulation with slightly grazing incidence. This is due to the fact that we use a 5X objective for illumination, so the angle of incidence is not strictly vertical, but a distribution. The three primary peaks related to the sample with 850 nm pitch can be related to coupled multipole Mie resonance - an electric dipole, a magnetic dipole and an electric quadrupole within the Ge pillar, respectively (Fig. 3). The peak related to electric quadrupole resonance vanishes under vertical illumination due to symmetry.

IV. Conclusion

We have demonstrated emission enhancement at the direct bandgap in intrinsic germanium up to a factor of 43, due to the use of resonant metasurface cavities. The resonances can be explained with multipole modes in coupled Mie resonators, and tuned based on geometry variation. Further research in cavity optimization and the modification of the process to include electrical contacts will be conducted in order to obtain Ge light emitting diodes in our 200 mm electronic-photonic integrated circuit pilot line.

Acknowledgments

We thank the German Ministry of Research, Technology and Space (BMFTR) for support under grant M077MB156.

References

[1] K. P. Kalinin, J. Gladrow, J. Chu, J. H. Clegg, D. Cletheroe, D. J. Kelly, B. Rahmani, G. Brennan, B. Canakci, F. Falck *et al.*, "Analog optical computer for ai inference and combinatorial optimization," *Nature*, vol. 645, no. 8080, pp. 354–361, 2025.

[2] E. M. Purcell, "Spontaneous emission probabilities at radio frequencies," in *Confined electrons and photons: new physics and applications*. Springer, 1995, pp. 839–839.

[3] A. Vaskin, R. Kolkowski, A. F. Koenderink, and I. Staude, "Light-emitting metasurfaces," *Nanophotonics*, vol. 8, no. 7, pp. 1151–1198, 2019.

[4] J. Schlipf, F. Berkmann, Y. Yamamoto, M. Reichenbach, M. Veleski, Y. Kawaguchi, F. Mörz, J. W. Tomm, D. Weißhaupt, and I. A. Fischer, "Robust si/ge heterostructure metasurfaces as building blocks for wavelength-selective photodetectors," *Applied Physics Letters*, vol. 122, no. 12, 2023.

[5] J. Schlipf and I. A. Fischer, "Rigorous coupled-wave analysis of a multi-layered plasmonic integrated refractive index sensor," *Optics Express*, vol. 29, no. 22, pp. 36 201–36 210, 2021.

[6] M. Moharam and T. K. Gaylord, "Rigorous coupled-wave analysis of planar-grating diffraction," *Journal of the Optical Society of America*, vol. 71, no. 7, pp. 811–818, 1981.

[7] I. H. Malitson, "Interspecimen comparison of the refractive index of fused silica," *Journal of the optical society of America*, vol. 55, no. 10, pp. 1205–1209, 1965.

[8] C. Schinke, P. Christian Peest, J. Schmidt, R. Brendel, K. Bothe, M. R. Vogt, I. Kröger, S. Winter, A. Schirmacher, S. Lim *et al.*, "Uncertainty analysis for the coefficient of band-to-band absorption of crystalline silicon," *Aip Advances*, vol. 5, no. 6, 2015.

[9] T. N. Nunley, N. S. Fernando, N. Samarasingha, J. M. Moya, C. M. Nelson, A. A. Medina, and S. Zollner, "Optical constants of germanium and thermally grown germanium dioxide from 0.5 to 6.6 ev via a multisample ellipsometry investigation," *Journal of Vacuum Science & Technology B, Nanotechnology and Microelectronics: Materials, Processing, Measurement, and Phenomena*, vol. 34, no. 6, p. 061205, 2016.

[10] C. Spindler, T. Galvani, L. Wirtz, G. Rey, and S. Siebentritt, "Excitation-intensity dependence of shallow and deep-level photoluminescence transitions in semiconductors," *Journal of Applied Physics*, vol. 126, no. 17, 2019.

GENERAL SESSION

Metamaterial-Based Devices

3 contributions · pp. 1341–1347

Monolithic integrated meta-mirror color filter for 5K PPI OLED pixel

Chi-Sun Hwang[1,*], Yong Hae Kim[1], Huynsu Cho[1], Sunghoon Hong[2]

[1]Reality Device Research Section, ETRI, S. Korea
[2]Smart Material Research Section, ETRI, S. Korea
*Corresponding author: hwang-cs@etri.re.kr

***Abstract*— Reflective-type color filters based on meta-atoms were monolithically integrated into the OLED pixel structure. The meta-mirror was optically and electrically integrated with the OLED pixel cavity. The OLED pixel pitch was 4.8 μm, corresponding to 5,000 PPI.**

***Keywords*— meta-mirror, OLED, monolithic integration, 5K PPI**

I. Introduction

In XR devices, microdisplays are required to achieve extremely high resolution within a very small area, leading to a growing demand for high-PPI panels. In the case of OLEDoS, products with pixel densities exceeding 4K PPI have already been commercialized [1], and ultimately, pixel densities on the order of 5K PPI are expected to be required [2].

However, implementing color using conventional approaches in such highly integrated OLEDoS panels is technically very challenging. Recently, a method for realizing color filters for 10K-PPI OLEDs using metasurfaces has been proposed [3]. While this approach achieves optical integration with OLED pixels, it lacks electrical integration, which is expected to pose significant challenges for practical panel-level fabrication and operation.

In this presentation, we propose a method for monolithically integrating metasurface-based color filters into the OLED pixel integration structure and present the corresponding experimental results..

II. Methods

Our approach to monolithically integrating metasurface-based color filters into OLED pixels is to utilize a reflective meta-filter as the anode of the OLED, while employing a transparent electrode material that is electrically conductive and optically transparent as the medium forming the metasurface.

Among transparent electrode materials commonly used in display applications, indium tin oxide (ITO) is known to provide the best combination of optical transparency and electrical conductivity. However, due to the relatively high optical refractive index of ITO, the effectiveness of dielectric-based metasurfaces is significantly reduced when ITO is used as the constituent medium.

As illustrated in Fig. 1, by constructing the metasurface using aluminum (Al) as a reflective electrode, it is possible to realize a high-efficiency reflective metasurface suitable for color filtering.

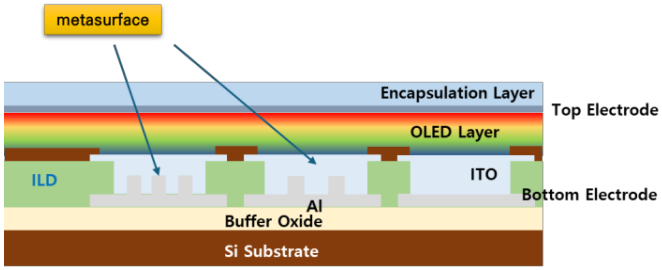

Fig. 1 Schematic of an OLED structure integrated with a meta-mirror–based color filter.

III. Results and Discussion

By tuning the Fabry–Pérot resonance modes through the phase delay introduced by the ITO layer and the phase modulation induced by the meta-mirror on the anode of the OLED device, pixel-level color control can be achieved. Considering the emission characteristics of the white OLED device and the reflectivity of the top metal electrode, the thickness of the ITO layer and the diameter of the meta-atoms were optimized to achieve optimal color gamut performance.

As a result, when the ITO thickness was fixed at 65 nm and the height of the cylindrical Al meta-atoms was fixed at 100 nm, red pixels were realized with a pitch of 351 nm and a diameter of 276 nm, while blue pixels were formed with a pitch of 400 nm and a diameter of 60 nm. For green pixels, replacing the metasurface with an ITO layer enabled a color gamut exceeding 85% of the DCI-P3 standard.

The fabrication process flow of the OLED pixels integrated with the metasurface is as follows. First, an Al layer used for

both the reflective layer and the metasurface was deposited, followed by meta-pattern formation using a nanoimprint lithography (NIL) process and patterning of the Al reflective layer. Next, an insulating layer was deposited, and only the pixel regions were etched to expose the reflective layer and the Al meta-atoms. An ITO layer was then deposited over the entire surface, followed by etching and planarization via chemical mechanical polishing (CMP), leaving ITO only in the pixel regions and electrically isolating adjacent pixels. Subsequently, banks were formed, after which the OLED functional layers and the top electrode were deposited, followed by encapsulation.

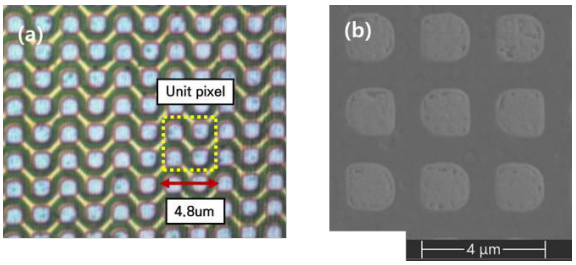

Fig. 2 Top-view images of the fabricated OLED pixel: (a) optical microscope image and (b) SEM image..

As shown in Fig. 2, an image of the pixel array obtained during the fabrication process prior to OLED layer deposition confirms a pixel pitch of 4.8 μm, corresponding to a pixel density of 5K PPI. Figure 3 presents a cross-sectional image of a pixel region, clearly showing the formation of an ITO resonance layer on top of the reflective layer.

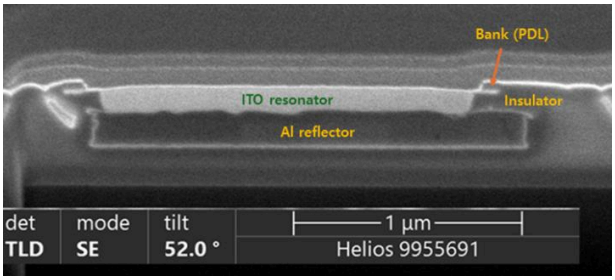

Fig. 3 Cross-sectional SEM image of the fabricated OLED pixel.

The fabricated devices exhibited good electroluminescent characteristics of the OLED, and detailed optical characterization results will be presented.

IV. Conclusion

By forming meta-atoms on the reflective layer of the OLED device and surrounding the meta-atoms with a transparent electrode material, a meta-mirror–based color filter was monolithically integrated into the OLED device. For a pixel structure corresponding to 5K PPI, a calculated color gamut of 85% was achievable. This integration of OLED devices with metasurfaces is expected to significantly contribute to the realization of future ultrahigh-resolution OLED pixel architectures..

Acknowledgments

This research was supported by the Nano & Material Technology Development Program through the National Research Foundation of Korea (NRF) funded by Ministry of Science and ICT (RS-2024-00408286).

References

[1] https://www.sony-semicon.com/en/products/microdisplay/oled.html0.
[2] https://www.insightmedia.info/samsungs-new-oled-on-silicon-microdisplays-at-ces-2026/
[3] W.-J. Joo, J. Kyoung, M. Esfandyarpour, S.-H. Lee, H. Koo, S. Song, Y.-N. Kwon, S. H. Song, J. C. Bae, A. Jo, M.-J. Kwon, S. H. Han, S.-H. Kim, S. Hwang, and M. L. Brongersma, "Metasurface-driven OLED displays beyond 10,000pixels per inch," Science, vol. 370, pp. 459–463, 2020.

Extreme field enhancement and anapoles in high-index tunable metamaterials

Zoltan Sztranyovszky[1,*], Nicolas Spiesshofer[2], Caleb Todd[2], Rakesh Arul[2], Jeremy J. Baumberg[2], Angela Demetriadou[1]

[1]School of Physics and Astronomy, University of Birmingham, Birmingham, B15 2TT, United Kingdom
[2]NanoPhotonics Centre, Cavendish Laboratory, University of Cambridge, Cambridge, CB3 0US, United Kingdom
*Corresponding author: z.sztranyovszky@bham.ac.uk

***Abstract*—We show that metamaterials made from gold nanoparticles self-assembled in layered aggregates with nanometer-sized gaps, exhibit remarkably high refractive index. When the aggregate is shaped into a disc it forms a resonator that hosts an anapole, which combined with the field enhancement from the nanogaps results in extreme light-matter interactions.**

***Keywords*— metamaterials, plasmonics, anapoles, high-index.**

I. Introduction

Metamaterials have transformed our ability to design devices with new and extreme optical properties, often not found in nature [1]. Frequently, top-down fabrication techniques (e.g. electron beam lithography) are employed to fabricate metamaterials and metasurfaces, since they give great control over the desired meta-atom shape and periodicity. However, with top-down techniques, feature or gap sizes between meta-atoms are limited to ∼5-10nm [2]. On the other hand bottom-up approaches provide an alternative way to fabricate metamaterials. Self-assembly-driven synthesis allows for both precise control of nanoparticle shapes and the sub-nanometer gaps between them by carefully choosing the spacer molecules binding the meta-atoms together [3], [4]. Here we consider metamaterials synthesized with gold nanoparticles, carefully self-assembled into aggregate layers, achieving a high and dispersionless effective refractive index in the mid-IR regime, while maintaining low loss. The high refractive index is tunable with the size of the nano-gaps, which also provide extreme field enhancement within them. By structuring the nanoparticle aggregates into disk shapes, we create resonators that support anapoles that provide an additional boost the field enhancement. This further enhances light-matter interactions, and paves the way towards metamaterial applications in sensing, enhancing non-linear processes, such as frequency conversion or lasing.

II. Methods

The effective parameters for the metamaterial are obtained via a standard retrieval method [5] using frequency domain simulations: a unit cell of an infinite metasurface made of gold spheres is modelled, the complex reflection and transmission coefficients are calculated and inserted into the analytic formulas for homogeneous slab, then inverted to obtain the effective refractive index.

We consider spherical gold nanoparticles of diameter $D = 100$nm arranged in a closed hexagonal packing and embedded in a chemical environment of refractive index $n_s = 1.5$ that enables for their self-assembly to occur, and surrounded by air, as illustrated on Fig.1.a. Current self-assembly methods can ensure extremely small gaps between the spherical nanoparticles, even with size of $g = 1$nm, for which we find the effective refractive index to be $n = 4.2 + 0.10i$ for a single layer aggregate at long wavelength [6], see Fig.1.b. This system has a resonance of the refractive index in the near-IR,

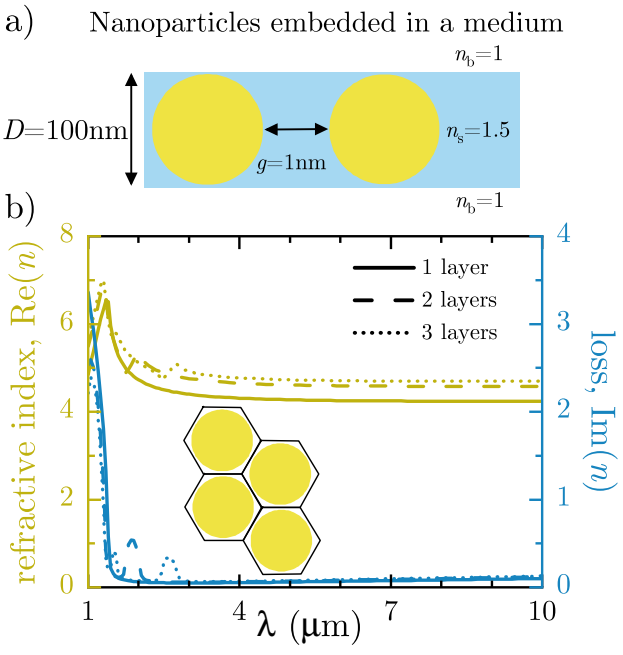

Fig. 1. a) Schematic illustration of the system with spherical nanoparticles of diameter D and gap size g embedded in a host medium with refractive index n_s and surrounded by air $n_b = 1$. b) Effective refractive index and loss of the metamaterial in the mid-IR as the number of tightly stacked layers increases. Inset shows the hexagonal packing of the nanoparticles.

and a nearly dispersion-less effective refractive index for a very broad frequency regime in the mid-IR. Additionally, the effective loss of this metamaterial is very low throughout the mid-IR regime. Therefore, this metamaterial behaves effectively as a low-loss dielectric for an extremely broad mid-IR regime and beyond, in stark contrast to the fact that is primarily made of metal (60% of volume is gold).

The stacking of additional layers of nanoparticles in close packing arrangement, increases slightly the refractive index to $n = 4.7 + 0.13i$ for a multilayer system, due the volume fraction of gold increasing in the unit cell. The gap size between the nanoparticles is controlled by the functionalization molecules that binds the nanoparticle together, with larger nanoparticle gap sizes reducing the field enhancement in the gaps and the effective polarizability of each nanoparticle, leading to a reduction in the effective refractive index [3], [4]. On the other hand, faceted nanoparticles increase the volume fraction of the gold in the unit cell and increase the effective refractive index [6]. For 1nm gaps the infinite metasurface structure provides a field enhancement factor of $EF \approx 90$ in the mid-IR region, and thus capable of enhancing non-linear processes by several orders of magnitudes.

III. Results and Discussion

We now shape the nanoparticle aggregate to form a disk resonator. The infinite metasurface at normal incidence excitation only support Fabry-Pérot resonances, however a disk resonator has a more complex mode spectrum. Such a structure supports anapoles, which are non-radiative states, characterised by a strong field confinement in the center of the resonator, and appear as strong dips in the scattering spectra [7], [8]. On Fig.2.b we show the scattering cross section spectra for a disk made of a single layer of nanoparticle aggregate. The spectrum of the homogenized disk (green line) shows a strong dip at $\lambda = 4\mu$m, and the field at this wavelength shows the typical features of an anapole, see Fig.2.b inset. Comparing this spectrum with the one for an inhomogeneous resonator made of gold spheres (gold line) we see a very good agreement between the two, suggesting the existence of an anapole in the inhomogeneous structure as well at the same frequency. The match in spectral position, but the small mismatch in amplitude suggest that the effective loss κ of the resonator is overestimated at longer wavelengths.

To confirm the existence of the anapole in the inhomogenous structure we plot the field along the radius of the resonator, parallel and perpendicular to the incoming field $\mathbf{E}_0$, see Fig.2.c and Fig.2.d. As the electric field is expelled from the metal, and confined to the gaps, it appears as sharp peaks on the plot. We also plot the field in the homogeneous resonator, which we scale up by a factor of 90, which is the enhancement factor in the infinite metasurface. We can see that the envelope of the peaks of the field in the inhomogeneous structure follows the field of the anapole in the homogeneous structure, confirming that an anapole exist in the inhomogeneous resonator. Importantly, the anapole is emerging across the whole resonator, and not just in a single unit cell as it is designed most often [9], [10], [11]. This means that the field enhancement in the nanogaps is further amplified by the anapole compared to what is found in the infinite metasurface to $EF \approx 300$, providing additional orders of magnitude boost to non-linear processes.

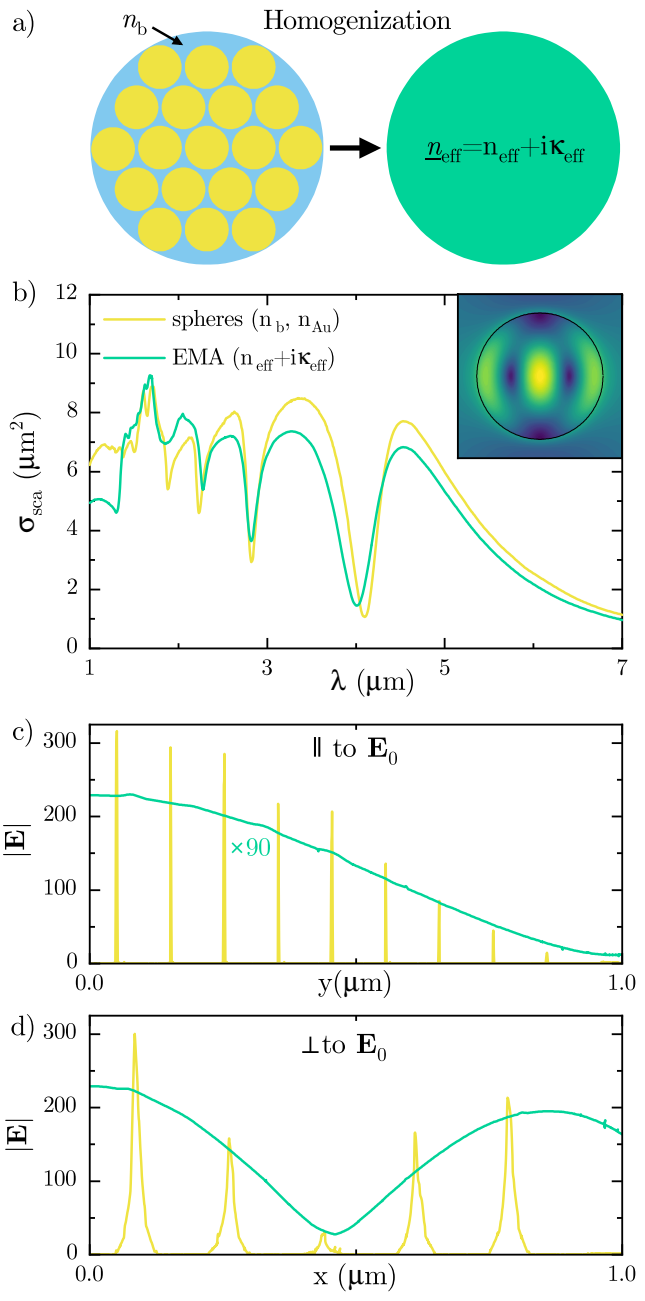

Fig. 2. a) Schematic illustration of the homogenization for the disk shaped resonator. b) Scattering cross section spectra for the homogenized resonator modelled with effective parameters, and the inhomogeneous resonator made of golds spheres. Inset shows the field amplitude inside the homogeneous disk at $\lambda = 4\mu$m. c) field inside the resonator along the radius parallel to the incoming field, which is polarized along the y direction. d) as c) but perpendicular to the incoming field.

IV. Conclusion

We have shown that self-assembled plasmonic nanoparticles behave as effective dielectrics with negligible dispersion or loss in the mid-IR. We have shown that when the aggregates is formed into a disk shape, the effective parameters obtained for an infinite metasurface remain valid despite the structure becoming finite. Importantly, the field enhancement due to the nano-gaps is amplified by the anapole in the disk resonator. The combined extreme field enhancement from this structure opens new pathways to enhance non-linear processes and light-matter interactions in the mid-IR region.

Acknowledgments

AD wishes to acknowledge support from the Royal Society University Research Fellowship URF\R1\180097 and URF\R\231024, Royal Society Research Fellows Enhancement Award RGF \EA\181038, funding from ESPRC grants EP/Y008774/1 and EP/X012689/1 from EPSRC for the CDT in Topological Design EP/S02297X/1.

References

[1] D. R. Smith, W. J. Padilla, D. C. Vier, S. C. Nemat-Nasser, S. Schultz. "Composite medium with simultaneously negative permeability and permittivity," *Physical Review Letters* vol. 84, pp. 4184, 2000.

[2] P. Wang, A. V. Krasavin, L. Liu, Y. Jiang, Z. Li, X. Guo, L. Tong, A. V. Zayats. "Molecular plasmonics with metamaterials," *Chemical Reviews* vol. 122, pp. 15031–15081, 2022.

[3] D. Doyle, N. Charipar, C. Argyropoulos, S. A. Trammell, R. Nita, J. Naciri, A. Pique, J. B. Herzog, J. Fontana. "Tunable subnanometer gap plasmonic metasurfaces," *ACS Photonics* vol. 5, pp. 1012–1018, 2017.

[4] R. Arul, DB. Grys, R. Chikkaraddy, N. S. Mueller, A. Xomalis, E. Miele, T. G. Euser, J. J. Baumberg. "Giant mid-IR resonant coupling to molecular vibrations in sub-nm gaps of plasmonic multilayer metafilms," *Light: Science & Applications* vol. 11, pp. 281, 2022.

[5] X. Chen, T. M. Grzegorczyk, BI. Wu, J. Pacheco Jr, J. A. Kong. "Robust method to retrieve the constitutive effective parameters of metamaterials," *Physical Review E* vol. 70, pp. 016608, 2004.

[6] N. Spiesshofer, E. Wyatt, Z. Sztranyovszky, C. Todd, T. V. Mykytiuk, J. W. Beattie, R. Davies, R. Arul, V. Lindo, T. F. Krauss, A. Demetriadou, J. J. Baumberg "Tailoring ultrahigh index plasmonic combinatorial metamaterials for SEIRA and SERS by tuning the fill fraction," *Optica* vol. 12, pp. 1357, 2025.

[7] A. E. Miroshnichenko, A. B. Evlyukhin, Y. F. Yu, R. M. Bakker, A. Chipouline, A. I. Kuznetsov, B. Luk'yanchuk, B. N. Chichkov, Y. S. Kivshar. "Nonradiating anapole modes in dielectric nanoparticles," *Nature Communiactions* vol. 6, pp. 8069, 2015.

[8] V. Savinov, N. Papasimakis, D. P. Tsai, N. I. Zheludev. "Optical anapoles," *Communications Physics* vol. 2, pp. 69, 2019.

[9] A. Tripathi, HR. Kim, P. Tonkaev, SJ. Lee, S. V. Makarov, S. S. Kruk, M. V. Rybin, HG. Park, Y. S. Kivshar. "Lasing Action from Anapole Metasurfaces," *Nano Letters* vol. 21 pp. 6563–6568,2021.

[10] A. C. Valero, E. A. Gurvitz, F. A. Benimetskiy, D. A. Pidgayko, A. Samusev, A. B. Evlyukhin, V. Bobrovs, D. Redka, M. I. Tribelsky, M. Rahmani, K. Z. Kamali, A. A. Pavlov, A. E. Miroshnichenko, A. S. Shalin. "Theory, Observation, and Ultrafast Response of the Hybrid Anapole Regime in Light Scattering," *Laser & Photonics Reviews* vol. 15, pp. 2100114, 2021.

[11] J. Yao, JY. Ou, V. Savinov, M. K. Chen, H. Y. Kuo, N. I. Zheludev, D. P. Tsai. "Plasmonic anapole metamaterial for refractive index sensing," *PhotoniX* vol. 3, pp. 23, 2022.

High-Efficiency Off-Grid-Positioned Metasurface Color Router for Sub-Micron CMOS Image Sensors

Po-Han Fu[1,*], Chin-Chuan Hsieh[1]

[1]Visera Technologies, Hsinchu, Taiwan

*Corresponding author: Pohan_Fu@viseratech.com

***Abstract*—We propose off-grid-positioned metasurface replacing traditional microlenses in 540 nm × 540 nm Bayer-pattern CMOS image sensors. By optimizing cylindrical meta-atom diameters and off-grid coordinates, our design efficiently routes visible light to corresponding color filters, mitigating severe diffraction and significantly enhancing overall optical efficiency.**

***Keywords*— CMOS image sensor, light routing, metasurface, off-grid positioning, sub-micron pixel.**

I. Introduction

As the demand for ultra-compact and high-resolution imaging continues to grow, the pixel size of CMOS image sensors (CIS) has aggressively scaled down into the deep sub-micron regime. At dimensions as small as 540 nm × 540 nm, the traditional optical stack encounters fundamental physical limitations. Specifically, conventional microlenses (MLs) suffer from severe diffraction at this scale, failing to focus light efficiently. Consequently, a large portion of the incident light is either scattered or directed into adjacent pixels, where it is subsequently absorbed by the color filter (CF) array. This traditional reliance on dye-based CFs to absorb unwanted spectral bands inherently wastes approximately two-thirds of the incident optical energy.

To overcome the diffraction limits of ML and the absorption losses of CFs, metasurface-based color routers have emerged as a highly promising solution. In this paper, we propose replacing the ML array with off-grid-positioned metasurface layered above the existing CF array. Unlike previous designs that restrict meta-atoms to a rigid periodic grid [1–3], our approach introduces spatial coordinates as continuous variables. This off-grid freedom provides unprecedented control over the phase profile, accurately redirecting specific wavelengths to their designated color filters, thereby minimizing absorption waste and maximizing pixel sensitivity [4].

II. Methods

The proposed metasurface is engineered for a standard 2 × 2 Bayer pattern unit cell, where each of the four sub-pixels occupies a 540 nm × 540 nm area, resulting in a total supercell footprint of 1.08 μm × 1.08 μm. The structure consists of TiO_2 cylindrical meta-atoms arranged on a transparent spacer layer directly above the CF array, as shown in Fig. 1.

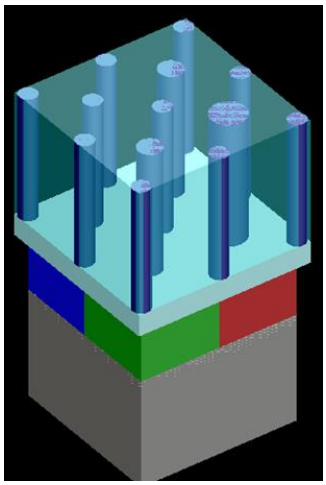

Fig. 1 Unit cell geometry of the proposed structure.

To intelligently exploit the design space, we employ a hybrid spatial arrangement of the meta-atoms across the supercell. Specifically, cylindrical meta-atoms located at the corners of the 540 nm × 540 nm pixel grid are fixed in both spatial coordinates and diameter (120 nm), serving as a structural baseline. Conversely, the meta-atoms positioned near the center of each sub-pixel are granted off-grid freedom; their diameters D_i and continuous spatial coordinates (x_i, y_i) are treated as free optimization variables, as shown in Fig. 2. This selective parameterization strategically balances computational efficiency with a highly non-linear design space. Because this expands the design into a highly non-linear and multi-dimensional parameter space, we utilize global optimization algorithms, (e.g., Genetic Algorithms), seamlessly coupled with rigorous 3D Finite-Difference Time-Domain simulations. The figure of merit is defined to maximize the optical transmission of target wavelengths into their respective CF regions while strictly penalizing inter-pixel crosstalk.

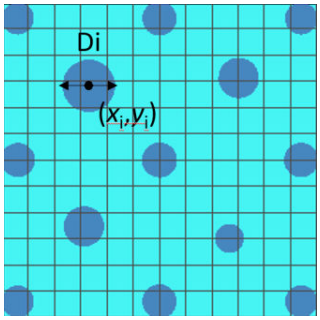

Fig. 2 Arrangement of proposed metasurface, D_i and (x_i, y_i) are treated as free optimization variables, i = 1, 2, 3, 4.

III. Results and Discussion

By simultaneously optimizing the off-grid positions and diameters, the freeform metasurface effectively shapes the incident wavefront to split and concentrate the broadband visible spectrum before it reaches the color filters. Removing the periodic grid restriction suppresses anomalous diffraction orders that typically plague sub-wavelength periodic structures, enabling a smoother and more precise phase gradient.

Numerical analyses demonstrate a dramatic enhancement in optical transmission compared to the traditional ML-CF stack, the transmittance spectra is shown in Fig. 3. Fig. 4 shows the electric field intensity of the monitor in the *xy* plane at wavelengths of 630 nm, 540 nm, and 450 nm, where the monitor is placed at the bottom of CF. Because the metasurface pre-sorts the photons, the incident light on each specific CF is already heavily weighted toward its transmission band. Consequently, the CFs function primarily as spectral purifiers rather than primary color separators, drastically reducing the amount of light they must absorb. This routing mechanism not only overcomes the severe diffraction limits of 540 nm MLs but also significantly boosts the overall quantum efficiency (QE) and reduces inter-pixel crosstalk.

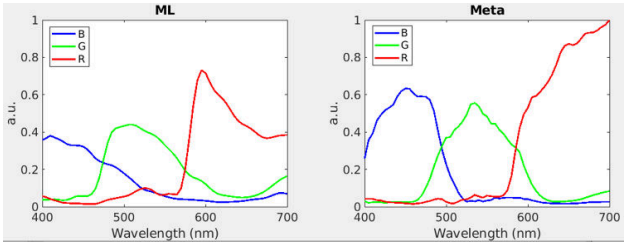

Fig. 3 Transmittance spectra of CIS with ML and proposed metasurface

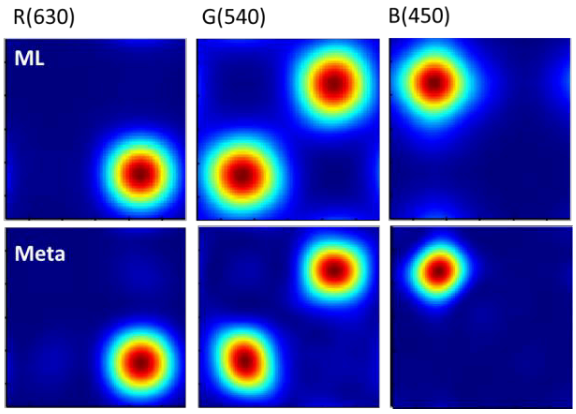

Fig. 4 Electric field intensity of the monitor in the *xy* plane at wavelengths of 630 nm (R), 540 nm (G), and 450 nm (B).

IV. Conclusion

We have demonstrated a high-efficiency metasurface color router tailored for sub-micron (540 nm × 540 nm) Bayer-pattern image sensors. By utilizing cylindrical meta-atoms with continuously optimized diameters and freeform, off-grid positions, the design achieves superior degrees of freedom for phase and dispersion control. Operating in tandem with the existing color filter array, this metasurface successfully replaces the traditional ML, pre-routing light to minimize dye-absorption losses and mitigating severe sub-micron diffraction. This freeform-positioning strategy provides a highly effective pathway for enhancing the sensitivity and color fidelity of next-generation ultra-compact CIS.

References

[1] M. Khorasaninejad, *et al*. "Metalenses at visible wavelengths: Diffraction-limited focusing and subwavelength resolution imaging," Science, vol. 352, pp. 1190–1194, 2016.

[2] X. Zou, *et al*. "Pixel-level Bayer-type colour router based on metasurfaces," Nature Communications, vol. 13, 3288, 2022.

[3] W. Hsu, *et al*. "Simplest but efficient design of a color router optimized by genetic algorithms," ACS Photonics, vol. 12, pp. 1402–1408, 2025.

[4] C. Kim, *et.al.* "Freeform metasurface color router for deep submicron pixel image sensors," Science Advances, vol. 10, 9000, 2024.

GENERAL SESSION

Photonic Crystals and Electromagnetic Bandgap Structures

3 contributions · pp. 1349–1355

Perovskite Anti-Resonant Reflection Optical Waveguide Fibre

Christian Johnson-Richards, Luke Cording and Noel Healy*

School of Mathematics, Statistics and Physics, Newcastle University, Newcastle Upon Tyne, NE1 7RU, United Kingdom

*Corresponding author: noel.healy@newcastle.ac.uk

***Abstract*—The use of meta-structures in fibre waveguides has allowed for designs that can improve light-matter interaction. In this work we present numerical characterisation of a perovskite ARROW fibre based on a commercially available fused silica template. It is shown to operate close to telecoms wavelengths and support low transmission loss.**

***Keywords*— metamaterials, photonic crystals, fibre optics, telecoms.**

I. Introduction

Photonic crystal fibres (PCFs) are a family of waveguides designed with periodic inclusions arranged transverse to the propagation direction [1]. PCFs have been demonstrated to improve upon some of the challenges faced with step-index fibres, for example the lattice structure can allow for tailored dispersion [2, 3] and they can be combined with exotic materials and shown to support light-matter interactions at low powers and long interaction lengths [4, 5]. An anti-resonant reflection optical waveguide (ARROW) fibre is an example of a PCF where guidance is provided by structures in the cladding that operate in an 'anti-resonant' regime and 'reflect' propagating light back into the core [6]. One fibre design that utilises ARROW guidance is the hollow core fibre, this design guides light in an air core with a very thin periodic silica framework cladding and because of this exhibits low dispersion and can support high power transmission [7]. Another ARROW fibre design employs a solid silica core construction with cladding inclusions of a high refractive index and is more suitable for non-linear applications due to the larger electromagnetic field locality near exotic material inclusions [8].

Perovskites have recently been demonstrated as an exciting material in optics due to their superlative properties. This is encompassed by their large refractive index [9], third order non-linear coefficient [10, 11] and high quantum efficiency [12]. However, one of the challenges with this material is the growth of large continuous single crystals in the confined spaces of small structured devices which may limit its applications in larger metamaterial devices. Typically perovskites are grown from solution in the process of inverse temperature crystallisation [13]. Presently, this process has been demonstrated in the manufacture of fibres with core sizes of hundreds of microns in diameter [14] and in the case of metal free perovskites a fibre core of ≈ 5 µm demonstrating that crystals of perovskite can be grown with large aspect ratios in confined spaces [15].

With this in mind, we propose a design for a $CsPbBr_3$ ARROW fibre that may be exploited for non-linear applications such as all-optical switching and frequency conversion. In this work ARROW guidance of this design is presented and an initial study is shown. From the results an analysis of the transmission loss and characteristic ARROW dispersion is presented. At the conference we will present an in depth study of the proposed silica-perovskite ARROW fibre, including a further study on the shifting of the transmission bands through non-linear processes and potential experimental work.

II. Methods

The wavelength at which to expect transmission bands in ARROW fibres can be approximated by the following equation [8]:

$$\lambda_m \approx \frac{2d\sqrt{(n_{\text{inc}})^2 + (n_{\text{silica}})^2}}{m + \sigma} \tag{1}$$

where n_{inc} is the inclusion index, n_{silica} is the index of silica, d is the inclusion diameter, λ_m is the wavelength of the mth mode and σ configures whether the system is on resonance ($\sigma = 0.5$) or anti-resonance ($\sigma = 0$). From this equation the required inclusion diameter to place an ARROW transmission band at a specific wavelength can be calculated. However, for this initial study the perovskite ARROW fibres were designed based on a commercially available Thorlabs ESM-12B endlessly single mode fibre (ESMF) template. These fibres are constructed out of fused silica with air inclusions placed in a hexagonal lattice. The inclusions make up a larger hexagonal structure around the core consisting of 9 periods wide with a missing inclusion in the centre. The ESMF template is modified where the air inclusions are replaced by $CsPbBr_3$. The lattice parameters of the ESMF template consists of a lattice constant of $a = 8$ µm and inclusion radius of, $r = 1.85$ µm (a schematic of the fibre is included as an insert in Fig. 1b). In the numerical study a dispersive material model for both the fused silica [16] and $CsPbBr_3$ [17] materials was considered. To model the band structure the Mode Analysis solver in COMSOL Multiphysics® was employed with a circular simulation domain with radius of 25 µm and surrounded with a perfectly matched layer (PML) of 10 µm thick. The PML was configured with cylindrical geometry and double symmetry was used so only one quarter of the domain

was simulated. In order to limit spurious modes, the solver was restricted in parameter space to a rectangle defined as $1.39 \leq n_{\text{eff}} \leq 1.52$ and $-1 \times 10^{-3} \leq \kappa_{\text{eff}} \leq 0$ for effective index and extinction coefficient respectively. Additionally, the solutions were filtered based on a mode overlap integral, Ω and compared to a hand selected solution where only solutions with a mode overlap of $\Omega \geq 65\%$ are considered.

III. Results and Discussion

Results of the numerical study are presented in Fig. 1a. Here the effective refractive index is presented in the upper part of the panel and each data point is coloured based on Ω. Additionally, the transmission loss T_{loss}, is displayed in the lower part of the panel. Here two ARROW bands are visible within the spectral window centred at $\lambda_1,\ \lambda_2 \approx 1.45,\ 1.70\ \mu\text{m}$ and with transmission loss of $T_{\text{loss}_1},\ T_{\text{loss}_2} \approx -0.013,\ -0.017\ \text{dB}\,\text{cm}^{-1}$ respectively. It is noted that the transmission loss is likely to be majorly attributed to the waveguide loss as the extinction coefficient for silica and perovskite is low at this wavelength. The transmission bands show good agreement with the analytical model from Eqn. 1 which is shown by vertical dashed lines where red (blue) corresponds to an anti-resonance (resonance) respectively. For each of the two bands the effective refractive index was fitted to a polynomial of order 5 and the results are shown as a red solid line. The polynomial fits were then used to calculate the dispersion coefficient, D, that is presented in Fig. 1b. Here a characteristic feature of ARROW fibres can be observed where for shorter (longer) wavelengths the dispersion tends towards $-\infty$ ($+\infty$) and at the band centre the dispersion is approximately zero.

IV. Conclusion

In this work we have presented the design of an ARROW fibre with $CsPbBr_3$ perovskite filled inclusions. Initial results show transmission bands near telecoms wavelengths, low transmission loss and ARROW fibre like dispersion. This platform may have potential in applications exploiting the highly non-linear nature of the perovskite inclusions and long interaction lengths that fibre optics provide, all while the perovskite remains encapsulated.

Acknowledgments

This work was supported by EPSRC (EP/S031103/1 and EP/2535904/1).

Fig. 1. (**a**) Retrieved solutions displayed as effective refractive index (upper) and transmission loss (lower), the effective refractive index data-points are coloured based on Ω and a 5th order polynomial fit is overlaid with a red solid line. (**b**) Calculated dispersion coefficient and schematic of the ARROW fibre core (inset). In both panels the analytic solutions from Eqn. 1 are overlaid as dashed lines for resonant (blue) and anti-resonant (red) cases.

References

[1] J. D. Joannopoulos, S. G. Johnson, J. N. Winn, and R. D. Meade. "Photonic Crystals: Molding the Flow of Light - Second Edition" *Princeton University Press*, 2011.

[2] C. Monat et al. "Slow light enhancement of nonlinear effects in silicon engineered photonic crystal waveguides" *Optics Express*, vol. 17, no. 4, p. 2944–2953, 2009.

[3] P. St. J. Russell, R. Beravat, and G. K. L. Wong. "Helically twisted photonic crystal fibres" *Philosophical Transactions of the Royal Society A: Mathematical, Physical and Engineering Sciences*, vol. 375, no. 2087, p. 20150440, 2017.

[4] X. Zhou, Q. Deng, W. Yu, K. Liu, and Z. Liu. "The Rise of Graphene Photonic Crystal Fibers" *Advanced Functional Materials*, vol. 32, no. 42, p. 2202282, 2022.

[5] A. Cheng, C. Wang, J. Xu, P. Zhang, Y. Zheng, and S. Dai. "Humidity Sensor Based on a Hollow Core Fiber Anti-Resonant Reflection Optical Waveguide" *Photonic Sensors*, vol. 15, no. 2, p. 250202, 2025.

[6] N. M. Litchinitser, A. K. Abeeluck, C. Headley, and B. J. Eggleton. "Antiresonant reflecting photonic crystal optical waveguides" *Optics Letters*, vol. 27, Issue. 18, p. 1592-1594, 2002.

[7] W. Ding, Y.-Y. Wang, S.-F. Gao, M.-L. Wang, and P. Wang. "Recent Progress in Low-Loss Hollow-Core Anti-Resonant Fibers and Their Applications" *IEEE Journal of Selected Topics in Quantum Electronics*, vol. 26, no. 4, p. 1-12, 2020.

[8] Healy, N. and Sparks, J. R. and He, R. R. and Sazio, P. J. A. and Badding, J. V. and Peacock, A. C. "High index contrast semiconductor ARROW and hybrid ARROW fibers," *Optics Express, OE*, vol. 19, pp. 10979–10985, 2011.

[9] M. C. Brennan, D. M. Krein, E. Rowe, C. L. McCleese, L. Sun, K. G.Berry, P. R. Stevenson, M. A. Susner, and T. A. Grusenmeyer, "Fundamental optical constants and anti-reflection coating of melt-grown, polished $CsPbBr_3$," *MRS Communications*, vol. 14, pp. 900-908, 2024.

[10] B. S. Kalanoor, L. Gouda, R. Gottesman, S. Tirosh, E. Haltzi, A. Zaban, and Y. R. Tischler, "Third-order optical nonlinearities in organometallic methylammonium lead iodide perovskite thin films," *ACS Photonics*, vol. 3, no. 3, pp. 361–370, 2016.

[11] I. Suárez, M. Vallés-Pelarda, A. F. Gualdrón-Reyes, I. Mora-Seró, A. Ferrando, H. Michinel, J. R. Salgueiro, and J. P. M. Pastor, "Outstanding nonlinear optical properties of methylammonium- and Cs-PbX_3 (X = Br, I, and Br-I) perovskites: Polycrystalline thin films and nanoparticles," *APL Materials*, vol. 7, no. 041106, 2019.

[12] A. Panda, C. Sudakar, and B. R. K. Nanda. "Enhancement of Quantum Efficiency in Perovskite Solar Cells Through Whispering Gallery Modes from Titanium Oxide Micro-Resonators" *Advanced Photonics Research*, vol. 5, no. 9, p. 2300339 2024.

[13] M. I. Saidaminov et al.. "High-quality bulk hybrid perovskite single crystals within minutes by inverse temperature crystallization" *Nature Communications*, vol. 6, no. 1, p. 7586, 2015.

[14] Y. Zhou, M. A. Parkes, J. Zhang, Y. Wang, M. Ruddlesden, H. H. Field-

ing, and Lei. Su, "Single-crystal organometallic perovskite optical fibers," *Science Advances*, vol. 8, no. 8629, 2022.
[15] H. C. L. Tsui et al. "Few-mode metal-free perovskite optical fiber with second-order optical nonlinearity" *APL Photonics*, vol. 9, no. 3, p. 036106, 2024.
[16] I. H. Malitson. "Interspecimen Comparison of the Refractive Index of Fused Silica*,†", *Journal of the Optical Society of America*, vol. 55, no. 10, p. 1205-1209, 1965.
[17] M. C. Brennan, D. M. Krein, E. Rowe, C. L. McCleese, L. Sun, K. G. Berry, P. R. Stevenson, M. A. Susner, T. A. Grusenmeyer. "Fundamental optical constants and anti-reflection coating of melt-grown, polished CsPbBr3", *MRS Communications*, vol. 14, no. 5, p. 900-908, 2024.

Effects of randomness on self-assembled photonic crystals

Duanduan Wan[1]

1 School of Physics and Technology, Wuhan University, Wuhan 430072, China

*corresponding author: ddwan@whu.edu.cn

***Abstract*—Randomness arising from thermal noise is almost inevitable in self-assembled colloidal crystals and is generally believed to be detrimental to photonic band gaps (PBGs). In this talk, I will present a counterintuitive example in which randomness actually enhances PBGs and discuss its effects on the width of PBGs.**

***Keywords*—photonic crystals, self-assembly, randomness.**

Unlike top-down design, self-assembly, as a bottom-up method, offers advantages such as low cost, low energy consumption, and the ability to produce crystals over large areas. However, randomness arising from thermal noise is almost inevitable in self-assembled colloidal crystals. In this talk, we will present a counterintuitive example where randomness actually benefits photonic band gaps (PBGs) and explore the effects of particle randomness on the width of PBGs. Additionally, we will discuss the realization of chiral photonic crystals using self-assembly approaches.

REFERENCES

1. D. Wan and S. C. Glotzer. “Unexpected dependence of photonic band gap size on randomness in self-assembled colloidal crystals”, Phys. Rev. Lett. 126, 208002 (2021).
2. Z. Qin, T. Liu, and D. Wan. “Effects of orientational and positional randomness of particles on photonic band gap”, Phys. Rev. B 107, 174110 (2023).
3. T. Liu, H.-K. Chan and D. Wan. “Chiral photonic crystals from sphere packing”, Soft Matter, 19, 7313, (2023). [Selected as the back cover]

Emergence of Rashba Spin-Orbit Coupling in Staggered-Gyromagnetic Photonic Crystals

Yao-Ting Wang[1,*], Wenlong Gao[2] and Hua-Shin Lin[1]

[1]Department of Photonics, National Sun Yat-sen University, Kaohsiung, 80424, Taiwan
[2]Eastern Institute for Advanced Study, Eastern Institute of Technology, Ningbo, China
*Corresponding author: ytwang@mail.nsysu.edu.tw

We report the Rashba spin–orbit coupling in a staggered-gyromagnetic photonic crystal with a modified honeycomb lattice. We confirm the emergence of a Rashba band structure and helical spin textures. Through both simulation and k-p theory. A positive-negative refraction through this structure has also been demonstrated.

***Keywords*— Rashba, spin-orbit couplings (SOC), staggered-gyromagnetic (SG) arrangement, photonic crystals.**

I. Introduction

Among all types of spin-orbit couplings (SOC), Rashba SOC represents a mechanism where inversion symmetry breaking and spin degrees of freedom give rise to spin-split band structures without external magnetic fields. Rashba SOC manifests itself in the splitting of degenerate bands into two branches shifted laterally in momentum space, forming a pair of parabolic dispersions with opposite spin orientations. The corresponding spin texture exhibits a helical pattern in momentum space. This spin-momentum locking results in two concentric iso-energy contours with opposite spin helicities.

In photonics, there has been a growing interest in the optical analogues of the Rashba effect. To date, a direct realization of Rashba-type SOC in photonic crystals, without relying on spatially engineered gauge fields or geometric-phase gradients, has remained elusive. In this article, we demonstrate that Rashba SOC can be realized in photonic crystals with staggered-gyromagnetic (SG) components and modified honeycomb lattice.

Breaking time-reversal-symmetry is essential for photons to realize Rashba (or Dirac cone) like dispersions. To this end, we derive an analytical expression of such system and introduce *k-p* theory to obtain the effective Hamiltonian near G point. The choice of gyromagnetic materials is yttrium iron garnet (YIG), which is an experimentally feasible matter due to its low loss property in microwave frequency range.

II. Methods

Fig. 1a depicts the schematic of the two-dimensional SG photonic crystals with modified honeycomb lattice. The unit cell is extended to a hexagon that contains six cylinders resulting in a four-fold Dirac point at G point because of the band folding of two Dirac degeneracies at K and K' points.

Since the SG arrangement causes the violation of reciprocity but remain the degeneracies, it makes the Dirac degeneracies at K and K' point respond at distinct frequencies. Thus, the band folding near G point facilitates two vertically split conical dispersions. Fig. 1b demonstrates how a four-fold Dirac point evolves. In a regular honeycomb lattice, the SG configuration splits the four-fold Dirac points into a nodal line. Then, the increase of distance of rods from the center of unit cell lifts a complete gap separating two photonic band branches.

The lattice constant of the photonic crystal is a and the radius of cylinders $r = 0.2R$, where R is the distance of each cylinder to the center of unit cell. In a regular honeycomb lattice, R = a/3, whereas R = 0.35a for a modified one. The permittivity of YIG rods $\varepsilon = 15$ and the permeability tensor takes the form

$$\begin{bmatrix} \mu_a & -i\mu_g & 0 \\ i\mu_g & \mu_a & 0 \\ 0 & 0 & 1 \end{bmatrix}. \tag{1}$$

When a 0.16T uniform magnetic field is applied, the approximate magnitude of $\mu_a = 14$ and $\mu_g = 12.4$ at frequency 4.281 GHz [1], the effect of material dispersion and loss are neglected.

In the presence of magnetic anisotropy, the TE $\left(H_x, H_y, E_z\right)$ polarization gives rise to a 2D master equation where the conventional band theory is applicable. By eliminating the magnetic fields from Maxwell's equations, one obtains

$$\nabla_\perp \cdot \xi(\mathbf{r}) \nabla_\perp E_z + i\left[\nabla_\perp \times \eta(\mathbf{r}) \nabla_\perp E_z\right]_z + \left(\frac{\omega}{c}\right)^2 \varepsilon(\mathbf{r}) E_z = 0, \tag{2}$$

where the elements of inverse permeability tensors $\xi(\mathbf{r}) = \mu_a / \left(\mu_a^2 - \mu_g^2\right)$ and $\eta(\mathbf{r}) = \mu_g / \left(\mu_a^2 - \mu_g^2\right)$.

Fig. 2a-c illustrate the evolution of the TE band diagram for the realistic SG photonic crystals. For a regular honeycomb lattice without SG component, Fig. 2a contains a G-point four-

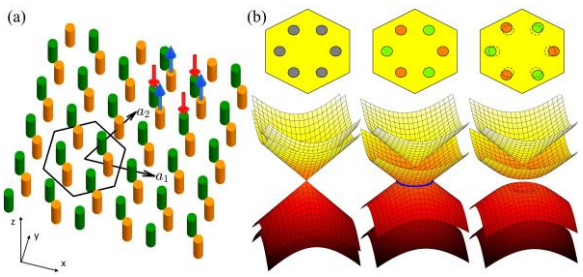

Fig. 1 Structure and band evolutions of a hexagonal photonic crystal composed of two alternating types of cylinders

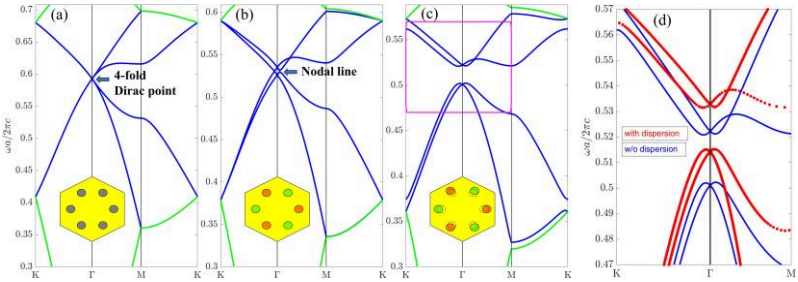

Fig. 2 Evolution of the photonic band structure under different perturbations.

fold Dirac degeneracy between the second and fifth bands at reduced frequency of 0.593. As mentioned previously, this degeneracy converts into a circular nodal line and two two-fold degeneracies when the SG material is employed, as shown in Fig. 2b. The nodal line is then lifted upon introducing a structural perturbation, thereby turning the entire four-band structure into a Rashba band diagram around reduced frequency of 0.52.

In Fig. 2d, it is evident that the influence the material dispersion is insignificant within the desired frequency range. This validates that the Rashba band splitting in Fig. 2d arises from the staggered gyromagnetic ordering (i.e., the specific structural arrangement) rather than from material dispersion, establishing the SG photonic crystal as a platform for realizing Rashba SOC in periodic media.

To construct a four-band reduced Hamiltonian near the Γ point, we use the Bloch wave function at $\mathbf{k}_0$ point as eigenbases. The Bloch state at $\mathbf{k}$ point near $\mathbf{k}_0$ point takes the form [2]-[4]

$$E_{z,n\mathbf{k}}(\mathbf{r}) = e^{i\mathbf{k}\cdot\mathbf{r}} u_{n\mathbf{k}}(\mathbf{r}) = \sum_j A_{nj}(\mathbf{k}) \exp\left[i(\mathbf{k}-\mathbf{k}_0)\cdot\mathbf{r}\right] E_{z,j\mathbf{k}_0} . \quad (3)$$

In here, the Bloch state $u_{n\mathbf{k}}(\mathbf{r})$ at $\mathbf{k}$ point has been expanded by the superposition of $u_{j\mathbf{k}_0}(\mathbf{r})$. Plugging (3) into (2) and employing orthonormal property of basis, we obtain the reduced Hamiltonian H_{lj} given by

$$H_{lj} = -(\mathbf{k}-\mathbf{k}_0)\cdot\mathbf{p}_{lj} + \left[\mathbf{t}_{lj}\times(\mathbf{k}-\mathbf{k}_0)\right]_z + (\mathbf{k}-\mathbf{k}_0)^2 q_{lj} , \quad (4)$$

where the indices $l, j = 1-4$.

In addition to the p and q coefficients that have been discussed in [3], [4], the t coefficient can be written as

$$\mathbf{t}_{lj} = A_c^{-1} \int_{u.c.} E^*_{z,l\mathbf{k}_0}(\mathbf{r})(\nabla\eta) E_{z,j\mathbf{k}_0}(\mathbf{r}) d^2\mathbf{r} . \quad (5)$$

with A_c denoting the area of the unit cell.

Since the desired bands are significantly separated from others, we only need to consider the two pairs of degeneracies around Γ point to obtain the dispersion relation.

Although the Eq. (4) does not explicitly appear as a direct sum of two conventional Rashba Hamiltonians owing to inter-band coupling among the four bands, it embodies a Rashba effect since the resulting band structure and spin texture are consistent with the nature of Rashba physics. To further validate whether the reduced Hamiltonian reflects underlying physics in our system, we compare the band structures calculated by Eq. (4) with the one calculated by COMSOL.

We then study the spin texture of each band. As stated in [5], the spin degrees of freedom in this six-rod structure are defined as $|\psi_n\rangle = [p_+, p_-, d_+, d_-]$, where $p_\pm = (p_x \pm ip_y)/\sqrt{2}$ and $d_\pm = \left(d_{x^2-y^2} \pm id_{xy}\right)/\sqrt{2}$. On this basis, the spin components can be evaluated through $s_i^{(n)} = \langle\psi_n|\mathbf{1}\otimes\mathbf{s}_i|\psi_n\rangle$, where $\mathbf{s}_i$ consists of three components of Pauli matrices.

III. Results and Discussion

As depicted in Fig. 3b-3d, the spin textures reveal how the pseudo-spin states of light evolve with the momentum of the photons in the SG photonic crystals. These spin textures describe that the photonic spin polarization, analogous to electron spin in the Rashba effect, is coupled to the momentum of the photons.

As k varies within the Brillouin zone, the direction of spin polarization of the photonic modes continuously rotates about the Brillouin center. This rotation of spin polarization is the main feature of Rashba SOC, which is a direct manifestation of the SOC in the system. For different photonic bands near the Γ point, the spin textures are visualized as a vortex-like structure with opposite rotating directions.

Fig. 4 illustrates the phenomenon of double refraction occurring in a SG photonic crystal slab illuminated by an obliquely incident electromagnetic wave at an angle of 20 degrees. The figure clearly demonstrates the splitting of the incident wave upon entry into the photonic crystal, generating two transmitted beams propagating at distinctly different angles.

The directional arrows depicted in the figure explicitly demonstrate the energy flow of the reflected and refracted beams, highlighting the doubly refractive behavior. This double refraction can be expressed by the following mechanism: The upper two branches of the Rashba dispersion can be expressed as $\omega_\pm(k) = Ck^2 \pm \alpha k$ in which C and a denote two constants related to structural geometry and materials. This dispersion yields the group velocities given by $\mathbf{v}_g = (2Ck \pm \alpha)\hat{\mathbf{k}}$.

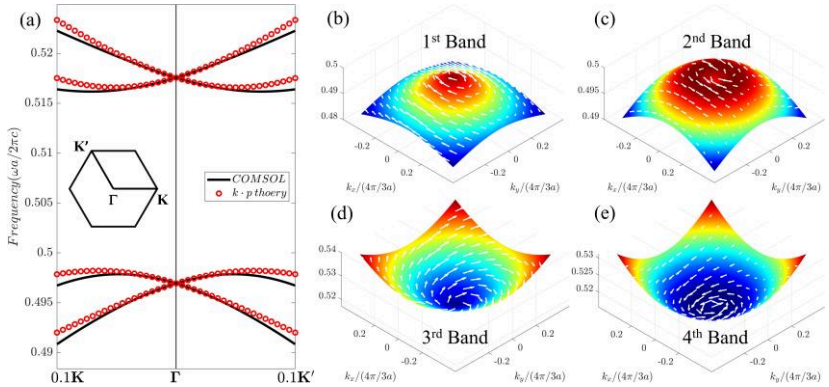

Fig. 3 Validation of the *k-p* band structure and the spin textures of eigenmode near the Dirac point.

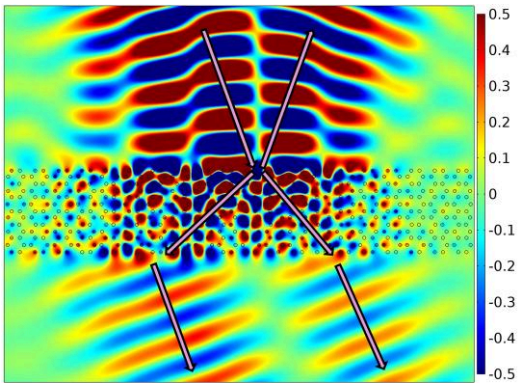

Fig. 4 Double refraction in a SG photonic crystal.

When the operating frequency corresponds to a region where the slopes $(2Ck \pm \alpha)\hat{\mathbf{k}}$ possess opposite signs, the two Rashba branches support energy flow in opposite directions. Consequently, both positive and negative refraction can occur simultaneously under this condition. Additionally, this anomalous double refraction is explained by analogy to the theory of resonant chiral media [6]. Since chiral resonance leads to Rashba-like band structure, the proposed SG structure produces similar conditions for spin states in photonic crystals.

IV. Conclusion

We have demonstrated that Rashba SOC can be effectively realized in SG photonic crystals with a modified honeycomb lattice structure.

By employing YIG rods in a staggered arrangement in a hexagonal lattice, we achieve nontrivial magneto-optical properties which are equivalent to spin-orbit interactions analogous to the electronic Rashba SOC. Using both numerical simulations and analytical *k-p* theory, we achieve photonic band dispersion and validated these findings through excellent agreement with COMSOL simulations.

Our analysis further reveals the formation of unique spin textures associated with each photonic mode near the Γ point. The spin polarization of the photonic modes continuously rotates around the Brillouin zone center, exhibiting a clear spin-dependent characteristic reminiscent of the Rashba effect.

Moreover, the double refraction behavior demonstrates their capability to manipulate electromagnetic wave propagation uniquely, reinforcing their significance for advancing understanding in photonics. Also, a quantitative extraction of the Rashba dispersion parameters based on effective-parameter retrieval is an interesting direction for future work.

Beyond photonics, the mechanism we reveal is universal to wave systems, suggesting a pathway to emulate Rashba-like effects across different branches of physics.

Acknowledgments

This work was supported by the National Science and Technology Council (NSTC) under Grant number: NSTC 113-2112-M-110-007-MY3 and National Natural Science Foundation of China (NSFC) under Grant number: 12474309.

References

[1] Z. Wang, Y. D. Chong, J. D. Joannopoulos, et. al., "Reflection-Free One-Way Edge Modes in a Gyromagnetic Photonic Crystal," Phys. Rev. Lett. 100, 013905 (2008).

[2] N. F. Johnson and P. M. Hui, "Theory of propagation of scalar waves in periodic and disordered composite structures," Phys. Rev. B, 48, 10118 (1993).

[3] J. Mei, Y. Wu, C. T. Chan, et. al., "First-principles study of Dirac and Dirac-like cones in phononic and photonic crystals," Phys. Rev. B, 86, 035141 (2012).

[4] Z.-G. Chen, X. Ni, Y. Wu, et. al., "Accidental degeneracy of double Dirac cones in a phononic crystal," Sci. Rep. 4, 4613 (2014).

[5] L.-H. Wu and X. Hu, "Scheme for Achieving a Topological Photonic Crystal by Using Dielectric Material," Phys. Rev. Lett. 114, 223901 (2015).

[6] J. B. Pendry, "A Chiral Route to Negative Refraction," Science 306, 1353-1355 (2004).

POSTERS

Symposia, Special-Session and Workshop Posters

72 contributions · pp. 1357–1520

On-chip Neural Network for High-speed, Energy-efficient and Integrated Computation

Xueyun Li[1], Shining Zhu[1], Tao Li[1,*]

[1]National Laboratory of Solid State Microstructures, Key Laboratory of Intelligent Optical Sensing and Manipulations, Jiangsu Key Laboratory of Artificial Functional Materials, College of Engineering and Applied Sciences, Nanjing University, Nanjing, 210093, China
*Corresponding author: taoli@nju.edu.cn

***Abstract*— We propose a novel architecture of waveguide-array optical neural network on the thin-film lithium niobate platform. The superior features of this design enable high-speed, energy-efficient, computationally dense and fabrication-robust performance on optical computation and machine learning inference, aiming at next-generation AI applications.**

***Keywords*— optical neural network, waveguide array, thin-film lithium niobate.**

I. Introduction

Optical neural network has been investigated widely in the recent years, targeting the solution of computational capacity, latency, energy efficiency of the conventional electric chips. Multiple on-chip architectures such as Mach-Zehnder interferometers (MZIs), micro-ring resonators (MRRs) and diffractive optical elements have been proposed, exhibiting the high speed, energy efficient and parallel processing features. However, there is still a challenge to simultaneously achieve all the exceptional performances above with a dense integration. And the tolerance of fabrication errors is also a hinder for optical computing. Herein, we demonstrate a waveguide-array optical neural network (WONN) on the thin-film lithium niobate (TFLN) platform, which enables the compact footprint, high computational density and fabrication robust leveraging the nature of the waveguide array and yields the high speed and energy efficiency by virtue of the characteristics of the TFLN.

II. Methods

The WONN is comprised of a multimode interference (MMI) splitting tree, electro-optic phase shifters, waveguide arrays and coupling gratings. As shown in Fig. 1, the 1550 nm-wavelength light is coupled into the chip and then split by the MMIs. The input features of the tasks are preprocessed and loaded onto the phase of the light. Subsequentially, the modulated light travels through the waveguide array, executing the matrix-vector multiplication, and the outputs of the selected ports give the final inference results. In this process, the waveguide array provides the desired weight matrix which is acquired in the training by adjusting the gap of the waveguides, or the coupling coefficient between the adjacent waveguides. Here, the coupled mode theory and the eigen mode expansion method are used to model the waveguide array and calculate its transmission matrix. By gradient descent optimization, the best arrangement of the waveguides is obtained for the identification tasks.

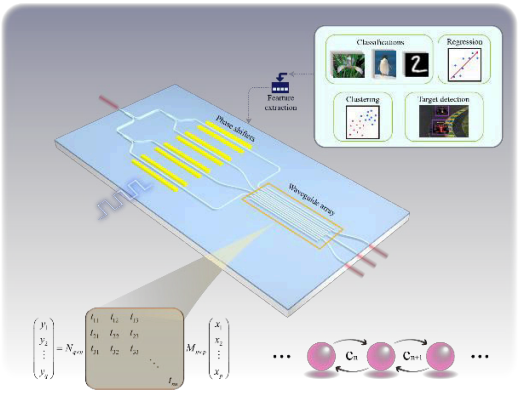

Fig. 1 Schematic diagram of the waveguide array optical neural network.

III. Results and Discussion

In the experiment, the WONN is designed for the iris flower identification task and the handwritten digit classification task, which achieves accuracies of 100% and 89.7% respectively. Moreover, the device maintains over 90% accuracy across a 75nm operating bandwidth in the iris flower identification task, demonstrating the wavelength insensitivity and superior robustness of the waveguide array. The computational metrics are also evaluated and shown a computing speed of 135.6 TOPS, an energy efficiency of 6.28 TOPS/W and a computational density of 9.48×10^4 TOPS/mm^2.

IV. Conclusion

We have demonstrated the matrix-vector multiplication of the waveguide array and constructed optical neural networks on the TFLN platform. The excellent performance of WONN

marks a leading position in the field of on-chip optical neural network and this architecture paves the way for dense, high-speed and energy-efficient optical processors for next-generation AI applications.

ACKNOWLEDGMENTS

The authors acknowledge the financial support from National Natural Science Foundation of China, Key Research and Development Program of Jiangsu Province, Natural Science Foundation of Jiangsu Province and the Fundamental Research Funds for the Central Universities. Tao Li thanks the support from Dengfeng Project B of Nanjing University.

REFERENCES

[1] Z. Wang, X. Li, J. Ji, et al., "Fast-speed and low-power-consumption optical phased array based on lithium niobate waveguides," Nanophotonics, vol. 13, pp. 2429-2436, 2024.

From Translucent to Transparent Wood

Ilya Sychugov

Department of Applied Physics, KTH Royal Institute of Technology, Stockholm
ilyas@kth.se

***Abstract*— Using spatiotemporal measurements of light propagation in transparent wood composites the main scattering mechanism was identified as refraction on cell wall interface with polymer filler. Based on this insight we show how by controlling the wood-polymer refractive index contrast and lumen shape a truly transparent wood composite can be realized.**

***Keywords*— hierarchical structure, cellulose, composite, light diffusion.**

I. Introduction

Transparent wood (TW) composites combining load-bearing and optical properties were developed a decade ago. Delignified cellulose matrix was impregnated with a refractive index matching polymer for optical transparency. It can host a variety of nanomaterials for advanced optical functions, such as luminescence [1]. However, the main obstacle in large-scale utilization of this novel composite is a high haze. It stems from wood hierarchical structure with pores at micro and nanoscales and multiple interfaces with the filling polymer [2]. In this paper we report on the mechanism of light propagation in such material as revealed by spatiotemporally resolved transmission. Main processes responsible for light scattering were identified and remedies for developing truly transparent wood, as opposite to hazy translucent wood, are outlined.

II. Methods

Using femtosecond laser pulses and a streak camera we detected light transmission through native, delignified and TW with ~ mm spatial and ~ ps temporal resolution for different wood species, cellulose treatment and filler polymers [3,4].

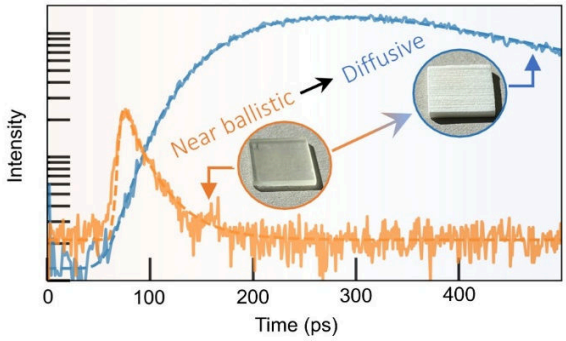

Fig. 1 Typical time-resolved transmission curves for delignified (blue) and transparent (red) wood samples 1 mm thick.

III. Results and Discussion

Time-resolved curves (Fig. 1) reveal that the transmission mechanism changes from diffusive for the native and delignified wood to nearly ballistic for the transparent wood. In addition, the spatial pattern for TW scattering is anisotropic with strong in-plane component. This can be attributed to refraction on the cell wall-polymer interface, as most lumen shapes in the wood are cylindrical [4]. Therefore, the light wavefront experiences high angles at the interfaces. This results in scattering even for a closely matched refractive indices of the wood (~ 1.536) and the polymer (~ 1.5 for PMMA).

To mitigate this unwanted effect both a better controlled refractive index contrast and the shape of the cell wall (lumen) should be considered. We show that some wood species possess more favorable lumen structure for this purpose, namely more rectangular/hexagonal lumens. The refractive index of the filler polymer can be modified by selected additives. Strategies to deal with remaining scattering (Mie or Rayleigh) on nanovoids in the cell wall as well as birefringent effects are discussed.

IV. Conclusion

We show that the high haze (80-90%), typical for translucent wood samples, can be mitigated using insights into the light propagation mechanism obtained from spatiotemporally resolved studies. Developments in this direction towards “wood glass” may offer lower embodied energy alternatives to monolithic glass, which today dominates building envelops.

Acknowledgments

This work was supported by Knut and Alice Wallenberg Foundation through the Wallenberg Wood Science Centre and grant KAW 2021.0311.

References

[1] Y. Li, S. Yu, J. G. C. Veinot, J. Linnros, L. Berglund, and I. Sychugov, "Luminescent Transparent Wood" Adv. Opt. Mater. **5**, 1600834 (2017).

[2] H. Chen, C. Montanari, R. Shanker, S. Marcinkevicius, L. A. Berglund, and I. Sychugov, "Photon Walk in Transparent Wood: Scattering and Absorption in Hierarchically Structured Materials" Adv. Opt. Mater. 10, 2102732 (2022).

[3] H. Chen *et al.*, "Green nanotechnology of cell wall swelling for nanostructured transparent wood of high optical performance" Small, 2406749 (2024).

[4] R. Shanker, M. Hoglund, H. Chen, L. A. Berglund, and I. Sychugov, "Spatiotemporally Resolved Light Propagation in Transparent Wood" Adv. Opt. Mater. *Editor's Choice*, e01789 (2025).

Multiscale QM/Classical Modeling of SERS Spectra in Amino Acids and Nucleobases

Sveva Sodomaco[1,*], Chiara Cappelli[1,2]

[1]Scuola Normale Superiore, Pisa, Italy

[2]Consorzio Interuniversitario Nazionale per la Scienza e Tecnologia dei Materiali (INSTM), UdR Pisa-SNS, Pisa, Italy

*Corresponding author: sveva.sodomaco@sns.it

***Abstract*—Our recently developed multiscale quantum mechanics/classical approach is presented for modeling surface-enhanced (SE) Raman scattering (SERS) spectra of amino acids and nucleobases near plasmonic nanostructures. Atomistic yet classical force fields describe the plasmonic properties of noble-metal nanostructures. SERS results are complemented by SE hyper-Raman spectra, together with experimental data.**

***Keywords*— atomistic modeling, multiscale, SERS, plasmonics, gold and silver nanostructures.**

I. Introduction

Surface-enhanced Raman scattering (SERS) exploits the intense local electromagnetic fields generated by localized surface plasmon resonances in metallic nanostructures, dramatically amplifying Raman signals down to the single-molecule level.[1][2] The optical response of plasmonic nanostructures can be tuned via their shape, size, composition, and surrounding environment, enabling precise control over the spectral features of adsorbed molecules.[3] Complementary techniques to SERS, such as surface-enhanced hyper-Raman scattering (SEHRS) and surface-enhanced infrared absorption (SEIRA), similarly leverage plasmonic field enhancement and are therefore fundamental for probing molecular behavior at nanostructured interfaces.[1]

In this work, we present a fully atomistic multiscale strategy to model the surface-enhanced spectroscopic response of (bio)molecules adsorbed on plasmonic nanostructures. Computed SERS spectra of representative DNA nucleobases and amino acids are compared with experimental data, and SEHRS spectra are calculated to provide complementary information on the bio-nano systems under investigation.

II. Methods

Theoretical modeling plays a crucial role in predicting and interpreting SERS spectra.[4] In recent years, multiscale approaches combining a quantum mechanical (QM) description of the molecule with atomistic, classical, and electromagnetic models of the plasmonic substrates have been proposed.[5]

In our approach, the target (bio)molecule is described at the (time-dependent) density functional theory [(TD)DFT] level, while the plasmonic environment is modeled classically using the atomistic, frequency-dependent Fluctuating Charges (ωFQ) and Fluctuating Dipoles (ωFQFμ) force fields[6][7] (see Fig. 1 for a schematic depiction of the QM/ωFQ(Fμ) model). These classical models capture Drude conduction, quantum tunneling, and interband transitions, providing an accurate yet efficient description of metallic and graphene-based nanostructures under external radiation across diverse sizes, morphologies, and compositions. [8, and references therein]. The QM/ωFQFμ method, initially developed for SERS of molecular subsystems adsorbed on noble-metal nanostructures[6], has also been extended to SEIRA [7] and SEHRS [9], thereby providing a more complete framework for simulating the linear and nonlinear vibrational responses of plasmon–molecule hybrid systems.

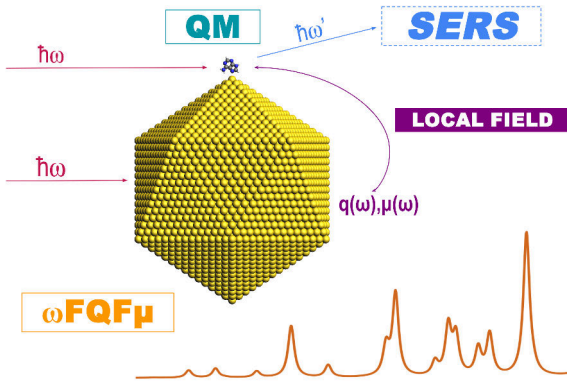

Fig. 1. Graphical representation of the QM/$\omega FQF\mu$ approach for SERS, explicitly including the local field contribution responsible for electromagnetic enhancement.

III. Results and Discussion

We first focus on the calculation of SERS spectra of the adenine nucleobase adsorbed on gold icosahedral nanoparticles, investigating how adsorption sites and molecular orientation influence spectral features and enhancement factors. The computed QM/$\omega FQF\mu$ SERS spectra are benchmarked against experimental data.[7] To identify the most likely adsorption geometries of adenine on gold, Fig. 2 compares the calculated spectra for the three proposed adsorption models (N1/N10, N7/N10, N3/N9) with experimental SERS data. The total averaged calculated spectra ("Calc") reproduce most experimental

features ("Exp"), indicating that N3/N9 and N7/N10 are the most probable adsorption configurations.

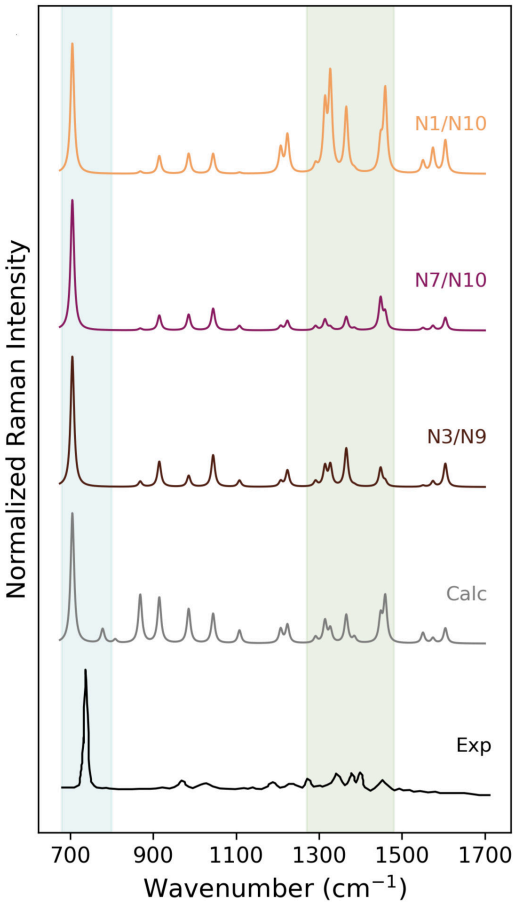

Fig. 2. Normalized QM/$\omega FQF\mu$ SERS spectra, calculated for N3/N9, N7/N10, N1/N10, and all (Calc) adsorption configurations of adenine nucleobase on a gold icosahedral nanoparticle, together with the experimental results (Reproduced from Ref. [10]. Copyright 2009 American Chemical Society.). The characteristic regions of the SERS spectra are highlighted.

SEHRS is a nonlinear technique complementary to SERS that, owing to its stronger electromagnetic field enhancement and distinct selection rules, can provide additional insight into biomolecule–surface interactions.[11] In the present work, computed SERS spectra are used in conjunction with SEHRS and compared with experimental data [12][13] to explore the effects of protonation states and hot-spot enhancement on the aromatic amino acid tryptophan, illustrating the potential of our multiscale simulations to investigate a broader range of biologically relevant molecules.[9]

IV. Conclusion

We have shown that the QM/$\omega FQF\mu$ approach provides an accurate and flexible framework for modeling SERS spectra of small biomolecules on plasmonic nanostructures, capturing the influence of molecular orientation, adsorption sites, substrate morphology, and environmental effects. Complementary SEHRS calculations further support the interpretation of SERS spectra, aiding the understanding of vibrational mode activation and molecule–surface interactions. Applications to representative nucleobases and amino acids demonstrate the predictive power of the method, highlighting its potential to guide the design of plasmonic biosensors and future surface-enhanced spectroscopic studies.

Acknowledgments

This work has received funding from the European Research Council (ERC) under the European Union's Horizon 2020 research and innovation programme (grant agreement No. 818064)

References

[1] M. Moskovits and K. Kneipp, *Surface-Enhanced Raman Scattering: Physics and Applications*, Springer, 2006.
[2] J. Langer et al., *ACS Nano*, vol. 14, pp. 28–117, 2020.
[3] K. Lance Kelly, E. Coronado, L. L. Zhao, and G. C. Schatz, *The Journal of Physical Chemistry B*, vol. 107, pp. 668–677, 2003.
[4] S. M. Morton, D. W. Silverstein, and L. Jensen, *Chemical Reviews*, vol. 111, pp. 3962–3994, 2011.
[5] J. L. Payton, S. M. Morton, J. E. Moore, and L. Jensen, *Accounts of Chemical Research*, vol. 47, pp. 88–99, 2014.
[6] P. Lafiosca, L. Nicoli, L. Bonatti, T. Giovannini, S. Corni, and C. Cappelli, *Journal of Chemical Theory and Computation*, vol. 19, pp. 3616–3633, 2023.
[7] S. Sodomaco, P. Lafiosca, T. Giovannini, and C. Cappelli, *The Journal of Physical Chemistry C*, vol. 130, pp. 1919–1930, 2026.
[8] T. Giovannini, P. G. Illobre, P. Lafiosca, L. Nicoli, L. Bonatti, S. Corni, and C. Cappelli, *Computer Physics Communications*, Art. no. 110035, 2026.
[9] S. Sodomaco, and C. Cappelli, *in preparation*, 2026.
[10] J. Kundu, O. Neumann, B. G. Janesko, D. Zhang, S. Lal, A. Barhoumi, G. E. Scuseria, and N. J. Halas, *The Journal of Physical Chemistry C*, vol. 113, pp. 14390–14397, 2009.
[11] F. Madzharova, Z. Heiner, and J. Kneipp, *Chemical Society Reviews*, vol. 46, pp. 3980–3999, 2017.
[12] F. Madzharova, Z. Heiner, and J. Kneipp, *The Journal of Physical Chemistry C*, vol. 121, pp. 1235–1242, 2017.
[13] F. B. Rahman, and J. Kneipp, *Journal of Raman Spectroscopy*, ASAP Article, 2026.

Topological edge-state waveguide fed slot antennas

Shih-Hui Gilbert Chang*

Department of Photonics, National Cheng-Kung University, Tainan, Taiwan
*Corresponding author: gilbert@mail.ncku.edu.tw

***Abstract*— Topological edge states based on the quantum spin Hall effect are implemented in a dual layer PEC structure to form a one-way propagation waveguide. A slot antenna fed by such a topological waveguide exhibits higher order resonant modes and leads to pseudospin flips. The properties of the topological protection, simulated by FDTD, are discussed.**

***Keywords*— photonic topological insultors, finite-difference time-domain method, nanoantennas.**

I. Introduction

Slot antennas used in phase array system are fed by transmission line within a dual-layer PEC structure. The opening of the slot introduces an additional impedance load to the transmission line, drastically altering the phase of the transmission channel. Consequently, designing a phased array with multiple slots requires phase compensators, making the system complex and inefficient. By adopting topological edge states based on quantum spin Hall effect as the transmission waveguide, the system benefits from topological protection. Because this protection is immune to defects such as the slot openings, it should successfully preserve the phase of the transmitted signal for the next slot antenna.

II. Methods

In this work, a dual-layered PEC structure is used to form a TM_0 waveguide, which is sandwiched with dielectric cylinders in a hexagonal lattice. Each unit cell consists of six dielectric cylinders with a fixed radius but varying center-to-center distances to form both trivial and nontrivial photonic topological insulators [1]. By using the order-N method alongside finite-difference time-domain(FDTD) simulations, we calculate the band structure of the trivial and nontrivial topological insulator to verify band inversion in the nontrivial case. A Wilson loop method is employed to calculate the Chern number and verify the system's topological properties. These two topological insulators are stitched together to form a zigzag interface supporting topologically protected edge states. The edge state dispersion is calculated, and its one-way propagation with pseudospin excitation is verified by the FDTD method. Exciting the pseudospin edge state at the interface forms a one-way propagating waveguide mode that is immune to defects and backscattering. Finally, by introducing a hexagonal opening on the upper PEC plane, a slot antenna is formed to extract the waveguide signal into free space. This slot antenna is designed to have a resonant peak at the center of the topological bandgap.

III. Results and Discussion

Analyzing the out-scattering spectrum of the slot antenna reveals two distinct peaks instead of a single broad resonant. An examination of the mode patterns indicates that these two peaks correspond to the m=0 and m=1 modes, respectively. These modes can be viewed as the photonic crystal defect modes introduced by the slot antenna. Underneath the opening of the PEC slot antenna, the periodic structure of the dielectric cylinders provides a stopband for mode confinement. When the pseudospin-up mode is excited as the right-going waveguide mode at the wavelength of the first peak, strong reflection occurs, whereas the second peak exhibits no reflection. Although the slot antenna breaks the Z_2 symmetry which typically leads to a spin flip, the symmetry of the m=1 resonant mode drastically reduced the effect and preserves the edge state mode.

IV. Conclusion

In conclude, by carefully designing the slot antenna and choosing the appropriate symmetry, a topological protected edge state waveguide can radiate an outgoing transmission without a spin flip, thereby maintaining topological protection. This work can provide a novel mechanism for phased array antenna design that avoids complicated phase and interference considerations.

Acknowledgments

This work was supported by the Taiwan National Science and Technology Council under Taiwan-Lithuania cooperation research project Grant number ：NSTC 113-2923-E-006-010-MY2.

References

[1] L.-H. Wu and X. Hu, "Scheme for achieving a topological Photonic Crystal by using dielectric material," Physical Review Letters, vol. 114, no. 22, p. 223901, 2015.

Gradient-Momentum Engineering in Metasurface for Continuous and Asymmetric Beam Steering

Su-Hsiu-Ping[1*], Po-Sheng Huang[1], and Pin Chieh Wu[1]

[1]*Department of Photonics, National Cheng Kung University, Tainan 70101, Taiwan*
* Corresponding author: samwii888@gmail.com

***Abstract*— Advanced optical sensing systems require continuous and high-resolution beam steering over a wide field of illumination (FOI). However, meeting these criteria in a compact transmissive device has yet to be achieved. Here, we develop a transmissive metasurface featuring spatially continuous, independently tunable in-plane momentum gradients, enabling wide FOI coverage of 100° and 70° in the horizontal and vertical directions, respectively. The proposed metasurface attains a theoretical deflection efficiency of 96% and an experimental efficiency of 58%, with a fine angular resolution of ~0.4°. By tuning the gradient momentum distribution, it enables precise control of the angular resolution and FOI along orthogonal axes, making this platform well suited for next-generation applications.**

***Keywords* — Active metasurface, LiDAR, All-dielectric metasurface.**

I. Introduction

With the rapid advancement of optical communications, LiDAR, and AR/VR technologies, there is a growing demand for nanophotonic devices that enable continuous beam steering while remaining highly compatible with existing platforms. Metasurfaces have emerged as a compelling solution due to their ability to manipulate optical properties such as phase, amplitude, and polarization at the subwavelength scale. To date, dynamic beam steering strategies have largely relied on phase-change materials, complicated physic principle, or integration with intricate circuits [1] to modulate the refractive index or the effective geometry of the device. Despite notable progress, these approaches often remain constrained by design complexity and limited operational efficiency.

In this work, we propose a transmissive metasurface that achieves asymmetric, high-efficiency, and continuous beam control with a wide asymmetric FOI at a wavelength of 940 nm [2]. The design principle is to engineer the in-plane momentum through a linear, spatially continuous gradient across the metasurface. Owing to the inherently continuous momentum distribution, the resulting beam steering is smooth and supports fine angular resolution. Furthermore, the momentum gradient can be tuned along selected directions, providing additional degrees of freedom for diverse application schemes. Experimentally, we demonstrate continuous beam deflection with an asymmetric FOI of 100° in the horizontal direction and 70° in the vertical direction, together with high theoretical steering efficiency, indicating strong potential for LiDAR and advanced optical sensing applications.

II. Methods

Continuous, asymmetric, and high-resolution beam steering can be realized using generalized Snell's law, where the spatial distribution of the phase gradient is intrinsically linked to the in-plane optical momentum which determines the direction of light propagation. By exploiting the vector nature of momentum, we design the momentum components independently along the x and y directions, thereby decoupling the deflection behavior along the orthogonal axes. The momentum can also be linearly combined to form a diagonal momentum vector, which enables arbitrary 2D steering trajectories.

Here, we assume linear relationships for the momentum gradients along the x and y directions characterized by distinct slope coefficients, respectively. Specifically, the momentum functions are defined as $k_x = k_0 ax$ and $k_y = k_0 by$ where k_0 is the free space wavevector and a, b denote the slope coefficients. For diagonal paths, the in-plane momentum is given by the vector sum of k_x and k_y. Consequently, the deflection angle can be tuned by shifting the incident beam position relative to the metasurface center, enabling customizable FOI range. Integrating the momentum functions gives the phase profile $\varphi(x, y) = k_0(ax^2 + by^2)$ where the coefficients are determined by the relations $a = \sin(\theta_{\Delta x})/L_x$, and $b = \sin(\theta_{\Delta y})/L_y$, where $\theta_{\Delta x} = \theta_{\Delta x_{max}} = 50°$, $L_x = 2268$ μm, $\theta_{\Delta y} = \theta_{\Delta y_{max}} = 35°$, and $L_y = 1715$ μm (the lateral dimensions L_x and L_y are the half length of the metasurface in x and y axis). Figure 1a and 1b illustrate the design phase distribution and the corresponding in-plane momentum map, respectively. Both exhibit anisotropic behavior, with a larger phase (momentum) variation along the horizontal direction.

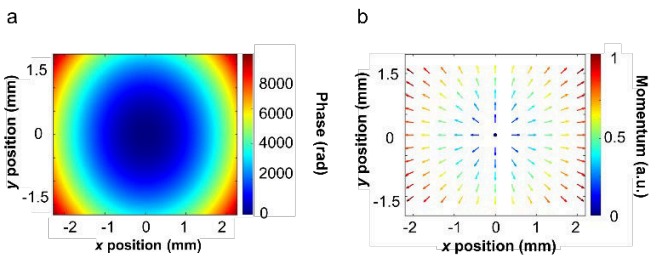

Fig. 1 (a) Design phase distribution which features an elliptical function confirming the asymmetric nature. (b) 2D momentum map for linear momentum design.

III. Results and Discussion

To validate the proposed concept, we performed both numerical simulations and experimental measurements. Figure 2a presents an optical microscope (OM) image together with scanning electron microscopy (SEM) images of the fabricated metasurface, confirming overall structural integrity and uniformity. Figure 2b shows the calculated deflection angles, which form an elliptical angular distribution that reflects the intentionally anisotropic design. The numerical and experimental deflection angles both demonstrate high deflection efficiency and continuous 2D steering, which are in good agreement with theoretical predictions. The discrepancies observed near the corners mainly arise from distortions of the deflected spots at larger steering angles, which hinder complete collection of the optical spot during measurement.

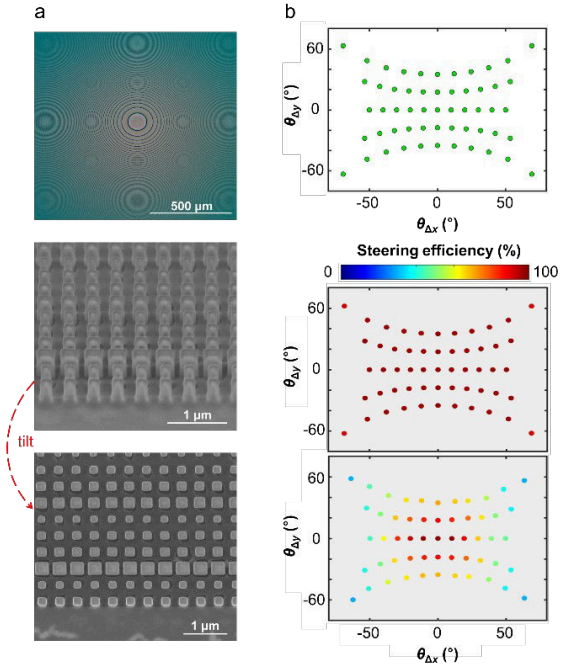

Fig. 2 (a) The OM image (top) and SEM image (center and bottom). (b) 2D map of theoretical deflection angles (top) compares with simulated (center) and experimental (bottom) deflection angles, where color indicates steering efficiency.

Figure 3a shows fine displacement scanning along the x, y, and diagonal directions, where the measured deflection angles follow the theoretical trend with high fidelity. To quantitatively assess the angular precision of the proposed metasurface, we define the angular resolution $\Delta\theta$ as the smallest displacement that yields a resolvable change in steering angle (Fig. 3b). The measured variations remain small and symmetrically distribute about the theoretical prediction line, with average values of 0.401°, 0.387°, and 0.392°, and corresponding standard deviations of 0.143°, 0.190°, and 0.155° for three scan directions. Notably, there is no observable drift or error accumulation across all displacement range. These results confirm that the metasurface maintains consistent beam steering accuracy through the entire scanning range.

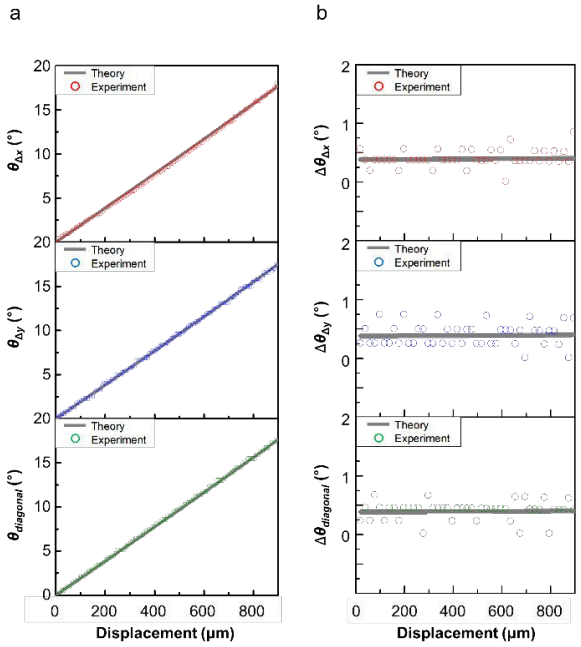

Fig. 3 (a) Beam steering corresponding to 5 μm incremental displacements of the incident beam along three directions. (b) Angular resolution with 20 μm beam displacement interval. Solid lines depict theoretical expectations, and the dots indicate experimental data.

IV. Conclusion

In this work, we develop and experimentally demonstrate a transmissive metasurface capable of continuous and high-resolution 2D beam deflection. By leveraging spatially linear and independently tunable in-plane momentum gradients along orthogonal directions, the proposed design achieves a wide and asymmetric FOI, covering 100° horizontally and 70° vertically, while maintaining high steering efficiency (~96% simulated average). Notably, sub-degree angular precision is obtained for beam steering in all directions, and dense spatial sampling confirms continuous 2D scanning without observable drift. This finding provides a compact, efficient, and versatile beam-steering platform, well suited for next-generation LiDAR, free-space communication and advanced sensing applications.

Acknowledgments

The authors gratefully acknowledge support from the National Science and Technology Council (NSTC), Taiwan, the Core Facility Center of National Cheng Kung University (NCKU), the Higher Education Sprout Project of the Ministry of Education (MOE) to the Headquarters of University Advancement at NCKU, the Center for Quantum Frontiers of Research & Technology (QFort) at NCKU.

References

[1] G. K. Shirmanesh, R. Sokhoyan, P. C. Wu and H. Atwater, "Electro-optically tunable multifunctional metasurfaces," *ACS Nano*, **vol. 14**, pp. 6912–6920, 2020.

[2] H.-P. Su, P.-S. Huang and P. C. Wu, "Gradient-momentum engineering in metasurface for continuous and asymmetric beam steering," *Laser & Photonics Reviews* **in press** (2026)

Multiscale analysis of anisotropic composites

Natalia Rylko

Faculty of Computer Science and Mathematics, Cracow University of Technology, Krakow, Poland

***Abstract*—A new two-dimensional polydisperse model for analyzing two-phase composites is developed. Verification of the model is performed using composite microstructures in which the local inclusion concentration is sufficiently uniform, ensuring that the material does not exhibit a graded structure. The examined microstructure is characterized at the macro-, meso-, and micro-scales through the structural sum e_2, which is equivalent to using the two-point correlation function. An anisotropy distribution $\varkappa(\mathbf{x})$ is then introduced through e_2 for meso-cells centered at position x. This new distribution $\varkappa(\mathbf{x})$ captures and aggregates the geometric features of the considered microstructure.**

***Keywords*— dispersed random composites, polydisperse model, macroscopic property tensor.**

I. Introduction

The classic homogenization theory and its constructive implementations are used to determine the effective constants of deterministic and random composites. Anisotropy is an intrinsic quality of composites arising from geometric structure. The macroscopic anisotropy is expressed by tensors corresponding to various constitutive equations for physical and mechanical fields. For simplicity, we restrict our attention to the two-dimensional conduction mathematically equivalent to the real dielectric permittivity.

II. Anisotropy coefficient

A complex variable for the plane coordinates will be used. Consider a composite with non-overlapping circular inclusions $|z-a_k|<r_k$ $(k=1,2,\dots,N)$ randomly distributed in the periodicity square unit cell and occupied by a material of conductivity σ_1. The conductivity of the host is normalized to $\sigma_0=1$. The truncated form for the normalized effective conductivity tensor for two-phase composites becomes [1]

$$\boldsymbol{\sigma}=(1+2\varrho f)I+\tfrac{2\varrho^2}{\pi}\sum_{k,m=1}^{N}f_kf_m\times \left(\begin{array}{cc}\mathrm{Re}\,E_2(a_m-a_k) & -\mathrm{Im}\,E_2(a_m-a_k)\\ -\mathrm{Im}\,E_2(a_m-a_k) & -\mathrm{Re}\,E_2(a_m-a_k)\end{array}\right)+O(f^{\frac{5}{2}}|\varrho|^3), \tag{1}$$

where I stands for the identity matrix, the contrast parameter $\varrho=\frac{\sigma_1-\sigma_0}{\sigma_1+\sigma_0}$, $E_2(z)$ is the Eisenstein function of second order. Here, $f_k=\pi r_k^2$ and $f=\sum_{k=1}^{N}f_k$ is the total concentration.

We introduce the local polydispercity anisotropy coefficient based on [1]. Let $\mathbf{x}$ be the center of the square cell. This cell will be considered a meso-cell. The local polydispersity anisotropy coefficient is introduced in the considered small square cell

$$\kappa(\mathbf{x})=\frac{1}{\pi}\sum_{k,m}f_m(\mathbf{x})f_k(\mathbf{x})\left[E_2(a_m-a_k)-\pi\right]. \tag{2}$$

The parameters $f_m(\mathbf{x})$ in the right part of (2) are calculated locally in a small cell, hence, depend on $\mathbf{x}$. The geometrical parameters in the brackets are calculated after the normalization to the unit square cell. We will consider the function $\kappa(\mathbf{x})$ from (2) as the global anisotropy value after the appropriate scaling. Thus, the function $\kappa(\mathbf{x})$ is formally defined for a discrete set of $\mathbf{x}$, the centers of meso-cells. It can be considered as a continuous function in $\mathbf{x}$ after a smoothing procedure. Below, we omit the argument $\mathbf{x}$ for shortness.

The macroscopic tensor can be written up to $O(|\varrho f|^3)$ in the form

$$\left(\begin{array}{cc}\sigma_{11} & \sigma_{12}\\ \sigma_{21} & \sigma_{22}\end{array}\right)=(1+2\varrho f)I+2\varrho^2+2\varrho^2f^2\left(\begin{array}{cc}\kappa_1 & -\kappa_2\\ -\kappa_2 & -\kappa_1\end{array}\right), \tag{3}$$

where $\sigma_{11}=1+2\varrho f+2\varrho^2f^2+\kappa_1$, $\sigma_{12}=\sigma_{21}=-\kappa_2$ and $\sigma_{22}=1+2\varrho f+2\varrho^2f^2-\kappa_1$. The principal conductivities are determined by its eigenvalues $1+2\varrho f+2\varrho^2f^2+|\kappa|$ and $1+2\varrho f+2\varrho^2f^2-|\kappa|$. The principal angle θ satisfies the following equation

$$\tan 2\theta=\frac{2\sigma_{12}}{\sigma_{11}-\sigma_{22}}=-\frac{\kappa_2}{\kappa_1}. \tag{4}$$

Two roots θ of equation (4) correspond to the inclinations of the major and minor axes to the original x-axis.

III. Conclusion

The main goal is to derive a formula that determines the anisotropy of phase distribution in composite materials, taking into account both the polydispersity of particle sizes and their location. A prominent application of this new formula is to explore anisotropy across macro-, meso-, and micro- scales following [2]. The obtained results can be extended to the complex-valued permittivity values following [3].

Acknowledgments

This work was supported by the COST Action CA23125.

References

[1] V. Mityushev, "Transport properties of doubly periodic arrays of circular cylinders and optimal design problems," *Applied Mathematics & Optimization*, vol. 44, 17–31, 2001.

[2] N. Rylko, M. Stawiarz, P. Kurtyka, P., V. Mityushev, "Study of anisotropy in polydispersed 2D micro and nano-composites by Elbow and K-Means clustering methods," *Acta Materialia*, vol. 276, 120116, 2024.

[3] V. Mityushev, T. Gric, R. Kycia, N. Rylko: Anisotropy of Metamaterials: Beyond Conventional Paradigms. Francis Taylor/CRC Press, 2025.

Spectral and Polarization Control of Smith-Purcell Radiation via Chiral Dielectric Gratings

Loris Cavenaile[1,*], Thomas Delplace[1], Muluneh G. Abebe[1], Bjorn Maes[1]

[1]Micro- and Nanophotonic Materials Group, Research Institute for Materials Science and Engineering, University of Mons, Place du Parc 20, 7000 Mons, Belgium

*Corresponding author: loris.cavenaile@umons.ac.be

***Abstract*—We utilize chiral materials to unlock Smith-Purcell radiation into modes typically forbidden in two-dimensional achiral structures. Via a Pasteur medium the modes hybridize, allowing excitation by the passing electron's evanescent field. This approach offers a new degree of freedom for wavelength and polarization control.**

***Keywords*— Smith-Purcell radiation, chiral materials, gratings.**

I. Introduction

The interaction between free electrons and periodic photonic structures enables the generation of tunable electromagnetic radiation, known as the Smith-Purcell (SP) effect [1]. This mechanism is fundamental for developing compact and novel light, e.g., in the terahertz and X-ray regimes. While initial designs relied on metallic gratings, recent advancements have shifted towards high-index dielectric structures. These offer lower losses and support resonances with high quality factors, allowing for maximal photon emission and optimized energy loss [2].

Current research focuses on tailoring these resonances to control the emission properties. Recent works have explored anomalous Doppler effects [3] and utilized geometric symmetry breaking, such as glide symmetry in coupled gratings, to direct radiation into specific half-spaces [4]. However, a persistent limitation in conventional two-dimensional (2D) SP devices is the polarization constraint: the electron beam naturally couples to Transverse Magnetic (TM) modes, leaving Transverse Electric (TE) modes largely inaccessible in standard 2D achiral models.

To overcome this limitation, we investigate the introduction of constitutive symmetry breaking via chirality [5]. Magneto-electric coupling in chiral (Pasteur) media is known to mix electric and magnetic dipoles, potentially allowing an electric source to excite TM modes [6].

In this work, we numerically demonstrate a Smith-Purcell source that combines a chiral layer ($n = 1.4$) with a silicon (Si) grating separated from a Si substrate. We show that the optical activity of the medium enables the excitation of a high-Q, TE-polarized resonance confined within the Si teeth, a mode forbidden in achiral counterparts. This approach thus offers a new degree of freedom for wavelength and polarization shaping in free-electron photonics.

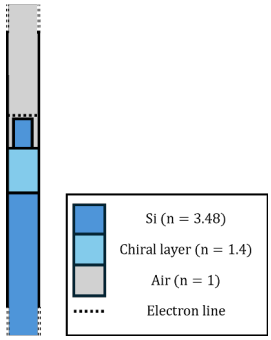

Fig. 1. Schematic of the unit cell geometry. The structure consists of a Si substrate ($n = 3.48$) coated with a chiral layer ($n = 1.4$) and periodic Si grating teeth. The electron beam (dashed line) passes above the grating, exciting Smith-Purcell radiation. In the chiral configuration, the chiral layer possesses a chirality parameter $\kappa = 0.05$.

II. Methods

The SP phenomenon can be efficiently simulated by employing only a single period of the structure. We use the finite-element commercial software COMSOL Multiphysics to solve the electromagnetic wave equation in the frequency domain. The unit cell geometry, see Fig. 1, consists of a Si substrate covered by a continuous chiral material. This chiral layer acts as the active medium ($\kappa = 0.05$), while all other materials remain achiral ($\kappa = 0$). The periodic grating modulation is provided by Si rectangles placed on top of the chiral layer. The upper surrounding background medium is air ($n = 1$).

The computational domain is truncated using Perfectly Matched Layers (PMLs) at the top and bottom boundaries to simulate semi-infinite open regions and suppress non-physical reflections. Floquet periodic boundary conditions are applied along the electron propagation direction (horizontal, x-axis) to mimic the infinite periodic array. The electron beam is modeled as a line current density flowing above the grating with a phase delay determined by the electron velocity, acting as the source term for the simulation [7].

III. Results and Discussion

We first investigate the spectral characteristics of the emitted radiation to assess the impact of chirality. Figure 2 compares the emitted energy density as a function of frequency for an

achiral structure ($\kappa = 0$) and a chiral structure ($\kappa = 0.05$). In the achiral case (Fig. 2a), the spectrum is dominated by a main resonance around 258 THz. As expected for conventional SP radiation arising from a standard grating, this emission is purely TM polarized (solid blue line), with no TE contribution.

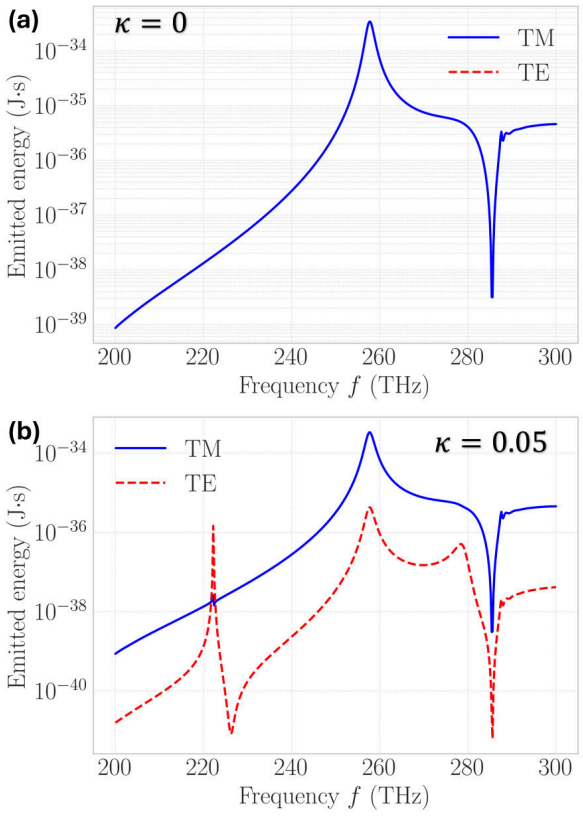

Fig. 2. Spectral density of emitted energy. (a) Achiral case ($\kappa = 0$): The emission is strictly TM-polarized (solid blue line) with a main resonance at 258 THz. (b) Chiral case ($\kappa = 0.05$): A sharp resonance emerges at 222 THz. The polarization decomposition reveals this peak is quasi-TE-polarized (dashed red line), demonstrating the magnetoelectric coupling.

The introduction of chirality in the chiral layer dramatically alters this behavior. As shown in Figure 2b, while the conventional TM peak is preserved, a new, sharp resonance emerges at $f = 222$ THz. Crucially, the polarization decomposition reveals that this chirality-induced peak is mainly TE-polarized (dashed red line). This observation confirms that the optical activity of the chiral medium breaks the symmetry, enabling a coupling to quasi-TE modes that are otherwise forbidden in standard achiral Smith-Purcell geometries. This mechanism offers a direct method to control the polarization and spectrum of the emitted light.

To understand the modes, we analyze the electromagnetic field distribution $|\mathbf{E}|$ at the resonance frequencies. Figure 3 compares the mode profiles for the TM peak and the TE chiral-induced resonance. At 258 THz (Fig. 3a), the TM-field is primarily distributed within the chiral layer and around the Si grating, exhibiting strong scattering and corner effects. In contrast, the chiral-induced TE resonance at 222 THz (Fig. 3b) reveals a field distribution strongly confined inside the Si grating tooth, with a decaying contribution in the chiral layer. This suggests that the chiral material hybridizes the TE mode, providing a channel for the electron beam TM current to couple into.

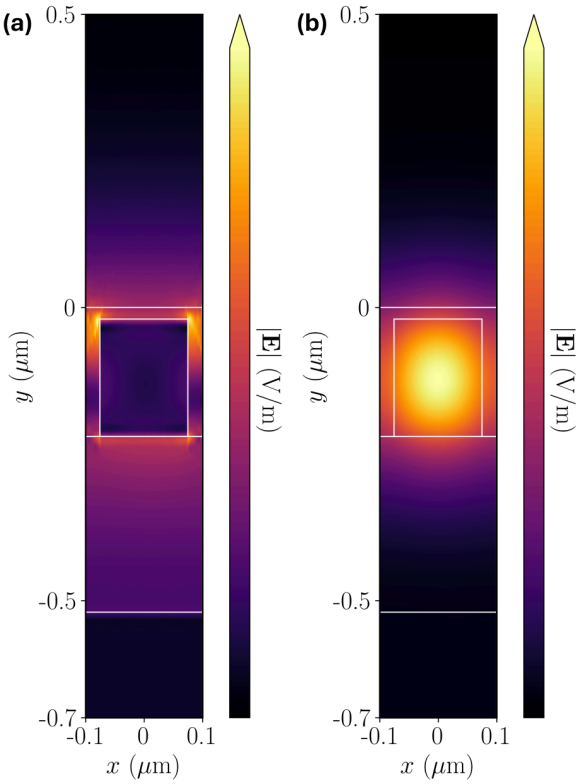

Fig. 3. Electric field norm $|\mathbf{E}|$ distributions (eigenmode analysis). (a) TM mode at 258 THz: The field is concentrated in the chiral layer with corner effects at the Si grating edges. (b) TE mode at 222 THz: The field is strongly confined inside the high-index Si tooth, with an exponential decay into the chiral layer beneath.

IV. Conclusion

We have numerically demonstrated a novel approach to tailor the spectrum and polarization of Smith-Purcell radiation by integrating chiral media into dielectric gratings. Our results show that the magnetoelectric coupling in a chiral layer enables the excitation of a sharp quasi-TE-polarized resonance forbidden in standard achiral geometries. This hybridization mechanism offers a new degree of freedom for free-electron photonics, paving the way for tunable, compact light sources in the terahertz and optical regimes.

Acknowledgments

This work was supported by the FRS-FNRS.

References

[1] S. J. Smith and E. M. Purcell, "Visible Light from Localized Surface Charges Moving across a Grating," *Phys. Rev.*, vol. 92, p. 1069, 1953.
[2] Y. Yang *et al.*, "Maximal spontaneous photon emission and energy loss from free electrons," *Nature Physics*, vol. 14, no. 9, p. 894, 2018.

[3] X. Zhang *et al.*, "Electron-beam-driven anomalous Doppler effects in Smith–Purcell radiation," *Photonics Research*, vol. 12, no. 1, p. 78, 2024.
[4] T. Delplace, I. Bouanati, G. Rosolen, and B. Maes, "Directional Smith-Purcell radiation via coupled high-index gratings," *Optics Express*, vol. 34, p. 2450, 2026.
[5] D. L. Jaggard, A. R. Mickelson, and C. H. Papas, "On electromagnetic waves in chiral media," *Applied Physics*, vol. 18, no. 2, pp. 211–216, 1979.
[6] H.-Y. Wu and F. Vollmer, "Coherent multipolar amplification of chiroptical scattering and absorption from a magnetoelectric nanoparticle," *Communications Physics*, vol. 6, 2023.
[7] A. Szczepkowicz, L. Schächter, and R. J. England, "Frequency-domain calculation of Smith–Purcell radiation for metallic and dielectric gratings," *Applied Optics*, vol. 59, no. 35, p. 11146, 2020.

Experimental Study of Mechanically Graded Tensegrity-Inspired Cellular Metamaterials

Anna Al Sabouni-Zawadzka[1,*], Adam Zawadzki[2], Wojciech Gilewski[1], Maciej Kołodziejczak[1]

[1]Faculty of Civil Engineering, Warsaw University of Technology, Poland
[2]Faculty of Automotive and Construction Machinery Engineering, Warsaw University of Technology, Poland
*Corresponding author: anna.zawadzka@pw.edu.pl

***Abstract*—This paper presents an experimental study of graded tensegrity-inspired metamaterials fabricated by additive manufacturing. Compression tests are performed under uniform and concentrated loads on simplex- and expanded octahedron-based lattices to demonstrate the influence of unit cell topology and cell gradation on their mechanical behaviour.**

***Keywords*— tensegrity, cellular metamaterials, additive manufacturing, graded materials.**

I. Introduction

Mechanical metamaterials derive their unusual and highly tunable behaviour from their internal architecture, enabling functionalities that are not attainable in conventional materials. In particular, lattice-based structures allow for the control of stiffness, load-bearing capacity, deformation modes, and the spatial distribution of mechanically stable regions through appropriate design and arrangement of unit cells [1].

Among the various design strategies, tensegrity-inspired lattices provide a compelling framework. Their mechanical response originates from infinitesimal mechanisms stabilised by self-stress states, which enable pronounced nonlinearity and strong sensitivity to geometric modifications [2]. Recent advances in additive manufacturing (AM) have made it possible to fabricate such architectures with rigid joints, while still retaining key features of ideal tensegrity systems [3], [4], [5].

Building on previous experimental and computational studies on two-dimensional (2D) tensegrity-inspired lattices with graded architectures [6], the present work extends these concepts to three-dimensional (3D) systems. The paper focuses on experimental investigation of additively manufactured 3D tensegrity-inspired metamaterials, with emphasis on the influence of gradation on stiffness, load-bearing capacity, and deformation modes. By systematically testing assemblies with varying geometry of unit cells and their arrangement, this study provides experimental information on the mechanical properties of 3D graded tensegrity-inspired metamaterials.

II. Methods

Tensegrity-inspired metamaterials considered in this paper are based on two different unit cells, whose geometry corresponds to that of two basic tensegrity modules: a four-bar simplex and an expanded octahedron. Using these modules, five different configurations of 3D lattices were designed for experimental testing:

- M.sim4.1.uni (Figure 1a) – regular simplex-based lattice,
- M.sim4.1.gra2 (Figure 1b) – graded simplex-based lattice with enhanced cells under concentrated load,
- M.oct1.1.uni (Figure 1c) – regular expanded octahedron-based lattice,
- M.oct1.1.gra1 (Figure 1d) – graded expanded octahedron-based lattice with enhanced lower and upper layers,
- M.oct1.1.gra2 (Figure 1e) – graded expanded octahedron-based lattice with enhanced cells under concentrated load.

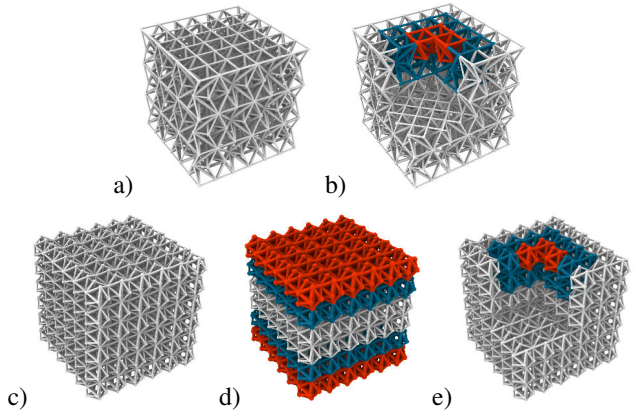

Fig. 1. 3D lattices: a) M.sim4.1.uni; b) M.sim4.1.gra2; c) M.oct1.1.uni; d) M.oct1.1.gra1; e) M.oct1.1.gra2. In b) and e) 1/8 of the model removed to show centric gradation inside the lattice.

All lattices were fabricated by AM using a ProJet® MJP 2500 Plus system (3D Systems). The used MultiJet Printing (MJP) process, which originates from inkjet-based technologies, builds parts by sequentially depositing layers of a UV-curable polymer together with a sacrificial wax support material. This manufacturing route is well suited for tensegrity-like architectures, as the supporting wax can be removed through thermal treatment, enabling effective cleaning of complex and slender structural features without inducing damage.

All specimens were produced using VisiJet® M2R-WT resin. According to the manufacturer's datasheet, the material exhibits a tensile modulus of 2000 MPa, a tensile strength of 39 MPa, and an elongation at break of 20%, determined following the ASTM D638 standard.

Mechanical testing was performed under uniaxial compression using an INSTRON 5567 universal testing machine fitted

with an INSTRON 2525-816 load cell with an accuracy of 0.5 N. The experimental setup is shown in Figure 2. All tests were carried out under displacement-controlled conditions at a constant velocity of 5 mm/min, with the applied force continuously recorded throughout the loading process. Two types of tests were performed: under uniform compression and under concentrated force. The concentrated load was realised using a small cube attached to the loading plate, which allowed the force to be applied to the central nodes of the upper face of the specimen.

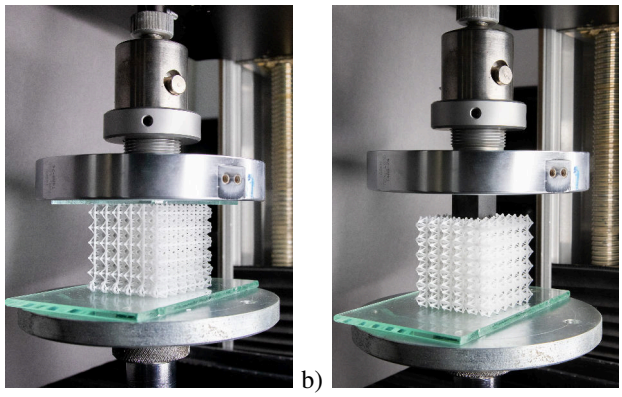

Fig. 2. Experimental setup: a) Expanded octahedron-based lattice under uniform load; b) Expanded octahedron-based lattice under concentrated load.

III. Results and Discussion

The results of the compression tests performed on regular lattices are presented in Figure 3 (each graph represents a mean curve obtained from five specimens), and the deformation of two selected expanded octahedron-based lattices is shown in Figure 4.

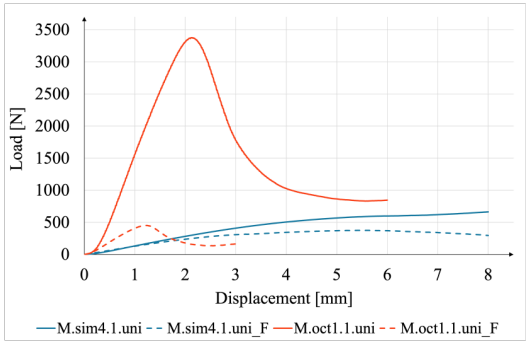

Fig. 3. Force-displacement graphs obtained for regular simplex and expanded octahedron-based lattices under uniform (continuous lines) and concentrated (dashed lines) load.

The expanded octahedron-based lattice exhibits significantly higher initial stiffness and load-bearing capacity under both the uniform and the concentrated load, followed by a sudden drop, which is caused by the loss of stability in two bottom or upper layers (uniform load) or localised damage in the centre of the upper layer (concentrated load). In contrast, the simplex-based lattice shows a more gradual increase in load, reflecting a more distributed deformation process, typical for soft metamaterials.

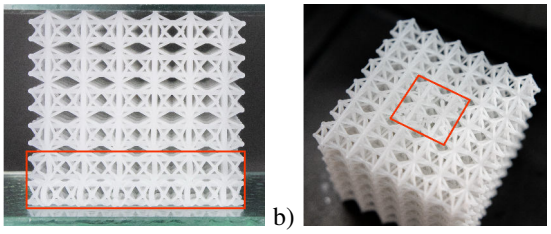

Fig. 4. Deformation of expanded octahedron-based lattices: a) under uniform load; b) under concentrated load. Areas with max. deformation marked in red.

Based on the results of compression tests performed on regular lattices, recommendations for designing graded metamaterials were made: two types of gradations in the expanded octahedron-based lattice and one in the simplex-based one (see Figure 1). The layer gradation in the simplex-based lattice subjected to uniform loading was not considered due to its uniformly distributed deformation – in this case, the gradation would not improve the mechanical behaviour of the structure.

IV. Conclusion

This study focused on the experimental investigation of mechanically graded tensegrity-inspired metamaterials fabricated by AM. Compression tests performed under uniform and concentrated loading conditions demonstrated that the mechanical response of the lattices is strongly governed by the unit cell topology. Expanded octahedron-based lattices exhibited high initial stiffness and load-bearing capacity, while simplex-based lattices showed a more progressive and distributed deformation response. Based on the observed behaviour of the regular lattices, mechanically graded configurations were designed to enhance performance under specific loading scenarios.

Acknowledgments

This research was funded in whole by National Science Centre, Poland, grant no. 2022/47/D/ST8/00466. For the purpose of Open Access, the author has applied a CC-BY public copyright licence to any Author Accepted Manuscript (AAM) version arising from this submission.

References

[1] J. U. Surjadi, L. Gao, H. Du, X. Li, X. Xiong, N. X. Fang, and Y. Lu, "Mechanical metamaterials and their engineering applications," *Advanced Engineering Materials*, vol. 21, no. 3, 2019.
[2] R. Skelton and M. Oliveira, *Tensegrity Systems*. Springer, 2009.
[3] Z. Vangelatos, A. Micheletti, C. P. Grigoropoulos, and F. Fraternali, "Design and testing of bistable lattices with tensegrity architecture and nanoscale features fabricated by multiphoton lithography," *Nanomaterials*, vol. 10, no. 4, 2020.
[4] H. Zeng, R. Mu, K. Huo, H. Zhao, K. Wang, and A. Wang, "A novel 3D-printable tensegrity-inspired metamaterial enabling dynamic attenuation," *International Journal of Mechanics and Materials in Design*, vol. 19, 2023.
[5] A. Al Sabouni-Zawadzka, A. Micheletti, M. Kołodziejczak, and A. Zawadzki, "Design and fabrication of modular tensegrity-like lattices with auxetic properties," *Materials & Design*, vol. 258, 2025.
[6] W. Gilewski, A. Zawadzki, M. Thammavong, and A. Al Sabouni-Zawadzka, "2D graded tensegrity-inspired metamaterials with hexagonal cells fabricated via additive manufacturing," *2D Materials*, vol. 12, 2025.

Dynamical superradiance in vibrationally dressed molecules

Lukas Freter[1,*], Piper Fowler-Wright[2], Javier Cuerda[1,3], Brendon Lovett[2], Jonathan Keeling[2], Päivi Törmä[1]

[1]Department of Applied Physics, Aalto University, Finland
[2]SUPA, School of Physics and Astronomy, University of St Andrews, UK
[3]Institute for Applied Physics, TU Darmstadt, Germany
*Corresponding author: lukas.freter@aalto.fi

***Abstract*—We study dynamical superradiance—the collective oscillation of energy between a cavity mode and emitters—in organic materials by solving the open Holstein-Tavis-Cummings model in the mean-field approximation. We show that superradiance survives for small vibrational coupling, and that for negative cavity detunings, vibrational coupling may even enhance superradiance.**

***Keywords*— vibrational coupling, strong light-matter coupling, cavity quantum electrodynamics, open quantum systems.**

I. Introduction

Superradiance, as first introduced by Dicke in 1954 [1], refers to the collective spontaneous emission of N closely spaced two-level systems in free space. One of the defining features of superradiance is the scaling of the peak emission rate as N^2, compared to N in the case of independent emitters. While in the original superradiance the emitters are in free space and interact with a continuum of electromagnetic modes, related phenomena also exist for emitters inside a cavity. One such phenomenon is termed dynamical superradiance—the subject of this paper—which describes the collective oscillation of energy between N initially excited emitters and the cavity mode. Dynamical superradiance is well understood if the emitters are treated as ideal two-level systems. In that case, the system is well described by the Tavis-Cummings model, and semi-analytical solutions in the large N limit predict that the photon number displays a train of hyperbolic secant pulses [2].

The two-level system approximation, however, does not hold in the case of organic molecules, where electronic degrees of freedom couple to vibrational modes of the molecule. In this work, we study dynamical superradiance in vibrationally dressed molecules using the open Holstein-Tavis-Cummings (HTC) model [3]. In Ref. [4], it was demonstrated that the open HTC model, when starting from a state with some initial coherence (i.e., a superradiant initial state), can be solved using mean-field theory. We show that the cavity detuning has a significant effect on the superradiant dynamics. Namely, for negative detunings, the superradiant photon emission is enhanced by including vibrational coupling, whereas for positive detunings, the photon emission is inhibited.

II. Methods

We consider a collection of N vibrationally dressed two-level systems coupled to a single cavity mode, which can be described with the HTC Hamiltonian ($\hbar = 1$)

$$\hat{H} = \omega_c \hat{a}^\dagger \hat{a} + \sum_{i=1}^{N} \Big[\frac{\omega_0}{2} \hat{\sigma}_i^z + g(\hat{a}\hat{\sigma}_i^+ + \hat{a}^\dagger \hat{\sigma}_i^-) + \omega_\nu \hat{b}_i^\dagger \hat{b}_i + \omega_\nu \sqrt{S}(\hat{b}_i + \hat{b}_i^\dagger)\hat{\sigma}_i^z \Big]. \quad (1)$$

Here, $\hat{a}$ and $\hat{a}^\dagger$ are the bosonic operators of the cavity mode with frequency ω_c, $\hat{\sigma}_i^{\pm,z}$ are the Pauli matrices describing the ith emitter satisfying $[\hat{\sigma}_i^z, \hat{\sigma}_j^\pm] = \pm 2\delta_{ij}\hat{\sigma}_i^\pm$, and $\hat{b}_i$ and $\hat{b}_i^\dagger$ are the bosonic operators for the vibrational mode of the ith emitter with frequency ω_ν. The vibrational coupling is determined by the Huang-Rhys parameter S, and g is the light-matter coupling constant. For $S = 0$, Eq. (1) reduces to the Tavis-Cummings model.

We include dissipation processes via a Gorini-Kossakowski-Sudarshan-Lindblad master equation for the density matrix ρ

$$\partial_t \rho = -\mathrm{i}[\hat{H} + \hat{H}_{\mathrm{LS}}, \rho] + \kappa \mathcal{L}[\hat{a}] + \sum_{i=1}^{N} \big(\gamma \mathcal{L}[\hat{\sigma}_i^-] + \gamma_\uparrow \mathcal{L}[\hat{b}_i^\dagger] + \gamma_\downarrow \mathcal{L}[\hat{b}_i] \big), \quad (2)$$

where $\mathcal{L}[\hat{X}] = \hat{X}\rho\hat{X}^\dagger - \{\hat{X}^\dagger\hat{X}, \rho\}/2$. The rate κ describes the loss of photons from the cavity mode, γ describes the individual loss of molecular excitations, and $\gamma_\uparrow = \gamma_\nu n_B, \gamma_\downarrow = \gamma_\nu(n_B + 1)$ are thermalization rates of the vibrations at a temperature T given by the mean phonon occupation number $n_B = (\mathrm{e}^{\omega_\nu/T} - 1)^{-1}$ (we set $k_B = 1$). The Lamb-shift term $\hat{H}_{\mathrm{LS}} = \mathrm{i}(\gamma_\nu/4)\sum_{i=1}^{N}(\hat{b}_i^\dagger \hat{b}_i^\dagger - \hat{b}_i \hat{b}_i)$ is included to introduce damping through the momentum coordinate [5].

We are interested in the dynamics starting from an initial state

$$\rho(0) = |\psi(\theta)\rangle\langle\psi(\theta)| \bigotimes_{i=1}^{N} \rho_{\mathrm{vib},i}, \quad (3)$$

where $|\psi(\theta)\rangle = |0\rangle \otimes \Big(\bigotimes_{i=1}^{N} \mathrm{e}^{-\mathrm{i}\theta\hat{\sigma}_i^x/2} |\uparrow\rangle_i \Big)$ and $\rho_{\mathrm{vib},i} = (1 - \mathrm{e}^{-\omega_\nu/T})\mathrm{e}^{-\omega_\nu \hat{b}_i^\dagger \hat{b}_i/T}$ ($k_B = 1$). At $t = 0$, there are zero photons

in the cavity mode, and the two-level systems are in an excited state (denoted by $|\uparrow\rangle_i$ for the ith emitter), which is coherently tilted by an angle θ. We term states with $\theta \neq 0$ superradiant initial states due to the initial coherence in the system, whereas states with $\theta = 0$ are termed superfluorescent. In the following, we solve Eqs. (1) and (3) for different values of vibrational coupling S and cavity detuning $\Delta = \omega_c - \omega_0$ using mean-field theory. We stress that we treat the vibrationally dressed emitters as $2N_\nu$-level systems, where N_ν is the number of vibrational levels included in the model; i.e., correlations between the electronic degrees of freedom and the vibrational mode are retained.

III. Results and Discussion

In Fig. 1, we show the numerical results for the average number of photons in the cavity mode obtained from mean-field theory for different values of S. All calculations were performed using the *QuantumCumulants.jl* package [6]. In Fig. 1(a), the cavity detuning is negative, whereas in Fig. 1(b) it is positive. All other parameters are given in the figure caption. The coupling to the vibrations enhances (inhibits) the dynamical superradiance for negative (positive) cavity detuning, which is evident from the fact that the number of photons in Fig. 1(a) increases with increasing S, while in Fig. 1(b) it decreases with increasing S.

To get an idea of the role the vibrations play in the emission process, we calculate the occupation of the νth energy level of the vibrational mode conditioned on the emitter being in the electronic ground state

$$p_\nu^{(g)} = \frac{\langle\downarrow,\nu|\,\rho_m\,|\downarrow,\nu\rangle}{\sum_\nu \langle\downarrow,\nu|\,\rho_m\,|\downarrow,\nu\rangle}, \tag{4}$$

where ρ_m is the reduced density matrix of a single emitter, which includes the electronic and vibrational degrees of freedom. In Fig. 2, we show the occupation for the ground state and the first five excited states of the phonon mode, conditioned on the emitter being in the electronic ground state. For $\Delta = -0.3\,\mathrm{eV}$, the probability of one or more phonons in the electronic ground state is significantly larger compared to $\Delta = 0.3\,\mathrm{eV}$, in which case almost exclusively the ground mode with zero phonons is occupied. This can be explained by the fact that for negative cavity detuning, the cavity frequency $\omega_c = \omega_0 + \Delta$ is smaller than the two-level system energy splitting. It is therefore more favorable for the molecule to undergo a transition from the excited-state manifold with zero phonons to the ground-state manifold with phonons.

IV. Conclusion

We have developed the theory of dynamical superradiance in organic materials, where electronic degrees of freedom couple to vibrational modes of the molecules. To model the many-emitter–cavity system, we have employed the Holstein-Tavis-Cummings Hamiltonian, which includes one vibrational mode per molecule, and added dissipative processes using a Gorini-Kossakowski-Sudarshan-Lindblad master equation. For superradiance initial conditions, mean-field theory is applicable, which allowed us to numerically solve the dynamics for a macroscopic number of molecules. We have shown that dynamical superradiance is possible for small vibrational couplings. If the cavity detuning is negative, vibrational coupling can even enhance the superradiant emission. For positive detunings, the opposite is the case, and superradiance is inhibited. The cavity detuning is an experimentally tunable quantity, which makes our findings experimentally accessible.

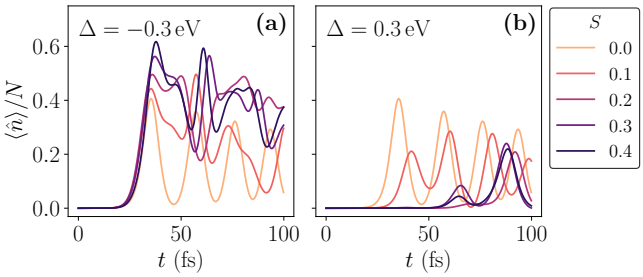

Fig. 1. Average number of photons in the cavity mode for different values of S obtained from mean-field theory. (a): $\Delta = -0.3\,\mathrm{eV}$, (b): $\Delta = 0.3\,\mathrm{eV}$. Other parameters: $g\sqrt{N} = 0.2\,\mathrm{eV}$, $\kappa = 0.01\,\mathrm{eV}$, $\gamma = 10^{-6}\,\mathrm{eV}$, $\omega_\nu = 0.15\,\mathrm{eV}$, $\gamma_\nu = 0.01\,\mathrm{eV}$, $\theta = 0.001\pi$, $T = 0.026\,\mathrm{eV}$.

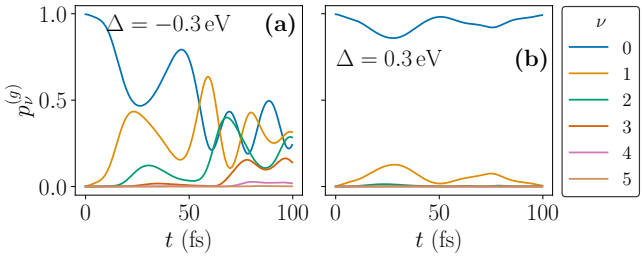

Fig. 2. Conditional probability for the phonon mode to be in the energy eigenstate ν given that the molecule is in the electronic ground state. (a): $\Delta = -0.3\,\mathrm{eV}$, (b): $\Delta = 0.3\,\mathrm{eV}$. Other parameters: $g\sqrt{N} = 0.2\,\mathrm{eV}$, $\kappa = 0.01\,\mathrm{eV}$, $\gamma = 10^{-6}\,\mathrm{eV}$, $\omega_\nu = 0.15\,\mathrm{eV}$, $\gamma_\nu = 0.01\,\mathrm{eV}$, $\theta = 0.001\pi$, $T = 0.026\,\mathrm{eV}$.

Acknowledgments

This work was supported by the Research Council of Finland under project number 339313, and by the Jane and Aatos Erkko Foundation. The work is part of the Research Council of Finland Flagship Programme, Photonics Research and Innovation (PREIN), decision number 346529, Aalto University.

References

[1] R. H. Dicke, "Coherence in spontaneous radiation processes," *Phys. Rev.*, vol. 93, pp. 99–110, 1954.
[2] R. Bonifacio and G. Preparata, "Coherent spontaneous emission," *Phys. Rev. A*, vol. 2, pp. 336–347, 1970.
[3] J. Roden, W. T. Strunz, K. B. Whaley, and A. Eisfeld, "Accounting for intra-molecular vibrational modes in open quantum system description of molecular systems," *J. Chem. Phys.*, vol. 137, p. 204110, 2012.
[4] L. Freter, P. Fowler-Wright, J. Cuerda, B. W. Lovett, J. Keeling, and P. Törmä, "Theory of dynamical superradiance in organic materials," *Nanophotonics*, vol. 14, pp. 5323–5336, 2025.

[5] J. R. Mannouch, W. Barford, and S. Al-Assam, "Ultra-fast relaxation, decoherence, and localization of photoexcited states in π-conjugated polymers," *J. Chem. Phys.*, vol. 148, p. 034901, 2018.
[6] D. Plankensteiner, C. Hotter, and H. Ritsch, "QuantumCumulants.jl: A Julia framework for generalized mean-field equations in open quantum systems," *Quantum*, vol. 6, p. 617, 2022.

Surface-Enhanced Raman Spectroscopic Observation of SuFEx Processes at Metal Surfaces

Aleksandra Miszczak[1], Justyna Grzęda[1], Hubert Sobiech[1], Jan Dudziński[1], Michał Barbasiewicz[1], Andrzej Kudelski[1], Aleksandra Szaniawska[1]*

[1]Faculty of Chemistry, University of Warsaw, Pasteura 1 Str., 02-093 Warsaw, Poland
*Corresponding author: aleksandra.szaniawska@uw.edu.pl

***Abstract*— Surface-enhanced Raman spectroscopy (SERS) was applied to investigate sulfur (VI) fluoride exchange reactions at metal–solution interfaces. The study demonstrates that SERS enables monitoring of click reaction, close proximity of metal surface does not significantly change the reaction and elegantly shows that structural changes of adsorbate influence their orientation on metal.**

***Keywords*—surface enhanced Raman spectroscopy, sulfur fluoride exchange, click chemistry, metal interfaces, adsorption geometry.**

I. Introduction

Sulfur fluoride exchange reactions have emerged as a robust and selective click chemistry platform for modular molecular construction in materials science and chemical biology. Their operational simplicity, tolerance to functional groups and predictable reactivity make them attractive for surface functionalization and interfacial chemistry.

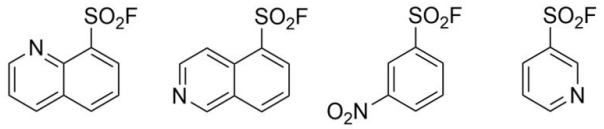

Fig.1 Structers of sulfonyl fluorides investigates in this study (8-quinolinesulfonyl fluoride, 5-isoquinolinesulfonyl fluoride, 3-nitrobenzenesulfonyl fluoride, 3-pyridinesulfonyl fluoride).

At the same time, metal nanostructures and plasmonic substrates provide unique opportunities for real time molecular characterization through surface enhanced Raman spectroscopy (SERS). SERS combines chemical specificity with extreme surface sensitivity and is therefore particularly suited for studying reactions occurring within the first molecular layer at metal solution interfaces.

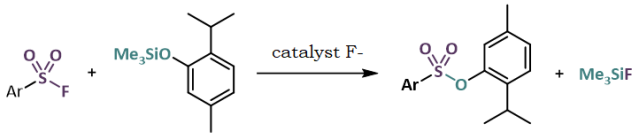

Fig.2 Scheme of the click reaction from this study.

Adsorption on metal surfaces induces specific orientation of reactants. Therefore, an important open question remains whether the close proximity of a plasmonic metal surface perturbs the intrinsic reactivity of sulfur fluoride exchange systems. In this work, we address this issue by systematically investigating sequential adsorption and reaction of sulfonyl fluoride derivatives with silyl protected phenolic substrates on silver electrodes.

II. Methods

Surface enhanced Raman spectra were recorded on electrochemically prepared silver substrates immersed in acetonitrile solutions. A heteroaromatic sulfonyl fluoride served as the electrophilic component (experiments have been performed for: 8-quinolinesulfonyl fluoride, 5-isoquinolinesulfonyl fluoride, 3-nitrobenzenesulfonyl fluoride, 3-pyridinesulfonyl fluoride). The nucleophilic partner was a silyl protected phenolic derivative (thymol trimethylsilyl ether, TMS-thymol). Tetrabutylammonium bifluoride was used as catalyst.

Sequential adsorption experiments were designed to separate adsorption phenomena from chemical transformation. The silver electrode was first exposed to the sulfonyl fluoride, rinsed with solvent and measured. Subsequently, the same surface was immersed either in the phenolic substrate solution or in the substrate solution containing catalyst. For reference, the isolated reaction product was independently synthesized and measured under identical SERS conditions.

To support assignments of Raman bands, density functional theory calculations were performed for the sulfonyl fluoride and reaction products. Geometry optimizations were carried out to determine energetically favorable conformations. Harmonic vibrational frequency calculations were then used to predict Raman active modes and corresponding band positions. Calculated frequencies were scaled and compared with experimental spectra to facilitate reliable assignment of characteristic vibrations, particularly in the fingerprint region and in modes associated with sulfur oxygen stretching and aromatic ring deformations.

III. Results and Discussion

The SERS spectrum of the adsorbed sulfonyl fluoride displayed distinct aromatic ring modes and characteristic vibrations related to the sulfur functional group. After solvent rinsing, these features remained stable, indicating strong adsorption on silver.

Upon exposure to the phenolic substrate, subtle but reproducible changes in selected fingerprint bands were observed (examples of spectral changes observed during the reaction of 5-isoquinolinesulfonyl fluoride and TMS-thymol are shown in Fig.1). Although the dominant sulfonyl fluoride features persisted, relative intensity variations suggested modification of adsorption geometry or local environment due to co adsorption.

Addition of catalyst resulted in the appearance of new spectral contributions that could not be described as a simple superposition of individual component spectra. Comparison with the SERS spectrum of the independently prepared product confirmed the formation of the sulfur fluoride exchange product at or near the metal interface.

The DFT calculated geometries provided insight into conformational preferences of both reactant and product when they do not interact with other molecules. Simulated Raman spectra reproduced the main experimental band positions and enabled assignment of key vibrational modes. In particular, calculated frequency shifts associated with transformation of the sulfonyl fluoride group to the sulfonate product were consistent with experimentally observed changes. This agreement supports the conclusion that the intrinsic reaction pathway is preserved in the vicinity of the metal surface.

At the same time, intensity differences between experimental and calculated spectra indicate that adsorption geometry plays a significant role in SERS enhancement. Structural conversion alters electron distribution and available coordination sites, leading to reorientation of the aromatic framework relative to the silver surface. These orientation effects are directly reflected in the relative enhancement of selected vibrational modes.

Overall, the combined experimental and theoretical approach allows discrimination between mere adsorption, co adsorption and true chemical conversion at the interface.

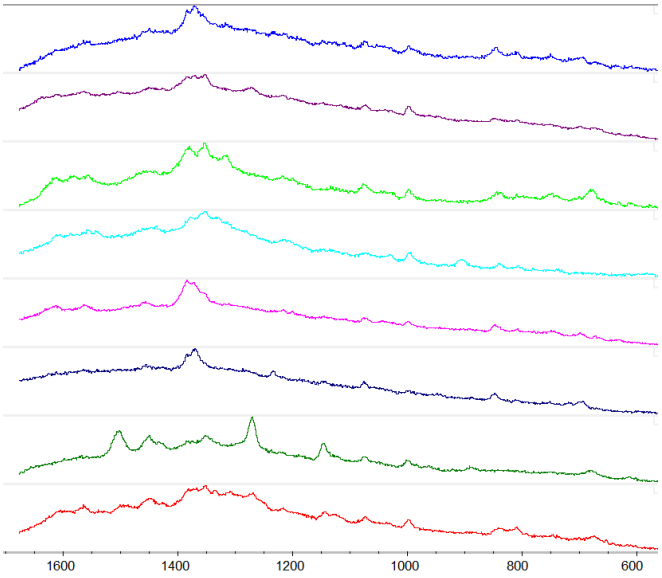

Fig. 3 SERS spectra of (from top to bottom): fluoride, fluoride + catalyst, fluoride + nucleophile, fluoride + catalyst + nucleophile, catalyst, final product, nucleophile, nucleophile + catalyst adsorbed on Ag electrode. As fluoride 5-isoquinolinesulfonyl fluoride was used, as nucleophile TMS-thymol, as catalyst - tetrabutylamonium bifluoride.

IV. Conclusion

Surface enhanced Raman spectroscopy combined with density functional theory provides a robust framework for investigating sulfur fluoride exchange reactions at metal solution interfaces. The results demonstrate that the reaction proceeds without fundamental alteration of its intrinsic pathway in the presence of silver. Structural transformation is accompanied by adsorption induced reorientation, which is reflected in characteristic spectral changes. The study highlights the value of integrating SERS and quantum chemical calculations for mechanistic analysis of interfacial click chemistry.

Acknowledgments

This work was supported by the Faculty of Chemistry, University of Warsaw.

References

[1] Jeremy Yatvin, Karson Brooks, Prof. Jason Locklin, “SuFEx on the Surface: A Flexible Platform for Postpolymerization Modification of Polymer Brushes”, Angew. Chem. Int. Ed, 2015, 54, 13370 –13373

[2] Dr. Jiajia Dong, Dr. Larissa Krasnova, Prof. M. G. Finn, Prof. K. Barry Sharpless, “Sulfur(VI) Fluoride Exchange (SuFEx): Another Good Reaction for Click Chemistry”, Angew. Chem. Int. Ed. 2014, 53, 9430 – 9448

Flat band Engineering in Polymer Acoustic Lieb Lattices

Anusha Rehman[1*], Riccardo C. Moroni[4], David Hutchins[1], Peter J. Thomas[1], Rudolf Roemer[2], Katarzyna Majewska[4], Stefano Laureti[3]

[1] School of Engineering, University of Warwick, UK
[2]Dept. of Physics, University of Warwick, UK
[3]DIMES Dept., University of Calabria, ITALY
[4]Institute of Fluid-Flow Machinery Polish Academy of Sciences, POLAND
*Corresponding author: anusha.rehman@warwick.ac.uk

***Abstract*— Flat band acoustic metamaterials enable interference-driven wave localization. Building on polymer Lieb lattices operating in the ultrasonic regime, a predictive scaling formulation for band tuning has been designed, together with extended Lieb architectures supporting multiple flat bands. Mechanically reconfigurable auxetic–Lieb structures are also demonstrated. These approaches provide scalable and tunable platforms for multi-frequency acoustic localization.**

***Keywords*— metamaterials, Lieb lattices, auxetic materials, phononic crystals.**

I. Introduction

Flat bands in periodic lattices provide a mechanism for wave localization governed by geometry and interference rather than material contrast. They arise from compact localized states (CLSs) [1], as can be seen readily within the tight-binding (TB) framework [2]. For such CLSs, destructive interference between hopping paths confines eigenstates to a small cluster of sites. This interference-driven confinement enables deterministic control of wave transport and spectral response in engineered acoustic metamaterials and phononic crystals [3,4].

In recent work [5] experimentally accessible polymer-based acoustic Lieb lattices operating in the sub-MHz ultrasonic regime were demonstrated, where site-selective vibrational enhancement consistent with flat-band behavior was observed. However, systematic frequency tuning, realization of multiple flat bands within a single structure, and dynamic reconfigurability remain open challenges. In this work, we establish a unified framework that combines predictive geometric scaling, extended Lieb architectures supporting multiple flat bands, and mechanically induced topological transformation through auxetic metamaterials. Together, these developments advance flat-band acoustic systems from static realizations toward scalable and tunable wave-engineering platforms.

II. Methods

A. Predictive Scaling Formulation

In a Cartesian coordinate system with coordinates x^*, y^*, z^* the problem is governed by the time-independent wave equation, known as the Helmholtz equation. The Helmholtz equation is given by[1] [6]:

$$\frac{\partial^2 p^*}{\partial x^{*2}} + \frac{\partial^2 p^*}{\partial y^{*2}} - k^{*2} p = 0 \quad (1)$$

where $p^* = p^*(x^*, y^*, z^*, \lambda^*)$ represents the sound pressure, and k^* is the wave vector defined as $2\pi/\lambda^*$. The wavelength of the mode is λ^*, with an associated frequency f^* in a material that has a speed of sound c^*.

To reveal the geometric scaling behavior of the system, we nondimensionalize the spatial coordinates using a characteristic lattice length L_1^*:

$$x = \frac{x^*}{L_1^*}, y = \frac{y^*}{L_1^*} \text{ and } z = \frac{z^*}{L_1^*} \quad (2)$$

and define the reduced frequency

$$f = \frac{L_1^* f^*}{c^*} \quad (3)$$

The characteristic lengths L_1, L_2,and L_3correspond to the principal geometric features of the unit cell (Fig. 1(a)), namely the resonator diameter, the connecting strut length, and the junction spacing between neighboring sites. These represent the natural geometric scales governing acoustic coupling in the lattice.

With this formulation, the dispersion relation depends only on geometric ratios rather than absolute dimensions. The frequency therefore becomes a function of nondimensional parameters L_i/L_1, allowing the sensitivity of the spectrum to geometric variations to be expressed as:

$$\frac{df}{dL_1} = \frac{\partial f}{\partial L_1} + \frac{1}{L_1}\left(\frac{\partial f}{\partial L_2}\gamma_2 + \cdots \frac{\partial f}{\partial L_n}\gamma_n\right) \quad (4)$$

where $\gamma_i = L_i^*/L_1^*$ denotes the relative scaling factors i.e. the scaling factors for each length scale, in relation to the primary length scale L_1^*.

[1] The asterisk superscript denotes dimensional quantities. The superscript is dropped for the corresponding nondimensionalized quantities

This scaling formulation allows flat-band frequencies to be predicted directly from geometric parameters. As demonstrated in Fig. 1(b), when the frequency axis is expressed in reduced form, the dispersion relations of two different lattice realizations collapse onto a single curve. The two datasets correspond to previously studied structures [5] denoted D4 and D6, which differ in their lattice dimensions but share identical geometric ratios.

The resulting sensitivity relations provide explicit measures of how each geometric parameter influences the dispersion curves and enable inverse design of lattice dimensions for a desired ultrasonic operating frequency.

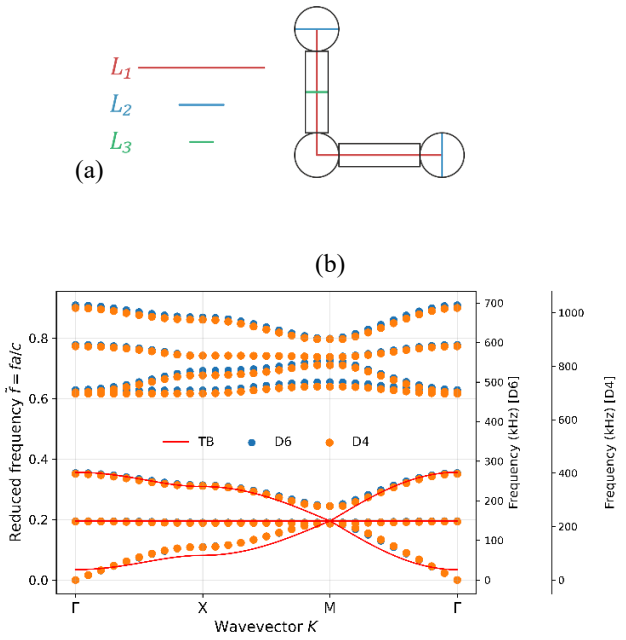

Fig.1 (a) Geometric parameters used in the nondimensional scaling formulation. Three independent characteristic length scales L_1, L_2, and L_3 are defined within the unit-cell geometry. (b) Band structure comparison between the tight-binding (TB) model and finite-element simulations for two lattice designs demonstrating that the dispersion relations of two geometrically scaled structures collapse onto a single reduced-frequency curve.

B. Extended Lieb Architectures

Motivated by this scaling framework, we designed enlarged Lieb unit cells that introduce additional symmetry-equivalent coupling pathways. The corresponding tight-binding description predicts the emergence of additional compact localized states, leading to multiple flat bands in the band structure.

Finite-element simulations were performed to compute the dispersion diagrams. The extended geometries generate several nearly flat bands separated by tunable band gaps. Representative pressure-field distributions for selected modes are shown in Fig. 2(a-b) along with their dispersion diagrams in Fig. 2(c-d), confirming spatial confinement characteristic of CLS behavior.

C. Auxetic–Lieb Transformation

To introduce mechanical reconfigurability, we developed a re-entrant auxetic metamaterial geometry [5] that transforms into a Lieb lattice under uniaxial tensile deformation.

The undeformed configuration, shown in Fig. 3(a), supports conventional dispersive propagation. Upon stretching, the geometry evolves toward Lieb connectivity, as illustrated in Fig. 3(b). Periodic simulations along the deformation direction were used to track the evolution of the band structure.

III. Results and Discussion

The nondimensional scaling formulation demonstrates that flat-band frequencies depend explicitly on geometric ratios, enabling controlled spectral positioning through systematic dimension variation. Numerical evaluation confirms that modest changes in resonator diameter or connection length led to predictable shifts in flat-band frequency without altering the underlying interference mechanism.

Extended Lieb lattices exhibit multiple flat bands within the same structure. The dispersion diagrams in Fig. 2(c–d) show additional flat bands compared to the standard three-site Lieb lattice. In particular, we investigated two extended configurations, denoted Lieb2 and Lieb3, corresponding to unit cells containing five and seven lattice sites, respectively. The tight-binding model predicts that these lattices support multiple compact localized states, leading to the emergence of two flat bands in the Lieb2 lattice and three flat bands in the Lieb3 lattice. For the symmetry-equivalent extended Lieb lattices studied here, the number of flat bands scales with the number of sites in the unit cell. A lattice containing N sites support $N_{FB} = (N-1)/2$ flat bands, corresponding to the number of independent compact localized states formed by destructive interference between the Lieb sublattice sites. The associated pressure distributions in Fig. 2(a-b) reveal distinct compact localized states corresponding to the first flat band of structures Lieb2 and Lieb3 respectively. These results demonstrate that interference-based localization can be engineered simultaneously at multiple frequencies in a single polymer architecture.

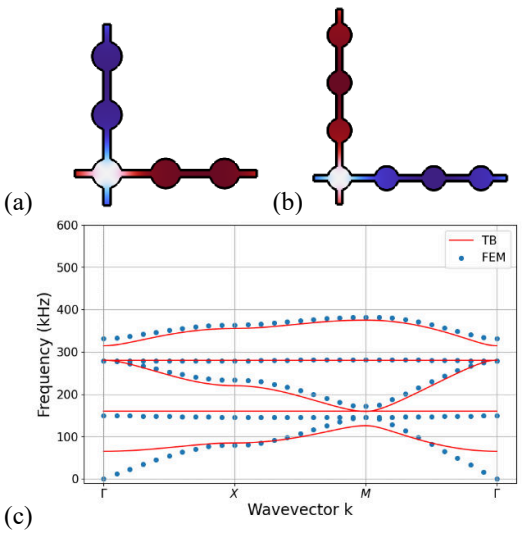

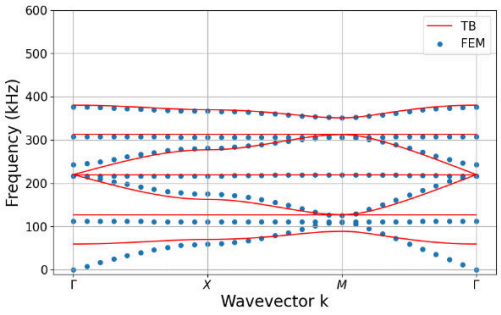

(d)

Fig. 2 (a–b) Unit-cell geometries of the Lieb2 and Lieb3 lattices containing five and seven sites per unit cell, respectively. (c–d) Corresponding dispersion relations obtained from tight-binding (TB) calculations and finite-element method (FEM) simulations.

For the auxetic–Lieb system, simulations reveal a change in the dispersion characteristics of the structure with applied strain. As the lattice is stretched, the negative Poisson-ratio geometry ($\nu \approx -0.5$) causes the internal connections to rotate outward, progressively approaching the orthogonal connectivity characteristic of the Lieb lattice. In our simulations, this configuration emerges at tensile strains of approximately $\varepsilon \approx 0.2$. The pressure fields simultaneously evolve toward compact localized patterns analogous to CLS modes, as shown in Fig. 3(b).

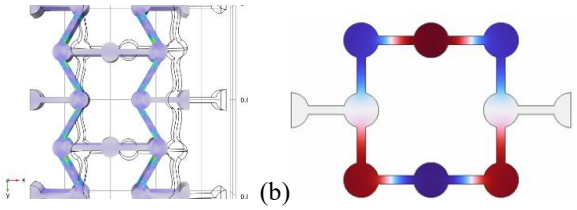

(a) (b)

Fig. 3 Mechanically reconfigurable auxetic–Lieb metamaterial. (a) Re-entrant auxetic lattice undergoing uniaxial tensile deformation. (b) Pressure-field distribution of a representative eigenmode in the deformed configuration, illustrating the emergence of Lieb-like connectivity and compact localized states.

The results establish a coherent strategy for flat-band engineering in acoustic polymer metamaterials. The nondimensional scaling formulation provides predictive frequency control, eliminating trial-and-error geometric tuning. Extended Lieb architecture demonstrates that flat-band localization is not restricted to a single spectral point but can be generalized to multi-band systems through unit-cell enlargement. The integration of auxetic deformation introduces mechanical tunability, enabling strain-controlled activation or modulation of flat-band behavior.

Operating in the sub-MHz ultrasonic regime, these polymer structures remain compatible with standard ultrasonic transducers while offering geometry-driven control of wave localization. The combination of predictive scaling, multi-flat-band realization, and mechanical reconfigurability represents a significant step toward adaptive acoustic devices based purely on structural interference. This unified approach bridges theoretical band engineering and experimentally accessible metamaterial design, opening pathways for tunable energy confinement and frequency-selective wave manipulation.

IV. Conclusion

This work extends polymer acoustic Lieb lattices toward predictive and adaptive flat-band engineering. A nondimensional scaling formulation enables deterministic tuning of flat-band frequencies through geometric parameters. Extended Lieb architectures demonstrate that multiple compact localized states and corresponding flat bands can be realized within a single structure. Furthermore, integrating auxetic geometries introduces mechanical reconfigurability, allowing strain-induced transformation into Lieb-like connectivity and the emergence of flat-band behavior. Together, these results establish a unified framework for geometry-driven acoustic band design, enabling scalable and tunable platforms for multi-frequency localization and adaptive wave control in ultrasonic metamaterials.

Acknowledgments

This project has received funding from the European Union's EU Framework Programme for Research and Innovation Europe Horizon (HORIZON TMA MSCA Doctoral Networks) under Grant Agreement No. 101119738 "MetacMed" (www.metacmed.eu). Views and opinions expressed are, however, those of the author(s) only and do not necessarily reflect those of the European Union. Neither the European Union nor the granting authority can be held responsible for them.

References

[1] D. Leykam, A. Andreanov, S. Flach, Artificial flat band systems: From lattice models to experiments (1 2018). doi:10.1080/23746149.2018.1473052

[2] N. W. Ashcroft, N. D. Mermin, Solid State Physics, Harcourt Brace, 1976..

[3] Wang, Xin-Tao, et al. "Mechanical properties of 3D re-entrant auxetic cellular structures." *International Journal of Mechanical Sciences* 131 (2017): 396-407.

[4] Lice Gao et al., Design and bandgap characteristics of acoustic metamaterials with crystal-like structures, Mechanics of Advanced Materials and Structures 1–13 (2025)

[5] A. Rehman, D.A. Hutchins, P.J. Thomas, R. Römer, K.E. Sopińska, J. Im, P. Sheffield, S. Laureti, An ultrasonic metamaterial based on Lieb lattice structures, International Conference on Metamaterials Photonic Crystals and Plasmonics. 1750-1751 (2025)

[6] Acoustics Module User's Guide, Tech. rep. (1998). URL www.comsol.com/blogs

Self-configuring linear diffractive optical networks for adaptive imaging through multimode fibres

Jérôme A. Don Jayamanne[1]*, José C. A. Rocha[1,2], Unė G. Būtaitė[1], J. Carpenter[2] and D. B. Phillips[1]

[1]Physics and Astronomy, University of Exeter, Exeter, EX4 4QL. UK.
[2]School of Electrical Engineering and Computer Science, The University of Queensland, Brisbane, QLD 4072, Australia
*Corresponding author: j.don-jayamanne@exeter.ac.uk

***Abstract*— When light propagates through complex media, its spatial modes become scrambled, hindering imaging and data transmission. Here we experimentally demonstrate how a linear diffractive optical network can be adaptively trained in-situ to efficiently reverse such scattering across multiple modes simultaneously.**

***Keywords*— diffractive optics, wavefront shaping, complex media, self-configuring**

When light propagates through complex media - such as biological tissue, turbulent air, or multimode optical fibre - the wavefront can be highly distorted, scrambling the spatial information it carries. This scrambling corrupts images and limits data transmission in these environments. Wavefront shaping is a versatile technique capable of reversing such distortions: the wavefront of a single spatial mode of light interacting with the complex medium is reshaped (typically using a spatial light modulator) to turn it back into its original state, thus 'undoing' the medium's effects [1,2]. However, uncorrelated spatial modes require different correction wavefront modulations, which cannot be efficiently multiplexed together onto a single-phase modulating surface. Thus, current wavefront shaping methods are often sequential in nature, dynamically correcting each spatial mode one after the other - and as such are yet to reach the full information capacity of data transmission through complex media.

In order to efficiently unscramble multiple uncorrelated modes at once, a 3D multi-modal beam shaping architecture is required [3,4,5]. In this work we explore how a self-optimising linear diffractive optical network can be used to tackle this problem. Our network consists of a cascade of phase modulating surfaces, each separated by free-space propagation – an optical system known as a multi-plane light converter [6,7,8]. To configure our network, we experimentally demonstrate a new technique we refer to as 'multi-plane wavefront shaping' which jointly optimises the phase profile of all phase planes in the network in-situ, to unscramble multiple different spatial modes simultaneously [4,9].

In our system there are tens of thousands of independently tuneable parameters to configure, so we devise a bespoke algorithm based on the transmission matrix formalism [2], that relies on light solely propagating forward through the device [9]. System convergence is accelerated to a timescale of minutes by constructing the network from a recently developed fast-switching piston-action MEMS phase light modulator operating at kHz rates [10,11] – with scope for substantial reductions in optimization time in the future. Our multi-plane wavefront shaping technique represents a versatile 'model-free' approach to the in-situ training of high-speed free-space linear diffractive optical networks [12], in this case enabling them to begin to adaptively reverse the scattering effects of transmissive complex media they are coupled to.

References

[1] Vellekoop et al. "Focusing coherent light through opaque strongly scattering media." Optics letters 32, no. 16 (2007): 2309-2311.
[2] Popoff et al. "Measuring the Transmission Matrix in Optics: An Approach to the Study and Control of Light Propagation in Disordered Media." Physical Review Letters 104, 10 (2010): 100601.
[3] Būtaitė et al. "How to build the "optical inverse" of a multimode fibre." Intelligent Computing (2022).
[4] Kupianskyi et al. "All-optically untangling light propagation through multimode fibers." Optica 11, no. 1 (2024): 101-112.
[5] SeyedinNavadeh et al. "Determining the optimal communication channels of arbitrary optical systems using integrated photonic processors." Nature Photonics 18, no. 2 (2024): 149-155.
[6] Labroille et al. "Efficient and mode selective spatial mode multiplexer based on multi-plane light conversion." Optics Express 22, no. 13 (2014): 15599-15607.
[7] Fontaine et al. "Laguerre-Gaussian mode sorter." Nature Communications 10, no. 1 (2019): 1865.
[8] Lin et al. "All-optical machine learning using diffractive deep neural networks." Science 361, no. 6406 (2018): 1004-1008.
[9] Rocha et al. "Self-configuring high-speed multi-plane light conversion." Nature Communications 17(73) (2025).
[10] Byrum et al. "Optimizing a micro-electro-mechanical system (MEMS) based phase-only light modulator (plm) for improved system performance." In Emerging Digital Micromirror Device Based Systems and Applications XVI, vol. 12900, SPIE, 2024.
[11] Rocha et al. "Fast and light-efficient wavefront shaping with a MEMS phase-only light modulator." Optics Express 32, no. 24 (2024): 43300-43314.

[12] Momeniet al. "Training of physical neural networks." Nature 645, no. 8079 (2025): 53-61.

Free-Electron Coupling to Surface Polaritons Mediated by Small Scatterers

Leila Prelat[1,*], Eduardo J. C. Dias[2], F. Javier García de Abajo[1,3]

[1] ICFO–Institut de Ciencies Fotoniques, The Barcelona Institute of Science and Technology, Barcelona, Spain
[2] POLIMA–Center for Polariton-driven Light–Matter Interactions, University of Southern Denmark, Odense, Denmark
[3] ICREA–Institució Catalana de Recerca i Estudis Avançats, Barcelona, Spain
*Corresponding author: leilaprelat@gmail.com

***Abstract*—We show that small scatterers enable low-energy electrons to excite surface polaritons even when direct coupling is kinematically forbidden. Maximum emission occurs at an optimum scatterer–surface distance, while periodic arrays produce directional polaritonic Smith–Purcell emission. Hexagonal boron nitride disks provide a practical route to spectrally selective excitation of graphene plasmons.**

***Keywords*— surface polaritons, free electrons, graphene plasmons, hexagonal boron nitride, dipolar scatterers, Smith–Purcell emission.**

I. Introduction

Surface polaritons (SPs) enable deep-subwavelength confinement and large near-field enhancement, making them attractive for nanoscale photonics, spectroscopy, and strong light–matter interactions [1]. However, their large in-plane momenta prevent direct far-field excitation. Free electrons offer a natural alternative because they generate broadband evanescent fields with nanometer localization. Still, direct electron–polariton coupling is subject to kinematic constraints: modes above the electron line in momentum–frequency space cannot be excited directly by a passing electron [4]. Here, we show that small nearby scatterers bridge this mismatch by converting the broadband electron field into a localized dipolar response containing the momentum components needed to launch SPs. We further show that periodic arrays of scatterers lead to directional in-plane Smith–Purcell emission of polaritons without patterning the polaritonic surface itself [3], [4].

II. Methods

We consider an electron moving parallel to a planar polariton-supporting surface at velocity $\mathbf{v} = v\hat{\mathbf{x}}$, in the presence of either a single small scatterer or a linear periodic array of scatterers. The surface is described through Fresnel reflection coefficients, while the particle is modeled by a frequency-dependent polarizability tensor. Starting from the frequency-resolved electron field near the interface, we calculate the self-consistent dipole induced on the scatterer, including the field reflected back by the surface. In the regime of strongly confined modes, the problem is treated in the electrostatic limit, which yields the SP emission probability from the imaginary part of the surface Green tensor weighted by the induced dipole amplitude [4].

For an ideal resonant particle, this formulation reveals the role of radiation damping and surface-mediated self-interaction in determining the effective polarizability and the emission maximum. For a realistic implementation, we consider graphene plasmons assisted by a thin hBN nanodisk deposited on a dielectric coating layer above graphene. The layered structure is incorporated through a modified reflection coefficient, while the disk is described by an effective in-plane polarizability obtained from an electrostatic modal expansion.

For periodic arrays with periodicity a, we consider the electron passing parallel to the dipole lattice with velocity $\mathbf{v} = v\hat{\mathbf{x}}$. We include dipole–dipole lattice interactions and determine the allowed n-th diffraction orders from the phase-matching condition $k_{nx} = \omega/v + 2\pi n/a$, which determines the emission direction of each polaritonic Smith–Purcell channel [4].

III. Results and Discussion

For a single scatterer, SP emission becomes possible even in spectral regions where direct electron excitation is forbidden. The emission probability is maximized at a finite scatterer–surface distance because reducing the separation strengthens the near-field coupling to the surface, but also enhances the self-interaction that suppresses the effective particle response. In the semi-analytical treatment of lossless resonant particles, this optimum distance follows the SP wavelength and yields a clean polaritonic signal under conditions where the bare electron does not excite the mode. These results are shown in Fig. 1 of Ref. [4].

A realistic realization is provided by hBN nanodisks coupled to graphene. The geometry under consideration is illustrated in Fig. 1(a), in which the electron passes above a small hBN disk of diameter D placed on top of a graphene layer coated by a dielectric of thickness z_0. The SP emission probability is calculated in Fig. 1(b) as a function of disk–2D-layer spacer z_0 and frequency. The optimum coating thickness z_0 is plotted on top as a yellow curve. The disk resonance near the upper Reststrahlen band filters the broadband electron spectrum and produces narrow-band plasmon generation around selected mid-infrared energies, shown as a dark blue spot in Fig. 1(b). Figure 1(c) also shows the emission rate

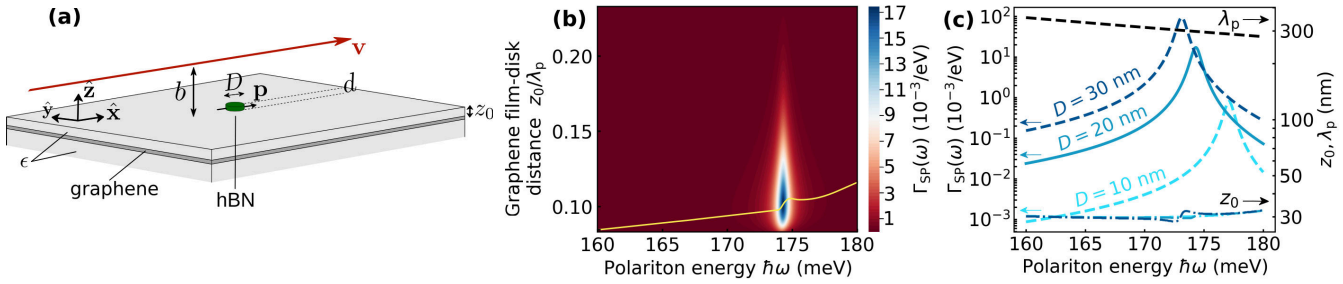

Fig. 1. **Free-electron excitation of graphene plasmons mediated by a hBN disk scatterer**. **(a)** Geometry under consideration, comprising a graphene film and an hBN disk of diameter D and thickness d. The disk is directly deposited on the top dielectric layer of thickness z_0. The electron passes at a distance b above the disk. The dielectric substrate and coating layer have a permittivity ϵ. **(b)** Spectrally resolved probability of graphene-plasmon emission $\Gamma_{SP}(\omega)$ under the conditions of (a) as a function of plasmon energy $\hbar\omega$ and coating-layer thickness z_0 for $D = 20$ nm, $d = 1$ nm, $\epsilon = 2$, $b = 10$ nm, and $v = 0.04\,c$. We set the graphene Fermi energy to $E_F = 1$ eV. **(c)** Maximum $\Gamma_{SP}(\omega)$ (left vertical scale, solid curve) and optimum coating thickness z_0 along with the SP wavelength λ_p (right scale) as a function of emission frequency under the conditions of (b). In (c), we also show results for the maximum $\Gamma_{SP}(\omega)$ with $D = 10$ nm and 30 nm (see labels).

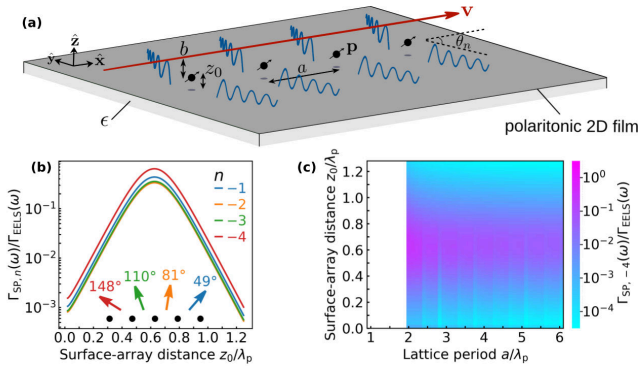

Fig. 2. **Polaritonic Smith–Purcell effect**. **(a)** Scheme with the geometry under consideration. A linear array of particles spaced by a period a along the direction of electron motion. The electron passes at a distance b above the array and induces a dipole moment $\mathbf{p}$ in each scatterer. The array is placed at a distance z_0 from a polaritonic 2D film. The in-plane emission angle θ_n is illustrated. **(b)** Probability of SPP emission $\Gamma_{SP,n}(\omega)$ for different orders n normalized per particle and divided by the self-standing-particle EELS probability $\Gamma_{EELS}(\omega)$ as a function of scaled array–surface distance z_0/λ_p for fixed frequency $\omega = 0.4\,\omega_D$. We assume perfect scatterers, a Drude film, and parameters $a/\lambda_p = 2$, $v = 2.2\,v_0 \approx 0.2\,c/(\epsilon+1)$, and $k_D b = 0.1$. The corresponding emission angles θ_n are indicated in the inset (top-view scheme). **(c)** Ratio $\Gamma_{SP,n=-4}(\omega)/\Gamma_{EELS}(\omega)$ as a function of a/λ_p and z_0/λ_p for $v/v_0 = 2.2$, with all other parameters the same as in (b). The white region corresponds to the condition that the $n = -4$ Smith–Purcell emission is kinematically forbidden. Figure adapted from Ref. [4].

spectra but for different values of the disk parameter D. There is a strong dependence on disk diameter, which tunes the spectral position and magnitude of the maximum. This behavior demonstrates that the scatterer not only enables otherwise forbidden coupling, but also introduces spectral selectivity to the launched graphene plasmons [2], [4].

When the individual scatterer is replaced by a periodic array aligned with the electron trajectory, as schematized in Fig. 2(a), the induced dipoles emit coherently into discrete in-plane diffraction orders n. The resulting polaritonic Smith–Purcell emission is highly directional and again displays an optimum array–surface distance. In Fig. 2(b), we calculate the normalized emission rate for different diffraction orders n as a function of the normalized surface-array distance z_0. As the figure shows, the different orders peak at similar normalized separations but radiate along distinct in-plane angles, indicated by colour-code arrows in the inset. The strongest emission occurs for the order whose propagation direction is closest to anti-parallel to the dipole array, provided it is not kinematically forbidden; in the present case, this corresponds to $n = -4$. Figure 2(c) shows the normalized emission for $n = -4$ as a function of z_0 and the lattice period a. The emission can be tuned through the lattice period, providing extra control over the directionality and efficiency of the launched SPs through the electron velocity and array spacing, while keeping the supporting surface translationally invariant [4].

IV. Conclusion

In summary, small scatterers provide an efficient interface between free electrons and highly confined SPs. They enable low-energy electrons to excite modes inaccessible by direct coupling, while resonant particles add spectral selectivity and periodic arrays provide directional control through polaritonic Smith–Purcell emission. hBN nanodisks illustrate the practical potential of this approach for launching graphene plasmons in realistic layered platforms [4].

Acknowledgments

This work was supported by the European Research Council (Advanced Grant 101141220-QUEFES), the European Commission (Horizon 2020 grants 101017720-eBEAM and 964591-SMART-electron), the Spanish MCIN, and the Catalan CERCA Program [4].

References

[1] M. I. Stockman, "Nanoplasmonics: the physics behind the applications," *Phys. Today*, vol. 64, pp. 39–44, 2011.
[2] S. Dai *et al.*, "Tunable phonon polaritons in atomically thin van der Waals crystals of boron nitride," *Science*, vol. 343, pp. 1125–1129, 2014.
[3] S. J. Smith and E. M. Purcell, "Visible light from localized surface charges moving across a grating," *Phys. Rev.*, vol. 92, pp. 1069–1069, 1953.
[4] L. Prelat, E. J. C. Dias, and F. J. García de Abajo, "Free-electron coupling to surface polaritons mediated by small scatterers," *Nanophotonics*, vol. 13, no. 25, pp. 4667–4681, 2024.

Long-range coupling through photonic molecules

Romina Abarca-Ramírez[1,2], Diego Román-Cortés[1,2], Rodrigo A. Vicencio[1,2*]

[1]Departamento de Física, Facultad de Ciencias Físicas y Matemáticas, Universidad de Chile, Chile
[2]Millenium Institute for Research in Optics - MIRO, Chile
*Corresponding author: rvicencio@uchile.cl

***Abstract*—We demonstrate the evanescent and resonant excitation of high transversal modes on long photonic molecules. By inserting the molecule as a link we observe long-range coupling of very distant waveguides. We use this on a one-dimensional lattice and demonstrate the emergence of a topological phase originated by third-order nearest-neighbour coupling.**

***Keywords*— evanescent coupling, transversal modes, femtosecond laser writing, photonic lattices.**

I. Introduction

A one-dimensional (1D) paraxial wave equation is, excepting constants, completely equivalent to a Schrödinger equation; therefore, we can directly interpret a photonic waveguide as an atom and a composed structure as a photonic molecule [1]. The larger structure allows higher-order states [2], depending on the excitation wavelength and propagation distance. Inter-orbital coupling among individual waveguides, which support a fundamental S and a first excited P state, was recently demonstrated in photonics in coupler configurations [3] fabricated using the femtosecond (fs) laser writing technique [4]. In that specific case, a fine-tuning protocol of the propagation constants was mandatory to achieve a resonant coupling among, otherwise, orthogonal states.

On the other hand, the hopping in solid-state-like (tight-binding) systems or the evanescent coupling in photonics is based on localized and exponentially decaying wavefunctions at specific sites. This naturally sets a cutoff for long-range interactions which decay exponentially with the distance [4]. Therefore, artificial lattices utilizing an evanescent coupling suffer from these limitations, leaving multiple interesting topological and transport phenomena out of reach.

II. Methods

We fabricate different photonic structures by means of the fs laser writing technique, as it is sketched in Fig.1(a). We tightly focus a pulse of $\sim$ 200 fs, with a wavelength of 1030 nm, inside a borosilicate glass wafer. The laser induces a weak modification of the refractive index contrast, estimated as $\Delta n \sim 10^{-3}$ over $n_0 = 1.48$ (wafer). A full waveguide is fabricated after translating the glass along its length (coordinate z), at a given writing velocity and power.

III. Results and Discussion

Photonic molecules are obtained by fabricating a sequence of closely spaced waveguides, with distances around 4 μm [see example in Fig.1(a)-inset]. A waveguide (atom) is inserted beside the molecule, at a distance larger than 15 μm to allow a standard evanescent coupling interaction [3]. Fig.1(b) shows different examples for short and long 1D molecules, with clear excitation of the 3rd, the 5th, the 6th, the 7th, the 9th and the 11th orbital molecular states. Fig.1(c) presents the extracted data for a molecule of width of $\sim$ 120 μm (formed by 31 waveguides), showing an almost perfect mode excitation at around specific optimal wavelengths. This data describes quite clearly a resonant-like picture, with very well-defined peaks around specific wavelengths and for different higher-order states. Therefore, the method shows an excellent and simple way of exciting higher-order states, for example as a way of spatial and wavelength multiplexing of optical information [5].

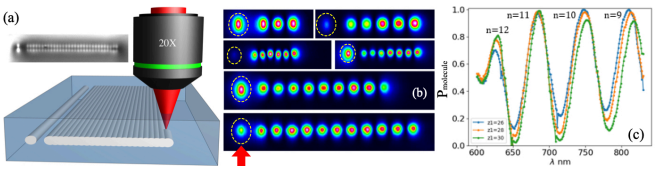

Fig. 1. (a) Illustration of the fs laser writing technique. Inset shows a microscope image of a fabricated 1D molecule composed of 31 single waveguides. (b) Output intensity profiles of different higher-order states excited at different photonic molecules and for different excitation wavelengths, after the excitation of the waveguide located beside each molecule (see red arrow and yellow circles). (c) Extracted data of the power at the 1D molecule versus the excitation wavelength, for three different propagation lengths z1 of the molecule.

Then, we explore two different applications using the resonant excitation of specific modes at the photonic molecule. A standard distance for fan-in and fan-out fiber optics operations inside a photonic chip is 127 μm. This distance allows to couple classical or quantum light coming from a given source using fibers, and then to fan-in to implement a given operation and fan-out to extract the result [6]. However, the curvature of waveguides introduces losses and, therefore, new solutions are always necessary. We specifically explore this idea using a photonic molecular link to connect waveguides which otherwise simply do not interact. Fig.2(a1) shows the sketch and Fig.2(a2) the result for a large wavelength to assure a large coupling. However, at this separation distance, the coupling is simply zero in practice for a 30 mm long glass. We introduce a long photonic molecule in between these two waveguides, as it is sketched in Fig.2(b1), and characterize its performance by a supercontinuum laser source. Fig.2(b2) shows the compiled results for the measured power at the opposite (right) waveguide (red curve) and the power at the molecule (black curve), for an excitation of the left

waveguide. We observe that the performance strongly depends on wavelength, with two optimal regions at around 685 and 770 nm [see Fig.2(b3)], and a $\sim 50/50$ beam splitter at 735 nm.

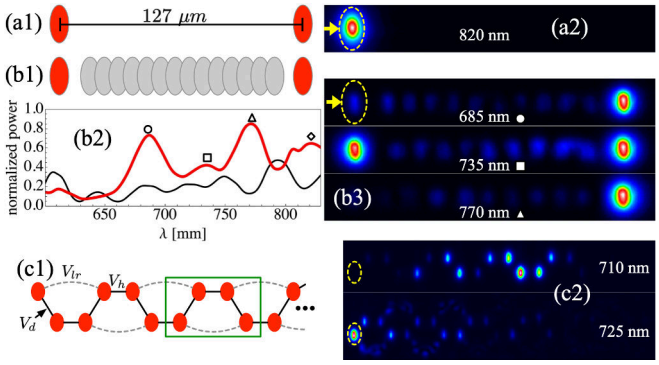

Fig. 2. (a) Sketch of two waveguides separated a distance $d = 127$ μm and (a2) output image at $\lambda = 820$ nm. (b1) Sketch of a coupler including a photonic molecule as a link. (b2) Extracted normalized power vs λ at the non-excited right waveguide (red) and the molecule (black). (b3) Output images at the indicated wavelengths. (c1) A 1D lattice with horizontal Vh, diagonal Vd, and long-range Vlr coupling constants. (c2) Output images, at the indicated wavelengths, after exciting the left edge site (yellow ellipses) of a trivial (top) and a non-trivial (bottom) lattice

Finally, we perform a second fundamental application on a lattice. An homogeneous one-dimensional lattice is trivial in any sense as it only contains a single dispersive band. This means that by exciting any site through the system, only dispersion will be observed as all the excited eigenmodes are spatially delocalized. The sketch in Fig.2(c1) shows a zig-zag-like configuration, and the lattice is completely trivial for $V_d = V_h$ and $V_{lr} = 0$. Fig.2(c2)-top shows the output dispersive profile obtained after the excitation of the left edge (yellow ellipse) with a propagation of 50 mm. We introduce long-range coupling V_{lr} by inserting photonic molecules as indicated with dashed lines in Fig.2(c1). These photonic link allows us to selectively couple specific lattice sites, in this case to the third nearest neighbour. This inclusion allows us to transform a trivial lattice into a topological one, which presents two topological transitions depending on the coupling ratio $V_{lr}/V_{d,h}$ [7]. In our experiments [2], we were able to obtain a ratio ~ 0.5, which allowed us to observe a first topological transition. This experimentally manifests on light localization at the edge, as it is clearly observed in Fig.2(c2)-bottom, with almost no light present at the photonic links.

IV. Conclusion

We have demonstrated the possibility of very long-distance coupling by means of femtosecond laser writing photonic links. This coupling is selectively determined by the excitation wavelength and propagation distance, and it has a resonant-like dependence which depends on the fabrication parameters. Therefore, a specific wavelength can be selectively tuned. This resonant evanescent interaction allowed us to effectively couple very distant waveguides, which otherwise will never interact (for waveguide distances larger than 50 μm, the coupling can be assumed as zero in practice). Our extracted data shows an excellent coupling of $\sim$ 85 % at $\lambda = 770$ nm. Finally, the use of long-range and selective coupling among specific sites allows us to increase the possibilities of lattice research in photonics. As new phenomena could emerge from this extra degree of freedom, new physics is now at hand to be explored. For example, we directly demonstrated a topological transformation of a standard trivial 1D lattice into a topologically non-trivial one by selectively inserting coupling links at third-nearest neighbours. The observation of edge localization at the topological phase constitutes an experimental proof of this transition.

Acknowledgments

This work was supported by ANID FONDECYT Grant 1231313 and Millennium Science Initiative Program ICN17_012.

References

[1] M. Mazanov, et al., "Photonic Molecule Approach to Multiorbital Topology," *Nano Letters*, vol. 24, pp. 4595, 2024.
[2] R. Abarca-Ramírez, et al., "Long/range evanescent coupling through photonic molecules," arXiv:2511.22718 [physics.optics], 2025.
[3] D. Guzm án-Silva, "Experimental observation of interorbital coupling," *Phys. Rev. Lett.*, vol. 127, pp. 066601, 2021.
[4] A. Szameit, et al., "Discrete nonlinear localization in femtosecond laser written waveguides in fused silica," *Optics Express*, vol. 13, pp. 10552, 2005.
[5] T. Mizuno and Y. Miyamoto, "High-capacity dense space division multiplexing transmission," *Optical Fiber Technology*, vol. 35, pp. 108, 2017.
[6] L. Sharma, et al., "Fiber-connectorized ultrafast-laser-inscribed K-band integrated optics beam combiner for the CHARA telescope array," *Applied Optics*, vol. 63, pp. 159, 2024.
[7] Y. Betancur-Ocampo, et al., "Twofold topological phase transitions induced by third-nearest-neighbor hoppings in one-dimensional chains," *Physical Review B*, vol. 109, pp. 104111, 2024.

Hyperbolic Super-Resonance and Long-Range Quantum Entanglement

Evgenii E. Narimanov[1] and Eugene A. Demler[2]
[1]School of Electrical and Computer Engineering and Birck Nanotechnology Center,
Purdue University, West Lafayette, Indiana 47907, USA
[2]Institute for Theoretical Physics, ETH Zurich, Wolfgang-Pauli-Str. 27, 8093 Zurich, Switzerland

***Abstract*—Hyperbolic materials support extreme momentum electromagnetic modes that enable deeply subwavelength field confinement and reshape light–matter interaction. We report the discovery of hyperbolic super-resonance, arising from clustered high-wavenumber modes in finite hyperbolic structures, which enables strong and even ultrastrong light–matter coupling and mediates strong long-range interaction between quantum emitters.**

I. Introduction

Hyperbolic materials provide an optical environment in which electromagnetic waves can access momenta exceeding those available in conventional dielectric media by several orders of magnitude.[1] Their anisotropic permittivity tensor, with opposite signs along orthogonal axes, produces open hyperbolic iso-frequency surfaces that support a continuum of high-wavenumber propagating modes. These waves enable deeply subwavelength field confinement, directional energy flow, and a divergent photonic density of states.[2] As a result, hyperbolic media have emerged as a powerful platform for controlling light–matter interaction at the nanoscale.

In a finite hyperbolic structure, the high-wavenumber modes of the hyperbolic medium form dense clusters of nearly degenerate states. In the effective-medium limit, these clusters collapse into distinct, sharply defined resonances – the phenomenon we refer to as the hyperbolic super-resonance.[3] The resulting field enhancement enables strong and even ultra-strong light–matter coupling for a single quantum emitter placed near the structure. Furthermore, these super-resonant modes also mediate strong long-range interaction between two distant quantum emitters.

II. Hyperbolic Super-Resonance

The physical origin of the hyperbolic super-resonance can be uncovered using a simple example: a long hyperbolic resonator with rectangular cross-section and a high-conductivity metal coating on its surface. The boundary conditions quantize the in-plane and out-of-plane wavevector components according to

$$k_x a_x = \pi n_x, \qquad k_z a_z = \pi n_z, \tag{1}$$

where n_x and n_z are integers. For a deeply subwavelength resonator ($a_x, a_z \ll \lambda_0$), the hyperbolic dispersion relation implies

$$k_x = \sqrt{-\frac{\epsilon_\parallel(\omega)}{\epsilon_\perp(\omega)}}\, k_z. \tag{2}$$

Combining these expressions yields the resonance condition

$$\sqrt{-\frac{\epsilon_\perp(\omega_r)}{\epsilon_\parallel(\omega_r)}} = \frac{a_x}{a_z}\,\frac{n_x}{n_z}. \tag{3}$$

Note that this condition is satisfied not only by a single pair (n_x, n_z), but by the entire integer ladder

$$(n_x, n_z) = (mn_1,\, mn_2), \qquad m = 1, 2, 3, \ldots, \tag{4}$$

all collapsing onto the same frequency; see Fig. 1. This resonance-frequency degeneracy, asymptotically exact in the quasistatic limit $a \ll \lambda_0$, is the *Hyperbolic Super-Resonance* (HSR) – the finite-size counterpart of the broadband hyperbolic super-singularity of infinite hyperbolic media.[2]

While this degeneracy formally extends over infinitely many integer multiples, material absorption suppresses the highest-order members of the ladder. Because the attenuation coefficient grows with the magnitude of the wavevector, higher-order super-resonances experience disproportionately stronger damping. As a result, the most robust and experimentally relevant HSRs arise from the lowest-order integer families.

This mechanism is not restricted to rectangular geometries. Infinite mode degeneracies appear in any hyperbolic resonator whose ray-optical dynamics is integrable – a condition that can be demonstrated by transforming the electromagnetic trajectories to action-angle variables, as in the Einstein-Brillouin-Kramers semiclassical quantization procedure.[4] For example, in a metal-clad cylindrical hyperbolic resonator (Fig. 1(a)), the resonance condition reduces to

$$\sqrt{-\frac{\epsilon_\perp(\omega_r)}{\epsilon_\parallel(\omega_r)}} = \frac{4R}{d}\, m, \tag{5}$$

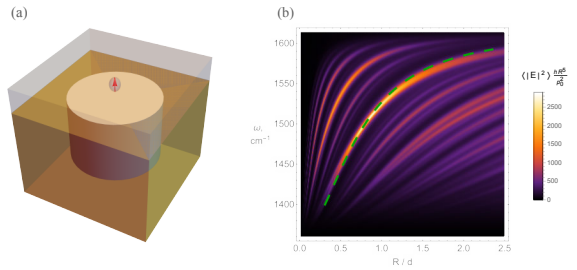

Fig. 1. **Average intensity of light emitted by a point dipole and trapped inside a hyperbolic resonator. (a)** Schematic of the system: a point dipole emitter positioned above a cylindrical hyperbolic resonator. Light-orange indicates the hyperbolic material, gold the metal cladding, and gray the supporting substrate. In a practical realization, the hyperbolic medium is hexagonal Boron Nitride (hBN), the cladding is gold, and the emitter is a donor impurity in silicon. **(b)** False-color plot of the average trapped intensity as a function of the resonator aspect ratio and emission frequency. The dielectric permittivity corresponds to hBN. The dashed green line marks the principal super-resonance defined by Eqn. (5). Note the negligible trapped intensity outside the hBN hyperbolic frequency band [5], [6] $1380\ \mathrm{cm}^{-1} < \omega < 1620\ \mathrm{cm}^{-1}$, and its dramatic enhancement at the super-resonance.

again yielding an asymptotically exact degeneracy over the integer ladder $m = 1, 2, 3, \ldots$

This mechanism concentrates electromagnetic energy into highly localized regions of the resonator, producing field enhancements far exceeding those achievable in dielectric or plasmonic structures of comparable size.

III. Light–Matter Interaction

The extreme mode degeneracy associated with the hyperbolic super-resonance has profound consequences for light–matter interaction. At the super-resonance, a point-like quantum emitter placed in the near field of a hyperbolic resonator couples simultaneously to an entire ladder of high-wavenumber electromagnetic modes whose frequencies collapse onto the same value. Their collective contribution produces an exceptionally large light-matter coupling strength.

A convenient quantitative measure of this interaction is the coupling coefficient g of the Jaynes-Cummings model.[7] For integrable hyperbolic geometries, the same semiclassical quantization that produces the super-resonance also yields a closed-form expression for g; for example, for the cylindrical resonator of Fig. 1,

$$\hbar g = \frac{1 - \cos\left(\frac{\pi m}{2}\right)}{2} \sqrt{\frac{p^2 \hbar \omega}{3 d\, h^2}}, \tag{6}$$

where the integer m is the order of the super-resonance (see Eq. (5)), h is the distance between the dipole and the resonator, and p is the characteristic dipole moment of the quantum emitter.

For a quantum emitter based on deep donor impurities in silicon, with $p \sim e \times 1\,\mathrm{nm}$, the dipole-resonator spacing $h \simeq 3\,\mathrm{nm}$ and cylinder length $d \sim 50\,\mathrm{nm}$, Eq. (6) yields $\hbar g \simeq 0.15\,\hbar\omega$ for the lower-frequency and $\hbar g \simeq 0.1\,\hbar\omega$ for the higher-frequency hyperbolic bands in hexagonal boron nitride.[5], [6] Thus, at the hyperbolic super-resonance, a single quantum emitter placed near a hyperbolic optical resonator naturally operates in the strong-coupling regime.

IV. Material Considerations

Hexagonal boron nitride (hBN) provides a natural platform for realizing hyperbolic super-resonance due to its strong phonon-polariton response and well-established fabrication pathways. The availability of isotopically purified hBN significantly reduces phonon scattering, enabling low-loss operation and enhancing the quality factor of the super-resonant mode.

Other hyperbolic materials – including semiconducting CrSBr [8] and metallic molybdenum oxychloride ($MoOCl_2$) [9], [10] – operate in the technologically important near-infrared range used in communications and information processing. These systems offer additional opportunities for realizing hyperbolic super-resonances and extend the accessible spectral range for the effect.

V. Conclusion

We have uncovered the hyperbolic super-resonance, a phenomenon arising from the clustering of high-wavenumber modes in finite hyperbolic structures. This effect produces strong – and even ultrastrong – light–matter coupling and mediates long-range interaction between quantum emitters, offering new opportunities for quantum nanophotonics and nonlinear optics.

References

[1] V. A. Podolskiy and E. E. Narimanov, "Strongly anisotropic waveguide as a nonmagnetic left-handed system," *Phys. Rev. B*, vol. 71, p. 201101(R), 2005).

[2] I. I. Smolyaninov, and E. E. Narimanov, "Metric Signature Transitions in Optical Metamaterials," *Phys. Rev. Lett.*, vol 105, p. 067402, 2010.

[3] E. E. Narimanov and E. A. Demler, "Hyperbolic Quantum Processor.," preprint axXiv:2412.14098

[4] M. Gutzwiller, *Chaos in Classical and Quantum Mechanics*, Springer; 1st edition (1990).

[5] J. Caldwell, A. Kretinin, Y. Chen *et al.*, "Sub-diffractional volume-confined polaritons in the natural hyperbolic material hexagonal boron nitride," *Nat. Commun.*, vol. 5, p. 5221, 2014.

[6] S. Dai, Q. Ma, T. Andersen *et al.*, "Subdiffractional focusing and guiding of polaritonic rays in a natural hyperbolic material," *Nat. Commun.*, vol. 6, p. 6963, 2015.

[7] E.T. Jaynes and F.W. Cummings, "Comparison of quantum and semiclassical radiation theories with application to the beam maser," *Proc. IEEE*, vol. 51, pp. 89 - 109, 1963.

[8] F. L. Ruta, S. Zhang, Y. Shao, *et al.*, "Hyperbolic exciton polaritons in a van der Waals magnet," *Nat. Comm.*, vol. 14, p. 8261, 2023.

[9] G. Venturi, A. Mancini, N. Melchioni, S. Chiodini, A. Ambrosio, "Visible-frequency hyperbolic plasmon polaritons in a natural van der Waals crystal," *Nat. Commun.*, vol. 15, p. 9727, 2024.

[10] F. L. Ruta, Y. Shao, S. Acharya *et al.*, "Good plasmons in a bad metal," *Science*, vol. 387, pp. 786 - 791, 2025.

Observing Exceptional Lines in Scattering Matrices

Jingyi Zhao[1,2], Xinhao Wang[2], Wenzhe Liu[1,2,3*], Lei Shi[1,2], C. T. Chan[3], and Jian Zi[1,2]

[1]State Key Laboratory of Surface Physics and Institute for Nanoelectronic Devices and Quantum Computing, Fudan University, China

[2]Key Laboratory of Micro- and Nano-Photonic Structures(Ministry of Education) and Department of Physics, Fudan University, China

[3]Department of Physics and Institute for Advanced Study, The Hong Kong University of Science and Technology, Hong Kong SAR

Corresponding author: wzliu@fudan.edu.cn

***Abstract*—We investigate topological singularities in scattering matrices of photonic structures in the visible spectrum. Using frequency and momentum as parameter space, we observe features consistent with exceptional lines through Mueller matrix spectroscopy. This approach enables investigation of non-Hermitian topology without complex structural requirements.**

***Keywords*— Exceptional lines, Non-Hermitian photonics, Scattering matrix, Mueller matrix spectroscopy.**

I. Introduction

Topological singularities in wave systems have attracted significant attention for their potential in photonic control and sensing applications. While isolated exceptional points have been demonstrated in various platforms ranging from microcavities to photonic crystals, extending these to higher dimensions remains challenging, particularly in the visible regime where material constraints and fabrication limitations become more pronounced. Exceptional lines, as one-dimensional extensions requiring three-dimensional parameter spaces, have been largely confined to microwave frequencies where complex structures can be more readily implemented through established fabrication techniques. The exploration of these topological features at optical frequencies has remained an outstanding challenge in the field of topological photonics. We present an approach that exploits scattering matrices of photonic structures, which naturally provide the required parameter space through frequency and momentum degrees of freedom, circumventing the need for elaborate structural engineering that would otherwise be necessary for three-dimensional architectures.

II. Theoretical Framework and Methods

We consider systems where the scattering matrix $S(\omega, \mathbf{k}_{\parallel})$ describes the optical response as a function of frequency and in-plane wavevector, providing a complete characterization of the system's reflective properties. For periodic structures with appropriate symmetries, this three-dimensional space can support singularities with non-trivial topology that manifest as characteristic features in the eigenvalue and eigenvector structure.

In systems with material absorption, which is inevitable in realistic photonic structures operating at visible frequencies, the interplay between resonant modes and symmetry breaking can lead to non-Hermitian degeneracies with unique properties. These degeneracies may exhibit characteristic features including distinctive eigenvalue structure with square-root dependencies and polarization properties that differ fundamentally from their Hermitian counterparts. The scattering matrix formalism provides a natural framework for describing these open systems, where energy exchange with the environment plays a crucial role in determining the system's optical response.

Our experimental platform combines Fourier-space optics with polarization-resolved spectroscopy to enable comprehensive characterization across the parameter space. A nanophotonic structure is characterized in the visible range using synchronized polarization control elements that generate multiple measurement configurations, providing complete information about the polarization-dependent scattering behavior. Spectroscopic imaging enables simultaneous access to both frequency and momentum dimensions, allowing efficient mapping of the three-dimensional parameter space without requiring mechanical scanning in multiple directions. Mueller matrix measurements across the parameter space are systematically performed and converted to scattering matrices in appropriate bases, enabling characterization throughout ω-$\mathbf{k}_{\parallel}$ space with high precision and resolution. This experimental methodology represents a significant advancement in the ability to probe topological features in optical systems, providing access to previously inaccessible information about the complete scattering behavior.

III. Results and Discussion

Experimental measurements reveal features in the scattering matrix eigenvalue structure that are consistent with theoretical predictions for topological singularities in non-Hermitian systems. Phase analysis of the scattering matrix elements shows vortex-like structures at certain locations in parameter space, providing direct evidence of the singular nature of these points. Different measurement configurations reveal complementary patterns in the phase and amplitude distributions, indicating polarization-dependent responses that are characteristic of chiral exceptional points with distinct handedness. The spatial distribution of these features suggests extended structures rather than isolated points, consistent with the expected one-dimensional nature of exceptional lines in three-dimensional parameter space.

Systematic scanning along different directions in momentum space traces trajectories that appear to form connected

curves in the three-dimensional parameter space, demonstrating the continuous nature of these topological features. Multiple regions in the frequency-momentum space exhibit similar characteristic signatures in both eigenvalue and eigenvector distributions, suggesting distinct classes of singularities with different physical origins related to the underlying resonance mechanisms. The observed eigenvalue behavior shows certain parameter dependencies near singular points that are consistent with theoretical predictions for exceptional points, including characteristic square-root scaling behavior. Eigenvector distributions exhibit variations consistent with theoretical predictions for such systems, showing evolution from linear to circular polarization states as one approaches the singular points. These features extend across spectral ranges spanning tens of terahertz, indicating inherent robustness in the parameter space and suggesting potential for broadband applications in photonic devices.

IV. Conclusion

This work demonstrates an approach for investigating topological features in optical scattering matrices using relatively simple and scalable photonic structures. By exploiting the natural parameter space available through frequency and momentum, we access phenomena typically requiring more complex implementations involving three-dimensional architectures or active tuning mechanisms. The observed signatures are consistent with higher-dimensional singularities in non-Hermitian systems, providing experimental evidence for these theoretical concepts in the visible regime. The experimental methodology based on Mueller matrix spectroscopy provides comprehensive characterization capabilities for such systems, enabling detailed investigation of both amplitude and phase properties across the full parameter space. The results suggest potential applications in areas where sensitivity to parameter variations or polarization-selective responses are desirable, including enhanced sensing schemes and chiral light-matter interactions. This framework may facilitate exploration of non-Hermitian topological physics at optical frequencies, contributing to both fundamental understanding of wave phenomena and practical photonic applications in communications and quantum technologies. The demonstration establishes a robust and accessible platform that bridges theoretical concepts with experimental accessibility in the visible spectrum, opening new possibilities for investigating complex topological phenomena in photonic systems.

Acknowledgments

This work was supported by the National Key R&D Program of China (2023YFA1406900, 2022YFA1404800), National Natural Science Foundation of China (12321161645, 12234007, 12221004, T2394480, T2394481), Science and Technology Commission of Shanghai Municipality (22142200400, 21DZ1101500, 2019SHZDZX01, 23DZ2260100), and Hong Kong RGC (CRS_HKUST601/23, AoE/P-502/20).

Nanopopcorn-Based SERS Nanosensors for Intracellular pH Mapping

Katarzyna Bogusz[1], Katarzyna Wleciał[1], Agnieszka Girstun[2], Andrzej Kudelski[1], Aleksandra Szaniawska[1]*

[1]Faculty of Chemistry, University of Warsaw, Pasteura 1 Str., 02-093 Warsaw, Poland
[2]Faculty of Biology, University of Warsaw, Miecznikowa 1 Str., 02-096 Warsaw, Poland
*Corresponding author: aleksandra.szaniawska@uw.edu.pl

***Abstract*— Surface enhanced Raman spectroscopy is investigated as a tool for probing intracellular pH and local chemical microenvironment using gold nanopopcorn nanostructures functionalized with pH sensitive Raman reporters. The work combines nanoparticle synthesis reporter comparison and cellular studies to evaluate how nanoscale architecture and biological environment determine intracellular SERS response.**

***Keywords*— surface enhanced Raman spectroscopy, intracellular pH, nanopopcorn, Raman reporters, cellular microenvironment.**

I. Introduction

Intracellular pH is a fundamental parameter regulating enzyme activity, metabolism, membrane trafficking, autophagy, and cell fate decisions. Although average cytosolic pH values are relatively well characterized, growing evidence indicates pronounced spatial and temporal pH heterogeneity at the subcellular level. Local pH gradients accompany endocytic maturation, lysosomal acidification, metabolic reprogramming, and stress adaptation. These processes occur on submicrometer length scales and evolve dynamically, making their quantitative characterization experimentally demanding.

Monitoring such local variations requires probes capable of operating within crowded and chemically complex intracellular environments. Fluorescence-based pH sensors are widely used but often suffer from photobleaching, spectral overlap, limited multiplexing capability, and sensitivity to probe concentration. In addition, fluorescence intensity-based measurements may be affected by local optical artifacts and intracellular scattering.

Surface enhanced Raman spectroscopy (SERS) offers an alternative approach providing molecularly specific vibrational information with high photostability and strong spatial confinement of the signal near plasmonic nanostructures. The spectral fingerprint character of Raman scattering allows direct discrimination between protonated and deprotonated forms of reporter molecules. In this work, we systematically evaluate nanopopcorn-type gold nanostructures together with different thiolated Raman reporters in order to develop a reliable and stable platform for intracellular pH measurements..

II. Methods

Gold nanopopcorn nanoparticles were synthesized using a seeded growth approach involving small gold seeds and controlled reduction of metal precursors. For comparison, conventional spherical gold nanoparticles of similar core diameter were prepared or obtained and subjected to identical functionalization and measurement protocols. The resulting anisotropic structures exhibit multiple protrusions and nanogaps that generate intense electromagnetic hot spots. Reaction parameters such as precursor concentration, reducing agent amount, and growth time were optimized to ensure reproducible morphology and colloidal stability.

Nanoparticles were functionalized with thiolated pH-sensitive Raman reporters including mercaptobenzoic acid isomers, mercaptopyridine, and aminothiophenol derivatives. Surface modification was performed under controlled conditions to ensure stable chemisorption via gold–sulfur bonds while minimizing aggregation. After functionalization, particles were purified and transferred into aqueous media compatible with cell culture experiments.

SERS calibration measurements were performed in buffer solutions covering physiologically relevant pH ranges, as well as in cell culture media to evaluate environmental effects. Raman spectra were collected using a confocal Raman microscope with visible or near-infrared excitation. Intensity ratios of selected vibrational bands corresponding to protonation-sensitive modes were used to construct calibration curves.

Cellular uptake, localization, and biocompatibility were assessed using transmission electron microscopy, confocal microscopy, and metabolic viability assays. Intracellular SERS spectra were collected from living cells incubated with functionalized nanoparticles at defined time points to probe pH-dependent spectral changes within endocytic compartments..

III. Results and Discussion

Nanopopcorn nanostructures exhibit substantially enhanced

SERS signals compared to conventional spherical gold nanoparticles of comparable size owing to their complex morphology and high density of electromagnetic hot spots. Direct comparison under identical experimental conditions demonstrates improved signal intensity, higher signal to noise ratio, and more robust intracellular detectability for the nanopopcorn architecture. The presence of sharp protrusions and nanoscale interstitial gaps increases electromagnetic field confinement, which translates into stronger enhancement of reporter vibrational modes.

When evaluated in buffer systems, both spherical and nanopopcorn nanoparticles show pH dependent spectral changes characteristic of the attached reporters. However, the dynamic range and apparent sensitivity are consistently higher for the nanopopcorn structures. In particular, intensity ratios of protonation sensitive bands display improved contrast across the physiological pH window. This difference becomes even more pronounced under biologically relevant conditions.

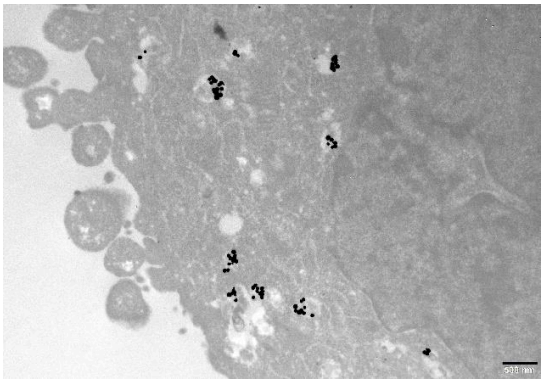

Fig.1 Transmission electron microscopy photography of HeLa cell with internalized gold nanoparticles.

In cell culture media and in living cells, spherical nanoparticles frequently produce weaker and less reproducible intracellular spectra, likely due to lower enhancement efficiency and partial signal masking by background contributions. In contrast, nanopopcorn based nanosensors maintain detectable reporter signatures inside endocytic compartments. The enhanced performance facilitates more reliable extraction of pH dependent band ratios from intracellular spectra.

Comparison of different Raman reporters further reveals that calibration behavior depends strongly on chemical structure. Carboxyl containing reporters show gradual intensity changes associated with acid base equilibria, whereas nitrogen containing heterocycles exhibit distinct band shifts and relative intensity redistribution. Importantly, calibration curves obtained in buffer solutions differ from those measured in cell culture media and inside cells. These shifts indicate that intracellular SERS response is influenced by protein corona formation, ionic strength, confinement effects, and reporter orientation on the nanoparticle surface. Consequently, the measured signal reflects an effective local microenvironment rather than bulk pH alone.

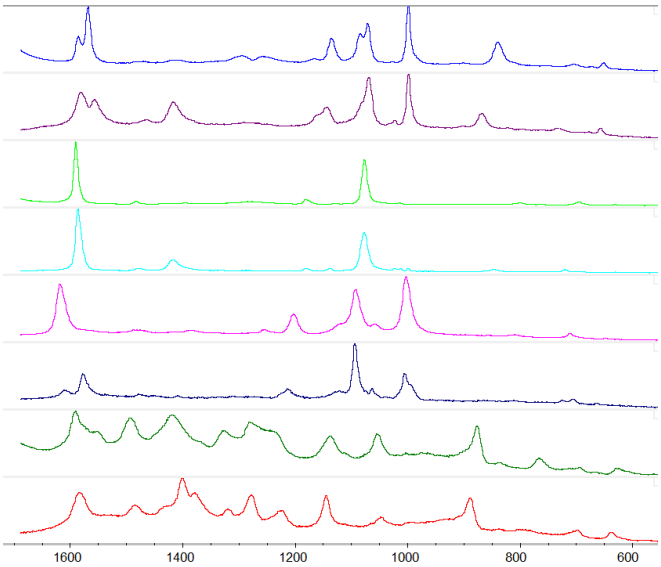

Fig.2 SERS spectra of 1,3 mercaptobenzoic acid (pH 1 and 12), 1,4-mercaptobenzoic acid (pH=1 and 12), 4-mercaptopyridine (pH=1 and 12) and 4-amine-3-mercaptobenzoic acid 9pH=1 and 12).

IV. Conclusion

This study demonstrates that nanopopcorn-based SERS nanosensors provide a versatile platform for probing intracellular pH and chemical microenvironment. Enhanced electromagnetic hot spots combined with carefully selected Raman reporters enable sensitive detection of protonation-dependent spectral changes in living cells.

Reliable interpretation of intracellular SERS measurements requires careful consideration of nanoparticle architecture, reporter chemistry, and biological context. The presented approach establishes a foundation for future development of quantitative SERS-based probes for studying dynamic cellular processes such as endocytic maturation, metabolic adaptation, and stress responses.

Acknowledgments

This work was supported by the National Science Centre, Poland, grant SONATA, No. UMO-2020/39/D/ST4/01973.

References

[1] A. Jaworska, K. Malek, A. Kudelski, Spectrochimica Acta Part A 251 119410 2021.
[2] J. R. Casey et al., Nature Reviews Molecular Cell Biology 11 50–61 2010.

Magnetic Properties and Applications of Glass-coated Ferromagnetic Microwires

Valentina Zhukova[1,2,3,*], Paula Corte-Leon[1,2,4], Mihail Ipatov[5], Juan Maria Blanco[2,3] and Arcady Zhukov[2,3,6]

[1]Dpto. de Polímeros y Materiales Avanzados, University of the Basque Country, EHU, San Sebastian, Spain
[2]Dpto. de Fisica Aplicada, EIG, University of the Basque Country, EHU, San Sebastian, Spain
[3]EHU Quantum Center, University of the Basque Country, EHU, Spain
[4]Dept. Mater. Science & Metallurgy, Univ. Cambridge, Cambridge CB3 0FS, UK
[5]General Magnetic Measurement Service of Advanced Research Facilities (SGIker), University of the Basque Country, EHU, San Sebastián, Spain
[6]IKERBASQUE, Basque Foundation for Science, Spain
*Corresponding author: valentina.zhukova@ehu.eus

***Abstract*—The impact of post-processing on soft magnetic properties and the giant magnetoimpedance (GMI) effect of Fe- and Co-based glass-coated microwires is evaluated. A remarkable improvement of magnetic softness and GMI effect is observed in Fe-rich glass-coated microwires subjected to stress annealing. Frequency dependence of GMI ratio of stress-annealed Fe-rich microwires has been discussed considering frequency dependence of the skin penetration depth, δ, as well as magnetic anisotropy distribution within the metallic nucleus. Annealed and stress-annealed Co-rich microwires present rectangular hysteresis loop and single and fast domain wall propagation. However, Co-based stress-annealed microwires present high magnetoimpedance ratio. Observed stress-induced anisotropy and related changes of magnetic properties are discussed considering internal stresses relaxation and "back-stresses"**

***Keywords*— metamaterials, terahertz, machine learning, photonic crystals.**

I. Introduction

Development of magnetic sensors is focused on the miniaturization of their size, improvement of their features and on finding of new materials. Among new magnetic materials a family of thin wire with reduced dimensions recently gained considerable attention [1]. Glass-coated magnetic microwires prepared using the Taylor-Ulitovsky technique with thin metallic nucleus (typically with diameters 0.5 to 50 μm) covered by flexible, insulating and biocompatible glass are therefore quite interesting for sensor applications [1]. This technique allows preparation of the thinnest rapidly quenched wires with amorphous or crystalline structure of metallic nucleus. Good magnetic properties can be observed either in crystalline or in amorphous magnetic wires, but amorphous magnetic wires present several advantages, such as superior mechanical properties, the absence of the microstructure defects (grain boundaries, crystalline texture, dislocations, point defects,…) [2] and hence precise post-processing is not required. Particularly, amorphous microwires can present giant magneto-impedance (GMI) or magnetic bistability. In the case of glass-coated microwires the magnetoelastic anisotropy contribution becomes relevant since the preparation process involves not only the rapid quenching itself, but also simultaneous solidification of the metallic nucleus surrounded by non-magnetic glass-coating with rather different thermal expansion coefficients [1].

The purpose of this paper is present last results on tailoring of soft magnetic properties and GMI effect in glass-coated microwires paying special attention to achievement of high GMI effect and on optimization of domain wall dynamics.

II. Methods

We studied glass-coated Fe and Co-rich ferromagnetic microwires with metallic nucleus diameter, d, between 10 μm, total diameter, D=22.2 μm, ρ =d/D= 0.88 produced by Taylor-Ulitovsky method described elsewhere [1,3].

Hysteresis loops of studied microwires have been measured using fluxmetric method previously described in details elsewhere [1]. We represent the hysteresis loops as the dependence of normalized magnetization, M/M_0 (where M is the magnetic moment at given magnetic field and M_0 is the magnetic moment of the sample at the maximum magnetic field amplitude) versus magnetic field, H.

The sample impedance, Z, in extended frequency range has been evaluated using the micro-strip sample holder from the reflection coefficient, S_{11}, obtained using Vector Network Analyzer (VNA), as previously described [3]. Such micro-strip holder with sample has been placed inside a long solenoid

producing homogeneous magnetic field, H. The GMI ratio, $\Delta Z/Z$, is obtained from $Z(H)$ dependence as:

$$\Delta Z/Z = [Z(H) - Z(H_{max})]/Z(H_{max}), \quad (1)$$

where H and H_{max} are given and maximum applied fields respectively.

III. Results and Discussion

Studied Co-rich and Fe-rich as-prepared microwires present rather different magnetic properties and hence GMI effect: $Fe_{75}B_9Si_{12}C_4$ microwires present perfectly rectangular hysteresis loops typical for Fe-rich microwires with high and positive magnetostriction coefficient, λ_s, ($\lambda_s \approx 35x10^{-6}$) exhibiting magnetic bistability. In contrast $Co_{69.2}Fe_{4.1}B_{11.8}Si_{13.8}C_{1.1}$ microwires present linear hysteresis loops previously reported for Co-based glass-coated microwires with low and negative λ_s ($\lambda s \approx -10^{-7}$) [3,4] (see Fig. 1a and Fig. 1b). Coercivity, H_c, of $Fe_{75}B_9Si_{12}C_4$ microwires (about 55 A/m) is about an order of magnitude higher that of $Co_{69.2}Fe_{4.1}B_{11.8}Si_{13.8}C_{1.1}$ microwires.

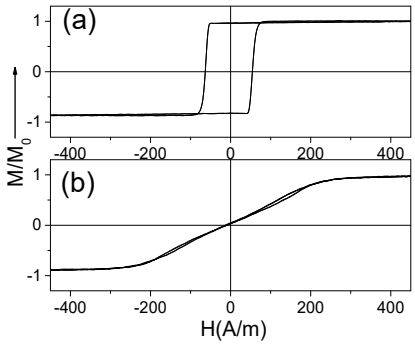

Fig 1. Hysteresis loops of as-prepared $Fe_{75}B_9Si_{12}C_4$ (a) and $Co_{69.2}Fe_{4.1}B_{11.8}Si_{13.8}C_{1.1}$ (b) microwires.

Accordingly, magnetically softer $Co_{69.2}Fe_{4.1}B_{11.8}Si_{13.8}C_{1.1}$ microwires exhibit an order of magnitude higher GMI ratio than $Fe_{75}B_9Si_{12}C_4$ microwires (see Fig. 2).

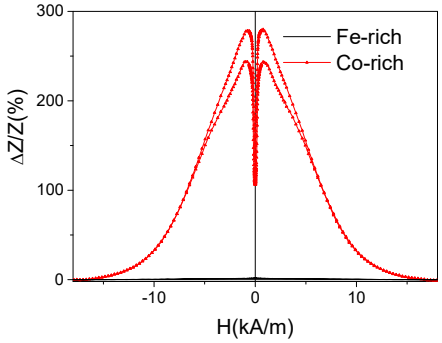

Fig. 2. $\Delta Z/Z(H)$ dependences of as-prepared $Co_{69.2}Fe_{4.1}B_{11.8}Si_{13.8}C_{1.1}$ and $Fe_{75}B_9Si_{12}C_4$ measured at 100 MHz.

Stress annealing of Fe based microwires allows considerable H_c decrease and inducing of transverse magnetic anisotropy, as can be observed from hysteresis loops measured in stress-annealed $Fe_{75}B_9Si_{12}C_4$ microwires (Fig. 3a).

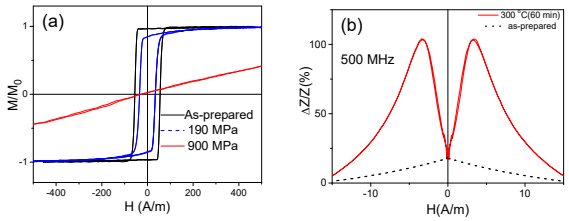

Fig. 3. Hysteresis loops (a) of as-prepared and stress-annealed at T_{ann}=300º C (upon σ =190 and 900 MPa) and $\Delta Z/Z(H)$ dependencies (b) of as-prepared and stress-annealed at T_{ann}=300º C (upon σ = 900 MPa) $Fe_{75}B_9Si_{12}C_4$ microwires.

Magnetic properties are considerably affected by the stress, σ, applied during the stress annealing: induced transverse magnetic anisotropy becomes more noticeable with increasing of σ -values. Accordingly, remarkable improvement of GMI ratio is observed in stress-annealed Fe–rich ($Fe_{75}B_9Si_{12}C_4$) microwires: improvement of $\Delta Z/Z$ –values by an order of magnitude is achieved.

Consequently, appropriate annealing of ferromagnetic microwires allows achievement of interesting combination of magnetic properties. In the Fe-rich microwires stress-annealing allows remarkable improvement of magnetic softness and GMI effect. On the other hand, a substantial GMI effect of Co-rich microwires can be also achieved. Thus, recently we reported $\Delta Z/Z$ –values up to 900% in annealed Co-rich microwires [4]

IV. Conclusion

We provide comparative studies of magnetic properties and GMI effect in Fe and Co-based microwires. Stress annealing allows remarkable improvement of magnetic softness and GMI effect in Fe-based microwires.

Acknowledgments

This work was supported by the Spanish MICIN, under PID2022-141373NB-I00 project, by EU (Horizon Europe) under "HARMONY", by the Government of the Basque Country, under Elkartek (MOSINCO and ATLANTIS) projects and by "Ayuda a Grupos Consolidados" (Ref.: IT1670-22).

References

[1] A.Zhukov, P. Corte-Leon, L. Gonzalez-Legarreta, M. Ipatov, J.M. Blanco, J. Gonzalez, V. Zhukova, "Advanced functional magnetic microwires for technological applications", J. Phys. D: Appl. Phys., vol. 55, p.253003, 2022.

[2] G. Herzer, "Amorphous and nanocrystalline soft magnets", in Proceedings of the NATO Advanced Study Insititute on Magnetic Hysteresis in Novel Materials, Mykonos, Greece, 1-12 July 1996 ed. George C. Hadjipanayis, NATO ASI Series (Series E:Applied Sciences) Vol. 338, pp.711-730. Kluwer Academic Publishers (Dordrecht/Boston/London) 1997.

[3] A. Zhukov, M. Ipatov and V. Zhukova, "Advances in Giant Magnetoimpedance of Materials", Handbook of Magnetic Materials, ed. K.H.J. Buschow, *Elsevier*, vol. 24, ch.2., pp. 139-236, 2015.

[4] A. Gonzalez, I. Skorvanek, M. Jakubcin, V. Zhukova, A. Zhukov, "Impact of elevated temperature on the Giant magnetoimpedance effect in Co-rich glass-coated microwires", Scr. Mater. vol.266. 116794, 2025.

Beyond optical chirality density: tensor descriptors of electromagnetic chirality

Ilia Smagin[1], Nikolay Gippius[1], Sergey Dyakov[1]

[1]Department of Physics, Skolkovo Institute of Science and Technology, Moscow, Russia

*Corresponding author: Ilia.Smagin@skoltech.ru

***Abstract*—Optical chirality density is commonly used to characterize chiral electromagnetic fields, but it is insufficient in anisotropic or structured media. We introduce tensorial descriptors of electromagnetic chirality based on the Lipkin formalism, clarify the physical meaning of their components, and demonstrate how multiple complementary measures of chirality naturally emerge in anisotropic consideration.**

***Keywords*— nanophotonics, optical chirality density, Lipkin tensor.**

I. Introduction

Optical chirality density is widely used as a scalar measure of the chiral properties of electromagnetic fields and their interaction with matter. However, in anisotropic and structured media, a single scalar quantity is generally insufficient to capture the full complexity of chiral field–matter coupling. In this work, we go beyond the conventional optical chirality density and introduce a set of tensor descriptors of electromagnetic chirality based on the Lipkin formalism [1]. These tensor quantities provide a richer and more physically transparent description of chiral electromagnetic fields, particularly in anisotropic environments. The physical meaning of individual tensor components is discussed, and their role in characterizing different aspects of electromagnetic chirality is clarified. In particular, we show that these tensor components naturally emerge when analyzing chiral light–matter interaction beyond isotropic approximations and can be directly linked to observable physical quantities.

II. Methods

To establish a direct link between electromagnetic chirality and observable physical quantities, we analyze molecular emission processes in chiral electromagnetic fields. Our approach builds upon the work of Tang and Cohen [2] and F. Fedorov formalism [3]. Specifically, we consider the period-averaged molecular emission rate in a monochromatic field:

$$A^{\pm} = \langle \mathbf{E}\cdot\dot{\mathbf{p}} + \mathbf{H}\cdot\dot{\mathbf{m}}\rangle = \frac{\omega}{2} Im(\mathbf{E}^*\cdot\mathbf{p} + \mathbf{H}^*\cdot\mathbf{m}) \qquad (1)$$

and use the expressions for dipole and magnetic moments in the anisotropic case [3], [5]:

$$p_\mu = \alpha_{\mu\nu}E_\nu - iG_{\mu\nu}H_\nu, \quad m_\mu = \chi_{\mu\nu}H_\nu + iG_{\mu\nu}E_\nu \qquad (2)$$

where $\alpha_{\mu\nu}$ is electric polarizability, $\chi_{\mu\nu}$ is magnetic susceptibility, and $G_{\mu\nu}$ is mixed electric-magnetic dipole polarizability or so-called optical activity tensor. Substituting (2) into (1) yields a generalized expression for the molecular emission velocity.

For modeling the interaction of chiral light with chiral matter we follow approaches [3], [4] that are expressed by the following material equations

$$\begin{aligned} D_\mu &= \varepsilon_{\mu\nu}E^\nu + \chi_{\mu\nu}H^\nu, \\ B_\mu &= \xi_{\mu\nu}E^\nu + \mu_{\mu\nu}H^\nu. \end{aligned} \qquad (3)$$

and use the Fourier modal method [6].

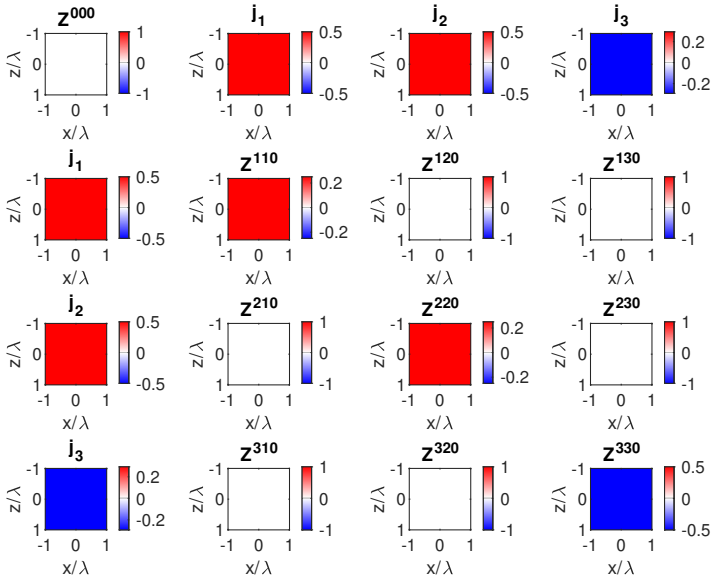

Fig. 1. The average Lipkin tensor components $Z^{\mu\nu 0}$. The optical chirality density $\rho_\chi = Z^{000}$ is equal to zero but diagonal density components and corresponding flux components are not.

III. Results and Discussion

Using the formalism described above, we derive an explicit expression linking molecular emission velocity to the components of the Lipkin density tensor. It appears that the emission velocity of a molecule in the monochromatic case can be represented in the form:

$$A^{\pm}_{ani} = \textit{nonchiral terms} \mp \sum_{m=1}^{6} w_m \overline{Z^{(m)}} \qquad (4)$$

Here $\overline{Z^{(m)}} = \mathcal{G}_{ab}^{(m)} Im(E_a^* H_b - H_a^* E_b) = \overline{Z^{ij0}}$ are one of the six realizations of the zilch tensor density components, $m = 1, ..., 6$ and the coefficients w_m quantify the weight of each chiral channel. Since the coefficients w_m are determined solely by molecular geometry, this expression generalizes the Tang–Cohen result: the chiral asymmetry in the excitation rate of a small molecule in an arbitrary anisotropic environment is proportional to the product of the molecular chirality and the corresponding component of the electromagnetic chirality encoded in the Lipkin tensor. We show that expression (4) in the isotropic case will match the Tang-Cohen result [2] with optical chiral density $\rho_\chi = \overline{Z^{000}}$

$$A_{iso}^{\pm} = \frac{\omega}{2}\left(\alpha''|\boldsymbol{E}|^2 + \chi''|\boldsymbol{H}|^2\right) \pm G''\omega Im(\boldsymbol{E}^* \cdot \boldsymbol{H}) \quad (5)$$

Moreover, the diagonal components of the Lipkin tensor admit a natural interpretation in terms of eigenfields of the chiral interaction operator, providing a basis-independent description of independent chiral channels. This provides a direct link between the Lipkin density tensor components and the molecular emission velocity, clarifying their physical meaning.

To illustrate the practical implications of this tensorial description, we consider a simple yet illustrative example of two plane monochromatic waves in a vacuum with different signs of circular polarization and spreading at different angles to the coordinate axes. The angles are chosen in such a way that the optical chiral density ρ_χ is equal to zero for the total field (see Fig. 1) but the diagonal density components and corresponding flux components are not. This demonstrates that the optical chiral density alone does not provide a complete characterization of electromagnetic chirality.

IV. Conclusion

In this work, we have demonstrated that optical chirality density, while useful, represents only a single component of a more general tensorial description of electromagnetic chirality. Using the Lipkin formalism, we introduced tensor descriptors that naturally arise in anisotropic and structured media and clarified their physical meaning through their connection to molecular emission processes.

We have shown that in anisotropic field configurations, the scalar optical chirality may vanish, even though other components of the Lipkin tensor remain finite and physically relevant. This shows that scalar measures alone can fail to capture essential aspects of chiral electromagnetic fields. In contrast, the tensorial approach provides a more complete and coordinate-resolved description of chirality, revealing contributions that are otherwise hidden.

References

[1] D. M. Lipkin,"Existence of a New Conservation Law in Electromagnetic Theory", *Journal of Mathematical Physics*, vol. 5, pp. 696–700, 1964.

[2] Y. Tang and A. E. Cohen, "Optical chirality and its interaction with matter", *Physical Review Letters*, vol. 104, 2010.

[3] F. I. Fedorov, "Theory of Gyrotropy", *Nauka i Tekhnika*, vol. 452, 1976.

[4] S. Dyakov, et al. "Strong coupling of chiral light with chiral matter: a macroscopic study." Optica 12.9 (2025): 1406-1416.

[5] L.D. Laurence, "Molecular light scattering and optical activity." Cambridge University Press, 2009

[6] I. Smagin, et al. "The Fourier modal method for gratings with bi-anisotropic materials." (2025) arXiv preprint arXiv:2510.05973.

Programmable synthetic frequency dimension platform for on-chip topological photonics

Xiaolong Su[1,*], Weiwei Liu[1], Bing Wang[1], Peixiang Lu[1]

[1] Wuhan National Laboratory for Optoelectronics and School of Physics, Huazhong University of Science and Technology, China

*Corresponding author: d202380097@hust.edu.cn

***Abstract*— More recently, photonic synthetic dimension has become an emerging paradigm. Specifically, the synthetic frequency dimension offers unique advantages due to flexibly reconfigurable gauge potential and long-range couplings. Here, we present the realization of programmable chiral edge states of the Hall ladder in synthetic frequency dimension.**

***Keywords*— synthetic dimension, Thin-film lithium niobate, topological photonics, photonic crystals.**

I. Introduction

Understanding chiral edge states is essential for probing spin-orbit coupling in topological systems, which play a prominent role in topological insulators, valleytronics, and topological photonics [1]. Experiments show that modulating these states via external fields leads to remarkable phenomena such as topological phase transitions, non-Abelian Aharonov-Bohm effects, and chiral Landau levels [2]. Although platforms like photonic crystals and metamaterials have enabled such studies through artificial gauge fields, their inflexibility and fabrication complexity limit the development of fully reconfigurable systems for controlling chiral edge states. The concept of photonic synthetic dimensions has emerged as a powerful strategy, using internal photon degrees of freedom—such as frequency [3], time [4], and orbital angular momentum—to create extra dimensions. Synthetic frequency dimensions have enabled chiral edge modes and spin-momentum locking through tailored gauge potentials. However, a fully reconfigurable and integrated photonic platform remains lacking, hindering further exploration and control of chiral edge states in synthetic dimensions.

II. Methods

In this work, we demonstrate a microring resonator supporting resonant frequency modes in both clockwise (CW) and counterclockwise (CCW) directions on an integrated thin-film lithium niobate (TFLN) photonic platform (Fig. 2). Through traveling-wave electro-optic modulation applied with phase control, we synthetically engineer frequency lattices for each pseudo-spin. The system is described by a tight-binding model:

$$H=-\sum_{m,s}\left[\omega_m a_{m,s}^{\dagger}a_{m,s}+\sum_{l=1}^{\infty}(J_s(t)a_{m,s}^{\dagger}a_{m-l,s}+H.c.)\right]-K\sum_{m}(a_{m,\uparrow}^{\dagger}a_{m,\downarrow}+H.c.),$$

where $a_{m,s}$ and $a_{m,s}^{\dagger}$ are the annihilation and production operators for the m-order frequency mode with pseudo-spin $s\in\{\uparrow(\mathrm{CW}),\downarrow(\mathrm{CCW})\}$. $J_s(t)$ and K represents coupling strength. We first construct a synthetic Hall ladder by applying phase-offset modulations, introducing an artificial magnetic flux. Band structure measurements reveal clear spin-momentum locking. Experimental spectra and current profiles align closely with theory. Furthermore, by applying asymmetric modulation signals, we create a misaligned interface that breaks symmetry between pseudo-spins, resulting in imbalanced chiral edge states. Next, we construct a coupled Hall ladder system supporting versatile chiral phases through next-nearest-neighbor coupling. By programming the phase parameters, we demonstrate several distinct regimes: chirality, single-pseudospin enhancement (SPE) and complete suppression. In conclusion, we have realized a programmable integrated photonic platform for synthesizing and controlling chiral edge states, paving the way for high-dimensional and reconfigurable topological photonic systems.

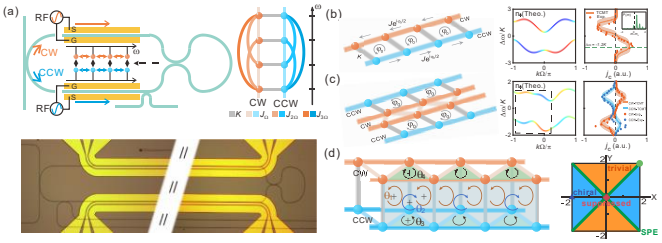

Fig. 1 Reconfigurable chiral edge states via synthetic dimensions in an integrated photonic platform.

III. Results and Discussion

Experimental results show:

- On-chip synthesis dimension platform
- Observation of band and chiral currents (Fig. 1)
- Programmatic Control of Chiral States

IV. Conclusion

We constructed an on-chip synthesis platform and synthesized Hall ladders, enabling observation and programmable modulation of chiral edges. This work establishes a programmable integrated photonic system for emulating and controlling chiral edge states in synthetic space.

Acknowledgments

This work was supported by the National Natural Science Foundation of China. The authors gratefully acknowledged the Center of Micro-Fabrication and Characterization (CMFC) of Wuhan National Laboratory for Optoelectronics (WNLO) for fabrication support.

References

[1] B. A. Bernevig and S. C. Zhang, "Quantum Spin Hall Effect," Phys. Rev. Lett. 96, 106802, 2006.
[2] H. Jia et al., "Experimental realization of chiral Landau levels in two-dimensional Dirac cone systems with inhomogeneous effective mass," Light: Sci. Appl. 12, 165, 2023.
[3] A. Dutt et al., "Experimental band structure spectroscopy along a synthetic dimension," Nat Commun 10, 3122, 2019.
[4] L. Yu et al., "Dirac mass induced by optical gain and loss," Nature 632, 63–68, 2024.

Angle-Induced Double Resonance of Quasi-Guided Modes for Enhanced Second-Harmonic Generation

Sooseong Ji[1], Jaesung Kim[1], Jongwon Lee[1,*]

[1]Department of Electrical Engineering, Ulsan National Institute of Science and Technology, Ulsan 44919, Korea

*Corresponding author: jongwonlee@unist.ac.kr

***Abstract*—We experimentally demonstrate angle-tunable double-resonant second-harmonic generation in a dielectric metasurface supporting quasi-guided modes. By adjusting the incident angle source, simultaneous resonances at both the fundamental and second-harmonic wavelengths are achieved, resulting in a 27-fold enhancement of the SHG signal.**

***Keywords*— Second-harmonic generation, guided mode, nonlocal.**

I. Introduction

All-dielectric metasurfaces have emerged as an effective platform for enhancing nonlinear light–matter interactions at the nanoscale. However, the relatively weak nonlinear response of dielectric materials often limits the efficiency of processes such as second-harmonic generation (SHG), motivating the development of resonant strategies capable of providing substantial field enhancement. One promising approach relies on high-Q resonances originating from leaky modes, such as quasi-bound states in the continuum (quasi-BICs) and quasi-guided modes (QGMs), where controlled structural perturbations introduce finite radiative coupling while preserving exceptionally large quality factors. QGMs engineered through modulation of grating width and periodicity have been reported to sustain high-Q resonances together with dispersive characteristics in momentum space [1]. The momentum-dependent characteristic of QGMs provides an additional degree of freedom for modal engineering. Exploiting this property, we design a dielectric grating metasurface supporting QGMs near the fundamental wavelength (800 nm) and its second harmonic (400 nm). By tuning the incident angle, corresponding to variation of the in-plane wavevector k_y, we identify a condition satisfying $k_{\mathrm{SH}} = 2k_{\mathrm{FF}}$, where the two QGMs become degenerate. Under this angle-selective degeneracy, simultaneous resonances at the fundamental and second-harmonic frequencies are achieved, resulting in a 27-fold enhancement of SHG efficiency.

II. Methods

The second-harmonic(SH) emission efficiency can be described by the modal overlap factor [2], which is expressed as

$$\beta = \frac{\int d\boldsymbol{r}\, \epsilon E_2^* E_1^2}{(\int d\boldsymbol{r} \epsilon_1 |E_1|^2)(\sqrt{\int d\boldsymbol{r} \epsilon_2 |E_2|^2})} \sqrt{\lambda_1^3}, \quad (1)$$

where E^{ω} and $E^{2\omega}$ denote the electric-field distributions at the fundamental and second-harmonic frequencies inside the structure, respectively. ε is the spatial permittivity distribution ε_{ω} and $\varepsilon_{2\omega}$ represent the permittivities. The SH intensity follows

$$I_{SH} \propto \left|\mathrm{X}_{(2)}\right|^2 |\beta|^2 \quad (2)$$

Indicating that the SHG efficiency increases as the modal overlap between the fundamental field distribution and the second-harmonic mode becomes stronger. Under double-resonant conditions, resonant enhancement at both frequencies increases E_{ω} and $E_{2\omega}$ simultaneously. When the degeneracy condition is satisfied, the modal overlap between the nonlinear source E_{ω}^2 and the second-harmonic mode is maximized, leading to stronger nonlinear coupling.

The dielectric grating metasurface was designed to support QGMs at both frequencies (fundamental and second-harmonic). The geometric parameters were optimized using finite-difference time-domain (FDTD) simulations. The final design consisted of TiO_2 grating with a width of 110 nm and a perturbation parameter $\alpha = 30$nm, arranged with a period of $2P = 390$nm.

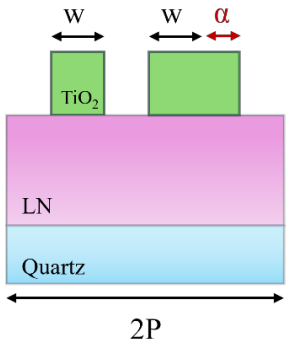

Fig. 1. Unit-cell geometry of the metasurface

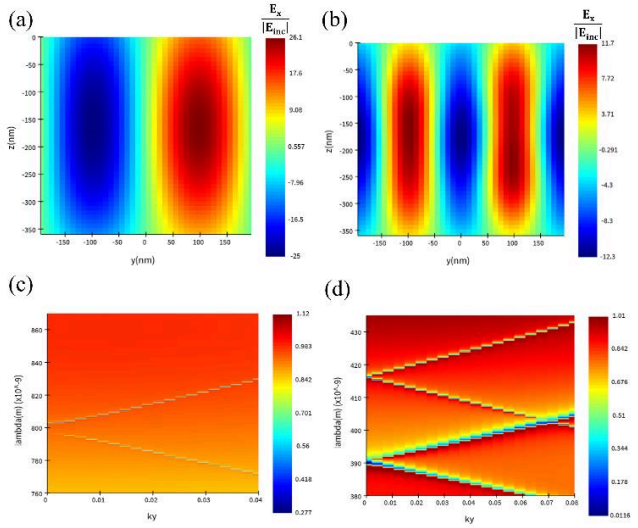

Fig. 2. Simulated QGMs at the fundamental (800 nm) and second-harmonic (416 nm) wavelengths. (a) and (b) Electric-field profiles in LN layer at 800 nm and 416 nm, respectively. (c) and (d) Corresponding dispersion relations

Angle-resolved linear spectrum was measured using a Fourier-plane filtering configuration to confirm the formation of the QGM. The transmitted beam was projected onto the Fourier plane, where each spatial position corresponds to a specific in-plane momentum k_y.

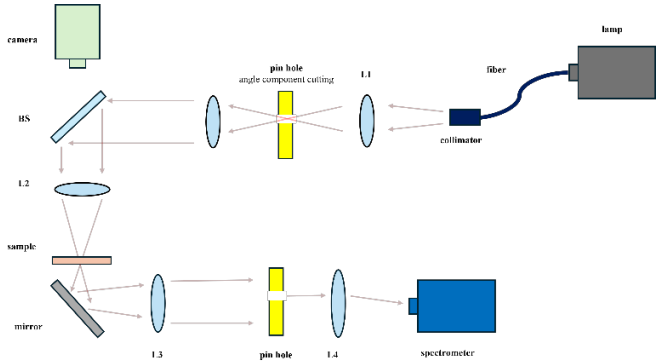

Fig. 3. Experimental setup for momentum-resolved linear spectroscopy. A pinhole placed at the Fourier plane selectively filters a specific in-plane momentum component.

And SHG measurements were performed using a pulsed excitation source and rotation stage.

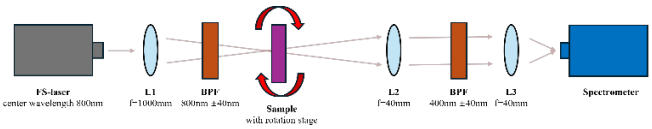

Fig. 4. Experimental setup for SHG measurements. The generated SH signal is spectrally filtered and collected for detection.

III. Results and Discussion

The measured linear transmission map reveals a clear dispersive resonance branch near 800 nm, exhibiting the same dispersion trend predicted by Fig. 2-(c).

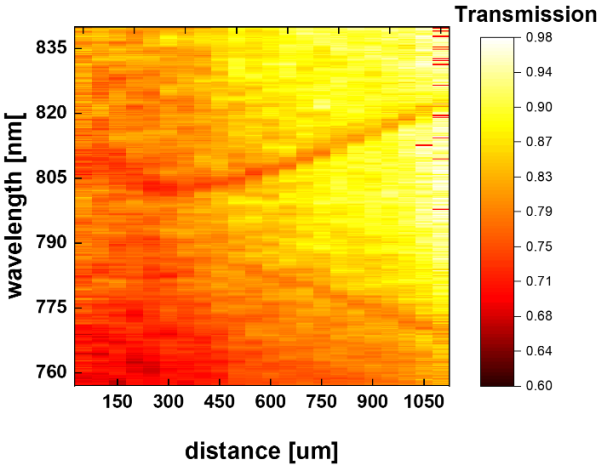

Fig. 5. Measured transmission spectrum. The transmission map is plotted as a function of wavelength and spatial position of pinhole in the Fourier plane (see Fig. 3).

The SH signal was experimentally measured for both an unpatterned reference and the patterned metasurface. This pronounced increase in SHG confirms that the patterned metasurface supports the designed resonant mode, leading to strong nonlinear enhancement.

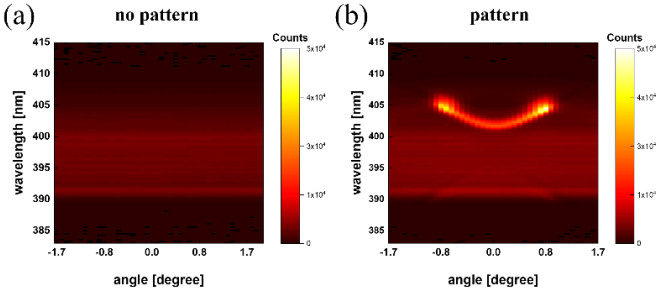

Fig. 6. Measured SHG result for (a) an unpatterned reference sample and (b) the TiO_2 grating patterned metasurface. A pronounced SHG enhancement is observed in the patterned.

In Fig. 7, The SHG enhancement factor was calculated by normalizing the measured SHG intensity of the patterned metasurface to that of the unpatterned reference. A pronounced peak is observed near angles of ± 0.83 degree where the enhancement factor reaches approximately 27.

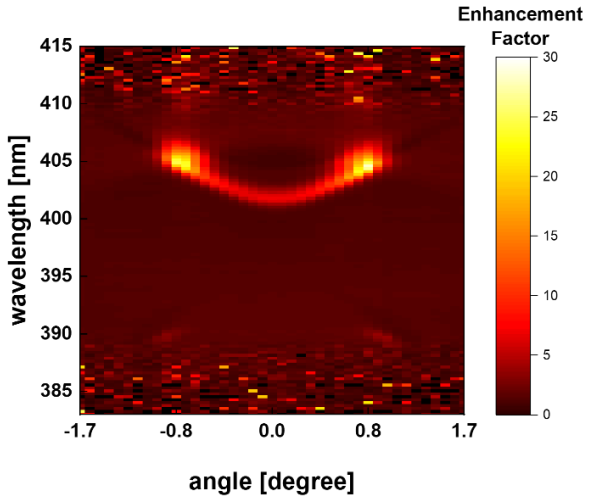

Fig. 7. Measured SHG enhancement factor of the patterned metasurface, defined as the ratio between the SHG intensity of the patterned structure and that of the unpatterned reference. A maximum enhancement factor of approximately 27 is observed near angles of ±0.83 degree

IV. Conclusion

We experimentally confirmed that a pronounced SHG peak is formed at the angle-induced double-resonant condition of the metasurface. By tuning the rotation angle, the dispersive QGMs at the fundamental and second-harmonic frequencies become simultaneously resonant, leading to a strong nonlinear enhancement with a maximum enhancement factor of 27. This result demonstrates that momentum-space engineering provides an effective route to access double-resonant operation without modifying the structural geometry.

Acknowledgments

This work was partly supported by Institute of Information & Communications Technology Planning & Evaluation (IITP) grant funded by the Korea government (MSIT) (RS-2023-00227854, RS-2023-00259676) and by the National Research Foundation of Korea (NRF) (2022R1A2C301189812, 2022M3H4A1A04096465).

References

[1] Jiang, Hui, et al. "Tunable Second Harmonic Generation with Large Enhancement in A Nonlocal All-Dielectric Metasurface Over A Broad Spectral Range." Advanced Optical Materials, p.2303229. (2024)

[2] Lin, Zin, et al. “Cavity-enhanced second-harmonic generation via nonlinear-overlap optimization.” Optica 3.3 233-238. (2016)

3D Stokes Polarimetry of Dipolar Near-Fields

Guillermo Serrera[1,*], Yael Gutiérrez[1], José J. Gil[2], Fernando Moreno[1]

[1]Applied Physics Department, University of Cantabria, Spain
[2]Independent researcher, 29620 Casares Costa, Spain
*Corresponding author: guillermo.serrera@unican.es

***Abstract*—Dipolar emitters constitute fundamental building blocks in nanophotonics, yet their polarization behavior outside the far-field approximation remains insufficiently characterized. In this work, we introduce the three-dimensional Stokes formalism as a unified framework to describe the complete polarimetric landscape of dipolar radiation across the near-, intermediate-, and far-field regimes.**

***Keywords*— Stokes, polarimetry, dipolar fields.**

I. Introduction

Dipolar emitters play a central role in nanoscale light–matter interactions, yet their polarization properties remain insufficiently characterized outside the far-field approximation. Conventional 2D Stokes analysis assumes purely transverse fields and therefore cannot capture the intrinsically three-dimensional, vectorial nature of dipolar radiation in the near- and intermediate-field regimes. Recent experimental advances have further underscored this limitation by demonstrating the measurement of full 3D polarization and optical spin in evanescent and near-field environments.[1] A rigorous description of these regimes is therefore essential for nanophotonic applications, where strongly inhomogeneous electromagnetic fields are ubiquitous.

In this work, we apply the 3D Stokes formalism to analyze the emission of a range of dipolar sources, including electric, magnetic, spinning, and chiral dipoles. We show how this formalism effectively describes all polarization phenomenology in real-space, in contrast with approaches based on the Angular Spectrum Representation.[2] Furthermore, we show how, for deterministic fields, the 3D Stokes formalism allows simplification to 2D representations, accomodating the interpretation of complex polarization landscapes to conventional polarimetric techniques.

II. Methods

Our analysis is based on the 3D polarization matrix constructed from the full vectorial electric field of dipolar emitters. The matrix is expanded using the Gell–Mann basis, yielding nine real-valued 3D Stokes parameters.[3] These parameters encode total intensity, linear and circular polarization content, and the relative weight of radial versus transverse field components.

III. Results and Discussion

For linear electric dipoles, the 3D Stokes formalism reveals a fully linear polarization in the near field, dominated by longitudinal components. In the intermediate field, non-zero circular Stokes parameters emerge despite uniform intensity, evidencing transverse optical spin in real space.[2] In the far field, the field becomes purely transverse and is well described by conventional 2D Stokes parameters.

Spinning electric dipoles exhibit uniform azimuthal symmetry and strong circular polarization signatures, with the formalism clearly capturing helicity inversion and the evolution of spin components across regimes.[4]

For chiral dipoles, the near field closely resembles that of an electric dipole, while magnetic contributions become significant in the intermediate regime. The 3D Stokes parameters distinguish chiral circular polarization from electric-dipole–induced polarization artifacts, highlighting potential pitfalls in chiral sensing.

Finally, we show how a reduction of 3D-to-2D polarization states can be achieved by finding an intrinsic system for each point in space. This allows to express the polarization state in terms of the usual 2D formalism, revealing the fundamental nature of evanescent linear and circular polarization components with respect to the energy flow.

IV. Conclusion

We have demonstrated that the 3D Stokes formalism provides a compact, intuitive, and fully analytical framework for characterizing the polarization structure of dipolar emission across near-, intermediate-, and far-field regimes. By explicitly accounting for longitudinal and transverse field components, the formalism captures polarization effects that are inaccessible to conventional 2D Stokes analysis. This approach offers a powerful and accessible alternative to angular-spectrum-based methods and is well suited for the analysis of nanoscale light–matter interactions involving inhomogeneous fields.

Acknowledgments

Y.G. acknowledges funding from a Ramon y Cajal Fellowship (RYC2022-037828-I). G.S. thanks the Spanish Ministry of Education for his predoctoral contract grant (FPU21/02296).

References

[1] Z. Dong, K. Saastamoinen, A. Norrman, J. Gil, Y. Chen, A. Friberg, and T. Setälä, "Nanoscattering measurement of 3D polarization and spin in a random evanescent wave," Optica 12, 1912-1918 (2025).
[2] M. Neugebauer, P. Banzer, and S. Nechayev, "Emission of circularly polarized light by a linear dipole," Sci. Adv. 5, eaav7588 (2019).
[3] J. J. Gil and R. Ossikovski, Polarized Light and the Mueller Matrix Approach, 2nd ed. (CRC Press, Boca Raton, 2022)
[4] Jörg S. Eismann, Martin Neugebauer, and Peter Banzer, "Exciting a chiral dipole moment in an achiral nanostructure," Optica 5, 954-959 (2018).

Flexible and Programmable Semiconductor Plasmonic Platforms for Near-Infrared Meta-Optics

Debmalya Mukhopadhyay[1] and Bivas Saha[1,2]

[1]Chemistry and Physics of Materials Unit and International Centre for Materials Science, Jawaharlal Nehru Centre for Advanced Scientific Research, Bangalore 560064, India
[2]School of Advanced Materials (SAMat), Jawaharlal Nehru Centre for Advanced Scientific Research, Bangalore 560064, India

Corresponding author: bsaha@jncasr.ac.in

Abstract: Semiconducting plasmonic platforms based on doped ScN and CdO thin films are demonstrated for near-infrared meta-optics. Flexible van der Waals heteroepitaxy enabled ScN exhibits tunable ENZ response, while Sc-doped CdO enables wide spectral programmability via carrier engineering. Attenuated total reflection reveals SPP modes, establishing complementary, low-loss, programmable plasmonic materials.

Keywords: Plasmonics, Dielectric permittivity, van der Waals heteroepitaxy, Surface plasmon polariton

Introduction: Plasmonic materials play a central role in meta-photonics by enabling subwavelength light confinement, enhanced light–matter interaction, and compact photonic integration. However, noble metals like gold and silver suffer from high optical losses, limited tunability, and poor compatibility with flexible or semiconductor platforms, restricting their use in the near-infrared (NIR) regime. These limitations have driven interest in alternative semiconducting plasmonic materials.

Degenerately doped semiconductors provide a powerful route to programmable plasmonics, where plasma frequency and optical response can be engineered via carrier concentration. Transition metal nitrides and transparent conducting oxides represent two complementary classes of low-loss semiconductor plasmonic materials. Scandium nitride (ScN), a refractory rocksalt semiconductor, exhibits epsilon-near-zero behaviour and mechanical robustness, while cadmium oxide (CdO) offers high carrier mobility and wide spectral tunability.

In this work, we present a unified semiconductor plasmonic platform combining flexible ScN and tunable CdO thin films. By controlling dopant incorporation and growth conditions, we demonstrate ENZ response and surface plasmon polariton excitation across a broad infrared range, highlighting their potential for near-infrared meta-optics.

Experimental methods: Flexible ScN thin films were grown on fluorophlogopite mica substrates using van der Waals heteroepitaxy in molecular beam epitaxy system (MBE), while epitaxial CdO films were deposited on MgO (001) substrates using DC magnetron sputtering system. Oxygen incorporation in ScN and Sc doping in CdO were employed to systematically tune carrier concentration.

Optical constants were extracted using variable-angle spectroscopic ellipsometry modelled with Drude and extended Drude approaches. Infrared reflectivity measurements were performed to identify ENZ wavelengths. Surface plasmon polaritons were excited using attenuated total reflection (ATR) in the Otto configuration with TM-polarized light.

Results and discussion: The plasmonic response is governed by the complex dielectric permittivity $\varepsilon(\lambda)=\varepsilon_1(\lambda)+i\varepsilon_2(\lambda)$. Near the plasma frequency, ε_1 crosses zero, yielding the ENZ condition, while negative ε_1 at longer wavelengths enables plasmonic behaviour.

Pristine ScN exhibits a carrier concentration of 3.4×10^{20} cm^{-3}, corresponding to an ENZ wavelength near 2.24 µm. Intentional oxygen doping increases the carrier concentration to 2.4×10^{21} cm^{-3}, shifting the ENZ to 1.14 µm within the NIR window (Figure 1a). Reflectivity minima observed near ENZ confirm plasmonic absorption arising from impedance matching (Figure 1b).

Similarly, pristine CdO shows an ENZ wavelength at ~6.63 µm due to a carrier concentration of 2.8×10^{19} cm^{-3}. Sc doping increases carrier density to 2.3×10^{20} cm^{-3}, shifting ENZ to 2.63 µm (Figure 1d, e). Both materials exhibit low optical loss near ENZ, favourable for meta-optical applications.

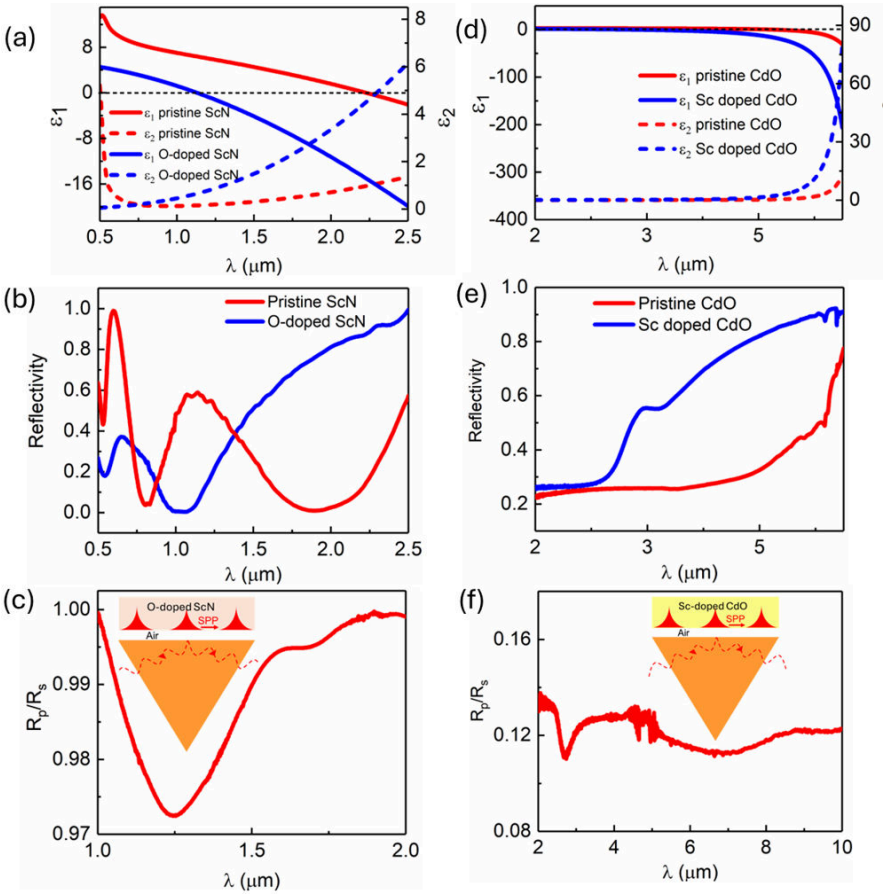

Figure 1. (a) Real (ε_1) and imaginary (ε_2) parts of the dielectric permittivity of pristine and O-doped ScN, showing doping-induced tuning of the ENZ wavelength in the NIR region. (b) Corresponding reflectivity spectra highlighting the ENZ-related reflectance minimum. (c) ATR reflectivity (R_p/R_s) of O-doped ScN in the Otto configuration, confirming SPP excitation at the ScN–air interface. (d) Dielectric permittivity of pristine and Sc-doped CdO illustrating carrier-dependent ENZ tunability in the mid-infrared regime. (e) Reflectivity spectra of CdO films showing doping-induced spectral shifts. (f) ATR spectra of Sc-doped CdO revealing propagating and hybridized SPP modes at the semiconductor–air interface.

Coupling of TM-polarized light with free electrons at a plasmonic material–dielectric interface gives rise to propagating surface electromagnetic waves known as surface plasmon polaritons (SPP). SPPs were excited using ATR in the Otto geometry (Inset of Figure 1c and

1f). For the ScN/air interface, a pronounced reflectivity dip at ~1.24 μm indicates SPP excitation (Figure 1c). CdO heterostructures exhibit two resonance minima at ~2.7 μm and ~7.0 μm, corresponding to hybridized symmetric and antisymmetric plasmonic modes arising from the air/CdO/MgO interfaces (Figure 1f).

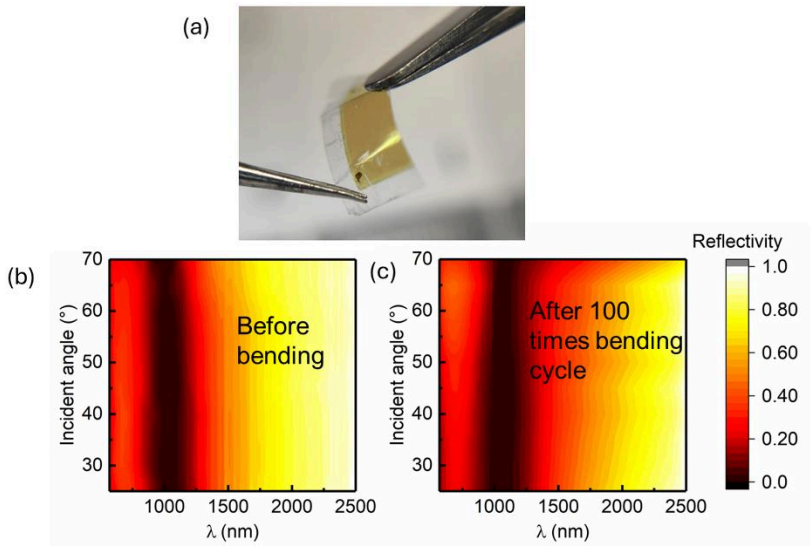

Figure 2. (a) Optical image of the exfoliated O-doped ScN/F-mica film demonstrating mechanical flexibility under bending. (b) Angle-dependent reflectivity map of the O- doped ScN/F-mica film. (c) Angle-dependent reflectivity map after 100 times bending cycle. The unchanged plasmonic response confirms the robustness of the ENZ resonance and surface plasmon behaviour under mechanical deformation.

After establishing the NIR plasmonic response of epitaxial O- doped ScN on F-mica, the mechanical flexibility of the film was examined by mechanically exfoliating the ScN layer with an approximately 5 μm mica support and bending it using tweezers (Figure 2a). Angle-resolved reflectivity maps measured before and after 100 times bending cycle show no noticeable variation in the plasmonic response, confirming the mechanical robustness and stability of the ENZ behaviour in the flexible ScN film (Figure 2b, c).

Conclusion: We demonstrate flexible and programmable semiconductor plasmonic platforms based on doped ScN and CdO thin films, supporting low-loss ENZ behaviour and surface plasmon polaritons across the near- and mid-infrared regimes. The combination of mechanical flexibility, carrier-controlled spectral tunability, and well-defined SPP modes establishes these materials as promising candidates for next-generation metasurfaces and near-infrared meta-optical devices.

References:

1. **D. Mukhopadhyay**, D. Rao, A. I. K. Pillai, M. Garbrecht and B. Saha, “van der Waals Heteroepitaxy Enabled Flexible Yet Refractory Near-Infrared Plasmon-Polaritons in Scandium Nitride” Nano Lett. 2024, 24 (45), 14493–14499.
2. **D. Mukhopadhyay**, S. Rudra, B. Biswas, P. Das, and B. Saha, “Surface Scattering-Dependent Electronic Transport in Ultrathin Scandium Nitride Films”, ***Appl. Phys. Lett.*** *123, 192101 (2023).*
3. **D. Mukhopadhyay**, J. Dhar, and B. Saha, “Symmetric and Antisymmetric Plasmonic Modes in Doped CdO Heterostructures”, *(Manuscript under preparation)*

A Dynamically Beam Steerable Metasurface Antenna with Sidelobe Suppression

Enez F. Cihan[1,2*], Nursel Akcam[2]

[1]Division of Radar, EW and Intelligence Systems, ASELSAN Inc., Ankara, Türkiye
[2]Dept. of Electrical and Electronics Engineering, Gazi University, Ankara, Türkiye
*Corresponding author: efcihan@aselsan.com.tr

***Abstract*— A dynamically beam-steerable metasurface antenna based on a substrate integrated waveguide is presented. Metasurface elements are loaded with PIN diodes to dynamically control the beam steering toward different directions. A modified sidelobe suppression method is also incorporated alongside beam steering and evaluated using analytical array factor calculations and full-wave simulations in ANSYS HFSS. The proposed antenna achieves up to 6 dB sidelobe reduction with minimal main-beam degradation while steering the beam from −25° to +30° in the Ku-band using only 24 elements.**

***Keywords*— metasurfaces, antennas, sidelobe suppression**

I. Introduction

Future wireless technologies are in search of cost-effective and dynamically adaptable beam angle control methods. Traditional phased array architectures are often accompanied by considerable system complexity as they often need highly sophisticated phase-shifting and feeding networks. On the other hand, emerging concepts such as dynamically reconfigurable metasurfaces represent two dimensional artificial electromagnetic (EM) structures engineered to manipulate and control EM wave propagation [1]-[3]. Enabling them to function as antenna radiators allows for the development of cost-effective new techniques for beamforming and beam shaping without additional design complexity [4-5]. When configured as an array of metasurface elements, the required phase shifts for beam steering are inherently derived from a propagating reference wave that travels across the metasurface aperture and a progressive phase to each metasurface element is then provided. By integrating a PIN diode into each metasurface element, the coupling behavior of each can be independently switched. Radiative metasurface antennas based on substrate integrated waveguide (SIW) employ subwavelength polarizable dipole-type metamaterial elements capable of dynamic radiation pattern reconfiguration. In [6], the authors achieved a dynamically reconfigurable metasurface antenna operating at 12 GHz with a gain of 8.35 dBi by employing PIN diodes. In [7], the authors introduced a two-dimensional metasurface antenna operating in the X-band, which achieves beam steering capability by utilizing varactor diodes for electronic tuning with a gain of 10 dBi.

In this work, a one-dimensional metasurface array based on a new metasurface geometry is proposed. Unlike most previous studies, sidelobe-level optimization is incorporated alongside beam steering, and the antenna performance is evaluated using a compact array with a small number of elements through analytical and full-wave analyses in ANSYS HFSS.

II. Substrate Integrated Waveguide Based Single Metasurface Antenna Design

The design methodology begins with the design of a low-loss SIW reference waveguide supporting the dominant TE_{10} mode, which serves as the excitation medium for the metasurface elements, which are complementary electric-LC (CELC) in this work. Subsequently, a single metasurface unit cell is designed and characterized to achieve ON–OFF radiation states using PIN diodes. The SIW can be regarded as a planar equivalent of a dielectric-filled rectangular waveguide, supporting the same dominant TE_{10} mode with an equivalent cut-off frequency [8], which can be calculated as shown in Eq. 1. Here, f_c denotes the cut-off frequency, ε_r is relative permittivity and A_r represents the SIW-width.

$$f_c = \frac{c}{2\sqrt{\varepsilon_r}} - \left(A_r - \frac{D^2}{0.95P}\right)^{-1} \quad (1)$$

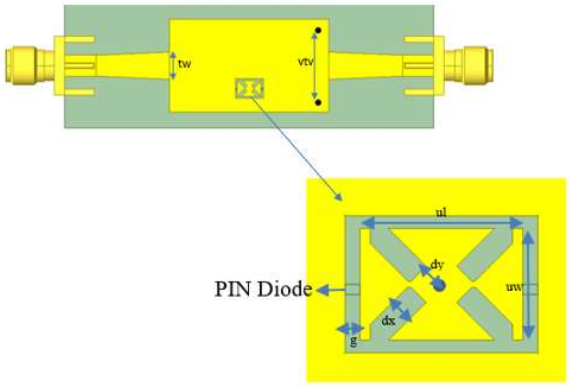

Fig 1. Proposed SIW-Based Metasurface Antenna Element

TABLE I. DIMENSIONS OF THE PROPOSED METASURFACE (IN MM)

uw	ul	dx	dy	g	tw	vtv
2.6	3.8	0.55	1.55	0.35	4.4	11.4

The continuous metallic sidewalls are replaced by two rows of metallized vias with diameter D, and an inter-via spacing P. A Rogers 4003 substrate (1.524 mm thick) is used with the via diameter and inter-via spacing are 0.8 mm and 1.1 mm, respectively. Those were chosen according to the proportional criteria derived in [9] to suppress electromagnetic leakage between adjacent vias. The metasurface dimensions were initially set to $\lambda/10$. A cutoff frequency was defined to cover the center operating frequency of 12.6 GHz, and the SIW width was chosen accordingly. After parameter optimizations, the values in Table 1 were selected as the final design parameters. As an example, Fig. 2 (a) illustrates how variations in the d_y spacing affect the transmission and reflection characteristics, and tune the resonance frequency, when the antenna element is in the open state (i.e., the PIN diode is off). This distance can be interpreted as the separation between the bias via—connected to the DC bias line and located near the center of the metasurface—and the rectangular slot etched on the surface. Variations in this distance directly affect the resonance frequency at which the metasurface unit cell couples to the reference wave. Fig. 2 (b) illustrates the variation in the reflection and transmission coefficients when the metasurface unit cell is offset from the center of the SIW. It can be observed that, as the metasurface offset increases, the return loss improves while the coupling to the reference wave decreases. Fig. 2 (c) demonstrates that the proposed metasurface exhibits a negative refractive index over the frequency range of 12.1–13.2 GHz and a negative group delay at 12.6 GHz when the element is nearly at center. As shown in Fig. 2 (d), the angular difference in the normalized gain of the metasurface element in its active and inactive states is analyzed in its principal plane, when the structure is assumed to be in one-dimensional array. It can be inferred that, within the angular range of −25° to +25°, the gain difference exceeds 8 dB, reaching a maximum value of 13 dB in this range.

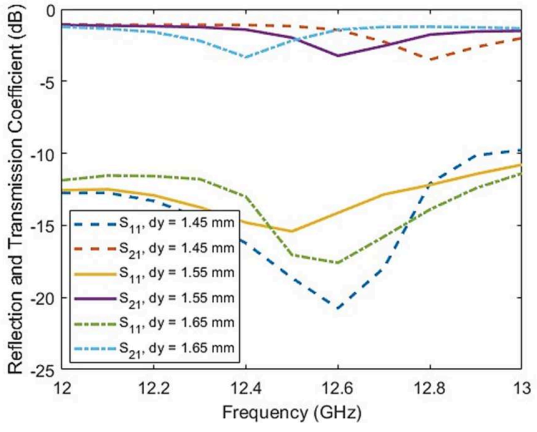

(a)

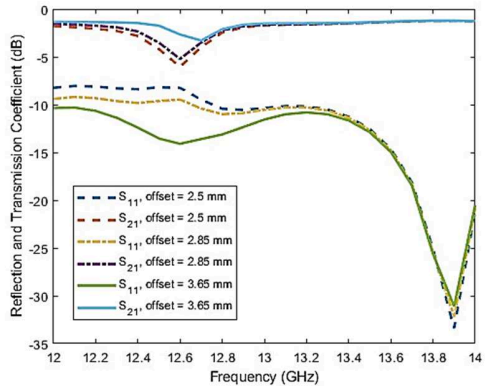

(b)

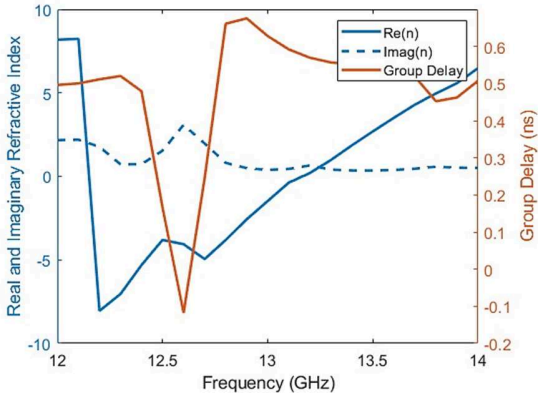

(c)

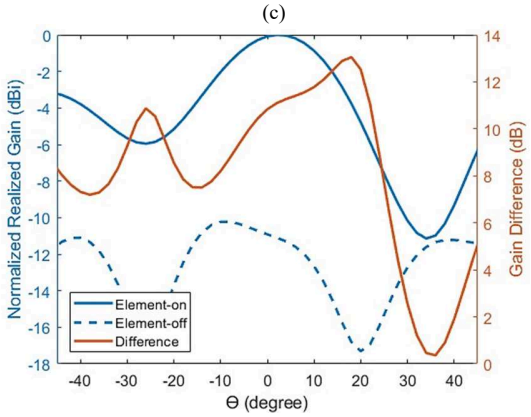

(d)

Fig. 2. Single metasurface antenna performance: (a) the optimization of *dy;* (b) the optimization of the metasurface offset; (c) negative refractive index and group delay; (d) gain in the on/off state of the antenna element

III. META-ARRAY ANTENNA DESIGN AND ANALYSES

To enhance radiation control and aperture efficiency, the metasurface is extended into an array configuration, enabling collective element behavior and improved overall antenna performance. Considering the array of 24-element metasurfaces, the inter-element spacing is regarded as a critical parameter, since excessive mutual coupling between adjacent elements is an undesirable effect that can degrade the overall radiation performance. With an inter-element spacing of $\lambda_o/4$, *d*, the array layer exhibits dimensions of 190 mm × 20 mm as shown in Fig. 3

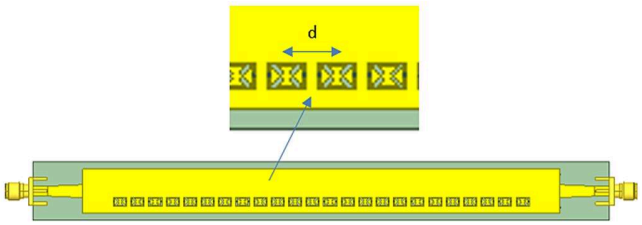

Fig. 3. Meta-array layer consists of 24 elements

As mentioned above, PIN diodes are employed to switch the metasurface elements between on and off states. The waveguide-fed metasurface elements radiate by coupling to the reference wave depending on their switching state. PIN diodes in the proposed design are MADP 000907-14020P by MACOM. It's modelled with a resistor of typically 5.2 Ω in the forward bias, and a capacitor of 0.025 pF in the reverse bias condition in HFSS. When determining the beam direction of the array structure, beam coding is formulated by associating the ON–OFF states of the metasurface elements with a binary coding scheme, where each element is assigned a binary amplitude coefficient (1 or 0) via PIN-diode control. These binary coefficients are then directly used as the amplitude weights in the 1-D array factor (AF) expression in broadside as follows [10]:

$$AF = \sum_{i=1}^{N} a_{m,i}(\omega)\, e^{-jx_i(\beta + k \sin \emptyset)} \qquad (2)$$

Where k is the wavenumber, β is the propagation constant, $a_{m,i}$ is the weighting coefficient of the i-th element, $\emptyset$ denotes the propagation angle normal to the surface of the antenna and x_i is the location of each element. The array factor is inherently dependent on the spatial configuration of the array elements and the phase excitation distribution across them as well as metasurfaces' polarizabilities, or weights. Accordingly, this binary weighting is incorporated into the array factor formulation by means of a unit step function as follows:

$$a_{m,i}(\omega) = \begin{cases} 0, & \text{if } \cos\left(x_i(\beta + k \sin \emptyset_0)\right) < 0 \\ 1, & \text{if } \cos\left(x_i(\beta + k \sin \emptyset_0)\right) > 0 \end{cases} \qquad (3)$$

The amplitude coefficients corresponding to the desired steering angle are calculated using this formulation through mathematical and scientific programming tools, and in this work, the beam codes are obtained using MATLAB. Based on these beam codes, a sidelobe suppression algorithm (SSA) is also applied similar to [11] with some modifications. At each iteration, a cancellation wave with amplitude and phase selected via nested for-loops is applied, and the array factor is recalculated with automatic sidelobe evaluation instead of pre-selection. Moreover, the modified algorithm monitors main-beam degradation during sidelobe suppression, and the optimal array factor is selected accordingly.

Increasing the number of elements introduces more and narrower sidelobes as shown in Fig. 4. However, these additional sidelobes generally exhibit lower amplitudes than those observed in arrays with fewer elements. Therefore, arrays with a higher number of elements may require relatively less sidelobe suppression effort compared to arrays with a smaller number of elements. From the sidelobe suppression perspective, the canceling wave is synthesized at the sidelobe angles of interest and superimposed with sufficient amplitude to suppress the targeted sidelobe and with a phase intentionally adjusted to be out of phase with it.

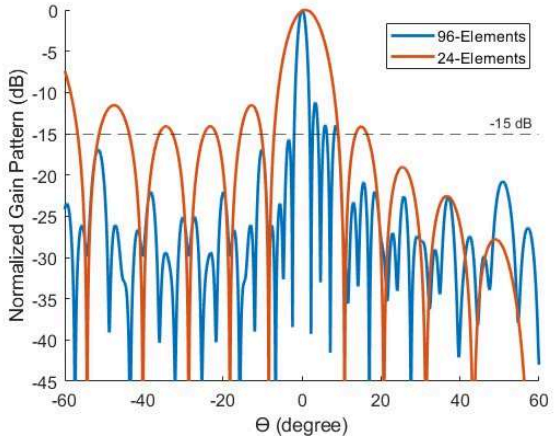

Fig. 4. Theoretical analysis of 24 elements vs 96 elements meta-array

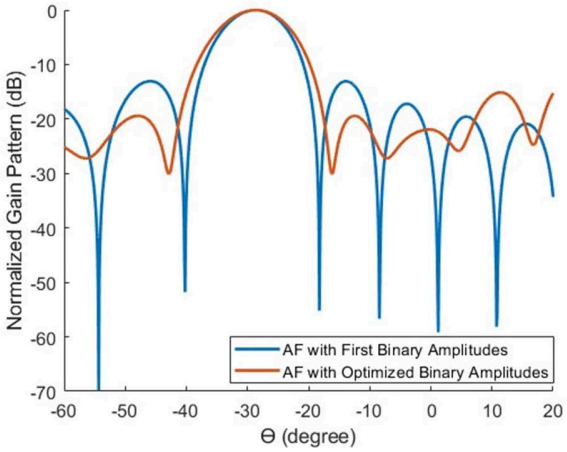

(a)

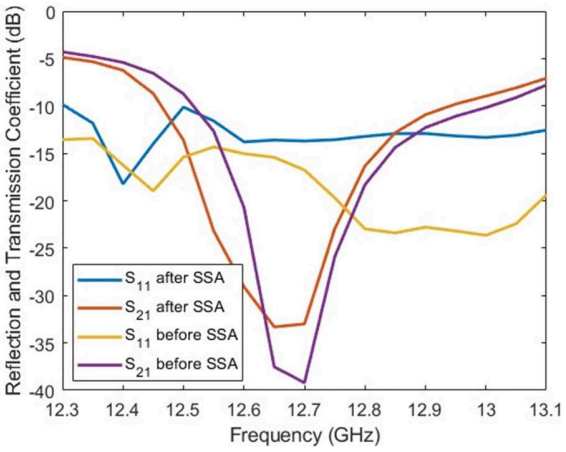

(b)

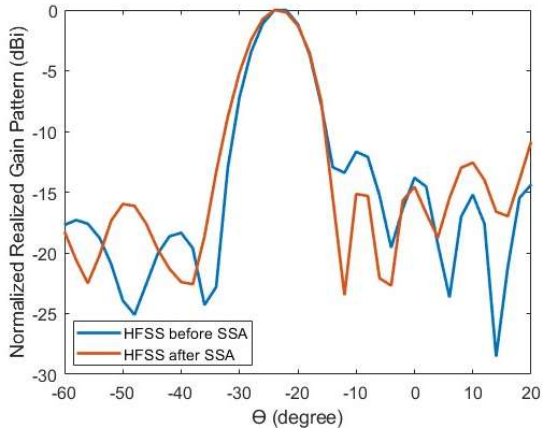

(c)

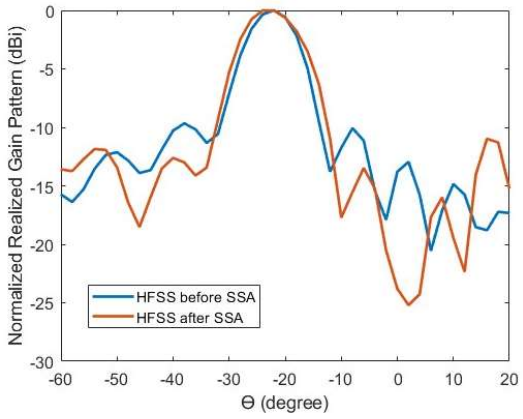

(d)

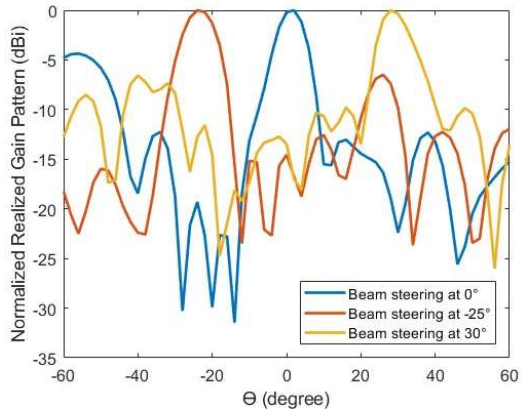

(e)

Fig. 5. Meta-array antenna performance: (a) Theoretical comparison before and after SSA at 12.5 GHz; (b) S-parameters; (c) Simulated radiation pattern at 12.5 GHz; (d) Simulated radiation pattern at 12.95 GHz; (e) Beam steering performance at 12.5 GHz. Each beam represents a separate simulation and beam code.

In Fig. 5 (a), after obtaining the above-mentioned binary amplitude coefficients for beam steering toward -25°, the corresponding theoretical array factor is presented. In the initial case, the SSA is not applied. Subsequently, the binary amplitude coefficients are processed using the SSA, and the resulting calculated array factor is plotted with the applied beam code given in Table II. It is observed that sidelobe reduction is achieved theoretically, particularly effective for the first sidelobes. To investigate the impact of SSA on the antenna return loss, the reflection and transmission coefficient

TABLE II. APPLIED BEAM CODES AND CORRESPONDING ANGLES

Beam To	Applied Beam Codes at 12.5 GHz
-25°	10001010101010101010110
0°	10010100101001011010 1101
+30°	11011001100100110010 0110

responses before and after SSA are presented in Fig. 5 (b). Since the applied beam code is modified by SSA, variations in these characteristics are expected. The extent of this variation is directly related to the degree of deviation from the initial beam code. Although the return loss slightly degrades after the application of SSA, it remains below −10 dB, indicating acceptable performance. Figure 5 (c) presents the normalized radiation pattern at 12.5 GHz. In the initial pattern, a sidelobe asymmetry is observed, with the sidelobe at −10° reaching a level close to 11 dB. After applying SSA, this sidelobe is suppressed by approximately 4 dB, reducing its level to around 15 dB. One noticeable effect after SSA is the emergence of a sidelobe at −50°, which is attributed to the algorithm; however, its level remains below 15 dB. Additionally, a slight reduction is observed in the main lobe at 0°. In contrast, the sidelobe at +10° increases in the SSA-applied case compared to the initial pattern. It should be noted that the increase in the sidelobe at +10° is consistent with the theoretical expectation presented in Fig. 5 (a). As a separate observation, the beamwidth is seen to broaden after the application of SSA, which is also consistent with theoretical expectations. Fig. 5 (d) presents the analysis of the same beam-code-based design at 12.95 GHz. At this frequency, a reduction of approximately 6 dB is achieved in the first sidelobes. The single-frequency beam steering performance of the antenna is analyzed in Fig. 5(e). Each beam is obtained from a separate simulation; therefore, the beam codes listed in Table II are individually applied for each steering angle. SSA is not applied for the 30° case, while the beams steered to −25° and 0° are SSA-optimized. As observed, without SSA, the sidelobe level remains slightly below 10 dB at best. From the analysis of these three beams, it can be concluded that for each steering angle, the sidelobes in the off–main-lobe region of approximately ±45° are maintained below 10 dB.

TABLE III. COMPARISONS WITH SOME OTHER WORKS

ID	Comparison Criteria				
	# of Elements	*Beam Steering with*	*Unit cell size*	*Freq. (GHz)*	*Sidelobe Suppression*
This work	24	PIN Diode	0.1λ x 0.15λ	12.5-13	6 dB
[4]	16	Water	0.15λ x 0.15λ	2.6	N/A
[5]	25	PIN Diode	0.12λ x 0.2λ	1.05	N/A
[6]	16	PIN Diode	0.12λ x 0.2λ	12	N/A
[7]	96	Var. Diode	0.12λ x 0.12λ	10	N/A

IV. Conclusion

A newly introduced metasurface element is designed and analyzed in a one-dimensional linear array with a limited number of elements, where a sidelobe suppression algorithm evaluated at multiple frequencies achieves about 6 dB first sidelobe reduction. Although a slight main-beam broadening is observed as an inherent trade-off of sidelobe suppression, the modified algorithm effectively monitors and minimizes main beam degradation, preserving beam integrity.

As summarized in Table III, unlike most previous works, which primarily focus on beam steering or reconfigurability without addressing sidelobe levels, this work demonstrates that meaningful sidelobe reduction can be realized concurrently with beam steering using binary-controlled metasurface elements. The beam steering to −25°, 0°, and +30° is successfully demonstrated using three distinct beam codes, confirming the robustness of the binary coding scheme and the effectiveness of the metasurface-based radiation control.

Although sidelobe suppression is achieved, slight discrepancies in sidelobe amplitudes and main beam pointing between the theoretically calculated array factor and the simulated radiation pattern are observed. These differences are mainly attributed to inter-element mutual coupling.

The results highlight that meaningful sidelobe suppression can be achieved even with a limited number of elements, which is particularly important for compact metasurface antenna implementations. The antenna can be extended to larger apertures or two-dimensional configurations in future work to further enhance radiation performance and beamforming flexibility.

References

[1] W. Li et al., “A reconfigurable polarization converter using active metasurface and its application in horn antenna,” IEEE Trans. Antennas Propag., vol. 64, no. 12, pp. 5281–5290, Dec. 2016.

[2] D. Darsena, F. Verde, I. Iudice and V. Galdi, "Design of Stacked Intelligent Metasurfaces With Reconfigurable Amplitude and Phase for Multiuser Downlink Beamforming," in IEEE Open Journal of the Communications Society, vol. 6, pp. 531-550, 2025

[3] H. L. Zhu, X. H. Liu, S. W. Cheung and T. I. Yuk, "Frequency-Reconfigurable Antenna Using Metasurface," in IEEE Transactions on Antennas and Propagation, vol. 62, no. 1, pp. 80-85, Jan. 2014.

[4] A. H. Naqvi and S. Lim, "A Beam-Steering Antenna With a Fluidically Programmable Metasurface," IEEE Trans. Antennas Propag., vol. 67, no. 6, pp. 3704-3711, 2019, doi: 10.1109/TAP.2019.2905690.

[5] A. Darvazehban, S. A. Rezaeieh, and A. M. Abbosh, ‘‘Programmable metasurface antenna for electromagnetic torso scanning,’’ IEEE Access, vol. 8, pp. 166801–166812, 2020, doi: 10.1109/ACCESS.2020. 3022870.

[6] S. Li, F. Xu, X. Wan, T. J. Cui and Y. -Q. Jin, "Programmable Metasurface Based on Substrate-Integrated Waveguide for Compact Dynamic-Pattern Antenna," in IEEE Transactions on Antennas and Propagation, vol. 69, no. 5, pp. 2958-2962, May 2021

[7] Boyarsky, M., Sleasman, T., Imani, M.F. et al. Electronically steered metasurface antenna. Sci Rep 11, 4693 (2021).

[8] Z. H. M. I. Nawaz and M. Kashif, "Substrate Integrated Waveguide (SIW) to Microstrip Transition at X band," Proc. of the Int. Conf. on Circuits, Systems and Control, pp. 61–63

[9] Deslandes, D.; Ke Wu, "Accurate modeling, wave mechanisms, and design considerations of a substrate integrated waveguide", IEEE Transactions on Microwave Theory and Techniques, vol.54, no.6, pp.2516,2526, June 2006

[10] D. R. Smith, O. Yurduseven, L. P. Mancera, P. Bowen, and N. B. Kundtz, “Analysis of a waveguide-fed metasurface antenna,” Physical Review Applied, vol. 8, no. 5, p. 054048,2017

[11] M. C. Johnson, S. L. Brunton, N. B. Kundtz, and J. N. Kutz, ‘‘Sidelobe canceling for reconfigurable holographic metamaterial antenna,’’ IEEE Trans. Antennas Propag., vol. 63, no. 4, pp. 1881–1886, Apr. 2

Quantisation of polariton modes for dispersive resonators

Jakub Skórka[1,*], Ben Yuen[1], Angela Demetriadou[1]

[1]School of Physics and Astronomy, University of Birmingham, UK
*Corresponding author: jss306@student.bham.ac.uk

***Abstract*—We describe a new way of quantising electromagnetic fields in the presence of dispersive, lossless resonators, based on normal mode expansion of the fields. This method is a generalisation of an existing approach, developed for non-dispersive media.**

***Keywords*— plasmonics, quantum optics, quantisation, polaritons.**

I. Introduction

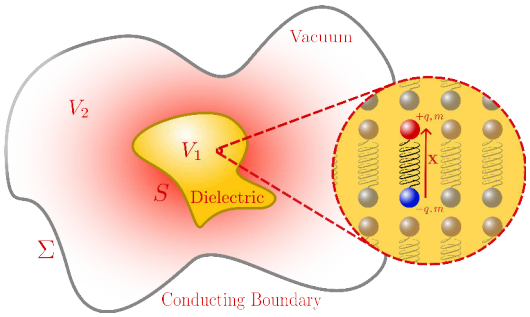

Fig. 1. Diagram of the system under study. An arbitrarily shaped piece of dielectric is surrounded by vacuum and enclosed by a perfectly conducting boundary. The dielectric material is described by the Hopfield model, as a continuous medium, with harmonic oscillator attached at every point.

Much of modern optical sciences focuses on investigating ways to control light and looking at their potential applications, in fields ranging from imaging to telecommunications. In particular, light is a very useful tool for interrogating and manipulating atoms, molecules, and nanostructures (collectively referred to as quantum emitters), due to the overlap between the energy scales of the processes occurring within these systems, and the energies of photons in the infrared to ultraviolet range. Spectroscopy is an obvious example of such a tool, being commonly employed, in its many varieties, to investigate chemical composition.

Coupling of light to individual quantum emitters is limited by the scale mismatch between light wavelengths and molecular dimensions. Plasmonics provides a way of bridging this gap, by coupling light to collective oscillations of conduction electrons in metallic nanostructures. Resulting hybrid modes, known as surface plasmon polaritons, are associated with strong, localised, electromagnetic near fields, bringing light down to the nanoscale, well below the diffraction limit. It has been demonstrated experimentally, that this approach can

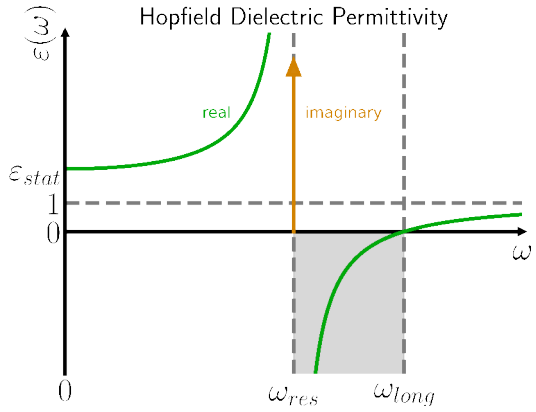

Fig. 2. Dispersion relation for a Hopfield dielectric. The real part of the permittivity varies rapidly near the resonance frequency of the medium oscillators, and becomes negative in a finite interval above it. The imaginary part of the permittivity is non-zero only at the resonance frequency.

give rise to strong coupling between light and individual dye molecules, resulting in mixed light-matter states[1].

Bringing light down to the nanoscale offers a possibility of investigating and exploiting quantum optical phenomena involving single quantum emitters. On the weakly coupled end of the scale, presence of a resonator can change the rate of spontaneous emission by influencing the vacuum field fluctuations in the vicinity of the emitter (Purcell effect). Going beyond spontaneous emission, if the interaction strength is sufficiently large, coupling to radiation can alter the nature of molecular eigenstates [2], shifting their energies (Lamb shift). Dynamically, this manifests itself through vacuum Rabi oscillations, where photons are emitted and reabsorbed by the molecule. The field of polaritonic chemistry is devoted to looking at how such coupling can be used to control chemical reactions[3].

In order to fully understand and exploit any of these phenomena, a rigorous understanding of the quantum behaviour of polaritons and their interaction with quantum emitters is necessary. For it to be complete, such understanding must include the effects of material dispersion and losses, which are of particular importance for metallic systems. Much work has been already devoted to this problem. The case of non-dispersive resonators has been comprehensively treated using normal modes expansion[4]. For uniform media, nor-

mal wave expansion provides a useful tool for quantising dispersive[5][6] and dispersive, lossy media[7]. For the non-uniform case an approach based on Green's functions has been developed[8][9][10]. Here, we describe a new way of quantising electromagnetic fields in the presence of dispersive, lossless dielectric resonators, based on the normal mode expansion.

II. Model

We consider an arbitrarily shaped, uniform, dielectric resonator surrounded by vacuum. Since it is convenient to work with a closed system, we introduce a perfectly conducting boundary around the resonator, not touching it at any point, whose size is eventually taken to be infinite. The dielectric material is described by the Hopfield model[5][6], as a continuous medium, with a single, isotropic, harmonic oscillator residing at each point. The oscillators are coupled to the electromagnetic fields through dipole moments proportional to their displacements. The resulting medium is linear, isotropic, dispersive and lossless. Its dispersion relation is shown on 2. The Lagrangian is a sum of three parts, describing the inside of the dielectric, the surrounding region of vacuum, and the interface between the two. It is given by:

$$\begin{aligned} L = \int_{\mathcal{V}_1} d^3\mathbf{r} \Bigg(\underbrace{\frac{\varepsilon_0}{2}\mathbf{E}^{(1)^2} - \frac{1}{2\mu_0}\mathbf{B}^{(1)^2}}_{\text{EM field}} + \underbrace{\frac{\rho}{2}\left(\partial_t \mathbf{X}\right)^2 - \frac{\rho\omega_{\text{res}}^2}{2}\mathbf{X}^2}_{\text{dielectric}} - \underbrace{\alpha\left(\mathbf{A}^{(1)}\cdot\partial_t\mathbf{X} + U^{(1)}\nabla\cdot\mathbf{X}\right)}_{\text{dielectric–EM coupling}} \Bigg) + \\ + \underbrace{\int_{\mathcal{V}_2} d^3\mathbf{r}\left(\frac{\varepsilon_0}{2}\mathbf{E}^{(2)^2} - \frac{1}{2\mu_0}\mathbf{B}^{(2)^2}\right)}_{\text{EM field}} + \underbrace{\oint_{\mathcal{S}} d^2S\,\alpha U^{(1)}\mathbf{n}\cdot\mathbf{X}}_{\text{dielectric–EM coupling}}, \end{aligned} \tag{1}$$

where $\mathbf{X}$ is a field describing the displacements of the medium oscillators, ρ is their mass density and α is a coupling constant. Through a suitable choice of gauge, the system can be separated into two decoupled parts, one interacting with the vector potential, and the other with the scalar potential.

III. Quantisation

The first step of the quantisation procedure is finding the normal modes of the system. These polariton modes comprise both an electromagnetic and material component. They are described either in terms of the electric field and the matter displacement field, as solutions to the following eigenvalue problem:

$$\begin{cases} \left(\frac{\mu_0\alpha^2}{\rho} + \nabla\times\nabla\times\right)\tilde{\mathbf{E}}^{(1)} + \mu_0\alpha\omega_X^2\tilde{\mathbf{X}} = k^2\tilde{\mathbf{E}}^{(1)} \\ \frac{\alpha}{c^2\rho}\tilde{\mathbf{E}}^{(1)} + \frac{\omega_X^2}{c^2}\tilde{\mathbf{X}} = k^2\tilde{\mathbf{X}} \end{cases} \\ \nabla\times\nabla\times\tilde{\mathbf{E}}^{(2)} = k^2\tilde{\mathbf{E}}^{(2)}, \tag{2}$$

or, alternatively, in terms of vector potential and matter momentum density field, with the eigenvalue problem taking the form:

$$\begin{cases} \left(\frac{\mu_0\alpha^2}{\rho} + \nabla\times\nabla\times\right)\tilde{\mathbf{A}}^{(1)} + \frac{\mu_0\alpha}{\rho}\tilde{\mathbf{P}} = k^2\tilde{\mathbf{A}}^{(1)} \\ \frac{\alpha\omega_X^2}{c^2}\tilde{\mathbf{A}}^{(1)} + \frac{\omega_X^2}{c^2}\tilde{\mathbf{P}} = k^2\tilde{\mathbf{P}} \end{cases} \\ \nabla\times\nabla\times\tilde{\mathbf{A}}^{(2)} = k^2\tilde{\mathbf{A}}^{(2)}. \tag{3}$$

The solutions, corresponding to different frequencies (eigenvalues), are orthogonal in the following sense:

$$\int_{V_1} d^3\mathbf{r}\left(\tilde{\mathbf{E}}_1^{(1)^*}\cdot\tilde{\mathbf{E}}_2^{(1)} + \frac{\rho\omega_X^2}{\varepsilon_0}\tilde{\mathbf{X}}_1{}^*\cdot\tilde{\mathbf{X}}_2\right) + \\ + \int_{V_2} d^3\mathbf{r}\,\tilde{\mathbf{E}}_1^{(2)^*}\cdot\tilde{\mathbf{E}}_2^{(2)} = 0, \tag{4}$$

$$\int_{V_1} d^3\mathbf{r}\left(\tilde{\mathbf{A}}_1^{(1)^*}\cdot\tilde{\mathbf{A}}_2^{(1)} + \frac{1}{\varepsilon_0\rho\omega_X^2}\tilde{\mathbf{P}}_1{}^*\cdot\tilde{\mathbf{P}}_2\right) + \\ + \int_{V_2} d^3\mathbf{r}\,\tilde{\mathbf{A}}_1^{(2)^*}\cdot\tilde{\mathbf{A}}_2^{(2)} = 0. \tag{5}$$

We can expand the fields in terms of both sets of modes. By substituting those expansions into the Hamiltonian and using the orthogonality relations, we can express the Hamiltonian, as that of a collection of uncoupled harmonic oscillators:

$$\hat{H} = \sum_{k\xi}\hbar ck\left(\hat{a}_{k\xi}^\dagger\hat{a}_{k\xi} + \frac{1}{2}\right). \tag{6}$$

Imposing the usual commutation relations on the creation and annihilation operators for these oscillators concludes the quantisation procedure.

IV. Conclusion

We have developed a new approach to quantising polaritons for lossless, dispersive resonators, based on the normal mode expansion of the fields. This method is akin to that already established for the non-dispersive case. It provides a new perspective on macroscopic electrodynamics, distinct to that offered by the Green's function method.

REFERENCES

[1] R. Chikkaraddy, et al., "Single-molecule strong coupling at room temperature in plasmonic nanocavities," *Nature*, vol. 535, pp. 127–130, 2016.

[2] P. Törmä and W. L. Barnes, "Strong coupling between surface plasmon polaritons and emitters: a review," *Reports on Progress in Physics*, vol. 78, p. 013901, 2014.

[3] J. Fregoni, F. J. Garcia-Vidal, and J. Feist, "Theoretical Challenges in Polaritonic Chemistry," *ACS Photonics*, vol. 9, pp. 1096–1107, 2022.

[4] R. J. Glauber, and M. Lewenstein, "Quantum optics of dielectric media," *Physical Review A*, vol. 43, pp. 467–491, 1991.

[5] J. J. Hopfield, "Theory of the Contribution of Excitons to the Complex Dielectric Constant of Crystals,", *Physical Review*, vol. 112, pp. 1555–1567, 1958.

[6] B. Huttner, J. J. Baumberg, and S. M. Barnett, "Canonical Quantization of Light in a Linear Dielectric," *Europhysics Letters*, vol. 16, p. 177, 1991.

[7] B. Huttner, and S. M. Barnett, "Quantization of the electromagnetic field in dielectrics," *Physical Review A*, vol. 46, pp. 4306–4322, 1992.

[8] T. Gruner, and D. -G. Welsch, "Green-function approach to the radiation-field quantization for homogeneous and inhomogeneous Kramers-Kronig dielectrics," *Physical Review A*, vol. 53, pp. 1818–1829, 1996.

[9] H. T. Dung, L. Knöll, and D. -G. Welsch, "Three-dimensional quantization of the electromagnetic field in dispersive and absorbing inhomogeneous dielectrics," *Physical Review A*, vol. 57, pp. 3931–3942, 1998.

[10] T. G. Philbin, "Canonical quantization of macroscopic electromagnetism," *New Journal of Physics*, vol. 12, p. 123008, 2010.

Chiral sensing along dielectric waveguides: effective index splitting and mode coupling

Alice De Corte[1], Tom T. C. Sistermans[2,3], Ankit K. Singh[2,3],
Bjorn Maes[1], and Alberto G. Curto[2,3]

[1] Micro- and Nanophotonic Materials Group, Research Institute for Materials Science and Engineering, University of Mons, 7000 Mons, Belgium
[2] Photonics Research Group, Ghent University-imec, 9052 Ghent, Belgium
[3] Center for Nano- and Biophotonics, Ghent University, 9052 Ghent, Belgium

*Corresponding author: alberto.curto@ugent.be

***Abstract*— The sensitive detection of chiral molecules is essential in biochemistry. We present a framework for understanding both optical rotation and circular dichroism in dielectric waveguides coated with chiral molecules. Our approach incorporates the Pasteur parameter into a mode solver to predict an effective index splitting explained by mode coupling theory.**

***Keywords*— circular dichroism, optical rotation, integrated photonics, waveguides.**

I. Introduction

Chiral light–matter interactions play a central role in optical spectroscopy and sensing, as many biomolecules and chemical compounds exhibit handedness-dependent responses. Enhancing the interaction between guided electromagnetic modes and chiral materials is therefore of considerable interest for integrated photonic sensing platforms. Dielectric waveguides provide a controlled environment in which light can interact with nanoscale analytes over extended propagation distances, offering a promising route toward compact and sensitive chiral detection [1-2].

Here, we provide a theoretical framework for predicting both optical rotation and circular dichroism induced by a chiral analyte, incorporated either as a coating or within the core of a cylindrical dielectric waveguide, for sensing applications.

II. Results and Discussion

We employ finite-element simulations to analyze core–shell waveguides with varying diameters and refractive indices. By adding the Pasteur (or chirality) parameter [3-4] to a mode solver, we compute the resulting splitting in the complex effective index of the fundamental guided modes for different Pasteur parameters for both circular polarizations. This effective index splitting directly quantifies the induced optical rotation and circular dichroism, thereby linking the modal

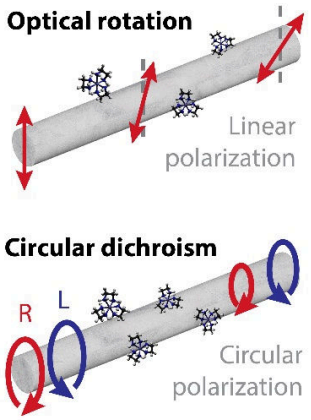

Fig. 1 Chiral sensing modalities for dielectric cylindrical waveguides covered by chiral molecules.

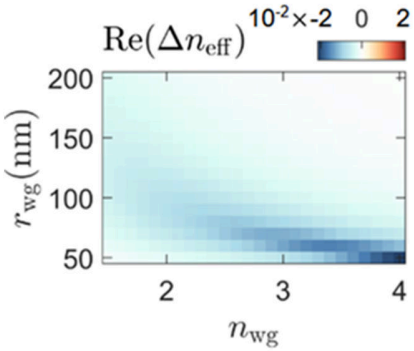

Fig. 2 Optical rotation along dielectric waveguides of different radius and refractive index shown as a difference in effective index for both circular polarizations.

properties to experimentally accessible quantities.

The goal is to determine the waveguide configuration most strongly influenced by material chirality. In our analysis, we identify clear trends in waveguide radius and refractive index contrast, and relate them to the underlying chiral coupling coefficients and chirality-induced mode interactions. In particular, high-index, small-radius waveguides exhibit enhanced sensitivity to nanoscale chiral inclusions. Both configurations—analyte confined to the core and analyte forming a surrounding shell—are examined and compared.

To validate the two-dimensional mode-solver model and account for finite propagation effects, we additionally perform full three-dimensional simulations. By calculating the associated optical rotation and circular dichroism, we can directly compare these results with the effective index splitting predictions of the two-dimensional model.

III. Conclusion

Our combined analysis clarifies the role of material chirality in mode dispersion and coupling, and provides design guidelines for dielectric waveguides optimized for integrated chiral sensing applications.

Acknowledgments

This work was financially supported by the Fund for Scientific Research FNRS through a FRIA grant and the European Research Council (ERC) under the European Union's Horizon 2020 Research and Innovation Program (Grant Agreement 948804, CHANSON).

References

[1] J. E. Vázquez-Lozano and A. Martínez, "Toward Chiral Sensing and Spectroscopy Enabled by All-Dielectric Integrated Photonic Waveguides". Laser & Photonics Reviews, vol. 14, pp. 1900422, 2020.

[2] S. K. Dezaki, A. N. Askarpour, and A. Abdipour, "Circular dichroism spectroscopy and chiral sensing in optical fibers", Opt. Express vol. 29, pp. 23096-23112, 2021.

[3] A. De Corte, M. Besbes, H. Benisty and B. Maes, "Chiral materials to control exceptional points in parity-time-symmetric waveguides", Phys. Rev. A vol. 109, pp. 023531, 2024.

[4] E. Mohammadi, T. V. Raziman and A. G. Curto, "Nanophotonic Chirality Transfer to Dielectric Mie Resonators", Nano Lett. vol. 23, 9, pp. 3978–3984, 2023.

Parametric studies to approximate configurations optimal for asymmetrical responses

Miklós Waldhauser[1], Ákos A. Sebők-Pap[1], Dávid Vass[1], András Szenes[1], Balázs Bánhelyi[2], Mária Csete[1,*]

[1]Department of Optics and Quantum Electronics, University of Szeged, Hungary
[2]Department of Computational Optimization, University of Szeged, Hungary
*Corresponding author: mcsete@physx.u-szeged.hu

***Abstract*— Multilayer metamaterial, consisting of periodic Babinet-complementary miniarray patterns in convex-concave-convex layers, was subject of parametric studies, by varying the configuration and topological parameters to achieve better Faraday-isolator properties. Wavelength dependent azimuthal orientation uncovers trade-off between nonreciprocal rotation and asymmetric transmission. Appropriate combination of crucial topological properties results in improvement.**

***Keywords*— metamaterials, topology, isolator, Faraday-rotation**

I. Introduction

Crescent-shaped metal nanostructures can support plasmonic resonances, with high localized fields around the sharp tips [1]. Designing periodic patterns of these nanostructures capable of resulting in metamaterials, with unique optical response. Bianisotropic nonreciprocal metamaterials enable to achieve unidirectional propagation, which is a result of magnetoelectric coupling [2]. Using ferromagnetic materials, the strength of the magnetoelectric coupling, as well as the asymmetric transmission can be significantly increased [3]. Modifying the topological properties of periodic patterns opens novel avenues in light-matter interaction, e.g. photonic topological insulators can be created [4]. Our previous studies on multilayers of convex and concave Babinet complementary patterns proved that negative index of refraction, asymmetric transmission and nonreciprocal rotation can be also achieved [5, 6].

II. Methods

Illuminating the tri-layer with linearly polarized light in plane of azimuthal orientation (γ=90°-α, measured from y-axis) in forward propagation direction, the orientation (β) and ellipticity (τ) of polarization ellipses were determined at the transmission side. In backward propagation direction, wavelength dependent azimuthal orientation was used, meeting the condition $\alpha_{backward}(\lambda) := \beta_{forward}(\lambda)$. The sum of forward and backward polarization rotations was determined for each inspected wavelength, which is the so called cumulative rotation (∑), along with the difference of forward incoming and backward outgoing orientations.

Our goal was for the cumulative rotation to be as close to 90° as possible, to fulfill conditions of a Generalized Faraday Rotator (GFR). In both propagation directions, orthogonal (co- & cross-polarized) transmission components were determined in bases corresponding to the incoming azimuthal orientations. Furthermore, the backward transmission components were also calculated in the corresponding forward coordinate-system. Different kind of asymmetrical transmissions were defined: $AT_{co}^{balanced}$ in order to map the transmission contrast of the structures in mixed bases, and $AT_{co}^{differential}$ to describe a Generalized Faraday Isolator (GFI) capability in the forward bases. Moreover, two figures of merits, GFR-FOM & GFI-FOM, were constructed as indicators of a GFR and GFI capabilities, incorporating $AT_{co}^{balanced}$ & $AT_{co}^{differential}$, respectively.

III. Results and Discussion

γ(λ) configurations

We examined the previously optimized tri-layer constructed with periodic patterns of Babinet complementary miniarrays for different incoming azimuthal orientations in [92°, 96°] interval, around the γ_{GFR} = 95.23°. In backward propagation direction, the azimuthal orientation of incoming linearly polarized light is strongly wavelength dependent in a narrow band, which is inherited from the polarization of beam outgoing in forward propagation direction.

As can be seen in the graphs for the entire inspected spectrum [600 nm, 800 nm], a cumulative rotation of around 90° is achievable only in a small spectral range. In the corresponding wavelength range a noticeable $AT_{co}^{balanced}$ peak is observable. Therefore, more detailed studies were performed with a wavelength step of 0.1 nm in this range [636 nm, 639 nm].

From these high resolution studies, it can be concluded that the optimal wavelengths of asymmetrical transmissions (both $AT_{co}^{balanced}$ and $AT_{co}^{differential}$) and ∑ are nearly identical, as both AT spectra reach their maximal value at 637.8 nm, while the ∑ approaches the 90° asymptote at 637.7 nm. Therefore, a well-defined peak is observable in GFR-FOM and GFI-FOM at this wavelength.

Considering these optimal wavelengths, increasing the azimuthal orientation from 92° to 93°, both AT maxima gradually decrease, while the ∑ better approximates 90°, though the forward ellipticity increases towards 45°. Between 93.5° and 94.5°, AT and forward ellipticity values are significantly smaller, while ∑ deviates more pronouncedly from 90°. Increasing the azimuthal orientation further from 95° to 96°, AT maxima begin increasing again, while the forward ellipticity decreases from 45°, however the ∑ moves away from 90°.

The symmetry with respect to the 94° azimuthal orientation is clearly visible in asymmetrical transmission as well as in forward rotation, forward and backward ellipticity and relative orientation spectra. For 0°≤x≤2° interval around this turning azimuthal orientation, both AT curves corresponding to 94°-x and 94°+x azimuthal orientations are mostly overlapping, while the corresponding forward rotation, forward and backward ellipticity curves are axial reflections of each other for the 0° line as axis of symmetry, as well as the relative orientation for the 90° value.

Although the aforementioned pairs of azimuthal orientations exhibit very similar $AT_{co}^{differential}$ maxima, considering cumulative rotations corresponding to azimuthal orientations in [95°, 96°] are slightly closer to 90° than for azimuthal orientations in [92°, 93°], the former are the optimal azimuthal orientations for achieving Generalized Faraday Isolation around 637.8 nm. However, as has been already established, forward ellipticity is large in this case, indicating a compromised performance. If we consider GFI-FOM, which also includes ellipticity, γ=96° azimuthal orientation seems to be even better at 638.9 nm, where both the forward and backward ellipticity are smaller than 2°, although $AT_{co}^{differential}$ is one-third of the maximum value, and ∑ is 5° away from 90°.

Combination of crucial topological properties

Based on the conclusions of parametric γ(λ) configuration studies on (i) a previously optimized tri-layer, the azimuthal orientation of 95.23° was selected for inspecting the impact of topological changes on the optical responses. Introducing certain novel DOFs, such as (ii) horizontal hexagonal nanocrescent-array orientation, were found favorable in AT and Σ, as well as GFR-FOM and GFI-FOM, therefore it was inherited in all inspected multilayers. Some DOFs have shown potential to construct a metamaterial outperforming the original structure in various measures. However, none was suitable for optimizing all measures simultaneously. Among the inspected multilayers (iii) tri-layer is that best meets the GFR criterion and results in the largest GFR-FOM and GFI-FOM, in which all nanocrescents were at an equal distance of 94.5 nm from the central nanoring.

Another topological property of the hexagonal miniarray, which was found to be the most promising in AT improvement at the expense of smaller Σ is a (iv) specific nanocrescent orientation of 65°, corresponding to **E**-field oscillation along the tips. Two tri-layers were created by introducing dimerization on triangular sub-lattices, (v) nanocrescent orientation of 65° without air, and (vi) with air filling in the holes of the concave layer.

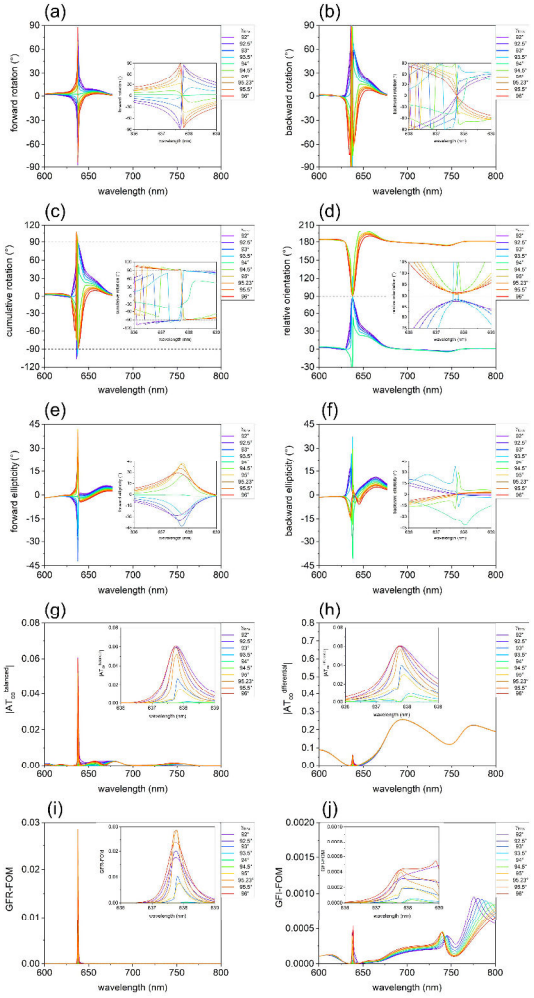

Fig. 1. Original structure. Polarization rotation for (a) forward and (b) backward propagation direction, (c) cumulative rotation (Σ), (d) difference of forward incoming and backward outgoing orientations, ellipticity in (e) forward and (f) backward propagation direction, (g) $AT_{co}^{balanced}$, (h) $AT_{co}^{differential}$, (i) GFR-FOM, (j) GFI-FOM.

However, these TRI-dimers were also compromised both in AT and Σ, though the ellipticity was small in forward /backward direction in (vi)/(v). Therefore, (vii) the elliptical deformation of the nanoring was realized, while keeping its circumference unchanged; which was combined with TRI-dimerization and air filling of the holes of the concave layer. The tri-layer (iv) and (vii) increased $AT_{co}^{balanced}$ and $AT_{co}^{differential}$ significantly, the latter (vii) served as the base of further studies due to its exceptional $AT_{co}^{differential}$ value.

In the following iterations, the advantageous topological properties of previously studied tri-layers were synthesized, namely the quadrumer was horizontal with a radius of 94.5 nm, while the nanoring was elliptical and the nanocrescent's orientation was always at 65°.

Iteration (1) created with elliptical nanoring deformation proved to be promising, despite the simple composition. In iteration (2) the parameters of the elliptical deformation of the nanoring were changed, while in iteration (3) TRI dimerization was introduced as well.

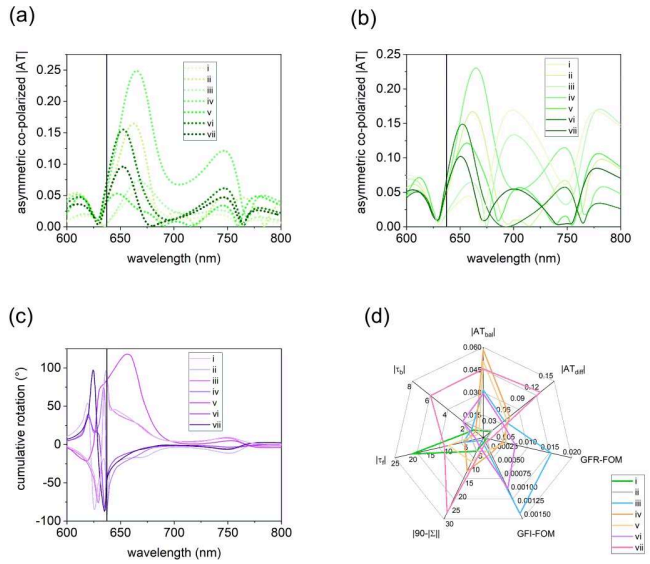

Fig. 2. Systems with parametric changes of topology compared to the originally optimized structure. (a) $AT_{co}^{balanced}$, (b) $AT_{co}^{differential}$, (c) cumulative rotation (Σ), (d) radar graph including $AT_{co}^{balanced}$, $AT_{co}^{differential}$, GFR-FOM, GFI-FOM, |90-|Σ|| and ellipticity in forward- and backward propagation direction.

Based on observations – to be elaborated on below – iteration (4-6) inherited the elliptical nanoring from iteration (1); in addition, in iteration (4) TRI dimerization was likewise for iteration (3); in iteration (5 and 6) air filling in the holes of the concave layer was realized; moreover in iteration (6) TRI dimerization was also inherited from iteration (3 and 4).

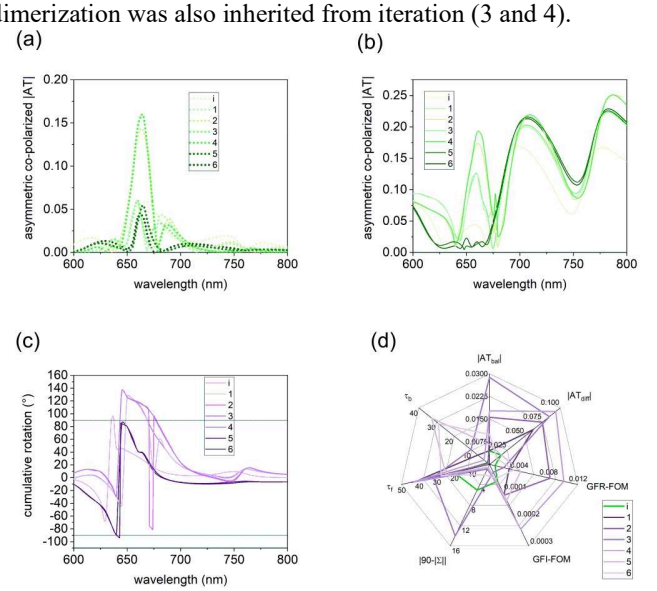

Fig. 3. Combined iterations. (a) $AT_{co}^{balanced}$, (b) $AT_{co}^{differential}$, (c) cumulative rotation (Σ), (d) radar graph including $AT_{co}^{balanced}$, $AT_{co}^{differential}$, GFR-FOM, GFI-FOM, |90-|Σ|| and ellipticity in forward- and backward propagation direction.

At 677 nm iteration (1) can produce the largest $AT_{co}^{differential}$, while having the 3rd best Σ value as well as the best GFR-FOM and GFI-FOM values. This confirms that (1) is the optimal system in all measures considered among the synthesized systems.

The wavelength corresponding to a cumulative rotation of 90° overlaps with an $AT_{co}^{differential}$ peak in this synthesized system, indicating that with topology variation it is possible to approximate 90° with good AT. Using specific elliptic deformation of the nanoring in iterations of (2/3) was particularly /reasonably efficient for achieving Σ~90°, although resulted in significantly larger τ_b values, than other compositions. Iteration (4) is only favorable concerning τ_b, the Σ in iteration (4) takes on the 90° value at a local maximum of $AT_{co}^{differential}$, similar to (1). Despite possessing the largest $AT_{co}^{balanced}$ value, iteration (5) rotates far beyond the desired Σ range, making it less favorable. After comparing the results of iterations (4 - to 5 and 6), air filling in the holes of the concave layer was considered to be disadvantageous based on FOMs. Considering (3 and 6) iterations are not the best in any quantity, conducting further research on these systems is not proposed.

IV. Conclusion

From the γ(λ) dependent studies, one can conclude that with a small change in the azimuthal orientation and wavelength, namely selecting 96° and 637.8 nm – instead of those from previous GFR optimization, – the cumulative rotation better approximates 90°, while the asymmetrical transmissions can further increase. Therefore, GFR and GFI-FOM values improve, despite the larger forward ellipticity. The main advantage of iterations (1&4) compared to the originally optimized structure is that their cumulative rotations not only approximate, but take on the 90° value in monotonously varying cumulative rotation inside a band, where larger $AT_{co}^{differential}$ values can be reached. However, the iterations exhibit larger ellipticity at their respective optimal wavelengths.

Acknowledgments

This work was supported by the National Research, Development and Innovation Office (NKFIH) of Hungary, projects: "Nanoplasmonic Laser Inertial Fusion Research Laboratory" (NKFIH-2022-2.1.1-NL-2022-00002) and "National Laboratory for Cooperative Technologies" (NKFIH-2022-2.1.1-NL-2022-00012) in the framework of the Hungarian National Laboratory program, as well as the Hurizont METAOPTQIP.

References

[1] H. Rochholz, N. Bocchio, and M. Kreiter, "Tuning resonances on crescent-shaped noble-metal nanoparticles," New Journal of Physics, vol. 9, p. 53, 2007.

[2] Y. Ra'di, V. S. Asadchy, and S. A. Tretyakov, "One-way transparent sheets," Physical Review B, vol. 89, p. 075109, 2014.

[3] I. Katsantonis, A. C. Tasolamprou, T. Koschny, E. N. Economou, M. Kafesaki, and V. Constantinos, "Giant enhancement of nonreciprocity in gyrotropic heterostructures," Scientific Reports, vol. 13, p. 21986, 2023.

[4] D. Smirnova, S. Kiriushechkina, A. Vakulenko, and A. B. Khanikaev, "Topological metasurfaces," Optical Materials Express, vol. 14, pp. 2065-2082, 2024.

[5] E. Tóth, B. Bánhelyi, O. Fekete, and M. Csete, "Metamaterial properties of Babinet complementary complex structures," Scientific Reports, vol. 13, p. 4701, 2023.

[6] E. Tóth, O. Fekete, B. Bánhelyi, M. Durach, Zs. Szabó, and M. Csete, "Layered Babinet complementary patterns acting as asymmetric negative index metamaterial," Scientific Reports, vol. 14, p. 29568, 2024.

Coupled nanolaser arrays: towards the realization of bright topological lasers

Amina Saadani[1], Kenneth Syddall[1], Kaiwen Ji[1], Juan Ariel Levenson[2],
Kamel BENCHEIKH[2], Alejandro YACOMOTTI[1]

[1]Laboratoire Photonique Numérique et Nanosciences, Université Bordeaux, CNRS, 33405 Talence, France
[2]Centre de Nanosciences et de Nanotechnologies, CNRS, Université Paris-Saclay, France
*Corresponding author: alejandro.giacomotti@institutoiptique.fr

***Abstract*— We realized a 1D coupled nanolaser chain enabling topologically protected bright zero modes. Our design exploits coupling sign inversion through photonic crystal barrier engineering. We present the design parameters, numerical simulation results, and preliminary experimental results from the first fabricated structures.**

***Keywords*— topological photonics; nanolasers; photonic crystals.**

I. Introduction

Topological photonics is a rapidly expanding field of research [1]. By combining light states within materials (bulk) and at interfaces (boundaries), it aims to create photonic modes that become robust against fabrication imperfections and mitigate the intrinsic limitations of classical systems. In particular, active systems based on coupled micro- or nanolasers can produce robust laser states, which falls within the research domain of topological lasers [2-3] (Fig. 1a-b).

However, these systems face several challenges that make their practical use difficult. Notably, the so-called zero modes protected by symmetry or by the topology of the lattice, are located at the center of photonic bandgaps and feature out-of-phase oscillation (dark modes) [4]. Consequently, their free-space radiation efficiency is very low and they are typically confined at boundaries (edge-states, Fig. 1d).

In this work we develop a new type of topological laser based on a 1D chain of coupled nanolasers in a photonic crystal (PhC), offering solutions to these issues. Specifically, in this work we have realized a Su-Schrieffer-Heeger (SSH) chain [5] based on a PhC geometry (Fig. 1c). Although similar PhC realizations have already been reported [6], our strategy relies on a unique property of our platform: the sign inversion of evanescent coupling between two adjacent coupled nanolasers [7] (see yellow regions in Fig. 1c). In addition, spatial distributions of gain produced by spatial light modulators (SLMs) enable localized sublattice pumping, and therefore selective lasing zero mode excitation [8-9]. Furthermore, the interplay between localized pumping and engineered coupling might enable bulk zero modes in future realizations [10].

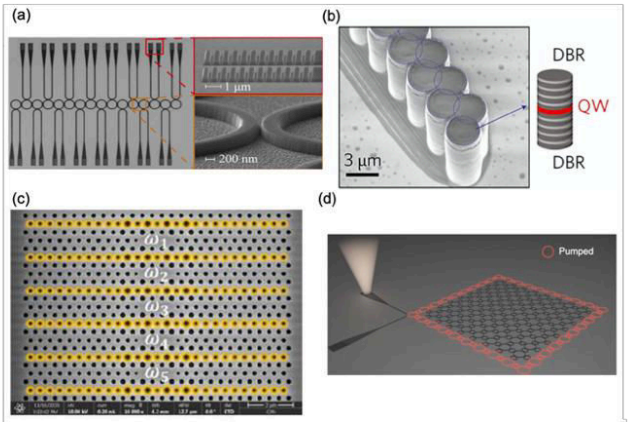

Fig 1: Topological laser arrays. a) Coupled microrings; b) coupled micropillars; c) coupled photonic crystal nanlasers, where regions in yellow highlight the photonic barriers (this work); d) topological edge mode.

II. Nanophotonic design and numerical simulations

We performed numerical simulations to design coupled nanolaser arrays in III-V semiconductor photonic crystals, specifically InP slabs with embedded InGaAsP quantum wells. Our model system is a SSH chain with N=9–10 coupled cavities, exploiting the coupling sign-inversion technique enabled by our photonic crystal platform [7]. This approach allows us to engineer in-phase topological zero modes that become bright, in contrast to conventional out-of-phase edge-localized modes.

Our simulations included: i) Electromagnetic modeling of the photonic crystal cavities to optimize resonance frequencies, mode overlap, and coupling strengths, by means of the Guided Mode Expansion (GME) method; ii) Coupled-cavity Maxwell-Bloch equations, as a nonlinear model for coupled lasers to predict mode dynamics, including gain saturation, and refractive index nonlinearities. We observe lasing zero modes

take a form of localized modes inside the band gaps of the 1D cavity chain, and are protected by either chiral symmetry in the case of N=9 cavities, or by topology in the case of N=10 cavity chains.

Preliminary simulation results confirm that topological lasing zero modes can be robustly excited utilizing localized pumping in one of the sublattices (Fig. 2a-c). Furthermore, by reverting the coupling sign every two sites, the zero modes become bright, in the sense that nanocavity field emission in one sublattice becomes phase locked (Fig. 1c).

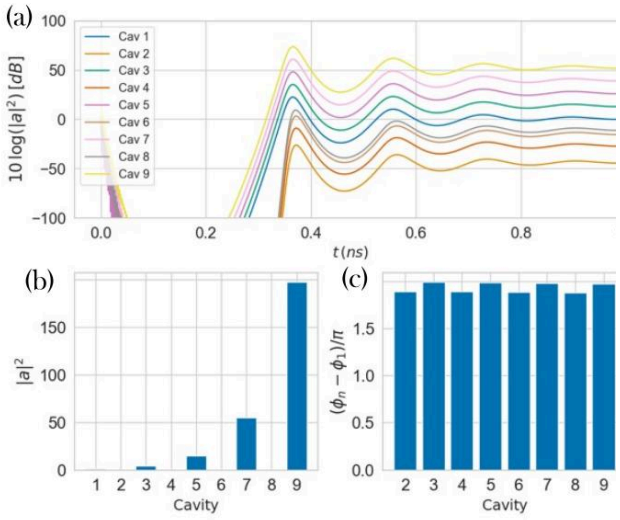

Fig 2: a) time trace of a numerical simulation of coupled Maxwell-Bloch equations under adiabatic elimination of the polarization (class-B lasers), and sublattice pumping in odd cavities ($|a|^2$ is photon number). Parameters are: gain linewidth Γ =1 THz, bare cavity linewidth Γ_{cav} =140.4 GHz, detuning between electronic band-gap and optical resonance δ =3 THz, light-matter coupling parameter g=13.6 GHz, cavity coupling parameters $\kappa_{odd\text{-}even}$= -28 Γ_{cav} and $\kappa_{even\text{-}odd}$ =15 Γ_{cav}, population inversion at lasing threshold ΔN_{th} = 7532, odd-cavity sublattice pumping ΔN_0 = 0.2 ΔN_{th}; b) cavity intensities at steady state, showing that the lasing mode is an edge mode; c) phase difference at steady state, showing that cavity fields in the pumped sublattice are phase locked.

III. Nanofabrication

We have fabricated photonic crystal nanolaser chains with inverted couplings on a suspended InP membrane containing quantum wells, with N=9 and N=10 coupled PhC L3 cavities. The fabrication process includes bonding the active layers onto Si substrates via BCB, electron-beam lithography, ICP etching, and ALD encapsulation. Structural quality and coupling fidelity were confirmed via scanning electron microscopy (SEM).

IV. Conclusion

We have designed and fabricated 1D PhC coupled nanolaser arrays featuring SSH geometry, containing 9 and 10 coupled nanocavities. The originality of our approach is the coupling sign inversion, that enables bright zero modes, which mitigates a serious drawback of standard zero modes: the out-of-phase oscillation becomes in-phase oscillation in our system. We have observed such lasing bright zero modes in numerical simulations, and the first fabricated samples have been obtained and characterized.

References

[1] L. Lu, J. D. Joannopoulos, and M. Soljacic, “Topological photonics”, Nat. Photon. 8, 821–829 (2014).
[2] Y. Ota, K. Takata, T. Ozawa, A. Amo, Z. Jia, B. Kante, B., ... and S. Iwamoto, Nanophotonics 9, 547 (2020).
[3] M. Parto, S. Wittek, H. Hodaei,... and M. Khajavikhan, Physical Review Letters 120, 113901 (2018).
[4] F. Hentinger, M. Hedir, B. Garbin, M. Marconi, L. Ge, F. Raineri, J. A. Levenson, and A. M. Yacomotti, “Direct observation of zero modes in a non-hermitian optical nanocavity array,” Photonics Research 10, 574 (2022).
[5] W. P. Su, J. R. Schrieffer, A. J. Heeger, “Solitons in Polyacetylene”,
[6] Phys. Rev. Lett. 42, 1698–1701, 1979.
[7] C. Han, M. Lee, S. Callard et al., “Lasing at topological edge states in a photonic crystal L3 nanocavity dimer array”, Light Sci Appl 8, 40 (2019).
[8] M. Hedir, K. Ji, J. A. Levenson, R. El-Ganainy, L. Ge, and A. M. Yacomotti, “Probing non-Hermitian zero modes in a nanophotonic trimer: from non-uniform to twisted coupling”, Phys. Rev. A 110, 043515 (2024).
[9] K. Ji, B. Garbin, M. Hedir, J. A. Levenson, and A. Yacomotti, “Non-hermitian zero-mode laser in a nanophotonic trimer,” Phys. Rev. A 107, L061502 (2023).
[10] K. Ji, Q. Zhong, L. Ge, G. Beaudoin, I. Sagnes, F. Raineri, R. El-Ganainy, and A. M. Yacomotti, “Tracking exceptional points above the lasing threshold,” Nature Communications 14 (2023).
[11] Alizadeh, M., Ozdemir, S.K., Yacomotti, A.M. et al. “Lasing zero modes are not always topological”, Commun Phys 8, 473 (2025).

Low-Contrast Bound States in the Continuum Metasurfaces Enabling Single Nanoparticle Sensing

Keisuke Watanabe[1,*], Samuel Crowther[2], Masanobu Iwanaga[3], Frank Vollmer[2], and Tadaaki Nagao[1,4]

[1]International Center for Materials Nanoarchitectonics (MANA), National Institute for Materials Science (NIMS), Japan
[2]Department of Physics and Astronomy, University of Exeter, UK
[3]Research Center for Electronic and Optical Materials, National Institute for Materials Science (NIMS), Japan
[4]Department of Condensed Matter Physics, Hokkaido University, Japan
*Corresponding author: watanabe.keisuke@nims.go.jp

***Abstract*—We present real-time sensing of single polystyrene nanoparticles using low-contrast bound states in the continuum metasurfaces with ultrahigh quality factors. Strongly confined electric fields in the shallow-etched geometry interact with virus-sized particles with a diameter of 100 nm, enabling the experimental observation of discrete wavelength steps.**

***Keywords*—metasurfaces, bound states in the continuum, silicon, biosensors.**

I. Introduction

Quasi-bound states in the continuum (qBICs) have attracted considerable attention for a wide range of applications owing to their high quality (Q) factors and strong electric field enhancement. The resulting enhancement of light–matter interactions has become among the key subjects of interest and stimulated particular interest in sensing applications in aqueous environment. Thus far, numerous label-free sensor geometries based on qBICs have been investigated, exploiting resonance wavelength shifts induced by changes in the refractive index of the surrounding medium. In particular, symmetry breaking of symmetry-protected BICs emerging at the Γ point of the Brillouin zone offers a significant advantage for sensing, as sharp resonances can be accessed under normal-incidence excitation from free space. Conventional design strategies for such sensors aim to simultaneously achieve a high Q factor and large refractometric sensitivity [1], capturing *global* refractive index variations in the environment. However, sensors capable of detecting *local* refractive index perturbations, such as the binding of a single nanometer-sized molecule [2], remain elusive and have not yet been demonstrated in BIC metasurfaces. This is because the Q factors of qBICs are highly susceptible to fabrication imperfections, and scattering losses caused by surface roughness restrict the potential for achieving ultrahigh Q factors. To overcome this challenge, we have recently demonstrated a BIC metasurface with Q factors exceeding 100,000 using a low-contrast geometry [3]. The ultrahigh Q factors originate from the inherently high radiative Q factors of a higher-order qBIC combined with reduced scattering losses enabled by shallow-etched designs. These features suggest that low-contrast BIC metasurfaces can simultaneously provide ultrahigh Q factors and small mode volumes, making them highly sensitive to *local* refractive index perturbations.

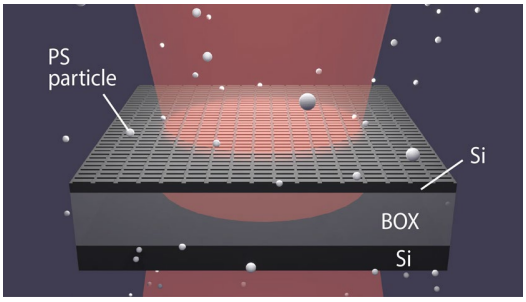

Fig. 1 Schematic illustration of single PS nanoparticle detection using a low-contrast BIC metasurface fabricated on a SOI wafer.

In this study, we demonstrate low-contrast BIC metasurfaces with the sensing resolution down to single nanoparticles. We show that the localized electric fields confined within the shallow-etched structures strongly interact with the virus-sized polystyrene (PS) particles (Fig. 1), manifesting as discrete wavelength steps.

II. Results and Discussion

The low-contrast metasurfaces were fabricated on a silicon-on-insulator (SOI) wafer with a 400-nm-thick top silicon layer. Only approximately 52 nm of the top silicon was dry-etched to form shallow pair-rod nanostructure arrays with a period P of 760 nm, as shown in Fig. 2a. Each unit cell consists of a pair of rods with lengths $L + 2\Delta L$ and $L - 2\Delta L$. The designed rod length L and the width are 640 nm and $L - P/2 = 260$ nm, respectively. By introducing this length asymmetry, the symmetry-protected BIC transforms into a qBIC with an asymmetry parameter $\alpha = 2\Delta L/L$, enabling the experimental observation of sharp qBIC resonances under normal-incidence excitation. Recently, we

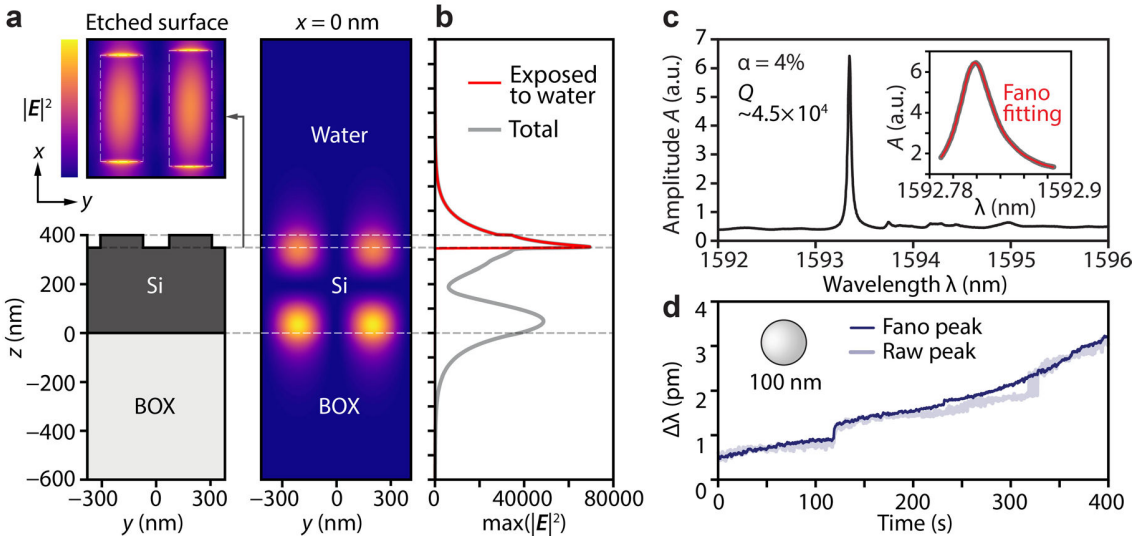

Fig. 2 (a) Cross-sectional schematic in the *yz*-plane (lower left) and simulated electric field intensity enhancement $|\boldsymbol{E}^2|$ at x = 0 nm (right), together with the field distribution in the *xy*-plane at the shallow-etched surface (upper left). (b) Maximum field intensity along the *z*-direction. (c) Representative transmittance spectrum measured in D_2O for the fabricated BIC metasurface with asymmetry parameter α = 4%. The inset shows the spectrum and its Fano fitting obtained under fine wavelength tuning using a piezo-controlled tunable laser. (d) Real-time resonance peak wavelength shift measured in a dispersion of unfunctionalized virus-sized PS particles (d = 100 nm), showing discrete wavelength steps corresponding to single nanoparticle binding events.

demonstrated that an optimal balance between a high Q factor and large resonance amplitude is achieved under the critical coupling condition, where the radiative and nonradiative Q factors are equal, thereby minimizing the impact of wavelength fluctuations [4]. In the present study, the critical coupling condition was experimentally determined to be α = 4%. Therefore, we only focus on this condition in the following discussion. As shown in the electric field distribution in the *yz*-plane (Fig. 2a), two antinodes exist along the *z*-direction, corresponding to a higher-order mode (TE_{122}) that is strongly confined within the top silicon layer and exhibits a large radiative Q factor. In the *xy*-plane at the shallow-etched surface, the electric fields are localized at the edges of both rods, which are exposed to the external medium (heavy water D_2O in our case) rather than to silicon (Fig. 2b). This field localization while keeping the Q factor is a key feature for sensing applications targeting molecular binding events. Fig. 2c shows the transmittance spectrum of the metasurface with α = 4%, measured in D_2O. The experimental Q factor was evaluated to be approximately 4.5×10^4 when a 10 Hz triangular wave piezo voltage was applied to the tunable laser (TSL210V, santec). Next, we injected unfunctionalized, virus-sized PS particles (d = 100 nm) diluted in D_2O containing 100 mM NaCl into a PDMS microfluidic channel and monitored the resonance peak wavelength shift in real-time. As shown in Fig. 2d, we observed discrete wavelength steps, as signatures of single particle binding events. This result can be attributed to the strong interaction between the localized electric field enhancement of the qBIC mode and nanoparticles occurring near the shallow-etched surface.

III. Conclusion

We have demonstrated, for the first time in BIC nanostructures, the detection of virus-sized single PS particles with a diameter of 100 nm in water using the ultrahigh-Q nature of a low-contrast geometry. This sensing capability arises from the strong interaction between the confined electric fields and nanoparticles located within the shallow-etched structures. Owing to the collective resonant behavior of relatively large-area periodic arrays, BIC metasurfaces are inherently position-insensitive and do not require precise alignment of the device. Moreover, normal-incidence excitation from free space provides direct access to sharp qBIC resonances. These advantages offer promising opportunities for simple, cost-effective, and highly sensitive detection of virions and other pathogenic nanoparticles with single nanoparticle resolution.

Acknowledgments

This work was financially supported by JSPS KAKENHI Grant Number JP22K20496, Iketani Science and Technology Foundation (Grant Number 0361252-A), and "Advanced Research Infrastructure for Materials and Nanotechnology in Japan (ARIM)" of the Ministry of Education, Culture, Sports, Science and Technology (MEXT). Proposal Number JPMXP1224NM5259, JPMXP1225NM5235.

References

[1] K. Watanabe and M. Iwanaga, "Nanogap enhancement of the refractometric sensitivity at quasi-bound states in the continuum in all-dielectric metasurfaces," *Nanophotonics*, vol. 12, no. 1, pp. 99–109, 2023.

[2] S. Arnold, M. Khoshsima, I. Teraoka, S. Holler, and F. Vollmer, "Shift of whispering-gallery modes in microspheres by protein adsorption," *Opt. Lett.*, vol. 28, no. 4, p. 272, 2003.

[3] K. Watanabe, T. Nagao, and M. Iwanaga, "Low-Contrast BIC Metasurfaces with Quality Factors Exceeding 100,000," *Nano Lett.*, vol. 25, no. 7, pp. 2777–2784, 2025.

[4] K. Watanabe and M. Iwanaga, "Optimum asymmetry for nanofabricated refractometric sensors at quasi-bound states in the continuum," *Appl. Phys. Lett.*, vol. 124, no. 11, p. 111705, 2024.

Externally Driven Quantum Dynamics in Plasmonic Nanocavities

Ishita Jena[1,*], Angus Crookes[1], Ben Yuen[1], Angela Demetriadou[1]

[1]School of Physics and Astronomy, University of Birmingham, UK

*Corresponding author: ixj384@student.bham.ac.uk

***Abstract*—Plasmonic nanocavities strongly couple to quantum emitters, but controlling this excitation with external illumination can be challenging. We propose a system of two couple nanocavities each hosting a single quantum emitter, to control the quantum dynamics of the system. This paves the way towards engineering quantum states in plasmonic systems.**

***Keywords*—nanoplasmonics, quantum dynamics, pulsed excitation.**

I. Introduction

Plasmonic nanocavities facilitate strong light-matter interactions due to their ability to extremely confine electromagnetic fields into subwavelength volumes. The field confinement arises from the excitation of plasmons formed by driving the free electrons of the surface of a metal with external electromagnetic fields . This phenomenon has led to several advances in spectroscopy, non-linear optics and sensing. In particular, the nanoparticle-on-mirror (NPoM) configuration formed by placing a nanoparticle above a metallic film, and separated by a dielectric spacer of just a few nanometers, has demonstrated strong coupling with a single molecule even at room temperatures [1]-[2]. It was recently shown that such nanocavities hosting multiple QEs are promising candidates to generate subradiant entangled states at ambient conditions, and the high radiative and Ohmic plasmonic losses in these systems enable the generation of the entangled states [3]-[4]. However, the system needs to be suitably prepared for the entangled states to emerge, which is experimentally difficult when two or more QEs reside in the same plasmonic nanocavity due to the very close proximity of the QEs of just a few nanometers [5]. Additionally, such systems need to be externally excited to prepare them for generating subradiant states which is not understood very well.

In this work, we first study the dynamics of a QE embedded in a nanoplasmonic system, where the cavity interacts with single frequency as well as broadband pulses of various durations, strengths and temporal shapes. Ohmic and radiative losses of the plasmonic system are taken into account with the Lindblad master equation (in the Markov approximation). After identifying the conditions for ambient excitation of the QE, we design a nanoplasmonic system composed of two coupled NPoM cavities, each hosting a single QE. The two nanocavities can be separated by several μm, and coupled with each other via propagating surface plasmon polaritons (SPPs) supported on the flat metallic surface. Since the nanocavity separation is at the micrometer scale, each nanocavity can be selectively excited, therefore initializing only one QE at an excited state as desired.

II. Methods

We start with a single mode plasmonic nanocavity hosting a quantum emitter in its nanogap. A schematic of the system is shown in Fig.1(a) which consists of a spherical gold nanoparticle with radii $R = 40$ nm and facet width $f_d = 16.6$ nm assembled on a gold mirror. The nanoparticle and the mirror are separated by a dielectric spacer of refractive index $n = 2.5$ and thickness $t = 1$ nm. The resonances of this plasmonic system are described by complex frequencies found using QNMEig method with COMSOL Multiphysics. $\tilde{\omega_\xi} = \omega_\xi - i\Gamma_\xi$. When the nanocavity is illuminated with an external pulse, the Hamiltonian of the system in a frame co-rotating with the pulse frequency ω_p is given by

$$\mathcal{H}_S = \Delta_c a^\dagger a + \frac{\Delta_d}{2}\sigma_z + g_\xi(r)(a\sigma_+ + a^\dagger\sigma_-) + \alpha(t)(a^\dagger + a) \quad (1)$$

$a(a^\dagger)$ is the annihilation (creation) operator for the plasmonic nanocavity. The QE is treated as a two-level system with resonant frequency ω_d obeying $[\sigma_-, \sigma_+] = 1$. $\Delta_c = \omega_\xi - \omega_p$ and $\Delta_d = \omega_d - \omega_p$ are the detunings of the nanocavity and the QE from the center frequency of the pulse. The coupling strength of the QE to mode ξ is given by: $g_\xi(r) = \sqrt{\omega_\xi/2\epsilon_0\epsilon V}\boldsymbol{\mu}.\mathbf{E}_\xi(r)$ and depends on the dipole moment of the QE: $\boldsymbol{\mu}$, the electric field eigenvector of the cavity mode at the location of the QE: $\mathbf{E}(r)$ and the mode volume of the cavity: V.

The pulse amplitude $\alpha(t) = \alpha_0 f(t)$, where α_0 is the maximum strength of the pulse and $f(t)$ is proportional to the pulse envelope. We use an open quantum system formalism to account accurately for the Ohmic and radiative loss channels present in the plasmonic system. Here, the density matrix ρ is described by a Lindblad master equation:

$$\frac{d\rho(t)}{dt} = -i[\mathcal{H}_S, \rho] + \sum_\xi \frac{\Gamma_\xi}{2}(2a_\xi\rho a_\xi^\dagger - a_\xi^\dagger a_\xi\rho - \rho a_\xi^\dagger a_\xi)$$

Fig.1(d) shows the time evolution of the QE population as the central pulse frequency ω_p is varied, which shows two peaks at $\omega_p = \omega_c \pm g_\xi$ corresponding to the vacuum Rabi splitting for the upper and lower polariton states $0, \pm$. The vacuum Rabi splitting also shows up as a mode hybridisation in the system's spectral response.

The populations of these states are explicitly plotted in Fig.1(c) for the cases when the pump is resonant with the upper and lower polaritons, respectively. To further populate the polariton states, we have to keep the pulse frequency resonant with either of them and increase the pump strength. The pulse amplitude α_0 and envelope $f(t)$ can be engineered to determine the final state of the system. When the drive is sufficiently weak and resonant with either polariton, the dynamics is restricted to a single excitation subspace given by $\{n,+,n,-,g,0\}$. The transition between the the upper polariton and the ground state of the system is described by the matrix element $\langle 0,+|\alpha(t)(\hat{a}^\dagger+\hat{a})|0,g\rangle = \langle 0,-|\alpha(t)(\hat{a}^\dagger+\hat{a})|0,g\rangle = \frac{\alpha(t)}{\sqrt{2}}$. Therefore, for a rectangular pulse as shown in Fig.1(e), when $\sqrt{2}\alpha_0 \int_0^T f(t)dt = (2n+1)\pi$ the conditions for a π pulse is fulfilled. As the pump strength is increased, higher photon transitions become more probable and the system can no longer be limited to the one excitation basis states. Fig.1(e) and (f) show the population dynamics with the plasmonic losses included.

The new plasmonic system is shown in Fig.2(a) and consists of two spherical gold nanoparticles assembled on a gold mirror. The nanoparticles and the mirror are separated by a dielectric spacer of refractive index $n = 2.5$ and thickness $t =$ 1 nm. The modes follow spherical harmonics nomenclature wherein each mode is labeled with (l, m) where $l = 0, 1, 2, 3...$ is the number of nodes and antinodes along the radial direction and $m = (-l, l)$ is the number of nodal lines intersecting at the poles [6][]. We also find that the propagating SPPs launched by each nanocavity interfere with each other either constructively or destructively, depending on the separation between the two nanocavities, leading to a "bonding mode" (denoted by +), and an "anti-bonding" mode, (denoted by -) for each (l, m) mode as shown in Fig.2(a). These bonding and anti-bonding modes emerge due to the coupling between the two nanocavities that leads to hybridized states. Fig.2(c) shows that the frequency splitting between the bonding and anti-bonding modes depends on the separation distance between the nanocavities and is also proportional to the propagating SPP field overlap from each nanocavity, demonstrating the destructive and constructive interferences.

We then obtain the quantum dynamics of this plasmonic system, where each nanocavity hosts one QE.

$$\begin{aligned}\mathcal{H}_S^{(2)} &= \sum_\xi \omega_\xi a_\xi^\dagger a_\xi + \sum_i \frac{1}{2}\omega_d^{(i)}\sigma_z^{(i)} \\ &\quad + \sum_{\xi,i} g_\xi(r^{(i)})\left(a_\xi^\dagger \sigma_-^{(i)} + a_\xi \sigma_+^{(i)}\right) \qquad (2)\end{aligned}$$

III. Results and Discussion

We have investigated the driven quantum dynamics of a quantum emitter strongly coupled to a plasmonic nanocavity, with particular emphasis on how tailored pulses can be used to control polaritonic states in the presence of plasmonic losses. Using a Jaynes–Cummings description combined with a Lindblad master equation, we analyzed the population dynamics under various pulse shapes accounting for both coherent light–matter coupling and dissipative processes intrinsic to plasmonic systems.

Fig. 1. (a) Schematic of the plasmonic system with external illumination having temporal profile $\alpha(t)$ (b)Population of QE in nanogap as a function of pulse detuning and time for a square pulse of duration 0.52 ps. (c) Quantum dynamics of the system when pump is resonant with the upper and lower polaritons.Population evolution of QE when nanocavity is illuminated with a square pulse of duration for varying pump strengths

Fig. 2. (a) Schematic of the system: excitation of SPP waves on a gold film by two gold nanoparticles, each hosting a QE. (b) Magnitude of electric field $\mathbf{E}_z(x, y, z = 0)$ in the x-y plane of the nanogap for d = 120 nm. (c) Frequency splitting between the bonding and anti-bonding modes is proportional to the overlap integral of the $\mathbf{E}_z$ component of the electric fields. (d) Population of QE_2 as a function of time and d.

The quantum dynamics of the coupled system show damped oscillations in the populations of the plasmonic modes and the QEs due to the presence of losses in the system with rates Γ_ξ and Γ_{vib} as shown in Fig.2(d). The oscillatory behavior in the time domain indicates that our plasmonic-QE system is well into the strong-coupling regime. We then excite the

first nanocavity with a Gauss-6 laser pulse and show the population of QE_2 as a function of time and separation between the nanocavities (Fig.2(d)). The population closely follows the variation seen in the different SPP interaction regimes, implying that the system dynamics is dependent on whether the second nanocavity is positioned at a maxima or minima of the electric field overlap. We further report on how one can customize the external pulsed excitation of the two nanocavities to engineer long-lived entangled states.

IV. Conclusion

We show that the two plasmonic nanocavities are coupled to each other even if they are separated by several μm from each other, due to the long range of propagating SPPs. We show that the interaction between the two nanocavities leads to "bonding" and "anti-bonding" modes that emerge from constructive and destructive interaction between the two nanocavities. This coupling between the two nanocavities directly impacts the quantum dynamics of the system, while the configuration of the system allows us to separately excite each NPoM nanocavity, paving the way for the generation of subradiant entanglement and the engineering of quantum states with nanoplasmonics at room temperature.

References

[1] J.J. Baumberg, J. Aizpurua, M.H. Mikkelsen, D.R. Smith, "Extreme nanophotonics from ultrathin metallic gaps," *Nature Materials,* vol. 18, no. 7, pp. 668-678, July 2019.

[2] R. Chikkaraddy, B. de Nijs, F. Benz, et al., "Single-molecule strong coupling at room temperature in plasmonic nanocavities," *Nature,* vol. 535, pp. 127–130, July 2016.

[3] F. Verstraete, M.M. Wolf, J. Ignacio Cirac, "Quantum computation and quantum-state engineering driven by dissipation," *Nature Physics,* vol. 5, no. 9, pp. 633-636, September 2009.

[4] A. Crookes, B. Yuen, A. Demetriadou, "Taming plasmonic nanocavities for persistent entanglement," *Physical Review B,* vol. 112, no. 8, p. 085427, August 2025.

[5] K. Bedingfield, B. Yuen, A. Demetriadou, "Subradiant entanglement in plasmonic nanocavities," *Physical Review B,* vol. 111, no. 7, p. 075420, February 2025.

[6] N. Kongsuwan, A. Demetriadou, M. Horton, R. Chikkaraddy, J.J. Baumberg, O. Hess, "Plasmonic Nanocavity Modes: From Near-Field to Far-Field Radiation," *ACS Photonics,* vol. 7, no. 2, pp. 463-471, February 19, 2020.

[7] A. Crookes, B. Yuen, A. Demetriadou, "Collective multimode strong coupling in plasmonic nanocavities," *Nanophotonics* vol. 14, no. 11, p. 2065-2073, June 2025.

Time-varying Metamaterials on a Drone Rotor Blade

Pavel Ginzburg[1,*] Dmytro Vovchuk[1],
Anna Mikhailovskaya[1], Konstantin Grotov[1], Mikhail Tsukerman[1], Omer Tsidki[1], Sergey Geyman[1],
Mykola Khobzei[2], Vladyslav Tkach[2], Toms Salgals[3], Natalja Muračova[3], Vjaceslavs Bobrovs[3]

[1]Department of Electrical Engineering, Tel Aviv University
[2]Yuriy Fedkovych Chernivtsi National University, Chernivtsi, Ukraine
[3]Institute of Telecommunications, Riga Technical University, 1048 Riga, Latvia
*Corresponding author: pginzburg@taux.tau.ac.il

***Abstract*— Time variation is a powerful degree of freedom that enables encoding, separation, and recognition of signals beyond what static scatterers can provide. A practical route to time-varying scattering is rotation. Rotating objects play a central role in radar signal analysis because rotor blades generate the micro-Doppler effect, which is widely used for target classification and is especially relevant for monitoring small drones. Here, we introduce a new approach in which rotor blades are tagged with engineered metamaterial scatterers that exhibit a strongly angle-dependent radar cross section. When driven in rotation, these resonant tags produce a large, deliberately shaped micro-Doppler signature, thereby increasing drone visibility and detectability to an interrogating radar. Beyond this immediate application, the same platform serves as a testbed for challenging classical scattering bounds through inverse design. We use multi-objective optimization and meta-learning strategies that operate under experimental constraints and jointly optimize the scattering cross-section, bandwidth, and operational angles, despite the inherent trade-offs among these parameters. We experimentally demonstrate advanced scattering performance in the laboratory and validate it in outdoor drone experiments.**

***Keywords*— Metamaterials, Time-varying metamaterials, Superscatterers, Radars, Wireless Communications.**

I. Introduction

The presentation is based on our recent work [1-8] and on a large set of unpublished data (several manuscripts under review). Furthermore, we will present a range of experimental findings obtained using outdoor radar. These experiments involve detecting airborne targets (small drones) equipped with our superscattering devices, which significantly enhance their visibility, making them highly detectable and thus facilitating surveillance and monitoring tasks.

Electromagnetic scattering on subwavelength structures has long been a subject of extensive investigation owing to both fundamental challenges and practical rewards associated with its maximization or suppression. Interaction with compact structures is well approximated by a multipole series, with lower orders typically sufficient for convergence. The maximal possible scattering into a single multipole is called a channel limit. In a vast majority of cases, a dipolar single channel limit (the maximal scattering cross-section, which a small resonant lossless dipole can approach) is considered. In this case, $3\lambda^2/(2\pi)$, where λ is a free space wavelength, is the value, versus which all the assessments will be made hereafter. Compact subwavelength structures that bypass the single-channel limit are called super-scatterers. While there is no fundamental upper bound on a scattering cross section, several theoretical limits, including the Cho-Harrington limit, which is the most used, have been proposed to account for practical considerations. Bypassing those limits requires accommodating several resonant multipoles that constructively interfere at nearly the same frequency. In this case, a significant near-field accumulation in the vicinity of lossy materials, accompanied by an extremely low fabrication tolerance, is the main known factor limiting the practical demonstration of super-scatterers. Nevertheless, several promising designs have been demonstrated over the last few years and will be reviewed hereinafter. Regardless of their particular realization, they all share the same design principles. The first one is the choice of a material platform. Since high near-field accumulation necessarily implies having high Ohmic losses, constitutive components should be carefully chosen. The second criterion is the capability to perform extensive electromagnetic optimization. In compact structures, internal resonances tend to repel one another, opening frequency gaps. To bypass those design challenges, optimization efforts are needed.

II. SUPERSCATTERING FOR TAGGING

We will present several conceptually distinct strategies for designing and experimentally demonstrating superscattering. Novel and conceptually different architectures will also be demonstrated at the conference. As a practical application, the emerging challenge of air traffic control is addressed. The rapid growth in drone air traffic calls for enhanced radar surveillance systems to ensure reliable detection in challenging conditions. Increasing the scattering cross-section, essential for radar visibility, can greatly improve detection reliability in civilian applications. Here, we introduce the concept of genetically designed metamaterials, specifically engineered to enhance scattering for end-fire incidence. Multi-layer stacks of arrays, encompassing strongly coupled electric and magnetic resonators, demonstrate broadband scattering exceeding 1 m^2 at 10 GHz, despite having an end-fire physical cross-section smaller than one squared wavelength. Despite its compact footprint, the structure achieves over 10% fractional bandwidth, meeting radar requirements where high-range resolution is essential. While the scattering cross-section and bandwidth are typically contradictory in resonant structures, this contradiction is circumvented by applying the resonance cascading principle, in which a series of closely spaced, spectrally aligned resonant multipoles creates a coherent response. The resonance

cascading is engineered using multi-objective optimization, implemented on top of a genetic algorithm operating in a large search space encompassing more than 100 independent variables. The experimentally realized parameters of the compact structure align with the typical scattering cross-sections observed in large airborne targets. Consequently, these performance characteristics enable the exploration of highly scattering structures as identifiers for small airborne targets, supporting effective radar-based air traffic monitoring in civilian applications. We demonstrate the worthiness of this objective through a series of outdoor experiments using the DJI Mini 2 drone. Lightweight, conformal add-ons with substantially high scattering cross-sections can serve as auxiliary tools to enhance passive monitoring systems, adding an additional layer of security in urban airspace.

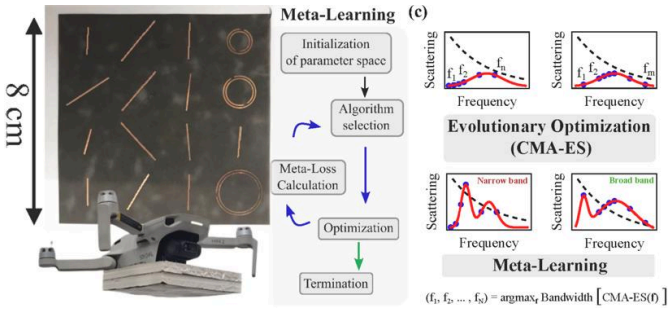

Fig. 1. Superscatterer: our state-of-the-art realization, an ML-based optimization algorithm to break through the Cho-Harrington limit, and the practical realization of a drone tagged with a superscatterer.

III. MICRO-DOPPLER TAGGING

We further extend the ideas of superscattering to rotor blade tagging toward micro-Doppler coding, where the blade rotation serves as a built-in time-varying encoder, and the metamaterial tag becomes an information-bearing scatterer. In this scheme, each blade is assigned a fixed index, and the presence or absence of a resonant sticker on that blade defines a binary state, so a multiblade platform naturally maps onto an 8-bit code word, for example, 11001010, with each bit set by whether the corresponding blade carries a tag. The coded signature arises from the strong angular dependence of the tag response and the time-dependent polarization mismatch between the resonant dipole axis and the incident field, which modulates the scattered signal during rotation and produces a structured micro-Doppler pattern that is much more pronounced than the native return from polymer blades. In practice, not every nominal code is uniquely observable because the radar typically lacks sufficient resolution to separate individual rotors in range and angular bins, and additional redundancies arise from platform symmetries and from different operational behavior of forward and rear blades, so the usable code space must be filtered by identifiability under realistic measurement constraints. To ensure robust decoding under noise and flight variability, the coded spectrograms are treated as inputs to a learning pipeline that includes convolutional neural network classification together with post-processing that quantifies code reliability as a function of signal-to-noise ratio, and dimensionality reduction tools such as PCA and UMAP that visualize code clustering and separation, guiding the selection of codes for outdoor validation. Overall, the approach converts small drones from weak, ambiguous micro-Doppler targets into strongly scattering, uniquely labeled objects, supporting stand-off detection and identification at kilometer-scale ranges, and providing a practical pathway to deployable, low-cost blade retrofits compatible with rapid transfer to industrial radar monitoring systems.

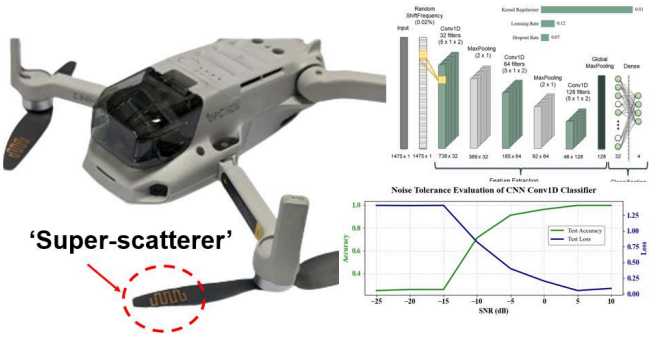

Fig. 2. Photograph of a tagged drone alongside a CNN-based radar processing layout and its performance, demonstrating reliable long-range detection below the noise level and exceeding conventional limits in radar monitoring.

IV. CONCLUSION

Beyond drone monitoring applications, the rotor blade platform provides a fundamental platform for studying rotating metamaterials as mechanically time-varying scatterers. Rotation converts a subwavelength resonator into a periodic spatiotemporal boundary condition, enabling controlled frequency mixing and engineered micro-Doppler spectra without active electronics, bias networks, or high-speed modulators. This framework connects classical micro-Doppler physics with modern metasurface and superscattering design, offering an experimentally accessible setting to explore how angular dispersion, modal interference, and optimization-driven geometry tailoring shape time domain scattering signatures. As a result, rotating metamaterials emerge as a general concept for low complexity spatiotemporal modulation, with applications spanning cooperative radar tags, reconfigurable beacons, and new measurement protocols for probing scattering bounds in dynamic electromagnetic systems.

REFERENCES

[1] K. Grotov et al., "Genetically Designed Wire Bundle Super-Scatterers," IEEE Trans Antennas Propag, 2022, 10.1109/TAP.2022.3177531.
[2] A. Mikhailovskaya *et al.*, "Superradiant Scattering Limit for Arrays of Subwavelength Scatterers," *Phys Rev Appl*, vol. 18, no. 5, p. 054063, 2022.
[3] S. Kosulnikov *et al.*, "Circular wire-bundle superscatterer," *J Quant Spectrosc Radiat Transf*, vol. 279, p. 108065, Mar. 2022,
[4] V. Kozlov, D. Vovchuk and P. Ginzburg, "Radar Range Deception With Time-Modulated Scatterers," in *IEEE TAP*. 71, no. 5, pp. 4486-4491, May 202
[5] V. Kozlov, D. Vovchuk, P. Ginzburg, "Direction of Arrival Deception With Time-Modulated Scatterers," in *IEEE Trans. on Radar Sys.*, vol. 1, .90-95, 2023
[6] D. Vovchuk, et. al., "Micro-Doppler-Coded Drone Identification", 2024.
[7] Kozlov V, et. al. Universal Software Only Radar with All Waveforms Simultaneously on a Single Platform. *Remote Sensing*. 2024; 16(11):1999.
[8] Vovchuk, D., Uziel, G., Machnev, A. *et al.* Genetically synthesized supergain broadband wire-bundle antenna. *Commun Eng* **3**, 101 (2024).

Metallic Nanohelices as Chiral Metasurfaces & Applications in Chiral Sensing

Thu Hac Huong Le
National Institute of Advanced Industrial Science and Technology (AIST), Japan
*Corresponding author: thu.le@aist.go.jp

***Abstract*— This study presents a wafer-scale self-assembly approach for the fabrication of metallic helices by engineering the residual stresses and gradient strains in thin films, which induce spontaneous folding and twisting. The resulting nanohelices, with submicrometer radii, exhibit pronounced chiroptical responses in the infrared regime, enabling practical applications in chiroptical spectroscopies.**

***Keywords*— nanohelices, chiral metasurfaces, chiral sensing, vibrational circular dichroism.**

I. Introduction

Chiral metasurfaces have emerged as promising platforms for enhancing chiroptical activity in spectroscopic and chiral chemistry applications. Recent theoretical and experimental studies have demonstrated that the chiroptical signals of chiral molecules can be significantly amplified through coupling with chiral metastructures. Among the various chiral architectures reported to date, helical structures are particularly attractive owing to their intrinsic optical chirality arising from their geometrical configuration.[1, 2] Their chirality enables strong light–matter interactions, making them especially suitable for applications such as chiral sensing and stereochemical reactions. However, despite their considerable potential, the fabrication and optical characterization of metallic helices remain relatively underexplored, primarily due to substantial technical challenges, including the tradeoff between precise structural control and scalable, efficient processing.

In this study, we present a self-assembly fabrication technique for nanohelices that offers precise feature control, wafer-scale production capability, and broad material compatibility. Our method involves the single-step transformation of metallic strips composed of multilayered thin films into helical geometries once released from the substrate. This transformation is driven by the nanoscale control of the residual stresses and gradient strains within the thin films, which spontaneously generate the necessary forces for folding and twisting. This technique facilitates the efficient fabrication of centimeter-scale samples, allowing for chiroptical characterization using standard commercial spectrometers. Experimental measurements and numerical simulations confirm strong chiroptical responses in the infrared (IR) region for helices with radii on the order of hundreds of nanometers.

II. Methods

The fabrication process begins with the preparation of micrometer-scale strips of multilayered metallic thin films on a Si substrate, using ultraviolet (UV) lithography, electron-beam evaporation, and lift-off techniques. The substrate is then coated with the electron-beam lithography (EBL) resist, and uniform nanoscale line-and-space patterns are written at a specific angle θ relative to the strip's axis. After development, selective wet etching is performed to partially remove the top metal layer. Upon removal of the EBL resist, microstrips with nanogroove patterns are formed. The substrate then undergoes isotropic reactive ion etching to eliminate the underlying silicon. As the Si beneath the strips is fully removed, the strips detach from the substrate. Residual stresses in the nanogrooves create a periodic strain gradient, causing the strips to fold and twist spontaneously into nanohelices.

III. Results and Discussion

Figure 1(a-b) shows the scanning electron microscope (SEM) images of nanohelices aligned in parallel to the Si substrate, fabricated from aluminum (Al)/titanium (Ti)/aluminum (Al) and gold (Au)/nickel (Ni)/aluminum (Al) trilayer films, respectively. The fabricated helices exhibit diameters ranging from approximately 800 nm to several micrometers, demonstrating the tunability of the structural dimensions achieved by this approach.

Based on the helical geometry, the pitch P between adjacent rings is related to radius R of helix by

$$P = \frac{2\pi R}{\tan\theta} \quad (1) \text{ and}$$

$$R \approx \frac{l}{|\alpha|} \quad (2);$$

where l is the periodicity of the nanogroove patterns and α is the folding angle induced at each nanogroove. These relationships indicate that structural parameters such as R and P can be precisely tuned by adjusting the nanogroove periodicity l, the folding angle α, and the alignment angle θ of the groove patterns. A key advancement of this technique is its ability to achieve wafer-scale fabrication within a relatively

short processing time. The realization of cm^2-sized samples has enabled the characterization of the chiroptical properties of metallic helices using standard spectrometers, eliminating the need for previously required microscope-based setups.

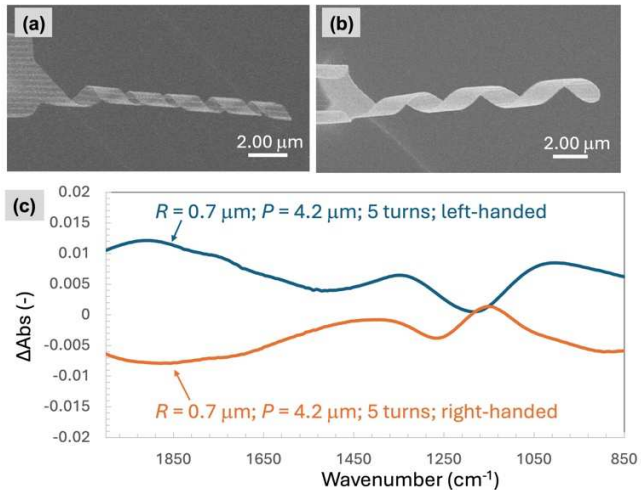

Fig. 1. SEM images of helices fabricated from (a) Al/Ti/Al and (b) Ni/Au/Al thin films, (c) IR-CD spectra of pairs of helices

To verify the chiral responses of the fabricated helices, we measured the extinction spectrum differences for incident circularly polarized light of opposite handedness in the IR range of 850 – 2000 cm^{-1}, using a standard Fourier transform-based IR circular dichroism (IR-CD) spectrometer. The resulting IR-CD spectra, shown in Fig. 1(c) for two Al helices with opposite handedness, reveal distinct circular dichroism (CD) peaks and dips at identical frequencies. The right- and left-handed structures exhibit opposite signs with nearly equal amplitudes, demonstrating the mirror-symmetric behavior characteristic of chiral systems. This can be attributed to the chiral eigenmodes arising from their intrinsic geometry.

The fabricated metallic nanohelices exhibit strong chiroptical responses in the infrared (IR) spectral range of 850–2000 cm^{-1}, which overlaps with the vibrational bands of many molecular functional groups. This spectral overlap makes the nanohelices particularly suitable for applications in chiroptical spectroscopy and chiral molecular sensing. Numerical simulations indicate the formation of a strongly enhanced chiral near field accumulated within the core of the helices, resulting in a high optical chirality density. This chiral near field gives rise to enantioselective interactions with nearby chiral molecules. To experimentally verify this effect, two samples consisting of geometrically identical nanohelices with opposite handedness (left- and right-handed) were uniformly coated with a thin layer of *L*-alanine molecules via thermal evaporation. Infrared transmission spectra were subsequently measured for both samples. The differential transmission spectrum between the left- and right-handed samples, shown in Fig. 2, exhibits a pronounced transmittance difference, including distinct peaks corresponding to the vibrational functional groups of alanine, despite identical molecular coverage on both samples. These observations confirm that chiral molecules interact differently with nanohelices of opposite handedness. Moreover, the results indicate that the nanohelices enable the simultaneous detection of molecular vibrational fingerprints and molecular chirality, providing information analogous to that obtained from vibrational circular dichroism (VCD) spectroscopy. Notably, this approach offer the VCD measurement through a single transmission measurement with enhanced sensitivity, in contrast to conventional techniques, which require complex experimental configurations and typically suffer from limited sensitivity and signal-to-noise ratios.

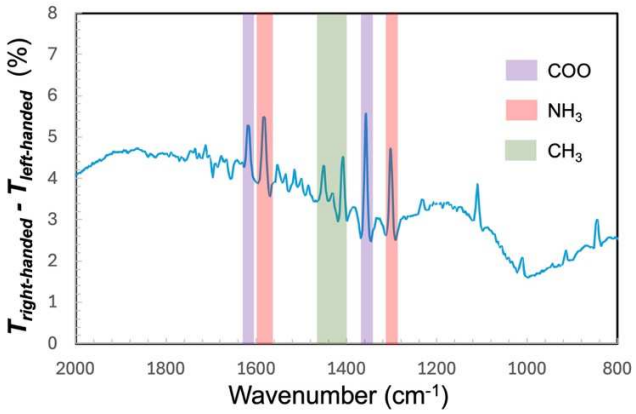

Fig. 2. Differential IR transmittance spectrum of *L*-alanine films covered on left- and right-handed helices revealing the VCD signals

IV. Conclusion

In summary, we have developed a robust and scalable approach for fabricating submicrometer metallic helices by engineering the stress and strain in metallic thin films. The wafer-scale realization of helical structures, together with tunable geometrical parameters and controllable optical responses, establishes this platform as a versatile and transformative chiral metasurface. Furthermore, we experimentally demonstrate the capability of these helices to perform the measurements of vibrational circular dichroism of chiral molecules. The developed metallic nanohelices therefore hold significant promise for practical applications in photonics, chiroptical spectroscopy, and stereochemistry, including chiral sensing, infrared inspection, stereochemical characterization, and enantioselective chemical reactions.

Acknowledgments

This study was supported by Fusion Oriented Research for disruptive Science and Technology (JPMJFR203Z) from The Japan Science and Technology Agency and Grant-in-Aid for Early-Career Scientists (21KK0256). The authors gratefully acknowledge the Nanotechnology Hub of Kyoto University, Japan for the support in nanofabrication processes.

References

[1] Gansel, J. K., Wegener, M, et al. “Gold helix photonic metamaterial as broadband circular polarizer”, Science 325, 1513-1515, 2009.

[2] Schäferling, M., Yin, X., Engheta, N., and Giessen, H. “Helical plasmonic nanostructures as prototypical chiral near-field sources”, ACS Photon. 6, 530-537, 2014.

Surface Light Localization in Topological Multilayers

Eva Otero,[1,*] Ivan Toftul,[2] Yuri Kivshar,[2] Crina Cojocaru,[1] Jose Trull[1]

[1]Department of Physics, Universitat Politècnica de Catalunya, Terrassa (Barcelona) Spain
[2]Nonlinear Physics Center, Research School of Physics, Australian National University, Canberra, Australia
*Corresponding author: eva.otero@upc.edu

***Abstract*—We numerically and experimentally study a photonic multilayer with SSH geometry supporting localized edge states. Comparison between two structures with identical periodicity but different topological phases show edge states only in the nontrivial phase. An absorber layer confirms the mode is confined to the surface rather than the bulk.**

***Keywords*—surface states, light localization, 1D photonic crystals, topological photonics, SSH, electric field enhancement**

I. INTRODUCTION

Surface states in periodic structures are of great interest in physics and photonics due to their ability to confine light at interfaces, enabling applications in sensing, lasing, and photonic devices. In recent decades, topological photonics has emerged as a promising field to achieve strong edge states that are robust against defects and disorder [1,2].

For one-dimensional (1D) topological systems, the most representative model is the Su-Schrieffer-Heeger (SSH) model [3]. It describes a periodic 1D chain with alternating weak and strong couplings between neighboring atoms. Depending on how the edge of a semi-infinite structure is truncated, two phases arise: topologically trivial and non-trivial. At the interface between different topological phases, a robust edge state is generated [1]. This model has been applied to photonic structures such as waveguides [4,5], ring resonators and nanoantenna arrays [6,7]. While numerical demonstrations exist for multilayer 1D photonic crystals [8], very few experimental demonstrations have been done so far.

In this work, we numerically and experimentally implement the SSH model in a 1D photonic crystal by fabricating two structures with identical periodicity but different edge truncations: structure A with a non-trivial phase, and structure B with a trivial phase.

II. DESIGN

The proposed structures consist of alternating layers of SiO_2 and Ta_2O_5, as schematically shown in Figure 1. The SSH geometry is introduced by alternating thin and thick SiO_2 layers, corresponding to strong and weak bonds (t and t'), respectively. Structure A has four periods and ends on a weak bond (t'), while Structure B includes two extra layers, ending on a strong bond (t). As air has a trivial phase, we expect only Structure A to support a topological edge mode at the surface.

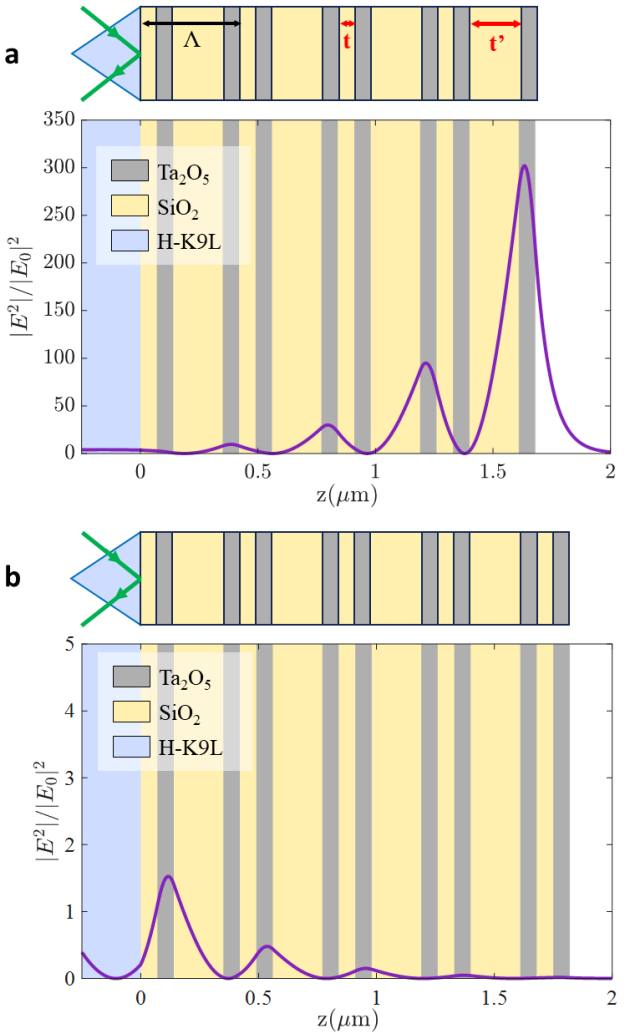

Fig. 2 **(a)** Type A and **(b)** Type B structures. **(Top of subfigures)** Simplified structure scheme (not real scale) of the structures with period Λ, surface termination bond is located at the right end. t corresponds to strong bond, t' to weak bond. **(Bottom of subfigures)** Simulations of the TE electric field intensity distribution normalized to the amplitude of the incident wave at 800nm for Type A structure and Type B structure at angle 68º.

In order to excite and detect the surface modes the multilayers were built on a prism, as seen in the schematics in fig. 1, with the experimental Kretschmann configuration, most known for detection of surface plasmon waves in metals but also used for Bloch surface waves detection in multilayers [9]. Light incident on the prism undergoes total internal reflection, generating an evanescent field that penetrates the multilayer. When angle and wavelength match the surface mode condition, energy couples into the mode. The coupling will lead to a decrease (dip) in the reflected intensity, facilitating the detection of the mode.

Transfer Matrix Method has been used to numerically calculate the electric field intensity distribution on the structures. Simulations in Fig. 1 show that at 800 nm and TE polarization, Structure A exhibits a highly localized surface state with a 300-fold field enhancement, while Structure B does not.

III. Results and Discussion

We measure the reflection spectra of both structures and we find that Structure A shows a resonance in reflection near 800 nm (precisely, at 798 nm) when the surface mode couples, while Structure B exhibits total reflection. To confirm the resonance originates from the surface rather than guided modes inside the multilayer, we coat the surface of the samples with a very narrow layer of absorbing dye. The absorption within the dye enhances the resonance without altering the mode, proving its surface nature. Figure 2 summarizes our experimental results: for the same angle of incidence, structure A without the absorber layer (blue plot) and with the absorber (yellow plot) present a resonance at the same wavelength, but we can clearly see that the presence of the absorber improves the resonance depth. For Structure B (orange plot), even with the absorber, no resonance appears, confirming that truncation determines the presence of the edge state.

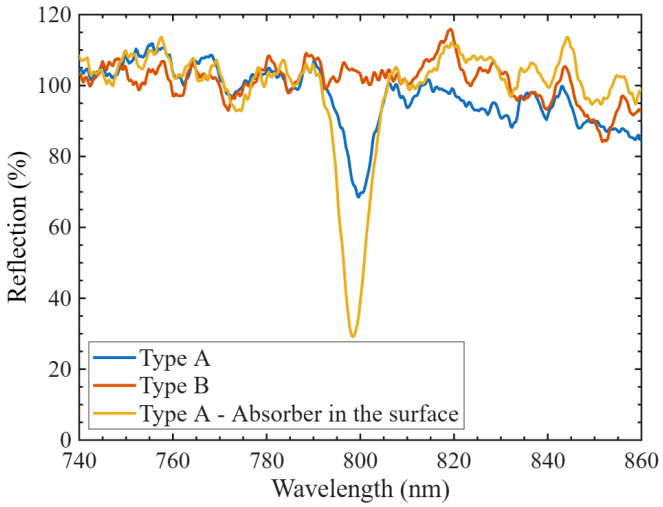

Fig. 2 Experimentally measured reflection spectrum of structure A for angle of incidence 67.9° without (blue line) and with (yellow line) the absorber layer on top and of structure B (orange line).

IV. Conclusion

In conclusion, we have constructed two multilayer structures following the SSH geometry and demonstrated, numerically and experimentally, that the choice of the end truncation at the edge of the structure defines whether a topological surface state emerges. Using the Kretschmann configuration and absorber coating, we verified that the detected mode is indeed a surface state, not an internal guided mode. This work provides an experimental pathway for implementing topological photonic concepts in 1D photonic crystals. Furthermore, the topological surface state exhibits large field enhancement at the interface, which in turn strengthens light–matter interactions in its vicinity. Such enhanced field localization makes these structures promising platforms for sensing technologies, where strong surface fields can boost sensitivity to refractive-index changes or molecular absorption.

Acknowledgments

E.O. acknowledges the predoctoral program AGAUR-FISDUR (2023 FISDU 0050) of the Secretariat of Universities and Research of the Department of Research and Universities of the Generalitat of Catalonia and the European Social Plus Fund. E.O., C.C. and J.T. acknowledge Spanish Agencia Estatal de Investigacion from Ministerio de Ciencia, Investigacion y Universidades (project PID2023-148620NB-I00 granted by MICIU/AEI/´10.13039/501100011033 and FEDER,UE). Also, they acknowledge M. Scalora for fruitful discussions.

References

[1] D. V. Zhirihin and Y. S. Kivshar, “Topological Photonics on a Small Scale,” Small Sci., vol. 1, no. 12, p. 2100065, Dec. 2021, doi: 10.1002/smsc.202100065.

[2] Z. Wang, Y. Chong, J. D. Joannopoulos, and M. Soljačić, “Observation of unidirectional backscattering-immune topological electromagnetic states,” Nature, vol. 461, no. 7265, pp. 772–775, Oct. 2009, doi: 10.1038/nature08293.

[3] W. P. Su, J. R. Schrieffer, and A. J. Heeger, “Solitons in Polyacetylene,” Phys. Rev. Lett., vol. 42, no. 25, pp. 1698–1701, Jun. 1979, doi: 10.1103/PhysRevLett.42.1698.

[4] Z. Zhang et al., “Experimental Realization of Multiple Topological Edge States in a 1D Photonic Lattice,” Laser Photonics Rev., vol. 13, no. 2, p. 1800202, Feb. 2019, doi: 10.1002/lpor.201800202.

[5] R. El-Ganainy and M. Levy, “Optical isolation in topological-edge-state photonic arrays,” Opt. Lett., vol. 40, no. 22, p. 5275, Nov. 2015, doi: 10.1364/OL.40.005275.

[6] H. Zhao et al., “Topological hybrid silicon microlasers,” Nat. Commun., vol. 9, no. 1, p. 981, Mar. 2018, doi: 10.1038/s41467-018-03434-2.

[7] L. Orsini et al., “Deep subwavelength topological edge state in a hyperbolic medium,” Nat. Nanotechnol., vol. 19, no. 10, pp. 1485–1490, Oct. 2024, doi: 10.1038/s41565-024-01737-8.

[8] H. Jiang et al., “Topological edge modes in one-dimensional photonic crystals containing metal,” OSA Contin., vol. 4, no. 5, pp. 1626–1639, May 2021, doi: 10.1364/OSAC.416906.

[9] W. M. Robertson and M. S. May, “Surface electromagnetic wave excitation on one-dimensional photonic band-gap arrays,” Appl. Phys. Lett., vol. 74, no. 13, pp. 1800–1802, Mar. 1999, doi: 10.1063/1.123090.

Revolutionizing semiconducting SERS application for resistant pollutants via nanoarchitectonics

Yunqing Kang[1], Yusuke Yamauchi[1,2,3], Julio Gutiérrez Moreno[4], Olga Guselnikova[5]

1 Department of Materials Process Engineering Graduate School of Engineering, Nagoya University, Nagoya 464–8603, Japan
2 Australian Institute for Bioengineering and Nanotechnology (AIBN), The University of Queensland, Brisbane, Queensland, 4072 Australia.
3 Department of Convergent Biotechnology & Advanced Materials Science, Kyung Hee University, 1732 Deogyeong-daero, Giheung-gu, Yongin-si, Gyeonggi-do 17104, South Korea
4 Barcelona Supercomputing Center, Plaça Eusebi Güell 1-3, 08034 Barcelona, Spain
5 Institute of Applied Physics, Vienna University of Technology, Vienna 1040, Austria

*Corresponding author: olga.guselnikova@tuwien.ac.at

***Abstract*— Amorphous Rh–Se mesoporous nanospheres synthesized via micellar self-assembly enable semiconducting SERS substrates with tunable composition, curvature, and amorphization, achieving sensitive detection of hexachlorobenzene and Teflon microplastics through electronic modulation, challenging high-surface-area paradigms and guiding design of advanced metal–selenium sensing materials for catalysis and electronics applications beyond conventional semiconductors worldwide.**

***Keywords*— Mesoporous metals; Amorphous alloys; Surface-enhanced Raman scattering; Chemical enhancement mechanism; Persistent organic pollutants**

I. Introduction

Amorphous materials provide unique advantages for catalysis and sensing because of their isotropic structure, high density of defect sites, and tunable electronic properties. However, producing amorphous nanostructures based on noble metals remains challenging due to their tendency to crystallize. Metal–selenium alloys provide a promising route to stabilize amorphous phases while introducing semiconducting behavior.

Surface-enhanced Raman spectroscopy (SERS) traditionally relies on plasmonic metals where electromagnetic enhancement dominates. Semiconductor SERS, in contrast, depends mainly on chemical enhancement via charge transfer between substrate and analyte. Despite progress, semiconductor substrates struggle to detect non-absorbing and weakly polarizable molecules because of limited adsorption and inefficient electronic coupling.

Here we demonstrate that combining amorphization with nanoscale curvature engineering in mesoporous Rh–Se nanospheres allows efficient detection of persistent pollutants such as hexachlorobenzene (HCB) and polytetrafluoroethylene (PTFE) microplastics. The results challenge the prevailing assumption that high surface area is the dominant factor in SERS performance and instead reveal electronic structure control as the key parameter.

II. Methods

Amorphous Rh–Se mesoporous nanospheres were synthesized using a one-step micellar self-assembly reduction approach. Diblock copolymers served as dynamic templates, enabling control over pore size and curvature. By varying polymer molecular weight, three curvature regimes were obtained corresponding to small, medium, and large pores.

Compositional control was achieved by tuning Rh/Se precursor ratios. Post-synthesis annealing under inert atmosphere allowed systematic control of crystallinity.

Structural characterization was conducted using SEM, TEM, XRD, XPS, BET surface analysis, and X-ray absorption spectroscopy. Surface electronic properties including work function and valence-band features were measured using Kelvin probe force microscopy and XPS.

SERS measurements were performed with 532 nm excitation after premixing substrates with analytes. Detection limits and enhancement factors were determined through calibration measurements. Adsorption and charge-transfer mechanisms were further examined using molecular dynamics and density functional theory simulation.

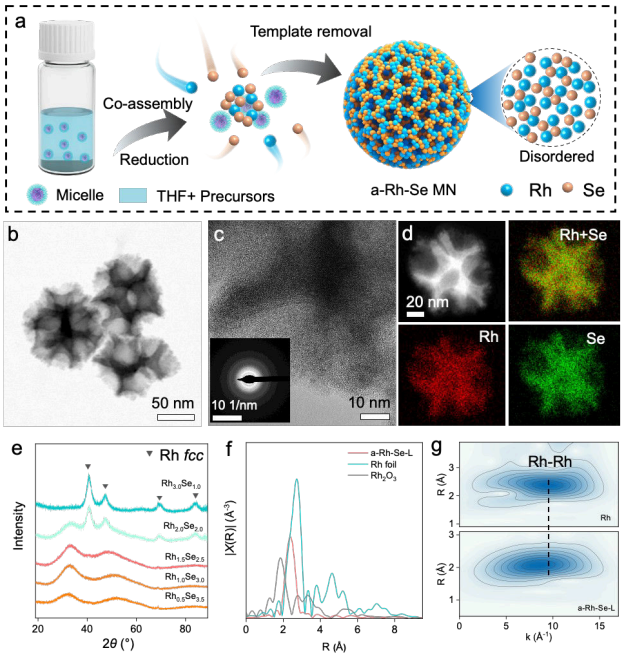

Figure 1. Schematic of material synthesis and characterization of a-Rh–Se-L MNs.

III. Results and Discussion

Curvature Engineering and Electronic Effects

Although higher curvature structures exhibit larger surface area, SERS experiments revealed that low-curvature mesostructures produce significantly stronger Raman enhancement. Surprisingly, the substrate with the lowest surface area delivered the highest enhancement factor.

Electronic measurements revealed that decreasing curvature shifts the d-band center closer to the Fermi level while reducing the work function. These changes promote efficient electron injection and improve orbital alignment between substrate and analyte, thereby enhancing chemical SERS mechanisms.

Thus, electronic structure modulation dominates over surface-area effects in determining SERS activity.

Role of Amorphization

Thermal annealing progressively transformed amorphous Rh –Se into crystalline phases. Increasing crystallinity caused strong reduction of SERS performance, confirming that amorphous disorder is critical for charge transfer.

Simulations showed that highly disordered structures provide stronger adsorption pockets and enhanced charge transfer to adsorbed molecules. Disorder-induced states facilitate carrier excitation and enable efficient photoinduced charge transfer under laser excitation.

Detection of Persistent Pollutants

The optimized amorphous low-curvature Rh–Se substrates enabled detection of HCB down to nanomolar concentrations with stable response across complex wastewater matrices. Signal reproducibility remained high over months of storage.

The platform also enabled quantitative detection of PTFE microplastics, which typically cannot be measured by conventional SERS due to low polarizability and poor adsorption. Compared to Au nanoparticles, Rh–Se substrates produced stronger and more uniform signals, indicating superior particle–substrate affinity.

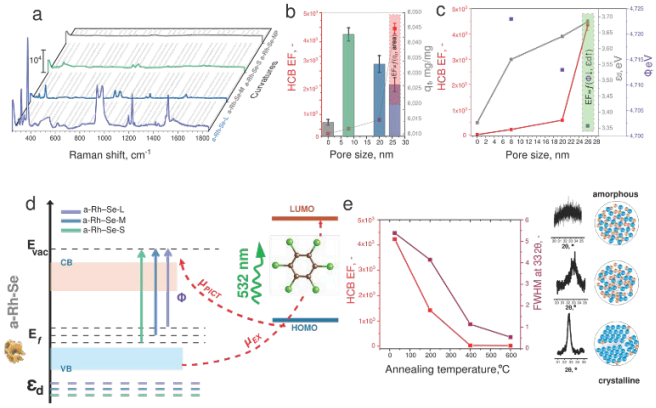

Figure 2. Probing SERS sensing of HCB on a-Rh-Se-S/M/L with different curvature degree.

D. Mechanistic Implications

Charge transfer processes contributing to enhancement include ground-state orbital hybridization, photoinduced electron transfer, and intramolecular excitation of adsorbed molecules. Amorphization and curvature jointly tune work function and electronic density of states, enabling resonant charge mobility and strong chemical enhancement.

Overall, the results overturn conventional SERS design strategies centered on maximizing surface area or electromagnetic hotspots.

IV. Conclusion

We developed amorphous mesoporous Rh–Se semiconductors with tunable curvature and crystallinity enabling efficient SERS detection of chemically resistant pollutants. Reduced curvature and enhanced amorphization modulate electronic descriptors, promoting charge transfer and chemical enhancement.

This strategy extends semiconductor SERS toward practical environmental sensing applications and provides design guidelines for future semiconductor-based SERS materials

Acknowledgments

The authors gratefully acknowledge the financial support of the JST-ERATO Yamauchi Materials Space-Tectonics Project (JPMJER2003) and ARC Laureate Fellowship (FL230100095). OG acknowledges FFG FO999923096 project.

High-performance Wide-angle Metalens for Optical Receiver

Wei-Hsiang Lai[1,*] and Pin Chieh Wu[1]

[1]Department of Photonics, National Cheng Kung University, Tainan 70101, Taiwan
*Corresponding author: a0905919411@gmail.com

***Abstract*—In this work, we present a 940nm metalens designed for integration with CCDs, enabling a significant reduction in system volume. The proposed metalens features a wide field of view of 93° while maintaining high modulation transfer function (MTF) performance. This ultra-compact solution enhances light collection efficiency for near-infrared optical receivers.**

***Keywords*— metalens, metasurface optics, optical receiver, wide-angel optics, ray-tracing and wave optics co-design.**

I. Introduction

Recently, the rapid development of optical sensing and communication systems has driven a strong demand for compact and highly integrated optical receivers. For these systems, achieving high optical collection efficiency over a wide field of view (FoV) is a critical requirement. However, conventional refractive or diffractive optical components often suffer from bulky form factors, limited FoV, and increased aberrations under large-angle incidence, which significantly constrain system-level integration and performance.

Metasurface lens (Metalens) provides a promising solution to overcome these limitations by enabling subwavelength wavefront manipulation within an ultrathin platform. Through spatially engineered phase responses, metalenses can achieve compact focusing functionalities that are difficult to realize with traditional optics. In particular, metalenses designed for a single operating wavelength offer enhanced flexibility in phase control, making them attractive candidates for wide-angle optical reception while maintaining high numerical aperture (NA). Nevertheless, realizing a wide-angle metalens at 940 nm that meets the practical requirements of optical receiver applications remains challenging, especially when off-axis performance and system-level efficiency must be simultaneously considered.

In this work, we present a wide-angle metalens operating at 940 nm, specifically optimized for optical receiver applications [1][2]. Our design framework integrates ray-tracing analysis with wave-optics-based metasurface modeling, allowing both geometric light collection behavior and electromagnetic wave effects to be consistently accounted for during the optimization process. Ray-tracing is employed to define the target phase profiles and evaluate angular response at the system level, while full-wave simulations are used to refine the meta-atom geometry and ensure accurate phase and amplitude control of metalens under oblique incidence. By combining these two complementary approaches, we demonstrate a metalens design that maintains stable focusing behavior and high reception efficiency across a wide FoV. The proposed methodology highlights an effective pathway for bridging system-level optical design and nanoscale wavefront engineering, offering practical insights for next-generation near-infrared optical receiver systems.

II. Methods

To meet the significant requirements of a compact optical receiver, a top-down hybrid design strategy was employed. This process consists of two stages: macroscopic optimization based on ray-tracing analysis, followed by physical implementation using Rigorous Coupled-Wave Analysis (RCWA).

A. Macroscopic Optimization via Ray Tracing

To model the properties of the metasurface, a binary 2 phase surface was utilized. The phase profile $\varphi(r)$ is defined by a rotationally symmetric polynomial expansion:

$$\varphi(r) = \sum_{i=1}^{N} A_i \left(\frac{r}{R_{norm}}\right)^{2i} \quad (1)$$

where R_{norm} is the normalization radius, and A_i is the aspheric phase coefficients. These coefficient (A_i) was set as variables in the optimization process. A merit function was constructed to minimize the root-mean-square spot size under various conditions of incidence and wavefront error while satisfying specific optical targets.

B. Physical Realization via RCWA

Based on the ray-tracing optimization, the optimized continuous-phase profile was discretized and mapped to physical nanostructures using the RCWA method. The meta-atoms consist of symmetric square nanopillars, ensuring polarization-independent optical response, making the device suitable for unpolarized light sources commonly used in

practical applications.

III. Results and Discussion

The macroscopic performance of the designed metalens was first evaluated using ray-tracing simulations. Figure 1 illustrates the ray-tracing optimization results of the metasurface. The system is optimized for a center wavelength of 940 nm with an effective focal length (EFL) of 1.513 mm and an F-number of 1.3. As shown in the ray trajectories, the metalens effectively focuses incident light across the entire field of view. The design supports a FoV of 93°. The distinct colored rays represent different field angles, confirming that the optimized phase profile successfully suppresses off-axis aberrations and directs light onto the sensor's active area.

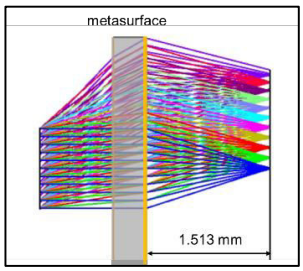

Fig. 1 optimization results of the 940-nm metalens system. The schematic shows the realized FoV of 93°, demonstrating effective focusing on the sensor plane.

Based on the ray-tracing optimization results of the metasurface, we subsequently use the RCWA method to design meta-atoms. Figure 2(a) depicts the schematic of the unit cell. The structure consists of amorphous silicon (a-Si) nanopillars on a SiO_2 substrate. Figure 2(b) shows the resulting transmittance (left) and phase shift (right) maps as functions of incident angle and width W. The transmittance map reveals that the unit cell maintains high efficiency across a broad range of widths, and the phase shift covers the full 2π range, satisfying the requirement for complete wavefront control.

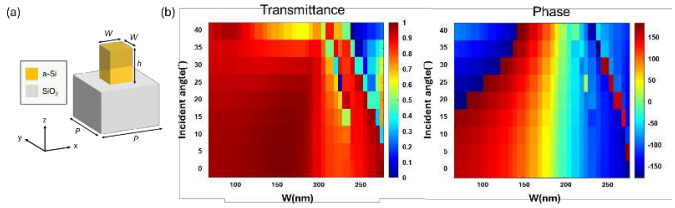

Fig. 2 (a) Schematic of the designed metasurface unit cell. The geometric parameters are defined as the lattice period P = 400 nm, pillar width W, and height h. (b) Simulation of transmittance and phase colormap of the unit cell as a function of nanopillar width W and incident angle at λ = 940 nm.

To strictly evaluate the imaging capability of the integrated metalens, we analyzed the intensity distribution and contrast transfer function at the sensor plane. Figure 3 presents the simulated focal spot intensity distributions for different incident angles. As the incident angle increases, slight coma and astigmatism develop, leading to a lateral spread of the spot profile. However, as shown in the intensity colormap, the optical energy remains highly concentrated within the central lobe. This confirms that the metalens effectively focuses light onto the active pixel area even at large field angles, ensuring sufficient signal-to-noise ratio (SNR) for optical sensor.

To further quantify the image quality, the modulation transfer function (MTF) was calculated, as shown in Fig. 4. The results demonstrate tangential and sagittal performance across the entire field of view. At a higher frequency of 100 cycles/mm, the MTF values for both on-axis and off-axis fields are maintained above 0.3. This indicates that the metalens design is successful for sensing applications.

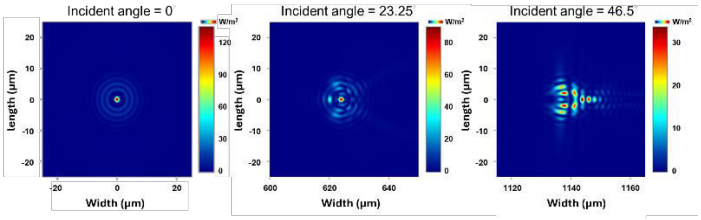

Fig. 3 Simulated point spread functions on the sensor plane for incident angles of 0°, 23.25°, and 46.5° at λ = 940 nm.

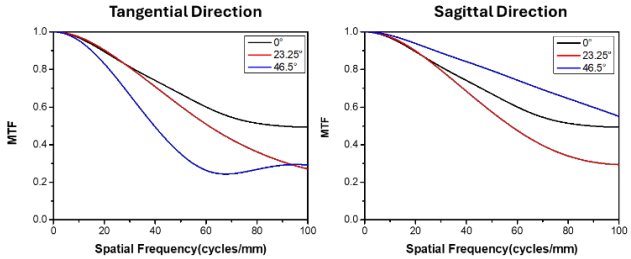

Fig. 4 Simulated MTF of the metalens for tangential and sagittal direction at λ = 940 nm, with incident angles of 0°, 23.25°, and 46.5°.

IV. Conclusion

In this work, we presented compact, high-performance metalens operating at 940 nm for optical receiver applications. By employing a hybrid design strategy combining macroscopic ray tracing with microscopic RCWA, we realized a polarization-independent device with a wide field of view (93°). The design ensures robust detection of unpolarized light with excellent focusing capabilities and superior MTF performance. Consequently, it offers a practical, scalable solution for next-generation space-constrained devices.

Acknowledgments

This work was supported by the National Science and Technology Council (NSTC), Taiwan. We also thank the Department of Photonics at National Cheng Kung University (NCKU) for providing the computational resources and technical support essential for this research.

References

[1] J. Deng, K. Wu, R. Fu, et al., "Full-space and wide field-of-view metalens based on 1D photonic crystal," *Opt. Laser Technol.*, vol. 182, pp. 112187, 2025

[2] B. Groever, W. T. Chen, and F. Capasso, "Meta-Lens Doublet in the Visible Region," *Nano Lett.*, vol. 17, pp. 4902−4907, 2017.

Structural Coloring via Hyperuniform Arrays of Tapered Si Nanostructures on Glass

Hanna Kylhammar[1, *], Mikko E. Kjellberg[1], Srinivasan Anand[1]

[1]Department of Applied Physics, KTH Royal Institute of Technology, Sweden
*Corresponding author: hannaky@kth.se

***Abstract*— High□index dielectric nanostructures provide a route to structural coloration without pigments. Here, we demonstrate color tuning in hyperuniform arrays of amorphous silicon (a□Si) nanodisks by controlling the nanodisks' sidewall angle, which results in a shift in the spectral position of the resonant scattering. Charged sphere lithography enables scalable hyperuniform pattern generation.**

***Keywords*— structural colors, all-dielectric metasurfaces, hyperuniform disorder, Mie resonators, charged sphere lithography**

Structural colors produced by dielectric nanostructures have emerged as a sustainable alternative to pigment□based coloration, which often relies on environmentally harmful chemical processes.[1] Beyond their ecological advantages, all□dielectric metasurfaces offer robust functionality for applications such as solar energy harvesting, decorative coatings, sensing, and display technologies.[2-6] Previous work has shown that tuning the size and geometry of high□index Mie resonators enables vivid colors. Beyond the size parameters, the tapering angle of nanostructures has recently been identified as a powerful degree of freedom for tailoring scattering responses in nanostructures.[7]

To translate coloured metasurface concepts into practical technologies, scalable and CMOS□compatible fabrication routes are essential. Silicon offers a low□loss, abundant, and CMOS□compatible platform, enabling scalable fabrication and seamless integration with established semiconductor processes. Here, we demonstrate structural colours generated by tapered amorphous□silicon (a-Si) nanodisks arrays on glass substrates. By systematically varying the taper angle, we demonstrate it as a parameter for colour tuning. The proposed methodology provides a scalable pathway toward high□performance dielectric colour metasurfaces.

The nanodisk arrays are fabricated using charged sphere lithography combined with reactive-ion etching. The a-Si/glass substrate is covered with a positively charged layer (PDDA). Negatively charged nanospheres are diluted in deionized water and drop-casted on the a-Si/glass substrate and bind electrostatically to the surface. Charged sphere lithography produces nearly hyperuniform disordered patterns (Fig. 1). We control the pattern density by increasing the ionicity of the charged sphere suspension.

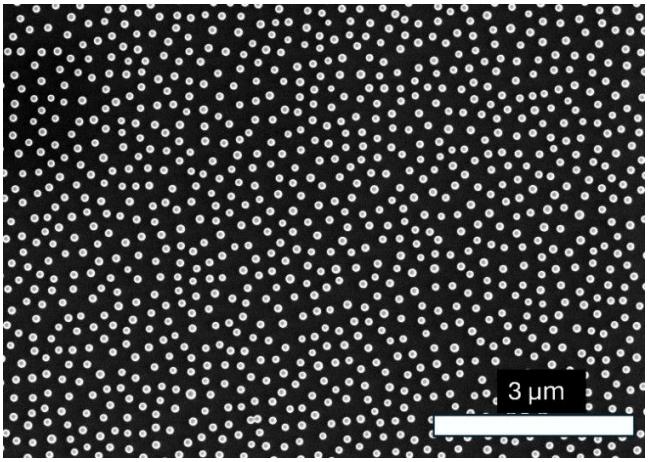

Fig. 1 SEM image of the top view of 100 nm diameter nanodisks as patterned by charged sphere lithography.

The nanostructures are etched in the a-Si are by reactive-ion etching using SF_6/C_4F_8 chemistry. Outward tapering of the structures is achieved by decreasing the gas ratio.[8] In Fig 2. the profiles of nanodisks etched with 30:80 SF_6/C4F8, with a sidewall angle of 90°, and nanodisks etched with 17:80 SF_6/C_4F_8, with a sidewall angle of 80°. We compare arrays of nanodisks of a-Si and c-Si to determine how material properties influence the fabrication of tapered nanodisks as well as the overall impact on structural color generation.

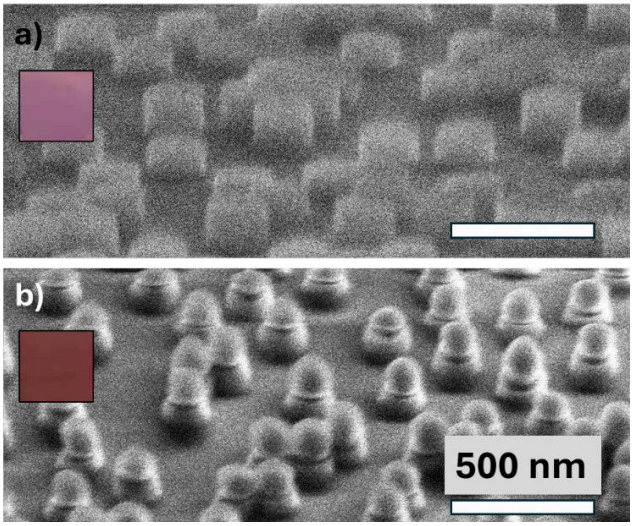

Fig. 2 SEM image of 200 nm top diameter nanodisks with a) 90° sidewall angle, etched with 30:80 SF_6/C_4F_8 and b) 80° sidewall angle, etched with 20:80 SF_6/C_4F_8. Inset are the reflected colours of the metasurfaces, photographed when placed on a black surface.

The scattering of the nanodisks is studied through finite-domain time-difference simulations and analysed by multipolar decomposition. [9,10] We show that the tapered geometry strongly influences the electric/magnetic dipole modes, shifting the spectral position of the resonant scattering which allows for continuous tuning across the visible spectrum.

Beyond the nanodisk geometry, we also investigate the impact on the colour appearance of the hyperuniform disordered arrangement. The disorder in the array results in stronger insensitivity to incident angle than for periodic arrays. The specular and diffuse reflectance and transmittance of the fabricated samples are measured.

The proposed coloured metasurfaces relies on low□cost, self□assembled patterns and that are compatible with large□area processing, opening pathways toward scalable coloration in a wide range of photonic devices.

ACKNOWLEDGMENTS

The work is supported by the Swedish Energy Agency – Energimyndigheten, grant no. P2023-01371.

REFERENCES

[1] Y. Wu, Y. Chen, Q. Song, S. Xiao, Dynamic Structural Colors Based on All-Dielectric Mie Resonators. *Adv. Optical Mater.* 2021, 9, 2002126. **https://doi.org/10.1002/adom.202002126**

[2] Yang, W., Xiao, S., Song, Q. *et al.* All-dielectric metasurface for high-performance structural color. *Nat Commun* **11**, 1864 (2020). https://doi.org/10.1038/s41467-020-15773-0

[3] Park, CS., Shrestha, V.R., Yue, W. *et al.* Structural Color Filters Enabled by a Dielectric Metasurface Incorporating Hydrogenated Amorphous Silicon Nanodisks. *Sci Rep* **7**, 2556 (2017). https://doi.org/10.1038/s41598-017-02911-w

[4] F. Vennberg, A.P. Ravishankar and S. Anand. Polarization dependent structural colors from tilted metalo-dielectric nanopillars, 2021 *Mater. Res. Express* **8** 046202

[5] A. Peralta Amores, A.P. Ravishankar and S. Anand, "Design and Modelling of Metal-Oxide Nanodisk Arrays for Structural Colors and UV-Blocking Functions in Solar Cell Glass Covers", *Photonics* **2022**, *9*(5), 273; **https://doi.org/10.3390/photonics9050273**

[6] Piechulla P.M., Fuhrmann B., Slivina E., Rockstuhl C., Wehrspohn R.B., Sprafke A.N. "Tailored Light Scattering through Hyperuniform Disorder in Self-Organized Arrays of High-Index Nanodisks," Adv. Optical Mater. 9, 2100186, (2021).

[7] A. V. Kuznetsov, A. Canós Valero, H. K. Shamkhi, P. Terekhov, X. Ni, V. Bobrovs, M. V. Rybin and A. S. Shalin, "Special scattering regimes for conical all-dielectric nanoparticles," *Sci. Rep.*, vol. 12, no. 1, p. 21904, Dec. 2022, doi: 10.1038/s41598-022-25542-2.

[8] F. Saffih, C. Con, A. Alshammari, M. Yavuz, and B. Cui, "Fabrication of silicon nanostructures with large taper angle by reactive ion etching," *J. Vac. Sci. Technol. B Nanotechnol. Microelectron. Mater. Process. Meas. Phenom.*, vol. 32, no. 6, p. 06FI04, Nov. 2014, doi: 10.1116/1.4901420.

[9] A. B. Evlyukhin and B. N. Chichkov, "Multipole decompositions for directional light scattering," Phys. Rev. B, vol. 100, no. 12, p. 125415, Sep. 2019, doi: 10.1103/PhysRevB.100.125415.

[10] A. B. Evlyukhin, T. Fischer, C. Reinhardt, and B. N. Chichkov, "Optical theorem and multipole scattering of light by arbitrarily shaped nanoparticles," Phys. Rev. B, vol. 94, no. 20, p. 205434, Nov. 2016, doi: 10.1103/PhysRevB.94.205434.

[11] S. Yu, C.-W. Qiu, Y. Chong, S. Torquato, and N. Park, "Engineered disorder in photonics," *Nat. Rev. Mater.*, vol. 6, no. 3, pp. 226–243, Mar. 2021, doi: 10.1038/s41578-020-00263-y.

Physically intuitive coupling engineering for realizing the proposed spectral response at the resonator with drop waveguide

Yae Jun Kim[1], Yu Sung Choi[1], Jae Won Ahn[1], and Jae Woong Yoon[1]*

[1]Department of Physics, Hanyang University, Seoul, 133-791, Korea
*Corresponding author: yoonjw@hanyang.ac.kr

***Abstract*— We present an analytically guided coupling engineering framework that maps coupling parameters to spectral characteristics in a resonator with a drop waveguide. By designing wavelength dependent coupling trajectories, we realize broadband uniform resonance output at the drop port and broadband critical coupling at the bus port.**

***Keywords*— Optical resonator, coupling trajectory, spectral response**

I. Introduction

Optical microring resonators are fundamental components in photonic integrated circuits because they provide compact and spectrally selective functionalities. Their performance in filtering, wavelength multiplexing, and on chip signal processing is determined by their resonance spectrum. In many practical systems, stable and predictable spectral characteristics over a broad wavelength range are required. However, spectral response exhibits strong wavelength dependence due to the dispersive coupling between the waveguides and the resonator, which leads to variations in resonance intensity, extinction ratio, and quality factor across the operating bandwidth.

In this work, we adopt a coupling centric perspective and establish an analytically guided framework that directly relates coupling parameters to spectral response. We explicitly analyze how the waveguide resonator coupling coefficients govern key spectral quantities. To extend the accessible coupling space, we consider a resonator coupled to both a bus and a drop waveguide. The presence of two independent coupling channels enables systematic exploration of a two-dimensional coupling parameter space and provides additional degrees of freedom for spectral engineering.

Within this framework, spectral design can be reformulated as trajectory engineering in the coupling parameter space. Desired spectral responses correspond to analytic conditions that define contours in this space. Broadband stabilization is achieved when the wavelength dependent evolution of the coupling parameters follows these contours. We formulate the coupling–response relation explicitly and show how target spectral characteristics can be predictively determined from analytic conditions.

II. Methods

To demonstrate the validity of the framework, we aim to realize the broadband uniform resonance output at the drop port as a first example. We first clarify the physical parameters that govern the spectral response. Figure 1a-1c present the physical model establishing the connection between the coupling parameters and spectral response. By analyzing how variations in coupling parameters influence the spectral response through the mapping, desired target response can be predictively designed from proper coupling engineering. The resonance output at the drop port is:

$$T_{drop,\max} = \frac{\alpha(1-t_1^2)(1-t_2^2)}{1+(\alpha t_1 t_2)^2 - 2\alpha t_1 t_2} \tag{1}$$

Therefore, the coupling parameter space can be directly mapped to the response. This mapping enables the derivation of the coupling trajectory which satisfies uniform resonance output at the drop port with enhanced stability of the quality factor. (Fig. 1d and Fig. 1e)

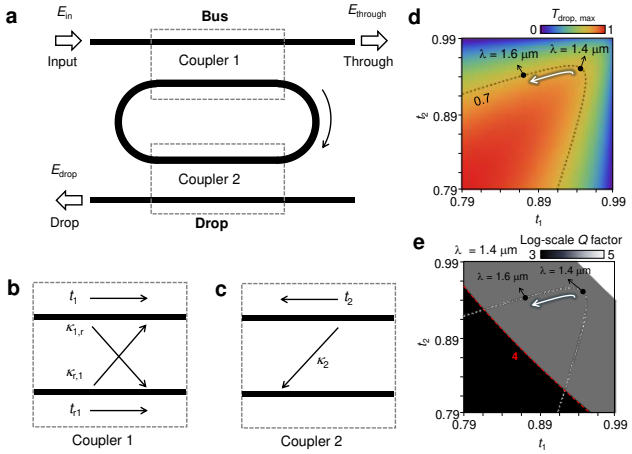

Fig. 1 Coupling system of a resonator with a drop waveguide to realize the broadband uniform resonance output at the drop port.

III. RESULTS

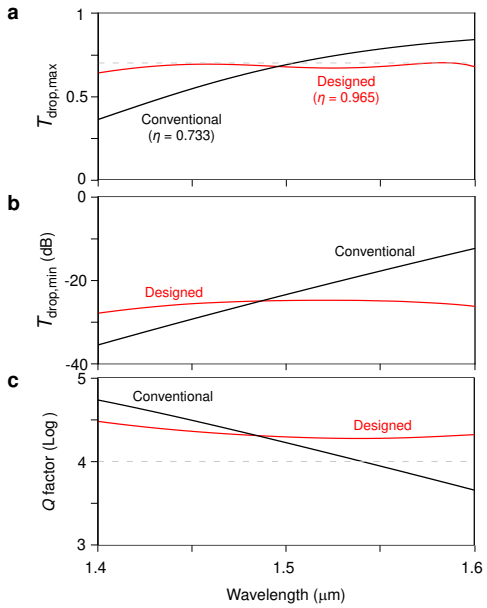

Fig. 2 Analytic calculation of the resonance output.

We calculate the resonance output and the quality factor from the coupling parameters from the given trajectories. Figure 2 illustrates the resonance output of the designed and conventional model. The designed model exhibits a nearly uniform resonance output, nearly constant in the 1.4 to 1.6 um wavelength range. Additionally, resonance dip of the designed model remains nearby -30 dB, with enhanced extinction ratio and uniform signal-to-noise ratios. Furthermore, quality factor of the designed model remains more than 10,000 in wide bandwidth. On the other hand, conventional model exhibits considerable fluctuation of the spectral responses in the same wavelength range.

We realize the broadband critical coupling at the bus port for the second example (Fig. 4). Using the same framework, the coupling trajectory which the critical coupling occurs can be derived. Figure 4 illustrates the physical analysis for realizing the broadband critical coupling at the bus port. The target model (Fig. 4c) shows that the critical coupling occurs in the broad wavelength range, 1.4 to 1.6 um. On the other hand, the conventional model (Fig. 4d) exhibits a narrow wavelength range of approximately 30 nm in which the resonance dip falls below -30dB.

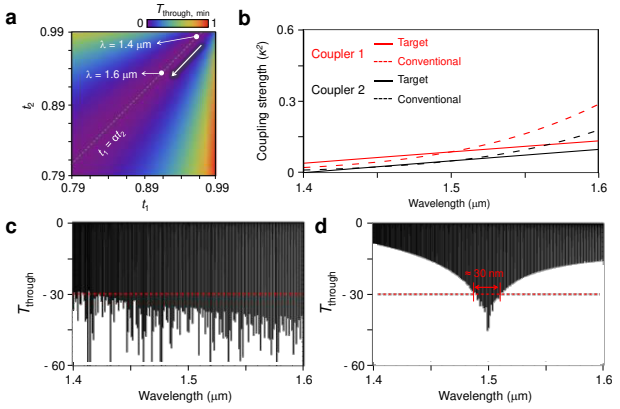

Fig. 3 Analysis of the broadband critical coupling at the bus port

IV. CONCLUSION

We verify the effectiveness of the proposed framework from realizing two representative examples, broadband uniform resonance output at the drop port, and the broadband critical coupling at the bus port. This work demonstrates that the proposed framework provides a general and predictive approach for designing a model with desired device performance.

ACKNOWLEDGMENTS

This research was supported by the Leader Researcher Program (NRF-2019R1A3B2068083) from the National Research Foundation of Korea.

REFERENCES

[1] Bogaerts, Wim, et al. "Silicon microring resonators." Laser & photonics reviews 6.1 (2012).

[2] Schwelb, Otto. "Transmission, group delay, and dispersion in single-ring optical resonators and add/drop filters-a tutorial overview." Journal of Lightwave Technology 22.5 (2004).

[3] Liu, Weijie, et al. "Observation of edge-to-edge topological transport in a photonic lattice." Physical Review A 105.6 (2022).

[4] Heebner, John, Rohit Grover, and Tarek Ibrahim. *Optical microresonators: theory, fabrication, and applications*. New York, NY: Springer New York, 2008.

Tunable Thermal Emissivity for Thermal Infrared Camouflage Enabled by a Zigzag Metallic Glass Structure

Yu-Ching Shih [1], Wei-Han Wang[1], Chia-Hsuan Lee[1], Hsuen-Li Chen[1,2,*]

[1] Department of Materials Science and Engineering, National Taiwan University, Taiwan
[2] Center of Atomic Initiative for New Materials, National Taiwan University, Taiwan
*Corresponding author: hsuenlichen@ntu.edu.tw

***Abstract*— Precise control of thermal infrared emissivity is critical for thermal management. Here, a single-layer zigzag metallic glass film fabricated by glancing angle deposition is demonstrated to provide precisely tunable emissivity. The structure induces strong optical anisotropy, enabling continuous emissivity modulation and effective thermal infrared camouflage of heated objects.**

***Keywords*— metallic glass, zigzag-type structure, anisotropic optical property, glancing angle deposition, thermal management, thermal infrared camouflage.**

I. Introduction

Precise control over thermal emissivity is essential for emerging applications in energy conservation, heat dissipation, and thermal infrared camouflage technologies. Effective modulation of emissivity enables regulation of radiative heat transfer and suppression of infrared signatures, which are critical for objects operating under elevated temperatures and variable environmental conditions.

Thin film metallic glasses possess intrinsically lossy optical characteristics arising from their amorphous atomic structure, which distinguishes them from conventional crystalline metals. Glancing-angle deposition enables the fabrication of anisotropic metastructures with well-defined geometry through self-shadowing, leading to pronounced optical anisotropy. However, the application of glancing-angle-deposited structures for precise control of thermal infrared emissivity remains largely unexplored.

In this work, we demonstrate a single-layer zigzag metallic glass film fabricated by glancing angle deposition that enables precisely tunable thermal infrared emissivity. The incorporation of a zigzag pattern enabled tunable optical behavior, enabling the film to adapt effectively to diverse thermal-infrared camouflage conditions. The lossy nature of metallic glass was leveraged to produce marked differences in thermal IR emissivity. By exploiting structure-induced optical anisotropy the thermal radiation of heated objects can be modulated, enabling stable thermal infrared camouflage under varying operating conditions.

II. Methods

Metallic glass films were deposited on silicon (Si) wafers via DC magnetron sputtering to fabricate the zigzag-type structure. To fabricate the zigzag structure, the first branch was deposited on the substrate at an α angle of 75°. Afterward, the substrate was rotated 180°, enabling the second branch to be deposited with the same α angle of 75°. This procedure was repeated to form the third and fourth branches. Thermal infrared images of the samples were captured with a thermal camera (FLIR T340) operating over a wavelength range of 7.5–13 μm.

III. Results and Discussion

Figure 1 schematically illustrates the zigzag-type metallic glass structure fabricated by glancing angle deposition and the experimental configuration used to characterize its thermal infrared response. Figure 1(a) depicts the atomic structure of a representative metallic glass (FeCrCoMoCBSi), which features a random and disordered atomic arrangement. This disordered structure leads to frequent electron scattering and increased conduction losses, resulting in the intrinsically lossy optical properties of metallic glass.

Figure 1(b) shows the zigzag-type structure based on FeCrCoMoCBSi. The zigzag pattern plays a key role in controlling the metastructure's optical anisotropy in the infrared. It significantly enhances the tunability of in-plane emissivity, enabling modulation of thermal emission under varying conditions.

To probe the angle-dependent optical behavior, a polarizer was introduced during the measurements, and three rotation angles, φ, θ, and ψ, were defined to describe the orientation of the zigzag structure relative to the incident radiation, as shown in Fig. 1(c). The angle φ is defined by the relative orientation between the transmission axis of the polarizer and the zigzag plane, while θ and ψ describe out-of-plane tilting of the sample. By adjusting these angles, the thermal infrared absorptance and emissivity of the zigzag-type metallic glass film can be effectively modulated.

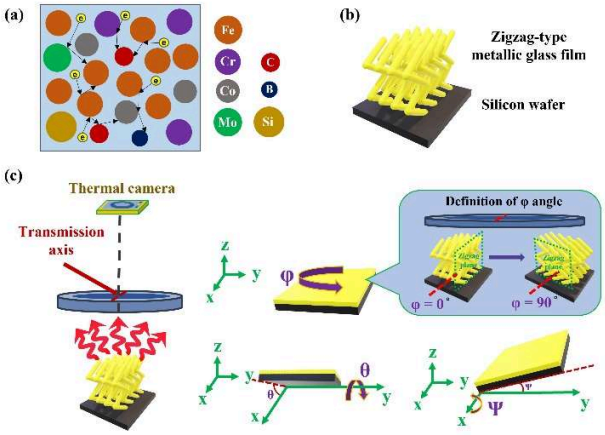

Fig. 1 (a) Atomic arrangement and free electron movement within the metallic glass (FeCrCoMoCBSi). (b) The zigzag-type structure of metallic glass can achieve tunable absorptance. (c) The schematic of the experimental setup for placing the zigzag-type film. For the two-parameter angular measurements

To further investigate this effect, a thermal camera was employed to capture the apparent temperature of the film at different φ, θ, and ψ angles, and thermal infrared images were analyzed to compare the corresponding emissivity. As shown in Fig. 2(a), the setup included a zigzag-type metallic glass film, a reference blackbody tape placed on a heated copper plate, and a polarizer positioned above. Fig. 2(b–g) illustrate the thermal emissivity at an object temperature of 73 °C, with emissivity values of 0.67, 0.59, 0.52, 0.40, 0.30, and 0.17, respectively. The zigzag-type metallic glass film exhibited significant changes in emissivity with variations in φ, θ, and ψ, demonstrating a continuously tunable thermal infrared response enabled by angular control.

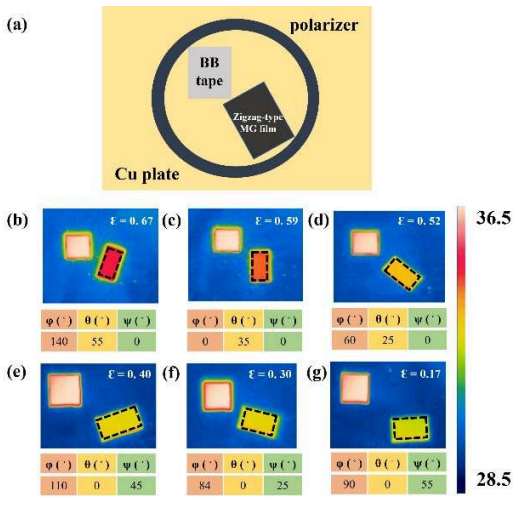

Fig. 2 (a) The schematic diagram and (b-g) thermal infrared images of zigzag-type metallic glass film at (φ, θ, ψ) of (b) (140°, 55°, 0°), (c) (0°, 35°, 0°), (d) (60°, 25°, 0°), (e) (110°, 0°, 45°), (f) (84°, 0°, 25°), and (g) (90°, 0°, 55°) at a blackbody tape apparent temperature of 73 °C.

As shown in Fig. 3(a), the experimental setup consisted of the zigzag-type metallic glass film and a reference blackbody tape placed on a heated copper plate, with soil and leaf used as background materials and observed through a polarizer.

Fig. 3(b–d) present thermal infrared images captured at different object temperatures. By selecting appropriate angular configurations, the apparent temperature of the zigzag-type metallic glass film can be adjusted to closely match that of the surrounding soil and leaf backgrounds, resulting in effective thermal infrared camouflage. In contrast, the copper plate remains clearly distinguishable from the background under the same conditions, highlighting the role of the tunable emissivity provided by the zigzag-type metallic glass structure.

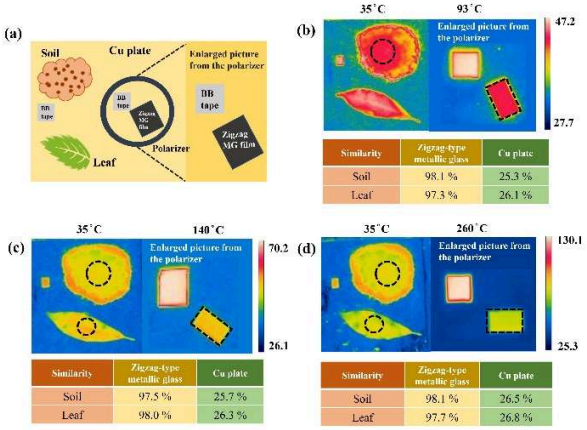

Fig. 3 (a) Schematic diagram of the experimental setup. Thermal infrared images and similarity with different heating temperatures of the samples, the temperatures of the blackbody tape are (b) 93 ˚C, (c) 140 ˚C, and (d) 260 ˚C.

IV. Conclusion

A zigzag-type metallic glass film fabricated by glancing-angle deposition is shown to enable controllable thermal infrared emissivity via angular tuning. The film's thermal radiation can be effectively modulated and applied to thermal infrared camouflage under various thermal conditions. These results highlight the potential of single-layer metallic glass metastructures as a practical platform for tunable thermal radiation control.

Acknowledgments

We thank the National Science and Technology Council, Taiwan, for supporting this study under contracts 112-2221-E-002 -087 -MY3, and 112-2221-E-002 -211 -MY3.

References

[1] Xiao, L., et al., Fast adaptive thermal camouflage based on flexible VO2/graphene/CNT thin films. Nano letters, 2015. 15(12): p. 8365-8370.

[2] .Lai, C. C., et al., Emissivity and Optical Properties of Thin-Film Metallic Glass in the Thermal Infrared Region. Advanced Optical Materials, 2023. 11(24): p. 2301517.

[3] Hawkeye, M.M. and M.J. Brett, Glancing angle deposition: Fabrication, properties, and applications of micro-and nanostructured thin films. Journal of Vacuum Science & Technology A, 2007. 25(5): p. 1317-1335.

Resonant dielectric metasurfaces in Silicon Nitride for enhanced third harmonic generation in the UV

Shroddha Mukhopadhyay[1,*], Maria A. Vincenti[2], Radu Malureanu[3], Crina Cojocaru[1], Michael Scalora[2], Jose Trull[1]

[1]Department of Physics, Universitat Politècnica de Catalunya, Rambla Sant Nebridi 22, 08222 Terrassa, Spain
[2]Department of Information Engineering – University of Brescia, Via Branze 38, 25123 Brescia, Italy
[3]DTU Nanolab, National Center for Nanofabrication and Characterization, Produktionstorvet, building. 426, rm. 120 Dk-2800, kg. Lyngby
*Corresponding author: shroddha.mukhopadhyay@upc.edu

***Abstract*—We present a combined experimental-theoretical study of third harmonic generation (THG) in plasma-etched silicon nitride metasurface gratings. Compared to a planar membrane, the resonant structures exhibit polarization-selective TE and TM responses. Under ultrafast near-infrared excitation, strong electromagnetic field localization enables two orders of magnitude THG enhancement, enabling efficient visible-to-UV upconversion.**

***Keywords*— nonlinear optics, silicon nitride, third harmonic generation, ultrafast laser, dielectric metasurface.**

I. Introduction

Silicon nitride (Si_3N_4) is a CMOS-compatible, wide-bandgap ($\sim 5eV$) dielectric with a moderately high refractive index ($n \approx 2$) and very low optical loss. A new generation of tunable metasurfaces, recently enabled by high-index semiconductor materials in their transparency windows, provides a versatile and efficient platform to simultaneously manipulate the near-field and far-field electromagnetic (EM) waves. In contrast to plasmonic systems with high thermal losses due to absorption, high index dielectric resonators can realize multipole electric or magnetic resonances with negligible thermal loss in their operating wavelength range. High-index dielectric resonators can realize near-field and far-field manipulation of EM waves with a high degree of freedom and thus provide a versatile high-performance platform to engineer the EM waves, such as manipulating the chirality, coherence, and topology of light [1]. On the other hand, nonlinear Si_3N_4 photonics offers unique abilities to generate, manipulate, and detect optical signals in nano-devices, with applications based on field localization and large third-order nonlinearity. These properties make it ideal for integrated nonlinear optical applications [2,3], especially in the in the near-infrared and telecom wavelength range, where its common adversary silicon suffers from two-photon absorption.

This study focuses on the third-order nonlinear optical properties of Si_3N_4, experimentally retrieved and quantified through THG from two distinct periodic nanogratings. The nanoscale gratings are fabricated by plasma etching from a planar Si_3N_4 membrane. Although intrinsically limited by subwavelength interaction lengths and very low nonlinear conversion efficiency, the flat membrane serves as a reference to quantify THG enhancement from the structured surfaces. We design and fabricate two types of resonant dielectric metasurfaces, exhibiting polarization-selective resonances under transverse electric (TE) and transverse magnetic (TM) polarizations. When driven by ultrafast near-infrared pulses under resonant conditions, these gratings strongly confine the EM field within the bulk of the structure, enhancing light–matter interaction and significantly increasing THG in the UV. Their characteristic resonances yield THG enhancements of more than two orders of magnitude. Our planar architectures are fully transparent, operate at normal or near-normal incidence, and provide a flexible design platform for the upconversion of visible light into the ultraviolet (UV) and deep-UV regimes with enhanced efficiency.

II. Methods

The nonlinear light-matter interactions in the thin film membrane is simulated using a microscopic, hydrodynamic model of linear and nonlinear optical properties of semiconductors that accounts for surface, magnetic and bulk nonlinearities extracted from equations of motion arising from free (Drude model) and bound electrons (Lorentz model) [5,6]. By fitting the THG characteristics of the planar membrane, we retrieve the wavelength dependent datasets of $\chi^{(3)}_{\omega}$ and $\chi^{(3)}_{3\omega}$, for our pump intensity and fixed laboratory environment. These datasets are then introduced into Comsol FEM platform as Si_3N_4 material properties, to simulate the linear transmission and the nonlinear transmitted THG from the structured materials. The linear transmission, E and H field localization maps are solved by the Maxwell's equation, while the THG conversion efficiencies are calculated by introducing the nonlinear polarization term into the same.

For experimental measurements, The pump used as a source for nonlinear wavelength dependant experiments is a femtosecond (fs) pulsed laser, wavelength tunable in the range of 650 nm - 2500 nm, with pulse width of 180 fs, pulse repeatition rate of 60 KHz, peak energy of $6\mu J/pulse$ and a maximum average power of 400 mWatt. The pump beam is focused on the sample plane using a plano-convex lens of f = 20 cm, in order to achieve intensities of $\sim 10GW/cm^2$. The transmitted signal is passed through a series of wavelength

selective optical elements such as a UV enhanced collimating lens, two "ultrafast harmonic separator" mirrors and a narrow bandpass filter centered at the THG frequency [4]. A Wollaston polarizer separates the TM and TE polarized THG signal and a photomultiplier tube is used to detect the harmonic signals. A detailed calibration procedure enables us to precisely quantify the THG conversion efficiencies, which are of the order of 10^{-6} down to 10^{-12}, and corroborate with our theoretical predictions in terms of shape, spectral width, and maximum amplitude of the spectral response.

III. Results and Discussion

The study begins with a Si_3N_4 membrane of thickness 380 nm (Fig.1(a)) which shows a Fabry-Perot resonance around 800 nm (Fig.1(d)). The corresponding THG spectral response, shown in Fig.1(g), gives a peak conversion efficiency of $\eta_T H = \frac{P_{THG}}{P_{Pump}} = 9 * 10^{-9}$.

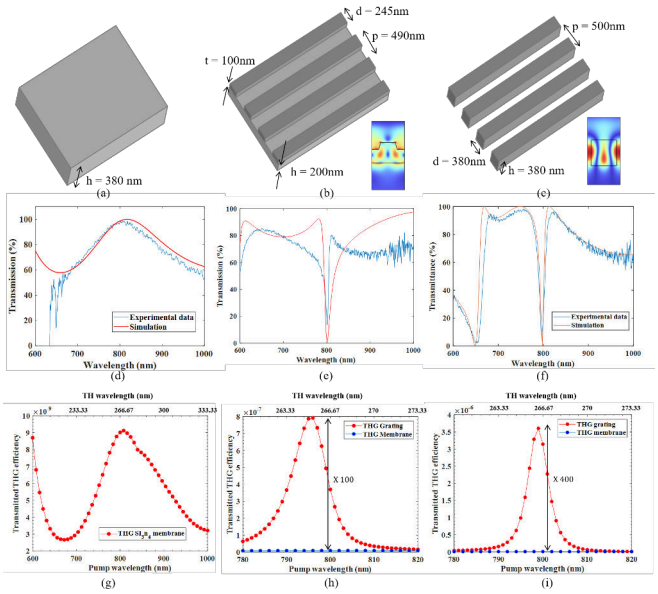

Fig. 1. Schematic diagram of the (a) Suspended membrane of Si_3N_4 (b) Suspended grating in Si_3N_4 and (c) Shallow etched grating. Linear transmission map of (d) Suspended membrane of Si_3N_4 (e) Suspended grating in Si_4N_4 and (f) Shallow etched grating. (g)-(i) Resonant THG spectral response and enhancement peak corresponding to each type of resonances.

The membrane is partially etched to fabricate a grating with corresponding design parameters indicated in Fig.1(b). This grating is designed to sustain a guided mode resonance at or near 800nm (Fig.1(e)). In this case, we achieve a resonant EM field localization (inset of 1(b)) due to the guided mode resonance, whose spectral position is highly dependant on the periodicity of the structure. Under TM polarized illumination, the EM mode field localization results into a THG spectral variation as theoretically predicted and shown in Fig1(h) with a peak enhancement factor of ~ 100 times, with respect to the flat membrane.

On the other hand, the membrane is fully etched to fabricate a second grating with dimensions as shown in Fig1(c), suspended in air. This grating is designed to sustain a characteristic Mie type resonance at or near 800nm (Fig.1(f)), under TE illumination, and the dip in the transmission spectra is once again a result of light localization in the bulk of the material (inset of 1(c)). This strong light localization corresponds to a resonant THG spectral variation as theoretically predicted, and shown in Fig.1(i), with a peak enhancement factor of ~ 400 times, with respect to the flat membrane.

IV. Conclusion

We report third-harmonic emission from two Si_3N_4 metasurfaces, comparing their resonant field localization and THG efficiencies with a flat Si_3N_4 membrane. Resonant, polarization-selective designs enhance conversion by over two orders of magnitude, with strong agreement between theory and experiment. The two gratings can be compared in terms of spectral properties of their characteristic resonances, resonant EM field localization, tunability and rebustness of the fabricated structure.

This study maps an important step towards understanding and showcasing Si_3N_4 metasurfaces as efficient, broadband photonic platforms operating from UV to IR and compatible with on-chip integration. Understanding their resonant properties and nonlinear dynamics enables compact UV/DUV/EUV light sources. With low losses, CMOS compatibility, high power handling, and hybrid integration (e.g., with InP), they support diverse applications from sensing to quantum technologies across an unprecedented spectral range.

Acknowledgments

SM, JT, and CC acknowledge the Spanish Agencia Estatal de Investigación from Ministerio de Ciencia, Investigación y Universidades (project PID2023-148620NB-I00 granted by MICIU/AEI/10.13039/501100011033 and FEDER, UE) and US Army Research Laboratory Cooperative Agreement No W911NF-22-2-0236 issued by US ARMY ACC-APG-RTP. S. M. acknowledges predoctoral grant FPI-UPC 2022, funded by Universitat Politècnica de Catalunya (Government of Catalunya). M. A. V. thanks NATO SPS Grant no. G5984 - RESPONDER for financial support.

References

[1] W. Liu, Z. Li, H. Cheng, and S. Chen, "Dielectric Resonance Based Optical Metasurfaces: From Fundamentals to Applications", *iScience*, vol. 23(12), pp. 101868, 2020.

[2] D. T. H. Tan, K. J. A. Ooi, and D. K. T. Ng, "Nonlinear optics on silicon-rich nitride—a high nonlinear figure of merit CMOS platform [Invited]," *Photon. Res.*, vol. 6, B50-B66, 2018.

[3] D. Moss, R. Morandotti, A. Gaeta, A. et al. "New CMOS-compatible platforms based on silicon nitride and Hydex for nonlinear optics", *Nature Photon*, vol. 7, pp. 597–607, 2013.

[4] S. Mukhopadhyay, A. Conde-Rubio, J. Trull, et al., "Gold-polymer hybrid metasurface for polarization-independent enhanced third harmonic generation in the ultraviolet", *Scientific Reports*, 2026. https://doi.org/10.1038/s41598-026-39260-6

[5] M. Scalora, M. A. Vincenti, and D. de Ceglia,et al, "Nonlinear Duffing oscillator model for third harmonic generation", *J. Opt. Soc. Am. B.*, vol. 32, pp. 2129-2138, 2015.

[6] K. A. Hallman, L. Rodríguez-Suné, J. Trull, et al, "Harmonic generation from silicon membranes at visible and ultraviolet wavelengths," *Opt. Express*, vol. 31, pp. 792-801, 2023.

Quantum Nanophotonic Control in Non-Perturbative Light-Matter Coupling Regimes

Erika Cortese[1,*], Johannes Bürger [2], Simone Di Muzio[3,*], Dario Ballarini[2], Simone De Liberato[2,3]

[1]School of Physics and Astronomy, University of Southampton, Southampton SO17 1BJ, UK
[2]CNR Nanotec, Institute of Nanotechnology, Via Monteroni, 73100 Lecce, Italy

[3]Istituto di Fotonica e Nanotecnologie, CNR, Piazza Leonardo da Vinci 32, Milano, Italy

*Corresponding author: e.cortese@soton.ac.uk

***Abstract*—Non-perturbative light–matter coupling in quantum nanophotonic platforms enables control of decay, dissociation, and electromagnetic confinement beyond geometry. We illustrate this across atomic, molecular, and nanophotonic systems, highlighting how structured multi-mode coupling provides new handles for controlling quantum optical functionality and spatial field distributions.**

***Keywords*— polaritons, quantum nanophotonics, ultrastrong coupling, photostabilization, nanophotonic waveguides, superstrong coupling.**

I. Introduction

Quantum nanophotonics exploits confined electromagnetic fields, tailored photonic environments, and strong light–matter interactions to engineer optical functionality at the nanoscale. In the non-perturbative regime, coupling to multiple photonic modes can modify intrinsic properties of both matter and light beyond what geometry alone determines. Here we present three realizations spanning atomic, molecular, and solid-state settings: (i) resonant laser driving stabilizes ionizing electronic transitions via AC Stark level repulsion [1]; (ii) multi-mode cavity coupling to a dissociative vibrational continuum suppresses photodissociation in diatomic molecular cations; and (iii) co-localized superstrong coupling (SSC) between an exciton and multiple photonic modes in visible nanophotonic waveguides provides direct control over real-space electromagnetic field distributions [2].

II. Results and Discussion

Laser-stabilized ionizing transitions

Resonant pumping of an ionizing transition above a critical intensity creates a metastable discrete resonance via AC Stark level repulsion—a semiclassical counterpart of the photon-bound exciton observed in microcavity-embedded doped quantum wells [3]. Unlike the Mollow triplet of a bound-to-bound transition, only two of the four emission channels survive; their spectral weights encode the hybridization with the continuum, and the state decays through two-photon ionization [1]. This demonstrates how structured light coupling can reshape decay pathways in an open quantum system.

Multi-mode photostabilization of molecular photodissociation

Extending the Lee–Friedrichs framework to diatomic cations (H_2^+, K_2^+), multi-mode cavity coupling to the dissociative vibrational continuum reshapes polaritonic potential energy surfaces. Franck–Condon overlaps with continuum modes, together with the coupling-strength dependence of the lower polariton energy, define a threshold above which cavity-induced stabilization suppresses photodissociation. These results show that quantum photonic environments can be used to control molecular instability and reaction channels through continuum engineering.

Co-localized superstrong coupling in visible nanophotonic waveguides

Co-localized SSC is the nanophotonic counterpart of multi-mode matter coupling: rather than one photon hybridizing with multiple matter excitations, one exciton hybridizes simultaneously with multiple photonic modes [2]. Because these modes possess distinct transverse field profiles, exciton-energy tuning becomes a direct handle on the spatial distribution of electromagnetic energy. Planar grating-coupled waveguides realize this mechanism in the visible range: restricting a 2D hybrid organic-inorganic perovskite active layer to 30% of the waveguide core yields full modal overlap between TE_0 and TE_1, producing multi-mode polaritons. RCWA simulations fitted with a generalized Hopfield model [2] confirm a characteristic S-shaped dispersion; coupling the lowest-order modes yields up to 44% higher coupling strength than higher-order pairs, and exciton tuning continuously switches the electromagnetic energy distribution between the bulk and the surface of the waveguide. This provides an in-situ route to field-profile engineering in integrated visible nanophotonic architectures.

III. Conclusion

These results frame non-perturbative multi-mode coupling as a resource for quantum nanophotonics. Across atomic, molecular, and waveguide platforms, coupling to a structured continuum enables control over decay, dissociation, and spatial field localization beyond conventional geometric design. This points toward nanophotonic strategies for quantum optical

devices based on continuum engineering, polaritonic mode shaping, and programmable electromagnetic confinement.

REFERENCES

[1] E. Cortese and S. De Liberato, "Laser-stabilized ionizing transitions," *Optica*, vol. 13, pp. 101–108, 2026.

[2] E. Cortese *et al.*, "Real-space nanophotonic field manipulation using non-perturbative light–matter coupling," *Optica*, vol. 10, p. 11, 2023.

[3] E. Cortese *et al.*, "Excitons bound by photon exchange," *Nature Physics*, vol. 17, pp. 31–35, 2021.

Effects of TE-TM splitting on bistability and nonlinear spin dynamics in resonantly driven spinor exciton-polaritons

Ting-Wei Chen[1,*], Szu-Cheng Cheng[2]

[1]Semiconductor Materials Science in Master Program of College of Science , National Pingtung University, Pingtung City, Taiwan
[2]Department of Optoelectric Physics, Chinese Culture University, Taipei, Taiwan
*Corresponding author: twchen@mail.nptu.edu.tw

***Abstract*—We study TE-TM splitting effects on resonantly driven spinor exciton-polariton bistability. TE-TM coupling modifies thresholds, hysteresis, and spin composition, suppressing circular polarization under elliptical pumping. Pump momentum and dispersion curvature govern nonlinear regimes. The intermediate branch is unstable but can show slow growth, enabling long-lived transient switching dynamics.**

***Keywords*— exciton-polaritons, microcavities, TE-TM splitting.**

I. Introduction

Exciton–polaritons are hybrid light–matter quasiparticles formed through the strong coupling between quantum-well excitons and cavity photons in semiconductor microcavities. Owing to their photonic component, polaritons possess an extremely small effective mass, while their excitonic component provides strong nonlinear interactions. This unique combination enables rich driven–dissipative nonlinear phenomena, including optical bistability, soliton formation, superfluid-like flow, and polarization multistability. Under coherent resonant pumping, interaction-induced blueshifts dynamically modify the effective detuning between the pump and the lower polariton mode, giving rise to S-shaped input–output characteristics and hysteresis behavior.

Beyond scalar nonlinear effects, polaritons carry a spin (polarization) degree of freedom associated with the cavity photon polarization. Spin-anisotropic interactions produce nonlinear polarization switching and multivalued steady states. An additional key mechanism affecting spin dynamics in planar microcavities is transverse-electric-transverse-magnetic (TE-TM) splitting. TE-TM splitting originates from polarization-dependent photon dispersion and introduces a momentum-dependent linear coupling between polarization components, effectively acting as a spin–orbit interaction for polaritons. While TE-TM splitting is known to play a central role in phenomena such as the optical spin Hall effect and spin textures, its systematic influence on bistability structure and dynamical stability in spatially homogeneous resonantly driven systems has not been fully clarified.

In this work, we investigate how TE-TM splitting reshapes bistability, polarization properties, and dynamical stability in a homogeneous spinor exciton–polariton system under continuous-wave resonant pumping. We demonstrate that TE-TM splitting strongly modifies switching thresholds, hysteresis width, and spin composition of steady states. Furthermore, although the intermediate branch of the hysteresis loop remains linearly unstable, its instability growth rate can be substantially reduced in certain parameter regimes, leading to long-lived transient dynamics.

II. Methods

We consider a one-dimensional, spatially homogeneous spinor exciton–polariton system described by coupled mean-field equations for the cavity photon field E_σ and exciton field Ψ_σ, where $\sigma = \pm$ denotes circular polarization components. The model incorporates photon dispersion, exciton–exciton nonlinear interactions, dissipation, coherent pumping, and TE-TM-induced spin mixing. The TE-TM contribution appears as a term proportional to $\beta\partial_x^2 E_{\bar{\sigma}}$, where β denotes the normalized TE-TM splitting strength and $\bar{\sigma}$ is the opposite spin component. Under plane-wave steady-state solutions at pump momentum k_p, this term scales as βk_p^2, explicitly showing that spin mixing increases quadratically with in-plane momentum.

Steady-state solutions are obtained by solving the coupled algebraic equations for fixed pump power P, detuning Δ, ellipticity χ, and pump momentum k_p. The spin-resolved exciton densities determine the degree of circular polarization (DoCP),

$$\mathrm{DoCP} = \frac{|\Psi_+|^2 - |\Psi_-|^2}{|\Psi_+|^2 + |\Psi_-|^2}.$$

In addition to full nonlinear numerical calculations, we derive an analytical linear-response expression for DoCP, demonstrating that the leading TE-TM-induced suppression scales as $(\beta k_p^2)^2$.

To determine dynamical stability, we perform a Bogoliubov analysis by linearizing the dynamical equations around steady states and constructing the corresponding non-Hermitian excitation matrix. The instability growth rate is defined as

$$\Gamma = \max_{j,q} \mathrm{Im}\, \mu_j(q),$$

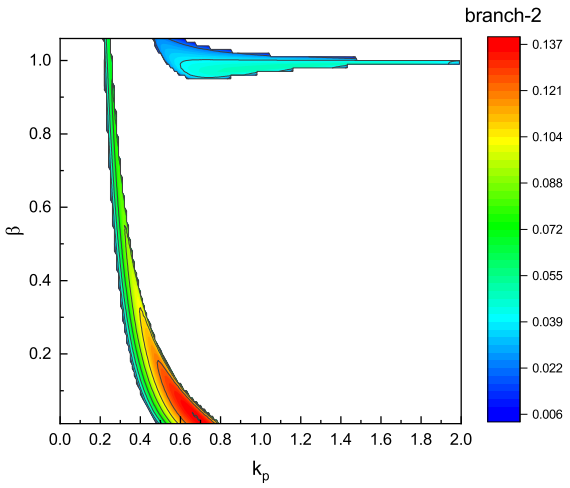

Fig. 1. Two-dimensional map of the growth rate Γ of branch-2 as a function of k_p and β. The slight jaggedness near the boundary originates from the finite parameter step size and data-boundary constrained interpolation, rather than physical discontinuities. Parameters: $\chi = 0.5$, $\gamma_{ph} = \gamma_{ex} = 0.1$, $\Delta = -0.32$, $P = 1.18$.

where $\mu_j(q)$ are Bogoliubov eigenvalues. The inverse growth rate $\tau_{\rm inst} = \Gamma^{-1}$ characterizes the instability timescale.

III. Results and Discussion

Our results show that TE-TM splitting substantially reshapes the nonlinear response of the system. In the absence of TE-TM splitting, bistability arises from interaction-induced renormalization of the effective detuning between the pump and the lower polariton mode. Finite β does not generate bistability by itself but significantly modifies switching thresholds and hysteresis width by introducing momentum-dependent spin mixing.

The pump momentum k_p plays a crucial role through its connection to the curvature of the lower polariton dispersion. Below the dispersion inflection point, interaction-induced blueshifts efficiently reduce the effective detuning, lowering bistability thresholds. Above the inflection point, bistability shifts toward higher pump powers and becomes narrower. This curvature-dependent behavior explains the strong momentum dependence of the hysteresis structure.

A central finding of this work is the strong suppression of circular polarization induced by TE-TM splitting. At normal incidence ($k_p = 0$), the DoCP is determined solely by the pump ellipticity and is independent of β. For finite momentum, however, TE-TM-induced spin mixing scales as βk_p^2, progressively reducing polarization contrast. At sufficiently large β or k_p, the steady states become nearly spin balanced even under elliptically polarized pumping. This behavior reflects competition between interaction-induced longitudinal spin splitting and TE–TM-induced transverse effective fields. At low β, interactions stabilize polarization on the lower branch, whereas at large β, transverse spin mixing dominates across all branches.

The pump detuning Δ further reshapes the bistability landscape. Near resonance, broad hysteresis regions appear over a wide momentum range. As the detuning becomes more negative, the bistable region shrinks and becomes increasingly sensitive to pump momentum. This behavior can be understood from the effective detuning

$$\Delta_{\rm eff}(n, k_p) = \omega_p - E_{\rm LP}(k_p) - gn,$$

where density-dependent energy shifts dynamically restore resonance. The efficiency of this restoration depends on dispersion curvature and detuning depth.

Although the intermediate branch of the hysteresis loop is always linearly unstable, the magnitude of the instability growth rate Γ varies significantly across parameter space. For certain combinations of moderate pump momentum and TE–TM splitting, Γ becomes much smaller than the intrinsic polariton decay rate. In these regimes, the instability develops over long timescales, and the system can transiently remain near the intermediate solution for experimentally relevant durations. TE–TM splitting modifies the Bogoliubov excitation spectrum and can substantially reduce instability growth rates without rendering the branch linearly stable. This demonstrates that TE–TM splitting provides a mechanism for controlling instability timescales and transient dynamics.

IV. Conclusion

We have systematically analyzed the influence of TE-TM splitting on bistability and nonlinear spin dynamics in resonantly driven spinor exciton-polaritons. TE-TM splitting modifies hysteresis thresholds and polarization properties through momentum-dependent spin mixing proportional to βk_p^2. The interplay between interaction-induced energy renormalization, dispersion curvature, and TE-TM coupling governs both steady-state structure and dynamical stability. While the intermediate branch remains linearly unstable, its instability growth rate can be dramatically reduced in selected parameter regimes, leading to long-lived transient states. These results establish TE-TM splitting as a powerful control parameter for nonlinear optical response and spin dynamics in polariton systems, with potential implications for polariton-based optical switching and spin-dependent photonic devices.

Acknowledgments

This work was supported by National Science and Technology Council of Republic of China under the contract number NSTC113-2112-M-034-001.

References

[1] O. A. Egorov, D. V. Skryabin, A. V. Yulin, and F. Lederer, "Bright Cavity Polariton Solitons," *Phys. Rev. Lett*, vol. 102, pp. 153904, 2009.
[2] A. V. Yulin, O. A. Egorov, F. Lederer, and D. V. Skryabin, "Dark polariton solitons in semiconductor microcavities," *Phys. Rev. A*, vol. 78, pp. 061801(R), 2008.

Near-field observation of energy transfer in nonlocal metasurfaces

Jie Ji[1,2*], Wouter J. Holman[1], Djero Peeters[3], Jaime Gomez Rivas[1,2]

[1]Department of Applied Physics and Science Education, Eindhoven University of Technology, Eindhoven, 5600 MB, the Netherlands

[2] Institute for Complex Molecular Systems, Eindhoven University of Technology, Eindhoven, 5600 MB, the Netherlands

[3]Department of Electrical Engineering, Eindhoven University of Technology, Eindhoven, 5600 MB, Netherlands

*Corresponding author: j.ji@tue.nl

***Abstract*—We demonstrate dipole–dipole energy transfer mediated by nonradiative bound states in the continuum in a terahertz metasurface. Using a custom THz near-field microscope, highly anisotropic long-range spatiotemporal coherence is revealed, enabling directional energy transfer and opening new pathways for controlling light–matter interactions at the mesoscale.**

***Keywords*— THz near-field microscopy, Energy transfer, Bound states in the continuum, THz metasurfaces**

I. Introduction

Long-range coherent energy transfer between spatially separated dipoles plays a central role in many physical, chemical and biological systems[1],[2]. In conventional electromagnetic environments, dipole–dipole interactions are typically limited to subwavelength distances due to radiative losses and rapid field decay[3]. Overcoming these constraints is essential for realizing scalable platforms for information processing, sensing, and energy routing. Metasurfaces provide a versatile framework for tailoring light–matter interactions through subwavelength structuring of electromagnetic resonators. By engineering collective resonances and symmetry properties, metasurfaces can support bound states in the continuum (BICs), which are nonradiative modes embedded within the radiation spectrum[4]. Owing to their symmetry protection or parameter tuning, BICs exhibit vanishing radiation loss and theoretically infinite quality factors in ideal structures, enabling strong field confinement and enhanced local density of optical states[5],[6].

Recent studies have shown that BIC-enabled metasurfaces can substantially enhance spontaneous emission[7], nonlinear optical processes[8], and near-field interactions[9]. However, the role of BICs in mediating long-range coherent energy transfer between spatially separated dipoles remains largely unexplored, particularly in the terahertz (THz) regime. The long wavelengths and weak intrinsic light–matter coupling at THz frequencies pose additional challenges for achieving efficient and controllable interactions. In this work, we investigate dipole–dipole energy transfer in a gold metasurface supporting BIC modes using a custom THz near-field microscope. By employing dipolar microprobes, we reveal millimeter-scale, highly anisotropic coherent energy transfer enabled by long-range collective resonances, highlighting the potential of BIC metasurfaces for low-loss and directional THz photonic technologies.

II. Methods

Terahertz (THz) near-field measurements were performed using a custom-built time-domain microscopy system, as illustrated in Fig.1(a). An ultrafast femtosecond laser (780 nm) was split into pump and probe beams using a beam splitter. The pump beam was focused onto a photoconductive-antenna microprobe to generate THz radiation, which served as the emitter. The probe beam, delayed by a mechanical delay stage, was focused onto a second microprobe for coherent detection. Both emitter (E) and detector (D) microprobes were mounted on independent three-dimensional translation stages, allowing precise control of their positions relative to the metasurface sample. The sample was mounted on an additional three-dimensional stage, enabling accurate alignment and scanning of the measurement region. Dipole-dipole interaction measurements were conducted using the two THz microprobes positioned on the metasurface, as shown in Fig. 1(b). The separation between the probes was systematically varied along the longitudinal (L_x) and transverse (L_y) directions. The THz electric field polarization was aligned parallel to the long axis of the metallic rods to selectively excite the relevant resonant modes. During measurements, the emitted THz near field from the source probe interacted with the metasurface and was detected by the receiver probe. The time-domain THz signals were recorded and Fourier-transformed to obtain spectral information. A camera system was used to monitor the relative positions of the probes and the sample in real time (Fig. 1(c)), ensuring stable alignment throughout the experiments. This setup enabled high-resolution mapping of spatiotemporal THz fields and direct characterization of long-range dipole-dipole energy transfer mediated by BICs.

The metasurface studied in this work consists of a periodic array of gold (Au) rod dimers fabricated on a substrate. Each unit cell contains two identical rods separated along the longitudinal direction, with a designed periodicity chosen to support symmetry-protected BICs. The metasurface is a square

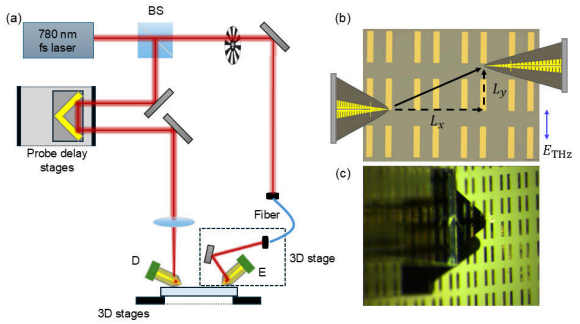

Fig. 1. (a) Illustration of the THz near-field microscopy setup. THz radiation is generated and detected by focusing ultrafast optical laser pulses onto photoconductive-antenna microprobes, which serve as the emitter and detector. The positions of the emitter and the measurement region on the sample are independently and precisely controlled using dedicated three-dimensional translation stages. (b) Conceptual schematic of dipole–dipole interaction measurements on a metasurface enabled by two THz microprobes, with the THz electric field oriented parallel to the long-axis direction of the rods. (c) Camera view of the sample and probes during the measurements.

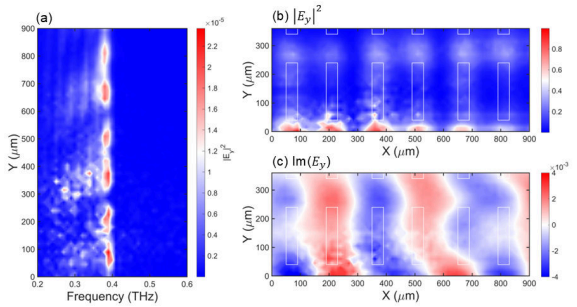

Fig. 2. (a) Two-dimensional color plot of the THz intensity $|E_y|^2$ as a function of frequency and relative displacement L_x between the emitter and the detector. (b) Spatial distribution of the THz intensity $|E_y|^2$ along L_x and L_y at the BIC frequency. (c) Spatial distribution of the imaginary part of the THz electric field, $\mathrm{Im}(E_y)$, as a function of relative displacement along L_x and L_y at the BIC frequency.

lattice with a lattice constant of 300 μm. Each rod has a length of 200 μm and a width of 40 μm, with a lateral separation of 120 μm between the two rods in one unit cell as shown in Fig. 1(b) and (c).

III. Results and Discussion

Fig. 2(a) presents the two-dimensional map of the THz intensity $|E_y|^2$ generated by the dipolar emitter and measured by the dipolar detector as a function of frequency and relative displacement L_x. A pronounced intensity enhancement is observed near 0.39 THz, corresponding to the BIC mode of the metasurface. Notably, this mode persists over a wide range of L_x, indicating robust long-range energy transfer between the emitter and detector probes mediated by the BIC mode. The localized intensity maxima along L_x demonstrate that energy transfer remains efficient over several hundred micrometers, far exceeding the typical near-field interaction range. Figure 2(b) shows the spatial distribution of $|E_y|^2$ in the L_x–L_y plane at the BIC frequency. The intensity is strongly confined and periodically modulated along the longitudinal direction L_x, following the arrangement of the rod dimers. In contrast, the field decays rapidly along the transverse direction L_y, revealing a highly anisotropic energy transfer behavior. This directional confinement reflects the collective nature of the BIC mode.

The phase characteristics of the energy transfer are further illustrated in Fig. 2(c), which displays the imaginary part of the electric field, $\mathrm{Im}(E_y)$, at the BIC frequency. A clear alternating phase pattern is observed along L_x, indicating coherent oscillations of the electromagnetic field across multiple unit cells. This extended phase correlation confirms the presence of long-range spatiotemporal coherence supported by the BIC mode. Meanwhile, the rapid phase variation along L_y further evidences the suppression of coupling in the transverse direction.

Together, these results demonstrate that the BIC resonance enables millimeter-scale coherent dipole–dipole energy transfer with strong directional selectivity. The simultaneous enhancement of field intensity and preservation of phase coherence along L_x indicate that the metasurface supports collective modes that effectively channel electromagnetic energy over long distances. This behavior stands in sharp contrast to conventional near-field interactions and arises from the nonradiative nature of the BIC mode.

IV. Conclusion

In conclusion, we have demonstrated millimeter-scale coherent dipole–dipole energy transfer in a terahertz metasurface mediated by nonradiative bound states in the continuum. Using a custom-built near-field time-domain microscopy system, we directly mapped the spatial evolution of THz fields and revealed highly anisotropic, long-range coherence along the longitudinal direction of the rod dimers. The pronounced intensity enhancement and preserved phase coherence confirm that BIC modes enable efficient and directional energy transfer far beyond conventional near-field limits. The demonstrated control of long-range coherent energy transfer opens new opportunities for the development of low-loss THz communication, sensing, and integrated photonic devices based on BIC-enabled metasurfaces.

Acknowledgments

This project has received funding from the PhotonDelta National Growth Fund programme.

References

[1] T. Pullerits and V. Sundstr¨om. Photosynthetic light-harvesting pigment-protein complexes: Toward understanding how and why. *Accounts of Chemical Research*, 8, 381–389, 1996.

[2] F. Wu, T. C. Nguyen-Phan, R. Cogdell, and T. Pullerits. Efficient cavity-mediated energy transfer between photosynthetic light harvesting complexes from strong to weak coupling regime. *Nature Communications*, 6, 5300, 2025.

[3] T. F¨orster. Zwischenmolekulare energiewanderung und fluoreszenz. *Annalen der Physik*, 437, 55–75, 1948.

[4] M. Kang, T. Liu, C. T. Chan, and M. Xiao. Applications of bound states in the continuum in photonics. *Nature Reviews Physics*, 10, 659– 678, 2023.

[5] N. J. Van Hoof, D. R. Abujetas, S. E. Ter Huurne, F. Verdelli, G. C. Timmermans, J. A. S´anchez-Gil, and J. G. Rivas. Unveiling the symmetry protection of bound states in the continuum with terahertz near-field imaging. *ACS Photonics*, 8, 3010–3016, 2021.

[6] J. Ji, J. A. S´anchez-Gil, D. Peeters, W. Holman, T. X. Hoang, D. van Mechelen, and J. G. Rivas. Near-field probing of the local density of optical states enhanced by bound states in the continuum in nonlocal metasurfaces. *Nature Communications*, 11, 11597, 2025.

[7] X. Li, J. Zhang, H. He, L. Liu, C. Dai, Y. Shi, S. Wan, Z. Wang, C. Zhou, X. Zhang, and Z. Li. Dynamic control of quasi-bic-driven emission enhancement via quantum dots-hydrogel integrated meta-crystal. *Advanced Materials*, 10, e12000, 2025.

[8] X. Zong and P. Shen. Merging bound states in the continuum for high-efficiency second-harmonic generation. *Physical Review A*, 12, 063528, 2024

[9] P. Xie, Y. Deng, L. Zeng, Z. Liang, S. Shen, Q. Ding, H. Zhang, Z. Zhou, and W. Wang. Tunable interactions of quasibound states in the continuum with cavity mode in a metasurface-microcavity hybrid. *Physical Review B*, 10, 165408, 2022.

Structural diversity of pentatwinned plasmonic nanoparticles

Ana Sánchez-Iglesias[1,*], Marek Grzelczak[1,]

[1]Centro de Física de Materiales (CFM-MPC), CSIC-EHU, Donostia – San Sebastián, Spain
*Corresponding author: anamaria.sanchezi@ehu.eus

***Abstract*—We report a universal approach to the colloidal synthesis of high-quality pentatwinned plasmonic nanoparticles with tailored optical properties.**

***Keywords*— gold nanoparticles, colloidal synthesis**

I. Introduction

Plasmonic nanoparticles with five-fold symmetry offer an important advantage over their single-crystalline analogs due to their superior structural stability at elevated temperatures. Although the family of pentatwinned nanoparticles is relatively rich, current experimental approaches can produce three main shapes: decahedra, rods, and bipyramids (Fig.1)

Gold decahedra are nearly isotropic, composed of five tetrahedral subunits sharing a common axis and joined along 111 twin planes, giving an overall ten-faceted shape. All exposed faces are of low-energy, making this morphology energetically favorable within a certain size range compared with single-crystal shapes.

Gold nanorods feature high synthetic tunability, allowing their longitudinal dipolar plasmon wavelength to be adjusted from the visible to the mid-infrared region by varying their aspect ratio.[1] They exhibit highly polarization-dependent absorption and scattering cross sections, large extinction cross sections, and intense electromagnetic field enhancement at their ends.

Finally, gold bipyramids are elongated nanoparticles composed of two pentagonal pyramids, base-stacked symmetrically.[2], [3] Unlike gold nanorods, which typically have rounded or flat ends, bipyramids have two sharp tips that facilitate the so-called ”lightning rod effect,” generating extremely large local electric-field enhancements and significantly larger optical cross-sections. Bipyramids exhibit highly tunable longitudinal dipolar plasmon resonance wavelengths that can be adjusted by aspect ratio. Gold bipyramids exhibit a narrower ensemble plasmon band, making them superior for surface-enhanced spectroscopies, and their nearly 100% photothermal conversion efficiency is critical for efficient catalysts for plasmon-powered chemical reactions.

Typically, regardless of shape, the concentration of Au seeds is the sole factor determining the size and/or aspect ratio, and thus the optical properties of the nanoparticles. That is, the fewer the seeds, the larger the nanoparticles. As a result, varying nanoparticle volumes while keeping their optical spectra unchanged remains a synthetically non-trivial task. Therefore, there is a need to simplify and unify current procedures to ultimately provide an experimental framework that enables facile tuning of structural properties. Here, we expand the chemical space for the synthesis of highly monodisperse penta-twinned gold nanoparticles (bipyramids, nanorods, and decahedra) and achieve yields approaching 100%. In particular, we found a unique role of bromide ions in tailoring the aspect ratio of gold bipyramids.

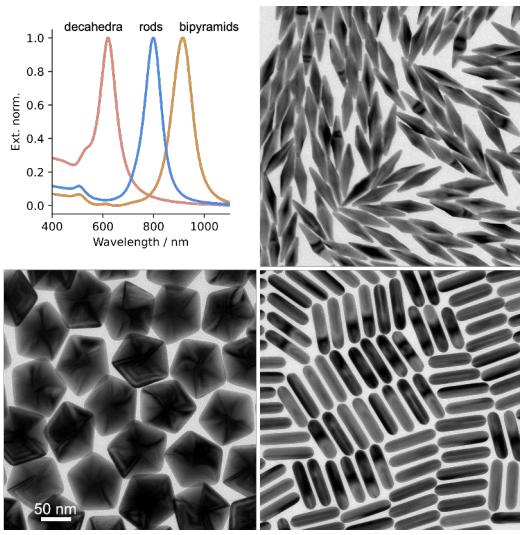

Fig. 1. Example of three types of pentatwinned gold nanoparticles, decahedra, rods, and bipyramids.

II. Methods

Our approach builds on our previous method, which starts with the synthesis of thermally aged 6 nm seeds with pentatwinned symmetry.[5] By further seeded growth in the presence of additives such as silver bromide or silver nitrate, we control the kinetics of gold precursor reduction, thereby producing nanoparticles of the desired shape and size. The final nanoparticles are characterized by UV-Vis-NIR spectroscopy and Transmission Electron Microscopy.

III. Results and Discussion

We expanded the parameter space for the synthesis of gold bipyramids, showing that both bromide ions and seed

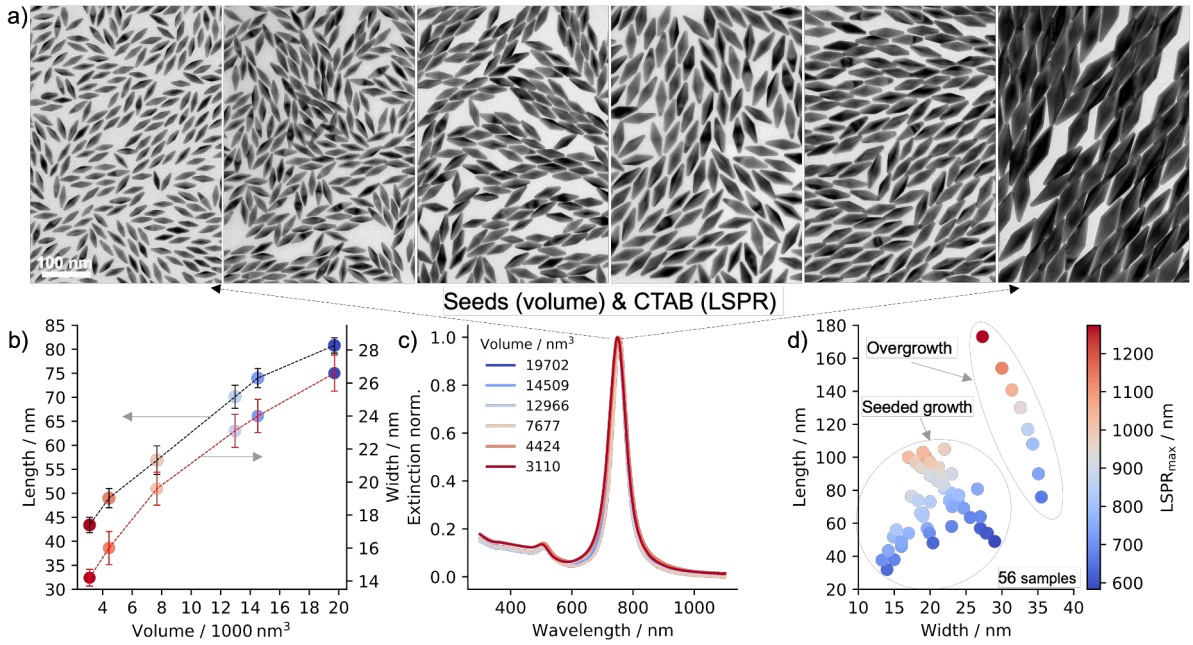

Fig. 2. Controlling the volume of gold bipyramids at constant position of longitudinal plasmon band. a) TEM images of nanoparticles featuring volumes ranging from 3110 to 19702 nm3 (from left to right) at constant aspect ratio. b) Change of length and width of nanoparticles demonstrating 6 fold reduction of volume at constant aspect ratio. c) UV–vis–NIR spectra of gold bypiramids featuring a constant plasmon band position at 750 nm. d) a collection of samples of gold bipyramids (56 in total) obtained through our new method.

concentration play complementary roles in tuning nanoparticle dimensions and thus their optical properties (Fig.2).[6] As a proof-of-concept experiments, we synthesized gold bipyramids with a fixed position of plasmon band at 750 nm and varying nanoparticle volume, a property that is not readily achievable with conventional methods. While the seed concentration was used to vary the volume of the final nanoparticles - the primary experimental parameter -, the bromide concentration was used to fine-tune the plasmon band position to the desired wavelength - the secondary experimental parameter. By carefully tuning these two parameters, we obtained six samples with the longitudinal surface plasmon band in nearly the same position. The same approach can be used for other nanoparticle shapes.

IV. Conclusion

We have expanded the chemical space in the synthesis of gold nanoparticles with pentatwineed symmetry. By carefully adjusting bromide and seed concentrations, we were able to produce nanoparticles with different dimensions but the same aspect ratio, thereby fixing the position of the plasmon bands. Our method unlocks the structural diversity of plasmonic nanoparticles, making them a suitable playground for evaluating plasmonic performance on the ensemble or single particle level.

Acknowledgments

A.S.-I. acknowledges the financial support received from the IKUR Strategy on behalf of the Department of Science, Universities and Innovation of the Basque Government. M.G. acknowledges the grant PID2022141017OB-100 funded by MCIN/AEI/10.13039/501100011033.

References

[1] Zheng, J.; Cheng, X.; Zhang, H.; Bai, X.; Ai, R.; Shao, L.; Wang, J. Gold Nanorods: The Most Versatile Plasmonic Nanoparticles. Chem. Rev. 2021, 121, 13342–13453

[2] Chow, T. H.; Li, N.; Bai, X.; Zhuo, X.; Shao, L.; Wang, J. Gold Nanobipyramids: An Emerging and Versatile Type of Plasmonic Nanoparticles. Acc. Chem. Res. 2019, 52, 2136–2146

[3] Ni, Y.; Kan, C.; Xu, J. Optimized Plasmonic Performances and Derivative Applications of Au Nanobipyramids. *Phys. Chem. Chem. Phys.* 2022, 24, 21522–21537

[4] Biswas, A.; Lemcoff, N.; Shelonchik, O.; Yesodi, D.; Yehezkel, E.; Finestone, E. Y.; Upcher, A.; Weizmann, Y. Photothermally Heated Colloidal Synthesis of Nanoparticles Driven by Silica-Encapsulated Plasmonic Heat Sources. Nat Commun 2023, 14, 6355.

[5] Sánchez-Iglesias, A.; Winckelmans, N.; Altantzis, T.; Bals, S.; Grzelczak, M.; Liz-Marzán, L. M. High-Yield Seeded Growth of Monodisperse Pentatwinned Gold Nanoparticles through Thermally Induced Seed Twinning. *J. Am. Chem. Soc.* 2017, 139, 107–110

[6] Sánchez-Iglesias, A.; Grzelczak, M. Expanding Chemical Space in the Synthesis of Gold Bipyramids. *Small* 2025, 21, 2407735.

Waveguide-Driven Nanoparticle-on-Mirror Nanocavities for Integrated On-Chip Raman Spectroscopy

D. Arenas-Ortega[1*], E. Pinilla-Cienfuegos[1], A. Martínez[1]

[1]Universitat Politècnica de València (UPV), Nanophotonics Technology Center (NTC)
*Corresponding author: dareort@upv.edu.es

***Abstract*— We demonstrate integrated Raman spectroscopy using a nanoparticle-on-mirror (NPoM) on top of a silicon nitride waveguide. TM modes efficiently excite the NPoM, producing strong nanogap-enhanced signals. Nanoparticles significantly enhance molecular Raman peaks, enabling sensitive, on-chip detection and potential chiral sensing. Guided measurements show with TM polarization 1.5× stronger than TE.**

***Keywords*— plasmonics, Nanoparticle on a Mirror (NPoM), guided Raman spectroscopy**

I. Introduction

Raman spectroscopy is a powerful optical technique used to probe the vibrational modes of molecules. By measuring the inelastic scattering of light, it provides detailed chemical fingerprints, enabling identification of molecular structures, composition, and interactions.

A nanoparticle-on-mirror (NPoM) consists of a metallic NP positioned above a metallic film, separated by a nanometer-scale gap. This configuration strongly confines light in the gap, creating intense electromagnetic hotspots that greatly enhance optical signals such as Raman scattering. NPoMs are ideal for single-molecule detection and nanoscale spectroscopy applications.

To make a compact design NPoM structure can be waveguide-coupled allowing the integration into photonic circuits, paving the way for portable, high-throughput sensing devices and lab-on-a-chip technologies that combine optical spectroscopy with microfluidics or other on-chip analytical tools. This structure would allow enantiomeric detection if it used with enantiomeric molecules and chiral nanoparticles [1].

We demonstrate waveguide-integrated Raman spectroscopy based on a nanoparticle-on-mirror (NPoM) plasmonic nanocavity fabricated directly on a silicon nitride waveguide. The NPoM nanogap, formed by a gold nanoparticle separated from a gold patch by a molecular monolayer, enables strong electromagnetic confinement and enhanced Raman scattering under guided excitation. Numerical and experimental results show that TM-polarized guided modes efficiently couple to the plasmonic cavity via evanescent excitation, producing significantly stronger nanogap-enhanced Raman signals compared to TE modes. Experimentally, TM excitation yields ~1.5× higher Raman intensity than TE polarization. The presence of the NP results in pronounced enhancement of the molecular vibrational peaks, confirming the critical role of nanogap formation for on-chip detection. This hybrid dielectric–plasmonic platform provides a compact architecture for sensitive integrated Raman spectroscopy and opens new opportunities for scalable molecular and potentially chiral sensing within photonic circuits.

II. Methods

The structures used in this study are composed of a silicon substrate and a strip silicon nitride waveguide (300 nm x 500 nm). Then a gold patch with 500 nm x 5 µm dimensions is placed on top of the silicon nitride waveguide. The gold surface is functionalized with a self-assembled monolayer (SAM) of biphenyl-4-thiol (BPT), finally using soft-lithography [2] a gold nanosphere with a diameter of 150 nm is deterministically transferred on top of the SAM. The NP enables the formation of a nanogap or even a picogap, between the two metallic structures, strongly confining the electromagnetic field and allowing highly sensitive molecular detection, potentially down to the single-molecule level [3]. The gold patches are placed on top of the waveguide, so we can couple light into the NPoM via evanescent field under TM-polarized guided modes, whose field components strongly overlap with the metallic nanostructure. The novelty on this configuration resides in enabling Raman spectroscopy through both reflection and transmission channels of the waveguide, allowing dual interrogation of the plasmonic nanocavity within a fully integrated configuration. This approach enables a systematic comparison between reflection and transmission channels, allowing us to evaluate their relative efficiency for Raman excitation and signal collection within the integrated platform. In figure 1, it is shown a scanning electron microscope (SEM) image of the mentioned structure.

The simulations are performed using finite-difference time-domain (FDTD) methods implemented in RSoft. We evaluate the enhancement factor (EF), defined as

$$EF(r, \lambda) \equiv |E(r, \lambda)|^2 / E_0(r, \lambda)|^2 \qquad (1)$$

where $E(r, \lambda)$ represents the electric field at position r in the presence of the complete metallic structure and $E_0(r, \lambda)$ corresponds to the field at the same position in the absence of the resonator structure (with the metal fully removed) [4].

We further define the waveguide transmission in Eq. (2) for the configuration including the gold patch, enabling quantitative evaluation of the insertion losses introduced by the plasmonic structure.

$$T(dB) = -10\, log_{10}\left(\frac{P_{in}}{P_{out}}\right) \qquad (2)$$

.

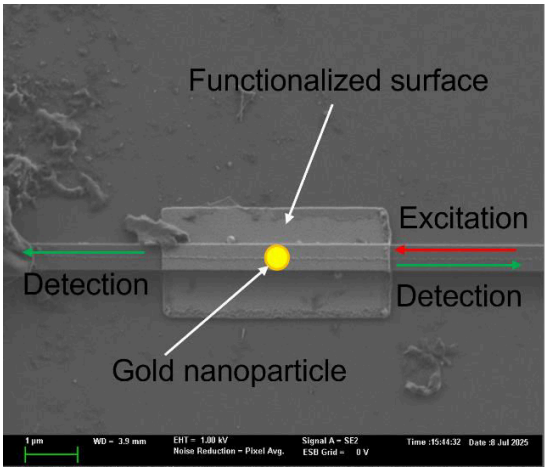

Fig. 1. SEM image. Example of the NPoM structure with gold patch on top. The gold surface is functionalized with a SAM of BPT, a gold nanosphere is placed on top to create the nanocavity. A SiN waveguide is used to excite and detect molecules.

For the Raman characterization of measurements is used a commercial Raman spectrometer from *WiTec.* The sample is placed vertically on a holder to couple light into the waveguide using the x100 microscope, as can be seen in fig 2.

Fig. 2. Optical microscope image of the experimental setup for guided Raman spectroscopy, showing the waveguide-coupled sample measured using a commercial Raman system.

III. Results and Discussion

III. a) Transmission and Enhancement Factor of the waveguide and the NPoM

The initial results are presented in Fig. 3, which shows the supported guided modes of the silicon nitride waveguide. The waveguide is designed to sustain TM-polarized modes that enable more efficient coupling into the NPoM cavity, as the plasmonic structure is positioned directly on top of the SiN core. The simulations are performed under continuous-wave excitation at 633 nm. A full spectral analysis will be addressed in future work.

Further optimization studies will investigate the influence of waveguide width, patch length, nanogap size between the nanoparticle and the gold film, and nanoparticle positioning. In the present study, however, the geometrical parameters are selected based on prior optimizations reported by our group [4,5].

For this configuration, the waveguide is designed to preserve the TM mode with less losses than the TE mode.

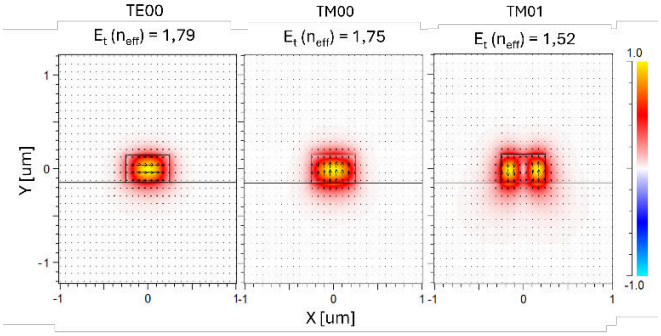

Fig. 3. Simulated transverse electric field profiles of the supported modes in the silicon nitride waveguide: TE00 (left), TM00 (center), and TM01 (right).

Table 1 summarizes the results from *full-wave* simulations, where the previously computed guided modes are used as the input field, to evaluate both propagation losses and field enhancement for the ideal configuration shown in Fig. 1, with the nanoparticle positioned above the waveguide. The simulations indicate that TE-polarized modes exhibit lower propagation losses than TM modes, as their electric field interacts only weakly with the gold patch. In contrast, TM excitation produces significantly stronger coupling to the plasmonic structure. The calculated enhancement factor is seven orders of magnitude higher for the TM mode compared to the TE mode, confirming that TM polarization more efficiently excites the plasmonic response of the patch due to its stronger evanescent field overlap with the metal interface.

	Transmission (dB)	EF
TE	0,73	0,0000001
TM	0,46	1,42

Table 1. Transmission and enhancement factors computed for the two polarizations.

III. b) Raman characterization of the NPoM

The structure is first characterized under free-space excitation. Figure 4(a) shows an optical microscope image of the fabricated NPoM, where the dark spot indicates the presence of a gold NP positioned on the metallic patch.

Figure 4(b) presents a Raman intensity map acquired at 1580 cm^{-1}, revealing a localized hotspot at the NP position. This enhanced signal originates from electromagnetic confinement within the nanogap cavity, which amplifies the Raman response of the molecular monolayer.

Figure 4(c) displays a representative Raman spectrum of the BPT monolayer within the nanogap. The characteristic vibrational peaks at 1090, 1280, and 1580 cm^{-1} are clearly resolved, confirming effective plasmonic enhancement.

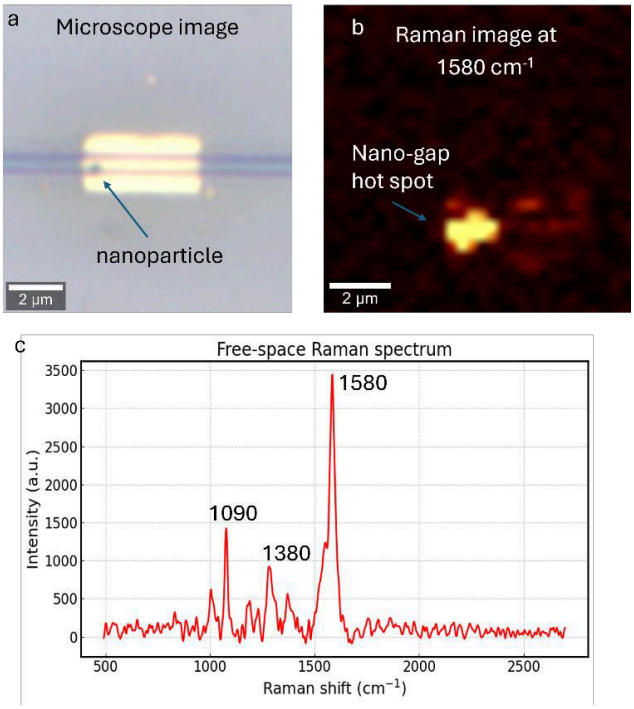

Fig. 4. a) Microscope image of the NPoM structure on top a silicon nitride waveguide. b) Raman mapping of the intensity of the 1580 cm^{-1} vibrational mode of the BPT molecule. c) Free-space Raman spectra of the BPT molecule highlighting the principal vibrational modes at 1090, 1280 and 1580 cm^{-1}.

Figure 5 compares the guided Raman spectra obtained from the complete NPoM structure and from a gold patch without the NP, where no nanogap is formed. In the absence of the NP, the vibrational peaks at 1090 and 1280 cm^{-1} are not detectable, and the intensity of the 1580 cm^{-1} mode is significantly reduced. When the nanogap cavity is created, the 1580 cm^{-1} peak increases by approximately a factor of three, clearly demonstrating the critical role of plasmonic nanogap formation in enhancing the Raman response [6].

This behavior is consistent with the expected operation of the NPoM cavity: without the NP, the electromagnetic field is not strongly confined, and the Raman signal from the BPT monolayer remains weak.

Although the guided Raman signal is lower in intensity compared to free-space measurements, it remains sufficiently strong to clearly resolve the characteristic molecular peaks. This confirms that the waveguide-coupled configuration enables effective on-chip Raman detection despite reduced excitation power and collection efficiency relative to free-space illumination.

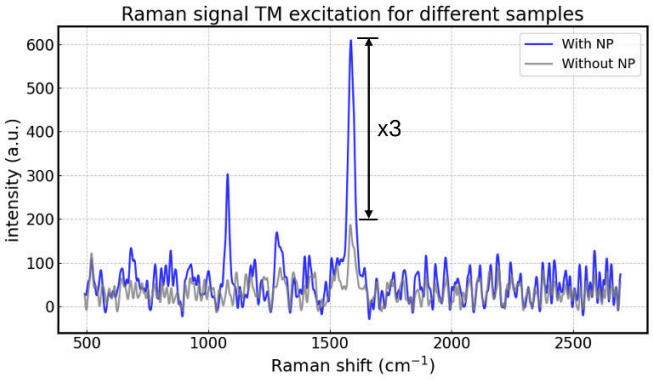

Fig. 5. Guided Raman signal of the NPoM structure measured with TM polarization (blue) vs the guided Raman signal of only gold patch with TM polarization (grey).

Figure 6 compares the guided Raman response under TE and TM excitation. Experimentally, TM polarization yields approximately 1.5× higher Raman intensity than TE, consistent with stronger coupling between the TM mode and the gold patch. This behavior can be attributed to the enhanced overlap of the TM mode's electric field component with the metallic structure, leading to more efficient plasmonic excitation of the nanogap cavity. However, in contrast to the simulations, which predict negligible enhancement for TE polarization, the experimental results show that TE excitation still produces a measurable Raman signal.

This discrepancy may arise from the fact that practical waveguide modes are not perfectly pure in polarization; a quasi-TE mode can retain non-negligible longitudinal or vertical field components that interact with the metallic patch. Additional full-vector and broadband simulations will be required to fully understand this behavior.

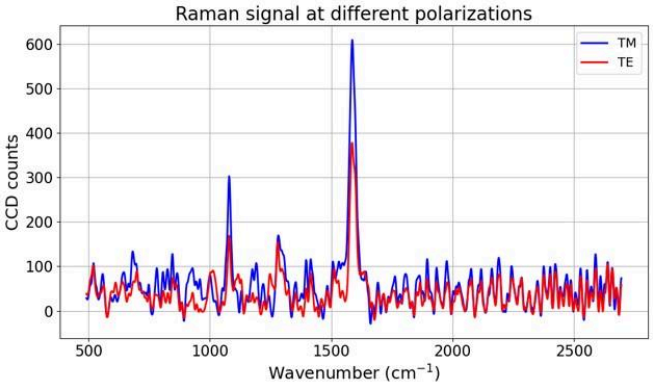

Fig. 6. Guided Raman signal of the NPoM structure measured with TM polarization (red) and TE polarization (blue).

IV. Conclusion

In this work, we have demonstrated both numerically and experimentally a novel waveguide-integrated configuration for Raman spectroscopy based on a NPoM nanocavity fabricated on top of a silicon nitride waveguide. Simulations confirm that TM-polarized guided modes efficiently couple to the plasmonic structure, producing strong local field enhancement within the nanogap. Although TE modes are predicted to exhibit weaker interaction with the gold patch, experimental results show that they still provide sufficient coupling to excite the nanocavity and detect the molecular signal.

Experimentally, guided Raman measurements collected through the waveguide clearly resolve the characteristic vibrational peaks of the BPT monolayer, demonstrating the viability of fully integrated excitation and collection. The formation of the nanogap via deterministic NP placement leads to a substantial increase in Raman intensity compared to a gold patch without NP, confirming the critical role of plasmonic confinement.

These results establish the NPoM–waveguide platform as a compact hybrid dielectric–plasmonic architecture for on-chip Raman spectroscopy, with strong potential for highly sensitive molecular detection and future implementations in chiral and enantiomeric sensing using engineered nanostructures.

Acknowledgments

We acknowledge funding from Generalitat Valenciana (GVA) under grant CIPROM/2022/14 (NIRVANA) and Agencia Estatal de Investigación, Ministerio de Ciencia, Innovación y Universidades (MCIN/AEI), through grant CNS2024-154922, funded by MICIU/AEI/10.13039/501100011033 and by the European Union NextGenerationEU/PRTR.

References

[1] M. Arabi *et al.*, «Chiral molecular imprinting-based SERS detection strategy for absolute enantiomeric discrimination», *Nat Commun*, vol. 13, n.º 1, p. 5757, sep. 2022, doi: 10.1038/s41467-022-33448-w.

[2] J. Redolat *et al.*, «Accurate Transfer of Individual Nanoparticles onto Single Photonic Nanostructures», *ACS Appl. Mater. Interfaces*, vol. 15, n.º 2, pp. 3558-3565, ene. 2023, doi: 10.1021/acsami.2c13633.

[3] J. Redolat *et al.*, "Synthesis and raman detection of 5-amino-2-mercaptobenzimidazole self-assembled monolayers in nanoparticle-on-a-mirror plasmonic cavity driven by dielectric waveguides," *Nano Lett.*, vol. 24, no. 12, pp. 3670–3677, Mar. 2024,

[4] J. E. Vázquez-Lozano, J. J. Baumberg, y A. Martínez, «Enhanced excitation and readout of plasmonic cavity modes in NPoM via SiN waveguides for on-chip SERS», *Opt. Express*, vol. 30, n.º 3, p. 4553, ene. 2022

[5] J. Redolat, D. Arenas-Ortega, Á. Barreda, A. Griol, E. Pinilla-Cienfuegos, y A. Martínez, «Polarization-insensitive integration of nanoparticle-on-a-slit cavities with dielectric waveguides for on-chip surface enhanced Raman spectroscopy», *npj Nanophoton.*, vol. 2, n.º 1, p. 17, may 2025, doi: 10.1038/s44310-025-00064-7.

[6] G.-H. Kim, J. Son, y J.-M. Nam, «Advances, Challenges, and Opportunities in Plasmonic Nanogap-Enhanced Raman Scattering with Nanoparticles», *ACS Nano*, vol. 19, n.º 3, pp. 2992-3007, ene. 2025, doi: 10.1021/acsnano.4c14557.

Inverse-Designed Ultra-Compact 1 x 3 Beam Splitter on a Cladding-Free Photonic Crystal Platform

Jinseong Bae[1], Donghyun Park[2], Minjin Kim[3], Sejeong Kim[4,*], and Haejun Chung[1,*]
[1]Department of Electronic Engineering, Hanyang University, Seoul, Korea
[2]Department of Artificial Intelligence Semiconductor Engineering, Hanyang University, Seoul, Korea
[3]Department of Artificial Intelligence, Hanyang University, Seoul, Korea
[4]Department of Electronic and Electrical Engineering, Sungkyunkwan University, Suwon, Korea
*Corresponding author: sejeongk@skku.edu, haejun@hanyang.ac.kr

***Abstract*— We demonstrate the first inverse-designed multi-port splitter for cladding-free photonic crystal waveguides, achieving 99.99% transmittance with 30:39:30% power splitting across three outputs within a 1.4 × 4.2 μm^2 footprint. Adjoint-based topology optimization with fabrication-aware projection filtering maintains 50 nm minimum feature size, enabling ultra-highdensity photonic integration without cladding layers.**

***Keywords*— Photonic Crystal, Adjoint Optimization, Inverse Design, Photonic-Integrated Circuit**

I. Introduction

Ultra-high-density photonic integrated circuits (PICs) require the elimination of every unnecessary spatial overhead. Recently, cladding-free photonic crystal (PhC) waveguides based on anisotropic rectangular lattices achieved zero-spacing waveguide arrays with negligible crosstalk by exploiting shifted spatial dispersions [1]. Unlike conventional waveguides that rely on total internal reflection or photonic bandgap cladding, this platform achieves mode isolation through deliberately mismatched iso-frequency contours between adjacent channels. Each waveguide simultaneously functions as a transmission channel and an effective cladding for its neighbors, completely removing micrometer-scale cladding layers and enabling unprecedented integration density.

However, functional circuit components, particularly multi-port power splitters have not been explored on this platform. A simple junction connecting one input to three output waveguides demonstrates limited transmission performance, achieving approximately 85% transmittance with a 17:66:17 power distribution [1], where the center channel dominates due to direct in-line coupling while the side channels receive minimal power.

Adjoint-based topology optimization has emerged as the leading method for compact, high-performance photonic device design [2], [3]. Recent advances include fabrication friendly frameworks guaranteeing design-rule compliance [4], broadband multi-port splitters on silicon [5], and silicon nitride platforms [6]. However, extending these capabilities to the cladding-free PhC platform presents unique challenges due to the anisotropic unit cell geometry and the fundamentally different waveguiding mechanism based on dispersion mismatch rather than index contrast.

In this work, we apply adjoint-based topology optimization to design the first inverse-designed 1×3 beam splitter on the cladding-free PhC platform, overcoming the severe limitations of intuitive junction designs.

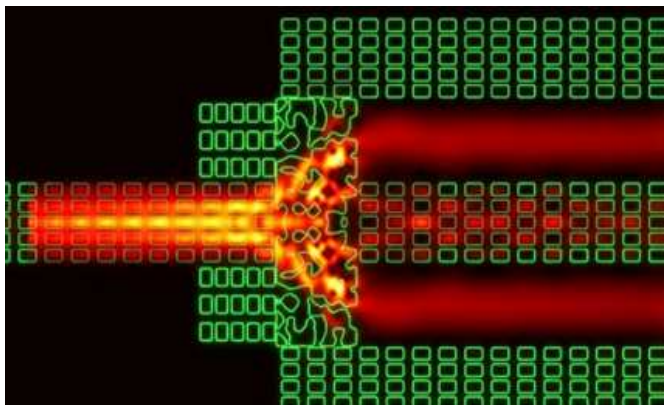

Fig. 1 *Schematic of the cladding-free photonic crystal 1×3 beam splitter. The rectangular dielectric rods ($\varepsilon = 12$) form an anisotropic lattice with periods a and $b = 0.6a$. One input waveguide (left) connects to three output waveguides (right) through the inverse-designed junction region. Green outlines indicate the PhC rod structure.*

II. Methods

A. Cladding-Free Photonic Crystal Platform

The PhC structure follows Ref. [1]: rectangular dielectric rods (ε = 12) in a rectangular lattice with horizontal period a and vertical period b = 0.6a. At a ≈ 460 nm, the operating frequency f = 0.2962(c/a) corresponds to λ ≈ 1.55 μm. The

anisotropic lattice shifts the iso-frequency contours of adjacent channels in momentum space, providing mode isolation without physical cladding [1]. The device consists of one input PhC waveguide connecting to three output waveguides through a 3a × 15b (≈ 1.4 µm × 4.2 µm) design region (Fig. 1). All simulations are performed in 2D for the TM polarization (Ez), consistent with the rod-type PhC operating within the first photonic bandgap.

B. Topology Optimization Framework

The design region is parameterized by a continuous density field ρ(x) ∈ [0, 1] mapped to permittivity: ε(x) = 1 + ρ(x) (εrod −1). The objective function jointly maximizes total transmission and splitting uniformity:

$$\mathcal{J} = \sum_{i=1}^{3} T_i - \alpha \sum_{i=1}^{3} (T_i - \bar{T})^2$$

where T_i is the transmitted power in port i, $\bar{T} = \frac{1}{3}\sum T_i$ is the mean, and α penalizes imbalance. Gradients are computed via the adjoint method in MEEP [2], requiring only two FDTD simulations per iteration regardless of the number of design variables.

As shown in Fig. 2, each iteration runs forward and adjoint simulations whose field overlap yields the sensitivity map. A gradient-based optimizer (Adam) updates the density, which is processed through a conic spatial filter and hyperbolic tangent projection:

$$\tilde{\rho} = \frac{\tanh(\beta\eta) + \tanh\big(\beta(\bar{\rho} - \eta)\big)}{\tanh(\beta\eta) + \tanh\big(\beta(1 - \eta)\big)}$$

where $\bar{\rho}$ is the filtered density, $\eta = 0.5$ is the projection threshold, and β controls binarization strength. A multi-stage β schedule (β: $1 \rightarrow 64$) gradually increases projection sharpness, allowing free exploration at low β before converging to a binary structure with minimum feature size ≥ 50 nm (Fig. 2, bottom).

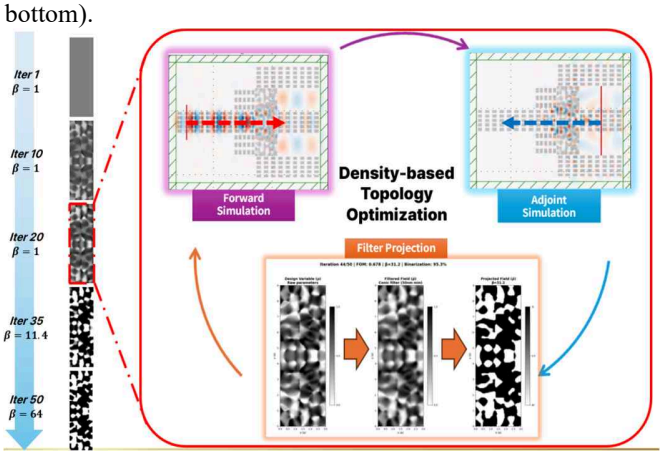

Fig. 2 *Density-based topology optimization workflow. Forward and adjoint FDTD simulations (top) compute gradients across the design region. The projection filter (bottom) progressively binarizes the design from grayscale ($\beta = 1$) to binary ($\beta = 64$), enforcing minimum feature size constraints.*

III. Results and Discussion

Performance Comparison with PhC-Based 1×3 Beam Splitters

Design	Trans.	Split Ratio	Feature	WG Pitch	Method
Ref. [1] (unopt.)	~85%	17:66:17	—	0.6a†	Manual
Jin *et al.* [7]	>96%	33:33:33	~100 nm	≥3a*	Simplex
This work	**99.99%**	**30:39:30**	**50 nm**	**0.6a†**	**Adj. TO**

†Cladding-free: zero-spacing waveguide array /
*Requires cladding rows between adjacent waveguides

- **99.99% total transmittance** with 30/40/30% power splitting
- **~5× higher channel density** than conventional PhC splitters (WG pitch 0.6a vs. ≥3a)
- **50 nm minimum feature size** maintained throughout the fully binarized design
- **Strong field confinement** with minimal scattering loss at the junction (Fig. 1)

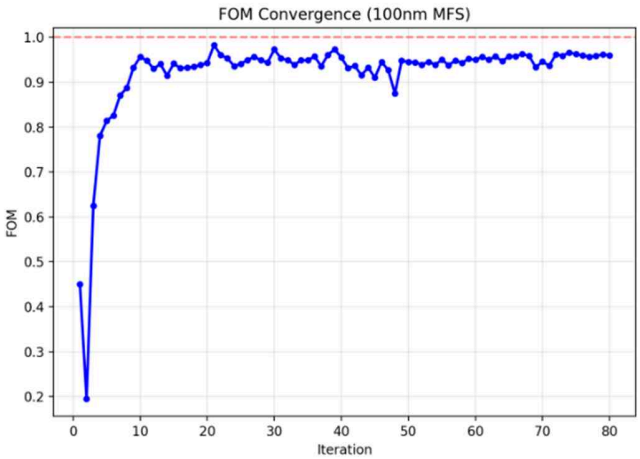

Fig. 3 *FOM convergence over 80 iterations. The dashed red line indicates the theoretical maximum.*

Fig. 3 shows the convergence of the figure of merit (FOM) over 80 iterations. The FOM rises rapidly during the initial low-β phase (iterations 1–10). Oscillations between iterations 20–60 correspond to β increments; each step sharpens binarization, temporarily degrading the FOM before reconvergence. The final FOM stabilizes near 0.97, reflecting high transmittance and improved uniformity with a fully binarized structure.

The 30:39:30 splitting ratio reflects the inherent T-junction geometry where the center channel receives slightly more power from direct in-line coupling. While not perfectly uniform, this represents a dramatic improvement over the 17:66:17 baseline and is sufficient for practical PIC applications including balanced detection and optical monitoring.

IV. Conclusion

We demonstrated the first inverse-designed multi-port component on a cladding-free PhC platform. The adjoint-optimized 1×3 beam splitter achieves 99.99% transmittance and 30:39:30 splitting within a $1.4 \times 4.2\ \mu m^2$ footprint with 50 nm minimum feature size. This establishes topology optimization as a viable methodology for cladding-free PhC circuits. Future work includes broadband optimization, robustness analysis (erosion/dilation), and experimental demonstration.

Acknowledgments

This work was supported by the National Research Foundation of Korea (NRF) grant funded by the Korean government (MSIT) (RS-2024-00338048)(RS-2024-00414119), (RS-2025-25463760), and also supported by the Republic of Korea's MSIT, under the Global Research Support Program in the Digital Field program (RS-2024-00412644) supervised by the IITP (Institute of Information and Communications Technology Planning & Evaluation) and also supported by Culture, Sports and Tourism R&D Program through the Korea Creative Content Agency grant funded by the Ministry of Culture, Sports and Tourism in 2024 (RS-2024-00332210) and also Artificial Intelligence Graduate School Program (No. RS-2020-II201373, Hanyang University) supervised by the IITP, and under the artificial intelligence semiconductor support program to nurture the best talents (IITP-(2025)-RS-2023-00253914) grant funded by the Korea government, and by the MSIT (RS-2025-02283217, RS-2025-25441264).

References

[1] T. Song, H. Xu, et al., "Ultracompact photonic circuits without cladding layers," Phys. Rev. X, vol. 12, p. 011053, 2022.
[2] A. M. Hammond, A. Oskooi, et al., "High-performance hybrid time/frequency-domain topology optimization for large-scale photonics inverse design," Opt. Express, vol. 30, pp. 4467–4491, 2022.
[3] R. E. Christiansen and O. Sigmund, "Inverse design in photonics by topology optimization: Tutorial," J. Opt. Soc. Am. B, vol. 38, pp. 496–509, 2021.
[4] J. Gedeon, et al., "Inverse design of photonic devices with strict foundry fabrication constraints," ACS Photonics, 2022.
[5] H. Chen, M. Zhang, and Y. Tong, "Always-feasible photonic inverse design with a differentiable conditional design generator," *ACS Photonics*, vol. 11, no. 10, pp. 4461–4471, 2024.
[6] J. L. Pita Ruiz, et al., "Integrated silicon nitride devices via inverse design," Nat. Commun., 2025.
[7] R. Jin, et al., "1×3 ultra-wideband photonic crystal waveguide power splitter designed by the downhill simplex algorithm," Appl. Opt., vol. 64, pp. 5021–5026, 2025.
[8] W. Bogaerts, et al., "Roadmapping the next generation of silicon photonics," Nat. Commun., vol. 15, p. 751, 2024.

Tunable nonlinearities of nonlocal free-electron gas in plasmonic heavily doped semiconductors

Huatian Hu[1,6], Gonzalo Álvarez-Pérez[1], Antonio Valletta[2], Marialilia Pea[3], Michele Ortolani[3,4,5], and Cristian Ciracì[1]
[1]Istituto Italiano di Tecnologia, Center for Biomolecular Nanotechnologies, Via Barsanti 14, 73010 Arnesano, Italy
[2]Istituto per la Microelettronica e Microsistemi, Consiglio Nazionale delle Ricerche, Via del Fosso del Cavaliere 100, Rome 00133, Italy
[3]Istituto di Fotonica e Nanotecnologie, Consiglio Nazionale delle Ricerche, Via del Fosso del Cavaliere 100, Rome 00133, Italy
[4]Department of Physics, Sapienza University of Rome, Piazzale Aldo Moro 5, 00185 Rome, Italy
[5]Istituto Italiano di Tecnologia, Center for Life Nano- and Neuro-Science, Viale Regina Elena 291, Rome 00161, Italy
[6]POLIMA—Center for Polariton-driven Light–Matter Interactions, University of Southern Denmark, Odense M, Denmark
*Corresponding author: huhu@mci.sdu.dk

***Abstract*— Nonlocal free-electron dynamics have a substantial contribution to the optical nonlinearity in heavily doped semiconductor systems, and is very tunable. We applied hydrodynamic method to explored the tunability third-harmonic generation and optical Kerr bistability.**

***Keywords*— hydrodynamics, mid-infrared, nonlocal optics, nonlinearities.**

I. Introduction

Understanding the nonlinear light-matter interaction at the nanoscale has been a long-standing fundamental target since it guides the design rule for minimized and integrated nonlinear photonic devices. Achieving a strong and ultrafast nonlinear optical response is essential for various fields such as optical information processing and artificial intelligence training. Yet, efficiently manipulating light with light is still challenging, leading to an urgent demand of exploring new physics for higher nonlinear interactions.

II. Methods

Our methodology used hydrodynamic theory to calculate the free-electron nonlinear interactions from the equation of the motion of the free-electron gases with the encapsulated energy functionals:

$$m_e\left(\frac{\partial}{\partial t}+\mathbf{v}\cdot\nabla+\gamma\right)\mathbf{v}=-e(\mathbf{E}+\mathbf{v}\times\mu_0\mathbf{H})-\nabla\frac{\delta G[n]}{\delta n}. \quad (1)$$

It will coupled with the wave equation for the linear and nonlinear optical responses

$$\nabla\times\nabla\times\mathbf{A}_j+\frac{\varepsilon_r}{c^2}\frac{\partial^2\mathbf{A}_j}{\partial t^2}+\mu_0\frac{\partial}{\partial t}(\mathbf{P}_j+\mathbf{P}_d^{\mathrm{NL}})=0. \quad (2)$$

with a field effect on the semiconductor considered by including the Poisson equation:

$$\nabla^2\varphi=-e(p_0(\mathbf{r})-n_0(\mathbf{r})+N_D^+-N_A^-)/\varepsilon_0\varepsilon_r. \quad (3)$$

On the left-hand side of Eq. (3) there is the Laplacian of the band bending φ, whereas the right-hand side accounts for the total charge density, including hole $p_0(\mathbf{r})$ and electron $n_0(\mathbf{r})$ densities, and ionized donor N_D^+ and acceptor N_A^- concentrations. $\varepsilon_0\varepsilon_r$ denotes the permittivity of the semiconductor.

III. Results and Discussion

Free electrons in plasmonic structures can provide extra degrees of freedom in modulating nonlinearities in the system when spatial nonlocality is considered. The hydrodynamic model reveals that the third-order nonlinearity due to the free electrons could even be orders of magnitude higher than that of the conventional bulk susceptibility when the equilibrium electron density is low.

Kerr nonlinearity is a third-order process that supports fascinating phenomena such as optical bistability and self-focusing. A high optical Kerr nonlinearity at the nanoscale is a crucial element in ultrafast optical neuromorphic computation devices as it can enable all-optical nonlinear activation functions. Employing a time-domain simulation within a finite-element framework, we could self-consistently solve electromagnetic wave equation and hydrodynamic formalism

with Kerr nonlinear contributions. We show that heavily doped semiconductor structures can provide strong free-electron Kerr nonlinearities supported by the longitudinal bulk plasmon mode, and is very tunable by the field effect. This high nonlinearity originates from the multibody properties of the free electron gas as the electron-electron interaction can be naturally taken into account in the hydrodynamic theory when proper kinetic energy functionals are considered. It can work as optical modulators in the mid-infrared.

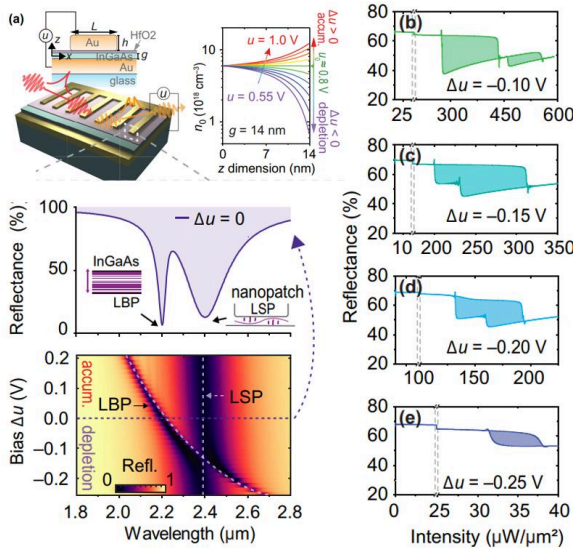

Fig. 1 Surface charge modulation of the heavily doped semiconductors that give rise to exceptional tunabilities for optical modulator in the mid-infrared.

IV. Conclusion

We applied multiphysical calculations involving quantum-corrected hydrodynamic theory with semiconductor and wave optics based on the finite-element method to explore a tunable and significant third-harmonic generation and optical Kerr bistability. We proposed a microscopic mechanism to electrically reconfigure the Kerr nonlinearity by modulating the concentration of free electrons in heavily doped semiconductors under a static bias. Our theory incorporates electrostatic and hydrodynamic frameworks to describe the electronic dynamics, demonstrating electrically tunable linear and nonlinear modulations. The power threshold of achieving optical bistability shows unprecedented tunability over 2 orders of magnitude. Varying biases, a charge depletion will significantly decrease the power threshold of the bistability from thousands of down to tens of $\mu W/\mu m^2$. On the contrary, charge accumulation will give rise to a wide (>70%) and high-contrast ($\sim 40\%$) bistability with a still decent threshold of several $mW/\mu m^2$. Moreover, we unveil that the often-neglected cascaded contributions in the Kerr effect can also be dominant in this system. Our findings open a viable avenue for active ultrafast nonlinear devices with low power consumption.

These findings offer insights into understanding and actively controlling Kerr nonlinearities, paving the way for efficient refractive-index engineering as well as the development of advanced linear and nonlinear electro-optical modulators

Acknowledgments

We acknowledge funding from the European Innovation Council through its Horizon Europe program with Grant Agreement No. 101046329. Views and opinions expressed are those of the authors only and do not necessarily reflect those of the European Union. Neither the European Union nor the granting authority can be held responsible for them.

References

[1] Rossetti†, Hu†, Venanzi† et.al, *Light Sci Appl* **14**, 192 (2025).
[2] Hu et.al, ACS Photonics 2024, 11, 11, 4812–4817
[3] Hu et.al, Phys. Rev. Applied 2025, **24**, 044006

Thermally Addressable Au/PDLC Multilayer metamaterial: A Platform for Tunable Epsilon-Near-Zero Response

Vimala Sridurai[1,2*], Geetha G Nair[1]

[1]Centre for Nano and Soft Matter Sciences, Bengaluru, India
[2] *Current Affiliation:* Dept. of Physics and Astronomy, The University of Manchester, UK

*Corresponding author: vimalags88@gmail.com

***Abstract*—We report a five- layer gold and polymer dispersed liquid crystal multilayer metamaterial exhibiting sub unity permittivity in the optical regime. Using spectroscopic ellipsometry and effective medium theory, we characterize this Epsilon near zero phenomenon. This architecture serves as a foundational platform for thermally switching the system towards hyperbolic dispersion.**

***Keywords*— Epsilon near zero, Active metamaterials, Hyperbolic metamaterial, Topological phase transition, Liquid crystal photonics.**

I. Introduction

Photonic metamaterials with Epsilon-Near-Zero (ENZ) and hyperbolic dispersion offer extraordinary control over light-matter interaction. However, many plasmonic-dielectric stacks are static[1]. By incorporating Polymer Dispersed Liquid Crystals (PDLC) as the active dielectric layer, we introduce a temperature-dependent refractive index into the system. This work focuses on the characterization of an Au/PDLC multilayer stack, identifying the specific spectral regions where the parallel permittivity component vanishes, marking the onset of the ENZ regime.

II. Methods

The system consists of a 5-layer stack (Au/PDLC/Au/PDLC/Au) on a glass substrate (Fig. 1). Au and PDLC layers were fabricated by sputtering and spin coating respectively. The PDLC was prepared with a mixture of nematic liquid crystal E7 and NOA68 in the ratio 70:30. After spin coating, the film was photo-polymerized with UV irradiation to form a polymer layer. The formation of PDLC was confirmed by polarizing optical microscopy. Nominal layer thicknesses are d_m = 55 nm for gold and d_d = 110 nm for PDLC. The layer thickness was confirmed by stylus profilometry. Spectroscopic ellipsometry was performed to collect Ψ (Psi) and Δ (Delta) parameters at three different incident angles, 65°, 70° and 75°. Data analysis was performed using the PyElli Python library, employing a multilayer model to fit the experimental Ψ and Δ profiles. Uniaxial Effective Medium Approximation (EMA) based on Maxwell-Garnet approach was employed to extract the permittivity[2]. The parallel and perpendicular permittivity components were calculated as:

$$\varepsilon_{\parallel} = \rho\varepsilon_m + (1-\rho)\varepsilon_d \quad (1)$$

$$\varepsilon_{\perp} = \frac{\varepsilon_m \varepsilon_d}{\rho\varepsilon_d + (1-\rho)\varepsilon_m} \quad (2)$$

where, ε_m and ε_d are permittivity of Au and PDLC layers, and ρ is the fill fraction of Au.

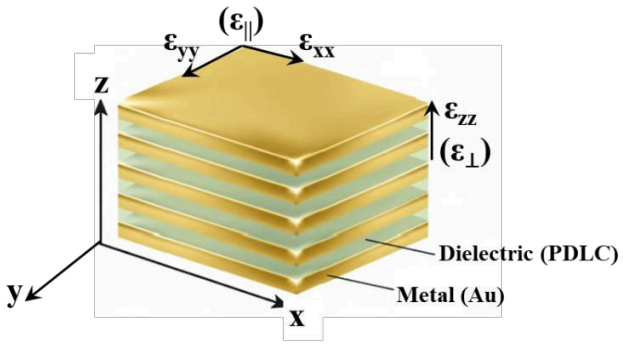

Fig. 1 Schematic representation of the Au/ PDLC multilayer metamaterial system.

III. Results and Discussion

The optical response of the five-layer Au/PDLC stack was characterized using spectroscopic ellipsometry. The extracted parallel and perpendicular effective permittivity components, $\varepsilon_{\parallel}$ and parallel $\varepsilon_{\parallel}$ and $\varepsilon_{\perp}$ perpendicular reveal a strong uniaxial anisotropy inherent to the multilayer geometry[3]. As shown in

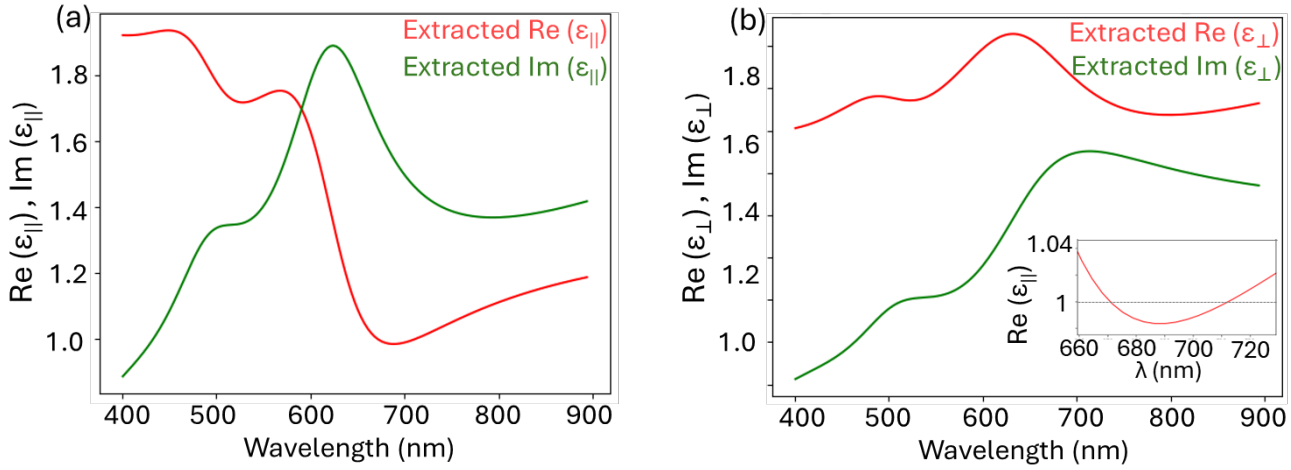

Fig. 2 Extracted Real and Imaginary permittivity of the Au/PDLC multilayer system in the direction (a) parallel to the layers and (b) perpendicular to the layers. Inset to (b) shows the Re $\varepsilon_{\parallel}$ drops below 1, thus exhibiting an ENZ behaviour

Fig. 2, the real part of $\varepsilon_{\parallel}$ (i.e., Re $\varepsilon_{\parallel}$) exhibits a significant decrease across the visible spectrum, reaching a sub-unity minimum of 0.98 at ~ 685 nm. This sub-unity value of $\varepsilon_{\parallel}$ signifies that the system is effectively acting as an Epsilon-Near-Zero (ENZ) medium, while the extent and wavelength range of ENZ is tunable by the nematic liquid crystal.

The proximity to zero indicates a highly balanced ratio between the plasmonic contribution of the gold layers and the

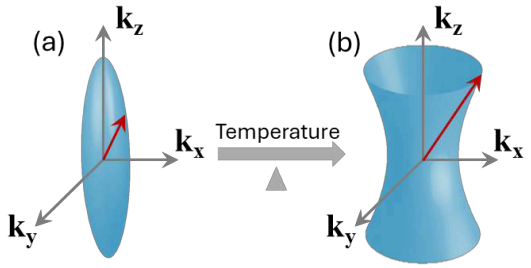

Fig. 3 Schematic representation of the Iso frequency surfaces representing the (a) ENZ behaviour exhibited by the Au/ PDLC multilayer system, (b) Hyperbolic metamaterial behaviour expected in the system upon increasing the temperature. The red arrow represents the direction of propagation of the k- vector

dielectric response of the PDLC. At this specific wavelength, the system operates at the topological threshold. The iso-frequency surface is currently an extreme prolate ellipsoid but is positioned to transition into hyperbolic dispersion[3]. The stability of this near-zero state validates our design and the accuracy of the effective medium approximation (EMA) for a five-layer metamaterial system. Unlike static metal-dielectric stacks, the current results represent a "pre-transition" state. Because the refractive index of the PDLC layers is highly sensitive to temperature, this Re $\varepsilon_{\parallel} \sim 0.98$ baseline suggests that a modest thermal modulation will drive the permittivity across the zero-axis, triggering a topological transition[4] to a hyperbolic regime (Re $\varepsilon_{\parallel} < 0$) as depicted in Fig. 3. This confirms the stack's potential as a thermally addressable photonic platform.

Conclusion

We have successfully designed, fabricated and characterized a five-layer gold and polymer-dispersed liquid crystal (Au/PDLC) multilayer metamaterial system. Spectroscopic ellipsometry analysis identifies a distinct sub-unity permittivity regime ($\mathrm{Re}(\varepsilon_{\parallel}) \approx 0.98$) in the nematic phase, confirming that the effective medium response is accurately captured by our 5-layer model. The achievement of an Epsilon near-zero state in the optical spectral regime serves as a critical threshold for active topological photonics.

Future work will focus on temperature-resolved ellipsometry to map the topological phase transition as the system crosses the nematic-to-isotropic transition. By thermally modulating the liquid crystal medium, we aim to demonstrate the active switching from an elliptical to a hyperbolic dispersion. This research provides a robust roadmap for the development of high-sensitivity thermal sensors and reconfigurable flat optics.

Acknowledgments

The corresponding author, VS, is thankful for the financial support from the project CRG/2018/000736 funded by SERB, Department of Science and Technology (DST), New Delhi, India. VS is also thankful for the funding from the European Union MSCA-PF- project 'MetaPhoton' under the grant agreement 101206740. The authors gratefully acknowledge the Central Research Facilities at the Centre for Nano and Soft Matter Sciences, Bengaluru, for the various experimental facilities used in the current study.

References

[1] I. Liberal and N. Engheta, "Near-zero refractive index photonics," Nature Photonics, vol. 11, no. 3, pp. 149–158, 2017.
[2] O. Reshef, I. De Leon, M. Z. Alam, and R. W. Boyd, "Anisotropic epsilon-near-zero metamaterials," Nature Reviews Materials, vol. 4, no. 8, pp. 535–551, 2019.

[3] P. Shekhar, J. Atkinson, and Z. Jacob, “Hyperbolic metamaterials: Fundamentals and applications,” Nano Convergence, vol. 1, no. 1, pp. 1–17, 2014.
[4] M. T. Sheldon, S. Wu, and N. Hogan, “Dynamic Control of Topological Phase Transitions in Active Plasmonic Systems,” Advanced Materials, vol. 36, no. 4, pp. 1120–1135, 2024.

Leveraging Stochastic Textures in Chiral Nematics for multi-modal Physical Unclonable Functions (PUFs)

Mauro D.L. Bruno[1,2], Giuseppe Nicoletta[1,2], Roberto Caputo[1,2], Maria Penelope De Santo[1,2,3], Riccardo C. Barberi[1,2,3], Antonio Ferraro[1,*]

[1]Dipartimento di Fisica - Università della Calabria, Via P. Bucci - cubo 33B, 87036 Rende, Italy
[2]Consiglio Nazionale delle Ricerche - Istituto di Nanotecnologia, Via P. Bucci - cubo 33C 87036 Rende, Italy
[3]Laboratorio di Preparazione Materiali Biologici - STAR IR, Università della Calabria, Via Tito Flavio, 87036 Rende, Italy
*Corresponding author: antonio.ferraro@cnr.it

***Abstract*—These studies explore the potential of Liquid Crystals (LCs) for the realization of security system based on the paradigm of Physical Unclonable Functions (PUFs). By exploiting the self-organizing nature of LCs and their sensitivity to external stimuli, we generate unique optical "textures" through different pathways. In parallel, the optical properties of LC allows to camouflage security system as PUF or Qre code which will be revealed only under specific conditions. Our results demonstrate the potential of LC to realized multi-modal security systems that significantly increase the barrier to unauthorized cloning.**

***Keywords*— physical unclonable function, liquid crystal, image recognition, optical encoding.**

I. Introduction

Traditional anti-counterfeiting measures, such as 2D holograms and RFID tags, often rely on secrets stored in digital memory or reproducible manufacturing patterns, making them vulnerable to sophisticated emulation. Physical Unclonable Functions (PUFs) offer a paradigm shift by deriving security from the inherent randomness of a physical medium.

Liquid crystals (LC), specifically chiral nematics, are ideal candidates for the generation of PUF primitives due to their stochastic self-assembly and sensitivity to stimuli like temperature, pressure, and electromagnetic fields. The obtained textures act as "physical-to-digital" bridges, where the microscopic complexity of molecular alignment provides a unique, non-deterministic signature that cannot be replicated even by the original manufacturer.

II. Results and Discussion

The experimental investigations yielded significant insights into the stochastic generation of liquid crystal textures across various physical configurations, establishing a robust basis for their use as Physical Unclonable Functions. In the first phase of the study, cholesteric liquid crystals (CLC) emulsioned with acqueos or Polydimethylsiloxane (PDMS) matrix were confined within spherical micro-cavities to observe the effects of multi-stimuli interaction. By applying controlled temperature variation, or mechanical stress, we successfully induced a series of highly complex, fingerprint-like textures. The latter were analyzed with image recognition algorithm yealding to identify more than 500 unique features in a single texture.

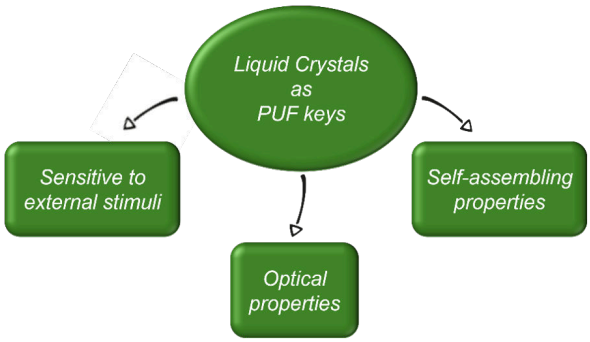

Fig. 1. Schematic of liquid crystal properties for the realization of PUF keys.

In parallel, our research into planar-aligned CLC revealed a critical discovery regarding molecular behavior in the regime immediately preceding the Fréedericksz transition. We observed that the application of sub-threshold voltages triggers a continuous and non-linear molecular rearrangement rather than a binary switch. This subtle movement results in a temporal sequence of unique textures that are governed by microscopic local variations in anchoring energy and field distribution. This phenomenon effectively creates a "kinetic" PUF, where the security key is defined irreproducible the texture's evolution over time. The discretization into different levels of the single unique image leads to the generation of a very large amount of secret key that can be used as One Time Password.

Finally, a polymer-dispersed liquid crystal (PDLC) architectures was optimized to provide a sophisticated method for optical camouflaging. The PDLC was realized on a multilayer structure which provide structural colors which are sensitive to incident and viewin angles. The results indicate that the light-scattering properties of the polymer matrix effectively

mask the underlying secret keys rendering the security device invisible to standard optical inspection. Upon the application of a temperature variation, the PDLC undergoes a transition from an opaque to a transparent state, revealing the key for verification. Furthermore, in the transparent state the structural colors are also visible. This dual-state functionality adds a vital ”stealth” layer to the authentication device, ensuring that the fingerprint is only exposed during the authorized reading phase, thereby significantly reducing the risk of unauthorized cloning or scanning.

III. Conclusion

This research establishes a versatile framework for utilizing Liquid Crystals in the fight against counterfeiting. By leveraging the sensitivity of LC textures to environmental and electrical stimuli, we have developed a suite of PUF keys that are both highly complex and easy to verify through standard optical methods. Furthermore PDLC matrices were optmized to realize a ”camouflage” layer that protects the key from unauthorized scanning. Future work will focus on the automated verification of these textures to ensure rapid, field-deployable authentication.

Acknowledgments

G.N. R.C. acknowledge the financial support from Project Poc “BiOt”, CUP C28H23000270002, Unical Pathways (UP), Piano Nazionale di Ripresa e Resilienza, NextGenerationEU. M.D.L.B. and A.F. acknowledge the financial support from project “PRIN2022 2022T3B4HS-PE11- Multi-step optical encoding in anticounterfeiting photonic tags based on liquid crystals (PHOTAG)” financed in the framework of Piano Nazionale di Ripresa e Resilienza(PNRR). M.P.D.S. acknowledges the financial support from project Poc “CHAOS”, CUP C28H23000300002, Unical Pathways (UP), Piano NazionalediRipresaeResilienza,NextGenerationEU. A.F. acknowledge the financial support from project “Ledger Assessment for Mobility, Batteries and AntiCounterfeiting - Certificazione dati basata sull’integrazione tra blockchain e funzioni fisiche non clonabili e per applicazioni nella mobilità e logistica (LAMBdA)” CUP: J39I24002050005 financed by Regione Calabria (Italy).

References

[1] M. D. L. Bruno, A. Ferraro, G. Palermo, R. C. Barberi, A. P. H. J. Schenning, M. P. De Santo “Cyber-attacks resistant Cholesteric Liquid Crystals based Physical Unclonable Function keys,” *Advanced Photonics Research*, 2026.

[2] M. D. L. Bruno, G. Nicoletta, C. P. Umeton, M. P. De Santo, A. Ferraro “Physical Unclonable Functions for One Time Password Generation based on the Exploitation of Cholesteric Liquid Crystals. Discover Materials,” *submitted*, 2026.

[3] G. Nicoletta, M. D. L. Bruno, P. Yu, Z. Wang, M. P. De Santo, R. Caputo, A. Ferraro, “Anti-Counterfeiting Tags with Camouflaged QR Codes on Nanocavities, Using Polymer-Dispersed Liquid Crystals,,” *Advanced Materials Technologies*, vol. 10, 2402055, 2025.

Exploring the coupling of TPMSs: What utility can they provide?

Alonso Cuartero Mondoño[1, 2,*], Andrea Bergamini[1]

[1]Swiss Federal Laboratories for Material Science and Technology (EMPA), Switzerland
[2]Federal Institute of Technology Zurich (ETHZ), Switzerland
*Corresponding author: alonso.cuartero@empa.ch

***Abstract*—Triply Periodic Minimal Surfaces (TPMS) offer lightweight, high-symmetry architectures with tunable mechanical properties. This study computationally investigates deformation coupling in TPMS-based beams under static and dynamic loading. Results reveal morphology-dependent behaviors, with sheet gyroids exhibiting strong bend–twist coupling and solid gyroids showing pull–twist responses. Coupling can be tailored via geometric modifications, enabling multifunctional, shape-adaptive structural design.**

***Keywords*— TPMS, deformation coupling, optimization**

I. Introduction

Triply Periodic Minimal Surfaces (TPMSs) have recently emerged as a versatile class of structured materials due to their high symmetry, exceptional stiffness-to-weight ratio, and large, tunable design space [1], [2]. Defined by smooth, zero-mean-curvature surfaces that partition space into two continuous and equivalent volumes, TPMSs can be efficiently described through parametric formulations and readily modified through grading, hybridization, or by modifying their equations [3] . While some research can be found studying their mechanical properties [4] and wave-propagation characteristics [5], [6], the potential of coupling effects—such as bend-twist and pull-twist interactions—remains comparatively underexplored.

II. Methods

This work investigates the utility of coupling in TPMS-based structures, with particular emphasis on the varying symmetry of the different geometries. Several TPMS-based structures are analyzed using finite element methods (FEM) to explore their deformation coupling in finite structures. The path followed looks at beams under static loading conditions and how the coupling they present can be tuned with a variety of techniques such as modifying the aspect ratio of the unit cells, al-tering their orientation or modifying their iso-surface. To effectively handle the complexity of these geometries in a computationally efficient manner, several geometry and simulation approaches have been used such as voxelization [7].

The testing campaign consists of both static and dynamic tests on polymeric, 3D-printed samples. The behavior of the resulting experiments is compared against the computational models and used to validate them.

III. Results and Discussion

Results demonstrate that different TPMS morphologies exhibit markedly distinct coupling behaviors. Figure 1 includes the static simulation of three different cantilever beams consisting of 1x1x10 unit cells and 20% volume ratio. Two different loading conditions, pure axial and pure bending, were applied to visualize and understand the deformation characteristics. The primitive acts as the control, lacking any type of coupling. On the other hand, the gyroid does couple deformation with a radically different type for the sheet and body variants. Figure 2 illustrates a quantitative measure of different TPMS types. The coupling coefficient, $C = r_{end}/d_{end}$, is a normalized ratio between the rotation and deformation at the end of the beam. it is apparent that different geometries have different coupling coefficients, with the gyroid being the most efficient at coupling bending-rotation, interesting for passively adaptive-airfoils [8].

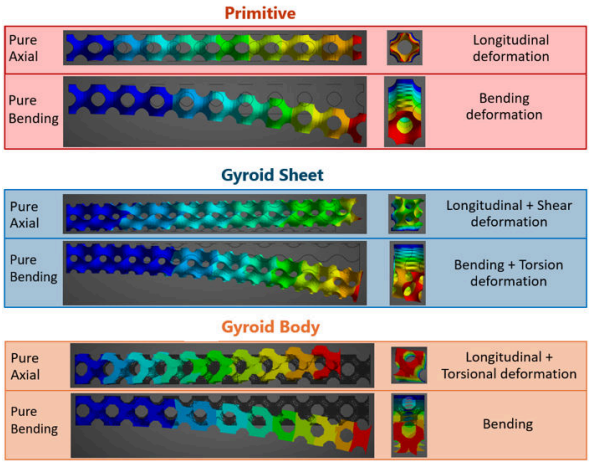

Fig. 1. Deformation coupling of different TPMS structures.

With this information, the finite structures can be modified to eliminate or enhance desired couplings increasing the design space of these types of structures. The impact of increasing the aspect ratio of the unit cells, modifying the iso-level surface of the TPMSs and the orientation of the unit cells have also been explored. These modifications result in different symmetries [7] with their respectively different stiffness

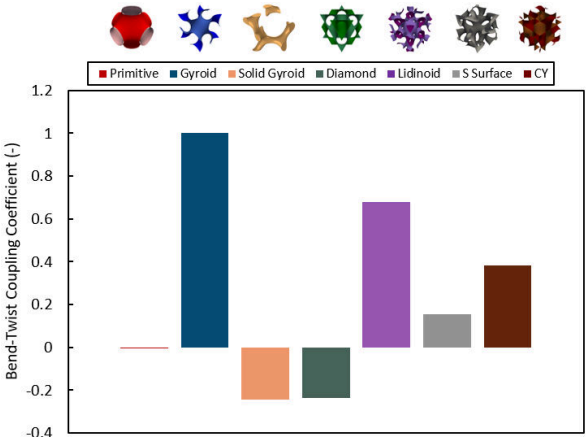

Fig. 2. Bend-Twist coupling coefficient of different geometries.

tensors allowing us to use properties such as anisotropy to our advantage [9]. These findings prove that TPMSs are not only effective structural materials but can also be engineered for multifunctional applications by exploiting coupling effects, such as passive shape-adaptive structures.

IV. Conclusion

This work demonstrates that TPMS-based beams exhibit morphology-dependent deformation coupling under static and dynamic loading. Finite element simulations, validated experimentally, confirm that coupling can be tuned through unit-cell aspect ratio, orientation, and iso-surface modifications. By leveraging symmetry and anisotropy, TPMS architectures can be systematically engineered to enhance or suppress targeted couplings. The gyroid resulted of particular interest for its hight coupling coefficient and tunability. These results expand the functional design space of TPMS structures, highlighting their potential for lightweight, multifunctional, and passively shape-adaptive applications.

Acknowledgments

This work was mostly carried out at EMPA within the department of Acoustics/Noise Control. The funding has been provided by the State Secretariat for Education, Research and Innovation, SERI, and the project takes place within the broader framework of a Marie Skłodowska-Curie Actions doctoral network called MetacMed.

References

[1] E. Kreyszig, "On the theory of minimal surfaces," in *The problem of Plateau: a tribute to Jesse Douglas and Tibor Radó*, World Scientific, 1992, pp. 138–164.

[2] A. H. Schoen, *Infinite periodic minimal surfaces without self-intersections*. National Aeronautics and Space Administration, 1970, vol. 5541.

[3] I. Maskery, A. O. Aremu, L. Parry, R. D. Wildman, C. J. Tuck, and I. A. Ashcroft, "Effective design and simulation of surface-based lattice structures featuring volume fraction and cell type grading," *Materials & Design*, vol. 155, pp. 220–232, 2018.

[4] R. Kumar, J. Ramkumar, and K. Balani, "Design and parametrization of tpms lattice using computational and experimental approach," *Engineering Research Express*, vol. 6, no. 3, p. 035 556, 2024.

[5] T. Gao et al., "Elastic wave manipulation via functional incorporation of air-solid phases in hybrid tpms," *Composites Communications*, vol. 44, p. 101 745, 2023.

[6] N. V. Viet, N. Karathanasopoulos, and W. Zaki, "Mechanical attributes and wave propagation characteristics of tpms lattice structures," *Mechanics of Materials*, vol. 172, p. 104 363, 2022.

[7] S. C. Kapfer, S. T. Hyde, K. Mecke, C. H. Arns, and G. E. Schröder-Turk, "Minimal surface scaffold designs for tissue engineering," *Biomaterials*, vol. 32, no. 29, pp. 6875–6882, 2011.

[8] H. Gu et al., "Tailored twist morphing achieved using graded bend–twist metamaterials," *Composite Structures*, vol. 300, p. 116 151, 2022.

[9] M. Zhang, J. Li, C. Liu, M. Deng, X. Liao, and D. Wang, "Study on the anisotropy of triply periodic minimal surface porous structures," *Coatings*, vol. 13, no. 7, p. 1206, 2023.

Topological Eutectic Heterostructures: Quantification of Their 2D-morphology

Krzysztof Markus[1], Kingshuk Bandopadhyay[1], Andrzej Materna[1], Andriy. M. Gusak[1], Dorota A. Pawlak[1]

[1]ENSEMBLE[3] Centre of Excellence, Wolczynska 133, 01-919 Warsaw, Poland
*Corresponding author: krzysztof.markus@ensemble3.eu

***Abstract*— Three-dimensional topological insulators (TIs) have attracted considerable attention due to their topologically protected gapless surface states. However, they have some disadvantages that limit their use. Here, we propose utilizing eutectic TI heterostructure composites as a platform for studying junctions between TIs and materials with complementary physical properties.**

***Keywords*— topological insulator, eutectic lamellar heterostructure, materials characterization.**

I. Introduction

The morphology of eutectic heterostructures is strongly influenced by crystal growth conditions. This dependence provides a powerful route to engineer and optimize microstructures for targeted applications. To understand and control these effects, a quantitative description of the relationship between growth parameters and resulting structural features is required. In this work, we investigate the morphological evolution of eutectic topological insulator heterostructures grown under different conditions and develop a methodology for their quantitative analysis.

II. Methods

The analyzed samples consisted of polycrystalline eutectic TI heterostructures, including Sb_2TeSe_2-Sb_2Se_3, Bi_2Te_3-BiTeI, grown using the vertical Bridgman method. For each material system, at least three different growth rates were employed. Samples were sectioned perpendicular to the growth direction and subsequently polished to obtain high-quality surfaces suitable for imaging. Morphological characterization was performed using scanning electron microscopy (SEM) in backscattered electron mode, providing enhanced phase contrast between the constituent materials.

The acquired SEM images were converted into binary matrices representing the two constituent phases. This enabled quantitative analysis using a digital image-processing algorithm developed by Gusak and Abakumov [1]. The algorithm determines structural parameters using two complementary approaches. The first method evaluates the number of phase transitions along image rows and columns, providing information on characteristic spacing and periodicity. The second method utilizes the total area of the minority phase and the interfacial boundary length to quantify phase distribution and interface complexity.

III. Results and Discussion

The analysis reveals a clear correlation between crystal growth rate and structural parameters, including lamellar thickness, interlamellar spacing, and interface morphology for each eutectic composition studied. The results confirm that the characteristic lamellar dimensions are strongly dependent on growth velocity. Increasing the growth rate leads to a significant reduction in lamellar size, enabling the transition from micrometer-scale to nanometer-scale structural features. This demonstrates the possibility of tailoring the microstructure through controlled solidification conditions.

IV. Conclusion

The study demonstrates that SEM imaging combined with the quantitative analysis algorithm developed by Gusak and Abakumov provides a reliable method for characterizing eutectic heterostructures, even when the constituent phases exhibit only small differences in atomic number.

Furthermore, we confirm that the morphology of eutectic topological insulator heterostructures can be systematically controlled through growth conditions. Such control enables the tuning of lamellar dimensions and material combinations, offering opportunities for phonon spectrum engineering and the enhancement of thermoelectric performance [2].

Acknowledgments

The authors thank ENSEMBLE3 Project (MAB/2020/14) which is carried out within the International Research Agendas Programme (IRAP) of the Foundation for Polish Science co-financed by the European Union under the European Regional Development Fund and Teaming Horizon 2020 programme (GA. No. 857543) of the European Commission and the project of the Minister of Science and Higher Education "Support for

the activities of Centers of Excellence established in Poland under the Horizon 2020 program" under contract No. MEiN/2023/DIR/3797.

REFERENCES

[1] A.M.Gusak, S.Abakumov. Modeling of pattern formation of the ordered intermediate phase during co-deposition of binary thin film. Cherkasy University Bulletin: Phys & Math Sciences, 2023, 1. 49-71. 10.31651/2076-5851-2023-49-71.

[2] Bandopadhyay, K., et al., Self-organized topological insulator heterostructures via eutectic solidification of Bi2Te3-Te. *Next Materials, 2024.* ***5****: p. 100252*

All-Dielectric Slotted-Disk Metasurface Sensor Based on quasi-Bound States in the Continuum

Jack Dobie[1,*], Oisin McCormack[1], Yongliang Zhang[1], Justin Schulz[1], A. Louise Bradley[1,*]

[1]School of Physics, Trinity College Dublin, Ireland

*Corresponding author: dobiej@tcd.ie, bradlel@tcd.ie

***Abstract*—An all-dielectric slotted-disk metasurface sensor supporting quasi-bound states in the continuum is presented. Symmetry-breaking enables high-Q resonance with strong, external E-field confinement, producing high refractive index sensitivity and figure-of-merit while offering a scalable platform for nanophotonic sensing application.**

***Keywords*— metamaterials, quasi-bound states in the continuum, metasurface, refractive index sensing.**

I. Introduction

Traditional biosensing methods frequently employ plasmonic nanostructures, utilizing localized surface plasmon resonances (LSPRs) for signal transduction. However, these structures often suffer from broad resonance peaks caused by inherent material losses, which lowers their quality factors [1].

The discovery of quasi-bound states in the continuum (q-BIC) resonances in dielectric metasurfaces presents interesting possibilities for sensing applications. q-BICs are sharp Fano resonant states with long optical lifetimes which can be manufactured and controlled by fabricating a small degree of asymmetry in the design of a nanoresonator.

In this work, we present a novel all-dielectric silicon metasurface design based on a slotted-disk nanostructure [2]. Compared to other designs, the slotted-disk is relatively easy to fabricate with enhanced control over the symmetry breaking, enabling very high Q-factors. As the slotted-disk is defined primarily by a single radius, whereas dimer-based metasurfaces specify complex positioning and ellipse requires both the minor and major axes.

This design exhibits a bulk refractive index sensitivity (S) of 450 nm/RIU in the IR spectrum, with a Q-factor $> 10^3$, E-field enhancement of 104 and a Figure-of-Merit (FOM) > 460. The quoted Q-factor is for a slot width of 100 nm offset by 10 nm from the center of the meta-atom. These dimensions fall well within fabrication limits of electron beam lithography and helium-ion lithography. The slot width can be further reduced with possibilities of Q $> 10^5$ achievable with the slotted-disk geometry. This work explores a new design space for advancing BIC-based nanophotonic sensors, which can be used for improved performance in real-world sensing applications.

II. Methods

Finite difference time domain (FDTD) simulations were performed using a commercial FDTD software (Lumerical Inc.) to numerically simulate the reflectance, transmittance and electric field maps of the metasurface using refractive index data. The transmittance spectra shown in Figure 3 can be described by the Fano formula. The Fano parameters are explicitly expressed through the material and geometrical parameters of the metasurface and dimensionless frequency [1].

$$T(\omega) = T_{bg}(\omega) + \frac{T_0}{1+q^2}\frac{(q+\bar{\omega})^2}{1+\bar{\omega}^2} \tag{1}$$

The dimensionless frequency is defined as $\bar{\omega} = \hbar(\omega - \omega_{\text{q-BIC}})/\gamma_{\text{q-BIC}}$, where $\omega_{\text{q-BIC}} = 2\pi c/\lambda_{\text{q-BIC}}$. Here, $\gamma_{\text{q-BIC}}$ denotes the half-linewidth of the q-BIC resonance, q is the Fano parameter, and c represents the speed of light in vacuum. The terms T_{bg} and T_0 correspond to the background contribution from non-resonant modes to the amplitude of the resonant peak and the offset, respectively.

Sensitivity is defined as $S = \Delta\lambda_{\text{res}}/\Delta n$, where $\Delta\lambda_{\text{res}}$ is the resonance shift induced by a refractive-index change Δn. The figure of merit is $\text{FOM} = S/\text{FWHM}$, with FWHM the resonance linewidth.

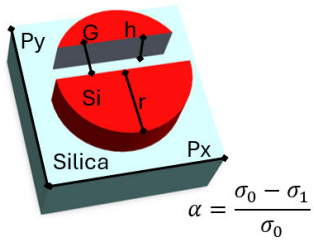

Fig. 1. Schematic of the Si slotted-disk meta-atom on a SOI (SiO_2) substrate. The parameters shown are the width of the slot, G, the radius of the disk, r, the periodicity of the meta-atom in the x and y directions, p_x and p_y, respectively and the height of the disk, h. The array of meta-atoms produces a metasurface that supports a q-BIC resonance. σ_0 and σ_1 are defined as the area of the larger and smaller hemispheres of the disk, respectively, and α is the asymmetry parameter.

III. Results and Discussion

A schematic diagram of the all-dielectric Si slotted-disk meta-atom can be seen in Figure 1, defining the unit cell of the metasurface with periodicity p_x and p_y in the x and y directions, respectively. The unit cell is composed of a cylinder of height h and radius r, with an off-center slot with width G, creating 2 asymmetrical hemispheres. The crucial structural

feature responsible for the realization of the q-BIC resonance is the off-center slot with width, G, between the hemispheres of the disk, as indicated in Figure 2 where the E-field map is shown. As seen in Figure 3, by tuning G, the FWHM of the resonance can be controlled, with a minimum full width at half maximum (FWHM) of 0.12 nm obtained with $r = 300$ nm, $G = 100$ nm, $p_x = p_y = 800$ nm and $h = 220$ nm, indicated by the dark blue line at 1539 nm in Figure 3 achieving a Q-factor $>$ 12,800.

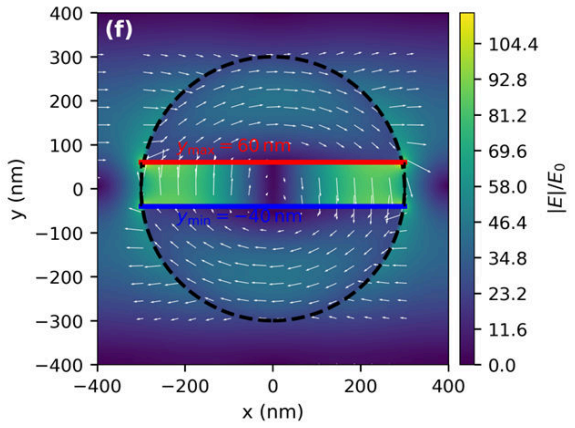

Fig. 2. Simulated electric field enhancement of the resonator, simulating the q-BIC resonance shown in Figure 3 located at 1544 nm with the positions of y_{min} and y_{max} shown.

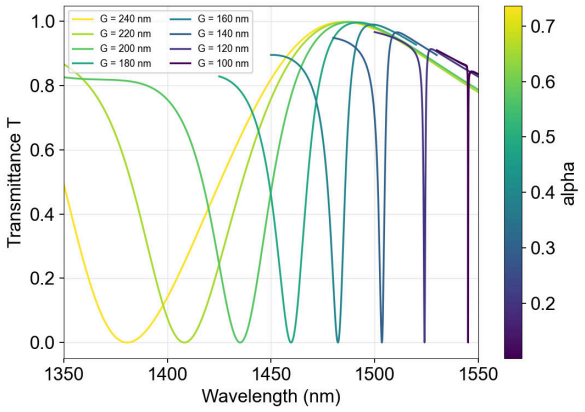

Fig. 3. Transmission spectra for a range of slot widths, with with one slot edge fixed at -40 nm and $r = 300$ nm, $p_x = p_y = 800$ nm and $h = 220$ nm.

The relationship between the slot width, the BRIS, the FOM, and Q-factor of the resonance was explored. It was shown that as the slot width increases, the sensitivity increases along with the FOM while a decrease in the Q-factor is observed. This is expected due to the $Q \propto \alpha^{-2}$ for q-BIC resonances. The sensitivity of the sensor was found to increase with the slot width, due to the increase in volume of the region of enhance dielectric field within the slot.

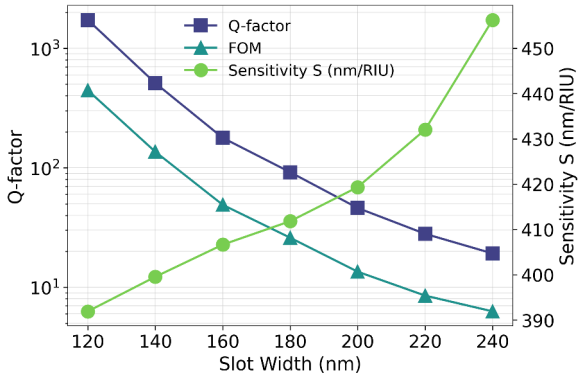

Fig. 4. FDTD simulations showing the FOM and sensitivity as a function of the slot width with $r = 300$ nm, $G = 120$ nm, $p_x = p_y = 800$ nm and $h = 220$ nm with the minimum of the slot kept at -40 nm.

TABLE I
SELECTED SILICON-BASED METASURFACE SENSORS WITH HIGH-PERFORMANCE SENSING METRICS.

Structure	Res.	λ (nm)	FOM	S (nm/RIU)
Dual Ellipses [3]	q-BIC	700–900	72.2	122
Chiral q-BIC [4]	q-BIC	940	163	48
Eight-Shaped [5]	Fano	1350–1550	444	404
Slotted Square [6]	q-BIC	1557	117000	58.9
This Work	q-BIC	1350–1550	450	460

IV. Conclusion

We have demonstrated an all-dielectric metasurface sensor which employs a q-BIC resonance. Table 1 shows a comparison between high performance silicon metasurfaces and our metasurface in a similiar spectral region. The Si slotted-disk metasurface shows the highest reported sensitivity and FOM for the wavelength range/

Acknowledgments

The authors acknowledge financial support by Research Ireland under grants 12/RC/2276_P2, SFI-21/FFP-P/10187 and 12/RC/2278_2. K. M. acknowledges the funding under PI-ADS: 18/EPSRC-CDT/3585 and acknowledges funding from the Marie Sklodowska Curie SPARKLE fellowship.

References

[1] J. Min, M. Nothing, B. Coble, et al., "Integrated biosensor for rapid and point-of-care sepsis diagnosis," *ACS Nano* 12, 3378–3384 (2018).
[2] O. McCormack, J. Dobie, et al, "Silicon nitride slotted-disk metasurfaces for refractive index sensing based on quasi-bound states in the continuum," *Opt. Express* 33, 49845-49859 (2025)
[3] W. Chen, M. Li, W. Zhang, and Y. Chen, "Dual-resonance sensing for environmental refractive index based on quasi-BIC states in all-dielectric metasurface," *Nanophotonics* 12, 1147–1157 (2023).
[4] J. Li, Q. Duan, X. Dong, et al., "Chiral quasi-bound states in the continuum for refractive-index sensing in metasurfaces," *Phys. Rev. Appl.* 22, 044035 (2024).
[5] X. Zhang, J. Li, C. Liu, et al., "Research on an all-medium two-parameter metasurface sensor based on fano resonance," *Biomed. Opt. Express* 16, 2415–2429 (2025).
[6] 21. J. F. Algorri, F. Dell'Olio, P. Roldán-Varona, et al., "Analogue of electromagnetically induced transparency in square slotted silicon metasurfaces supporting bound states in the continuum," *Opt. Express 30*, 4615 (2022).

Mid-Infrared Metasurfaces for Exosome-Based Liquid Biopsy in Hepatocellular Carcinoma

R. Di Santo [1,2], B. Niccolini [1], F. Di Giacinto [1,2], M. De Spirito [1], R. Polito [3], A. Notargiacomo [3], M. Ortolani [4,3], A. Di Gaspare [5], F. Pizzolante [6], G. Ciasca [1,*],M. Pea [3,*]

[1] Dipartimento di Neuroscienze, Sezione di Fisica, Università Cattolica del Sacro Cuore & Fondazione Policlinico Universitario "A. Gemelli", IRCCS, Rome, Italy

[2] Dipartimento di Scienze della Vita, della salute e delle Professioni sanitarie, Link Campus University, Rome, Italy

[3] Istituto di Fotonica e Nanotecnologie, Consiglio Nazionale delle Ricerche IFN-CNR, Via Del Fosso Del Cavaliere 100, 00133, Rome, Italy

[4]Department of Physics, Sapienza University of Rome, Piazzale Aldo Moro 2, 00185, Rome, Italy

[5]NEST, CNR - Istituto Nanoscienze and Scuola Normale Superiore, Piazza San Silvestro 12, 56127, Pisa, Italy

[6] CEMAD, Medical and Surgery Sciences, Fondazione Policlinico Universitario A.Gemelli IRCCS, Università Cattolica del Sacro Cuore,

Rome, Italy

*Corresponding author: Gabriele.Ciasca@unicatt.it, marialilia.pea@cnr.it

***Abstract*—We propose a double-resonant mid-infrared plasmonic metasurface for label-free spectroscopic analysis of circulating exosomes in hepatocellular carcinoma. The device is designed to enhance protein vibrational bands and to provide a refractive-index-sensitive readout, as a candidate characterization module for a future exosome-based liquid biopsy platform.**

***Keywords*— plasmonic metasurfaces, mid-infrared spectroscopy, extracellular vesicles, exosomes, liquid biopsy, hepatocellular carcinoma.**

I. Introduction

Mid-infrared spectroscopy provides label-free access to vibrational fingerprints of nucleic acids, proteins, and lipids, making it highly attractive for biosensing and cancer diagnostics. Its use in complex biofluids, however, is limited by weak biomolecular absorption cross-sections and strong water background, which reduce sensitivity and restrict in-liquid measurements. Surface-enhanced infrared absorption using plasmonic metasurfaces has emerged as an enabling technology to overcome mid-infrared limitations, by exploiting lithographically defined metal nanoantennas to concentrate the electromagnetic field and amplify selected vibrational modes. In parallel, recent studies have demonstrated that similar double-resonant metasurface architectures can also be applied to real-time monitoring of live cells under drug treatment, further supporting their robustness and versatility. Extracellular vesicles (EV), and exosomes in particular, are nanoscale lipid vesicles secreted by most cell types that carry molecular cargo reflecting the physiological or pathological state of their parental cells. They are abundantly released in blood and other fluids and are increasingly recognized as promising biomarkers for liquid biopsy in oncology, including hepatocellular carcinoma.

In this work we present a double-resonant gold nanoantenna metasurface tailored for mid-infrared characterization of circulating exosomes from hepatocellular carcinoma patients. We show how our nanoantenna based device enhances diagnostically relevant amide bands, provides a refractive-index-sensitive readout for monitoring immunocapture, and fits as the core characterization module of future multifunctional platform for exosome isolation and machine-learning-driven spectral classification

In a future implementation, this metasurface module could operate alone or downstream of an exosome isolation unit (e.g. ZnO-nanowire based microfluidic module) and be coupled to machine-learning analysis of mid-IR spectra for automated classification of healthy, cirrhotic, and HCC samples.

II. Methods

The sensing platform is based on a double-resonant gold nanoantenna array fabricated on CaF_2 and optimized for mid-IR operation in liquid. The chip is conceived for reflection measurements on a commercial FTIR spectrometer using back-side illumination: the mid-IR beam impinges on the dry

side of the CaF_2 substrate at an oblique angle and is reflected by the nanoantennas in contact with the liquid sample. This geometry minimizes direct interaction with water, maintains exosomes in a hydrated environment, and enables large-area probing of the metasurface.

Gold nanoantenna metasurfaces are patterned on a 1 mm-thick CaF_2 substrate by electron-beam lithography using a 300 nm thick PMMA resist layer. The unit cell of the pattern includes two parallel rod types: long rods ($L \approx 1.8$ μm) resonant in the Amide I–II region, and shorter rods ($L \approx 1.0$ μm) responsible for a sharp reflectance dip around 1900 cm^{-1}. After PMMA exposure and development, a 10 nm Cr / 80 nm Au bilayer is deposited by e-beam evaporation and lifted off, leaving the rod array directly on CaF_2. Final cleaning involves organic solvent rinses and brief oxygen plasma to remove resist residues. Exosomes are isolated from plasma of healthy, cirrhotic, and HCC subjects using polymer-based precipitation and are characterized by TEM and NTA to confirm vesicle size and morphology. The gold metasurface is functionalized with a biotin-PEG thiol layer, NeutrAvidin, and biotinylated antibodies to enable selective immunocapture of exosome subpopulations directly on the antennas.

III. Results and Discussion

Mid-IR analysis of extracellular vesicles isolated from plasma of cirrhotic and HCC patients evidences that discriminative information is concentrated in the vesicle fraction rather than in bulk plasma.

The double-resonant nanoantenna architecture is designed to enhance exactly these diagnostically relevant regions and to introduce an additional refractive-index-sensitive observable. Long antennas are tuned to the Amide I–II bands, maximizing near-field enhancement for protein-related vibrations, while shorter antennas generate a sharp reflectance dip around 1900 cm^{-1} in a spectral interval with negligible intrinsic biomolecular absorption. This configuration enables a dual-mode readout: i) enhanced vibrational absorption in the amide bands, suitable for extracting spectral markers such as the 1538 cm^{-1} feature; ii) a mass- and refractive-index-sensitive shift of the reflectance dip, which can be used to monitor the extent and kinetics of exosome immunocapture on the metasurface. Our results show differences in EV-enriched samples between cirrhotic and HCC patients, revealing tumor-related changes and identifying key spectral targets.

In the context of the proposed platform, the metasurface and the EV measurements are therefore conceived as a single integrated system: EV spectroscopy defines the relevant bands for HCC vs cirrhosis discrimination, and the antenna design is optimized to amplify those bands and to add a quantitative surface-binding metric. Subsequent integration with dedicated isolation modules and machine-learning-based analysis is foreseen as a future development.

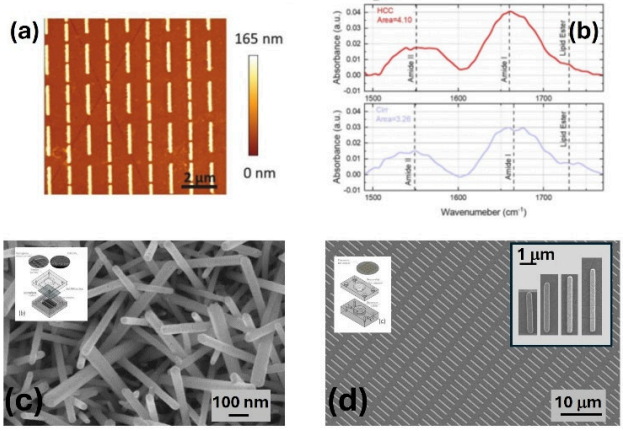

Fig. 1. (a) AFM image of double-resonant gold nanoantenna array on CaF_2. (b) Representative Amide I–II spectra of EV-enriched samples from cirrhotic (blue) and HCC (red) patients. (c) SEM image of ZnO nanowires used in the isolation module (shown in the inset), (d) SEM images of DNA/RNA-resonant nanoantennas, with the plasmonic characterization module shown in the inset.

IV. Conclusion

We have presented a design concept for a mid-infrared double-resonant plasmonic metasurface intended for label-free spectroscopic analysis of circulating exosomes in hepatocellular carcinoma. The device targets simultaneous enhancement of amide bands and refractive-index-sensitive monitoring of immunocapture on a commercial FTIR spectrometer.

In future developments, the double-resonant platform will be engineered to address both protein and DNA/RNA bands, to increase sensitivity towards tumour-specific molecular targets. Within this conceptual framework, the plasmonic metasurface is envisioned as the core characterization element of a modular platform that will also include a ZnO nanowire-based isolation/elution unit, essential to enrich and purify clinically relevant exosome subpopulations and to deliver them in a controlled manner to the metasurface, and machine-learning-assisted spectral analysis for exosome-based liquid biopsy.

Acknowledgments

This work is supported by PRIN 2022 project MUNE (Multifunctional Micro-Nanostructured Platform for Exosome-based Liquid Biopsy in Cancer Diagnosis, 2022E5J859).

References

[1] R. Di Santo et al., "Exploring novel circulating biomarkers for liver cancer through extracellular vesicle characterization with infrared spectroscopy and plasmonics," Analytica Chimica Acta, 1319, 342959,

[2] B. Niccolini *et al.*, "Dual-mode mid-infrared plasmonic metasurface for real-time label-free analysis of live cells," Talanta, 301, 129240, 2026

Colloidal lithography for correlated disorder light-trapping structures

Laura de Almeida[1,*], Jean-Baptiste Doucet[1], Guilhem Almuneau[1], Stéphane Collin[2,3], Inès Revol[1]

[1]LAAS-CNRS, Université de Toulouse, CNRS, 31400 Toulouse, France
[2]Centre for Nanoscience and Nanotechnology (C2N), CNRS, Université Paris-Saclay, 91120 Palaiseau, France
[3]Institut Photovoltaïque d'Ile-de-France (IPVF), 91120 Palaiseau, France
*Corresponding author: laura.de-almeida@laas.fr

***Abstract*—We demonstrate that, using colloidal lithography with carboxyl-functionalized polystyrene particles, we can control the correlations in the particle arrangement and tune the pseudo-period between 260 and 980 nm. Such correlated disordered nanostructures show promise in enhancing light scattering outside the escape cone and effectively trapping light in solar cells.**

***Keywords*— Colloidal lithography, correlated disorder, light trapping, self-assembly**

I. Introduction

Disordered photonic structures have emerged as a promising strategy to increase light trapping in ultrathin silicon solar cells [1]. Self-assembly processes such as colloidal lithography allow fabricating disordered structures on large surface areas. Previous works on PMMA (poly(methyl methacrylate)) [2] and PS (PolyStyrene) [3] particles have already shown homogeneous patterns with correlated disorder and studied how to vary the arrangement parameters. However, one aspect that has been overlooked in the literature is the impact of particles functionalization.

In this study, modifying the functionalization of the particle surface allows us to obtain an homogeneous arrangement for rather large nanoparticles (200 and 500 nm), while maintaining a simple process. We showed that using different strategies, we can tune the pseudo-periods between 260 nm and 980 nm, thereby opening the way to tailored optical properties for enhanced light-trapping in the visible and near-infrared range in a wide range of applications, and in particular solar energy conversion.. This tunability is achieved through a simple process based on PS particles and the control of particle and salt concentration. We discuss an in-depth investigation of the impact of experimental conditions on correlated disorder based on the pair correlation function and structure factor, which are directly related to the scattering optical properties.

II. Methods

A. Colloidal lithography:

A 0.2 wt% PDDA (poly(diallyl dimethylammonium chloride)) solution was deposited via dropcasting for 30 seconds, and then rinsed for 30 seconds on clean p-type silicon substrates. PS-Latex beads (0.2 wt%) were deposited using the same dropcasting method. Adsorption times were optimized based on bead diameter: 2 minutes for 0.2 µm beads and 7 minutes for 0.5 µm beads, following a protocol adapted from Hanarp et al. [4]. Before nitrogen drying, the sample was rinsed with boiling water for 1 minute, followed by an IPA (IsoPropyl Alcohol) rinse to reduce aggregation [5].

B. Image analysis

SEM (Scanning Electron Microscope) images are used to detect particle centers and diameters through custom Python-based image processing. We then calculated several metrics to analyze the particle arrangements (% aggregates, density of particles). We calculated the pair correlation function g(r) [6] to assess the pseudo-period of the particle arrangement. We used the plots of the static structure factor and its angular average [7] as qualitative tools to study the correlated disorder in the particle arrangement.

III. Results and Discussion

A. Functionalization of particle surfaces

Most studies on colloidal lithography use polystyrene particles with sulfate functionalization [4], [3]. In this study, we tested alternative functionalizations on the particle surface: carboxyl and CML.

Figure 1(a-c) shows the SEM images of the arrangement obtained with the three functionalizations used in our study, and the associated structure factor in Figure 1 (d-f). Firstly, we note that the CML (modified carboxylate) functionalization does not exhibit a correlated arrangement anymore, as observed in the SEM images. This is confirmed by the absence of the correlation ring found in sulfate et carboxyl functionalization, which we seek to preserve. The pseudo-periods of our two arrangements, calculated using the pair correlation function, are similar: 352 nm for the sulfate and 362 nm for the carboxyl. The main difference observed is the percentage of aggregates. The calculated aggregate percentage is 11% for the arrangement with sulfate functionalization and 3.8% for carboxyl. Carboxyl functionalization therefore allows us to obtain more homogeneous and reproducible arrangements.

B. Tuning the pseudo-period

As highlighted in Figure 2(c), we investigated different strategies to tune the pseudo-period on a wide range of values.

Fig. 1. Impact of surface functionalization on the arrangement obtained by colloidal lithography (a-c) SEM images of the arrangement obtained with (a) sulfate, (b) carboxyl and (c) CML particles functionalization. (d-f) 2D-plots of structure factor for the arrangement obtained with (a) sulfate, (b) carboxyl and (c) CML particles functionalization.

Fig. 2. Impact of tuning the pseudo-period with addition of ions or dillution of the colloidal suspension. (a-b) SEM images of the arrangement obtained with 200 nm diameter carboxyl-functionalized particles (a) with the addition of NaCl and (b) dilution of the colloidal suspension. (c) Pair correlation function of different arrangements made with 200 and 500 nm particles, with the addition of NaCl, or with dilution of the colloidal suspension.

On one hand, the addition of NaCl to reduce the pseudo-period, studied for sulfate functionalization, has not been studied for carboxyl functionalization. We prepared samples with an addition of 4mmol/L and 40mmol/L of NaCl in the suspension of carboxyl-functionalised particles. In Figure 2 (a), the SEM image shows the arrangement obtained by adding NaCl (4 mmol/L) to the colloidal suspension. Our results matched our expectations, with a clear reduction in the pseudo-period from 360 nm to 262 nm (with an addition of 40 mmol/L of NaCl).

On the other hand, we have investigated the dilution of the colloidal suspension as a way to increase the pseudo-period. We prepared 4 samples with 4 different colloidal concentrations ranging from 0.1 to 0.02 wt%. Figure 2 (b) shows the arrangement obtained with carboxyl-functionalized particles (200 nm diameter) at a concentration of 0.05 wt%. Through this dilution, we successfully increased the pseudo-period from 362 nm to 556 nm. However, this increase in pseudo-period was accompanied by a reduction in particle surface density, which may be detrimental for application to light trapping.

IV. Conclusion

In conclusion, we have demonstrated the potential of carboxyl surface functionalization of polystyrene particles, not previously reported in the literature, in order to obtain homogeneous arrangements. We demonstrated our ability to tune the pseudo-period of the particle arrangement between 260 nm and 980 nm, see Figure 2 (c), which allows for a wide range of possible applications. In this study, modifying the functionalization of the particle surface allows us to obtain an homogeneous arrangement for rather large particles (200 and 500 nm), while maintaining a simple process.

Acknowledgments

The authors acknowledge the support of the French Agence Nationale de la Recherche (ANR), under grant ANR-22-PETA-0005 (PEPR TASE, project IOTA). This work is also partly supported by LAAS-CNRS micro and nanotechnologies platform, member of the French RENATECH network.

References

[1] V. Depauw, C. Trompoukis, I. Massiot, W. Chen, A. Dmitriev, P. Roca i Cabarrocas, I. Gordon, J. Poortmans, "Sunlight-thin nanophotonic monocrystalline silicon solar cells", *Nano Futures*, 1 021001, 2017

[2] P. M. Piechulla, B. Fuhrmann, E. Slivina, C. Rockstuhl, R. B. Wehrspohn, and A. N. Sprafke, "Tailored light scattering through hyperuniform disorder in self-organized arrays of high-index nanodisks," *Advanced Optical Materials*, 9(17), 2021

[3] C. Trompoukis, I. Massiot, V. Depauw, O. El Daif, K. Lee, A. Dmitriev, I. Gordon, R. Mertens, and J. Poortmans, "Disordered nanostructures by hole-mask colloidal lithography for advanced light trapping in silicon solar cells" *Optics Express*, 24(2) :A191, 2015

[4] Hanarp, P. and Sutherland, D. and Gold, J. and Kasemo, B., "Control of nanoparticle film structure for colloidal lithography," *Colloids and Surfaces A: Physicochemical and Engineering Aspects*, 2003.

[5] Zemmour, C. and Torchinsky, I. and Breiman, N. and Oginets, A. and Vakahi, A. and Benny, O., “Enhanced control of particle distribution in colloidal lithography for Janus metal-capped nanoparticles,” *Colloids and Surfaces A: Physicochemical and Engineering Aspects*, v. 710, 136203, 2025.

[6] Terao, T. and Nakayama, T., ”Crystallization in quasi-two-dimensional colloidal systems at an air-water interface” *Physical Review E*, vol. 60, pp. 7157–7162, 1999

[7] Lalanne, P. and Chen, M. and Rockstuhl, C. and Sprafke, A. and Dmitriev, A. and Vynck, K., ”Disordered optical metasurfaces: basics, properties, and applications”, *Advances in Optics and Photonics*, 2025, Version Number: 3.

Meta-devices based on liquid photonic devices

Yin Zhou[1, *], Zihan Geng[2], Mu Ku Chen[1]

[1]Department of Electrical Engineering, City University of Hong Kong, Hong Kong, China
[2]Institute of Data and Information, Tsinghua Shenzhen International Graduate School, Tsinghua University, Shenzhen, China
*Corresponding author: yzhou695-c@my.cityu.edu.hk

***Abstract*—Metasurfaces demonstrate unprecedented advantages in multi-functional imaging, but their tunability is still severely limited in the visible band. Joint optimization of metasurfaces and liquid photonic devices can enable tunable, multifunctional imaging, opening new avenues for metasurface development.**

***Keywords*— metasurfaces, liquid photonic devices, tunability, imaging.**

I. Introduction

Three-dimensional imaging is a key technology for capturing the three-dimensional information of objects and is widely applied in fields such as machine vision, medical plastic surgery, and cultural heritage protection. Although the structured light projection based on the metasurface offers a large field of view and a large depth of field, its spatial sampling rate is fixed after fabrication and cannot be improved, which limits reconstruction resolution. To solve this problem, this work proposes a meta-device with tunable point-cloud projection, composed of an mmeta-lens array and a tunable focus objective lens, for collaborative optimization. This meta-device can dynamically adjust the distribution of the projected point cloud, thereby achieve multiple samplings of the object's spatial information and effectively improving the spatial resolution of three-dimensional reconstruction.

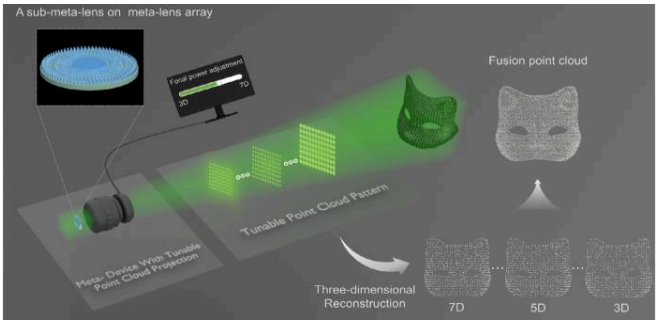

Fig. 1 Schematic of the proposed meta-device.

II. Methods

The proposed meta-device consists of two main parts: a diffraction-free meta-lens array that generates approximately 3600 focal points to form the initial points pattern; and a variable-focus projection objective based on a liquid lens, used to zoom and project the point cloud. By adjusting the optical power of the liquid lens, the point cloud pattern can continuously change radially, achieving multiple sampling of the object surface without introducing defocus blur. The system adopts a binocular stereo vision architecture, combining the Hough transform to extract point centers, epipolar-line constraint-based matching, and depth calculation based on the triangulation principle. Finally, it fuses the multi-focus point clouds to achieve high-density three-dimensional reconstruction.

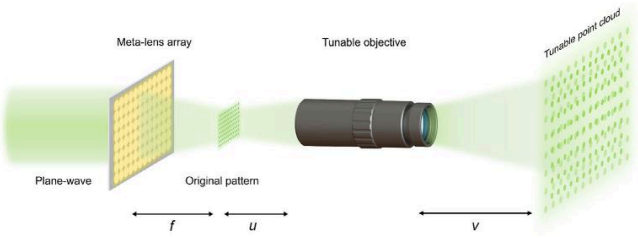

Fig. 2 Working principle of tunable point cloud projection based on the meta-device.

III. Results and Discussion

Figure 3 illustrates the experimental process of high-resolution depth estimation using a binocular stereoscopic imaging system based on meta-devices. Figure 3a is a schematic diagram of the experimental setup, including the laser illumination, the meta-device, and the binocular cameras. Figure 3b shows the images captured by the left and right cameras under different focal lengths. Figure 3c matches the point clouds in the left and right views through epipolar constraints. Figure 3d presents the contraction of the projected point cloud patterns and the extraction results of the center point as the optical focal length changes. Figure 3e compares the point cloud density of a single optical focal length with that after multi-focus fusion, verifying the effectiveness of the fusion strategy in improving spatial resolution.

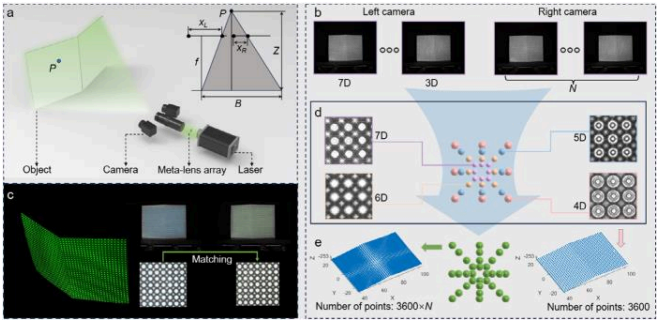

Fig. 3 High-resolution depth estimation of 3D objects.

To evaluate the depth perception capability of the proposed meta-device in three-dimensional imaging, this study first used a standard ceramic flat plate as the test object and conducted multi-position quantitative accuracy experiments, as shown in Fig.4. In the experiment, the plate was placed at four radial positions, and point cloud images at different optical focal lengths were collected using a binocular system, and depth information was calculated using the triangulation principle. The results showed that the reconstruction error distribution at each position was highly consistent, with root-mean-square errors (RMSEs) of 0.0365 mm, 0.0320 mm, 0.0353 mm, and 0.0356 mm, respectively, and an average accuracy of 0.035 mm. This high precision was mainly attributed to the system's longer baseline (128.8 mm) and its sub-pixel-level point-center extraction capability. Moreover, because the point cloud pattern remained focused across different optical focal lengths, the system could still stably output high-precision depth information while maintaining a large depth-of-field characteristic, verifying its consistent and reliable imaging performance across the full field of view.

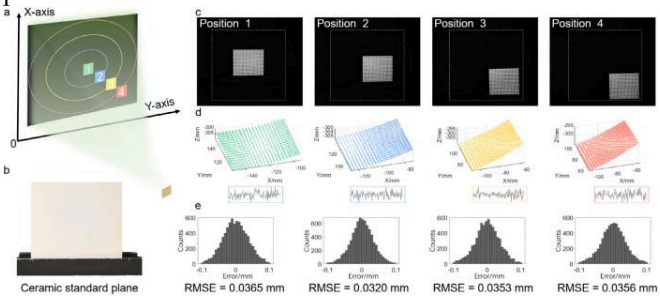

Fig. 4 3D imaging of a standard ceramic plate at four positions.

To further verify the improvement in spatial resolution from adjustable-focus projection, the experiment selected complex-shaped head portrait sculptures as test objects, as shown in Fig. 5. By adjusting the liquid lens's optical power, the system successively collected point clouds at multiple focal states and merged them into a high-density point cloud model. The experimental results showed that the point cloud in a single optical power could only reconstruct the rough outline of the object, with a large amount of surface details missing; while after fusing multiple optical power point clouds, the model details were significantly enhanced, especially in areas such as facial contours and hair textures, showing a higher geometric fidelity. Taking the head portrait sculpture as an example, the point cloud density increased to 3600×17 points, and the spatial sampling rate increased by approximately 17 times.

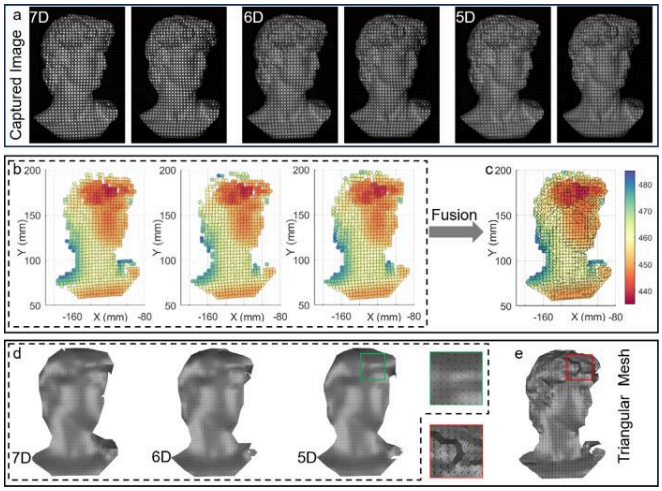

Fig. 5 3D reconstruction results of the head statue.

IV. Conclusion

We present a tunable point-cloud-projection meta-device, designed collaboratively as a meta-lens array and a liquid lens. It achieves high-resolution three-dimensional imaging without mechanical movement, wide spectral adaptation, and large depth of field. The system maintains a small footprint while significantly improving spatial and depth resolution, achieving a reconstruction accuracy of 0.035 mm. It provides a new technical path for fields such as augmented reality, face recognition, and human-computer interaction.

Acknowledgments

This work is supported by the Guangdong Basic and Applied Basic Research Foundation [2025A1515011846], University Grants Committee / Research Grants Council of the Hong Kong Special Administrative Region, China [CRF Project: C5031-22G, GRF Project: CityU11310522; CityU11300123], City University of Hong Kong [Project No. 9610628], the Shenzhen Research Institute, City University of Hong Kong [R-IND27901].

References

[1] Y. Zhou, Z. Chen, J. Cheng, Q. Zhang, Z. Geng, Z. Wu, & M. K. Chen, "High - Resolution 3D Imaging with Tunable Point Cloud Projection Based on Meta - Device," Laser & Photonics Reviews, 20(2), e01327, 2026.

[2] Y. Zhou, L. Li, J. Zhang, J. Cheng, X. Liu, Y.Gao, Z. Geng, L. Li & M. K. Chen, "Meta - Device for Field - of - View Tunability via Adaptive Optical Spatial Differentiation," Advanced Science, 12(9), 2412794,2025.

Breaking Reciprocity with Self-Oscillators

Alexander K. Stoychev[1,*], Ulrich Kuhl[1,2], Nicolas Noiray[1,*]

[1]ETH Zürich, Department of Mechanical and Process Engineering, CAPS, 8092 Zürich, Switzerland
[2]Université Côte d'Azur, CNRS, Institut de Physique de Nice (INPHYNI), 06200, Nice, France
*Corresponding authors: astoychev@ethz.ch; noirayn@ethz.ch

***Abstract*—We demonstrate nonreciprocal acoustic scattering by using weakly nonlinear self-oscillators whose internal synchronization state controls the system behavior, without bias, modulation, or strong nonlinearity. The meta-atom scattering is modeled by modified nonlinear coupled mode theory and validated experimentally. A two meta-atom unit cell yields directional transmission and reflection.**

***Keywords*— acoustic scattering, synchronization, limit cycle.**

I. Introduction

Reciprocity in passive linear wave media dictates that source and receiver are interchangeable under the assumptions of (microscopic) time-reversal symmetry and time-invariance, implying that an unidirectional transmission (e.g. diodes, insulators, circulators, etc.) requires bias or nontrivial material properties. Specific strategies to break reciprocity have been classified [1] into: (i) momentum bias (breaking time-reversal) [2], (ii) spatio-temporal modulations (breaking time-invariance) [3], and (iii) structural asymmetry with nonlinearity (breaking linearity) [4].

We propose a fundamentally different approach (Fig. 1), which relies on weakly nonlinear self-oscillators and their internal synchronization state rather than bias, spatio-temporal modulation, band topology, or conventional nonlinearity. Specifically, we employ autonomous, saturable-gain elements, whose individual steady state is a stable limit cycle emitting a single dominant frequency, which can be phase- and frequency-locked by an external drive [5], or another such element [6], inside a subset of amplitude–frequency space (i.e., the synchronization region or Arnold tongue [7, Chap. 3.1.2]).

Crucially, the two self-oscillators do not need to be precisely adjusted, it is sufficient that the driving frequency-amplitude pair is in the range of the joint synchronization region, and importantly, the self-oscillators lock to the injected signal, hence, phase relations are fixed. This mechanism is generic to systems supporting weakly nonlinear limit cycles and is compatible with the modified temporal coupled mode theory (TCMT) developed next.

II. Results

A nominally stable shear layer is able to amplify acoustic perturbations at certain frequencies and the coalescence of the Helmholtz mode with this amplifying frequency range is the physical mechanism driving the self-sustained cavity oscillations in our system [Fig. 1(a)]. However, this behavior eventually saturates due to nonlinear effects and the systems flips from finite linear gain at low amplitudes to finite linear loss at high ones. To model this phenomenon we utilise a saturable gain given by $(1+a^2)^{-1}$, hence, the nonlinear temporal coupled mode theory (TCMT) describing the scattering at a single meta-atom reads [5]

$$\frac{\mathrm{d}a}{\mathrm{d}\tau} = \left(i\frac{1-\Omega^2}{2\Omega} + \frac{\mu}{2}\frac{1-|a|^2}{1+|a|^2}\right)a - \frac{i}{2\Omega}\left\langle\kappa\middle|s_j^+\right\rangle , \tag{1}$$

$$\left|s_k^-\right\rangle = \left|s_j^+\right\rangle S_{kj} + |\kappa\rangle\, a\,, \tag{2}$$

where $\mathrm{d}/\mathrm{d}\tau$ represents the derivative with respect to time, normalized by the self-oscillation frequency $\tau = f_0 t$, i denotes the imaginary unit, and $a = A\exp i\varphi$ is the complex envelope of the normalized limit cycle [normalized pressure inside the whistle in Fig. 1(a)]. Additionally, μ incorporates the radiation and viscous losses, $\langle\kappa| = \kappa\,\langle 1| + \kappa\,\langle 2|$ stands for the coupling matrix and $\left|s_j^+\right\rangle = s\,|j\rangle\cos\Omega\tau$ represents the injected signal,

Fig. 1. Schematic representation of (a) the experimental setup and (b) the scattering process of a single meta-atom. The (acoustic) limit cycle is implemented as a whistle, which is arranged as a side branch of a one dimensional waveguide. The latter results in a fully transmissive direct process.

Fig. 2. Scattering matrix of (a) the passive resonator and (b) the (reciprocal) self-oscillating meta-atom. Markers represent experimental measurements and lines are predictions of Eqs. (1)–(2). Blue and red colors correspond to transmission and reflection, respectively. Note that the behavior transitions from fully transmissive in the passive case (a) to fully reflective when waves are scattered by the limit cycle (b).

Fig. 3. Schematic representation of (a) the experimental setup and (b) the scattering process of the unit cell consisting of two coupled nonlinear self-oscillators. The (acoustic) limit cycles are arranged as side branches of a one dimensional waveguide and are separated by approximately quarter of a wavelength. The fully transmissive direct process in combination with a relative phase shift of about $\pi/2$ between them results in unidirectional radiation. The phase shift can be controlled by tuning the air flows $\dot{Q}_1$ and $\dot{Q}_2$.

with s being the normalized magnitude and $\Omega = f/f_0$ the ratio of injected to self-oscillation frequency. $\mathbf{S}$ denotes the (reciprocal) scattering matrix of the direct process [cf. Fig. 1(b)], with S_{11} and S_{21} being reflection and transmission, respectively.

Note that Eqs. (1)–(2) are evolving in a time dependent reference frame, and contain terms deviating from classical temporal coupled mode theory. Specifically, we perform asymptotic averaging in a coordinate system moving in-phase with the incident wave, i.e., $|s^+\rangle = |1\{2\}\rangle\, s$ with $s = \text{const}$, which introduces an asymmetric detuning term, $j(1-\Omega^2)/2\Omega$, and multiplicative forcing factor, $j/2\Omega$ [5]. With the aforementioned modifications we can qualitatively and quantitatively capture the physical processes involved as shown in Fig. 2.

Next we introduce a second self-oscillator, and as a consequence of the mutual synchronization between the two the scattering behavior is governed by the relative phase of the locked limit cycles (Fig. 3). In particular, by separating the whistles by about quarter of a wavelength [Fig. 3(a)] and detuning them via the air flows $\dot{Q}_1$ and $\dot{Q}_2$ as to achieve roughly $\pi/2$ phase difference, we establish a synchronization state heavily favoring one of the propagation directions. Specifically, since the physical separation introduces a $\pi/2$ phase delay, radiation from the limit cycle which is $\pi/2$ radians behind will accumulate a phase of π as it reaches its counterpart, hence, resulting in destructive interference in this direction. Conversely, the self-oscillator which is $\pi/2$ radians ahead will get delayed by quarter of a cycle as it reaches its counterpart, resulting in a constructive interference in the opposite direction [Fig. 3(b)].

Since opposite injection ports can favor or resist the stable synchronization branch, waves incident from opposite directions experience dramatically different transmission, i.e., destructive interference in one direction yet not in the other [Fig. 4]. The resulting synchronization pattern governs the reciprocity breaking, where the bandwidth is set by the width

Fig. 4. Scattering matrix of the (nonreciprocal) self-oscillating unit cell. Markers represent experimental measurements with blue and red colors corresponding to transmission and reflection, respectively. Shaded regions indicate the synchronization bandwidth where high nonreciprocity is achieved. The data itself illustrates a highly nonreciprocal behavior, with superradiant transmission and negligible reflection in the direction favored by the synchronization sate and vice versa in the opposite direction. The depicted magnitude measurements reveal transmission ratios of up to $(|S_{21}|/|S_{12}|)_{\max} \approx 50$, which corresponds to $(|S_{21}|^2/|S_{12}|^2)_{\max} \approx 2500$ in terms of power.

of the joint synchronization region, while the weak nonlinearity filters out small perturbations. Even for the simple setup in Fig. 3(a) this effect readily achieves transmission ratios of up to $(|S_{21}|/|S_{12}|)_{\max} \approx 50$ in terms of magnitude, or alternatively $(|S_{21}|^2/|S_{12}|^2)_{\max} \approx 2500$ in terms of power.

Finally, we can model this behavior by a temporal coupled mode theory similar to Eqs. (1)–(2)

$$\frac{\mathrm{d}a_1}{\mathrm{d}\tau} = \left(i\Delta_1 + \frac{\mu}{2}\frac{1-|a_1|^2}{1+|a_1|^2}\right) a_1 - \frac{i}{2\Omega}\left\langle\kappa\middle|s_1^+\right\rangle + \frac{1}{2\Omega}\left\langle\kappa\middle|s_{\mathrm{in}}^-\right\rangle, \tag{3}$$

$$\frac{\mathrm{d}a_2}{\mathrm{d}\tau} = \left(i\Delta_2 + \frac{\mu}{2}\frac{1-|a_2|^2}{1+|a_2|^2}\right) a_2 - \frac{i}{2\Omega}\left\langle\kappa\middle|s_2^+\right\rangle + \frac{1}{2\Omega}\left\langle\kappa\middle|s_{\mathrm{in}}^+\right\rangle, \tag{4}$$

$$\left|s_1^-\right\rangle = \left|s_1^+\right\rangle S_{11} - i\left|s_{\mathrm{in}}^-\right\rangle S_{21} + |\kappa\rangle\, a_1\,, \tag{5}$$

$$\left|s_{\mathrm{in}}^+\right\rangle = \left|s_1^+\right\rangle S_{21} - i\left|s_{\mathrm{in}}^-\right\rangle S_{11} + |\kappa\rangle\, a_1\,, \tag{6}$$

$$\left|s_{\mathrm{in}}^-\right\rangle = \left|s_2^+\right\rangle S_{21} - i\left|s_{\mathrm{in}}^+\right\rangle S_{11} + |\kappa\rangle\, a_2\,, \tag{7}$$

$$\left|s_2^-\right\rangle = \left|s_2^+\right\rangle S_{11} - i\left|s_{\mathrm{in}}^+\right\rangle S_{21} + |\kappa\rangle\, a_2\,, \tag{8}$$

where a_1 and a_2 are the complex envelopes of the normalized pressure of the first and second meta-atom, respectively [Fig. 3]. Additionally, $\Delta_1 = (1-\Omega^2)/2\Omega$ and $\Delta_2 = (\delta - \Omega^2)/2\Omega$, with $\delta = f_{0,1}/f_{0,2}$ being the frequency detuning between the two self-oscillators.

III. Conclusion

We introduce a reciprocity-breaking mechanism for acoustic scattering that is rooted in the internal synchronization state of weakly nonlinear self-oscillators rather than external bias, spatio-temporal modulation, topological edge states, or strong nonlinearity, and which is fundamentally different from the synchronization topology approach reported in [6]. Using self-oscillating meta-atoms implemented as "whistling" side branches of a one-dimensional waveguide, we show that a modified nonlinear TCMT with saturable gain captures the experimentally observed scattering of a single reciprocal element. Subsequently coupling two such limit-cycle meta-atoms illustrates highly nonreciprocal transport, where mutual phase locking sets a stable relative phase that, together with a quarter-wavelength separation, enforces constructive interference in one propagation direction and destructive interference in the other. The resulting unit cell exhibits strongly asymmetric transmission and reflection over a bandwidth governed by the joint synchronization region, while remaining robust to small perturbations due to the weakly nonlinear, saturated dynamics. These results establish synchronization as a generic and tunable route to nonreciprocal acoustic devices and provide a predictive TCMT framework for scaling toward more complex active metamaterial architectures.

References

[1] H. Nassar, B. Yousefzadeh, R. Fleury, M. Ruzzene, A. Alu, C. Daraio, A. N. Norris, G. Huang, and M. R. Haberman, "Nonreciprocity in acoustic and elastic materials," *Nature Review Materials,* vol. 5(9), p. 667–685, 2020.

[2] R. Fleury, D. L. Sounas, C. F. Sieck, M. R. Haberman, and A. Alu, "Sound isolation and giant linear nonreciprocity in a compact acoustic circulator," *Science,* vol. 343(6170), p. 516–519, 2014.

[3] Y. Wang, B. Yousefzadeh, H. Chen, H. Nassar, G. Huang and C. Daraio, "Observation of nonreciprocal wave propagation in a dynamic phononic lattice," *Physical Review Letters,* vol. 121(19), p. 194301, 2018.

[4] B. Liang, X. Guo, J. Tu, D. Zhang, and J. Cheng, "An acoustic rectifier," *Nature Meterials,* vol. 9(12), p. 989–992, 2018.

[5] A.K. Stoychev, X. Guo, U. Kuhl and N. Noiray, "Synchronization driven acoustics: The nonlinear scattering of a self-oscillating meta-atom," *Physical Review E,* pending production, arXiv:2508.14819, 2025.

[6] A.K. Stoychev, U. Kuhl and N. Noiray, "Synchronization driven reciprocity breaking," *arXiv preprint,* arXiv:2508.14810, 2025.

[7] A. Pikovsky, M. Rosenblum, and J. Kurths, *Synchronization: a universal concept in nonlinear science,* 1st edition, Cambridge, UK: Cambridge University Press, 2001.

Generalized Space-Time reconfigurable Metasurfaces in synthetic dimension

Yinglan Li[1*], Chengzhi Qin [1], Bing Wang[1] and Peixiang Lu[1]

[1]School of Physics and Wuhan National Laboratory for Optoelectronics and, Huazhong University of Science and Technology, Wuhan 430074, China.
[*]corresponding author: lylan@hust.edu.cn

Abstract: We implement a synthetic discrete photonic lattice based on a dual fiber loop system and construct dynamically reconfigurable temporal metasurface within this platform. By introducing electro-optic linear phase modulation at temporal interfaces, we experimentally realize discrete-light temporal refraction and perfect imaging. We further observe refraction and reflection in spatial and spatiotemporal metasurfaces, where phase gradients evolve in space or vary jointly in space and time.

Main results:

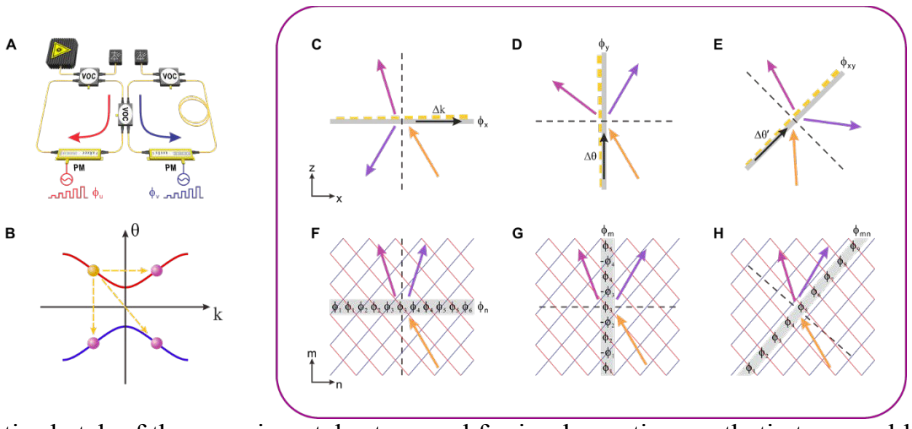

Fig. 1. A. Schematic sketch of the experimental setup used for implementing synthetic temporal lattice. **B.** Schematic diagram of the band structure. **C-E.** Refraction and reflection in the spatial coordinate system. **F-H.** Refraction and reflection in the spatiotemporal coordinate system.

As illustrated in Fig. 1, applying electro-optic linear phase modulation to the long and short fiber loops induces temporal metasurface in the synthetic temporal lattice, leading to the change in momentum within the Floquet bands. Similarly, spatial metasurface and spatiotemporal metasurface influence the evolution of the light beam through the tangential momentum generated at the corresponding interfaces.

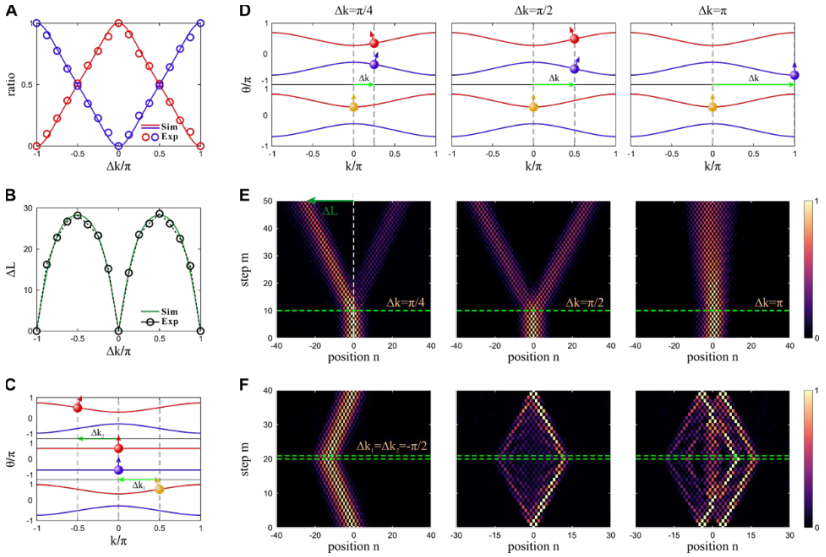

Fig. 2. A. Measured (circle) and theoretical (solid line) upper band (red) and lower band (blue) occupancies versus Δk as the wave packet crosses temporal metasurface. **B.** Measured (circle) and theoretical (solid line) splitting distance ΔL versus Δk as the wave packet crosses temporal metasurface. **C.** Band structures schematic of the sandwich configuration, the structure consists of two cascaded temporal metasurfaces and a flat band. **D,E.** Band structure schematic and the corresponding pulse intensity evolutions for $\Delta k = \pi/4$, $\pi/2$ and π. **F.** Measured pulse intensity evolutions for a wave packet incidence and n-site excitation.

Based on the discrete-time photonic lattice discussed above, we first introduce an electro-optic linear phase modulation $\phi(n) = \Delta k \cdot n$, which varies linearly with the space position "n", at a specific time step "m" to construct temporal metasurface. We observe discrete time refraction and reflection in a single-layer temporal metasurface, and then extend to double-layer configurations to realize negative refraction and perfect imaging.

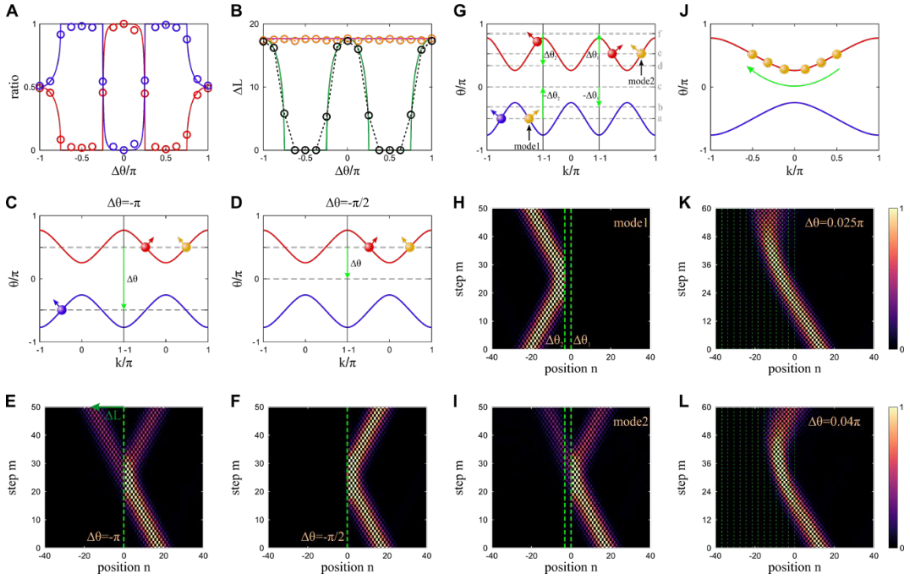

Fig. 3. A. Measured (circle) and theoretical (solid line) upper band (red) and lower band (blue) occupancies versus $\Delta\theta$ as the wave packet crosses spatial metasurface. **B.** Measured (circle) and theoretical (solid line) splitting distance ΔL versus $\Delta\theta$ as the wave packet crosses spatial metasurface. **C-F.** Band structure schematic and the corresponding pulse intensity evolutions for $\Delta\theta = -\pi$ and $-\pi/2$. **G.** Band structure schematic of two cascaded spatial metasurfaces. **H,I.** Measured pulse intensity evolutions for different incident modes. **J.** Band structure schematic of mode translation in multilayer spatial metasurfaces. **K,L.** Measured pulse intensity evolutions for $\Delta\theta = 0.025\pi$ and 0.04π at each layer of the metasurfaces.

We extend this concept to spatial metasurface, which is constructed by applying the gradient phase modulation $\phi(m) = \Delta\theta \cdot m$ in the time evolution direction. To be more precise, we create an equivalent temporal interface between $n = -1$ and $n = 0$. We experimentally demonstrate discrete spatial refraction and reflection in a single-layer spatial metasurface, followed by the implementation of multilayer configurations to achieve asymmetric transmission and beam bending.

Acknowledgements: This work is supported by the National Natural Science Foundation of China (No. U25D8017, No. 12374305, No. 12474381).

References

1. Yinglan Li *et al*., "Generalized Space-Time reconfigurable Metasurfaces in synthetic dimension," under preparation.
2. Nanfang Yu *et al*., "Light Propagation with Phase Discontinuities: Generalized Laws of Reflection and Refraction," Science 334, 333-337 (2011).

Inverse Designed Metasurfaces for Spatially Isolated Optical Skyrmions

Donghyun Park[1], Jinseong Bae[2], Jiwoo Kim[3], Sejeong Kim[4,*], Haejun Chung[1, 2, 3,*]

[1]Department of Artificial Intelligence Semiconductor Engineering, Hanyang University, Korea
[2]Department of Electrical Engineering, Hanyang University, Korea
[3]Department of Artificial Intelligence, Hanyang University, Korea
[4]Department of Electronic and Electrical Engineering, Sungkyunkwan University, Korea
[*]Corresponding authors: Sejeong Kim (sejeongk@skku.edu), Haejun Chung (haejun@hanyang.ac.kr)

***Abstract*—Optical skyrmions exhibit structured polarization textures, but extended side lobes hinder spatial isolation. We design a compact silicon metasurface generating a spatially confined skyrmion using a truncated Bessel target and full-wave adjoint optimization. The device achieves field overlap above >88% and a skyrmion number $N_{\mathrm{sk}} \approx 0.97$ at $\lambda = 1550$ nm.**

***Keywords*— optical skyrmion, metasurface, inverse design, adjoint optimization, topological photonics.**

I. Introduction

Optical skyrmions are vector fields carrying structured polarization textures that have attracted growing interest in topological photonics [1], [2], [4]. These textures have been observed in free-space beams, surface plasmon fields, and guided modes, offering a route toward compact polarization-based field encoding [1], [3], [4]. Dielectric metasurfaces are well suited to shape such textures with subwavelength control [13].

However, confining these textures within a clear radial boundary remains difficult. Many skyrmion generators rely on vortex-type modes, including Bessel beams, whose oscillating side lobes extend well beyond the main lobe [5]. The ambiguous boundary that results limits applications where multiple skyrmion channels must coexist without crosstalk.

Here, we design a metasurface that produces a skyrmion field confined within a spatial boundary. We define a target field that vanishes outside a chosen radius and optimize a compact silicon structure using full-wave adjoint methods [6], [7].

II. Methods

Figure 1(a) illustrates the simulation schematic. A normally incident Gaussian beam (beam waist $w_0 = 1.15\,\mu$m) at $\lambda = 1550\,$nm illuminates a silicon metasurface on a silica substrate. The metasurface consists of a $1\,\mu$m thick silicon layer patterned within a $6.0\,\mu$m diameter disk. The transmitted field is recorded on a focal plane located $1.55\,\mu$m from the metasurface exit.

The target field is composed of two circularly polarized Bessel-mode components of different orders. The RCP channel follows a zeroth-order Bessel profile J_0, exhibiting a bright central lobe with nearly uniform phase, while the LCP channel

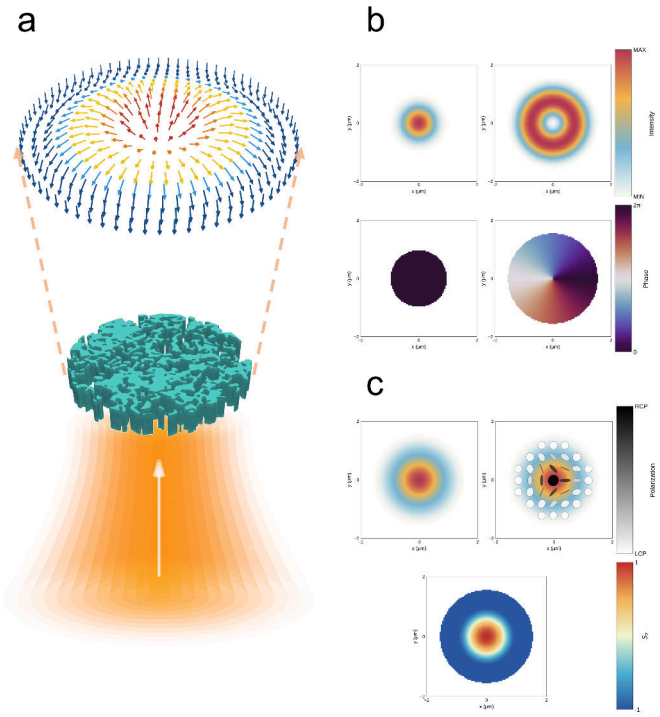

Fig. 1. Simulation schematic and desired field definition.

follows a first-order profile J_1, forming a ring-shaped intensity with a 0 to 2π azimuthal phase winding [Fig. 1(b)]. Both components share a numerical aperture $\mathrm{NA} = 0.61$, giving a radial wave vector $k_r = 2\pi\,\mathrm{NA}/\lambda \approx 2.47\,\mu\mathrm{m}^{-1}$. To enforce spatial isolation, both profiles are truncated by a radial mask at $r_1 = j_{1,1}/k_r \approx 1.55\,\mu$m, where $j_{1,1} \approx 3.832$ is the first zero of J_1. In polar coordinates (r, φ), the target reads

$$\mathbf{E}_{\mathrm{tar}}(r,\varphi) = \left[J_0(k_r r)\,\hat{\mathbf{e}}_R + J_1(k_r r)\,e^{i\varphi}\,\hat{\mathbf{e}}_L\right]\Theta(r_1 - r), \quad (1)$$

where $\hat{\mathbf{e}}_{R/L}$ are circular basis vectors and $\Theta(\cdot)$ is the Heaviside step function. This truncation removes the extended side lobes of ideal Bessel beams [5], confining both the amplitude and polarization texture within a compact disk.

From the coherent superposition of the two channels, we evaluate the total intensity, the polarization ellipse map, and the normalized spin density [Fig. 1(c)]

$$S_z = \frac{|E_R|^2 - |E_L|^2}{|E_R|^2 + |E_L|^2}, \tag{2}$$

which equals $+1$ for pure RCP and -1 for pure LCP. The polarization ellipse map visualizes the local circularity consistent with S_z, where the background shading reflects local intensity.

We quantify the topological quality through the skyrmion number [1], [3], [4]

$$N_{\mathrm{sk}} = \frac{1}{4\pi} \iint \mathbf{n} \cdot \left(\frac{\partial \mathbf{n}}{\partial x} \times \frac{\partial \mathbf{n}}{\partial y} \right) dx\, dy, \tag{3}$$

where $\mathbf{n}$ is the normalized Stokes vector.

The metasurface is optimized through three-dimensional FDTD simulations (Meep) [8] with the adjoint gradient method [9], [10]. The spatial resolution is 50 pixels/μm. The permittivity distribution is iteratively updated using the Adam optimizer, and fabrication constraints are enforced through spatial filtering and threshold projection with a minimum feature and gap size of 80 nm [11]. The objective function is a normalized overlap between the simulated and target fields evaluated inside the truncation radius r_1.

III. Results and Discussion

Simulation results show:

- Field overlap integral of 95 percent between the simulated output and the truncated Bessel target inside r_1 (Fig. 2)
- Skyrmion number $N_{\mathrm{sk}} \approx 0.97$, indicating near-unity topological purity
- Field leakage of 8 percent outside the region of interest ($r > r_1$), confirming effective spatial isolation

After optimization at $\lambda = 1550\,\mathrm{nm}$, the resulting metasurface is a compact, aperiodic silicon pattern in which the smallest features and gaps satisfy the 80 nm fabrication constraint. Figure 2(a) shows the top view of the optimized binary structure within the 6.0 μm diameter disk, where black regions denote silicon and white regions denote air. The pattern exhibits a spiral-like, freeform topology that is characteristic of adjoint-optimized metasurfaces and cannot be reduced to a periodic unit-cell description.

The simulated output field on the focal plane is decomposed into its circularly polarized components in Fig. 2(b). The RCP component displays a compact central intensity lobe with a nearly flat phase front, closely reproducing the target J_0 profile. The LCP component forms a ring-shaped intensity distribution with a clear 0-to-2π azimuthal phase winding, consistent with the target $J_1\, e^{i\varphi}$ profile. In both channels, the field amplitude drops rapidly near the designed boundary at $r_1 \approx 1.55\,\mu$m, with negligible intensity outside this radius compared to the central region. This confirms that the truncated target successfully suppresses the side lobes characteristic of ideal vortex-type modes [5].

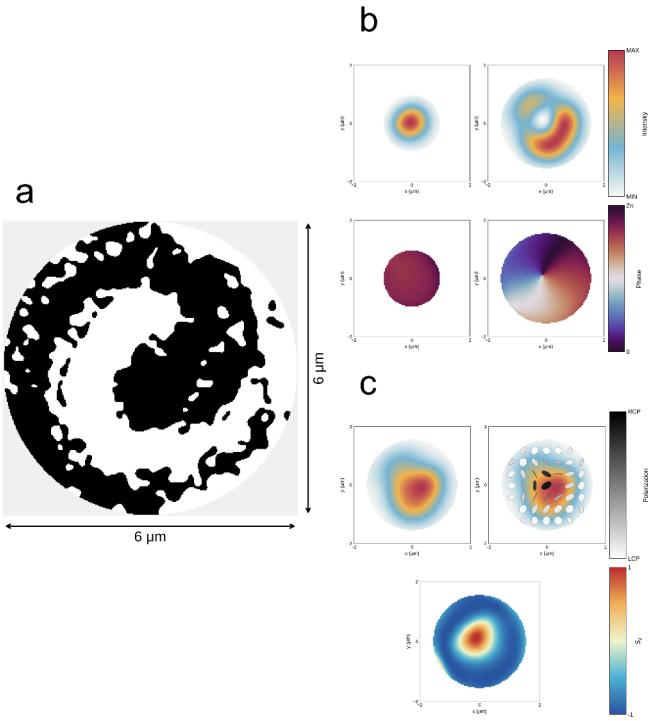

Fig. 2. Optimization result and output skyrmion characterization.

Figure 2(c) presents the skyrmion properties of the output field. The total intensity profile shows a well-confined distribution that vanishes smoothly at the target boundary, demonstrating effective spatial isolation. The polarization ellipse map reveals a continuous texture that winds from right-circular polarization at the center to left-circular polarization in the outer ring, reproducing the intended skyrmion topology. The normalized spin density S_z transitions from $+1$ (pure RCP) at the core to -1 (pure LCP) at the periphery, in agreement with the target defined in Eq. (1) and consistent with prior optical skyrmion reports [3], [4].

Although a strict radial truncation can in principle introduce diffraction artifacts, the freeform nature of the inverse-designed metasurface allows near-field coupling and multiple scattering to suppress the field outside the target radius while preserving fidelity inside the disk [6], [7].

IV. Conclusion

We have designed a compact silicon metasurface that generates a spatially isolated optical skyrmion with a well-defined edge. The design uses a truncated target built from two circularly polarized Bessel-mode components and is realized through full-wave adjoint optimization. The resulting 6.0 μm device achieves a field overlap above 88% and a skyrmion number of 0.97 within the target region. This approach may benefit dense photonic architectures such as optical communication arrays or holographic multiplexing, where crosstalk between neighboring channels must be minimized.

ACKNOWLEDGMENTS

This work was supported by the National Research Foundation of Korea (NRF) grant funded by the Korean government (MSIT) (RS-2024-00338048)(RS-2024-00414119), (RS-2025-25463760), and also supported by the Republic of Korea's MSIT, under the Global Research Support Program in the Digital Field program) (RS-2024-00412644) supervised by the IITP (Institute of Information and Communications Technology Planning & Evaluation) and also supported by Culture, Sports and Tourism R&D Program through the Korea Creative Content Agency grant funded by the Ministry of Culture, Sports and Tourism in 2024(RS-2024-00332210) and also Artificial Intelligence Graduate School Program (No. RS-2020-II201373, Hanyang University) supervised by the IITP, and under the artificial intelligence semiconductor support program to nurture the best talents ((IITP-(2025)-RS-2023-00253914) grant funded by the Korea government, and by the MSIT (RS-2025-02283217, RS-2025-25441264). This research was supported by Basic Science Research Program through the National Research Foundation of Korea(NRF) funded by the Ministry of Education(RS-2025-25432434).

REFERENCES

[1] S. Tsesses, E. Ostrovsky, K. Cohen, B. Gjonaj, N. H. Lindner, and G. Bartal, "Optical skyrmion lattice in evanescent electromagnetic fields," *Science*, vol. 361, pp. 993–996, 2018.

[2] L. Du, A. Yang, A. V. Zayats, and X. Yuan, "Deep-subwavelength features of photonic skyrmions in a confined electromagnetic field with orbital angular momentum," *Nat. Phys.*, vol. 15, pp. 650–654, 2019.

[3] Y. Shen, E. C. Martínez, and C. Rosales-Guzmán, "Generation of optical skyrmions with tunable topological textures," *ACS Photonics*, vol. 9, pp. 296–303, 2022.

[4] Y. Shen, Q. Zhang, P. Shi, L. Du, X. Yuan, and A. V. Zayats, "Optical skyrmions and other topological quasiparticles of light," *Nat. Photonics*, vol. 18, pp. 15–25, 2024.

[5] J. Durnin, J. J. Miceli, Jr., and J. H. Eberly, "Diffraction-free beams," *Phys. Rev. Lett.*, vol. 58, pp. 1499–1501, 1987.

[6] S. Molesky, Z. Lin, A. Y. Piggott, W. Jin, J. Vučković, and A. W. Rodriguez, "Inverse design in nanophotonics," *Nat. Photonics*, vol. 12, pp. 659–670, 2018.

[7] A. Y. Piggott, J. Lu, K. G. Lagoudakis, K. Petykiewicz, T. M. Babinec, and J. Vučković, "Inverse design and demonstration of a compact and broadband on-chip wavelength demultiplexer," *Nat. Photonics*, vol. 9, pp. 374–377, 2015.

[8] A. F. Oskooi, D. Roundy, M. Ibanescu, P. Bermel, J. D. Joannopoulos, and S. G. Johnson, "Meep: A flexible free-software package for electromagnetic simulations by the FDTD method," *Comput. Phys. Commun.*, vol. 181, pp. 687–702, 2010.

[9] C. M. Lalau-Keraly, S. Bhargava, O. D. Miller, and E. Yablonovitch, "Adjoint shape optimization applied to electromagnetic design," *Opt. Express*, vol. 21, pp. 21693–21701, 2013.

[10] T. W. Hughes, M. Minkov, I. A. D. Williamson, and S. Fan, "Adjoint method and inverse design for nonlinear nanophotonic devices," *ACS Photonics*, vol. 5, pp. 4781–4787, 2018.

[11] A. Y. Piggott, J. Petykiewicz, L. Su, and J. Vučković, "Fabrication-constrained nanophotonic inverse design," *Sci. Rep.*, vol. 7, Art. no. 1786, 2017.

[12] T. Ozawa *et al.*, "Topological photonics," *Rev. Mod. Phys.*, vol. 91, Art. no. 015006, 2019.

[13] N. Mata-Cervera, Z. Xie, C. Li, H. Yu, H. Ren, Y. Shen, and S. A. Maier, "Tailoring propagation-invariant topology of optical skyrmions with dielectric metasurfaces," *Nanophotonics*, vol. 14, pp. 4069–4077, 2025.

Optimization of Broadband Sound Absorber Consisting of Helmholtz Resonator Array

Jia-Hong Sun[1,*], Yu-Shao Chang[2], Jin-Chen Hsu[2]

[1]Department of Mechanical Engineering, Chang Gung University, Taiwan
[2]Department of Mechanical Engineering, National Yunlin University of Science and Technology, Taiwan
*Corresponding author: jhsun@mail.cgu.edu.tw

***Abstract*— This paper studied the optimization of Helmholtz resonator arrays to achieve broadband high absorption. The interaction between adjacent resonant cavities was studied using finite-element methods. Then genetic algorithm combined with the theoretical model helps optimize arrays of nine resonators. A 0.95 averaged absorption was observed in the 300-490 Hz range.**

***Keywords*— Acoustic metamaterials, Helmholtz resonator, genetic algorithm.**

I. Introduction

Acoustic Metamaterials (AMs) are materials consisting of designed artificial microstructures that can manipulate acoustic waves. AMs are currently studied to control the reflection, transmission, and absorption of sound [1]. Helmholtz resonators (HRs) are one of the commonly used microstructures in AMs [2-4]. An HR contains a cavity and a neck connecting the atmosphere and the cavity. By modifying the geometric sizes of HRs, the resonant frequency of air inside the cavity changes, and thus HR absorbs sound of different tones. HRs with different sizes may have the same resonant frequency, and a small HR can absorb low-frequency sound with a high absorption rate, so it has received attention and a lot of research in recent years.

In fact, an HR only has a narrow absorption frequency bandwidth; therefore, array structures were proposed to extend the high absorption frequency range. Designing a proper HR array actually consumes much computation. Thus, this paper studies the optimization of designing a wide-band and high absorption HR array.

II. Methods

We studied the absorption spectrum of and interaction between adjacent resonant cavities by finite-element method (FEM) firstly. A model of an HR in an impedance tube was defined in COMSOL as shown in Fig. 1(a). The HRs with an extended neck in Fig. 1(b) are used in this study. Then the absorbing coefficient α can be evaluated based on the instruction in ASTM-E-1050-08.

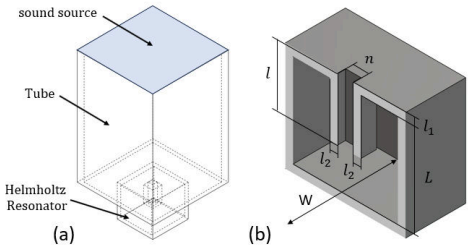

Fig. 1 (a) The model to evaluate absorption in FEM. (b) Geometry of the extended neck HR.

The theoretical resonant frequency of a single HR has be studied [2-3] and can be estimated as

$$f_r = \frac{c}{2\pi}\sqrt{\frac{A_0}{l_0 V_0}}, \tag{1}$$

where c is the sound velocity, A_0 the cross section area of the neck, l_0 the length of the neck, and V_0 the volume of the cavity.

Then the AM made of an HR array can be defined. Fig. 2 shows an example consisting of nine HRs to expand the absorption frequency range. To form a high-performance AM, these HRs should have discrete resonant frequencies in the high-absorption range.

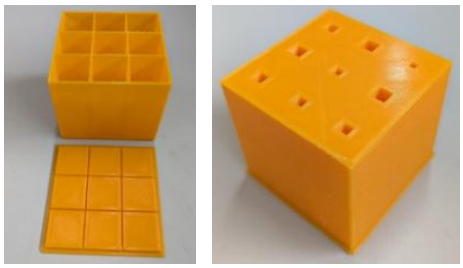

Fig. 2 The AM made of nine-HR array.

However, the adjacent resonant cavities interact with each other and change the spectrum. Therefore, the genetic algorithm was adopted to search for the design of high-performance HR arrays. To accelerate the process, we proposed a two-phase

optimization method. Firstly, we use Eq. (1) to build the cases of the initial population and find the geometric sizes of every single cavity in the array. Then the results in the first phase became the initial population of the nine-cavity array and the best design was evaluated at the end of the second phase. Finally, a specimen of an array with nine HRs was fabricated and the experimental absorption was measured to verify its performance.

III. Results and Discussion

In the FEM simulation, we observed that the interaction of two or more HRs is complex. There can be constructive or destructive results in the absorption spectrum. Therefore, optimization is a considerable issue in designing an HR-array AM.

In the optimization of the HR-array, we give the nine cavities the same W=19mm and L= 50 mm (defined as shown in Fig. 1(b)), and let the algorithm search for the best dimensions for l and n. The value of l is limited between 3 and 6 mm, and n is between 4 and 48mm. The requested high absorption range is 300-480 Hz. In the GA, the initial population is set as 40 after several trials. We first let GA optimize 18 dimensions synchronously. After 40 generations, the average absorption is 0.9, shown as the case "General GA" in Table 1. To accelerate the process, the two-phase GA as mentioned was executed. In the first phase, the target frequencies are 300, 310, 320, 340, 370, 400, 430, 360 and 490 Hz, respectively. All of them reached 0.85 absorption after 10 generations. Using the results as the initial population, the second phase GA gets a higher absorption of 0.95 after 5 generations. The total time is obviously less than the General GA. The final performance is shown in Fig. 3.

Table 1. Acceleration of two GA method

Method	Freq. (Hz)	$\alpha_{ave.}$	Time (h.)
General GA	300–480	0.9	189.8
Two-Phase GA	300–490	0.95	68.9

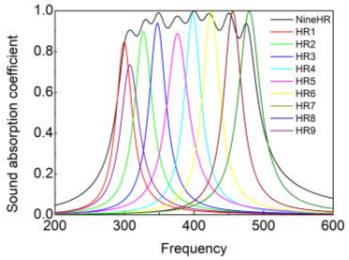

Fig. 3 The absorption spectrum of the HR array optimized by the two-phase GA. The absorption of individual HR are also shown.

After the GA optimization, we fabricated the specimen (as shown in Fig. 2) and then measured the absorbing coefficient α according to ASTM-E-1050-08. We also measured the absorption of a porous material, a sponge, with the same thickness. The spectra were plotted in Fig. 4, and the result shows a high absorption in a wide frequency range. Further, the thickness of this AM is only 1/20 of the wavelength of the lowest frequency sound.

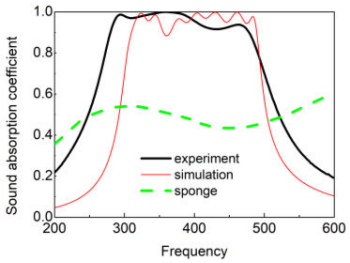

Fig. 4 The experimental result of HR array comparing to the numerical result.

IV. Conclusion

We have demonstrated the optimization of designing a broadband sound absorber based on Helmholtz resonators. The interaction of HRs in an array is complex, and thus an optimization algorithm is necessary. GA was adopted in this research, and further, a two-phase method was proposed and examined. The result shows more efficient optimization and a better design in a shorter time. This paper shows the potential of using an HR-array as an AM to absorb low-frequency noise. Future work will extend the design to minimize the thickness of AM devices.

Acknowledgments

The authors gratefully thank the financial support from National Science and Technology Council, Taiwan (NSTC 112-2221-E-182-057).

References

[1] B. Assouar, et al., "Acoustic metasurfaces," Nature Reviews Materials, Vol. 3, 460-472, 2018.
[2] Panton, R. L., and Miller, J. M., "Resonant frequencies of cylindrical Helmholtz resonators," The Journal of the Acoustical Society of America, 57, 1533–1535, 1975.
[3] Chanaud, R. C., "Effects of geometry on the resonance frequency of Helmholtz resonators," Journal of Sound and Vibration, 178, 337–348, 1994.
[4] Selamet, A., and Lee, I., "Helmholtz resonator with extended neck," The Journal of the Acoustical Society of America, 113, 1975–1985, 2003.

Causality and free-space propagation for the second quantization of radiative nanophotonic systems

Luke Hands [1,*], Ben Yuen[1], Angela Demetriadou [1]

[1]School of Physics and Astronomy, University of Birmingham, UK

*Corresponding author: lxh897@student.bham.ac.uk

***Abstract*—We introduce a new framework for quantizing radiative nanophotonic systems with arbitrarily positioned quantum emitters. The framework produces free-space propagation and decay terms, enforcing causality. Applying our framework to spherical nanoparticles captures position-dependent, non-Markovian dynamics, providing a complete picture of near- and far-field interactions essential for designing quantum nanophotonic devices.**

***Keywords*— Quantum Photonics, Non-Markovian Physics, Quantum Light-Matter Interactions.**

I. Introduction

Recent advances in quantum nanophotonics have enabled quantum light sources to be coupled to increasingly compact and complex radiative nanophotonic structures operating at deeply subwavelength scales. In the strong-coupling regime [1], these systems offer promising platforms for integrated quantum technologies operating under ambient conditions [2]. However, designing these systems requires precise control over radiative losses and open quantum dynamics. It is therefore crucial to develop an accurate theoretical understanding of radiative nanophotonic systems. However, the strongly radiative nature of these systems presents a fundamental challenge in obtaining a full description of the quantum dynamics that govern their light-matter interactions.

Recently [3], we introduced an *exact* and *complete* framework for describing the quantum dynamics of radiative nanophotonic systems using a second quantization approach that preserves the often-overlooked non-Markovian contributions. Here, we extend this framework to nanophotonic systems coupled to a Quantum Emitter (QE) positioned within the free space continuum, revealing additional terms corresponding to free-space propagation and decay. Our formulation enforces causality intrinsically, without requiring externally imposed conditions, which we demonstrate through its application to a nanophotonic system consisting of a spherical nanoparticle. By comparing emitter dynamics at different spatial positions relative to the nanoparticle surface, we show how these terms reduce to known expressions for free space decay while revealing tail effects characteristic of non-Markovian dynamics. Finally, we demonstrate how these additional terms impact the quantum dynamics of radiative nanophotonic systems.

II. Methods

Second quantization is a formalism which describes a system by treating its fields as fundamental degrees of freedom. Each mode is represented by creation and annihilation operators that account for discrete energy quanta allowing the full field to be described through their combination. In the case of a closed photonic system, a discrete set of well-defined normal modes can be constructed straightforwardly from boundary conditions. In an open system however, as energy can propagate to a continuum of far-field modes, there is additional complexity in defining a discrete and normalizable set of modes.

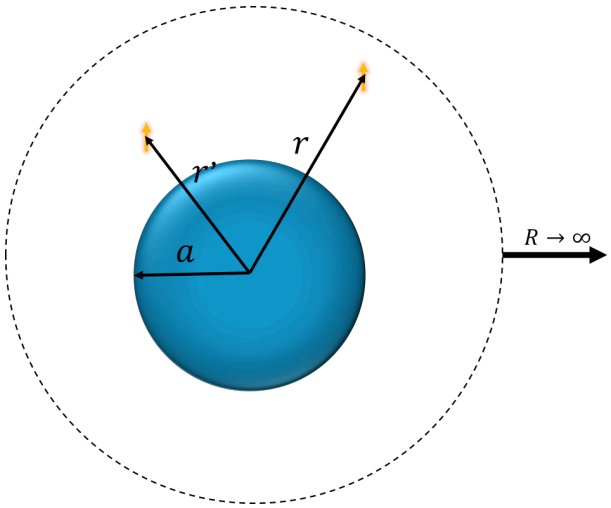

Fig. 1. The layout of the nanophotonic system studied. A spherical nanoparticle of radius a is coupled to a quantum emitter at position $\mathbf{r}$ and detector at $\mathbf{r}'$. The system is enclosed within a spherical boundary which is taken to infinity when convenient modeling radiative losses.

To quantize a radiative nanophotonic system, we start by considering its closed analogue. By enclosing it within a boundary shell matching its geometry, a set of well-defined normal modes, $\mathbf{u}_\xi(k, \mathbf{r})$ can be obtained. To recover a description applicable to an open, radiative system, we let the radius of the boundary tend to ∞. The continuum that arises as a result is handled by transforming [3], [4] the resulting continuous normal modes into a set of complex pseudomodes, $\mathbf{v}_{\xi n}(\mathbf{r})$,

using the generalized pseudomode transformation given (for a time τ) by:

$$\int_0^\infty dk\; k\rho(k)\mathbf{u}_\xi\left(k,\mathbf{r}\right)\mathbf{u}_\xi\left(k,\mathbf{r}'\right)e^{-ick\tau} = \Theta\left(\tau,\mathbf{r},\mathbf{r}'\right)\sum_n z_{\xi n}\mathbf{v}_{\xi n}\left(\mathbf{r}\right)\mathbf{v}_{\xi n}\left(\mathbf{r}'\right)e^{-icz_{\xi_n}\tau} + f_{fs}(\mathbf{r},\mathbf{r}';\tau), \quad (1)$$

where each of the (ξ, n)th pseudomodes resonates at complex frequency $z_{\xi n}$ and the $\Theta\left(\tau,\mathbf{r},\mathbf{r}'\right)$ term introduces a time delay on the pseudomodes ensuring causality. By solving the integral in Eq. 1, we now obtain an additional f_{fs} term when the quantum emitter is positioned away from the nanoparticle. This describes the free space propagation for times prior to light propagating from $\mathbf{r}$ to $\mathbf{r}'$ via the nanoparticle, ensuring causality is preserved for the QE positioned away from the surface.

This generalized transformation allows the full quantum dynamics of radiative system to be described through the coupled equations:

$$i\dot{\tilde{c}}_0(t) = \Theta_1\omega_{fs}\tilde{c}_0(t) + \Theta_2\sum_{\xi,n} e^{i(\omega_0 - cz_{\xi,n})t}\bar{g}_{\xi,n}\tilde{b}_{\xi,n} \quad (2)$$

$$i\dot{\tilde{b}}_{\xi,n}(t) = \bar{g}_{\xi,n}e^{-i(\omega_0 - cz_{\xi,n})t}\tilde{c}_0(t) \quad (3)$$

Here $\tilde{c}_0(t)$ is the scaled probability amplitude of the QE, oscillating at bare frequency ω_0. $\tilde{b}_{\xi,n}(t)$ is the probability amplitude of the (ξ, n)th pseudomode and $\bar{g}_{\xi,n}$ is the coupling strength between the QE and each pseudomode. The free space terms cause an additional complex contribution, ω_{fs}, which modifies the bare frequency of the QE, representing free space propagation and decay. The functions $\Theta_{1,2}$ correspond to Heaviside step functions that ensure relevant terms act either before or after sufficient time has occurred for light to propagate from $\mathbf{r}$ to $\mathbf{r}'$ via the nanoparticle. These terms enforce causality for our description and naturally arise from the solutions to Eq. 1.

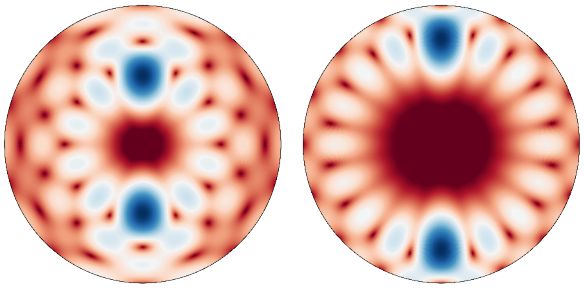

Fig. 2. The intensity of the $(5, 4)$ [left] and $(8, 3)$ [right] pseudomodes within the nanoparticle. Both resonate at the same frequency, w_r and their profiles show remarkable similarity to the normal modes of a spherical system demonstrating the close mapping between the two.

III. Results and Discussion

We apply our framework to a spherical silicon nanoparticle of radius $a = 1\mu m$ coupled with a two-level QE aligned radially so only the TE modes contribute. The quantum dynamics

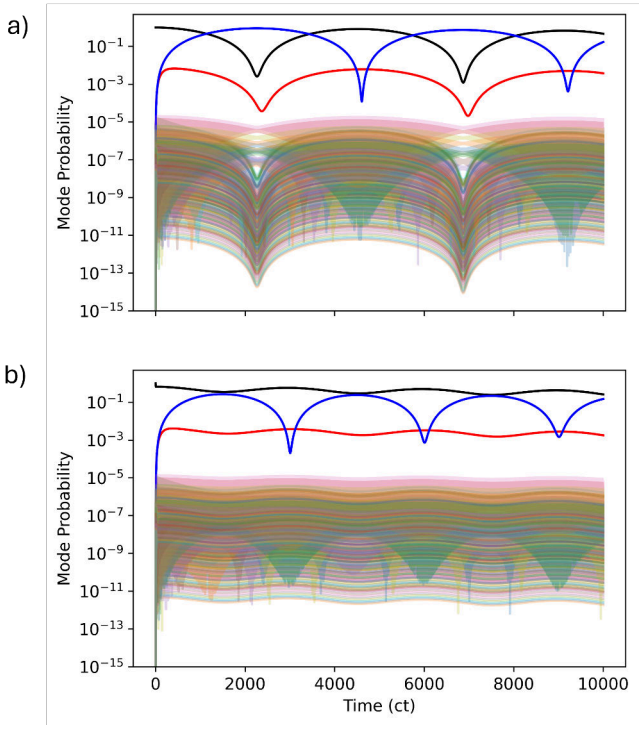

Fig. 3. The population dynamics for the spherical nanoparticle system with a QE placed (a) on the surface and at (b) $2\mu m$ from the $1\mu m$ silicon nanoparticle. The QE is tuned to be on resonance with the $(8, 3)$ mode with a dipole moment $d = 1000D$. The population of the QE is plotted in black, the resonant $(5, 4)$ and $(8, 3)$ pseudomodes in red and blue respectively, with fainter lines showing off resonant pseudomodes.

are calculated for various QE positions both on and away from the nanoparticle surface. Fig. 2 shows the normalized intensity profiles of two pseudomodes ($(\xi, n) = (8, 3)$ and $(5, 4)$) which share a similar resonant frequency, ω_r.

Evaluating Eq. 1 for arbitrary positions of $\mathbf{r}$ and $\mathbf{r}'$ results in solutions containing the previously unaccounted for free-space terms. To compute the pseudomode dynamics, we take the limit $\mathbf{r} \to \mathbf{r}'$ keeping the non-divergent components of f_{fs}. This results in terms that describe the free-space behavior of the QE. The imaginary component of these terms, $Im(f_{fs}) \propto \omega^3 d^2/3\pi c^3\hbar\varepsilon_0$ agrees with standard results predicted by other quantum theories for a dipole decaying in free space. Additionally, position dependent phase shifts of the probability amplitude oscillations arise, affecting the coupling between QE and pseudomodes. Additional tail effects broaden the interaction as light reaches the surface of the nanoparticle demonstrating the non-Markovian effects our framework preserves.

Fig. 3 shows quantum dynamics obtained using our generalized pseudomode framework for two different QE positions. For short times in 3b there is a strong initial decay, occurring before light can return information about the nanoparticle. In this scenario, the real part of f_{fs} shifts the frequencies, enhancing coupling to the radiative channels of the off resonant modes as can be seen. This same shift simultaneously

weakens coupling to the resonant modes resulting in the smaller oscillation amplitudes observed.

At longer times, the dynamics obtained for both QE positions exhibit both Markovian and non-Markovian behavior. The resonant $(8, 3)$ pseudomode exhibits out of phase vacuum Rabi-oscillations, a signature of non-Markovian dynamics, while the $(5, 4)$ pseudomode oscillates in phase with the QE reflecting Markovian behavior.

IV. Conclusion

We have demonstrated a generalized pseudomode framework for the exact second quantization of radiative nanophotonic systems with emitters placed at arbitrary positions. By applying our framework, we have shown it naturally accounts for causality through additional terms representing free space propagation and decay. Using this method, we obtain a *complete* picture of the near- and far-field quantum dynamics that incorporates overlooked non-Markovian effects.

References

[1] Chikkaraddy, R., de Nijs, B., Benz, F. et al. "Single-molecule strong coupling at room temperature in plasmonic nanocavities," *Nature,* 535, 127–130 (2016).

[2] Hu, S., Huang, J., Arul, R. et al." Robust consistent single quantum dot strong coupling in plasmonic nanocavities," *Nat Commun* 15, 6835 (2024).

[3] B. Yuen and A. Demetriadou., "Exact Quantum Electrodynamics of Radiative Photonic Environments," *Physical Review Letters,*6 (2025).

[4] B. M. Garraway., "Nonperturbative decay of an atomic system in a cavity," *Physical Review A,* 55 (1997)

Light emission from metals - photluminescence and electroluminescence

Imon Kalyan[1], Ieng-Wai Un[1], Kaiqiang Lin[2], John M. Lupton[2], Sebastian Bange[2], Yonatan Sivan[1]
[1] *School of Electrical and Computer Engineering, Ben-Gurion University of the Negev, Beer-Sheva, Israel*
[2] *Institut für Experimentelle und Angewandte Physik, Universität Regensburg, Germany*

Abstract: We provide a single line analytic theory for photoluminescence and electroluminescence from metal nanostructures under CW and pulsed illumination which allows us to explain a long series of seemingly contradicting experimental reports. We then describe the signature of our predictions in old and new measurements.

Photoluminescence (PL) from metals is one of the most fundamental aspects of light-matter interactions – it involves the 2-step process in which an incoming photon gets absorbed in a material, and consequently emitted spontaneously. In the context of metals, this phenomenon was disputed for many decades, with contradicting experimental reports on every possible aspect – the emission statistics (fermionic/bosonic, thermal/non-thermal), its dependence on electric field (polynomial/power law with integer/non-integer exponent), on structure size (grows/decreases with increasing size), its quantum efficiency, the underlying microscopic mechanism (electronic Raman scattering/simple recombination) etc. etc. [1]. These radically different behaviours were not accompanied by a complete theory because of the lack of knowledge of the hard-to-calculate electron non-equilibrium distribution under illumination.

Here, we remedy this problem by providing a complete quantitative theory for this important, decades-old, yet unresolved problem of (nonlinear) photoluminescence (PL) from metals for both continuous-wave (CW) and pulsed illumination. Based on our the *steady-state* non-equilibrium electron distribution in metals [2], we first compute the electron and lattice temperatures and the emission from metals illuminated by *CW* light [3]. This solution reveals what is to our knowledge, the first ever explanation of the dependence of the metal emission on the electric field, and its dependence on the electron temperature; we show that the emission is a primarily *non-thermal* phenomenon, and identify the unique signatures of the deviation from thermal equilibrium on the emission spectra and electric field dependence. The theory is then shown to match experimental data and used to clarify open questions associated with the use of the PL as a temperatre probe.

We then analyze *transient* nonlinear PL following illumination by intense *ultrashort pulses*. Our detailed calculations and a simplified heuristic model enable us to elucidate the crossover from the non-thermal emission characteristic of weak (CW-like) illumination to thermal emission occurring after illumination by strong shorter pulses [4]. Specifically, we identify the characteristics of nonthermal and thermal emission in the transient emission spectra and its dependence on the illumination frequency and intensity. These findings, specifically, the weak 3 photon absorption, were then verified in measurements from various sets of Au rods (see Fig. 1(a)). In that regard, our work puts to rest the many decades-long arguments on the statistics and electric field dependence of the emission [1].

Then, based on the extension of our point-emission theory [3,4] to macroscopic bodies using the extension of the local Kirchhoff's law to non-equilibrium distributions [5], we reconcile seemingly contradicting behaviour of the PL as a function of the metal structure size (for nanospheres and nanofilms), see Fig. 1(b)-(d) [6].

Finally, we describe the analogous theory for light emission under bias voltage (with and without illumination), and discuss our novel findings and their relation to the state-of-the-art theory and to experimental measurements.

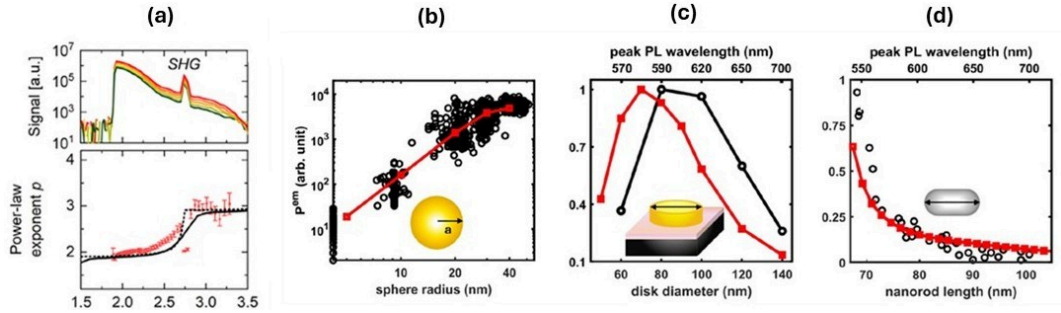

Figure 1: (a,top) Measured spectra at various illumination intensities and (a,bottom) the corresponding power-law exponent extracted from the measured data; an excellent match to the theoretical prediction (black line) is observed. (b)-(d) Measured PL from various different metal nanoparticles (Au spheres, discs, Ag rods), showing opposing size dependence, all explained by our single line quantitative theory (red).

References

[1] G. Baffou, ACS Nano 15, 5785 (2021).
[2] Y. Dubi, Y. Sivan, Light: Science & Applications 8, 89 (2019). Y. Sivan *et al.*, Faraday Discussion 214, 215 (2019).

[3] Y. Sivan, Y. Dubi, ACS Nano 15, 8724 (2021).
[4] Y. Sivan, I.W. Un, I. Kalyan, K. Lin, J. Lupton, S. Bange, ACS Nano 17, 11439 (2023).
[5] J.-J. Greffet *et al.*, Phys. Rev. X, 8, 021008 (2018). A. Pelous-Loirette, J.-J. Greffet, ACS Nano 18, 31823 (2024).
[6] I. Kalyan, I.W. Un, G. Rosolen, N. Shitrit, Y. Sivan, ACS Nano 19, 29181 (2025).

Phase-Change Extraordinary Optical Transmission Metasurfaces for Reconfigurable Spatial Filtering in the Mid-Infrared

S. Kendall, J. Shields, J. Pady, C. Ruiz de Galarreta, J. Bertolotti[1], C. D. Wright[*]

Centre for Metamaterials Research and Innovation, University of Exeter, Exeter, EX4 4QF, UK

*Corresponding author: david.wright@exeter.ac.uk

***Abstract*— Reconfigurable spatial filters comprising phase-change materials integrated into extraordinary optical transmission metasurfaces are designed and fabricated. Near-zero transmission in the crystalline state coupled with high amorphous transmission deliver spatial filters that can be written and re-written. Example functionalities of reconfigurable high and low-pass spatial filters are demonstrated.**

***Keywords*— phase-change metasurface, extraordinary optical transmission.**

I. Introduction

Analogue optical computing is experiencing increased attention as a result of inherent advantages it possesses over digital computing, including spatial parallelism, ultra-high bandwidth and low-loss transmission [1]. Previous work in the field has demonstrated both free-space and integrated photonic systems for a range of uses that include optical neural networks [2] and parallelized matrix-vector multiplication [3]. Here we present a design for a reconfigurable spatial filter metasurface within a free-space system. The metasurface utilises phase-change materials (PCMs) to allow for reconfigurability by writing into the spatial filter regions of high and near-zero transmission, corresponding, respectively, to amorphous and crystalline regions of the PCM layer. In this manner, a variety of optical spatial filters can be realized, including high-pass, low-pass, band-pass and band-reject, in a single reconfigurable device.

Our devices are designed to be used in the classic 4f spatial filter arrangement, as shown in Fig. 1a. The reconfigurability of the metasurface is achieved via the integration of chalcogenide phase-change materials into an extraordinary optical transmission (EOT) metasurface. The EOT effect is a phenomenon in which massively enhanced light transmission occurs at the resonant wavelength of a sub-wavelength array of holes in a metallic film [4]. The device developed here consists of a thin film of $Ge_2Sb_2Te_5$ (GST) deposited atop a gold film patterned with an array of sub-wavelength holes (see Fig. 1b). GST offers vastly contrasting optical properties (n and k) between its amorphous and crystalline phases [5]; changing the phase of the GST shifts the spectral position of the EOT array's resonant wavelength. Switching of the PCM phases can be achieved via a heat stimulus, e.g. by using ex-situ laser excitation or in-situ embedded microheaters [6]. Arbitrary patterns can thus be written into the GST layer of the device such that a variety of reconfigurable spatial filters can be realized by selectively switching desired regions of the PCM-EOT metasurface to deliver, for example, the low-pass, high-pass, band-reject and band-pass spatial filters shown schematically in Fig. 1c.

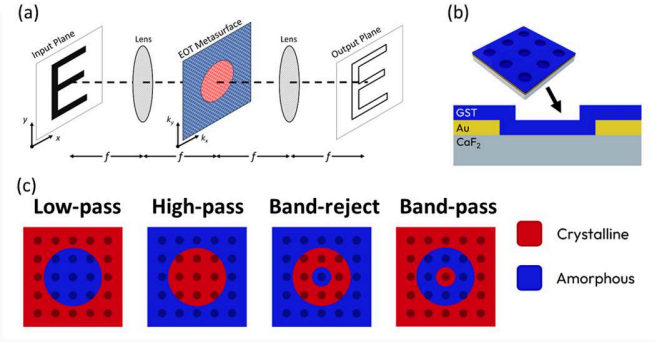

Fig. 1. (a) Schematic of a 4f system with the phase-change EOT metasurface placed at the shared focal point of the lenses; this example shows the metasurface acting as a high-pass filter. (b) A schematic of the phase-change ($Ge_2Sb_2Te_5$, or GST) EOT device design. (c) Schematics of metasurface devices with amorphous (blue) and crystalline (red) regions written into the phase-change layer to produce the spatial filter functionalities of low-pass, high-pass, band-reject and band-pass filters.

II. Results and Discussion

Phase-change EOT devices were fabricated using magnetron sputtering and electron beam lithography. An SEM image of an exemplar device is shown (prior to the deposition of the PCM layer) in Fig. 2a, here with geometric dimensions designed to provide functionality in the mid-infrared waveband. The

transmission spectra of the fabricated devices were measured using Fourier transform infrared spectroscopy (FTIR). Typical experimental transmission spectra are shown Fig. 2b, for the phase-change layer in both its amorphous and crystalline states. As expected, switching the phase-state of the PCM layer shifts to the position of the EOT peak, due to the change in refractive index (n) on switching. An increase in extinction coefficient (k) leads to slight reduction peak transmission in the crystalline case, as compared to that of the amorphous state. It can also be seen in Fig. 2b that the minimum (near-zero) in the crystalline transmission occurs almost directly below the maximum in the amorphous transmission, such that the device demonstrates the desired properties for use as a reconfigurable spatial filter along the lines previously discussed.

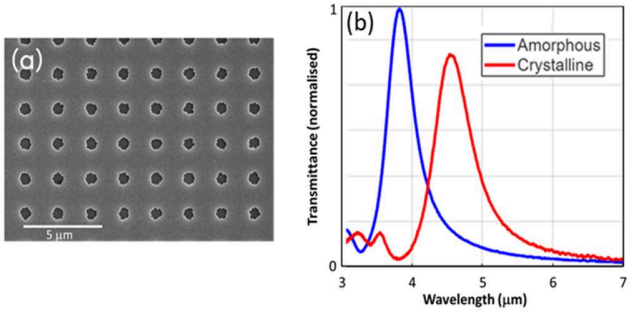

Fig. 2. (a) SEM image of an exemplar as-fabricated EOT array (Au on CaF_2) designed for use in the mid-infrared. (b) Experimental (FTIR) spectra of a phase-change EOT array with the PCM layer in both the amorphous (blue) and crystalline (red) states.

To test the likely performance of the device shown in Fig.2, its operation as a spatial filter in a 4f system, for both high-pass and low-pass filtering, was simulated (in Matlab). The results are shown in Fig. 3 for example cases of high-pass and low-pass filtering. The input image is the letter 'E', and with the PCM layer configured to deliver a high-pass response (central region crystalline, outer region amorphous) the filter emphasizes the edges of the input image, acting as a form of edge detector, so revealing a high-pass functionality (Fig. 3b). With the device reconfigured to provide a low-pass response (central region amorphous, outer region crystalline), the output image shows evidence of smoothing/blurring (Fig. 3c), as expected from a low-pass filter. These functionalities are further clarified in the output image cross-sections shown in Figs. 3d and 3e. These experimental results demonstrate the viability of the PCM EOT metasurface device to function as a reconfigurable spatial filter in the mid-infrared.

III. Conclusion

We have presented device designs based around phase-change extraordinary optical transmission metasurfaces that can provide a form of reconfigurable optical spatial filtering. Experimental transmission results of as-fabricated devices revealed properties suitable for such reconfigurable spatial filtering. Simulations based on experimental transmission responses successfully demonstrated, as a proof-of-concept, both high-pass and low-pass spatial filtering of test images.

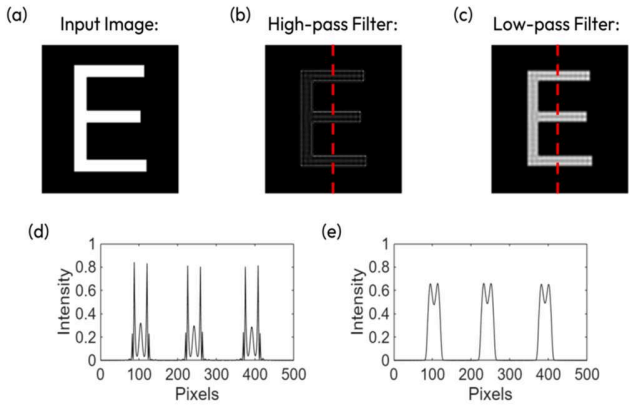

Fig. 3. Simulated device functionality for high and low-pass filters using experimentally measured phase-change EOT device transmission values: (a) the input image, (b) the output image with the device configured as a high-pass filter and (c) as a low-pass filter. (c) and (d) show (scaled) cross-sections through the output images from (b) and (c) respectively.

Acknowledgments

Funding is acknowledged via EPSRC projects A-META (EP/W003341/1), APT-NuCOM (EP/W022931/1) and MetaHUB (UKRI1255), as well as the Marie Sklodowska-Curie Postdoctoral Fellowship 101068089 (METASCALE).

References

[1] McMahon, P. L. (2023). The physics of optical computing. Nature Reviews Physics, 1-18.
[2] Lin, X. et al. (2018). All-optical machine learning using diffractive deep neural networks. Science 361, 1004-1008.
[3] Feldmann, J. et al. (2021). Parallel convolutional processing using an integrated photonic tensor core. Nature 589, 52–58.
[4] Ebberson, T. W. et al. (1998). Extraordinary transmission through sub-wavelength hole arrays. Nature 391, 667-669.
[5] Ruiz de Galarreta C. et al. (2020). Tunable optical metasurfaces enabled by chalcogenide phase-change materials: from the visible to the THz. Journal of Optics 22, 114001.
[6] Popescu, C. C. et al., (2024). Electrically Reconfigurable Phase-Change Transmissive Metasurface. Advanced Materials 36, 2400627.

Structural and Electronic Transitions in Pure and Au-Decorated VO_2 Nanoporous Thin Films under Thermal and Photothermal Excitations

Claudia P. Hallqvist[1,*], Charlotte L.O. Nani[1], Edoardo Casadei[1], Cristina Mancarella[1], Francesco Bisio[2], Michele Magnozzi[3], Maurizio Canepa[3], Andrea Li Bassi[1]

[1]NanoLab, Department of Energy, Politecnico di Milano- Milano, Italy
[2]CNR-SPIN, Genova, Italy
[3] OptMatLab, Dipartimento di Fisica, Università di Genova - Genova, Italy
*Corresponding author: claudiapernilla.hallqvist@polimi.it

***Abstract*— Vanadium dioxide nanoporous films and Au–VO_2 nanocomposites were fabricated by pulsed laser deposition. The nanoporous VO_2 shows anisotropic optical properties and a thermally driven structural-phase and insulator-to-metal transition. Incorporating Au nanoparticles enables photo-thermal activation of the structural-phase transition under continuous-wave illumination, demonstrating a pathway toward switchable VO_2-based photonic devices.**

***Keywords*— vanadium dioxide, phase change material, nanoporous thin films, photo-thermal switching, Au nanoparticles, optical anisotropy.**

I. Introduction

Vanadium dioxide (VO_2) is a phase-change material exhibiting a reversible insulator-to-metal transition (IMT) coupled to a structural phase transition (SPT) at ~68 °C, leading to pronounced changes in its optical and electrical properties. These features make VO_2 highly attractive for photonic, plasmonic, and smart photothermal applications. However, its practical implementation is hindered by the relatively high transition temperature (T_C) and by synthesis challenges arising from the multiple oxidation states of vanadium.[1] Recent studies have shown that nanoscale control of VO_2 thin films—particularly in terms of morphology and doping—enables effective tuning of their thermochromic response. In this context, nanoporous VO_2 has emerged as a promising architecture: the high surface-to-volume ratio can accommodate the structural distortions associated with the SPT, resulting in a reduced T_C.[2] Moreover, the enhanced surface area of nanoporous VO_2 is advantageous for sensing and energy-storage applications. This morphology also facilitates the incorporation of metal nanoparticles (NPs), such as gold. Au-VO_2 nanocomposites have been reported to further decrease T_C through thermoplasmonic heating, nanoantenna effects, and possible carrier injection at the Au/VO_2 interface, although the dominant mechanism remains under debate.[3,4] Furthermore, such Au-VO_2 systems have been mainly investigated under thermal excitation or ultrafast optical pumping, whereas photo-induced phase transitions driven by continuous-wave optical illumination remain less explored.

Therefore, in this work, a pure nanoporous VO_2 thin film and an Au-VO_2 nanocomposite were fabricated by pulsed laser deposition (PLD). The nanoporous VO_2 thin film exhibited a smooth SPT transition from the VO_2 (M1) phase to the VO_2 (R) phase, beginning near 70 °C and ending near 90 °C. Furthermore, the nanoporous VO_2 grew preferentially along the vertical direction, forming a columnar-like structure that displayed optical anisotropy between the in-plane and out-of-plane directions, further tunable with temperature: two positive (dielectric) and negative (metallic) ε_1 values at room temperature and high temperature, respectively. Finally, the Au nanoparticles embedded in the VO_2 nanoporous matrix were shown to be essential for photo-inducing the VO_2 SPT.

II. Methods

The VO_2 thin film and Au-VO_2 nanocomposite were deposited by pulsed laser deposition (PLD). The morphology was investigated by scanning electron microscopy (SEM). The insulator-to-metal transition of the pure VO_2 thin film was investigated by room and high temperature ellipsometric measurements. The thermally induced structural phase transition (SPT) of VO_2 was investigated by variable-temperature Raman measurements using a 532 nm laser with a power <1 mW to avoid thermal contribution coming from the Raman laser. Conversely, the photo-induced SPT of the VO_2 and Au-VO_2 nanocomposite was studied through variable-power Raman measurements at room temperature.

III. Results and Discussion

During growth, the nanoporous pure VO_2 thin film exhibited a preferential vertical growth, forming a columnar-like structure characterized by an approximate uniaxial anisotropy (Fig. 1a). In this case, the dielectric constants are equal in the in-plane directions but differ along the out-of-plane direction (i.e. $\varepsilon_{xx} = \varepsilon_{yy} \neq \varepsilon_{zz}$). The SPT investigated by variable, Raman

temperature measurements is reported in Fig. 1b. The main Raman peaks of the insulating VO_2 (M1) phase progressively decreased in intensity with increasing temperature and completely transformed into the metallic VO_2 (R) phase at 90 °C. The IMT investigated by room temperature (RT) and high temperature (HT) ellipsometric measurements is shown in Fig. 1c and 1d. At RT, the VO_2 film exhibits a dielectric-like behaviour, with different dielectric constants along the in-plane (*xx*) and out-of-plane (*zz*) directions. Conversely, at HT the real permittivity (ε_1) becomes negative in the near-infrared region. The in plane and out-of-plane dielectric functions show different plasma frequencies, hinting at possible hyperbolic behaviour.

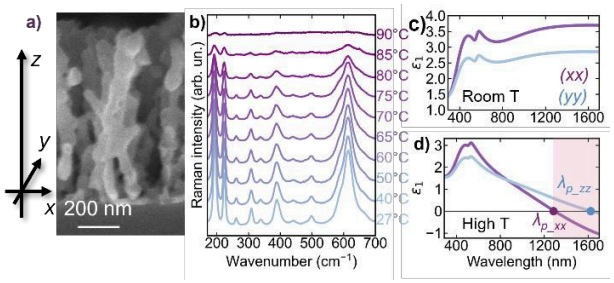

Fig. 1 (a) Cross-sectional SEM image of a nanoporous VO_2 thin film. (b) Temperature-dependent Raman spectra. (c,d) Ellipsometric measurements at room temperature and high temperature.

Subsequently, the nanoporous VO_2 thin film was decorated with Au NPs to photo-induce the VO_2 transition and investigate the role of Au under continuous-wave optical excitation (Fig. 2a). The photo-induced transition was studied using power-dependent Raman measurements with a 532 nm laser wavelength resonant with the Au NPs (Fig. 2b). The Raman signal of the VO_2 (M1) phase initially increases with laser power up to 2 mW. At higher powers, the VO_2 (M1) Raman peaks progressively decrease in intensity and completely disappear for powers >20 mW. This reduction in peak intensity can be clearly observed by focusing on the VO_2 (M1) mode at 190 cm^{-1} (see Fig. 2c). By fitting the peak-intensity trend, the onset of the photo-induced SPT can be identified at the maximum of the curve, around 2.3 mW. In contrast, a pure nanoporous VO_2 thin film does not exhibit any photo-induced transition under the same excitation conditions (here not shown), highlighting the crucial role of Au NPs in triggering the VO_2 phase transition.

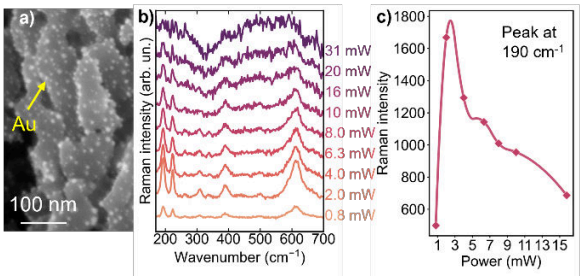

Fig. 2 (a) Cross-sectional SEM image of the Au-decorated VO_2 film. (b) Power-dependent Raman spectra of the Au-VO_2 system. (c) Peak intensity vs power of the VO_2 M1 peak at 190 cm^{-1}.

IV. Conclusion

We successfully deposited a pure VO_2 thin film with a nanoporous morphology, which exhibited anisotropic optical properties and switchable behavior. At room temperature, the film showed a fully positive real permittivity, whereas at high temperature it displayed a negative real permittivity, confirming its insulator-to-metal transition. In addition, we demonstrated that combining the VO_2 thin film with Au nanoparticles enables photo-thermal switching of the VO_2 phase. These results pave the way for the development of VO_2-based devices that exploit morphology-driven properties for active thermal and photo-thermal switching applications.

Acknowledgments

C.M. and A.L.B. acknowledge funding by the project funded under the National Recovery and Resilience Plan (NRRP), Mission 4 Component 2 Investment 1.3 – Call for tender No. 341 of 15.03.2022 of Ministero dell'Università e della Ricerca (MUR); funded by the European Union NextGenerationEU - Award Number: project code PE0000021, Concession Decree No. 1561 of 11.10.2022 adopted by Ministero dell'Università e della Ricerca (MUR), CUP D43C22003090001, Project title "Network 4 Energy Sustainable Transition (NEST)".

References

[1] Y. Wang et al. "Phase-Change VO_2 Enabled Optoelectronic Devices With Switching Dynamics." Advanced Optical Materials 13.36 (2025): e02649.

[2] HX. Xu et al. "Effect of porous morphology on phase transition in vanadium dioxide thin films." Journal of Vacuum Science & Technology A 33.6 (2015).

[3] Z. Fang et al. "Plasmon-enhanced photothermal sensing through coupled VO_2/Au nanodisks." Surfaces and Interfaces 62 (2025): 106145.

[4] G. XU et al. "Electron injection assisted phase transition in a nano-Au-VO_2 junction." Applied Physics Letters 93.6 (2008).

Equivalent Circuit Analysis of a Time-Varying Edge-Coupled Split-Ring Resonator

Theocharis T. Manassis[1,2 *], Guido Valerio[1,2], Theodosios D. Karamanos[1,2]

[1]Sorbonne Université, CNRS, Laboratoire de Génie Electrique et Electronique de Paris (GeePs), France
[2]Université Paris-Saclay, CentraleSupélec, CNRS, GeePs, France
*Corresponding author: theocharis.manassis@sorbonne-universite.fr

***Abstract*—This paper presents an equivalent circuit model of a time-varying Edge-Coupled Split-Ring Resonator. Time modulation is imposed by a varactor diode connected between the two rings of the scatterer and enables the generation of scattered wave harmonics, as predicted by the provided circuit model.**

***Keywords*— space-time metamaterials, time-varying media, electromagnetic modeling, polarizabilities, scattering**

I. Introduction

Time-varying metasurfaces have recently gained considerable interest due to their broad range of applications. These include photonic time crystals [1], [2], frequency mixing [3], absorbers [4], power combing [5], filtering and isolation [6], beamforming [7] and more. A common method the analysis of a metasurface is by modeling the multipolar response of its constituting scatterers [8]. However, this process is quite difficult for time-varying metasurfaces due to the complex nature of their respective time-varying scatterers. Therefore, the analytic calculation of polarizability/T matrices of time-varying scatterers is possible only for simple geometrical shapes via Mie theory [9]. As a result, the dipole response of the time-varying resonators is usually approximated via equivalent circuit models [10]. Nevertheless, those circuit models for more complicated time-varying resonator setups are still unavailable, and their development would expand the design and optimization processes for time-varying media.

This work proposes a circuit model for the time-varying Edge-Coupled plit-ring resonator (EC-SRR). The EC-SRR is modulated by means of two varactors diodes, corresponding to a time-modulated capacitance. Afterwards, a well-known equivalent RLC-circuit approach for the computation of the (dipole) polarizability matrix in the passive or stationary case [11] is expanded to incorporate the time modulation provided by the varactors [10]. Assuming a periodic capacitance modulation with an instantaneous response, the current induced along the rings can be derived from the voltage across the rings and, consequently, from the external excitation, enabling the calculation of the polarizabilities. Due to the periodic time modulation, the current is expressed in terms of its harmonic components, leading to a matrix formulation of the problem. Then, the generation of harmonic frequencies by an illuminated time-varying EC-SRR is demonstrated and, eventually, the presented results are validated by rigorous and demanding time-domain numerical simulations.

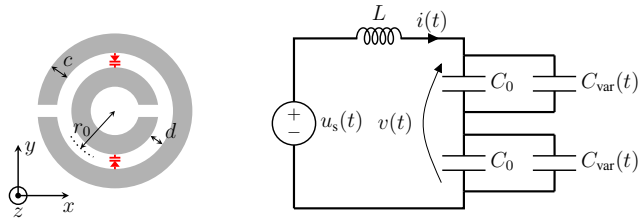

(a) (b)

Fig. 1. (a) Geometry of the time-varying EC-SRR, where $r_0 = 2.3$ mm, $c = 0.8$ mm and $d = 0.2$ mm. All metallic parts are considered, in this work, as PEC. The origin of the axes O(0,0,0) is placed at the center of the EC-SRR. (b) The RLC equivalent circuit of the resonator under study.

II. Equivalent Time-Varying Circuit Model

A time-modulated EC-SRR, as shown in Fig. 1(a), consists of two metallic circular strips of equal thickness c connected through two varactors, placed perpendicularly along the y-axis. The scatterer is modeled as a series connection of two halves, so the use of two varactors is necessary for the analysis to hold. Assume that the largest dimension of the EC-SRR, i.e. its diameter, remains electrically small, below $\lambda/5$. Thus, the response of the particle can be represented as an equivalent assortment of only electric/magnetic dipoles. Under this dipole approximation, the scattered fields of an EC-SRR can be modeled by two electric dipole moments p_x, p_y and a magnetic dipole moment m_z. Due to the geometry of the particle, the induced dipoles are connected with the incident fields on the particle via five non-zero polarizabilities, through [11]

$$\begin{bmatrix} p_x \\ p_y \\ c^{-1}m_z \end{bmatrix} = \begin{bmatrix} a_{\mathrm{ee}}^{xx} & 0 & 0 \\ 0 & a_{\mathrm{ee}}^{yy} & a_{\mathrm{em}}^{yz} \\ 0 & a_{\mathrm{me}}^{zy} & a_{\mathrm{mm}}^{zz} \end{bmatrix} \begin{bmatrix} \varepsilon_0 E_{x,\mathrm{i}} \\ \varepsilon_0 E_{y,\mathrm{i}} \\ c^{-1}H_{z,\mathrm{i}} \end{bmatrix}. \quad (1)$$

The particle is modeled, herein, as an equivalent RLC-circuit, as shown in Fig. 1(b). Each capacitance branch consists of a static capacitance C_0 (the capacitance between the rings in the absence of varactors), and a time-varying capacitance due to the varactor C_{var} placed in parallel. The total capacitance is therefore the sum of two terms: $C_{\mathrm{t}}(t) = \frac{1}{2}\left[C_0 + C_{\mathrm{var}}(t)\right]$. As the capacitance of a varactor can be expressed as the sum of constant and a modulated component, the total capacitance of the time-modulated EC-SRR can be expressed as $C_{\mathrm{t}}(t) = \frac{1}{2}C_{\mathrm{s}}[1 + M\cos(\Omega_{\mathrm{p}}t)]$. Here, Ω_{p} is the modulation frequency, M the modulation strength value, and C_{s} is the stationary capacitance consisting of the capacitance of the half ring, C_0, and the constant capacity of the varactor.

From circuit theory the following equation holds: $u_{\mathrm{s}}(t) = R\,i(t) + L\frac{\mathrm{d}i}{\mathrm{d}t} + v(t)$ [10], [11], with L the system inductance, $R = 0$, as losses are neglected, and $v(t)$ the voltage on the total capacitance C_{t}. In the time-invariant case, $M = 0$ and the analysis is straightforward, as the induced current is linearly related to the derivative of the voltage between the rings: $i(t) = \frac{C_{\mathrm{s}}}{2}\frac{\mathrm{d}v(t)}{\mathrm{d}t}$. However, when the capacitance is temporally modulated, the current turns to $i(t) = \frac{\mathrm{d}}{\mathrm{d}t}\left[C_{\mathrm{t}}(t)v(t)\right]$. In this case, a frequency-domain relation can be found between the current $I(\Omega)$ and the capacitance voltage $V(\Omega)$ [10]:

$$I(\Omega) = \frac{j\Omega}{2\pi}\int_{-\infty}^{+\infty} C_{\mathrm{t}}(\omega, \Omega-\omega)\,V(\omega)\,d\omega. \tag{2}$$

Assuming that the periodic time-modulation is instantaneous (i.e., the absence of frequency dispersion), the capacitance is expressed as a series of harmonics,

$$C_{\mathrm{t}}(t) = \sum_{m=-\infty}^{+\infty} c_m e^{\,jm\Omega_{\mathrm{p}}t}, \tag{3}$$

where, due to the cosine dependence defined above, the only non-zero terms are $c_0 = C_{\mathrm{s}}/2, \quad c_1 = c_{-1} = MC_{\mathrm{s}}/4$, yielding a discrete Fourier spectrum. Assuming a time-harmonic voltage source, the voltage can be expressed as an expansion of exponential functions as

$$v(t) = \Re\mathrm{e}\left\{\sum_{n=-\infty}^{+\infty} V_n\, e^{j\Omega_n t}\right\}, \tag{4}$$

which allows the current in the ring in (2) to be written in discrete form [10] as a series:

$$I = \sum_m \sum_n j\left[\Omega_0 + (n+m)\,\Omega_p\right] c_m\, V_n. \tag{5}$$

Having established the relationship between the current and voltage in the frequency domain, the current in (5) can be rewritten for arbitrary excitation in a matrix form as

$$[I] = -j\,[\Omega]\,[K]^{-1}\,[\Sigma] \tag{6}$$

where the matrix $[K]$ is

$$[K] = \begin{bmatrix} \Omega_{-N}^2 L - q_{11} & -q_{12} & \cdots & -q_{1n} \\ -q_{12} & \Omega_{1-N}^2 L - q_{22} & \cdots & -q_{2n} \\ \vdots & \vdots & \ddots & \vdots \\ -q_{1n} & -q_{2n} & \cdots & \Omega_N^2 L - q_{nn} \end{bmatrix} \tag{7}$$

q_{ij} being entries of the inverse of the matrix relating the voltage and current from (5), and the matrix $[\Omega]$ being a diagonal matrix containing the harmonics Ω_n in (4). It should be noted that the a finite truncation of harmonics must be performed, introducing a negligible inaccuracy, provided that the number of harmonics considered is large enough.

Having established the relation between the current and the excitation, the polarizabilities can be found, following a similar approach as done in [11], as

$$[a_{\mathrm{mm}}^{zz}] = -\mu_0\,\pi^2\,r_0^4\,[\Omega]\,[K]^{-1}\,[\Omega] \tag{8a}$$

$$[\alpha_{\mathrm{ee}}^{xx}] = \frac{16}{3}\,r_{\mathrm{ext}}^3 \tag{8b}$$

$$[a_{\mathrm{em}}^{yz}] = 4j\,\eta_0\,r_0^2\,d_{\mathrm{eff}}\,[K]^{-1}\,[\Omega] \tag{8c}$$

$$[a_{\mathrm{me}}^{zy}] = -4j\,\eta_0\,r_0^2\,d_{\mathrm{eff}}\,[\Omega]\,[K]^{-1} \tag{8d}$$

$$[a_{\mathrm{ee}}^{yy}] = [\alpha_{\mathrm{ee}}^{xx}] - \frac{16\,d_{\mathrm{eff}}^2}{\varepsilon_0\pi^2}[K]^{-1} \tag{8e}$$

where r_0 is the mean radius of the scatterer, $r_{\mathrm{ext}} = r_0 + \frac{d}{2} + c$ is the exterior radius and $d_{\mathrm{eff}} = c + d$.

A scatterer must satisfy the condition of energy conservation for the system. For passive scatterers, this requirement is known as the Sipe–Kranendonk condition [12]. In time-varying systems there is additional energy actively pumped into the balance. However, this pumped energy is expressed by the calculated moments and so it is present in the power absorbed and radiated by the scatterer. In order to correctly add the radiation term into the quasi-polarizability calculated in (8), as in [12], a new, dynamic polarizability $3(N+1)\times 3(N+1)$ matrix, N being the number of retained harmonics, is constructed. It contains every polarizabilty tensor for all frequencies considered, as well as their mutual coupling induced by the time modulation. This way, the quasi-static polarizability matrices $[a]_{\mathrm{st}}$ can be inversed in order for the dumping term to be added, resulting in the dynamic polarizability matrix to be found as

$$[a]_{\mathrm{dyn}}^{-1} = [a]_{\mathrm{st}}^{-1} + \frac{j}{6\pi}[k]^3. \tag{9}$$

III. Results and Discussion

A full-wave simulation was performed via the transient solver of COMSOL Multiphysics [13], in order to validate the equivalent circuit model that was presented above. An SMD capacitor was inserted into the simulation setup, with a periodic electric permittivity variation, $\varepsilon = \varepsilon_{\mathrm{s}}[1 + w\cos(\Omega_{\mathrm{p}}t)]$ with ε_{s} the static permittivity and $w = MC_{\mathrm{s}}/C_{\mathrm{var}}$ the SMD's modulation strength, in order to emulate the behaviour of a varactor. The capacitance value of the SMD was first evaluated with the AC/DC solver of COMSOL, and two such identical capacitors were then placed between the rings of the scatterer [see Fig. 1(a) and its caption for the relevant coordinate system]. The subsequent modulated EC-SRR was excited by an elementary electric dipole, located in the zx plane at the point $A = (a, 0, a)$ with $a = 1$ cm, and its scattered field calculated at an observation point in the xy plane at the point $B = (-b, b, 0)$ where $b = 3.54\,r_0$. A modulated Gaussian pulse is used at the source electric dipole, centered at $f_{\mathrm{c}} = 4.5$ GHz with a spectral deviation set to $\sigma = 1/(1.5f_{\mathrm{c}})$. Additionally, for the purpose of verification, a fast modulation frequency of $\Omega_{\mathrm{p}} = 2\pi f_c/3$ was chosen. The electric permittivity was defined with $\varepsilon_s = 10$ and $w = 0.5$, resulting in the system's total modulation strength $M = 0.125$. Finally, in order to compare the two models, the scattered field at the observation point B is normalized by the spectral peak value of the incident field at B, as

$$\text{normalized } E_{\mathrm{sc}}(f) = \frac{|E_{\mathrm{sc}}(f)|}{\max_f\left\{|E_{\mathrm{i}}(f)|\right\}} \tag{10}$$

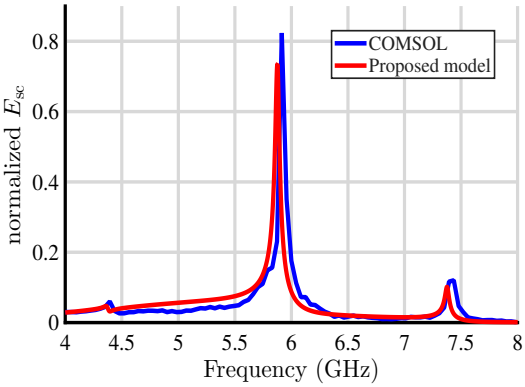

Fig. 2. Comparison of circuit equivalent and numerical results for the scattered field by a time-varying EC-SRR.

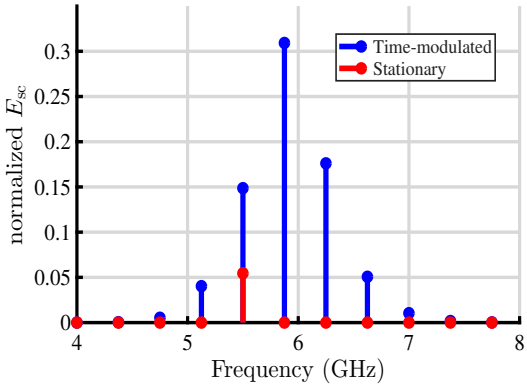

Fig. 3. Normalized scattered fields from a time-varying EC-SRR via the proposed method for a monochromatic excitation.

The comparison, seen in Fig. 2, shows good agreement with a slight frequency shift and a small amplitude deviation. The frequency shift is primarily influenced by small discrepancies in the capacitance value of the SMD capacitor when finally inserted in the EC-SRR setup, i.e. parasitic capacitances or inadequate local mesh density. Moreover, one can also notice the generated resonances. The central one corresponds to the resonance frequency of the EC-SRR, while the others are the harmonics, as indicated in the analysis of the previous section.

As outlined above, the time-varying EC-SRR is generally expected to generate harmonics obtained through the mixing of the modulation and the illumination frequencies. To evaluate this behaviour, the scatterer is excited by a modulated Gaussian pulse centered at $f_c = 5.5$ GHz with a very narrow frequency spectrum, in order to emulate a monochromatic excitation or almost delta function in frequency domain. Additionally, a slow modulation was investigated with $\Omega_p = \Omega_c/14.6$ GHz, while the modulation strength is $M = 0.125$. If we maintain the same points A and B for the dipole source and observation points respectively, the calculated polarizabilities from (8) and (9) lead to the normalized scattered field depicted on Fig. 3, along with the results for an unmodulated or stationary EC-SRR. The creation of harmonics is clearly visible, with some having greater amplitude than the central one, due to being closer to resonant frequency of the EC-SRR. Finally, Fig. 3 shows significantly more powerful scattered waves, reaching approximately four times when comparing with the central scattered frequency without modulation. This behavior is attributed to the time-varying capacitance pumping energy into the system, as an active circuit.

Regarding the numerical validation procedure, a finer mesh density of the numerical simulation will possibly lead to better agreement between the two models. Nevertheless, the COMSOL simulations lasted for about 12 hours running on 128 Gigabytes of RAM, in contrast to the equivalent circuit developed above needing approximately 1 minute.

IV. Conclusion and Future Work

In this paper, an efficient equivalent circuit model of a time-varying EC-SRR was presented and validated. Future work will build on the proposed model by incorporating it into the analysis of time-varying metasurfaces. Finally, the same analysis framework can be applied to other geometries of time-varying resonators, whose equivalent circuit can be determined in the passive case.

References

[1] L. Zeng, J. Xu, C. Wang, J. Zhang, Y. Zhao, J. Zeng, and R. Song, "Photonic time crystals," *Scientific Reports*, vol. 7, no. 1, p. 17165, 2017.

[2] E. Galiffi, R. Tirole, S. Yin, H. Li, S. Vezzoli, P. A. Huidobro, M. G. Silveirinha, R. Sapienza, A. Alù, and J. B. Pendry, "Photonics of time-varying media," *Advanced Photonics*, vol. 4, no. 1, pp. 014 002–014 002, 2022.

[3] Z. Li, X. Ma, A. Bahrami, Z.-L. Deck-Léger, and C. Caloz, "Space-time fresnel prism," *Physical Review Applied*, vol. 20, no. 5, p. 054029, 2023.

[4] M. Mostafa, A. Díaz-Rubio, M. Mirmoosa, and S. Tretyakov, "Coherently time-varying metasurfaces," *Physical Review Applied*, vol. 17, no. 6, p. 064048, 2022.

[5] X. Wang, V. S. Asadchy, S. Fan, and S. A. Tretyakov, "Space–time metasurfaces for power combining of waves," *ACS Photonics*, vol. 8, no. 10, pp. 3034–3041, 2021.

[6] X. Wu, X. Liu, M. D. Hickle, D. Peroulis, J. S. Gómez-Díaz, and A. Á. Melcón, "Isolating bandpass filters using time-modulated resonators," *IEEE Transactions on Microwave Theory and Techniques*, vol. 67, no. 6, pp. 2331–2345, 2019.

[7] S. Taravati and G. V. Eleftheriades, "Full-duplex nonreciprocal beam steering by time-modulated phase-gradient metasurfaces," *Physical Review Applied*, vol. 14, no. 1, p. 014027, 2020.

[8] A. Rahimzadegan, T. D. Karamanos, R. Alaee, A. G. Lamprianidis, D. Beutel, R. W. Boyd, and C. Rockstuhl, "A comprehensive multipolar theory for periodic metasurfaces," *Advanced Optical Materials*, vol. 10, no. 10, p. 2102059, 2022.

[9] G. Ptitcyn, A. Lamprianidis, T. Karamanos, V. Asadchy, R. Alaee, M. Müller, M. Albooyeh, M. S. Mirmoosa, S. Fan, S. Tretyakov *et al.*, "Floquet–mie theory for time-varying dispersive spheres," *Laser & Photonics Reviews*, vol. 17, no. 3, p. 2100683, 2023.

[10] G. Ptitcyn, M. S. Mirmoosa, A. Sotoodehfar, and S. A. Tretyakov, "A tutorial on the basics of time-varying electromagnetic systems and circuits: Historic overview and basic concepts of time-modulation," *IEEE Antennas and Propagation Magazine*, vol. 65, no. 4, pp. 10–20, 2023.

[11] R. Marqués, F. Mesa, J. Martel, and F. Medina, "Comparative analysis of edge-and broadside-coupled split ring resonators for metamaterial design-theory and experiments," *IEEE Transactions on antennas and propagation*, vol. 51, no. 10, pp. 2572–2581, 2003.

[12] S. Albaladejo, R. Gómez-Medina, L. S. Froufe-Pérez, H. Marinchio, R. Carminati, J. Torrado, G. Armelles, A. García-Martín, and J. J. Sáenz, "Radiative corrections to the polarizability tensor of an electrically small anisotropic dielectric particle," *Optics Express*, vol. 18, no. 4, pp. 3556–3567, 2010.

[13] "Comsol multiphysics® v. 6.3," https://www.comsol.com, 2024, cOMSOL AB, Stockholm, Sweden.

Optimising Microwave Cavities for nonzero Helicity with Machine Learning

E. C. I. Paterson[1,*], J. Bourhill[1], M. Goryachev[1]
[1]Quantum Technologies and Dark Matter Labs
University of Western Australia, Australia
*Corresponding author: emma.paterson@research.uwa.edu.au

***Abstract*—We present a machine-learning-driven inverse design framework that replaces heuristic cavity design with boundary-shape optimisation to engineer three-dimensional microwave resonators supporting large electromagnetic helicity. This approach systematically explores complex parameter spaces, revealing non-intuitive high-helicity geometries, and is demonstrated on smooth, edge-free cavity families using two gradient-free optimisation strategies.**

***Keywords*— inverse design, microwave cavities, electromagnetic helicity, genetic algorithm, Bayesian optimisation, robustness.**

I. Introduction

Electromagnetic helicity, $\mathscr{H}$, defined as the projection of electromagnetic spin onto linear momentum [1], [2], [3], [4], provides a quantitative measure of field handedness. Modes with non-zero $\mathscr{H}$ enable strong coupling to chiral matter, offering versatile platforms for enantioselective microwave spectroscopy [5], [6], axion dark-matter searches [7], [8], and chiral quantum sensing [9].

Although microwave cavities supporting non-zero $\mathscr{H}$ have been demonstrated using heuristic design principles [8], [10], [11], [12], such approaches offer limited guidance for systematically maximising $\mathscr{H}$. The $\mathscr{H}$ figure of merit (FoM) depends on the full three-dimensional field distribution and can be highly sensitive to small boundary perturbations. These challenges motivate the adoption of inverse-design methodologies.

Over the past decade, inverse design has transformed nanophotonic device development, shifting from intuition-driven geometries to algorithmically optimised structures that maximise prescribed performance metrics. By coupling flexible geometric parameterisations with rigorous electromagnetic solvers and optimisation engines [13], [14], [15], these methods enable systematic exploration of large design spaces.

Here, we extend these principles to fully three-dimensional microwave cavity resonators. Metallic boundary shapes are optimised to maximise a $\mathscr{H}$-based FoM evaluated via finite-element eigenmode analysis. Gradient-free optimisation techniques, genetic algorithms (GA) and Bayesian optimisation (BO), enable systematic discovery of strongly helical cavity modes. The framework is applied to multiple cavity families composed of smooth, edge-free components compatible with metal additive manufacturing and electropolishing.

II. Methods

A. Helicity Figure of Merit

For a monochromatic resonant mode i, the global electromagnetic helicity is

$$\mathscr{H}_i = \frac{2\,\mathrm{Im}\left[\int \vec{\mathbf{E}}_i(\vec{r}) \cdot \vec{\mathbf{H}}_i^*(\vec{r})\, dV\right]}{\sqrt{\int \vec{\mathbf{E}}_i \cdot \vec{\mathbf{E}}_i^* dV \int \vec{\mathbf{H}}_i \cdot \vec{\mathbf{H}}_i^* dV}}, \tag{1}$$

where $\vec{\mathbf{E}}_i$ and $\vec{\mathbf{H}}_i$ denote the electric and magnetic fields.

For a parameterised geometry $\mathbf{x} \in [-1, 1]^d$, eigenmodes are computed and the fitness is defined as

$$F(\mathbf{x}) = |\mathscr{H}_m|, \tag{2}$$

where m denotes the most helical mode.

B. COMSOL–Python Optimisation Loop

Each cavity family is implemented in COMSOL Multiphysics®. A Python routine generates $\mathbf{x}$, maps it to physical parameters, injects them via the Java API, performs an eigenfrequency study, and computes $\mathscr{H}_i$. Non-convergent simulations are penalised to prevent propagation of invalid designs. This is demonstrated in the block diagram in Fig. 1.

To compare families, models are scaled to maintain constant surface-to-volume ratio. Surface-loss performance is quantified using the geometric factor

$$\tilde{G}_i = \frac{\iiint_V \mu_0 |\mathbf{H}_i|^2 dV}{\mu_0 \iint_S |\mathbf{H}_i^\tau|^2 dS}. \tag{3}$$

C. Optimisation Strategies

Two gradient-free optimisers are employed:

Genetic Algorithm (GA): A population-based evolutionary algorithm that iteratively refines cavity parameters via selection, crossover, and mutation to maximise $F(\mathbf{x})$.

Bayesian Optimisation (BO): A Gaussian Process surrogate model is trained on COMSOL results to guide evaluations toward promising regions, reducing the number of required simulations.

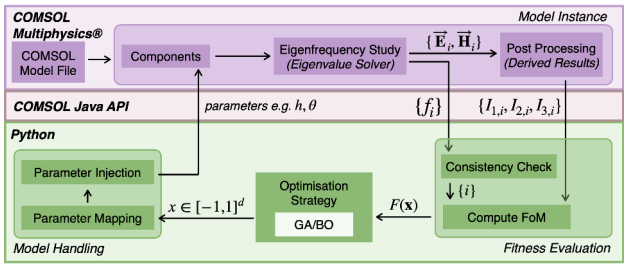

Fig. 1. Inverse-design loop linking Python optimisation to COMSOL eigenmode analysis. A normalised design vector $\mathbf{x} \in [-1,1]^d$ is mapped to geometric parameters, simulated in COMSOL, and scored via the $\mathscr{H}$-based fitness $F(\mathbf{x}) = |\mathscr{H}_m|$ for the most helical mode. The post processing integrals are $I_{1,i} = \int \vec{\mathbf{E}}_i \cdot \vec{\mathbf{H}}_i^* \, dV$, $I_{2,i} = \int \vec{\mathbf{E}}_i \cdot \vec{\mathbf{E}}_i^* \, dV$, $I_{3,i} = \int \vec{\mathbf{H}}_i \cdot \vec{\mathbf{H}}_i^* \, dV$.

TABLE I
OPTIMISED PERFORMANCE METRICS ACROSS CAVITY FAMILIES.

Cavity	f (GHz)	$\mathscr{H}$	$\tilde{G}$ (mm)	$\mathcal{R}$
EF twisted linear (GA, baseline)	8.57	1.03	5.26	1.02
EF twisted linear (BO, baseline)	9.15	1.02	4.57	—
EF twisted linear (GA, expanded)	9.42	1.10	6.32	0.635
EF twisted ring (GA)	9.99	1.47	14.2	1.29
Prism intersection (GA)	12.0	−0.900	8.27	0.735
Sphere-subtracted cyl. (GA)	17.1	−0.958	3.83	0.707
Sphere-subtracted cyl. (BO)	6.23	−0.750	7.38	—
Param. surface (GA)	20.0	−0.673	2.90	0.113

D. Mesh Convergence and Robustness

The optimal cavity geometry is validated through mesh-refinement analysis, in which the maximum element size is progressively reduced until relative changes in $F(\mathbf{x})$ fall below a stringent convergence threshold.

Fabrication tolerance is assessed by independently perturbing design parameters with Gaussian uncertainty and sampling the resulting space using Latin hypercube sampling. We report the mean $\bar{F}$, standard deviation σ_F, 5th percentile $F_{0.05}$, minimum $F_{\min}$, and robustness index $\mathcal{R} = \bar{F} - 2\sigma_F$, which penalises sensitivity to geometric variation.

III. RESULTS

A. Cavity Families and Optimised Performance

We investigated multiple smooth, edge-free cavity families suitable for additive manufacturing, including globally twisted cavities (linear and ring), orthogonal prism intersections, sphere-subtracted cylinders, and parametrised surface resonators.

A concise comparative summary of representative optimised cavities is given in Table I. Across explored design spaces, the EF twisted family consistently achieved the largest $|\mathscr{H}_i|$, with the ring configuration emerging as the top-performing geometry across $\mathscr{H}_i$, $\tilde{G}_i$, and $\mathcal{R}$ metrics.

B. Mechanisms for Large Helicity

Two mechanisms emerge:

Local-feature-driven helicity: Sharp curvature can create strong local helicity hotspots but is highly sensitive to geometric perturbations and may degrade surface-loss performance.

Global-twist-driven helicity: Smooth, continuous twist maintains constructive overlap of electric and magnetic fields throughout the volume, enabling robust $\mathscr{H}_i$ enhancement.

The EF twisted ring benefits from global twist and the absence of endcaps, improving $\mathcal{R}$ and $\tilde{G}_i$.

IV. CONCLUSION

We demonstrate that machine-learning-driven inverse design provides a systematic approach to engineering microwave cavity resonators with large electromagnetic helicity, surpassing previously studied heuristic twisted geometries. Rather than relying on physical intuition and incremental geometric adjustments, this framework systematically identifies smooth, edge-free resonator geometries that support strongly helical modes. In contrast to most inverse-design efforts in quasi-two-dimensional photonics, our method operates on fully three-dimensional metallic microwave cavities compatible with additive manufacturing.

The framework can be readily extended to alternative or composite figures of merit, such as field-gradient enhancement or joint optimisation of $|\mathscr{H}_i|$ and $\tilde{G}_i$, offering a flexible pathway for tailored chiral-field engineering. Machine learning thus provides a general and scalable route for designing highly chiral, low-loss microwave resonators with complex yet manufacturable three-dimensional metallic boundaries, enabling applications in enantioselective spectroscopy, parity-violation experiments, axion haloscopes, and beyond.

ACKNOWLEDGEMENTS

This work was funded by the Australian Research Council Centre of Excellence for Engineered Quantum Systems (CE170100009) and the Centre of Excellence for Dark Matter Particle Physics (CE200100008).

REFERENCES

[1] F. Alpeggiani, K. Y. Bliokh, F. Nori, and L. Kuipers, Phys. Rev. Lett. **120**, 243605 (2018).
[2] K. Y. Bliokh, Y. S. Kivshar, and F. Nori, Phys. Rev. Lett. **113**, 033601 (2014).
[3] J. Martínez-Romeu, I. Diez, S. Golat, F. J. Rodríguez-Fortuño, and A. Martínez, Photon. Res. **12**, 431 (2024).
[4] K. Y. Bliokh, A. Y. Bekshaev, and F. Nori, New J. Phys. **15**, 033026 (2013).
[5] Y. Tang and A. E. Cohen, Science **332**, 333 (2011).
[6] E. Hendry, T. Carpy, J. Johnston, M. Popland, R. V. Mikhaylovskiy, A. J. Lapthorn, S. M. Kelly, L. D. Barron, N. Gadegaard, and M. Kadodwala, Nat. Nanotechnol. **5**, 783 (2010).
[7] P. Sikivie, Rev. Mod. Phys. **93**, 015004 (2021).
[8] J. F. Bourhill, E. C. I. Paterson, M. Goryachev, and M. E. Tobar, Phys. Rev. D **108**, 052014 (2023).
[9] L. A. Völker, K. Herb, E. Janitz, C. L. Degen, and J. M. Abendroth, J. Chem. Phys. **158**, 161103 (2023).
[10] E. C. I. Paterson, J. Bourhill, M. E. Tobar, and M. Goryachev, Phys. Rev. A **112**, 013530 (2025).
[11] E. C. I. Paterson, J. Bourhill, M. E. Tobar, and M. Goryachev, arXiv:2510.01217 (2025).
[12] E. C. I. Paterson, M. E. Tobar, M. Goryachev, and J. Bourhill, arXiv:2506.07320 (2025).
[13] L. Su, D. Vercruysse, J. Skarda, N. V. Sapra, J. A. Petykiewicz, and J. Vučković, Appl. Phys. Rev. **7**, 011407 (2020).
[14] A. Y. Piggott, J. Petykiewicz, L. Su, and J. Vučković, Sci. Rep. **7**, 1786 (2017).
[15] M. F. Schubert, A. K. C. Cheung, I. A. D. Williamson, A. Spyra, and D. H. Alexander, ACS Photonics **9**, 2327 (2022).

Polarisation Conversion in Bulk Hyperbolic Crystals

Katherine Stevens [1,*], Rebecca Craig[1], Mark Cunningham[1], Sonja Franke-Arnold[2], Rair Macêdo[1]

[1]James Watt School of Engineering, Electronics & Nanoscal Engineering Division, University of Glasgow, Glasgow, United Kingdom

[2]School of Physics & Astronomy, University of Glasgow, Kelvin Building, Glasgow, United Kingdom

*Corresponding author: k.stevens.2@research.gla.ac.uk

***Abstract*—We investigate polarisation control of an infrared beam reflected off the surface of a hyperbolic crystal. We illustrate the mechanism using calcite as our example material. We calculate the reflection coefficients using the 4×4 transfer matrix method, and from this obtain the Stokes vector which characterises the reflected beam.**

***Keywords*— hyperbolic dispersion, infrared, polarisation.**

I. Introduction

The control of the polarisation of radiation is a critical in many established and emerging technologies, from the original BB84 protocol, to edge enhancement imaging using vector vortex beams [1], [2]. Recently, metamaterials have been used as an alternative to traditional optical components, to provide tailored polarisation control for a variety of applications, including structured light, integrated circuits, and polarisation imaging [3], [4], [5]. However, these are often highly specific to polarisation states, where device parameters must be changed in order to tune the output, or rely on expensive nanofabrication techniques [6], [7], [8].

Here, we suggest the use of anisotropic crystals exhibiting hyperbolic behaviour, such as calcite, for polarisation control. In this crystal, hyperbolic behaviour emerges from infrared-active phonon resonances, which drive the principal components of the dielectric tensor to opposite signs. As a result, phenomena such as negative refraction, surface polaritons, and cross polarisation conversion can emerge [9], [10], [11]. For cases where the incident beam comprises both TE- and TM-polarised components (or where there is cross-polarisation conversion), these polarised components will interact differently with the dielectric tensor components, resulting in a change of phase difference between them and, as a consequence, lead to an overall polarisation state change.

II. Methods

We investigate polarisation changes that occur on reflection from an infrared beam in the xz plane incident on a semi-infinite anisotropic crystal as shown in Fig. 1, and where the crystal's optical axis is defined relative to the x, y, and z directions, and lies parallel to the x direction. We consider a general incident polarisation, described as a linear combination of the TE- and TM-polarised components with respect to the incidence plane, also referred to as s- and p-polarisation, respectively. In our case the incident beam contain equal s- and p-polarised components. Therefore, the total reflectance R can be obtained using a 4×4 transfer matrix method and can be expressed in terms of the reflectivity components for each polarised output as:

$$R = \frac{|r_{pp}|^2 + |r_{ps}|^2 + |r_{sp}|^2 + |r_{ss}|^2}{2}, \tag{1}$$

where r_{pp} is the reflection coefficient of the p-polarised components, r_{ss} is the reflection coefficient of the s-polarised component, and r_{ps}, r_{sp} are the reflection coefficients of the crossed polarised components (p-polarised to s-polarised and s-polarised to p-polarised respectively).

Assuming fully coherent radiation, the polarisation of the incident radiation can be represented by either a Jones vector or a Stokes vector. The Jones vector can be defined as any two complex electric field components that are mutually orthogonal with the propagation direction. Here we use the

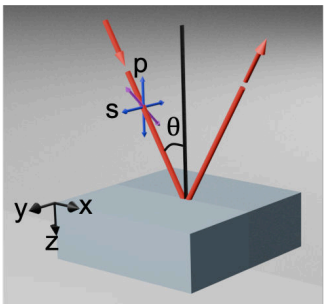

Fig. 1: Diagram showing crystal geometry of incidence in the xz plane, where θ is the angle of incidence, the p- and s-polarised components are shown by blue arrows (that lie in the yz plane) and the incident polarisation is +45° (with respect to the p- and s-polarised components) shown by a purple arrow.

s- and p-polarised components (2) as this allows for the calculation of the Jones matrix of the crystal without additional rotational matricies. The Jones vector of the incident radiation propagating along the $xz-$plane can be defined as:

$$\hat{\mathbf{E}}(\hat{\mathbf{d}}, t) = \begin{bmatrix} E_s \\ E_p \end{bmatrix} \tag{2}$$

where $\hat{\mathbf{d}}$ defines the propagation direction, E_s is the electric field of the s-polarised component (parallel to the crystal surface and referred to as the horizontal direction), and E_p is the electric field of the p-polarised component (perpendicular

to the crystal surface and referred to as the vertical direction). The Jones matrix (Equation 3) is calculated for the crystal, from which the Jones vector of the reflected ray can be calculated as $\hat{\mathbf{E}}_{\text{reflected}} = \hat{\mathbf{J}} \cdot \hat{\mathbf{E}}_{\text{incident}}$, where:

$$\hat{\mathbf{J}}_{\text{crystal}} = \begin{bmatrix} r_{ss} & r_{sp} \\ r_{ps} & r_{pp} \end{bmatrix}. \tag{3}$$

As the Jones vector includes the phase of both electric field components, it cannot be directly determined by intensity measurements. Therefore, we use the Stokes vector to allow for experimental verification. The Stokes vector is defined by four intensity measurements of the form:

$$\hat{\mathbf{S}} = \begin{bmatrix} S_0 \\ S_1 \\ S_2 \\ S_3 \end{bmatrix} = \begin{bmatrix} I_0 \\ I_{\text{horizontal}} - I_{\text{vertical}} \\ I_{+45} - I_{-45} \\ I_{\text{right-circular}} - I_{\text{left-circular}} \end{bmatrix}, \tag{4}$$

where I_0 is the total reflected intensity, $I_0 = RI_{\text{incident}}$ for a case where the incident polarisation has s- and p-polarised components.

The Stokes vector to be calculated from our Jones vector as:

$$\hat{\mathbf{S}} = \begin{bmatrix} S_0 \\ S_1 \\ S_2 \\ S_3 \end{bmatrix} = \begin{bmatrix} |E_s|^2 + |E_p|^2 \\ |E_s|^2 - |E_p|^2 \\ 2\ \mathrm{Re}(E_s {E_p}^*) \\ -2\ \mathrm{Im}(E_s {E_p}^*) \end{bmatrix}. \tag{5}$$

This allows the incident Jones vector to be defined and the experimentally measurable stokes vector to be calculated.

Stokes vectors can be graphically represented using the Poincaré sphere, where each unique polarisation state is determined by polar angle (ψ) and azimuthal angle (ϕ), and the radius $r = S_0$. When the Stokes vectors are normalised with respect to S_0, all polarisations states correspond to a position on the resultant sphere surface, where σ determines the ellipticity and ϕ determines the rotation angle of the major axis of the polarisation ellipse. This means that all linear polarisation states lie along the $S3 = 0$ axis of the sphere, and right and left circularly polarised states correspond to the $S1, S2 = 0, S3 = \pm 1$ axis respectively.

III. Results

The 4×4 transfer matrix method is used to obtain the Fresnel reflection coefficients for the s- and p-polarised components [12], [13], from which the reflected Stokes vector is calculated based on a chosen incident Jones vector. Calculations are performed with the optical axis along x as defined in Fig. 1, an incident polarisation of +45° with respect to the p- and s-polarised components and an angle of incidence of $\theta = 30°$, for wavenumbers in the range 800−1700 cm^{-1} (corresponding to 12.5−5.88 μm). The normalised Stokes vectors are plotted onto the Poincaré sphere which is shown in Fig. 2, where the stokes vector for each wavenumber is represented by a different colour. We can see that in the regions of 875−900 cm^{-1} and 1545−1570 cm^{-1}, small changes in wavenumber result in large changes in polarisation – this is a direct consequence of hyperbolic behaviour.

At a wavenumber of 800 cm^{-1}, the reflected polarisation remains linear, however is rotated to an angle of 18.8° [shown in inset (a)]. Increasing the wavenumber rotates the rotation angle. When nearing the phonon resonance the ellipticity is introduced, and the polarisation starts to rapidly change. Between 875−900 cm^{-1} the ellipticity goes from −7.8° to −8.2° and the rotation goes from −77.0° to −26.4°, passing through a minimum ellipticity of −16.0° (with corresponding rotation of −86.7°) which is shown in inset (c). The polarisation returns to linear at 1005 cm^{-1}, with a rotation of −37.7° shown on inset (f). In the second hyperbolic region, ellipticity is introduced, with a maximum ellipticity of −14.8° (with corresponding rotation of 0.7°) shown in inset (e), and a minimum ellipticity of −30.7° (with corresponding rotation of 38.1°). We then return close to a linear polarisation with a rotation of −77.1° (with corresponding ellipticity of 0.7°), increasing the wavenumber range would allow a linear polarisation to be reached.

It can be seen from Fig. 2, outside of the regions of hyperbolic dispersion, polarisation changes are dominated by amplitude differences between the reflected s- and p-polarised components, and there are only small phase changes that occur, resulting in the reflected polarisation state being of similar type to the incident state, but rotated to a new rotation angle. However within the regions of hyperbolic dispersion the introduced phase difference between the s- and p-polarised components results in elliptical polarisations, (with greater ellipticity in the larger wavenumber band due to larger dielectric tensor components). Larger changes in the amplitudes of the s- and p-polarised components also results in much larger rotation changes than in the non-hyperbolic regions.

IV. Conclusion

We have shown how the polarisation state of a reflected beam can be drastically modified by a hyperbolic crystal. Such changes could be exploited for polarisation control or sensing applications, and more complex crystal geometries could increase the control over the polarisation states. The full characterisation of these interactions is also vital when utilising hyperbolic crystals in polarisation sensitive systems.

Acknowledgments

K.S. acknowledges funding from the Engineering and Physical Sciences Research Council (EPSRC) under grant number EP/S023321/1.

References

[1] C. H. Bennett and G. Brassard, "Quantum cryptography: Public key distribution and coin tossing," *Theoretical computer science*, vol. 560, no. Journal Article, pp. 7–11, 2014.

[2] H. Ahmed, M. A. Ansari, L. Paterson, X. Yang, and X. Chen, "Vector Vortex Beam-Enabled Edge Microscopy with Dynamic Orientation Selectivity," *ACS Photonics*, vol. 12, no. 12, pp. 7013–7019, Dec. 2025.

[3] V. Aita, D. J. Roth, A. Zaleska, A. V. Krasavin, L. H. Nicholls, M. Shevchenko, F. J. Rodríguez-Fortuño, and A. V. Zayats, "Longitudinal field controls vector vortex beams in anisotropic epsilon-near-zero metamaterials," *Nature Communications*, vol. 16, no. 1, p. 3807, Apr. 2025.

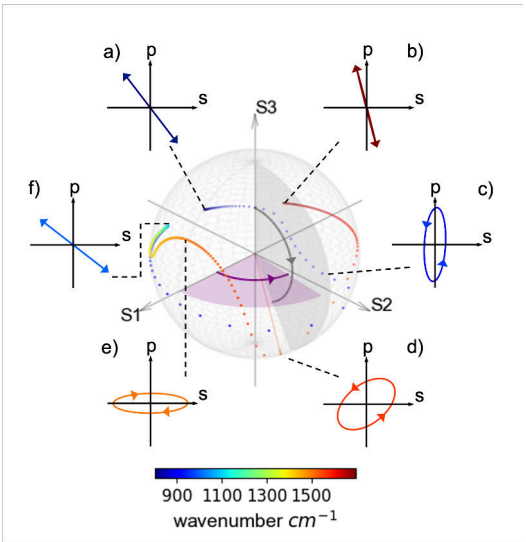

Fig. 2: Normalised Stokes parameters plotted on the Poincaré sphere, for an incident polarisation of +45° and an angle of incidence of $\theta = 30°$ where the optical axis is aligned with the x-direction, for a wavenumber range of 800-1700cm^{-1}. For a wavenumber of 1560 cm^{-1} the ψ is shown by the purple shaded region and ϕ is shown by the grey shaded region. Insets (a)-(f) show the polarisation ellipse for wavenumbers 800, 890, 1005, 1500, 1560 and 1700 cm^{-1} respectively.

[4] Y. Zhao, J. Xiang, A. He, Y. He, X. Guo, and Y. Su, "Metamaterial-enabled Fully On-Chip Polarization-Handling Devices," *Laser & Photonics Reviews*, vol. 17, no. 11, p. 2300320, 2023.

[5] T. Zhu, L. Wang, W. Jing, J. Deng, J. Ye, Y. Zhang, Z. Chu, J. Zhou, X. Chen, X. Li, W. Lu, and X. Shen, "Circular Polarimetric Imaging with a Metamaterial Integrated Long-Wavelength Infrared Focal Plane Array," *Advanced Science*, vol. 12, no. 39, p. e09292, Jul. 2025.

[6] J. Chen, F. Yu, X. Liu, Y. Bao, R. Chen, Z. Zhao, J. Wang, X. Wang, W. Liu, Y. Shi, C.-W. Qiu, X. Chen, W. Lu, and G. Li, "Polychromatic full-polarization control in mid-infrared light," *Light: Science & Applications*, vol. 12, no. 1, p. 105, May 2023.

[7] X. Shi, Z. Liang, F. Yang, S. Guo, X. Wei, Z. Wu, W. Sun, X. Chen, and H. Xu, "Universal polarization control with metasurfaces," *Applied Physics Letters*, vol. 126, no. 15, p. 151701, Apr. 2025.

[8] T.-Y. Lin, S.-H. Huang, P.-C. Chen, Y.-C. Lin, C.-P. Lin, S.-Y. Chen, and P. C. Wu, "Nearly Full-Stokes Polarization Control Enabled by Geometric Polarization in Broadband Metasurfaces," *Nano Letters*, vol. 25, no. 26, pp. 10 579–10 587, Jul. 2025.

[9] T. Dumelow, R. R. da Silva, R. M. da Silva, J. A. P. da Costa, S. B. Honorato, and A. P. Ayala, "Negative Refraction of Far-Infrared Radiation in Quartz," *Optics and Photonics News*, vol. 22, no. 12, pp. 42–42, Dec. 2011.

[10] W. Ma, G. Hu, D. Hu, R. Chen, T. Sun, X. Zhang, Q. Dai, Y. Zeng, A. Alù, C.-W. Qiu, and P. Li, "Ghost hyperbolic surface polaritons in bulk anisotropic crystals," *Nature*, vol. 596, no. 7872, pp. 362–366, Aug. 2021.

[11] X. Wu, C. A. McEleney, Z. Shi, M. González-Jiménez, and R. Macêdo, "Asymmetric Reflection Induced in Reciprocal Hyperbolic Materials," *ACS Photonics*, vol. 9, no. 8, pp. 2774–2782, Aug. 2022.

[12] P. Yeh, "Optics of anisotropic layered media: A new 4 × 4 matrix algebra," *Surface Science*, vol. 96, no. 1, pp. 41–53, Jun. 1980.

[13] R. Chipman, W. S. T. Lam, and G. Young, *Polarized Light and Optical Systems*. Boca Raton: CRC Press, Jul. 2018.

Towards a BIC-based optomechanical polarization modulator

Chiara Brugnoni[1,*], Giuseppe E. Lio[1], Grazia Salerno[1], Simone Zanotto,[2] Alessandro Tredicucci[1,2], Alessandro Pitanti[1,2]

[1]Department of Physics, University of Pisa, Italy
[2]CNR - Nanoscience institute, Pisa, Italy
*Corresponding author: c.brugnoni@studenti.unipi.it

***Abstract*—This work proposes a polarization modulator in the infrared range, exploiting optomechanical interaction of Bound-states-In-the-Continuum (BICs) electromagnetic resonances and vibrational modes in MicroElectroMechanical Systems (MEMS). BICs topological nature, forming polarization vortices in the reciprocal space, enables rapid polarization switching through controlled mechanical tilting of the device.**

***Keywords*— optomechanics, Bound states In the Continuum, MEMS, polarization modulation, infrared photonics**

I. Introduction

In recent years, optical metasurfaces have revealed powerful control over all the parameters of electromagnetic radiation. Among the others, interesting topological modes can be designed by patterning semiconductor slabs: Bound-states-In-the-Continuum (BICs) are a prime example of this, since their far-field radiation forms polarization vortices in the reciprocal space, making them suitable for quasi-static control and manipulation of the polarization of light [1]. Combined with their high Q-factor, this makes the use of these modes very appealing for advanced light manipulation. Albeit flexible-by-design, standard operation of optical metasurfaces offers static control, whereas dynamical effect would be favorable for advanced applications. To address this issue, optomechanical polarization modulators based on optical metasurfaces have been recently reported [2], opening the route for advanced dynamical control of the rotational degree of freedom of light via mechanical resonances, which can be controlled introducing Micro-Electro-Mechanical Systems (MEMS) actuators [3].

This work proposes a novel concept for a polarization modulator, operating in the infrared range and exploiting the optomechanical interaction of BICs electromagnetic resonances and MEMS vibrational modes. The topological nature of BICs can be exploited to rapidly switch the polarization of its eigenmodes by tilting the suspended resonator via one of its torsional mechanical modes.

II. Methods

Our work towards the realization of a BIC-based optomechanical polarization modulator started with designing the device via numerical simulations. We computed numerical simulations with Comsol Multiphysics, a partial differential equation solver based on the finite element method. Our model was based on Si_3N_4 trampoline membrane resonators, which have revealed exceptional mechanical properties with ultra-high Q-factors [4]. Despite the material reduced refractive index with respect to silicon, silicon nitride thin films can support near-infrared light guided modes, which have been exploited in integrated devices with different functionalities [5].

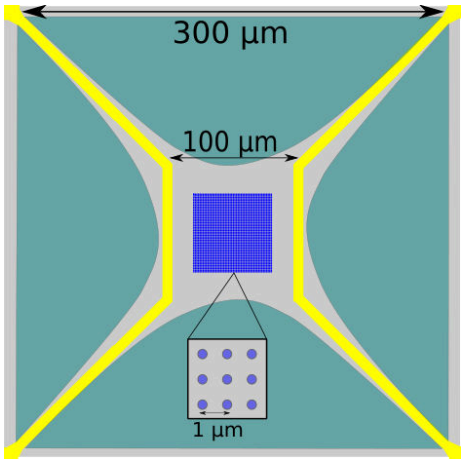

Fig. 1. **Sketch of the hybrid device.** Schematics of the Si_3N_4 trampoline membrane (grey area) composed of a central square pad, on which surface a square array of circular holes with radius $r = 150$ nm (blue circles) is inscribed, and connected to the substrate through four narrow legs on which run the electric contacts (yellow segments).

The sketch of the hybrid device is shown in Fig. 1. It is composed by a square trampoline membrane whose central plate has been patterned with a square lattice of cylindrical holes. Furthermore, we considered a possible deposition of metallic contacts upon the trampoline tethers to exploit Lorentz-based forcing when the device is placed within a planar magnetic field, a standard technique for MEMS resonators [6]. The geometrical parameters of the final device have been identified employing numerical simulations. A frequency-domain analysis of the mechanical motion, upon

Lorentz-force driving a single contact, allowed us to identify the frequency of the first excited eigenmode, which laterally tilts the membrane central plate as sketched in the inset of Fig. 2. A quantification of the tilt angle as a function of the applied voltage, assuming a contact resistance of $\sim$ 200 Ω and a homogeneous static field of $\sim$ 200 mT, can be further extracted from the simulation. Final results have been reported in Fig. 2, where we can appreciate a substantial tilt, both considering low-stress and high-stress 300 nm thick silicon nitride films, characterized by a film planar stress of 200 and 900 MPa and a resonance frequency of 885 kHz and 1667 kHz, respectively.

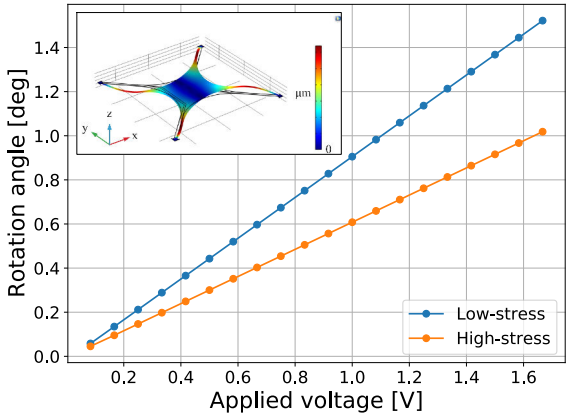

Fig. 2. **Calibration of the trampoline deflection from numerical results.** Plot obtained from numerical results, for both low-stress (blue) and high-stress (orange) Si_3N_4, showing the linear relation between the deflection angle of the trampoline central pad with respect to the driving voltage applied to actuate its torsional mode (inset).

As a second step, we simulated the photonic characteristics of an optical metasurface designed by patterning the central plate of the trampoline membrane. We performed photonic eigenfrequency simulations considering the unit cell of a square lattice of cylindrical holes; sweeping the Bloch periodic conditions at the cell outermost edges we can obtain the photonic band structure. The best set of parameters, reported in Tab. I, give two BICs within the range of the available NIR laser; their frequency dispersion around the Γ point can be seen in Fig. 3 (a). One of the hints towards their BIC nature can be seen by evaluating their radiative Q-factors, reported in Fig. 3 (b), which diverge at the Γ point as expected by symmetry-protected BICs.

While these results have been obtained by considering a one-dimensional path in the reciprocal space crossing Γ along k_x, the topological nature of the BICs can be unveiled by considering their polarization in the far-field at different wavectors in the k_x-k_y plane. Employing a real dielectric constant for the material slab and a $\hat{z}$-symmetric device, we constrain the far-field polarization to be linear. The polarization vectors with their own orientation have been plotted in the quiver plots of

TABLE I
SIMULATION PARAMETERS

Material: Si_3N_4	
Density	3100 kg m^{-3}
Young's modulus	250 GPa
Poisson's ratio	0.23
Refractive index	2
Intrinsic stress (high)	900 MPa
Intrinsic stress (low)	200 MPa
Geometry: suspended trampoline	
Thickness	300 nm
Outer frame size	300 μm
Tethers width	5 μm
Central plate size	100 μm
Holes radius	150 nm
Lattice constant	1 μm

Fig. 3 (c) and (d): it is evident to see the polarization rotation around Γ, highlighting two polarization vortices with winding numbers ± 1, respectively.

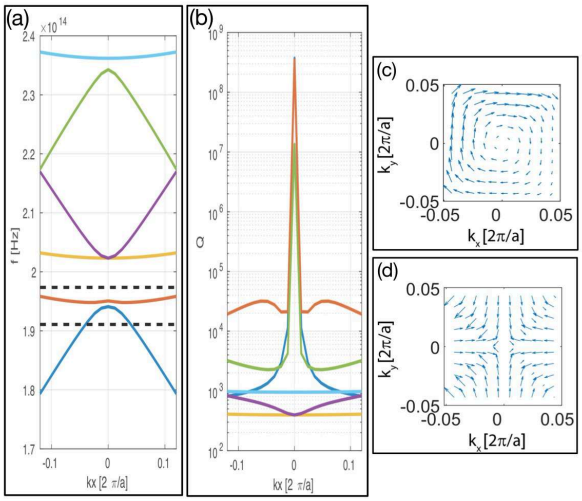

Fig. 3. **Photonic bands structure with relative Q-factors and BIC polarization vortices.** Photonic bands structure of the simulated photonic pattern (a) and relative Q-factors (b), with quiver plots of the far-field polarization state of the two BICs (red and blue curves) in the reciprocal space (c,d).

III. Results and Discussion

Mechanical and optical designs can be combined in a hybrid optomechanical device such as the one shown in Fig. 1. Combining typical driving voltages around 1 V_{RMS} to excite the first excited mode, which tilts the membrane in the $\hat{x} - \hat{z}$ plane with static tilting along the orthogonal plane $\hat{y} - \hat{z}$, one can expect a $\pi/2$ polarization rotation at MHz frequency, strongly competing with commercial polarization modulators based on macroscopic moving optical elements ceiling at an operating frequency of $\sim$ 1 kHz.

As a preliminary step before the realization of the final device, we combined the designed photonic structure with a

trampoline membrane resonator. To this end, we prepared a Si_3N_4/Si/Si_3N_4 chip with thicknesses 300nm/250μm/300nm, by spin-coating AR-P 6200 resist (CSAR). The resist layer has been exposed by an Electron Beam Lithography (EBL) to a 30 keV accelerated electron beam to define the desired mask. The silicon nitride layer has been removed by a Reactive Ion Etching (RIE) with an Inductively Coupled Plasma (ICP) step based on SF_6 and performed by a private company (CamGraphic). The final step was performed by wet etching with an hot KOH 30% solution which completely suspended the device by removing the silicon underneath. A Scanning Electron Microscope (SEM) image of the sample after this final step is reported in Fig. 4.

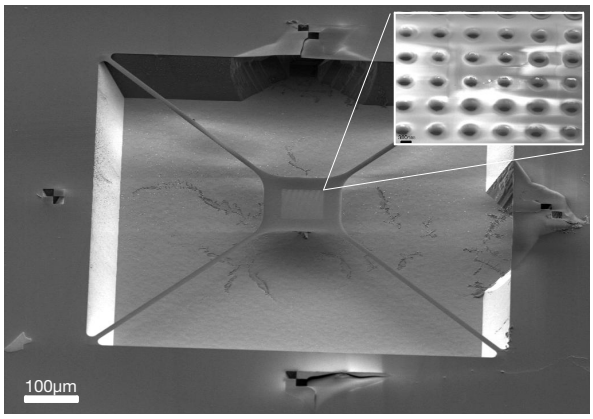

Fig. 4. **SEM image of the final device.** Released structure of the trampoline resonator, composed of a square central pad suspended through four narrow legs, and a portion of the photonic pattern of nanometric circular holes etched on its central pad (inset).

While the combination of mechanical and optical structures is promising for the realization of the final device, which would also include electrical contacts, the possibility of exploiting geometrical mechanical nonlinearities such as the Duffing one makes the metal-free membrane also interesting. By driving the fundamental membrane motion via a piezo-actuator well into the nonlinear regime, it is possible to couple higher order modes which would determine a metasurface tilt resulting in polarization modulation through BICs control.

IV. Conclusions

This work aimed at developing a device able to dynamically modulate the polarization of light in a controlled way.
The numerical results demonstrated the potential of the device as a linear polarization modulator, showing large deflection angles, when exciting the first excited vibrational mode of the square trampoline, and BIC states hosted by the photonic pattern realized in the material of the final device. The fabrication process, which followed to realize the desired device, resulted in an overall yield of about 30%, which is a promising starting point to obtain a device working in the right frequency range. As a future perspective, we plan to fabricate the final sample combining interesting photonic structures with trampoline resonators, which can be actuated in a versatile fashion using embedded metallic contacts.
Although the achievable membrane tilts are small, the extreme sensitivity of BICs is expected to ensure strong effects. Furthermore, mechanical vibrations in the MHz range would make this system highly attractive for fast polarization control, far surpassing macroscopic optical elements limited to ~ 1 kHz. Finally, the possibility of exploiting geometrical mechanical nonlinearities makes the metal-free membrane also interesting, since it makes it possible to couple higher order modes determining a metasurface tilt which would result in polarization modulation through BICs control.

References

[1] M. Kang et al., "Coherent full polarization control based on bound states in the continuum", *Nature Communications*, vol. 13, 2022.
[2] S. Zanotto, A. Tredicucci, D. Navarro-Urrios, M. Cecchini, G. Biasiol, D. Mencarelli, L. Pierantoni, and A. Pitanti, "Optomechanics of Chiral Dielectric Metasurfaces", *Advanced Optical Materials*, vol. 8, 2020.
[3] C. Meng et al., "Dynamic piezoelectric MEMS-based optical metasurfaces", *Science Advances*, vol. 7, 2021.
[4] Y. Tsaturian et al., "Ultracoherent nanomechanical resonators via soft clamping and dissipation dilution", *Nature Nanotechnology*, vol. 12, 2017.
[5] L. Vicarelli, A. Tredicucci, and A. Pitanti, "Micromechanical bolometers for subterahertz detection at room temperature", *ACS Photonics*, vol. 01, 2022.
[6] M.H. Chien et al., "Nanoelectromechanical position-sensitive detector with picometer resolution", *ACS Photonics*, vol. 7, 2020.

Elasticity-Driven Wrinkled PDMS Structures for Tailoring Optical Properties Across the Hyperspectral Range

Urszula Malecka[1,*], Patrycja Wytrych[1], Tomasz Stefaniuk[1]

[1] Faculty of Physics, University of Warsaw, Pasteura 5, Warsaw, Poland
*Corresponding author: u.malecka@student.uw.edu.pl

***Abstract*—We present a controllable and scalable approach for fabricating tunable photonic structures based on patterned PDMS and angle-dependent PVD deposition. The optical response of structures can be tailored across the hyperspectral range by applying mechanical strain after fabrication. This strategy enables precise control of properties and supports versatile optical devices.**

***Keywords*— PDMS, slot-die coating, metamaterials, wrinkled plasmonic metastructures, elastic polymers, self-organization, tunability.**

I. Introduction

Tailoring the optical properties of a photonic structure over a wide wavelength range holds significant potential for industrial applications, for example, in passive radiative cooling. However, large-scale structuring is often costly, and post-fabrication tuning of the optical properties remains challenging. We propose a mechanism based on an elastic polymer with periodic metasurfaces, which would allow for mechanical modifications of the optical properties of the structure throughout the hyperspectral range.

In our approach, large-scale patterning is enabled by combining mechanical strain and oxygen plasma treatment. When PDMS is exposed to oxygen plasma, reactive oxygen species attack methyl groups on the surface. Further oxidation leads to the formation of silanol ($Si-OH$) groups. The mechanical properties of treated PDMS differ from those of the untreated polymer. Silanol groups have a glass-like structure, making the topmost oxidized layer stiffer and more brittle. Thus, treated samples exhibit substantial differences in Young's modulus between the surface and the inner part, causing mechanical stress at the interface [1], [2]. To relieve this tension, the surface of the polymer buckles, forming a sinusoidal pattern. In order to ensure that the wrinkles are parallel to each other, mechanical strain is induced during the plasma treatment.

Theoretically, the period of the wrinkles depends on the thickness of the topmost glass-like film h_f and on Young's moduli of this stiff film E_f and of unoxidised PDMS E_s:

$$\lambda = 2\pi h_f \left(\frac{E_f \left(1-\nu_s^2\right)}{3E_S \left(1-\nu_f^2\right)} \right)^{\frac{1}{3}}. \tag{1}$$

The Poisson's ratios of the stiff layer ν_f and pure PDMS ν_s are sometimes also taken into account, although they are often neglected for simplicity [3], [4]. According to this model, the wrinkle period should scale linearly with the thickness of the oxidized topmost layer. Consequently, it is expected to increase with plasma treatment time, although the relationship between oxidation time and layer thickness is not necessarily linear. The Young's modulus of PDMS depends on the concentration of the curing agent and the polymerization conditions [5].

The wrinkle morphology can be further tuned after fabrication by applying mechanical strain to the elastomeric substrate. Stretching the material modifies the wrinkle amplitude and wavelength, providing an additional degree of control over the optical response of the structure. However, this approach alone is insufficient to enable tuning across the full spectral range. Therefore, a viable mechanism for tailoring the optical response of the samples involves utilizing the shadow effect to deposit metal-oxide layers on the hills of sinusoidal wrinkles (see Fig 1).

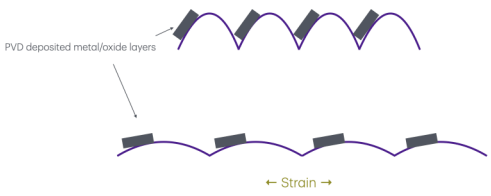

Fig. 1: Tunability scheme.

Stretching of the polymer leads to reorientation of the deposited layers, which changes the optical response of the structure. However, for this mechanism to be efficient, the deposited structure must exhibit a strong angular dependence of the optical response, preferably occurring simultaneously

in different spectral ranges. Therefore, resonant structures are favored, as their optical response relies strongly on the constructive interference of incident light. The optical path inside the structure depends on the angle of incidence, which can either promote or suppress constructive interference. Moreover, structures with well-defined resonance peaks are easier to investigate using optical methods.

II. Methods

Polydimethylsiloxane (PDMS) was prepared using the Sylgard 184 Silicone Elastomer Kit according to the manufacturer's instructions. The structuring process consisted of several steps. First, the PDMS solution was coated onto a glass substrate. The sample was then placed in a vacuum furnace and polymerized for 24 h at $80\,^{\circ}\mathrm{C}$. After polymerization, the sample was removed from the furnace and placed in a water bath. The separated polymer film was subsequently mounted in a custom-made stretching apparatus. After applying the desired strain, the sample was clamped between two rigid frames to maintain the deformation. It was then removed from the stretching apparatus and placed in a plasma cleaner (Diener Zepto 200 W) for oxygen plasma treatment. In the final step, the strain was released after plasma treatment, revealing a self-organized wrinkled structure (see Fig. 2). The resulting structural coloration was visible to the naked eye, as the sample exhibited opalescence similar to that of a diffraction grating.

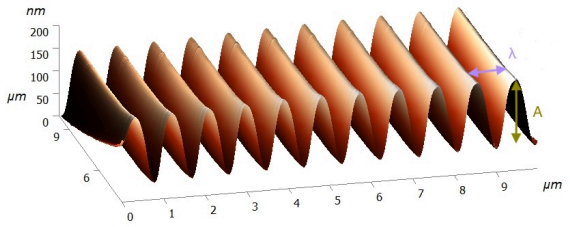

Fig. 2: AFM 3D image of the wrinkled sample. The surface profile can be approximated by a sinusoidal function characterized by the period λ and amplitude A.

The subsequent step involved depositing metal–oxide layers on top of the periodic samples in order to test the proposed tunability mechanism. For this purpose, physical vapor deposition of the following exemplary stack was performed: 40 nm Ag / 160 nm SiO_2 / 25 nm Ag (Kurt J. Lesker PVD75). This coating was chosen due to its resonances in the visible spectral range and its relatively high transmittance. Otherwise, transmittance measurements using an ellipsometer would not be possible, as both coated and uncoated samples exhibit strong scattering and diffraction, while reflectance is difficult to measure accurately without the use of an integrating sphere. The presence of an optical resonance in the visible range enables direct, naked-eye evaluation of the color change induced by mechanical stretching. The samples were placed in custom 3D-printed holders oriented at an angle to achieve the so-called "shadow effect." After the deposition process was completed, the samples were coated with a thin layer of PDMS to secure the metal–oxide layer in place.

The final stage of the study focused on optical measurements of the previously characterized samples. As the RC2 ellipsometer (J.A. Woollam) provides a fast and reliable platform for optical characterization, it was used to perform transmission measurements of the samples. Each sample was measured three times: with the deposited layer, under applied strain, and after releasing the strain, for both horizontal and vertical orientations of the wrinkles.

III. Results and Discussion

Parameters of the periodic structures were found to be controllable and repeatable. The resulting self-organized wrinkles exhibited periods ranging from 300 nm to 1.65 μm and amplitudes between 40 nm and 350 nm, depending on the process conditions. Moreover, the independence of the structural parameters from the sample thickness was established. It is understandable, since according to the literature, they depend on Young's modulus, which is not connected in any way with the dimensions of the sample, but is rather an intrinsic property of the material. Additionally, a relation between said parameters and the percentage of curing agent in the solution was established.

Transmittance measurements, performed using an ellipsometer, were preceded by observations with the naked eye. At first sight, the unstretched sample is red in transmission with strong turquoise hues when the angle is altered (Fig.3a and 3b). Its colours change with the angle of observation because different wavelengths interfere constructively within the metal-dielectric-metal layer relative to normal incidence. The lamp in the background remains clearly visible. Upon applying strain, however, the sample becomes white and opaque (Fig.3c). Scattering from the uneven surface is presumably to account for this behaviour, suggesting the temporary formation of large cracks in the deposited layer. When the strain is released sample looks intact, as the protective polymer overlayer holds the whole structure in place. This particular optical response mechanism is supported by the transmission measurements, confirming the significant reduction of transmitance.

In the case of wrinkled samples deposited at an angle, mechanical deformation led to a substantial reduction in peak intensities and the disappearance of higher-order spectral features. These observations indicate that applied strain modifies the effective geometry of the structure and alters the optical path within the resonant system. The optical response is inherently complex due to scattering, diffraction, and geometric non-uniformities. Nevertheless, the experiments demonstrate that mechanically induced structural changes lead to measurable modifications of the spectral behaviour. The

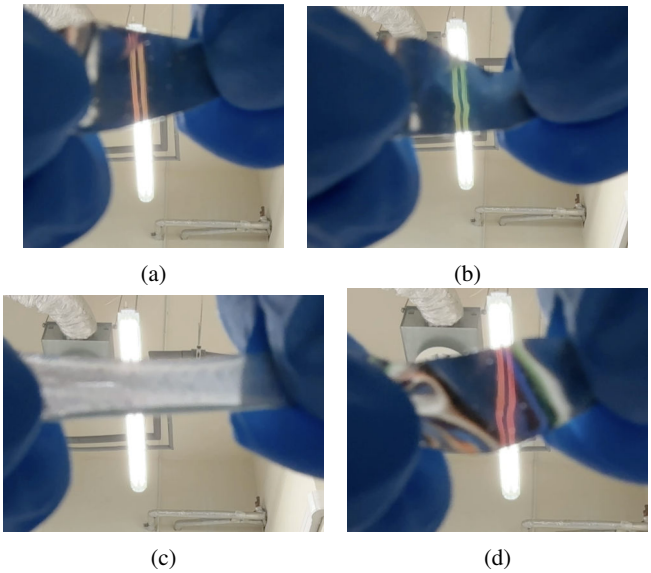

Fig. 3: A photo of PDMS film covered with 40 nm Ag/160 nm SiO_2/25 nm Ag and a protective layer of polymer on top before and during the stretching procedure stages (a) - (d). No damage to the sample was observed after releasing the strain.

colour changes observed in the visible range further support the presence of strain-dependent interference effects.

IV. Conclusion

A systematic investigation demonstrated that the wrinkle period and amplitude depend on plasma treatment time, oxygen concentration, and curing agent ratio, while remaining independent of the overall film thickness. Optical measurements confirmed the feasibility of angle-dependent deposition and revealed the emergence of a shadowing effect above $65\,^{\circ}\mathrm{C}$, enabling controlled modification of the optical response. Optical characterization was performed using ellipsometric transmittance measurements, which showed pronounced angular- and strain-dependent spectral features. Mechanical deformation was found to significantly modify the optical response of the system.

Although complex light–structure interactions were observed in periodically structured samples and require further investigation for a detailed understanding, this study establishes a scalable fabrication route and demonstrates the concept of mechanically tunable optical behaviour in wrinkled PDMS-based systems. The obtained results provide a solid experimental basis for further optimization and modelling of elastomeric photonic structures.

Acknowledgments

This study was financially supported by the National Science Center, Poland under the research project no 2022/46/E/ST5/00381.

References

[1] D. B. H. Chua, H. T. Ng, and S. F. Y. Li, "Spontaneous formation of complex and ordered structures on oxygen-plasma-treated elastomeric polydimethylsiloxane," *Applied Physics Letters*, vol. 76, no. 6, pp. 721–723, 2000. [Online]. Available: https://doi.org/10.1063/1.125873

[2] J. Genzer and J. Groenewold, "Soft matter with hard skin: From skin wrinkles to templating and material characterization," *Soft Matter*, vol. 2, pp. 310–323, 2006. [Online]. Available: http://dx.doi.org/10.1039/B516741H

[3] A. Knapp, L. J. Nebel, M. Nitschke, O. Sander, and A. Fery, "Controlling line defects in wrinkling: a pathway towards hierarchical wrinkling structures," *Soft Matter*, vol. 17, pp. 5384–5392, 2021. [Online]. Available: http://dx.doi.org/10.1039/D0SM02231D

[4] N. Bowden, W. T. S. Huck, K. E. Paul, and G. M. Whitesides, "The controlled formation of ordered, sinusoidal structures by plasma oxidation of an elastomeric polymer," *Applied Physics Letters*, vol. 75, no. 17, pp. 2557–2559, 1999. [Online]. Available: https://doi.org/10.1063/1.125076

[5] H. Hocheng, C.-M. Chen, Y.-C. Chou, and C.-H. Lin, "Study of novel electrical routing and integrated packaging on bio-compatible flexible substrates," *Microsystem Technologies*, vol. 16, no. 3, pp. 423–430, 2010. [Online]. Available: https://doi.org/10.1007/s00542-009-0930-2

Ultrasonic Needle Beam Generation in Water Using a Complex-Amplitude-Encoded Polymer Trapped-Air Acoustic Mirror

Hafiz Muhammad Imran[1,*], Marco Ricci[2], Rocco Zito[1], Dr. Stefano Laureti[1]

Dipartimento di Ingegneria Informatica, Modellistica, Elettronica e Sistemistica, University of Calabria, Italy
[2] Department of Information Engineering, Electronics and Telecommunications, Sapienza University of Rome, Italy
*Corresponding author: muhammad.imrnahafiz@dimes.unical.it

***Abstract*— This research presents a complex amplitude encoded reflective acoustic mirror that integrates super-unit phase encoding with a parabolic geometry to generate ultrasonic needle beams in water at a given focal distance. The mirror, fabricated in PLA with air trapped inside, combines phase-only modulation with geometric focusing, enabling extended depth of focus and controlled beam shaping for ultrasonic underwater imaging applications.**

Keywords— acoustic metamaterials, complex amplitude encoding, parabolic mirror, ultrasonic needle beam, water acoustics.

I. Introduction

Extended depth-of-focus ultrasonic beams are critical for biomedical imaging, nondestructive testing, and underwater sensing. Recently, complex amplitude encoding metalenses (CAEM) have demonstrated the ability to generate arbitrary ultrasonic needle beams using super-unit phase decomposition [1]. Separately, broadband reflective focusing using parabolic mirrors has been modeled through impulse-response formulations treating the mirror as a distributed secondary source [2]. In this work, we merge these two concepts by embedding CAEM phase encoding into a reflective parabolic mirror operating in water. Furthermore, the mirror is realized with plastic, exploiting the so-called trapped-air concept to overcome low impedance mismatch between water and plastic, thus preserving the intended functionality [3]. The objective is to realize a compact, passive, single-sided reflective metasurface capable of generating uniform needle beam for sound manipulation.

II. Methods

A. Complex Amplitude Encoding

The target transmission function is expressed as:

$$T(x,y) = A_0(x,y)e^{i\varphi_0(x,y)} \quad (1)$$

Here both amplitude $A_o(x,y)$ and phase $\varphi_o(x,y)$ are space varying as shown in the Figure 1. Following the CAEM strategy, the complex amplitude is decomposed into two phase-only components:

$$A_o(x,y)e^{\{i\varphi_o(x,y)\}} = 1/2\,A_{max}\,(e^{i\varphi_1(x,y)} + e^{i\varphi_2(x,y)}) \quad (2)$$

Here A_{max} is the maximum amplitude of A_o and such as $\varphi_{1,2}(x, y) = \varphi_0 \pm \theta$ where $\theta(x, y) = cos^{-1}[A_o(x, y)/A_{max}]$. These phase distributions are spatially interleaved using complementary binary masks within super-units, ensuring statistical blending and effective amplitude control [1].

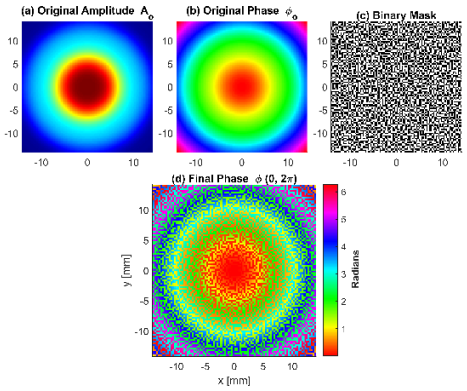

Figure 1: Complex Amplitude Encoding (a) Original Amplitude $A_o(x,y)$; (b) Original Phase φ_o (x,y); (c) Binary Mask (Complementary Mask) for super units and, by combining all of them, the (d) Final Phase φ(x,y)

B. Reflective Parabolic Mirror Model

Unlike transmissive CAEM plates, our design embeds the encoded phase distribution onto a parabolic reflector. The reflected field is modeled using the impulse response method described for plane piston reflection [2].

$$h(\mathbf{r},t) = \int \frac{\delta(t - R/c)}{2\pi R}\, dS \quad (3)$$

Here, $h(\mathbf{r},t)$ denotes the impulse response at position $\mathbf{r}$ and time t, R is the distance between the surface element dS and the observation point, c is the speed of sound, and $\delta(\cdot)$ is the propagation delay [2]. Each point on the mirror acts as a secondary source as shown in Fig.2, and the desired reflected pressure distribution is obtained via superposition of

appropriate phase delays, obtained by realizing different path-length between the mirror surface and the trapped air volume, according to the profile of Fig.1(d).

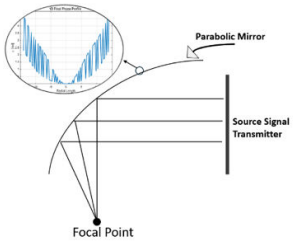

Figure 2: Schematic Diagram of the Parabolic Modulated Reflector

The geometric parabolic condition ensures equal optical path to the focal axis, while the encoded phase introduces additional spatial phase modulation to generate extended needle beam. In addition, a clever trapping of an air layer inside within the parabolic profile ensures the mirror to act as a rigid acoustic reflector in water [3].

III. Results and Discussion

Results were obtained via FEM simulations in COMSOL using full-wave acoustic modeling. The acoustic field produced by the proposed device operating in water was analyzed for input planar pressure fields with frequencies from 100 kHz to 1 MHz. The results show a focus condition over an extended frequency range, fully agreeing with the results shown in [2]. On top of that, a uniform ultrasonic needle beam is generated along the optical axis, as illustrated in Figure 3, because of the additional coded phase delay [1]. Note that at the present stage, the needling behavior is simulating by modulating the pressure field to reflect the desired phase delay. The design also demonstrates suppression of sidelobe oscillations through super-unit phase blending, as shown in Figure 4, which improves beam quality and reduces unwanted acoustic interference. The beam length can be tuned by optimizing the distribution of focal positions in the complex amplitude encoding process. Compared to purely geometric focusing, this approach enables programmable beam shaping while maintaining a compact passive structure. The design supports both single and off-axis needle beams without requiring multiple transducers or active arrays. Full simulations including explicit phase encoding on the mirror surface will be addressed in the extended version of this work.

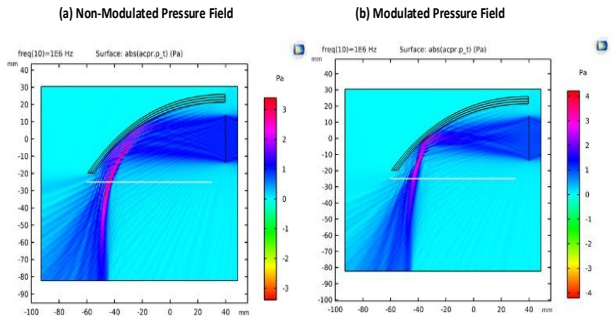

Figure 3: FEM of parabolic reflector (a) without and (b) with the complex amplitude encoded pressure. The white line is the reference cut baseline for Fig.4.

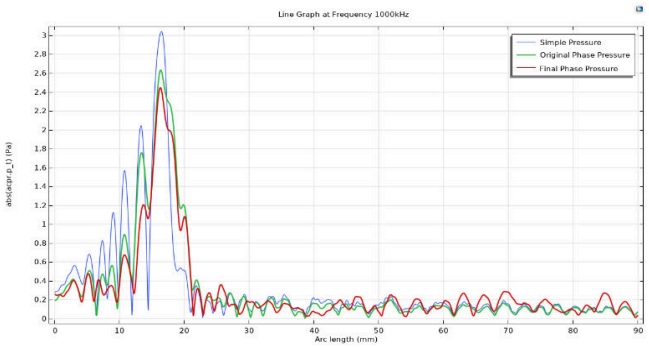

Figure 4: Line graph of Pressure field obtained at the cut-line using the different pressure field input, as per Fig.1.

IV. Conclusions

A hybrid reflective acoustic metasurface integrating complex amplitude encoding with a parabolic mirror geometry is proposed. Operating in water and fabricated in PLA exploiting the trapped-air concept, the structure enables programmable ultrasonic needle beam generation. This approach bridges transmissive acoustic metalenses and reflective focusing systems, opening pathways toward compact underwater imaging systems and single-sided broad-band pulse-echo applications. Future work includes experimental validation, ultra broadband optimization, and integration with single-element transducers for medical and underwater imaging.

Acknowledgments

This project has received funding from the European Union's EU Framework Programme for Research and Innovation Europe Horizon (HORIZON TMA MSCA Doctoral Networks) under Grant Agreement No. 101119738 "MetacMed" (www.metacmed.eu). Views and opinions expressed are however those of the author(s) only and do not necessarily reflect those of the European Union. Neither the European Union nor the granting authority can be held responsible for them.

References

[1] Y.-H. Lv, X. Chen, J. Yao, X.-F. Zhu and D.-J. Wu, "Complex amplitude encoding metalens realizing arbitrary ultrasonic needle beams," *Ultrasonics,* vol. 152, p. 107645, 2025.

[2] A. Neild, D. A. Hutchins, T. J. Robertson and D. W. Schindel, "A model for the radiated field of a plane piston after reflection from a curved surface," *Journal of the Acoustical Society of America,* vol. 116, no. 5, pp. 2793-2801, 2004.

[3] S. Laureti et al., "Trapped air metamaterial concept for ultrasonic sub-wavelength imaging in water," *Scientific Reports,* vol. 10, p. 10601, 2020.

Finite Element Simulation of Strain Measurement in Auxetic Materials via FBG Sensors

Katarzyna Majewska[1,*], Riccardo C. Moroni[1], Stefano Laureti[2]

[1]Institute of Fluid-Flow Machinery, Polish Academy of Sciences, 14 Fiszera Street 80-231 Gdańsk, Poland
[2] DIMES Department, University of Calabria, Rende, 87036, Italy
*Corresponding author: k.majewska@imp.gda.pl

***Abstract*—Auxetic materials are increasingly used in biomedical and aerospace applications. Fibre Bragg grating sensors are well-known in non-destructive testing for their precision. This work simulates a tensile test of two auxetic specimens with embedded sensors and compares the results with experimental data to validate the model.**

***Keywords*— metamaterials, auxetic, NDT/SHM, FBG sensor.**

I. Introduction

Auxetic materials are a class of metamaterials that, as a defining feature, have a negative Poisson ratio [1]. It means that these materials, under tension, expand in the directions orthogonal to the applied load. Conversely, under compression, they collapse in directions perpendicular to the applied load. A schematic of auxetic behaviour compared with normal material under tension is shown in Fig.1 As a consequence

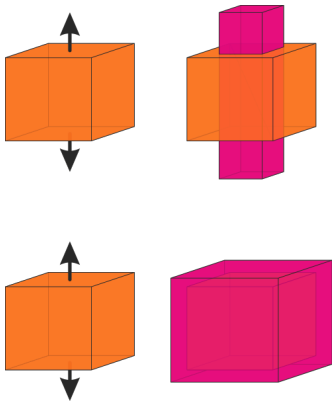

Fig. 1. On top normal material behaviour. Below auxetic material behaviour.

of this peculiar behaviour, these materials exhibit interesting features, such as increased shear, indentation and fracture resistance; synclastic behaviour, which means that if these structures are subjected to an out-of-plane bending moment, they show a dome shape; moreover, due to their deformation method, it is possible to exploit them as a variable permeability [2]. Fibre Bragg Grating (FBG) sensors are composed of an optical fibre in which a grating is inscribed. To obtain the grating, the refractive index of the fibre is modified to form a periodic pattern. As a result, this structure can reflect light with a specific wavelength. It is possible to calculate the exact reflected wavelength using the following formula [3]:

$$\lambda_B = 2n\Lambda, \tag{1}$$

in this formula, λ_B represents the Bragg wavelength, which is the reflected wavelength, n is the effective refractive index, and Λ is the periodicity of the sensor. As it is possible to infer from the formula, this kind of sensors are sensitive to deformation. In fact, when the fibre is stretched, the reflected wave shows a redshift (the reflection happens for a higher wavelength). On the contrary, during compression, the reflected wave shows a blueshift (the reflection happens for a lower wavelength). This is caused by the action of the deformation on the periodicity of the grating and on the effective refractive index. Furthermore, these sensors are sensitive to temperature, which is because temperature can also affect the periodicity of the grating through the thermal expansion coefficient and the effective refractive index through the thermal-optic effect. The relationship between the Bragg wavelength, strain and temperature is made explicit in the following formula [4]:

$$\frac{\Delta\lambda}{\lambda_B} = (1-p)(\epsilon + \alpha\Delta T) + \xi\Delta T, \tag{2}$$

where $\Delta\lambda$ represents the shift of the reflected wavelength, λ_B the Bragg wavelength, p the coefficient of the photoelatic effect, ϵ the deformation, α the thermal-expansion coefficient, ΔT the temperature difference, and ξ the thermal-optic coefficient. The possibility of monitoring auxetic materials using FBG sensors could have some potential due to the increasing importance of auxetic materials and the interesting features of FBG sensors. Nevertheless, this possibility is still poorly explored in the literature. In this paper, we want to investigate the possibility of simulating the behaviour of an FBG sensor attached to the surface of an auxetic material for measuring the stretching of the structure.

II. Methods

In previous work [5], it was demonstrated that it is feasible to attach a Fiber Bragg Grating (FBG) sensor to the surface of an auxetic structure without significantly altering its mechanical behaviour. Building upon this foundation, the present study aims to develop a comprehensive numerical model of an FBG sensor using COMSOL Multiphysics, with the objective of

simulating the sensor's response under tensile strain. The modeling process will proceed in several steps. First, the FBG sensor will be represented as a discrete element with appropriate material properties and geometrical parameters. a picture on the grating modelled in COMSOL is shown in Fig. 2. Subsequently, the auxetic specimen will be simulated under

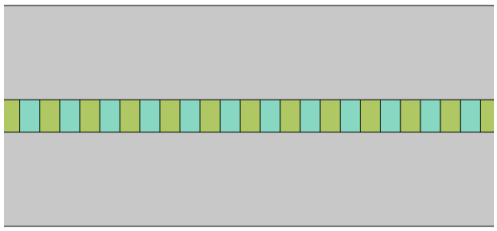

Fig. 2. Schematic of the grating geometry implemented in COMSOL.

controlled tensile loading conditions, providing a detailed map of the strain distribution at the location where the sensor is attached. Using the obtained deformation field, we will then apply the corresponding strain to the FBG model in order to predict the resulting Bragg wavelength shift, based on the well-known relationships that link strain to changes in the optical response of the sensor. This approach enables a direct correlation between the mechanical deformation of the structure and the optical signal generated by the FBG. Figure 3 shows the redshift predicted by the model for a simple tensile simulation, and the blueshift resulting from a compression simulation. Finally, the simulated wavelength shifts

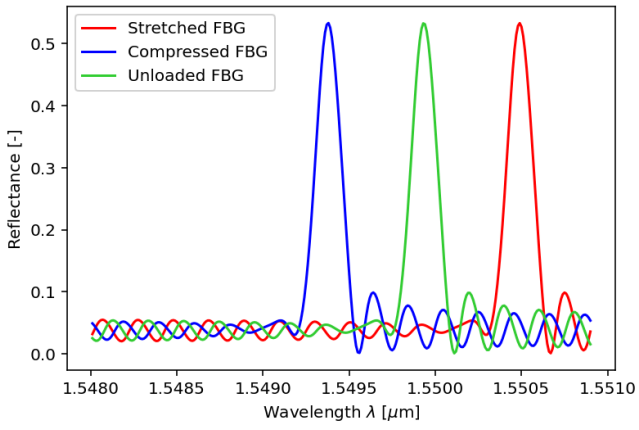

Fig. 3. FBG reflectance peak shifts under mechanical load: compression (blue) causes a blueshift, tension (red) induces a redshift, and the unloaded state (green).

will be processed to calculate the corresponding measured strains. These numerical predictions will be compared with experimental data obtained from physical testing of the sensor-embedded auxetic specimens. Through this comparison, we aim to validate the accuracy of the FBG model. The outcomes of this study will not only provide a validated computational framework for simulating FBG sensors in complex structures but also enhance the understanding of the interplay between auxetic deformation and optical sensing, paving the way for more advanced structural health monitoring applications.

III. Conclusion

This work proposes a numerical approach for simulating the behaviour of a Fibre Bragg Grating sensor attached to an auxetic structure under tensile loading. The developed model, implemented in COMSOL Multiphysics, aims to establish a correlation between the strain field generated in the auxetic material and the corresponding Bragg wavelength shift of the sensor. At this stage, the study focuses on defining the modelling strategy and the procedure that will be used to predict the optical response of the FBG based on the mechanical deformation of the structure. The comparison with future experimental results will allow validation of the proposed framework and assessment of its reliability. The presented methodology represents a preliminary step toward the integration of FBG sensors in auxetic materials for structural health monitoring applications.

Acknowledgments

This work has received funding from the European Union's EU Framework Programme for Research and Innovation Europe Horizon (HORIZON TMA MSCA Doctoral Networks) under Grant Agreement No. 101119738 "MetacMed" (www.metacmed.eu). Views and opinions expressed are, however, those of the author(s) only and do not necessarily reflect those of the European Union. Neither the European Union nor the granting authority can be held responsible for them.

References

[1] A. S. Shuaibu, J. Deng, C. Xu, V. P. Ade-Oke, A. Aliyu, and D. Momoh, "Advancing auxetic materials: Emerging development and innovative applications," *Reviews on Advanced Materials Science*, vol. 63, no. 1, 2024, Art. no. 0021, doi: 10.1515/rams-2024-0021.

[2] X. Ren, R. Das, P. Tran, T. D. Ngo, and Y. M. Xie, "Auxetic metamaterials and structures: A review," *Smart Materials and Structures*, vol. 27, no. 2, 2018, Art. no. 023001, doi: 10.1088/1361-665X/aaa61c.

[3] J. K. Sahota, N. Gupta, and D. Dhawan, "Fiber Bragg grating sensors for monitoring of physical parameters: A comprehensive review," *Optical Engineering*, vol. 59, no. 6, 2020, Art. no. 060901, doi: 10.1117/1.oe.59.6.060901.

[4] X. Li, J. Long, S. Guo, M. Yang, T. Zhang, C. An, and Y. Pei, "Experimental study on FBG sensing technology-based stress monitoring at the corners of reinforced soil retaining walls," *Science Progress*, vol. 105, no. 4, 2022, doi: 10.1177/00368504221135380.

[5] R. Moroni, A. Andrearczyk, and K. Majewska, "Monitoring auxetic structure with FBG sensor," *e-Journal of Nondestructive Testing*, vol. 31, no. 2, 2026, doi: 10.58286/32439.

Fabry–Pérot and Friedrich–Wintgen Bound States in the Continuum in a Plasmonic Double T-Cavity

A. Rezzouk[1], S. Khattou[1], M. Amrani[1,*], A. Noual[1], E.H. El Boudouti[1] and B. Djafari-Rouhani[2]

[1]LPMR, Département de Physique, Faculté des Sciences, Université Mohammed I, 6000 Oujda, Morocco
[2]IEMN, UMR CNRS 8520, Département de Physique, Université de Lille, 59655 Villeneuve d'Ascq, France
*Corresponding author: m1.amrani@ump.ac.ma

***Abstract*—We demonstrate the coexistence of twin Friedrich–Wintgen and Fabry–Pérot bound states in the continuum in a plasmonic metal–insulator–metal double T-cavity. Analytical Green's function formalism and finite-element simulations reveal the existence of multi-BICs and their transformation to Fano resonance for sensing and filtering.**

***Keywords*— FW-BIC, FP-BIC, Plasmonic cavity.**

I. Introduction

Bound states in the continuum (BICs) [1] constitute a special class of resonant modes with infinite lifetimes that remain spatially localized within a structure despite their eigenfrequencies lying inside the radiation continuum. BICs are commonly classified according to their physical formation mechanisms into three main categories [2]: symmetry-protected (or separability-protected) BICs (SP-BICs) [3], Friedrich-Wintgen (FW) BICs [4], and Fabry-Pérot (FP) BICs [5]. More recently, another type, known as twin BICs (T-BICs), has been reported in two-dimensional FP-type resonators [6]. BICs have attracted considerable attention due to their high impact on nanophotonic structures, enabling high-performance sensing platforms through enhanced light–matter interaction at the nanoscale [7]. Recently, increasing attention has been devoted to the interaction mechanisms between FP- and FW-BICs in multi-cavity systems [8]. Among such configurations, the T-shaped cavity has been investigated in photonic and plasmonic platforms to realize FW-BICs [9].

In this work, we show that a plasmonic metal–insulator–metal (MIM) double-T cavity can support the simultaneous existence of FW- and FP-BICs. The MIM waveguide system studied here is composed of two identical T-shaped cavities separated by a distance d_4 (see the illustration of the double T-cavity in Figs. 1 and 2). Each T-shaped cavity consists of two lateral arms with lengths d_1 and d_2, connected to an infinite MIM waveguide by a stub of length d_3.The total length of the horizontal waveguides is kept constant, $d = d_3 = d_1 + d_2$ = 540 nm. The detuning between the two waveguides is defined as $\delta = d_2 - d_1$, which is treated as a tunable parameter. Using both the analytical Green's function formalism [10] and finite-element simulations (COMSOL Multiphysics), we investigate the coexistence and interplay of FW-BICs and FP-BICs in this structure as a function of the geometrical parameters. Each T-cavity supports a FW-BIC, resulting from destructive interference between two resonant modes within the same cavity [9]. The coupling between these FW-BICs in the double T-structure leads to the formation of doubly degenerate BICs, referred to as T-BICs. In addition, FP-BICs appear for discrete values of the separation between cavities, corresponding to a round-trip phase accumulation equal to an integer multiple of 2π. When the BIC conditions are slightly broken, these modes evolve into Fano resonance.

II. Results and Discussion

First, we consider the symmetric case $\delta = 0$ (i.e., $d_1 = d_2$). To examine the coexistence and interaction between T-BICs and FP-BICs, Fig. 1(a) shows the transmission as a function of frequency and the separation d_4. The horizontal line at $f = 198$ THz corresponds to T-BICs, which is independent of d_4. Two additional resonances shift to lower frequencies as d_4 increases and collapse at $d_4 = 540$ nm and $d_4 = 1080$ nm, forming FP-BICs. Their intersection with the T-BICs at $f = 198$ THz results in triple-degenerate BICs. Figures 1(b)–(d) present transmission spectra for selected d_4 values. The analytical results obtained by the Green's function method (blue solid lines) are in good agreement with the numerical results using Comsol Multiphysics (red open circles). For $d_4 = 430$ nm, a Fano resonance appears whose linewidth decreases as d_4 approaches 540 nm. At $d_4 = 540$ nm, the resonance collapses into an FP-BIC, coexisting with the T-BIC and forming a triple-degenerate BIC. Increasing d_4 beyond this value reopens the resonance as a Fano line shape. The spatial magnetic-field distributions corresponding to the T-BIC, FP-BIC, and Fano resonance are shown in Figs. 1(e)–(g) under a local magnetic excitation (red arrow). For $f = 198$ THz and $d_4 = 430$ nm, the degenerate T-BICs (Fig. 1(e)) exhibit strong localization within the lateral arms of the T-cavities without extending into the surrounding waveguides. In contrast, the Fano resonance (Fig. 1(f)) displays significant field leakage throughout the structure, enabling transmission across the system. The field map of the FP-BIC (Fig. 1(g)) reveals a mode tightly confined within the double T-cavity, with no radiation escaping when the excitation is applied in the waveguide of length d_4.

Next, the symmetry of the cavity is broken by setting $\delta \neq 0$. Figure 2(a) shows the transmission as a function of frequency and d_4 for $\delta = 80$ nm. As d_4 varies, the linewidths of

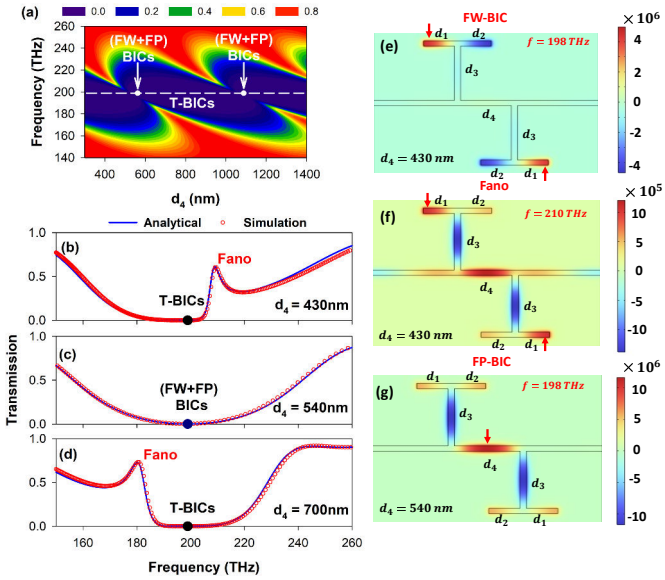

Fig. 1. (a) Variation of the transmission magnitude versus the frequency and d_4, for d_3 = 540 nm and δ = 0 nm. (b)–(d) Transmission spectra as a function of the wavelength for three values of d_4. The blue and red curves indicate the analytical and numerical results, respectively. Magnetic (H_z) field maps of (e) the FW-BIC, (f) the Fano resonance for d_4 = 430 nm and (g) the FP-BIC for d_4 = 540 nm. The positions of the excitations are shown by the red arrows.

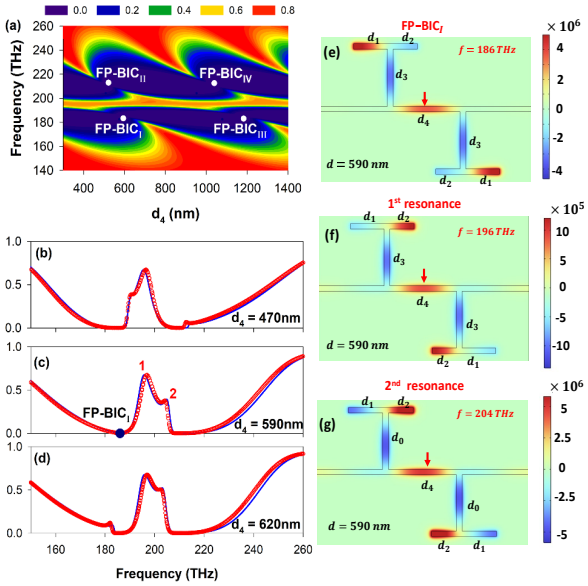

Fig. 2. (a) Variation of the transmission magnitude versus the frequency and d_4. (b)–(d) Transmission spectra at representative values of d_4. Magnetic field maps of (e) FP-BIC$_I$ at $f = 186$ THz and $d_4 = 590$ nm, (f) and (g) of the Fano resonances at $f = 196$ THz (mode 1) and $f = 204$ THz (mode 2) for $d_4 = 590$ nm, under local excitation applied at the waveguide d_4.

the symmetric and antisymmetric FP resonances progressively vanish, leading to the formation of FP-BIC$_I$ and FP-BIC$_{II}$ around $d_4 = d_3 = d = 540$ nm and FP-BIC$_{III}$ and FP-BIC$_{IV}$ around $d_4 = 2d_3 = 2d = 1080$ nm. Figures 2(b)–(d) show transmission spectra as a function of frequency for selected values of d_4. For $d_4 = 470$ nm (Fig. 2(b)), three resonances appear. The second one, around $f = 200$ THz, is broad and remains nearly unchanged as d_4 varies. In contrast, the lowest Fano resonance at $f = 189$ THz gradually evolves into a FP-BIC$_I$ at $f = 186$ THz Fig. 2(c)). Increasing d_4 further to 620 nm (Fig. 2(e)) reopens the resonance, producing a Fano line shape near $f = 182$ THz. The magnetic field map associated with FP-BIC$_I$ at $f = 186$ THz (Fig. 2(e)) clearly shows that this mode is tightly confined within the double T-cavity. The field map of the two resonant modes 1 and 2 in Figs. 2(f) and (g) are fully excited and propagate through the entire structure, resulting in full transmission.

III. Conclusion

In conclusion, we investigated the coexistence of FW- and FP-BICs in a plasmonic MIM double T-cavity operating in the infrared regime. Analytical Green's-function modeling, supported by finite-element simulations, reveals twin FW-BICs localized in each T-cavity and FP-BICs appearing for discrete cavity separations. Their interaction can produce triple degenerate BICs, while breaking the BIC conditions leads to Fano and plasmon-induced reflection (PIR) resonances [11]. These results provide insight into multi-BIC formation in plasmonic waveguides and highlight their potential for compact sensing and integrated photonic filtering devices. Further, BICs enhance light–matter interaction and can produce strong emission when the BIC condition is slightly broken. Indeed, the transformation from a FW-BIC to a quasi-FW-BIC can lead to far-field enhanced radiation outside the double T-cavity, originating from the coherent collective emission of the leaky modes (for more details, see Ref. [11]).

References

[1] J. von Neumann et al., Uber merkwurdige diskrete Eigenwerte, Phys. Z. **30**, 465 (1929).
[2] C. W. Hsu et al., Bound states in the continuum, Nat. Rev. Mater. **1**, 16048 (2016).
[3] Z. F. Sadrieva et al., Experimental observation of a symmetry-protected bound state in the continuum in a chain of dielectric disks, Phys. Rev. A **99**, 053804 (2019).
[4] H. Friedrich et al., Interfering resonances and bound states in the continuum, Phys. Rev. A **32**, 3231 (1985).
[5] D. C. Marinica et al., Bound states in the continuum in photonics, Phys. Rev. Lett. **100**, 183902 (2008).
[6] N. M. Shubin et al., Twin Bound States in the Continuum in a Waveguide Fabry-Pérot Resonator, JETP Lett. **118**, 401–407 (2023).
[7] D. N. Maksimov et al., Enhanced sensitivity of an all-dielectric refractive index sensor with an optical bound state in the continuum, Phys. Rev. A **105**, 033518 (2022).
[8] Y. Rezzouk et al., Fabry-Pérot and Friedrich-Wintgen bound states in the continuum in a photonic triple-stub cavity, Phys. Rev. B **109**, 235431 (2024).
[9] S. Khattou et al., Friedrich-Wintgen bound states in the continuum in a photonic and plasmonic T-shaped cavity: Application to filtering and sensing, Phys. Rev. Appl. **20**, 044015 (2023).
[10] L. Dobrzynski et al., Photonics, Elsevier (2020).
[11] A. Rezzouk et al., Coexistence and interplay of Fabry-Pérot and twin Friedrich-Wintgen bound states in the continuum in a plasmonic double T-cavity, J. Appl. Phys. (accepted).

Auxetic Materials for Biomimicry: Designing for Tendon-Like Behavior

Riccardo C. Moroni*, Katarzyna Majewska

Institute of Fluid-Flow Machinary, Polish Academy of Science, Gdańsk, Poland
*Corresponding author: rmoroni@imp.gda.pl

***Abstract*—Tendon healing is slow and rarely restores full functionality. Studies show that in the toe region, up to 2% deformation, tendons behave as auxetic materials. This work aims to optimize a 2D re-entrant auxetic cell to replicate tendon Poisson ratio and stiffness for improved biomechanical performance.**

***Keywords*—metamaterials, auxetic materials, tendon, biomimicry.**

I. Introduction

The physiological role of tendons is to transmit load from muscles to bones to permit the body movement. They are composed by a hierarchical structure of collagen fibres. The hierarchical structure of the tendon is illustrated in Fig. 1. Over 30 million tendon interventions happened every year

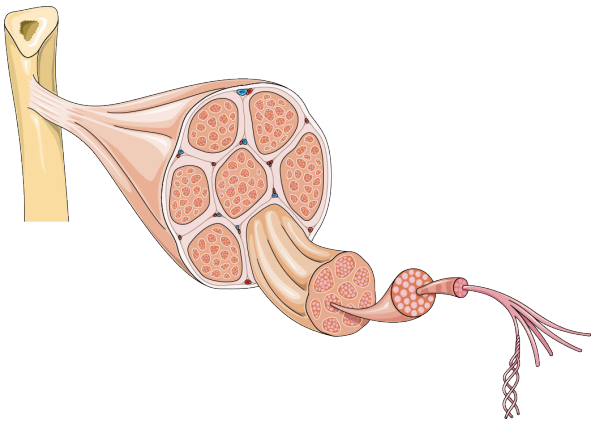

Fig. 1. Hierarchical structure of tendons. Image credit: Smart Servier licensed under CC BY 4.0.

worldwide [1]. Despite the increased possibility of modern medicine, it is still impossible to achieve a full restoration of the pre-injured performance of the tendon, for example the tensile strength of a healed tendon can be 30% less then the healthy one [2]. As a consequence the risk of recurrence is high and the functionality of the tendon can be reduce according to the severity of the residual damage. In 2015 Gatt et al. [3] report that tendons shows an auxetic behaviour. Auxetic material are a class of mechanical metamaterial that present a negative Poisson ratio. Under tensile loading, they expand perpendicular to the applied force, while under compressive loading, they contract laterally. This study focuses on biomimicry, a design approach inspired by natural structures and processes. The term "biomimicry" comes from the Greek words "bios" (life) and "mimesis" (imitation), reflecting the goal of replicating efficient strategies found in nature. Tendon deformation can be divided in three phases. The first one is called toe region (between 0-2% of deformation), in this phase tendon shows a wave-form shape which disappear increasing strain. *In vivo* tendon usually deform in this zone. The second phase is the strain region (between 2-6% of deformation) in this phase collagen fibre are no more crimped and they are strained by the applied load. The third phase is associated with the tendon rupture [4]. Fig. 2 provides a schematic representation of the stress–strain behaviour of tendons. Specifically, Gatt et al. demonstrate that in the toe region Achilles tendon exhibit a negative Poisson ratio. Integrating auxeticity in the design of artificial substitute can result in a more effective device. The primary objective of this research is to develop

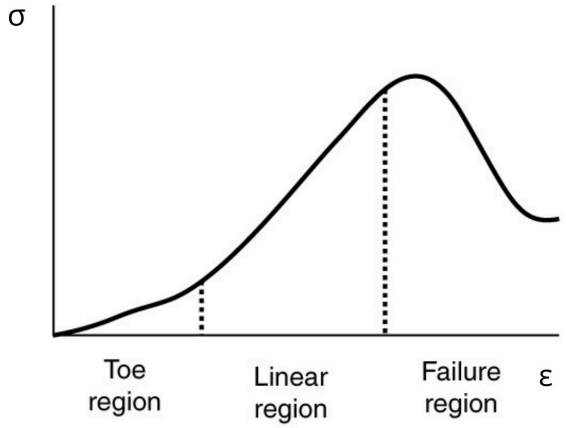

Fig. 2. Schematic representation of the stress–strain behavior of the tendon. Image credit: OpenStax licensed under CC BY 4.0.

and optimize a re-entrant unit cell capable of emulating the characteristic stress–strain response of tendons, particularly in the initial toe region and the subsequent linear elastic region. Achieving this goal could enable the design of bio-inspired auxetic structures that better replicate tendon mechanics and improve the performance of artificial tendon substitutes.

II. Methods

Firstly, among all possible auxetic mechanisms, a re-entrant mechanism was selected due to its simplicity and the fact

that it is the most widely studied and characterized in the literature. Consequently, a 2D re-entrant honeycomb structure was chosen as the basis for optimization. Once the base geometry was defined, the parameters requiring optimization were identified. The study focused on three main objectives: optimizing the Poisson's ratio in the toe region, adjusting the Young's modulus in the linear strain region, and limiting the auxetic behavior to the toe region. The initial geometry was constructed starting from a "Z"-shaped configuration, which provides the characteristic re-entrant profile. The parameters considered for optimization included the length of each rib (L1, L2, L3), the cross-sectional dimensions of each rib (height (H) and base (B) length, assuming a rectangular section), and the re-entrant angle of the cell(α). A schematic representation of the unit cell is shown in Fig. 3. These parameters were chosen because they directly influence the mechanical response, including stiffness, auxeticity, and the transition between the toe and linear strain regions.

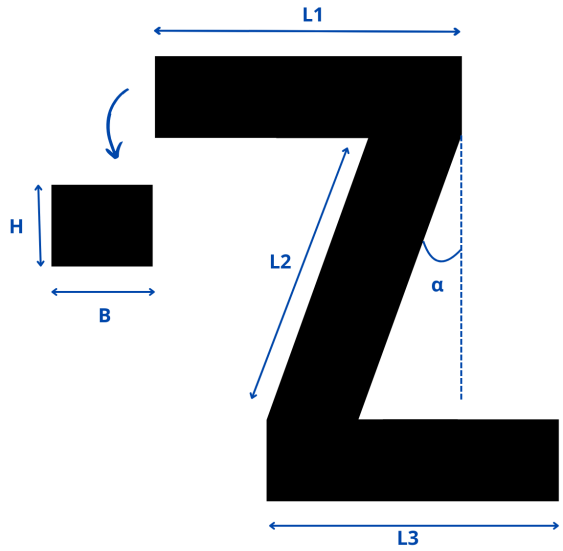

Fig. 3. Schematic representation of the unit cell and the parameter which charcterize it.

III. Conclusion

Tendons play a fundamental role in transmitting loads from muscles to bones, allowing body movement, thanks to their hierarchical structure of collagen fibers. The discovery of auxetic behavior in tendons, particularly in the toe region, opens new possibilities for the design of artificial substitutes. By developing and optimizing a re-entrant unit cell, it is possible to reproduce the tendon's characteristic stress–strain response, controlling both the Poisson's ratio in the toe region and the stiffness in the linear strain region. Implementing these bio-inspired auxetic structures in artificial tendons could improve their mechanical performance, reduce the risk of failure, and bring them closer to the behavior of natural tendons.

Acknowledgments

This work has received funding from the European Union's EU Framework Programme for Research and Innovation Europe Horizon (HORIZON TMA MSCA Doctoral Networks) under Grant Agreement No. 101119738 "MetacMed" (www.metacmed.eu). Views and opinions expressed are however those of the author(s) only and do not necessarily reflect those of the European Union. Neither the European Union nor the granting authority can be held responsible for them.

References

[1] A. J. Lomas, C. N. M. Ryan, A. Sorushanova, N. Shologu, A. I. Sideri, V. Tsioli, G. C. Fthenakis, A. Tzora, I. Skoufos, L. R. Quinlan, G. O'Laighin, A. M. Mullen, J. L. Kelly, S. Kearns, M. Biggs, A. Pandit, and D. I. Zeugolis, "The past, present and future in scaffold-based tendon treatments," *Advanced Drug Delivery Reviews*, vol. 84, pp. 257–277, 2015, doi:10.1016/j.addr.2014.11.022.

[2] S. A. Müller, A. Todorov, P. E. Heisterbach, I. Martin, and M. Majewski, "Tendon healing: an overview of physiology, biology, and pathology of tendon healing and systematic review of state of the art in tendon bioengineering," *Knee Surgery, Sports Traumatology, Arthroscopy*, vol. 23, no. 7, pp. 2097–2105, 2013, doi:10.1007/s00167-013-2680-z.

[3] R. Gatt, M. Vella Wood, A. Gatt, F. Zarb, C. Formosa, K. M. Azzopardi, A. Casha, T. P. Agius, P. Schembri-Wismayer, L. Attard, N. Chockalingam, and J. N. Grima, "Negative Poisson's ratios in tendons: An unexpected mechanical response," *Acta Biomaterialia*, vol. 24, pp. 201–208, 2015, doi:10.1016/j.actbio.2015.06.018.

[4] M. Beldjilali-Labro, A. G. Garcia, F. Farhat, F. Bedoui, J. F. Grosset, M. Dufresne, and C. Legallais, "Biomaterials in tendon and skeletal muscle tissue engineering: Current trends and challenges," *Materials*, vol. 11, no. 7, 2018, doi:10.3390/ma11071116.

Photonic Fiber Bragg Grating Sensor Network for Detection and Micro-Doppler Characterization of Small UAVs

Rodions Marstupa[1], Aleksandrs Olins[1], Mykola Khobzei[1,2], Vladyslav Tkach[1,2], Serhii Haliuk[1,2], Sandis Migla[1], Janis, Braunfelds[1], Toms Salgals[1], Vjaceslavs Bobrovs[1], Dmytro Vovchuk[1,*]

[1] Riga Technical University, Department of Telecommunications, Riga, Latvia
[2] Yuriy Fedkovych Chernivtsi National University, Department of Radio Engineering and Information Security, Chernivtsi, Ukraine
*Corresponding author: dimavovchuk@gmail.com

***Abstract*— This work presents a fiber Bragg grating (FBG) sensor network for detection and motion analysis of low-slow-small (LSS) unmanned aerial vehicles (UAVs). Spatiotemporal responses of distributed sensors are processed using STFT and FFT to identify drone trajectories and extract propeller micro-Doppler signatures. Experiments demonstrate reliable detection and estimation of rotor rotation characteristics.**

***Keywords*— optical fiber, FBG sensor network, micro-Doppler, drone detection.**

I. Introduction

The rapid growth of UAVs in civil, commercial, and defense domains creates challenges for reliable detection, identification, and classification. Conventional radars, including optical and acoustic [1], are limited by small radar cross-section (RCS), environmental clutter, and others. Both require new approaches to recognize the so-called Low-Slow-Small (LSS) targets, such as small plastic drones used for various delivery and monitoring tasks in the concept of 'smart cities' for a drone swarm delivery, where their concentration in one place is expected to grow over time [2].

Using information gathered from a FBG sensor network, this research suggests a machine learning-based algorithmic framework for LSS UAV detection and trajectory tracing. The suggested method uses the spatiotemporal response patterns of FBG sensors array to infer UAV positioning data and short-term motion dynamics with analysis in time and frequency domains with further prospective involving machine learning.

II. Setup and Frequency Domain Analysis

The block diagram and the appropriate experimental setup-under-test are shown in Fig. 1a, b, respectively. It consists of the consists of FBG sensor network integrated into an optical fiber, each sensor of which is distributed by 100 mm with the reflected wavelength range 1520 to 1565 nm. The fiber is connected to SCN-80 S-line Scan 800 from Sylex measurement tool with sampling rate up to 5 kHz and includes consists of a superluminescent light emitting diode (SLED) as a local oscillator to trig an optical circulator (OC) and transfers light to the FBG sensors via a single mode optical fiber (SMF). The reflected signals are read by the measurement device is fully controlled from a personal computer (PC), allows recording the data after passing the optical spectrometer and digital signal processor (DSP) for each sensor separately. Whole setup is placed over the platform with a 2D coordinate system each cell squared by 200 × 200 mm. – the size is fitted to the size potential drones-under-test (from Crazyflie 2.1+ sized 92 × 92 × 29 mm – was used for this experiment, to DJI Mini 2 sized 131 × 81 × 58 mm).

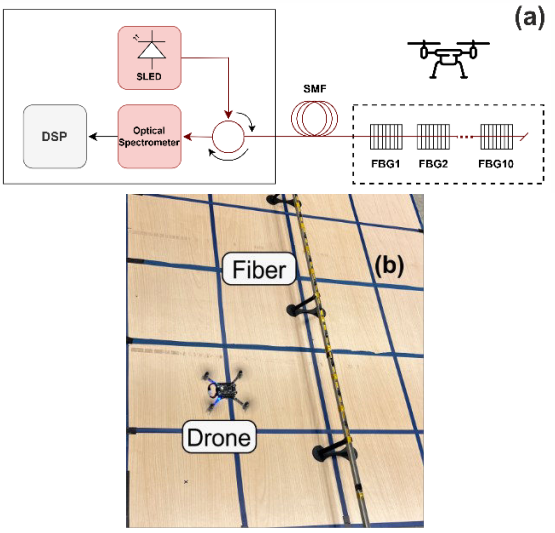

Fig. 1 The block diagram (a) and experimental setup (b) that include an optical fiber FBG sensor network and special measurement tool with full control from a PC.

The first set of assessments engages spectrograms (short-time Fourier transformation – STFT) post-processing analysis. The drone was flying along the fiber back and forth 500 mm over (Fig. 1b). From the normalized STFT diagrams one can clearly see the drone detection and his movement trajectory

where each sensor is trigged one by one (Fig. 2a). The detection process is fully reproducible, considering the STFT of the drone flying in the backward direction where sensors react in reverse order (Fig. 2b) that confirm the measurement system operability.

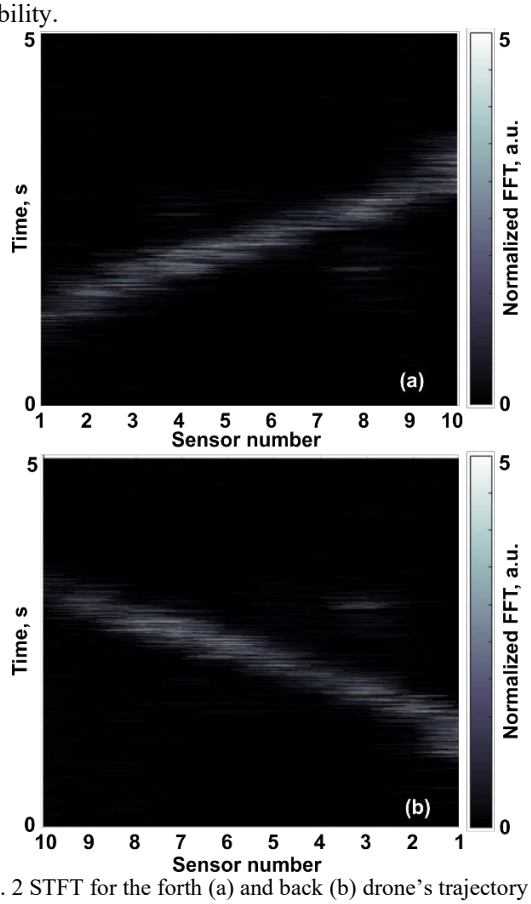

Fig. 2 STFT for the forth (a) and back (b) drone's trajectory flight.

III. Time-Domain Analysis and Micro-Doppler Detection

The analysis in time domain opens a possibility to detect and analyze a unique characteristic of the flying-over drone such as micro-Doppler. It is modern approach in radar technologies for target detection, identification and classification [3-4]. As the LSS UAVs has a very low RCS, their Doppler characteristics is often comparable to birds around [5]. The micro-Doppler combs (appear as a scattering from UAV's propellers) characterization allows such misunderstanding as different UAVs has difference propeller rotation speed, length, material, and so on.

The time series signals, recorded by the used measurement system, are shown in Fig. 3a. It is clearly seen the short 'flashes' of the backreflected signals from each sensor of FBG network for the direct drone flight along the fiber. Meanwhile, the simple Fast-Fourier Transform analysis (Fig. 3b) demonstrate two peaks around 150 and 450 Hz that correspond to the 2nd and 6th micro-Doppler harmonics, thus the speed of propeller rotation can be estimated.

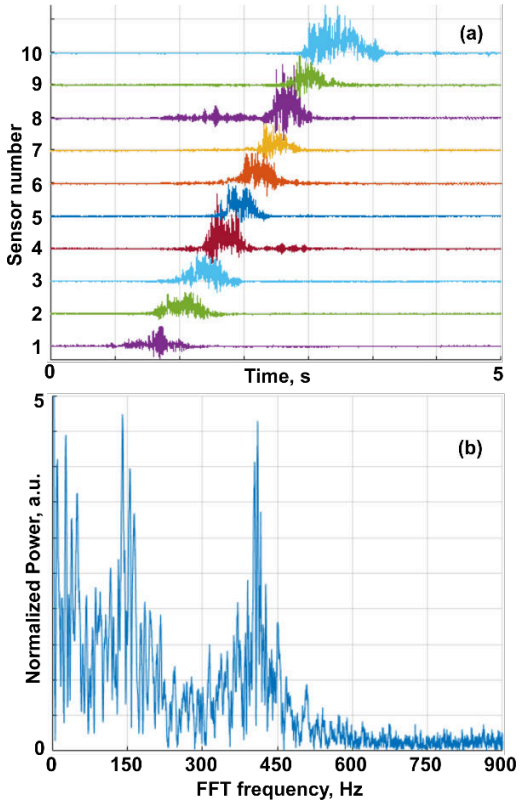

Fig. 3 Time series of the backreflected signals from FBG sensors (a) and the normalized FFT of the measured signal on sensor number 6 (b).

IV. Conclusion

A FBG sensor network was demonstrated as an alternative sensing approach for detection and characterization of LSS UAVs. Spectrogram analysis revealed the drone trajectory through sequential activation of sensors, confirming reliable spatial detection. Time-domain analysis enabled extraction of micro-Doppler signatures associated with propeller rotation. The measured frequency components allowed estimation of rotor rotational dynamics, highlighting the capability of optical fiber sensing systems for UAV monitoring. The proposed approach opens perspectives for integrating machine learning algorithms for improved detection accuracy, classification of aerial targets, and trajectory reconstruction in smart-city environments.

References

[1] Khan, M.A.; Menouar, H.; Eldeeb, A.; Abu-Dayya, A.; Salim, F.D. On the Detection of Unauthorized Drones—Techniques and Future Perspectives: A Review. IEEE Sensors J. 2022, 22, 11439–11455.

[2] K. Kuru, D. Ansell, W. Khan and H. Yetgin, "Analysis and Optimization of Unmanned Aerial Vehicle Swarms in Logistics: An Intelligent Delivery Platform," in IEEE Access, vol. 7, pp. 15804-15831, 2019.

[3] Lei, J. & Lu, C. Target classification based on Micro-Doppler signatures. IEEE Int. Radar Conf. 2005, 1–5 (2005).

[4] D. Vovchuk et al., "Micro-Doppler-Coded Drone Identification via Resonant Tagging," in IEEE Transactions on Antennas and Propagation, vol. 73, no. 6, pp. 3917-3927, June 2025.

[5] Narayanan, R. M., Tsang, B. & Bharadwaj, R. Classification and discrimination of birds and small drones using radar MicroDoppler spectrogram images'. Signals (2023).

POSTERS

Plasmonics, Nano-Optics and Nanophotonics

36 contributions · pp. 1522–1611

META 2026 · Dublin, Ireland · ISSN 2429-1390

Control of Chiroptical Response with Chiral Plasmonic Nanoparticles on Dielectric Substrate

Ruiqian Zhang[1,*], Xiaolu Zhuo[2], Jianfang Wang[1]

[1]Department of Physics, The Chinese University of Hong Kong, Shatin, Hong Kong SAR, China

[2]School of Science and Engineering, The Chinese University of Hong Kong, Shenzhen, Guangdong, China

*Corresponding author: zhangrq@link.cuhk.edu.hk

***Abstract*— This work investigated the chiroptical response of chiral plasmonic nanoparticles via structural and substrate design. The plasmonic nanohelix exhibits distinct mode-dependent chiroptical far-field properties. Plasmonic helicoid with high-refractive-index substrate shows remarkable enhancement in g-factor and peak separation between absorption and scattering g-factor spectra, attributed to strong plasmon hybridization.**

***Keywords*— chiral nanoparticles, chiroptical responses, plasmon.**

I. Introduction

Chiral plasmonic nanoparticles enable on-chip CPL devices but rely on substrates. Low-index dielectrics minimally affect their chiroptical properties,[1,2] whereas high-index semiconductors induce image charges similar to NPoM systems. For chiral LSPRs, circular polarization can generate rotating image dipoles that enhance or cancel optical chirality. Substrates strongly modulate chiral signals, with plasmon hybridization and superchiral fields adding complexity.

We systematically simulate dielectric substrates' effects on individual chiral plasmonic nanoparticles using Au helicoids. Increasing substrate refractive index notably amplifies the g-factor and induces an abnormal peak separation between absorption and scattering g-factors.[3,4] This rare phenomenon arises from the enhanced near-field optical chirality confined at the nanoparticle–substrate gap, driven by energy differences between bonding and antibonding quadrupole modes. The mechanism, supported by near-field analysis, is applicable across other metals like Ag and Cu.

II. Methods

The simulations were performed using FDTD Solutions developed by Ansys Lumerical. Two total-field scattered-field plane-waves with orthogonal polarizations and a phase difference of $\pm\pi/2$ were used to generate the RCP or LCP excitation source. Mesh size of 1.0 nm was utilized to calculate the spectra and the electric field enhancement. The dielectric functions of Au, Ag and Cu were set by fitting the measured data of Johnson and Christy, Palik and CRC, respectively.

III. Results and Discussion

To investigate the substrate effect, we performed FDTD simulations on the Au helicoids with an edge length of 150 nm supported by the dielectric substrates with different refractive indexes. For substrates with refractive indexes of $n = 1.5$ and $n = 4.0$, Fig. 1(b) and 1(c) show the scattering and absorption cross-sections under LCP/RCP excitation, along with the resulting g-factor defined as

$$g=2\times\frac{\sigma_R-\sigma_L}{\sigma_R+\sigma_L} \quad (1)$$

where σ_R and σ_L are the cross-sections under RCP and LCP excitation.

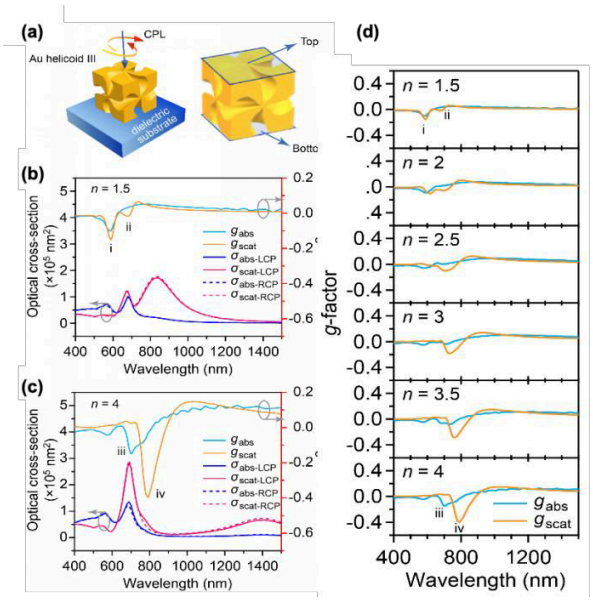

Fig. 1 (a) Schematic of Au helicoid supported by a dielectric substrate under the in-plane CPL excitation. (b),(c) Calculated optical cross-section and g-factor spectra for the substrate with refractive index of $n = 1.5$ (b) and $n = 4$ (c). (d) Calculated g-factor spectra for the substrate with different refractive indexes under the in-plane CPL excitation.

The absorption cross-section shows minor peak shifts but distinct intensity differences for LCP vs. RCP. Scattering

spectra reveal a broad low-energy peak and a sharp high-energy peak. With increasing substrate refractive index, the low-energy peak redshifts and weakens, while the high-energy peak shifts little and strengthens, indicating mode-dependent nanoparticle–substrate coupling.

Moreover, when the Au helicoid is supported by a high-refractive-index substrate, g_{scat} is enhanced from 0.15 to 0.39, and that of g_{abs} also increases from 0.09 to 0.15. Especially, there is a notable separation in the peak positions of g_{abs} and g_{scat}, which is an uncommon phenomenon among various chiral plasmonic nanoparticles.[5–7]

The enhanced chiroptical responses are also evident in the near field. Fig. 2(a) shows the differential optical chirality enhancement ($C_{LCP}/|C_{CPL}|$-$C_{RCP}/|C_{CPL}|$), which indicates the position where the chiral signal is located, and the differential electric field enhancement ($|E_{LCP}|/|E_{CPL}|$-$|E_{RCP}|/|E_{CPL}|$), which is related to the enhancement of the chiroptical response of peaks iii and iv, with the optical chirality enhancement defined by[44]

$$\frac{C(r)}{|C_{CPL}(r)|} = -\frac{c\times \mathrm{Im}[\boldsymbol{E}^{*}(r)\cdot\boldsymbol{B}(r)]}{|\boldsymbol{E}_{CPL}(r)|^{2}} \qquad (2)$$

where c is the speed of light, r is the displacement vector, $\boldsymbol{E}$ and $\boldsymbol{B}$ represent the electric and magnetic field. C_{CPL} and $\boldsymbol{E}_{CPL}$ are the optical chirality density and electric field obtained under CPL excitation without the helicoid, respectively.

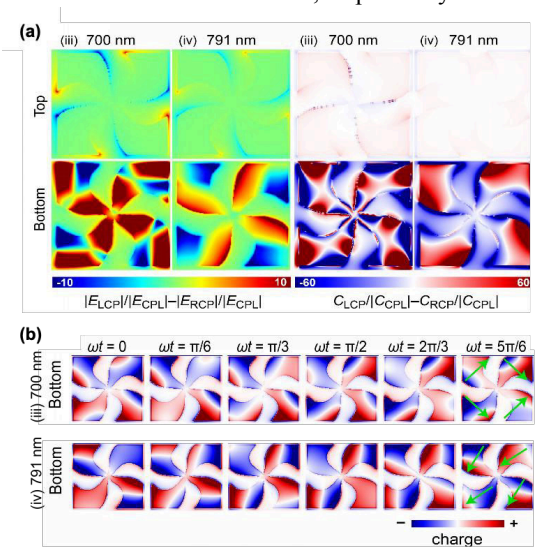

Fig 2 (a) Differential optical chirality distribution and electric field enhancement; (b) Charge distribution contours at different phases and resonance wavelengthsfor the substrate with refractive index of n = 4 under in-plane RCP excitation.

To ascertain the evolution of these chiroptical peaks, we further refine our calculations by varying the substrate refractive indexes from 1.5 to 4 with a step of 0.5. We focus on the in-plane excitation to figure out the physical origins behind the g-factor enhancement and the abnormal peak separation [Fig. 1(d)]. The two g_{scat} peaks i and ii that initially appear for the low-refractive-index substrate of n = 1.5 gradually merge into one dominant peak iv as the substrate refractive index increases. Peak ii gradually redshifts with its intensity largely enhanced, while peak i becomes much weaker even disappears. As the g-factor spectra mainly exhibit negative response, all the charge distributions in Fig. 2(b) are calculated under the in-plane RCP light. For the refractive index of n = 4, the low-energy g_{abs} peak iii is attributed to a bonding quadrupolar mode while the g_{scat} peak iv at 791 nm corresponds to an antibonding quadrupolar mode [Fig. 2(b)]. Symmetry breaking induced by the high-refractive-index substrate enables the excitation of the antibonding quadrupolar mode, leading to the appearance of a bump in the scattering spectrum [Fig. 1(c)]. The observed separation between the g_{scat} and g_{abs} peaks therefore, originated from the mode splitting in the interaction between the Au helicoid and the dielectric substrate.

IV. Conclusion

Chiroptical response modulation is achieved by structural and substrate design. Dielectric substrates with plasmonic helicoid induce symmetry breaking, enhancing chiral response. g_{scat} increases from 0.15 to 0.39 as refractive index rises from 1.5 to 4. Plasmon hybridization of quadrupolar-quadrupolar modes causes separation of gabs and gscat peaks. These findings facilitate precise manipulation of chiral light and facilitate applications in nanophotonics.

Acknowledgments

This work was supported by the National Natural Science Foundation of China (62575185, 62205223), Guangdong Basic and Applied Basic Research Foundation (2023A1515110091, 2023A1515011455), Department of Science and Technology of Guangdong Province (2023QN10C200, 2023QN10X082), and Science and Technology Innovation Commission of Shenzhen (20231121120748002, JSGGKQTD20221101115701006). The authors acknowledge the Guangdong Basic Research Center of Excellence for Aggregate Science at CUHK-Shenzhen.

References

[1] X. T. Kong, L. V. Besteiro, Z. Wang, and A. O. Govorov, “Plasmonic chirality and circular dichroism in bioassembled and nonbiological systems: theoretical background and recent progress,” Advanced Materials, vol. 32, pp. 1801790, 2020.

[2] K. Saito, Y. Nemoto, and Y. Ishikawa, “Circularly polarized light-induced chiral growth of achiral plasmonic nanoparticles dispersed in a solution,” Nano Letters, vol. 24, pp. 12840–12848, 2024.

[3] C. K. K. Choi, X. Zhuo, Y. T. E. Chiu, H. Yang, J. Wang, and C. H. J. Choi, “Polydopamine-based concentric nanoshells with programmable architectures and plasmonic properties,” Nanoscale, vol. 9, pp. 16968-16980, 2017.

[4] G. Zheng, J. He, V. Kumar, S. Wang, I. Pastoriza-Santos, J. Pérez-Juste, L. M. Liz-Marzán, and K. Y. Wong, “Discrete metal nanoparticles with plasmonic chirality,” Chemical Society Reviews, vol. 50, pp. 3738-3754, 2021.

[5] Y. Chen, J. Zheng, L. Zhang, S. L, Y. Chen, K. K. Chui, W. Zhang, L. Shao, and J. Wang, “Inversion of the chiroptical responses of chiral gold nanoparticles with a gold film,” ACS Nano, vol. 18, pp. 383-394, 2023.

[6] F. Spreyer, J. Mun, H. Kim, R. M. Kim, K. T. Nam, J. Rho, and T. Zentgraf, “Second harmonic optical circular dichroism of plasmonic chiral helicoid-III nanoparticles,” ACS Photonics, vol. 9, pp. 784-792, 2022.

[7] J. Zheng, C. Boukouvala, G. R. Lewis, Y. Ma, Y. Chen, E. Ringe, L. Shao, Z. Huang, and J. Wang, “Halide-assisted differential growth of chiral nanoparticles with threefold rotational symmetry,” Nature Communications, vol. 14, pp. 3783, 2023.

Harmonizing Plasmonic and Photonic Effects to Boost Photocatalytic H_2 Production

Tharishinny Raja Mogan[1], Jiajia Zhang[1], Li Shiuan Ng[1], Siew Kheng Boong[1], Carice Chong[1], Jinn-Kye Lee[1], Haitao Li[2], Hiang Kwee Lee[1,3*]

[1]Division of Chemistry and Biological Chemistry, School of Chemistry, Chemical Engineering and Biotechnology, Nanyang Technological University, 21 Nanyang Link, Singapore 637371, Singapore.
[2]School of Chemistry and Chemical Engineering, Yangzhou University, Yangzhou, 225002, PR China.
[3]Institute of Materials Research and Engineering, The Agency for Science, Technology and Research (A∗STAR), 2 Fusionopolis Way, #08-03, Innovis, 138634, Singapore.

*Corresponding author: hiangkwee@ntu.edu.sg

***Abstract*— This work demonstrates a plasmonic photonic architecture using an optically inert silica opal framework to confine light efficiently. Spectral alignment between photonic and plasmonic modes amplifies electromagnetic fields, enabling exceptionally high solar driven hydrogen generation without semiconductors or cocatalysts and establishing a general design principle for plasmonic catalysis.**

***Keywords*— plasmonic, slow photons, photonic, hydrogen evolution, photocatalysis**

I. Introduction

The development of efficient solar-driven hydrogen production technologies is a central challenge in the transition toward a sustainable energy economy. Plasmonic catalysis has attracted increasing interest as an alternative to conventional semiconductor photocatalysis, as noble metal nanostructures are capable of concentrating visible light through localized surface plasmon resonance (LSPR) and generating energetic hot carriers that can participate directly in chemical transformations.[1,2] Despite these advantages, standalone plasmonic nanoparticles generally exhibit limited catalytic efficiency, primarily due to weak electromagnetic field confinement and rapid hot-carrier recombination.[3-5]

To enhance light-matter interactions, plasmonic nanoparticles are frequently coupled with photonic crystals, which possess periodic refractive index modulations capable of supporting photonic bandgaps and slow photon effects.[6-7] Nevertheless, many reported plasmonic photonic systems employ photoabsorbing semiconductor backbones, resulting in complex optical competition among photoabsorption, plasmonic scattering, and photonic effects. Such competition often suppresses slow photon formation and diminishes the effective electromagnetic field enhancement. The present work synthesizes a design strategy that mitigates these issues by harmonizing plasmonic and photonic effects through the use of a non-photoabsorbing photonic framework.

II. Methods

Synthesis of silica nanoparticles

The preparation of SiO_2 particles was carried out following the modified Stober's method.[8] Briefly, 37.61 mL of ethanol, 6.75 mL of ultrapure water and 1.2 mL of ammonium hydroxide solution were added in conical flask and stirred at 500 rpm for 15 minutes. Then 1.55 mL, 2 mL or 4 mL of tetraethyl orthosilicate was added dropwise into the ethanolic solution to obtain SiO_2 nanoparticles with diameter of 210 nm, 270 nm, and 400 nm, respectively. The solution was stirred for 6 hours in room temperature. The solution was then centrifuged (8000 rpm, 10 minutes) to obtain the resulting SiO_2 particles. The particles were washed with ultrapure water and ethanol and dried in vacuum.

Fabrication of SiO_2 opal

3D powdered opal was formed by a self-assembly method. Self-assembly of SiO_2 particles was performed by sedimentation aided with centrifugation approach.[9] 1wt% of SiO_2 particles were dispersed in ethanol and sonicated for 10 minutes. The SiO_2 particles was sedimented by long and slow centrifugation process (2000 rpm, 12 minutes). Then, the supernatant was removed and the assembled particles were dried in vacuum. The self-assembled opals were calcined at 300 ºC for 2 hours to strengthen the mechanical stability.

Deposition of silver nanoparticles to form Ag/SiO_2 opal

SiO_2 opal was soaked in 0.1 M sodium borohydride solution for 10 minutes. The excess sodium borohydride solution was removed. Then, 2 mL of 0.2 M silver nitrate solution was added

and allowed to infiltrate the SiO_2 opal under vacuum pressure for 15 minutes for each cycle. This led to in-situ formation of silver nanoparticles deposited on/within the SiO_2 opal. The resulting Ag/SiO_2 opal was washed thrice using ultrapure water.

Photocatalytic hydrogen evolution reaction (HER) using plasmonic photonic opal

The photocatalytic HER setup was carried out by using 12 mL transparent quartz tube secured with septum seal. 15 mg of photocatalyst was placed in the quartz tube in the presence of 3 mL of 10% methanol solution serving as hole scavenger. The reaction solution was purged with argon (Ar) gas for 15 minutes to remove air prior to the reaction. The samples were irradiated with 100 W white light LED (400 - 750 nm) to initiate the HER. The temperature of the photocatalytic setup was maintained at room temperature with a turbo fan. The evolved gas was analyzed by injecting 0.8 mL of the reactor's headspace gas into a gas chromatograph (SRI Multiple Gas Analyzer #5) equipped with a thermal conductivity detector (GC-TCD). All experiments were repeated at least thrice to ensure the reproducibility of the results.

III. Results and Discussion

Our plasmonic photonic architecture consists of a non-photoabsorbing SiO_2 opal backbone integrated with Ag nanoparticles as plasmonic catalysts (Figure 1). Monodisperse SiO_2 nanoparticles with diameters of 210 ± 15 nm, 270 ± 20 nm, and 400 ± 10 nm were synthesized via the Stober method and assembled into three-dimensional photonic crystals by centrifugation-assisted sedimentation. The resulting opal structures exhibit a face-centered cubic arrangement with thicknesses exceeding 10 micrometers, enabling strong multiscattering and pronounced photonic effects. The periodicity of each opal corresponds directly to the SiO_2 particle size, allowing systematic tuning of the photonic bandgap and the spectral region for slow-photon generation. Ag nanoparticles were uniformly deposited throughout the opals using an in-situ reduction approach, yielding spherical Ag particles of approximately 37 nm with consistent size distributions and mass loadings across all samples. Structural integrity of the photonic crystals was preserved after Ag deposition, ensuring reliable comparison of photonic effects.

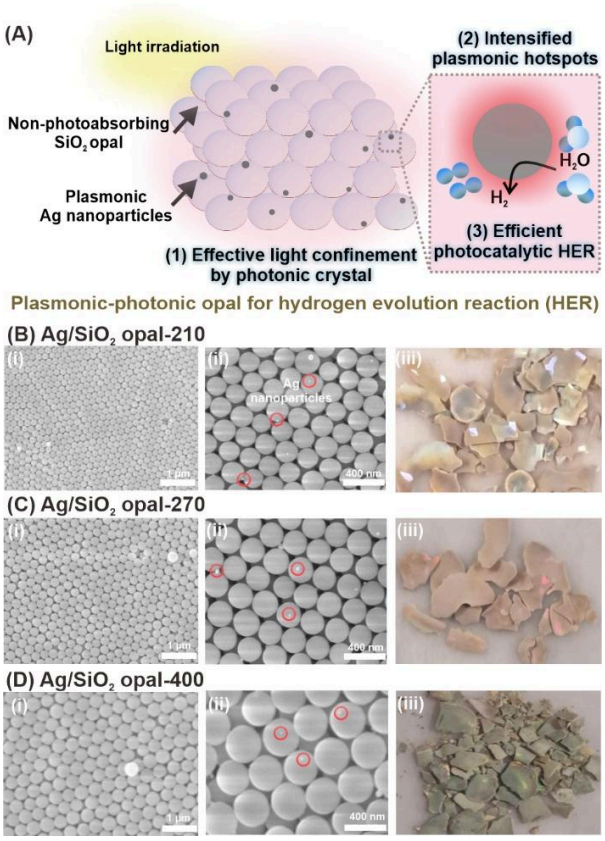

Figure 1. (A) Design of an opal-like plasmonic photonic crystal with superior light concentration ability and its application for efficient photocatalytic hydrogen production. (B – D) Plasmonic photonic crystals composed of Ag nanoparticles deposited onto SiO_2 opal-like structures with nanoparticle diameters of (B) 210 nm (Ag/SiO_2 opal-210), (C) 270 nm (Ag/SiO_2 opal-270), and (D) 400 nm (Ag/SiO_2 opal-400). (i) Overview and (ii) magnified SEM images of various platforms. Ag nanoparticles are highlighted using the red circles. (iii) Digital images showing the distinct color iridescences from the different plasmonic photonic crystals.

Optical characterization confirms that all Ag/SiO_2 opals retain distinct photonic bandgaps, as evidenced by angle-dependent reflectance and diffuse reflectance spectroscopy. The broad photonic features observed arise from random crystal orientation and angle-dependent bandgap dispersion inherent to three-dimensional photonic crystals, enabling access to a wide range of slow-photon wavelengths across the visible spectrum (Figure 2). The localized surface plasmon resonance of Ag nanoparticles is centered near 450 nm and overlaps partially with the photonic bandgaps depending on opal periodicity. Surface-enhanced Raman spectroscopy reveals that Ag/SiO_2 opal-270 exhibits the strongest electromagnetic field enhancement, attributed to concurrent excitation of plasmonic resonance and slow photon modes. In contrast, misaligned photonic bandgaps result in weaker plasmonic enhancement, while standalone Ag nanoparticles show negligible field amplification, highlighting the essential role of the photonic crystal in light confinement.

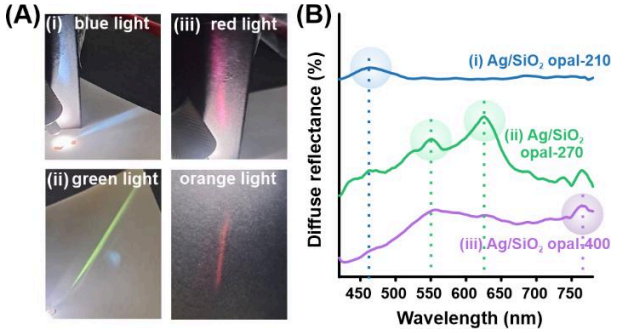

Figure 2. (A) Optical images showing the characteristic stop band reflection of specific light wavelength by various plasmonic photonic crystals upon white light irradiation. (i) Ag/SiO_2 opal-210, (ii) Ag/SiO_2 opal-270, and (iii) Ag/SiO_2 opal-400. (B) Diffuse reflectance spectra recorded from Ag/SiO_2 opal-210, Ag/SiO_2 opal-270, and Ag/SiO_2 opal-400. The dotted line and associated shaded region indicate the position of photonic bandgap (PBG) and estimated slow photons range, respectively. For (A) and (B), the angle-dependent measurement is set at ~40° with respect to the samples.

Application of these architectures to visible-light-driven hydrogen evolution demonstrates that optimized spectral alignment yields hydrogen production rates exceeding 550 mmol $h^{-1}g_{Ag}^{-1}$ under visible light irradiation (Figure 3). Control experiments confirm that neither bare SiO_2 opals nor standalone Ag nanoparticles are effective, underscoring the synergistic requirement of both plasmonic and photonic effects. Disordered Ag/SiO_2 assemblies exhibit significantly lower activity due to the absence of slow photon generation. Further mechanistic analysis indicates that increasing plasmonic nanoparticle loading does not lead to proportional performance gains. Elevated plasmonic content introduces pronounced optical screening and random scattering, which disrupt slow photon formation and reduce light confinement within the photonic crystal. These observations underscore that effective photonic field management, rather than increased photoabsorbing material, governs the efficiency of plasmonic catalysis.

Collectively, these results highlight the critical role of a non-photoabsorbing photonic backbone in harmonizing plasmonic and photonic effects within hybrid architectures, thereby maximizing electromagnetic field enhancement. This conclusion is further supported by apparent quantum efficiency measurements under monochromatic irradiation. The Ag/SiO_2 opal-270 achieves photocatalytic hydrogen evolution rates that surpass most reported systems, outperforming other plasmonic, photonic, and hybrid platforms by up to 280-fold. These comparisons indicate that strengthening photonic effects is more effective for enhancing carrier generation than increasing photocatalyst loading.

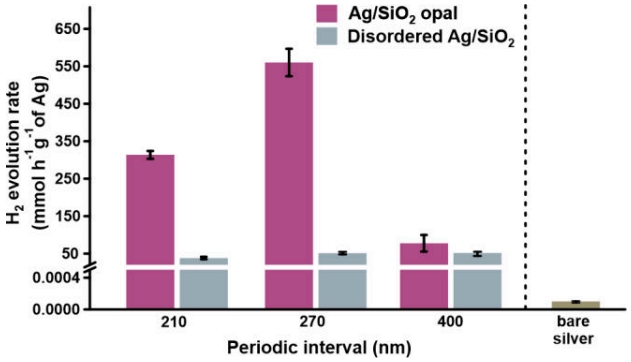

Figure 3. H_2 evolution rate from water when in presence of Ag/SiO_2 opals, disordered Ag/SiO_2 platforms, or bare Ag nanoparticles under light irradiation.

IV. Conclusion

The findings summarized here establish non-photoabsorbing photonic backbones as effective platforms for amplifying plasmonic electromagnetic fields through the preservation and exploitation of slow photons. Deliberate harmonization of photonic and plasmonic effects enables highly efficient visible-light-driven hydrogen evolution without reliance on semiconductor absorbers or additional co-catalysts. The design principles discussed offer broadly applicable guidelines for engineering electromagnetically enhanced plasmonic catalysts and may be extended to a wide range of light-driven chemical and energy-conversion processes.

This paper summarizes previously published work and is submitted solely to meet conference submission requirements. No new experimental data or unpublished results are reported.

References

[1] J. Mo, E. C. M. Barbosa, S. Wu, Y. Li, Y. Sun, W. Xiang, T. Li, S. Pu, A. Roberston, T.-S. Wu, Y.-L. Soo, T. V. Alves, P. H. C. Camargo, W. Kuo, S. C. E. Tsung, "Atomic-Precision Tailoring of Au–Ag Core–Shell Composite Nanoparticles for Direct Electrochemical-Plasmonic Hydrogen Evolution in Water Splitting," Adv. Funct. Mater., vol. 31, pp. 1–11, 2021.

[2] N. Jiang, X. Zhuo, J. Wang, "Active Plasmonics: Principles, Structures, and Applications," Chem. Rev. vol. 118, pp. 3054–3099, 2018.

[3] M. Ijaz, "Plasmonic hot electrons: Potential candidates for improved photocatalytic hydrogen production," Int. J. Hydrogen Energy, vol. 48, pp. 9609–9619, 2023.

[4] C.Hu, X. Chen, J. Jin, Y. Han, S. Chen, H. Ju, J. Cai, Y. Qiu, C.Gao, C. Wang, Z. Qi, R. Long, L. Song, Z. Liu, Y. Xiong, "Surface Plasmon Enabling Nitrogen Fixation in Pure Water through a Dissociative Mechanism under Mild Conditions," J.Am. Chem. Soc. vol. 141, pp. 7807–7814, 2019.

[5] M. J. Kale, T.Avanesian, P. Christopher, "Direct Photocatalysis by Plasmonic Nanostructures," ACS Catal., vol. 4, pp.116–128, 2014.

[6] L. Zhang, C-Y. Lin, V. K. Valev, E. Reisner, U. Steiner, J. J. Baumberg, "Plasmonic Enhancement in $BiVO_4$ Photonic Crystals for Efficient Water Splitting," Small, vol. 10, pp. 3970–3978, 2014.

[7] T. Raja Mogan, E. Kowalska, B. Ohtani, "Photonic Crystals for Plasmonic Photocatalysis," Catalysts vol.10, pp. 1–20, 2020.

[8] W. Stöber, A. Fink, E. Bohn, "Controlled growth of monodisperse silica spheres in the micron size range," J. Colloid Interface Sci., vol. 26, pp. 62-69, 1968.

[9] J. Liu, M. Nero, K. Jansson, T. Willhammar, M. H. Sipponen, "Photonic crystals with rainbow colors by centrifugation-assisted assembly of colloidal lignin nanoparticles," Nat. Commun., vol. 14, pp. 1-9, 2023.

Carbon Nanodot Superparticles as a new family of Optical Metamaterials

C. Tortorici,[1] R. Rubino,[1] L. Roffi,[2] V. De Michele,[2] R. Szostak,[3] F. Messina,[1] A. Sciortino[1]*

[1]Physics and Chemistry department – Emilio Segrè, University of Palermo, Italy

[2] Universite´ Jean Monnet, CNRS, IOGS, Laboratoire Hubert Curien, France

[3] Brazilian Synchrotron Light Laboratory (LNLS), Brazil

*Corresponding author: alice.sciortino02@unipa.it

Carbon nanodot superparticles were fabricated via emulsion-templated assembly using bare and PEGylated nanodots. PEG functionalization modulates interparticle spacing, leading to emission blueshifts and longer lifetimes. Structural uniformity is confirmed by electron microscopy, while humidity induces emission quenching and structural degradation.

***Keywords*— carbon metamaterials, carbon superparticles, fluorescent carbon dots**

I. Introduction

Carbon nanodots (CDs) are fluorescent carbon-based nanoparticles characterized by tunable optical properties and high photostability making them attractive for optoelectronic and photonic applications. However, aggregation-induced quenching strongly limits their use in solid-state devices.[1]

One promising strategy to overcome this limitation is the hierarchical assembly of CDs into superparticles (SPs), where, similarly to what is observed for other types of nanomaterials [2-3], collective optical properties may emerge from controlled interparticle interactions. Thereby, the successful emulsion-templated assembly of CDs would enable the formation of spherical superstructures with micrometric dimensions and preserved luminescence in the solid state.

In this work, we investigate how surface functionalization with polyethylene glycol (PEG) chains of different molecular weights affects the internal organization and photophysics of CD-based metamaterials. By tuning interparticle distance using PEG400 and PEG3000, we modulate the coupling within the superparticles. Additionally, we explore the stability of these materials under environmental humidity, which is fundamental for real-world application, discovering that the presence of water in the atmosphere compromises the emission properties of the metamaterials.

II. Methods

Carbon nanodots were synthesized by microwave method starting from citric acid and urea, and then purified by column chromatography to obtain a narrow size distribution prior to assembly.[4] Three types of CDs were used: non-functionalized CDs, PEG400-functionalized CDs, and PEG3000-functionalized CDs. To achieve the pegylation of the surface, the non-functionalized CDs were allowed to react in autoclave at 180°C with PEG400 or PEG3000 for 24 hours.

Following a strategy typically used to achieve the self-assembly of semiconductor quantum dots [1], CD superparticles were fabricated via a water-in-oil emulsion-templated self-assembly process in presence of a surfactant (SPAN80) using toluene as the oil phase. The spontaneous evaporation of water droplets induced the hierarchical aggregation of CDs into spherical superstructures.

Morphological characterization was performed using scanning electron microscopy (SEM) and transmission electron microscopy (TEM). Optical properties were investigated through steady-state photoluminescence spectroscopy and time-resolved photoluminescence measurements in the ps–ns time range, at the level of individual superstructure. Photobleaching kinetics were measured under controlled atmospheric conditions, comparing dry air and humid environments at level of single superstructure.

III. Results and Discussion

Optical and structural characterization was first performed on isolated carbon nanodots prior to assembly. Bare CDs exhibit an average diameter of approximately 4 nm and show bright photoluminescence in solution. Upon surface functionalization with PEG chains, a small blueshift of the emission band is observed, accompanied by an increase in photoluminescence quantum yield and a longer excited-state lifetime. These effects are likely associated with a screening of the CD surface from the external environment provided by the PEG shell.[4]

After the assembly, morphological study has been performed by SEM and TEM. The images reveal that all types of CDs self-assemble into well-defined spherical superparticles with a quite large distribution of diameters which spans from 150 nm to few um, independent of surface functionalization (examples are

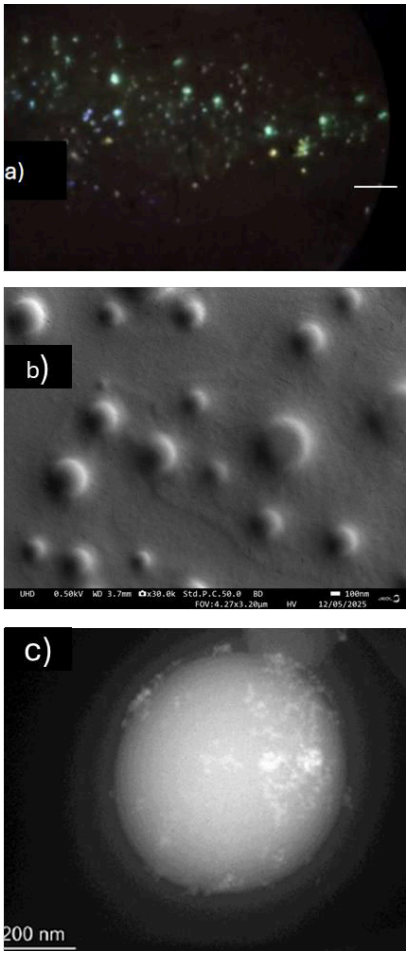

Figure 1: (a) Micrograph of Superstructures deposited on a glass substrate upon 405 nm excitation (the white bar indicates a scale of 50 um). (b) SEM images of non-pegylated superstructures. The scale bar is 100 nm (c) TEM images on a single PEG400-superstructure. The scale bar is 200 nm.

shown in Figure 1). The superstructures appear compact and homogeneous, indicating successful emulsion-templated assembly.

Optical measurements on superstructures deposited on a substrate show that the optical properties of isolated CDs and PEG-CDs are preserved upon self-assembly. PEGylated-CD superparticles display a small but reproducible blueshift of the emission band compared to bare-CD superparticles, but also an increased emission QY and a longer lifetime. Overall, the optical function is preserved (Figure 2a-2b) despite the aggregation of carbon nanoparticles which typically causes a dramatic quenching of the emission. This suggests that a controlled assembly is fundamental to control the structure of microparticles, paving the way to a new family of photoluminescent metamaterials.

We performed environmental stability tests on the optical properties of superstructures. Water vapor has a detrimental effect on the metamaterials. In fact, in humid air, the emission undergoes quenching effect as demonstrated by the photobleaching kinetics in Figure 2c. In contrast, the optical properties are preserved for a longer time in nitrogen atmosphere. This behavior suggests that water penetration disrupts interparticle interactions and partially destroys the superparticle architecture, highlighting the importance of encapsulation strategies for practical applications.

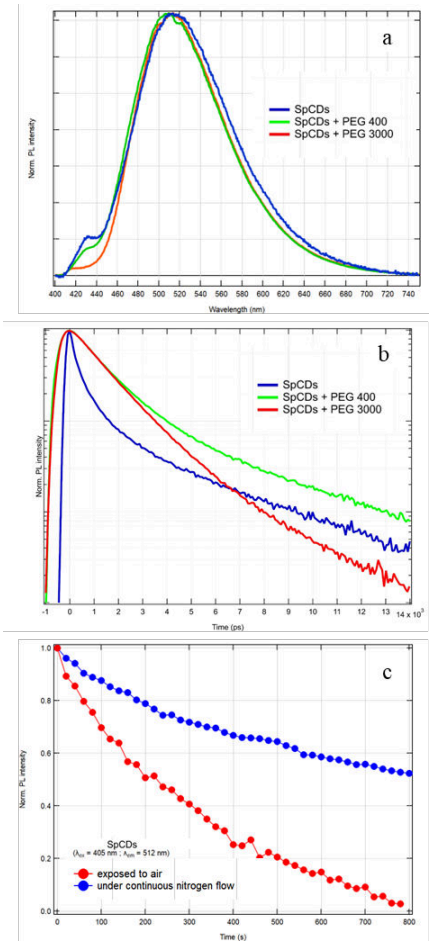

Figure 2: (a) Steady-state emission spectra of single superstructures excited at 405 nm. (b) Emission lifetime of single superstructures excited at 405 nm. (c) Emission photobleaching kinetics of non-pegylated superparticles in ambient air and upon nitrogen atmosphere.

IV. Conclusion

These results demonstrate that emulsion-templated assembly enables the formation of compact CD-based superparticles that retain the intrinsic optical properties of the individual nanodots. PEGylation plays a key role by preserving emissive behavior upon aggregation, leading to higher quantum yield, longer lifetimes, and a reproducible blueshift without aggregation-induced quenching. At the same time, the sensitivity of the superstructures to humid environments reveals that their optical performance is closely linked to the integrity of the assembled architecture.

Acknowledgments

L.R., A.S. acknowledge Project PRIN 2022-20223CWFZT "Vertically Oriented Graphene Assembled Nanostructures for

WATER purification".

REFERENCES

[1] Sciortino, A. et al., *C*, **4**, 67 (2018).
[2] Marino, E. et al., *Advanced Materials*, **30**, 1803433 (2018).
[3] Marino, E. et al., *ACS Nano*, **14**, 13806–13815 (2020).
[4] Reale, M. et al., *Nanoscale*, **17**, 9380 (2025).

Optical Control of Lasing Modes in Quantum Dot Superparticles

Marco Reale[1,2*], Pietro Castronovo[1], Marco Cannas[1,2],
Emanuele Marino[1], Alice Sciortino[1], Fabrizio Messina[1]

[1]Department of Physics and Chemistry "E. Segrè", University of Palermo, Italy
[2]Consorzio Interuniversitario Scienza e Tecnologia dei Materiali INSTM, Florence, Italy
*Corresponding author: marco.reale@unipa.it

***Abstract*— We report excitation-controlled lasing from individual CdSe/CdS quantum dot superparticles. By tuning the pump wavelength, reversible selection of whispering-gallery modes is achieved. This provides a purely optical route to dynamically reconfigurable and compact microlasers.**

***Keywords*— Quantum Dot Superparticles; Tunable lasing; Whispering-Gallery Modes Microresonators.**

I. Introduction

Systems combining strong light confinement, optical gain, and tunability are of growing interest in photonics for applications ranging from compact light sources to sensing and adaptive optical components. While high-quality resonances can be readily achieved in dielectric microcavities, their spectral properties are often fixed once the structure is fabricated, limiting dynamic control of their optical response.

Semiconductor quantum dots (QDs) provide a versatile platform for active photonics due to their size-dependent absorption and emission, near-unity photoluminescence quantum yields, and compatibility with bottom-up fabrication. Beyond individual emitters, the self-assembly of colloidal QDs into mesoscale superparticles (SPs) enables collective optical behavior that cannot be attributed to single nanocrystals. In spherical QD SPs, the global geometry supports whispering-gallery modes (WGMs), providing resonant optical feedback coexisting with distributed optical gain.

Lasing from QD SPs has been previously reported, establishing these systems as compact and efficient microlasers. However, dynamic tuning of lasing modes without modifying the physical structure of the resonator remains largely unexplored, even if essential for adaptive and multifunctional photonic platforms.

Here, we present a systematic optical study of lasing in individual SPs assembled from CdSe/CdS core/shell QDs. We show that lasing can be reversibly tuned by controlling the excitation wavelength, owing to the wavelength-dependent penetration of the pump light and the resulting modulation of the spatial overlap between optical gain and WGMs. This mechanism provides a simple and robust route to optical reconfiguration of microlasers.

II. Methods

Superparticle preparation: CdSe/CdS core/shell QDs with thick shells were synthesized to enhance optical gain and suppress non-radiative recombination. Controlled self-assembly yielded spherical SPs with micrometer-scale diameters and smooth outer surfaces, favorable for supporting WGMs with low optical losses.

Optical characterization: Individual SPs were optically excited using pulsed laser source with tunable wavelength. Emission spectra were collected as a function of excitation fluence to identify lasing thresholds and mode structure. Time-resolved photoluminescence measurements were employed to probe emission dynamics and gain evolution below and above the lasing threshold, providing insight into the role of excitation conditions on mode formation.

III. Results and Discussion

Red-emitting quantum dot SPs with diameters of approximately 10 μm were produced via a source-sink emulsion process applied to CdSe/CdS core/shell quantum dots (Fig. 1a). The resulting SPs exhibit a highly spherical morphology and a dense internal packing of emitters, enabling them to act as luminescent optical microcavities (see Fig. 1b). Their circular geometry and refractive index contrast naturally support WGMs, as evidenced by the dense series of narrow peaks superimposed to the photoluminescence spectra of individual SPs (Fig. 1c).

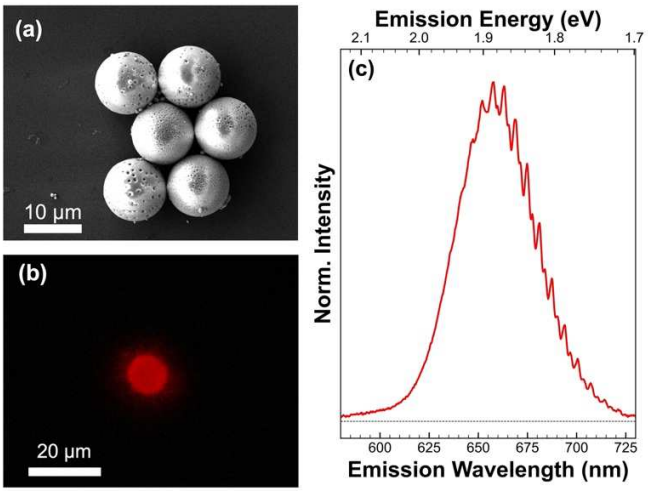

Fig. 1 (a) SEM image of QD SPs. (b) Photoluminescence imaging and (c) spectrum of an individual SP. Adapted from ref [3].

The emission properties of individual SPs were investigated in detail under optical pumping, both below and above the lasing threshold. As shown in Fig. 2, upon increasing excitation fluence, a clear transition from spontaneous emission to stimulated emission is observed, marked by a nonlinear increase in output intensity and the appearance of narrow spectral peaks associated with WGM-lasing. Depending on the specific SP and excitation conditions, single-mode or multi-mode lasing can be achieved, reflecting the balance between gain, cavity losses, and mode competition. Interestingly, lasing spectra are extremely sensitive to the morphology and the environment of each individual SP.

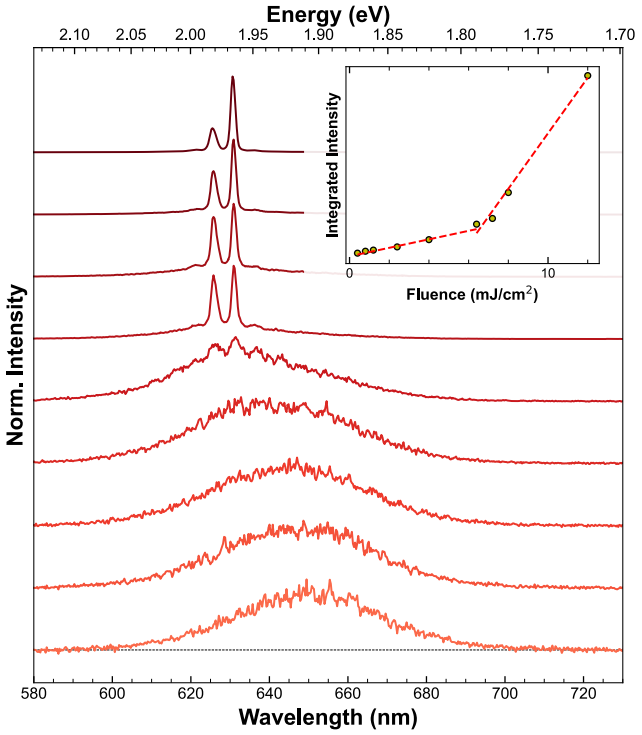

Fig. 2 Single-SP emission spectra for increasing pump fluences. Inset shows intensity of SP emission vs excitation fluence.

A key result of this work is that the lasing emission from individual SPs is spectrally tunable through the excitation wavelength (Fig. 3). By varying the pump wavelength, we observe reversible transitions in the lasing pattern. This tunability arises from the wavelength-dependent absorption profile of the CdSe/CdS quantum dots, which determines whether the optical excitation predominantly addresses the core or the shell region. As a consequence, the spatial distribution of optical gain within the SP is modified, altering the overlap between the gain region and the electromagnetic field profiles of different WGMs.

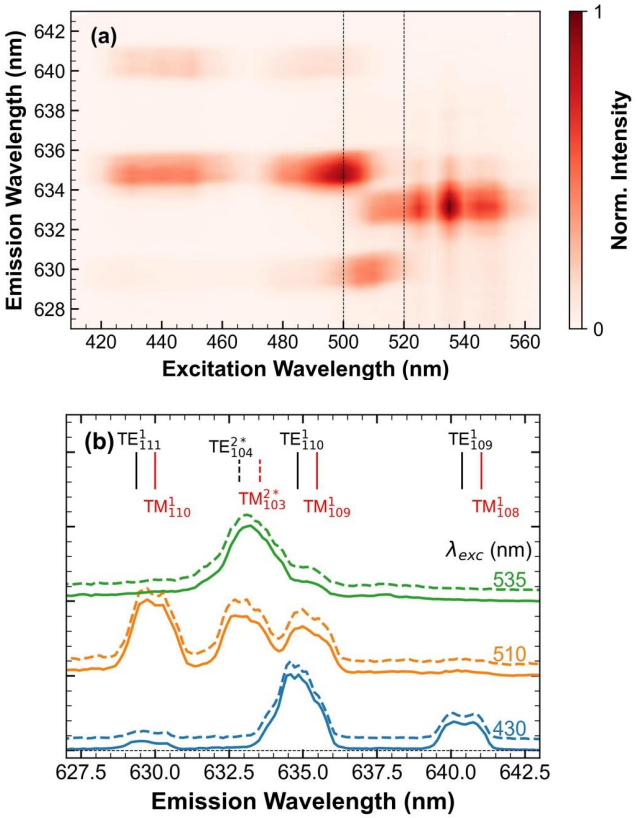

Fig. 3 (a) Lasing excitation-emission map of an individual SP. (b) Lasing spectra at three representative pump wavelength. Adapted from ref [3].

Time-resolved photoluminescence measurements further support this interpretation, revealing excitation-dependent emission dynamics and gain buildup. Shorter-wavelength excitation leads to more localized absorption near the outer regions of the SPs, whereas longer-wavelength excitation penetrates deeper into the structure, activating a larger effective gain volume. Since different WGMs exhibit distinct spatial field distributions, changes in gain localization result in selective amplification of specific modes, enabling excitation-controlled mode selection. This mechanism, corroborated also by numerical simulations, provides a simple and robust route to dynamically reconfigure the lasing response of the SP without modifying its geometry or surrounding environment.

Finally, we achieved both physical and optical coupling to an

optical fiber producing a microlaser that can be easily integrated with existing photonic technologies.

IV. Conclusion

We have demonstrated reversible, excitation-wavelength-dependent lasing in individual CdSe/CdS quantum dot superparticles. The tunability arises from excitation-controlled modulation of the optical gain distribution and its overlap with whispery-gallery-modes, enabling purely optical reconfiguration of micro-resonant emission. Moreover, the strong sensitivity of the lasing spectra to superparticle morphology and environment yields distinctive spectral fingerprints, highlighting potential of these self-assembled microlasers for photonics and optoelectronic applications including sensing and anticounterfeiting.

Acknowledgments

This work was supported by the PRIN projects 2022H8LE9P and 20223CWFZT.

References

[1] F. Montanarella, D. Urbonas, L. Chadwick, P. G. Moerman, P. J. Baesjou, R. F. Mahrt, A. van Blaaderen, T. Stöferle and D. Vanmaekelbergh, "Lasing Supraparticles Self-Assembled from Nanocrystals", ACS Nano, vol. 12, pp. 12788-12794, 2018.

[2] E. Marino, S. W. van Dongen, S. J. Neuhaus, W. Li, A. W. Keller, C. R. Kagan, T. E. Kodger and C. B. Murray, "Monodisperse Nanocrystal Superparticles through a Source–Sink Emulsion System", Chemistry of Materials, vol. 34, pp. 2779-2789, 2022.

[3] M. Reale, P. Castronovo, M. Cannas, E. Marino, A. Sciortino and F. Messina, "Excitation-Wavelength-Tunable Lasing in Individual Quantum Dot Superparticles", Advanced Optical Materials, vol. 13, pp. 2500838, 2025.

Increased hot carrier generation and separation in porous golden nanorods

Katarzyna Kluczyk-Korch [1], Tomasz J. Antosiewicz[1]
[1]Faculty of Physics, University of Warsaw, Poland
*Corresponding author: k.kluczyk-korch@uw.edu.pl

***Abstract*—The enhanced photocatalytic performance of porous gold compared to bulk gold has been examined using atomistic simulations. A correlation has been identified between the larger number of low-coordinated surface gold atoms and an increased generation of hot carriers within the plasmonic nanostructure.**

***Keywords*— hot carrier generation, photocathalysis, gold nanoparticles.**

I. Introduction

Porous gold is known to possess higher catalytic activity than in bulk. This behaviour is commonly attributed to an increased surface-to-volume ratio resulting in a high presence of gold atoms with low coordination numbers, and a higher density of so-called "hot spots," i.e. regions of strongly enhanced electromagnetic field intensity. For certain reactions, the catalytic performance of gold is further linked to the direct transfer of highly energetic charge carriers into the reactants. These carriers arise from the decay of coherent collective electron oscillations, known as plasmons, which are excited in a nanoparticles (NPs). In the present paper, we verify the hypothesis an increased generation rate of hot carriers in porous NPs compared to solid homogeneous NPs.

II. Methods

We investigate the optical and electronic characteristics of porous gold nanorods using Density Functional Theory (DFT) and Real-Time Time-Dependent DFT (RT-TDDFT). All simulations are performed with the GPAW package [1], employing the LCAO scheme for both ground-state DFT [2] and RT-TDDFT [3]. The calculations rely on uniform real-space grids and a finite-difference discretization.

Ground-state properties are obtained using the Gritsenko-van Leeuwen-van Lenthe-Baerends (GLLB-sc) exchange–correlation functional, which offers a substantially improved description of d-electron states in noble metals compared with the conventional Perdew-Burke-Ernzerhof (PBE) functional. The time-dependent response is then evaluated within the adiabatic PBE approximation. Photoabsorption spectra are generated via the δ-kick method [4] in the linear-response regime, using the dipole approximation to describe light–matter coupling. The time-dependent density functional theory (TDDFT) implementation is interfaced with post-processing tools that decompose resonances into electron–hole transition contributions and represent them as transition contribution maps (TCMs) [5]. Hot carrier generation rates are obtained following the procedure of Rossi et al. [6], which enables the analysis of ultrafast plasmon decay through Landau damping in the time domain and yields both the energetic and spatial distribution of hot carriers prior to any electron–electron or electron–phonon scattering.

III. Results and Discussion

We study the optical response of Au nano rods (NRs) with a number of holes inside introduced by systematic removal of chosen atoms (see the insets in fig.1). The geometry of the holes, i.e. size and shape, is kept constant and the number is increased from zero to five.

The TCMs, presented in fig. 1, show a spread of low-energy, in phase plasmonic transitions, into a larger area of energies, i.e., the energy broadening of plasmonic transitions, somewhat similarly as in small metallic clusters like Ag_{55}. There is also a slight increase in single-particle transitions resonant with excitation (transitions resonant with excitation lines on the black diagonal line), suggesting increased damping due to the extended surface of the NR. The out of phase, blue, transitions involving high energetic holes illustrate the contribution from d states present in Au. With an increase in the surface to volume ratio, the contribution of transitions from deep d states decreases. This is accompanied by a shrinking of the width of d-band.

Hot carriers are generated in the process of plasmon decay into single-particle-like transitions, which are resonant with the excitation. In consequence, their energy distribution resembles the density of states (DOS), resulting in highly energetic holes, formed by transitions of the d to sp states. The probability of the total per-atom hot carrier occupation as a function of the excitation energy is shown in fig. 2. Although in a narrow, 5x5 atom wide, NRs hot carrier generation does not follow a systematic evolution, interestingly, in the case of a wider, 7x7 atom wide, NRs we observe a steady increase of carrier per-atom occupation probability. The following analysis of spatial distribution of hot electrons and holes reveals that hot electrons tend to accumulate at the regions of high electromagnetic field intensity, while the hot holes surplus is find at the regions of low electromagnetic field intensity.

IV. Conclusion

The presence of the d states provides a reservoir of electrons that can be promoted to sp states, leading to the formation of high-energy hot holes. The projected density of d states varies

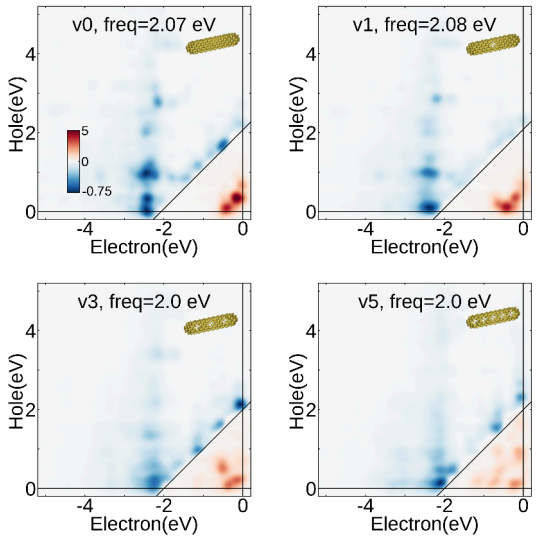

Fig. 1. The TCMs to photoabsorption calculated at the plasmon resonance frequencies for Au NRs with increasing number of pores. The excitation field is aligned with the long axis of rods.

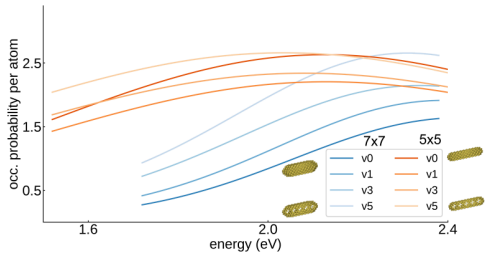

Fig. 2. Hot electron/hole occupation probability per atom as a function of pulse energy.

depending on the arrangement of voids. As the number of pores increases, more distinct electronic transitions contribute to plasmon oscillations, which broaden the energy distribution of hot carriers. Consequently, highly porous NRs produce a larger overall number of hot carriers. Excess hot electrons are concentrated near the NR surface in regions of strongly enhanced electromagnetic fields, whereas hot holes preferentially accumulate at low-coordinated atomic sites in these regions.

Acknowledgments

We acknowledge the support of the National Science Centre, Poland, via the project 2023/51/D/ST3/02731. The computations were enabled by resources provided by the Interdisciplinary Center for Mathematical and Computational Modelling of the University of Warsaw via project #GC84-51.

References

[1] J. Enkovaara, C. Rostgaard, J. Mortensen, J. Chen, M. Dulak, L. Ferrighi, J. G. an C. Glinsvad, V. Haikola, H. Hansen, H. Kristoffersen, M. Kuisma, A. Larsen, L. Lehtovaara, M. Ljungberg, O. Lopez-Acevedo, P. Moses, J. Ojanen, T. Olsen, V. Petzold, N. Romero, J. Stausholm-Moller, M. Strange, G. Tritsaris, M. Vanin, M. Walter, B. Hammer, H. Hakkinen, G. Madsen, R. Mieminen, J. Norskov, M. Puska, T. Rantala, J. Schiotz, K. Thygesen, and K. Jacobsen, "Electronic structure calculations with gpaw: a real-space implementation of the projector augmented-wave method," *J. Phys.: Condens. Matter*, vol. 22, p. 253202, 2010.

[2] A. Larsen, M. Vanin, J. Mortensen, K. Thygesen, and K. Jacobsen, "Localized atomic basis set in the projector augmented wave method," *Phys. Rev. B*, vol. 80, p. 195112, 2009.

[3] M. Kuisma, A. Sakko, T. Rossi, A. Larsen, J. Enkovaara, L. Lehtovaara, and T. Rantala, "Localized surface plasmon resonance in silver nanoparticles: Atomistic first-principles time-dependent density-functional theory calculations," *Phys. Rev. B*, vol. 91, p. 115431, 2015.

[4] K. Yabana and G. F. Bertsch, "Time-dependent local-density approximation in real time," *Phys. Rev. B*, vol. 54, pp. 4484–4487, 1996.

[5] T. P. Rossi, M. Kuisma, M. J. Puska, R. M. Nieminen, and P. Erhart, "Kohn-sham decomposition in real-time time-dependent density-functional theory: An efficient tool for analyzing plasmonic excitations," *Journal of Chemical Theory and Computation*, vol. 13, p. 4779, 9 2017.

[6] T. Rossi, P. Erhart, and M. Kuisma, "Hot-Carrier Generation in Plasmonic Nanoparticles: The Importance of Atomic Structure," *ACS Nano*, vol. 14, no. 8, pp. 9963 – 9971, 2020. [Online]. Available: https://doi.org/10.1021/acsnano.0c03004

Exciton-Plasmon Strong Coupling in Gold Nano-Bipyramid Arrays

Kseniia Mamaeva[1,3,*], Hodjat Hajan[1], Jamie Somers[1], Teodora Faraone[2], Colm Delaney[2], Larisa Florea[2], A. Louise Bradley [1,3,*]

[1]School of Physics, Trinity College Dublin, Ireland
[2]School of Chemistry, Trinity College Dublin, Ireland
[3]IPIC, Tyndall National Institute, Ireland
*Corresponding author: kmamaeva@tcd.ie, bradlel@tcd.ie

***Abstract*— We demonstrate deterministic room-temperature strong coupling between single CdSe/ZnS quantum dots (QDs) and gold nano-bipyramid tips using plasmon-triggered two-photon polymerization. Gold bipyramids are patterned via EBL/drop-casting, then photosensitive QD-loaded resin selectively polymerizes at plasmonic hotspots. Scattering reveals 265 meV Rabi splitting, photoluminescence shows characteristic polariton emission. This reproducible platform overcomes stochastic positioning limitations, and is a potential route to scalable bright nonlinear single-photon sources for integrated quantum photonic circuits and nanolasers.**

***Keywords*— strong coupling, quantum dots, localized sur-face plasmon polaritons, two-photon polymerization, gold nano-bipyramids.**

I. Introduction

Strong light–matter coupling between individual quantum emitters and optical nanocavities is a cornerstone of scalable quantum photonics, enabling hybrid polaritons for single-photon nonlinearities, thresholdless nanolasers, and deterministic entanglement generation.[1,2] Solid-state emitters such as nitrogen-vacancy centers and colloidal quantum dots (QDs) offer photostability and integration potential, yet bare QDs suffer broad linewidths (~50–100 meV) and modest brightness that limit spectral purity and indistinguishability.[3,4] Plasmonic nanocavities offer ultrasmall mode volumes ($V_m \sim 10^{-4}\left(\lambda/n\right)^3$) and room-temperature strong coupling ($g > k, \gamma$) evidenced by Rabi splitting $\hbar\Omega = 2g$ in scattering spectra.[5,6]

Recent advances for plasmonic nanoresonators coupled to single QDs include bow-tie cavities (Ω~100 meV), nanoparticle-on-mirror (NPoM) geometries (Ω~200 meV), and wedge nanogaps (Ω~240 meV), yet stochastic self-assembly or serial nanopositioning hinders scalability.[7,8] Plasmon-triggered two-photon polymerization (P-2PP) offers a deterministic alternative, selectively localizing emitters in plasmonic hotspots *via* near-field enhancement.[9]

Here, we demonstrate room-temperature strong coupling between single CdSe/ZnS QDs and gold nano-bipyramids (BPs)—nanostructures with sharp tips (~4 nm radius) enabling extreme field enhancement [10]. Using P-2PP, we precisely position QDs at a single BP tip hotspot, yielding scattering spectra with clear Rabi splitting, polariton-modified photoluminescence, and verified single-photon emission ($g^{(2)}(0)$=0.3). This hybrid platform provides a reproducible route to bright, nonlinear single-photon sources for integrated quantum technologies.

II. Methods

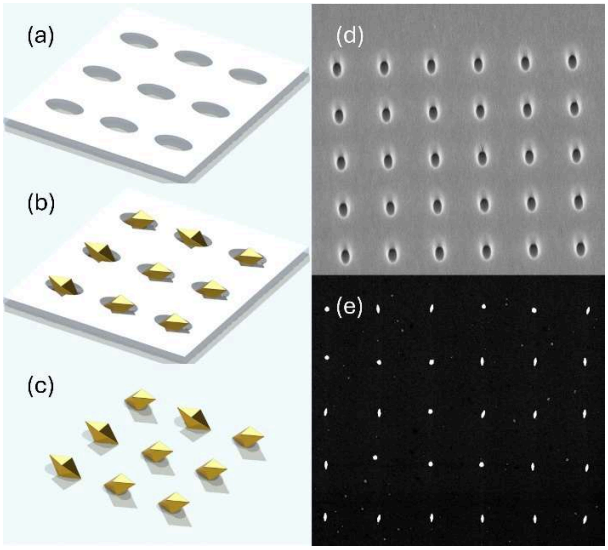

Fig. 1 (a,b,c) Schematic illustration of BPs placement in arrays (d) SEM image of elliptical shaped holes pattern after EBL (e) SEM image of BPs array on silicon substrate.

Our methodology for positioning single excitons at nanoparticle tips consists of two stages. First, we arrange gold BPs into arrays to characterize their plasmonic resonances prior to coupling. Second, we use 2PP to place QDs at the BP tips and achieve strong coupling [11].

The polymer-coated substrate is patterned with elliptical holes by electron beam lithography (EBL) (Fig. 1a,d). A solution of chemically synthesized BPs is drop-cast onto the patterned surface (Fig. 1b), and after solvent evaporation the sample is rinsed in acetone so that only BPs trapped inside the holes remain (Fig. 1c,e).

Next, a solution containing a polymerizable resin with embedded QDs isdeposited onto the BP array. To localize QDs near the tips of the Au BPs, we employ 2PP with the laser power set just below the bulk polymerization threshold, so that polymerization occurs only in regions of locally enhanced intensity due to the plasmonic near field. Finally, the unpolymerized solution is removed, leaving QDs selectively positioned at the BP tips.

III. Results and Discussion

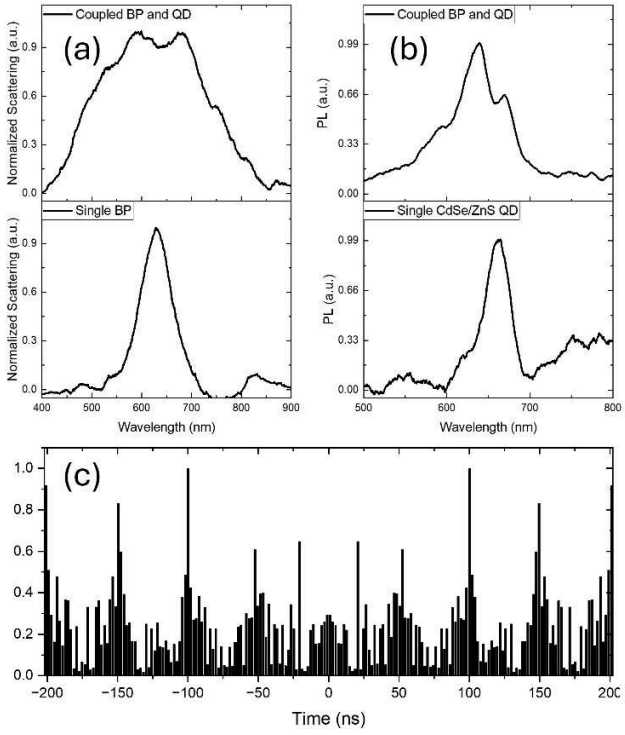

Fig. 2 Strong coupling signatures in QD–BP nanocavities. (a) Scattering: single BP plasmon (black, bottom) vs. Rabi splitting (top). (b) PL: uncoupled QD (bottom) vs. polariton emission (top). (c) $g^{(2)}(0)=0.3$ antibunching from single QD. All measurements are made at room temperature.

The fabricated QD–BP nanostructures exhibit clear optical signatures of room-temperature coupling between the localized surface plasmon mode and the QD exciton. In dark-field scattering, an isolated BP displays a single broad plasmon resonance (Fig. 2a, bottom). When single or few CdSe/ZnS QDs are positioned at the BP tip *via* plasmon-triggered 2PP, the spectra develop characteristic double-peaked profiles with a pronounced central energy dip, revealing Rabi splitting of 265 meV (Fig. 2a, top). This confirms coherent coupling where the exciton–plasmon interaction strength g exceeds the combined linewidths of the uncoupled modes.

Photoluminescence (PL) provides complementary evidence with reduced splitting of 93 meV, as expected from strong coupling theory. An uncoupled reference QD displays a single emission peak (Fig. 2b, bottom), while the coupled QD–BP system exhibits broadened emission redistributed across polariton branches (Fig. 2b, top). The smaller PL splitting (~35% of scattering value) arises because PL probes incoherent spontaneous emission dominated by the lower polariton branch, whereas scattering captures symmetric coupling of both upper and lower branches—a well-established distinction in hybrid nanosystems [12,13].

The single-photon nature of the emitter was independently verified through time-correlated single-photon counting on a reference CdSe/ZnS QD, yielding clear antibunching with $g^{(2)}(0)=0.3$ (Fig. 2c). Together, the 265 meV scattering splitting, 93 meV PL polariton emission, and confirmed single-photon statistics demonstrate deterministic realization of strongly coupled single-emitter plasmonic nanocavities at room temperature.

IV. Conclusion

Our plasmon-triggered two-photon polymerization method transforms gold nano-bipyramid arrays—fabricated *via* EBL-defined elliptical traps—into deterministic single-emitter plasmonic nanocavities. The observed 265 meV Rabi splitting in scattering, alongside polariton-modified photoluminescence, establishes room-temperature strong coupling previously limited by stochastic positioning. This hybrid platform is a route to scalable quantum plasmonic devices with unprecedented reproducibility for next-generation photonic quantum technologies.

Acknowledgments

This work was supported through funding from the Research Ireland under grants 21/FFP-P/10187, 12/RC/2276_P2, 12/RC/2278_2 and 18/EPSRC-CDT/3585.

References

[1] P. Vasa and C. Lienau, "Strong Light–Matter Interaction in Quantum Emitter/Metal Hybrid Nanostructures," *ACS Photonics*, vol. 5, pp. 2–23, 2018.

[2] E. Pelucchi et al., "The potential and global outlook of integrated photonics for quantum technologies," *Nat. Rev. Phys.*, vol. 4, pp. 194–208, 2022.

[3] P. Senellart, G. Solomon, and A. White, "High-performance semiconductor quantum-dot single-photon sources," *Nat. Nanotechnol.*, vol. 12, pp. 1026–1039, 2017.

[4] R. Uppu et al., "Scalable integrated single-photon source," *Sci. Adv.*, vol. 6, p. eabc8268, 2020.

[5] P. Törmä and W. L. Barnes, "Strong light-matter coupling and Fano-like interference phenomena," *Rep. Prog. Phys.*, vol. 78, p. 013901, 2014.

[6] H. Groß et al., "Near-field strong coupling of single quantum dots," *Phys. Rev. Lett.*, vol. 121, p. 077401, 2018.

[7] J. Lawless et al., "Influence of Gold Nano-Bipyramid Dimensions on Strong Coupling with Excitons of Monolayer MoS_2," *ACS Appl. Mater. Interfaces*, vol. 12, pp. 46406–46415, 2020.

[8] S. Hu et al., "Robust consistent single quantum dot strong coupling in plasmonic nanocavities," *Nat. Commun.*, vol. 15, p. 7119, 2024.

[9] D. Ge et al., "Hybrid plasmonic nano-emitters with controlled single quantum emitter positioning on the local excitation field," *Nat. Commun.*, vol. 11, p. 3414, 2020.
[10] T. Shegai et al., "Strong Light–Matter Coupling between Plasmons in Individual Gold Bipyramids and Excitons in Mono- and Multilayer WSe_2," *Nano Lett.*, vol. 18, pp. 5938–5945, 2018.
[11] K. Mamaeva "Integration of quantum dots at the tips of single plasmonic bipyramids," *arXiv:2511.03409*, 2025.
[12] M. Wersäll et al, “Observation of Mode Splitting in Photoluminescence of Individual Plasmonic Nanoparticles Strongly Coupled to Molecular Exciton” *Nano Letters*, vol. 1, 551-558, 2017
[13] Y. Niu et al., "Unified Scattering and Photoluminescence Spectra for Strong Plasmon-Exciton Coupling," *Phys. Rev. Lett.* 128, 167402, 2022

Deterministic Photon Addition in a Waveguide Mode

Kristina L. Malinowski[1,*], Holland Frieling[1], Benjamin E. C. Koltenbah[2], Pankaj K. Jha[3,4], Harry A. Atwater[1]

[1] Thomas J. Watson Laboratories of Applied Physics, California Institute of Technology, MS 128-95, Pasadena CA, USA
[2] Boeing Technology Innovation, Seattle, WA, USA
[3] Quantum Technology Laboratory<Q|T|L>, Department of Electrical Engineering and Computer Science, Syracuse University, Syracuse, NY, USA
[4] Institute for Quantum & Information Sciences, Syracuse University, Syracuse, NY, USA
*Corresponding author: kmalinow@caltech.edu

EXPORT CONTROLLED – ECCN EAR99 - This technology or software is subject to the U.S. Export Administration Regulations (EAR), (15 C.F.R. Parts 730-774). No authorization from the U.S. Department of Commerce is required for export, re-export, in-country transfer, or access EXCEPT to country group E:1 or E:2 countries/persons per Supp.1 to Part 740 of the EAR.

***Abstract*— We report on emitter-waveguide modeling results investigating stimulated emission during single photon addition. We design and fabricate a coupled emitter-waveguide device, representing significant progress towards an experimental demonstration of deterministic single photon addition.**

***Keywords*— quantum photonics, 2D materials, quantum emitters.**

I. Introduction

Pushing chip-based nanophotonics to the quantum limit relies on the availability of waveguide-coupled single photons. This is true both for commercializable technologies such as quantum photonic computing and networking and fundamental investigations of non-classical photon interactions. Photon addition, creating a superposition of an initial thermal or coherent state with a Fock state, is a particularly interesting model for both creating non-Gaussian states as a resource for quantum technologies and probing under-studied photon interactions including stimulated emission in a waveguide mode.

Photon addition was theoretically proposed over 30 years ago as a mechanism for generating squeezed light [1]. Today, there are multiple experimental demonstrations of heralded single-photon and multiple-photon addition using probabilistic single photon sources including spontaneous parametric down conversion (SPDC) [2-5] and optical parametric amplification (OPA) [6-8]. The existing work has yielded squeezed light and arbitrary quantum state generation. Further, the authors have proposed that photon addition can be used to amplify the signal to noise ratio (SNR) of weak signals by over 2x the classical limit [9-10].

While probabilistic photon addition is an effective way to generate indistinguishable photons and permits post-processing detected light by single photon events using the heralded photon, it is intrinsically rate limited. As the nonlinear component is pumped at higher powers, the single photon purity degrades [11]. Typical single photon rates from probabilistic sources are on the order of 10 to 100 Hz [7]. Deterministic solid state single photon emitters (SPEs) emit at significantly higher single photon rates. Specifically, hexagonal boron nitride (hBN) is a promising SPE host due to high quantum efficiencies, photon purity, Debye-Waller factors and single photon count rates (>10^6, 10^4x more than common probabilistic sources) [12,13]. hBN SPEs have also been shown to be electrostatically tunable, near lifetime-limited [14], and indistinguishable [15]. Further, hBN emitters have been coupled to nanophotonic structures both in monolithic hBN photonic platforms [16] and hybrid silicon nitride (Si_3N_4) platforms [17].

II. Methods

For our physically robust model, we embed a two-level emitter into the solution for a 1D waveguide (1DWG) in the spatial domain, following a similar derivation to existing models [18,19]. In Eq. 1, derived from considering two excitations in the model, we determine the number of right traveling photons (N_R) at a fixed point by integrating the photon number density (n_R) (defined by Eq. 2) over time.

$$N_R(x) = v_g \int_{t_1}^{t_2} dt\, n_R(x,t) \tag{1}$$

$$n_R(x,t) = |\beta_R(x,t)|^2 + 4\int dx' \left|\gamma_{RR}(x,x',t)\right|^2 + 4\int dx' \left|\gamma_{RL}(x,x',t)\right|^2 \tag{2}$$

$\beta_R(x,t)$ is the complex probability density denoting the combined probability of a single R-traveling photon and the excited state of the emitter. The functions $\gamma_{ij}(x_1,x_2,t)$ represent complex probability densities of the combinations of two photons and the ground state of the emitter. v_g is the group velocity. The limits of integration in Eq. 2 span a detection time gate. Our model of one and two excitations is based upon Ref. 10 and 19. We also include additional number of excitations and perform further statistical calculations.

To advance towards experimental demonstration of deterministic photon addition in a waveguide, we design in simulation an hBN nanowaveguide structure to promote high coupling to a single-mode Si_3N_4 waveguide. Full-wave simulations were performed using a finite difference time domain (FDTD) optical simulation (Tidy3D FDTD). The hBN refractive index was modeled as a custom diagonal anisotropic material using Phillips–van Vechten model and experimental parameter fitting [20]. A downloadable Jupyter Notebook with full simulation details can be found at Ref 21.

To fabricate this device, we first exfoliate hBN flakes onto thin film low pressure chemical vapor deposited Si_3N_4 on a silicon dioxide and silicon substrate. To form SPE defects in the hBN we anneal at atmospheric pressure while flowing argon at 850°C for 30 min. SPEs are characterized with photoluminescent (PL) spectroscopy and second order correlation measurements in a homebuilt mapping confocal microscope. The nanowaveguide pattern is aligned to an individual defect. We use electron-beam lithography and reactive ion etching to fabricate the hBN nanowaveguide and Si_3N_4 waveguide.

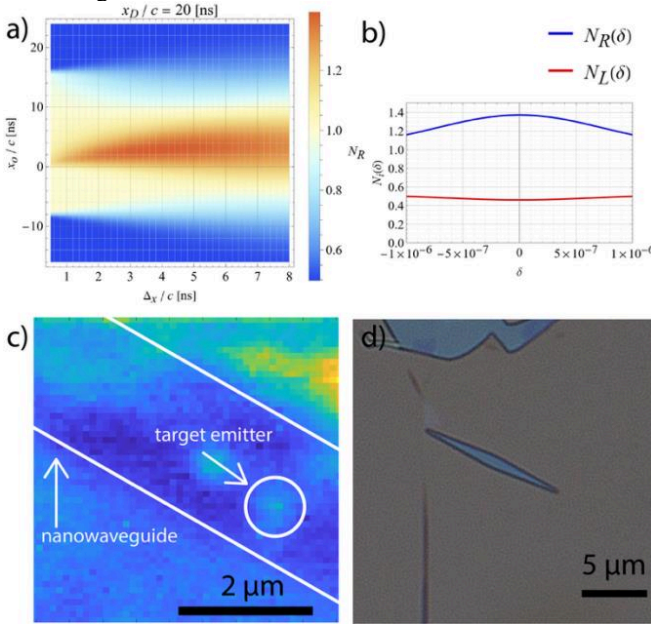

Fig. 1 (a) Parameter plot showing the number of R-traveling photons as integrated through time at a fixed observation point with spatial offset on the y-axis and linewidth detuning on the x-axis. (b) Simulated time-gated photon number measurements for the detuned pulse interacting with the initially excited emitter. (c) PL map of hBN SPE coupled in nanowaveguide. (d) Optical image of patterned and etched active hBN nanowaveguide.

III. Results and Discussion

In this work, we advance the theoretical understanding of stimulated photon addition through the interaction of an emitter and one-dimensional waveguide (1DWG) and make progress towards high coupling between an hBN SPE and a Si_3N_4 waveguide [10]. We use the model described in Methods to simulate photon addition using a nominal case in which the two-level emitter is excited, and a right traveling photon pulse interacts with the emitter. Qualitatively, increasing the spatial overlap between the pulse and emitter significantly alters the emission dynamics with respect to the spontaneous emission case, consistent with stimulated emission. This model can also be integrated into a photon statistic framework like the one used in previous work with a more simplistic numerical model [10]. This allows us to begin addressing questions regarding the ratio of spontaneous to stimulated emission during a deterministic photon addition event, which remains a critical and unanswered question. We also use this model to investigate the effect of detuning the pulse linewidth with respect to the emitter lifetime and the pulse frequency, with the number of right-traveling photons qualitatively relating to stimulated emission. As shown in Fig. 1(a), the emission dynamics and number of right-traveling photons are sensitive to the spatial overlap, showing the greatest number of right-traveling when the pulse is overlaps the emitter by an offset equivalent to around one emitter lifetime of 3 ns. The tolerance increases slightly for wider pulse widths. The dynamics are fairly robust to linewidth detuning (Fig. 1(a)) and frequency detuning (Fig. 1(b)) (only varying by 15% over a span of detuning commensurate with the coupling strength).

Working towards validating these theoretical predictions experimentally, we design and fabricate an emitter-containing a hBN nanowaveguide coupled to a Si_3N_4 waveguide. For a simulated spontaneous dipole emission, this design has 34% coupling in one direction. We have successfully fabricated a passive (no emitter) hBN nanowaveguide on top of a Si_3N_4 waveguide using electron-beam lithography and an active (emitter-containing) hBN nanowaveguide on a Si_3N_4 thin film (Fig. 1(c-d)). Further fabrication of a Si_3N_4 waveguide and grating coupler beneath the active hBN nanowaveguide will yield a favorable platform for experimentally probing deterministic photon addition in a waveguide. Through a robust analysis of photon statistics as we have previously demonstrated with hBN SPEs [22], we will characterize photon addition by examining detected photon distributions for non-classical peaks like those in Ref. 3. Using this device we will validate our theoretical results, particularly those assessing the impact of spatial mode overlap and frequency detuning on the photon addition mechanism and stimulated emission dynamics.

IV. Conclusion

Through our emitter-1DWG modeling and highly coupled emitter-waveguide device design we make significant advancements towards experimental deterministic photon addition. A deterministic photon addition platform provides a foundation for significantly increased experimental photon addition rates. Better photon addition rates enable more

efficient non-Gaussian state generation as a quantum computing or networking resource. Deterministic photon addition is also an ideal system to experimentally demonstrate theoretical predictions for quasi-lossless SNR enhancement of weak signals, whereas probabilistic photon addition may not provide sufficient photon additions to significantly amplify SNR. Finally, the higher photon addition coincidence rate of deterministic photon addition provides a pathway towards multiple sequential photon additions, which enables more exotic state generation and further SNR enhancement. While significant challenges remain in the pursuit of multiple sequential photon additions, with deterministic photon addition this becomes and engineering challenge rather than an intrinsic limitation. As such, the first experimental demonstration will represent a monumental step towards efficient cascaded single photon addition modules.

ACKNOWLEDGMENTS

This research was in part financially supported by the DARPA Photon-Efficient Nanoscale Optical Metrology (PhENOM) program (DARPA-PA-23-03-09). This work is also funded in part through the Boeing University Partnership Program under the direction of the Disruptive Computing, Networking & Sensing Group. K. M. recognizes support by the Department of Defense (DoD) through the National Defense Science & Engineering Graduate (NDSEG) Fellowship Program. P. K. J. also acknowledges the Syracuse University Startup Funds, which partially supported this research.

REFERENCES

[1] G. S. Agarwal, K. Tara, "Nonclassical properties of states generated by the excitations on a coherent state," *Phys. Rev. A* **43**, 492 (1991).
[2] A. Zavatta *et al.*, "Quantum-to-classical transition with single-photon-added coherent states of light," *Science* **306**, 5696 (2004).
[3] V. Parigi *et al.*, "Probing quantum commutation rules by addition and subtraction of single photons to/from a light field," *Science* **317**, 5846 (2007).
[4] A. Zavatta *et al.*, "A high-fidelity noiseless amplifier for quantum light states," Nature Photon **5**, 52–56 (2011).
[5] R. Kumar *et al.*, "Experimental Characterization of Bosonic Creation and Annihilation Operators," Phys. Rev. Lett. **110**(13), 130403 (2013).
[6] J. Wenger *et al*., "Non-Gaussian Statistics from Individual Pulses of Squeezed Light," *Phys. Rev. Lett.* **92**, 153601 (2004).
[7] J. Fadrný *et al*., "Experimental preparation of multiphoton-added coherent states of light," *Npj Quantum Inf* **10**, 1–9 (2024).
[8] M. Barbieri *et al*., "Non-Gaussianity of quantum states: An experimental test on single-photon-added coherent states," *Phys. Rev. A* **82**, 063833 (2010).
[9] C. G. Parazzoli *et al.,* "Enhanced thermal images of faint objects via photon addition / subtraction," *2016 CLEO* (2016)
[10] K. Malinowski *et al*., "Overcoming the Classical Signal-to-Noise Ratio Limit Through On-Chip Photon Addition," *APL Quantum* In Review (2026).
[11] W. Wasilewski *et al*., "Statistics of multiphoton events in spontaneous parametric down-conversion," *Phys. Rev. A* **78**, 033831 (2008).
[12] J. D. Caldwell *et al.*, "Photonics with hexagonal boron nitride," *Nat. Rev. Mater.* **4**, 552 (2019).
[13] T. T. Tran *et al.*, "Quantum emission from hexagonal boron nitride," *Nat. Nanotechnol.* **11**, 37 (2016).
[14] H. Akbari *et al.*, "Lifetime limited and tunable quantum light emission in h-BN via electric field modulation," *Nano Lett.* **22**, 7798 (2022).
[15] C. Fournier *et al.*, "Two-Photon Interference from a Quantum Emitter in Hexagonal Boron Nitride," *Phys. Rev. Applied* **19**, 041003 (2023).
[16] C. Li *et al.*, "Integration of hBN Quantum Emitters in Monolithically Fabricated Waveguides," *ACS Photonics* **8,** 2966-2972 (2021)
[17] D. Yamashita *et al.*, "Spatially Deterministic Integration of hBN Single-Photon Emitters on SiN Waveguides Via Femtosecond Laser Processing." *Adv. Optical Mater.* **13**, 27 (2025)
[18] E. Rephaeli, and S. Fan, "Stimulated Emission from a Single Excited Atom in a Waveguide," *Phys. Rev. Lett.* **108**, 143602 (2012).
[19] O.A. Chuikin *et al.*, "Single-photon stimulated emission in waveguide quantum electrodynamics," *Eur. Phys. J. B* **97**, 159 (2024).
[20] A. Segura *et al.*, "Natural optical anisotropy of h-BN: Highest giant birefringence in a bulk crystal through the mid-infrared to ultraviolet range," *Phys. Rev. Mater.* **2**, 024001 (2018).
[21] K. Malinowski, and A. Targholizadeh, "Modeling Photon Transfer from Silicon Nitride Waveguide to Hexagonal Boron Nitride Nanowaveguide and Niobium-Titanium-Nitride Nanowire," https://www.flexcompute.com/tidy3d/4cEyzxjHEx (2026).
[22] H. Akbari *et al.*, "Photon statistics analysis of h-BN quantum emitters with pulsed and continuous-wave excitation," *APL Quantum.* **1**, 026116 (2024).

Pole expansion of the optical scattering matrix via rescaled scattering channels

Elias Fösleitner[1,*], Adrià Canós Valero[1], Zoltan Sztranyovszky[2], Egor A. Muljarov[3], Kirill Koshelev[4], Thomas Weiss[1]

[1]Institute of Physics, University of Graz, and NAWI Graz, Universitätsplatz 5, 8010 Graz, Austria
[2]School of Physics and Astronomy, University of Birmingham, Birmingham B15 2TT, United Kingdom
[3]School of Physics and Astronomy, Cardiff University, Cardiff CF24 3AA, UK
[4]Department of Electronic Materials Engineering, Research School of Physics, Australian National University, Canberra, ACT, Australia
*Corresponding author: elias.foesleitner@uni-graz.at

***Abstract*—The pole expansion of the optical scattering matrix provides a fast and insightful route to investigate nanophotonic systems. However, conventional scattering channels from Mie theory result in matrices that exponentially diverge in the complex frequency plane, preventing simple pole expansions. We discuss different rescaling approaches to regularize the scattering channels.**

***Keywords*— scattering matrix, resonant states, pole expansion, metamaterials**

I. Introduction

In this work, we investigate the optical scattering matrix and its pole expansion in terms of optical resonances for spherical particles. The scattering matrix, which connects the incoming and outgoing waves of a scatterer, plays a central role in describing light-matter interaction at the nanoscale [1]–[7]. Since analytic solutions for the scattering matrix are only available for few systems, theoretical calculations typically rely on computing fullwave simulations of Maxwell's equations. However, such calculations are time-consuming and provide little insight into the underlying physics.

Recently, the pole expansion of the scattering matrix has been established as a powerful tool for replacing full-wave simulations [5], [8]–[14]. This type of expansion based on the optical resonances of the system, also known as resonant states or quasi-normal modes, is not only faster than conventional calculations of the scattering matrix, but also provides additional insight into resonant dynamics [15], [16].

However, to apply the pole expansion the scattering matrix have to satisfy certain prerequisites. This is particularly crucial for the Mittag-Leffler expansion — a variant of the pole expansion that only requires knowledge about poles and residues as well as one background term. While the ML expansion is often successfully applied in literature, its validity is rarely considered rigorously from first principles. Remarkably, the prerequisites for the Mittag-Leffler expansion are not fulfilled for the most-commonly known scattering matrix from Mie theory [17], since this scattering matrix exhibits exponential divergences in the complex plane, as shown in Fig. 1(a) and (b).

Fig. 1. Pole structure in the complex kR plane (left panels) and asymptotic behavior for $kR \to \pm i\infty$ (right panels) of the optical scattering matrix S for different regularizations of the analytic scattering matrices $S^{\mathrm{Mie}}_{\mathrm{TE},\ l=3}$, $S^{\mathrm{R1}}_{\mathrm{TE},\ l=3}$ and $S^{\mathrm{R2}}_{\mathrm{TE},\ l=3}$. The left panels show $|S(k)|$ in the complex plane, where red circles indicate poles originating from optical resonances (Ω_{p}), and black squares indicate poles introduced by the regularization of the channels (Ω_{c}). (a) $S^{\mathrm{Mie}}_{\mathrm{TE},l}$ with channels commonly used in Mie theory. The gray dashed line indicates the cut along the imaginary axis for which $S^{\mathrm{Mie}}_{\mathrm{TE},l}$ is depicted in (b), showing the asymptotically exponential divergence of $S^{\mathrm{Mie}}_{\mathrm{TE},l}$ for $kR \to i\infty$. (c), (d): Asymptotically regularized $S^{\mathrm{R1}}_{\mathrm{TE},l}$ channel that removes exponential divergence. (e), (f): Global regularization $S^{\mathrm{R2}}_{\mathrm{TE},l}$, which also removes the exponential divergence but introduces artificial poles coming from the underlying channels.

II. Results

We demonstrate that a Mittag-Leffler expansion of the scattering matrix becomes possible through an appropriate rescaling of the basis, i.e., the incoming and outgoing waves, and provide a rigorous framework on how this rescaling of the basis affects the scattering matrix. We show that appropriate rescalings make it possible for the scattering matrix $S(k)$ to fulfill the prerequisite of the (first-order) Mittag-Leffler theorem on its asymptotics, which is

$$\lim_{k\to\infty} |S(k)/k| = 0, \tag{1}$$

where k is the wavenumber. We refer to the process of removing divergences of $S(k)$ in the complex k plane as

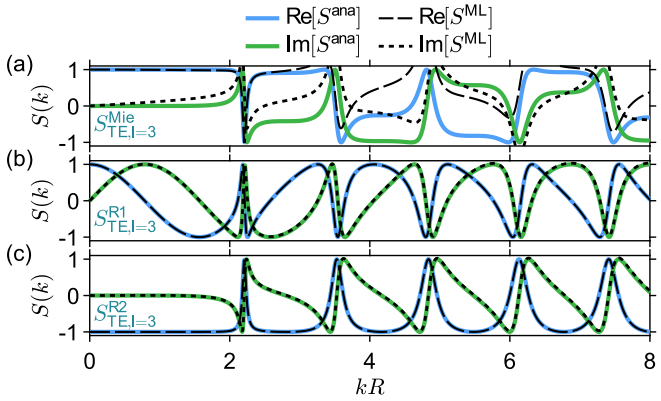

Fig. 2. Real (blue) and imaginary parts (green) of the different analytic scattering matrices $S^{\mathrm{ana}} \in \{S^{\mathrm{Mie}}_{\mathrm{TE},l=3}, S^{\mathrm{R1}}_{\mathrm{TE},l=3}, S^{\mathrm{R2}}_{\mathrm{TE},l=3}\}$ for real kR, compared with the pole expansions S^{ML} (black). Here, S^{ML} denotes the Mittag-Leffler (ML) expansions, where for (a) and (b) only physical poles were used while for (c) additionally the channel poles are used. Note that the residues also differ for the three cases and, thus, both S^{ana} and S^{ML} depend on the channels, so that even the analytic reference differs in all three cases. The pole expansions were computed using 201 physical poles.

regularization and we show that this enables the application of the Mittag-Leffler theorem to the scattering matrix.

Moreover, we demonstrate that the choice of rescaling is not unique and that certain choices can fundamentally alter the analytic continuation of the scattering matrix. We identify the emergence of additional, regularization-dependent poles, referred to as channel poles, that do not originate from the optical resonances of the system, as shown by the black squares in Fig. 1(e). Furthermore, we demonstrate that other regularizations do not require such channel poles, rendering them as a convenient choice in most practicable applications, as displayed in Fig. 1(c) and (d).

Figure 2(a) shows that the Mittag-Leffler expansion fails to describe the real-valued spectra of channels derived from Mie theory, whereas it accurately reproduces the regularized channels, as illustrated in Fig. 2(b) and (c).

III. Conclusion

In conclusion, we have shown that, by rescaling the channels of the scattering matrix, one can modify its analytic continuation to the complex frequency plane in distinct ways. Our results suggest that the regularization of the scattering matrix can enable efficient pole expansion schemes for more complex three-dimensional scatterers, thereby broadening the range of systems accessible to modal analysis in photonics.

Acknowledgments

Austrian Science Fund (FWF) (P12296). K.K. acknowledges the the Australian Research Council via Discovery Early Career Researcher Award DE250100419.

References

[1] H. M. Nussenzveig, *Causality and Dispersion Relations*, ser. Mathematics in Science and Engineering. New York, London: Academic Press, 1972, vol. 95.

[2] P. T. Kristensen, K. Herrmann, F. Intravaia, and K. Busch, "Modeling electromagnetic resonators using quasinormal modes," *Adv. Opt. Photon.*, vol. 12, no. 3, pp. 612–708, Sep 2020. [Online]. Available: https://opg.optica.org/aop/abstract.cfm?URI=aop-12-3-612

[3] D. M. Whittaker and I. S. Culshaw, "Scattering-matrix treatment of patterned multilayer photonic structures," *Phys. Rev. B*, vol. 60, pp. 2610–2618, Jul 1999. [Online]. Available: https://link.aps.org/doi/10.1103/PhysRevB.60.2610

[4] T. Weiss, N. A. Gippius, S. G. Tikhodeev, G. Granet, and H. Giessen, "Derivation of plasmonic resonances in the fourier modal method with adaptive spatial resolution and matched coordinates," *J. Opt. Soc. Am. A*, vol. 28, no. 2, pp. 238–244, Feb 2011. [Online]. Available: https://opg.optica.org/josaa/abstract.cfm?URI=josaa-28-2-238

[5] T. Weiss and E. A. Muljarov, "How to calculate the pole expansion of the optical scattering matrix from the resonant states," *Phys. Rev. B*, vol. 98, p. 085433, 8 2018. [Online]. Available: https://link.aps.org/doi/10.1103/PhysRevB.98.085433

[6] S. G. Tikhodeev, A. L. Yablonskii, E. A. Muljarov, N. A. Gippius, and T. Ishihara, "Quasiguided modes and optical properties of photonic crystal slabs," *Phys. Rev. B*, vol. 66, p. 045102, Jul 2002. [Online]. Available: https://link.aps.org/doi/10.1103/PhysRevB.66.045102

[7] N. A. Gippius, S. G. Tikhodeev, and T. Ishihara, "Optical properties of photonic crystal slabs with an asymmetrical unit cell," *Phys. Rev. B*, vol. 72, p. 045138, Jul 2005. [Online]. Available: https://link.aps.org/doi/10.1103/PhysRevB.72.045138

[8] F. Alpeggiani, N. Parappurath, E. Verhagen, and L. Kuipers, "Quasinormal-mode expansion of the scattering matrix," *Phys. Rev. X*, vol. 7, p. 021035, 6 2017. [Online]. Available: https://link.aps.org/doi/10.1103/PhysRevX.7.021035

[9] M. Benzaouia, J. D. Joannopoulos, S. G. Johnson, and A. Karalis, "Quasi-normal mode theory of the scattering matrix, enforcing fundamental constraints for truncated expansions," *Phys. Rev. Res.*, vol. 3, p. 033228, 9 2021. [Online]. Available: https://link.aps.org/doi/10.1103/PhysRevResearch.3.033228

[10] R. Colom, R. McPhedran, B. Stout, and N. Bonod, "Modal expansion of the scattered field: Causality, nondivergence, and nonresonant contribution," *Phys. Rev. B*, vol. 98, p. 085418, Aug 2018. [Online]. Available: https://link.aps.org/doi/10.1103/PhysRevB.98.085418

[11] S. V. Lobanov, W. Langbein, and E. A. Muljarov, "Resonant-state expansion of three-dimensional open optical systems: Light scattering," *Phys. Rev. A*, vol. 98, p. 033820, Sep 2018. [Online]. Available: https://link.aps.org/doi/10.1103/PhysRevA.98.033820

[12] H. Zhang and O. D. Miller, "Quasinormal coupled mode theory," *arXiv preprint arXiv:2010.08650*, 2020. [Online]. Available: https://arxiv.org/abs/2010.08650

[13] J. Defrance and T. Weiss, "On the pole expansion of electromagnetic fields," *Opt. Express*, vol. 28, no. 22, pp. 32 363–32 376, 10 2020. [Online]. Available: https://opg.optica.org/oe/abstract.cfm?URI=oe-28-22-32363

[14] V. Grigoriev, A. Tahri, S. Varault, B. Rolly, B. Stout, J. Wenger, and N. Bonod, "Optimization of resonant effects in nanostructures via weierstrass factorization," *Phys. Rev. A*, vol. 88, p. 011803, Jul 2013. [Online]. Available: https://link.aps.org/doi/10.1103/PhysRevA.88.011803

[15] S. Both and T. Weiss, "Resonant states and their role in nanophotonics," *Semiconductor Science and Technology*, vol. 37, no. 1, p. 013002, dec 2021. [Online]. Available: https://doi.org/10.1088/1361-6641/ac3290

[16] P. Lalanne, W. Yan, K. Vynck, C. Sauvan, and J.-P. Hugonin, "Light interaction with photonic and plasmonic resonances," *Laser & Photonics Reviews*, vol. 12, no. 5, p. 1700113, 2018. [Online]. Available: https://onlinelibrary.wiley.com/doi/abs/10.1002/lpor.201700113

[17] G. Mie, "Beiträge zur optik trüber medien, speziell kolloidaler metallösungen," *Annalen der Physik*, vol. 330, no. 3, pp. 377–445, 1908. [Online]. Available: https://onlinelibrary.wiley.com/doi/abs/10.1002/andp.19083300302

Can real motion be synthetically emulated ?

Kyan Louisia†*, Francisco J. Rodríguez-Fortuño†,
†Department of Physics and London Centre for Nanotechnology, King's College London, WC2R 2LS UK
*Corresponding author: kyan.louisia@gmail.com

***Abstract*—Advances in spatiotemporal material modulation have enabled synthetic motion, emulating electromagnetic responses of moving objects without physical displacement. We assess how faithfully synthetic motion reproduces true motion, using both Galilean and Lorentz protocols. By analysing wave reflection and hybrid real–synthetic motion, we isolate which dynamical effects are genuinely reproduced.**

***Index Terms*—time-varying metamaterials, Galilean and Lorentz synthetic motion, spacetime modulation.**

I. Introduction

Recent work in space-time modulated metamaterials suggests stationary structures can reproduce relativistic phenomena like Doppler shifts. [1] However, it remains unclear in which ways synthetic motion may be electromagnetically equivalent to genuine physical motion. A moving interface alters scattering via frame transformation, whereas synthetic motion relies on explicit modulation of material parameters. Although both generate similar frequency shifts, the underlying mechanisms are distinct. This work compares reflection of a normally incident plane wave from (i) a physically moving surface, (ii) a surface in Galilean synthetic motion and (iii) a surface in Lorentz synthetic motion to determine the limits of this equivalence. Our work lies in parallel to other investigations of spacetime modulation [2] [3].

II. METHODS

We consider a normally incident monochromatic TE plane wave (electric field along $\hat{y}$) impinging on a planar interface at $z = 0$ as in Figure 1. Region 1 ($z > 0$) is vacuum, while Region 2 ($z < 0$) is a non-magnetic dielectric with spatially periodic permittivity

$$\varepsilon_r(x) = \varepsilon_b + \Delta\varepsilon \sin(Kx).$$

Due to the spatial periodicity, the fields are expanded into discrete Floquet diffraction orders. [4] In Region 1, the reflected field is written as a superposition of these orders, with longitudinal components determined by the vacuum dispersion relation, distinguishing propagating and evanescent modes.

In Region 2, Fourier expansion of the permittivity and field converts the Helmholtz equation into a coupled system in diffraction-order space. For sinusoidal modulation, only nearest neighbours couple. The system is written in matrix form and solved via a Bloch eigenvalue problem, yielding the longitudinal propagation constants and modal structure of the periodic medium.

Enforcing continuity of the field and its normal derivative at the interface leads to a linear system for the reflection

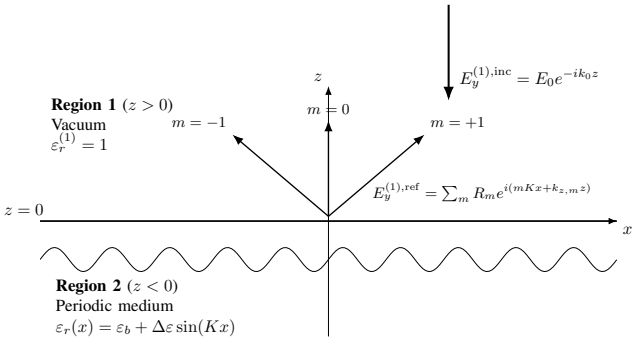

Fig. 1: Normal-incidence TE scattering from a sinusoidally modulated permittivity interface.

amplitudes, from which a closed matrix expression for the reflected-order vector is obtained.

$$\boxed{\mathbf{R} = (M - K_z)^{-1} \left[-(k_0 I + M)\, \mathbf{e}^{(\mathrm{inc})} \right]}$$

Here:

- $K_z = \mathrm{diag}(k_{z,m})$ contains the longitudinal reflected wavenumbers,
- I is the identity matrix,
- $\mathbf{e}^{(\mathrm{inc})}$ has only the $m = 0$ component equal to the incident amplitude E_0,
- M encodes the Bloch-mode response of the periodic medium.

In practice the Floquet expansion is truncated at a finite maximum order to obtain numerical solutions.

Dynamic extensions of the system are constructed directly from the static solution described above. For a surface translating along x, the problem is treated in the instantaneous rest frame of the interface, where the modulation is static and the incidence becomes oblique. The reflected modes are computed using the same formalism and then Lorentz-transformed back to the laboratory frame, yielding Doppler-shifted frequencies and modified reflection angles.

Synthetic motion is introduced through travelling-wave modulation of the permittivity, $\varepsilon_r(x) = \varepsilon_b + \Delta\varepsilon \sin(Kx - \Omega t)$, rendering the system periodic in both space and time. The field is therefore expanded in double Floquet indices, producing a coupled system in spatial and temporal orders derived from Maxwell's equations. In the Lorentz synthetic case, relativistic length contraction is incorporated into the modulation profile,

Fig. 2: The left plot corresponds to the reflected modes in $k-\omega$ space for the case of real physical motion. On the right, the same phase space diagram is plotted for Lorentz synthetic motion. The larger points represent propagating modes and the smaller ones are evanescent. The colours represent the amplitude of the modes.

$\varepsilon_r(x) = \varepsilon_b + \Delta\varepsilon \sin(\gamma K(x - vt)$, while the coupled-mode structure remains formally unchanged.

We introduce a hybrid configuration, where physical motion and synthetic modulation both occur with equal and opposite velocity. The resulting space–time scattering problem is solved in the surface frame and subsequently transformed back to the laboratory frame.

III. RESULTS AND DISCUSSION

Physical and synthetic motion are compared through the spectral structure (Figure 2) and energy distribution of the reflected field. In the frequency–momentum diagrams, the most intense modes produced by Lorentz synthetic modulation follow the same qualitative structure as those of genuine motion, although they do not coincide exactly. In hybrid configurations with equal and opposite velocities, the dominant modes become approximately monochromatic, indicating some form of cancellation for the leading Doppler shifts.

The distinction becomes clearer in the angular and energetic response. Lorentz synthetic modulation captures the principal trends of physical motion more faithfully than the Galilean protocol, yet discrepancies remain in the intensity distribution across diffraction orders. These differences persist in the total reflected power. We also investigate whether synthetic motion may be used for amplification purposes.

IV. CONCLUSION

We have examined to what extent synthetic motion can reproduce the electromagnetic response of genuine physical motion. Although both Galilean and Lorentz protocols reproduce Doppler-like frequency shifts, only the Lorentz construction can combine with physical motion to cancel certain features associated with motion. Even then, the agreement is largely confined to the most intense modes.

Crucially, discrepancies persist in the modal amplitudes and the reflected power. These differences indicate that matching dispersion relations is not sufficient to establish dynamical equivalence. Genuine motion corresponds to a Lorentz-covariant transformation of the full electromagnetic constitutive response, whereas synthetic implementations, so far, have only been able to modulate a scalar permittivity.

Synthetic motion can therefore reproduce certain aspects of moving interfaces, but it does not establish full physical equivalence. These results help delineate both the reach and the limitations of space–time modulation as a surrogate for genuine motion.

ACKNOWLEDGMENT

This work was supported by the Engineering and Physical Sciences Research Council (EPSRC), grant number EP/Y015673.

REFERENCES

[1] A. C. Harwood, S. Vezzoli, T. V. Raziman *et al.*, "Space-time optical diffraction from synthetic motion," *Nature Communications*, vol. 16, p. 5147, 2025.

[2] P. A. Huidobro, M. G. Silveirinha, E. Galiffi, and J. B. Pendry, "Homogenization Theory of Space-Time Metamaterials," *Phys. Rev. Applied*, vol. 16, 014044, 2021.

[3] A. Alex-Amor, C. Molero, and M. G. Silveirinha, "Analysis of Metallic Space-Time Gratings Using Lorentz Transformations," *Phys. Rev. Applied*, vol. 20, 014063, 2023.

[4] E. Galiffi, R. Tirole, S. Yin, H. Li, S. Vezzoli, P. A. Huidobro, M. G. Silveirinha, R. Sapienza, A. Alù, and J. B. Pendry, "Photonics of time-varying media," *Advanced Photonics*, vol. 4, no. 1, 014002, 2022.

Probing Strongly Coupled Multi-Resonant Plasmonic Cavities and Excitons in ITR-PEEM

Sacha Schwarz[1,*], Raphael Gherman[2,3], Alex Currie[1,4], Jean-François Bryche[2,3], Guillaume Beaudin[2,3], Dominique Drouin[2,3], Serge Ecoffey[2,3], François Fillion-Gourdeau[1,4], Pierre Levesque[1], Paul G. Charette[2,3], Steve G. MacLean[1,4,5]

[1]Infinite Potential Laboratories, Waterloo, Ontario, N2L 0A9, Canada
[2]Institut Interdisciplinaire d'Innovation Technologique (3IT), Université de Sherbrooke, 3000 Boulevard de l'université, Sherbrooke, J1K OA5 Québec, Canada
[3] Laboratoire Nanotechnologies Nanosystèmes (LN2)-IRL3463, CNRS, Université de Sherbrooke, INSA Lyon, École Centrale de Lyon, Université Grenoble Alpes, Sherbrooke, J1K 0A5 Québec, Canada
[4] INRS-Energie, Matériaux et Télécommunications, Varennes, Québec, J3X 1S2, Canada
[5] Institute for Quantum Computing, University of Waterloo, Waterloo, Ontario, N2L 3G1, Canada
*Corresponding author: sacha.schwarz@iplabs.ca

***Abstract*—We present strong coupling between excitonic and both localized and delocalized plasmonic modes in the near-field of a multi-resonant nanoparticle-on-mirror array integrated with a WSe_2 monolayer using interferometric time-resolved photoemission electron microscopy.**

***Keywords*— hybrid plasmon-photon modes, transition metal dichalcogenides, strong coupling, plasmonic cavity, photoemission electron microscopy.**

The combination of metallic nanostructures and two-dimensional transition metal dichalcogenides (TMDs) has steadily gained momentum as a robust platform to form hybrid light-matter states by strongly coupling excitons with plasmonic resonances. TMDs are particularly interesting because of their evolution to a direct bandgap at the monolayer level, enabling light absorption and emission through excitonic transitions [1]. When combined with nanostructures, and thus forming metasurfaces, these materials can be tuned to address and manipulate their photoemission by coupling with resonant optical nanocavities and arrays [2], [3], [4]. The tunability of these devices has been of great interest in various fields, such as single photon generation [5], [6], light manipulation [7] and sensing [8], [9], with applications in surface-enhanced Raman spectroscopy (SERS) [10], ultra-fast optical switching [11], [12] and biosensing [13].

In light-matter coupling, we distinguish between weak and strong coupling regimes. The weak coupling regime in monolayered TMD based nanostructures emerges primarily as an increase in photoluminescence intensity without a significant change in the emission spectrum. This enhancement is a result of the Purcell effect, which improves the quantum yield by boosting the local density of optical states [14]. This effect is highly dependent on the nanocavity Q-factor and the effective mode volume V. Gap plasmonic modes, which arise in the nanometric spacers between plasmonic components, are of special interest here due to their ability to achieve extreme field confinement and small mode volumes.

Moving into the strong coupling regime requires overcoming the high dissipative losses inherent in plasmonic cavities. This regime is fundamentally defined by a distinct spectral splitting into upper and lower polariton branches, resulting in a characteristic anti-crossing signature in the energy-momentum dispersion when the exciton and plasmonic cavity modes are in resonance. To address the dissipative challenges in achieving strong coupling, the nanoparticle-on-mirror (NPoM) geometry serves as a particularly interesting architecture [15]. In our NPoM array system [16], the localized surface plasmon (LSP) is created by the intense field enhancement within the sub-nanometer gap between the gold nanoparticle and the underlying metallic film. Simultaneously, the periodic or semi-infinite nature of the mirror surface allows for the excitation of delocalized propagating surface plasmon polaritons (SPPs) that can be tuned via the illumination angle. First, we show LSP-SPP hybridization in our NPoM array that enables both low mode volume (gap mode) and manageable dissipation. Secondly, we integrate a WSe_2 monolayer in this multi-resonant cavity and measure an effective coupling strength of 140 meV between excitons and coupled LSP-SPP, which surpasses Rabi splittings in typical individual nanorod layouts on WSe_2 flakes of approximately 106 meV [17].

To probe these dynamics, we employ interferometric time-resolved photoemission electron microscopy (ITR-PEEM), an advanced imaging technique that bypasses the diffraction limits of traditional optics. While far-field spectroscopy offers an ensemble-averaged view of energy shifts, ITR-PEEM enables a direct way to capture the precise spatial distribution of the electromagnetic fields and thus a direct measure of light absorption. By employing ultra-short laser pulses in an interferometric configuration, we resolve the ultrafast dephasing of excitonic and plasmonic modes with femtosecond timing

resolution, while directly capturing their spatiotemporal propagation dynamics across the surface.

ACKNOWLEDGMENTS

This work was supported by the Natural Sciences and Engineering Research Council of Canada (NSERC) and Infinite Potential Laboratories LP (Waterloo, ON).

LN2 is a French-Canadian joint International Research Laboratory (IRL 3463) funded and co-operated by CNRS, Université de Sherbrooke, INSA Lyon, École Centrale Lyon (ECL) as well as Université Grenoble Alpes (UGA). It is also supported by the Fonds de Recherche du Québec Nature et Technologie (FRQNT). LN2 is principally operated at the Institut Interdisciplinaire d'Innovations Technologiques (3IT) at Sherbrooke.

Dominique Drouin, Serge Ecoffey, and Paul G. Charette benefit from their affiliation to the RQMP - Regroupement Québécois sur les Matériaux de Pointes (10.69777/309032).

Infinite Potential Laboratories LP (IPL) is a company under the umbrella of Quantum Valley Investments located in Waterloo, Ontario, that supports research and commercialization activities associated with Quantum Information Science. IPL wishes to take advantage of the latest progress in quantum materials and nano-fabrication science to develop new technologies for vacuum-based applications in quantum information processing.

REFERENCES

[1] S. Z. Butler, S. M. Hollen, L. Cao, Y. Cui, J. A. Gupta, H. R. Gutiérrez, T. F. Heinz, S. S. Hong, J. Huang, A. F. Ismach, E. Johnston-Halperin, M. Kuno, V. V. Plashnitsa, R. D. Robinson, R. S. Ruoff, S. Salahuddin, J. Shan, L. Shi, M. G. Spencer, M. Terrones, W. Windl, and J. E. Goldberger, "Progress, Challenges, and Opportunities in Two-Dimensional Materials Beyond Graphene," *ACS Nano*, vol. 7, no. 4, pp. 2898–2926, Apr. 2013. [Online]. Available: https://pubs.acs.org/doi/10.1021/nn400280c

[2] J. Qin, Y.-H. Chen, Z. Zhang, Y. Zhang, R. J. Blaikie, B. Ding, and M. Qiu, "Revealing Strong Plasmon-Exciton Coupling between Nanogap Resonators and Two-Dimensional Semiconductors at Ambient Conditions," *Physical Review Letters*, vol. 124, no. 6, p. 063902, Feb. 2020. [Online]. Available: https://link.aps.org/doi/10.1103/PhysRevLett.124.063902

[3] T. W. Lo, X. Chen, Z. Zhang, Q. Zhang, C. W. Leung, A. V. Zayats, and D. Lei, "Plasmonic Nanocavity Induced Coupling and Boost of Dark Excitons in Monolayer WSe2 at Room Temperature," *Nano Letters*, vol. 22, no. 5, pp. 1915–1921, Mar. 2022, publisher: American Chemical Society. [Online]. Available: https://doi.org/10.1021/acs.nanolett.1c04360

[4] J. Fang, S. Huang, K. Yao, T. Zhang, M. Terrones, W. Huang, Y. Pan, and Y. Zheng, "Tunable Couplings of Photons with Bright and Dark Excitons in Monolayer Semiconductors on Plasmonic-Nanosphere-on-Mirror Cavities," *The Journal of Physical Chemistry C*, vol. 127, no. 19, pp. 9105–9112, May 2023. [Online]. Available: https://pubs.acs.org/doi/10.1021/acs.jpcc.3c01019

[5] B. Munkhbat, C. Piccinini, A. Paralikis, J. Neto, A. Madigawa, P. Wyborski, V. Remesh, L. Vannucci, and N. Gregersen, "High-purity and stable single-photon emission in bilayer WSe2 via phonon-assisted excitation," Aug. 2024. [Online]. Available: https://www.researchsquare.com/article/rs-4809013/v1

[6] A. Paralikis, C. Piccinini, A. A. Madigawa, P. Metuh, L. Vannucci, N. Gregersen, and B. Munkhbat, "Tailoring polarization in WSe2 quantum emitters through deterministic strain engineering," *npj 2D Materials and Applications*, vol. 8, no. 1, p. 59, Sep. 2024. [Online]. Available: https://www.nature.com/articles/s41699-024-00497-2

[7] Y. Yang, J. Seong, M. Choi, J. Park, G. Kim, H. Kim, J. Jeong, C. Jung, J. Kim, G. Jeon, K.-i. Lee, D. H. Yoon, and J. Rho, "Integrated metasurfaces for re-envisioning a near-future disruptive optical platform," *Light: Science & Applications*, vol. 12, no. 1, p. 152, Jun. 2023. [Online]. Available: https://www.nature.com/articles/s41377-023-01169-4

[8] S. Butun, E. Palacios, J. D. Cain, Z. Liu, V. P. Dravid, and K. Aydin, "Quantifying Plasmon-Enhanced Light Absorption in Monolayer WS2 Films," *ACS Applied Materials & Interfaces*, vol. 9, no. 17, pp. 15 044–15 051, May 2017, publisher: American Chemical Society. [Online]. Available: https://doi.org/10.1021/acsami.7b01947

[9] J. Li, Z. Xie, T. Zhao, H. Li, D. Wu, and X. Yu, "Metasurface-Enhanced Infrared Photodetection Using Layered van der Waals MoSe2," *Nanomaterials*, vol. 15, no. 12, p. 913, Jun. 2025. [Online]. Available: https://www.mdpi.com/2079-4991/15/12/913

[10] J.-F. Bryche, M. Vega, A. Tempez, T. Brulé, T. Carlier, J. Moreau, M. Chaigneau, P. G. Charette, and M. Canva, "Spatially-Localized Functionalization on Nanostructured Surfaces for Enhanced Plasmonic Sensing Efficacy," *Nanomaterials*, vol. 12, no. 20, p. 3586, Oct. 2022. [Online]. Available: https://www.ncbi.nlm.nih.gov/pmc/articles/PMC9609756/

[11] A. Genco and G. Cerullo, "Optical nonlinearity goes ultrafast in 2D semiconductor-based nanocavities," *Light: Science & Applications*, vol. 11, no. 1, p. 127, Dec. 2022. [Online]. Available: https://www.nature.com/articles/s41377-022-00827-3

[12] C. Huang, B. Xu, S. Peng, H. Y. Fu, and Q. Li, "Strong coupling and ultrafast switching in hybrid epsilon-near-zero-plasmonic metasurfaces," *Applied Optics*, vol. 64, no. 23, pp. 6657–6665, Aug. 2025, publisher: Optica Publishing Group. [Online]. Available: https://opg.optica.org/ao/abstract.cfm?uri=ao-64-23-6657

[13] G. Wu, F. Yan, L. Liang, X. Du, W. Wang, T. Li, J. Tian, X. Yan, H. Yao, Z. Wang, and M. Wang, "Exciton-Photon Coupling Microcavity as a Selective Biosensing Platform for Nonlocal Terahertz Metamaterials," *Advanced Science*, vol. 12, no. 16, p. 2416951, Apr. 2025. [Online]. Available: https://advanced.onlinelibrary.wiley.com/doi/10.1002/advs.202416951

[14] M. Pelton, S. D. Storm, and H. Leng, "Strong coupling of emitters to single plasmonic nanoparticles: exciton-induced transparency and Rabi splitting," *Nanoscale*, vol. 11, no. 31, pp. 14 540–14 552, 2019. [Online]. Available: http://xlink.rsc.org/?DOI=C9NR05044B

[15] N. Kongsuwan, A. Demetriadou, M. Horton, R. Chikkaraddy, J. J. Baumberg, and O. Hess, "Plasmonic Nanocavity Modes: From Near-Field to Far-Field Radiation," *ACS Photonics*, vol. 7, no. 2, pp. 463–471, Feb. 2020, publisher: American Chemical Society. [Online]. Available: https://doi.org/10.1021/acsphotonics.9b01445

[16] R. Gherman, S. Schwarz, J.-F. Bryche, G. Beaudin, A. Currie, P. Levesque, F. Fillion-Gourdeau, S. G. MacLean, D. Drouin, S. Ecoffey, and P. G. Charette, "A comprehensive study of plasmonic mode hybridization in gold nanoparticle-over-mirror (NPoM) arrays," *Nanophotonics*, Dec. 2025. [Online]. Available: https://www.degruyterbrill.com/document/doi/10.1515/nanoph-2025-0437/html

[17] R. Ai, X. Xia, H. Zhang, K. K. Chui, and J. Wang, "Orientation-Dependent Interaction between the Magnetic Plasmons in Gold Nanocups and the Excitons in WS_2 Monolayer and Multilayer," *ACS Nano*, vol. 17, no. 3, pp. 2356–2367, Feb. 2023. [Online]. Available: https://pubs.acs.org/doi/10.1021/acsnano.2c09099

Detection and Quantification of Mid-Infrared through Raman thermometry in Plasmonic Bilayer Metasurface

Anju Sajan[1, *], Christopher Sumner[1], Rohit Chikkaraddy[1]

[1]Department of Physics and Astronomy, University of Birmingham, United Kingdom
*Corresponding author: axs2370@student.bham.ac.uk

***Abstract*— Room-temperature manipulation of mid-infrared radiation is hindered by weak light–matter coupling and thermal dissipation. We design and fabricate a plasmonic bilayer resonant metasurface that enhances absorption in the mid-IR and enables quantitative evaluation of the resulting temperature rise, offering a pathway toward improved photonic sensing and thermal detection.**

***Keywords*— Metamaterials, Plasmonics, mid-IR detection, SERS**

I. Introduction

The mid-infrared (mid-IR) spectral range (2–20 μm) in the electromagnetic spectrum is of significant importance due to its applications in various fields, including molecular sensing, gas sensing, atmospheric monitoring, biomedical imaging, free-space communication, and energy harvesting. Unlike the visible or near-infrared regions, mid-IR radiation is challenging to detect due to its low photon energy and the influence of thermal noise, which complicates room-temperature detection and limits practical applications.

Recent developments in mid-IR detector technologies, particularly those based on emerging materials and metasurface engineering, offer promising pathways toward more efficient and cost-effective mid-IR sensing solutions and allow wavelength selective detection. Plasmonic Metamaterials are interesting due to their ability to convert light into heat through localized surface plasmons resonance (LSPR) and propagating surface plasmon resonance (PSPR).

Here we designed and fabricated plasmonic Mid-Infrared Disc-Coupled Hole Array (MDHA) system and investigated its mid-IR thermosensing properties using anti-Stokes Raman thermometry.

II. Methods

The MDHA, consisting of array of polymer micropillars with gold disks on the top and a perforated hole-film at the bottom seperated by a dielectric layer (Figure 1), fabricted using two photon polymerization techniques followed by sputtering of gold.

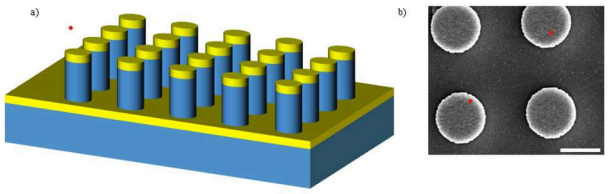

Figure 1: a) Geometry of MDHA The structure consists of a periodic array of cylindrical pillars with a diameter (D) of 5 μm, height (H) of 5 μm, and periodicity (Λ) of 10 μm. b) SEM image of the fabricated structure. The scale bar is 5 μm.

The designed MDHA structure facilitates two channel coupling of mid-IR and NIR light coupling. The mid-IR light (4.6μm) illuminated from the top side couples directly with the MDHM modes whereas tightly focused NIR light at 785nm is coupled through the glass substrate and through the polymer pillar (Figure 2 a). Thus, mid-IR light resonantly gets absorbed on the disc and forms temperature gradient between the top disc layer and the bottom hole film.

The difference in the temperature to top and bottom layer is measured through Surface-Enhanced Raman scattering (SERS) thermometry. The temperature rise induced by the mid-IR laser is estimated from the ratio of the anti-Stokes intensity measured with and without mid-IR excitation using the following equation,

$$\ln\left(\frac{I_m}{I_0}\right) = \frac{\Delta E}{k_B}\left(\frac{1}{T_0} - \frac{1}{T_M}\right) \quad (1)$$

Here T_0 is the refererence temperature, we use $T_0 = 300\ K$ and T_M is the temperature introduced in the presnce of mid-IR, I_m and I_0 are the anti-Stoke intensity with and without the presence of mid-IR radiation, k_B is the Boltzman constant and ΔE is energy difference between incident and scattered photon.

III. Results and Discussion

Upon illumination with the mid-IR laser, a temperature rise (ΔT) of approximately 2 K was observed between the top disc and the bottom film aperture, originating from absorption of the incident radiation by the gold disc. By linearly increasing the excitation power and monitoring ΔT, we find a proportional relationship, indicating that higher mid-IR input leads to greater absorption within the MDHA and a corresponding linear conversion of optical energy into heat.

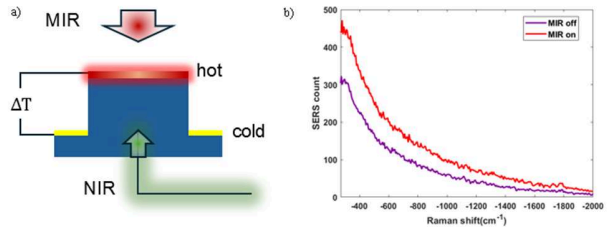

Figure 2: a) Experimental configuration for mid-IR thermosensing measurements using a Raman spectrometer. The MDHA array is illuminated with a mid-IR laser (λ=4.6 μm) from the top metal disc and a near-infrared (NIR) laser (λ=785 nm). b) Anti Stoke SERS spectra with and without mid-IR showing a change in background due to mid-IR absorption.

Under an incident optical power density of $0.727\,\frac{\mu W}{\mu m^2}$, the structure exhibits a detectable temperature modulation corresponding to a thermal response on the order of $10^{-6}\,\frac{W}{\sqrt{Hz}}$, indicating its potential sensitivity at room temperature.

IV. Conclusion

We designed and fabricated a plasmonic bilayer resonant metasurface to enhance mid-IR absorption through engineered optical confinement. The structure supports spectrally selective resonances that increase the interaction between incident radiation and the absorbing layer, leading to a measurable photothermal response under ambient conditions. Local temperature rises induced by mid-IR absorption are quantified using non-contact Raman thermometry, allowing direct evaluation of the thermal response without perturbing the system. Potential applications include thermal imaging, chemical sensing, and mid-IR energy harvesting.

Acknowledgments

This work was supported by Centre for Doctoral Training in Topological Design and Engineering and Physical Sciences Research Council (EPSRC).

References

[1] Dao, Thang Duy, et al. "Hole array perfect absorbers for spectrally selective midwavelength infrared pyroelectric detectors." *Acs Photonics* 3.7 (2016): 1271-1278

[2] Jones, Steven, et al. "Photothermal heating of plasmonic nanoantennas: Influence on trapped particle dynamics and colloid distribution." *ACS Photonics* 5.7 (2018): 2878-2887.

Direct Laser Writing of Ag-Au Thin Films for Plasmonic Sensing Platform

Kernius Vilkevičius[1,*], Tomas Rakickas[2], Evaldas Stankevičius[1]

[1]Department of Laser Technologies, Center for Physical Sciences and Technology, Lithuania
[2]Department of Nanoengineering, Center for Physical Sciences and Technology, Lithuania
*Corresponding author: kernius.vilkevicius@ftmc.lt

***Abstract*— Periodic plasmonic nanostructures were fabricated on silver, gold, and silver-gold thin films using single ultrashort laser pulses. Grating-coupled resonances exhibit sharp spectral peaks and a high refractive-index sensitivity up to 930 nm/RIU. The Ag-Au nanobump arrays demonstrate enhanced performance stability and repeatability, highlighting their potential for scalable plasmonic sensing platforms.**

***Keywords*— plasmonics, direct laser writing, sensing, periodic arrays.**

I. Introduction

Plasmonic nanostructures arranged in a periodic manner have gained significant attention owing to their distinctive optical response and strong light-matter interaction at the nanoscale. For large-scale applications and integration into practical devices, a reliable, rapid, and highly reproducible method is essential. Conventional lithographic and chemical approaches, while providing high resolution, often suffer from limited throughput, scalability, or multi-step process complexity. Therefore, alternative strategies are actively sought. Direct laser writing (DLW) technique based on single femtosecond pulse exposure of thin metallic films represents a promising single-step approach and is employed in this work for the production of periodic plasmonic arrays with high precision and repeatability [1]. Localized laser irradiation induces melting of the thin metallic films, and subsequent resolidification under strong thermal stresses results in the formation of complex nanostructures, including hemispherical bumps, pyramid-shaped cones, and jets having a sharp spike [2]. Periodic arrangement of these nanostructures results in the excitation and hybridization of several plasmonic modes, leading to the enhanced optical characteristics. Upon interaction with electromagnetic radiation, structures exhibit strong local field enhancement and increased absorption at resonant frequencies. These phenomena are fundamental to application in surface-enhanced Raman spectroscopy (SERS) and plasmonic sensing. Therefore, the fast production with flexible tuning of the properties is in demand.

Plasmonic sensing exploits the sensitivity of nanostructured metallic surfaces to local refractive index (RI) variations near the metal-dielectric interface. Changes in the surrounding RI led to spectral resonance shifts, enabling real-time and label-free detection of DNA, biomolecules, analytes, or liquids [3]. In the latter applications, variations in concentration directly lead to RI changes, allowing rapid and accurate detection of pollutants. Performance of such sensors depends on the plasmonic coupling, therefore strategies aimed at reducing the linewidth of the resonances are actively pursued. Metallic gratings produce sharp and narrow resonant peaks arising from hybridization of plasmonic modes, while also offering device compactness since the bulky prism used in conventional plasmonic sensors is eliminated. By implementing DLW for such platform fabrication, free-form, easily scalable, and large-area sensing zones can be manufactured in a rapid manner with tailored optical responses of required parameters [4]. Here, we present a single-step DLW-based fabrication of a plasmonic sensing platform and its characterization using a glycerol solution of various concentrations.

II. Methods

Ultrafast fs laser (Pharos, Light Conversion) with a 343 nm wavelength was used for nanostructure fabrication in metallic films. Thin gold (50 nm), silver (50 nm), and silver-gold (25-25 nm) layers were deposited on microscopic soda-lime glasses using a magnetron sputter coater. The laser beam was then tightly focused onto the surface using a high-NA objective (NA=0.5) into a spot of 0.8 μm in diameter. Thin films were modified using pulse energies in the range of 0.46-0.55 nJ to produce hemispherical nanobumps. Laser scanning with an implemented pulse picker was employed to produce a square 3×3 mm^2 array with 0.8 μm period. The samples were characterized using a scanning electron microscope and an optical microscope. Finally, the sensing platform (Figure 1a) was finished by attaching an adhesive chamber (HybriWell-FL) over the structured area.

For sensing measurements, ultrapure water and glycerol solution in water of 4 different concentrations were used. Ellipsometric measurements were performed to determine the RI of the measured liquids at 658 nm wavelength, and the Sellmeier equation was used to calculate the dispersions for the whole investigated wavelength range. Sensing performance was determined by measuring the reflection with a spectrophotometer in the range of 600-1400 nm with a step of 1 nm. Response was measured for both s- and p-polarization at

an 8° angle, with additional measurements at 15°, 30°, 45°, and 60°. The whole characterization consisted of a reflectance measurement in an air environment, liquid infusion into a chamber, reflectance measurement in a liquid environment, and a liquid extrusion. Such a cycle was repeated for 3 times to ensure the stability of the platform.

The platform was evaluated by calculating the quality factor of the resonant peaks, as well as the figure of merit (FOM) and sensitivity. The latter was described as:

$$S = \frac{\Delta \lambda_{res}}{\Delta n}, \#(1)$$

where $\Delta\lambda_{res}$ is the resonant peak shift, and Δn is the change in RI. Meanwhile, the FOM was determined by dividing S by the full width of the resonant peak at its half depth.

III. Results and Discussion

The periodic arrays of gold, silver, and silver-gold bilayer nanobumps were produced on 50 nm thick layers with a grating period of 0.8 µm. The geometrical dimensions of the structures were intentionally kept similar to ensure that variation in height and shape would not impact the optical response, thereby allowing a direct comparison of different metallic samples. By measuring the spectral response in air, water, and glycerol solutions of 1.7%, 3.4%, 5.1%, and 6.8%, a clear resonance redshift with increasing RI was observed (Figure 1b). Detailed analysis showed that each diffraction-based resonant peak (m=±1 in *s*-polarization and m=-1 and m=+1 at *p*-polarization) exhibits a slightly different shift and is evaluated individually. Among these, the m=-1 peak demonstrated the highest sensitivity, with values up to 870 nm/RIU. The metal comparison revealed that while silver nanobumps exhibit the largest sensitivity values, the bilayer sample shows intermediate sensitivities, with better performance than gold grating. This suggests that the Ag-Au configuration is optimal for a sensing platform, as the upper gold layer protects the silver from oxidation while the bimetallic combination enhances plasmonic properties. Consecutive measurements confirmed excellent repeatability and demonstrated that the platform provides a stable performance.

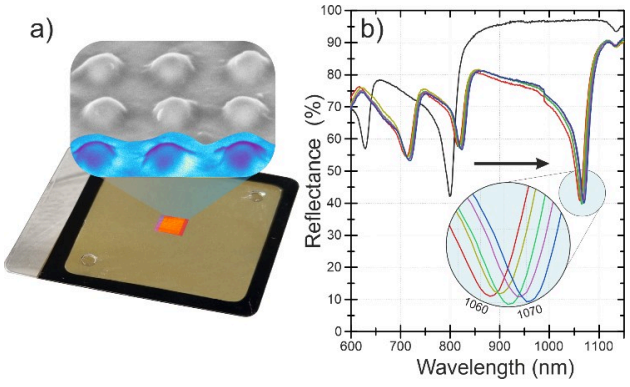

Fig. 1 a) Nanobump sensing platform. b) Reflectance spectrum with a resonance shift.

After determining the optimal metal configuration, additional measurements were carried out for the Ag-Au sample at varying angles of incidence. Since grating-coupled resonances are highly angle-dependent, both resonance position and sensing performance were influenced by this parameter. With increasing angle of incidence, peak qualities, sensitivities, and FOMs either increased or decreased depending on the resonance diffractive origin. For the m=±1 peak, the sensitivity increased up to 933 nm/RIU at 60° angle. However, this was accompanied by peak broadening, resulting in reduced FOM. In contrast, the m=-1 resonance exhibited a slight decrease in sensitivity while maintaining its width with a remarkable redshift, leading to an increase in FOM from 25 RIU^{-1} to 57 RIU^{-1}. It was also observed that, at certain angles, some resonant peaks overlapped with water absorption zones, thus limiting their applicability.

Finally, the durability and reusability of the sample were investigated by performing spectral measurements after 6 months. Despite the storage for a long time, the resonance positions remained unchanged with similar peak sensitivities and highly repeatable results. These findings confirm the robustness of the sensing platform and its suitability for prolonged measurements.

IV. Conclusion

We have demonstrated periodic nanobump arrays fabricated using direct laser writing on gold, silver, and silver-gold bilayer films and evaluated their performance as refractive index sensing platforms. Grating-coupled resonances have pronounced dips in reflectance spectra, which exhibit accurate redshifts with increasing RI of the surrounding medium. Among the investigated structures, the silver-gold bilayer showed the greatest sensing parameters with combined favorable properties of both plasmonic metals. Individual resonant peaks demonstrate distinct sensitivities, which can be improved even more by tuning the angle of incidence. This allows reaching the sensitivity of 933 nm/RIU and FOM of 57 RIU^{-1}. The platform also demonstrates high stability and repeatability of the results over an extended period of time. Overall, the results highlight direct laser writing as a rapid and scalable technique for high-performance plasmonic sensors suitable for environmental and biochemical applications. Future work will extend the platform application for biomolecule binding to the surface and their detection.

Acknowledgments

The authors acknowledge the Research Council of Lithuania (LMTLT) for the received funding under project No. S-TPP-23-14.

References

[1] E. Stankevičius, K. Vilkevičius, M. Gedvilas, E. Bužavaitė-Vertelienė, A. Selskis, Z. Balevičius, "Direct Laser Writing for the Formation of Large-Scale Gold Microbumps Arrays Generating Hybrid Lattice Plasmon Polaritons in Vis-NIR Range", Advanced Optical Materials, vol. 9, pp. 2100027, 2021.

[2] K. Vilkevičius, G. D. Tsibidis, A. Selskis, E. Stratakis, E. Stankevičius, "Formation of Highly Tunable Periodic Plasmonic Structures on Gold

Films Using Direct Laser Writing," Advanced Optical Materials, vol. 12, pp. 2400172, 2024.
[3] A. Minopoli, A. Acunzo, B. DellaVentura, R. Velotta, "Nanostructured Surfaces as Plasmonic Biosensors: A Review", Advanced Materials Interfaces, vol. 9, pp. 2101133, 2022.
[4] K. Vilkevičius, T. Rakickas, E. Stankevičius, "High-quality plasmonic Ag-Au bilayer nanobump grating sensor", Advanced Materials Technologies, vol. 10, pp. e01199, 2025.

Benchmark Study Using Machine Learning Surrogate Models for Predicting Optical Spectra of Tungsten Bronze Nanospheres Based on Mie Theory

Yuanchao Lu[1], Ruixing Li[1,*]

[1]School of Materials Science and Engineering, Beihang University, China
*Corresponding author: 1499149583@qq.com

***Abstract* — We compared three regression models for predicting absorption spectra of tungsten bronze nanospheres with anisotropic dielectric response, approximated by two independent isotropic Mie calculations. The Random Forest achieved higher accuracy than the Multilayer Perceptron and XGBoost under interpolation. All models lost predictive ability when extrapolating beyond the training radius range.**

***Keywords*— machine learning, Mie theory, surrogate model, tungsten bronze.**

I. Introduction

Nanoscale tungsten bronzes (M_xWO_3, M = alkali metal, $0 < x < 1$) exhibit strong localized surface plasmon resonance (LSPR) in the near-infrared region, showing potential for applications in areas such as smart windows, photothermal therapy, and selective absorbers[1]. The optical absorption of nanoparticles is generally sensitive to particle size and morphology[2]. For ideal spherical particles, Mie theory provides an analytical solution to Maxwell's equations and can be used to calculate absorption spectra[3]. In practice, tungsten bronze nanoparticles often exhibit faceted or non-spherical anisotropic morphologies, for which the analytical solution of Mie theory is, strictly speaking, no longer applicable, and numerical methods such as the finite-difference time-domain (FDTD) method are usually needed[4]. On the other hand, if the particle shape is temporarily approximated as a sphere, two independent isotropic Mie calculations can be performed using the dielectric functions along the a-axis and c-axis, respectively. This provides a large amount of accurate analytical training data for benchmarking surrogate models in an exactly solvable system.

Machine learning surrogate models can learn the mapping from structural parameters to spectra from a modest amount of simulation data, significantly accelerating predictions.[5] However, most existing studies test only a single model or report successful cases, and a systematic understanding of the performance differences and applicable ranges of different methods in similar systems is still lacking[6]. Before directly dealing with complex real systems where shape and dielectric anisotropy are coupled, we believe it is necessary to first carry out a comparison within a controllable, analytically tractable, and idealized framework.

Inspired by the experimental practice of separately measuring and averaging spectra under different polarization directions to analyze anisotropic particles, we decompose the dielectric anisotropy of hexagonal tungsten bronze into two independent isotropic Mie scattering problems, phenomenologically defined by the principal dielectric functions: ε_a and ε_c[7]. This gives two independent, noise-free, idealized spectral mapping problems. The two problems follow similar variation trends, yet the distinct principal dielectric parameters introduce subtle differences, together forming a fundamental benchmark for testing the ability of regression models to capture spectral features and generalize. With this simplification, we can clearly evaluate the interpolation accuracy and extrapolation limits of different models on data with zero numerical noise, thereby offering a preliminary reference for future applications of surrogate models in more realistic systems.

In this work, three widely used regression models—Multilayer Perceptron (MLP), Random Forest (RF), and XGBoost (XGB)—are benchmarked. These three models span different algorithm families—neural networks, bagging, and boosting—allowing a comparison of their suitability for spectral surrogate modeling. Using Mie-theory-calculated spectra as the training and test datasets, and considering the optical absorption properties and application requirements of tungsten bronzes, this study is confined to the visible–near-infrared range of 350–2000 nm, with the spectral responses based on the a-axis and c-axis treated separately.

II. Methods

2.1 Dataset Generation

Standard Mie theory calculations were performed using the a-axis dielectric function ε_a and the c-axis dielectric function ε_c, respectively. The resulting absorption cross sections C_{abs} were volume-normalized to give the volume absorption coefficient α_{abs}; this removes the volume scaling effect of particle size on the absorption cross section and highlights the intrinsic absorption strength of the material, making the results more directly comparable with experimentally measured bulk absorption spectra. Calculations were carried out for radii from 1 to 200 nm with a step size of 1 nm, yielding 200 radius samples. The experimental values of ε_a and ε_c were both taken from Ref. [7].

For each radius, we performed Mie calculations using ε_a and ε_c separately, producing two independent spectra. Although in typical experiments an ensemble of randomly oriented nanocrystals yields a polarization-averaged spectrum, we kept these two independent spectra in the training set to capture as much of the intrinsic optical anisotropy of the material as possible. All spectra were initially calculated at 1 nm intervals over the 350–2000 nm range, covering the LSPR of tungsten bronzes and the visible–near-infrared region relevant to applications.

Figure 1 shows the absorption spectra calculated using ε_a at several selected radii. All spectra exhibit a clear absorption peak at around 1100 nm, which is the LSPR peak arising from the collective oscillation of free carriers driven by the incident electromagnetic field. As the particle radius increases from 20 nm to 160 nm, the peak redshifts and its intensity increases, a trend described by Mie theory, while the secondary absorption peaks that gradually appear in the visible region originate from higher-order multipole contributions. The spectra calculated using ε_c have similar line shapes and trends, with only slight shifts in peak position and intensity due to the different dielectric function.

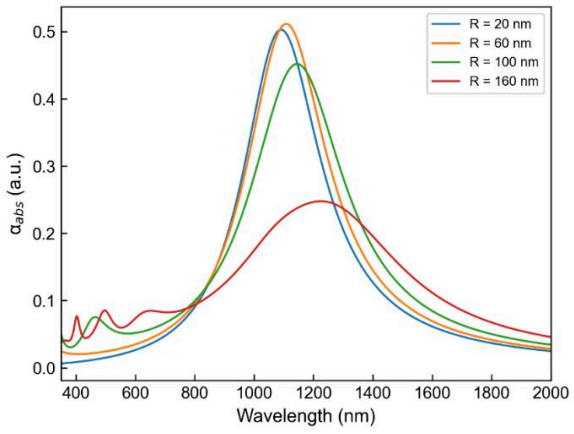

Fig. 1 Volume absorption coefficient spectra of tungsten bronze nanospheres at selected radii calculated using ε_a

2.2 Machine Learning Models

The dataset described in Section 2.1 was used for both interpolation and extrapolation training. For interpolation, the dataset was randomly split into a training set of 160 radii (80%) and a test set of 40 radii (20%). For extrapolation, radii from 1 to 150 nm were used as the training set, and radii from 151 to 200 nm as the test set.

Three regression models were implemented using Python and the scikit-learn and XGBoost libraries:

- **Multilayer Perceptron (MLP).** A feedforward neural network with three hidden layers of sizes 128, 64, and 32, all using ReLU activation. Training used the Adam optimizer with L2 regularization (α = 0.001), early stopping, and a batch size of 32.
- **Random Forest (RF).** An ensemble of 100 decision trees using bootstrap aggregation, with scikit-learn default hyperparameters.
- **XGBoost (XGB).** A gradient-boosted tree model with 100 estimators and a learning rate of 0.1. A multi-output regressor wrapper was used to handle the high-dimensional spectral output.

For all models, the input feature was the nanoparticle radius, and the target was a vector formed by concatenating the a-axis and c-axis absorption spectra (3302 points in total). The input features for the MLP model were standardized; the tree-based models were trained on the raw radius values. Model performance was evaluated using the coefficient of determination (R^2) and root mean square error (RMSE) on the test set. The three models were chosen for their complementarity: MLP represents neural networks that can learn highly nonlinear mappings; RF is generally robust on small datasets; and XGBoost offers another popular boosting-tree scheme.

III. Results and Discussion

3.1 Interpolation test

Table 1 summarizes the predictive performance of the three models on the test set.

Table 1. Performance metrics of the multilayer perceptron (MLP), random forest (RF), and XGBoost models on the test set

Model	Axis	R^2	RMSE($\times 10^{-3}$ m^{-1})
MLP	a	0.9071	6.18
	c	0.9112	11.53
RF	a	0.9991	0.81
	c	0.9993	2.89
XGB	a	0.9966	1.57
	c	0.9973	5.69

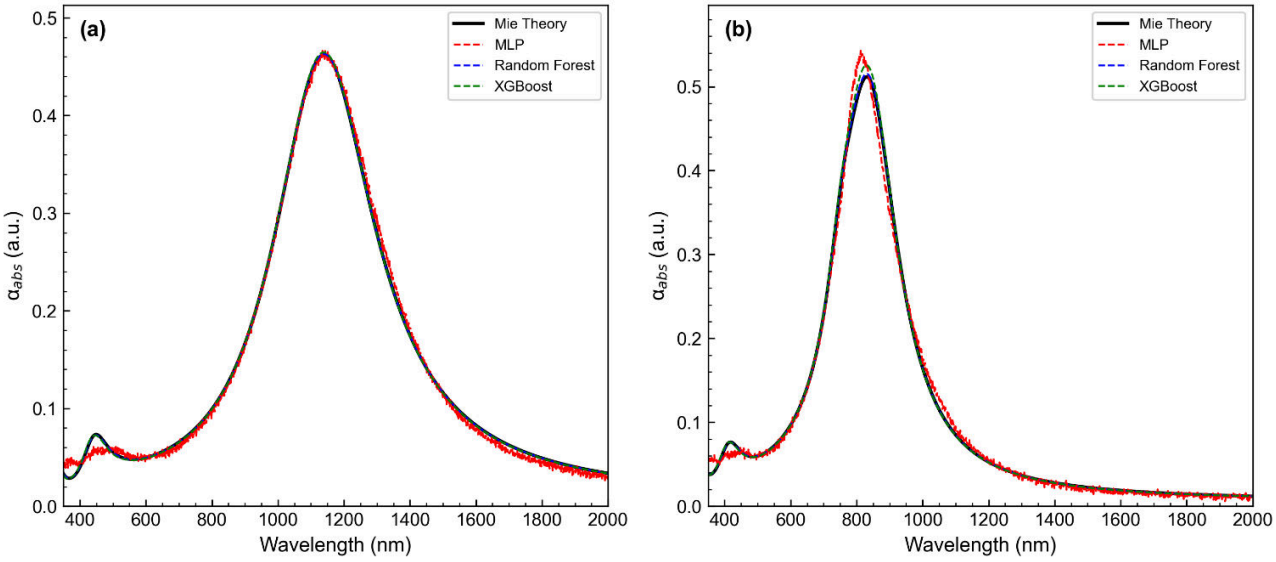

Fig. 2 Comparison of predicted and Mie-theory-calculated volume absorption coefficient spectra for a test radius of 96 nm: (a) a-axis and (b) c-axis

Among the three models, RF performed the best, achieving the highest R^2 and the lowest RMSE for both the a-axis and c-axis directions. XGB followed, also maintaining an R^2 above 0.99. In contrast, MLP, a method commonly used for learning nonlinear mappings, achieved lower accuracy than RF and XGB in this task.

To illustrate the prediction quality visually, a representative sample with a radius of 96 nm is examined. Figure 2 presents the predicted volume absorption coefficient spectra from the three models compared with the Mie theory spectra in the 350–2000 nm range, for both the a-axis and c-axis. The red dashed lines represent the MLP predictions: the agreement at the main LSPR peak around 1100 nm is acceptable, but the accuracy for the c-axis is lower than for the a-axis. The prediction deviations of MLP at the secondary peak near 500 nm are clearly larger than those of RF and XGB. The blue and green dashed lines correspond to the RF and XGB predictions, respectively; both fit the main LSPR peak and the 500 nm secondary peak well, clearly outperforming MLP. The slightly weaker performance of XGB on the c-axis is consistent with its higher RMSE value.

3.2 Extrapolation test

When the models trained on volume absorption coefficient spectra for radii 1–150 nm were applied to the unseen radius interval of 151–200 nm, the R^2 values of all models dropped to negative values, indicating a loss of predictive ability. The R^2 of MLP dropped to -9.91, while those of RF and XGB decreased to -3.56 and -3.40, respectively. The negative R^2 values mainly arise because the models cannot extrapolate features beyond the training range; at the same time, the significantly enhanced contribution of higher-order multipoles in the extrapolation interval further worsens the prediction performance.

IV. Conclusion

This work presents a benchmark study, under interpolation and extrapolation settings, of three regression models—Multilayer Perceptron (MLP), Random Forest (RF), and XGBoost (XGB)—for predicting the absorption spectra of anisotropic tungsten bronze nanospheres based on particle radius. Under interpolation, RF achieved higher accuracy than MLP and XGB. Within the extrapolation interval considered here, none of the models gave valid predictions for radii in the 151–200 nm range (negative R^2), indicating that purely data-driven surrogate models fail to capture changes in physical mechanisms beyond the training parameter space. These results suggest that when applying machine learning surrogate models in nanophotonics, it is important to carefully evaluate their applicable range, and direct extrapolation to unseen parameter regimes should be avoided.

References

[1] C. Guo, S. Yin, and T. Sato, “Tungsten Oxide-Based Nanomaterials: Morphological-Control, Properties, and Novel Applications,” *Reviews in Advanced Sciences and Engineering*, vol. 1, pp. 235–263, 2012

[2] A. Agrawal, I. Kriegel, and D. J. Milliron, “Shape-Dependent Field Enhancement and Plasmon Resonance of Oxide Nanocrystals,” *J. Phys. Chem. C*, vol. 119, pp. 6227–6238, 2015.

[3] G. Mie, “Beiträge zur Optik trüber Medien, speziell kolloidaler Metallösungen,” *Annalen der Physik*, vol. 330, pp. 377–445, 1908

[4] Kane Yee, “Numerical solution of initial boundary value problems involving maxwell’s equations in isotropic

media," *IEEE Trans. Antennas Propagat.*, vol. 14, pp. 302–307, 1966

[5] K. Yao and Y. Zheng, *Nanophotonics and Machine Learning: Concepts, Fundamentals, and Applications*, vol. 241. in Springer Series in Optical Sciences, vol. 241. Cham: Springer International Publishing, 2023

[6] A. Movsesyan, L. V. Besteiro, Z. Wang, and A. O. Govorov, "Mie Sensing with Neural Networks: Recognition of Nano-Object Parameters, the Invisibility Point, and Restricted Models," *Advcd Theory and Sims*, vol. 5, p. 2100369, 2022

[7] J. Kim, A. Agrawal, F. Krieg, A. Bergerud, and D. J. Milliron, "The Interplay of Shape and Crystalline Anisotropies in Plasmonic Semiconductor Nanocrystals," *Nano Lett.*, vol. 16, pp. 3879–3884, 2016

Enhanced Strong Coupling in Two-Dimensional Dichalcogenide Materials and a Bowtie Nanoantenna Plasmonic Array

Na Jia[1,2*], Bhera Ram Tak[3], Luke Doolan[1,2], Yongliang Zhang[1], Riley Gatensby[2], Jonathan N. Coleman[1,2], Richard Hobbs[3] and A. Louise Bradley[1,2*]

[1]School of Physics, Trinity College Dublin, Ireland
[2]Trinity College Dublin, The University of Dublin, Centre of Doctoral Training for Advanced Characterization of Materials, CRANN & AMBER, Dublin, Ireland
[3]School of Chemistry, Trinity College Dublin, Ireland *Corresponding author: jian@tcd.ie, bradlel@tcd.ie

***Abstract*—We demonstrate large strong coupling between a Au bowtie nanoantenna array enabling and monolayer WS_2. Using a PMMA layer to engineer the dielectric environment enhances local fields and increases the Rabi splitting from 84 to 135 meV, visible in both scattering and emission spectra. Experimental results agree well with simulations.**

***Keywords*— Bowtie nanoantenna, Plasmon–exciton interaction, Rabi splitting, Strong coupling.**

I. Introduction

Strong coupling at room temperature between narrow-band excitonic transitions in monolayer transition metal dichalcogenides (TMDCs) and plasmonic modes has attracted significant interest due to its importance for manipulating light –matter interactions in advanced photonic devices [1-3]. In this work, we investigate strong plasmon–exciton coupling in a hybrid system composed of a bowtie nanoantenna array and monolayer WS_2 [4, 5]. Varying the bowtie nanoantenna dimensions enables precise tuning of the plasmonic nanocavity modes, while the sharp tips provide strong near-field confinement, facilitating efficient interaction with WS_2 excitons. The robust excitonic resonance of monolayer WS_2 supports stable room-temperature coupling, resulting in enhanced optical absorption in the hybrid structure [6, 7].

By varying the bowtie geometry, the plasmonic resonance is tuned from 590 to 690 nm, allowing systematic control of the detuning between plasmonic and excitonic modes and leading to the observation of strong coupling at room temperature [8, 9]. A Rabi splitting energy of 84 meV is achieved in the WS_2-coupled Au bowtie nanoantenna. After introducing a PMMA overlayer, the plasmonic resonance exhibits an experimentally observed redshift of approximately 20 nm, accompanied by a pronounced enhancement of the local electric field as seen in the numerical simulations. Experimentally, the Rabi splitting energy increases to 135 meV, in excellent agreement with the simulated value of 138 meV. These results confirm that PMMA layer provides effective dielectric environment engineering and strengthens plasmon–exciton coupling through the enhanced electric field[10, 11].

II. Methods

The bowtie nanoantenna structures are designed and numerically simulated using Lumerical FDTD Solutions. The nanoantennas are fabricated on fused silica substrates by electron-beam lithography (EBL), followed by metal deposition and lift-off [12]. To improve pattern resolution, the sample was developed in a 1:3 MIBK: IPA solution at 0 °C for 30 s using a thermoelectric cold plate with stirring, followed by nitrogen drying. Metal deposition was then performed using a Temescal FC-2000 system. For Au deposition, a 1 nm Ti adhesion layer was introduced, with deposition rates of 1 Å s^{-1} for Ti and 0.5 Å s^{-1} for Au. The patterned structures were transferred to the substrate via lift-off in N-methyl pyrrolidone (NMP) at 55 °C for 45 min, followed by rinsing in acetone and IPA and nitrogen drying. Monolayer WS_2 is obtained from a commercial supplier (Six Carbon Technology) and transferred onto the fabricated nanoantenna arrays using a dry transfer method. A PMMA overlayer with controlled thickness is subsequently deposited by spin coating.

Raman and photoluminescence (PL) measurements are performed using 532 nm continuous-wave laser excitation under ambient conditions. Scattering spectra are collected using an optical microscopy system (Olympus) in a dark-field configuration.

III. Results and Discussion

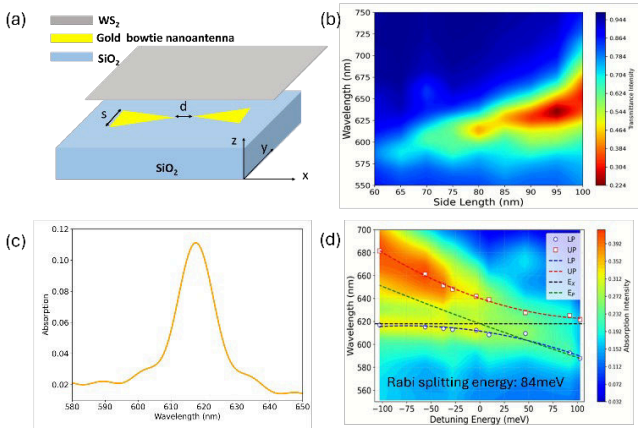

Fig. 1(a) Schematic of the WS_2/bowtie nanoantenna/fused silica hybrid structure. (b) Color map of simulated plasmonic resonance spectra as a function of the bowtie side length. (c) Simulated absorption spectrum of monolayer WS_2. (d) Absorption colormap of the WS_2/bowtie nanoantenna/fused silica system as a function of detuning energy. The horizontal black dashed line denotes the WS_2 exciton energy E_x, while the green dashed line represents the plasmonic resonance energy E_p. The triangle side length s (nm) is varied to tune E_p, yielding an energy detuning $\Delta=E_p-E_x$. The red and blue dashed curves show the fitted dispersion of the lower polariton (LP) and upper polariton (UP) branches obtained from coupled-mode theory (CMT), resulting in a Rabi splitting $\hbar\Omega$ of 84 meV [13].

The schematic of the designed strong-coupling architecture is shown in Fig. 1a, where a monolayer WS_2 is placed on top of a Au bowtie nanoantenna. By varying the side length of the individual triangular elements, the plasmonic resonance can be continuously tuned from 590 to 690 nm (Fig. 1b). As shown in Fig. 1c, monolayer WS_2 exhibits an absorption peak at 616 nm, corresponding to the A exciton peak used for strong coupling with the bowtie nanoantenna mode. The absorption color-map of the WS_2/bowtie nanoantenna hybrid system reveals a clear anti-crossing behavior. By extracting the upper polariton (UP) and lower polariton (LP) branch energies, a Rabi splitting energy of 84 meV is obtained (Fig. 1d).

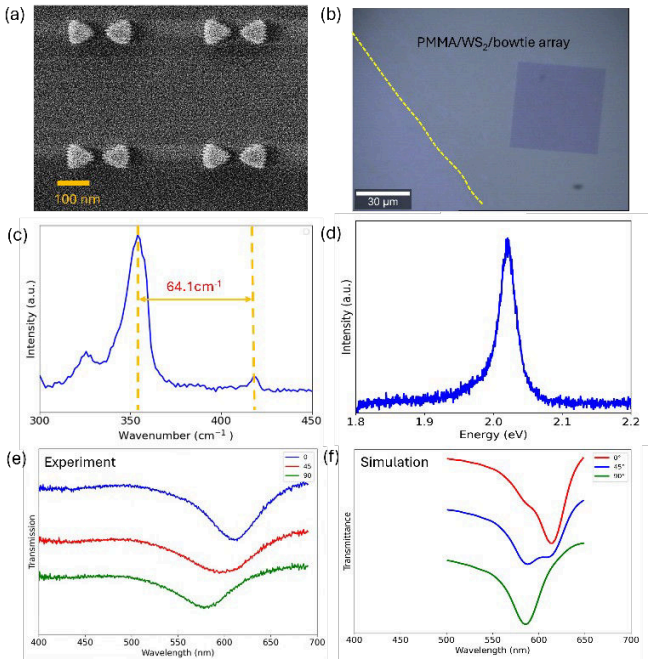

Fig. 2 (a) SEM image of bowtie nanoantennas fabricated by electron-beam lithography (EBL). (b) Optical micrograph of the PMMA/WS_2/bowtie nanoantenna structure. (c) Raman spectrum of monolayer WS_2 showing the E_{2g}^1 and A_{1g} vibrational modes. (d) Photoluminescence (PL) spectrum of monolayer WS_2. Polarization-dependent resonance spectra obtained from (e) experiments and (f) simulations at polarization angles of 0°, 45°, and 90°.

A SEM image of the fabricated bowtie nanoantennas is shown in Fig. 2a. Subsequently, a monolayer WS_2 film was transferred onto the patterned substrate *via* a dry-transfer process (Fig. 2b). The Raman spectrum (Fig. 2c) exhibits two characteristic vibrational modes, with the E_{2g}^1 mode at 353.8 cm^{-1} (red dashed line) and the A_{1g} mode at 417.9 cm^{-1} (green dashed line), with frequency separation $\Delta\approx$ 64.1 cm^{-1} The PL spectrum shows a pronounced emission peak at 2.023 eV, corresponding to the A-exciton transition of WS_2 (Fig 2d). These results confirm the monolayer nature of the WS_2. Polarization-dependent measurements of the bowtie nanoantenna reveal that the plasmonic resonance at 612 nm gradually weakens and eventually vanishes as the polarization angle is varied from 0° to 90° (Fig. 2e), in excellent agreement with the simulated results (Fig. 2f).

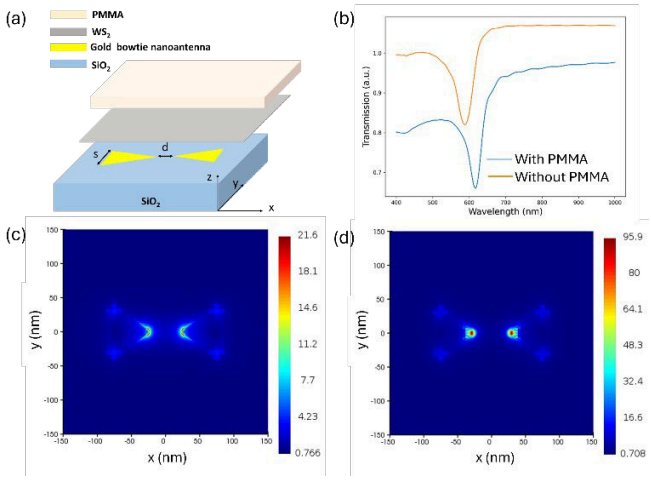

Fig. 3(a) Schematic illustration of the PMMA/WS_2/bowtie nanoantenna/fused silica hybrid structure. (b) Simulated transmittance spectra of the system with and without a PMMA overlayer. (c, d) Simulated in-plane electric field intensity distributions on the top surface of the bowtie nanoantenna (c) without and (d) with the PMMA layer.

To enhance the Rabi splitting energy, a PMMA overlayer was introduced into the hybrid coupling system, as schematically illustrated in Fig. 3(a). After incorporating the PMMA layer, numerical simulations show that the plasmonic resonance of the bowtie nanoantenna redshifts from 598 nm to 617 nm (Fig 3b), and the in-plane (x–y) electric field intensity on the top of the plasmonic is also significantly enhanced, increasing from 21.6 to 95.9 (Fig. 3 c, d).

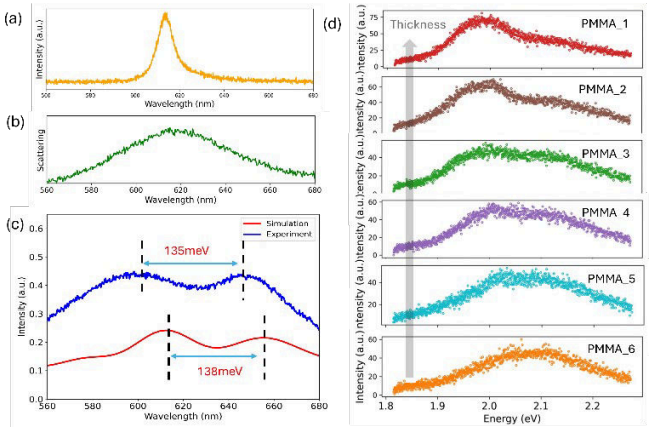

Fig. 4 (a) PL spectrum of monolayer WS_2 and (b) the Au bowtie nanoantenna. (c) Comparison of simulated and experimental scattering spectra of the PMMA/WS_2/bowtie nanoantenna/fused silica hybrid system. The bowtie nanoantenna array parameters are periodicity = 300 nm, side length = 65 nm, thickness = 40 nm, and gap = 40 nm. (d) PL spectra of the PMMA/WS_2/bowtie nanoantenna/fused silica system with varying PMMA thicknesses.

The monolayer WS2 exhibits a peak at 616nm in the PL spectrum, after introducing the PMMA layer (100nm) onto the bowtie nanoantennas array, the plasmonic scattering resonance occurs at 622 nm, see Fig. 4b. The scattering spectrum of the PMMA/WS_2/bowtie nanoantenna hybrid system (blue curve in Fig. 4c) presents a clear splitting, indicating strong coupling, with a calculated Rabi splitting energy of 135 meV. This value is in close agreement with the simulated transmittance-based Rabi splitting of 138 meV (red curve). PL characterization of the hybrid system was further performed (Fig 4d). Different PMMA thicknesses produce distinct PL curves, each showing clear splitting. The Rabi splitting energy extracted from the PL spectra is 135 meV.

IV. Conclusion

In conclusion, a bowtie nanoantenna array was fabricated using electron-beam lithography (EBL). By adjusting the antenna arm length, the plasmonic resonance can be tuned across the visible spectrum. Numerical simulations indicate that strong coupling with a WS_2 monolayer produces a Rabi splitting of 84 meV. Upon capping the structure with a 100 nm PMMA layer, the resonance wavelength redshifts by 20 nm, accompanied by a 4.4 times enhancement of the in-plane electric field amplitude, leading to an increased Rabi splitting of 138 meV. Experimental measurements after PMMA deposition yielded a splitting of 135meV in both the scattering and PL spectra, in excellent agreement with the simulations.

Acknowledgments

This work was supported by Science Foundation Ireland 18/EPSRC-CDT-3581 and the Engineering and Physical Sciences Research Council EP/S023259/1. YZ and ALB acknowledge financial support by Research Ireland under awards SFI-21/FFP-P/10187.

References

[1] M. Geisler, X. Cui, J. Wang, T. Rindzevicius, L. Gammelgaard, B. S. Jessen, P. A. D. Gonçalves, F. Todisco, P. Bøggild, and A. Boisen, "Single-crystalline gold nanodisks on WS2 mono-and multilayers for strong coupling at room temperature," *Acs Photonics,* vol. 6, no. 4, pp. 994-1001, 2019.

[2] P. Törmä, and W. L. Barnes, "Strong coupling between surface plasmon polaritons and emitters: a review," *Reports on Progress in Physics,* vol. 78, no. 1, pp. 013901, 2014.

[3] F. Stete, W. Koopman, and M. Bargheer, "Signatures of strong coupling on nanoparticles: revealing absorption anticrossing by tuning the dielectric environment," *Acs Photonics,* vol. 4, no. 7, pp. 1669-1676, 2017.

[4] X. Chen, H. Wang, N.-S. Xu, H. Chen, and S. Deng, "Resonance coupling in hybrid gold nanohole–monolayer WS2 nanostructures," *Applied Materials Today,* vol. 15, pp. 145-152, 2019.

[5] K. Santhosh, O. Bitton, L. Chuntonov, and G. Haran, "Vacuum Rabi splitting in a plasmonic cavity at the single quantum emitter limit," *Nature communications,* vol. 7, no. 1, pp. ncomms11823, 2016.

[6] L. Liu, L. Y. Tobing, X. Yu, J. Tong, B. Qiang, A. I. Fernández-Domínguez, F. J. Garcia-Vidal, D. H. Zhang, Q. J. Wang, and Y. Luo, "Strong plasmon–exciton interactions on nanoantenna array–monolayer WS2 hybrid system," *Advanced Optical Materials,* vol. 8, no. 5, pp. 1901002, 2020.

[7] J. Sun, Y. Li, H. Hu, W. Chen, D. Zheng, S. Zhang, and H. Xu, "Strong plasmon–exciton coupling in transition metal dichalcogenides and plasmonic nanostructures," *Nanoscale,* vol. 13, no. 8, pp. 4408-4419, 2021.

[8] S. Butun, E. Palacios, J. D. Cain, Z. Liu, V. P. Dravid, and K. Aydin, "Quantifying plasmon-enhanced light absorption in monolayer WS2 films," *ACS Applied Materials & Interfaces,* vol. 9, no. 17, pp. 15044-15051, 2017.

[9] B. Munkhbat, D. G. Baranov, A. Bisht, M. A. Hoque, B. Karpiak, S. P. Dash, and T. Shegai, "Electrical control of hybrid monolayer tungsten disulfide–plasmonic nanoantenna light–matter states at cryogenic and room temperatures," *ACS nano,* vol. 14, no. 1, pp. 1196-1206, 2020.

[10] X. Han, K. Wang, X. Xing, M. Wang, and P. Lu, "Rabi splitting in a plasmonic nanocavity coupled to a WS2 monolayer at room temperature," *ACS Photonics,* vol. 5, no. 10, pp. 3970-3976, 2018.

[11] M.-E. Kleemann, R. Chikkaraddy, E. M. Alexeev, D. Kos, C. Carnegie, W. Deacon, A. C. de Pury, C. Große, B. de Nijs, and J. Mertens, "Strong-coupling of WSe2 in ultra-compact plasmonic nanocavities at room temperature," *Nature communications,* vol. 8, no. 1, pp. 1296, 2017.

[12] P. Muñoz, Y. Yong, M. Dijkstra, F. Segerink, and S. García-Blanco, "Double metal layer lift-off process for the robust fabrication of plasmonic nano-antenna arrays on dielectric substrates using e-beam lithography," *Optical materials express,* vol. 9, no. 5, pp. 2046-2056, 2019.

[13] J. Lawless, C. Hrelescu, C. Elliott, L. Peters, N. McEvoy, and A. L. Bradley, "Influence of gold nano-bipyramid dimensions on strong coupling with excitons of monolayer MoS2," *ACS Applied Materials & Interfaces,* vol. 12, no. 41, pp. 46406-46415, 2020.

Spatial Dispersion in Optical Properties of Planar Lattices of Plasmonic Nanoparticles Revealed by Müller Matrix Ellipsometry

Eugene Bortchagovsky[1,2], Fang Dai[3], Monika Fleischer[3], Dietrich R.T. Zahn[2,4,*]

[1]V. Lashkaryov Institute of Semiconductor Physics of NAS of Ukraine, Ukraine
[2]Semiconductor Physics, Chemnitz University of Technology, Germany
[3]Institute for Applied Physics and Center LISA$^+$, Eberhard Karls Universität Tübingen, Germany
[4]Center for Materials, Architectures, and Integration of Nanomembranes (MAIN), Chemnitz University of Technology, Germany
*Corresponding author: zahn@physik.tu-chemnitz.de

***Abstract*— We demonstrate the vital role of spatial dispersion in the optical properties of planar ordered lattices of plasmonic nanoparticles, which cannot be described by any standard dielectric tensor, and demonstrate the orientational dependence of the optical properties opening a new way for tuning their optical response by the orientation.**

***Keywords*— spatial dispersion, plasmonic nanoparticles, polarizability, effective anisotropy.**

I. Introduction

The properties of any complex system are defined not only by the individual properties of constituting elements but their mutual interactions. In optics such interactions occur via the electromagnetic field generated by a polarizable particle in the place of other particles modifying the local field in relation to the external exciting field [1]. It results in the concept of the local field and effective polarizability.

The external field cannot change the physical polarizability of an individual particle, which is defined by the material, size, and shape of this particle and the dipole moment ($\boldsymbol{P}$) generated on the particle is also an objective physical value independent on the way of its calculation. By definition, it is defined by the physical polarizability (α_0) and the field exciting the particle. However, the exciting field is not the external one ($\boldsymbol{E}_0$) but the unknown local one ($\boldsymbol{E}_{loc}$) at the position of the particle and defined by the external field and fields generated by all other constituting elements. On the other side, it is more convenient to determine the dipole moment via the known external field if we are not interested in the internal field distribution and consider our system as one object. We can do this by introducing an effective polarizability (α_{eff}), which takes into account the interactions between all particles. So, we can write

$$\boldsymbol{P} = \alpha_0 \boldsymbol{E}_{loc} = \alpha_{eff} \boldsymbol{E}_0. \quad (1)$$

Any interaction modifies such effective polarizability via the known canonical expression [1,2]

$$\alpha_{eff}^{n+1} = \frac{1}{\left(\alpha_{eff}^{n}\right)^{-1} - M_n}, \quad (2)$$

where M_n is the matrix element of the corresponding interaction.

It is necessary to note that all interactions are directional meaning that the response of one particle depends on the other particles and fields at their position. So, interactions introduce non-locality in the system, which, in turn, results in spatial dispersion of the resulting optical properties of the system [3], *i.e.* the dependence of optical properties on the wavevector of the exciting light. Such effects of spatial dispersion are proportional to the ratio of the interparticle separation to the wavelength [4], which explains their invisibility in solids.

However, it is worth to note that even optical anisotropy observed for anisotropic materials is the result of spatial dispersion as it stems from interparticle interactions between isotropic objects arranged non-symmetrically in contrary to isotropic materials. Even conventionally used refractive index and dielectric tensor are convenient parameters for the description of the response of media defined by interparticle interactions [5].

II. Peculiar Optical Properties of Planar Systems of Interacting Particles

Even though it is known for more than half a century that optical properties of planar layers of particles depend on the angle of incidence of the exciting light [6], it is usually not taken into account in the treatment of data obtained at different angles of incidence. We attracted attention to this fact and

demonstrated a remarkable dependence of the optical response of lattices of nanoparticles on the angle of incidence, which changes the interactions and effective polarizabilities [1,7]. It was also proven that taking into account the phase retardation reveals the creation of an effective planar optical anisotropy also dependent on the angle of incidence and observed in experiments [8].

However, another effect influencing the optical response of ordered lattices of interacting nanoparticles was demonstrated in Ref. [7], namely the dependence of the optical properties of lattices on their orientation in relation to the plane of incidence.

Considering the direct sum of dipolar fields, it is easy to demonstrate that any two identical particles/dipoles situated symmetrically with respect to the plane of symmetry of the lattice, which coincides with the plane of incidence do not generate any cross-polarized field on particles situated on the plane of symmetry. Analogous considerations but for 4 or 8 symmetrically arranged dipoles were made in Ref. [7].

Recollecting the effective planar anisotropy of such lattices with perpendicular optical axes, the absence of cross-polarization means that the system is illuminated along one of their optical axes. However, square lattices have four planes of symmetry, while hexagonal ones – six. Such a behavior is absolutely peculiar from the point of view of standard crystal optics. According to standard anisotropic considerations, each optically anisotropic lattice has one set of optical axes defined by its Bravais vectors, while symmetrical considerations demonstrate that for planar lattices the number of sets of optical axes is more for the same system.

In contrast to standard ellipsometry determining the two ellipsometric angles Ψ and Δ defined by the Fresnel reflection coefficients for different polarizations [9]

$$tan\Psi e^{i\Delta} = \frac{r_p}{r_s}, \tag{3}$$

Müller matrix ellipsometry allows determining whether cross-polarization is present in the system of interest or not [10] by non-zeroing or zeroing of the values of elements in the non-diagonal block matrices 2x2.

We investigated a number of square lattices of plasmonic nanoparticles prepared by electron beam lithography in dependence on their orientation in relation to the plane of incidence by imaging spectral microscopic ellipsometer Accurion ep4 (Park System). Starting from the orientation of rows of squares along the plane of incidence (angle 0°) the angle was varied up to 90°. The results for the m_{13} element of the Müller matrix for a lattice with a pitch of 350 nm and a diameter of the gold nanodiscs of 260 nm measured at two different angles of incidence (45° and 60°) together with differential spectra of the angle Ψ (*i.e.* in relation to the spectra for the bare substrate without nanoparticles) are presented in Fig. 1.

The main obvious result for the m_{13} element (also revealed for other Müller matrix elements) is the zeroing of its value for any wavelength at illumination along the planes of symmetry of the lattice (0° and 90° correspond to the illumination along columns or rows of squares while 45° to the illumination along a diagonal). This confirms previous symmetry considerations and proves the existence of more than one set of axes of the effective planar anisotropy.

Non-zero values coincide with the spectral position of plasmonic resonances determined by the extrema in the differential spectra of the ellipsometric angle Ψ [11]. It unambiguous demonstrates that interparticle interactions enhanced at plasmonic resonances are responsible for the creation of cross-polarization.

One more result exhibited in Fig. 1 is the hybridization and splitting of different resonances. As the change of the angle of incidence shifts the spectral position of the Rayleigh anomaly it reveals at an angle of incidence 45° a part of a plasmonic mode at about 600 nm (m_0) almost hidden by the Rayleigh anomaly at 60° angle of incidence. Approaching the next plasmonic resonance the Rayleigh anomaly hybridizes with it and changes its spectral position shown by its non-horizontal shape.

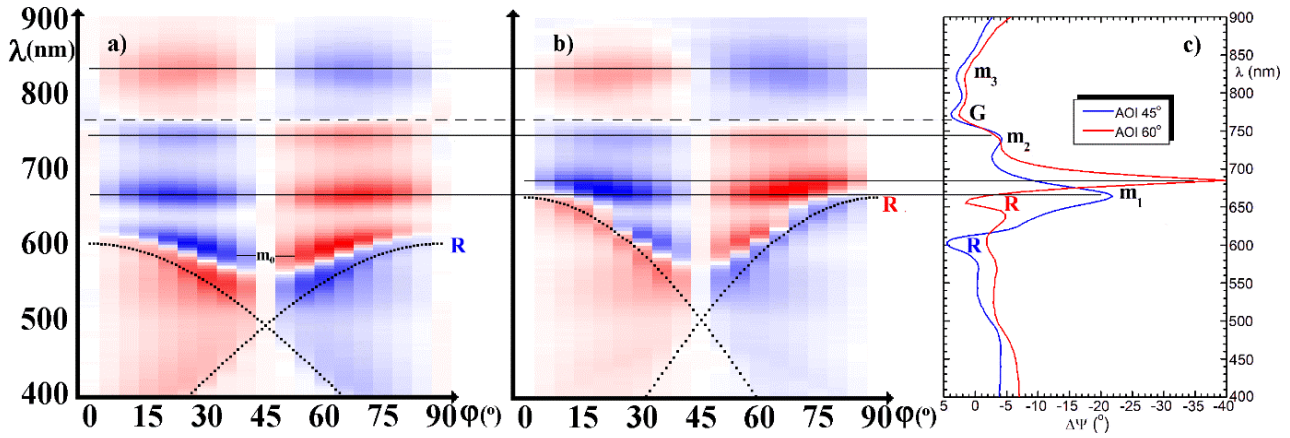

Fig. 1 Color coded value of the m_{13} element of the Müller matrix for a square lattice of gold discs with a period of 350 nm and diameter of 260 nm versus the orientational angle and differential ellipsometric spectra measured at the orientation along the side of squares.

III. Conclusion

We proved experimentally theoretical considerations about the vital influence of interactions leading to spatial dispersion (dependence on the wavevector) in the optical response of planar lattices of interacting particles. The spatial dispersion leads to the creation of a few sets of axes of effective planar optical anisotropy for a nominally isotropic structure.

Acknowledgments

This work was inspired by the cooperation of all coauthors in the COST Action MP1302 "Nanospectroscopy". We appreciate the support from the bilateral DFG (Germany) – SFFRU (Ukraine) project "Microellipsometric investigation of ordered plasmonic nanostructures," under DFG Grant Nos. ZA 146/43-1 and FL 670/8-1 and NRFU Grant No. Ф81/41842.

References

[1] E. Bortchagovsky, Yu. Demydenko, *et al.*, "Microellipsometry study of plasmonic properties of Metal-Insulator-Metal structures with ordered lattices of nanoparticles," Journal of Applied Physics, vol. 129, 123104, 2021.

[2] V. G. Kravets, A. V. Kabashin, W. L. Barnes, and A. N. Grigorenko, "Plasmonic surface lattice resonances: A review of properties and applications," Chemical Reviews, vol. 118, pp. 5912-5951, 2018.

[3] F. Monticone, N. A. Mortense, *et al.*, "Nonlocality in photonic materials and metamaterils: roadmap", Opt. Mater. Express, vol. 15, pp. 1544-1709, 2025.

[4] V. M. Agranovich and V. L. Ginzburg, *Crystal optics with spatial dispersion and excitons*, Springer-Verlag, 1984.

[5] V. A. Kizel, *Reflection of light*, Moscow: Nauka, 1973 (in Russian).

[6] S. Yamaguchi, "Theory of the optical properties of very thin inhomogeneous films," Journal of Physical Society of Japan, vol. 17, pp. 184-193, 1962.

[7] E. Bortchagovsky, F. Dai, *et al.*, "Ordered arrays of metal nanostructures on insulator/metal film: Dependence of plasmonic properties on lattice orientation," Nano Express, vol. 6, 025011, 2025.

[8] T. Yamaguchi, S. Yoshida, and A. Kinbara, "Effect of retarded dipole-dipole interaction between island particles on the optical plasma-resonance absorption of a silver-island film," Journal of the Optical Society of America, vol. 64, pp. 1563-1568, 1974.

[9] R. N. M. Azzam and N. M. Bashara, *Ellipsometry and polarized light*, North-Holland, 1977.

[10] H. Fujiwara, *Spectroscopic ellipsometry: Principles and applications*, Willey, 2007.

[11] E. Bortchagovsky and T. Mishakova, "Exhibition of a film's resonances in ellipsometric spectra and the Berreman effect," Applied Optics, vol. 62, pp. 904-913, 2023.

Eigenmodes of Finite Rectangular Lattices

Jussi Kelavuori[1,*], Roman Calpe[2], Benjamin Asamoah[2], Tommi Hakala[2], Mikko Huttunen[1]

[1]Faculty of Engineering and Natural Sciences, Tampere University, Finland

[2]Faculty of Science, Forestry and Technology, University of Eastern Finland, Finland: jussi.kelavuori@tuni.fi

***Abstract*—We investigate eigenmodes forming in finite, rectangularly periodic 2D arrays, and their effect on the optical response. We experimentally demonstrate optimal far-field coupling and eigenmode engineering that favors Hermite-Gaussian modes over plane waves. Furthermore, we show how traditional band diagrams are discretized to discrete resonance energies in finite structures.**

***Keywords*— metamaterials, surface lattice resonances, finite-size effects, discrete dipole approximation**

I. Introduction

Periodic structures have been used in optical applications for centuries. In recent research, they form the foundation of metamaterials capable phenomena such as lasing, nonlinear optical responses, and beam modulation. Typically, periodicity in these structures is modeled using periodic boundary conditions, which effectively assume an infinitely extended system. This assumption, however, does not accurately represent the physical behavior of real, finite structures. Recent studies have demonstrated deviations in the extinction efficiency of individual particles when compared to predictions based on infinite lattices [1], [2]. Moreover, finite lattices have been shown to support lasing modes that are not captured by periodic boundary condition models [3]. In this work, we investigate both computationally and experimentally the eigenmodes that arise due to the finite size of periodic arrays.

II. Methods

We utilize the discrete dipole approximation (DDA), in which each nanoparticle is modeled as an electric dipole, while higher-order electric and magnetic multipolar contributions are neglected. Within this framework, the optical response of an array is obtained by solving for the dipole moments $\vec{p}$,

$$\vec{E} = \varepsilon_0 \varepsilon_r A \vec{p}, \tag{1}$$

through inversion of the interaction matrix A. We determine the eigenvalues and eigenvectors of this matrix, which reveal the self-consistent spatial distributions of dipole moments supported by the array. Examples of such modes are shown in Fig. 1a.

Furthermore, we extend the DDA framework into the complex frequency plane to identify poles in the eigenvalues (see Fig. 1b). These poles correspond to quasi-normal modes (QNMs), enabling incorporation of mode losses into our analysis. This approach is well suited for inverse design of nanoparticle arrays with tunable degrees of freedom, such as individual particle sizes (and corresponding scattering cross sections) and particle positions, enabling systematic eigenmode engineering.

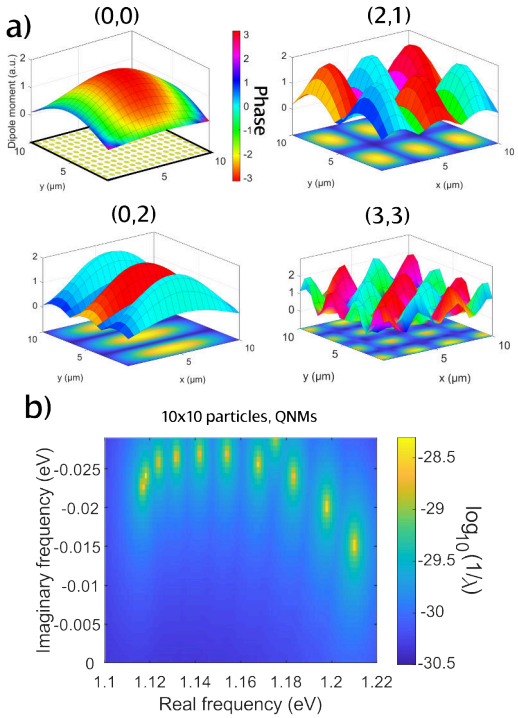

Fig. 1. a) Example eigenmodes found in a 20×20 particle lattice. b) QNM analysis of 10×10 lattice with QNMs from (0,0) to (9,0) for x-polarization shown.

III. Results and Discussion

We experimentally demonstrated selective coupling to distinct finite-size eigenmodes of a lattice by employing Hermite–Gaussian (HG) free-space modes as excitation fields. HG modes were chosen due to their close correspondence and high mode-overlap integrals with the lattice eigenmodes. The results shown in Fig. 2a compare resonance positions obtained under HG-mode excitation with eigenmode resonance energies calculated using DDA, revealing good agreement.

We next measured the quality factor (Q factor) of the lattice under excitation with Gaussian beams of varying waist sizes. Results are depicted in Fig. 2b. As expected, the Q factor increases with increasing beam size, but only up to the physical dimensions of the array. Optimal coupling is achieved when the incident field closely matches the fundamental (0,0) eigenmode of the lattice. Further increasing the beam size leads to a reduction in the Q factor, as additional eigenmodes with nearby resonance energies become simultaneously excited.

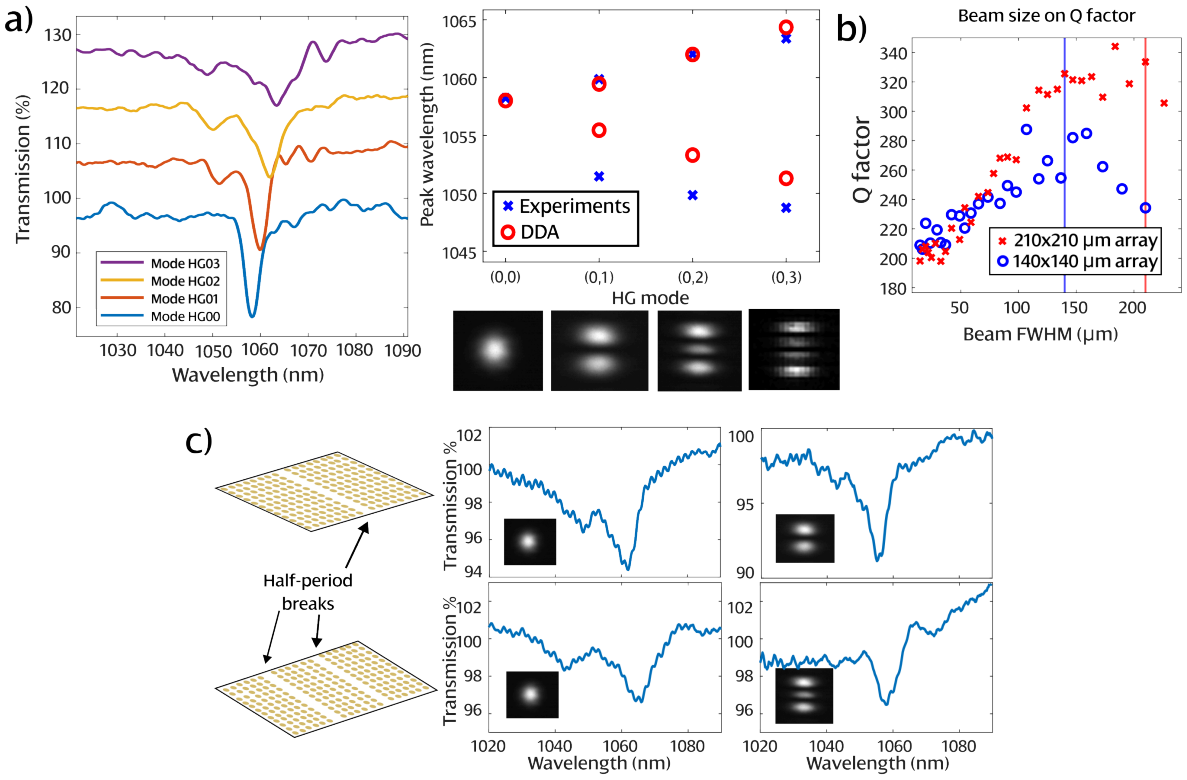

Fig. 2. a) Experiments exciting 210×210μm lattice with different HG modes compared to DDA eigenmode analysis on a lattice of equal size. b) Beam size effect on Q factor on two different-sized arrays. c) Eigenmode engineering using half-period breaks in lattice to favor HG modes over normal Gaussian excitation.

This behavior contrasts with the commonly held assumption that plane-wave excitation provides the optimal coupling to lattice modes [4].

Finally, we experimentally demonstrated eigenmode engineering by introducing half-period defects within the lattice (see Fig. 2c). These defects shift the fundamental eigenmode to exhibit a Hermite–Gaussian–like phase profile while preserving low-loss characteristics. This mode-engineering strategy may enable applications such as mode-cleaning devices and mode-selective flat lasers.

References

[1] L. Zundel and A. Manjavacas, 'Finite-size effects on periodic arrays of nanostructures', Journal of Physics: Photonics, vol. 1, no. 1, p. 015004, Dec. 2018.

[2] A. S. Kostyukov, I. L. Rasskazov, V. S. Gerasimov, S. P. Polyutov, S. V. Karpov, and A. E. Ershov, 'Multipolar Lattice Resonances in Plasmonic Finite-Size Metasurfaces', Photonics, vol. 8, no. 4, 2021.

[3] T. K. Hakala et al., 'Lasing in dark and bright modes of a finite-sized plasmonic lattice', Nature Communications, vol. 8, no. 1, p. 13687, Jan. 2017.

[4] M. S. Bin-Alam et al., 'Ultra-high-Q resonances in plasmonic metasurfaces', Nature Communications, vol. 12, no. 1, p. 974, Feb. 2021.

Single-Particle Study of Spin Crossover Compounds for Reconfigurable Photonic Integration

Lucas Mascaró Burguera[1,*], Ramón Torres-Cavanillas[2], Alejandro Regueiro[2], J. Ignacio Echevarria[4], Eugenio Coronado[2], Jorge Parra[3], Pablo Sanchis[1], Javier Hernández-Rueda[4], Elena Pinilla-Cienfuegos[1].

[1]Nanophotonics Technology Center, Universitat Politècnica de València, Spain
[2]Instituto de Ciencia Molecular, Universitat de València, Spain.
[4]Universidad Complutense de Madrid, Spain
*Corresponding author: lmasbur@ntc.upv.es

***Abstract*— We demonstrate single particle characterization of spin crossover nanoparticles using a quadrupole Paul trap combined with polarization resolved optical scattering. Laser and pressure control reveal reversible volumetric expansion and bistability. Integration into silicon micro ring resonators confirms their potential as active materials for reconfigurable integrated photonic devices.**

***Keywords*— spin crossover, phase change materials, spin transition, reconfigurable photonics, quadrupole trap, integrated photonics.**

I. Introduction

Reconfigurable nanophotonic platforms require active materials capable of large and controllable refractive index modulation with low energy consumption and high stability. Conventional phase change materials such as chalcogenides or vanadium oxides rely on structural transitions that often introduce optical losses, high switching thresholds, or limited endurance [1].

Spin crossover (SCO) materials provide an alternative molecular mechanism based on reversible electronic transitions between low spin and high spin states. This transition is accompanied by significant volume change and optical contrast while preserving bistability at the nanoscale. Such properties make them promising candidates for integrated photonic switching and nonvolatile optical functionalities [2].

However, the implementation of SCO nanoparticles (SCO-NPs) in photonic circuits requires precise understanding of their behavior at the single particle level. Most previous studies rely on ensembles embedded in matrices or deposited on substrates, preventing accurate isolation of intrinsic optomechanical responses [3,4].

Here, we introduce a substrate free single particle platform based on a quadrupole Paul trap combined with polarization resolved optical scattering, enabling controlled optical and environmental characterization of individual nanoparticles and facilitating their integration into silicon photonic devices [5].

II. Methods

SCO NPs of $Fe(NH_2trz)_3(NO_3)_2$ were synthesized using a reverse micelle method to obtain size-controlled particles between 100 and 300 nanometers [6]. Structural and magnetic characterization confirmed bistable spin transition behavior. SCO NPs were embedded in a polymer matrix to determine their optical constants and refractive index contrast across the transition.

Single particle measurements were then performed using a quadrupole Paul trap integrated inside a vacuum chamber (see Figure 1.c). The SCO-NPs dispersed in ethanol were introduced via electrospray and trapped using radiofrequency electric fields. A polarization resolved multispectral scattering microscope monitored individual trapped NPs under controlled optical excitation.

A blue laser induced the spin transition, while red and near infrared probe beams enabled size dependent scattering analysis. Particle dimensions were extracted by fitting experimental visibilities to Mie scattering calculations. Environmental control was achieved by varying chamber pressure.

For device level validation, a SCO polymethyl methacrylate (SCO/PMMA) nanocomposite was prepared and deposited onto silicon micro ring resonators. Resonance spectra were monitored under controlled temperature to evaluate refractive index driven modulation.

III. Results and Discussion

Magnetic measurements of the Fe(NH2trz)3(NO3)2 compound confirm a thermally driven spin transition with a bistable window of about 10 K between 310 and 320 K (Fig 1.a). This transition produces clear optical signatures, including disappearance of the low spin absorption band near 520 nm and a refractive index contrast measured by ellipsometry of approximately $\Delta n = 0.0123$ in the SCO/PMMA nanocomposite (Figure 1.b). Single particle measurements in a quadrupole Paul

trap reveal optically induced size expansion of approximately 5±1%, corresponding to nearly 10% volumetric change, consistent with typical values for SCO compounds, directly confirming cooperative switching at the nanoscale. We also demonstrate that a pressure reduction to 0.1 mbar induces a 4–6% increase in particle size, highlighting environmental tunability (Figure 1.f).

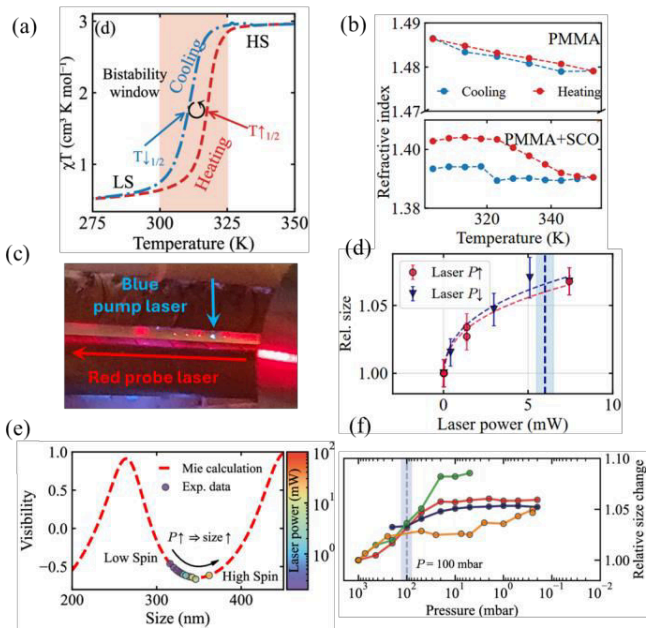

Figure 1: All figures are adapted from Pinilla-Cienfuegos et al., ACS Nano, 2026, under CC-BY license. (a) SQUID measurement of the SCO NPs. (b) Refractive index ellipsometry measurements for the nanocomposite, in comparison to those of a thin film of PMMA. (c) Picture of NPs suspended in the trap. (d) Relative laser-induced size change of trapped SCO NPs as a function of laser power at λ = 488 nm. (e) Visibility of trapped SCO NPs as a function of their size for different laser intensity, plotted over the theoretical Mie calculations. (f) Relative particle size change, as a function of ambient pressure.

Finally, integration onto silicon micro ring resonators demonstrates hysteretic resonance wavelength shifts near room temperature, validating the material as an active platform for nonvolatile and energy efficient photonic switching.

Conclusion

We have demonstrated a substrate free platform for the controlled manipulation and characterization of individual SCO NPs using a quadrupole Paul trap combined with polarization resolved optical scattering. The approach enables three-dimensional metrology, direct measurement of optically induced volumetric expansion, and environmental control at the single particle level.

The observed refractive index contrast and cooperative nanoscale expansion translate into measurable hysteretic resonance shifts when integrated onto silicon micro ring resonators, validating SCO materials as viable active elements for integrated photonics.

These results establish critical operational parameters for implementing molecular phase change materials in reconfigurable photonic architectures and open the path toward energy efficient, nonvolatile optical switching and sensing platforms.

Acknowledgments

E. P. C. acknowledges funding from Generalitat Valenciana (Grant No. SEJIGENT 2021 039) and Agencia Estatal de Investigación of Ministerio de Ciencia e Innovación (PID2021 128442NA I00 and CNS2024 154922, funded by MICIU AEI 10.13039 501100011033). J. H. R. acknowledges funding from the Programa de Atracción de Talento de la Comunidad Autónoma de Madrid, Modalidad 1 (Project 2020 T1 IND 19951).

The authors acknowledge funding from the European Commission (Pathfinder 4D NMR 101099676) and the Spanish Ministerio de Ciencia e Innovación, including the Unit of Excellence María de Maeztu grant CEX2024 001467 M, PID2023 149309OB I00, and PID2020 117264GB I00, funded by MICIU AEI 10.13039 501100011033.

This study forms part of the Advanced Materials program and was supported by MCIU with funding from the European Union NextGenerationEU PRTR C17 I1 and by Generalitat Valenciana (MFA 2022 050 and MFA 2022 025).

E. C. acknowledges Generalitat Valenciana (PROMETEO Program CIPROM 2024 51) and the European Union NextGenerationEU Cátedras PERTE Chip Program (TSI 069100 2023 0012).

References

[1] Ko, J. H.; Yoo, Y. J.; Lee, Y.; Jeong, H.-H.; Song, Y. M. A review of tunable photonics: Optically active materials and applications from visible to terahertz. *iScience* 2022, *25*, No. 104727

[2] Galán-Mascarós, J. R.; Coronado, E.; Forment-Aliaga, A.; Monrabal-Capilla, M.; Pinilla-Cienfuegos, E.; Ceolin, M. Tuning Size and Thermal Hysteresis in Bistable Spin Crossover Nanoparticles. Inorg. Chem. 2010, 49, 5706−5714.

[3] Molnár, G.; Rat, S.; Salmon, L.; Nicolazzi, W.; Bousseksou, A. Spin Crossover Nanomaterials: From Fundamental Concepts to Devices. Adv. Mater. 2017, 30, No. 1703862.
for photonic crystal optimization," Journal of Made-Up Science, vol. 12, pp. 200–215, 2019.

[4] Salmon, L.; Catala, L. Spin-crossover nanoparticles and nanocomposite materials. C. R. Chim. 2018, 21, 1230−1269.

[5] Pinilla-Cienfuegos, E.; Mascaró-Burguera, L.; Torres-Cavanillas, R.; Echavarría, J. I.; Regueiro, A.; Coronado, E.; Hernandez-Rueda, J. Unveiling Spin Transition at Single-Particle Level in Levitating Spin Crossover Nanoparticles. ACS Nano 2026. https://doi.org/10.1021/acsnano.5c18794.

[6] Torres-Cavanillas, R.; Lima-Moya, L.; Tichelaar, F.; Zandbergen, H.; Giménez-Marqués, M.; Coronado, E. Downsizing of robust Fe-triazole@ SiO 2 spin-crossover nanoparticles with ultrathin shells. Dalton Trans. 2019, 48, 15465−15469.

Design of exotic plasmonic lattice dispersions

Joel Lehikoinen[1,*], Päivi Törmä[1]

[1]Department of Applied Physics, Aalto University School of Science, P.O. Box 15100, Aalto, FI-00076, Finland
* Corresponding author: joel.s.lehikoinen@aalto.fi

***Abstract*—We use the empty lattice approximation to design plasmonic nanoparticle arrays with exotic dispersions. As a case example, we study the bullseye lattice made out of individual nanoparticles, and show analytically and numerically that it has similar beaming properties as plasmonic bullseye antennas.**

***Keywords*— diffraction, plasmonics, bullseye antenna**

I. Introduction

Plasmonic bullseye antennas—concentric ring arrangements of metallic nanostructures—provide a compact route to shaping emission through the controlled interplay of localized plasmonic scattering and radial phase engineering [1]. Owing to their rotational symmetry, bullseye lattices can convert radiation into a narrow, highly directional beam along the surface normal. In emitter-integrated architectures, this enables enhanced brightness in a target direction, improved collection efficiency, and deterministic control over the far-field pattern without requiring macroscopic optics. Beyond simple collimation, the radial geometry also supports polarization- and wavelength-selective emission features [2], and can be implemented in a planar, lithographically scalable format.

Surface lattice resonances (SLRs) in arrangements of metallic nanoparticles arise from the coherent radiative coupling of localized surface plasmon resonances to diffractive lattice modes near Rayleigh anomalies [3]. This collective coupling strongly suppresses radiative damping relative to isolated nanoparticles, producing spectrally narrow resonances with high quality factors, long-range phase coherence, and pronounced dispersion in angle-resolved spectra. The resulting band structure depends on the array geometry.

Here, we employ the empty lattice approximation to design nanoparticle lattices with exotic dispersions. As a case example, we present the dispersion of a bullseye antenna constructed out of individual nanoparticles. Despite the differences in the underlying physics (surface plasmon polaritons vs. SLRs), a similar beaming property to plasmonic bullseye antennas is uncovered. This paper is a summary of the full work, where we present also other, exotic lattice geometries. [4]. Furthermore, in the full work, we also demonstrate lasing from these arrays [5].

II. Methods

The following description of the methods is paraphrased from Ref. [5]. To calculate the band structures of the investigated lattices, we use the empty lattice approximation, which consists of superposing the dispersion of each diffracted order weighted by its structure factor [6]. The structure factor $S(\mathbf{k})$ of the mode characterized by the wavevector $\mathbf{k}$ is defined as

$$S(\mathbf{k}) = \frac{1}{N^2}\left|\sum_{n=0}^{N-1} e^{i\mathbf{k}\cdot\mathbf{r}}\right|^2 \equiv \frac{1}{N^2}\left|A(\mathbf{k})\right|^2, \tag{1}$$

where N is the number of lattice sites and $\mathbf{r}_n$ denotes the position of the nth lattice site. The choice of the normalization factor N^{-2} ensures that the structure factor takes values between zero and one. The dispersion of light in a homogeneous, linear, isotropic optical background for in-plane modes is

$$E = \frac{\hbar c_0}{n}\sqrt{k_x^2 + k_y^2}, \tag{2}$$

where $\hbar$ is the reduced Planck constant, c_0 the speed of light in vacuum, and n the refractive index of the background medium. In the (k_x, k_y, E) space, this dispersion describes the surface of a light cone emanating from the point $(k_x, k_y, E = 0)$. Thus, modes that can scatter light to a particular point (k_x, k_y, E) lie on a ring centered at (k_x, k_y) with the radius determined by E. The total scattering intensity is thus proportional to the weighted sum of these modes

$$I(\mathbf{k}_\parallel, E) \propto \int S(\mathbf{k}')\delta(|\mathbf{k}' - \mathbf{k}_\parallel| - \kappa)d\mathbf{k}', \tag{3}$$

where the integration is over the k_x-k_y plane, $\mathbf{k}_\parallel = (k_x, k_y)^{\mathrm{T}}$, and $\kappa = \frac{n}{\hbar c_0}E$ is the wavevector magnitude corresponding to the energy E. Numerically, the above integral is computed by discretizing the k space and summing $S(\mathbf{k})$ over the points for which $||\mathbf{k}' - \mathbf{k}_\parallel| - \kappa| \leq \frac{\Delta E}{2}$, where ΔE is the energy discretization parameter.

III. Results and Discussion

We consider bullseye lattice consisting of individual nanoparticles. First, we consider the scattering amplitude [$A(\mathbf{k})$ in Eq. (1)] of a continuous, isotropic 2D distribution $\rho(\mathbf{r}) = \rho(r)$. The scattering amplitude of $\rho(r)$ is given by its Fourier transform:

$$A(\mathbf{k}) = \int \rho(r)e^{i\mathbf{k}\cdot\mathbf{r}}d^2r = \int_0^\infty \int_0^{2\pi} \rho(r)e^{ikr\cos(\theta-\varphi)}rd\theta dr, \tag{4}$$

where $\mathbf{k} = k(\cos\varphi, \sin\varphi)^{\mathrm{T}}$.
On the other hand, the zeroth-order Bessel function of the first kind $J_0(z)$ is defined by

$$\int_0^{2\pi} e^{iz\cos\alpha}d\alpha = 2\pi J_0(z). \tag{5}$$

Because $\rho(r)$ is isotropic, it can be taken outside of the angular integral and Eq. (4) rewritten as

$$A(\mathbf{k}) = 2\pi \int_0^\infty r\rho(r) J_0(kr) dr. \tag{6}$$

Our goal is to construct a lattice that scatters light at a specific wavelength to the normal direction. To this end, we select

$$\rho(r) = \sum_{t=1}^{T} \frac{w_t}{2\pi r_t} \delta(r - r_t), \tag{7}$$

where w_t is a weighting factor for the tth term in the sum. Plugging this into Eq. (4) gives

$$\begin{aligned} A(\mathbf{k}) &= \int_0^\infty \int_0^{2\pi} r\rho(r) e^{ikr\cos(\theta-\varphi)} d\theta dr \\ &= \sum_{t=1}^{T} \frac{w_t}{2\pi r_t} \int_0^\infty \int_0^{2\pi} r e^{ikr\cos(\theta-\varphi)} \delta(r - r_t) d\theta dr \\ &= \sum_{t=1}^{T} \frac{w_t}{2\pi} \int_0^{2\pi} e^{ikr_t\cos(\theta-\varphi)} d\theta = \sum_{t=1}^{T} w_t J_0(kr_t). \end{aligned} \tag{8}$$

The Bessel function $J_0(z)$ has an approximation (Debye asymptotic expansion) for $z \gg 0$

$$J_0(z) \approx \sqrt{\frac{2}{\pi z}} \cos\left(z - \frac{\pi}{4}\right) \equiv D(z). \tag{9}$$

The validity of the approximation for $z \gtrsim 1.2$ is confirmed by Figure 1; we will be interested in values $z \geq 2\pi$.

Inserting this approximant into the expression for the amplitude $A(\mathbf{k})$ yields

$$A(\mathbf{k}) = \sum_{t=1}^{T} w_t \sqrt{\frac{2}{\pi k r_t}} \cos\left(k r_t - \frac{\pi}{4}\right). \tag{10}$$

Next, we set

$$r_t = \Delta r \cdot t, \tag{11}$$

where Δr is the constant spacing between consecutive rings. With this, the amplitude can be written as

$$A(\mathbf{k}) = \sqrt{\frac{2}{\pi k}} \sum_{t=1}^{T} \frac{w_t}{\sqrt{\Delta r \cdot t}} \cos\left(k\Delta r \cdot t - \frac{\pi}{4}\right). \tag{12}$$

The sum is maximized when the cosine terms interfere constructively, i.e.,

$$k\Delta r = m \cdot 2\pi, \; m \in \mathbb{Z}. \tag{13}$$

Finally, to have a maximum in the amplitude (structure factor) at $k = m \cdot k_0, \; m \in \mathbb{N}$, we set

$$\Delta r = \frac{2\pi}{k_0}. \tag{14}$$

This gives a structure factor with concentric rings, which corresponds to scattering of a certain wavelength to the normal direction.

To transform the continuous distribution $\rho(r)$ into a discrete lattice, we generate the lattice by the following algorithm:

1) Select the number of rings T, the lattice constant (ring spacing) R and the number of lattice sites on the first ring N_1.
2) For each ring $t \in [1, \ldots, T]$:
   a) Calculate the number of points as $N_t = \lceil \sqrt{t} N_1 \rceil$ (this, together with the normalization of $1/N$ is the weighting factor w_t).
   b) Set the coordinates of the points as (tR, θ), where θ is a uniformly distributed random number, $\theta \in [0, 2\pi)$.

An example lattice generated by the above algorithm is shown in Figure 2.

Figure 3 shows the dispersion of a bullseye lattice calculated using the empty lattice approximation. It shows a strong feature at the Γ-point. Because of the isotropy of the lattice, by symmetry, the dispersion must be the same along any other line in the k_x-k_y-plane. The lattice thus scatters incident light strongly to the normal direction, similar to the plasmonic bullseye antennas.

The weighting factor that appears in Eqs. (7)–(12) is related to the number of particles in the tth ring over the total number of particles N_t/N, $N = \sum_t N_t$. By choosing $N_t = \lceil \sqrt{t} N_1 \rceil$, we compensate for the $t^{-\frac{1}{2}}$ scaling in the amplitude in Eq. (12).

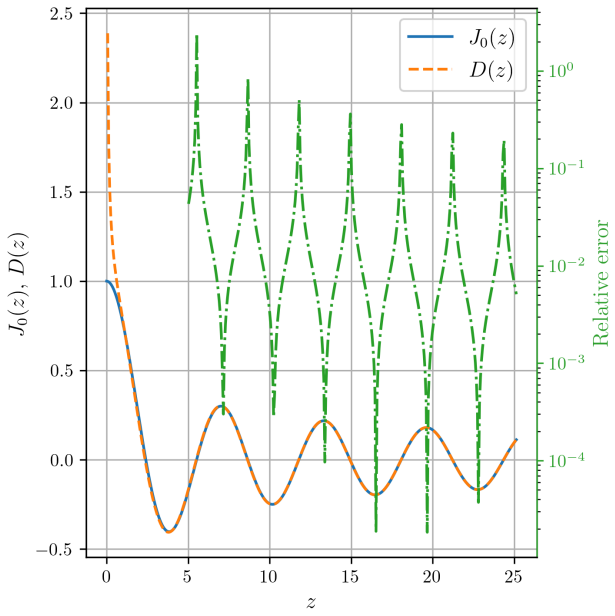

Fig. 1. Plots of the Bessel function $J_0(z)$, the Debye asymptotic expansion $D(z)$ (Eq. (9)) and the relative error. The graph shows that the $D(z)$ approximates $J_0(z)$ well at sufficiently high values of z and away from the zeros of $J_0(z)$.

IV. Conclusion

Using analytical and numerical methods, we have shown that the empty lattice approximation predicts that bullseye

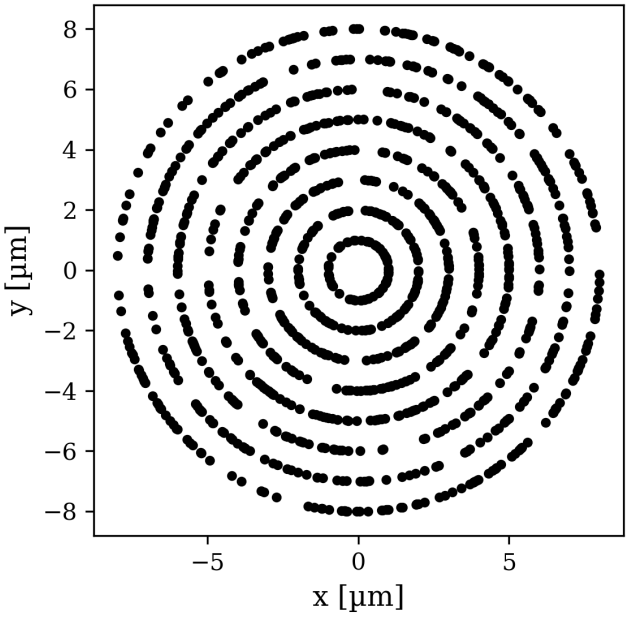

Fig. 2. Example of a bullseye lattice with 1 µm ring spacing.

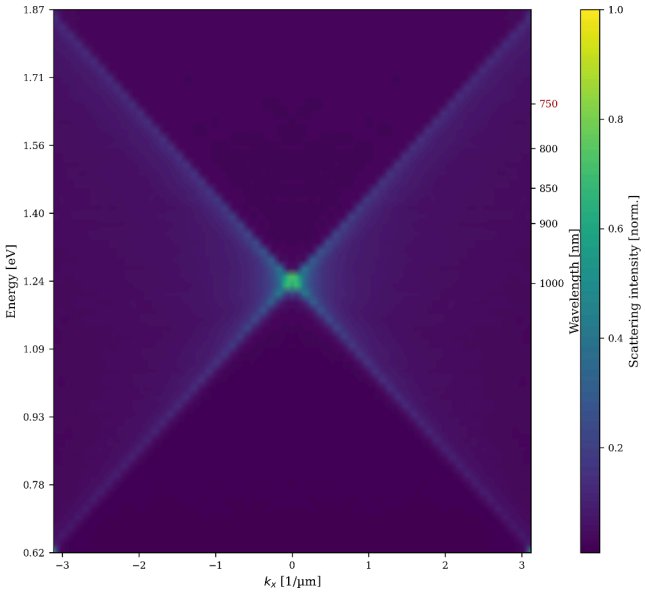

Fig. 3. Dispersion of a bullseye lattice (with more particles than the lattice of Fig. 2). The dispersion shows a strong feature at the Γ point at the wavelength corresponding to the ring spacing of 1 µm with background refractive index $n = 1$.

lattices consisting of isolated nanoparticles have similar beaming properties as plasmonic bullseye antennas consisting of continuous, concentric rings. The work showcases that the empty lattice approximation is useful also for computing the dispersions of exotic and aperiodic lattice geometries.

Acknowledgments

Funded by the European Union. Views and opinions expressed are however those of the author(s) only and do not necessarily reflect those of the European Union or the European Innovation Council and the SMEs Executive Agency (EISMEA). Neither the European Union nor the granting authority can be held responsible for them (SCOLED, Grant Agreement No. 101098813).

References

[1] H. J. Lezec, A. Degiron, E. Devaux, R. A. Linke, L. Martin-Moreno, F. J. Garcia-Vidal, and T. W. Ebbesen, "Beaming light from a subwavelength aperture," *Science*, vol. 297, pp. 820–822, 8 2002.

[2] C. I. Osorio, A. Mohtashami, and A. F. Koenderink, "K-space polarimetry of bullseye plasmon antennas," *Scientific Reports*, vol. 5, p. 9966, 4 2015.

[3] V. G. Kravets, A. V. Kabashin, W. L. Barnes, and A. N. Grigorenko, "Plasmonic surface lattice resonances: A review of properties and applications," *Chemical Reviews*, vol. 118, pp. 5912–5951, 6 2018.

[4] J. Lehikoinen, R. Heilmann, A. J. J. Dahlberg, E. Härmä, M. Mahmoudi, A. Dutta, K. S. Daskalakis, and P. Törmä, 2026, submitted.

[5] R. Heilmann, J. Lehikoinen, S. Eyvazi, E. A. Mamonov, and P. Törmä, 2026, submitted.

[6] R. Guo, T. K. Hakala, and P. Törmä, "Geometry dependence of surface lattice resonances in plasmonic nanoparticle arrays," *Physical Review B*, vol. 95, p. 155423, 4 2017.

Interparticle Spacing–Driven Ultrafast Dynamics in Gold Nanoparticle Superlattices

Pietro Castronovo,[1] Cristian Gonzalez,[2] Giuseppe Ammirati,[3] Shengsong Yang,[2]

Daniele Catone,[3] Alessandra Paladini,[3] Patrick O'Keeffe,[3] Cherie R. Kagan,[2,4,5]

Christopher B. Murray,[2,4] Antonio Emanuele,[1] Emanuele Marino,[1] Fabrizio Messina,[1,6] and Alice Sciortino,[1,6,]*

[1]Physics and Chemistry Department, University of Palermo, Italy
[2] Department of Chemistry, University of Pennsylvania, USA
[3] Istituto di Struttura della Materia – CNR, Italy
[4] Department of Materials Science and Engineering, University of Pennsylvania, USA
[5] Department of Electrical and Systems Engineerin, University of Pennsylvania, USA
[6] ATeN Center, University of Palermo, Italy
**Corresponding author: alice.sciortino02@unipa.it*

The collective optical response of plasmonic nanoparticle assemblies is strongly governed by interparticle interactions. Here, we investigate gold nanoparticle superlattices with tunable interparticle spacing, demonstrating that reduced spacing induces a plasmon blueshift and slows electron–phonon relaxation due to enhanced near-field coupling and hot-carrier population.

I. Introduction

Plasmonic metal nanoparticles exhibit localized surface plasmon resonances (LSPRs) arising from collective oscillations of conduction electrons, leading to strong light–matter interactions and enhanced electromagnetic fields.[1] Beyond individual nanoparticles, assembling plasmonic building blocks into ordered superstructures enables access to collective optical phenomena governed by interparticle coupling.[2]

While plasmon coupling in small nanoparticle clusters has been investigated, dense three-dimensional superstructures remain comparatively unexplored, particularly with respect to their ultrafast photodynamics. Interparticle distance is expected to play a critical role, yet systematic studies correlating precise structural control with ultrafast carrier dynamics at the single-superparticle level are scarce.[3]

In this work, crystalline gold superparticles are employed as a model system to investigate how interparticle spacing governs plasmonic spectral features and hot-carrier relaxation dynamics. By combining structural characterization with ultrafast transient absorption microscopy, we elucidate the relationship between nanoscale architecture and collective photophysical behavior.[3]

II. Methods

Gold superparticles (AuSPs) were prepared via emulsion-templated self-assembly by mixing AuNPs in toluene (5 mg mL^{-1}) with an aqueous SDS solution, followed by vortexing and slow solvent evaporation at 30 °C.

Ligand exchange was performed by drop-casting AuSPs onto glass substrates, removing residual SDS by acetonitrile rinsing, and immersing the samples in a 3 mM thiol solution in acetonitrile for 10 min. Samples were subsequently washed, vacuum-dried, and stored for characterization.

Structural characterization was carried out using transmission electron microscopy (TEM) and small-angle X-ray scattering (SAXS). TEM imaging was performed at 120–200 kV, while SAXS measurements were collected under vacuum using an 8 keV X-ray source and analysed to determine lattice symmetry and interparticle spacing.

Optical properties were investigated by ensemble UV–vis spectroscopy and ultrafast transient absorption microscopy (TAM). TAM measurements employed 50 fs laser pulses, with a 400 nm pump and broadband probe, achieving ~2 μm spatial and ~80 fs temporal resolution. Kinetic traces were obtained

by averaging multiple pump–probe scans and corrected for dispersion and nonlinear artifacts.

III. Results and Discussion

Gold nanoparticles with an average diameter of ~6 nm were assembled into spherical superparticles via emulsion-templated self-assembly. Transmission electron microscopy (Figure 1a) confirms the formation of compact, highly packed superparticles with diameters around 160 nm. Small-angle X-ray scattering (Figure 1b) reveals a face-centered cubic (FCC) superlattice extending throughout the entire superparticle volume.

Interparticle spacing was systematically tuned through ligand exchange using alkanethiols of varying chain length. Changes in the surface-to-surface nearest-neighbour distance were quantitatively determined from the shift of the FCC (111)

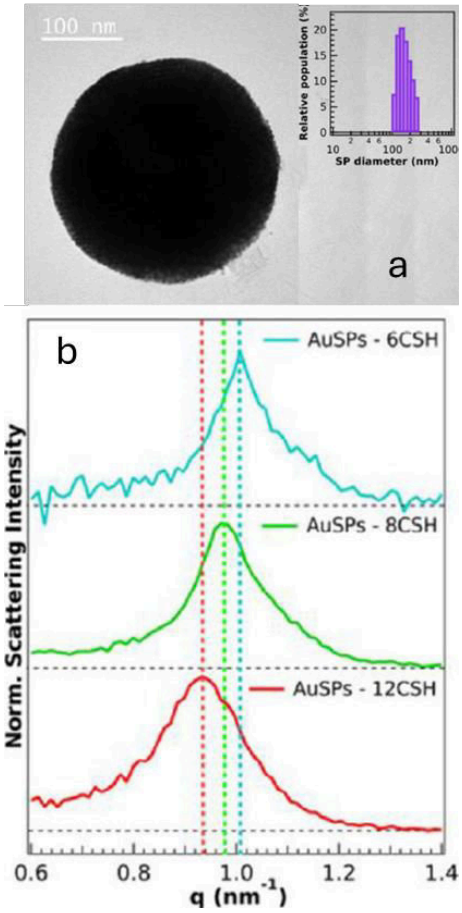

SAXS reflection (Figure 1b). Structural characterization confirms that ligand exchange enables precise control over interparticle spacing while preserving long-range crystalline order. As expected, as the ligand length decreases, the nearest-neighbour distance is reduced, and this could lead to stronger interparticle coupling.

Figure 1: (a) TEM image of a single AuSP; inset AuSPs size distribution.(b) SAXS pattern of AuSPs as a function of ligands.

Optically, assembled superparticles exhibit a blueshift of the static LSPR compared to isolated nanoparticles (Figure 2a) which highlights the interaction between the nanoparticles.

Then, we studied the ultrafast photodynamics using transient absorption microscopy, enabling simultaneous femtosecond temporal resolution and micrometer-scale spatial selectivity, thereby isolating the response of individual superparticles. AuSPs show a systematic redshift of the plasmonic peak when the interparticle distance increases (Figure 2b). These trends indicate that long-range plasmonic interactions dominate the collective response of the superlattice, in contrast to the redshifts typically associated with short-range coupling.

Moreover, transient absorption microscopy kinetics (Figure 2c) reveal pronounced differences in ultrafast dynamics as a function of spacing. Following photoexcitation the electron–phonon relaxation time increases significantly as interparticle distance decreases. This counterintuitive slowdown is attributed to enhanced near-field coupling, which increases the

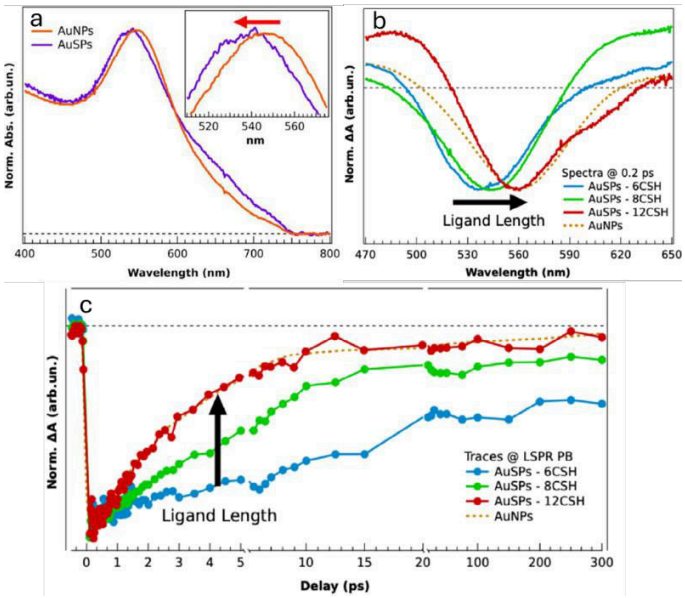

Figure 2: (a) Absorption spectra of Au nanoparticles and AuSPs, the inset highlights the blueshift. (b) Transient absorption spectra of AuSPs as a function of ligands at 0.2 ps. (c) Transient absorption kinetics of AuSPs as a function of ligands on the plasmonic peak.

local population of hot carriers and delays their thermalization with the lattice.

Together, these observations demonstrate that both spectral and dynamical plasmonic properties can be finely tuned through nanoscale structural control.

IV. Conclusion

This study demonstrates that interparticle spacing is a key parameter governing the collective plasmonic response of gold nanoparticle superlattices. Reduced spacing induces a blueshift of the plasmon resonance and significantly slows electron–phonon relaxation due to enhanced near-field interactions. These findings provide fundamental insight into ultrafast

dynamics in dense plasmonic assemblies and offer design guidelines for tunable nanophotonic materials.

ACKNOWLEDGMENTS

E.M. and A.E. acknowledge funding received from the European Union – NextGenerationEU – funding MUR D.M. 737/2021 – project "REFINE." E. M. acknowledges travel support from the European Union – Horizon Europe – Next Generation Internet Enrichers programme, grant agreement no. 101070125. E. M. is grateful to the European Union – NextGenerationEU – funding MUR D. M. 737/2021 for funding his position at Unipa. The authors acknowledge funding received from Unipa through "Fondo Finalizzato alla Ricerca di Ateneo" (FFR) 2022–2024. Open access publishing facilitated by Università degli Studi di Palermo, as part of the Wiley - CRUI-CARE agreement.

REFERENCES

[1] L. Wang, et al *Adv. Funct. Mater.* **2020**, *30*, 2005400
[2] P. Castronovo et al *Nano Lett.* **2025**, *25*, 5828.
[3] P. Castronovo et al. *Adv Opt Mater*, **2025**, e02501

Temporal Interfaces in a Kretschmann–Raether Geometry

Harry Donegan [1,*], M. J. Bhaseen[1], Francisco Rodríguez Fortuño[1], Anatoly Zayats[1]

[1]Department of Physics, King's College London, United Kingdom

*Corresponding author: harry.donegan@kcl.ac.uk

***Abstract*—We explore the conversion of a surface plasmon polariton (SPP) into propagating radiation due to a time-varying plasma frequency. We consider a temporal interface using integral transforms and finite-difference-time-domain (FDTD) simulations to benchmark the results. We apply these results to an instantaneous frequency shift in indium tin oxide.**

***Keywords*— time-varying materials, plasmonics.**

I. Introduction

Time-varying metamaterials offers a fascinating counterpart to conventional electrodynamics in static media [1]. In recent years, the field has seen a surge of interest, both theoretical and experimental, driven by the discovery of strong nonlinearities in transparent conducting oxides (TCOs) [2]. Under ultrafast optical pumping these materials undergo rapid and strong electron redistribution, leading to significant modifications to their permittivities.

When the permittivity changes, an initial wave ceases to be an eigenmode of Maxwell's equations and decomposes into a superposition of new eigenmodes. This temporal modulation not only produces refracted and reflected waves, but also breaks frequency conservation. Near-field modes such as surface plasmon polaritons, which are ordinarily confined to interfaces, can convert into propagating radiation that escapes to the far field [3].

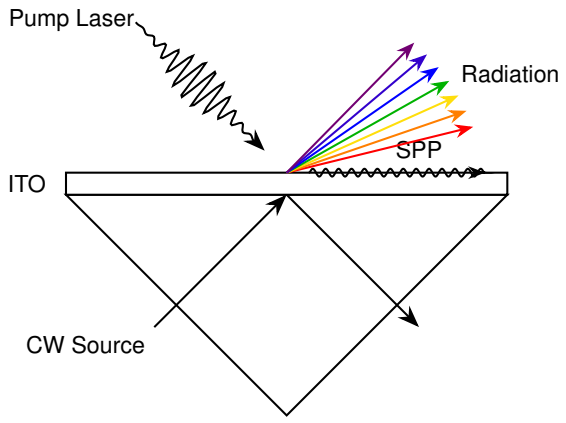

Fig. 1. A surface plasmon polariton (SPP), excited by a continuous wave (CW) source, propagating along an indium tin oxide (ITO)–air interface undergoes mode conversion when the plasma frequency is modified. This temporal perturbation results in the generation of broadband radiation, with frequencies up-shifted from the original SPP frequency.

Here, we consider the idealisation of a rapid plasma frequency change of indium tin oxide (ITO) in the Kretschmann-Rather configuration by considering temporal interfaces. We focus on the characteristics of the far-field radiation in the vacuum half-space. This consists of a continuous frequency spectrum, in contrast to spatial scattering where frequency is conserved, as shown in Fig 1. Our results demonstrate how a temporal interface for an excited SPP undergo conversion under moderate plasma frequencies changes.

II. Methods

Our theoretical model consists of a quasi-1D system where a plane wave in a glass prism with wavevector k_x is incident on an ITO slab (described by a Drude permittivity) with an air half-space above. Excitation by a pump laser redistributes the electrons changing the plasma frequency. We model this by a time-varying effective mass [4]. We solve Maxwell equations with

$$\frac{d\mathbf{J}}{dt} = \epsilon_0 \omega_p^2 f(t)\mathbf{E} - \left(\gamma - \frac{1}{f(t)}\frac{df}{dt}\right)\mathbf{J}, \tag{1}$$

where $f(t) = 1 + \Delta\omega_p^2(t)$ is the modulation function of the plasma frequency.

Time evolving the system, we analyse the conversion to radiation via the total energy emitted in the far-field

$$W_R = \int_{-\infty}^{\infty} dt\, E_x H_y^*. \tag{2}$$

As the parallel wavevector is conserved the radiative frequency ω is directly related to the angle of emission θ.

In the limit that $f(t)$ is much faster than the optical period, the modulation can be treated as stepwise and we can solve the time evolution using the Laplace transform method. We performed FDTD simulations that are in agreement with our analytical results.

III. Results and Discussion

Our system parameters are chosen to model a 6% plasma frequency redshift of which is inline with achievable experimental results for ITO [5]. The Poynting flux as a function of time is shown in Fig 2 showing the coincidence of the analytical and numerical results. Not visible on this scale, but shown in the inset, are oscillations present in the signal; the overall envelope displays a significant peak. By integrating this signal over time, we can calculate the total radiated energy and

compare it to the initial fields giving a conversion efficiency η of about 1%.

Fig. 2. Poynting flux S_z of far-field radiation from surface plasmon polariton conversion under a sudden 6% redshift of the plasma frequency Both the Laplace transform method and numerical method converge. Not visible on this scale are the oscillations present in the flux.

Using the Poynting flux, we can calculate the angular distribution of the far field finding agreement between the numerical and analytical approaches. Both forward and backward propagating radiation can be produced but at the moderate plasma frequencies we consider only the forward fields are present. Furthermore, the angles at which this radiation is produced is shallow suggesting that the bulk of the radiative frequencies are found near the lightline.

IV. Conclusion

We have employed analytical and numerical methods to handle temporal interfaces for SPPs in the Kretschmann-Raether configuration. Working with a moderate change in plasma frequency based on ITO under effective mass modulation, we have analysed the conversion efficiency. We seek to further this work by considering by considering smooth modulations and how this affects both the quantity of radiation and its distribution.

Acknowledgments

HD is funded by the EPSRC Research Council, part of the EPSRC DTP, Grant Ref: EP/W524475/1. MJB, FRF and AZ are supported by EPSRC grant META4D (EP/Y015673). We thank J. Wu and M. Rai for helpful discussions and ongoing collaboration.

References

[1] E. Galiffi et al., "Photonics of time-varying media," *Advanced Photonics*, vol. 4, 014002–014002, 2022.
[2] M.Z. Alam, I. De Leon, R.W. Boyd, "Large optical nonlinearity of indium tin oxide in its epsilon-near-zero region," *Science*, vol. 25, p.p. 795-797, 2016.
[3] X. Wang, M.S. Mirmoosa and S.A. Tretyakov, "Controlling surface waves with temporal discontinuities of metasurfaces," *Nanophotonics*, vol. 12, pp. 2813-2822 .
[4] E. Galiffi et al., "Electrodynamics of photonic temporal interfaces," *Light: Science and Applications*, vol. 14, 2023.
[5] J. Bohn et al., "All-optical switching of an epsilon-near-zero plasmon resonance in indium tin oxide,"" *Nature Communications*, vol. 25, 2021.

Mode and Pitch Multiplexed Guided-Mode Resonance Active Metasurfaces, for Multi-Wavelength Control

Julie Belleville [1,*], Martin Thomaschewski [1], Harry A. Atwater [1]

[1]Thomas J. Watson Laboratories of Applied Physics, California Institute of Technology
Pasadena, CA 91125, United States
*Corresponding author: jbellevi@caltech.edu

***Abstract*—We report designs for multi-wavelength operation of active metasurfaces, based on guided-mode resonances on tunable electro-optic thin films. We simulate diffractive switching efficiencies of 60% at 625 and 545 nm for titanium dioxide multi-mode waveguides on thin-film barium titanate and demonstrate three-wavelength control through two superposed perturbation pitches.**

***Keywords*— active metasurfaces, electro-optic, guided-mode resonances, multi-wavelength control.**

I. Introduction

Metasurfaces offer a lightweight, versatile approach to complex wavefront control [6]. In many applications which might benefit from such control, such as communication apertures and AR/VR red-green-blue projection, the ability to manipulate light across multiple wavelengths is essential. As such, many approaches—group delay engineering [3], spatial multiplexing [1], or multi-layer stacks [2]—have been used to make either broadband or discrete multi-wavelength passive metasurfaces. However, these solutions fall short when it comes to active metasurfaces. Group delay engineering is incompatible with the use of resonances to amplify the device response to small index changes. Spatial multiplexing increases the challenges of active addressing while reducing either the efficiency by dividing the aperture, or the achievable field of view by interleaving elements. Finally, active metasurfaces tend to be less efficient than passive ones, increasing losses in cascaded systems.

In this work, we report a novel design approach for multi-wavelength, programmable metasurfaces, building on previous work on electro-optically tunable guided-mode resonances [7] [8]. Motivated by recent developments in the fabrication of thin-film barium titanate (BTO) and the material's high Pockels coefficient ($r_{42} \approx 1000pm/V$) [4][9], we consider visible light designs on thin-film BTO. However, our currently on-going fabrication efforts aimed at proving the concepts of this paper will first use lithium niobate (LNO), since it is a more mature and commercially available platform.

II. Methods

GMR metasurfaces locally modify the amplitude and phase of a wavefront through propagation along the waveguide axis, defined here as the y-axis (Fig. 1(a)). We select the wavelength of operation by picking a perturbation pitch in y such that the in-plane momentum matching condition for normally incident light satisfies

$$n_{eff} = a\frac{\lambda_0}{p_y} \tag{1}$$

at the desired wavelength, where $a \in \mathbb{Z}$, n_{eff} is the waveguide effective index, λ_0 is the free space wavelength, and p_y is the period of perturbation along y. Figure 1(a) shows the perturbation as a notch of size (dx, dy).

Our simulated devices shown in Fig.1(a, c) use titanium dioxide (TiO_2) as the waveguide (red), BTO as the active material (light grey), silicon dioxide (SiO_2) to provide the index contrast which localizes the waveguide mode (orange), and a silver backreflector (dark grey). We design our waveguides such that their modes (Fig.1(b)) overlap the electro-optic material. This enables active control of the resonance position through strip electrodes (yellow) which change the refractive index of the electro-optic material. Shifting the resonance changes the local phase and amplitude response of the metasurface. To first order, the target resonance shifts according to

$$\Delta n_{eff} = a\frac{\Delta\lambda_0}{\Lambda} \tag{2}$$

Using the Tidy3D mode solver, we design the metasurface waveguide elements to support two local modes (Fig. 1(b)) with distinct effective indices $n_{eff}(\lambda_0)$. This enables us to satisfy Eqn. 1 at multiple wavelengths, enabling wavelength multiplexing. We also consider an alternate multiplexing scheme in which perturbations of distinct periodicity $p_{y1} \neq p_{y2}$ are superposed onto a single waveguide (Fig. 1(c)).

Finally, approximating the index shift in BTO as uniform within a unit cell, we use Tidy3D's full-wave FDTD simulations to calculate the tunable phase and amplitude response of waveguide elements and simulate diffractive switching.

We also target an initial experimental proof-of-concept demonstration using silicon waveguides on LNO. This effort is currently underway.

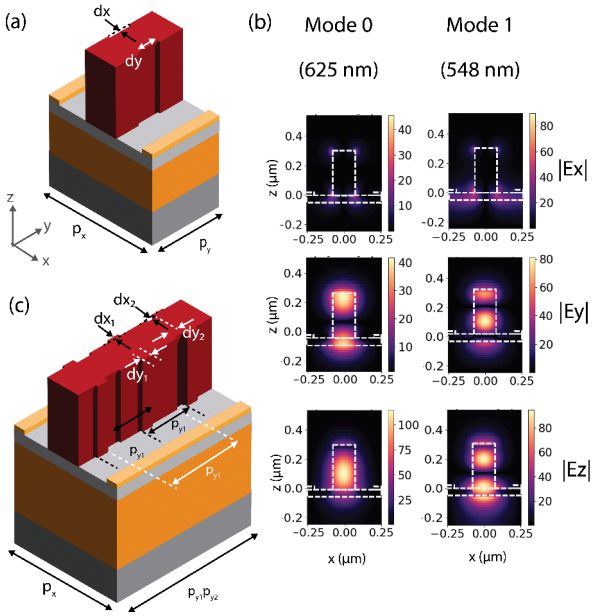

Fig. 1. (a) Guided-mode resonance (GMR) metasurface unit cell. A ridge waveguide (red) is built on an electro-optic material (grey) such that the effective indices of waveguide modes depend on the electrically tuned electro-optic material index. The electrical tuning is applied by the strip electrodes (yellow). p_y periodic perturbations of size (dx, dy) create a momentum matching condition from free space into the waveguide. (b) Two modes which satisfy the momentum matching condition at different wavelengths $\lambda_0^0 = 625nm, \lambda_0^1 = 548nm$. This allows dual-wavelength tunability. The white outline is the xz cross section of the metasurface unit cell. (c) Alternate approach for satisfying the momentum-matching condition at multiple wavelengths, in which two separate perturbation pitches are superposed in a single GMR structure.

III. Results and Discussion

We first confirm in simulation that tuning the BTO index shifts the mode indices at both wavelengths of interest by more than the resonance linewidth. Then, we simulate diffractive switching efficiency in Fig. 2(a) for BTO index shifts of $\Delta n = \pm 0.04$ in adjacent unit cells. We consider three different perturbation sizes, which produce the Q factors noted in the figure, and predict a diffractive switching efficiency of 60% for the lowest Q design.

We simulate devices with different Q factors because the shift in wavelength achieved by index modulation must exceed the linewidth of the resonance to provide significant modulation. Thus, devices with higher Q can be tuned with lower index shifts. Here, we nominally assume an achievable $\Delta n = \pm 0.04$, but these higher Q simulations indicate that our devices will work with smaller index changes, with some efficiency cost. We attribute the lower steering efficiency at higher Q factors to increased inter-waveguide coupling due to longer interaction times between modes in adjacent waveguides [5].

This motivates the use of BTO, with its much higher Pockels coefficient, over lithium niobate (LNO). For a fixed applied voltage, we expect a greater index shift, which in turn enables lower Q, more efficient operation.

Finally, we note that waveguide geometry limits the number of modes and engineering of their dispersion, which limits the number and relative position of tunable wavelengths. In Fig. 2(b), we overcome this limitation and add a third controllable wavelength by introducing a second set of perturbations with a different period, as depicted schematically in Fig. 1(c). The two shorter wavelengths (450 nm, 600 nm) are coupled into mode 1 using two different perturbation periods, and the longest wavelength (640 nm) is coupled into mode 0.

In simulation, the computational cost of large simulations constrains us to periods p_{y1}, p_{y2} which share a small least common multiple. In experiment, we are working towards fabricating silicon on LNO structures with arbitrary periods to demonstrate arbitrary selection of wavelengths of operation.

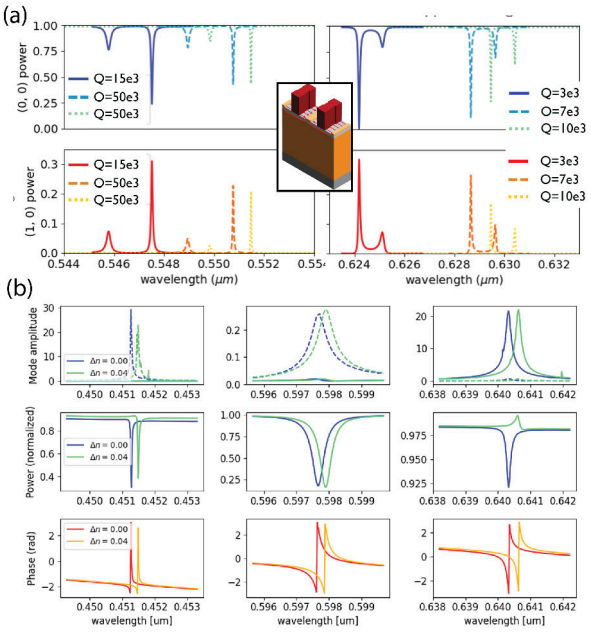

Fig. 2. (a) Simulated diffractive switching at 625 nm and 550 nm, for varying quality (Q) factor resonances. The varying Q factors are produced by varying perturbation sizes (dx, dy), with smaller perturbations corresponding to higher Q factors. Inset shows the effective unit cell used for switching. (b) Shift in resonance with a change of index $\Delta n = 0.04$ in the BTO, at 450 nm, 600 nm, and 640 nm, for a structure with two superposed perturbation pitches.

IV. Conclusion

We present GMR metasurface designs which use thin-film BTO for multi-wavelength active control and steering of light. Unlike previous approaches, these designs do not increase the complexity of electronic addressing, increase the pitch of elements, or decrease efficiency of operation through cascading. We demonstrate diffractive splitting with a simulated efficiency of 60% across both wavelengths and show up to 3 separate tunable wavelengths. We anticipate a first experimental demonstration of these concepts on LNO.

ACKNOWLEDGMENTS

This work was supported by the Air Force Office of Scientific Research Meta-Imaging MURI Grant No. FA9550-21-1-0312 (J.B., M.T., H.A.A.). J.B. acknowledges the support of the Natural Sciences and Engineering Research Council of Canada (NSERC) through the Postgraduate Scholarship-Doctoral program.

REFERENCES

[1] Ehsan Arbabi et al. "Multiwavelength metasurfaces through spatial multiplexing". en. In: *Scientific Reports* 6.1 (Sept. 2016). Number: 1, p. 32803. ISSN: 2045-2322. DOI: 10.1038/srep32803. URL: https://www.nature.com/articles/srep32803 (visited on 02/27/2024).

[2] Ori Avayu et al. "Composite functional metasurfaces for multispectral achromatic optics". en. In: *Nature Communications* 8.1 (Apr. 2017), p. 14992. ISSN: 2041-1723. DOI: 10.1038/ncomms14992. URL: https://www.nature.com/articles/ncomms14992 (visited on 05/28/2025).

[3] Wei Ting Chen et al. "A broadband achromatic metalens for focusing and imaging in the visible". en. In: *Nature Nanotechnology* 13.3 (Mar. 2018), pp. 220–226. ISSN: 1748-3395. DOI: 10.1038/s41565-017-0034-6. URL: https://www.nature.com/articles/s41565-017-0034-6 (visited on 05/28/2025).

[4] Yu Cao et al. "A Barium Titanate-on-Oxide Insulator Optoelectronics Platform". en. In: *Advanced Materials* 33.37 (Sept. 2021), p. 2101128. ISSN: 0935-9648, 1521-4095. DOI: 10.1002/adma.202101128. URL: https://onlinelibrary.wiley.com/doi/10.1002/adma.202101128 (visited on 09/28/2025).

[5] Elissa Klopfer et al. "High-Quality-Factor Silicon-on-Lithium Niobate Metasurfaces for Electro-optically Reconfigurable Wavefront Shaping". In: *Nano Letters* 22.4 (Feb. 2022), pp. 1703–1709. ISSN: 1530-6984. DOI: 10.1021/acs.nanolett.1c04723. URL: https://doi.org/10.1021/acs.nanolett.1c04723 (visited on 02/28/2025).

[6] Prachi Thureja et al. "Toward a universal metasurface for optical imaging, communication, and computation". en. In: *Nanophotonics* 11.17 (Aug. 2022), pp. 3745–3768. ISSN: 2192-8614. DOI: 10.1515/nanoph-2022-0155. URL: https://www.degruyter.com/document/doi/10.1515/nanoph-2022-0155/html (visited on 10/03/2022).

[7] Sahil Dagli et al. "GHz-Speed Wavefront Shaping Metasurface Modulators Enabled by Resonant Electro-Optic Nanoantennas". en. In: *Advanced Materials* 37.40 (2025). _eprint: https://advanced.onlinelibrary.wiley.com/doi/pdf/10.1002/adma.202506790, e06790. ISSN: 1521-4095. DOI: 10.1002/adma.202506790. URL: https://onlinelibrary.wiley.com/doi/abs/10.1002/adma.202506790 (visited on 11/23/2025).

[8] Martin Thomaschewski et al. "Ferroelectric nanophotonics: electro-optic active metasurfaces". In: *High Contrast Metastructures XIV*. SPIE, 2025, PC133780U. URL: https://www.spiedigitallibrary.org/conference-proceedings-of-spie/PC13378/PC133780U/Ferroelectric-nanophotonics-electro-optic-active-metasurfaces/10.1117/12.3043953.short (visited on 06/16/2025).

[9] Prachi Thureja et al. "Spalled Barium Titanate Single Crystal Thin Films for Functional Device Applications". In: *Nano Letters* 25.28 (July 2025), pp. 11089–11096. ISSN: 1530-6984. DOI: 10.1021/acs.nanolett.5c02279. URL: https://doi.org/10.1021/acs.nanolett.5c02279 (visited on 07/16/2025).

Wavelength-Guided Plasmonic Control of CO_2 Reduction: From Model Nanostructures to Gold Dendritic Electrodes

Anjalie Edirisooriya[1*], Manuka Suriyage[1], Zelio Fusco[1], Ning Lyu[1,2], Shenyou Zhao[3], Christin David[4], Fiona Beck[1]
[1]School of Engineering, Australian National University, Canberra ACT2600, Australia
[2]IFTO, Friedrich-Schiller-Universität Jena, 07743 Jena, Germany
[3]School of Electronic Engineering, Xi'an University of Posts and Telecommunications, China
[4]University of Applied Sciences Landshut, Am Lurzenhof 1, 84036 Landshut, Germany
[*]corresponding author: Anjalie.Edirisooriya@anu.edu.au

***Abstract* - Selective CO_2 reduction to multi-carbon products requires localized excitation and repeated electron transfer. We present a wavelength-guided plasmonic strategy linking controlled optical modes in gold nanostructures to scalable gold dendritic electrodes. Structure–optical relationships identified in simplified geometries are translated to complex morphologies, enabling optical control of CO_2 reduction processes**

INTRODUCTION

The conversion of CO_2 into value-added chemicals is central to sustainable energy and carbon-neutral manufacturing. While capture technologies continue to advance, selectively reducing CO_2 into multi-carbon (C_2^+) products such as ethylene and ethanol remains challenging. These reactions involve multiple coupled electron and proton transfer steps and must compete with kinetically favored pathways including hydrogen evolution and CO formation under practical operating conditions.

Plasmonic nanostructures offer a complementary route to addressing these challenges by enabling optical control over interfacial reaction environments[1]. Upon illumination, localized surface plasmon resonances concentrate electromagnetic energy into nanoscale regions and generate energetic charge carriers at metal–electrolyte interfaces. These localized excitation conditions can influence adsorption, charge transfer, and reaction pathways in ways that are not accessible through purely thermal or electrochemical activation.

However, achieving selective CO_2 reduction using plasmonic catalysts requires more than increasing light absorption[2]. Reaction outcomes depend on how optical energy is distributed spatially and spectrally, how near-fields are localized, and how these excitation conditions align with the requirements of multi-electron chemistry. Establishing clear structure-optical-reactivity relationships is therefore essential for translating plasmonic concepts into rational catalyst design.

I. Methods and Results

To identify optical excitation conditions relevant to selective CO_2 reduction, we adopt a hierarchical strategy that progresses from simplified plasmonic geometries to complex, scalable dendritic electrodes. Our approach combines electromagnetic simulations (BEM, FEM), nanoscale optical characterization, cathodoluminescence (CL) spectroscopy, and in situ surface-enhanced Raman spectroscopy (SERS) to probe plasmon-mediated excitation and charge-transfer processes.

Gold nanotriangles are employed as a model plasmonic platform to establish wavelength-selective excitation behavior. Their well-defined geometry supports tunable localized surface plasmon resonances, enabling systematic control over resonance energy, near-field localization, and absorption. Electromagnetic simulations are used to correlate triangle dimensions with spectral shifts and field enhancement, providing a controlled

framework for isolating optical effects that are difficult to disentangle in disordered systems.

This simplified-geometry approach is motivated by experimental CL mapping of gold nano-dendrites(Fig. 1 c, d), which reveals that plasmonic hot-spots are strongly localized at sharp tips and high-curvature junctions[3]. These observations suggest that the spectral behavior of dendritic hot-spots is governed primarily by local geometry rather than the full interconnected morphology. Using model structures therefore allows efficient identification of key features controlling near-field localization and wavelength response while capturing qualitative trends observed experimentally.

Raman spectroscopy using molecular probe systems is employed as a sensitive reporter of plasmonic activity and wavelength-dependent excitation effects[4], providing mechanistic insight into plasmon-mediated charge transfer without directly probing CO_2 intermediates. These optical benchmarks establish excitation conditions relevant to multi-electron chemistry and guide interpretation of more complex catalytic measurements.

Building on these insights, we investigate self-assembled gold nano-dendrites fabricated via scalable electrodeposition. These hierarchical architectures exhibit sharp features and complex junctions that support broadband and spatially heterogeneous plasmonic modes. Such excitation landscapes naturally generate localized near-fields and enhanced carrier flux at multiple sites, conditions that are well suited to driving repeated electron-transfer events required for multi-electron CO_2 reduction.

Photocatalytic and photo-assisted electrochemical measurements are used to assess how plasmonic excitation modifies reaction behavior in dendritic electrodes. While wavelength-dependent selectivity can be clearly demonstrated in model plasmonic systems, extending deterministic wavelength control to dendrites remains an active area of investigation due to their multi-mode optical response. Ongoing work focuses on correlating wavelength-resolved excitation with changes in reaction rate and product distribution, guided by optical trends established in simplified geometries.

II. Conclusion

This work establishes a wavelength-guided plasmonic design framework for CO_2 reduction that connects controlled optical modes in simplified nanostructures with scalable gold dendritic electrodes. By using model geometries to identify excitation conditions relevant to complex plasmonic morphologies, we define a clear pathway toward optical control of multi-electron CO_2 reduction. These results position plasmonic dendrites as a promising platform for future wavelength-selective and optically programmable CO_2 conversion.

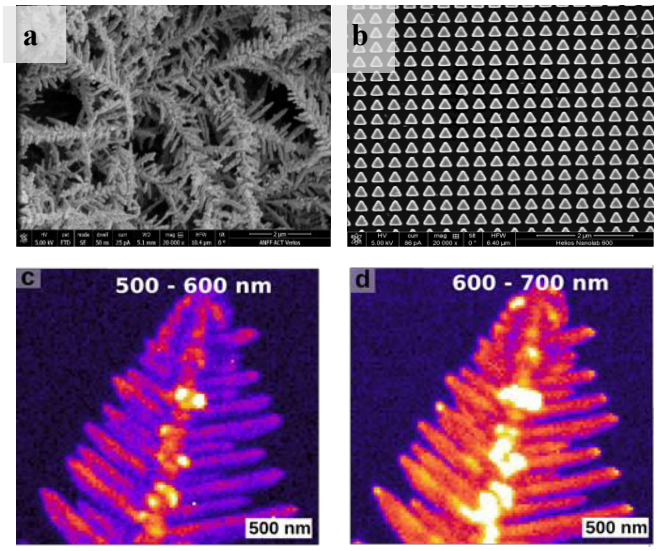

Figure 1. SEM images of *(a)* Au nano-dendrites and *(b)* Au nanotriangle array. *(c,d)* CL maps of a dendrite integrated over 500–600 nm and 600–700 nm, showing wavelength-dependent plasmonic emission at high-curvature regions.

References

1. Fusco, Z.; Beck, F. J. Nanophotonics 2024, 13, 387–417
2. Fusco, Z.; Catchpole, K.; Beck, F. J. J. Mater. Chem. C 2022, 10, 7511–7524
3. Fusco, Z.; Riaz, A.; David, C.; Beck, F. J. Adv. Mater. Interfaces 2023, 10, 2202236
4. Lyu, N. *et al. ACS Nano* **19**, 25821–25829 (2025).

Cd(Zn)O gap antennas on polar substrates

Maria Villanueva-Blanco[1], Pablo Ibañez-Romero[1], Julia Ingles-Cerrillo[1], Javier Yeste[2], Vicente Muñoz-Sanjosé[2], Maria del Carmen Martínez-Tomás[2], Miguel Montes Bajo[1], Adrian Hierro[1]*

[1]ISOM, ETSI Telecomunicación, Universidad Politécnica de Madrid, Madrid, Spain
[2]Departament de Física Aplicada i Electromagnetisme, Universitat de València, Spain
*Corresponding author: adrian.hierro@upm.es

CdO stands out as the best plasmonic semiconductor in the mid infrared. Here, we evaluate its plasmonic characteristics on two polar substrates, SiC and sapphire, and show large enhancements of the near-field from the interaction between surface phonon polaritons from the substrate and localized surface plasmon polaritons from CdO stripes.

***Keywords*— metamaterials, semiconductors, plasmonics, Oxides.**

I. Introduction

CdO stands out in the mid infrared (IR) range thanks to its low optical losses and high carrier concentration [1]. CdO has a tunable plasma frequency that can be changed with the alloying of other metals like Zn [2]. The possibility to grow it over polar substrates, like SiC and sapphire, together with the recent advances in gap antenna processing [3], opens the door to the coupling of localized surface phonon and plasmon polaritons (LSPhP and LSPP, respectively) leading to very large near field amplifications.

The plasmonic properties of CdO and $Cd_{1-x}Zn_xO$ thin films have been studied in a great variety of substrates. Polar dielectrics, like sapphire, can support surface phonon polaritons, which are highly propagative low-loss modes. When hybridized with the CdO antisymmetric mode in sufficiently thin films, the modes show a large enhancement of the propagation length. [4]. Additionally, in the case of CdO nanostructured thin films over sapphire substrates, the localized surface plasmons can couple with the localized surface phonon polaritons hosted on sapphire, causing significant amplification of the near-field [3].

Unfortunately, sapphire is very insulating, which can be a serious limitation for the integration of CdO on active devices. Hence, a substrate that can host active devices would be most desirable. In this context, SiC is an interesting substrate as it is already present in a variety of commercial devices [5]. Like sapphire, it is a wide-gap polar semiconductor. But, unlike sapphire, its electrical characteristics can be manipulated by doping. In this work we will study the viability of using SiC as a polar active substrate for CdZnO thin films and investigate the near-field amplification in gap-antennas.

II. Methods

$Cd_{1-x}Zn_xO$ thin films were grown by metal organic chemical vapor deposition (MOCVD) on 4H-SiC and r-sapphire. Conventional reflectance and attenuated total reflectance (ATR) in the Otto configuration were performed using a Fourier transform infrared (FTIR) spectrometer.

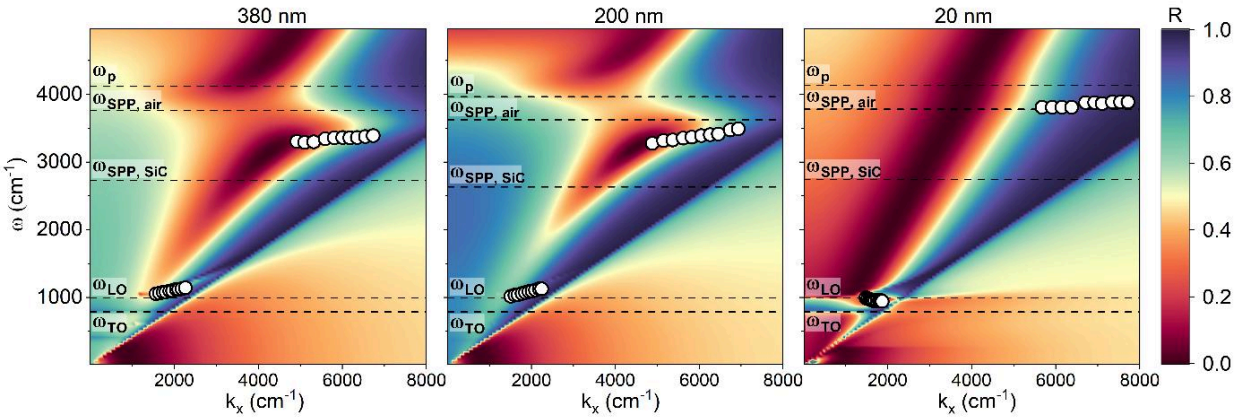

Figure 1: Simulated reflectance contour plots and experimentally determined SPP frequencies (white circles) for CdZnO/SiC structures for different layer thicknesses. The Zn content was 10 % for all three samples.

Gap antennas were processed using standard e-beam lithography followed by ICP etching.

Reflectance dispersion curves on the CdZnO thin films were calculated using a homemade program based on the transfer matrix method (TMM). Near-field amplification maps and surface average amplification in nanostructured CdO stripes were calculated using the commercial software COMSOL Multiphysics.

III. Results and Discussion

Figure 1 shows the simulated ATR contour plots and the experimental SPP resonance frequencies for a series of CdZnO thin films grown on SiC. As seen in previous studies on r-sapphire [4], the dispersion curves show two different polaritonic branches, symmetric and antisymmetric. The decrease in film thickness triggers a repulsion between the two modes. While the symmetric mode is essentially plasmonic in nature and rises to higher frequencies until it reaches the plasma frequency (ω_p), the antisymmetric hybridized mode tends toward lower energies and at low values of k_x remains pinned at the LO-phonon frequency of SiC.

As shown in Figure 2, the plasmonic quality in each of the substrates is quite similar. They both have very low optical losses, but while the symmetric mode behaves similarly in sapphire and SiC, the antisymmetric mode in SiC exhibits lower dispersion throughout k_x and zero group velocity. Overall, these particularities make SiC promising as an epsilon near zero (ENZ) material in the IR range.

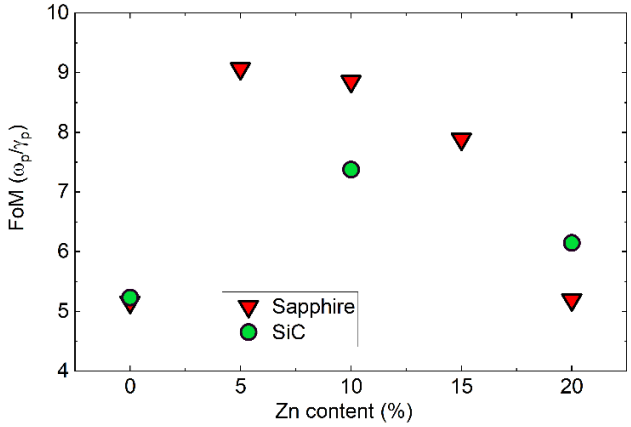

Figure 2:Figure of merit (FoM) of samples with different nominal Zn content. The data for the calculation of the FoM in sapphire substrates was obtained from [6].

In the case of CdO on sapphire our group has recently demonstrated gap antennas [3] with very large near field amplification. This processing technology hence opens the door to reaching very large couplings between the LSPhP from CdO and LSPhP from the polar substrate. As shown in Figure 3, by controlling the stripe size one can tune the LSPP frequency to that of the LSPhP, yielding an anticrossing behavior around the LSPhP frequency, and very large field enhancements around the gap antenna. Results from current ongoing work on processed CdO gap antennas on both sapphire and SiC will be presented.

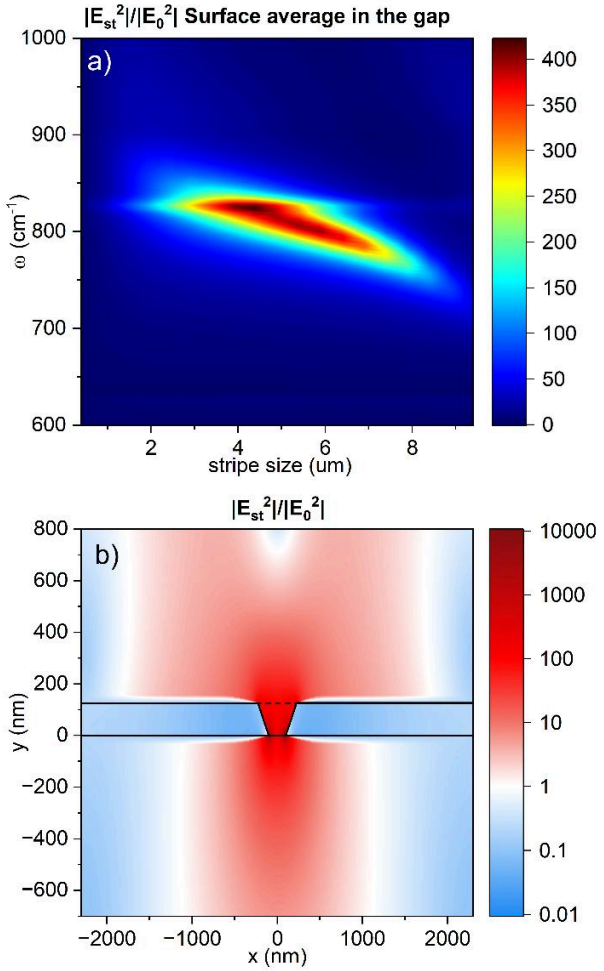

Figure 3: a) Gap near-field surface average for varying stripe widths and equal gap size ω =830 cm^{-1} b) Near-field simulation for the grid with gap size = 200 nm and stripe size = 4400 nm.

IV. Conclusion

We have demonstrated the presence of two surface plasmon polariton resonances in the CdZnO/SiC structures, correspondent to the symmetric and antisymmetric modes. We have shown the combination of the CdZnO antisymmetric mode with the LO phonon in SiC results in a hybrid surface plasmon-phonon polariton also found in sapphire. In this way we have shown the viability of SiC as a substrate for CdZnO thin films while maintaining plasma frequencies and optical losses comparable to those found in sapphire.

We have calculated the optimum grid geometry for maximum near-field amplification in a CdO/sapphire gap antenna, yielding an enhancement of the integrated near-field in the gap of $\times 422$ Furthermore, the enhancement extends hundreds of nm outside the gap nanoantenna too, facilitating its use in applications such as surface enhanced infrared absorption (SEIRA). The experimental results from the processed design will be presented.

ACKNOWLEDGMENTS

This work was partly supported by Projects PID2024-156706OB-C2 funded by MICIU/AEI/10.13039/501100011033/FEDER,UE and PDC2023-145827-C2 funded by MICIU/AEI/10.13039/501100011033 and by European Union Next Generation EU/ PRTR, and by Generalitat Valenciana under Project No. PROMETEU/2021/066.

REFERENCES

[1] J. D. Caldwell, L. Lindsay, V. Giannini, I. Vurgaftman, T. L. Reinecke, S. A. Maier and O. J. Glembocki, "Low-loss, infrared and terahertz nanophotonics using surface phonon polaritons", Nanophotonics, vol. 4, n.º 1, pp. 44-68, 2015.

[2] J. Tamayo-Arriola, A. Huerta-Barberà, M. Montes Bajo, E. Muñoz, V. Muñoz-Sanjosé, and A. Hierro, "Rock-salt CdZnO as a transparent conductive oxide", Appl. Phys. Lett., vol. 113, n.º 22, p. 222101, 2018.

[3] P. Ibañez-Romero, M. Villanueva-Blanco, J. Yeste, F. Gonzalez-Posada, T. Taliercio, V. Muñoz-Sanjosé, M. Montes Bajo and A. Hierro, "Near-Field Enhancement via Plasmon–Phonon Polariton Coupling with CdO Stripes", Adv. Opt. Mater., 2026.

[4] J. Tamayo-Arriola, E. Martínez Castellano, M. Montes Bajo, A. Huerta-Barberà, E. Muñoz, V. Muñoz-Sanjosé and A. Hierro ,"Controllable and Highly Propagative Hybrid Surface Plasmon–Phonon Polariton in a CdZnO-Based Two-Interface System", ACS Photonics, vol. 6, n.º 11, pp. 2816-2822, 2019.

[5] B. J. Nel and S. Perinpanayagam, "A Brief Overview of SiC MOSFET Failure Modes and Design Reliability", Procedia CIRP, vol. 59, pp. 280-285, 2017.

[6] J. Tamayo Arriola, "Infrared intersubband detection and plasmonics with (Zn,Mg)O and (Cd,Zn)O compounds", PhD Thesis, Universidad Politécnica de Madrid, 2019.

Switchable n-type conducting polymer nanoantennas

Suraya Kazi, Pravallika Bandaru, Yulong Duan, Shangzhi Chen, Magnus Jonsson*

Laboratory of Organic Electronics, Department of Science and Technology, Linköping University, Norrköping, SE-60174, Sweden
*Corresponding author: magnus.jonsson@liu.se

***Abstract*— We establish n-type conducting polymer poly(benzodifurandione) (PBFDO) as a switchable organic plasmonic system. In doped state, PBFDO becomes optically metallic above 700 nm and supports plasmonic resonances when nanostructured, which can be reversibly turned on/off electrically/chemically. This stretches the horizon and functionalities of plasmonics for dynamic metasurfaces and adaptive optical devices.**

***Keywords*— conducting polymers, n-type nanoantennas, organic plasmonics, electro-tunable.**

SUMMARY

We have recently introduced p-type conducting polymers as a new class of materials for dynamically tunable plasmonics[1], [2]. In contrast to traditional metals, conducting polymers can reversibly switch between metallic behavior (negative permittivity) and dielectric behavior (positive permittivity) through changes in their redox state. Nanoantennas fabricated from these polymers can therefore exhibit plasmonic resonances that can be turned on or off on demand.

In our recent work [3], we showed for the first time that nanostructures made from an n-type conducting polymer named poly(benzodifurandione) (PBFDO)[4] support plasmon-like resonances [3] similar to p-type conducting polymers. We fabricated PBFDO thin film onto a substrate by spincoating and measured permittivity by ellipsometry. We observed negative permittivity in the near infrared for doped-conductive state, but positive permittivity for dedoped-dielectric state (See Fig. 1a) which shows promise for switchable plasmonic system. To realize PBFDO nanoantennas, we later patterned the film into nanodisk arrays using colloidal lithography. Spectroscopic measurements on the nanodisks showed size-dependent extinction peak-shift (see Fig. 1b) as expected for plasmonic resonance. This resonance was modulated through electrical or chemical control of the polymer's doping state (see Fig. 1c) governed by its charge carrier density. This work extends redox-tunable plasmonics beyond previously studied p-type systems. Integrating metasurfaces made of both p type and n type conducting polymers in tandem devices can enable new functionalities, including tunable p–n junction concepts for dynamic metaoptics.

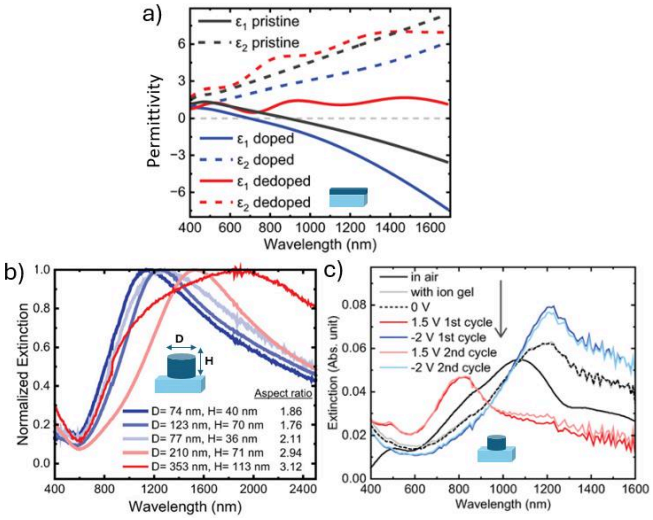

Fig. 1 a) Permittivity of PBFDO thin film at different redox state. b,c) Experimental spectra of PBFDO nanoantennas for different diameter, D and height, H (b) and during electrochemical switching (c) from Ref. [3].

ACKNOWLEDGMENTS

The authors acknowledge support from the Swedish Research Council, the Knut and Alice Wallenberg Foundation, the European Research Council, the Basic and Applied Basic Research Major Program of Guangdong Province, and the Swedish Government Strategic Research Area in Materials Science on Functional Materials at Linköping University.

REFERENCES

[1] S. Chen *et al.*, "Conductive polymer nanoantennas for dynamic organic plasmonics," *Nat. Nanotechnol.*, vol. 15, no. 1, pp. 35–40, 2020, doi: 10.1038/s41565-019-0583-y.

[2] A. Karki *et al.*, "Electrical Tuning of Plasmonic Conducting Polymer Nanoantennas," *Adv. Mater.*, vol. 34, p. 2107172, 2022, doi: 10.1002/adma.202107172.

[3] S. Kazi *et al.*, "n-Type redox-tuneable conducting polymer optical nanoantennas," *J. Mater. Chem. C*, vol. 12, no. 43, pp. 17469–17474, 2024, doi: 10.1039/D4TC03038A.

[4] H. Tang *et al.*, "A solution-processed n-type conducting polymer with ultrahigh conductivity," *Nature*, vol. 611, no. 7935, pp. 271–277, 2022, doi: 10.1038/s41586-022-05295-8.

Vortex Excited Plasmon Resonances in Metal Nanodisks Governed by Symmetry and Size

Daisuke Tanaka[1,*], Kayn A. Forbes[2], David L. Andrews[2]

[1]Department of Electrical and Electronic Engineering, National Institute of Technology, Oita College, Japan

[2]School of Chemistry, University of East Anglia, UK

*Corresponding author: d-tanaka@oita-ct.ac.jp

***Abstract*— Optical vortices with different total angular momentum excite LPRs in gold nanodisks, studied by DDA. In circular disks, resonance wavelengths depend strongly on diameter and show an optimal excitation band. In polygonal disks, rotational symmetry controls excitable modes, and spectra switch with even/odd angular-momentum parity.**

***Keywords*— plasmonics, optical vortex, angular momentum, mode selectivity, plasmonic filter.**

I. Introduction

Structured light provides additional degrees of freedom to control localized plasmon resonances (LPRs) beyond conventional scalar illumination. Optical vortex beams have orbital angular momentum (OAM) according to the topological charge ℓ and spin angular momentum (SAM) according to the circular polarization helicity σ. It is possible to selectively excite a given multipole mode in an LPR through tailoring the total angular momentum (TAM) [1,2] of the incident beam. Figure 1 shows a conceptual diagram. We term this TAMSE: total-angular-momentum-selective excitation of LPRs under vortex illumination. More recently, cylindrical vector beams were shown to selectively excite bright and dark plasmon modes in triangular gold nanodisks by matching the spatial symmetry of the incident field to the mode character [3]. Despite these advances, a systematic comparison of continuous versus discrete rotational symmetry under vortex excitation, and its impact on TAM-dependent spectral shifts, mode order selection, and excitation efficiency, remains incomplete. Here we address this gap and further highlight a passive TAM-to-intensity mapping concept for plasmonic filters.

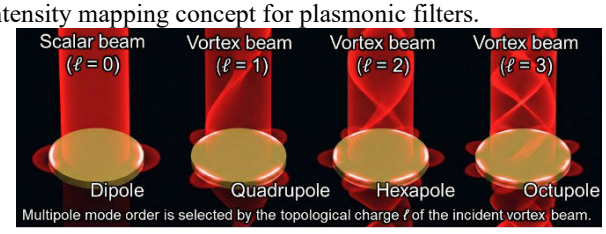

Fig. 1 Conceptual illustration of TAMSE. Under LCP vortex illumination, the dominant multipolar response can change with ℓ+σ, as identified by azimuthal lobe patterns in near-field distributions.

II. Methods

We performed electromagnetic simulations using the discrete dipole approximation based on DDSCAT [4] with custom optical vortex illumination. The target structures are 30-nm-thick metallic nanodisks: circular nanodisks with diameters from 200 to 600 nm and an equilateral triangular disk with a side length of 300 nm. The incident beam is a left-circularly polarized (LCP; σ=+1) optical vortex with topological charge ℓ. We compute extinction spectra and identify resonance mode order from distributions of electric field intensity at peak wavelengths using azimuthal lobe patterns.

III. Results and Discussion

Figure 2 shows the extinction spectra of circular gold nanodisks with diameters of 300, 400, and 600 nm under incident optical vortices with topological charges ℓ=+1 to +4, where the phase singularity of the vortex beam is aligned with the disk center. As ℓ increases, the resonance peak shifts systematically to shorter wavelengths. For a fixed ℓ, increasing the disk diameter causes a redshift of the resonance together with spectral broadening. The peak extinction is largest when the resonance wavelength lies in the 600−700 nm range, indicating a wavelength region where the excitation efficiency is maximized for these structures.

Size-dependent spectral shifts are common in confined optical systems. In molecules there is no universal rule linking molecular dimensions to absorption wavelength, although within analogous series a general trend toward longer wavelengths with increasing size is often observed. Simple models such as the quantum particle-in-a-box capture this qualitative behavior by predicting smaller energy level spacings for larger systems, though they are only crude approximations for real molecules. A closer analogy arises in semiconductor quantum dots, where Brus theory explicitly predicts size-dependent transition energies due to quantum confinement. The TAMSE response of nanodisks is similarly governed by confinement of the electromagnetic field at the surface; the disk effectively acts as a two-dimensional resonant cavity, so

increasing its physical dimensions lowers the resonance frequency and produces the observed redshift.

Figure 3 presents the near-field intensity maps at each peak wavelength for a 200-nm-diameter gold nanodisk. The results show that the resonant mode order increases from dipole to decapole mode with increasing TAM. The observed dependence of the resonance mode order on the TAM is independent of variations in disk diameter. Overall, these findings indicate that by tuning the disk size, plasmon resonances can be excited with the desired mode order while maximizing the excitation efficiency.

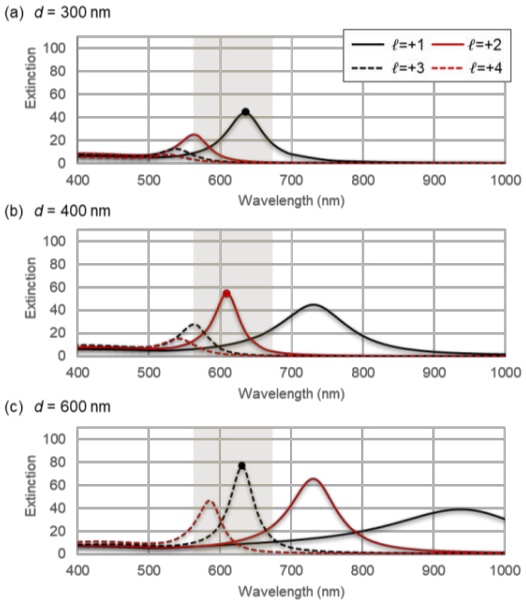

Fig.2 DDA-calculated extinction spectra of 30 nm thick circular nanodisks with different diameters under LCP vortex illumination (ℓ=+1 to +4). The filled circles indicate peak wavelengths. The shaded region indicates the wavelength band where the excitation efficiency (peak extinction) is maximized.

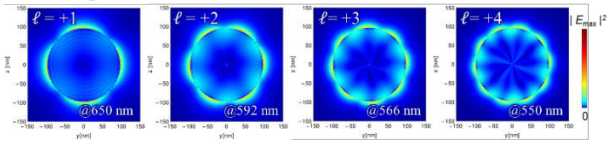

Fig. 3 Simulated field distribution maps at peak wavelengths for a single circular nanodisk with a diameter of 200 nm.

Fig. 4 shows the TAMSE of a single triangular nanoplate. Fig. 4(a) shows the schematic of the simulation conditions, and Fig. 4(b) shows the simulated extinction spectra at each ℓ. The extinction spectra have two peaks at around 550-700 nm and 910 nm. Examining the shorter wavelength side, the spectral shape varies depending on whether ℓ is even or odd, indicating that the excitable modes differ depending on the total angular momentum. At longer wavelengths, the peak value of the extinction spectra decreases linearly as ℓ increases, and the resonance wavelength remains unchanged regardless of ℓ. The order of resonance modes also remains in all cases (shown in Fig. 4(c)). We found that this typical characteristic was observed only for the triangular configuration. Comparing the electric-field maps and extinction spectra for the triangular and circular nanodisks indicates that the mode order plays a key role in determining the resonance wavelength. In the plane perpendicular to the incident beam, a circular disk exhibits continuous rotational symmetry about the beam axis. In contrast, a triangular disk has only threefold rotational symmetry together with a limited set of mirror symmetries. This reduction in symmetry lifts degeneracies present in the circular case and modifies the allowed modal structure, which likely accounts for the differences observed in the resonance states.

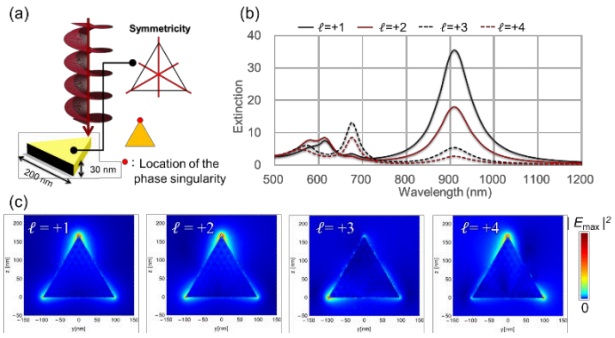

Fig.4 TAMSE of a single triangular gold nanodisk. (a) Schematic of on-axis optical-vortex illumination (vortex axis aligned to the disk edge) for a 30-nm-thick nanodisk. (b) Corresponding extinction spectra under vortex beams with ℓ=+1, +2, +3, +4, showing symmetry-dependent mode selectivity and distinct resonance features. (c) Near-field intensity maps at the long side peak wavelengths (910 nm) for each ℓ, where the azimuthal lobe patterns reveal the excited multipolar order. The color scale denotes the normalized field magnitude.

IV. Conclusion

We simulated the optical response of single circular and triangular gold nanodisks under optical vortex illumination to investigate TAMSE. The results show that the optical characteristics associated with TAMSE depend strongly on both the symmetry and size of the nanostructure. In particular, for triangular nanodisks, the extinction peak intensity varies linearly with the vortex topological charge ℓ under appropriate excitation conditions. This behavior suggests that such structures could function as passive transmission-type nano-filters that convert TAM states into measurable intensity contrasts for mode discrimination. Preliminary simulations further indicate that the same TAM-based selection principle may extend to other geometries, including to square and regular pentagonal nanodisks as well as multi-ring nanostructures, pointing to broader applicability of the approach.

Acknowledgments

This work was supported in part by JSPS KAKENHI 22K04975 and Iketani Science and Technology Foundation.

References

[1] K. Sakai, K. Nomura, T. Yamamoto, and K. Sasaki, "Excitation of Multipole Plasmons by Optical Vortex Beams", *Sci. Rep.*, **5**, 8431 (2015).

[2] D. Tanaka, S. Harajiri, Y. Fujita, K. A. Forbes, T. T. Pham, D. L. Andrews "Multipole Excitation of Localized Plasmon Resonance in Asymmetrically Coated Core–Shell Nanoparticles Using Optical Vortices", *Laser and Photo. Rev.*, **18**, 2300536 (2024).

[3] S. Hasegawa, H. Ichikawa, K. Imura, "Selective Excitation of Dark Plasmon Modes Using Cylindrical Vector Beams Studied by Microscopic Imaging of Nonlinear Photoluminescence", *J. Phys. Chem. C*, **128**, 2536 (2024).

[4] B. T. Draine, and P. J. Flatau, "Discrete-dipole approximation for scattering calculations", *J. Opt. Soc. Am. A*, **11**, 1491 (1994).

Single-photon generation from strongly coupled Au-metasurface-WSe2 monolayers via photon blockade

Andergachew Mekonnen Berhe[1,*], Haroldo T. Hattori[1], and Andrey E. Miroshnichenko[1,*],
[1]School of Engineering and Technology, University of New South Wales at Canberra, Northcott Drive, Canberra ACT 2610, Australia
*Corresponding author: a.berhe@unsw.edu.au and andrey.miroshnichenko@unsw.edu.au

***Abstract*— In this study, we demonstrated the application of quantum nanophotonics, specifically single-photon emission (SPE), in a strongly coupled Au plasmonic metasurface and a monolayer of WSe_2 at room temperature. The demonstrated SPE has high purity with an equal-time second-order correlation function $g^{(2)}(\tau = 0) = 0.00035$ at $\Omega_c = 0.5$ meV, via photon blockade.**

***Keywords*— metasurfaces, strong coupling, photon blockade, single-photon purity.**

I. Introduction

Quantum nanophotonics offers a versatile platform for confining and coherently controlling individual quanta of light and matter at deeply subwavelength scales. This enables on-chip quantum functionality and deterministic single-photon generation. In quantum communication and photonic quantum computing, single photons serve as a universal resource for qubit encoding. To develop scalable, integrable SP emitters that operate at room temperature, they should exhibit high emission efficiency and purity.[14] The purity of these photons can be measured via the second–order correlation function at zero delay, g(2)(0), with an ideal value of $g^{(2)}(\tau = 0) = 0$, corresponding to unity purity defined as $P = 1 - g^{(2)}(\tau = 0) = 1$.

A promising approach for single-photon generation with high brightness and purity involves cavity quantum electrodynamics (cQED). Despite advancements, achieving room-temperature SPSs with high purity remains a significant challenge, prompting new strategies in materials and device design. Here, we theoretically demonstrate that a strongly coupled hybrid platform composed of a compact Au plasmonic metasurface and a monolayer of WSe_2 enables scalable single-photon emission (SPE) at room temperature. After confirming strong coupling, both conventional photon blockades (CPB) at low drive strength and unconventional photon blockade (UnPB) using a two-tone coherent drive that causes destructive interference between two-photon excitation pathways were implemented in QuTiP.

As a result, the calculated equal-time second-order correlation function $g^{(2)}(\tau = 0)$ is resulted 0.0267 via CPB at lower drive. Moreover, due to the destructive quantum interference, the UPB induced higher purity with $g^{(2)}(\tau = 0) = 0.00035$ at $\Omega_c = 0.5$ meV.

II. Methods

Our methodology combines Lumerical simulation and modeling. The optical response of the WSe2 monolayer (thickness 0.7 nm) was modeled using a Lorentz oscillator formalism to describe its in-plane excitonic permittivity.[1]

The uncoupled Au metasurface was analyzed through multipole decomposition across various geometric parameters, revealing that the dominant plasmonic resonance is controlled by an electric quadrupole (EQ) mode. Then, the optical properties of the individual components and their hybrid configuration were simulated using the finite-difference time-domain (FDTD) method in Lumerical (Ansys). We used periodic boundary conditions in the x- and y-directions and a perfectly matched layer in the z-direction. A plane wave, incident along the z-axis and polarized along the y-axis, was employed in the simulations. Finally, numerical modeling was carried out using a Python-based quantum toolbox (QuTiP).

III. Results and Discussion

Strong coupling in the Au–WSe_2 heterostructure (Fig. 1(a-b)) was confirmed by extracting the polariton dispersion through thickness-dependent tuning of the Au nanostructure and fitting the resulting anticrossing behaviour using a coupled-oscillator model. [1,2]

$$\begin{pmatrix} E_P + i\gamma_P & g \\ g & E_X + i\gamma_X \end{pmatrix} \begin{pmatrix} \alpha \\ \beta \end{pmatrix} = E \begin{pmatrix} \alpha \\ \beta \end{pmatrix} \quad (1)$$

where $\hbar = 1$, E_P, and E_X are the resonance energies of the plasmon and exciton modes, g is the coupling strength, and Γ_P and Γ_X are the half-widths at half-maximum (HWHM) of the plasmon and exciton modes, respectively. The calculated Rabi splitting of Au-WSe_2 heterostructures strongly depends on the

catenary-like field enhancement induced by the Au cavity, resulting in a room-temperature coupling strength of $g = 36.26$ meV. It was confirmed that the calculated Rabi splitting of the system is nonvanishing and can be experimentally measured.

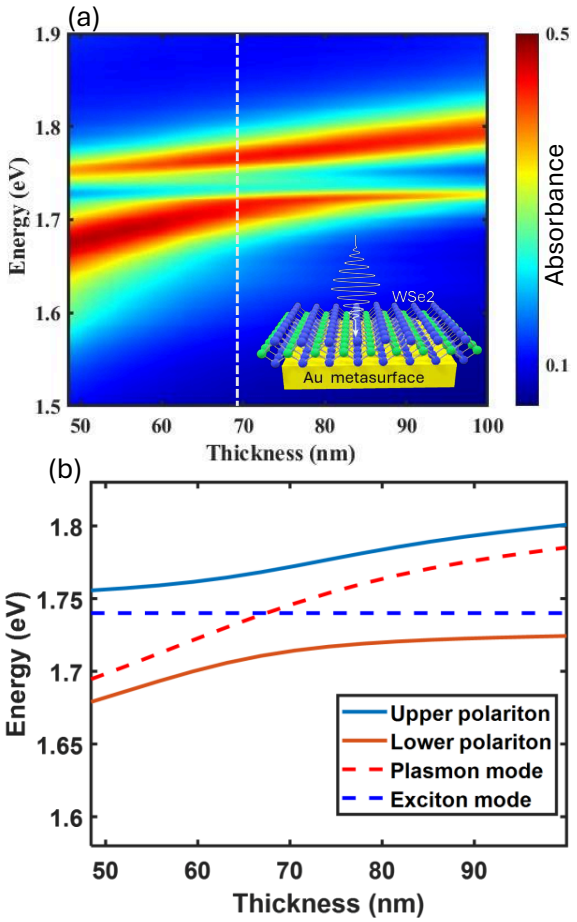

Fig. 1: Single-photon emission from a strongly coupled Au-WSe2 monolayer. (a) Absorbance map of the Au-WSe2 monolayer as a function of Au metasurface thickness. (b) The corresponding polariton dispersion curve [1]. The vertical dashed line in panel (a) indicates detuning.

After confirming the strong coupling in the EQ-mode of Au metasurfaces-WSe_2 monolayer, we simulated the quantum master equation for the second-order correlation function, $g^{(2)}(\tau)$ using QuTiP. The demonstrated strong coupling in the Au cavity–WSe_2 monolayer shown in Fig. 1 reveals that the system is highly anharmonic. Therefore, we first applied conventional photon blockades (CPB) at low drive strength and unconventional photon blockade (UnPB) using a two-tone coherent drive that induces destructive interference between two-photon excitation pathways (see Fig. 2). As a result, at a drive strength of $\Omega_c = 0020$ meV of the CPB, the calculated equal-time second-order correlation function $g^{(2)}(\tau = 0)$ is resulted 0.0267. Moreover, due to the destructive quantum interference, the UPB induced $g^{(2)}(\tau = 0) = 0.00035$ at $\Omega_c = 0.5$ meV. The results demonstrated are much larger than those of a single-photon purity, a strongly coupled few-layer hBN film, and a high-Q bound-state-in-the-continuum (BIC) cavity.[3] These findings demonstrate that Au-metasurface–WSe_2 monolayers are a scalable route to high-purity, room-temperature single-photon sources for integrated quantum photonics and quantum communication.

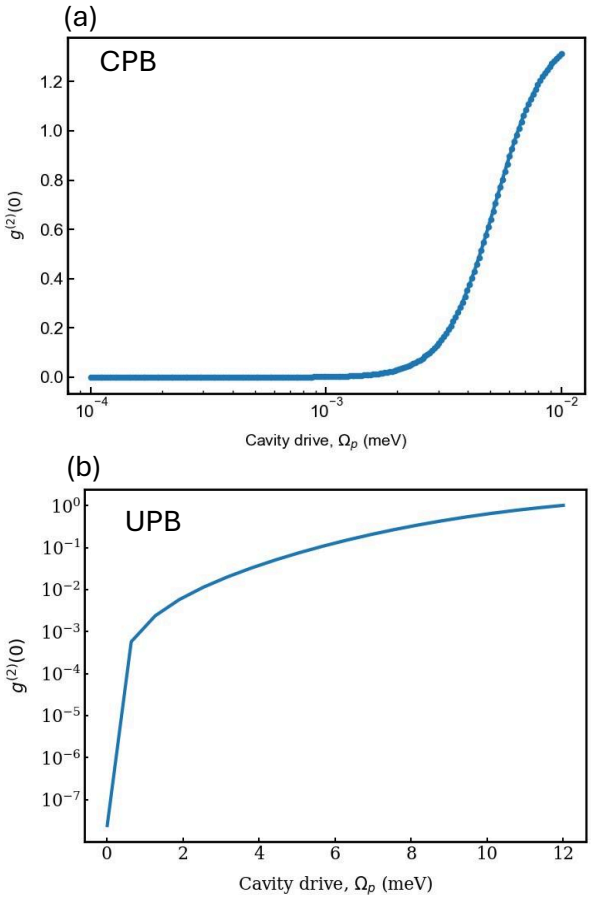

Fig. 2: Effect of drive strength on $g^{(2)}(\tau = 0)$ at the same coupling strength via (a) CPB and (b) UPB.

IV. Conclusion

We have demonstrated that compact, scalable single-photon emission can be achieved in a strongly coupled plasmonic metasurface with an EQ mode and a WSe2 monolayer. By fabricating the metasurface in a clean room using electron-beam lithography (EBL) and transferring the monolayer, the proposed design and modeling could provide a viable pathway toward integrated quantum light sources for quantum key distribution and low-power photonic quantum interconnects.

Acknowledgments

This work was supported by the Australian Research Council Discovery Project (DP200101353).

References

[1] Berhe AM, As'ham K, Al-Ani I, et al. "Strong coupling and catenary field enhancement in the hybrid plasmonic metamaterial cavity and TMDC monolayers," Opto-Electron Adv 7, 230181(2024).

[2] A. M. Berhe, A. A. Odebowale, K. Koshelev et al. “Enhanced Rabi Splitting of Exciton-Polaritons and Plasmon-Polaritons in Lithium Niobate Metasurface,“ Laser Photonics Rev. 2026, 20, e01825.
[3] T. T. H. Do, M. Nonahal, C. Li *et al*., “Room-temperature strong coupling in a single-photon emitter-metasurface system ” Nature Communications 2024, 15, 1 2281.

TMOKE Enhancement via Hybrid Fabry–Perot-Plasmonic Modes in Magnetoplasmonic Multilayers

Elkin D. Sepúlveda[1,*], Edgar J. Patiño[1], Mario Zapata[2]

[1]Department of Physics, Superconductivity and Nanodevices Laboratory, University of Los Andes, Colombia
[2] Donostia International Physics Center, San Sebastian, Spain
*Corresponding author: e.sepulvedaa@uniandes.edu.co

***Abstract*—We demonstrate enhanced transverse magneto-optical Kerr effect (TMOKE) in magnetoplasmonic multilayers via hybrid Fabry–Perot-plasmonic modes. Coupling evanescent plasmonic fields with propagating cavity resonances enables co-localized field enhancement within the magneto-active layer. Tuned multilayer heterostructures exhibit stronger TMOKE than single-mode designs, confirmed by modeling, simulations, and experiments.**

***Keywords*— TMOKE, magnetoplasmonics, Fabry-Perot resonances, plasmonic modes, multilayer structures, mode hybridization.**

I. Introduction

Plasmonic, a branch of photonics, investigates the interaction between electromagnetic radiation and conduction electrons at metal-dielectric interfaces. Such interactions give rise to collective surface electron oscillations known as surface plasmons (SPs)[1], coupled with incident photons. Due to their ability to confine light to scales below the diffraction limit and their high sensitivity to dielectric variations, SPs have enabled the development of diverse optoelectronic devices[2]. As we will show, Fabry-Perot (FP) microcavities together with plasmonic architectures allow the enhancement of internal electromagnetic fields through constructive interference between cavity and plasmonic modes.. This results in the enhancement of transverse magneto-optical Kerr effect (TMOKE).

Multilayered metal-dielectric-metal systems have proven to be versatile structures, in which both propagating and localized plasmon modes can coexist and couple with cavity modes, for example, FP-type resonances. This coupling enhances field confinement and enables spectral tunability and hybridization of optical modes in magneto-plasmonic multilayers. Nevertheless, previous studies have largely focused on symmetric and antisymmetric plasmonic modes in metal-insulator-metal (MIM) microcavities and on alternative routes to TMOKE enhancement[3], leaving the transverse magneto-optical Kerr Effect in the presence of FP resonances largely unexplored.

Here, we address these effects by investigating one of the architectures proposed in [4] of a multilayer magneto-plasmonic heterostructure in which propagating SP modes are phase-matched to FP cavity modes. This is achieved using two metallic layers that act as mirrors to generate FP modes together with the excitation of SPs modes. By tuning layer thicknesses and refractive-index contrast, we co-localize cavity antinodes and plasmonic near fields to achieve resonance overlap and constructive interference. To realize and test this concept, we employ a Prism/Metal/Dielectric/Metal/Ferromagnet/Dielectric (P/M/D/M/F/D) system and assess the impact of FP modes and propagating SP modes on TMOKE.

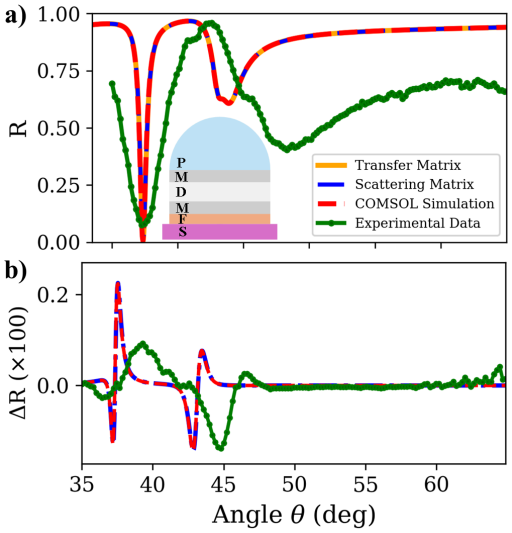

Fig. 1. **a)** Reflectance (R) and **b)** Reflectivity difference, $\Delta R = R(+M) - R(-M)$, as a function of the angle of incidence (θ) for the heterostructure. The experimental data (green line) is compared with theoretical models using the Transfer Matrix Method (TMM, blue solid line) and the Scattering Matrix Method (SMM, orange dashed line), as well as with numerical simulations (COMSOL, red dashed line).

II. Methods

We study a multilayer heterostructure in a Prism/Metal/Dielectric/Metal/Ferromagnet/Dielectric (P/M/D/M/F/D) configuration through a combined theoretical, numerical, and experimental approach (see figure 1):

1) **Analytical Modeling (TMM & SMM):**
   - The Transfer Matrix Method (TMM) models the system's isotropic optical response.

- Under an external magnetic field, the Scattering Matrix Method (SMM) calculates the TMOKE signal and reflectivity, accounting for the magneto-optical anisotropy.

2) **Numerical Simulation (FEM – COMSOL Multiphysics):**
   - Finite Element Method (FEM) simulations map the electric field profiles to physically characterize the modes.
   - This distinguishes between evanescent plasmonic modes (symmetric/antisymmetric) and propagating Fabry-Perot cavity modes.
3) **Validation:**
   - SMM/TMM results are cross-verified with FEM simulations.
   - Final model accuracy is confirmed by comparing numerical spectra with experimental laboratory data.

REFERENCES

[1] A. V. Zayats, I. I. Smolyaninov, and A. A. Maradudin, "Nano-optics of surface plasmon polaritons," *Physics Reports*, vol. 408, no. 3–4, pp. 131–314, 2005.

[2] E. Ferreiro-Vila, J. M. García-Martín, A. Cebollada, G. Armelles, and M. U. González, "Magnetic modulation of surface plasmon modes in magnetoplasmonic metal-insulator-metal cavities," *Optics Express*, vol. 21, no. 4, pp. 4916–4930, 2013.

[3] Z. A. Mohamed, "Refractive index sensor using perfect plasmonic absorber based on metamaterial Fabry-Perot cavity," *Optics Communications*, vol. 591, p. 132110, 2025.

[4] E. J. Patiño and P. Quiroga, "PLASMONIC DEVICE, SYSTEM AND METHOD," *U.S. Patent No. 17/161,195*, 2021.

The Topography Makes the Potential: A Covariant Wave Equation for Surface Plasmon Polaritons on Arbitrary Weakly Curved Interfaces

Florian Bönsel[1,2,*] and Flore K. Kunst[1,2]

[1]Max-Planck-Institute for the Science of Light, 91058 Erlangen, Germany
[2]Department of Physics, Friedrich-Alexander-Universität Erlangen-Nürnberg, 91058 Erlangen, Germany
*Corresponding author: florian.boensel@mpl.mpg.de

***Abstract*—We derive a 2D wave equation for surface plasmon polaritons on curved metal surfaces via a perturbative Maxwell expansion. Two linear curvature potentials emerge, distinguishing convex from concave surfaces. Applying our results to excited emitters on spheroids, we demonstrate curvature driven frequency shifts and superradiance.**

***Keywords*— Surface Plasmon Polaritons, Extrinsic Curvature, Geometric Potentials, Superradiance.**

I. Introduction

Surface plasmon polaritons (SPPs) at metal-dielectric interfaces enable rich photonic phenomena ranging from nanofocusing and enhanced biosensing to topological plasmonic lattices [1], [2], [3]. Advances in nanofabrication allow the realization of smooth metallic interfaces with prescribed curvature profiles [4], [5], motivating a systematic theoretical understanding of how curvature shapes SPP dynamics.

The defining feature of the SPP field is that the mode decays much more rapidly into the metal than into the dielectric. In contrast, light confined to a thin dielectric layer decays symmetrically, so that bending convexly or concavely yields identical physics, producing geometric potentials only at second order in curvature [6], [7], [8]. For SPPs, this symmetry is not present, and geometry-induced corrections can appear already at first order in the curvature [9], [10]. Prior work addressed this in specific geometries using paraxial or ray-based methods [9], [11], [12], [13], but a general two-dimensional wave equation valid for any smooth and weak surface modulation has been lacking.

II. Surface Helmholtz Equation on Curved Interfaces

We derive such an equation by expanding Maxwell's equations in the Lorenz gauge in coordinates adapted to the curved interface, parametrized by two tangential surface coordinates q_a ($a = 1, 2$) and a normal coordinate q_3. Working in a gauge where the tangential vector potential components vanish on a flat interface, and using the rescaled field $\mathcal{A}^i = \sqrt{\Omega}\, A^i$ with $\Omega = 1 - 2Hq_3$, the 3D metric near the interface expands as $g_{ab} = \gamma_{ab} - 2q_3 h_{ab}$, with γ_{ab} being the intrinsic surface metric and h_{ab} the second fundamental form [7].

The perturbative expansion parameter is H/k_{spp}, the ratio of the surface extrinsic curvature H to the flat-surface SPP wavenumber

$$k_{\mathrm{spp}} = k_0 \sqrt{\frac{\epsilon_m \epsilon_d}{\epsilon_m + \epsilon_d}}. \tag{1}$$

The SPP field samples the normal direction on a scale $|q_3| \sim \kappa_{d,m}^{-1} \sim k_{\mathrm{spp}}^{-1}$, so the curvature correction experienced by the mode is of order H/k_{spp}. Crucially, we retain a finite normal coordinate q_3, in contrast to the thin-layer limit $q_3 \to 0$ used in many dielectric waveguide studies [6], [7]. It is this q_3-dependent coupling to curvature, captured by the operator $2q_3\, h^{ab}\nabla_a\nabla_b$, that generates the linear-in-curvature potentials.

After a perturbative order-by-order expansion of the wave equations and curvature-modified boundary conditions, we obtain the effective two-dimensional wave equation for the transverse magnetic SPP mode ψ on the interface as

$$\left[\Delta_\gamma + k_{\mathrm{spp}}^2 + V_H + V_\sigma\right]\psi = 0, \tag{2}$$

with the two geometry-induced potential (operators)

$$V_H = \underbrace{\frac{k_0(\epsilon_d^2 + \epsilon_d\epsilon_m + \epsilon_m^2)}{(\epsilon_d + \epsilon_m)\sqrt{-(\epsilon_d + \epsilon_m)}}}_{C_H} H, \tag{3}$$

$$V_\sigma = -\underbrace{\frac{\epsilon_d^2 + 3\epsilon_d\epsilon_m + \epsilon_m^2}{k_0\epsilon_d\epsilon_m\sqrt{-(\epsilon_d + \epsilon_m)}}}_{C_\sigma} \sigma^{ab}\nabla_a\nabla_b. \tag{4}$$

Here, Δ_γ is the Laplace-Beltrami operator, $H = \frac{1}{2}\gamma^{ab}h_{ab}$ the mean curvature, and $\sigma^{ab} = h^{ab} - H\gamma^{ab}$ the traceless part of the second fundamental form.

The prefactor $C_H < 0$ for any material combination supporting SPPs. Consequently, a convex metal surface ($H < 0$) blue-shifts the SPP dispersion, while a concave surface ($H > 0$) red-shifts it [11], [12]. The anisotropic potential V_σ vanishes on isotropic surfaces (spheres and flat interfaces) and acts as a curvature-induced birefringence on surfaces with unequal principal curvatures.

The prefactor C_σ, in contrast to C_H can have different sign depending on the permittivities.

We verify that Eq. (2) reproduces established results for the sphere and cylinder as special cases, recovering the curvature-corrected wavenumbers of Refs. [13], [11] for the sphere and the paraxial Schrödinger equation of Ref. [9] for the cylinder.

III. SPP-Mediated Collective Radiance on a Curved Spheroid

As an application of Eq. (2), we study cooperative emission from an ensemble of quantum emitters interacting via SPPs on a macroscopically curved metal surface, a regime not previously analyzed. SPP-mediated superradiance and subradiance are well understood for planar interfaces [14], [15] and nanowire geometries [16], [17], but the effect of macroscopic curvature on the collective spectrum has not been addressed.

We consider N identical two-level emitters with normally oriented dipole moments placed in a ring near the pole of a silver–air spheroidal interface. For the special case of a spherical surface, the collective spectrum of $N = 9$ emitters is asymmetric with respect to $H = 0$, which means that convex and concave geometries redistribute the N collective eigenmodes differently between superradiant and subradiant channels, and the cooperative frequency shifts change sign depending on the curvature sign. This asymmetry is a direct consequence of the linear-in-curvature potential V_H.

For a spheroidal surface with fixed equatorial radius and varying polar radius, deviations from the spherical shape activate the anisotropic potential V_σ. As the aspect ratio moves away from unity (oblate or prolate deformation), the collective eigenvalues evolve asymmetrically around the spherical case. Decay rates are more sensitive to the deformation than frequency shifts and a selected mode can be driven from near-dark (subradiant) to bright (superradiant) by varying the eccentricity.

IV. Conclusions

We have derived a covariant surface Helmholtz equation for SPPs on weakly curved metal-dielectric interfaces, containing two geometric potential terms linear in the extrinsic curvature. The scalar potential V_H distinguishes convex from concave bending and shifts the effective SPP momentum uniformly, while the anisotropic potential V_σ introduces direction-dependent momentum and acts as a curvature-induced birefringence. Both effects have no analogue in symmetric waveguide systems and vanish in the thin-layer limit. Applied to emitters on a metallic spheroid, the equation predicts that macroscopic surface curvature can redistribute superradiant and subradiant decay channels and produce sign-dependent cooperative frequency shifts, offering a geometric knob for engineering plasmon-mediated light-matter interactions.

Acknowledgments

We acknowledge funding from the Max Planck Society's Lise Meitner Excellence Program 2.0.

References

[1] M. I. Stockman, "Nanofocusing of optical energy in tapered plasmonic waveguides," *Physical review letters*, vol. 93, no. 13, p. 137404, 2004. [Online]. Available: https://doi.org/10.1103/PhysRevLett.93.137404

[2] H. Lee and D. Kim, "Curvature effects on flexible surface plasmon resonance biosensing: segmented-wave analysis," *Optics Express*, vol. 24, no. 11, pp. 11 994–12 006, 2016. [Online]. Available: https://doi.org/10.1364/OE.24.011994

[3] T. B. Smith, C. Kocabas, and A. Principi, "Topological plasmonic waveguides in triharmonic metal gratings," *Journal of Physics: Condensed Matter*, vol. 33, no. 26, p. 265003, 2021.

[4] N. Lassaline, R. Brechbühler, S. J. Vonk, K. Ridderbeek, M. Spieser, S. Bisig, B. Le Feber, F. T. Rabouw, and D. J. Norris, "Optical fourier surfaces," *Nature*, vol. 582, no. 7813, pp. 506–510, 2020. [Online]. Available: https://doi.org/10.1038/s41586-020-2390-x

[5] P. Nagpal, N. C. Lindquist, S.-H. Oh, and D. J. Norris, "Ultrasmooth patterned metals for plasmonics and metamaterials," *Science*, vol. 325, no. 5940, pp. 594–597, 2009.

[6] S. Batz and U. Peschel, "Linear and nonlinear optics in curved space," *Physical Review A - Atomic, Molecular, and Optical Physics*, vol. 78, no. 4, p. 043821, 2008. [Online]. Available: https://doi.org/10.1103/PhysRevA.78.043821

[7] R. da Costa, "Quantum mechanics of a constrained particle," *Physical Review A*, vol. 23, no. 4, p. 1982, 1981. [Online]. Available: https://doi.org/10.1103/PhysRevA.23.1982

[8] M. Carmi, M. Roth, and R. Bekenstein, "Photon-mediated atomic interactions in curved surface settings," *arXiv preprint arXiv:2503.19635*, 2025. [Online]. Available: https://doi.org/10.48550/arXiv.2503.19635

[9] G. Della Valle and S. Longhi, "Geometric potential for plasmon polaritons on curved surfaces," *Journal Of Physics B: Atomic, Molecular and Optical Physics*, vol. 43, no. 5, p. 051002, 2010. [Online]. Available: https://doi.org/10.1088/0953-4075/43/5/051002

[10] A. Libster-Hershko, R. Shiloh, and A. Arie, "Surface plasmon polaritons on curved surfaces," *Optica*, vol. 6, no. 1, pp. 115–118, 2019. [Online]. Available: https://doi.org/10.1364/OPTICA.6.000115

[11] S. Ancey, Y. Décanini, A. Folacci, and P. Gabrielli, "Surface plasmon polaritons and surface phonon polaritons on metallic and semiconducting spheres: Exact and semiclassical descriptions," *Journal of the Optical Society of America B*, vol. 26, no. 6, pp. 1176–1187, 2009. [Online]. Available: https://doi.org/10.1364/JOSAB.26.001176

[12] R. Spittel, P. Uebel, H. Bartelt, and M. A. Schmidt, "Curvature-induced geometric momenta: the origin of waveguide dispersion of surface plasmons on metallic wires," *Optics Express*, vol. 23, no. 9, pp. 12 174–12 188, 2015. [Online]. Available: https://doi.org/10.1364/OE.23.012174

[13] M. V. Perel and D. Y. Zaika, "Asymptotics of surface plasmons on curved interface," in *Proceedings of the International Conference Days on Diffraction 2011*. IEEE, 2011, pp. 149–156.

[14] R. Chance, A. Prock, and R. Silbey, "Molecular fluorescence and energy transfer near interfaces," *Advances in chemical physics*, vol. 37, pp. 1–65, 1978.

[15] Z. Jalali-Mola, S. Asgarnezhad-Zorgabad, and O. Hess, "Collective quantum dynamics with distant quantum emitters in slow-wave nanoplasmonic waveguides," *APL Quantum*, vol. 1, no. 4, 2024. [Online]. Available: https://doi.org/10.1063/5.0217702

[16] D. Chang, A. S. Sørensen, P. Hemmer, and M. Lukin, "Quantum optics with surface plasmons," *Physical review letters*, vol. 97, no. 5, p. 053002, 2006. [Online]. Available: https://doi.org/10.1103/PhysRevLett.97.053002

[17] D. Dzsotjan, A. S. Sørensen, and M. Fleischhauer, "Quantum emitters coupled to surface plasmons of a nanowire: A green's function approach," *Physical Review B–Condensed Matter and Materials Physics*, vol. 82, no. 7, p. 075427, 2010. [Online]. Available: https://doi.org/10.1103/PhysRevB.82.075427

Mixing Lateral Casimir Forces: Rotating Particle Above a Moving Surface

Stéphane Azar[1], Francisco. J. Rodríguez-Fortuño[1,*],

[1]Department of Physics and London Centre for Nanotechnology,
King's College London, Strand, London WC2R 2LS, UK
*Corresponding author: francisco.rodriguez_fortuno@kcl.ac.uk

***Abstract*—We study the lateral Casimir force experienced by a particle rotating above a planar surface in uniform motion. Working with fluctuational electrodynamics, we investigated the conditions under which the total lateral Casimir force vanishes under different regimes and analysed to what extent it mimics a classical wheel rolling.**

***Keywords*— Casimir lateral force, quantum fluctuations, moving interfaces.**

I. Introduction

Fluctuation-induced forces, generally referred to as Casimir forces, emerge from vacuum and thermal fluctuations of virtual electromagnetic interactions. They are usually attractive and acts along the normal of the interacting surfaces. However, if two surfaces parallel to each other are set in relative motion, a new force component appears parallel to the surface [1], [2], commonly referred to as lateral Casimir force. Furthermore, a polarizable particle moving above a surface also experiences a lateral Casimir force [2], [3], [4], which depends linearly with respect to speed for non-zero temperatures and to the third power for zero temperature [5]. Moreover, other approaches have shown that linear motion is not the only possibility to create Casimir Lateral forces. Indeed, a rotating polarizable particle will interact with the vacuum and thermal electromagnetic fields differently based on the handedness of the field, creating an imbalance in the circularly polarized components which results in asymmetric fluctuations inducing a lateral Casimir force [6]. In the case of metallic materials, this "rotation" force was shown to be proportional to the particle's rotation frequency for non-zero temperature, and to its cube for zero temperature. This rotation frequency dependence behavior with respect to temperature is reminiscent of the speed dependence for a moving particle mentioned above. This raises a question, how would the lateral Casimir forces originating from rotation and linear motion interact, and under which conditions would they cancel out? In this work we consider both types of lateral Casimir forces simultaneously, studying them in different regimes and different assumptions for the particle polarizability. Finally, we analyse to which extent it mimics the behavior of a classical wheel rolling on a surface. This analogy was raised in Ref. [6] since their force and torque were satisfying the relation expected from a wheel in classical mechanics.

II. Analytical Model

In this work, we consider a spherical nanoparticle particle of temperature T_1 and radius R placed at a centre-to-surface distance d above a planar surface of temperature T_0 (see Fig. 1). Assuming the particle is small enough we can adequately describe it within the dipolar limit through a frequency-dependent polarizability $\alpha(\omega)$. We allow the particle to rotate along the y-axis at a frequency Ω which induces a lateral Casimir force along the x-axis [6], we refer to it as the rotation force. Furthermore, we assume the surface to be in uniform motion with velocity $\mathbf{v} = v\hat{\mathbf{x}}$, and calculate its reflection coefficients according to Ref. [7]. As shown in [7], in the case of a metallic surface, the surface's motion introduces an asymmetry in its surface modes dispersion relation, creating a momentum imbalance along the direction of motion, which induces a Casimir friction force along the x-axis, which we refer to as the friction force.

It is clear that the friction force induced by the moving surface is directed along the surface motion, we could imagine the surface trying to drag the particle with it. Therefore, by choosing wisely, we are able to counteract the force induced by rotation, and eventually cancel it.

Fig. 1. Schematic of the system under study. A spherical particle rotates at angular frequency Ω at a centre-to-surface distance d above the surface. The surface itself moves with a uniform velocity $\mathbf{v}$. Both, particle rotation and surface motion, induce a Casimir lateral force on the particle.

As an example, let's consider the particle and the surface to be made of the same metallic material, whose response at low frequencies, well below interband transitions, can be described in terms of the static conductivity σ_0. Using a Drude dielectric function $\varepsilon_r(\omega) = 1 + i\frac{\sigma_0}{\varepsilon_0\omega}$. When the relevant frequencies Ω, $k_x v$ and $k_b T/\hbar$ are much smaller than σ_0, we can approximate the polarizability, $\mathrm{Im}\{\alpha(\omega)\} \approx 12\pi R\varepsilon_0^2\omega/\sigma_0$, and the reflection coefficient $\mathrm{Im}\{r_p(\omega - k_x v)\} \approx 2\varepsilon_0(\omega - k_x v)/\sigma_0$. Using these, and considering the surface and particle to be at the same non-zero temperature ($T_1 = T_0 = T > 0$), it is possible to calculate the total force on the particle along the x-axis as follow,

$$F_{x,\mathrm{tot}} = \frac{3\pi\varepsilon_0^2 R^3 k_b^2 T^2}{2\hbar\sigma_0^2 d^4}\left(\Omega + \frac{1}{A}\frac{v}{d}\right) \tag{1}$$

where A is a constant coefficient which changes depending on the regime considered and polarizability model used. Considering the zero temperature limit, the force would behave as

$$F_{x,\mathrm{tot}} \propto \left[\Omega^3 + \frac{1}{B}\left(\frac{v}{d}\right)^3\right] \tag{2}$$

where B is also a regime dependant constant. Overall, we see that the lateral Casimir force experienced by the particle cancels out when,

$$v = -\eta\,\Omega d \tag{3}$$

with η is a positive constant replacing A and B. In analogy, a classical wheel rolling on a surface without sliding would satisfy $\eta = 1$. It is interesting to note that the equilibrium speed at which the force cancels does not depend on the radius of the particle, but rather on the centre-to-surface distance. This could be imagined as a ghost wheel with radius ηd rolling, strengthening the analogy with classical mechanics and rolling wheels.

III. Discussion

Our aim is to study various sceneries and determine how closes they mimic a classical wheel. The two main path corresponding to the thermal regime ($T > 0$) and vacuum regime ($T = 0$). In the thermal regime we can safely approximate the total force as a sum of a rotation force experienced by a rotating particle above a static surface, and a friction force experienced by a static particle above a moving surface, with no cross terms. However, in the zero-temperature limit (vacuum regime) the interplay becomes unavoidable, and both, friction and rotation force, have to be treated together. Furthermore, at higher temperature, we expect the total force to slightly deviate from the analytical model, as was observed for the rotation force in Ref. [6].

Aside from the temperature dependence, Casimir forces are know to be very model-dependent [2], [4]. For instance Ref. [4] considered a polarizable particle moving above a static surface, and included radiative damping in the particle's polarizability, in contrast with a static conductivity. Under this assumption, the speed and distance dependences change by a factor of $(v/d)^2$ with respect to a static conductivity. Therefore, it is mandatory for us to explore various assumptions. It is also interesting to explore different materials that are not described by a simple Drude model and study how it impacts the lateral forces.

Another possible path of study is the distance dependence. In Ref. [6] it was shown that for large nanoparticle of silicon carbide (with radius of 500nm) the force would oscillate as a function of distance. We may expect a similar behavior with the friction force decaying faster than the rotation force with respect to distance.

We are currently working on the subject and will explore all the available tracks in the future.

IV. Conclusion

We extend the previous research on Casimir lateral force by mixing two sources, a rotating particle and a moving surface. Mixing these we arrive at a condition to completely cancel the forces experienced by the particle, leading to a close analogy with a rolling wheel in classical mechanics. We explore all the different regimes and assumptions which can impact the lateral forces, in order to get a more complete understanding of the phenomenon.

Acknowledgments

S. A. is supported by EPSRC through an NMESFS-2024 scholarship. F.J. R.-F. was supported by the Engineering and Physical Sciences Research Council (EPSRC) grant META4D (EP/Y015673).

References

[1] J. B. Pendry, "Shearing the vacuum - quantum friction," *Journal of Physics: Condensed Matter*, vol. 9, pp. 10301–10320, 11 1997.

[2] K. Milton, J. Høye, and I. Brevik, "The reality of casimir friction," *Symmetry*, vol. 8, p. 29, 4 2016.

[3] F. Intravaia, R. O. Behunin, and D. A. R. Dalvit, "Quantum friction and fluctuation theorems," *Physical Review A*, vol. 89, p. 050101, 5 2014.

[4] J. S. Høye, I. Brevik, and K. A. Milton, "Casimir friction between polarizable particle and half-space with radiation damping at zero temperature," *Journal of Physics A: Mathematical and Theoretical*, vol. 48, p. 365004, 9 2015.

[5] J. S. Høye and I. Brevik, "Casimir friction at zero and finite temperatures," *The European Physical Journal D*, vol. 68, p. 61, 3 2014.

[6] A. Manjavacas, F. J. Rodríguez-Fortuño, F. J. G. D. Abajo, and A. V. Zayats, "Lateral casimir force on a rotating particle near a planar surface," *Physical Review Letters*, vol. 118, 3 2017.

[7] S. Azar, F. J. Rodríguez-Fortuño, and S. Golat, "Fresnel reflection coefficients in the fourier domain for a planar surface in uniform motion parallel to its interface," *Scientific Reports*, vol. 15, p. 45755, 12 2025.

Fast Computation of Hot-Spot–Enhanced Hot-Carrier Generation in Plasmonic Nanoclusters

Pablo M. Uribe-Pizarro[1,*], Alan McGaughey[2], Francisco V. Ramirez-Cuevas[1]

[1]Science and Engineering Faculty, Adolfo Ibañez University, Chile
[2]School of Mechanical Engineering, Carnegie Mellon University, USA
*Corresponding author: pauribe@alumnos.uai.cl

***Abstract*—Plasmon-induced photochemistry exploits metallic nanostructures to concentrate light into localized electromagnetic energy, enabling otherwise inaccessible photochemical pathways. Hot-carrier generation is inherent to plasmonic nanoparticles and enhanced by morphology, composition, and interparticle coupling; this work targets the latter in nanoclusters via an efficient semi-analytical framework connecting plasmon modes to energy-resolved yields for photocatalytic design.**

***Keywords*— plasmonics, hot carriers, photocatalysis, hot spots.**

I. Introduction

Metallic nanostructures concentrate light below the diffraction limit through localized surface plasmon resonances (LSPR), whose spectral and spatial characteristics are governed by particle geometry and interparticle coupling [1], [2], [3], [4]. The non-radiative decay of these resonances produces non-equilibrium electron–hole pairs—so-called hot carriers—capable of driving photocatalytic reactions [5], [6], [7]. In nanoparticle clusters, plasmon hybridization gives rise to collective eigenmodes with modified field distributions and, consequently, altered carrier generation profiles [8], [9], [10]. As cluster complexity grows, efficient frameworks that link the electromagnetic response to energy-resolved hot-carrier production become essential [11], [12], [13].

II. Methods

We combine a semi-analytical treatment of cluster electrodynamics with Fermi's golden rule, linking plasmonic field enhancement directly to hot-carrier generation rates.

A. Boundary-Charge Method for Plasmon Hybridization

We obtain the plasmon-induced potential through the boundary-charge method (BCM). Given a cluster of N metallic spheres, the induced surface charge $\rho_i(\boldsymbol{r}_i)$ on each surface S_i that interact with every sphere j is determined by:

$$\frac{1}{2}\frac{\varepsilon_i+\varepsilon_h}{\varepsilon_i-\varepsilon_h}\rho_i(\boldsymbol{r}_i) - \sum_j^N \int_{S_j} \frac{\hat{\boldsymbol{n}}_i\cdot(\boldsymbol{r}_i-\boldsymbol{r}'_j)}{4\pi\|\boldsymbol{r}_i-\boldsymbol{r}'_j\|^3} \times \rho_j(\boldsymbol{r}'_j)\,dS'_j = \varepsilon_0\hat{\boldsymbol{n}}_i\cdot\hat{\boldsymbol{E}}_{\text{ext}}(\boldsymbol{r}_i). \quad (1)$$

Expanding ρ_i in spherical harmonics $Y_{\ell m}$ reduces this integral equation to a linear system, yielding semi-analytical expressions for the scalar potential $\phi(\boldsymbol{r},\omega)$ inside every particle for arbitrary cluster structures and illumination polarizations [14], [15], [16].

B. Hot-Carrier Generation via Fermi's Golden Rule

The resulting potential drives interband electronic transitions. The energy-resolved electron generation rate at final-state energy ε_f under monochromatic illumination at frequency ω reads:

$$\Gamma_e(\varepsilon_f,\omega) = \sum_i \mathcal{F}(\varepsilon_i)[1-\mathcal{F}(\varepsilon_f)]\frac{4}{\tau} \times\left[\frac{|M_{fi}(\omega)|^2}{(\hbar\omega-\varepsilon_f+\varepsilon_i)^2+\hbar^2/\tau^2} + \frac{|M_{if}(\omega)|^2}{(\hbar\omega-\varepsilon_i+\varepsilon_f)^2+\hbar^2/\tau^2}\right], \quad (2)$$

where $M_{fi} = \langle\psi_f|\phi|\psi_i\rangle$ are matrix elements of the BCM potential between electronic states, $\mathcal{F}$ is the Fermi–Dirac distribution, and τ is a phenomenological lifetime that broadens the energy-conserving delta functions [17], [6]. An analogous expression yields the hole generation spectrum. Together, these rates provide the energy-resolved hot-carrier distributions needed to evaluate photocatalytic figures of merit.

III. Results and Discussion

We illustrate the framework on a silver nanosphere heptamer illuminated at $\lambda = 374.5$ nm. This compact cluster supports a rich set of hybridized plasmon eigenmodes arising from the strong coupling between the central and peripheral spheres. Figures 1a and 1b show the external and internal normalized electric-field intensities obtained from the BCM expansion at the selected wavelength.

The external field (Fig. 1a) reveals pronounced hot spots in the six gaps between the central and peripheral particles as well as between adjacent satellites, with enhancements reaching $|E|^2/|E_0|^2 \approx 35$, characteristic of the bright dipolar mode of the heptamer. Inside the particles (Fig. 1b), the field is strongly redistributed toward the gap-facing hemispheres of the peripheral spheres, where enhancements exceed $|E_{\text{int}}|^2/|E_0|^2 \approx 60$. This asymmetric internal redistribution directly shapes the spatial profile of interband transitions and, consequently, the hot-carrier generation landscape.

Figure 2 presents the spectral hot-carrier generation rate Γ_e for a $D = 7$ nm silver nanoparticle, together with the

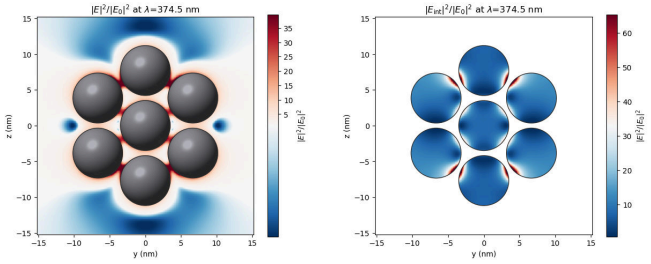

(a) (b)

Fig. 1: Normalized electric-field intensity at $\lambda = 376.9$ nm for a silver nanosphere dimer computed via the BCM. (a) External field $|E|^2/|E_0|^2$ showing hot spots at the gap and outer poles. (b) Internal field $|E_{\text{int}}|^2/|E_0|^2$ showing redistribution toward the gap-facing region.

absorption cross-section Q_{abs} and the thresholded rate for electrons above 1.2 eV. Two dominant resonances appear near 3.2 eV and 3.65 eV; the total generation rate closely tracks the absorption peaks, confirming that resonant modes govern carrier production. Importantly, only a fraction of the generated carriers exceed the energy threshold at each resonance, highlighting the need for mode-selective engineering to maximize useful hot-carrier yields.

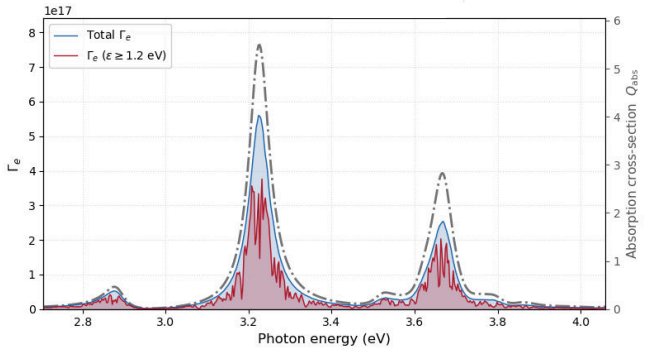

Fig. 2: Spectral hot-electron generation rate Γ_e (blue) and thresholded rate for $\varepsilon \geq 1.2$ eV (red) for a $D = 7$ nm silver nanoparticle with $\tau = 500$ fs. The absorption efficiency Q_{abs} (right axis) confirms that carrier generation peaks track plasmonic resonances.

These results demonstrate that the framework efficiently links near-field distributions to energy-resolved carrier metrics even for multi-particle clusters with dense mode spectra, providing a practical tool for scanning cluster geometries and identifying configurations that optimize photocatalytic performance.

IV. Conclusion

We have presented an efficient semi-analytical framework that connects plasmon hybridization in metallic nanoclusters to energy-resolved hot-carrier generation. By combining the boundary-charge method with Fermi's golden rule, the approach maps the plasmon-induced internal fields of arbitrary cluster geometries directly onto spectral carrier distributions. Applied to a silver nanosphere heptamer ($D = 7$ nm, gap ~ 0.5 nm), the framework captures the strongly enhanced internal fields arising from multi-particle hybridization and resolves two distinct plasmonic resonances that govern hot-carrier production. The computational efficiency of the method enables systematic scanning of cluster configurations, interparticle separations, and illumination conditions, providing a practical design tool for optimizing hot-carrier yields in photocatalytic and energy-harvesting applications.

Acknowledgments

The authors thank Professor Francisco V. Ramirez-Cuevas for valuable guidance and discussions throughout this work.

References

[1] M. L. Brongersma, N. J. Halas, and P. Nordlander, "Plasmon-induced hot carrier science and technology," *Nat. Nanotechnol.*, vol. 10, pp. 25–34, 2015.
[2] P. Nordlander, C. Oubre, E. Prodan, K. Li, and M. I. Stockman, "Plasmon hybridization in nanoparticle dimers," *Nano Lett.*, vol. 4, pp. 899–903, 2004.
[3] N. J. Halas, S. Lal, W.-S. Chang, S. Link, and P. Nordlander, "Plasmons in strongly coupled metallic nanostructures," *Chem. Rev.*, vol. 111, pp. 3913–3961, 2011.
[4] J. Khurgin, A. Yu. Bykov, and A. V. Zayats, "Hot-electron dynamics in plasmonic nanostructures: fundamentals, applications and overlooked aspects," *eLight*, vol. 4, p. 15, 2024.
[5] C. Clavero, "Plasmon-induced hot-electron generation at nanoparticle/metal-oxide interfaces for photovoltaic and photocatalytic devices," *Nat. Photonics*, vol. 8, pp. 95–103, 2014.
[6] A. Manjavacas, J. G. Liu, V. Kulkarni, and P. Nordlander, "Plasmon-induced hot carriers in metallic nanoparticles," *ACS Nano*, vol. 8, pp. 7630–7638, 2014.
[7] R. Verma, G. Sharma, and V. Polshettiwar, "The paradox of thermal vs. non-thermal effects in plasmonic photocatalysis," *Nat. Commun.*, vol. 15, p. 7816, 2024.
[8] L. V. Besteiro and A. O. Govorov, "Amplified generation of hot electrons and quantum surface effects in nanoparticle dimers with plasmonic hot spots," *J. Phys. Chem. C*, vol. 120, pp. 19329–19339, 2016.
[9] H. Harutyunyan *et al.*, "Anomalous ultrafast dynamics of hot plasmonic electrons in nanostructures with hot spots," *Nat. Nanotechnol.*, vol. 10, pp. 770–774, 2015.
[10] A. Muravitskaya *et al.*, "Hot electrons and electromagnetic effects in the broadband Au, Ag, and Ag–Au nanocrystals: the UV, visible, and NIR plasmons," *ACS Photonics*, vol. 11, pp. 68–84, 2024.
[11] L. V. Besteiro, X.-T. Kong, Z. Wang, G. Hartland, and A. O. Govorov, "Understanding hot-electron generation and plasmon relaxation in metal nanocrystals: quantum and classical mechanisms," *ACS Photonics*, vol. 4, pp. 2759–2781, 2017.
[12] E. Y. Santiago, L. V. Besteiro, X.-T. Kong, M. A. Correa-Duarte, Z. Wang, and A. O. Govorov, "Efficiency of hot-electron generation in plasmonic nanocrystals with complex shapes: surface-induced scattering, hot spots, and interband transitions," *ACS Photonics*, vol. 7, pp. 2807–2824, 2020.
[13] M. Vanzan and M. Marsili, "Theoretical approaches for the description of plasmon generated hot carriers phenomena," *npj Comput. Mater.*, vol. 10, p. 252, 2024.
[14] L. Novotny and B. Hecht, *Principles of Nano-Optics*, 2nd ed. Cambridge University Press, 2012.
[15] J. D. Jackson, *Classical Electrodynamics*, 3rd ed. Wiley, 1998.
[16] F. J. García de Abajo, "Optical excitations in electron microscopy," *Rev. Mod. Phys.*, vol. 82, pp. 209–275, 2010.
[17] A. O. Govorov, H. Zhang, and Y. K. Gun'ko, "Theory of photoinjection of hot plasmonic carriers from metal nanostructures into semiconductors and surface molecules," *J. Phys. Chem. C*, vol. 117, pp. 16616–16631, 2013.

Room-Temperature Lasing in quasi-2D Perovskite Coupled with High-Q Plasmonic Metasurfaces

Yen-Yu Wang[1,2,3], Xing-Hao Lee[1,2], Lin-Chyn Yuan[1,2], Chia-Yu Lai[4], Jia-Wern Chen[2], Chen-Yu Wang[1,2], Tzu-Yu Peng[1,2], Chu-Chen Chueh[3], Yu-Jung Lu[*1,2]

[1]*Department of Physics, National Taiwan University, Taipei, Taiwan.*
[2]*Research Center for Applied Sciences, Academia Sinica, Taipei, Taiwan.*
[3]*TIGP-Nano Programs, Academia Sinica, Taipei, Taiwan*
[4]*Department of Chemical Engineering, National Taiwan University, Taipei, Taiwan.*

*Email: D13222021@ntu.edu.tw

Abstract — We demonstrate room-temperature lasing in a quasi-2D perovskite integrated with a high-Q plasmonic metasurfaces supporting a Γ-point quasi-bound state in the continuum mode. To clarify the nature of the lasing mode, we analyze the emission characteristics using polarization-resolved k-space spectroscopy and compare them with the calculated photonic band structure.

***Keywords* — High-Q plasminic metasurfaces, quasi-2D perovskite, room-temperature lasing, plasmonic quasi-BIC**

I. Introduction

Plasmonic surface lattice resonances (SLRs), supported by periodic arrays of metallic nanoparticles, have emerged as a representative high-Q plasmonic metasurface platform, providing robust optical cavities that can sustain high-quality-factor resonances at room temperature[1]. It has been widely utilized in applications ranging from refractive index sensing[2] to strong light-matter coupling[3] and nanoscale lasing[4]. The hybridization between localized surface plasmons (LSPRs) and diffracted orders in these periodic structures yields complex photonic band structures[5], hosting rich physical phenomena such as Bose-Einstein condensation[6] and nontrivial topological characteristics[7]. However, inherent ohmic losses in metallic components remain a fundamental limitation. When the electromagnetic field is tightly confined to the metal surface, substantial energy is dissipated as heat. To mitigate this, dark modes within the SLR cavity—often associated with optical bound states in the continuum (BICs)—have attracted considerable attention[8,9]. While quasi-BIC (q-BIC) SLR lasing has been demonstrated across various lattice geometries, the majority of these implementations rely on liquid-phase dye solutions as the gain medium, which limits their integration into on-chip photonic devices.

Building upon our previous demonstration of room-temperature SLR lasing using a quasi-2D perovskite (PVSK) film [9], this work we further presents an engineered square lattice design where a symmetry-protected BIC is spectrally aligned with the gain profile of the quasi-2D PVSK. We experimentally realize solid-state q-BIC lasing with a threshold of 56 μJ/cm^2 and utilize momentum-resolved (k-space) spectroscopy to reveal the photonic band structure. Furthermore, by employing polarization-resolved k-space spectroscopy, we analyze the far-field polarization states to investigate the modal characteristics associated with the BIC point.

II. Methods

- Sample fabrication

The High Q plasmonic metasurfaces were fabricated using a standard electron-beam lithography (EBL) and lift-off process. The square lattice patterns were defined on a positive ZEP-520 resist using an EBL system (Elionix ELS-BODEN 100). Subsequently, an aluminum (Al) film was deposited *via* evaporation on quartz substrate, followed by a lift-off procedure to form the Al nanoparticle arrays (aka SLR cavity). The quasi-2D PVSK film was spin-coated onto the designed structure, and the entire process was carried out in a glove box.

III. Results and Discussion

The SLR laser consists of a 70-nm-thick Ruddlesden-Popper phase quasi-2D PVSK layer ($PEA_2Cs_{n-1}Pb_nBr_{3n+1}$, with n=5)[10], and aluminum nanoparticles (54 nm in diameter and 60 nm in height) arranged in a periodic array with a pitch of 330 nm as shown in the Fig. 1A. Fig. 1B shows the calculated photonic band structure obtained by FDTD simulations, with the incident angle varied from 0° to 20°, where the angle is defined with respect to the surface normal. The calculated transmission spectra at θ = 0° and 1° in Fig. 1C are extracted from the photonic band structure reveals the resonant modes. More importantly, we calculated the mode distribution and define the dipole mode (560 nm) and the quadrupole mode (526 nm), as shown in Fig. 1D. Fig. 1E shows the measured k-space spectrum of the fabricated sample under 405 nm continuous-wave (CW) laser excitation. Details of the fabrication process can be found in the Methods section. The photoluminescence from the quasi-2D perovskite couples into the SLR modes, and the angle-resolved photon emission reveals the photonic band

Proceedings of META 2026 · Dublin, Ireland · 14–17 July 2026 · ISSN 2429-1390 · pp. 1597–1599
1597

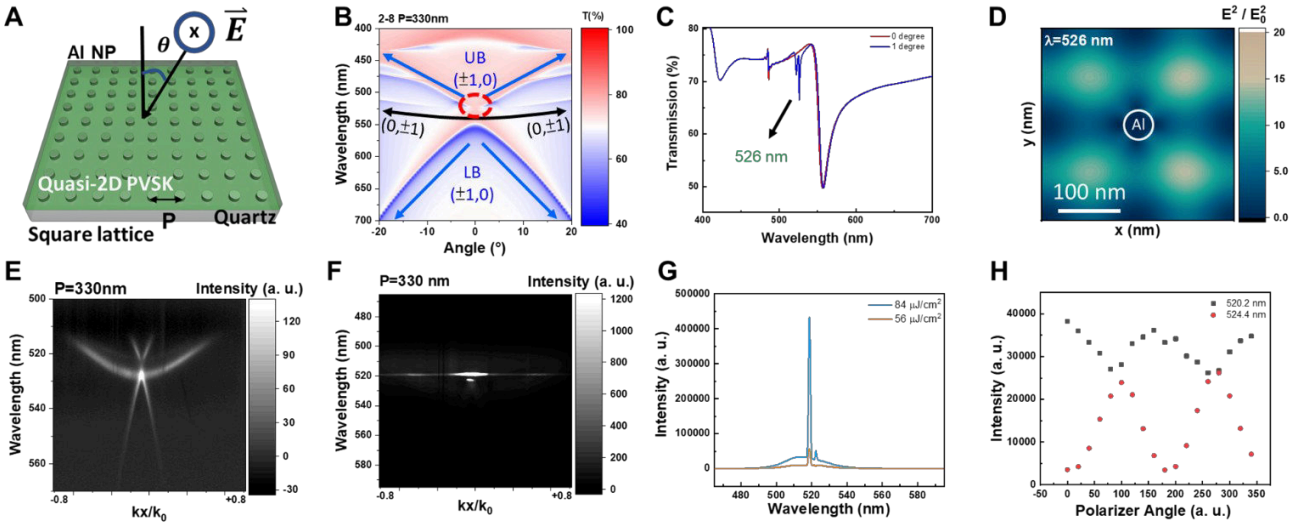

Fig. 1 Room-temperature lasing in quasi-2D PVSK coupled with high Q plasmonic metasurfaces. (A) Schematic of the designed SLR structure. A quasi-2D PVSK film (green layer) was spin-coated on top of the Al nanoparticle array fabricated on a quartz substrate. The angle θ in the inset indicates the electric field polarization used in the simulation. P stand for the period of the nanoparticle array. (B) FDTD-simulated angle-dependent transmission spectra of the designed device. The blue arrows and the black curves indicate the (±1, 0) and (0, ±1) modes of the SLR cavity, respectively. A Γ-point BIC can be observed inside the red dashed circle. **(C)** Simulated transmission spectra extracted from (A) at incident angles of 0° and 1°. **(D)** Calculated electric field distribution of the q-BIC at 526 nm (quadrupole mode). **(E)** Measured k-space spectrum under 405 nm continuous-wave (CW) laser excitation. **(F)** Measured k-space spectrum under lasing conditions with pulsed laser excitation. **(G)** Lasing signals of the q-BIC and dipole modes at an excitation fluence of 56 and 84 μJ/cm² respectively. **(H)**

structure of the fabricated device. The experimental data align perfectly with the simulation results (Fig. 1B). Not only the bandgap separating the upper branch (UB) and lower branch (LB) evident is in both the experiment and simulation, but the BIC at the Γ point of the UB is also clearly observed. To summarize, the fundamental difference between the UB and LB lies in their electric field distributions. The UB operates as a quadrupolar dark mode, whereas the LB acts as a dipolar bright mode.

When the sample is excited by a 400 nm ultrafast pulsed laser (1 kHz, 100 fs), a sharp q-BIC SLR lasing peak emerges at 520.4 nm with a full-width at half-maximum (FWHM) of ~1 nm under an excitation power of 56 μJ/cm², as shown in Fig. 1F and 1G. Additionally, a second sharp peak is observed at 524.4 nm, also exhibiting an FWHM of ~1 nm. The shorter-wavelength peak appears at the Γ point of the upper branch (UB), but its emission is not fully concentrated at 0° in the k-space spectrum. This offset is a characteristic trait of q-BIC lasing, as the mode cannot radiate exactly at normal incidence.

Due to the high quality factor of the q-BIC mode, the lasing threshold for the 520.2 nm peak is lower than that of the 524.4 nm peak (~84 μJ/cm²), which corresponds to classical SLR bright-mode lasing. Finally, in the light-in-light-out (L-L) curve from the power-dependent photoluminescence (PL) experiment, a superlinear transition in PL intensity, accompanied by linewidth narrowing, occurs at a pump fluence of 56 μJ/cm². These characteristics confirm that the sharp peak originating from the upper branch is indeed a q-BIC lasing signal.

Furthermore, we measured the polarization-dependent k-space spectra of these two lasing peaks, as shown in Fig. 1H. While the 520.2 nm peak exhibited a minimum intensity at a polarizer angle of approximately 90°, the 524.4 nm peak showed a maximum intensity. The polarization ratio defined by the eq. (1) are 76% and 17 % respectively. These polarization results indicate that the origins of these peaks are distinct, as their lasing polarizations are mutually orthogonal. Ultimately, these lasing characteristics reflect the difference in the electric field distributions between the quadrupole (dark) mode and the dipole (bright) mode.

$$P = \frac{(I_{max} - I_{min})}{(I_{max} + I_{min})} \quad (1)$$

IV. Conclusion

In summary, we successfully demonstrated plasmonic q-BIC lasing by integrating an aluminum SLR cavity with a novel quasi-2D PVSK. Our investigation demonstrates that the q-BIC originates from a quadrupolar dark mode at normal incidence, which transforms into a radiating bright state through in-plane symmetry breaking. The measured k-space spectra and the extracted photonic band structure exhibit excellent agreement with our FDTD simulation predictions. Under pulsed laser excitation, lasing action with difference polarization was definitively confirmed by a superlinear transition in the light-in-light-out (L-L) curve, accompanied by distinct linewidth narrowing. Furthermore, the lasing threshold for the 520.2 nm q-BIC mode was determined to be approximately 56 μJ/cm².

Benefiting from the high Q factor of the q-BIC, this threshold is lower than that of the classical dipolar SLR bright mode lasing at 524.4 nm (~84 μJ/cm²). Moreover, polarization-dependent measurements confirmed that these two lasing modes possess mutually orthogonal polarizations. This directly verifies their distinct physical origins, reflecting the fundamental difference in the electric field distributions between the quadrupolar and dipolar modes. These findings provide a concrete experimental and theoretical framework for manipulating bound states in the continuum within plasmonic architectures, offering a reliable platform for studying light-matter interactions.

V. Acknowledgments

The authors acknowledge financial support from the National Science and Technology Council, Taiwan (Grant No. NSTC-114-2112-M-001-005, NSTC-114-2124-M-001-011), and Academia Sinica of Taiwan (AS-TP-113-M02, AS-GCS-114-M06, and AS-NTU-114-05).

References

1 Kravets, V. G., Kabashin, A. V., Barnes, W. L. & Grigorenko, A. N. Plasmonic Surface Lattice Resonances: A Review of Properties and Applications. *Chemical Reviews* **118**, 5912–5951 (2018). https://doi.org/10.1021/acs.chemrev.8b00243

2 Yang, A. *et al.* Real-time tunable lasing from plasmonic nanocavity arrays. *Nature Communications* **6**, 6939 (2015). https://doi.org/10.1038/ncomms7939

3 Hong, C., Zheng, Z., Patel, S. K. & Odom, T. W. High-Chirality Polariton Lasing from Symmetry-Broken Plasmonic Lattices. *ACS Nano* **19**, 18824–18832 (2025). https://doi.org/10.1021/acsnano.5c04290

4 Wang, Y.-Y. *et al.* Plasmon-enhanced exciton relocalization in quasi-2D perovskites for low-threshold room-temperature plasmonic lasing. *Science Advances* **11**, eadu6824 https://doi.org/10.1126/sciadv.adu6824

5 Weick, G., Woollacott, C., Barnes, W. L., Hess, O. & Mariani, E. Dirac-like Plasmons in Honeycomb Lattices of Metallic Nanoparticles. *Phys. Rev. Lett.* **110**, 106801 (2013).

6 Hakala, T. K. *et al.* Bose–Einstein condensation in a plasmonic lattice. *Nature Physics* **14**, 739–744 (2018). https://doi.org/10.1038/s41567-018-0109-9

7 Arjas, K., Salerno, G. & Törmä, P. Topological invariants and topological charges in photonic systems. *Physical Review B* **112**, 235428 (2025). https://doi.org/10.1103/kr1j-fx1p

8 de Gaay Fortman, N. *et al.* Spontaneous symmetry breaking in plasmon lattice lasers. *Science Advances* **10**, eadn2723 https://doi.org/10.1126/sciadv.adn2723

9 Hakala, T. K. *et al.* Lasing in dark and bright modes of a finite-sized plasmonic lattice. *Nature Communications* **8**, 13687 (2017). https://doi.org/10.1038/ncomms13687

10 Lin, Y.-K. *et al.* Realizing High Brightness Quasi-2D Perovskite Light-Emitting Diodes with Reduced Efficiency Roll-Off via Multifunctional Interface Engineering. *Advanced Science* **10**, 2302232 (2023). https://doi.org/https://doi.org/10.1002/advs.202302232

Tip-Enhanced High-Harmonic Generation in an STM Nanojunction Driven by Mid-Infrared Pulses

Atsunori Sakurai[1,2*], Shota Takahashi[1], Tatsuto Mochizuki[1,2], Tsuneto Kanai[1], and Toshiki Sugimoto[1,2]

[1]Institute for Molecular Science, Japan
[2]Graduate Institute for Advanced Science, SOKENDAI, Japan
*Corresponding author: asakurai@ims.ac.jp

***Abstract*—The fourth- and fifth-harmonic generation of mid-infrared pulses (3500 nm), accompanied by a broad luminescence from the gap-mode plasmon excitation in an STM nanojunction, was observed through the tip-enhanced process. This demonstrates that mid-IR field enhancement and visible plasmon resonance work together efficiently in tip-enhanced high-harmonic generation at the nanoscale.**

***Keywords*—tip-enhanced spectroscopy, high harmonic generation, plasmonic nanogap, strong-field phenomena.**

I. Introduction

Electric-field enhancement in plasmonic nanostructures has proven effective for amplifying nonlinear optical phenomena and inducing strong-field effects [1]. In particular, high-harmonic generation (HHG) has been demonstrated in periodic metallic nanostructures [2, 3]. However, such periodic structures inevitably lead to signal averaging over the focal spot on a micrometer scale. In contrast, plasmonic nanogaps formed between a metallic tip and a substrate confine optical fields to a single nanoscale hot spot beyond the diffraction limit, thereby enabling nanoscale chemical analysis, as exemplified by tip-enhanced Raman spectroscopy [4].

Although most tip-enhanced spectroscopy (TES) studies employ continuous-wave lasers, we have combined TES with ultrashort pulsed lasers and demonstrated tip-enhanced second-harmonic generation (TE-SHG) with near-infrared (IR) pulses [5, 9] and tip-enhanced sum-frequency generation (TE-SFG) [6–9] with both near-IR and mid-IR pulses. Through these studies, we have elucidated two enhancement mechanisms underlying TES: (i) incident field enhancement as the incident field is collected by the tapered shaft of the tip and guided to the apex (antenna effect); (ii) radiation efficiency enhancement arising from the gap-mode plasmon within the nanogap (plasmon resonance). Numerical simulations have revealed that the antenna effect becomes more pronounced at longer wavelengths, indicating that the mid-IR region provides significant enhancement of the incident field, whereas plasmon resonance enhances the radiation efficiency in the visible region [5, 6] (Fig. 1). This result suggests that tip-enhanced HHG (TE-HHG), driven by a mid-IR pulsed laser and generated in the visible region, provides a promising platform for probing strong-field phenomena at the nanoscale.

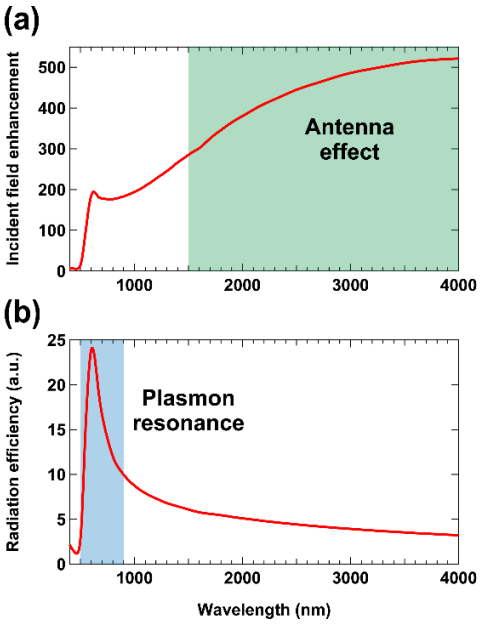

Fig. 1 (a) Enhancement of the incident field at the nanogap between a gold tip and a gold substrate, calculated using electromagnetic field simulations. (b) Radiation efficiency from the dipole in the nanogap, monitored at a position corresponding to the far-field. Details are described in Refs. [5, 6].

II. Methods

The experimental setup of the TE-HHG system is schematically illustrated in Fig. 2. In this system, the output from a mode-locked Yb:KGW laser (1029 nm, 108 fs, 140 nJ, 50 MHz) was used to pump an optical parametric oscillator (OPO), which generated two output beams: a signal (1.3–2 μm) and an idler (2.1–5 μm). The idler beam passed through a telescope to expand the beam diameter and compensate for its divergence, and subsequently through a pair of polarizers to adjust the beam intensity. The idler pulses (3500 nm, 0.8 nJ, 50 MHz) were then focused onto the nanojunction between a gold

tip and a gold substrate in a scanning tunneling microscope (STM) system at an incident angle of 55°. The beam was linearly polarized along the tip axis (*p*-polarization) to effectively excite the gap-mode plasmon. Two identical CaF_2 aspherical lenses were employed to focus the incident beam and collect the emitted signals. A dichroic mirror (reflective over 730–920 nm and transmissive over 2.5–8 μm) was placed in the incident beam path to collect the backward-scattered signal. Both the forward- and backward-scattered signals were focused by an achromatic doublet, passed through a short-pass filter (transmissive over the 500–900 nm range), and coupled into separate branches of a bifurcated optical fiber bundle, thereby enabling their simultaneous detection. The fiber-coupled signals were spectrally dispersed by a spectrometer and detected using an electronically cooled CCD camera.

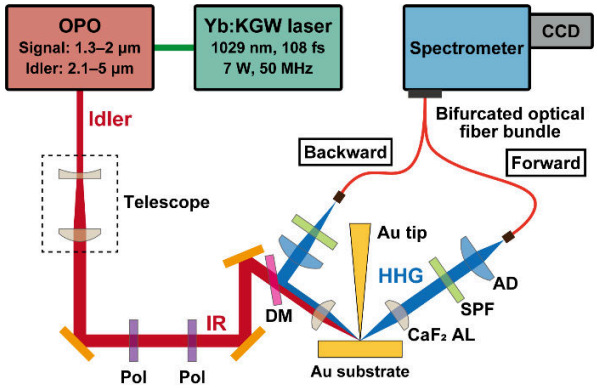

Fig. 2 Experimental setup of the TE-HHG system. Pol: polarizer, CaF_2 AL: CaF_2 aspherical lens, SPF: short-pass filter, AD: achromatic doublet. A dichroic mirror (DM) and a bifurcated optical fiber bundle were employed to simultaneously collect both forward- and backward-scattered signals.

III. Results and Discussion

The spectra of the (a) forward- and (b) backward-scattered signals are shown in Fig. 3. The black curves correspond to spectra obtained with the Au substrate retracted by 50 nm from the Au tip, which show almost no signal or spectral features. In contrast, the red curves correspond to spectra obtained with the Au substrate positioned within ~1 nm of the Au tip, which show two distinct peaks superimposed on a broadband luminescence. These two peaks correspond to the fourth- and fifth-harmonic generation (4HG/5HG) of the incident mid-IR pulses (3500 nm). The broadband luminescence is attributed to gap-mode plasmon excitation in the STM nanojunction. The luminescence induced by tunneling electrons in STM nanojunctions is known as STM luminescence, whereas in the present case, the luminescence is induced by irradiation with mid-IR pulses. A similar phenomenon has been reported under THz irradiation in the form of THz-field-driven STM luminescence [10]. The backward-scattering signal was approximately three times stronger than the forward-scattering signal; however, the intensity distribution varied significantly depending on the specific tips used. This variation originates from the nanoscale morphology of the tip apex, which critically influences near-field generation in the nanogap and thereby affects both the signal radiation efficiency and the emission direction, as previously reported for STM luminescence [11]. The simultaneous observation of 4HG/5HG and broadband luminescence, together with the different intensity distributions between the forward- and backward-scattered signals, suggests an enhancement of the radiation efficiency of HHG signals due to the plasmon resonance. This result demonstrates that the hybrid enhancement mechanism (i.e., the incident mid-IR field enhancement by the antenna effect and the radiation efficiency enhancement by the plasmon resonance) operates efficiently in the TE-HHG process.

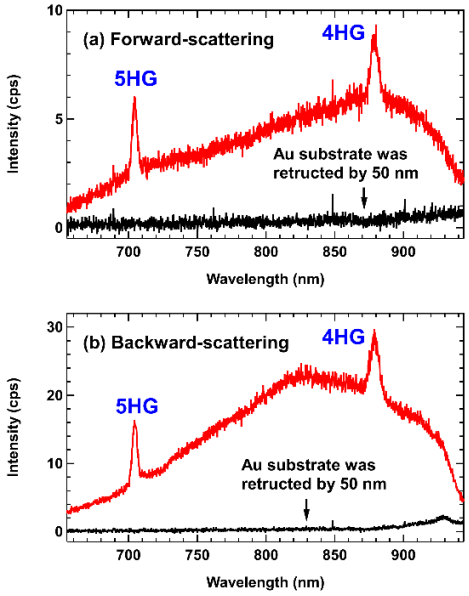

Fig. 3 Spectra of the (a) forward- and (b) backward-scattered signals. The black curves correspond to spectra obtained with the Au substrate retracted by 50 nm from the Au tip, whereas the red curves correspond to spectra obtained with the Au substrate positioned within ~1 nm of the Au tip, which show two distinct peaks corresponding to the 4HG and 5HG of the incident mid-IR pulses (3500 nm), superimposed on a broadband luminescence attributed to gap-mode plasmon excitation in the STM nanojunction. Intensities are normalized to counts per second (cps).

IV. Conclusion

We have demonstrated TE-HHG in an STM nanojunction between a Au tip and a Au substrate. Two distinct peaks were observed at the 4th and 5th harmonics of the incident mid-IR pulses, accompanied by a broad luminescence arising from gap-mode plasmon excitation in the STM nanojunction. This result indicates that the hybrid enhancement mechanism (the incident mid-IR field enhancement by the antenna effect and the radiation efficiency enhancement by the plasmon resonance) operates efficiently in the TE-HHG process at the nanoscale.

Acknowledgments

This work was supported by JST (PRESTO: JPMJPR1907; CREST: JPMJCR22L2), JSPS KAKENHI (Scientific Research

(A):19H00865 and 22H00296; Transformative Research (A): 24H02205; Scientific Research (B): 23K26548 and 23K26570; Challenging Research (Exploratory): 24K21759; JSPS Fellows: 22KJ309), the Matsuo Foundation for Science Promotion, the Amada Foundation (General Research and Development Grant: AF-2022234-B3), and the International Research Exchange Support Program of the National Institutes of Natural Sciences (314150403).

REFERENCES

[1] P. Dombi, Z. Pápa, J. Vogelsang, S. V. Yalunin, M. Sivis, G. Herink, S. Schäfer, P. Groß, C. Ropers, and C. Lienau, "Strong-field nano-optics," *Review of Modern Physics*, vol. 92, pp. 025003 [66 pages], 2020.

[2] M. Sivis, M. Duwe, and C. Ropers, "Extreme-ultraviolet light generation in plasmonic nanostructures," Nature Physics, X. F. Smith and Y. T. Lee, "Terahertz metamaterials: design and applications," Fictional Photonics Letters, vol. 9, pp. 304–309, 2013.

[3] G. Vampa, B. G. Ghamsari, S. S. Mousavi, T. H. Hammond, A. Olivieri, E. Lisicka-Skrek, A. Y. Naumov, D. M. Villeneuve, A. Staudte, P. Berini, and P. B. Corkum, "Plasmon-enhanced high-harmonic generation from silicon," *Nature Physics*, vol. 13, pp.659–662, 2017.

[4] J. Lee, K. T. Crampton, N. Tallarida, and V. A. Apkarian, "Visualizing vibrational normal modes of a single molecule with atomically confined light," *Nature*, vol. 568, pp. 78–82, 2019.

[5] S. Takahashi, A. Sakurai, T. Mochizuki, and T. Sugimoto, "Broadband Tip-Enhanced Nonlinear Optical Response in a Plasmonic Nanocavity," *The Journal of Physical Chemistry Letters*, vol. 14, pp. 6919–6926, 2023.

[6] A. Sakurai, S. Takahashi, T. Mochizuki, and T. Sugimoto, "Tip-Enhanced Sum Frequency Generation for Molecular Vibrational Nanospectroscopy," *Nano Letters*, vol. 14, pp. 6390–6398, 2025.

[7] S. Takahashi, K. Kumagai, A. Sakurai, T. Mochizuki, T. Hirano, A. Morita, and T. Sugimoto, "Tip-Enhanced Sum-Frequency Vibrational Nanoscopy beyond the Diffraction Limit," *The Journal of Physical Chemical C*, vol. 130, pp. 373–385, 2026.

[8] A. Sakurai, S. Takahashi, T. Mochizuki, T. Hirano, A. Morita, and T. Sugimoto, "Tip-Enhanced sum frequency generation spectroscopy using temporally asymmetric pulse for detecting weak vibrational signals," *The Journal of Chemical Physics*, vol. 164, pp. 074202 [12 pages], 2026.

[9] S. Takahashi, A. Sakurai, T. Mochizuki, and T. Sugimoto, "Giant near-field nonlinear electrophotonic effects in an angstrom-scale plasmonic junction," *Nature Communications*, vol. 17, pp. 2012 [10 pages], 2026.

[10] K. Kimura, Y. Morinaga, H. Imada, I. Katayama, K. Asakawa, K. Yoshioka, Y. Kim, and J. Takeda, "Terahertz-Field-Driven Scanning Tunneling Luminescence Spectroscopy," *ACS Photonics*, vol. 8, pp. 982–987, 2021.

[11] S. Cui, T.-H. Kim, and U. Ham," Influence of the Tip Shape on Scanning Tunneling Luminescence Spectra: Implications for Nanomaterial Characterization," *ACS Applied Nano Materials*, vol. 4, pp. 29–32, 2020.

Enhanced Raman scattering on tip-on-mirror platforms

V. Camús[1,*], D. Arenas-Ortega[2], A. Martínez[2], E. Pinilla-Cienfuegos[2], A. Cros[1], N. Garro[1]

[1]Institut de Ciència dels Materials (ICMUV), Universitat de València, Paterna, 46980, València, Spain

[2]Nanophotonics Technology Center, Universitat Politècnica de València, València, 46022, Spain.

*Corresponding author: victor.camus@uv.es

***Abstract*— Comparative studies of nanoplasmonic cavities formed in the interspace between gold microdisks and either a gold-coated AFM tip or a gold nanoparticle are presented based on enhanced Raman scattering of molecular self-assembled monolayers. These measurements deepen our understanding of plasmonic interactions and contribute to new sensing and photonic devices.**

***Keywords*— TERS, SERS, Raman spectroscopy, plasmonics, NPoM.**

I. Introduction

Nanoparticle-on-mirror (NPoM) platforms are stable, robust, and reproducible systems where light is squeezed into sub-nanometer volumes. They are made up of a metal nanoparticle (NP) over a metallic substrate. This system forms a plasmonic cavity, where the interaction between the localized surface plasmons of the NPs and the underlying substrate creates a highly confined electromagnetic field. The field not only enhances significantly the Raman signal from the molecules underneath, enabling detailed spectroscopic analysis at the nanoscale, but can also trigger photocatalytic reactions acting as nanoreactors. Despite the increasing amounts of promising applications [1,2], active surface sites of NPoMs remain hard to control, adding imprecision to these nanostructures.

Here we propose an alternative architecture where the metal NP is substituted by a metalized atomic force microscopy (AFM) tip. Such tip-on-mirror (ToM) cavities can be spatially scanned and combines the spatial resolution of AFM with the chemical specificity of tip-enhanced Raman spectroscopy (TERS). We have used a ToM to scan a NPoM platform and in this way compare the performance of both systems regarding their enhancement factors, spectral features, and stabilities.

II. Methods

Raman spectroscopy maps of a NPoM sample were measured using a ToM set-up to obtain both TERS and surface-enhanced Raman scattering (SERS) spectra. The sample consisted of a 24×24 array of gold disks, each with a height of 120 nm and a diameter of 12 µm. The surface of these disks was functionalized with a self-assembled monolayer (SAM) of biphenyl-4-thiol (BPT). A single 150 nm gold NP was placed on the surface of each disk following a procedure reported by Redolat *et al.* [1].

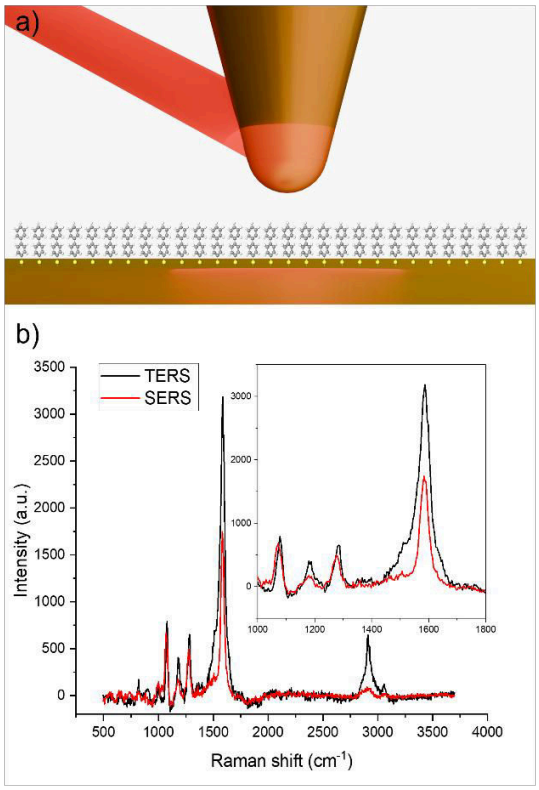

Fig. 1 a) Diagram showing the AFM tip over the BPT SAM. The laser is focused on the tip apex, and it excites the plasmon of the tip-surface system. The confined light, in turn, excites the vibrational modes of the molecules before being scattered. b) Comparison between TERS and SERS spectra. TERS measurements were taken at 200 µW laser power, and SERS at 500 µW.

TERS is a spectroscopic technique that integrates scanning

probe microscopy (SPM) with Raman spectroscopy to achieve nanoscale spatial resolution, surpassing the limitations imposed by the optical diffraction limit. This enhancement is accomplished by focusing a laser onto the apex of a metallic-coated scanning probe tip, exciting localized surface plasmons that generate a highly confined electromagnetic field. This field, in turn, amplifies the vibrational modes of molecules located beneath the tip, enabling precise molecular characterization at the nanoscale. This configuration is represented in the diagram in Fig. 1a.

SERS is another spectroscopic technique that makes use of the same underlying mechanism to enhance the measured signal. In this case, light is focused on a golden NP, exciting its surfaced plasmon and confining it in the nanocavity formed in the tight gap between the NP and the substrate. It does not improve the spatial resolution of regular Raman spectroscopy, but it can be done using the same microscope setup.

III. Results and Discussion

Experimental results show that the intensity enhancement in both SERS and TERS (Fig. 1b) are comparable, although TERS' enhancement factor is about 2 to 5 times higher than in SERS. We have also observed that TERS peaks are narrower than SERS peaks and appear shifted towards higher frequencies (Table 1).

BPT Mode	Mag (cm^{-1})	TERS	SERS
1080 cm^{-1}	Center	1078 ± 1	1071 ± 2
	FWHM	10 ± 2	20 ± 3
1280 cm^{-1}	Center	1282 ± 1	1276 ± 4
	FWHM	13 ± 3	28 ± 4
1580 cm^{-1}	Center	1588 ± 1	1583 ± 4
	FWHM	26 ± 3	33 ± 4

Table 1 Average magnitudes derived from the statistical analysis of the TERS and SERS maps' fitted peaks. The TERS data has been measured on zones of the golden disk with no NPs. TERS peaks appear narrower than SERS peaks. They are also slightly shifted towards higher frequencies.

TERS and SERS spectra are different due to their different plasmonic nanocavity geometries. The laser incidence direction and its polarization are different, and so are the shape of the excited plasmons. This changes the Raman selection rules and influences the measured spectra. TERS measurements have about 50 times better spatial resolution and can be done anywhere on the golden microdisks, while SERS measurements are confined to the area around the NPs.

TERS spectra around the NPs are significantly changed (Fig. 2). They are also affected by a change in the cavity geometry, as there are three bodies in this system: the tip, the substrate and the golden NP; and the interaction between their plasmons makes an effect on the dispersed light. It has also been reported that the citrate capping agent used to stop the growth of the NPs can degrade into graphitic or amorphous carbon after being heated up by the intense EM fields SERS measurements produce in a NPoM platform [3].

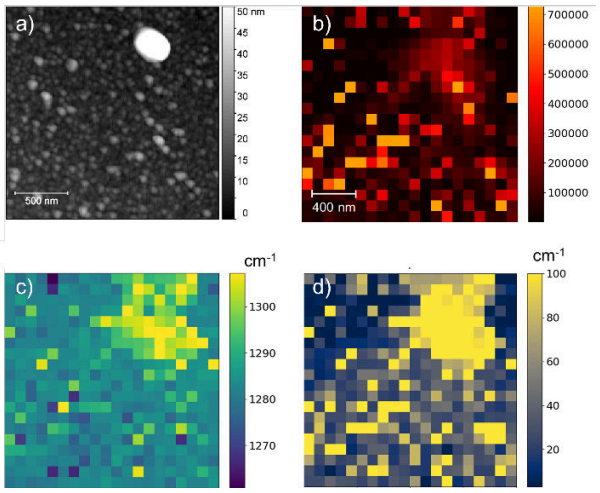

Fig. 2 TERS mapping over a gold NP. a) AFM topography image. b) TERS total spectral intensity. c) 1280 cm^{-1} mode peak center map. d) 1280 cm^{-1} mode peak FWHM map. The peak is broader and shifts towards higher frequencies around the NP.

IV. Conclusion

ToM platforms can be used to study and compare NPoM systems. We have been able to measure the Raman spectra of a BPT SAM using both TERS and SERS. TERS has shown better spatial resolution and enhancement factor, and a slight change in the spectra that can be explained by the different geometry of the plasmonic nanocavities. The change in spectra around the NPs hints toward the catalysis of chemical reactions in the NPoM system induced by the strong EM fields involved. These results open the door to the precise and detailed characterization of advanced sensing devices and deepen our understanding of the physical and chemical processes underlying the manipulation of light at the nanoscale, paving the way for the design and implementation of advanced sensing devices and photonic integrated circuits.

Acknowledgments

This work was supported by grant PID2024-161277OB-I00 financed by MICIU/AEI/10.13039/501100011033/ERDF, EU. Víctor Camús acknowledges the funding from the 'Atracció de Talent' program of the Universitat de València.

References

[1] J. Redolat, M. Camarena-Pérez, A. Griol, M. Kovylina, A. Xomalis, J. J. Baumberg, A. Martínez, and E. Pinilla-Cienfuegos, "Accurate Transfer of Individual Nanoparticles onto Single Photonic Nanostructures," ACS Applied Materials & Interfaces, vol. 15 (2), pp. 3558-3565, 2023.

[2] G. Kang, S. Hu, C. Guo, R. Arul, S. M. Sibug-Torres and J. J. Baumberg, "Design rules for catalysis in single-particle plasmonic nanogap reactors with precisely aligned molecular monolayers," Nature Communications, vol. 15, 9220, 2024

[3] D. Oliveira de Souza, J.-S. Girardon, D. J. Hoffmann and E. Berrier, "Dynamics of Citrate Coordination on Gold Nanoparticles Under Low Specific Power Laser-Induced Heating," ChemPhysChem, vol. 24, e202200744, 2023.

Ultranarrow Linewidth Surface Lattice Resonances in Aluminum Bowtie Metasurfaces

Bhera Ram Tak*, Robert O'Meara, Nebras Alattar, Hodjat Hajian, Richard G. Hobbs

School of Chemistry, Trinity College Dublin, Ireland, D02W085

Advanced Microscopy Laboratory, Centre for Research on Adaptive Nanostructures and Nanodevices, Trinity College Dublin, Ireland, D02W9K7

*Corresponding author: takb@tcd.ie

***Abstract*— We report surface lattice resonances in the 460 to 580 nm range in aluminum bowtie nanoantennas fabricated by electron beam lithography. Without post-annealing or symmetric refractive index material coating, fabricated arrays exhibit ultra-narrow 3.4 nm linewidth. These metasurfaces can support strong coupling for photocatalysis and quantum emitters.**

***Keywords*— metasurface, bowtie, surface lattice resonance, plasmonic gap.**

I. Introduction

Plasmonic nanoparticles can locally amplify optical fields within nanoscale volumes, making them functional for enhancing light-matter interactions in fields of photocatalysis, sensing and nanoscale light sources.[1,2,3] However, localized surface plasmon resonances (LSPRs) in metal nanoparticles typically exhibit low quality factor resonances arising from optical losses and plasmon damping.[4] Surface lattice resonances (SLRs) can be generated by arranging plasmonic nanoparticles in periodic arrays and can support higher quality factor resonances than LSPRs by suppressing radiative damping. The narrow linewidths, and consequently the higher quality factors of the SLRs, make them practical for surface-enhanced Raman spectroscopy, lasing, and strong coupling to molecular resonances and quantum emitters.[5] In particular, SLRs in arrays of aluminum (Al) nanoparticles are of interest, because they provide a route to access resonances in the blue and UV regions of the spectrum, which may not be achievable using typical lithography techniques on plasmonic metasurfaces based on noble metals.. Furthermore, the coupling of LSPRs and SLRs with guided mode resonances (GMRs), supported by a high-index buffer layer between the Al metasurface and the substrate, can generate hybrid modes with narrow linewidth features in the optical extinction spectra, which can be effectively utilized in the applications listed above.[6] Previously, surface plasmon resonances have been reported in the blue region of the spectrum using silver nanostructures, however, the plasmonic properties deteriorated with time due to oxidation and sulfidation of silver in air.[7,8] Here, we have experimentally demonstrated and numerically verified that periodic arrays of Al bowtie nanoantennas can support narrow-linewidth (FWHM 3.4-5 nm) SLRs in the green and blue regions of the spectrum.

II. Methods

The Al metasurface consists of bowtie nanoantennas made of equilateral triangles with side lengths of 85 nm, a bowtie gap of 15 nm, a thickness of 20 nm, and varying pitches ranging from 280 to 380 nm. The structures were simulated by finite element method using COMSOL Multiphysics. These bowtie nanoantennas were fabricated over 50 µm × 50 µm areas with high placement accuracy of a nanometer using electron beam lithography. The entire Al metasurface is fabricated on a 100-nm-thick ITO film on an SiO_2 substrate. The Al metal deposition was performed at low base vacuum of 5×10^{-8} Torr to reduce oxidation. A 0.07 N.A. lens was used for normal incidence excitation. All the absorption spectra were recorded in high resolution mode of Andor spectrometer (Kymera 328i) with 10 µm slit width and 500 l/mm grating that is blazed at 600 nm.

III. Results and Discussion

The high-index ITO film acts as a slab waveguide, supporting hybrid plasmonic-GMR resonances. A red shift in the SLR peak was observed from 460 to 580 nm with increasing bowtie period (figure 1a). SLR peak positions also found to match close to the simulated results which validates the high quality of fabricated structures. A quality factor of about 117 was measured for the SLR peak at 542 nm with a narrow spectral width of 4.6 nm. The linewidth of SLRs also depends on the bowtie counts and further reduced to 3.4 nm (for 461 nm SLR peak) with increasing counts as shown in figure 1b which is the among the best reported for Al nanoantenna arrays in this spectral region.[9] In addition to the observed narrow linewidth SLRs, we have also observed strong coupling between the LSPR of the bowtie nanoantennas and guided modes in the ITO film. The coupling of the LSPRs and guided modes in the ITO film result in hybrid modes separated by an energy equivalent

to a Rabi splitting of 259 meV, indicating a robust coupling regime.

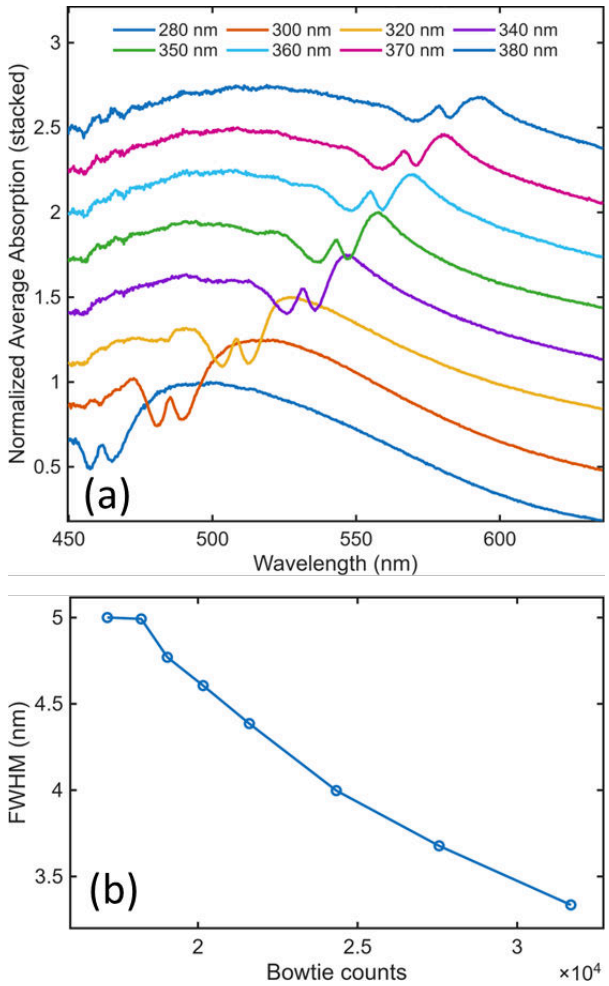

Figure 1 (a) Experimentally measured extinction spectra for arrays of Al nanoantennas with different pitches (b) the surface lattice resonance linewidth as a function of bowtie counts. The SLR peak at 461 nm has an observed FWHM of 3.4 nm.

IV. Conclusion

Overall, this report provides a route to obtain geometrically tunable SLRs in the blue/green region of the spectrum with narrow SLR modes within the broad LSPR modes. We believe that our findings in this study can contribute to the development of the field of strong light-matter interaction, particularly when photocatalysis or quantum emitters are strongly coupled to the Al metasurface.

Acknowledgments

RGH acknowledges the support of Science Foundation Ireland (SFI) through The Advanced Materials and Bioengineering Research Centre (AMBER, grant 12/RC/2278_2) and the Royal Society-Science Foundation Ireland University Research Fellowship (15/RS-URF/3306).

References

[1] Siwei Li, Peng Miao, Yuanyuan Zhang, Jie Wu, Bin Zhang, Yunchen Du, Xijiang Han, Jianmin Sun, and Ping Xu, 33 (6), 2000086 (2021).
[2] Na Liu, Martin Mesch, Thomas Weiss, Mario Hentschel, and Harald Giessen, Nano Letters 10 (7), 2342 (2010).
[3] Jae Yong Suh, Chul Hoon Kim, Wei Zhou, Mark D. Huntington, Dick T. Co, Michael R. Wasielewski, and Teri W. Odom, Nano Letters 12 (11), 5769 (2012).
[4] Baoqing Wang, Peng Yu, Wenhao Wang, Xutao Zhang, Hao-Chung Kuo, Hongxing Xu, and Zhiming M. Wang, Adv Opt Mat 9 (7), 2001520 (2021).
[5] V. G. Kravets, A. V. Kabashin, W. L. Barnes, and A. N. Grigorenko, Chemical Reviews 118 (12), 5912 (2018).
[6] S. Linden, J. Kuhl, and H. Giessen, Phys Rev Lett 86 (20), 4688 (2001).
[7] Q. Le-Van, E. Zoethout, E. J. Geluk, M. Ramezani, M. Berghuis, and J. G. Rivas, Adv Opt Mater 7 (6) (2019).
[8] M. Rycenga, C. M. Cobley, J. Zeng, W. Y. Li, C. H. Moran, Q. Zhang, D. Qin, and Y. N. Xia, Chem Rev 111 (6), 3669 (2011).
[9] A. Yang, A. J. Hryn, M. R. Bourgeois, W.-K. Lee, J. Hu, G. C. Schatz, T. W. Odom, Proc. Natl. Acad. Sci. USA, 113, 14201 (2016).

Plasmonic Response in Mg-Al Bimetallic Nanoparticles

Marwan Alam[1], Katarzyna Kluczyk-Korch[1], Tomasz J. Antosiewicz[1,*]

[1]Faculty of Physics, University of Warsaw, Poland

*Corresponding author: tomasz.antosiewicz@fuw.edu.pl

***Abstract*—First-principles study of Mg-Al icosahedral clusters (0-100% Al) reveals starkly different photoabsorption spectra for clustered vs. random atomic arrangements. Random alloys exhibit a single, progressively broadening peak that evolves continuously from Mg to Al character. However, clustered configurations display multiple distinct peaks. Composition and atomic ordering enable controlled plasmonic properties.**

***Keywords*— metamaterials, Magnesium-aluminum alloys, icosahedral clusters, photoabsorption spectra, plasmonics, density functional theory, atomic configuration effects.**

I. Introduction

Bimetallic nanoparticles have emerged as versatile metamaterials for gearing optical, electronic, and catalytic properties by controlled manipulation of composition, size, and atomic arrangement [1]–[3]. Magnesium-aluminum (Mg-Al) alloys are particularly important among the several binary systems being studied because of their low density, high specific strength, and potential uses in lightweight structural materials, hydrogen storage, and plasmonics [4]–[6]. The optical behavior of Mg-Al nanoparticles, specifically the impact of atomic-scale chemical ordering on their photoabsorption spectra, is still largely unknown, despite the fact that the thermodynamic and mechanical properties of bulk Mg-Al alloys are well understood [7]. The plasmonic response of metallic nanoparticles is exceptionally sensitive to the local dielectric environment and electron density distribution [8]. Alloying introduces compositional and spatial degrees of freedom, which modulates the average electron density and the dielectric landscape whether randomly mixed or phase separated into distinct domains [9], [10]. Understanding how these factors interplay is crucial for designing nanoparticles with targeted optical responses. In this work, we present a comprehensive first-principles investigation of the structural relaxation and photoabsorption spectra of 147-atom icosahedral Mg-Al clusters across the complete compositional range (0-100% Al). We construct two distinct atomic configurations at each composition: clustered arrangements, where Al atoms aggregate into a contiguous domain mimicking early-stage phase separation, and random arrangements, representing homogeneous solid solutions. (Fig. 1)

II. Methods

All atomic structures and calculations were performed using the Atomic Simulation Environment (ASE) [11] in conjunction with the GPAW package [12], [13], using time-dependent density functional theory (TDDFT) utilizing the projector-augmented wave (PAW) method. The initial structure consisted of a 147-atom icosahedral magnesium cluster, constructed using ASE's cluster building tools. 81.63, 88.44, 95.24, and 100 at.% Al): (i) Random configurations, where Al atoms were substituted randomly at Mg sites, and (ii) Clustered configurations, where substitutions were biased to nearest-neighbor sites around an initial randomly chosen Al atom, creating a contiguous Al-rich domain. All structures were fully relaxed using the (Broyden Fletcher Goldfarb Shanno) BFGS optimizer in ASE. The Perdew–Burke–Ernzerhof (PBE) exchange–correlation functional [4] was employed, with a grid spacing of 0.2 and 0.3 $\AA$ for relaxation and groundstate calculations and the GPAW default setup for Mg and Al PAW datasets. Electronic temperatures were smeared using the Fermi–Dirac scheme with a width of 0.05 eV. Photoabsorption spectra were computed within the linear response regime using the dipole transition matrix elements between occupied and unoccupied Kohn–Sham states, with the imaginary part of the dielectric function broadened by a Lorentzian of width 0.1 eV to yield continuous spectra. To extract quantitative peak parameters—position (E_0), full width at half maximum (Γ), and oscillator strength (A)—all spectra were fitted with single or multiple Lorentzian functions as appropriate.

$$L(E) = \frac{A}{\pi} \frac{\Gamma/2}{(E - E_0)^2 + (\Gamma/2)^2} \tag{1}$$

where E_0 is the center of the peak, Γ is the full width at half maximum (FWHM) and A is the area under the peak (related to oscillator strength). For multiple overlapping peaks, a sum of Lorentzians is used:

$$\sigma(E) = \sum_j \frac{A_j}{\pi} \frac{\Gamma_j/2}{(E - E_{0,j})^2 + (\Gamma_j/2)^2}. \tag{2}$$

III. Results and Discussion

Computational results show:

- The photoabsorption spectra of the icosahedral Mg-Al clusters exhibit systematic evolution with aluminum concentration. To quantify the trends in the absorption spectrum, we fitted all spectra with Lorentzian functions (single or multiple peaks, as appropriate). (Fig. 2)

Fig. 1. Structures of Cluster (first row) and Random (second row) Mg-Al alloys. The green atoms are Mg and the grey atoms are Al

Fig. 2. Absorption spectrum of Cluster (first row) and Random Mg-Al (second row) Bimetallic system. In the top-left corner of each subplot we have Al percentage. The red line is lorentzian fit and the black line represent the absorption spectra of each system.

- We calculated the spectrum of pure Mg and pure Al particles; their respective sharp resonance peaks emerged at 4.80eV and 7.84eV, which are characteristics of collective plasmon excitation in these nanostructures. They have minimal damping in these homogeneous metallic systems.
- In random system the Mg and Al peaks hybridize and become broadened, this broadening reflects increased electron scattering due to disorder and the breakdown of translational symmetry.
- In cluster system we see multiple resonance peaks, with different intensities depending on majority atoms. The peaks tend to overlap at approximately 75% of the Al atoms and become broadened, indicating a strong electronic hybridization between the Mg and Al subsystems resulting in collective excitation that reaches the entire cluster.

IV. Conclusion

This comprehensive study of icosahedral Mg-Al clusters reveals that atomic-scale chemical ordering fundamentally dictates the photoabsorption response. Random solid-solution alloys exhibit a single, smoothly evolving plasmon peak that progressively broadens and shifts from Mg-like to Al-like character with increasing Al content—a homogeneous electronic response reflecting composition-averaged dielectric behavior. In contrast, clustered configurations produce multiple distinct absorption peaks throughout intermediate compositions (10-70% Al), arising from spatially separated Mg-rich and Al-rich domains that support independent plasmonic excitations. These multi-peak features persist until a critical concentration of approximately 75% Al, where the Al-rich domain percolates through the cluster, merging the separate resonances into a single hybrid peak. Our findings demonstrate that composition and atomic configuration provide dual, independent tuning knobs for engineering optical properties: random arrangements yield homogeneous single-resonance behavior adjustable by composition, while clustered arrangements enable heterogeneous multi-resonance response from identical compositions. The Mg-Al system thus offers a versatile platform for designing plasmonic materials with tailored spectral features for applications in sensing, broadband absorption, and nanophotonics.

Acknowledgments

We acknowledge support from the National Science Center, Poland, via the project 2019/35/B/ST5/02477. The computations were enabled by resources provided by the Interdisciplinary Center for Mathematical and Computational Modelling of the University of Warsaw via project #GC84-51 as well as using resources provided by the National Academic Infrastructure for Supercomputing in Sweden (NAISS), partially funded by the Swedish Research Council through grant agreement no. 2022-06725.

References

[1] R. Ferrando, J. Jellinek, and R. L. Johnston, "Nanoalloys: From theory to applications of alloy clusters and nanoparticles," *Chemical Reviews*, vol. 108, no. 3, pp. 845–910, 2008.

[2] M. B. Cortie and A. M. McDonagh, "Synthesis and optical properties of hybrid and alloy plasmonic nanoparticles," *Chemical reviews*, vol. 111, no. 6, pp. 3713–3735, 2011.

[3] K. D. Gilroy, A. Ruditskiy, H.-C. Peng, D. Qin, and Y. Xia, "Bimetallic nanocrystals: Syntheses, properties, and applications," *Chemical Reviews*, vol. 116, no. 18, pp. 10 414–10 472, 2016.

[4] T. D. Dao, K. Chen, S. Ishii, A. Ohi, T. Nabatame, M. hiro Kitajima, and T. Nagao, "Aluminum infrared plasmonic perfect absorbers fabricated by colloidal lithography," *2015 Conference on Lasers and Electro-Optics Pacific Rim*, p. 25E3_7, 2015.

[5] I. Jain, C. Lal, and A. Jain, "Hydrogen storage in mg: A most promising material," *International Journal of Hydrogen Energy*, vol. 35, no. 10, pp. 5133–5144, 2010.

[6] I. J. Polmear, "Magnesium alloys and applications," *Materials Science and Technology*, vol. 10, no. 1, pp. 1–16, 1994.

[7] H. Su, M. Harmelin, P. Donnadieu, C. Baetzner, H. Seifert, H. Lukas, G. Effenberg, and F. Aldinger, "Experimental investigation of the mg-al phase diagram from 47 to 63 at.

[8] K. L. Kelly, E. Coronado, L. L. Zhao, and G. C. Schatz, "The optical properties of metal nanoparticles: the influence of size, shape, and dielectric environment," *The Journal of Physical Chemistry B*, vol. 107, no. 3, pp. 668–677, 2003.

[9] G. Barcaro and A. Fortunelli, "A magic pd- ag binary cluster on the fs-defected mgo (100) surface," *The Journal of Physical Chemistry C*, vol. 111, no. 30, pp. 11 384–11 389, 2007.

[10] L.-L. Wang, T. L. Tan, and D. D. Johnson, "Configurational thermodynamics of alloyed nanoparticles with adsorbates," *Nano Letters*, vol. 14, no. 12, pp. 7077–7084, 2014.

[11] A. Hjorth Larsen, J. Jørgen Mortensen, J. Blomqvist, I. E. Castelli, R. Christensen, M. Dułak, J. Friis, M. N. Groves, B. Hammer, C. Hargus, E. D. Hermes, P. C. Jennings, P. Bjerre Jensen, J. Kermode, J. R. Kitchin, E. Leonhard Kolsbjerg, J. Kubal, K. Kaasbjerg, S. Lysgaard, J. Bergmann Maronsson, T. Maxson, T. Olsen, L. Pastewka, A. Peterson, C. Rostgaard, J. Schiøtz, O. Schütt, M. Strange, K. S. Thygesen, T. Vegge, L. Vilhelmsen, M. Walter, Z. Zeng, and K. W. Jacobsen, "The atomic simulation environment—a python library for working with atoms," *Journal of Physics: Condensed Matter*, vol. 29, no. 27, p. 273002, jun 2017.

[12] J. J. Mortensen, L. B. Hansen, and K. W. Jacobsen, "Real-space grid implementation of the projector augmented wave method," *Phys. Rev. B*, vol. 71, p. 035109, Jan 2005.

[13] J. Enkovaara, C. Rostgaard, J. J. Mortensen, J. Chen, M. Dułak, L. Ferrighi, J. Gavnholt, C. Glinsvad, V. Haikola, H. A. Hansen, H. H. Kristoffersen, M. Kuisma, A. H. Larsen, L. Lehtovaara, M. Ljungberg, O. Lopez-Acevedo, P. G. Moses, J. Ojanen, T. Olsen, V. Petzold, N. A. Romero, J. Stausholm-Møller, M. Strange, G. A. Tritsaris, M. Vanin, M. Walter, B. Hammer, H. Häkkinen, G. K. H. Madsen, R. M. Nieminen, J. K. Nørskov, M. Puska, T. T. Rantala, J. Schiøtz, K. S. Thygesen, and K. W. Jacobsen, "Electronic structure calculations with gpaw: a real-space implementation of the projector augmented-wave method," *Journal of Physics: Condensed Matter*, vol. 22, no. 25, p. 253202, jun 2010.

Lithium Niobate Photonic Moiré Superlattice for Telecoms Wavelengths

Romae Grierson-Copeland[1], Christian Johnson-Richards[1], Noel Healy[1,*]

[1]School of Mathematics, Statistics and Physics, Newcastle University, Newcastle Upon Tyne, NE1 7RU, United Kingdom
*Corresponding author: Noel.Healy@newcastle.ac.uk

***Abstract*—A 2D simulation studying photonic Moir´e superlattices made from triangular lattices of holes in lithium niobate is conducted. Field enhancement is observed due to flatbands in the photonic bandstructure. The lattice constant has a negative correlation with the flatband frequency, with 576nm enhancing the field at telecoms wavelengths in simulation.**

I. Introduction

Moiré patterns are the result of two or more periodic lattices of inclusions that are overlapped with each other by a twist angle, θ, creating long-range patterns. These structures have found applications in areas from condensed matter physics [1] to photonics, using twisted bilayer graphene and photonic crystals for quantum applications [2,3]. Our design takes inspiration from previous works [4][5], utilising 2 triangular lattices of holes to create a Moiré superlattice with hexagonal unit cells in a dielectric medium. This results in a field enhancement at the center of the superlattice unit cell, and this locality of the optical modes is essential to increase light-matter interaction at low operating powers. This has been shown to improve the interaction between excitons in single QDs [6], increase the yield of entangled photons from second order non-linear materials [7,8], and is a key step toward large-scale integrated quantum photonic circuits [9,10]. This light confinement is a result of a long wavelength periodic potential that can fold the electric band structure into a Moiré mini-Brillouin zone [11], capable of giving rise to the formation of flat bands in the photonic bandstructure. The implication of this leads to the emergence of linear photonic states which are completely localized in space [12]. When photons exist in these flat bands they do not propagate through the materials as they would in regular bands, behaving in a non-dispersive manner. Having a larger field enhancement contributing to the light matter interaction in an essentially 2 dimensional material also negates the requirement of phase matching for many quantum mechanical processes [13]. Lithium Niobate ($LiNbO_3$) is a versatile synthetic crystal widely used for its electro-optic, piezoelectric and nonlinear optical properties [14]. The interest in this material is also owed to the commercial availability of thin-film lithium niobate, as well as its second order non-linear susceptibility [15]. $LiNbO_3$ has been used in the extension of electric field poling techniques to two-dimensional lattices, enabling the demonstration of purely non-linear photonic crystals [16]. This, however, requires the material to be periodically poled to allow quasi-phase matching, a process that could be omitted through our design. In this work we investigate the possibility of designing a Moire superlattice using $LiNbO_3$. Taking advantage of the field enhancement in superlattice structures we propose a platform that drastically improves the efficiency in accessing the large second order non-linearity of $LiNbO_3$ for quantum and photonic applications. To do this we present an initial design in 2D and show changing the lattice constant of the triangular lattice can effect the position of the flatband in the band structure.

II. Methods

The simulation was designed using the eigensolver in the COMSOL Multiphysics RF module. The hexagonal superlattice was designed with periodic boundary conditions on all 6 sides. The solutions were retrieved for interpolated wavevectors encompassing the irreducible brillouin zone, tracing the unit cell's high symmetry points. In the initial study, we modelled the structure in 2D, which is expected to shift the bandstructure down in frequency and disregard losses. This allows us to rapidly prototype designs with less computational resources, to investigate trends in results. In the initial simulation, the model was designed with a lattice constant, a = 500 nm, a twist angle, θ = 6.01 degrees, the holes were sized with radius r = 0.24a. The period of the superlattice is therefore $a/2sin(\theta/2)$. The structure was configured as lithium niobate with a dispersive model [17] and air holes with refractive index n = 1. A parameter sweep was then conducted, in which the triangular lattice constant was varied to find out how this affects the frequency at which the flatband occurs to shift the flatband frequency, f_{flat}, to the desired operating range $\approx$ 190THz (1550nm).

III. Results and Discussion

The results of the 2D study are shown in Fig. 1, where the electric field distribution for the wavevector k is shown in Fig.1a and the band structure is shown in Fig.1b. The expected flatband in the bandstructure (highlighted by the red box) is present, showing that non-dispersive nature in the field distribution. The light confinement mechanism is in agreement with previous works [4], with the majority of the field distribution in the central 3 holes. The results for

Fig. 1. (a) Schematic of the superlatice including the magnetic field distribution for a solution in the flatband at K and with an f_{flat} around 222THz. (b) The complete band structure of the superlattice with a = 500nm and θ = 6.01 . The flatband is highlighted by a red box.

the lattice constant parameter sweep are presented in Fig. 2, here it is shown that there is a negative relationship between the lattice constant and flatband frequency that appears to be linear, with the red line in the figure presenting a linear fit. The dashed black line of the graph represents the telecoms band (λ = 1550nm), and using the linear fit a lattice constant for which the telecoms frequency of light will be confined can be estimated to be around a = 583nm, used to find the actual value a = 576nm. For the use of spontaneous parametric down conversion, the generated photons would need to be of telecoms wavelength as opposed to the input. Using the linear fit, a triangular lattice constant a = 273nm is extrapolated outside the range of tested results. A comprehensive study of the structure will be discussed including field enhancement at the center of the moire superlattice. A larger range of results will be shown for a more accurate fit and allow an improved estimate of the enhancement of nonlinear optical processes. The design will also be extended to demonstrate a suspended 3D slab.

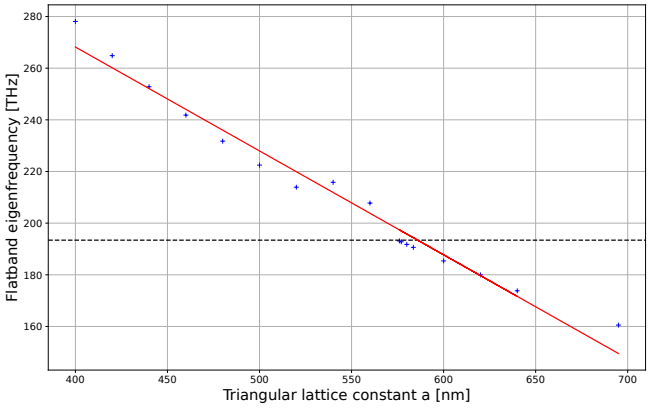

Fig. 2. The eigenfrequencies presenting the flatband of interest for different triangular lattice constants is represented by blue data points. The red linear fit has equation f_{flat} = -0.4023a + 429.0992. The black dashed line corresponds to a frequency in the telecoms band of λ = 1550nm.

IV. Conclusion

In this work we have demonstrated the design of a $LiNbO_3$ based Moiré superlattice and shown the dependence of the lattice constant on the flat-band frequency. As an example, the band structure and field distribution at the flatband of a superlattice designed with a = 500nm is shown. This work is the first step in designing a $LiNbO_3$ based platform for that may be exploited in producing entangled photons for use in quantum applications. an estimate of a design for spontaneous parametric down conversion that should output photon pairs of frequency in the telecoms band is found to have $a \approx$ 273nm.

Acknowledgments

This work was supported by the Engineering and Physical Sciences Research Council (DTP Studentship).

References

[1] Kennes, D.M., Claassen, M., Xian, L. et al. *Moiré heterostructures as a condensed-matter quantum simulator.* Nat. Phys. 17, 155–163 (2021). https://doi.org/10.1038/s41567-020-01154-3

[2] Oudich, M., Kong, X., Zhang, T. et al. *Engineered moiré photonic and phononic superlattices.* Nat. Mater. 23, 1169–1178 (2024). https://doi.org/10.1038/s41563-024-01950-9

[3] L. Du, M.J.R. Molas, Z. Huang, G. Zhang, F. Wang, Z. Sun, *Moiré photonics and optoelectronics*, 31 March 2023, DOI: 10.1126/science.adg0014

[4] T. Ning, L. Zhao, Y. Huo , Y. Cai, Y. Ren, *Giant enhancement of second harmonic generation from monolayer 2D materials placed on photonic moiré superlattice*, 10 October 2023, DOI: https://doi.org/10.1515/nanoph-2023-0124

[5] Mao, XR., Shao, ZK., Luan, HY. et al. *Magic-angle lasers in nanostructured moiré superlattice*. Nat. Nanotechnol. 16, 1099–1105 (2021). https://doi.org/10.1038/s41565-021-00956-7

[6] Yan, S., Li, H., Yang, J. et al. *Cavity quantum electrodynamics with moiré photonic crystal nanocavity.* Nat Commun 16, 4634 (2025). https://doi.org/10.1038/s41467-025-59942-5

[7] Q. Lin, H. Fang, A. Kalaboukhov, Y. Liu et al. *Moiré-engineered light-matter interactions in MoS2/WSe2 heterobilayers at room temperature*. Nat commun 15, 8762 (2024). https://doi.org/10.1038/s41467-024-53083-x

[8] C. J. R. Duncan, A. C. Johnson, I. Maity, A. Rubio et al *Photoinduced twist and untwist of moiré superlattices* Nature 647, 619–624 (2025). https://doi.org/10.1038/s41586-025-09707-3

[9] Bao, J., Fu, Z., Pramanik, T. et al. *Very-large-scale integrated quantum graph photonics.* Nat. Photon. 17, 573–581 (2023). https://doi.org/10.1038/s41566-023-01187-z

[10] Arrazola, J.M., Bergholm, V., Brádler, K. et al. *Quantum circuits with many photons on a programmable nanophotonic chip.* Nature 591, 54–60 (2021). https://doi.org/10.1038/s41586-021-03202-1

[11] Andrei, E.Y., MacDonald, A.H. *Graphene bilayers with a twist.* Nat. Mater. 19, 1265–1275 (2020). https://doi.org/10.1038/s41563-020-00840-0

[12] Rodrigo A. Vicencio Poblete (2021) *Photonic flat band dynamics*, Advances in Physics: X, 6:1, 1878057, DOI: 10.1080/23746149.2021.1878057

[13] B. Sain, C. Meier, T. Zentgraf *Nonlinear optics in all-dielectric nanoantennas and metasurfaces: a review* Advanced Photonics, Vol. 1, Issue 2, 024002 (April 2019). https://doi.org/10.1117/1.AP.1.2.024002

[14] A Boes et al. *Lithium niobate photonics: Unlocking the electromagnetic spectrum.* .DOI:10.1126/science.abj4396

[15] . DeSalvo, A. A. Said, D. J. Hagan, E. W. Van Stryland and M. Sheik-Bahae, *Infrared to ultraviolet measurements of two-photon absorption and n/sub 2/ in wide bandgap solids* IEEE Journal of Quantum Electronics, vol. 32, no. 8, pp. 1324-1333, Aug. 1996, doi: 10.1109/3.511545]

[16] V. Berger *Nonlinear Photonic crystals* DOI: https://doi.org/10.1103/PhysRevLett.81.4136

[17] D. E. Zelmon, D. L. Small, D. Jundt *Infrared corrected Sellmeier coefficients for congruently grown lithium niobate and 5 mol.% magnesium oxide doped lithium niobate*. https://doi.org/10.1364/JOSAB.14.003319

POSTERS

Metamaterials, Metasurfaces and Their Applications

41 contributions · pp. 1613–1716

META 2026 · Dublin, Ireland · ISSN 2429-1390

Temporal Disorder in Two-Dimensional Phononic Time Crystals: A Numerical Study

Takamichi Terao[1]

[1]Department of Electrical, Electronic and Computer Engineering, Gifu University, Japan
*Corresponding author: terao.takamichi.x0@f.gifu-u.ac.jp

***Abstract*— Numerical simulations of a 2D mass–spring lattice with time-varying stiffness reveal parametric amplification of vibrational waves. The exponential growth depends on the modulation interval and temporal disorder. The Fourier analysis shows selective amplification of specific wavenumbers governed by momentum bandgaps that can be tuned or suppressed by temporal disorder.**

***Keywords*— time-varying metamaterials, momentum bandgaps, temporal disorder, phononic crystals.**

I. Introduction

In recent years, research on wave propagation characteristics at temporal boundaries in time-varying materials has attracted significant attention [1-4]. The importance of the physical problems posed by temporal boundaries was first proposed by Morgenthaler [5]. Subsequently, these phenomena were studied as the temporal analogy of spatial boundaries. With respect to this field, research on photonic time crystals (PTCs) has been actively pursued. Whereas photonic crystals are systems in which the permittivity varies periodically in space, in PTCs, the permittivity of the system varies periodically in time. Furthermore, attention is being focused on the wave characteristics in systems in which the material properties undergo nonperiodic temporal variations.

In reference [6], a one-dimensional (1D) phononic lattice was realized using repulsively coupled ring magnets that provided nonlinear intersite interactions. A time-varying medium was implemented by placing current-driven coils near the lattice sites. This electromechanical stiffness modulation enabled parametric wave phenomena such as amplification and modulation-induced bandgap formation. Analogous concepts can be applied to elastic waves rather than electromagnetic waves, namely phononic time crystals (PNTCs) [7,8].

Prior theoretical studies on time-varying media predominantly focused on 1D systems. In this study, numerical simulations were performed to elucidate the amplification characteristics of vibrational waves in higher-dimensional time-varying media.

II. Methods

This study analyzes systems in which the elastic modulus can be modulated by external fields, as introduced in the Introduction section, using a lattice model. Our calculations investigate lattice vibrations in a mass-spring model on a two-dimensional (2D) square lattice. This study adopts a scalar elasticity model [9] and incorporates uniform weak damping at each site.

In a scalar model, the equation of motion for (i,j) mass with displacement $u_{i,j}(t)$ can be written as follows:

$$m\frac{d^2}{dt^2}u_{i,j}(t) = k(t)\left(u_{i+1,j}(t) + u_{i-1,j}(t) + u_{i,j+1}(t) + u_{i,j-1}(t) - 4u_{i,j}(t)\right) - c\frac{d}{dt}u_{i,j}(t) \quad (1)$$

where c is a damping constant, and spring constant $k(t)$ in this model is time-dependent, unlike in conventional scalar elastic models. In this study, this is defined as follows:

$$k(t) = \begin{cases} K & (t_{2p} \le t < t_{2p+1}) \\ K + \Delta K & (t_{2p+1} \le t < t_{2(p+1)}) \end{cases} \quad (2)$$

where p is an integer, and $t_n = (n + \alpha\gamma_n)$ (T denotes a time interval, and $\{\gamma_n\}$ denotes a uniformly distributed real random number between 0.0 and 1.0). Furthermore, α is a parameter representing the magnitude of the temporal disorder, satisfying the condition, $0 \le \alpha < 1$. For the initial conditions, displacements $u_{i,j}(t=0)$ were set to be uniformly random between -0.5 and 0.5, whereas velocities $v_{i,j}(t=0)$ were set to zero. Periodic boundary conditions were applied in both the x and y directions.

III. Results and Discussion

In the following calculations, the system size was set to $L = 1024$. $K = 1.0$ and $\Delta K = 0.5$ were set for the spring constant, and the damping coefficient was set to $c = 2.0 \times 10^{-3}$. The time step was set to $\Delta t = 1.0 \times 10^{-4}$, and the time evolution of the system was numerically investigated.

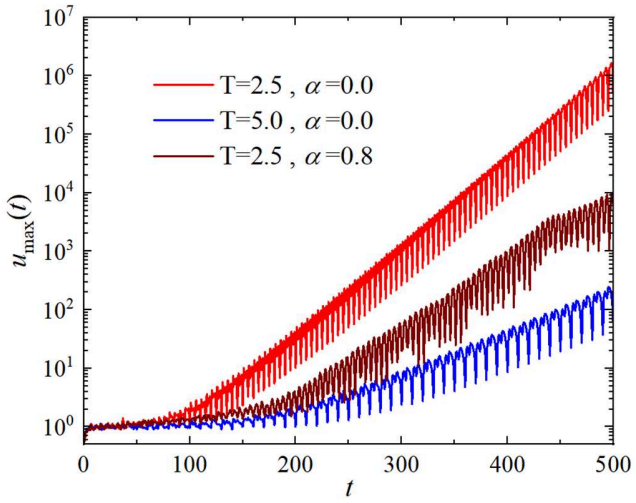

Fig. 1 Time development of maximum displacement $u_{\max}(t)$

Figure 1 shows the calculated time evolution of maximum displacement $u_{\max}(t)$. The red, blue, and brown lines represent the results for (T, α) = (2.5, 0.0), (5.0, 0.0), and (2.5, 0.8), respectively. In all the cases, the displacement exhibited exponential growth after a sufficient amount of time had elapsed. Furthermore, exponent λ, that represents the degree of amplification, depended on both interval T and temporal randomness α.

To further elucidate the amplification properties of the oscillating waves, a spatial Fourier transform of displacement $u_{i,j}(t)$ was performed to identify the amplified wavenumber components. Subsequently, $\{u_{ij}\}$ was analyzed based on the numerical results of the time evolution of the system described by Eq. (2) up to $t = 500.0$. Figures 2(a), and 2(b) show calculated Fourier components $F(k_x, k_y)$ for $(T, \alpha) = (2.5, 0.0)$ and $(2.5, 0.4)$, respectively. The values of $F(k_x, k_y)$ were normalized such that the maximum value was 1.0. The horizontal and vertical axes represent wavenumbers k_x and k_y, respectively. The yellow regions in the figures correspond to the wavenumber components where wave amplification occurs.

The results, as shown in Fig. 2(a), indicated that two distinct wave curves with different wavenumbers were amplified; these components propagated isotropically in all directions rather than in specific orientations. The deviation from circularity in the outer curve (where the wavenumber magnitude was approximately 2.0) was attributed to the anisotropy of the underlying square lattice that became more pronounced at shorter wavelengths. Figure 2(b) presents the results for the system when temporal randomness is introduced ($\alpha > 0$). By comparing this with Fig. 2(a), evidently, the outer curve—corresponding to the higher wavenumber—had vanished. Figure 2(c) shows the calculation results of $F(k_x, k_y)$ for a system with a larger interval T without temporal randomness. These results demonstrated that wave amplification occurred at lower wavenumbers in this regime.

The series of calculation results revealed that the wavenumber components undergoing amplification could be controlled by modulating the temporal variations of the spring constants. This wave amplification was attributed to the presence of a momentum bandgap. The disappearance of wave amplification at higher wavenumbers, as shown in Fig. 2(b), suggested that the momentum bandgap corresponding to these wavenumbers collapsed owing to the introduction of temporal disorder.

In this regard, the widths of the wavenumber regions where wave amplification occurred were examined. Figure 3 shows the k_x-dependence of $F(k_x, 0)$. Figures 3 corresponds to the wavenumber ranges associated with the inner and outer amplification regions, respectively, as observed in Fig. 2(a). Vertical axis represents the value of $F(k_x, 0)$. These results indicated that the wavenumber range of the amplification narrowed, as shown in Fig. 3(a), owing to the introduction of the temporal disorder, whereas the amplification region itself completely disappeared, as shown in Fig. 3(b). This result was qualitatively consistent with the numerical results, as presented in Fig. 2(b).

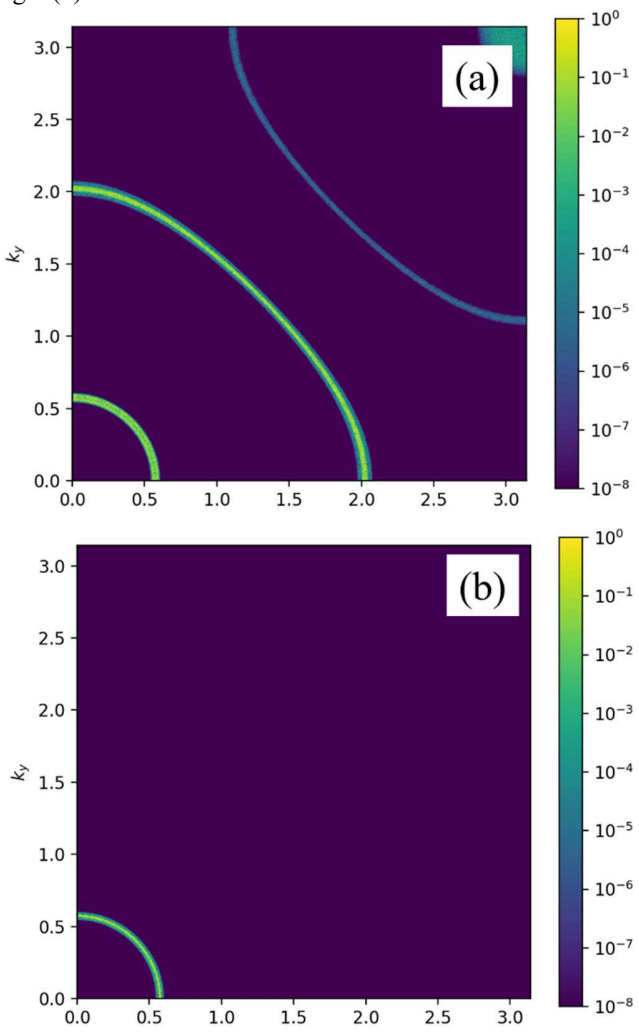

Fig. 2 Fourier transform of displacement $u_{i,j}(t)$ (a) $T = 2.5, \alpha = 0.0$ (b) $T = 2.5, \alpha = 0.4$

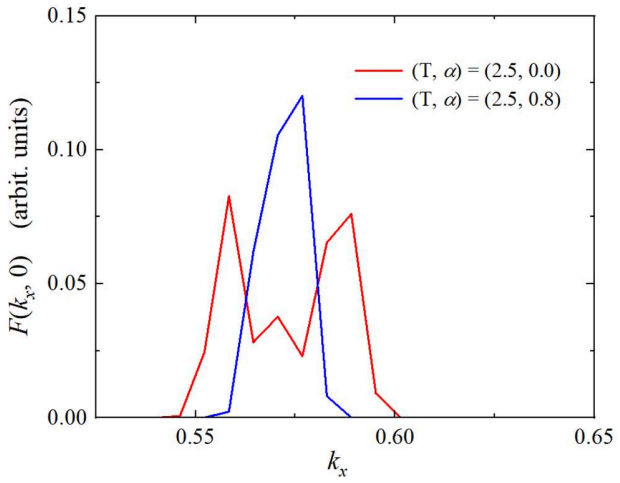

Fig. 3 Dependence of $F(k_x, 0)$ on temporal disorder α

Finally, this paper discusses time-varying media in uniform three-dimensional (3D) systems. This study focused on the analytical results of 2D time-varying phononic metamaterials. However, the author also conducted similar investigations on 3D phononic metamaterials and reported that the conclusions obtained were qualitatively consistent with those for the 2D systems presented here.

IV. Conclusion

In this study, the effects of the temporal disorder on phononic time crystals were clarified using numerical simulations. Whereas prior theoretical research on time-varying metamaterials—involving both electromagnetic and elastic waves—was largely limited to 1D spatial systems, this study elucidated their behavior in higher-dimensional systems. Given that the wave amplification characteristics can be controlled by modulating the functional form of the temporal variations in the medium, further advancements in this field are highly anticipated.

Acknowledgments

The author acknowledges the Supercomputer Centers of Nagoya University for allowing the use of their facilities. This study was supported by the JSPS KAKENHI (Grant Number 24K14976).

References

[1] E. Galiffi, R. Tirole, S. Yin, H. Li, S. Vezzoli, P. A. Huidobro, M. G. Silveirinha, R. Sapienza, A. Alù, and J. B. Pendry, "Photonics of time-varying media," Advanced Photonics, vol. 4, pp. 014002, 2022.

[2] M. M. Asgari, P. Garg, X. Wang, M. S. Mirmoosa, C. Rockstuhl, and V. Asadchy, "Theory and applications of photonic time crystals: a tutorial," Advances in Optics and Photonics, vol. 16, pp. 958-1063, 2024.

[3] N. Engheta, "Four-dimensional optics using time-varying metamaterials," Science, vol. 379, pp. 1190-1191, 2023.

[4] S. A. R. Horsley, E. Galliffi, and Y.-T. Wang, "Eigenpulses of dispersive time-varying media", Physical Review Letters, vol. 130, pp. 203804, 2023.

[5] F. Morgenthaler, "Velocity modulation of electromagnetic waves", IRE Transactions on Microwave Theory and Techniques, vol. 6, pp. 167-172, 1958.

[6] B. L. Kim, C. Chong, and C. Daraio, "Temporal Refraction in an Acoustic Phononic Lattice", Physical Review Letters, vol. 133, pp. 077201, 2024.

[7] K. S. Eswaran, A. E. Kopaei, and K. Sacha, "Anderson localization in photonic time crystals", Physical Review B, vol. 111, pp. L180201, 2025.

[8] Y. Sharabi, E. Lustig, and M. Segev, "Disordered Photonic Time Crystals", Physical Review Letters, vol. 126, pp. 163902, 2021.

[9] C. Monthus and T. Garel, "Anderson localization of phonons in dimension d=1,2,3: Finite-size properties of the inverse participation ratios of eigenstates", Physical Review B, vol. 81, pp. 224208, 2010.

Research on Hydrogel-Based Flexible Underwater Acoustic Metamaterials

Haoyu Zhao[1], Lei Zuo[1,2,3,4], Jinxin Zhao[4] , Kai Zhang[1,2,3,4,*]

[1]School of Aerospace Engineering, Beijing Institute of Technology, Beijing 100081, China
[2]Tangshan Research Institute, Beijing Institute of Technology, Tangshan, 063000, China
[3]State Key Laboratory of Environment Characteristics and Effects for Near-space, Beijing Institute of Technology, Beijing 100081, China
[4]Beijing Ningji New Materials Technology Co., Ltd, Beijing 100081, China
*Corresponding author: zhangkai@bit.edu.cn

***Abstract*—We develop a novel hydrogel-based flexible acoustic metamaterial for underwater carpet cloaking. To elucidate the underlying mechanism of the proposed microstructure, the effects of anisotropic stiffness and anisotropic density are investigated. It suppresses shear waves and utilizes a longitudinal wave-dominant coupling mode, enabling excellent cloaking performance confirmed by simulations and experiments.**

***Keywords*—Hydrogel, Flexible Acoustic Metamaterial, Underwater Carpet Cloak, Wave Manipulation.**

I. Introduction

Hydrogels, with their high water content and matched acoustic impedance to water, show significant potential for underwater acoustic applications [1-4]. While traditional acoustic cloaks face challenges in eliminating acoustic-solid coupling and balancing performance with structural integrity, hydrogels offer a promising solution. Their unique properties, such as flexibility and load-bearing capacity, enable the design of advanced metamaterials. This study develops a flexible acoustic metamaterial based on hydrogels, and systematically validates its outstanding performance in underwater acoustic wave manipulation through a combination of theoretical analysis, numerical simulations, and experimental investigations.

II. Methods

This study designs a novel hydrogel-based flexible unit cell and proposes a rigid unit cell for comparative analysis. Both unit cell microstructures are designed based on a composite material paradigm, featuring a coupling of flexible hydrogel and rigid solid materials. As shown in the rigid cell in Fig. 1(a), which are connected to each other by solid materials. As shown in the flexible cell in Fig. 1(b), which are connected to each other by hydrogels.

For example, apply the designed unit cell to the underwater acoustic carpet cloak. Following the acoustic transformation theory under linear mapping, rigid (Fig. 2(a)) and flexible (Fig. 2(b)) underwater acoustic carpet cloaks were respectively designed based on these two unit cells, with steel employed as the solid material.

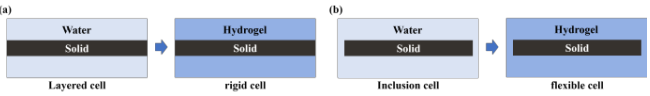

Fig. 1 (a)-(b) Design strategy of hydrogel-based unit cell microstructure.

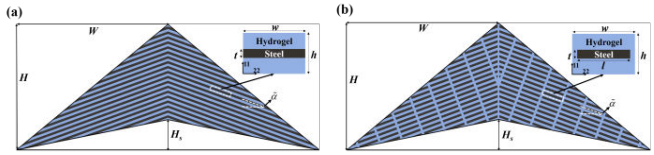

Fig. 2 (a) Rigid hydrogel-based unit cell and its assembled acoustic carpet cloak; (b) Flexible hydrogel-based unit cell and its constructed acoustic carpet cloak.

III. Results and Discussion

Firstly, we elucidate the transverse wave attenuation mechanism in the proposed acoustic metamaterial through the analysis of anisotropic stiffness and anisotropic density. It reveals that flexible hydrogel-steel unit achieves comparable effective mass density and modulus to rigid counterpart, while anisotropic stiffness analysis demonstrates a reduction in shear modulus and suppressed shear wave modes. Besides, anisotropic density analysis further identifies a single acoustic-solid coupled longitudinal wave mode in flexible unit cell, contrasting with multiple modes in rigid structures that cause parasitic scattering. .

Secondly, we investigated the scattering control performance of the designed hydrogel-based flexible underwater acoustic carpet cloak for plane waves incident at different angles using finite element simulations. As shown in Fig. 3, the scattered acoustic fields are presented for plane-wave incidence at 20 kHz across angles ranging from 0° to 90° in steps of 15°, comparing three types of underwater acoustic carpet cloaks.

The results indicate that the designed flexible acoustic carpet cloak achieves scattering control comparable to that of an ideal homogeneous carpet across the full angular range.

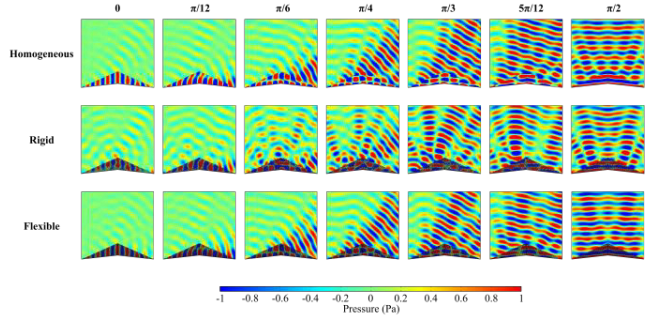

Fig .3. Acoustic wave fields demonstrating scattering control for 20 kHz plane waves under 7 incident angles.

Finally, the experimental results demonstrate the practical cloaking performance of the flexible underwater acoustic carpet cloak (Fig. 4(a)). As illustrated in Fig. 4(b), the experimental setup consists of a cylindrical transducer emitting Gaussian wave packet signals and six hydrophones receiving both incident waves and structural backscattering. Three scenarios were tested: (i) reference field (a flat empty surface without any test objects), (ii) uncloaked field (a stainless steel triangular prism scatterer placed on the flat surface), and (iii) cloaked field (the same scatterer covered with the fabricated flexible underwater acoustic carpet cloak). The incident signal was a 10 kHz–18 kHz Gaussian wave packet containing two cycles. To quantitatively evaluate the robustness of the theoretical cloaking performance of the designed flexible underwater acoustic carpet cloak, we adopted the RCS metric defined in Eq. (1) [5] was adopted to quantitatively evaluate the cloaking performance:

$$\zeta_{\mathrm{RCS}} = \oint_{\Omega} \left(\frac{\left| P_{\mathrm{Cloaked}} - P_{\mathrm{Reference}} \right|^2}{\left| P_{\mathrm{Uncloaked}} - P_{\mathrm{Reference}} \right|^2} \right) d\Omega \qquad (1)$$

Here, $P_{\mathrm{Reference}}$, P_{Cloaked}, and $P_{\mathrm{Uncloaked}}$ denote the instantaneous acoustic pressure values in the reference, cloaked, and uncloaked scenarios, respectively, while Ω represents the measured region.

Figure 4(c) shows the average RCS calculated over the echo time window from 0.4 ms to 0.9 ms, which remains below 0.25 across the 10 kHz–18 kHz frequency range, confirming that the flexible underwater acoustic carpet cloak effectively suppresses strong scattering induced by the object and achieves notable acoustic stealth performance.

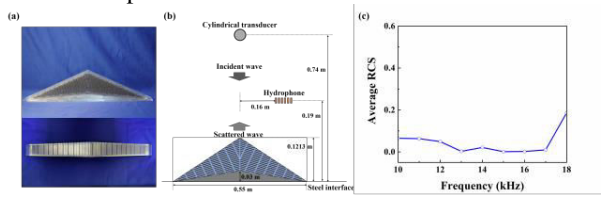

Fig. 4(a) Physical specimen of the flexible underwater acoustic carpet cloak: The specimen is composed of hundreds of stainless steel sheets wrapped with hydrogel material and the scattering body is made of stainless steel material; (b) Schematic diagram of the underwater acoustic experiment scene; (c) The average RCS experimental test values of the acoustic stealth carpet cloak in the range of 10 kHz to 18 kHz.

IV. Conclusion

Leveraging the unique properties of hydrogels, such as their near-perfect impedance matching with water, inherent load-bearing capability, and structural flexibility, we designed a novel flexible acoustic metamaterial based on hydrogels for underwater carpet cloaking, which possesses sufficient autonomous load-bearing capacity. Experimentally validated prototype demonstrates superior acoustic cloaking performance (RCS < 0.25) by minimizing shear wave interference within the microstructure. Subsequent discussions further confirmed the broadband and wide-angle cloaking capability of the designed flexible underwater acoustic carpet cloak. This approach enables advanced underwater wave manipulation and expands the scope for hydrogel applications in complex acoustic regulation structures.

Acknowledgments

This work was supported by the National Natural Science Foundation of China (Grant Nos. 12272041 and 12202055).

References

[1] H. Yuk, S. Lin, C. Ma, M. Takaffoli, N. X. Fang, and X. Zhao, "Hydraulic hydrogel actuators and robots optically and sonically camouflaged in water," Nature Communications, vol. 8, p. 14230, 2017.

[2] K. Zhang, C. Ma, Q. He, S. Lin, Y. Chen, Y. Zhang, et al., "Metagel with broadband tunable acoustic properties over air–water–solid ranges," Advanced Functional Materials, vol. 29, p. 1903699, 2019.

[3] R. Guo, R. Liu, H. Liu, L. Zuo, Q. Zhang, and K. Zhang, "Tunable metamaterial lens for ultra-broadband hydroacoustic focusing," Journal of Applied Mechanics, Transactions of the ASME, vol. 92, p. 051009, 2025.

[4] J. Zhang, N. Zhou, E. Dong, C. Zhang, Z. Song, S. Liu, et al., "Soft bio-metamaterials with high acoustic transparency and gradient refractive index for tunable acoustic beamformer," Matter, vol. 7, pp. 3857–3875, 2024.

[5] Y. Yang, L. Jing, B. Zheng, R. Hao, W. Yin, E. Li, et al., "Full-polarization 3D metasurface cloak with preserved amplitude and phase," Advanced Materials, vol. 28, pp. 6866–6871, 2016.

Diversity-Optimized Dataset Generation Pipeline for High-Reflectivity Metamirror Inverse Design

Swarali Talele[1,2*], Liam Shelling Neto[1,2], Stefanie Kroker[1,2,3]

[1]Technische Universität Braunschweig, Institut für Halbleitertechnik, Hans-Sommer-Str. 66, Braunschweig, Germany
[2]Laboratory for Emerging Nanometrology, Langer Kamp 6a-b, Braunschweig, Germany
[3]Physikalisch-Technische Bundesanstalt, Bundesallee 100, Braunschweig, Germany
*Corresponding author: swarali.talele@tu-braunschweig.de

***Abstract*—Designing complex multispectral metamirrors for cavities requires precise control of phase and reflectivity across subwavelength metaatoms. Diffusion-based generative models enable inverse design for such structures but are limited by dataset quality, especially when crucial regions are underpopulated. We present a pipeline that generates validated candidate geometries, yielding an enriched dataset.**

***Keywords*— metamirrors, multispectral cavities, diffusion, dataset enrichment, high reflectivity, inverse design.**

I. Introduction

Ultrastable optical cavities, fundamental to a wide range of precision measurement applications, are limited by Brownian thermal noise in conventional dielectric mirror coatings, affecting their performance [1]. A promising alternative to overcome this limitation is metamirrors-based cavity (Fig.1), which offers a route toward reducing coating-induced noise [2]. A metamirror consists of an array of subwavelength metaatoms designed to provide both high reflectivity and a prescribed spatial phase profile, allowing a curved optical wavefront to be realized on a planar surface and enabling compact cavity architectures. Additionally, it also allows for complex functionalities such as multispectral operation [3]. The need for multispectral cavities is observed in applications such as gravitational-wave detectors [4] or quantum photonic systems [5]. Designing the desired metamirrors poses a highly constrained inverse problem, as each metaatom geometry must simultaneously satisfy reflectivity and phase requirements at one or more target wavelengths. Recently, deep generative models, in particular diffusion-based architectures, have emerged as powerful tools for inverse nanophotonic design by learning to generate metaatom geometries conditioned on desired optical responses [6]. The effectiveness of these models, however, is critically dependent on the quality and structure of the training dataset [7].

A dataset constructed through random sampling of the geometric parameter space does not provide uniform coverage of phase and reflectivity, since high-reflectivity designs occupy only a small and highly structured region of the design space. To increase the number of useful samples, optimization-based filtering or targeted sampling toward high reflectivity is commonly employed. This strategy, however, introduces a new limitation: most optimization procedures converge toward a small number of similar geometries, leading to datasets that are biased not only toward high performance but also toward a narrow set of structural configurations, thereby severely reducing geometric diversity [8]. Such collapse of diversity in the high-reflectivity region restricts the ability of generative inverse design models to produce multiple distinct solutions for a given optical target.

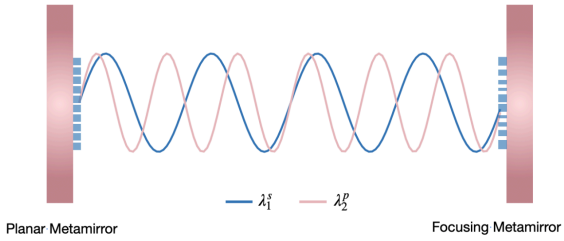

Fig. 1. Schematic representation of a non-conventional metamirrors-based cavity designed for different wavelengths and polarization states.

While surrogate-assisted sampling [8] and active learning [9] have been applied to inverse design problems and dataset acquisition for nanophotonics, existing methods do not focus on targeting and enriching rare high-performance regions with explicit response-space coverage goals. In this work, we investigate the construction of metaatom datasets, with a particular focus on balancing performance bias and geometric diversity. We introduce a dataset generation approach aimed at selectively enriching the high-reflectivity region of the design space, thus enabling the formation of an enriched dataset containing both a sufficient concentration of high-reflectivity samples and a broad range of distinct metaatom geometries.

II. Methods

Here we present our pipeline (Fig.2) which combines surrogate-guided sampling with phase/reflectivity binning to systematically populate the high-reflectivity region with

diverse optical responses, addressing a gap in current dataset construction strategies. This is the proposed pipeline:

- An initial dataset is generated by sampling the geometry and the corresponding optical responses (phase and reflectivity), for two wavelengths using rigorous coupled-wave analysis (RCWA) [10].
- The dataset is used to train a surrogate forward model that approximates the mapping from metaatom geometry to electromagnetic response.
- The predicted and simulated responses are analyzed to characterize the distribution of samples in phase–reflectivity–wavelength space and to identify regions of dense and sparse coverage.
- The dataset is filtered to high-performance samples by applying a reflectivity threshold ($R \geq 97\%$). These samples are discretized into bins according to phase and wavelength to quantify coverage of the high-reflectivity response space. Underpopulated or empty bins are designated as target response regions for further sampling.
- Additional candidate geometries are generated by random sampling through RCWA and evaluated using the surrogate model, and only those falling within the target response regions are retained.
- The selected candidates are simulated with RCWA for validation. Redundant geometries are removed using a similarity criterion to avoid near-duplicate samples.
- The newly validated samples are incorporated into the existing dataset.
- The surrogate model is retrained on this new dataset, and the procedure is iterated until the high-reflectivity region of the response space exhibits sufficient coverage and diversity.
- Finally, a diffusion model is trained on both the original dataset and the new enriched dataset to test its feasibility.

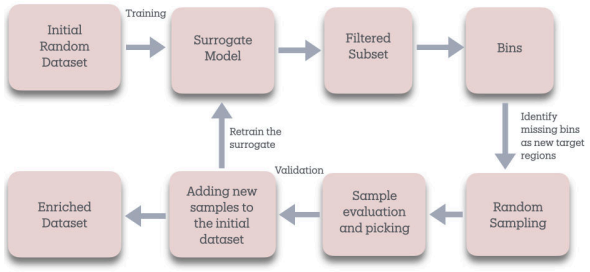

Fig. 2. Overview of the pipeline for dataset enrichment

III. Results and Discussion

We report on the behavior of the proposed dataset construction pipeline in terms of its ability to populate and uniformly cover the high-reflectivity region of the response space. In addition, we assess the practical feasibility of the method and analyze its computational efficiency when applied to large-scale dataset generation for inverse nanophotonic design.

Acknowledgments

This work was supported by the Deutsche Forschungsgemeinschaft (DFG, German Research Foundation) under Germany's Excellence Strategy within the Cluster of Excellence PhoenixD (EXC 2122, Project No. 390833453) and EXC 2123/2 QuantumFrontiers – 390837967.

References

[1] S. Kroker, J. Dickmann, C. B. Rojas Hurtado, D. Heinert, R. Nawrodt, Y. Levin, and S. P. Vyatchanin, "Brownian thermal noise in functional optical surfaces," *Phys. Rev. D*, vol. 96, no. 2, p. 022002, 2017.

[2] J. Dickmann, S. Sauer, J. Meyer, et al., "Experimental realization of a 12,000-finesse laser cavity based on a low-noise microstructured mirror," *Communications Physics*, vol. 6, p. 16, 2023.

[3] L. Shelling Neto, J. Dickmann, S. Sauer, and S. Kroker, "Bispectral optical cavity based on twin metamirrors," *J. Eur. Opt. Soc. Rapid Publ.*, vol. 20, p. 3, 2024.

[4] J. Ding, E. Capocasa, I. Ahrend, F. Liu, Y. Zhao, and M. Barsuglia, "Performance of multiple filter-cavity schemes for frequency-dependent squeezing in gravitational-wave detectors," *arXiv preprint*, arXiv:2506.02222 [gr-qc], 2025.

[5] Y. Cai, J. Roslund, V. Thiel, et al., "Quantum enhanced measurement of an optical frequency comb," *npj Quantum Inf.*, vol. 7, p. 82, 2021.

[6] L. Hen, E. Yosef, D. Raviv, R. Giryes, and J. Scheuer, "Inverse design of diffractive metasurfaces using diffusion models," *ACS Photonics*, vol. 13, no. 1, pp. 38–46, 2026.

[7] Y. Qin, H. Zheng, J. Yao, M. Zhou, and Y. Zhang, "Class-balancing diffusion models," *arXiv preprint*, arXiv:2305.00562, 2023.

[8] W. Ma, F. Cheng, and Y. Liu, "Deep learning for the design of nanophotonic structures," *Nature Photonics*, vol. 15, pp. 77–90, 2021.

[9] D. Lee, Y.-C. Chan, W. W. Chen, L. Wang, A. van Beek, and W. Chen, "t-METASET: Tailoring property bias of large-scale metamaterial datasets through active learning," *Journal of Mechanical Design*, vol. 145, no. 3, p. 031704, 2023.

[10] W. Jin, W. Li, M. Orenstein, and S. Fan, "Inverse design of lightweight broadband reflector for relativistic lightsail propulsion," *ACS Photonics*, vol. 7, no. 9, pp. 2350–2355, 2020.

Chiral Meta-atoms for Geometric-phase Manipulation in Metasurfaces Operating in the Visible Range

M. Giloan

MG Data, Cluj-Napoca, Romania
Corresponding author: mircea_giloan@yahoo.com

***Abstract*— The geometric phase method enables phase manipulation of circularly polarized incident light. We investigate the ability of chiral meta□atoms with specific geometries to convert incident circularly polarized light into its orthogonal handedness in transmission. Such meta□atoms can be used to design efficient, polarization□insensitive metasurfaces.**

***Keywords*— metasurfaces, chiral meta-atoms, geometric phase.**

I. Introduction

Optical devices require a specific phase distribution on a plane surface. The geometric phase method enables phase manipulation of circularly polarized incident light when the cross-polarized component is transmitted [1]. Chiral meta-atoms have been used to efficiently convert circularly polarized light into its cross-polarized component in transmission, enabeling the design of metasurfaces operating in the infra redrange [2].

In this theoretical study, chiral meta-atom with different geometries are investigated to identify the most suitable design for efficiently converting incident circularly polarized light into its cross-polarized transmitted component in the visible range.

II. Methods

The studied meta-atoms consist of TiO_2 structures on a SiO_2 substrate. Three-dimensional finite-difference time-domain simulations were performed [3]. The propagation of circularly polarized light normally incident on the metasurface was simulated. Figure 1 depicts the xy-plane cross-section of a meta-atom within a square unit cell of length 400 nm. The incident light propagates along z-axis. Periodic boundary conditions were applied along the x and y directions, while absorbing layers were used along the z direction. All depicted lengths are expressed in micrometers. The meta-atom geometry is chiral, since its mirror image cannot be superimposed onto itself. The height of meta-atom and the thickness of the substrate were set to 600 nm and 100 nm, respectively. The refractive index of the dielectric materials used in simulations, TiO_2 and SiO_2, were set to 2.41 and 1.45, respectively.

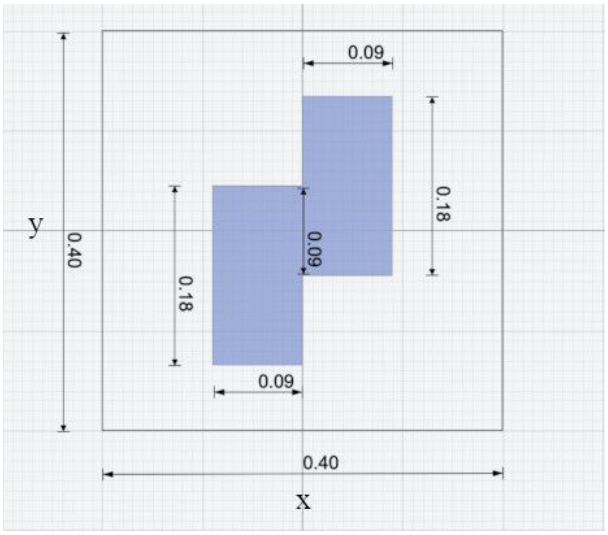

Fig. 1 Geometry of the studied chiral meta-atom, depicted in an xy-plane cross-section.

III. Results and Discussion

Figure 2 shows the real part of the electric-field component along z-axis for left-circularly polarized incident light at a wavelength of 568 nm. The distribution was computed in an xy-plane cross-section passing through the midpoint of the meta-atom height.

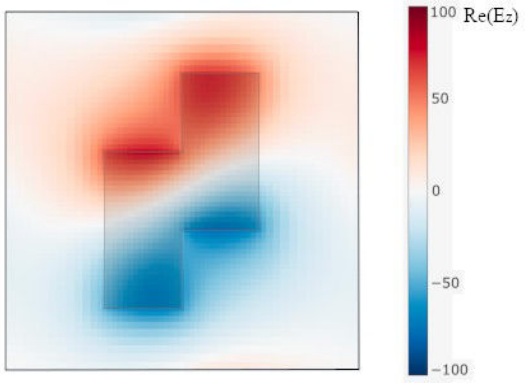

Fig. 2 Real part of the electric-field component along the z-axis for LCP incident light, shown in an xy-plane cross-section.

Figure 3 shows the real part of the electric-field component along z-axis for right-circularly polarized incident light at a wavelength of 568 nm. The distribution was computed in an xy-plane cross-section passing through the midpoint of the meta-atom height.

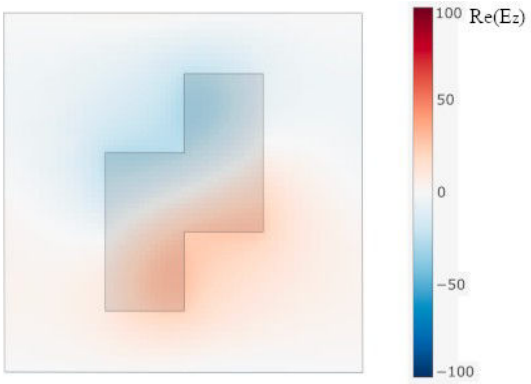

Fig. 3 Real part of the electric-field component along the z-axis for RCP incident light, shown in an xy-plane cross-section.

The difference in intensity observed in Figures 2 and 3 reflects the asymmetric transmission of left- and right-circularly polarized light produced by the studied meta-atom design.

IV. Conclusion

In this study, we analyzed the optical response of chiral dielectric meta-atoms designed for operation in the visible range using three-dimensional FDTD simulations. The investigated geometries exhibit asymmetric transmission for left- and right-circularly polarized incident light, enabling efficient conversion into cross-polarized component. The simulated field distributions and transmission spectra demonstrate that the meta-atom geometry strongly influences the achievable polarization-conversion efficiency. These findings confirm that properly engineered chiral dielectric meta-atoms are promising building blocks for metasurfaces based on the geometric-phase method, offering a viable route toward high-performance phase-manipulation devices in the visible spectrum.

References

[1] N. Yu and F. Capasso, “Flat optics with designer metasufaces,” Nature Mater., vol. 13, no. 2, pp. 139–150, 2014.
[2] Z. Ma, Y. Li, Y. Li, Y. Gong, S. A. Maier, and M. Hong, “All-dielectric planar chiral metasurface with gradient geometric phase,” Optics Express, vol. 26, no. 5, pp. 6067–6078, 2018.
[3] W. Shin, A. F. Oskooi, and S. G. Johnson, “Accelerating large-scale electromagnetic simulations with Tidy3D,” arXiv:2105.00965, 2021.

Mid-infrared Hyperbolic Metamaterial for the Silicon-Germanium Technology Platform

Jon Schlipf[1,*], Enrico Talamas Simola[2], Fritz Berkmann[3], Leonetta Baldassare[4], Giovanni Capellini[1,2], Monica de Seta[2], Luciana di Gaspare[2], Inga A. Fischer[1,3], Damiano Marian[5], Michele Ortolani[4], Michele Virgilio[5]

[1]IHP - Leibniz Institute for High Performance Microelectronics, Frankfurt (Oder), Germany
[2]Dipartimento di Scienze, Università degli Studi Roma Tre, Roma, Italy
[3]Chair of Experimental Physics and Functional Materials, BTU Cottbus-Senftenberg, Cottbus, Germany
[4]Dipartimento di Fisica, Sapienza Università di Roma, Roma, Italy
[5]Dipartimento di Fisica 'E Fermi', Università di Pisa, Pisa, Italy
*Corresponding author: schlipf@ihp-microelectronics.com

***Abstract*—We present anisotropic metamaterials based on SiGe layers with alternating doping. They were grown by chemical vapour deposition and characterized using Fourier-transform infrared spectroscopy. Measured reflectance spectra show excellent agreement with full-wave simulations, indicating the presence of a hyperbolic metamaterial near the plasma edge.**

***Keywords*— hyperbolic metamaterial, germanium, fourier-transform infrared spectroscopy.**

I. Introduction

When the components of the dielectric permittivity tensor of a metamaterial along different axes have opposite signs, the isofrequency surfaces in its dispersion relation become hyperboloids instead of the typical ellipsoids (or spheres in the isotropic case)[1]. Such hyperbolic metamaterials enable propagation of waves with very large in-plane k-vectors that would normally be evanescent. This leads to a virtually-infinite local density of optical states.

Among other approaches, hyperbolic metamaterials can be realized as planar periodic multilayer structures featuring sufficiently thin metals and dielectrics. Effective medium theory predicts anisotropic materials in this case, with hyperbolic behaviour near the plasma frequency of the metallic component.

The mid infrared (MIR) spectral range is important for a number of practical applications, including spectroscopy, imaging, thermal detection, and optical communication. As metals in MIR feature excessive negative permittivities, they can not be leveraged for hyperbolic metamaterials. Instead one can rely on heavily doped semiconductors. MIR hyperbolic metamaterials have been demonstrated using GaAs/AlInAs heterostructures[2]. Striving to bring MIR hyperbolic metamaterials in line with more established silicon photonic technologies for improved applicability[3], here we propose and investigate hyperbolic metamaterials based on Si_5Ge_{95} stacks with alternating intrinsic and highly doped layers.

II. Methods

We model the permittivity of doped and undoped Si_5Ge_{95} layers using a Drude model

$$\epsilon(\omega) = \epsilon_{\infty,Si5Ge95}(1 - \frac{\omega_p^2}{\omega^2 + i\omega\gamma}). \quad (1)$$

Here, $\epsilon_{\infty,Si5Ge95} = 16.36$ and $\omega_p^2 = \frac{N_D e^2}{\epsilon_0 m_{eff}}$ is the squared plasma frequency. m_{eff} is the effective mass of electrons, e is the elemental charge, ϵ_0 is the vacuum permittivity and N_D is the concentration of active dopants.

Based on effective medium theory, the effective in-plane and out-of-plane permittivity of the layer stack of intrinsic ϵ_d and doped ϵ_m material can be modeled as

$$\epsilon_{||} = (1-f)\epsilon_d + f\epsilon_m \quad (2)$$
$$\epsilon_{\perp} = \epsilon_m\epsilon_d/(f\epsilon_d + (1-f)\epsilon_m), \quad (3)$$

where the filling factor f stands for the relative thickness of the doped region with respect to the multilayer period. To simulate light propagation in the full layer stack, we use the rigorous coupled wave analysis[4], considering only the 0^{th} Fourier order and assuming non-dispersive substrate materials, $\epsilon_{Si} = 11.7$ and ϵ_{Ge}=16.6.

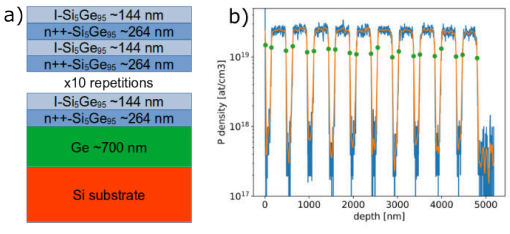

Fig. 1. (a) Sketch of the nominal structure of the sample. (b) SIMS measurements of the p dopant concentration in the grown sample.

We grew 10 repetitions of nominally 264 nm highly doped ($2.5 \cdot 10^{19}\mathrm{cm}^{-3}$) and 144 nm intrinsic Si_5Ge_{95} layers on a 700 nm Ge virtual substrate on Si by ultrahigh-vacuum chemical

vapour deposition, using SiH_4, GeH_4 and PH_3 as precursors (Fig. 1a)). Typically, one can expect about two thirds of the dopant atoms to be active. Secondary-ion mass spectroscopy (Fig. 1b)) confirms successful creation of steep doping profiles. Both doped and undoped layers are 20% thicker than their nominal values at 330±3 nm and 150±4 nm, respectively.

Fourier-transform infrared (FTIR) spectroscopy was performed in vacuum with a BRUKER VERTEX 70V spectrometer equipped with an angle-resolved reflectance setup, a wideband silicon beam splitter, a globar source and a pyroelectric detector with integrated preamplifier.

III. RESULTS AND DISCUSSION

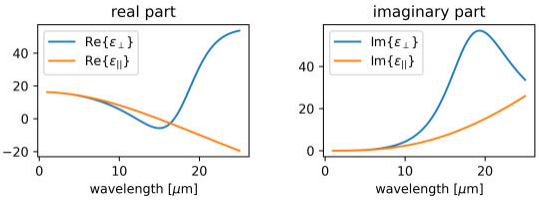

Fig. 2. Calculated real and imaginary parts of the in-plane and out-of-plane components of the relative permittivity of the metamaterial.

The calculated in-plane and out-of-plane permittivity for a metamaterial with $f = 0.68$ and $N_D = 1.8 \cdot 10^{19}\text{cm}^{-3}$ is shown in Fig. 2. The real parts of the out-of-plane and in-plane permittivity cross zero at $\lambda = 12\mu\text{m}$ and $\lambda = 15\mu\text{m}$, respectively. Between these, only the out-of-plane permittivity is negative, and we expect a hyperbolic metamaterial.

Fig. 3. Heatmaps of a) measured and b) simulated ratios of TE and TM reflectance as a function of wavenumber and angle of incidence. The red lines represent the wavenumber-dependent pseudo-Brewster angle (solid) and the numerical minimum of the dichroic ratio as shown in the heatmap (dashed) as a function of frequency. Black vertical lines mark the zero crossings of real parts of the in-plane and out-of-plane permittivity at 12 and 15 μm.

Experimental and full-wave simulated ratios of TM and TE reflectance as a function of angle of incidence θ and angular frequency ω are shown in Fig. 3. Agreement between them is best for lower angles of incidence. For the dielectric regime ($\lambda < 12\ \mu\text{m}$), we observe Fabry-Perot thickness oscillations, related to the thickness of the metamaterial layer. The singular Bragg peak at $\lambda = 3.6\ \mu\text{m}$ is caused by the periodic stack of doped and intrinsic layers.

We computed the pseudo-Brewster angle, which is the angle of minimized TM reflectance of a hypothetical infinite-thickness metamaterial slab in effective-medium approximation, thus disregarding Fabry-Perot and Bragg effects, shown in Fig.2a-b) as a red solid line. In hyperbolic metamaterials, one expects a discontinuity at the pseudo-Brewster angle at the onset of hyperbolic regime[2], at $\lambda = 12\ \mu\text{m}$ in our case. The fact that we only observe a dip in pseudo-Brewster angle, followed by an increase at the plasma edge, and no discontinuity, is due to considerable losses induced by the very high doping concentration(Fig.2b). A discontinuity can be observed when artificially increasing the electron mobility by a factor of 10 in simulation.

In addition to magnitudes, we also measured relative phase between TE and TM reflectance in a configuration similar to periodic ellipsometry, with a polarizer before the sample at 45° with respect to the plane of incidence and an analyzer after the sample rotated in increments of 5°. With this additional information we were able to fit our simulation model to the experimental data, with N_D and layer thicknesses as free parameters. From the fit, we obtain in $N_D = 1.62 \cdot 10^{19}\text{cm}^{-3}$, which is lower than expected but still high enough for a hyperbolic metamaterial according to our analytical model.

IV. CONCLUSION

We have grown anisotropic metamaterials as epitaxial silicon-germanium multilayer stacks with modulated doping. Experimental measurements strongly agree with simulations and fits on experimental data yield parameters close to nominal values, indicating hyperbolic optical properties in the mid-infrared regime. Typical optical features are obscured by losses in reflectance, and we intend a stronger demonstration of hyperbolic properties in transmission[5] or in layer stacks featuring less doping tailored to lower frequencies.

ACKNOWLEDGMENTS

We thank the German Federal Ministry of Research, Technology and Space (BMFTR) for support under grant M077MB156.

REFERENCES

[1] V. A. Podolskiy and E. E. Narimanov, "Strongly anisotropic waveguide as a nonmagnetic left-handed system," *Physical Review B—Condensed Matter and Materials Physics*, vol. 71, no. 20, p. 201101, 2005.

[2] A. J. Hoffman, L. Alekseyev, S. S. Howard, K. J. Franz, D. Wasserman, V. A. Podolskiy, E. E. Narimanov, D. L. Sivco, and C. Gmachl, "Negative refraction in semiconductor metamaterials," *Nature Materials*, vol. 6, no. 12, pp. 946–950, 2007.

[3] I. A. Fischer, M. Brehm, M. De Seta, G. Isella, D. J. Paul, M. Virgilio, and G. Capellini, "On-chip infrared photonics with si-ge-heterostructures: What is next?" *APL Photonics*, vol. 7, no. 5, p. 050901, 2022.

[4] J. Schlipf and I. A. Fischer, "Rigorous coupled-wave analysis of a multi-layered plasmonic integrated refractive index sensor," *Optics Express*, vol. 29, no. 22, pp. 36 201–36 210, 2021.

[5] M. A. Noginov, Y. A. Barnakov, G. Zhu, T. Tumkur, H. Li, and E. E. Narimanov, "Bulk photonic metamaterial with hyperbolic dispersion," *Applied Physics Letters*, vol. 94, no. 15, p. 151105, 2009.

Needle-beam metalens-enabled large-volume super-resolution photoacoustic neuron imaging of expanded tissue

Yongjae Jo[1, #], Inki Kim[1, 2, *]

[1] Department of Biophysics, Institute of Quantum Biophysics, Sungkyunkwan University, Korea

[2] Departments of MetaBioHealth, Biopharmaceutical Convergence, Sungkyunkwan University, Korea

*Corresponding author: Inki.kim@skku.edu

***Abstract*—Needle-beam metalens photoacoustic microscopy has emerged as a promising approach due to its extended depth of focus, which enables volumetric imaging with minimal axial resolution degradation. Despite this advantage, conventional PAM is constrained by limited axial resolution, hindering quantitative three-dimensional analysis at the cellular scale. To address, expansion microscopy was adopted with a needle-beam metalens PAM platform to enhance effective spatial resolution while preserving large-volume imaging capability. A modified phase design was further introduced to improve optical efficiency, yielding approximately two-fold higher brightness than conventional needle-beam configurations. A 2 mm metalens was fabricated on a 1 μm-thick silicon nitride substrate, and imaging was conducted using a custom-built transmission-mode photoacoustic system. Selective pigment-based labeling enabled neuron-specific photoacoustic contrast following tissue expansion. The proposed approach was evaluated using carbon nanoparticle phantoms and neuronal tissue samples. he results demonstrated an effective resolution improvement of 4–20× and enabled quantitative assessment of neuronal density changes after amyloid-beta treatment. Overall, this study highlights the potential of metalens-enabled PAM for high-resolution three-dimensional cellular imaging.**

***Keywords*— Needle beam metalens, photoacoustic microscopy, deep tissue imaging**

I. Introduction

Needle-beam metalens-based photoacoustic imaging has recently gained attention owing to its extended depth of focus, which enables volumetric imaging over large depths with minimal degradation in axial resolution. In addition, photoacoustic imaging offers rapid signal acquisition along the acoustic axis, making it well suited for high-speed three-dimensional imaging. However, conventional approaches are constrained by limited spatial resolution, particularly along the axial direction, which restricts quantitative analysis of fine structures in three dimensions. To address this limitation, expansion microscopy was incorporated into a needle-beam metalens-based photoacoustic imaging system to enhance effective spatial resolution while preserving large-volume imaging capability. Furthermore, a modified needle-beam metalens was introduced to improve optical efficiency, achieving approximately two-fold higher brightness compared with conventional designs. In neuroscience applications, resolving fine neuronal structures distributed in three-dimensional space is essential for understanding cellular function and organization. To validate the proposed imaging strategy, neuronal imaging experiments were conducted to assess its capability for high-resolution structural visualization.

II. Methods

In this study, a 2 mm diameter needle-beam metalens was fabricated on a 1 μm-thick silicon nitride substrate using electron-beam lithography followed by development and etching. Conventional needle-beam metalenses are implemented by randomly multiplexing phase maps corresponding to single-focus metalenses with different focal lengths. However, this approach suffers from reduced optical efficiency, as the intensity decreases proportionally to the square of the number of multiplexed phase components. Here, a newly developed phase design was introduced to overcome this limitation, enabling approximately two-fold enhancement in optical efficiency. The proposed 2 mm needle-beam metalens was validated through both numerical simulations and

experimental characterization.

Imaging experiments were conducted using a custom-built transmission-mode photoacoustic microscopy system. A 532 nm pulsed laser operating at 20 kHz and a 19 MHz ultrasound transducer were employed, achieving an axial resolution of approximately 100 μm and a lateral resolution of ~2 μm with a single-shot imaging depth of up to 1 mm. To address the intrinsic resolution limitation of photoacoustic microscopy, expansion microscopy was incorporated to physically enlarge the sample and enable high-resolution imaging. While conventional expansion microscopy relies on fluorescence labeling, it is not directly compatible with photoacoustic contrast generation. To overcome this limitation, antigen–antibody reactions combined with pigment-based staining were utilized to selectively deposit absorbing labels on neuronal structures. The proposed approach was evaluated using carbon nanoparticle phantoms and three-dimensional neuronal tissue imaging. Resolution changes associated with the use of needle-beam excitation and tissue expansion were systematically analyzed to demonstrate the effectiveness of the method. Furthermore, quantitative analysis of three-dimensional neuronal distributions following amyloid-beta treatment confirmed the applicability of this technique for structural analysis at the cellular level.

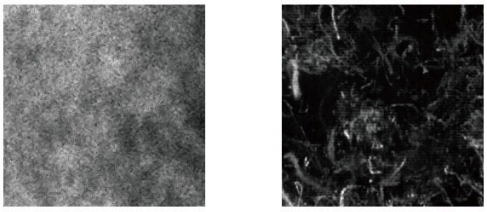

Fig. 1 Photoacoustic imaging of neurons. Conventional PAM (left) and proposed system (right)

III. Results and Discussion

Optical-resolution photoacoustic microscopy enables diffraction-limited imaging at the focal plane but suffers from defocus-induced blurring away from focus due to limited axial resolution and optical focusing constraints. By combining expansion microscopy with a needle-beam metalens, both effective resolution and depth of focus are enhanced, enabling high-resolution imaging over an extended axial range. In addition, the high sampling rate of ultrasound detection allows rapid axial data acquisition without mechanical scanning, supporting large-volume three-dimensional imaging. To validate this concept, imaging experiments were performed using carbon nanoparticle phantoms and neuronal tissues. With Gaussian-beam excitation, particles appeared increasingly blurred and enlarged with defocus, whereas needle-beam illumination provided uniform and sharp imaging over a depth of approximately 1 mm.

For biological validation, neuronal and glial structures were labeled and imaged to resolve fine three-dimensional architectures. A neurodegenerative condition was further mimicked via amyloid-beta treatment to assess whether structural alterations could be detected and quantified. Before expansion, limited resolution hindered clear discrimination of cellular morphology. After expansion combined with needle-beam imaging, fine structural details became clearly resolvable. The effective resolution improvement ranged from approximately 4× to 20×, enabling cellular-level imaging that is difficult to achieve with conventional photoacoustic approaches. In the disease model, three-dimensional imaging enabled quantitative analysis of neuronal density. An increase in neuronal density in the amyloid-beta-treated group was detected and quantified using the proposed method. These results demonstrate that needle-beam metalens-based photoacoustic imaging enables high-resolution three-dimensional visualization at the cellular scale. While expansion alone is limited by the short depth of focus of Gaussian beams, the needle-beam metalens provides uniform axial resolution, highlighting the potential of this approach for advanced optical imaging applications.

IV. Conclusion

We have demonstrated feasibility of modified needle beam metalens for thick tissue PAM imaging in expanded samples. Future work will extend the utilization of our system for high-resolution 3D PA imaging.

Acknowledgments

This work was supported by the Samsung Research Funding & Incubation Center of Samsung Electronics under Project Number SRFC-IT2401-01 and by National Research Foundation (NRF) grants (RS-2026-25479531 and RS-2024-00462912) funded by the Ministry of Science and ICT (MSIT) of the Korean government. Y.J. acknowledges the NRF Sejong Science Fellowship (RS-2026-25473628) funded by the MSIT of the Korean government.

References

[1] Barulin, Aleksandr, et al. "Axially multifocal metalens for 3D volumetric photoacoustic imaging of neuromelanin in live brain organoid." *Science advances* 11.3 (2025): eadr0654.

[2] Rui, et al. "Optical-resolution photoacoustic microscopy with a needle-shaped beam." *Nature photonics* 17.1 (2023): 89-95.

[3] Jo, Yongjae, et al. "Image scanning microscopy based on multifocal metalens for sub-diffraction-limited imaging of brain organoids." *Light: Science & Applications* 14.1 (2025): 367.

[4] Chen, Fei, Paul W. Tillberg, and Edward S. Boyden. "Expansion microscopy." *Science* 347.6221 (2015): 543-548.

[5] Mu, Xuan, et al. "On-demand expansion fluorescence and photoacoustic microscopy (ExFLPAM)." *Photoacoustics* 38 (2024): 100610.

Autoregressive Transformer for Inverse Design of Optical Multilayer Thin-Film Structures

Kewen Ding[1†], Peng Dai[1†], Mike Pivnenko[1], Daping Chu[1*]

[1]Centre for Photonic Devices and Sensors,
University of Cambridge, 9, JJ Thomson Avenue, CB3 0FA, England, United Kingdom

*Corresponding author: dpc31@cam.ac.uk
Contributing authors: kd507@cam.ac.uk; pd566@cam.ac.uk; mp380@cam.ac.uk;
†These authors contributed equally to this work.

***Abstract*—We propose an encoder-decoder Transformer for inverse design of optical multilayer thin-film structures. A decoupled tokeniser predicts materials and thicknesses as separate tokens, achieving 1 nm thickness resolution. The model attains a mean absolute error of 0.0785 on 50,000 test samples at 511 designs per second.**

***Keywords*— metamaterials, thin-film optics, inverse design, Transformer, autoregressive generation.**

I. Introduction

Multilayer thin-film structures modulate reflectance through interference and are widely used in Distributed Bragg Reflector (DBR), dielectric mirror and anti-reflective coatings. However, inverse design of such structures remains challenging in practice due to the dimensional curse as the layer count increases. Early optimisation-based approaches are computationally expensive [1], scale poorly with increasing design complexity, and typically require physical prior and design experience to begin at a reasonable initial design to avoid low-quality local optima.

Data-driven deep learning models have been explored as alternatives for photonic inverse design. Nevertheless, the conventional single-step neural predictor is inherently limited when the structure contains a variable layer count, since the output dimensionality of the neural network is fixed. This constraint motivates reformulating multi-layer structure inverse design as a sequence-generation problem, where an autoregressive model predicts the structure token by token [2], [3].

Building on this idea, OptoGPT introduced an autoregressive framework for inverse design of multilayer structures using Transformer [4], demonstrating the ability to design structures with variable layer counts. Despite this progress, its tokenisation couples material and thickness into a single token, constraining thickness resolution to 10 nm or requiring a further thickness fine-tune.

To address the aforementioned issues, we propose an encoder–decoder Transformer architecture that supports flexible wavelength windows and employs a decoupled tokeniser, enabling material and thickness tokens to be predicted separately. This strategy increases thickness precision and reduces the vocabulary size. As the thickness is conditioned on material, this prediction order introduces more physical causality, improving both modelling efficiency and adaptability across design settings.

II. Results and Discussions

The schematic of the proposed model is illustrated in Fig. 1a. The encoder takes the wavelengths and spectral values, then outputs a contextual representation. The decoder autoregressively generates the structure conditioned on the encoder output via cross-attention.

We trained the model using the standard teacher-forcing method in the Large Language Model (LLM) [5]. The losses and accuracies are shown in Fig. 1b. The training loss dropped significantly within the first 1000 steps, and then gradually converged. The validation loss followed the training loss closely, indicating no overfitting occurred. The accuracy validated the loss trend, which indicated the performance improvement of the model during training.

A. Autoregressive Generation

The structure generation started from a special token BoS, and proceeded token by token. At each step, logits were temperature-scaled and masked to enforce the alternating material–thickness order. For example, at the turn of material prediction, the probabilities of thickness were set to zero, and vice versa. We used the nucleus (top-p) strategy with $p = 0.9$ to sample tokens and appended them to the generated sequences. The special token EoS served as the signal to stop the generation, which enabled variable layer counts.

In the test set with 50,000 samples, the trained model achieved an average MAE of 0.0785. Fig. 2a presents the MAE histogram, which is strongly right-skewed, indicating high design accuracy, with 95% of predictions achieving MAE < 0.164. We selected a representative design result (MAE $= 0.049998$) that demonstrated closely aligned spectral reconstruction, as shown in the Fig. 2b, validating the model's precision for multilayer inverse design. The structures of the ground truth and the predicted are listed in Table I. The first two layers showed high similarity, while the later layers had certain degrees of differences in thickness or material. An

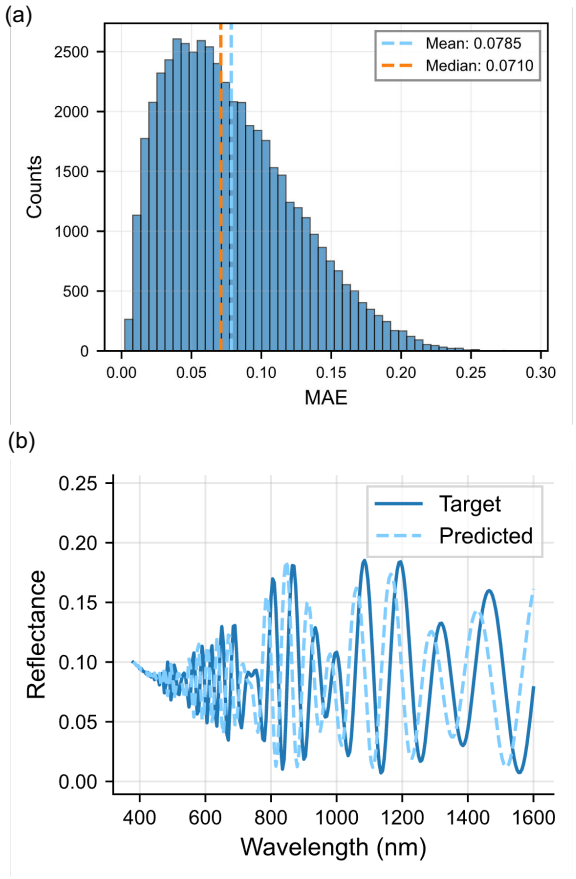

Fig. 1. (a) Schematic of the encoder–decoder Transformer. The encoder embeds the input reflectance spectrum into a spectral context, which the decoder attends to via cross-attention while autoregressively generating the multilayer structure. (b) The training, validation losses and accuracies show that the model converges efficiently.

Fig. 2. (a) MAE distribution of over 50,000 test samples. The distribution is strongly right-skewed; 95% of predictions achieve MAE < 0.165. (b) The representative design of a random target spectrum; the predicted spectrum has a similar distribution to the target.

inference throughput of 511 designs/s enables practical real-time optical design workflows.

TABLE I
GROUND TRUTH AND PREDICTED STRUCTURES FOR SPECTRAL IN FIG.2B. THICKNESSES ARE IN NM. BOTH STRUCTURES CONTAIN 8 LAYERS.

	Ground Truth		Predicted	
Layer	**Material**	**t (nm)**	**Material**	**t (nm)**
1	ZnO	521	ZnO	972
2	ZnO	355	ZnO	687
3	ZnO	762	Al_2O_3	964
4	Al_2O_3	911	MgF_2	456
5	CaF_2	439	Al_2O_3	69
6	Al_2O_3	166	Al_2O_3	83
7	TiO_2	357	Ta_2O_5	372
8	SiO_2	592	MgF_2	11

III. CONCLUSION

We have presented an encoder–decoder Transformer for inverse design of optical multilayer thin-film structures. By decoupling material and thickness tokens, the proposed architecture achieves 1 nm thickness resolution, and the design order is more physically intuitive. The model attained a mean absolute error of 0.0785 at an inference throughput of 511 designs/s using a single GPU NVIDIA RTX 5090, enabling practical real-time design workflows. Future work will extend the framework to include real-time physical guidance into the model and use reinforcement learning to enhance the accuracy.

ACKNOWLEDGMENTS

This work was supported by the Cambridge Trust and the Chinese Scholarship Council.

REFERENCES

[1] D. Liu, Y. Tan, E. Khoram, and Z. Yu, "Training deep neural networks for the inverse design of nanophotonic structures," vol. 5, no. 4, pp. 1365–1369. [Online]. Available: https://doi.org/10.1021/acsphotonics.7b01377

[2] H. Wang, Z. Zheng, C. Ji, and L. Jay Guo, "Automated multi-layer optical design via deep reinforcement learning," vol. 2, no. 2, p. 025013. [Online]. Available: https://doi.org/10.1088/2632-2153/abc327

[3] P. Dai, K. Sun, X. Yan, O. L. Muskens, C. H. K. d. Groot, X. Zhu, Y. Hu, H. Duan, and R. Huang, "Inverse design of structural color: finding multiple solutions via conditional generative adversarial networks," vol. 11, no. 13, pp. 3057–3069. [Online]. Available: https://www.degruyterbrill.com/document/doi/10.1515/nanoph-2022-0095/html

[4] T. Ma, H. Wang, L. J. Guo, Department of Physics, University of Michigan, Ann Arbor, Michigan 48109, USA, and Department of Electrical Engineering and Computer Science, University of Michigan, Ann Arbor, Michigan 48109, USA, "OptoGPT: A foundation model for inverse design in optical multilayer thin film structures," vol. 7, no. 7, pp. 240 062–240 062. [Online]. Available: http://www.oejournal.org//article/doi/10.29026/oea.2024.240062

[5] R. J. Williams and D. Zipser, "A learning algorithm for continually running fully recurrent neural networks," vol. 1, no. 2, pp. 270–280. [Online]. Available: https://doi.org/10.1162/neco.1989.1.2.270

Hyperbolic metamaterials for efficient single photon emission

Manobina Karmakar[1,*], Pavel Klok[2], Katarina Rovenská[2], Peter Kepič[2], Thomas Possmayer[1], Beáta Idesová[2], Filip Ligmajer[2] and Leonardo de Souza Menezes[1,*]

[1]Chair in Hybrid Nanosystems, Nanoinstitute Munich, Faculty of Physics, Ludwig-Maximilians-Universität München, Königinstraße 10, 80539 München, Germany
[2]Institute of Physical Engineering, Faculty of Mechanical Engineering, Brno University of Technology, Technická 2, 616 69 Brno, Czech Republic
*Corresponding author: Manobina.Karmakar@lmu.de, L.Menezes@physik.uni-muenchen.de

***Abstract*— Hyperbolic metamaterials (HMMs) offer ultrahigh photonic density of states for enhancing solid-state single-photon emitters. Using analytical and FDTD simulations, we evaluate Purcell factors and photon collection efficiencies for metal–dielectric HMM stacks coupled to two-dimensional emitters. We show that high Purcell enhancement often accompanies strong non-radiative losses, while surface gratings significantly improve far-field photon out-coupling.**

***Keywords*— Hyperbolic metamaterials, single photon emitters, photon extraction.**

I. Introduction

Solid-state single-photon emitters (SPEs) are essential building blocks for scalable photonic quantum information processing [1-2]. Despite deterministic single-photon generation, compatibility with nanophotonic architectures, currently available SPEs face several challenges like low emission rate, fast decoherence and less external control that hinder practical deployment [3]. A general strategy to address these challenges is to embed SPEs in nanostructured photonic environments with elevated photonic density of states (PDOS), thereby enhancing light-matter interactions [4]. The increased PDOS provides additional decay channels, enabling brighter single photon emission. Recent approaches using quantum dots in Bragg reflectors have demonstrated moderately bright and pure single photons, but face two drawbacks: (i) fabrication is complex due to selective emitter placement, and (ii) the enhancement of spontaneous emission remains modest. Hyperbolic metamaterials (HMMs), composed of alternating metal–dielectric layers, offer much higher PDOS compared to Bragg reflectors [5]. Light-matter coupling is strong at the HMM surface, making surface-integration of atomically thin 2D emitters ideal for achieving high Purcell enhancement. Defect-bound excitonic states in monolayer transition-metal dichalcogenides, such as WSe_2, provide reliable single-photon emission with sub-nanometer confinement [2], and are ideal candidates to be integrated on the HMM surface with minimal separation.

A plethora of experimental and theoretical studies have highlighted Purcell factor, given by $\frac{P_r + P_{nr}}{P_0}$ (P_r: radiative power dissipation, P_{nr}: non-radiative power dissipation, P_{tot}: total power dissipation in vacuum) as indicators of photon emission enhancement. However, as the definition suggests, Purcell enhancement includes radiative as well as non-radiative pathways. Often the latter is strong enough to have poor photon out-coupling. Therefore, depiction of PF alone is not enough for judging enhancements in emitter properties. In this study, we simulate PF as well as photon collection probabilities of hyperbolic metamaterials in order to account for non-radiative losses in the system that most studies overlook. We explore properties of photon emitters coupled to HMMs through analytical and Finite Difference Time Domain (FDTD) electromagnetic simulations. We consider HMM stacks with various dielectric and metal pairs and investigate their suitability to enhance single-photon emitters based on two-dimensional materials like tungsten selenide (WSe_2) and hexagonal boron-nitride (hBN).

II. Methods

To estimate the PDOS of a dispersive medium, we rely on the depiction of isofrequency surface that is defined by a surface in the k-space where all points correspond to states with same frequency ω (i.e., ω(k) = constant). In an isotopic medium, the linear dispersion leads to propagating waves with a spherical isofrequency surface given by the following equation: $k_x^2 + k_y^2 + k_z^2 = \epsilon\frac{\omega^2}{c^2}$; where, the propagating wavevector is $\boldsymbol{k} = (k_x, k_y, k_z)$, ϵ is the dielectric permittivity of the medium and ω is the frequency of light (Fig. 1(a)). If we consider an anisotropy, the isofrequency surface for a TM polarized wave reads as $\frac{k_x^2+k_y^2}{\epsilon_{zz}} + \frac{k_z^2}{\epsilon_{xx}} = \frac{\omega^2}{c^2}$ with an assumed dielectric tensor $\epsilon = (\epsilon_{xx} = \epsilon_{||}, \epsilon_{xx} = \epsilon_{||}, \epsilon_{zz} = \epsilon_{\perp})$. In such a case, the isofrequency surface is an ellipsoid. Interestingly, if there is an anisotropic material where the parallel and perpendicular components have different signs, that is $\epsilon_{||}.\epsilon_{\perp} < 0$, the isofrequency surface becomes an open hyperboloid. Such materials can be fabricated artificially by incorporating hybrid designs of metals and dielectrics and are termed as hyperbolic metamaterials (HMMs)

[6-7]. Interestingly the high k-waves that become evanescent in isotropic materials and decay exponentially are allowed to propagate in HMMs. The presence of high-k modes enhances the overall photonic density of states. A single photon emitter directly coupled to the higher PDOS of the HMMs display higher spontaneous emission rates and hence, stronger emission.

First, we identify the proportion ratios of metal and dielectric needed for hyperbolicity from Effective Medium Theory and thereafter, use analytical solutions and finite difference time domain (FDTD) simulations to find field enhancements, Purcell factors and photon collection efficiencies corresponding to artificial, multi-layered HMM stacks.

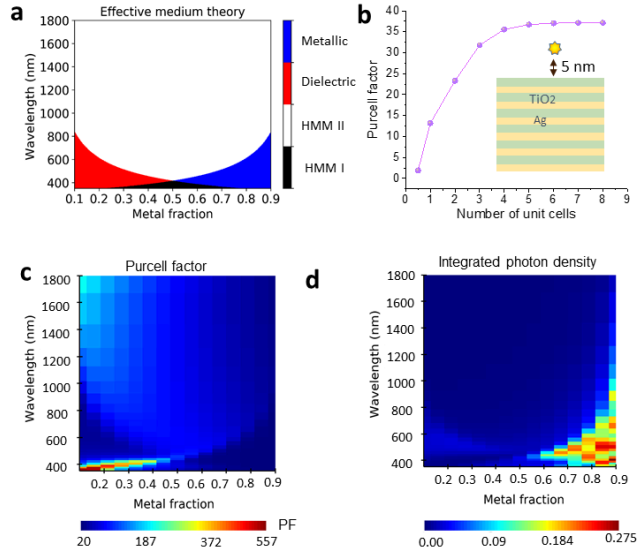

Fig. 1 (a) Estimation of metallic, dielectric, hyperbolic type-I and type-II regions as a function of metallic fraction and wavelength for TiO_2/Ag stack using effective medium theory. (b) Convergence test for Purcell factor of a horizontal dipole placed 5 nm above the stack as a function of number of unit cells consisting of a metal and a dielectric layer. Analytically calculated (c) Purcell factor and (d) integrated photon density as a function of metal fraction and wavelength.

III. Results and Discussion

We apply EMT to find the suitable wavelength regions of enhancement in a stack made of titanium oxide and silver. As seen from Fig. 1(a), this stack offers hyperbolic states in the visible spectrum for selected metal fractions around 0.5 and offers hyperbolicity in the near-infrared region throughout all metal fractions studied here. Prior to estimating the PF of the structure with various metal fractions and wavelengths, we perform a convergence test for the same and as depicted in Fig. 1(b), six unit cells comprising of a metal and dielectric material show optimized PF. We use this set-up for further calculations. To investigate the potential spontaneous emission enhancement through coupling with the HMM, we calculate the PF of TiO_2/Ag stack corresponding to varying metal fraction of Ag and spanning visible to the near infrared frequencies. To perform these simulations, we consider a horizontal dipole placed 5 nm above the metamaterial stack. As the analytical calculations reveal, the spectral and metal fraction regions corresponding to higher PF correlates strongly with the EMT map, as expected. Since the PF indicates the enhancement of spontaneous emission rate originating from both radiative and non-radiative channels, we also calculate the angle-integrated photon intensity and plot in Fig. 1(d). This allows distinction of the radiative contributions. Surprisingly enough, the higher photon collection probabilities are correlated with lower PFs, as clearly visible from Fig. 1(c) and (d). This stems from the non-radiative loss of the high-k modes taking place in the metal-dielectric interfaces of the stack. To overcome non-radiative losses, one must introduce a coupling element into the structure—such as a grating or a photonic crystal—so that high-k modes can be coupled out to the far field [8].

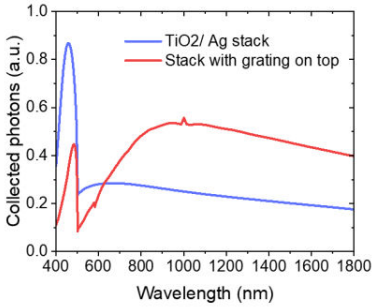

Fig. 2: Blue curve: Collected photon intensity at a far-field location above a HMM stack of TiO_2/Ag (20 nm/5 nm) with metallic fraction of 0.2, as a function of wavelength of dipole emission - estimated from FDTD. Red curve: same quantity with a 2D photonic crystal of etched on top TiO_2 surface (height: 20 nm). The etched PhC consists of square array of a period of 100 nm with radius of each pillar being 40 nm.

We perform FDTD electromagnetic simulations with a HMM stack with unit cells of 20 nm TiO_2 and 5 nm Ag and a horizontal dipole placed 5 nm above surface. We calculate the total photons collected at far-field as a function of emission wavelength which matches well with analytical result (metal fraction 0.2 in Fig. 1(d)). Next, we introduce a 2D photonic crystal array consisting of etched holes into the top TiO_2 surface layer and calculate the same quantity. As Fig. 2 depicts, we observe about a two-fold enhancement of the photon collection by introducing the etched grating structure. This result highlights the importance of a grating to out-couple the high-k modes that contribute to the high PDOS and strong light-matter interaction of the dipole emitter. Further, we study other combinations of materials and observe tunability in the photon out-coupling using two phase-change materials, namely-vanadium dioxide and antimony-sulfide.

IV. Conclusion

In this study, we explore the hyperbolic metamaterials from scratch and identify the important figures of merit for designing and fabricating a single photon emitter coupled to a hyperbolic metamaterial stack. We uncover that high PF is not a sufficient criterion for enhancing spontaneous emission rate of an emitter: the drawback being non-radiative losses in the metal-dielectric interfaces. Such bottleneck is overcome by enabling out-coupling of high-k modes of light through a photonic crystal on top of the metasurface stack. In addition, we investigate multiple materials and their suitability to enhance single photon emission from two-dimensional material based emitters.

ACKNOWLEDGMENTS

This work was supported by the *Joint Czech-Bavarian Research Projects 2024 – 2026* from the Bavarian-Czech Academic Agency – BTHA.

REFERENCES

[1] Science 318, 1567 (2007)
[2] The Journal of Physical Chemistry Letters 14 (13), 3274-3284 (2023)
[3] Rep. Prog. Phys. 68, 1129 (2005)
[4] Adv. Optical Mater. 11, 2202759 (2023)
[5] J. of Optics 14, 063001 (2012)
[6] Science 336, 205-209 (2012)
[7] Nature Photon 7, 948–957 (2013)
[8] Nature Nanotech 9, 48–53 (2014)

Dual-Band Beam-Switching Cavity-Excited Antenna Based on Scattering Constellations

Yumeng Wang[1], Zeqiang Lin[1], Alex M. H. Wong[1,2,*]

[1]Department of Electrical Engineering, City University of Hong Kong, Hong Kong SAR, China
[2]State Key Laboratory of Terahertz and Millimeter Waves, City University of Hong Kong, Hong Kong SAR, China
*Corresponding author: alex.mh.wong@cityu.edu.hk

***Abstract*—A mechanically reconfigurable, dual-band cavity-excited antenna is designed based on scattering constellations composed of metallic rods. The reconfigurability originates from modulating the sparse distribution of metallic rods inside the cavity, which offers vast design freedom. A hybrid BPSO-LS algorithm is employed to optimize the rod layout for target radiation patterns. By using only two distinct scattering constellations, the design enables dual-band beam switching between 0° and 30° at both 7 GHz and 12 GHz. Full-wave simulations validate the concept, demonstrating high-precision beam control.**

***Keywords*— dual band, beam switching, reconfigurable antenna, optimized algorithm, scattering constellation.**

I. Introduction

With the rapid evolution of wireless communication systems, reconfigurable antennas (RAs) have become a widely adopted approach for achieving functional agility. Traditional reconfiguration (p-i-n diodes [1], varactors [2], MEMS [3]) often introduces significant parasitic effects and ohmic losses, which can severely degrade the antenna's radiation performance. Moreover, complex biasing circuits make antenna design more expensive and complex [4]. Compared to electric reconfigurable techniques, mechanical solutions offer higher radiation efficiency and less interference. However, mechanical mechanisms often result in bulky, costly designs and offer limited structural freedom.

Among various mechanical reconfigurable architectures, the cavity-excited antenna based on scattering constellation emerged as a robust, all-metal structure [5]. Its design can offer immense degrees of freedom for reconfiguration and realize diverse radiation functionalities only by modulating the rods inside the cavity. The all-metal structure also simplifies fabrication.

In this work, we propose a dual-band beam switching scheme for a cavity-excited antenna based on the concept of scattering constellations. For illustration, the antenna is designed to operate at 7 GHz (C-band) and 12 GHz (Ku band). To achieve this design, an optimization algorithm is employed to determine the optimal sparse layout of the metallic rods, with the electric field characterized by a semi-analytical model. The proposed design is validated using two distinct scattering constellations: Constellation A generates a radiation beam at 0° for both 7 GHz and 12 GHz, while Constellation B directs the beam at 30° at the same frequencies. Simulation results confirm that dual-band beam switching between 0° and 30° is achieved by switching between the two constellations, with stable radiation performance at both frequencies. Moreover, the directivity of Constellation A matches well with that of an ideal uniform aperture of the same size, and the measured S11 values are below -10 dB at both frequencies, verifying excellent impedance matching for dual-band design.

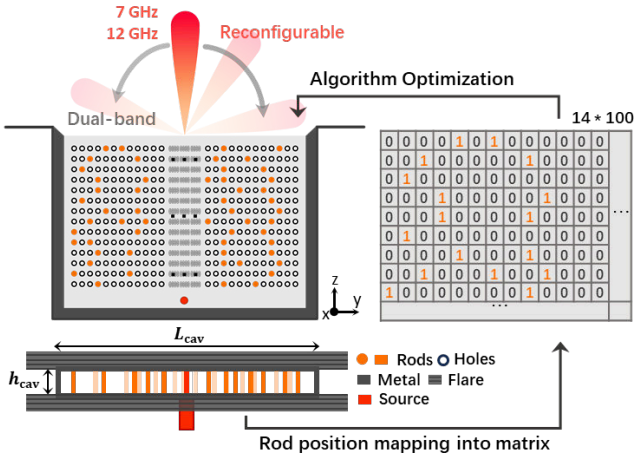

Fig. 1. Configuration of the cavity-excited antenna and the design procedure. Beam switching can be achieved simply by changing the rods distribution (constellations) inside the cavity.

II. Methods

The configuration of the cavity excited antenna is shown in Fig. 1. The antenna comprises a metallic cavity with a single radiation aperture, with the remaining five walls enclosed in metal. To minimize propagation discontinuities and ensure a smooth impedance transition, flare structures are integrated at the top and bottom edges of the aperture. Both the upper and lower metallic plates of the cavity are uniformly distributed with a 14×100 array of holes. These holes are precisely aligned between the two layers, such that the insertion of metallic rods establishes a reliable electrical connection between the top and bottom walls.

The cavity can be considered as a 2D configuration ($\partial/\partial x = 0$). The total field on the aperture can be considered as the sum

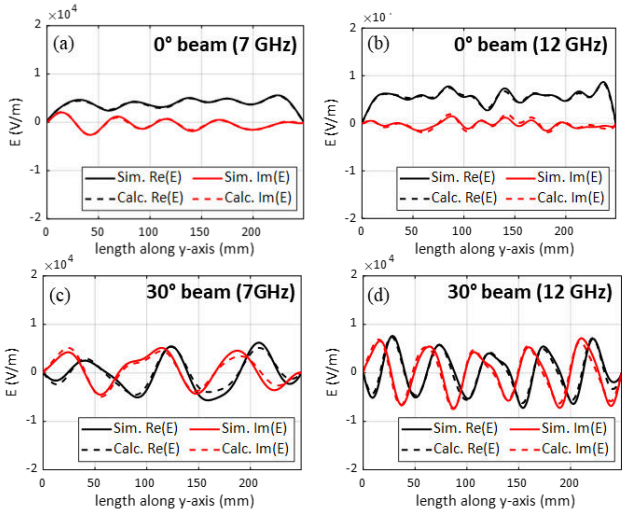

Fig. 2. Calculated E-field based on semi-analytical model and full-wave simulated E-field along the aperture at 7 GHz and 12 GHz.

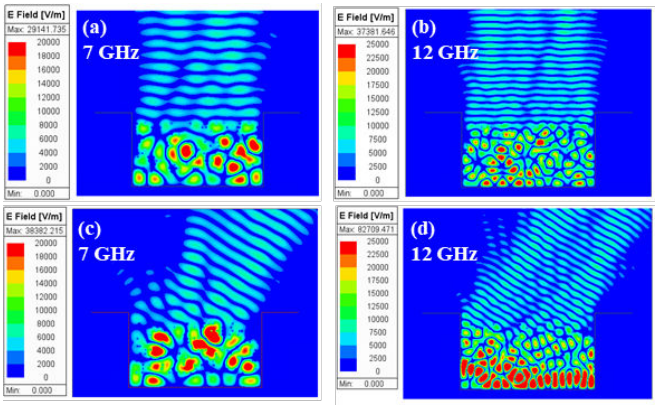

Fig. 3. The simulated field distributions for (a) 0° single-beam radiation and at 7 GHz, (b) 0° single-beam radiation at 12 GHz, (c) 30° single-beam radiation and at 7 GHz, and (d) 30° single-beam radiation at 12 GHz. The results in (a) and (b) are realized by the same antenna constellation, while those in (c) and (d) are achieved by another constellation.

of the E field from the source and the E field from the metallic rods:

$$E^{total}(y, z_{ap}) = E_x^{(s)}(y, z_{ap}) + \sum_{i=1}^{N_{rod}} E_x^{(i)}(y, z_{ap}) \quad (1)$$

Where $E_x^{(s)}$ represents E field from source, $E_x^{(i)}$ represents E field from rods. N_{rod} is the total number of rods inside the cavity, y is the location along the y-axis, and z_{ap} is the location of the aperture along the z-axis. So, different functions can be realized simply by changing the positions of the rods. We do not need to design the structure of every element.

The cavity's radiation state is dynamically reconfigured by inserting or removing metallic rods into these holes. This physical setup is represented by a binary matrix model, where each matrix element corresponds to a location: a 0 indicates an empty hole, and a 1 indicates a hole filled with a metallic rod. As a result, the algorithm's optimization goal is to find the best binary matrix (the ideal rod distribution) that achieves the desired dual-band radiation.

To optimize the sparse rod distribution within the vast 2^{1400} search space, a hybrid algorithm combining Binary Particle Swarm Optimization (BPSO) and Local Search (LS) is implemented. For the first 400 iterations, BPSO is utilized to navigate the high-dimensional landscape and prevent premature convergence to local optima. For the last 100 iterations with the total rod count fixed, the algorithm performs a localized search to fine-tune rod positions, ensuring convergence to the optimal configuration. The cost function is set as the sum of the differences between the calculated E-field using the semi-analytical equation and the ideal E-field.

III. Results and Discussion

To validate the method, two constellations are presented: Constellation A produces the single beam radiation at 0° at 7 GHz and 12 GHz, and Constellation B realizes a beam directed towards 30° at the same two frequencies. The distribution of the cavity-excited antenna rods (scattering constellations) is optimized using the method mentioned above. Antennas with optimized rod distributions are also simulated in HFSS. Results calculated from the semi-analytical model and simulated from HFSS are both obtained under a quasi-2D scenario. For the full-wave simulation setup, the metacavity is integrated within a parallel plate waveguide, and this configuration yields identical radiation performance to the 3D scenario with integrated flare structures.

The real and imaginary parts of the calculated results, compared with full-wave simulation results, along the cavity aperture are shown in Fig. 2, which exhibit high agreement. The level of correspondence between the two can be further enhanced by increasing the number of modes in the analytical model. The full-wave simulated electric field distributions for the two cases are presented in Figs. 3(a-d). Corresponding normalized radiation patterns are shown in Fig. 4. For cases (a) and (b), the main beam is directed at 0°, while for cases (c) and (d), it is steered to 30°. These results show excellent agreement with the design objectives. The full-wave simulations confirm that the optimized cavity design can precisely steer EM waves to the desired angles.

To characterize the performance of the proposed cavity-excited scattering constellation antenna, the directivity for Constellation A (0° beam) at 7 GHz and 12 GHz is compared in Fig. 5 against the theoretically calculated ideal uniform aperture of identical physical dimensions as the antenna's exit facet.

The maximum directivity of Constellation A reaches 9.73 dB and 14.55 dB at 7 GHz and 12 GHz, respectively, while the theoretical maximum directivity of the ideal uniform aperture is 10.09 dB and 14.78 dB. The main lobe profiles of the two are nearly identical, and this minimal directivity discrepancy verifies highly consistent directional radiation performance

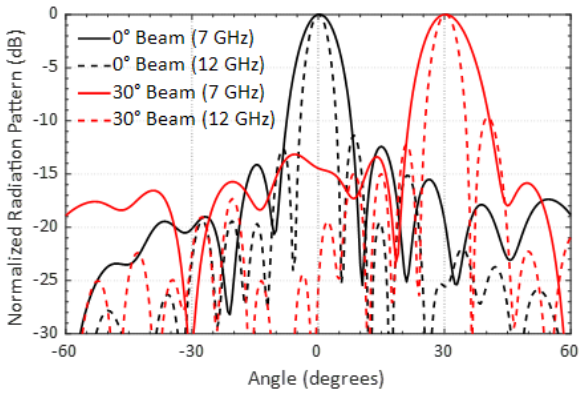

Fig. 4. Normalized radiation patterns for single-beam steering to 0° (black line) and 30° (red line) simultaneously achieved at both 7 GHz (solid line) and 12 GHz (dashed line).

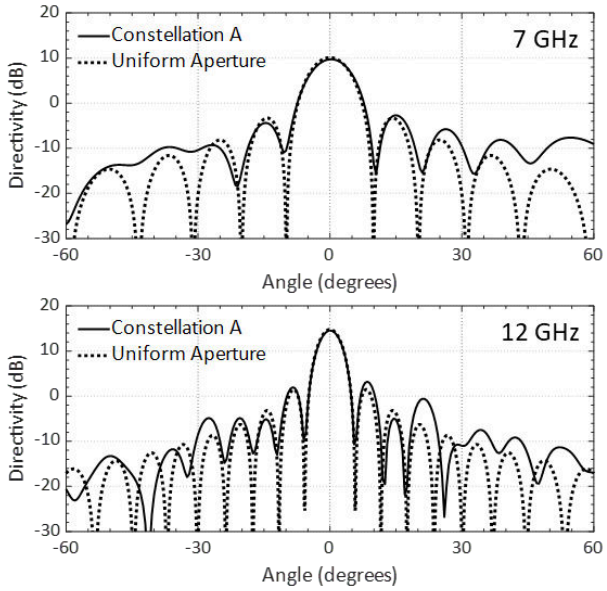

Fig. 5. Comparison of unnormalized directivity between constellation A (solid line) and an ideal uniform aperture (dashed line) at 7 GHz and 12 GHz.

between the proposed design and the ideal benchmark. Besides directivity, the S11 parameter of Constellation A was measured, with values of -12.40 dB at 7 GHz and -13.67 dB at 12 GHz.

IV. Conclusion

In conclusion, we have proposed and validated a dual-band beam-steering antenna based on a cavity-excited scattering constellation. A semi-analytical model enables efficient aperture field calculation, and a hybrid BPSO-LS algorithm successfully optimizes the binary rod distribution across the vast design space. The final design demonstrates the capability to independently steer a single main beam to 0° or 30° across two frequency bands with wide spectral separation, as confirmed by full-wave simulations. This work showcases a low-loss, mechanically reconfigurable approach to achieving multi-functionality in a single aperture. Future work may focus on expanding the functionality and implementing an automated mechanical control system for robust reconfiguration.

Acknowledgments

This work was supported by the Research Grants Council of the Hong Kong SAR, China, under Project AoE/E-101/23-N.

References

[1] X. Jin, S. Liu, Y. Yang and Y. Zhou, "A Frequency-Reconfigurable Planar Slot Antenna Using S-PIN Diode," *IEEE Antennas and Wireless Propagation Letters*, vol. 21, no. 5, pp. 1007-1011, May 2022.

[2] Q. Chen, J. Ala-Laurinaho, A. Khripkov, J. Ilvonen, R. M. Moreno and V. Viikari, "Varactor-Based Frequency-Reconfigurable Dual-Polarized mm-Wave Antenna Array for Mobile Devices," *IEEE Transactions on Antennas and Propagation*, vol. 71, no. 8, pp. 6628-6638, Aug. 2023.

[3] Z. Deng, Y. Wang, C. Lai. "Design and analysis of pattern reconfigurable antenna based on RF MEMS switches,"*Electronics*, vol. 12, no. 14, pp. 3109, 2023.

[4] H. L. Zhu, S. W. Cheung, X. H. Liu, and T. I. Yuk, "Design of Polarization Reconfigurable Antenna Using Metasurface," *IEEE Transactions on Antennas and Propagation*, vol. 62, no. 6, pp. 2891–2898, 2014.

[5] Z. Lin, A. M. H. Wong, "Reconfigurable cavity antenna based on metallic pins," *in Proceedings of the 2025 IEEE International Symposium on Antennas and Propagation and North American Radio Science Meeting*, 2025.

Retrieving colors hidden in a grey Fabry-Pérot cavity through coherent absorption

Giuseppe E. Lio[1], Giulio Carotta[2], Lorenzo Lavista[3], Andrea Camposeo[1], Giacomo Venturi[2], Agnese Guernieri[2], Alessandro Pitanti[3], Simon A. R. Horsley[4], Giuseppe C. La Rocca[5], Alessandro Tredicucci[3], Simone Zanotto[1*]

[1]Istituto Nanoscienze – CNR, and Laboratorio NEST – SNS, Pisa, Italy
[2]Dipartimento di Fisica "E. Fermi", Università di Pisa, Pisa, Italy
[3]Dipartimento di Fisica "E. Fermi", Università di Pisa and Istituto Nanoscienze – CNR, Pisa, Italy
[4]School of Physics and Astronomy, University of Exeter, Devon, UK
[5]NEST, Scuola Normale Superiore, Pisa, Italy
*Corresponding author: simone.zanotto@nano.cnr.it

***Abstract*—A dielectric slab coated with thin metal films is the prototypical Fabry-Pérot cavity, featuring defined reflectance and transmittance spectral resonances. Here we challenge this common acquisition, showing that an appropriately chosen metal coating washes out the Fabry-Pérot resonances, that can be however fully retrieved by a coherent absorption measurement.**

***Keywords*— Fabry-Pérot, coherent absorption, cryptography.**

I. Introduction

Dielectric thin films are well known to exhibit structural colors, ultimately originating from the Fabry-Pérot spectral features. It is usually acknowledged that coating the two sides of the dielectric slab with metal thin films further enhances the resonant behavior, leading to high-finesse spectral peaks visible in transmittance and in reflectance. However, it was to date overlooked that a specially matched thin film, whose surface conductivity is purely real, plays exactly the opposite role, washing out any resonant behavior from the system, and resulting in spectrally flat reflectance and transmittance.

II. Methods and Results

The phenomenon relies upon a special case of the reflectance/transmittance formulas for a dielectric slab sandwiched between thin conducting interfaces. These formula read

$$r = -\frac{\alpha_{+-}\,\alpha_{--}\,e^{ikd} - \alpha_{-+}\,\alpha_{++}\,e^{-ikd}}{\alpha_{--}^2\,e^{ikd} - \alpha_{++}^2\,e^{-ikd}},$$

$$t = \frac{\alpha_{-+}\,\alpha_{--} - \alpha_{+-}\,\alpha_{++}}{\alpha_{--}^2\,e^{ikd} - \alpha_{++}^2\,e^{-ikd}},$$

where

$$\alpha_{++} = n + 1 + \sigma Z_0, \qquad \alpha_{+-} = n + 1 - \sigma Z_0,$$

$$\alpha_{-+} = n - 1 + \sigma Z_0, \qquad \alpha_{--} = n - 1 - \sigma Z_0.$$

Here, n is the refractive index of the slab, σ is the conducting interface sheet conductivity, Z_0 is the vacuum impedance, $k = 2\pi n/\lambda_0$ is the wavevector in the dielectric, and d is the dielectric thickness. If the ordinary, uncoated slab is considered, σ must be set to 0, leading to wavelength dependent reflectance and transmittance (Fig.1a). In general, a finite value of σ leads also to λ-dependent spectra, possibly with sharp features. However, if the special value

$$\sigma_M = \frac{n-1}{Z_0}$$

is employed, α_{--} becomes zero, and drastically simplified formulas emerge:

$$r = \frac{1-n}{n}, \qquad t = \frac{e^{ikd}}{n}.$$

Taking the moduli squared, the phase factor disappears, meaning wavelength- and thickness- independent reflectance and transmittance spectra (Fig. 1b). Nonetheless, a *kd*-dependent phase factor is still present in the *t* coefficient; intriguingly, this can be accessed through a coherent measurement performed by illuminating both sides of the cavity simultaneously with phase-locked beams (Fig. 1c).

If the double-beam absorptance is defined as $A_{db}=1-I_{out,I}-I_{out,II}$, being $I_{out,I(II)}$ the intensity recorded at detectors placed at either sides of the cavity, for the matched cavity one gets

$$A_{db} = A_{sb}\,(1 - \cos(kd)\cos(\phi))$$

having defined the single-beam absorptance $A_{sb}=1-|r|^2-|t|^2 = 2(n-1)/n^2$, and being ϕ the phase difference between the input

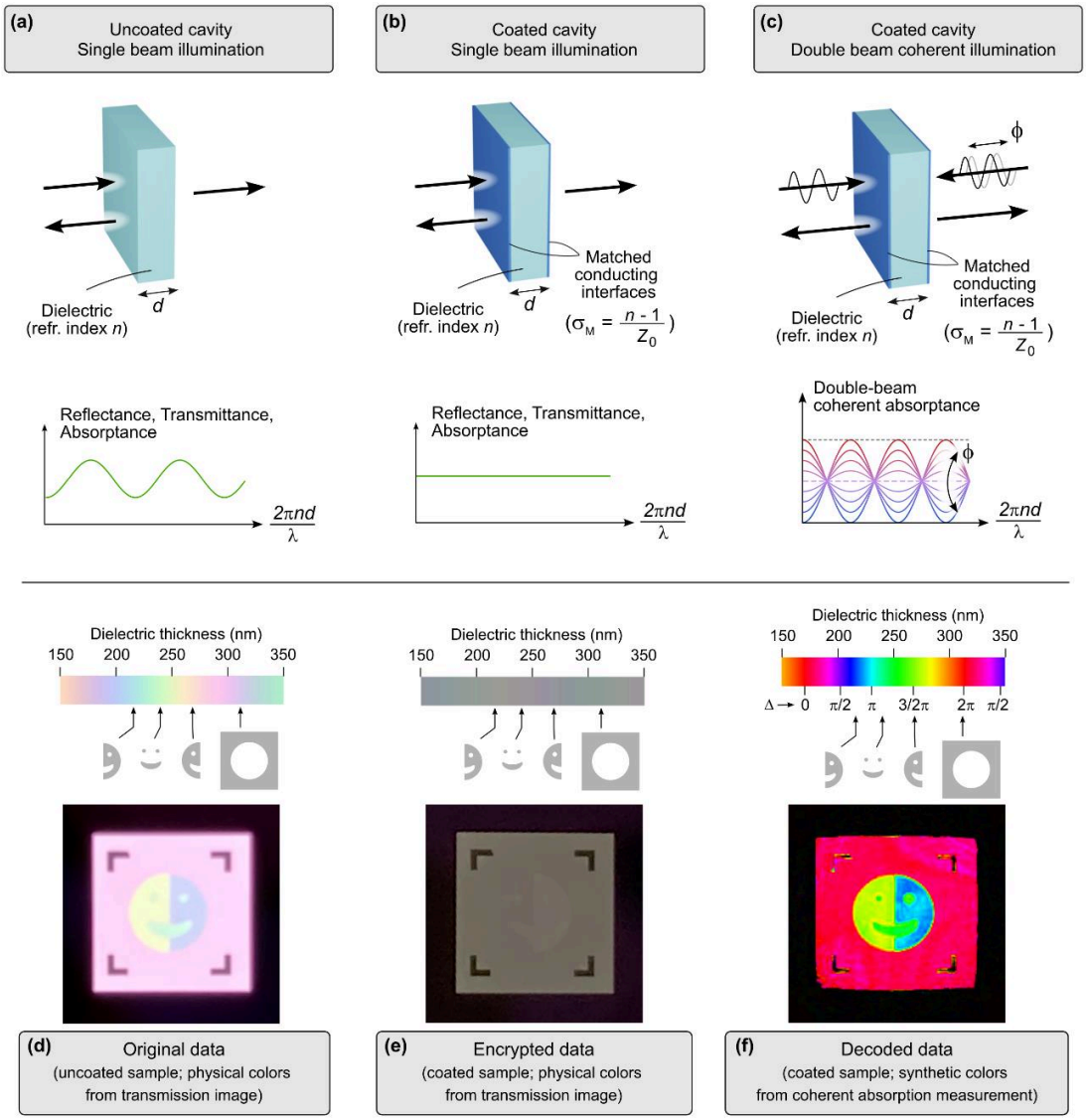

Figure 1. (a-c), concepts of spectrally flat, conductivity matched Fabry-Pérot cavity, and its interrogation through coherent absorption. (d-f), proposed application of the aforementioned phenomenon for cryptographic purposes.

beams. As illustrated in Fig. 1c, this implies the retrieval of spectral features originally present in the uncoated system; however, such features are now accessible only through a coherent-absorption scheme that grant access to A_{db}. Better yet, instead of relying upon measuring the total output intensity, one could consider that the individual intensities found at either sample sides follow the law

$$I_{\mathrm{out},I} = \frac{1}{2}\left(|r|^2 + |t|^2 + 2|rt|\cos(\phi + \frac{\Delta}{2})\right)$$

$$I_{\mathrm{out},II} = \frac{1}{2}\left(|r|^2 + |t|^2 + 2|rt|\cos(\phi - \frac{\Delta}{2})\right)$$

where $\Delta = 2kd$. By comparing the signals at the two detectors collected upon a sweep of input phase ϕ, one can strightforwardly and robustly determine the value of Δ and hence the dielectric thickness d.

This phenomenon, besides having a fundamental physics character, lends itself to applications in cryptographic schemes, where a piece of information is concealed to undesired recipients, while being still recoverable only by those agents who know a specific protocol. To demonstrate that, we fabricated a thin-film silicon nitride membrane, with lateral size 5x5 mm, featuring various areas with different thicknesses, such that the resulting spectral colors create a “smiley” image, see Fig. 1d. The chosen thicknesses fall within the 220-310 nm range, such that the spectra present a few oscillations in the visible spectral range, and ultimately resulting in well-defined spectral colors that can be observed by naked eye and captured by an ordinary smartphone camera (Fig. 1d).

After coating the sample with a thin Cr/Au film (4/6 nm thickness), which is the closest practical implementation to the

matching conductivity σ_M, the "smiley" feature is almost completely washed out, as visible in Fig. 1e. Here, all the sample is characterized by an extremely weakly saturated, low-brightness grey shade, consistently with the theroretical prediction that yields a spectrally flat transmittance amounting to $T = (1/n)^2 \approx 1/5$, having considered the typical value of silicon nitride refractive index.

However, we have been able to retrieve the data physically encoded in the sample, by performing coherent absorption imaging. Here, two He-Ne laser beams with variable phase delay are shone on either side of the sample, and the phase Δ is measured point-by-point. By mapping such phase on a properly chosen cyclic hue scale, the original appearance of the "smiley" can be recovered, although it was concealed from any single-beam measurement.

III. Conclusion

In summary, we have studied a simple yet powerful mechanism to conceal the spectral colors intrinsic to a thin dielectric film, by coating it on both sides with a conductivity-matched thin film. Notably, the hidden information can be retrieved with a specialized measurement scheme that amounts to illuminating the sample with phase-swept coherent beams. We believe that this results illustrates a fundamental photonic concept, and meanwhile a viable protocol for secure information transfer.

References

[1] Lio, G. E., Carotta, G., Lavista, L., Camposeo, A., Venturi, G., Guernieri, A., ... & Zanotto, S. (2025). Coherent absorption reveals colors hidden in a grey Fabry-Pérot cavity. *arXiv preprint arXiv:2510.13637*.

Broadband tunable second-harmonic generation using local-to-nonlocal intersubband polaritonic metasurfaces

Jaesung Kim[1], Gerhard Boehm[2], Mikhail A. Belkin[2] and Jongwon Lee[1]*
[1]Department of Electrical Engineering, Ulsan National Institute of Science and Technology (UNIST)
[2]Walter Schottky Institute, Technical University of Munich, Germany
*Corresponding author: jongwonlee@unist.ac.kr

***Abstract*— We demonstrate local-to-nonlocal intersubband polaritonic metasurfaces that enable broadband two-dimensional control of second-harmonic generation. A local resonance enhances excitation at the fundamental frequency, while a nonlocal resonance governs dispersive emission at the second harmonic. Voltage and incident angle independently modulate the SH spectral response, enabling broadband two-dimensional control of SHG.**

***Keywords*— nonlinear metasurface, nonlocal metasurface, second harmonic generation, electrical tuning, angle tuning.**

I. Introduction

Electrically tunable nonlinear metasurfaces based on intersubband transitions in multiple quantum wells (MQWs) are a powerful platform for mid-infrared frequency conversion, providing strong out-of-plane nonlinearity and electrical tunability.[1] In many existing architectures, however, electrical bias primarily changes the generated SH intensity through modulation of the fundamental-field enhancement and the nonlinearity of MQW layer, while the SH spectral position is largely constrained by structure-oriented local resonance condition. In parallel, nonlocal resonances in periodic metasurfaces—such as guided-mode resonances, quasi-bound states in the continuum, and lattice resonances—offer narrowband spectral selectivity and strong angular dispersion, enabling wavelength tuning through incident-angle control.[2] Yet in nonlinear implementations, achieving both high conversion efficiency and additional tunability can be challenging because high-Q nonlocal resonances are sensitive to absorption loss of material.

In this work, we propose and demonstrate a hybrid SHG strategy that explicitly assigns two different modal roles within a single SHG process. A local resonance is used to induce excitation at the fundamental frequency (FF), maximizing nonlinear polarization inside MQWs under electrical control, while a nonlocal resonance is used at the second-harmonic frequency to obtain dispersive outcoupling and spectral positioning under angle tuning. This separation of functions enables two independent tuning knobs—voltage and angle—that map onto two distinct outputs: SH peak amplitude and SH peak wavelength.[3] The result is two-dimensional control of the SH spectrum, rather than a single-parameter tuning trajectory.

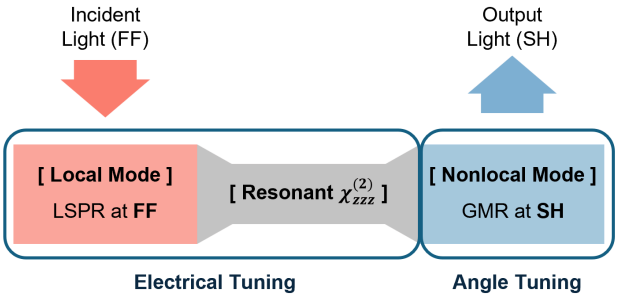

Fig. 1 A hybrid SHG scheme in intersubband polaritonic metasurfaces with local and nonlocal modes for dual tuning knobs.

II. Metasurface Design and Tunability

The metasurface is designed so that the unit cell supports a plasmonic local resonance at the FF (localized surface plasmon resonance) and an angle-dispersive nonlocal resonance at the SH frequency (TM guided mode resonance). Figure 2 shows the meta-atom geometry and the field distributions at both frequencies. A key design objective is to secure a nonzero overlap factor between the driven nonlinear polarization distribution inside the MQW layer and the radiative SH mode supported by the nonlocal resonance. Because nonlocal modes can exhibit highly symmetric field profiles that may lead to far field cancellation, the field distribution of the local resonance at the FF is asymmetrically shaped through the line connection of the upper side of the meta atoms and then it results to non-centrosymmetric field product. This design strategy ensures nonzero modal overlap factor as shown in Figure 2d which can be calculated by the equation (1),

$$\chi_{yxx}^{(2)\mathrm{eff}}(V,\theta) \approx \chi_{zzz}^{(2)\mathrm{MQW}}(V) \cdot \left[\int_{v_{\mathrm{MQW}}} \frac{E_z^{2\omega}(\theta)}{E_{y,inc}^{2\omega}} \frac{E_z^{\omega}(V)}{E_{x,inc}^{\omega}} \frac{E_z^{\omega}(V)}{E_{x,inc}^{\omega}} dv\right] / v_{\mathrm{unit}} \quad (1)$$

where the effective second order nonlinear susceptibility is the product of MQW nonlinearity and modal overlap factor. The integral term indicates modal overlap factor in equation (1).

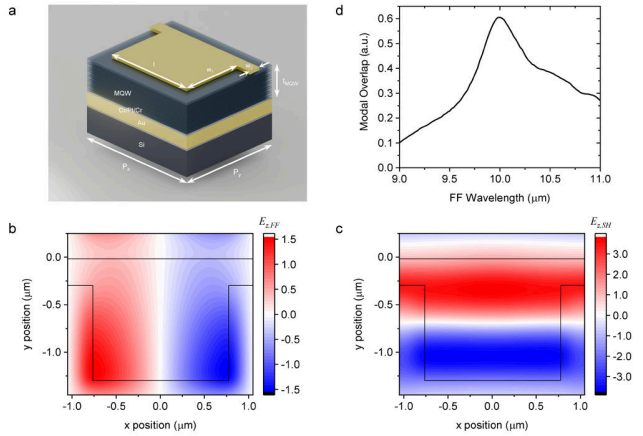

Fig. 2 a) Unit-cell geometry of the metasurface designed to support both local and nonlocal modes. b,c) Simulated E_z field distribution for b) the local mode under x-polarized FF excitation and c) the nonlocal mode under y-polarized SH excitation. d) Calculated modal overlap factor spectrum plotted versus the fundamental wavelength.

Figure 3a shows the electrical tuning which tunes the intersubband transition energies by quantum confined Stark effect (QCSE) that modulates the reflection spectrum at the FF due to strong coupling between local resonance and intersubband transition. Figure 3b shows the angle tuning which controls in-plane momentum and shifts the nonlocal resonance at the SH frequency through its angular dispersion. The detector position in the Fourier plane is directly translated into in plane momentum, which indicates the incident angle θ. And as a result, modal overlap factor and corresponding effective nonlinear susceptibility become a function of two independent variables, V and θ, which can be expressed as the equation (1).

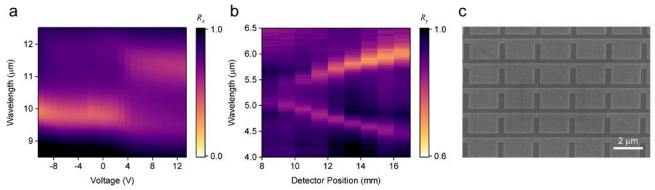

Fig. 3 a) Measured x-polarization reflection spectra of the fabricated sample as a function of applied voltage. b) Measured y-polarization reflection spectra of the fabricated sample as a function of detector position in the Fourier plane. c) SEM image of the fabricated sample.

III. Results and Discussion

Figure 4 summarizes the key outcome by comparing the effect of each tuning knob and their combination. Voltage tuning alone moves the SH response mainly along an amplitude axis at nearly fixed peak wavelength, while angle tuning alone moves it along a wavelength axis following the dispersive nonlocal resonance. Each tuning knob therefore traces an essentially one-dimensional trajectory in the space of 'SH peak wavelength versus amplitude'. When both angle and bias are used together, the accessible operating points expand into a two-dimensional region, enabling selection of target combinations of SH peak wavelength and amplitude rather than being restricted to a single tuning path. We experimentally achieved peak wavelength control from 10.04 μm to 9.66 μm, and 36% of peak amplitude modulation depth of SH response.

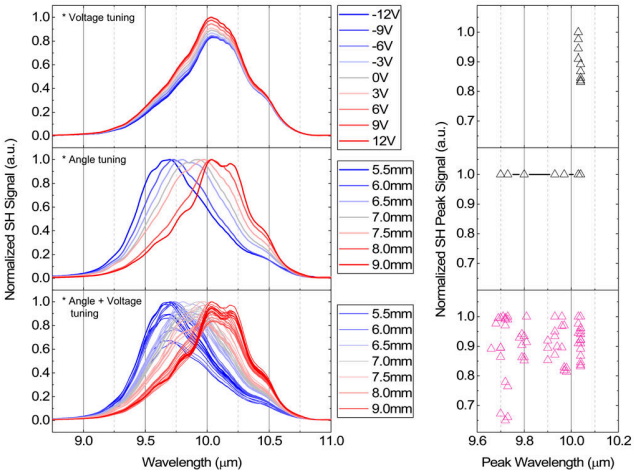

Fig. 4 Comparison of the impact of dual tunability enabled by the hybrid SHG process for 2D control of the SH spectrum. The panels on the left side represent normalized SH spectra, and the panels on the right side represent accessible peak positions of normalized SH spectra. top) Voltage tuning of SH spectra (single tunability). middle) Angle tuning of SH spectra (single tunability). bottom) Angle, voltage tuning of SH spectra (dual tunability). The legends of angle tuning indicate the pump laser position that represent corresponding incident angle tuning through the high NA lens.

IV. Conclusion

In conclusion, we demonstrate a hybrid SHG strategy in intersubband polaritonic metasurfaces where a local resonance is used to enhance excitation at the fundamental frequency while a nonlocal resonance governs dispersive emission at the second harmonic. This separation of roles provides two independent external controls: electrical bias predominantly modulates the SH amplitude by tuning the excitation strength in the MQW, whereas incident angle shifts the SH peak wavelength through the angular dispersion of the nonlocal emission channel. By combining these two knobs, we achieve two-dimensional control of the SH spectrum, enabling programmable selection of SH peak wavelength and amplitude beyond the one-dimensional tuning trajectories available in

conventional nonlinear metasurfaces with local or nonlocal modes. This approach establishes a general design principle for multifunctional nonlinear metasurfaces that require both strong frequency conversion and flexible spectral programmability.

ACKNOWLEDGMENTS

This work was partly supported by Institute of Information & Communications Technology Planning & Evaluation (IITP) grant funded by the Korea government (MSIT) (RS-2023-00227854, RS-2023-00259676) and by the National Research Foundation of Korea (NRF) (2022R1A2C301189812, 2022M3H4A1A04096465).

REFERENCES

[1] Krakofsky, Jonas H., Sarma, Raktim, Brener, Igal, Alù, Andrea, Lee, Jongwon and Belkin, Mikhail A. "Flat nonlinear optics with intersubband polaritonic metasurfaces" Nanophotonics, vol. 14, no. 23, pp. 3709-3721, 2025.

[2] Shastri, K., Monticone, F., “Nonlocal flat optics”, Nat. Photon. 17, 36–47, 2023.

[3] J. Kim, H. Chung, S. Lee, G. Boehm, M. A. Belkin, and J. Lee, “Local-to-Nonlocal Second-Harmonic Generation from Electrically Tunable Intersubband Polaritonic Metasurfaces.” Adv. Sci., e18776, 2025.

Fundamental Limits to the Design of Achromatic Metasurfaces

Nicolas Kossowski[1,*], Roman Buisine[1], Adelin Patoux[1], Rémi Colom[1], Patrice Genevet[1,2], Samira Khadir[1]

[1]Université Côte d'Azur, CNRS, CRHEA, Rue Bernard Gregory, Valbonne, 06650, France

[2] Physics Department, Colorado School of Mines, 1523 Illinois Street, Golden CO, 80401, USA

*Corresponding author: nicolas.kossowski@crhea.cnrs.fr

***Abstract*—This work establishes rigorous conditions for designing achromatic metasurfaces, defining two regimes: achromatic (unitary Strehl ratio) and pseudo-achromatic (near-achromatic behavior via aberration compensation). It derives size limits and performance metrics, validated using FDTD simulations, to guide the design of broadband metasurfaces for applications like augmented reality and imaging.**

***Keywords*— metamaterials, metasurfaces, achromaticity**

I. Introduction

Metasurfaces start to be widely spread and are reaching the industrial levels. Conventionally, metasurfaces are designed at a single frequency, meaning that outside of this operating frequency the optical performances quickly drops. For several applications, such as for augmented reality or in imagery system, it is preferable to have large bandwidth operations, i.e. the optical function should remain the same at all frequencies with equal optical performances. Designing such componenents is challenging as it supposes to engineer and control the phase dispersion of each meta-elements constituting the metasurface.

In light of these challenges, several works have been realized to estimate limits in terms of size or optical performances of such achromatic metasurfaces in function of its constitutive parameters [1], [2], [3], [4].

In this work, we establish rigorous conditions to be satisfied by the phase dispersion of the meta-atoms in order to realize an achromatic metasurface. Based on those conditions, we define different regimes of operation of achromatic metasurfaces, (i) an achromatic regime garanteeing unitary Strehl ratio, (ii) pseudo-achromatic regime, where appropriate choice of meta-atoms leads to the compensation of the different chromatic aberrations and so to a near-achromatic behavior. We clarify how the previous limits compare with each others as well as to our approach.

II. Methods

In our theoretical framework, we consider metasurface introducing an optical-path difference $g(\boldsymbol{r})$ associated with phase function $\varphi(\boldsymbol{r},\omega) = \frac{\omega}{c} g(\boldsymbol{r})$. We show that in order to realize an achromatic metasurface with wavefront $g(\boldsymbol{r})$, the phase dispersion $\tilde{\varphi}_p$ of the meta-atoms should satisfy the *achromatic conditions*, for any meta-atoms (p, q),

$$\begin{cases} \tilde{\varphi}_p(\omega) - \tilde{\varphi}_q(\omega) = \dfrac{\omega}{c}[g(\boldsymbol{r}_p) - g(\boldsymbol{r}_q)], & \text{(1a)} \\ \dfrac{d\tilde{\varphi}_p}{d\omega}(\omega) - \dfrac{d\tilde{\varphi}_q}{d\omega}(\omega) = \dfrac{1}{c}[g(\boldsymbol{r}_p) - g(\boldsymbol{r}_q)], & \text{(1b)} \\ \dfrac{d^n\tilde{\varphi}_p}{d\omega^n}(\omega) - \dfrac{d^n\tilde{\varphi}_q}{d\omega^n}(\omega) = 0 \quad \text{for} \quad n \geq 2. & \text{(1c)} \end{cases}$$

Assuming those conditions we can derive the maximal size of an achromatic metasurface with unitary Strehl ratio from a certain dataset,

$$\frac{\Delta g}{h} + \Delta n_0 = \Delta n, \tag{2}$$

where Δn_0 is the dispersion, over the bandwidth, of a reference meta-atom placed at the center of the metasurface, and Δn the maximal variation of effective refractive index in this subset of meta-atoms, as illustrated in Fig. 1.

To validate our theory, we generated a dataset composed of more than 10000 elements of $1\mu m$-thick GaN pillars on Sapphire simulated with a FDTD software (Lumerical). We show the phase dispersion $\tilde{\varphi}_p$ of the p-th meta-atoms can be approximated over the whole visible range by a Taylor expansion at the second order with relatively small error. Consequently, each meta-atom can be represented by the triplet its phase, phase delay and phase delay dispersion at the central frequency, $\left(\tilde{\varphi}_p(\omega_c),\ \frac{d\tilde{\varphi}_p}{d\omega}\Big|_{\omega_c},\ \frac{d^2\tilde{\varphi}_p}{d\omega^2}\Big|_{\omega_c}\right)$ as in Fig. 1 (b-c).

To quantify how the optical perfomances are affected by the chromatic aberrations, we derived an expansion of the Strehl ratio in terms of chromatic wavefront aberrations δ_p, cf Fig. 1 (d),

$$S(\omega) \approx 1 - V_{0,0} - 2(\omega-\omega_c)V_{0,1} - (\omega-\omega_c)^2(V_{1,1}+V_{0,2}) - (\omega-\omega_c)^3 V_{1,2} - \frac{(\omega-\omega_c)^4}{4}V_{2,2},$$

with $V_{m,n}$ the covariance between the chromatic aberration of the wavefront of order m and n,

$$V_{m,n} = \langle \delta_m \delta_n \rangle - \langle \delta_m \rangle \langle \delta_n \rangle . \tag{3}$$

Fig. 1. **a.** Schematic representation of an achromatic metalens. **b.** Meta-atoms dataset representation in terms of phase $\Delta\beta_{p,0} = \tilde{\varphi}_p(\omega_c) - \tilde{\varphi}_0(\omega_c)$ and group delay $\Delta\beta_{p,1} = \frac{d\tilde{\varphi}_p}{d\omega}(\omega_c) - \frac{d\tilde{\varphi}_0}{d\omega}(\omega_c)$, relative to the reference meta-atoms. **c.** Meta-atoms dataset representation in terms of group delay $\Delta\beta_{p,1}$ and group delay dispersion $\Delta\beta_{p,2} = \frac{d^2\tilde{\varphi}_p}{d\omega^2}(\omega_c) - \frac{d^2\tilde{\varphi}_0}{d\omega^2}(\omega_c)$, relative to the reference meta-atoms. In **b.** and **c.** the red points are the targeted value and the blue points are the selected meta-atoms. **d.** Strehl ratio in function of the wavelength (top panels) as well as expansion coefficients (bottom panels).

III. Results and Discussion

Based on our framework, we identified at least two regimes of operation to realize an achromatic metasurface:

1) The first regime corresponds to the *achromatic regime*, where we are able to find meta-atoms of the dataset meeting the achromaticity conditions (1a)-(1c). In this regime, the Strehl ratio of the metasurface is unitary since the phase profile of metasurface matches exactly the targeted phase profile. Therefore we can rigorously calculate a maximum size for the achromatic metasurface and this size is independent from the bandwidth under consideration.
2) The second regime corresponds to the *pseudo-achromaticity regime*, where the achromaticity conditions are not strictly met but thanks to the correlations between the different aberrations, the overall performances of the metasurface remains good over the bandwidth. In this regime, determining the maximal size in function of the optical performances remains challenging as it depends on how the meta-atoms are chosen.

IV. Conclusion

We have derived rigorous conditions that must be satisfied by the meta-atoms in order to realize an achromatic metasurface. Based on those conditions, we identified several regime of operation. Our work aims at clarifying the physics of achromatic metasurfaces and help identify design guidelines.

Acknowledgments

This work was supported by the European defense fund Mini-bot (EDF-2021-OPEN-R) and the ANR Astrid Millesime 2 (ANR-21-0014-02).

References

[1] F. Presutti and F. Monticone, "Focusing on bandwidth: Achromatic metalens limits," *Optica*, vol. 7, no. 6, pp. 624–631, Jun. 2020.
[2] S. Shrestha, A. C. Overvig, M. Lu, A. Stein, and N. Yu, "Broadband achromatic dielectric metalenses," *Light: Science & Applications*, vol. 7, no. 1, p. 85, Nov. 2018.
[3] E. Arbabi, A. Arbabi, S. M. Kamali, Y. Horie, and A. Faraon, "Controlling the sign of chromatic dispersion in diffractive optics with dielectric metasurfaces," *Optica*, vol. 4, no. 6, p. 625, Jun. 2017.
[4] W. T. Chen, A. Y. Zhu, V. Sanjeev, M. Khorasaninejad, Z. Shi, E. Lee, and F. Capasso, "A broadband achromatic metalens for focusing and imaging in the visible," *Nature Nanotechnology*, vol. 13, no. 3, pp. 220–226, Mar. 2018.

Transmissive Metasurface for Efficient Underwater Sound Focusing with a Wide Incident Angle

Jin-Chen Hsu[1,*], Jia-Feng Lai[1], Jia-Hong Sun[2]

[1]Department of Mechanical Engineering, National Yunlin University of Science and Technology, Taiwan

[2]Department of Mechanical Engineering, Chang Gung University, Taiwan

*Corresponding author: hsujc@yuntech.edu.tw

***Abstract*—An underwater acoustic metasurface for wide-angle and efficient focusing in transmission mode is designed. Numerical results show that the metasurface can focus oblique-incident waves up to 45° at the same power level as the normal-incident case. The metasurface also exhibits good achromatic capability with a large spatial incident angle view.**

***Keywords*—metasurfaces, local resonance, underwater sound, transmission, focusing.**

I. Introduction

Metasurfaces, the two-dimensional counterpart of volumetric metamaterials, have attracted enormous attentions owing to its excellent abilities to arbitrarily reshape the wavefront of the incident waves. Relying on the abrupt shift of field amplitude and phase within subwavelength scale, metasurfaces have been created for various interesting devices, such as metalens, meta-coupler, holograms, beam splitters, and many others. Among various fascinating applications of metasurfaces, metasurfaces to act as a flat lens which can transform incident plane wave to a predesigned circular one are particularly of interest because of its ultra-compact design compared to the conventional bulky lenses which rely on the spatial variation of refractive index. Metasurfaces hold promise in many practical applications, such as controlling ambient sound fields. Depending on the specific design of the meta-atoms, metasurfaces can operate in reflective or transmissive mode. The design of transmissive metasurfaces is more challenging. Despite the great success of metasurfaces in the past years for efficiently focusing airborne sound, few attention and efforts have been made to apply them to spatial focusing of waterborne sound. Furthermore, metasurfaces are mostly designed at specific normal incidence with an incident angle θ_i=0° according to the generalized Snell's laws. However, for some practical applications, metasurfaces operating with a wide oblique incident angle range are highly desirable and can also greatly enhance the performance of conventional metalens.

This paper presents a highly efficient wide-angle acoustic metasurface for underwater sound. The proposed meta-atom is based on a locally resonant unit, and a large phase shift can be achieved by varying its geometric dimensions, with an average transmittance exceeding 90%. The final metasurface consists of three unit layers (total thickness approximately 0.26λ, where λ is the operating wavelength) and can efficiently focus obliquely incident plan waves continuously to one side, with an incident angle of up to 45°. Numerical results show that this metasurface exhibits good achromatic properties and a large spatial incident angle.

II. Methods

Compared to reflective metasurfaces, the main challenge in designing transmissive ones lies in simultaneously considering high transmission rate and full-range phase shift. The proposed unit cell is a perforated metal plate with a mechanical resonator (a composite of metal mass and rubber spring) attached to its sidewall. The transmission performance and phase shift depend on structural parameters, including the plate thickness, channel width, metal mass width and thickness, rubber spring width and thickness, and lattice period. Here, the element is proposed for high-efficient focusing and the working frequency is designed at 5 kHz.

To design a metasurface capable of converting incident plane waves into transmitted circular waves, the phase compensation by the designed acoustic metasurface should follow a parabolic distribution dependent on its spatial position. Commonly used phase formulas only apply to the case of normal incidence along the axis with an incident angle $\theta_i = 0°$. Based on the generalized Snell's law, here we use the universal phase distribution of the metasurface for both normal and oblique incidence along the x-axis, namely:

$$\phi(x) = k_0\left(\sqrt{(x-x_0)^2 + L^2} - L - (x-x_0)\sin\theta_i\right) + \phi_0 \qquad (1)$$

where L is the focal length, and ϕ_0 is the phase at the midpoint. The general phase distribution for wide-angle focusing includes incident angle θ_i which is dependent on the off-axis distance as indicated by x_0. For normal incidence, the general expression (1) can be degraded to the widely-used form with $\theta_i = 0$ and $x_0 = 0$ for on-axis focusing.

III. Results and Discussion

Firstly, to achieve full-range phase shift on metasurfaces for

efficient focusing, a meta-atomic structure consisting of stacked three-layer unit cells was constructed in the simulation setup. For the target frequency, the meta-atom thickness is 26 mm, the channel width is 10 mm, and the period is 20 mm. The widths of the rubber and the mass of the resonator (with a fixed ratio of 0.5) were used to adjust the phase shift. Figure 1 shows the simulated results using finite element method, demonstrating that a high transmission rate of over 0.9 and a full 2π phase shift are achieved within the parameter range.

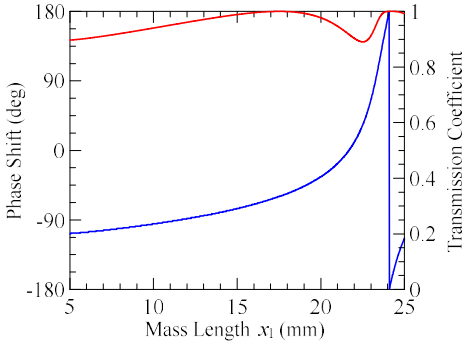

Fig. 1. Simulated results of transmission coefficient and phase shift of the meta-atom with three-layer unit cell as a function of mass length of the resonators.

Based on formula (1), the phase distribution along the x-axis for the normally incident pressure wave was designed under the conditions of wavelength $\lambda = 0.3$ m and focal length $L = 4\lambda$. As shown in Fig. 2, the focusing performance of normal incidence by the metasurface is given, and then its focusing performance under oblique incidence is further examined.

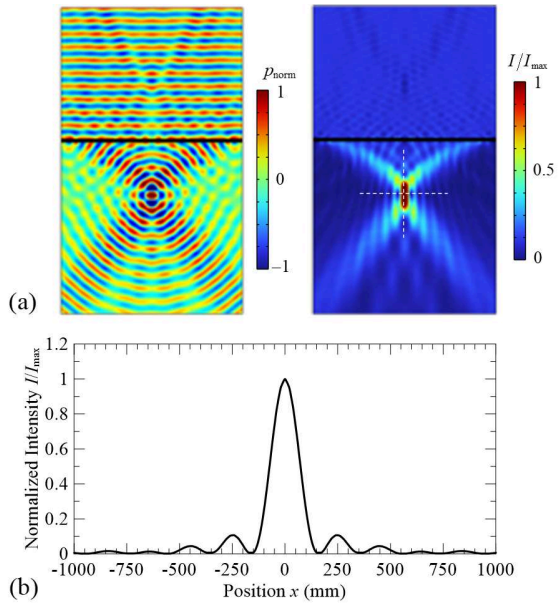

Fig. 2. Focused acoustic pressure field for the normally incident wave achieved by the designed phase-gradient metasurface.

Figure 2(a) shows the simulated focused acoustic pressure field for the normally incident wave in the $+y$ direction. The metasurface, composed of three layers of stacked unit cells, has a thickness of only 0.26λ (= 78 mm). It can be observed that a significant focusing effect is achieved at the predetermined distance $L = 4\lambda$. Furthermore, the acoustic pressure intensity at the focused spot is more than four times that of the incident pressure intensity, demonstrating the highly efficient sound focusing performance of the proposed metasurface. Figure 2(b) plots the normalized focusing pressure distribution along the x-direction (shown by the horizontal white dashed line) through the focused spot. Its full width at half maximum (FWHM) is approximately 0.46λ, indicating diffraction-limited focusing characteristics.

Figures 3(a–c) show the focused pressure fields at incident angles $\theta_i = 15°$, 30°, and 45°, respectively. It can be seen that, compared to the case of normal incidence, the metasurface can also focus obliquely incident waves well, maintaining good focusing performance even at incident angles as large as 45°. Comparing the focused pressure field distributions shows that their FWHM values remain almost unchanged even at oblique incident angles up to 45°, indicating that the proposed acoustic metasurface exhibits good achromatic properties at large spatial incident angles.

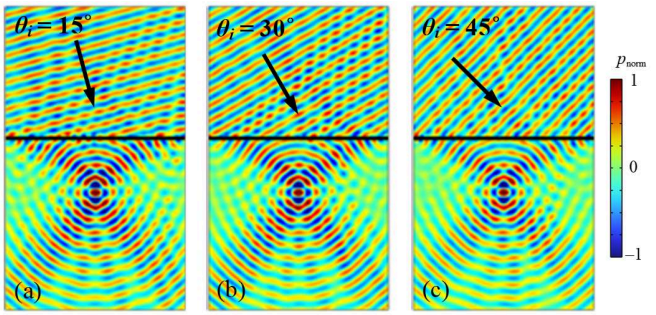

Fig. 3. Focused pressure fields by the designed metasurface at incident angles $\theta_i = 15°$, 30°, and 45°, showing that the metasurface can well focus obliquely incident waves with a wide incident angle.

IV. Conclusion

This paper presents an ultrathin metasurface lens with wide-angle and high-efficiency focusing capability. This wide-angle metasurface lens is based on the abrupt phase change of meta-atoms along the normal incident direction at the subwavelength scale, which conforms to the generalized Snell's law. It exhibits high-efficiency focusing performance, achromatic properties, and a wide incident angle.

Acknowledgments

This work was financially supported by the National Science and Technology Council, Taiwan (112-2221-E-224-044-MY3).

References

[1] B. Assouar, B. Liang, B., Y. Wu, Y. Li, J. C. Cheng, and Y. Jing, "Acoustic metasurfaces," Nature Reviews Materials, vol. 3, pp. 460-472, 2018.

[2] C. Kim, J. Kim, and W. Jeon, "Realization of an acoustic metalens exhibiting broadband high transmission," Journal of Sound and Vibration, 529, 116910, 2022.

Transfer Learning for Data-Efficient Modeling of Composite Metasurface Unit Cells

Alexander Wolff[1], Lukas Mueller[1], Steffen Klingel[1], and Marco Rahm[1]
[1]RPTU Kaiserslautern-Landau, Department of Electrical and Computer Engineering and Research Center OPTIMAS, Kaiserslautern, D-67663, Germany
*Corresponding author: alexander.wolff@rptu.de

***Abstract* — Training data is scarce when developing neural networks to model geometry-dependent scattering parameters of metamaterials. By applying transfer learning, we reduced the training data required for a neural surrogate model of a tunable composite metasurface more than twentyfold and demonstrate the approach's generalizability across different composite and fundamental structures.**

***Keywords* — metamaterials, transfer learning, inverse design, machine learning, tunable metasurface**

I. INTRODUCTION

Neural networks have the potential to accelerate the design process of artificial electromagnetic materials (AEM) by several orders of magnitude [1]. Yet, training an accurate neural network requires a substantial amount of training data to be obtained beforehand. This training data is typically specific to a particular set of geometrical and material parameters of the described AEM. However, transfer learning allows us to generalize training data from one AEM problem to another [1, 2, 3].

We use transfer learning to design a metasurface unit cell intended to enhance 5G/6G wireless links. In this setting, metasurfaces can boost a mobile user's signal-to-noise ratio by steering and concentrating the electromagnetic field onto the user [4]. Reducing side-lobe levels requires the phase of the reflected wave to be tunable over the full 0°–360° range while maintaining nearly constant reflectivity. This can be realized with composite unit cells consisting of two varactor-tuned dipoles [5]. Several dipole configurations can be considered for such a composite unit cell. Three example layouts are shown in Fig. 1(b-d).

II. RESULTS

All of these composite unit cells are based on the same fundamental structure, a single varactor-tuned dipole on top of an FR-4 substrate with a completely closed ground plane on the bottom layer of the substrate (see Fig. 1(a)). During the early design stage, we ignored the bias network for the varactors to accelerate training data generation, although the network is indicated as dashed lines in Fig. 1(a). The single dipole structure has four degrees of freedom (C, D, L, H), where C is the bias-voltage-dependent capacitance of the varactor diode (MACOM MAVR-011020-1411).

The composite unit cells are comprised of two of these varactor-tuned dipoles of different length. Fig. 1(b) shows a collinear configuration of the two dipoles. Their distance d is tunable, resulting in seven degrees of freedom for this structure (C_1, C_2, D, L_1, L_2, H, d). Figure 1(c) shows a parallel configuration of the dipoles. Finally, Fig. 1(d) displays another collinear dipole configuration, where we replaced the varactor diode with one of lower ohmic resistance (MACOM MGV 125-08).

We started our study with the collinear configuration from Fig. 1(b). The goal was to investigate whether transfer learning could reduce the number of simulations of this dual-dipole structure as inherently needed to train a direct model of the structure. This was examined by comparing the required simulations for training a direct model (multi layer perceptron, MLP) to those needed when first training a model on the single dipole (see Fig. 1(a)) and then applying a transfer model to learn the coupling between two dipoles, ultimately describing the same composite structure.

The objective of the transfer learning process was to train a model to accurately characterize the S_{11}-parameters of a single dipole, before feeding them into a transfer model designed to learn the coupling effects between two dipoles to describe the S_{11}-parameters of the composite structures. For this purpose, we first simulated and extracted the S_{11}-parameters of a single dipole dependent on the four parameters (C_i, D, L_i, H). Based on this data, we trained an MLP to output the S_{11}-parameters of a single dipole in a frequency range between 18 GHz and 34 GHz. The MLP had 4 input neurons, 4 hidden layers with 200 neurons each and 706 output neurons that represented the concatenation of $\mathrm{Re}(S_{11})$ and $\mathrm{Im}(S_{11})$ at 353 discrete frequency samples. In order to train the transfer model regarding the coupling between two dipoles, we used the S_{11}-parameters of the single dipole model as input for a second MLP of the same size that learned the dipole-dipole coupling dependent on the distance d between the two dipoles. The second MLP was trained on simulation data obtained from numerically simulating the S_{11}-parameters of the composite unit cell in Fig. 1(b).

In order to evaluate the benefit of this transfer learning scheme, we calculated the mean squared error (MSE) of the transfer-learned MLP over a test dataset for different sizes of training datasets. The result is illustrated by the solid blue line in Fig. 2. We see that the MSE reaches 0.05 with only 64 training simulations. In comparison, the dashed blue line in Fig. 2 represents a reference MLP of the direct model of the structure in Fig. 1(b). This reference network requires 1,280

simulations to yield an MSE of 0.05. As a result, the transfer-learning scheme requires 20 times fewer training samples of the composite unit cell than the directly trained reference model.

Although transfer learning requires additional simulations to train the single dipole, these simulations are typically faster due to the smaller and less complex geometry. Furthermore, the simulations of the single dipole can be recycled for composite unit cells with different coupling geometries between the dipoles.

We illustrate this fact with the parallel and the low-resistance collinear dipole configurations shown in Figs. 1(c) and (d). From the comparison of the training-data dependence of the test MSE in Fig. 2 - red and yellow lines - we find that transfer learning can decrease the training set size of the composite unit cells by up to a factor of 25. Hence, the method provides similarly substantial benefits as for the collinear unit cell.

In further investigations involving different fundamental structures, such as split-ring resonators and infinitely long wires, we likewise confirmed the advantages of the transfer learning approach, thereby establishing a data-efficient pathway toward automated, modular metasurface unit cell design.

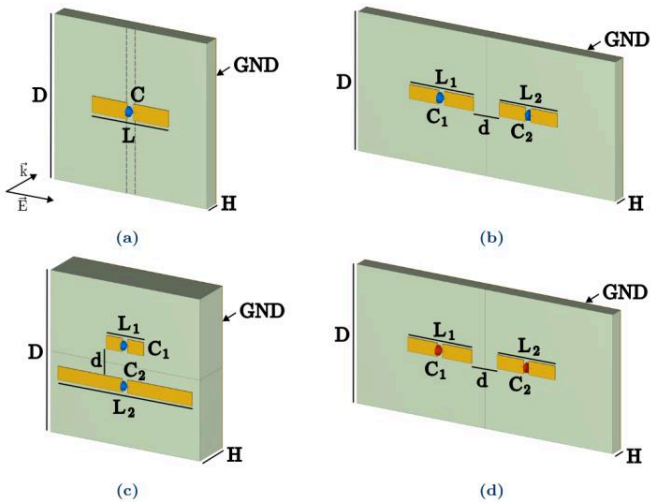

Figure 1: Singe-dipole and composite unit cell designs. (a) shows the single-dipole unit cell and the features (C, D, L, H) that were altered during the training data generation. Drafted in blue is the varactor diode. $\vec{E}$ and $\vec{k}$ indicate the polarization and the propagation direction of the incident plane wave. The dashed gray lines display the position of the bias lines, although they were omitted in the simulations. (b) shows the collinear dipole unit cell. (c) displays the parallel dipole unit cell. (d) illustrates the low resistance collinear dipole unit cell. It is identical to the collinear dipole unit cell but for the chosen varactor diodes (red) modeled with a resistance of 2.65 Ω to simulate the characteristics of the varactor diode MGV125-08 by MACOM. All three composite unit cells have the feature set (C_1, C_2, D, L_1, L_2, H, d) [3].

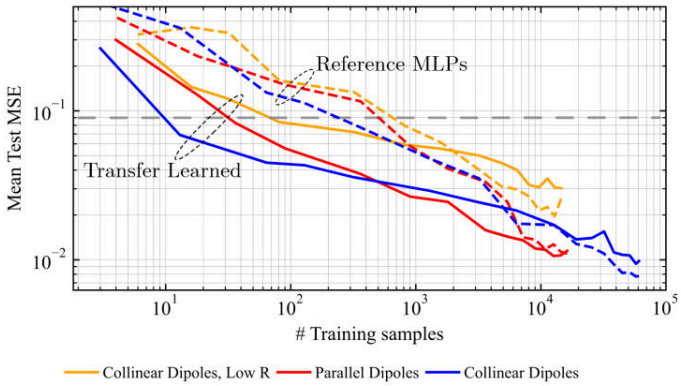

Figure 2: Log-log plot of the test MSE (prediction error) of different forward models versus the applied training set size. Solid lines depict the results of the transfer-learned models, whereas dashed lines illustrate the corresponding results of the reference directly learned models. The colors indicate the type of composite unit cell. Blue: collinear dipole unit cell; red: parallel dipole unit cell; orange: low resistance collinear dipole unit cell. The transfer-learned forward model requires up to 25 times fewer training data to achieve a test MSE of 0.09 (see gray dashed line). [3].

III. Conclusion

We demonstrated a transfer-learning framework for data-efficient forward modeling of composite metasurface unit cells. By leveraging pre-trained neural networks of simpler single-dipole structures, our method significantly reduces the amount of training data required to model more complex dual-dipole configurations. We showed that the proposed architecture can reduce training data demands by up to a factor of 25 while maintaining sufficient accuracy for practical applications, with mean squared errors below 0.09. Additionally, we extended the transfer learning approach to other fundamental unit cell structures, such as split-ring resonators and infinitely long wires, and obtained similarly promising results.

Acknowledgments

The authors acknowledge the financial support by the Federal Ministry of Research, Technology and Space of Germany in the project “Open6GHub” (grant number: 16KISK004).

References

[1] Khatib, O., Ren, S., Malof, J. and Padilla, W. J., “Deep Learning the Electromagnetic Properties of Metamaterials – A Comprehensive Review,” Advanced Functional Materials, Vol. 31, No. 31, 2101748, 2021.

[2] Peng, R., Ren, S., Malof, J. and Padilla, W. J., “Transfer Learning for Metamaterial Design and Simulation,” Nanophotonics, Vol. 13, No. 13, 2323–2334, 2024.

[3] Wolff, A., Mueller, L., Klingel, S. and Rahm, M., “Transfer learning for data-efficient modeling of composite metasurface and FSS unit cells,” Journal of Materials Science: Materials in Engineering, Vol. 21, No. 1, p. 16, 2026.

[4] Wu, Q., Zhang, S., Zheng, B., You, C. and Zhang, R., “Intelligent Reflecting Surface-Aided Wireless Communications: A Tutorial,” IEEE Transactions on Communications, Vol. 69, No. 5, 3313-3351, 2021.

[5] Zhu, B. O., Zhao, J. and Feng, Y., “Active impedance metasurface with full 360° reflection phase tuning,” Scientific Reports, Vol. 3, No. 1, 3059, 2013.

Spatial Electric-Field-Induced Chiral Discrimination in Planar Plasmonic Nanostructures

Chung-Kai Tseng[1], Tang-Chun Liu[1], Almudena Marti Morant[2], Chao-Yi Tai[1]*

[1]Department of Optics and Photonics, National Central University, Taiwan
[2]CNRS, L2CM (UMR 7053), Université de Lorraine, France
*Corresponding author: cytai@dop.ncu.edu.tw

***Abstract*— In this work, we investigate the relationship between chiral dependent forces on chiral particles and the spatial distribution of electric fields that generate optical chiral field. Through analysis on planar plasmonic structures, we identify specific electric field distributions that significantly enhance the contrast between chiral dependent and independent forces.**

***Keywords*— metamaterials, plasmonic, chiral discrimination.**

I. Introduction

Optical chiral fields have long been studied in systems involving surface-localized plasmonic enhancements [1-3] or evanscent waves [4], due to their inherent phase-delay properties. The spatial overlap between electric fields and magnetic fields gives rise to optical chiral fields, which can be further enhanced or concentrated through nanophotonic structures. Since the optical chirality is a conserved quantity, strong localization of optical chiral fields can lead to enhanced chiral related gradient forces. However, strongly localized electric fields not only generate highly chiral fields, but also induce strong achiral gradient forces through the electric-field gradient. The achiral component of the optical forces therefore becomes an obstacle to chiral discrimination of molecular enantiomers.

To improve and optimize the design of plasmonic meta-material for chiral molecular discrimination, we identify spatial phase distributions as a critical factor. In particular, properly engineered phase gradients enhance chiral optical forces while suppressing achiral force contributions.

II. Methods

In this work, two kinds of nanostructures are discussed, including dimers and dislocated double-slit pairs. The generalized multipole Mie-solution (GMM) [5] is applied to the dimer structures, while for the dislocated double slit is simulated using finite-difference time-domain method (FDTD) in Lumerical. The generalized multipole Mie-solutions are Fortran-based codes developed from Professor Xu, Yu-lin's work, which have been wildly used for multipole and multi-particle solutions.

The simulation of structures considered in this work are shown in Fig. 1. The Mie scattering coefficients (a_n, b_n) not only provide results such as scattering cross sections and scattered fields, but also provide information on the scattering field of different orders that appear in the total scattering fields, as shown in the equation below, where $\vec{N}$ and $\vec{M}$ are vector spherical wave functions derived in Mie theory.

$$\vec{E}_s = \sum_{n=1}^{\infty} E_n(ia_n\vec{N}_{e1n}^{(3)} - b_n\vec{M}_{o1n}^{(3)}) \quad (1)$$

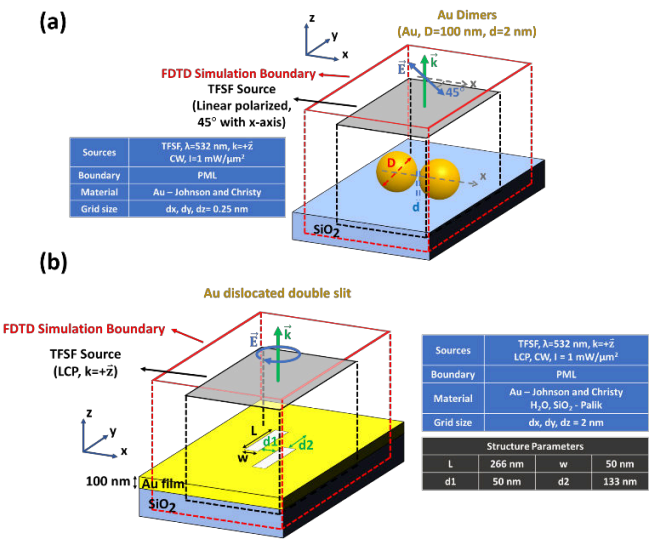

Fig. 1. Simulation setups and parameters

III. Results and Discussion

Fig. 2 (b) shows the simulation results of the total optical forces calculated by FDTD at λ=532 nm. The total optical forces include achiral reactive and dissipative forces, as well as chiral reactive and dissipative forces [6]. The reactive forces are the dominated terms, as shown below. Here, α, β, χ are the electric, magnetic and chiral polarizabilities of the chiral molecule, respectively, and ω is the angular frequency of light. C denotes the optical chirality, while $W_E = \|E\|^2(\varepsilon_m/4)$ represents the electric energy density and $W_H = \|H\|^2(\mu_d/4)$ represents the magnetic energy density.

$$F_{\alpha,\beta}^{reac} = \mathrm{Re}[\alpha]\nabla W_E + \mathrm{Re}[\beta]\nabla W_H \quad (2)$$

$$F_{\chi}^{reac} = \mathrm{Re}[\chi] \cdot \frac{c}{\omega} \nabla C \quad (3)$$

$$C = \frac{\omega}{2c^2} \mathrm{Im}[\vec{E} \cdot \vec{H^*}] \quad (4)$$

We found that under monochromatic illumination at λ=532 nm, the difference between the total optical forces of right/left-handed molecules is the largest. In our case, the right-handed molecules are attracted to the center, whereas left-handed molecules are not. This observation raises our interest. As shown in Fig. 2(a), λ=532 nm does not correspond to dimer's electric dipole mode or monomer's dipole mode. Instead, it corresponds to monomer's quadrupole (a_2, b_2) peak in the GMM analysis [7]. The spatial distributions of both monomers' quadrupole modes in the center region of the dimer also form quadrupole-like distributions.

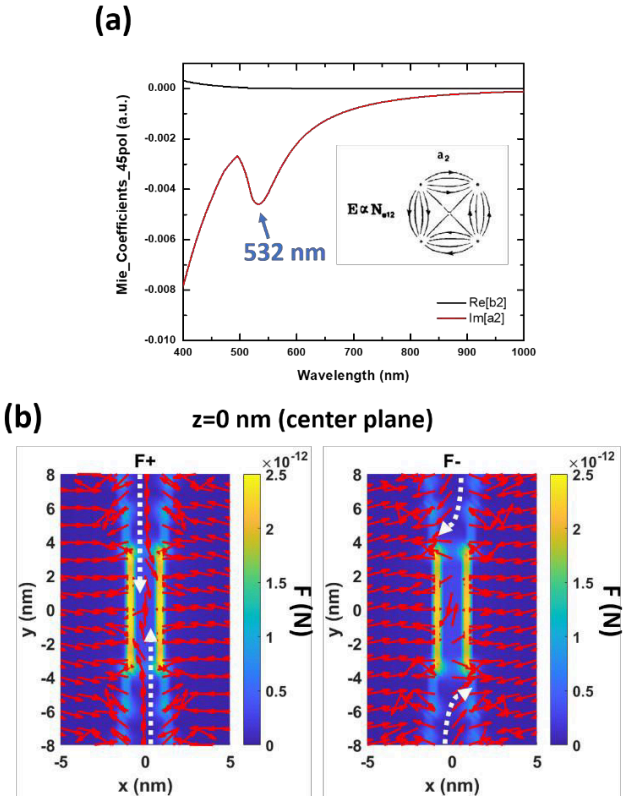

Fig. 2. Dimer simulation results (a) Mie scattering coefficient a_2 intensity and it's corresponding field distribution [ref] (b) Total optical forces (λ=532 nm) for chiral enantiomers of right-handed (F+) and left-handed (F-)

As we found the spatial phase distributions' effect on the difference in chiral optical forces, we attempted to generate a spatial electric quadrupole-like distribution. Coincidently, we found a previous work [8] that uses a dislocated double-slit to generate an overlap of electric field and magnetic field in the center region, thereby generating a high optical chiral field. However, we found that this configuration can generate not only a high optical chiral field, but also strong chiral optical forces, since the spatial phase in the central region forms an electric quadrupole-like distribution.

Notably, the largest difference between the chiral forces (F+/F-) in our simulations appears precisely at the phase-delay wavelength (λ = 2L), whereas the enhancement of the optical chirality field reported in previous works occurs at different wavelengths. This indicates that the chiral force difference observed here is governed by spatial phase distributions rather than by the maximization of optical chirality alone.

In Fig. 3(a), the maximum difference in optical forces occurs at 532 nm, which corresponds to the wavelength where the spatial phase delay induces an electric quadrupole-like distribution. As a result, within the separation region surrounded by the electric quadrupole-like distribution, vertically propulsion forces act on right-handed molecules, while vertically attraction forces act on left-handed molecules.

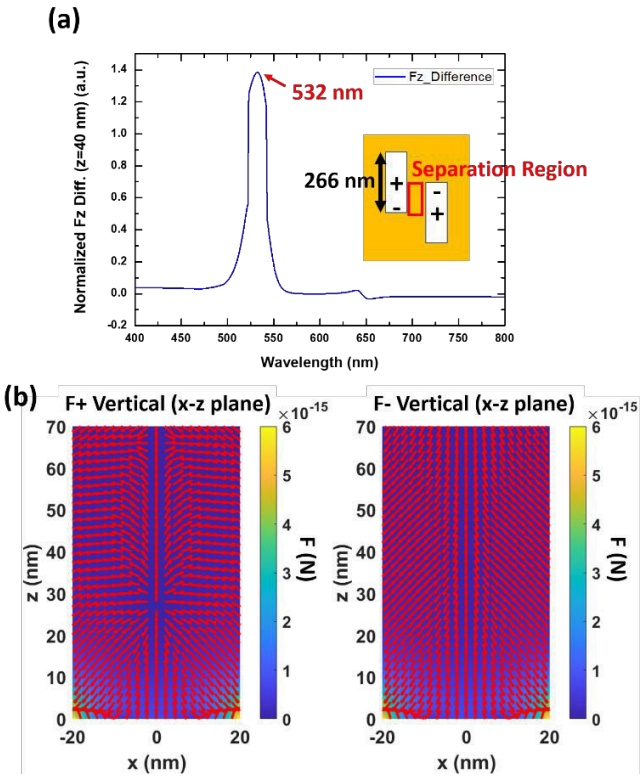

Fig. 3. Dislocated double slit simulation results (a) F+ / F-difference along z-axis at z=40 nm above (b) Total optical forces (λ=532 nm) for chiral enantiomers of right-handed (F+) and left-handed (F-) at center of separation region (y=0, x-z plane)

Fig. 3(b) shows the vertically total optical force difference on the center plane at λ=532 nm. Similar vertical force differences are observed throughout the entire separation region.

IV. Conclusion

From the results above, we identify the importance of the electric quadrupole effect on chiral optical forces. To form a single chirality trap in spatial domain, a single peak or valley of chirality is required. As mentioned previously, we focus on optimizing the spatial phase distribution to achieve a single chirality peak, motivated by the conservation property of optical chirality. From our perspective, the spatial phase distribution induced by the electric quadrupole is more directly related to the physical meaning of helicity, as it corresponds to the phase difference between right- and left-circularly polarized

(RCP and LCP) components. Under monochromatic excitation conditions, optical chirality and helicity are proportional to each other, further supporting this interpretation.

Interestingly, we find that the quadrupole plays a role not only in coupling the molecular quadrupole moment to the gradient of the optical chirality, as reported in previous studies [9, 10], but also in generating suitable chirality distributions that enhance chiral discrimination

REFERENCES

[1] Y. Zhao, A. A. E. Saleh, J. A. Dionne, "Enantioselective Optical Trapping of Chiral Nanoparticles with Plasmonic Tweezers," ACS Photonics, vol. 3, pp. 304-309, 2016.

[2] T. Cao, Y. Qiu, "Lateral sorting of chiral nanoparticles using Fano-enhanced chiral force in visible region," Nanoscale, vol. 10, pp. 566-574, 2018.

[3] S. Zu, Y. Bao, Z. Fang, "Planar plasmonic chiral nanostructures," Nanoscale, vol. 8, pp. 3900-3905, 2016.

[4] A. Hayat, J. P. B. Mueller, F. Capasso, "Lateral chirality-sorting optical forces," Proceedings of the National Academy of Sciences, vol. 112, pp. 13190-13194, 2015.

[5] Y.-L. Xu, B. Å. S. Gustafson, "A generalized multiparticle Mie-solution: further experimental verification," Journal of Quantitative Spectroscopy and Radiative Transfer, vol. 70, pp. 359-419, 2001.

[6] A. Canaguier-Durand and C. Genet, "Chiral route to pulling optical forces and left-handed optical torques," Physical Review A, vol. 92, 2015.

[7] C. F. Bohren and D. R. Huffman, *Absorption and scattering of light by small particles*, John Wiley & Sons, 2008.

[8] E. Hendry, R. V. Mikhaylovskiy, L. D. Barron, M. Kadodwala and T. J. Davis, "Chiral Electromagnetic Fields Generated by Arrays of Nanoslits," Nano Letter, vol. 12, pp. 3640-3644, 2012.

[9] R. P. Cameron, S. M. Barnett and A. M. Yao, "Discriminatory optical force for chiral molecules," New Journal of Physics, vol. 16, 2014.

[10] R. P. Cameron, A. M. Yao, S. M. Barnett, "Diffraction Gratings for Chiral Molecules and Their Applications," The Journal of Physical Chemistry A, vol. 118, pp. 3472-3478, 2014.

Towards Tunable Nanophotonics Filters using Quantum Confined Stark Effect

Tanneguy Blandin[1,*], Mathieu Arribat[1], Antoine Monmayrant[1], Aurélie Lescestre[1], Jean-Yves Duboz[2] and Olivier Gauthier-Lafaye[1]

[1]LAAS-CNRS, Université de Toulouse, CNRS
[2]Université Côte d'Azur, CNRS, CRHEA
*Corresponding author: tanneguy.blandin@laas.fr

***Abstract*—We experimentally demonstrate the refractive index modulation of a n-i-n doped GaAs/AlGaAs Quantum Confined Stark Effect based structure. Usage of a similar structure for the fabrication of Cavity Resonator Integrated Guided-Mode Resonance Filter (CRIGF) is demonstrated. The loss induced by the GaAs contact layers are evaluated.**

***Keywords*— CRIGF, Active-Metasurface, Quantum Confined Stark Effect**

I. Introduction

Cavity Resonator Integrated Guided-Mode Resonance Filters (CRIGFs) are a novel class of sub-wavelength-grating-based optical filters [1].

They are based on a guided mode confined in between two DBR mirrors, coupled to a propagating focused beam via a grating coupler (GC), thus giving rise to a Fano resonance. This type of structure is represented by a schematic figure 1.

Fig. 1. Schematic of a CRIGF structure.

Their responses are driven by the excitation of localized Fabry-Pérot modes, resulting in fixed-wavelength narrow band optical filters, with Q-factors that can exceed several thousand [2]. Combined with their angular tolerance [3], they are highly attractive for many applications.

Unlike other grating techniques (diffractive Volume Bragg Gratings (VBG) or Guided Mode Reflecting Filter (GMRF)), CRIGFs are spectrally insensitive to angular tuning. Achieving wavelength tunability thus requires either modifying the microcavity's geometric parameters or altering its waveguide's effective refractive index.

Electrically tunable CRIGF filters have been demonstrated on Thin Film Lithium Niobate, relying on its electro-optic sensitivity. However, the bias voltage required for optical tuning was in the hundreds volts range [4].

As pointed out by [5] in their metasurface studies, using Quantum Confined Stark Effect (QCSE), can lead to strong optical index modulation with low voltage. In this work, we investigate the possibility of combining CRIGF structures with QCSE using GaAs/AlGaAs materials.

II. Optical index modulation by QCSE in n-i-n structures

As compared to a previously demonstrated approach [5], based on a p-i-n doped heterostructure, we choose to use a n-i-n doped scheme. This configuration provides a flat band alignment at a zero voltage bias. It turns out that this configuration maximises the index modulation. The main drawback of such an approach is that n-i-n unipolar structures are known to be leaky at room temperature. In order to test this approach, a first structure was designed. It is presented in table I. A thick stack of 29 quantum wells (QWs) will provide the QCSE index modulation. It is embedded in between two $Al_{.4}Ga_{.6}As$ layers that act as electrical barriers to minimize the current leakage. Their thickness was optimized to maximise the stack reflectivity variation upon index modulation of the QW.

TABLE I
Stack used to measure the optical index modulation. The Quantum Wells are 10nm layers of GaAs spaced by 10nm $Al_{.15}Ga_{.85}As$ barriers. Both contacts layers are N-doped. All others layers are non intentionally doped (NID).

Layer role	Layer material	Thickness [nm]	Doping scheme
Top contact	GaAs	499	N_{++}
Barrier	$Al_{.4}Ga_{.6}As$	173	NID
QWs	$\overset{\text{barrier}\times 30}{\underset{\text{QWs}\times 29}{}}$	592	NID
Barrier	$Al_{.4}Ga_{.6}As$	200	NID
Bot. contact	GaAs		N_{++}

Reflectivity measurements under electrical modulation were conducted and are presented in figure 2. A comparison between these measurements and an optical model (that will be presented) allowed us to estimate an optical index modulation of 0.02 at 5V, in good agreement with theoretical predictions.

This rather large index modulation is interesting for applications such as actively tunable metamaterials. However the highly doped layers required for the electrical contacts may lead to absorption losses wich are not compatible with design of resonant meta-atomes used in metamaterials.

Fig. 2. Measured optical reflectance variation depending of the voltage applied to the stack described in table I

III. CRIGF WITH N-I-N INDEX MODULATION STRUCTURES

To evaluate the losses induced by the contact layers, we designed a Cavity Resonator Integrated Filter (CRIGF) [1] based on a similar structure. Those filters are know to be highly sensitive to absorption losses of the material [2].

A waveguide was designed to accommodate those requirements and the QCSE modulation scheme. Its vertical structure is depicted on table II. The waveguide is made of an active part, which is a stack of 31 QWs, embedded in between 90 nm $Al_{.4}Ga_{.6}As$ barriers, and top and bottom contact layers. It is optically isolated from the substrate by a thick low index $Al_{.95}Ga_{.05}As$ cladding layer.

TABLE II
STACK USED FOR THE DESIGN AND THE FABRICATION OF THE CRIGF. IT WAS EPITAXIED ON A GAAS N+ SUBSTRATE. THE QUANTUM WELLS ARE 10 NM LAYERS OF GAAS SEPARATED BY 10 NM $AL_{.15}GA_{.85}AS$ BARRIERS. ONLY THE CONTACT LAYERS ARE INTENTIONALLY N+ DOPED.

Layer role	Layer material	Thickness [nm]	Doping scheme
Top contact	GaAs	200	N_{++}
Barrier	$Al_{.4}Ga_{.6}As$	90	NID
QWs	$\begin{matrix}\text{barrier} \times 31\\ \text{QWs} \times 30\end{matrix}$	630	NID
Barrier	$Al_{.4}Ga_{.6}As$	90	NID
Bot. contact	GaAs	200	N_{++}
Cladding	$Al_{.95}Ga_{.05}As$	2500	NID
Substrate	GaAs		N_{++}

From numerical modeling, we decided to use a DBR and GC with a corrugation depth of 250 nm. The GC is 61 periods long, each period measuring 272 nm. The DBRs are 300 periods long with a period of 136 nm. The phase shift between GC and DBR is set at 102 nm.

The sample was fabricated in a clean room using standard III–V technological processes. First, a hard mask of SiO_2 was deposit by ICPECVD. A spin-coated layer of PMMA was then exposed by a Raith150 electron-beam lithography machine. After development in MIBK-IPA mixture, this mask was transferred to the SiO_2 using fluorinated ICP-RIE. GaAs etching was then made with chlorine ICP-RIE. Images figure 3 were made just before the removal of the SiO_2 mask with hydrofluoric acid. The Focused Ion Beam (FIB) etched view reveals an Aspect Ratio Dependent Etching (ARDE) as the GC is etched for 250 nm but the DBR is only etched for 205 nm.

Fig. 3. Images of the fabricated CRIGF. On the left, a FIB transverse view shows the profile of the etching. The red strip represents 300 nm, the view is tilted at 52°. On the right part is an optical microscopic view of the final CRIGF, the black strip represents 20 µm.

After fabrication, the CRIGF was characterised by reflectometry using a focused tunable Broadsweeper Laser in sweeping mode.

IV. FANO RESONANCE OPTICAL MEASUREMENT

The reflectivity of the structure is presented in figure 4. It showcases a sharp Fano resonance at 896.5 nm. The amplitude of the resonance is measured to be 45%. The full width at half maximum is of 0.70 nm.

Fig. 4. Reflectivity spectra of the fabricated CRIGF

We simulated the expected reflectivity using the RCWA simulation free software Nannos [6] on a standard workstation.

The optical indices considered for the $Al_xGa_{1-x}As$ are those published by K. Papatryfonos et al. in 2021 [7]. This simulation was run with different values of the imaginary part of the refractive index of the GaAs. It is presented figure 5. The amplitude of the resonance strongly varies with the absorption. It is at 45% for an imaginary part of the optical index of 4×10^{-4}.

Fig. 5. Simulated reflectivity of the crigf depending on the imaginary part of the optical index k for he contact layers.

Neither the etching profile geometry nor the ARDE were taken into account in our simulations to lower the computation cost. Would they be simulated, they could account for additional optical losses.

The influence of doping concentration on absorption in GaAs has been studied for some times [8]. As the doping goes up, the gap is shifted towards higher energies. Thus near the gap, in the transparency region, at a given wavelength, doping decreases the absorption.

This effect could relax the constrains on the realization of a unipolar based QCSE modulated CRIGF.

V. Conclusion

In this work, we demonstrated a QCSE based refractive index modulation on a n-i-n structure. Furthermore, a highly resonant CRIGF structure was fabricated and caracterized. Its resonance allowed us to evaluate the imaginary part of the optical index of the contact layers.

In our presentation, we will show electrically tuned resonance of CRIGF. This demonstration should open the door towards n-i-n structures QCSE modulated metasurfaces.

Acknowledgments

This work was supported by LAAS-CNRS micro and nanotechnologies platform, a member of the Renatech french national network.

Autors aknowledge financial support from the Agence Nationale de la Recherche under grant ANR-22-CE24-005 (ANR Sweet).

References

[1] K. Kintaka, T. Majima, J. Inoue, K. Hatanaka, J. Nishii, and S. Ura, "Cavity-resonator-integrated guided-mode resonance filter for aperture miniaturization," *Opt. Express*, vol. 20, no. 2, pp. 1444–1449, Jan 2012.

[2] E. Hemsley, O. Gauthier-Lafaye, A. Monmayrant, P. Dubreuil, S. Calvez, A.-L. Fehrembach, and E. Popov, "Critical coupling in cavity-resonant integrated-grating filters (crigfs)," *Optics Express*, vol. 31, no. 17, p. 27274, Jul. 2023.

[3] X. Buet, E. Daran, D. Belharet, F. Lozes-Dupuy, A. Monmayrant, and O. Gauthier-Lafaye, "High angular tolerance and reflectivity with narrow bandwidth cavity-resonator-integrated guided-mode resonance filter," *Optics Express*, vol. 20, no. 8, p. 9322, Apr. 2012.

[4] A. Monmayrant, S. Calvez, P.-F. Calmon, P. Dubreuil, S. Charlot, A.-L. Fehrembach, E. Popov, and O. Gauthier-Lafaye, "Cavity resonator-integrated guided-mode resonance filters with on-chip electro- and thermo-optic tuning," *Optics Express*, vol. 30, no. 10, p. 16669, Apr. 2022.

[5] P. C. Wu, R. A. Pala, G. K. Shirmanesh, W.-H. Cheng, R. Sokhoyan, M. Grajower, M. Z. Alam, D. Lee, and H. A. Atwater, "Dynamic beam steering with all-dielectric electro-optic III–V multiple-quantum-well metasurfaces," *Nat. Com.*, vol. 10, 2019.

[6] B. Vial, "nannos," 2022. [Online]. Available: https://doi.org/10.5281/zenodo.11658672

[7] K. Papatryfonos, T. Angelova, A. Brimont, B. Reid, S. Guldin, P. R. Smith, M. Tang, K. Li, A. J. Seeds, H. Liu, and D. R. Selviah, "Refractive indices of MBE-grown AlxGa(1-x)As ternary alloys in the transparent wavelength region," *AIP Advances*, vol. 11, no. 2, Feb. 2021.

[8] W. Sritrakool, V. Sa-yakanit, and H. R. Glyde, "Absorption near band edges in heavily doped gaas," *Physical Review B*, vol. 32, no. 2, pp. 1090–1100, Jul. 1985.

Inducing anisotropy in time via spacetime interfaces

Andrew M. Naylor[1] and Victor Pacheco-Peña[1*]

[1]School of Mathematics, Statistics and Physics, Newcastle University, Newcastle Upon Tyne, NE1 7RU, UK

*Corresponding author: Victor.pachecopena@gmail.com

***Abstract*— Four-dimensional media have become an interesting paradigm for the manipulation of wave propagation in multiple dimensions. Here, we present a mechanism to induce isotropic-to-anisotropic time interfaces from entirely isotropic spacetime modulations.**

***Keywords*—spacetime metamaterials, photonic time interfaces.**

I. Introduction

The ability to manipulate electromagnetic (EM) waves in space has been at the core of multiple fields [1-3], with many applications benefiting from the advancements in this area. To that end, metamaterials [4-6] have been of particular interest, to further control EM propagation [7- 28]. Recent efforts by the scientific community have also demonstrated interesting features of time-varying materials. By considering a material that has optical properties [permittivity (ε) and permeability (μ)] that change in time [$\varepsilon(t)$ and $\mu(t)$], wave propagation can be controlled not only in space (x,y,z) but also in both space and time (x,y,z,t) [29-31].

An example of time modulated media is the case of time interfaces, which [32] consider a rapid variation in time of $\varepsilon(t)$ and/or $\mu(t)$. When doing so, a set of forward (FW) and backward (BW) waves are generated, which are now considered as the temporal analogue of the transmitted and reflected waves produced at a spatial interface between two materials of different impedances [3]. Time interfaces have recently been studied by different groups demonstrating exotic physical phenomena [33-44]. Importantly, experimental demonstrations have begun to emerge [45-48]. Among the different types of time interfaces, it has been recently shown that when they involve isotropic-to-anisotropic modulations (a change from ε_{r1}, to a tensor, $\overline{\overline{\varepsilon_{r2}}}$ [49-53]), the direction of the Poynting Vector, $\boldsymbol{S}$, is modified, while the wavenumber, $\boldsymbol{k}$, is invariant (as expected) [52,53].

Motivated by the interesting effects and applications of time interfaces and, in particular, photonic isotropic-to-anisotropic time interfaces, here, we present our recent efforts in emulating them using solely isotropic spacetime modulations[54]. To do this, multiple isotropic-to-isotropic time interfaces are applied at the same time in such a way that a spatially subwavelength multilayer structure is formed. As it will be shown, this performance can then be described by an effective permittivity tensor of the form $\overline{\overline{\varepsilon_{r2}}} = \{\varepsilon_{reff,z}, \varepsilon_{reff,x}\}$.

II. Methods

A schematic representation of the proposed scenario is shown in Fig. 1 with the case of an isotropic-to-anisotropic time interface presented in Fig. 1a. This scenario was discussed in [24] but we present it here to put our system into context. For times $t < t_0$, a monochromatic signal is propagating within an unbounded isotropic (ε_{r1}) medium with an angle θ_1 (i.e., the wavenumber $\boldsymbol{k}$ and Poynting vector $\boldsymbol{S}$ are parallel). Then, at

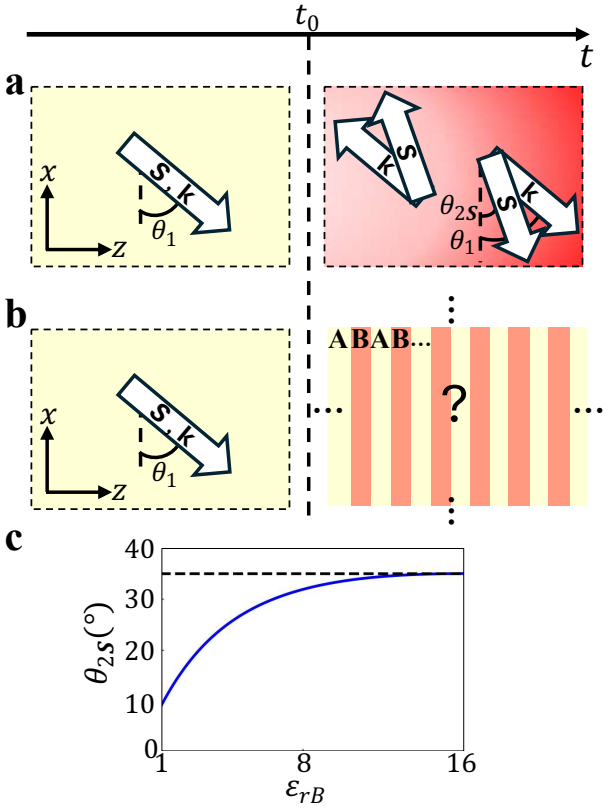

Fig. 1 Schematic of **a.** (left) a wave propagating in an unbounded, isotropic (ε_{r1}) medium with an incident angle θ_1 for $t < t_0$. (right) An anisotropic time interface is then induced at $t = t_0$. **b.** (left) same as panel **a** but in this case multiple isotropic-to-isotropic time interfaces are created in different spatial regions (right). **c.** Poynting vector for the case from panel **b.** when $\theta_1 = 35°$, $\varepsilon_{r1} = \varepsilon_{rA} = 16$ and $\widetilde{\Delta x_1} = 0.5$.

$t = t_0$, an isotropic-to-anisotropic interface is induced, meaning that for times $t > t_0$ we have, $\overline{\overline{\varepsilon_{r2}}}$ and $\theta_1 = \theta_{2k} \neq \theta_{2S}$, as explained in [24].

To emulate this response, we propose the scenario from Fig. 1b where isotropic spacetime modulations are used instead. For times $t < t_0$, the same incident signal, as in Fig. 1a, is propagating in the isotropic medium. Then, at $t = t_0$, multiple isotropic-to-isotropic time interfaces are created, forming spatially subwavelength multilayers. As will be shown in the conference, and presented schematically in Fig. 1b, one of the considered cases is when the spatial layers 'A' have the same permittivity as the initial medium for $t < t_0$ while layers 'B' vary (i.e. $\varepsilon_{r1} = \varepsilon_{rA} \neq \varepsilon_{rB}$). This structure can produce effective permittivity values such that $\varepsilon_{reff,z} \neq \varepsilon_{reff,x}$ [42]. This means that the proposed structure can be used to mimic isotropic-to-anisotropic time interfaces and its related effects (such as the change of direction of energy propagation in real time).

To illustrate an example, we provide in Fig. 1c the theoretical calculations of the direction of the Poynting vector, for the scenario shown in Fig. 1b at times $t > t_0$, as a function of the permittivity of layers B when layers A are time-independent ($\varepsilon_{r1} = \varepsilon_{rA} = 16$). In these calculations a filling fraction of $\widetilde{\Delta x_1}$=0.5 is used with $\widetilde{\Delta x_1} = \Delta x_1/(\Delta x_1 + \Delta x_2)$, $\Delta x_1, \Delta x_2$ as the absolute thicknesses of layer A and B, respectively. The incident angle is $\theta_1 = 35°$ for times $t < t_0$. As it can be observed in this figure, the Poynting vector varies depending on ε_{rB} (i.e., using isotropic spacetime modulations). Moreover, when $\varepsilon_{rB} = \varepsilon_{rA}$, the direction of the Poynting vector is not changed, as expected, as this will account for an isotropic-to-isotropic time interface instead. As shown in Fig.1b,c, here we consider the creation of vertical multilayers in time. The case where horizontal multilayers are induced in time will also be presented during the conference, as well as detailed discussion of the effect of the filling fraction on the overall performance of the proposed spacetime structure.

III. Conclusion

In summary, we have proposed a mechanism to emulate isotropic-to-anisotropic interfaces using isotropic spacetime modulations. The method involves multiple isotropic-to-isotropic time interfaces produced at the same time but in different spatial regions. This results in a spatially subwavelength multilayer structure that can be described by an effective permittivity tensor.

Acknowledgments

This work was supported by the Leverhulme Trust under the Leverhulme Trust Research Project Grant scheme (No. RPG-2023-024).

References

[1] M. Born *et al.*, *Principles of Optics*. Cambridge University Press, 1999.

[2] S. A. Maier, *Plasmonics : fundamentals and applications*. Springer, 2007.

[3] D. M. Pozar, *Microwave engineering*. John Wiley & Sons Incorporated, 2013.

[4] N. Engheta and R. W. Ziolkowski, *Metamaterials: physics and engineering explorations*. John Wiley & Sons, 2006.

[5] M. Kadic, G. W. Milton, M. van Hecke, and M. Wegener, "3D metamaterials," *Nature Reviews Physics*, vol. 1, pp. 198–210, 2019.

[6] Y. Liu and X. Zhang, "Metamaterials: a new frontier of science and technology," *Chemical Society Reviews*, vol. 40, p. 2494, 2011.

[7] T. Knightley, A. Yakovlev, and V. Pacheco-Peña, "Neural Network Design of Multilayer Metamaterial for Temporal Differentiation," *Advanced Optical Materials*, vol. 11, 2023.

[8] F. Zangeneh-Nejad, D. L. Sounas, A. Alù, and R. Fleury, "Analogue computing with metamaterials," *Nature Reviews Materials*, vol. 6, pp. 207–225, 2020.

[9] A. Silva, F. Monticone, G. Castaldi, V. Galdi, A. Alù, and N. Engheta, "Performing Mathematical Operations with Metamaterials," *Science*, vol. 343, pp. 160–163, 2014.

[10] Y. Li, I. Liberal, C. Della Giovampaola, and N. Engheta, "Waveguide metatronics: Lumped circuitry based on structural dispersion," *Science Advances*, vol. 2, 2016.

[11] M. Miscuglio *et al.*, "Approximate analog computing with metatronic circuits," *Communications Physics*, vol. 4, 2021.

[12] R. G. MacDonald, A. Yakovlev, and V. Pacheco-Peña, "Solving partial differential equations with waveguide-based metatronic networks," *Advanced Photonics Nexus*, vol. 3, 2024.

[13] M. Barbuto, F. Trotta, F. Bilotti, and A. Toscano, "Horn Antennas With Integrated Notch Filters," *IEEE Transactions on Antennas and Propagation*, vol. 63, pp. 781–785, 2015.

[14] G. Minatti *et al.*, "Modulated Metasurface Antennas for Space: Synthesis, Analysis and Realizations," *IEEE Transactions on Antennas and Propagation*, vol. 63, pp. 1288–1300, 2015.

[15] B. A. F. Esmail, S. Koziel, L. Golunski, H. B. A. Majid, and R. K. Barik, "Overview of Metamaterials-Integrated Antennas for Beam Manipulation Applications: The Two Decades of Progress," *IEEE Access*, vol. 10, pp. 67096–67116, 2022.

[16] H. Tao *et al.*, "Metamaterials on Paper as a Sensing Platform," *Advanced Materials*, vol. 23, pp. 3197–3201, 2011.

[17] H.-G. Kim, S. Hajra, H. Lee, N. Kim, and H. J. Kim, "Additively Manufactured Mechanical Metamaterial-Based Pressure Sensor with Tunable Sensing Properties for Stance and Motion Analysis," *Advanced Engineering Materials*, vol. 25, 2023.

[18] T. Nakanishi, T. Otani, Y. Tamayama, and M. Kitano, "Storage of electromagnetic waves in a metamaterial that mimics electromagnetically induced transparency," *Physical Review B*, vol. 87, p. 161110, 2013.

[19] E. Almeida, O. Bitton, and Y. Prior, "Nonlinear metamaterials for holography," *Nature Communications*, vol. 7, p. 12533, 2016.

[20] M. Huang, J. Yang, and A. Petrin, "Microwave sensor using metamaterials," *Wave propagation*, vol. 13, p. 36, 2011.

[21] R. Maas, J. Parsons, N. Engheta, and A. Polman, "Experimental realization of an epsilon-near-zero metamaterial at visible wavelengths," *Nature Photonics*, vol. 7, pp. 907–912, 2013.

[22] V. Pacheco-Peña *et al.*, "Mechanical 144 GHz beam steering with all-metallic epsilon-near-zero lens antenna," *Applied Physics Letters*, vol. 105, 2014.

[23] M. Koivurova, T. Hakala, J. Turunen, A. T. Friberg, M. Ornigotti, and H. Caglayan, "Metamaterials designed for enhanced ENZ properties," *New Journal of Physics*, vol. 22, p. 093054, 2020.

[24] V. Pacheco-Peña, M. Beruete, P. Rodríguez-Ulibarri, and N. Engheta, "On the performance of an ENZ-based sensor using transmission line theory and effective medium approach," *New Journal of Physics*, vol. 21, p. 043056, 2019.

[25] T. Brunet *et al.*, "Soft 3D acoustic metamaterial with negative index," *Nature Materials*, vol. 14, pp. 384–388, 2015.

[26] S. A. Tretyakov, "Meta-materials with wideband negative permittivity and permeability," *Microwave and Optical Technology Letters*, vol. 31, pp. 163–165, 2001.

[27] S. Hrabar, J. Bartolic, and Z. Sipus, "Waveguide miniaturization using uniaxial negative permeability metamaterial," *IEEE Transactions on Antennas and Propagation*, vol. 53, pp. 110–119, 2005.

[28] R. W. Ziolkowski and E. Heyman, "Wave propagation in media having negative permittivity and permeability," *Physical Review E*, vol. 64, p. 056625, 2001.

[29] E. Galiffi *et al.*, "Photonics of time-varying media," *Advanced Photonics*, vol. 4, 2022.

[30] C. Caloz and Z.-L. Deck-Leger, "Spacetime Metamaterials—Part I: General Concepts," *IEEE Transactions on Antennas and Propagation*, vol. 68, pp. 1569–1582, 2020.
[31] C. Caloz and Z.-L. Deck-Leger, "Spacetime Metamaterials—Part II: Theory and Applications," *IEEE Transactions on Antennas and Propagation*, vol. 68, pp. 1583–1598, 2020.
[32] F. R. Morgenthaler, "Velocity Modulation of Electromagnetic Waves," *IEEE Transactions on Microwave Theory and Techniques*, vol. 6, pp. 167–172, 1958.
[33] C. Rizza, G. Castaldi, and V. Galdi, "Short-Pulsed Metamaterials," *Physical Review Letters*, vol. 128, p. 257402, 2022.
[34] G. Castaldi, C. Rizza, N. Engheta, and V. Galdi, "Multiple actions of time-resolved short-pulsed metamaterials," *Applied Physics Letters*, vol. 122, 2023.
[35] V. Pacheco-Peña, M. Fink, and N. Engheta, "Temporal chirp, temporal lensing, and temporal routing via space-time interfaces," *Physical Review B*, vol. 111, p. L100306, 2025.
[36] V. Pacheco-Peña and N. Engheta, "Antireflection temporal coatings," *Optica*, vol. 7, p. 323, 2020.
[37] I. Liberal, J. E. Vázquez-Lozano, and V. Pacheco-Peña, "Quantum Antireflection Temporal Coatings: Quantum State Frequency Shifting and Inhibited Thermal Noise Amplification," *Laser & Photonics Reviews*, vol. 17, 2023.
[38] M. Antyufeyeva and V. Pacheco-Peña, "Emulating time refraction at photonic time interfaces via smooth temporal transitions," *Physical Review Applied*, vol. 24, p. 034004, 2025.
[39] J. E. Sustaeta-Osuna, F. J. García-Vidal, and P. A. Huidobro, "Quantum Theory of Photon Pair Creation in Photonic Time Crystals," *ACS Photonics*, vol. 12, pp. 1873–1880, 2025.
[40] P. A. Huidobro, M. G. Silveirinha, E. Galiffi, and J. B. Pendry, "Homogenization Theory of Space-Time Metamaterials," *Physical Review Applied*, vol. 16, p. 014044, 2021.
[41] V. Pacheco-Peña and N. Engheta, "Effective medium concept in temporal metamaterials," *Nanophotonics*, vol. 9, pp. 379–391, 2020.
[42] V. Pacheco-Peña and N. Engheta, "Merging Effective Medium Concepts of Spatial and Temporal Media: Opening new avenues for manipulating wave-matter interaction in 4D," *IEEE Antennas and Propagation Magazine*, vol. 65, pp. 39–49, 2023.
[43] D. Ramaccia, A. Alù, A. Toscano, and F. Bilotti, "Temporal multilayer structures for designing higher-order transfer functions using time-varying metamaterials," *Applied Physics Letters*, vol. 118, 2021.
[44] M. J. Mencagli, D. L. Sounas, M. Fink, and N. Engheta, "Static-to-dynamic field conversion with time-varying media," *Physical Review B*, vol. 105, p. 144301, 2022.
[45] R. Tirole *et al.*, "Double-slit time diffraction at optical frequencies," *Nature Physics*, vol. 19, pp. 999–1002, 2023.
[46] H. Moussa, G. Xu, S. Yin, E. Galiffi, Y. Ra'di, and A. Alù, "Observation of temporal reflection and broadband frequency translation at photonic time interfaces," *Nature Physics*, vol. 19, pp. 863–868, 2023.
[47] J. Bohn, T. S. Luk, S. Horsley, and E. Hendry, "Spatiotemporal refraction of light in an epsilon-near-zero indium tin oxide layer: frequency shifting effects arising from interfaces," *Optica*, vol. 8, p. 1532, 2021.
[48] M. Koukouraki, P. Petitjeans, A. Maurel, and V. Pagneux, "Characterization of temporal aiming for water waves with an anisotropic metabathymetry," *Physical Review B*, vol. 112, p. 214301, 2025.
[49] G. Ptitcyn and N. Engheta, "Temporal twistronics," *arXiv preprint arXiv:2403.10477*, 2024.
[50] G. Ptitcyn, D. M. Solís, M. S. Mirmoosa, and N. Engheta, "Temporal interface in dispersive hyperbolic media," *Nanophotonics*, 2025.
[51] A. Akbarzadeh, N. Chamanara, and C. Caloz, "Inverse prism based on temporal discontinuity and spatial dispersion," *Optics Letters*, vol. 43, p. 3297, 2018.
[52] V. Pacheco-Peña and N. Engheta, "Temporal aiming," *Light: Science and Applications*, vol. 9, 2020.
[53] V. Pacheco-Peña and N. Engheta, "Temporal equivalent of the Brewster angle," *Physical Review B*, vol. 104, 2021.
[54] A. M. Naylor and V. Pacheco-Peña, "Anisotropic photonic time interfaces via isotropic spacetime modulations," *in preparation*, 2026.

Fundamental Study on Lamb Wave Control Using Resonator-Based Acoustic Metasurfaces

Kent Hora[1], Toshihiko Sugiura[1,*]

[1]Keio University, Japan

*Corresponding author: sugiura@mech.keio.ac.jp

***Abstract*— Previous studies numerically demonstrated that lamb-wave propagation can be suppressed by controlling boundary conditions using resonator-based acoustic metasurfaces. This study aims to experimentally verify this effect and explore its application to a pseudo band-pass filter, demonstrating attenuation characteristics and the feasibility of such filtering using resonator-based metasurfaces.**

***Keywords*— acoustic metasurfaces, lamb wave, resonator.**

I. Introduction

Acoustic metamaterials are artificial structures that exhibit properties not found in nature, and they are known to suppress the propagation of specific acoustic waves due to these properties. Such structures that especially focus on surface configurations are referred to as acoustic metasurfaces. Technologies for controlling acoustic waves are expected to find applications in noise reduction and nondestructive testing. Unlike conventional soundproofing and vibration-damping materials, these approaches offer advantages such as compact device size and ease of installation and modification. Previous studies have focused on mode conversion induced by resonators under specific boundary conditions for lamb waves propagating along boundaries, and numerical simulations have demonstrated that the propagation of particular modes can be suppressed by realizing certain boundary conditions using resonators [1]. This study demonstrates these effects experimentally and also investigates their applicability to a structural pseudo band-pass filter for lamb waves by combining resonators of different heights.

II. Theory

For lamb waves, the phase velocity dispersion curves shown in Fig. 1 as blue lines are obtained under stress-free boundary conditions on both surfaces of the thin plate. In this study, attention is focused on the fundamental modes S0 and A0 that occur in the low-frequency region.

As in Ref. [1], this study applies the following Mindlin boundary condition to the upper surface of the thin plate, as shown in Fig. 2:

$$w = \sigma_{31} = 0 \quad (z = h) \tag{1}$$

The dispersion characteristics of the wave mode propagating under this condition, hereafter referred to as the X mode, are shown by the red lines in Fig. 1. Furthermore, it has been reported that when the Mindlin boundary condition is applied only to a portion of the surface, the S0 mode is converted into the X0 mode with a similar phase velocity and propagates, whereas the A0 mode does not propagate because no corresponding mode with a similar phase velocity exists [1]. Although the Mindlin boundary condition can be readily expressed mathematically, resonators are attached to the surface in order to realize this condition in practice.

III. Numerical Analysis and Experiment

The Mindlin boundary condition can be reproduced by utilizing the anti-resonance of a resonator [1]. The resonator in this study is made of aluminum and has dimensions of 5 × 5 × 33.7 mm³.

In the simulations, models for free vibration and forced vibration were prepared, as shown in Fig. 2, and finite element analysis was performed using COMSOL. In the free-vibration model, the natural frequencies of the resonator were analyzed, while in the forced-vibration model, the displacement of the bottom surface was obtained as a frequency response function when excitation at frequency f was applied in the direction normal to the bottom surface, assuming the A0 mode. As a result, consistent with Ref. [1], the free-vibration model was found to exhibit a natural frequency at 38 kHz, corresponding to the anti-resonance frequency of the resonator. This indicates that the Mindlin boundary condition can be realized by the resonator at 38 kHz.

The model used for the transient analysis is shown in Fig. 3. To verify the filtering effect, the second resonator was introduced, and comparative investigations were conducted for models with one and two resonators. The second resonator indicated by the dashed line in Fig. 3 has a height of 10.6 mm so that its anti-resonance frequency is 120 kHz. In addition, a flat plate model of the same size without resonators was also prepared to evaluate the attenuation of the A0 mode induced by the resonators. Excitation was applied in the z direction from both sides of the plate with the same phase using a continuous sinusoidal wave, so that only the A0 mode propagated within the plate. The amplitude ratio of the metasurface to the flat plate was calculated. The results are shown in Figs. 4 and 5.

Experiments were performed using a similar model to verify whether attenuation of the A0 mode occurs in practice. A normal-incidence transducer was used for transmission to apply out-of-plane excitation, and the same transducer was employed for reception. The transmitted signal was a five-cycle sinusoidal burst with a Hanning window. The amplitude obtained from the measurements was used to perform the same calculations as in Figs. 4 and 5, and the results are shown in Figs. 6 and 7.

IV. Discussion

The trends observed in Figs. 4 and 6 for the single-resonator case are similar. In both cases, suppression of A0-mode propagation is confirmed in frequency bands different from the anti-resonance frequency of 38 kHz. This is considered to be due to differences in the applied stress conditions. In the frequency response function analysis, a uniform stress normal to the bottom surface is applied, whereas in the transient analysis, a propagating wave results in a nonuniform stress distribution. In contrast, for the two-resonator case shown in Figs. 5 and 7, suppression of A0-mode propagation is observed near the anti-resonance frequencies of 38 and 120 kHz. This is presumed to be because the resonator on the transmitting side reduces the nonuniformity of the applied stress. In addition, attenuation is reduced at frequencies between the anti-resonance points, specifically around 70 and 80 kHz.

V. Conclusion

For the single-resonator model, suppression of A0-mode propagation was confirmed in frequency bands different from the anti-resonance frequency through both numerical analysis and experiments. In contrast, for the two-resonator model, propagation suppression was observed at the anti-resonance frequencies, while attenuation was reduced in the frequency band between the anti-resonance points, demonstrating the functionality of a pseudo band-pass filter.

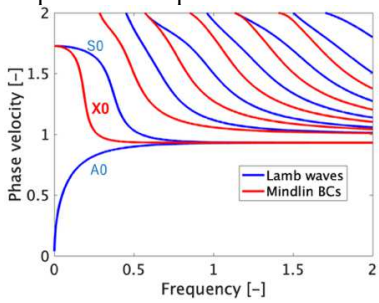

Fig. 1. Phase velocity curves for Mindlin BCs and lamb waves.

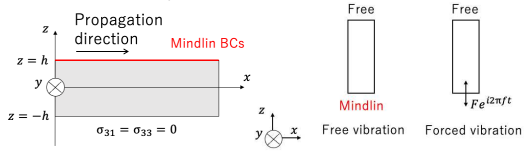

Fig. 2. Schematic of Mindlin BCs and the resonator models.

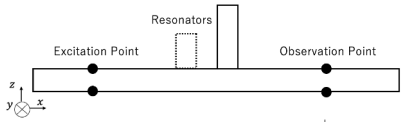

Fig. 3. Dimensions and position of the metasurface models in transient analysis

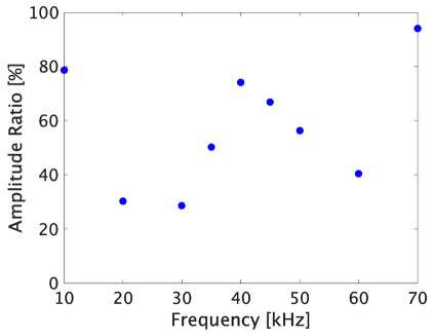

Fig. 4. FEM results showing normalized amplitude with one resonator.

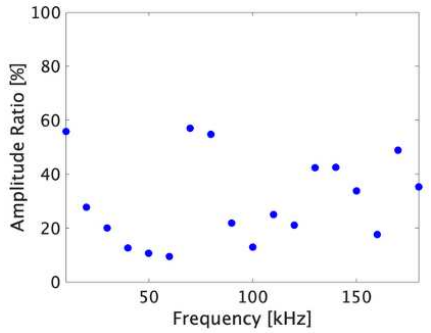

Fig. 5. FEM results showing normalized amplitude with two resonators.

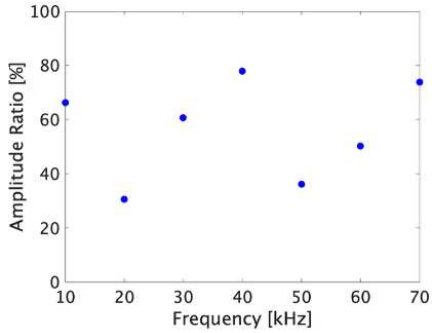

Fig. 6. Experimental results showing normalized amplitude with one resonator.

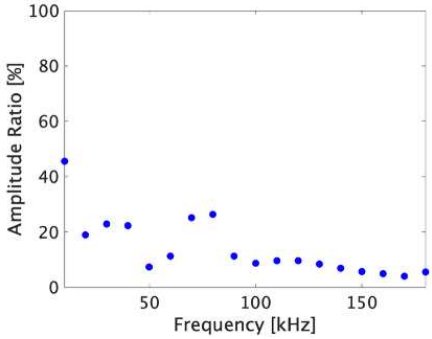

Fig. 7. Experimental results showing normalized amplitude with two resonators.

References

[1] C. J. Lissenden, C. N. Hakoda, P. Shokouhi, “Control of low-frequency lamb wave propagation in plates by boundary condition manipulation,” *Journal of Applied Physics*, vol. 129, p. 094903, 2021.

Genetic Algorithm-based 3D-Metamaterials for Radar Range Extension

Dmytro Vovchuk[1,2,*], Dmitry Dobrykh[1], Konstantin Grotov[1], Anna Mikhailovskaya[1], Mykola Khobzei[2,3], Vladyslav Tkach[2,3], Anton Kharchevskii[1], Toms Salgals[2], Vjaceslavs Bobrovs[2], Pavel Ginzburg[1]

[1] Tel Aviv University, Department of Electrical Engineering, Tel Aviv, Israel
[2] Riga Technical University, Department of Telecommunications, Riga, Latvia
[3] Yuriy Fedkovych Chernivtsi National University, Department of Radio Engineering and Information Security, Chernivtsi, Ukraine
*Corresponding author: dimavovchuk@gmail.com

***Abstract*— Drone utilization for different areas such as delivery, monitoring etc. suffers the rapid growth that causes air traffic and thus requires proper navigation and control. The most challenging are targets with the comparable to clutter or critically low radar cross-section (RCS) value. Therefore, we introduce a concept of evolutionarily designed metamaterial structure in the form of multilayer stacks array of strongly coupled electric and magnetic resonators that provide a broadband end-fire backscattering RCS approaching 1 m² (a human comparable) at 10 GHz and, despite their compact footprint, achieve over 10% fractional bandwidth, meeting essential radar requirements for high-range resolution. We have demonstrated 1.5-5 times range detectability enhancement based on DJI Mini 2 drone tagged with genetically designed volumetric metastructures.**

***Keywords*— metamaterials, machine learning, range extension, scattering maximization.**

I. Introduction

Electromagnetic wave interactions with matter remain a key research area, evolving with applications in telecommunications, medical imaging, and radar [1-2]. Metamaterials enable wave manipulation, with negative index materials used for radar cloaking [3-4]. Early designs relied on homogenization approaches, but modern computational power and machine learning allow direct optimization of complex structures [5].

This work focuses on volumetric structures maximizing electromagnetic scattering for emerging wireless applications. These structures, composed of electric and magnetic resonators, are referred to as evolutionarily designed metamaterials [6]. A major application is UAV detection in urban radar environments. Small drones are difficult to detect, and while active transponders are mandated, passive labels improve monitoring without power demands. The design must balance radar cross-section (RCS) enhancement with aerodynamic and size constraints.

Traditional retroreflectors (e.g., corner reflectors, Luneburg lenses, and Van-Atta arrays) provide high RCS but are often too large. For X-band radar, a UAV's RCS (~10 cm²) is significantly lower than the ~1 m² target, necessitating compact solutions. Superscatterers, highly resonant subwavelength structures, offer enhanced scattering via resonance cascading, overcoming conventional bandwidth and size trade-offs. However, their near-field energy accumulation makes them sensitive to material losses and fabrication tolerances.

Optimization, particularly via genetic algorithms, is essential for designing superscatterers, allowing exploration of novel geometries [7]. This study investigates 3D architectures using near-field coupled resonators, demonstrating the impact of volumetric design on scattering performance.

II. Design and Experimental Validation

In this work, we propose a radar range enhancement strategy based on superscatterer-enabled drones, where engineered electromagnetic structures are used to deliberately amplify the backscattered radar signature. We introduce evolutionarily optimized volumetric metamaterials implemented as compact multilayer stacks of strongly coupled electric and magnetic resonators. The optimization search space includes discrete choices and three continuous parameters per pixel (position and rotation), resulting in a 135-dimensional space for a 2×2×2 and 3×3×3 structures (Fig. 1). The objective function maximizes radar cross-section (RCS) over a 10% bandwidth in the X-band (8-12 GHz), commonly used for radar monitoring. We employ the Covariance Matrix Adaptation Evolution Strategy (CMA-ES) algorithm, optimizing RCS over selected frequency points to ensure broadband performance.

The structures were fabricated with a conventional printed circuit board (PCB) methodology following chemical etching of copper elements on a very thin dielectric substrate Rogers 3003 ($\varepsilon_r = 3$, $tan(\delta) = 0.001$) with a thickness of 0.127 mm. Each fabricated layer was separated by foam breaks, material of which is transparent for EM wave propagation at the investigation frequency range. The fabricated structure – 2x2x2

is then used for experiment (Fig. 2), while the 3x3x3-dimentional structure and results of its measurements will be demonstrated during the presentation.

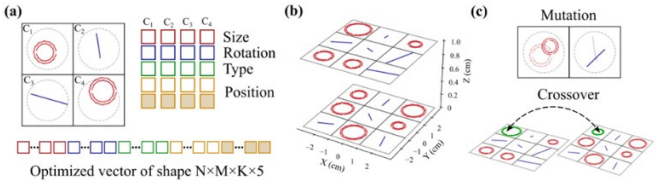

Fig. 1 Genetical algorithm principle for 3D-scatterer design and optimization based on electric (straight wires) and magnetic dipoles (split-ring resonators) (a). The algorithm considers layered structures 2x2x2 and 3x3x3-dimentional structures spaced by 1 cm along Z-axis (b) and perform mutation and crossover for searching for the best backscattering performance (c).

Experimental validation using a DJI Mini 2 drone equipped with genetically designed volumetric metastructures (Fig. 2) was outdoor with a custom-made continuous wave (CW) radar, based on Keysight P9374A Network Analyzer 300 kHz - 20 GHz (Fig. 2(b)). The 2-ports PNA, operated by Matlab, was connected to Tx and Rx broadband horn antennas (NATO IDPH-2018, 2-18 GHz). Horizontal polarization related to the terrain was maintained. The output power (at Tx) was 20 dBm. A low-noise amplifier (LNA, MWA-020180-1-4019, 2-18 GHz) was applied at the Rx. To avoid a feedback loop between transmit and receive channels, the antenna isolation was maintained at more than a 30 dB level, which was checked by monitoring the S_{21} spectrum before introducing the drone. This is the reason why Tx and Rx were taken apart, compared to the laboratory experiments. The bandpass filter (VHF-6010+, 6.3-15 GHz) was used to suppress noise at frequencies irrelevant to the experiment. Photographs of untagged and tagged drones appear in Fig. 2(c and d).

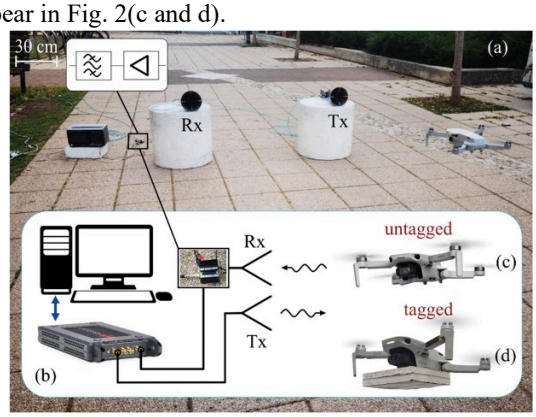

Fig. 2 Experimental setup for outdoor measurements that depict the photo (b) schematic of the CW radar as well as untagged (c) and tagged (d) drone with 2x2x2 designed scatterer.

Finally, to explore additional capabilities of tagging and relate it to real distances, the following analysis has been done. First, the measured drone velocity (e.g., from Doppler maps in Fig. 3) was translated to the distance in meters considering the nonuniform accelerated motion. This mapping with the CW radar is made possible since the target flies toward the radar and co-locates with it at a known time. The Doppler filter was adjusted to fit the 7–9m/sec drone's velocity. Results demonstrate a 1.5-fold increase in radar detection range for the equipped by the 2x2x2 scatterer UAV, considering the take-off payload ability of the used UAV. In the case of 3x3x3 scatterer, the 5-fold increase in radar detection range, in direct agreement with radar equation predictions. The presented results establish a practical and scalable approach to extending radar coverage for small drone detection in next-generation airspace monitoring systems.

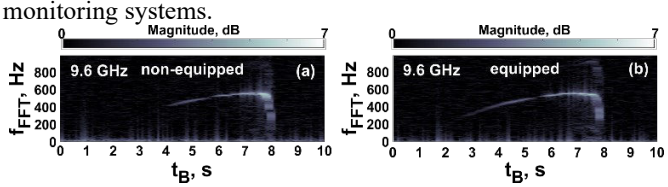

Fig. 3 Short-Time Frequency Transform for the untagged (a) and (b) tagged drone flights at different carrier frequencies of the used CW at 9.6 GHz – maximum of the tag's scattering.

III. Conclusion

We proposed an evolutionarily optimized metamaterial design for enhancing radar scattering in end-fire incidence scenarios. The structure consists of multi-layered arrays of near-field coupled electric and magnetic resonators. A multi-objective genetic optimization algorithm was employed to maximize radar cross-section (RCS) while maintaining a high fractional bandwidth. The resulting design achieves broadband scattering of ~1 m^2 at 10 GHz with over 10% fractional bandwidth. Despite its compact broadside dimensions, the metamaterial scatterer maintains a sub-wavelength end-fire cross-section.

For practical validation, UAV monitoring in urban environments was selected as a demonstration case. We showed that the inherent ~10 cm^2 RCS of a small drone can be enhanced by three orders of magnitude using the metamaterial scatterer. Outdoor experiments confirmed a two-fold increase in detection range with a minimal-sized scatterer attached to the drone.

References

[1] V. M. Shalaev, "Optical negative-index metamaterials," Nature Photonics 2006 1:1, vol. 1, no. 1, pp. 41–48, Jan. 2007.

[2] N. Engheta and R. W. Ziolkowski, Electromagnetic Metamaterials: Physics and Engineering Explorations. Wiley-IEEE Press; 1 edition, 2006.

[3] V. Kozlov, D. Vovchuk, and P. Ginzburg, "Broadband radar invisibility with time-dependent metasurfaces," Scientific Reports 2021 11:1, vol. 11, no. 1, pp. 1–11, Jul. 2021.

[4] D. Ramaccia, D. L. Sounas, A. Alu, A. Toscano, and F. Bilotti, "Phase-Induced Frequency Conversion and Doppler Effect with Time-Modulated Metasurfaces," IEEE Trans Antennas Propag, vol. 68, no. 3, pp. 1607–1617, Mar. 2020

[5] W. Li et al., "Machine Learning for Engineering Meta-Atoms with Tailored Multipolar Resonances," Laser Photon Rev, vol. 18, no. 7, p. 2300855, Jul. 2024

[6] A. Mikhailovskaya *et al.*, "Superradiant Scattering Limit for Arrays of Subwavelength Scatterers," *Phys Rev Appl*, vol. 18, no. 5, p. 054063, Nov. 2022.

[7] A. W. Powell, A. P. Hibbins, and J. R. Sambles, "Multiband superbackscattering via mode superposition in a single dielectric particle," *Appl Phys Lett*, vol. 118, no. 25, p. 251107, Jun. 2021

High-Index Plasmonic Metamaterials for Mid-Infrared Upconversion

Caleb Todd[1,*], Nicolas Spiesshofer[1], Zoltan Sztranyovszky[2], Rakesh Arul[1], Angela Demetriadou[2], Jeremy J. Baumberg[1]

[1]NanoPhotonics Centre, Cavendish Laboratory, Department of Physics, JJ Thomson Avenue, University of Cambridge, Cambridge, CB3 0US, UK

[2]School of Physics and Astronomy, University of Birmingham, Birmingham B15 2TT, UK

*Corresponding author: cat64@cam.ac.uk

***Abstract*—A self-assembled plasmonic metamaterial composed of aggregated gold nanoparticles promotes nonlinear mixing between mid-infrared and visible light. By enhancing and co-localizing the fields in nanometer gaps containing $\chi^{(2)}$-active molecules, sum-frequency generation is observable even from low-power CW illumination. This offers an avenue for broadband, room-temperature mid-infrared detection.**

***Keywords*—metamaterials, mid-infrared, plasmonics, sum-frequency generation.**

I. Introduction

The mid-infrared region of the electromagnetic spectrum contains a wealth of information about molecular composition, structure, interactions, and dynamics. However, these insights are obscured by the limitations of existing mid-infrared (MIR) detectors, which (in contrast with their optical domain counterparts) are typically slow, cumbersome to use, cryogenically cooled, and suffer from high noise levels. One way around this problem is to upconvert MIR photons to the visible regime (where excellent single-photon detectors exist) via nonlinear optical processes such as sum- or difference-frequency generation (SFG and DFG) [1], [2]. If the MIR frequency is tuned to a simultaneously Raman- and infrared-active molecular vibration, optomechanical coupling improves the efficiency of the conversion process (illustrated in the Fig. 1 top inset). Nevertheless, only a tiny percentage of MIR photons will undergo upconversion under typical circumstances.

Plasmonic systems — with their characteristic small mode volumes and large electric field enhancements — can enormously improve the efficiencies of these nonlinear processes. In this paper, we present results on a plasmonic metamaterial composed of self-assembled multilayer aggregates (MLaggs) of close-packed gold nanoparticles, separated by ∼1nm gaps scaffolded with 4-nitrothiophenol (4NTP), as illustrated in Fig. 1. Although composed of ∼65% gold, MLaggs can be modeled as a high-refractive-index, surprisingly-low-loss dielectric at MIR wavelengths. These aggregates exhibit dual resonances in the visible and MIR regimes, simultaneously enhancing and co-localizing both electric fields onto the scaffolding molecule within the gaps, which possesses a strongly Raman- and MIR-active vibrational mode that provides a large nonlinear coupling. We demonstrate MIR-to-visible upconversion in this system under CW illumination with microwatts of power. The MLaggs, consequently, act as broadband, room-temperature detectors for MIR light.

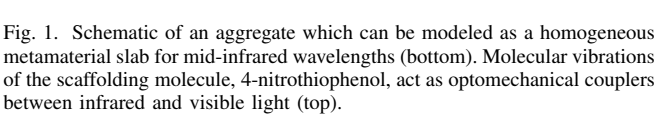

Fig. 1. Schematic of an aggregate which can be modeled as a homogeneous metamaterial slab for mid-infrared wavelengths (bottom). Molecular vibrations of the scaffolding molecule, 4-nitrothiophenol, act as optomechanical couplers between infrared and visible light (top).

II. Methods

Multilayer aggregates are formed using a self-assembly process similar to that reported in e.g. [3]. First, 500µL of colloidal gold nanoparticles (250nm diameter, citrate capped, BBI Solutions) are added to 500µL of chloroform in an Eppendorf tube. The two immiscible solutions remain distinct and form a liquid-liquid interface. Next, we add 400µL of 1mM 4NTP (Sigma Aldrich) solution and shake for one minute. The 4NTP glues the nanoparticles into a 3D aggregate which then settles at the chloroform interface. Excess solutes can be washed by repeated dilution with deionised water. Most of the remaining water is then extracted, leaving a droplet with a 2D nanoparticle aggregate on the surface. Drop-casting this droplet and drying on the surface of a MIR-transparent

CaF_2 substrate (Crystran) leaves 1–2 layers of random-close-packed gold nanoparticles separated by ∼1nm gaps scaffolded by 4NTP. The aggregate is then immersed for ∼16 hours in 10mM 4NTP to ensure saturation of the plasmonic nanogaps. Excess 4NTP is washed away with ethanol and the sample is dried using an N_2 gun.

Mid-infrared spectroscopy and characterization of the MLaggs was performed in an FTIR microscope (Shimadzu AIM-9000 FTIR microscope, liquid nitrogen cooled MCT detector, Cassegrain 15X objective 0.7N.A., 20µm spot size, Happ-Genzel apodization). Modeling of the resulting MIR reflectance spectra used a custom transfer-matrix method code, treating the MLagg as a homogeneous slab whose dielectric constant is the fit parameter.

Upconversion experiments used a tuneable QCL MIR pump laser (LaserTune, Block Ltd.) operating at a 5% duty cycle. This was focused onto the sample from below through a 0.5NA, 40x reflective objective (Thorlabs). A 785nm diode laser (MatchBox, Integrated Optics Ltd.) was passed through an AOM operating at a 15% duty cycle synchronised to the QCL to temporally overlap the MIR and visible/near-infrared beams, before being focused onto the sample from above through a 0.9NA 100x dark field objective in a customised commercial microscope (BX51, Olympus). Light was collected in reflectance from above and sent through notch filters (785–20 NNF, Iridian) to remove Rayleigh scattered light. The remaining light was passed through a monochromator (i303, Shamrock) and dispersed by a 150 lines/mm grating onto an EMCCD (Newton, Andor).

III. Results and Discussion

Fourier-transform infrared spectroscopy of 4NTP-aggregated MLaggs reveals strong surface-enhanced infrared absorption (SEIRA) signals from the molecule. From this we can confirm its presence within the plasmonically active gaps between nanoparticles. The metamaterial possesses a Fabry-Perot resonance whose spectral positions comes in discrete steps based on the number of layers present in the sample. By modeling the aggregate as an effective dielectric arranged as a homogeneous slab, allowing the refractive index

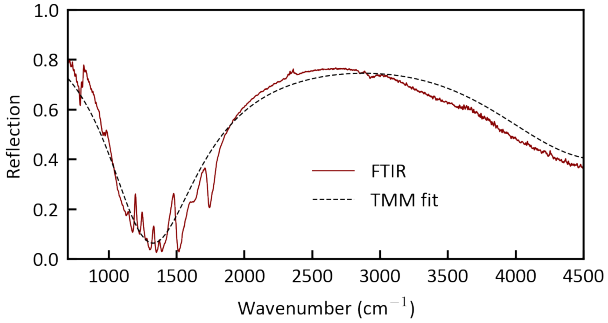

Fig. 2. FTIR spectrum of a nanoparticle aggregate with a transfer-matrix method fit using $n \approx 4.7 + 0.1i$.

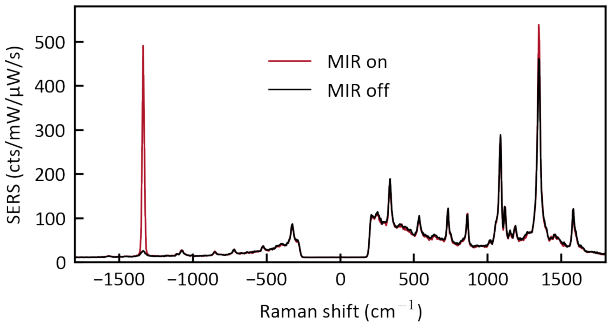

Fig. 3. Spectra of a 4NTP MLagg with (red curve) and without (black curve) a MIR beam tuned to the 1338cm^{-1} molecular vibrational resonance.

to vary but setting the aggregate thickness to that expected from a close-packed stack, we can use the transfer-matrix method to fit our FTIR spectra and calculate an experimental value for the dielectric constant. An example is shown in Fig. 2 with a refractive index of $n \approx 4.7 + 0.1i$, but much larger values should be achievable [4].

To perform nonlinear mixing on these samples, we illuminated them with CW light: 23µW of 785nm near-infrared (NIR) from above, and 220µW of 1338cm^{-1} MIR from below (tuned to the vibrational energy of the 4NTP NO_2 functional group). In Fig. 3, we compare spectra taken with MIR off (black curve) and on (red curve). The signal is unchanged except for a large increase at the sum-frequency, which is a signature of coherent SFG.

Next, we varied the MIR wavenumber to evaluate the relative importance of resonant and non-resonant contributions to the SFG (i.e. that from the vibration and that from the background $\chi^{(2)}$). The bright diagonal in Fig. 4a where the anti-Stokes Raman shift equals the MIR pump wavenumber demonstrates completely broadband SFG. A line-cut across that diagonal (as well as the equivalent diagonal on the Stokes side) is shown in Fig. 4b, where it is easier to see the Fano lineshape of the SFG near vibrational resonances. This is due to interference between the aforementioned resonant and non-

Fig. 4. (a) Metamaterial difference spectra (MIR on minus MIR off) as the MIR wavenumber is scanned from 960cm^{-1} to 1630cm^{-1}. (b) Line-cuts of the Raman shift equals MIR wavenumber diagonals on the Stokes (DFG, red curve) and anti-Stokes (SFG, blue curve) sides from the scan in (a), plotted on the same scale but vertically offset for clarity.

resonant contributions, whose relative phase shifts by π as the MIR wavenumber crosses a particular vibration. Further to this, we can see that the DFG signal (red curve), although similar in magnitude, is significantly noisier than the SFG signal.

IV. Conclusion

We have showcased a self-assembled plasmonic metamaterial with the capacity for extraordinary nonlinear mixing between MIR and visible/NIR light. Close-packed layers of gold nanoparticles separated by 4NTP molecules act as an effective dielectric in the MIR with a large refractive index and low loss. The Fabry-Perot resonances from such structures can be observed in FTIR spectroscopy and modeled using the transfer-matrix method to extract experimental values for the measured refractive indices, which sit near $n \approx 4.7 + 0.1i$. The plasmonic enhancement of MIR and NIR light within the metamaterial enables remarkably strong nonlinear mixing between the two fields, generating easily detectable SFG signals even under CW illumination at 20μW of 785nm and 220μW of 1338cm^{-1}. These signals are detectable broadband, making it a feasible avenue for future room-temperature MIR detectors.

Acknowledgments

AD wishes to acknowledge support from the Royal Society University Research Fellowship URF/R1/180097 and URF/R/231024, Royal Society Research Fellows Enhancement Award RGF/EA/181038, funding from ESPRC grants EP/Y008774/1 and EP/X012689/1 from EPSRC for the CDT in Topological Design EP/S02297X/1.

References

[1] A. Xomalis, X. Zheng, R. Chikkaraddy, Z. Koczor-Benda, E. Miele, E. Rosta, G. A. E. Vandenbosch, A. Martínez, and J. J. Baumberg, "Detecting mid-infrared light by molecular frequency upconversion in dual-wavelength nanoantennas," *Science*, vol. 374, Issue 6572, pp. 1268–1271, 2021.

[2] W. Chen, P. Roelli, H. Hu, S. Verlekar, S. P. Amirtharaj, A. I. Barreda, T. J. Kippenberg, M. Kovylina, E. Verhagen, A. Martínez, and C. Galland, "Continuous-wave frequency upconversion with a molecular optomechanical nanocavity," *Science*, vol. 374, Issue 6572, pp. 1264–1267, 2021.

[3] D.-B. Grys, M. Niihori, R. Arul, S. M. Sibug-Torres, E. W. Wyatt, B. de Nijs, and J. J. Baumberg, "Controlling Atomic-Scale Restructuring and Cleaning of Gold Nanogap Multilayers for Surface-Enhanced Raman Scattering Sensing," *ACS Sensors*, vol. 8, Issue 7, pp. 2879-2888, 2023.

[4] N. Spiesshofer, E. Wyatt, Z. Sztranyovszky, C. Todd, T. V. Mykytiuk, J. W. Beattie, R. Davies, R. Arul, V. Lindo, T. F. Krauss, A. Demetriadou, and J. J. Baumberg, "Tailoring ultrahigh index plasmonic combinatorial metamaterials for SEIRA and SERS by tuning the fill fraction," *Optica*, vol. 12, pp. 1357-1366, 2025.

Efficient bio-sensor based on terahertz metasurface

Pradeep Tiwari, Deepak Kala, Maciej Sakowicz
CENTERA Laboratories, Institute of High Pressure Physics PAS, 01-142 Warsaw, Poland
e-mail address: pradeep.tiwari@unipress.waw.pl

***Abstract*-Terahertz metasurfaces enable safe, label-free biosensing with sensitivity to water and weak molecular interactions. Micrometer gaps concentrate fields, overcoming wavelength–biomatter mismatch. Simulations show that low-index PMP substrates maximize response. An H-split metasurface achieves 800 GHz/RIU, experimentally validated with BSA, delivering 31.25 µg/mL LOD and 343 GHz/(ng/mm²) sensitivity via reduced mode volume and increased light–matter interaction**.

Keywords — metasurfaces; terahertz; biosensing; COMSOL

I. INTRODUCTION

Sensors based on terahertz metasurfaces (THz MSs) are starting to get big attention in sensors community [1]. The main focus is in bio-sensing because of properties of the THz radiation. It is non-ionizing (safe for biological samples and operator [2]), sensitive to water content and week molecules interactions (resonances of hydrogen and van der Waals bonds lay in the THz spectral region as well) [3,4]. Also rotational and vibrational modes of molecules all lay in this spectral region.

A THz metasurface usually has a dielectric substrate with a repeating metallic pattern on top of it. This kind of structure helps with one of the biggest problems with THz biosensing: the difference in size between biological objects like cells, bacteria, viruses, proteins, and DNA (which are smaller than a micrometer) and the THz wavelength (which is hundreds of micrometers) [5]. Subwavelength gaps in the metallic pattern that are usually a few micrometers wide govern the electromagnetic response [6]. These narrow gaps strongly confine electromagnetic fields and enhances light-matter interaction with bio-molecules.

The substrate critically influences sensor performance. Important parameters include substrate thickness, refractive index, and dielectric loss. Since most of THz sensors operate in transmission mode, researchers widely use low-loss substrates like high-resistivity silicon and polymers such as polyethylene (PE), polytetrafluoroethylene (PTFE), and polymethyl pentene (PMP). Thinner substrates make things more sensitive, while thicker, higher-index materials add capacitance that can hide spectral changes caused by analytes. To get the most sensitive detection, low-refractive-index substrates are the best choice [7]. The current work is focused on how low and high refractive index substrates influence the sensitivity of metamaterial.

Bovine serum albumin (BSA) is a common model protein used to study how biomolecules interact with surfaces. When BSA sticks to a THz metasurface, it changes the dielectric environment around it and moves the resonance frequency. It makes it possible to detect biomolecules very easily.

II. METHOD

The numerical response of the THz MS is modelled using COMSOL Multiphysics with RF module, using the finite element method. In the simulation, x-polarized light travels along the z-axis and is incident normal to the metasurface. To ensure accurate simulations, periodic boundary conditions are enforced in the x- and y-directions, while perfectly matched layers are employed to truncate the infinite space along the z-direction. The dielectric constant of metal (gold) is described by the Drude-Lorentz model $\boldsymbol{\varepsilon = 1 - \frac{\omega_p^2}{(\omega^2 + i\gamma\omega)}}$ in which we take the plasma frequency $\frac{\omega_p}{2\pi}$ = 2175 THz and the collision frequency $\frac{\gamma}{2\pi}$ = 9 THz [8]. A thickness of 110 nm was used for the metal and we took 500 µm as a thickness of both the substrates in the simulations. To study the sensitivity of our metasurfaces in the simulations we put onto the metasurface a layer of dielectric (10 µm thick) with various dielectric constants (from 1 to 2). This will simulate covering the metasurface with bio-matter. For our investigations we used two designs of THz MSs (Fig. 1). Among other we used previously studied metasurface to have additional verification of our simulations.

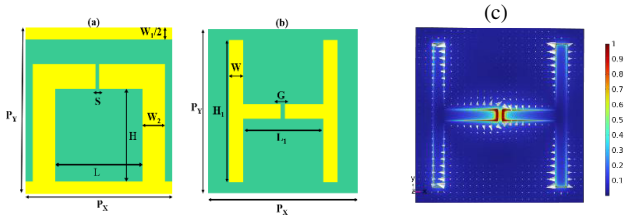

Fig. 1. (a) Schematic of unit cell of the metallic Fano resonance structure. (b) H-split structure. The Fano structure (a) are characterized by specific dimensions: both PX and PY measure 40 µm, W1 is 8 µm, W2 is 6 µm, L is 24 µm, H is 22 µm, and the gap width is denoted as S=1.5µm. (b) H-split structure has the dimension PX= PY=55 µm, G=2µm L1=36 µm, W=4 µm and H1=45 µm. (c) electric field intensity of on the PMP substrate in the XY plane (scolor scale) and current distribution at the resonance (arrows)

As we can observe in Fig. 2, there is a redshift in the frequency of the resonance as we vary refractive index (n) from 1 to 2. It can be seen that sensitivity defined as the frequency shift per refractive index unit (RIU) decreases as we move from PMP to the silicon. This behavior is due to the following factors: (i) the increase in non-radiative losses associated with substrates of higher permittivity, (ii) the enhancement of electromagnetic field confinement within the substrate, rather than extending into the surrounding medium

where the analyte is present. In the case of silicon, high refractive index pulls the field much deeper into the substrate. This confinement reduces the overlap between the evanescent fields of the metasurface and the analyte layer, decreasing the interaction volume and, consequently, the sensor's sensitivity[9]. From linear fit to simulation data of resonance shift we obtained sensitivity of 800 GHz/RIU.

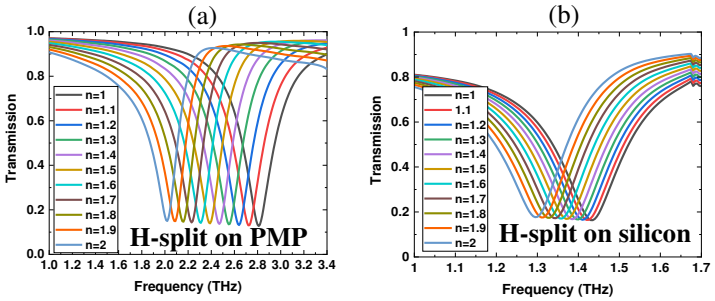

Fig. 2. The H-split structure: (a) simulation result of transmission magnitude on the PMP substrate; (b) simulation result of transmission magnitude on the silicon substrate.

III. Result and Discussion

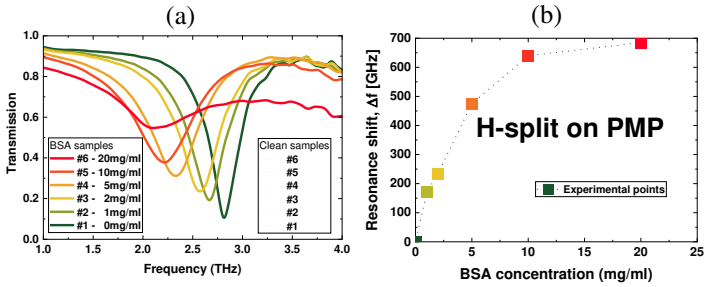

Fig. 3. (a) Transmission spectra for six samples of H-split structure on PMP with varying BSA concentrations (thick solid lines). (b) Resonance shift as a function of BSA concentration, derived from data in the panel (a).

The validate our method and the results of simulations we conducted BSA detection experiments. One of four experimental results is presented in Fig. 3, where we show resonance shift (Fig. 3b) as a function of BSA protein concentration, derived from the transmission spectra of H-split structure on PMP (Fig. 3a). This simulates covering the metasurface with a material of increasing refractive index, as in the simulations. The observed shift (Δf) saturates at 685 GHz for the highest BSA concentration of 20 mg/ml. This shift corresponds to the simulation result for a refractive index of 1.86 (Δn = 0.86). Notably, this value matches the value reported for BSA (n = 1.8) in the literature [24,25]. So to obtain the experimental sensitivity in GHz/RIU, one should divide experimental Δf (in GHz) by 0.8 RIU. This gives experimental sensitivity of 856 GHz/RIU.

VI. Conclusion

In conclusion, we experimentally demonstrated an ultrasensitive H-split design-based meta-biosensor, achieving an exceptional sensitivity of 800 GHz/RIU.

The increased sensitivity comes from the low-refractive-index substrate, which supports tighter electromagnetic confinement and lower mode volume, resulting in stronger light-matter interaction and higher sensing capabilities. The simulations were experimentally validated and compared with previous experimental studies on Fano resonance structures [10]. Our results represent a crucial step toward the development of next-generation high-sensitivity sensing platforms. The proposed H-split metasurface presents an approach for developing ultrasensitive biological sensors, nonlinear photonic devices, and platforms for enhanced light-matter interaction.

Acknowledgement

This research was funded by the National Science Centre, Poland, grant number 2020/38/E/ST7/00476 and "International Research Agendas" program of the Foundation for Polish Science, cofinanced by the European Union under the European Regional Development Fund for CENTERA Lab (No. MAB/2018/9).

References

[1] Zhang, Zhongquan, Zhao, Rui, Cong, Mengyang and Qiu, Jianfeng. "Developments of terahertz metasurface biosensors: A literature review" Nanotechnology Reviews, vol. 13, no. 1, 2024, pp. 20230182. https://doi.org/10.1515/ntrev-2023-0182.

[2] Zhan X, Liu Y, Chen Z, Luo J, Yang S, Yang X. Revolutionary approaches for cancer diagnosis by terahertz-based spectroscopy and imaging. Talanta. 2023;259:124483.

[3] Qin J, Ying Y, Xie L. The detection of agricultural products and food using terahertz spectroscopy: A review. Appl Spectrosc Rev. 2013;48(6):439.

[4] Ryder MR, Van de Voorde B, Civalleri B, Bennett TD, Mukhopadhyay S, Cinque G, et al. Detecting molecular rotational dynamics complementing the low-frequency terahertz vibrations in a zirconium-based metal-organic framework. Phys Rev Lett. 2017;118(25):255502

[5] Ahmadivand A, Gerislioglu B, Ahuja R, Kumar Mishra Y. Terahertz plasmonics: The rise of toroidal metadevices towards immunobiosensings. Mater Today. 2020;32:108–30.

[6] Yu, Liu and Hao, Liu and Meiqiong, Tang and Jiaoqi, Huang and Wei, Liu and Jinying, Dong and Xueping, Chen and Weiling, Fu and Yang, Zhang, "The medical application of terahertz technology in non-invasive detection of cells and tissues: opportunities and challenges", RSC Adv., 2019, vol. 9, p. 9354-9363.

[7] J. Liu, W. Lyu, X. Deng, Y. Wang, H. Geng and X. Zheng, "Material and thickness selection of dielectrics for high transmittance terahertz window and metasurface, " *Opt. Mater.*, vol. 127, pp. 112219, 2022.

[8] Ordal, Mark A., Robert J. Bell, Ralph W. Alexander Jr, Larry L. Long, and Marvin R. Querry. "Optical properties of Au, Ni, and Pb at submillimeter wavelengths." *Applied Optics* 26, no. 4 (1987): 744-752.

[9] Lopato, P.; Herbko, M.; Mescheder, U.; Kovacs, A. "Influence of a thin dielectric layer on resonance frequencies of square SRR metasurface operating in THz band." *Open Eng.* 2023, *13*, 20220400

[10] Tiwari, Pradeep, Deepak Kala, and Maciej Sakowicz. "The optimal substrate choice for effective biosensors based on THz metasurfaces." *Scientific Reports* 15, no. 1 (2025): 29749.

Polarization dynamics of waves propagating in complex media: application to moving media

Aymeric Braud* and Renaud Gueroult

LAPLACE, Université de Toulouse, CNRS, INPT, UPS, 31062 Toulouse, France
*Corresponding author: aymeric.braud@laplace.univ-tlse.fr

***Abstract*—We use an extended geometrical optics theory to derive an evolution equation for polarization in complex media. Considering moving media, we show that motion affects polarization via new spin-orbit mechanisms. Because they arise from properties bestowed to the medium by motion, these effects should also manifest in static complex media.**

***Keywords*—spin-orbit interaction, light polarization, geometrical optics, moving medium**

I. Introduction

Propagation of electromagnetic waves in a medium is modified when the medium is moving. Historically Fizeau [1] showed that medium motion can affect the phase velocity of light. Later Player [2] and Jones [3] demonstrated that both the group velocity, hence the trajectory of light rays, and the polarization of light were also affected by motion. Although as demonstrated by original studies [3], [4] these effects are small in dielectrics under normal conditions, more recent experiments showed large rotations of a light beam image propagating in a rotating medium under slow-light conditions [5], or in a rotating plasma [6].

The emergence of such manifestations of light in moving media can be explained by the fact that a moving medium appears, for an observer in the lab frame, as a complex medium manifesting for example (bi)anisotropy [7], magneto-electric coupling and spatial dispersion [8]. Because of this complexity, most of the studies, both theoretical [2], [9], [10], [11], [12] and experimental [3], [4], [5], [6], were carried out in very specific and simple geometrical configurations. It thus remains to be seen how motion may, when considering a more generic problem, lead to new wave manifestations.

In the present communication, we make use of a very general eikonal theory to model the propagation of waves in moving media in more general configurations. A key building block of this model is the Extended Geometrical Optics (XGO) theory derived by Ruiz and Dodin [13], [14] to solve wave equations asymptotically assuming quasi-plane wave solutions in the limit of short wavelengths. Supporting mode conversion, this theory describes how the modes amplitudes evolve along light rays and then the dynamics of the wave envelope. Going further, we extend this work to derive a transport equation for the wave polarization, that is an equation capturing the dynamics of polarization along the ray. This important equation allows us to identify which physical effects contribute to variations of the wave polarization.

By applying this model to electromagnetic waves in moving media, we can capture light polarization dynamics in very general configurations. Doing so, we not only confirm known dynamical effects of motion and extend them to more general geometrical configurations [15], we also interestingly predict new effects of motion beyond those accessible in the specific configurations that had previously been considered [15], [16]. Precisely, we find that motion is responsible for a spin-orbit interaction (SOI) of light leading to polarization rotation. Importantly, we demonstrate that, if the medium is time dispersive at rest, a SOI can be induced even if the ray is straight [16], in contrast to the classically studied SOI of light for which a redirection of the ray trajectory is usually required [17].

Looking beyond moving media, it stands to reason that such effects should be at play in other complex media, even at rest, if they present similar properties such as anisotropy, magneto-electric coupling or spatial dispersion. This is particularly true of spacetime modulated metamaterials mimicking moving media [18], [19] or in other metamaterials exhibiting magneto-electric coupling. More generally, the versatility of XGO makes it interesting for studying wave propagation, especially polarization dynamics, in such media.

In this communication, we first introduce the XGO theory, starting with a brief introduction to usual Geometrical Optics (GO) to then expose how the first-order equations capture spin-orbit interactions and gradient corrections. Secondly, we show how a moving medium can be treated like any other medium at rest with complex properties, and from there review what XGO applied to this problem can tell on the effects of motion on polarization.

II. Extended geometrical optics theory

Extended Geometrical Optics (XGO) as presented here is based on the theory derived by Ruiz & Dodin [14], [20], [13] but finds its roots in short-wavelength asymptotic theories like eikonal theory, WKB approximation, semiclassical approximation, polarized geometrical optics or post-geometrical optics which share basically the same asymptotic structure and are already largely used in optics, quantum mechanics, acoustics and seismology.

A. Classical geometrical optics

Because XGO is an extension of the usual GO we recall here first the basic underlying principles. Both are based on the same assumption, that is that the wavelength λ is small compared to the characteristic lengths L of the medium variations [21] ($\epsilon \doteq \lambda/L \ll 1$). Locally the medium then appears homogeneous. In this limit one may look for local plane-wave solutions $\propto e^{i\epsilon^{-1}(\omega t - \boldsymbol{k}\cdot\boldsymbol{x})}$ with local frequency ω and wavevector $\boldsymbol{k}$. The corresponding algebraic equation, which importantly should not include gradients of the medium properties, gives the dispersion matrix [21]. The eigenvalues and the eigenvectors of this matrix are respectively the dispersion functions and the polarization states of the wave modes. Using the dispersion function as the Hamiltonian in Hamilton equations gives the ray tracing equations of GO. The solutions to these equations are rays describing the trajectory of the energy of the propagating waves. The group velocity $\boldsymbol{v}_g$ is then a vector tangent to the ray.

In this procedure the mode polarization states are defined up to a phase whose choice amounts to fixing a non-physical gauge [22]. Moreover, this zeroth-order approach (gradient of the medium properties have so far been neglected) does not give dynamical equation for the complex amplitudes of the modes. To have the full gauge-independent dynamics of the wave envelope, one has to perform a proper asymptotic expansion of the wave equation in ϵ and consider the next order, as done below.

B. Extended geometrical optics

To capture the wave envelope dynamics, XGO assumes solutions in the form of quasi-plane waves. This wave form is locally a plane wave but allows the envelope $\boldsymbol{\mathcal{E}}$ to vary slowly compared to the dynamical phase Φ. It is written

$$\boldsymbol{E}(\boldsymbol{x},t) = \boldsymbol{\mathcal{E}}(\boldsymbol{x},t)e^{i\epsilon^{-1}\Phi(t,\boldsymbol{x})} \tag{1}$$

with $\boldsymbol{\mathcal{E}} = \underline{\boldsymbol{\Xi}}\boldsymbol{a}$ the wave envelope composed of the vector $\boldsymbol{a}$ of the complex amplitudes of the resonant modes, i.e. modes that have the same dispersion relation to zeroth order, and the polarization matrix $\underline{\boldsymbol{\Xi}}$ gathering the eigenvectors of these modes [14]. While classical GO describes the dynamics of the dynamical phase Φ, XGO describes in addition the dynamics of $\boldsymbol{\mathcal{E}}$ including the dynamics of the wave polarization. For that, by considering the first-order terms in the ϵ-expansion, XGO provides a transport equation for $\boldsymbol{a}$ along the ray that governs the evolution of the complex amplitude of the modes. These may be coupled in the presence of mode conversion [14].

C. Polarization evolution equation

The unit polarization vector of the quasi-plane wave, describing the wave polarization state and direction, is defined as [23], [15]

$$\hat{\boldsymbol{e}} = \boldsymbol{E}e^{-i\Phi}/|\boldsymbol{E}|. \tag{2}$$

From the equation for $\boldsymbol{a}$ we derive a transport equation for $\hat{\boldsymbol{e}}$ that writes [15]

$$\frac{d\hat{\boldsymbol{e}}}{ds} = \text{parallel transport term} + \text{gradient corrections}. \tag{3}$$

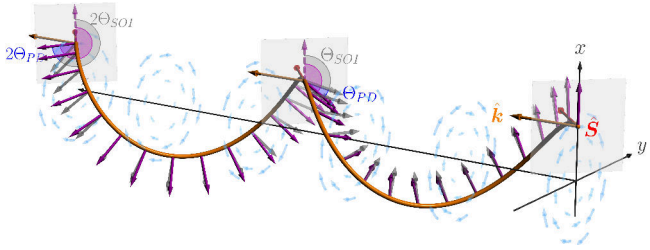

Fig. 1. In a rotating isotropic non-dispersive medium, the ray trajectory (orange) is dragged so that it can be a helix and hence have a non-zero torsion. Since the polarization plane (gray) is redirected, a spin-redirection Berry phase is accumulated and the polarization (purple) undergoes a Rytov rotation by an angle Θ_{SOI} after each cycle. In addition to this purely geometrical effect, a dynamical effect called polarization drag makes the polarization rotates in its plane of an angle Θ_{PD}. The total polarization rotation is then the combination of these two phenomena.

The first term describes the parallel transport of the polarization vector $\hat{\boldsymbol{e}}$ along the ray parameterized by s, and the second term captures changes of $\hat{\boldsymbol{e}}$ induced by non-uniformities (gradients) of the medium properties.

III. Predicted Effects of Motion on Polarization

We apply here the above XGO theory to moving media to understand how the dynamics of polarization is affected by motion. First, we show how the moving medium as seen from the lab frame can be seen as an equivalent effective medium at rest [24]. Equipped with this result, we then introduce the new polarization effects induced by motion.

A. Description of medium motion as a magneto-electric coupling

In order to describe the moving medium as an equivalent effective medium at rest, the flow velocity field $\boldsymbol{v}(\boldsymbol{x}) = \boldsymbol{\beta}(\boldsymbol{x})c$ is considered as a vector property of the medium, which introduces locally a preferred direction and hence anisotropy [7]. As a result, a medium that is isotropic at rest will appear from the lab frame to be anisotropic when in motion. Just like other medium properties, GO assumptions require that the velocity field varies slowly in space compared to the wavelength [25]. Consequently, the wave sees locally a uniform rectilinear motion and special relativity is then valid locally and instantaneously [25]. To have the medium response to the wave, it is then possible to perform local Lorentz transformations $\mathcal{L}$ in the rest frame constitutive relations according to Minkowski's theory [26]. For example for an isotropic medium this procedure gives

$$\begin{cases} \boldsymbol{D}' = \varepsilon'\boldsymbol{E}' \\ \boldsymbol{B}' = \mu'\boldsymbol{H}' \end{cases} \overset{\mathcal{L}}{\Longrightarrow} \begin{cases} \boldsymbol{D} = \varepsilon'\boldsymbol{E} + (\varepsilon'\mu'c^2 - 1)\boldsymbol{\beta}\times\boldsymbol{H}/c \\ \boldsymbol{B} = \mu'\boldsymbol{H} - (\varepsilon'\mu'c^2 - 1)\boldsymbol{\beta}\times\boldsymbol{E}/c \end{cases} \tag{4}$$

We see here that the obtained lab-frame constitutive relations exhibit anisotropy and a magneto-electric coupling. Propagation in a moving medium can accordingly be treated using XGO like propagation in any other medium at rest, with the difference that the medium considered is an equivalent

effective medium with additional properties compared to this same medium at rest [24].

B. Spin-orbit effects

When computing the polarization evolution equation (3) for the moving medium, we find a parallel transport term that is entirely due to motion, revealing a SOI induced by motion [15] which as usual is associated with the accumulation of a Berry phase [27]. Precisely, we identify this Berry phase caused by motion to be a spin-redirection phase, similarly to that observed for example in twisted optical fibers [28]. For moving media though, we find that this spin-redirection phase can have two distinct origins as explained now.

1) Ray-redirection Berry phase induced by motion: In a non-dispersive isotropic medium, through light-dragging effects [29], [30], a non-uniform motion is able to bend light rays [31], [32] and even to render them non-planar [15] as represented in Fig. 1. As a consequence, analogously to gradient-index media at rest [23], [33], the polarization plane, which is normal to the ray trajectory, is redirected and a spin-redirection Berry phase is then accumulated [15]. This phase originates from the parallel transport of the polarization in the parameter space since this latter has a curved geometry. Since this effect is caused by the redirection of the ray we call this phase *ray-redirection Berry phase* [16]. However, unlike in most of the existing studies on SOI of light that are focused on media at rest [23], [34], ray redirection is led by $\boldsymbol{w} = \boldsymbol{k} + (n'^2 - 1)\omega/c\boldsymbol{\beta}$ [15], instead of $\boldsymbol{k}$, due to light-dragging effects [24]. This novelty introduced by motion shows that a spin-redirection SOI is possible even if $\boldsymbol{k}$ is not redirected as it is the case in Fig. 1. Yet, the effect of this SOI on the polarization remains the well-known Rytov rotation [35], [20], [13], that is a rotation of the polarization in its plane due to parallel transport along a ray with non-zero torsion as depicted in Fig. 1.

2) Spin-deviation-redirection Berry phase induced by motion: Spin-redirection Berry phase is often believed to require non-planar rays, as discussed above. Yet, we find through the same formalism that motion combined with time dispersion can in fact induce a spin-redirection Berry phase with rays with zero torsion [16]. To see this, consider the particular case of a moving unmagnetized cold plasma, for which rays are singularly not affected by motion [36], [24], i.e. there is no transverse drag. In this case, as illustrated in Fig. 2, rays are straight lines just as in a homogeneous plasma, and hence there cannot be ray-redirection SOI. Yet, we find that there is still a spin-redirection SOI: this is because the polarization plane is redirected by motion, and as a result is no longer normal to the ray. This deviation of the polarization plane from the ray, shown in Fig. 2, constitutes an additional degree of freedom for its redirection. A non-uniform motion can then redirect the polarization plane independently from the ray. Reflecting its origin, that is a geometric phase due to the redirection of the polarization plane even if the ray is straight, we call this contribution *spin-deviation-redirection Berry phase* [16]. As a spin-redirection phase it also is classically associated with a Rytov rotation of the polarization.

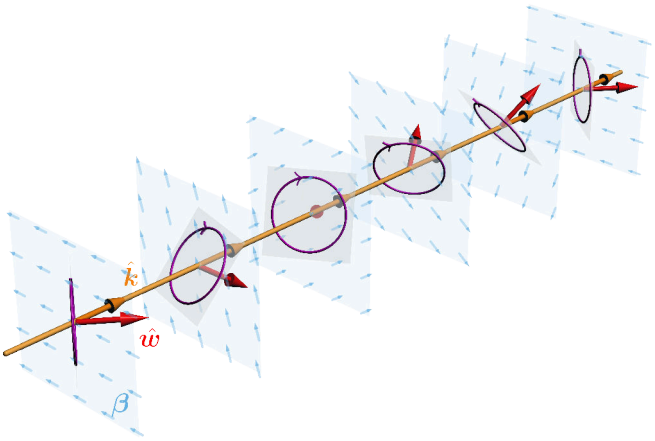

Fig. 2. In a moving unmagnetized cold plasma, the ray (orange) is not affected by motion (blue) and is therefore a straight line if the plasma is homogeneous. However, the motion makes the polarization plane normal (red) deviate from the ray tangent being $\boldsymbol{k}$ (orange). Its redirection by a non-uniform motion leads to a novel type of SOI – the *spin-deviation-redirection SOI* – and induces a Rytov-like rotation of the polarization.

C. Dynamical effects

The spin-orbit effects described above are purely geometrical effects. However, motion also induces a dynamical effect named polarization drag [37] that leads to an additional rotation of the polarization in its plane, which, as shown in Fig. 1, can compete with or add to Rytov rotation. This effect is well-known but was only studied for rigid-body rotation in the case where the wavevector is aligned with the rotation axis [4], [9], [38], [39], [40]. The gradient correction term in Eq. (3) now captures this effect for an arbitrary velocity field $\boldsymbol{\beta}(\boldsymbol{x})$ in a general configuration, i.e. for a wavevector $\boldsymbol{k}$ with an arbitrary direction [15]. We find that the intensity of this effect depends on the local vorticity of the flow and on the angle between the latter and the polarization plane normal. As expected this results reduces to the historical result for a non-dispersive isotropic medium [37], [4], [9] and to the result that has more recently been predicted for a rotating unmagnetized plasma [41].

IV. Conclusion

We exploited a very general asymptotic theory named *Extended Geometrical Optics* (XGO), rigourously developed using Wigner-Weyl formalism, to derive an evolution equation for the dynamics of wave polarization along the rays, obtained using classical geometrical optics. This equation is very general and can therefore be used to study the behavior of light polarization in media with complex properties including anisotropy, magneto-electric coupling and spatial dispersion. Because it captures mode conversion, this theory can also handle degenerate or resonant modes.

As a particular case and making use of its versatility, we apply this formalism to describe the dynamics of light polarization in moving media. We then find that the polarization is governed by two contributions. The first one, a geometrical effect, captures a parallel transport of the polarization in the parameter space. The second one, a dynamical effect named polarization drag, acts to rotate the polarization in its plane.

The first effect is a spin-orbit interaction of spin-redirection type. Yet, the mechanism at play in moving media differs from that in gradient-index media at rest where SOI of light have been classically studied. Specifically, for a moving non-dispersive isotropic medium, the spin-redirection Berry phase does not depend on the redirection of the wavevector $\boldsymbol{k}$, but rather on the redirection of the group velocity $\boldsymbol{v}_g$ [15]. Even more interestingly, when the medium is dispersive at rest, for instance in a plasma, the polarization plane normal can deviate from the ray. This additional degree of freedom then allows for SOI even if rays are straight, since the polarization plane can be redirected independently from the ray. We called this effect *spin-deviation-redirection SOI* [16] as it requires a deviation of the polarization plane normal from the ray, and a variation of this deviation along the ray.

This new flavor of spin-redirection SOI is particularly interesting in that it can be tuned independently from the ray trajectory, whereas up until now spin-redirection SOI essentially required engineering the ray trajectory. This added control in turn offers new possibilities for light manipulation. Importantly, it is expected that this added control may be enabled beyond moving media, in particular in static metamaterials, and notably in spacetime modulated metamaterials mimicking moving [18], [19].

Acknowledgments

This work is supported by the Agence Nationale de la Recherche (ANR) through the WaRP project (ANR-21- CE30-0002). This work has been carried out within the framework of the EUROfusion Consortium, via the Euratom Research and Training Programme (Grant Agreement No 101052200 – EUROfusion). Views and opinions expressed are however those of the authors only and do not necessarily reflect those of the European Union or the European Commission.

References

[1] H. Fizeau, "Sur les hypothèses relatives à l'éther lumineux," *Comptes Rendus*, vol. 33, pp. 349–355, 1851.

[2] M. A. Player, "Dispersion and the transverse aether drag," *Proc. R. Soc. Lond. A.*, vol. 345, pp. 343–344, 1975.

[3] R. V. Jones, "'Aether drag' in a transversely moving medium," *Proc. R . Soc. Lond. A.*, vol. 345, pp. 351–364, 1975.

[4] ——, "Rotary 'aether drag'," *Proc. B. Soc. Lond. A.*, vol. 349, pp. 423–439, 1976.

[5] S. Franke-Arnold, G. Gibson, R. W. Boyd, and M. J. Padgett, "Rotary Photon Drag Enhanced by a Slow-Light Medium," *Science*, vol. 333, no. 6038, pp. 65–67, Jul. 2011.

[6] R. Gueroult, S. Tripathi, J. Han, P. Pribyl, J.-M. Rax, and N. J. Fisch, "Image Rotation in Plasmas," *Physical Review Letters*, vol. 134, no. 24, p. 245101, Jun. 2025.

[7] M. McCall and D. Censor, "Relativity and mathematical tools: Waves in moving media," *American Journal of Physics*, vol. 75, no. 12, pp. 1134–1140, Dec. 2007.

[8] E. D. Lopez, "Dispersion process of electromagnetic waves in a moving medium," *Radiophysics and Quantum Electronics*, vol. 39, no. 1, pp. 84–89, Jan. 1996.

[9] M. A. Player, "On the dragging of the plane of polarization of light propagating in a rotating medium," *Proceedings of the Royal Society of London. A. Mathematical and Physical Sciences*, vol. 349, no. 1659, pp. 441–445, Jun. 1976.

[10] M. Padgett, G. Whyte, J. Girkin, A. Wright, L. Allen, P. Öhberg, and S. M. Barnett, "Polarization and image rotation induced by a rotating dielectric rod: an optical angular momentum interpretation," *Optics Letters*, vol. 31, no. 14, p. 2205, Jul. 2006.

[11] J. B. Götte, S. M. Barnett, and M. Padgett, "On the dragging of light by a rotating medium," *Proceedings of the Royal Society A: Mathematical, Physical and Engineering Sciences*, vol. 463, no. 2085, pp. 2185–2194, Sep. 2007.

[12] J. Langlois and R. Gueroult, "Contribution of fictitious forces to polarization drag in rotating media," *Physical Review E*, vol. 108, no. 4, p. 045201, Oct. 2023.

[13] D. E. Ruiz and I. Y. Dodin, "Extending geometrical optics: A Lagrangian theory for vector waves," *Physics of Plasmas*, vol. 24, no. 5, p. 055704, May 2017, arXiv:1612.06184 [physics].

[14] I. Y. Dodin, D. E. Ruiz, K. Yanagihara, Y. Zhou, and S. Kubo, "Quasioptical modeling of wave beams with and without mode conversion. I. Basic theory," *Physics of Plasmas*, vol. 26, no. 7, p. 072110, Jul. 2019.

[15] A. Braud and R. Gueroult, "Spin-orbit interactions induced by light drag in moving media," *Physical Review A*, vol. 112, no. 4, p. 043505, Oct. 2025.

[16] ——, "Spin-redirection Berry phase with planar rays," Jan. 2026, arXiv:2601.18624 [physics]. [Online]. Available: http://arxiv.org/abs/2601.18624

[17] M. V. Berry, "Interpreting the anholonomy of coiled light," *Nature*, vol. 326, no. 6110, pp. 277–278, Mar. 1987.

[18] P. A. Huidobro, E. Galiffi, S. Guenneau, R. V. Craster, and J. B. Pendry, "Fresnel drag in space–time-modulated metamaterials," *Proceedings of the National Academy of Sciences*, vol. 116, no. 50, pp. 24 943–24 948, Dec. 2019.

[19] A. Bahrami, Z.-L. Deck-Léger, and C. Caloz, "Electrodynamics of Accelerated-Modulation Space-Time Metamaterials," *Physical Review Applied*, vol. 19, no. 5, p. 054044, May 2023.

[20] D. E. Ruiz and I. Y. Dodin, "First-principles variational formulation of polarization effects in geometrical optics," *Physical Review A*, vol. 92, no. 4, p. 043805, Oct. 2015.

[21] E. R. Tracy, Ed., *Ray Tracing and Beyond: phase space methods in plasma wave theory*. Cambridge: Cambridge Univ. Press, 2014.

[22] A. Venaille, Y. Onuki, N. Perez, and A. Leclerc, "From ray tracing to waves of topological origin in continuous media," *SciPost Physics*, vol. 14, no. 4, p. 062, Apr. 2023.

[23] K. Y. Bliokh, "Geometrodynamics of polarized light: Berry phase and spin Hall effect in a gradient-index medium," *Journal of Optics A: Pure and Applied Optics*, vol. 11, no. 9, p. 094009, Sep. 2009.

[24] A. Braud, J. Langlois, and R. Gueroult, "Geometrical optics methods for moving anisotropic media: a tool for magnetized plasmas," *Comptes Rendus. Physique*, vol. 26, no. G1, pp. 7–23, Jan. 2025.

[25] D. Censor, "Ray tracing in weakly nonlinear moving media," *Journal of Plasma Physics*, vol. 16, no. 3, pp. 415–426, Dec. 1976.

[26] H. Minkowski, "Die Grundgleichungen für die elektromagnetischen Vorgänge in bewegten Körpern," *Mathematische Annalen*, vol. 68, no. 4, pp. 472–525, Dec. 1910.

[27] M. V. Berry, "Quantal Phase Factors Accompanying Adiabatic Changes," *Proceedings of the Royal Society of London. Series A, Mathematical and Physical Sciences*, vol. 392, no. 1802, pp. 45–57, 1984.

[28] A. Tomita and R. Y. Chiao, "Observation of Berry's Topological Phase by Use of an Optical Fiber," *Physical Review Letters*, vol. 57, no. 8, pp. 937–940, Aug. 1986.

[29] A. Bourgoin, "General expansion of time transfer functions in optical spacetime," *Physical Review D*, vol. 101, no. 6, p. 064035, Mar. 2020.

[30] J. Langlois, A. Braud, and R. Gueroult, "Fresnel drag in a moving magnetised plasma," *Journal of Plasma Physics*, vol. 91, no. 2, p. E47, Apr. 2025.

[31] U. Leonhardt and P. Piwnicki, "Optics of nonuniformly moving media," *Physical Review A*, vol. 60, no. 6, pp. 4301–4312, Dec. 1999.

[32] J. Langlois and R. Gueroult, "Light drag in nonuniformly moving anisotropic media through the lens of gradient-index optics," Dec.

2025, arXiv:2512.01718 [physics]. [Online]. Available: http://arxiv.org/abs/2512.01718
[33] K. Y. Bliokh, F. J. Rodríguez-Fortuño, F. Nori, and A. V. Zayats, "Spin–orbit interactions of light," *Nature Photonics*, vol. 9, no. 12, pp. 796–808, Dec. 2015.
[34] Z.-L. Zhang and R.-Y. Liu, "The Twisting of Radio Waves in a Randomly Inhomogeneous Plasma," *The Astrophysical Journal*, vol. 975, no. 2, p. 260, Nov. 2024.
[35] S. M. Rytov, "Sur la transition de l'optique ondulatoire à l'optique géométrique," *Dokl. Akad. Nauk SSSR*, vol. 18, no. 4-5, pp. 263–266, 1938.
[36] H. C. Ko and C. W. Chuang, "On the passage of radiation through moving astrophysical plasmas," *The Astrophysical Journal*, vol. 222, pp. 1012–1019, 1978.
[37] E. Fermi, "On the rotation of the plane of polarization in a rotating medium," *Rend. Mat. Acc. Lincei*, 1923.
[38] R. Gueroult, Y. Shi, J.-M. Rax, and N. J. Fisch, "Determining the rotation direction in pulsars," *Nature Communications*, vol. 10, no. 1, p. 3232, Jul. 2019.
[39] R. Gueroult, J.-M. Rax, and N. J. Fisch, "Enhanced tuneable rotatory power in a rotating plasma," *Physical Review E*, vol. 102, no. 5, p. 051202, Nov. 2020.
[40] ——, "Wave propagation in rotating magnetised plasmas," *Plasma Physics and Controlled Fusion*, vol. 65, no. 3, p. 034006, Mar. 2023.
[41] J. Langlois and R. Gueroult, "Manifestations of inertia on light dragging revealed in plasmas," *Proceedings of the Royal Society A: Mathematical, Physical and Engineering Sciences*, vol. 480, no. 2301, p. 20240300, Nov. 2024.

Parity Resolved Origin Optimization for Efficient Multipolar Modeling of Metasurfaces

Hossein Allahverdizadeh[1,*], Karim Achouri[2]

[1,2]École Polytechnique Fédérale de Lausanne (EPFL),Lausanne, Switzerland
*Corresponding author: hossein.allahverdizadeh@epfl.ch

***Abstract*—Understanding and controlling the scattering response of metasurfaces often relies on expressing their electromagnetic behavior in terms of multipolar contributions, but redundant higher-order moments can unnecessarily increase the complexity of the model. Here, we identify an optimal decomposition origin for both even and odd parity components to minimize excess multipoles contributions for each. This strategy enables accurate reproduction of the full scattering behavior with a reduced dipolar description.**

***Keywords*— metamaterials, Multipolar decomposition, GSTC, Optimal origin.**

I. Introduction

A multipolar approach offers a clear physical picture of the scattering mechanisms responsible for metasurface functionalities, including the Kerker effect, symmetry-protected or accidental bound states in the continuum, and beam steering. The practical use of multipolar expansions, therefore, demands careful control over the number of retained moments. This aspect is therefore fundamental to multipolar metasurface modeling and designing; otherwise, an excessive number of redundant multipole moments increases model complexity and computational cost.

Several factors govern how many multipolar moments are required to accurately capture the response of a metasurface, including the electrical size and geometry of the unit cell, lattice couplings, the symmetry origin (Wyckoff position), incident angle and the selected coordinate origin for the decomposition [1].

In this work, we identify an optimal coordinate origin for multipolar decomposition that minimizes higher order contributions and corresponds to an equilibrium position of the moments. To accommodate moments with different equilibrium positions, we further separate the response into even and odd parity components, allowing better flexibility in the choice of multiple origin [2]. This parity separation ensures that shifting the origin of one set of moments acts orthogonally to the other and leaves the total response unchanged. With effective electric and magnetic boundary conditions defined at these equilibrium positions, the metasurface scattering can be accurately reproduced using fewer multipolar contributions, ultimately reducing the description to a dipolar level.

II. Methods

We can model the electromagnetic properties of metasurfaces using generalized sheet transition conditions (GSTCs) through effective boundary conditions. For TE-polarized illumination, the GSTCs reduce to the following relations involving the y-component of $\Delta\mathbf{E}$ and the x-component of $\Delta\mathbf{H}$ [2]

$$\Delta\mathbf{E}_y^{\mathrm{TE}} = \tilde{M}_x + \tilde{Q}_{yz}^{(\mathrm{e})} + \tilde{Q}_{xx}^{(\mathrm{m})} + \tilde{Q}_{zz}^{(\mathrm{m})} + \tilde{O}_{yzx}^{(\mathrm{e})}, \tag{1a}$$

$$\Delta\mathbf{H}_x^{\mathrm{TE}} = \tilde{P}_y + \tilde{M}_z + \tilde{Q}_{xz}^{(\mathrm{e})} + \tilde{Q}_{yx}^{(\mathrm{e})}\tilde{O}_{yxx}^{(\mathrm{e})} + \tilde{O}_{yzz}^{(\mathrm{e})}. \tag{1b}$$

and corresponding scattering parameters as [2]

$$r^{\mathrm{TE}} = \frac{E_y^{\mathrm{r}}}{E_y^{\mathrm{i}}} = \frac{1}{2}\left(\Delta\mathbf{E}_y^{\mathrm{TE}} - Z_{yy}\Delta\mathbf{H}_x^{\mathrm{TE}}\right), \tag{2a}$$

$$t^{\mathrm{TE}} = \frac{E_y^{\mathrm{t}}}{E_y^{\mathrm{i}}} = 1 - \frac{1}{2}\left(\Delta\mathbf{E}_y^{\mathrm{TE}} + Z_{yy}\Delta\mathbf{H}_x^{\mathrm{TE}}\right). \tag{2b}$$

Here, $\tilde{P}$, $\tilde{M}$, $\tilde{Q}$, and $\tilde{O}$ denote normalized electric dipole, magnetic dipole, quadrupole, and octupole contributions, respectively; $\Delta\mathbf{E}$ and $\Delta\mathbf{H}$ are the tangential field discontinuities, Z_{yy} is the TE wave impedance, and r^{TE} and t^{TE} are the reflection and transmission coefficients.

It can be shown that shifting the coordinate origin leaves $\Delta\mathbf{E}_y$ and $\Delta\mathbf{H}_x$ invariant, affecting only their phase. This behavior is expected, since the boundary conditions already encode the full scattering information, and scattering is inherently independent of the choice of origin. Exploiting this property, different origins can be selected for each boundary condition, with each one associated with a specific multipolar parity. In earlier approaches, the choice of origin was restricted to a single global point, requiring a compromise that reduced redundant multipoles only for specific terms [1]. Here, by treating even and odd parity contributions separately, we lift this restriction and allow independent optimization of the origin for each parity, enabling a more efficient and physically transparent description.

III. Results and Discussion

We modeled a bianisotropic cone [Fig. 1 (a)] under normal incidence and applied multipolar decomposition using Eqs. (1a) and (1b). This formulation enables the extraction of effective boundary conditions for the structure within different parity channels. By independently shifting the decomposition origin for each boundary condition, we identify the minima of higher order contributions for the electric (odd-parity) and

Fig. 1: (a) Unit-cell geometry of the proposed metamaterial and (b,c,d) corresponding multipolar decomposition for different origins. (e) Optimum dipolar moments at each positions and (f) retrieved scattering parameters from optimal multipolar response compared with full wave simulations.

magnetic (even-parity) moments, respectively. The multipolar decomposition evaluated at the center of mass is shown in Fig. 1 (d), while the decompositions at the optimal electric and magnetic origins are presented in Fig. 1 (b) and Fig. 1 (c), respectively. As observed, the center of mass decomposition contains both electric and magnetic quadrupoles, as well as higher order contributions such as octupoles. In contrast, at the parity optimized electric and magnetic positions, the response is dominated by dipolar contributions. The gray diagrams correspond to multipoles that are not associated with the selected parity or boundary condition; although these modes formally exist at the chosen origin, only the moments consistent with the parity of the corresponding boundary condition are retained in the model. In Fig. 1 (e), we show that the response of the structure can be accurately captured using only dipolar moments. In Fig. 1 (f), an excellent agreement is observed between the scattering parameters retrieved from full-wave simulations and those obtained using the double-origin method described above.

IV. Conclusion

In conclusion, we demonstrated that separating the metasurface response into parity resolved channels enables independent optimization of the multipolar decomposition origin. This approach significantly suppresses redundant higher order contributions and allows the full scattering behavior to be accurately captured at the dipolar level. The resulting framework provides a physically transparent and computationally efficient route for modeling bianisotropic metasurfaces.

References

[1] A. V. Kildishev, K. Achouri, and D. Smirnova, "The art of finding the optimal scattering center(s)", Adv. Opt. Mater. **13**(4), 2402787 (2025).
[2] H. Allahverdizadeh and K. Achouri, "Multipolar angular scattering of substrated metasurfaces", Phys. Rev. B **112**(24), 245420 (2025).

Scattering properties of a cylindrical scatterer with time-modulated permittivity

J. Yan[1,*], I. Katsantonis[1], M. Mostafa[2], V. Asadchy[2] and M. Kafesaki[1]

[1]Institute of Electronic Structure and Laser, Foundation for Research and Technology-Hellas, Crete, Greece
[2]Department of Electronics and Nanoengineering, School of Electrical Engineering, Aalto University, Finland
*jiaruo.yan@iesl.forth.gr

***Abstract*—We investigate the scattering behavior of a cylinder, with infinite length, whose permittivity is periodically modulated in time. By exploiting the interference among scattering coefficients associated with different temporal harmonics and multipolar orders, the radiation pattern can be engineered through appropriate adjustment of the modulation parameters.**

I. Introduction

Modulating a medium's material properties in time provides additional degrees of freedom for tailoring the wave–matter interactions [1]. Such modulation can be discontinuous, aperiodic, or periodic variations [2], [3]. When the modulation is periodic in time, the Floquet theory offers a suitable analytical framework. It has been demonstrated that a homogeneous medium subject to periodic temporal modulation of its electromagnetic properties exhibits the formation of momentum bandgaps [4], [5]. Moreover, scatterers of various geometries and time-varying material properties have been reported in the literatures [6], [7], [8].

In this work, we examine cylindrical scatterers with time-modulated relative permittivity. We discuss our analytical results for the parametric Mie resonances, and identify the required modulation conditions. Furthermore, we explore how the far-field radiation pattern can be engineered by tailoring the interference among different scattered harmonics.

II. Formalism

We consider a dielectric cylinder of infinite length, whose relative permittivity, ε_r, varies sinusoidally in time as follows:

$$\varepsilon(t) = \varepsilon_{r0} + \Delta\varepsilon\cos(\omega_{\mathrm{m}}t) = \sum_{n=-N}^{N} \varepsilon(n)\exp(in\omega_{\mathrm{m}}t) \quad (1)$$

Here, ε_{r0} denotes the reference permittivity of a time-invariant system, and $\Delta\varepsilon$ represents the modulation amplitude. The terms $\varepsilon(n)$ correspond to the Fourier coefficients, with the series truncated at a maximum harmonic order N. The modulation angular frequency is $\omega_{\mathrm{m}} = 2\pi/T_{\mathrm{m}}$, where T_{m} is the modulation period. The scattered field components contain harmonics at frequencies $f - nf_m$, where f is the incident frequency, n is the scattered harmonic order. Using the Floquet theory, the electric and magnetic fields can be expressed as Fourier series in time. By substituting these field expansions, together with the expanded form of ε_r, into Maxwell's equations, we obtain an eigenvalue problem that characterizes the periodically time-modulated homogeneous medium, given as follows:

$$\mu_c(2\pi\frac{f-nf_m}{c})^2 \sum_{\nu=-N}^{N} \varepsilon(n-\nu)\mathbf{E}^{(\nu)} = q^2\mathbf{E}^{(n)}. \quad (2)$$

Here μ_c denotes the permeability of the medium, assumed to be $\mu_c = 1$. q is the square root of the eigenvalues, and corresponds to the permitted wavenumbers in the time-modulated medium. The associated eigenvectors $\mathbf{v}_\nu$, each consisting of $2N+1$ elements representing the amplitudes of the scattered harmonics.

For a cylindrical scatterer with time-modulated permittivity, the total fields in both the host medium and inside the cylinder are represented using cylindrical wave expansions. To illustrate this, we present the expressions of the transverse electric (TE) polarization, in which the electric field is normal to the cylinder axis. The corresponding expressions for the electric field are given below.

$$\mathbf{E}_{\mathrm{h}}^{(n)}(\mathbf{r}) = i\sum_{l}\left[a_l^0\mathbf{m}_l(k_0,\mathbf{r})\delta_{n0} + a_{l+}^{(n)'}\,\mathbf{m}_l'(q_{\mathrm{h}n},\mathbf{r})\right] , \quad (3)$$

$$\mathbf{E}_{c}^{(n)}(\mathbf{r}) = i\sum_{\nu=-N}^{N} v_\nu(n)\sum_{l} a'_{l;\nu}\mathbf{m}_l(q_\nu,\mathbf{r}) \ . \quad (4)$$

Here $\mathbf{m}_l$ denotes the vector cylindrical harmonic of order l. The quantity $a_{l+}^{(n)'}$ represents the scattering coefficient of the n-th harmonic generated by the time modulation. When normalized to the incident coefficient a_l^0, it is expressed as $a_{l+}^{(n)} = a_{l+}^{(n)'}/a_l^0$. The wavenumber of the n-th harmonic in the host medium (assumed hereafter to be free space) is given by $q_{hn} = \frac{\omega - n\omega_m}{c}$, while k_0 denotes the wavenumber of the incident wave in the host medium. The magnetic field components are formulated in a similar way using vector cylindrical harmonics - also expressed in terms of Bessel functions—and are omitted here for brevity.

Under the boundary conditions ar $r = R$, which is the radius of the cylinder, based on the tangential components of $\mathbf{E}$ and $\mathbf{H}$, we arrive at,

$$\sum_{\nu=-N}^{N} a_{l;\nu}\, v_\nu(n)\frac{\partial J_l(q_\nu R)}{\partial(q_\nu R)} = \frac{\partial J_l(k_0R)}{\partial(k_0R)}\delta_{n0} + a_{l+}^{(n)}\frac{\partial H_l(q_{\mathrm{h}n}R)}{\partial(q_{\mathrm{h}n}R)} \ , \quad (5)$$

$$\sum_{\nu=-N}^{N} b_{l;\nu}\, v_\nu(n) J_l(q_\nu R) = J_l(k_0 R)\delta_{n0} + b_{l+}^{(n)} H_l(q_{\mathrm{h}n} R)\ , \tag{6}$$

where J_l, H_l are the Bessel and Hankel function (of order l), respectively. With the relationships $a_{l+}^{(n)} = \sqrt{\mu_h/\varepsilon_h}\, b_{l+}^{(n)}$, we have $2(2N+1)$ variables that can be solved numerically.

The total scattering efficiency is then defined as,

$$Q_{\mathrm{sc}} = \sum_{n=-N}^{N} Q^{(n)} = \sum_{n=-N}^{N} \frac{2}{|q_{\mathrm{h}n}|R} \sum_l \frac{2}{1+\delta_{l0}} |a_{l+}^{(n)}|^2\ . \tag{7}$$

We should note that if $N = 0$, the above formalism reduces to the classical problem of scattering from a time-invariant infinite cylinder [9].

III. Results and Discussion

Following the method outlined in Section II, and setting the modulation frequency to $f_m = 2f$, we find that, under the assumption of weak modulation, the dominant scattered harmonics at parametric resonances are $n = 0, 1$. These correspond to frequencies $f_{n=0,1} = \pm f$. In this case, the system of equations in Eq.,(5) simplifies to four coupled equations, supplemented by the eigen-condition in the absence of incident excitation. Nontrivial solutions for the scattering coefficients are obtained by solving this truncated eigenvalue problem, which yields the required modulation strength for each modulation frequency (with $f_m = 2f$ thoughout).

With parameters $\varepsilon_{r0} = 12$, $R = 5\,\mathrm{mm}$, the semi-analytical results are shown in Fig.,1. The upper and lower panels correspond to TE and TM polarizations, respectively, with colored solid curves indicating different multipolar orders l. These curves are referenced to the left vertical axis in each subplot. Also plotted is the scattering efficiency as a function of incident frequency, in black dashed lines for a static cylinder with $\varepsilon_{r0} = 12$, referenced to the right vertical axis. Distinct Mie resonances of various orders are clearly observed within the selected frequency range.

The threshold modulation strength, $\Delta\varepsilon_{th}$ (upper curves), for each multipolar order l reaches its minimum at the frequency f corresponding to the Mie resonance of the static reference cylinder ($\varepsilon_r = \varepsilon_{r0} = 12$). Notably, this minimum decreases with increasing l, which can be attributed to the lower losses associated with higher-order Mie resonances, as reflected by the increasingly sharp peaks of the dashed curves at higher frequencies.

For TE polarization, an alternative method was employed to determine the required modulation strength $\Delta\varepsilon_{th}$ for achieving parametric resonance. This approach is based on the coupled equations in Eqs.,(5) and (6) and incorporates higher-order scattered harmonics up to $N = 3$. The results for different multipolar orders l are shown as colored dots in Fig.,1, on top of the predictions from the truncated eigenvalue problem. Larger discrepancies appear at higher $\Delta\varepsilon_{th}$, as stronger modulation produces non-negligible higher-order scattered harmonics, reducing the accuracy of the truncated approximation. The overlapped dots of different colors indicate modulation conditions where different multipoles can be excited simultaneously. For instance, in the TE-polarized case around 12 GHz with $\Delta\varepsilon \approx 5.5$, both the electric dipole and quadrupole are simultaneously excited, producing backward radiation for specific modulation parameters, as illustrated by the field distribution in Fig.,2. The interplay between different modes, combined with the phase relationships among the harmonics generated by the time modulation, enables the engineering of diverse far-field radiation patterns.

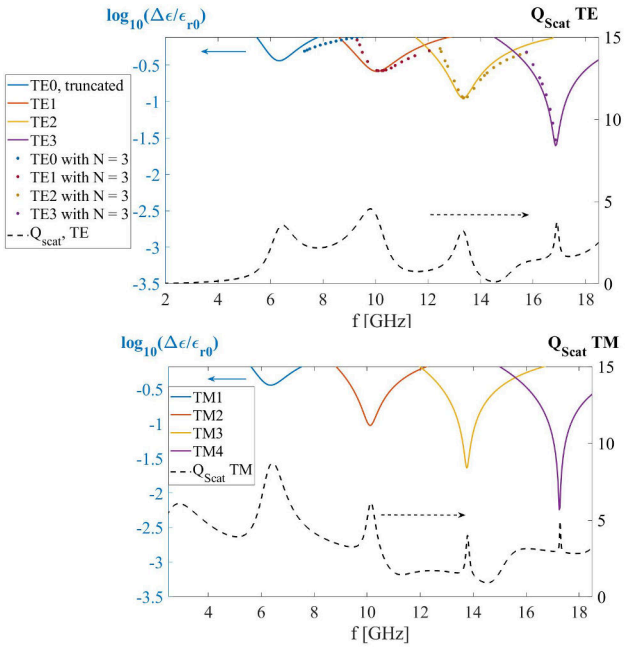

Fig. 1. Left axes (both panels): Logarithmic scale of the ratio between the threshold modulation strength $\Delta\varepsilon_{th}$ required for parametric resonance at $f_m = 2f$ and the reference relative permittivity $\varepsilon_{r0} = 12$ ($R = 5$mm) shown as colored solid curves versus the incident frequency f. Right axes: Scattering efficiency of a static system of $\varepsilon_{r0} = 12$ versus frequency on a linear scale, plotted as black dashed curves. Upper panel: TE polarization; colored dots show results from Eqs.,(5) and (6) including harmonics up to third order. Lower panel: TM polarization.

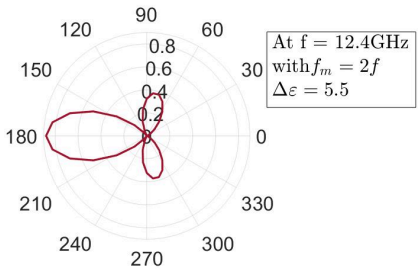

Fig. 2. Farfield distribution $|E|^2$, for a time-modulated cylinder of $\varepsilon_{r0} = 12$, $R = 5\,\mathrm{mm}$, $f = f_m/2 = 12.4\,\mathrm{GHz}$, $\Delta\varepsilon = 5.5$.

IV. Conclusion

We have studied an infinitely long cylindrical scatterer with periodically time-modulated relative permittivity. Semi-analytical calculations of the scattering properties, based on Floquet–Mie theory and the relevant spatial boundary conditions, show that the modulation parameters required to achieve parametric Mie resonances are closely linked to the resonant characteristics of the corresponding static scatterer. Multipolar modes of different orders can be simultaneously excited, enabling the design of a variety of far-field radiation patterns. Future work will extend this analysis to plasma cylinders with time-varying plasma properties, which could be implemented by controlling the plasma ignition or sustainment sources in practice. Such time-modulated scatterers could be arranged into dynamic metamaterial structures, with potential applications in wavefront shaping and related areas.

Acknowledgments

This work was supported by the European Union under the call "EIC Pathfinder Open 2022" (Project PULSE, project no. 101099313).

References

[1] C. Caloz and Z.-L. Deck-Leger, "Spacetime metamaterials—part ii: Theory and applications," *IEEE Trans- actions on Antennas and Propagation*, vol. 68, no. 3, pp. 1583–1598, 2019.

[2] F. R. Morgenthaler, "Velocity modulation of electromagnetic waves," *IRE Transactions on microwave theory and techniques*, vol. 6, no. 2, pp. 167–172, 2003.

[3] E. Galiffi, R. Tirole, S. Yin, et al., "Photonics of time-varying media," *Advanced Photonics*, vol. 4, no. 1, pp. 014 002–014 002, 2022.

[4] M. M. Asgari, P. Garg, X. Wang, M. S. Mirmoosa, C. Rockstuhl, and V. Asadchy, "Theory and applications of photonic time crystals: A tutorial," *Advances in Optics and Photonics*, vol. 16, no. 4, pp. 958–1063, 2024.

[5] X. Wang, P. Garg, M. Mirmoosa, A. Lamprianidis, C. Rockstuhl, and V. Asadchy, "Expanding momentum bandgaps in photonic time crystals through resonances," *Nature Photonics*, vol. 19, no. 2, pp. 149–155, 2025.

[6] I. Stefanou, P. A. Pantazopoulos, and N. Stefanou, "Light scattering by a spherical particle with a time-periodic refractive index," *Journal of the Optical Society of America B*, vol. 38, no. 2, pp. 407–414, 2021.

[7] G. Ptitcyn, A. Lamprianidis, T. Karamanos, et al., "Floquet–mie theory for time-varying dispersive spheres," *Laser & Photonics Reviews*, vol. 17, no. 3, p. 2 100 683, 2023.

[8] V. Asadchy, A. Lamprianidis, G. Ptitcyn, et al., "Parametric mie resonances and directional amplification in time-modulated scatterers," *Physical Review Applied*, vol. 18, no. 5, p. 054 065, 2022.

[9] C. P. Mavidis, A. C. Tasolamprou, E. N. Economou, C. M. Soukoulis, and M. Kafesaki, "Polaritonic cylin- ders as multifunctional metamaterials: Single scattering and effective medium description," *Physical Review B*, vol. 102, no. 15, p. 155 310, 2020.

Ultrashort Bright Envelope Solitons in Ferromagnetic Metamaterials Placed in High-Intensity Magnetic Biased Fields

Feodor Yu. Ogrin[1,2,*], Alexandra V. Zhabova[3], Mariya D. Amel'chenko[3], Sergei V. Grishin[3], and Sergei A. Nikitov[3,4]

[1]School of Physics and Astronomy, University of Exeter, Exeter, UK
[2]MaxLLG Ltd., University of Exeter, Exeter, UK
[3]Institute of Physics, Saratov State University, Saratov, Russia
[4]Kotelnikov Institute of Radioengineering and Electronics of Russian Academy of Science, Moscow, Russia
*Corresponding author: F.Y.Ogrin@exeter.ac.uk

***Abstract*— The paper presents numerical simulation results of the ultrashort bright envelope solitons in a normally magnetized parallel-plate waveguide completely filled with a nonlinear ferromagnetic metamaterial. It is shown that in high-intensity magnetic biased fields, the soliton width of an "extraordinary" slow forward electromagnetic wave reaches several hundreds of picoseconds.**

***Keywords*— microwave metamaterials, solitons.**

I. Introduction

In 2005, Dewar suggested to embed a periodic lattice of the dielectrically insulated thin metal wires inside a dielectric ferromagnet (FM) host and described his model the so-called "left-handed" FM metamaterial (MM) [1] The model was based on the effective medium approximation and did not take into account the spatial dispersion of the periodic lattice. In 2023, Amel'chenko with coauthors, utilizing the MaxLLG software [2], carried out the numerical simulation of a parallel-plate waveguide (PPWG) completely filled with Dewar's FM MM thin plate placed in two (normal or longitudinal) magnetic biased field H_0 orientations [3]. The numerical simulations were conducted for slow-intensity magnetic biased fields (of about 0.1 T) and they confirmed the existence of a backward electromagnetic wave (BEMW) in such double negative (DNG) (ε_{eff}<0, μ_{eff} <0) medium for both types of H_0 orientation. In 2025, the same authors showed that the bandwidths of two slow EMWs (the BEMW existing at the frequencies corresponding to DNG-medium and a forward EMW (FEMW) existing at the frequencies of double positive (DPS) (ε_{eff} >0, μ_{eff}>0) medium) have opposite magnetic field dependencies [4]. So, the BEMW bandwidth is decreased and the FEMW bandwidth is increased with the increasing of the magnetic biased field strength.

In addition to its dispersive properties, a FM is also a nonlinear medium that possesses the formation of bright envelope solitons (BESs) [5]. These are formed on the magnetostatic spin waves and have durations of about several tens of nanoseconds. In the paper, it is demonstrated that the BESs can be formed on the slow FEMW existing in the FM MM and have the subnanosecond durations at high-intensity magnetic biased fields.

II. Methods

Fig. 1(a) represents the schematic diagram of a normally magnetized PPWG completely filled with FM MM plate containing the dielectrically insulated wire inclusions. The dispersion equation for the transversely magnetized FM MM has the following form [1]:

$$k - k_0^2 \varepsilon_{eff\perp} \mu_{eff\perp} = 0, \tag{1}$$

where k - is a wavenumber of EMW propagating in FM MM, $k_0 = \omega/c$ - is a wavenumber of EMW propagating in vacuum, $\mu_{eff\perp} = (\mu^2 - \mu_a^2)/\mu$, $\mu = (\omega_\perp^2 - \omega^2)/(\omega_{||}^2 - \omega^2)$, $\mu_a = \omega_M \omega/(\omega_{||}^2 - \omega^2)$, $\omega_\perp = \omega_{||}\omega_{ar}$ is a ferromagnetic resonance (FMR) frequency for transverse magnetization, $\omega_{ar} = \omega_{||} + \omega_M$ is a frequency of anti-FMR, $\omega_{||} = \gamma H_0$ is a FMR frequency for longitudinal magnetization, γ is a gyromagnetic ratio, $\omega_M = 4\pi\gamma M_0$, $4\pi M_0$ is saturation magnetization;

$$\varepsilon_{eff\perp} = \varepsilon_r\left[1 - \omega_{p\perp}^2/(\omega^2 + i\alpha_\perp)\right],$$
$$\omega_{p\perp}^2 \cong 2\pi/\langle \varepsilon_f T^2 \mu_0 \{ln(r_2/r_1) + \mu_{eff\perp}[\ln(T/r_2) - (3 + \ln 2 - \pi/2)/2]\}\rangle,$$

$\alpha_\perp = \varepsilon_f \omega \omega_{p\perp}^2/\sigma_{eff}$, $\varepsilon_f = \varepsilon_0\varepsilon_r$ – is the absolute permittivity, $\varepsilon_0 = 1/(\mu_0 c^2)$ is the vacuum constant, μ_0 is the vacuum permeability, $\sigma_{eff} = \pi r_1^2 \sigma/T^2$ is the effective conductivity of the wire array, σ is the conductivity of the wires, T is an array period, r_1 is a wire radius and r_2 is an outer radius of the cladding material.

For a nonlinear model it is assumed that the longitudinal component M_y of the magnetization vector depends on the square of the alternating magnetic field amplitude $|\varphi|^2$, and this dependence has the following view:

$$M_y \approx M_0(1 - a|\varphi|^2), \tag{2}$$

where $a = (1 + \omega_H^2/\omega^2)/2$.

The nonlinear Schrodinger equation (NSE) was obtained from the nonlinear dispersion equation. The NSE has the following form:

$$j\left(\frac{\partial}{\partial t} + V_g\frac{\partial}{\partial z}\right)\varphi + \beta\frac{\partial^2\varphi}{\partial z^2} - \chi|\varphi|^2\varphi = 0, \tag{6}$$

where $V_g=\partial\omega/\partial k$ is the slow FEMW group velocity, $\beta=\partial^2\omega/\partial k^2$ is the dispersion of the slow FEMW group velocity, $\chi=\partial\omega/\partial|\varphi|^2$ is the wave nonlinearity coefficient. To obtain the soliton solutions, the values of the dispersion β and nonlinearity χ coefficients of NSE must satisfy the Lighthill criterion ($\beta\chi$<0) and have the opposite signs.

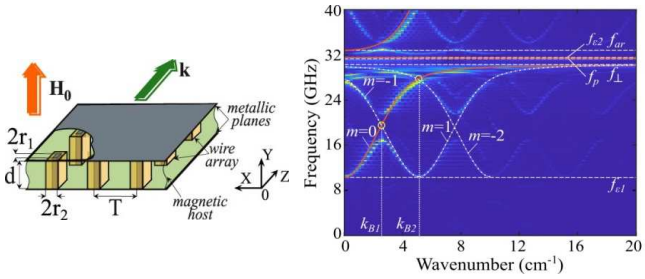

Fig. 1 (a) A scheme of normally magnetized PPWG completely filled with FM MM plate. (b) Dispersion responses of the EMWs existing in the FM MM thin plate at H_0=1 T. The solid red lines correspond to the Dewar's analytical theory. The calculations were performed for $4\pi M_0$=1750 G, ε_r=16, r_1=0.01 cm, r_2=0.03 cm, T=0.2 cm, d=0.05 cm, and $\sigma=10^8$ S/m.

III. Results and Discussion

The simulation results of the dispersion responses (DRs) of the EMWs in the normally magnetized PPWG completely filled with a FM MM thin plate are presented in Fig. 1 (b). They are obtained by the use of the MaxLLG software. It can be seen that the frequency band of the zero spatial harmonic of the slow FEMW increases to 20 GHz in the magnetic biased field with the strength of 1 T. On the contrary, the frequency band of the zero spatial harmonic of the BEMW decreases.

Fig. 2 demonstrates the bright envelope soliton train that is formed on the zero spatial harmonic of the slow FEMW, when the NSE was solved numerically with periodic boundary conditions. In simulation, the soliton generation frequency was outside the frequency band of the first Bragg resonance and the FEMW wavenumber was higher than the Bragg wavenumber. For such frequency, the Lighthill criterion was satisfied. The FEMW bright envelope solitons have the 250 ps-duration that is two oders of magnitude shorter than the duration of MSW bright envelope solitons.

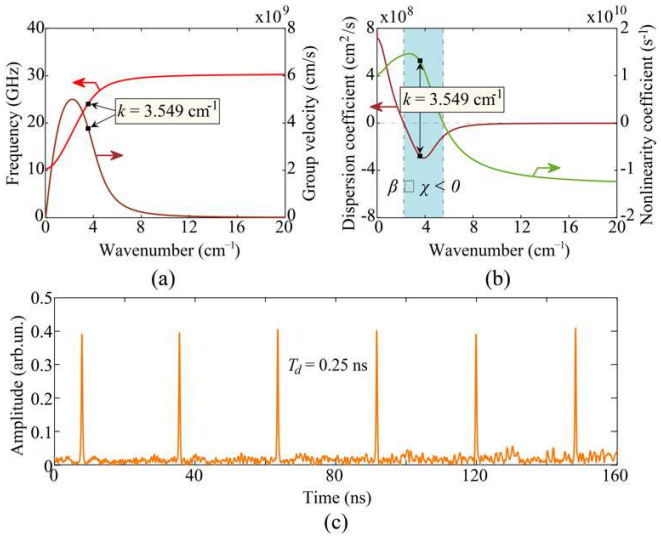

Fig. 2. (a) DR and group velocity of the slow FEMW; (b) the coefficients of dispersion β and nonlinearity χ as the functions of wavenumber k; (c) the envelope wave front evolution in the Dewar's FM MM. The calculations were made for:H_0=1 T, $4\pi M_0$=1750 G, ε_r=16, r_1=0.01 cm, r_2=0.03 cm, T=0.2 cm, and f=24 GHz.

IV. Conclusion

We have demonstrated that in the FM MM layer, which is a dielectric FM thin plate, containing a periodic lattice of the dielectrically insulated metal wires in high-intensity magnetic biased fields, a bandwidth of the "extraordinary" slow FEMW reaches several octaves in microwave range. The FEMW bright envelope solitons obtained by the use of nonlinear Schrodinger equation have duration of about two hundreds of picoseconds.

Acknowledgments

This work was supported by the Russian Science Foundation grant No. 23-79-30027, https://rscf.ru/project/23-79-30027/

References

[1] G. Dewar, "Minimization of losses in a structure having a negative index of refraction," New J. Phys., vol. 7, p. 161, Aug. 2005.
[2] High Frequency Magnetics Software [Electronic resource]. Devon, UK. Available from: https://www.maxllg.com.
[3] M. D. Amel'chenko, S. V. Grishin, F. Yu. Ogrin, and S. A. Nikitov, "Micromagnetic simulation of ferromagnetic metamaterials with wire inclusions," Phys. Rev. B, vol. 108, p. 224401, Dec. 2023.
[4] M. D. Amel'chenko, S. V. Grishin, F. Yu. Ogrin, and S. A. Nikitov, "Ultra-wideband ferromagnetic metamaterials in high-intensity magnetic biased fields," Appl. Phys. Lett., vol. 126, p. 101702, March 2025.
[5] B. A. Kalinikos, N. G. Kovshikov, and A. N. Slavin, "Experimental observation of magnetostatic wave envelope solitons in yttrium iron garnet films," Phys. Rev. B, vol. 42, pp. 8658-8660, Nov. 1990.

Robust Design of a Reconfigurable Linear-to-Circular Polarization Metasurface via LHS

Gregorio J. Molina-Cuberos[1*], Ángel J. García-Collado[2], Ismael Barba[3], José Margineda[1]

[1]Departamento de Electromagnetismo y Electrónica, Universidad de Murcia, 30100 Murcia, Spain
[2]Grupo de Investigación en Telecomunicaciones Avanzadas, Universidad Católica de Murcia, 30107 Murcia, Spain
[3]Departamento de Electricidad y Electrónica, Universidad de Valladolid, 47011 Valladolid, Spain
*Corresponding author: gregomc@um.es

***Abstract*—A design-space exploration of a mechanically reconfigurable linear-to-circular polarization (LTC) metasurface is presented. Latin Hypercube Sampling with full-wave simulations is employed to map broadband LTC behavior beyond single-point optimization. Extended high-performance regions and a bandwidth–robustness trade-off are identified, enabling selection of tolerant and reliable metasurface designs.**

***Keywords*— metasurface, circular polarization, linear-to-circular converter, broadband microwave, microwave polarization control, reconfigurable electromagnetic devices.**

I. Introduction

Linear-to-circular polarization (LTC) devices are key components in modern electromagnetic systems, as circular polarization improves robustness against misalignment and mitigates multipath effects [1]. Transmissive LTC metasurfaces are particularly attractive for multilayer and conformal architectures; however, achieving broadband conversion in transmission while maintaining low loss and structural simplicity remains challenging [2].

In previous work, a mechanically reconfigurable transmissive LTC metasurface based on dual-layer L-shaped resonators was demonstrated [3]. The structure enables handedness switching through a 90° mechanical rotation while providing approximately 26% relative bandwidth under the 3 dB axial-ratio criterion. Although the design was optimized using conventional parametric sweeps, the global structure of the design space and the robustness of high-performance solutions were not systematically analyzed.

In this work, a statistical design-space exploration based on Latin Hypercube Sampling (LHS) [4], [5] is employed to investigate the dominant geometrical parameters of the converter. In contrast to conventional parametric optimizations—where the geometry is tuned to maximize bandwidth around a single best-case design—the proposed approach maps the design space, identifies high-performance regions, and evaluates the robustness of the LTC response. Rather than pursuing an isolated optimum, the objective is to identify extended regions of the design space that preserve broadband LTC behavior under geometrical variations, thereby providing depper insight into the design methodology of mechanically reconfigurable polarization converters.

II. Methodology

The analyzed structure consists of a dual-layer arrangement of L-shaped metallic resonators located on opposite faces of a low-permittivity dielectric slab (foam). The resonators are made of low-carbon steel wire (AWG-25), with a total length of 20 mm and a 90° bend forming two equal arms. Electromagnetic coupling between the orthogonal current modes supported by the two resonators produces the quadrature phase shift required for circular polarization conversion. A 90° mechanical rotation interchanges the resonators' orientation with respect to the incident field, thereby reversing the handedness of the transmitted wave [3].

The global design space is explored by varying the lateral dimension of the unit cell, p, and the dielectric thickness, t, while keeping the size and shape of the resonators constant to target LTC operation around the X-band. The operating frequency band can be shifted by properly scaling the resonator geometry. The exploration begins with 100 configurations generated using an LHS distribution within predefined parameter ranges. An additional refinement sampling is subsequently performed to focus on the regions exhibiting the highest performance.

For each configuration, the polarization-conversion performance is evaluated using full-wave simulations (CST Studio Suite 2025, frequency solver). The relative bandwidth (RBW), defined as the continuous frequency interval over which the axial ratio (AR) remains below 3 dB, is used as the primary performance metric. Additional statistical descriptors of the AR response are computed to quantify robustness and stability of the LTC behavior.

All results reported in this work are obtained from full-wave numerical simulations. Experimental validation is not repeated here, since the same metasurface configuration was experimentally characterized in [3], where measurements confirmed both the preservation of the relative bandwidth and the robustness of the mechanical RHCP/LHCP switching mechanism.

III. Results and Discussion

Figure 1 shows the RBW distribution across the explored parameter space. A well-defined high-performance ridge is observed around $p \approx 17$ mm, extending over dielectric thickness values between approximately $t \approx 4$ and 8 mm.

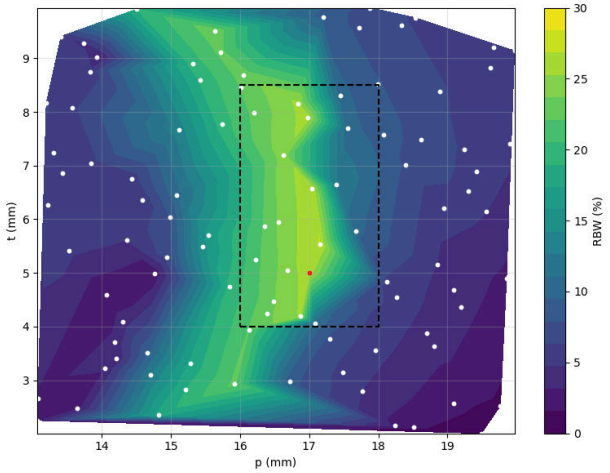

Fig. 1. Relative bandwidth (RBW) obtained from the Latin Hypercube Sampling (LHS) exploration over the design space defined by the unit-cell size p and dielectric thickness t. White markers indicate simulated configurations. A continuous high-performance ridge associated with broadband LTC conversion is observed. The previously reported configuration ($p = 17$ mm, $t = 5$ mm) [3] is highlighted with a red marker and lies within the primary ridge. The black dashed rectangle indicates the region selected for local refinement sampling.

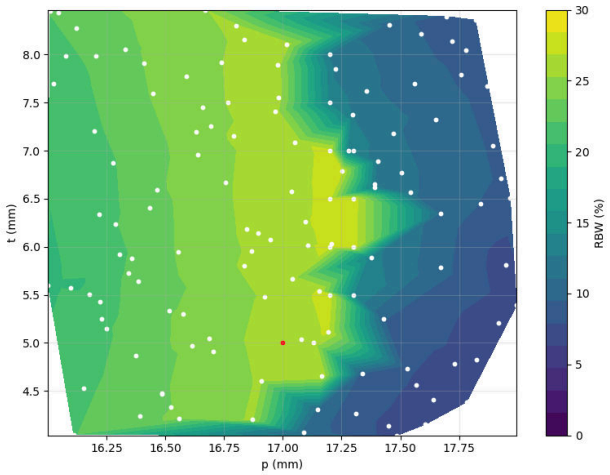

Fig. 2. Local refinement of the primary RBW ridge using an additional LHS sampling restricted to the region indicated in Fig. 1.

The configuration previously reported in [3] ($p = 17.0$ mm, $t = 5.0$ mm) lies within this ridge, confirming that the reference design is located near the the dominant high-performance domain.

To resolve the local structure of this region, a refinement sampling was carried out within the parameter window marked in Fig. 1. The zoomed map in Fig. 2 shows that the primary ridge forms a relatively broad plateau rather than a narrow peak. This behavior indicates that the wideband polarization conversion is preserved under moderate variations of p and t, suggesting inherent robustness and relaxed manufacturing tolerance within the identified parameter domain.

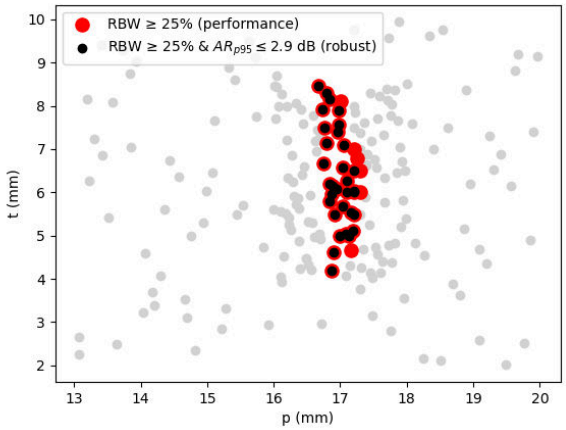

Fig. 3. Global distribution of LTC configurations obtained from the LHS exploration. Grey markers correspond to all simulated geometries. Red circles indicate configurations with RBW≥25%, and black markers denote the subset that additionally satisfies the stability requirement $AR_{p95} \leq 2.9$ dB.

To quantitatively assess performance and robustness among the LTC solutions, a sequential filtering strategy was applied. First, a performance criterion was imposed by selecting configurations with RBW≥25%, matching the bandwidth level of the reference design in [3]. This filter isolates a set of broadband configurations concentrated along the main ridge identified in the RBW maps.

Although RBW captures the extent of the LTC band, it does not quantify the statistical stability of the axial ratio inside that band. A second stage was therefore introduced by requiring the 95th percentile of the axial-ratio distribution to satisfy $AR_{p95} \leq 2.9$ dB. This constraint ensures that the vast majority of frequency samples within the LTC band remain comfortably below the 3 dB threshold, providing a margin against degradation due to fabrication tolerances and modeling uncertainties.

The global distribution of the configurations satisfying these criteria is shown in Fig. 3. Grey markers represent the full LHS dataset, red circles denote the subset meeting the RBW requirement, and black markers indicate the subset that additionally satisfies the robustness condition. The robustness filter removes only a limited fraction of high-bandwidth solutions, confirming that broadband LTC behavior is not confined to an isolated optimum but instead distributed along an extended region centered around $p \approx 17$ mm and $t \approx 6$ mm.

Notably, the robustness criterion tends to exclude some configurations exhibiting the absolute maximum RBW values (close to 28%). This observation suggests a bandwidth–robustness trade-off: solutions optimized to maximize RBW operate closer to the axial-ratio threshold and consequently exhibit larger AR excursions within the operating band. In contrast, slightly reduced RBW values are typically associated with smoother AR responses and improved statistical stability.

Overall, the combined analysis indicates that the proposed

TABLE I
REPRESENTATIVE LTC CONFIGURATIONS IDENTIFIED IN THE LHS EXPLORATION.

Case	p (mm)	t (mm)	f_0 (GHz)	RBW (%)	$\overline{AR}$ (dB)	σ_{AR} (dB)	AR_{p95} (dB)
Original	17.0	5.0	11.76	26.0	1.96	0.57	2.52
Max RBW	17.3	6.5	11.65	27.7	2.25	0.57	2.97
Most robust	17.0	5.7	11.70	26.0	1.88	0.44	2.40

metasurface supports broadband LTC conversion over a wide and tolerant region of the design space. This characteristic is advantageous for practical implementations, since it relaxes fabrication constraints while maintaining high polarization-conversion performance.

To facilitate a direct comparison of representative solutions, Table I summarizes three configurations: (i) the reference design reported in [3], (ii) the configuration achieving the maximum RBW within the explored set, and (iii) the most robust configuration, defined as the case with the minimum AR_{p95} among those satisfying RBW$\geq$25%. In addition to the geometrical parameters and RBW, the mean axial ratio $\overline{AR}$ and its standard deviation σ_{AR} are reported to characterize the stability of the polarization response.

All three configurations exhibit similar center frequencies, with $f_0 \approx 11.7 \pm 0.1$ GHz, indicating that variations of p and t within the dominant ridge primarily affect the quality and robustness of the LTC response while leaving the operating band essentially unchanged. The maximum-bandwidth case achieves the largest RBW (27.7%), but shows the poorest robustness metrics, with AR_{p95} approaching the 3 dB limit and increased $\overline{AR}$ and σ_{AR}. This confirms that the highest RBW values are obtained at the expense of operating closer to the LTC conversion threshold.

In contrast, the most robust configuration preserves the RBW of the reference design (26%) while improving the AR statistics, with lower $\overline{AR}$ and reduced variability. This result confirms that slightly reduced RBW values can yield a more stable circular-polarization response across the operating band. Overall, the LHS-based analysis shows that broadband LTC conversion is supported over an extended and tolerant region of the design space rather than around a single finely tuned optimum, highlighting the value of statistical design-space exploration beyond conventional parametric sweeps.

IV. CONCLUSIONS

A Latin Hypercube Sampling (LHS)–based design-space exploration has been applied to a mechanically reconfigurable linear-to-circular polarization (LTC) metasurface. The analysis reveals that broadband LTC conversion is not limited to a single optimal configuration but occurs over an extended region of the (p, t) parameter space.

Designs optimized exclusively for maximum bandwidth tend to exhibit reduced robustness, whereas alternative configurations achieve comparable relative bandwidth with improved polarization stability. These results demonstrate that statistical exploration provides a practical and effective approach to balancing bandwidth and robustness in mechanically reconfigurable polarization converters.

ACKNOWLEDGMENTS

This research was funded by the Spanish Ministry of Science and the European Union: MCIN/AEI/10.13039/501100011033/FEDER, UE, grant number PID2022-137619NB-I00.

REFERENCES

[1] C. A. Balanis, *Antenna Theory: Analysis and Design*, 4th ed. Wiley, 2016.
[2] H.-T. Chen, A. J. Taylor, and N. Yu, "A Review of Metasurfaces: Physics and Applications," *Reports on Progress in Physics*, vol. 79, Art. no. 076401, 2016. https://doi.org/10.1088/0034-4885/79/7/076401
[3] G. J. Molina-Cuberos, Á. J. García-Collado, I. Barba, and J. Margineda, "A Reconfigurable Metasurface for Linear-to-Circular Polarization Conversion Using Mechanical Rotation," *Electronics*, vol. 14, no. 18, Art. no. 3639, 2025. https://doi.org/10.3390/electronics14183639
[4] M. D. McKay, R. J. Beckman, and W. J. Conover, "A Comparison of Three Methods for Selecting Values of Input Variables in the Analysis of Output from a Computer Code," *Technometrics*, vol. 21, pp. 239–245, 1979. https://doi.org/10.1080/00401706.1979.10489755
[5] Stein, M. Large Sample Properties of Simulations Using Latin Hypercube Sampling. *Technometrics*, 29, 143–151, 1987. https://doi.org/10.1080/00401706.1987.10488205

Optically Transparent Metasurface Reflector for Radar Visibility Enhancement of Vehicles

S. Geyman[1,*], D. Vovchuk[1,2], D. Kolchanov[1], M. Khobzei[2,3], V. Tkach[2,3], V. Bobrovs[2], H. Gilon[4], E. Cohen[4], E. Yungar[4] and P. Ginzburg[1]

[1]School of Electrical Engineering, Tel Aviv University, Tel Aviv, Israel
[2]Institute of Photonics, Electronics and Telecommunications, Riga Technical University, Riga, Latvia
[3]Department of Radio Engineering and Information Security, Yuriy Fedkovych Chernivtsi National University, Chernivtsi, Ukraine
[4]DR Utilight Ltd., Yavne, Israel
*Corresponding author: sergeigeiman@mail.tau.ac.il

***Abstract*— Automotive radar detection depends on vehicle radar cross-section (RCS), yet modern vehicles lack dedicated reflectors. We propose an optically transparent metasurface integrated on the rear windshield, formed by conductive wires satisfying the first Bragg condition. A 10×10 cm² prototype achieves ~90% optical transparency and an RCS of 8 m².**

***Keywords*— metamaterials, RCS, radar.**

I. Introduction

Ensuring road safety relies on ADAS sensors, with radar being primary due to its robustness in adverse conditions. Automotive radars (77–81 GHz) assist in collision avoidance and object detection but face challenges like limited angular resolution and multipath effects. A key factor in detection reliability is the target's RCS, which for passenger vehicles typically ranges from 10 to 100 m^2 [1]-[3]. RCS enhancement, widely used in maritime applications, can significantly improve radar detection, increasing the effective range and signal-to-noise ratio [4].

Despite its advantages, integrating radar reflectors into vehicle design remains a challenge due to aesthetic and space constraints. The rear windshield, largely unused apart from defogging elements, presents a viable alternative for a functional backscatter reflector. A 1 m^2 windshield, modeled as a square plate, theoretically yields an RCS of 1000 m^2 at 80 GHz, highlighting the potential for enhanced detectability.

Maintaining optical transparency is crucial. Transparent antennas and reflectors find applications in automotive wireless communication, wearable electronics, and security [5]-[8]. Technologies like transparent conductive oxides, metal meshes, and pattern transfer printing (PTP) enable fabrication of optically transparent yet conductive surfaces. We employ PTP with silver pastes to print sub-millimeter conductive patterns onto glass, ensuring both transparency and high radar reflectivity.

II. Methods

The proposed structure for increasing the radar cross section (RCS) magnitude is based on a well-studied wire grid [9]. The fabricated metasurface with selected geometrical parameters provides a significant increase in vehicle visibility - Fig. 1(a). The insets in Fig. 1(a) schematically describe the scattering process and an example of the resulting radar map.

In order to achieve an in-phase response from an array of parallel wires, it is necessary that the path difference to neighbouring elements is a multiple of the wavelength [10]: $2d\sin(\theta) = \lambda$.. In this equation, d is the period of the reflector, θ is the angle of incidence of the plane wave and λ is the wavelength in the medium. For the considered frequency range and typical angle of inclination of a car window ($\theta = 45$ degrees), the period d=2.65 mm was selected. In order to demonstrate the performance of the proposed concept, a sample was simulated and fabricated on a glass of thickness 4 mm with a dielectric permittivity 6 with dimensions of 10*10 cm^2 and with thickness of conductive strips of 0.02 mm. All numerical simulations were performed in CST Microwave Studio, with a linearly polarized plane wave as the source.

Fig. 1(b) shows the 3D pattern of bistatic RCS at 80 GHz. The plane wave was incident on the sample surface at an angle of 45 degrees, while the electric vector E remained co-directional with the wires. Since the system is optimized for such parameters, four beams are expected: two reflected from the plane of the metasurface and two passed through it. The insets in Fig. 1(b) show the direction of incidence of the plane wave on the structure and the color scale of the RCS magnitude in m^2. The beam returning back to the radar is quite narrow - the RCS value attenuates by 6 dB over a range of 1.8 degrees from the original direction.

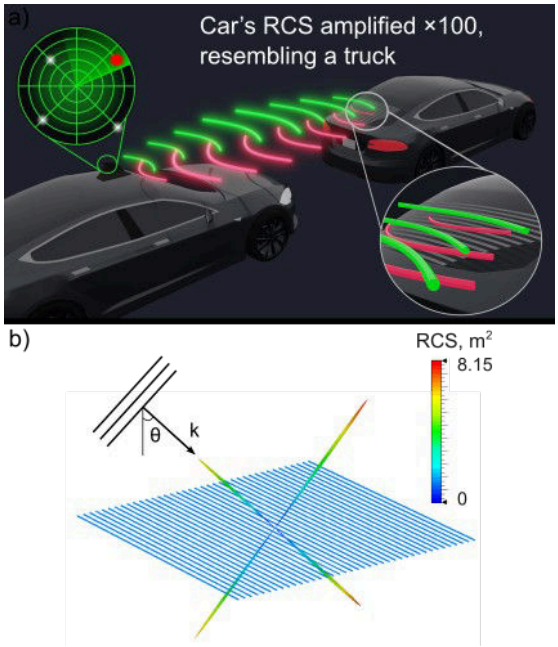

Fig. 1 Illustration of the proposed concept for increasing the RCS of a vehicle (a). The metasurface on the rear window of a vehicle significantly improves its visibility to radars. The 3D bistatic RCS pattern for angle of incidence θ = 45 degrees at 80 GHz carrier frequency (b).

III. Results and Discussion

The optical properties of the SUTs were investigated using a standard method to confirm the transparency of the glass samples. A collimated visible light beam illuminated the sample, and the transmitted light was collected into an optical fiber and analyzed using an Avantes spectrometer. The transmission spectrum (Fig. 2(a)), normalized to the lamp signal, showed that plain glass had approximately 90% transparency at lower wavelengths, while the deposition of a transparent polarizer reduced it by about 2%, indicating minimal optical loss.

The result of a numerical simulation of the scattering of a developed metasurface at different incident plane wave angles for different frequencies is shown in Fig. 2(b). The incident wave angle was varied from 0 to 60 degrees with a step of 1 degree, and the carrier frequency was varied from 75 to 110 GHz with a step of 0.1 GHz. The figure highlights a narrow maximum at normal incidence (θ = 0 degrees) and an additional line at the 30–45-degree section.

Considering the Bragg condition and the simulation results, the reflection measurements were conducted in an anechoic chamber (Fig. 2(c)). The setup includes a PNA controlled via MATLAB, with the SUT placed at the center of a rotating styrofoam table. The SUT consists of conductive wires on a glass substrate. Measurement was performed for azimuthal rotations of 0:1:60 degrees and fixed elevation angle 0 degrees (wires parallel to the vertically polarized antenna). Strong reflection was observed across 75–110 GHz for 0 degrees azimuth and 0 degrees elevation and additional reflections appeared between 30–45 degrees azimuth due to Bragg condition optimization (Fig. 2(d)).

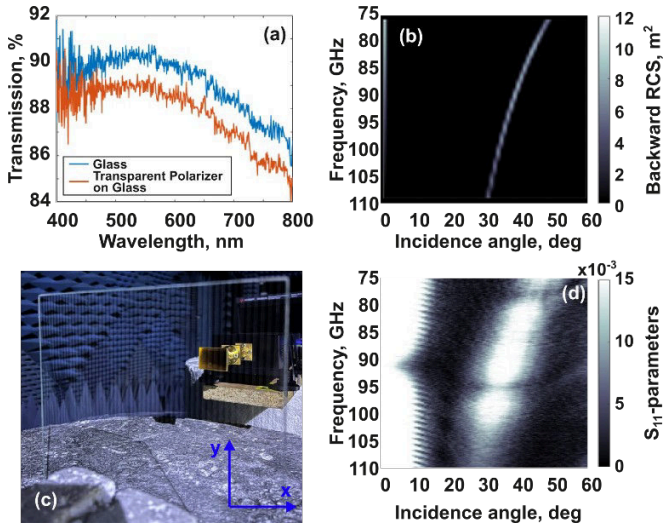

Fig. 2 Experimental result in the optical laboratory for glass SUT in the visible wavelength range (a). Simulation results - dependence of the backward RCS in linear scale on the frequency and angle of incidence of a plane wave (b). Experimental setup for measurement the S_{11}-parameters (c)-(d).

IV. Conclusion

We have demonstrated a 3D-printed optically transparent metasurface designed to enhance automotive radar visibility while maintaining high optical transparency. The metasurface, composed of conductive wire arrays, was optimized to satisfy the Bragg condition, ensuring strong radar reflections in the 77–81 GHz band. Both simulations and experimental measurements confirmed a significant increase in RCS, with a fabricated 10*10 cm^2 sample achieving an RCS of 8 m^2. Extrapolating this to a full rear windshield suggests an RCS of up to 1,000 m^2, improving vehicle detectability by nearly two orders of magnitude. The proposed approach offers a scalable solution for integrating electromagnetic functionality into automotive glass, with potential applications in radar sensing, wireless communication, and smart infrastructure.

References

[1] T. Schipper, J. Fortuny-Guasch, D. Tarchi, L. Reichardt, T. Zwick, "RCS measurement results for automotive related objects at 23-27 GHz," Proceedings of the 5th European Conference on Antennas and Propagation (EUCAP), pp. 683-686, Rome, Italy, 11-15 April 2011.
[2] E. Bel Kamel, A. Peden and P. Pajusco, "RCS modeling and measurements for automotive radar applications in the W band," Proceedings of 11th European Conference on Antennas and Propagation (EUCAP), pp. 2445-2449, Paris, France, 19-24 March 2017.
[3] M. Dudek, D. Kissinger, R. Weigel, and G. Fischer, "A millimeter-wave FMCW radar system simulator for automotive applications including nonlinear component models," Proceedings of 8th European Radar Conference, pp. 89-92, Manchester, UK, 12-14 October 2011.
[4] M. I. Skolnik, Introduction to Radar Systems, 3rd edition, McGraw-Hill, 2001.

[5] A.R. Chishti, A. Aziz, M.A. Qureshi, M.N. Abbasi, A.M. Algarni, A. Zerguine, N. Hussain, and R Hussain, “Optically transparent antennas: a review of the state-of-the-art, innovative solutions and future trends,” Applied Sciences, 13, no. 1: 210, 2023.
[6] A. Katsounaros, Y. Hao, N. Collings, and W. A. Crossland, “Optically transparent ultra-wideband antenna,” Electronics Letters, vol. 45, no. 14, pp. 722–723, 2009.
[7] L. Kannappan, S. K. Palaniswamy, M. Kanagasabai, J. K. Pakkathillam, S. Kumar, and M. I. Hussein, “Quad-port multiservice integrated optically transparent automotive antenna for vehicular classification applications,” Sci Rep, vol. 13, no. 1, 2023.
[8] Y. Morimoto, S. Shiu, I. W. Huang, E. Fest, G. Ye, and J. Zhu, “Optically transparent antenna for smart glasses,” IEEE Open Journal of Antennas and Propagation, vol. 4, pp. 159–167, 2023.
[9] S. Tretyakov, Analytical Modeling in Applied Electromagnetics, Artech, 2003.
[10] R. K. Chourasia and A. Katti, Bragg Fibers, Springer Cham, 2024.

300-µm Gaussian Beams from Meta-Grating Couplers for Ultra-Stable Lasers

Max Schittenhelm[1,2*], Mika Gaedtke[1,2], Steffen Sauer[1,2], Sebastian Häfner[1,2], and Stefanie Kroker[1,2,3]

[1]Technische Universität Braunschweig, Institut für Halbleitertechnik, Hans-Sommer-Str. 66, 38106 Braunschweig, Germany

[2]Laboratory for Emerging Nanometrology, Langer Kamp 6a/b, 38106 Braunschweig, Germany

[3]Physikalisch-Technische Bundesanstalt, Bundesallee 100, 38116 Braunschweig, Germany

*Corresponding author: max.schittenhelm@tu-braunschweig.de

***Abstract*—We present a framework for interfacing an ultra-stable laser resonator with photonic integrated circuits via low-noise resonator mirrors and show initial simulation and experimental results of large-area grating couplers with near-Gaussian beam diameters of 300 µm at λ = 1.55 µm on an SOI-platform.**

***Keywords*— ultra-stable lasers, grating couplers, photonic integrated circuits, optical resonators**

I. Introduction

Ultra-stable lasers (USLs) are a key enabling technology driving the quantum revolution. They provide the stable frequencies needed for precise interrogation of narrow atomic transitions in atoms or ions. Additionally, they are indispensable for precision measurements in fields such as gravitational wave detection [1] and tests of fundamental physics [2]. Current state-of-the-art USLs operated at 1.55 µm achieve a sub-10 mHz linewidth, limited by the fundamental thermal Brownian noise of the mirror coatings [3]. The bulky design of conventional USLs, requiring extensive thermal shielding, also necessitates large optical systems for operation [4]. While integrated lasers based on micro-ring resonators [5] and chip-coupled micro-resonators [6] offer compact solutions, they still lack the mid- and long-term stability often required. To overcome these limitations, our novel resonator approach leveraging multifunctional mirrors and integrated photonics aims to meet the stringent SWaP (size, weight, and power) requirements of the quantum revolution. While coupling and stabilizing on-chip laser light to mm-scale micro-resonators has been recently demonstrated [6], ultra-stable laser resonators (USLRs) exhibit lengths on the cm-scale. These cm-scale resonator lengths, however, demand large, Gaussian output beams emitted from the chip with mode field diameters in the range of several hundreds of micrometers.

In this work, we present the design approach and experimental data of fully-etched grating couplers on a 220 nm silicon-on-insulator platform emitting large mode field diameter Gaussian beams at 1.55 µm wavelength suitable to be directly coupled into cm-scale USLRs. Figure I displays the envisioned approach, where the resonator mirror (center) consists of multiple vertically stacked functional layers, with the photonic integrated circuit (PIC) at the very bottom. This

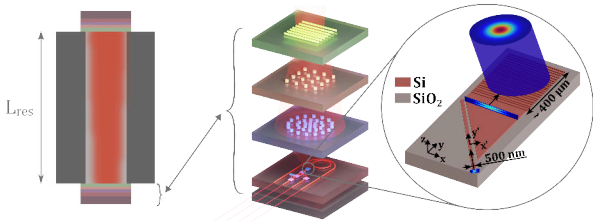

Fig. 1. A macroscopic, optical resonator (left) with L_{res} on the order of centimeters is interfaced to a photonic chip which is integrated into the lower mirror substrate. The proposed vertical structure of the chip and mirror (center) consists of the photonic integrated circuit (dark red), two layers for beam shaping (blue, brown) and finally the low-noise meta mirror (green).

PIC provides the light in- & out coupling, routing, and light modulation necessary for locking a laser to the resonator. The following description of the design and experimental realization of large-area grating couplers marks the first step towards multifunctional low-noise resonator mirrors, interfacing integrated photonics with free-space USLRs.

II. Methods

The geometry, i.e. the length of the resonator and the curvature of the second mirror, dictates the spatial distribution of its fundamental mode: for a fixed resonator length of $L_{res} = 4$ cm consisting of one flat mirror and one focusing mirror, the fundamental mode will depend on the radius of curvature of the focusing mirror. As a starting point, a radius of curvature of 100 mm was chosen, corresponding to a beam waist diameter of 300 µm at the plane mirror. Since the plane mirror defines a perpendicular propagation vector in respect to its surface, it is chosen as the incoupling mirror with the PIC attached to the back of it. The resulting emission diameter of the grating coupler located on the PIC thus needs to equal this beam waist diameter of 300 µm. The required local coupling strength κ of a grating, which emits a beam intensity profile $S(y) \propto |E(y)|^2$, can be expressed through

$$\kappa(y) = \frac{S(y)}{P(-\infty) - \int_{-\infty}^{y} S(t)dt}, \quad (1)$$

where $P(-\infty)$ is the initial power in the waveguide. For classical chip to SM-fiber (≈10 µm mode diameter) coupling

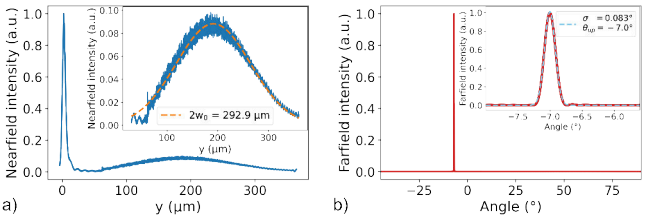

Fig. 2. (a) Nearfield and (b) farfield emission profiles of the cherry-picked sub-wavelength grating coupler extracted from a 2D-FDTD simulation. The simulated beam diameter is 292.9 µm with an emission angle of $-7°$.

applications, the coupling strengths need to be on the order of $10^{-2}...10^{0}$ µm^{-1}. However, for beam diameters of several hundreds of microns, small coupling strengths down to 10^{-4} µm^{-1} are required. To achieve such large output diameters, a sub-wavelength grating-based approach was chosen, as the coupling strength can be tuned to almost arbitrarily small values [7]. FDTD-simulation sweeps were performed over large design spaces and the coupling strength for each design was recorded. Designs of these sweeps were cherry-picked to best fit the required coupling strength-function according to Eq. 1, where $S(y)$ is the Gaussian intensity profile with a beam waist diameter of $2w = 300\,\mu\text{m}$. While a Gaussian beam is advantageous for a USLR, the present design concept enables the realization of arbitrarily shaped intensity profiles defined by $S(y)$.

In addition to the grating coupler, an evanescent mode converter (Figure I, right) was analytically designed to convert the waveguide mode to a slab mode with a width of 300 µm to obtain a circular Gaussian beam emission from the grating coupler, similar to the design process shown in [8]. The resulting gap function between the waveguide and the slab is then expressed by

$$g(y') = -\frac{1}{b}\ln\left(\frac{\lambda_0}{\sqrt{2}aw\pi^{3/2}}\frac{e^{-2\frac{(y'-L)^2}{w^2}}}{1-\text{erf}\left\{\sqrt{2}\frac{y'-L}{w}\right\}}\right) \quad (2)$$

where a, b are parameters derived from the effective mode index, w is the desired waist of the slab mode, L is the center of the slab mode and y' the spatial coordinate along the waveguide (see Figure I for reference).

III. Results and Discussion

Different cherry-picked gratings for a beam diameter of 300 µm at different emission angles have been designed and fabricated. The simulated 2D-FDTD response of a design for an emission angle of $-7°$ is shown in Figure 2. The emitted beam exhibits a broad Gaussian shape, spanning over several hundreds of microns with a fitted beam diameter of 292.2 µm in the nearfield 2 µm above the grating and an upwards transmission efficiency of 47 %. Due to the symmetric nature of the fully-etched gratings, the upper limit of the efficiency lies at 50 %. The distinct emission peak at the beginning of the grating is attributed to the abrupt change in the effective refractive index of the mode when it transitions from the slab waveguide to the grating. As the design emission angle approaches 0°, the grating enters the Bragg-reflection regime, where most of the light is reflected back into the input slab. Since the emission angle should ideally be 0° for efficient resonator-coupling, an angle-correcting meta surface similar to the one in [9] will be employed in future steps.

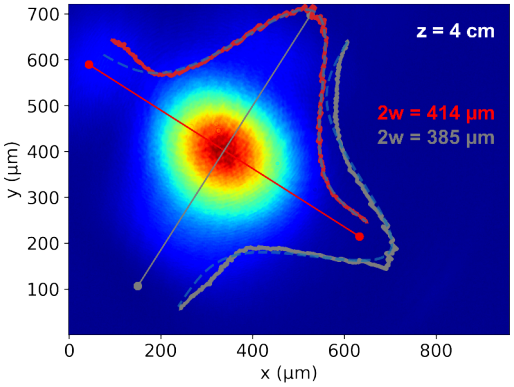

Fig. 3. (a) Experimentally measured beam profile at a height of z = 4 cm above the chip with two line profiles along the grating ridges (gray) and perpendicular to them (red). The ellipticity of the beam is due to the non-zero emission angle.

Figure 3 displays the experimentally acquired cross section profile of the emitted beam at a height of 4 cm above the grating coupler, corresponding to the location of the curved resonator mirror. The emission angle relative to the chip's surface normal was experimentally determined to be $-10.9°$. Due to additional refraction at the SiO_2/air-interface, the expected emission angle in air is $\theta_{\text{up}}^{\text{air}} = \arcsin(\frac{1.444}{1}\sin(-7°)) = -10.1°$, which closely matches the experimental value of $-10.9°$. This non-vertical emission accounts for the elliptical beam profile in cross-sections parallel to the chip's surface. Thus, the actual beam waist diameter $2w$ along the red axis in Figure 3 is 414 µm · cos(10.9°) = 407 µm, while the waist diameter of 385 µm along the gray axis does not need adjustment since this axis is oriented along the grating ridges. The resulting ellipticity of this design is therefore $e = 385\ \mu\text{m}\ /\ 407\ \mu\text{m} \approx 0.95$ at a height of $z = 4$ cm.

IV. Conclusion

In conclusion, we have shown a pathway and first steps towards designing compact ultra-stable laser resonators by employing a multi-functional resonator mirror approach. We experimentally demonstrated the feasibility of our cherry-picking design method for designing and fabricating fully-etched grating couplers on an SOI-platform that can emit collimated, large-scale Gaussian beams on the order of hundreds of micrometers.

Acknowledgments

This project has received funding from the European Research Council (ERC) under the European Union's Horizon Europe research and innovation program (Project Number [101170022]). This work is partially funded by the Deutsche

Forschungsgemeinschaft (DFG, German Research Foundation) under Germany's Excellence Strategy – EXC-2123 Quantum-Frontiers – 390837967.

REFERENCES

[1] R. X. Adhikari, "Gravitational radiation detection with laser interferometry," *Reviews of Modern Physics*, vol. 86, 121-151 (2014).
[2] M. Nagel et al., "Direct terrestrial test of Lorentz symmetry in electrodynamics to 10^{-18}," *Nature Communications*, vol. 6, 8174 (2015).
[3] D.G. Matei et al., "1.5 µm Lasers with Sub-10 mHz Linewidth," *Physical Review Letters*, vol. 118, 263202 (2017).
[4] S. Häfner et al., "$8{\cdot}10^{-17}$ fractional laser frequency instability with a long room-temperature cavity," *Optics Letters* vol. 40, pp. 2112-2115 (2015).
[5] Roy Zektzer et al., "On-chip multi spectral frequency standard replication by stabilizing a microring resonator to a molecular line," *Applied Physics Letters*, vol. 109, 2016
[6] H.Cheng et al., "Harnessing micro-Fabry–Pérot reference cavities in photonic integrated circuits," *Nature Photonics*, vol. 19, pp. 992-998, 2025
[7] M. Barona-Ruiz et al., "Large Beam Size Grating Coupler in Silicon-on-Insulator Using Fully Etched Subwavelength Gratings," *Laser Photonics Reviews* vol. 19, 2401775 (2025).
[8] S.Kim et al., "Photonic waveguide to free-space Gaussian beam extreme mode converter," *Light: Science and Applications*, vol. 7, 72 (2018)
[9] A. Yulaev et al., "Chip-scale Doppler atomic spectroscopy enabled by a metasurface integrated photonic emitter," *Applied Physics Letters*, vol. 125, 121114 (2024)

Elimination of Beam Walk-off in Second Harmonic Generation

Edvinas Aleksandravičius[1,*], Darius Gailevičius[1], Kęstutis Staliūnas[1,2,3]

[1]Vilnius University, Faculty of Physics, Laser Research Center, Saulėtekio Ave. 10, Vilnius, Lithuania

[2]ICREA, Passeig Lluís Companys 23, 08010, Barcelona, Spain

[3]UPC, Dep. de Fisica, Rambla Sant Nebridi 22, 08222, Terrassa (Barcelona), Spain

*Corresponding author: edvinas.aleksandravicius@ff.vu.lt

***Abstract*— We show that periodic modulation of the refractive index of a nonlinear material on the wavelength scale can modify the angular dispersion of the interacting waves. This modification improves the phase-matching conditions and can significantly reduce beam walk-off. As a result, the efficiency of second-harmonic generation can be enhanced.**

***Keywords*— metamaterials, second harmonic generation, nonlinear optics, photonic crystals.**

I. Introduction

Efficient second-harmonic (SH) generation critically depends on the fulfillment of the Phase-Matching (PM) condition, which ensures that the interacting fundamental (FW) and harmonic waves propagate with matched phase velocities. In birefringent nonlinear media, exact phase matching is realized for a specific propagation direction (incidence angle) corresponding to a given fundamental frequency. In the present work, we restrict our analysis to the two-dimensional (2D) case; in a fully three-dimensional (3D) geometry, the phase-matching condition is satisfied along closed curves -typically circles or ellipses - in the azimuthal and polar angular domains.

In the vicinity of the PM point, the phase mismatch exhibits a linear dependence on the angular deviation from the phase-matching direction, as illustrated schematically in Fig. 1. In the angular (spatial Fourier) domain, this dependence defines the angular bandwidth of efficient SH generation. In the corresponding spatial domain, the linear phase mismatch manifests as a walk-off between the interacting fundamental and second-harmonic beams, arising from the anisotropic refractive index of the birefringent medium. This spatial walk-off leads to a progressive separation of the interacting beams and, consequently, to a reduction in the effective nonlinear interaction length. In the absence of walk-off, the SH intensity increases quadratically with the interaction distance, reflecting perfect phase matching over the interaction length. By contrast, when the walk-off is present, the overlap between the interacting beams diminishes with distance, and the SH conversion efficiency grows only linearly with the crystal length.

Here, we demonstrate that periodic modulation of the refractive index on a wavelength scale within a nonlinear crystal, implemented in both longitudinal and transverse directions, can substantially modify the fundamental phase-matching condition and profoundly alter the beam walk-off behavior. The underlying concept of this work is based on the well-established principle that periodic modulation of the refractive index on a scale comparable to the optical wavelength can significantly modify the spatial dispersion properties of propagating waves. This effect becomes particularly pronounced when both the longitudinal and transverse modulation periods approach specific resonant conditions, known as Talbot resonances. In the vicinity of such resonances, the periodic modulation induces strong coupling between spatial harmonics, leading to substantial modifications in the effective dispersion relations of the interacting waves.

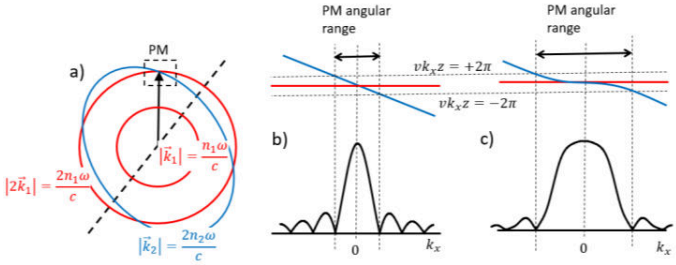

Fig. 1 a) The SH generation is at PM at a particular direction of the incident beam propagation (black arrow) at a PM angle with respect to the axis of birefringent media. b). In the vicinity of the PM point the dispersions of interacting waves can be approximated as linear ones with respect to k_x, crossing at a particular angle. This intersection angle results in a finite PM angular range of the second harmonics. c) The idea is to deform the dispersion curve in the vicinity of the PM point, in order to obtain a broader phase matching angular range.

II. METHODS

We employ the split-step beam propagating method to simulate the beam propagation, dispersion, and SH generation. The photonic crystal was estimated as being sinusoidally modulated along the transverse x and longitudinal z dimensions as a phase mask:

$$Mask = \Delta n \cdot \cos(\frac{x}{a_x}) \cdot \sin(\frac{z}{a_z}).$$

The complex beam envelope u was propagated along the photonic crystal by iterating:

$$u_{l+1} = \mathcal{F}^{-1}\left(e^{i \cdot Difr} \cdot \mathcal{F}(u_l \cdot e^{i \cdot Mask})\right),$$

where *Difr* is the normal, unmodulated dispersion that is either circular for the FW or a rotated ellipse for the SH.

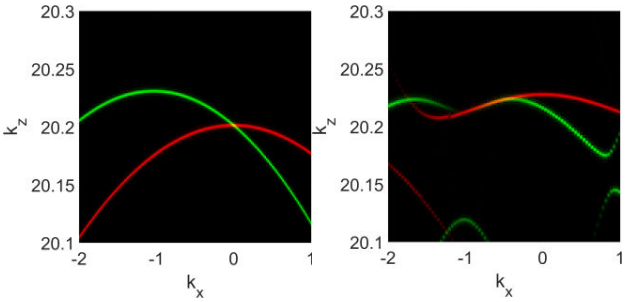

Fig. 2 Spatial dispersion curves of the FW (red) and the SH (green). The left image shows normal dispersion, whereas the right image shows engineered dispersion with a significantly greater overlap between the FW and SH.

Nonlinear coupling between the FW and SH is introduced as first-order finite-difference terms:

$$u_{l,\omega} = u_{l,\omega} + i \cdot k_\omega \cdot \frac{d_{eff}}{n_\omega} \cdot {u_{l,\omega}}^* \cdot u_{l,2\omega},$$

$$u_{l,2\omega} = u_{l,2\omega} + i \cdot k_{2\omega} \cdot \frac{d_{eff}}{n_{2\omega}} \cdot {u_{l,\omega}}^2,$$

where d_{eff} is the effective nonlinear coefficient.

III. RESULTS AND DISCUSSION

Broadening of the PM angle can be achieved for many configurations of the photonic crystal. One such example for β-BBO, corresponding to the dispersion curves shown in Fig. 2, is:

- $a_x = 2$ µm;
- $a_z = 26$ µm;
- $\lambda_{FW} = 1.03$ µm.

The equivalent angular conversion efficiency is shown in Fig. 3. The photonic crystal shifts the central PM angle by 2 degrees while broadening it from 0.12 degrees to 1.7 degrees. The peak SH generation efficiency in the photonic is approximately 43% of the unmodulated case.

It should be noted that this decrease in peak conversion efficiency is not exclusive to this particular example but rather a common factor for all configurations. This is because in a photonic crystal part of the radiation may project into dispersion bands other than the one exhibiting PM.

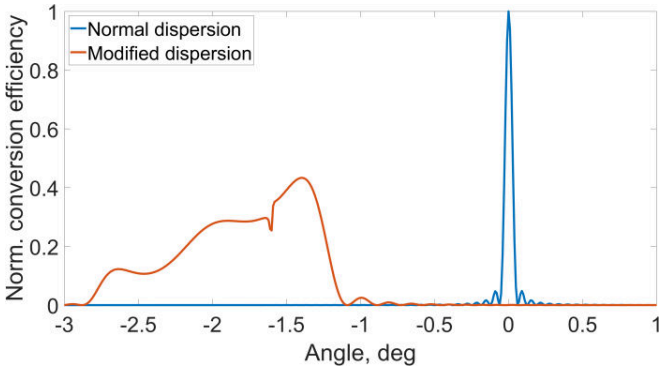

Fig. 3 Angular dependence of the normalized conversion efficiency for $a_x = 2$ µm; $a_z = 26$ µm, $\lambda_{FW} = 1.03$ µm. The crystal length is 5 mm.

While peak angular conversion efficiency is reduced, this may be less relevant for somewhat focused beams. In this case, rather than peak efficiency, the determining factor would instead be the integral of angular efficiency. Assuming the beam covered the entire PM area in each case, the modulated dispersion results in a 6.3 times higher total conversion efficiency.

IV. CONCLUSION

We have demonstrated control of spatial dispersion to enhance phase matching in second second-harmonic generation by the use of photonic crystals. The angular range of phase matching is increased by up to 14 times, while total conversion efficiency is increased by up to 6.3 times.

ACKNOWLEDGMENTS

E.A., D.G., and K.S. were supported by the project from the Research Council of Lithuania (LMTLT), agreement No. S-MIP-24-10. K.S. was supported by Spanish Ministry of Science, Innovation and Universities (MICINN) under the project PID2022-138321NB-C21.

Zero-angle polarizers based on periodically structured dielectric thin films

Julianija Nikitina[1,*], Rytis Buzelis[1], Kęstutis Staliūnas[2,3], Lina Grinevičiūtė[1]

[1]Center for Physical Sciences and Technology, Vilnius, Lithuania
[2]ICREA, Passeig Lluís Companys 23, 08010, Barcelona, Spain
[3]UPC, Rambla Sant Nebridi 22, 08222, Barcelona, Spain
*Corresponding author: julianija.nikitina@ftmc.lt

Abstract **— Zero angle of incidence polarizers in reflection/transmission based on Fano resonances in periodically nanostructured dielectric thin films are analyzed. Its main optical characteristics for 1064 nm wavelength are investigated in the context of laser applications, including laser damage evaluation with a discussion of resonance-related electric field distribution.**

Keywords**— polarization control, all dielectric structure, conformal deposition, optical damage, electric field distribution.**

I. Introduction

Linear polarizers are a kind of optical filter whose optical properties, as transmission/reflection, depend on the polarization state of incident radiation. The simplest example of polarization selectivity can be obtained with a plain glass substrate tilted at the Brewster angle, allowing partial reflection only for *S* polarization, but polarization contrast falls way below what a full-fledged polarizer must demonstrate. Up-to-date linear polarizers comprise a wide diversity, such as absorptive, birefringent or thin-films polarizers. These optical elements can provide an outstanding polarization extinction ratio of $>10^3$:1 [1]. However, most of them have exploitation inconveniences, coming from their inner structure: selective absorption-based polarizers have low laser-induced damage threshold (LIDT), excluding high-power applications; birefringent and thin-film polarizers are for non-normal incidence and are bulky solutions for space-limited optical systems. Considering these drawbacks, such already well-established polarizing elements can hardly be integrated into the resonators of constantly developing microlasers, such as microchip lasers or semiconductor VECSELs. Thus, there is an evident lack of compact radiation-resistant polarizers suitable for normal incidence.

Following this discussion, in this work, we explore and demonstrate ultra-compact, zero-angle polarizers, based on the waveguiding structure of dielectric nano-modulated thin films. The design of our polarizing structure consists of a high-index dielectric coating layer on a periodically patterned surface, as schematically shown in Fig. 1. Its main optical characteristics are investigated in the perception of the laser applications, including laser damage evaluation and its correlation with resonance-related electric field distribution within the structure.

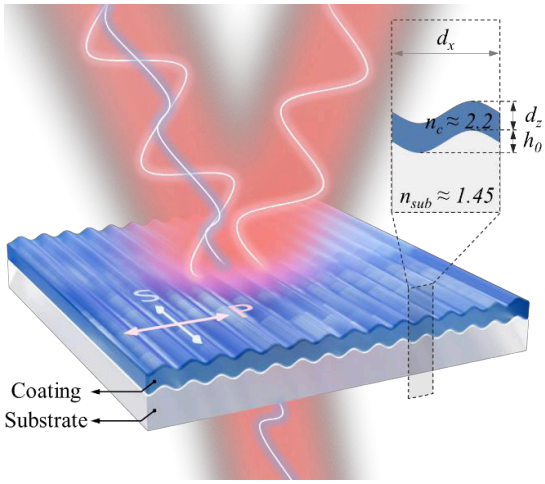

Fig. 1 Schematic representation of the geometry for the resonant coupling between normal incident waves and planar waveguiding modes [2].

II. Methods

Our methodology includes numerical simulations of the waveguiding structure's optical characteristics, optimization, followed by fabrication of the element and its experimental characterization. Target optical properties of the polarizing element were set for radiation of 1064 nm wavelength incident at 0° angle. Numerical simulations of the periodically structured polarizing element were calculated by a commercial solver of Maxwell-Bloch equations MC Grating [3]. Two distinct designs of single-layer and multilayer structures were created and experimentally realized via conformal deposition of dielectric layers on a pre-patterned substrate (with $d_x = 625$ nm, $h_0 = 200$ nm, variable layer thickness d_z) by ion beam sputtering technology.

Optical characterization included measuring transmission spectra for two orthogonal linear polarizations in the spectral range of 400 – 1400 nm for a normal angle of incidence. Optical resistance was evaluated with a laser-induced damage test for single-shot nanosecond pulses (1-on-1 test). After exposure, the surface was inspected with an optical microscope to verify the presence of damage and investigate its morphology.

Additionally, the contact profilometer was used to determine the damage profile.

III. Results and Discussion

A simple design of a thin single-layer coating of a high refractive index dielectric material, such as niobium oxide, was realized at subwavelength linear grating features a polarization-dependent Fano-like resonance. As a result, as shown in Fig. 2 (a, b), optimized thickness of the layer can form a high polarization contrast region around the target wavelength. Simulated transmittance values at 1064 nm are 0.0022 % and 98.12 %, while measured transmittance values are 96.22 % and 0.01 % for *P* and *S* polarizations, respectively. These experimental results correspond to an averaged polarization contrast of approximately 1:1000, with a more precise extinction ratio of 1:962. The discrepancy in transmittance for *P* polarization is attributed to back reflection of several per cent from the rear surface of the glass sample, which is not taken into account in the numerical evaluation.

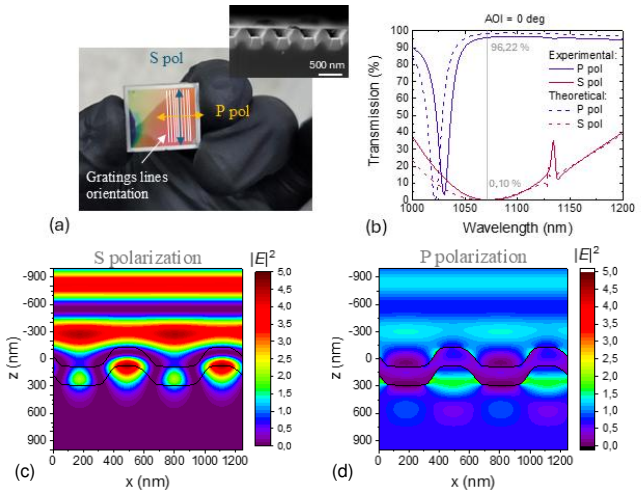

Fig. 2 Experimental realization of the polarizing waveguiding structure: (a) a photograph of the sample and an SEM cross-section of the fabricated structure; (b) Transmittance at 0° angle of incidence for *S* and *P* polarizations; (c, d) simulated electric field distribution within the single-layer structure for perpendicular polarizations for 1064 nm wavelength [2].

Considering laser applications, another important aspect to discuss is the laser damage, which is tightly connected to the distribution of the electric field within the structure. As it is known, strong field localization can lead to a significant intensity enhancement, which increases the probability of structural damage and thus lowers the laser-induced damage threshold (LIDT).

The LIDT measurement of the presented single-layer polarizing structure showed values of 0,7 J/cm² for *S* polarization and 3,1 J/cm² for *P* polarization. The correlation for both polarizations coincides with the respective field distributions within the structure, which are shown in Fig. (c, d). Since the architecture of the waveguiding structure is optimized for operation at *S* polarization resonant condition, its higher field enhancement (evident from the color scale) within the coating results in optical damage at lower laser fluence, compared with the off-resonance condition for *P* polarization at target wavelength. Nevertheless, these LIDT values are already higher than those reported for commercial 0° angle-of-incidence polarizers [4].

Since a single-layer thin film structure does not possess much optimization freedom in order to improve the optical resistance, the multilayer architecture was realized. Experimentally formed multilayer structure showed a slight improvement of LIDT and a more evident correlation of laser-induced damage and electric field distribution within the coating, which will be discussed during the presentation.

IV. Conclusion

The main conclusion is that an ultracompact thin-film polarizer has been proposed, designed, and experimentally demonstrated. The polarizer shows theoretically unlimited contrast for monochromatic plane waves at normal incidence and has experimentally achieved values as high as approximately 1:1000. Polarization-selective resonant phenomena occurring in subwavelength high refractive index structures cause increased electric field intensity, favouring lower laser-induced damage threshold values. As this investigation suggests, further work is ongoing to optimize the architecture of the polarizer and its electric field distribution in order to further enhance the polarization contrast ratio and LIDT.

Acknowledgments

This work has received funding from the Research Council of Lithuania (LMTLT), agreement No. S-LT-TW-24-9.

References

[1] "Thorlabs, Inc." Accessed: Dec. 04, 2022. [Online]. Available: https://www.thorlabs.com/

[2] L. Grineviciute, J. Nikitina, and K. Staliunas, "Understanding all-dielectric periodically modulated coatings for normal-incidence polarization control," *Optical Materials, under review*.

[3] N. Lyndin and B. Usievich, "Modal and C Methods Grating Software." Accessed: Dec. 11, 2022. [Online]. Available: https://mcgrating.com/

[4] "Thorlabs Polymer Linear Polarizer - LPNIRE050-B | MEETOPTICS." Accessed: Feb. 12, 2026. [Online]. Available: https://www.meetoptics.com/polarization-optics/linear/polymer-linear-polarizer/s/thorlabs/p/LPNIRE050-B

Optical properties of Ge metasurfaces realized on a Si photonics platform for wavelength-selective absorption

Paul Oleynik[1,*], Wei-Han Chen[2], Jon Schlipf[2], Oliver Skibitzki[2], Christian Wenger[2], Inga A. Fischer[1]

[1]Chair of Experimental Physics and Functional Materials, BTU Cottbus-Senftenberg, Cottbus, Germany
[2]IHP- Leibniz Institute for High Performance Microelectronics, Frankfurt (Oder), Germany

*Corresponding author: paul.oleynik@b-tu.de

***Abstract*—We report optical characterization results of complementary-metal-oxide-semiconductor compatible Ge metasurfaces fabricated on 200 mm SOI wafers. Optical properties of our metasurfaces are geometry-dependent and exhibit a large degree of homogeneity across the wafer. The metasurfaces will be used in wavelength-dependent photodetectors directly integrated on the Si photonics platform.**

***Keywords*— metasurface, selective epitaxy, photodetection, short-wave-infrared, CMOS**

I. Introduction

Optical metasurfaces as two-dimensional structures composed of subwavelength-sized nanoscatterers, commonly referred to as meta-atoms, can be used to tailor light-matter interaction for applications, e.g., in sensing or multispectral photodetection. [1] Metasurfaces offer remarkable control over the phase and propagation of light, their fabrication on 300 mm substrates has been successfully demonstrated. However, the front-end-of-line integration into device fabrication processes on the cost-effective complementary-metal-oxide-semiconductor (CMOS) platform remains challenging. [2] Possible advantages of integrating metasurfaces as functional layers directly into devices comprise realizing new device functionality such as wavelength- or polarization-selectivity while simultaneously harnessing electromagnetic field enhancement within the metasurface for absorptance enhancement compared to bulk photodiodes with the same thickness of the absorbing layer.

II. Methods

The fabrication of our CMOS compatible Ge metasurfaces (Fig. 1) was performed in a state-of-the-art 0.13 µm SiGe BiCMOS technology pilot line for 200 mm wafers [3], by structuring an oxide/nitride mask using deep ultraviolet photolithography and reactive ion etching. Subsequently, selective epitaxial growth of Ge was carried out by reduced pressure chemical vapor deposition (RPCVD) [4]. Ge metasurfaces with footprints of 3x3 mm^2 were obtained, with pitches ranging from 490 nm to 1165 nm and diameters of the individual Ge pillars ranging from 245 nm to 850 nm.

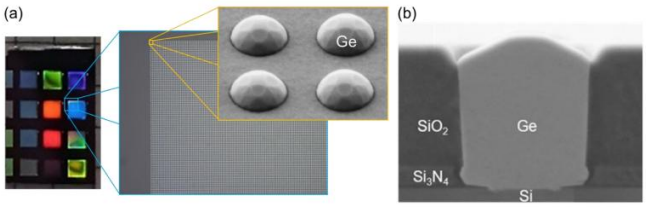

Fig. 1 (a) Images of metasurfaces as well as the constituent meta-atoms obtained from optical and scanning electron microscopy. (b) Cross-sectional scanning electron microscopy image of a single meta-atom of the metasurface fabricated using chemical vapor deposition of Ge into a nanostructured SiO_2/Si_3N_4 mask. Epitaxial growth of the Ge nanostructures on the Si wafer has been achieved.

Optical characterization was carried out using a Bruker Invenio Fourier-transform infrared (FTIR) spectrometer coupled to a Bruker Hyperion II FTIR microscope with an InGaAs detector. Absorptance spectra of the metasurfaces on substrate were derived from transmittance and reflectance measurements. Transmittance measurements of an adjacent unstructured substrate area enabled the separation of wafer absorption from metasurface absorption and Fabry-Pérot inferences of the SiO_2. The metasurface absorptance was obtained using a de-embedding approach [5]. Additionally, the absorptance of the metasurface was simulated using the rigorous coupled-wave analysis (RCWA) method [6].

Reflectance spectra at incidence angles of 10°, 15° and 20° with p-polarization were measured using a LAMBDA 1050+ UV/Vis/NIR spectrometer with a Si-detector for the 1000 nm - 1100 nm wavelength region and a n InGaAs detector for the 1100 nm - 2000 nm wavelength region.

III. Results and Discussion

Our metasurface is designed as the absorbing layer of a wavelength-selective photodetector in the near-infrared range. A full device integration requires in particular the realization of a top electrode. In this work, we focus on FTIR and wavelength-dependent reflectance spectroscopy measurements of the metasurface itself. The metasurface's optical behavior arises from the interplay between Mie resonances of the individual meta-atoms, collective lattice resonances due to their mutual coupling and diffraction grating effects. Here, the optical properties are investigated as a function of pitch (P) and diameter (D).

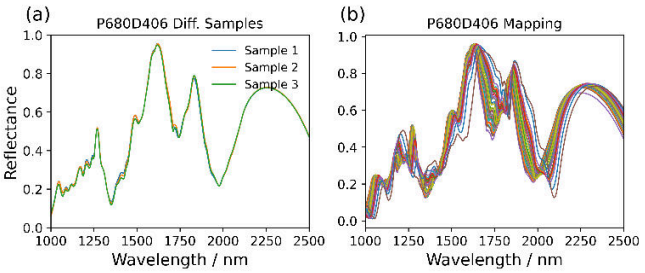

Fig. 2 (a) Reflectance spectra measured by Fourier-transform infrared (FTIR) spectroscopy on (a) the center of different metasurfaces with the same geometry from different positions on a 200 mm wafer and (b) at 30 different positions on the same 3 x 3 mm^2 metasurface (mapping).

Reflectance measurements demonstrate the homogeneity of optical properties when comparing different metasurfaces with the same geometry at different positions on the wafer (Fig. 2 (a)). Furthermore, 30 measurements taken on the same 3 x 3 mm^2 metasurface with an illumination spot size of 100 µm × 100 µm show good agreement (Fig. 2 (b)).

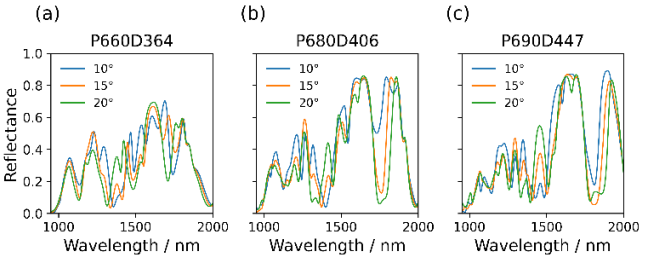

Fig. 3 Measured reflectance spectra at different angles of incidence for metasurfaces with different pitch (P) and diameter (D) (a) P = 660 nm and D = 364 nm, (b) P = 680 nm and D = 406 nm, and (c) P = 690 nm and D = 447 nm.

Reflectance measurements of the metasurfaces under varying angles of incidence show a large dependence of the reflectance on the angle of incidence (Fig. 3). This is also relevant for the measured absorptance spectra. The absorptance spectra of the metasurfaces are predicted by simulation to exhibit multiple absorption peaks governed by the optical resonances (Fig. 4 (a-c)). Increasing diameter and pitch shifts the absorptance peaks to higher wavelengths. In the measured absorptance spectra, the drop in absorption at wavelengths corresponding to the bandgap of Ge is well reproduced, however, no clearly defined peaks are visible. We attribute the difference between measurement and simulation mainly to a variation in the angle of incidence induced by the objective of our FTIR measurement setup. This aspect will be addressed in future metasurface designs.

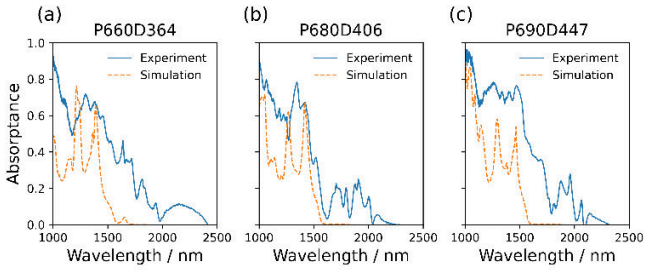

Fig. 4: Measured and simulated absorptance spectra for metasurfaces with different pitch (P) and diameter (D) (a) P = 660 nm and D = 364 nm, (b) P = 680 nm and D = 406 nm, and (c) P = 690 nm and D = 447 nm.

IV. Conclusion

We present first results of the optical characterization of CMOS compatible Ge-based metasurfaces with geometry-dependent absorption spectra in the near-infrared range. Our results are the starting point for the development of wavelength-dependent photodetectors for wavelengths up to 1600 nm on the Si photonics platform.

Acknowledgments

The authors gratefully acknowledge the computing time granted by the Resource Allocation Board and provided on the supercomputer Emmy/Grete at NHR-Nord@Göttingen as part of the NHR infrastructure. The calculations for this research were conducted with computing resources under the project bbp00044. This work is part of a collaborative project OASYS between different research groups and funded by the Federal Ministry of Research, Technology and Space, Germany, via grants 16ME0420K and 16ME0868K.

References

[1] H.-T. Chen, A. J. Taylor, and N. Yu, "A review of metasurfaces: Physics and applications," *Rep. Prog. Phys*., vol. 79, no. 7, 2016.

[2] L. Augel, F. Berkmann, J. Schlipf, O. Skibitzki, and I. A. Fischer, "Integration of nanophotonic structures with optoelectronic devices on the Si platform," *APL Photon.*, vol. 11, no. 2, 2026.

[3] C. Mai, A. Peczek, A. Kroh, J. Jose, S. Reiter, C. Wenger, and I. A. Fischer, "Towards a CMOS compatible refractive index sensor: Cointegration of TiN nanohole arrays and Ge photodetectors in a 200 mm wafer silicon technology," *Opt. Express*, vol. 32, pp. 29099–29110, 2024.

[4] Y. Yamamoto, P. Zaumseil, T. Arguirov, M. Kittler and B. Tillack, "Low threading dislocation density Ge deposited on Si (100) using RPCVD," *Solid-State Electron.,* vol. 60, no. 1, pp. 2-6, 2011.

[5] J. Schlipf, F. Berkmann, Y. Yamamoto, M. Reichenbach, M. Veleski, Y. Kawaguchi, F. Mörz, J. W. Tomm, D. Weishaupt, and I. A. Fischer, "Robust Si/Ge heterostructure metasurfaces as building blocks for wavelength-selective photodetectors," *Appl. Phys. Lett*., vol. 122, no. 12, 2023.

[6] J. Schlipf and I. A. Fischer, "Rigorous coupled-wave analysis of a multilayered plasmonic integrated refractive index sensor," *Opt. Express*, vol. 29, no. 22, pp. 36201–36210, 2021.

Optical responses from zero optical-path-length object

Da Yong Lee[1,†], Moongul Byun[1,†], Robert Magnusson[2], Jae Woong Yoon[1,*]

[1] Department of Physics, Hanyang University, Seoul 133-791, Korea
[2] Department of Electrical Engineering, University of Texas – Arlington, TX 76019, United States
*Corresponding author: yoonjw@hanyang.ac.kr

***Abstract*— We address a fundamental question – What is the ultimately minimal embodiment of optical objects that produce useful optical effects? We show that such an object does not require non-zero physical and optical-path-length volume. Two-dimensional polarizing sheets are the minimal optical objects and practically realizable using 2D materials or polarizing ceramics.**

***Keywords*— low-dimensional materials, photonic lattices, guided-mode resonances.**

I. Introduction

A common intuition in optics is that a structure becomes optically inactive when its optical path length and physical thickness simultaneously approach zero. In such an extreme sparsity limit, no phase delay can be accumulated within the material, and the elementary processes that give rise to reflection, diffraction, and scattering are therefore expected to disappear. From this perspective, a system with strictly vanishing optical path length would conventionally be regarded as incapable of producing any meaningful optical response.

Nevertheless, recent developments in atomically thin material systems challenge this conventional notion that finite optical path length is necessary for producing substantial optical effects. Experiments on atomic monolayer of transition-metal dichalcogenide and graphene sheets have demonstrated guided propagation of visible and infrared waves even as their characteristic optical path length effectively vanishes, indicating that optical functionality may persist in the limit of vanishing OPL.

In this study, we examine the limiting case of a susceptibility distribution whose optical path length is strictly zero. We show that zero-OPL δ(x) susceptibility is a conceptually minimal embodiment capable of supporting the fundamental processes of reflection, diffraction, and guided propagation, as well as their coherent combinations. Furthermore, when such zero-OPL sheets are arranged into resonant periodic arrays, their individual responses combine to yield pronounced and functionally useful optical effects that extend beyond previously reported single-sheet waveguiding phenomena. We briefly discuss the relevance of these findings to lower-frequency spectral regimes, where material platforms with exceptionally large polarizability are more readily available.

II. Results

We begin by considering a planar slab composed of a fictitious dielectric medium whose permittivity is defined to scale inversely with its physical thickness h such that

$$\varepsilon_s = 1 + L_\delta h^{-1}, \quad (1)$$

as schematically illustrated in Fig. 1A. When the slab thickness enters the deep-subwavelength regime $h \ll \lambda$, this construction approaches the behavior of a two-dimensional material whose optical path length becomes effectively vanishing. In the limit $h \to 0$, OPL thickness $h_{OPL}=\varepsilon_s^{1/2}h=(h^2+L_\delta h)^{1/2}$ of the slab tends to zero while the susceptibility integrated across the slab thickness, *i.e.*, $\int\chi\cdot dx = \int(\varepsilon_s-1)\cdot dx = L_\delta$, remains a non-zero constant at L_δ, as shown in Fig. 1B. Thus, even though h_{OPL} disappears in this limit, the persistence of this finite integrated susceptibility suggests that appreciable optical response may still arise from the slab. Surface dipole density S_P under unit applied electric field is determined by $S_p=\varepsilon_0\int\chi\cdot dx=\varepsilon_0 L_\delta$ which does not depend on h. Therefore, the vanishing-OPL thickness of this fictitious slab can be interpreted as a medium compression of 3D dielectric medium in to a 2D material while conserving the total electric dipoles of the medium which serves as the fundamental origin of optical effects.

More rigorous argument can be obtained directly from mathematical principles of the classical electrodynamics. By introducing an ideal zero-OPL δ-dielectric sheet into the Maxwell equations and imposing corresponding interface conditions, a noteworthy feature emerges: a discontinuity appears in the first-order spatial derivative of the tangential field normally across the sheet. This jump in the first-order derivative constitutes the electromagnetic signature of the zero-OPL δ-dielectric sheet and give rise to significant partial reflection even though the sheet has vanishing h_{OPL}. For plane-wave incidence on a zero-OPL δ-dielectric sheet, non-zero reflection coefficient $r_{s/p}$ are obtained for both transverse-electric (TE) and transverse-magnetic (TM) polarizations as

$$r_s = i\sin u_s \exp(iu_s) \text{ and } r_p = -i\sin u_p \exp(iu_p), \quad (2)$$

where the parameter $u_{s/p}$ is given by $u_s=\tan^{-1}(\sigma_\delta \sec\theta)$ and $u_s=\tan^{-1}(\sigma_\delta \cos\theta)$ with $\sigma_\delta=\pi\varepsilon_b^{-1/2}(L_\delta/\lambda)$.

Beyond reflection, zero-OPL δ-dielectric sheet also supports optical guiding for TE polarization. A fundamental TE guided-mode solution with effective index

$$n_f = n_b\sqrt{1+\sigma_\delta^2} \quad (3)$$

This guiding effect persists even in the weak-polarizability regime $\sigma_\delta << 1$ where $n_f \approx n_b(1+\sigma_\delta^2/2) > n_b$, ensuring that the guided mode remains robust.

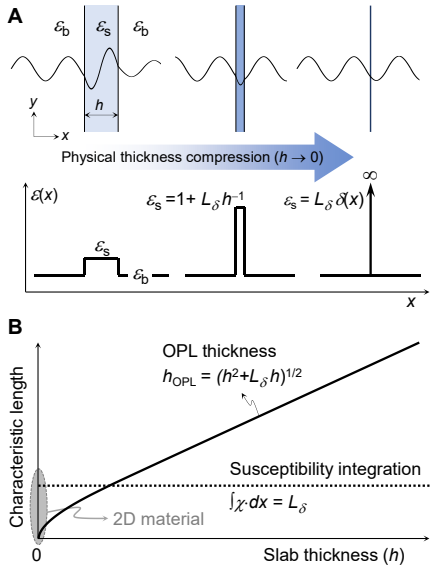

Figure 1 . Concept of a zero-OPL δ-dielectric sheet. A) Schematic representation of a fictitious dielectric slab which gradually morphs into a 2D dielectric material in its vanishing thickness limit ($h \to 0$). B) Essential h-dependence of the OPL thickness and susceptibility integration length of the fictitious dielectric slab.

We further investigate horizontal arrays of zero-OPL δ-dielectric sheets under TE-wave incidence. In this configuration, the elementary responses of individual sheets combine coherently across the array, giving rise to pronounced collective optical behavior.

We consider a subwavelength-periodic array structure schematically illustrated in Fig. 2A. Because each sheet produces partial reflection, as discussed earlier, the periodically arranged segments modulate the incoming wave and generate a set of discrete diffracted components propagating at well-defined angular orders. Under appropriate phase-matching conditions, one of these diffracted orders can couple to a guided mode supported by the zero-OPL sheet, producing a guided-mode resonance (GMR). This resonance manifests as a sharp spectral feature accompanied by strong variations in both the amplitude and phase of the reflected and transmitted fields. The phase-matching occurs when the in-plane wavevector of a diffraction order coincides with the effective propagation constant of the guided mode, leading to the pronounced resonant response characteristic of guided-mode resonance.

To validate the analytical prediction, we compare it with numerical simulations performed using rigorous coupled-wave analysis (RCWA). Since an ideal δ-function permittivity profile cannot be directly implemented within a conventional RCWA framework, we instead employ an approximate model in which each δ-sheet is replaced by an ultrathin high-index dielectric slab consistent with Eq. (1) in the deep-subwavelength OPL-thickness limit of $\varepsilon_s^{1/2}h << \lambda$. We confirm that, in a deep-subwavelength thickness limit of $h/\lambda < 10^{-2}$, this approximate-slab accurately yields propagation constants and mode profiles that closely match those of the ideal guided mode described by Eq. (3). This agreement confirms that the RCWA model faithfully captures the physics of the zero-OPL sheet in the vanishing-thickness limit

The predicted GMR clearly appears in our sufficiently converged RCWA model, as shown in Figure 2B for the angular spectrum map and Figure 2C for the spectral profile at angle of incidence θ = 20°. The simulated resonance exhibits characteristic GMR signatures, including an asymmetric Fano-like lineshape and the formation of a spectral gap near normal incidence. The detailed parameter values used in the simulation are summarized in the figure caption.

The RCWA spectra are in close agreement with the theoretical dispersion obtained from the phase-matching condition. In Fig. 2B, the calculated dispersion curves are overlaid and accurately trace the loci of the observed resonances. Furthermore, field distributions shown in Figs. 2D and 2E at λ/Λ=1.66 demonstrate that the resonant fields in the RCWA structure correspond closely to the guided mode supported by the ideal zero-OPL δ-dielectric sheet. This comparison confirms that the observed GMR originates from coupling to the underlying guided mode of the zero-OPL interface.

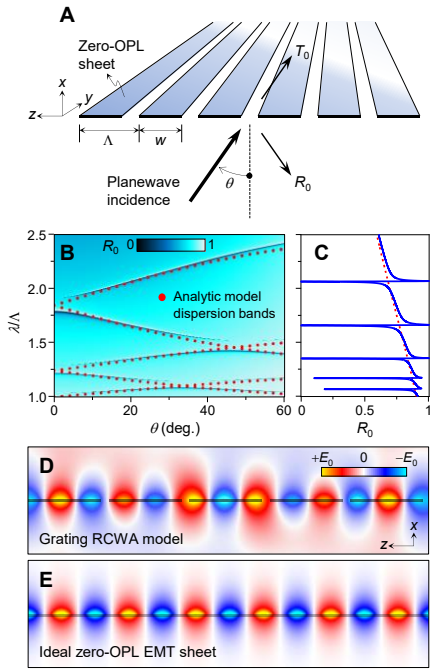

Figure 2. Horizontal guided-mode resonance. (a) Schematic

of a horizontal periodic array composed of zero-OPL δ-dielectric sheets. (b) Reflectance map calculated for an approximate-slab grating model (Λ = 1.5 μm, w = 1.35 μm, ε_s = 1+10^4, h = 0.15 nm) as a function of incidence angle θ and normalized wavelength λ/Λ. The overlaid red dots indicate analytic model dispersion bands for the fundamental guided mode supported in an ideal zero-OPL EMT sheet (L_δ = 1.35 μm). (c) Spectral reflectance profile (blue solid curve) extracted from (b) at θ = 20° compared with the non-resonant reflectance spectrum (red dotted curve) of an ideal zero-OPL EMT sheet predicted by Eq. (2). (d) Spatial distribution of electric field component Ey at the resonance center at λ/Λ = 1.66 and θ = 20° obtained from the RCWA model. (e) Corresponding guided-mode field profile Ey for the ideal zero-OPL EMT sheet at λ/Λ = 1.66.

III. Conclusion

We have identified a zero-OPL polarizing sheet as a conceptually minimal embodiment capable of producing fundamental optical responses. When such a sheet is appropriately structured to sustain resonant excitations, it can generate pronounced and practically useful optical functionality despite possessing vanishing optical-path-length thickness. An intuitive model and a corresponding theoretical framework have been developed to describe elementary processes such as partial reflection and guided propagation in this idealized zero-OPL limit.

Using rigorous numerical simulations, we confirm both the fundamental characteristics predicted by the idealized theory and the emergence of pronounced optical responses in horizontal arrays of zero-OPL sheets, arising from guided-mode excitations that operate in essentially the same manner as in their three-dimensional structural counterparts.

Intriguingly, our result suggest a conceptual framework for realizing optical or electromagnetic components that occupy minimal physical volume while remaining mechanically flexible and dynamically responsive. Such functionality may be implemented using 2D material platforms or other media exhibiting strong electric polarizability. In particular, dielectric constants on the order of 10^2 – 10^3 in the MHz–GHz frequency range are available in several ceramic systems, including $CaCu_3Ti_4O_{12}$, $Cu_2Ta_4O_{12}$, and $La_{15/8}Sr_{1/8}NiO_4$. Taking the approximation scheme in Eq. (1) into account, compact and lightweight optical components can be constructed while maintaining strong electromagnetic response.

Acknowledgments

This research was supported by the Leader Researcher Program (NRF-2019R1A3B2068083) from the National Research Foundation of Korea

References

[1] M. Lee, H. Hong, J. Yu, F. Mujid, A. Ye, C. Liang, and J. Park, "Wafer-scale δ waveguides for integrated two-dimensional photonics," Science, vol. 381, pp. 648–653, 2023.

[2] A. P. Ramirez, M. A. Subramanian, M. Gardel, G. Blumberg, D. Li, T. Vogt, and S. M. Shapiro, "Giant dielectric constant response in a copper-titanate," Solid State Commun., vol. 115, pp. 217–220, 2000.

[3] S. S. Wang and R. Magnusson, "Theory and applications of guided-mode resonance filters," Appl. Opt., vol 32, pp. 2606–2613 (1993).

[4] M. G. Moharam and T. K. Gaylord, "Rigorous coupled-wave analysis of planar-grating diffraction," J. Opt. Soc. Am., vol 71, pp. 811–818, 1981.

[5] J. W. Yoon, K. J. Lee, and R. Magnusson, Ultra-sparse dielectric nanowire grids as wideband reflectors and polarizers, Opt. Express 23, 28849 (2015).

Anomalous Reflecting Nonlocal Metasurfaces

Marten Musiol[1,2,*], Liam Shelling Neto[1,2], Steffen Sauer[1,2], Sebastian Häfner[1,2], Stefanie Kroker[1,2,3]

[1]Institute of Semiconductor Technology, TU Braunschweig, Braunschweig, Germany
[2]LENA Laboratory for Emerging Nanometrology, Braunschweig, Germany
[3]Physikalisch-Technische Bundesanstalt, Braunschweig, Germany
*Corresponding author: marten.musiol@tu-braunschweig.de

***Abstract*—This work presents an optimized nonlocal metasurface for anomalous reflection at a wavelength of $1550\ \mathrm{nm}$. Using optimization and Bezier-defined geometries, we achieved $90.92\ \%$ reflectivity at 38.5°. This approach enables compact, on-chip folded beam paths for gas sensing and enhanced rubidium and cesium isotope analysis by significantly increasing interaction lengths.**

***Keywords*— Anomalous Reflection, Nonlocal Metasurfaces, Semicontinuous Metaatoms, Rigorous Coupled-Wave Analysis (RCWA), Gas Sensing**

I. Introduction

Metasurfaces are thin optical devices, that can influence the phase, amplitude, and polarization of light. As those properties can be tailored precisely along the surface, a metasurface can reflect light with a defined angle of incidence θ_i to an arbitrarily defined angle of reflection θ_r. The ability to reflect light in a direction that deviates from the conventional law of reflection is the defining feature of anomalous reflecting metasurfaces. Metasurfaces with this behavior are called anomalous reflecting metasurfaces or anomalous reflecting metamirrors.

Anomalous reflecting metamirrors can be divided into two categories: local and nonlocal. The behavior of local metasurfaces is dictated by individual meta-units [1]. This means that the optical response of each element depends exclusively on its own geometry and is not influenced by interactions with neighboring structures. As a result, the entire metasurface can be considered as an array of independent building blocks. Though this approach does impose limitations of reflectivity on the anomalous reflecting metasurface.[2].

To overcome these limitations, nonlocal metasurfaces can be utilized. Here each individual structure contributes to the formation of one collective mode across multiple adjacent meta-units. The physical principle underlying nonlocal metasurfaces is the interaction of energy with evanescent surface waves traveling along the surface. While the metasurface modifies the electromagnetic field, these surface waves act as energetic channels that transport energy along the metasurface. The interference of these surface waves with the incident and transmitted fields results in a targeted redistribution of power density at the surface. This directs the energy in the desired direction and reflects it back into the free space [3]. In this way, the energy can not only be redistributed locally but also actively directed back toward the desired direction, theoretically, without causing energy losses. These mechanisms of energy circulation along the surface are essential for passively and losslessly realizing sophisticated functions such as anomalous reflection or directional changes [3].

Therefore, the response of the surface to the incident light for nonlocal metasurfaces is tailored by the interacting meta-units [1]. One meta-unit can be a distinct metaatom or one section of a larger metaatom. This holistic approach allows for higher precision in the description of the forming mode at the surface. Hence, the reflectivity can be increased compared to local anomalously reflecting metasurfaces. However, to design a highly efficient anomalous reflecting metasurface the dimensions of all meta-units have to be very precise. Hence, to consider all meta-unit interactions and design the perfect mode at the surface, simulations with optimization approaches are most promising.

Highly efficient anomalous reflecting metasurfaces allow for increasing the optical beam length in space-limited setups. Herriott cells are one configuration where an increased beam length is achieved by a folded light path. To shape this light path, Herriott cells use concave mirrors. Since metasurfaces are planar and significantly thinner than concave mirrors, they are better suited for compact integration. Hence, metasurfaces are a promising alternative to decrease the thickness of the cells and simplify the ability to integrate these cells into on-chip devices.

Another field of application is rubidium and cesium isotope analysis. Here, a folded light path is able to increase the interaction length between the light and the alkali vapor, similar to the approach proposed in [4]. This increased interaction length enhances the sensitivity of the measuring system and thereby lowers the limit of detection. These systems exploit the high absorption cross-sections of the alkali atoms at their respective D1 and D2 transitions. Consequently, the anomalous reflecting metamirrors must be designed specifically for these target wavelengths: $794.98\ \mathrm{nm}$ (D1) and $780.24\ \mathrm{nm}$ (D2) for rubidium, and $894.59\ \mathrm{nm}$ (D1) and $852.35\ \mathrm{nm}$ (D2) for cesium. Given the narrow linewidths of these transitions, the operation frequency of the metamirrors has to fit these wavelengths for maintaining high reflectivity at the exact resonance frequencies.

An example of a configuration that increases the beam length is shown in Figure 1. The beam path starts at the incoupling point. Afterwards it hits the first anomalous reflecting metasurface normally. The reflection of the anomalous

metasurface is now under an angle. This directs the beam path into a zig-zag configuration formed by regular reflecting metasurfaces. At the end of this section is another anomalous reflecting metasurface, which reflects the incoming light. The incoming light is incident under an angle and gets reflected normal to the surface. Now the light can couple back out into free space or be reflected back into another zig-zag configuration in the same way described. Each transition between two zig-zag configurations can be used as a point to rotate the next zig-zag path to the previous one. Thereby, the square shape depicted in Figure 1 can be achieved.

As described earlier, the rubidium and cesium analysis operates at distinct wavelengths. The same accounts for gas sensing applications that utilize Herriott cells. They have to operate at wavelengths matched to the absorption of the gases detected. Each wavelength needs a specific metasurface with distinct dimensions and materials designed for the exact wavelength. In this work, we focus on a design wavelength of $1550\ \mathrm{nm}$. This choice is motivated by the high maturity of silicon-on-insulator (SOI) fabrication processes, which allows for sub-nanometer control over the Bezier-defined geometries. By utilizing this established platform, we can precisely characterize the physical limits and challenges of nonlocal mode excitation. The methodology and the resulting design rules are inherently scalable, providing a direct blueprint for the realization of metasurfaces at the specific resonance frequencies required for rubidium and cesium analysis.

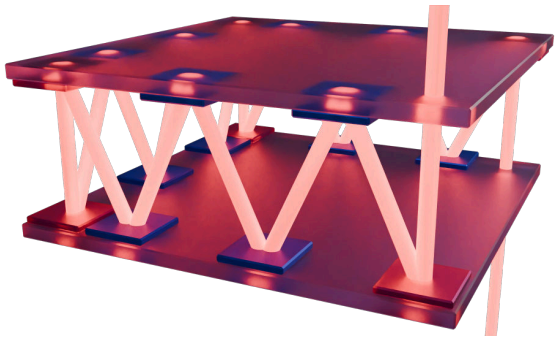

Fig. 1. Schematic configuration of the folded beam path utilizing anomalous reflecting metasurfaces. Inspired by the Herriott cell design, this setup increases the interaction length by folding the beam between two parallel substrates. The anomalous reflecting metasurface pairs in the corners (red) redirect the beam and rotate the propagation plane by $90°$, while regular reflecting metamirrors (blue) maintain the periodic zig-zag pattern.

II. Methods

The design of a nonlocal anomalous reflecting metasurface requires a holistic approach, as the individual contributions of each meta-unit and their mutual interactions must be fully accounted for. A high number of degrees of freedom is necessary to tailor both the meta-atoms and the gaps between them to excite the specific surface modes required. Since a single parameter change can influence the entire mode profile, even slight dimensional variations in one meta-unit may alter the overall functionality of the surface. This interdependency results in complex meta-atom geometries and necessitates a dedicated optimization approach, where the dimensions of each meta-unit serve as independent degrees of freedom.

The primary objective is to maximize the reflectivity of the metasurface at a specific anomalous angle, which serves as the figure of merit for the optimization. For this task, Rigorous Coupled-Wave Analysis (RCWA) offers several distinct advantages. Since the metasurface is treated as a periodic arrangement, RCWA leverages the Floquet-Bloch theorem to solve Maxwell's equations in Fourier space. This approach eliminates the need for full-volume meshing, thereby significantly reducing memory overhead and execution time compared to FDTD or FEM. Furthermore, RCWA inherently calculates the complex amplitudes of specific diffraction orders. For an anomalous reflector, this allows for the direct extraction of power flow into the target angle, bypassing the need for additional near-field to far-field transformations. Finally, as a frequency-domain method, RCWA provides high accuracy for monochromatic sources, such as the $1550\ \mathrm{nm}$ wavelength used in this work, while avoiding the dispersive errors or long stabilization times often encountered in time-domain simulations.

The optimization focuses on the shape and fill factor of each unit cell to define the diameter of each meta-unit. These parameters are defined by 20 control points, as illustrated in Figure 2. They are spaced equally along the y-direction with an optimizable lateral gap. To ensure symmetry along the x-axis, the points are mirrored across the y-axis. All points are connected using Bezier curves to prevent fabrication inaccuracies typically associated with sharp corners.

Fig. 2. Schematic visualization of the design approach for the Bezier-shaped metaatom. The unit cell is shown in gray and the metaatom in orange. Red markers indicate the control points used for optimization, while the purple line represents the resulting Bezier curve. For clarity, only 10 control points are displayed, whereas 20 points are utilized in the full optimization process. The incident wave propagates along the negative z-direction, and the reflected wave propagates along the positive z- and positive y-direction

III. Results and Discussion

To satisfy the design restraint of the anomalous reflecting metasurfaces described in Figure 1, the angle of incidence of the simulation is set to zero degrees. For this configuration the highest anomalous reflectivity the optimization was able to achieve so far is $R_{an} = 90.92\ \%$ for an angle of $38.5°$. It corresponds to the geometry shown in Figure 3. This figure also shows the angular reflectivity distribution. A fraction of the incident power is still redirected into parasitic diffraction orders, specifically the 0^{th} and the -1^{st} orders. Given that

the total reflectance of the metasurface is $R_{\mathrm{total}} = 93.51\ \%$, it follows that $2.59\ \%$ of the total intensity is shifted into these unwanted orders.

However, the optimization result is limited by several factors. The described power redistribution along the surface does not perfectly transfer to the desired reflection order if the geometry does not precisely match its condition. The constraints on the unit cell size and the height of the metaatom lower the degrees of freedom for the optimization and thereby limit the power redistribution. Additionally, the number of generations of the optimization was limited as well to save computational time. Future optimization runs with a higher number of generations are expected to further enhance the anomalous reflectivity.

Fig. 3. Visualization of the shape of the optimized metaatom (left) and corresponding Polar-Plot of the angle dependant reflectivity (right). The peak anomalous reflectivity for a wavelength of $1550\ \mathrm{nm}$ of $90.92\ \%$ is achieved at $38.5°$.

IV. Conclusion

In this work, we have developed an optimization-based design for a nonlocal anomalous reflecting metasurface at $1550\ \mathrm{nm}$. By utilizing a semicontinuous metaatom geometry defined by Bezier curves and a TPE optimization approach, we achieved an anomalous reflectivity of $R_{an} = 90.92\ \%$ for an angle of $38.5°$.

The ability to steer light at normal incidence with high efficiency is a crucial step toward the realization of compact, on-chip folded beam paths. Such setups, inspired by the Herriott cell, can significantly increase the interaction length for gas sensing or isotope analysis while maintaining a minimal footprint. The detection sensitivity can be increased by this increased interaction length.

Future work will focus on scaling the optimization to a higher number of generations to further suppress parasitic diffraction orders and approach the ideal lossless reflection regime. Additionally, the robustness of the optimized geometries against fabrication tolerances will be investigated. Following the experimental characterization of the fabricated metasurfaces, the measured performance data will be reintegrated into the optimization loop to further refine the designs and achieve even higher reflectivities.

Acknowledgments

This project has received funding from the European Research Council (ERC) under the European Union's Horizon Europe research and innovation program (Project Number [101170022]).

References

[1] S. C. Malek, A. C. Overvig, S. Shrestha and N. Yu, "Active nonlocal metasurfaces." *Nanophotonics*, vol. 10, no. 1, pp. 655–665, 2020.

[2] V. S. Asadchy, M. Albooyeh, S. N. Tcvetkova, A. Díaz-Rubio, Y. Ra'Di, and S. A. Tretyakov, "Perfect control of reflection and refraction using spatially dispersive metasurfaces," Phys Rev B, vol. 94, no. 7, 2016.

[3] A. Epstein and G. v. Eleftheriades, "Synthesis of Passive Lossless Metasurfaces Using Auxiliary Fields for Reflectionless Beam Splitting and Perfect Reflection," Phys Rev Lett, vol. 117, no. 25, 2016.

[4] G. Qi, Y. B. Huang, J. Huang, X. J. Lu, T. Yang and Z. S. Cao, "Highly sensitive spectral measurement of rubidium isotopes using open multi-pass cell in tunable diode laser absorption spectroscopy." *Journal of Analytical Atomic Spectrometry*, vol. 39(3), pp. 935–941, 2024.

Multi-frequency Amplification of Underwater Acoustic Signals

C. W. Park[1], H. J. Lee[1], J. H. Park[1], W. Choi[1,2,*]

[1] Korea Research Institute of Standards and Science (KRISS), Nondestructive Metrology Group, 267 Gajeong-ro Yuseong-gu, 34113, Daejeon, South Korea
[2] University of Science and Technology (UST), Department of Precision Measurement, 217 Gajeong-ro Yuseong-gu, 34113, Daejeon, South Korea
*Corresponding author: w.choi@kriss.re.kr

***Abstract*— Underwater detection of airborne sound is challenging because acoustic waves significantly attenuate when propagating from air into water. We present a meta-acoustic sensor combining a piezoelectric element and a perforated 3D-printed cavity. Quarter-wave resonance selectively amplifies weak airborne acoustic signals at multiple target frequencies underwater while suppressing background noise.**

***Keywords*— metamaterials, multi-frequency, signal amplification, underwater, acoustic waves.**

I. Introduction

Detecting airborne acoustic sources from underwater environments is challenging because acoustic waves undergo strong reflection and severe attenuation when propagating from air into water [1,2]. Resonant acoustic structures offer a potential solution by selectively amplifying weak signals at target frequencies. In particular, quarter-wave resonance cavities can enhance acoustic pressure through standing-wave formation within confined structures. Here, we propose a metastructure-based underwater acoustic sensor that exploits quarter-wave resonance to selectively amplify weak acoustic signals at multiple target frequencies. The sensor integrates a piezoelectric element with a perforated cavity structure designed to support multiple resonant modes. Our results demonstrate significant signal enhancement, achieving a maximum 43-fold increase in voltage response compared with a conventional configuration.

II. Methods

The proposed sensor is composed of a 3D-printed structure containing an off-center slit, which promotes bending-dominated deformation of the structure. Because bending stiffness is substantially lower than compressive stiffness, this deformation mode effectively reduces the acoustic wave speed within the structure. The resulting slow-wave effect enables quarter-wavelength resonance within a subwavelength cavity. Depending on the resonance order, mechanical stress is either concentrated or suppressed at the location where the piezoelectric element is attached. Specifically, stress maxima occur at odd multiples of the quarter-wavelength resonance, while stress minima appear at even multiples, enabling simultaneous amplification and suppression of multiple frequency components. The resulting stress modulation is converted into electrical signals by the piezoelectric element, producing frequency-selective signal amplification and suppression.

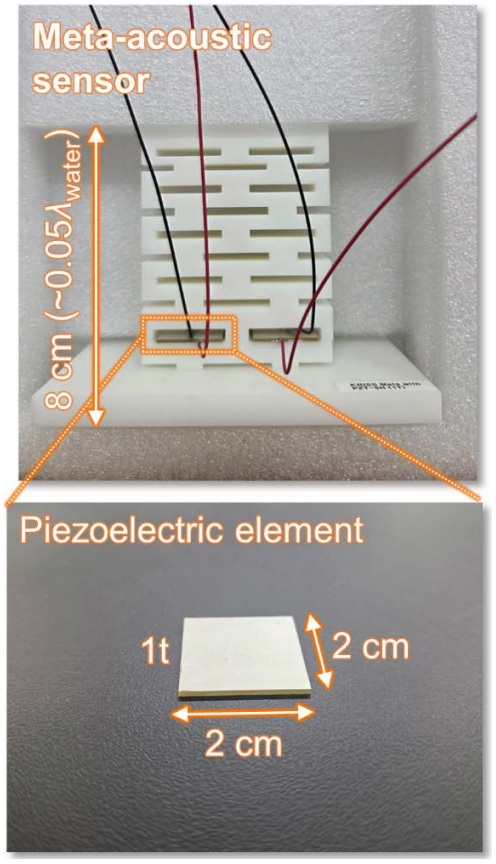

Fig. 1 Geometry of the meta-acoustic sensor composed of a metastructure integrated with a piezoelectric element.

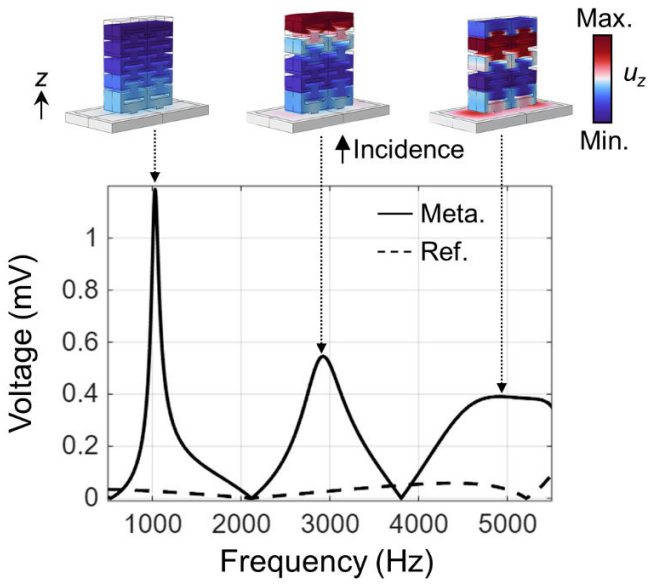

Fig. 2 Voltage response of meta-acoustic sensor. The pressure wave is incident along the z-direction, and the corresponding displacement distribution in the z-direction at the peak frequency is presented. "Meta." and "Ref." denote the metastructure-integrated sensor and the reference sensor without the metastructure, respectively.

III. Results and Discussion

- Selective amplification near 1, 3, and 5 kHz corresponding to odd multiples of the quarter-wave resonance, with suppression near 2 and 4 kHz.
- Up to a 43-fold increase in voltage response compared with the reference sensor without the metastructure.

IV. Conclusion

This study presented an underwater acoustic sensing strategy for enhancing weak airborne acoustic signals in underwater environments. The signal amplification mechanism of the metastructure-based acoustic sensor, arising from structural resonance, was systematically investigated. Our results confirmed that the proposed meta-acoustic sensor provides significantly improved sensitivity compared with a reference acoustic sensor. These results suggest that the proposed approach offers a promising pathway for high-sensitivity underwater detection and may be extended to advanced underwater sensing systems for airborne source monitoring.

Acknowledgments

This work was supported by the National Research Foundation of Korea (NRF) grand funded by the Korea government (MSIT,DAPA) (RS-2024-00464563).

References

[1] R. J. Urick, Principles of Underwater Sound, 3rd ed. (McGraw-Hill, 1983)..

[2] E. Bok, J. J. Park, H. Choi, C. K. Han, O. B. Wright, and S. H. Lee, Phys. Rev. Lett. 120, 044302 (2018).

Temporal Coupled Mode Theory for a Single Floquet-Sheet Resonator

Yao-Ting Wang* and Hsu-Hui Chou

Department of Photonics, National Sun Yat-sen University, Kaohsiung, 80424, Taiwan
*Corresponding author: ytwang@mail.nsysu.edu.tw

We develop a rigorous Temporal Coupled-Mode Theory (TCMT) specifically tailored for a single Floquet-sheet resonator governed by time-modulated conductivities. By invoking photon-number conservation during frequency conversion, we derive characteristic radiative decay rates and coupling coefficients that account for the frequency ratio between channels. We establish a systematic bridge to the Floquet Transfer Matrix Method (TMM), providing closed-form analytical expressions that map scattering parameters to the Drude-type physics of the sheet. Our model explicitly captures the resonant coupling between the 0th-order propagating channel and the -1st-order surface-mode channel. Validated by COMSOL numerical simulations, the theory remains robust even when intrinsic material loss is incorporated. This framework offers an intuitive pole-expansion representation for designing time-varying photonic interfaces.

***Keywords*— Temporal Coupled-Mode Theory, Transfer Matrix Method, Floquet-sheet resonator, time-varying media.**

I. Introduction

In the latest decade, the field of photonics has witnessed a major transition from spatially inhomogeneous structures to temporally modulated systems. Time-varying materials have opened up unprecedented avenues for controlling light-matter interactions, such as temporal aiming [1], multiple light conversion [2]. By modulating the constitutive parameters of a medium, on a timescale comparable to the optical cycle, researchers have demonstrated exotic phenomena including adiabatic frequency conversion [3], topological effects in photonic time crystals [4], and the electronic circuit for time-reversal wavefronts [5]. While conventional metamaterial/photonic crystals rely on spatial periodicity to control the wavevector, time-varying media utilize temporal modulations to redistribute energy across the frequency spectrum.

To provide a unified and analytically tractable description of these resonant systems, TCMT has emerged as a cornerstone in the photonic community. TCMT was firstly proposed by Fan and colleagues [6][7][8] to describe systems with energy conservation and time-reversal symmetry. In their a series of seminal articles, a resonator is characterized by its eigenfrequency, radiative decay rates, and coupling coefficients to external ports. For time-modulated systems, TCMT can be used as a powerful tool to separate different modal coupling. It allows for the description of frequency conversion as a resonant process, where energy is exchanged between different Floquet channels through a discrete set of coupling equations, ensuring that the complex physics of time-varying systems can be understood through a compact, intuitive pole-expansion representation.

Despite the success of TCMT in describing various time-varying photonic resonators, its application to Floquet-sheet resonators, specifically those governed by time-modulated conductivities/Drude weight, remains unexplored. While numerical approach like transfer matrix method (TMM) can simulate these systems, a rigorous analytical bridge that connects the macroscopic scattering parameters to the microscopic physics of the sheet is still missing. Particularly, the relationship between the surface modal excitation in the -1st Floquet channel and the resulting scattering in the 0th channel has not been fully formulated within a TCMT framework. This paper seeks to fill this gap by developing a TCMT model specifically tailored for a single Floquet sheet and establishing a systematic connection to the TMM. Furthermore, the underlying concepts and the mapping procedure established herein are generalizable to a wide range of other time-varying resonant systems.

II. Methods

Figure 1 illustrates a Floquet sheet whose surface current density obeys a lossless Drude-type dynamic equation $dJ/dt = \eta_0^{-1} W_p(t) E_x$, where η_0 is vacuum impedance and the Drude weight $W_p(t)$ is temporally modulated as

$$W_p(t) = W_{p0}\left(1 + 2\alpha\cos\Omega t\right). \quad (1)$$

If the surface modal excitation is described by a complex amplitude a, then the excitation dynamics induced by the Floquet sheet with modulation frequency Ω can be written in the coupled-mode form

$$\frac{da}{dt} = \left(-i\omega_s + \gamma_s\right)a + e^{i\Omega t}\boldsymbol{\kappa}^T \mathbf{s}_+ \quad (2)$$

where ω_s is the eigenfrequency of the surface mode, γ_s accounts for radiative leakage of the surface mode into the external scattering channels, and $\boldsymbol{\kappa}$ denotes the coupling coefficient between the incident waves and the surface excitation. The amplitude is normalized so that $|a|^2$ equals the energy stored in the surface mode. In the ideal lossless limit considered here, the intrinsic dissipation rate γ_i is set to be zero. In addition, the radiation from the Floquet sheet back into the propagating channels is described by

$$\mathbf{s}_- = C\mathbf{s}_+ + e^{-i\Omega t}\mathbf{d}a \quad (3)$$

where C is the direct S-matrix pertaining to the incoming and outgoing waves of the sheet, and **d** characterizes how the resonant surface excitation radiates into the external channels. The explicit time factors in Eq. (2) and (3) are introduced to satisfy the frequency matching condition to connect the input channel at ω_0 and the surface mode channel at $\omega_{-1} = \omega_0 - \Omega$.

When the incident wave $\mathbf{s}_+$ impinges on the Floquet sheet at a frequency ω_0, the time modulation enables frequency conversion between the propagating channels at ω_0 and the surface-mode channel centered around $\omega_{-1} = \omega_0 - \Omega$ so that the detuning entering the resonance denominator is $\omega_0 - \Omega - \omega_s$. Solving Eq. (2) and (3) in the frequency domain then yields the scattering relation

$$\mathbf{s}_- = S\mathbf{s}_+ = \left[C + \frac{\mathbf{d}\boldsymbol{\kappa}^T}{\gamma_s - i\left(\omega_0 - \Omega - \omega_s\right)}\right]\mathbf{s}_+ \quad (4)$$

To determine the radiative decay rate γ_s and the coupling vector **d** under our chosen normalization of the surface-mode amplitude, we invoke photon-number conservation for the frequency-conversion process. Although the sheet is temporally modulated and electromagnetic energy is not required to be conserved, a monochromatic conversion event still allows one to enforce conservation of the number of photons exchanged between the surface excitation at ω_s and the radiated waves at ω_0. With the normalization $|a|^2$ representing the energy stored in the surface mode, we define the surface-mode photon number as $N_s = |a|^2/\omega_s$. For the propagating channels, the photon flux is proportional to $N_0 = |\mathbf{s}|^2/\omega_0$. Hence, photon-number conservation requires

$$\frac{d}{dt}\left(\frac{|a|^2}{\omega_s}\right) = \frac{|\mathbf{s}_-|^2 - |\mathbf{s}_+|^2}{\omega_0} \quad (5)$$

The left-hand side represents the change of surface modal photon numbers in time, whereas the right-hand side is the photon numbers after the interaction with single Floquet-sheet resonator. Substituting Eq. (2) and its time-conjugate into the left-hand side of Eq. (5), it becomes

$$\frac{d}{dt}\left(\frac{|a|^2}{\omega_s}\right) = \frac{2\gamma_s|a|^2 + e^{i\Omega t}a^*\boldsymbol{\kappa}^T\mathbf{s}_+ + e^{-i\Omega t}a\boldsymbol{\kappa}^\dagger\mathbf{s}_+^*}{\omega_s} \quad (6)$$

Next, from Eq. (3), the intensity of the outgoing wave can be written as

$$|\mathbf{s}_-|^2 = |C|^2|\mathbf{s}_+|^2 + |\mathbf{d}|^2|a|^2 + e^{i\Omega t}a^*\mathbf{d}^\dagger C\mathbf{s}_+ + e^{-i\Omega t}a\mathbf{s}_+^\dagger C^\dagger\mathbf{d} \quad (7)$$

In the lossless background S-matrix, $|C| = 1$. By plugging Eq. (3) into the right-hand side of Eq. (5) yields

$$\frac{|\mathbf{s}_-|^2 - |\mathbf{s}_+|^2}{\omega_0} = \frac{|\mathbf{d}|^2|a|^2 + e^{i\Omega t}a^*\mathbf{d}^\dagger C\mathbf{s}_+ + e^{-i\Omega t}a\mathbf{s}_+^\dagger C^\dagger\mathbf{d}}{\omega_0} \quad (8)$$

Equating Eq. (6) and (8) for arbitrary $(a, \mathbf{s}_+)$ then fix the coefficients uniquely

$$2\gamma_s = \left(\omega_s/\omega_0\right)|\mathbf{d}|^2 \quad (9a)$$

$$\boldsymbol{\kappa}^T/\omega_s = \mathbf{d}^\dagger C/\omega_0 \quad (9b)$$

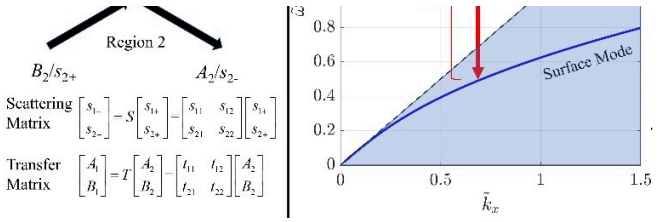

Fig. 1: (a) Schematic of the incident and outgoing wave components across the conducting sheet in region 1 and region 2. The corresponding scattering matrix *S* and transfer matrix *T* definitions are provided below. (b) Normalized dispersion diagram ($\tilde{\omega} = \omega/W_{p0}$ and $\tilde{k}_x = ck_x/W_{p0}$) illustrating the light line, the supported surface mode, and the frequency modulation process $\tilde{\Omega}$ coupling a propagating wave to the surface state.

III. Results and Discussion

It is noteworthy that we covers the functional form of the seminal temporal coupled-mode theory proposed by Fan et. al., [6]

$$S = \begin{bmatrix} r_0 & t_0 \\ t_0 & r_0 \end{bmatrix} - \frac{\gamma_s\left(r_0 + t_0\right)}{\gamma_s - i\left(\omega_{-1} - \omega_s'\right)}\begin{bmatrix} 1 & 1 \\ 1 & 1 \end{bmatrix} \quad (10)$$

where

$$\gamma_s = \left(\frac{\omega_s}{\omega_0}\right)\frac{2\alpha^2\eta_1^{-1}W_{p0}/\cos\theta_i}{\left(2\eta_1^{-1}/\cos\theta_i\right)^2 + \left(W_{p0}/\omega_0\right)^2} \quad (11a)$$

$$\omega_s' = \omega_s\left[1 - \frac{\alpha^2\left(W_{p0}/\omega_0\right)^2}{\left(2\eta_1^{-1}/\cos\theta_i\right)^2 + \left(W_{p0}/\omega_0\right)^2}\right] \quad (11b)$$

This correspondence is underpinned by the 2π phase difference between the reflection coefficient r_0 and transmission coefficient t_0, i.e., $r_0 + t_0 = e^{i\phi}\left(|r_0| + i|t_0|\right)$, under

the condition of identical surrounding materials. This structural identity demonstrates how the surface modal resonance within the -1st Floquet channel facilitates resonant scattering into the 0th channel.

Eq. (11a) also quantitively links the square of the modulation strength α^2, Drude weight W_{p0}, and the incident angle θ_i with the radiative rate, thereby elucidating the physical origin of the resonance in temporally modulated conducting sheet. Additionally, Eq. (11b) reveals that the surface-mode frequency ω_s' undergoes a subtle shift due to the temporal modulation. To ensure a well-defined resonance with minimal frequency deviation, maintaining a small W_{p0}/ω_0 ratio is essential, which necessitates that the modulation frequency Ω remains sufficiently higher than the excitation.

In Fig. 2, it is evident that the numerical results from COMSOL and the analytical predictions from the TCMT model exhibit an excellent fit across the entire frequency range, which validates the TCMT model. As the modulation strength α increases, the resonance peak in reflectance and the corresponding dip in transmittance broaden, indicating that stronger temporal modulation enhances the radiation loss and strengthens the coupling between the surface mode and the incident free-space wave.

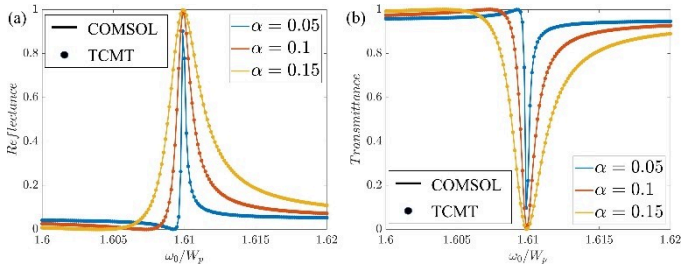

Fig. 2: (a) Reflectance and (b) transmittance as a function of the normalized frequency ω_0/W_p for various modulation strengths $\alpha =$ 0.05, 0.1, and 0.15. The solid lines represent the numerical results obtained from COMSOL Multiphysics, while the dot markers denote the analytical results derived from the TCMT.

IV. Conclusion

In conclusion, we have developed a comprehensive TCMT description for a single Floquet-sheet resonator and established a systematic connection to a Floquet transfer-matrix formulation. To determine the key parameters of the resonator, we introduce photon-number conservation for the frequency-conversion process, which necessitates a characteristic frequency ratio correction in the coupling coefficients to ensure physical consistency. This structural identity demonstrates how the surface modal resonance within the -1st Floquet channel facilitates resonant scattering into the 0th channel, effectively recovering the functional form of seminal TCMT while successfully incorporating the complexities of temporal modulation.

The analytical expressions derived via TMM provide a quantitative link between the modulation strength, Drude weight, and incident angle with the radiative decay rate, thereby elucidating the microscopic physical origin of the resonance in time-modulated-sheet systems. Our investigation into the effects of intrinsic material loss confirms that the simplified resonance form remains robust, with analytical predictions matching full-wave numerical results across a wide range of loss parameters. Furthermore, the symmetry of the coupling vectors confirms that the surface excitation maintains an even distribution due to the inherent mirror symmetry of the sub-wavelength sheet. The mapping procedure and underlying concepts established in this work are generalizable to a broad spectrum of time-varying resonant systems. These results provide a vital theoretical foundation for future explorations into multi-sheet configurations, non-reciprocal topological interfaces, and advanced periodic synthetic spaces in the frequency domain.

Acknowledgments

The authors acknowledge financial support from the National Science and Technology Council under Grant No. NSTC 113-2112-M-110-007-MY3.

References

[1] V. Pacheco-Peña, N. Engheta, Temporal aiming. Light Sci Appl 9, 129 (2020).
[2] X. Guo, Y. Ding, Y. Duan, & Xingjie Ni, Nonreciprocal metasurface with space–time phase modulation, Light Sci Appl 8, 123 (2019).
[3] K. Pang, M. Z. Alam, Y. Zhou, C. Liu, O. Reshef, K. Manukyan, M. Voegtle, A. Pennathur, & A. E. Willner, Adiabatic frequency conversion using a time-varying epsilon-near-zero metasurface. Nano Letters, 21(14), 5907-5913 (2021)
[4] E. Lustig, Y. Sharabi, & M. Segev, Topological aspects of photonic time crystals. Optica, 5(11), 1390-1395 (2018)
[5] H. Moussa, G. Xu, S. Yin, E. Galiffi, Y. Ra'di, & A. Alù, Observation of temporal reflection and broadband frequency translation at photonic time interfaces. Nature Physics, 19(6), 863-868 (2023)
[6] S. Fan, W. Suh, & J. D. Joannopoulos, Temporal coupled-mode theory for the Fano resonance in optical resonators. Journal of the Optical Society of America A, 20(3), 569-572 (2003)
[7] S. Fan, Photonic crystal theory: Temporal coupled-mode formalism. In: Photonic Crystals: Physics, Fabrication and Applications, edited by K. Inoue and K. Ohtaka, Springer, 431-456 (2004)
[8] Z. Zhao, C. Guo, & S. Fan, Connection of temporal coupled-mode-theory formalisms for a resonant optical system and its time-reversal conjugate. Physical Review A, 99(3), 033839 (2019)

Beam Steering in the Sub-Terahertz Band Using a Microbridge-Array Based Reconfigurable Intelligent Surface

Steffen Klingel[1,*], Lars Franke[1], and Marco Rahm[1]

[1]Department of Electrical and Computer Engineering and Research Center OPTIMAS, RPTU Kaiserslautern-Landau, Germany

*Corresponding author: steffen.klingel@rptu.de

***Abstract*—We present a MEMS-based reconfigurable intelligent surface (RIS) with switchable microbridges for sub-THz beam control. Simulations demonstrate a phase tuning range of 300° at 100 GHz with a reflection magnitude over 0.9 and a usable bandwidth exceeding 4 GHz. A 10x10 unit cell prototype was fabricated, demonstrating the feasibility of our design.**

***Keywords*— beam steering, wireless communication, MEMS, RIS.**

I. Introduction

As wireless communication systems move toward increasingly higher operating frequencies, extending into the terahertz (THz) range to support higher data rates, they encounter new challenges. These include shorter propagation distances and frequent blockage of line-of-sight links caused by obstacles such as buildings and vegetation [1,2]. Reconfigurable intelligent surfaces (RIS) have emerged as a promising approach to mitigate these limitations by enabling signals to be redirected around obstacles and dynamically focused toward one or multiple users [1-6]. This functionality is realized through a large array of RIS unit cells, each with individually controllable electromagnetic properties. By independently adjusting the phase of the reflected signal at every unit cell, the overall wavefront can be engineered to perform operations such as beamforming, beam steering, and beam splitting.

Traditional RIS implementations typically employ varactor diodes [5,6], which provide continuous capacitance tuning through a DC bias voltage, or PIN diodes, which allow only two discrete phase states [3,4]. However, when operating in the sub-THz frequency range, designing diode-based unit cells capable of achieving a phase tuning range close to 180° over a sufficiently wide bandwidth becomes increasingly challenging. This difficulty is often accompanied by a noticeable reduction in reflection amplitude. Consequently, the beamforming performance of RIS operating at sub-THz and THz frequencies remains significantly limited.

To address these limitations, we propose a MEMS-based RIS consisting of an array of switchable microbridges. The microbridges are fabricated from SiO_2 and copper on a silicon substrate with a metallized backside, which enables the application of a DC voltage between the bridges and the ground plane. By varying this voltage, a quasi-continuous mechanical deflection of the microbridges is induced. This mechanical actuation allows continuous tuning of the electromagnetic response of each unit cell, providing functionality analogous to varactor diodes used at lower frequencies. Figure 1 shows a drawing of the unit cell design with and without a voltage applied between the bridges and substrate backside.

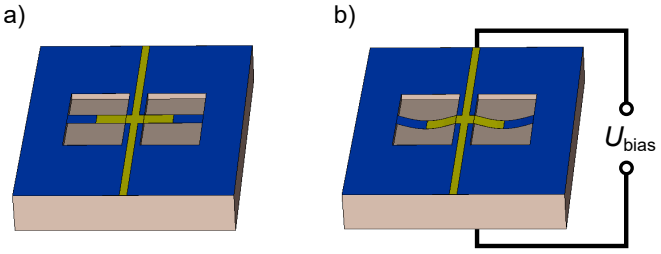

Fig. 1. Unit cell design based on two half-side metallized microbridges a) without applied voltage and b) with applied voltage.

II. Methods

First, we analyzed the S_{11}-parameters of the microbridge-based RIS unit cells in CST Microwave Studio to identify a geometry that enables a near-360° reflection phase shift at 100 GHz while maintaining a reflection magnitude $\geq$0.9.

After identifying a suitable geometry, we fabricated a prototype RIS consisting of 10×10 unit cells using standard lithography on 200 μm-thick, (100)-oriented silicon wafers. We dry-oxidized the wafers to form a 300 nm-thick SiO_2 layer. Fig. 2 shows a flowchart of the fabrication process.

First, we applied a positive photoresist (Microchemicals AZ1512HS) to the wafer and patterned it using a direct laser writer (Microtech LW405D). We then transferred the resulting pattern into the oxide layer via HF etching with buffered oxide etch (7:1), thereby defining the eventual lengths of the microbridges.

Next, we cleaned the wafer with acetone and isopropyl alcohol and applied a second layer of positive photoresist. We patterned this layer again with the direct laser writer and carefully aligned it to the holes in the oxide. Subsequently, we coated the wafer with 50 nm of titanium followed by 200 nm of copper using an electron beam evaporator (Pfeiffer Classic

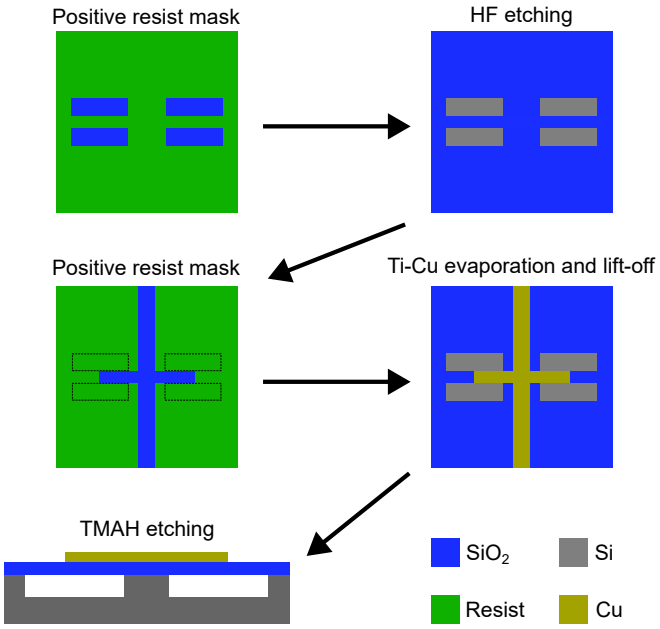

Fig. 2. Flowchart for the fabrication of a microbridge-based RIS. The upper and middle row show a top-view of the sample, the lower row a cross-section through the silicon wafer.

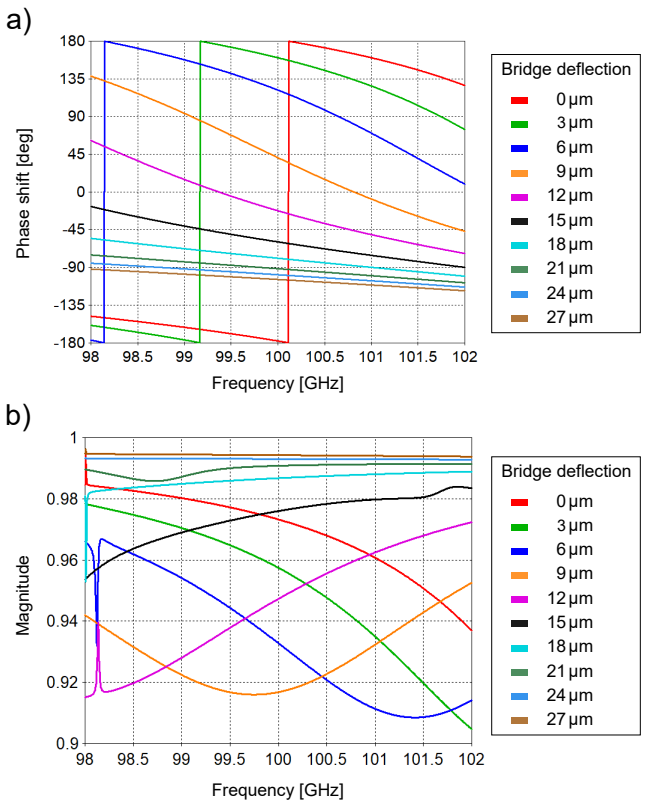

Fig. 3. Simulated S_{11}-parameters of the radiation reflected from a microbridge-based unit cell array shown in terms of a) phase shift and b) magnitude. Each curve corrresponds to a different maximum deflection of the bridges. The bridges are 750 μm long and 80 μm wide, with a 50 μm gap between them. The unit cells have a length and width of 1750 μm each. The silicon substrate is 200 μm thick.

500L). After performing a lift-off process, we obtained the transmission line and the half-side metallization of the bridges.

We then etched the exposed silicon in a 10% aqueous TMAH solution at 70°C for 75 minutes, which produced an etch depth of 30 μm. We rotated the unit cells by 45° with respect to the wafer flat, which allowed the TMAH solution to underetch the bridges. After etching, we first immersed the wafer in isopropyl alcohol and then dried it in air instead of using a nitrogen spray gun in order to protect the extremely thin bridges. Finally, we completed the fabrication of the RIS by flipping the wafer and coating the entire backside with 50 nm of titanium and 200 nm of copper using the electron beam evaporator.

III. Results and Discussion

From the unit cell simulations, we found that the deflection of the microbridges produces a phase shift in the reflected radiation, as expected. Figure 3a) illustrates the phase shift for microbridges with different maximum deflections as a function of the radiation frequency. In this configuration, the bridges have a length of 750 μm and a width of 80 μm, while the gap between adjacent bridges is 50 μm. The unit cell itself has dimensions of 1750 μm × 1750 μm. The thickness of the silicon substrate was fixed at 200 μm, corresponding to the thickness of the available wafers.

At an operating frequency of 100 GHz, the phase shift can be tuned over a range of approximately 300°, with the highest sensitivity observed at small deflections. Across the full simulated frequency range from 98 GHz to 102 GHz, the tuning range remains above 240°. In this range, the magnitude exceeds 0.9, indicating a usable bandwidth exceeding 4 GHz. Outside this range, the phase shift may still exceed 180°, which is sufficient for beam steering applications [7], but the reflection magnitude decreases to values below 0.9.

Since the geometry described above proved to be optimal in terms of both phase shift range and reflection magnitude, a first 10 × 10 unit cell RIS prototype was fabricated. Because the bridges required a width of 80 μm for best performance, while the desired etch depth was only 30 μm, complete underetching was geometrically not feasible. Therefore, holes with dimensions of 5 μm × 10 μm were etched into the oxide layer along the entire length of the bridges. This enabled the TMAH solution to underetch the microbridges independently of their size.

Figure 4 shows a microscope image of a single RIS unit cell before the final etching step in TMAH, as well as an SEM image of a bridge after TMAH etching and air drying. While the overall fabrication process was successful, the bridges exhibit a larger-than-expected initial bending toward the substrate. We suspect this to be caused by the surface tension of isopropyl alcohol pulling the bridges toward the silicon during drying.

Since the highest sensitivity of the bridges occurs at small deflections, and almost no phase shift is observed when the

bridge is bent more than 15 μm toward the substrate, this RIS prototype is not yet suitable for beam steering applications. To overcome this issue, we intend to repeat the fabrication process using a critical point dryer to evaporate the isopropyl alcohol, thereby significantly reducing the effects of surface tension.

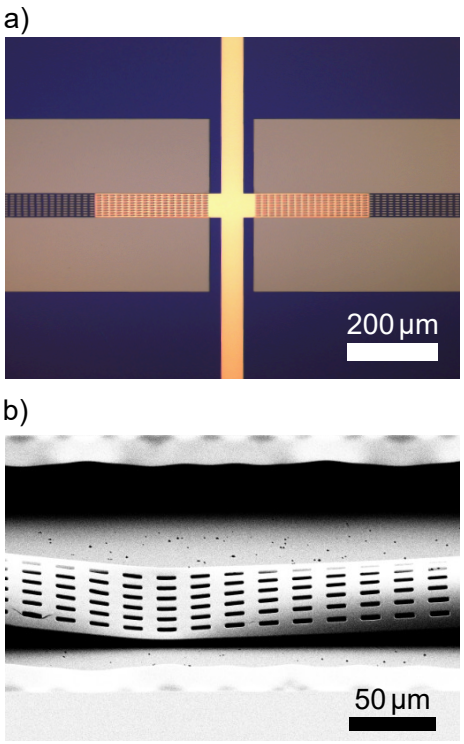

Fig. 4. a) Microscope image of a single unit cell before TMAH etching, b) SEM image of a bridge after TMAH etching and drying in air.

IV. Conclusion

We have presented the design, simulation, and initial fabrication of a MEMS-based RIS using switchable microbridges. Simulations demonstrated that the microbridge deflection enables a phase shift of up to 300° at 100 GHz and a usable bandwidth exceeding 4 GHz. A 10×10 unit cell prototype was successfully fabricated, validating the proposed fabrication approach. However, surface tension during air drying caused a large initial bending of the bridges, severely limiting the achievable phase tuning and rendering the current prototype unsuitable for beam steering applications. Future work will focus on optimizing the fabrication process using critical point drying to minimize surface tension effects, enabling fully functional RIS devices capable of dynamic beam control at sub-THz frequencies.

References

[1] C. Pan et al., "Reconfigurable Intelligent Surfaces for 6G Systems: Principles, Applications, and Research Directions," in *IEEE Communications Magazine*, vol. 59, no. 6, pp. 14-20, June 2021.

[2] M. Di Renzo et al., "Smart Radio Environments Empowered by Reconfigurable Intelligent Surfaces: How It Works, State of Research, and The Road Ahead," in *IEEE Journal on Selected Areas in Communications*, vol. 38, no. 11, pp. 2450-2525, Nov. 2020.

[3] X. Wan et al., "Reconfigurable Sum and Difference Beams Based on a Binary Programmable Metasurface," in *IEEE Antennas and Wireless Propagation Letters*, vol. 20, no. 3, pp. 381-385, March 2021.

[4] J. -B. Gros, V. Popov, M. A. Odit, V. Lenets and G. Lerosey, "A Reconfigurable Intelligent Surface at mmWave Based on a Binary Phase Tunable Metasurface," in *IEEE Open Journal of the Communications Society*, vol. 2, pp. 1055-1064, 2021.

[5] Alexander Wolff, Lars Franke, Steffen Klingel, Janis Krieger, Lukas Mueller, Ralf Stemler, and Marco Rahm, Continuous beam steering with a varactor-based reconfigurable intelligent surface in the Ka-band at 31 GHz. *J. Appl. Phys.* 21 September 2023; 134 (11): 114502.

[6] da Silva LG, Chu Z, Xiao P and Cerqueira S Jr. A (2023) A varactor-based 1024-element RIS design for mm-waves. *Front. Comms. Net*, 4:1086011.

[7] L. Cao, H. Yin, L. Tan and X. Pei, "RIS With Insufficient Phase Shifting Capability: Modeling, Beamforming, and Experimental Validations," in *IEEE Transactions on Communications*, vol. 72, no. 9, pp. 5911-5923, Sept. 2024

Assessing Monolithic and Thin-Film Silicon Metasurfaces for Ultrafast Pulse Applications

Klaudijus Midveris[1], Gvidas Klyvis[1], Erika Jonaitytė[1], Tomas Klinavičius[1], Andrius Žutautas[1], Mindaugas Juodėnas[1,*]

[1]Institute of Materials Science, Kaunas University of Technology, Lithuania
*Corresponding author: mindaugas.juodenas@ktu.lt

***Abstract*— This study evaluates crystalline and amorphous silicon metasurfaces as compact optics for ultrafast lasers. Using a 1030 nm, 270 fs laser, both platforms demonstrated over 90% spatial shaping efficiency. Although moderate temporal dispersion, increased pulse duration, and damage thresholds limit high-fluence use, this proves their relevance for low-power applications.**

***Keywords*— silicon metasurfaces, ultrafast optics, beam shaping, group delay dispersion, laser-induced damage threshold**

I. Introduction

Ultrafast lasers have become indispensable tools across various scientific and industrial domains, making a profound impact on laser processing of materials, spectroscopy, and imaging.[1–3] However, the traditional transmissive optical components required to manipulate these light fields present significant limitations; the complex optical setups required for these systems are often costly, bulky, and challenging to align.

Optical metasurfaces—dense 2D arrays of subwavelength metaatoms—offer a revolutionary alternative to traditional optics.[4–6] By engineering the phase, amplitude, and polarization response of these nanostructures, metaoptics allows for the combination of multiple functions in one essentially flat optical component.[7,8] Furthermore, this technology is highly compatible with standard semiconductor nanofabrication techniques, allowing for unprecedented precision.

Despite these transformative capabilities, most metasurface research until now has focused on continuous wave lasers, and applications for ultrafast lasers are still largely uncharted.[9,10] Deploying metasurfaces in the ultrafast regime requires overcoming specific spatiotemporal challenges, most notably the management of group delay dispersion (GDD) to prevent temporal pulse broadening and ensuring a sufficiently high laser-induced damage threshold (LIDT) to withstand intense peak powers.

To address this research gap, we present a comparative feasibility study of two distinct silicon-based metasurface platforms for ultrafast pulse applications: monolithic crystalline silicon (c-Si) and thin-film amorphous silicon (a-Si). While c-Si allows for the fabrication of high-aspect-ratio geometries, amorphous silicon offers a highly accessible, lower-profile alternative. By evaluating the LIDT and temporal dispersion characteristics of both platforms, we aim to demonstrate their viability as compact, passive elements for spatiotemporal beam shaping in integrated ultrafast systems.

II. Methods

To fabricate the metasurfaces, we employed standard electron beam lithography (EBL) followed by a lift-off process to define the etching mask. The silicon nanostructures were subsequently patterned using a continuous inductively coupled plasma reactive ion etching (ICP-RIE) process with a fluorine-based mixed gas chemistry of SF_6 and C_4F_8. This exact protocol was utilized for both the thin-film a-Si samples on fused silica substrates and the monolithic c-Si samples. For the latter, the absence of an etch-stop layer typically introduces aspect-ratio-dependent etching (ARDE) challenges. However, this effect was effectively mitigated by employing the Pancharatnam-Berry (PB) phase delay configuration; because the local pattern density remains uniform across the device in a PB design, we successfully achieved uniform final aspect ratios of approximately 10.

Experimental characterization of the metasurfaces was performed using a Yb:KGW ultrafast laser system (Pharos, Light Conversion) operating at a fundamental wavelength of 1030 nm with a pulse duration of 270 fs in a custom micro-spectroscopy setup. To precisely evaluate the temporal effects of the metasurfaces on the transmitted pulses, temporal pulse broadening were measured using a scanning autocorrelator (GECO, Light Conversion) and frequency-resolved optical gating (FROG). A single diffraction order was spatially filtered in a conjugate back-focal plane and fed into the autocorrelator, ensuring that the temporal measurements explicitly isolated the specific beam generated by the metasurface, eliminating background interference. Finally, the laser-induced damage threshold (LIDT) for both silicon platforms was evaluated using the standard S-on-1 testing protocol to determine their power-handling capabilities and overall feasibility for practical ultrafast applications.

III. Results and Discussion

The spatial wavefront shaping capabilities were validated by analyzing the back focal plane images of the transmitted 1030 nm beam. Using PB-phase metasurfaces, we encoded a variety of phase profiles, including spherical, cylindrical lenses, OAM generators, axicons, and computer-generated holograms. To evaluate the efficiency of these elements, we measured the amount of light deflected into a diffraction order by a simple linear phase gradient—a deflector. Both the monolithic c-Si and thin-film a-Si platforms achieved a relative efficiency of >95%. This excellent performance closely aligned with the theoretical efficiency predicted by numerical simulations when optimizing the metaatoms as half-waveplates.

S-on-1 testing was performed to determine the power-handling capabilities of both silicon platforms using the 1030 nm, 270 fs laser source. The monolithic c-Si metasurfaces exhibited a robust damage threshold of 32.8 mJ/cm^2 (99.0 mJ/cm^2 unstructured reference substrate). The thin-film a-Si metasurfaces demonstrated a slightly lower, yet highly practical, LIDT of 11.1 mJ/cm^2 (41.3 mJ/cm^2 unstructured reference substrate). Both values fall comfortably within the operational fluences of typical ultrafast oscillators and amplifiers used in micro-spectrometry, confirming the feasibility of both platforms without rapid structural and optical degradation.

To evaluate the temporal effects of the metasurfaces, one transmitted diffraction order of the PB-based deflector device was isolated using the micro-spectrometry setup. Autocorrelation and FROG measurements of the pulses passing through both the a-Si and c-Si metasurfaces revealed a deflection angle dependent temporal broadening. At low deflection angles (<10 deg) the added temporal FWHM is negligible and is comparable to reference Si slab (~270 fs). Beyond 10°, the FWHM increases non-linearly to approx. 320 fs at 20° deflection. This finding demonstrates that such passive flat optics sufficiently maintains temporal integrity of the ultrafast pulses.

When comparing the two platforms, a practical trade-off emerges. Monolithic c-Si avoids the constraints of an etch-stop layer and exhibits a moderately higher laser-induced damage threshold (LIDT). Conversely, thin-film a-Si offers a more accessible, cost-effective, and substrate-versatile fabrication route while matching the spatial and temporal optical performance of its crystalline counterpart.

However, a candid evaluation of the measured LIDT values dictates the immediate practical scope of these devices. While these thresholds are reasonable for nanoscale silicon structures, they fundamentally cannot compete with the damage resistance of macroscopic, low-index refractive optics or specialized dielectric mirror coatings used in high-energy laser amplifiers. Consequently, the deployment of these metasurfaces as direct replacements in high-peak-power beamlines is currently unfeasible.

Instead, the true potential of these silicon metasurfaces lies in low-power ultrafast pulse applications. Because they can combine multiple optical functions—such as simultaneous beam deflection, focusing, and polarization control—into a single, compact element, they are perfectly suited for integration into systems where fluences are low, space is tight, and alignment of multiple closely spaced components is cumbersome. Future work will focus on implementing these ultrafast-grade metasurfaces into integrated low-power devices, such as custom-built multiphoton microscopy assemblies, or compact ultrafast spectroscopy systems. By targeting these specific low-energy regimes, silicon metasurfaces can successfully reduce the footprint, cost, and alignment complexity of ultrafast optical setups without risking optical damage.

Acknowledgments

This project has received financial support from the Research Council of Lithuania (LMTLT), agreement No. S-MIP-24-4. This work was supported in part by EU Horizon Europe under the INFRACHIP project, grant No. 101131822.

References

[1] Syubaev, S. et al. “Direct laser printing of chiral plasmonic nanojets by vortex beams,” Optics Express, vol. OE 25, pp. 10214–10223, 2017.
[2] Jin, Y. et al. “Dynamic modulation of spatially structured polarization fields for real-time control of ultrafast laser-material interactions,” Optics Express, vol. OE 21, pp. 25333–25343, 2013.
[3] Kontenis, G., Gailevičius, D., Jonušauskas, L. & Purlys, V. “Dynamic aberration correction via spatial light modulator (SLM) for femtosecond direct laser writing: towards spherical voxels,” Optics Express, vol. OE 28, pp. 27850–27864, 2020.
[4] Kamali, S. M., Arbabi, E., Arbabi, A. & Faraon, A. “A review of dielectric optical metasurfaces for wavefront control,” Nanophotonics, vol. 7, pp. 1041–1068, 2018.
[5] Ding, F., Pors, A. & Bozhevolnyi, S. I. “Gradient metasurfaces: a review of fundamentals and applications,” Reports on Progress in Physics, vol. 81, pp. 026401, 2017.
[6] Yu, N. et al. “Light Propagation with Phase Discontinuities: Generalized Laws of Reflection and Refraction,” Science, vol. 334, pp. 333–337, 2011.
[7] Chen, W. T., Zhu, A. Y. & Capasso, F. “Flat optics with dispersion-engineered metasurfaces,” Nature Reviews Materials, vol. 5, pp. 604–620, 2020.
[8] Balthasar Mueller, J. P., Rubin, N. A., Devlin, R. C., Groever, B. & Capasso, F. “Metasurface Polarization Optics: Independent Phase Control of Arbitrary Orthogonal States of Polarization,” Physical Review Letters, vol. 118, pp. 113901, 2017.
[9] Shcherbakov, M. R. et al. “Ultrafast all-optical tuning of direct-gap semiconductor metasurfaces,” Nature Communications, vol. 8, pp. 17, 2017.
[10] Divitt, S., Zhu, W., Zhang, C., Lezec, H. J. & Agrawal, A. “Ultrafast optical pulse shaping using dielectric metasurfaces,” Science, vol. 364, pp. 890–894, 2019.

Physics-Guided Inverse Design of Broadband Low-Frequency Underwater Acoustic Metamaterials

Krupali Donda[1], Vatsal Patel[1], Yash Shah[1], Vimi Patel[1,*]

[1] Faculty of Engineering Sciences and Technology, Adani University, Ahmedabad

*Corresponding author: vimi8720@gmail.com

***Abstract*—Broadband low-frequency acoustic absorption is constrained by large wavelengths and high-dimensional design complexity. We propose a physics-guided inverse design framework using a Conditional Invertible Neural Network (cINN) for a 20-parameter multilayer acoustic metamaterial absorber. Trained on one million Latin Hypercube Sampling (LHS) samples and validated via Transfer Matriacx Method (TMM), it achieves $< 0.3\%$ error.**

***Keywords*— Acoustic metamaterials, low frequency absorption, machine learning, inverse design.**

I. Introduction

Recent advancements in machine learning have drastically changed the design paradigm of acoustic metamaterials by enabling data-driven exploration of complex design spaces. However, conventional design methodologies still largely rely on forward simulations and large-scale parametric sweeps to estimate desired responses, which are computationally expensive and often constrained by intuition-driven exploration [1]. While gradient- based and evolutionary optimization methods have enhanced automation, they still remain reliant on the use of iterative numerical computations and become inefficient in case of highly dimensional and multi-constrained design spaces. Additionally, the traditional absorber architecture based on canonical resonators restricts bandwidth, tunability, and structural diversity. To mitigate the effect of these limitations, a robust inverse model that can directly relate the target functionality to structural parameters is essential. Data-driven neural models offer a promising solution by learning complex nonlinear relationships between geometry and the acoustic response, while incorporating physics-driven loss functions to enforce governing physical constraints and ensure physically consistent predictions [2].

In this work, we propose a physics-guided inverse design framework based on a Conditional Invertible Neural Network (cINN) for a 20-parameter multilayer AMA. The model directly retrieves structural parameters from a target absorption spectrum while ensuring physical consistency. The presented method opens new avenues for automating the metasurface design process and enables a more generalized and broader scope of optimal designs beyond acoustic applications by incorporating physics-based loss functions to ensure physically consistent and realistic solutions.

II. Methods

The proposed approach aims to develop an inverse design framework to predict the structural parameters for a given spectrum of absorption coefficients in the frequency range of 1-1000 Hz. The following subsections provide a comprehensive elucidation for each stage of the adopted pipeline.

A. Metamaterial Parameterization And Acoustic Response

Each unit of the employed structure consists of 10 layers of rubber substrate with a few hollow layers and a rigid backing at the bottom [3], as illustrated in Fig. 1 (a). Each layer of the coating is perceived as a combination of multiple layers of rubber with distinct equivalent parameters [3] (Fig. 1 (b) and (c)).

The entire structure possesses 16 distinct geometric parameters and 4 material parameters, which were primarily utilized in computing the broadband absorption spectrum with careful examination and strict adherence to the analytical derivation of the complex absorption determination presented in [3]. Subsequently, an extensive dataset was constructed consisting of 1,000,000 rows of the aforementioned 20 sensitive parameters and the corresponding computed absorption coefficients. This dataset was generated randomly using the Latin Hypercube Sampling (LHS) method while ensuring compliance to their respective predefined structural limits and their corresponding absorption coefficient values.

B. Computational Model And Implementation

Following data generation, we trained the conditional Invertible Neural Network (cINN) to build the aforementioned inverse design framework. Fig. 1 (d) illustrates the workflow of the developed model. The proposed network includes a spectrum encoder that transforms the 1000-frequency absorption spectrum into a 128-dimensional embedding vector, forcing the network to learn essential spectral features instead of memorizing the noise. Subsequently, the 20-dimensional parameter sets and the embedded vector from the training subset were utilized to train 8 identical conditional affine coupling blocks for 250 epochs. Each block comprises a 3-layer Multi-Layer Perceptron (MLP) with LeakyReLU activations, responsible for transforming the input parameter sets. These blocks collectively function in two possible directions: the forward pass during training and the reverse pass during testing.

Fig. 1. Physics-guided inverse design framework for broadband underwater acoustic metamaterials. (a–c) Multilayer unit-cell configuration with 20 design parameters (16 geometric, 4 material). (d) Conditional Invertible Neural Network (cINN) architecture mapping 1000-point absorption spectra (1–1000 Hz) to structural parameters, generating 20 candidate designs per target. (e) Predicted absorption spectra demonstrating high-fidelity full-spectrum reconstruction.

For each training epoch, we employed the Negative Log-Likelihood (NLL) as the loss function, averaged across the entire training batch, which is given by (1).

$$\text{NLL} = \text{mean}\left(\frac{1}{2}\|\mathbf{z}\|^2 - \log|\det(\mathbf{J})|\right) \tag{1}$$

Here, $\frac{1}{2}\|\mathbf{z}\|^2$ represents the squared L_2 norm of the latent variable, and $-\log|\det(\mathbf{J})|$ is the log-determinant of the Jacobian matrix that accounts for volume distortion during the transformation. Cosine annealing was consequently applied after each epoch to control the learning rate and fine-tune the optimization process.

Each target spectrum, alongside 20 independent Gaussian vectors, undergoes reverse processing through the entire network, producing 20 different parameter sets, each conditioned for the same target, explicitly addressing the one-to-many mapping between geometry and acoustic absorption, and thereby exploring different regions of the solution space.

C. Theoretical Validation

With the intent to evaluate the performance of the model, we constructed a Transfer Matrix Method (TMM) physics engine, based on the analytical derivation of the absorption spectra proposed in [3], to compute the absorption spectra using the predicted candidate sets. Since the proposed framework yields 20 possible solutions to a target, the deterministic physics engine was implemented to select the best configuration among them. This engine computes the predefined acoustic equations and compares the Root Mean square error (RMSE) of each candidate, thereby identifying the parameter set with minimal spectral variance. The use of this evaluation measure was mainly to filter the final result, ensuring the candidate isolation which best represents the extreme resonance points and general topology of the target spectrum.

III. Results and Discussion

This section analyses the trained conditional Invertible Neural Network (cINN) model on unknown test samples. To strictly assess the effectiveness of the model, we inspected several different evaluation measures on the entire test data. The mean spectral relative error of the proposed model came out to be 0.2932%, with the minimum value of 0.0046% respectively. Moreover, the model achieved a full-spectrum average Root Mean Square Error (RMSE) of 0.00108624 and a Mean Absolute Error (MAE) of 0.00076246. Subsequently, Fig. 1 (e) compares the absorption spectra for the top three performing designs of two representative test samples, where each candidate successfully replicates the targeted spectrum with high precision, thereby demonstrating the fidelity and robustness of the proposed model.

IV. Conclusion

In this work, we proposed a cINN-based inverse design framework for broadband underwater acoustic metamaterials

across 1–1000 Hz. On 100,000 unseen samples, the model achieves a mean spectral RMSE of 0.00109, MAE of 0.00076, and a mean relative error of 0.29%. Unlike ref. [3], that employs MLP limited to a single averaged absorption metric, our framework solves the full-spectrum inverse problem and generates 20 diverse candidate designs per target, addressing the one-to-many nature of inverse design. Coupled with a TMM-based physics filter, the pipeline delivers validated absorber configurations in a single inference pass.

REFERENCES

[1] G. Ma and P. Sheng, "Acoustic metamaterials: From local resonances to broad horizons," *Science Advances*, vol. 2, no. 2, p. e1501595, 2016.

[2] K. Donda, P. Brahmkhatri, Y. Zhu, B. Dey, and V. Slesarenko, "Machine learning for inverse design of acoustic and elastic metamaterials," *Current Opinion in Solid State and Materials Science*, vol. 35, p. 101218, 2025.

[3] N. Gao, M. Wang, X. Liang, and G. Pan, "On-demand prediction of low-frequency average sound absorption coefficient of underwater coating using machine learning," *Results in Engineering*, vol. 25, p. 104163, 2025.

Conditional Diffusion Modeling for Low-Frequency Underwater Acoustic Absorber Design

Vatsal Patel[1], Vimi Patel[1], Yash Shah[1], Krupali Donda[1,*]

[1] Faculty of Engineering Sciences and Technology, Adani University, Ahmedabad

*Corresponding author: krupali.donda@adaniuni.ac.in

***Abstract*—Broadband low-frequency acoustic absorption is constrained by high-dimensional design complexity and inverse-problem non-uniqueness. We propose a physics-guided Conditional Diffusion Model (CDM) for inverse design of a 20-parameter underwater acoustic metamaterial absorber. Trained on 1,000,000 LHS samples and validated via TMM, the framework achieves 0.1065% best-of-20 error on 100,000 test samples.**

***Keywords*— Acoustic metamaterials, Inverse design, Conditional diffusion model, Physics-guided learning**

I. Introduction

The attenuation of low-frequency underwater noise remains challenging due to long acoustic wavelengths and impedance mismatch between water and conventional absorbers [1]. Multilayer acoustic coatings with internal cavities have shown strong absorption performance in the 1–1000 Hz range. A representative multilayer rubber coating proposed by Gao et al. [2] depends on twenty geometric and material parameters, making exploration of the design space computationally expensive despite accurate forward prediction using equivalent medium theory and the TMM.

Recent machine learning approaches have accelerated forward prediction and inverse design of acoustic metamaterials [3]. However, deterministic models such as feed-forward neural networks, tandem networks, and conditional variational autoencoders reduce the inherently one-to-many inverse problem to a single solution. This limitation becomes more significant when only the average absorption coefficient is used, as spectral information is lost and multiple distinct structures may produce identical responses. To address this challenge, this work proposes a physics-guided Conditional Diffusion Model for inverse design of underwater acoustic metamaterial coatings, capable of generating multiple physically consistent candidate designs for a target average absorption coefficient.

II. Methods

The proposed inverse design framework is illustrated in Fig. 1(a). The material architecture follows a 10-layer configuration with rigid backing and hollow sub-layers, represented by 20 sensitive variables (16 geometric and 4 mechanical parameters). We adopt the analytical TMM formulation of [2] to compute the average absorption coefficient and build a large-scale dataset using LHS.

A lightweight Multi-Layer Perceptron (MLP) surrogate is first trained to map normalized parameters to absorption coefficient and then frozen. During diffusion training, this frozen surrogate provides physics guidance through a consistency term, while the conditional denoiser uses timestep and target-conditioned embeddings with Feature-wise Linear Modulation (FiLM) blocks under a cosine noise schedule. Two pivotal losses were examined for computing the gradients: the noise prediction loss and the physics loss carried out by the frozen surrogate model. Subsequently, The total training loss is given by

$$\mathcal{L}_{\text{total}} = \mathcal{L}_{\text{noise}} + \lambda\, \mathcal{L}_{\text{physics}}, \tag{1}$$

where $\mathcal{L}_{\text{noise}}$ is the denoising score-matching loss, $\mathcal{L}_{\text{physics}}$ is the MSE between surrogate-predicted and target absorption, and λ is linearly ramped over the first 40 training epochs. At inference, the model generates 20 candidate parameter sets for each target, and the best candidates are selected using TMM verification, enabling one-to-many inverse design with physical consistency.

An extensive dataset of 1,000,000 samples was generated using Latin Hypercube Sampling (LHS) within the predefined parameter bounds, each entry comprising the 20 structural parameters and the corresponding TMM-computed average absorption coefficient.

A. Conditional diffusion model and implementation

Following dataset construction, a CDM was trained on the normalised 20-parameter space. The conditional denoiser employs sinusoidal timestep embeddings and a target-conditioned embedding fused via Feature-wise Linear Modulation (FiLM) blocks, which adaptively scale and shift intermediate feature maps based on the target absorption value. A cosine noise schedule governs the forward diffusion process over $T{=}500$ timesteps. Training optimises Eq. (1) with λ ramped over 40 epochs. The forward surrogate achieves $R^2{>}0.99$, confirming its suitability as a differentiable physics proxy. At inference, 20 candidate sets are generated by independently denoising 20 Gaussian noise vectors conditioned on the same target.

B. Theoretical validation

A TMM physics engine based on [2] computes the average absorption coefficient for each of the 20 predicted parameter sets. The candidate with minimum absolute relative error relative to the target is retained, enforcing physical correctness independently of the learned model.

Fig. 1. Physics-guided Conditional Diffusion Model for inverse design of broadband low-frequency underwater acoustic metamaterials. (a) Multilayer unit-cell configuration with 20 design parameters (16 geometric, 4 material). (b) CDM architecture: frozen MLP surrogate provides physics guidance via composite loss ($\mathcal{L}_{\text{noise}} + \lambda\mathcal{L}_{\text{physics}}$) with FiLM-conditioned denoiser under cosine noise schedule. (c) Embedded design space showing structured variation with target absorption coefficient. (d) Heatmap of TMM-validated spectra across target levels 0.1–1.0. (e) Best-of-20 reconstructed absorption spectra demonstrating accurate target recovery.

III. Results and Discussion

The trained CDM was evaluated on 100,000 unseen test samples using TMM-verified best-of-20 selection. Model performance is quantified by two complementary metrics. The mean *single-sample* relative error, the raw performance of one generated design without selection is 2.9634%, establishing the intrinsic generative quality of the model. The *best-of-20* mean relative error, where the TMM physics filter selects the optimal candidate from 20 independently generated designs, is 0.1065%, with a minimum of 0.00% and a maximum of 5.0718%. The model further achieves RMSE of 0.000422 and MAE of 0.000298 on the best-of-20 selected designs (Fig. 1(e)).

IV. Conclusion

A physics-guided CDM is proposed for inverse design of low-frequency underwater acoustic metamaterials (1–1000 Hz). On 100,000 unseen samples, it achieves a best-of-20 mean relative error of 0.1065%, Root Mean Square Error (RMSE) of 0.000422, and MAE of 0.000298 using TMM-verified candidate selection. Unlike [2], the proposed CDM directly solves the inverse problem and generates 20 diverse candidate designs per target without iterative optimization. Future work will address full spectral targets and experimental validation.

References

[1] N. Gao and K. Lu, "An underwater metamaterial for broadband acoustic absorption at low frequency," *Applied Acoustics*, vol. 169, p. 107500, 2020.

[2] N. Gao, M. Wang, X. Liang, and G. Pan, "On-demand prediction of low-frequency average sound absorption coefficient of underwater coating using machine learning," *Results in Engineering*, vol. 25, p. 104163, 2025.

[3] K. Donda, P. Brahmkhatri, Y. Zhu, B. Dey, and V. Slesarenko, "Machine learning for inverse design of acoustic and elastic metamaterials," *Current Opinion in Solid State and Materials Science*, vol. 35, p. 101218, 2025.

Actively Tunable EIT in Strongly Coupled Toroidal Terahertz Metamaterials

Lavi Kumar Vaswani[1,*], Bhagwat Singh Chouhan[2], Rohith K M[2], Sirsendu Ghosal[2], Anuraj Panwar[1], P.K. Giri[2] and Gagan Kumar[2,3]

[1]Department of Physics and Materials Science and Engineering, Jaypee Institute of Information Technology, Noida, 201309, Uttar Pradesh, India

[2]Department of Physics, Indian Institute of Technology Guwahati, Guwahati, 781039, Assam, India

[3]Department of Physics, Indian Institute of Technology Ropar, Rupnagar, 140001, Punjab, India

*Corresponding author: lavivaswani37@gmail.com

***Abstract*—Active controlled metamaterials are crucial for advancement of terahertz technology. This study demonstrates actively tunable electromagnetically induced transparency, achieved by modulating phase of vanadium dioxide through temperature variation. Active transmission modulation of approximately 85% is observed. These results indicate strong potential for developing active components in toroidal terahertz photonics.**

***Keywords*— metamaterials, terahertz, active tunable metamaterial, toroidal.**

I. Introduction

Electromagnetically induced transparency (EIT) in terahertz photonics is the key research interest in recent years. It is caused by the destructive interference between the probe and pump beams and is usually explained by a three-level atomic system [1]. EIT results in a narrow transparency window in an otherwise opaque medium [2], thus it has enormous application in non-linear devices and slow light devices [3], [4], [5], [6]. The applications of traditional EIT are elusive due to rigorous conditions such as very low temperature, high-intensity laser, etc. Recently, artificially designed materials, commonly known as metamaterials (MM) are used to mimic the EIT-like effect at room temperature.

The studies so far have largely focused on the passively tunable EIT behavior. The active tunability of EIT is highly desirable for various applications, such as photoconductive material, thermally controlled superconducting metamaterials, and graphene. Numerous researchers have shown the modulation of EIT by integrating graphene-based patterns in metamaterials [7]. But very few studies focus on phase-changing materials like vanadium dioxide (VO_2).

In this paper, we experimentally demonstrated the actively controlled EIT in the THz regime. The metamaterial comprises of two toroidal resonators. Both resonators couple together and open an EIT window at 0.55 THz. A VO_2 layer is grown on quartz substrate and sandwiched between quartz and polyimide substrate. The external temperature of VO_2 is increased gradually to achieve the modulation of EIT. An on-to-off modulation is observed in simulation results.

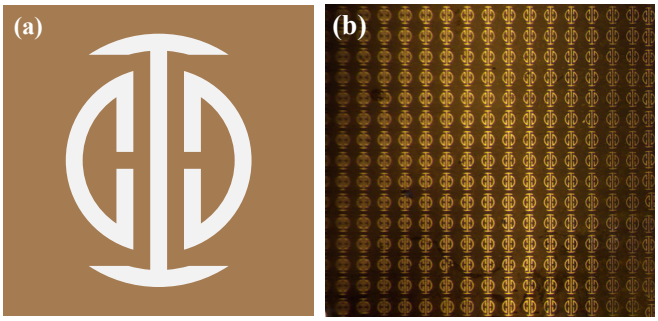

Fig. 1. (a) Unit cell geometry of the proposed metamaterial. (b) Microscopic image of fabricated metamaterial.

II. Methods

Our geometry consists of 2 main parts: firstly, the substrate and metal-based MM, the design consists of two toroidal resonators shown in unit cell (see Fig. 1(a)). These two resonators couple together and an EIT-like effect is observed. Secondly, the VO_2 layer over a quartz substrate, which is used to actively tune the EIT effect. The designed MM and the arrangement of MM, polyimide, VO_2 and quartz. The MM structure is of aluminum and has a thickness, $t = 200nm$, and VO_2 layer is 1.5 μm thick. The microscopic image of experimentally fabricated sample is shown in Fig. 1(b). The optical properties of VO_2 is described using Drude model which is expressed as [8]:

$$\varepsilon(\omega) = \varepsilon_\infty - \frac{\omega_p^2}{\omega^2 + i\gamma\omega} \tag{1}$$

$$\omega_p = \sqrt{\frac{\sigma}{\sigma_0}}\,\omega_p(\sigma_0) \tag{2}$$

Where, $\varepsilon_\infty = 12$, and ω_p is the plasma frequency, equation 1 is utilized to plot real and imaginary part dielectric constant versus frequency at different conductivities to achieve active modulation of EIT response.

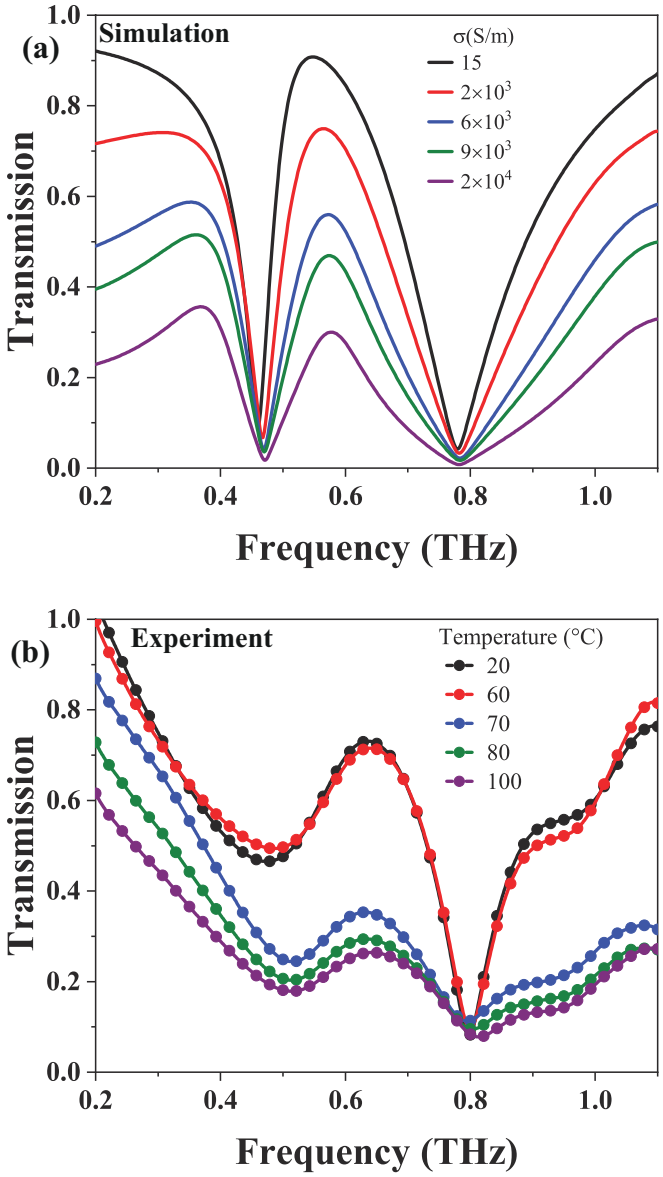

Fig. 2. (a) Modulation of Transmission with variation of conductivity in simulation. (b Modulation of transmission with variation of environmental temperature in the experiment.

III. Results and Discussion

The transmission spectrum of the complete geometry and its modulation with varying conductivity of VO_2 is depicted in Figure 2. The transmission window at 0.55 THz arises due to the frequency detuning of bright-bright mode resonators. The black solid trace represents the transmission spectrum for the proposed metamaterial (MM) at a conductivity of 15 S/m. In contrast, the violet trace shows the transmission spectrum when the conductivity of VO_2 is 20,000 S/m, representing the insulating and conductive phases, respectively. The transmission spectra for different conductivity values are illustrated in Figure 2 (a). Figure 2 (b) demonstrates experimental modulation of transmission response with varying temperature, the black circle trace shows transmission at room temperature, and the violet circle trace shows transmission at 100°C.
It clearly shows that as the conductivity of VO_2 increases, the EIT window is diminishes. This active tuning is achieved experimentally by increasing the external temperature. As we know, VO_2 is a phase transition material, and changes its phase from dielectric to conductive at a transition temperature of 67°C, which is further validated by experimental results.

IV. Conclusion

In conclusion, we experimentally demonstrated an actively tunable EIT by bright-bright mode coupling in toroidal THz metamaterials. The bright-bright mode coupling results in a narrow transparent window at 0.55 THz. Additionally, VO_2 is employed with the MM structure to actively control the EIT-like effect by varying its conductivity. In this case, the peak of the EIT window can be controlled. It is noted that the transparency peak of the EIT effect reduces from 90% at the insulating phase to 30% at the conductive phase. Ultimately, we can tune the EIT window by actively using VO2, which can be greatly utilized in the fabrication of modulators, switches, and slow light devices.

Acknowledgments

The authors AP and GK acknowledge Science and Engineering Research Board (SERB), India, under Grant CRG/2021/002187. The author LKV wishes to acknowledges INUP I2I under Grant 5(1)/2021-NANO, in part by the Centre for Nanotechnology, IIT Guwahati, & MeitY for the kind support. LKV further acknowledge Council for Scientific and Industrial Research (CSIR), India, for senior research fellowship (SRF).

References

[1] K.-J. Boller, A. Imamoğlu, and S. E. Harris, "Observation of electromagnetically induced transparency," *Physical Review Letters*, vol. 66, no. 20, pp. 2593, 1991.
[2] S. Zhang, D. A. Genov, Y. Wang, M. Liu, and X. Zhang, "Plasmon-induced transparency in metamaterials," *Physical review letters*, vol. 101, no. 4, pp. 047401, 2008.
[3] Z. Wei, X. Li, N. Zhong, X. Tan, X. Zhang, H. Liu, H. Meng, and R. Liang, "Analogue electromagnetically induced transparency based on low-loss metamaterial and its application in nanosensor and slow-light device," *Plasmonics*, vol. 12, no. 3, pp. 641–647, 2017.
[4] P. Pitchappa, M. Manjappa, C. P. Ho, R. Singh, N. Singh, and C. Lee, "Active control of electromagnetically induced transparency analog in terahertz MEMS metamaterial," *Advanced Optical Materials*, vol. 4, no. 4, pp. 541–547, 2016.
[5] A. A. Kutuzova, S. Li, B. Ma, Q. Li, and M. V. Rybin, "Polarization-independent BIC-based electromagnetically induced transparency," *ACS Photonics*, vol. 12, no. 8, pp. 4289–4295, 2025.
[6] B. X. Wang, Y. Sun, W. Zhou, Y. Chen, G. Yang, H. Xiong, and Z. Huang, "Metamaterial-Based Electromagnetically Induced Transparency," *Advanced Functional Materials*, pp. 2508025, 2025.
[7] S. Qu, and Y. Gao, "Design of a graphene-based plasmonic-induced transparency structure for optical switching, sensing, and slow-light applications," *Optics Express*, vol. 33, no. 21, pp. 45267–45280, 2025.
[8] Q. Zhang, G. Zhang, Z. Che, J. Zhu, Y. Feng, and R. Qiu, "Polarization-insensitive electromagnetically induced transparency-like and dual-band absorption based on graphene and vanadium dioxide metamaterials," *Optics Communications*, vol. 530, pp. 129164, 2023.

Interference Induced Complex Nonlinearities in Metal-ITO Metasurfaces

Christopher Stevens[1,2], Matthew Klein[1,2], Ashley Luo[2], Dennis Walker[2], Joshua R. Hendrickson[2], Ivan Avrutsky[3], Shivashankar Vangala[2,*], Maxim Sukharev[4,5]

[1]KBR, Beavercreek, OH, USA
[2]Air Force Research Laboratory, Sensors Directorate, Wright-Patterson AFB, OH, USA
[3]Dept. of Electrical and Computer Engineering, Wayne State University, Detroit, MI, USA
[4]College of Integrative Sciences and Arts, Arizona State University, Mesa, AZ, USA
[5]Department of Physics, Arizona State University, Tempe, AZ, USA
*Corresponding author: shivashankar.vangala.2@us.af.mil

***Abstract*— We show that Lorentz-dispersive nonlinearities are essential to describe the second- and third-harmonic responses from a metal-ITO metasurface with high fidelity. Details of a nonlinear-oscillator model that yields closed form angular dependences for second- and third-harmonic generation to describe the experimentally measured angular resolved spectra are presented.**

***Keywords*— metasurfaces, nonlinearities, indium-tin-oxide, hydrodynamic model, second-harmonic generation.**

I. Introduction

Nonlinear metasurfaces offer a compact platform for frequency conversion, enabling precise control over second-harmonic and third-harmonic generation [1]. A particularly effective architecture combines plasmonic resonators with epsilon-near-zero (ENZ) media like indium tin oxide (ITO), which exhibit large, tunable nonlinear responses near their ENZ wavelength [2]. These metal-dielectric-metal structures can strongly confine optical energy and support multiple, interfering radiation pathways.

However, accurately predicting the behavior of these systems is a significant challenge. Simplified models that neglect the frequency dependence (dispersion) of the material's nonlinear coefficients, $\chi^{(2)}$ and $\chi^{(3)}$, often fail. Near the ENZ point, treating these parameters as static constants misrepresents the phase of the nonlinear polarization, leading to incorrect predictions of interference effects and the final angular emission pattern. This work investigates resonant split-ring resonator (SRR)/ITO/Au metasurfaces using a combined numerical and analytical approach.

II. Methods

The study utilized a metasurface composed of gold split-ring resonators (SRRs) fabricated on an indium-tin-oxide (ITO) film, which was deposited on a continuous gold ground plate to ensure reflection-only operation (Fig. 1). The device's nonlinear optical response was characterized using a tunable femtosecond laser in a reflection-geometry microscope. Second- and third-harmonic generation (SHG and THG) signals were collected and analyzed for various input polarizations. Angle-resolved datasets between the SRR orientation and the input laser polarization were acquired not by moving the sample, but by rotating the polarization. Rigorous calibration, background subtraction, and power-scaling tests were performed to ensure data accuracy and confirm the perturbative nature of the harmonic generation.

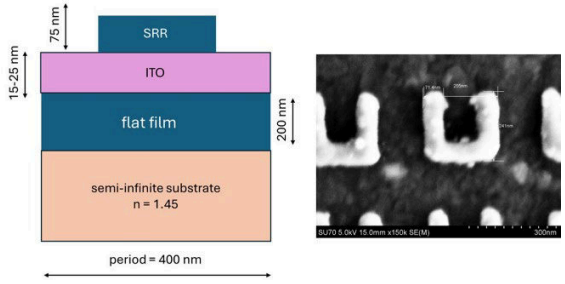

Fig. 1 Schematic of the (SRR)/ITO/Au structure along with an SEM image of the fabricated split-ring resonator.

The modeling framework employs an FDTD solver where gold is described by a nonlinear hydrodynamic model [3-4]. The crucial ITO layer is modeled with three increasing levels of fidelity: as a linear dielectric, then by adding static nonlinear susceptibilities ($\chi^{(2)}$, $\chi^{(3)}$), and finally by implementing frequency-dispersive Lorentz-pole nonlinearities.

III. Results and Discussion

A comparison between experimental second-harmonic generation (SHG) spectra and simulations reveals the critical

role of material properties in accurately modeling the metasurface's response. The experimental data shows two distinct SHG peaks corresponding to orthogonal pump polarizations (Fig. 2). Models that only account for nonlinearities from the metallic components, or that treat the indium tin oxide (ITO) layer with a simple, frequency-independent nonlinearity, fail to reproduce these results. Specifically, a model with a static, non-dispersive $\chi^{(2)}$ for the ITO layer also fails to match the measured polarization contrast and the relative amplitudes of the harmonic peaks, demonstrating that a more sophisticated description is necessary.

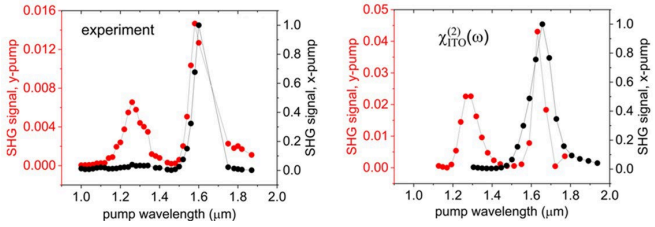

Fig. 2 Total SHG versus pump wavelength for x polarized (black circles, right axis) and y polarized (red circles, left axis) excitation. (left) experiment (right) simulations with a dispersive $\chi^{(2)}$ for ITO.

The key insight is that excellent agreement with the experiment is only achieved when the ITO's second-order susceptibility, $\chi^{(2)}$, is modeled as a dispersive, frequency-dependent parameter as described by equation 1. This advanced model correctly captures the position, relative intensity, and spectral shape of the SHG peaks.

$$\chi^{(n)}(\omega) = \frac{B_n}{\Omega_n^2 - \omega^2 - i\gamma_n\omega} \quad (1)$$

Expanding on this, we demonstrate that a model incorporating Lorentz-dispersive nonlinearities for ITO is essential to reproduce not only the spectra but also the experimentally measured angular patterns for both SHG and THG, whereas simpler, static models consistently fail. Our analysis reveals that the enhanced harmonic generation arises not from ENZ field concentration alone, but from the complex interplay between the SRR-induced modal fields and the intrinsically dispersive ITO nonlinearities [5].

To provide a physically interpretable framework, we developed a compact analytical model that treats the metasurface as a driven nonlinear oscillator. This model consists of coupled equations of motion for the x and y axes, each with distinct effective mass, damping, and restoring forces to capture the SRR's structural anisotropy. A weak cubic anharmonic potential is introduced to the system, which, when perturbed by the linear motion driven by the pump field, generates the second- and third-harmonic responses. By solving these equations perturbatively, we derive closed-form expressions for the SHG and THG intensities as functions of the input polarization angle. The most critical feature of this model is that the coefficients for the angular basis functions are treated as complex numbers. This complexity is not merely a fitting parameter but is physically significant: the magnitude and phase of each coefficient encode the intricate interference between different radiation pathways, capturing phase delays arising from material dispersion, propagation within the multilayer stack, and geometry-dependent radiation patterns. By fitting this model to the experimental data, we can extract these complex amplitudes, allowing us to deconstruct the final angular emission patterns into the fundamental contributions and their relative phases.

IV. Conclusion

In conclusion, this work demonstrates that accurately modeling the metasurface's second- and third-harmonic generation requires incorporating the dispersive nature of ITO's nonlinearities, as simpler static models fail. This approach is successful because it correctly captures the complex phase interference between different radiation pathways, which governs the observed angular emission patterns. This physical picture is further validated by a compact, driven nonlinear oscillator model that relies on complex coefficients to encapsulate the crucial phase relationships between these interfering pathways. This framework not only reconciles experiment and theory but also provides a practical route for the inverse design of metasurfaces with tailored, angle-dependent nonlinear emission.

Acknowledgments

This work was supported by the U.S. Air Force Office of Scientific Research. All simulations were made possible through the DOD High Performance Computing Modernization Program.

References

[1] Krasnok, A.; Tymchenko, M.; Alù, A. Nonlinear Metasurfaces: A Paradigm Shift in Nonlinear Optics. Materials Today 2018, 21 (1), 8–21.

[2] Reshef, O.; De Leon, I.; Alam, M. Z.; Boyd, R. W. Nonlinear Optical Effects in Epsilonnear-Zero Media. Nat Rev Mater 2019, 4 (8), 535–551.

[3] Ciracì, C.; Pendry, J. B.; Smith, D. R. Hydrodynamic Model for Plasmonics: A Macroscopic Approach to a Microscopic Problem. ChemPhysChem 2013, 14 (6), 1109–1116.

[4] Clark, M. R.; Shah, S. A.; Piryatinski, A.; Sukharev, M. Harnessing Complexity:Nonlinear Optical Phenomena in L-Shapes, Nanocrescents, and Split-Ring Resonators. J Chem Phys 2024, 161 (10), 104107.

[5] Stevens, C.E., Klein, M., Luo, A., Vatrano, G., Walker Jr, D.E., Vangala, S.R., Hendrickson, J.R., Avrutsky, I. and Sukharev, M., Interference-Engineered Metal-ITO Metasurfaces for Tailored Second- and Third-Harmonic Emission. ACS Applied Optical Materials 2025, 3(12), 2910-2922.

POSTERS

Photonic Crystals, Lasers and Photonic Devices

11 contributions · pp. 1718–1747

Enhancement of Spontaneous Decay Rate in Hybrid Photonic Nanocavities

Themistoklis Deloudis[1,*], Angus Crookes [1], Angela Demetriadou [1]

[1]School of Physics and Astronomy, University of Birmingham, UK
*Corresponding author: txd383@student.bham.ac.uk

***Abstract*—Structured optical environments modify the spontaneous decay rate of quantum emitters. Ultra high emission rates are often hindered by either the diffraction limit or material losses. We design a hybrid photonic nanocavity with extreme enhancement of the spontaneous decay rate, not often seen in diffraction-limited photonic cavities. Our new design can easily form a quantum network, with applications in quantum technology.**

***Keywords*— hybrid cavities, Purcell factor, emission rate enhancement, photonic crystal, plasmonic antenna.**

I. Introduction

Optical environments modify the spontaneous emission rate of quantum emitters, either enhancing or suppressing it [1]. Spontaneous emission in a photonic environment is quantified by the Purcell factor

$$F_P^m = \frac{3}{4\pi^2}\left(\frac{\lambda_m}{n}\right)^3 Q_m Re\left[\frac{1}{\tilde{V}_m}\right] \quad (1)$$

where λ_m corresponds to the wavelength of the m^{th} photonic mode, n refers to the refractive index of the environment surrounding the emitter and Q_m,$\tilde{V}_m$ are the quality factor and the mode volume of the mode experiences, respectively.

While many different photonic environments exist, one can classify them into two broad categories: dielectric and plasmonic. Here, we concentrate on nanocavities (i.e. cavities with nanosized features). Dielectric nanocavities, for example formed with photonic crystals, retain photons for long times, but they are diffraction limited. On the other hand, plasmonic nanocavities confine light into deep subwavelength scales, but exhibit high ohmic and radiative losses. To address these limitations, hybrid photonic nanocavities have been proposed [2]. In this work, a scalable hybrid photonic design is proposed, operating in the optical frequencies which demonstrates unprecedented enhancement of the spontaneous enhancement of the spontaneous decay rate. In contrast to other hybrid designs [7], a plasmonic dimer antenna is integrated inside a photonic nanobeam, at the point where the electric field of the latter is maximum. In this way, the scattering losses are mostly mitigated, enabling simultaneously ultra-high Q factor and subwavelength mode volume to achieve extremely high Purcell factors.

II. Hybrid Cavity Design

Our design operates at 780nm and combines a periodically patterned photonic nanobeam made of Si_3N_4 [3] and a gold dimer antenna integrated in the central air hole of the former, as graphically shown in Fig. 1a) and b). The radius of each air hole is $r = 52.67$nm, while the photonic crystal lattice constant is $\alpha = 262$nm. The cavity has a constant height of $h = 300$nm and is wider in the center; namely $b_0 = 558$nm, gradually tapered down to $b_m = 458$nm to the edges. This introduces a band gap at the edges of the waveguide, preventing photons of $\lambda = 780$nm from escaping and, therefore, minimising scattering losses and forming a cavity. In the absence of plasmonic components, the nanobeam exhibits resonant cavity modes at $\lambda = 780$nm, $\lambda = 767$nm and $\lambda = 756$nm. The lowest order mode, depicted in Figure 1c), corresponds to $\lambda = 780$nm and has a quality factor $Q = 1.3 \times 10^7$ and mode volume $V = 1.1\lambda^3$. The plasmonic component is a gold dimer antenna that consists of two identical faceted spheres of radius $r_p = 24$nm and facet radius $r_f = 6$nm. The distance between the spheres is set to 1nm, which yields extremely strong electric fields. By placing a dielectric spacer of permittivity ϵ_{sp}^{rel} between the facets, we can tune the resonant frequencies of the plasmonic antenna and, thus, control the detuning with respect to the nanobeam modes.

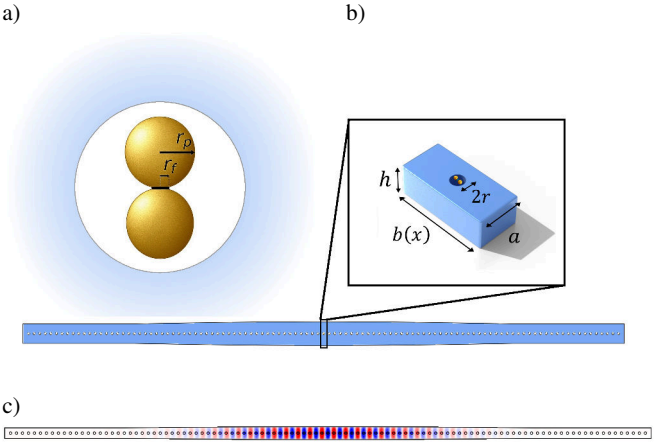

Fig. 1: a) Close up view of the central air hole of the hybrid photonic - plasmonic nanocavity. b) Depiction of the central unit cell. c) Lowest order mode of the isolated photonic nanobeam, at $\lambda = 780$nm

III. Spontaneous Decay Rate Enhancement

It is often desirable to decompose a photonic system into normal modes, especially if one wants to explore its interaction with quantum emitters. However, to account for the dispersive and lossy nature of gold, we use Quasi Normal Mode (QNM) formalism [4]. This approach allows for the computation of both the total and each QNM's contribution to the spontaneous decay rate of an emitter using [5]:

$$\frac{\gamma}{\gamma_0} = \sum_m F_P^m \frac{\Omega_m^2}{\omega} \frac{(\Gamma_m/2)^2}{(\omega-\Omega_m)^2+(\Gamma_m/2)^2} \times \left[1 + 2Q_m \frac{\omega-\Omega_m}{\Omega_m} \frac{\mathrm{Im}(\tilde{V}_m)}{\mathrm{Re}(\tilde{V}_m)}\right] \tag{2}$$

where m idexes the mode with eigenfrequency

$$\omega_m = \Omega_m - i\Gamma_m/2 \tag{3}$$

where Q_m, $\tilde{V}_m$, F_P^m referring to the quality factor, mode volume and Purcell factor defined in Equation (1) of the m^{th} mode respectively, and Ω_m and Γ_m being the resonant frequency and decay rate of the corresponding QNM [5]. The mode volume is defined as follows [5]:

$$\tilde{V}_m = \frac{1}{2\epsilon_0 n^2 \left(\tilde{\mathbf{E}}_m(\mathbf{r}_0)\cdot\mathbf{u}\right)^2} \tag{4}$$

where $\tilde{\mathbf{E}}_m(\mathbf{r}_0)$ declares the normalised electric field at $\mathbf{r}_0$, $\mathbf{u}$ is the unitary vector along the emitter's dipole moment.

Figure 2 depicts the modes of the hybrid cavity QNMs, as ϵ_{sp}^{rel} increases, with the area of each dot being commensurate with F_p, computed at the centre of the hybrid cavity, using Equations (1). The QNM splitting occurring when the detuning between the dimer and the nanobeam is low indicates that the two constituents are coupled. Examining the response of

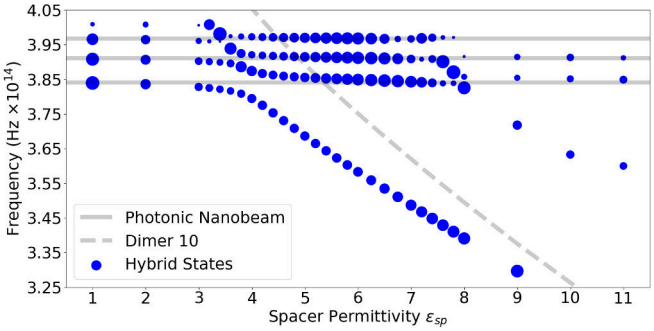

Fig. 2: Dispersion relation of hybrid QNMs in a broad range of spacer electric permittivity values. The dot size is proportional to the Purcell factor of the corresponding QNM. The spectral positions of the isolated waveguide modes and the (10) mode of the isolated antenna are added for reference.

the hybrid cavity, it clearly surpasses its isolated constituents, when these are detuned. To explicitly show this, we use Equation (2) to compute the increment of the spontaneous emission rate both for the hybrid cavity and its isolated constituents. The same rate is also computed classically by dividing the power emitted by a dipole placed in the cavity by the power it emits in free space. Figure 3 depicts how the γ/γ_0 varies throughout the red and near infrared part of the spectrum when the antenna is strongly blue - detuned with respect to the nanobeam (top panel) and when the (10) mode of the antenna is on resonance with the nanobeam (bottom panel). The former case is captured by simulating a hybrid cavity with $\epsilon_{sp}^{rel} = 1$, and results in a threefold increase of γ/γ_0 in comparison to with the isolated photonic nanobeam. The increase when the dimer and the nanobeam are brought on resonance is strongly suppressed compared to the detuned case [6].

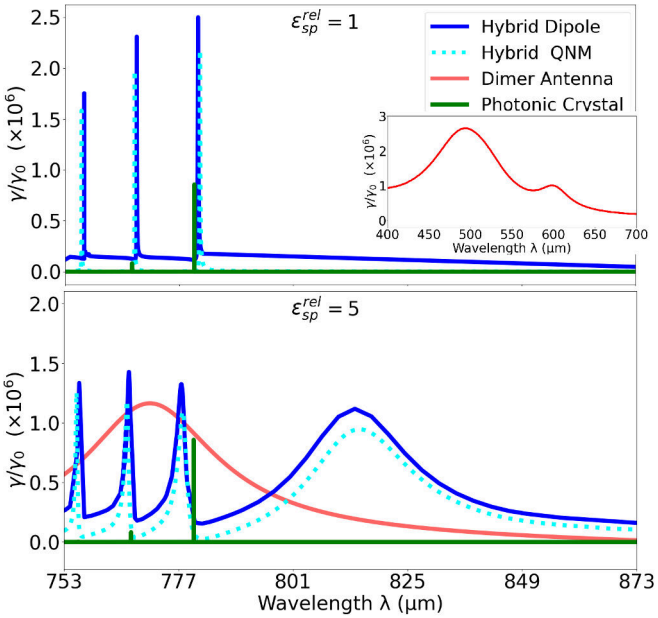

Fig. 3: Spontaneous emission rate, computed in the middle of the hybrid photonic cavity. Top panel demonstrates the enhancement achieved when the dimer antenna is blue detuned with respect to the nanobeam ($\epsilon_{sp}^{rel} = 1$). The inset depicts the isolated, spacerless antenna response. Bottom panel demostrates the case where the nanobeam being on resonance with the (10) mode of the antenna, which corresponds to $\epsilon_{sp}^{rel} = 5$. The enhancement attained with the isolated nanobeam and antenna are added for reference.

IV. Conclusion

In conclusion, we have designed a hybrid photonic nanocavity by integrating a gold dimer antenna inside a silicon nitride nanobeam to create an optical environment that significantly enhances the spontaneous decay rate of quantum emitters, operating at 780nm. This property makes it an ideal optical environment for specific quantum emitters, such as cold Rubidium atoms. The emission rate enhancement can reach as high as $2.5 \cdot 10^6$, a threefold increase in comparison to the enhancement attained by its isolated photonic waveguide. Furthermore, the size and shape of the nanocavity makes it an

excellent candidate as the building block of a long network of coupled waveguides. Atoms can be easily adsorbed to the metal surface and placed in the hot point, where the electric field and, subsequently, the emission rate enhancement is maximum. Ultimately, the geometry of the cavity makes rescaling possible, to make the device operate at different wavelengths, making it eligible for a plethora of emitters.

ACKNOWLEDGMENTS

AD gratefully acknowledges support from the Royal Society University Research Fellowship URF\R1\180097 and URF\R\231024, Royal Society Research grants RGS \R1\211093, funding from ESPRC grants EP/Y008774/1 and EP/X012689/1. AD acknowledges support from Royal Society Research Fellows Enhancement Award RGF \EA\181038, and AD, AC acknowledge funding from EPSRC for the CDT in Topological Design EP/S02297X/1.

REFERENCES

[1] E. M. Purcell, "Spontaneous emission probabilities at radio frequencies," *Phys. Rev.*, vol. 69, pp. 681, 1946.

[2] X. Yang, A. Ishikawa, X. Yin, and X. Zhang., "Hybrid Photonic-Plasmonic Crystal Nanocavities" *ACS Nano*, vol. 5.4, pp. 2831–2838, 2011.

[3] A. Crookes, B. Yuen, S. M. Hanham, and A. Demetriadou, "Multi-partite entanglement in extreme nanophotonic cavities" *APL Quantum*, vol. 2, pp. 046115, 2025.

[4] W. Yan, R. Faggiani, and P. Lalanne, "Rigorous modal analysis of plasmonic nanoresonators" *Physical Review B*, vol. 97, pp. 205422, 2018.

[5] P. Lalanne, W. Yan, K. Vynck, C. Sauvan, and J. P. Hugonin, "Light Interaction with Photonic and Plasmonic Resonances" *Laser & Photonics Reviews*, vol. 12, pp. 1700113, 2018.

[6] H. M. Doeleman, E. Verhagen, and A. F Koenderink, "Antenna - Cavity Hybrids: Matching Polar Opposites for Purcell Enhancements at Any Linewidth" *ACS Photonics*, vol. 3, pp. 1943–1951, 2016.

[7] I. M. Palstra, H. M. Doeleman, and A. F Koenderink, "Hybrid cavity-antenna systems for quantum optics outside the cryostat" *Nanophotonics*, vol. 8, pp. 1513–1531, 2019.

Solution-processed microcavities incorporating luminescent hybrid Copper(I) iodides

Federica Bortoletto[1,*], Emma Contini[2], Ullrich Steiner[1,3], Andrea Dodero[1,3]

[1]Adolphe Merkle Institute, University of Fribourg, Switzerland
[2]Department of Chemistry 'Giacomo Ciamician', University of Bologna, Italy
[3]NCCR Bio-Inspired Materials, Adolphe Merkle Institute, Fribourg, Switzerland
*Corresponding author: federica.bortoletto@unifr.ch

***Abstract*—Luminescent hybrid crystals are grown via organic ligand evaporation within a CuI-containing polymeric layer. This emissive layer can serve as defect layer in solution-processed microcavities, whose photonic bandgap and cavity mode are tuned to spectrally match the hybrid crystals emission, to the end of narrowing and enhancing it.**

***Keywords*— optical microcavities, photonic crystals, luminescence, hybrid coordination polymers.**

I. Introduction

Photonic crystals (PCs) are low-loss materials featuring periodic modulation of the refractive index, which gives rise to a photonic band gap (PBG), i.e. a frequency range in which light propagation is forbidden along specific directions and which is responsible for the PC chromatic response. The simplest examples of PCs are planar multilayer stacks of alternating dielectric layers, with high (n_H) and low (n_L) refractive indices, whose periodicity ($d_H + d_L$) is on the order of UV, visible, or infrared wavelengths. These structures are commonly referred to as distributed Bragg reflectors (DBRs). The reflectance of the first order PBG is maximized when the quarter-wavelength condition is satisfied:

$$\frac{\lambda_{PBG}}{4} = n_H d_H = n_L d_L \quad (1)$$

When the symmetry of the DBR is broken by introducing a defect layer (cavity) with a specifically designed optical thickness, allowed photonic states appear within the bandgap, giving rise to a narrow transmission peak (Fig. 1b). The thickness L_C and refractive index n_C of the cavity layer must be tuned such that the cavity supports a standing wave of wavelength λ_C comprised in the bandgap [1], according to:

$$2n_C L_C = m\lambda_C \quad (2)$$

where m denotes the cavity mode order. A microcavity (MC) is thus formed, consisting of DBRs sandwiching a defect layer in which the optical field is strongly confined. If an active emissive material is introduced into the cavity (Fig. 1a), it experiences an enhanced local electromagnetic field and a modified photonic density of states [2]. Consequently, its emission spectrum is altered, with increased intensity and spectral redistribution around the cavity resonance (Fig. 1c). To exploit this effect for applications ranging from lasing to optical sensing and filtering [2], the MC must be properly engineered such that the cavity mode spectrally overlaps the emission of the active material.

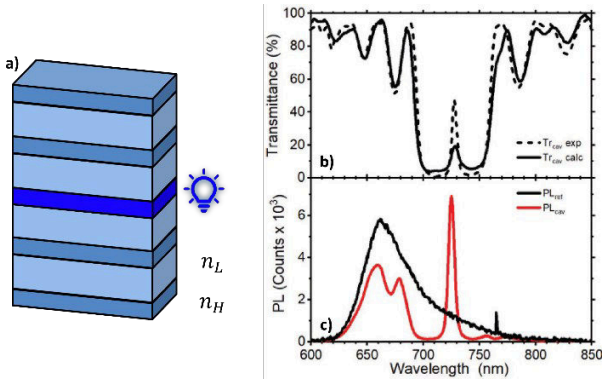

Fig. 1 Scheme of a planar MC with an emissive material embedded in the defect layer a). Experimental (continuous line) and calculated (dashed line) transmission b) and emission spectra c) of a MC (red) and a reference sample (black) for a all-polymer MC containing Perylene BisimideJ-aggregates. Adapted from [1].

Hybrid coordination polymers (HCPs) are an emerging class of materials whose photoluminescence properties can be tuned through the appropriate selection of their constituent building blocks. HCPs are coordination compounds containing inorganic clusters or inorganic polymeric subunits [3]. In these materials, the infinite repetition of the coordination entity is provided by the inorganic component, while the overall dimensionality (Fig. 2) depends on the binding sites of the organic ligand [3]. Among HCPs, copper(I) iodide-based hybrids display a wide variety of molecular structures, often showing stimuli-responsive emissive properties [3] and high luminescence efficiency [4].

In this work, luminescent copper(I) iodide hybrids are used as active materials within the cavity layer of solution-processed organic microcavities. Ligand evaporation is employed to promote crystal growth directly within the cavity layer of a pre-fabricated MC. The inherently broad emission of the HCP is

expected to be reshaped by the MC, resulting in enhanced emission intensity and spectral narrowing, potentially amplifying any stimuli-responsive behavior.

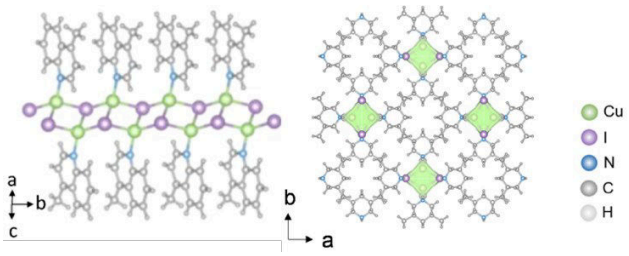

Fig. 2 Example of 1D and 2D crystal structures of Copper(I) iodide hybrids materials. Adapted from [4].

II. Methods

Wet-chemistry and solution-processing techniques are used to fabricate both the organic DBRs and the cavity layer composing the MC. The DBRs are deposited on glass substrates by dynamic spin-coating of alternating low-refractive-index (cellulose acetate, CA, in diacetone alcohol) and high-refractive-index (polyvinylcarbazole, PVK, in toluene) polymer solutions, followed by annealing at 70°C. The cavity layer is fabricated by spin-coating a CA solution in acetonitrile containing 0.1 M CuI, which acts as the inorganic node of the emissive HCP. The complete microcavity is then exposed for 24 h to vapors of an organic ligand, which binds to the CuI nodes within the cavity layer, leading to the formation of confined emissive HCP crystals. Depending on the specific HCP emission, the DBR bandgap and cavity-mode spectral positions are tuned using Eq. (1) and Eq. (2), to achieve overlap with the emission band of the hybrid crystals.

III. Results and Discussion

Fig. 3 shows the reflectance spectra of PVK:CA DBRs fabricated by spin-coating polymeric solutions with different concentrations, resulting in photonic band gaps centered at approximately 450 nm, 550 nm and 650 nm. These results demonstrate that the PBG can be continuously tuned across the visible spectrum by adjusting the layer thicknesses, enabling adaptation to the emission wavelength of a target CuI hybrid coordination polymer.

Several organic ligands capable of coordinating CuI nodes to form emissive hybrid crystals were investigated. Here, we focus on 4-methylquinoline. Fig. 4 shows the photoluminescence emission spectrum of a three-layer sample (PVK:CA–CuI:PVK) exposed to 4-methylquinoline vapors. The appearance of an emission peak at approximately 575 nm confirms the formation of emissive hybrid crystals. However, this emission is red-shifted compared to literature values [4], possibly due to polymer–crystal interactions or the formation of a different crystal polymorph. Further investigations are required to clarify this behavior. Based on the measured emission spectrum (Fig. 4, red curve), a microcavity with a cavity mode spectrally overlapping the emission was successfully fabricated (Fig. 4, black curve).

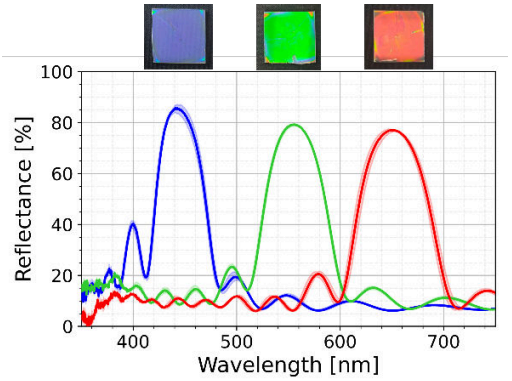

Fig. 3 Reflectance measurements of blue, green, and red PVK:CA DBRs obtained by tuning the layer thicknesses. Inset photographs show the structural color of each DBR.

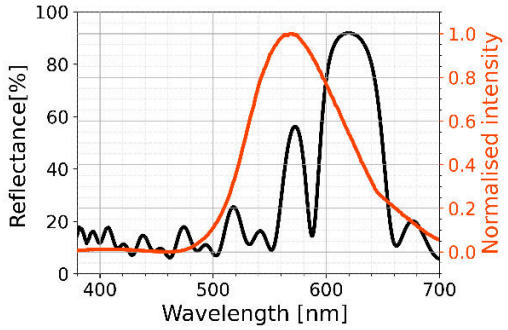

Fig. 4 Photoluminescence emission spectrum (red, excitation at 365 nm) of a PVK:CA–CuI:PVK stack after exposure to 4- methylquinoline vapors. Reflectance spectrum (black) of a microcavity engineered to spectrally match the emission band.

IV. Conclusion

We have demonstrated the formation of emissive CuI-based hybrid crystals grown directly within a CuI-containing polymeric layer via ligand evaporation. Furthermore, a solution-processed microcavity with a photonic bandgap and cavity mode spectrally overlapping the hybrid emission (~575 nm) was successfully fabricated. Future work will focus on the growth of emissive crystals directly within the cavity layer of the completed microcavity. Key-challenges include controlling ligand permeation through the DBR layers, which may alter the refractive indices and consequently the MC optical response. A carefully tuned additional annealing step, designed to preserve the emissive crystals, may promote ligand desorption from the DBRs layers and mitigate this effect.

Acknowledgments

This work was financially supported by an SNSF Sinergia grant (number 216659) and an SPS NATO grant (number G6238).

References

[1] P. Lova, “Advances in functional solution processed planar 1D photonic crystals,” Adv. Optical Mater., vol. 6, p. 1800730, 2018.

[2] H. Megahd, D. Comoretto, and P. Lova, “(INVITED) Planar microcavities: Materials and processing for light control,” Optical Materials: X, vol. 13, p. 100130, 2022.
[3] L. Contini, “Stimuli responsive hybrid coordination polymers based on copper iodide as luminescent mechanochromic materials,” Master’s thesis, Photochemistry and Molecular Materials, 2022.
[4] S. Wang, E. E. Morgan, S. Panuganti, L. Mao, P. Vishnoi, G. Wu, Q. Liu, M. G. Kanatzidis, R. D. Schaller, and R. Seshadri, “Ligand control of structural diversity in luminescent hybrid copper(I) iodides,” Chemistry of Materials, vol. 34, pp. 3206–3216, 2022.

Multimode Waveguiding Photonic-Crystal Gratings

Lucciano A. Letelier[1,*], Lina Grineviciute[1], Simas Melnikas[1], Kestutis Staliunas[2,3]

[1]Center for Physical Sciences and Technology (FTMC), Vilnius, Lithuania
[2]Catalan Institution for Research and Advanced Studies (ICREA), Barcelona, Spain
[3]Universitat Politècnica de Catalunya (UPC), Barcelona, Spain
*Corresponding author: lucciano.letelier@ftmc.lt

***Abstract*— We investigate multilayer photonic crystal gratings in which stacked layers replicate a periodic surface pattern, enabling multimode waveguiding and angle-selective diffraction in reflection. An FDTD-based design approach clarifies the influence of the grating period, refractive index contrast, and layer sequence. Samples fabricated using ion beam sputtering technology experimentally confirm a narrowband, angle-selective response under oblique illumination.**

***Keywords*—photonic crystal gratings, multilayer structures, multi waveguiding, diffraction filtering, FDTD.**

I. Introduction

Unlike conventional one-dimensional gratings, Multimode Waveguiding Photonic-Crystal Gratings are periodically modulated multilayer structures that enable angular selectivity in diffraction through the combined effects of surface modulation and Bragg-type resonances. These structures can improve the spatial quality of reflected diffracted beams. Similar spatial filtering mechanisms based on periodic refractive-index modulation and photonic crystal concepts have previously been demonstrated in both transmission and reflection configurations [1-3].

In this work, we investigate multilayer photonic crystal gratings formed by depositing dielectric layers onto a corrugated substrate (see Fig. 1a). Their angular and spectral responses are analyzed using finite-difference time-domain simulations, which guide the design and fabrication of the structure.

II. Methods

Our methodology combines analytical modeling, numerical simulations, and experimental validation (see Fig. 1b) to study angular-selective diffraction and spatial filtering in multilayer photonic crystal gratings formed by periodically replicated layers on a corrugated substrate. The structure is modeled as a two-dimensional periodic system with transverse and longitudinal periods d_x and d_z.

$$\lambda_{m_x,m_z}=\frac{2d_xd_z\left(m_xd_z\sin\theta+m_zd_x\cos\theta\right)}{m_x^2d_z^2+m_z^2d_x^2},$$

The resonance conditions of the multiple diffracted and guided modes are obtained from elastic wave-vector conservation in reciprocal space, leading to a unified multimode diffraction relation which simultaneously describes Bragg resonance, when constructive interference in reflection occurs between the waves scattered by the periodic planes, transverse resonance, when the diffractive coupling condition to a transverse (lateral) mode of the structure is satisfied in reflection or transmission, and Littrow-type resonance, which occurs when both resonances occur simultaneously, sending the light back along the incident direction (see Fig. 1c); these regimes can be described through the integers m_x and m_z.

A four-wave coupled-mode formulation is further introduced to describe the interaction between the incident wave, the Bragg-backwards reflected wave, and the forward and backward diffracted waves. Most interesting for us are backward diffracted wave, which is supposed to propagate at approximately the Littrow direction. We expect that this diffraction component will lead strongest angular filtering. Based on this framework, the grating parameters are chosen to reach a multimode resonance regime.

Finite-difference time-domain (FDTD) simulations are used to validate the analytical model and to refine the design. The simulations start by defining a unit cell with the corresponding geometry and by applying Bloch boundary conditions along the periodic directions. A Broadband Fixed-Angle Source Technique (BFAST) is used to model non-normal incidence.

The multilayer thicknesses and the longitudinal period are optimized for oblique incidence using a generalized quarter-wave condition. The Nb_2O_5/SiO_2 gratings fabricated by ion beam sputtering (IBS) technology [4] were previously studied in the non-diffractive regime [3]. In this work, the diffracted light orders are experimentally characterized and compared with theoretical predictions.

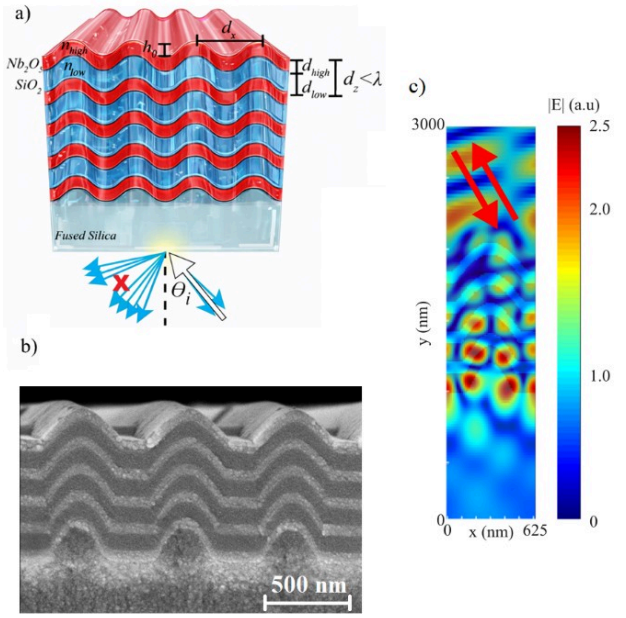

Fig. 1. (a) Schematic of multilayer grating, defining the transverse and longitudinal periods and the incidence angle. (b) Cross-sectional SEM image of the fabricated the Nb_2O_5/SiO_2 structure on fused silica substrate. (c) FDTD electric-field amplitude distribution under resonant illumination.

III. Results and Discussion

Experimental measurements at 633 nm under S polarization reveal a strong angular redistribution of the reflected and transmitted diffraction orders produced by the fabricated multilayer grating. As shown in Fig. 2, the first reflected order R_1dominates over a broad angular range around 29° - 32°, while the specular reflection R_0 is strongly suppressed in the same region.

A complementary behavior is observed for the transmitted orders, indicating efficient angular-selective coupling between reflection and diffraction channels. The total measured power remains close to 97% over the entire angular range, confirming low losses and good fabrication quality. These results demonstrate experimentally the angular-selective response and spatial filtering capability predicted by the analytical model and numerical simulations.

IV. Conclusion

We have theoretically and experimentally demonstrated angular selective diffraction and spatial filtering in multilayer photonic crystal gratings fabricated on corrugated substrates. The measured redistribution of reflected and transmitted diffraction orders and the high overall efficiency confirm the validity of the analytical and numerical design approach. These results highlight the potential of multilayer grating photonic crystals for compact diffractive and spatial filtering optical components.

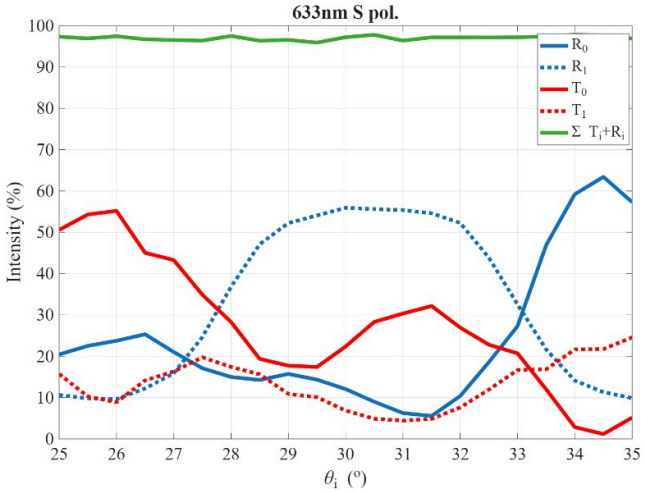

Fig. 2. Measured angular dependence of the reflected and transmitted diffraction efficiencies R_0, R_1, T_0, and T_1 at $\lambda = 633$nm under S polarization for the fabricated multilayer photonic crystal grating. The green curve shows the total measured efficiency $\sum_i (R_i + T_i)$.

Acknowledgments

This work has received funding from the Research Council of Lithuania (LMTLT), agreement No. S-LT-TW-24-9.

References

[1] K. Staliunas and V. J. Sánchez-Morcillo, "Spatial filtering of light by chirped photonic crystals," Phys. Rev. A, vol. 79, p. 053807, 2009.

[2] K. Staliunas, R. Herrero, and G. J. de Valcárcel, "Subdiffraction and spatial filtering due to periodic spatial modulation of the refractive index," Phys. Rev. A, vol. 75, no. 1, p. 011804, 2007.

[3] L. Grineviciute, C. Babayigit, D. Gailevičius, M. Peckus, M. Turduev, T. Tolenis, M. Vengris, H. Kurt, and K. Staliunas, Nanostructured Multilayer Coatings for Spatial Filtering, Adv. Optical Mater., 2001730 (2021).

[4] L. Grinevičiūtė, S. Melnikas, J. Nikitina, M. Drazdys, A. Selskis, and D. Astrauskytė, "Optical coating deposition on submicron-patterned surfaces," Coatings, vol. 15, no. 4, p. 372, 2025, doi: 10.3390/coatings15040372.

Spatially coherent quantum dot emission using guided mode resonances

Nimisha Ramprasad[1,*], Harry A. Atwater[2]

[1]Thomas J. Watson Laboratory of Applied Physics, California Institute of Technology, Pasadena, CA, USA, 91125
*Corresponding author: nrampras@caltech.edu

***Abstract*—We design guided-mode-resonant gratings to enable spatially coherent quantum-dot emission in the visible, with applications to emissive luminescent solar concentrators. This single-mode waveguide device enables high angular selectivity and asymmetric diffraction, establishing a new architecture for off axis focusing, enabling high efficiency concentrators.**

***Keywords*— metamaterials, visible, guided-mode-resonator, quantum dots, solar technology**

I. Introduction

The current world demand for energy requires the expansion of renewable solar energy. The Space Solar Power Project aims to increase access to clean energy by harvesting power at large from space via ultra-light, efficient photovoltaic (PV) devices and transmitting it back to Earth through RF enabled wireless power transfer [1]. Luminescent solar concentrators (LSCs) are one such class of PV concentrator devices that leverages the Stokes shift [2] to achieve 10^5 times greater light concentration than traditional bulk optics methods [2]. Typically, LSCs are waveguide devices with isotropic emitters non-deterministically dispersed within a slab waveguide, such that their luminescence is transmitted via total internal reflection (TIR) to an attached PV cell. However, TIR - based strategies in the optical regime are inefficient, leading to $> 25\%$ photon loss [3].

To mitigate these losses, we propose a redesign of the LSC architecture that facilitates controlled free space optical outcoupling from the waveguide to the PV cell instead. This Emissive Luminescent Solar Concentrator (eLSC) model comprises an ensemble of quantum dots placed within a waveguide resulting in a spatially and temporally incoherent source, with a spatially isotropic emission profile. However, by coupling the quantum dot emission to a guided mode resonance, we enforce a single spatial phase profile along the aperture, thus establishing a degree of spatial coherence to an ensemble of incoherent emitters [4].The confined light is then outcoupled via a momentum matched resonant grating structure.

II. Methods and Results

The eLSC is designed to span 20 cm; 2 mirrored devices of 10 cm each. The quantum dots used are CdSe/CdS that that absorb broadly up to ~ 600 nm and emit at 635 nm ± 15 nm. The corresponding PV cell(s) is to be placed above one end (i.e., at -10 cm and $+10$ cm) of the waveguide grating structure, as seen in 1a), which then dictates two crucial design considerations: a) the grating structure must be quasi-aperiodic to outcouple light at a range of diffraction angles with respect to the PV cell and b) at each grating period, the emission profile must be asymmetric such that maximum energy is transmitted towards the closer PV cell.

To address these challenges, we use FDTD electromagnetic simulations to design the waveguide and grating structure, optimizing for maximum coupling efficiency along the optical path: quantum dots to guided mode, guided mode to free space. To evaluate the overall outcoupling performance, two orthogonally polarized dipoles were placed along the axis of the propagation, exciting both forward and backward guided modes. For the waveguide, sputtered TiO_2 $(n \sim 2.35)$ was chosen as the core, and SiO_2 $(n = 1.44)$ as the substrate for their high refractive index contrast and ease of fabrication. The waveguide dimensions were determined to be 200nm tall and 400nm wide, resulting in a unidirectional coupling efficiency of 70% and a Purcell factor of 30 for the TM polarized dipole. This indicates an enhancement of specific radiative decay channels into the guided mode, which translates to the dominance of a single mode (in this case, TM_0) within the waveguide, establishing spatial coherence to incoherent quantum dot luminescence.

To outcouple the confined light, we introduce periodic perturbations along the surface of the waveguide in the form of symmetric TiO_2 grating elements that satisfy the following phase matching condition:

$$n_{eff} \quad = \quad n_1 \sin\theta_i - m\frac{\lambda_0}{\Lambda} sin\phi, \tag{1}$$

here, n_1, n_2, n_3 refer to the refractive index of the upper cladding (in this case air), waveguide material (TiO_2), and the substrate material (SiO_2), respectively. θ_{inc} is the angle of diffraction into free space, λ_0 is the wavelength of operation. n_{eff} refers to the effective index of the mode within the waveguide medium and Λ refers to the grating period of the grating element.

Equation 1 states that the periodic perturbations of the grating supplies discrete momentum such that light confined in the guided mode, i.e., outside the light line, is folded back into the light line, allowing free space outcoupling. However, to satisfy requirement a) mentioned above, the grating period

Fig. 1. a) The overall eLSC design with quasi-aperiodic arrays of guided mode resonators. b) A single period of 660nm with 4 sub-periods, each of $\Lambda' = 165$nm. c) Asymmetric emission profile from 2 orthogonal dipole excitation d) Asymmetric emission profile from randomized, incoherent dipole sources e) 66μm aperture (= 100 periods) simulation, confirming beam steering at finite, large apertures.

must change with respect to the desired outcoupling angle (as per Equation 1), requiring a range of grating periods to cover the full range of the proposed 10 cm device while remaining optically coupled to the PV cell. Each period is thus repeated a finite number of times over few centimeters before "stepping" to the next period, creating a quasi-periodic array on the wavelength scale, and aperiodic array in the macroscopic scale 1a).

In the presence of a bi-directional guided mode, both the $+1$ and -1 diffraction conditions are satisfied, leading to symmetric transmission intensities in both directions (requirement b)). We address this issue by designing a metasurface with a blazed phase profile. By dividing a single period into n equal sub-periods, each containing a structure contributing $2\pi/n$ phase, it is possible to create a phase ramp that enhances one diffraction order, while suppressing the other, via constructive and destructive interference, respectively. Thus, for incoherent emitters with established spatial coherence via the single mode waveguide, the relative spatial/phase profile along the waveguide remains well-defined, allowing the phase ramp to create some asymmetry in the transmission intensity [5].

For our case, we divide the period into 4 sub-periods (1b)), and use a Bayesian optimization algorithm to determine the parameters of each sub-structure, optimizing for maximum transmission to the $-1(+1)$ order and penalizing transmission to parasitic orders. For the 660 nm period, the addition of the blazed phase profile demonstrated angular selectivity, and allowed for 62.5% emission into the -1 order, with the remaining 37.5% considered as loss, from the $+1$ and $0th$ order as seen in 1c).

Finally, for a more realistic model, we simulate incoherent emitters using 100 dipoles of randomized phase, polarization, and location, placed along the propagation axis of the waveguide, and the transmission to the -1 order observed. The simulation was then iterated 10 times, each with a new set of randomized dipoles, and averaged to determine the emergent behavior. Analyzing the phase contribution of the individual sub-structures revealed a low relative phase delay, with an average delay across the period of $5\pi/6$ instead of the expected 2π. Despite the lack of a phase gradient however, the device design maintained the high angular selectivity, and asymmetric emission under incoherent excitation, as seen in 1d), e).

III. Conclusion

In conclusion, we demonstrate high angular selectivity, and preferential outcoupling to the -1 order of non-equilibrium, incoherent emission. The use of a guided mode resonator facilitated the re-establishment of spatial coherence, allowing for directional emission in the visible. Further work includes expanding current models to full wave simulations, including tiling together the full aperiodic structure to demonstrate the "off axis focusing" of the diffracted beam.

Acknowledgments

This work was supported by the Space Solar Power Project and the National Science Foundation Graduate Research Fellowship Program. The authors would like to thank Dr. Simo Pajovic, Julie Belleville, and Yae-Chan Lim for their discussions and support.

References

[1] O. Mizrahi, et.al., "Space solar power generation: A viable system proposal and technoeconomic analysis", *Joule* 9, 6 (2025).
[2] E. Yablonovitch, "Thermodynamics of Fluorescent Planar Concentrator", *JOSA* 70, 11 (1980).
[3] H.C. Bauser, et.al., "Photonic Crystal Wavegides for ¿90% Light Trapping Efficiency in Luminescent Solar Concentrators", *ACS Photonics*, 7, 8 (2020).
[4] J.-J. Greffet, et.al., "Coherent emission of light by thermal sources", *Nature*,416, 61-64 (2002).
[5] S. Inampudi, et,al., "Unidirectional thermal radiation from a SiC metasurface", *J. Opt.Soc.Am*, 39-46 (2018).

Stabilization of Whispering Gallery Microresonators by Hidden Solvent Dynamics

Marco Reale[1,2*], Antonino Madonia[1], Simonpietro Agnello[1,3], Marco Cannas[1,2], Emanuele Marino[1], Alice Sciortino[1], Fabrizio Messina[1]

[1]Department of Physics and Chemistry "E. Segrè", University of Palermo, Italy
[2] INSTM, Florence, Italy
[3]Aten Center, University of Palermo, Palermo, Italy
*Corresponding author: marco.reale@unipa.it

***Abstract*— Whispering-gallery microresonators offer ultrasensitive optical fingerprints but can suffer from long-term spectral drifts. Combining experiments and modeling, we trace this instability to slow solvent release from quantum-dot-loaded polystyrene microparticles. Harnessing this understanding, we develop a simple stabilization protocol that locks resonances, enabling reliable WGM-based photonic labels, sensors, and microscale self-trackers.**

***Keywords*— Whispering-Gallery Modes Microresonators; Photonic labels; Optical Memory.**

I. Introduction

Whispering gallery mode (WGM) microresonators provide ultrasensitive optical fingerprints that are ideally suited for photonic labeling and for detecting minute variations in size and refractive index. These resonances arise from the repeated total internal reflection of light confined along the periphery of dielectric microstructures, resulting in long optical path lengths and high quality factors. When coupled to a luminescent gain medium, WGM microcavities can be directly probed through their emission, enabling compact and highly sensitive optical platforms with ultrasharp spectral features. Such luminescent WGM microresonators can be fabricated through self-assembly approaches, for instance by incorporating luminescent molecules or nanomaterials into dielectric microspheres.

Among the different material platforms, polymer microspheres loaded with semiconductor quantum dots represent a particularly attractive architecture. Polystyrene microbeads provide a low-cost, optically transparent, and easily processable dielectric host with well-defined spherical geometry, while quantum dots offer high photostability, size-tunable emission, and efficient coupling to cavity modes owing to their large absorption cross-section and high quantum-yields. His combination enables fully self-emissive WGM microresonators that do not require external evanescen coupling schemes and can be fabricated in a scalable and versatile way.

WGM microresonators have attracted considerable interest for applications in optical sensing, photonic tagging, and microscale tracking of physicochemical changes. In most experimental and theoretical descriptions, their optical response is implicitly assumed to be passive and reversible, governed solely by instantaneous parameters such as temperature, refractive index, and resonator geometry. Within this framework, long-term spectral drifts are typically regarded as undesirable artifacts that compromise performance and must be suppressed. However, despite their sharp spectral signatures, polymer-based WGM microresonators often exhibit pronounced thermal and temporal instabilities that limit their practical applicability. The physical origin of these drifts has remained poorly understood.

In this work, we combine experiments and modeling to show that these instabilities originate from slow internal dynamics within the microresonator material. In particular, we demonstrate that the gradual release of residual solvent trapped inside the polymer matrix during fabrication induces a continuous and irreversible evolution of the effective refractive index and a progressive shrinking of the microparticles, which can be directly monitored via WGM spectroscopy. As a result, the optical spectrum of the resonator does not solely reflect its instantaneous state, but progressively encodes information about its preparation conditions and environmental history. By identifying and controlling this mechanism, we establish a simple protocol to suppress long-term spectral drift, locking WGM resonances into stable, sharply defined modes. More broadly, our results reveal that commonly used WGM microresonators operate as non-equilibrium optical systems, in which slow internal processes couple to confined optical modes. This insight provides a new perspective on WGM resonators, advancing their reliable use as robust optical platforms, for photonic labeld, noninvasive sensors, and precise self-trackers of microscale physicochemical changes, while opening new opportunities for micro-optical memories.

II. Methods

Microresonator Fabrication: Whispering gallery

microresonators were realized by loading colloidal quantum dots into polystyrene microspheres, a widely adopted architecture for active WGM systems. The loading procedure relies on solvent-assisted diffusion of emitters into the polymer matrix, yielding intense photoluminescence coupled to high-Q optical modes.

Optical characterization: Optical spectra were acquired using high-resolution photoluminescence spectroscopy, allowing individual WGM resonances to be tracked over time with sub-nanometer precision. Measurements were performed over extended time windows (hours to days) and under controlled thermal conditions to disentangle fast thermal effects from slow temporal evolution.

III. Results and Discussion

Single-particle spectroscopy reveals that QD-polystyrene microparticles exhibit sharp and distinctive WGM fingerprints that evolve in time under ambient conditions. Monitoring the emission spectrum of an individual microparticle as a function of time elapsed after dropcasting, we initially observe a relatively low mode density, which progressively increases while displaying a systematic blueshift of the resonances (Figure 1b). This behaviour indicates a gradual modification of the optical cavity parameters, mainly associated with the change of the refractive index constrast with respect to the environment, where external solvent layers evaporate. However, the shift persists for several hours and becomes even more pronounced under mild vacuum conditions, as evidenced by the spectra reported in Figure 1c, which suggest the involvement of slow structural relaxation.

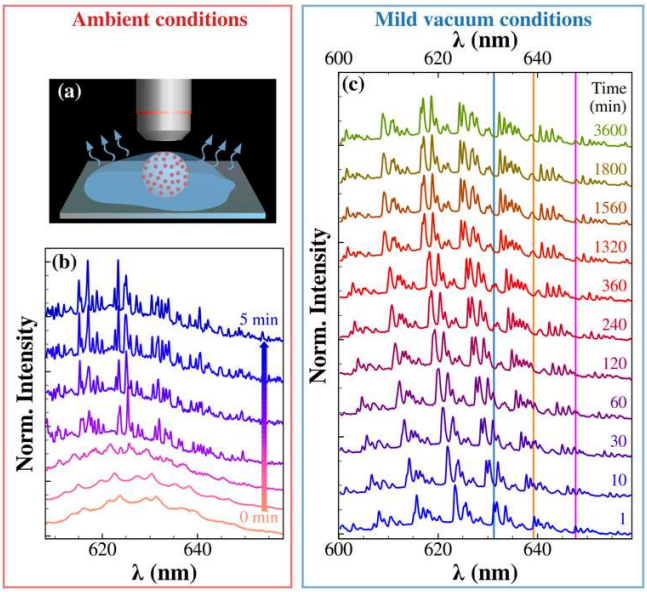

Fig. 1 (a) Illustration of the optical configuration employed to record PL spectra from a single QD-PSμP in air during solvent evaporation. (b) Temporal progression of the PL spectrum measured from the same microparticle following drop-casting under ambient conditions. (c) Time-dependent PL spectrum of an individual QD-PSµP maintained under mild vacumm (0.15 bar). Colored markers and shaded areas emphasize the systematic blueshift of three selected modes.

To elucidate the origin of this effect, the temporal evolution of WGM positions was analyzed within a model linking resonance shifts to variations in the effective refractive index and microsphere radius. The analysis corroborates a gradual shrinkage of the particle overt time, consistent with the slow release of residual solvent molecules trapped within the polymer matrix during the quantum dot loading process. As the solvent diffuses out, the the local dielecric environment experienced by the confined optical modes evolves concurrently with a reduction of the cavity size, leading to a continous and irreversible modification of the WGM spectrum.

Based on these observations, we implemented a thermal protocol aimed at accelerating solvent release to produce spectrally-stable photonic microtags. After this treatment, WGM spectra exhibit a marked suppression of long-term drift, with resonance positions remainng stable over extended measurements times and reproducible after prolonged storage, as shown in Figure 2. The thermal treatment effectively drives the system toward a steeady optical configuration, where both the internal refractive index and the resonator size reach a quasi-equilibrium state.

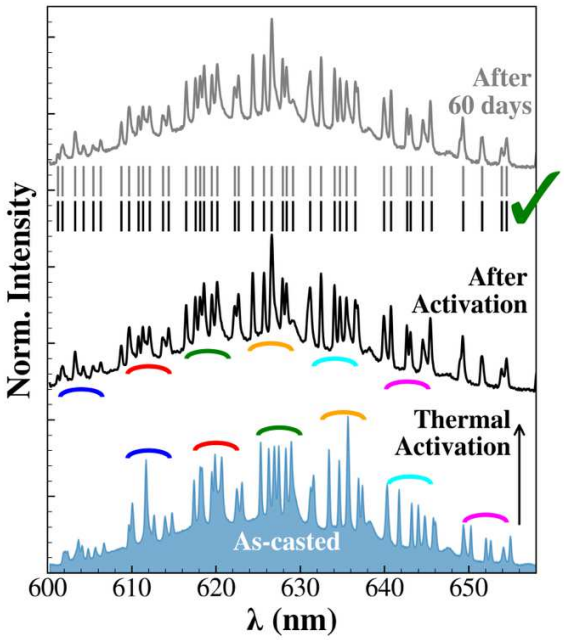

Fig. 2 µ-PL spectrum of a QD-PSµP recorded shortly after drop-casting (blue-filled) and following thermal treatment (black line), displaying a clear blueshift of the main WGM clusters (indicated by colored arcs). The gray spectrum shows the same sample measured 60 days later, after storage in ambient conditions. The WGM positions remain stable after thermal activation, making them suitable as a robust photonic barcode.

These findings reveal that polymer-based WGM microresonators operate as non-equilibrium optical systesm, in which slow internal structural dynamics are intrinsically coupled to confined optical modes. Rather than representing a limitation, this coupling can be harnessed as an additional

degree of freedom in photonic labeling and sensing, enabling microresontars whose optical spetra encode not only their present environment, but also their prior structural evolution.

IV. Conclusion

We have investigated whispering gallery modes in hybrid QD-polystyrene microparticle microcavities, showing that their unique spectral fingerprints sensitively encode environmental changes. Time-resolved tracking reveals irreversible blueshift driven by residual solvent evaporation, which are fully suppressed by a simple, thermal treatment requiring no additional fabrication steps. After stabilization, the resonators exhibit low thermal sensitivity due to near-compensation between thermal expansion and thermo-optic effects. Beyond secure photonic labeling, this platform enables noninvasive, real-time probing of structural dynamics in soft photonic materials and reconfigurable microresonators.

Acknowledgments

This work was supported by the PRIN projects 2022H8LE9P and 20223CWFZT, the ERC Starting Grant REFINE2LASE (grant agreement n. 101202342), the University of Palermo Funds – EUROSTART 2025 Call, SuperMAQ project.

The authors acknowledge ATeN Center for the μPL measurements.

References

[1] S. Jana, X. Xu, A. Klymchencko, A. Reisch, T. Pons, “Microcavity-Enhanced Fluorescence Energy Transfer from Quantum Dot Excited Whispering Gallery Modes to Acceptor Dye Nanoparticles”, ACS Nano, vol. 15, pp. 1445-1453, 2021.

[2] J. Wang, J. Li, S. Sun, H. Dong, L. Wu, E. Zhao, F. He, X. Ma, Y. S. Zhao, “Revealing Molecular Diffusion Dynamics in Polymer Microspheres by Optical Resonances”, Sci. Adv., vol 9, 2023.

[3] M. Reale, A. Madonia, S. Agnello, M. Cannas, E. Marino, A. Sciortino, F. Messina, “A Versatile Approach to Stabilize Whispering Gallery Microresonators Toward Reliable Photonic Labeling”, JPCL, ASAP, 2026.

Topological Transitions in Bilayer Photonic Crystal Slabs

Bo Wang *, Junjie Li,

Institute of Physics, Chinese Academy of Sciences, 100190 Beijing, China

*Corresponding author: wangbo2014@iphy.ac.cn

***Abstract*—We theoretically and experimentally demonstrate that merely tuning the spacer thickness of the bilayer photonic crystal slabs induces a topological transition from a fundamental charge ($\nu = 1$) to a high-order charge ($\nu = -2$) without modifying symmetry. This topological transistion is triggered by bilayer destructive interferences of quasi-BICs.**

***Keywords*— photonic crystal slabs, BIC, topological transitions.**

I. Introduction

Topological photonics has emerged as a vibrant frontier, with bound states in the continuum (BICs) being paradigmatic topological states in photonic crystal slabs(PhCs). BICs emerge as polarization vortices carrying quantized topological charges defined by the winding of far-field polarization vectors[4]. They have enabled numerous applications in lasing, sensing, and polarization control. Spatial symmetry strictly quantizes the charges at Γ points; e.g -symmetric systems require $\nu = 3n + 1$ ($n \in Z$)[4]. Although high-order charges such as $\nu = -2$ have been realized in C_6-symmetricstructures[1], prior works have largely isolated fundamental ($n = 1$) charges. A deterministic transition from fundamental to high-order charges—especially under preserved symmetry—remains unrealized.

Here, we theoretically propose and experimentally demonstrate symmetry-preserved tuning of at-Γ BICs in bilayer PhCs, realizing a topolgical transition from fundamental ($\nu = 1$) to high-order ($\nu = -2$) charges while maintaining C_3 symmetry[3].Via perturbation theory, we analytically reveal that destructive interference between bilayer radiation can completely suppress the first-order far-field correction upon tuning the spacer thickness. This drives a topological transition and the Q-factor scaling of near-Γ resonances changes from $\mathcal{O}^{-2}$ to$\mathcal{O}^{-4}$, with k the Bloch wavenumber. Full-wave simulations and angle-resolved measurements validate the predicted transition.

II. Theory

Figure 1(a) shows the structure of our BM. Each layer is composed of a triangular lattice of TiO_2 ($n = 2.46$) nanopillars. All the dimensional parameters for the two layers remain the same, but the top layer (tL) is shifted along the y-axis by p relative to the bottom layer (bL). The tL and bL are vertically separated by $2s$. The individual layers are governed by D_{6h} ($C_{6v} \times C_{1h}$) point group and hence support symmetry-protected at-Γ BIC, carrying polarization singularity with $\nu = +1$. The stack of the two layers breaks the C_6 and up-down mirror symmetry, resulting in the D_{3d} ($C_{3v} \times C_{1i}$) point group. Due to the symmetry breaking, the eigenstates of the two single layers, $|\mathbf{u}_{t,b}\rangle \equiv \mathbf{u}_{t,b}(\boldsymbol{\rho}, z \mp s)$, become mixed, where ($\boldsymbol{\rho}$,$z$) is the coordinate. Using group representation theory, we find that $|\mathbf{u}_s\rangle \equiv |\mathbf{u}_b\rangle + |\mathbf{u}_t\rangle$ ($|\mathbf{u}_a\rangle \equiv |\mathbf{u}_b\rangle - |\mathbf{u}_t\rangle$) is associated with the A_{2g} (A_{1u}) irreducible representation of the D_{3d} group. Therefore, $|\mathbf{u}_{s,a}\rangle$ are the eigenstates at the Γ points of the bilayer PhCs. We call photonic bands related to $|\mathbf{u}_s\rangle$ and $|\mathbf{u}_a\rangle$ symmetric band(SB) and antisymmetric band (AB), respectively. Since both $|\mathbf{u}_t\rangle$ and $|\mathbf{u}_b\rangle$ of the single layers are BICs, their linear superpositions, i.e., $|\mathbf{u}_{s,a}\rangle$, are BICs, exhibiting polarization singularity in the momentum spaces with the topological charges generally obeying $\nu = 3n + 1$ ($n \in \mathbb{Z}$) because of the C_3 symmetry. Although $|\mathbf{u}_{s,a}\rangle$ have vanished far-field radiation, the so-called quasi-BICs near the Γ point will radiate. This radiation, contributed from both the tL and bL, is expected to interfere constructively or destructively as s varies.

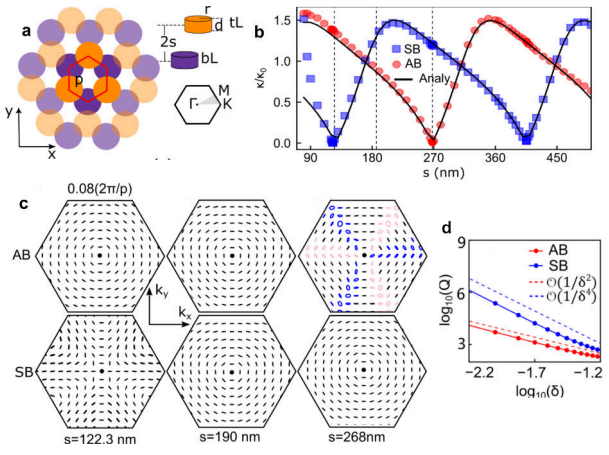

Fig. 1. **a** Schematic of the bilayer PhCs. The parameters are $r = 0.6p$, $d = 0.4p$ and $p = 300$ nm. **b** Simulated and analytical coupling coefficients for the SB and AB. **c** Polarization vector patterns of the far-field radiation from the SB and AB. **d** Q factors and their evolution trends with δ when $s = 122.3$ nm.

To reveal the interference behavior of the surrounding

radiative states around the BICs and the evolutions of the topological charges, we use perturbation theory to directly solve the far-field polarization vectors at a near-Γ Bloch wavevector $\boldsymbol{\alpha} = \frac{2\pi\delta}{p}[\ \cos\theta \quad \sin\theta\ ]^T$, where θ is the angle between $\boldsymbol{\alpha}$ and the x-axis, and δ is the perturbation parameter. We show that the $\mathbf{d}_1^+$ can be calculated from

$$\begin{bmatrix} d_{1y}^+ \\ d_{1x}^+ \end{bmatrix} = M\kappa_{s,a} \begin{bmatrix} \cos\theta \\ -\sin\theta \end{bmatrix} \tag{1}$$

where $\kappa_{s,a} = \langle \mathbf{u}_{y*}^+ | \mathcal{L}_{1x} | \mathbf{u}_{s,a} \rangle = \frac{1}{\sqrt{2}} \langle \mathbf{u}_{y*}^+ | \mathcal{L}_{1x} | \mathbf{u}_b \pm \mathbf{u}_t \rangle$ and M is a normalization parameter. The global coupling parameter $\kappa_{s,a}$ which relates the far-field polarization vectors of all the near-Γ states $|\mathbf{u}_{s,a}\rangle + \delta |\mathbf{u}_1(\theta)\rangle$ with the at-Γ states $|\mathbf{u}_{s,a}\rangle$, where θ spans 0–2π. According to Eq.(1), $\nu = +1$ ($n = 0$) for the SB and AB if $\kappa_{s,a}$ are nonzero[4]. Note that $\kappa_{s,a}$ are contributed from the tL and bL. we derive a detailed form of $\kappa_{s,a}$ to reveal how they vary with s,

$$\kappa_{s,a} = \frac{\kappa_0}{\sqrt{2}} e^{is\gamma} \frac{1 \mp e^{-i(2s\gamma+\varphi)}}{1 \mp \tilde{r}_0 e^{-2is\gamma}} \tag{2}$$

where κ_0 is the coupling coefficient of the single layer; $\varphi = \angle(r_0 - t_0)$, r_0 (t_0) is the normal reflection (transmission) coefficient of the single layer. Equation (2) indicates that when $2s\gamma+\varphi = 2N\pi$, $\kappa_s = 0$ and that when $2s\gamma+\varphi = (2N+1)\pi$, $\kappa_a = 0$, where N is an integer. We have demonstrated in theory that far-field radiation of the resonant states near BICs from two separated layers can produce destructive bilayer interference.

Figure 1(b) shows the calculated results of $\kappa_{s,a}$. The squares mark the simulated results according to the definition $\kappa_{s,a} = \langle \mathbf{u}_{y*}^+ | \mathcal{L}_{1x} | \mathbf{u}_{s,a} \rangle$. The solid curves denote the analytic results from Eq.(2), consistent with the simulation results. Our collective interference theory successfully predicts the destructive interferences at $s = 122.3$ nm for the SB and $s = 268$ nm for the AB. Figure 1(c) show the polarization vector patterns when $s = 122.3$ nm, $s = 190$ nm and $s = 268$ nm. One can find that when the destructive interference conditions are satisfied, i.e, $s = 122.3$ nm for the SB and $s = 268$ nm for the AB , the ν becomes -2 ($n = -1$). When $\kappa_{a,s}$ deviate far from zero, $\nu = +1$ ($n = 0$) for both the SB and AB. These results indicate that the topological charges can transition from $+1$ to -2 by changing s without breaking or boosting symmetry. We show in Fig.1(d) that when the condition for the destructive interferences is met, the Q factors scale with δ^{-4} near the Γ point.

III. Experiments

We fabricated the designed BMs with their spacer thickness of $s \sim 120$ nm and $s \sim 190$ nm based on the alignment lithography[2]. The scanning electron microscope (SEM) images shown in Fig.2(a) and 2(b) confirm the fine alignment and the precise control of the spacing layers. We use a commercial angle-resolved spectrometer(ARMS, Ideaoptics) to reveal the topological transition of the BICs. Figure 2(c,e) shows the measured spectra when $s \sim 120$ nm and $s \sim 190$ nm. The dispersions of the resonant modes in the SB and AB are clearly

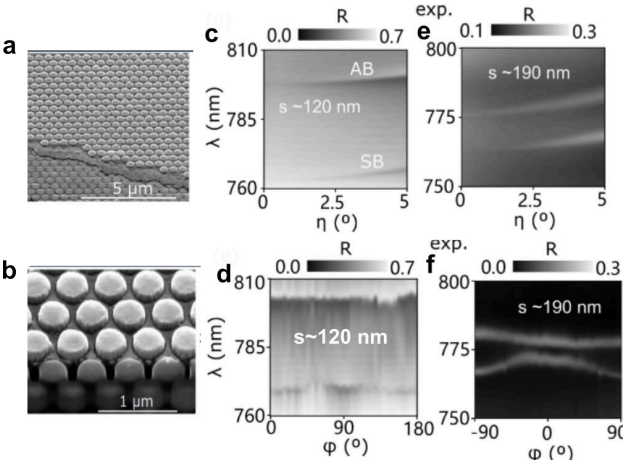

Fig. 2. **a, b** SEM images of the fabricated bilayer PhCs. **c, e** Experimental and simulated angle-resolved reflection spectra. **d, f** Experimental and simulated azimuth-angle dependence of the reflection spectra.

presented. When η approaches 0°, the Fano resonant structures disappear, indicating the existence of BICs. The resonance linewidth of the SB is noticeably narrower than that of the AB when $s \sim 120$ nm, which provides preliminary evidence for destructive interference.

We then rotated the samples and recorded the reflection spectra under the illumination of s-polarized input lights at a fixed η of 4°. The reflectance peak amplitudes scale with $R_{peak} \propto \cos^2\beta$, where β is the angle between the input light polarization and the major axis of the polarization ellipses. Consider that the sample azimuth angle is φ, the input polarization vector is then $[\ -\sin\varphi \quad \cos\varphi\ ]^T$. If the topological charge is $+1$ (-2), the polarization vectors is $[\ -\sin\varphi \quad \cos\varphi\ ]^T$ ($[\ -\cos 2\varphi \quad \sin 2\varphi\ ]^T$) and then $R_{peak} \sim 1$ ($R_{peak} \sim \sin^2 3\varphi$). Hence, as the samples are rotated by 180°, the reflectance at the resonances remains unchanged when $\nu = +1$ while R_{peak} oscillates by 3 cycles when $\nu = -2$. Figure 2(d) and 2(f) shows the measured φ-dependent reflection spectra. It can be seen that when $s = 120$ nm, the resonant peaks for the SB oscillate 3 times while those for the AB remain nearly unchanged. When $s = 190$ nm, the resonant peaks for both bands do not oscillate. These results indicate that we observed a topological transition of polarization singularities simply by changing the thickness of the BM spacer layer.

IV. Conclusion

We demonstrate theoretically and experimentally that the topological charges ($\nu = 3n + 1$) of BICs in C_3-symmetric bilayer metasurfaces can be dynamically tuned from fundamental charges ($n = 0$) to high-level charges ($n = -1$) by adjusting the spacer thickness. Our work provides a symmetry-preserved approach to control BIC topological charges and quasi-BIC Q factors, critical for tunable vortex lasers, ultrasensitive sensors, and other vortex-based devices.

ACKNOWLEDGMENTS

This work was supported by the National Natural Science Foundation of China(Grants No. 12304463, and No. 12074420)

REFERENCES

[1] M. Kang, L. Mao, S. Zhang, M. Xiao, H. Xu, and C. T. Chan. Merging bound states in the continuum by harnessing higher-order topological charges. *Light: Science & Applications*, 11(1):228, 2022.

[2] J. Tan, R. Pan, Y. Xiang, Z. Tang, B. Wang, and J. Li. Unilateral asymmetric radiation in bilayer metasurfaces. *Advanced Functional Materials*, n/a(n/a):2501156, 2025.

[3] B. Wang, R. Pan, L. Yang, X. Ji, H. Yang, and J. Li. Destructive interference mediated topological transitions in bilayer metasurfaces. *Physical Review Letters*, 136(4):043801, 2026.

[4] B. Zhen, C. W. Hsu, L. Lu, A. D. Stone, and M. Soljačić. Topological nature of optical bound states in the continuum. *Phys. Rev. Lett.*, 113:257401, Dec 2014.

Thermal optical and mechanical tuning in all-silicon and hybrid nanopillars

Victor Gonzalez-Morote[1,*], David Alonso-Tomas[1], Nestor E. Capuj[2], Albert Romano-Rodriguez[1] and Daniel Navarro-Urrios[1]

[1]MIND-IN2UB, Electronics and Biomedical Engineering Department at University of Barcelona, Spain
[2]Depto. Física, Universidad de La Laguna, 38200 San Cristóbal de La Laguna, Spain
*Corresponding author: vgonzalezmorote@ub.edu

***Abstract*—Nanopillar optomechanical cavities are sensitive to absorption driven heating. We compare monolithic silicon and hybrid pillars with a silicon dioxide base using optical tuning and pump probe readout. Thermal simulations, including full cavity models, identify dominant dissipation pathways and relate them to thermooptic shifts and changes in transduced mechanical spectra.**

***Keywords*— optomechanics, photonic crystals, nanopillar cavities, thermal dissipation, thermo optic effect.**

I. Introduction

Nanopillar-based optomechanical cavities (OMCs) provide an attractive platform for co-localizing high-Q optical resonances with multiple mechanical modes in a sub-wavelength footprint [1]. These devices are promising for compact displacement and force sensing, as nanopillars offer high mechanical compliance while photonic-crystal confinement enables efficient optical transduction [2], [3]. While monolithic silicon implementations provide strong optomechanical performance [2], hybrid architectures integrating a silicon dioxide base on silicon-on-insulator (SOI) substrates facilitate low-loss waveguide integration and robust optical access [3]. The introduction of vertical material asymmetry and additional thermal interfaces is expected to modify heat-transport pathways.

In these high-field nanophotonic devices, residual optical absorption leads to localized heating, triggering thermo-optic (TO) shifts and free-carrier effects that distort the optical response [4]. Absorption-driven temperature gradients can also induce thermoelastic stresses and photothermal backaction, modifying the mechanical dynamics and the transduced radio-frequency (RF) spectra, with consequences for stability and calibration [5].

Thermal tuning and relaxation have been investigated in silicon optomechanical crystal cavities [6]. For nanopillar-based 1D photonic-crystal cavities, however, a quantitative identification of the dominant heat-loss pathways and their simultaneous optical and mechanical signatures remains missing.

Here we compare monolithic Si and hybrid Si/SiO_2 nanopillar cavities to identify dominant heat-loss channels. Combining power-dependent optical tuning, frequency-domain pump–probe measurements, and mechanical spectral analysis with finite-element (FEM) simulations, we connect thermal dissipation dynamics to thermo-optic shifts and changes in mechanical readout, extending beyond relaxation-focused comparisons [7].

II. Methods

A. Optomechanical cavities under study

We investigate one-dimensional photonic-crystal nanopillar cavities implemented in two material platforms: (i) monolithic silicon nanopillars and (ii) hybrid nanopillars with a silicon top segment and a silicon dioxide base on a silicon-on-insulator substrate. In both designs, the optical cavity is formed by a longitudinal modulation of the pillar geometry to create an adiabatic defect, resulting in strong optical confinement near the upper portion of the pillars and enabling optical transduction of their mechanical motion [2], [3]. Unless otherwise stated, the unit-cell geometry follows Fig. 1.

B. Experimental setup and readout

Optical and mechanical mode tuning. Optical resonances are probed with a tunable infrared laser coupled to the cavity via evanescent fiber-loop coupling (Fig. 2). Power-dependent optical tuning is obtained by monitoring the transmitted signal while sweeping the laser wavelength. Under increased optical excitation, absorption-driven heating produces thermo-optic shifts and free-carrier related effects that distort and shift silicon cavity resonances [4]. Mechanical motion is read out through optomechanical transduction of the transmitted light: the transmission is detected with a fast photodiode and the radio-frequency (RF) power spectral density is measured with a spectrum analyzer.

Frequency-domain pump–probe thermal response. Thermal relaxation is extracted using a frequency-domain pump–probe method (Fig. 3). The cavity supports at least two optical modes. A pump laser is tuned into resonance with one mode and intensity-modulated to generate periodic absorbed power and temperature modulation. A low-power probe laser is tuned to a second mode and converts the thermally-induced spectral shift into an amplitude modulation of the transmitted probe via the thermo-optic effect. The probe modulation at the pump modulation frequency is measured with a vector network

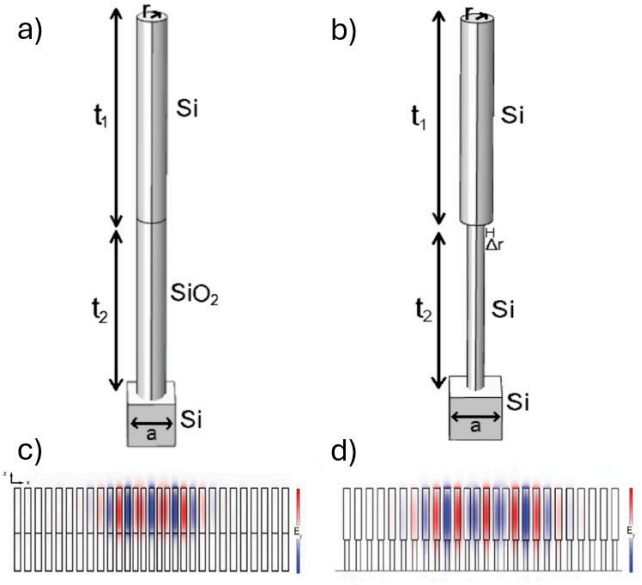

Fig. 1. Nanopillar unit-cell geometries and optical mode localization used for thermal modeling. (a) Hybrid nanopillar with a silicon top segment and a silicon dioxide bottom segment. (b) Monolithic silicon nanopillar with a radius step Δr between bottom and top segments. Parameters: $t_1 = t_2 = 1500$ nm, $a = 350$ nm, $r = 105$ nm, and $\Delta r = 50$ nm (monolithic). (c) FEM simulation of the E_y field component of the fundamental TM cavity mode (side view). (d) Same for the second-order TM cavity mode, showing similar localization near the pillar top.

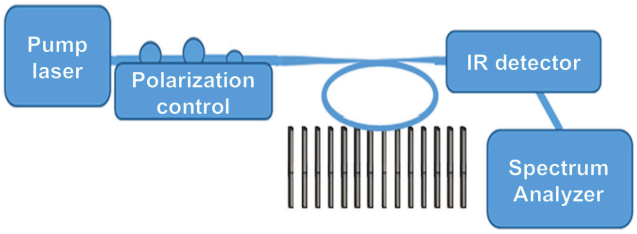

Fig. 2. Setup for optical transmission and mechanical readout under optical heating. A tunable IR laser is coupled to the cavity using a fiber-loop; the transmitted signal is detected on a fast photodiode and analyzed with a spectrum analyzer to obtain the RF power spectral density.

analyzer (VNA). We fit the magnitude response to a first-order low-pass transfer function,

$$|H(\Omega)| = \frac{1}{\sqrt{1 + (\Omega\tau_{\mathrm{th}})^2}}, \tag{1}$$

and extract τ_{th} and the cutoff frequency $1/\tau_{th} = 1/(2\pi\tau_{\mathrm{th}})$.

C. Finite-element thermal simulations

Thermal transport is modeled in COMSOL Multiphysics using time-dependent finite-element simulations (Heat Transfer in Solids),

$$\rho C_p \frac{\partial T}{\partial t} = \nabla \cdot (k\nabla T) + Q(\mathbf{r}, t), \tag{2}$$

where $Q(\mathbf{r}, t)$ represents an effective heat source associated with optical absorption localized near the upper pillar region,

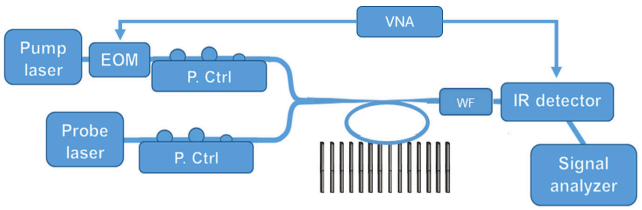

Fig. 3. Frequency-domain pump–probe setup to extract the thermal time constant. A modulated pump induces absorption-driven heating; a weak probe monitors thermo-optic detuning of a second mode. A wavelength filter separates probe and pump at the output; the VNA measures the probe magnitude response versus modulation frequency.

motivated by the optical mode localization in both platforms [2], [3]. We first employ a reduced single-pillar (unit-cell) model to capture the dominant relaxation dynamics. Simulations are run to steady state under constant heating and then the heat source is switched off to obtain the transient thermal decay. The local temperature at a monitoring point near the optical mode maximum is fitted to

$$T(t) = T_{\mathrm{amb}} + \Delta T\, e^{-t/\tau_{\mathrm{th}}}, \tag{3}$$

providing τ_{th}. To identify dominant dissipation pathways, we compare simulation variants including air-mediated dissipation (convection / heat exchange with an air domain) versus purely solid conduction through the substrate stack. We also develop full-cavity electromagnetic and thermal simulations to emulate the experimental measurements and evaluate collective effects on the entire cavity geometry.

III. Results and Discussion

A. Optical mode tuning

We characterize the optical response under increasing excitation by recording power-dependent transmission spectra of the cavity resonance (Fig. 4). For both monolithic Si and hybrid Si/SiO_2 nanopillar cavities, increasing input power induces a redshift and progressive lineshape distortion, consistent with absorption-driven heating and carrier-related nonlinearities reported in silicon photonic-crystal resonators [4], [6].

For comparable excitation conditions, the hybrid platform shows a larger effective redshift and more pronounced nonlinear distortion, suggesting a higher temperature rise at the mode location. This is consistent with reduced thermal extraction expected from the vertically asymmetric stack and additional thermal interfaces, and agrees with the slower thermal response extracted from pump–probe measurements (Sec. III-C).

B. Mechanical mode tuning

Mechanical motion is read out via optomechanical transduction of the transmitted field. Figure 5 summarizes the evolution of the transduced RF spectra under optical heating. In monolithic Si cavities, the dominant mechanical resonances remain largely stable over the explored range.

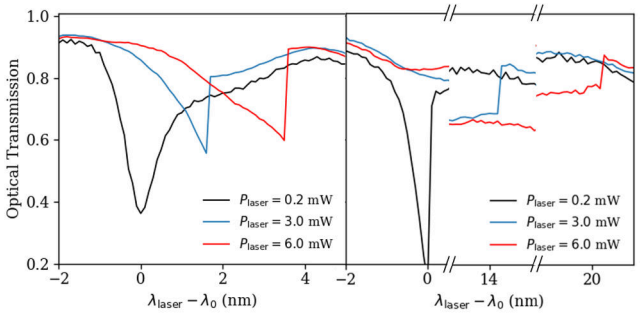

Fig. 4. Power-dependent optical transmission spectra for monolithic Si and hybrid Si/SiO_2 nanopillar cavities. Increasing excitation induces a redshift and lineshape distortion consistent with absorption-driven thermal effects and carrier-related nonlinearities.

In hybrid Si/SiO_2 devices, most resonances remain stable; however, selected modes exhibit reproducible frequency upshifts as optical heating is increased. This behavior is unexpected and is currently under investigation. When two resonances approach each other, we observe signatures consistent with mode hybridization (avoided crossing), which becomes more apparent as heating modifies mechanical detuning (Fig. 6).

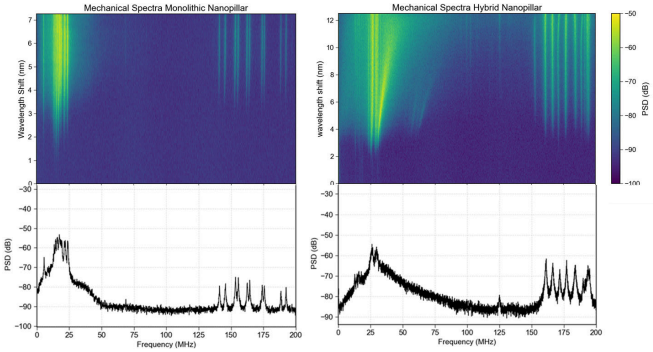

Fig. 5. Mechanical spectra under optical heating for monolithic Si and hybrid Si/SiO_2 cavities.

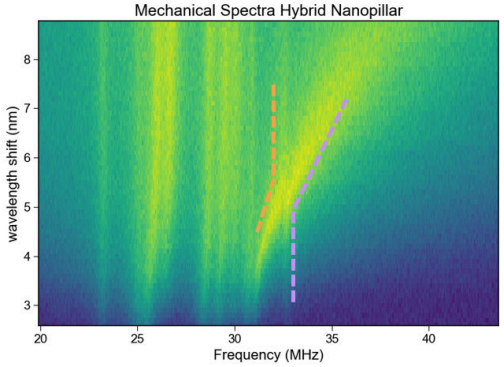

Fig. 6. Example of two mechanical resonances approaching and exhibiting an avoided-crossing-like behavior consistent with mode hybridization.

C. Thermal relaxation measurements

Heat dissipation is quantified with a frequency-domain pump-probe method. Figure 7 shows the probe magnitude response versus modulation frequency, which is fitted to a first-order low-pass fit [8], yielding $1/\tau_{th} \sim 11$ MHz (monolithic Si) and $1/\tau_{th} \sim 2$ MHz (hybrid Si/SiO_2), a markedly slower thermal response in the hybrid platform.

Figure 8 shows the time-domain FEM transients on a reduced unit-cell model, which provide consistent values ($f_c \sim$ 7.67 MHz and $\sim$ 2.22 MHz), supporting the observed trend.

FEM control simulations indicate that, in the hybrid geometry, heat dissipation through the base of the pillar is greatly obstructed by the low thermal conductivity of SiO_2, leading to a much slower conduction-only decay. When an air domain is included, heat exchange with air significantly accelerates the relaxation, becoming a major contribution to the effective decay rate (Fig. 9).

Full-cavity coupled electromagnetic and thermal simulations are being developed to capture the coupled thermal–optical dynamics and collective effects in the complete cavity.

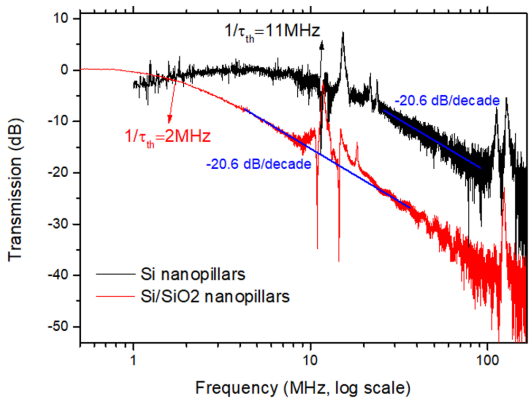

Fig. 7. Frequency-domain pump–probe thermal response for monolithic Si and hybrid Si/SiO_2 nanopillar cavities. The probe magnitude response shows a first-order roll-off, from which an effective thermal relaxation rate is extracted.

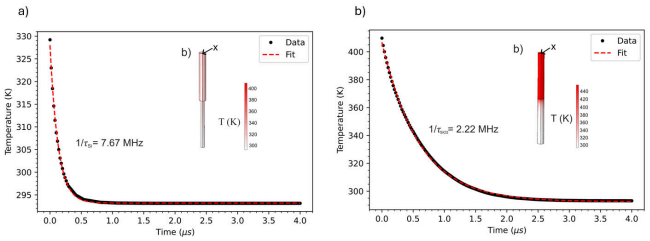

Fig. 8. The average temperature of the top of the nanopillar as a function of time for both geometries.

IV. Conclusion

We compared monolithic Si and hybrid Si/SiO_2 nanopillar optomechanical cavities under absorption-driven heating. Pump–probe measurements and FEM transients show a slower

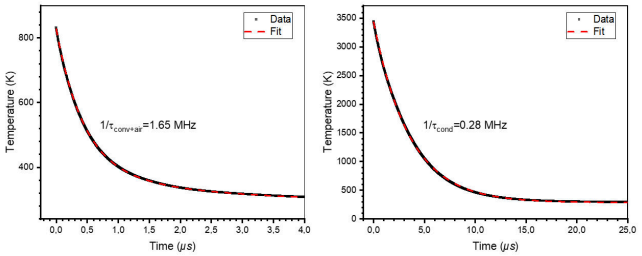

Fig. 9. FEM dissipation rate for (a) air domain enabled (convection/air exchange) and (b) purely solid conduction.

thermal response in the hybrid platform, consistent with reduced heat extraction through the SiO_2 segment. This enhanced thermal response correlates with larger optical resonance shifts and with mode-dependent changes in the transduced mechanical spectra, highlighting the role of the material stack in thermal–optical–mechanical behavior.

ACKNOWLEDGMENTS

This work was supported by the MCINN through the projects ALLEGRO (Grants No. PID2021-124618NBC22 and PID2021-124618NB-C21), MOCCASIN-2D (Grant No. TED2021-132040B-C21), and an FPU fellowship (FPU23/00690) awarded to D.A.T.

REFERENCES

[1] M. Aspelmeyer, T. J. Kippenberg, and F. Marquardt, "Cavity optomechanics," *Rev. Mod. Phys.*, vol. 86, pp. 1391–1452, Dec 2014. [Online]. Available: https://link.aps.org/doi/10.1103/RevModPhys.86.1391

[2] J. Jaramillo-Fernandez, M. Poblet, D. Alonso-Tomás, C. V. Bertelsen, E. López-Aymerich, D. Arenas-Ortega, W. E. Svendsen, N. Capuj, A. Romano-Rodríguez, and D. Navarro-Urrios, "Strong cavity-optomechanical transduction of nanopillar motion," *ACS Nano*, vol. 18, no. 35, pp. 24 550–24 557, 2024, pMID: 39167712. [Online]. Available: https://doi.org/10.1021/acsnano.4c09014

[3] M. Poblet, Berte:contentReference[oaicite:4]index=4er, E. Alonso-Tomás, David:contentReference[oaicite:5]index=5 López-Aymerich, J. Goldschmidt, K. Schmitt, M. Dimaki, W. E. Svendsen, A. Romano-Rodríguez, and D. Navarro-Urrios, "Hybrid sio2/si pillar-based optomechanical crystals for on-chip photonic integration," *Nanophotonics*, vol. 14, no. 17, pp. 2953–2961, 2025.

[4] P. E. Barclay, K. Srinivasan, and O. Painter, "Nonlinear response of silicon photonic crystal microresonators excited via an integrated waveguide and fiber taper," *Optics Express*, vol. 13, no. 3, pp. 801–820, 2005.

[5] A. G. Primo, C. M. Kersul, R. Benevides, N. C. Carvalho, M. Ménard, N. C. Frateschi, P.-L. De Assis, G. S. Wiederhecker, and T. P. Mayer Alegre, "Accurate modeling and characterization of photothermal forces in optomechanics," *APL photonics*, vol. 6, no. 8, 2021.

[6] D. Navarro-Urrios, J. Gomis-Bresco, N. E. Capuj, F. Alzina, A. Griol, D. Puerto, A. Martínez, and C. M. Sotomayor-Torres, "Optical and mechanical mode tuning in an optomechanical crystal with light-induced thermal effects," *Journal of Applied Physics*, vol. 116, p. 093506, 2014.

[7] V. González-Morote, D. Alonso-Tomás, M. Poblet, N. E. Capuj, A. Romano-Rodríguez, and D. Navarro-Urrios, "Thermal dissipation in pillar-based optomechanical resonators: Comparing monolithic silicon and hybrid silicon-silicon dioxide nanopillars," in *META 2025: International Conference on Metamaterials, Photonic Crystals and Plasmonics*, Málaga, Spain, 2025.

[8] C. Shakespeare, A. S. Kumar, and J. T. Muhonen, "Thermal relaxation time and photothermal optomechanical force in sliced photonic crystal silicon nanobeams," *Opt. Express*, vol. 32, no. 21, pp. 36 824–36 834, Oct 2024. [Online]. Available: https://opg.optica.org/oe/abstract.cfm?URI=oe-32-21-36824

Independent control of dispersion band and linewidth of guided-mode resonances by using dual-ridge unit-cell structures

Joong Hyeon Pyo[1,*], Yu Sung Choi[1,*], Robert Magnusson[2], and Jae Woong Yoon[1,‡]

[1]*Department of Physics, Hanyang University, Seoul 04763, Korea*
[2]*Department of Electrical Engineering, University of Texas - Arlington, Arlington, TX 76019, United States*
[*]These authors contributed equally to this work.
[‡]Correspondence should be addressed to yoonjw@hanyang.ac.kr

***Abstract*—We present a dual-ridge unit cell enabling deterministic, independent tuning of guided-mode resonance frequency and linewidth. A closed-form parametric search space maps geometry to spectral metrics, removing trial-and-error. The framework supports multi-metric design and uncovers emergent non-Hermitian and topological features, including exceptional points and Fermi arcs.**

***Keywords*— metamaterials, guided-mode resonance, photonic crystals, dual-ridge unit-cell.**

I. Introdunction

Guided-mode resonances (GMR) near the second-order band-gap condition are of particular interest because they can yield strong spectral signatures such as near-unity reflection/transmission, symmetry-protected bound states in the continuum (BIC), and topological edge states under near-normal incidence.

However, practical GMR device design frequently requires the independent tuning of multiple spectral metrics. To increase degrees of freedom, designers typically introduce additional parameters such as material index, ridge height, and layer thickness. Nevertheless, it remains difficult to predict and decouple each parameter's influence on resonance position and linewidth, which makes optimization slow and frequently suboptimal.

Here, we present a comprehensive study of dual-ridge compound unit cells and propose a deterministic tuning strategy based on a coupled-mode-theory (CMT) model with closed-form geometric relations. We further validate the feasibility of the method through rigorous numerical analysis.

II. Simplified Model Description

Our model is based on the CMT formulation introduced by Kazarinov and Henry [1]. For the considered geometry, the coupled-mode description reduces to an eigenvalue problem of the form

$$\mathbf{H}|\psi\rangle = (\omega - \omega_{\mathrm{B}})|\psi\rangle, \tag{1}$$

for GMR state $|\psi\rangle = [a_+\ a_-]^{\mathrm{T}}$, where $a_\pm$ denote the amplitudes of guided modes propagating along $\pm x$. Here, ω_{B} is the frequency corresponding to the second-order Bragg condition of the guided mode, and the effective Hamiltonian is written as

$$\mathbf{H} = \begin{bmatrix} vk+\delta & m_+ \\ m_- & -vk+\delta \end{bmatrix}. \tag{2}$$

where v is group velocity of the guided mode and k is Bloch wave vector along x. The two counter-propagating guided modes couple to each other through second-order Bragg reflection with rates $m_\pm$.

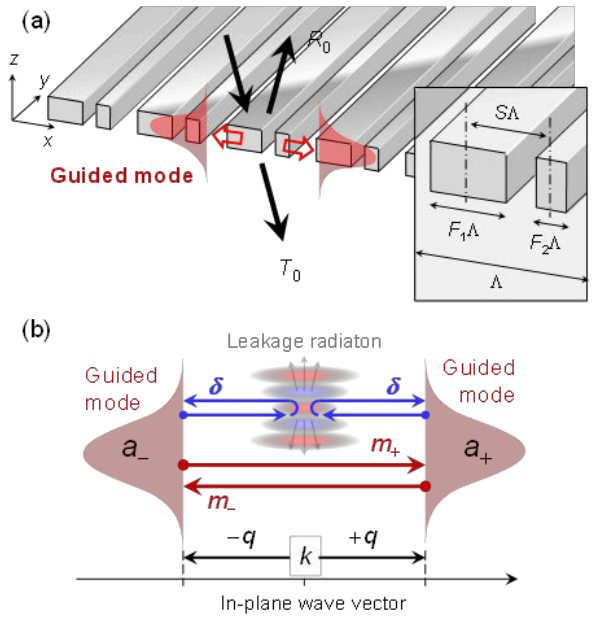

Fig. 1. GMR in dual-ridge compound unit-cell structure.

Importantly, $m_\pm$ and the detuning parameter δ are directly linked to the unit-cell geometry, enabling geometry-driven

design strategies that target the band-gap width and linewidth in a controlled manner. They can be expressed using the Fourier coefficients $\{\varepsilon_n\}$ of the dielectric function in the grating region as

$$m_{\pm} = \varepsilon_{\pm 1}{}^{2}\kappa_1 - \varepsilon_{\pm 2}\kappa_2 , \tag{3}$$

$$\delta = \varepsilon_{+1}\varepsilon_{-1}\kappa_1 , \tag{4}$$

where κ_1 and κ_2 are diffraction-rate coefficients associated with the first- and second-order diffraction processes of the guided mode, respectively. Detailed expressions are provided in our previous work [2].

To exploit a convenient constant-F subspace, we introduce the ridge-width difference factor $\chi = F_1 - F_2$, which sets the individual fill factors as by $F_1 = (\mathrm{F}-\chi)/2$ and $F_2 = (\mathrm{F}+\chi)/2$, together with the ridge center-distance factor S. With these parameters, the real and imaginary parts of the Fourier coefficients $\{\varepsilon_n\}$ admit explicit expressions:

$$\mathrm{Re}(\varepsilon_{n\neq 0}) = \frac{2\Delta\varepsilon}{n\pi}\sin\left(\frac{n\pi \mathrm{F}}{2}\right)\cos\left(\frac{n\pi\chi}{2}\right)\cos\left(n\pi S\right), \tag{5}$$

$$\mathrm{Im}(\varepsilon_{n\neq 0}) = \frac{2\Delta\varepsilon}{n\pi}\cos\left(\frac{n\pi \mathrm{F}}{2}\right)\sin\left(\frac{n\pi\chi}{2}\right)\sin\left(n\pi S\right). \tag{6}$$

Substituting these relations into the model equations yields closed-form expressions for the linewidth ω_g and the linewidths $\Delta\omega_{\pm}$, which can be conveniently visualized on the χ-S plane. The independent-control scheme is then constructed by using gradient directions or equi-level contours of ω_g and $\Delta\omega_{\pm}$, as described next.

III. Rigorous Numerical Analysis

To quantify the degree of independent tunability, we define the parametric-gradient cosine $c_{\pm}$ on χ-S plane as

$$c_{\pm} = \frac{\nabla\omega_g \cdot \nabla\Delta\omega_{\pm}}{|\nabla\omega_g||\nabla\Delta\omega_{\pm}|}, \tag{7}$$

where the parametric gradient operator is $\nabla = \mathbf{e}_{\chi}(\partial/\partial\chi)+\mathbf{e}_S(\partial/\partial S)$. Independent control is poorly achievable in regions where $c_{\pm} \approx \pm 1$ while maximally efficient for $c_{\pm} \approx 0$.

We further demonstrate several practical examples of independent parametric control in Figs. 2(c)–3(e). Figure 2(c) shows a band-gap-preserving linewidth modulation. The angle-resolved transmittance spectra simultaneously visualize the dispersion bands and their linewidth distributions. Notably, the dispersion curve remains nearly fixed while the linewidth varies substantially. In Fig. 2(d), we highlight a particularly strong linewidth modulation: the linewidth changes by a factor of 65 while the resonance wavelength remains fixed at 1.259 μm. Conversely, resonance-position tuning with nearly fixed linewidth is also readily achievable, as shown in Fig. 2(e), where the linewidth is maintained at 0.5 nm while the resonance wavelength shifts from 1.247 μm to 1.297 μm.

Importantly, these demonstrations are achieved while holding other structural parameters constant, including the net fill factor F, period, and ridge height. Therefore, the dual-ridge compound unit-cell approach enables highly efficient and practical independent control of GMR metrics.

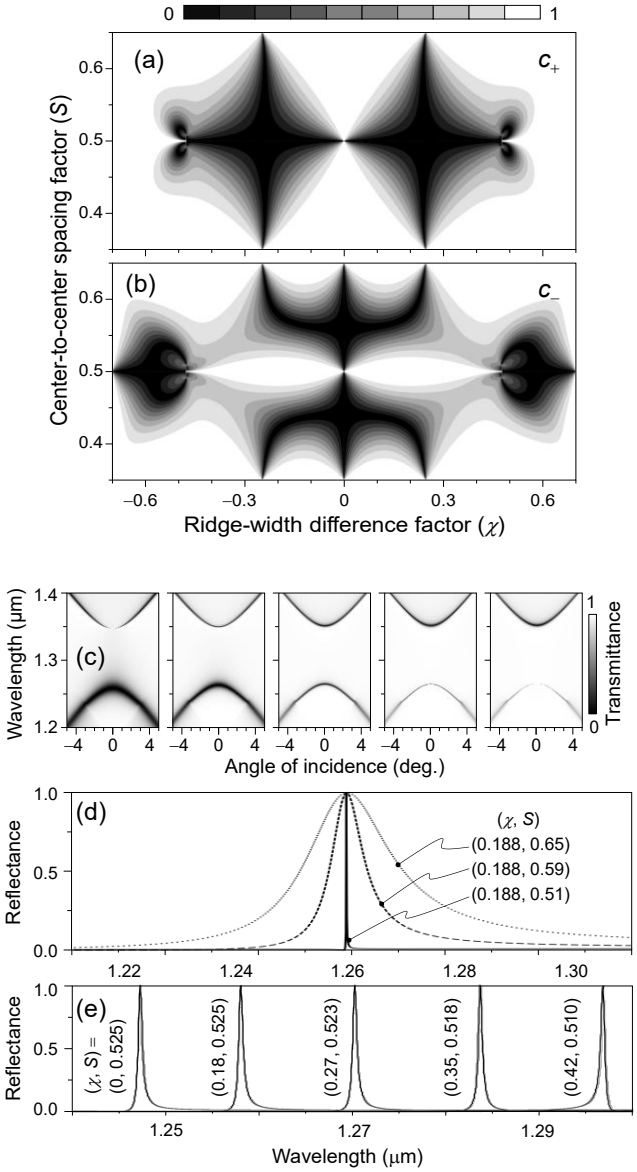

Fig. 2. Fully independent parametric control of resonance position and linewidth.

IV. Additional Feature: Fermi Arc Condition

Beyond independent tunability, the χ-S maps reveal additional emergent features. In the distributions of $\Delta\omega_{\pm}$, we observe arc-like loci where the linewidths of the upper and lower bands coincide, i.e., $\Delta\omega_{+} = \Delta\omega_{-}$. These loci are indicated by the blue curves in Fig. 3(a). Within the simplified model of Eqs. (1)–(4), these arcs correspond to a loop defined by the condition $\mathrm{Im}(m_{+}m_{-}) = 0$, which can be expressed in terms of the Fourier coefficients $\{\varepsilon_n\}$ as

$$\mathrm{Re}(\kappa_1) = \mathrm{Re}(\varepsilon_2 / \varepsilon_1^{\,2})\kappa_2 \,. \tag{8}$$

Using Eqs. (5) and (6), this condition can be evaluated explicitly on the χ-S plane, producing the loop shown in Fig. 3(a). Here we note that κ_1 is generally complex-valued, whereas κ_2 is purely real for lossless structures, which is used in deriving Eq. (8). As a result, nearly uniform linewidth can be obtained across the entire GMR bands, as illustrated in Fig. 3(b) (angle-resolved transmittance) and Fig. 3(c) (reflection spectra). Remarkably, an extremely narrow resonance can persist over a broad range of incident angles and wavelengths, which occurs for parameter sets on the blue segment of the loop in Fig. 3(a).

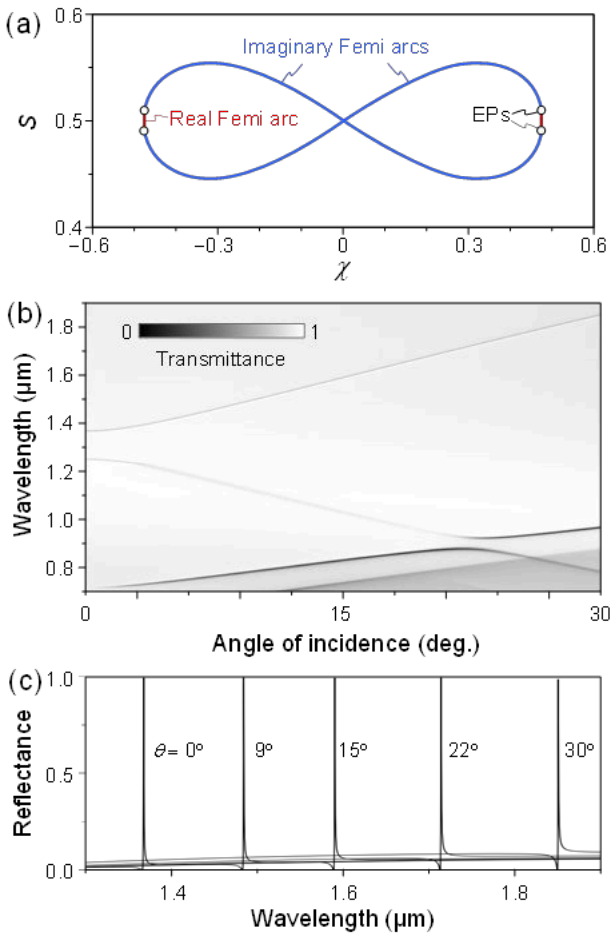

Fig. 3. Fermi arcs in GMR spectra.

V. Conclusion

We have presented a comprehensive description of key GMR metrics in explicit terms of unit-cell design parameters and proposed a deterministic design methodology for targeted resonance properties. In particular, a dual-ridge compound unit cell enables fully independent tuning of dispersion-band location and resonance linewidth, offering a highly efficient approach for practical GMR devices such as filters, sensing templates, and surface-emitting light sources.

Moreover, we find that the dual-ridge design provides direct access to emergent physics associated with non-Hermitian dynamics and topological wave effects, including EP singularities, Fermi arcs, and band-topological phase transitions. These advantages originate from enhanced parametric controllability over the complex-valued Fourier coefficients $\{\varepsilon_n\}$, which fundamentally determine the coupling strengths and phases of elementary diffraction processes. This framework can be further extended to develop new GMR elements involving BICs, topological localization, beam shaping, and related functionalities.

Acknowledgments

This research was supported in part by the Leader Researcher Program (NRF-2019R1A3B2068083).

References

[1] R. Kazarinov and C. Henry, "Second-order distributed feedback lasers with mode selection provided by first-order radiation losses," *IEEE Journal of Quantum Electronics*, vol. 21, no. 2, pp. 144–150, 2003.

[2] K. Y. Lee et al., "Topological guided-mode resonances at non-Hermitian nanophotonic interfaces," Nanophotonics, vol. 10, no. 7, pp. 1853–1860, 2021.

Controlling topologically-protected edge states via synthetic space manipulation in photonic crystals

Bartosz Janaszek[1,2*], Tomasz Śmiarowski[1,2], Anna Tyszka-Zawadzka[1], Paweł Szczepański[1,2]

[1]Institute of Microelectronics and Optoelectronics, Warsaw University of Technology, Warsaw, Poland

[2]National Institute of Telecommunications, Warsaw, Poland

*Corresponding author: Bartosz.janaszek@pw.edu.pl

***Abstract*— We propose a design framework for controlling topologically protected edge states, illustrated by Tamm Plasmon Polaritons in 1D planar photonic crystals. By emulating Weyl points in synthetic-parameter space, robust interface modes can be engineered on demand. This strategy opens up new pathways toward resilient, multifunctional photonic platforms.**

***Keywords*: topological photonics, photonic crystal, topological edge states, synthetic space.**

I. Introduction

Topologically protected edge states are typically associated with Weyl points—three-dimensional band degeneracies originally identified in semimetals and defined in momentum space. While such features are conventionally studied in fully three-dimensional systems, it has recently been shown that analogous topological singularities can be engineered in synthetic parameter spaces constructed from controllable structural or temporal degrees of freedom [1].

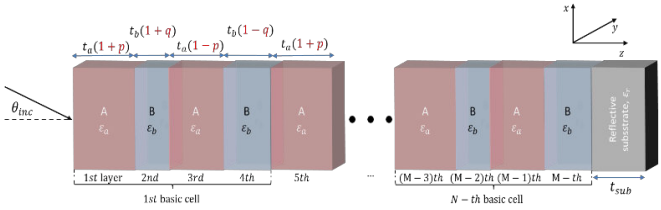

Fig. 1 Schematic of a parametrized 1D topological PC emulating Weyl point.

Here, we introduce a systematic design approach that enables controlled realization of topologically protected edge states, which we demonstrate by example of topologically-protected Tamm Plasmon Polaritons existing at the interface between a parametrized PC (depicted in Fig.1) and a highly reflective substrate/superstrate. The method is based on the approach proposed by Wang et al. [2] and emulates a Weyl point in a one-dimensional periodic system with a parametrized four-layer unit cell composed of materials A and B (isotropic or anisotropic).

II. Design Approach

By independently tuning two unit-cell geometrical parameters and combining them with a wavevector component, we construct an effective three-dimensional synthetic space. Within this space, linear band degeneracies emerge, accompanied by characteristic phase vortices in the reflection response.

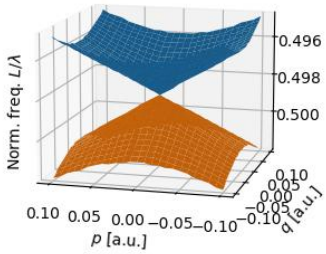

Fig. 1 Linear degeneracy around for a wave of Weyl frequency in the assumed synthetic space

Importantly, this synthetic-space framework serves not merely as a theoretical construct but as a predictive design tool: it directly determines the conditions under which robust interface states fulfill the resonance condition and must arise in real space. In particular, we demonstrate how these synthetic Weyl points guarantee the formation of topologically protected Tamm plasmon polaritons at the boundary between the photonic crystal and a reflective truncation. The approach therefore provides an intuitive and scalable route for engineering high-quality, polarization-independent interface resonances with built-in robustness against structural perturbations.

III. Results and Discussion

The results presented confirm that the synthetic-space design framework provides direct control over the formation and physical properties of topologically protected interface states. The first set of colormaps (Fig. 3(a–c)) illustrates transmission, reflection, and absorption as functions of the synthetic-space parameters p and q.

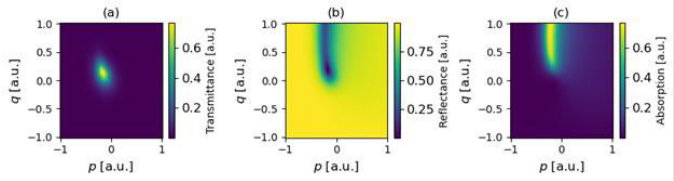

Fig. 3 Colormaps of power transmission (a), reflection (b), and absorption (c) plotted vs. synthetic space parameters.

Distinct arc-like regions are visible in all three maps, corresponding to Fermi-arc states that originate from the emulated Weyl point in synthetic space. These arcs indicate parameter combinations for which a robust interface resonance exists. Importantly, while the reflectance map exhibits a clearly defined dip along the arc, corresponding to the presence of the interface state, the transmission and absorption maps reveal that the energy redistribution between these channels strongly depends on the chosen synthetic-space coordinates.

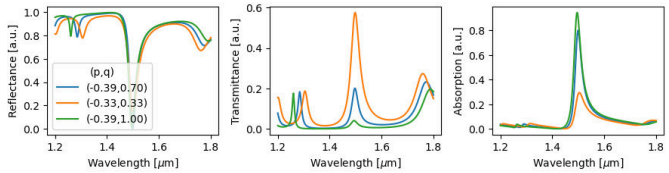

Fig. 4 Spectra of transmission (a), reflection (b) and absorption (c) for different *pq* pairs.

The corresponding spectral responses shown in the Fig. 4, further clarify this behavior. For different synthetic-space parameters located along the Fermi arc, a reflectance minimum is preserved at approximately the same spectral position, confirming the topological nature of the interface state. However, the depth and spectral redistribution of energy between transmission and absorption vary significantly. In some configurations, the interface state is predominantly absorptive, whereas in others it enables enhanced transmission. This demonstrates that the proposed approach does not merely guarantee the existence of a state but allows its optical properties to be engineered.

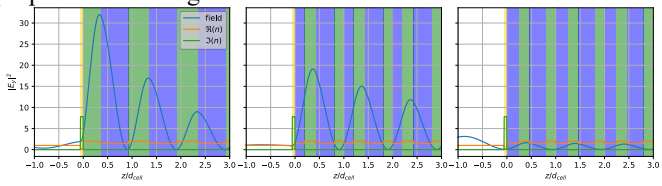

Fig. 5 Field distribution for absorption-dominated (a), transmission-enhanced (b) and weakly confined configuration (c).

Along with transmission and absorption, spatial field distributions can also be engineered by an appropriate choice of synthetic-space parameters, see Fig. 5. The results show strong localization of the electromagnetic field at the interface, characteristic of a Tamm plasmon polariton. Crucially, the magnitude and spatial profile of the local field enhancement differ across parametrizations. By appropriately selecting the synthetic parameters, one can tailor the degree of field confinement and peak intensity while maintaining the reflectance dip associated with the topological state. This capability is particularly attractive for enhancing nonlinear effects and optimizing sensing performance while maintaining the guaranteed existence of the interface state.

IV. Conclusion

This work demonstrates that topology in photonics can move beyond an abstract concept toward function-driven design. By emulating Weyl points in a synthetic parameter space, we transform a simple one-dimensional multilayer into a platform where the existence of interface states is guaranteed by topology, yet their functionality remains fully engineerable. The resulting Tamm plasmon polaritons combine robustness with tunability: the reflectance dip persists as a topological invariant, while transmission, absorption, and local field enhancement can be deliberately tailored through synthetic-space parameter selection. Rather than designing resonances that must be delicately optimized and are vulnerable to fabrication imperfections, we begin with a state that is topologically secured and subsequently tailor its propertties. In this sense, synthetic space becomes a powerful design framework for creating robust and customizable photonic responses. The implications extend beyond the specific system studied here. In sensing, topologically protected resonances provide stable spectral markers whose field enhancement can be engineered for maximum interaction with active or analyte materials [3]. In nonlinear photonics, controllable interfacial confinement enables enhanced Kerr or saturable effects, paving the way for intensity discriminators, compact optical limiters, and elements for all-optical signal processing [4]. Looking forward, expanding the synthetic-space concept to alternative parameter manifolds—including gain–loss balance, anisotropy, temporal modulation, electrostatic bias, or nonlinear coefficients—opens the possibility of topology tailored to functionality. Extension to two-dimensional photonic configurations further enriches the design landscape, enabling directional robustness, higher-order topological states, and scalable integration within photonic circuits.

Ultimately, this approach bridges abstract topological physics and practical device engineering. It suggests a future in which photonic components are not merely optimized against imperfections, but are fundamentally designed to be robust, adaptable, and multifunctional by construction.

Acknowledgments

This work was supported by WUT's AEEiTK Scientific Discipline Council grant.

References

[1] L. Yuan, Q. Lin, M. Xiao, and S. Fan, "Synthetic dimension in photonics," Optica **5**, 1396-1405 (2018)

[2] Wang, Q., Xiao, M., Liu, H., Zhu, S., & Chan, C. T. (2017). Optical interface states protected by synthetic Weyl points. Physical Review X, 7(3), 031032.

[3] B. Janaszek, A. Tyszka-Zawadzka, and P. Szczepański. "Utilizing Fermi arc states in photonic crystals for ultrasensitive gas detection." *Optics Express* 33.24 (2025): 51319-51334.

[4] B. Janaszek and P. Szczepański. "Optical Intensity Discrimination with Engineered Interface States in Topological Photonic Crystals." Micromachines 17.2 (2026): 165.

Floquet-Engineered Switching of Dissipation between Driven and Undriven States

Hidemasa Yamane[1,*]

[1]Osaka Research Institute of Industrial Science and Technology, Japan
*Corresponding author: yamane.hidemasa@orist.jp

***Abstract*—We study two atoms coupled to a continuum and analytically reveal a mechanism for selective dissipation induced by external driving. By tuning only the driving parameters, an undriven atom can decay remotely while the driven atom remains long-lived. Numerical simulations demonstrate controllable switching between dissipation and suppression.**

***Keywords*— quantum photonics, Floquet engineering, dissipation control, waveguide QED**

I. Introduction

Structured photonic environments provide powerful platforms for controlling dissipation [1], [2]. In systems such as photonic crystal waveguides, coupled-resonator optical waveguides, and waveguide-QED platforms, the finite bandwidth of the continuum and the density of states near band edges strongly modify radiative processes, giving rise to a variety of open-system dynamics including non-Markovian effects and bound-state formation [2], [3]. If the lifetime of a particular state among multiple discrete degrees of freedom coupled to such a continuum can be selectively controlled, it would be useful for tasks such as state initialization and reset.

Periodic driving provides an additional control knob for this purpose [4]. Within Floquet theory, a time-periodic Hamiltonian is described in an extended Hilbert space [5], where the drive creates additional channels in the energy structure of both discrete states and the continuum [6], [7]. As a result, dissipation pathways that do not exist in the static system may be opened or closed.

In this work, we consider a minimal model consisting of two atoms (discrete states) coupled to a one-dimensional tight-binding continuum, where only one of the states is subjected to a time-periodic modulation of its transition energy. Using the Wannier–Stark basis, we construct the Floquet Hamiltonian and analyze the complex spectrum by the Brillouin–Wigner–Feshbach projection method [8]. We show that, by tuning only the parameters of the external drive while keeping all system parameters fixed, it is possible to selectively induce dissipation either in the driven state or in the undriven state.

II. Theoretical Formulation

We consider a Fano–Anderson-type model [9] in which two discrete states $|d_A\rangle$ and $|d_B\rangle$ are coupled to a one-dimensional tight-binding continuum, while only A is subjected to periodic driving. In the Bloch basis $|k\rangle$, the time-dependent Hamiltonian is written as

$$\hat{H}(t) = \hat{H}_{\rm tb} + \hat{H}_{\rm d}(t) + \hat{H}_{\rm int} \tag{1}$$

$$\begin{cases} \hat{H}_{\rm tb} \equiv \displaystyle\int_{-\pi}^{\pi} dk\, \varepsilon_k |k\rangle\langle k|, \qquad \varepsilon_k = -\beta\cos k, & (2)\\ \hat{H}_{\rm d}(t) \equiv (e_A + \alpha\cos\omega t)\,|d_A\rangle\langle d_A| + e_B|d_B\rangle\langle d_B|, & (3)\\ \hat{H}_{\rm int} \equiv \dfrac{g_A}{\sqrt{2\pi}}\displaystyle\int_{-\pi}^{\pi} dk\ (|d_A\rangle\langle k| + \text{H.c.}) \\ \qquad\quad + \dfrac{g_B}{\sqrt{2\pi}}\displaystyle\int_{-\pi}^{\pi} dk\ (|d_B\rangle\langle k| + \text{H.c.})\,. & (4) \end{cases}$$

Here, β is the parameter that determines the bandwidth of the static continuum. The bare energies e_A and e_B are placed outside this band. The constants g_A and g_B denote the coupling strengths of A and B to the continuum, respectively. Throughout this work we mainly focus on the weak-coupling regime, $g_A \sim g_B \sim g \ll \beta$. The drive amplitude and frequency are denoted by α and ω, and we define $\chi \equiv \alpha/\omega$.

To exploit the time periodicity, we introduce the extended Floquet space and use the Fourier basis $|\cdot, n\rangle\!\rangle \equiv |\cdot\rangle \otimes e^{in\omega t}$ with Floquet index n [6], [7]. For the driven state A, we further introduce the Wannier–Stark basis

$$|\phi_A^{(n)}\rangle\!\rangle = \sum_{\nu} J_{n-\nu}(\chi)\,|d_A, \nu\rangle\!\rangle, \tag{5}$$

where $J_n(\chi)$ is the Bessel function of the first kind. Using this basis, the Floquet Hamiltonian $\hat{\mathcal{H}} = \hat{H}(t) - i\partial_t$ can be decomposed, in the same way as the original Hamiltonian [10], as

$$\hat{\mathcal{H}} = \hat{\mathcal{H}}_{\rm tb} + \hat{\mathcal{H}}_{\rm d} + \hat{\mathcal{H}}_{\rm int}. \tag{6}$$

$$\begin{cases} \hat{\mathcal{H}}_{\rm tb} = \displaystyle\sum_n \int_{-\pi}^{\pi} dk\,(\varepsilon_k + n\omega)\,|k, n\rangle\!\rangle\langle\!\langle k, n|, & (7)\\ \hat{\mathcal{H}}_{\rm d} = \displaystyle\sum_n (e_A + n\omega)\,|\phi_A^{(n)}\rangle\!\rangle\langle\!\langle \phi_A^{(n)}| \\ \qquad\quad + \displaystyle\sum_n (e_B + n\omega)\,|d_B, n\rangle\!\rangle\langle\!\langle d_B, n|, & (8)\\ \hat{\mathcal{H}}_{\rm int} = \dfrac{g_A}{\sqrt{2\pi}}\displaystyle\sum_{n,n'}\int_{-\pi}^{\pi} dk\, J_{n'-n}(\chi)\left[|\phi_A^{(n')}\rangle\!\rangle\langle\!\langle k, n| + \text{H.c.}\right] \\ \qquad\quad + \dfrac{g_B}{\sqrt{2\pi}}\displaystyle\sum_n\int_{-\pi}^{\pi} dk\ [|d_B, n\rangle\!\rangle\langle\!\langle k, n| + \text{H.c.}]\,. & (9) \end{cases}$$

As shown in Fig. 1, the continuum forms the band $[-\beta + n\omega, \beta + n\omega]$ in the nth Floquet mode, while the discrete ladders of A and B appear at $e_A + n\omega$ and $e_B + n\omega$, respectively. The ladder of A can couple different Floquet modes through the Bessel weight $J_{n'-n}(\chi)$, whereas the ladder of B remains mode-diagonal, namely $|d_B, n\rangle\!\rangle$ couples only to $|k, n\rangle\!\rangle$. Therefore, B cannot change the Floquet index by itself, and in order to reach an open continuum band in a neighboring Floquet mode, it must pass through the driven ladder of A. In the following, the complex spectrum of the Floquet Hamiltonian is analyzed by the Brillouin–Wigner–Feshbach projection method [8]; a finite imaginary part of the A-like or B-like pole corresponds to decay of the corresponding state. Within the projection formalism, the A-like and B-like poles are obtained from the projected resolvent in the discrete subspace.

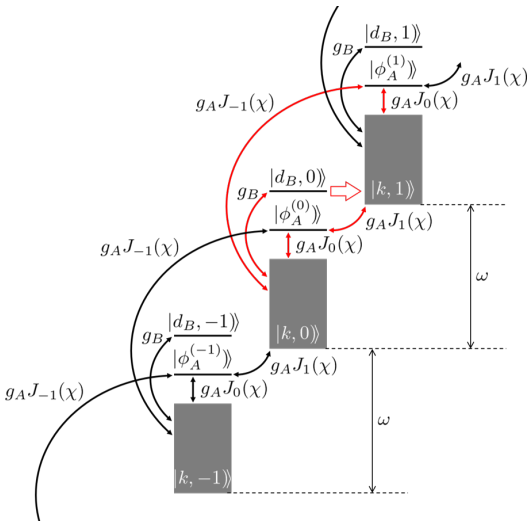

Fig. 1. Schematic energy structure in the physical and extended Floquet representations. The tight-binding continuum forms a finite band in each Floquet mode, while the driven discrete ladder $\{|\phi_A^{(n)}\rangle\!\rangle\}$ couples to different Floquet modes with Bessel-weighted amplitudes $J_{n'-n}(\chi)$. The undriven ladder $\{|d_B, n\rangle\!\rangle\}$ couples to the continuum without changing n. This structure allows photon-assisted pathways, mediated by the driven ladder, that connect the undriven state to a neighboring continuum Floquet mode.

III. Results and Discussion

We now interpret the two representative cases shown in Fig. 2 on the basis of the energy structure in Fig. 1. As a time-domain observable, we use the survival probability

$$P_X(t) = |\langle d_X | U(t,0) | d_X \rangle|^2 \tag{10}$$

for the initial state $|d_X\rangle$ $(X = A, B)$, where $U(t,0)$ is the time-evolution operator associated with the time-dependent Hamiltonian $\hat{H}(t)$. The numerical results are obtained by direct integration of the time-dependent Schrödinger equation. The common parameters are $\beta = 1$, $e_A = 1.25$, $e_B = 1.30$, and $g_A = g_B = 0.05$. In this case, the continuum band in the nth Floquet mode is $[-\beta + n\omega, \beta + n\omega]$.

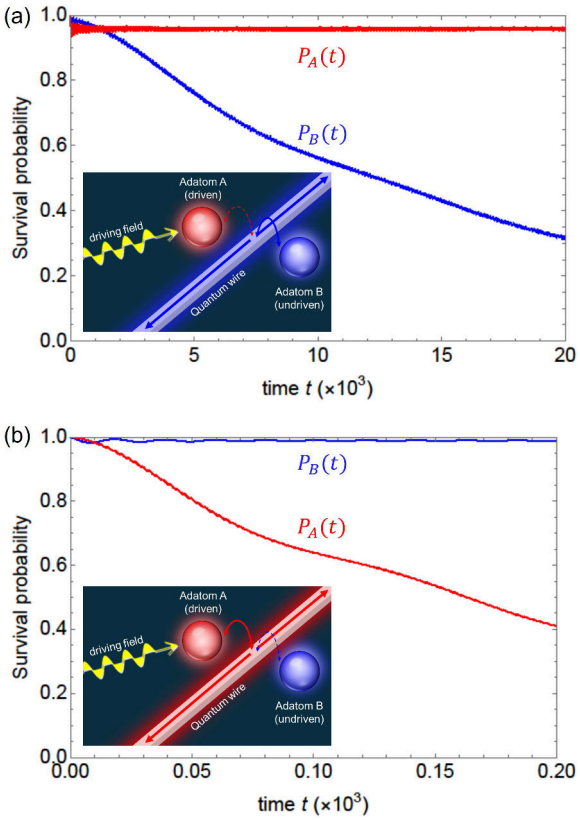

Fig. 2. Selective dissipation controlled by local driving. (a) Remote dissipation of the undriven state: $P_A(t)$ remains close to unity while $P_B(t)$ decays for $\omega = 2.3025$ and $\chi = 1.08$. (b) Switching and suppression of the remote channel: choosing χ near the first zero of J_0 suppresses the decay of B, while the driven state A decays for $\omega = 2.2$ and $\chi = 2.40$. The internal parameters are $\beta = 1$, $e_A = 1.25$, $e_B = 1.30$, and $g_A = g_B = 0.05$.

We first consider the condition corresponding to Fig. 2(a), namely $\omega = 2.3025$, $\chi = 1.08$. In this case, the lower edge of the first Floquet mode is very close to e_B. By contrast, e_A is still below this edge, so A is not yet sufficiently inside the open continuum band. Moreover, for $\chi = 1.08$, the product $|J_0(\chi)J_1(\chi)|$ is large, so the weight of the indirect pathway for B is strong. Therefore, as can be read from the energy diagram in Fig. 1, the undriven state $|d_B, 0\rangle\!\rangle$ first couples to $|k, 0\rangle\!\rangle$ with amplitude g_B, then to the driven ladder state $|\phi_A^{(0)}\rangle\!\rangle$ with amplitude $g_A J_0(\chi)$, and finally to the continuum state $|k, 1\rangle\!\rangle$ in the first Floquet mdoe with amplitude $g_A J_1(\chi)$. The effective amplitude of this remote pathway is thus weighted by $g_A^2 g_B J_0(\chi) J_1(\chi)$. Once this channel is open, the B-like pole acquires a finite imaginary part. Accordingly, the induced linewidth appears at order $O(g_A^4 g_B^2)$, namely $O(g^6)$ for $g_A \sim g_B \sim g$. In contrast, A is still far from an open dissipation channel into which it can decay directly. As a result, in Fig. 2(a), the driven state A remains long-lived, while only the undriven state B decays appreciably.

We next consider the condition corresponding to Fig. 2(b), namely $\omega = 2.2$, $\chi = 2.40$. In this case, both e_A and e_B lie inside the continuum band of the first Floquet mode.

From the energy structure alone, both A and B may appear energetically allowed to decay. However, when the pathway structure in Fig. 1 is also taken into account, their behaviors are very different. Since A can directly transition from $|\phi_A^{(0)}\rangle\rangle$ to $|k,1\rangle\rangle$ with amplitude $g_A J_1(\chi)$, the A-like linewidth appears at $O(g^2)$, and $P_A(t)$ indeed decays rapidly. On the other hand, the dominant indirect pathway of B is proportional to $J_0(\chi)J_1(\chi)$. Under this condition, $J_0(\chi) \simeq 0$, so that its principal pathway is closed. Therefore, although B is located near the continuum band of the first Floquet mode, the main photon-assisted pathway leading to that dissipation channel is supplessed. Consequently, in Fig. 2(b), A decays, whereas the remote dissipation of B is suppressed and B remains long-lived.

These two results show that which state decays is determined not only by simple energetic overlap, but also by whether the Floquet pathway leading to the corresponding continuum band is actually open. While A can decay at low order because it can directly cross Floquet modes under the drive, B depends on an indirect pathway mediated by A, so its dissipation can be selectively opened or closed by changing only the drive condition.

IV. Conclusion

In this work, we theoretically studied a system in which only one of two discrete states coupled to a finite-band continuum is subjected to local periodic driving. Starting from the Hamiltonian in the k-representation, we described the Floquet Hamiltonian in terms of $\hat{\mathcal{H}}_{\rm tb}$, $\hat{\mathcal{H}}_{\rm d}$, and $\hat{\mathcal{H}}_{\rm int}$ using the Wannier–Stark basis, thereby making clear which Floquet modes couple to which discrete states. Furthermore, by means of the Brillouin–Wigner–Feshbach projection method, we analyzed the complex spectrum associated with the A-like and B-like poles. This analysis shows that the linewidth of the driven state appears at low order through a direct pathway to an open Floquet mode, whereas the linewidth of the undriven state arises from a higher-order photon-assisted pathway mediated by the driven state.

In particular, when the energy of the undriven state is located near an open continuum band in a neighboring Floquet mode, especially near its edge, and at the same time the driven state is arranged so as not to decay directly, only the undriven state undergoes remote dissipation. By contrast, when an open Floquet mode is directly available for the driven state, while the dominant indirect pathway for the undriven state is suppressed by a Bessel weight such as $J_0(\chi) \simeq 0$, only the driven state decays and the remote dissipation of the undriven state is supplessed. Direct numerical integration of the time-dependent Schrödinger equation clearly reproduced both of these selectively dissipative situations.

These results show that Floquet analysis together with complex-spectrum analysis provides a quantitative understanding of how local periodic driving remotely controls the dissipation of an undriven state coupled to a common continuum. The mechanism presented here offers a useful design principle for state-selective reset and dissipation engineering in structured photonic environments.

Acknowledgments

This work was supported by JSPS KAKENHI (Grant Number JP24K00933).

References

[1] H.-P. Breuer and F. Petruccione, *The theory of open quantum systems*. OUP Oxford, 2002.

[2] A. S. Sheremet, M. I. Petrov, I. V. Iorsh, A. V. Poshakinskiy, and A. N. Poddubny, "Waveguide quantum electrodynamics: Collective radiance and photon-photon correlations," *Reviews of Modern Physics*, vol. 95, no. 1, p. 015002, 2023.

[3] A. Yariv, Y. Xu, R. K. Lee, and A. Scherer, "Coupled-resonator optical waveguide: a proposal and analysis," *Optics letters*, vol. 24, no. 11, pp. 711–713, 1999.

[4] N. Yamada, K.-i. Noba, S. Tanaka, and T. Petrosky, "Dynamical suppression and enhancement of instability for an unstable state by a periodic external field," *Physical Review B—Condensed Matter and Materials Physics*, vol. 86, no. 1, p. 014302, 2012.

[5] T. Petrosky, I. Prigogine, and S. Tasaki, "Quantum theory of non-integrable systems," *Physica A (Theoretical and Statistical Physics);(Netherlands)*, vol. 173, no. 1/2, 1991.

[6] J. H. Shirley, "Solution of the Schrödinger equation with a Hamiltonian periodic in time," *Physical Review*, vol. 138, no. 4B, p. B979, 1965.

[7] H. Sambe, "Steady states and quasienergies of a quantum-mechanical system in an oscillating field," *Physical Review A*, vol. 7, no. 6, p. 2203, 1973.

[8] H. Feshbach, "Unified theory of nuclear reactions," *Annals of Physics*, vol. 5, no. 4, pp. 357–390, 1958.

[9] K. Friedrichs, "On the perturbation of continuous spectra," *Communications on Pure and Applied Mathematics*, vol. 1, no. 4, pp. 361–406, 1948.

[10] H. Yamane and S. Tanaka, "Ultrafast dynamics of high-harmonic generation in terms of complex floquet spectral analysis," *Symmetry*, vol. 10, no. 8, p. 313, 2018.

Nonlinear Topological States in Photonic Crystals: Modal Structure and Intensity-Dependent Optical Response

Tomasz Śmiarowski[1,2*], Bartosz Janaszek[1,2], Paweł Szczepański[1,2]

[1]Institute of Microelectronics and Optoelectronics,
Warsaw University of Technology, Warsaw, Poland
[2]National Institute of Telecommunications, Warsaw, Poland
*Corresponding author: t.smiarowski@il-pib.pl

***Abstract*— We theoretically investigate how Kerr-type nonlinearity modifies topological Bloch and interface states in 1D and 2D photonic crystals, and how these changes manifest in intensity-dependent transmission and reflection characteristics.**

***Keywords*: topological photonics, photonic crystal, topological edge states, nonlinear optics.**

I. Introduction

Topological photonics offers a powerful paradigm for controlling light via states robust against structural disorder. In photonic crystals (PhCs), this allows for the engineering of protected edge and interface states. Utilizing synthetic dimensions enables the realization of these phenomena even in 1D systems, leading to highly localized optical modes, such as topological Tamm plasmon polaritons (TPPs) [1]. Integrating Kerr-type optical nonlinearity, particularly through graphene in the terahertz (THz) regime enables dynamic, intensity-dependent control over the spectral position of these states. Despite rapid advancements, the interplay between topology and nonlinearity remains only partially understood, especially regarding how nonlinear effects modify the underlying modal structure. In this work, we present a theoretical investigation of nonlinear topological PhCs in 1D and 2D configurations. We analyze the formation of topological interface states within synthetic parameter spaces and examine how Kerr nonlinearity influences their transmission and reflection properties.

II. Numerical Analysis

The numerical framework combines rigorous frequency-domain techniques to investigate the interplay between photonic topology and Kerr-type nonlinearity. First, the linear dispersion characteristics, including the engineering of topological bandgaps and the exploration of synthetic parameter spaces, are calculated using the Plane Wave Expansion Method (PWEM) [6]. By solving the electromagnetic eigenvalue problem, PWEM allows for the precise identification of frequency regimes supporting protected edge and interface states. To evaluate optical response and the excitation of highly localized modes, such as TPPs, we employ the Transfer Matrix Method (TMM) for strictly 1D stratified configurations and Rigorous Coupled-Wave Analysis (RCWA) for structures with 2D lateral periodicity [7]. Crucially, to accurately model the intensity-dependent Kerr nonlinearity elements, the scattering algorithms are augmented with a self-consistent spatial discretization scheme. Because the nonlinear dielectric response is linked to the spatially varying local electric field intensity, the nonlinear regions are subdivided into a series of the sub-layer stripes (Fig. 1) along the propagation axis [5]. Within each stripe, the optical properties are assumed to be locally uniform and are iteratively updated based on the confined field distribution. This iterative feedback loop ensures self-consistency between the internal electromagnetic field profile and the material's dynamic response.

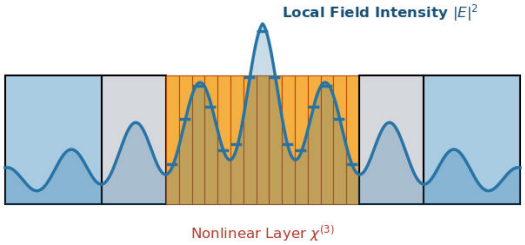

Fig. 1 Spatial discretization of the nonlinear layer in the 1D model, comparing the continuous field profile with its piecewise-averaged approximation for each strip.

By correlating these rigorously calculated nonlinear transmission and reflection spectra with the PWEM-derived band structures, we can directly map how incident light intensity modulates the spectral position and coupling conditions of the topological interface states.

III. Results and Discussion

Here, we analyze a 1D photonic crystal truncated with a nonlinear defect layer based on graphene. The basic cell of the considered structure consists of 4 layers of two dielectric materials and thickness that are parametrized with geometrical parameters p and q, which allows to obtain a synthetic parameter space with so-called Fermi-arc states translated into

real-space TPPs [2]. To establish the topological nature of our structure, we first calculated the linear band dispersion. As shown in Fig. 2, the cross-section of the dispersion relation with the assumed synthetic space (for a $q = 0$) exhibits a Dirac-like linear degeneracy at the intersection between the first and second bands, signifying the presence of a Weyl point. Subsequently, numerical simulations (Fig. 3) of a state belonging to the Fermi arc, arbitrarily chosen to be at p=-0.53 q=1.00, reveal a non-monotonic, intensity-dependent transmission response. At low optical intensities, a clear transmission channel emerges. However, due to the dispersive Kerr-type nonlinearity of graphene, increasing the incident intensity dynamically shifts the phase of the reflected waves. This effect bends the transmission channel and leads to an abrupt suppression of transmittance, driving the device into a highly reflective state.

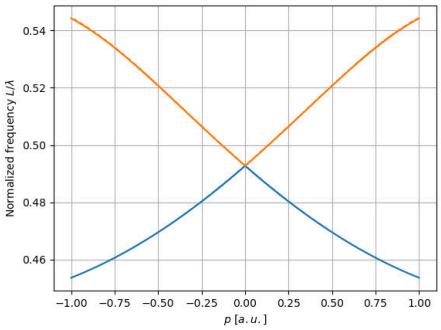

Fig. 2 Calculated band structure exhibiting a Dirac-like degeneracy. The linear crossing signifies a topological phase transition.

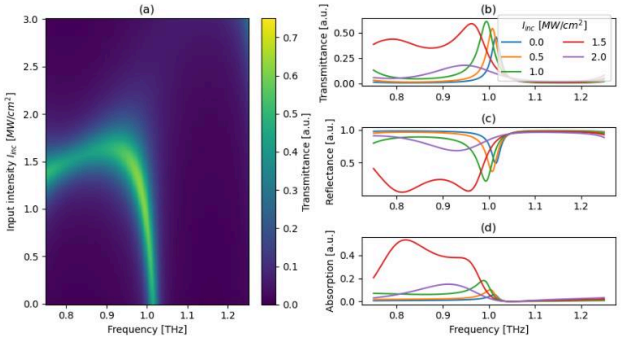

Fig. 3 (a) Transmittance colormap plotted as a function of frequency and incident intensity. Spectral characteristics of (b) transmittance, (c) reflectance, and (d) absorption for selected incident intensities

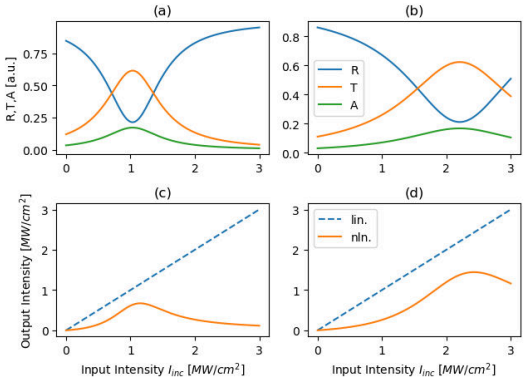

Fig. 4 Power-limiting performance of the proposed structure. Relative redistribution of optical power among reflectance, transmittance, and absorption (a, b), and absolute output versus input intensity characteristics (c, d) for two different graphene electrostatic biasing levels.

Importantly, this power-limiting threshold can be actively tuned via electrostatic biasing of the graphene layer; higher bias voltages decrease the effective nonlinear sensitivity, shifting the cut-off to higher incident intensities. These characteristics demonstrate the platform's potential as a compact, electrically tunable nonlinear distributed Bragg reflector (DBR), highly suitable for optical power limiting and passive pulse shaping in THz laser cavities.

IV. Conclusion and Future Outlook

We theoretically demonstrate the dynamic, intensity-dependent control of TPPs in THz photonic crystals utilizing the ultrafast Kerr nonlinearity of integrated graphene. By combining PWEM with self-consistent nonlinear TMM/RCWA models, we capture the spectral modulation of these robust interface states, driven by strong local-field enhancement. The observed interplay between topological protection and nonlinear field confinement provides a versatile platform for active nanophotonic devices. These include ultrafast optical limiters, all-optical switches, and highly sensitive, label-free THz sensors based on novel intensity-interrogated detection schemes.

While the present study focuses on 1D structures, ongoing work extends this framework toward higher-dimensional photonic crystals, where richer topological phenomena and additional degrees of freedom are expected to emerge. In particular, future efforts will emphasize a more comprehensive analysis of the underlying modal structure, including Bloch, edge, and interface states in 2D systems, and their role in shaping nonlinear optical response. These directions will be further explored and presented during the conference.

References

[1] L. Yuan, Q. Lin, M. Xiao, and S. Fan, "Synthetic dimension in photonics," Optica **5**, 1396-1405 (2018)

[2] Wang, Q., Xiao, M., Liu, H., Zhu, S., & Chan, C. T. (2017). Optical interface states protected by synthetic Weyl points. Physical Review X, 7(3), 031032.

[3] B. Janaszek, A. Tyszka-Zawadzka, and P. Szczepański. "Utilizing Fermi arc states in photonic crystals for ultrasensitive gas detection." *Optics Express* 33.24 (2025): 51319-51334.

[4] B. Janaszek and P. Szczepański. "Optical Intensity Discrimination with Engineered Interface States in Topological Photonic Crystals." Micromachines 17.2 (2026): 165.

[5] A. Mossakowska-Wyszyńska, P. Witoński, and P. Szczepański, "Nonlinear operation of an FP laser with PT symmetry active medium," Opt. Express 31, 8518-8534 (2023)

[6] Joannopoulos, J. D., Johnson, S. G., Winn, J. N., & Meade, R. D. (2008). *Photonic Crystals: Molding the Flow of Light* (2nd ed.). Princeton University Press.

[7] Moharam, M. G., Grann, E. B., Pommet, D. A., & Gaylord, T. K. (1995). Formulation for stable and efficient implementation of the rigorous coupled-wave analysis of binary gratings. *Journal of the Optical Society of America A*, 12(5), 1068-1076.

POSTERS

Micro/Nano Fabrication and Characterization

9 contributions · pp. 1749–1775

Establishing a Library of Metasurface Building Blocks through Coherence-Controlled Holographic Microscopy

Ondřej Červinka[1,2], Vlastimil Weiss[1], Martin Hrtoň[1,2], Petr Bouchal[1,2], Petr Liška[1,2], Filip Ligmajer[1,2], Tomaš Šikola[1,2], Petr Viewegh[1,2]

[1]*Institute of Physical Engineering, Brno University of Technology, Brno, Czech Republic Central European*
[2]*Institute of Technology (CEITEC), Brno University of Technology, Brno, Czech Republic*
**Corresponding author: ondrej.cervinka1@ceitec.vutbr.cz*

Abstract — We demonstrate coherence-controlled holographic microscopy (CCHM) as a robust tool for creating experimental metasurface building block libraries. By measuring the experimental response of TiO_2 nanostructures across varying wavelengths, polarizations, and numerical apertures, we identify critical discrepancies between simulations and real-world performance caused by fabrication-induced internal voids in modified damascene nanofabrication process.

Keywords — metasurfaces, holographic microscopy, TiO_2 nanostructures, phase characterization, building block library.

I. INTRODUCTION

Optical metasurfaces are next generation for state-of-the-art free-space and on-chip devices. While dielectric materials like TiO_2 and Si have pushed light-scattering efficiencies over 90%, their design often relies solely on numerical simulations (FDTD, RCWA). These simulations frequently overlook real-world fabrication imperfections, such as rounding, size deviations, surface roughness, or material density variations.

Existing characterization methods, such as far-field intensity inspection, evaluate overall response but fail to identify specific sources of functional imperfections. While scattering-type scanning near-field optical microscopy (s-SNOM) offers high resolution, it is limited by slow imaging speeds and small fields of view. In this work, we propose coherence-controlled holographic microscopy (CCHM) as a practical, single-snapshot alternative for establishing experimental libraries that account for all fabrication and material imperfections.

II. METHODS

Our experimental setup utilizes a modified CCHM (based on the Telight Q-Phase microscope) [1]. The system was modified with a monochromator for wavelength sweeps (600–740 nm) and a rotatable linear polarizer. This configuration provides amplitude and direct phase imaging using light of arbitrary spatial and temporal coherence. We compare the experimentally acquired data with commercial FDTD (Lumerical) and RCWA (Python [2]) implementations.

Sample Fabrication: Anisotropic TiO_2 building blocks, pictured in Fig. 1, were fabricated on a fused silica substrate using electron beam lithography and atomic layer deposition (ALD), similar to [3]. The sample consists of 20×20 µm fields with widths and lengths ranging from 130 to 330 nm, a constant period of 450 nm, and a height of 500 nm. Fabrication accuracy was verified via Atomic Force Microscopy (AFM) and SEM.

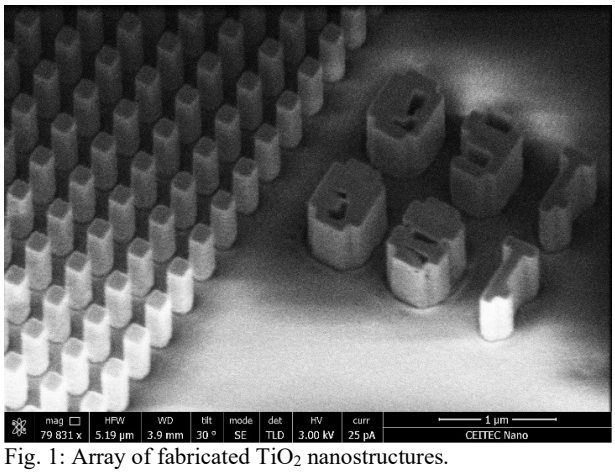

Fig. 1: Array of fabricated TiO_2 nanostructures.

III. RESULTS AND DISCUSSION

Wavelength Dependence

We conducted a spectral sweep from 600 to 740 nm. As can be seen in Fig. 2, the experimental phase values are found to saturate at 1.25 π, whereas numerical simulations (RCWA/FDTD) predicted coverage up to 2π. This discrepancy is critical for forward design, as simulated half-wave plates (HWPs) may only function as quarter-wave plates (QWPs) in practice.

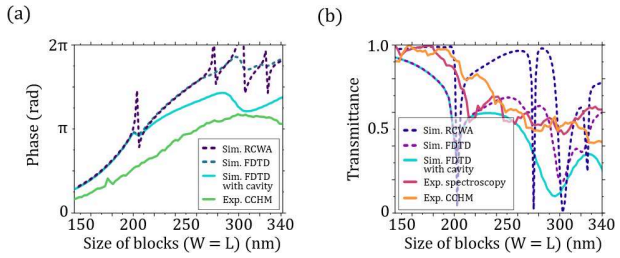

Fig. 2: Comparison of experimental and simulated a) phase and b) amplitude response.

Identification of Internal Voids

Investigation into the phase discrepancy revealed that it was not caused by changes in the material's dielectric function or rounding of edges. Instead, Focused Ion Beam (FIB) cross-sections confirmed the formation of hollow spaces within the high-aspect-ratio nanostructures. These voids, caused by limited ALD precursor diffusion, significantly reduce the phase shift and shift resonant spectral positions.

Polarization and Numerical Aperture Effects

Including the linear polarizer showed a polarization sensitive phase response of the nanostructures, proving the versatility of the CCHM. Furthermore, experimental testing showed that varying the numerical aperture of the condenser lens (0.05 to 0.5) had an insignificant impact on the phase response, suggesting the robustness of the building blocks under varying illumination conditions.

IV. CONCLUSION

We have demonstrated that CCHM is an effective and robust tool for validating metasurface building blocks. By identifying systematic fabrication defects like internal voids that are invisible to non-destructive techniques, CCHM allows for the creation of experimental true response "metalibraries". This approach is essential for high-performance metasurface design, ensuring that fabricated devices meet their intended phase and amplitude specifications and can also be used for metasurface validation.

ACKNOWLEDGMENTS

This work was supported by the Grant Agency of the Czech Republic (20-01673S), and Brno University of Technology (FSI-S-23-8336 and CEITEC VUT-J-24-8583). This work was supported by the project Quantum materials for applications in sustainable technologies (QM4ST), funded as project No. CZ.02.01.01/00/22_008/0004572 by OP JAK, call Excellent Research. We also acknowledge CzechNanoLab Research Infrastructure supported by MEYS CR (LM2018110) and the Biophotonics Core Facility, CEITEC Brno University of Technology, Czech Republic supported by MEYS CR (LM2023050 Czech-BioImaging).

REFERENCES

1. P. Kolman and R. Chmelík, "Coherence-controlled holographic microscope," Optics Express, Vol. 18, Issue 21, pp. 21990-22004 18(21), 21990–22004 (2010).

2. "inkstone · PyPI," https://pypi.org/project/inkstone/.

3. R. C. Devlin, M. Khorasaninejad, W. T. Chen, J. Oh, and F. Capasso, "Broadband high-efficiency dielectric metasurfaces for the visible spectrum," Proc. Natl. Acad. Sci. U. S. A. 113(38), 10473–10478 (2016).

Retrieving structural and optical parameters of 2D photonic crystals through angle-resolved spectroscopy: Addressing the electron microscope limitations

A. Anand Eswara Rao,[1,2] and P. Viswanath,[1,2*]
[1] Center for Nano and Soft Matter Sciences (CeNS), Shivanapura, Bengaluru 562 162, India
[2]Academy of Scientific and Innovative Research (AcSIR), Ghaziabad 201 002, India
*Corresponding author: viswanath@cens.res.in

***Abstract*— We demonstrated angle-resolved spectroscopy as precise, non-invasive metrology for characterizing self-assembled 2D photonic crystals in close-packed and non-close-packed states. By analyzing diffraction, retroreflection, and interference, we retrieved the structural parameters and effective refractive indices. This framework overcomes limitations of electron microscopy, such as need for conductive coatings and vacuum conditions.**

***Keywords*— 2D photonic crystal, self-assembly, angle-resolved spectroscopy, diffraction, retroreflection**

I. Introduction

Self-assembled two-dimensional colloidal spheres, which function as 2D photonic crystals, play a significant role in nanophotonics [1], [2]. In this work, polystyrene (PS) sphere monolayers were fabricated via interfacial self-assembly, which offers a superior approach for large-scale production on a wide range of substrates [3]. Reactive ion etching (RIE) is employed to transform polystyrene (PS) monolayers from the close-packed (CP) state to the non-close-packed (NCP) state [2]. While these systems are often characterized by electron microscopy, the need for conductive coatings and a vacuum environment limits usability. Since the optical properties of these 2D photonic crystals are strictly dependent on the lattice geometry and effective refractive index[4], spectroscopy offers a strong pathway to solve the inverse problem. By systematically analysing the spectral response of these 2D photonic crystals, one can rigorously deduce the underlying structural and optical parameters non-invasively. However, interpreting the spectral response is non-trivial, as it involves an interplay of three optical phenomena: lattice diffraction [5], thin-film interference [6], and guided-mode resonances [7]. Since the substrate's refractive index is higher than the PS monolayer's effective refractive index ($n_{Si} > n_{eff}$), the optical modes along the monolayer are not entirely confined and may leak into the substrate, resulting in leaky mode resonances (LMR) [8]. These LMRs are often accompanied by broad interference and diffraction patterns, making it challenging to distinguish resonant features against the background.

II. Methods

In the present work, we fabricated PS sphere ($\approx 1000\ nm$) monolayers on silicon substrates via surfactant-assisted self-assembly at the air-water interface [9]. Further, we generated a library of NCP test structures with varying sphere size (d_f) through RIE. To characterize the complex optical response of the PS monolayers, we used three complementary geometries: fixed-incidence diffraction, retroreflection, and symmetric reflection (Fig. 1). Through this approach, we distinguished the respective contributions of diffraction, retroreflection, and thin-film interference.

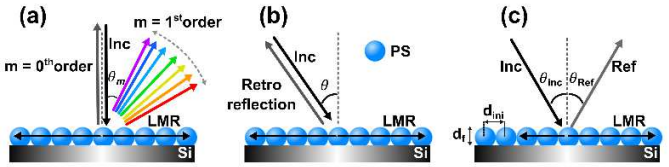

Fig. 1. Schematic representation of the optical measurement geometry exploring (a) diffraction, (b) retroreflection, and (c) interference phenomena in a PS monolayer deposited on a silicon substrate. Here, LMR refers to leaky mode resonance.

III. Results and Discussion

First, by tracking the angular evolution of the dominant diffraction peak, the iridescence of the 2D photonic crystals was quantified (Fig. 2 a and b). Second, to uniquely extract the lattice parameter and identify the underlying lattice symmetry, we fit the grating phase-matching condition to the angular dispersion of multiple orders in retroreflection spectra (Fig. 2 c). Finally, by performing a global fit of the theoretical thin-film model to multi-order symmetry reflection spectra (Fig. 2 d), we determined the evolution of the reduced sphere size (d_f) and effective refractive index (n_{eff}) as a function of etch duration.

Finally, we identified the anomalous spectral dips observed across the aforementioned optical spectra as LMR (Fig. 2 b - c). We compared the optically retrieved structural parameters with field emission scanning electron microscope (FESEM) data, demonstrating that the proposed method is a cost-effective, robust, and non-invasive alternative for precise structural characterization. From Fig. 3, we observed that the geometric sizes extracted from FESEM (black circles) exhibit a systematic offset of about $115\ nm$ ($\approx 11\%$) compared to the optical measurements (black triangles). This deviation is attributed to calibration issues and charging-induced edge blooming in FESEM. Furthermore, the discrepancy in the n_{eff}

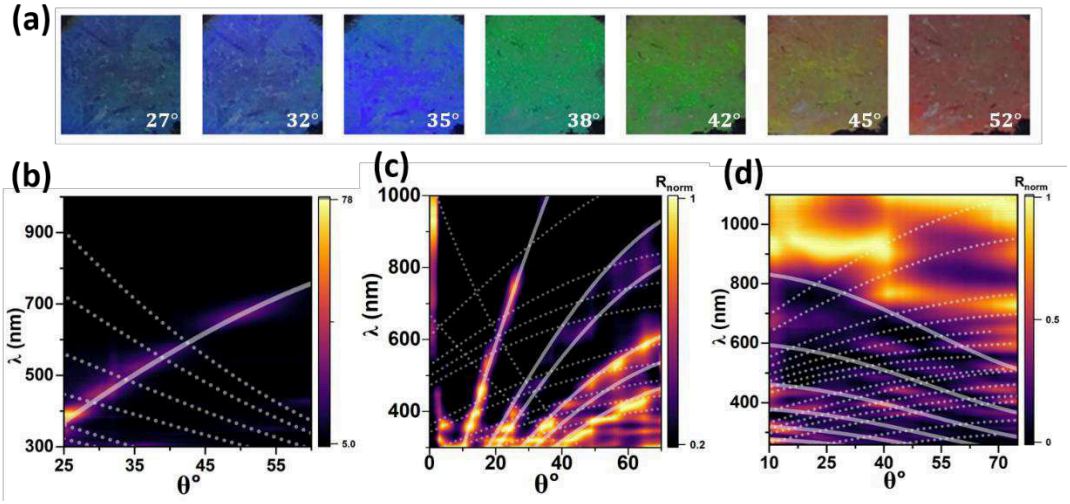

Fig. 2. (a) Photographs of the PS monolayers captured by varying the camera viewing angle (θ_m) for fixed-incidence ($\theta_{ini} = 0°$). The field of view of each images is 1.5×1.5 cm^2. Color maps indicate the experimental spectra of (b) diffraction, (c) retroreflection, and (d) symmetry reflection. (b-c) continuous lines are the analytical phase-matching and thin-film fits, while the dotted lines are plotted from the LMR dispersion relation.

increases significantly with RIE duration (from $\Delta n_{eff} \approx 0.03$ in the CP state to $\Delta n_{eff} \approx 0.09$ after 420 s of RIE) is attributed to the anisotropic nature of the etching process.

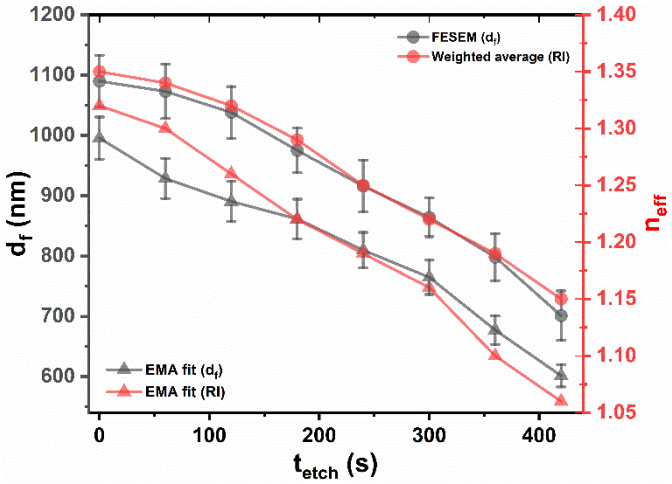

Fig. 3. The sphere size (d_f) and effective refractive index (n_{eff}) obtained from FESEM images and the weighted average index are compared with values obtained from the analytical thin-film model for different RIE durations.

IV. Conclusion

In this work, we have demonstrated a facile, non-invasive, and robust approach to measure the lattice periodicity, effective refractive index, and reduced sphere size of a 2D photonic crystal with angle-resolved optical spectroscopy. We quantified the iridescence using fixed-incidence surface diffraction. Using the retroreflection geometry, the lattice symmetry and the lattice parameter of the colloidal assembly are precisely determined. The evolution of the reduced sphere size and effective refractive index with respect to etching duration was rigorously quantified by globally fitting the interference spectra obtained in symmetric reflection geometry. Furthermore, the anomalous spectral dips observed in all these optical phenomena are attributed to leaky mode resonances. Using the appropriate dispersion relation, the dispersive trajectories of these LMR resonances for multiple reciprocal lattice vectors were accurately predicted. The lattice periodicity obtained from three different optical studies is in excellent agreement with the manufacturer's specifications. Our study highlights a significant discrepancy between sphere sizes measured via FESEM and those retrieved optically. We attributed this discrepancy to calibration issues and charge-induced blooming in FESEM. The identification of the leaky-mode resonance signatures in all three optical phenomena provides a comprehensive understanding of the electromagnetic modes supported by 2D photonic crystals. Since colloidal monolayers are increasingly used as a sacrificial mask in NSL, our non-invasive optical approach serves as an essential quality-control step, ensuring the integrity of sphere geometry and lattice order. Beyond static structural characterization, this framework can be extended to real-time monitoring of lattice evolution under external stimuli, including mechanical strain, thermal expansion, and chemical-induced swelling. Our findings establish that angle-resolved spectroscopy serves not only as an alternative to electron microscopy but also as a versatile metrology platform for the development of active photonic sensors.

Acknowledgments

The authors thank the Central Research Facilities of CeNS, Bengaluru, and are grateful to the Department of Science and Technology, GoI, for the funding.

References

[1] V. Lotito and T. Zambelli, "Approaches to self-assembly of colloidal monolayers: A guide for nanotechnologists," Aug. 01, 2017, *Elsevier B.V.* doi: 10.1016/j.cis.2017.04.003.

[2] B. Malani S and P. Viswanath, "Impact of ordering of gold nanohole arrays on refractive index sensing," *Journal of the Optical Society of America B*, vol. 35, no. 10, pp. 2501–2508, Oct. 2018, doi: 10.1364/josab.35.002501.

[3] A. Anand Eswara Rao and P. Viswanath, "Angle-dependent optical studies on size-reduced monolayer of self-assembled polystyrene spheres," *J. Appl. Phys.*, vol. 137, no. 13, p. 133103, Apr. 2025, doi: 10.1063/5.0255027.

[4] J. Lawall, Y. Bao, and J. J. Gorman, "Accurate measurement of the photonic crystal slab period using diffraction in the Littrow configuration," *Opt. Express*, vol. 29, no. 23, p. 37091, Nov. 2021, doi: 10.1364/OE.438308.

[5] T. Liu and M. J. Solomon, "Reconfigurable grating diffraction structural color in self-assembled colloidal crystals," *Small*, vol. 19, no. 37, p. 2301871, Sep. 2023, doi: 10.1002/smll.202301871.

[6] N. Vogel, S. Goerres, K. Landfester, and C. K. Weiss, "A convenient method to produce close- and non-close-packed monolayers using direct assembly at the air-water interface and subsequent plasma-induced size reduction," *Macromol. Chem. Phys.*, vol. 212, no. 16, pp. 1719–1734, Aug. 2011, doi: 10.1002/macp.201100187.

[7] S. G. Romanov, "Light diffraction features in an ordered monolayer of spheres," *Physics of the Solid State*, vol. 59, no. 7, pp. 1356–1367, Jul. 2017, doi: 10.1134/S1063783417070216.

[8] M. Khokhar, S. Sharma, S. K. Saini, and R. V Nair, "Enhancing spontaneous emission using structural resonances of self-assembled monolayers," *Journal of Optics*, vol. 23, no. 8, p. 085004, Aug. 2021, doi: 10.1088/2040-8986/ac0ff2.

[9] X. Li, Y. Zhang, M. Li, Y. Zhao, L. Zhang, and C. Huang, "Convex-meniscus-assisted self-assembly at the air/water interface to prepare a wafer-scale colloidal monolayer without overlap," *Langmuir*, vol. 37, no. 1, pp. 249–256, Jan. 2021, doi: 10.1021/acs.langmuir.0c02851.

Structural Colour Transmission of Novel Superimposed Gratings Fabricated via Two-Photon Polymerisation

Jamie Somers[1,*], Jing Qian[2], Colm Delaney[2], Pascal Landais[3], A. Louise Bradley[1,*]

[1]Department of Physics, Trinity College Dublin, Ireland
[2]Department of Chemistry, Trinity College Dublin, Ireland
[3]School of Electronic Engineering, Dublin City University, Ireland
*Corresponding author: jsomers@tcd.ie, bradlel@tcd.ie

***Abstract*— Direct laser writing continues to develop for photonic applications. The technique can produce complex structures using low refractive index polymer materials. The superimposed phase grating structure presented demonstrates improved colour saturation across the visible spectrum, with examples shown at 390 nm, 470 nm and 700 nm.**

***Keywords*— Structural Colour, Direct Laser Writing, Phase Grating, Optimization Algorithm.**

I. Introduction

Square wave gratings have been proven to be ideal candidates for producing structural colour using two photon polymerization [1]. Previous works have investigated the characteristics of these gratings as well as their applications for sensing in liquid and vapour environments [2][3]. Transmission in certain wavelength ranges can require pillars of 4 µm or taller with pillar widths of 0.5 µm. Such large height-width aspect ratios are challenging to achieve from a fabrication standpoint and are less robust. Taller pillars also support more colours in their zeroth order modes which affects the purity of colour achievable. The superimposed grating design is motivated by producing transmission within the visible spectrum range with improved colour purity at all wavelengths. This implies that there is a minimized number of spectral components transmitted outside a given colour range. The structure presented comprises a superposition of multiple phase square wave gratings which cause constructive interference to produce a saturated form of the desired wavelength while destructively interfering to suppress contributions from any other part of the visible spectral range. This superimposed grating design allows for the fabrication of structures with smaller pillar heights proportional to the pillar widths which has the added benefit of improving the ease of fabrication along with achieving more spectrally pure and saturated structures.

II. Methods

Our methodology integrates Finite-Difference Time-Domain (FDTD) simulations, a Particle Swarm Optimization (PSO) algorithm, and experimental feedback to design the optimal structures needed to produce saturated colour at each targeted wavelength. The gaussian spectra with a full width half maximum of 23.5 nm centered at the target wavelengths (Fig. 1a) are plotted on a CIE 1931 chromaticity diagram which provides target chromaticity coordinates (x_t, y_t) for each wavelength. The zeroth order transmission spectrum for the optimized gratings is computed using Lumerical with a minimum mesh step of 0.125 nm and a step time less than 0.06 fs, these designs are optimised using the dimension limitations imposed by the two-photon lithography method. The cost function to be minimized is defined as the Euclidean distance between the target and simulated chromaticity coordinates:

$$Cost = (x - x_t)^2 + (y - y_t)^2 \qquad (1)$$

where x denotes the simulated x coordinate, x_t the target x coordinate, y the simulated y coordinate, and y_t the target y coordinate. As can be seen in Fig 1.b, the closer the optimized transmissions (white dots) are to the target spectra (black dots), the lower the value of the cost function.

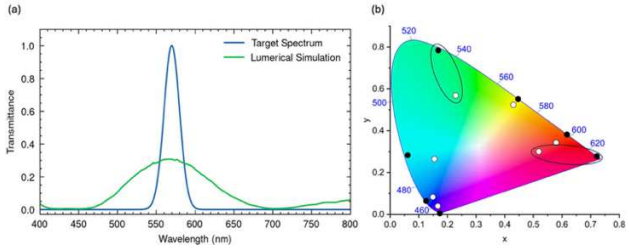

Figure 1: (a) Target spectrum in blue and optimised spectrum in green produced by the zeroth order of a superimposed grating designed to achieve yellow (570 nm), (b) The target colour is represented by black dots and the colour of the optimised structure is represented by white dots.

III. Results and Discussion

A schematic of the superimposed phase grating design is given in Fig. 2a. It is composed of elementary square gratings of various heights, generating multiple filters simultaneously. Pillars 1, 2, 4 and 5 have an identical width of 0.75 µm (labelled w1, w2, w4 and w5), pillar 3 has a width (w3) of 1 µm and hence the gap between pillar 3 and 4 or pillar 3 and 2 is 1 µm. The total of these widths gives a period of 6 µm. The height of pillars 2 and 4 (h2 and h4) are identical, the height of pillars 1 and 5 (h1 and h5) are also identical and finally pillar 3 has a height denoted by h3. With this approach, there are only three degrees of freedom, the heights h1, h2 and h3. This number is motivated by simplicity in the fabrication and keeping the computation time relatively short. The dimensions of the fabrication are verified experimentally using SEM as seen in Fig. 2b.

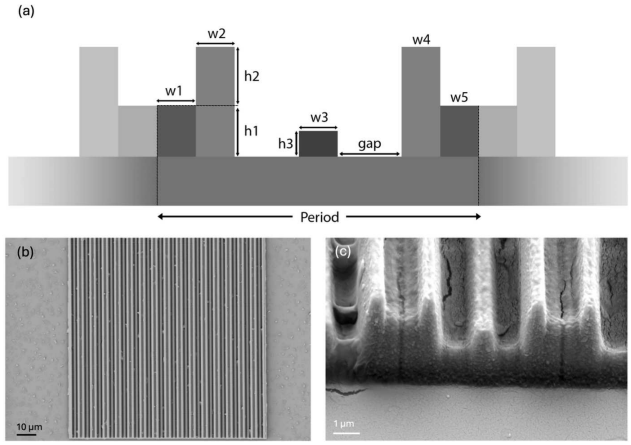

Figure 2: (a) Simple schematic of superimposed gratings with 3 pillars of height h1, h1 + h2 and h3 respectively. SEM images show (b) a top-down view of the superimposed grating for 470 nm and (c) 45-degree view of superimposed grating for 470 nm.

Experimental characterization is carried out using optical measurements taken on a home-built angle resolved setup to capture zero-order transmittance spectra for both the square wave grating and superimposed grating designs at 390 nm, 470 nm and 700 nm. The images of the gratings in transmission are obtained using a 4x objective lens coupled with a microscope focused into a CCD camera [3].

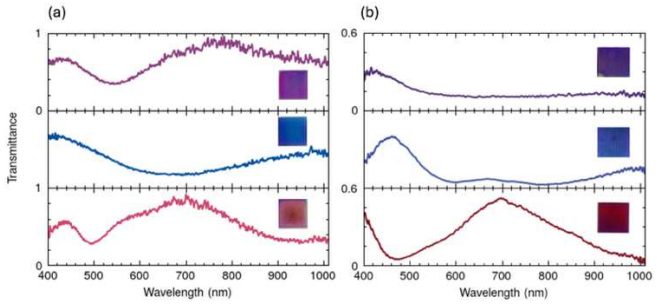

Figure. 3: (a) Comparison between the square wave and (b) superimposed grating zeroth-order transmission spectra for 390 nm, 470 nm and 700 nm, respectively.

Fig. 3 shows a comparison between the square wave grating zeroth-order transmissions and that of the superimposed gratings. We can clearly see from the experimental spectra that the contributions of other wavelengths have been greatly reduced leading to better agreement between fabrication and targeted wavelength. In the case of square wave gratings, the 700 nm fabricated sample lacks a distinct red colour and instead appears pink to the eye as there are larger contributions being made by wavelengths such as 470 nm contributing to a colour mixing affect between red and blue. Samples such as 390 nm have a clearly defined peak at 390 nm in both square wave and superimposed gratings but the superimposed grating design has managed to entirely suppress any wavelength higher than 500 nm meanwhile the square wave grating has a secondary more intense peak at 700 nm and beyond, leading to a colour mixing of purple and red.

Finally, we compared the height width aspect ratio and cost function for both experimental designs.

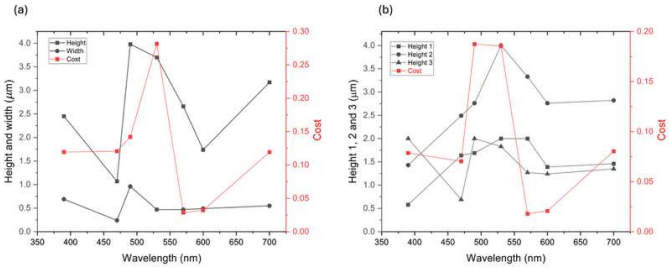

Figure 4: Dependence of the heights h, h1, h2, h3 and the cost function value as a function of wavelength for the (a) square wave and (b) superimposed grating.

In the case of the square wave grating at 390 nm, 470 nm and 700 nm the cost function value is 0.119, 0.121 and 0.119, respectively, whereas for the superimposed grating a lower cost function value is achieved of 0.079, 0.070 and 0.080 respectively, clearly demonstrating that the zeroth order transmissions realized by this novel design are closer to the target spectrum.

IV. Conclusion

In this work, we have demonstrated the design and experimental realization of polymer-based phase gratings by direct laser printing optimized for colour-selective transmission using a PSO algorithm coupled to rigorous FDTD simulations. The optimization strategy, based on minimizing the Euclidean distance between simulated and target spectra in the CIE 1931 colour space, enabled precise tuning of grating geometries to achieve desired chromatic responses.

Acknowledgments

This project is funded as part of a Research Ireland Centre for Doctoral Training in Advanced Characterisation of Materials (18/EPSRC-CDT/3581) The parts and samples for this project (18/EPSRC-CDT/3581) were manufactured using facilities in the Additive Research Laboratory at the AMBER centre, CRANN Institute, Trinity College Dublin. The

imaging/analysis for this project (18/EPSRC-CDT/3581) was carried out at the Advanced Microscopy Laboratory (AML) at the AMBER centre, CRANN Institute, Trinity College Dublin.

REFERENCES

[1] Wang, J., Yu, H., Zheng, J. et al. Nanograting-Based Dynamic Structural Colors Using Heterogeneous Materials. Nano-Micro Lett. 17, 59 (2025).

[2] C. Delaney, J. Qian, X. Zhang, et al., "Direct laser writing of vapour-responsive photonic arrays," Journal of Materials Chemistry C 9, 11674-11678 (2021).

[3] J. Qian, S. Kolagatla, A. Pacalovas, et al., "Responsive Spiral Photonic Structures for Visible Vapor Sensing, Pattern Transformation and Encryption," Advanced Functional Materials n/a, 2211735 (2023).

Wrinkle-Mediated Plasmonic Metasurfaces for Large-Area Photoresponsive Devices

Swagato Sarkar[1,2,*], Tobias A.F. König[1], Andreas Fery[1]

[1] Leibniz-Institut für Polymerforschung Dresden e. V., Dresden, Germany
[2] Institute of Radiopharmaceutical Cancer Research, Helmholtz-Zentrum Dresden-Rossendorf, Dresden, Germany
*Corresponding author: sarkar@ipfdd.de

***Abstract*— Wrinkle-mediated plasmonic metasurfaces provide a scalable route to anisotropic light-matter interaction without complex lithography. Here, large-area 1D plasmonic gratings fabricated via mechanical instabilities and oblique-angle metal deposition are presented. Surface plasmon polaritons and localized plasmon modes enable deformation-stable optical sensing and photoresponsive device functionalities.**

***Keywords*— wrinkled plasmonic metasurfaces, surface plasmon polaritons, localized surface plasmon resonances, anisotropic optical response, photoresponsive devices.**

I. Introduction

Large-area plasmonic metasurfaces can exhibit strong, tunable light-matter interactions, with applications in optical sensing and photodetection. However, conventional top-down nanofabrication techniques, such as electron-beam lithography, can impose severe limitations on scalability and throughput, which is why cost-effective, scalable alternative fabrication strategies are often sought. In this regard, wrinkling induced by mechanical instabilities in elastomeric substrates has emerged as an attractive bottom-up approach for realizing periodic 1D surface relief gratings over centimeter-scale areas [1,2]. By combining metal deposition, such wrinkled templates can produce continuous and discrete plasmonic metasurfaces that support surface plasmon polariton (SPP) and localized surface plasmon resonance (LSPR) modes, respectively. These wrinkle-mediated architectures offer a versatile platform for engineering anisotropic optical responses and photoresponsive functionalities without relying on complex lithographic processes.

II. Methods

We fabricated wrinkled templates by plasma-oxidizing elastomeric substrates, thereby inducing periodic surface modulations via controlled mechanical instabilities [1,2]. The wrinkle periodicity and amplitude were tuned through plasma exposure conditions and substrate parameters. Plasmonic metasurfaces were realized by oblique angle deposition (OAD) of metallic layers on top of these wrinkled substrates under both normal and oblique incidence, to further ensure the selective formation of surface- and edge-dominated plasmonic gratings [1]. The wrinkle fabrication process, resulting surface morphology, and subsequent plasmonic grating formation are schematically summarized in Fig. 1.

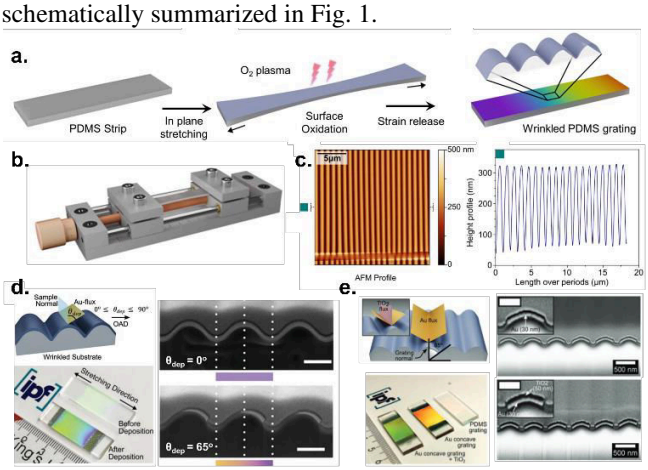

Fig. 1. Wrinkle fabrication, surface topology, and plasmonic grating formation. (a) Schematic illustration of wrinkled PDMS fabrication via in-plane stretching, O2 plasma oxidation, and strain release. (b) Custom-built stretching device used [3]. (c) Surface topology of wrinkled PDMS showing an AFM height map and the corresponding line profile extracted along the indicated direction [1]. (d) Wrinkled PDMS as a template for plasmonic grating fabrication, showing OAD of metal layer and centimeter-scale uniformity. Corresponding FIB-SEM cross-sections show Au surface gratings deposited at 0° and Au edge gratings deposited at 65° [1]. (e) Formation of concave plasmonic gratings using symmetric OAD at 65°. Photographs of large-area samples and cross-sectional SEM images show concave Au and Au/TiO2 gratings, with insets highlighting a single grating period [3].

For photoresponsive device architectures, we fabricated metal-semiconductor hybrid gratings by integrating plasmonic metals with further deposited semiconductor layers to allow electrical readout of plasmon-induced photoresponses [3]. Optical characterization was performed using polarization-resolved UV-visible-NIR spectroscopy to probe anisotropic plasmonic resonances. We conducted photoresponse

measurements under controlled illumination conditions with different excitation wavelengths, including angular dependence. Finite-difference time-domain simulations were employed to analyze electromagnetic field distributions and plasmonic mode characteristics [1-3].

III. Results and Discussion

Wrinkle-mediated plasmonic metasurfaces exhibit pronounced anisotropic optical responses arising from their 1D periodic geometry. Depending on the deposition configuration, the metasurfaces supported propagating SPP modes along continuous metallic features or LSPR-dominated modes localized at metal edges [2]. Polarization-resolved spectroscopy revealed distinct resonance features associated with these plasmonic modes, with strong sensitivity to incident light polarization and wavelength. Figure 2 provides an overview of the functional performance of the wrinkled plasmonic metasurfaces, including refractive index sensing and photoresponsive device operation.

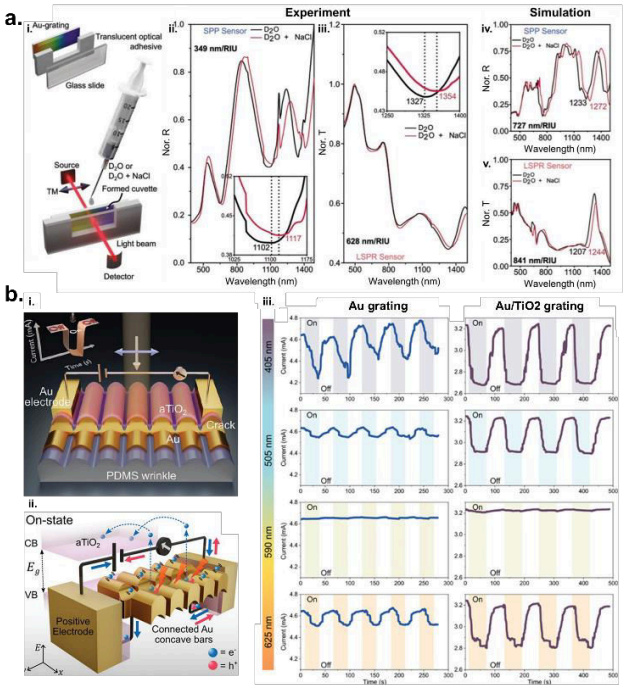

Fig. 2. Plasmonic sensing and photoresponsive behavior of wrinkled plasmonic metasurfaces. (a) RI sensing study, showing the cavity-based liquid measurement setup, experimentally measured spectral shifts of SPP modes in Au surface gratings and LSPR modes in Au edge gratings upon RI variation from D2O to D2O + NaCl, along with FDTD simulations [1]. (b) Photoresponsive device operation based on wrinkled plasmonic gratings, showing the device architecture with Au and Au/TiO2 concave bars forming the active channel between electrodes, the operating principle illustrated by band alignment and hot-electron-mediated charge transport under illumination, and time-dependent photocurrent responses for different LED excitations, where shaded regions indicate periods of light exposure [3].

Importantly, the plasmonic response of the wrinkled metasurfaces remained stable under mechanical deformation, enabling deformation-tolerant optical sensing [1]. Changes in the surrounding refractive indices led to measurable shifts in plasmonic resonance positions, demonstrating the suitability of these metasurfaces for large-area, flexible optical sensing applications.

Beyond passive sensing, metal-semiconductor wrinkled gratings also exhibited pronounced photoresponsive electrical behavior under illumination [3]. The interconnected plasmonic structures facilitate efficient light absorption and hot-carrier generation, resulting in a measurable photoresistive response. The interplay between plasmonic excitation, charge transport across metal-semiconductor interfaces, and carrier recombination dynamics governed the magnitude and sign of the photoresponse. These results established wrinkle-mediated plasmonic metasurfaces as a versatile platform for photoresponsive devices combining anisotropic optical functionality with electrical readout.

IV. Conclusion

Overall, these wrinkle-mediated plasmonic metasurfaces provide a scalable and lithography-free route to large-area photoresponsive devices with anisotropic optical and electrical properties. By exploiting mechanically induced surface instabilities and controlled metal deposition, plasmonic metasurfaces supporting SPP and LSPR modes are realized with high robustness and deformation stability. This approach offers a general framework for future plasmonic sensing and photoresponsive technologies based on large-area metasurfaces.

Acknowledgments

Tobias A.F. König acknowledges Volkswagen Foundation for financial support through the Freigeist Fellowship. Andreas Fery acknowledges the financial support of DFG, German Research Foundation, for the funding of project 451785257 (GRK 2767-‘Supracolloidal Structures’) and project BA 4986/10.

References

[1] A. K. Ghosh, S. Sarkar, L. J. Nebel, O. Aftenieva, V. Gupta, O. Sander, A. Das, J. Joseph, S. Wießner, T. A. König, and A. Fery, “Exploring plasmonic resonances toward large-scale flexible optical sensors with deformation stability,” Advanced Functional Materials, vol. 31, no. 30, p. 2101959, 2021.

[2] Z. Yu, S. Sarkar, S. Seçkin, N. Sun, A. K. Ghosh, S. Wießner, Z. Zhou, and A. Fery, “Two-dimensional wrinkle-assisted zigzag plasmonic chains for isotropic SERS enhancement,” Scientific Reports, vol. 15, no. 1, p. 3662, 2025.

[3] A. K. Ghosh, S. Sarkar, T. Tsuda, M. Hoffmann, A. Fery, and T. A. König, “Plasmonic photoresistor based on interconnected metal–semiconductor grating,” Advanced Functional Materials, vol. 33, no. 6, p. 202210172, 2023.

Hybrid Silica-Perovskite Microcavities for High Quality-Factor Whispering-Gallery Resonance

Luke Cording[1], Christian Johnson-Richards[1], Hei Chit Leo Tsui[1], Pablo Docampo[2], and Noel Healy[1,*]

[1]School of Mathematics, Statistics and Physics, Newcastle University, Newcastle Upon Tyne, NE1 7RU, United Kingdom

[2]BCMaterials, IKERBASQUE, Basque Foundation for Science, Bilbao, 48009, Spain

*Corresponding author: Noel.Healy@ncl.ac.uk

***Abstract*—Current realisations of perovskite whispering-gallery mode resonators suffer from relatively low quality factor, restricted coupling geometries, and instability in air. We present a high-Q hybrid microcavity platform that addresses all three of the bottlenecks in state-of-the-art perovskite resonators, providing a route to accessing the promising optical properties of perovskites.**

***Keywords*— whispering-gallery resonators, perovskites, fabrication, ion migration**

I. Introduction

Metal halide perovskites, have recently been established as promising emergent materials for optics and photonics due to their large refractive index [1], high photoluminescent quantum efficiency [2], and strong reported third-order optical nonlinearity [3], [4]. These qualities make perovskites interesting candidates for use in devices that facilitate high intensity fields at low powers, such as whispering-gallery mode (WGM) resonators [5]. To date, works have realised perovskite optical resonators via solution-processed crystals grown on substrate; however, WGM resonators fabricated so far have been subject to relatively low quality factor (Q-factor) on the order of $\sim$1000 and are limited to relatively inefficient free-space coupling of light into the cavity [6], [7], [8]. Additionally, the sensitivity of perovskites to air exposure, which has been shown to cause optical degradation [9], poses an additional engineering challenge; however, in other perovskite devices such as solar cells, encapsulation of the perovskite layer has been shown to result in substantial improvements to device lifetime [10].

Here, we iterate on the perovskite WGM devices demonstrated thus far by integrating a solution-grown lead-halide perovskite with a silica template of few-micron wall thickness to produce a hybrid layered core-cladding structure. A diagram of our device is given schematically in figure 1 [11]. Our fabricated WGM resonators support higher Q-factor operation than previous demonstrations of devices composed solely of perovskite, and permit evanescent coupling of light into the cavity via tapered optical fibre. These qualities allow us to explore the effect of photo-induced ion migration, which is a unique effect in perovskites which has been previously identified to occur over timescales on the order of seconds to minutes [12]. In our devices, this effect results in a time-dependent modulation of the measured transmission spectrum. Additionally, our device geometry offers encapsulation of active region of the resonator, protecting it from the environment.

II. Methods

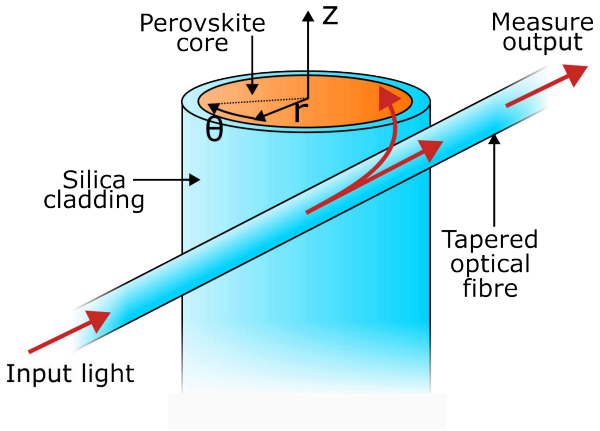

Fig. 1. Schematic representation of perovskite-based WGM resonator, showing perovskite core surrounded by thin silica layer, shown with tapered optical micro-fibre for coupling of light. Shown with cylindrical coordinates system with radial (r), azimuthal (θ), and axial (z) directions.

The silica cladding templates used here were fabricated from commercially available Polymicro fused silica capillary tubing. To prepare the capillary, a multi-stage heat-and-pull tapering process was used, employing both an electric arc and a butane flame along with translational stages to reduce the outer diameter of the capillary by over an order of magnitude to $\sim$50 µm and below. This allows for the tuning of resonator parameters such as free spectral range (FSR) as well as reduces the thickness of the external silica layer, promoting mode localization to the perovskite core. A precursor solution of $MAPbBr_3$ was drawn into the templates via capillary action, from which crystals were grown using an inverse temperature crystallization process [13], resulting in a layered core-cladding structure.

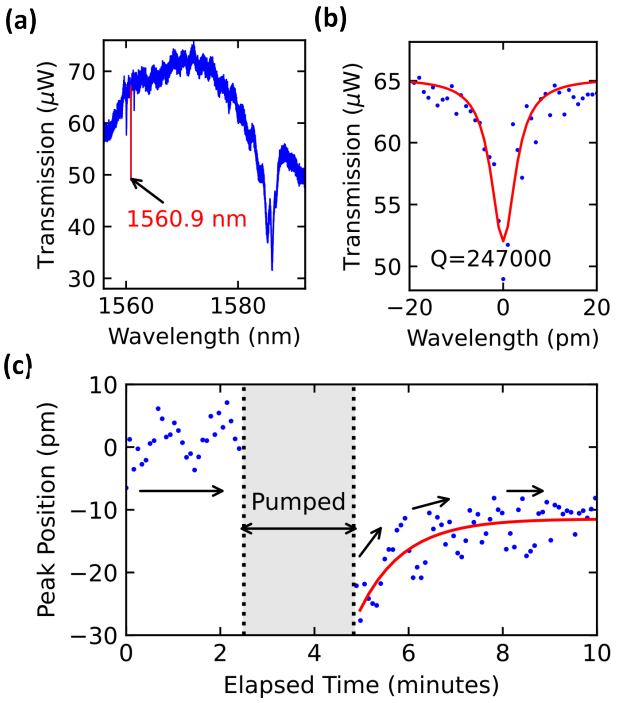

Fig. 2. Transmission spectrum characterisation of $MAPbBr_3$ WGM resonator, with highlighted high-Q mode (a). Lorentzian fit to highlighted mode, adjusted such that the center of the peak is located at zero wavelength, producing estimated Q-factor of 247000 (b). Time-dependent measurement in $MAPbBr_3$ WGM resonator, showing modulation of central peak position as a function of time before and after being pumped with high power pulsed source (c).

III. Results and Discussion

The fabricated $MAPbBr_3$ WGM resonators are characterised using a bespoke mode-hop free telecommunications characterisation rig, which employs a continuous-wave source of 400 kHz bandwidth tunable in the 1520-1630 nm range. The cross-section of the silica wall is sufficiently narrow so as to allow light to be introduced to the perovskite core via evanescent coupling from a tapered optical fibre (TOF) of diameter $\sim$1 μm. To produce a transmission spectrum, the TOF is pumped with the tunable source whilst positioned close enough to the resonator to induce coupling. The output power of the TOF is measured whilst scanning the wavelength of the tunable source to produce the transmission spectra such as the one shown in figure 2(a). To assess the performance of the device, the resonance peak located at 1560.9 nm is fitted with a Lorentzian, which is shown in figure 2(b). In doing so, a Q-factor of 247000 is identified.

To examine the role of the presence of the perovskite core in device operation, a resonator was pumped with high power light from a transform-limited pulsed source with a central wavelength of 1560 nm, a pulse width of 200 fs, and a repetition rate of 80 MHz. It was noted that, rather than returning to their original spectral position after the pump was switched off, the resonances had translated to a position that was blue-shifted from their original values. Such a measurement is given in figure 2(c). After being pumped for a duration of $\sim$2 minutes, the peak position was displaced to a position of -30 pm relative to its original value. Then, over a period of five minutes, the peak recovers to a position of -10 pm. The experimental data are fitted to an exponential model yielding a time constant of 56 s. This behaviour can be attributed to refractive index modulation caused by ion migration taking place within the core.

IV. Conclusion

In this work we have iterated upon methods for the fabrication of perovskite waveguide devices, presenting WGM resonators comprising a hybrid layered silica-perovskite structure. In our devices, we demonstrate a resonance with a Q-factor of 247000, exceeding previous examples of perovskite WGM resonators by approximately two orders of magnitude, as well as the ability to affect the transmission spectrum over protracted time periods via refractive index modulation as a result of ion migration in the perovskite core.

Acknowledgments

This work was supported by funding from the EPSRC through EP/S031103/1 & EP/Z535904/1.

References

[1] M. C. Brennan, D. M. Krein, E. Rowe, C. L. McCleese, L. Sun, K. G.Berry, P. R. Stevenson, M. A. Susner, and T. A. Grusenmeyer, "Fundamental optical constants and anti-reflection coating of melt-grown, polished $CsPbBr_3$," *MRS Communications*, vol. 14, pp. 900-908, 2024.

[2] X. Liu, W. Xu, S. Bai, Y. Jin, J. Wang, R. Friend, and F. Gao, "Metal halide perovskites for light-emitting diodes," *Nature Materials*, vol. 20, pp. 10–21, 2021.

[3] B. S. Kalanoor, L. Gouda, R. Gottesman, S. Tirosh, E. Haltzi, A. Zaban, and Y. R. Tischler, "Third-order optical nonlinearities in organometallic methylammonium lead iodide perovskite thin films," *ACS Photonics*, vol. 3, no. 3, pp. 361–370, 2016.

[4] I. Suárez, M. Vallés-Pelarda, A. F. Gualdrón-Reyes, I. Mora-Seró, A. Ferrando, H. Michinel, J. R. Salgueiro, and J. P. M. Pastor, "Outstanding nonlinear optical properties of methylammonium- and Cs-PbX_3 (X = Br, I, and Br-I) perovskites: Polycrystalline thin films and nanoparticles," *APL Materials*, vol. 7, no. 041106, 2019.

[5] G. Lin, A. Coillet, Y. K. Chembo, "Nonlinear photonics with high-Q whispering-gallery mode resonators," *Advances in Optics and Photonics*, vol. 9, no. 4, pp. 828–890, 2017.

[6] X. Li, K. Wang, M. Chen, S. Wang, Y. Fan, T. Liang, Q. Song, G. Xing, and Z. Tang, "Stable whispering gallery mode lasing from solution-processed formamidinium lead bromide perovskite microdisks," *Advanced Optical Materials*, vol. 8, no. 2000030, 2020.

[7] X. Tian, L. Wang, W. Li, Q. Lin, and Q. Cao, "Whispering Gallery Mode Lasing from Perovskite Polygonal Microcavities via Femtosecond Laser Direct Writing," *ACS Applied Material Interfaces*, vol. 13, pp. 16952-16958, 2021.

[8] J. Yang, Z. Liu, M. Pi, H. Lin, F. Zeng, Y. Bian, T. Shi, J. Du, Y. Leng, and X. Tang, "High Efficiency Up-Conversion Random Lasing from Formamidinium Lead Bromide/Amino-Mediated Silica Spheres Composites," *Advanced Optical Materials*, vol. 8, no. 2000290, 2020.

[9] C. C. Boyd, R. Cheacharoen, T. Leijtens, M. D. McGehee, "Understanding Degradation Mechanisms and Improving Stability of Perovskite Photovoltaics," *Chemical Reviews*, vol. 119, no. 5, pp. 3418-3451, 2019.

[10] Q. .Q. Chu, Z. Sun , D. Wang, B. Cheng, H. Wang, C. Wong, and B. Fang, "Encapsulation: The path to commercialization of stable perovskite solar cells," *Matter*, vol. 6, no. 11, pp. 3838-3863, 2023.

[11] L. Cording, C. Johnson-Richards, H. C. L. Tsui, P. Docampo, N. Healy, "Photonic and Ionic Control of High-Q Organometallic Halide Perovskite Micro-Resonators," *In Preparation*, 2026.
[12] Y. Liu, A. V. Ievlev, N. Borodinov, M. Lorenz, K. Xiao, M. Ahmadi, B. Hu, S. V. Kalinin, and O. S. Ovchinnikova, "Direct Observation of Photoinduced Ion Migration in Lead Halide Perovskites," *Advanced Function Materials*, vol. 31, no. 2008777, 2021.
[13] M. I. Saidaminov, A. L. Abdelhady, B. Murali, E. Alarousu, V. M. Burlakov, W. Peng, I. Dursun, L. Wang, Y. He, G. MacUlan, A. Goriely, T. Wu, O. F. Mohammed, and O. M. Bakr, "High-quality bulk hybrid perovskite single crystals within minutes by inverse temperature crystallization," *Nature Communications*, vol. 6, no. 7586, 2015.

Uniformity-Enhanced Gas-Phase Catalyst Etching of Silica Glass for Metalens Fabrication

Yusuke Kataoka, Kohei Sano, Yoshitaka Ono, Yasuo Hayashi

Innovative Technology Laboratories, AGC Inc., Japan
*Corresponding author: yusuke.kataoka@agc.com

***Abstract*— We investigate gas-phase catalyst etching of silica glass under reduced pressure for metalens fabrication. Vacuum conditions improve etching uniformity by enhancing reactive gas diffusion, while reducing etch rate. High-aspect-ratio, vertically etched nanoscale structures with excellent uniformity are demonstrated, indicating suitability for visible and ultraviolet metalens applications.**

***Keywords*— Metalens, glass, dry etching.**

I. Introduction

Metalens fabricated using nanoscale fabrication technologies have attracted attension as nest generation optical elements because they can realize small and thin optical components. In infrared region, these have been achieved by silicon processed by using semiconductor processes and have been applied as sensing devices such as thermal camera[1] and LiDAR[2]. More recently, metalens for visible and more high frequency light are proposed. Especially, silica glass has been investigated as a promising substrate material in ultraviolet region.[3]

Reactive ion etching (RIE) is generally used to fabricate fine structures in silica glass. However, since the mask material is simultaneously etched by ion bombardment during the RIE process, achieving vertical sidewall is challenging. On the other hand, the verticality of the meta-atoms which are components of metalens affects the optical performance of the metalens. Therefore, in order to realize metalens targeting ultraviolet region, process technology capable of forming vertical fine structures with high-aspect-ratio is required.[4]

We have reported a new anisotropic etching process for SiO_2 materials, using catalyst and HF gas. This process enables vertical etching independent of conventional selectivity etching ratio by inducing a localized reaction at the interface between the catalyst and the surface of SiO_2 substrate. As a result, it is expected that nanostructures with high verticality suitable for meta-atom can be fabricated.[5]

Because the etching reaction occurs in the gas-phase catalyst etching without plasma, etching properties are expected to be controlled by the gas environment conditions. In this study, we investigated the effects of process gas pressure on etching rate and its uniformity in gas-phase catalyst etching assuming eight-inch-scale process.

II. Methods

Silica glass substrates were prepared and cleaned by ultraviolet ozone treatment for 15 minutes. Then the substrates treated by hexamethyldisilazane and coated with photoresists which is positive-tone novolac type (THMR-iP5700, Tokyo Ohka Kogyo, Japan) at 3000 rpm for 30 s. Micrometer-scale patterns (~10 μm) and nanoscale line patterns were exposed on the substrate using a maskless photolithography system (DL-1000A2, Nano System Solutions, Japan). The patterns were developed by using an alkaline developer solution (NMD-W, Tokyo Ohka Kogyo, Japan). Subsequently, the substrates were cleaned by ultraviolet ozone treatment again to remove organic contaminants from the surface without the photoresist.

The gas treatment was carried out using a tube furnace equipped with a vacuum system. The samples were placed on the furnace and heated to above 200 °C. A mixture of HF and N_2 was introduced into the furnace for from 5 minutes to 60 minutes. After the treatment, photoresist was removed by O_2 plasma treatment.

The etched structures were observed by a scanning electron microscope (SU8000, Hitach, Japan).

III. Results and Discussion

Figure 1 and Figure 2 show cross-sectional image of the etched structure and the depth distribution of the patterns respectively. Vertical hole structure without noticeable tapering is observed in Figure 1. The standard deviation of the etched depth was approximately 2.5% relative to the average as shown in Figure 2. In gas-phase catalyst etching, HF is consumed on the contact interface through inside of the catalyst in the reaction. Therefore, gas exchange must occur at the catalyst surface located at the bottom of etched holes. The reduced-pressure atmosphere enhances the diffusion of reactive gas species in the chamber and the bottom of etched feature. The gas concentration becomes uniform immediately in such reduced-pressure atmosphere. Therefore, it allows that fresh HF gas is supplied effectively and stably to all reactive areas.

Figure 3 shows the etching rate under atmospheric pressure and at 250 Torr. The rate under vacuum conditions decreases to approximately 20% of that at atmospheric pressure. Since the amount of HF per volume decreases in reduced-pressure atmosphere, the number of times it comes into contact with the catalyst decreases. This indicates that the etching reaction depends on the supply of HF and its speed is determined by the contact frequency between HF and the catalyst.

Figure 4 presents a cross-sectional image of a nanoscale pitch line structure fabricated by gas-phase catalyst etching under vacuum conditions. The achieved aspect ratio is approximately 10. All nanoscale features are etched uniformly with high vertically, demonstrating that the gas-phase catalyst etching enables the formation of high-aspect-ratio nano structures with high uniformity.

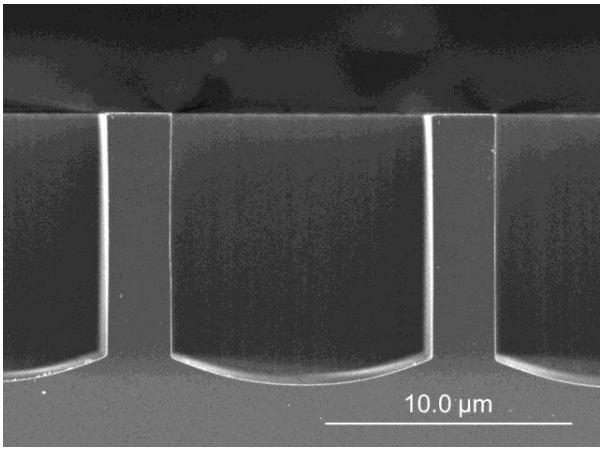

Figure 1. Cross sectional scanning electron microscopy (SEM) image of etched the micro-scale structures by gas-phase catalyst etching.

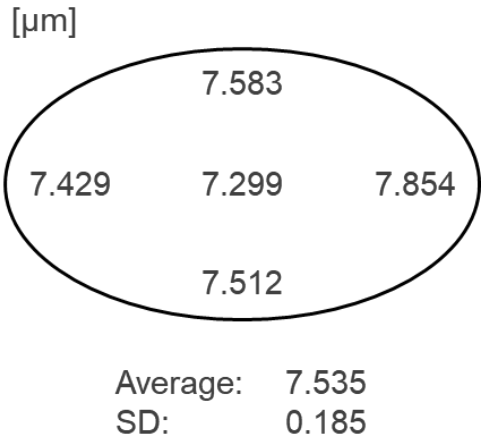

Figure 2. Depth distribution of the micro-scale structures in eight inches area.

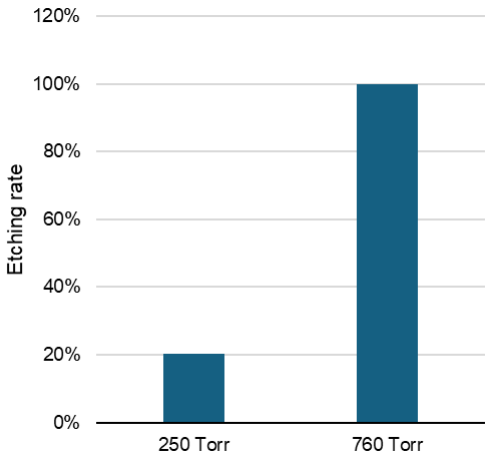

Figure 3. Etching rate of the micro-scale structures under atmospheric pressure and 250 Torr.

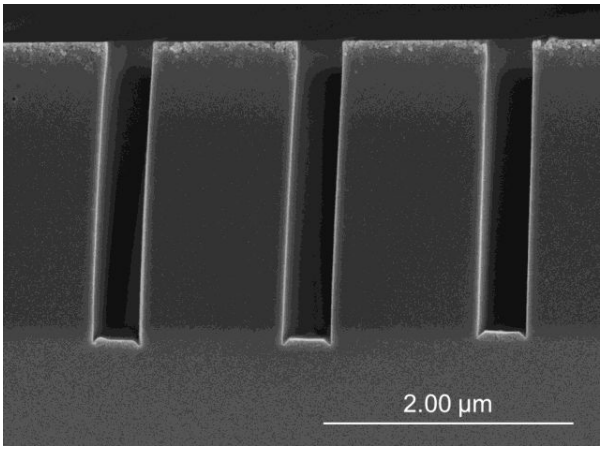

Figure 4. Cross sectional SEM image of a nano scale pitch line structures by gas-phase catalyst etching.

IV. Conclusion

We have demonstrated gas-phase catalysts etching under vacuum atmosphere and shown that the process enables the fabrication of vertical nanoscale structures with high uniformity. This technology is expected to contribute to metalens for visible or ultraviolet regions.

References

[1] L. Huang et al., “Long wavelength infrared imaging under ambient thermal radiation via an all-silicon metalens”, Optical Materials Express, vol. 11, No. 9, pp. 2907–2914, 2021.

[2] Zhang et al. “A dual-mode LiDAR system enabled by mechanically tunable hybrid cascaded metasurfaces” Light: Science & Applications 14 287, 2025.

[3] J S Park et al., “All-Glass, Large Metalens at Visible Wavelength Using Deep-Ultraviolet Projection Lithography”, Nano Lett, 19, pp 8673-8682, 2019.

[4] X Shi et al., “Integrated Deep Ultraviolet Doublet Metalens for Projection Imaging”, Appl Sci, 14, 1316, 2024.

[5] K Sano et al., “Atmospheric Gas-Phase Catalyst Etching of SiO2 for Deep Microfabrication Using HF Gas and Patterned Photoresist”, ACS Appl. Mater. Interfaces 16, pp22657−22664, 2024.

Automated SEM-Based Metrology for Wafer-Scale Characterization of Nanostructured Metamaterials

A. Peyyety[1*], E. Butzen[2], I. Harder[2], T Waldsauer[1], S. Bauerdick[1], K Gieb[1]

[1]GenISys GmbH, Unterhaching, Germany
[2]Max Planck Institute for Science of Light, Erlangen, Germany

*Corresponding author: peyyety@genisys-gmbh.com

Abstract— We present an automated scanning electron microscopy workflow for quantitative characterization of nanostructured metamaterials. The approach combines layout-based navigation, robust alignment, and autofocus to enable reproducible wafer scale measurements. Experiments demonstrate high throughput acquisition, consistent critical dimension (CD) extraction, and statistical analysis capabilities suitable for metamaterial design, fabrication optimization, and process monitoring.

Keywords— metamaterials, scanning electron microscopy, automated metrology, nanostructures, wafer-scale characterization.

I. Introduction

Scanning electron microscopy (SEM) remains a key technique for critical dimension measurements and nanoscale structural inspection in modern nanofabrication workflows [1]. While dedicated CD-SEM systems provide highly automated and precise metrology [2], their cost and limited versatility restrict widespread use, particularly in shared research facilities. Consequently, conventional SEM platforms are still frequently operated manually, limiting throughput and reproducibility. These limitations are especially relevant for nanostructured metamaterials, where functionality is critically governed by geometric fidelity and dimensional variability. Systematic and reproducible SEM-based characterization is therefore essential for validating fabricated structures. Software-defined SEM metrology platforms extend conventional SEM platforms toward high-throughput measurement systems, enabling layout-based navigation, automated image acquisition, and direct image-to-layout comparison.

II. Methods

The automated SEM imaging and metrology workflow was implemented using a commercial SEM (Zeiss Gemini 560) with metrology upgrade kit (GenISys InSPEC software), which provides digital interfacing with conventional SEM, including stage control, scan coordination, and detector signal access. The platform enables layout-based navigation, automated alignment, and reproducible image acquisition across large sample areas. Image-to-layout matching allows direct comparison between fabricated nanostructures and nominal metamaterial target design. Geometric parameters are extracted relative to intended layout features, enabling systematic evaluation of dimensional deviations, process variation bands, and spatially resolved fabrication changes.

III. Results and Discussion

Automated image acquisition enables statistically meaningful characterization of fabricated metamaterial arrays. Image-to-layout comparison reveals systematic deviations from nominal geometry, while aggregated datasets support quantitative evaluation of process variation bands. Spatial trends and dimensional distributions provide direct feedback for fabrication optimization, device reproducibility, and tolerance-based metamaterial design.

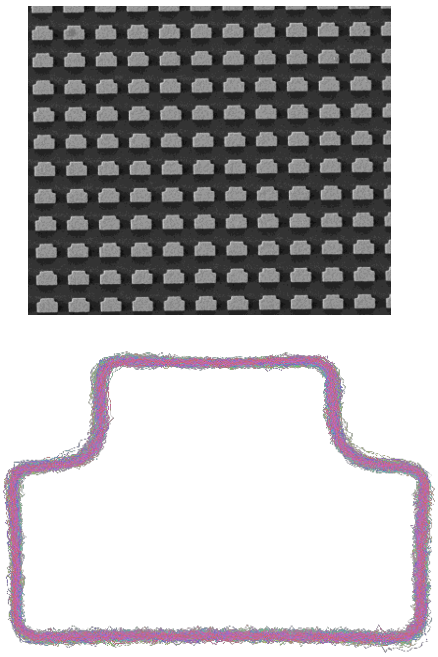

Fig. 1 Top view SEM image of metastructures (top) and superposition of extracted contours (bottom).

Structural variability and layout comparisons:

- Extracted structural contours are aggregated and centered to construct process variation tolerance bands (Fig. 1)
- Waferscale uniformity is evaluated through image-to-layout matching, incorporating systematic corrections including lateral shift, scaling, and rotation (Fig. 2)
- Direct quantitative comparison with layout primitives enables evaluation of dimensional bias and variability (Fig. 3 and Fig. 4)

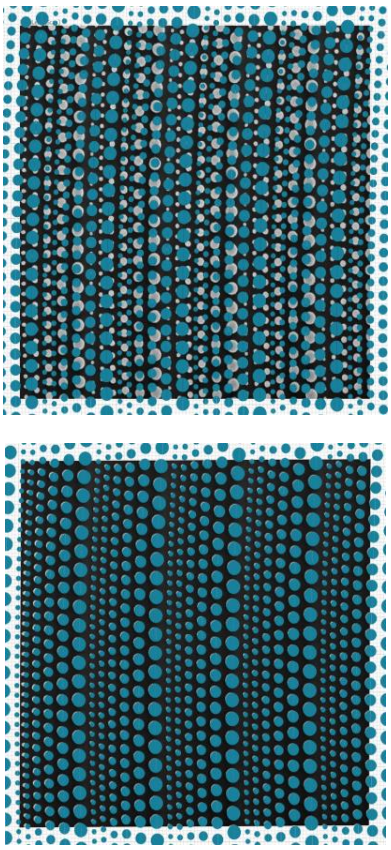

Fig. 2 Image-to-layout comparison before (top) and after (bottom) shift, scaling, and rotation corrections applied to metalens structure

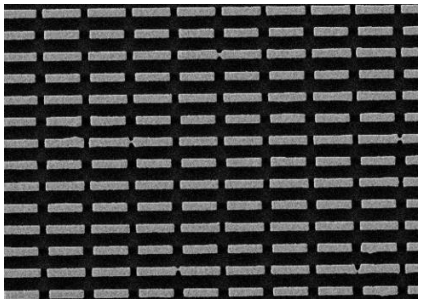

Fig. 3 Top view SEM image of rectangular metastructures

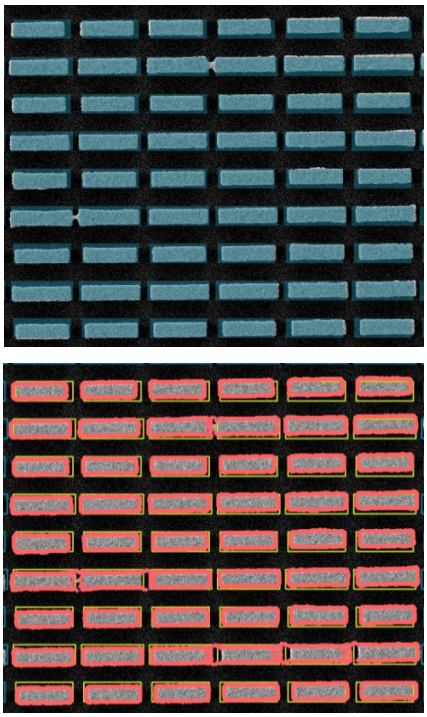

Fig. 4 Layout-overlaid SEM image from Fig 3. (top) and contour-based comparison with layout primitives (bottom).

Table 1 CD bias and variation relative to layout primitives

Width (µm)	Height (µm)	Width Bias (nm)	Width σ (nm)	Height Bias (nm)	Height σ (nm)
0.764	0.260	-50.4	7.1	-58.1	4.3
0.830	0.260	+12.5	94.0	-55.9	2.9

Table 1 summarizes the quantitative deviations obtained from comparison with layout primitives, including design bias and variability metrics relevant for lithography feedback.

IV. Conclusion

Automated SEM-based metrology provides a scalable and reproducible approach for wafer-scale characterization of nanostructured metamaterials using conventional SEM. The demonstrated workflow enables high-throughput data acquisition and statistical analysis, supporting reliable evaluation of pattern fidelity and process variation effects. Beyond the discussed results, the methodology offers a pathway toward advanced characterization capabilities, including edge roughness analysis, feature placement, and advanced layout comparison like EPE. The framework further supports curvilinear geometries and contour export into layout files, enabling direct integration with electromagnetic simulations.

ACKNOWLEDGMENTS

The authors gratefully acknowledge Chad Eichfeld at Penn State University, US for support with metalens measurements and valuable cooperation. The authors also thank Changjin Son and Katrin Ludwig at the Max Planck Institute for the Science of Light for providing the T-shaped and double bar metasurfaces design and ebeam lithography exposure support, respectively.

REFERENCES

[1] J. A. Liddle and G. M. Gallatin, "Lithography, metrology and nanomanufacturing," *Nanoscale*, vol. 3, pp. 2679–2688, 2011.

[2] T. Iwamatsu *et al.*, "High precision critical dimension measurement using CD-SEM," *Journal of Vacuum Science and Technology B*, vol. 19, pp. 1264–1268, 2001.

Meta-lenses phase characterization by phase retrieval

Jialuo Cheng[1], Bowen Liu[2], Yin Zhou[1], Lei Shi[2], Zihan Geng[3], Mu Ku Chen[1,4*]

[1]Department of Electrical Engineering, City University of Hong Kong, Kowloon, Hong Kong SAR, China

[2]State Key Laboratory of Surface Physics, Key Laboratory of Micro- and Nano-Photonic Structures (Ministry of Education) and Department of Physics, Fudan University, 200433 Shanghai, China

[3]Institute of Data and Information, Tsinghua Shenzhen International Graduate School, Tsinghua University, 518071 Shenzhen, Guangdong, China

[4]State Key Laboratory of Terahertz and Millimeter Waves, City University of Hong Kong, Kowloon, Hong Kong SAR, China.

*Corresponding author: mkchen@cityu.edu.hk

***Abstract*— A robust multi-distance phase retrieval system based on optical field scanning is presented to characterize meta-lens phase modulation. Validated in the near-infrared spectrum, our method analyzes focal length, aberrations, and defect impacts. We also demonstrate phase variation across different media (air vs. ethanol), offering a straightforward tool for metalens optimization.**

***Keywords*— Phase retrieval, meta-lens, computational imaging.**

I. Introduction

Meta-lenses are highly efficient, compact optical metasurfaces capable of modulating the amplitude, phase, and polarization of incoming light. While their design and fabrication have seen significant advancements, characterization techniques remain limited. Precise measurement of phase distribution is crucial for evaluating and optimizing meta-lens performance, yet direct measurement in the optical frequency band is challenging. Traditional methods like light field scanning and electron microscopy fail to simultaneously capture localized optical field modulation and structural topography. Furthermore, existing phase measurement techniques, such as quadriwave lateral shearing interferometry (QLSI) and off-axis interferometry, are constrained by low energy utilization, complex optical setups, and strict coherence requirements. To address these challenges, we introduce a meta-lens phase-measurement system based on multi-distance phase retrieval (MDPR). This method effectively calculates the phase distribution by measuring light intensity across various distances on the sample's exit plane, offering a simpler and more robust alternative. We evaluate the system's convergence and noise sensitivity. Using this MDPR approach, we successfully measured the phase distributions of a near-infrared (NIR) meta-lens and a 405 nm metalens immersed in ethanol. The retrieved phase data enables the precise calculation of wave aberrations and other critical parameters.

II. Methods

The multi-distance phase retrieval (MDPR) system addresses the fundamental computational holography problem of determining missing phase information from intensity measurements. It achieves this through measurement encoding, capturing intensity distributions at various distances governed by free-space angular spectrum diffraction. In practice, a collimated laser illuminates the sample, and a sequence of intensity images is captured at equal intervals moving away from the surface.

Mathematically, the imaging process can be expressed as

$$\boldsymbol{y} = |\boldsymbol{A}\boldsymbol{x}|^2, \tag{1}$$

where $\boldsymbol{x}$ denotes the complex amplitude modulation of the sample, and $\boldsymbol{y}$ denotes the intensity profile captured by the camera. $\mathbf{A}$ denotes the linear measurement operator which is calculated based on the angular spectrum propagation and can

be further expressed as$\boldsymbol{A} = \boldsymbol{F^{-1}H_lF}$, where $\boldsymbol{F}$and$\boldsymbol{F^{-1}}$denote the Fourier transform and inverse Fourier transform, respectively. The transfer function at a given distance l is given by

$$\boldsymbol{H}_l(f_x, f_y) = \begin{cases} exp\left(j\frac{2\pi}{\lambda}l\sqrt{1-\lambda^2 f_x^2-\lambda^2 f_y^2}\right), & f_x^2+f_y^2 \le \frac{1}{\lambda^2}, \\ 0, & \text{otherwise}, \end{cases} \quad (2)$$

where f_x and f_y denote the spatial frequency coordinates.

To retrieve the phase, the system utilizes an iterative algorithm based on far-field amplitude-only speckle transfer. The core process unfolds in a continuous sequence of steps. First, a random complex field is initialized at the sample plane and propagated forward to the N measurement distances. Second, at each distance, the calculated phase is retained while the computed intensity is replaced with the physically measured intensity. Next, these N updated fields are propagated back to the sample plane and averaged to integrate the multi-distance information. Finally, the measured sample surface intensity is incorporated using a Kalman filtering method to refine the averaged field. By continuously repeating these steps—aided by double-feedback and selective filtering of erroneous images—the algorithm progressively converges to the meta-lens's true complex optical field, as shown in Fig. 1.

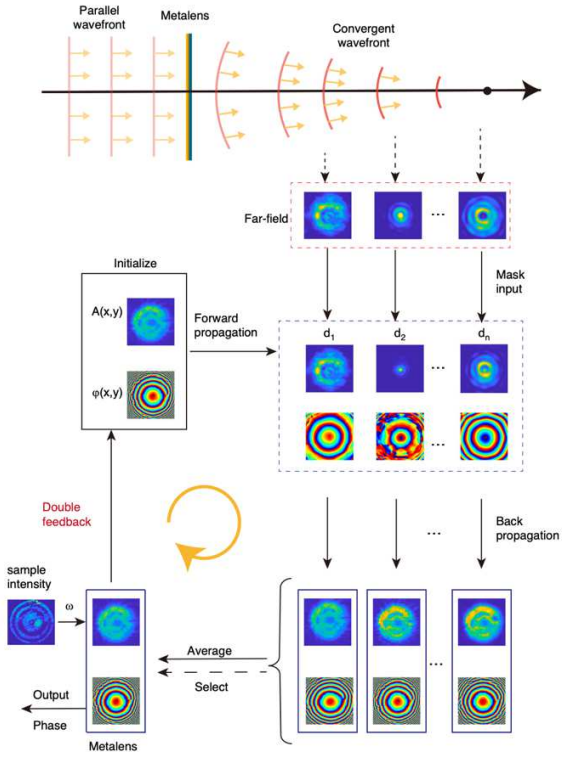

Fig. 1 Algorithmic flowchart for phase retrieval from intensity images captured at different positions

III. Results and Discussion

Two identical 1560 nm meta-lenses (design focal length 220 μm, NA 0.2) are evaluated using a supercontinuum laser. One sample contained physical defects (scratches, stains, layer penetrations), while the other was defect-free. Using 30 scanned images, the system successfully retrieved the phase distributions for both samples, revealing stark differences in their key performance metrics. Physical defects significantly hampered focusing efficiency, dropping it from 0.51 in the defect-free sample to just 0.27. Furthermore, the actual focal lengths shifted to 250 μm for the defective lens and 243 μm for the defect-free one. Consequently, the defective lens exhibited a higher wave aberration variance (0.13 compared to 0.06) and a correspondingly lower Strehl ratio (0.86 versus 0.94). The retrieved phase maps allowed us to directly correlate physical anomalies with specific aberrations. Broad stains caused significantly lower-order spherical aberrations (the 9th Zernike term), whereas localized scratches had minimal impact on these modes. Additionally, even the defect-free sample exhibited high-order spherical aberrations (the 16th term) induced by the inherent 0-2π phase jumps in the meta-lens design, as shown in Fig. 2.

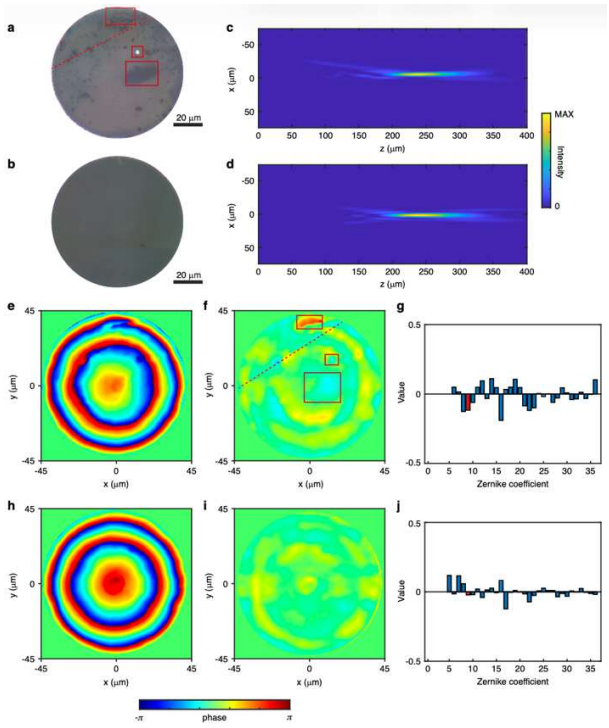

Fig. 2 Phase measurement for meta-lens working at 1560 nm. a, b Optical microscope images depicting the sample with defects and the defect-free sample. c, d Experimentally measured optical eld distributions for the sample with defects and the defect-free sample. Phase distribution, wave aberration, and Zernike expansion coefficients are illustrated for the sample with defects in (e–g) and the defect-free sample in (h–j)

IV. Conclusion

In this study, we developed a multi-distance phase retrieval (MDPR) system to measure meta-lens phase distributions. By extracting phase from intensity maps, our approach minimizes

laser coherence requirements, allowing versatile applications across various wavelengths and working mediums. We successfully demonstrated this by measuring near-infrared meta-lenses, subsequently deriving critical optical properties like focal length and wave aberration. Additionally, we quantified the phase modulation variations of a meta-lens operating in ethanol versus air. Finally, we introduced a simulation-based paradigm to analyze the system's convergence and robustness, ensuring adaptable stability and data reliability for characterizing diverse meta-lens samples.

Acknowledgments

This work is financed by the Guangdong Basic and Applied Basic Research Foundation [2025A1515011846], the University Grants Committee/Research Grants Council of the Hong Kong Special Administrative Region, China (CRF Project: C5031-22G; and GRF Project: CityU11310522; CityU11300123); City University of Hong Kong (Project No. 9610628 and No. 7020142).

References

[1] Liu, B., Cheng, J., Zhao, M., Yao, J., Liu, X., Chen, S., ... & Chen, M. K. (2024). Metalenses phase characterization by multi-distance phase retrieval. Light: Science & Applications, 13(1), 182.

[2] Cheng, J., Zhou, Y., Gao, Y., Liu, B., Liu, X., Shi, L., ... & Chen, M. K. (2025). Quantitative phase imaging for meta‐lenses by phase retrieval. Advanced Optical Materials, 13(9), 2402833.

Effective Optical Response of Multilayer Thin Films Using a Single-Layer Model for Photonic Applications

M. F. Al-Kuhaili, Reem Abubaker*

Physics Department, King Fahd University of Petroleum and Minerals, Dhahran 31261, Saudi Arabia
*Corresponding author: g202204020@kfupm.edu.sa

***Abstract*—A single-layer model is proposed to extract effective optical constants of multilayer thin films from transmittance spectra. Applied to MoO_3/WO_3 bilayers, the method accurately describes the optical response and shows excellent agreement with effective-medium theory, providing a simple approach for photonic and electromagnetic applications.**

***Keywords*—multilayers, optical constants, thin films, photonic applications, effective medium.**

I. Introduction

A multilayer is an ordered array of thin films deposited on substrates or certain functional elements. The properties of these structures can be controlled via the choice of materials comprising the films, resulting in unique mechanical, thermal, and optical characteristics that have profound potential in various fields of science and engineering. Multilayers are crucial elements in several applications, including microelectronics, anticorrosion coatings, sensors, and thermal barrier coatings [1-4]. Such multilayer systems are also of significant interest in photonic and optoelectronic applications, where precise control of light–matter interaction is essential. However, the focus of this work is on the optical applications of multilayers, which include anti-reflection coatings, highly reflective coatings, beam splitters, interference filters, and X-ray imaging [5-7]. Traditionally, these coatings have been deposited on lenses, mirrors, prisms, and other optical substrates and integrated into optical elements and instruments such as telescopes, microscopes, diffraction gratings, interferometers, and laser output couplers. Recent optical applications of multilayers include antireflection coatings in solar cells [8] and extreme ultraviolet lithography [9], transparent electrodes [10], high-capacity optical data storage [11], tunable optical filters [12], spatial filtering (imaging) [13], optical sensors [14], electrochromic applications [15], and smart windows [16]. Multilayer optical coatings are based on interference of light rays reflected from the interfaces between constituent layers, which can be designed to yield constructive or destructive interference, thereby enhancing or suppressing reflection from (or transmission through) the multilayer structure at a specific wavelength or over a band of wavelengths [17]. Therefore, the performance of a multilayer is dependent on the following properties of its layers: their number, composition, periodicity, refractive index, and thickness; performance also depends on the angle of incidence of light [7]. The design and fabrication of multilayers for optical applications necessitate accurate knowledge of the optical constants (refractive index and extinction coefficient) of the layers. Optical modeling of multilayers has been established using the transfer matrix method, which is based on Fresnel coefficients that connect electromagnetic field components at an interface [18,19]. The transfer matrix method requires precise knowledge of the optical constants and layer thicknesses to calculate the system's transmittance and reflectance. The values of these parameters are optimized to maximize or minimize the optical function over the desired wavelength range. Here, the inverse problem is investigated, in which the measured normal-incidence transmittance is used to determine the effective optical constants and thickness of a multilayer using a single-layer model. Instead of using a priori knowledge of the optical constants to design a multilayer system for specific performance, the optical performance of an existing system is examined. The proposed model is applied to a bi-layer consisting of a molybdenum oxide (MoO_3) film deposited on a tungsten oxide (WO_3) film. The validity of this methodology is verified using the effective-medium theory. The proposed model simplifies the optical characterization of complex multilayer photonic structures, particularly when the number of layers or their nature is unknown. Furthermore, the model is easily extendable to any number of layers.

II. Experimental Details

Thin film deposition was carried out in a Leybold L560 system using thermal evaporation from a molybdenum boat. The starting materials were 99.99% pure powders of WO_3 or MoO3. Three sets of samples were prepared: pure WO_3 thin films, pure MoO_3 thin films, and MoO_3/WO_3 multilayer thin films. The multilayer was deposited using two boats without breaking the

Proceedings of META 2026 · Dublin, Ireland · 14–17 July 2026 · ISSN 2429-1390 · pp. 1770–1775

vacuum: first, a WO_3 layer was deposited on the substrate, followed by a MoO3 layer. The system was initially pumped to a base pressure of 2×10^{-5} mbar. Prior to evaporation, the powders were slowly outgassed. Deposition was performed on unheated fused-silica and tantalum substrates; the latter were used for chemical analysis. To ensure better film uniformity, the substrates were rotated during deposition. The evaporation rate (0.2 nm/s) and film thickness were controlled using a quartz crystal (QC) thickness monitor. For all layers, the thickness set by the QC was 150 nm. However, the real thickness was found by optical fitting.

X-ray diffraction revealed that all of the films were amorphous. The chemical properties of the single films were studied using X-ray photoelectron spectroscopy (XPS) performed in a Thermo Scientific Escalab 250Xi spectrometer equipped with a monochromatic Al K_α (1486.6 eV) X-ray source. To minimize electrostatic charging of the samples, the films deposited on the tantalum substrates were used for XPS analysis. The surface carbon 1s peak at 284.5 eV was used as the binding energy reference. For the multilayer film, the elemental distribution across the film thickness was obtained by a sequence of ion etching followed by XPS measurements. Etching was performed using a 2-keV Ar+ ion beam, and the ion current at the sample surface was less than 1 μA. The optical properties of the films were determined by measuring their normal-incidence transmittance over the wavelength range 200–800 nm using a Jasco V-570 spectrophotometer.

III. Results and Discussion

Chemical Properties:

The tungsten XPS W 4*f* core level spectrum consists of two sublevels ($4f_{5/2}$ and $4f_{7/2}$) due to spin-orbit splitting, as shown in **Fig. 1a**. In order to determine the binding energies of these peaks, the spectrum was fitted using a non-linear least squares algorithm with a Shirley background and a Gaussian-Lorentzian mixed line shape. The binding energies of the W $4f_{7/2}$ and the W $4f_{5/2}$ peaks were 36.0 eV and 38.1 eV, respectively. These values are identical to those of tungsten in the W^{6+} oxidation state (WO3) [20], indicating that our tungsten oxide films were stoichiometric. Similarly, the molybdenum XPS Mo 3*d* core-level spectrum consists of two sublevels ($3d3/2$ and $3d_{5/2}$) due to spin-orbit splitting (**Fig. 1b**). The binding energies of the Mo $3d5/2$ and Mo $3d_{3/2}$ peaks were 232.7 eV and 235.8 eV, respectively. These values are in close agreement with those of molybdenum in the Mo^{6+} oxidation state (MoO_3) [20]. Therefore, our molybdenum oxide films were stoichiometric. The O 1*s* spectrum (**Fig. 1c**) of both oxides was resolved into two components. The first is a low-binding-energy (LBE) component, which is attributed to oxygen bound to W or Mo. The second high-binding-energy (HBE) component may be attributed to oxygen species (such as water vapor or OH species) adsorbed at the film surface.

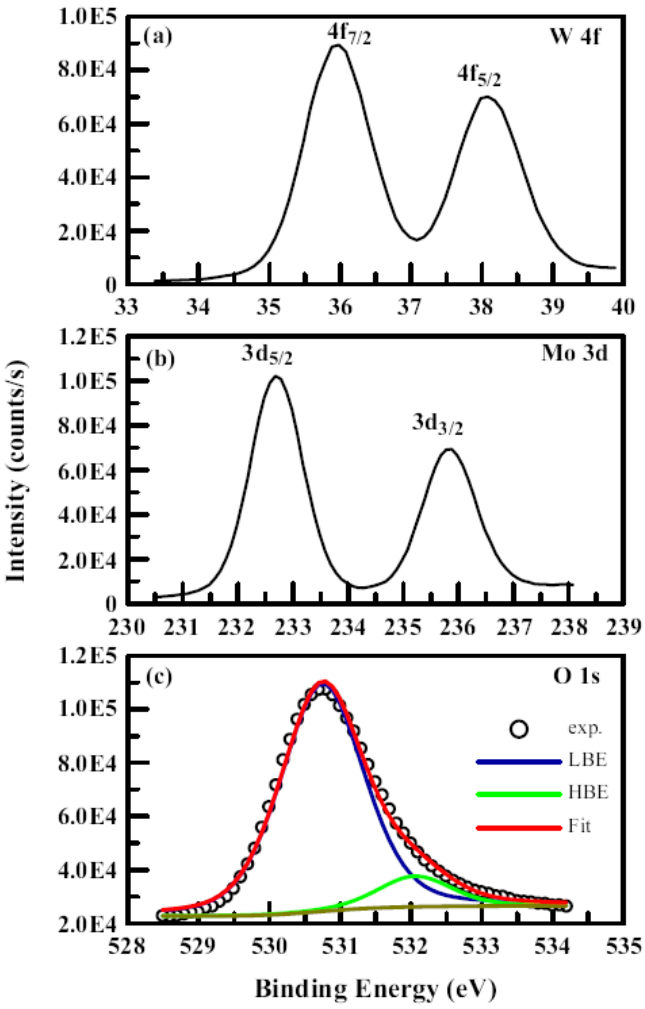

Fig. 1: XPS spectra of the pure oxide (single-layer) films: (a) W 4*f* core-level spectrum of the WO3 film; (b) Mo 3*d* core-level spectrum of the MoO3 film; (c) O 1*s* core-level spectrum, resolved into its two components.

The binding energies of these two components were 530.7 ± 0.1 eV, and 532.0 ± 0.1 eV, for the LBE and HBE components, respectively.

XPS depth profiling was used to investigate the spatial distribution and diffusion of the metals (W or Mo) across the multilayer structure. Several tungsten XPS peaks overlap with those of molybdenum or tantalum. Therefore, the Mo 3*d* and W 4*d* peaks were selected for our depth profile investigation. These two peaks are well separated, yet they are very close in binding energy. This situation makes it possible to simultaneously monitor their evolution as a function of etching time, as shown in **Fig. 2**. To achieve a better fit, it was necessary to deconvolute each of these peaks into five components (**Fig. 2**). The area under each peak (i.e. the sum of the areas of the five components) was used as a measure of the concentration of the metal at that depth. Etching was conducted until no signal was observed from the W 4*d* peak. The relative concentration of each metal was normalized with respect to the maximum intensity obtained for that metal, and the results are shown

in Fig. 3. It is evident from this Figure that the interface between the two layers was not sharp, and inter-diffusion of WO_3 and MoO_3 occurred, which resulted in a junction layer that accounted for nearly 1/6 of the total thickness of the multilayer structure. Etching the molybdenum oxide layer took less time because the Mo etching rate (0.44 nm/s) was higher than that of W (0.33 nm/s) [21].

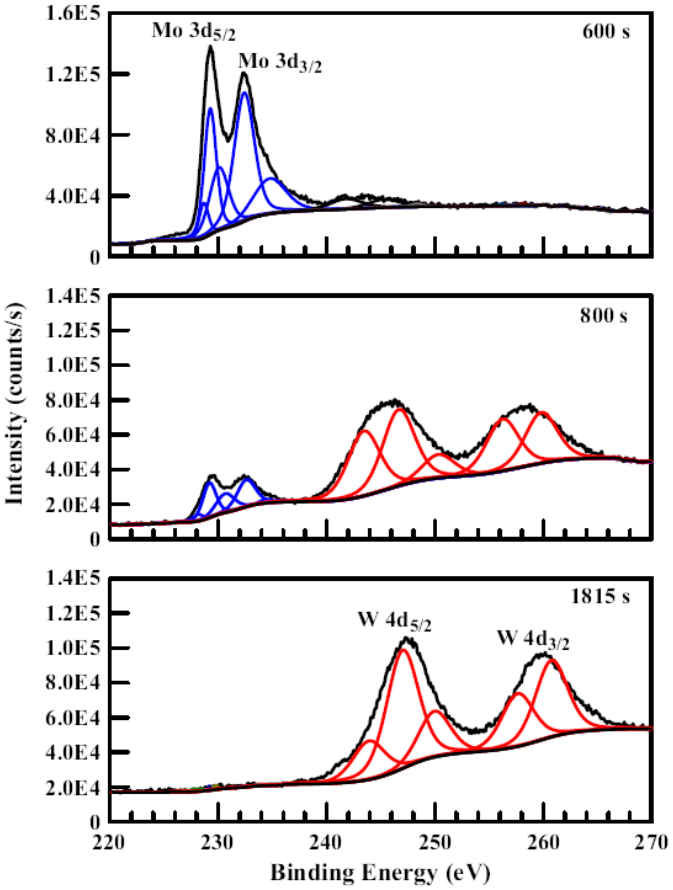

Fig. 2: X-ray photoelectron spectra of the multilayer structure in the W 4*d* and Mo 3*d* core level regions showing the evolution of the spectra as a function of etching time. The black curve is the experimental spectrum, and the blue and red curves indicate the component peaks under each spectrum.

Optical Properties:

The normal-incidence transmittance spectra of the films are shown in Fig. 4. The films were transparent throughout the visible region. These spectra were used to extract the optical constants of the films. In the transparency region of the films (wavelength, $\lambda \geq 400$ nm), the transmittance (T) spectra of the single films were fit using the formula for the transmittance of a thin film on a transparent substrate [22,23]:

$$T = \frac{16\, n_s(n^2+k^2)\beta}{A + B\beta^2 + 2\beta\left[C\cos\left(\frac{4\pi nd}{\lambda}\right) + D\sin\left(\frac{4\pi nd}{\lambda}\right)\right]} \qquad (1)$$

with

$$B = [(n-1)^2 + k^2][(n-n_s)^2 + k^2]$$
$$C = -(n^2 - 1 + k^2)(n^2 - n_s^2 + k^2) + 4k^2 n_s$$
$$D = 2kn_s(n^2 - 1 + k^2) + 2k(n^2 - n_s^2 + k^2)$$

where n, k, and d are the refractive index, extinction coefficient, and thickness of the film, respectively, n_s is the refractive index of the substrate, and $\beta = exp(-4\pi kd/\lambda)$. In order to fit the experimental transmittance spectra using Eq. (1), models for the dispersion of n and k must be used. The refractive index of the films was modeled using a Cauchy dispersion formula:

$$n(\lambda) = n_0 + \frac{A_1}{\lambda^2} + \frac{A_2}{\lambda^4} \qquad (2)$$

where n_o, A_1, and A_2 are constants. The extinction coefficient of the films was modeled by an exponential law for absorption below the band gap:

$$k = k_o + k_1 e^{-\kappa\lambda} \qquad (3)$$

where k_o, k_1, and κ are constants. Such an equation for k can account for band-tail absorption as well as absorption due to scattering and defects. The least-squares method was used to fit the experimental transmittance spectra of the single films using Eq. (1), with Eqs. (2) and (3) as the models for the optical constants. The fitting parameters were n_o, A_1, A_2, d, k_o, k_1, and κ. The best-fit parameters are listed in Table 1, and were used to calculate the optical constants of the films, as shown in Fig. 5. The accuracy of this technique is ± 0.02 for n, ± 2×10^{-4} for k, and ± 10 nm for d. Our values of the refractive index were comparable to those previously reported for MoO_3 and WO_3, as shown in Fig. 5.

Optical Properties of Multilayers – Effective Layer Method

The multilayer is treated as a single layer with effective optical constants (n_{eff} and k_{eff}) and overall thickness d_{eff}. The single-layer model (Section 3.2) was used to fit the experimental transmittance spectrum of the multilayer, with (n, k, d) replaced with (n_{eff}, k_{eff}, d_{eff}). An excellent fit of the experimental transmittance spectrum was noted, as shown in Fig. 6, and the corresponding best-fit parameters are listed in Table 1. The effective optical constants of the multilayer using this method are shown in Fig. 7 and are compared with those of the single films.

The effective refractive index of the multilayer is assumed to lie between those of the individual layers and is largely influenced by the layer adjacent to the substrate. The reason for this trend is that the difference in the refractive index (Δn) between WO_3 and the substrate is larger than Δn between WO_3 and MoO_3. In the visible region, the extinction coefficient of the multilayer was higher than that of the single layers. This could be due to light scattering at the junction layer. Given the thicknesses of the single layers found in Section 3.2 (Table 1), the overall thickness of the multilayer should be 232 nm. However, the effective thickness obtained from the fit was 183 nm. X-ray photoelectron spectroscopy depth profiles (Fig. 3) indicated that the thickness of the junction layer between MoO_3 and WO_3 was approximately ⅙ of the total thickness. Therefore, the effective thickness of the multilayer is ⅚ × 232 = 193 nm, which is close to the value of 183 nm obtained from the fit.

The validity of the new model was tested using effective-medium theory, which was developed to study the dielectric properties of heterogeneous media consisting of several phases or components [26]. This theory has also been used to investigate the effective optical properties of multilayers [27-

29]. Several effective medium models have been developed, including the parallel model and the series model [26]. In the parallel model, the effective dielectric function (ϵ_{eff}) is treated as a linear combination of the dielectric functions (ϵ_1, ϵ_2) of the two layers [26]:

$$\epsilon_{eff} = \xi_1\epsilon_1 + \xi_2\epsilon_2 \quad (4)$$

where ξ_j is the contribution of the j^{th} layer to the total dielectric function, such that

$$\xi_1 + \xi_2 = 1$$

The series model expresses the effective dielectric function as [26]:

$$\frac{1}{\epsilon_{eff}} = \frac{\xi_1}{\epsilon_1} + \frac{\xi_2}{\epsilon_2} \quad (5)$$

These equations can be expressed for the refractive index by noting that the complex dielectric function ($\tilde{\epsilon} = \epsilon_r + i\epsilon_i$) and the complex index of refraction ($\tilde{n} = n + ik$) are related by $\tilde{\epsilon} = \tilde{n}^2$, where ϵ_r and ϵ_i are the real and imaginary parts of the dielectric function. Therefore, $\epsilon_r = n^2 - k^2$ and $\epsilon_i = 2nk$. For the region of interest ($\lambda \geq 400$ nm), $k^2 \ll n^2$, and thus $n^2 \approx \epsilon_r$. The parallel and series models can then be written, respectively, as:

$$n_{eff} = \sqrt{\xi_1 n_1^2 + \xi_2 n_2^2} \quad (6)$$

$$n_{eff} = \left[\frac{\xi_1}{n_1^2} + \frac{\xi_2}{n_2^2}\right]^{-1/2} \quad (7)$$

Both models were applied to fit the effective refractive index of the multilayer, taking n_{eff} from **Fig. 7**, and n_1 (MoO_3) and n_2 (WO_3) from **Fig. 5a**. Excellent fits were obtained, with ξ_1 = 0.45 ± 0.05 and ξ_2 = 0.55 ± 0.02.

Bandgap

The band gap of a semiconductor is closely related to its band structure. It is also related to the optical constants via the absorption coefficient (α), given by $\alpha = 4\pi k/\lambda$. The absorption coefficient of the films was calculated using the equation: $\alpha = (1/d)\ ln\ (1/T)$. For semiconductors with indirect bandgaps, such as MoO_3 and WO_3 [30,31], the absorption coefficient is related to the band gap (E_g) via the relation $\sqrt{\alpha E} = b\ (E - E_g)$ where b is a constant, and E is the incident photon energy. The band gap of the films was obtained by plotting $(\alpha E)^{1/2}$ vs. E (Tauc plot), as shown in **Fig. 8**. Extrapolation of the linear portions of the curves to the energy axis yielded the band-gap values. The band gap values were 2.75, 3.29, and 3.06 eV for MoO_3, WO_3, and multilayer thin films, respectively. These values are close to those reported in the literature for MoO_3 [30] and WO_3 [31] thin films. The multilayer film assumed a band gap value that was intermediate between those of MoO_3 and WO_3, which may be written as:

$$E_g\ (multilayer) = \eta_1\ E_g(MoO_3) + \eta_2\ E_g(WO_3) \quad (8)$$

with η_1 = 0.45 and η_2 = 0.55, the same as obtained for the refractive index using effective-medium theory.

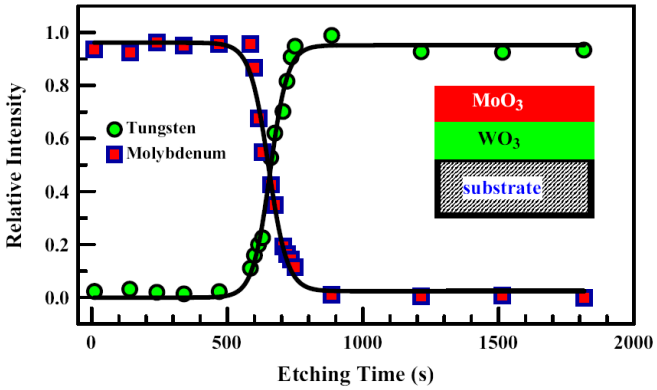

Fig. 3: X-ray photoelectron spectroscopy depth profile showing the distribution of Mo and W across the thickness of the multilayer structure.

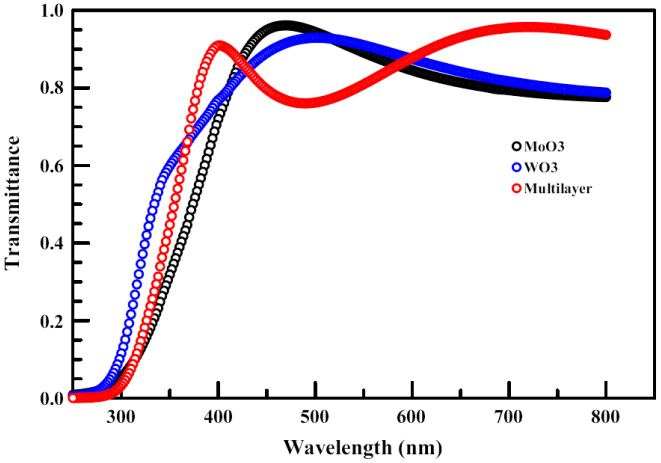

Fig. 4: Normal-incidence transmittance spectra of the single films and multilayer structure.

IV. Conclusion

A new model was proposed to determine the optical properties of a multilayer structure. This model uses the equation for the transmittance of a single layer to derive the effective optical constants of the multilayer, free of considerations of the individual layers comprising the structure. The model was applied to a two-layer system consisting of the dielectrics MoO_3 and WO_3. The structural, chemical, and optical properties of the single films were investigated, and the individual dielectric layers were found to be stoichiometric and transparent. Moreover, the optical constants of these layers were determined. Elemental depth profiling was used to probe the distribution of the elements across the thicknesses of the films in the multilayer structure, and this analysis revealed a significant overlap between the two layers. The new model was then used to obtain the effective optical constants of the multilayer. The validity of the new model was tested on the basis of effective-medium theory, which indicated an excellent fit to the experimental transmittance spectrum using the obtained optical constants. Finally, the band gaps of the films were determined, and the

multilayer structure yielded an intermediate band gap that was consistent with effective-medium theory.

ACKNOWLEDGMENTS

The support for this work by the Physics Department of King Fahd University of Petroleum and Minerals is acknowledged.

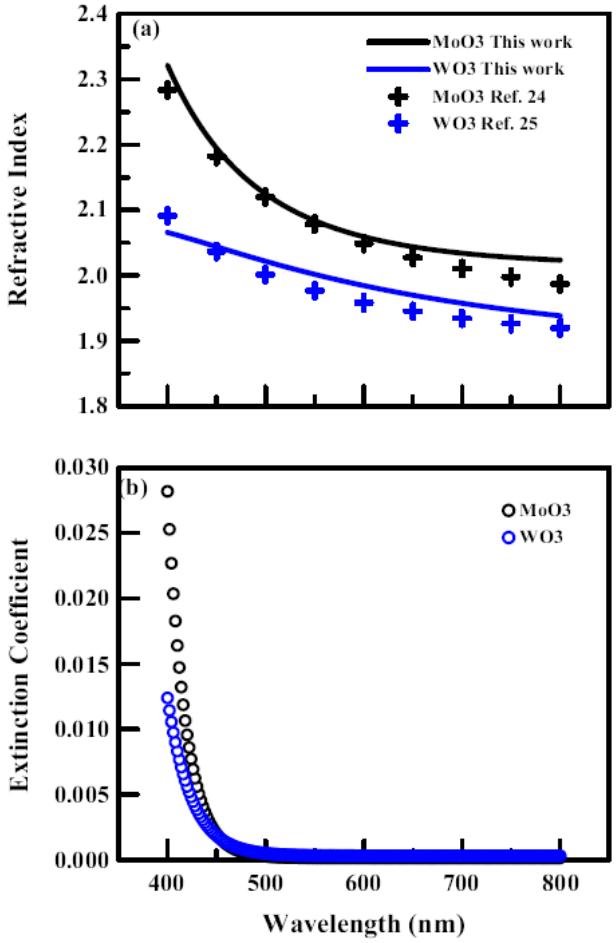

Fig. 5: Dispersion curves of the optical constants of the single oxide films: (a) Refractive index of the films. A comparison with literature values is also presented; (b) Extinction coefficient of the films.

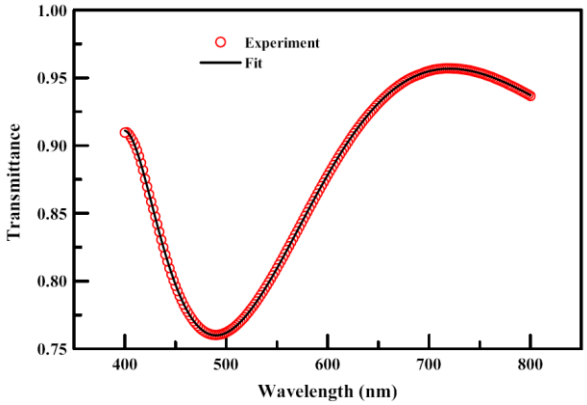

Fig. 6: Fitting the transmittance spectrum of the multilayer structure using the newly proposed effective-layer method.

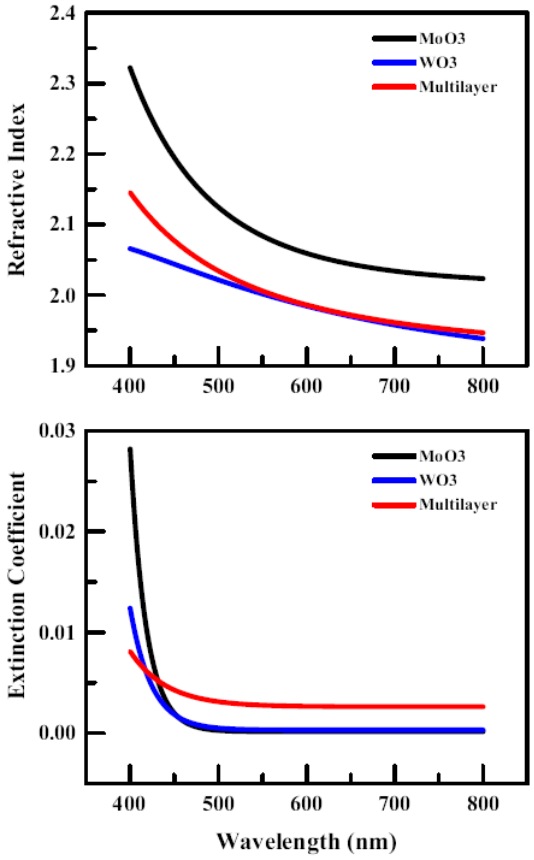

Fig. 7: Dispersion curves of the optical constants of the multilayer structure using the effective layer method compared with the optical constants of the single oxide films.

Table 1: Optical parameters of the films.

Material	n_o	A_1 (nm^2)	A_2 (nm^4)	k_o	k_1	κ (nm^{-1})	d (nm)
MoO_3	2.02	-1.34×10^4	9.86×10^9	2.00×10^{-4}	8.45×10^7	0.0546	108
WO_3	1.87	5.15×10^4	-3.11×10^9	3.00×10^{-4}	1.72×10^5	0.0412	124
Multilayer	1.91	2.01×10^4	2.85×10^9	2.60×10^{-3}	77.7	0.0239	183

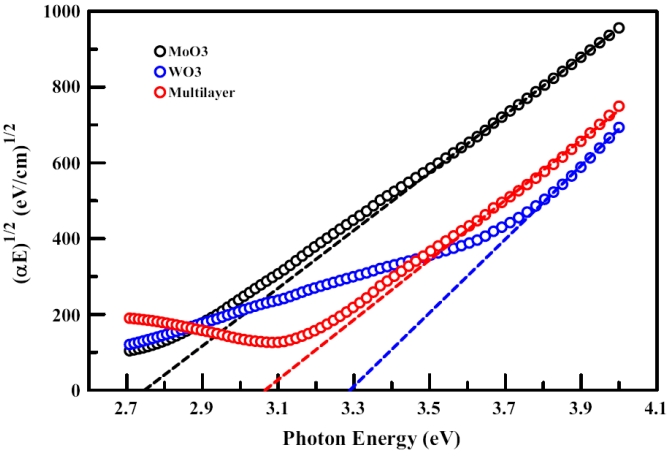

Fig. 8: Tauc plots showing the band gaps of the films.

REFERENCES

[1] M. Heikkinen, R. Ghiyasi, and M. Karppinen, "Layer-engineered functional multilayer thin-film structures and interfaces through atomic and molecular layer deposition," *Adv. Mater. Interfaces*, vol. 12, p. 2400262, 2025.

[2] M. Aliofkhazraei *et al.*, "Development of electrodeposited multilayer coatings: A review of fabrication, microstructure, properties and applications," *Applied Surface Science Advances*, vol. 6, p. 100141, 2021.

[3] T. Y. Rai and A. C. Hegde, "Development of high corrosion resistant (Ni-Fe) alloy coatings from a low concentration bath through multilayer approach," *Mater. Sci. Technol.*, vol. 41, pp. 77–89, 2025.

[4] E. J. Gildersleeve and R. Vaßen, "Thermally sprayed functional coatings and multilayers: A selection of historical applications and potential pathways for future innovation," *J. Therm. Spray Technol.*, vol. 32, pp. 778–817, 2023.

[5] A. Piegari and F. Flory, *Optical Thin Films and Coatings: From Materials to Applications*. Woodhead Publishing, 2013.

[6] O. Stenzel, "The Physics of Thin Film Optical Spectra: An Introduction," vol. 44, 2016.

[7] H. A. MacLeod, *Thin-film optical filters, fourth edition*, 4th ed. Boca Raton, FL: CRC Press, 2010.

[8] C. Ji *et al.*, "Recent applications of antireflection coatings in solar cells," *Photonics*, vol. 9, p. 906, 2022.

[9] H. Wang, S. Gao, Y. Li, L. A. Gubanova, and H. A. Tsyganok, "Simulation and analysis of multilayer film for EUV lithography," in *Optical Design and Testing XIV*, 2024, p. 49.

[10] F. Turkoglu *et al.*, "Development of ZTO/Ag/ZTO transparent electrodes for thin film solar cells," *J. Mater. Sci.: Mater. Electron.*, vol. 33, pp. 10955–10964, 2022.

[11] D. Dai, Y. Zhang, S. Yang, W. Kong, J. Yang, and J. Zhang, "Recent advances in functional materials for optical data storage," *Molecules*, vol. 29, p. 254, 2024.

[12] L. C. Lohithakshan and P. Kannan, "Realisation of optical filters using multi-layered thin film coatings by transfer matrix model simulations," *Mater. Today*, vol. 66, pp. 1671–1677, 2022.

[13] Y. Man *et al.*, "Versatile optical spatial filtering based on multilayer film flat optics," *Laser Photon. Rev.*, vol. 20, no. 3, 2026.

[14] D. Kim *et al.*, "Ti/TiO_2/SiO_2 multilayer thin films with enhanced spectral selectivity for optical narrow bandpass filters," *Sci. Rep.*, vol. 12, p. 32, 2022.

[15] M. Yaseen *et al.*, "State-of-the-art electrochromic thin films devices, fabrication techniques and applications: a review," *Nanocomposites*, vol. 10, no. 1, pp. 1–40, 2024.

[16] L. Yao *et al.*, "Long-lived multilayer coatings for smart windows: Integration of energy-saving, antifogging, and self-healing functions," *ACS Appl. Energy Mater.*, vol. 2, pp. 7467–7473, 2019.

[17] A. Jiang, Y. Osamu, and L. Chen, "Multilayer optical thin film design with deep Q learning," *Sci. Rep.*, vol. 10, p. 12780, 2020

[18] T. Baenas and M. Machado, "Optical model for multilayer glazing systems: application to laminated glass and photovoltaic modules," *Sol. Energy*, vol. 125, pp. 256–266, 2016.

[19] M. Bass *et al.*, *Handbook of optics, third edition volume IV: Optical properties of materials, nonlinear optics, quantum optics (set)*, 3rd ed. McGraw-Hill Education, 2009.

[20] "NIST X-ray photoelectron spectroscopy database," *Nist.gov*. [Online]. Available: https://srdata.nist.gov/xps/. [Accessed: 19-Mar-2026].

[21] MicroFab, Inc. (http://www.microfabnh.com/index.php).

[22] O. S. Heavens, *Optical Properties of Thin Solid Films*, Dover Publications (1991).

[23] J. C. Manifacier, J. Gasiot, J. P. Fillard, *A simple method for the determination of the optical constants n, k and the thickness of a weakly absorbing thin film*, J. Phys. E 9 (1976) 1002-1004.

[24] R. A. Mohamed, M. M. El-Nahass, M. Y. El-Bakry, E.-S. A. El-Dahshan, E. H. Aamer, D. M. Habashy, *Investigation of optical properties of molybdenum trioxide (MoO_3) thin films using neural networks*, Eur. Phys. J. Plus 139 (2024) 378.

[25] D. Davazoglou, A. Donnadieu, *Study of optical dispersion parameters of WO_3 polycrystalline thin films*, J. Appl. Phys. 72 (1992) 1502-1511.

[26] B. Ansari, A. N. Kalhoro, S. Shah, F. Memon, A. Ali, S. Afridi, *Ability and limitations of the effective medium theory in terms of the filling fraction and number of layers for hyperbolic metamaterials*, Appl. Opt. 64 (2025) 2497-2503.

[27] A. J. Abu El-Haija, *Effective medium approximation for the effective optical constants of a bilayer and multilayer structure based on the characteristic matrix technique*, *J. Appl. Phys.* 93 (2003) 2590-2594.

[28] D. M. Pereze, *General effective medium model for the complex permittivity extraction with an open-ended coaxial probe in the presence of a multilayer material under test*, PhD thesis, Bologna University, Italy (2012).

[29] T Zhao, *Effective medium modeling and experimental characterization of multilayer dielectric with periodic inclusion*, PhD thesis, Iowa State University, USA (2015).

[30] A. V. Juan-Arturo, A. Leonel Mendoza-Martínez, G. Morales-Luna, M. Morales-Luna, *Exploring the optical properties of molybdenum trioxide: approach of theory modeling and depositions techniques*, Adv. Phys. X 10 (2025) 2451687

[31] R. J. Sáenz-Hernández, G. M. Herrera-Pérez, J. S. Uribe-Chavira, M. C. Grijalva-Castillo, J. T. Elizalde-Galindo, J. A. Matutes-Aquino, *Correlation between thickness and optical properties in nanocrystalline γ-monoclinic WO_3 thin films*, Coatings 12 (2022) 1727

Author Index

Gonzalo A-Perez **1170**
Pablo Cencillo Abad **901**
Jaime Abad-Arredondo **405**
Gregory Abadias **759**
F. Javier García de Abajo **108, 676, 1137, 1176, 1192, 1381**
Romina Abarca-Ramirez **1383**
M. Abbarchi **997**
Ali Abbas **1109**
Philippe Ben Abdallah **124**
Muluneh G. Abebe **723, 1366**
Hamed Abiri **141, 503**
Mahmoud A. A. Abouelatta **272**
Reem Abubaker **1770**
Eslam Abubakr **361**
Diego Romero Abujetas **1183**
Younes Achaoui **381**
Sandra Achieng **491**
Karim Achouri **272, 714, 1670**
T. Ackemann **694**
Guillermo Acuna **1209**
Giorgio Adamo **329, 467**
Alexandra Adams **387**
Sadhvikas Addamane **435**
Ali Adibi **141, 503**
Albert Adserias **148**
Badri Aekbote **902**
Andrei Afanasev **451**
Dmytro Afanasiev **322**
Adeel Afridi **114**
Louis Agard **208**
Girish Agarwal **130**
Gonzague Agez **164, 324**
Nada Aghad **1109**
Vincenzo Aglieri **753**
Simonpietro Agnello **1728**
Diogo Aguiam **697, 832, 1121**
Igor Aharonovich **1281**
Zeeshan Ahmad **942**
Hammad Ahmed **304, 441**
Arik Ahmed **762**
Sungmo Ahn **327**
Geun Ho Ahn **1116**
Jae Won Ahn **1436**
Jouni Ahopelto **612, 646, 672**
Misbah ul Ain **181**
Vittorio Aita **105**
Javier Aizpurua **243, 1154, 1203, 1211**
Nursel Akçam **1404**
Evelijn Akerboom **1215**
Serap Aksu **276**
Vladimir Aksyuk **273**
Mohammad Al-Kuhaili **1770**
Alessandro Alabastri **405, 1052**
Abdullah Alabbadi **894**
Ahmadreza Alaeddini **1070**
Badrul Alam **1070**
Marwan Alam **1607**
Nebras Alattar **1605**
Pablo Albella **364, 1200, 1209**
Nicolas Albenge **145**
Edoardo Albisetti **400**
Wiebke Albrecht **1215**
Edvinas Aleksandravičius **1686**
Andrea Alessandrini **401**
Jose Francisco Algorri **868**
Ghada Alharbi **942**
Farhan Ali **425**
Amir Rajabpoor Alisepahi **629**
Hossein Allahverdizadeh **1670**
Maryam Allamki **407**
B. Alloing **694**
Laura de Almeida **1473**
Guilhem Almuneau **1473**
Isabel Alonso **871**
Pablo Alonso-Gonzáles **1160**
Pablo Alonso-González **911**
Carlos Alonso-Ramos **330**
David Alonso-Tomas **1734**
Andrea Alù **506, 830**
Francesc Xavier Alvarez **1256**
Gonzalo Alvarez-Perez **730, 842, 1158, 1458**
Gonzalo Álvarez-Pérez **1160**
Ramon A. Alvarez-Puebla **201**
Cristiana F. Alves **646**
Alessio Amaolo **705, 707**
A. Ambrosio **524**
Mariya D. Amel'chenko **1675**

Author Index (cont.)

Tomohiro Amemiya **432**
Vincenzo Amendola **1045**
Giuseppe Ammirati **1570**
Madiha Amrani **264, 1515**
Srinivasan Anand **1434**
Hjalmar Andersson **1336**
David González Andrade **344**
David Andrews **1584**
Francesco De Angelis **1086, 1222**
Costantino De Angelis **1092**
Steven Anlage **260, 947**
Ferdinanda Annesi **1062**
Matthieu Ansquer **1006**
Mauro Antezza **686, 687**
Alexander Antonov **550**
Thomas M. Antonsen **260, 947**
Tomasz Antosiewicz **1533, 1607**
Nicklas Anttu **1206**
Roman Anufriev **1261**
Dogukan Apaydin **1336**
Ashod Aradian **413, 927**
Nobuhiro Arai **581**
Olivier Arcizet **1266**
Gianluigi Ardissino **1065**
Raffaele Ardito **109**
Daniel Arenas-Ortega **1603**
Christos Argyropoulos **578**
Kristian Arjas **715**
Paolo Arosio **1233**
Guillermo Arregui **342**
Mathieu Arribat **1650**
Rakesh Arul **1203, 1343, 1660**
Anand Eswara Rao Aryasomayajula **1751**
Viktar Asadchy **1207, 1672**
Benjamin Asamoah **1563**
Shun Asano **1012**
Yuto Ashida **1017**
Bülent Aslan **252**
Stella Aslanoglou **1055**
Rita Asquini **1070**
Luca Assogna **476**
A. S. Astrakhantseva **1324**
Darija Astrauskyte **751**
Harry Atwater **117, 1538, 1575, 1726**
Yannick Augenstein **1003**
V. Averbukh **818**
Rémi Avriller **1203**
Ivan Avrutsky **1715**
David Ayuso **543, 801, 802, 819**
D. Ayuso **818**
Abul Azad **293, 305**
Jose Azana **690**
Stéphane Azar **1593**
Antoine Azéma **164**
Maria Azhar **566**
Enrique Azuaje-Hualde **854**
Antton Babaze **1154**
Mohamed Babiker **356**
David Babonneau **759**
Nicolas Baboux **390**
Alberto Bacci **704**
Romain Bachelard **937**
Renaud Bachelot **176, 198, 203**
Tereza Bačová **838**
Youssef El Badri **381**
Jinseong Bae **1029, 1455, 1483**
Gabriela Báez **623**
Guillaume Baffou **212, 446**
Silvia Bagnoli **1233**
Mustapha Bahich **381**
Olha Bahrova **694**
Mohamad Bahsoun **194**
Elise Bailly-Rioufreyt **1129**
Michela Baiocchi **1070**
M. Bajcsy **597**
Miguel Montes Bajo **1293, 1299, 1580**
Christopher Baker **999**
Manjunath Balagopalan **646**
Damián Baláž **1135**
Ilko Bald **1221**
Leonetta Baldassare **1622**
Ilaria Micol Baldi **1222**
Pietro Baldin **231**
Antonio Balena **1055, 1082**
Adam Ball **481**
Dario Ballarini **1168, 1442**
John Ballato **348**
Carlos Gonzalez Ballestero **519**

Author Index (cont.)

Enkeleda Balliu **348**
S. C. Baltogiannis **632**
Pravallika Bandaru **1583**
Kingshuk Bandopadhay **1109**
Kingshuk Bandopadhyay **391, 922, 1467**
Rimi Banerjee **939**
Arnab Banerjee **945**
Francesco Banfi **669**
Sebastian Bange **1491**
Balázs Bánhelyi **965, 1414**
Peter Banzer **484, 530, 1024**
Yiliang Bao **273**
Lifeng Bao **291**
Larysa Baraban **188**
Denis Baranov **514, 572**
Ismael Barba **1677**
Michał Barbasiewicz **1374**
Riccardo Cristoforo Barberi **1463**
Tiago Barbosa **1152**
Ingrid Barcelos **1152**
Matias Bargheer **1239**
Hani Barhom **593**
Hani Barhum **1059**
Saika Muntaha Bari **491**
Stephen M. Barnett **184**
Thierry Baron **291**
Alexandre Baron **413, 1296**
Nicolae Barsan **145**
David Barton **507**
Zahra Basiri **1131**
Andrea Li Bassi **1495**
Mathieu Bastide **209**
Enrico Baù **458**
Enrico Bau **1158**
Emmanuel Baudin **1275**
Anne-Laure Baudrion **185**
Gerrit Bauer **126**
S. Bauerdick **1764**
Jeremy J. Baumberg **102, 910, 1203, 1343, 1660**
T. Baumert **818**
Jérémie Béal **759**
Albert Beardo **1256**
Guillaume Beaudin **1545**
Gregoir Beaudoin **1158**
Fiona Beck **346, 358, 1578**
Chris Beckerleg **996**
Erik Beji **1068**
Robel Bekele **506**
Cherif Belacel **1265**
A. Belardini **935**
Ali Belarouci **276**
Mikhail A. Belkin **1308, 1638**
Joel Bellessa **924**
Julie Belleville **117, 1575**
L. Belliard **632**
Anila Bello **1224**
Dhimiter Bello **1224**
Philippe Ben-Abdallah **684, 713**
Kamel Bencheikh **1417**
Filippo Bencivenga **1258**
Ileana-Cristina Benea-Chelmus **1131**
Stefania Benedetti **453**
Jean Michel Benoit **924**
Fouad Bentata **390**
Ivonne Bente **835**
Taha Benyattou **156**
Stéphane Berciaud **1213**
Andrea Bergamini **1465**
Matthijs Berghuis **929**
Alexander Bergmann **484**
Lotfi Berguiga **156, 390**
Andergachew Berhe **1586**
Pierre Berini **724, 787**
Fritz Berkmann **1622**
Sarah Berman **507**
Peter Bermel **945**
Silvie Bernatova **334**
Martin Bernier **348**
Nathan Berrit **614, 1263**
Aurélie Bertaux **222, 224, 239**
Jacopo Bertolotti **830, 1493**
Valentina Bessi **1233**
Lucas Vazquez Besteiro **179**
Lucas Vázquez Besteiro **203**
Lucas Besteiro **218**
Yonatan Betancur-Ocampo **623**
Sylvain Betoule **801**
Daniel Beysens **394**

Author Index (cont.)

Pavel Bezrukov **593, 1059**
Miraculous Joseph Bhaseen **1573**
Harish Bhaskaran **419, 830, 835**
Yudhajit Bhattacharjee **219**
Biswajit Bhattacharyya **1221**
Lei Bi **574**
Stefano Biasi **252**
Manuel Bibes **844**
Sébastien Bidault **881, 1296**
Jonas Biechteler **458**
Alessandro Bile **154**
Joel Billermann **834**
Ilario Bisignano **151**
Francesco Bisio **397, 1495**
Sudipta Biswas **491**
Aritra Biswas **901, 905**
Kushal Biswas **1224**
Eric R. Bittner **1273**
Cédric Blanchard **721**
Paul-Édouard Blanchard **1015**
Nicholas Blanchard **1269**
Valérie Blanchet **801**
Juan Maria Blanco **1391**
Tanneguy Blandin **1650**
Vjaceslavs Bobrovs **1424, 1519, 1658, 1680**
D. Bobylev **694**
Gerhard Boehm **1308, 1638**
Elizabeth Boer-Duchemin **1181, 1213**
Hilario Boggiano **1265**
Katarzyna Bogusz **1043, 1389**
Jan Bolek **932**
Monica Bollani **727, 1142**
Paul de Bollivier **163**
Margherita Bolognesi **1068**
Alexandra Boltasseva **101, 425, 455, 473, 726**
Alessandro di Bona **453**
Caroline Bonafos **194**
Igor Bondarev **498**
Nicolas Bonod **161**
Florian Bönsel **1591**
Siew Kheng Boong **1524**
Andrei G. Borisov **1154**
João Borlido **832, 1121**
Martina Borreani **440**
Lille Borresen **910**
Redouane Borsali **921**
Eugene Bortchagovsky **1560**
Federica Bortoletto **1721**
Paolo Bortolotti **844**
Nicholas J. Borys **762**
Muriel Botey **783, 790**
Roberto A. Boto **1203**
M. Bouabdellaoui **997**
Arthur Bouamra **279**
Petr Bouchal **1749**
S. Bouchoule **694**
E. H. El Boudouti **264, 1515**
Alexandre Bouhelier **222, 224, 239**
Souhir Boujday **161**
Rabah Boukherroub **264**
Olivier Bourgeois **1249**
Jeremy Bourhill **816, 1010, 1500**
Gilles Bourret **934**
Adel Bousseksou **1158**
Eric G Bowes **360**
Robert Boyd **121**
Olga Boyko **632**
Andrey Bozhko **744**
A. Louise Bradley **127, 854, 967, 1326, 1469, 1535, 1556, 1754**
Rudolf Bratschitsch **416**
Aymeric Braud **1665**
Timo Braun **145**
Benjamin Braun **401**
Paul Braun **741**
Giovanni Breglio **1077**
Samuel Brem **1156**
Igal Brener **134, 1287**
Sean Bresler **273**
Fernando Bresme **1200**
Hope M Bretscher **1275**
Maurizio Brigotti **1065**
Nicole Brimhall **1004**
Christelle Brimont **694**
Boris Brisuda **1249**
Mark L. Brongersma **499**
Julie Brown **1000**
Chiara Brugnoni **1505**

Author Index (cont.)

Marco Brühlmann **519**
Mauro Daniel Luigi Bruno **1463**
Jean-François Bryche **150, 1545**
Thalia Dominguez Bucio **291**
Stefan Yoshi Buhmann **562**
Roman Buisine **1641**
Ida Juliane Bundgaard **883**
Johannes Bürger **1168, 1442**
Jorge Burgos **917**
Lucas Mascaro Burguera **1565**
Thomas W. Burkle **286**
Luca Bursi **453**
Edgar Bustamante **1114**
Unė G. Būtaitė **1379**
Johannes Bütow **530**
E. Butzen **1764**
Rytis Buzelis **1688**
Alessio Buzzin **1070**
Anton Bykov **910**
Niall Byrnes **951**
Moongul Byun **1692**
Javiera Cabezas **535**
Raquel Fernández de Cabo **330, 344**
Karen Caicedo **927, 1084**
Soraya Caixeiro **1054**
Joshua D. Caldwell **1133, 1135**
Vincenzo Caligiuri **440, 457, 1062**
C. Callegari **818**
Roman Calpe **159, 1563**
Gabriele Calusi **342, 438**
Arrigo Calzolari **453**
Filipe Camarneiro **697, 1121**
E. Cambril **694**
Sophie Camelio **759**
Angela Campo **166**
Leonardo Campos **1152**
Andrea Camposeo **1635**
Víctor Camús **1603**
Angela Candreva **1062**
Maurizio Canepa **397, 1495**
Marco Cannas **1530, 1728**
Diego Martin Cano **879**
Michael Canva **150**
Jian Cao **825**
Xiaoyu Cao **860**
Federico Capasso **100, 473**
Giovanni Capellini **1338, 1622**
Chiara Cappelli **1228, 1360**
Nestor Eduardo Capuj **1734**
Roberto Caputo **151, 452, 1463**
Christian Carbogno **1135**
Ioana Cârdan **1226**
Giulia Cardinali **1336**
Simão Cardoso **1152**
Luca Carletti **1169**
Remi Carminati **713**
R. Carminati **1289**
Marciano Palmo do Carmo **1046**
Antonio Carone **915**
Giulio Carotta **1635**
Joel Carpenter **1379**
Lucciano Antonio Letelier Carreño **1724**
Edoardo Casadei **1495**
Justin Case **777**
Mathias Casiulis **426**
Eric Cassan **825**
Davide Cassara **473**
Giuseppe Castaldi **306**
Eduardo Martínez Castellano **1299**
Beatriz Castillo **1183**
R. Margoth Cordova Castro **1290**
Pietro Castronovo **1305, 1530, 1570**
Daniele Catone **1570**
Sébastien Cavalaglio **921**
Ramón Torres Cavanillas **1565**
Loris Cavenaile **585, 1366**
Marcello Cazzola **109**
Domenico de Ceglia **154, 425, 455, 1315**
Michele Celebrano **727, 1142**
Daniele Ceneda **154, 192**
Marco Centini **154, 192**
M. Centini **935**
Luis Cerdán **963**
Alexander Cerjan **435, 1103**
Francisco Cervera **671**
Ondrej Cervinka **1749**
G. Cesarini **935**
Tiziana Cesca **954**

Author Index (cont.)

Fernando Chacon-Sanchez **839, 913**
Mohand Chalal **1041**
Yann Chalopin **1254**
Eng AIk Chan **329**
Che Ting Chan **544, 1387**
Nolan Chan **1006**
Debashis Chanda **480, 901, 905**
Jiu Chang **141**
Wei-Shun Chang **181**
Chun-Chieh Chang **293, 305, 478**
Taeyong Chang **329**
Ming-Li Chang **544**
Shih-Hui Gilbert Chang **1362**
Yu-Shao Chang **1486**
Pengning Chao **705**
Gregory Chaplain **673**
Robert Chapman **1129**
P-Olivier Chapuis **731**
Paul Charette **150, 1545**
Rémi Chassagnon **174**
Anjali Chaudhary **1334**
Nicolas Chauvin **1129**
André Jorge Chaves **1152**
Cecile Chazot **906**
Pavel Cheben **787, 825, 993**
Zhigang Chen **113**
Minyu Chen **203**
Jui-Hung Chen **279**
Chong Chen **291**
Hou-Tong Chen **293, 305, 478**
Xianzhong Chen **304, 441**
Hao Chen **310**
Chun-Wei Chen **348**
Yijun Chen **408**
Xuewen Chen **468**
Yong P. Chen **570**
Hongsheng Chen **604**
Cong Chen **637**
Hong-Gen Chen **659**
Yuheng Chen **726**
Weijian Chen **779**
Jianlong Chen **794**
Wen Chen **884**
Yilin Chen **979**
Zhongyi Chen **979**
Qizhe Chen **991**
Xue-Wen Chen **1145**
Mu Ku Chen **1332, 1476, 1767**
Hsuen-Li Chen **1438**
Ting Wei Chen **1444**
Shangzhi Chen **1583**
Jia-Wern Chen **1597**
Wei-Han Chen **1690**
Wen-Hui (Sophia) Cheng **295**
Qian Cheng **631**
Han-Hsiang (Michael) Cheng **681**
Zheyu Cheng **939**
Szu-Cheng Cheng **1444**
Jialuo Cheng **1767**
Alexey Chernikov **1156**
Alexandre Chevillot-Biraud **185, 866**
Dmitry Chigrin **736**
Rohit Chikkaraddy **1547**
S. Chiodini **524**
Choonlae Cho **327**
Sangyeon Cho **462**
Hui Jae Cho **1330**
Hyunsu Cho **1341**
Yu Sung Choi **1436, 1738**
W. Choi **1698**
Yidong Chong **939, 1117**
Carice Chong **1524**
Yu-Hsun Chou **970**
Hsu-Hui Chou **1700**
Bhagwat Singh Chouhan **1713**
Rasmus Christiansen **741**
Louis Christienne **1259**
Demetrios N. Christodoulides **335**
E. A. Christou **818**
Cheng Hung Chu **489**
Daping Chu **1626**
Chu-Chen Chueh **1597**
Andrii Chumak **519**
Haejun Chung **1029, 1455, 1483**
Hyeongju Chung **1308**
Anastasiia Chyzhykova **1019**
Gabriele Ciasca **1471**
Sara Cibella **1158**

Author Index (cont.)

Francesco Ciccarello **884**
Elena Pinilla Cienfuegos **1451, 1565**
Joachim Ciers **1336**
Enez Furkan Cihan **1404**
Cristian Ciracì **730**
Cristian Ciraci **1158, 1170, 1458**
Emilio Ciusani **1235**
Alasdair Clark **902**
Daniel D. A. Clarke **985**
Karen De Clerck **723**
Bruno Clerckx **1088**
Adolfo Cobo **868**
Yovan de Coene **204**
Dan Cogan **1014**
Eyal Cohen **1680**
Crina Cojocaru **365, 775, 1428, 1440**
Justin Cole **1103**
Jonathan N. Coleman **1556**
Liam Collard **1082**
Stephane Collin **1473**
Ornella Colmegna **840**
Rémi Colom **1641**
Raffaele Colombelli **1158**
Giada Colombo **648, 653**
Lukas Conrads **357**
Lucian A. Constantin **1167**
Gloria Conte **612, 646**
Alessandra Contestabile **306**
Emma Contini **1721**
Lucia Conzatti **397**
Brain Corbett **1326**
Luke Cording **1349, 1759**
Alberto Corigliano **109**
Stefano Corni **709, 1170, 1220**
Eugenio Coronado **1565**
Alessandra Corrado **1082**
José Correia **832**
Alice de Corte **1412**
Paula Corte-Leon **591, 1391**
Emiliano Cortés **982**
Erika Cortese **1168, 1442**
Diego Costa **1152**
Robin Cours **194**
Christophe Couteau **759**
Joel D. Cox **1164, 1171, 1192**
Rebecca Craig **1502**
Dominic Craske **1334**
Caterina Credi **1233**
Benjamin Crockett **690**
Angus Crookes **1421, 1718**
Ana Cros **1603**
Giulia Crotti **231**
Gavin Crowder **696**
Samuel Crowther **1419**
Thierry Crozes **1249**
Aurélien Crut **614, 1263**
Andrea Csaki **230**
Mária Csete **965, 1414**
Marzia Cuccu **1156**
Aurélien Cuche **164, 324**
Sébastien Cueff **156, 390, 840**
Javier Cuerda **1371**
Joao Cunha **697, 1121**
Mark Cunningham **1502**
Alex Currie **1545**
Alberto G. Curto **200, 364, 383, 1049, 1412**
Andrea Cusano **868, 1077**
Maria Alessandra Cutolo **1077**
Alessia Cutri **1235**
Sergio D'Addato **453**
Gervasio D'Anzieri **825**
Amalia D'Avino **1065, 1078, 1080**
Annachiara D'Urso **1235**
Ceren Dag **586**
E. Daher **997**
Yunyun Dai **973**
Peng Dai **1626**
Giulia Dall'Osto **1220**
Caterina Dallari **1233**
Luca DalNegro **900**
Diego A. R. Dalvit **293, 305**
Sameer Dambal **1273**
Jiri Damborsky **894**
Caterina Damiano **433**
Benjamin Damilano **1293**
Alexandre Danescu **1129**
Hamid Reza Darabian **391**
Principia Dardano **283**

Author Index (cont.)

Trishita Das **566**
Akash Das **588**
Prasanta Kumar Datta **901**
Christin David **346, 358, 1578**
Rowena Davies **359**
Joshua Davis **1296**
Matthew W. Day **1275**
Jonathan Dearlove **419**
Dominique Decamps **801**
Piero Decleva **801**
Massimo La Deda **433, 1062**
Lex M. Dedding **364**
Pascal Del'Haye **894**
Colm Delaney **854, 1535, 1754**
Kaveh Delfanazari **407**
R. Delgado-Buscalioni **1187**
Florian Dell'ova **222**
Florian Dell'Ova **224**
Kevin Delmote **897**
Themistoklis Deloudis **1718**
Thomas Delplace **585, 1366**
Guillaume Demesy **161**
Angela Demetriadou **1284, 1343, 1409, 1421, 1488, 1660, 1718**
Hilmi Volkan Demir **190, 375, 1061**
Eugene Demler **1385**
Zilan Deng **251**
Huiwen Deng **291**
Juan Ramon Deop-Ruano **753, 1149**
Olivier Deparis **897**
Quentin Deplano **1203**
Sina Abedini Dereshgi **507**
Valentin Develay **694**
Chiara Devescovi **302**
Ancin M. Devis **1046**
Rob Devlin **116**
Arnaud Devos **1247**
Kevin Dhaliwal **387**
Abdelhak Dhibi **1041**
Eduardo J.C. Dias **1137, 1162, 1192, 1381**
Eduardo J. C. Dias **1176**
Jon Canosa Diaz **1249**
Wayne Dickson **170**
Michele Diego **1261**
Michel J. F. Digonnet **348**
Fei Ding **471**
Kun Ding **940**
Kewen Ding **1626**
Benjamin Diroll **481**
Laurent Divay **844**
Bahram Djafari-Rouhani **264, 268, 381, 661, 1515**
Nadia Djaker **1041**
Khanh-Van Do **176**
J. Dobie **127**
Jack Dobie **967, 1326, 1469**
Dmitry Dobrykh **1658**
Pablo Docampo **1759**
Andrea Dodero **1721**
Yoshiyasu Doi **1016**
Chloe Doiron **435**
Mathias Dolci **866**
Rafael Fuentes Dominguez **756**
Maria G. Donato **334**
Krupali Donda **1708, 1711**
Harry Donegan **1573**
Hao-Wen Dong **659**
Zhen-Chao Dong **978**
Hatou Yvelin Donkeng **704**
Luke Doolan **1556**
Bernardo Dores **832**
Ali Douaki **457**
Jean-Baptiste Doucet **1473**
Cattleya Dousset **1266**
James Downing **716**
L. Doyennette **694**
Ioannis Draganidis **832**
Peter D. Dragic **348**
Bogdan Dragnea **1251**
Dominique Drouin **1545**
Mingde Du **419**
Jiahua Duan **842**
Yulong Duan **899, 1302, 1583**
Jean-Yves Duboz **1650**
Jan Dudziński **1374**
Scott Duhey **303**
Rembert Duine **518**
Erik Dujardin **174, 222, 224, 239**
Jean-Yves Duquesne **1259**

Author Index (cont.)

Blas Durá-Azorín **956**
Brandon K. Durant **195**
Emek Goksu Durmusoglu **375**
Thomas Dursap **1129**
Ghada Dushaq **420**
Eitan Dvorquez **1105**
Ranjeet Dwivedi **413**
Sergey Dyakov **514**
K. R. Dzhikirba **1324**
Alvaro Rodriguez Echarri **1197**
J. Ignacio Echevarría **1565**
Christian J. Eckhardt **1275**
Serge Ecoffey **1545**
Mahmoud Eddrief **1259**
Kofi Edee **761**
Jacob Edginton **802, 819**
Anjalie Edirisooriya **346, 358, 1578**
Anatoly Efimov **293, 305**
A. Efimova **524**
Jörg S. Eismann **530**
Ihab Fathy El-Kady **1114**
Ramy ElGanainy **1108**
Chase Ellis **195**
Mahmoud Elsawy **737**
Antonio Emanuele **1570**
Md Tanvir Emrose **341**
Seyed Enjavi **503**
Sven Enns **409**
Taisuke Enomoto **882**
Nathan Epalle **174**
Jared Erb **947**
Said Ergoktas **147**
Daniel Erkensten **1156**
Alper Erturk **615**
Carlos Alberto Maciel Escudero **308**
Juan Pablo Escudero **635**
Martin Esmann **616**
Ruben Esteban **1203**
Aitzol Garcia Etxarri **302**
Karin Everschor-Sitte **566**
Davide Faccialà **818**
Yeshaiahu (Shaya) Fainman **340**
Jérôme Faist **1033, 1275**
Andrea di Falco **425**
Shanhui Fan **341**
Tongmiao Fan **858**
Dai Fang **1560**
Teodora Faraone **1535**
Cosmin Farcau **1226**
Henna Farheen **733**
Nikolaos Farmakidis **419, 830, 835**
Natalia Del Fatti **614, 1263**
Olga Favale **1062**
Ivan Favero **1265**
Letizia Fede **801**
Daniel Feferman **218**
Eyal Feigenbaum **486**
Armin Feist **1194**
Nordin Felidj **185, 866**
Nordin FELIDJ **1041**
Marcos D. Vozer Felisberto **286**
Simon Félix **611**
Alexander P. Fellows **1135**
Dou Feng **1334**
Mónica Fernandez-Arias **394**
Ivan Fernandez-Corbaton **582, 1201**
Antonio Fernández-Domínguez **405**
Antonio I. Fernandez-Dominguez **879, 956**
Louis-Henri Fernandez-Mouron **270**
Patrick Ferrand **446**
Carino Ferrante **476**
Antonio Ferraro **151, 452, 1463**
Catarina Ferreira **883**
Marcello Ferrera **284, 306, 425, 455, 1315**
Lydie Ferrier **156**
Vivian Ferry **483**
Andreas Fery **188, 201, 1757**
Robert Fickler **159**
Saskia Fiedler **1215**
Marco Filice **1062**
François Fillion-Gourdeau **1545**
Marco Finazzi **727, 1142**
Simona Fine **906**
Andrea Fiore **279, 342, 438**
Inga Anita Fischer **1338, 1622, 1690**
Jamie Fitzgerald **308, 1179**
Baptiste Fix **385**
J. Pierce Fix **762**

Author Index (cont.)

Julien Flamant **446**
Benedetta Flebus **515**
Monika Fleischer **145, 1560**
Guillaume Fleury **921**
Larisa Florea **854, 1535**
P. C. Flores **818**
Enrique Flores-Olmedo **623**
Marian Florescu **399, 438**
Vincent Flynn **515**
Angelica Focardi **1070**
Michael Foltýn **298**
Dhruv Fomra **481**
Kayn A. Forbes **184, 1584**
Matthew Foreman **951**
Jens Förstner **733**
Franck Fortuna **1259**
Elias Fösleitner **1541**
Frederic Fossard **385**
Antonino Foti **334**
Frank Fournel **164**
Piper Fowler-Wright **1371**
Ilia Fradkin **514**
M. Di Fraia **818**
Agostino Di Francescantonio **727, 919, 1142**
Alfredo Franco **1200**
Alejandro Franco-Medrano **623**
Gérard Colas des Francs **222, 224, 229, 239**
Lars Franke **720, 1703**
Sonja Franke-Arnold **1502**
Jonas Fransson **516**
Jesse Frantz **506**
Sonia Freddi **727, 1142**
Maximilian Frenzel **1174**
Lukas Freter **1371**
Georg von Freymann **409**
Holland Frieling **1538**
Wolfgang Fritzsche **230**
Bruno Frka-Petesic **915**
Thomas Fromentèze **1092**
Colton B. Fruhling **425**
Hongyan Fu **464**
PoHan Fu **1346**
David Fuard **921**
adam Fuchs **716**
Minoru Fujii **928, 1209, 1215**
Manato Fujimoto **581**
Yuri Fukaya **628**
Hiroshi Funaki **605**
Keita Funayama **663**
Zelio Fusco **346, 358, 1578**
Michael Fusella **1000**
Alessio Gabbani **1217**
Nikolaj Gadegaard **184**
Mika Gaedtke **1683**
Shashank Kumar Gahlaut **1221**
D. Gailevicius **780**
Darius Gailevičius **1686**
Carlota Ruiz de Galarreta **830, 1493**
Vincenzo Galdi **306**
Francesco Galeotti **1077**
Henning Galinski **933**
Christophe Galland **884, 1140**
Bruno Gallas **161**
Manuel Gallego **994**
Emma Gallo **433**
Sarra Gam-Derouich **866**
Maria Gambelli **1158**
Lin Gan **377**
Qiaoqiang Gan **991**
Ramy El Ganainy **957**
Marco Gandolfi **1092**
Yajun Gao **506**
Yang Gao **581**
Hanyu Gao **902**
Weibo Gao **1021**
Wenlong Gao **1353**
Eloise Garcelon **185**
D. Garcia **632**
Pedro David García **917**
Ángel J. García-Collado **1677**
Antonio García-Martín **1183**
Francisco García-Vidal **405**
Frederic Gardes **291**
Puneet Garg **1207**
Erik C. Garnett **1305**
Denis Garoli **457**
Miquel Garriga **871**
Núria Garro **1603**

Author Index (cont.)

Arian Gashi **303**
Alessandra Di Gaspare **1471**
Luciana di Gaspare **1622**
Riley Gatensby **1556**
James Gates **291**
Caroline Gauchotte-Lindsay **902**
Olivier Gauthier-Lafaye **1650**
Gian Carlo Gazzadi **453**
Chiara Gazzola **109**
Li Ge **957**
Ailsa Geddis **1076**
Sergei Geiman **1680**
Jozefien Geltmeyer **723**
Emanuele Gemo **835**
Patrice Genevet **390, 1641**
Zihan Geng **1476, 1767**
Davy Gérard **185, 203**
Davy Gerard **198, 759**
L. Germeroth **818**
David Gershoni **1014**
Lydia Federica Gervasini **1235**
Sergey Geyman **1424**
Mohamed El Ghafiani **264**
Ch. Ghaisas **632**
Monika Ghalawat **218**
Katayoun Gharagozloo-Hubmann **1135**
Ana Maria Mihaela Gherman **1226**
Raphael Gherman **1545**
Sirsendu Ghosal **1713**
J. Ghosh **818**
Flavio Di Giacinto **1471**
Alejandro M. Giacomotti **957**
Lorenzo Giannini **1070**
Brant C. Gibson **1105**
K. Gieb **1764**
Harald Giessen **458**
Gabriel Gil **1170**
José J. Gil **1400**
Cristina Gila **721**
Wojciech Gilewski **754, 1369**
Valeria Giliberti **1158**
Mircea Giloan **1620**
Hagit Gilon **1680**
Pablo Ginel-Moreno **993**
Pavel Ginzburg **593, 1059, 1424, 1658, 1680**
Valentina Giordano **1258**
Isabella Giovannelli **260**
Tommaso Giovannini **1228**
Nikolay Gippius **514**
Theo Girerd **156**
P. K. Giri **1713**
Agnieszka Girstun **1043, 1389**
Valerio Di Giulio **1194**
Sergei Gladyshev **312**
David Globosits **312**
Sandra Glocker **145**
Claire F. Gmachl **994**
Dongwook Go **534**
Alexis Gobe **737**
Rasmus H. Godiksen **364**
Sebastian Golat **576**
Sandeep Yadav Golla **825**
Brandon Gomes **821**
P. André Gonçalves **1166**
Juan Sebastian Totero Gongora **418**
José González **411**
Alvaro Gonzalez **591**
Pablo Alonso González **842**
Xavier Gonzalez **1051**
Francisco González **1200**
Cristian Gonzalez **1570**
David González-Andrade **330**
Javier González-Colsa **1200**
Javier Gonzalez-Colsa **1209**
Fernando Gonzalez-Posada **1299**
Fernando Gonzalez-Posada-Flores **385**
Camilla Gonzini **342, 438**
Majid Goodarzi **690**
George Gordon **756**
Maxim Gorkunov **550**
Jason Gorman **273**
Yuri Gorodetski **588**
Sean Gorsky **900**
Maxim Goryachev **816, 1010, 1500**
Nadav Goshen **520**
Sumit Goswami **481**
Kazuhiro Gotoh **874**
Jörg B. Götte **184**

Author Index (cont.)

Stephan Gotzinger **1288**
Masoumeh Goudarzi **929**
A. Gourdin **997**
Catherine Gourdon **1259**
Alexander O. Govorov **181, 201, 203, 218, 584**
Pasha Goz **588**
Eva-Maria Graefe **792**
Duncan Graham **359**
Nicoletta Granchi **342, 438**
Mathys Le Grand **270, 716**
Rachel Grange **103, 379, 1129**
Annabella La Grasta **1082**
Luc Le Gratiet **616**
Sarina Graupeter **1336**
Sasan V. Grayli **148**
Lorenzo Graziotto **1033, 1275**
Andrew D. Greentree **1105**
Heather F. Greer **915**
Stefano Gretter **252**
Tatjana Gric **1110**
Romae Grierson-Copeland **1610**
Lina Grineviciute **751, 1688, 1724**
L. Grineviciute **780**
Sergei V. Grishin **1675**
Jean-Philippe Groby **635**
Jesse Groenen **194**
Jorik van de Groep **499**
Caspar Groiseau **879**
Nicolas Gros **222, 224, 239**
Thierry Grosjean **163**
David Grosso **997**
Konstantin Grotov **1424, 1658**
Pawel Gruszecki **555**
Dmytro Gryb **550**
Justyna Grzeda **1043, 1374**
Marek Grzelczak **864, 1449**
Fengzhi Gu **208**
Chunying Guan **859**
Davide Guarnera **704**
Pietro Giuseppe Gucciardi **334**
Abdellatif Gueddida **138**
Agnese Guernieri **1635**
Renaud Gueroult **1665**
Timothée Guerra **721**
Luca Guerrini **1219**
Lili Gui **310**
Bryan Guilcapi **1065, 1078, 1080**
Victor Guillemot **713**
Thierry Guillet **694**
Brahim Guizal **687**
Michele Guizzardi **453**
Muhammad Gulzari **665**
Alexander Gumennik **286**
Kenan Gundogdu **349**
Durdu Guney **1133**
Pieter Gunnink **518**
Xinxin Guo **625**
Xuhan Guo **796**
Tianyi Guo **901**
Vaibhav Gupta **201**
Clément Gureghian **385**
Andriy. M. Gusak **1467**
Olga Guselnikova **173, 1430**
P. A. Gusikhin **1324**
Olga Guskova **201**
Bjarne Gutbrod **145**
Yael Gutiérrez **848, 1400**
Heonhak Ha **500**
Fabian Haake **933**
Mojtaba Karimi Habil **928**
Jordan A. Hachtel **1039, 1176**
Lisa Hackett **435**
Emebet Woldu Hadgu **1092**
Sebastian Häfner **1683, 1695**
Michael Haftel **777**
Jesse Hagelstein **1275**
Tuomas Haggren **858**
Asa Haglund **1336**
Rudolf Haindl **1194**
Hodjat Hajan **1535**
Hodjat Hajian **1326, 1605**
Tommi Hakala **159, 1563**
Naomi J. Halas **1052**
Lucy Hale **1033**
Robert Halir **993**
Serhii Haliuk **1519**
Gloria Halka **117**
Claudia Pernilla Hallqvist **1495**

Author Index (cont.)

Tetsuya Hama **874**
Ryo Hamano **528**
Ryusuke Hamazaki **944**
Manfred Hammer **733**
Kyunghun Han **273**
Yanjun Han **377**
Yaqi Han **464**
Luke Hands **1488**
Stephen Hanham **353**
Nicolas Hanine **1070**
Zhibiao Hao **377**
Tianyi Hao **787**
Jiang Hao **1021**
I. Harder **1764**
Jade Hardouin **1261**
Muhammad Haris **206**
Joren Harms **518**
Abdelmounaim Harouri **616**
Shun Hashiyada **184, 889**
Jamshid Hassanpour **141**
Yusuke Hata **628**
Toshiaki Hattori **407**
Haroldo Hattori **1586**
Raphael Hauer **430**
Yasuo Hayashi **1762**
Tina M. Hayward **1004**
Haonan He **407**
Liangshu He **658**
Fei He **756**
Noel Healy **1349, 1610, 1759**
Bert Hecht **133**
Melissa Hedir **957**
Hendrik H. Heenen **1135**
Jacob Terndrup Heiden **1162**
R. Heilemann **818**
Connor Heimig **458, 550**
Reza Hekmati **370**
Mohamed Helal **370**
Manfred Helm **1156**
Felix Helmrich **1033, 1275**
Joshua Hendrickson **1715**
Vicente Cutanda Henriquez **610**
Olivier Henrotte **214**
Joel Henzie **206, 959**
Philip Heringlake **1266**
Svenja Hermann **636**
Carlos Hernandez-Garcia **280**
Pedro Ludwig Hernandez-Martinez **190**
Tobias Herr **894**
Hector Pascual Herrero **494**
Ramon Herrero **783**
Dorothee Herrmann **1275**
Ortwin Hess **985**
Lucia Hidalgo-Orteaga **1183**
Adrian Hierro **1293, 1299, 1580**
Nina Hildenhagen **906**
Christian Hill **430**
Rainer Hillenbrand **1189, 1211**
T. X. Hoang **688**
Richard G. Hobbs **1556, 1605**
David Hoey **854**
J. Hofkens **1187**
Sven Höfling **370**
Mirjam Hofmaier **201**
Ulrich Hohenester **430, 1144**
Nils Holle **834**
Jennifer Hollingsworth **360**
W. Holman **688**
Wouter Holman **1446**
Christof Holzer **582**
Sunghoon Hong **1341**
Kent Hora **1656**
Michal Horák **298, 1039**
Simon A. R. Horsley **1635**
Yuya Hoshimiya **258**
Yaonan Hou **291**
Philipp del Hougne **1089**
Anya Houk **597**
Fayçal Houssaini **239**
Martin Hrtoň **1749**
Chin-Chuan Hsieh **1346**
Po-Chun Hsu **350**
Jin-Chen Hsu **1486, 1643**
Han Htoon **360**
Xiaoyong Hu **282**
Liyan Hu **432**
Xiao Hu **432**
Gengkai Hu **637**

Author Index (cont.)

Huatian Hu **730, 1158, 1170, 1458**
Shanshan Hu **1096**
Shu Hu **1203**
Chen Huang **760**
Shengxi Huang **1124**
Yunfei Huang **1275**
Po-Sheng Huang **1363**
Lorenz Huber **1144**
Tobias Huber-Loyola **370**
Coleman Huetz **999**
Paloma A. Huidobro **1046, 1203**
Matjaž Humar **747**
David Hutchins **1376**
Mikko Huttunen **159, 1563**
Yunyoung Hwang **519**
Chi-Sun Hwang **1341**
Maria Antonia Iatì **334**
Pablo Ibañez-Romero **1299, 1580**
Martin Ibarias **671**
Beáta Idesová **1629**
Umberto Iemma **648, 653**
Lucia Iglesias **844**
Hideo Iizuka **663**
Hiroyuki Ikagawa **1230**
Tatsuhiko Ikeda **605**
Ivanina Ilieva **582**
Andrea C. Illana **1299**
Pablo Grobas Illobre **1228**
Atac Imamoglu **1033**
Hafiz Muhammad Imran **1511**
Julia Ingles-Cerrillo **1293, 1580**
Francesca Intonti **342, 438**
Mihail Ipatov **1391**
Andrea Irace **1077**
Takuya Ishida **872**
Hajime Ishihara **526, 1230**
Yoshie Ishikawa **180**
Salim Benadouda Ivars **783**
Masanobu Iwanaga **1419**
Vaishnavi Iyer **726**
Fadil Iyikanat **1176**
Chukwunaedum Patrick Izediuno **942**
Eric Jackson **195**
Nishaant Jacobus **1273**
Wallace Jaffray **284, 425, 455, 1315**
Chennupati Jagadish **858**
Lukas A. Jakob **1203**
Cécile Jamois **156**
Bartosz Janaszek **1741**
Maxwell H. Jancich **286**
Min Seok Jang **474, 500, 1162**
Jaewon Jang **1330**
Mohammed Janneh **868, 1077**
Juliana Jaramillo **917**
Saeed Javadizadeh **503**
Jérôme Don Jayamanne **1379**
Mohammad Mahdi Jafarizadeh Jazi **766**
Line Jelver **1152, 1171**
Ishita Jena **1421**
Heonsu Jeon **328**
Woong Bae Jeon **393**
Lakjong Jeong **328**
Hyeon-Ho Jeong **1057**
Hu Young Jeong **1162**
Sangmin Jeong **1224**
Youssef Jeyar **687**
Pankaj Jha **1538**
Jie Ji **688, 1446**
Kaiwen Ji **781, 957, 1417**
Sooseong Ji **1397**
N. Jia **127**
Wenhe Jia **1129**
Na Jia **1326, 1556**
Quanbo Jiang **212**
Hao Jiang **408**
Tao Jiang **550**
Zhaoqi Jiang **859**
Yabin Jin **658**
Keyu Jin **857**
Yucheng Jin **908**
Sunghwan Jo **929**
Yongjae Jo **1624**
Elsa Jöchl **1033**
Maryam Hojjat Jodaylami **1076**
Ben John **1135**
Sancenia Johnson **256**
Isaac Johnson **291**
Neil Johnson **804**

Author Index (cont.)

Christian Johnson-Richards **1349, 1759**
Erika Jonaitytė **1706**
Tabitha Jones **910**
Magnus Jonsson **824, 899, 1302, 1583**
Sebastien Joulié **194**
Safi Jradi **203**
Adrian Juan-Delgado **1203**
Lucas Judéaux **1266**
Gabriel Juelg **1131**
Mindaugas Juodėnas **206, 959, 1706**
Jiří Kabát **838, 1039**
Malcolm Kadodwala **184, 217**
Maria Kafesaki **595, 1672**
Sota Kagami **395**
Hibiki Kagami **764**
Cherie R. Kagan **1305**
Cherie K. Kagan **1570**
Thomas Kainz **379**
Robin Kaiser **937**
Matti Kaivola **317**
Kotaro Kajikawa **434**
Karol Kakarenko **932**
Deepak Kala **1663**
Samane Kalhor **407**
Mikael Käll **446**
Imon Kalyan **1491**
Khosro Kamali **446**
Atsushi Kamegaya **889**
Eugene Kamenetskii **1035**
Tetsuo Kan **361**
Warren Kut King Kan **825**
Tsuneto Kanai **1600**
Ajay R. S. Kandada **1273**
Young Soo Kang **277**
Jiwon Kang **500**
Seung-Kyun Kang **773**
Evan S. Hyunkoo Kang **925**
Yicui Kang **982**
Chanik Kang **1029**
Yunqing Kang **1430**
Vage Karakhanyan **163**
Omer Can Karaman **919, 1140**
Theodosios Karamanos **1497**
Helmut Karl **840**
Manobina Karmakar **458, 901, 1629**
Ayon Jyoti Karmakar **901**
Paul-Ludovic Karsenti **150**
Muhammad Fayyaz Kashif **1055, 1082**
Takanari Kashiwagi **407**
Natalia Kasian **932**
Linda Kasiarova **894**
Yusuke Kataoka **1762**
Yuichiro Kato **423**
Ioannis Katsantonis **699, 1672**
Jochen Kaupp **370**
Kohei Kawabata **939**
Daiki Kawasaki **891**
Kodo Kawase **692**
Mohammadrahim Kazemzadeh **1055**
Suraya Kazi **1302, 1583**
Jonathan Keeling **1371**
Jussi Kelavuori **1563**
Aidar Kemelbay **303**
Stuart Kendall **830, 835, 1493**
Dante M. Kennes **1275**
Oded Kenneth **1014**
Peter Kepič **838, 1039, 1629**
Sebastien Kerdiles **194**
B. Kerzabi **997**
Sivasruthi Kesavan **1275**
Kirill Khabarov **1222**
Samira Khadir **1641**
Anousha Khamsavi **391**
Alexander Khanikaev **1025**
Anton Kharchevskii **1658**
Manita Khatri **181**
Soufyane Khattou **1515**
Amin Khavasi **503**
Nadzeya Khinevich **959**
A. R. Khisameeva **1324**
Amine Khitous **205, 209, 222, 224, 239**
Mykola Khobzei **1424, 1519, 1658, 1680**
D. A. Khudaiberdiev **1324**
Jacob Khurgin **1139**
Piran R. Kidambi **1135**
Alexander V. Kildishev **726**
Ufuk Kilic **578**
Sema G. Kilic **578**

Author Index (cont.)

Soo Jin Kim **245**
Chang Woo Kim **277**
Dongsung Kim **305**
Jaekwan Kim **327**
Dong Ha Kim **368**
Kyu-Young Kim **393**
Je-Hyung Kim **393**
Andrew Kim **435**
Junhyung Kim **500**
Shin-Sung Kim **681**
Donghyun Kim **1029**
Kyungmin Kim **1029**
Doeun Kim **1057**
Juhwan Kim **1057**
Gyurin Kim **1057**
Minhyuk Kim **1162**
Byunggi Kim **1261**
Beomjoon Kim **1308**
Yong Hae Kim **1341**
Jaesung Kim **1397, 1638**
Yae Jun Kim **1436**
Minjin Kim **1455**
Sejeong Kim **1455, 1483**
Jiwoo Kim **1483**
Inki Kim **1624**
Itamar Kimchi **563**
Alexey V. Kimel **322**
Yuki Kimura **874**
Nathaniel Kinsey **481, 1133**
Ioannis Kiorpelidis **642**
Gunda Kipp **1275**
Daisuke Kitayama **764**
Yuri Kivshar **1428**
Mikko Kjellberg **1434**
Michael A. Klatt **994**
Matthew Klein **1715**
Tomas Klinavičius **206, 1706**
Steffen Klingel **720, 1645, 1703**
Pavel Klok **1629**
Katarzyna Kluczyk-Korch **1533, 1607**
Gvidas Klyvis **206, 959, 1706**
Ross Knapman **566**
Michael Kneissl **1336**
Nurten Koc **276**
Toshiyuki Kodama **522**
Yumiko Kodama **874**
Tobias A. F. Koenig **188, 1757**
Martin Kogelschatz **921**
Monika Devi Koijam **661**
Emmanouil Theodoros Kokkinakis **335**
Karol Kolataj **1209**
Denis Kolchanov **593, 1680**
Purbita Kole **1135**
Radoslaw Kolkowski **317**
P. Kolorenc **818**
Benjamin Koltenbah **1538**
Svitlana Kondovych **565**
Andrea Konečná **1039, 1176**
Jinseok Kong **500**
Tobias A. F. Konig **201**
Kuniaki Konishi **764**
Maciej Kołodziejczak **754, 1369**
Zala Korenjak **747**
Wilton J. M. Kort-Kamp **293, 305**
Thomas Koschny **1098**
Kirill Koshelev **1541**
Ethan Koskas **1275**
Nicolas Kossowski **1641**
Sergei Kostcheev **176, 198**
Nicholas A. Kotov **201, 915**
Konstantinos Kouderis **391**
Stefanos Koufidis **802**
Demosthenes Koutsogeorgis **1334**
Natalia Kowalska **932**
Ryan A. Kowalski **1135**
Rafał Kowerdziej **151**
Anna Kozanecka-Szmigiel **932**
Valentina Krachmalnicoff **713, 1289**
Roman Krahne **440, 457**
Nouh Krai **138**
Rudin Kraja **1025**
Vlastimil Křápek **1039**
Alexey Krasavin **799**
Mira Kreßler **1135**
Janis Krieger **720**
Artemijs Krimovs **1049**
Stefanie Kroker **1618, 1683, 1695**
Arkadii Krokhin **655, 671, 744**

Author Index (cont.)

Sergey Kruk **841**
Wakana Kubo **171**
Andrzej Kudelski **1043, 1073, 1374, 1389**
András Kufcsák **387**
Ulrich Kuhl **625, 1478**
Karolina Kukrálová **233**
I. V. Kukushkin **1324**
Julius Kullig **1108**
Gagan Kumar **1713**
Flore K. Kunst **1126, 1591**
Yuichi Kurashima **395**
Patryk Kusch **1135**
Kateryna Kusyak **1275**
Junyoung Kwon **915**
Hanna Kylhammar **1434**
Ouassila Narsis Labbani **224, 239**
Hachim Lahbib **825**
Yun Lai **703**
Wei-Hsiang Lai **1432**
Chia-Yu Lai **1597**
Jia-Feng Lai **1643**
Florian Laible **145**
Paula Laborda Lalaguna **184**
G. Lalle **935**
Jacob LaMountain **821**
Hassan Lamsaadi **324**
Pascal Landais **1754**
Andrea Lanfranchi **1131**
Andrew Lang **195**
Sara Maria Langner **1275**
Stéphane Lanteri **737**
Christian Lanza **842**
Norberto Daniel Lanzillotti-Kimura **616, 840, 1245**
Capucine Laprais **390**
Maria Cristina Larciprete **154, 192**
M. C. Larciprete **935**
Nicolas Large **1241**
Vincent Larrey **164**
Guilhem Larrieu **164**
Noëlle Lascoux **614, 1263**
Ivan Latella **573**
Claudia Lattebovio **1055**
Stéphanie Lau-Truong **185, 866**
Maël Laupretre **924**
Elysé Laurent **1213**
Stefano Laureti **619, 1376, 1511, 1513**
Lorenzo Lavista **1635**
Andrei Lavrinenko **250**
Benjamin Lawrie **1036**
Thu Hac Huong Le **395, 1426**
Gary Leach **148**
G. Leahu **935**
Michael Leamy **1101**
Thomas LeBrun **273**
Yonas Lebsir **883**
Tomas Lednicky **230**
Seunghoon Lee **178**
Bong Jae Lee **244**
Junho Lee **327**
Sooyeon Lee **327**
Tae-Yun Lee **328**
Hansol Lee **328**
Jin Hee Lee **393**
Changhyoup Lee **393**
Elizabeth M. Y. Lee **494**
Myung-Joon Lee **617**
Howard Lee **908**
Seunghyun Lee **1029**
Kyoungpyo Lee **1135**
Jongwon Lee **1308, 1397, 1638**
Chia-Hsuan Lee **1438**
JinnKye Lee **1524**
Hiang Kwee Lee **1524**
Ning-Hao Lee **1597**
Da Yong Lee **1692**
H. J. Lee **1698**
Julien Legendre **832**
Joel Lehikoinen **1567**
Bing Lei **860**
Sheng Lei **1094**
Marina Leite **496**
Aristide Lemaitre **616, 924**
Aristide Lemaître **1245**
Unai Arregui Leon **231**
Thibault Leportier **681**
Aurélie Lescestre **1650**
Piotr Lesiak **932**
Antonio Calà Lesina **740**

Author Index (cont.)

Xavier Letartre **156, 390**
Juan Ariel Levenson **1417**
Gaëtan Lévêque **138, 264, 268**
Pierre Levesque **1545**
Wiktor Lewandowski **932**
Baihui Li **230**
Fengjun Li **251**
Xiangping Li **251**
Hongtao Li **377**
Lin-Han Li **440**
Jinxiang Li **467**
Qian Li **488**
Qitong Li **499**
Xiaomeng Li **604**
Zhanyu Li **637**
Jensen Li **673**
Ge Li **781**
Wenjia Li **859**
Jie Li **860**
Hong Li **921**
Tao Li **1096, 1357**
Xiaoqin Li **1135**
Hua Li **1140**
Xinyu Li **1275**
Hongliang Li **1321**
Xueyun Li **1357**
Yinglan Li **1481**
Haitao Li **1524**
Ruixing Li **1552**
Junjie Li **1731**
Shusen Liao **405**
Kun Liao **437**
Iñigo Liberal **419**
Simone De Liberato **1168, 1442**
Tim Liedl **414**
Filip Ligmajer **838, 1629, 1749**
Viktor Aadland Lilja **1119**
Yae-Chan Lim **117**
Geunweon Lim **690**
Miao-Ling Lin **440, 974**
Dongqing Lin **899**
Harvey Lin **908**
Shuxin Lin **939**
Hua-Shin Lin **1353**
Kaiqiang Lin **1491**
Zeqiang Lin **1632**
Sarah Lindner **530, 1024**
Giuseppe Emanuele Lio **151, 452, 1505, 1635**
Johannes Lischner **750**
Petr Liška **1749**
Franziska Lissel **201**
Natalia Litchinitser **821**
Weizhen Liu **204**
Tao Liu **259**
Huiyun Liu **291**
Tzu-Hsiang Liu **295**
Hong Liu **300**
Dawei Liu **358**
Kaihui Liu **760**
Guangyan Liu **794**
Xinxin Liu **1222**
Wenzhe Liu **1387**
Weiwei Liu **1395**
Tang-Chun Liu **1647**
Bowen Liu **1767**
Rodrigas Liudvinavicius **763**
Esther Alarcón Lladó **112**
Ares Lládos **917**
Hsuan Lo **1117**
Andrea Locatelli **704, 1092**
Eva Loccufier **723**
Matteo Lodde **342, 438**
Ishaan Lohia **359**
A. G. Lohr **818**
Alexander Löhr **819**
David Long **273**
Guilherme Lopes **230**
Ceferino López **917**
Etienne Lorchat **1213**
Salvatore Lorenzo **1305**
Andrea Lorenzoni **1068**
Simona Losio **397**
Maria Losurdo **848**
Charalambos Louca **910**
B. Louis **1187**
Kyan Louisia **1543**
Brahim Lounis **1203**
Brendon Lovett **1371**

Author Index (cont.)

Bin Lu **114**
Yu-Jung Lu **132, 1597**
Ya Yan Lu **679**
Zihao Lu **915**
Peixiang Lu **1395, 1481**
Yuanchao Lu **1552**
Antonio De Luca **1062**
Luca Lucia **1158**
Frieder Lucklum **607, 610**
Andrea Lucotti **1235**
I. Lukosiunas **780**
Shaun Lung **311**
Yi Luo **377**
Yuan Luo **489**
Yun Luo **866**
Zhendong Luo **1332**
Ashley Luo **1715**
John M. Lupton **1491**
Ecole Centrale de Lyon **390**
Ning Lyu **346, 358, 1578**
Rohith K. M. **1713**
Jinyong Ma **311, 858**
Yungui Ma **444**
Dongchen Ma **574**
Jihong Ma **629**
Guancong Ma **640, 652**
Xinyu Ma **860**
Jessica Ma **915**
Wei Ma **1112**
Pranshu Maan **726**
Roberto Macaluso **192**
Kevin MacDonald **355, 467**
Ross Macdonald **1311**
Rair Macedo **1502**
Ricardo Machado **832**
Andrey Machnev **286, 593**
Aleida Machorro-Ortiz **1052**
Demetrio Macias **198**
David Mack **1046**
Steve MacLean **1545**
Finlay MacNab **148**
Luke Madden **854**
Angela Madeo **140**
Dorotheé Mader **1160**
Antonino Madonia **1728**
Andreas Maeder **1129**
Sebastian F. Maehrlein **1174**
Bjorn Maes **585, 723, 1366, 1412**
Alejandro Maese-Novo **993**
Tiago E. C. Magalhaes **612**
Alessandro Magazzù **334**
Michele Magnozzi **397, 1495**
Robert Magnusson **1692, 1738**
Benoit Mahler **1269**
Stefan A. Maier **458, 1046**
P. Martin Maier **818**
Giuseppe Di Maio **433**
Yann Mairesse **801**
Agnes Maitre **208**
Damien Maitre **270, 716**
Katarzyna Majewska **1376, 1513, 1517**
Apratim Majumder **1004**
Tapani Makkonen **672**
Konstantinos G. Makris **335, 642, 785**
Urszula Malecka **1508**
Ermin Malic **308, 1156, 1179**
Uzair Malik **994**
Kristina Malinowski **1538**
Guillaume Malpuech **694**
Radu Malureanu **1440**
K. Mamaeva **127**
Kseniia Mamaeva **1535**
Theocharis Manassis **1497**
Cristina Mancarella **1495**
A. Mancini **524**
Andrea Mandanici **334**
Fabien Mandorlo **156**
Hicham Mangach **138, 268, 381**
Claire Mangeney **866**
Florian Mangold **458**
Bryan Manjarrez-Montañez **623**
Alejandro Manjavacas **753, 956, 1149**
Andrew Mannix **499**
Zakaria Mansouri **851**
Marques Manuel **339**
Onofrio Maria Maragò **334**
Massimiliano Marangolo **1259**
Cecile Marcelot **194**

Author Index (cont.)

Amandine Marchand **897**
Valentina Marchesano **1065, 1078, 1080**
Valérie Marchi **174**
Marzia Marciello **1062**
Willy Daney de Marcillac **208**
David Marco **280**
Giulia Marcucci **418**
Martin Marek **894**
José Margineda **1677**
Jérémie Margueritat **1269**
Sylvie Marguet **203, 209, 614, 1263**
Jon-Paul Maria **1133**
Damiano Marian **1622**
Andrea Marini **401, 476**
Emanuele Marino **1305, 1530, 1570, 1728**
Obren Markovic **161**
Gil Markovich **218**
Krzysztof Markus **922, 1109, 1467**
Zakaria Marmri **212**
M. I. Marques **1187**
Rodions Marstupa **1519**
Daniele Martella **372**
Christian Martella **1104**
Baptiste Marthy **446**
Almudena Marti-Morant **1647**
Nicolas Martin **163**
Jerome Martin **185**
Léo Martin **222, 224, 239**
Aitana Tarazaga Martín-Luengo **842, 1160**
Javier Martín-Sánchez **325, 842, 1160**
Hannah Martinelli **148**
Andrés Guerrero Martínez **450**
Alejandro Martínez **1451, 1603**
Angel Martínez-Argüello **623**
Miguel Angel Martinez-Garcia **879**
Virginia Martínez-Martínez **1281**
Maria del Carmen Martínez-Tomás **1580**
Stefano Martiniani **426**
Hugo Lourenço Martins **324**
Sofia Martins **727**
Diego Martın-Cano **1203**
Reza Marzban **141, 503**
Cristina Masoller **781**
Amir Hossein Masominia **825**
Jean-Francois Masson **1076**
Giulio Mastrototaro **1055**
Koji Masuda **894**
H. Masuhara **1187**
Luigi Matera **844**
Andrzej Materna **922, 1109, 1467**
Mohan C. Mathpal **1105**
Osamu Matsuda **656**
Mamoru Matsuo **605**
Toru Matsuyama **1275**
Giovanni Mattei **266, 954**
Francesco Mattioli **1158**
A. Maurizi **935**
Giorgio Sebastiano Mauro **704**
Anna De Girolamo Del Mauro **1078**
Jeronimo R. Maze **1105**
Gabrielle Mazevet-Schargrod **1261**
Yarden Mazor **520**
Stanislav Mazurenko **894**
Federico Mazzola **922**
Silvia Mazzoleni **1258**
Gerard McCaul **418**
Oisin McCormack **1326, 1469**
Alexander McDonald **1015**
Alan McGaughey **1595**
David McGee **999**
James McIver **1275**
D. van Mechelen **688**
Alex Meek **399**
Michael Meeker **195**
Elham Mehdi **1245**
Ting Mei **851**
Guido Meier **1275**
Moritz Meinecke **370**
Madona Mekhael **159**
Daniele Melati **330, 344, 825**
N. Melchioni **524**
Paula Mellado **535**
Christopher J. Mellor **851**
Simas Melnikas **1724**
Bruno de Melo **114**
Gaetan Membrez **1275**
Sergey G. Menabde **1162**
Rafael Mendez-Sanchez **623**

Author Index (cont.)

Jose Mendoza-Carreño **871**
Elizabeth Mendoza-Sandoval **954**
Giuseppe Meneghini **308**
Leonardo de S Menezes **458, 550, 1629**
Vinod Menon **1000**
Rajesh Menon **1004**
Martina Mercurio **192**
Moritz Merklein **369**
Holger Merlitz **201**
Jean-Sebastien Mérot **385**
Lars Meschede **985**
Andrea Mescola **453**
I. Meskelaite **780**
Riccardo Messina **684, 713**
Fabrizio Messina **1305, 1527, 1530, 1570, 1728**
Nadine Meyer **114**
Roya Ebrahimi Meymand **341**
Qiwei Miao **851**
Alberto Micco **1077**
Marios H. Michael **1275**
Lior Michaeli **117**
Vincenzo De Michele **1527**
Johannes Michl **370**
Klaudijus Midveris **206, 1706**
Sandis Migla **1519**
Agustín Mihi **658, 871, 929**
Anna Mikhailovskaya **1424, 1658**
Maiken Mikkelsen **504**
J. Mikosch **818**
Alessia Milano **1065, 1078, 1080**
Sarah Miller **1213**
Florian Millo **1259**
Ben Mills **355**
Bumki Min **135**
Olga Minakova **1174**
Philippe Minard **174**
Sota Mine **692**
Marco Miniaci **109, 138, 650**
Maryam Mirahmadi **457**
M. Mirahmadi **818**
Bruno Miranda **283, 303**
Andrey Miroshnichenko **1586**
Nasim Mirzajani **1135**
Aleksandra Miszczak **1043, 1374**
Vladimir Mityushev **769**
Mathieu Mivelle **161, 1296**
Vahagn Mkhitaryan **1176**
Khaled Mnaymneh **337**
Séverine Le Moal **1213**
Eric Le Moal **1213**
Vito Mocella **303, 1084**
Jun Mochida **1017**
Masahito Mochizuki **528**
Tatsuto Mochizuki **886, 1600**
Jérémy Moeyaert **291**
Tharishinny Raja Mogan **1524**
Aditi Raman Moghe **1213**
Habib Mohamad **716**
Ershad Mohammadi **364**
Abdenbi Mohand-Ousaid **239**
Zindine Mokeddem **825**
Yuriy Mokrousov **521, 534**
Sean Molesky **705**
Gregorio J. Molina-Cuberos **1677**
Iñigo Molina-Fernández **993**
Céline Molinaro **150, 205, 209**
Alessandro Molle **1104**
Mohammadhossein Momtazpour **851, 1334**
Alonso Cuartero Mondoño **1465**
Anne Mongruel **394**
Loriane Monin **1215**
Antoine Monmayrant **1650**
Jose Luis Montaño-Priede **864**
Carlos Montenegro **1245**
Cinzia Montinaro **1055, 1082**
Alexander Mook **518**
Stefano Morabito **1065**
Antonio Morales-Perez **302**
Miltos Moralis-Pegios **291**
Martina Morassi **616, 1245**
Julien Moreau **150**
Fernando Moreno **848, 1400**
Julio Gutiérrez Moreno **1430**
Alonso Moreta **927**
Keisuke Moriasa **928**
Yuto Moritake **254, 289**
Riccardo Carlo Moroni **1376, 1513, 1517**
Víctor González Morote **1734**

Author Index (cont.)

Benedict Morris **176, 228**
Sean Morrison **821**
N. Asger Mortensen **1152, 1162**
Salvatore Moschetto **1068**
T. Moschos **291**
Mohamed Mostafa **1672**
Filipa Mota **832**
Taisei Motomura **395**
Sébastien Mouchet **897**
Sara Moujdi **851**
Artur Movsesyan **201**
Owen Moynihan **1326**
Kai Mueller **572**
Lukas Mueller **720, 1645**
Niclas Sven Mueller **1135, 1160, 1203**
Samyobrata Mukherjee **505**
Shroddha Mukhopadhyay **365, 775, 1440**
Debmalya Mukhopadhyay **1401**
Egor A. Muljarov **312, 1541**
Jonas Muller **164**
Martin Müller **201**
Jeremy Munday **497**
Haridas Mundoor **1000**
Battulga Munkhbat **250**
Francisco Muñoz **535**
Carlos Sanchez Munoz **879**
Vicente Muñoz-Sanjosé **1299, 1580**
Natalja Muračova **1424**
Shunsuke Murai **158, 882, 930**
Shuichi Murakami **581**
Ryo Murakami **1016**
Kosuke Murate **692**
V. M. Muravev **1324**
Christopher B. Murray **1305, 1570**
Mohammad Musavinezhad **1288**
Marten Musiol **1695**
Otto L. Muskens **422**
Simone Di Muzio **1168, 1442**
Monika Mycroft **519**
Jason Myers **506**
Nojoon Myoung **373**
Christos Mystilidis **1147**
Mengxing Na **322**
Youn Ju Na **1057**
Andrew E. Naclerio **1135**
Benedetta Nacmias **1233**
Hiroki Nada **874**
Tadaaki Nagao **319, 1419**
Arun Nagpal **117**
Gopal Narmada Naidu **227**
Geetha G. Nair **1460**
Masaru Nakagawa **874**
Jungmin Nam **244**
L. Nan **524**
Charlotte Lea Oceane Nani **1495**
Alfonso Nardi **727, 1142**
Evgeniy Narimanov **1318, 1385**
Aurimas Narkevicius **915**
Ouassila Labbani Narsis **222**
Douglas Natelson **405**
Miguel Navarro-Cía **1334**
Daniel Navarro-Urrios **670, 1734**
Andrew Naylor **1311, 1653**
Gabriel Nedelea **341**
Fran Nekvapil **1226**
Arash Nemati **506**
Svetlana Neretina **167**
Matteo Nerini **1088**
Kyle S. Netherwood **363**
Liam Shelling Neto **1618, 1695**
Ofer Neufeld **600**
Li Shiuan Ng **1524**
Thien Duc Ngo **319**
Trang Nguyen **181**
Vinh Nguyen **506**
Tô Nguyet **264**
Benedetta Niccolini **1471**
Mathieu Nicolas **161**
Giuseppe Nicoletta **452, 1463**
Christophe Nicolle **222, 224, 239**
Jens Niegemann **681**
Iris Niehues **1211**
Richarda Niemann **1133, 1160**
Brendan Nieukirk **167**
Hiromasa Niinomi **874**
Bart de Nijs **359, 982**
Maxim Nikitin **250**
Alexey Y. Nikitin **842, 1189, 1281**

Author Index (cont.)

J. Nikitina **780**
Julianija Nikitina **1688**
Sergei A. Nikitov **1675**
Frank Niklaus **1222**
Yoshiaki Nishijima **258**
Sara Nocentini **372**
Valeria Nocerino **283**
Flavio Nogueira **1019**
Nicolas Noiray **625, 1478**
Masahiro Nomura **1261**
Peter Nordlander **1052**
Alexander Norman **989**
Andrea Notargiacomo **1158, 1471**
Jelena Notaros **827**
Masaya Notomi **254**
Adnane Noual **1515**
Tobia Nova **1033**
Martin Nørgaard **1162**
Sara Nuñez-Sánchez **917**
Alice Nyaga **239**
Deirdre O'Carroll **1001**
Patrick O'Keeffe **1570**
Robert O'Meara **1605**
Roger Bresoli Obach **1187**
L. Oberti **818**
Mahiro Ochiai **770**
Feodor Yu. Ogrin **540, 1675**
Sang Soon Oh **363, 942**
Il-Kwon Oh **617**
Joo Hwan Oh **644**
Makoto Ohashi **258**
Taisuke Ohta **435**
S. Okada **432**
Hiromi Okamoto **129, 143**
Koichi Okamoto **158, 930**
Yoshihiro Okamura **1020**
Paul Oleynik **1338, 1690**
Marek Olifierczuk **151**
Aleksandrs Olins **1519**
Irene Olivares **330**
Edson Rafael Cardozo de Oliveira **616, 1245**
Jesus Olivera **591**
Davide Olivieri **252**
Luana Olivieri **418**
Jorge Olmos **878**
J. Olmos **1187**
Takashige Omatsu **561**
Yoshitaka Ono **1762**
Mathieu Opprecht **194**
Andres Ordonez **801**
Andrés Ordóñez **819**
Régis Orobtchouk **270**
Daniel Arenas Ortega **1451**
Angel Ortega-Gomez **419**
Alejandro Ortega-Moñux **993**
Omar Ortiz **616**
Dolores Ortiz **1200**
Michele Ortolani **1158, 1458, 1471, 1622**
Daniel Osborne **902**
Stefano Luigi Oscurato **990**
Tomoya Oshikiri **874**
Johann Osmond **727, 1142**
Paolo Maria Ossi **1235**
Eva Otero **1428**
Tadele Orbula Otomalo **1082, 1170**
Taiichi Otsuji **391**
Jun-Yu Ou **422**
Daigo Oue **248**
Oscar Avalos Ovando **181**
Adam Overvig **506, 1150**
Nobuaki Oyamada **884**
Sahin Ozdemir **1133**
Mustafa Ozlu **425**
Viswanath P **1751**
Alexander Paarmann **1135, 1160**
Haydee Pacheco **1001**
Victor Pacheco-Peña **710, 1311, 1653**
Pawel Packo **658**
Willie Padilla **443**
M. Padovani **818**
Joe Pady **830, 1493**
Joseph Pady **835**
Karthik Pagadala **473**
Simone Paganelli **401**
Vincent Pagneux **611, 635**
Stéphane Pailhès **1258**
Vincent Paillard **164, 324**
Simo Pajovic **293, 305**

Author Index (cont.)

Norbert Pałka **151**
Umapada Pal **277**
Vishwa Pal **1004**
Robert Pal **1049**
Alessandra Paladini **1570**
Swaroop Palai **164**
Etienne Palleau **164**
Andrew Palmer **908**
Roberta Palmeri **704**
Bruno Palpant **176, 228**
Clément Panais **614, 1263**
Adam Pander **764**
Kartikey Pandey **866**
Nicolae-Coriolan Panoiu **363**
Anuraj Panwar **1713**
Georgia Papadakis **832**
Constantine Papakonstantinou **825**
Michelle Paparella **291**
Nikitas Papasimakis **678**
Konstantinos Papatryfonos **616**
Kyoungweon Park **166**
Won Park **182**
Jaeseong Park **291**
Hyunsung Park **327**
Dong Hyun Park **393**
Suk-In Park **393**
Tae Gwan Park **478**
Hong-Gyu Park **961**
Mingyu Park **1029**
Donghyun Park **1029, 1455, 1483**
Yeonsang Park **1330**
C. W. Park **1698**
J. H. Park **1698**
Camilla Parmeggiani **372**
Jorge Parra **1565**
Polette Parra-Palavecino **949**
Stefan Partel **842**
Thomas G. Parton **915**
Régis Parvaud **174**
Sheikh Parvez **762**
S. Patchkovskii **818**
Vatsal Patel **1708, 1711**
Vimi Patel **1708, 1711**
Emma Paterson **816, 1010, 1500**
Edgar J. Patino **1589**
Adelin Patoux **1641**
Lorenzo Pavesi **252**
Santi Concetto Pavone **704**
Francesco Saverio Pavone **1233**
Dorota Anna Pawlak **391, 922, 1109, 1467**
María Blanco de Paz **1149**
Nicolas Pazos-Perez **201**
Marialilia Pea **1158, 1458, 1471**
Jane Peabody **762**
Domantas Peckus **206, 959**
D. Peeters **688**
Djero Peeters **1446**
Julian Peiro **844**
Ovidio Peña-Rodríguez **277**
Ruwen Peng **99, 285**
Siying Peng **472**
Tzu-Yu Peng **1597**
Giora Peniakov **370**
Yan Pennec **138, 264, 268, 381, 661**
Lieven Penninck **996**
José Penuelas **1129**
Raul Perea-Causin **1156**
Sinuhe Perea-Puente **915**
Keshan Perera **1001**
Nuno Peres **1152**
Nicolas Pazos Perez **262**
Jesus Zuniga Perez **694**
Diego Pérez **848**
Luis A. Pérez **871**
Mateo Perez **927**
J. Gonzalo Wanguemert Perez **993**
Wolfram Pernice **835**
George Perrakis **595**
Anthony Perri **902**
Thomas Pertsch **311**
Raphael Pestourie **351**
Rapha¨el Pestourie **1092**
Ke-Sean J. Peter **1133**
Jeroen Peters **1068**
Stéphane Petit **801**
Camille Petit-Etienne **921**
Emilija Petronijevic **238**
E. Petronijevic **935**

Author Index (cont.)

Lucia Petti **1065, 1078, 1080**
William Peveler **902**
Naga Anirudh Peyyety **1764**
Andreas Pfenning **370**
Mathew Philippou **1000**
David B. Phillips **830, 1379**
R. Pierrat **1289**
Benjamin Pigeau **1266**
Alessandro Pignedoli **566**
A. Pimenov **1324**
J. Luke Pimlott **421**
Anatoliy Pinchuk **777**
Felipe Pinheiro **900, 937**
Elena Pinilla-Cienfuegos **1603**
Felipe A. Pinto **1105**
Piotr Piotrowski **1109**
Matteo Pirro **1261**
Giuseppe Pirruccio **954**
Andrei Piryatinski **1273**
Ferruccio Pisanello **439, 1055, 1082, 1170**
Marco Pisco **868, 1077**
Linda Piscopo **1055, 1082**
Alessandro Pitanti **529, 1505, 1635**
Mike Pivnenko **1626**
Fabrizio Pizzolante **1471**
Jérôme Plain **759**
Luis Plaja **280**
O. Plekan **818**
Nikos Pleros **291**
Viktor Podolskiy **821**
Wilfrid Poirier **713**
Raffaella Polito **1158, 1471**
Albert Polman **1215**
Zoya Polshchykova **1129**
Thomas Pons **208**
Bernard Pons **801**
Jacopo Maria De Ponti **109**
Luisa Ponticelli **1233**
Gregor Posnjak **414**
Thomas Possmayer **1629**
Sneha Pottekad **1055**
Alexander M. Potts **1275**
Juan Pou **394**
Pablo Pou-Alvarez **394**
Jean-Marie Poumirol **164, 194, 324**
Baptiste Poursat **902**
Marcello Pozzi **933**
Marcus Prado **937**
Jordi Tur Prats **1256**
Leila Rocio Prelat **1137, 1381**
Thomas Prieur **150**
K. Prince **818**
Patrick T. Probst **201**
Mario Prosa **1068**
Demetri Psaltis **785**
Jorge Puebla **519**
Magali Putero **849**
M. Putero **997**
Achmad Putranto **921**
Oleksandr Pylypovskyi **568**
Joong Hyeon Pyo **1738**
Jingbo Qi **332**
Xiaoyu Qi **871**
Limin Qi **977**
Jing Qian **854, 1754**
Li Qiang **363**
Dun Qiao **291**
Jun Qin **574**
Meibao Qin **851**
Chengzhi Qin **1481**
Xiwen Qiu **858**
Antonio Qualtieri **1055**
Christine Joy Querebillo **359**
Giuseppe Quero **1077**
Romain Quidant **114**
Tom Quinn **387**
Luis Quiroga **804**
Viktoriia Radovskaia **322**
Edik Rafailov **445**
Regina Ragan **494**
Emeline Raguin **915**
Aso Rahimzadegan **915**
Marco Rahm **720, 1645, 1703**
Mohsen Rahmani **851, 1334**
Valerica Raicu **1031**
Shima Rajabali **1128**
Debobrata Rajak **801**
Tomas Rakickas **1549**

Author Index (cont.)

Aliaksandra Rakovich **1046**
Yury Rakovich **1281**
Lukas Ramalis **751**
Mohammad Ramezani **929**
Francisco Ramirez-Cuevas **1595**
Carlos Alonso Ramos **344**
Carlos Ramos **825**
Raphael Ramos **921**
Nimisha Ramprasad **117, 1726**
Lora Ramunno **696**
Theodore Rangarajan **291**
Omid R. Ranjbar-Naeini **646**
Omid R. Ranjbar-Naeni **672**
Anish Rao **864**
Theo H. Rasing **322**
Venugopal Raskatla **467**
Theis Rasmussen **1192**
Mahmoud Rasras **420**
Daniel C. Ratchford **195**
Jonas Rathgeb **145**
Bogdan-Petrin Ratiu **363**
Miha Ravnik **747**
Bart Jan Ravoo **906**
Shivakh Rawat **505**
Ethan Ray **507**
Søren Raza **364**
T. V. Raziman **364**
Luca Razzari **743**
Charlie Readman **359**
Marco Reale **1305, 1530, 1728**
Lukas Rebholz **1201**
Laura Rego **819**
Philippe Regreny **1129**
Alejandro Regueiro **1565**
Anusha Rehman **1376**
Christian Reichl **1275**
Bjoern Reinhard **602**
Erwin Reisner **359**
Xifeng Ren **404**
Haoran Ren **458**
Jie Ren **626**
Ivo Rendina **303, 1084**
Jan Renger **1288**
Marco Di Renzo **1093**
Rostislav Řepa **1039**
Josef Resl **848**
Laurence Ressier **164**
Yorick Reum **370**
Karsten Reuter **1135**
Bar Reuven **218**
Inès Revol **1473**
Alejandro Reyes-Coronado **1190**
Hamid Reza-Darabian **1109**
Houssem Rezgui **612**
Amina Rezzouk **1515**
Tânia Ribeiro **612**
Francesco Riboli **372**
Marco Ricci **1511**
Christian Richards-Johnson **1610**
Phillip Richerme **286**
Denis Rideau **716**
Denis Ridzal **1114**
Susan A Rigter **1305**
Massimo Rippa **1065, 1078, 1080**
Emanuele Riva **615**
J. Gomez Rivas **688**
Jaime Gomez Rivas **929, 1446**
Antonio Riveiro **394**
Nicholas Rivera **1009**
Carlo Rizza **306, 455, 1315**
Bavo Robben **996**
Ann Roberts **701**
Jean-François Robillard **1249**
Isabel Pascual Robledo **1211**
Giuseppe C. La Rocca **1635**
José C. A. Rocha **1379**
Carsten Rockstuhl **582, 1185, 1201, 1207**
José Rodrigues **832**
Jean-Baptiste Rodriguez **385**
Alejandro Rodriguez **705**
F. J. Rodríguez **804**
Aude Rodriguez **819**
Luis Rodriguez-Cobo **868**
Álvaro Rodríguez-Echarri **1192**
Francisco J. Rodriguez-Fortuno **576**
Francisco Rodriguez-Fortuño **1046**
Francisco J. Rodríguez-Fortuño **1543, 1573, 1593**
Santiago Rodríguez-Jiménez **359**

Author Index (cont.)

Philippe Roelli **1211**
Rudolf Roemer **1376**
Laureline Roffi **1527**
Andrey Rogach **1281**
Benoit Rogez **212**
Junior Rognon **1261**
Sookyoung Roh **327**
Isabel Y. Rojas-Martinez **1190**
Ricardo Javier Peña Roman **1213**
Diego Roman-Cortes **949, 1383**
Silvia Romano **303, 1084**
Albert Romano-Rodriguez **1734**
Mayela Romero-Gomez **170**
A. Roos **818**
Peter Ropač **747**
Claus Ropers **1194**
Charles Roques-Carmes **680**
Roberto Rosati **1179**
Jana Rosenkranzova **235**
Michael Ross **1224**
Thijs van Rossum **1098**
Habib Rostami **421**
Nir Rotenberg **1283**
Diane J. Roth **1046**
Stefan Rotter **312**
Bahram Djafari Rouhani **138**
Katarina Rovenská **1629**
Pauline Rovillain **1259**
Connor Rowe **690**
Lee Rozema **401**
Olivier Rozenbaum **721**
M. Ruberti **818**
Riccardo Rubino **1527**
Guillermo González Rubio **450**
Angel Rubio **1275**
Javier Hernández Rueda **1565**
Anna Rumyantseva **176, 198**
Kristina Rusimova **1075**
Natalia Rylko **1365**
Diana Ryzhak **1338**
Victor Ryzhii **391**
M. S. Ryzhkov **1324**
Amina Saadani **1417**
Chirine Saadi **390**
Foster Sabatino **1025**
Anna Al Sabouni-Zawadzka **754, 1369**
Katarzyna Sadecka **1109**
Grégoire Saerens **1129**
Domenico Sagnelli **1065, 1078, 1080**
Isabelle Sagnes **616, 1158, 1245**
Abhirupa Saha **503**
Bivas Saha **1401**
Maximilian Saiko **484**
Sudhir K. Saini **440**
Guillaume Saint-Girons **390**
Hugo Saint-Olive **208**
Koichiro Saito **180**
Saito Saito **361**
Jose M. Saiz **1200**
Anju Sajan **1547**
Maciej Sakowicz **1663**
Atsunori Sakurai **886, 1600**
Fabio Della Sala **1167, 1170**
Natalia Salakhova **514**
Akbar Salam **532**
Elie Salemeh **611**
Grazia Salerno **427, 715, 1505**
Nunzio Salerno **704**
Toms Salgals **1424, 1519, 1658**
Sarra Salhi **825**
Martin Salinga **834**
Roland Salut **163**
Ermelinda Salvaggio **759**
Marcella Salvatore **990**
Alejandro Sánchez Sánchez **344**
Miguel Sánchez Sánchez **411**
Sara Núñez Sánchez **1182**
Jose Sanchez-Dehesa **671**
Jose Sanchez-Gil **688**
José Antonio Sánchez-Gil **1183**
Ana Sánchez-Iglesias **864, 1449**
Alejandro Sánchez-Sánchez **330**
Pablo Sanchis **1565**
Sathyan Sandeep **616**
Elliot Sandell **291**
Gabriel Sanderson **851**
Vahid Sandoghdar **1288**
Hannah Sanford-Crane **903**

Author Index (cont.)

Ryotaro Sano **605**
Kohei Sano **1762**
Omar Jesus Franca Santiago **562**
Maria Penelope De Santo **1463**
Riccardo Di Santo **1471**
Edgardo Gabriel Santoro **277**
Luis Dos Santos **176**
Paulo Santos **529**
Gonzalo Santos **848**
Maria Sanz-Paz **1209**
Luca Sapienza **900**
Renata Saramak **1000**
Sina Saravi **311**
Radwan M. Sarhan **1221**
Swagato Sarkar **188, 1757**
Jayanta Sarkar **373**
Siddhartha Sarkar **629**
Subhajit Sarkar **1151**
José Dario Sarmiento-Merenguel **993**
Sandeep Sathyan **840, 1245**
Masatoshi Sato **247**
Masahiro Sato **558**
Steffen Sauer **1683, 1695**
Lucien Saviot **1238**
Kei Sawada **542**
Giacomo Scalari **1033, 1275**
Michael Scalora **306, 365, 425, 455, 727, 775, 1142, 1315, 1440**
Christian Schaefer **572**
Peter Schall **1305**
Frank Scheffold **426**
Martina Schenkel **749**
Christoph Scheurer **1135**
Rudolf Schick **902**
Andrea Schirato **231**
Max Schittenhelm **1683**
Alexander Schleusener **440**
Jon Schlipf **1338, 1622, 1690**
Jens H. Schmid **787, 825, 993**
William Schmid **1052**
Peter C. Schmitz **534**
A. Schneider **818**
Alexander Schossmann **484**
Oliver Schraidt **646**
Eva Schubert **578**
Mathias Schubert **578**
Benedikt Schulte **1275**
J. Schulz **127**
Julian Schulz **409**
Justin Schulz **967, 1326, 1469**
Julian Schwab **458**
Adam M. Schwartzberg **303**
Ulrich Theodor Schwarz **1336**
Sacha Schwarz **1545**
Catherine Schwob **161**
Leah Schynowski **145**
Beniamino Sciacca **920**
Alice Sciortino **1305, 1527, 1530, 1570, 1728**
Jordan Scott **422**
Eric Seabron **195**
Ákos Sebők-Papp **1414**
Hooman Barati Sedeh **821**
Alwyn Seeds **291**
Sagar Sehrawat **317**
Akihiko Sekine **1016**
Skyler Selvin **499**
Behrooz Semnani **597**
Raja Sen **1243**
A. Senftleben **818**
Michael Sentef **1275**
Dongjin Seo **1029**
I. Septembre **694**
Elkin Sepúlveda **1589**
Babak Seradjeh **286**
Andriy Serebryannikov **373**
Rostyslav Serha **519**
Oleksandr Serha **546**
Rosalia Serna **839, 913**
João Câmara Serra **1025**
Valerie Serradeil **716**
Juan Jose Alvarez Serrano **753**
Diana Serrano **846**
Guillermo Serrera **364, 1209, 1400**
Monica De Seta **1158**
Monica de Seta **1622**
Rebecca Setford **902**
Sohan Seth **387**
Frank Setzpfandt **311**

Author Index (cont.)

Fabrizio Sgrignuoli **900**
Ilya Shadrivov **249**
Yash Shah **1708, 1711**
Tigran Shahbazyan **256**
Nadav Shaibe **947**
Tashfin Shaife **148**
Mohammad Imran Shaik **1269**
Sandra Shaju **566**
Diana Shakirova **554**
Vladimir M. Shalaev **120, 425, 455, 473, 726**
Nianze Shang **760**
Lei Shao **980**
Boris Shapiro **1318**
Vijay Kumar Sharma **1061**
Anupam Sharma **1259**
Komron Shayegan **117**
Matthew Sheldon **220**
Hsin-Yu Shen **295**
Yijie Shen **566**
Lian Shen **857**
Andriy Shevchenko **317**
Chengzhi Shi **651**
Jinhui Shi **859**
Jianhua Shi **860**
Lei Shi **1387, 1767**
Jun Shibayama **683**
Joe Shields **830, 835, 1493**
Aaron Shih **426**
Yu-Ching Shih **1438**
Saniya Shinde **311**
Alexey Shkarin **1288**
Oksana Shramkova **274**
Xuewen Shu **296**
Yi Shuai **574**
Alexey Shuvaev **1324**
Gennady Shvets **505**
Dmitrii Shymkiv **655, 671**
Vira Shyta **1019**
C. Sibilia **935**
Nicole Siegel **1209**
Tomáš Šikola **298, 1039, 1749**
Mário Silveirinha **248, 1025**
Matteo Silvestri **476**
Marko Šimić **530**
Enrico Talamas Simola **1158, 1622**
Stelios Simos **291**
Kamal P. Singh **1004**
Ankit K. Singh **1412**
Vidhi Singla **181**
Chad Sipperley **902**
Tom T.C. Sistermans **364, 383, 1049, 1412**
Yonatan Sivan **1151, 1491**
Josef Sivic **894**
Jelena Sjakste **1243**
Ilias Skandalos **291**
Oliver Skibitzki **1690**
Jakub Skorka **1409**
C. Skubisz **935**
Ilia Smagin **514, 1393**
Tomasz Śmiarowski **1741, 1746**
Badreddine Smiri **921**
O. Smirnova **818**
Olga Smirnova **819**
Raymond Smith **578**
David R. Smith **729, 1091**
Steve Smith **762**
Peter Smowton **291**
Hubert Sobiech **1043, 1374**
Krzysztof Sobucki **555**
Sveva Sodomaco **1360**
Kentaro Soeda **764**
Muhammad Sohaib **753**
David Ramirez Solana **665**
Fernando Soldevila **658**
Théo Soler **1215**
Diego M. Solís **1149**
Dmitry Solnyshkov **694**
M. Soltani **597**
Luca Somboli **1275**
Jamie Somers **1535, 1754**
L. Soncin **1289**
Junyeob Song **273**
Subeom Song **327**
Jin Dong Song **393**
Qinghua Song **469**
Jung-Hwan Song **499**
Junchao Song **835**
JinDong Song **900**

Author Index (cont.)

Jialu Song **928**
Olivier Soppera **150, 205, 209**
Gino Sorbello **704**
Maira Perez Sosa **929**
Clivia M. Sotomayor-Torres **612, 646**
Mahdi Soudi **901**
H. Souissi **694**
Patrícia C. Sousa **1121**
Anton Souslov **660**
Christina Spaegele **677**
Barbara Spagnolo **1055**
Chris Sparling **801**
Sara Spaziani **1077**
Mark S. Spector **926**
Joni Spencer **494**
Michael Spencer **1174**
Justin Sperling **902**
Nicolas Spiesshofer **910, 1343, 1660**
Marco De Spirito **1471**
Emma Spotorno **397**
Ali Sraj **185**
Sneha Sreekumar **1001**
Vimala Sridurai **1460**
Kartik Srinivasan **273**
Ken Ssennyimba **405**
Philippe St-Jean **1015**
Paola Stagnaro **397**
Kestutis Staliunas **780, 783, 1688, 1724**
Kęstutis Staliūnas **1686**
Elli Stamatopoulou **1185**
Evaldas Stankevicius **763**
Evaldas Stankevičius **1549**
Tobias Stauber **411**
Theresa Stecher **933**
Tomasz Stefaniuk **1508**
Luca De Stefano **283**
Anja Maria Steiner **201**
Ullrich Steiner **379, 1721**
Ralf Stemler **720**
Sven Stengel **284, 425, 455, 1315**
Katherine Stevens **1502**
Christopher Stevens **1715**
Kriss Stokkereit **399**
Kris Stokkereit **438**
Irena Stolic **330**
James Stone **387**
Michael Stoneman **1031**
Rebbeca Storck **148**
Alexander Stoychev **1478**
Erik Strandberg **1336**
Giuseppe Strangi **111**
Rhonda Stroud **195**
W. Strupinski **373**
Felix Sturm **1275**
Zu-En Su **1014**
Hsiu-Ping Su **1363**
Xiaolong Su **1395**
Miguel A. Suarez **163**
Xitlali G. Suarez **195**
Toshiki Sugimoto **886, 1600**
Hiroshi Sugimoto **928, 1209, 1215**
Toshihiko Sugiura **1656**
Jae Yong Suh **315**
Myoung-Gyun Suh **722**
Maxim Sukharev **1715**
Andrey Sukhorukov **311, 858**
Christopher Sumner **1547**
Ningwei Sun **201**
Changzheng Sun **377**
Jingbo Sun **403**
Fang-Wen Sun **406**
Kai Sun **422, 629**
Hao Sun **690**
Zhipei Sun **760, 796**
Qiang Sun **1105**
Xiaoxiao Sun **1156**
Jia-Hong Sun **1486, 1643**
Manuka Suriyage **1578**
Duncan Sutherland **1051**
Hironori Suzuki **361**
Yuta Suzuki **581**
Takehito Suzuki **770**
Ilya Sychugov **863, 1359**
Kenneth Syddall **1417**
Jacob Syme **148**
Clémentine Symonds **924**
Alexander Szameit **789**
Aleksandra Szaniawska **1043, 1374, 1389**

Author Index (cont.)

Paweł Szczepański **1741**
András Szenes **965, 1414**
Rodrigo Szostak **1527**
Pascal Szriftgiser **268**
Zoltan Sztranyovszky **1343, 1541, 1660**
Virág Szünstein **965**
Andres Valladares Y Tacchi **231**
Omar Tada **687**
Nima Taghipour **910**
Giulia Tagliabue **227, 919, 1140**
Atsushi Taguchi **552**
Behnood Taheri **733**
Chao-Yi Tai **1647**
Laure Tailpied **385**
Bhera Ram Tak **1556, 1605**
Junichi Takahara **712**
Youtarou Takahashi **517**
Hiroyuki Takahashi **764**
Shota Takahashi **886, 1600**
Akafumi Takamizawa **395**
Osamu Takayama **250**
Ryohei Takei **395**
Nahid Talebi **771**
Swarali Talele **1618**
Thierry Taliercio **385, 1299**
B. Tallon **632**
Ülle-Linda Talts **379**
Philippe Tamarat **1203**
Asta Tamulevičienė **206**
Tomas Tamulevičius **206, 959**
Sigitas Tamulevičius **206, 959**
Mamoru Tamura **1230**
Ping-Heng Tan **440, 974**
Jiaren Tan **821**
Hark Hoe Tan **858**
Yoshito Y. Tanaka **184, 512, 889**
Takuo Tanaka **465, 891**
Hiroya Tanaka **663**
Yuta Tanaka **770**
Katsuhisa Tanaka **882**
Daisuke Tanaka **1584**
Runze Tang **167**
Mingchu Tang **291**
Chao Tang **391**
Hong Tang **634**
Takeshi Taniguchi **1156**
Takashi Taniguchi **1275**
Anna Tasolamprou **595, 699**
Philippe Tassin **417, 1098, 1119, 1336**
Gen Tatara **510**
Tetsu Tatsuma **872**
Thomas Taubner **357**
Michael A. D. Taylor **1278**
Davide Tedeschi **476**
Albert Teoh **908**
Enrique Teran-Garcia **1160**
Takamichi Terao **1613**
J. Terentjevas **818**
Justas Terentjevas **819**
Roberto Termine **433**
Martin Thämer **1135**
Laura Thévenard **1259**
Franck Thibaudau **212**
Angel Thomas **181**
Rijil Thomas **1198**
Peter J. Thomas **1376**
Martin Thomaschewski **117, 1575**
Jesse Thompson **696**
Nicholas Thompson **1000**
Yuan Tian **406**
Klaas-Jan Tielrooij **1107, 1256**
Nunzio Timpanaro **192**
Giulio Tirabassi **781**
Joseph Tischler **195**
Andreas Tittl **187, 458, 550, 1158**
Pradeep Tiwari **1663**
Vladyslav Tkach **1424, 1519, 1658**
Vlad Tkach **1680**
Michael Tobar **136, 816, 1010**
Caleb Todd **1343, 1660**
Stefano Toffanin **1068**
Michael Tofferl **484**
Ivan Toftul **1428**
Yoshihiko Togawa **169**
Maxwell J. Tolchin **1133**
Andrea Toma **753**
David Alonso Tomás **670**
Alessandro Tomasino **1131**

Author Index (cont.)

Monika Tomczyk **1109**
Satoshi Tomita **1028**
Matteo Tommasini **1235**
Päivi Törmä **715, 1371, 1567**
Daniel Torrent **658**
Clivia M. Sotomayor Torres **661, 672**
Francesca Torrini **1233**
Giuseppe Torrisi **704**
Caterina Tortorici **1527**
Johann Toudert **839, 913**
Yousra Traouli **578**
Jean-Baptiste Trebbia **1203**
Alessandro Tredicucci **1505, 1635**
Mona Tréguer-Delapierre **1296**
Loumi Trémas **270**
Loumi Tremas **716**
Ana Isabel F. Tresguerres-Mata **713, 842, 1160**
Girish Tripathy **418**
Brandon Triplett **473**
Oliver Trojak **900**
Liudmila Trotsiuk **174, 185**
Chiara Trovatello **401**
Jose Trull **365, 775, 1428, 1440**
Sebastiano Trusso **1235**
Aleksandra Trzaskowska **373**
Costas Tsakonas **1334**
Joshua T. Y. Tse **882**
Shuo-Yen Tseng **279**
Chung-Kai Tseng **1647**
Christos Tserkezis **883, 1147**
Omer Tsidki **1424**
Yekaterina Tskhe **854**
Hei Chit Leo Tsui **1759**
Mikhail Tsukerman **1424**
Kenji Tsuruta **628**
Shohei Tsuzuki **683**
Sophia Turean **908**
Nina Tverdokhleb **201**
Anna Tyszka-Zawadzka **1741**
K. Ueda **818**
Lukas Uhlig **1336**
Nathan Ullberg **446**
Soobin Um **1029**
Kirankumar Karkihalli Umesh **409**
Ieng-Wai Un **1151, 1491**
Pascal Urard **270, 716**
Matthias Urban **230**
Joanna M. Urban **1174**
Michal Urbánek **549**
Pablo M. Uribe-Pizarro **1595**
Jonathan A. Urrutia-Anguiano **1190**
Agathe Urvoas-Cisse **174**
Andrey Ushkov **593**
Roberto Utzeri **397**
Richard Vaia **166**
Patrizio Vaiano **868**
Costas Valagiannopoulos **699**
José Valderrama-Botia **224**
Guido Valerio **1497**
Marielle Valerio-Lepiniec **174**
Adrià Canós Valero **312, 554, 1541**
Ventsislav Valev **160**
Giuseppe Della Valle **231**
Antonio Valletta **1458**
Shivashankar Vangala **1715**
Gearht VanVoorhis **1000**
Sebin Varghese **1256**
Thomas Vasileiadis **1246**
Igor Vasilevskiy **411**
Dávid Vass **965, 1414**
Nathalie Vast **1243**
Lavi Kumar Vaswani **1713**
Marlo Vega **150**
Julia Vehndel **834**
Aitor Villafranca Velasco **330, 344**
René P. J. van Veldhoven **279, 342**
Alessandro Veltri **927**
Tommaso Venanzi **1156, 1158**
Thirumalai Venkatesan **481**
Valeria Vento **1140**
G. Venturi **524**
Giacomo Venturi **1635**
Thierry Verbiest **204**
Maia G. Vergniory **302**
Georgios Veronis **341**
Olena Vertsanova **749**
Milo Vescovo **684**
Benjamin Vest **475**

Author Index (cont.)

Frank Vewinger **409**
Stéphane Vézian **1293**
Rodrigo Vicencio **949, 1383**
Luis Moreno Vicente-Arche **844**
Eliana Vieira **832**
Petr Viewegh **1749**
Silvia Vignolini **915**
Pieter Vijn **279**
Kernius Vilkevicius **763**
Kernius Vilkevičius **1549**
Andrea Villa **453**
Maria Villanueva-Blanco **1293, 1299, 1580**
Leone Di Mauro Villari **401**
Gregory Vincent **385**
Maria Antonietta Vincenti **306, 425, 455, 727, 775, 1142, 1315, 1440**
Patricia Vindel-Zandbergen **819**
Paul Virally **705**
Tersilla Virgili **453**
Michele Virgilio **1622**
Miriam Serena Vitiello **1106**
Massimo De Vittorio **439, 1055, 1082**
Prisca Viviani **109**
Laurent Vivien **825**
Tamie Vo **181**
Viola Vogler-Neuling **379**
Josh Vogwell **819**
Niklas Vollmar **834**
Frank Vollmer **894, 1419**
Kirill Voronin **842, 1189**
Roberto Li Voti **935**
Dmytro Vovchuk **1424, 1519, 1658, 1680**
C. Vozzi **818**
Jelena Vuckovic **123**
Sunil Vyas **489**
Kevin Vynck **413, 915**
Miklós Waldhauser **965, 1414**
T. Waldsauer **1764**
Sebastian Walfort **834**
Dennis Walker **1715**
Gregory Q. Wallace **359**
Emma Wallace-Wilmot **908**
Finlay Walton **902**
Duanduan Wan **259, 1352**
Chao Wan **794**
Mu Wang **99, 285**
Shaojun Wang **168**
Zhiming Wang **201**
Ji Tong Wang **363**
Jian Wang **377**
Lai Wang **377**
Long Wang **406**
Qianshuo Wang **432**
Xingxiang Wang **432**
Alan Wang **491**
Xiangrong Wang **537**
Jialong Wang **574**
Zuojia Wang **604**
Xulong Wang **640**
Yue-Sheng Wang **659**
Shubo Wang **735**
Kaizhi Wang **796**
Mengyun Wang **830**
Wei Wang **860**
Kaiyuan Wang **951**
Jianfang Wang **976, 979, 1522**
Shengyan Wang **979**
Yuhang Wang **1112**
Qi Jie Wang **1117**
Chuntao Wang **1224**
Yao-Ting Wang **1353, 1700**
Xinhao Wang **1387**
Bing Wang **1395, 1481**
Wei-Han Wang **1438**
Yen-Yu Wang **1597**
Chen-Yu Wang **1597**
Yumeng Wang **1632**
Bo Wang **1731**
Louis Waquier **1265**
Sören Wasserroth **1160**
Keisuke Watanabe **319, 1419**
Hogara Watanabe **558**
Kenji Watanabe **1156, 1275**
James Watkins **449**
Benoit Wattellier **1006**
Mike Weaver **1000**
Sébastien Weber **324**
Jonathan Weber **481**

Author Index (cont.)

Nils Weber **834**
L. Weber **997**
Werner Wegscheider **1275**
Yu-Chen Wei **929**
Hong Wei **981**
Eva Weig **1252**
Helena Weigand **1129**
Udo Weimar **145**
Thomas Weiss **312, 554, 1541**
Vlastmil Weiss **1749**
Maximilian Weissflog **311**
Hugo Weltz **1266**
Jisen Wen **1321**
Jianyu Weng **860**
Jerome Wenger **212**
Christian Wenger **1690**
Tim Wernicke **1336**
Daron Westly **273**
Peter R. Wiecha **164**
Jan Wiersig **779, 1108**
Diederik Wiersma **372**
Maciej Wiesner **373**
Edith Wietek **1156**
Yannick De Wilde **713**
Y. De Wilde **1289**
Gabrielle Williams **256**
Liam Wilson **902**
Shawn Wimer **578**
Stephan Winnerl **1156**
Katarzyna Wleciał **1389**
Katarzyna Wlecial **1043**
Ondřej Wojewoda **549**
Martin Wolf **1135, 1160, 1174**
Alexander Wolff **720, 1645**
Tomasz Woliński **932**
Rachel Won **912**
Wai Chun Wong **673**
Stephan Wong **942, 1103**
Alex Man Hon Wong **1094, 1632**
Aklilu Worku **166**
Thomas Wright **387**
Terry Wright **756**
C. David Wright **830, 835, 1493**
Jerzy Wróbel **151**
Hung-Yi Wu **295**
Enzong Wu **604**
Heng Wu **974**
Yina Wu **1176**
Pin Chieh Wu **1363, 1432**
Matthias Wuttig **357**
Patrycja Wytrych **1508**
Han-Rong Xia **259**
Chushuang Xiang **616**
Zong Xiang **860**
Meng Xiao **259**
Di Xiao **581**
Yang Xiao **1321**
Kexin Xie **405**
Minjun Xie **447**
Dajie Xie **741**
Yuanyang Xie **799**
Zhe Xie **860**
Zhiyuan Xie **884**
Xiaochen Xin **825**
Bing Xiong **377**
Bo Xiong **447**
Tao Xu **203**
Yiyuan Xu **310**
Kun Xu **310**
Xiulai Xu **415**
Fenghao Xu **499**
Athena Xu **597**
Zhenwei Xu **625**
Lei Xu **851, 1334**
Eli Yablonovitch **119**
Alejandro M. Yacomotti **781, 1417**
Yoshinori Yamaguchi **764**
Raku Yamaji **432**
Ai Yamakage **605**
Kazuki Yamamoto **944**
Yuji Yamamoto **1338**
Hidemasa Yamane **1743**
Junsuke Yamanishi **876**
Yusuke Yamauchi **1430**
Xingzhao Yan **422**
Peng Yan **557**
Dong Yan **794**
Jin Yan **908**

Author Index (cont.)

Jiaruo Yan **1672**
Youichi Yanase **1012**
Shuhui Yang **161**
Morris M. Yang **473**
Yuanmu Yang **490**
Guoce Yang **830**
Tao Yang **1135**
Fan Yang **1173**
Shengsong Yang **1570**
Dapeng Yao **510**
Andre Yaroshevsky **588**
Kenichi Yatsugi **663**
Dmitriy Yavorskiy **151**
Qian Ye **405, 1052**
Winnie N. Ye **825**
Yuning Ye **1321**
J. Andrew Yeh **489**
Stephanos Yerolatsitis **387**
Javier Yeste **1299, 1580**
Cetin Yilmaz **621**
Bo Yin **201**
Cuifeng Ying **1334**
Yaroslava G. Yingling **201**
Oili Ylivaara **612, 646, 672**
Taiki Yoda **254**
Jae Woong Yoon **1436, 1692, 1738**
Bingying You **383**
Leila Yousefi **766**
X. Yu **291**
Alvine Yu **494**
Zongfu Yu **1003**
Jianbo Yu **1117**
Xuechao Yu **1321**
Xinyi Yuan **427**
Lin-Chyn Yuan **1597**
Ben Yuen **1409, 1421, 1488**
Junji Yumoto **764**
Kuk Hyun Yun **244**
Yongseob Yun **327**
Seokho Yun **327**
Eran Yungar **1680**
Okan Yurduseven **1091**
A. A. Zabolotnykh **1324**
Luiz Fernando Zagonel **1213**
Dietrich R. T. Zahn **1560**
Kelment Zahoaliaj **1068**
Vadim Zakomirnyi **198**
Anastasiia Zaleska **105, 170**
Amin Zamani **851**
Ashkan Zandi **503**
Simone Zanotto **547, 1505, 1635**
Mario Zapata **243, 1589**
Adam Zawadzki **754, 1369**
Anatoly Zayats **105, 170, 799, 821, 1573**
Marc Zelsmann **921**
Brielle Zemer **999**
Shuwen Zeng **176**
Vladimir A. Zenin **1162**
Alexandra V. Zhabova **1675**
Y. Zhang **127, 632**
X. Zhang **127**
Chunmei Zhang **304**
Wenhan Zhang **355**
Mingqi Zhang **407**
Minming Zhang **408**
Zhenrong Zhang **463**
Bohan Zhang **490**
Zhepeng Zhang **499**
Qing Zhang **574**
Yu Zhang **598, 1273, 1278**
Kai Zhang **794, 1616**
Yufeng Zhang **796**
Lu Zhang **851**
Wending Zhang **851**
Baile Zhang **939**
Yongliang Zhang **967, 1326, 1469, 1556**
Ruiqian Zhang **979, 1522**
Yezhezi Zhang **994**
Yan Zhang **1021**
Pu Zhang **1145**
Shunping Zhang **1148**
Xia Zhang **1326**
Peng Zhang **1332**
Jiajia Zhang **1524**
Shenyou Zhao **358, 1578**
Yang Zhao **493, 1332**
Miao Zhao **1046**
Jingyi Zhao **1387**

Author Index (cont.)

Haoyu Zhao	**1616**
Jinxin Zhao	**1616**
Nikolay I. Zheludev	**107, 329, 467**
Ze Zheng	**320, 851**
Yu Zheng	**406**
Shuang Zheng	**408**
Yuruo Zheng	**821**
Harry Zheng	**945**
Di Zheng	**1082**
Xuezhi Zheng	**1147**
Qi Zhong	**1108**
Ziwei Zhou	**201**
Ming Zhou	**341**
Ji Zhou	**403**
Xiaoming Zhou	**637**
Lu Zhou	**1065**
Qiang Zhou	**1145**
Hongli Zhou	**1148**
Yin Zhou	**1476, 1767**
Jie Zhu	**631**
Xinyi Zhu	**690**
Zheng Zhu	**859**
Changyan Zhu	**1117**
Fangjia Zhu	**1209**
Shining Zhu	**1357**
Arcady Zhukov	**591, 1391**
Valentina Zhukova	**591, 1391**
Xiaolu Zhuo	**979, 1522**
Jian Zi	**1387**
Peter Zijlstra	**1074**
Attilio Zilli	**727, 1142**
Gianluigi Zito	**303, 1084**
Rocco Zito	**1511**
Dimitris Zografopoulos	**868**
Yongyu Zou	**407**
Runzhi Zou	**1145**
Lei Zuo	**1616**
Andrius Žutautas	**1706**

Session Index

Plenary Presentations 98
Keynote Presentations 104
Tutorial 142
Hybrid Nanomaterials and Metastructures for Photonics, Sensing and Energy 144
New trends in nanophotonics and advanced materials 242
Advanced passive and active metasurfaces and zero-index materials 461
Chirality, magnetism, and magnetoelectricity: Separate phenomena and joint effects in metamaterial structures 509
Phononics and acoustic metamaterials 606
Advanced Techniques for Computational Electromagnetics 675
Metamaterials: novel trends and applications 746
Parity-Time and quasi-normal modes in Photonics, Plasmonics, Acoustics 778
New Advances in Metamaterials and Their Functional Applications 793
Chiral fields and ultrafast chiral spectroscopy 798
Functional materials for tunable and reconfigurable photonics 823
Quantum metaphotonics 856
Enhanced light-matter interactions: fundamentals and sensing applications 862
Bio-Inspired Nanophotonics 896
When ‘meta' meets ‘materials': innovative materials, fabrication, functionalities 909
Non-Hermitian Photonics - Topological, Disordered and Quantum systems 936
Nano-Lasers, Spasers, and Nanostructures with Quantum Elements 953
Plasmonics and Nanophotonics: Fundamentals and Applications 972
Commercialization of Metasurface and Nanophotonic Devices 988
Towards chiral and magnetoelectric quantum electrodynamics 1008
Plasmonic Nanomaterials for Bio-diagnostics, Environmental Monitoring and Food Safety 1038
Metamaterials and Metasurfaces as Platforms for Next-Generation Electromagnetics: Fundamentals, Applications and Future Trends 1087
Topological Insulator Metamaterials 1100
Inverse design, topology optimization, and machine learning 1111
Quantum Matter and Dynamics in Hybrid Metamaterial Platforms 1123
Nonlocal and nonlinear nanophotonics 1127
New trends in light-matter interaction at the nanoscale 1178
Surface-Enhanced Raman Scattering: Integrating Theoretical and Experimental Perspectives 1218
Nanoscale Phononics : Energy Transport, Light-Matter Coupling, and Emerging Applications 1237
Cavity Quantum Materials and Polaritonic Devices: From Microscopic Theory to Functionality 1272
META Quantum Nanophotonics Workshop 1280
Plasmonics and Nano-Optics 1292
Nanophotonics and Plasmonics Applications: Optical Antennas, Quantum Photonic Devices, and Beyond 1304
Chiral and Hyperbolic Metamaterials 1314
Metasurfaces: Flat Optics, FSS, HIS, and Beyond 1320
Metamaterial-Based Devices 1340
Photonic Crystals and Electromagnetic Bandgap Structures 1348
Symposia, Special-Session and Workshop Posters 1356
Plasmonics, Nano-Optics and Nanophotonics 1521
Metamaterials, Metasurfaces and Their Applications 1612
Photonic Crystals, Lasers and Photonic Devices 1717
Micro/Nano Fabrication and Characterization 1748

Country Index

Australia **136, 249, 311, 346, 358, 369, 458, 701, 816, 858, 1010, 1046, 1105, 1281, 1379, 1428, 1500, 1541, 1578, 1586**

Austria **173, 312, 401, 430, 484, 519, 530, 554, 572, 680, 842, 848, 934, 1024, 1144, 1324, 1430, 1541**

Belgium **200, 204, 364, 383, 585, 723, 897, 996, 1049, 1187, 1366, 1412**

Brazil **900, 937, 1152, 1213, 1527**

Canada **148, 150, 337, 348, 597, 681, 690, 696, 705, 724, 743, 787, 825, 903, 993, 1015, 1076, 1283, 1290, 1545**

Chile **535, 949, 1105, 1383, 1595**

China **99, 113, 168, 201, 203, 251, 259, 282, 285, 296, 310, 332, 358, 377, 403, 404, 406, 408, 415, 432, 437, 440, 444, 447, 464, 468, 469, 472, 488, 490, 537, 544, 557, 574, 581, 604, 605, 626, 631, 637, 640, 652, 658, 659, 679, 703, 735, 760, 794, 796, 842, 851, 857, 858, 859, 860, 884, 940, 973, 974, 977, 978, 979, 980, 981, 1065, 1094, 1096, 1112, 1145, 1147, 1148, 1151, 1173, 1281, 1321, 1326, 1332, 1352, 1353, 1357, 1387, 1395, 1476, 1481, 1522, 1524, 1552, 1578, 1616, 1632, 1731, 1767**

Colombia **804, 1589**

Czech Republic **233, 235, 298, 549, 818, 838, 894, 1039, 1176, 1629, 1749**

Denmark **250, 364, 471, 504, 607, 610, 741, 883, 1051, 1137, 1147, 1152, 1162, 1164, 1166, 1171, 1192, 1381, 1440, 1458**

Ecuador **927**

Finland **159, 317, 373, 427, 612, 646, 672, 715, 760, 796, 841, 1206, 1207, 1371, 1563, 1567, 1672**

France **124, 138, 150, 156, 161, 163, 164, 174, 176, 185, 194, 198, 203, 205, 208, 209, 212, 222, 224, 228, 229, 239, 264, 268, 270, 274, 276, 291, 324, 330, 344, 381, 385, 390, 394, 413, 446, 475, 611, 614, 616, 625, 632, 635, 661, 669, 684, 686, 687, 694, 713, 716, 721, 731, 737, 759, 761, 781, 801, 825, 840, 844, 846, 849, 866, 881, 915, 920, 921, 924, 927, 937, 957, 997, 1006, 1041, 1082, 1089, 1092, 1129, 1154, 1158, 1181, 1203, 1209, 1213, 1238, 1243, 1245, 1247, 1249, 1254, 1258, 1259, 1263, 1265, 1266, 1269, 1275, 1289, 1293, 1296, 1299, 1417, 1473, 1497, 1527, 1641, 1647, 1650, 1665**

Germany **133, 140, 145, 187, 188, 201, 214, 219, 230, 308, 311, 346, 357, 358, 370, 409, 414, 416, 458, 518, 521, 529, 534, 546, 550, 562, 565, 566, 568, 572, 582, 636, 720, 733, 736, 740, 749, 771, 779, 789, 801, 818, 819, 834, 835, 840, 894, 901, 906, 915, 982, 994, 1019, 1108, 1126, 1135, 1156, 1158, 1160, 1174, 1179, 1185, 1194, 1198, 1201, 1203, 1207, 1211, 1221, 1239, 1252, 1275, 1288, 1308, 1338, 1491, 1560, 1578, 1591, 1618, 1622, 1629, 1638, 1645, 1683, 1690, 1695, 1703, 1757, 1764**

Greece **291, 335, 595, 642, 699, 785, 868, 1672**

Hong Kong **976, 979, 1332, 1476, 1767**

Hungary **801, 965, 1414**

India **164, 864, 901, 1004, 1151, 1334, 1401, 1460, 1708, 1711, 1713, 1751**

Ireland **127, 665, 715, 854, 967, 985, 1326, 1469, 1535, 1556, 1605, 1754**

Israel **218, 520, 588, 593, 600, 1014, 1035, 1059, 1151, 1318, 1424, 1491, 1519, 1658, 1680**

Italy **109, 138, 151, 154, 192, 231, 238, 252, 266, 283, 303, 306, 334, 342, 365, 372, 397, 400, 401, 425, 427, 433, 438, 439, 440, 452, 453, 455, 457, 476, 524, 529, 547, 615, 619, 648, 650, 653, 704, 709, 715, 727, 730, 753, 775, 801, 818, 835, 842, 848, 868, 922, 927, 935, 954, 990, 1045, 1055, 1062, 1065, 1068, 1070, 1077, 1078, 1080, 1082, 1084, 1086, 1092, 1104, 1106, 1131, 1142, 1158, 1160, 1167, 1168, 1169, 1170, 1217, 1220, 1222, 1228, 1233, 1235, 1258, 1305, 1315, 1360, 1376, 1440, 1442, 1458, 1463, 1465, 1471, 1495, 1505, 1511, 1513, 1527, 1530, 1570, 1622, 1635, 1721, 1728**

Japan **126, 129, 143, 151, 158, 169, 171, 180, 184, 206, 247, 248, 254, 258, 289, 319, 361, 391, 395, 407, 423, 432, 434, 465, 510, 512, 517, 519, 522, 526, 528, 542, 552, 558, 561, 570, 581, 605, 628, 656, 663, 681, 683, 692, 712, 764, 770, 818, 872, 874, 876, 882, 886, 889, 891, 928, 930, 939, 944, 959, 1012, 1016, 1017, 1020, 1028, 1156, 1209, 1215, 1230, 1261, 1275, 1419, 1426, 1430, 1584, 1600, 1613, 1656, 1743, 1762**

Korea **135, 178, 244, 245, 277, 327, 328, 368, 373, 393, 474, 500, 534, 617, 644, 773, 900, 915, 925, 961, 1029, 1057, 1162, 1308, 1330, 1341, 1397, 1436, 1455, 1483, 1624, 1638, 1692, 1698, 1738**

Latvia **1424, 1519, 1658, 1680**

Lithuania **206, 751, 763, 780, 959, 1110, 1549, 1686, 1688, 1706, 1724**

Mexico **277, 623, 954, 1190**

Morocco **264, 381, 1515**

Netherlands **112, 279, 322, 342, 364, 438, 518, 688, 929, 1068, 1074, 1107, 1128, 1192, 1197, 1215, 1256, 1305, 1446**

Country Index (cont.)

Poland **151, 373, 391, 555, 658, 754, 769, 922, 932, 1043, 1073, 1109, 1246, 1365, 1369, 1374, 1376, 1389, 1467, 1508, 1513, 1517, 1533, 1607, 1663, 1741, 1746**

Portugal **248, 612, 646, 661, 697, 832, 1025, 1121, 1152**

Romania **1226, 1620**

Russia **514, 550, 572, 1324, 1393, 1675**

Saudi Arabia **991, 1770**

Singapore **190, 300, 329, 375, 467, 499, 566, 688, 939, 951, 1021, 1061, 1117, 1524**

Slovenia **747**

Spain **108, 179, 201, 203, 218, 243, 262, 277, 280, 302, 325, 330, 339, 344, 364, 365, 394, 405, 411, 419, 450, 573, 591, 658, 670, 671, 676, 688, 721, 727, 753, 775, 780, 781, 783, 790, 819, 832, 839, 842, 848, 864, 868, 871, 878, 879, 911, 913, 917, 929, 956, 963, 993, 1046, 1062, 1137, 1142, 1149, 1154, 1160, 1176, 1182, 1183, 1187, 1189, 1192, 1200, 1203, 1209, 1211, 1219, 1256, 1281, 1293, 1299, 1381, 1391, 1400, 1428, 1430, 1440, 1449, 1451, 1565, 1580, 1589, 1603, 1677, 1686, 1734, 1759**

Sweden **348, 417, 446, 516, 824, 863, 879, 899, 1098, 1119, 1156, 1222, 1302, 1336, 1359, 1434, 1583**

Switzerland **103, 114, 227, 272, 342, 379, 426, 625, 714, 785, 884, 919, 933, 1033, 1129, 1131, 1140, 1209, 1233, 1275, 1385, 1465, 1478, 1635, 1670, 1721**

Taiwan **132, 279, 295, 489, 970, 1187, 1346, 1353, 1362, 1363, 1432, 1438, 1444, 1486, 1597, 1643, 1647, 1700**

Turkey **276, 621, 1404**

Ukraine **1424, 1560**

United Arab Emirates **420**

United Kingdom **102, 105, 107, 147, 160, 170, 184, 217, 284, 291, 302, 304, 306, 312, 320, 329, 348, 353, 355, 356, 359, 363, 387, 399, 407, 418, 419, 421, 422, 425, 438, 441, 445, 455, 467, 540, 543, 576, 660, 673, 678, 681, 694, 710, 750, 756, 766, 792, 799, 801, 802, 818, 819, 821, 830, 835, 851, 894, 900, 902, 910, 912, 915, 942, 982, 1046, 1049, 1054, 1075, 1082, 1088, 1091, 1093, 1168, 1200, 1203, 1284, 1311, 1315, 1334, 1343, 1349, 1371, 1376, 1379, 1409, 1419, 1421, 1442, 1460, 1488, 1493, 1502, 1541, 1543, 1547, 1573, 1584, 1593, 1610, 1626, 1635, 1653, 1660, 1675, 1718, 1759**

USA **100, 101, 111, 116, 117, 119, 120, 121, 123, 130, 134, 141, 166, 167, 181, 182, 195, 201, 203, 218, 220, 256, 260, 273, 286, 293, 303, 305, 315, 335, 340, 341, 348, 349, 350, 351, 360, 390, 405, 425, 426, 435, 443, 449, 451, 455, 462, 463, 473, 478, 480, 481, 483, 486, 491, 493, 494, 496, 497, 498, 499, 503, 505, 506, 507, 515, 532, 549, 563, 578, 581, 584, 586, 598, 602, 615, 629, 634, 651, 655, 671, 677, 705, 707, 722, 726, 729, 741, 744, 762, 777, 779, 781, 804, 819, 821, 827, 830, 900, 902, 905, 906, 908, 915, 926, 942, 945, 947, 957, 989, 994, 999, 1000, 1001, 1003, 1004, 1009, 1025, 1029, 1031, 1036, 1039, 1052, 1091, 1092, 1098, 1101, 1103, 1108, 1114, 1116, 1117, 1124, 1133, 1135, 1139, 1150, 1160, 1176, 1213, 1224, 1241, 1251, 1273, 1275, 1278, 1287, 1305, 1318, 1385, 1538, 1570, 1575, 1595, 1635, 1641, 1692, 1715, 1726, 1738**

META 2026

The 16th International Conference on
Metamaterials, Photonic Crystals and Plasmonics

DUBLIN, IRELAND • 14–17 JULY 2026

SUPPORTED BY OUR SILVER SPONSORS

metaconferences.org

Join us at the next META conference

© 2008–2026 META Conference • All rights reserved